ECCOMAS
European Community on Computational Methods in Applied Sciences

ECCOMAS Thematic Conference

COMPDYN 2013

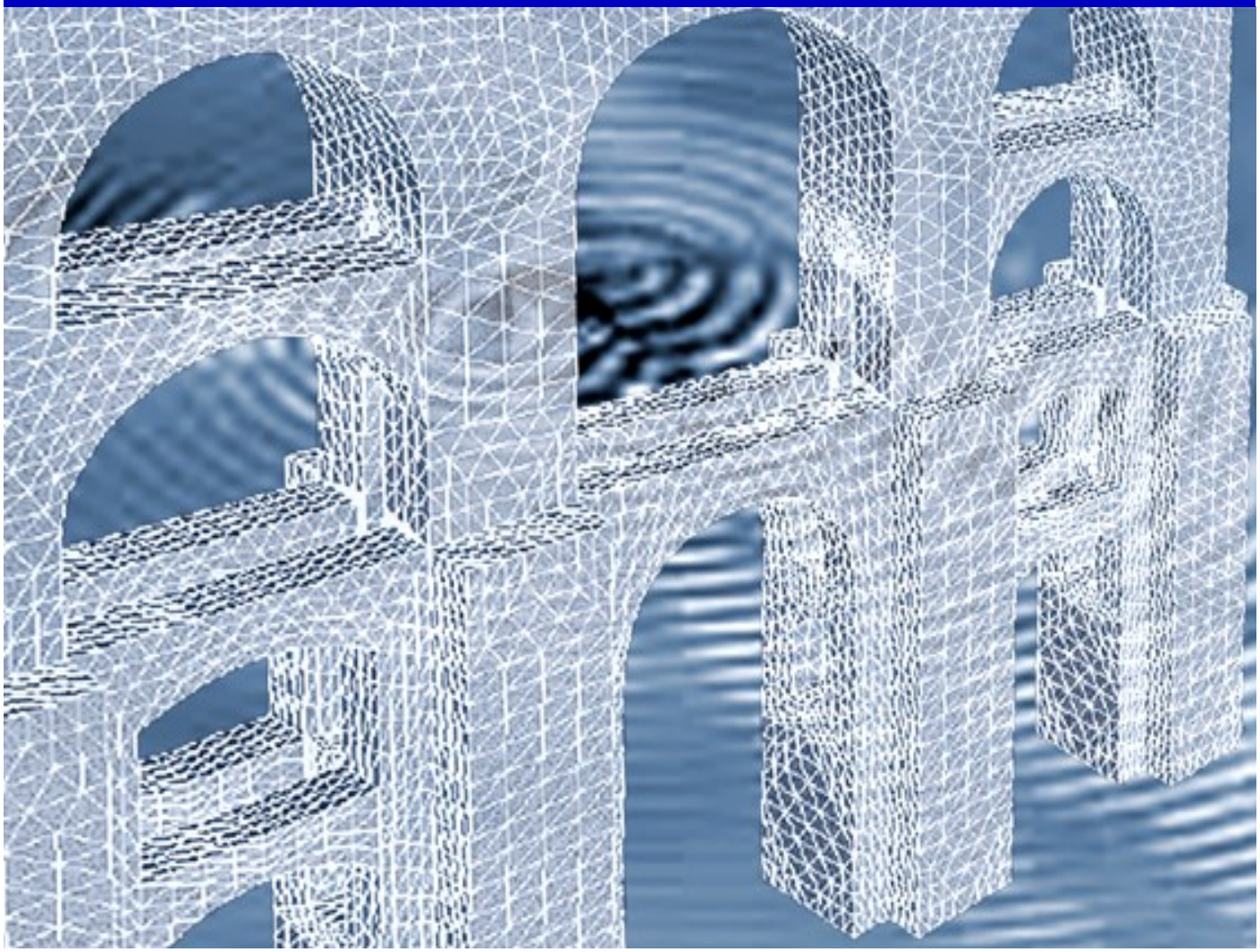
4th International Conference on

Computational Methods in Structural Dynamics And Earthquake Engineering

PROCEEDINGS

An IACM Special Interest Conference

M. Papadrakakis, V. Papadopoulos, V. Plevris (Eds)



COMPDYN 2013
Computational Methods in Structural Dynamics and Earthquake Engineering

Proceedings of the 4th International Conference on Computational
Methods in Structural Dynamics and Earthquake Engineering
Held in Kos Island, Greece
12-14 June 2013

Edited by:

M. Papadrakakis
National Technical University of Athens, Greece

V. Papadopoulos
National Technical University of Athens, Greece

V. Plevris
School of Pedagogical and Technological Education, Athens, Greece

A publication of:

Institute of Structural Analysis and Antiseismic Research
School of Civil Engineering
National Technical University of Athens (NTUA)
Greece

COMPDYN 2013
Computational Methods in Structural Dynamics and Earthquake Engineering
M. Papadrakakis, V. Papadopoulos, V. Plevris (Eds)

First Edition, February 2014

© The authors

ISBN: **978-960-99994-2-7**

PREFACE

This volume contains the full-length papers presented in the 4th International Conference on Computational Methods in Structural Dynamics and Earthquake Engineering (COMPDYN 2013) that was held on June 12-14, 2013 on the Kos Island, Greece.

COMPDYN 2013, one of the thematic Conferences of the European Community on Computational Methods in Applied Sciences (ECCOMAS), is a Special Interest Conference of the International Association for Computational Mechanics (IACM) and has been promoted by the European Committee on Computational Solid and Structural Mechanics (ECCSM) of ECCOMAS. The purpose of the Conference is to bring together the scientific communities of Computational Mechanics, Structural Dynamics and Earthquake Engineering in an effort to facilitate the exchange of ideas in topics of mutual interests and to serve as a platform for establishing links between research groups with complementary activities. The communities of Structural Dynamics and Earthquake Engineering will benefit from this interaction, acquainting them with advanced computational methods and software tools which can highly assist in tackling complex problems in dynamic/seismic analysis and design, while also giving the Computational Mechanics community the opportunity to become more familiar with very important application areas of great social interest. The COMPDYN 2013 Conference is supported by the National Technical University of Athens (NTUA), the European Association for Structural Dynamics (EASD), the European Association for Earthquake Engineering (EAEE), the Greek Association for Computational Mechanics (GRACM) and the John Argyris Foundation.

The editors of this volume would like to thank all authors for their contributions. Special thanks go to the colleagues who contributed to the organization of the Minisymposia and to the reviewers who, with their work, contributed to the scientific quality of this e-book.

M. Papadrakakis
National Technical University of Athens, Greece

V. Papadopoulos
National Technical University of Athens, Greece

V. Plevris
School of Pedagogical and Technological Education, Athens, Greece

ACKNOWLEDGEMENTS

The conference organizers acknowledge the support towards the organization of the "4th International Conference on Computational Methods in Structural Dynamics and Earthquake Engineering", to the following organizations:

- European Community on Computational Methods in Applied Sciences, ECCOMAS
- International Association for Computational Mechanics (IACM)
- School of Civil Engineering, National University of Athens
- Greek Association for Computational Mechanics (GRACM)
- European Association for Earthquake Engineering (EAEE)
- John Argyris Foundation
- Information Technologies & Digital Engineering, Ioannina, Greece
- TWT Science &Innovation, Stuttgart, Germany
- STRUDL Europe
- Greek National Tourism Organisation, Greece

Plenary Speakers and Invited Session Organizers

We would also like to thank the Plenary and Semi-Plenary Speakers and the Minisymposia Organizers for their help in the setting up of a high standard Scientific Programme.

Plenary Speakers: Alain Combescure, Kumar Tamma, Shinobu Yoshimura

Semi-Plenary Speakers: Dan Givoli, Isaac Harari, Muneo Hori, Hector Jensen, Boris Jeremic, Makoto Ohsaki, K. C. Park, Constantinos Stavrinidis

MS Organizers: Guglielmo Aglietti, Antonio Arede, Panagiotis Asteris, Alessandro Baratta, Michele Barbato, Rui Carneiro Barros, Noureddine Bouhaddi, Elsa Caetano, Rui Calcada, Adriano Calvi, Gian Paolo Cimellaro, Álvaro Cunha, Panos Dakoulas, Guido de Roeck, Reimundo Delgado, Pedro Delgado, Matjaz Dolšek, S.E. Dritsos, Michalis Fragiadakis, Seriani Geza, Roger Ghanem, Dan Givoli, George Hatzigeorgiou, Muneo Hori, Mohamed Ichchou, Alexander Idesman, Boris Jeremic, Andrea Kappos, Spyros Karamanos, Theodore Karavasilis, Ioannis Kougioumtzoglou, Dimitrios Lignos, Asterios Liolios, Nikos Makris, George Manos, George Mylonakis, Arvid Naess, Dan Negrut, Makoto Ohsaki, Stavroula Pantazopoulou, Costas Papadimitriou, Vissarion Papadopoulos, Edoardo Patelli, Ioannis Psycharis, Vitomir Racic, James Ricles, Masato Saitoh, Evangelos Sapountzakis, Gerhart Schueller, Anastasios Sextos, Ahmed Shabana, Castorina Silva Vieira, Christian Soize, Sergey Sorokin, Aram Soroushian, Constantine Spyrakos, George Stavroulakis, Božidar Stojadinović, Hiroyuki Sugiyama, Mahdi Taiebat, Arturo Tena-Colunga, Yiannis Tsompanakis, Enrico Tubaldi, Dimitrios Vamvatsikos, Peter van den Broeck, Ioannis Vayas, Shinobu Yoshimura, Farzin Zareian

SUMMARY

Preface..... iii

Acknowledgements..... iv

Contents..... ix

Semi-plenary Lectures 1

Minisymposia

MS 1: Progress and Challenges in Performance-Based Earthquake Engineering 29
Organized by Farzin Zareian and Dimitrios Lignos

MS 2: Computational Contact Mechanics - Seismic Interaction (Pounding) Between Adjacent Structures 77
Organized by Asterios Liolios, George Hatzigeorgiou and George Stavroulakis

MS 3: Progress and Challenges in Spacecraft Structural Dynamics 101
Organized by Adriano Calv and Guglielmo Aglietti

MS 4: Performance-Based Engineering And Reliability-Based Design 196
Organized by Michele Barbato and Enrico Tubaldi

MS 5: Control of Vibrations in Civil Engineering by Passive, Active and Semi-Active Devices 298
Organized by Rui Carneiro Barros and Alessandro Baratta

MS 6: Low Cost Methods for Robust Design in Structural Dynamics and Vibroacoustics 345
Organized by Noureddine Bouhadd and Mohamed Ichchou

MS 7: Dynamic Effects on High-Speed Railway Tracks 373
Organized by Rui Calcad and Reimundo Delgado

MS 8: Resilience Based-Design of Communities and Infrastructures 471
Organized by Gian Paolo Cimellaro

MS 9: Wind Effects on Structures 527
Organized by Álvaro Cunh and Elsa Caetano

MS 10: Seismic Analysis and Design of Industrial Facilities and Pipelines 597
Organized by Spyros Karamanos, Panos Dakoulas, Vissarion Papadopoulos and Michalis Fragiadakis

MS 11: Probabilistic Methods in Design and Assessment of Structures: Concepts and Applications 608
Organized by Matjaz Dolšek and Dimitrios Vamvatsikos

MS 12: Advances in Numerical Methods for Linear and Non-Linear Dynamics 746
Organized by Alexander Idesman

MS 13: Dynamic Soil Structure Interaction Modeling and Simulation ……801
Organized by Boris Jeremic and Mahdi Taiebat

MS 14: Seismic Assessment and Retrofit of Bridges ……823
Organized by Andrea Kappos and S.E. Dritsos

MS 15: Numerical Simulation and Experimental Verification on Problems in the Field of Earthquake Engineering and Structural Dynamics …… 978
Organized by George Manos

MS 16: Recent Advances in Experimental Pile Dynamics & Soil-Structure Interaction ……1145
Organized by George Mylonakis and Masato Saitoh

MS 17: Risk Assessment and Quantification in Engineering: a Multi-Disciplinary Perspective ……1230
Organized by Edoardo Patelli, Ioannis Kougioumtzoglou and Arvid Naess

MS 18 : Seismic Assessment of Herritage Structures and Monuments Through Simulation ……1339
Organized by Stavroula Pantazopoulou

MS 19: Identification Methods in Structural Dynamics ……1421
Organized by Costas Papadimitriou

MS 20: Seismic Behaviour and Design of Precast Structures ……1469
Organized by Ioannis Psycharis

MS 21: Seismic Behaviour and Retrofitting of Monuments and Historical Buildings ……1615
Organized by Ioannis Psycharis

MS 22: Advances in Computational Methods for Resilient Structural Systems Under Extreme Hazards …… 1758
Organized by James Ricles and Theodore Karavasilis

MS 23: Advances In Structural Vibrations ……1816
Organized by Evangelos Sapountzakis

MS 24: Advances in Modeling of Wave Propagation and Applications ……1898
Organized by Dan Givoli and Seriani Geza

MS 25: Software Development in the Field of Earthquake Engineering and Structural Dynamics ……1920
Organized by Anastasios Sextos

MS 26: Computational Multibody System Dynamics ……1975
Organized by Ahmed Shabana, Dan Negrut and Hiroyuki Sugiyama

MS 27: Uncertainty Quantification in Computational Dynamics ……1991
Organized by Christian Soize, Roger Ghan and Gerhart Schueller

MS 28: Periodicity Effects and Periodicity-Based Methods in Vibro-Acoustics and Structural Dynamics 2103
Organized by Sergey Sorokin

MS 29: Accuracy and Computational Efficiency in Dynamic/Seismic Structural Analysis 2232
Organized by Aram Soroushian

MS 30: Robust Modeling and Control for Smart Structures 2313
Organized by George Stavroulakis, Amalia Moutsopoulou and Anastasios Pouliezos

MS 31: Seismic Isolation of Industrial and Essential Facilities (Power Plants-Equipment, Chemical/Oil Plants-Equipment, Hospitals) 2330
Organized by Arturo Tena-Colunga

MS 32: Seismic Analysis and Design of Irregular Buildings 2345
Organized by Arturo Tena-Colunga

MS 33: Steel and Composite Steel Reinforced Concrete Structures Under Dynamic and Seismic Loading 2360
Organized by Ioannis Vayas

MS 35: High-Performance Computing for Structural Mechanics and Earthquake Engineering 2422
Organized by Shinobu Yoshimura, Muneo Hori and Makoto Ohsaki

MS 36: Seismic Safety Assessment of Structures 2443
Organized by Raimundo Delgado, Antonio Arede and Pedro Delgado

MS 38: Human Induced Vibrations 2565
Organized by Guido De Roeck, Peter van den Broeck and Vitomir Racic

MS 39: Recent Advances and Challenges in Geotechnical Earthquake Engineering 2650
Organized by Castorina Silva Vieira and Yiannis Tsompanakis

MS 40: Structural Dynamics and Earthquake Engineering of Rocking Structures 2751
Organized by Božidar Stojadinović and Nikos Makris

MS 41: Brick-Infilled RC Frames: Seismic Behavior and Retrofit 2931
Organized by Constantine Spyrakos and Panagiotis Asteris

MS 42: Religious Monuments: Seismic Behavior and Retrofit 2997
Organized by Constantine Spyrakos and Panagiotis Asteris

Regular Sessions

RS 1: Active-Passive Control 3030

RS 3: Computational Seismic Structural Analysis 3049

RS 4: Constitutive Modelling Under Dynamic and Seismic Actions 3179

RS 5: Design Methods Under Dynamic and Seismic Actions 3217

RS 6: Dynamics of Coupled Problems 3278

RS 7: Dynamics of Micro Systems 3328

RS 8: Geotechnical Earthquake Engineering 3350

RS 10: Identification Methods in Structural Dynamics 3448

RS 12: Masonry Structures 3496

RS 13: Numerical Methods for Linear and Nonlinear Dynamics 3523

RS 14: Optimum Design in Structural Dynamics and Earthquake Engineering 3637

RS 15: Passive Active and Semi-Active Devices 3672

RS 16: Performance-Based Engineering 3736

RS 17: Reinforced Concrete Structures 3799

RS 18: Reliability of Dynamic Systems 3989

RS 19: Repair and Retrofit of Structures 4002

RS 20: Seismic Assessment of Heritage Structures and Monuments Through Simulation 4039

RS 21: Seismic Design and Assessment of Bridges 4050

RS 22: Seismic Performance Evaluation Under Uncertainty 4095

RS 23: Seismic Risk and Reliability Analysis 4135

RS 24: Seismic Safety Assessment of Structures 4179

RS 25: Simulation Methods for Dynamic Problems 4234

RS 26: Simulation of Sound and Vibration 4334

RS 27: Soft Computing Applications 4348

RS 28: Soil Dynamics 4361

RS 29: Soil-Structure Interaction 4404

RS 31: Steel Structures 4545

RS 32: Structural Health Monitoring 4568

RS 33: Waves and Computation 4578

CONTENTS

Semi-plenary Lectures

THE USE OF BAYESIAN MODEL UPDATING IN STOCHASTIC DESIGN PROBLEMS 1
Jensen Hector, Vergara Camila

APPLICATION OF HPC TO EARTHQUAKE ENGINEERING - SEISMIC STRUCTURE RESPONSE ANALYSIS AND URBAN AREA EARTHQUAKE SIMULATION 12
Hori Muneo, Tanaka Seizo, Ichimura Tsuyoshi, Lalith Maggededaera, Miyamura Tomoshi, Ogino Masao, Okazawa Shigenobu

Minisymposia

MS 1: PROGRESS AND CHALLENGES IN PERFORMANCE-BASED EARTHQUAKE ENGINEERING

ACCOUNTING FOR NEAR-SOURCE EFFECTS IN THE DISPLACEMENT COEFFICIENT METHOD FOR SEISMIC STRUCTURAL ASSESSMENT 29
Baltzopoulos Georgios, Chioccarelli Eugenio, Iervolino Iunio

COLLAPSE CAPACITY SPECTRA BASED ON AN IMPROVED INTENSITY MEASURE 40
Tsantaki Styliani, Adam Christoph

AN OUTLOOK INTO TIME-DEPENDENT AFTERSHOCK VULNERABILITY ASSESSMENT 54
Ebrahimian Hossein, Jalayer Fatemeh, Asprone Domenico, Lombardi Anna, Marzocchi Warner, Prota Andrea, Manfredi Gaetano

MS 2: COMPUTATIONAL CONTACT MECHANICS - SEISMIC INTERACTION (POUNDING) BETWEEN ADJACENT STRUCTURES

NON-SMOOTH ANALYSIS OF THE EARTHQUAKE-INDUCED POUNDING IN SKEW BRIDGES 77
Dimitrakopoulos Elias

MITIGATION MEASURES FOR SEISMIC POUNDING EFFECTS ON ADJACENT BUILDINGS RESPONSES 89
Abdel Raheem Shehata

MS 3: PROGRESS AND CHALLENGES IN SPACECRAFT STRUCTURAL DYNAMICS

CHARACTERIZATION AND SYNTHESIS OF RANDOM ACCELERATION VIBRATION SPECIFICATIONS 101
Wijker Jaap, Ellenbroek Marcel, de Boer Andre

SINE TEST PREPARATION & MANAGEMENT INVOLVING A LARGE NUMBER OF CHANNEL COUNTS 131
Kiley Andrew

REDUCTION OF OVERTESTING DURING BASE-DRIVE RANDOM VIBRATION TESTS FOR THE EUCLID SPACECRAFT HARDWARE 167
Calvi Adriano

AN EASY-TO-IMPLEMENT COMPUTATIONAL METHOD FOR THE SPACECRAFT SINE TEST-PREDICTION WITH PARTICULAR EMPHASIS ON THE MODAL CONTRIBUTIONS 181
Nali Pietro, Mucciante Luigi, Caccamo Luca

MS 4: PERFORMANCE-BASED ENGINEERING AND RELIABILITY-BASED DESIGN

GRADIENT-BASED STUDY ON SEISMIC PERFORMANCE REDUCTION OF STEEL BRACED FRAMES DUE TO IRREGULAR BRACE OVER-STRENGTH DISTRIBUTIONS 196
Dall'Asta Andrea, Zona Alessandro, Ragni Laura

PREDICTING FLOOR RESPONSE SPECTRA FOR RC FRAME STRUCTURES 208
Lucchini Andrea, Cheng Yin, Mollaioli Fabrizio, Liberatore Laura

CONCEPT OF RISK-BASED SEISMIC DESIGN OF BUILDINGS USING METHODS OF NONLINEAR ANALYSIS 220
Dolšek Matjaž

STRUCTURAL MODELLING ISSUES IN SEISMIC PERFORMANCE ASSESSMENT OF INDUSTRIAL STEEL BUILDINGS 231
Della Corte Gaetano, Iervolino Iunio, Petruzzelli Fabio

SEISMIC RESPONSE ANALYSIS OF EXISTING NON-DUCTILE BUILDINGS RETROTIFFED WITH BRBS 244
di Sarno Luigi, Chiodi Remo, Manfredi Gaetano

INFLUENCE OF STRUCTURAL AND FRAGILITY MODELING DECISIONS IN THE LOSS ASSESSMENT OF RC FRAME BUILDINGS 257
Welch David, Sullivan Timothy

DESIGN AND ASSESSMENT OF STEEL AND STEEL-CONCRETE COMPOSITE STRUCTURES: EFFICACY OF EN1998 DESIGN PROCEDURE 272
Braconi Aurelio, Caprili Silvia, Degée Hervé, Guendel Max, Hjaij Mohammed, Hoffmeister Benno, Karamanos Spyros, Rinaldi Valerie, Salvatore Walter

MS 5: CONTROL OF VIBRATIONS IN CIVIL ENGINEERING BY PASSIVE, ACTIVE AND SEMI-ACTIVE DEVICES

MODIFICATION OF MODAL PROPERTIES OF A SYSTEM WITH NON-PROPORTIONAL DAMPING DUE TO VIBRATION ABSORBERS AND SUB-SOIL INTERACTION 298
Náprstek Jiří , Hračov Stanislav

COMPARISONS OF A TALL LATTICE WIND TOWER RESPONSE WITH AND WITHOUT A TMD 316
Henriques Jorge, Barros Rui

METHODS TO DESIGN A GUIDED TOWER CONCERNING DYNAMIC BEHAVIOR 332
Mendonça Cecília, Barros Rui

MS 6: LOW COST METHODS FOR ROBUST DESIGN IN STRUCTURAL DYNAMICS AND VIBROACOUSTICS

EFFICIENT CALCULATION OF THE RESPONSE OF A STRUCTURAL ACOUSTIC SYSTEM UNDER AERODYNAMIC EXCITATIONS 345
Chronopoulos Dimitrios, Ichchou Mohamed, Troclet Bernard

REDUCTION METHOD APPLIED TO VISCOELASTICALLY DAMPED FINITE ELEMENT MODELS 362
Zghal Souhir, Bouazizi Mohamed Lamjed, Nasri Rachid, Bouhaddi Noureddine

MS 7: DYNAMIC EFFECTS ON HIGH-SPEED RAILWAY TRACKS

EFFICIENT DYNAMIC INTERACTION ANALYSIS OF HIGH-SPEED TRAIN AND RAILWAY STRUCTURE DURING AN EARTHQUAKE 373
Tanabe Makoto, Sogabe Masamichi, Wakui Hajime, Matsumoto Nobuyuki, Tanabe Yasuko

HOW TO QUANTIFY THE VIBRATION REDUCTION OF RAILWAY TRACKS 384
Auersch Lutz

HIGH-SPEED TRAIN PASSAGE EFFECTS IN BUILDINGS: VIBRATION ASSESSMENT AND ISOLATION 403
Romero Ordóñez Antonio, Solís Muñiz Mario, Galvín Barrera Pedro

A NONLINEAR VEHICLE STRUCTURE INTERACTION METHODOLOGY WITH WHEEL RAIL DETACHMENT AND REATTACHMENT 416
Montenegro Pedro Aires, Neves Gonçalves Moreira Sérgio, Azevedo Ferreira Marques Álvaro, Calçada Rui

A SHEET PILING WALL AS A WAVE BARRIER FOR TRAIN INDUCED VIBRATIONS 430
Dijckmans Arne, Ekblad Alf, Smekal A., Degrande Geert, Lombaert Geert

A NUMERICAL STUDY OF SUBGRADE STIFFENING AS A MITIGATION MEASURE FOR RAILWAY INDUCED VIBRATIONS THROUGH 2.5D AND 3D FE-BE MODELS 447
Coulier Pieter, François Stijn, Degrande Geert, Lombaert Geert

MS 8: RESILIENCE BASED-DESIGN OF COMMUNITIES AND INFRASTRUCTURES

A COMPREHENSIVE METHODOLOGY FOR THE EVALUATION OF INFRASTRUCTURE INTERDEPENDENCIES 471
Solari Daniele, Cimellaro Gian Paolo

EVALUATING THE POST-EARTHQUAKE ACCESSIBILITY OF HOSPITALS FOR MITIGATION STRATEGY DECISION SUPPORT BY FRAGILITY AND CONNECTIVITY MODELLING 493
Kongar Indranil, Verrucci Enrica, Rossetto Tiziana, Bevington John

SECURING COMMUNITY RESILIENCE BY MODERN INFRASTRUCTURE DESIGN 507
Pickering Thomas, Dunn Sarah, Wilkinson Sean

DAMAGE REPORT WITH SMARTPHONES DURING EMILIA EARTHQUAKE, 2012 517
Arcidiacono Vincenzo, Cimellaro Gian Paolo

MS 9: WIND EFFECTS ON STRUCTURES

NUMERICAL INVESTIGATION OF WIND INDUCED OVALLING VIBRATIONS IN SILO GROUPS 527
Hillewaere Jeroen, Degroote Joris, Rezayat Ali, Vanlanduit Steve, Lombaert Geert, Vierendeels Jan, Degrande Geert

CHARACTERISATION OF THE AERODYNAMIC BEHAVIOUR OF THE GRANDE RAVINE VIADUCT FROM PROTOTYPE MONITORING 546
Bastos Fernando , Caetano Elsa, Cunha Ãlvaro, Cespedes Xavier, Arquier Mathieu, Flamand Olivier

CHARACTERISATION OF THE AERODYNAMIC BEHAVIOUR OF THE BRAGA STADIUM SUSPENSION ROOF FROM PROTOTYPE MONITORING 564
Caetano Elsa, Martins Nuno, Cunha Ãlvaro

WIND CHARACTERISTICS AROUND AND EFFECTS ON A SEA-CROSSING BRIDGE BASED ON MONITORING DATA 581
Sun Limin, Zhou Yi, Min Zhihua

MS 10: SEISMIC ANALYSIS AND DESIGN OF INDUSTRIAL FACILITIES AND PIPELINES

RELIABILITY ASSESSMENT OF PIPE NETWORKS UNDER SEISMIC LOADS 597
Fragiadakis Michalis, Christodoulou Symeon

MS 11: PROBABILISTIC METHODS IN DESIGN AND ASSESSMENT OF STRUCTURES: CONCEPTS AND APPLICATIONS

SEISMIC BEHAVIOR OF DAMAGED BUILDINGS: A COMPARISON OF STATIC AND DYNAMIC NONLINEAR APPROACH 608
Polese Maria, Gaetani D'Aragona Marco, Prota Andrea, Manfredi Gaetano

INVESTIGATION INTO ANALYTICAL VULNERABILITY CURVES DERIVATION ASPECTS CONSIDERING MODELING UNCERTAINTY FOR INFILLED RC BUILDINGS 626
Meslem Abdelghani, D'Ayala Dina

DEAGGREGATION OF SEISMIC SAFETY IN THE DESIGN OF THE REINFORCED CONCRETE BUILDINGS USING EUROCODE 8 641
Žižmond Jure, Dolšek Matjaž

APPLICATION OF THE RISK-BASED SEISMIC DESIGN PROCEDURE TO A REINFORCED CONCRETE FRAME BUILDING 655
Lazar Nuša, Dolšek Matjaž

ISSUES ON THE USE OF TIME-HISTORY ANALYSIS FOR THE DESIGN AND ASSESSMENT OF MASONRY STRUCTURES 669
Penna Andrea, Rota Maria, Mouyiannou Amaryllis, Magenes Guido

NEW DAMAGE MODELS FOR PERFORMANCE-BASED EARTHQUAKE ENGINEERING 687
Haukaas Terje, Javaherian Yazdi Abbas

RISK ASSESSMENT OF REINFORCED CONCRETE BUILDINGS CONSIDERING THE EARTHQUAKE DIRECTIONALITY EFFECTS 714
Vargas Alzate Yeudy Felipe, Luis Gonzaga Pujades Beneit, Alex Horia Barbat, Hurtado Gomez Jorge Eduardo

SEISMIC FRAGILITY AND VULNERABILITY ASSESSMENT USING SIMPLIFIED METHODS FOR THE GLOBAL EARTHQUAKE MODEL 725
Vamvatsikos Dimitrios, Kazantzi Athanasia

MEASURING BIAS IN INCREMENTAL DYNAMIC ANALYSIS USING BOOTSTRAP 737
Zacharenaki Athanasia, Fragiadakis Michalis, Papadrakakis Manolis

MS 12: ADVANCES IN NUMERICAL METHODS FOR LINEAR AND NON-LINEAR DYNAMICS

EXTERNAL COUPLING OF FE CODES FOR STRUCTURAL DYNAMICS 746
Brun Michael, Gravouil Anthony, Combescure Alain, Limam Ali

FINITE ELEMENT MODELING OF LINEAR ELASTODYNAMICS PROBLEMS WITH EXPLICIT TIME-INTEGRATION METHODS AND LINEAR ELEMENTS WITH REDUCED DISPERSION. COMPARATIVE STUDY OF DIFFERENT FINITE ELEMENT TECHNIQUES USED FOR ELASTODYNAMICS 759
Idesman Alexander

APPLICATIONS OF VARIATIONALLY CONSISTENT SELECTIVE MASS SCALING IN EXPLICIT DYNAMICS 777
Tkachuk Anton, Bischoff Manfred

STUDIES IN NUMERICAL STABILITY OF EXPLICIT CONTACT-IMPACT ALGORITHM TO THE FINITE ELEMENT SOLUTION OF WAVE PROPAGATION PROBLEMS 787
Kopačka Ján, Gabriel Dušan, Kolman Radek, Plešek Jiří, Ulbin Miran

MS 13: DYNAMIC SOIL STRUCTURE INTERACTION MODELING AND SIMULATION

EFFECT OF NEAR-FAULT GROUND MOTIONS ON SEISMIC RESPONSE OF DEEP BASEMENT WALLS 801
Amirzehni Elnaz, Taiebat Mahdi, Finn Liam, Devall Ronald

EARTHQUAKE RESPONSE ANALYSES OF SOIL-STRUCTURE INTERACTION SYSTEM USING NONLINEAR ENERGY TRANSMITTING BOUNDARY 812
Nakamura Naohiro

MS 14: SEISMIC ASSESSMENT AND RETROFIT OF BRIDGES

EMULATIVE COLUMN-FOOTING CONNECTIONS FOR SEISMIC DESIGN IN ACCELERATED BRIDGE CONSTRUCTION 823
Haber Zachary, Saiidi Saiid, Sanders David

SPECTRUM RESPONSE AND CODES EVOLUTION CASE STUDY - POST-COMPRESSED GIRDER BRIDGE 831
Bucur Carmen, Bucur Victor Mircea

BRIDGES WITH FIXITIES AND BEARINGS VS ISOLATED SYSTEMS 845
Mitoulis Stergios

SEISMIC RESPONSE OF BRIDGE ABUTMENTS ON SURFACE FOUNDATION SUBJECTED TO COLLISION FORCES 860
Argyroudis Sotirios, Mitoulis Stergios, Pitilakis Kyriazis

PARAMETRIC INVESTIGATION FOR THE OPTIMIZATION OF A LONGITUDINAL SEISMIC RESTRAINING SYSTEM CONSISTING OF STRUTS-TIES FOR CONCRETE BRIDGES 879
Markogiannaki Olga, Tegos Ioannis

OPTIMUM SELECTION OF RETROFIT MEASURES FOR R/C BRIDGES USING FRAGILITY CURVES 894
Stefanidou Sotiria, Kappos Andreas

ASSESSMENT OF EC 8 PROCEDURES FOR THE ASYNCHRONOUS EXCITATION OF BRIDGES BASED ON NUMERICAL ANALYSIS AND RECORDED DATA 912
Papadopoulos Savvas, Lekidis Vassilios, Sextos Anastasios, Karakostas Christos

SHEAR STRENGTH ASSESSMENT OF REINFORCED CONCRETE COLUMNS 927
Chasioti Stamatina, Megalooikonomou Konstantinos, Pantazopoulou Stavroula

NUMERICAL MODELLING OF A FOUR-SPAN BRIDGE, BI-AXIALLY TESTED ON THREE SHAKE TABLES .. 941
Isakovic Tatjana, Saiidi Saiid, Fischinger Matej

ASSESSMENT AND DESIGN OF SEISMICALLY ISOLATED BRIDGES IN PROXIMITY OF MAJOR FAULTS AND LOCATED ON LIQUEFIABLE SOILS 953
Ozkaya Cenan , Gercek Mete

RESTRAINED CONCRETE SHRINKAGE IN CASE OF STRENGTHENED BRIDGE PIERS BY CONCRETE JACKETING 967
Lampropoulos Andreas, Tsioulou Ourania, Dritsos Stephanos

MS 15: NUMERICAL SIMULATION AND EXPERIMENTAL VERIFICATION ON PROBLEMS IN THE FIELD OF EARTHQUAKE ENGINEERING AND STRUCTURAL DYNAMICS

STUDY OF THE IN-PLANE BEHAVIOUR OF GROUND FLOOR REINFORCED CONCRETE (R/C) FRAMES RETROFITTED WITH JACKETING AND AN ENCASED R/C PANEL IN ORDER TO WITHSTAND SEISMIC FORCES 978
Manos George, Soulis Vasilios, Katakalos Kostas, Koidis George

IN-PLANE BEHAVIOUR OF MASONRY INFILLS WITHIN MULTI-STOREY R/C FRAMES SUBJECTED TO SEISMIC TYPE LOADS AND THEIR UTILIZATION IN RETROFITTING 991
Manos George, Soulis Vasilios, Thauampteh Jafar

NUMERICAL AND EXPERIMENTAL STUDY OF THE ROCKING RESPONSE OF UNANCHORED BODY TO HORIZONTAL BASE EXCITATION 1011
Manos George, Petalas Apostolos, Demosthenous Milton

EXPERIMENTAL RESEARCH ON THE CAPACITY OF BRIDGE SHEAR KEYS 1025
Mitoulis Stergios, Tegos Ioannis, Malekakis Andreas

ANALYTICAL AND EXPERIMENTAL INVESTIGATION ON THE SEISMIC EFFICIENCY OF A NEW RESTRAINING SYSTEM FOR LIMITING THE SEISMIC MOVEMENTS OF THE BRIDGE DECK 1040
Tegou Sevasti, Tegos Ioannis

SHAKING TABLE STUDY OF THE SEISMIC INTERACTION OF AN ISOLATED BRIDGE DECK WITH THE ABUTMENT UTILIZING SMALL-SCALE MODELS AND NUMERICAL SIMULATIONS 1054
Mitoulis Stergios, Manos George, Tegos Ioannis

EXPERIMENTAL AND NUMERICAL INVESTIGATION OF RECTANGULAR R/C BEAMS RETROFITTED AGAINST SHEAR UTILISING FRP STRIPS 1064
Manos George, Katakalos Konstantinos, Theofanous Marios, Kozikopoulos Evaggelos

DYNAMIC BEHAVIOUR OF GREEK POST-BYZANTINE CHURCHES WITH FOUNDATION DEFORMABILITY AND EVALUATION OF THEIR EARTHQUAKE PERFORMANCE – EXPERIMENTAL INVESTIGATION OF STONE MASONRY MATERIAL PROPERTIES 1075
Manos George, Kotoulas Labros, Matsou Vassiliki, Felekidou Olimbia

THE EARTHQUAKE DESIGN OF LOW-RISE HOMES MADE BY EITHER REINFORCED CONCRETE, PARTIALLY REINFORCED MASONRY OR A NOVEL STEEL COMPOSITE SYSTEM 1095
Manos George, Katakalos Konstantinos, Theofanous Marios, Nalbadidou Alexandra, Tsakalidis Valerio, Stathi Christina

INFLUENCE OF THE LOADING RATE ON THE AXIAL COMPRESSIVE BEHAVIOR OF CONCRETE SPECIMENS CONFINED WITH SRG JACKETS 1107
Thermou Georgia, Katakalos Konstantinos, Manos George

DESIGN AND VERIFICATION OF A DYNAMIC EXPERIMENTAL CAMPAIGN ON ANCHORING SYSTEMS THROUGH MACRO AND MICRO NUMERICAL MODELS 1123
Mazzon Nicola, Tecchio Giovanni, Abate Marco, Alì Santoro Daniele, Gualano Daniele, Modena Claudio

SEISMIC RELIABILITY OF REINFORCED CONCRETE BRIDGE COLUMNS BASED ON LOCAL AND GLOBAL DAMAGE APPROACHES 1133
Benamer Mohamed, Feng Yatin

MS 16: RECENT ADVANCES IN EXPERIMENTAL PILE DYNAMICS & SOIL-STRUCTURE INTERACTION

APPLICABILITY OF PRINCIPLE OF SUPERPOSITION IN OBTAINING HORIZONTAL IMPEDANCE FUNCTIONS OF PILE GROUPS UNDER SOIL NON-LINEARITY 1145
Goit Chandra, Saitoh Masato, Mylonakis George

EXPERIMENTAL AND NUMERICAL INVESTIGATION OF THE SEISMIC BEHAVIOR OF RECTANGULAR TUNNELS IN SOFT SOILS 1152
Tsinidis Grigorios, Pitilakis Kyriazis, Heron Charles, Madabhushi Gopal

FULL-SCALE TESTING OF A MODEL STRUCTURE IN EUROSEISTEST TO STUDY SOIL-FOUNDATION-STRUCTURE INTERACTION 1175
Pitilakis Kyriazis, Anastasiadis Anastasios, Pitilakis Dimitris, Rovithis Emmanuil

PILES-INDUCED FILTERING ACTION AND ITS EFFECT ON THE SEISMIC RESPONSE OF BUILDINGS 1189
Caterino Nicola, de Sanctis Luca, di Laora Raffaele, Maddaloni Giuseppe

EXPERIMENTAL INVESTIGATION OF DYNAMIC BEHAVIOUR OF CANTILEVER RETAINING WALLS 1204
Kloukinas Panos, Scotto di Santolo Anna*, Penna Augusto, Bhattacharya Subhamoy, Dietz Matthew, Dihoru Luiza, Evangelista Aldo, Simonelli Armando, Taylor Colin, Mylonakis George*

SEISMIC PILE-SOIL INTERACTION: EXPERIMENTAL RESULTS VS. NUMERICAL SIMULATIONS 1218
Durante Maria Govanna, di Sarno Luigi, Sica Stefania, Mylonakis George, Taylor Colin, Simonelli Armando

MS 17: RISK ASSESSMENT AND QUANTIFICATION IN ENGINEERING: A MULTI-DISCIPLINARY PERSPECTIVE

STOCHASTIC RESPONSE DETERMINATION AND RELIABILITY ASSESSMENT OF A NONLINEAR CABLE NET STRUCTURAL SYSTEM 1230
Kougioumtzoglou Ioannis, Vassilopoulou Isabella, Gantes Charis

PROBABILISTIC PERFORMANCE-BASED SEISMIC DESIGN OF BRIDGE COLUMNS 1249
Saini Amarjeet, Vosooghi Ashkan, Saiidi Mehdi

SYSTEM RELIABILITY ANALYSIS OF SLENDER NETWORK ARCH BRIDGES 1258
Rønnquist Anders, Naess Arvid

NUMERICAL INVESTIGATION OF THE PARAMETRIC PENDULUM UNDER FILTERED RANDOM PHASE EXCITATION 1272
Alevras Panagiotis, Yurchenko Daniil, Naess Arvid

VISK: A GIS-COMPATIBLE PLATFORM FOR MICRO-SCALE ASSESSMENT OF FLOODING RISK IN URBAN AREAS 1281
de Risi Raffaele, Jalayer Fatemeh, Iervolino Iunio, Manfredi Gaetano, Carozza Stefano

A SIMPLIFIED METHODOLOGY TO OBTAIN RELIABILITY INDEXES FOR CALIBRATION OF DESIGN CODE FOR BUILDINGS 1303
Pérez-Rocha Luis Eduardo, Fernández Marco Aurelio, Manjarrez Lorena Elizabeth, Maldonado Jiménez David, Esteva L.

A BAYESIAN MODEL UPDATING PROCEDURE FOR DYNAMIC HEALTH MONITORING 1321
Patelli Edoardo, Broggi Matteo, Beaurepaire Pierre

THE RATIONAL IMPERATIVE OF PROFESSIONAL RISK MANAGEMENT 1332
Nathwani Jatin, Lind Niels

MS 18 : SEISMIC ASSESSMENT OF HERRITAGE STRUCTURES AND MONUMENTS THROUGH SIMULATION

DERIVATION OF FRAGILITY CURVES FOR TRADITIONAL TIMER-FRAMED MASONRY BUILDINGS USING NONLINEAR STATIC ANALYSIS 1339
Kouris Leonidas, Kappos Andreas

SEISMIC LOAD ASSESSMENT FOR MASONRY MONUMENTAL BUILDINGS 1349
Salonikios Thomas, Morfidis Konstantinos, Lekidis Vasilios

ANALYTICAL PROCEDURE FOR SEISMIC ASSESSMENT OF MASONRY BUILDINGS WITH HISTORICAL VALUE 1360
Pardalopoulos Stylianos, Kontari Maria, Pantazopoulou Stavroula

SEISMIC ASSESSMENT OF A NON – SYMMETRIC STONE MASONRY BUILDING WITH FLEXIBLE FLOORS ... 1377
Karantoni Fillitsa, Manalis I.C.

REHABILITATION OF A PARTIALLY COLLAPSED MASONRY TRADITIONAL TOBACCO WAREHOUSE OF THE LATE 19TH CENTURY 1389
Chalioris Constantin, Favvata Maria, Alexandri Venetia, Karayannis Chris

RECORDING HISTORIC MASONRY BUILDINGS USING PHOTOGRAMMETRY - TWO CASE STUDIES 1401
Chalioris Constantin, Tsioukas Vassilios, Favvata Maria, Karayannis Chris

STRUCTURAL UPGRADING OF A 3-STOREY HERITAGE STRUCTURE OF 1925 IN THESSALONIKI 1410
Karayannis Chris, Chalioris Constantin, Favvata Maria

MS 19: IDENTIFICATION METHODS IN STRUCTURAL DYNAMICS

ESTIMATING THERMAL INERTIA AND TEMPERATURE DISTRIBUTION CONSISTENT WITH MONITORED DATA FROM A RAILWAY BRIDGE 1421
Casciati Fabio, Casciati Sara, Faravelli Lucia, Bortoluzzi Daniele, Messervey Thomas

FINITE ELEMENT MODEL UPDATING OF A FOOTBRIDGE BASED ON STATIC AND DYNAMIC MEASUREMENTS 1432
Solís Mario, He Leqia, Lombaert Geert, de Roeck Guido

UKF ESTIMATION OF SP-TAR MODELS FOR THE IDENTIFICATION OF TIME-VARYING STRUCTURES 1450
Spiridonakos Minas, Chatzi Eleni

MODE SHAPE ASSEMBLY FOR AMBIENT MODAL ANALYSIS USING A TWO-STAGE BAYESIAN SPECTRAL DENSITY APPROACH 1460
Yan Wang-Ji, Katafygiotis Lambros

MS 20: SEISMIC BEHAVIOUR AND DESIGN OF PRECAST STRUCTURES

DESING OF ONE STOREY BUILDING WITH PRECAST CONCRETE SANDWICH PANELS IN EARTHQUAKE REGIONS 1469
Christou Andreas

SAFECAST PROJECT: EUROPEAN RESEARCH ON SEISMIC BEHAVIOUR OF THE CONNECTIONS OF PRECAST STRUCTURES 1482
Toniolo Giandomenico

EARTHQUAKE EXPERIENCE OF TURKISH PRECAST INDUSTRY 1494
Ozden Sevket, Barka Gunkut, Atakoy Hakan, Hancıoğlu Baykal, Ozkan Umit

ANALYTICAL PREDICTION OF THE SHEAR RESISTANCE OF PRECAST RC PINNED BEAM-TO-COLUMN CONNECTIONS 1502
Kremmyda Georgia, Fahjan Yasin, Psycharis Ioannis

SEISMIC BEHAVIOUR OF THE BEAM-TO-COLUMN DOWEL CONNECTIONS: FEM ANALYSIS 1515
Zoubek Blaz, Fischinger Matej, Isakovic Tatjana

SEISMIC BEHAVIOR OF THE BEAM-TO-COLUMN DOWEL CONNECTIONS: MACRO MODELLING 1523
Fischinger Matej, Zoubek Blaz, Isakovic Tatjana

NUMERICAL MODELING OF SINGLE-STOREY PRECAST FRAME'S PINNED CONNECTIONS WITH A SPECIAL DAMPER 1533
Soydan Cihan, Yüksel Ercan, İrtem Erdal

SINGLE STORY PRECAST STRUCTURES IN SEISMIC ZONES - I 1550
Karadogan Faruk, Yüce Serkan, Yüksel Ercan, Bal I.E., Hasel F.B

SHAKE TABLE TESTING OF A FULL-SCALE FIVE-STORY BUILDING: SEISMIC PERFORMANCE OF PRECAST CONCRETE CLADDING PANELS 1569
Pantoli Elide, Chen Michelle, Hutchinson Tara, Underwood Glen, Hildebrand Mark

SEISMIC PERFORMANCE EVALUATION OF A POST-TENSIONED FRAME BUILDING 1588
Hancıoğlu Baykal, Kırçıl Murat Serdar, Ulusoy Seyit Ismail

THE EMILIA EARTHQUAKES: REPORT AND ANALYSIS ON THE BEHAVIOR OF PRECAST INDUSTRIAL BUILDINGS FROM A FIELD MISSION 1600
Bournas Dionysios, Negro Paolo, Taucer Fabio

MS 21: SEISMIC BEHAVIOUR AND RETROFITTING OF MONUMENTS AND HISTORICAL BUILDINGS

THE EFFECT OF MULTIPLE EARTHQUAKE EXCITATIONS IN SEQUENCE ON ANCIENT MULTI-DRUM STRUCTURES 1615
Papaloizou Loizos, Komodromos Petros

SEISMIC PERFORMANCE OF ANCIENT MASONRY BUILDINGS: A SENSITIVITY ANALYSIS 1624
Mendes Nuno, B. Lourenço Paulo

POST-EARTHQUAKE ASSESSMENT OF A MASONRY TOWER BY ON - SITE INSPECTION AND OPERATIONAL MODAL TESTING 1639
Saisi Antonella, Gentile Carmelo, Cantini Lorenzo

SEISMIC RELIABILITY ASSESSMENT OF CLASSICAL COLUMNS SUBJECTED TO NEAR SOURCE GROUND MOTIONS 1651
Psycharis Ioannis, Fragiadakis Michalis, Stefanou Ioannis

EFFECT OF DAMAGE ON THE DYNAMIC CHARACTERISTICS OF ST. NICHOLAS CATHEDRAL IN CYPRUS 1665
Votsis Renos, Kyriakides Nicholas, Tantele Elia, Chrysostomou Christis

SEISMIC PROTECTION OF MONUMENTS AND HISTORICAL BUILDINGS BY A SUSTAINABLE REDUCTION SYSTEM OF THE SEISMIC INPUT MOTION 1675
Carydis Panayotis, Giannopoulos Vasileios, Athanasiou Egkolfios, Lebesis Nikolaos

PERFORMANCE-BASED ASSESSMENT OF THE ARSENAL DE MILLY OF THE MEDIEVAL CITY OF RHODES .. 1699
Cattari Serena, Karatzetzou Anna, Degli Abbati S., Gkoktsi K., Pitilakis Dimitris, Negulescu Caterina

EARTHQUAKE BEHAVIOR OF HISTORICAL MINARETS IN ISTANBUL 1718
Çakti Eser, Oliveira Carlos, Lemos Jose V., Saygili Özden, Görk Serkan, Zengin Esra

EARTHQUAKE PROTECTION OF HISTORICAL BUILDINGS ACCORDING TO PROHITECH 1731
Mazzolani Federico

MS 22: ADVANCES IN COMPUTATIONAL METHODS FOR RESILIENT STRUCTURAL SYSTEMS UNDER EXTREME HAZARDS

DETAILED COMPONENT MODELLING OF A SELF-CENTERING ENERGY DISSIPATIVE BRACE SYSTEM 1758
Erochko Jeffrey, Christopoulos Constantin, Tremblay Robert

RY-μ-Tn RELATIONS FOR SEISMICALLY ISOLATED STRUCTURES 1771
Tsiavos Anastasios, Vassiliou Michalis, Mackie Kevin, Stojadinović Božidar

MINIMAL-DAMAGE STEEL FRAMES USING POST-TENSIONED CONNECTIONS WITH WEB HOURGLASS SHAPE PINS: DESIGN AND ASSESSMENT 1782
Dimopoulos Athanasios, Karavasilis Theodore, Vasdravellis George, Uy Brian

MONTE CARLO ANALYSIS FOR THE BLAST RESISTANCE DESIGN AND ASSESSMENT OF A REINFORCED CONCRETE WALL 1803
Olmati Pierluigi

MS 23: ADVANCES IN STRUCTURAL VIBRATIONS

INVERSE ANALYSIS FOR DETERMINING THE REINFORCED CONCRETE FLEXURAL STIFFNESS OF A STRUCTURE UNDER STRONG COMPRESSION 1816
Wahrhaftig Alexandre, Brasil Reyolando

SEISMIC SOIL-PILE INTERACTION - INFLUENCE OF SOIL INELASTICITY 1825
Kampitsis Andreas, Sapountzakis Evangelos, Giannakos Spyros, Gerolymos Nikos

MULTI-SCALE ENERGY PUMPING BETWEEN A MAIN OSCILLATOR INCLUDING SAINT-VENANT TERM AND A NONLINEAR ENERGY SINK 1839
Weiss Mathieu, Ture Savadkoohi Alireza, Lamarque Claude-Henri

LIQUID FREE VIBRATION ANALYSIS IN A CIRCULAR CYLINDRICAL RIGID CAVITY USING THE h-p FINITE ELEMENT METHOD 1857
Ouissi Mohammed Nabil, Hamza Cherif Sidi Mohammed

NONLINEAR DYNAMIC ANALYSIS OF PLATES STIFFENED BY PARALLEL BEAMS WITH DEFORMABLE CONNECTION 1867
Dourakopoulos John, Sapountzakis Evangelos

NONLINEAR VIBRATIONS OF ROTATING 3D TAPERED BEAMS WITH ARBITRARY CROSS SECTIONS 1883
Stoykov Stanislav, Margenov Svetozar

MS 24: ADVANCES IN MODELING OF WAVE PROPAGATION AND APPLICATIONS

COUPLING OF FINITE ELEMENTS AND HIERARCHICAL BOUNDARY ELEMENTS FOR DYNAMIC SOIL-STRUCTURE INTERACTION PROBLEMS 1898
Coulier Pieter, François Stijn, Lombaert Geert, Degrande Geert

MS 25: SOFTWARE DEVELOPMENT IN THE FIELD OF EARTHQUAKE ENGINEERING AND STRUCTURAL DYNAMICS

BRIDGE-WIZARD: EXPERT SYSTEM FOR FINITE ELEMENT MODELING AND POST PROCESSING OF BRIDGE STRUCTURES 1920
Sextos Anastasios, Lesgidis Nikolaos

ROBUSTNESS, REPEATABILITY AND RESILIENCE OF INTERCONTINENTAL DISTRIBUTED COMPUTING FOR THE PURPOSES OF SEISMIC ASSESSMENT OF BRIDGES 1930
Taskari Olympia, Sextos Anastasios

CABLE-STAYED BRIDGES SUBJECTED TO NEAR-FAULT VERTICAL MOTION 1941
Kuleli Muge, Elnashai Amr

VALIDATION OF NUMERICAL MODELS FOR RC COLUMNS SUBJECTED TO CYCLIC LOAD 1958
del Vecchio Ciro, di Sarno Luigi, Kwon Oh-Sung, Prota Andrea

MS 26: COMPUTATIONAL MULTIBODY SYSTEM DYNAMICS

RIGID BODY DYNAMICS USING A NOVEL APPROACH BASED ON LIE GROUP THEORY 1975
Paraskevopoulos Elias, Natsiavas Sotirios

MS 27: UNCERTAINTY QUANTIFICATION IN COMPUTATIONAL DYNAMICS

UNCERTAINTY ANALYSIS ON A PUMP ASSEMBLY USING COMPONENT MODE SYNTHESIS 1991
Audebert Sylvie, Fall-Lo Fatou

DYNAMICAL BEHAVIOR OF TRAINS EXCITED BY A NON-GAUSSIAN VECTOR VALUED RANDOM FIELD 2001
Perrin Guillaume, Soize Christian, Duhamel Denis, Funfschilling Christine,

GENERATION OF RESPONSE SPECTRUM COMPATIBLE ACCELEROGRAMS USING THE MAXIMUM ENTROPY PRINCIPLE 2016
Batou Anas, Soize Christian

UNCERTAINTY QUANTIFICATION OF THE NONLINEAR DYNAMICS OF ELECTROMECHANICAL COUPLED SYSTEMS 2026
de Queiroz Lima Roberta, Sampaio Rubens

UNCERTAINTIES IN MULTI-STAGE ROTORS MODELED BY THE POLYNOMIAL CHAOS EXPANSION 2050
Seguí Bartolomé, Faverjon Béatrice, Jacquet-Richardet Georges

STABILITY AND RESPONSE ANALYSIS OF A PIPE WITH INTERNAL FLOW ANALYZED WITH AN UNCERTAIN COMPUTATIONAL MODEL 2057
Ritto Thiago, Soize Christian, Rochinha Fernando, Sampaio Rubens

FORMULATION OF A STOCHASTIC SEMI ANALYTICAL FINITE ELEMENT METHOD FOR UNCERTAIN MEDIA 2069
Bouchoucha Faker, Ichchou Mohamed, Haddar Mohamed

CHARACTERIZATION OF THE INFLUENCE OF RAIL WEAR ON TRAIN DYNAMICS 2080
Lestoille Nicolas, Perrin Guillaume, Funfschilling Christine

DISCONTINUOUS GALERKIN METHODS FOR HIGH-DIMENSIONAL FOKKER-PLANCK EQUATIONS IN STOCHASTIC DYNAMICS 2093
Loerke Friederike, Nackenhorst Udo

MS 28: PERIODICITY EFFECTS AND PERIODICITY-BASED METHODS IN VIBRO-ACOUSTICS AND STRUCTURAL DYNAMICS

ANALYSIS OF OSCILLATIONS OF ONE-DIMENSIONAL SPATIALLY PERIODIC STRUCTURES. AN UNCONVENTIONAL APPROACH AND SOME NEW EFFECTS 2103
Sorokin Vladislav

ON THE EFFECT OF DAMPING ON DISPERSION CURVES IN PLATES 2118
Manconi Elisabetta, Sorokin Sergey

INFINITE PERIODIC STRUCTURE OF LIGHTWEIGHT ELEMENTS: REPRESENTATION OF WAVE PROPAGATION 2133
Domadiya Parthkumar, Andersen Lars Vabbersgaard, Sorokin Sergey

MULTIMODE CHARACTER OF DYNAMICAL SYSTEMS AS A CAUSE OF THEIR COMPLEX ("CHAOTIC") BEHAVIOR 2145
Blekhman Iliya

INFLUENCE OF STRUCTURAL PERIODICITY ON VIBRATION TRANSMISSION IN A MULTI-STOREY WOODEN BUILDING 2158
Andersen Lars Vabbersgaard

ON OPTIMUM DESIGN AND PERIODICITY OF BAND-GAP STRUCTURES 2178
Olhoff Niels, Niu Bin, Cheng Gengdong

EXCITATION OF PARAMETRIC RESONANCE IN MICRO BEAMS BY JOULE'S HEATING 2204
Sibgatullin Timur, Schreiber David, Krylov Slava

THE LOCATION OF PASS AND STOP BANDS OF AN INFINITE PERIODIC STRUCTURE VERSUS THE EIGENFREQUENCIES OF ITS FINITE SEGMENT CONSISTING OF SEVERAL "PERIODICITY CELLS" 2220
Filippenko Georgy

MS 29: ACCURACY AND COMPUTATIONAL EFFICIENCY IN DYNAMIC/SEISMIC STRUCTURAL ANALYSIS

A SIMPLE APPROACH TOWARDS FURTHER ACCURACY IN STRUCTURAL DYNAMIC ANALYSIS 2232
Soroushian Aram

ON THE RESPONSE OF THE SMALL BUILDINGS TO VIBRATIONS 2244
Munteanu Ligia, Chiroiu Veturia, Sireteanu Tudor

MORE VERSATILITY FOR AN INTEGRATION-STEP-SIZE-ENLARGEMENT TECHNIQUE IN TIME INTEGRATION ANALYSIS 2265
Sabzei Ahmad, Reziakolaei Ali Yahyapour, Soroushian Aram

ON THE PERFORMANCE OF A STRUCTURAL ANALYSIS COST REDUCTION TECHNIQUE WHEN APPLIED TO RESIDENTIAL BUILDINGS 2275
Reziakolaei Ali Yahyapour, Sabzei Ahmad, Soroushian Aram

CYCLIC BEHAVIOR MODELING OF RECTANGULAR RC BRIDGE PIERS USING OPENSEES 2286
Attarchian Nahid, Kalantari Afshin, Moghaddam AbdoReza Sarvghad

THEORETICAL STUDY ON THE REDUCTION AND RECOVERING METHOD 2296
Kurata Mitsuharu, Gan Buntara Sthenly, Nouchi Eiji

SIMPLIFICATION OF EARTHQUAKE ACCELEROGRAMS FOR RAPID TIME HISTORY ANALYSIS BASED ON THE IMPULSIVE LOAD CONCEPT 2304
Hosseini Mahmood, Mirzaei Iman

MS 30: ROBUST MODELING AND CONTROL FOR SMART STRUCTURES

DESIGN AND IMPLEMENTATION OF A LINEAR CONTROLLER ON A REDUCED MODEL OF A SMART STRUCTURE 2313
Ghareeb Nader, Schmidt Ruediger

MS 31: SEISMIC ISOLATION OF INDUSTRIAL AND ESSENTIAL FACILITIES (POWER PLANTS-EQUIPMENT, CHEMICAL/OIL PLANTS-EQUIPMENT, HOSPITALS)

INFLUENCE OF SOIL-STRUCTURE INTERACTION ON ISOLATED BUILDINGS FOR SF6 GAS-INSULATED SUBSTATIONS 2330
Pérez-Rocha Luis Eduardo, Aviles López J., Tena Colunga Arturo, Cordero Macías C.

MS 32: SEISMIC ANALYSIS AND DESIGN OF IRREGULAR BUILDINGS

ROT INDEX FOR ASSESSING THE TORSIONAL EFFECT ON THE SEISMIC PERFORMANCE OF RC BUILDINGS 2345
Stathi Chrysanthi, Bakas Nikolaos, Lagaros Nikos, Papadrakakis Manolis

MS 33: STEEL AND COMPOSITE STEEL REINFORCED CONCRETE STRUCTURES UNDER DYNAMIC AND SEISMIC LOADING

SEISMIC BEHAVIOUR OF INNOVATIVE ENERGY DISSIPATION SYSTEMS FUSEIS 1-2 2360
Dimakogianni Danai, Dougka Georgia, Vayas Ioannis, Karydakis Phaedon

SEISMIC BEHAVIOUR OF INNOVATIVE ENERGY DISSIPATION SYSTEMS FUSEIS 1-1 2375
Dougka Georgia, Dimakogianni Danai, Vayas Ioannis, Karydakis Phaedon

ESTIMATION OF THE BEHAVIOR FACTOR OF STEEL STORAGE PALLET RACKS 2389
Adamakos Konstantinos, Avgerinou Stella, Vayas Ioannis

DESIGN AND PERFORMANCES OF STEEL-CONCRETE HYBRID COUPLED SHEAR WALLS IN SEISMIC CONDITIONS 2404
Bogdan Teodora, Zona Alessandro, Leoni Graziano, Dall'Asta Andrea, Braham C. , Degée Hervé

MS 35: HIGH-PERFORMANCE COMPUTING FOR STRUCTURAL MECHANICS AND EARTHQUAKE ENGINEERING

HIGH-PRECISION FINITE-ELEMENT ANALYSIS OF RUBBER BEARING FOR BASE-ISOLATION OF BUILDING STRUCTURES 2422
Ohsaki Makoto, Miyamura Tomoshi, Kohiyama Masayuki, Yamashita Takuzo, Yamamoto Masashi, Nak Naohiro

DYNAMIC COLLAPSE ANALYSIS OF FOUR-STORY STEEL FRAME USING E-SIMULATOR 2431
Miyamura Tomoshi, Ohsaki Makoto, Yamashita Takuzo, Isobe Daigoro, Kohiyama Masayuki

MS 36: SEISMIC SAFETY ASSESSMENT OF STRUCTURES

DESIGN OF DISSIPATIVE BRACES FOR AN EXISTING STRATEGIC BUILDING WITH A PUSHOVER BASED PROCEDURE 2443
Bergami Alessandro Vittorio, Nuti Camillo

HEURISTIC APPROACH IN STRUCTURAL STRENGTH EVALUATION AND RETROFITTING OF EXISTING BUILDINGS IN SEISMIC AREAS 2454
Gluck Nicolae, Farhat Rina, Eid Rami, Tzadka Uri

EVALUATION OF DAMAGE IN REINFORCED CONCRETE COLUMNS UNDER BIAXIAL LOADING 2466
Rodrigues Hugo, Arêde António, Varum Humberto, Costa Aníbal

EXPERIMENTAL AND NUMERICAL STUDY OF RC COLUMNS UNDER BIAXIAL LOADING: AS BUILT 2480
Silva José Pedro, Rodrigues Hugo, Arêde António, Rocha Patrício, Monteiro André

ESTIMATING ROOF-LEVEL ACCELERATION SPECTRA FOR SINGLE STOREY BUILDINGS 2491
Sullivan Timothy, Calvi Paolo, Welch David

A CASE STUDY OF COLLAPSE DURING THE 2009 L'AQUILA (ITALY) EARTHQUAKE 2500
Mulas Maria Gabriella, Martinelli Luca, Perotti Federico

EXPERIMENTAL CYCLIC TESTS OF HOLLOW PIERS WITH DIFFERENT RETROFIT STRATEGIES 2514
Delgado Pedro, Rocha Patrício, Arêde António, Vila Pouca Nelson, Costa Aníbal, Delgado Raimundo

EXPERIMENTAL EVALUATION OF THE OUT-OF-PLANE BEHAVIOUR OF TRADITIONAL STONE MASONRY BUILDINGS IN AZORES, PORTUGAL 2524
Arêde António, Costa Aníbal, Costa Alexandre, Ferreira Tiago, Gomes Ana, Varum Humberto

STUDY ON THE DEFINITION OF ANALYTICAL FRAGILITY FUNCTIONS FOR CONCRETE BUILDINGS 2532
Marques Mário, Amorin Epiphanie, Martins Luís, Araújo Miguel, Delgado Raimundo

INFLUENCE OF CODE-BASED RECORD SELECTION METHODS ON THE SEISMIC ASSESSMENT OF EXISTING STEEL BUILDINGS 2549
Araújo Miguel, Macedo Luís, Castro José Miguel, Delgado Raimundo

MS 38: HUMAN INDUCED VIBRATIONS

CHARACTERISATION OF WALKING LOADS FROM INERTIAL MOTION TRACKING 2565
van Nimmen Katrien, van den Broeck Peter, Lombaert Geert, de Roeck Guido

ANALYTICAL AND NUMERICAL ESTIMATE OF FOOTBRIDGES' MAXIMUM DYNAMIC RESPONSE TO UNRESTRICTED PEDESTRIAN TRAFFIC 2576
Tubino Federica, Piccardo Giuseppe

AN OPTICALLY BASED ASSESSMENT OF PEDESTRIAN BALANCE BEHAVIOUR WHILE WALKING ON A LATERALLY OSCILLATING TREADMILL 2590
Carroll Sean, Owen John, Hussein Mohammed

HUMAN INDUCED VIBRATIONS IN A PEDESTRIAN TIMBER BRIDGE 2609
Casciati Sara, Faravelli Lucia, Bortoluzzi Daniele

DYNAMIC LOADING FACTORS OF INDIVIDUAL JOGGING FORCES 2619
Racic Vitomir, Brownjohn James, Pavic Aleksandar

DYNAMIC ANALYSIS OF STEEL-CONCRETE COMPOSITE TUBULAR FOOTBRIDGES SUBMITTED TO HUMAN WALKING 2627
Debona Gilvan Lunz, Santos da Silva José Guilherme, Sieira Ana Cristina Castro Fontenla

QUANTIFICATION OF THE STRUCTURAL RESPONSE OF A STAIRCASE DAMPED BY THE PRESENCE OF PEOPLE: NUMERICAL MODEL AND EXPERIMENTAL TESTS 2639
Cappellini Anna, Manzoni Stefano, Vanali Marcello

MS 39: RECENT ADVANCES AND CHALLENGES IN GEOTECHNICAL EARTHQUAKE ENGINEERING

3-D CONVOLUTIONAL PERFECTLY MATCHED LAYER MODELS FOR DYNAMIC SOIL-STRUCTURE INTERACTION ANALYSIS IN THE FINITE ELEMENT TIME-DOMAIN 2650
Xu Bo-Qing, Tsang Hing-Ho, Lo S.H.

APPLICABILITY OF TOTAL STRESS SEISMIC GROUND RESPONSE ANALYSIS UNDER LARGE EARTHQUAKES 2666
Yoshida Nozomu

THE STABILITY OF THE GENERALISED-α METHOD IN SOIL-PORE FLUID COUPLED FORMULATION 2681
Han Bo, Zdravković Lidija, Kontoe Stavroula

EFFECTS OF ARTIFICIAL LANDFORM CHANGE TO WATER PIPELINE DAMAGE IN SENDAI CITY DURING THE 2011 TOHOKU OFFSHORE JAPAN EARTHQUAKE 2696
Wakamatsu Kazue, Nagata Shigeru, Maruyama Yoshihisa

BEHAVIOUR OF A GEOSYNTHETIC REINFORCED STEEP SLOPE CONSTRUCTED WITH COHESIVE BACKFILL UNDER EARTHQUAKE LOADING 2708
Silva Vieira Castorina, Lopes Maria de Lurdes

SITE RESPONSE ANALYSIS FOR VERTICAL GROUND MOTION 2722
Kontoe Stavroula, Christopoulos Antonios, May Robert

OPTIMUM DESIGN OF CANTILEVER WALLS RETAINING LINEAR ELASTIC BACKFILL BY USE OF GENETIC ALGORITHM 2731
Papazafeiropoulos George, Plevris Vagelis, Papadrakakis Manolis

MS 40: STRUCTURAL DYNAMICS AND EARTHQUAKE ENGINEERING OF ROCKING STRUCTURES

A NEW PERFORMANCE-BASED DESIGN METHODOLOGY FOR CONTROLLED ROCKING STEEL FRAMES ... 2751
Wiebe Lydell, Christopoulos Constantin

ROCKING RESPONSE AND STABILITY ANALYSIS OF AN ARRAY OF FREE-STANDING COLUMNS CAPPED WITH A FREE-STANDING RIGID BEAM 2764
Makris Nicos, Vassiliou Michalis

ROCKING RESPONSE OF SLENDER, FLEXIBLE COLUMNS UNDER PULSE EXCITATION 2786
Vassiliou Michalis, Mackie Kevin, Stojadinović Božidar

TOWARDS A UNIFIED DESCRIPTION OF ROCKING STRUCTURES 2802
DeJong Matthew, Dimitrakopoulos Elias

ROCKING RESPONSE OF FREE-STANDING FURNITURES UNDER EARTHQUAKE FLOOR MOTIONS 2813
Chiriatti Marco, Cimellaro Gian Paolo

FINITE ELEMENT MODELING OF "ROCKING WALLS" 2831
Belleri Andrea, Torquati Mauro, Riva Paolo

SHAKING TABLE TESTS ON UNREINFORCED LOAD-BEARING MASONRY WALLS – COMPARISON WITH SIMPLE ROCKING MODELS. 2849
Mordant Christophe, Dietz Matthew, Degée Hervé

SEISMIC RESPONSE OF POST-TENSIONED STEEL ROCKING CONCENTRICALLY BRACED FRAMES WITH VARIOUS ASPECT RATIOS 2866
Chancellor Brent, Sause Richard, Ricles James, Tahmasebi Ebrahim, Akbas Tugce

COMPUTATIONAL MODELLING OF SELF-CENTERING PRECAST CONCRETE WALLS 2880
Watkins Jonathan, Henry Richard, Sirtharan Sri

BALANCING THE BENEFICIAL CONTRIBUTIONS OF FOUNDATION ROCKING AND STRUCTURAL YIELDING TO IMPROVE STRUCTURAL SEISMIC RESILIENCE 2892
Liu Weian, Hutchinson Tara, Kutter Bruce, Hakhamaneshi Manouchehr, Gavras Andreas- Gerasimos

ROCKING RESPONSE OF TALLER REINFORCED CONCRETE WALLS 2909
Lemieux Marc- André, Koboevic Sanda

SEISMIC PERFORMANCE OF PRE-STRESSED SHEAR WALLS WITH BOTTOM HORIZONTAL SLITS AND BUCKLING RESTRAINED REINFORCEMENT 2922
Xiangliang Dang, Ying Zhou, Xilin Lu

MS 41: BRICK-INFILLED RC FRAMES: SEISMIC BEHAVIOR AND RETROFIT

LOCAL EFFECTS IN THE SEISMIC DESIGN OF RC FRAME STRUCTURES WITH MASONRY INFILLS 2931
Hak Sanja, Morandi Paolo, Magenes Guido

ESTIMATION OF EFFECTIVE STIFFNESS OF INFILL PANELS AT DAMAGE LIMITATION LIMIT STATE FOR LOW- AND MID-RISE INFILLED RC FRAMES 2944
de Risi Maria Teresa, Ricci Paolo, Verderame Gerardo Mario, Manfredi Gaetano

ANALYSIS OF LOCAL SHEAR EFFECTS IN BRICK MASONRY INFILLED RC FRAMES 2962
Cavaleri Liborio, di Trapani Fabio, Papia Maurizio

VALIDATION OF ANALYTICAL MODELS FOR THE ASSESSMENT OF BRICK-INFILLED RC FRAMES STRENGTHENED WITH FRPS 2978
Spyrakos Constantine, Maniatakis Charilaos, Psycharis Ioannis, Smyrou Eleni, Asteris Panagiotis

MS 42: RELIGIOUS MONUMENTS: SEISMIC BEHAVIOR AND RETROFIT

SEISMIC ANALYSIS OF VAULTED MASONRY STRUCTURES THROUGH THE FINITE ELEMENT MODEL "BLOCK-JOINT" 2997
Pugi Francesco

SEISMIC EVALUATION OF THE HISTORIC CHURCH OF ST.NICHOLAS IN PIRAEUS BEFORE AND AFTER INTERVENTIONS 3015
Spyrakos Constantine, Francioso Alessio, Kiriakopoulos Panagiotis, Papoutsellis Stavros

Regular Sessions

RS 1: ACTIVE-PASSIVE CONTROL

OPTIMAL CONTROL DESIGN BY ADJOINT-BASED OPTIMIZATION FOR ACTIVE MASS DAMPER WITH DRY FRICTION 3030
Guida Domenico, Nilvetti Fabio, Pappalardo Carmine Maria,

RS 3: COMPUTATIONAL SEISMIC STRUCTURAL ANALYSIS

BASIC DISPLACEMENT FUNCTIONS IN DYNAMIC ANALYSIS OF AN ARCH DAM AS A CURVED BEAM RESTING ON A CONTINUES ELASTIC FOUNDATION 3049
Hashemi Ashkan, Attarnejad Reza, Zarinkamar Shermineh

CONTACT INTERFACE MODELING IN THE DYNAMIC RESPONSE OF RIGID BLOCKS SUBJECTED TO BASE EXCITATION 3060
Ardila-Giraldo Oscar, Reyes Juan Carlos, Smith-Pardo J. Paul

NUMERICAL MODELLING OF PILES GROUP UNDER SEISMIC LOADING IN COHESIVE SOILS : INCLINATION EFFECT 3072
Hage Chehade Fadi, Sadek Marwan, Bachir Douaa

AN ANALYTICAL APPROACH FOR ASSESSMENT OF THE EFFECTS OF INFILL PANELS IN RC FRAMES .. 3084
Casolo Siro, Porco Francesco, Uva Giuseppina

A THREE DIMENSIONAL MULTISCALE FORMULATION FOR THE NONLINEAR DYNAMIC ANALYSIS OF MASONRY STRUCTURES 3101
Triantafyllou Savvas, Chatzi Eleni

ALTERNATIVE INTEGRATORS AND PARALLEL COMPUTING FOR EFFICIENT NONLINEAR RESPONSE HISTORY ANALYSES 3116
Mosalam Khalid, Liang Xiao, Günay Selim, Schellenberg Andreas

A COMPARATIVE STUDY BETWEEN ACCELERATION AND ENERGY-BASED SEISMIC DEMAND SPECTRA COMPUTED BY AN EXTENSIVE COMPUTER ALGORITHM ON A GRID COMPUTER 3137
Dindar Ahmet Anil, Yalcin Cem, Yüksel Ercan, Ozkaynak Hasan, Buyukozturk Oral

NON-LINEAR DYNAMICS OF ELECTRICAL EQUIPMENT CABLES 3144
Oliveto Nicholas, Sivaselvan Mettupalayam

DISCRETE IMPEDANCE MATRIX FOR FLEXIBLE SURFACE FOUNDATIONS 3153
Maravas Andreas , Mylonakis George, Karabalis Dimitris

ENVELOPE PRINCIPLE IN MULTI-MODE PUSHOVER PROCEDURE FOR RC BUILDINGS 3162
Mihanović Ante, Balić Ivan, Trogrlić Boris

RS 4: CONSTITUTIVE MODELLING UNDER DYNAMIC AND SEISMIC ACTIONS

EXPERIMENTAL STUDY AND NUMERICAL RESPONSE PREDICTION OF A STEEL MOMENT-FRAME WITH TAKING FATIGUE DAMAGE INTO ACCOUNT 3179
Saranik Mohammad, Jézéquel Louis, Lenoir David

NUMERICAL MODELING OF DYNAMIC COMPACTION IN DRY SAND USING DIFFERENT CONSTITUTIVE MODELS 3195
Pourjenabi Majid, Ghanbari Elham, Hamidi Amir

THE APPLICATION OF FEM/DEM METHOD IN ANALYSIS OF RC BEAM-COLUMN JOINTS 3203
Nikolić Željana, Živaljić Nikolina, Smoljanović Hrvoje

RS 5: DESIGN METHODS UNDER DYNAMIC AND SEISMIC ACTIONS

DYNAMICS OF MARINE STATIONARY PLATFORM UNDER ACTION OF HORIZONTAL SEISMIC LOADING 3217
Shekhovtsov Alexey, Shekhovtsov Vyacheslav, Tovstik Petr, Tovstik Tatiana

ECCENTRIC STEEL BUILDINGS DESIGNED FOR UNIFORM DUCTILITY DEMANDS UNDER EARTHQUAKE ACTIONS 3228
Kyrkos Miltiadis, Anagnostopoulos Stavros

INCLUSION OF GEOMETRIC NONLINEARITY IN CALCULATING SEISMIC BUILDING FRAMES 3243
Martinez Valle Jose Miguel, Martinez Jimenez Jose Miguel, Martinez Jimenez Pilar

ANALYSIS AND DESIGN OF STAIRCASES AGAINST SEISMIC LOADINGS 3259
Tegos Ioannis, Panoskaltsis Vassilis, Tegou Sevasti

RS 6: DYNAMICS OF COUPLED PROBLEMS

DYNAMIC EFFECT OF RAILWAY VEHICLE ON SEISMIC RESPONSE OF RAILWAY STRUCTURE 3278
Tokunaga Munemasa, Minoura Shintaro, Sogabe Masamichi

DYNAMIC COMPUTATION AND DESIGN OF A WORLD'S RECORD DEATH-RIDE 3289
Denoël Vincent, Canor Thomas, Demanet Johan

MODELLING A LARGE-SCALE UNIAXIAL SHAKING TABLE FACILITY 3300
Ceresa Paola, Brezzi Franco, Calvi Gian Michele

ON NUMERICAL MODELING OF DYNAMICS OF IRREVERSIBLE DEFORMING AND FRACTURE OF OIL-BEARING LAYER IN THE VICINITY OF A BOREHOLE 3316
Kiselev Alexey, Zacharov Pavel

RS 7: DYNAMICS OF MICRO SYSTEMS

NONLOCAL MODAL ANALYSIS FOR NANOSCALE DYNAMICAL SYSTEMS 3328
Adhikari Sondipon, Gilchrist Daniel, Murmu Tony, McCarthy Michael

RS 8: GEOTECHNICAL EARTHQUAKE ENGINEERING

STABILITY OF EARTH RETENTION SYSTEM IN DRY COHESIONLESS SOIL UNDER STATIC AND SEISMIC CONDITION 3350
Chowdhury Subha Sankar, Deb Kousik, Sengupta Anirudhha

STABILITY ANALYSIS OF STEEP NAILED SLOPES IN SEISMIC CONDITIONS: NUMERICAL APPROACH 3356
Sahoo S, Manna B, Sharma K. G

STABILITY ANALYSIS OF A ROCK MASS IN SEISMIC CONDITIONS: CASE STUDY IN LEBANON 3366
Abdallah Mirvat, Shahrour Isam, Hage Chehade Fadi

STATISTICAL EVALUATION OF THE SEISMIC SERVICE ABILITY OF A BULLET TRAIN ALONG THE DEAD SEA FAULT 3383
Uchida Shun, Klar Assaf

FUNDAMENTAL STUDY ON EVALUATING ROCK SLOPE STABILITY BY VIBRATION MEASUREMENTS USING REMOTE VIBRATION MEASURING SYSTEM 3403
Minoura Shintaro, Uehan Fumiaki, Saito Hideki

EFFECT OF COUPLING EXCESS PORE PRESSURE AND SOIL DEFORMATION ON THE NONLINEAR RESPONSE 3415
Montoya-Noguera Silvana, Lopez-Caballero Fernando

ROLE OF SLIDING BLOCK ROTATION ON EARTHQUAKE-INDUCED PERMANENT DISPLACEMENT OF EARTH SLOPES 3430
Lashgari Ali, Jafarian Yaser

FRAGILITY CURVES FOR ASSESSING THE SEISMIC VULNERABILITY OF GRAVITY QUAY WALLS 3439
Miraei M., Jafarian Yaser

RS 10: IDENTIFICATION METHODS IN STRUCTURAL DYNAMICS

SYSTEM IDENTIFICATION OF A 13-STORY REINFORCED CONCRETE BUILDING THROUGH AMBIENT AND FORCED VIBRATION 3448
Beskhyroun Sherif, Wotherspoon Liam, Ma Quincy

DYNAMIC IDENTIFICATION AND EVALUATION OF THE SEISMIC SAFETY OF A MASONRY BELL TOWER IN THE SOUTH OF ITALY 3459
Colapietro Domenico, Fiore Alessandra, Netti Adriana, Fatiguso Fabio, Marano Giuseppe, de Fino Mariella, Cascella Davide, Ancona Antonio

IDENTIFICATION OF REINFORCED CONCRETE BEAM PARAMETERS USING INVERSE MODELING TECHNIQUE AND MEASURED DYNAMIC RESPONSES FOR STRUCTURAL HEALTH MONITORING 3471
Waeytens Julien, le Corvec Véronique, Lévèque Philippe, Siegert Dominique, Bourquin Frédéric

IDENTIFYING THE DAMPING CONTRIBUTION OF BUILDING COMPONENTS BASED ON MEASURED TOP VIBRATION 3479
van den Berg Ronald, Steenbergen Raphaël

RS 12: MASONRY STRUCTURES

A MACRO-ELEMENT MODEL FOR THE NONLINEAR ANALYSIS OF MASONRY MEMBERS INCLUDING SECOND ORDER EFFECTS 3496
Penna Andrea, Galasco Alessandro

A 2-DOF MODEL FOR THE DYNAMIC ANALYSIS OF UNREINFORCED MASONRY WALLS IN OUT-OF-PLANE BENDING 3510
Gabellieri Rocco, Landi Luca, Diotallevi Pier Paolo

RS 13: NUMERICAL METHODS FOR LINEAR AND NONLINEAR DYNAMICS

APPLICATION OF GENERALIZED PLASTICITY MODEL IN SQUARE CFT COLUMN ANALYSIS 3523
Kostic Svetlana, C. Filippou Filip, Deretic-Stojanovic Biljana

CONTROL OF THE EIGENSOLUTIONS OF A HARMONICALLY DRIVEN COMPLIANT STRUCTURE 3536
Peters Hugo J., Tiso Paolo, Goosen Johannes F.L., van Keulen Fred

DEVELOPMENT OF AN EFFICIENT UNSTRUCTURED FINITE VOLUME SOLVER FOR A NEW CONSERVATION LAW IN FAST STRUCTURAL DYNAMICS 3550
Aguirre Miquel, Gil Antonio, Bonet Javier, Lee Chun Hean

REDUCTION METHOD APPLIED TO VIBRATIONS OF VISCOELASTIC SANDWICH SHELLS 3560
Duigou Laëtitia, Boumediene Faiza, Cadou Jean-Marc, Daya El Mostafa

EFFECT OF POUNDING ON THE SEISMIC RESPONSE OF TWO ADJACENT ASYMMETRIC BUILDINGS UNDER SINGLE UNI-DIRECTIONAL GROUND MOTION 3568
Fiore Alessandra, Marano Giuseppe

A NUMERICAL SCHEME FOR TIME-DOMAIN FE ANALYSIS OF VISCOELASTIC STRUCTURES WITH FRACTIONAL DERIVATIVE CONSTITUTIVE EQUATIONS 3580
Deü Jean-François, Matignon Denis

A NEW COROTATIONAL ELEMENT FOR NONLINEAR DYNAMIC ANALYSIS OF 3D BEAMS 3586
Le Thanh-Nam, Battini Jean-Marc , Hjiaj Mohammed

RIGID BODY TIME INTEGRATION BY CONVECTED BASE VECTORS WITH IMPLICIT CONSTRAINTS 3609
Krenk Steen, Nielsen Martin

TRANSIENT RESPONSE OF FUNCTIONALLY GRADED BEAMS UNDER ARBITRARY DYNAMIC LOADING ... 3618
Villamil Pedro D., Zhang Chuanzeng, Chen Weiqiu

FINITE ELEMENT FORMULATION FOR AN ARCH STRUCTURE FORMED BY USING BUILT-UP BEAMS ELEMENT 3628
Nouchi Eiji, Kurata Mitsuharu, Gan Buntara Sthenly

RS 14: OPTIMUM DESIGN IN STRUCTURAL DYNAMICS AND EARTHQUAKE ENGINEERING

OPTIMAL DESIGN OF VIBRATING RING-STIFFENED CYLINDRICAL SHELL 3637
Filippov Sergei, Naumova Natalia

COMPUTATIONAL ASSESSMENT OF THE PROGRESSIVE COLLAPSE OF A FIVE STOREY STRUCTURE CONSIDERING TWO DIFFERENT BUILDING CODES 3647
Oliveira Cláudio, Berke Péter, Silveira Ricardo, Massart Thierry

NON LINEAR STATIC ANALYSIS OF A PLAN IRREGULAR BUILDING ACCORDING TO EC8 PROVISIONS ... 3662
Magliulo Gennaro, Maddaloni Giuseppe, Cosenza Edoardo

RS 15: PASSIVE ACTIVE AND SEMI-ACTIVE DEVICES

EXPERIMENTAL AND NUMERICAL ANALYSIS OF MR DAMPERS 3672
Braz-César Manuel, Barros Rui

EFFECTIVENESS AND ROBUSTNESS OF A SEMI-ACTIVE CONTROL STRATEGY BASED ON SEISMIC EARLY WARNING INFORMATION 3691
Maddaloni Giuseppe, Caterino Nicola

REGIONAL-BASED CONTROL ALGORITHMS USING EARLY WARNING INFORMATION FOR SEISMIC PROTECTION OF A HIGHWAY BRIDGE 3704
Maddaloni Giuseppe, Caterino Nicola, Nestovito Gianluca, Occhiuzzi Antonio

SHAKING TABLE TESTS TO COMPARE SEMI-ACTIVE CONTROL ALGORITHMS FOR VARIABLE DAMPERS 3717
Caterino Nicola, Spizzuoco Maria-Cristina, Occhiuzzi Antonio

RESPONSE TIME OF MR DAMPERS FOR SEISMIC SEMIACTIVE CONTROL: EXPERIMENTAL MEASURES AND POSSIBLE PREDICTION 3727
Caterino Nicola, Spizzuoco Maria-Cristina

RS 16: PERFORMANCE-BASED ENGINEERINGI

VULNERABILITY ASSESSMENT OF RC BUILDINGS TO LANDSLIDE DISPLACEMENTS. APPLICATION TO CORNIGLIO CASE HISTORY, ITALY. 3736
Fotopoulou Stavroula, Callerio Alberto, Pitilakis Kyriazis

PERFORMANCE-BASED SEISMIC DESIGN OF A RETAINING WALL 3754
Jurado Carlos

MECHANISM BASED ASSESSMENT OF DAMAGED BUILDING'S RESIDUAL CAPACITY 3763
Polese Maria, Marcolini Marco, Prota Andrea, Zuccaro Giulio

IMPROVED PROCEDURE FOR DESIGN AND EVALUATION OF STRUCTURES: SINGLE-DEGREE-OF-FREEDOM BILINEAR SYSTEMS 3780
Chikh Benazouz, Moussa Leblouba, Mehani Youcef, Zerzour Ali, Bechtoula Hakim, Benyoucef Abdelkader

EXPERIMENTAL RESEARCH OF SHEAR STRENGTH MODELS FOR REINFORCED CONCRETE MEMBERS ... 3790
Syntzirma Despina, Pantazopoulou Stavroula

RS 17: REINFORCED CONCRETE STRUCTURES

LOCAL AND NON LOCAL APPROACHES FOR SIMULATING CFR PREINFORCED CONCRETE SHEAR WALLS UNDER MONOTONIC LOADS 3799
le Nguyen Khuong, Brun Michael, Limam Ali, Ferrier Emmanuel, Michel L.

AN INNOVATIVE PROPOSAL FOR THE IMPROVEMENT OF DURABILITY OF SLABS ON SOIL 3815
Bantias Alexandros, Tegos Ioannis, Chrysanidis Theodoros, Athanatopoulou Asimina

NON-LINEAR SEISMIC ANALYSIS OF RC FRAMED BUILDING DESIGNED ACCORDING TO EC-8 3828
Nikolić Željana, Nikolić Mijo

ASSESSMENT OF THE RELIABILITY OF STRUCTURAL CONCRETES DURING EXECUTION PHASES 3837
Porco Francesco, Uva Giuseppina

COMPARATIVE EVALUATION OF DIFFERENT DAMAGE MEASURES FOR R/C BUILDINGS CONSIDERING VARIABLE INCIDENT ANGLES 3850
Morfidis Konstantinos, Kostinakis Konstantinos, Karakostas Christos

IMPACT OF SEISMIC CODES ON BUILDING PERFORMANCE IN THE CARIBBEAN 3864
Redmond Laura, Stroecker Rebecca, DesRoches Reginald

EFFECTS OF TORSION ON THE BEHAVIOUR OF NON-STRUCTURAL COMPONENTS MOUNTED ON IRREGULAR REINFORCED CONCRETE MULTI-STOREY BUILDINGS 3875
Aldeka Ayad, Chan AHC, Dirar S.

RAPID EVALUATION OF NON-DUCTILE MULTISTORY RC FRAME BUILDINGS 3884
Thermou Georgia, Palaioxorinou Anastasia

INFLUENCE OF LOW-CYCLE FATIGUE AND CORROSION PHENOMENA ON THE DUCTILE BEHAVIOUR OF STEEL REINFORCING BARS 3915
Braconi Aurelio, Braga Franco, Caprili Silvia, Gigliotti Rosario, Salvatore Walter

STRUCTURAL ANALYSIS OF MULTISTORY BUILDING USING COUPLED BEM-STIFFNESS MATRIX 3948
Mohareb Ramez, Rashed Youssef, Wagdy Mina, Mobasher Mostafa

NONLINEAR SEISMIC ANALYSIS OF INFILLED RC FRAMES WITH AN EQUIVALENT STRUT MODEL 3975
Landi Luca, Tardini Annalisa, Diotallevi Pier Paolo

RS 18: RELIABILITY OF DYNAMIC SYSTEMS

TRANSIENT FOKKER-PLANCK EQUATION WITH SPH METHOD - APPLICATION IN SEISMIC DESIGN 3989
Canor Thomas, Denoël Vincent

RS 19: REPAIR AND RETROFIT OF STRUCTURES

IMPROVING THE SEISMIC PERFORMANCE OF EXISTING OLD PILOTIS TYPE BUILDINGS BY STRENGTHENING ONLY THE GROUND STORY 4002
Antonopoulos Themistocles, Anagnostopoulos Stavros

STUDY OF THE BEHAVIOR OF RC COLUMNS STRENGTHENED WITH RC JACKETS CONTAINING DOWELS AND DIFFERENT CONFINEMENT RATIOS. 4018
Achillopoulou D. V., Tasiopoulos T.P.K., Karabinis A.I

INVESTIGATION OF FORCE TRANSFER MECHANISMS IN RETROFITTED RC COLUMNS WITH RC JACKETS CONTAINING WELDS SUBJECTED TO AXIAL COMPRESSION. 4029
Achillopoulou D. V., Pardalakis T.A., Karabinis A.I.

RS 20: SEISMIC ASSESSMENT OF HERITAGE STRUCTURES AND MONUMENTS THROUGH SIMULATION

DYNAMICAL CHARACTERIZATION OF TYPICAL MEXICAN COLONIAL CHURCHES 4039
Peña Fernando, Manzano Julio, Robles Laura

RS 21: SEISMIC DESIGN AND ASSESSMENT OF BRIDGES

BRIDGES WITH SIMPLY SUPPORTED DECKS: A SIMPLIFIED VULNERABILITY ASSESSMENT 4050
Raffaele Domenico, Mezzina Mauro, Tosto Antonio

EFFECT OF SPATIALLY VARIABLE GROUND MOTIONS ON THE SEISMIC FRAGILITY OF BOX GIRDER CONTINUOUS BRIDGES 4062
Elhowary Hesham, Ramadan Osman, Mehanny Sameh

AN ANALYTICAL TECHNIQUE FOR THE SEISMIC RESPONSE ASSESSMENT OF SLENDER BRIDGE PIERS ... 4079
Tubaldi Enrico, Tassotti Luca, Dall'Asta Andrea, Dezi L.

RS 22: SEISMIC PERFORMANCE EVALUATION UNDER UNCERTAINTY

A COMPARATIVE STUDY OF SEISMIC FRAGILITY ESTIMATES USING DIFFERENT NUMERICAL METHODS 4095
Mandal Tushar, Pujari Nikil, Ghosh Siddhartha

EVALUATION OF THE EFFECT OF MODELING UNCERTAINTIES ON THE SEISMIC RESPONSE OF EXISTING MASONRY BUILDINGS 4104
Rota Maria, Bracchi Stefano, Penna Andrea, Magenes Guido

TIME-DEPENDENT SEISMIC VULNERABILITY ASSESSMENT OF RC BUILDINGS CONSIDERING SSI AND AGING EFFECTS 4117
Karapetrou Sotiria, Filippa Argyro, Fotopoulou Stavroula, Pitilakis Kyriazis

RS 23: SEISMIC RISK AND RELIABILITY ANALYSIS

INSTRUCTIONS OVERVIEW ON THE REGIONAL SCALE ANALYSIS OF SCHOOL BUILDINGS IN PUGLIA (ITALY) 4135
Raffaele Domenico, Mezzina Mauro, Tosto Antonio

AN ANALYSIS OF METHODS FOR DERIVING MAGNITUDES OF HISTORIC EARTHQUAKES THAT ARE BASED ON PHYSICAL PRINCIPLES 4147
Belsham Christopher

CONDITIONS FOR MEASURING SEISMIC SHOCKS AND THEIR ANALYSIS AND RESPONSE ON BUILDINGS AND INDUSTRIAL STRUCTURES 4166
Ziaran Stanislav, Musil Milos, Cekan Michal

RS 24: SEISMIC SAFETY ASSESSMENT OF STRUCTURES

QUANTIFICATION OF RESIDUAL AXIAL CAPACITY OF BEAM-COLUMN JOINTS IN EXISTING CONCRETE BUILDINGS UNDER SEISMIC LOAD REVERSALS 4179
Hassan Wael, Moehle Jack

ROCKING AND SLIDING OF UNANCHORED BODIES SUBJECTED TO SEISMIC LOAD ACCORDING TO CONVENTIONAL AND NUCLEAR RULES 4194
Schau Henry, Johannes Micheal

EFFECTS OF “REINFORCED” INFILLED FRAMES ON EXISTING RC BUILDINGS 4213
Fiore Andrea, Uva Giuseppina

SEISMIC FRAGILITY ANALYSIS OF A NUCLEAR PRIMARY CONTAINMENT STRUCTURE 4226
Lala Sayantani, Ghosh Siddhartha, Pujari Nikil

RS 25: SIMULATION METHODS FOR DYNAMIC PROBLEMS

SIMULATION OF STRUCTURAL POUNDING WITH THE SEARS IMPACT MODEL 4234
Khatiwada Shushil, Chouw Nawawi, Larkin Tam

FREE VIBRATIONS OF A CYLINDRICAL SHELL MADE OF AN ANISOTROPIC MATERIAL 4247
Tovstik Petr, Tovstik Tatiana

AN EFFICIENT NUMERICAL APPROACH FOR THE PARAMETRIC INVESTIGATION OF THE EFFECTS OF POUNDING ON THE 3D DYNAMIC RESPONSE OF BUILDINGS DURING EARTHQUAKES 4263
Polycarpou Panayiotis, Komodromos Petros

PHENOMENOLOGICAL MODELING OF DEFORMATION OF POROUS AND CELLULAR MATERIALS TAKING INTO ACCOUNT THE INCREASE IN STIFFNESS BECAUSE OF THE COLLAPSE OF PORES 4277
Sadovskii Vladimir, Sadovskaya Oxana

REAL-TIME ERROR CORRECTION IN FAST PSEUDODYNAMIC TESTING: A NUMERICAL STUDY 4287
Gultom Ronald, Ma Quincy

A NUMERICAL INVESTIGATION INTO THE BEHAVIOUR OF FLEXIBLE UPLIFTING STRUCTURES WITH SLIP-FRICTION CONNECTORS UNDER EARTHQUAKE LOADING 4295
Loo Wei Yuen, Quenneville Pierre, Chouw Nawawi

MATH SIMULATION OF CONTACT INTERACTION DURING SPACECRAFT DOCKING AND ROBOTIC ASSEMBLY OPERATIONS 4304
Yaskevich Andrey

A PROCEDURE TO SELECT TIME-HISTORIES FOR SHAKING TABLE TESTS ON NONSTRUCTURAL COMPONENTS 4321
Magliulo Gennaro, Maddaloni Giuseppe, Petrone Crescenzo

RS 26: SIMULATION OF SOUND AND VIBRATION

AN IMPROVED METHODOLOGY FOR THE VIRTUAL POINT TRANSFORMATION OF MEASURED FREQUENCY RESPONSE FUNCTIONS IN DYNAMIC SUBSTRUCTURING 4334
van der Seijs Maarten, van den Bosch Dennis, Rixen Daniel, de Klerk Dennis

RS 27: SOFT COMPUTING APPLICATIONS

A SIMPLIFIED ALGORITHM FOR EVALUATING THE SEISMIC RETURN PERIOD OF STRUCTURAL CAPACITY 4348
Raffaele Domenico, Fiore Andrea

RS 28: SOIL DYNAMICS

A MULTI-DIRECTIONAL ABSORBING LAYER FOR SEISMIC WAVE PROPAGATION IN UNBOUNDED DOMAIN BY USING HETEROGENEOUS MULTI-TIME STEP SUBDOMAIN METHODS 4361
Zafati Eliass, Brun Michael, Irini Djeran-Maigre

PERFECTLY MATCHED LAYER (PML) FOR TRANSIENT WAVE PROPAGATION IN A MOVING FRAME OF REFERENCE 4379
Madsen Stine, Krenk Steen, Hededal Ole

COMPARISON OF TWO ELASTIC-PLASTIC APPROACHES TO CYCLIC SOIL MODELING 4389
Pisanò Federico, Jeremić Boris

RS 29: SOIL-STRUCTURE INTERACTION

AN INSIGHT INTO THE INFLUENCE OF CONSTRUCTION METHODS ON THE LATERAL LOAD CAPACITY OF DRILLED DEEP FOUNDATIONS 4404
Bezgin Özgür

THREE-DIMENSIONAL FINITE ELEMENT MODELLING OF DYNAMIC PILE-SOIL-PILE INTERACTION IN TIME DOMAIN 4426
Kouroussis Georges, Anastasopoulos Ioannis, Gazetas George, Verlinden Olivier

PERFORMANCE-BASED SEISMIC DEMAND OF SOIL-FOUNDATION-STRUCTURE SYSTEMS 4440
Karatzetzou Anna, Pitilakis Dimitris

STRUCTURE-SOIL INTERACTION FOR FRAMED STRUCTURES UNDER DYNAMICS LOADING CAUSED BY RECIPROCATING COMPRESSOR 4451
Viana Eduardo, Roehl Deane

A PROCEDURE FOR EVALUATING THE SOIL-STRUCTURE INTERACTION EFFECTS ON THE SYSTEM PERIOD AND DAMPING OF PILE-SUPPORTED STRUCTURES 4463
Medina Cristina, Aznárez Juan J., Padrón Luis A., Maeso Orlando

NON-LINEAR DYNAMIC ANALYSIS OF MASONRY TOWERS UNDER NATURAL ACCELEROGRAMS ACCOUNTING FOR SOIL-STRUCTURE INTERACTION 4488
Casolo Siro, Uva Giuseppina

GENERATION OF INCOHERENT GROUND MOTIONS FOR SOIL-STRUCTURE INTERACTION APPLICATIONS 4507
Tran Phuong, Wang Fan, Clouteau Didier

DYNAMIC SOIL-STRUCTURE INTERACTION ANALYSIS OF A TELESCOPE AT THE JAVALAMBRE ASTROPHYSICAL OBSERVATORY 4525
François Stijn, Galvin Pedro, Museros Pedro, Lombaert Geert, Degrande Geert

ACCOUNTING FOR NONLINEAR DYNAMIC SOIL-STRUCTURE INTERACTION IN EARTHQUAKE ENGINEERING 4538
Nieto Ferro Alex, Greffet Nicolas, Devésa Georges, Clouteau Didier

RS 31: STEEL STRUCTURES

BLAST RESPONSE OF FIELD OBJECTS 4545
Chen Anqi, Louca Luke, Elghazouli Ahmed

COMPARATIVE ASSESSMENT OF BUILDINGS WITH PURE STEEL OR STEEL-CONCRETE COMPOSITE COLUMNS USING STRUCTURAL DESIGN OPTIMIZATION 4557
Papavasileiou Georgios, Nikolaou Nikolas, Charmpis Dimos

RS 32: STRUCTURAL HEALTH MONITORING

GRAPHICAL MODAL ANALYSIS AND EARTHQUAKE STATICS OF LINEAR ONE-WAY ASYMMETRIC SINGLE-STORY STRUCTURE 4568
Faggella Marco

RS 33: WAVES AND COMPUTATION

COMPUTATIONAL MODELING OF THE WAVES PROPAGATION IN A BLOCK MEDIUM WITH VISCOELASTIC INTERLAYERS 4578
Sadovskaya Oxana, Sadovskii Vladimir, Varygina Mariya

COMPDYN 2013
4th ECCOMAS Thematic Conference on
Computational Methods in Structural Dynamics and Earthquake Engineering
M. Papadrakakis, N.D. Lagaros, V. Plevris (eds.)
Kos Island, Greece, 12–14 June 2013

THE USE OF BAYESIAN MODEL UPDATING IN STOCHASTIC DESIGN PROBLEMS

H.A. Jensen and C. Vergara

Department of Civil Engineering, Santa Maria University, Valparaiso, Chile
e-mail: hector.jensen@usm.cl

Keywords: Bayesian Updating, Robust Analysis, Simulation Methods, Structural Reliability

Abstract. *This work focuses on the effect of using updated reliability measures in the context of stochastic structural dynamical systems. A Bayesian probabilistic methodology for model updating is first implemented for the purpose of updating the structural model using dynamic data. The updated distribution of the system model parameters is then used to implement a strategy for updating the system reliability. The effect of the updated information on the reliability and design of dynamical systems under stochastic excitation is illustrated by an example problem.*

1 INTRODUCTION

During operation conditions structural systems may deteriorate from a number of reasons, such as fatigue, corrosion, damage induced in structural elements by strong wind loads or earthquakes, etc. These conditions may lead to significant reduction of the structural reliability. Therefore, the re-assessment of the reliability of a structure after it has been built by monitoring the dynamic response is of paramount importance. The updated reliability may be used to identify potentially unsafe structures, to schedule repairs, maintenances or inspection intervals, or to design retrofitting or control strategies [1, 2]. In this work a strategy for updating structural reliability using dynamic data is considered. For this purpose, a Bayesian probabilistic framework for model updating is integrated with advanced simulation tools [3]. In particular, a multi-level Markov chain Monte Carlo algorithm is adopted here [4]. In this framework, a revised information about the uncertainties in the system parameters is obtained, which is expressed by posterior probability density functions. Using the updated characterization of the system model, a strategy is implemented for computing the reliability of structural systems under future excitations characterized by means of stochastic processes. In this context, the probability that design conditions are satisfied within a particular reference period is used as reliability measure. Such measure is referred as the first excursion probability and quantifies the plausibility of the occurrence of unacceptable behavior of the structural system [5]. The strategy is based on subset simulation and it uses a Markov chain Monte Carlo technique based on the Metropolis algorithm for generating conditional samples [6]. Based on the proposed strategy for updating the structural reliability it is the objective of this work to study the effect of the updated information on the reliability and design of dynamical systems under stochastic excitation.

2 BAYESIAN UPDATING USING DYNAMIC DATA

2.1 General Considerations

Let M be the probabilistic model class of structural models parameterized by the vector of uncertain model parameters $\boldsymbol{\theta} \in \Theta \subset R^{n_p}$, and D the measured dynamic data from the system. The objective of Bayesian model updating is to define the posterior probability density function of $\boldsymbol{\theta}$ conditioned on D, $p(\boldsymbol{\theta}/M, D)$, as (Bayes' Theorem) [7]

$$p(\boldsymbol{\theta}/M, D) = \frac{p(D/M, \boldsymbol{\theta})\ p(\boldsymbol{\theta}/M)}{p(D/M)} \tag{1}$$

where $p(\boldsymbol{\theta}/M)$ is the initial (prior) probability density function of $\boldsymbol{\theta}$, $p(D/M, \boldsymbol{\theta})$ is the likelihood function, and $p(D/M)$ is the evidence of M. The prior probability distribution reflects the relative plausibility of each model in the model class M before utilizing the data D. The term $p(D/M, \boldsymbol{\theta})$ gives the probability of obtaining the data D based on a model specified by the model parameters $\boldsymbol{\theta}$. Finally, the normalizing constant $p(D/M)$ corresponds to the evidence for the model class M given by the data D. The likelihood function gives a measure of the agreement between the system response and the corresponding structural model output. This measure of the data fit of each model in the model class M, i.e. the value of the likelihood function for each parameter vector $\boldsymbol{\theta}$, is given by the probability model established for the system output. The probability model class for the prediction error $\mathbf{e}(t_n, \boldsymbol{\theta})$, that is, the difference between the measured response and the model response, considered in the present formulation is based on the maximum entropy principle which yields a multi-dimensional Gaussian distribution with zero mean and covariance matrix $\boldsymbol{\Sigma}_e$. In particular, the prediction error $\mathbf{e}(t_n, \boldsymbol{\theta})$ is modeled as a

discrete zero mean Gaussian white noise process, that is,

$$E[\mathbf{e}(t_n, \boldsymbol{\theta})] = 0 \ , \ E[\mathbf{e}(t_n, \boldsymbol{\theta})\mathbf{e}(t_m, \boldsymbol{\theta})^T] = \boldsymbol{\Sigma}_e \ \delta_{nm} \tag{2}$$

where $E[\cdot]$ denotes expectation, δ_{nm} denotes the kronecker delta function, $\boldsymbol{\Sigma}_e$ denotes the $N_o \times N_o$ covariance matrix which is assumed to have the form $\boldsymbol{\Sigma}_e = \sigma_e^2 \mathbf{I}_o$, where $\mathbf{I}_o$ is the identity matrix, and N_o is the number of observed degrees of freedom of the structural model. The above assumption implies equal variances and stochastic independence of the prediction errors for different channels of measurements. Using the above probability model for the prediction error it can be shown that the likelihood function $p(\boldsymbol{D}/\boldsymbol{M}, \boldsymbol{\theta})$ can be expressed in terms of a measure-of-fit function $J(\boldsymbol{\theta}/\boldsymbol{M}, \boldsymbol{D})$ between the measured response and the model response at the measured degrees of freedom. Such function is given by [8, 9]

$$J(\boldsymbol{\theta}/\boldsymbol{M}, \boldsymbol{D}) = \frac{1}{N_t N_o} \sum_{n=1}^{N_t} \parallel \mathbf{e}(t_n, \boldsymbol{\theta}) \parallel^2 \tag{3}$$

where $\parallel \cdot \parallel$ denotes the Euclidian norm of a vector and N_t is the number of available data in time.

2.2 Simulation-based Methods

For a large number of available data it has been found that the most probable model parameters $\hat{\boldsymbol{\theta}}$ are obtained by minimizing $J(\boldsymbol{\theta}/\boldsymbol{M}, \boldsymbol{D})$ over all parameters in Θ that it depends on [10]. In this regard one of the difficulties of model updating is that the problem is potentially ill-posed, that is, there may be more than one optimal solution. The problem becomes even more challenging when only some degrees of freedom of the model are measured and when modeling errors are explicitly considered. Under certain conditions, ie. global or local identifiable cases, methods based on asymptotic approximations have been successful used in resolving the aforementioned difficulties [8, 9, 10]. For the general case more flexible methods such as simulation-based Bayesian model updating techniques should be used. In particular, an efficient method called transitional Markov chain Monte Carlo is implemented in this work [4]. Validation calculations have shown the effectiveness of this approach in a series of practical Bayesian model updating problems [11]. The method can be applied to a wide range of cases including high-dimensional posterior probability density functions, multimodal distributions, peaked probability density functions, and probability density functions with flat regions.

2.3 Transitional Markov Chain Monte Carlo Method

For completeness the basic ideas of the transitional Markov chain Monte Carlo method are presented in this section. The method iteratively proceeds from the prior to the posterior distribution. It starts with the generation of samples from the prior distribution in order to populate the space in which also the most probable region of the posterior distribution lies. For this purpose a number of intermediate distributions are defined as $p_j(\boldsymbol{\theta}/\boldsymbol{M}, \boldsymbol{D}) = c\ p(\boldsymbol{\theta}/\boldsymbol{M}) p(\boldsymbol{D}/\boldsymbol{M}, \boldsymbol{\theta})^{\alpha_j}$ $j = 0, 1, ..., m,$, $0 = \alpha_0 < \alpha_1 < ... < \alpha_m = 1$, where the index j denotes the step number, and c is a normalizing constant. The exponent α_j can be interpreted as the percentage of the total information provided by the dynamic data which is incorporated in the j^{th} iteration of the updating procedure. The first step ($j = 0$) corresponds to the prior distribution and in the last stage ($j = m$) the samples are generated from the posterior distribution. The idea is to choose the values of exponents α_j in such a way that the change of the shape between two adjacent intermediate distributions be small. This small change of the shape makes it possible to efficiently

obtain samples from $p_{j+1}(\boldsymbol{\theta}/M,D)$ based on the samples from $p_j(\boldsymbol{\theta}/M,D)$. The samples are obtained by generating Markov chains where the lead samples are selected from the distribution $p_j(\boldsymbol{\theta}/M,D)$ by computing their plausibility weights with respect to $p_{j+1}(\boldsymbol{\theta}/M,D)$ which are given by

$$w(\boldsymbol{\theta}_j^k) = \frac{p(\boldsymbol{\theta}_j^k/M)\ p(D/M,\boldsymbol{\theta}_j^k)^{\alpha_{j+1}}}{p(\boldsymbol{\theta}_j^k/M)\ p(D/M,\boldsymbol{\theta}_j^k)^{\alpha_j}} = p(D/M,\boldsymbol{\theta}_j^k)^{\alpha_{j+1}-\alpha_j} \qquad k=0,1,...,N_j \tag{4}$$

where the upper index $k = 1,...,N_j$ denotes the sample number in the j^{th} iteration step $(\boldsymbol{\theta}_j^k, k = 1,...,N_j)$. Each sample of the current stage is generating using the Metropolis-Hastings algorithm [6, 12]. The starting point of the Markov chain is a sample from the previous step that is selected according to the probability equal to its normalized weight $\bar{w}(\boldsymbol{\theta}_j^k) = w(\boldsymbol{\theta}_j^k)/\sum_{l=1}^{N_j} w(\boldsymbol{\theta}_j^l)\ ,\ k=1,...,N_j$. The proposal probability density function for the Metropolis-Hastings algorithm is a Gaussian distribution centered at the preceding sample of the chain and with a covariance matrix equal to the scaled version of the estimated covariance matrix of the current intermediate distribution. The previous steps are repeated until $\alpha_j = 1$ is reached (samples generated from the posterior distribution). At the last stage the samples $(\boldsymbol{\theta}_m^k, k = 1,...,N_m)$ are asymptotically distributed as $p(\boldsymbol{\theta}/M,D)$. For a detailed implementation of the transitional Markov chain Monte Carlo method the reader is referred to [4].

3 SYSTEM RELIABILITY

The updating procedure presented in the previous section is now used to update the system reliability. As previously pointed out, the focus is in stochastic structural dynamical systems where the reliability is defined in terms of a first excursion probability, that is the probability that design conditions are satisfied within a particular reference period. In this context, a failure domain F can be defined as

$$F(M) = \{(\mathbf{z},\boldsymbol{\theta}) \mid \max_{j=1,...,n_j}\max_{t\in[0,T]} \frac{\mid r_j(t,\mathbf{z},\boldsymbol{\theta}) \mid}{r_j^*} > 1\} \tag{5}$$

where $\mathbf{z}$ represents the vector of random variables that specifies the stochastic excitation, $[0,T]$ is the time interval of analysis, $r_j(t,\mathbf{z},\boldsymbol{\theta}), j = 1,...,n_j$ are the response functions associated with the failure event that defines the failure domain F, and r_j^* is the corresponding critical threshold level. The response functions $r_j(t,\mathbf{z},\boldsymbol{\theta}), j = 1,...,n_j$ are obtained from the solution of the equation of motion that characterizes the structural model.

4 UPDATED RELIABILITY

To estimate the failure probability that takes into account the updated information a weighted integral of conditional failure probabilities over the whole parameter space must be evaluated. The weighting function in the integral is the posterior probability density function $p(\boldsymbol{\theta}/M,D)$. Thus the updated failure probability can be written as

$$P(F/M,D) = \int_\Theta P(F/M,\boldsymbol{\theta}) p(\boldsymbol{\theta}/M,D) d\boldsymbol{\theta} \tag{6}$$

where $P(F/\boldsymbol{M},\boldsymbol{\theta})$ is the conditional failure probability, that is the probability using known model parameters $\boldsymbol{\theta}$. Alternatively, Eq.(6) can be re-written in terms of the indicator function as

$$P(F/\boldsymbol{M},D)=\int_{\Theta}\int_{\Omega_z}\Pi_F(\mathbf{z},\boldsymbol{\theta}/\boldsymbol{M})\;f(\mathbf{z})\;p(\boldsymbol{\theta}/\boldsymbol{M},D)\;d\mathbf{z}\;d\boldsymbol{\theta} \tag{7}$$

where $f(\mathbf{z})$ is the probability density function that characterizes the vector of random variables $\mathbf{z}$, and $\Pi_F(\mathbf{z},\boldsymbol{\theta}/\boldsymbol{M})$ is the indicator function, that is, $\Pi_F(\mathbf{z},\boldsymbol{\theta}/\boldsymbol{M})=1$ if $(\mathbf{z},\boldsymbol{\theta}/\boldsymbol{M})\in F$ and $\Pi_F(\mathbf{z},\boldsymbol{\theta}/\boldsymbol{M})=0$ otherwise. The above probability integral usually involve a large number of random variables (hundreds or thousands) in the context of dynamical systems under stochastic excitation. Therefore, this integral represents a high-dimensional reliability problem which is difficult to evaluate. An approach based on the set of samples generated at the last stage of the transitional Markov chain Monte Carlo method is implemented in the present contribution [13].

5 APPLICATION

5.1 Description

The objective of this application problem is to evaluate the effect of the additional information gained about the structure from measured data on the reliability and design of a passive energy dissipation system. For this purpose, the two-story reinforced concrete structure under earthquake loading shown in Figures (1) and (2) is considered. Forty eight columns of square cross section support each floor. The dimension of the columns are equal to 0.57 m and 0.53 m for the first and second floor, respectively. Both floors have a constant height of 3.0 m. The mass of each floor is equal to 1260 ton. The behavior of the reinforced concrete structure is characterized by considering a Young's modulus equal to $E=2.5\times10^{10}$ N/m^2 and Poisson ratio $\nu=0.3$. Damping ratios equal to 3% are assuming for the vibrational modes that contribute significantly to the response. This model may be interpreted as the structural model obtained during the design phase. The structure is excited horizontally by a ground acceleration applied at 45° with respect to the axis x. The ground acceleration is modeled as a non-stationary stochastic process. In particular, a point-source model characterized by a moment magnitude and epicentral distance is considered here [15, 16]. The model is a simple, yet a powerful means for simulating ground motions which has been successfully applied in the context of earthquake engineering. The sampling interval and the duration of the excitation are taken equal to $\Delta t=0.01$ (s) and $T=20.0$ (s), respectively. Based on this information and according to the excitation model the generation of each ground motion involves more than 2000 random variables. For an improved earthquake performance the structure is reinforced with friction hysteretic devices at each floor. The devices follow the restoring force law $r(t)=k_d\Big(\delta(t)-\gamma^1(t)+\gamma^2(t)\Big)$, where k_d denotes the stiffness of the device, $\delta(t)$ is the relative displacement between floors, and $\gamma^1(t)$ and $\gamma^2(t)$ denote the plastic elongations of the friction device. Using the supplementary variable $s(t)=\delta(t)-\gamma^1(t)+\gamma^2(t)$, the plastic elongations are specified by the nonlinear differential equations [17]

$$\begin{aligned}\dot\gamma^1(t)&=\dot\delta(t)H(\dot\delta(t))\Big[H(s(t)-s_y)\frac{s(t)-s_y}{s_p-s_y}H(s_p-s(t))+H(s(t)-s_p)\Big]\;,\\ \dot\gamma^2(t)&=-\dot\delta(t)H(-\dot\delta(t))\Big[H(-s(t)-s_y)\frac{-s(t)-s_y}{s_p-s_y}H(s_p+s(t))+H(-s(t)-s_p)\Big]\end{aligned} \tag{8}$$

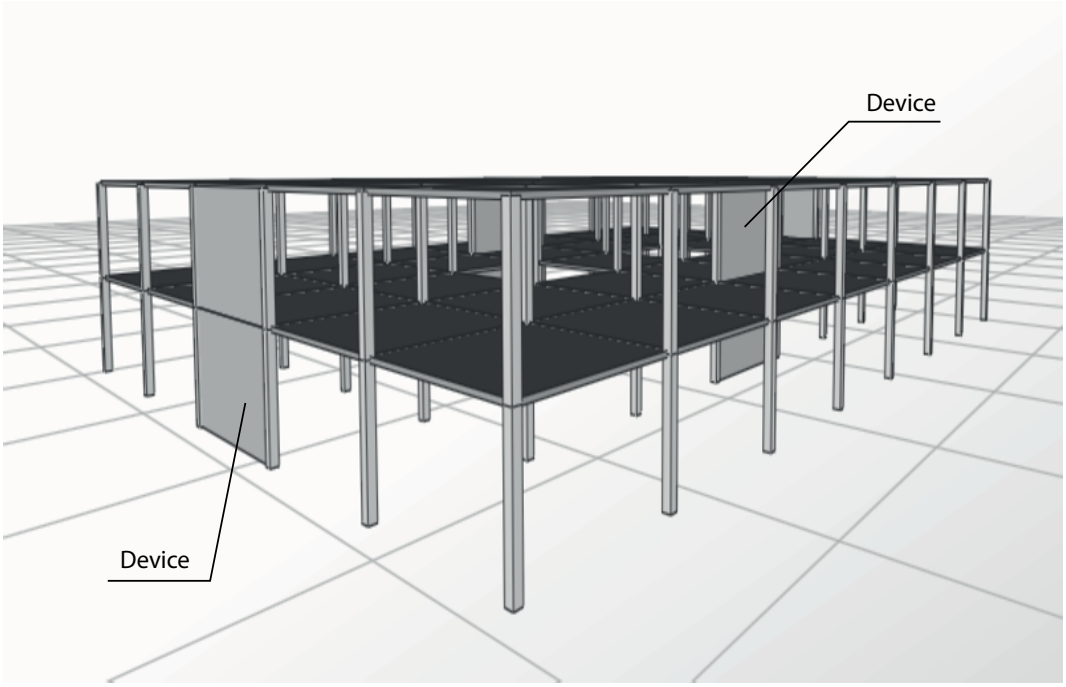


Figure 1: Isometric view of the structural model

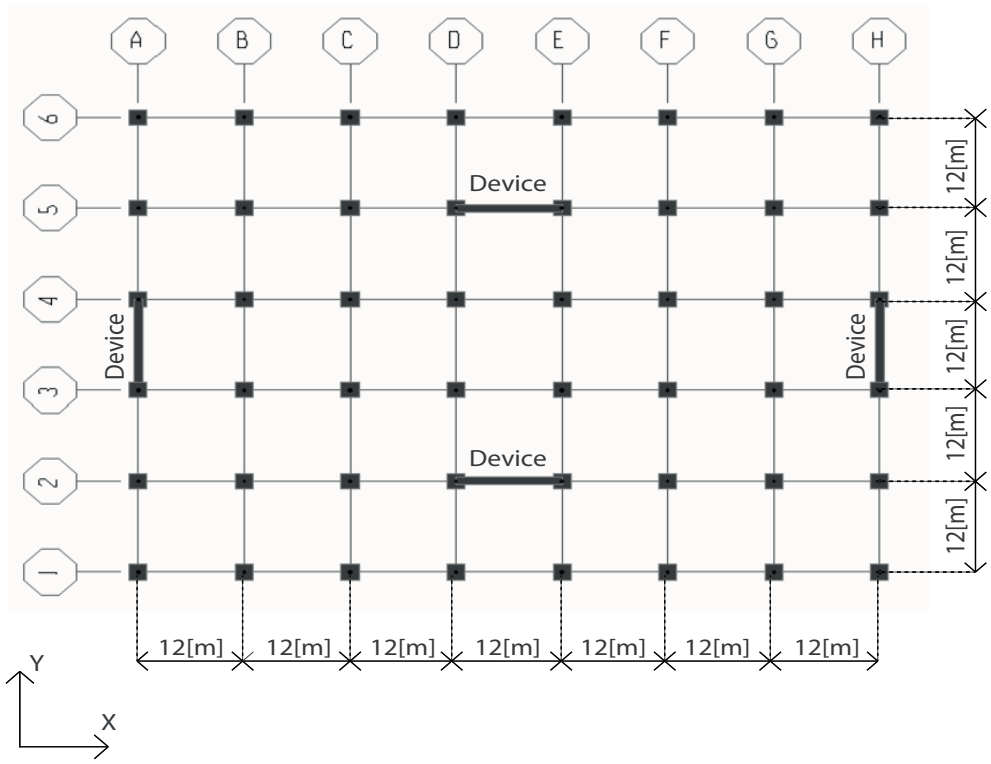


Figure 2: Plan view of the structural model

where $H(\cdot)$ denotes the Heaviside step function, s_y is a parameter specifying the onset of yielding, and k_d s_p is the maximum restoring force of the friction device. The values $s_p = 0.006$

m and $s_y = 0.0042$ m are used in this case. Because of the yielding, energy dissipation due to hysteresis is introduced in the structural response.

5.2 Identification Process

For identification purposes, the following class of structural models M is considered. It is assumed that each floor may be represented as rigid within the $x - y$ plane when compared with the flexibility of the columns. Hence, each floor is represented by three degrees of freedom, i.e. two translatory displacements in the direction of the x and y axis, and a rotational displacement. Due to modeling errors the rigidities of the actual class of models are parameterized as: $EI_{1x} = \theta_1 E\bar{I}_{1x}$, $EI_{2x} = \theta_2 E\bar{I}_{2x}$, $EI_{1y} = \theta_3 E\bar{I}_{1y}$, and $EI_{2y} = \theta_4 E\bar{I}_{2y}$, where $\bar{I}_{ix}$ and $\bar{I}_{iy}, i = 1, 2$ represent the nominal moment of inertia of the columns of the i floor in the x and y direction, respectively. These nominal values correspond to the columns of the nominal system previously described. The model updating is based on measurements of the ground acceleration at the base and the absolute acceleration at the first and second floor of the structure. Simulated measured data are used in this application The actual structure used to generate the measured data corresponds to a finite element model with about 5000 degrees of freedom, which includes beam, column and shell elements. The moment of inertia of the columns are defined in terms of the nominal properties as: $I_{1x} = 0.8\bar{I}_{1x}$, $I_{2x} = 0.9\bar{I}_{2x}$, $I_{1y} = 0.9\bar{I}_{1y}$, and $I_{2y} = 0.95\bar{I}_{2y}$. Note that the actual structure does not correspond to any model in the class of models considered. This actual structure may correspond to the structural system already built where changes in the stiffness have occurred due to, for example, large response levels. The input ground acceleration history for model identification is taken as the N-S component of the 2012 Chilean earthquake, Concepcion record shown in Fig. (3) and applied at 45° with respect to the x axis. The measured response is simulated by first calculating the absolute acceleration response of the actual structure at the first and second floor (in the x and y direction) and then adding 15% *RMS* Gaussian white noise. The responses are computed at the center of mass of each floor.

Thirty seconds of data with sampling interval $\Delta t = 0.01$ s are used, given a total of $N_t = 3000$ data points. Independent uniform prior distributions are assumed for the parameters θ_1, θ_2, θ_3, and θ_4 over the range $[0.5, 1.5]$. The transitional Markov chain Monte Carlo method with $N_j = 1000, j = 1, ..., m$ is implemented for the identification process. The four components of the samples corresponding to the rigidity parameters are shown in Fig. (4) in two groups: θ_1 versus θ_2 and θ_3 versus θ_4. The values of the parameters of the nominal system are also indicated in the figure. The posterior samples are concentrated around the reference values $(0.8, 0.9)$ and $(0.9, 0.95)$, respectively, leading to a relatively peaked posterior probability density function. Recall that the reference values correspond to the rigidity of the model used to generate the measure data (actual structure). From Fig. (4) it is also observed that the data is strongly correlated along certain directions in the parameter space. Actually, there is a line of maximum likelihood estimates in the vicinity of the reference values in the $\theta_1 - \theta_2$ and $\theta_3 - \theta_4$ spaces. Note that the lines have negative slopes, which is reasonable since for example an increase in the stiffness of the first floor in the x direction is compensated by a decrease in the stiffness of the second floor in the x direction during the updating process. In other words, all points along that direction correspond to structural models that have almost the same response at the measured degrees of freedom.

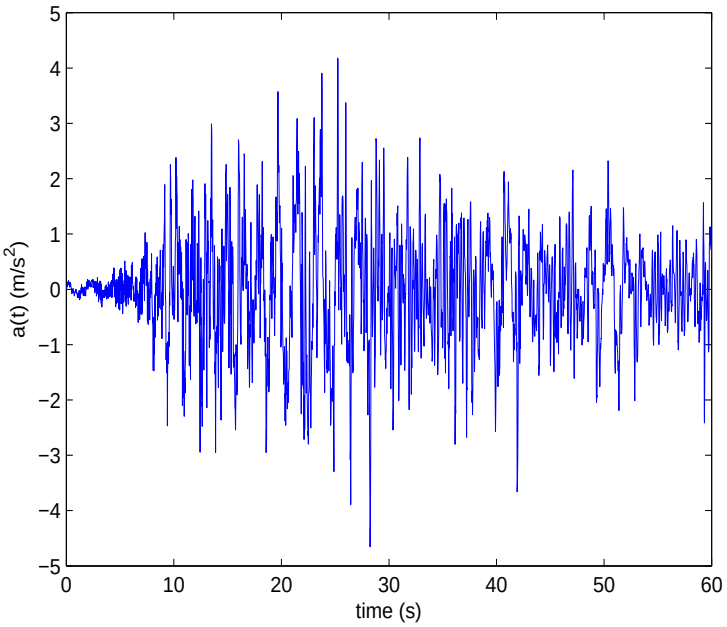


Figure 3: Ground acceleration time history for model identification

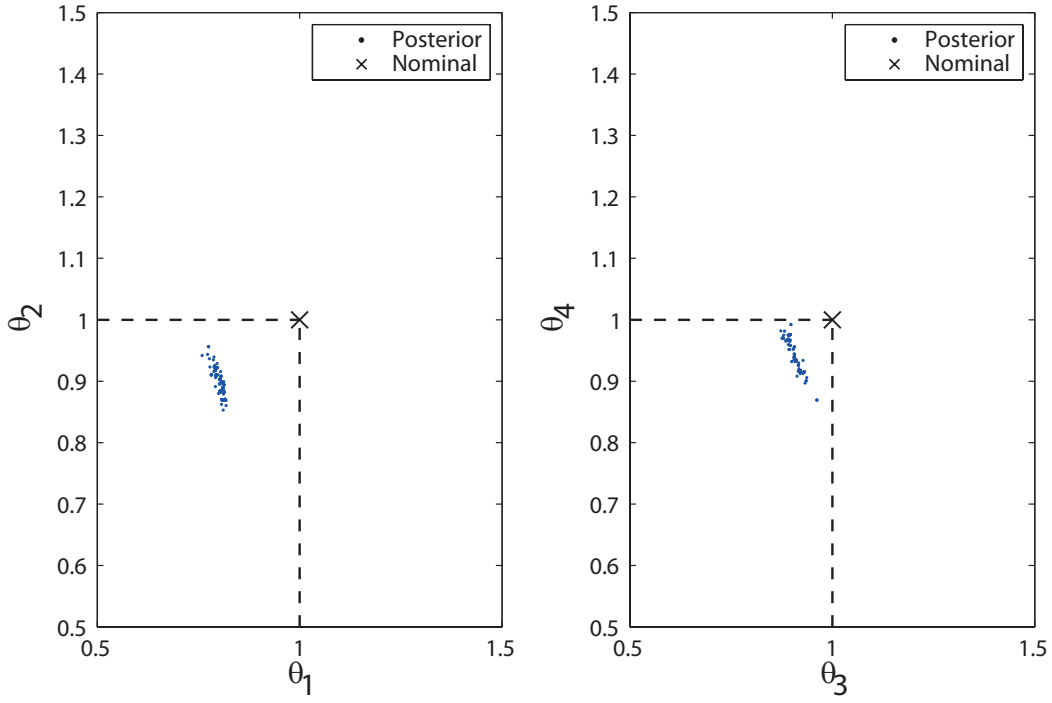


Figure 4: Samples of the rigidity parameters obtained by the transitional Markov chain Monte Carlo method

5.3 System Reliability

To evaluate the reliability of the structural system the following failure domain is considered

$$F(\boldsymbol{M}) = \{(\mathbf{z}, \boldsymbol{\theta}) \mid \max_{j=1,2} \max_{t\in[0,T]}\{\frac{\mid r_{jx}(t, \mathbf{z}, \boldsymbol{\theta}) \mid}{r_x^*}, \frac{\mid r_{jy}(t, \mathbf{z}, \boldsymbol{\theta}) \mid}{r_y^*}\} > 1\} \tag{9}$$

where $r_{jx}(t, \mathbf{z}, \boldsymbol{\theta})$ and $r_{jy}(t, \mathbf{z}, \boldsymbol{\theta})$ represent the relative displacement between the $(j-1, j)th$ floor in the x and y direction, respectively, and r_x^* and r_y^* are the corresponding threshold levels. The critical response levels are calibrated such that the probability of failure of the reinforced nominal system is equal to 10^{-4}. The estimation of the failure probabilities represents a high-dimensional reliability problem since more than two thousand random variables are involved in the corresponding multidimensional probability integrals in this case. Figure (5) shows the failure probability of the nominal and updated models in terms of the stiffness of the nonlinear devices. The same properties are assumed for the devices placed in the first and second floor. A range between 0 and $20 \times \bar{k}_d$ is considered in the figure, where $\bar{k}_d$ is a percentage of the stiffness of the first floor in the x direction. In this case a 1% is considered. Note that zero stiffness corresponds to the linear model, i.e. the structural system without the hysteretic devices. It is observed that the probability of failure decreases as the stiffness of the nonlinear devices increases for both cases. This is reasonable since the structural model becomes stiffer when the stiffness increases and at the same time the devices introduce additional energy dissipation capacity to the structural system. In this regard, the use of friction hysteretic devices constitutes an effective control strategy.

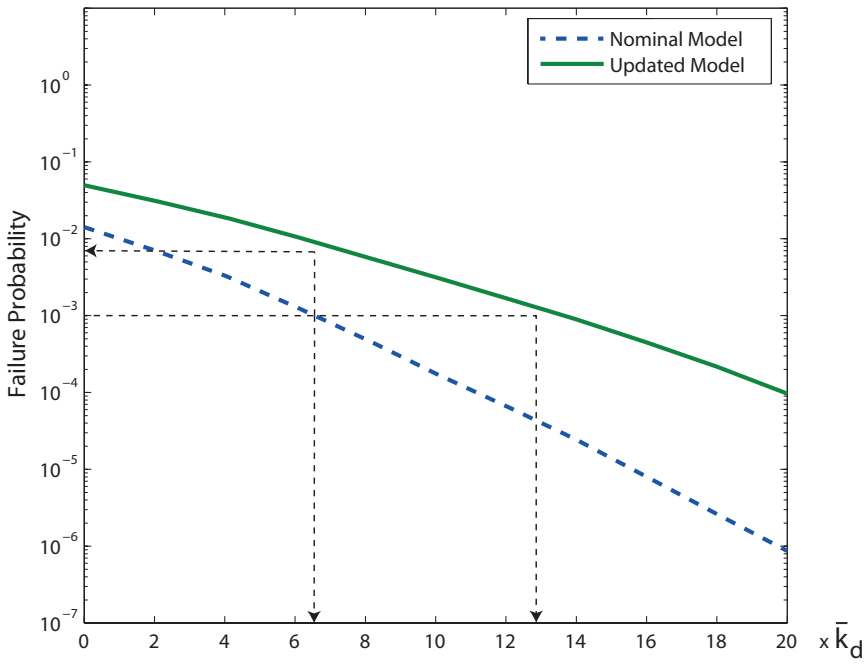


Figure 5: Failure probability of the nominal and updated models in terms of the stiffness of the hysteretic devices

Comparison of the curves obtained by the updated model and the nominal system demon-

strates the effect of new information on the system failure probability. The failure probability of the updated model is significantly larger than the corresponding to the nominal system. For example, if a probability of failure equal to 10^{-3} is imposed as a design requirement the stiffness of the devices required in the nominal system is approximately $7 \times \bar{k}_d$ while devices with stiffness equal to $13 \times \bar{k}_d$ are required for the updated system. In other words, the updated structural model reinforced with the devices used in the nominal system is not feasible under the prescribed reliability requirement since the failure probability would be close to 10^{-2} (see Figure 5). Then, the reliability of the structural system computed before and after using dynamic data can differ significantly. Consequently, the effect of the additional information on the design of the hysteretic devices can be considerable.

6 Conclusions

The use of updated reliability measures in the context of stochastic structural dynamical systems has been explored. A simulation-based Bayesian framework for system identification is used to update the structural models using dynamic response data. The updated distribution of the system model parameters is then used to implement a methodology for estimating the system reliability which incorporates knowledge from the test data. Numerical results show that the structural reliability computed before and after using dynamic data can differ significantly. In fact, monitoring data makes an important difference in the design of structural systems. Therefore measured responses, whenever available, should be used.

Acknowledgments

The research reported here was supported in part by CONICYT (National Commission for Scientific and Technological Research) under grant number 1110061 and by the European Union Project PIRSES-GA-2010-269222: Analysis and Design of Earthquake Resistant Structures (ADERS) of the FP7-PEOPLE-2010-IRSES, Marie Curie Actions. This support is gratefully acknowledged by the authors.

REFERENCES

[1] H. Shoji, M. Shinozuka and S. Sampath. A Bayesian evaluation of simulation models of multiple-site fatigue crack. *Probabilistic Engineering Mechanics*, 16:355–361, 2001.

[2] P. Beaurepaire, M.A. Valdebenito, G.I. Schuëller and H.A. Jensen. Reliability-based optimization of maintenance scheduling of mechanical components under fatigue. *Computational Methods in Applied Mechanics and Engineering*, 221-222:24–40, 2012.

[3] K. V. Yuen. *Bayesian methods for structural dynamics and civil engineering*, John Wiley & Sons. 2010.

[4] J. Ching and Y.C. Chen. Transitional Markov chain Monte Carlo method for Bayesian updating, model class selection, and model averaging. *Journal of Engineering Mechanics*, 133:816–832, 2007.

[5] L.D. Lutes and S. Sarkani. *Random Vibrations: Analysis of structural and mechanical systems*, Elsevier B-H. Oxford, UK. 2004

[6] W. Hastings. Monte Carlo sampling methods using Markov chains and their applications. *Biometrika*, 57(1):97–109, 1970.

[7] E. Jaynes. *Probability Theory: The Logic of Science*, Cambridge University Press, 2003

[8] J. Beck and L. Katafygiotis. Updating models and their uncertainties. I: Bayesian statistical framework. *Journal of Engineering Mechanics*, 124(4):455–461, 1998.

[9] L. Katafygiotis and J. Beck. Updating models and their uncertainties. II: Model Identifiability. *Journal of Engineering Mechanics*, 124(4):463–467, 1998.

[10] C. Papadimitriou, J.L. Beck and L. Katafygiotis. Updating robust reliability using structural test data. *Probabilistic Engineering Mechanics*, 16:103–113, 2001.

[11] B. Goller, M. Broggi, A. Calvi and G.I. Schuëller. A stochastic model updating technique for complex aerospace structures. *Finite Elements in Analysis and Design*, 47:739–752, 2011

[12] N. Metropolis, A. Resenbluth, M. Resenbluth, A. Teller and E. Teller. Equations of state calculations by fast computing machines. *Journal of Chemical Physics*, 21(6):1087–1092, 1953.

[13] H.A. Jensen, C. Vergara and E. Millas. The use of Bayesian model updating in reliability-based optimal design. *11th Joint Specialty Conference on Probabilistic Mechanics and Structural Reliability*, University of Notre Dame, 17-20 June, IN, USA, 2012

[14] S.K. Au and J.L. Beck. Estimation of small failure probabilities in high dimensions by subset simulation. *Probabilistic Engineering Mechanics*, 16(4):263–277, 2001.

[15] G.M. Atkinson and W. Silva. Stochastic modeling of California ground motions. *Bulletin of the Seismological Society of America*, 90(2):255–274, 2000.

[16] D.M. Boore. Simulation of ground motion using the stochastic method. *Pure and Applied Geophysics*, 160(3-4):635–676, 2003.

[17] H.A. Jensen, M.A. Valdebenito, G.I. Schuëller, and D.S. Kusanovic. Reliability-based optimization of stochastic systems using line search. *Computer Methods in Applied Mechanics and Engineering*, 198(49-52):3915–3924, 2009.

COMPDYN 2013
4th ECCOMAS Thematic Conference on
Computational Methods in Structural Dynamics and Earthquake Engineering
M. Papadrakakis, V. Papadopoulos, V. Plevris (eds.)
Kos Island, Greece, 12–14 June 2013

APPLICATION OF HPC TO EARTHQUAKE ENGINEERING – SEISMIC STRUCTURE RESPONSE ANALYSIS AND URBAN AREA EARTHQUAKE SIMULATION –

Muneo Hori[1], Seizo Tanaka[1], Tsuyoshi Ichimura[1], Maggededaera Lalith[1], Tomoshi Miyamura[2], Masao Ogino[3], and Shigenobu Okazawa[4]

[1]Earthquake Research Institute, University of Tokyo
Yayoi 1-1-1, Bunkyo, Tokyo 113-0032, Japan
e-mail: {hori, stanaka, ichimura, lalith}@eri.u-tokyo.ac.jp

[2] College of Engineering, Nihon University,
Nakagawara, Tokusada, Tamuramachi, Koriyama, Fukushima, 963-8642, Japan
e-mail: miyamura@cs.ce.nihon-u.ac.jp

[3] Information Technology Center, Nagoya University Furo-cho, Chikusa-ku, Nagoya, 464-8601, Japan
e-mail: masao.ogino@cc.nagoya-u.ac.jp

[4] Graduate School of Engineering, Hiroshima University Kagamiyama 1-4-1, Higashi-Hiroshima,
Hiroshima 739-8527, Japan. e-mail: okazawa@hiroshima-u.ac.jp

Keywords: High Performance Computing, Seismic Structure Response Analysis, Urban Area Earthquake Simulation.

Abstract. *This paper presents two examples of applying high performance computation (HPC) to earthquake engineering problems. One example is for the seismic structure response simulation, which improves the accuracy of estimating the structure seismic performance. A finite element method which is tuned for K computer is explained and results of trial simulation made in K computer are presented. The second example is for the urban area earthquake simulation. Explained are the urban area seismic response simulation which analyzes seismic response of all the building and the mass evacuation simulation that uses multi agent simulation. Illustrative examples of these simulations are presented.*

1 INTRODUCTION

Seismic design is improved if structure seismic performance is evaluated more accurately; see, for instance, Fardis[1] for the seismic design of concrete buildings. However, accurate evaluation is not trivial, since, for an extremely large ground motion, seismic responses often induce residual deformation but the deformation should not reach the level at which structure collapse happens. Currently, experiments are used for accurate evaluation of seismic performance, though these are time consuming and require sophisticated large experimental apparatus. Numerical analysis will be a substitute, if it is able to evaluate local damage and global failure.

Earthquake disaster assessment[2, 3] is used to make an earthquake disaster mitigation plan for an urban area. A more accurate assessment is required to make a more rational mitigation plan. Unlike the structure seismic performance, the earthquake disaster assessment involves non-physical processes such as mass evacuation, recovery works of damaged structures, and so on. Numerical simulation is a unique tool of evaluating such non-physical processes since no experiment can be made for these processes. It is thus necessary to development reliable codes.

High performance computing (HPC)[4] plays a key role in carrying out larger numerical computation for the accurate evaluation of seismic structure performance and for the accurate assessment of urban area earthquake disaster. This is because more accurate evaluation and assessment requires more sophisticated model and simulation, which inevitably results in larger amount of numerical computation.

The authors have been seeking to apply HPC to two major problems of earthquake engineering, namely, the seismic structure response analysis and the urban area earthquake simulation, which are used for the seismic structure performance evaluation and the earthquake disaster assessment, respectively. In this paper, we present several examples of applying HPC to the earthquake engineering problems, demonstrating the potential of the HPC application.

This paper is organized as follows: first, we summarize our perspective of numerical computation that is currently used in solving the two problems of earthquake engineering. Next, we present recent achievement of applying HPC to solve the problems. For the problem of the seismic structure analysis, developed is a general purpose finite element method (FEM), which is able to solve high fidelity model of a structure subjected to ground motion. For the problem of the urban area earthquake simulation, the urban area seismic response simulation and the mass evacuation simulation are explained.

2 CURRENT STATE OF NUMERICAL COMPUATION IN EARTHQUAKE ENGINEERING

As mentioned, earthquake engineering has two major numerical problems, the seismic structure response analysis and the urban area earthquake simulation. The seismic structure responses analysis is aimed at evaluating structure seismic performance, by considering various factors such as soil-structure interaction, cyclic loading, or local damage and failure. The urban earthquake simulation is used to make a rational disaster mitigation plan, by considering possible structure damages which induce fire, injuries and casualties as well as regional and domestic economic loss.

It is most difficult to numerically analyze dynamic processes of non-linear structure seismic response which could reach local or overall damage. In practice, therefore, used are experimental studies of a scaled model of structure members, and numerical analysis that takes advantage of the experiment results to evaluate the structure seismic performance. As the higher level

of accuracy is sought from these experiments, the cost and time required become higher and longer; the number of the infrastructures with required facilities decreases, too.

FEM with solid elements is a substitute of experimental study, if it is able to analyze local damage of a structure. Since the zone of local damages is several orders of magnitudes smaller than the size of a structure, an analysis model is required to consist of multitudes of solid elements. This is the major reason that HPC is needed for the seismic structure response analysis. It should be noted that reinforced concrete (RC) structure shares a large portion of buildings, and hence FEM for an RC structure is a major target of the HPC application. The HPC application should account for the two characteristics of concrete material, namely, complicated elasto-plastic properties and brittle cracking of various sizes.

Urban area earthquake simulation is not a new subject; there are open software for the simulation of ground motion distribution and induced structure damages. The present simulation relies on empirical relations, since it must analyze ground of large area and all buildings located in a target area. Inter- or extrapolation of data of past disaster is also used to make assessment of a possible disaster, provided that the situation at future earthquake will be similar to the one at the past.

If a *physical* model is built for underground structure and a set of building in a target city, processes of ground motion generation and resulting building responses are computed for a given scenario of an earthquake. Such numerical simulation is a good application of HPC, since it requires large amount of numerical computation. A key element is the construction of an urban area model. A sequence of damage such as mass evacuation could be simulated if a suitable model and analysis method is developed. This is a good application of HPC as it is aimed at simulating behavior of all residents in the target area.

3 HPC FOR SEISMIC STRUCTURE RESPONSE ANALYSIS

In this section, we present recent achievement of applying HPC to the seismic structure response analysis. A general purpose seismic response simulation is being developed; it is an extension of an FEM package which has high parallel computation performance. A major target of the simulation is non-linear dynamic responses of an RC structure, and modules of concrete elasto-plasticity and failure analysis are implemented.

3.1 FEM for Structure Seismic Response Simulation

ADVENTURE-K, which is an extended version of ADVENTURE_Solid[6] and specially tuned for K computer, is used for the structure seismic response simulation. We should mention that ADVENTURE_Solid is a general purpose FEM package and has high parallel computation performance in several computer environments. It is a solver that plays a key role in achieving higher parallel computation performance when a large scale model is analyzed; most of computation time is used to solve a matrix equation of FEM. A key characteristic of ADVENTURE-K's solver is a domain decomposition method (DDM) which is specially tuned with preconditioning of balanced domain decomposition (BDD). Most of efforts made to tune ADVENTURE_solid to ADVENTURE-K have been put to improve the solver.

Architecture of a massive parallel computer like K computer (in which around 88,000 nodes each of which has 8 cores are installed) favors structured grid computation rather than non-structured grid computation. FEM has inherent disadvantage in achieving high scalability by taking full advantage of structured communication topology of supercomputers. In view of this, we evaluate the parallel computation performance of ADVENTURE-K's solver as fairly satis-

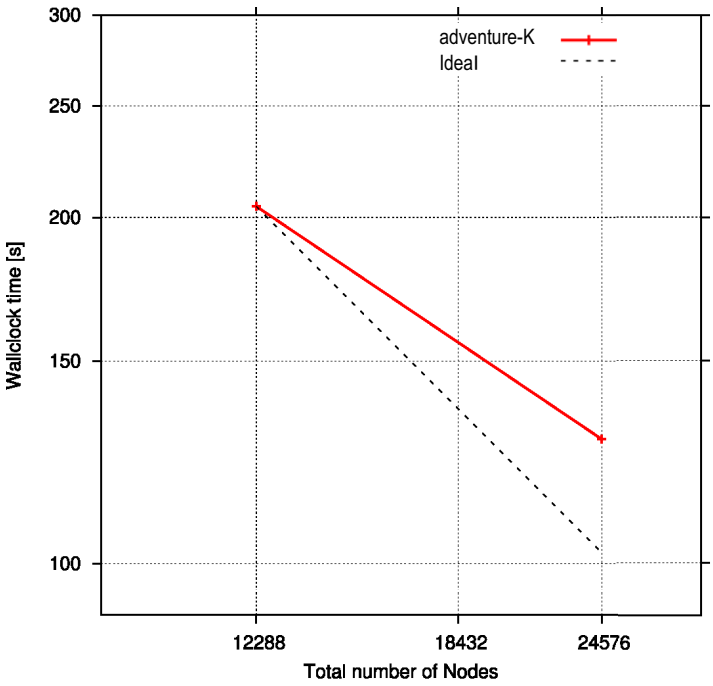


Figure 1: Strong scaling of ADVNENTURE-K in K computer environment.

Table 1: Parallel Computation Performance of ADVENTURE-K in K computer environment.

# Nodes	Total Time(s)	Peak [TFLOPS]	Peak ratio [%]	Efficiency [%]
12,288	204.5	89.7	5.71	-
24,576	128.3	151.3	4.81	79.6

factory in K computer environment, due to the implementation of DDM with preconditioning of BDD. In Table 1 and Fig. 1, basic parallel computation performance of ADVENTURE-K is summarized; the peak speed is 151.3 TFLOPS, which corresponds to the peak ratio of 4.81% of K computer, and the efficiency in strong scaling is 79.7% when the performance of 24,576 nodes is compared with that of 12,288 nodes.

3.2 Example of RC Structure Simulation

A major target of the structure seismic response simulation is an RC structure. Modules which deal with the two characteristics of concrete material (i.e., elasto-plastic constitutive relation and failure analysis) are implemented into ADVENTURE-K. In this subsection, we explain these modules, and present results of numerical computation for a RC pier.

3.2.1 Modules to deal with concrete material

Elasto-plastic constitutive relation which depends on confining pressure and loading history is a key characteristic of concrete material. The relation developed by Maekawa *et al.*[7] is used since it is known as one of the most accurate and reliable relations in the field of concrete engineering. To implement this constitutive relation into ADVENTURE-K, we have to make the following two efforts[8]:

Table 2: Material properties of sample of shear connector experiment.

	concrete	steel
Young modulus [MPa]	21820.0	208000.0
Poisson ratio	0.3	0.29
yield stress [MPa]	-	370.0
hardening [MPa]	-	2080.0
compressive strength [tMPa]	21.4	-

1. Reformulation of the constitutive relation in the form that correspond to standard rate form of elasto-plasticity.

2. Development of a new algorithm to solve the elasto-plastic constitutive relation.

The reformulation makes it easy to implement the constitutive relation into the code. The new algorithm is essential since the constitutive relation of concrete has a negative slope between strain and stress increments after concrete reaches its maximum strength; the negative slop results in the loss of the positive-definiteness in the matrix of the discretized equation and the conjugate gradient method is not applicable.

Initiation and propagation of cracks of various sizes is a key characteristic of concrete material. Crack surfaces observed in concrete are complicated, and it is difficult to apply ordinary numerical analysis method, such as extended FEM[9] or element-free Galerkin method[10], to compute cracks of such complicated configuration. We employ a new discretization scheme, called Particle Discretization Scheme (PDS)[11, 12], to discretize a displacement field with discontinuities that correspond to cracks. This scheme uses a set of discontinuous basis function and bifurcation and branching of discontinuities is easily expressed. The failure analysis that uses this scheme is straightforward as it easily computes the crack initiation and propagation by using the inherent discontinuities of the basis functions.

3.2.2 Trial numerical simulation of shear connector

In order to examine the usefulness the two modules of the elasto-plastic constitutive relation and the failure analysis, we make trial numerical computation of a shear connector problem; a shear connector is used to connect two RC structure members, and its capacity is strongly influenced by non-linear elasto-plastic deformation as well as cracking which stems from the connector. A schematic view of a shear connector problem is presented in Fig. 2 which is an experiment sample[13], and Table 2 summarizes the material properties of the experiment sample.

In the numerical computation, studied are the effects of smoother which is put in the interface between the RC slab and the main beam and the effects of re-contact of cracked concrete. Smoother decreases shear friction on the interface; shear friction on the interface may lead to cracking in concrete near the interface; and re-contact transmits stress in cracked concrete, which, in our view, is a mechanism of concrete near the connector to hold concentrated stress. The results are shown in Fig. 3; a) gives the load-displacement curve when the smoother is included, and b) is cracking pattern when re-contact is included. As is seen, introducing smoother, we can improve the agreement of the synthesized load-displacement curve with the experimental data. Also, re-contact of cracked concrete spatially distributes the initiation of cracks near the shear connector, which appears more realistic.

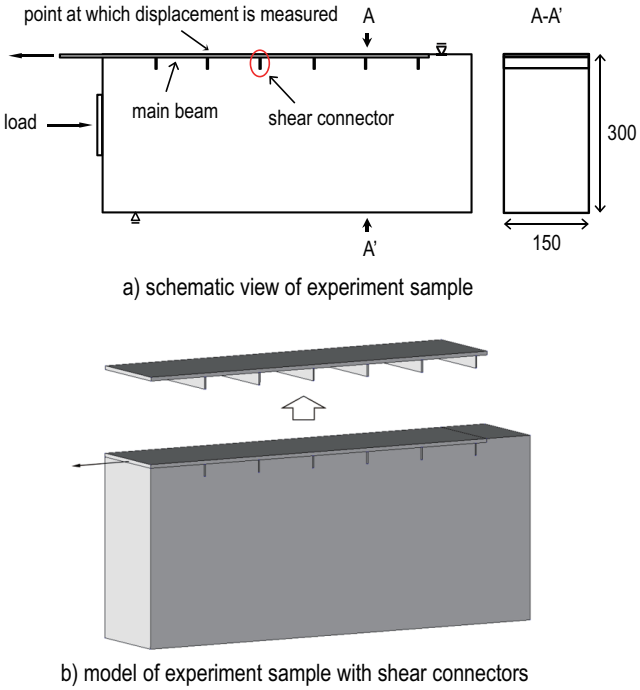


Figure 2: Experiment sample for shear connector.

A typical cracking pattern is presented in Fig. 4. Cracking takes place at the tip of shear connector, and each crack has its own length and arc length. The pattern of this cracking is similar to the one observed in the experiment.

The major role of shear connector is to transmit force between two RC structure members. The numerical simulation is thus required to reproduce the dependence of the transmitted force on the properties of the shear connectors. In Fig. 5, the dependence of the transmitted force via the shear connector on its number and spacing is plotted and compared with the experimental results; smoother and re-contact are used in the simulation. As is seen, the agreement of the numerical simulation with the experiment data is satisfactory in a wide range of the number and spacing of shear connector. We should emphasize that these results are reproduced by FEM analysis of massive solid elements, which requires small scale experiments in order to determine material properties.

3.2.3 Numerical simulation RC pier

Since the trial simulation produces good results, we move to study the seismic performance of an RC pier, using ADVENTURE-K. We have to emphasize that no validation is made to the results of the present simulation unlike the trial simulation. We are planning to make validate the simulation results with the experiment data made in E-DEFENSE[14], a shaking table that is operated by National Research Institute for Earth Science and Disaster Prevent, Japan; the pier analyzed in this simulation is the one that was used in an actual experiment of E-DEFENSE. An analysis model consists of an RC pier (which is the combination of concrete and reinforcemenet), its pile foundation and surrounding soil, so that soil-structure interaction effects are fully taken into consideration. The analysis model and the material properties are summarized in Fig. 6 and Table 3, respectively. As is seen, all the components of the RC pier are densely discretized.

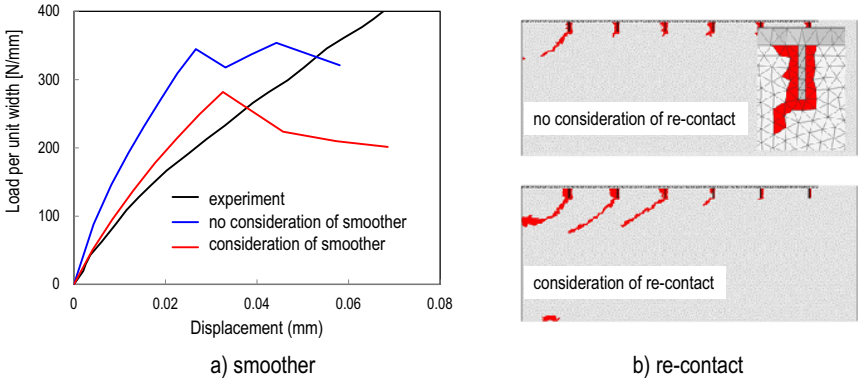


Figure 3: Effects of smoother and re-contact.

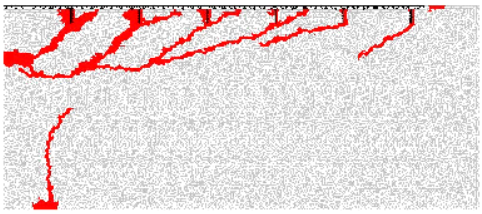


Figure 4: Pattern of cracking; a crack is initiated from each shear connector and extends.

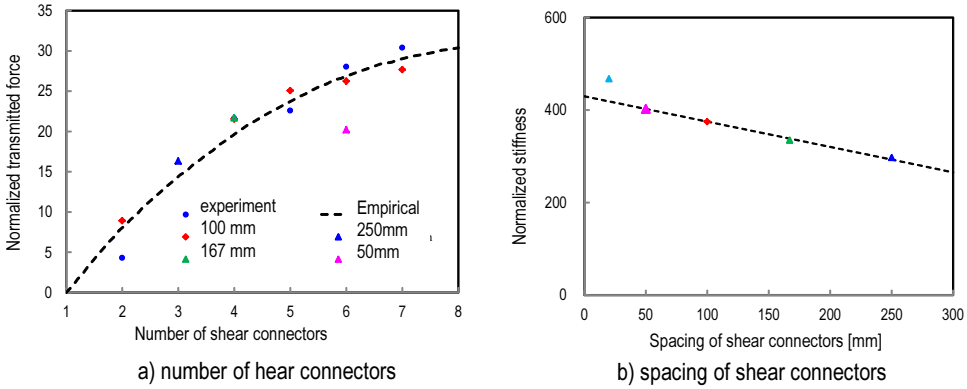
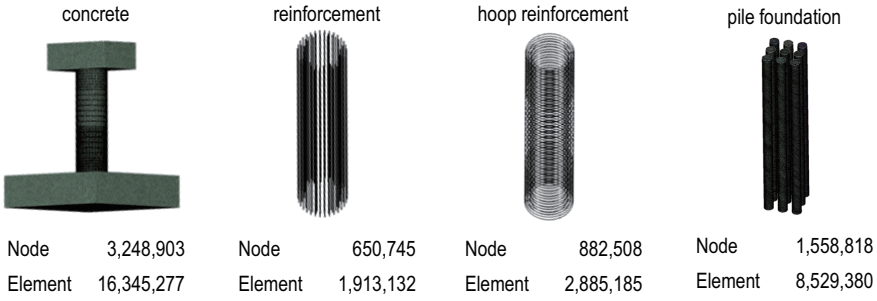


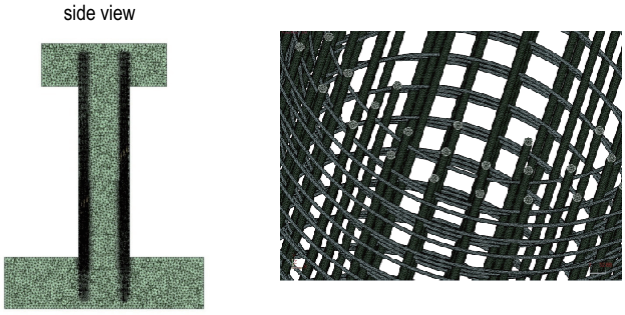
Figure 5: Dependence of transmitted force on shear connector.

Table 3: Material properties of RC pier.

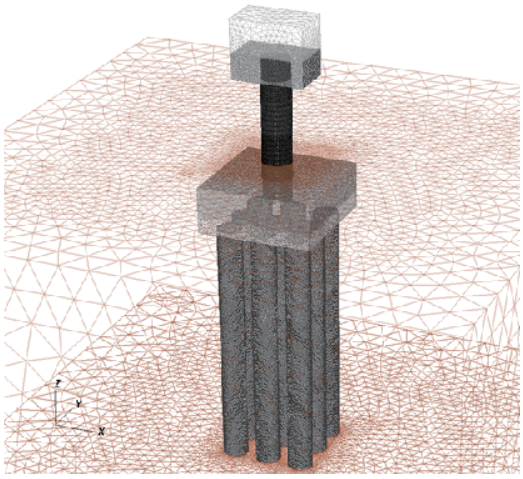
	concrete	steel
Young modulus [kN/mm^2]	25000.0	200000.0
Poisson ratio	0.3	0.3
hardening [kN/mm^2]	1000.0	20000.0
yield stress [kN/mm^2]	30.0	350.0
density [ton/mm^3]	2.3e-0.9	7.5e-0.9



a) major parts of RC pier



b) details of reinforcement



c) whole view of RC pier model standing on its pile foundation embedded in soil

Figure 6: Analysis model of RC pier.

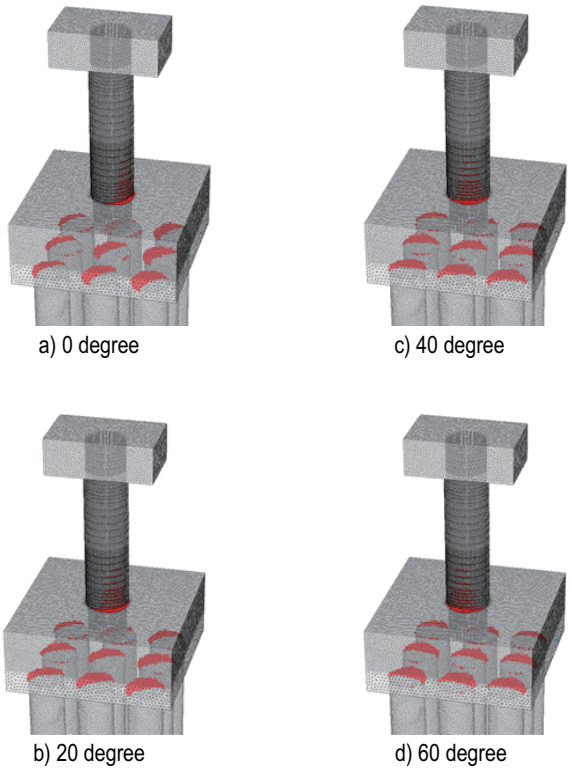


Figure 7: Cracking pattern of RC pier subjected to ground motion at different input angle.

An advantage of applying HPC to the structure seismic response simulation is the fact that it allows us to study a detailed model as shown in Fig. 6 which has a large number of degree-of-freedom. As another advantage, we point out that it allows us to accurately evaluate the seismic performance of a structure, by considering various cases of input ground motion. Experimental study surely has limitation in the number of experiment samples, unlike numerical study in which we can reuse one analysis model several or many times. In the present simulation, we study the performance of the RC pier subjected to JR Takatori ground motion, which was observed in 1995 Great Kobe Earthquake, by changing the direction of the ground motion.

As an illustrative example of the numerical simulation for the seismic performance evaluation, we present cracking pattern of the RC pier due to different input ground motion in Fig. 7. As is seen, the location of cracked concrete (the crack surfaces are colored in red) change as the direction of the input ground motion changes. While the area of the crack surfaces appears more or less the same even when subjected to input ground motion of different direction, it is not identical. As expected, the structure behavior is not *isotropic*, in the sense that the behavior changes depending on the loading direction. Due to this anisotropy, therefore, more accurate evaluation of the seismic performance can be made by analyzing the seismic response with various input ground motion. HPC is surely an important element to realize such numerical simulation which requires large amount of numerical computation as well as efficient and fast computation for practical purpose.

4 HPC FOR URBAN AREA EARTHQUAKE SIMULATION

Unlike the structure seismic response simulation, there are few numerical analysis methods which can be used for urban area earthquake disaster assessment. This is mainly because numer-

ical computation required for the assessment is huge. The progress of computer hardware and software is solving this difficulty. In this section, we briefly mention a system, called *Integrated Earthquake Simulation* (IES)[4, 15, 16], which uses a set of numerical analysis methods for urban area earthquake disaster assessment, and present two examples of the numerical analysis methods which are put in the system.

4.1 Summary of IES

IES is aimed at providing a tool for urban area earthquake disaster assessment, by carrying out a series of numerical simulation. The target of the simulation is the three phases of earthquake disaster, namely, the ground motion generation, the urban area seismic response and the disaster reaction. For an urban area, analysis models are constructed for each phase, and distinct codes are used for physical or non-physical processes of the phases. It should be noted that output of one simulation of one phase is converted to input of another simulation of the next phase, so that the three phases will be seamlessly simulated for a given scenario of earthquake.

HPC is surely a core element of IES. Simulation of the three phases requires larger amount of numerical computation as more sophisticated codes and more detailed models are used; for instance, an analysis model of a building will eventually become the one shown in the preceding section. We should point out that, beside for the code and model, handling of input and output should be being improved in order to make larger and faster computation, by using most updated I/O hardware and software. At this moment, data generated in one phase reach 100 TB when a large urban area is simulated. IES is able to simulate various cases of earthquake disaster for one urban area, by considering many earthquake scenarios, which increases the data size of IES simulation.

In the following two subsections, we explain the urban area seismic response simulation and the mass evacuation simulation, for the phase of the urban area seismic response and the disaster reaction, respectively. The urban area seismic simulation uses an urban area model which consists of a set of building models and a non-linear seismic response code is applied to each of the building model. In the mass evacuation simulation, Multi Agent Simulation (MAS)[17, 18, 19, 20] is employed; agents are used as a model of human being who escapes in an urban area.

4.2 Urban Area Seismic Response Simulation

There have been developed numerous codes for non-linear seismic response simulation, which has sufficient accuracy, reliability and functionalities. The major task of the urban area seismic response simulation is not to develop a new code for the seismic structure response, but to construct an analysis model for each building, using available data so that we can take advantage of the existing codes. At this moment, Geographic Information System (GIS) which contain configuration data of buildings is available. We develop a code which automatically constructs an analysis model for one building, extracting necessary data from GIS and converting the data to the model.

A schematic view of the automatic construction is presented in Fig. 8. GIS which we are using has configuration data of different floors, and analysis models of different complexity are generated from one set of configuration data stored in GIS. Material properties as well as structure properties are *guessed* in constructing these analysis models. This is the limitation of the current module for the data construction.

There are some buildings which have quite complicated configurations in an urban area. It

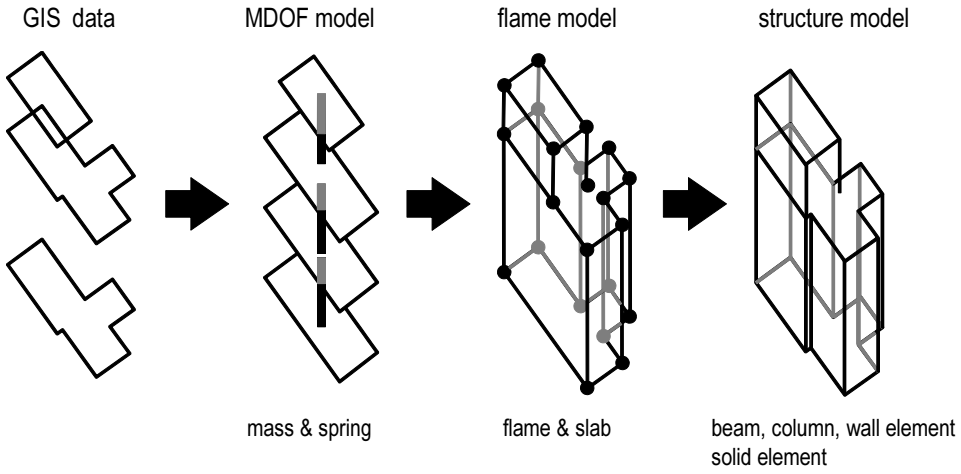


Figure 8: Construction of building model of different complexity from GIS data.

is not an easy task to make automated construction of an analysis model from the configuration data of such complicated building; in general, data stored in GIS are a set of point locations, and does not include information about connectivity. To deal with building with complicated configuration, we utilize a set of templates of floor arrangement. An analysis model is made from the template that best fits the building configuration. In Fig. 9, presented is the use of template sets to make a model for one building; the template is found by comparing the similarity in shape, and the model is constructed from the template. Some approximations are included in the process of constructing an analysis model from the template, not the structure configuration; for instance, the floor area cannot be computed exactly. However, the use of template set has high robustness in dealing with building of complex configuration, and the robustness is increased by adding new templates, which correspond to more complicated buildings.

As a typical example, we construct an urban area model of Tokyo Metropolis, for the urban area seismic response simulation. The non-linear one-component model is automatically constructed for around 2,000,000 buildings. We have to point out that the quality of the constructed models is not checked, since the number of the model is too large; we are planning to investigate natural frequencies of the generated model as the first step of checking the model quality. Seismic structure response is computed by analyzing each model for a given ground motion. This computation is so called *embarrassing parallel*, since it does not need inter-node communication. The parallel computation performance is highest, except for handling a large number of input and output data. Two snapshots of the urban area responses are presented in Fig. 10. The color legend is for the norm of displacement vector, and it is shown that higher buildings are shaken more than lower ones.

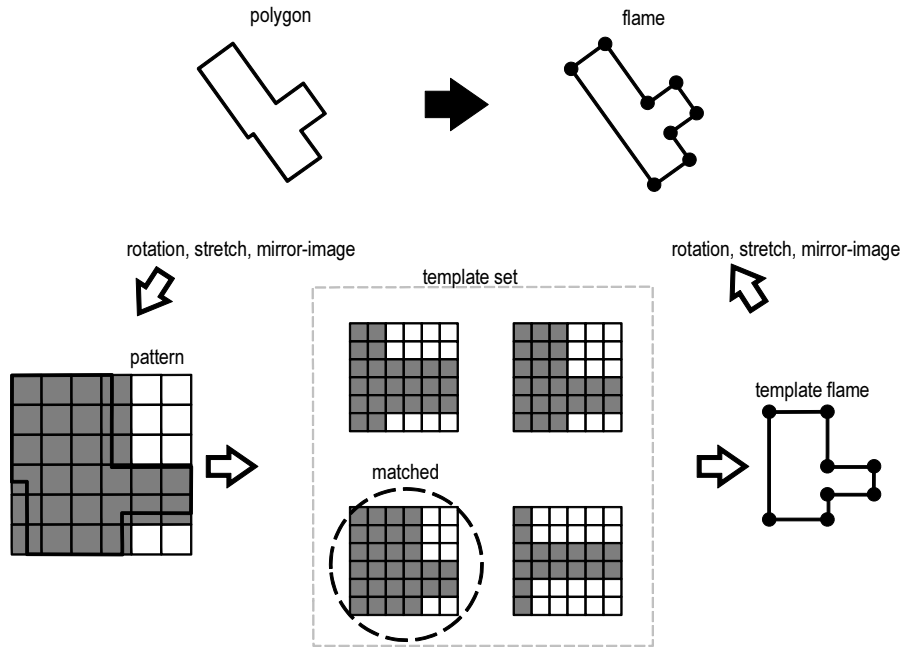
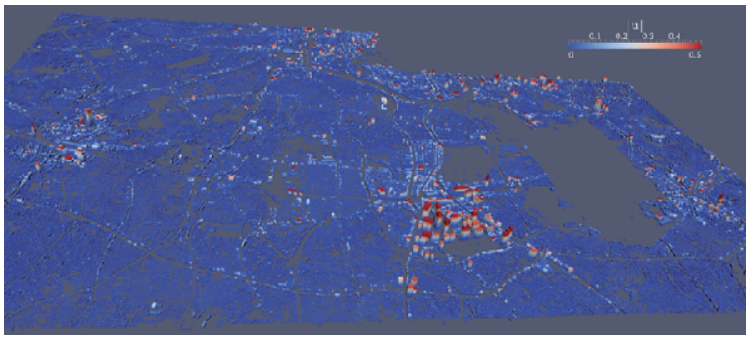
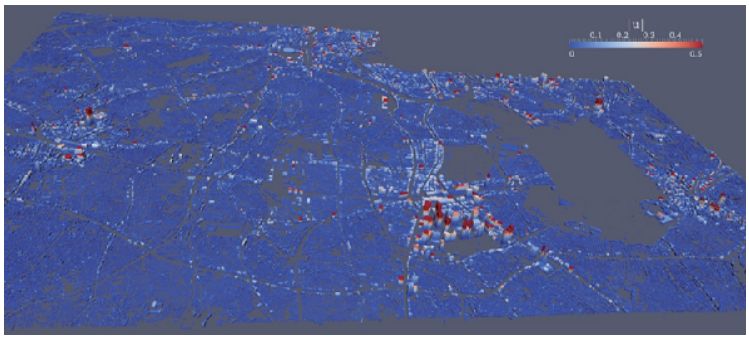


Figure 9: Use of template to make analysis model of building with complicated configuration.



a) 500 time step



b) 520 time step

Figure 10: Snapshot of urban area seismic response of urban area model for Tokyo Metropolis.

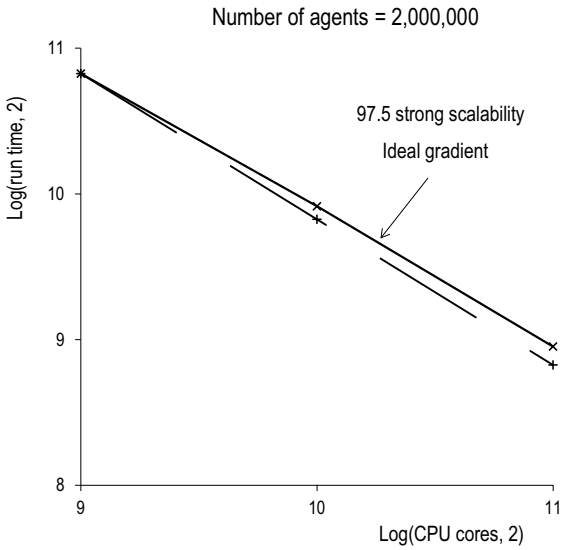


Figure 11: Parallel computation performance of MAS.

4.3 Mass Evacuation Simulation

As mentioned, IES employs MAS for the mass evacuation simulation[21], which, we think, is suitable to deal with situation in which *heterogeneous* persons escapes in a disorganized manner; the heterogeneity corresponds to the walking speed, the familiarity to the directory. An agent is designed to have `physical` and `intellectual` data, together with three functionalities of `seeing`, `thinking` and `moving`. It spontaneously moves in an evacuation route model interacting with the surrounding agents and finding the best route for the evacuation. In the mass evacuation simulation, a set of agents are generated in the evacuation route model, and the agents are activated to move towards pre-determined safe place or direction. The evacuation time, in which agents exit from the model, is an output of the simulation.

In Fig. 11, the parallel computation performance of MAS is plotted. While the number of the node is small, the performance of the code is satisfactory; it shows almost ideal strong scaling. Special cares are taken for the decomposition of analysis domain each of which is analyzed by one node. We should emphasize that since the code is written C++, which is not well supported by the current version of K computer system, the performance in the K computer environment is worse than the PC cluster environment; the use of C++ or other object oriented programing language is preferred in developing a code for MAS.

As a typical example of the output of the mass evacuation simulation, Fig. 12 shows snapshots of agents which move in the urban area model of evacuation routes; the model is constructed for Kochi City in Japan. Heterogeneous agents move smoothly, going from the top to the bottom of the figure. While overall movement of the agents is smooth, there are local conflicts created in the simulation. An agent stops or passes over other agents when it enters a crowded place. In very crowded situation, therefore, the current MAS produces less smooth movement of the agents.

While the primary objective of the mass evacuation simulation is more accurate assessment of earthquake disaster, it can be used for other purposes. As an example of such purpose, we consider the mass evacuation simulation in which *official* agents are introduced. The official agent seeks to find other agents which do not start evacuation and to make them do so. In view of 2011 Tohoku Earthquake, the importance of shortening preparation time for the tsunami

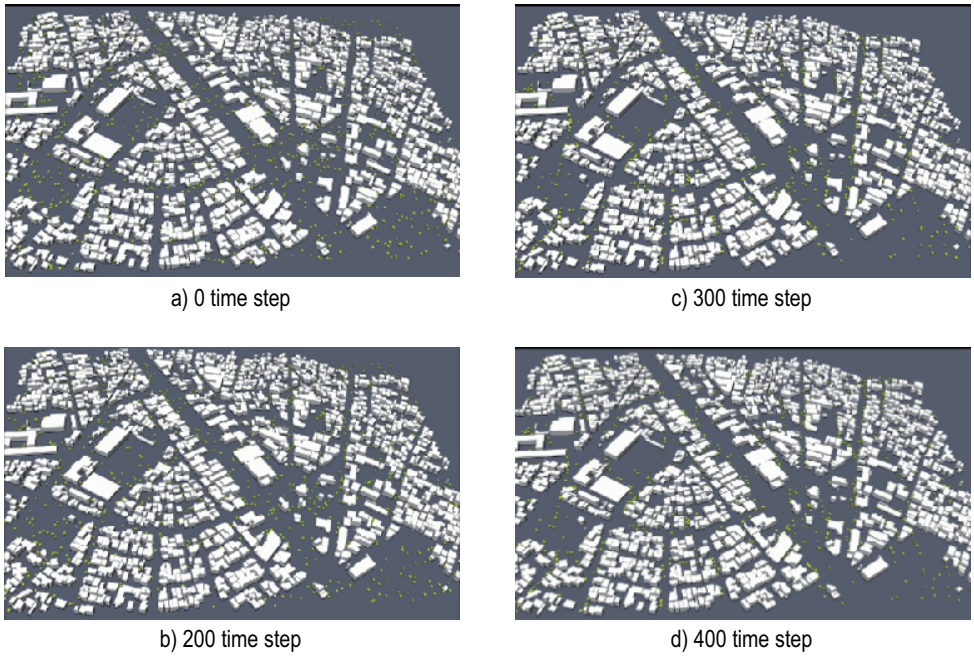


Figure 12: Snapshot of evacuating agents in mass evacuation simulation.

Table 4: Problem setting of official agent in mass evacuation simulation.

a) agent characteristics

Average moving speed [m/s]	1.4 (Normal) 1.1 (Slow)
S.D of moving speed [m/s]	0.6 (Normal) 0.3 (Slow)
Moving Speed of officials [m/s]	3.0
Average preparation time [s]	1000
S.D of preparation time [s]	240

b) setting of 5 cases

CASE	PET	OR (%)
1	No	-
2	Varying	0.0
3	Varying	0.5
4	Varying	1.0
5	Varying	3.0

PET Pre-Evacuation Time
OR Official Agent Ratio

evacuation is pointed out, and the official agent plays a role of an authority which guides residents. Snapshots of the official agents interacting other agents are presented in Fig. 13. It is shown that the official agents succeed to find agents which stop and make them move.

The mass evacuation simulation will give an answer to the question of "how many authorities are required in an urban area, in order to fasten tsunami evacuation." We study the reduction of the tsunami evacuation time by introducing the official agent. The problem setting is summarized in Table 4, and the results are shown in Fig. 14; the evacuation time for the ideal case (no preparation time) to the worst case (no authorities guiding evacuation) is plotted. As the ratio of the official agent increases, the evacuation time is decreased. However, the relation between the reduced time and the official agent ratio is not simple; it depends on the whole number of agents. The relation also depends on the complicatedness of the evacuation routes as well as the properties of the other agents. Many cases should be simulated in order to find a suitable ratio of the official agents.

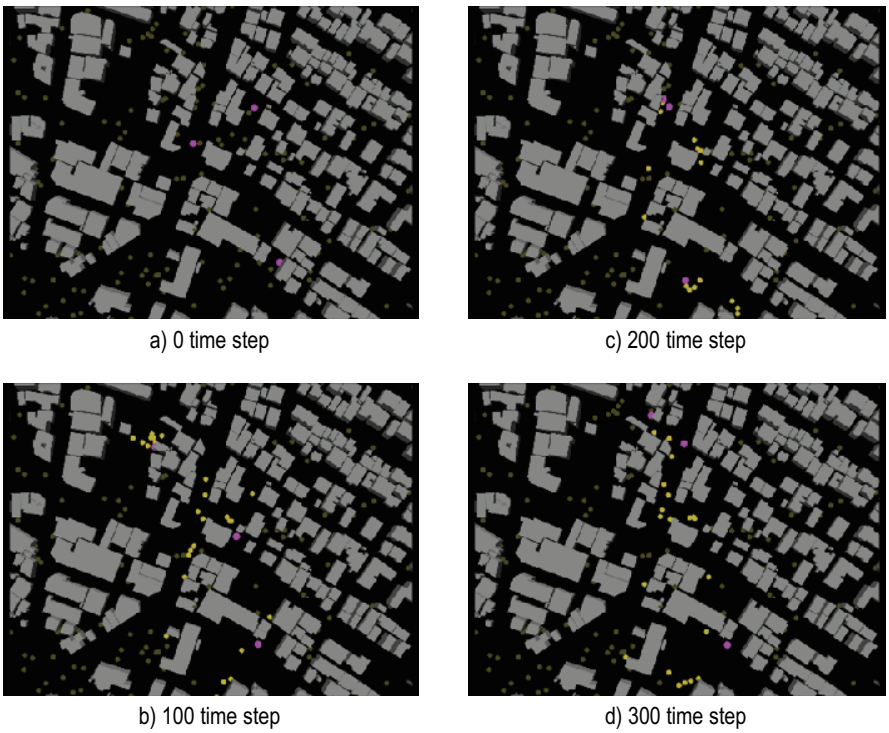


Figure 13: Snapshot of official agent guiding agents which do not start evacuation.

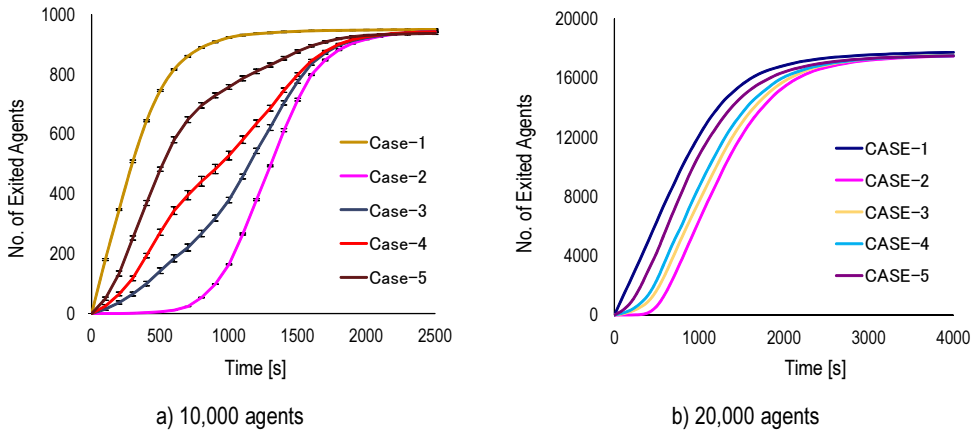


Figure 14: Evacuation time shortened by introducing official agent.

5 CONCLUDING REMARKS

This paper presents examples of applying HPC to two earthquake engineering problems, namely, the seismic structure response simulation and the urban area earthquake simulation. Strictly speaking, we are finishing code tuning that is required for the use of K computer; the validation of the computation results will be made when the tuning tasks are fully accomplished. Still, the results presented here show the potential advantage of applying HPC to solve the earthquake engineering problem.

Further development and improvement of the analysis codes is needed for the seismic structure response simulation and the urban area earthquake simulation. Beside for the code development, we need to construct a more reliable analysis model for a structure and an urban area. Although human efforts are inevitable to improve or correct the analysis model, most of tasks in constructing a model from a given set of data must be automated. We need to develop software for such model generation.

Acknowledgment. This work is supported by the MEXT grant for HPCI. Strategic Program Field No. 3. A part of the results is obtained by early access to K computer at the RIKEN-AICS.

REFERENCES

[1] Fardis, M. N.: *Seismic Design, Assessment and Retrofitting of Concrete Buildings: based on EN-Eurocode 8,* Springer, 2013.

[2] The Federal Emergency Management Agency Hazus, http://www.fema.gov/hazus.

[3] Global Earthquake Model, GEM, http://www.globalquakemodel.org/.

[4] Hori, M.: *Introduction to computational earthquake engineering*, 2nd edition, Imperial College Press, 2011.

[5] RIKEN Advanced Institute for Computational Science, http://www.aics.riken.jp/en/.

[6] ADVENTURE Project, http://adventure.sys.t.u-tokyo.ac.jp/.

[7] Maekawa, K., Pimanmas, A. & Okamura, H.: *Nonlinear mechanics of reinforced concrete*, Taylor & Francis Group., 2003.

[8] Yamashita, T., Hori, M., Oguni, K., Okazawa, S. & Maki, H.: Reformulation of non-linear constitutive relations of concrete for large-scale finite element method analysis, *Journal of Japan Society of Civil Engineering*, **67:1**, 145–154, 2011.

[9] Moes, N., Dolbow, J., & Belytschko, T.: A finite element method for crack growth without remeshing, *International Journal for Numerical Methods in Engineering*, **46**, 131–150, 1999.

[10] Belytschko, T., Lu, Y. Y. & Gu, L.: Element-free Galerkin method, *International Journal for Numerical Methods in Engineering*, **37**, 229–256, 1994.

[11] Hori, M. Oguni, K. & Sakaguchi, H.: Proposal of FEM implemented with particle discretization for analysis of failure phenomena, *Journal of the Mechanics and Physics of Solids*, **53**, 681–703, 2005.

[12] Wijerathne, M. L. L., Oguni, K. & Hori, M.: Numerical analysis of growing crack problem using particle discretization scheme, *International Journal for Numerical Methods in Engineering*, **80**, 46–73, , 2009.

[13] Chuah, C. L., Shima, H. & Virach, R.: Load-displacement relationship of plate shear connector in steel-concrete composite structures, *Proc. of JSCE*, **15**, 433, 223–229, 1991.

[14] National Research Institute for Earth Science and Disaster Prevent, E-DEFNESE, http://www.bosai.go.jp/hyogo/ehyogo/index.html.

[15] Hori, M., Oguni, K. & Ichimura, T.: Integrated simulation for earthquake hazard and disaster prediction, *Journal of Earthquake and Tsunami*, **3**, **2**, 121–141, 2009.

[16] Hori, M., Sobhaninejad, G., Ichimura, T. & Lalith, M.: Enhancement of integrated earthquake simulation with high-performance computing, *Journal of Earthquake and Tsunami*, **5**, **3**, 271–282, 2011.

[17] Wooldridge, M.: *An Introduction to MultiAgent Systems*, John Wiley & Sons, 2002.

[18] Vlassis, N.: *A Concise Introduction to Multiagent Systems and Distributed Artificial Intelligence*, Morgan & Claypool Publishers, 2007.

[19] Kirchner, A. & Schadschneider, A.: Simulation of evacuation processes using a bionics-inspired cellular automaton model for pedestrian dynamics, *Physica*, **A312**, 260–276, 2002.

[20] Farinelli, A., Grisetti, G., Iocchi, L., Lo Cascio, S. & Nardi, D.: Using the RoboCup-Rescue Simulator in an Italian Earthquake Scenario, the 1st International Workshop on Synthetic Simulation and Robotics to Mitigate Earthquake Disaster, Padua, Italy, 2003.

[21] Inukai, Y., Oguni, K., & Hori, M.: Developmenmt of measurement-based multiagent simulator for evacuation process, *Journal of Applied Mechanics*, JSCE, **8**, 323–330, 2005 (in Japanese).

COMPDYN 2013
4th ECCOMAS Thematic Conference on
Computational Methods in Structural Dynamics and Earthquake Engineering
M. Papadrakakis, V. Papadopoulos, V. Plevris (eds.)
Kos Island, Greece, 12–14 June 2013

ACCOUNTING FOR NEAR-SOURCE EFFECTS IN THE DISPLACEMENT COEFFICIENT METHOD FOR SEISMIC STRUCTURAL ASSESSMENT

Georgios Baltzopoulos, Eugenio Chioccarelli and Iunio Iervolino

Dipartimento di Strutture per l'Ingegneria e l'Architettura, Università degli Studi di Napoli Federico II
Via Claudio 21, 80125, Naples, Italy.
e-mail: georgios.baltzopoulos@unina.it, eugenio.chioccarelli@unina.it, iunio.iervolino@unina.it

Keywords: directivity, performance-based seismic design.

Abstract. *Non-linear static procedures are well-established analytical tools for performance-based seismic design and assessment. On the other hand, near-source (NS) ground motions are emerging as relevant to structural engineering because they may be characterized by seismic demand larger and systematically different than that typically induced by so-called ordinary records. This is the result of phenomena such as rupture forward directivity (FD), which may lead to the appearance of distinct velocity pulses in the ground motion velocity time-history. Lately, effort was put towards the framework necessary for taking FD into account in probabilistic seismic hazard analysis (PSHA). The objective of the present study is to discuss the extension of non-linear static procedures, such as the displacement coefficient method (DCM), with respect to the inelastic demand associated with FD. In this context, the DCM is implemented to estimate NS seismic demand by making use of the results of NS-PSHA, developed for single-fault-case scenarios. A predictive model for NS-FD inelastic displacement ratios, previously developed by the authors, is employed. An illustrative application of the DCM, with explicit inclusion of NS-pulse-like effects, is given for a plane R/C frame designed under modern code provisions.*

1 INTRODUCTION

Sites located in the vicinity of seismic faults may experience ground motions which can be considered *atypical* due to phenomena collectively known as near-source (NS) effects. Most important among these effects, is forward rupture directivity (FD). During fault rupture, shear dislocation may propagate at velocities similar to the shear wave velocity; as a result, there is a probability that at sites aligned along the direction of rupture propagation, shear wave-fronts generated at different points along the fault arrive at the same time, delivering most of the seismic energy in a single double-sided pulse registered early in the velocity recording. Such impulsive behavior, which is actually the result of constructive interference of horizontally polarized waves, is most prominent in the fault-normal component of ground motion [1]. These pulses, which characterize FD ground motions, have an appreciable effect on spectral pseudo-acceleration (S_a) at periods around the pulse duration (or pulse period, T_p) [2].

Recently, advances have been made allowing such NS effects to be consistently included in probabilistic seismic hazard analysis (PSHA) [3,4], which refers to elastic structural demand. Moreover, inelastic structural response to pulse-like ground motions may be systematically different from that to non-impulsive, or *ordinary*, records, exhibiting heightened displacements at structural periods around one-half to one-third of T_p [5].

In this study, a discussion of the application of recent results about pulse-like seismic demand to non-linear static structural analysis procedures is addressed. The following is structured so that an introductory presentation of the displacement coefficient method (DCM) is first given. Then, evaluation of NS elastic (hazard) and inelastic seismic demand is described. Finally, the DCM in NS conditions is illustrated by means of an example and the outcome is discussed with respect to the ordinary case.

2 NON-LINEAR STATIC PROCEDURES

Estimating non-linear structural response is essential in the context of performance-based seismic design and assessment. Due to the relative inadequacy of elastic analysis on one hand, and the daunting complexity of non-linear dynamic analysis on the other, approximate procedures based on static non-linear analysis of structures were developed towards that end. Prominent among these are the DCM introduced in [6,7] and improved upon in [8] and the capacity spectrum method (CSM) [9].

The concept, which lies at the core of these methods, is that one first obtains a capacity (or "pushover") force-displacement curve by loading a non-linear model of the structure with a predetermined profile of lateral forces which are gradually increased up to a point of collapse. This curve is subsequently used as the starting point to approximate the structure as a (typically bilinear) yielding single degree of freedom (SDoF) oscillator, whose spectral inelastic response (given the elastic demand) is used to estimate that of the original structure.

Inelastic response spectra required in the procedure mentioned above are traditionally derived from the statistical treatment of the responses of yielding SDoF oscillators subjected to a suite of recorded ground motions. These are usually presented in the form of strength reduction factor - ductility - period (R-μ-T) relations (e.g., [10]), or inelastic displacement ratio spectra (e.g., [11]) applicable in the DCM, as elaborated in the following sections.

3 DISPLACEMENT COEFFICIENT METHOD

3.1 Method description

The DCM attempts to estimate the inelastic displacement demand of the structure, which corresponds to a degree of freedom of reference and is termed the target displacement, δ_t, by

applying a succession of modification factors upon the elastic spectral response of an *equivalent* SDoF system, Equation (1):

$$\delta_t = C_0 \cdot C_1 \cdot C_2 \cdot C_3 \cdot S_a \cdot \frac{T^2}{4\pi^2} \tag{1}$$

S_a is the intensity measure chosen to represent elastic demand and forms the basis for design. It is derived from seismic hazard corresponding to the performance level considered; i.e., from design spectra. Thus $S_a \cdot \left(T^2/4\pi^2\right)$ represents elastic spectral displacement of the equivalent SDoF system having elastic period equal to T. Coefficients $C_i \left\{i = 0,1,2,3\right\}$ are intended to transform this elastic response to inelastic structural response in a modular manner.

C_0 converts the displacement of the equivalent SDoF system into that of the original multiple degree of freedom (MDoF) structure and is given by Equation (2), where [M] is the lumped mass matrix of the structure, {r} is a vector coupling foundation motion with degrees of freedom of the structure, and vector {φ} is the generalized displacement used for the SDoF approximation, normalized so that unit value corresponds to the degree of freedom the target displacement refers to (e.g., the roof displacement). C_0 is the modal participation factor when {φ} is an eigenvector of the system.

$$C_0 = \frac{\{\varphi\}^T [M] \{r\}}{\{\varphi\}^T [M] \{\varphi\}} \tag{2}$$

C_1 is termed the inelastic displacement ratio and is defined as the peak displacement response $S_{d,inel}$ of an inelastic SDoF system divided by the displacement of an indefinitely elastic SDoF oscillator with the same initial period, Equation (3).

$$C_1 = \frac{S_{d,inel}}{S_a \cdot \left(T^2/4\pi^2\right)} \tag{3}$$

In [8] it was recommended that C_1 be estimated from Equation (4), where the inelastic displacement ratio is given as a function of the period of vibration, strength reduction factor R and a site subsoil-dependent parameter α.

$$C_1 = 1 + \frac{(R-1)}{\alpha \cdot T^2} \tag{4}$$

The R factor appearing in Equation (4) is the reciprocal of structural yield strength normalized with respect to ground motion intensity and is given by Equation (5), where W is the weight of the structure, V_y is the base shear causing conventional yielding of the structure (to follow) and g is the acceleration of gravity. C_m is the percentage of total mass activated when the structure vibrates according to the displacement vector {φ}.

$$R = \frac{S_a/g}{V_y/W} \cdot C_m = \frac{S_a/g}{V_y/W} \cdot C_0 \cdot \frac{\{\varphi\}^T [M] \{r\}}{\{r\}^T [M] \{r\}} \tag{5}$$

C_2 is intended to account for the effect stiffness and/or strength degrading hysteretic behavior can have on maximum inelastic displacement.

Lastly, coefficient C_3 is intended to account for increased inelastic displacements in cases where second order (or P-Δ) effects become an important factor.

3.2 Inelastic displacement ratio of near-source pulse-like ground motions

In [12,13] and elsewhere, it was discussed that C_1 from Equation (4) is not explicitly representative of inelastic displacement ratios in the case of pulse-like ground motions in NS conditions. In [5], Equation (6) was proposed for the (constant-strength) inelastic displacement ratio C_R, based on a dataset of pulse-like FD ground motions identified as such in previous works [2,12]. Ordinary least squares estimators obtained for the parameters $\theta_i \{i = 1,2,3,4,5\}$ appearing in Equation (6) are reported in [5].

$$C_R = \frac{S_{d,inel}}{S_a \cdot \left(T^2/4\pi^2\right)} = 1 + \theta_1 \cdot \left(T_p/T\right)^2 \cdot \left(R-1\right) + \theta_{2\cdot} \cdot \left(T_p/T\right) \cdot \exp\left\{\theta_3 \cdot \left[\ln\left(T/T_p - 0.08\right)\right]^2\right\} + \\ + \theta_4 \cdot \left(T_p/T\right) \cdot \exp\left\{\theta_5 \cdot \left[\ln\left(T/T_p + 0.5 + 0.02 \cdot R\right)\right]^2\right\} \quad (6)$$

A graphical representation of Equation (6) is provided in Figure 1. The most important feature of this analytical model for C_R, is the use of normalized period T/T_p as a predictor variable in order to capture the spectral regions of amplification of inelastic response.

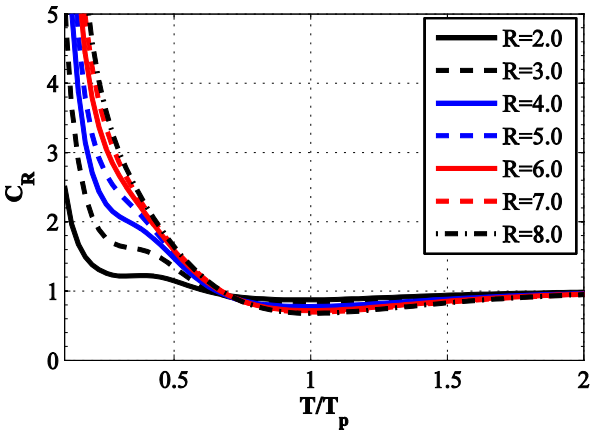


Figure 1: Model for the inelastic displacement ratio C_R of near-source pulse-like ground motions [5].

3.3 Other coefficients of displacement modification in NS conditions

The effect of cyclic structural degradation on peak inelastic displacement was investigated at the SDoF level in [13]. This effect would correspond to C_2 in the DCM. It was found that there is palpable increase in inelastic displacement for values of T/T_p less than 0.5, especially for cases of severe strength and stiffness degradation.[*] The present study deals with a code-conforming structure in the illustrative example given below, and the C_2 coefficient is constrained to unity in what follows.

In [14] it is reported that pulse-like ground motions may be more sensitive to phenomena of dynamic instability due to P-Δ effects than non-pulse-like ground motions. However, this issue being outside the scopes of the study, the C_3 coefficient is also taken as unity herein.

[*] In [13] it is also reported that such effects as there are, they tend to wane with increasing strength reduction factors. This is in contrast with the trend of the equation suggested in [8].

4 NEAR-SOURCE SEISMIC HAZARD AND INELASTIC DEMAND

4.1 Near-source probabilistic seismic hazard analysis

Near-source probabilistic seismic hazard analysis (NS-PSHA [3,4]) at present state computes the mean annual frequency (λ) of exceedance of an intensity measure value, spectral acceleration hereafter, as a linear combination of two hazard terms, one accounting for absence of pulse $\left(\lambda_{S_a,\text{no pulse}}\right)$ and one for pulse occurrence $\left(\lambda_{S_a,\text{pulse}}\right)$ as shown in Equation (7).

$$\lambda_{S_a}\left(s_a\right)=\lambda_{S_a,\text{no pulse}}\left(s_a\right)+\lambda_{S_a,\text{pulse}}\left(s_a\right) \tag{7}$$

In the NS case, the first term on the right-hand side of Equation (7) is calculated by implementing some modifications to classical PSHA [15] resulting in the integral shown in Equation (8a) for a single fault scenario. The contribution of pulse-like ground motions to hazard is expressed by the second right-hand term of Equation (7) which is given in Equation (8b).

$$\lambda_{S_a,\text{no pulse}}\left(s_a\right)=\nu\cdot\int_{m}\int_{\underline{z}}P\left[\text{nopulse}\,|\,m,\underline{z}\right]\cdot G_{S_a|M,\underline{Z}}\left(s_a\,|\,m,\underline{z}\right)\cdot f_{M,\underline{Z}}\left(m,\underline{z}\right)\cdot dm\cdot d\underline{z} \tag{8a}$$

$$\lambda_{S_a,\text{pulse}}\left(s_a\right)=$$
$$\nu\cdot\int_{m}\int_{z}\int_{t_p}P\left[\text{pulse}\,|\,m,\underline{z}\right]\cdot G_{S_a,\text{mod}|M,\underline{Z},T_p}\left(s_a\,|\,m,\underline{z},t_p\right)\cdot f_{T_p|M,\underline{Z}}\left(t_p\,|\,m,\underline{z}\right)\cdot f_{M,\underline{Z}}\left(m,\underline{z}\right)\cdot dm\cdot d\underline{z}\cdot dt_p \tag{8b}$$

In these equations ν is the annual rate of event occurrence on the source, and M is the moment magnitude (not to be confused with the mass matrix appearing in Section 3). A relationship between M and rupture dimensions is used in order to derive the joint probability density function, or PDF, $f_{M,\underline{Z}}$ [16]. In this case, source-site distance is only one of the variables included in the vector of rupture-site geometry parameters, $\underline{z}$, which is required in order to evaluate the probability of pulse occurrence, $P\left[\text{pulse}\,|\,m,\underline{z}\right]$ [17]. Additionally, G_{S_a} indicates a complementary cumulative distribution function (CCDF) defined by an ordinary ground motion prediction equation (GMPE), while $G_{S_a,\text{mod}}$ represents a GMPE suitably modified to account for NS-FD spectral shape [2][†]. The PDF $f_{T_p|M,\underline{Z}}$ is taken from an empirical model of T_p [12]. More details on NS-PSHA are in [4].

4.2 Hazard disaggregation and near-source inelastic demand

Once NS-PSHA calculations are completed, disaggregation of seismic hazard can be carried out for any s_a. This procedure provides the probability distribution of the covariates appearing in Equations (8a,b) conditional, for example, on exceedance of s_a [4]. In this case, the distribution of pulse period $f_{T_p|S_a(T)>s_a}$ (implicitly also conditional on pulse occurrence) is relevant in the implementation of the DCM in NS conditions, since pulse period T_p enters Equation (6) determining expected inelastic demand.

However, NS hazard includes contributions from pulse-like ground motions with infinite in number possible pulse periods. Therefore, one needs the probability density $f_{T_p|S_a(T)>s_a}$ in order to marginalize the expectation function of C_R according to Equation (9).

[†] In a recent paper [18], a modified GMPE was proposed for the non-impulsive case as well.

$$E\left[C_R \mid S_a(T) > s_a\right] = \int_{t_p} E\left[C_R \mid S_a(T) > s_a, T_P = x\right] \cdot f_{T_p \mid S_a(T) > s_a}(x) \cdot dx \tag{9}$$

Apart from the marginal PDFs of pulse period, one more useful result can be obtained from disaggregation of NS hazard, namely, the conditional probability of pulse occurrence given that $S_a > s_a$. This may be used to also estimate the NS inelastic demand $\delta_{t,NS}$, via the conditional expectation theorem, as an average of two separate contributions, target displacements given pulse occurrence $\delta_{t,pulse}$ and absence thereof $\delta_{t,no\ pulse}$. These two terms are weighted by their probability of occurrence conditional to the scenario of interest, Equation (10).

$$\delta_{t,NS} = \delta_{t,pulse} \cdot P\left[pulse \mid S_a > s_a\right] + \delta_{t,no\ pulse} \cdot \left(1 - P\left[pulse \mid S_a > s_a\right]\right) \tag{10}$$

A simpler alternative could be to assume the target displacement equal to the largest estimate between impulsive and non-impulsive inelastic demand. Note, however, that this may be conservative since, even in sites particularly prone to directivity effects, marginal pulse occurrence probability is hardly close to one [17].

5 ILLUSTRATIVE APPLICATION

5.1 Design scenario in NS conditions

For the purpose of the present study, a NS design scenario was considered, where the site to source configuration is prone to FD effects – intentionally so. This is illustrated in Figure 2(a), which shows a plan view of a 200 km long strike-slip fault and a site of interest perfectly aligned with the fault at a distance of 5 km off the tip.

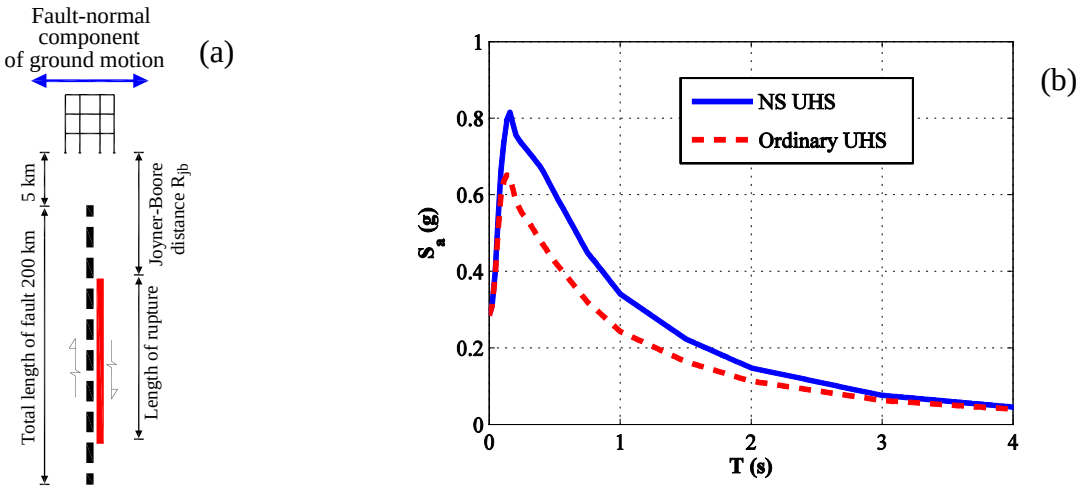


Figure 2: Schematic representation of design scenario (a) and UHS for a 2475 yr return period resulting from NS and ordinary PSHA (b).

Subsoil conditions at the site were taken to correspond to stiff soil deposits and an annual rate of event recurrence on the fault $\nu = 0.20$ was arbitrarily assumed, along with unit negative slope for the Gutenberg-Richter [19] relationship defined between M 4.5 and M 7.5. Seismic hazard was calculated through modified NS-PSHA (from Section 4) resulting in the 2475 yr uniform hazard spectrum (UHS) in Figure 2(b); in the figure the UHS derived by ordinary PSHA is also reported.

Given that in the following section a structure with a first-mode natural period of vibration T = 0.75s is considered, disaggregation of NS hazard was sought conditional on exceedance of s_a from the 2475 yr UHS at this period. The PDF of T_p thus obtained is shown in Figure 3.

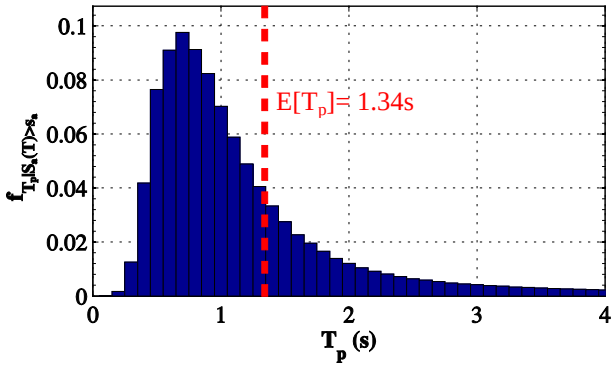


Figure 3: Probability density function resulting from NS hazard disaggregation conditional on pulse occurrence and $S_a(T) > s_a$, referring to 2745yr return period at the site, for T = 0.75s (histogram normalized to unit area).

5.2 Implementation of the displacement coefficient method in near-source conditions

For an illustrative application of the DCM in NS conditions, a specific structure was considered at the fictitious site described in the above section. The structure in question is a 5-storey bare (non-infilled) reinforced concrete (R/C) frame corresponding to the internal frames of a perfectly symmetric building (Figure 4). This frame was chosen to correspond to a first-mode period of natural vibration T_1 = 0.75s (in the direction normal to the fault's strike, Figure 2). Furthermore, structure geometry was selected so that this plane frame would exhibit first-mode dominated dynamic elastic response (first mode participation ratios in excess of 80%) and flexure-dominated inelastic response.

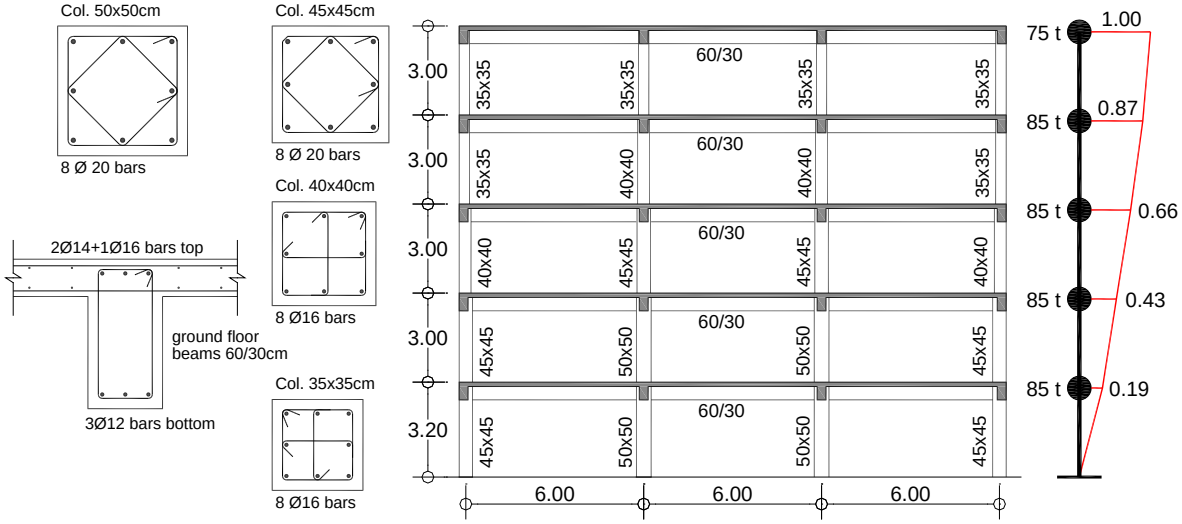


Figure 4: Summary of design details and MDoF model characteristics for a 5-storey plane R/C frame used in this study corresponding to a first mode period of vibration T = 0.75s.

The structure was designed according to modern codes [20,21] against gravity loads and seismic actions. The design spectrum was considered to be a site-specific UHS obtained by classical PSHA. More specifically, the frame was designed for inelastic response corresponding to a *behavior factor* ≈ 3.0 under the actions of a 475 yr return period (T_R) ordinary UHS.

Material qualities assumed for design were C20/25 for concrete and S500/550 for reinforcing steel [20]. A sample of the resulting detailing can also be seen in Figure 4.

Given that a modern-code-designed structure possessing significant reserves of over-strength is unlikely to exhibit inelastic response corresponding to a large strength reduction factor for a *life safety* performance level (T_R = 475 yr), the following example focuses on a *collapse prevention* performance level (T_R = 2475 yr).

First, a pushover (base shear – roof displacement) curve was obtained for the structure (shown in Figure 5 as gray dashed line). The non-linear structural model built for this inelastic static analysis, used lumped plasticity multi-linear moment-rotation envelopes and a smeared crack approach for modeling elastic stiffness of R/C members. Moment-rotation relationships for each member were estimated using mean strength and stiffness properties for confined concrete [22] and reinforcing steel. The bilinear approximations of the resulting relations used the *collapse prevention* limiting values recommended in [7] for ultimate rotation capacity.

The non-linear static analysis was carried out by applying a gradually increasing lateral deformation profile which remained unchanged throughout the analysis and corresponds to the structure's first mode eigenvector (shown in Figure 4).

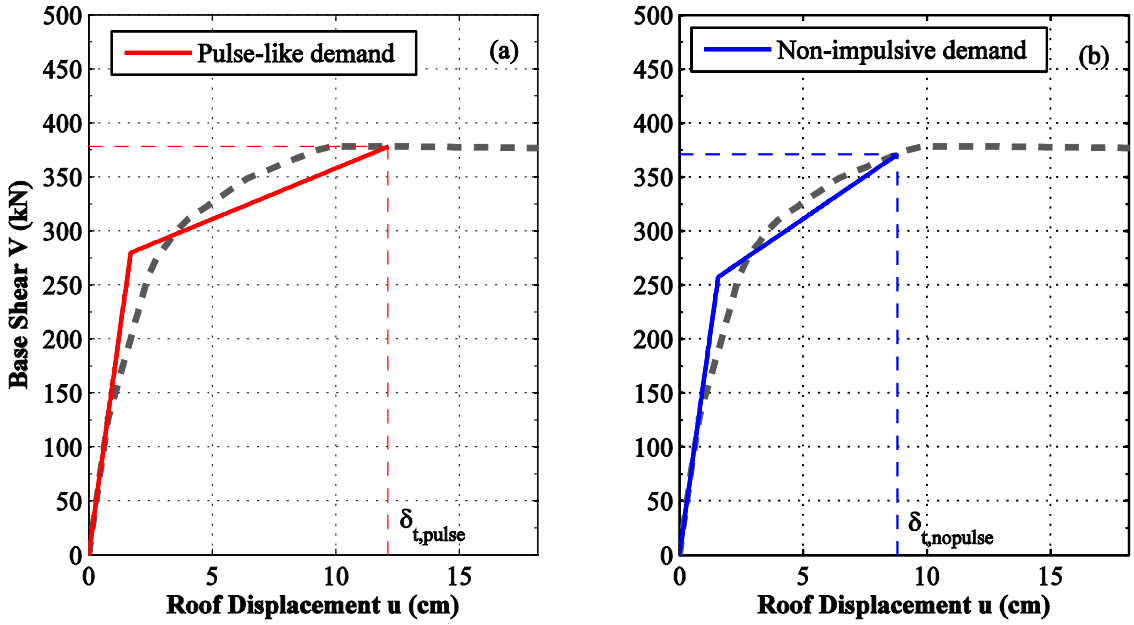


Figure 5: Graphical representation of application of the DCM static non-linear procedure for the 5-storey R/C frame considered. Target displacement estimates for the collapse prevention performance level considering impulsive (a) and non-impulsive contributions (b).

In estimating the right-hand-side of Equation (10), the non-impulsive contribution $\delta_{t,\text{no pulse}}$ was obtained by simple implementation of the DCM using Equation (4) for coefficient C_1, taking subsoil coefficient α to correspond to NEHRP class C [8]. The same process was repeated for the impulsive contribution $\delta_{t,\text{pulse}}$, with the difference that Equation (6) and Equation (9) have to be used to substitute coefficient C_1 with the inelastic displacement ratio C_R for FD ground motions.

In order to calculate these target displacements using the DCM, a bilinear approximation of the capacity (pushover) curve was constructed according to the methodology suggested in [7]. This method requires the bilinear approximation to intersect the pushover curve at δ_t thus resulting in some (usually) positive post-yield stiffness or hardening. This hardening behavior is

typically ignored when estimating C_1 via Equation (4); however, this matter will not be discussed here. Additionally, this bilinearization method implies that the point corresponding to conventional yield base shear V_y is dependent on target displacement δ_t, thus requiring some iterations before convergence to an R and corresponding δ_t value. A graphical representation (corresponding to the converged iteration) for each of the two contributions considered in Equation (10), is provided in Figure 5. Both operations described above use the NS UHS of Figure 2 to calculate elastic demand.

For reasons of comparison, an ordinary target displacement $\delta_{t,ord}$ was also evaluated using the classical DCM and the non-impulsive UHS (red dashed line in Figure 2b) for elastic demand. It is worth noting that $\delta_{t,no\ pulse}$ and $\delta_{t,ord}$ are both derived by following the same procedure applied to different estimates of elastic demand (NS and ordinary UHS respectively), which means that $\delta_{t,no\ pulse}$ would be the target displacement if NS conditions were only accounted for during hazard calculations.

To obtain the final estimate of target displacement $\delta_{t,NS}$ for the considered site, one also requires the pulse occurrence probability conditional to the hazard threshold, which is equal to 0.747. Thus from Equation (10), $\delta_{t,NS}$ is found to be equal to 113 mm, which is 85% more than $\delta_{t,ord}$. All numerical results are summarized in Table 1.

$\delta_{t,pulse}$ (mm)	$\delta_{t,no\ pulse}$ (mm)	$P\left[\text{pulse}\middle\vert S_a > s_a\right]$	$\delta_{t,NS}$ (mm)	$\delta_{t,ord}$ (mm)	$\frac{\delta_{t,NS}-\delta_{t,ord}}{\delta_{t,ord}}$
121	88	0.747	113	61	85%

Table 1: Summary of target displacement estimate resulting from DCM application. All values refer to collapse prevention limit state (i.e. T_R = 2475yr).

Instead of using entire probability densities obtained from disaggregation of seismic hazard, as in Equation (9), a first moment approximation may be obtained by using the average pulse period, $E[T_p]$, from Figure 3 as per Equation (11).

$$E\left[C_R \mid S_a(T) > s_a\right] \approx E\left[C_R \mid S_a\left(T\right) > s_a, T_P = E\left[T_P\right]\right] \tag{11}$$

In the present example, Equation (9) resulted in $E[C_R] = 1.47$ while the approximation of Equation (11) would give $E[C_R] \approx 1.33$, resulting in an estimated inelastic displacement, due to impulsive ground motions, of 109 mm – compare that with 121 mm in Table 1.

6 CONCLUSIONS

The study dealt with implementing static non-linear procedures in order to estimate inelastic structural demand in near-source conditions. First, a brief overview of the original procedure for estimating target displacement using the DCM was given. Subsequently, the modifications required in order to account for NS conditions were discussed, both in terms of elastic (i.e., seismic hazard) and inelastic displacement demand. Then, a procedure for the implementation of the DCM in a NS context was outlined, considering a single-fault NS design scenario and finally, an illustrative example was provided.

The structure considered in the example was a code-conforming R/C frame designed against seismic demand corresponding to ordinary site-specific hazard. The site was intentionally assumed to have a disadvantageous location with respect to expected directivity ef-

fects. After computing UHS from ordinary- and NS-PSHA, a non-linear static analysis of the frame was carried out and the capacity curve obtained was used to derive a bilinear SDoF approximation of the structure. Furthermore, NS hazard disaggregation was calculated conditional on $S_a(T) > s_a$ at the period corresponding to the SDoF approximation and for a return period of 2475 yr. The resulting PDF of pulse period was combined with a predictive model for inelastic SDoF response to pulse-like ground motions in order to estimate NS displacement demand.

It was shown that, in the case examined, NS inelastic structural demand can considerably exceed demand as computed without accounting for FD in non-linear static analysis procedures.

ACKNOWLEDGMENTS

The study presented in this paper was developed within the activities of Rete dei Laboratori Universitari di Ingegneria Sismica (ReLUIS) for the research program funded by the Dipartimento della Protezione Civile (2010-2013).

REFERENCES

[1] P.G. Somerville, N.F. Smith, R.W. Graves, N.A. Abrahamson, Modification of empirical strong ground motion attenuation relations to include the amplitude and duration effects of rupture directivity. *Seismological Research Letters*, **68**, 199-222, 1997.

[2] J.W. Baker, Identification of near-fault velocity and prediction of resulting response spectra. *Proceedings of Geotechnical Earthquake Engineering and Structural Dynamics IV*, Sacramento, CA, 2008.

[3] P. Tothong, C.A. Cornell, J.W. Baker, Explicit directivity-pulse inclusion in probabilistic seismic hazard analysis. *Earthquake Spectra,* **23**, 867-891, 2007.

[4] E. Chioccarelli, I. Iervolino, Near-source seismic hazard and design scenarios. *Earthquake Engineering & Structural Dynamic*s, **42**, 603-622, 2013.

[5] I. Iervolino, E. Chioccarelli, G. Baltzopoulos, Inelastic Displacement Ratio of Near-Source Pulse-like Ground Motions. *Earthquake Engineering & Structural Dynamics,* **41**, 2351-2357, 2012.

[6] BSSC, *NEHRP guidelines for the seismic rehabilitation of buildings,* FEMA-273, developed by ATC for FEMA, Washington, D.C., 1997.

[7] ASCE, *Prestandard and Commentary for the Seismic Rehabilitation of Buildings*, FEMA-356, developed by ASCE for FEMA, Washington, D.C., 2000.

[8] FEMA, Improvement of nonlinear static seismic analysis procedures, FEMA-440 prepared by ATC, Washington, D.C., 2005.

[9] P. Fajfar, Capacity Spectrum Method Based on Inelastic Demand Spectra. *Earthquake Engineering and Structural Dynamics*, **28**, 979-993, 1999.

[10] T. Vidic, P. Fajfar, M. Fischinger, Consistent Inelastic Design Spectra: Strength and Displacement. *Earthquake Engineering & Structural Dynamics*, **23,** 507-521, 1994.

[11] J. Ruiz-García, E. Miranda, Inelastic displacement ratios for evaluation of existing Structures. *Earthquake Engineering and Structural Dynamics,* **32**(9), 1237-1258, 2003.

[12] E. Chioccarelli, I. Iervolino, Near-source seismic demand and pulse-like records: A discussion for L'Aquila earthquake. *Earthquake Engineering and Structural Dynamics*, **39**, 1039-1062, 2010.

[13] J. Ruiz-García, Inelastic Displacement Ratios for Seismic Assessment of Structures Subjected to Forward-Directivity Near-Fault Ground Motions. *Journal of Earthquake Engineering*, **15**(3), 449-468, 2011.

[14] B. Alavi, H. Krawinkler, Behavior of moment-resisting frame structures subjected to near-fault ground motions. *Earthquake Engineering and Structural Dynamics*, **33**(6), 687–706, 2004.

[15] L. Reiter, *Earthquake hazard analysis, issues and insights*. NY: Columbia University Press, 1990.

[16] D.L. Wells, K.J. Coppersmith, New empirical relationships among magnitude, rupture length, rupture width, rupture area, and surface displacement. *Bulletin of the Seismological Society of America*, **87**(4), 974-1002, 1994.

[17] I. Iervolino, C.A. Cornell, Probability of occurrence of velocity pulses in near-source ground motions. *Bulletin of the Seismological Society of America*, **98**(5), 2262–2277, 2008.

[18] S. Shahi, and J.W. Baker, An empirically calibrated framework for including the effects of near-fault directivity in probabilistic seismic hazard analysis. *Bulletin of the Seismological Society of America*, **101**(2), 742-755, 2011.

[19] B. Gutenberg, C.F. Richter, Frequency of Earthquakes in California. *Bulletin of the Seismological Society of America*; **34**, 185-188, 1944.

[20] CEN, *EN 1992-1-1 Design of concrete structures. General rules and rules for buildings*, European Committee for Standardization, Brussels, 2004.

[21] CEN, *EN 1998-1 Design of structures for earthquake resistance – Part 1: General rules seismic actions and rules for buildings*, European Committee for Standardization, Brussels, 2004.

[22] J.B. Mander, M.J.N. Priestley, R. Park, Theoretical Stress-Strain Model for Confined Concrete. *Journal of Structural Engineering*, **114**(8), 1804-1826, 1988.

COMPDYN 2013
4th ECCOMAS Thematic Conference on
Computational Methods in Structural Dynamics and Earthquake Engineering
M. Papadrakakis, V. Papadopoulos, V. Plevris (eds.)
Kos Island, Greece, 12–14 June 2013

COLLAPSE CAPACITY SPECTRA BASED ON AN IMPROVED INTENSITY MEASURE

S. Tsantaki[1], and C. Adam[1]

[1] Unit of Applied Mechanics, University of Innsbruck
Technikerstr. 13, 6020 Innsbruck, Austria
{styliani.tsantaki, christoph.adam}@uibk.ac.at

Keywords: Averaged Spectral Acceleration, Collapse Capacity, Earthquake Excitation, Improved Intensity Measure, P-Delta Effect, Reduced Dispersion.

Abstract. *A collapse capacity spectrum represents the seismic collapse capacity of highly inelastic non-degrading single-degree-of-freedom systems vulnerable to the destabilizing effect as a function of characteristic structural parameters. In this paper collapse capacity spectra with reduced dispersion due to record-to-record uncertainties are presented. This reduction is achieved utilizing an improved intensity measure, based on the spectral acceleration averaged in a certain period band between the structural period and an elongated period. It is shown that the "optimal" elongated period, which is related to the smallest achievable dispersion, depends primarily on the structural period. Based on extensive parametric studies, an analytical expression for the optimal ratio between elongated and structural period is derived. This analytical period ratio is constant for systems with a period larger than 0.15 s. In several examples the superiority of the presented collapse capacity spectra with respect to the related dispersion is shown and quantified.*

1 INTRODUCTION

The dispersion of the seismic response due to record-to-record (RTR) uncertainties depends on various factors such as the considered set of earthquake ground motions, the type of structure (regularity, etc.), the considered response quantity, and the choice of the intensity measure (IM).

In this paper the latter issue is addressed when predicting the collapse capacity of highly inelastic single-degree-of-freedom (SDOF) systems vulnerable to second-order effects of gravity. The considered systems exhibit a negative post-yield stiffness, however, material degradation is assumed to be negligible. Fundamental studies of the P-delta effect on inelastic SDOF systems subjected to strong motion earthquakes have been presented e.g. in [1, 2]. Recently, in the research group of the authors of the subsequently presented study the collapse capacity of P-delta sensitive SDOF systems has been assessed qualitatively and quantitatively for a set of characteristic parameters [3, 4]. The presentation of the collapse capacity and its dispersion has been referred to as collapse capacity spectra, providing a compact and easily applicable tool for the practicing engineer [3]. In [3, 4] the 5% damped spectral pseudo-acceleration at the structural period serves as IM. In [5] the effect of other "standard" IMs on the collapse capacity has been investigated. However, the so far applied IMs result in a quite large dispersion of the collapse capacity.

In this study, the influence of a recently proposed IM [6] on the RTR randomness of collapse capacity spectra is investigated by conducting extensive parametric Incremental Dynamic Analyses (IDAs) [7]. Following an idea of [6] the geometric mean of pseudo-spectral acceleration ordinates over a certain range of periods is employed as IM, taking into consideration the period elongation of inelastic SDOF systems. A slightly modified version of this IM is applied, at which the structure's period serves as the lower limit of this period range. In [8] it has been shown that for the considered systems the "optimal" period range, i.e. the period range leading to the smallest dispersion, depends highly on the structure's period. Thus, the optimal period range is identified as a function of the structure's period. In [9] collapse fragility curves are presented, and compared with outcomes of the corresponding benchmark study [3] on the same systems, based on the 5% damped spectral pseudo-acceleration at the structural period as IM. As a main outcome of the presented investigation an analytical formulation of the "optimal" elongated period is derived, which is a function of the structural period only. Simultaneously, the dependence of the RTR variability on the viscous damping coefficient is investigated.

2 DEFINITIONS AND FRAMEWORK

2.1 P-delta effect on an inelastic SDOF System

In an inelastic SDOF system the gravity load generates a shear deformation of its hysteretic force-displacement relationship. Characteristic displacements (such as the yield displacement) of this relationship remain unchanged, whereas the characteristic forces (such as the strength) are reduced. As a result, the slope of the curve is decreased in its elastic and post-elastic branch of deformation. The magnitude of this reduction can be expressed by means of the so-called stability coefficient θ [2]. θ is a function of the gravity load, geometry, and stiffness. Figure 1 visualizes the P-delta effect on the non-dimensional hysteretic behavior of a SDOF system with non-deteriorating bilinear characteristics. In this example, the post-yield stiffness is negative, because the stability coefficient θ is larger than the hardening ratio α.

A negative slope of the post-yield stiffness, expressed by the difference of the stability coefficient θ and the strength hardening coefficient α, $\theta - \alpha$, is the essential condition that the

structure may collapse under severe earthquake excitation. In [3] it is shown that collapse of inelastic SDOF systems vulnerable to P-delta is mainly governed by the following parameters:

- The negative slope of the post-yield stiffness expressed by $\theta - \alpha$,
- the elastic structural period of vibration T_1,
- the viscous damping coefficient ζ (usually 5%), and
- the shape of the hysteretic loop.

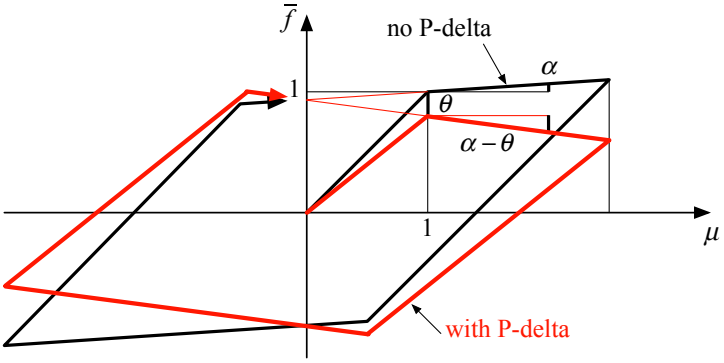


Figure 1: Normalized bilinear cyclic behavior with and without destabilizing effect of gravity loads [3].

2.2 Utilized intensity measure

In the present study, a slightly modified form of the IM defined in [6] is employed, which is based on the geometric mean of the 5% damped spectral pseudo-acceleration over the period range ΔT,

$$\Delta T = T_n - T_1, \quad T_n > T_1 \tag{1}$$

between the structural period T_1 and an elongated period T_n of T_1 (note that T_n is not the nth structural period). At equally spaced discrete periods T_i within of ΔT,

$$T_i = T_1 + (i-1)\delta T, \quad i = 1,...,n \quad , \quad \delta T = \frac{\Delta T}{n-1} = \frac{T_n - T_1}{n-1} \tag{2}$$

the corresponding discrete spectral pseudo-accelerations $S_a(T_i)$ ($i = 1,...,n$) are combined according to [6]

$$S_{a,gm}(T_1, T_n) = \left(\prod_{i=1}^{n} S_a(T_i) \right)^{1/n} \tag{3}$$

An appropriate IM should comply with the following properties [6]:

- Hazard compatibility, i.e. the IM quantifies appropriately the ground motion hazard at the site
- Efficiency, which is defined as the dispersion of the IM values associated with a given response quantity level
- Sufficiency, i.e. the IM is conditionally statistically independent of ground motion characteristics such as magnitude, distance, epsilon, etc.
- Scaling robustness

In [6] it is shown that $S_{a,gm}(T_1,T_n)$ is statistically independent from ground motion characteristics and scaling factors, and thus, it complies with the IM properties sufficiency and scaling robustness.

In the following considerations the accelerated efficiency of the IM $S_{a,gm}(T_1,T_n)$ with respect to the reduction of collapse capacity dispersion of P-delta sensitive SDOF systems due to the RTR variability is investigated, compared to the efficiency of the conventional IM $S_a(T_1)$ (spectral pseudo-acceleration at the period of the structure).

2.3 Ground motion scaling

In this study, RTR uncertainties are captured employing the 44 far-field ground motions of the ATC63-FF record set described in FEMA P-695 [10]. The records of the ATC63-FF set originate from severe seismic events of magnitude between 6.5 and 7.6 and closest distance to the fault rupture larger than 10 km. Thereby, only strike-slip and reverse sources are considered. The 44 records of this set were recorded on NEHRP site classes C (soft rock) and D (stiff soil). For further details see [10].

To obtain comparable results, the ground motion records must be scaled. When using Equation 3 as IM, scaling of the original *j*th ground acceleration $\ddot{x}_{g,unscaled}^{(j)}$ must be performed over the period range ΔT according to

$$\ddot{x}_{g,scaled}^{(j)} = \frac{S_{a,gm}^{ref}(T_1,T_n)}{S_{a,gm}^{(j)}(T_1,T_n)} \ddot{x}_{g,unscaled}^{(j)} \tag{4}$$

to account for the spectral shape within ΔT. Thereby, $S_{a,gm}^{ref}(T_1,T_n)$ is the target mean spectral acceleration, which is the same for all ground motions of the considered record set.

2.4 Collapse capacity

The collapse capacity is defined as the maximum ground motion intensity at which the structure still maintains dynamic stability [11]. Most generally, the IDA procedure is applied to predict the collapse capacity. In an IDA for a given structure and a given acceleration time history of an earthquake record dynamic time history analyses are performed repeatedly, at which in each subsequent run the intensity of the ground motion is incremented [7]. As an outcome a characteristic IM is plotted against the corresponding maximum characteristic structural response quantity for each analysis. The procedure is stopped, when the response grows to infinity, i.e. structural failure occurs. The corresponding IM is referred to as collapse capacity of the considered structure for this specific ground motion record (subsequently denoted by *j*). In this study, the relative collapse capacity related to the *j*th ground motion record corresponds to the suggested IM $S_{a,gm}^{(j)}(T_1,T_n)$ at collapse divided by the gravity and base shear coefficient γ,

$$CC_j\Big|_{S_{a,gm}} = \frac{S_{a,gm}^{(j)}(T_1,T_n)\Big|_{collapse}}{g\gamma} \quad , \quad \gamma = \frac{f_y}{mg} \tag{5}$$

f_y is the yield strength, m the mass of the SDOF system, and g denotes the gravity. Since the inherent RTR variability leads to different collapse capacities for different ground motion records, the collapse capacities are determined for all records of a ground motion set, and subsequently evaluated statistically. In [12, 13] good arguments are provided for representing a set of corresponding collapse capacities by a log-normal distribution. A log-normal distribu-

tion is characterized by the median of the individual collapse capacities CC_i (referred to as CC), and the 16th and 84th percentiles of the collapse capacities denoted as CC_{16} and CC_{84}, respectively. In the following, the dispersion quantity s^* [3]

$$s^* = \ln\sqrt{s_u s_l} \;\;,\;\; s_u = \frac{CC_{84}}{CC} \;\;,\;\; s_l = \frac{CC}{CC_{16}} \tag{6}$$

is utilized as a representative measure of the RTR variability of the individual collapse capacities. Note that in the log-domain s^* corresponds to the standard deviation, $\sigma \approx s^*$ [14].

2.5 Collapse capacity spectrum

In a collapse capacity spectrum the representative collapse capacity of a P-delta sensitive and non-deteriorating SDOF system with given negative post-yield stiffness ratio $\theta - \alpha$, viscous damping ζ, and hysteretic loop is presented as a function of the structural period T_1 [3]. As an example, Figure 2 shows 5% damped median collapse capacity spectra in the period range from $T_1 = 0.1$ to $T_1 = 5$ s based on the conventional IM $S_a(T_1)$ for bilinear SDOF systems with various negative post-yield stiffness ratios $\theta - \alpha$. These spectra are based on the 44 records of the ATC63-FF ground motion set [3].

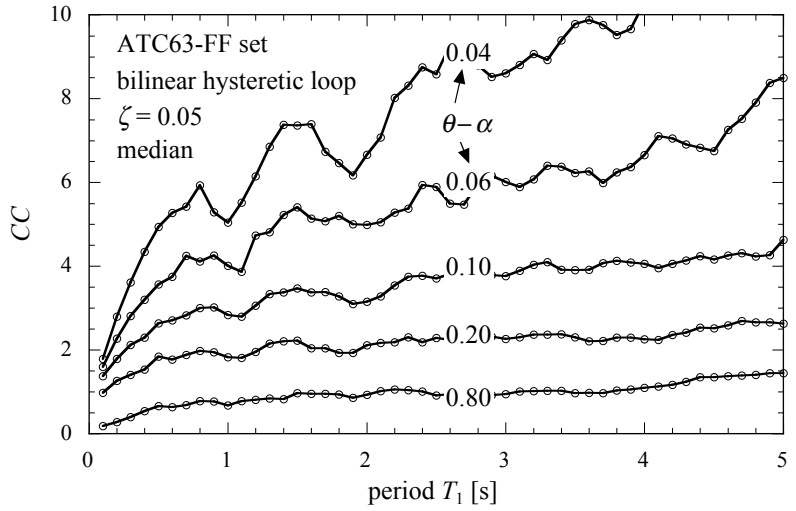


Figure 2: Median collapse capacity spectra CC based on the conventional IM $S_a(T_1)$ [3].

3 DISPERSION OF THE COLLAPSE CAPACITY

3.1 Record-to-record variability for various intensity measures

Subsequently, the effect of the proposed IM $S_{a,gm}(T_1,T_n)$ on the dispersion parameter s^* of the collapse capacity, Equation 5, is investigated. In particular it is of interest to reveal the impact of the period band ΔT on s^* in dependence of the characteristic structural parameters specified in Section 2.1. As reference solution serve the outcomes based on the conventional IM, i.e. the 5% damped spectral acceleration $S_a(T_1)$ at the initial structural period T_1 [3]. All subsequent studies are based on bilinear cyclic behavior of the SDOF system. Viscous damping ζ is set to 5%, unless otherwise indicated.

In an initial study SDOF systems exhibiting a negative post-yield stiffness ratio of $\theta - \alpha = 0.20$ and structural periods T_1 in the range between 0 and 5.0 s are considered. For each structural configuration (T_1) the collapse capacity is determined for all records of the

ATC63-FF ground motion set by IDA, and parameter s^* is evaluated. This analysis is conducted for period bands ΔT = 0.4 s, 0.6 s, 0.8 s, 1.0 s, 1.2 s, and 1.4 s.

A graphical representation of the derived dispersion parameter s^* with respect to the structural period T_1 is shown in Figure 3 [9]. The solid line in red corresponds to s^* of the original base case study [3] using the conventional IM $S_a(T_1)$. Black lines provided with different markers represent outcomes utilizing the proposed IM according to Equation 3 for various period ranges ΔT, as specified in the figure. For very stiffness systems up to period of T_1 = 0.22 s the conventional IM renders the smallest dispersion. As discussed in [4], a rigid system (T_1 = 0) does not exhibit any aleatory uncertainty, i.e. s^* = 0, when using the spectral acceleration at T_1 as IM. However, this IM leads to the largest dispersion for moderately stiff and flexible systems with T_1 > 0.8 s. If the structural period T_1 becomes larger, the accelerated efficiency of the proposed IM in reducing the dispersion s^* becomes obvious. While for systems with initial periods between 0.22 and 0.9 s the period band ΔT = 0.4 s for averaging the spectral acceleration leads to the smallest dispersion, for more flexible systems with T_1 > 1.58 s the period band ΔT = 1.4 s gives the smallest dispersion. However, the difference between the outcomes based on ΔT = 1.2 s and ΔT = 1.4 s is negligible. It is interesting to note that for this particular structural configuration efficiency of the proposed IM is largest for systems with periods T_1 between 2.6 s and 3.0 s. Here, the reduction of s^* is more than 50%, compared to the outcome using the conventional IM. For larger periods the ability of IM $S_{a,gm}(T_1,T_n)$ to decrease s^* becomes lower, because acceleration response spectra become almost horizontal for such flexible systems.

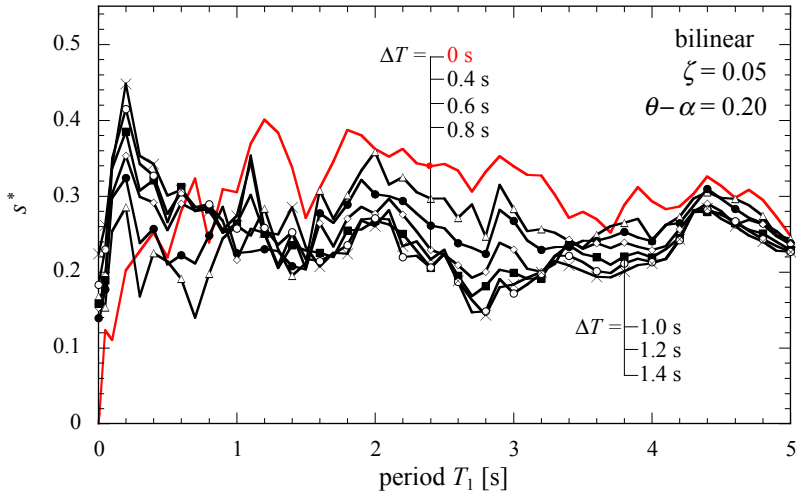


Figure 3: Dispersion parameter s^* of the collapse capacity as a function of the structural period T_1 for different period ranges ΔT. Discrete negative post-yield stiffness ratio $\theta-\alpha$ = 0.20.

In order to reveal a general trend of the effect of the proposed IM on the dispersion parameter s^* in a further step the study is extended considering a series of negative post-yield stiffness ratios $\theta-\alpha$. In particular, the following discrete values of $\theta-\alpha$ are assigned to the SDOF systems: $\theta-\alpha$ = 0.04, 0.06, 0.08, 0.10, 0.20, 0.30, 0.40, 0.50, 0.60, 0.80. Additionally, period bands ΔT of 1.8 s, 2.4 s, 3.0 s, and 4.0 s are taken into account. Then, from the individual outcomes of s^* mean values with respect to the negative post-yield stiffness ratio $\theta-\alpha$ and to the period T_1, respectively, are determined.

Figure 4 shows the mean of s^*, derived from all individual outcomes comprising the entire set of parameter $\theta-\alpha$, for each IM separately as a function of the structural period. The solid

line in red corresponds to the mean of s^* based on the conventional IM $S_a(T_1)$, whereas lines in black and blue represent the mean dispersion parameter for different period bands ΔT of the proposed IM. The results of this figure confirm in a large extent the findings of Figure 3. Except for very stiffness structures, the conventional IM leads to a mean dispersion s^* of the collapse capacity of about 0.4, while the dispersion s^* with the underlying proposed IM exhibits an average minimum of about 0.25, considering only the most efficient period band ΔT at different periods T_1. From the results of this figure it can be concluded that there is no "optimal" IM for the entire range of structural periods, because the "optimal" period band ΔT is a function of T_1. I.e., the larger T_1 becomes, the larger is the required ΔT to render the minimum achievable dispersion parameter s^*. The relation between T_1 and the "optimal" period band ΔT will later be studied in more detail.

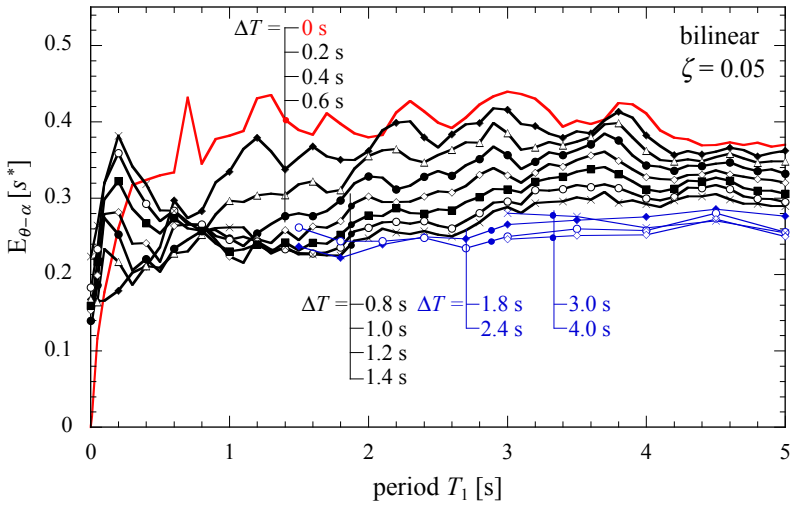


Figure 4: Mean values of the dispersion parameter s^* with respect to the considered discrete post-yield stiffness ratios $\theta-\alpha$ as a function of the structural period T_1 for various period ranges ΔT.

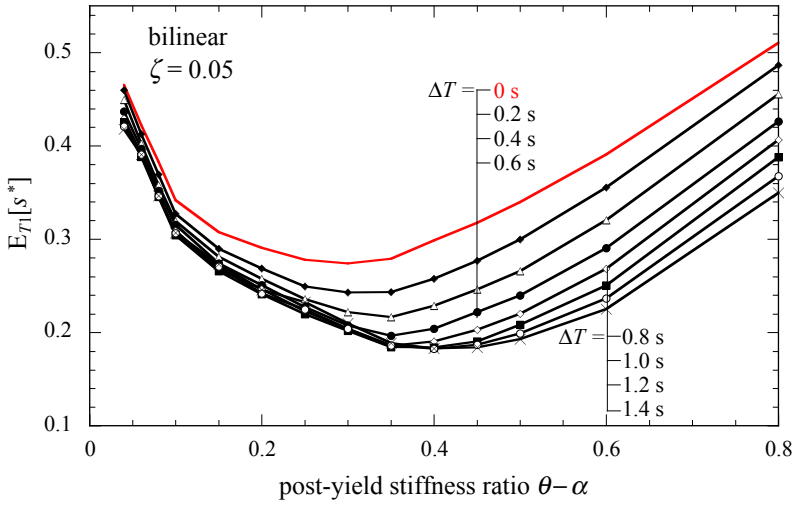


Figure 5: Mean values of the dispersion parameter s^* with respect to the structural period range $0 \le T_1 \le 5$ s as a function of the post-yield stiffness ratio $\theta-\alpha$ for various period ranges ΔT.

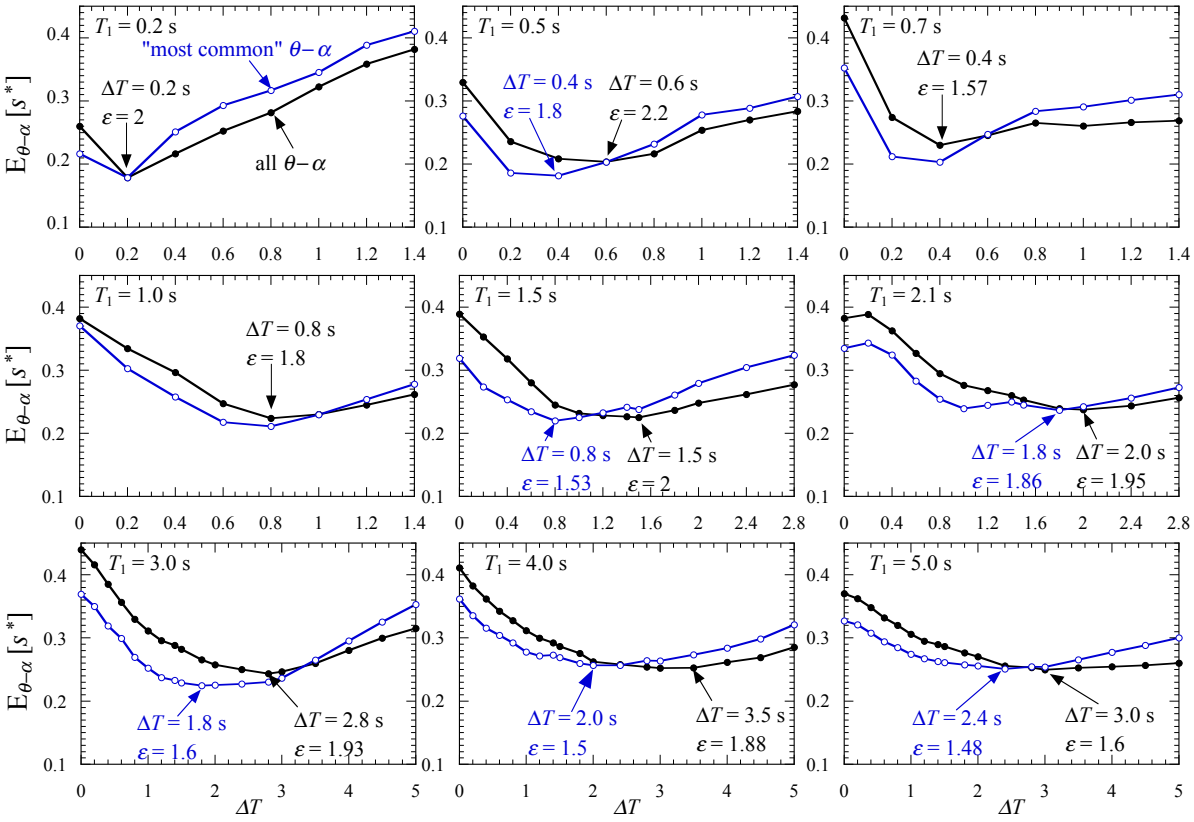


Figure 6: Mean values of the dispersion parameter s^* with respect to the post-yield stiffness ratios $\theta-\alpha$ as a function of period range ΔT for nine discrete structural periods T_1. Black graphs: mean from all considered discrete values of $\theta-\alpha$. Blue graphs: mean from discrete values of $\theta-\alpha$ in the range of $0.08 \le \theta-\alpha \le 0.40$.

However next, the overall trend of the dispersion parameter s^* with respect to the negative post-yield stiffness ratio $\theta-\alpha$ is discussed for IMs with different ΔT ($0 \le \Delta T \le 1.4$ s). Figure 5 displays mean values of s^* with respect to the structural period T_1 (in the range between 0 and 5.0 s equally spaced with increments of 0.1 s) as a function of the negative post-yield stiffness ratio $\theta-\alpha$. In this representation, the conventional IM leads to the poorest performance in the entire range of $\theta-\alpha$. Thereby, the minimum mean dispersion s^* of 0.275 exhibits the systems with a negative post-yield stiffness ratio of 0.30. With increasing period band ΔT the achievable minimum of mean s^* is reduced up to 0.18, and the minimum is shift to $\theta-\alpha$ = 0.40 (for ΔT = 1.4 s). It is readily observed that for small $\theta-\alpha$ ($\theta-\alpha$ < 0.10) the reduction of mean s^* (based on IM $S_{a,gm}(T_1,T_n)$) is quite small compared to the corresponding outcomes for the conventional IM $S_a(T_1)$.

Figure 6 shows for nine discrete structural periods (T_1 = 0.2 s, 0.5 s, 0.7 s, 1.0 s, 1.5 s, 2.1 s, 3.0 s, 4.0 s, 5.0 s, respectively) the mean dispersion parameter s^* (with respect to $\theta-\alpha$) plotted against period band ΔT of the underlying proposed IM $S_{a,gm}(T_1,T_n)$. Thereby, on the one hand the mean of s^* is determined comprising the complete set of considered post-yield stiffness ratios $\theta-\alpha$. The corresponding results are depicted in black. On the other hand, only the collapse capacities of $\theta-\alpha$ in the range of $0.08 \le \theta-\alpha \le 0.40$ (referred to as "most common $\theta-\alpha$) are used to calculate the mean dispersion parameter s^*. Blue graphs represent these outcomes. In this set of $\theta-\alpha$ extreme values are excluded, which might distort the general trend of the response behavior. Exemplarily, Figure 7 shows for a system with T_1 = 1.5 s parameter s^* both for discrete $\theta-\alpha$ values and the proposed mean values. It can be readily observed that the trend of the dispersion for systems with an extremely large ratio of

$\theta-\alpha = 0.80$ is very different from the other depicted cases. The results of Figure 6 confirm that the "optimal" period band ΔT strongly depends on the structural period T_1. As already observed in Figure 4, the optimal value of ΔT becomes larger with increasing T_1. In all subplots period band ΔT leading to the minimum mean dispersion is specified. For example, for T_1 = 1.0 s the minimum mean dispersion is 0.21 (all $\theta-\alpha$), compared to 0.38 for the conventional IM (i.e. $\Delta T = 0$). For the minimum mean s^* the corresponding ΔT is about 0.8 s. It is interesting to note that the ratio ε between the elongated period T_n and initial structural T_1,

$$\varepsilon = \frac{T_n}{T_1} \tag{7}$$

lies for "optimal" ΔT in the range between 1.4 and 2.0.

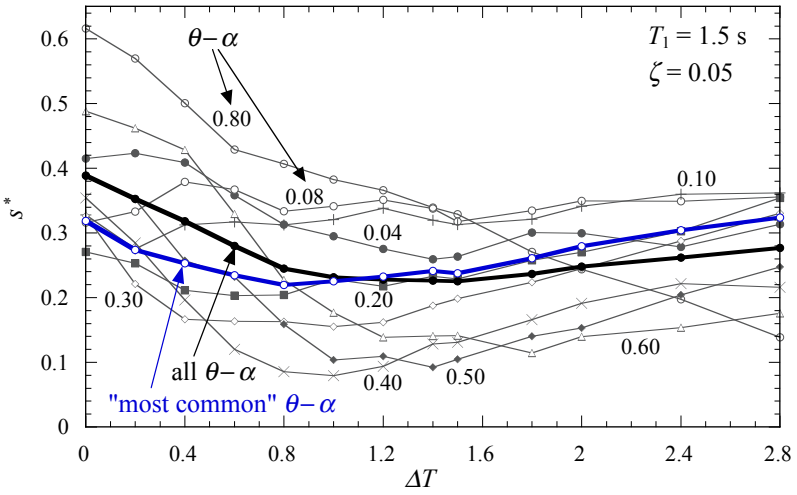


Figure 7: Dispersion parameter s^* for various post-yield stiffness ratios $\theta-\alpha$ as a function of period range ΔT. Structural periods $T_1 = 1.5$ s. Black graph: mean from all considered discrete values of $\theta-\alpha$. Blue graph: mean from discrete values of $\theta-\alpha$ in the range of $0.08 \le \theta-\alpha \le 0.40$.

3.2 "Optimal" intensity measure

Based on the observation of the results presented in Figure 6, in the subsequent section an attempt is made to derive a simple analytical expression for an "optimal" IM $S_{a,gm}(T_1,T_n)$, which leads globally to the smallest dispersion of the collapse capacities. Starting point is the consideration the "optimal" (i.e. the minimum) dispersion parameter s^* for IM $S_{a,gm}(T_1,T_n)$, identified from extensive parametric IDA studies. In Figure 8 the mean of this quantity with respect to the considered negative post-yield stiffness parameters $\theta-\alpha$ is shown in solid lines as a function of the structural period T_1. Additionally to 5% damped SDOF systems also the outcomes for undamped and 2% damped systems are displayed. It is readily observed that the minimum of mean s^* is in average about 0.24 in almost the entire period range T_1. This value remains the same considering the complete set of $\theta-\alpha$ and, alternatively, the set including the "most common" $\theta-\alpha$. Additionally, dashed lines represent the mean dispersion of the collapse capacities based on the conventional IM $S_a(T_1)$. Here, the mean s^* is in average about 0.4, which proofs the superiority of the proposed IM $S_{a,gm}(T_1,T_n)$ in reducing the RTR uncertainty. Furthermore, the results of Figure 8 show that the dispersion is globally unaffected from the amount of viscous damping, independent from the underlying IM.

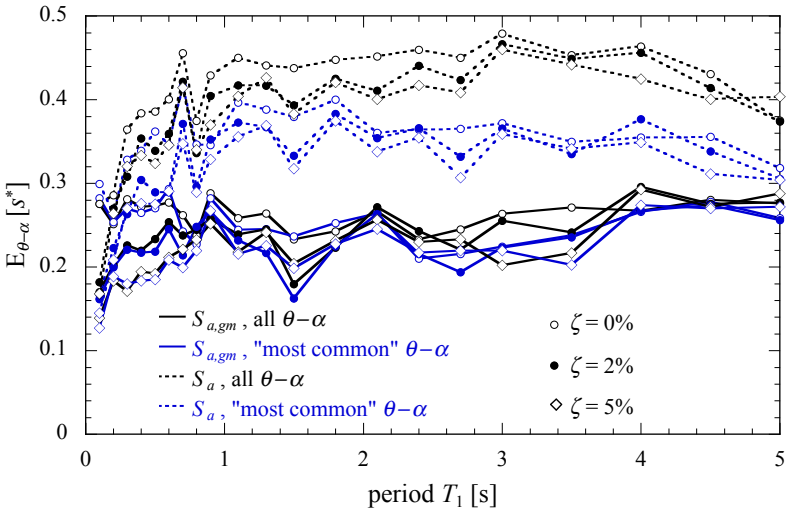


Figure 8: Mean with respect to the considered set of negative post-yield stiffness ratios $\theta-\alpha$ of the dispersion parameter s^* as a function of T_1. Dispersion based on the conventional IM $S_a(T_1)$, and smallest obtained dispersion parameter based on the proposed IM $S_{a,gm}(T_1,T_n)$. Results for viscous damping of 0%, 2%, and 5%.

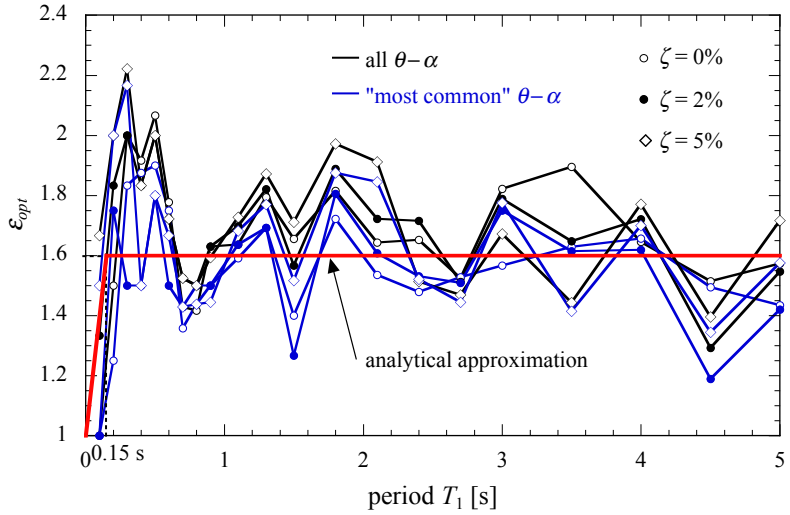


Figure 9: Ratio ε_{opt} between the "optimal" elongated period T_n and the initial structural period T_1 leading to the minimum mean dispersion s^* as a function of T_1. Results for viscous damping of 0%, 2%, and 5%.

Figure 9 shows the ratios (according Equation 7) between the "optimal" elongated period $T_{n,opt}$ and the initial period T_1,

$$\varepsilon_{opt} = \frac{T_{n,opt}}{T_1} \tag{8}$$

as a function of T_1. Thereby, the "optimal" elongated period $T_{n,opt}$ corresponds to the minimum of the mean dispersion s^* displayed in Figure 8. It is readily observed that for rigid systems this ratio is 1, because for this structure type the dispersion is 0 when using the conventional IM $S_a(T_1)$, as already discussed before [4]. Then follows a sharp rise of ε_{opt} up to 2.2. For periods $T_1 > 0.8$ s ε_{opt} fluctuates around a mean value of 1.6.

Based on this observation, the following analytical approximation for ε_{opt},

$$\varepsilon_a(T_1) = \begin{cases} 4T_1 + 1 & 0 \le T_1 \le 0.15\,\text{s} \\ 1.6 & T \ge 0.15\,\text{s} \end{cases} \tag{9}$$

is proposed in an effort to provide for a simple but reliable "optimal" IM $S_{a,gm}(T_1, T_n)$. This simple expression is independent of viscous damping parameter $0 \le \zeta \le 0.05$, and negative post-yield stiffness ratio $\theta - \alpha$. Thus, the recommended elongated period for the proposed IM is determined according to

$$T_{n,a} = \varepsilon_a T_1 \tag{10}$$

Consequently, the corresponding IM $S_{a,gm}(T_1, T_{n,a})$ is subsequently referred to "recommended IM".

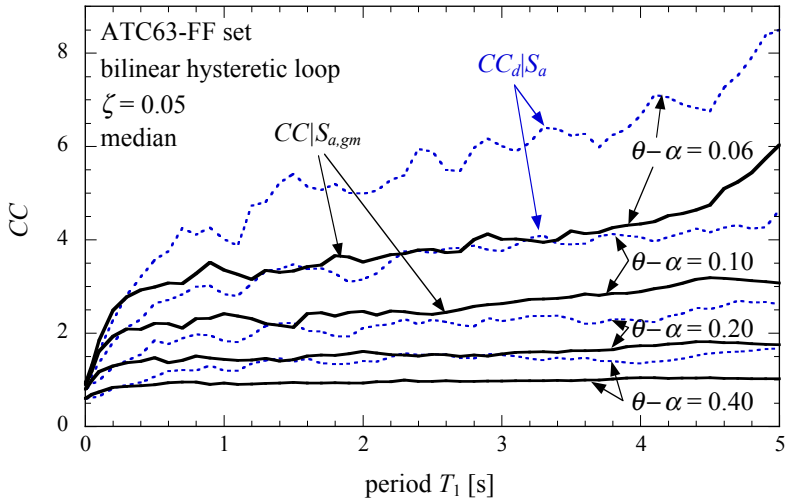


Figure 10: Median collapse capacity spectra for four different negative post-yield stiffness ratios $\theta - \alpha$. Solid black lines: spectra based on the recommended IM $S_{a,gm}(T_1, T_{n,a})$. Dashed blue lines: spectra based on the conventional IM $S_a(T_1)$.

4 COLLAPSE CAPACITY SPECTRA BASED ON "OPTIMAL" INTENSITY MEASURE

Figure 10 shows median collapse capacity spectra for four selected post-yield stiffness ratios $\theta - \alpha$ = 0.06, 0.10, 0.20, and 0.40. Viscous damping ζ is set to 5%. Spectra displayed by solid black lines are based on the recommended IM $S_{a,gm}(T_1, T_{n,a})$, compare also with Equation 10. Additionally, the corresponding "conventional" collapse capacity spectra, relying on the spectral acceleration $S_a(T_1)$ at the initial period as IM, are set in contrast. Dashed blue lines represent these spectra. At $T_1 = 0$ enhanced and conventional spectra coincide, since for rigid structures the period ratio $\varepsilon_a = 1$, see Equation 9. Enhanced median spectra exhibit in the period range $T_1 > 0.2$ s a smaller median collapse capacity compared to the conventional counterparts. This is a result of "averaging" the spectral acceleration in the period band ΔT in the descending branch of this quantity. However, the trend of the enhanced spectra with respect to T_1 remains similar to the original ones.

In Figure 11 dispersion parameters s^*, which correspond to these median spectra, are plotted against the initial structural period T_1. It is readily observed that for systems with $T_1 = 0$ the dispersion is zero, as discussed in [4]. However, stiff and more flexible systems exhibit for all considered structural configurations a reduced dispersion in the almost entire period range

when using the proposed IM. This reduction becomes more pronounced the larger the negative post-yield stiffness ratio $\theta-\alpha$ is. While for $\theta-\alpha = 0.06$ the decrease of s^* is in average 15%, for $\theta-\alpha = 0.40$ parameter s^* for IM $S_{a,gm}(T_1,T_{n,a})$ is in general less than 50% of its counterpart for IM $S_a(T_1)$. This result shows that the dispersion magnitude not only depends on period T_1 but also on the negative post-yield stiffness ratio $\theta-\alpha$.

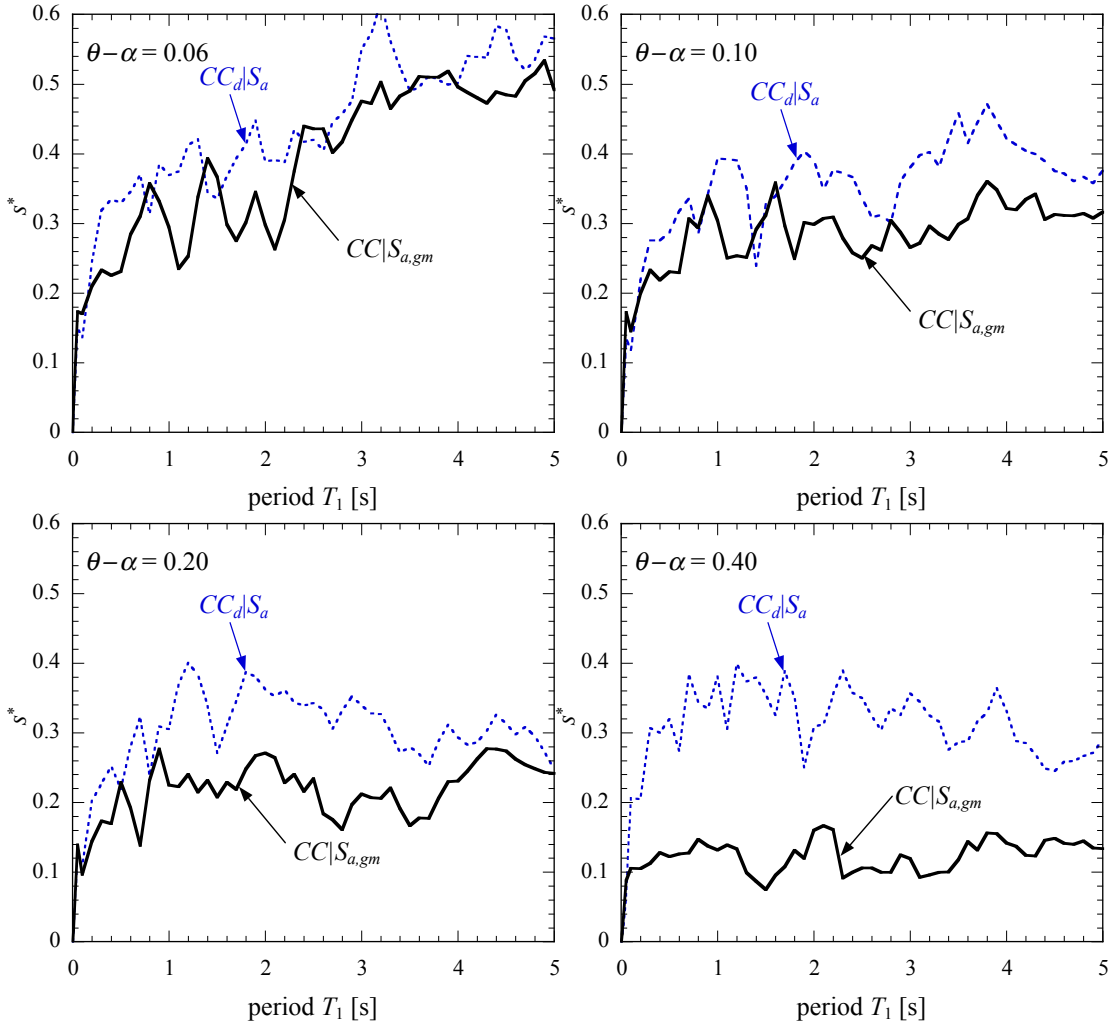


Figure 11: Dispersion parameter of the collapse capacities based on the recommended IM $S_{a,gm}(T_1,T_{n,a})$ (solid black lines) and on the conventional IM $S_a(T_1)$ for four different negative post-yield stiffness ratios $\theta-\alpha$.

5 CONCLUSIONS

It has been shown that an intensity measure (IM) based on the averaged spectral acceleration of a certain period band between the structural period and a corresponding elongated period reduces considerably the record-to-record (RTR) variability of the seismic collapse capacity of highly inelastic single-degree-of-freedom systems vulnerable to the P-delta effect. From the results of extensive parametric studies the "optimal" elongated period has been identified. The "optimal" elongated period is related to the smallest achievable dispersion of a system with certain assigned characteristic structural parameters. It has been shown that this "optimal" period depends primarily on the initial structural period, and is more or less unaffected by viscous damping, and the negative post-yield stiffness ratio of the SDOF system. In general, the more flexible a system becomes, the larger is the period band between the elon-

gated and the initial period that renders the smallest dispersion. However, this may not be the case for systems with a period larger than 3 s, since in this period range the acceleration response spectrum is almost horizontal. An analytical expression of the ratio between the "optimal" elongated period and the structural period has been derived. As an outcome, this ratio is constant for systems with a period larger than 0.15 s. In several applications, the reduction of the dispersion has been quantified. The largest reduction of the dispersion compared with the outcomes based on the conventional IM, i.e. the spectral acceleration at the initial structural period, can be achieved for systems with a negative post-yield stiffness ratio of 0.40. For those systems, the dispersion is reduced by more than 50%. In contrast, for systems with a mild negative post-yield stiffness ratio the reduction of the dispersion is quite small. The derived collapse capacity spectra based on the enhanced IM are valid for non-deteriorating bilinear cyclic behavior only. The effect of other constitutive laws such as pinching and peak-oriented hysteretic loops on the RTR variability of the collapse capacity spectra will be addressed in further studies.

ACKNOWLEDGEMENT

S. Tsantaki conducted the research for this paper as a student of the Doctoral School (FWF DK-plus) "Computational Interdisciplinary Modelling", which is based at the University of Innsbruck and substantially funded by the Austrian Science Fund (FWF).

REFERENCES

[1] D. Bernal, Amplification factors for inelastic dynamic P-Δ effects in earthquake analysis. *Earthquake Engineering and Structural Dynamics*, **15**, 635-651, 1987.

[2] G.A. MacRae, P-Δ effects on single-degree-of-freedom structures in earthquakes. *Earthquake Spectra*, **10**, 539-568, 1994.

[3] C. Adam, C. Jäger, Seismic collapse capacity of basic inelastic structures vulnerable to the P-delta effect. *Earthquake Engineering and Structural Dynamics*, **41**, 775-793, 2012.

[4] C. Jäger, C. Adam, Influence coefficients for collapse capacity spectra. *Journal of Earthquake Engineering*, accepted for publication.

[5] C. Adam, C. Jäger, Dynamic instabilities of simple inelastic structures subjected to earthquake excitation. H. Irschik, M. Krommer, A. Belyaev eds. *Advanced Dynamics and Model-Based Control of Structures and Machines*, pp. 11-18. Springer Wien, New York, 2012.

[6] M. Bianchini, P. Diotallevi, J.W. Baker, Prediction of inelastic structural response using an average of spectral accelerations. *10th International Conference on Structural Safety and Reliability* (*ICOSSAR 09*), Osaka, Japan, September 13-19, 2009, 8 pp.

[7] D. Vamvatsikos, C.A. Cornell, Incremental dynamic analysis. *Earthquake Engineering and Structural Dynamics*, **31**, 491-514, 2002.

[8] S. Tsantaki, C. Jäger, C. Adam, Improved seismic collapse prediction of inelastic simple systems vulnerable to the P-delta effect based on average spectral acceleration. *15th World Conference on Earthquake Engineering (15 WCEE)*, Lisbon, Portugal, September 24-28, 2012, digital paper, paper no. 0287, 10 pp., 2012.

[9] C. Adam, S. Tsantaki, Seismic collapse fragility of structures vulnerable to the P-delta effect. Submitted for publication *11th International Conference on Structural Safety & Reliability (ICOSSAR 2013)*, Columbia University, New York, June 16-20, 2013.

[10] FEMA P-695, *Quantification of building seismic performance factors*. Federal Emergency Management Agency, 2009.

[11] H. Krawinkler, F. Zareian, D.G. Lignos, L.F. Ibarra, Prediction of collapse of structures under earthquake excitations. M. Papadrakakis, N.D. Lagaros, M. Fragiadakis eds. *2nd International Conference on Computational Methods in Structural Dynamics and Earthquake Engineering (COMPDYN 2009)*, Rhodes, Greece, June 22-24, 2009, CD-ROM paper, paper no. CD449.

[12] L.F. Ibarra, H. Krawinkler, *Global collapse of frame structures under seismic excitations*. PEER Report 2005/06. University of California at Berkeley, California, Pacific Earthquake Engineering Research Center.

[13] L. Ibarra, H. Krawinkler, Variance of collapse capacity of SDOF systems under earthquake excitations. *Earthquake Engineering and Structural Dynamics*, **40**, 1299-1314, 2011.

[14] E. Limpert, W.A. Stahel, M. Abbt, Log-normal distributions across the sciences: Keys and clues. *BioScience*, **51**, 341-352, 2001.

COMPDYN 2013
4th ECCOMAS Thematic Conference on
Computational Methods in Structural Dynamics and Earthquake Engineering
M. Papadrakakis, V. Papadopoulos, V. Plevris (eds.)
Kos Island, Greece, 12–14 June 2013

AN OUTLOOK INTO TIME-DEPENDENT AFTERSHOCK VULNERABILITY ASSESSMENT

Hossein Ebrahimian[1], Fatemeh Jalayer[1], Domenico Asprone[1], Anna M. Lombardi[2], Warner Marzocchi[2], Andrea Prota[1], and Gaetano Manfredi[1]

[1] Department of Structures for Engineering and Architecture, University of Naples Federico II, Naples, Italy
e-mail: ebrahimian.hossein@unina.it, fatemeh.jalayer@unina.it

[2] Istituto Nazionale di Geofisica e Vulcanologia (INGV), Rome, Italy

Keywords: Aftershock hazard, Time-dependent vulnerability assessment, Daily rate of exceedance, Sequential cloud analysis, Modified Omori model, ETAS model.

Abstract. *Operative seismic aftershock risk forecasting is particularly useful as support for rapid decision-making in the presence of an ongoing aftershock sequence. Arguably, an operative forecasting framework can be built on the basis of adaptive time-dependent seismic aftershock risk assessment. In such a context, the fragility curves represent the progressive state of damage in a structure. Focusing on adaptive time- and event-dependent fragility assessment, this work explores various issues related to probability-based performance assessment in the immediate post main-shock environment. A fragility curve is expressed herein as the daily probability of (first-excursion) exceeding of a prescribed limit states given the first-mode spectral acceleration. A time-dependent structural performance variable, defined as the ratio of residual demand to residual capacity, is adopted in order to measure the cumulative damage in the structure. The sequence of event-dependent fragility curves are calculated by evolutionary linear logarithmic regression of the structural performance variable versus spectral acceleration, called herein as the sequential cloud method. It is demonstrated that the aftershock recurrence model used to estimate the daily number events of interest significantly affects the resulting fragility curves. Two alternative aftershock occurrence models based on the ETAS model and the modified Omori are studied herein. The sequence of daily fragility curves for a given limit state are finally integrated together with daily aftershock hazard curves (based on above-mentioned aftershock models) in order to calculate the daily aftershock risk. As a numerical example, the daily aftershock risk is calculated for the L'Aquila 2009 aftershock sequence (central Italy). An equivalent single-degree-of-freedom structure with cyclic strength and stiffness degradation is used in order to evaluate the progressive damage caused by the sequence of aftershock events.*

1 INTRODUCTION

The first few days after the occurrence of a strong earthquake are crucial in decision-making between different actions such as search and rescue, evacuation, inspection, building stabilization and repair, retrieval of possessions, or re-occupation in an aftershock-prone zone. This issue can be further complicated by progressive deterioration in the structures, induced by an ongoing sequence of aftershock events. An operational aftershock damage forecasting framework can provide a quantified support basis for rapid decision-making. Such a framework can be built based on analytic predictions of structural performance as a function of the time elapsed after the main earthquake event. The mean daily rate of exceeding a prescribed limit state can be regarded as an operational and probability-based proxy for time-dependent structural performance. This work focuses on the issues that can arise in time-dependent performance-based fragility assessment in the presence of an ongoing aftershock sequence.

Recently, many studies have been conducted in order to address the time-dependent issues related to seismic aftershock risk assessment. Li and Ellingwood [1] proposed a probabilistic approach for post-earthquake performance assessment of steel frame buildings. In the absence of ground motion records to describe the main shock-aftershocks sequence, it was assumed that the aftershocks are modeled by ensembles of the main-shock ground motions to be appropriately scaled using relations established between the main-shock and aftershock intensities. They concluded that the characteristics of the aftershocks have a significant influence on the structural damage pattern. Yeo and Cornell [2] have proposed a decision-making framework based on stochastic dynamic programming which minimizes the expected life-cycle cost subjected to acceptable life-safety constraints. As a proxy for life-safety, they have employed an equivalent constant collapse rate for the main-shock damaged structure (Yeo and Cornell [3]). Goda and Taylor [4] studied the peak ductility demand for inelastic single degree of freedom (SDOF) systems using both real and artificially generated main shock-aftershock sequences based on seismological models. They showed that by using the real sequences, the incremental effects of aftershocks on the peak ductility demand were relatively small. Meanwhile, using artificially-generated sequences, the additional aftershock effects on the peak ductility demand were found to be significant.

Jalayer et al. [5] proposed a probabilistic methodology, based on successive applications of the Total Probability theorem [6], for calculating the rate of exceeding a prescribed *limit state* (*LS*) in the time elapsed after the occurrence of the main event. In this approach, the time-variant daily rate of exceeding the *collapse* limit state is adopted as a proxy for life-safety considerations. In this study, the main-shock-after-shock sequence was approximated by a sequence of strong-motion events. The present study is based on a modified version of the methodology presented in [5] which is adapted to an operation forecasting framework. A non-linear time-dependent performance variable, defined as the ratio of maximum demand increment to residual capacity, is adopted herein to represent the evolution in structural performance. Daily fragility curves, expressed as the conditional probability that the performance variable exceeds unity in a 24 hour interval (given seismic intensity), are used to represent the time-dependent vulnerability of the structure. The daily fragility curves are calculated as a sum of a sequence of *event-based* fragility curves that are weighted by the probability that a certain number of aftershock events take place in the considered interval. The event-based fragilities are calculated by linear logarithmic regression of the structural performance variable versus seismic intensity (represented by the first-mode spectral acceleration) subjected to a series of plausible seismic sequences in order to model the record-to-record uncertainty in structural response assessment. This method is referred to herein as the *sequential cloud analysis* since it is inspired from a non-linear dynamic structural analysis procedure known as the

cloud method [7].The set of seismic sequences are selected through alternative approaches, namely, (a) permutation of real aftershock events taken from the ongoing sequence; (b) ”cloning“ of real aftershock events (repeating the same wave-form for a number of times); (c) permutation of a set of strong-motion wave-forms scaled so that their median is equal to the median spectral acceleration of the real aftershocks (i.e., the so-called *cloud scaling*, described later); (d) cloning of a set of strong-motion wave-forms ”clone-scaled“ to the median spectral acceleration of the real aftershocks. The probability that a certain number of aftershock events of interest take place in a 24 hour time interval is calculated from two alternative aftershock occurrence models. These occurrence models are based on, (a) an epidemiologic space-time point process model known as ETAS [8, 9]; (b) the modified Omori model assuming a non-homogenous Poisson occurrence [10]. The mean daily rate of exceeding a given limit state is calculated next by integrating the daily rate of exceeding a given spectral acceleration (probabilistic aftershock hazard analysis, PASHA, see [11]) and the daily fragility curve for the limit state in question.

As a numerical example, daily forecasts of the mean rate of exceeding two ultimate *LS*'s are performed for the L'Aquila aftershock sequence (2009, central Italy). As the structural model, an equivalent SDOF model with cyclic strength and stiffness deterioration is used in order to study the damage induced as a result of the sequence of aftershocks. The first excursion points for both *LS*'s due to the L'Aquila sequence are also used as a benchmark for the calculations.

1.1 Definition of daily forecasting

In an operational forecasting framework, daily fragility curves for a given limit state can be predicted for a time interval (usually equal to or less than 24 hour) defined as $[T_{start}, T_{end}]$ for the *j*th day, $j = 1, \ldots, N_{\text{day}}$ (where N_{day} denotes the number of days of interest for decision-making purposes). The sequence aftershock wave-forms (registered in a temporary catalog) in the time elapsed between the main-shock until T_{start} is denoted as $\mathbf{seq}$. However, the aftershock events occurring in the *forecasting interval* $[T_{start}, T_{end}]$ need to be generated (as will be discussed hereafter). These generated sequences are denoted by $\mathbf{seq}_{\text{gen}}$.

2 TIME-DEPENDENT VULNERABILITY ASSESSMENT

2.1 Structural performance variable *Y*

Residual drift demands are recognized as key response parameters in the short- and long-term performance-assessment of existing buildings [12-14]. Let N_{as} be the number of aftershock events taking place in the forecasting interval $[T_{start}, T_{end}]$ associated with *j*th day after the main event. Each event n, $n = 1, \ldots, N_{\text{as}}$, may lead to an increase in the peak and residual drift demands in the damaged structure, based on its amplitude and frequency content as well as the hysteretic characteristics of the structure (see [15, 16]). Arguably, the structural response to the *n*th event is significantly affected by the residual (permanent) drift demand due to (*n*-1) previous events.

In this work, a novel scalar time-dependent performance variable, suitable for sequential evaluation of demand and capacity in the structure, is introduced as the ratio of maximum demand increment due to the sequence of *n* events and the residual drift capacity in the structure:

$$Y_{LS}^{(n)} = \frac{D_{\max}^{(n)} - D_{\mathrm{r}}^{(n-1)}}{C_{LS} - D_{\mathrm{r}}^{(n-1)}} \tag{1}$$

where $D_{\max}^{(n)}$ is the maximum drift demand due to the sequence of *n* events, $D_r^{(n-1)}$ is the residual drift demand corresponding to the sequence of (*n*-1) events, and C_{LS} is the capacity of the (intact) structure for the desired limit state. The term $D_{\max}^{(n)} - D_r^{(n-1)}$ can be interpreted as the maximum increment in the story drift due to the *n*th event; meanwhile, the term $C_{LS} - D_r^{(n-1)}$ can be viewed as the structural residual drift capacity right after the sequence of (*n*-1) events. Note that at the onset of *LS*, the maximum drift demand is equal to the *LS* capacity (i.e., $D_{\max}^{(n)} = C_{LS}$). Hence, the performance variable Y_{LS} is equal to unity at the onset of the *LS*. It is interesting to note that the performance variable in Equation (1), which derived for maximum inter-story drift, can be generalized (see [17]) in order to take into account a range of potential failure mechanisms (*cut-sets*):

$$Y_{LS}^{(n)} = \max_{l=1}^{N_{\mathrm{mech}}} \min_{m=1}^{N_l} Y_{m,l}^{(n)} \tag{2}$$

where N_{mech} is the number of potential failure mechanisms; N_l is the number of components in the *l*th mechanism; and $Y_{m,l}^{(n)}$ is the structural performance index for the *m*th component of the *l*th mechanism, defined in Equation (1). This generalized performance variable can be interpreted as the component demand to capacity ratio that brings the system closer to the first *LS* excursion (see [17] for more detail). This generalized formulation can be quite useful for shear-critical structures.

2.2 A probabilistic performance-based framework for aftershock forecasting

A probabilistic performance objective for aftershock forecasting can be achieved by ensuring that the daily rate of exceeding a prescribed limit state denoted by λ_{LS} is smaller than or equal to an admissible rate denoted by λ_{admis}:

$$\lambda_{LS} = \lambda\left(Y_{LS} \geq 1\right) \leq \lambda_{\mathrm{admis}} \tag{3}$$

where the mean daily rate of exceeding a limit state is equal to the mean daily rate that the performance variable Y_{LS} corresponding to *LS* is greater than or equal to unity. In order to take into account only the aftershock events of interest, the daily limit state rate λ_{LS} can be written as:

$$\lambda_{LS} = \lambda\left(Y_{LS} \geq 1\right) = \lambda\left(M \geq M_l\right) \cdot P\left(Y_{LS} \geq 1 \,|\, M \geq M_l\right) \tag{4}$$

where $\lambda\left(M \geq M_l\right)$ is the time-dependent daily rate of occurrence of aftershocks with magnitude larger than or equal a cut-off magnitude M_l and $P\left(Y_{LS} \geq 1 \,|\, M \geq M_l\right)$ is the probability of exceeding the limit state *LS* given $M \geq M_l$, referred to as the seismic aftershock risk hereafter.

2.3 Time-dependent risk assessment

let $\mathbf{I}_j$ denote the following information[1]: A **seq** of aftershock events with $M \geq M_l$ in the forecasting interval $[T_{start}, T_{end}]$ corresponding to the *j*th day. The probability of exceeding a specified *LS* can be expanded as follows (using the Total Probability Theorem):

$$P\left(Y_{LS} \geq 1 | \mathbf{I}_j\right) = \sum_{n=1}^{N_{as}} P\left(Y_{LS} \geq 1 | n, \mathbf{I}_j\right) P\left(n | \mathbf{I}_j\right) \tag{5}$$

where N_{as} denotes the maximum number of aftershock events in the forecasting interval; $P\left(Y_{LS} \geq 1 | n, \mathbf{I}_j\right)$ is the probability of exceeding the *LS* given that exactly n aftershock events take place; and $P\left(n | \mathbf{I}_j\right)$ is the probability that exactly n events take place in the prescribed time interval. The term $P\left(LS | n, \mathbf{I}_j\right)$ can be further decomposed[2] by introducing the spectral acceleration *x* as an interface variable:

$$P\left(Y_{LS} \geq 1 | n, \mathbf{I}_j\right) = \int_x P\left(Y_{LS} \geq 1 | x, n, \mathbf{I}_j\right) \left| \mathrm{d}P\left(S_a(T) > x | n, \mathbf{I}_j\right) \right| \tag{6}$$

where $P\left(Y_{LS} \geq 1 | x, n, \mathbf{I}_j\right)$ is the structural *fragility* defined as a function of the spectral acceleration at the specified period $S_a(T) = x$; $P\left(S_a(T) > x | n, \mathbf{I}_j\right)$ is the probability that an aftershock event has a spectral acceleration greater than *x*[3]. It is interesting to note that

$$\mathrm{d}\lambda\left(x | \mathbf{I}_j\right) = \lambda\left(M \geq M_l | \mathbf{I}_j\right) \cdot \mathrm{d}P\left(S_a(T) > x | \mathbf{I}_j\right) \tag{7}$$

where $\lambda\left(M \geq M_l | \mathbf{I}_j\right)$ is the time-dependent daily rate of occurrence of aftershocks with $M \geq M_l$ and $\lambda\left(x | \mathbf{I}_j\right)$ is the mean daily rate of exceedance of a given level of $S_a(T)$ equal to x (also referred to as daily forecasting of aftershock hazard, [11]).

2.3.1 *Estimating the number of events P(n|I_j)*

As mentioned in the introduction, this work employs two well-established earthquake occurrence models suitable for daily seismicity forecasts associated with the evolution of an aftershock sequence; the Modified Omori's aftershock model (MO) [10] with updated parameters based on the aftershocks that have already occurred, i.e. the **seq**, (see [5, 11]) and the Epidemic Type Aftershock Sequence (ETAS) model [8, 9, 18]. The daily seismic aftershock hazard $\lambda\left(x | \mathbf{I}_j\right)$ can be calculated based on both occurrence models [11]. Accordingly, the probability $P\left(n | \mathbf{I}_j\right)$ that exactly *n* events take place in the forecasting interval on *j*th day (i.e. Equation 5) can be estimated based on both MO and ETAS occurrence models.

---

[1] This is done for simplifying the formulation and will be used to remind that the risk calculations are conditioned on background information $\boldsymbol{I_j}$. Needless to say, also $\boldsymbol{I_j}$ represents a time-dependent set of information.

[2] Using the Total Probability Theorem

[3] It is assumed that knowing the exact number of aftershock events *n* with magnitude greater than or equal to a lower cut-off level is not going to affect the aftershock hazard. Therefore the dependence on *n* is dropped hereafter. This assumption may be justified by the fact that the forecasted hazard for the *j*th day is does not take into account the events occurring within the forecasting time window (see [11]).

ETAS: ETAS model accounts for the triggering effect of all the events that have occurred before T_{start} and those that will occur during the forecasting interval $\left[T_{start}, T_{end}\right]$. Since the latter are unknown at the moment of the forecast, they can be simulated. For instance, Marzocchi and Lombardi [9] have simulated N=500 different synthetic daily catalogs by using the "thinning method" proposed by Ogata [18]. Based on the N simulated catalogs and the **seq**, the N different realizations of the number of events N_{as} (occur in the forecasting interval) can be obtained based on ETAS model [11]. Therefore, $P\left(n \mid \mathbf{I}_j\right)$ can be estimated with an empirical probability distribution for the various realizations of N_{as}.

Modified Omori (MO): $P\left(n \mid \mathbf{I}_j\right)$ can also be estimated by a non-homogenous Poisson probability distribution with the time-decaying rate based on the MO model:

$$P\left(n \mid \mathbf{I}_j\right) = \frac{\lambda_{\text{MO}}\left(M \geq M_l \mid \mathbf{I}_j\right)^n e^{-\lambda_{\text{MO}}\left(M \geq M_l \mid \mathbf{I}_j\right)}}{n!} \tag{8}$$

where $\lambda_{\text{MO}}\left(M \geq M_l \mid \mathbf{I}_j\right)$ is the daily rate of having aftershock events with $M \geq M_l$ based on the MO occurrence model (for more details see [5, 11]).

2.3.2 *Time-dependent vulnerability assessment*

The fragility term $P\left(Y_{LS} \geq 1 \mid x, n, \mathbf{I}_j\right)$ in Equation (6) can be calculated by taking into account the set of mutually exclusive and collectively exhaustive (MECE) events that the *LS* is exceeded at one and just one of the previous aftershock events (first excursion, see also [19]):

$$P\left(Y_{LS} \geq 1 \mid x, n, \mathbf{I}_j\right) = P\left(C_1 + \overline{C_1}C_2 + \overline{C_1 C_2}C_3 + \ldots + \overline{C_1 C_2 \ldots C_{n-1}}C_n \mid x, n, \mathbf{I}_j\right) \tag{9}$$

where $C_k, k = 1{:}n$ is defined as:

$$\begin{cases} C_k \equiv Y_{LS} \geq 1 \text{ after } k\text{th event} \\ \overline{C}_k \equiv Y_{LS} < 1 \text{ after } k\text{th event (read as not } C_k) \end{cases} \tag{10}$$

Since the events $\overline{C_1 C_2 \ldots C_{k-1}}C_k, k = 1{:}n$ are MECE, Equation (9) can be re-written by summing up the probabilities for each separate term[4]:

$$P\left(Y_{LS} \geq 1 \mid x, n, \mathbf{I}_j\right) = \sum_{k=1}^{n} P\left(\overline{C_1 C_2 \ldots C_{k-1}}C_k \mid x, \mathbf{I}_j\right) \tag{11}$$

where $P\left(\overline{C_1 C_2 \ldots C_{k-1}}C_k \mid x, \mathbf{I}_j\right)$ represents the sequence of fragility terms identified by the fact that the first *LS* excursion takes place at *k*th event This fragility term can be expanded as[5]:

[4] Note that the dependence on *n* is dropped for simplicity. In any case, the fact that *n* events have taken place is already reflected in the summation.

[5] In the previous articles by the authors [5] and [20], it was assumed that the C_k's are stochastically independent. Therefore, the formulation presented in Equation (12) is general and is obtained based on the *product rule* in probability [21].

$$P\left(\overline{C_1C_2....C_{k-1}}C_k \mid x,\mathbf{I}_j\right)=P\left(C_k \mid \overline{C_1C_2....C_{k-1}},x,\mathbf{I}_j\right)P\left(\overline{C_1C_2....C_{k-1}} \mid x,\mathbf{I}_j\right) \quad (12)$$

where $P\left(C_k \mid \overline{C_1C_2....C_{k-1}},x,\mathbf{I}_j\right)$ denotes the structural fragility when the first *LS* excursion takes place after the occurrence of the *k*th event, and $P\left(\overline{C_1C_2....C_{k-1}} \mid x,\mathbf{I}_j\right)$ is the probability that the structure has not exceeded the limit state after the (*k*-1)th event. The latter can be further expanded as (by following the same logics as in Equations 10 and 12):

$$P\left(\overline{C_1C_2....C_{k-1}} \mid x,\mathbf{I}_j\right)=\left[1-P\left(C_{k-1} \mid \overline{C_1C_2....C_{k-2}},x,\mathbf{I}_j\right)\right]P\left(\overline{C_1C_2....C_{k-2}} \mid x,\mathbf{I}_j\right) \quad (13)$$

In a recursive manner, one can obtain the following expression:

$$P\left(\overline{C_1C_2....C_{k-1}} \mid x,\mathbf{I}_j\right)=\prod_{i=1}^{k-1}\left[1-P\left(C_i \mid \overline{C_1C_2....C_{i-1}},x,\mathbf{I}_j\right)\right] \quad (14)$$

Thus, substituting $P\left(\overline{C_1C_2....C_{k-1}} \mid x,\mathbf{I}_j\right)$ from Equation (14) in Equation (12):

$$P\left(\overline{C_1C_2....C_{k-1}}C_k \mid x,\mathbf{I}_j\right)=P\left(C_k \mid \overline{C_1C_2....C_{k-1}},x,\mathbf{I}_j\right)\prod_{i=1}^{k-1}\left[1-P\left(C_i \mid \overline{C_1C_2....C_{i-1}},x,\mathbf{I}_j\right)\right] \quad (15)$$

Finally, substituting $P\left(\overline{C_1C_2....C_{k-1}}C_k \mid x,\mathbf{I}_j\right)$ from Equation (15) in Equation (11), one can calculate the *event-dependent* fragility $P\left(Y_{LS}\geq 1 \mid x,n,\mathbf{I}_j\right)$:

$$P\left(Y_{LS}\geq 1 \mid x,n,\mathbf{I}_j\right)=\sum_{k=1}^{n}\left(P\left(C_k \mid \overline{C_1C_2....C_{k-1}},x,\mathbf{I}_j\right)\cdot\prod_{i=1}^{k-1}\left[1-P\left(C_i \mid \overline{C_1C_2....C_{i-1}},x,\mathbf{I}_j\right)\right]\right) \quad (16)$$

The *event-dependent* fragility term $P\left(Y_{LS}\geq 1 \mid x,n,\mathbf{I}_j\right)$ is estimated herein by a novel nonlinear dynamic analysis procedure presented herein as the *sequential cloud analysis* procedure.

3 SEQUENTIAL CLOUD ANALYSIS

The sequential cloud analysis procedure outlined in this section leads to the calculation of the sequence of fragility terms $P\left(\overline{C_1C_2....C_{k-1}}C_k \mid x,\mathbf{I}_j\right),\ k\in\langle 1,\ldots,n\rangle$ in Equation (11).

Let N_{seq} be the number of wave-form sequences $\mathbf{seq}_{\text{gen}}$ generated to model the sequence of aftershocks taking place in the forecasting interval. In the operational forecasting context, this means that the generated sequences $\mathbf{seq}_{\text{gen}}$ are going to be applied to the structure that has been already subjected to the sequence of events preceding the forecasting window denoted as **seq** beforehand (i.e., structural state at T_{start}). Each sequence $\mathbf{seq}_{\text{gen}}$ consists of N_{as} waveforms that generically substitutes/represents the number of events *k*. While the structure is subjected to N_{seq} suites of sequences $\mathbf{seq}_{\text{gen}}$, for each aftershock event *k*, a set of N_{seq} structural performance variables $Y_{LS}^{(k,m)},\ m\in\langle 1,\ldots,N_{\text{seq}}\rangle$ can be calculated.

The performance variable $Y_{LS}^{(k,m)}$ is calculated by subjecting the structure (damage state at T_{start}) to the *m*th sequence of *k* events in the suite of N_{seq} sequences generated. The spectral acceleration value corresponding to $Y_{LS}^{(k,m)}$ and denoted by $S_a^{(k,m)}$ is defined as the elastic

small-amplitude[6] spectral acceleration of the last (*k*th) aftershock event in the *m*th sequence of events. However, in order to create the condition $\overline{C_1 C_2 ....C_{k-1}} C_k$, those $Y_{LS}^{(k,m)}$ values for which the structure has already exceeded the *LS* threshold in the previous $(k-1)$ steps are not taken into account. This entails a sample reduction and the effective cloud sample size may be reduced from N_{seq} to $N_{\text{seq}}^{\text{red}}(k)$. In short, the cloud analysis, given *k* aftershock events, leads to a suite of $Y_{LS}^{(k,m)}$ values, $m \in \langle 1, \ldots, N_{\text{seq}}^{\text{red}}(k) \rangle$.

Assuming that the (conditional) distribution of critical demand-to-capacity ratio Y_{LS} for a given level of $S_a(T) = x$ is described by a lognormal distribution, the *k*th fragility term $P\left(C_k \mid \overline{C_1 C_2 ....C_{k-1}}, x, \mathbf{I}_j\right)$ in Equation (16), can be expressed as:

$$P\left(C_k \mid \overline{C_1 C_2 ....C_{k-1}}, x, \mathbf{I}_j\right) = P\left(Y_{LS}^{(k)} \geq 1 \mid x, \mathbf{I}_j\right) = 1 - \Phi\left(\frac{-\ln \eta_{Y|Sa}^{(k)}(x)}{\beta_{Y|Sa}^{(k)}}\right) \tag{17}$$

where (see [22]):

$$\ln \eta_{Y|Sa}^{(k)}(x) = a + b \ln(x)$$
$$\beta_{Y|Sa}^{(k)} = \sqrt{\frac{\sum_{m=1}^{N_{\text{cloud}}^{\text{red}}(k)} \left[\ln\left(\frac{Y_{LS}^{(k,m)}}{a \cdot \left(S_a^{(k,m)}\right)^b}\right)\right]^2}{N_{\text{cloud}}^{\text{red}}(k) - 2}} \tag{18}$$

where $N_{\text{cloud}}^{\text{red}}(k)$ is the effective cloud sample size given *k* aftershock events; *a* and *b* are the coefficients of the logarithmic linear regression (see [5, 22] for more details). $\eta_{Y|Sa}^{(k)}$ and $\beta_{Y|Sa}^{(k)} = \sigma_{\ln Y|Sa}^{(k)}$ are the conditional median and the conditional standard deviation of the natural logarithm of $Y_{LS}^{(k)}$ given spectral acceleration and that *k* aftershock events have occurred; $Y_{LS}^{(k)}$ is the structural performance variable given a sequence of *k* aftershock events.

4 NUMERICAL EXAMPLE

The methodology described in Sections 2 and 3 is applied in order to perform an adaptive performance-based aftershock risk assessment for an SDOF system, representative of an existing RC building.

4.1 The L'Aquila aftershock sequence

On April 6, 2009, at 1:32 AM UTC (i.e., Universal Time Coordinated), an earthquake with local magnitude (Ml) equal to 5.9 struck central Italy in the Abruzzo region underneath the town of L'Aquila which is located approximately 6 km from the epicenter. The large shock triggered a vigorous aftershock sequence, which spread within the first twenty-four hours over

[6] It is noteworthy that using the spectral acceleration at the secant period of the damaged structure due to the deteriorating effects of previous events (i.e. those within the **seq**) might provide a better correlation with the performance variable. However, it has been decided herein to use the elastic small-amplitude period spectral acceleration as the seismic intensity measure.

a secondary seismogenetic structure north of L'Aquila. The reference structure's hypothetic site is located near the recording station "L'Aquila - V. Aterno - Aquil Park Ing" (AQK), ITDPC network (Italian ACcelerometric Archive, ITACA, http://itaca.mi.ingv.it/ItacaNet/).

In order to generate operative daily earthquake occurrence forecasts based on ETAS and MO models (which are directly implemented in the probabilistic aftershock hazard analysis, PASHA), a provisional and quasi real-time catalog used by Marzocchi and Lombardi [9] is utilized by the authors (see also [11]). This is to reflect the fact that immediately after a main-shock, one often needs to make reference to a provisional catalog. In addition to the catalog, the waveform archive of L'Aquila aftershock sequence registered between 30 March 2009 and 30 April 2009 is used. This archive consists of recordings by DPC-RAN (Rete Accelerometrica Nazionale) (35 stations) and by INGV (Istituto Nazionale di Geofisicae Vulcanologia) (29 stations) permanent and temporary seismic networks. The database of wave-forms is one of the products related to the Project S5 "High-resolution multi-disciplinary monitoring of active fault test-site areas in Italy" in Task 4 UR6 WP 4.3 (http://dpc-s5.rm.ingv.it/en/S5.html). Consequently, the waveforms corresponding to each aftershock events listed within the catalog are post-processed and extracted from long-format time-windows [11].

The sequence of aftershock events **seq** consists of the aftershock wave-forms registered in the above-mentioned catalog after the main-shock up to 6:00 AM UTC of the upcoming day (i.e. *j*th day). The sequence **seq** is used to: (a) estimate the time-decaying parameters of the MO model [11]; (b) estimate the time dependent rate $\lambda\left(M \geq M_l \,|\, \mathbf{I}_j\right)$ based on both ETAS and MO models, as shown in the subsequent section (see also [11]); (c) perform time-dependent PASHA; (d) obtain the distribution $P\left(n \,|\, \mathbf{I}_j\right)$ based on both ETAS and MO models; and (e) construct the suite of ground motion sequences $\mathbf{seq}_{\text{gen}}$.

4.1.1 *The estimated number of events*

The number of registered aftershock events per day with magnitude greater than or equal to 3.3 is illustrated in Figure 1 in the time period from April 6, 2009, at 6:00 UTC, (i.e., a few hours after the main event) up to May 10, 2009. The forecasted of number of events with $M \geq 3.3$ per day based on both MO and ETAS models are also shown in the figure. It can be depicted from Figure 1 that both models perform quite well in capturing the trend in the number of aftershocks. Moreover, it can be observed that the ETAS tends to provide an upper-bound estimate of the number of events.

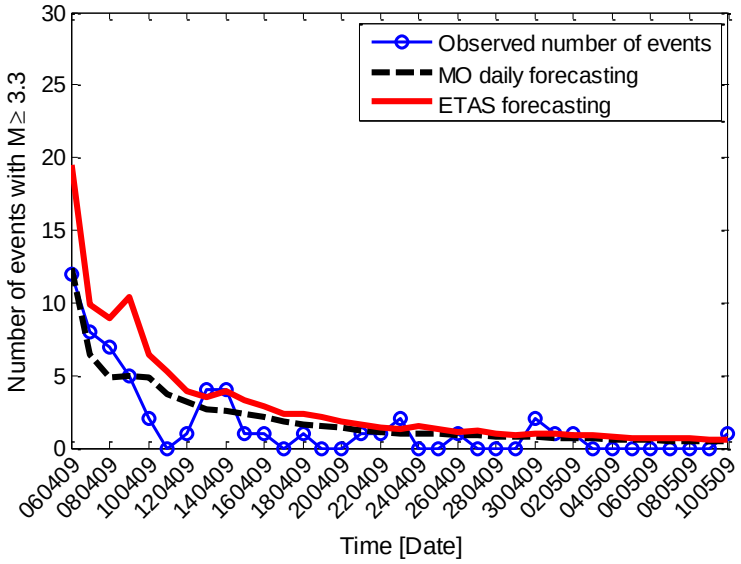


Figure 1: The observed and forecasted number of events ($M \geq 3.3$) per day.

4.2 The limit states

The performance objectives for post-earthquake assessment of the case-study structure are defined in terms of discrete *LS*'s of *Serviceability*, *Damage Limitation* (DL), *Significant Damage* (SD) and *Near Collapse* (NC). The last three *LS*'s are based on the European standard EC8-3 [23]. The *LS*'s are distinguished herein in terms of increasing levels of the maximum displacement for the equivalent SDOF system. In this study, it has been assumed that the ultimate displacement corresponding to a 20% drop in strength is representative of the NC limit state. Table 1 outlines the maximum displacements for the equivalent SDOF system identifying these *LS*'s.

LS	Maximum Displacement (meters)
Serviceability	0.01
Damage Limitation (DL)	0.02
Significant Damage (SD)	0.05
Near Collapse (NC)	0.07

Table 1: *LS*'s threshold for the equivalent SDOF

4.3 The structural model

An equivalent degrading (SDOF) system is utilized as the structural model. The case-study system is a modified version of the SDOF model which has been extensively used by the authors in previous works (see [5, 20, and 24]). The reference building is a generic five-story RC frame structure designed to resist seismic actions. The equivalent SDOF system has period $T = 0.58\text{sec}$, damping $\zeta = 5\%$, yield displacement $D_y = 0.02$ (meters), ultimate displacement $D_u = 0.15$ (meters), strength reduction factor $R = 2$, ductility $\mu = 2.5$, post yield stiffness ratio $\alpha_h = 0.17$, and no residual deformations. Based on the resulting equivalent pushover (capacity) curve, a non-linear degrading hysteresis model for the equivalent SDOF system is constructed. Figure 2a demonstrates the capacity curve for the equivalent SDOF

system where the onset of various limit states is marked. The figure also shows the maximum and residual displacement demand induced due to L'Aquila 2009 main event. It can be observed that the structure has exceeded the state of DL while it falls below the SD limit state. Moreover, the residual displacement of the system has exceeded the Serviceability limit state and it is just a little lower than the state of DL. This equivalent SDOF system seems to represent the category of structures that can be quite vulnerable to the aftershocks. In other words, although the structure has not experienced very high level of damages due to the main-shock, it has the growing potential of moving toward higher damage levels under the sequentially-applied aftershock events.

The sequential time history analyses are performed with the Open System for Earthquake Engineering Simulation (OPENSEES, http://opensees.berkeley.edu) by employing a hysteresis model with pinching that exhibits cyclic degradation in unloading and reloading stiffness as well as strength degradation (Pinching4 Material). Figure 2b represents the hysteresis behavior of the structure in response to a periodic loading protocol.

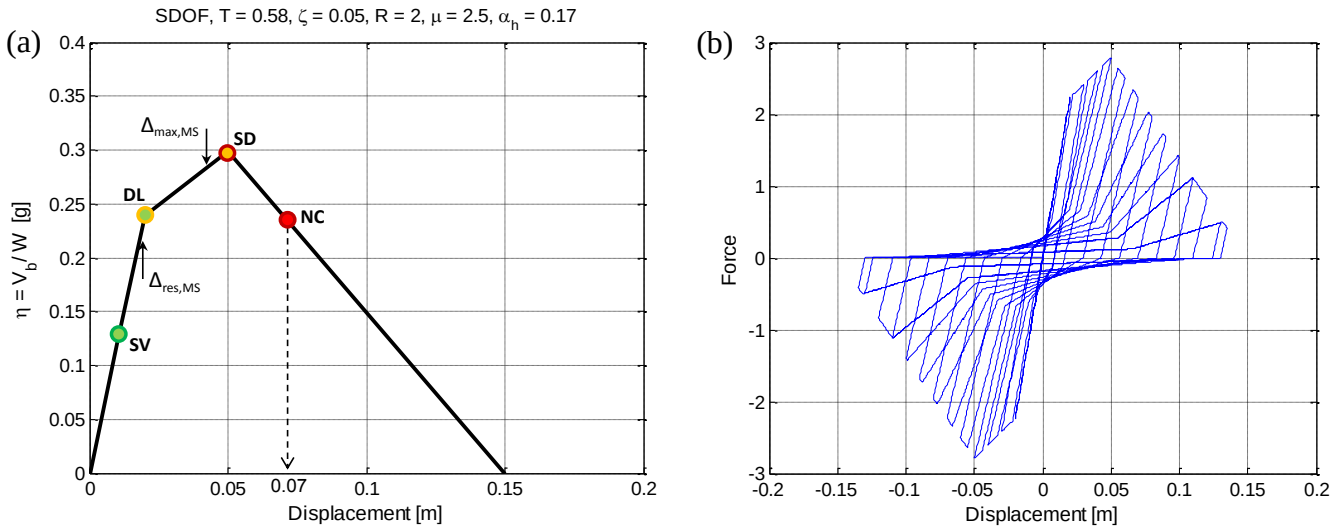


Figure 2: Equivalent SDOF system (a) the capacity curve, (b) the hysteresis behavior

4.4 Estimating number of aftershocks per day

As mentioned before, the probability distribution for the number of events $P\left(n \mid \mathbf{I}_j\right)$ can be estimated based on both MO and ETAS occurrence models (see Section 2.3.1). Figure 3 illustrates the histogram for the number of ETAS forecasted events with $M \geq 3.3$ [9] for date 06/04/09. This histogram can also be used in order to estimate the number of aftershocks N_{as} that are expected to happen per day. For example, a best-estimate of N_{as} for the forecasting interval of 06/04/09 can be calculated as $\left(\text{mean} + \sqrt{3}\,\text{sigma}\right)$ for the distribution $P\left(n \mid \mathbf{I}_j\right)$ based on ETAS model (as shown in Figure 3). Accordingly, $P\left(n \mid \mathbf{I}_j\right)$, $n = 1, \ldots, N_{as}$ are shown in Figure 4 for the first 4 days elapsed after the main event, namely, from 06/04/09 up to date 09/04/09. Equation (8) is used to estimate the probability distribution for the number of events based on a non-homogenous Poisson distribution (MO).

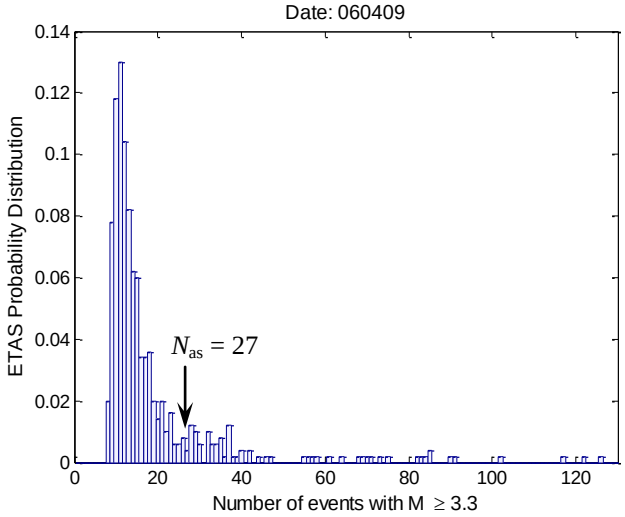


Figure 3: The histogram of the ETAS forecasted number of events for the day 06/04/09. N_{as} is a best-estimate for the number of events based on ETAS model

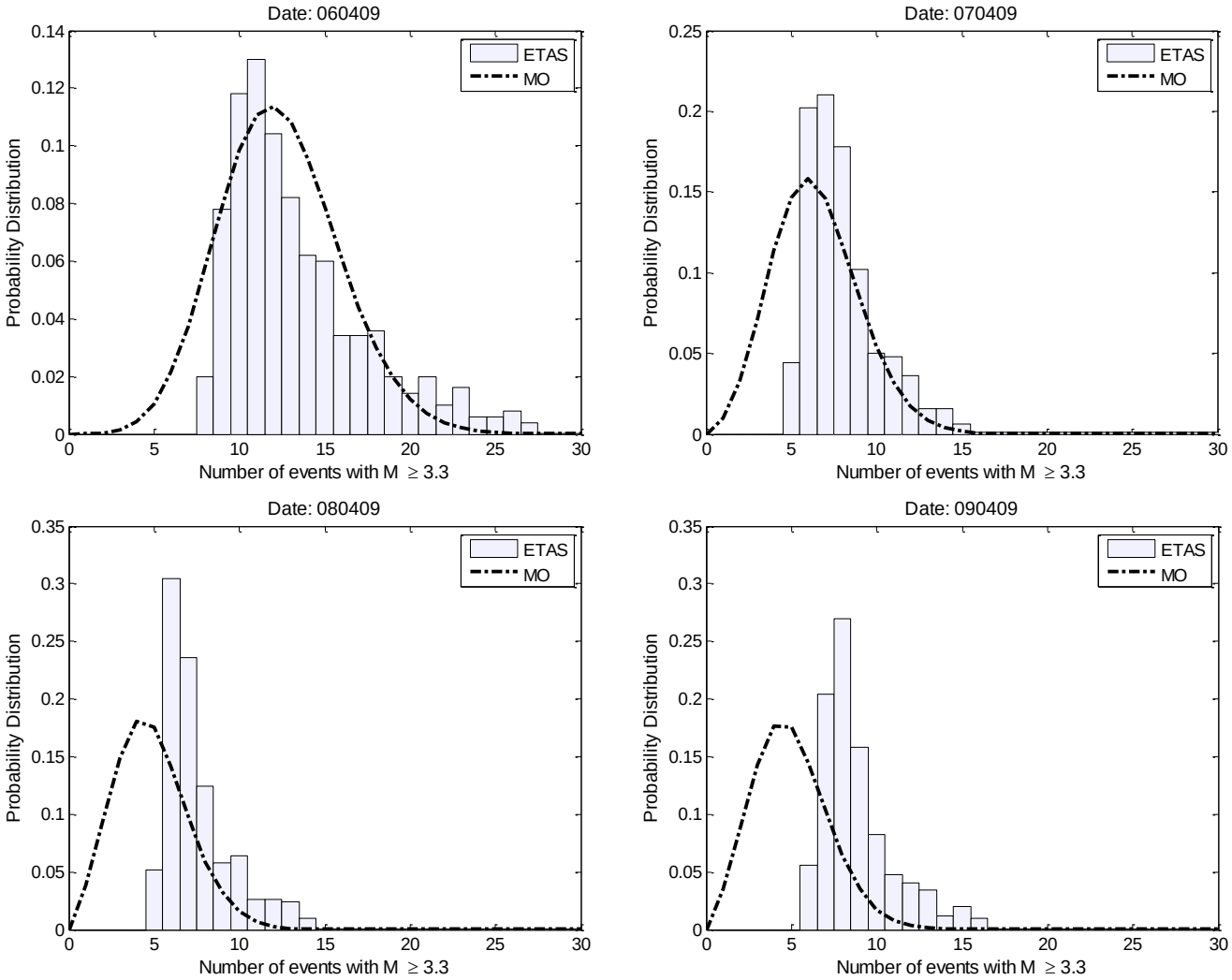


Figure 4: The distribution of the number of events per day based on MO and ETAS models

It can be observed that the ETAS predictions for the number of events are systematically larger than those of non-homogenous Poisson distribution based on MO model. Moreover, it can be seen that the MO Poisson model assigns a non-zero probability to having very few aftershock events (i.e., in the order of 5-10). On the contrary, ETAS assigns zeros probability to the possibility of having very few aftershock events. This is expected to affect the daily fragility curves which are going to be calculated as a weighted sum, equal to $P\left(n \mid \mathbf{I}_j\right)$, of event-dependent fragilities.

4.5 The selection of the suite of aftershock sequences

In the sequential cloud analysis, the selection of the suites of the aftershock records denoted as $\mathbf{seq}_{\text{gen}}$ is expected to play an important role. Previous studies on the effect of seismic sequences on the response of structures typically employed artificial sequences using the main-shock wave-form as a seed for simulating the aftershocks based on two different schemes: the so-called *back-to back* approach, and randomization (see [13] for an extensive review of these approaches). It is also interesting to study the possibility of employing recorded ground motions. The archive of L'Aquila sequence waveforms within the first month after the main event provides an opportunity to study the issues related to ground motion record selection for the non-linear dynamic analysis procedures such as the sequential cloud. In this work 4 different ground motion selections strategies, relying in real ground motion recordings, are studied:

a. Generate N_{seq} suites of ground motion sequences $\mathbf{seq}_{\text{gen}}$ of N_{as} records by random permutation (with replacement) of the wave-forms recorded in the available sequence $\mathbf{seq}$. As mentioned before, the sequence $\mathbf{seq}$ consists of records registered before the forecasting interval $\left[T_{start}, T_{end}\right]$.
b. Generate N_{seq} suites of ground motion sequences $\mathbf{seq}_{\text{gen}}$ of N_{as} records by repeating N_{as} times (also referred to as *cloning*) the various wave-forms recorded in the available sequence $\mathbf{seq}$. As the sequence evolves, there are more records available to select.
c. Generate N_{seq} suites of ground motion sequences $\mathbf{seq}_{\text{gen}}$ of N_{as} records by random permutation (with replacement) of a selection of strong-motion wave-forms that are scaled so that their median spectral acceleration $S_a(T)$ is equal to the median of the spectral acceleration values for the aftershock records registered within $\mathbf{seq}$.This is referred to hereafter as the *cloud-scaling*.
d. Generate N_{seq} suites of ground motion sequences $\mathbf{seq}_{\text{gen}}$ of N_{as} records by repeated cloning of a selection of strong-motion wave-forms that are cloud-scaled to the median $S_a(T)$ of the aftershocks within $\mathbf{seq}$.

The outcome of the sequential cloud method depends clearly on the choice of the parameters N_{as} and N_{seq}. For record selection based on the wave-forms within $\mathbf{seq}$, more and more records become available as days pass. Therefore, N_{seq} can be increased in order to increase the precision of the cloud method. On the other hand, the expected number of aftershock per

day is going to decrease with time. Table 2 outlines the values adopted for N_{as} and N_{seq} in the first four days elapsed after the main event.

Target Date	Best estimate for the number of events, N_{as}	Number of events within the **seq**, N_{seq}
06/04/09	27	15
07/04/09	15	22
08/04/09	14	29
09/04/09	16	38

Table 2: N_{as} and N_{seq} values for the first 4 days after the main-shock

4.6 The daily fragility curves

It is described herein how the daily fragility curves for the limit state of SD for the second day (j=2) elapsed after the main event can be calculated[7]. As it can be observed from Table 2, $N_{\text{as}} = 15$ and $N_{\text{seq}} = 22$. The step-by-step approach for fragility assessment is outlines below:

1. The sequence of fragility curves $P\left(C_k \mid \overline{C_1 C_2 .... C_{k-1}}, x, \mathbf{I}_2\right)$, $k \in \langle 1, \ldots, n \rangle$ is first calculated from Eq. (17) by employing the sequential cloud analysis described in Section 3. Figure 5 illustrates the sequence of N_{as} fragility curves calculated for the second day based on record selection strategy (a) (described in the previous section).
2. The sequence of event-dependent fragility curves $P\left(Y_{LS} \geq 1 \mid x, n, \mathbf{I}_2\right)$, $n \in \langle 1, \ldots, N_{\text{as}} \rangle$ are calculated next from Eq. (16), based on the fragility sequence calculated in the previous step. Figure 6 shows the sequence of fragility curves $P\left(Y_{LS} \geq 1 \mid x, n, \mathbf{I}_2\right)$.
3. The fragility curve for the second day $P\left(Y_{LS} \geq 1 \mid x, \mathbf{I}_j\right)$ can be finally calculated from Equations (5) and (6) as a weighted sum of $P\left(n \mid \mathbf{I}_2\right)$ (see Figure 4) and $P\left(Y_{LS} \geq 1 \mid x, n, \mathbf{I}_2\right)$. Figure 6 also demonstrates forecasted fragility curve for the second day based on both ETAS and MO models. Note that the difference between the forecasted fragility curves can be attributed to the difference between their associated probability distributions $P\left(n \mid \mathbf{I}_2\right)$, as shown in Figure 4.

As a benchmark for the forecasted fragility curves, the first-excursion point for the SD is marked with probability 1 on Figure 6. For the previous events, a point with probability zero is shown on the figure. Note that this benchmark points are created by means of *hind-sight*[8] based on the records registered in the forecasting time interval. Clearly, these records are not available for calculating the daily fragility forecasts. According to this Figure, the first excursion of the SD threshold is triggered by the 4th record (an event with $M = 5.3$). As it can be

[7] The time window between 6:00 UTC 07/04/09 until 6:00 UTC 08/04/09.
[8] By doing a back analysis on the sequence.

observed, the forecasted fragility curves (both ETAS and MO), predict that the limit state is going to be exceeded with probability 1 at $S_a(T)$ close to 0.14g.

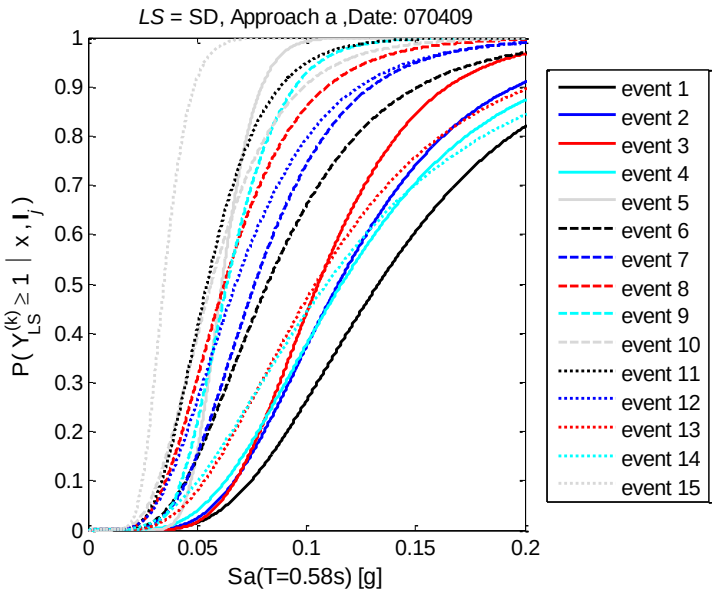


Figure 5: The sequence of fragility curves associated with Equation (17), approach "a", for day 07/04/09

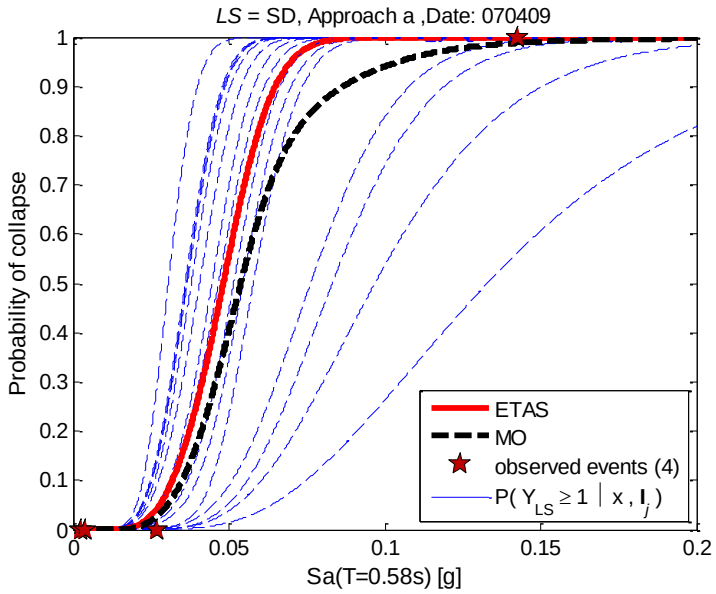


Figure 6: Forecasted fragility curves, based on both ETAS and MO models, approach "a", for day 07/04/09

4.6.1 *Comparison of daily fragility curves based on permutation and cloning*

Figure 7 illustrates the forecasted daily fragilities for SD and NC limit states for the first four days (j=1:4). It is important to note that the daily forecasts for any prescribed limit state are provided up to the day in which the first limit state excursion takes place. For example, the results for SD are only reported for the first two days elapsed after the main event (first excursion for SD takes place in the second day). These fragility curves are calculated through the first two record selection strategies (a) and (b) outlined in Section 4.5, namely, based on per-

mutation (black lines) and cloning (red lines) of aftershock records registered in **seq**, based on ETAS (solid lines) and MO (dashed lines) models.

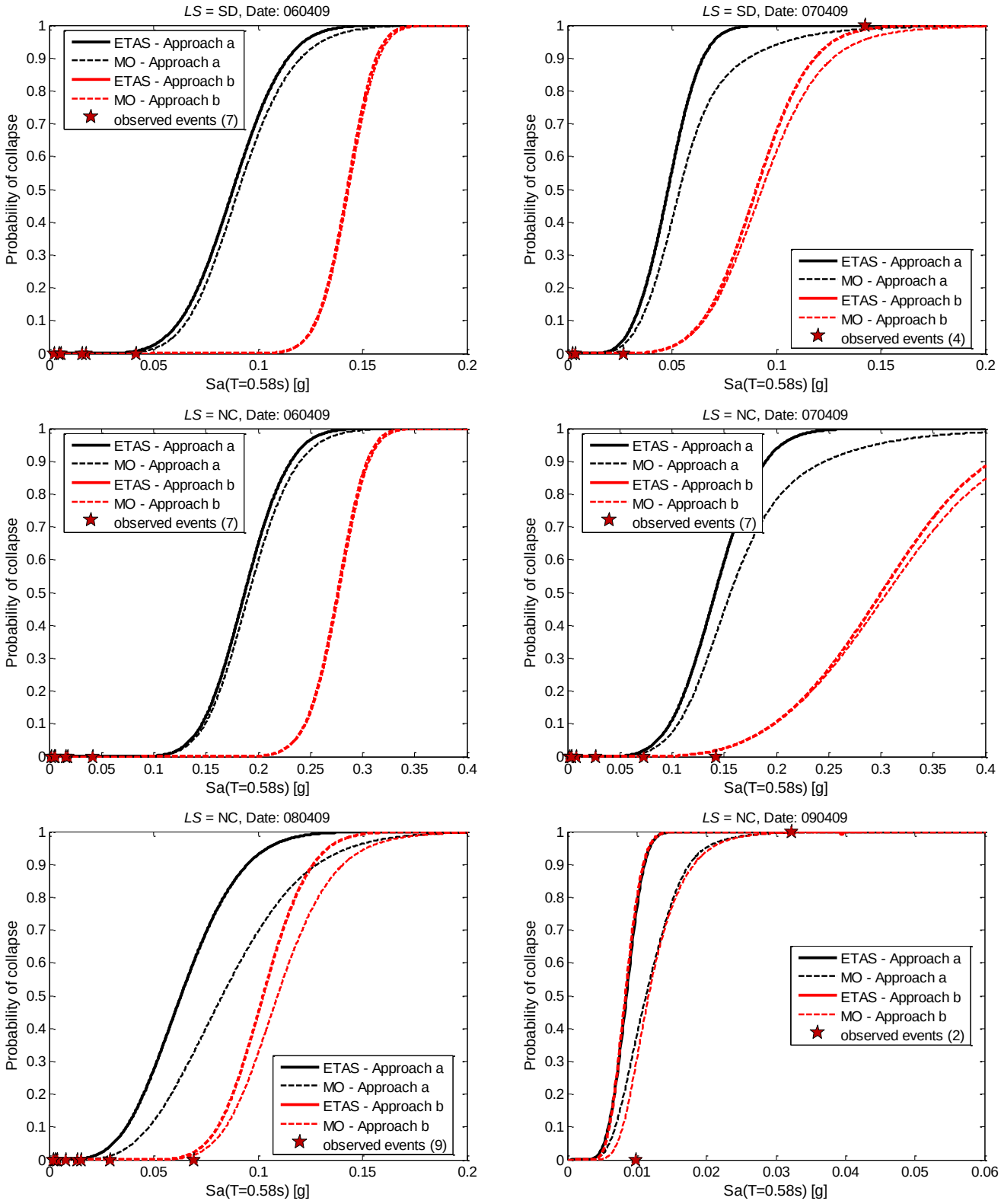


Figure 7: Forecasted daily fragility curves for the first four days, and both SD and NC limit states, based on ETAS (solid lines) and MO (dashed lines); ground motion selections strategy "a" (black lines), and "b" (red lines)

It can be depicted that the daily fragility curves based on cloning of the aftershock events are generally lower than those calculated based on permutation. This can be explained by the fact that the majority of the aftershock events are quite weak and the sequence generated by cloning them will be quite weak. Such a sequence, may fail to emulate the gradual increase in residual displacements in a real aftershock sequence. In this sense, the permutation strategy seems to provide a more realistic picture of the accumulation of damage due to a sequence of events with different magnitudes.

However, it should be kept in mind that the generated sequence $\mathbf{seq}_{\text{gen}}$ is created by selecting the previous registrations within the $\mathbf{seq}$. Given the time-dependent decreasing trend in the aftershock sequence, the permutation strategy may over-estimate the damage[9]. It is also observed that the daily fragility curves based on permutation and cloning in the fourth day are quite close. This can be attributed to the fact that the structure is very close to the onset of the limit state. This will make it vulnerable even to weaker aftershock sequences.

Discussion: From the engineering point of view, the forecasted fragility curves obtained through permutation seem to provide more robust predictions of the accumulation for residual damage in the structure. For instance, take the second-day event with local magnitude of 5.3 and $S_a\left(0.58\text{s}\right)=0.143g$ that causes the first SD limit state excursion. This is a key aftershock event which stimulates further residual deformations pushes the structure closer to the onset of NC limit state. It can be detected that the fragility curves (permutation strategy based on both ETAS and MO) predict NC first-excursion with probabilities ranging from 40% (MO) to around 50% (ETAS). This is true also for the third-day 5.1 magnitude aftershock event with $S_a\left(0.58\text{s}\right)=0.07g$ that leads to further accumulation of residual deformations and takes the structure even closer to the onset of NC. The fragility curve obtained through permutation predicts the NC first-excursion with probability 60% (ETAS-based). This is while fragility curve obtained through cloning predicts NC first-excursion with a small probability (around 2%).

4.6.2 *The daily fragility curves based on ETAS and MO methods*

Figure 8 illustrates the decrease in the structural vulnerability for DS (the first two days) and NC (the first four days) based on ETAS and MO models, adopting the permutation strategy, i.e. approach "a" in Section 4.5. It can be observed that the fragility curves obtained based on the two aftershock occurrence models are significantly different. The effect of the aftershock model on fragility estimation manifests itself through the probability distribution $P\left(n\,|\,\mathbf{I}_j\right)$. As demonstrated in Figure 4 (Section 4.4), the probability distributions $P\left(n\,|\,\mathbf{I}_j\right)$, built based on the two aftershock models ETAS and MO are quite different. As it was mentioned in Section 4.4, the ETAS model assigns zero probability to the event-dependent fragilities for n=0 to 5 ~10. Consequently, the ETAS model systematically shifts the probability content towards larger number of aftershocks per day. This means that the event-dependent fragilities for larger n are going to have a larger weight. This manifests itself into systematically larger fragility predictions based on ETAS compared to MO.

[9] In general, a stronger suite of records may manifest different frequency content characteristics with respect to the weaker records. As far as it concerns the cloud method, the domain of regression (i.e., the range of spectral acceleration values) is going to be shifted towards larger spectral acceleration values.

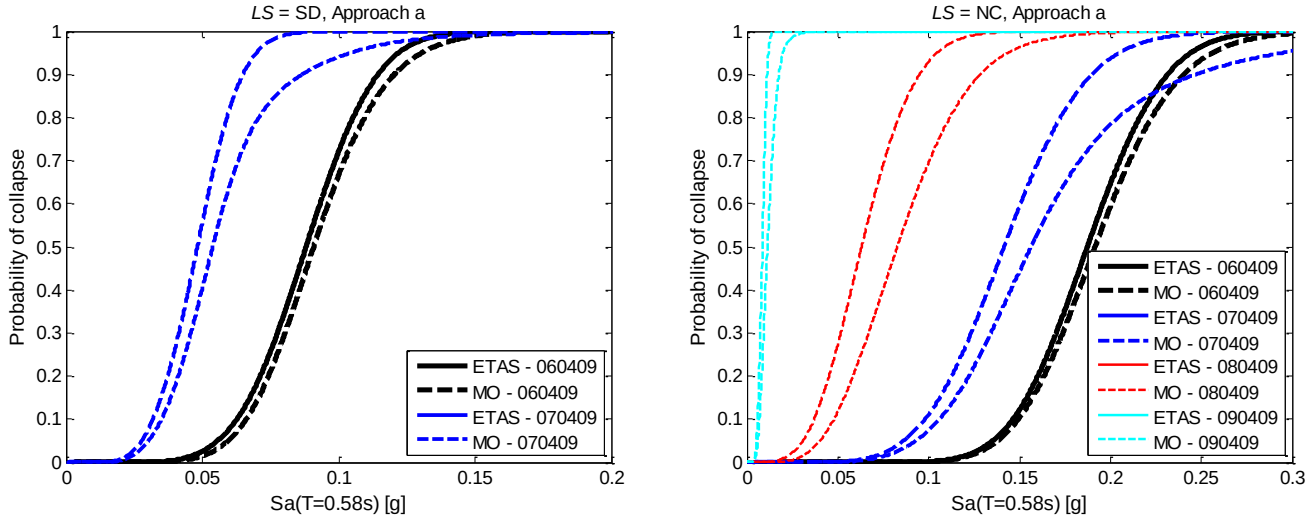


Figure 8: Forecasted daily-fragility curves (based on ETAS and MO models) for the first four days, and both for SD and NS limit states, ground motion selections strategy "a" (permutation)

4.6.3 *The daily fragility curves based on scaled strong motion recordings*

It is interesting to investigate if adopting a set of scaled ground motion records (instead of the registered aftershock records) as per [1, 12-13]) would also lead to reasonable results. In fact, this issue is addressed through strategies (c) and (d) for generating $\mathbf{seq}_{\text{gen}}$, outlined in Section 4.5. This simplifies the application of sequential cloud since it does not rely on after-shock records from the same sequence. Herein, a set of 15 European ground motion records ($N_{\text{seq}} = 15$) are chosen [5]. As mentioned in Section 4.5, these strong motion records are cloud-scaled so that their median spectral acceleration is equal to that of the ground motions within **seq**. Figure 10 illustrates the ETAS-based daily fragility curves (strategy (c): permutation, dashed lines) for limit states NC (first four days) and SD (first two days) compared to those based on strategy (a) (solid lines).

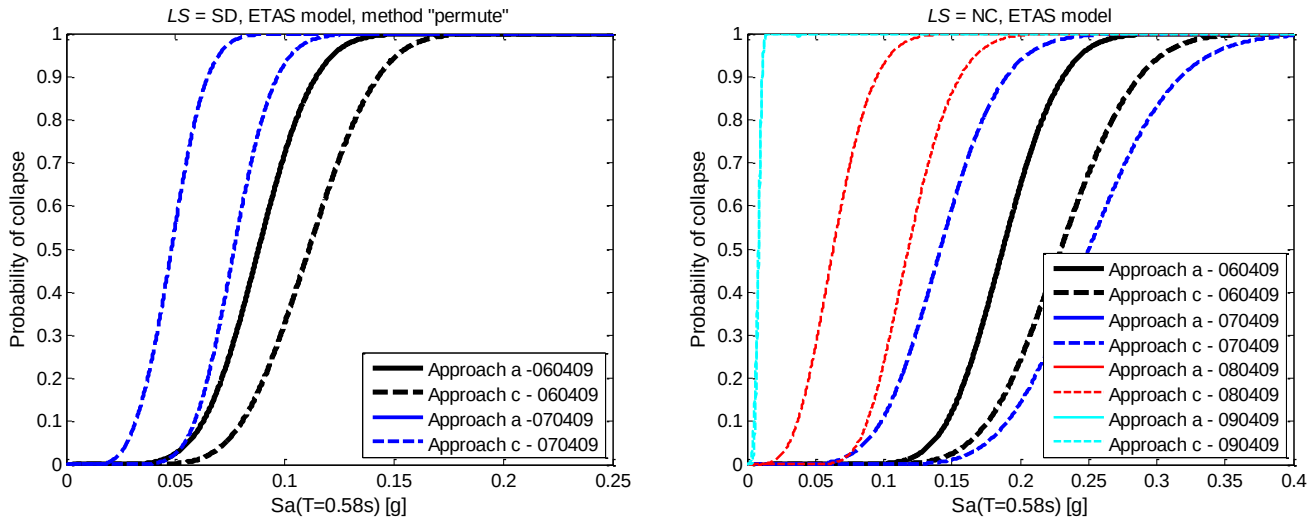


Figure 9: Forecasted daily fragility curves (ETAS) through strategy (a) and strategy (c) for SD (left) and NC (right) limit states

It can be observed that using the scaled strong motions systematically under-estimates the fragilities. This may be attributed to the change in the frequency content of the strong- and weak-motion records.

4.7 Daily aftershock risk forecasting

In this section daily aftershock risk, expressed in terms of the mean daily rate of exceeding limit states *SD* and *NC*, is calculated. This is done by the integration of the corresponding daily fragility and hazard curves. Figure 10 below illustrates the forecasted daily aftershock hazard curves, expressed in terms of mean daily rate of exceeding various levels of $S_a(0.58\text{s})$, denoted as $\lambda(x|\mathbf{I}_j)$ in Equation (7), for $3.3 \le M \le 7.5$ within the first four days after the main event (PASHA, see [11] for more details). It is should be noted that the parameters of the MO model (labeled as *seq-based*) as well as the ground motion prediction relation (Sabetta and Pugliese [25], labeled as *updated SP96*) are updated daily based on the L'Aquila sequence. In contrast to ETAS model hazard curves (solid lines) which take into account the spatio-temporal evolution of seismicity, the MO hazard curves (dashed lines) are based on the assumption of uniform seismicity in the aftershock zone (labeled as *uniform*). It can be seen that the ETAS-based hazard curves are larger than the MO-based ones, especially in the first few days elapsed after the main event. This is in line with the corresponding predictions for the number of events in Figure 4.

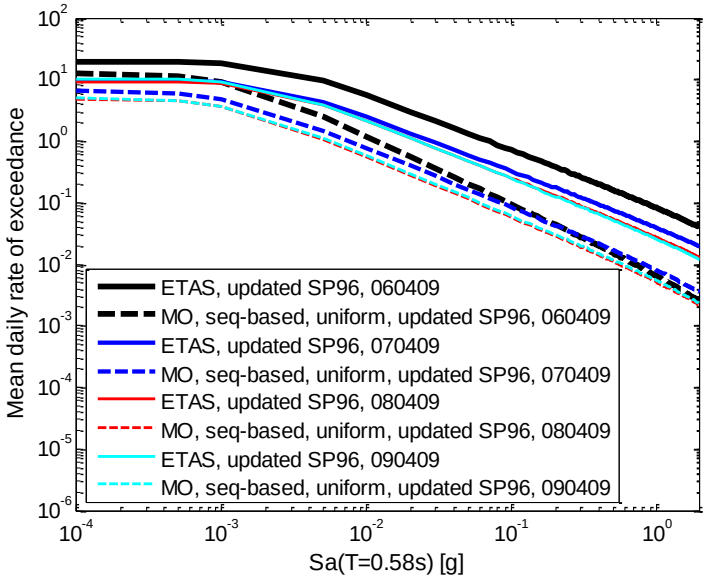


Figure 10: The mean daily rate of exceeding various levels of S_a(0.58s) based on MO and ETAS from 06/04/09 up to 09/04/09

Figure 12 illustrates the daily risk forecasts for two limit states SD and NC. The left-most column represents the ETAS-based results and the right-most column is dedicated to the MO-based results. The risk estimates obtained through strategies (a), (b), (c) and (d) are plotted as circles (black), squares (blue), triangles (red) and stars (cyan), respectively. The following observations can be made:

- The difference between the daily risk predictions based on MO and ETAS models arises from both the difference in the daily fragility and hazard forecasts. The MO model leads to systematically lower values.

- As it can be seen, the first-excursion of NC limit state in the fourth day is accurately predicted by both models. Both models predicts first-excursion of NC between during between day 3 and day 4 (i.e., when the mean day rate is equal to 1/day).
- On the other hand, the first-excursion of SD limit state is not signaled as accurately. The ETAS model (strategy (a)) predicts the risk around 0.65/day (sufficiently alarming); meanwhile the MO model (strategy (a)) predicts the risk around 0.20/day. This under-estimation can be attributed to the hazard forecasting. That is, in the second day elapsed after the main event, another seisimo-genetic structure became active and none of the two models managed to predict the hazard very well for this particular day (although ETAS did better than MO).
- The risk predictions based on ETAS method reveal higher sensitivity to the sequential cloud analysis strategies compared to MO model. In general, the strategy (a), which is based on selecting records from the ongoing sequence and generating the sequence by permutation, lead to the highest risk estimates.

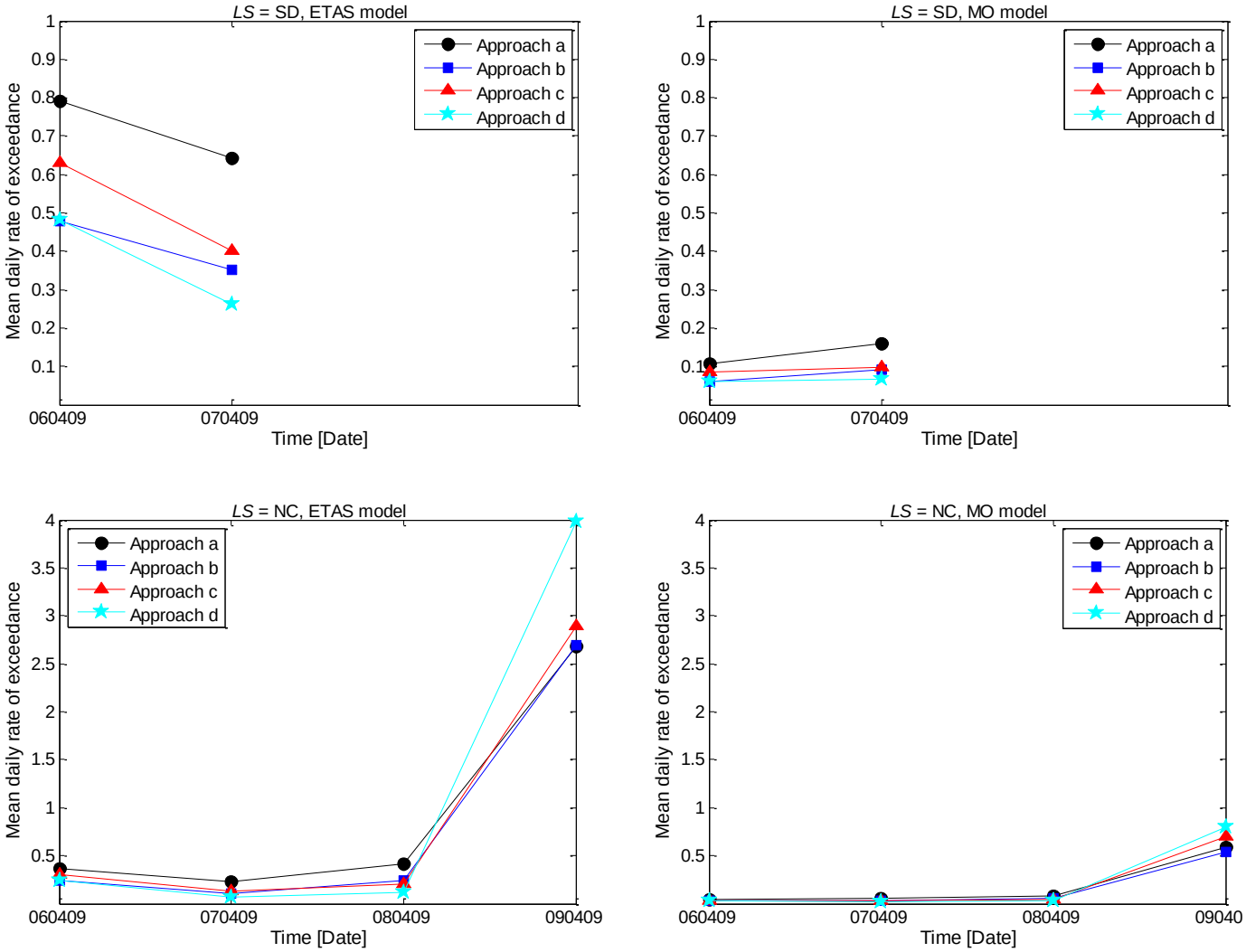


Figure 12: Daily risk forecasting for SD (upper-most row) and NC (lower-most row) limit states for the first four days from 06/04/09 to 09/04/09 based on ETAS (left-most column) and MO (right-most column)

5 CONCLUSIONS

This paper explores the various issue related to performance-based time-dependent vulnerability assessment in the presence of an ongoing aftershock sequence. This is done in the framework of operation aftershock risk forecasting. Arguably, operational risk forecasting provides a quantified support basis for rapid decision making the immediate post main event environment. The structural vulnerability in such a framework can be represented by daily fragility curves, conditional first-excursion probabilities given seismic intensity, for prescribed structural limit states. The performance objective for each limit state is defined through adoption of a novel structural performance variable. This variable is defined as the time-dependent ratio of maximum demand increment to residual limit state capacity and is equal to unity at the onset of the limit state in consideration.

An existing time-dependent risk assessment methodology proposed in [5] and [20] is modified and improved in order to construct the daily fragility curves. In this methodology, the daily fragility curves are calculated as a weighted sum of event-dependent fragility curves (the conditional first-excursion probability given that exactly *n* events have taken place). The weights are equal to the probability that exactly *n* aftershock events take place in each given day. This probability distribution is constructed based on two established aftershock recurrence models, namely, Epidemic Type Aftershock Sequence (ETAS) and Modified Omori (MO). The event-based fragility curves are calculated next through a recursive formulation as the sum of a sequence of probabilities that the first-excursion takes place after the occurrence of a certain event (within the *n* events). A non-linear dynamic analysis procedure entitled sequential cloud analysis is developed in order to calculate the latter sequence of first-excursion probabilities. In this method, the record sequence selection/generation is done by adopting four different strategies: (a) generation of a sequence by permutation of aftershock events registered previously in the ongoing sequence; (b) generation of a sequence by back-to-back repeating (cloning) of aftershock events registered previously in the ongoing sequence; (c) generation of a sequence by permutation of cloud-scaled strong motion records; (d) generation of a sequence by cloning of cloud-scaled strong motion records.

Finally, daily risk predictions, expressed in terms of the mean daily rate of limit-state first-excursion, are calculated by integrating daily hazard and fragility predictions. The daily hazard predictions are furnished from a previous work of the authors [11]. In general, the following observations can be made with regard to the case-study application demonstrated for the L'Aquila 2009 seismic sequence:

- The daily fragility predictions are quite sensitive to both the underlying aftershock model and the alternative sequence generation strategies. Overall, it seems that adopting ETAS as the underlying aftershock model and sequence generation by permutation of previous events within the ongoing sequence (strategy a) lead to the best estimates. The structural response to the real sequence is used as a benchmark for comparison.
- In particular, the probability distributions for the number of aftershock events per day, which are used as weights in the calculation of daily fragilities, significantly affect the results.
- For the example SDOF system studied herein, risk forecasting based on both ETAS and MO models manages to capture the first-excursion of near collapse NC limit state in the fourth day elapsed after the main event.
- However, for the limit state of severe damage SD neither of the two methods can provide accurate estimates of risk in the second day (although both methods signal a critical situa-

tion). This can be attributed to the short-coming of both methods in predicting the seismic hazard in the second day, due to the activation of a second fault structure.

As a final word for near future developments, it would be interesting to apply the present methodology for a range of generic SDOF and MDOF structural models in order to gain a better insight into the factors that affect the time-dependent fragility assessment in the presence of an ongoing seismic sequence.

REFERENCES

[1] Q. Li, B.R. Ellingwood, Performance evaluation and damage assessment of steel frame buildings under main shock-aftershock sequences. *Earthquake Engineering and Structural Dynamics*, **36**, 405-427, 2007.

[2] G.L. Yeo, C.A. Cornell, Post-quake decision analysis using dynamic programming. *Earthquake Engineering and Structural Dynamics*, **38**, 79-93, 2009.

[3] G.L. Yeo, C.A. Cornell, Equivalent constant rates for post-quake seismic decision making. *Structural Safety*, **31**, 443-447, 2009.

[4] K. Goda, C.A. Taylor, Effects of aftershocks on peak ductility demand due to strong ground motion records from shallow crustal earthquakes. *Earthquake Engineering and Structural Dynamics*, **41**(15), 2311-2330, 2012.

[5] F. Jalayer, D. Asprone, A. Prota, G. Manfredi, A decision support system for post-earthquake reliability assessment of structures subjected to aftershocks: an application to L'Aquila earthquake, 2009. *Bulletin of Earthquake Engineering*, **9**(4), 997-1014, 2011.

[6] J.R. Benjamin, C.A. Cornell, *Probability, statistics and decision for civil engineers*. McGraw Hill, 684pp, 1970.

[7] C.A. Cornell, F. Jalayer, R.O. Hamburger, D.A. Foutch, Probabilistic Basis for the 2000 SAC Federal Emergency Management Agency Steel Moment Frame Guidelines. *ASCE Journal of Structural Engineering*, **128**, 526-533, 2002.

[8] Y. Ogata, Statistical models for earthquake occurrences and residual analysis for point processes. *Journal of the American Statistical Association*, **83**, 9-27, 1988.

[9] W. Marzocchi, A.M. Lombardi, Real-time forecasting following a damaging earthquake, *Geophysical Research Letters*, **36**, L21302, 2009, doi 10.1029/2009GL040233.

[10] T. Utsu, A statistical study of the occurrence of aftershocks. *Geophysical Magazine*, **30**, 521-605, 1961.

[11] H. Ebrahimian, F. Jalayer, D. Asprone, A.M. Lombardi, W. Marzocchi, A. Prota, G. Manfredi, Adaptive Daily Forecasting of Seismic Aftershock Hazard. *Bulletin of Seismological Society of America*, **submitted**.

[12] N. Luco, P. Bazzurro, C.A. Cornell, Dynamic versus static computation of the residual capacity of mainshock-damaged building to withstand an aftershock. In: *Proceedings 13th World Conference on Earthquake Engineering*, Vancouver, B.C., Canada, August 1-6, 2004, Paper No. 2405.

[13] J. Ruiz-García, J.C. Negrete-Manriquez, Evaluation of drift demands in existing steel frames under as-recorded far-field and near-fault mainshock–aftershock seismic sequences. *Engineering Structures,* **33**, 621-634, 2011.

[14] J. Ruiz-García, E. Miranda, Probabilistic estimation of residual drift demands for seismic assessment of multi-story framed buildings. *Engineering Structures,* **32**, 11-20, 2010.

[15] J. Ruiz-García, J.Y. Moreno, I.A. Maldonado, Evaluation of existing Mexican highway bridges under mainshock–aftershock seismic sequences. In: *Proceedings of the 14th World Conference on Earthquake Engineering*, Beijing, China, October 12-17, 2008, Paper No. 05-02-0090.

[16] G.D. Hatzigeorgiou, A.A. Liolios, Nonlinear behaviour of RC frames under repeated strong ground motions. *Soil Dynamics and Earthquake Engineering*, **30**, 1010-1025, 2010.

[17] F. Jalayer, P. Franchin, P.E. Pinto, A scalar damage measure for seismic reliability analysis of RC frames. *Earthquake Engineering and Structural Dynamics*, **36**, 2059-2079, 2007.

[18] Y. Ogata, Space-time point-process models for earthquake occurrences. *Annals of the Institute of Statistical Mathematics*, **50** (2), 379-402, 1998.

[19] H. Ebrahimian, F. Jalayer, D. Asprone, A.M. Lombardi, W. Marzocchi, A. Prota, G. Manfredi, Adaptive post-earthquake reliability assessment of structures subjected to aftershocks. *11th International Conference on Structural Safety & Reliability (ICOSSAR 2013*), Columbia University, New York, NY, June 16-20, 2013.

[20] F. Jalayer, D. Asprone, A. Prota, G. Manfredi, Multi-hazard upgrade decision making for critical infrastructure based on life-cycle cost criteria. *Earthquake Engineering and Structural Dynamics*, **40**(10), 1163-1179, 2011.

[21] E.T. Jaynes, *Probability Theory: The Logic Of Science*. Cambridge University Press, 2004.

[22] F. Jalayer, C.A. Cornell, A Technical Framework for Probability-Based Demand and Capacity Factor Design (DCFD) Seismic Formats. *Pacific Earthquake Engineering Center* (*PEER*) 2003/08, November 2003.

[23] CEN. *Eurocode 8: design of structures for earthquake resistance. Part 3: assessment and retrofitting of buildings.* EN 1998-3, CEN, Brussels, March 2005.

[24] D. Asprone, F. Jalayer, A. Prota, G. Manfredi, Proposal of a probabilistic model for multi-hazard risk assessment of structures in seismic zones subjected to blast for the limit state of collapse. *Structural Safety* **32**(1), 25-34, 2010.

[25] F. Sabetta, A. Pugliese, Estimation of response spectra and simulation of nonstationary earthquake ground motions. *Bulletin of Seismological Society of America*, **86**(2), 337-352, 1996.

COMPDYN 2013
4th ECCOMAS Thematic Conference on
Computational Methods in Structural Dynamics and Earthquake Engineering
M. Papadrakakis, V. Papadopoulos, V. Plevris (eds.)
Kos Island, Greece, 12–14 June 2013

NONSMOOTH ANALYSIS OF THE EARTHQUAKE-INDUCED POUNDING IN SKEW BRIDGES

Elias G. Dimitrakopoulos[1]

[1]Hong Kong University of Science and Technology
Department of Civil and Environmental Engineering, Kowloon, Clear Water Bay, Hong Kong
ilias@ust.hk

Keywords: skew bridges, oblique impact, unilateral contact, concrete bridges, linear complementarity problem, nonsmooth dynamics.

Abstract. *Skew bridges with separation/expansion joints are one of the most common types of existing bridges worldwide. Earthquake reconnaissance reports indicate that skew bridges often rotate in the horizontal plane, increasing the chances of unseating at their acute corners. This behaviour is triggered by the oblique, in-deck, contact which leads in coupling of the longitudinal and the transverse response, binding in one of the obtuse corners and subsequently rotation in the horizontal plane, in such a way that the skew angle increases. Despite the recorded evidence from previous earthquakes, and most empirical vulnerability methodologies, which acknowledge skew as a primary vulnerability factor of bridges, the relevant literature lacks a thorough theoretical study and is mostly confined to empirical descriptions of the phenomenon. This study examines both the case of deck-abutment impact, as well as, the impact between adjacent deck segments, of skew bridges. It shows that the coupling, and hence the unseating during an earthquake excitation, after deck-abutment collisions is not a factor of the skew angle alone, but rather of the total geometry in plan plus the contact parameters. Finally, it offers closed-form solutions for all physically feasible post-impact states observed in skew bridges.*

.

1 INTRODUCTION

The present paper examines the in-deck, as well as, the deck-abutment impact of skew bridges. On the same time, it belongs to a broader study [1]–[5] on the problem of the earthquake-induced pounding in (straight and skew) bridges. The aim of this research is to shed light on the impact-induced rotations in skew bridges deploying a nonsmooth dynamics methodology.

Skew bridges with expansion joints are one of the most common types of existing bridges worldwide. The recorded evidence from previous earthquakes [6] indicates that skew bridges often rotate (during earthquake excitation) in the horizontal plane, tending to drop off the supports at their acute corners [7] (Fig. 1). This behavior is triggered primarily by the oblique, impact at the expansion/separation joints and leads in coupling of longitudinal and transverse response, binding in one of the obtuse corners and subsequently rotation about that corner in such a way that the skew angle increases (Fig. 1).

The phenomenon of oblique multi-contact is the main gap in the existing knowledge regarding the seismic response of skew bridges. The recorded evidence from previous earthquakes and the empirical vulnerability methodologies that acknowledge skew as a primary vulnerability factor in bridges, create incentive to comprehend this mechanism. Impact in skew bridges has been primarily tackled with the contact element (or "compliance") approach [8], [9]. This study though, offers an in-depth analysis of the oblique and frictional impact of skew bridges within the context of nonsmooth dynamics. To this end, the study deploys a fully nonsmooth rigid body approach and uses set-valued force laws [10]. The proposed formulation captures all physically feasible impact states (such as multi-impact, multi-slip or stick) through a linear-complementarity problem.

The motivation for this research originates from (i) the need to elucidate the seismic response of skew bridges, (ii) the importance of this non-conventional behavior, manifested by empirical evidence, and (iii) the large number of existing bridges of this type worldwide.

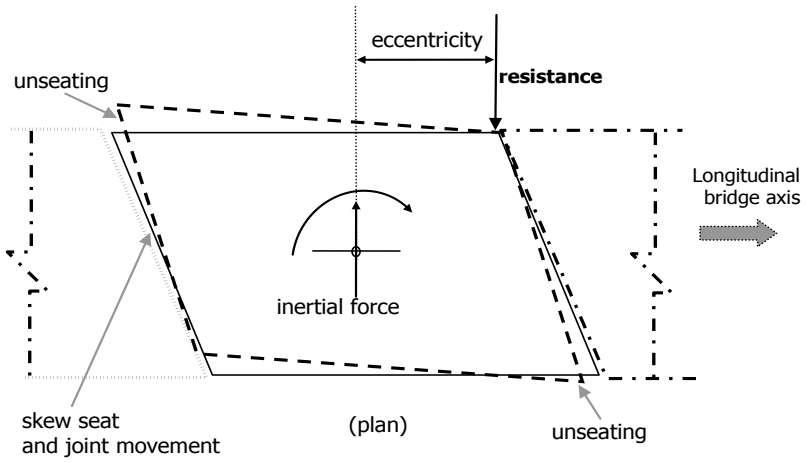


Figure 1: Rotation mechanism of skew bridges – potential unseating, adopted from [7].

2 PROPOSED NONSMOOTH DYNAMICS APPROACH

This study considers the individual bridge deck segments (in-between two successive separation/expansion joints) as rigid bodies moving on the horizontal plane and the abutments as inelastic half-spaces. The study further assumes that the interaction between adjacent segments, or between the deck and the abutment, is a unilateral contact and adopts the simplest impact laws, in a set-valued form [11], to describe this interaction.

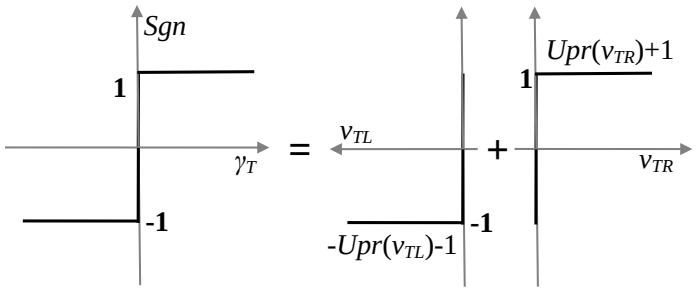


Figure 2: Set-valued friction force law.

In particular, the unilateral primitive *Upr* (e.g. Fig. 2, right) and Newton's coefficient of restitution $\varepsilon_N \in [0,1]$ describe the behavior in the normal direction of contact. A different set-valued map, the *Sgn*(x) function, enforces the Coulomb's friction law in the tangential direction of contact: $-\Lambda_{Ti} \in \mu_i \Lambda_{Ni}\,\mathrm{Sgn}\left(\gamma_{Ti}^{+}\right)$ where μ is the coefficient of friction and Λ_{Ti} the tangential impulse at contact *i*. The *Sgn*(x) function differs from the standard *sgn* function at the point x = 0, where the former yields a set of values: *Sgn*(*x* = 0) = [−1, 1], instead of a single value *sgn*(x = 0) = 0. Key role in this approach holds the decomposition of Fig. 2, which restores the complementarity conditions in the tangential direction of impact [4].

In integrated form the Newton – Euler equations are:

$$\mathbf{M}(\mathbf{u}^{+} - \mathbf{u}^{-}) = \mathbf{W}_{\mathrm{N}}\boldsymbol{\Lambda}_{\mathrm{N}} + \mathbf{W}_{T}\boldsymbol{\Lambda}_{T} \tag{1}$$

where $\mathbf{M}$ is the mass matrix and $\mathbf{W}$ are the direction matrices of the impulse vectors $\boldsymbol{\Lambda}$. Throughout this paper, superscript "+" refers to the post-impact state and super-script "–" to the pre-impact state, while sub-indexes *N, T* indicate the normal and the tangential direction of contact respectively. For the generalized velocities $\mathbf{u}$ and the generalized coordinates $\mathbf{q}$, $\dot{\mathbf{q}} = \mathbf{u}$ holds in an "*almost everywhere"* sense of functional analysis [11].

The relative (contact) velocities in the normal γ_N and the tangential γ_T direction are given by:

$$\begin{aligned} \boldsymbol{\gamma}_N^{+} - \boldsymbol{\gamma}_N^{-} &= \mathbf{G}_{NN}\boldsymbol{\Lambda}_{\mathrm{N}} + \mathbf{G}_{NT}\boldsymbol{\Lambda}_{T} \\ \boldsymbol{\gamma}_T^{+} - \boldsymbol{\gamma}_T^{-} &= \mathbf{G}_{TN}\boldsymbol{\Lambda}_{\mathrm{N}} + \mathbf{G}_{TT}\boldsymbol{\Lambda}_{T} \end{aligned} \tag{2}$$

where the "G" matrices are:

$$\begin{aligned} \mathbf{G}_{NN} &= \mathbf{W}_N^{T}\mathbf{M}^{-1}\mathbf{W}_{\mathrm{N}} \quad \mathbf{G}_{NT} = \mathbf{W}_N^{T}\mathbf{M}^{-1}\mathbf{W}_{T} \\ \mathbf{G}_{TN} &= \mathbf{W}_T^{T}\mathbf{M}^{-1}\mathbf{W}_{N} \quad G_{TT} = \mathbf{W}_T^{T}\mathbf{M}^{-1}\mathbf{W}_{T} \end{aligned} \tag{3}$$

Following the procedure outlined in [1], [4] the problem of the frictional multi-impact is formulated as a *linear complementarity problem* (LCP):

$$\begin{pmatrix} \mathbf{v}_N \\ v_{TR} \\ \Lambda_{TL} \end{pmatrix} = \begin{pmatrix} \mathbf{G}_{NN} - \mathbf{G}_{NT}\bar{\bar{\boldsymbol{\mu}}} & \mathbf{G}_{NT} & \mathbf{0} \\ \mathbf{G}_{TN} - G_{TT}\bar{\bar{\boldsymbol{\mu}}} & G_{TT} & 1 \\ 2\bar{\bar{\boldsymbol{\mu}}} & -1 & 0 \end{pmatrix} \begin{pmatrix} \boldsymbol{\Lambda}_N \\ \Lambda_{TR} \\ v_{TL} \end{pmatrix} + \begin{pmatrix} \left(\bar{\bar{\varepsilon}}_{\mathrm{N}} + \mathbf{E}\right)\boldsymbol{\gamma}_N^{-} \\ \gamma_T^{-} \\ 0 \end{pmatrix} \tag{4}$$

with the pertinent complementarity conditions being:

$$\begin{pmatrix} \mathbf{v}_N \\ v_{TR} \\ \Lambda_{TL} \end{pmatrix} \geq 0, \begin{pmatrix} \mathbf{\Lambda}_N \\ \Lambda_{TR} \\ v_{TL} \end{pmatrix} \geq 0, \quad \begin{pmatrix} \mathbf{v}_N \\ v_{TR} \\ \Lambda_{TL} \end{pmatrix}^T \begin{pmatrix} \mathbf{\Lambda}_N \\ \Lambda_{TR} \\ v_{TL} \end{pmatrix} = 0 \tag{5}$$

In which v_{TR} and v_{TL} are the right and left velocity-parts of the post-impact tangential velocity: $\gamma_{Ti}^{+} = v_{TRi} - v_{TLi}$, Λ_{TR} and Λ_{TL} are the corresponding impulses (Fig. 2) and $\mathbf{E}$ is the identity matrix. The proposed LCP (4), (5) encapsulates a great variety of impact states such as "slip", "stick", reversal of sign and nonimpulsive behaviour both for single-impact and multi (point)-impact (see section 4).

3 SKEW DECK-ABUTMENT IMPACT

The present section examines the different, deck-abutment, impact states that might occur within the deck of a skew bridge. The discussion starts from the (simpler) frictionless case, then focuses on double (point) frictional impact and finally summarizes single (point) impact as a special case of the pertinent double impact case. Section 4 presents, in a similar fashion, the in-deck impact of adjacent skew deck segments.

3.1 Double frictionless impact

When the pre-impact rotation is zero $\theta^{-}=0$ full-edge impact occurs between the deck (rigid body) and the abutment (inelastic half-space). Herein, full-edge impact (Fig. 3) is modeled (and referred to) as double impact due to the rigid body assumption.

In order to determine the unknown generalized velocities after impact, $\mathbf{u}^{+}$, one has to calculate first the corresponding impulses Λ_N. From Newton's impact law it follows that:

$$\mathbf{\Lambda}_N = -\mathbf{G}_{NN}^{-1}(\mathbf{E} + \bar{\bar{\boldsymbol{\varepsilon}}}_N)\boldsymbol{\gamma}_N^{-} \tag{6}$$

For the frictionless double impact of Fig. 3, Eqn (6) yields:

$$\begin{pmatrix} \dfrac{\Lambda_{N1}}{m\gamma_N^{-}} \\ \dfrac{\Lambda_{N2}}{m\gamma_N^{-}} \end{pmatrix} = -(1+\varepsilon_N) \begin{pmatrix} -\dfrac{r_2}{r_1 - r_2} \\ \dfrac{r_1}{r_1 - r_2} \end{pmatrix} = -\frac{(1+\varepsilon_N)}{2} \begin{pmatrix} 1-\eta_0 \\ 1+\eta_0 \end{pmatrix} \tag{7}$$

Equation (7) gives impulses Λ_{N1} and Λ_{N2} as a function of the geometry (α, L, W, *see* Fig. 3), the coefficient of restitution in the normal direction ε_N, and the translational mass m. However, Eqns.(7) are incomplete without the physical inequality constraint $\Lambda_N \geq 0$ which accounts for the unilateral nature of impact. Taking into account that by definition: $m(1+\varepsilon_N) > 0$, and that in order for contact to occur the relative velocity must be negative (which denotes an approach process), the sign of impulse depends solely on the dimensionless criterion, η_0, proposed in [1] which relates the ratio of the two sides in plan (L,W) with the skew angle, α, as follows:

$$\eta_0 = \frac{\sin 2\alpha}{2(W/L)} \tag{8}$$

For $\eta_0 > 1$, impulse at the acute corner is negative $\Lambda_{N1} < 0$ (Eqn.7), which violates the unilateral character of dry impact. The physical interpretation of a negative impulse, in this case, is that contact at that particular point is lost and hence the formulation of the impact problem

as double impact does not hold. Instead, when $\eta_0 > 1$, the impact problem should be treated as a single impact at the obtuse corner at which the impulse is always positive, $\Lambda_{N2} > 0$ (Eqn. 7). Hence, two distinct deck-abutment impact response patterns emerge: when $\eta_0 < 1$ (Fig. 3 top), the angular momentums of the two impulses Λ_{N1} and Λ_{N2} about the centre of mass (C.M.) are of a different sense and cancel out; as a consequence no (post-impact) angular velocity is developed [1]. On the contrary, when $\eta_0 > 1$ (Figure 6 bottom) impulse at the acute corner is lost, impact is effectively a single-impact, solely at the obtuse corner, and as a result angular velocity is developed due to impact. These observations unveil a complex, non-intuitive impact behavior that has not received the attention it deserves in relevant literature.

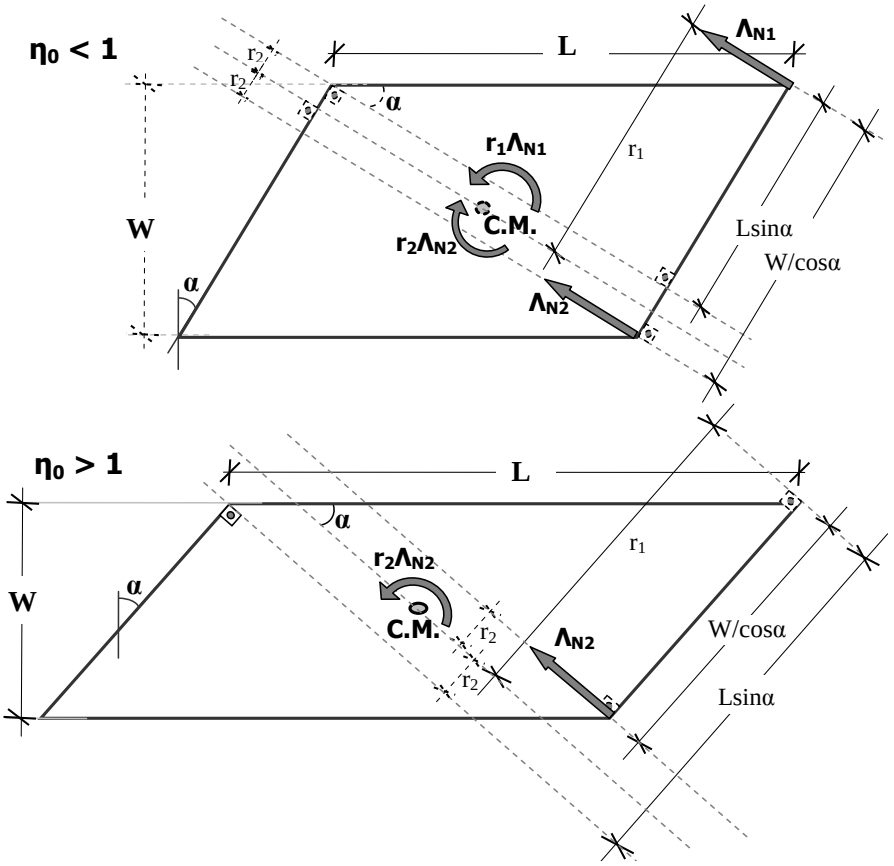


Figure 3: Geometry of the rocking masonry wall for (a) positive and (b) negative rotations.

3.2 Double frictional impact

In order to obtain a more realistic description of the deck-abutment impact of skew bridges, this section takes into account the presence of friction during impact. For the examined double frictional impact problem, the proposed LCP Eqns.(4 ,5) yields a great variety of potential solutions, in particular: three impact-states (backward slip, forward slip and stick) for each of the two contact points, when only one contact point is active (i.e. six single-impact states in total) and, in addition, three impact states when both contact points are active (double backward slip, double forward slip and double stick). Double impacts for which $\Lambda_N = 0$ holds at both impact points, lack physical interpretation and are not considered.

Friction perplexes the formulation of the double-impact problem of Fig. (3). The main difficulty lies in the linear dependency of the two impacts in the tangential direction, which

causes the appearance of singular matrices. The present study offers (in Section 4.2) a rational method to avoid the singularities arising from dependent constraints.

The response of the examined oblique frictional multi-impact configuration depends on (a) the geometry (in the form of the proposed dimensionless criterion η_0) and (b) on the kinematics (the tangential and the normal pre-impact velocity ratio) and the contact parameters (ε_N and μ). The former (a) determines if a contact point is active, while the latter (b) whether the double impact is forward/backward slip or stick.

The impulse and the tangential velocity for all physically feasible post-impact states can be summarized as follows:

Double slip: When double slip occurs $\Lambda_{N1} >0$, $\Lambda_{N2} >0$ and $\Lambda_T = \mp\mu\left(\Lambda_{N1}+\Lambda_{N2}\right)$, the impulses in the normal direction of the two (active) contact points are calculated from the LCP (Eqns. 4 and 5) as:

$$\begin{pmatrix} \dfrac{\Lambda_{N1}}{m\gamma_N^-} \\ \dfrac{\Lambda_{N2}}{m\gamma_N^-} \end{pmatrix} = \left(1+\varepsilon_{\mathrm{N}}\right) \begin{pmatrix} \dfrac{r_2 \pm \mu r_T}{r_1 - r_2} \\ \dfrac{r_1 \pm \mu r_T}{r_2 - r_1} \end{pmatrix} \tag{9}$$

The corresponding post-impact tangential velocity is (Eqns. 4 and 5):

$$\frac{\gamma_T^+}{\gamma_N^-} = \frac{1}{\varepsilon_N}\frac{\gamma_T^-}{\gamma_N^-} \pm \frac{-1-\varepsilon_N}{\varepsilon_N}\mu \tag{10}$$

In Eqns. (9) and (10) the positive sign (+) holds for backward slip and the negative sign (-) for forward slip.

Double stick: The impulses in the normal direction of the two (active) contact points ($\Lambda_{N1} >0$, $\Lambda_{N2} >0$) and the resultant impulse in the tangential direction $\left|\Lambda_T\right| < \mu\left(\Lambda_{N1}+\Lambda_{N2}\right)$ are given by Eqns. (20) (presented later in Section 4.2 and in [4]). The final expressions, which agree with the results of a different ad-hoc approach [1], are :

$$\begin{pmatrix} \dfrac{\Lambda_{N1}}{m\gamma_N^-} \\ \dfrac{\Lambda_{N2}}{m\gamma_N^-} \end{pmatrix} = \begin{pmatrix} \dfrac{r_T}{r_1 - r_2}\dfrac{\gamma_T^-}{\gamma_N^-} + \dfrac{r_2}{r_1 - r_2}\left(1+\varepsilon_N\right) \\ -\dfrac{r_T}{r_1 - r_2}\dfrac{\gamma_T^-}{\gamma_N^-} - \dfrac{r_1}{r_1 - r_2}\left(1+\varepsilon_N\right) \end{pmatrix} \text{ and } \frac{\Lambda_T}{m\gamma_N^-} = -\frac{\gamma_T^-}{\gamma_N^-} \tag{11}$$

Single slip: when impact takes place (solely) at the obtuse corner ($\Lambda_{N2} >0$, $\Lambda_{N1} =0$, and $\Lambda_T = \mp\mu\Lambda_{N2}$) the normal impulse is (Eqns. 4 and 5):

$$\frac{\Lambda_{N2}}{m\gamma_N^-} = -\frac{1+\varepsilon_N}{1+\dfrac{r_2^2 \pm \mu r_2 r_T}{I/m}} \tag{12}$$

Where I is the mass moment of inertia of the rigid body (deck-segment). Again in Eqns. (15) the positive sign (+) holds for backward slip and the negative sign (-) for forward slip. The corresponding post-impact tangential velocity is then:

$$\frac{\gamma_T^+}{\gamma_N^-} = \frac{\gamma_T^-}{\gamma_N^-} - \frac{r_2 r_T \pm \mu\left(I/m + r_T^2\right)}{I/m + r_2^2 \pm \mu r_2 r_T}\left(1+\varepsilon_N\right) \tag{13}$$

Note that backward slip at the acute corner ($\Lambda_{N1} >0$, $\Lambda_{N2} =0$, and $\Lambda_T = +\mu\Lambda_{N1}$) is not physically feasible [1].

Single Stick: When stick at the obtuse corner occurs ($\Lambda_{N2} >0$, $\Lambda_{N1} =0$, and $|\Lambda_T| < \mu\Lambda_{N2}$), the impulses in the normal and the tangential direction are (Eqns. 4 and 5):

$$\frac{\Lambda_{N2}}{m\gamma_N^-} = \frac{-\left(I/m + r_T^2\right)\left(1+\varepsilon_N\right) + r_2 r_T \dfrac{\gamma_T^-}{\gamma_N^-}}{I/m + r_2^2 + r_T^2} \qquad \frac{\Lambda_T}{m\gamma_N^-} = \frac{r_2 r_T\left(1+\varepsilon_N\right) - \left(I/m + r_2^2\right)\dfrac{\gamma_T^-}{\gamma_N^-}}{I/m + r_2^2 + r_T^2} \tag{14}$$

Slip/stick at the acute corner is described also by Eqns. (12 and 13)/(14 and 15) substituting lever r_2 with lever r_1.

3.3 Single frictional impact

When the pre-impact rotation of the rigid body (deck-segment) is non-zero, single point impact takes place. The proposed LCP (Eqns. 4, 5) describes also single frictional impacts, as a special case when only one impact point is active (i.e. $\Lambda_N > 0$ holds at that point). In particular, the closed-form solutions of Section 3.2 for single-impacts hold provided the appropriate levers r_1, r_2 and r_T are used. Figure 4 presents sample results of the existential conditions of the three distinct (single) impact states (forward slip, backward slip and stick).

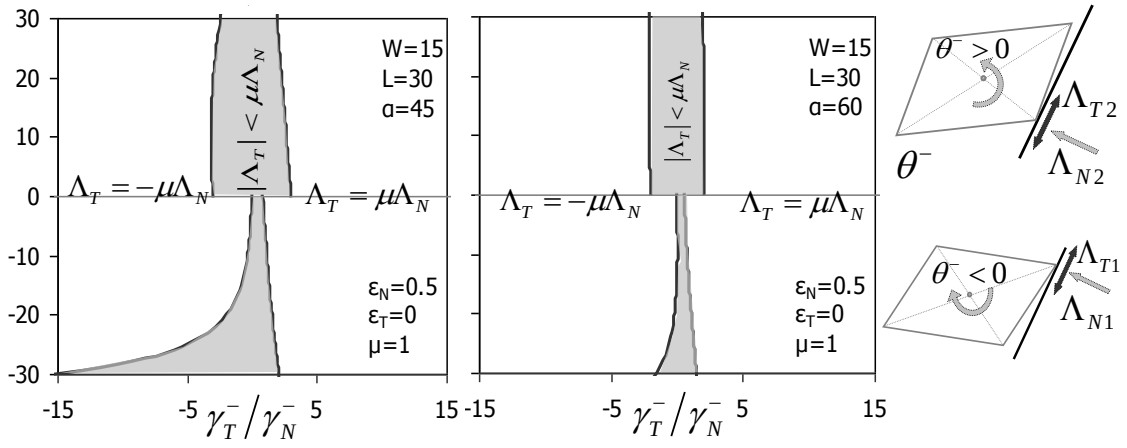


Figure 4: The three distinct single frictional impact states in the $\gamma_T^-/\gamma_N^-, \theta^-$ plane for coefficient of restitution ε_N = 0.5, skew angle α =45° (left), 60° (right), coefficient of friction μ = 1.

4 IN-DECK SKEW BRIDGE IMPACT

This section describes the impact between two adjacent skew bridge-segments (Fig. 5). A detailed discussion of the kinematics of a pair of skew rigid bodies (adjacent deck segments) is offered in [4]. The present study though focuses on the description of the physically feasible post-impact conditions for the configuration of Fig. 5.

4.1 Double frictionless impact

Again, utilizing the rigid body assumption, full-edge impact is modeled as a double-point impact and the discussion starts with the frictionless case. With reference to Fig. 5, full-edge contact occurs when the two bodies come to contact while their pre-impact rotations are the same $\theta_1^- = \theta_2^-$. In the following, without loss of generality it is as assumed that: $\theta_1^- = \theta_2^- = 0$.

Inequalities (16) give the conditions under which the sign of the two point impulses is positive, or in other words, the corresponding contact point is active.

$$\begin{aligned} \Lambda_{N1} > 0 &\Rightarrow \frac{I_1}{I_2} > \frac{\eta_1 - 1}{\eta_2 + 1} \\ \Lambda_{N2} > 0 &\Rightarrow \frac{I_2}{I_1} > \frac{\eta_2 - 1}{\eta_1 + 1} \end{aligned}, \quad \eta_j = \frac{\sin 2\alpha}{2\left(W/L_j\right)}, \quad j = 1,2 \tag{15}$$

Compared with the case of (skew) deck- abutment impact (Fig. 3), the impact mechanism of in-deck impact (Fig. 5) is considerably more complicated. In particular, the signs of the impulses depend not only on the geometry (the proposed dimensionless criteria η_1, η_2), but also on the ratio of the mass moments of inertial of the two bodies I_1/I_2. A simple parametric analysis shows that in most cases of practical interest both contact points are active. The solution of the Newton-Euler equations (1) shows that, unlike the deck-abutment case, in-deck double impact causes both rigid bodies (deck-segments) to rotate in the direction of increasing the skew angle, but with equal post-impact angular velocities. However, when impact is effectively single-point impact the two bodies develop different post-impact angular velocities and hence different rotations.

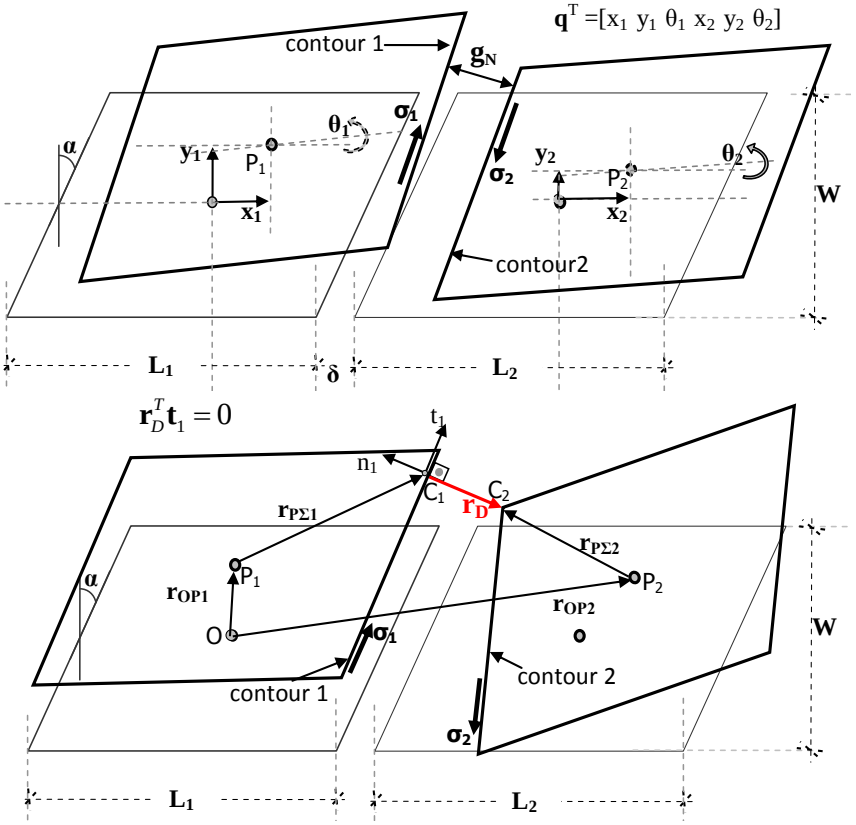


Figure 5: Geometry of two planar rigid bodies – simulating adjacent skew bridge segments.

4.2 Double frictional impact

Consider the frictional full-edge impact of two adjacent skew deck segments (Fig. 6). The "conventional" simulation approach is to consider the normal and the tangential impulses of each contact point explicitly: $\mathbf{\Lambda}_T = \left(\Lambda_{T1} \quad \Lambda_{T2}\right)^T$. This formulation of the double impact problem, neglects that the two (point) impacts are linearly dependent in the tangential direction and, as a consequence $\mathbf{G}_{NT}$, $\mathbf{G}_{TN}$ and $\mathbf{G}_{TT}$ (3) are all singular matrices (of size 2x2). This is a typical case of overconstrainted impacts which arise often in multibody dynamics with multi-contacts. The present study proposes an alternative description of the double impact, which does not over-constrain the problem and, on the same time, allows for a closed-form solution avoiding all singularities during solution of the LCP. Instead of examining the tangential impulse in each point explicitly, the proposed simulation considers solely the resultant (scalar) tangential impulse Λ_T (Fig. 6) resulting in $\mathbf{G}_{NT} = \mathbf{G}_{TN}^T$, $\mathbf{G}_{NT} \in \mathbb{R}^{2\times1}$, $\mathbf{G}_{TN} = \mathbf{G}_{NN}^T \in \mathbb{R}^{1\times2}$ and $G_{TT} \in \mathbb{R}^{1\times1}$.

Again, two conditions govern the post-impact state of the frictional multi-impact problem of Fig. 6: (i) the geometrical and inertial properties determine which contact points are active (the pertinent normal impulse is positive $\Lambda_N > 0$) and (ii) the kinematical conditions together with the contact parameters (ε_N and μ) determine whether the impact results in (forward/backward) slip or stick.

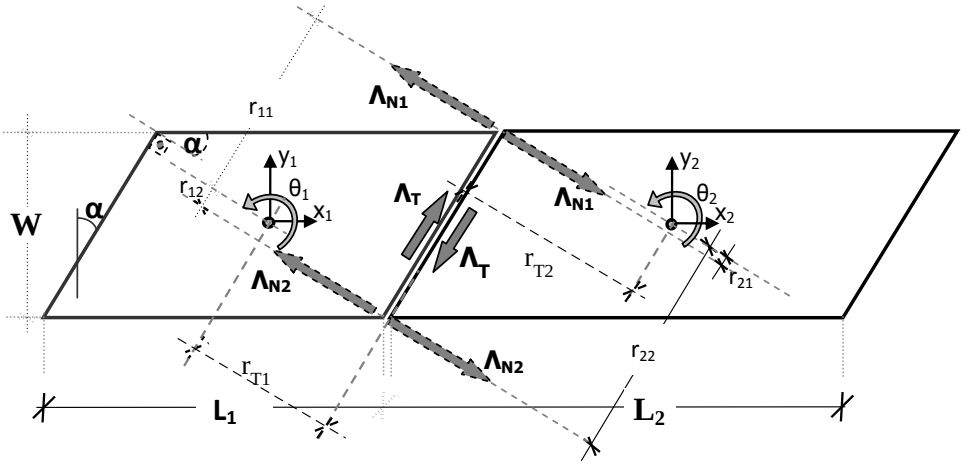


Figure 6: Full-edge frictional impact between two skew deck segments (considered as rigid bodies).

Double slip: with reference to Fig.6 (which shows levers r_{11}, r_{12}, r_{21}, r_{22}, r_{T1} and r_{T2}) the impulses in the normal direction of the two (active) contact points are (Eqns. 4 and 5):

$$\begin{pmatrix} \dfrac{\Lambda_{N1}}{\gamma_N^- M} \\ \dfrac{\Lambda_{N2}}{\gamma_N^- M} \end{pmatrix} = -\left(1+\varepsilon_N\right) \begin{pmatrix} \dfrac{\left(r_{12}-r_{11}\right)\left(r_{12} \pm \mu r_{T1}\right)}{I_1} + \dfrac{\left(r_{22}-r_{21}\right)\left(r_{22} \pm \mu r_{T2}\right)}{I_2} \\ \dfrac{\left(r_{11}-r_{12}\right)\left(r_{11} \pm \mu r_{T1}\right)}{I_1} + \dfrac{\left(r_{21}-r_{22}\right)\left(r_{21} \pm \mu r_{T2}\right)}{I_2} \end{pmatrix} \tag{16}$$

Where I_1, I_2 are the mass moment of inertias of the two bodies (deck-segments). The corresponding post-impact tangential velocity is:

$$\frac{\gamma_T^+}{\gamma_N^-}=\frac{\gamma_T^-}{\gamma_N^-}-(1+\varepsilon_N)M\left\{\begin{matrix}\frac{\mu}{\bar{m}}\left[\frac{(r_{11}-r_{12})^2}{I_1}+\frac{(r_{21}-r_{22})^2}{I_2}\right]+\\ \frac{1}{I_1I_2}\left[(r_{21}-r_{22})r_{T1}+\right]\left[(r_{21}-r_{22})\mu r_{T1}+\right.\\ \left.(r_{12}-r_{11})r_{T2}\right]\left[(r_{12}-r_{11})\mu r_{T2}\pm(r_{12}r_{21}-r_{11}r_{22})\right]\end{matrix}\right\} \tag{17}$$

Where $\bar{m}=\frac{m_1m_2}{m_1+m_2}$ and:

$$\frac{1}{M}=\frac{1}{\bar{m}}\left[\frac{(r_{11}-r_{12})^2}{I_1}+\frac{(r_{21}-r_{22})^2}{I_2}\right]+\frac{r_{12}r_{21}-r_{11}r_{22}}{I_1I_2}\left[\begin{matrix}\pm(r_{21}-r_{22})\mu r_{T1}\pm(r_{12}-r_{11})\mu r_{T2}\\ +r_{12}r_{21}-r_{11}r_{22}\end{matrix}\right] \tag{18}$$

In Eqns. (17) to (19) the positive sign (+) holds for backward slip and the negative sign (-) for forward slip respectively.

Double stick: When $\Lambda_{N1}>0$, $\Lambda_{N2}>0$ and $|\Lambda_T|<\mu(\Lambda_{N1}+\Lambda_{N2})=\bar{\bar{\boldsymbol{\mu}}}\boldsymbol{\Lambda}_N$, double stick takes place and the corresponding post-impact velocities are zero. The impulses in the normal direction of the two (active) contact points and the resultant impulse in the tangential direction are (Eqns. 4 and 5):

$$\begin{aligned}\boldsymbol{\Lambda}_N&=\frac{1}{G_{TT}-\mathbf{G}_{TN}\mathbf{G}_{NN}^{-1}\mathbf{G}_{NT}}\left[\mathbf{G}_{NN}^{-1}\mathbf{G}_{NT}\gamma_T^--\left[\begin{matrix}\mathbf{G}_{NN}^{-1}\mathbf{G}_{NT}\mathbf{G}_{TN}+\\ \left(G_{TT}-\mathbf{G}_{TN}\mathbf{G}_{NN}^{-1}\mathbf{G}_{NT}\right)\mathbf{E}\end{matrix}\right]\mathbf{G}_{NN}^{-1}\left(\bar{\bar{\varepsilon}}_N+\mathbf{E}\right)\boldsymbol{\gamma}_N^-\right]\\ \Lambda_T&=\frac{\mathbf{G}_{TN}\mathbf{G}_{NN}^{-1}\left(\bar{\bar{\varepsilon}}_N+\mathbf{E}\right)\boldsymbol{\gamma}_N^--\gamma_T^-}{G_{TT}-\mathbf{G}_{TN}\mathbf{G}_{NN}^{-1}\mathbf{G}_{NT}}\end{aligned} \tag{19}$$

Single slip: When slip takes place at point 1 (solely) the normal impulse is (Eqns. 4 and 5):

$$\frac{\Lambda_{N1}}{\bar{m}\gamma_N^-}=-\frac{1+\varepsilon_N}{1+\frac{r_{11}^2\pm\mu r_{11}r_{T1}}{I_1/\bar{m}}+\frac{r_{21}^2\pm\mu r_{21}r_{T2}}{I_2/\bar{m}}} \tag{20}$$

Whereas the tangential post-impact velocity is given by (Eqns. 4 and 5):

$$\frac{\gamma_T^+}{\gamma_N^-}=\frac{\gamma_T^-}{\gamma_N^-}-\frac{\pm\frac{\mu}{\bar{m}}+\frac{r_{11}r_{T1}\pm\mu r_{T1}^{\ 2}}{I_1}+\frac{r_{21}r_{T2}\pm\mu r_{T2}^{\ 2}}{I_2}}{\frac{1}{\bar{m}}+\frac{r_{11}^2-\mu r_{11}r_{T1}}{I_1}+\frac{r_{21}^2-\mu r_{21}r_{T2}}{I_2}}(1+\varepsilon_N) \tag{21}$$

Again, sign (+) holds for backward slip and sign (-) corresponds to forward slip. For impact at point 2 one has to replace levers r_{12} and r_{22} with r_{11} and r_{21} respectively.

Single stick: When stick occurs at point 1 (Fig.6) the normal and tangential impulses are:

$$\frac{\Lambda_{N1}}{\bar{m}\gamma_N^-}=\frac{1}{\bar{m}}\frac{\left(\frac{r_{11}r_{T1}}{I_1}+\frac{r_{21}r_{T2}}{I_2}\right)\frac{\gamma_T^-}{\gamma_N^-}-\left(\frac{1}{\bar{m}}+\frac{r_{T1}^{\ 2}}{I_1}+\frac{r_{T2}^{\ 2}}{I_2}\right)\left(1+\varepsilon_N\right)}{\left(\frac{1}{\bar{m}}+\frac{r_{11}^2}{I_1}+\frac{r_{21}^2}{I_2}\right)\left(\frac{1}{\bar{m}}+\frac{r_{T1}^{\ 2}}{I_1}+\frac{r_{T2}^{\ 2}}{I_2}\right)-\left(\frac{r_{11}r_{T1}}{I_1}+\frac{r_{21}r_{T2}}{I_2}\right)^2}$$

$$\frac{\Lambda_{T}}{\bar{m}\gamma_N^-}=\frac{1}{\bar{m}}\frac{\left(\frac{r_{11}r_{T1}}{I_1}+\frac{r_{21}r_{T2}}{I_2}\right)\left(1+\varepsilon_N\right)-\left(\frac{1}{\bar{m}}+\frac{r_{T1}^{\ 2}}{I_1}+\frac{r_{T2}^{\ 2}}{I_2}\right)\frac{\gamma_T^-}{\gamma_N^-}}{\left(\frac{1}{\bar{m}}+\frac{r_{11}^2}{I_1}+\frac{r_{21}^2}{I_2}\right)\left(\frac{1}{\bar{m}}+\frac{r_{T1}^{\ 2}}{I_1}+\frac{r_{T2}^{\ 2}}{I_2}\right)-\left(\frac{r_{11}r_{T1}}{I_1}+\frac{r_{21}r_{T2}}{I_2}\right)^2} \quad (22)$$

Where $\bar{m}=m_1m_2/\left(m_1+m_2\right)$. For impact at point 2 (Fig.6) one has to replace levers r_{12} and r_{22} with r_{11} and r_{21} respectively.

4.3 Single frictional impact

When the pre-impact rotations of the two rigid bodies (deck-segments) are different, single point impact takes place. Again, the proposed LCP (Eqns. 4, 5) describes also single frictional impacts, as a special case when only one impact point is active (i.e. $\Lambda_N > 0$ holds at that point). In particular, the closed-form solutions of Section 4.2 for single-impacts hold provided the appropriate levers r_{11}, r_{21}, r_{21}, r_{22}, r_{T1} and r_{T2} are used [4].

5 CONCLUSIONS

The aim of the present paper is to bring forward the impact mechanism during in-deck collisions in skew bridges. To this end, the study adopts a fully nonsmooth rigid body approach and examines in depth the impact response of a planar skew (rigid) body against an inelastic half-space, as well as, the impact of a pair of planar rigid bodies. Key features of the present approach are the proposed linear complementarity problem, which encapsulates all physically feasible impact states, and the use of set-valued force laws.

The analysis of the rotation mechanism associated with oblique impact shows that the tendency of skew bridges to rotate depends on the total geometry of the body in plan, and not on the skew angle alone, as it is commonly considered. In addition, the post-impact state depends on the contact parameters, the inertial properties of the two segments (for impact between adjacent deck segments) and on the pre-impact kinematics. Further, the study elaborates on the conditions under which oblique (frictionless or frictional) impact triggers deck rotation in skew bridges. It shows that post-impact rotation is more common for impact between adjacent deck-segments than deck-abutment impact. It also verifies that in most cases, post-impact rotation is in the direction of increasing the skew angle. For each physically feasible impact state (single slip/stick at either corner of a skew deck segment, or double slip/stick along the whole edge of a segment), it offers pertinent closed-form solutions which yield the unknown impulses in the normal and the tangential direction of contact and the post-impact velocities when the latter are unknown (slip post-impact states).

ACKNOWLEDGEMENTS

The author gratefully acknowledges the financial support for this research provided by the Research Grants Council of Hong Kong, under grant reference number DAG12EG03.

REFERENCES

[1] E. G. Dimitrakopoulos, Analysis of a Frictional Oblique Impact Observed in Skew Bridges, *Nonlinear Dynamics*, **60**, 575–595, 2010.

[2] E. G. Dimitrakopoulos, N. Makris, and A. J. Kappos, Dimensional analysis of the earthquake-induced pounding between inelastic structures, *Bulletin of Earthquake Engineering*, **9**(2), 561–579, 2011.

[3] E. G. Dimitrakopoulos, Seismic response analysis of skew bridges with pounding deck–abutment joints, *Engineering Structures*, **33**(3), 813–826, 2011.

[4] E. G. Dimitrakopoulos, Nonsmooth Analysis of the Impact Between Successive Skew Bridge-segments, *Nonlinear Dynamics*, **under review 2013**.

[5] E. G. Dimitrakopoulos, N. Makris, and A. J. Kappos, Dimensional analysis of the earthquake-induced pounding between adjacent structures, *Earthquake Engineering Structural Dynamics*, **38**(7), 867–886, 2009.

[6] A. S. Elnashai, B. Gencturk, O.-S. Kwon, Y. M. A. Hashash, S. J. Kim, S.-H. Jeong, and J. Dukes, The Maule (Chile) earthquake of February 27, 2010: Development of hazard, site specific ground motions and back-analysis of structures, *Soil Dynamics and Earthquake Engineering*, **42**, 229–245, 2012.

[7] M. J. N. Priestley, G. M. Calvi, and F. Seible, *Seismic design and retrofit of bridges*. Wiley, 1996.

[8] Y. Huo and J. Zhang, Effects of Pounding and Skewness on Seismic Responses of Typical Multi-Span Highway Bridges Using Fragility Function Method, *Journal of Bridge Engineering*, doi:10.1061/(ASCE)BE.1943-5592.0000414.

[9] P. Kaviani, F. Zareian, and E. Taciroglu, Seismic behavior of reinforced concrete bridges with skew-angled seat-type abutments, *Engineering Structures*, **45**, 137–150, 2012.

[10] C. Glocker, *Set-valued force laws : dynamics of non-smooth systems*. Springer, 2001.

[11] M. Payr and C. Glocker, Oblique Frictional Impact of a Bar: Analysis and Comparison of Different Impact Laws, *Nonlinear Dynamics*, **41**(4), 361–383, 2005.

COMPDYN 2013
4th ECCOMAS Thematic Conference on
Computational Methods in Structural Dynamics and Earthquake Engineering
M. Papadrakakis, V. Papadopoulos, V. Plevris (eds.)
Kos Island, Greece, 12–14 June 2013

MITIGATION MEASURES FOR SEISMIC POUNDING EFFECTS ON ADJACENT BUILDINGS RESPONSES

Shehata E. Abdel Raheem[1, 2]

[1]Civil Engineering Department, Faculty of Engineering, Assiut University, Assiut, Egypt
[2]Taibah University, Universities road, Madinah Munawarh, Saudi Arabia
shehataraheem@yahoo.com

Keywords: Seismic pounding, Adjacent buildings, Mitigation measures, Separation distance, Time history analysis.

Abstract. *Investigations of past and recent earthquake damage have illustrated that the building structures are vulnerable to severe damage and/or collapse during moderate to strong ground motion. Among the possible structural damages, seismic induced pounding has been commonly observed in several earthquakes. A parametric study on buildings pounding response as well as proper seismic hazard mitigation practice for adjacent buildings is carried out. Three categories of recorded earthquake excitation are used for input. The effect of impact is studied using linear and nonlinear contact force model for different separation distances and compared with nominal model without pounding consideration. Pounding produces acceleration and shear at various story levels that are greater than those obtained from the no pounding case, while the peak drift depends on the input excitation characteristics. Also, increasing gap width is likely to be effective when the separation is sufficiently wide practically to eliminate contact. It is effective to provide a shock absorber for the mitigation of impact effects between adjacent buildings with relatively narrow seismic gaps. The sudden changes of stiffness during poundings can be smoothed by using a natural rubber shock absorber, which prevents, to some extent, the acceleration peaks due to impact. The pounding forces exerted on the adjacent buildings can be satisfactorily reduced.*

1 INTRODUCTION

A quake with a magnitude of six is capable of causing severe damage. Several destructive earthquakes have hit Egypt in both historical and recent times from distant and near earthquakes. The annual energy release in Egypt and its vicinity is equivalent to an earthquake with magnitude varying from 5.5 to 7.3. Adjacent buildings subjected to seismic excitations collide against each other when the separation distance is not large enough to accommodate the displacement response of the structures relative to one another. As shown by field observations and by numerical models, seismic pounding can cause severe damage on the affected structures. Investigations of past and recent earthquakes damage have illustrated several instances of pounding damage in both building and bridge structures [1 - 5]. Pounding damage was observed during the 1985 Mexico earthquake, the 1988 Sequenay earthquake in Canada, the 1992 Cairo earthquake, the 1994 Northridge earthquake, the 1995 Kobe earthquake and 1999 Kocaeli earthquake, 2011 Tohoku earthquake [6 - 10]. Extensive pounding damage was observed in low-rise unreinforced masonry buildings that were constructed with no building separation. Modern buildings were also endangered by pounding when building separations were in-filled with solid architectural flashings [11, 12]. Significant pounding was observed at sites over 90 km from the epicenter thus indicating the possible catastrophic damage that may occur during future earthquakes having closer epicenters. Pounding of adjacent buildings could have worse damage as adjacent buildings with different dynamic characteristics, which vibrate out of phase and there is insufficient separation distance or energy dissipation system to accommodate the relative motions of adjacent buildings.

Past seismic codes did not give definite guidelines to preclude pounding, because of this and due to economic considerations including maximum land usage requirements, especially in the high-density populated areas of cities, there are many buildings worldwide which are already built in contact or extremely close to another that could suffer pounding damage in future earthquakes. A large separation is controversial from both technical (difficulty in using expansion joint) and economical (loss of land usage) views. The highly congested building system in many metropolitan cities constitutes a major concern for seismic pounding damage. For these reasons, it has been widely accepted that pounding is an undesirable phenomenon that should be prevented or mitigated [4, 13 - 16]. Numerical and experimental studies have shown that, in case of structural poundings, both floor accelerations and inter-story deflections are significantly amplified, threatening the functionality of the structure, as well as sensitive equipment that may be housed in the building [17, 18]

Moreover, a new generation of structural design codes defines requirements for the design of buildings against earthquake action, new seismic zonations have been defined, the new earthquake zones in connection with the corresponding design ground acceleration values will lead in many cases to earthquake actions which are remarkably higher than defined by the design codes used up to now. Pounding between buildings during earthquakes has been recently intensively studied using different models of colliding structures [19 -24].

The most simplest and effective way for pounding mitigation and reducing damage due to pounding is to provide enough separation but it is sometimes difficult to be implemented due to detailing problem and high cost of land. An alternative to the seismic separation gap provision in the structure design is to minimize the effect of pounding through decreasing lateral motion [25 - 29], which can be achieved by joining adjacent structures at critical locations so that their motion could be in-phase with one another or by increasing the pounding buildings damping capacity by means of passive structural control of energy dissipation system. Certain mitigation measures have already been proposed by several

researchers who investigated this problem in buildings and bridge decks in an effort to alleviate the detrimental effects of structural poundings. A potential mitigation measure for the pounding problem is the incorporation of layers of soft material, such as rubber, which can act as collision bumpers, in order to prevent the sudden impact pulses [5, 30 - 31].

The focus of this study is the development of an analytical model and methodology for the formulation of the adjacent building-pounding problem based on the classical impact theory, an investigation through parametric study to identify the most important parameters is carried out. The main objective and scope are to evaluate the effects of structural pounding on the global response of building structures; to determine proper seismic hazard mitigation practice for already existing buildings as well as new buildings and to develop and provide engineers with practical analytical tools for predicting pounding response and damage. A realistic pounding model is used for studying the response of structural system under the condition of structural pounding during moderate to strong earthquakes. An analytical technique based on the contact force-based approach is developed, where the contact element is activated when the structures come into contact. A spring with high stiffness is used to avoid overlapping between adjacent structures. Two adjacent multi-story buildings are considered as a representative structure for potential pounding problem. A simplified nonlinear analytical model is developed to study the response of multi-story building subject to earthquake excitation.

2 NONLINEAR DYNAMIC ANALYSIS PROCEDURES

2.1 Equilibrium equation solution technique

The governing nonlinear dynamic equation of motion for the structure response can be derived by the principle of energy that the external work is absorbed by the work of internal, inertial and damping forces for any small admissible motion that satisfies compatibility and boundary conditions. By assembling the element dynamic equilibrium equation for the time $t+\Delta t$ over all the elements, the incremental FEM dynamic equilibrium equation can be obtained as:

$$[M]\{\ddot{u}\}^{t+\Delta t}+[C]\{\dot{u}\}^{t+\Delta t}+[K]^{t+\Delta t}\{\Delta u\}^{t+\Delta t}=\{F\}^{t+\Delta t}-\{F\} \quad (1)$$

where [M], [C] and $[K]^{t+\Delta t}$ = system mass, damping and tangent stiffness matrices at time $t+\Delta t$. The tangent stiffness considers the material nonlinearity through bilinear elastic-plastic constitutive model, $\ddot{u}$, $\dot{u}$ and Δu = accelerations, velocities, and incremental displacements at time $t+\Delta t$, respectively; and $\{F\}^{t+\Delta t}-\{F\}^{t}$ = unbalanced force vector. The Newmark's step-by-step integration method is used for the integration of the equation of motion. These equations for the building structure system subjected to earthquake ground motion input are assembled and numerically solved for the incremental displacement using the Newton-Raphson iteration method. In this study, an equivalent viscous damping is explicitly introduced in the system in the form of damping matrix [C]. A spectral damping scheme of Rayleigh's damping is used to form damping matrix as a combination of mass and stiffness matrices, which effectively captures the building damping and is also computationally efficient.

2.2 Input ground motion

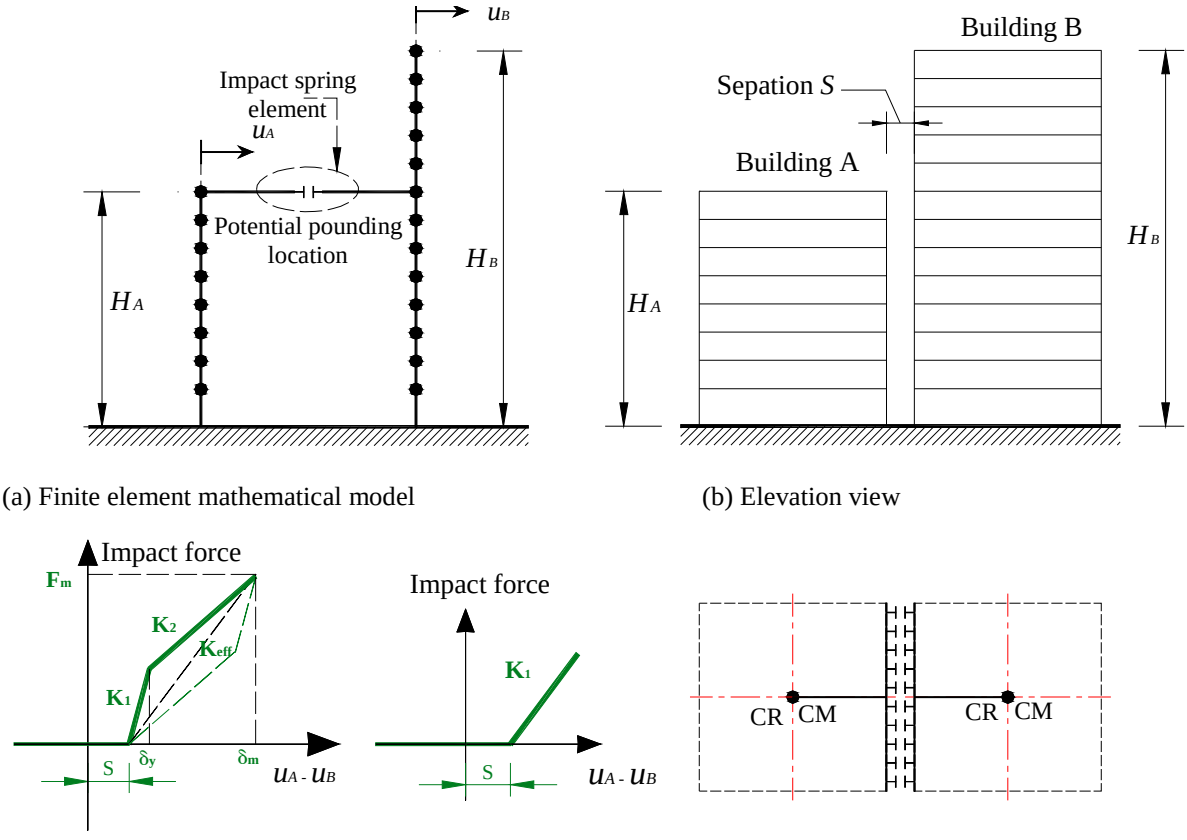
A suite of nine-ground motion records from seven different earthquakes [32 is selected for the purpose of understanding the input ground motion effect, as listed in **Table 1**. The ground motion records are grouped into three levels depending on the peak ground acceleration as,

low (0.1g up to 0.3g), moderate (0.4g up to 0.6g) and high (0.7g up to 0.9g). The records are chosen such that the period ratio (T_1/T_g and T_2/T_g; adjacent buildings period over the ground motion characteristic period) has a wide range.

3 FINITE ELEMENT MODELLING

3.1 Building model

This study investigates pounding of adjacent building structures from an analytical perspective. A simplified nonlinear model of a multi-story building is developed incorporating the effects of geometric and material nonlinearities. A three-dimensional (3D) finite element model has been defined and 3D non-linear time-history analyses have been performed. A new formulation is proposed to model pounding between two adjacent building structures, with natural periods T_A and T_B and damping ratios ζ_A and ζ_B under earthquake excitation, as linear and nonlinear contact force based impact between two multi-degree-of-freedom oscillators. Steel moment resistant frame building of 8-story (building *A*, period = 0.72) is assumed to collide with and adjacent 13-story (building *B*, Period = 1.22), as shown in **Figure 1**. In this model, the building floor is assumed to be infinitely rigid in its own plane. The entire mass of the structure is uniformly distributed at the floor level. The model has coincident CR (Rigidity/stiffness Center) and CM (Mass Center) that is located at the geometric center of the floor. For the purpose of evaluating the effect of torsion, a torsional unbalanced model is defined where the mass center lies at a distance *e* from the center of rigidity, and the model has the same stiffness and mass distribution.



(a) Finite element mathematical model (b) Elevation view

(c) Truss contact element for pounding simulation (d) Plan view

Figure 1 Pounding potential problem modeling

PGA Level	PGA (g)	Input wave	M_w	Earthquake / Station	Φ°	EPD (km)	PGV (cm/s)	PGD (cm)	T_g (s)
Low	0.21	1MVH	6.0	N. Palm Springs, 1986 / Morongo Valley	135	10.1	40.9	15.0	1.90
	0.30	2A-GRN	6.0	Whittier narrows, 1987 / E-Grand Ave	180	9.0	23.0	3.3	0.70
	0.29	3G06	6.2	Morgan Hill, 1994 / Gilroy Array #6	090	11.8	36.7	6.1	1.20
Moderate	0.48	4CYC	6.9	Loma Prieta, 1989 / Coyote Lake Dam	285	21.8	39.7	15.2	0.65
	0.51	5STG	6.9	Loma Prieta, 1989 // Saratoga-Aloha Ave	000	11.7	41.2	16.2	1.80
	0.59	6NPS	6.0	N. Palm Springs, 1986 / 5070 N-Palm Spring	210	8.2	73.3	11.5	1.10
High	0.60	7D-PVY	5.8	Coalinga, 1983 / Pleasant Valley P.P.	045	17.4	34.8	8.1	0.65
	0.84	8RRS	6.7	Northridge, 1994 / Rinaldi	228	7.1	166.1	28.8	1.05
	1.04	9CPM	7.1	Cape Mendocino, 1992 / Cape Mendono	090	8.5	42.0	12.4	2.00

Table 1 Suite of earthquake ground motion records

3.2 Impact model

Pounding is simulated using contact force-based model such as linear and nonlinear springs. In addition, a nonlinear contact model accounting for impact energy dissipation is also introduced to model impact. A bilinear truss contact model with a gap is considered for representing impact between closely spaced adjacent structures, as shown in **Figure 1**. The model parameters such as the stiffness properties and the yield deformation of the truss element are determined using the Hertz contact law for the effective stiffness and by equating the element hysteresis area to the energy dissipated during impact [32, 33].

4 REQUIRED SEISMIC SEPARATION DISTANCE TO AVOID POUNDING

Seismic pounding occurs when the separation distance between adjacent buildings is not large enough to accommodate the relative motion during earthquake events. Seismic codes and regulations worldwide specify minimum separation distances to be provided between adjacent buildings, to preclude pounding, which is obviously equal to the relative displacement demand of the two potentially colliding structural systems. For instance, according to the 2000 edition of the International building code and in many seismic design codes and regulations worldwide, minimum separation distances [34] are given by ABSolute sum (ABS) or Square Root of Sum of Squares (SRSS) as follow:

$$\text{ABS:} \qquad S = U_A + U_B \tag{2}$$

$$\text{SRSS:} \qquad S = \sqrt{u_A^2 + u_B^2} \tag{3}$$

where S = separation distance and u_A, u_B = peak displacement response of adjacent structures A and B, respectively. Previous studies have shown that they give poor estimates of S, especially when the natural periods of the adjacent structures are close to each other. In these cases, the ABS and SRSS rules give excessively conservative separation distances, which are very difficult to effectively implement because of maximization of land usage. A more rational approach that is usually referred to as the Double Difference Combination (DDC) rule, for estimation of the critical required separation distance, which is obviously equal to the peak relative displacement response [34, 35], is given by:

$$S = u_{Rel}(t) = \sqrt{u_A^2 + u_B^2 - \rho_{AB} u_A u_B} \tag{4}$$

where u_A, u_B and u_{Rel} = mean peak values of $u_A(t)$, $u_B(t)$ and $u_{Rel}(t)$, respectively. The correlation coefficient, ρ_{AB} depends on the period on the period ratio $r = T_B / T_A$, as well as ζ_A and ζ_B, (Lopez Garcia 2004, Penzien 1997) and is given by

$$\rho_{AB} = \frac{8\sqrt{\zeta_A \zeta_B}\left(\zeta_A + r\,\zeta_B\right) r^{1.5}}{\left(1 - r^2\right)^2 + 4r\,\zeta_A \zeta_B \left(1 + r^2\right) + 4\left(\zeta_A^2 + \zeta_B^2\right) r^2} \tag{5}$$

where T_A, ζ_A and T_B, ζ_B are natural periods and damping ratios of systems A and B, respectively. The DDC rule is much more accurate than the ABS and SRSS rules, although it gives somewhat un-conservative results when TA and TB are well separated [34,35]. Four different criteria to calculate the separation necessary to prevent seismic pounding between nonlinear hysteretic structural systems were examined. none of the criteria evaluated in this study is completely satisfactory in the sense that none of them provides separations that are consistently exact or somewhat conservative. Observations indicate that there is still a need to adequately characterize the correlation between displacement responses of nonlinear hysteretic systems [36].

Input Earthquake	u_A (m)	u_B (m)	u_{Rel} (m)	u_{Rel} / max. (u_A & u_B)	u_{Rel} /(u_A + u_B)
1MVH	0.06	0.10	0.13	1.30	0.81
2A-GRN	0.24	0.45	0.65	1.45	0.94
3G06	0.09	0.04	0.11	1.22	0.85
4CYC	0.11	0.19	0.27	1.42	0.90
5STG	0.09	0.17	0.19	1.18	0.73
6NPS	0.15	0.14	0.24	1.71	0.83
7D-PVY	0.08	0.13	0.21	1.62	1.0
8RRS	0.13	0.06	0.14	1.08	0.74
9CPM	0.09	0.16	0.19	1.19	0.76

Table 2 Non-pounding and relative pounding displacements for different input earthquakes

5 NUMERICAL RESULTS AND DISCUSSION

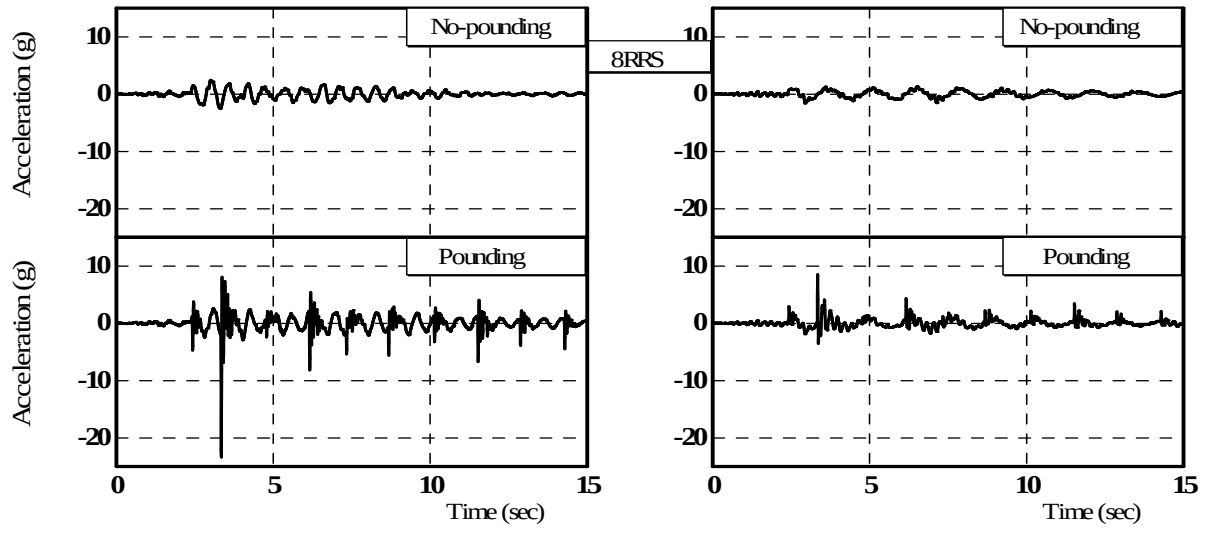
5.1 Pounding and spacing size effects

In order to achieve an acceptably safe structural performance during seismic events, a correct seismic design should take into account the relative displacements calculated by means of a nonlinear time history analysis. The maximum displacement for the non-pounding case for stiff and flexible buildings u_A, u_B and the relative pounding displacement u_{Rel} for different input excitation are listed in **Table 2**. Since the absolute sum (ABS) approach assumes complete out-of-phase motion of the adjacent buildings, so the ratio of u_{Rel} to the sum of u_A and u_B could be taken as a measure of out-of-phase of adjacent buildings, which range from 0.73 to 1.0 depending on the input earthquakes characteristic. The out of phase movement between building *A* and *B* is clearly observed due to different periods of the building. The positive and negative peak displacements are essential to determine the degree of biased response of the pounding system. Therefore, seismic poundings between adjacent

buildings may induce unwanted damages even though each individual structure might have been designed properly to withstand the strike of credible earthquake events.

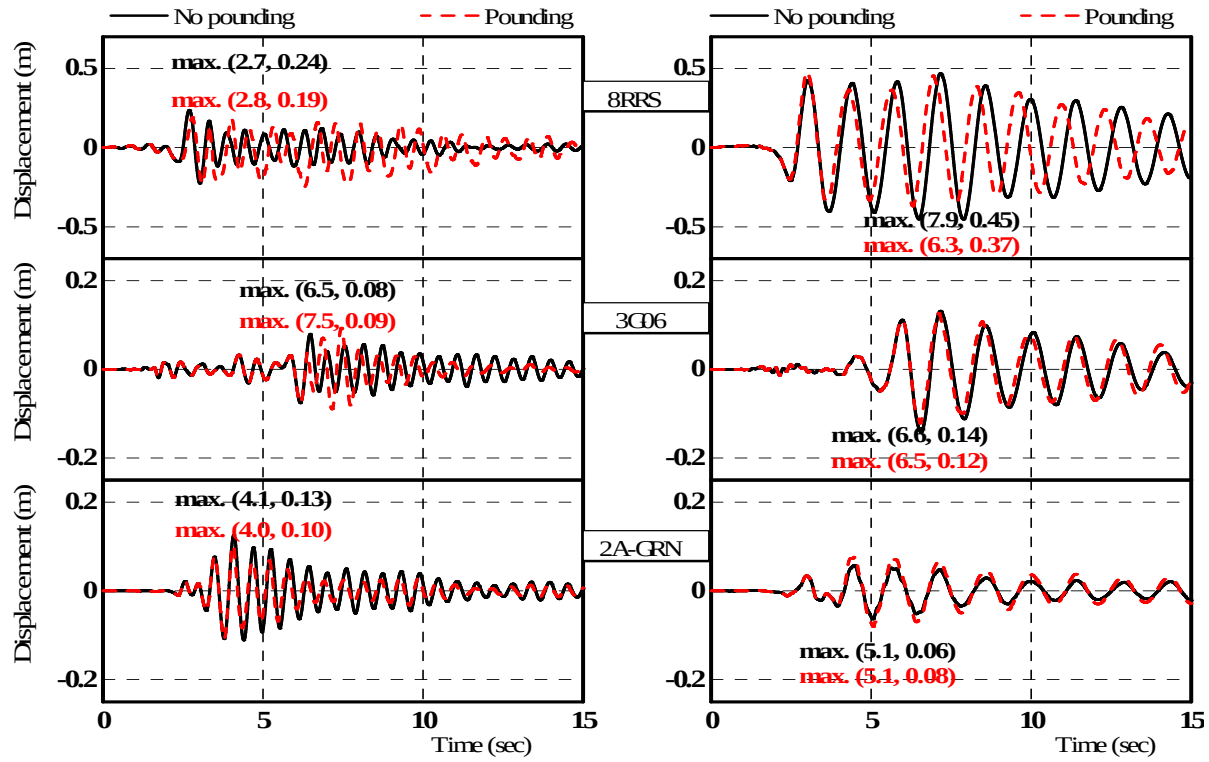
The acceleration variation at the top level of shorter building during impact between adjacent structures under different earthquakes is computed to study the behavior of the building during impact. Pounding is a severe load condition that could result in high magnitude and short duration floor acceleration pulses in the form of short duration spikes, which in turn cause greater damage to building contents. A sudden stopping of displacement at the pounding level results in large and quick acceleration pulses in the opposite direction. The acceleration increases due to impact with adjacent structure and can be more than 10 times those from no-pounding case, as illustrated in **Figure 2**. The time history of inward displacements and their extreme values for the pounding and no pounding cases shows that pounding reduces the building response when vibrating near the characteristic period of the ground motion and increases the adjacent building response, as shown in **Figure 3**. The flexible 13-story building vibrates near the dominant frequency of the 3G06 input earthquake; pounding response is increased in the flexible building while pounding response of the stiff building is reduced. Conversely, the stiff 8-story building demand increases and the flexible building demand decreases due to pounding for the 2A-GRN input earthquake that has dominant period near the fundamental period of stiff building. Pounding slightly decreases both building responses for 8RRS input earthquake. The amplification in building response is a function of each of adjacent buildings vibration period and their ratio as well as the dominant frequency of input excitation.

Furthermore, pounding can amplify the global response of participating structural systems. The effects of impact are found to be severe for both of adjacent buildings. Pounding produces acceleration response and shear force at various story levels that are greater than those from the no pounding case, as shown in **Figure 4**, while the peak drift depends on the input excitation characteristics. Flexible 13-story building pounding increases shear above impact level and below the third floor slab as well as acceleration at the vicinity of impact, while stiff 8-story building pounding almost increases the peak shear over the entire height. The increase of spacing from 0.12 to 0.25m has the capability for reducing impact effects and could reduce the number of pounding's occasion. Also, increasing gap width is likely to be effective when the separation is sufficiently wide practically to eliminate contact.



(a) 8-story building (8th level) (b) 13-story building (8th level)

Figure 2 Acceleration time histories at pounding level (Pounding problem versus no-pounding case)



(a) 8-story building (8th level) (b) 13-story building (8th level)

Figure 3 Displacement time histories at pounding level (Pounding problem versus no-pounding case)

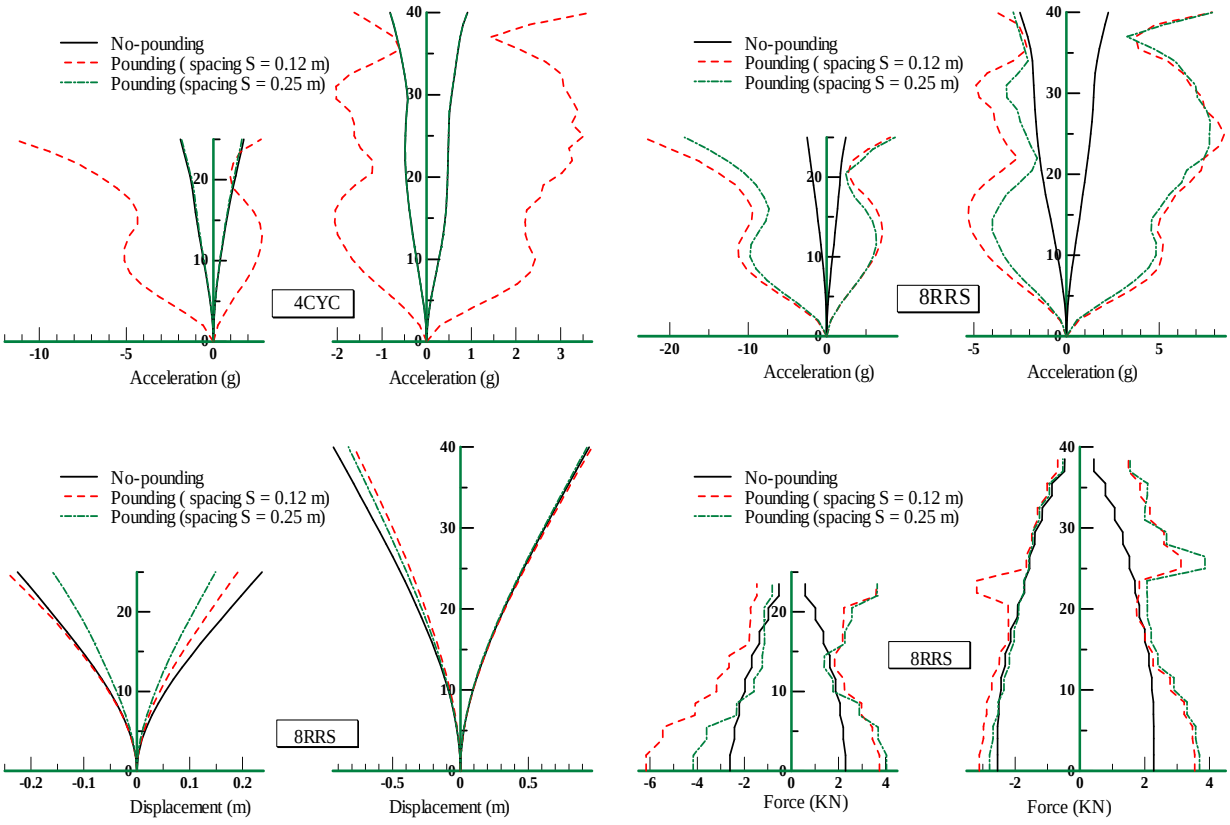


Figure 4 Response envelops for different spacing size between adjacent buildings

5.2 Impact energy dissipation effect

The nonlinearity and dissipated energy associated with impact are illustrated by the shear response envelop and acceleration time history response at short building top level for linear and nonlinear impact modeling, **Figures 5** and **6**. An increase in the damping energy absorption capacity of the pounding element results in reduction of the acceleration amplification, impact force and building global responses. The pounding element can be activated every time for energy absorption whenever the buildings vibrate. Consequently, impact force can be significantly reduced. The failure of buildings occurs not only from the increase of lateral loading, but also from vertical failure. Building upholds their structural integrity by providing a continuous load path to their foundation. As the building displaces laterally the columns are caused to deflect from the p-δ effect, causing them to inadequately transfer the loads of the floors. These deformed members could buckle from the floors weight. The response discloses the significance of the use of the energy dissipation system. Hence, it is clear that an energy dissipation system installed at potential pounding level could be an effective tool to reduce the effect of impact upon adjacent buildings. Consideration of impact energy dissipation through nonlinear impact model amplifies pounding displacement reduces the impact forces and promotes the impact eccentricity due one direction yielding that could lead to localized damage at corners of building.

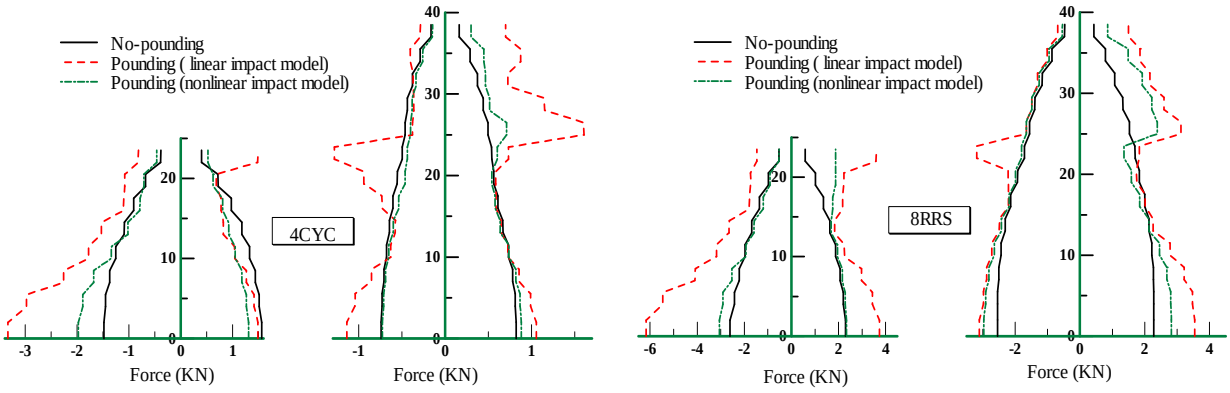
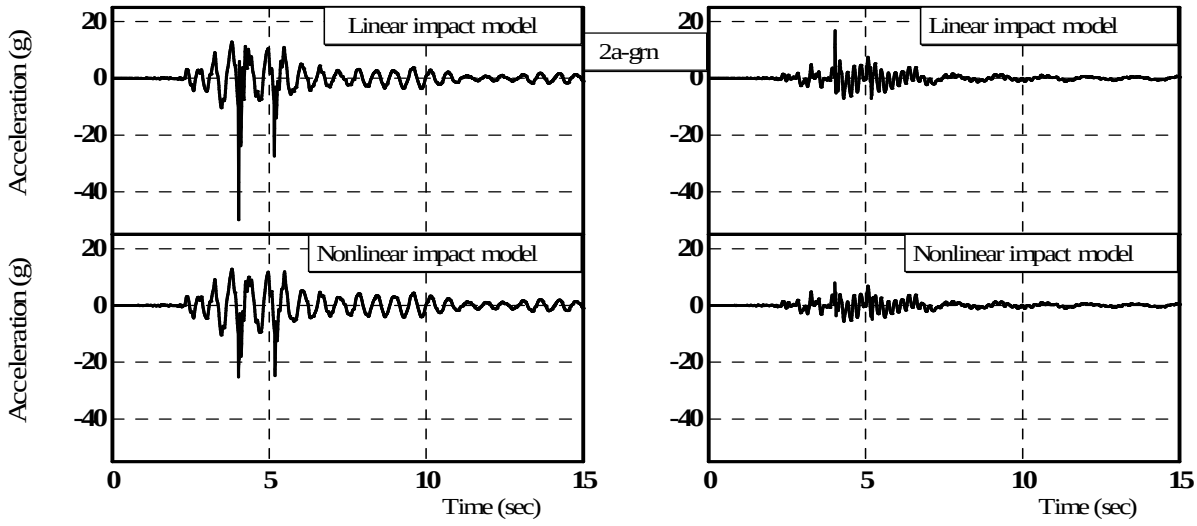


Figure 5 Shear response envelops for linear and nonlinear impact modeling



(a) 8-story building (8th level) (b) 13-story building (8th level)

Figure 6 Acceleration time history response for linear and nonlinear impact modeling

6 CONCLUSIONS

In this study, a mathematical modeling of adjacent building pounding has been demonstrated and its implementation in a finite element nonlinear seismic analysis is presented. Numerical investigation, aiming at accurate description and evaluation of colliding adjacent structures real behavior and its effects on global response has been conducted. It studies the relative importance of dynamic characteristics of adjacent building structures in causing relative responses. The effect of vibration properties of adjacent structures is significant to those of high-rise adjacent structures if they have noticeably different vibration periods.

Pounding is a highly nonlinear phenomenon and a severe load condition that could result in significant structural damage, high magnitude and short duration floor acceleration pulses in the form of short duration spikes, which in turn cause greater damage to building contents. A sudden stopping of displacement at the pounding level results in large and quick acceleration pulses in the opposite direction. Furthermore, pounding can amplify the global response of participating structural systems. The vertical location of pounding significantly influences the distribution of story peak responses through the building height. The acceleration response at pounding level indicate that pounding is especially harmful for equipment or secondary systems having short periods, where the existing industrial design spectra does not cover this effect. More importantly, pounding can amplify the building displacement demands beyond those typically assumed in design. Existing design procedure should account for dynamic impact. Adjacent building period ratio should be carefully selected to reduce the pounding effects.

Analyses of pounding have shown that there is considerable scatter in the amplification of action effects caused by pounding. This study clearly shows the sensitivity of the system response to parameters affecting the pounding phenomenon, i.e., characteristics of buildings, plan layout, structural system and frequency content of the input ground motions. The results depend on the excitation characteristics and the relationship between the buildings fundamental period. The impulse found when pounding occurs increases suddenly the acceleration and the velocity. These accelerations generated by the impacts may cause significant damage to the structural components, especially in the contact area of pounding. Non-structural components (electrical/mechanical units and architectural features) in some buildings are important to the building's function.

The results depend on the excitation characteristics and the relationship between the buildings fundamental period. In addition, unwanted period shift of an existing structure imposed by the construction of a new building in its neighborhood may lead to unprepared and unexpected damages of the former during earthquakes. Therefore, seismic poundings between adjacent buildings may induce unwanted damages even though each individual structure might have been designed properly to withstand the strike of credible earthquake events. Pounding produces acceleration and shear at various story levels that are greater than those from the no pounding case, while the peak drift depends on the input excitation characteristics. An increasing gap width is likely to be effective when the separation is sufficiently wide practically to eliminate contact.

REFERENCES

[1] A. Astaneh-Asl, B. Bolt, K. McMullin, R.R. Donikian, D. Modjtahedi and S.W. Cho, *Seismic performance of steel bridges during the 1994 Northridge earthquake*. Report No. UCB/CEE-Steel-94/01, University of California, Berkeley, 1994.

[2] Northridge Reconnaissance Team, "*Northridge earthquake of January 17, 1994, Reconnaissance report*", EERI, Oakland, California, 25- 47, 1996.

[3] K. Kasai, B.F. Maison, V. Jeng, D.J. Patel and P.C. Patel, A study of earthquake pounding between adjacent structures. *Proceeding of 6th Canadian Conference of Earthquake Engineering*, Toronto, Canada, 93-100, 1991.

[4] S. E. Abdel Raheem, Seismic Pounding between Adjacent Building Structures, *Electronic Journal of Structural Engineering – EJSE, The University of Melbourne*, **6**, 66 -74, 2006..

[5] S. E. Abdel Raheem, Pounding Mitigation and unseating prevention at expansion joint of isolated multi-span bridges. *Engineering Structures*, **31**(10), 2345-2356, 2009.

[6] J.P. Moehle, Northridge earthquake of January 17, 1994: Reconnaissance report. Volume 1– Highway bridges and traffic management. *Earthquake Spectra*, **11**(C), 287–372, 1995.

[7] V.V. Bertero, Implications of observed pounding of buildings on seismic code regulations. *11th World Conference on Earthquake Engineering, 11WCEE*, Acapulco, Mexico, Paper No. 2102, 23-28 June 1996.

[8] Committee of Earthquake Engineering, *The 1995 Hyogoken-Nanbu earthquake, investigation into damage to civil engineering structures*, Japan Society of Civil Engineers, 1996.

[9] A.W. Sadek, A. Solaiman and M.A. Baraka, GIS-based earthquake damage analysis in the greater Cairo area. *12th World Conference on Earthquake Engineering, 12WCEE*, Auckland, New Zealand, Paper No. 2255, 30 January - February 2000.

[10] A.G. Gillies, D.L. Anderson, D. Mitchell, R. Tinawi, M. Saatcioglu, N.J. Gardner and A. Ghoborah, The August 17, 1999, Kocaeli (Turkey) earthquake — lifelines and preparedness. *Canadian Journal of Civil Engineering*, **28**, 881–890, 2001.

[11] G.L. Cole, R.P. Dhakal and F. M. Turner, Building pounding damage observed in the 2011 Christchurch earthquake. *Earthquake Engineering and Structural Dynamics*, **39,** 595-611, 2011.

[12] I. Takewaki, S. Murakami, K. Fujita, S. Yoshitomi and M. Tsuji, The 2011off the Pacific coast of Tohoku earthquake and response of high-rise buildings under long period ground motions. *Soil Dynamics and Earthquake Engineering*, **31**, 1511–1528, 2011.

[13] K. Kasai, and B.F. Maison, Observation of structural pounding damage from 1989 Loma Prieta earthquake. *Proceeding of 6th Canadian Conference of Earthquake Engineering*, Toronto, Canada, 735-742, 1991.

[14] C.P. Pantelides and X. Ma, Linear and nonlinear pounding of structural systems. *Computers & Structures*, **66(**1), 79-92, 1998.

[15] H. Hao and S. Zhang, Spatial ground motion effect on relative displacement of adjacent building structures. *Earthquake Engineering and Structural Dynamics*, **28**, 333-349, 1999.

[16] T. Hayashikawa, T. Hirooka, K. Ikeda and S.E. Abdel Raheem, Dynamic behavior of viaducts with PC cables in consideration of pounding of girders and energy absorption. *Proceedings of Hokkaido Chapter of the Japan Society of Civil Engineers (JSCE),* **59**, 50-53, 2002.

[17] P. Komodromos, P. Polycarpou, L. Papaloizou, M.C. Phocas, Response of seismically isolated buildings considering poundings, *Earthquake Engineering and Structural Dynamics*, **36**, 1605–1622, 2007.

[18] A. Masroor, G. Mosqueda, Experimental simulation of base-isolated buildings pounding against moat wall and effects on superstructure response. *Earthquake Engineering and Structural Dynamics*, **41** (14), 2093-2109, 2012.

[19] S.A. Anagnostopoulos, Pounding of buildings in series during earthquakes. *Earthquake Engineering and Structural Dynamics*, **16, 443**-456, 1988.

[20] R.O. Davis, Pounding of buildings modelled by an impact oscillator. *Earthquake Engineering and Structural Dynamics*, **21**,253-274, 1992.

[21] K.T. Chau, X.X. Wei, Pounding of structures modelled as non-linear impacts of two oscillators. *Earthquake Engineering and Structural Dynamics*, **30**, 633-651, 2001.

[22] A. Ruangrassamee, K. Kawashima, Relative displacement response spectra with pounding effect. *Earthquake Engineering and Structural Dynamics*, **30**(10), 1511-1538, 2001.

[23] R. Jankowski, Non-linear viscoelastic modelling of earthquake-induced structural pounding, *Earthquake Engineering and Structural Dynamics*, **34,** 595-611, 2005.

[24] R. Jankowski, Pounding force response spectrum under earthquake excitation. *Engineering Structures*, **28**, 1149-1161, 2006.

[25] K. Kasai, A.R. Jagiasi, and V. Jeng, Inelastic vibration phase theory for seismic pounding mitigation. *Journal of Structural Engineering*, **122** (10), 1136-1146, 1996.

[26] R. Jankowski, K. Wilde and Y. Fujino, Reduction of pounding effects in elevated bridges during earthquakes. *Earthquake Engineering and Structural Dynamics*, **29**, 195-212, 2000.

[27] K. Kawashima and G. Shoji, Effect of restrainers to mitigate pounding between adjacent decks subjected to a strong ground motion. *Proceeding of the 12th World Conference on Earthquake Engineering*, Auckland, New Zealand, paper No. 1435, 2000.

[28] M. M. Abdullah, J. H. Hanif, A. Richardson and J. Sobanjo, Use of a shared tuned mass damper (STMD) to reduce vibration and pounding in adjacent structures. *Earthquake Engineering and Structural Dynamics*, **30**, 1185-1201, 2001.

[29] A. Ruangrassamee and K. Kawashima, Control of nonlinear bridge response with pounding effect by variable dampers. *Engineering Structures*, **25**, 593-606, 2003.

[30] P. C. Polycarpou and P. Komodromos, Numerical investigation of potential mitigation measures for poundings of seismically isolated buildings, *Earthquakes and Structures*, 2 (1), 1-24, 201 1

[31] P.C. Polycarpou, P. Komodromos and A.C. Polycarpou, A nonlinear impact model for simulating the use of rubber shock absorbers for mitigating the effects of structural pounding during earthquakes, *Earthquake Engineering and Structural Dynamics*, **42**, 81–100, 2013.

[32] S. Muthukmar and R. DesRochs, Evaluation of impact models for seismic pounding. *Proceeding of the 13th World Conference on Earthquake Engineering*, Vancouver, B.C., Canada, Paper No. 235, 2004.

[33] S. Muthukmar, *A contact element approach with hysteresis damping for the analysis and design of pounding in bridges*. Ph. D Thesis Presented to The Academic Faculty, Civil and Environmental Engineering, Georgia Institute of Technology, November 2003.

[34] D. Lopez Garcia, Separation between adjacent nonlinear structures for prevention of seismic pounding. *Proceeding of the 13th World Conference on Earthquake Engineering*, Vancouver, B.C., Canada, paper No. 478, 2004.

[35] J. Penzien, Evaluation of building separation distance required to prevent pounding during strong earthquakes. *Earthquake Engineering and Structural Dynamics*, **26**, 849-858, 1997.

[36] D. Lopez-Garciaand T.T. Soong, Evaluation of current criteria in predicting the separation necessary to prevent seismic pounding between nonlinear hysteretic structural systems. *Engineering Structures*, **31**, 1217- 1229, 2009.

COMPDYN 2013
4th ECCOMAS Thematic Conference on
Computational Methods in Structural Dynamics and Earthquake Engineering
M. Papadrakakis, N.D. Lagaros, V. Plevris (eds.)
Kos Island, Greece, 12–14 June 2013

CHARACTERIZATION AND SYNTHESIS OF RANDOM ACCELERATION VIBRATION SPECIFICATIONS

J.J. Wijker[1], M.H.M. Ellenbroek[2], and A. de Boer[1]

[1]University Twente
Drienerlolaan 5, 7522 NB Enschede, The Netherlands
e-mail: j.j.wijker@utwente.nl

[2] Dutch Space, University Twente
Leiden, Enschede, The Netherlands
e-mail: m.ellenbroek@dutchspace.nl, a.deboer@utwente.nl

Keywords: Random vibrations, random vibration testing, random response analysis, damage response spectra.

Abstract. *Random acceleration vibration specifications for subsystems, i.e. instruments, equipment, are most times based on measurement during acoustic noise tests on system level, i.e. a spacecraft and measured by accelerometers, placed in the neighborhood of the interface between spacecraft and subsystem. Tuned finite element models can be used to predict the random acceleration power spectral densities at other locations than available via the power spectral density measurements of the acceleration.*

The measured and predicted power spectral densities do represent the modal response characteristics of the system and show many peaks and valleys.

The equivalent random acceleration vibration test specification is a smoothed, enveloped, peak-clipped version of the measured and predicted power spectral densities of the acceleration spectrum.

The original acceleration vibration spectrum can be characterized by a different number response spectra: Shock Response Spectrum (SRS) , Extreme Response Spectrum (ERS), Vibration Response Spectrum (VRS), and Fatigue Damage Spectrum (FDS). An additional method of non-stationary random vibrations is based on the Rayleigh distribution of peaks. The response spectra represent the responses of series of SDOF systems excited at the base by random acceleration, both in time and frequency domain.

The synthesis of equivalent random acceleration vibration specifications can be done in a very structured manner and are more suitable than equivalent random acceleration vibration specifications obtained by simple enveloping. In the synthesis process Miles' equation plays a dominant role to invert the response spectra into equivalent random acceleration vibration spectra.

A procedure is proposed to reduce the number of data point in the response spectra curve by dividing the curve in a numbers of fields. The synthesis to an equivalent random acceleration

spectrum is performed on a reduced selected set of data points. The recalculated response spectra curve envelops the original response spectra curves.

A real life measured random acceleration spectrum (PSD) with quite a number of peaks and valleys is taken to generate, applying response spectra SRS, ERS, VRS, FDS and the Rayleigh distribution of peaks, equivalent random acceleration vibration specifications. Computations are performed both in time and frequency domain.

1 INTRODUCTION

Subsystems (instruments, equipment, boxes) are to be qualified against rather severe mechanical random acceleration vibration test specifications as discussed in [11]. The random acceleration vibration test specifications are, in general, enforced accelerations at the interface between spacecraft and subsystems. The random vibrations are mainly induced by the acoustic loads exposed to the spacecraft during launch and performing acoustic tests, representing the launch environment. The acoustic loads (sound pressures) are assumed to be diffuse and are simulated in a reverberant chamber, like the Large European Acoustic Facility (LEAF) at ESA/ESTEC, Noordwijk, The Netherlands.

The measured random accelerations and or similar predictions are broad-banded and shows many peaks as shown in Fig. 1 (blue line). These random acceleration measurements and predictions are converted into more or less equivalent smooth random acceleration vibration test specification, which represent as good as possible the underlying measured and calculated random acceleration responses. The equivalent random acceleration vibration test specification shall not lead to under-testing or significant over-testing of the test-item. An enveloping test random acceleration vibration specification is illustrated in Fig. 1 (black line), which is such severe that over-testing of the test item will certainly occur.

Several methods are available to reconstruct and characterize in a very structured manner the equivalent random acceleration vibration test specification from the measured and predicted random response data. The following characterization methods are discussed in this paper:

- Shock Response Spectrum (SRS) [19], Extreme Response Spectrum (ERS) [21]. Both response spectra are based on extreme responses of SDOF systems excited by enforced random accelerations, the first in the time and and the second in frequency domain.

- Vibration Response Spectrum (VRS) [16]. The VRS is the response spectrum based on the 3σ responses of series of SDOFs, with varying natural frequency, excited at the base by random acceleration in the frequency domain.

- Fatigue Damage Spectrum (FDS) [21]. This damage response spectrum represents the cumulative damage due to the random responses of series of SDOF systems, with varying natural frequency, excited by random acceleration, both in the time and frequency domain.

Another method to synthesize the equivalent random vibration spectra is a method applied to pseudo stationary random vibration [8, 23], and is based on Rayleigh distribution of peaks (damage-potential) [36].

Miles' equation [24] is in the synthesis process of equivalent random acceleration vibration specifications from the different response spectra of great importance.

2 PREVIOUS WORK

The SRS was already mentioned by M.A. Biot in 1933 [4] and later in 1941 [5]. The theoretical description of the SRS was done within the frame of earthquake engineering. A mechanical analyzer was developed to predict stresses in structural systems under transient impulse. The concept of SRS of accelerations is nowadays still in use in spacecraft structure engineering to characterize the severity of high frequency transient accelerations, such as separation of launch vehicle stages, shroud and the separation of spacecraft [34]. In SVM-5 [19] the principles and methods to analyze shocks are discussed in depth. Smallwood developed in [30] a very

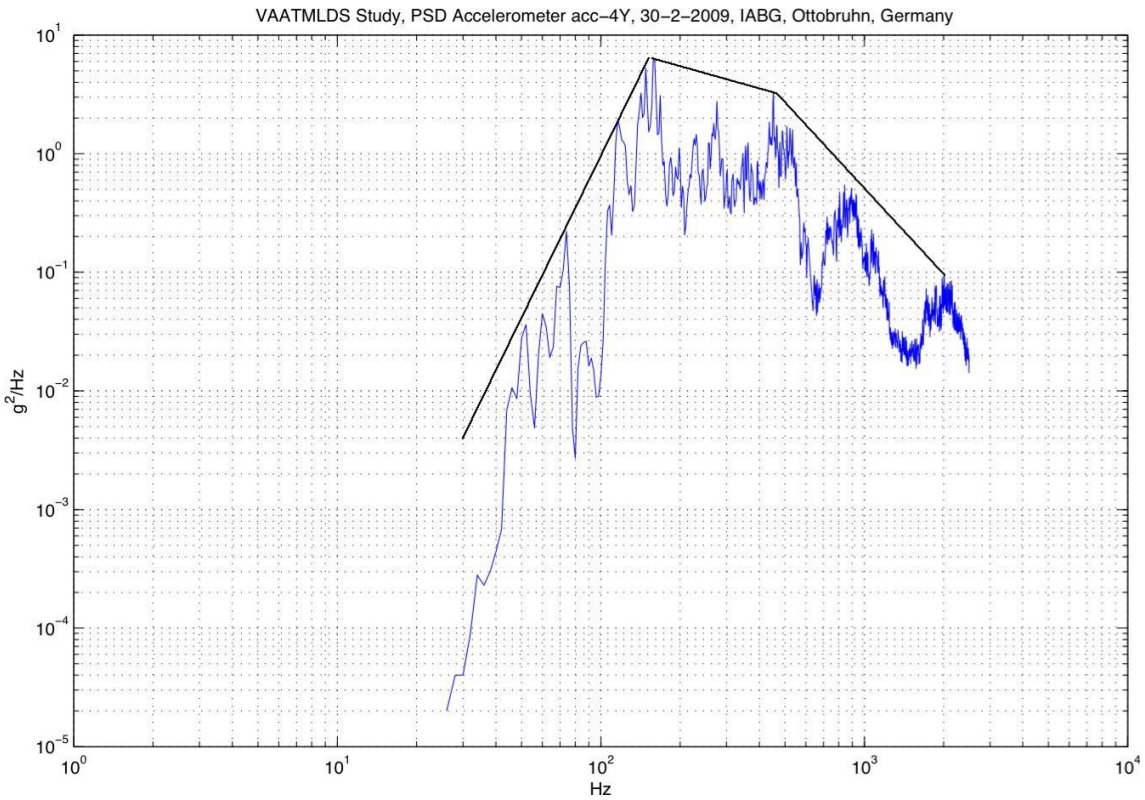


Figure 1: Schematic random acceleration vibration test specification (black) representing measured PSD responses (blue) g^2/Hz

efficient recursive formula to calculate the SRS. In [1, 32] the Smallwood recursive method (z-transform) was presented as a Matlab® or Octave® script. This script is applied to calculate the acceleration SRS in the time domain.

Lalanne discussed in his book "Specification Development" [21] the principle of the ERS and FDS for both sinusoidal and random vibration and the FDS for shocks as well.

Halfpenny et al discussed in their paper [13] the application of the SRS, ERS for peak accelerations and the FDS, to represent the cumulative fatigue damage caused by relative displacements (stresses), to describe new methods for vibration qualification of equipment on aircraft. Equivalent ERS and FDS are calculated for the proposed qualification random acceleration vibration test specification, which envelopes the flight ERS and SRS. The ERS is calculated in the frequency domain using numerical integration of the vibration spectrum and/or Miles' equation [24]. The peak values of stationary Gaussian process are discussed in detail in [27, 28]. In [13] the FDS is accurately obtained by numerical integration of the response spectrum or can be approximated applying Miles' equation. The approximate equation is used to calculate the equivalent random acceleration vibration spectrum.

Halfpennny described in his paper [12] the calculation of the the FDS of random vibrations both in the time and frequency domain. The random acceleration vibration spectrum is synthesized into the time domain by the summation of sine waves and the associated frequency, which in turn are applied to calculate the FDS in the time domain. The rain flow counting method is made available in Matlab® scripts, however, a number of rain flow counting methods are discussed in [3]. The synthesized random vibration test spectrum is calculated from the FDS, both in time and frequency domain, using the Miles' approximation for the FDS. The FDS is based

on the relative displacements of the SDOF systems base excited by the random accelerations.

McNeil described in his paper [23] the application of the FDS, however, not based on the relative displacement, but on the relative pseudo-velocities of the SDOF systems. He stated that at resonance the pseudo-velocity is roughly proportional to the stress. The FDS is calculated both in the frequency and time domain. In the time domain rain flow counting is used to extract amplitudes and associated number of cycles. The equivalent random vibration spectrum is calculated inverting the FDS based on Miles' approximation. The second method discussed in this paper is based upon the Rayleigh distribution of peaks for non stationary random accelerations.

Eaton [10] described in his paper presented on the 2012 SCLV Conference a test tailoring methodology for equipment based on the ERS and FDS.

Dimaggio et al [8] mentioned the Rayleigh distribution of peaks a damage-based approach. The synthesis of the equivalent random vibration spectrum is again based on Miles' equation. Irvine presented on the 2012 SCLV conference a paper [18] a comparison of the damage potential method twith the SRS, ERS and VRS methods.

The VRS is described by Irvine in [16], which is used to synthesize random vibration spectra by enveloping the VRS. Miles' equation is applied to obtain synthesized random vibration spectra. The VRS spectrum is very similar to the ERS.

In the previous referenced papers (e.g. [8]) it was recommended to vary the amplification factor and Basquin's exponent of the s-N curve, such that $Q = 10, 25, 50$ and $b = 4, 8, 12$. The worst synthesized random vibration spectra shall be applied to testing.

3 RESPONSE SPECTRUM

In this section a number of response spectra will be briefly discussed. The SRS is based on deterministic transient inputs and responses, while the VRS, ERS are based on the random PSD acceleration inputs and r.m.s. responses of SDOF systems. and the FDS is based on the response of SDOF systems both in the time and frequency domain. The random acceleration input is assumed to be weakly stationary and Gaussian. Mean values of responses are assumed to be zero.

3.1 Shock Response Spectrum (SRS)

The SRS was first introduced by Biot [4, 5] within the frame of earthquake engineering, and has been in existence for a long time.

The SRS is a graphical representation of an arbitrary transient acceleration input, how a single degree of freedom system (SDOF) (mass-spring-damper) responds to that input. Actually it shows the peak acceleration response in principle of an infinite number of SDOF systems, each of which has different natural frequencies ($\omega_i = 2\pi f_i,\ i = 1, 2, \cdots$). This illustrated in Fig. 2, where the SDOF systems are mass normalized. In fact, the SRS analysis is the maximum response of a series of SDOF systems having the same damping to a given transient signal. In practice a damping ratio $\zeta = 0.05$ ($Q = 10$) is assumed.

The analysis procedure to compute the SRS is described in [1, 32], where a MATLAB® script has been presented based on the recursive formula proposed by Smallwood [30].

3.2 Vibration Response Spectrum (VRS)

Tom Irvine introduced the VRS in [16], which is similar to the SRS, however, the transient acceleration input is now replaced by random acceleration PSD input $W_{\ddot{u}}(f)$ (g^2/Hz) and the transient maximum responses are replaced by the 1σ absolute responses of the SDOF systems.

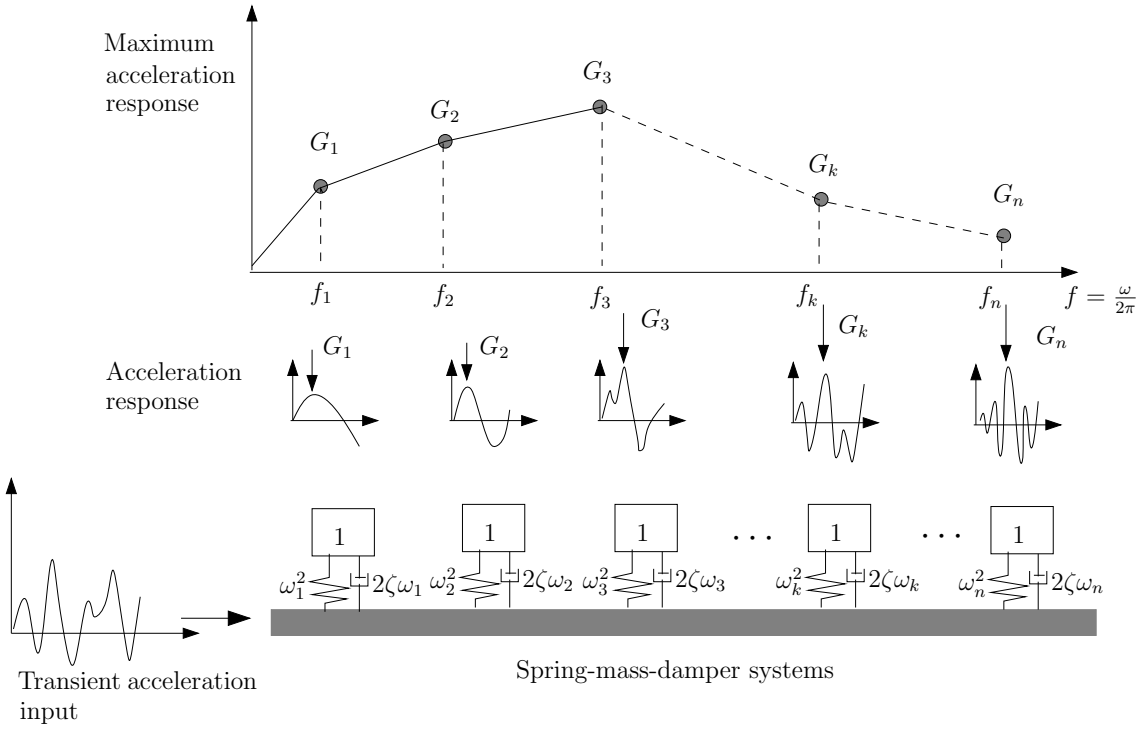


Figure 2: How a shock response spectrum is developed

In general, the damping ratio is taken $\zeta = 0.05$ ($Q = 10$) and is the same for all SDOF systems.

The graphical representation of the VRS is illustrated in Fig. 3. The SDOF systems are mass normalized. The standard deviation of the response of the SDOF system enforced at the base by random acceleration input can be calculated by the following expression

$$\sigma_i = \sqrt{\int_0^\infty |H_i(f)|^2 W_{\ddot{u}}(f) df} \approx \sqrt{\sum_{f_{min}}^{f_{max}} |H_i(f)|^2 W_{\ddot{u}}(f) \Delta f},\ i = 1, 2, \cdots, N, \tag{1}$$

where the frequency transfer function (FRF) $H_i(f)$ is given by

$$H_i(f) = \frac{1 + 2j\zeta f/f_i}{1 - (f/f_i)^2 + 2j\zeta f/f_i}, \tag{2}$$

and $f_i = \omega_i/2\pi$ is the natural frequency.

If the input PSD $W_{\ddot{u}}(f)$ is relatively flat at frequencies near the natural frequency f_i equation (15) can be approximated by Miles' equation [35]:

$$\sigma_i \cong \sqrt{\frac{\pi f_i W_{\ddot{u}}(f_i)(1 + 4\zeta^2)}{4\zeta}} \approx \sqrt{\frac{\pi f_i Q W_{\ddot{u}}(f_i)}{2}},\ i = 1, 2, \cdots, N. \tag{3}$$

The VRS is defined as

$$VRS(f_i) = 3\sigma_i,\ i = 1, 2, \cdots, N. \tag{4}$$

The VRS equivalent random acceleration vibration specification $W_{\ddot{u}}(f_i)$ for the enforced acceleration can be calculated by inverting of (3)

$$W_{VRS,\ddot{u}}(f_i) = \frac{2(VRS)^2(f_i)}{9\pi f_i Q},\ i = 1, 2, \cdots, N. \tag{5}$$

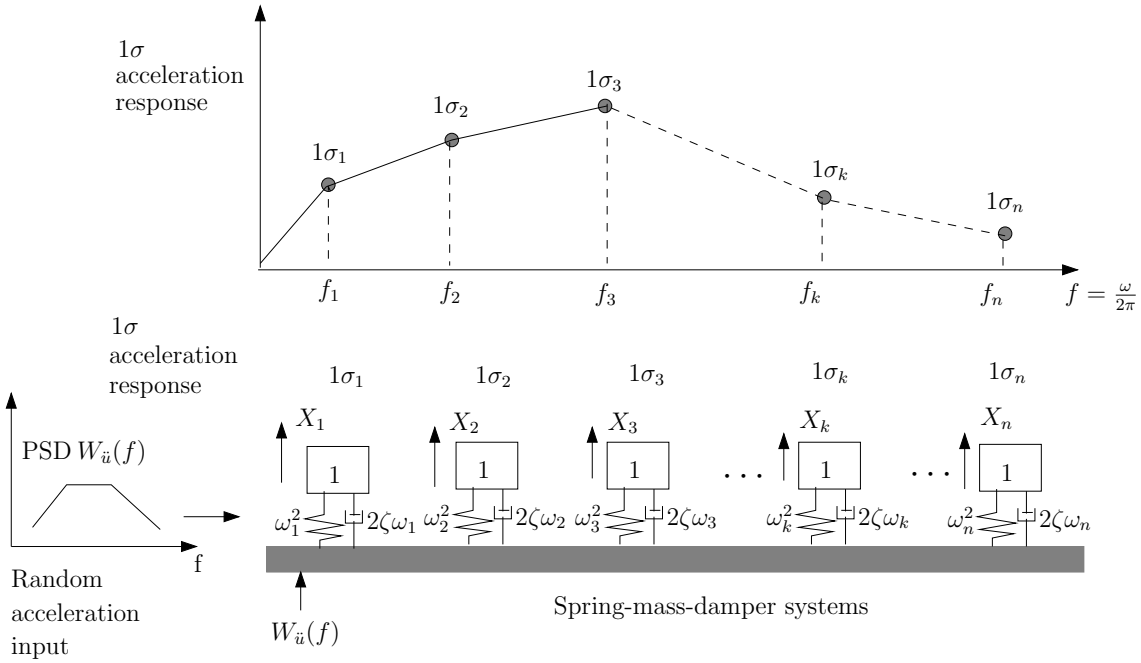


Figure 3: How a vibration response spectrum is developed

3.3 Extreme (Peak) Response Spectrum (ERS)

The ERS is similar to the SRS because peak values of the SDOF random response are depicted graphically in the ERS. Lalanne already discussed in [21] the ERS for random vibrations. The $1\sigma_i$ response of the SDOF system "i" is multiplied by a random peak factor C_i. The expected value of the peak factor of the random response of the SDOF system is given by [28]:

$$E[C_i] = \sqrt{2\ln(f_i T)} + \frac{\gamma}{\sqrt{2\ln(f_i T)}}, \tag{6}$$

and the standard deviation of the peak factor is

$$\sigma[C_i] = \frac{\pi}{\sqrt{6}} \frac{1}{\sqrt{2\ln(f_i T)}}, \tag{7}$$

where f_i is the natural frequency of the SDOF system, T the time duration of the random accelerations process and $\gamma = 0.5772$ is the Euler constant [9]. Further it is assumed that $f_i T \gg 1$, and

- the random response X_i of the SDOF system has a Gaussian distribution, and
- the peak values of the random response of the SDOF system are statically independent. The statistically independence assumption is acceptable if $E[C_1]/\sigma[C_1] > 3.5$ and $f_i T > 250$ for a Gaussian process [14].

With a given standard deviation σ_i of the random response of the SDOF system the maximum expected extreme (peak) acceleration response spectrum $ERS_a(f_i)$ can be calculated using:

$$ERS_a(f_i) = E[C_i] * \sigma_i, \; i = 1, 2, \cdots, N. \tag{8}$$

The expected peak values for the displacement, the $ERS_d(f_i)$ displacement spectrum, is given by [13]

$$ERS_d(f_i) = 9.81^2 \frac{E[C_i] * \sigma_i}{\omega_i^2},\ i = 1, 2, \cdots, N, \tag{9}$$

in case the PSD input spectrum $W_{\ddot{u}}(f)$ is specified in g^2/Hz.

The ERS equivalent random acceleration vibration specification $W_{ERS,\ddot{u}}(f_i)$ for the enforced acceleration can be calculated with the aid of inverting (8)

$$W_{ERS,\ddot{u}}(f_i) = \frac{2ERS^2(f_i)}{E(C_i)^2 \pi f_i Q},\ i = 1, 2, \cdots, N. \tag{10}$$

Because the SRS is also based on peak responses, the equivalent random acceleration vibration specification can be obtained using (10),

$$W_{SRS,\ddot{u}}(f_i) = \frac{2SRS^2(f_i)}{E(C_i)^2 \pi f_i Q},\ i = 1, 2, \cdots, N. \tag{11}$$

3.4 Fatigue Damage Spectrum (FDS)

In this section the fatigue damage spectrum will be based on the relative displacements FDS$_d$ and pseudo-velocities [23] FDS$_{pv}$.

3.4.1 FDS$_d$ in Frequency Domain

The expected cumulative fatigue damage $E[D(T)]$ (in one SDOF system) involves the Palgren-Miner fatigue accumulation rule [20, 22] in combination of the s-N curve $N_k s_k^b = C$ (N_k is the number of allowable cycles at stress level s_k) for a narrow-banded Gaussian process the cumulative damage and is given by [7, 36] for $f_1,\ i = 1, 2, \cdots N$:

$$E[D(T, f_i)] = \frac{f_i T}{C} (\sqrt{2}\sigma_s)^b \Gamma\left(1 + \frac{b}{2}\right), \tag{12}$$

where C is a material constant (Basquin coefficient), b is the fatigue exponent (Basquin's exponent), f_i is the natural frequency of the SDOF system, T the time duration, σ_s is the standard deviation of the stress, and Γ is the gamma function.

The stress s is proportional to the relative displacement of the SDOF multiplied by a constant K. The standard deviation of the stress $\sigma_{s,i}$ can be obtained as follows:

$$\sigma_{s,i} = K \frac{9.81}{(2\pi f_i)^2} \sqrt{\frac{\pi}{2} f_i Q W_{\ddot{u}}(f_i)}, \tag{13}$$

because the PSD spectrum $W_{\ddot{u}}$ of the enforced random acceleration is most times specified in g^2/Hz.

The FDS$_d$ corresponding to the natural frequency of the SDOF system "i" is now defined for $f_i,\ i = 1, 2, \cdots N$:

$$FDS_d(T, f_i) = f_i T \frac{K^b}{C} \left[\frac{9.81^2 Q W_{\ddot{u}}(f_i)}{2(2\pi f_i)^3}\right]^{\frac{b}{2}} \Gamma\left(1 + \frac{b}{2}\right). \tag{14}$$

In general, the constants are taken as $K = C = 1$, the exponent $b = 4, 8, 12$, and the amplification factor $Q = 10, 25, 50$.

Instead of using Miles' equation, the standard deviation of the relative displacement response $\sigma_{d,i}$ of the SDOF system can be computed as follows

$$\sigma_{d,i} = \sqrt{\int_0^\infty |H_{d,i}(f)|^2 W_{\ddot{u}}(f) df} \approx \sqrt{\sum_{f_{min}}^{f_{max}} |H_{d,i}(f)|^2 W_{\ddot{u}}(f) \Delta f}, \; i = 1, 2, \cdots, n, \tag{15}$$

where the frequency transfer function (FRF) $H_i(f)$ is given by

$$H_{d,i}(f) = \frac{1}{(2\pi f_i)^2} \frac{1}{(1 - (f/f_i)^2 + 2j\zeta f/f_i)}. \tag{16}$$

The standard deviation of the stress s_i is $\sigma_{s_i} = 9.81 K \sigma_{d,i}$. The mean value of the stress is assumed to be zero.

The synthesized equivalent random acceleration vibration spectrum $W_{FDS_d,\ddot{u}}(f_i)$ can be calculated by the inverse of (14)

$$W_{FDS_d,\ddot{u}}(f_i) = \frac{2(2\pi f_i)^3}{9.81^2 Q} \left[\frac{C \; FDS_d(f_i)}{K^b f_i T \Gamma \left(1 + \frac{b}{2}\right)} \right]^{\frac{2}{b}}, \; i = 1, 2, \cdots, N. \tag{17}$$

3.4.2 FDS$_d$ in Time Domain

If the random acceleration is provided in the time domain or is synthesized into the time domain, the the cumulative damage D is given by the Palgren Miner rule, which tells us that cumulative damage D is

$$D = \sum_{k=1}^{N} \frac{n_k}{N_k}, \tag{18}$$

where n_k is the number of stress oscillations at stress level s_k, and N_k is the number of allowable oscillation at stress level s_k given by the $s - N$ curve

$$s_k^b N(s_k) = C. \tag{19}$$

The generation of the FDS$_d$ in the time domain is symbolically illustrated in Fig. 4. The random enforced transient acceleration is applied to the base of each of the SDOF systems. From the calculated random relative displacements $z(t)$, per SDOF system, the numbers of cycles and associated "stress" peaks are extracted using a rain flow counting procedure [2, 26]. Using "stress" peaks and cycles the fatigue damage spectrum can be obtained. Again the stress constant and the Basquin's coefficient are assumed to be $K = C = 1$ and the Basquin exponent may vary $b = 4, 8, 12$.

3.4.3 FDS$_{pv}$ in Frequency Domain (Spectral Method)

in [23] the pseudo-velocity $pv(t)$ of the SDOF system is applied to calculate the FDS$_{pv}$, because the pseudo-velocity is roughly proportional to stress for many structures, a scale factor exists between the stress σ and the pseudo-velocity pv, $\sigma = Kpv$, [6, 17]. The maximum strain amplitude ϵ is proportional to the "vibration Mach number" v/c, where v is the maximum

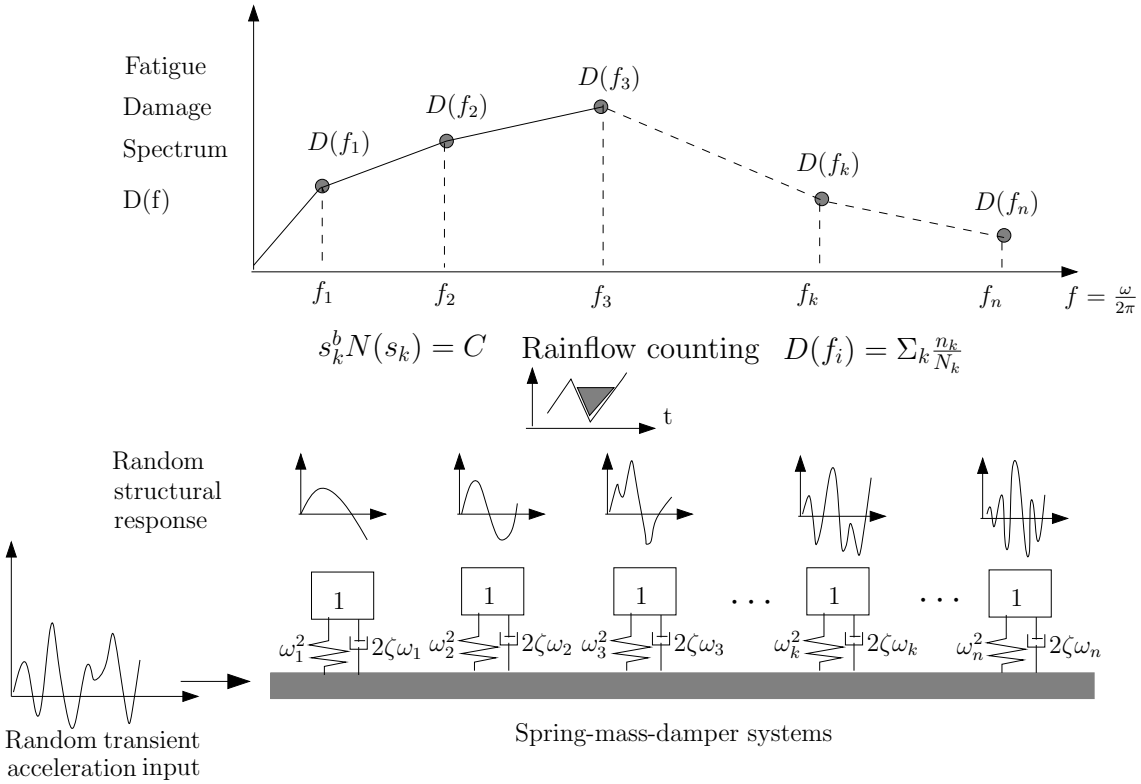


Figure 4: How a time domain damage fatigue spectrum is developed

vibratory velocity and c is the speed of sound in the material. The maximum strain is given by $\epsilon = k(v/c)$, where $k = 0.145 - 2.00$ for many different configurations [6].

The pseudo-velocity is defined as the relative displacement response $z(t)$ of the SDOF system multiplied by the natural frequency of that SDOF, $pv(t) = z(t) * (2\pi f_i)$.

The expected cumulative fatigue damage $E[D(T)]$ involves the Palgren-Miner fatigue accumulation rule [22] in combination of the s-N curve $N_k s_k^b = C$ (N_k is the number of allowable cycles at stress level s_k) for a narrow-banded Gaussian process the expected cumulative damage of FDS and is given by [7, 36], for $f_1,\ i = 1, 2, \cdots N$

$$FDS_{pv}(f_i) = E[D(T, f_i)] = \frac{f_i T}{C}(\sqrt{2}\sigma_s)^b \Gamma\left(1 + \frac{b}{2}\right) = \frac{f_i T}{C} K^b (2\sigma_{pv}^2)^{\frac{b}{2}} \Gamma\left(1 + \frac{b}{2}\right). \quad (20)$$

The standard deviation of pseudo-velocity $\sigma_{pv,i}$ is expressed as follows:

$$\sigma_{pv,i} = 9.81\sqrt{\frac{1}{8\pi f_i} Q W_{\ddot{u}}(f_i)}, \quad (21)$$

where the PSD function $W_{\ddot{u}}$ is most times given in g^2/Hz.

In general, the constants are taken as $K = C = 1$, the exponent $b = 4, 8, 12$, and the amplification factor $Q = 10, 25, 50$.

Instead of using Miles' equation, the standard deviation of the pseudo-velocity response $\sigma_{pv,i}$ of the SDOF system can be numerically calculated as follows

$$\sigma_{pv,i} = 9.81\sqrt{\int_0^\infty |H_{pv,i}(f)|^2 W_{\ddot{u}}(f) df} \approx \sqrt{\sum_{f_{min}}^{f_{max}} |H_{pv,i}(f)|^2 W_{\ddot{u}}(f) \Delta f},\ i = 1, 2, \cdots, n, \quad (22)$$

where the frequency transfer function (FRF) $H_{pv,i}(f)$ is given by

$$H_{pv,i}(f) = \frac{1}{(2\pi f_i)} \frac{1}{(1-(f/f_i)^2 + 2j\zeta f/f_i)}. \tag{23}$$

The standard deviation of the pseudo-velocity s_i is $\sigma_{s_i} = K\sigma_{pv,i}$. The mean value of the stress is zero.

The PSD values $W_{FDS_{pv}\ddot{u}}(f_i), i = 1, 2, \cdots, N$ of the random acceleration vibration specification can be obtained inverting (20) in combination with (21). Thus we get

$$\sigma_{pv}^2(f_i) = \frac{1}{2}\left(\frac{C\ FDS_{pv}(f_i)}{f_i T K^b \Gamma(1+\frac{b}{2})}\right)^{\frac{2}{b}}, \tag{24}$$

and

$$W_{FDS_{pv}\ddot{u}}(f_i) = \frac{8\pi f_i \sigma_{pv}^2(f_i)}{9.81^2 Q},\ i = 1, 2, \cdots, N. \tag{25}$$

3.4.4 FDS$_{pv}$ in Time Domain

The calculation of FDS$_{pv}$ is identical to calculation of the FDS$_d$, however, the stress is now proportional to the pseudo-velocity. If the random pseudo-velocity is provided in the time domain the the cumulative damage D is given by the Palgren Miner rule, which tells us that cumulative damage D is

$$D = \sum_{k=1}^{N} \frac{n_k}{N_k} = \frac{K^b}{C} \sum_{k=1}^{N} n_k p v_k^b, \tag{26}$$

where n_k is the number oscillations at pseudo-velocity level pv_k, and N_k is the number of allowable oscillation at pseudo-level level pv_k given by the $s-N$ curve

$$s_k^b N(s_k) = K^b p v^b N(pv) = C. \tag{27}$$

The constants are taken $K = C = 1$ and, in general, the exponent $b = 4, 8, 12$.

The calculation procedure for FDS$_{pv}$ is the similar to the calculation of FDS$_d$ as shown in Fig. 4.

3.5 Pseudo Stationary Random Vibration, Damage Potential

The method of pseudo stationary random vibration described in this section was discussed in [8, 23], however, McNeil applied this method using pseudo velocities, as discussed in sections 3.4.3 and 3.4.4.

The acceleration response of a lightly damped SDOF system excited by a zero-mean, stationary Gaussian white noise excitation is narrow banded and the probability of peak values is a Rayleigh distribution function and given by

$$f(A) = \left(\frac{A}{\sigma^2}\right) \exp\left(\frac{-A^2}{2\sigma^2}\right),\ A \geq 0, \tag{28}$$

where A is the amplitude and σ is the standard deviation. For a zero-mean response the standard deviation is equal to the r.m.s. value of the response. The probability the amplitude is grater then A, $A >$ can be obtained by integrating the probability density function from A to ∞

$$P(A >) = \int_A^{\infty} f(a)da = \exp\left(\frac{-A^2}{2\sigma^2}\right). \tag{29}$$

If we consider a stationary test of duration T_o, the total time $T(A >)$, or cumulative duration, spent during which response cycles with amplitudes exceeding A occur is

$$T(A >) = T_o \exp\left(\frac{-A^2}{2\sigma^2}\right). \tag{30}$$

For a SDOF system, with natural frequency f_i, the mean square acceleration response to a broad-band Gaussian excitation with a power spectral density W (g^2/Hz) is approximated by Miles' equation

$$\sigma^2 = \frac{\pi}{2} f_i Q W(f_i). \tag{31}$$

Taking the natural logarithme of both sides of (30) and substituting (31) yields

$$\ln\left(\frac{T_o}{T(A >)}\right) = \frac{1}{\pi f_i W(f_i)} \frac{A^2}{Q}. \tag{32}$$

For a particular natural frequency f_i, the function (32) appears as a straight line on a plot of $\ln T(A >)$ versus linear A^2/Q as shown in Fig. 5. In Fig. 5, A_{max} is the expected maximum amplitude at the exceedence duration of one period $1/f_i$. Prescribing a test based on an en-

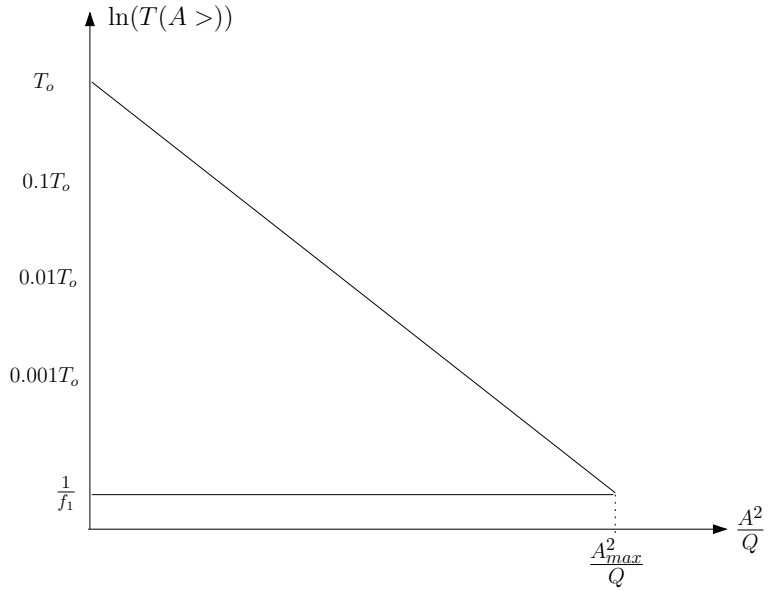


Figure 5: Cumulative duration plot for Rayleigh distributed Maxima

veloping Rayleigh line guarantees that the damage potential of the test, for a resonance of that frequency, envelops the damage potential of flight loads over the range of damping uncertainty. The Rayleigh line starts at T_o and $A^2/Q = 0$ and goes to a minimum time, the duration of the period $1/f_i$, associated with A^2_{max}/Q. The total time $T_o = n_{A_{min}>}/f_i$, where $n_{A_{min}>}$ the number of cycles with amplitudes $A \geq A_{min>}$. The number of cycles can be obtained by the rain flow counting method. The equivalent power spectral density $W_{DP,\ddot{u}}(f_i)$ corresponding to the the line T_o to A^2_{max}/Q can be calculating by the following expression

$$W_{DP,\ddot{u}}(f_i) = \frac{(A^2_{max}/Q)}{\pi f_i \ln(f_i T_o)}. \tag{33}$$

To construct the Rayleigh line (Fig. 5) the following step by step procedure is to be done:

1. Translate the power spectral density spectra of the random vibration into a time domain random excitation.

2. Determine the absolute random acceleration response of the SDOF system, with natural frequency f_1, excited by the random excitation in the time domain.

3. Perform a rain flow counting to analyze the spectrum of amplitudes and corresponding number of cycles

4. Select a number of amplitudes $A_k,\ k = 1, 2, \cdots$, analyze the number of cycles $n(A_k >),\ k = 1, 2, \cdots$ and calculate the durations $T(A_k >) = n(A_k >)/f_i,\ k = 1, 2, \cdots$. The minimum number of cycles beyond A_{max} is $n(A_{max} >) = 1$, with $T(A_{min} >) = 1/f_i$, and the number of cycles beyond A_{min} is $n(A_{min} >= T_o/f_i$. This step is illustrated in Fig. 6.

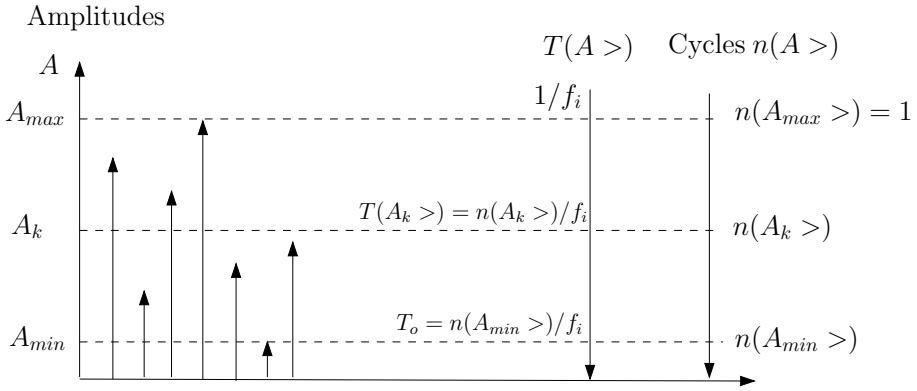
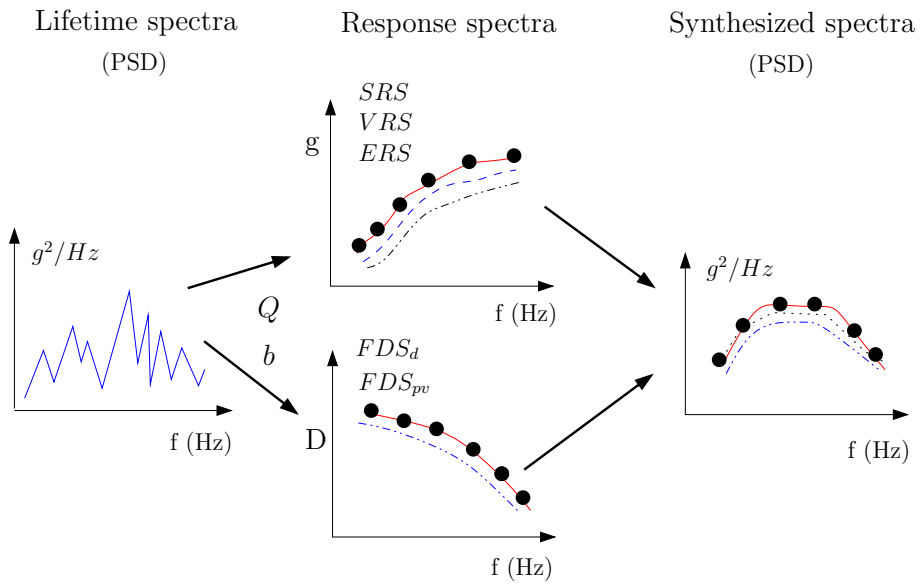


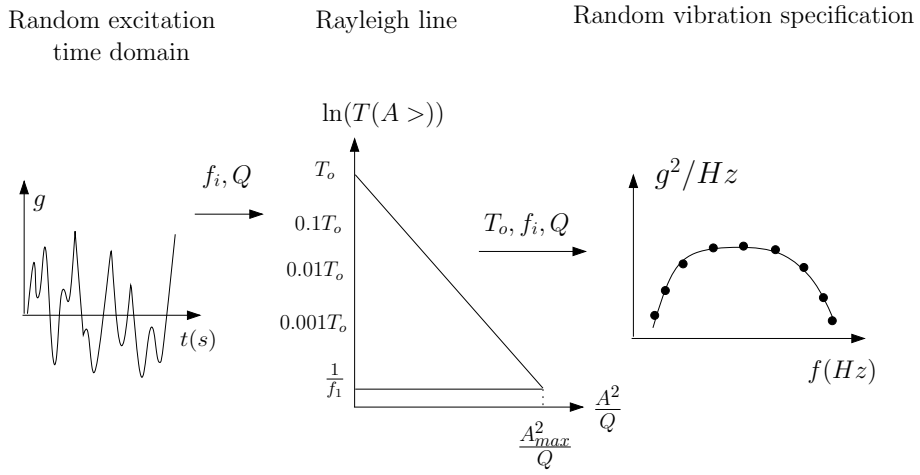
Figure 6: The evaluation of $T(A >)$ versus the amplitude A

4 SYNTHESIS OF EQUIVALENT RANDOM ACCELERATION VIBRATION SPECIFICATION

It is assumed that the equivalent random acceleration vibration spectra represent the same amount of (fatigue) damage as expected for the original measured or calculated spectrum. The reconstruction or synthesis of an equivalent random acceleration vibration specification $W_{\ddot{u}}(f)$ can be done using the response spectra; SRS, VRS, ERS, FDS$_d$, FDS$_{pv}$ and the Rayleigh line (damage potential). The response spectra computing in the time domain can be used as well. For that purpose the equations (5), (10), (11), (17), (25), and (33) can be applied. Miles' equation has a key role computing the equivalent random acceleration specifications. The procedure to reconstruct the equivalent random acceleration vibration specification is illustrated in Fig. 7 (a and b). In order to address the variations in damping and s-N curve fatigue exponent b , the response spectra and Rayleigh line shall be computed with amplification factor values of $Q = 10, 25, 50$ and exponents $b = 4, 8, 12$ for each natural frequency f_i of the SDOF systems. The greatest power spectral density value of $W_{\ddot{u}}(f_i)$ over the 3-9 variations of Q and b is used as the random equivalent vibration specification level at frequency $f = f_i$. Finally, the complete random acceleration vibration specification is established. However, engineering judgement is still needed.



(a)



(b)

Figure 7: Schemes to synthesize the random acceleration vibration specification

5 APPLICATION

5.1 Random Vibration Measurement during a Acoustic Test

Within the frame of the ESA/TRP study: "Vibro-Acoustic Analysis Test methods for Large Deployable Structures" (VAATMLDS) [33] acoustic tests were performed on the VAATMLDS Bread Board solar array wing in the acoustic reverberant chamber of IABG [15].

The read-out of accelerometer Acc-4Y (Fig. 9) is the random acceleration spectrum, for which a smooth and shaker controllable random vibration acceleration test spectrum should be generated, as illustrated in Fig. 1. The read-out of accelerometer Acc-4Y is in fact the raw random acceleration vibration specification. The number of data points is 1251 and the frequency increment $\Delta f = 2$Hz. The generation of the random acceleration vibration test specification will be performed in a more or less structured manner applying the response spectra; SRS, ERS, VRS, FDS and the Rayleigh distribution of peaks. To account for uncertainties in damp-

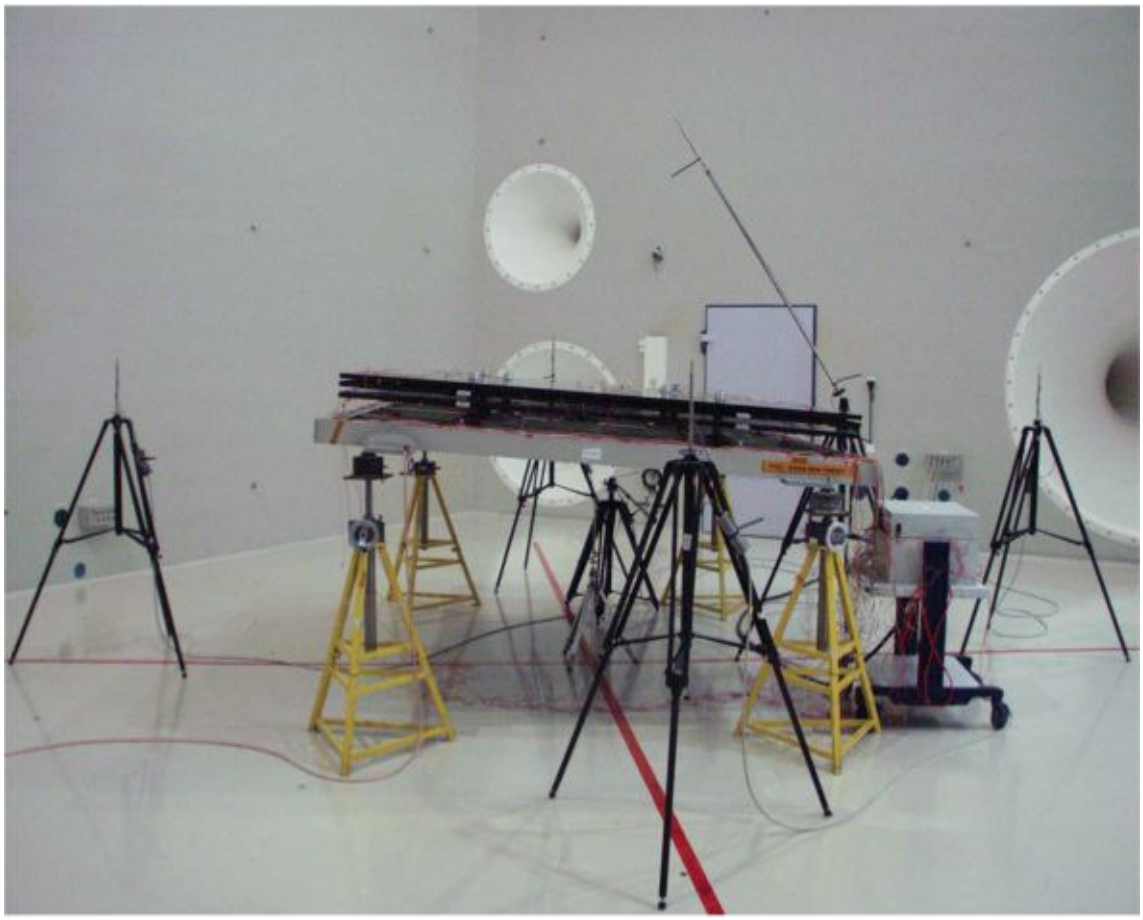


Figure 8: VAATMLDS bread board 3 panel solar array wing in IABG acoustic chamber

ing and Palgren-Miner cumulative damage rule, the amplification factor (quality factor) will be varied $Q = 10, 25, 50$ and fatigue exponent $b = 4, 8, 12$. Matlab® is applied to perform all computations.

The random acceleration spectrum is synthesized into the time domain (waveform) using the method described in [29], in combination with the Fourier transform [25]. The synthesized equivalent signals in the time domain are shown Fig. 10. It should be noticed that the synthesized time domain accelerations are random and will vary from analysis to analysis, however, having the same mean and standard deviation. This is due to the random frequency shifts in the arguments of the sine waves. The time increment $\delta t = 1/2f_{max} = 2.0 \times 10^{-4}$s, and the total time $T = 2N\delta t = 0.5004$s. The mean value of the all time domain signals is $\mu = 0$, and the standard deviation $1\sigma = r.m.s. = 24.98$g. In case the time domain random acceleration is a Gaussian process the skewness $\lambda = 0$ and the kurtosis $\gamma = 3$ [31]. A skewness $\gamma > 3$ will result in higher peaks and a skewness $\gamma < 3$ will result in lower peaks compared to the ideal Gaussian process.

The measured accelerations of accelerometer Acc-4Y, during the acoustic test, are now available both in the frequency and time domain. The response spectra: SRS, ERS, VRS, FDS$_d$, FDS$_{pv}$ and the distribution of Rayleigh peaks (damage potential) can now be computed.

The response spectra will be divided into N_{field} fields containing each n_{field} data points. This is illustrated in Fig. 11. The parameter N_{field} is set to $N_{field} = 100$. In each field

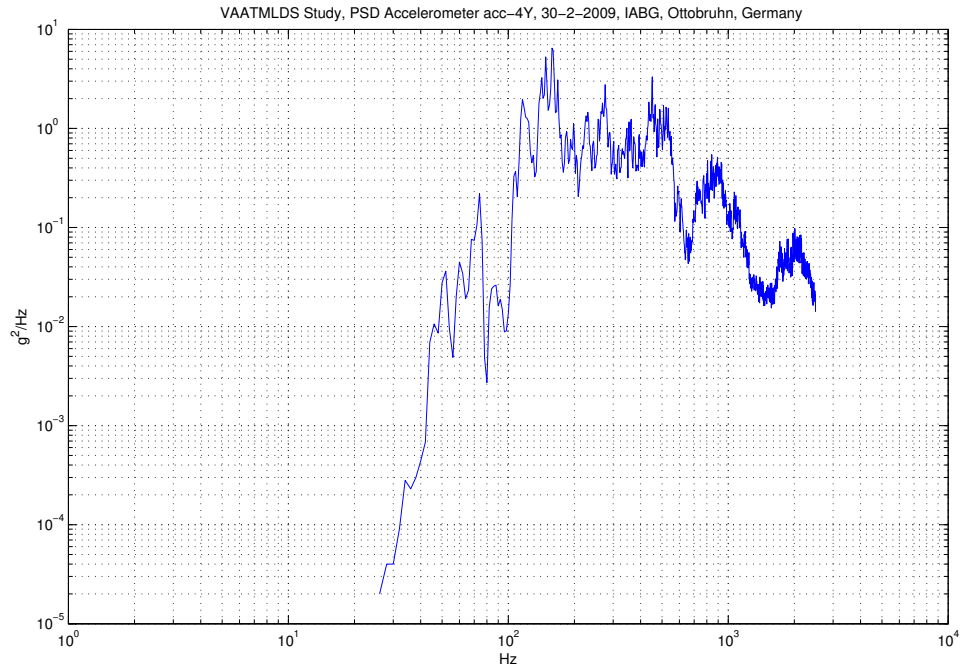


Figure 9: PSD measurement of accelerometer 4-Y, Grms=24.98g

the maximum value of the spectrum, and corresponding frequency, is detected and used to calculate the synthesized PSD of the random acceleration vibration specification. The local maximum may be an internal point or at the boundaries of the field. The first and last data point of the complete spectrum are considered too. The synthesized PSD's at the detected points are connected to each other assuming the log-log scales for the spectra and corresponding frequencies, respectively. Internal PSD values can be obtained by the following expression

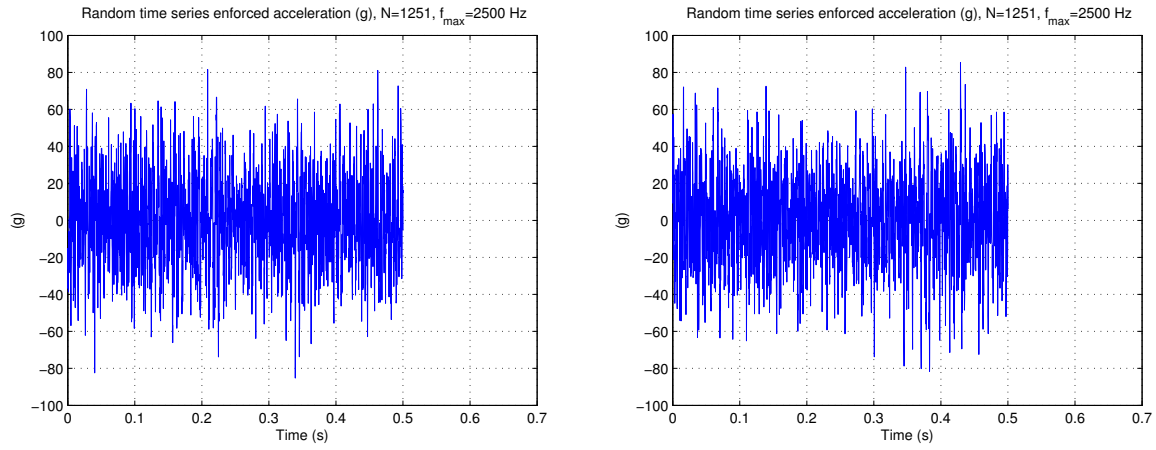
$$N = \log\left(\frac{W_2}{W_1}\right) / \log\left(\frac{f_2}{f_1}\right),\ W_i = W_1\left(\frac{f_i}{f_1}\right)^N = W_1\left(\frac{f_i}{f_1}\right)^{\frac{m}{3}}, \tag{34}$$

where W_1 and W_2 are the PSD values of the extreme points, f_1 and f_2 are the associated frequencies and m is the slope of the spectrum in dB/octave. Index i indicates a point with frequency f_i in between the extreme points. Equation (34) is applied to calculate the area (mean square) under the synthesized equivalent PSD spectrum.

5.2 Synthesis of Random Acceleration Vibration Specification from SRS and ERS

In this section the synthesized equivalent random acceleration vibration specification is calculated based on the SRS and ERS spectra. The SRS and ERS have 1251 and 2481 data points, respectively. Both are ranging from 20-2500Hz. The SRS and ERS are computed in accordance to the methods mentioned in sections 3.1 and 3.3. The VRS is common to the ERS, and therefor not considered. The computed ERS and SRS are shown Fig. 12(a).

The SRS and ERS overlay each other very well. Instead of computing the SRS in the time domain the ERS is a very good representative shock spectrum. Most times in spacecraft structures engineering the 3σ VRS spectrum is used, however, it is recommended to use the ERS as the SRS for a given random acceleration vibration specification.



(a) (b)

Figure 10: Synthesized time domain random accelerations, $\mu = 0$, $1\sigma = 24.98$g, $\lambda = 0.01$, $\gamma = 2.97$ (λ, γ mean values 10 samples) [31]

The SRS and ERS are divided into $N_{field} = 100$ fields. For each field the maximum value of the SRS and ERS is detected and applied to synthesize the reduced number of data points of the SRS and the ERS into PSD of the random acceleration vibration specification using (11) and (10), respectively. Both random acceleration vibration specifications are shown in Fig. 12(b). Further, the synthesized random acceleration vibration specifications W_{SRS} and W_{ERS} are compared to the original response spectrum of accelerometer Acc-4Y in Fig. 12(c). The

Table 1: Synthesis random acceleration vibration specification from ERS and SRS

	Q		
	10	25	50
W_{ERS} r.m.s.	26.1	26.3	26.9
W_{SRS} r.m.s. μ	24.0	23.1	22.5
W_{SRS} r.m.s. σ	0.8	0.6	0.4
Acc-4Y	25.0 G_{rms}		

PSD spectra W_{SRS} and W_{ERS} are computed varying the amplification factor $Q = 10, 25, 50$. The synthesized random accelerations are calculated from the original spectrum as shown in Fig 9, although, mean and standard deviation remain the same, but the distribution of the peaks alters in time, due to random arguments in the sine waves representation of the original PSD spectrum. That means that the SRS and W_{SRS} are more or less random. Therefor the mean and standard deviation of W_{SRS} is calculated from 10 samples. The PSD spectrum W_{ERS} will not change. The r.m.s. values of the PSD spectra W_{SRS} and W_{ERS} are given in Table 1. The synthesized r.m.s. values of PSD spectra of W_{SRS} under estimate the r.m.s. value of the original PSD spectrum and the synthesized r.m.s. values of the PSD spectrum of W_{ERS} show a higher r.m.s. values compared to the original PSD spectrum of the accelerometer Acc-4Y.

A further simplification of the random acceleration vibration spectra W_{SRS} and W_{ERS} can be achieved dividing the SRS and ERS spectra into less fields, however, this will result in higher r.m.s. values of the equivalent random acceleration vibration specifications.

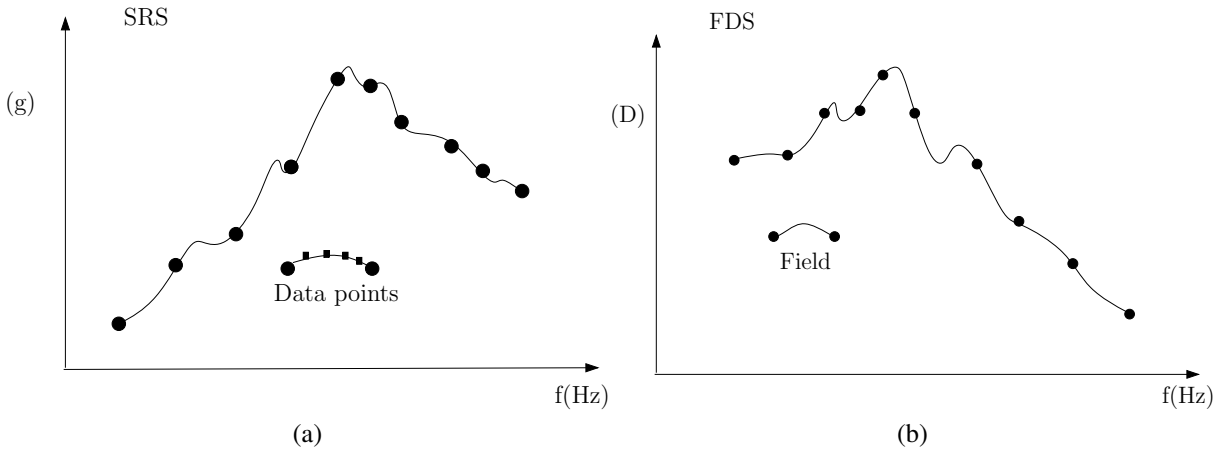


Figure 11: Division of spectra in fields

In Fig. 12 (d) the equivalent ERS from the equivalent W_{ERS} is computed for $Q = 10$ and compared to the original ERS.

5.3 Synthesis of Random Acceleration Vibration Specification from FDS$_d$

The FDS$_d$ spectrum is computed both in the frequency and time domain. In the time domain the rain flow counting method (RF), as provided in Matlab®, is used. The number of data points of the FDS$_d$ in the frequency domain is 2481 and in the time domain 1251. The number of data point in the original spectrum is namely 1251 too. The FDS$_d$ is computed varying the amplification factor $Q = 10, 25, 50$ and the fatigue exponent $b = 4, 8, 12$. For $Q = 10$ and $b = 8$ the FDS$_d$ are shown in Fig. 13(a). To compute the equivalent random acceleration vibration specifications from the FDS$_d$, the spectra are divided into $N_{field} = 100$ fields. W_{Freq} is the synthesis of the random acceleration vibration specification taken from the FDS$_d$ spectrum and W_{RF} is the synthesis of FDS$_{d,RF}$. For $Q = 10$ and $b = 8$ both synthesized FDS are shown in Fig. 13(b). In Fig. 13(c) both synthesized random acceleration vibration specifications are compared to the random acceleration spectrum of Accelerometer Acc-4Y.

All computed data are given in Table 2. The mean values and the standard deviations of the W_{RF} PSD spectra are calculated using 10 samples. The figures in between the brackets are the standard deviations.

Again it is noticed that the synthesized random acceleration vibration specifications W_{RF} (time domain) are below the original spectrum of accelerometer Acc-4Y.

Table 2: Synthesis random acceleration vibration specification from FDS$_d$

	b					
	4		8		12	
Q / r.m.s.	W_{Freq}	W_{RF} (RF*)	W_{Freq}	W_{RF}	W_{Freq}	W_{RF}
10	26.1	24.0(0.3)	26.2	23.8(0.5)	26.2	23.1(0.4)
25	26.2	24.2(0.4)	26.7	23.9(0.4)	26.7	22.9(0.5)
50	27.0	24.4(0.4)	27.4	24.0(0.4)	27.4	22.8(0.5)
Acc-4Y	25.0 G_{rms}					

* RF is Rain flow counting

5.4 Synthesis of Random Acceleration Vibration Specification from FDS$_{pv}$

The FDS$_{pv}$ is quite similar to the FDS$_d$. The FDS$_{pv}$ spectrum is computed both in the frequency and time domain. In the time domain the rain flow counting method (RF) was used. The number of data points of the FDS$_{pv}$ in the frequency domain is 2481 and in the time domain 1251. The FDS$_{pv}$ is computed varying the amplification factor $Q = 10, 25, 50$ and the fatigue exponent $b = 4, 8, 12$. For $Q = 10$ and $b = 8$ the FDS$_{pv}$ are shown in Fig. 14(a). To compute the synthesized random acceleration vibration specifications the FDS$_{pv}$ spectra are divided in $N_{field} = 100$ fields. W_{Freq} is the synthesis of the random acceleration vibration specification taken from the FDS$_{pv}$ spectrum and W_{RF} is the synthesis of FDS$_{pv,RF}$. For $Q = 10$ and $b = 8$ both synthesized FDS are shown in Fig. 14(b). In Fig. 14(c) both synthesized random acceleration vibration specifications are compared to the random acceleration spectrum of Acc-4Y accelerometer.

All computed data are given in Table 3. The mean values and the standard deviations of the W_{RF} PSD spectra are calculated using 10 samples. The figures in between the brackets are the standard deviations.

It is again noticed that the r.m.s. values of the synthesized random acceleration vibration specifications W_{RF} (time domain) are below the r.m.s. value of the original spectrum of accelerometer Acc-4Y.

Table 3: Synthesis random acceleration vibration specification from FDS$_{pv}$

	b					
	4		8		12	
Q / r.m.s.	W_{Freq}	W_{RF} (RF*)	W_{Freq}	W_{RF}	W_{Freq}	W_{RF}
10	26.1	23.9(0.2)	26.1	24.1(0.4)	26.1	23.2(0.5)
25	26.4	24.3(0.5)	26.4	24.3(0.4)	26.4	23.3(0.3)
50	27.5	25.0(0.6)	27.5	24.5(0.4)	27.5	23.2(0.4)
Acc-4Y	25.0 G$_{rms}$					

* RF is Rain flow counting

5.5 Synthesis of Equivalent Random Acceleration Vibration Specification based on Rayleigh Distribution of Peaks

Table 4: Equivalent random acceleration vibration specification from Rayleigh distribution of peaks

	Q		
W_{DP}	10	25	50
Mean r.m.s. μ	26.0	25.4	24.8
Std-dev r.m.s. σ	0.7	0.4	0.2
Acc-4Y	25.0 G$_{rms}$		

The analysis of the Rayleigh distribution of peaks (damage potential) is completely done in the time domain on a transient random acceleration as illustrated in Fig. 10. The rain flow method as provided by Matlab®, is used to extract from the transient signal the amplitudes and corresponding number of cycles. The minimum value A_{min} of the distribution of

peaks is used to calculate the number of positive crossings n_0 through A_{min}. The total time $T_{A>A_{min}} = n_o/f_i,\ i = 1, 2, \cdots$, where f_i is one the frequency in the range of the spectrum (20-2500Hz). The number of crossings (spectrum of crossings) n_0 is shown in Fig. 15(a). In the application the total time is $T = 0.5004$s, in fact the duration of the random transient signal. The total equivalent random acceleration vibration spectrum is computed from (33). The random acceleration vibration spectrum is divided in $N_{field} = 100$ fields, and maximum values of that spectrum in these fields and associated frequencies are indicated and applied to generate the reduced equivalent random acceleration vibration specification W_{DP}. The full and reduced synthesized equivalent random acceleration spectra are shown in Fig. 15(b). The comparison to the original random acceleration vibration spectrum of accelerometer Acc-4Y is provided in Fig. 15(c). The presentation of Figures 15 are based on an amplification factor $Q = 10$.

The amplification factors are varied $Q = 10, 25, 50$ and the results of the calculation are presented in Table 4. The mean values and standard deviations of the r.m.s values of W_{test} are calculated from 10 samples.

5.6 All equivalent random acceleration vibration specifications in one plot

All synthesized equivalent random acceleration vibration specification from SRS, ESR, FDS$_d$, FDS$_{pv}$ and from the damage potential (Rayleigh distribution of peaks) are depicted in Fig 16 (a) and (b). It can be seen that all equivalent random acceleration specifications have the same shape and about the same r.m.s values of the spectra, however, the r.m.s. values of the equivalent spectra computed from the frequency domain are somewhat higher than calculated in the time domain.

5.7 Influence Number of Fields N_{field}

The number of fields N_{field} defines to a high extent the details kept in the equivalent random acceleration vibration specification, although in combination with the number of available data points in the response spectra. In previous sections the computations of the equivalent vibration spectra was based on a number of fields $N_{field} = 100$. The original random acceleration spectra of accelerometer Acc-4Y (Fig. 9) is rather smoothened in the lower frequency range, but in the higher frequencies the spectra still exhibit a number of peaks and valleys (i.e Fig 12). If we decrease the number of fields $N_{field} = 50, 25, 10, 5$, the equivalent random acceleration vibration specification becomes more smoothened, however, the r.m.s. value will increase, and at the other hand the vibration specification becomes more severe. This will be illustrated by an example computing the equivalent acceleration vibration specification from the original ERS assuming an amplification factor $Q = 10$. The figures are shown in Table 5. The mean and standard deviation of the equivalent vibration spectrum W_{SRS} is computed using 10 samples. If the number of fields $N_{field} < 10$, then it becomes difficult to get an envelope of the response

Table 5: Equivalent random acceleration vibration spectra (r.m.s.) from ERS, SRS with varying N_{field}.

	N_{field}, $Q = 10$				
	100	50	25	10	5
W$_{ERS}$ r.m.s.	26.1	27.2	28.0	30.9	23.5
W$_{SRS}$ r.m.s. μ	24.0	25.0	26.0	27.8	26.6
W$_{SRS}$ r.m.s. σ	0.8	0.9	0.8	1.1	1.6

spectra and a r.m.s. value of the equivalent random acceleration spectrum below the r.m.s. value of the original spectrum (Fig. 9) will be achieved. It is recommended to keep $N_{field} = 10 - 20$ as a minimum. In Fig. 17(a) the synthesized equivalent random acceleration vibration specifications, based on the ERS, SRS and $N_{field} = 10$ are shown.

6 CONCLUSIONS

In this paper a number of damage spectra are discussed to characterize measured or computed random acceleration vibration spectra, most times defined in PSD (g^2/Hz). The characterization is based on equivalent damage caused by extreme peaks (SRS, ERS, VRS and Rayleigh distribution of peaks or cumulative damage (FDS), using relative displacements and pseudo-velocities. The response spectra are all based on the response of SDOF systems exited to random accelerations, both in the time and frequency domain. The principles to compute the response spectra are illustrated in the Figures 2, 3, 4 and 5.

For random acceleration vibration it is shown numerically, that the ERS is the same as the SRS (i.e. Fig. 12(a)). The ERS is calculated in the frequency domain, but the SRS is calculated in the time domain, therefor the computation of the ERS is more straight forward then the calculation of the SRS. Nowadays in spacecraft structure engineering practice the VRS is applied to compare to the SRS, however, it is recommended to use the ERS instead of the VRS., because the ERS match better with the SRS then the VRS.

The FDS_d and FDS_{pv} spectra are quite the same.

Miles' equation fulfills a key role in the synthesis process to generate equivalent random acceleration vibration specifications, however, this equation represents the r.m.s. acceleration response of a SDOF system excited at the base by white noise random acceleration, which is an idealization of the real random acceleration spectrum. The application of Miles' equation in the synthesis process is an approximation!

An envelope of the damage response spectrum is achieved by dividing the spectrum into a number of fields N_{field}. The lower N_{field} to more severe and smoother the equivalent random acceleration vibration specification becomes. This process is shown in Fig. 11.

All damage response spectra result in about the same equivalent random acceleration vibration specifications (see Fig. 16).

The methods described in this paper are applied to a real life problem, the random acceleration spectrum (PSD) measured during an acoustic noise test of an accelerometer placed on the outside panel of the VAATMLDS bread board solar array wing.

To handle uncertainties in damping and material properties the amplification factor Q and the Basquin's exponent b in the s-N curve have to be varied, in general, $Q = 10, 25, 50$ and $b = 4, 8, 12$. The worst case equivalent random acceleration vibration specification shall be selected, however, engineering judgement of the engineer is still needed.

The synthesized random transient signal derived from the Acc-4Y random spectrum has an invariant mean and standard deviation, however, the distribution of the peaks and the skewness and kurtosis show small variations.

REFERENCES

[1] Ahlin, K. (2006) Comparison of Test Specifications and Measured Field Data, *Sound and Vibration*, September, pages 22-24

[2] Amzallag, C., Geray, J.P., Robert, J.L., Bahuaud, J. (1994) Standardization of Rain flow Counting Method for Fatigue Analysis, *Fatigue*, Vol 16, June, pages 287-293

[3] Benasciutti, D. (2004) *Fatigue Analysis of Random Loadings*, PhD University of Ferrara, Department of Engineering

[4] Biot, M.A. (1933) Theory of Elastic Systems Vibrating under Transient Impulse with an Application to Eartquake-Proof Buildings, *Proceedings of the National Academy of Sciences*, Vol. 19, No. 2, February, pages 261-268

[5] Biot, M.A. (1941) A Mechanical Analyzer for the Prediction of Earthquake Stresses, *Bulletin of the Seismological Society of America*, Vol. 31, No. 2, April, pages 150-171

[6] Crandall, S.H.(1962) *Relation between Strain and Velocity in Resonant Vibration*, Journal of Acoustical Society of America, Vol. 34(12), pages 160-1961

[7] Crandall, S.H., Mark, W.D. (1973) *Random Vibration in Mechanical Systems*, Academic Press

[8] DiMaggio, S.J., Sako, B.H. Rubin, S. (2003) Analysis of Non-stationary Vibroacoustic Flight Data using a Damage-Potential Basis, *Journal of Spacecraft and Rockets*, Vol. 40 No. 5, pages 682-689

[9] Dunham, W. (1999) *Euler The Master of Us All*, The Mathematical Society of America, ISBN 0-88385-328-0

[10] Eaton, R., Caro, E. (2012) Test Tailoring Methodology for Equipment Qualification, *2012 Spacecraft and launch Vehicle Dynamic Environments Workshop*, June 19-21 El segundo, Ca, USA, pages 37

[11] Girard, A., Imbert, J.F., Moreau, D. (1989) Derivation of European Satellite Equipment Test Specification from Vibro-Acoustic Test data, *Acta Astronautica*, Vol 10, No. 10, pages 797-803

[12] Halfpenny, A. (2006) Methods for Accelerating Dynamic Durability, *9th Int. Conf. Recent Advances in Structural Dynamics*, Southampton, UK, pages 18

[13] Halfpenny, A., Walton, T.C. (2010) New Techniques for Vibration Qualification of Vibrating Equipment on Aircraft, *Aircraft Airworthiness & Sustainment 2010*, pages 19

[14] Henderson, G.R., Piersol, A.G. (2003) Evaluating Vibration Environments Using the Shock Response Spectrum, *Sound and Vibration*, April, pages 18-20

[15] *IABG, Space Division, Survey of Facilities,* TN-TR-1000, Issue 12, may 2012

[16] Irvine, T. (2009) An Introduction to the Vibration Response Spectrum, Revision D, *Vibrationdata*, June 16, pages 20

[17] Irvine, T. (2012) Shock and Vibration Stress as a Function of Velocity, Revision C, *Vibrationdata*, May 21, pages 66

[18] Irvine, T. (2012) An Alternate Damage Potential Method for Enveloping Nonstationary Random Vibration, *2012 Spacecraft and launch Vehicle Dynamic Environments Workshop*, June 19-21 El segundo, Ca, USA, pages 28

[19] Kelly, R.D., Richman, G. (1969) *Principles and Techniques of Shock Data Analysis*, SVM-5, The Shock and Vibration Information Center, US MOD

[20] Lalanne, C. (2002) *Mechanical Vibration & Shock, Fatigue Damage Volume V*, HPS, ISBN 1-9039-9606-6

[21] Lalanne, C. (2002) *Mechanical Vibration & Shock, Specification Development, Volume V*, HPS, ISBN 1-9039-9607-4

[22] Madayag, A.F. (1969) *Metal fatigue: Theory and Design,* John Wiley & Sons, ISBN 471-56315-3

[23] McNeill, S.I. (2008) Implementing the Fatigue Damage Spectrum and Fatigue Equivalent Vibration Testing, *Sound and Vibration, 79th Shock and Vibration Symposium, October 26-30, Orlando, Florida* pages 1-20

[24] Miles, J.W. (1954), On structural fatigue under random loading, *Journal of the Aeronautical Sciences*, Vol. 21, 753-762

[25] Miles, R.N. (1992) Effect of Spectral Shape on Acoustic Fatigue Life Estimation, *Journal of Sound and Vibration*, Vol. 153 No. 2, pages 376-386

[26] Nieslony A. (2008) Determination of fragments of multi-axial service loading strongly influencing the fatigue of machine components, *Mechanical Systems and Signal Processing*, Vol. 23(8) pages. 2712-2721

[27] Ochi, M.K. (1981) Principles of Extreme ValuesStatistics and their Application, *Paper presented at Extreme Loads response Analysis Symposium*, Arlington, VA, October 19-20, pages. 15-30

[28] Preumont A. (1985) On the Peak Factor of Stationary Gaussian Processes, *Journal of Sound and Vibration*, **100**(1), pages 15-34

[29] Shinozuka, M., Jan, C.M. (1972) Digital Simulation of Random Processes and Its Applications, *Journal of Sound and Vibration* , **25** (1), pages 111-128

[30] Smallwood, D.O. (1981) An Improved Recursive Formula for Calculating Shock Response Spectra, Shock and Vibration Bulletin, No. 51, pages 4-10

[31] Steinwolf, A., White, R.G. (1997) Probability Density Functions of Acoustically Induced Strains in Experiments with Composite Plates, *AIAA Journal*, Vol. 35 No. 12, pages 1583-1861

[32] Tůma, J., Koči, P. (2009) Calculation of Shock Response Spectrum, Colloquium "Dynamics of Machines" 2009, Prague, February 3-4, pages 6

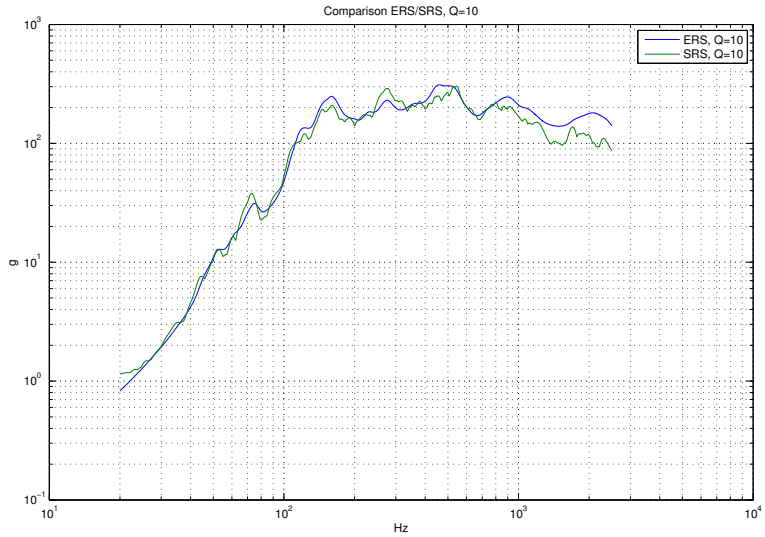
[33] Wijker, J.J. (2011) Final Presentation '*Vibro-Acoustic Analysis Test Methods for Large Deployable Structure*' (VAATMLDS), ESA/TRP Study Contract AO/1-5659/08/NL/EM, Noordwijk, February 20, 2011.

[34] Wijker, J.J. (2008) *Spacecraft Structures*, Springer, ISBN 978-3-540-75552

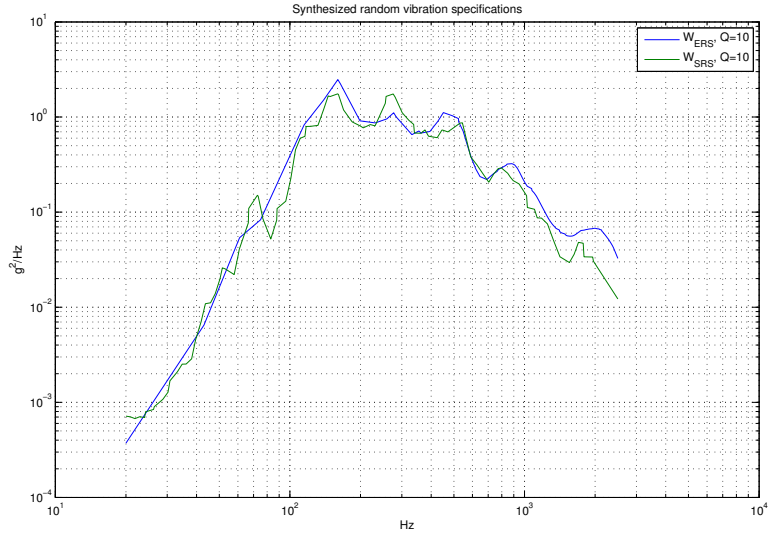
[35] Wijker, J.J. (2009) *Random Vibrations in Spacecraft Structures Design*, Springer, ISBN 978-90-2727-6

[36] Wirsching, P.H., Paez, T.L., Ortiz, H. (1995) *Random Vibrations, Theory and Practice*, John Wiley and Sons Inc., ISBN 0-471-58579-3

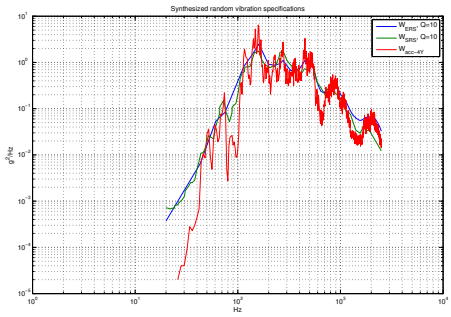
[37] Wood, W.L.. (1990) *Practical Time-stepping Schemes*, Clarendon Press, ISBN 0-19-859677



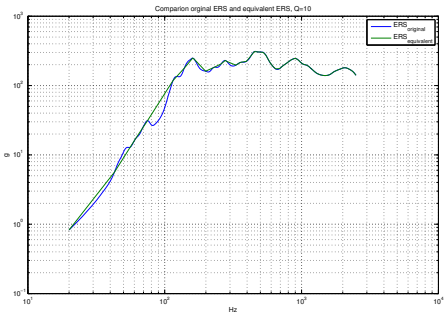
(a) SRS/ERS



(b) W_{SRS}, W_{ERS}

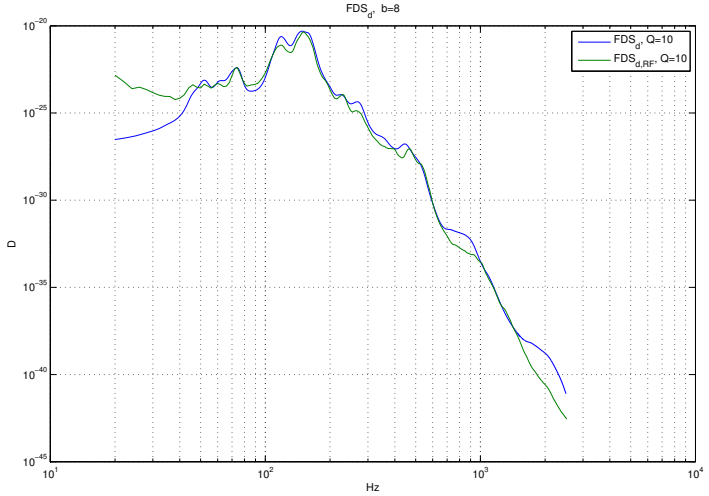


(c)

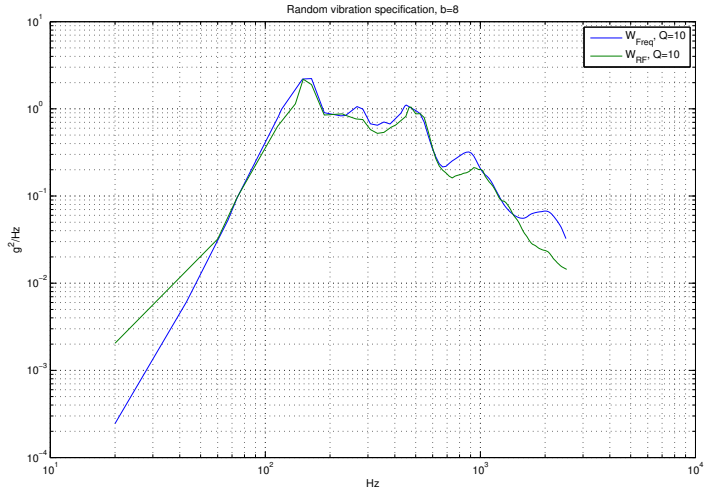


(d) ERS

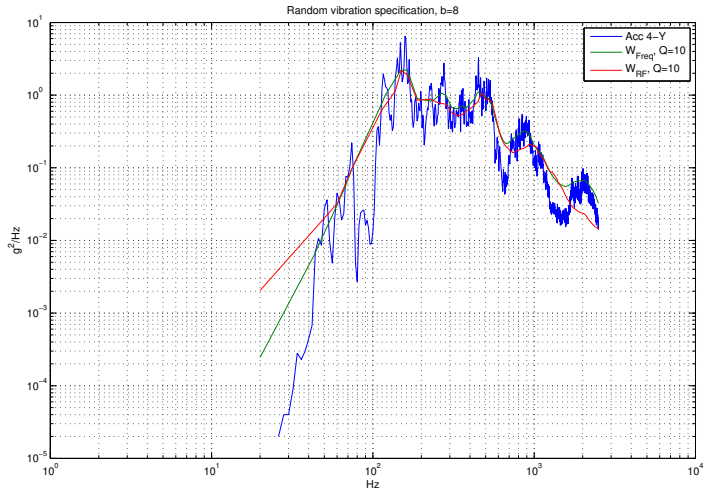
Figure 12: Synthesis of equivalent random acceleration vibration specification from SRS/ERS



(a)

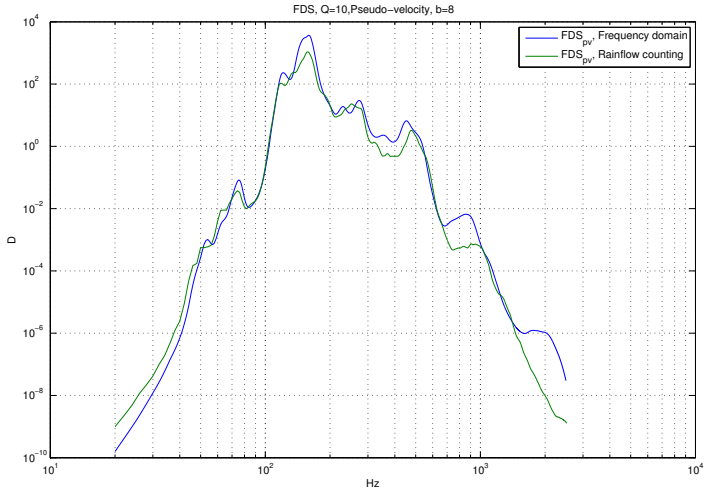


(b)

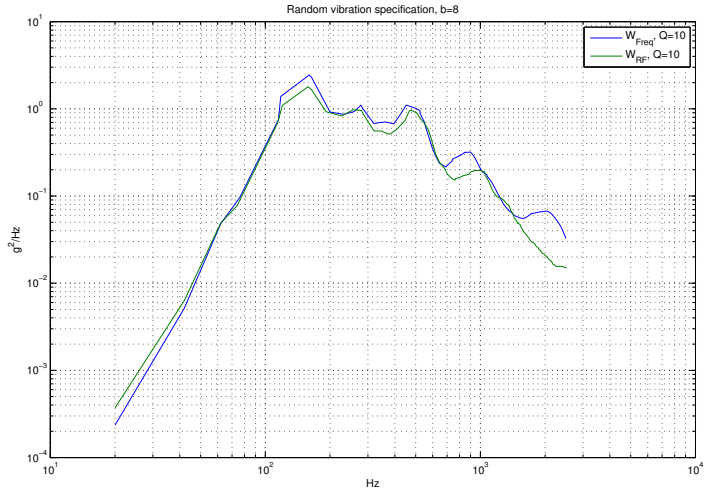


(c)

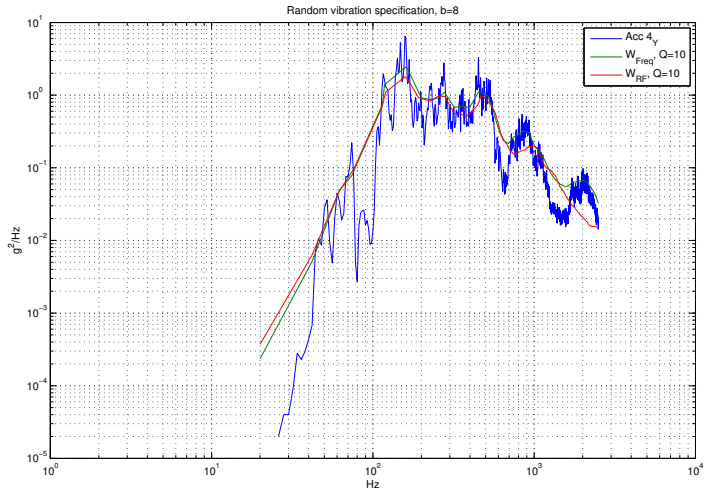
Figure 13: Synthesis of random acceleration vibration specification from FDS_d (RF is rain flow counting)



(a)

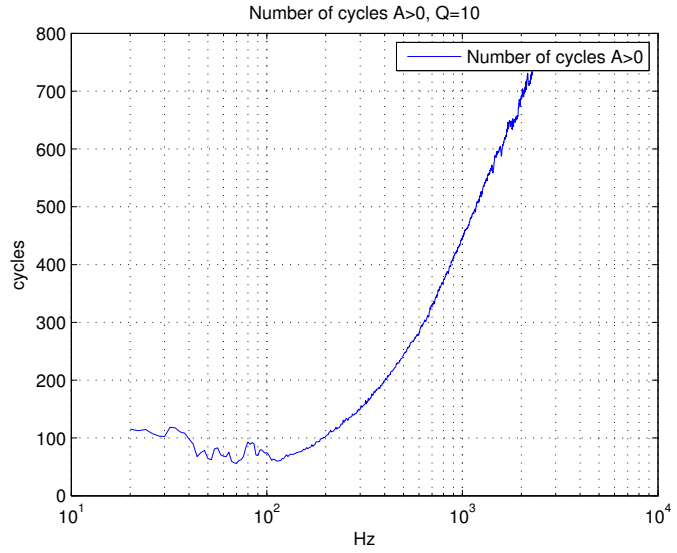


(b)

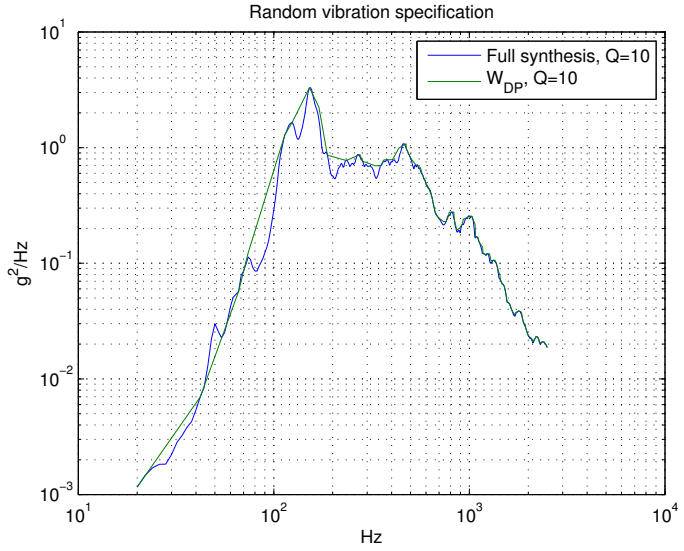


(c)

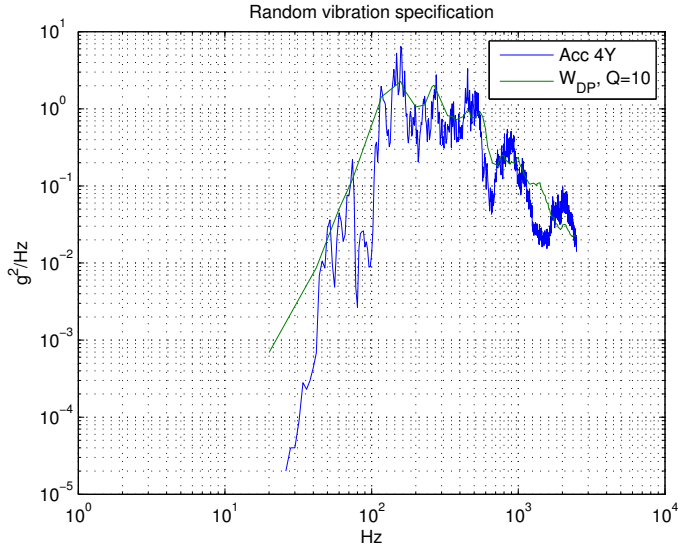
Figure 14: Synthesis of random acceleration vibration specification from FDS$_{pv}$ (RF is rain flow counting)



(a)

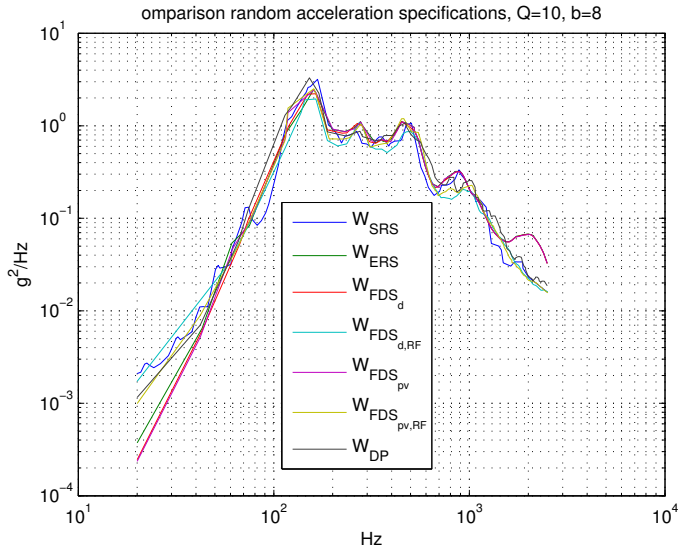


(b)

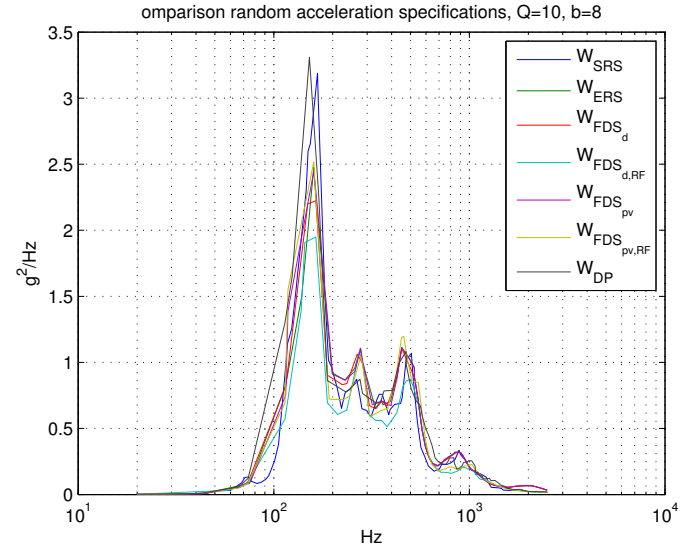


(c)

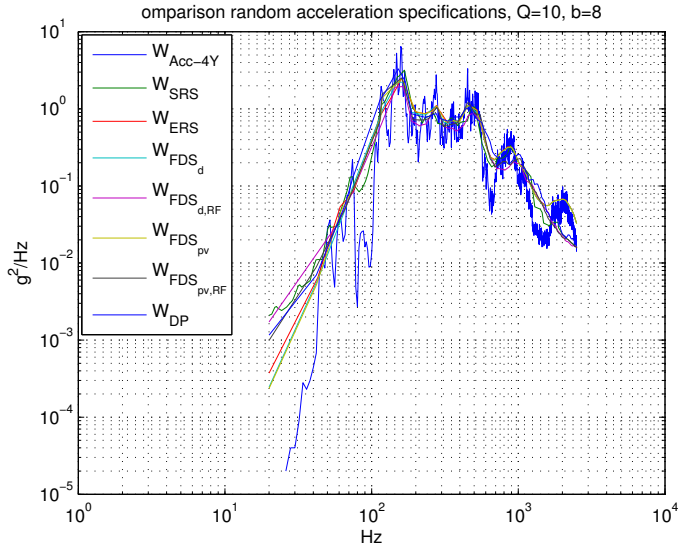
Figure 15: Synthesis of random acceleration vibration specification from potential damage (Rayleigh distribution of peaks)



(a)

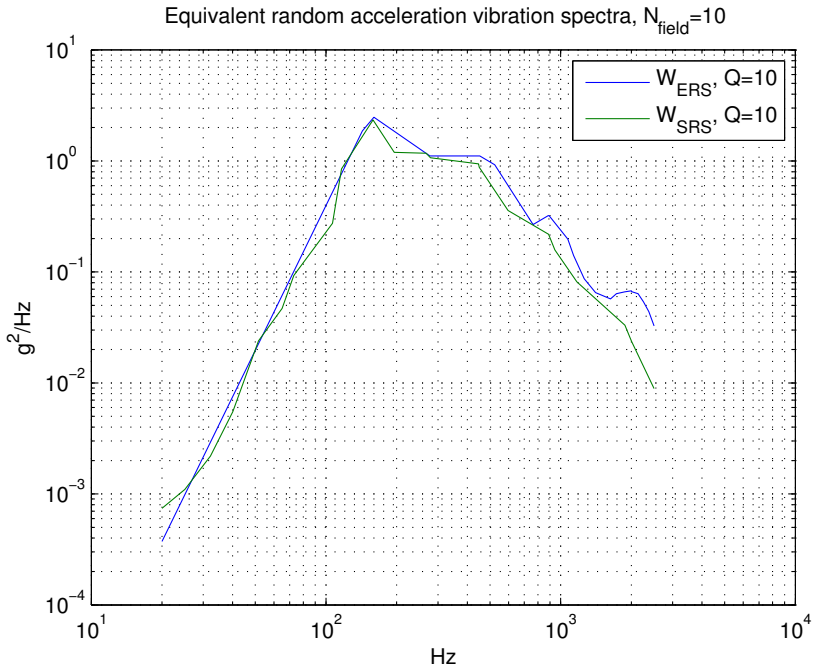


(b)

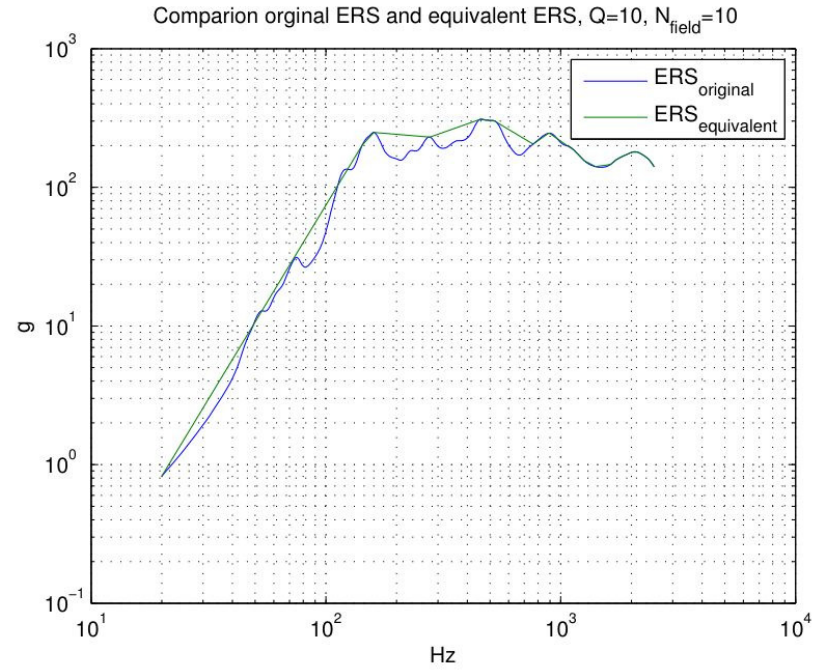


(c)

Figure 16: Presentation of all equivalent random acceleration vibration specifications



(a)



(b)

Figure 17: Equivalent random acceleration vibration spectra, $N_{field} = 10$

COMPDYN 2013
4th ECCOMAS Thematic Conference on
Computational Methods in Structural Dynamics and Earthquake Engineering
M. Papadrakakis, N.D.Lagaros, V. Plevris (eds.)
Kos Island, Greece, 12–14 June 2013

SINE TEST PREPARATION & MANAGEMENT INVOLVING LARGE NUMBER OF CHANNEL COUNTS.

Andrew Kiley BSc MSc Senior Specialist.

EADS-Astrium Ltd, Stevenage, Herts. United Kingdom.
e-mail: andy.kiley@astrium.eads.net

Keywords: Bepi-Colombo, sine test management, ECCOMAS Thematic Conference, Structural Dynamics, Earthquake Engineering, Proceedings.

Abstract. *Bepi Colombo represents an ESA corner stone mission in collaboration with JAXA in Space science and exploration. The purpose of the mission is to fly two (2) planetary orbiters to Mercury with the aims of magnetospheric and planetary surface mapping.*

The paper presented here is intended to convey to the wider community considerations and experiences relating to both preparing and conducting a sine test with a large acquisition count. The test specimen comprises of a stack of three Spacecraft modules: a propulsion Spacecraft at the launcher interface and two (2) planetary orbiters stacked one on top of the other. The total test specimen mass was 6400kg comprising 3900kg (structure), 2400kg (test adapter) with the remaining mass allocated to a Force Measurement Device (FMD) and ancillaries. Over 512 channels were instrumented (441 accelerometers, 69 strain gauges, 6 FMD channels) along with a further 49 Virtual Channels combining physical acquisitions to produce angular accelerations, direct force outputs, local bending moment outputs (both from strain gauges) to enable management of sine input levels and monitor integrity of the structure.

During pre-test preparation, activity is focused towards preparation of the test technical management plan whose purpose is to define a justification for sine input levels, how the test is to be managed in terms of technical strategy and collation / establishment of the acceptable upper and lower limits which the test must achieve and not exceed to avoid compromising the structural specimen. The paper also discusses preparation of the test support tool and highlights a number of points including factors such as the need to validate data phase acquisition checks. Simulation (dry runs) of on-test activities is seen as critical to a successful test to ensure that the process is robust, tools/software are adequately de-bugged and ensuring the data analysis team responsibilities are well understood.

For the Bepi Colombo sine test campaign Astrium deliberately maintained the same acquisitions during each axis of sine test, thus trading complexity of data analysis versus improvement in acquisition management. Typically re-configuration of acquisitions between sine test axes is accompanied by a number of re-patching issues which is discussed further in the paper. Using in-house tools written into DYNAWORKS, Astrium confidently managed the large number of acquisitions and data analysis successfully within the tight timeframes imposed during such campaign. The paper concludes with a discussion of the lessons learnt covering both successes and areas for future improvement for the final flight model sine test campaign.

1 INTRODUCTION

Bepi Colombo represents an ESA corner stone mission in collaboration with JAXA in Space science and exploration. Launch is scheduled for 2015 on Ariane 5, the purpose of the mission is to fly two planetary orbiters to Mercury with the aims of magnetospheric and planet surface mapping. Figure 1 shows the Structural Thermal Model (STM) in readiness for longitudinal sine testing at ESTEC within ESA ETS facility. The test specimen comprises of a stack of three (3) Spacecraft modules: a propulsion Spacecraft at the launcher interface and two (2) planetary orbiters stacked one on top of the other. The overall test specimen mass is 6400kg comprising 3900kg (structure), 2400kg (test adapter) with the remaining mass allocated to a Force Measurement Device (FMD) and ancillaries. Over 512 channels were instrumented (441 accelerometers, 69 strain gauges, 6 FMD channels) along with a further 60 Virtual Channels combining physical acquisitions to produce angular accelerations, direct force outputs, local bending moment outputs (both from strain gauges) to enable management of sine input levels and monitor integrity of the structure.

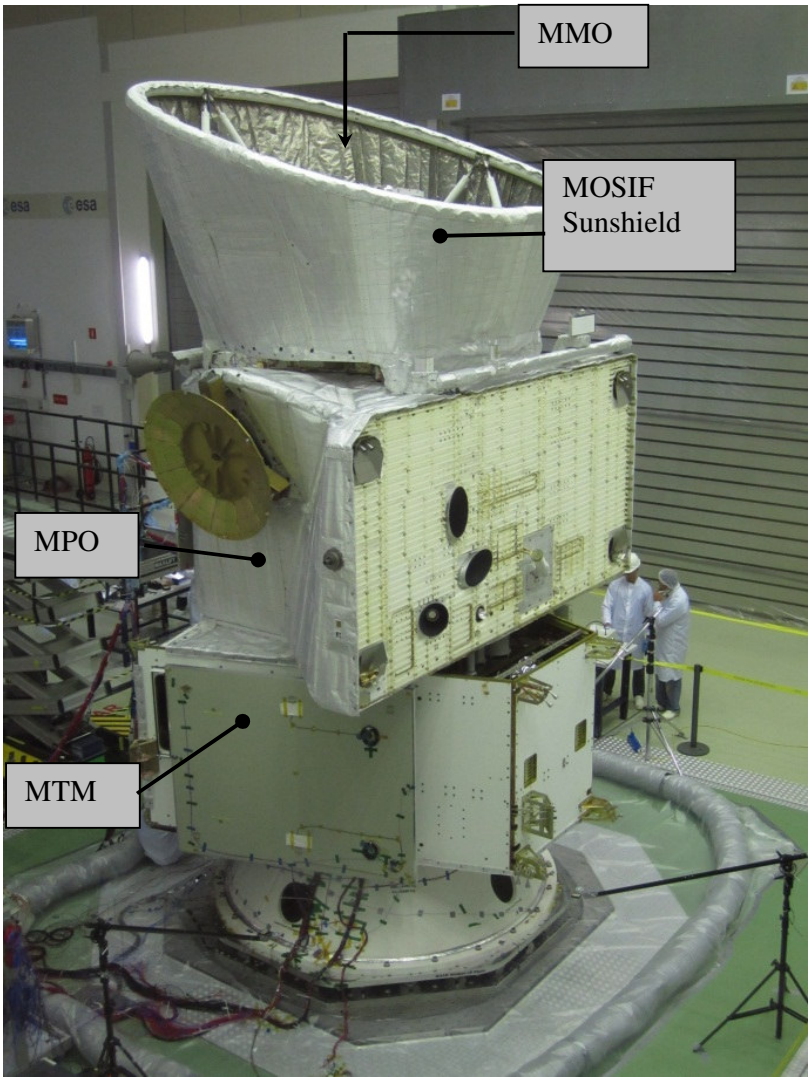


Figure 1. Bepi-Colombo STM stack in readiness for longitudinal sine test on ETS Quad shaker.



Figure 2. Spacecraft integration and stack preparation prior to installation onto ETS QUAD shaker for longitudinal Sine test. MOSIF & Sunshield are shown removed showing MMO STM at top of stack.



Figure 3. MOSIF adapter (right with MMO mass dummy) and sunshield structure with MLI removed. Photographs courtesy of RUAG Space.

2 SPACECRAFT ARCHITECTURAL OVERVIEW.

2.1 Overview.

The composite stack comprises of three (3) Spacecraft modules:

- Mercury Transfer Module (MTM) which provides autonomous propulsion after launch injection by Ariane 5.
- Mercury Planetary Orbiter (MPO): This supports a complement of instruments for planetary mapping.
- Mercury Magnetospheric Orbiter (MMO): that is furnished by JAXA. This module supports magnetic field characterization of Mercury and other science objectives highlighted below.

This section gives a brief overview of the stack complement together with a description of how the Spacecraft modules are coupled together to form a single contiguous structure.

2.2 Mercury Transfer Module (MTM).

The MTM provides the primary interface to the Launch Vehicle Adapter (LVA) through a conventional 1666mm clampband interface through a central honeycomb composite cone. This module contains the fuel tanks for the transit to Mercury after release from the Launch Vehicle. CPS and Xenon tanks are located outside the central structure. The structure is closed by conventional honeycomb panels linked to the central structure via vertical shear walls.

2.3 Mercury Planetary Orbiter (MPO).

The MPO module is located immediately on top of the MTM and is mounted via four (4) point cup and cone separation interfaces. The cup/cone arrangements are geometrically arranged on a square pitch of 870mm with each mating cup/cone preloaded in excess of 160kN to resist launch inertia loads. Separation is achieved by sequential 'firing' of low shock separation devices of the NEA fuse wire type. Local coil springs provide motive force to de-mate and separate umbilical connections between the Spacecraft module bodies.

The MPO construction is of aluminium honeycomb panels based on a double H section central structure and contains its own propulsion system for orbital management above Mercury's surface. This Spacecraft module supports a payload of eleven (11) instrument packages for mapping the surface of Mercury, measuring heights of features, detecting ions and particles in the exosphere and measuring its magnetic field. The instrument complement is:

- BELA (Bepi Colombo Laser Altimeter): a topographic mapping instrument.
- ISA (Italian Spring Accelerometer): non–gravitational accelerations of the spacecraft
- MERMAG: detailed description of planetary magnetic field, its source and interaction with the solar wind.
- MERTIS (Radiometer and Thermal Imaging Spectrometer): global mineralogical mapping (7-14 μm), surface temperatures and thermal inertia.
- MGNS (Mercury Gamma-Ray and Neutron Spectrometer): elemental surface and sub-surface composition, volatile deposits on polar areas.
- MIXS (Mercury Imaging X-ray Spectrometer): elemental surface composition, global mapping and composition of surface features.
- MORE (Mercury Orbiter Radio Science Experiment): core and mantle structure, Mercury orbit, fundamental science, gravity field.

- PHEBUS (Probing of Hermean Exosphere by Ultraviolet Spectroscopy): UV spectral mapping of the exosphere.
- SERENA (Search for Exospheric Refilling and Emitted Natural Abundances): Study of composition, distribution, source and sink processes of the neutral and charged particle environment.
- SIMBIO-SYS (Spectrometers and Imagers for MPO Bepi Colombo Integrated Observatory): HRIC, STC, VIHI Optical high resolution and stereo imaging, Near-IR (<2.0μm) imaging spectroscopy for global mineralogical mapping.
- SIXS (Solar Intensity X-ray and particle Spectrometer): monitor solar X-ray intensity and solar particles in support of MIXS

2.4 MOSIF Adapter and Sunshield.

The MOSIF adapter is located immediately on top of the MPO and provides a structural interface between the MPO and MMO Spacecraft Modules. The adapter is a simple box section cruciform structure manufactured from riveted aluminium alloy sections which is coupled to the MPO by NEA's preloading cup/cones in a similar fashion to the MTM/MPO interface (nominal preload 72kN).

Supported on top of the adapter cruciform is a Sunshield and thermal blanket whose interfaces circumscribe the NEA cup/cone interfaces and the MMO. The Sunshield structure resembles an inverted cone and comprises of thin walled riveted aluminium tubes and end fittings as shown in Figure 3.

2.5 Mercury Magnetospheric Orbiter (MMO).

The MMO Spacecraft Module is provided by the Japanese space agency JAXA. The MMO supports five (5) instruments whose primary functions are plasma and magnetic field measurement.

- MO/MGF Magnetometer: whose function is to establish a detailed description of the magnetosphere and relation and interaction with solar wind and planetary magnetic field.
- MPPE (Mercury Plasma Particle Experiment): to support the study of low and high energetic particles in the magnetosphere.
- PWI (Mercury Plasma Wave Instrument): This instrument provides detailed analysis of the structure and dynamics of magnetosphere.
- MSASI (Mercury Sodium Atmospheric Spectral Imager).
- MDM (Mercury Dust Monitor): whose function is to establish the distribution of interplanetary dust in Mercury orbit.

2.6 Inter Module Hardware (IMH).

The Spacecraft inter-module separation planes at the MTM/MPO and MPO/MOSIF are coupled by a four (4) point mounting arrangement shown sectioned in Figure 4. Each of these device modules are referred to programmatically as Inter Module Hardware (IMH) designed and qualified by Astrium. Each device is consists of single NEAs providing preload to a cup/cone interface through a single tension 'bolt' member with an integrated ejection mechanism. External to the device are ejection devices for Spacecraft module separation.

The four (4) point IMH is contained within the primary load path for launch and has obtained special focus for overall structure qualification as a result of the devices functional

criticality. This point of criticality is addressed further in later sections in terms overall load management, sine data processing and critical modes of the structure.

Each of the eight (8) IMHs integrated into the stack were instrumented with two (2) groups of four (4) uni-axial strain gauges as shown in Figure 5. The functions of each group of strain gauges are:

- *Preload stability gauges*: to monitor static preload status and its stability following swept sine loads. Status checks made prior to and immediately after each sine test to confirm no change of preload.
- *Dynamic load gauges:* to establish the external axial force, component bending moments and resultant bending moments exerted during the sine test. In this context each IMH unit was an integrated load cell. Strain gauge frequency response outputs acquired during sine tests were post-processed as Virtual Channels to establish resultant applied axial force and bending moments.

Integration of these load monitoring features was implemented relatively late in the design process hence further improvement to the static preload monitoring could be envisaged if applied early in the design. Prior to stack level STM testing the IMHs were subject to their own static qualification campaign to ensure compliance with specification integrity, stiffness, shock, life test, motorization margins and inertial injection on the stack; such requirements are appropriate to a critical mechanism structural element.

Characterization tests were also performed at IMH level to provide global calibration data for use during the system level sine test campaign thus translating strain output in terms of resultant axial force and bending moment.

In terms of system level preparation activities prior to conducting the sine test campaign, the IMHs received special focus not only in terms of understanding unit level behaviour but also in terms of formulation of test management schemes. An important point of note with respect to establishing a stack level test management philosophy was that at no time prior to test was total reliance on the ability of the IMH integrated load cell adopted. As a back-up strategy in the event of poor strain gauge outputs on test, redundant load management approaches were formulated to provide in essence an ‘over-constraint’ on such limit parameters. These redundant analytical limitations are discussed later. As a general philosophy when developing and testing analytical test control strategies, personal emphasis was always placed on the FEM uncertainty. A philosophy of *the only certainty given to the FEM was its potential uncertainty* provides a good basis for success since the engineer is always working in mode of risk management which maximizes potential for process robustness.

This general philosophy served the test campaign well in that the aim was to apply robust analysis observations and the over-constraint of parameters served to provide a degree of margin on safely conducting a complex test.

A final key message of experience would be relaying the key point of: Redundancy! Redundancy! Redundancy! whether it be a process, individual expertise, computing support hardware or associated networks or sine test control. If every aspect of the test and its process has inherent redundancy then the possibility of a successful test campaign is maximised.

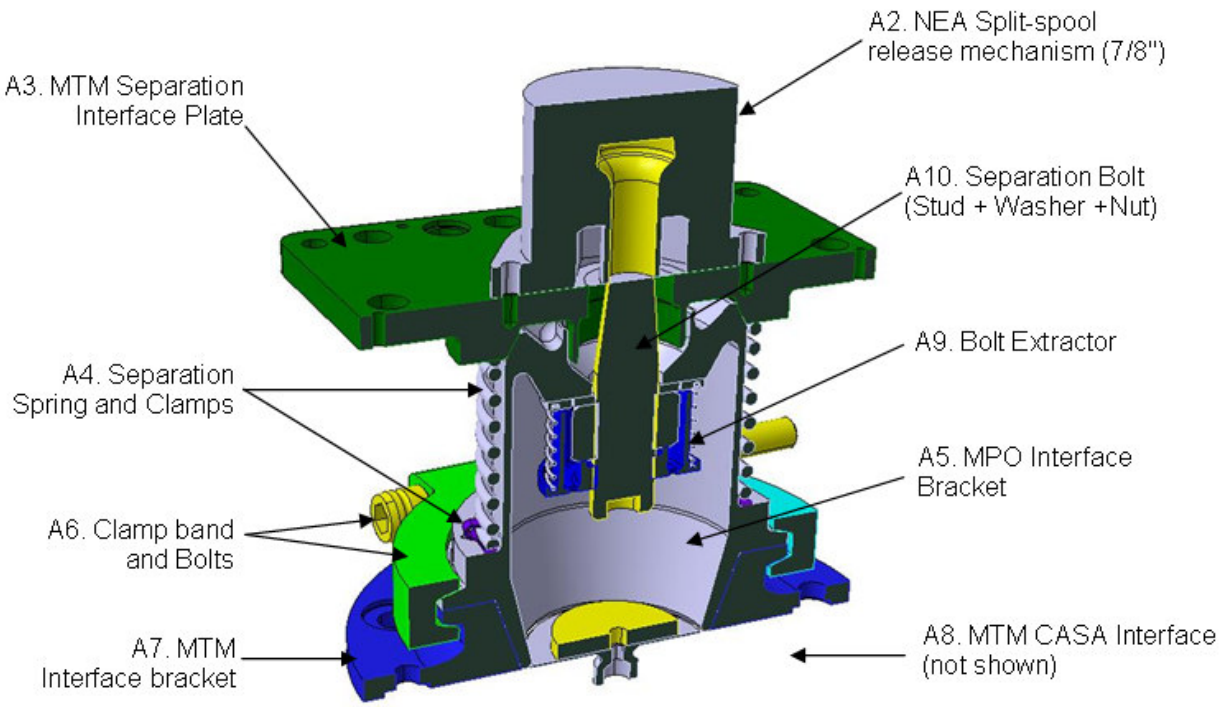


Figure 4. Sectioned illustration of MTM/MPO Inter Module Hardware (IMHs). A similar four (4) point arrangement exists at the MOSIF/MPO interface.

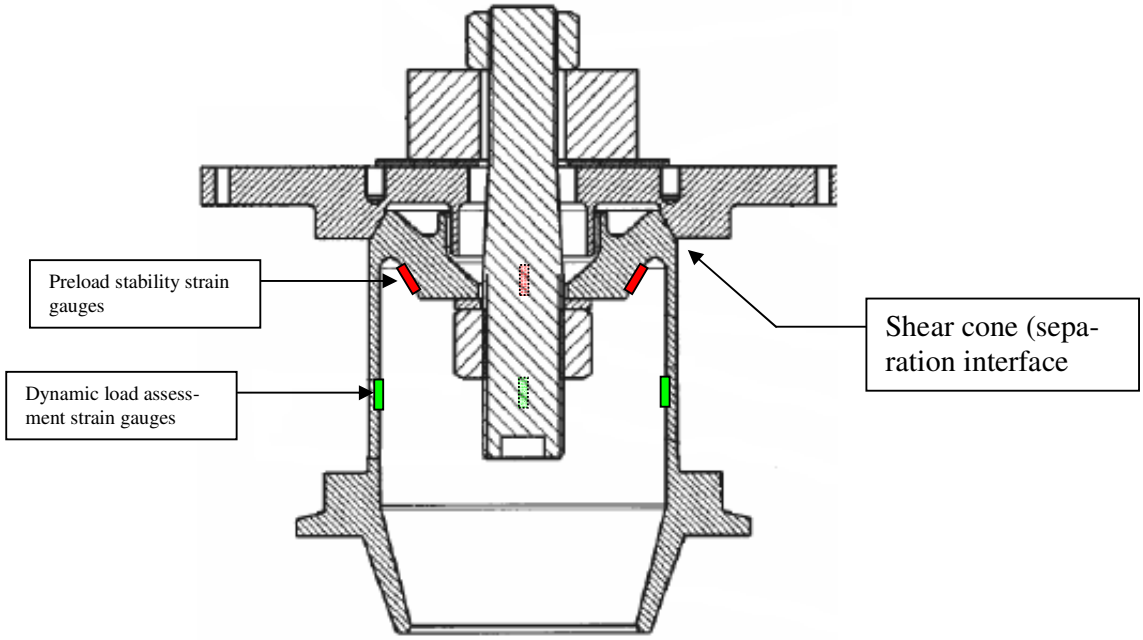


Figure 5. Four point equi-spaced uni-axial strain arrangement for static preload monitoring local to applied preload load path. Gauge purpose is to confirm preload stability pre- and post dynamic loading. Four point uni-axial strain gauge system on external body for external dynamic load measurement during sine testing.

3 DYNAMIC TEST CAMPAIGN.

Bepi Colombo's dynamic test campaign is centered on the needs to fulfill the requirements of an Ariane 5 launch and has been tailored around distinct Structural/Thermal test model (STM) and proto-flight model (PFM) philosophy where only the PFM is scheduled to fly.

In spite of the STM being non-flight, the structure did comprise of certain flight structural elements namely: the MOSIF adapter/Sunshield structure and secondary thermal support structures on the MTM. The JAXA supplied MMO is an STM.

The STM test campaign conducted during July 2012 comprised of sequence tests as dictated by an Ariane 5 launch:

- ***Sine test***: three (3) axis independent at 2 octs/min:
  - Longitudinal:- 5.6-50Hz 1.25g, 50-100Hz 1g.
  - Lateral:- 6.4-25Hz 1g, 25-100Hz 0.8g.
  - Notching both primary and secondary applied.
- ***Acoustic***: Levels [1] +3dB for Qualification
- ***Shogun*** and ***Clampband*** shock tests.
- ***Appendage*** and ***equipment release shock firings:*** characterization shock emission tests.

4 INSTRUMENTATION OVERVIEW.

Subsystem/Module	Instrumentation	No. of Channels for Sine Test	Notes
MMO	Accelerometer	31	
MOSIF	Accelerometer.	35	
MPO	Accelerometer.	219	
MTM	Accelerometer.	153	
FMD/LVA/shaker i/f	Accelerometer.	26	
TOTAL ACCELEROMETERS		**464**	
MMO	Strain gauge	4	Strain gauges on interface ring at clampband to monitor interface loads
MOSIF	Strain gauge	8	Mounted on discrete struts to monitor bending.
MPO	Strain gauge	15	Tank support struts, tank interface brackets, optical bench iso-static mounts.
MTM	Strain gauge	10	
IMH	Strain gauge	32	To assess global axial force and bending moments
TOTAL STRAIN GAUGES		**69**	
FORCE MEASUREMENT DEVICE (FMD)		**6**	24 load cells supporting an interface plate below the VTA.

LVA: Launcher vehicle adapter.

VTA: Vibration test adapter. A cylindrical structure of high relative stiffness with respect to the test specimen. Upper end provides clampband interface. Lower end interfaces to adapter plates on the FMD.

Table 1. Total numbers of channels and types of instrumentation.

5 TEST PREPARATION.

5.1 Recipe for success.

Successful test campaigns are based upon:

- Preparation.
- Test management philosophy supported by back-up test control strategies or “flexible” limitations.
- Pre-agreed limitations and working tolerance defining the safe working perimeter for the test.
- Effective test time management.
- Achievable, measurable & readily identifiable pre-agreed test success criteria.
- Redundancy, redundancy & redundancy! –in ALL elements of the process and support infra-structure.

5.2 Sine test preparation overview.

The typical scope of activities associated with preparation for a major sine test campaign is shown schematically illustrated in Figure 6. Effort is grouped into three principal blocks starting with:

- Establishing and defining test needs.
- Performing analysis to establish a plan for test implementation and management and documenting such process.
- Planning and simulation of the process.

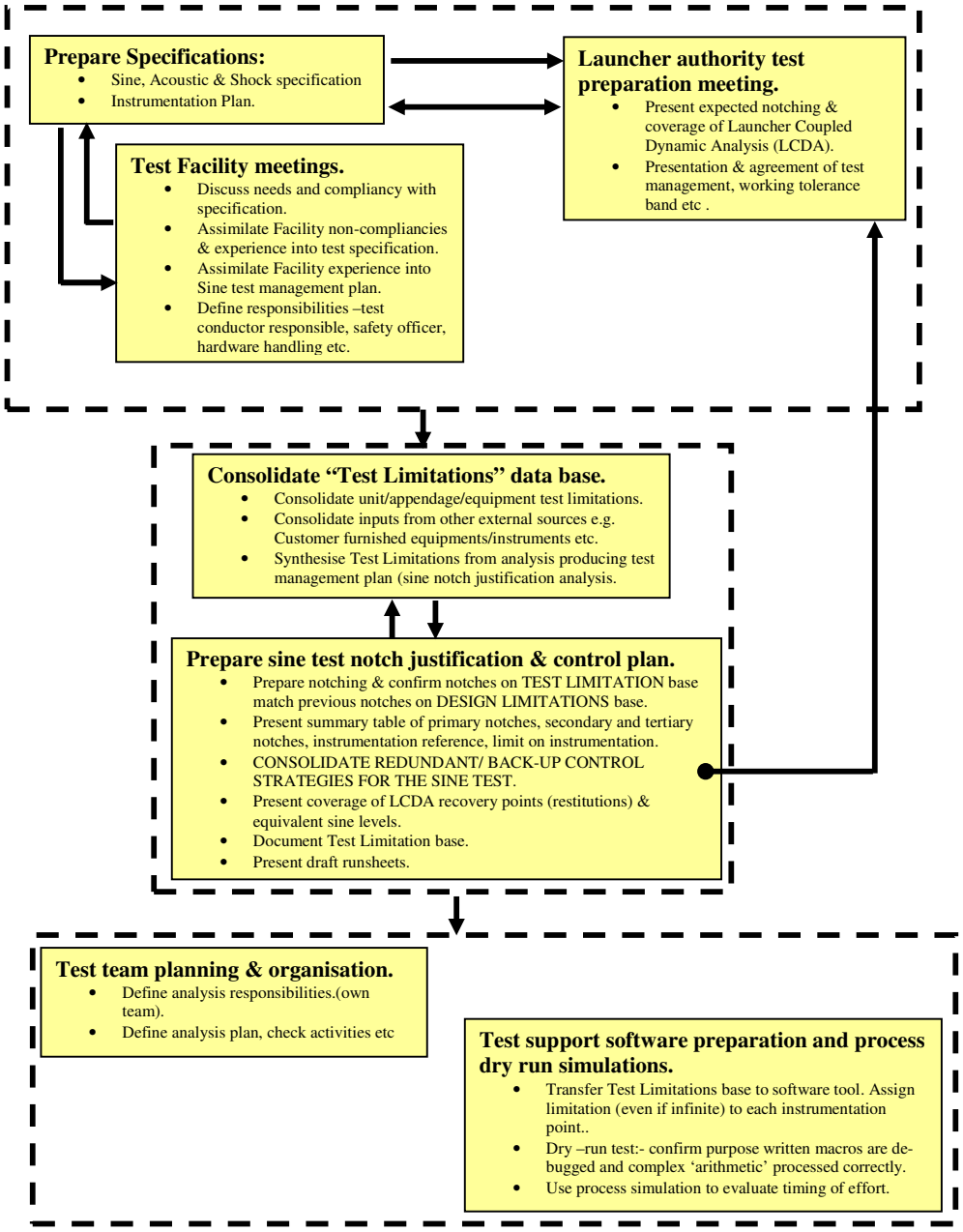


Figure 6. Test preparation activity –schematically illustrated.

5.3 Planning the test.

Experience, planning and effective preparation is of paramount importance in achieving a successful test campaign. This paper has attempted to provide an outline of most of these key points but if these were to be summarized further then principal points which should be focused on can be summarized by a small number of bullet points:

- *Ensure measurable test specific success criteria are in place:* the criteria should be specific to the test and should be closable within the framework of the test activity. Success criteria not specifically linked to the test (e.g. FEM correlation criteria) should where possible be rejected.

- *Ensure all Test Limitations are in place* and every instrumentation point has an assigned limit for its output. Some instrumentation locations may not be critical to the test and may be included for information only, for such locations limits may be assigned to be "infinite".
- *Ensure appropriate endorsements are in place:* from the customer and launcher authority in terms of test tolerance philosophy, predicted notching etc.
- *Ensure the test needs have been discussed with the test facility:* such interface meetings are a two-way process of understanding, provide a means of realizing a rational specification and enable an early understanding of compliancy with the test specification. Include within such meetings (and test specification) needs such as the analysis environment and the means and format of data transfer. For some unknown reason the mechanisms of data transfer always seem to be complicated by political reasons. It is important that a minuted understanding is reached.
- *Ensure all steps of the test support process have been subject to dry runs and the support tools de-bugged.* The aim should be to ensure that all members of the team understand their own responsibilities and are able if necessary to fulfill other member roles. Leave no process to chance and ensure the process is planned and mapped out. For Bepi Colombo this planning process was support by a process flow diagram which was taken and displayed on test.
- *Redundancy, redundancy and redundancy*! This message cannot be over emphasized in terms of its importance. All aspects associated with the test should be reviewed from the point of redundancy or process back-up. This applies to:
  - Personnel expertise.
  - Analysis hardware and software particularly non-reliance on network connections which invariably fail in spite of being "sold" to the test team as robust!
  - Data transfer from the facility to test team computer hardware.
  - Back-up test control strategies and redundant limitations. At the start of the Bepi Colombo test campaign (TRR) it became evident that certain strain gauges would not support management of their associated interfaces. Redundant analytically based limits, established at system level, had been synthesized which were able to address poor instrumentation implementation. Assessment of the second order cantilever mode responses and *applying angular acceleration* limits established during the sine test notch justification and test control plan analysis activity, provided this redundancy in terms of monitoring the interface concerned.

    For purpose of example, other illustrations of such redundant strategies could be catering for correlation errors in boom type structures where an acceleration limit and associated frequency is concerned. In this case of poor advance correlation, such acceleration limits can be corrected to relative deflection limits subject to correcting for frequency and relative response differences.
  - Key non-accessible instrumentation. Invariably accelerometers installed on tanks are typical locations where for various reasons instrumentation function is lost prior to or during a test. Usually tank response limits are critical to the test hence it is recommended that such locations which may be non-accessible for rectification include redundancy or redundant averaging for interpolation to c of g location is required.

5.4 Sine test notch justification and test control plan.

The output resulting from the test preparation analysis activity should be a document or plan (*sine test notch justification and test control plan*) which defines the test control plan, justification of primary and secondary notching and data or perimeters defining limits of response with the instrumentation defined by the measurement point plan.

Content of this notch justification and management plan would normally compose:

- *Definition of predicted notching.*
- *A definition of the test working tolerance band.*
- *A database of Test Limitations providing the perimeter of responses for conducting the test.*
- *Coverage and margins against the LCDA recoveries and equivalent sine inputs.*
- *Support analyses defining test control /management approaches and analyses synthesizing specific Test Limitation base entries.*
- *Summary tables defining governing notch locations, test instrumentation limits, associated frequency bands.*

The test working tolerance band:

For Bepi Colombo the generic working tolerance was proposed as the minimum band based upon experience for managing responses and overshoot of responses (+2.5dB). The generic applied tolerances are shown illustrated in Figure 7. The lower limit provides the target (auto) notch specification given on the run sheet and the upper limit defines the prescribed run sheet abort limit. It should be noted that it is Astrium's practice to contain the abort limit within specification limits compatible with the system's design specification so that any response achieved between notch assignment and abort does not entail justification in terms of imparted load exceedance. On test the low limit may be subject to reduction based upon observations of response overshoot from intermediate levels.

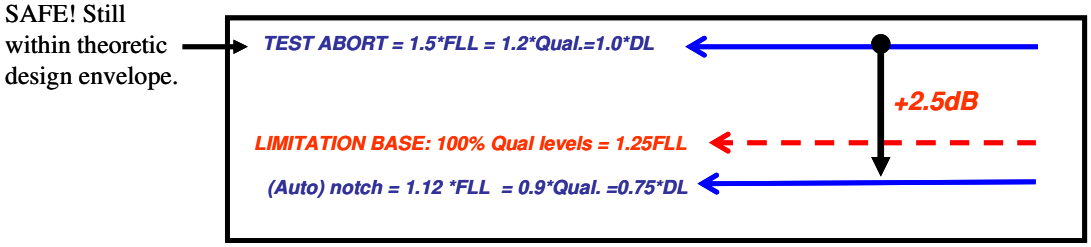


Figure 7. Schematic illustration of the sine test control band between notch specification and abort. The 2.5dB band is based upon experience in terms of management of response overshoots. FLL=flight limit load. DL=Design Limit load (excluding FoS).

A database of Test Limitations providing the perimeter of responses for conducting the test.

Experience has shown that the consolidation effort required to formulate this data base of limits should not be underestimated particularly for subsystems that are not under the Prime's responsibility.

It should be noted that a clear distinction exists between the Test Limitations and the Design Limitations specified in the system design specifications. The majority of the Test Limitations are defined by the design specifications but not all. Some inputs are consolidated from various institutional bodies into one database while others have to be specifically computed from the analysis framework that produces the test control/management plan. In essence the

Test Limitation data base comprises of those limits assigned to the sine test instrumentation and may be an indirect to monitor a Design Limit value.

Definition of predicted notching.

The plan should provide a justification of the notching projected for the test and withstand scrutiny from both the Customer and launcher authority. Since the notching presented is based upon Test Limitations, the notching should be consistent with notching predictions established by application of the Design Limitations. Normally manual notch proposals would be projected on to the computed notching as part of the overall presentation of test control and for forwarding to the launcher authority for endorsement prior to the Test Readiness Review (TRR). The pre-test projected notching for Bepi Colombo is shown in Figure 8 which is shown for one lateral axis and the longitudinal case. These curves show the predicted notch density for the program.

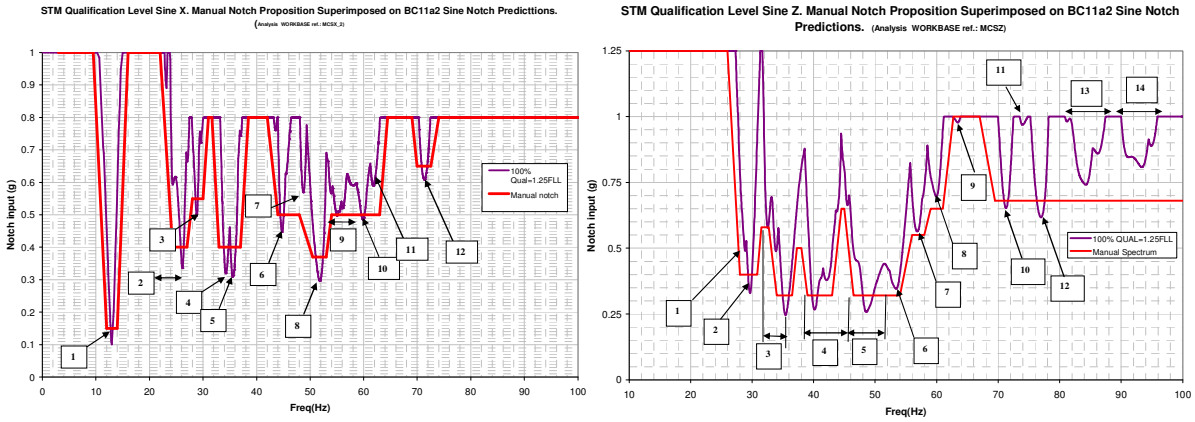


Figure 8. Pre-test predictions illustrate predicted notch density. Notches governed by primary structure main bending modes in the low frequency domain, composite limits suited to virtual channel assignment and single value notch limits are typically at higher frequencies.

5.5 Control of primary modes.

For Bepi Colombo the primary limitations associated with the fundamental cantilever modes and main axial mode are those associated with the Spacecraft interface loads at the LVA derived from the launcher qualification level quasi-static specification [1]. During pre-test sine notch justification/prediction analysis the main LVA longitudinal force limit associated with the main axial mode was predicted to be covered by other internal limitations which generated there own governing notch. For the first cantilever modes the analysis predicted a primary notch governed by the quasi-static interface loads marginally covering secondary notches associated with IMH bending moment limits.

Management of base loads was greatly simplified by use of ETS' force measurement device (FMD) which is shown in Figure 9. This device was installed between the slip table or head expander and the VTA and consists of annular interface plates and twenty-four (24) piezo-electric load cell elements capable of providing six-dof resultant load output on it reference plane. Evaluation of data provided by ETS in advance of the test gave confidence that the gross specimen mass and associated centre of gravity offset would not reduce the fundamental modes or degrade the boundary conditions for the test.

Piloting for all sine tests was specified at the VTA/LVA interface which was of the order of 1.0m above the slip table or FMD reference plane. Due to this height offset two(2) options for interface load management thus existed:

- Generate a DYNAWORKS Virtual Channel (see later for applied Virtual Channel) by transformation of the FMD reference planes *complex* loads to the VTA /LVA reference plane. Such a process would produce 'exact' computed loads at the plane of interest but would need to be transformed to the FMD plane for run sheet specification.
- On the assumption that both the FMD and VTA are rigid relative to the Spacecraft, to *statically* transform the quasi-static LVA interface load limits to the FMD reference plane with a small allowance based upon a small phase angle of the static mass of the VTA and FMD interface plate sprung mass on the load cells. This approach meant that the Test Limitation could be assigned a load limit directly assignable to the FMD and directly assignable to the run sheet. For the Bepi Colombo sine test campaign, this approach was adopted and endorsed by the customer and launcher authority.

As a consequence of incorporation of an FMD into the instrumentation plan, this provided several options in terms of control strategies for managing Spacecraft base loads. During pre-test facility meetings ETS indicated that on a previous program the fundamental cantilever modes were controlled by direct auto-notching on the FMD with no manual notch back-up. Such an approach prior to test was considered by Astrium but it was decided to apply the well trodden path of specifying accelerometer limits on the top of the stack with a manual notch back-up. In addition the FMD limits were also specified on the run sheet with appropriate margin to avoid control hand-overs. This approach of control functioned perfectly adequately and safely on the Bepi lateral sine tests potentially as a result adequate damping on the fundamental cantilever modes (>2% critical viscous). Other programs of similar overall Spacecraft mass but greater centre of gravity height offset (e.g. Metop-A, Metop-B, Metop-C) were more difficult to control on the first cantilever mode's exit from resonance, this was believed as a result of low damping (<1% critical viscous). Hence although initial inspection of the architecture for Bepi indicated a complex structural definition it is believed that multiple interface assisted damping and control during the sine test.

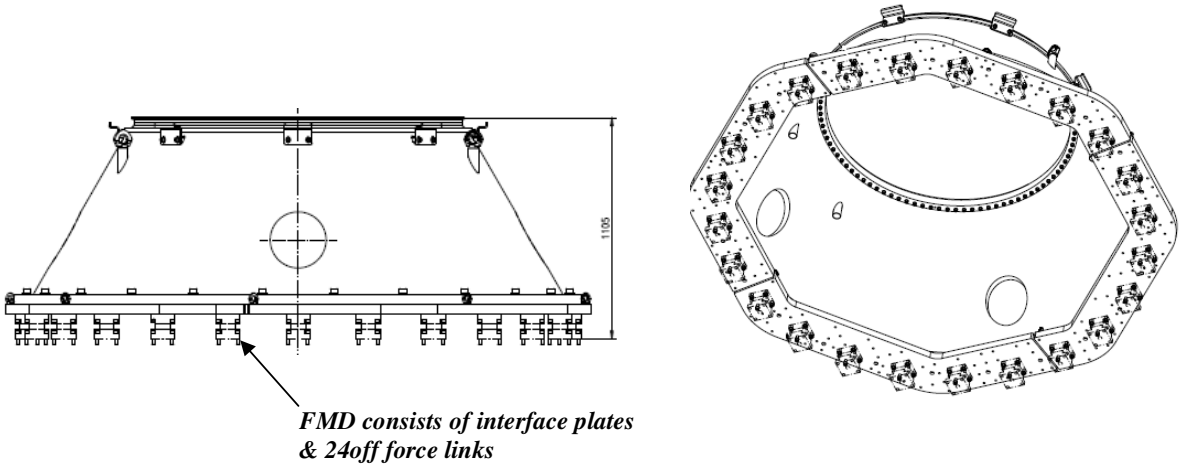


Figure 9. FMD / VTA architecture:- 24off Kistler force links at VTA interface.

5.6 Specific test limitations, management of second order cantilever bending modes and use of DYNAWORKS to formulate constants of proportionality between differing spectral entities.

A powerful feature of DYNAWORKS is its simplicity with regard to application of manipulation of complex variables and its ability to formulate strategies for indirect approaches of managing certain design limits. The "Signal Analysis" window (see Figure 10) is similar to a spreadsheet but with the advantage that a single cell can store a complex quantity such as a complete frequency response function. Thus instead of needing three (3) columns as in a spreadsheet to store XYdata: X, Re(Y) and Im(Y) all of this data can be stored and manipulated within a single cell.

Management of the IMH loads was critical to the success of Bepi Colombo sine test campaign. The primary means for controlling the loads (specifically bending moment components and their resultants) was from strain gauges thus each IMH was an integrated load cell precalibrated against IMH qualification static tests.

Prior to test knowledge of the potential quality of frequency response output from the strain gauges was an unknown and as a consequence a redundant strategy for IMH load monitoring was established as a back-up approach to managing their loads. Again in line with robust focus, the strategy needed robust 'physics' and needed to account for FEM uncertainty. The principal modes governing major IMH loads were the first and second order cantilever modes (see Figure 11 for 2nd order mode). To this end the 'firm physics' of the approach is recognizing that the second order cantilever mode is a firm expected outcome from the test, but when relating differing response quantities the uncertainty is the quality of the FEM mode shape to provide links in terms of constants of proportionality between differing response quantities within a frequency band. Since the aim was a redundant back-up to the main means of controlling IMH load, by direct load measurement, then the limited uncertainty is acceptable. Also since the governing modes are associated with lower order modes their predictability in terms of quality of mode shape should be well established from the FEM.

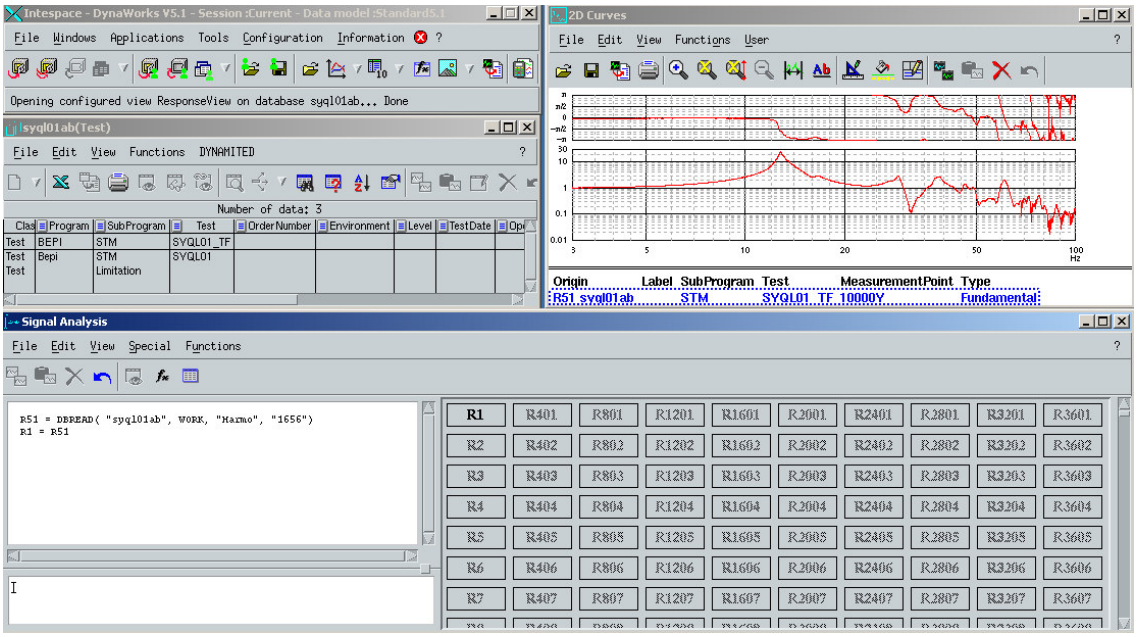


Figure 10. The DYNAWORKS environment.

Figure 11 shows the characteristics of the second cantilever mode. This mode (predicted circa 28Hz for both YZ and XZ planes) shows the upper MMO rotating in the opposite direction to the remainder of the cantilevered structure. Through the assumption that the predicted mode shape quality is adequate to formulate limits, it is possible to link various load quantities that are of interest in the mode to measured *angular acceleration* responses: IMH bending moment, IMH axial force and MMO bending moments for example.

From analysis of the pre-test predictions it was evident that the *angular* response (off axis Z responses) of the MMO was a suitable means to establish these load parameters. An advantage of response differencing in this manner to obtain "scaled" (*) angular accelerations is that the analytical sensitivity is increased, since the difference of out-of-phase responses is amplified, and the differencing approach filters in-phase characteristics.

(*) "Scaled" because the geometry separating these accelerometers can be ignored.

Figures 12 and 13 show example over-plots of the angular accelerations Δ(10001Z,10011Z)(*) Transfer Functions (TF) versus the IMH bending moment TFs and MMO interface bending moment TF.

10001Z and 10011Z denote labels assigned to accelermeters.

Figure 12: *MOSIF/IMH fixation plane result B.M. envelope:*

$$MO_IFL^*_MXY \approx 42^* (10001Z - 10011Z) \text{ ----------(1)}$$

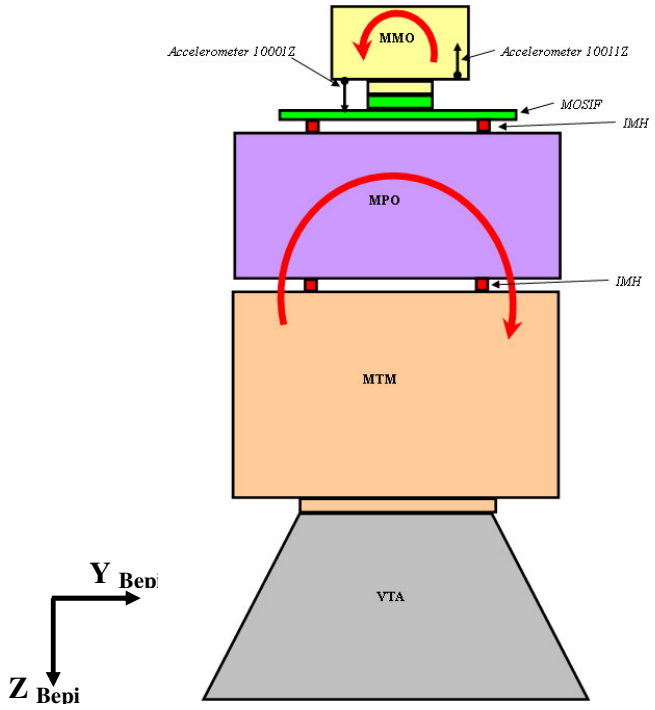


Figure 11. Schematic of 2nd cantilever mode. MMO lower floor accelerometers differenced for angular response characterization of this mode.

It can be seen from Figure 12 that the relation (1) provides a good approximation over the frequency band 20-46Hz except for a narrow band below the main peak of 26.2Hz where the relation is not conservative. To address this, two options exist:

- Modify the constant of proportionality until this region is covered. This will produce a more conservative function but would result in relation which would generate a deeper notch at the 26.22Hz peak.
- Extend the main notch computed at 26.2Hz so that it spans the region not covered by the redundant function.

For test application a combination of these two(2) options was recommended along with a specification of a manual notch covering a region +/- 3Hz centered on the main peak. At 1Hz below the main peak at 26.2Hz the error in correlation of the redundant function with the predicted B.M is predicted as 20%, factoring the constant of proportionality by this factor:

$$MO_IFL^*_MXY \approx 50.4^* (10001Z - 10011Z)\ Nm \quad 20Hz \leq f \leq 40Hz \text{ ----------(2)}$$

For an MXY limit of 616Nm:

$$\Delta(10001Z - 10011Z) \leq 12.2g \qquad \text{----------(3)}$$

The relation and limitations here on the differential Δ(10001Z,10011Z) cannot be directly applied to the run sheet for control purposes. The expressions are therefore on-test analytic and must then be transferred to one or both of the channels 10001Z and 10011Z on the run sheet i.e.:

$$10001Z = 0.58^* 12.2g = 7.08g \qquad \text{----------(4)}$$
$$10011Z = 0.419^*12.2g = 5.11g$$

The previous example linking MMO angular accelerations to IMH bending moments gives some insight to the power of DYNAWORKS to iteratively assess spectral limitations. With raw response quantities such as multiple IMH component bending moments, by a single macro function it is possible to define a new response quantity which is maximum spectral envelope of numerous loads at different IMH locations. From this step it is relatively easy to correct this quantity to a TF and iteratively amend constants of proportionality until the analysis shows good coverage of the measured relation relative to the load entity of interest.

As a point of note, with measured loads obtained the IMH integrated load cells, the above parameters are able to be correlated in "real time" during the test.

Figure 13: *MMO interface bending moment for Sine X excitation:*

Shows a similar process applied for evaluating acceleration limits for establishing MMO interface bending moments generated by Sine X excitation. Such redundant analytical methods compensated for poor MMO strain gauge outputs.

Additional evaluations are presented in Table 2 linking relations between measured IMH axial force 'Fz' and different bending moment quantities on the MTM/MPO and MOSIF/MPO IMH interfaces. The analysis here shows that adoption of measured 10kN limitation ensures that all IMH bending constraints remain with the static qualification perimeter established from unit level static tests.

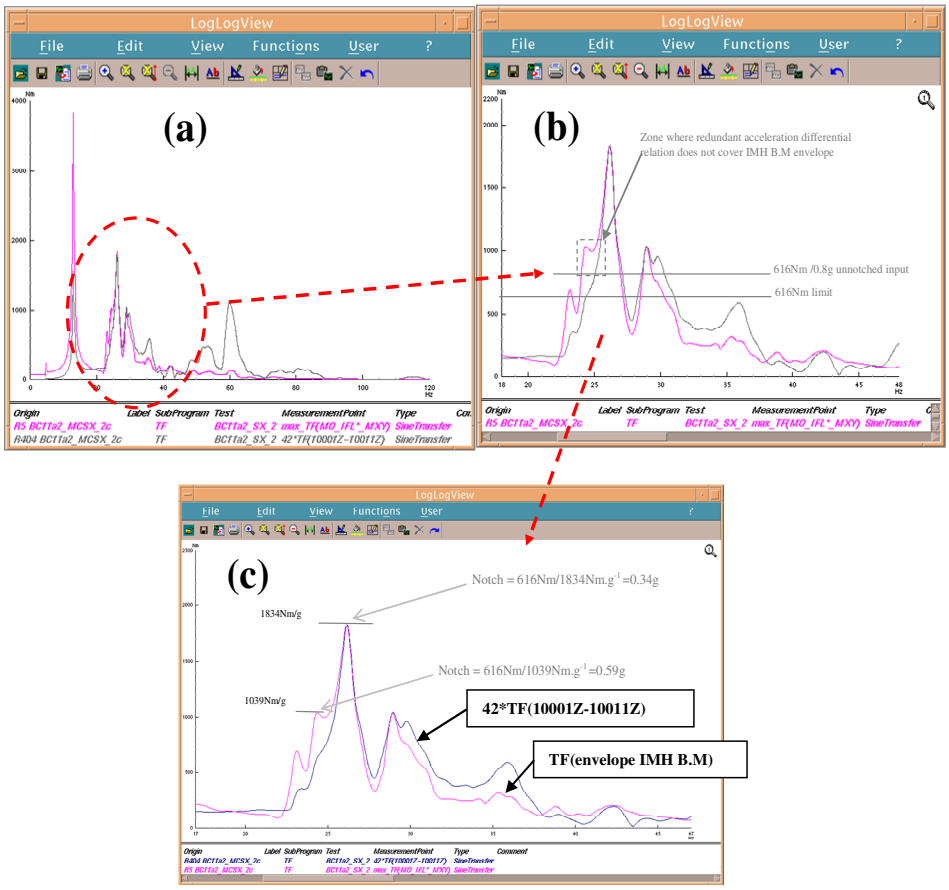
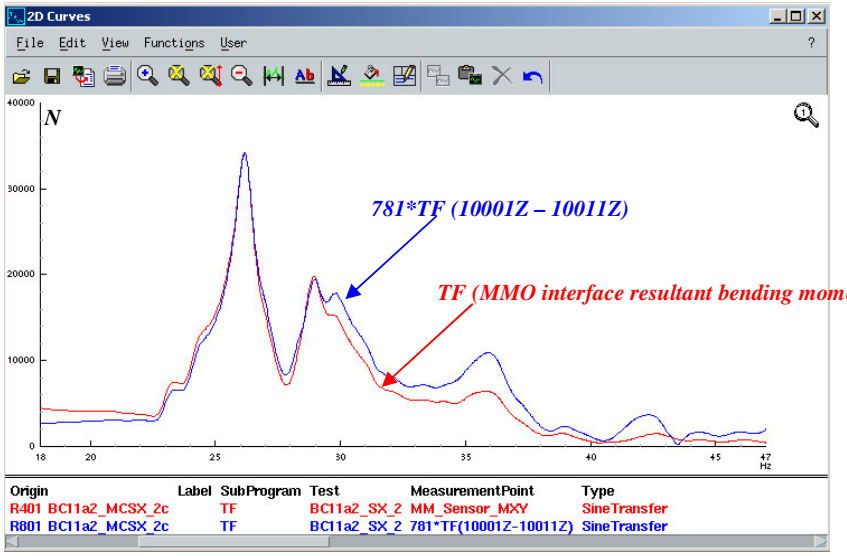


Figure 12. Spectral coverage of IMH maximum bending moment, envelope of four (4) IMH locations, and a synthesized CONSTANT* acceleration differential Δ(10001Z,10011Z) accelerometer references.



MXY = 781(10001Z -100011Z) = 17g for limitation =13322Nm (20 ≤ f ≤ 47Hz)*

Figure 13. CONSTANT* Δ(10001Z,10011Z) related to MMO interface bending moment T.F. (MM_Sensor_MXY).

Case	Variable	I/F description	Const. proportionality (Nm/N)	Qual. Limitation (Nm)	Qual. Limit Fz (N)	Notes
SINE X	max TF(MO_IFL*_MXY)	MOSIF /IMH fixation	13.9	616	8562.4	max. TF(MP_IFU*_FZ)=13.9*max TF(MO_IFL*_MXY)
	max TF(MP_IFU*_MXY)	MOSIF/ MPO cup/cone	30.2	355	10721	max. TF(MP_IFU*_FZ)=30.2* max TF(MP_IFU*_MXY)
	max TF(MP_IFL*_MXY)	MPO/MTM cup/cone	17.4	861	14981.4	max. TF(MP_IFU*_FZ)=17.4* max TF(MP_IFL*_MXY)
				min. cup/cone=	**10721**	Limitation Fz PER IMH
				min overall=	**8562.4**	
SINE Y	max TF(MO_IFL*_MXY)	MOSIF /IMH fixation	23.7	616	14599.2	max. TF(MP_IFU*_FZ)=23.7*max TF(MO_IFL*_MXY)
	max TF(MP_IFU*_MXY)	MOSIF/ MPO cup/cone	38.3	355	13596.5	max. TF(MP_IFU*_FZ)=38.3* max TF(MP_IFU*_MXY)
	max TF(MP_IFL*_MXY)	MPO/MTM cup/cone	21.4	861	18425.4	max. TF(MP_IFU*_FZ)=21.4* max TF(MP_IFL*_MXY)
	max TF(MP_IFL*_MX)	MPO/MTM cup/cone	21.9	440	9636	max. TF(MP_IFU*_FZ)=21.9*max TF(MO_IFL*_MX)
				min. cup/cone=	**9636**	Limitation Fz PER IMH
				min overall=	**9636**	

Table 2. Summary of narrow band (20-45Hz) constants of proportionality of MOSIF/MPO IMH axial Fz force versus various IMH bending moments.

5.7 Asymmetry of boundary conditions .influencing measurement point locations.

For a limited number of units/payloads, pre-test analysis indicated the sensitivity of the exact assigned location of accelerometers relative to the unit. System architects (may) prefer instrumentation specified at the base of the unit for direct comparison with unit level specifications while the engineer performing the inertial load assessment may conflict with this in terms of preference with a response through a unit's centre of gravity. For flight items, surface coatings or configuration may preclude such a response through the c of g, but instances where the unit is a mass dummy or the boundary conditions are highly asymmetric then sensitivity to accelerometer position assignment may need to be addressed in advance of the test.

One such example was noted on one of the MTM large avionics units. The foot print of this unit is rectangular but the supports on each boundary are significantly different. Depending on which boundary the accelerometer was mounted then the assumed inertia load could be significantly different.

On one foot edge the unit was immediately adjacent to a shear wall hence the out-of-plane response of the unit was propped by this panel. Similarly the next edge clockwise was propped by floor panel while the diametrically opposite edge was a free edge. The final foot edge was remote from any support and tended towards a panel centre type response. For this unit as a mass dummy was defined the only way of confidently establishing the units interface load was instrumentation through the unit's c of g.

5.8 Virtual channels.

In the context of this paper a "Virtual Channel" represents a new channel of data computed by combining or processing of a set physical data acquisitions. Such channels may be embedded into the notching analysis performed on test by expanding the *raw* acquisitions data set prior to TF computation and subsequent notch computation effort. In the previous discussion

one such Virtual Channel has already been highlighted namely combining accelerometer differentials to derive an angular acceleration for which a Test Limitation would be prescribed. It should be noted that the Virtual Channel retains the original complex basis in terms of Real and Imaginary content from the physical acquisition from which it is generated.

During the Bepi Colombo sine test data analysis some forty-nine (49) extra Virtual Channels were synthesized by pre-prepared DYNAWORKS macros. On receipt of the frequency response data from the facility, a suite of three (3) macros were run making generation of the Virtual Channels automatic. Table 3 lists the supplementary Virtual Channels created, the list has been condensed by grouping like channels.

*MO_IFL*_MXY*: -see previous section 5.6. Limits are assigned angular accelerations.

*QSL_MT_S*_Z*: average Solar Array dummy panel responses to establish in-plane accelerations effective through the dummy centre of gravity. Limitation is based upon specification quasi-static design limits for the dummy and the structure interfaces.

*QSL_MP_TK*_XY:* resultant accelerations through specific propellant tank c of g's.

MP_MIXS_TY, QSL_MP_OPTB_Z:, QSL_MP_OPTB_Z: responses for one of the MPO instruments and the MPO optical bench equipments. Constants of proportionality established during sine test preparation analysis.

MT_TMY_PXMZ_TXYZ: establishes the resultant (XYZ) accelerations for specific MTM thrusters from a local triax on each thruster.

QSL_MT_TPA3_XY: establishes a response for lateral acceleration resultant through the SEPs thrusters c of g.

QSL_MM_Z: Similar quantity as MO_IFL*_MXY constants of proportionality convert angular acceleration quasi-static equivalent interface bending moment on the MMO.

MP_TK_AUX_*_TRQ: virtual channel computing: *(angular acceleration * polar moment of inertia)* to establish reaction torque on the polar mounted tanks –see Figure 14.

IMH_MO_PXPY_Fz: virtual channel averaging four(4) strains on each MOSIF/MPO IMH. Limits retained as strain but calibration factor for this average strain to resultant axial force Fz = 86.5N/με. 'Calibration' constant derived from local static testing / qualification of the IMHs

IMH_MO_PXPY_M:* three Virtual Channels per IMH covering two (2) component bending moments and resultant at the MOSIF/MPO interface. Bending moment components established from differential strains in diametric opposing strain gauges. Calibration constant =1.86Nm/με.

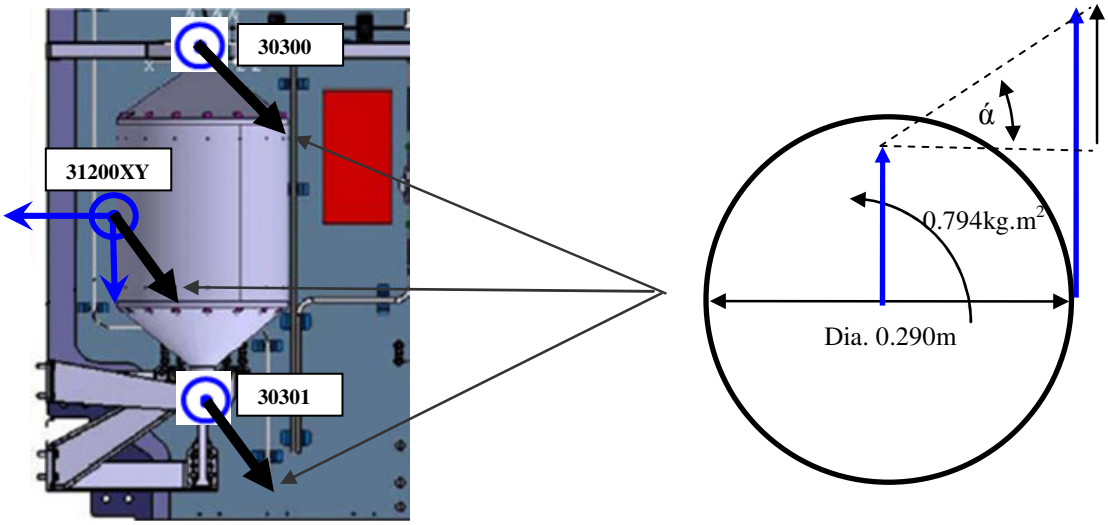
IMH_MT_PXPY_*: IMH virtual channels monitors but for MPO/MTM interface Fz and Mx,My and Mxy loads as MOSIF/MPO.

In terms of implementing these differential limits and other virtual quantities to the sine test run sheet, the compound spectra of combined responses must be prescribed to a single physical channel. For angular acceleration based limits this not a problem as this entails selection of one of the pair channels used for differencing while the other channel may be used as a redundant back-up.

5.9 Preparation of test calibration support data.

Irrespective of certification, engineers always perceive it to be good practice to validate information against a quantifiable reference i.e. "*the back of envelope approach*". Load cells typically fall into this domain, armed with basic mass information and low frequency responses (*tending to quasi-static*) it is possible to establish a level of confidence in the data acquired.

For transducer sets such as the FMD such basic calibration can be made during bare fixture tests. For integrated load cells such as the IMHs preparation of mass property data of Space-craft modules or pre-test 1g load distributions fulfill the quality check.



$\Delta a_1 = ((0.5*(30300Y+30301Y)) - 31200Y)$
Test management parameters:
Tank diameter= 0.290m
Tank mass dummy Polar Moment of Inertia= 0.794kg. m²

$Torq = I \,.\, \acute{\alpha} = 0.794 \,.\, \Delta a_j / (0.290 * 0.5)$

Torque Limit (100% Qual Limit) = 158Nm
100% Δa_j Limit = 2.94g (ALL sine cases X,Y,Z)

Figure 14. Virtual channels for complex computational assessment of propellant tank reaction torques evaluated by differential responses for angular accelerations. 30300Y,3030Y and 31200Y define accelerometer labels from the measurement point plan.

Virtual channel ref.	No. channels	Location	Unit	Limitation	Calculation
MO_IFL*_MXY	2	MO IMH MXMY OP	g	**12.2, 10.4**	=(10001Z – 10011Z) & (10006Z-10007Z) range of validity: *20Hz*≤ f ≤40Hz
QSL_MT_S*_Z	2	MTM SA PX IF IP	g	12.5	=(AvZ^2+AvY^2)^0.5 , AvZ= (40601Z+40602Z)/2 AvY=(40601Y+40602Y)/2
QSL_MP_TK*_XY	2	MPO Hyd. Tank QS IP	g	5	=(31000X^2+31000Y^2)^0.5
MP_MIXS_TY	1	MPO MIXS Ave. OOP	g	9	=(1.7*30706Y+30752Y)/2.7
QSL_MP_OPTB_Y	1	MPO OPTB QS IP Y	g	13.7	=(30150Y+30152Y+30153Y)*1.23 / 3
QSL_MP_OPTB_Z	1	MPO OPTB QS IP Z	g	10.38	=(30150Z+30152Z+30153Z)*1.3 / 3
MT_TMY_PXMZ_TXYZ	4	MT TMY PX MZ RXYZ	g	28.7	=(40114X^2+40114Y^2+40114Z^2)^0.5
QSL_MT_TPA3_XY	1	MTM TPA3 QS IP	g	6.25	40106XY=(40106X^2+40106Y^2)^0.5
QSL_MM_Z	1	MMO/MPO IF QS OP	g	11.25	=(10001Z+….+10011Z) *0.7 / 11 f ≤ 60Hz
MP_TK_AUX_*_TRQ	2	MY Tank reaction torque	Nm	158	(AVG(30401Y,30400Y) - 31202Y)*9.81 *0.794/(0.145), Tank moment of inertia I = 0.794 Tank radius r = 0.145
IMH_MO_PXPY_FZ	4	MO/MP PXPY FZ	uStrain	116	Refer to chapter 11.2 µS1(-X) = S50002 , µS2(+X) = S50000 µS3(-Y) = S50003 , µS4(+Y) = S50001 Strain limit = av(S50001,S50002,S50003,S50004) Fz= 86.5N/µέ
IMH_MO_PXPY_MX	4	MO/MP PXPY MX	uStrain	191	Refer to chapter 11.2 µS3(-Y) = S50003 , µS4(+Y) = S50001 MX=1.86Nm/uE * (S50003-S50001) /2 Nm
IMH_MO_PXPY_MY	4	MO/MP PXPY MY	uStrain	191	Refer to chapter 11.2 µS1(-X) = S50002 , µS2(+X) = S50000 MY=1.86Nm/uE * (S50002-S50000) /2 Nm
IMH_MO_PXPY_MXY	4	MO/MP PXPY MXY	uStrain	191	= (MX^2+MY^2)^0.5
IMH_MT_PXPY_FZ	4	MT/MP PXPY FZ	uStrain	983	Refer to chapter 11.2 µS1(-X) = S50033 , µS2(+X) = S50031 µS3(-Y) = S50034 , µS4(+Y) = S50032 Strain limit = av(S50031,S50032,S50033,S50034) Fz= 86.5N/uE
IMH_MT_PXPY_MX	4	MT/MP PXPY MX	uStrain	237	Refer to chapter 11.2 µS3(-Y) = S50034 , µS4(+Y) = S50032 MX=1.86Nm/uE * (S50034-S50032) /2 Nm
IMH_MT_PXPY_MY	4	MT/MP PXPY MY	uStrain	272	Refer to chapter 11.2 µS1(-X) = S50033 , µS2(+X) = S50031 MY=1.86Nm/uE * (S50033-S50031) /2 Nm
IMH_MT_PXPY_MXY	4	MT/MP PXPY MXY	uStrain	272	= (MX^2+MY^2)^0.5

Table 3. Summary of Virtual Channels (49 channels total)

5.10 Test support software preparation and 'dry run' process simulations.

Software preparation, de-bugging and process simulations should enable a level to be reached by the data analysis engineer where usage of the tool within a planned process is second nature. Experience has shown most tests that 'fail' in terms of perceived inefficiency of management usually as a result of complex analysis processes or lack in depth familiarization of the tool at hand. The aim of any preparation is to ensure that test focus is directed to considering the information that is presented by the test and that mental effort is *not* expended in the demands of driving the software or data analysis tool.

The principal elements associated with preparation of the data analysis software are:

- *Transfer the Test Limitation base into the software*: for Bepi Colombo a Test Limitation was defined for every instrumentation channel. For some instrumentation 'infinite' limits were assigned when the channel was included for information only, post test correlation support etc. The Test Limitations defined in the software are the reference limits to which the computed *TFs * un-notched base sine input* are compared so that a notch curve is produced for each instrumentation point. The overall predicted notching is then the minimum of each curve at each discrete frequency point. For Intermediate sine levels i.e. sine inputs between the first low level and qualification, scaled limits may be defined so that Intermediate responses may be directly (automatically) compared with the factored limits. This analysis provides a check to confirm no limits have been exceeded by this preparatory run before qualification.
- *Generate program specific macros to compute Virtual Channels*: such channels have been discussed previously in some detail.
- *Test the macros functions and Test Limitations base:* during Bepi Colombo test preparation activity, two(2) tests were designed to ensure Test Limitations and their labeling were free of errors and to confirm the arithmetic operations of the macros:
  - *Test 1:* simulated test data was generated by converting NASTRAN data into a test format. This was achieved by simply changing FE related identifiers from grids or element I.Ds to the actual instrumentation identifier.
  - *Test 2*: to modify existing sine test data so that instrumentation identifiers matched those for the forth coming test. The complex data operated on here was not intended to produce notch simulations but test operation of macros and that the 'arithmetic' on the complex data was performed correctly.

The value of these tests was only apparent when the actual Bepi Colombo sine test was performed, no data bugs manifested during the test data analysis. The value of dry runs cannot be over emphasized. A 'killer consequence' in terms of effective analysis management is managing analysis time. All Spacecraft test campaigns are subject to progress chaser activity and time constraints lead ultimately to pressure on the analyst. For Bepi Colombo process tests on site prior to test enabled a good understanding of the turn-around time on analytical support.

5.11 A key trade-off: reducing the effort of data acquisition check.

The sine test involves acquiring a significant amount of data, much of which is for downstream information, but the objective is to narrow this large amount of data to a relatively small number of channels to those critical for managing or monitoring the sine inputs and specification on the run sheet. Normally this process of data analysis and criticality filter is achieved by purpose written software to project notch needs controlled by a select number of channels.

Historically tests were often pressed to perform with the minimum amount of acquisition which often meant acquiring different channels on different axes of test. Such an approach has two(2) main disadvantages:

- Re-patching of channels and incorporation of new channels often brings with data management issues relating to repeated validation of data and instrumentation disturbance resulting in data channels becoming defective or providing data of uncertain content resulting in exhaustive and repeated patch checks.
- If a channel whose response is initially evaluated in an off-axis context then full validation is often only possible if that channel is ultimately checked as an on-axis response i.e. X response for X direction of sine input.

Experience from previous sine test campaigns has shown that defective channel management should not be underestimated in terms of time and effort required to rectify such bad data.

The first activity the mechanical analyst is responsible for when receiving new data from the facility is to confirm the data as received is acceptable in terms of:

- On axis responses are clearly on-axis and no errors in orientation assumptions are evident.
- There are no defective channels.
- The quality of the frequency responses is acceptable i.e. free of noise/spikes.
- The data is of the correct level confirming correct charge sensitivity settings on the acquisition.

The management process here involves recording observations or 'bad' data log deficiencies, generating appropriate non-conformance reports, performing rectification, validating the fix and tracking; this entire activity is a time consuming process.

On Bepi-Colombo Astrium were confident that a high channel could easily be managed analytically by the DYNAWORKS tool set, hence this conventional approach of dedicated channels per axis was disposed of and consistent acquisitions were specified for each axis of sine input. As a consequence it was accepted that some channels would be of very low order response for certain directions of sine excitation but the resulting high channel count was traded-off against the benefits of potential reduced channel management. As result of reduced disturbance to the patched channels it was found during the Bepi Colombo sine test campaign that management effort rapidly diminished after the first rectification exercise and that the decision to adopt such a philosophy was vindicated.

A secondary advantage of maintaining consistent acquisitions through the X,Y and Z axis tests was that ultimately an on-axis response check was able to be performed which might not be the case for different acquisitions on different test axes. For post-test data processing and FEM correlation this ability to validate accelerometer bonded orientation or labeling can be important.

5.12 Test axis sequence planning.

The sequence that tests are performed must be considered where Virtual Channels are computed. When inter-data phasing is important, such as computation of angular response variables, then data phase validation with respect to macro summations is important. Generally data can only be validated when it is known to be an 'on-axis' response. As a consequence the sequence that tests are performed can be important in this respect.

5.13 Team planning and organization.

Time management on test and individual understanding of responsibilities is a key element for success. A clear danger during any test campaign is failure to correctly plan for parallel

analysis activities or redundancy in roles of individuals. As a general policy, test redundancy not only applies to control strategies and instrumentation but also to personnel roles. Most test analysis activities fail primary as a result of poor planning, preparation of tools and analysis of test data being processed by a single individual who treats the activity as one long in-series process. Every effort must be made in the planning stage to define roles and responsibilities within the team and to parallelize effort within the team. Astrium advocates a planning flow-chart showing the analysis focus through the sine test campaign. The core main stream process can be regarded as generic irrespective of the project while off-line parallel activities may be project specific involving detail data acquisition checks.

5.14 Sine test data analysis planning.

Analysis planning is critical to test success. The goals of the plan should be to:

- Ensure that the test support analysis does not become a serial process through a single individual.
- To establish a plan for parallel activities to offload effort on any single individual and to define clearly understood domains of responsibility on each person in the test data analysis team.
- To obtain a 'time and motion' understanding of effort associated with the data analysis activity.
- To capture program specific data checks and assign them to a given individual. Examples of such data validations have already been discussed e.g. data phase checks to confirm accelerometer bonded orientation (mechanical installation phase) to ensure correct 'sign' of response are programmed into macro computations. Other program specific checks included FUNDAMENTAL /GLOBAL response comparisons on accelerometers adjacent to the IMHs. The purpose of such checks was to establish if the IMHs were structurally stable in terms of no noise/shock source indicating global slippage or gapping of the devices (*highly undesirable*).
- To provide visual reference or process refresher to team member during the test. On the Bepi Colombo sine test campaign, the process flow charts were pinned on the office wall as source of reference.

5.15 Facility pre- test meetings.

The propose of these meetings is to ensure a number of key aims are understood by all parties involved in the test campaign:

- The industrial and institutional teaming responsibilities are understood on all sides. During such meeting identification of test conductor, test hardware interfacing constraints, safety person etc is some of the key responsibilities that have to be understood and specified prior to test.
- Such meetings ensure status of compliancy against the test specification are understood and that the needs on both sides have been discussed and properly recorded.
- Through such meetings the specification may be subject amendment or update.

5.16 Launcher interface meetings.

During this meeting the Prime contractor would normally present the sine notch justification including the proposal for test control, working test control tolerances on the Test Limitations base and the specific limitations governing requested notches. As part of the sine notch justification effort the Prime contractor would normally demonstrate to the Launcher Author-

ity that their flight predictions through the LCDA are covered. From the Prime contractor's side, the main outcome from such meeting is a provisional endorsement or sanctioning of the test management approach and expected notches.

6 TEST ANALYSIS INFRA-STRUCTURE.

The analysis infra-structure for the Bepi Colombo test campaign is shown in Figure 15 with the aim of reinforcing the point on redundancy consideration. Notching is performed by designated team members on one lap top, the remaining lap top provides redundancy and data back-up potential. The principal lap top has a node locked license capability so that further redundancy from the local network is provided in the event of network or connection to home site loss.

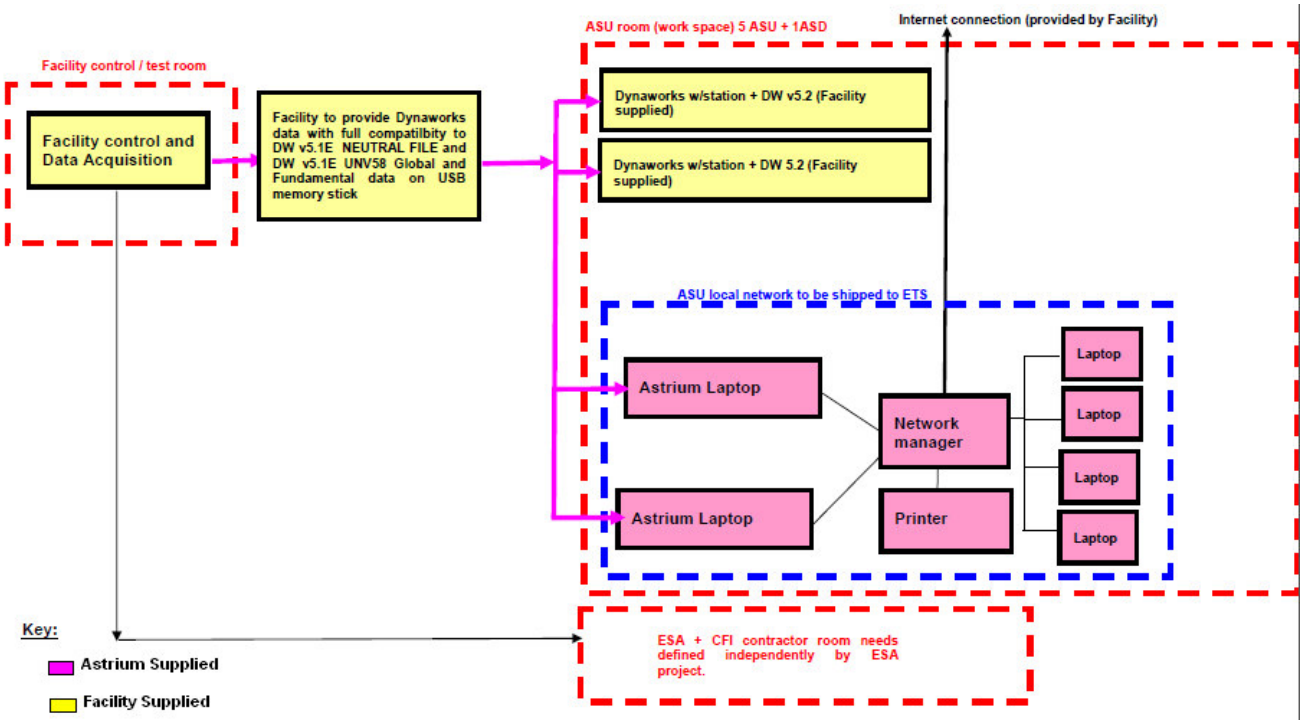


Figure 15. The analysis environment and infra-structure.

7 THE DATA ANALYSIS PROCESS DURING TEST.

The test analysis that is conducted is as result of the necessary trade-off between risk, analysis robustness, confidence in the process and data at hand and most importantly time. A sufficient amount of analysis of the test data has to be performed, prior to committing to the next level of input, to avoid compromising integrity of the test specimen. An early trade-off must be made with allocated time to conduct this analysis and the time need to progress testing. As a consequence the analysis must be focused and effort must be directed solely to data evaluation and *not* mentally applying thought to driving any support tools.

Experience has shown that poor time management has direct affect on success or perceived success outcome. Time pressures force mistakes, undermine external confidences and reflect badly on the industrially responsible team.

The basic philosophies behind successful test management are very simple: knowledge of specimen's perimeter of loading (Test Limits) and to establish where and what frequencies the limitations are most prevalent. On the latter point it is the function of the notching analysis software to provide this filtered focus, the transducer set (*both physical and virtual*) may be large (>500 channels) but its purpose of the notching software to filter this set to small set of critical locations that can be selected to manage the test or specify on the run sheet.

In general analysis effort diminishes during any given axis of test after evaluation of the first low run data and becomes more efficient through the test campaign as confidence in the structures behaviour increases. Figure 16 *schematically* outlines the process of analysis of the Bepi Colombo sine test for any given axis. This schematic is a simplification of the analysis plan (flow chart) discussed previously and forms the basis of the test analysis process plan. Certain data checks clearly diminish through the overall test campaign, for example, certain phase checks implemented to validate summation assumptions in specific macros performing the Virtual Channel calculations may only need to be performed once and not repeated for each axis of test.

The general core process is based upon experience and trade-off on efficient test time management. For Bepi Colombo the process was expanded and further analysis was conducted in support of test abort margins. The decision to conduct this additional analysis was vindicated by the time saved resulting from no abortive sine runs.

The schematic shown in Figure 16 comprises of the following elements:

- Parallelised check / validation effort within the team.
- Data checks, recording and tracking of bad channels requiring rectification.

Low level sine:

- Notching analysis based upon the first low level Sine data operating on the *Test Limitation* base. Notching is "mapped" and this map is critically evaluated to establish if deep notching can be elevated by exercising known stress margins of safety. Mapping involves transferring to the notch diagram labeling for each feature providing the notch along with notches hidden by these primary notches.
- Establishing a draft control plan and test the run sheet by repeating the notching analysis on the *run sheet values*.
- Assessing abort margins based upon pilot inaccuracy.

Intermediate and Qualification data review:

- Analysis is focused on confirming the acceptability of the previous control philosophy in terms of confirming no responses exceedances and confirmation of overshoot allowance where necessary.
- For the Qualification data the analysis aim is to principally confirm that all response were maintained within the agreed limits ideally avoiding the need to justify acceptability of responses that exceed advise limits.

Final low level comparisons:

- A dynamic comparison of final low level signatures with the initial responses recorded at the start of testing on a given axis.

Confirm IMH preload strains (stability check)

OK? → STOP

Yes

Start Low Level Sine

Prepare 'blank' DYNAWORKS bases to receive data.

Receive data from Facility

CHECK FORMAT
- Check format compliant with specification.
- Format data for import into DYNAWORKS.

DYNAWORKS (DW) IMPORT DATA & ACQUISTION CHECKS. Bad data channels?

DYNAWORKS (DW) IMPORT DATA & ACQUISTION CHECKS. Bad data channels?

BAD CHANNEL LIST PROFORMA
- Complete proforma listing bad data channels. Action remedy / check/track
- Supply list to Facility /AIT.

RUN DW MACROS GENERATE VIRTUAL CHANNELS

Export data to other analysts for parallel evaluations.

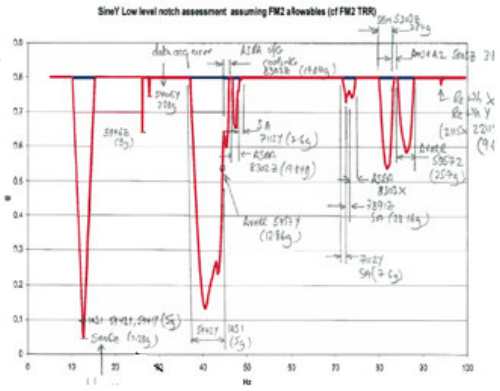
RUN ASTRIUM TEST SUPPORT MACROS.
- Generate TF on selected control strategy (MAX PILOTS)
- Compute notches on TEST LIMITATIONS data-base.

Global/Fundamental data comparisons:
- ALL data
- Accelerometers adjacent to IMHs. (to indicate gapping)
- All virtual channel inputs.

Virtual Channel checks:
- ALL input acquisitions—check low freq. phases for correct 'sign' assumptions in macros.
- Calibration (confidence) checks – IMH low freq (q-static) loads versus known mass properties.

CONFIDENCE CHECKS ON IMH LOADS.

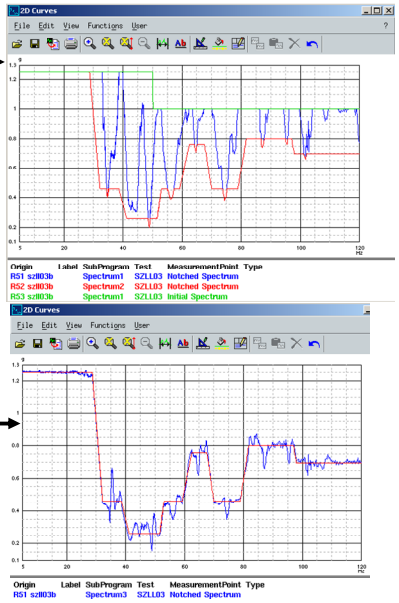
MAP NOTCHES:
- Notch minima and those covered notches.
- Critique notches and limitations – evaluate scope for limitation increase based upon known margins



DRAFT RUNSHEET & PROPOSED MANUAL NOTCH PROFILE

Continued next page

RUN ASTRIUM TEST SUPPORT MACROS.
- Compute notches based on DRAFT RUNSHEET specification..
- Confirm notching is in-line with notching based upon TEST LIMITATIONS



RUN ASTRIUM TEST SUPPORT MACROS.
- Compute notches DRAFT RUNSHEET specification –INCLUDE PILOT INACCURACY.
- Assess ABORT margins.

PREPARE PROPOSED RUNSHEET & CONSOLIDATE WITHIN INDUSTRIAL TEAM.

PRESENT RUNSHEET PROPOSAL TO CUSTOMER, DISCUSS,AGREE, JUSTIFY CONTROL APPROACH. Consolidate inputs from AGENCY & AGENCY CONTRACTORS.

NOTCHES & RUNSHEET PROPOSAL PRESENTED TO THE LAUNCHER AUTHORITY BY THE AGENCY/CUSTOMER.

Confirm IMH preload strains (stability check) → OK? → STOP

Yes

INTERMEDIATE SINE RUN

Prepare 'blank' DYNAWORKS bases to receive data.

Receive data from Facility

CHECK FORMAT
- Check format compliant with specification.
- Format data for import into DYNAWORKS.

DYNAWORKS (DW) IMPORT DATA & ACQUISTION CHECKS. Bad data channels?

DYNAWORKS (DW) IMPORT DATA & ACQUISTION CHECKS. Bad data channels?

BAD CHANNEL LIST PROFORMA
- Complete proforma listing bad data channels. Action remedy / check/track
- Supply list to Facility /AIT.

RUN DW MACROS GENERATE VIRTUAL CHANNELS

Global/Fundamental data comparisons:
- Accelerometers adjacent to IMHs. (to indicate ga

COMPARE RESPONSES WITH TEST LIMITATIONS AT 50%QL
COMPARE RESPONSES WITH 0.8* 50%QL TEST LIMITATIONS
- Generate assessment for presentation to Customer.

UPDATE PROPOSED RUNSHEET & CONSOLIDATE WITHIN INDUSTRIAL TEAM.

PRESENT RUNSHEET PROPOSAL TO CUSTOMER, DISCUSS,AGREE, JUSTIFY CONTROL APPROACH. Consolidate inputs from AGENCY & AGENCY CONTRACTORS.

NOTCHES & RUNSHEET PROPOSAL PRESENTED TO THE LAUNCHER AUTHORITY BY THE AGENCY/CUSTOMER.

Continued next page

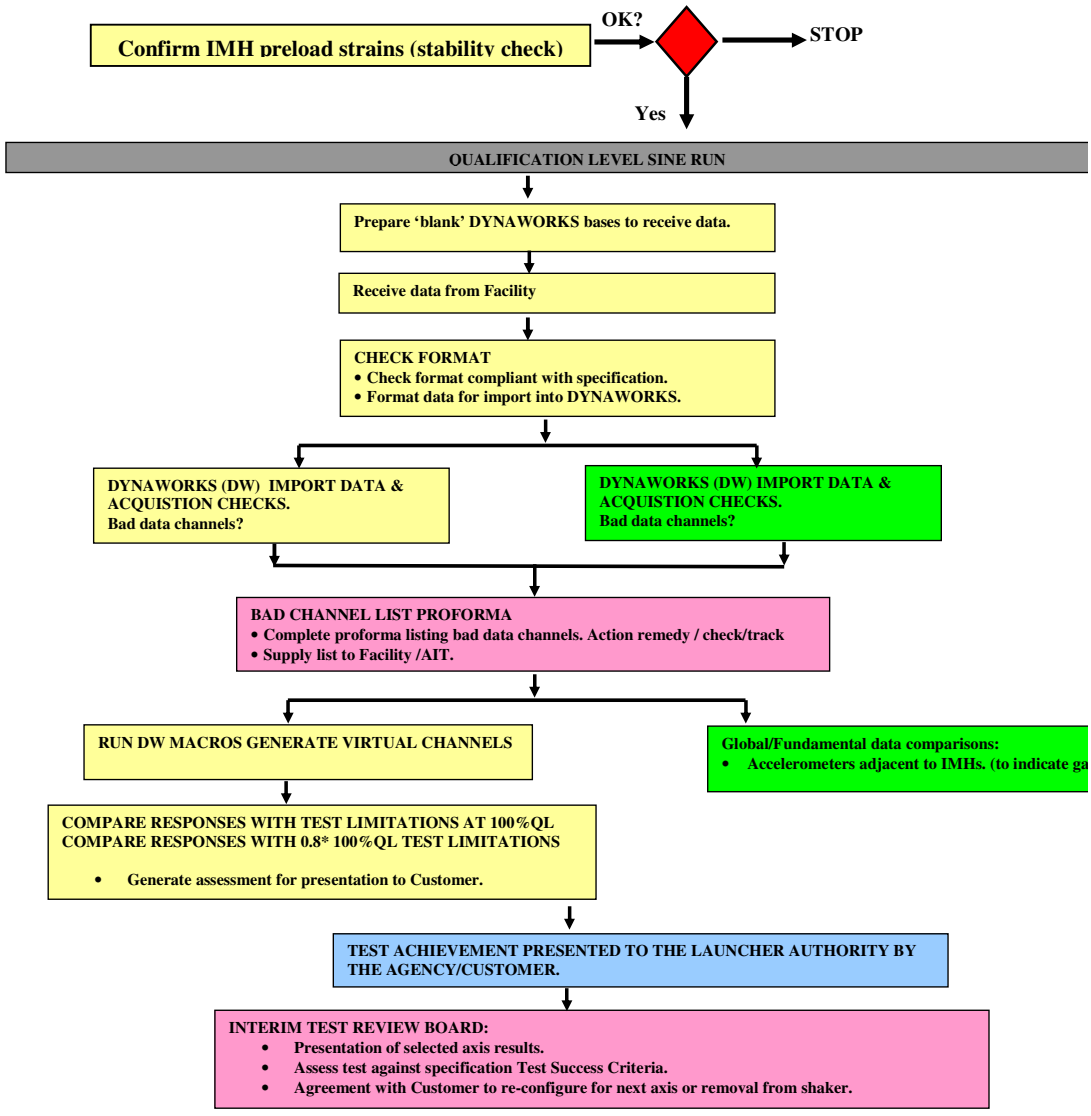


Figure 16. Schematic outline of test analysis and management. Note visual inspections and feedback from 'bad' acquisition tests/checks not shown.

8 LESSONS LEARNT.

Irrespective of an individuals experience all test campaigns provide a new set of lessons learnt. The principal lessons learnt from Bepi Colombo's sine test campaign are summarized below:

Instrumentation:

- A key part of the lessons learnt process reflection on decisions made during the program. On reflection the decision to integrate static and dynamic load cell capability into the IMHs in advance of the Spacecraft stack test was of paramount importance to both management and structural qualification. By incorporating the strain measurement systems into the STM stack test this provided an element of closure to concerns associated

with the functionality and endurance of the IMH system. The IMH systems have been subject, rightly, to close scrutiny during unit level design reviews. The STM test campaign has demonstrated that:

- *The static preload state* was stable in terms of comparison of state prior to and subsequent to dynamic loading. No relaxation in load was observed across the whole sine campaign.
- *The dynamic response of the strain gauges (and associated virtual load channels)* yielded frequency response outputs of high quality in spite of relatively low strain outputs. Confidence in data quality from the integrated IMH load cells was established from the analysis of the first data outputs from the sine test campaign. High quality low noise FRFs along with good low frequency correlation of output load with respect to predicted static load distributions from the known support module masses on each interface gave early confidence in the integrated IMH load cells-see Figures 17 and 18. A key lesson learnt here was that of effective screening of the strain gauge cabling which is in contrast to a selected few strain gauges pre-installed elsewhere. At these other locations gauge outputs were not usable due to high signal / noise resulting from interference from lack of screening.
- *Global and Fundamental comparisons:* comparisons of the Fundamental (narrow band pass FRFs) with the unfiltered Global FRFs of accelerometers in the vicinity of the IMHs were made to obtain confidence that no gapping or gross slippage was evident in the IMH system. Polar mounted propellant tank instrumentation is often characterized by noise generation from tank mounting interface and this is evident by such comparisons. This phenomenon was used not necessarily as a definitive means of confirming the structural stability of the IMHs but indicative. It should be noted that no Global / Fundamental anomalies were evident on IMH local transducers.

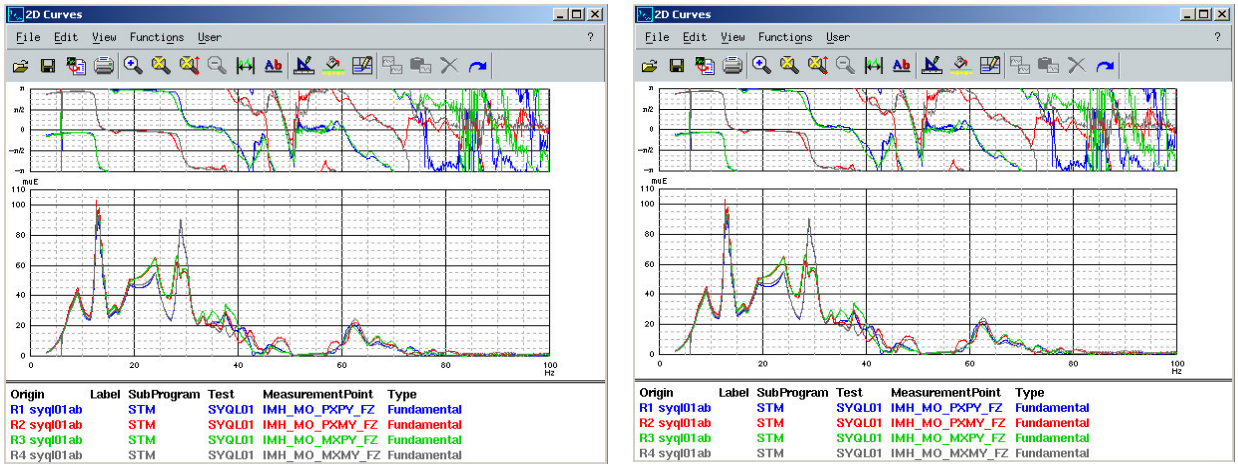


Figure 17. IMH Virtual Channel output for IMH axial force (in terms of µstrain sum) for MOSIF/MPO interface (LEFT) and MTM/MPO interface (RIGHT). Data shown for notched lateral qualification sine Y.

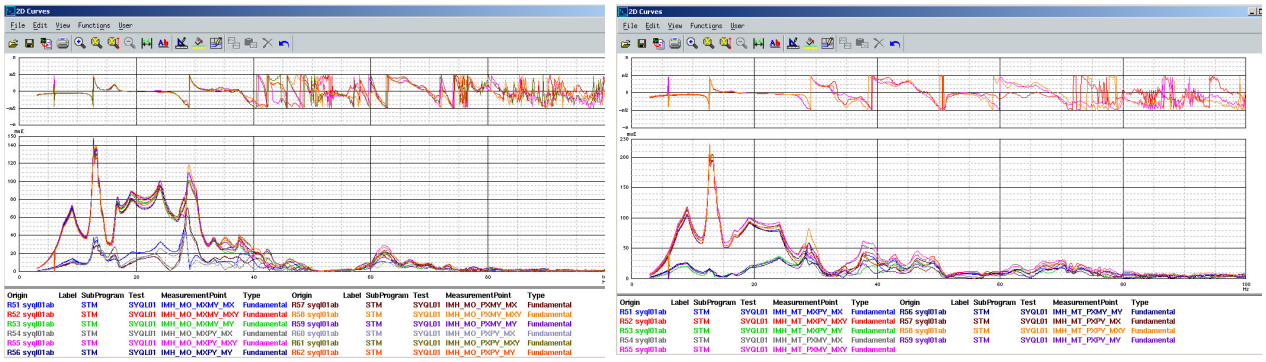


Figure 18. IMH Virtual Channel output for IMH bending moment components and resultants. (in terms of µstrain) for MOSIF/MPO interface (LEFT) and MTM/MPO interface (RIGHT). Data shown for notched lateral qualification sine Y.

Working practice:

- Prior to conducting one of the Intermediate level sine runs, following self / control loop check but before data acquisition was active, the shaker was subject to a transient voltage spike which introduced as a short duration transient motion. Since no data acquisition was active then input into the Spacecraft was not measured. Limited peak hold data was available along with video footage of the motion which enabled estimates quantifying response input.

  As a consequence of this 'non-quantified' anomaly, Astrium has modified its generic test specification policy to ensure that some form of data acquisition is maintained at all times when the shaker drive amplifiers are active.
- Previous discussion has highlighted that in advance of the test campaign it was decided to minimize channel re-patching to minimise corrective effort in rectifying and validating defective channels. The trade-off with respect to increased channel count versus potential reduced effort associated with such management was deemed validated and is expected to be applied during subsequent PFM testing.
- A notable success attained during the sine test campaign was that there were no test aborts recorded during the whole campaign with the exception of a sweep down run on a low level sine survey that was included for information only. For a complex stacked structure such as Bepi Colombo this was deemed a testimony to the planning and management. Repeated control aborts are undesirable because they introduce time management pressures on the analysis team and often detract from team credibility in terms of technical management. Success in terms of lack of aborts can be attributed to the factors below:
  - The analysis effort was extended by assessing abort margins using purpose written macros in DYNAWORKS centered on accounting for pilot dispersion or inaccuracy with respect to base manual notch profile. By extending the amount of analysis the team traded-off this extended analysis effort against the cost of abortive runs, repeated set-up and re-presentation of strategy to the customer. The tool and results were used to support judgment as opposed to provide definitive margin assessment but were deemed of sufficient value to warrant some limited extended effort in analysis.

- Maintaining a credible margin between the notch specification and abort so that some no response overshoots triggered an abort. As rule of thumb a minimum margin of 2.0-2.5dB has been found from experience as adequate to cover uncertainty in output response.
- Characterising overshoots from Intermediate sine runs. To some extent testing entails trust and confidence in the known limits or the perimeter of integrity within which the test is to be conducted. To this end it is possible to introduce a healthy margin or tolerance between the run sheet notch prescription and abort at Intermediate levels compared with the final qualification run. Specifying the run sheet auto-notch limits to be compatible with the Intermediate level at hand but maintaining ABORTs at the qualification limits increases the effective tolerance for the Intermediate run and enables the qualification strategy to be fully tested. In addition by replicating fully the desired qualification level control strategy, it is possible to obtain the best estimates for overshoot when the tolerance between notch and abort is reduced for the qualification run. A key philosophy when considering an intermediate run is maintenance of the control philosophy between the lower level input and the subsequent higher level input which is the next target. On Bepi Colombo only one Intermediate level was applied per axis hence effectively each axis consisted only of: a low level swept sine survey, Intermediate (50% Qualification level), Qualification sine followed by the final low level sine survey. An Intermediate level of 50%QL was specified in advance of test as this was deemed compatible with 2.5dB margins or possible expected overshoot of response. Post Intermediate sine analysis confirmed there were no unexpected exceedances relative to 50% QL limits by direct comparison of each measured and virtual response versus the 50%QL spectral limit profiles and by comparison of 0.8*50% QL limits to indicate if any other limits approached limits and were worthy of note. Overshoot characteristics in terms of 'X'dB overshoot were noted and incorporated as reductions for subsequent auto-notch specification on the following Qualification Level run sheet.

- This paper has emphasized the need during pre-test preparation to establish redundant strategies in all aspects associated with the test. During the Bepi Colombo sine test campaign this preparatory focus was vindicated when it was found the strain gauges monitoring MMO interface loads were not operable. To cover this interface management the analytical preparation discussed earlier with respect to management of the second order cantilever mode of the stack were used with effect.

Management and planning effectiveness:

- The test planning, preparatory de-bugging of the process and software, personnel planning and definition of individual responsibilities was a "*one-hundred percent*" success. No macro errors were evident and the use of tools and implementation of the process was instinctive due the repeated dry runs simulations of the process prior to test. During the test a white board was useful means of providing a visual record to the team of analysis findings that needed further consideration or a prompt to provide reminders for activities to be completed before committing to the next crucial runs.

Test control:

- Prior to test the complex stacked nature of the Spacecraft system was anticipated to bring with it complexities of test management in terms of control related issues. Stacked (tandem) Spacecraft of smaller overall size have been previously tested by Astrium where configurations such as a Science spacecraft stacked on top of a single propulsion module have been recently tested, but no experience exists where a stack of four(4) major modules (MOSIF and Sunshield considered here) has been tested. On reflection the

stacked nature actually assisted management of the test in that due to integration of a number of major structural bodies the structure was acceptably damped in all of main primary structure modes. In comparison with another large Spacecraft such as Metop-A, -B and –C; these Spacecraft exhibited relatively low damping (<1% critical viscous) in their first-cantilever modes and this presented control issues even at 2-octaves/minute sweep as the structure passed through resonance of the first main bending modes.

- During the final lateral axis tests, control of one local 10N thruster (panel corner response) was the only the only area were notable control issues were observed. No active auto-notching was initiated during this run for this location but subsequent notching analysis on this low level data indicated potential criticality with respect to assigned response limits. For the Intermediate sine run auto-notch limits were prescribed that resulted in active auto-notching for the 10N thruster location. The depth of the notch generated exceeded that projected from the low level analysis. As a consequence of the deeper notch finding on the Intermediate it was decided to remove the auto-notching on this channel and prescribe an abort only limit on the run sheet (*this is implemented by a notch specification at -0.1dB relative to abort*). The test was passed successfully and the resulting notch depth was significantly less than that which would have introduced by assignment of an auto-notch. It was clear after the Qualification Level run that controlling an off axis channel (*Z response for X sine input*) for local mode that was very lightly damped the control system was not able to react sufficiently to manage such characteristics. This observation will be carried forward in due course for the PFM test.

Cross talk observations at the piloted interface during longitudinal sine tests :

- Sine test piloting was implemented at the VTA/LVA interface plane which was approximately 1m above the FMD interface plane. For the longitudinal test the lateral cross talk (*lateral responses on the piloting plane)*is shown in Figure 19. The cross-talk above 35Hz can be seen to be significant i.e. the off-axis response at the LVA approaches or even exceeds input. In terms of managing the longitudinal tests the cross talk generally did not present any technical difficulties in terms of conducting the test safely. The issues resulting from this phenomena were expected to arise in later sine test correlation effort and filtering out the influence of these responses to obtain a pure fixed base understanding.

  In terms of a lesson learnt relative to pre-test statements of compliancy against the dynamic test specification, confirmation of lateral stability of the header expander and test fixture could be given in advance of the main test campaign by early blank fixture tests. The practicality on future programs for this early confirmation will be considered in the future by Astrium.
- The previous point highlighted for the longitudinal test the boundary condition for the Spacecraft was potentially removed from that of a pure encastre condition. Further evidence of this was found in the small degree of coupling between the fundamental cantilever modes and the axial excitation. Lateral sine tests confirmed that the first bending modes were circa 13Hz for both XZ and YZ plane cantilever modes. Low level coupling between these modes and axial excitation was predicted and is not sole consequence of the lateral cross talk. The test TFs for the longitudinal sine in terms of FMD bending moments (Mx,My) and certain lateral responses at the top of stack showed this coupling to exist at circa 10.5Hz which indicates that the boundary flexibility, lack of base inertia or clearance in the longitudinal guidance system has resulted in relatively significant drop in frequency. Such an observation is readily apparent but less apparent is influence of the boundary condition on higher order modes for the longitudinal case. The implications are as stated previous and mainly affect post test correlation effort.

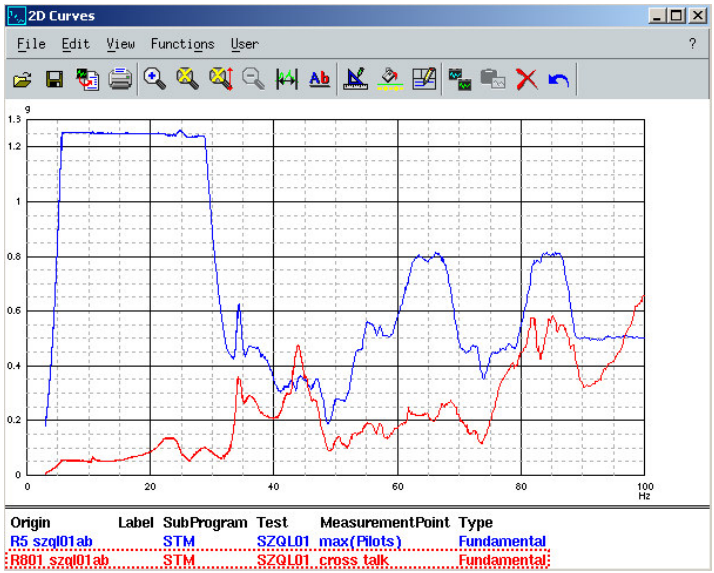


Figure 19. Qualification level Longitudinal Sine Z. Pilot maximum [envelope of four (4) pilots] versus cross talk [off axis response on pilot plane-maximum envelope of eight (8) channels].

Test support infra-structure (redundancy):

- Information technology is invariably sold to engineers as a robust and reliable commodity. One of the key messages this paper has tried to convey is that the concept of redundancy should be considered or applied to all domains of the process, infra-structure, personnel, control strategies etc. In support of the Bepi Colombo test campaign, the Astrium test support team utilized an in-house designed secure portable network solution providing an off-site office capability. This network capability provided the capability to access tools, including DYNAWORKS, by remote connection to the Astrium home site. The redundancy in-built into this infra-structure was the ability on at least one PC to run stand alone with no network using local software licenses. This capability was used when a short duration network failure manifested.

Test specimen hardware:

- Propellant tank mass dummy design has historically provided sources for lessons learnt. On Bepi Colombo a degree of geometric representation was made in that the tanks were designed essentially diametrally representative. For the polar mounted tanks (no internal baffling), the tank dummy polar moment of inertia introduced non-representative reaction torques relative to a fluid filled tank. This characteristic was recognized well in advance of the test and was managed by specific monitoring –see Virtual Channel listing Table 3.
- Astrium's sine test specification required that specific checks should be made to the interface flatness of the Vibration Test Adapter (VTA) as result of lessons learnt on previous test campaigns. Such checks were made but checks were omitted on the interface plates between the adapter and FMD. Delay to the test was incurred when it was found that these plates did not meet flatness needs. Consideration should therefore be given to early fit-checks to ensure advance inspections are completed to avoid impact on test delay.

9 CONCLUSIONS

By virtue of the complex structural nature of the test specimen in terms of stacked module arrangement the test management and outcome was a resounding success. The fundamental reasons for this success are governed by the principles reported in this paper: careful preparation and planning, process simulation and mapping, the software tool supporting data analysis (DYNAWORKS coupled with Astrium's purpose written macros) and of course redundancy, redundancy and redundancy!

It is hoped that the messages and experiences detailed here will support the wider community in terms of their needs and preparation.

REFERENCES

[1] Arianespace. Ariane 5 User Manual Issue 5 Rev.1.

[2] Background and further information relating to the Bepi Colombo--see www.esa.int and search Bepi Colombo.

COMPDYN 2013
4th ECCOMAS Thematic Conference on
Computational Methods in Structural Dynamics and Earthquake Engineering
M. Papadrakakis, V. Papadopoulos, V. Plevris (eds.)
Kos Island, Greece, 12–14 June 2013

REDUCTION OF OVERTESTING DURING BASE-DRIVE RANDOM VIBRATION TESTS FOR THE EUCLID SPACECRAFT HARDWARE

Adriano Calvi[1]

[1] European Space Agency
Keplerlaan 1, Noordwijk, The Netherlands
e-mail: Adriano.Calvi@esa.int

Keywords: Random vibration, Overtesting, Notching, Spacecraft Mechanical Loads, Euclid Project.

Abstract. *The purpose of random vibration testing is generally to verify strength and structural life by introducing random vibration through the mechanical interface. Typical applications are electrical components, instruments and small spacecraft for which acoustic testing is ineffective. The base-drive vibration test is conducted with the test item sitting on a moving platform that is driven by a shaker which introduces vibration typically up to 2000 Hz in three single-axis tests. The base-drive configuration is commonly employed to achieve test levels comparable to the launch environment. This conventional approach to testing has been known for decades to potentially overtest the test article at its own resonance frequencies. For this reason "notching" (i.e. reduction) of the specified input spectrum is often necessary.*

Notching on the input spectrum can be considered as far as it does not "jeopardise" the aim of the test, for example the qualification of the test specimen. As a consequence, one of the main issues for the structural engineer is to define a minimum threshold for the input notching. Special attention is paid to the "phenomenology" of secondary notching, which is related to level reduction on critical areas inside the test specimen. This paper provides some guidelines for assessing the notched profile in random vibration testing. In particular the importance and the benefits of performing a vibro-acoustic analysis of the complete spacecraft is illustrated with an example.

The paper is based on some author's contributions to the ECSS Spacecraft Mechanical Loads Analysis Handbook [1], and his experiences with the a number of European Space Agency projects. A critical investigation of the overall approach from the definition of the test specification to the quantification of the notching is shortly presented. The guidelines should be used in the frame of the Euclid spacecraft hardware verification when base-drive random vibration testing will be performed to show compliance to the random vibration and vibro-acoustic environment requirements.

1 INTRODUCTION

Some spacecraft load environments are treated as random phenomena, when the forces involved are controlled by non-deterministic parameters. Examples include high frequency engine thrust oscillation, aerodynamic buffeting of fairing, and sound pressure on the surfaces of the payload.

Random vibration analysis describes the forcing functions and the corresponding structural response statistically. It is generally assumed that the phasing of vibration at different frequencies is statistically uncorrelated. The amplitude of motion at each frequency is described by a power spectral density (PSD) function. In contrast to transient analysis which predicts time histories of response quantities, random vibration analysis generates the power spectral densities of these response quantities. From the power spectral density, the root mean square (rms) amplitude of the response quantity is calculated. The root-mean-square acceleration is the square root of the integral of the acceleration PSD over frequency. Random vibration limit loads are typically taken as the "3-sigma load" (obtained by multiplying the rms load by 3).

Random vibration testing helps demonstrate that space hardware can withstand the broadband high frequency vibration environment. The tests are conducted on an electrodynamic vibration machine or "shaker", which consists of a mounting table for the test item rigidly attached to a drive-coil armature. A control system energizes the shaker to the desired vibration level. Feedback for the control system is provided by a series of accelerometers, which are mounted at the base of the test item. Similarly to sine testing, adequate control approaches and strategies are used to avoid overtesting and to ensure realistic structural responses.

Heritage flight data, test data and analytical methods are used to predict vibration test levels. In most cases the predicted environments are verified later with system-level acoustic tests.

2 THE EUCLID PROJECT

Euclid is the ESA's mission to understand dark energy and dark matter within our universe. The spacecraft will start its journey in 2020 towards “L2”, the second Earth-Sun Lagrange point (Figure 1). It will be launched on a Soyuz rocket from Kourou.

The Euclid spacecraft is composed of a Service Module (SVM) and a Payload Module (PLM). The SVM includes the sunshield. The PLM consists of a large three mirror Korsch telescope feeding two instruments, the VIS visible imager and the NISP near-infrared spectrophotometer. The two instruments deliver Euclid's science, VIS for precise visible-light images of distant galaxies, and NISP for near-infrared spectro-photometry. They lie within Euclid's Payload Module (Figure 2) which provides mechanical and thermal interfaces to the instruments (radiating areas and heating lines). The VIS instrument is delivered in several separate units with dedicated mechanical and thermal interfaces with the payload module: the VIS focal plane assembly including proximity electronics, the readout shutter unit and the calibration unit. The NISP instrument is delivered as a standalone instrument. Both instruments have warm electronics located on the SVM to minimize thermal dissipation on the cold PLM.

The payload module development relies on Structural and Thermal Model (STM), built at flight standard, used to qualify the PLM with respect to the mechanical environment. After integration on the SVM STM, it is used to check the mechanical and thermal coupling, and thermal model predictions. A PLM Flight Model (FM) undergoes a full proto-qualification programme before delivery to Prime contractor.

The hardware of the Euclid spacecraft has to be qualified with respect to the random vibration and vibro-acoustic environments. For this reason a number of base-drive random vibra-

tion tests will be performed. The overtesting should be avoided or limited, without "jeopardizing" the objectives of the test.

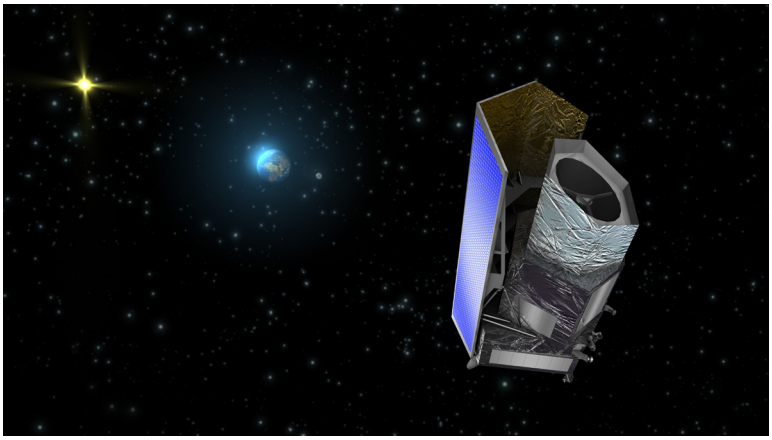


Figure 1: Euclid at L2 – Artist impression (source ESA)



Figure 2: VIS and NISP instruments integrated in the baseplate of the Euclid payload module (source Astrium)

3 CRITERIA FOR RANDOM VIBRATION LOADS AND ENVIRONMENTS

3.1 General aspects

The parameter most commonly used in the industry to define the motion of a mechanical system is the acceleration. The reason is mainly that accelerations are directly related to forces/stresses and "easy" to specify and measure. In practice accelerations are used as a measure of the severity of the mechanical environment. The loads are usually specified in terms of power spectral densities (usually of the acceleration), for the broad band random vibrations.

The main parameters are levels but also durations. The duration is a significant parameter for random vibrations. Of course the damage potential depends both on the load levels and duration, the latter being especially relevant for structural life verification.

3.2 Equivalence criteria

The subject of the equivalence criteria for dynamic environments, which are often crucial for establishing appropriate loads, is very complex, and normally the "equivalence" is limited and it can have some drawbacks. Since in general the equivalence has some limitations, enveloping techniques and conservativeness are often applied. In the following just some basic concepts about equivalence criteria are recalled. Relevant information can also be found in [2].

It should be noted that a very first "equivalence criterion" is implicit in the way the loads are defined. For example it is implicitly assumed that two random vibration environments are "equivalent" if they are represented by the same PSD of the input accelerations and duration, regardless the differences in the time histories. On the other hand, it is a common mistake to use the rms value of the input acceleration as a measure of its severity. The problem with the rms value is that it depends strongly on the values of the PSD at very high frequencies and on the upper frequency limit, which are often irrelevant. The most appropriate measure of the severity of a random vibration test is the PSD value at the resonant frequencies of the item. The maximum PSD value is important only if it is related to the main resonances.

Establishing an equivalence between different environments, or identifying which is the most severe, typically involves the evaluation and comparison of the (expected) structural responses. This is very important since on the basis of environment comparisons, decisions can be made, for example, on the status of compliance or on the most adequate tests which should be performed and included in the structural verification plan.

The equivalence criteria which allow establishing the equivalence between the base-drive random vibration environment with the vibro-acoustic environment are also very important in practical applications. The "equivalence" which can be established is indeed rather limited since the two environments are intrinsically different due to the different physical nature, i.e. purely mechanical and acoustic, of the excitation. In practice, for large spacecraft, it should be noted that the specified levels and duration for the acoustic noise test are, usually, highly conservative. On the basis of that assumption, the base-drive random vibration environments for lower levels of assembly (e.g. instruments and units) can be derived by enveloping the predicted response in terms of acceleration PSDs, when the spacecraft is loaded by the vibro-acoustic environment specified by the launcher authority for the acoustic noise test. For small and compact spacecraft, random tests can be more severe on some areas than the acoustic noise test.

In a number of situations, for example for primary or secondary notching definitions (see paragraph 4.1), it is crucial to compare the random vibration environment with the quasi-static loads (QSL) specified for the structural item. It is a common mistake, and unfortunately an usual industrial approach, to consider the "3-sigma" output acceleration as equivalent (or in any case comparable) to a quasi-static load. This is in general incorrect since:

- QSL are equivalent accelerations at the CoG, this is not usually the case for the random acceleration considered.
- The rms value of the acceleration depends strongly on the values of the PSD at very high frequencies and on the upper frequency limit, which are often irrelevant.

This can be illustrated by the following considerations.

The response displacement, as well as force and stress, spectral densities have the same "general shape" as the response acceleration spectral densities but their higher-frequency peaks are, in general, significantly lower in proportion to the lower-frequency peaks. In other words the first modes account for nearly all of the total displacement, force and stress. In mathematical terms it can be explained by noting that the displacement PSD is proportional to

the acceleration PSD by a factor $1 / \omega^4$. In more "physical" terms, this effect can also be explained by considering that the fundamental modes, e.g. the ones that have the largest effective masses and that establish the "force-link", are usually at lower frequency. Finally a global argument is the following: QSL and random loads do not have the same distribution in the item, depending on the frequency content compared to the eigenmodes. In other words, QSL implies a "quasi-rigid" behaviour which is not far from the first global mode in each direction, but the quasi-rigid behaviour is quite different with respect to the other modes, i.e. upper global modes and local modes.

In industrial applications often two mechanical environments are considered equivalent if they have the same shock response spectrum (SRS) [1], or similarly, for random vibrations, the same random response spectrum (RRS) (also known as vibration response spectrum [3]). In this case the equivalence is established on the base of the single-degree-of-freedom (SDOF) response. This criterion is often applied to structure with base excitation.

Another criterion is based on the evaluation and comparison of the structural response to the mechanical environments. The comparison is often performed in terms of accelerations and interface forces. In this case the equivalence is established on the base of the response of the actual structure.

Both criteria are based on structural responses, either from the SDOF system or from the actual structure. The advantage of the SDOF system is that it is a simple and "standard" structure which can be used not only to characterize the environment but also to estimate the response of the actual structure, albeit with assumptions. The advantage of using the response of the actual structure is that the solution is "exact", but the calculations are more costly and the results are valid only for the given structure. The practice depends on the industrial context, schematically:

- If the structure is "unknown", the SRS approach should be applied. This approach is simple but with assumptions, so with some risk.
- If the structure is "known", it is recommended to compute its actual response. This approach is more costly but also more reliable.

As a conclusive remark on equivalent loads and environments, in general it is always dangerous to replace an environment by another of different type and relevant structural analyses of the item should be performed.

3.3 Verification criteria

The following criteria are normally applied for strength verification of structures exposed to random vibration environments [1]:

- Verification by analysis: margins of safety greater than or equal to zero.
- Verification by test (qualification by acoustic or random vibration testing): test environments are compared with random-vibration environments derived from system-level acoustic testing. In other words this is evidence that the applied random vibration test levels, at lower level of assembly, were high enough, including qualification margins.

3.4 Some inconsistencies of the loads verification process

Some "inconsistencies" and potential issues in the verification process of random vibration loads are here summarized:

• Uni-axial vibration test facilities while the dynamic environments for space vehicle hardware are typically multiple-axis. In practice, tests are performed axis by axis.

• Infinite mechanical impedance of the shaker and the standard practice of specifying the input acceleration as the frequency envelope of the flight interface acceleration (despite the presence of antiresonances or dips in the flight configuration). This is the major cause of over testing in aerospace vibration tests.

• Vibro-acoustic environment often simulated at the subsystem and units assembly level using a random vibration test.

• Test levels largely based on computational analyses. For this reason it is important to validate critical loads analyses.

4 NOTCHING IN RANDOM VIBRATION TESTING

4.1 General aspects

Notching is the reduction of acceleration input levels around resonant frequencies, to avoid over testing. "Notching" can be distinguished in "primary notching" and "secondary notching". The primary notching is performed to limit the shaker-test specimen interface forces to the target values, normally qualification or acceptance loads. This is basically the same as to limit the equivalent accelerations to the centre of gravity (CoG) of the test item. The secondary notching is performed to limit local accelerations inside the test item with the purpose of protecting equipment, instruments or sub-systems.

Primary notching in random vibration testing of space hardware is mainly justified by the fact that the real environment in flight is simulated on shaker by an acceleration PSD based on an envelope of the interface levels foreseen in the considered frequency band, typically from 20 to 2000 Hz. This envelope doesn't account for the possible reactions of the test item which can produce level reductions in some frequency bands.

These potential level reductions (with respect to a rigid test item) are due to a high test item dynamic mass at the interface (with the "flight" mounting structure) which reduces the effect of the exciting forces according to the Newton's law. This high dynamic mass is generated by eigenmodes with high effective masses with respect to the interface. As the primary notching is related to interface forces, the unique criterion for mode selection in this case should be based on the modal effective masses [1].

The secondary notching is related to level reduction on critical areas inside the test item. In this case, the frequency response function involved is the test item dynamic transmissibility between the considered area and the test item interface, and the unique criterion for mode selection should be based on the modal effective transmissibilities [1].

4.2 Basic principles

Notching can be considered when it can be demonstrated that an "unreasonable" over testing with respect to the target loads (e.g. qualification loads) occurs if an adequate reduction of the input spectrum in some frequency bands is not applied.

In this context the term "unreasonable" is important. In fact by using random vibration tests the risk of overtesting (as well as undertesting) with respect to the maximum expected flight environment (including margin) cannot be completely removed. This is due to differences between "flight" and "test" conditions which can hardly be removed (e.g. base drive random test used to simulate vibro-acoustic environment, multi-axis excitations vs. single axis test facilities, differences in boundary conditions).

In order to minimize the risk of under testing, and then of mission failure, the general recommendation of minimizing the practice of notching can often be imposed by explicit (or "implicit") requirements, for example by the launcher authority or by the customer. On the

other hand it should be noted that, especially in the case of flight hardware, it is normally a "common interest" to limit as much as possible any overtesting and unjustified risk of structural failures.

Other important aspects are the following. The need for primary notching is generally "well understood", i.e. it is due to the specific dynamic behaviour of the test specimen on the shaker produced by the modes with large effective masses. In addition the frequency bands involved are normally narrows and relatively easy to localize. The agreement on the depth and width of the notches is usually rather straightforward.

More complex is the scenario for the definition of the secondary notching. In fact the secondary notching is, in its own essence, a revision of the applicable mechanical environment; it means a change of the applicable test specifications. The arguments are then not only technical, but also contractual, since they involve the sharing of responsibility and risk between customer and contractor. However, within a cooperative scenario, the crucial question remains technical: is the test specimen, or part of it, going to suffer an unreasonable overtesting, if the notching is not applied?

In practice secondary notching opens the door to a systematic reassessment of the test specifications by comparing the predicted dynamic response in the test with the expected "flight" mechanical environment. This is potentially in conflict with the logic of producing the test specifications by "enveloping" the expected mechanical environment at the interface, which has demonstrated during the years to be a robust approach. Moreover the systematic reassessment of the mechanical loads induced by the possibility of performing secondary notching generally induces inefficiencies and complexities in the process of mechanical analyses. This explains why it is often recommended to limit the practice of secondary notching to the critical items which indeed need to be protected.

In short, the notching on the input spectrum can be considered as far as it does not "jeopardise" the aim of the test, for example the qualification of the test specimen. However the application of the basic principles is not straightforward. Adequate approaches and criteria are crucial and some of them are hereafter reported.

4.3 Response and force limiting

To alleviate the overtesting problem and to define the notched spectra, two basic approaches are used:

- methods based on measurement of accelerations, also referred as "response limiting"
- methods based on measurement of forces, also referred as "force limiting"

Response-limiting consists of analytically predicting, usually through coupled loads analysis, the in-flight response at critical locations on the test article, measuring these responses during the test, and reducing or notching the input acceleration at the critical resonance frequencies so that measured responses do not exceed the predicted limits.

The main problems or disadvantages with the response limiting approach are reported for example in [1].

In the force limited vibration approach, response-limiting is replaced by limiting the reaction force at the interface between the test article and the shaker. The force limited vibration notching approach has a number of advantages [1].

In the industrial practice often a hybrid approach which includes both response and force-limiting is implemented.

4.4 Criteria for notching justification

Notching should be accepted when:

- Loads coming from the coupled system are demonstrated (with margins)
- Target loads of the tests would be exceeded

In practice for random vibration tests the assessment is based on the following approach. The random test analytical predictions (and during the test campaign the expected structural response based on lower level test runs) are compared to the results of the system-level vibro-acoustic analysis. Typically the comparison is performed in terms of PSDs of the interface forces, interface accelerations and accelerations at critical locations. Unfortunately reliable and detailed analyses are not always available.

The general criterion of not exceeding the QSL during the vibration test is generally accepted, however the accurate evaluation of the equivalent acceleration at CoG can be a difficult task, especially for secondary notching.

Specific criteria which are generally accepted are hereafter reported.

For primary notching in random vibration test:

- Criterion 1: Primary notching based on measured interface forces can be considered when they are predicted to be higher than the target loads.
- Criterion 2: Primary notching based on measured accelerations can be considered when the adequacy of the I/F forces estimation method can be proved.
- Criterion 3: Width and depth of the notches in the relevant frequency bands should be identified with the goal of minimizing the risk of under testing.

For secondary notching in random vibration test:

- Criterion 1: Secondary notching in random vibration tests can be considered when it can be demonstrated that the severity of the structural response of the test item during the random vibration test is expected to be higher than the acoustic response which is intended to simulate (e.g. satellite acoustic noise qualification test). It means that measured accelerations PSDs in critical locations are expected to be higher than the predicted acceleration PSDs in the system-level vibro-acoustic analysis.
- Criterion 2: Secondary notching in random vibration test should be minimized in order to reduce the risk of under testing within the concerned frequency bands. It means that moderate over testing is acceptable if positive margins can be shown. It should be noted that local dynamic response higher than the “internal item” QSL does not necessarily mean that the QSL (i.e. equivalent CoG accelerations) are exceeded.

4.5 Practical aspects of notching and verification of compliance in random vibration

Qualification of structures in the random environment raises several specific problems such as difficulties in numerical analysis for test prediction due to the extended frequency range, and the choice between mechanical base-excitation and acoustic excitation.

The evaluation (both by structural analysis and test measurements) of the CoG net acceleration of the component is properly performed by means of the external forces. For example, for a pure translation, by Newton’s second law, the CoG net acceleration is simply equal to the measured external force divided by the total mass. Attempts to measure the CoG acceleration with an accelerometer usually overestimate the CoG response at resonances, so limiting these measurements to the CoG criterion (notching in a vibration test) results in an undertest.

The signal processing bandwidth is a common source of misunderstanding in random vibration testing [1]. In the space industry today, an enormous number of samples of random vibration data are taken with many different measurement techniques and processed in many different ways. In particular with the popularity of digital signal processing, the frequency bandwidth can be very narrow and PSD curves often show very high and sharp peaks. These phenomena sometimes create "problems", specifically when comparing PSD curves. Two typical situations are:

- when controlling, within specified tolerances, the test environment at the base of the item with respect to the specified ("target") PSD;
- when processing data from system level acoustic test to arrive at PSDs for comparison with those used to test components.

These "problems" in some cases can be irrelevant since created by the high resolution processing. To be consistent the processing resolution in the vibration test should match the one used to establish test conditions or the processing resolution of the test data should be converted with that used to derive the specified environment.

In case the acoustic test measurement peaks exceed the specification, before taking a decision about retesting the item, the following approaches are used:

- Peak clipping. A commonly used rule is that all narrowband spectral peaks should be clipped by 3 dB [2]. Sharp peaks or peaks with a relatively small bandwidth of exceeding the unit's power spectral density specification might be clipped if the exceedance is not more than 3dB. This approach is based on the following justification. The acoustic test measurements are usually much lower than the unit's power spectral density specification next to the peak. Then it can be assumed that in the relevant frequency band the random input (usually flat for a wide frequency band at left and right of the peak found) is at least equivalent to the corresponding energy input resulting from the higher peak but taking into account the significantly smaller random levels next to the peak (see [1] for the analytical discussion of the approach). However perhaps the best approach "to remove" the narrowband spectral peaks is to compute all spectra with a resolution bandwidth that is proportional to frequency (e.g., a 1/6 octave bandwidth), and then envelope all peaks without clipping [2].
- Application of random response spectrum (RRS). For example [3] shows how the RRS of a typical power spectral density specification is compared with the actual peaky measurements and how it can be then shown that the specification covers the measurements even if there might be large exceedances. An approximate evaluation of the RRS can be performed by applying the Miles' equation with varying the natural frequency from 20 to 2000 Hz, which is the typical random vibration frequency range.
- There could be the chance to compare the unit's internal responses measured during the system acoustic noise test with the ones measured during the random vibration base-drive test at unit's level. In this case the internal responses should be checked first. In fact the incompatibility of the unit's random test excitation with the corresponding acoustic test measurement at the interface of the unit does not exclude a potential compatibility of the respective internal responses, which might depend much on the mounting conditions of the unit on the satellite as compared to the shaker test. In practice, if measurements of unit's internal responses are available from the acoustic test then these responses should be taken into account and, where relevant, the proposed approaches should be adapted accordingly to the comparison of the internal responses. Of course the aim is to verify that the unit's random vibration test has been performed with sufficient excitation alt-

hough an incompatibility with respect to the acoustic test measurements at the unit interface was noted.

However it should be noted that at the time of taking decisions on the adequacy of the notching , the results of the system level acoustic test are normally not available. On the other hand, recent developments in the area of computational mechanics allow performing vibro-acoustic response analysis of a complete spacecraft. The analysis can be performed by combining the FE method and the BE method with SEA approach, and allows the random levels on units and instruments to be compared to technical specifications or qualification levels. In particular an important advantage of performing a vibro-acoustic analysis at spacecraft level is that the results can be compared to the ones from a base drive random vibration test predictions, for example of an instrument, and to assess if some adjustments of the levels (e.g. secondary notching) are possible, for example before the qualification run.

5 EXAMPLE: SLSTR

5.1 General aspects

In the following some data concerning the qualification test campaign of the structural and thermal model (STM) of the Sea Land Surface Temperature Radiometer (SLSTR) are reported. SLSTR (see Figure 3) is one of the instruments of the ESA satellite Sentinel 3. The test article was instrumented with 21 load cells which allowed to recover the interface forces.

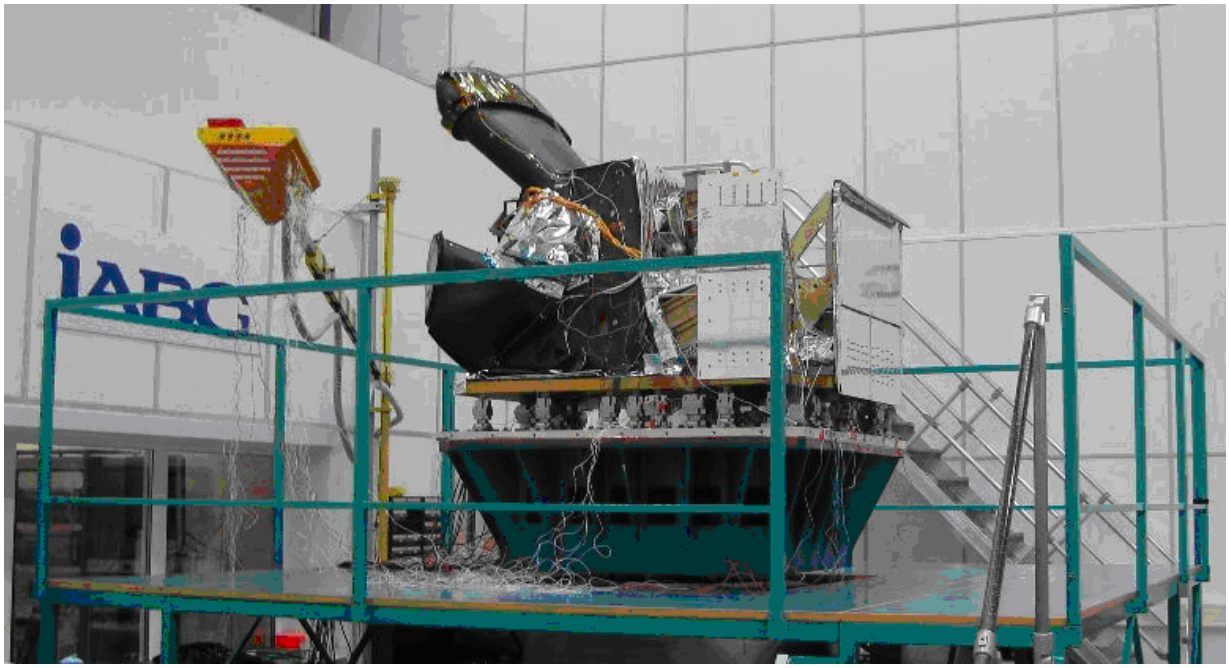


Figure 3: SLSTR STM on the shaker – X axis configuration.

Before starting the test campaign a finite element analysis of the base-drive random vibration was performed to predict the dynamic response of the test item on the shaker and, specifically, to predict if notching of the input spectra would have been necessary. An overview of the finite element model is shown in Figure 4.

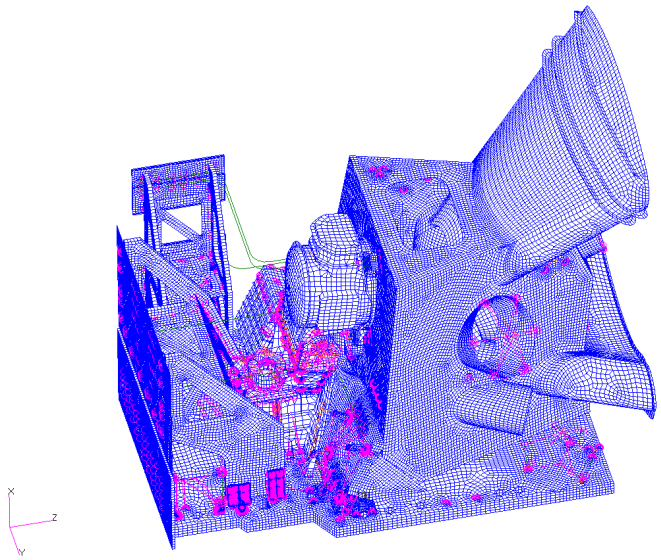


Figure 4: SLSTR STM Finite Element Model (source: SLSTR Industrial Consortium)

The results of the vibro-acoustic analysis at spacecraft level were also available at the time of the test campaign and the structural response was recovered at a number of critical locations of the instrument. In practice a number of comparisons have been possible since during the test the structural response was measured at relevant locations. In particular, the following criteria have been investigated before applying the full qualification levels:

- The interface load levels (expected to be) reached during the qualification test should cover with margins the ones predicted by the vibro-acoustic analysis (acceleration PSDs and forces if available).
- The test item "internal accelerations" (expected to be) reached during the qualification test should cover with margins the ones predicted by the vibro-acoustic analysis, both in terms of PSD levels and, consequently, root mean square.

Figure 5 shows the comparison between the initial test specification level in lateral direction Z (green profile) and the nominal spectrum applied during the test (blue profile). It should be noted that both secondary notchings and a general reduction of the vibration levels have been applied.

Figure 6 reports the nominal qualification levels in Z direction (red profile: "pilot") compared to the levels predicted by the vibro-acoustic analysis at the interface between the instrument and the spacecraft. The comparison is performed in terms of acceleration PSDs at relevant recovery points of the mathematical models, i.e. some restitution nodes distributed around the interface of the SLSTR. It can be concluded that the applied levels should be adequate to qualify the structure with respect to the vibro-acoustic flight environment.

Figure 7 shows an example of structural response in a critical location of the instrument. The extrapolated response at qualification level for the test run in Y direction is compared to the response computed by vibro-acoustic analysis. The root mean square value expected during the test is $5.7g_{rms}$ versus a predicted value equal to $2.2g_{rms}$.

In conclusion the final levels have been agreed mainly on the basis of the results of the vibro-acoustic analysis of the complete spacecraft and the expected structural response at qualification level in the random vibration test run. The latter has been extrapolated on the basis of the structural response measured during the test run at intermediate level.

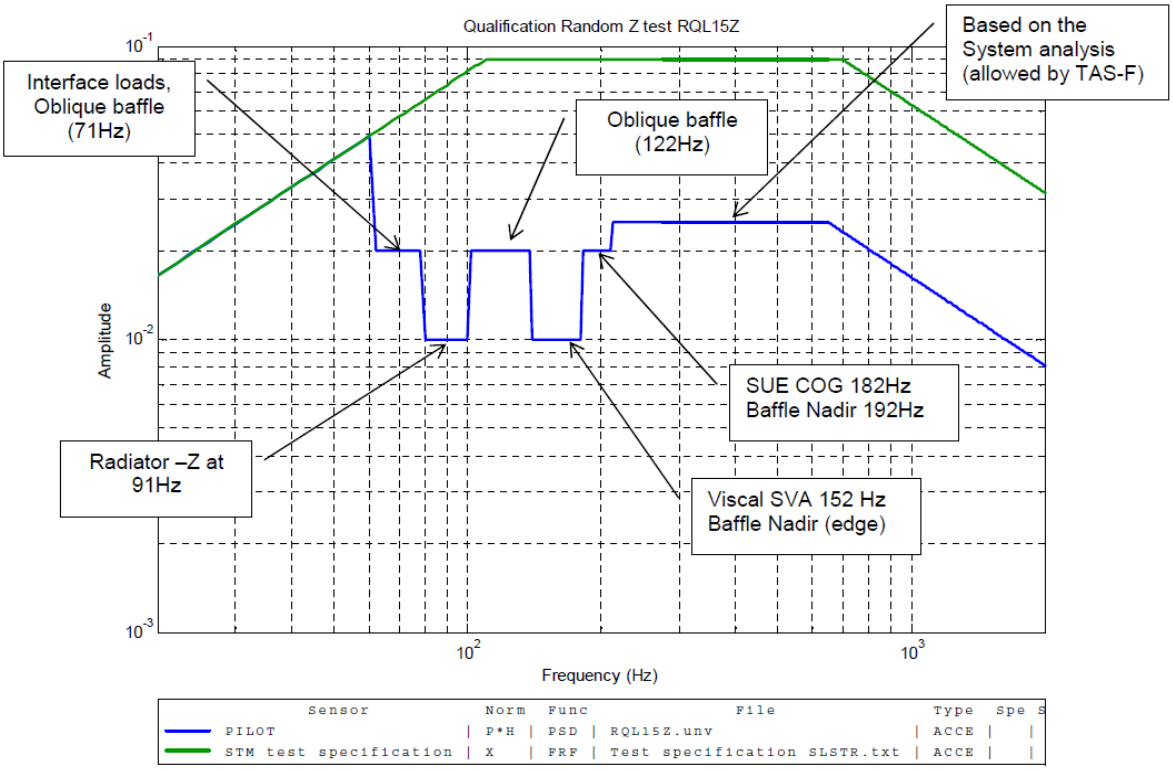


Figure 5: Random vibration test in Z: nominal input profile compared to specification (source TAS-F)

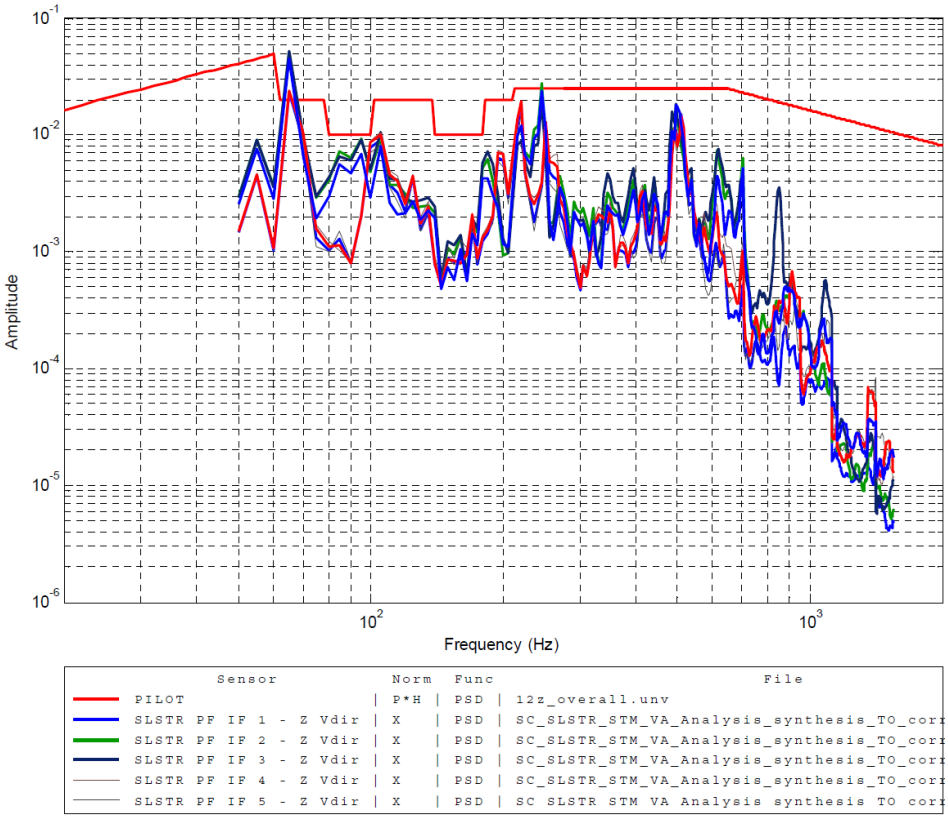


Figure 6: Nominal qualification levels (Z direction) compared to PSD levels calculated by vibroacoustic analysis (source TAS-F)

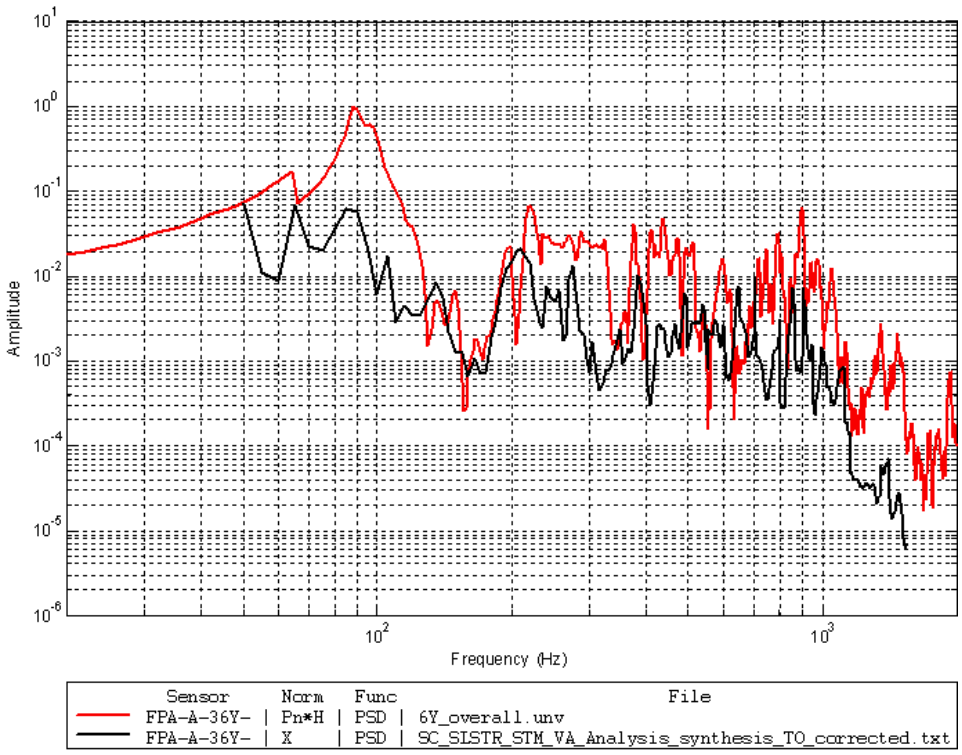


Figure 7: Location FPA-A-36Y: expected response at qualification level run in Y direction - red curve - vs. computed response by vibroacoustic analysis - black curve (source TAS-F)

5.2 Additional remarks

It should be pointed out that the calculated random response coming from the vibro-acoustic analysis (acoustic excitation of the spacecraft mathematical model which includes the one of the instrument), has been compared to the response from a base-drive random vibration test on a "rigid" interface (assuming an infinite mechanical impedance of the shaker).

The response at the instrument interface recovered by the vibro-acoustic analysis can include the contribution of modes of the interface not necessarily related to a significant response inside the instrument. So, trying to reach the same interface levels with the test item mounted on a rigid interface (i.e. the shaker), with a different transmissibility, can increase the risk of over-testing the subsystems.

In principle a conservative approach should be to apply test levels covering the ones predicted at the instrument/spacecraft interface recovered from the vibro-acoustic analysis. This is often the approach used for non-flying hardware (e.g. STM), where often the levels to apply are "as high as possible". The reason is to keep some margins which can cover the uncertainties related to the (non-validated) mathematical models, in particular of the test item. In fact that uncertainties can also affect the predictions obtained by the vibro-acoustic analysis.

In some cases this conservative approach could be not feasible without the risk to damage something and it is perhaps also not necessary. In fact even if the test levels applied at the interface of the item are apparently somewhat low in some frequency bands, the response (PSD) obtained on a critical location could be globally much higher than the one coming from the vibro-acoustic analysis.

6 CONCLUSIONS

The purpose of random vibration testing is generally to verify strength and structural life by introducing random vibration through the mechanical interface. The base-drive configuration is commonly employed to achieve test levels comparable to the launch environment. This conventional approach to testing has been known for decades to potentially overtest the test article at its own resonance frequencies. For this reason "notching" of the input spectrum is often necessary.

In this paper a critical investigation of the overall approach from the definition of the test specification to the criteria to justify the notching has been presented. Special attention has been paid to the "phenomenology" of secondary notching, which is related to level reduction on critical areas inside the test item. In this case, the frequency response function involved in the notching quantification is the "test item" dynamic transmissibility between the considered area and the test item interface. Another important aspect of the secondary notching is that it should be quantified based on the predicted equivalent CoG acceleration of the specific "internal item" which needs protection. However the mentioned CoG acceleration is difficult to evaluate, mainly because the relevant interface force is normally not available (i.e. not measured) during the test.

On the other hand, recent developments in the area of computational mechanics allow performing vibro-acoustic response analysis of a complete spacecraft. The analysis allows the random levels on units and instruments to be compared to technical specifications or qualification levels. In particular an important advantage of performing the vibro-acoustic analysis is that the results can be compared to the responses from base drive random vibration test predictions (calculated by analysis or by extrapolation of measured levels) to assess if some adjustments of the levels (e.g. secondary notching) are possible.

An example which illustrates the importance and the benefits of performing a vibro-acoustic response analysis at spacecraft level has been reported. Of course a crucial aspect of the approach is that, since the assessments are largely based on computational analyses, it is fundamental to validate the relevant mathematical models.

The presented guidelines should be used in the frame of the Euclid spacecraft hardware verification when base-drive random vibration testing will be performed to show compliance to the random vibration and vibro-acoustic environment requirements.

Acknowledgements

The author would like to thank the colleagues from Industry and the companies that have been involved in the design and verification of SLSTR STM. The companies are: Thales-Alenia Space France (F), Selex Galileo (I), Jena-Optronik (D), CarboFibretec (D) and Studiel (F). The test was performed at IABG (D) premises in November 2011.

REFERENCES

[1] *Spacecraft Mechanical Loads Analysis Handbook*, ECSS-E-HB-32-26A, February 2013, Noordwijk, The Netherlands

[2] *Dynamic Environmental Criteria*, NASA-HDBK-7005, March 2001

[3] T. Irvine, An Introduction to the Vibration Response Spectrum, Revision D, www.vibrationdata.com, June 2009

COMPDYN 2013
4th ECCOMAS Thematic Conference on
Computational Methods in Structural Dynamics and Earthquake Engineering
M. Papadrakakis, V. Papadopoulos, V. Plevris (eds.)
Kos Island, Greece, 12–14 June 2013

AN EASY-TO-IMPLEMENT COMPUTATIONAL METHOD FOR THE SPACECRAFT SINE TEST-PREDICTION WITH PARTICULAR EMPHASIS ON THE MODAL CONTRIBUTIONS

P. Nali[1], L. D. Mucciante[1] and L. Caccamo[1]

[1]Thales Alenia Space Italy
Strada antica di Collegno, 253 - 10146, Turin, Italy
e-mail: {pietro.nali,luigi.mucciante,luca.caccamo}@thalesaleniaspace.com

Keywords: Sine Tests, Structural Dynamics, Base-motion, Interface Forces, FRA.

Abstract. *A methodology useful for calculating the frequency response functions in terms of interface forces and local accelerations of a hard-mounted structure subjected to base-shake sine tests is described in this work. The structure is specifically a SC and will be called SC01. Reference to basic structural dynamics is done. The proposed easy-to-implement procedure permits to calculate the SC interface forces to the base and the SC local accelerations by post treating the results of the hard-mounted normal mode analysis. As a consequence of that, dedicated frequency response runs are not necessary. In accordance with the mode superposition approach, the normal mode analysis outputs are processed by accounting each modal contribution independently from the others. The relevance of each mode on the SC responses is thus explicitly quantified. This can favour a focused design refinement aiming to produce the main impact on the natural frequencies and mode shapes of interest. The critical responses can thus be modified and this can produce some advantages along the preliminary definition of the sine test notching plan. A complete set of numerical result comparisons is detailed along the paper in order to assess the accuracy of the methodology presented.*

1 Introduction

Low-frequency base-shake sine tests, hereafter shortly called sine tests, are usually performed in the aerospace industry for identifying the modal characteristic, qualifying the structural design and verifying the structural integrity of a SpaceCraft (SC) [1]-[3]. The aim of the qualification sine tests is to make the SC reaching the qualification level of SC InterFace (I/F) loads and of some local accelerations of interest (typically related to subsystems or units).
The launch vehicle (LV) users manuals (e.g. [4],[5]) provide the Quasi-Static Loads (QSL) specification from which the qualification LV/SC I/F loads can be calculated [6]. The qualification LV/SC I/F loads are usually intended to be the I/F longitudinal force and lateral moments. The corresponding I/F in-line loads and overfluxes might also be verified.
The Sine Test Vibration Specification (STVS) is provided in the LV users manual and it is a conservative envelope of the launch transients. The STVS do not take into account the amplification factor existing around the SC most significant natural frequencies [6]. It follows that the SC I/F loads and local accelerations that could be reached during the sine test by applying the STVS input profile would significantly exceed the corresponding qualification values. Some limitations, called notching, are thus commonly introduced to the STVS in order to avoid overtesting. The notching can be considered as far as it does not jeopardise the aim of the test, that is, in this specific case, the SC sine test qualification. See work [7]-[9] for an overview of the main issues of overtesting during the sine tests.
For what concerns modeling and computations, the sine tests I/F load and acceleration responses are usually predicted in the numerical sine test-prediction through dedicated Finite Element (FE) Frequency Response Analysis (FRA), where the STVS is provided as input loading. See the work [10] for a complete overview of the Finite Element Method (FEM).
During the sine test-prediction, the so-called "primary notching strategy" is defined in order to limit the SC I/F loads that would be reached during the sine tests to the LV/SC I/F loads calculated from to the QSL specification. Also a "secondary notching" is typically defined in order to limit the acceleration or the load levels at some particular locations of the spacecraft. The limits used for computing the secondary notching correspond normally to the qualification levels of the interested subsystems or units.
It is understood that the numerical sine test-prediction plays a significant role in the SC qualification for low-frequency environment. Moreover, a large number of FE FRA might be iteratively performed in order to predict the SC structural responses to the STVS, when operating some SC structural design refinements. Each sine test-prediction imply three different FRA runs, that is one run for each axis of excitation. The SC FE model can involve a considerable number of Degree Of Freedoms (DOFs). As a consequence, each SC FRA might be rather time expensive and demanding in the computational point of view.
In this work, an easy-to-implement methodology useful for performing the sine test-prediction for the three axis of excitation is presented. The advantage of following the proposed approach is that dedicated FRA runs are not required, being the structure responses obtained by processing the output of the hard-mounted normal mode analysis through a code implemented by the authors in the Matlab numerical computing environment. The assumption of low sine sweep rate during test is made and the sine sweep rate effect [11],[12] is thus neglected.
Since the computational method presented is based on the mode superposition approach and each modal contribution is considered independently from the others, the relevance of each mode on the SC responses can be easily quantified. This can eventually provide some useful information when some structural design refinements are needed. Along this paper, the results

obtained with the proposed methodology are assessed and compared with the FE FRA results obtained with MSC Nastran commercial software. Reference is made to the real case of a SC, hereafter called SC01.

2 Base motion of SDOF system

The complex equation for relative motion of a Single DOF (SDOF) system, when no force is applied to the mass, is given below [13].

$$m\ddot{\overline{u}} + c\dot{\overline{u}} + k\overline{u} = c\dot{\overline{z}} + k\overline{z}, \tag{1}$$

where the overline indicates a complex quantity, $\overline{u}$ is the displacement of the mass, $\overline{z}$ is the displacement of the moving base and the dot denotes differentiation with respect to time. m, c and k are the mass, the coefficient of viscous damping and the spring constant, respectively. The hypothesis of linear oscillations is done.
If the base undergoes the simple harmonic motion $z = Zcos(\Omega t)$, where Ω and t indicate respectively the excitation frequency and the time, moving to the complex domain implies that $z = Re(\overline{z}) = Re(Ze^{i\Omega t})$, where $i = \sqrt{-1}$ is the imaginary unit. The following complex steady state response is assumed:

$$\overline{u} = \overline{U}e^{i\Omega t}.$$

It is convenient to divide Eq. (1) by m and rewrite it as

$$\ddot{\overline{u}} + 2\zeta\omega_n\dot{\overline{u}} + \omega_n^2\overline{u} = 2\zeta\omega_n\dot{\overline{z}} + \omega_n^2\overline{z}, \tag{2}$$

where ω_n is the undamped circular natural frequency and $\zeta = \frac{c}{c_{cr}}$ is the viscous damping factor, with $c_{cr} = 2\sqrt{km}$.
It is useful to rearrange Eq. (2) as

$$\left(-\Omega^2 + 2\Omega i\zeta\omega_n + \omega_n^2\right)\overline{U} = \left(2\Omega i\zeta\omega_n + \omega_n^2\right)Z, \tag{3}$$

so that $\overline{U}/Z$ takes the following form:

$$\frac{\overline{U}}{Z} = Tr\left(\frac{\Omega}{\omega_n}\right), \tag{4}$$

where

$$Tr\left(\frac{\Omega}{\omega_n}\right) = \frac{1 + 2i\zeta\frac{\Omega}{\omega_n}}{1 - \left(\frac{\Omega}{\omega_n}\right)^2 + 2i\zeta\frac{\Omega}{\omega_n}}. \tag{5}$$

The function $Tr\left(\frac{\Omega}{\omega_n}\right)$ of Eq. (5) is commonly called transmissibility [13] and keeps its validity also for the subsequent derivatives of $\overline{U}$ and Z. That is, Eq. (5) is also the ratio between the acceleration imposed to the base and the acceleration felt by the mass: $\ddot{\overline{U}}/\ddot{Z}$. By multiplying the latter accelerations by m it follows that Eq. (5) gives also the ratio between the interface force transmitted to the base dynamically $m\ddot{\overline{U}} = \overline{F}_{dyn}$ and the force $m\ddot{Z} = F_{st}$ that would be transmitted to the base in the case of infinitely-stiff spring, that is in the case of static behaviour. By taking the absolute value of Eq. (5) leads to

$$\frac{\left|\overline{F}_{dyn}\right|}{F_{st}} = \frac{\sqrt{1 + \left(2\zeta\frac{\Omega}{\omega_n}\right)^2}}{\sqrt{\left(1 - \left(\frac{\Omega}{\omega_n}\right)^2\right)^2 + \left(2\zeta\frac{\Omega}{\omega_n}\right)^2}}. \tag{6}$$

Figs. 1 and 2 show respectively the curves of magnitude and phase of the transmissibility in Eq. (6), with varying ζ.

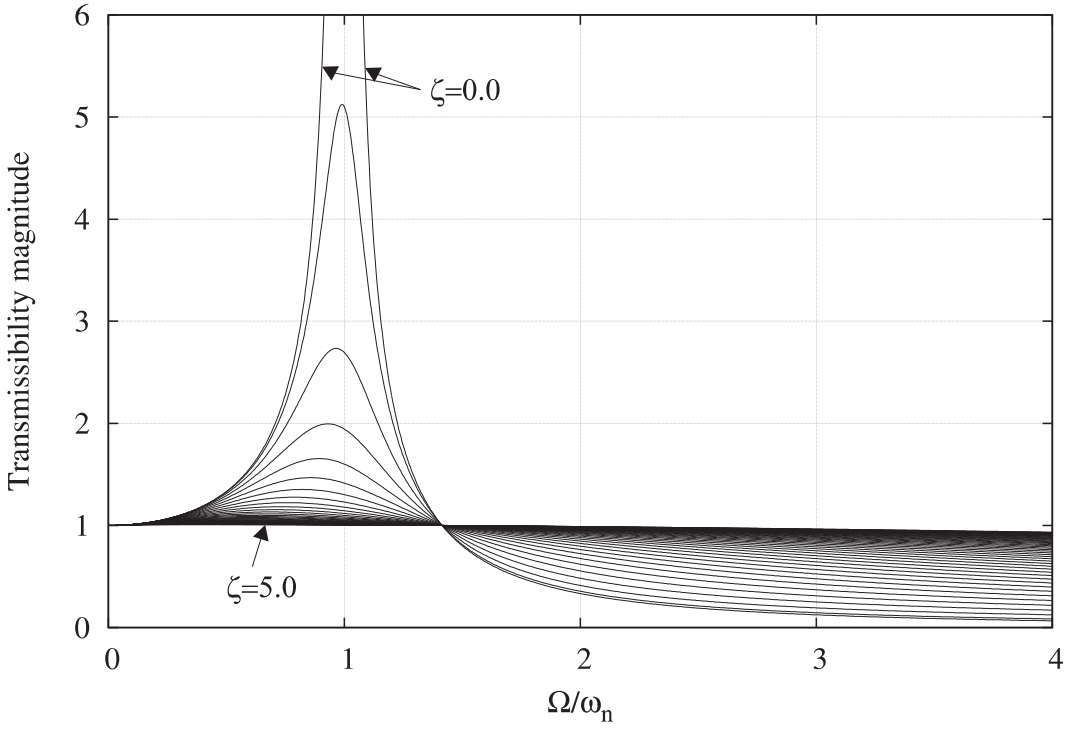


Figure 1: Transmissibility magnitude curves with ζ increasing from 0.0 to 1.5 with step of 0.1.

3 Base motion interface forces of mDOF systems

The interface forces between the moving base and a multi DOF (mDOF) system may be written as

$$\overline{\boldsymbol{F}}_{dyn} = \boldsymbol{M}_{app}\,\ddot{\overline{\boldsymbol{z}}}, \tag{7}$$

where bold letters denote arrays.
The apparent mass matrix $\boldsymbol{M}_{app}$ is usually written in the following form [3],[14]:

$$\boldsymbol{M}_{app} = \boldsymbol{M}_0 + \sum_{j=1}^{n} \boldsymbol{M}_j^{\text{eff}} \frac{1}{-1 + \left(\frac{\omega_{nj}}{\Omega}\right)^2 + 2i\zeta_j \frac{\omega_{nj}}{\Omega}}. \tag{8}$$

$\boldsymbol{M}_0$ is the rigid-body mass matrix and $\boldsymbol{M}_j^{\text{eff}}$ is the effective mass matrix associated to the jth mode.
Since $\sum_{j=1}^{n} \boldsymbol{M}_j^{\text{eff}} = \boldsymbol{M}_0$ [3], Eq. (8) becomes

$$\boldsymbol{M}_{app} = \sum_{j=1}^{n} \boldsymbol{M}_j^{\text{eff}} \left(1 + \frac{1}{-1 + \left(\frac{\omega_{nj}}{\Omega}\right)^2 + 2i\zeta_j \frac{\omega_{nj}}{\Omega}}\right). \tag{9}$$

After imposing common denominator and multiplying numerator and denominator by $(\frac{\Omega}{\omega_{nj}})^2$, Eq. (9) takes the form of Eq. (10), where the transmissibility ratio in Eq. (5) is recalled for the

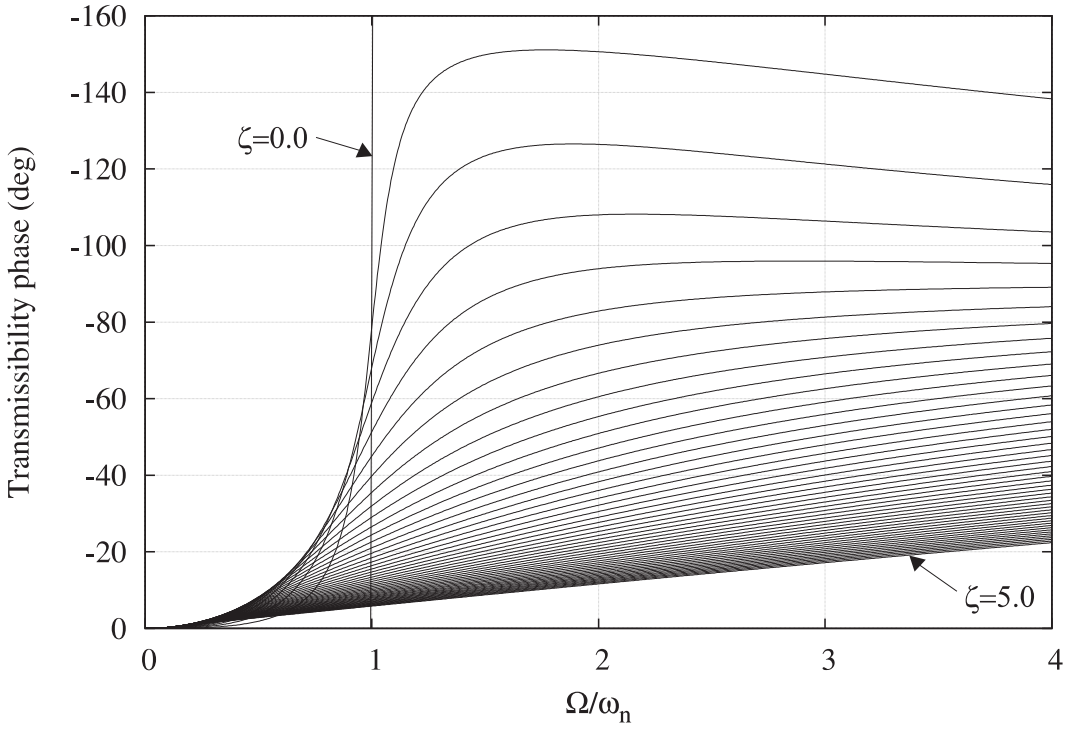


Figure 2: Transmissibility phase curves with ζ increasing from 0.0 to 1.5 with step of 0.1.

jth modal contribution.

$$\boldsymbol{M}_{app} = \sum_{j=1}^{n} \boldsymbol{M}_j^{\text{eff}} \, Tr\left(\frac{\Omega}{\omega_{nj}}\right). \tag{10}$$

The effective mass residual matrix $\boldsymbol{M}_{res}^{\text{eff}}$ could be added to $\boldsymbol{M}_{app}$. In so doing, the modal contributions with $j > n$ would be considered statically when calculating the interface forces.

4 Acceleration response of mDOF systems

Considering the base-motion excitation vector $\ddot{\overline{\boldsymbol{z}}}$, according to structural dynamics basic theory [3],[14], the displacement vector $\ddot{\overline{\boldsymbol{u}}}$ is given by Eq. (11).

$$\ddot{\overline{\boldsymbol{u}}} = \boldsymbol{\Phi}\ddot{\overline{\boldsymbol{z}}} + \sum_{j=1}^{n} \boldsymbol{\Psi}_j \frac{1}{m_{jj}} \frac{1}{-1 + \left(\frac{\omega_{nj}}{\Omega}\right)^2 + 2i\zeta_j \frac{\omega_{nj}}{\Omega}} \boldsymbol{L}_j \ddot{\overline{\boldsymbol{z}}}, \tag{11}$$

where $\boldsymbol{\Phi}$ is the rigid-body matrix, $\boldsymbol{\Psi}_j$ is the jth fixed-base eigenvector, m_{jj} is the generalized mass of the jth mode and $\boldsymbol{L}_j$ is the jth mass modal participation factor.
By assuming that the eigenvectors are mass normalized leads to $m_{jj} = 1$. Moreover, by restricting the analysis only to the translational DOFs of $\ddot{\overline{\boldsymbol{u}}}$, hereafter denoted with the subscript tr, Eq. (11) becomes

$$\ddot{\overline{\boldsymbol{u}}}_{tr} = \left(\boldsymbol{\Phi}_{tr} + \sum_{j=1}^{n} \boldsymbol{\Psi}_j \frac{1}{-1 + \left(\frac{\omega_{nj}}{\Omega}\right)^2 + 2i\zeta_j \frac{\omega_{nj}}{\Omega}} \boldsymbol{L}_j \right) \ddot{\overline{\boldsymbol{z}}}_{tr}, \tag{12}$$

where the columns of $\boldsymbol{\Phi}_{tr}$ are given by the translational rigid-body modes. A rigid-body mode corresponds to the displacement vector produced by imposing the unit value to a DOF of the

moving base and setting the remaining DOFs of the moving base to zero. It follows that the cells of $\mathbf{\Phi}_{tr}$ are unitary or null, depending on the direction. Eq. (12) can be written in the form of Eq. (13), where the transmissibility ratio of Eq. (4) is recalled for the jth modal contribution.

$$\ddot{\overline{\boldsymbol{u}}}_{tr} = \mathbf{\Phi}_{tr} + \sum_{j=1}^{n} \mathbf{\Psi}_j \left(Tr \left(\frac{\Omega}{\omega_{nj}} \right) - 1 \right) \boldsymbol{L}_j \ddot{\overline{\boldsymbol{z}}}_{tr}. \tag{13}$$

5 Numerical results

Within the space community, MSC Nastran is recognized as the commercial software of reference for the FEM mechanical analyses. The numerical results obtained for the sine test-prediction of the SC01 are considered in this section. A Matlab code has been developed by the authors. The code reads the natural frequencies, modal effective masses, eigenvectors and mass modal participation factors from the MSC Nastran F06 file. The latter file is the output file of the hard-mounted normal mode analysis of the SC, performed with the SOL 103 of MSC Nastran. The interested responses are thus calculated by processing the information read from the F06 file, according to Eqs. 10 and 13. Several assessments are proposed in Secs. 5.1 and 5.2 in order to provide a comparison between the I/F forces and local acceleration responses obtained with the SOL 111 of MSC Nastran (modal frequency response analysis) and the same responses calculated through the Matlab code. The responses of the longitudinal I/F force Tz and the lateral I/F moments Mx and My are calculated for the SC base-excitation along the x,y and z-axis. The x,y and z-DOF local acceleration responses of eight nodes (mainly located in the upper zone of the SC) are calculated too. If not differently specified, the SC base-excitation is the sinusoidal input profile of 1 [g], for each axis of excitation. In Sec. 13 an example of footprint showing which modal contributions do more significantly contribute to generate Tz is provided and discussed. In Sec. 5.4 the notching plan of SC01 obtained by using the Matlab code is illustrated. All the responses are computed by encompassing the first 300 modal contributions. The residuals are not taken into account in the calculations. The 300th natural frequency is equal to 116.3 [Hz]. The summation of the first 300 effective masses pertaining to the translational excitation and response along the z-axis leads to the 95.7 % of the SC mass. The frequency range from 0 to 100 [Hz] is considered in the plots.

5.1 I/F forces response assessment

The frequency responses of Tz, Mx and My I/F forces of SC01, respectively obtained with the excitation along the z,y and x-axis, are illustrated in the Fig. 3, where the results obtained with the Matlab code are compared with those calculated with MSC Nastran. All the I/F forces curves are plotted with the frequency step of 0.05 [Hz]. A good agreement between the two set of results is confirmed in terms of magnitude. A satisfactory agreement is obtained for the response phases at low frequencies, while some differences can be detected above 60 [Hz]. The reason of such discrepancies is not clear to the authors. Additional investigations would be required in order to verify the consistency of the methodology based on Eqs. 10 and 13 with the computational process of MSC Nastran. Since the results of the sine test-prediction are not significantly sensitive to the phase differences above discussed, the agreement between the I/F forces responses obtained with the Matlab code and those calculated with MSC Nastran is considered to be satisfactory for the purpose of this work.

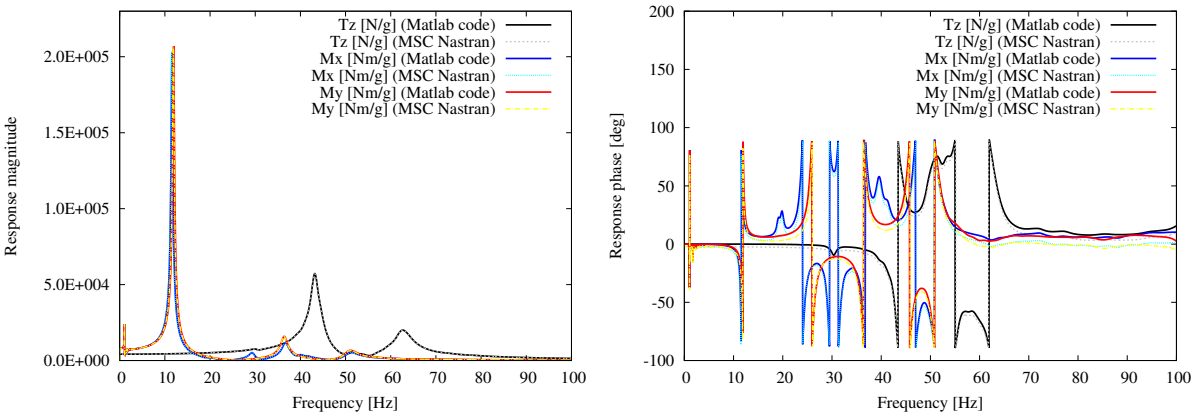


Figure 3: Frequency responses of Tz, Mx and My I/F forces of SC01: comparison of the results obtained with the Matlab code with those calculated with MSC Nastran.

5.2 Local accelerations response assessment

The local acceleration responses of the SC01 eight nodes under study are illustrated in Figs. 4-12. Figs. 4-6 show respectively the acceleration responses of the x,y and z-DOFs to the excitation along the x-axis. Figs. 7-9 and 10-12 show the same results in case of excitation along the y-axis and z-axis, respectively. The responses calculated with the Matlab code are plotted with the frequency step of 0.1 [Hz] while the responses obtained in MSC Nastran are plotted with the frequency step of 0.05 [Hz]. Figs. 4,8 and 12 show the in-axis responses (that is the responses of the DOFs which are parallel to the axis of excitation). Figs. 5,6,7,9,10 and 11 gives the cross-axis responses (that is the responses of the DOFs not parallel to the axis of excitation). If the magnitude plots are addressed, a good agreement is confirmed between between the results calculated with the Matlab code and those obtained in MSC Nastran. Differently, some discrepancies can be detected along the curves of the phase responses. Such differences can appear along all the considered frequency range. Concerning the reasons of such discrepancies, the comment made in Sec. 5.1 for the I/F forces responses is valid also in this case. Since the results of the sine test-prediction are not significantly sensitive to the phase differences above discussed, the agreement between the local accelerations responses obtained with the Matlab code and those calculated with MSC Nastran is considered to be satisfactory for the purpose of this work.

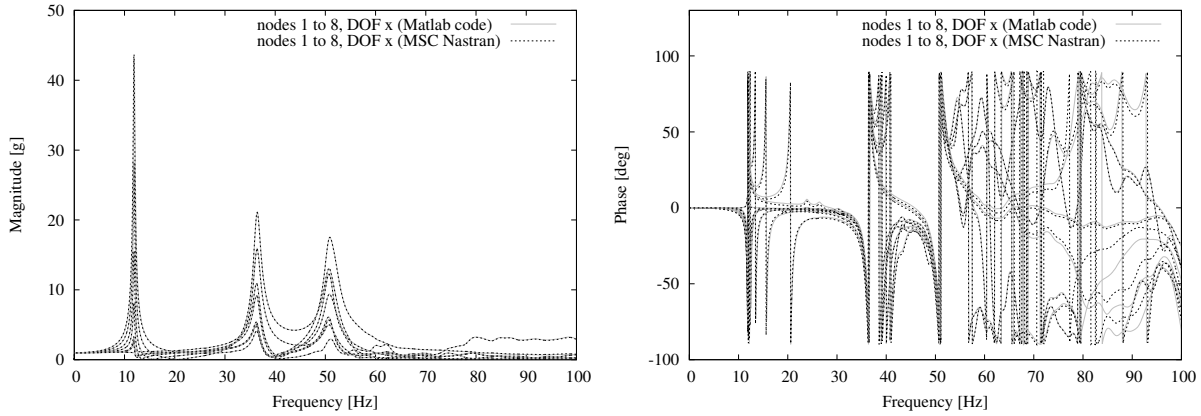


Figure 4: Frequency responses of the DOFs parallel to the x-axis to the sinusoidal enforced acceleration of 1 [g] along the x-axis.

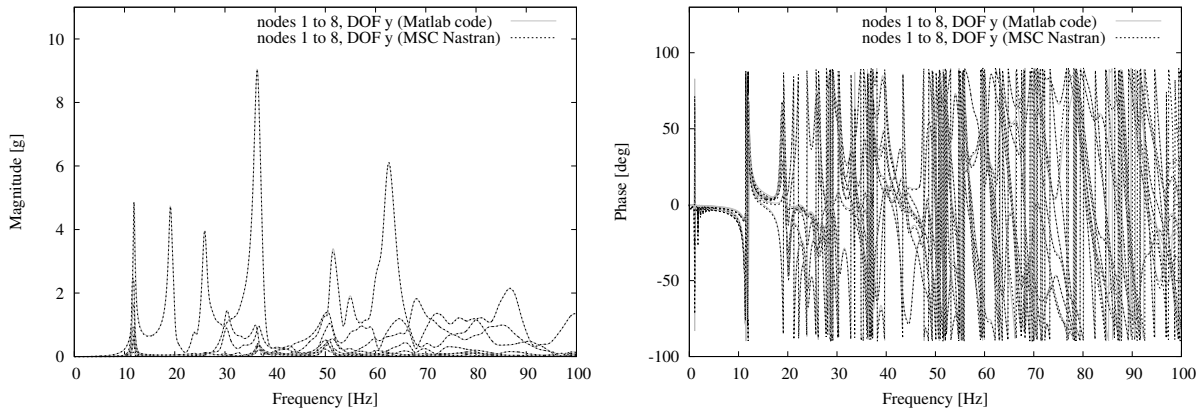


Figure 5: Frequency responses of the DOFs parallel to the y-axis to the sinusoidal enforced acceleration of 1 [g] along the x-axis.

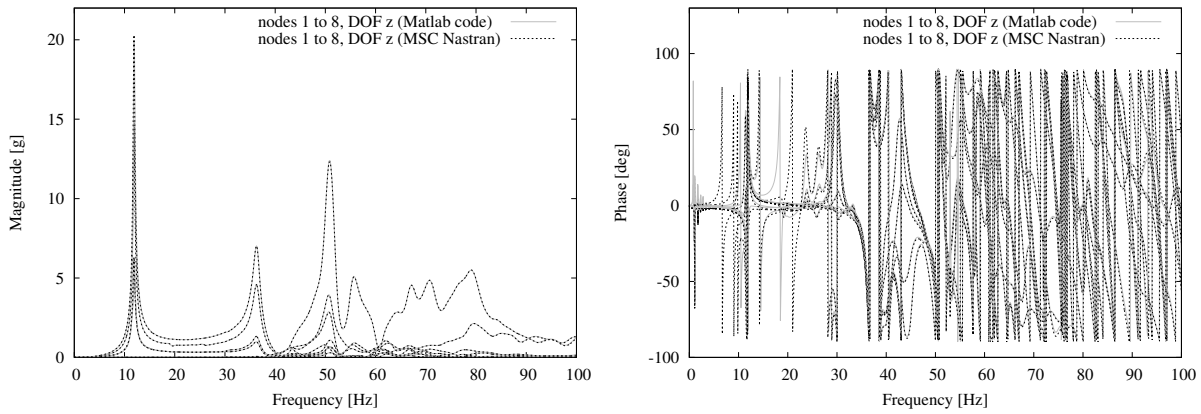


Figure 6: Frequency responses of the DOFs parallel to the z-axis to the sinusoidal enforced acceleration of 1 [g] along the x-axis.

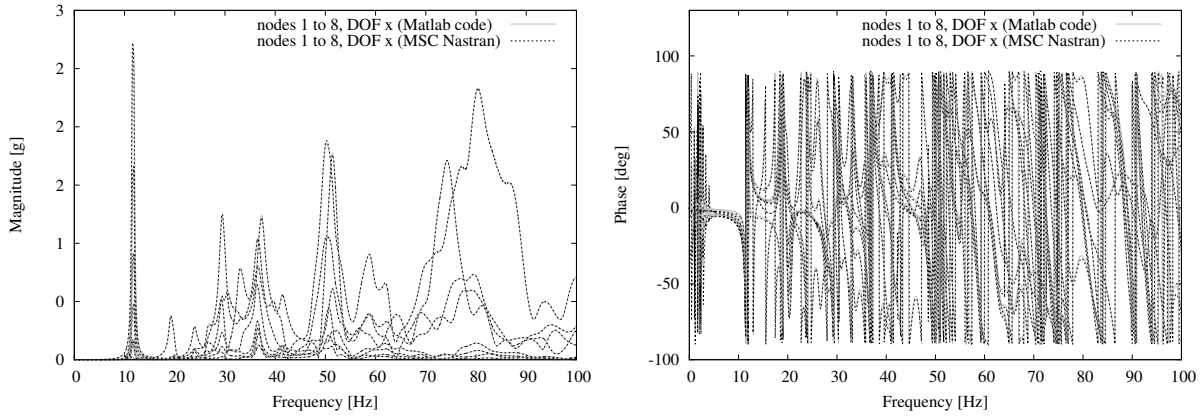


Figure 7: Frequency responses of the DOFs parallel to the x-axis to the sinusoidal enforced acceleration of 1 [g] along the y-axis.

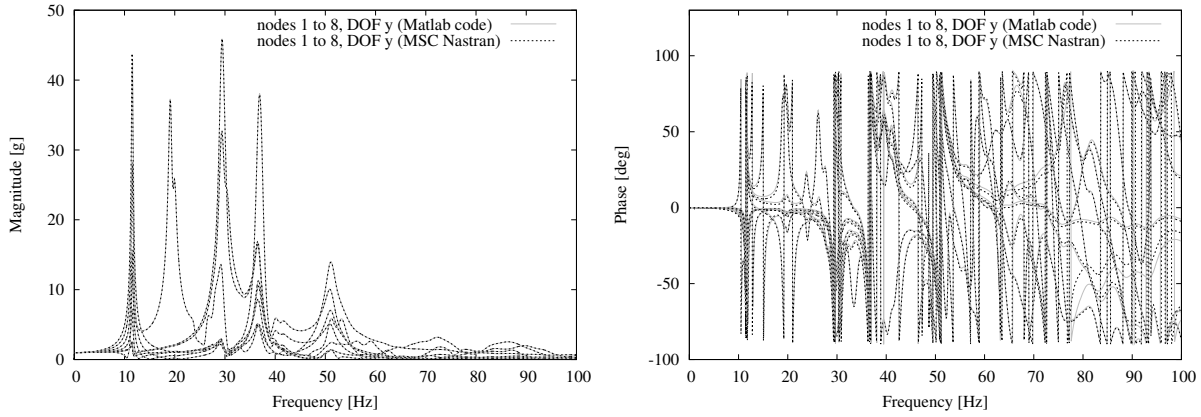


Figure 8: Frequency responses of the DOFs parallel to the y-axis to the sinusoidal enforced acceleration of 1 [g] along the y-axis.

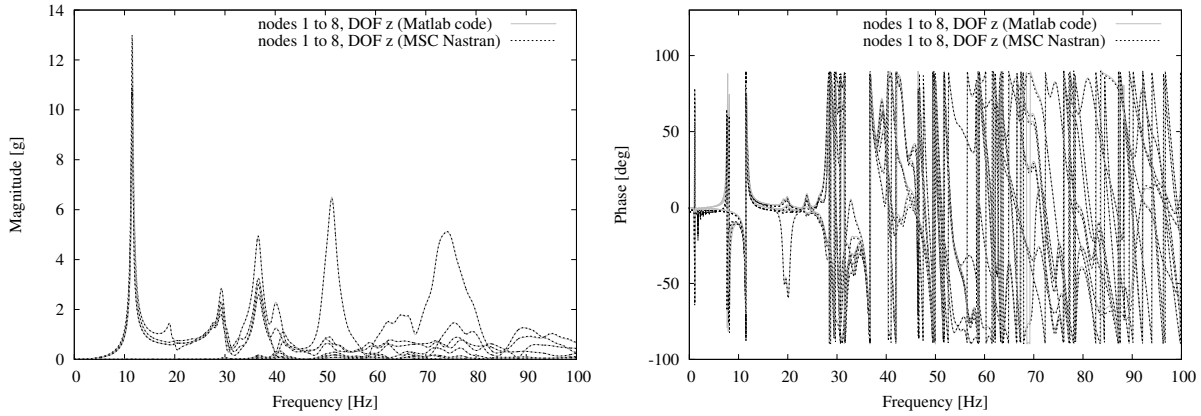


Figure 9: Frequency responses of the DOFs parallel to the z-axis to the sinusoidal enforced acceleration of 1 [g] along the y-axis.

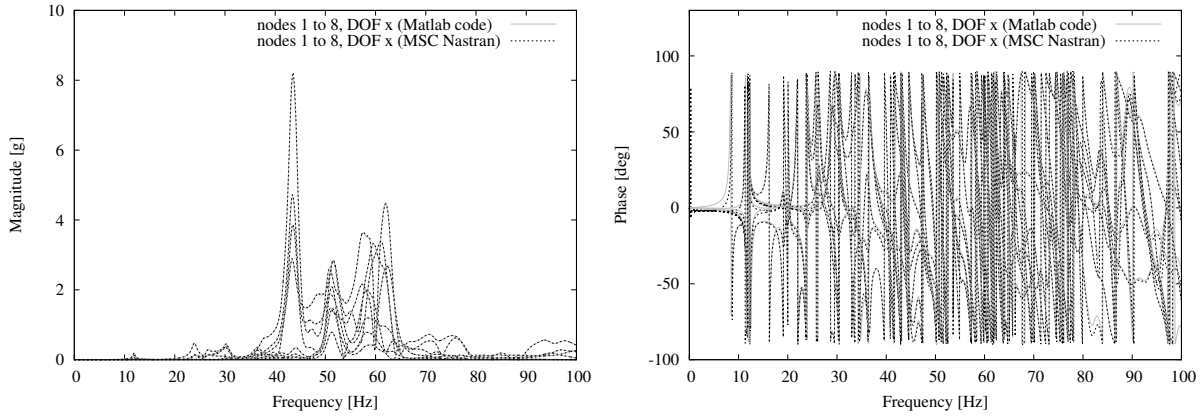


Figure 10: Frequency responses of the DOFs parallel to the x-axis to the sinusoidal enforced acceleration of 1 [g] along the z-axis.

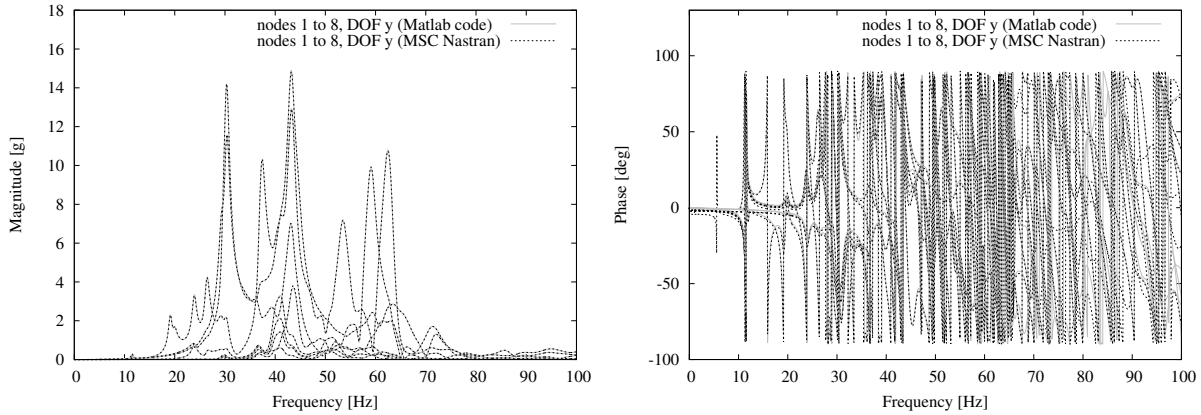


Figure 11: Frequency responses of the DOFs parallel to the y-axis to the sinusoidal enforced acceleration of 1 [g] along the z-axis.

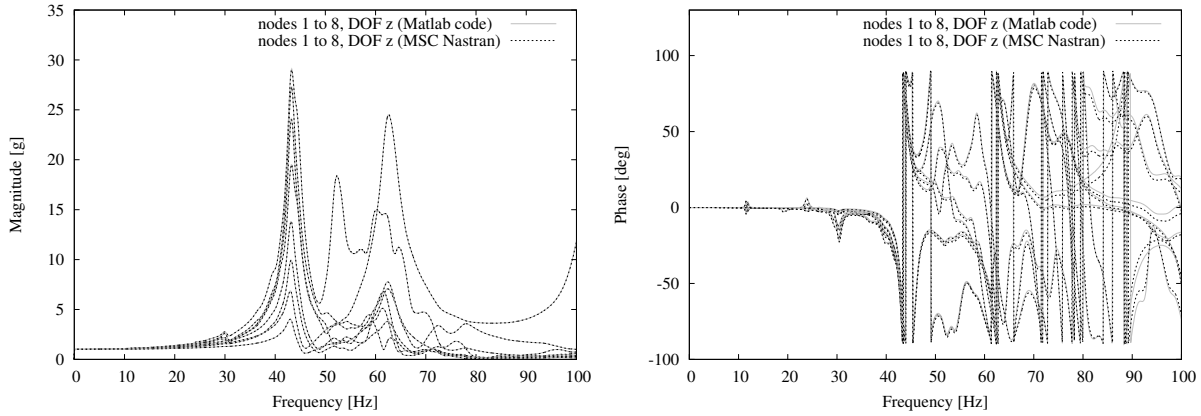


Figure 12: Frequency responses of the DOFs parallel to the z-axis to the sinusoidal enforced acceleration of 1 [g] along the z-axis.

5.3 Quantification of modal contributions vs frequencies

The Fig. 13 provides some information regarding the modal contributions whose summation leads to the Tz I/F response to the sinusoidal enforced acceleration of 1 [g] along the z-axis. Each point of the surface of Fig. 13 is given by the result of Eq. (7), when only the jth modal contribution for a particular frequency implying a specific $\frac{\Omega}{\omega_{nj}}$ ratio is considered. The surface provides a self-explaining footprint of the modes which most significantly contribute to rise the value of the Tz I/F force vs the corresponding frequency. The same kind of plot can be obtained for the remaining I/F forces/moments or the local accelerations. In the latter case, Eq. (12) should be considered and the obtained footprint would reveal the modes most significantly contributing to rise the value of the interested local acceleration response vs the corresponding frequency. It is understood that such footprints can be useful in the SC design phase, when some targeted structural design refinements might are required with the aim of reducing some I/F forces and/or local acceleration responses. A critical interpretation of those surfaces might help finding design solutions which limit/shift the responses associated to particular modal contributions. In practise this could be achieved by stiffening/softening the modes of interest or simply trying to update the design in order to modify the corresponding mode shape. A few iterations may be required before freezing the design.

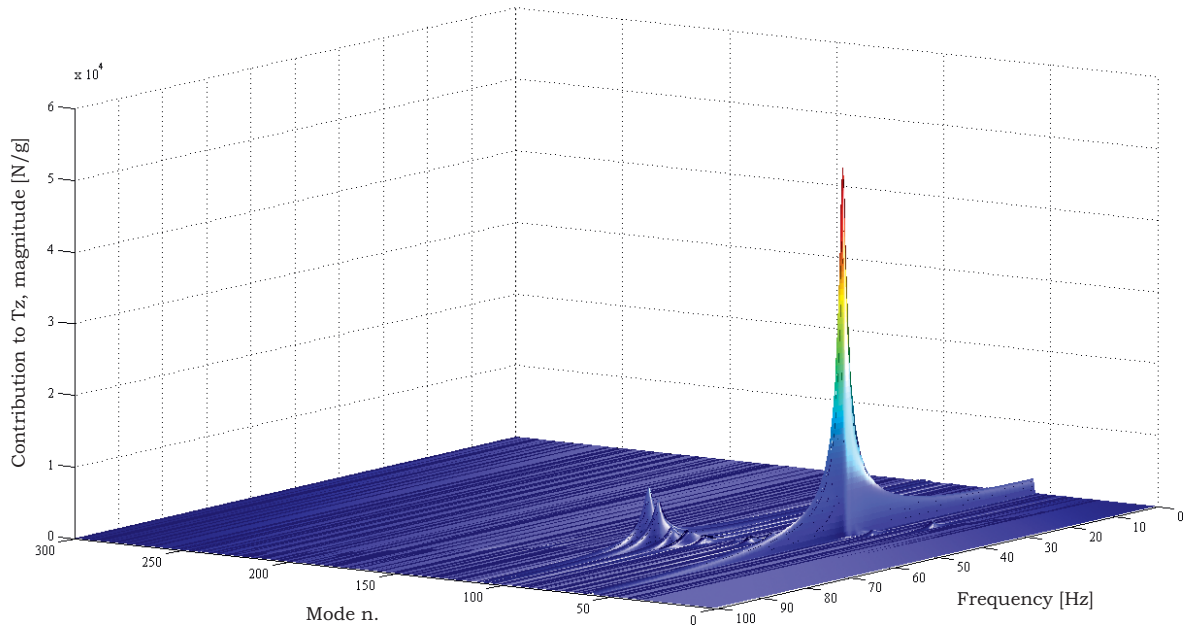


Figure 13: Surface indicating the magnitude of each modal contribution to Tz vs frequencies.

5.4 The notching plan of SC01

The sine test notching plan of SC01 is illustrated in this section for the three axis of excitation. The STVS input profile provided in the LV user manual is considered. The I/F force and local acceleration responses are calculated in accordance with the methodology proposed in this work by using the Matlab tool developed by the authors. The QSL provided in the LV user manual leads to the qualification LV/SC I/F loads. That is, the primary notching limitations are calculated for Mx, My and Tz. The secondary notching limitations are provided

by the qualification levels of the subsystems or units associated to the interested nodes. Each node and DOF representing a subsystem or unit with a secondary notching limitation should have an appropriate sensor placed in the corresponding position of the testing structure. Fig. 14 illustrates the notched input profile for the x-axis. The limitation on My gives the primary notching while the limitations on local accelerations provide the secondary notching. Only one secondary notching cross-axis limitation is present (node 1 acceleration along the z-axis). The remaining five secondary notchings are in-line limitations (along the x-axis). Fig. 15 shows the notched input profile for the y-axis. In this case the primary notching is given by Mx while no secondary notching cross-axis limitations are present, being all the eight limitations in-line (along the y-axis). Fig. 16 gives the notched input profile for the z-axis. In this case the primary notching is given by Tz and three secondary notching cross-axis limitations are present (node 3,4 and 6 acceleration along the y-axis). The remaining seven secondary notching are in-line limitations (along the z-axis).
In this specific case, concerning the SC01 qualification sine tests, a manual notching enveloping both primary and secondary notches will be defined for all the three axis of excitation in order to simplify the test control.

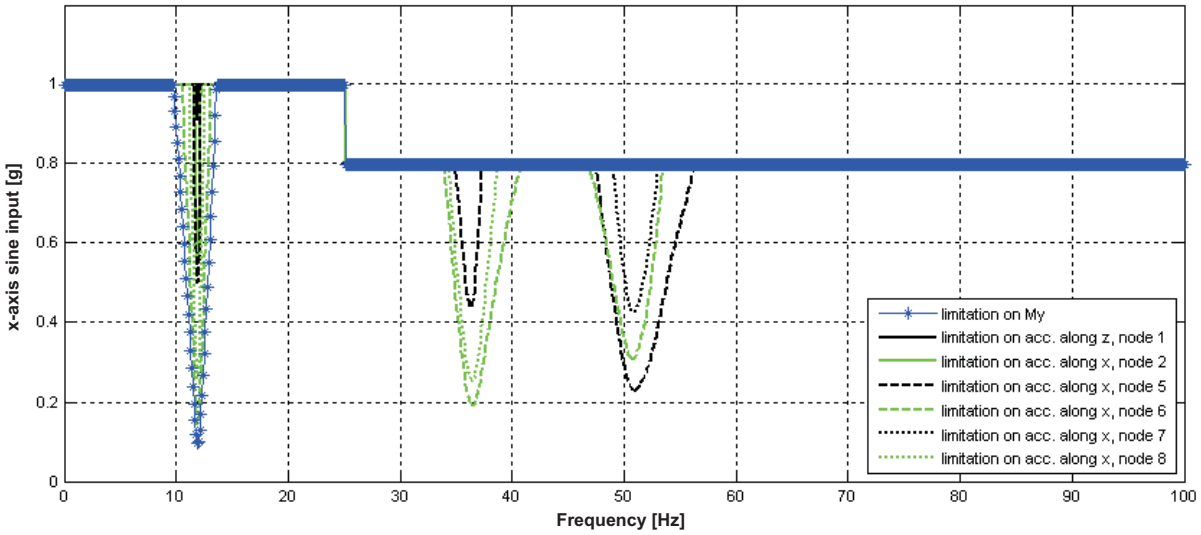


Figure 14: Primary and secondary notching profiles, x-axis.

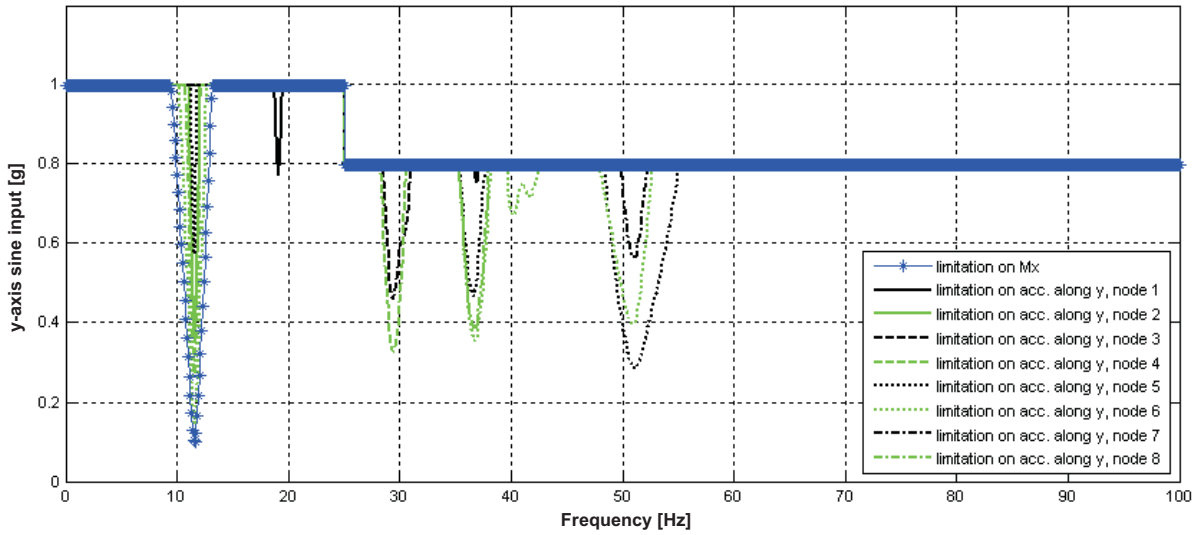


Figure 15: Primary and secondary notching profiles, y-axis.

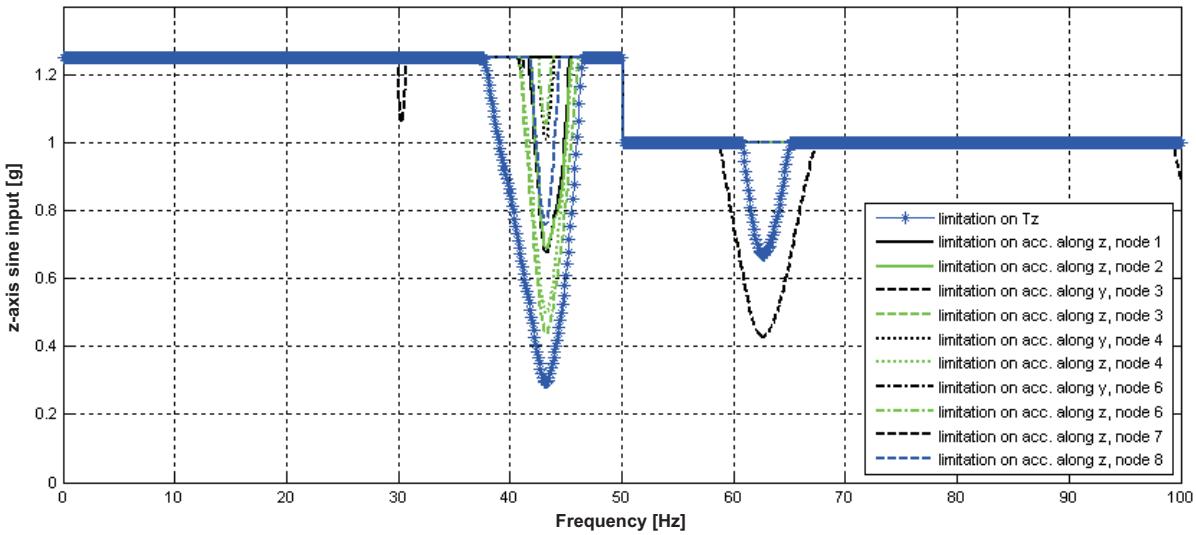


Figure 16: Primary and secondary notching profiles, z-axis.

6 Conclusions

In this work an easy-to-implement methodology useful for calculating the frequency response functions in terms of I/F forces and local accelerations of a hard-mounted structure subjected to base-shake sine tests was proposed. The assumption of no sine sweep rate effect was made. After a theoretical introduction recalling some basics concepts of structural dynamics, the equations useful for the implementation of the methodology discussed were obtained and commented. The implementation of the methodology described was made by the authors in Matlab. Several result assessments and comparisons with MSC Nastran FRA solutions were reported in order to confirm the accuracy of the Matlab code. The advantage of the approach presented in this work is that the frequency responses to the x, y and z-axis sinusoidal excitations are calculated by simply processing the output of the mode analysis. The example of SC01 sine test-prediction was studied, where the SC01 frequency responses for the three directions of excitations were calculated with the Matlab code. The file provided as input was the F06 file of the normal mode MSC Nastran analysis of the hard-mounted structure of SC01. No dedicated MSC Nastran FRA runs were thus required for performing the sine test-prediction and defining the primary and secondary notching plans. An additional advantage of the methodology proposed is that the relevance of each mode on the SC responses can be explicitly quantified both for interface forces and local accelerations. This can be particularly useful in the SC design phase, when some targeted structural design refinements might be required in order to reduce some I/F forces and/or local acceleration responses.

REFERENCES

[1] C. Lalanne, *Mechanical vibration & shock analysis, Vol 1: Sinusoidal Vibrations, 2nd Edition*. John Wiley & Sons, 2009.

[2] A Girard and N. Roy, *Structural dynamics in industry*. ISTE Ltd and John Wiley & Sons, ISBN: 978-1-84821-004-2, 2008.

[3] J. Wijker, *Mechanical vibrations in spacecraft Design*. Springer, 2004.

[4] *Rockot User's Guide*. Issue 05, August 2011.

[5] *Ariane 5 Users Manual*. Issue 05 Revision 1, July 2011.

[6] *Spacecraft mechanical loads analysis handbook*. ECSS-E-HB-32-26A, 2013.

[7] Y. Soucy and A Côté, Reduction of overtesting during vibration tests of space hardware. *Canadian Aeronautics and Space Journal*, Vol. 48, No 1, March 2002.

[8] P. Nali and A. Calvi, An investigation on the spacecraft design loads cycles and sine vibration test. *TEC-MCS/2006/1362/ln/AC, ESA*, Noordwijk, The Netherlands, March 2006.

[9] A. Calvi and P. Nali, Some remarks on the reduction of overtesting during base-drive sine vibration tests of spacecraft. *ECCOMAS Conf. on Computational Methods in Structural Dynamics and Earthquake Engineering*, Rethymno, Crete, Greece, June 2007.

[10] O.C. Zienkiewicz and R.C. Taylor, *The finite element method, Vol. 1, 4th Edition*. McGraw Hill, 1989.

[11] J. A. Lollock, The effect of a swept sinusoidal excitation on the response of a single-degree-of-freedom oscillator. *43rd AIAA Structures, Structural Dynamics, and Materials Conference*, Denver, Colorado, 22-25 March, 2002.

[12] N. Roy and A. Girard, Revisiting the effect of sine sweep rate on modal identification. *European Conference on Spacecraft Structures, Materials and Environmental Testing*, Noordwijk, The Netherlands, 20-23 March, 2012.

[13] R.R. Craig, *Structural dynamics, an introduction to computer methods*. John Wiley & Sons, 1981.

[14] R. Sedaghati, Y. Soucy and N. Etienne, Efficient estimation of effective mass for complex structures under base excitations. *Canadian Aeronautics and Space Journal*, 49(3):135–143, 2003.

COMPDYN 2013
4th ECCOMAS Thematic Conference on
Computational Methods in Structural Dynamics and Earthquake Engineering
M. Papadrakakis, V. Papadopoulos, V. Plevris (eds.)
Kos Island, Greece, 12–14 June 2013

GRADIENT-BASED STUDY ON SEISMIC PERFORMANCE REDUCTION OF STEEL BRACED FRAMES DUE TO IRREGULAR BRACE OVER-STRENGTH DISTRIBUTIONS

Andrea Dall'Asta[1], Alessandro Zona[1] and Laura Ragni[2]

[1] School of Architecture and Design, University of Camerino
Viale della Rimembranza, Ascoli Piceno, 63100 Italy
andrea.dallasta@unicam.it , alessandro.zona@unicam.it

[2] Department of Civil and Building Engineering and Architecture, Marche Polytechnic University
Via Brecce Bianche, Ancona, 60131 Italy
laura.ragni@univpm.it

Keywords: Braced Frames, Buckling-Retrained Braces, Dissipative Braces, Gradient Methods, Sensitivity Analysis, Steel Frames.

Abstract. *In this paper a general sensitivity-based gradient methodology developed to investigate the relation between seismic performance reduction and regularity of brace over-strength distributions is used for performance-based design and assessment of braced steel frames. A range of variation of the brace over-strength is defined and the brace over-strength patterns that are the most unfavorable for each response parameter are identified. Then, the relationship between the brace over-strength used in the seismic design and the maximum seismic performance reduction is obtained. Results for a case study considering a realistic buckling-restrained braced frame are presented and discussed showing the practical use of the developed sensitivity-based gradient methodology.*

1 INTRODUCTION

Seismic design of structures and relevant codes of practice are often based on the reduction factor method. The success of this approach is undoubtedly due to its simplicity as it permits approaching the seismic problem by a linear structural analysis, even though some drawbacks in its application have been highlighted, especially in the retrofit of existing structures. The reduction factor method aims at establishing a relation between the linear elastic behaviour of a structure and its ultimate post-elastic capacity under seismic actions, assuming that all necessary provisions are taken to provide a pre-defined yielding path in the structure (global ductility) and to ensure a sufficient ductility of critical yielded zones (local ductility). While it is possible to control the local ductility by means of specific design and detailing provisions, it is usually more difficult to ensure the desired global ductility that is influenced by two main issues. The first issue concerns the ratio between the seismic demand and the strength capacity in the yielding portions of the structure, such a ratio should be as uniform as possible in order to attain yielding in all the expected yielding parts. The second issue concerns the structural elements that must remain elastic, target commonly accomplished by making these elements more resistant than the yielding elements. The former issue is a quite critical point in the practical applications of the reduction factor design procedure, as it is often very difficult to obtain a satisfactory uniformity in the design of real structures and irregularity has significant negative effects on the seismic performance, in particular for low redundant structures. Steel braced frames are very sensitive to this problem and all the most diffused typologies show a significant tendency to soft story formation during seismic events in consequence of a not regular distribution of over-strength in bracings, as shown for concentrically braced frames (CBFs), e.g. [1][2][3], eccentrically braced frames (EBFs), e.g. [4][5], and more recently buckling-restrained braced frames (BRBFs), e.g. [7][8][9][10]. This significant influence is mainly due to the low redundancy of these systems and becomes particularly high when the frames coupled with the bracings are very deformable, as in the case of pinned beam-column connections. Overall, the studies available in the technical literature delineate the need to further examine the influence of the brace over-strength on the structural seismic performance as well as the effectiveness of current code recommendations.

This study aims at establishing a rational and consistent relation between the global reduction factor and the over-strength regularity, completing the approach presented in [11] with information that can be directly applied in performance-based engineering. This should be a first step towards a more safe use of this popular design method and towards the definition of new rules capable to overcome some drawbacks of current provisions that are often difficult to be applied in practice or may be ineffective and lead to excessively expensive solutions. The first objective of this paper consists of defining a general methodology to investigate the relation between seismic reduction factor and over-strength distributions. The method is based on sensitivity analysis of dynamic response and linearization of functional operators. A specific formulation to study the influence of brace over-strength distributions on the reduction factor of steel braced structures is presented, including the random nature of the seismic input. The actual nonlinear variations of specific demand measures of interest in seismic response, i.e., engineering demand parameters (EDPs), as well as their linearly approximated variations, are derived. A second objective, more practically oriented, concerns the definition of the maximum expected decrement of the reduction factor within an accepted range of variability in the over-strength coefficients. To this extent, it is assumed an over-strength domain as suggested by Eurocode 8 (hyper-cube) and the most unfavourable patterns are identified together with the corresponding decrement of the reduction factor. The solution is determined by constrained optimization tools supported by the problem gradient defined in the sensitivity analy-

sis. Selected results for a BRBF used as case study are presented and discussed in order to illustrate the practical application of the proposed methodology.

2 RELATION BETWEEN SEISMIC PERFORMANCE AND BRACE OVERSTRENGTH DISTRIBUTIONS: METHODOLOGY

2.1 Seismic demand sensitivity analysis of nonlinear structures

It is assumed that the motion of the structural system is described by the following differential equations and relevant initial conditions:

$$\dot{\boldsymbol{\chi}}(\boldsymbol{\theta};t) = \mathbf{a}(\boldsymbol{\chi}(\boldsymbol{\theta};t),\boldsymbol{\theta}) + \mathbf{p}(t) \qquad \boldsymbol{\chi}(\boldsymbol{\theta};0) = 0 \tag{1}$$

where $\boldsymbol{\theta} \in \Re^m$ is a vector collecting m parameters defining material and geometric properties of the structural system, $\boldsymbol{\chi} : \Re^m \times [0,T] \mapsto \Re^s$ is a vector-valued function describing the evolution of the s state variables, e.g., displacement, velocity and state variables of history-dependent constitutive material models, $t \in [0,T]$ is the time and T the duration of the dynamic analysis, a superposed dot represents one derivative with respect to time, $\mathbf{p} : [0,T] \mapsto \Re^s$ is a function describing the seismic input, $\mathbf{a} : \Re^m \times \Re^s \mapsto \Re^s$ a vector-valued nonlinear function describing the response of the structure. It is assumed that **a** and **p** are continuous functions and that **a** is not an explicit function of time. Given a reference motion $\boldsymbol{\chi}_0 : [0,T] \mapsto \Re^s$ corresponding to assigned values of the material and geometric parameters collected in $\boldsymbol{\theta}_0$, the variation of the motion in consequence of a variation $\hat{\boldsymbol{\theta}}$ of the parameters can be linearized in the neighbourhood of the reference motion, i.e., for $\|\hat{\boldsymbol{\theta}}\| \to 0$, by means of the following series expansion:

$$\boldsymbol{\chi}(\boldsymbol{\theta}_0 + \hat{\boldsymbol{\theta}};t) = \boldsymbol{\chi}_0(t) + \mathbf{S}_0(t)\hat{\boldsymbol{\theta}} + \mathrm{o}(\|\hat{\boldsymbol{\theta}}\|) \quad \forall t \in [0,T] \tag{2}$$

where $\mathbf{S}_0 : [0,T] \mapsto \Re^s \times \Re^m$ is the sensitivity matrix at $\boldsymbol{\chi}_0$ defined by the condition

$$\mathbf{S}_0(t)\mathbf{e} = \lim_{\lambda \to 0} \frac{\boldsymbol{\chi}(\boldsymbol{\theta}_0 + \lambda\mathbf{e};t) - \boldsymbol{\chi}_0(t)}{\lambda} \quad \forall \mathbf{e} : \|\mathbf{e}\| = 1 \tag{3}$$

and whose components $S_{0ij}(t) = \partial\chi_i(\boldsymbol{\theta};t)/\partial\theta_j\big|_{\boldsymbol{\theta}=\boldsymbol{\theta}_0}$ describe the ratio between the variation of the i-th component $\chi_i(t)$ of $\boldsymbol{\chi}$ due to the variation of the j-th component θ_j of $\boldsymbol{\theta}$ when $\boldsymbol{\theta} = \boldsymbol{\theta}_0$ and at the considered time instant t, o( ) is the "little-o" Landau symbol, i.e. given a function $f(x)$ and a positive function $\phi(x)$, then $f = \mathrm{o}(\phi)$ means that $f/\phi \to 0$. Similarly, the response of the perturbed structural system in the neighbourhood of the reference motion $\boldsymbol{\chi}_0$ may be written as (time dependence omitted for the sake of brevity):

$$\mathbf{a}(\boldsymbol{\chi}(\boldsymbol{\theta}_0 + \hat{\boldsymbol{\theta}}), \boldsymbol{\theta}_0 + \hat{\boldsymbol{\theta}}) = \mathbf{a}\big|_0 + \nabla_{\chi}\mathbf{a}\big|_0 \mathbf{S}_0\hat{\boldsymbol{\theta}} + \nabla_{\vartheta}\mathbf{a}\big|_0 \hat{\boldsymbol{\theta}} + \mathrm{o}(\|\hat{\boldsymbol{\theta}}\|) \quad \forall \mathbf{e} : \|\mathbf{e}\| = 1 \tag{4}$$

where the symbol $\big|_0$ attached after a function means that that function is evaluated at the reference motion $\boldsymbol{\chi}_0$ corresponding to $\boldsymbol{\theta} = \boldsymbol{\theta}_0$. The sensitivity matrix can be deduced from the differential equation:

$$\dot{\mathbf{S}}_0 = \nabla_{\boldsymbol{\chi}}\mathbf{a}\big|_0 \mathbf{S}_0 + \nabla_{\vartheta}\mathbf{a}\big|_0 \tag{5}$$

obtained differentiating Equation (2) with respect to time, using Equation (1) and then comparing the result to Equation (4). Equation (5) is solved and $\mathbf{S}_0$ determined, the motion variation $\hat{\boldsymbol{\chi}}$ directly and linearly related to the small variations $\hat{\boldsymbol{\theta}}$ of the structural parameters:

$$\hat{\boldsymbol{\chi}} \cong \mathbf{S}_0 \hat{\boldsymbol{\theta}} \tag{6}$$

Commonly, in seismic analysis the structural performance is evaluated by one or more EDPs. An EDP is a positive scalar d giving a measure of the structural damage occurring during the motion produced by the earthquake and it is a derived quantity of $\boldsymbol{\chi}$:

$$d = \mathsf{D}(\boldsymbol{\chi}) \tag{7}$$

where $\mathsf{D}: U_{\boldsymbol{\chi}} \to \Re$ is a functional operator acting on the space of motions $U_{\boldsymbol{\chi}}$. Consequently, the previous sensitivity analysis must be extended to evaluate the EDP variations $\hat{d}$ due to the small variations $\hat{\boldsymbol{\theta}}$ of the model parameters through the difference:

$$\hat{d} = \mathsf{D}\left(\boldsymbol{\chi}_0 + \mathbf{S}_0 \hat{\boldsymbol{\theta}}\right) - \mathsf{D}(\boldsymbol{\chi}_0) \tag{8}$$

The relationship between d and the motion $\boldsymbol{\chi}$ is usually nonlinear. Coherently with the sensitivity approach, oriented to investigate the neighbourhood of the reference motion, the relationship between d and $\boldsymbol{\chi}$ may be linearized:

$$\hat{d} = \mathsf{L}_0 \mathbf{S}_0 \hat{\boldsymbol{\theta}} + \mathrm{o}\left(\left\|\hat{\boldsymbol{\theta}}\right\|\right) \tag{9}$$

introducing the operator L_0 defined as the derivative of D:

$$\mathsf{L}_0 \hat{\boldsymbol{\chi}} = \lim_{\lambda \to 0} \frac{\mathsf{D}(\boldsymbol{\chi}_0 + \lambda \mathbf{c}) - \mathsf{D}(\boldsymbol{\chi}_0)}{\lambda} \qquad \forall \mathbf{c} : \|\mathbf{c}\| = 1 \tag{10}$$

In this way a complete overview of the effects on the seismic demand due to any combination of the variations of the structural parameters $\boldsymbol{\theta}$ is obtained. This is a qualitative and quantitative information that is quite important in understanding the structural behaviour as well as in studying the propagation of uncertainties of $\boldsymbol{\theta}$ to the structural response. In addition, structural design requires precise information on the entity of seismic performance reduction, measured by the EDPs, due to possible deviations from the reference design solution. It is thus crucial for the sake of safety: (i) to establish the range of the potential deviations from the design solution, and (ii) to assess the largest performance reduction to be expected within the set of admissible deviations. To this end, it is essential to complete the sensitivity analysis with a constrained extreme problem where the EDP is the objective function:

$$\begin{aligned} &\mathsf{D}\left(\boldsymbol{\chi}_0 + \mathbf{S}_0 \hat{\boldsymbol{\theta}}^*\right) - \mathsf{D}(\boldsymbol{\chi}_0) = \max \\ &\mathbf{g}\left(\hat{\boldsymbol{\theta}}^*\right) \geq \mathbf{0} \\ &\mathbf{n}\left(\hat{\boldsymbol{\theta}}^*\right) \leq \mathbf{0} \end{aligned} \tag{11}$$

and $\hat{\boldsymbol{\theta}}^*$ is the most dangerous variation of $\boldsymbol{\theta}$ which must be found within the set defined by the constraints $\mathbf{g}$ and $\mathbf{n}$. Clearly, the problem solution becomes simpler when both the EDP expression and the constraint equations are linear.

The formulation presented above assumes a deterministic seismic input **p** while it is well-known that the seismic input is affected by an high level of randomness that cannot be neglected in the design. Various code provisions, e.g., Eurocode 8, suggest the description of the seismic input uncertainty with the use of response results averaged over the response results obtained from a sufficiently large number of accelerograms. According to this approach, the EDPs variations is evaluated by a mean sensitivity function $\mathbf{S}_0$ obtained from the analyses performed using an adequately large set of accelerograms. Different and more advanced treatments of the seismic input randomness are beyond the objectives of this study.

The seismic response analysis of nonlinear structures is commonly performed through the finite element (FE) method where the structure motion is reduced to the time histories of a set of discrete variables, i.e., the generalized displacements and velocities of the nodes of the FE model and the required state variables of the inelastic material models. The computation of the response sensitivities within the FE framework has been investigated in the past and several methods are available, such as the Direct Differentiation Method (DDM) and the Finite Difference Method (FDM) [12][13][14].

2.2 Sensitivity of seismic capacity and seismic reduction factor

Let $\mathbf{p}_0(t)$ be a reference seismic input, $\alpha \in \Re$ a multiplying factor, and the dynamic problem be posed in the form:

$$\dot{\boldsymbol{\chi}} = \mathbf{a}(\boldsymbol{\chi}, \boldsymbol{\theta}) + \alpha \mathbf{p}_0(t) \tag{12}$$

The value $\alpha_0(\boldsymbol{\theta}_0)$ corresponds to the multiplier providing the maximum value of acceptable damage d_0 and can be interpreted as a measure of the seismic capacity of the structural system for the assigned values $\boldsymbol{\theta}_0$ of the system parameters.

It is also assumed that the dynamic system shows a linear elastic behaviour for motions sufficiently small to produce a damage measure smaller than d_y. In other words, if $\boldsymbol{\chi}$ is such that $\mathsf{D}(\boldsymbol{\chi}) \le d_y$ then a linear operator $\mathbf{A}(\boldsymbol{\theta}_0)$ such that $\mathbf{a}(\boldsymbol{\chi}, \boldsymbol{\theta}_0) = \mathbf{A}(\boldsymbol{\theta}_0)\boldsymbol{\chi}$, exists. The attention is now focused on two particular values of the multiplying parameter: the value $\alpha_y(\boldsymbol{\theta}_0)$ providing the damage value d_y bounding the system linear range, and the smallest value $\alpha_0(\boldsymbol{\theta}_0)$ providing the maximum value d_0 acceptable for the damage.

The seismic reduction factor is defined as the following ratio

$$R_0 = \frac{\alpha_0(\boldsymbol{\theta}_0)}{\alpha_y(\boldsymbol{\theta}_0)} \tag{13}$$

The nonlinear problem at the ultimate condition

$$\dot{\boldsymbol{\chi}}_0 = \mathbf{a}(\boldsymbol{\chi}_0, \boldsymbol{\theta}_0) + \alpha_0 \mathbf{p}_0 \tag{14}$$

is the reference solution of the sensitivity analysis and its behavior in the neighborhood of the solution $\boldsymbol{\chi}_0$ were already studied in the previous section. By a little change in this perspective, the perturbed (linear) motion $\boldsymbol{\chi}_0 + \bar{\boldsymbol{\chi}}$ deriving both from small variations of system parameters $\bar{\boldsymbol{\theta}}$ and a small variation of the input scaling factor $\bar{\alpha}$ has the expression

$$\dot{\boldsymbol{\chi}}_0 + \dot{\bar{\boldsymbol{\chi}}} = \mathbf{a}_0 + \nabla_{\chi}\mathbf{a}\big|_0 \bar{\boldsymbol{\chi}} + \nabla_{\vartheta}\mathbf{a}\big|_0 \bar{\boldsymbol{\theta}} + (\alpha_0 + \bar{\alpha})\mathbf{p}_0 \tag{15}$$

that can be simplified as

$$\dot{\overline{\boldsymbol{\chi}}} - \nabla_{\chi}\mathbf{a}\big|_0 \overline{\boldsymbol{\chi}} \cong \nabla_{\vartheta}\mathbf{a}\big|_0 \overline{\boldsymbol{\theta}} + \overline{\alpha}\mathbf{p}_0 \tag{16}$$

The solution $\overline{\boldsymbol{\chi}}$ of the linear problem is the sum of a contribution due to parameter variations and a contribution due to data variation. The former one may be denoted as $\overline{\boldsymbol{\chi}}^*$ and it is the result of the sensitivity analysis. In particular, the perturbation directly due to the worst parameter variation $\hat{\boldsymbol{\theta}}^*$, previously defined, is

$$\overline{\boldsymbol{\chi}}^* = \mathbf{S}_0 \hat{\boldsymbol{\theta}}^* \tag{17}$$

The latter contribution, denoted as $\overline{\alpha\boldsymbol{\chi}}_p$, can be expressed as the product of the scaling factor $\overline{\alpha}$ and the solution of the linear problem

$$\dot{\overline{\boldsymbol{\chi}}}_p - \nabla_{\chi}\mathbf{a}\big|_0 \overline{\boldsymbol{\chi}}_p = \mathbf{p}_0 \tag{18}$$

Within a linear approximation, $\overline{\boldsymbol{\chi}} = \overline{\boldsymbol{\chi}}^* + \overline{\alpha\boldsymbol{\chi}}_p$ describes the relation between motion variation and seismic intensity, when the variation of the parameters is the worst one. Also for what concerns the damage, the linearization results of the previous section, Equation (9), can be used to evaluate the change close to the reference solution

$$\hat{d} \cong \mathbf{L}_0 \overline{\boldsymbol{\chi}}^* + \overline{\alpha}\mathbf{L}_0 \overline{\boldsymbol{\chi}}_p \tag{19}$$

so that it is possible to found the seismic intensity variation providing the ultimate value of damage d_0 in the parameter-varied system, simply by posing a null damage in Equation (19). This leads to

$$\overline{\alpha}\left(\hat{\boldsymbol{\theta}}^*\right) \cong -\frac{\mathbf{L}_0 \mathbf{S}_0 \hat{\boldsymbol{\theta}}^*}{\mathbf{L}_0 \overline{\boldsymbol{\chi}}_p} \tag{20}$$

that is usually a negative value expressing a reduction of the seismic capacity performance.

A new reduction factor can consequently be determined for the varied parameters, by evaluating the elastic limit $\alpha_y\left(\boldsymbol{\theta}_0 + \hat{\boldsymbol{\theta}}^*\right)$ corresponding to the linear operator $\mathbf{A}\left(\boldsymbol{\theta}_0 + \hat{\boldsymbol{\theta}}^*\right)$; the variation in the reduction factor has the form

$$\hat{R} \cong \frac{\alpha_0(\boldsymbol{\theta}_0) + \overline{\alpha}\left(\hat{\boldsymbol{\theta}}^*\right)}{\alpha_y\left(\boldsymbol{\theta}_0 + \hat{\boldsymbol{\theta}}^*\right)} - R_0 \,. \tag{21}$$

3 APPLICATION EXAMPLE

3.1 Geometry and data

A realistic 4-storey steel frame is considered as case study structure. Interstorey height h = 3.4 m is constant between adjacent floors; columns are continuous with pinned beam-to-column connections and hinge restraints at the base. Four V-bracing systems (BRBs) for each direction are the only seismic resistant components (Figure 1a), their preliminary design was based on the procedure described in [15]. Masses from vertical live and superimposed dead loads are 1200 kNs^2/m for each floor. The yield length of BRBs (L_y) is one third of the overall length (L_d) of diagonal braces (Figure 1b). The design yield stress of the BRBs is 275 MPa, columns and beams are made of steel with design yield stress equal to 355 MPa. Seismic de-

sign was based on spectrum type 1 of Eurocode 8 for ground type B with design ground acceleration $a_g = 0.35g$). A simplified model was used to reduce the dimensions of the finite element model (Figure 1b). Details on geometric properties are reported in Table 1 while additional data not given here can be found in [11].

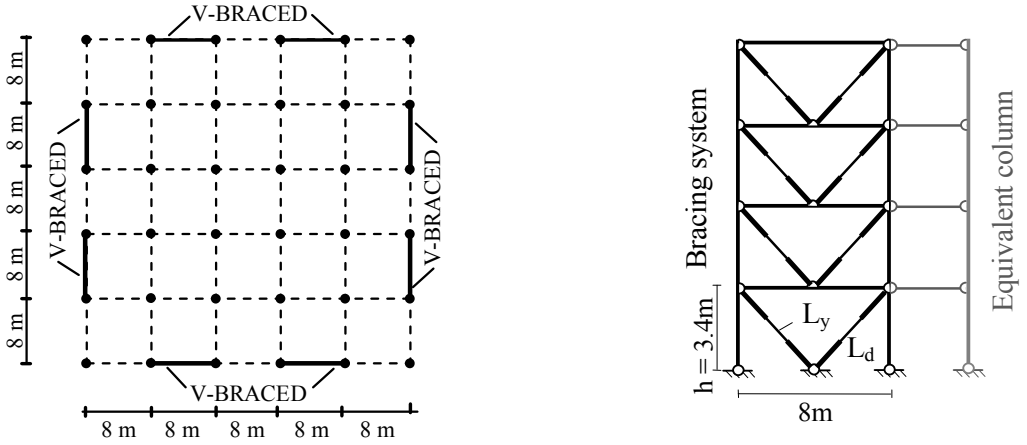


Figure 1: Case study: (a) floor configuration with arrangement of bracing system; (b) simplified planar model of the bracing system (bracing system and equivalent column).

Storey #	Bracing system columns		BRBs	Equivalent column	
	Area (cm^2)	Inertia (cm^4)	Area (cm^2)	Area (cm^2)	Inertia (cm^4)
4	58	4099.3	15.55	406	17637.3
3	101	12733.4	24.47	587	29457.9
2	141	35151.8	30.44	787	70325.6
1	192	45760.0	35.17	1069	91876.7

Table 1: Case study: geometric data of the 4-storey bracing system and equivalent column.

Beams and columns were modelled using geometric nonlinear (moderate rotations theory) Euler-Bernoulli frame FEs with linear elastic steel (elastic modulus E = 210 GPa). The BRBs were modelled with truss elements having rigid links to represent the unrestrained non yielding segments in 2/3 of the brace total length. An elastoplastic constitutive model based on a simple rheological scheme, specifically developed for steel BRBs [16], was used in this study for the yielding segments of trusses representing the BRBs. Such BRB model has only one internal variable, i.e., plastic strain, and was formulated in order to replicate the experimental behaviour (isotropic hardening and tension-compression asymmetry), as well as to include some highly desired requirements (explicit computation of the plastic component of the deformation as required in BRB capacity models, smoothness of the elastic-to-plastic transition to improve convergence rate, limited number of parameters to facilitate its implementation and use in response sensitivity analysis). In addition to the damping provided by the dissipative elastoplastic braces, a global damping for the structure was included using the Rayleigh model, with the damping matrix proportional to the mass matrix and updated stiffness matrix, and 5% of the critical damping assigned to the first and second vibration modes. The constant average acceleration method with constant time step $\Delta t = 0.01$ s, in conjunction to the Newton-Raphson iterative procedure, was used in all the dynamic analyses performed.

3.2 Seismic response results

The behaviour of the case study was studied through time history analyses having as seismic input 28 natural ground motions selected from the PEER strong motion database and scaled so that the elastic response spectra for the records matched the Eurocode 8 elastic spectrum at the first natural period $T_1 = 0.746$ s. More details on the selected ground motions can be found in [11]. Incremental dynamic analyses (IDA) were performed to assess the performance of the bracing systems. The multiplier of the scaled selected ground motions leading to a maximum interstorey drift, averaged over the 28 ground motions, equal to the design value (1% of the story height) is 0.94 corresponding to the elastic spectrum with $a_g = 0.33g$. This acceleration is very close to the design one, notwithstanding the record to record variability, the possible concentration of inelastic deformation at some story levels, and the effects of the geometric nonlinearity included in the FE model. Response results, i.e., interstorey drifts and BRB cumulative ductility at each story are reported in Table 2 in terms of mean values (averaged over the 28 ground motions) and coefficients of variations (COVs) of the absolute peak values. For each nonlinear time history analysis it was verified that beams and columns remained within their elastic range.

	Interstorey drift		BRB cumulative ductility	
Storey #	Mean	COV	Mean	COV
4	0.78%	22.18%	66.23	47.34%
3	0.69%	23.25%	50.10	37.47%
2	0.88%	35.18%	59.15	41.59%
1	0.99%	35.22%	76.28	43.62%

Table 2: Response results at $a_g = 0.33$g for the considered set of 28 ground motions.

3.3 Seismic response sensitivity results

Response sensitivities of the selected EDPs, i.e., ζ_i (interstorey drift at the i-th floor normalized with respect the interstorey height h) and μ_i^c (cumulative plastic strain at the i-th floor normalized with respect to the BRB yield strain ε_y) were computed with respect to the independent sensitivity parameters $\theta_k = A_k / A_{0k}$, being A_k the actual core area and A_{0k} the core area of the reference design solution of each of the two BRBs at the k-th floor. For ζ_i attention is limited to the sensitivities of each EDP when its peak value is attained, whereas for μ_i^c the value attained at the end of the ground motion is considered. The local response sensitivity results could be questioned being derivatives of the peak response and thus representative of the local effect of small variations of the sensitivity parameters θ_k. In order to clarify this issue, the global sensitivities of the peak values of the considered EDPs, computed with respect to θ_k using the FDM for finite variations $\Delta\theta_k = 0.125$ and 0.250, are also shown in this study. In addition, the FDM with $\Delta\theta_k = 0.1$, 0.01, and 0.001 was used to approximate local sensitivities, showing that the convergence of the FDM approximation is achieved with $\Delta\theta_k = 0.01$ without incurring in the step-size dilemma. When FDM is used, the sensitivities are computed from the maximum values of the EDPs in the reference and perturbed motion, even if the maximum values are attained in different time instants. Despite the inevitable differences in structural response obtained from the various seismic inputs, similar qualitative trends were observed for the sensitivity results, regardless of the ground motion considered.

Response sensitivity results (averaged over the set of 28 ground motions) with the normalized interstorey drifts as EDPs of interest are summarized in Figure 2. The local response sensitivities, i.e., $\partial\zeta_i/\partial\theta_k$, are depicted in Figure 2a, the global response sensitivities, i.e.,

$\Delta\zeta_i/\Delta\theta_k$, in Figures 2b,c. Comparisons between local and global sensitivities, i.e., between Figures 2a and 2b,c, reveals some (typically minor) numerical differences. However, it is important to observe that the qualitative results are basically the same. Thus the response sensitivities (local derivatives) of the interstorey drifts with respect to the sensitivity parameters θ_k, are to some extent representative of the effects of finite variations of θ_k, and thus of finite variations of the BRB core areas. A positive (negative) value of the sensitivity means an increment (decrement) of the relevant EDP due to the increment of the sensitivity parameter considered. Thus, the results shown in Figure 2 allow the quantification of the increments and decrements of peak interstorey drifts due to the sensitivity parameters. In addition to such quantification, qualitative considerations can be deduced. For example, it is observed that the increment of the internal core area of the BRBs of a given floor causes a notable reduction of the peak interstorey drift of that same floor and a smaller increment of the peak drift values of all the other floors.

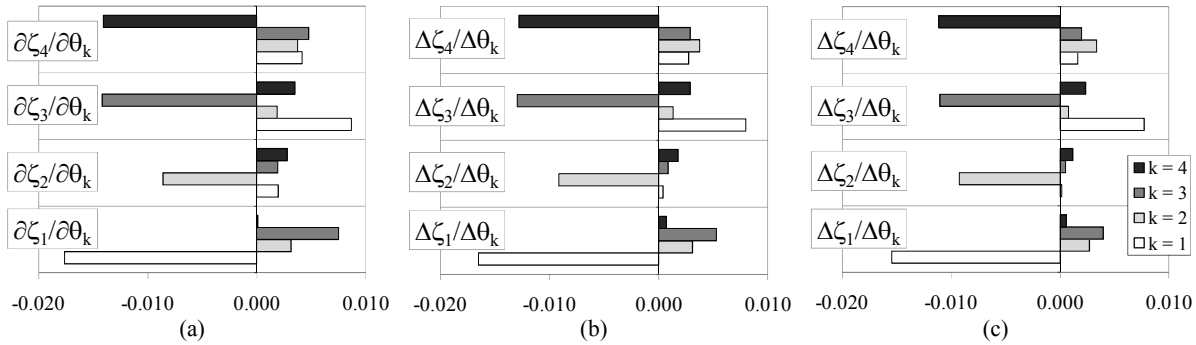


Figure 2: (a) local normalized sensitivities of the maximum interstorey drifts; (b) global (ΔA_k / A_k = 12.5%) normalized sensitivities of the maximum interstorey drifts; (c) global (ΔA_k / A_k = 25.0%) normalized sensitivities of the maximum interstorey drifts.

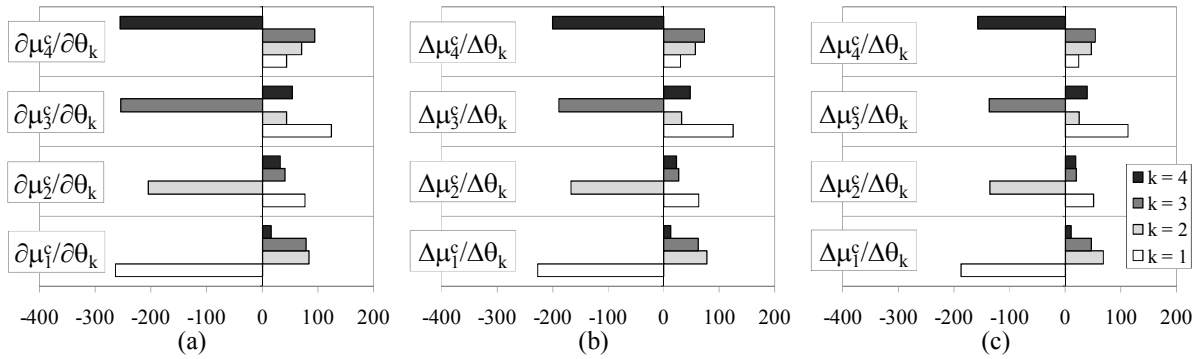


Figure 3: (a) local normalized sensitivities of the BRB cumulative ductility; (b) global (ΔA_k / A_k = 12.5%) normalized sensitivities of the BRB cumulative ductility; (c) global (ΔA_k / A_k = 25.0%) normalized sensitivities of the BRB cumulative ductility.

Similar trends of the local and global sensitivities (averaged over the set of 28 ground motions) are observed when the EDPs related to the seismic demand on the BRBs are considered, i.e., local ($\partial\mu_i^c/\partial\theta_k$) and global ($\Delta\mu_i^c/\Delta\theta_k$) response sensitivities of the cumulative ductility (Figure 3). It is observed that the increment of the core area of the BRBs at a given floor decreases the seismic demand on the BRBs of that same floor and typically increases the seismic demand on the other BRBs, with increment amplitude usually smaller than the amplitude of the decrement.

3.4 Effects of over-strength distributions and relevant seismic performance reduction

Response sensitivity diagrams shown in Figures 2 and 3 can be used to identify the variation of the sensitivity parameters (BRB core areas) resulting in largest increment in the EDPs considered. The most unfavourable combination of sensitivity parameters is found according to the linearized formulation and set of variations described section 2. In this way, the response sensitivities assume a role similar to influence lines: whereas influence lines permit to locate moving loads in bridge analysis so to attain the largest effects, response sensitivity diagrams permit to estimate the worst combination of the variation of the BRB core areas to attain the largest EDP increment. For example, if the goal is to evaluate the maximum interstorey drift at the first floor of the considered case study, then the brace areas of the second, third and fourth floors must be increased (positive sensitivity) and the brace areas at the first floor left unchanged (negative sensitivity), as depicted in Figure 4.

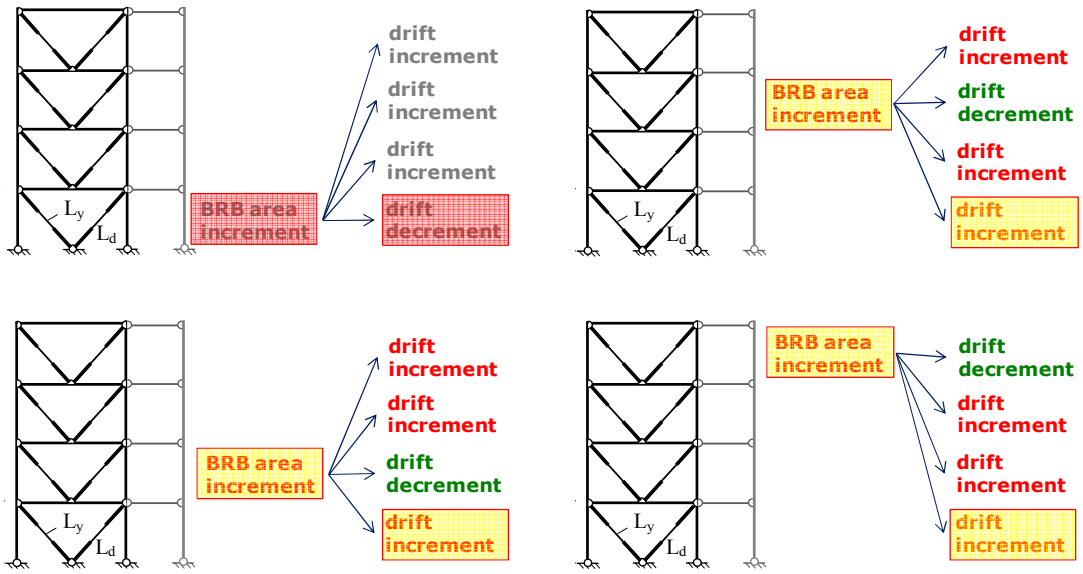


Figure 4: Use of response sensitivity results to identify the worst distributions of brace over-strength.

Results derived from the set of variations with amplitudes spanning from 0 to 25%, are henceforth reported and commented. Results (averaged over the set of 28 ground motions) for the interstorey drift as EDP are given in Figure 5a. For comparison purposes, results obtained with an homogeneous amplification of all sensitivity parameters θ_k are reported in Figure 5b. Additionally, in order to verify the validity of the linear approximations based on the local response sensitivity calculations, the same Figure 5 also show the actual EDP variations obtained from the nonlinear analysis with finite increments of BRB areas. It is observed that the linear approximations based on the local response sensitivity results give fairly accurate predictions of the actual variations, in particular when the amplifications in the BRB areas are below 12.5%. The results in Figure 5 show significant differences between the maximum interstorey drifts derived from the most adverse combinations of BRB over-strengths and those derived from uniform BRB over-strengths. The BRB uniform over-strength reduces the interstorey drifts. On the other hand, the worst combination of BRB over-strength for the *i*-th interstorey drift significantly increases the *i*-th interstorey drift, e.g., the minimum interstorey increment is about 10% in floor #2 for 25% parameter increment. In addition, the worst combination of BRB over-strength for the *i*-th interstorey drift has the effect of reducing the other interstorey drifts (results not shown in the presented figures for the sake of brevity) with reductions in the range from 1% to 30%, always smaller than the increments in the *i*-th intersto-

rey drift. Results similar to those of the interstorey drift are observed for the BRB cumulative ductility (Figure 6). The increment of BRB cumulative ductility under its most adverse combinations of BRB over-strength is more important that those noted for the interstorey drift.

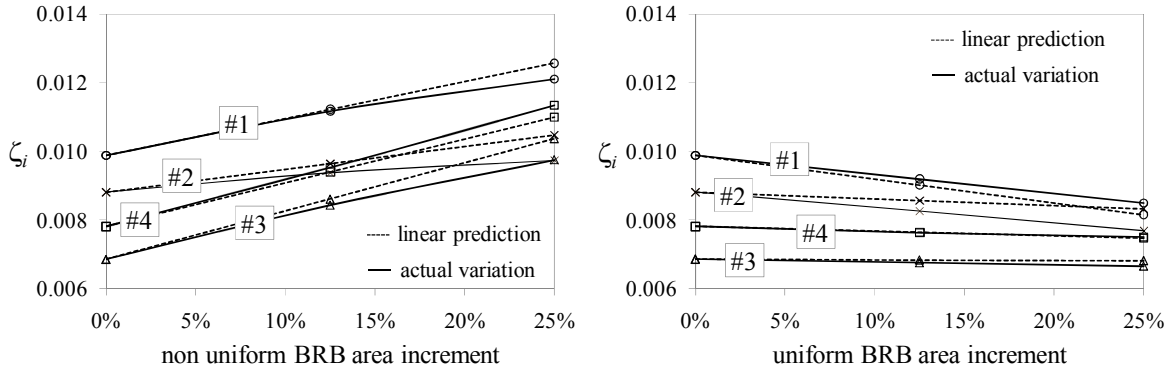


Figure 5: (a) variation of the maximum interstorey drift from the worst combination of the increment of BRB areas; (b) variation of the maximum interstorey drift from the uniform increment of BRB areas.

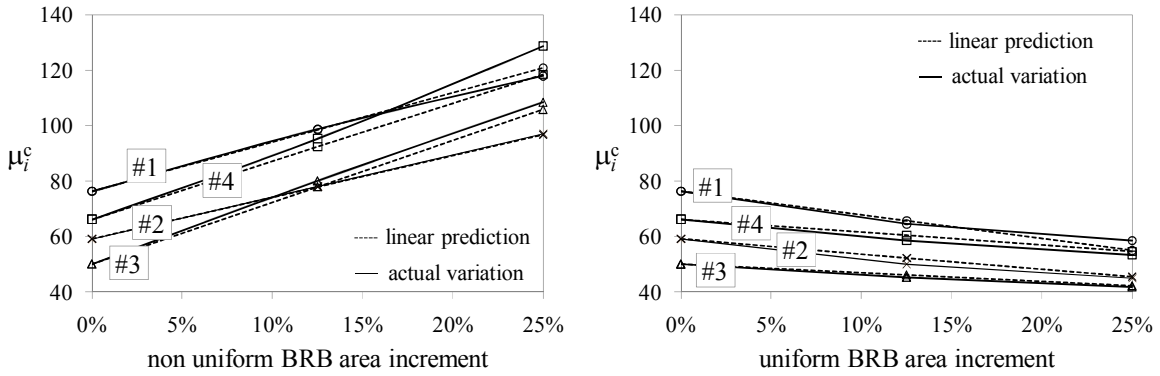


Figure 6: (a) variation of the BRB cumulative ductility from the worst combination of the increment of BRB areas; (b) variation of the BRB cumulative ductility from the uniform increment of BRB areas.

The variation of the reduction factor of the reference design solution (R_0 = 4.86) due to the worst combination of the increment of BRB areas as determined based on sensitivity results is quite significant. Using the described methodology, the obtained values are R = 3.62 for the 12.5% worst variation amplitude of the BRB area increment and R = 2.37 for the 25% worst variation amplitude of the BRB area increment.

4 CONCLUSIONS

In this paper a general sensitivity-based gradient methodology developed to investigate the relation between seismic performance reduction and regularity of brace over-strength distributions was presented for performance-based design and assessment of braced steel frames. Seismic response and response sensitivity analyses were performed using as input a given set of natural accelerograms. The sensitivity analysis results averaged over the considered set of accelerograms were used to identify the most unfavourable brace over-strength patters for each EDP, and the relevant worst possible increments of each EDP with respect to the reference design solution were predicted using a linear approximation based on local sensitivities and compared to the actual increments computed from nonlinear analysis. Afterwards, the maximum expected decrement of the reduction factor was determined within an accepted range of variability in the over-strength amplitude. In this way it was highlighted how re-

sponse sensitivity results are a powerful and relatively simple strategy to better understand the structural seismic response, and an efficient tool for more effective seismic designs.

REFERENCES

[1] R. Tremblay, Inelastic response of steel bracing members. *Journal of Constructional Steel Research*, **58**, 665-701, 2002.

[2] R. Tremblay, Achieving a stable inelastic seismic response for braced steel frames. *AISC Engineering Journal*, **40**, 111-129, 2003.

[3] A.Y. Elghazouli, Assessment of European seismic design procedures for steel framed. *Bulletin of Earthquake Engineering*, **8**(1), 65-89, 2010.

[4] P.P. Rossi, A. Lombardo,. Influence of the link overstrength factor on the seismic behaviour of eccentrically braced frames. *Journal of Constructional Steel Research*, **63**, 1529-1545, 2007.

[5] M. Bosco, P.P. Rossi, Seismic behaviour of eccentrically braced frames. *Engineering Structures*, **31**,664-674, 2009.

[6] R. Sabelli, S. Mahin, C. Chang, Seismic demands on steel braced frame building with buckling-restrained braces. *Engineering Structures*, **25**, 655-666, 2003.

[7] C.M. Uang, M. Nakashima, K.C. Tsai, Research and application of buckling restrained braced frames. *International Journal of Steel Structures*, **4**, 301-313, 2004.

[8] S. Kiggins, C.M. Uang, Reducing residual drift of buckling-restrained braced frames as a dual system. *Engineering Structures*, **28**, 1525-1532, 2006.

[9] L.A. Fahnestok, J.M. Ricles, R. Sause, Experimental evaluation of a large-scale buckling-restrained braced frames. *Journal of Structural Engineering*, **133**,1205-1214, 2007.

[10] C. Ariyaratana, L.A. Fahnestock, Evaluation of buckling-restrained braced frame seismic performance considering reserve strength. *Engineering Structures*, **33**,77-89, 2011.

[11] A. Zona, L. Ragni, A. Dall'Asta, Sensitivity-based study of the influence of brace overstrength distributions on the seismic response of steel frames with BRBs. *Engineering Structures*, **37**,179-192, 2012.

[12] M. Kleiber, H. Antunez, T.D. Hien, P. Kowalczyk, *Parameter Sensitivity in Nonlinear Mechanics: Theory and Finite Element Computations*. Wiley, 1997.

[13] J.P.Conte, P.K. Vijalapura, M. Meghella, Consistent finite-element response sensitivity analysis. *Journal of Engineering Mechanics*, **129**, 1380-1393, 2003.

[14] M. Barbato, A. Zona, J.P. Conte, Finite element response sensitivity analysis using three-field mixed formulation: general theory and application to frame structures. *International Journal for Numerical Methods in Engineering*, **69**,114-161, 2007.

[15] L. Ragni, A. Zona, A. Dall'Asta, Analytical expressions for preliminary design of dissipative bracing systems in steel frames. *Journal of Constructional Steel Research*, **67**, 102-113, 2011.

[16] A. Zona, A. Dall'Asta, Elastoplastic model for steel buckling-restrained braces. *Journal of Constructional Steel Research*, **68**, 118-125, 2012.

COMPDYN 2013
4th ECCOMAS Thematic Conference on
Computational Methods in Structural Dynamics and Earthquake Engineering
M. Papadrakakis, N.D.Lagaros, V. Plevris (eds.)
Kos Island, Greece, 12–14 June 2013

PREDICTING FLOOR RESPONSE SPECTRA FOR RC FRAME STRUCTURES

A. Lucchini[1], Y. Cheng[1], F. Mollaioli[1], and L. Liberatore[1]

[1]Department of Structural and Geotechnical Engineering, Sapienza University of Rome
Via Antonio Gramsci 53, Rome, Italy
andrea.lucchini@uniroma1.it, yin.cheng@uniroma1.it,
fabrizio.mollaioli@uniroma1.it, laura.liberatore@uniroma1.it

Keywords: Non-structural Elements, Floor Response Spectra, Intensity Measures, Frame Buildings

Abstract. *In the framework of performance-based earthquake engineering, a fundamental step in the assessment of buildings is the definition of models for the prediction of the seismic demand, namely, the definition of functional relationships between Engineering Demand Parameters of interest (EDPs) and an earthquake Intensity Measure (IM). While many studies focused on EDP representative of the structural response, only few investigated EDP well correlated with the non-structural response. The objective of this paper is to evaluate commonly used IMs, which are currently available in the literature, with respect to their capability to predict Floor Response Spectra, EDPs usually adopted for defining the seismic demand in acceleration-sensitive non-structural elements. Selected for the study are two RC frame structures, characterized by different number of stories and masonry infill wall configurations, subjected to a large number of ordinary natural accelerograms.*

1. INTRODUCTION

Non-structural elements are those buildings' components supported by the structure, such as architectural elements (e.g., ceilings, partitions and paneling) and mechanical and electrical equipment (e.g., elevators, tanks, pipes, antennas, transformers and emergency systems), that do not contribute to carrying gravity loads. Reducing seismic damage to these elements is of primary importance not only for economic reasons, since in most buildings they account for a large percentage of the building total replacement cost, but also for maintaining the functionality of the building immediately after the earthquake. Non-structural damage, in fact, can both produce significant economic losses and make the building unusable for a period of time that can vary from few weeks to several months. The usability aspect is crucial especially for buildings with emergency management functions, such as hospitals or police stations, which need to remain fully operational after frequent and rare seismic events. In addition, damage to non-structural elements caused by earthquakes can increase casualty risk. Potential threats to the safety of the occupants can be caused, for example, by falling of chimneys and ceiling panels and also by fire triggered by the pipe gas leaks that may ignite and explode. Based on these premises it is apparent that an accurate evaluation of the dynamic behavior of non-structural elements during earthquake events is essential.

In the framework of performance-based earthquake engineering, a fundamental step in the assessment of buildings is the definition of probabilistic seismic demand models (PSDM), namely, of functional relationships between Engineering Demand Parameters of interest (EDPs) and an earthquake Intensity Measure (IM). Most of the research work on PSDM that can be found in the literature focuses on the response prediction of regular structures and on EDPs well correlated to structural damage only. Recently investigations have been carried out also on types of structures different than regular moment resisting frames. Among these studies deserve to be mentioned those of Lucchini et al. [9], [10] and Asgarian et al. [1] on torsional and tall buildings, respectively, and the work of Mollaioli et al. on base-isolated frames [14]. Only a few studies, however, has focused on the prediction of EDPs well correlated to non-structural damage. In such works, the response parameters usually adopted for defining the demand in acceleration-sensitive non-structural elements are the floor response spectra. In Clayton and Medina [2] only the spectral acceleration of the ground motion at the first-mode period of the supporting structure is investigated. In Taghavi and Miranda [17] the PGA and the second-mode ordinate of the spectrum are also considered as well as a combination of them. Elenas and Meskouris [7] evaluated several IMs from the literature, but using in the analyses a limited number of ground motions and focusing on peak floor accelerations only.

The objective of this paper is to investigate the floor response spectra predictive capability of IMs that are commonly used in seismic assessment of buildings. Selected for the study are two RC frame structures characterized by different number of stories and masonry infill wall configurations. Studies [5] [6] have shown, in fact, that infills walls may affect significantly the seismic response of framed systems, and can modify both spectral shape and amplitude of the floor response spectra [12] [13]. A large number of ordinary natural records are used for exciting the buildings. For each considered IM, the predictive capability is evaluated as follows. First, a large number of ordinary natural records are used for exciting the buildings. Then, the floor response spectra are calculated using the obtained floor acceleration responses of the structures, and their ordinate values correlated to the values of the ground motion IMs. The predictive capability of the IMs is finally estimated by evaluating the results of the regression/correlation analyses.

2. CASE STUDIES

2.1 Studied structures

The selected buildings are a 2-bay 4-storey and a 2-bay 6-storey ductile reinforced concrete frame structures (see Figure 1), which are characterized by strong beams and weak columns. The frames are designed according to the seismic code in force in Italy between 1996 and 2008 that lacks any capacity design provision. The two frames are characterized by two infill walls configurations: bare and with brick infill walls at all stories. The infill walls are meant to represent internal partitions or weak perimeter walls. The four frames will be called 4b, 4w, 6b, and 6w, where the number indicates the stories and the letters "b" and "w" stands for bare and walled, respectively. Both buildings are characterized by a regular stiffness and mass distribution, and by a design lateral base shear capacity equal to 35% of the total weight. The masses of the walls are included also in the bare frame models. The length of each bay and the height of each story are identical in all four models. Table 1 shows the results of modal analyses run with linear models of the bare frames built by using for structural members the effective stiffness to yielding.

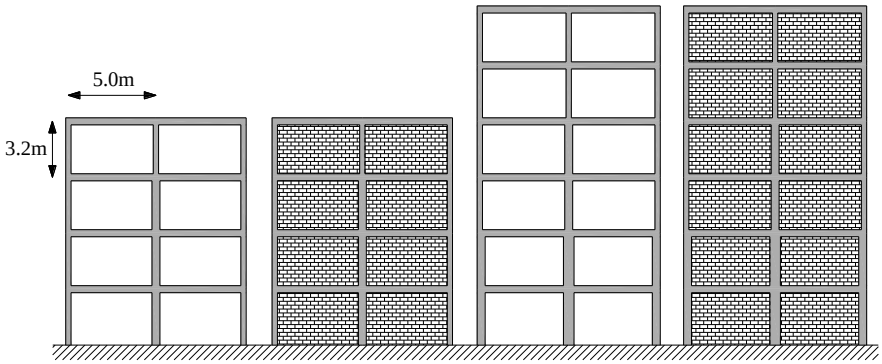


Figure 1: Schematic front view of the studied bare and infilled frame RC structures of 4- and 6-storey buildings.

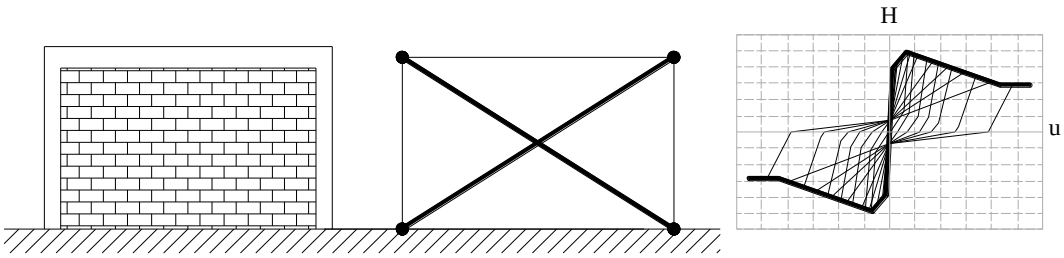


Figure 2: Infill wall model: struts system and horizontal force-displacement (H-u) constitutive behavior.

	4b		6b	
Mode	T	PMR	T	PMR
1	1.30s	80%	1.50s	75%
2	0.49s	11%	0.54s	11%
3	0.29s	5%	0.32s	5%

Table 1: Periods (T) and participating mass ratios (PMR) of the first three modes of vibration obtained with models built with the effective stiffness to yielding of structural members.

The nonlinear seismic response of the buildings is evaluated using finite element models built in OpenSees [11]. Structural members are modeled with force-based nonlinear elements characterized by distributed inelasticity, while contribution of the infill walls is represented using the equivalent strut model proposed by Decanini and Fantin [3]. The model consists of a system of diagonal struts connected to the nodes of the frame that act only in compression and with a hysteretic behavior characterized by stiffness degradation, strength deterioration, and loop pinching (Figure 2). The parameter values were calibrated after the work by Decanini et al. [4] on typical infill walls frequently used in Italy. These walls are made of 120 mm thick hollow bricks and a mixture of cement, sand and lime mortar, characterized by a compressive and shear strength (the latter evaluated through diagonal compressive test) equal to 1.2 and 0.2 MPa, respectively, and an initial elastic modulus of 1,050 MPa. A Rayleigh damping proportional to the mass and tangent stiffness matrix is considered with coefficients calibrated to provide a 5% damping at the first and third mode periods of the undamaged structures. The effects of geometric nonlinearities are not considered.

2.2 Ground motion database

The dynamic response of the studied buildings is evaluated via time-history analyses that use an ensemble of 72 ground motions from 26 worldwide earthquakes with magnitude ranging from 5.0 to 7.6 (see Figure 3). All the selected accelerograms are extracted from the Pacific Earthquake Engineering Research (PEER) Next Generation Attenuation (NGA) database [15]. All of them have a "usable" frequency range that brackets the frequency range of the response of these buildings. They are characterized by the same NEHRP soil condition type C-D. In general, they consist of far-field "standard" records that do not include any recognizable pulse in the velocity trace.

Not all obtained responses are used in the following correlation analyses. Responses corresponding to maximum inter-storey drift ratio values greater than 5% are excluded because considered to be associated, for the studied buildings, to deformations close to those expected at the onset of collapse. For this range of responses, the seismic demand evaluation of non-structural elements is, of course, not a major concern and, thus, the prediction of the floor response spectra is not of interest. As a consequence, in the case of the bare frames the results of only 65 time-histories are used in the regression analyses, while in the case of the infilled frames the used results are only those from 71 time-histories.

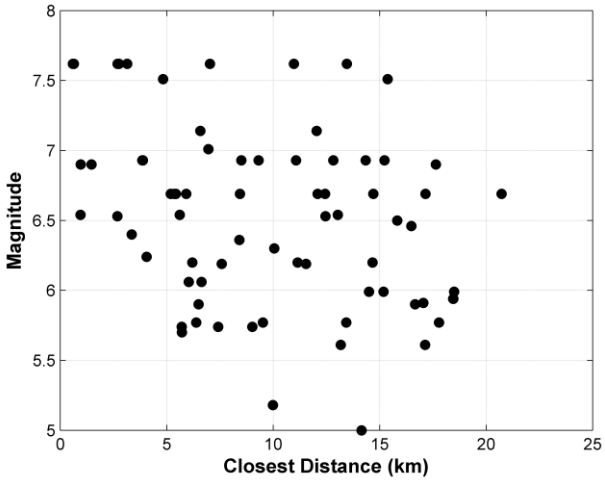


Figure 3: Earthquake magnitude and distance range for the 72 ordinary ground motions used in the analyses.

3. INTENSITY MEASURES AND ENGINEERING DEMAND PAPAREMTERS

3.1 Intensity measures

The IMs investigated in the present paper are: the Peak Ground Acceleration (PGA) and the Peak Ground Velocity (PGV); the compound acceleration-related IM (Ia), proposed by Riddell and Garcia [16], whose definition is given in Equation (1); the pseudo-spectral acceleration at the first- and second-mode period of the structure ($S_{pa}(T_1)$ and $S_{pa}(T_2)$, respectively); the Housner Intensity (I_H) [8], as defined in Equation (2); the Velocity and the Acceleration Spectrum Intensity (VSI and ASI, respectively) [19], derived from the absolute velocity and pseudo-acceleration response spectra as described in Equation (3) and (4).

$$\begin{gathered} I_a = PGA \cdot t_d^{1/3} \\ t_d = t_2 - t_1; t_1 = t(5\%AI);\ t_2 = t(95\%AI) \\ AI = \text{Arias Intensity} \end{gathered} \tag{1}$$

$$I_H = \int_{0.1}^{2.5} S_{pv}\, dT \tag{2}$$
$$S_{pv} = 5\%\ \text{damp. pseudo-velocity spectrum}$$

$$VSI = \int_{0.1}^{2.5} S_v\, dT \tag{3}$$
$$S_v = 5\%\ \text{damp. absolute velocity spectrum}$$

$$ASI = \int_{0.1}^{0.5} S_{pa}\, dT \tag{4}$$
$$S_{pa} = 5\%\ \text{damp. pseudo-acceleration spectrum}$$

A modified version of the ASI (MASI), obtained by simply changing the periods range of integration from 0.1s-0.5s to 0.1s-2.5s, is investigated as well. This different range is considered so as to include periods of the pseudo-acceleration response spectrum that can significantly affect the response of the studied RC frames. The definition of ASI given in Equation (4), in fact, was proposed for predicting the response of dams, structures which are characterized by values of the fundamental period that are usually lower than 0.5s.

3.2 Engineering demand parameters

A flexible non-structural element experiences maximum acceleration when its period of vibration is close to one of those of the modes of vibration of the supporting structure. Based on this observation, the parameters selected in this study to be representative of the non-structural seismic demand are the following: the Peak Floor Acceleration (PFA), used to represent infinitely (or almost infinitely) rigid elements, and the maximum ordinate of the Floor Acceleration response Spectrum within the short-period region (FAS_2) and the fundamental-region (FAS_1). In accordance with the approach adopted in Clayton and Medina [2], the boundaries of these two regions are 0, $0.5T_1$ and $2.0T_1$, where T_1 denotes the fundamental period of the structure.

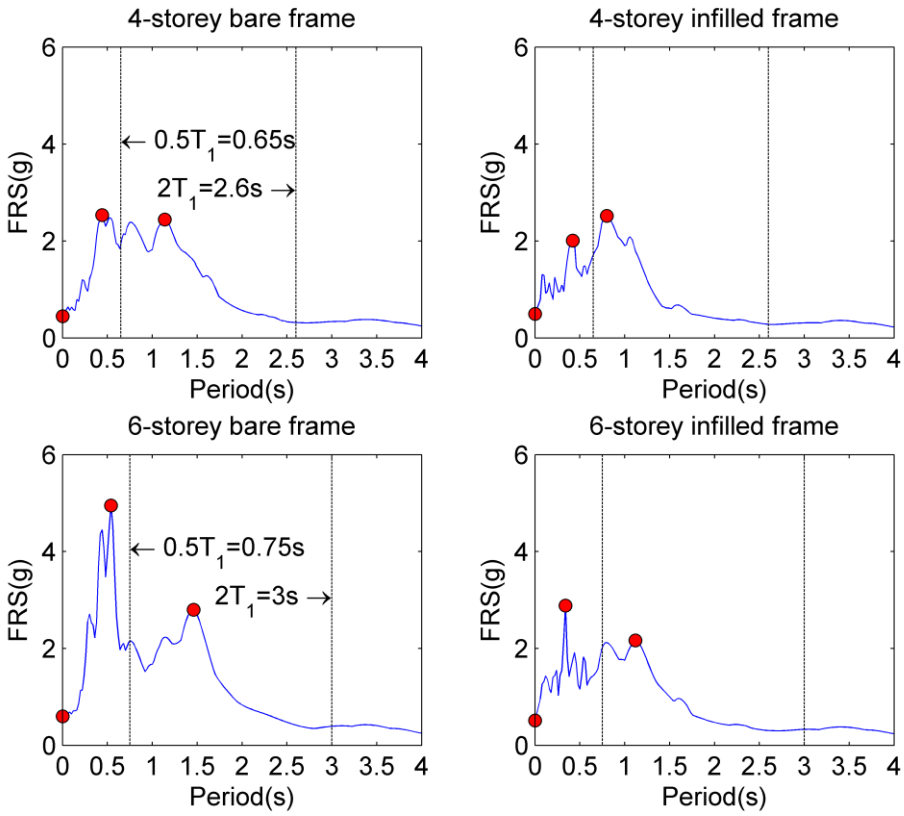


Figure 4: Floor Response Spectra obtained with one record of the ensemble. In red the spectral ordinates corresponding to PFA, FAS_1 FAS_2.

Many studies have shown that in medium- and low-rise buildings maximum non-structural accelerations usually occur at top floor. For such a reason, in the present investigation only the Floor Response Spectra (FRS) at the roof are calculated. In Figure 4 those obtained with one record from the used ensemble are shown. In the same Figure the considered fundamental- and short-period regions and ordinates of the spectra corresponding to PFA, FAS_2 and FAS_1 are also reported.

4. REGRESSION ANALYSES

4.1 Predictive models

Several are the properties that are usually investigated for evaluating the predictive capabilities of an IM (e.g., see Tothong and Luco [18]). Those considered in this study are the efficiency and the sufficiency. These properties are evaluated by first running non-linear dynamic analyses on the structures, and then by carrying out regression analyses between the obtained EDP values and the IM values of the used earthquake records. In all the regression analyses the used functional form is the following:

$$\ln(\mathrm{EDP}) = \ln(a) + b \cdot \ln(\mathrm{IM}) \tag{5}$$

Among the statistical parameters calculated in the regressions, the standard error of residuals σ_ε is used for measuring the predictive efficiency of the IM. IMs resulting in EDPs standard errors of the order of 0.20-0.30 are normally considered as having a good efficiency, while the range 0.30-0.40 is still considered as reasonably acceptable. The regression

residuals $\varepsilon|_{IM}$, instead, are used for evaluating the IM sufficiency. If the following predictive models are used for correlating $\varepsilon|_{IM}$ with magnitude (M) and distance (R):

$$\varepsilon|_{IM} = \alpha_M + \beta_M \cdot M, \ \varepsilon|_{IM} = \alpha_R + \beta_R \cdot R \tag{6}$$

the sufficiency can be directly measured by the p-value for the estimated slope coefficient β. A smaller p-value of β indicates a less sufficient IM, where M or R have significant influence on residuals of EDP. Generally, IM is considered sufficient when the p-value is more than 0.05.

4.2 Results

By looking at the results of the correlation analyses between IMs and PFA reported in Figure 5, it can be observed that in general the most efficient predictor for this EDP is MASI. The values of the standard error of residuals obtained with this IM are lower than 0.2 for all the studied buildings. Only for the 4w, the σ_ε values of the PGA-PFA regressions are slightly lower. This finding is in accordance with those of other studies from the literature that have demonstrated how efficient the PGA can be in predicting the response of structures with fundamental periods in the short-period (acceleration-controlled) region of the spectrum. The results of the present work show that in case of the PFA prediction, MASI can become much more efficient than the PGA with the increase of the flexibility of the structure (see in particular the results obtained with the 6b building).

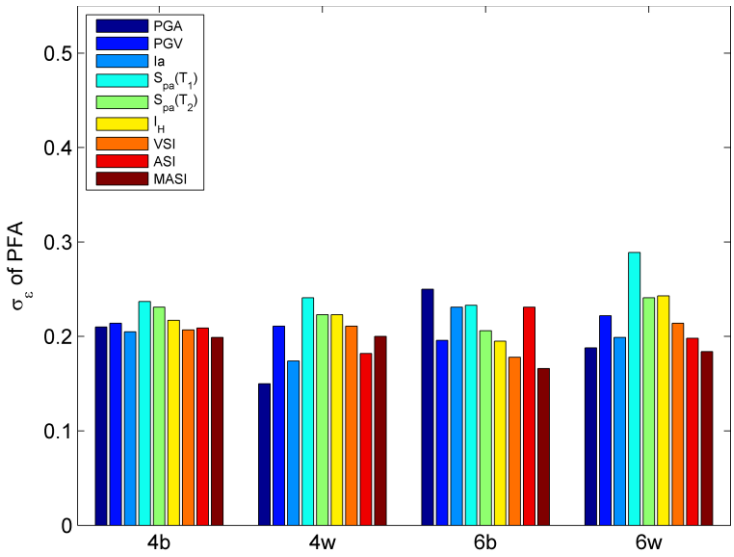


Figure 5: Standard error of residuals σ_ε obtained in the IMs-PFA correlation analyses.

In Figure 6, the standard errors of residuals of the IMs-FAS_1 regressions are reported. By comparing the plots of Figure 5 and Figure 6, it can be noticed that in the FAS_1 predictions the efficiency of all the IMs gets significantly worse. If the σ_ε values obtained with the different predictors are compared to each other, it can be found that the best IM is $S_{pa}(T_1)$. Also the efficiency of I_H, VSI and MASI is reasonably acceptable, being very close to that of $S_{pa}(T_1)$ for all the studied buildings except the 6b. About ASI and MASI, it can be observed that for the case of the 4-storey structures the predictive efficiency is almost the same, while for the case of the more flexible 6-storey buildings by using the modified IM than the existing one significant improvement in the FAS_1 predictions can be obtained.

The analyses results of the IMs-FAS_2 regressions are given in Figure 7. Analogously to what observed in the FAS_1 predictions, the most efficient predictor for this EDP is $S_{pa}(T_2)$. The standard errors of residuals obtained with $S_{pa}(T_2)$ are always close to the minimum observed values, being lower than 0.3 in all of the studied cases. For the 4-storey buildings, the σ_ε obtained with all the IMs are actually very similar. For the 6-storey frames, instead, the predictors efficiencies are much more different: in particular, for the bare frames the most efficient IM results to be $S_{pa}(T_2)$ while for the infilled frames is I_a. The predictive efficiency of ASI and MASI is in this case pretty the same.

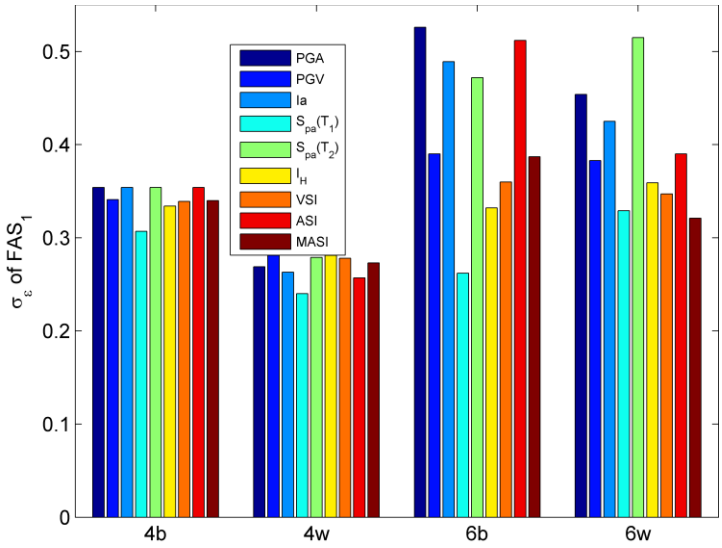


Figure 6: Standard error of residuals σ_ε obtained in the IMs- FAS_1 correlation analyses.

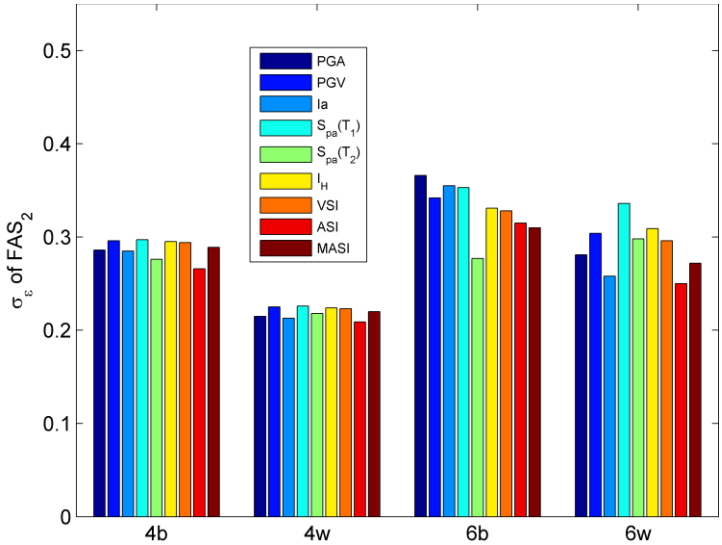


Figure 7. Standard error of residuals σ_ε obtained in the IMs- FAS_2 correlation analyses.

In Table 2 and Table 3 the p-values of β_M and β_R calculated for the evaluation of the IMs sufficiency are reported. In general, it can be observed that the only IMs that are sufficient for all the studied cases with respect to both magnitude and distance and for all the considered EDPs are $S_{pa}(T_1)$ and I_H. Also PGV and VSI are characterized in many cases by high p-values. The prediction errors obtained with MASI are much less correlated to magnitude and distance than those obtained with ASI.

In particular, by observing the results of the IMs-PFA regressions only, it can be observed that between the two most efficient IMs, namely, PGA and MASI, only the latter is sufficient for all the studied cases. The PGA is sufficient only when predicting the response of the 4w building. In the FAS_1 predictions, $S_{pa}(T_1)$ and I_H are always sufficient while VSI and MASI are not sufficient in two cases only. In the FAS_2 predictions, both $S_{pa}(T_2)$ and I_a result to be sufficient.

p-value for β_M		PGA	PGV	I_a	$S_{pa}(T_1)$	$S_{pa}(T_2)$	I_H	VSI	ASI	MASI
Prediction of PFA	4b	**0.00**	0.79	0.13	0.54	**0.02**	0.96	0.96	**0.01**	0.95
	4w	0.06	0.51	0.47	0.68	0.20	0.70	0.48	0.20	0.34
	6b	**0.00**	0.99	**0.03**	0.69	**0.00**	0.65	0.61	**0.00**	0.76
	6w	**0.00**	0.27	0.91	0.90	0.14	0.32	0.15	**0.01**	0.06
Prediction of FAS_1	4b	**0.00**	**0.01**	**0.00**	0.18	**0.00**	0.05	**0.02**	**0.00**	**0.01**
	4w	**0.00**	0.35	**0.02**	0.47	**0.00**	0.77	0.56	**0.00**	0.50
	6b	**0.00**	**0.00**	**0.00**	0.24	**0.00**	0.10	**0.03**	**0.00**	**0.00**
	6w	**0.00**	0.22	**0.00**	0.50	**0.00**	0.78	0.46	**0.00**	0.23
Prediction of FAS_2	4b	0.13	0.16	0.38	0.06	0.45	0.19	0.24	0.47	0.45
	4w	0.66	0.44	0.66	0.42	0.83	0.69	0.88	1.00	0.88
	6b	**0.00**	0.52	0.09	0.42	0.30	0.88	0.83	**0.03**	0.98
	6w	**0.00**	0.66	0.56	0.28	0.09	0.74	0.87	**0.02**	0.85

Table 2: Prediction of the $\varepsilon|_{IM}$ residuals obtained in the IMs-EDPs regressions: p-values for the slope coefficient β_M (in bold the values lower than 0.05).

p-value for β_R		PGA	PGV	I_a	$S_{pa}(T_1)$	$S_{pa}(T_2)$	I_H	VSI	ASI	MASI
Prediction of PFA	4b	0.98	0.52	0.39	0.91	0.53	0.57	0.51	0.78	0.33
	4w	0.80	0.80	0.39	0.33	0.09	0.88	0.90	0.21	0.74
	6b	0.48	0.15	0.39	0.93	0.24	0.19	0.13	0.24	0.10
	6w	0.08	0.78	0.89	0.18	**0.01**	0.89	0.84	0.01	0.62
Prediction of FAS_1	4b	0.26	0.87	0.59	0.73	0.55	0.81	0.99	0.42	0.97
	4w	**0.03**	0.66	0.28	0.29	**0.01**	0.79	0.72	**0.02**	0.71
	6b	**0.01**	0.64	0.18	0.53	**0.02**	0.81	0.87	**0.01**	0.61
	6w	**0.01**	0.96	0.20	0.34	**0.01**	0.74	0.86	**0.00**	0.93
Prediction of FAS_2	4b	0.79	0.58	1.00	0.41	0.81	0.59	0.66	0.79	0.87
	4w	0.53	0.98	0.24	0.97	0.79	0.78	0.64	0.52	0.48
	6b	0.46	0.78	0.97	0.75	0.72	0.68	0.67	0.59	0.50
	6w	0.22	0.77	0.86	0.20	0.07	0.67	0.80	0.09	0.96

Table 3: Prediction of the $\varepsilon|_{IM}$ residuals obtained in the IMs-EDPs regressions: p-values for slope coefficient β_R (in bold the values lower than 0.05).

5. SUMMARY AND CONCLUSIONS

In the present work, the seismic response of four buildings characterized by different number of stories and infill wall configurations were analyzed by using a large number of ground motions. Floor response spectra at top floor were evaluated with the objective of evaluating the capability of several intensity measures from the literature in predicting the acceleration response of non-structural elements. Different regions of the spectra were investigated by using the three following engineering demand parameters:

- PFA, the spectral ordinate of the spectrum corresponding to a period of vibration of the non-structural element T equal to 0;
- FAS_2, the maximum ordinate of the spectrum in the short-period region $0s<T<0.5T_1$, where T_1 is the fundamental period of the structure;
- FAS_1, the maximum ordinate of the spectrum in the fundamental-period region $0.5 T_1<T<2.0T_1$.

For each intensity measure both the predictive efficiency and sufficiency were investigated. Such properties were estimated by evaluating the results of correlation analyses between the values of the ground motion intensity measures and the obtained values of the considered engineering demand parameters. The main findings of the analyses can be summarized in the following:

- intensity measures are in general much less efficient in predicting the acceleration response of non-structural elements than that of the structure;
- the predictive capability of the acceleration spectrum intensity ASI can be significantly improved by changing the periods range of integration from 0.1s-0.5s to 0.1s-2.5s;
- the best intensity measure for predicting PFA is MASI, namely, the modified version of the acceleration spectrum intensity investigated in this study;
- for short-period structures only, such as the infilled frames investigated in this work, peak ground acceleration is also a good predictor for PFA;
- the best intensity measure for predicting FAS_1 is $S_{pa}(T_1)$, namely, the pseudo-spectral acceleration at the first-mode period of the structure;
- the best predictor for FAS_2 is $S_{pa}(T_2)$, namely, the pseudo-spectral acceleration at the second-mode period of the structure;
- the best option for predicting all of the regions of the floor response spectra with one intensity measure only is to use $S_{pa}(T_1)$, I_H or MASI;
- $S_{pa}(T_1)$, even if not always among the most efficient predictors, was found to be sufficient for all of the studied cases;
- Housner intensity I_H and MASI were found to be the most robust predictors, that is, the most efficient ones regardless of the considered engineering demand parameter and of the supporting structure properties;
- among I_H and MASI, the first one were found to be in general more sufficient while the latter slightly more efficient.

The above listed findings can be used as a guide for the selection of the best intensity measure for predicting floor response spectra of frame buildings. It is important to underline that the results obtained in the present investigation can be applied, in principle, only to structures with dynamic properties similar to those of the studied frames.

ACKNOWLEDGEMENTS

This work has been partially carried out under the program “Dipartimento di Protezione Civile – Consorzio RELUIS”, signed on 2009-09-24 (no. 823), Line RS 2. The financial

support of the Ministry of the Instruction, University and Research of Italy (MIUR) is gratefully acknowledged. The authors are grateful to Prof. Giorgio Monti for his valuable suggestions.

REFERENCES

[1] B. Asgarian, R.M. Nojoumi, P. Alanjari, Performance-based evaluation of tall buildings using advanced intensity measures (case study: 30-story steel structure with framed-tube system). *The Structural Design of Tall and Special Buildings*, published online: 6 June, 2012. DOI: 10.1002/tal.1023.

[2] J.S. Clayton, R.A. Medina, Proposed Method for Probabilistic Estimation of Peak Component Acceleration Demands. *Earthquake Spectra*, **28**, 55-75, 2012.

[3] L.D. Decanini, G.E. Fantin, Modelos simplificados de la mamposteria incluida en porticos. Caracteristicas de rigidez y resistencia lateral en estado limite. *Jornadas Argentinas de Ingenieria Estructural*, Buenos Aires, Argentina, **2**, 817-836, 1986. (in spanish).

[4] L.D. Decanini, F. Mollaioli, A. Mura, R. Saragoni, Seismic Performance of Masonry Infilled R/C frames. *Proc. of 13th WCEE*, Paper 165, Vancouver, Canada, August 1-6, 2004.

[5] L.D. Decanini, A. De Sortis, L. Liberatore, F. Mollaioli, Estimation of near-source ground motion and seismic behaviour of RC framed structures damaged by the 1999 Athens earthquake. *Journal of Earthquake Engineering*, **9:3**, 1-27, 2005.

[6] L.D. Decanini, L. Liberatore, F. Mollaioli. Damage potential of the 2009 L'Aquila, Italy, earthquake. *Journal of Earthquake and Tsunami*, **6:3**, 1250032:1-32, 2012.

[7] A. Elenas, K. Meskouris, Correlation study between seismic acceleration parameters and damage indices of structures. *Engineering Structures*, **23**, 698-704, 2001.

[8] G.W. Housner, Spectrum Intensities of Strong-Motion Earthquakes. *Proc. Symp. Eathquake and Blast Effects on Structures*, EERI, Los Angeles, California, June, 1952.

[9] A. Lucchini, F. Mollaioli, G. Monti, Intensity measures for response prediction of a torsional building subjected to bi-directional earthquake ground motion. *Bulletin of Earthquake Engineering*, **9:5**, 1499-1518, 2011.

[10] A. Lucchini, F. Mollaioli, G. Monti, S. Kunnath, Seismic response of asymmetric RC frames subjected to bi-directional ground motions. *fib Syposium on Concrete Engineering for Excellence and Efficiency*, Prague, Czech Republic, 8-10 June, 2011.

[11] F. McKenna, G.L. Fenves, M.H. Scott, OpenSees: open system for earthquake engineering simulation. http://opensees.berkeley.edu, PEER, University of California, Berkeley, CA, 2007.

[12] F. Mollaioli, A. Lucchini, P. Bazzurro, S. Bruno, A. De Sortis, Floor horizontal acceleration demand in reinforced concrete frames. *fib Syposium on Concrete Engineering for Excellence and Efficiency*, Prague, Czech Republic, 8-10 June, 2011.

[13] F. Mollaioli, A. Lucchini, S. Bruno, A. De Sortis, P. Bazzurro, Floor acceleration demand in reinforced concrete frame structures with masonry infill walls. *9th US national and 10th Canadian conference on earthquake engineering*, Toronto, Canada, July 25-29, 2010.

[14] F. Mollaioli, A. Lucchini, Y. Cheng, G. Monti, Intensity Measures for the Seismic Response Prediction of Base-Isolated Buildings. *Bulletin of Earthquake Engineering*, DOI: 10.1007/s10518-013-9431-x, Pages 1-26, 2013.

[15] Pacific Earthquake Engineering Research Center (PEER). PEER Ground Motion Database – Beta Version, 2011, http://peer.berkeley.edu/peer_ground_motion_database/site, 2011.

[16] R. Riddell, J. Garcia, Hysteretic energy spectrum and damage control. *Earthquake Engineering and Structural Dynamics*, **30:12**, 1791-1816, 2001.

[17] A. Taghavi, E. Miranda, Probabilistic Seismic Assessment of Floor Acceleration Demands in Multi-Story Buildings. *The John A. Blume Earthquake Engineering Center*, Department of Civil and Environmental Engineering, Stanford University, Report No. 162, June, 2006.

[18] P. Tothong, N. Luco, Probabilistic seismic demand analysis using advanced ground motions intensity measures. *Earthquake Engineering and Structural Dynamics*, **36:13**, 1837-1860, 2007.

[19] J.L. Von Thun, L.H. Roehm, G.A. Scott, J.A. Wilson, Earthquake ground motions for design and analysis of dams. *Proceedings of the Earthquake Engineering and Soil Dynamics II-Recent Advances in Ground Motion Evaluation*, Geotechnical Special Publication, 20, ASCE, New York, 463-481, 1988.

COMPDYN 2013
4th ECCOMAS Thematic Conference on
Computational Methods in Structural Dynamics and Earthquake Engineering
M. Papadrakakis, V. Papadopoulos, V. Plevris (eds.)
Kos Island, Greece, 12–14 June 2013

CONCEPT OF RISK-BASED SEISMIC DESIGN OF BUILDINGS USING METHODS OF NONLINEAR ANALYSIS

Matjaž Dolšek[1]

[1] University of Ljubljana, Faculty of Civil and Geodetic Engineering
e-mail: mdolsek@fgg.uni-lj.si

Keywords: Performance-based Earthquake Engineering, Risk-based Design, Nonlinear Response Analysis, Envelope-based Pushover Analysis, Seismic Hazard, Seismic Risk.

Abstract. *Development of nonlinear methods of analysis and powerful software for simulation of seismic response of structures offered a possibility to overcome shortcomings of the standards for earthquake-resistant design of structures. Firstly, these shortcomings are briefly addressed, followed by an overview of the nonlinear methods for seismic performance assessment of buildings. An emphasis is given on the envelope-based pushover analysis procedure, which was recently developed, and assumes that the seismic demand for each response parameter is controlled by a predominant system failure mode that may vary according to the ground motion and intensity level. The second part of the paper deals with the concept of risk-based design procedure, which is an iterative process based on different methods for seismic performance assessment of buildings. The proposed design procedure involves definition of the initial structure, which is then assessed in order to check whether the seismic risk is below the acceptable/tolerable level. However, since several or many iterations will be needed in order to fulfill the criteria of acceptable/tolerable risk it is foreseen that this step of the risk-based design procedure will be based on approximate procedures for seismic performance assessment. The next step of the proposed design procedure will utilize the nonlinear response history analysis, which would be performed for few ground motions from a set of hazard-consistent ground motions. The risk-based design will be possible only by further development of comprehensive software for computational simulation. The paper is concluded with presenting pros and cons of the proposed design procedure. It is foreseen that, the risk-based seismic design of structures will represent a major step towards scientifically oriented design procedures employing high level of technology.*

1 INTRODUCTION

Earthquakes endanger built environment and consequently human lives more as it can be perceived in everyday life. For example, only the earthquake in Turkey (1999) caused more than eighteen thousand deaths [1] or in Haiti (2010), the earthquake caused estimated three hundred thousand deaths, displaced more than a million people, and damaged nearly half of all structures in the epicentral area [2]. Tohoku Earthquake (2011) caused the second largest

nuclear disaster in the world and revealed weakness and vulnerability of urban cities and modern society in Japan, which were thought to be one of the most earthquake-prepared nations in the world [3]. Although in Europe such great earthquake is not expected, the vulnerability of urban cities is not negligible. Recently, L'Aquila earthquake (2009) caused 308 losses of human lives [4], 1500 people were injured and 65000 homeless. Direct economic losses were around 4 billion Euros. Losses due to earthquakes in the last twenty years were observed also on the territory of Slovenia. The strongest earthquake in this period occurred on 12th of April 1998 in the upper Posočje region. This earthquake damaged over 4000 buildings. All these experiences from recent earthquakes around the world show that the risk of loss of life and property due to earthquakes is too high, if structures are not properly designed. This finding is not new although many societies associated earthquakes with mythological creatures and religion up to about 1755 Lisbon event [5], which produced profound change in the interpretation of the cause of earthquakes.

As mentioned above, the awareness of too high seismic risk in the case if structures are not properly designed has triggered development of regulatory documents for design of structures in seismic areas. Currently many different building codes and guidelines for earthquake-resistant design of structures exist, which were developed to reduce seismic risk, but due to the complexity of the problem they still involve many simplifications and assumptions. However, the first generation of Performance-based Earthquake Engineering (PBEE) procedures was implemented already in regulatory guidelines and standards such as ATC-40 [6], FEMA 273 [7], ACI 318-11 [8], Eurocode 8 [9], and others. Those regulatory documents were developed to reduce seismic risk, but building codes often prescribe the capacity design procedure for a given design earthquake. Therefore it cannot be claimed that the current building codes for earthquake-resistant design of structures control seismic risk to such an extent that would be acceptable for all types of structures and for all investors. However, comprehensive methodologies for probabilistic performance assessment of buildings exists (e.g. [10]), but its use in design phase of building is limited.

One component of the next-generation performance-based seismic design procedures should involve assessment of seismic risk, which is an essential ingredient of risk-informed management decisions [11], but it is still insufficiently communicated between structural engineers and facility stakeholders. The major contribution to the development of the new methodology has been made in the PEER Center [12]. The methodology is probabilistic and permits consistent characterization of the inherent uncertainties throughout the process. There are many variants of the PEER methodology. Probably the simplest closed-form solution for seismic risk assessment, expressed in terms of the mean annual frequency of exceeding a given limit state, was proposed by Cornell [13]. This approach was later further developed [14] by incorporating the epistemic uncertainties through a confidence level approach, which is one of the two approaches discussed elsewhere (e.g. [15,16]). However, recent studies have shown that a more general treatment of the epistemic uncertainty increases dispersion, but also affects the median seismic response parameters (e.g. [15, 17, 18]). Since seismic risk assessment is a complex problem, several simplified procedures have been proposed (e.g. [19, 20]), which could be used in the iterative process of design.

However, the final goal of earthquake engineering research community is that the structural performance will be assessed by using nonlinear response history analysis. Such an approach requires definition of an appropriate set of ground motions, as discussed by Evangelos et al. [21]. The most basic procedures for selection of records involve criteria associated with the earthquake magnitude and distance of the rupture zone from the location of the building of the interest. However, these procedures were not found to be very efficient in terms of nonlinear response of structure [22]. Thus selection of ground motion records based on magnitude

and distance is often enhanced by spectral matching. A conservative version of this approach is adopted in the codes for seismic-resistant design of buildings, e.g. in Eurocode 8 [9], which prescribes that the uniform hazard spectrum should be used as a target spectrum. Baker [23] proposed an alternative target spectrum, termed a conditional mean spectrum (CMS). He showed that structural responses from ground motions matching the more probabilistically consistent conditional mean spectrum are significantly smaller than the response from ground motion matching the uniform hazard spectrum. However, Bradley [24] identified limitation of the CMS approach and proposed a generalized conditional intensity measure approach (GCIM) that allows determination of the conditional distribution of any arbitrary ground-motion intensity measure. All these methods do not address the issue of number of records required for sufficiently accurate prediction of seismic response of a structure. This issue was partly solved by introducing precedence list of ground motion records, which was firstly used for progressive incremental dynamic analysis (PIDA) [25].

Development of nonlinear methods of analysis and powerful software for simulation of seismic response of structures (e.g. [26]) offered a possibility to overcome shortcomings of the standards for earthquake resistant design of structures. Recently, Slovenian Research Agency approved three-year project entitled Design of structures for tolerable seismic risk using non-linear methods of analysis. The objective of the proposed project is development of procedures and tools for design of structures for a tolerable level of seismic risk. It is foreseen that the innovative procedure for design of structures will represent a major step towards scientifically oriented design procedures employing high level of technology. This paper basically represents a brief overview of the project proposal with an emphasis on design procedure for collapse safety, which is one of the fundamental requirements of standards for earthquake-resistant design of structures.

Firstly, the shortcomings of current practice for earthquake-resistant design are addressed, followed by an overview of the nonlinear methods for seismic performance assessment of buildings. An emphasis is given on the envelope-based pushover analysis procedure [27], which was recently developed, and assumes that the seismic demand for each response parameter is controlled by a predominant system failure mode that may vary according to the ground motion and intensity level. The concept of the risk-based design procedure as foreseen in the project is then explained. The paper concludes with addressing pros and cons of the proposed procedure with an emphasis on underdeveloped components of the proposed risk-based design procedure.

2 CURRENT APPROACH FOR EARTHQUAKE-RESISTANT DESIGN OF BUILDINGS

Standard for earthquake resistant design of structures (Eurocode 8) [9] prescribes that structures are sufficiently designed if they are capable to withstand a design seismic action, which is defined for an earthquake recurrence interval associated with a limit state of interest. Usually design procedures involve elastic analysis method and design acceleration spectrum, which implicitly takes into account the ability of inelastic energy absorption of the structural system. Thus, seismic risk of newly designed structures is only implicitly controlled through the q-factor (R-factor) concept and capacity design procedure. Therefore current standards for earthquake-resistant design of buildings do not control seismic risk to such an extent that would be acceptable for all types of structures and for all stakeholders.

A study which addresses the factors of safety in design of reinforced concrete frames using Eurocode 8 is presented in this conference [28]. The objective of the study was to show how different safety measures contribute to global parameters of structure, such as yield strength,

ductility corresponding to the near-collapse limit state, and the so-called structural performance parameters, such as the peak ground acceleration causing near-collapse limit state, or the return period of the near-collapse limit state ($T_{R,NC}$). For this purpose the code-conforming buildings were analyzed on the basis of the pushover analysis. The requirements of Eurocode 2 and 8 were gradually taken into account, whereas the design assumptions were gradually excluded in the performance assessment of buildings. Such approach resulted in six variants of the structure, which gradually take into account the effect of design seismic action, the effect of redundancy and the minimum requirements for dimensions and reinforcement of structural elements according to Eurocode 2, the minimum requirements for dimensions and reinforcement of structural elements according to Eurocode 8, the effect of partial factors of the strength of material, the effect of the difference between actual (selected) and required (calculated) reinforcement, and the effect of the capacity design principles. More details regarding the variants of the building and the assessment procedure are given elsewhere [28]. However, interesting results were obtained. For the 11-storey building located in the region with moderate seismicity and designed for ductility class medium it was shown that the seismic action has the major impact on the yield strength of code-conforming building and on the peak ground acceleration causing near collapse limit state, whereas its contribution to the return period of the near collapse limit state is only minor. Furthermore, the capacity design principles practically did not contribute to any of structural parameter or to performance parameters, but their implementation in design process requires a lot of labour. Based on this study it can be concluded that partial safety factors of strength of material contributed around 50% to overall structural safety, whereas the factors corresponding to redundancy, minimum requirements of Eurocode 2 and 8, partial safety factors of material strength and the ratio between the actual and required reinforcement contributed 90% to overall safety of the building (see Figure 7 in [28]). Therefore it is argued that it would be better to make the nonlinear model of the building and explicitly design the building for tolerable risk based on several iterations rather to use capacity design approach in conjunction with elastic intensity-based assessment.

However, the above-described argument is only one of a series of arguments which lean towards the risk-based or performance-based design procedures. According to FEMA P-58 [10] the limitations in present-generation of earthquake-resistant design of structures are associated with questions regarding the accuracy and reliability of available analytical procedures in predicting actual building response, the level of conservatism present in acceptance criteria, the inability to reliably and economically apply performance-based procedures to the design of new buildings, and the need for alternative ways of communicating performance to stakeholders that is more meaningful and useful for decision-making purpose. This issue can be solved by adequate estimation of seismic risk in the design process of a building, which would probably be the best approach for mitigation of earthquake losses in the future. However, such approach requires use of nonlinear methods in the process of design.

3 OVERVIEW OF NONLINEAR METHODS FOR SEISMIC PERFORMANCE ASSESSMENT

Nonlinear analysis is basically classified in static and response history (dynamic) analysis. In the case of static analysis, the equilibrium equations are independent of time, which does not allow sufficient simulation of seismic response of a building. From a theoretical point of view this issue was solved by introducing the nonlinear response history analysis, which is capable of simulating the damage in the structure and the dynamic effects, which are important in the case of earthquake actions on a structure. Therefore the nonlinear response history analysis is the most advanced analysis for the simulation of structural response under seismic

action. However, when the seismic performance assessment of a building is performed on the basis of nonlinear response history analysis, several issues have to be adequately considered. Firstly, the response history analysis is computationally extremely demanding. For this reason alone it is necessary to use simplified nonlinear models of structural elements, which are partly based on the empirical evidence. Furthermore, use of response history analysis requires hazard-consistent selection of ground motion, (e.g. [23, 24]), which is in itself quite complex procedure, selection of damping model as well as the numerical integration scheme of the equations of motion. All these ingredients of the response history analysis have impact on the analysis results and consequently affect the final design. Additionally, response history analysis of complex structural systems often becomes the subject of numerical non-convergence. For a practical application of response history analysis in the design process it is therefore necessary to develop appropriate software tools, guidelines for determination of structural models, procedures for selection of ground motions and methods which would enable predicting structural response with sufficient accuracy using only a small number of ground motions.

Due to the above-mentioned reasons it is foreseen that the nonlinear response history can be used only in final step of the risk-based design process, since seismic design based on nonlinear analysis requires iterations. The pushover-based methods could be used in the intermediate step of the design. Over the last two decades, the pushover-based methods become popular among both researchers and engineers, but these methods have several limitations. Many different procedures have been developed [29-35]. For brevity, the detailed description of these pushover-based methods is omitted in this paper. However, an overview of recently introduced envelope-based pushover analysis procedure [27] is given in the following subsection. This procedure involves nonlinear response history analysis for equivalent single-degree-of-freedom models, which correspond to pushover analyses based on invariant force vectors associated with the first three vibration modes. A new feature of the envelope-based pushover analysis procedure is the use of so-called failure-based SDOF models, which are capable of predicting approximate seismic response of buildings in the case if ground motions cause system failure modes which are significantly different to that observed for 'first-mode' pushover analysis.

3.1 Background and overview of envelope-based pushover analysis procedure

The variation of system failure modes, observed in the response history analysis, can be quite large due to the ground-motion randomness. Some ground motions would cause the system failure mode which is very similar to that corresponding to the 'first-mode' pushover analysis. In this case the basic-pushover based methods would provide sufficiently accurate estimate of collapse fragility. However, for some ground motions from a set, the system failure modes observed in the response history analysis cannot be simulated by the 'first-mode' pushover analysis. For this reason, the modal-based SDOF model becomes inaccurate in order to estimate the collapse fragility [27]. This awareness is not new. A similar conclusion was made by Bobadilla and Chopra [36] when evaluating the ability of the MPA procedure to estimate the seismic demands of reinforced concrete frame buildings. They concluded that the 'first-mode' SDOF models can estimate the median roof displacement to a useful degree of accuracy, whereas this may not be true in the case when the roof displacement is estimated for an individual ground motion. This inability of the modal-based SDOF model motivated Brozovič and Dolšek [27] to perform a detailed study in order to better understand when the 'first-mode' SDOF model provides inaccurate estimates of global response of structures. They came to an interesting conclusion, that for particular ground motions, the 'first-mode' SDOF model always provides sufficiently accurate estimate of global response of buildings regardless how tall the building is, whereas for some other ground motions, the response of build-

ings based on the 'first-mode' SDOF model cannot be simulated with useful degree of accuracy even for buildings having only four stories. Based on this finding, Brozovič and Dolšek proposed envelope-based pushover analysis procedure which involves so-called failure-based SDOF models [27]. The failure-based SDOF models utilize the displacement vectors corresponding to the system failure modes of the 'second-mode' and 'third-mode' pushover curves. This is the only difference in definition of the failure-based SDOF models and the modal-based SDOF models. Consequently the seismic demand given ground-motion intensity is greater in the case of failure-based SDOF model in comparison to corresponding modal-based SDOF model. This makes the failure based SDOF models capable of predicting the global response of structure with sufficient accuracy for the case when the 'first-mode' SDOF model provides inaccurate estimates.

The envelope-based pushover analysis procedure as introduced in [27] involves following steps:

1) **Pushover analyses:** perform pushover analyses for first, second and third mode distributions of lateral forces. This step is the same as in the case of the modal pushover analysis procedure [30].
2) **Equivalent SDOF models:** define modal-based SDOF model corresponding to idealized force-displacement relationship of the 'first-mode' pushover curve and the failure-based SDOF models corresponding to the idealized force-displacement relationships of the 'second-mode' and 'third-mode' pushover curves. Definition of the equivalent SDOF models is consistent with the N2 method [29]. However, the effective mass, period and the transformation factor of the failure-based SDOF model are calculated by using the displacement vectors corresponding to the system failure modes as defined elsewhere [27].
3) **Seismic demand for equivalent SDOF model:** perform nonlinear response history analysis for the modal-based and failure-based SDOF models.
4) **Seismic demand at structural level:** calculate the target displacement for each SDOF model and ground motion by multiplying the displacement demand of the SDOF model times the corresponding transformation factor. This step is the same as in the case of the N2 method [29], but it is performed for three SDOF models instead of one. Obtain the total seismic demand for each response parameter and for a particular ground motion by enveloping results associated with the target displacement and corresponding pushover analysis.

The envelope-based pushover analysis procedure therefore assumes that each response parameter is controlled by the predominant system failure mode caused by a ground motion. Brozovič and Dolšek [27] have shown that the envelope-based pushover analysis procedure enables sufficiently accurate prediction of collapse fragility parameters even for taller buildings, which may collapse in several different modes. Since the procedure is not computationally demanding, it can be used in the concept of risk-based design procedure, which is described in the following Section.

4 CONCEPT OF RISK-BASED SEISMIC DESIGN

The proposed design procedure is decomposed in several steps as presented in the flowchart (Figure 1). Firstly, the initial structure has to be defined. It is foreseen that the good approximation of final design could be achieved by taking into account the minimum requirements for dimensions and reinforcement of structural elements as defined by current building codes and by using engineering judgment, which could be used for approximate determination of the expected amount of reinforcement with consideration of seismicity of the region, the structural system, regularity of the building and other factors. However, initial de-

sign could also be based on simple design checks, such as the criteria for the level of normalized axial force in vertical structural elements in order to obtain basic dimensions of their cross sections, or eventually by designing the building using software which supports current building codes.

The second step of the proposed design procedure is quite important since it involves determination of the nonlinear structural model. Since the results of performance assessment of structures are highly sensitive to the features of the nonlinear structural model, several guidelines will be needed in order to help the analyst to construct a simple yet sufficiently accurate nonlinear model of structure. Simplified nonlinear models could be used since it is sufficient that the models will be capable of simulating the most important system failure modes. The non-simulated failure modes, such as shear failure of structural elements and joints, could be designed on the basis of demand hazard analysis in order to prevent such failures in the case of great earthquakes and in order to guarantee that the simplified nonlinear model provides sufficiently accurate results.

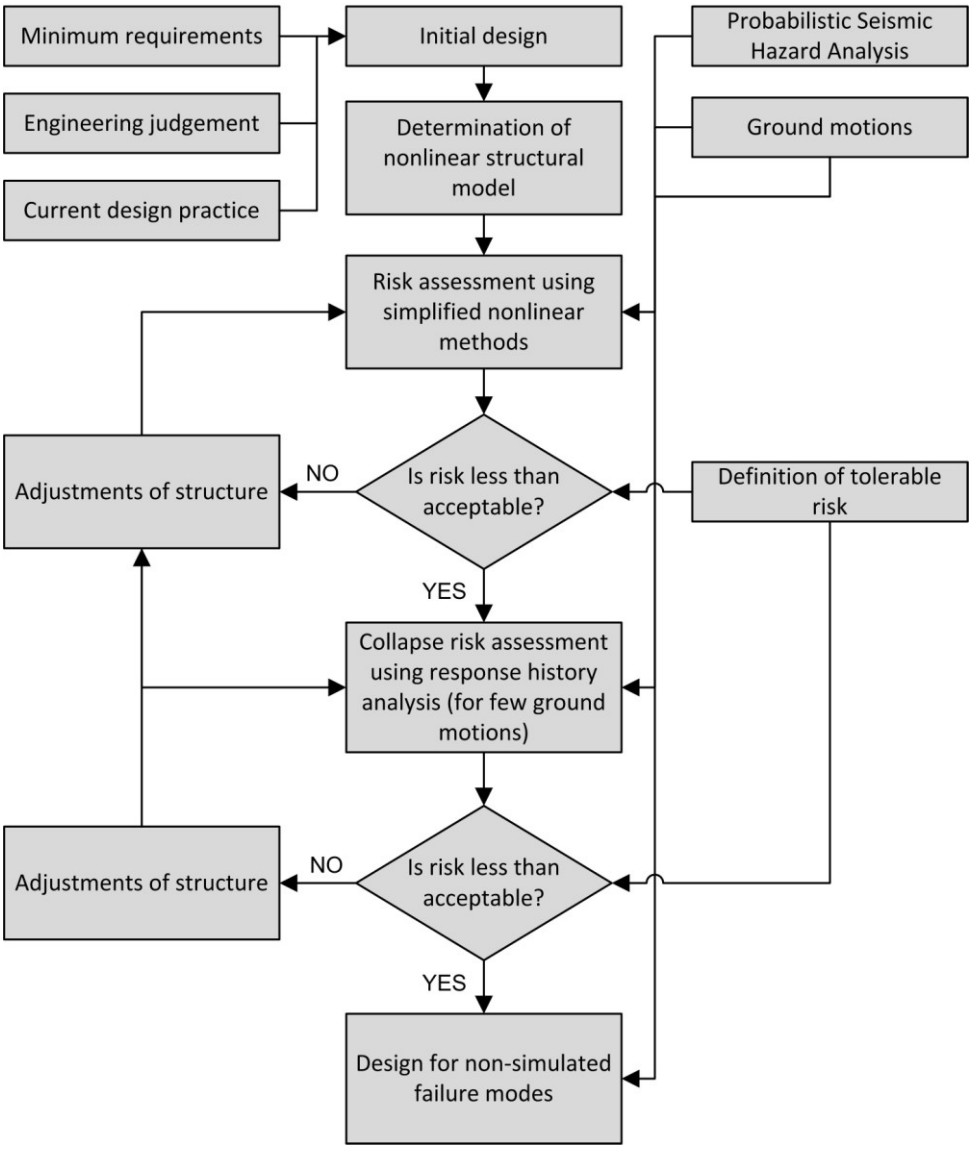


Figure 1: Flowchart of the proposed risk-based seismic design of buildings.

The simplified nonlinear model will be used for risk assessment of the initial structure. This is the third step of the proposed procedure, which requires additional information. In general detailed results of probabilistic seismic hazard analysis are needed in order to assess seismic risk of a structure with sufficient accuracy. It is foreseen that in this step the simplified nonlinear method will be used, since this type of method is not computationally demanding. In the case if envelope-based pushover analysis procedure (Section 3.1) will be used, a set of hazard-consistent ground motions will be needed. Based on results of EPA, ground motions could be further selected in order to be used later on for checking the adequacy of final design on the basis of response history analysis. However, an important ingredient of the proposed design procedure, which is important for decision-making, is the model of acceptable/tolerable risk. The most basic criterion for determination of acceptable or tolerable risk is related, respectively, to the probability of collapse of the facility or to the probability of loss of life. Several models for determination of acceptable risk are available. Some of them are briefly discussed in [37].

Most probably several iterations will be needed in order to satisfy the criteria for acceptable risk. Since risk assessment in this step will involve simplified nonlinear methods, iterative design procedure could be applied to realistic structures. However, the efficiency of the design procedure in terms of the number of iterations will depend on the ability of the analyst to adopt the best decisions regarding structural adjustments of the current structural variant (Step 4: Structural adjustments). Rather to use genetic algorithms or optimization methods, it is proposed to develop simple guidelines for structural adjustment in order to meet the criteria of acceptable risk with the smallest number of iterations and to achieve high utilization rate for all structural parts of the building. Such guidelines could be developed using the results of a sensitivity analysis for different types of structures aiming to assess which parameters of structural configuration has the greatest impact on the global seismic response parameters and consequently on seismic risk. In this step of the proposed design procedure the creative work of the designer will be encouraged, since this iterative design process will offer excellent insight into the nonlinear response for different structural variants of the building. Such approach will enable most effective decisions regarding the design adjustments which would eventually optimally increase the strength and ductility of the building.

Once the final structure will be obtained on the basis of the iterative design process, it is foreseen that the final design will be checked by performing response history analysis for few ground motions (Step 5), which will be carefully selected using the results of the envelope-based pushover analysis. The Step 5 of the design procedure will be performed in combination with the Step 6 in order to increase the utilization rate in the case if some parts of the building will be ‘over-designed’ or to check the accuracy of the simplified nonlinear methods used in the previous step. However, Step 6 is intended to provide demand for those components, which will not be simulated with the simplified nonlinear model. Based on this demand, the non-simulated failure modes, such as shear failure of structural elements or joints, will be prevented with a reasonably low exceedance rate.

Although the proposed procedure is in the initial stage of development, it was preliminary used to design an eight-storey reinforced concrete frame building. For an interested reader, detailed description of this illustrative example is given in paper No. 1249, which is also presented in this conference [37].

5 PROS AND CONS OF THE PROPOSED PROCEDURE AND FUTURE DEVELOPMENT

The main advantage of the proposed risk-based seismic design procedure is that it involves use of variety of nonlinear analysis methods, which enable predicting actual building response

and seismic risk. Therefore the analyst will get insight into the redistribution of internal forces in building, better information regarding the critical building's parts, which can suffer the most severe damage in the case of major earthquakes, and an excellent understanding how different structural adjustments affect seismic performance of the building. Additionally, the results of the design will be expressed in terms of probability. However, such approach will offer alternative ways of communicating performance to stakeholders that is more meaningful and useful for decision-making purpose, which is one of the shortcomings of current building codes [10].

However, design of structures for acceptable seismic risk requires information, which are highly uncertain (seismic hazard, nonlinear model, simplified nonlinear analyses, response history analysis, ground motions) and subjective (acceptable risk). Uncertainties should be appropriately taken into account. Therefore the treatment of uncertainties represents a disadvantage of the proposed concept of design in comparison to that incorporated in current building codes. Additionally, the risk-based design of realistic buildings is possible by using specific and powerful software and hardware. Therefore, algorithms and software tools aimed at facilitating the design process will have to be developed in the framework of the proposed research.

6 CONCLUSIONS

The concept of the iterative design procedure for acceptable/tolerable risk is presented in this paper. The proposed procedure is in the development stage within the basic research project Design of structures for tolerable seismic risk using non-linear methods of analysis, which is supported by the Slovenian Research Agency. The main objective of the proposed project is development of procedures and tools for design of structures for an acceptable/tolerable level of seismic risk. It is foreseen that the innovative procedure for the design of structures will overcome shortcomings of the current building codes and thus make a contribution towards scientifically oriented design procedures employing high level of technology and expert knowledge.

ACKNOWLEDGEMENT

The results presented in this paper are based on work supported by the Slovenian Research Agency. This support is gratefully acknowledged. The author appreciate the comments prepared by Nuša Lazar and Marko Brozovič, which contributed to improvement of the this paper.

REFERENCES

[1] P.G. Bakir, H.M. Boduroglu. Earthquake Risk and Hazard Mitigation in Turkey. *Earthquake Spectra*, **18**(3), 427-447, 2002.

[2] R. DesRoches, M. Comerio, M. Eberhard, W. Mooney, G.J. Rix. Overview of the 2010 Haiti Earthquake. *Earthquake Spectra*, **27**(S1):1-21, 2011.

[3] K. Goda, A. Pomonis, S.C. Chian, M. Offord, K. Saito, P. Sammonds, S. Fraser, A. Raby, J. Macabuag. Ground motion characteristics and shaking damage of the 11th March 2011 Mw9.0 Great East Japan earthquake. *Bull Earthquake Eng*, **11**, 141–170, 2013.

[4] D. D'Ayala, M. Dolce. Guest editorial: L'Aquila earthquake: seismic sequence of the 6th April 2009, Abruzzo, Italy. *Bull Earthquake Eng*, **9**, 1-10, 2011.

[5] Severn R.T. (2012). Understanding earthquakes: from myth to science. *Bulletin of Earthquake Engineering*, **10**, 361-366.

[6] ATC. Seismic Evaluation and Retrofit of Concrete Buildings (ATC-40), Applied Technology Council, Redwood City, California, 1996.

[7] FEMA. NEHRP guidelines for the seismic rehabilitation of buildings (FEMA publication 273),Washington, DC, 1997.

[8] Amer. Conc. Inst. (ACI). Building code requirements for structural concrete and commentary. ACI 318-11, Farmington Hills, MI, 2011.

[9] CEN. Eurocode 8: design of structures for earthquake resistance. Part 1: general rules, seismic actions and rules for buildings, 2004.

[10] FEMA. Seismic Performance Assessment of Buildings Volume 1- Methodology, FEMA P-58/Pre-Release, Federal Emergency Management Agency, August 2012.

[11] B.R. Ellingwood. Risk-informed condition assessment of civil infrastructure: state of practice and research, *Struct. and Infrastruct. E.*, **1**(1), 7-18, 2005.

[12] G. Deierlein. Overview of a comprehensive framework for earthquake performance assessment, Performance-Based Seismic Design – Concepts and Implementation, Fajfar P., Krawinkler H. eds., PEER Report 2004/05:15-26, Berkeley, 2004.

[13] C.A. Cornell. Calculating building seismic performance reliability, a basis for multi-level design norms. *Proc. of the 11th WCEE*, P.No. 2122, 1996.

[14] C.A. Cornell, F. Jalayar, R.O. Hamburger, D.A. Foutch. Probabilistic basis for 2000 SAC Federal Emergency Management Agency Steel Moment Frame Guidelines. *J. of Struct. Eng.* (ASCE), **128**(4), 526–533, 2002.

[15] A.B. Liel, C.B. Haselton, G.G. Deierlein, J.W. Baker. Incorporating modeling uncertainties in the assessment of seismic collapse risk of buildings. *Structural Safety*, **31**, 197-211, 2009.

[16] F. Zareian, H. Krawinkler, L. Ibarra, D. Lignos. Basic concepts and performance measures in prediction of collapse of buildings under earthquake ground motions. *The struc. design of tall and special build.*, **19**(1-2), 167-181, 2010.

[17] Dolšek M. Incremental dynamic analysis with consideration of modeling uncertainties. *Earthquake Engineering and Structural Dynamics*, **38**(6), 805–825, 2009.

[18] D. Vamvatsikos, M. Fragiadakis. Incremental dynamic analysis for estimating seismic performance sensitivity and uncertainty. *Earthquake Engineering and Structural Dynamics*, **39**, 141–163, 2010.

[19] M. Dolšek. Simplified method for seismic risk assessment of buildings with consideration of aleatory and epistemic uncertainty. *Struc. and I. Eng.*, **8**(1), 1-25, 2012.

[20] P. Fajfar, M. Dolšek. A practice-oriented estimation of the failure probability of building structures. *Earth. Eng. Struct. Dyn.*, **41**(3), 531-547, 2012.

[21] I. Evangelos, I. Katsanos, A.G. Sextos, G.D. Manolis. Selection of earthquake ground motion records: A state-of-the-art review from a structural engineering perspective. *Soil Dynamics and Earthquake Engineering*, **30**(4), 157-169, 2010.

[22] I. Iervolino, C.A. Cornell. Record selection for nonlinear seismic analysis of structures. *Earthquake Spectra*, **21(**3), 685-713, 2005.

[23] J.W. Baker. Conditional mean spectrum: Tool for ground-motion selection. *Journal of Structural Engineering*, **137**(3), 322-331, 2011.

[24] B.A. Bradley. A generalized conditional intensity measure approach and holistic ground-motion selection. *Earth. Eng. Struct. Dyn.*, **39**, 1321-1342, 2010.

[25] A. Azarbakht, M. Dolšek. Progressive incremental dynamic analysis for first-mode dominated structures. *Journal of Structural Engineering* **137**(3), 445-455, 2011.

[26] OpenSees. Open system for earthquake engineering simulation, PEER Center, Univ. of California, Berkeley, http://opensees.berkeley.edu/, 2012.

[27] M. Brozovič, M. Dolšek. Envelope-based pushover analysis procedure for the approximate seismic response analysis of buildings. *Submitted to Earthquake Engineering & Structural Dynamics* (in review), 2013.

[28] J. Žižmond, M. Dolšek. Deaggregation of seismic safety in the design of reinforced concrete buildings using Eurocode 8. 4th International Conference on Computational Methods in Structural Dynamics and Earthquake Engineering, COMPDYN 2013, Paper No. 1226, 2013.

[29] P. Fajfar. A nonlinear analysis method for performance-based seismic design. *Earthquake Spectra*, **16**, 573-592, 2000.

[30] A.K. Chopra, R.K. Goel. A modal pushover analysis for estimating seismic demands for buildings. *Earthquake Engineering and Structural Dynamics*, **31**, 561-582, 2002.

[31] M.N. Aydinoğlu. An incremental response spectrum analysis based on inelastic spectral displacement for multi-mode seismic performance evaluation. *Bulletin of Earthquake Engineering*, **1**, 3-36, 2003.

[32] S. Antoniou, R. Pinho. Development and verification of a displacement-based adaptive pushover procedure. *Journal of Earthquake Engineering*, **8**, 643-661, 2004.

[33] H. Sucuoğlu, M.S. Günay. Generalized force vectors for multi-mode pushover analysis. *Earthquake Engineering and Structural Dynamics*, **40**(1), 55-74, 2011.

[34] C.J. Reyes, A.K. Chopra. Three-dimensional modal pushover analysis of buildings subjected to two components of ground motion, including its evaluation for tall buildings. *Earthquake Engineering and Structural Dynamics*, **40**(7), 789–806, 2011.

[35] M. Kreslin, P. Fajfar. The extended N2 method taking into account higher mode effects in elevation. *Earthquake Engineering and Structural Dynamics*, **40**(14), 1571–1589, 2011.

[36] H. Bobadilla, A.K. Chopra. Evaluation of the MPA procedure for estimating seismic demands: RC-SMRF buildings. *Earthquake Spectra*, **24**(4), 827-845, 2008.

[37] N. Lazar, M. Dolšek. Application of the risk-based seismic design of buildings using nonlinear methods of analysis. 4th International Conference on Computational Methods in Structural Dynamics and Earthquake Engineering, COMPDYN 2013, Paper No. 1226, 2013.

COMPDYN 2013
4th ECCOMAS Thematic Conference on
Computational Methods in Structural Dynamics and Earthquake Engineering
M. Papadrakakis, N.D. Lagaros, V. Plevris (eds.)
Kos Island, Greece, 12–14 June 2013

STRUCTURAL MODELLING ISSUES IN SEISMIC PERFORMANCE ASSESSMENT OF INDUSTRIAL STEEL BUILDINGS

G. Della Corte[1], I. Iervolino[1], and F. Petruzzelli[1]

[1] Università degli Studi di Napoli Federico II
Via Claudio 21, 80125 Napoli
e-mail: {gaetano.dellacorte,iunio.iervolino,fabio.petruzzelli}@unina.it

Keywords: Dynamic Analysis, Risk Assessment, Seismic Response, Steel Structures.

Abstract. *The paper presents part of a study on the probabilistic seismic performance assessment of an existing industrial facility featuring a steel structure as the main building. The building is located in central Italy and is composed of structures having different construction ages. One portion was designed and built in the early 1970s and expanded in the late 1970s. In the early 1990s, a new portion was built close to the former but separated by means of gaps. All the structures are very similar in concept, though they are different in detailing and structural behavior. Six models were built up for the existing structures, four two-dimensional (2D) and two three-dimensional (3D) models. The four 2D models represent four distinct frames, one per each of the two main plan directions of the two structures (the older, i.e. the 1970s', and the newer, i.e. the 1990s'). The two 3D models are variants of a model of the newer building: the difference is the modeling options of roof truss joints. Non-linear dynamic analyses of the six structural models were carried out. Ground acceleration records were specifically selected consistent with disaggregation of seismic hazard at the site. The probability distribution of demands was then investigated, considering both global and local failure modes. This paper, in particular, presents and discusses results for only the global response assessment, in terms of peak transient and residual roof drifts. The structural modeling issues are discussed with a focus on the effects that different modeling options may have on assessment of seismic fragility and risk. The main conclusions drawn are: (i) roof truss failure might occur in the form of instability of a group of members, a failure mode – triggered by local out-of-plane truss vibrations and P-Delta effects – that can be only captured by a 3D model; (ii) including residual drifts, along with peak transient values, in the evaluation of the probability of failure can be of utmost importance if the structure is relatively stiff (thus experiencing small peak drift) but weak (thus easily experiencing inelasticity). The first conclusion above is specific for industrial steel buildings but applicable to all those characterized by a roof truss with the possibility of out-of-plane joint displacements, while the second conclusion appears to have general validity for the seismic risk assessment of structures.*

1 INTRODUCTION

The industrial building stock of many countries is significantly contributed by steel structures. Although the latter are generally relatively lightweight structures and, in most of cases, designed for wind actions, the assessment of their seismic performance is important for the estimation of the possible consequences of earthquakes, in terms of direct damage and/or business interruption. On the other hand, it is known that assessing the performance of existing structures is a task quite different with respect to the design of a new one. An especially relevant issue is the need for models to be able to capture all the potential failure modes, especially those reflecting brittle behavior. Old steel structures are frequently characterized by partial-strength connections, whose contribution to the system's inelastic response cannot be neglected. In the special case of industrial steel buildings, the undesired failure modes may involve also the roof structure, whose design is generally dominated by gravity and wind loading. Besides, the roof structure is frequently a complex three-dimensional system, whose dynamics may involve modes of failure different from the case of horizontal rigid floor diaphragms.

The analysis of the above issues was tackled in the study presented in the following, within the context of probabilistic risk assessment and performance-based earthquake engineering. The study was carried out with reference to a case study industrial steel building, which is characterized by constructional details (columns, connections, roof members, roof bracing) that are common for this structural type. Therefore, investigations may allow tracing comments and drawing conclusions applicable to similar structures.

The following Sections give first a short description of the building structures and of the models set-up. Subsequently, seismic hazard at the building site is described by means of results from a site-specific probabilistic seismic hazard analysis (PSHA); ground motion records were consequently selected from available databases. The selected ground motions were then used to analyze seismic demands to the investigated building structures. Results from nonlinear dynamic analyses of multiple two-dimensional (2D) and three-dimensional (3D) structural models are presented and commented in this paper with reference to structural fragility and seismic risk represented by means of annual failure probability.

2 THE BUILDING STRUCTURES

Figure 1a shows an aerial view of the whole building, while Figure 1b illustrates schematically the structural plan layout. There are four building structures, separated by gaps. The white area in Figure 1b refers to the oldest structure, built in 1971 and separated into two portions by a longitudinal joint parallel to the direction X. In 1979 these two portions were enlarged with no separation between the new and old constructions (light grey shaded area in Figure 1b). Considering that additions were built using the same materials and structural dimensions as those of the previous 1971 structures, these will be referred to as 1971/79 structures. Finally, the most recent parts were built in 1991, as indicated by the dark grey shadow in Figure 1b. Both the 1971/79 and the 1991 structures were designed according to old seismic codes [1], with significant underestimation of design seismic intensities with respect to current design seismic actions based on probabilistic hazard at the site. Codes and Standards used for the design of the existing structures were based on the *Allowable Stress* method without any account of *Capacity Design* principles. The latter were in fact enforced only very recently [2] for the Italian design professionals. The expected consequence is that no control was taken of the location of plastic zones, which may therefore involve also relatively brittle failure modes.

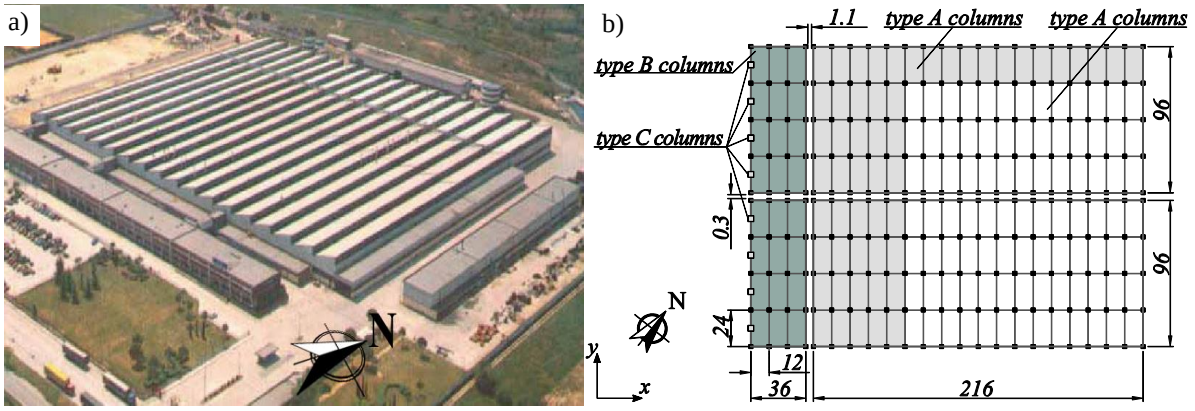


Figure 1: Aerial view of the whole facility (a) and schematic drawing illustrating the plan layout (units: m) (b).

Parts made in different years have similar columns and roof structures. The latter are made of shed-type trusses in direction X and Pratt trusses in direction Y. Sample structural cross sections of trusses in directions X and Y, as recorded in the original design drawings, are reproduced in Figures 2a, 2b and 2c. Figures 2a and 2b show typical cross sections of roof trusses for internal frames. Figure 2c shows a cross section of the truss located onto the south-west side perimeter frame. Such a perimeter frame is characterized by additional columns with respect to other frames (Fig. 1b), and a smaller free length of columns because the corresponding roof truss is at a smaller height (Fig. 2c). A sample of some details of roof joints is illustrated in Figure 2d. As mentioned, detailing (bolts pitch, hole-to-bolt diameter tolerance, etc.) follows outdated Italian regulations about the design of steel structures [1]. The roof structure is completed by in-plane sub-horizontal X-bracing and minor elements supporting the roof panels.

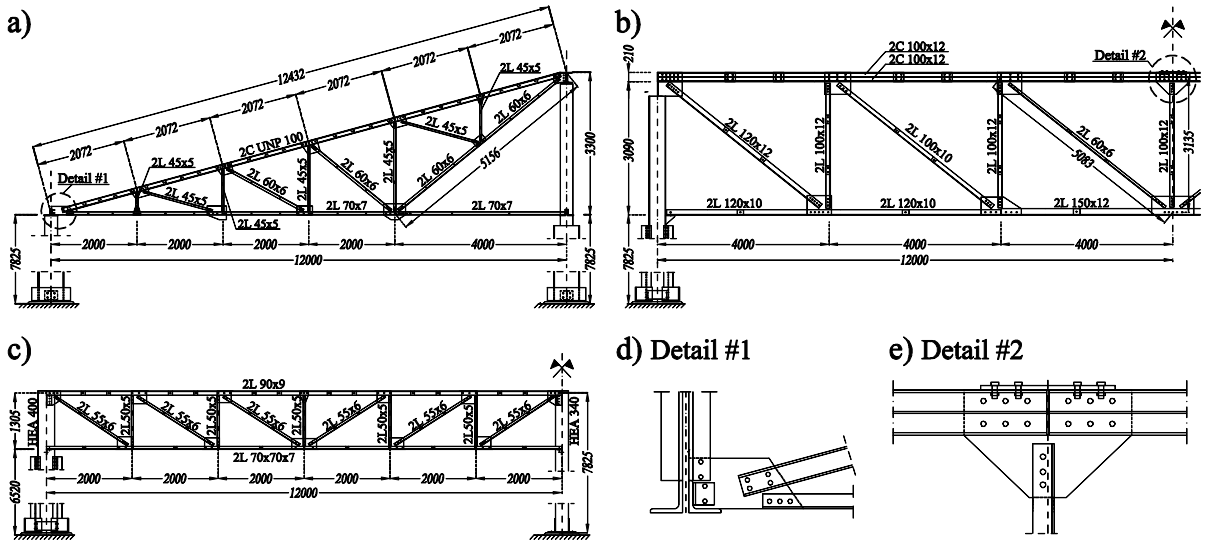


Figure 2: Sample structural cross-sections of trusses in direction X (a) and Y (b, c); sample (qualitative) details of roof member joints (d).

Vertical resisting members, which are both sustaining the roof structure and resisting horizontal forces, are composite battened columns. In the portions of the structure built in 1971/79, composite columns are made of two IPE 360 shapes, reinforced on the flanges with 15 mm thick plates and coupled together by battens consisting of plates welded to the flanges of the two profiles (Fig. 3a). A HE A 240 shape is welded at the top-end of the battened column in

order to connect the roof trusses. These composite columns will be hereafter referred to as columns of type A, whose plan location is shown in Figure 1b. In the 1991 building, the main columns, referred to as type B (Fig. 1b), are also composite members, obtained by battening IPE 600 shapes. Battens of type-B columns were obtained by cutting pieces from hot-rolled profiles with HE A 500 cross-section and bolting their flanges to the web of the main column members, as shown in Figure 3b. A hot-rolled HE A 400 shape is placed at the top-end of the column, connecting the latter to the roof trusses. Flanges of the HE A 400 shape are connected to the web of the composite column members by means of bolts, as made for battens (Fig. 3c). In addition to the above, there are also columns consisting of a single hot-rolled HE A 340 shape (type C, Fig. 3d), located at the left-hand side perimeter frame shown in Figures 1b and 2c. These type-C columns are located in the middle of each main span, whose length is therefore reduced to one-half (12 m) of the value in other frames parallel to the direction Y.

Figure 3 also shows details of the connections to the foundation for different types of columns. For type A columns (Fig. 3a), the connection is provided by a single 20 mm thick steel plate with four anchor bolts (diameter = 30 mm). For type B columns (Fig. 3b), the connection is constituted of two distinct 30 mm thick base plates, each one with three anchor bolts (diameter = 30 mm). The connection of type C columns to the foundation (Fig. 3d) is comprised of a steel plate (thickness = 30 mm) and four anchor bolts (diameter = 30 mm). In each of the cases described above, base plate stiffeners with thickness varying between 15 and 20 mm were used.

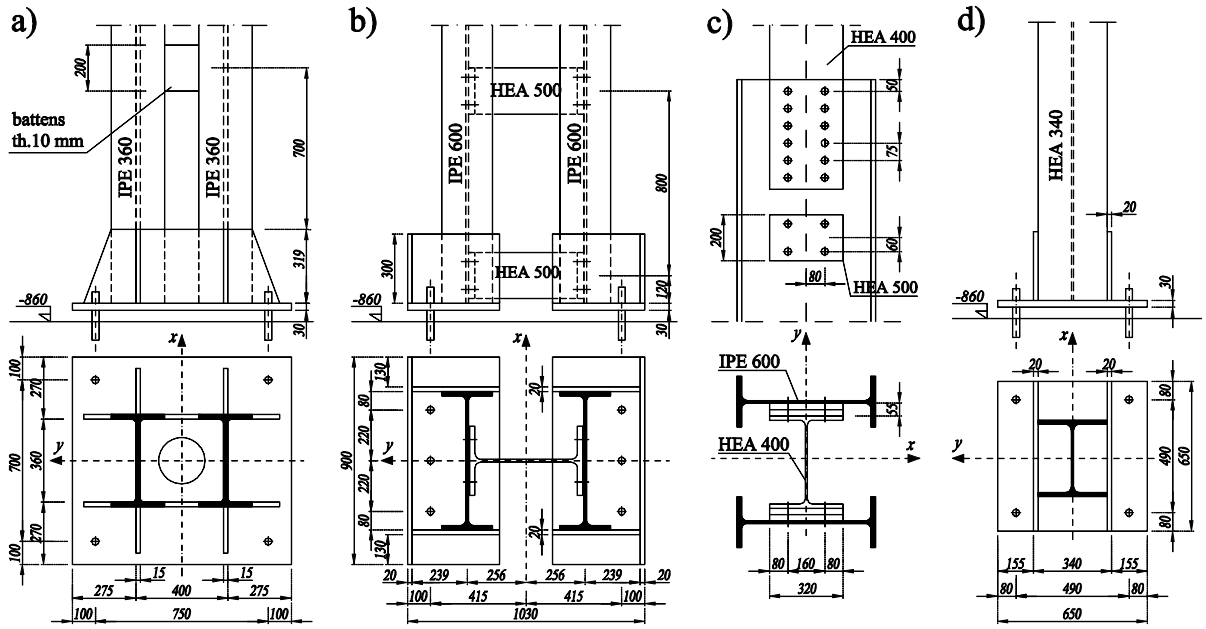


Figure 3: Columns and base connections: a) type A, b) type B, c) details at the top of type B columns, d) type C.

Based on the available information, it is inferred that building foundations are made of isolated reinforced concrete blocks. Original design documents indicate that the soil can be assumed as class B according to the Italian Seismic Code [2]. Soil type B is a quite stiff soil, which is characterized by average shear wave velocity in the first 30 m of depth from ground surface ($V_{S,30}$) in the range 360 m/s to 800 m/s. Soil-structure interaction is expected to be not significant for such soil conditions and it was neglected in the analysis.

As-built data collection is always important for a reliable assessment of the performance of existing constructions. Generally, expected average material properties are used to evaluate the seismic strength and to estimate the seismic deformation demand. According to the cur-

rent Italian seismic code [2], the expected average values of steel yield strength are about 1.10-1.20 times the characteristic values, depending on the grade. No information is provided by the code about average-to-characteristic strength ratio of bolts, which are considered non-dissipative elements for the design of new structures. However, as shown in the next Sections, in the case study structures as-built column base connections are partial-strength. Column base connection failure occurs with a mixed failure mode involving failure of bolts in tension. Therefore, a necessary (but cautious) modeling choice was to use the characteristic strength of bolts in the calculation of column base connection strength. In order to be consistent with the use of characteristic values of bolt strength, it was decided to use always the characteristic value of material strengths. The latter, due to the relatively small variability of yield strength, is close to the mean value and therefore it is expected to have a minor effect on the bias in the failure probability as computed in Section 6. However, to check the eventual occurrence of some failure modes (e.g., failure of base plate welds or failure of column battens), peak values of column base strength were estimated using commonly adopted material and strain-hardening factors, with a total overstrength factor assumed equal to about 1.3. The original design documents report the following characteristic values of the material strengths: yield strength of members f_{ym} = 235 MPa; yield strength of column base plates f_{yp} = 275 MPa; yield strength of roof gusset plates f_y = 355 MPa; grade 8.8 for bolts; grade C20/25 for concrete [3].

3 STRUCTURAL MODELS

This Section highlights a few aspects relevant to the modeling for seismic performance assessment of the case study structures. Figure 4 illustrates schematically the numerical models: four two-dimensional (2D) frame models, one per direction (X and Y) for each of the structures built in 1971/79 and 1991; two three-dimensional (3D) models for the 1991 building, here analyzed for earthquakes acting along direction Y. The two 3D models built up for the 1991 building structure are differing for the modeling hypotheses of roof truss joints, as further discussed in the following.

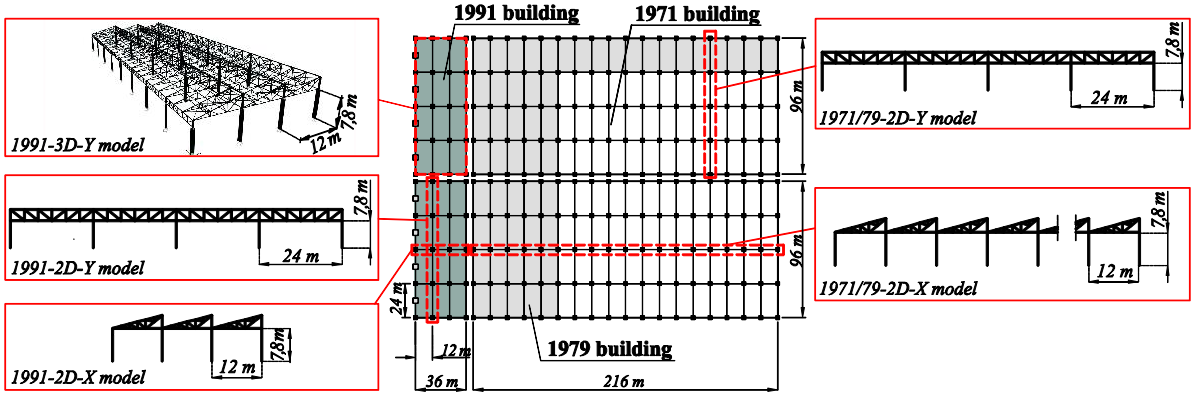


Figure 4: Structural models for 1991 and 1971/79 portions of the case study buildings.

The 1991 structures are characterized by the type B column base connections (Fig. 3b), which are appreciably different from the standard types covered by Eurocode 3 (EC3) [3]. However, using the same principles at the basis of the EC3 *component method*, but slightly adapting/interpreting the rules given in the code, component contributions to the total rotational stiffness and strength were derived [4].

An issue common to all the investigated numerical models is the representation of the hysteresis response of plastic zones, especially with reference to cyclic degradation phenomena. Previous studies [5, 6, 7] have shown that in-cycle strength degradation, such as the one due

to P-Delta effects, has a much more pronounced effect on the evaluation of seismic response than cyclic strength degradation, especially for flexible structures. Generally, the development of accurate models representing the hysteretic response of plastic zones involves significant efforts, even in case of standard geometries for which several experimental results are available. In the specific case studies, column base connections of type B are characterized by geometry for which there are no experimental test results available. Based on the above arguments, the cyclic moment-rotation response of column base connections was approximated by the *Pivot* hysteresis model [8] including pinching of hysteresis loops but no cyclic degradation. The moment-rotation response of flexural plastic hinges in hot rolled members was approximated by an elastic-perfectly-plastic model.

Failure of battens in composite columns was checked to be not a concern by verifying that they were able to sustain the maximum internal actions corresponding to the peak column shear force associated with the flexural strengths at the top and bottom ends. Consequently, composite columns were treated as linear elastic elements, taking into account the increase of shear elastic deformability due to the discontinuous and flexible web connections [3].

It is finally to remark that pounding of adjacent frames was not explicitly modeled, because displacement demand from the analysis of individual frame models (Section 5) showed that relative joint displacements would never be large enough to close the existing gap prior to the occurrence of global frame collapse.

3.1 3D vs. 2D models

The behavior of single-storey industrial steel buildings is generally affected by the roof deck diaphragm, which is almost always comprised of a thin-walled cold-formed trapezoidal sheet. The shear flexibility of such deck diaphragm is not negligible, generally leading to an increase of the building period of vibration with respect to a model based on rigid diaphragm assumption [9]. However, it has also been proved that nonstructural components may reduce appreciably the period of vibration with respect to predictions based on a model including the steel deck only [10]. It is noted that the contribution of nonstructural components may be difficult to be quantified in practice. On the other hand, a typical practice in the design consists of neglecting the stiffening contribution of the roof deck diaphragm while using roof braces, an option also selected for the case study building. However, such roof braces are characterized by high slenderness leading to buckling for relatively low levels of seismic intensity. Whether roof braces buckle, the coupling of response of parallel 2D frames obviously reduces and the system response approaches the one of isolated 2D frames. In addition, consideration has to be given to the feature of a 3D model to explicitly and automatically capture buckling of the roof structure. 2D models are unable to represent out-of-plane buckling of the roof trusses and they therefore may be missing important information about the possible failure modes of the structure. Out-of-plane buckling modes are sensitive to end-restraint conditions. Members of roof trusses are commonly modeled as perfectly pinned at their ends when in-plane structural analysis is to be carried out. This is generally motivated because the truss response is dominated by axial forces: neglecting bending moments removes one source of stiffness and strength thus resulting into conservative global response assessment. However, out-of-plane end-restraints may be essential in case of transverse vibrations of plane trusses: releasing transverse end moments may result in such a case into an unstable structure.

Therefore, the issue of 3D versus 2D model predictions has been investigated. In particular, the importance of modeling of roof joints was investigated by analyzing two alternative 3D models: (i) a model where all roof joints were assumed to be fully continuous (labeled as *fully continuous*) and (ii) a model where all moments were released for those members interrupting at a joint (labeled as *partially continuous*). Results from analyses of 3D models are subse-

quently also compared with those from 2D models, which have the advantage of being much less cumbersome from the points of view of the computational time and effort. In the 3D model the roof bracing elements were assumed to be linear elastic but with P-Delta effects activated. Therefore, the 3D model is able to capture elastic buckling but it is not able to capture inelastic buckling or failure of connections, which must be checked separately based on peak force demand.

4 SEISMIC HAZARD AND GROUND MOTIONS

The site of interest (that cannot be disclosed for confidentiality) is located in central Italy, in the middle of Appennines and its seismic hazard was computed ad-hoc. In fact, although hazard is made available by the *Istituto Nazionale di Geofisica e Vulcanologia* (INGV) [11] for a dense grid covering the country, such an information is only for site class A (rock), which does not correspond to the local geological conditions of the facility. Therefore, hazard curves were computed via the software described by Convertito *et al.* [12], employing the seismic source zone model for Italy of Meletti *et al.* [13]; the latter is also adopted for the official nationwide hazard assessment by INGV. The parameters associated to each of the zones in terms of minimum and maximum magnitude, rate of occurrence, and b-value of the Gutenberg-Richter relationships, were given by Barani *et al.* [14].

For the purposes of dynamic structural analysis, the spectral accelerations at the fundamental period of the structures and 5% damping ratio, $S_a(T_1)$, have been adopted as the ground motion intensity measures (IMs). Therefore, specific hazard curves for 1 s and 1.6 s (the fundamental periods of the 1991 and 1971/79 structures, respectively) were developed for *stiff soil* considered as a proxy for B-type site class. The resulting hazard curves are given in Figure 5 and served as a basis for the risk assessment discussed in Section 6.

In fact, hazard was also used, via disaggregation, for ground motion (GM) record selection. Disaggregation was carried out in terms of magnitude, M, and source-to-site distance, R. Disaggregation changes with the IM-value considered and therefore with the return period T_R. To cover a wide range of IM-values, the hazard for four levels of $S_a(1s)$, corresponding to 50, 475, 975 and 2475 yrs. return periods, was disaggregated. This allowed to determine the *design earthquakes* for each T_R and both IMs, using the same procedure as in Iervolino *et al.* [15]. Table 1 reports the M and R bins and strong motion databases in which records were selected via the REXEL software [16]. Sets of 30 one-component records were selected for each bin [4]. These sets were employed as an input for incremental dynamic analysis (IDA) [17] at intensity levels around that of the return period they correspond to [4]. The records of the selected sets were scaled in a way the elastic spectral acceleration at the fundamental period of vibration of each structure is equal to the target intensity level in all the IDA steps.

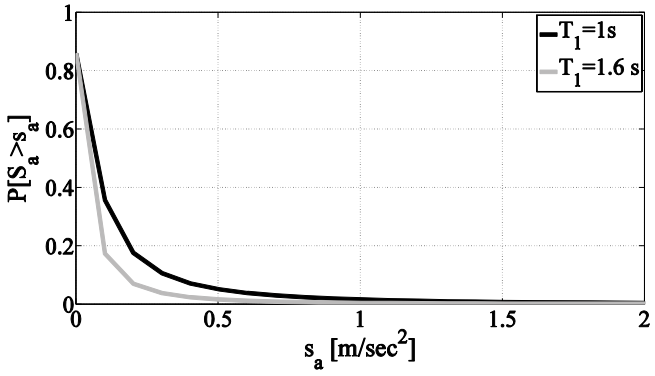


Figure 5: Seismic hazard for the site in terms of annual exceedance probability for the IMs of interest.

T_R [yr]	S_a(1s) [g]	R [km]	M	Database
50	0.10	0-20	5-6	ITACA
475	0.30	0-30	5.3-6.5	ITACA
975	0.37	5-25	6-7	ESD
2475	0.50	0-40	6-7.5	ESD

Table 1: Record selection bins consistent with disaggregation of seismic hazard at the facility site. ITACA is the Italian ACcelerometric Archive, and ESD is the European Strong-motion Database [16].

5 NON LINEAR DYNAMIC ANALYSES

Results of IDAs are summarized hereafter by showing the relationships between the assumed IM and the selected engineering demand parameters (EDPs). The latter were peak transient and residual roof drift ratios (ratios of displacement and corresponding height on the ground) for the global response assessment. Results were obtained using lumped plasticity finite element models analysed by means of SAP 2000 v.14 [18].

Figure 6 shows results in terms of drift ratio demand to the four 2D structures for all the selected earthquake intensities and GMs. Both peak transient (full dot) and residual (empty dot) drift demands are shown. Median drift demands are also illustrated with solid line (transient) and dashed line (residual). Figures 6a and 6b allow comparing the response of the 1971/79 frames, in the X and Y directions respectively. It is noted that the X-direction frame is characterized by an appreciable (non-zero) value of the drift under gravity loads (i.e. for $S_a = 0$). This is due to the asymmetry of the 2D frame, which is swaying laterally under gravity loading. It is also noted that at relatively small values of seismic intensity, the ratio of median residual to peak transient demand to the X-direction frame (Fig. 6a) is larger than it is for the Y-direction frame (Fig. 6b). This is an aspect having an influence on the probability to exceed a given limit state expressed either in terms of residual drift or transient drift or in terms of both quantities (see next Section). Figures 6c and 6d allow comparing the X and Y direction response of the 1991 building. Similarly to the 1971/79 frames, the ratio of residual to peak transient drift is larger for the X-direction than it is for the Y-direction frame. Differently from the 1971/79 frame, the X-direction frame is characterized by a small initial (gravity-induced) drift. This will have consequences on fragilities and probabilities of failure calculated considering both residual and transient drifts as discussed in the next Section.

Figure 7 illustrates the median drift demands to the 1991-3D-Y models. The median drift demand to the 1991-2D-Y frame is also reported in Figure 7 in order to compare the global performance predicted from 3D and 2D models. For spectral accelerations up to about 0.5g, all models show a similar median drift demand. At larger spectral accelerations the behavior changes radically. In case of a 3D model, the number of GMs inducing global collapse increases much more rapidly than it does for a 2D model. Such a large difference in response is due to the activation of a different collapse mechanism. Collapse of the 1991-2D-Y frame occurs with a column-sway mode (Fig. 8a). The same type of collapse mechanism is also exhibited by the X-direction 2D frames (Fig. 8b). The collapse mechanism of the 1991-3D-Y model is instead characterized by relatively complex three-dimensional instability of roof trusses (Fig. 8c), a mode of response which cannot be captured by 2D models. The details of the collapse mode depend on the GM, because high-frequency modes of transverse vibration of planar trusses are activated depending on the GM frequency content. Clearly, the *fully continuous* 3D model leads to a better structural response than the *partially continuous* 3D model, because roof instability is delayed at larger levels of spectral acceleration by introducing continuity of the joint bending moments. Thus, the *fully continuous* 3D model approaches the response of the 2D model for which such roof instability is *a priori* excluded.

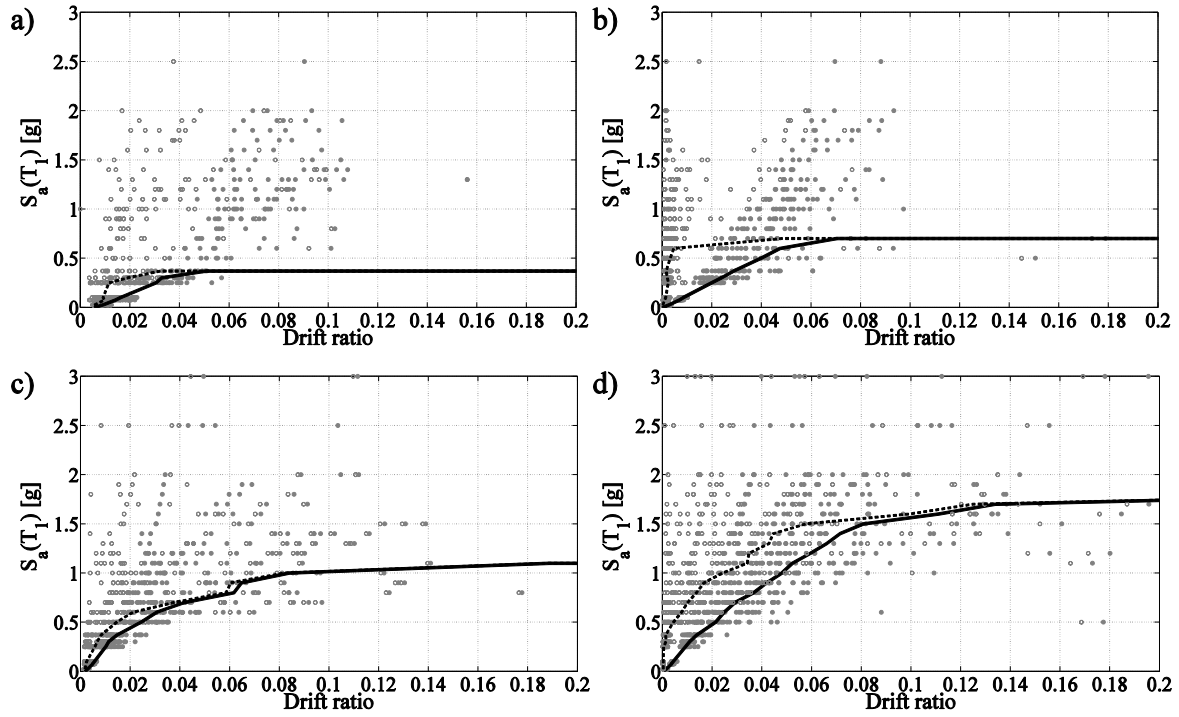


Figure 6: Peak transient and residual drift ratio for 2D frames: (a) 1971/79-2D-X; (b) 1971/79-2D-Y; (c) 1991-2D-X; (d) 1991-2D-Y.

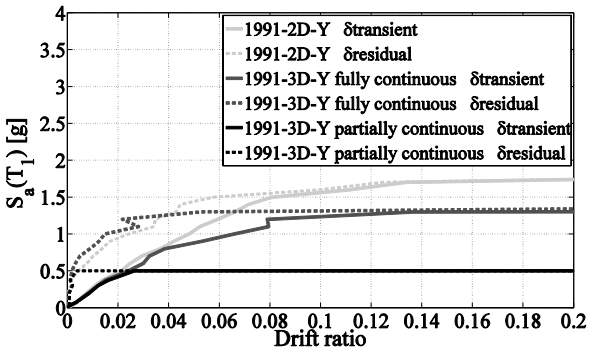


Figure 7: Peak transient drift ratio for the 1991-3D-Y models and the corresponding 1991-2D-Y frame.

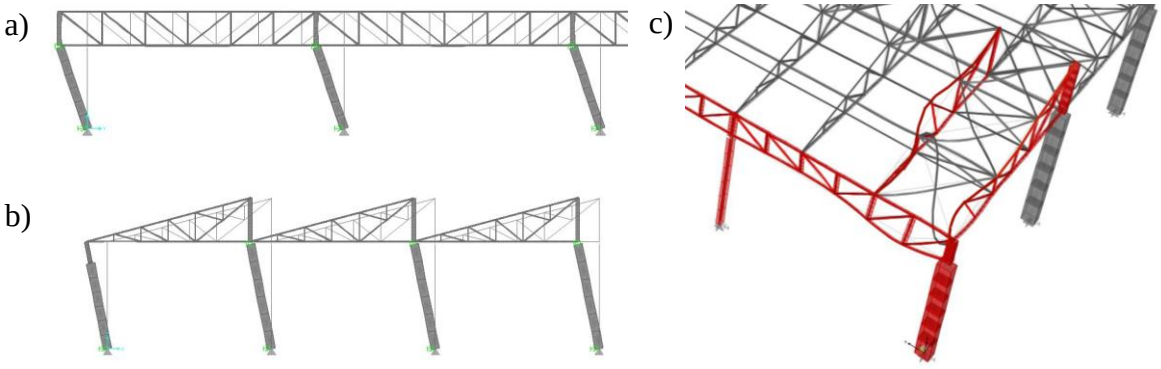


Figure 8: Collapse mechanisms: (a) 1991-2D-Y frame; (b) 1991-2D-X frame; (c) 1991-3D-Y model.

6 FRAGILITIES AND FAILURE PROBABILITIES

Three limit states were considered: Immediate Occupancy (IO), Life Safety (LS) and Collapse Prevention (CP) [19]. For global performance assessment, such limit states are defined in terms of limit values of residual drifts and/or peak transient drifts. Transient drift ratio capacities corresponding to the IO, LS and CP performance levels were assumed equal to 0.0075, 0.025 and 0.05. The residual drift ratio capacity at the CP limit state coincides with the peak transient capacity, while it was assumed equal to 0.01 at the LS limit state. According to ASCE [19], the residual drift must be *negligible* at the IO limit state. It was assumed that this means that the residual drift must be smaller than or equal to the initial drift due to gravity loading (i.e., the pre-earthquake drift). A composite rule was used to define global *collapse*, considering either numerical instability or the transient drift being larger than 0.1, a limit introduced to exclude entering a region where the model is not trustworthy [17].

Figure 9 shows example comparisons of fragility curves obtained on the basis of only the peak transient drift ratio (*univariate* distribution of demands) and those calculated considering limits on the residual drifts also (*bivariate* distribution of demands). Figure 9a shows fragilities computed for the 1971/79-2D-X frame (based on IDA results illustrated in Figure 6a), while Figure 9b is relevant to the 1991-2D-X frame (IDA results in Figure 6c). For both structures, at the CP limit state, the two types of fragility curves (for *univariate* and *bivariate* distributions) are practically coincident, because the residual drift demand is always smaller than the transient drift demand, while capacity limits [19] are coincident. The largest effect of including limitations on the residual drifts is expected to appear in the calculation of fragilities for the LS and, especially, the IO limit states. However, the changes in the calculated fragilities can be either large or small, because of the structure peculiar response. For example, Figure 9a shows no significant effect at the IO limit state, while Figure 9b shows large difference. Indeed, the 1971/79-2D-X frame is subject to a relatively large initial (gravity induced) drift (Fig. 6a). As mentioned above, such an initial drift is the assumed residual drift capacity at the IO limit state; it is relatively large and close to the peak drift capacity for the 1971/79-2D-X frame. On the other hand, median residual drift demands resulted to be relatively small with respect to median transient demands (Fig. 6a), because of the flexibility of the structure associated with large peak drifts and small inelasticity. Thus, introducing a limit to the residual drift did not change significantly the total seismic fragility of the 1971/79-2D-X frame. An opposite trend is revealed by the 1991-2D-X frame: the ratio of residual and transient drift capacity is small while the ratio of the median residual and transient drift demand is large (Fig. 6c). Consequently, the frequency of exceeding the IO limit state because of an excessive residual drift had a strong effect on the total computed fragility (Fig. 9b).

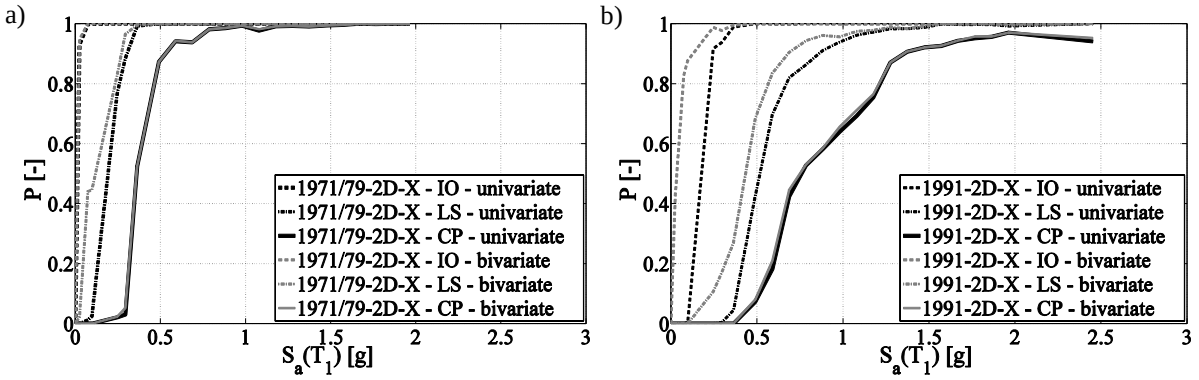


Figure 9: Fragility curves: a) 1971/79-2D-X frame; b) 1991-2D-X frame.

Given the hazard (Section 4) and the fragilities discussed above, the annual probability of failure (P_f) was computed [4]. The P_f calculated on the basis of the peak transient drifts are reported in Table 2, while Table 3 gives percentage variations obtained when also residual drifts were included in the analysis. Tables 2 and 3 permit appreciating the seismic reliability of the analyzed structures, the influence of the model adopted, as well as the importance of including residual drifts in the assessment.

Table 2 shows that that Y-direction frames are generally more reliable than X-direction frames: this is because of the larger stiffness and strength observed for Y-direction frames. It is worth remembering that this paper discusses only the global response in terms of roof drift ratios and the above conclusion is based on only such response parameters. A more comprehensive assessment must necessarily include local failure modes; e.g., failure of roof members and connections [4, 20, 21]. (It has to be noted that differences between results reported in Table 2 and those presented in [21] are generally due to refinements made to the numerical fragility curves at low levels of spectral accelerations. In addition, the 3D model previously analyzed [20] was characterized by different joint restraint modeling assumptions.)

Table 3 confirms the results of Figure 9. If transient and residual drift capacities are close each other, the inclusion of residual drifts in the calculation of P_f must obviously have a minor effect, because the residual drift demand is always smaller than the transient value. If the residual drift capacity is significantly smaller than the transient value, the influence of including residual drifts in the calculations will still depend on the distribution of demands. At a given level of spectral acceleration, if the median residual and transient drift demands are relatively similar, which is the case for stiff but weak structures, then the limit imposed to the residual drift is expected to have a remarkable influence on the calculated P_f. On the contrary, if the median transient drift demand is larger than the median residual drift demand, as in case of flexible and strong structures, the influence will be smaller though it may still be significant.

Frame	IO	LS	CP
1971/79-2D-X	3.7E-02	1.2E-03	2.0E-04
1971/79-2D-Y	5.7E-03	3.3E-04	7.0E-05
1991-2D-X	5.1E-03	4.7E-04	1.9E-04
1991-2D-Y	5.0E-03	3.9E-04	1.1E-04
1991-3D-Y “fully continuous”	5.9E-03	4.2E-04	1.7E-04
1991-3D-Y “partially continuous”	6.0E-03	4.3E-04	3.4E-04

Table 2: Probabilities of failure based on only the peak transient drift.

Frame	IO	LS	CP
1971/79-2D-X	1.26	454.30	2.74
1971/79-2D-Y	113.40	3.62	0.13
1991-2D-X	1182.59	152.06	4.97
1991-2D-Y	1.81	6.92	8.33
1991-3D-Y “fully continuous”	6.48	0.55	0.35
1991-3D-Y “partially continuous”	4.14	0.79	0.38

Table 3: Variations of probabilities of failure due to inclusion of residual drifts; the table gives the percentage differences with respect to values shown in Table 2.

7 CONCLUSIONS

This paper has presented failure mode considerations versus modeling assumptions in the probabilistic seismic global performance assessment of a case study industrial steel building.

Results of dynamic nonlinear analyses of different frame models extracted from the case study buildings have been discussed. The analyses were based on sets of ground motion records consistent with site-specific probabilistic seismic hazard analysis. Integrating the hazard and the fragility curves for different limit states, annual probabilities of failure were obtained. The following are the main conclusions drawn from the study.

- Using a 3D model highlighted the possibility of roof truss failure in the form of complex three dimensional instability modes, involving groups of roof truss members. Such failure modes cannot be predicted using 2D models, because of the intrinsic 3D features of transverse vibrations of planar trusses. The latter vibrations are triggering local P-Delta effects, which are responsible of the instability modes. This conclusion is valid for all industrial steel buildings featuring a roof truss structure with out-of-plane joint displacements.
- Including both residual and peak transient drifts in the seismic risk assessment could be either very important or rather unessential depending on the structural characteristics and the relative magnitude of limits on residual and transient drifts. Results obtained within this study suggests that, generally, residual drifts should be included in the analysis, unless it can be anticipated by clear reasoning that they would have a minor effect on the probability of failure. The results presented in this paper might be helpful in identifying the latter cases. Such comments on the influence of residual drift limitations are clearly valid beyond the specific case study of industrial buildings.

ACKNOWLEDGEMENTS

This work was partially supported by AXA-MATRIX, within the AXA-DIST 2010-2013 research program, and partially by ReLUIS, within the ReLUIS-DPC 2010-2013 research program.

REFERENCES

[1] CS.LL.PP. (1996). D.M. 16.01.1996: Norme Tecniche per le Costruzioni in Zona sismica, 29, 5 febbraio 1996 (in Italian).

[2] CS.LL.PP. (2008). D.M. 14.01.2008: Norme Tecniche per le Costruzioni. *GU della Repubblica Italiana*, 29, 4 febbraio 2008 (in Italian).

[3] CEN (2005). *EN 1993-1-1, Eurocode 3: Design of steel structures – Part 1-1: General rules and rules for buildings*. European Committee for Standardization, Brussels.

[4] F. Petruzzelli, *Scale dependent procedures for seismic risk assessment and management of industrial building portfolios*. PhD Thesis in Seismic Risk, University of Naples Federico II, Advisor: I. Iervolino, 2013.

[5] G. Della Corte, G. De Matteis, R. Landolfo, F.M. Mazzolani, Seismic analysis of MR steel frames based on refined hysteretic models of connections. *Journal of Constructional Steel Research*, **58**, 1331-1345, 2002.

[6] L.F. Ibarra, H. Krawinkler, *Global collapse of frame structures under seismic excitations.* Report No. 152, The John A. Blume Earthquake Engineering Center, Department of Civil and Environmental Engineering, Stanford University, 2005.

[7] ATC, *Improvement of nonlinear static seismic analysis procedures (FEMA 440)*. Prepared by Applied Technology Council, Redwood City, California, for Federal Emergency Management Agency, Washington, D.C., 2005.

[8] R.K. Dowell, F.S. Seible, E.L. Wilson, Pivot hysteretic model for reinforced concrete members. *ACI Structural Journal,* **95**, 607–617, 1998.

[9] R. Tremblay, C. Rogers, E. Martin, W. Yang, Analysis, testing and design of steel roof deck diaphragms for ductile earthquake resistance. *Journal of Earthquake Engineering*, **8(5)**, 775–816, 2004.

[10] S. Mastrogiuseppe, C.A. Rogers, R. Tremblay, C.D. Nedisan, Influence of nonstructural components on roof diaphragm stiffness and fundamental periods of single storey steel buildings. *Journal of Constructional Steel Research,* **64**, 214227, 2008.

[11] M. Stucchi, C. Meletti, V. Montaldo, H. Crowley, G.M. Calvi, E. Boschi, Seismic hazard assessment (2003-2009) for the Italian building code. *B. Seismol. Soc. Am.*, **101**, 1885–1911, 2011.

[12] V. Convertito, I. Iervolino, A. Herrero, The importance of mapping the design earthquake: insights for southern Italy. *Bulletin of the Seismological Society of America*, **99(5)**, 2979–2991, 2009.

[13] C. Meletti, F. Galadini, G. Valensise, M. Stucchi, R. Basili, S. Barba, G. Vannucci, E. Boschi, A seismic source zone model for the seismic hazard assessment of the Italian territory. *Tectonophysics*, **450**, 85–108, 2008.

[14] S. Barani, D. Spallarossa, P. Bazzurro, Disaggregation of probabilistic ground motion hazard in Italy. *Bulletin of the Seismological Society of America,* **99**, 2638–61, 2009.

[15] I. Iervolino, E. Chioccarelli, V. Convertito, Engineering design earthquakes from multimodal hazard disaggregation, *Soil Dynamics and Earthquake Engineering*, **31(9)**, 1212–1231, 2011.

[16] I. Iervolino, C. Galasso, E. Cosenza, REXEL: computer aided record selection for code-based seismic structural analysis. *Bulletin of Earthquake Engineering*, **8**, 339–362, 2010.

[17] D. Vamvatsikos, C.A. Cornell, Incremental dynamic analysis. *Earthquake Engineering and Structural Dynamics*, **31**, 491–514, 2002.

[18] E.L. Wilson, *Three-dimensional static and dynamic analysis of structures.* Berkeley (CA, USA). Computers & Structures, Inc., 2002.

[19] ASCE, Pre-standard and Commentary for the Seismic Rehabilitation of Buildings. *Report No. FEMA 356*. Reston, VA: American Society of Civil Engineers prepared for the Federal Emergency Management Agency, 2000.

[20] F. Petruzzelli, G. Della Corte, I. Iervolino, Seismic risk assessment of an industrial steel building. Part I: Modelling and analysis. *Proceedings of the 15th World Conference on Earthquake Engineering*, Paper No. 3088, Lisbon, Portugal, 2012.

[21] F. Petruzzelli, I. Iervolino, G. Della Corte, Seismic risk assessment of an industrial steel building. Part II: Fragility and failure probabilities. *Proceedings of the 15th World Conference on Earthquake Engineering*, Paper No. 3086, Lisbon, Portugal, 2012.

COMPDYN 2013
4th ECCOMAS Thematic Conference on
Computational Methods in Structural Dynamics and Earthquake Engineering
M. Papadrakakis, V. Papadopoulos, V. Plevris (eds.)
Kos Island, Greece, 12–14 June 2013

SEISMIC RESPONSE ANALYSIS OF EXISTING NON-DUCTILE BUILDINGS RETROTIFFED WITH BRBS

L. Di Sarno[1*], R. Chiodi[2], G. Manfredi[2]

[1]University of Sannio
Department of Engineering, Piazza Roma, 21, 82100 Benevento, Italy
ldisarno@unisannio.it

[2]University of Napoli "Federico II"
Department of Structural Engineering, via Claudio 21, 80125 Napoli, Italy
remo.chiodi@unina.it; gamanfre@unina.it

Keywords: Reinforced Concrete, Frames, Seismic Performance, Retrofitting, Buckling Restrained Braces.

Abstract. *The paper assesses the seismic performance of typical reinforced concrete (RC) existing framed structures designed for gravity loads only. Such structures exhibit high seismic vulnerability, i.e. low lateral stiffness, strength along with limited translation ductility; thus retrofitting strategies are employed to augment the seismic system capacity. Metallic dissipative braces, namely buckling restrained braces (BRBs), may utilized as cost-effective rehabilitation schemes for existing RC framed buildings. The braces can be conveniently installed along the perimeter frames of the multi-storey buildings to lower the seismic demand on the existing structure and regularize its dynamic response. The design approach assumed herein postulates that the global response of the inelastic framed structure is the sum of the elastic frame (primary system) and the system comprising perimeter diagonal braces (secondary system). Displacement-based approaches were employed to design the BRBs and the needs to improve existing code provisions and design guidelines are emphasized. Analysis and further design research needs, such as the effects of the effects of masonry infill panels and the beam-to-column joint modeling on the seismic performance of the retrofitted frames are also discussed.*

1 INTRODUCTION

Framed systems are extensively used for buildings structures in earthquake-prone regions because of their high capability of energy absorption and dissipation. However a large number of existing reinforced concrete (RC) framed building structures was designed in the last decades for gravity loads only and hence they do not possess satisfactory lateral stiffness and resistance; seismic detailing is also lacking. Surveys carried out in the aftermath of recent major

earthquakes, especially in countries of Southern Europe, such as Greece, Italy [1, 2] and Turkey [3]; they have emphasized the widespread brittle failure of RC members, caused by inadequate reinforcement bar details especially in shear walls and deep columns, as for example shown in Figure 1.



Figure 1: Field surveys carried out in the aftermath of the 2011 Van (Turkey): (a) brittle failure of a typical shear wall (b) inset of the reinforcement details, (c) failure at the base and at the top (d) of deep RC columns in residential buildings.

The data collected in the earthquake reconnaissance investigations have pointed out that numerous existing RC framed buildings are not conforming as they exhibit inadequate earthquake resistance and hence require retrofitting or rehabilitation to conform to the current seismic design provisions. Seismic retrofitting of existing structures may result, however, not straightforward due to the complex response of the as-built structures, either in RC or in steel and composite steel and concrete. Innovative materials and technologies, such as base isolation and supplemental damping (e.g. [4, 5] among many others) tend to be highly beneficial to upgrade reliably the existing structures at an affordable cost [6].
In order to design properly the retrofit scheme and minimize the intervention cost, it is of paramount importance to determine accurately the actual capacity and characterize the failure mechanisms of structural systems. The seismic vulnerability of existing RC framed buildings

designed for gravity loads is significantly endangered by the lack of plan and elevation regularity, insufficient stiffness and strength of flooring systems, short column effects and inadequate structural detailing. As a result, the response of the structural system may possess insufficient local and global ductility. Additionally, the seismic vulnerability assessment of RC structures is a challenging task as it involves the interaction between several local and global mechanisms. Shear response, axial load-flexure-shear interaction, local buckling of steel reinforcement bars, bond slip and fixed-end mechanisms require sound models to predict reliably the inelastic static and dynamic response of RC framed systems. Reliable seismic performance assess is of paramount importance to select and design cost-effective intervention schemed for non-conforming RC framed buildings.

Concentrically braced frames (CBFs), which possess a lateral stiffness significantly higher than that of unbraced frames, e.g. moment resisting frames are efficiently used as lateral.resisting systems. Nevertheless, due to buckling of the metal compression members and material softening due to the Bauschinger effect, the hysteretic behaviour of CBFs with traditional steel braces is unreliable. Several recent experimental tests and numerical simulations (e.g. [7, 8, 9, 10, 11] among many others) have shown that multi-storey framed building structures may be efficiently retrofitted by using unbonded or buckling restrained braces (BRBs). A typical BRB consists of a steel ductile core designed to yield both in tension and compression. The core is placed within a hollow section member, filled with either mortar or concrete. The outer tube prevents the occurrence of the buckling of the brace. The confinement of the outer tube may also increase the compressive resistance of the braces. Such braces provide higher hysteretic energy dissipation than traditional metal braces due to the prevention of global buckling [5]. Stable hysteretic response is of vital importance in seismic design and/or re-design to absorb and dissipate large amount of earthquake-induced energy. The occurrence of plastic hinges in the existing RC frame is, indeed, prevented.

Buckling restrained braces are suitable for seismic applications in damage controlled structures [12] where the bare RC frame (existing system) responds elastically and the braces (added system) are the dissipative components of the system. The global response of the inelastic structural system can be assumed as the sum of the elastic frame (also termed primary structural system) and the system formed by the diagonal braces (secondary system) that absorbs and dissipates large amount of hysteretic energy under earthquake ground motion. The primary system is capable to withstand vertical loads and behaves elastically under earthquake loads. The secondary system includes the dissipative members and is thus designed to damp the seismic lateral actions and deformations. Dissipative members, such as BRBs, may be installed in the exterior frames of multi-storey buildings and can be thus easily replaced in the aftermath of a devastating earthquake. Primary and secondary systems act as a parallel system; the lateral deformation of the structure as a whole corresponds to the deformation of both primary and secondary systems.

The present work illustrates the design issues concerning the application of BRBs for the seismic retrofitting of typical non-conforming RC existing framed structures designed for gravity loads only. Two sample RC buildings, located in earthquake-prone areas with different risk, namely high and moderate, are selected as case studies; the BRBs are conveniently placed along the perimeter frames to limit the downtime for the occupancy of the buildings and lower the seismic demand on the existing structure and regularize its dynamic response. Nonlinear static (pushover) and dynamic (response history) analyses were carried out for both the as-built and retrofitted structures to investigate the efficiency of the adopted intervention strategy. The numerical models used to simulate the structural response of the bare and retrofitted systems were validated with respect to full-scale experimental test results of typical low-storey RC non-conforming frames. The outcomes of the inelastic analyses carried out on

the sample structures demonstrate that, under moderate and high magnitude earthquakes, the damage experienced by the retrofitted structural system is concentrated in the added dampers and the response of the existing RC framed structure is chiefly elastic. Finally, analysis and further design research needs, such as the effects of the effects of masonry infill panels and the beam-to-column joint modeling on the seismic performance of the retrofitted frames are also discussed herein.

2 DESIGN OF BRBS FOR SEISMIC RETROFITTING OF RC STRUCTURES

The retrofitting of existing RC framed buildings with BRBs generally requires:

- The estimation of the optimum parameters for the dissipative braces, which may be conveniently performed by using simplified analysis methods;
- The application of capacity design checks for all members of the structure under the expected ultimate force induced by the dissipative braces, e.g. the yielding force of the BRBs;
- The compliance with the design performance requirements, which is preferably carried out through nonlinear response history analyses.

Numerous displacement-based design methods ofr BRBs have also been formulated but they refer primarily to steel structures, e.g. [13, 14], among many others. The design methodology typically employed within the framework of damage controlled structures is an iterative strategy based on response spectra and an equivalent viscous damping (ξ) used to quantify the effective hysteretic global response of the earthquake-resistant. The selected damping can be utilized to estimate both design spectral accelerations and displacements. A versatile design method has been recently formulated by employing an equivalent elastic static approach based on a mixed force- and deformation-based scheme employing. The step-by-step design procedure can be found in [5]. The aforementioned design method accounts for the energy dissipation capacity through the equivalent viscous damping; such damping is employed to reduce the acceleration and displacement response spectra. Alternatively, adequate response modification factors (R- or q-factors) may be employed; values of R ranging between 4.5 and 6.5 have been proposed in [15]. Values of R-factors have been recently investigated experimentally for existing RC structures retrofitted with BRBs (*see* [9]).

3 CALIBRATION OF NUMERICAL MODELS

3.1 Model description

Two full scale RC framed systems were employed to calibrate the numerical models used to investigate the effectiveness of BRBs as innovative retrofitting scheme for typical multi-storey non ductile frames. The benchmark structures include a bare system and a similar frame retrofitted with BRBs in the loading direction; their width is 5m, the depth is 6m and the roof height is 7.35m. The beams are 30x50cm deep and the columns employ square sections (30x30cm). The tested specimens employ typical details of gravity load design, i.e. smooth bars (fym=330MPa), intermediate concrete compression strength (fcm=19MPa), hooks and large spacing stirrups. Two types of BRBs were employed to retrofit one of the bare RC frame at first and second floor; both BRBs exhibit maximum strokes of ±20mm. They are connected to tubular pipe of diameter 80mm and a thickness of 7.2mm and 7.4mm, for the first and top floor, respectively. The yield force of the BRADs at base is Fy,b =75 kN, the maximum force is Fmax,,b = 90 kN; the displacement is dmax,b = ±15mm and the elastic axial stiffness kel,b = 90 kN/mm. For the top floor, Fy,t = 40 kN, the maximum force is

Fmax,t = 55 kN; the displacement is dmax,t = ±14mm and the elastic axial stiffness kel,t = 90 kN/mm. Further details on the layout, material properties and structural details of the sample RC buildings can be found in [9].

3.2 Model calibration

The sample frames were modelled with both lumped and fiber-based numerical discretizations; the finite element (FE) programs utilized are SAP2000 [16] and SeismoStruct [17]. The latter FE platform is capable of predicting the large displacement response of spatial frames under static or dynamic loading, taking into account both geometric and material nonlinearities. The spread of inelasticity along the member length and across the section depth is explicitly modelled, allowing for accurate estimation of damage distribution. In SAP2000, the inelasticity is lumped in zero-length plastic hinges placed at the both ends of the frame elements. Trilinear models were employed to define the inelastic response of beam-columns in SAP2000. Interaction between axial load and bending moment is accounted for in the columns. Non linear material modelling was utilized in SeismoStruct; the concrete was modelled with a nonlinear constant confinement. For the sample structures, values of the confinement factor k were assumed equal to 1.2 and 1.0 for confined (core) and unconfined (shell) concrete, respectively. A bilinear model with kinematic strain-hardening was utilized to simulate the inelastic response of steel longitudinal bars of the cross-sections of RC beams and columns. A strain hardening equal to 0.001 was assumed for the post-yield response. The distribution of material nonlinearity across the section area is accurately modelled in FE simulation due to the selection of 200 fibres employed in the spatial analysis of the sample structural systems. Two integration Gauss points per element are then used for the numerical integration of the governing equations of the cubic formulation (stress/strain results in the adopted structural model refer to these Gauss Sections, not to the element end-nodes). The spread of inelasticity along member length is accurately estimated because four 3D inelastic frame elements are utilized to model both beams and columns. At least two Gauss points were located in the inelastic regions in order to investigate adequately the spreading of plasticity in the critical regions and within structural members. Modelling of the local (beam-column effect) and global (large displacements/rotations effects) sources of geometric nonlinearity is carried out through the employment of a co-rotational formulation.

In the retrofitted system the dissipative buckling restrained braces (BRBs) were modelled using 3D inelastic truss elements. The BRBs employed for the retrofitting of the sample RC frame are connected in series with traditional steel hollow section braces. Equivalent mechanical properties were thus derived to replace the BRBs and the connected diagonal braces with equivalent steel inelastic truss elements. A bilinear model with kinematic strain-hardening was employed to model the structural steel of the braces.

The modal response analysis carried out using the FE models provide a close match of the frequencies estimated with both ambient noise and instrumented hammer, especially for translational modes of vibration. The values computed with Seismostruct are closer to those estimated experimentally. The discretization of the sample framed system with Seismostruct and the adopted formulation of the beam-column elements is more accurate than that implemented in SAP 2000. The values of the fundamental frequencies measured after the pushover tests, i.e. elongation of periods of vibrations of about 50-55%, demonstrate that the bare RC frames has experienced widespread damage in beams and columns. The numerical models used for the pre- and post-test analyses are sufficiently accurate and reliable for the seismic assessment of the sample building structures. Experimental and preliminary numerical results computed for the bare and retrofitted framed systems are shown in Figures 2 and 3. The results show the

hysteretic response of the each floor and the global cyclic behaviour of the frames. High inelastic demand is concentrated at ground floor level. Soft storey and, in turn, global frame instability, was observed in the bare RC frame.

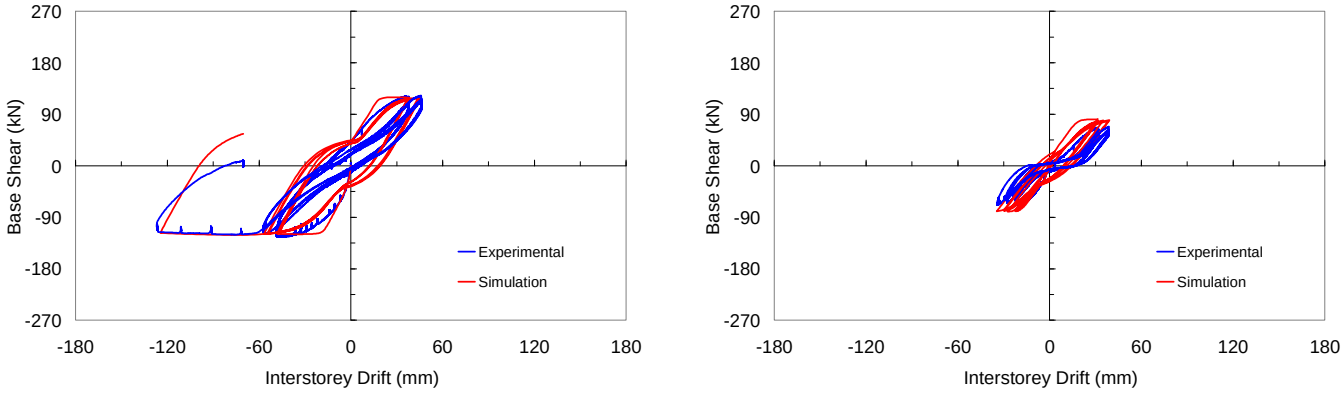


Figure 2. Experimental and simulation hysteretic response of the bare frame: 1st floor (*left*) and 2nd floor (*right*) response.

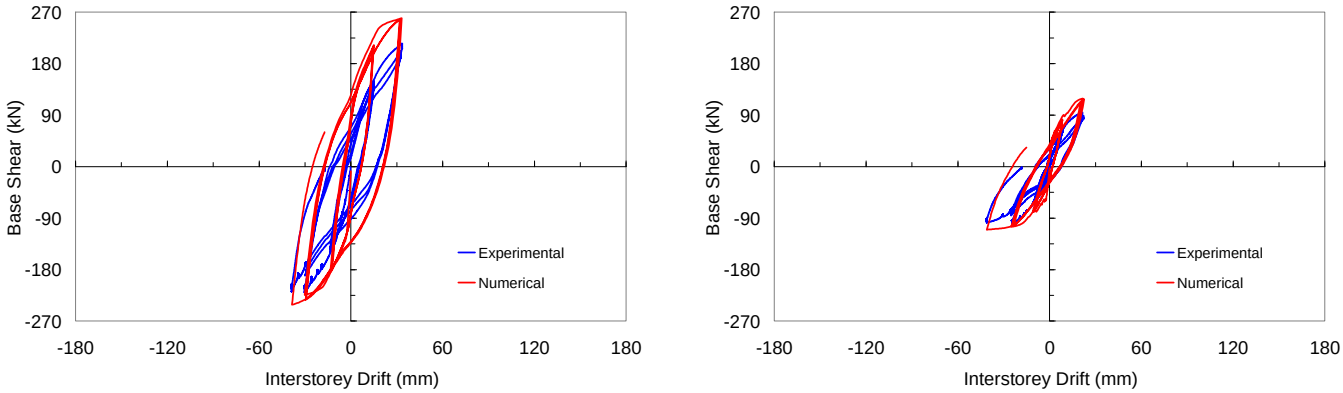


Figure 3. Experimental and simulation hysteretic response of the retrofitted frame: 1st floor (*left*) and 2nd floor (*right*) response.

The hysteretic response corresponds to the cyclic pushover loading applied to the buildings during the experimental tests. Pinching effects are not adequately modelled and further improvements, especially for concrete in tension, are deemed necessary. Notwithstanding, the simulated hysteretic loops provide close matches of the energy dissipation of the assessed systems.

4 SAMPLE BUILDING STRUCTURES

The first sample structure consists of a typical two-storey RC framed school building located in the South of Italy (area with high seismic hazard); it was designed in the late ‘60s to resist primarily gravity loads. The plan layout of the building is irregular; it consists of three main blocks: two T-shape block and a rectangular block. The T-shape unit is about 31m long, it has a width of 28.5m, the web thickness of 14.7m and two 7m-long offsets. Seismic joints were utilized to separate the three main blocks of the sample building. The ground floor of the structure is 3.08m high; the first and second floors are 3.65m high. The top floor has an in-

clined tiled roof: its height varies between 0.2m and 1.90m. Detailed fiber-based models were implemented in Seismostruct [17] to simulate the spreading of inelasticity within the structural members. Further details can also be found in [9].

The second sample building is an existing RC framed building which was built in the late 1930s in Tuscany, North-East of Italy, area of moderate seismic risk. The structural system frames located along a single direction only; the stairs are located in a slightly eccentric position. The 4-storey building has large interstorey heights in the range between 4.58 m and 5.10 m; the floors are placed at a height of 5.10 m, 9.86 m, 14.62 and 19.2 m. The floor slabs consist of 21 cm and 23 cm deep cast in situ concrete and brick decks at the first floor and all the other floors, respectively. The solid slab thickness is 5 cm at all floors; thus diaphragmatic behavior may be assumed for the assessed framed structure. The as-built framed system employs deep foundations consisting of plinths on piles, the piles are connected with tie-beams. Refined three-dimensional (3D) finite element models were employed to analyze the sample framed as-built and retrofitted structures under earthquake loading. The lumped plasticity models as implemented in SAP2000 code [16] were used to investigate the earthquake performance of the bare and retrofitted buildings. Further details can be found in [18].

5 EARTHQUAKE RESPONSE ANALYSIS

The seismic input was defined for the sample structures with reference to the 5% viscous damping acceleration response spectra evaluated for the four limit states compliant with the recent Italian code of practice [19], namely the operational (SLO), damageability (SLD), life safety (SLV) and collapse (SLC) limit states. Static (pushover) and dynamic (response history) nonlinear dynamic analyses were carried out on the refined 3D structural models to assess they earthquake elastic and inelastic response. The outcomes of such analyses are presented hereafter.

5.1 Framed Building located in high seismicity zone

The computed response (pushover) curves are provided in Figure 4 for the X and Y-directions. Two force distributions were considered: modal (or inverted triangular) and uniform distributions. The points corresponding to the onset of displacement demands at damage limit state (DL), life safety limit state (LS) and collapse prevention limit state (CP) are also included in the plots in Figure 4; such points are indicated with solid triangle, square and circle on the response curves. The results show that the existing frame exhibits a soft storey located at ground floor along the X-direction. The dimensionless global seismic resistance, i.e. ratio of the base shear and the seismic weight, of the as-built frame varies between 15% and 20%; the existing frame possesses similar global strength along X and Y directions. However, the seismic response is significantly influenced by the lateral load distribution along the X-direction. The modal response evidenced an irregular dynamic response along the latter direction. The maximum global displacement demand, expressed as roof drift, is 1.3%.

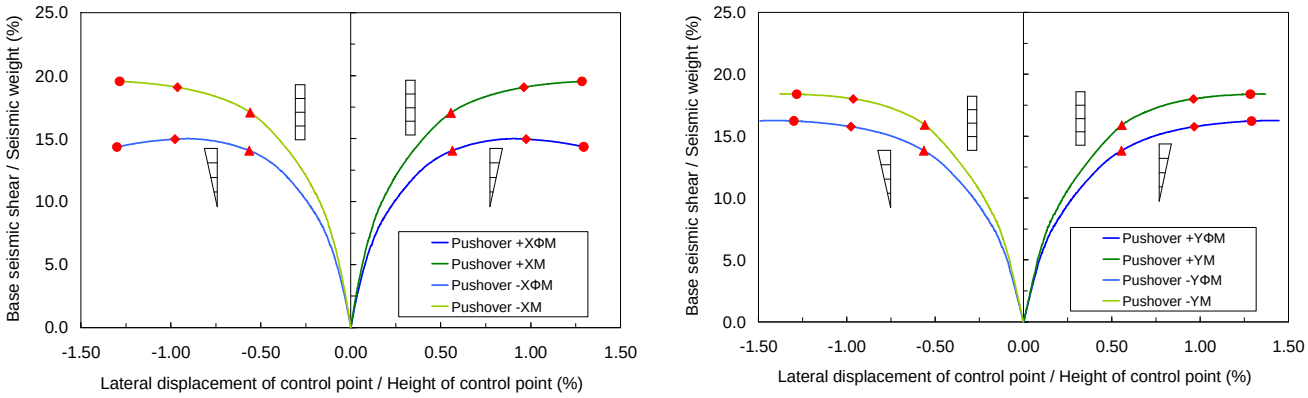


Figure 4. Response curve of the as-built structure: X-direction (*top*) and Y-direction (*bottom*)
Note: Triangle = DL; Square LS; Circle = CP.

For the retrofitted system, the computed results show a significant increase of the global over-strength of the structural system (about 30%) and a reduction of the displacement demand imposed on the structure at different limit states (Figure 5). The dimensionless global seismic resistance is about 45%; the displacement demand is lower than 1.0% (the estimated global drift is 0.8%). The post-peak stiffness and strength degradation observed along the X-direction of the as-built structure is also prevented thus enhancing the energy absorption and dissipate especially under high magnitude earthquake ground motions. The results of the pushover analyses provided in Figure 5 demonstrate that the retrofitted structure is not significantly affected by the lateral load pattern, especially with respect to the lateral strength. The variations between the results computed with the inverted triangular horizontal force distribution and those relative to uniform force distributions are lower than 10%.

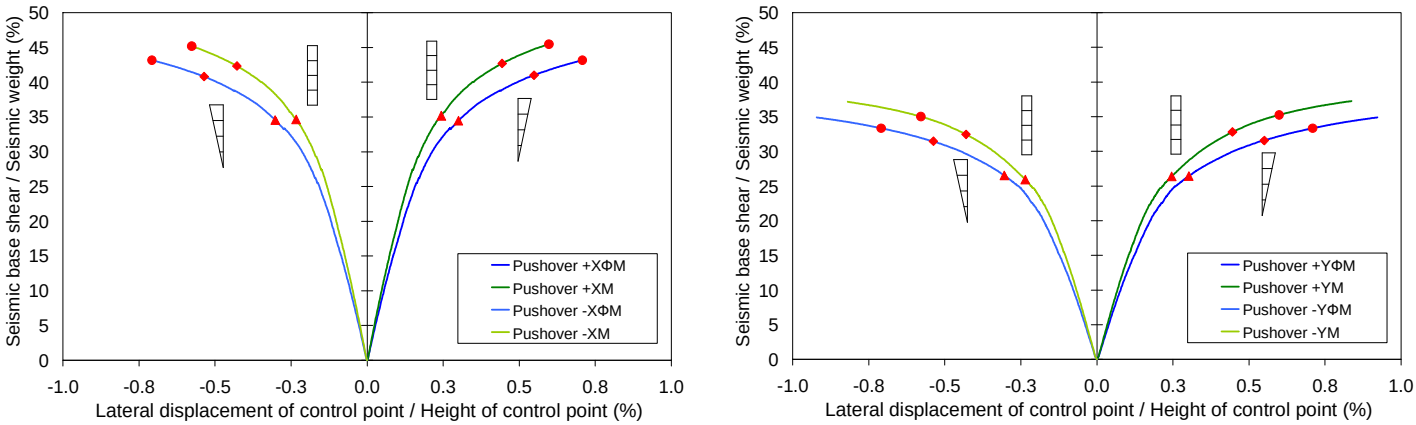


Figure 5. Response curve of the retrofitted structure: X-direction (*top*) and Y-direction (*bottom*)
Note: Triangle = DL; Square LS; Circle = CP.

The inelastic seismic performance of the as-built and retrofitted structures was further investigated through nonlinear dynamic analyses. Such analyses were conducted with respect to suites of seven different groups of earthquake natural records scaled linearly for each of the code-compliant limit states.

Table 1 summarizes the maximum interstorey drifts for the X- and Y-directions at damageability (serviceability) limit. The table provides also the average values of interstorey drift (σ), the standard deviations (δ) and coefficients of variation (COV).

Table 1. - Maximum interstorey drift at damageability limit state for existing and retrofitted buildings

		Existing Building				Retrofitted Building			
		Direction X		Direction Y		Direction X		Direction Y	
		1st Floor	2nd Floor	1st Floor	2nd Floor	1st Floor	2nd Floor	1st Floor	2nd Floor
$d_{r\,1}/h$	(%)	0.259	0.389	0.272	0.387	0.094	0.098	0.156	0.159
$d_{r\,2}/h$	(%)	0.189	0.320	0.346	0.452	0.095	0.108	0.115	0.111
$d_{r\,3}/h$	(%)	0.162	0.227	0.263	0.284	0.082	0.090	0.124	0.110
$d_{r\,4}/h$	(%)	0.288	0.373	0.197	0.221	0.148	0.143	0.118	0.130
$d_{r\,5}/h$	(%)	0.161	0.232	0.258	0.277	0.173	0.188	0.132	0.135
$d_{r\,6}/h$	(%)	0.210	0.291	0.260	0.334	0.127	0.142	0.149	0.148
$d_{r\,7}/h$	(%)	0.273	0.417	0.380	0.468	0.100	0.109	0.164	0.164
σ	(%)	0.220	0.321	0.282	0.346	0.117	0.125	0.137	0.137
δ	(%)	0.049	0.070	0.057	0.086	0.031	0.032	0.018	0.020
COV	(%)	22.30	21.80	20.20	24.90	26.50	25.40	13.20	14.60

The results provided in Table 1 demonstrate that the interstorey displacements estimated for the retrofitted structure are considerably lower than the counterparts values computed for the existing structure, especially at the second floor, where the storey mechanism is detected at ultimate limit state.

The time history of two typical devices is provided in Figure 6 with respect to the axial force and axial displacement response. The computed results demonstrate the large amount of energy dissipation and its cyclic stability under moderate-to-high magnitude earthquakes.

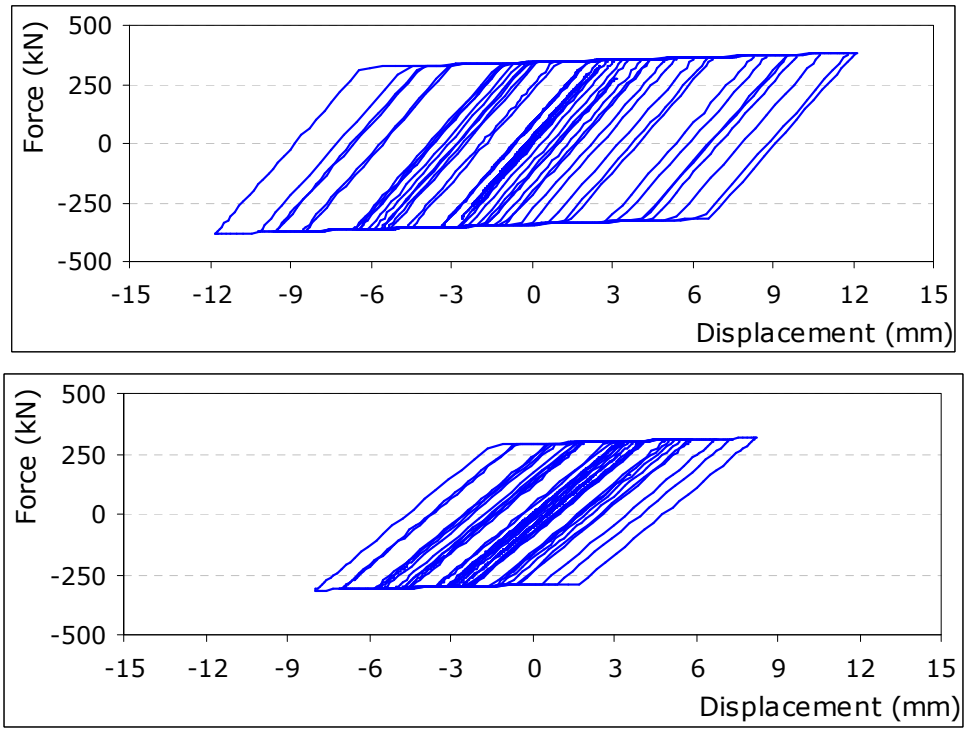


Figure 6 – Inelastic response history for typical hysteretic buckling restrained braces.

The maximum axial ductility of the BRBs is often a critical design parameter. For the sample structure located in the region with high seismicity, it can be assumed equal to 10 for both first and second floor. The computed value of maximum translation ductility is, however, compliant with BRBs available on the market.

5.2 Framed Building located in moderate seismicity zone

Modal and uniform load pattern distributions were employed to investigate the inelastic (static) response of the framed building located in the region with moderate seismic risk. Figure 7 provide the Acceleration Displacement Response Spectrum (ADRS) of the as-built and retro-fitted structures, respectively; they are calculated along the X- and Y- direction, for positive and negative directions of the lateral loadings. It is noted that conventional viscous damping coefficients equal to 4% and 10% have been assumed for the as-built and retrofitted structures, respectively. The performance points at operational life safety (LS) limit states with respect to both shear and moment beams and columns capacities are also included. The computed results showed that the as-built system is characterized by a low stiffness and ductility along X-direction, that is the weaker direction due to the lack of frames.

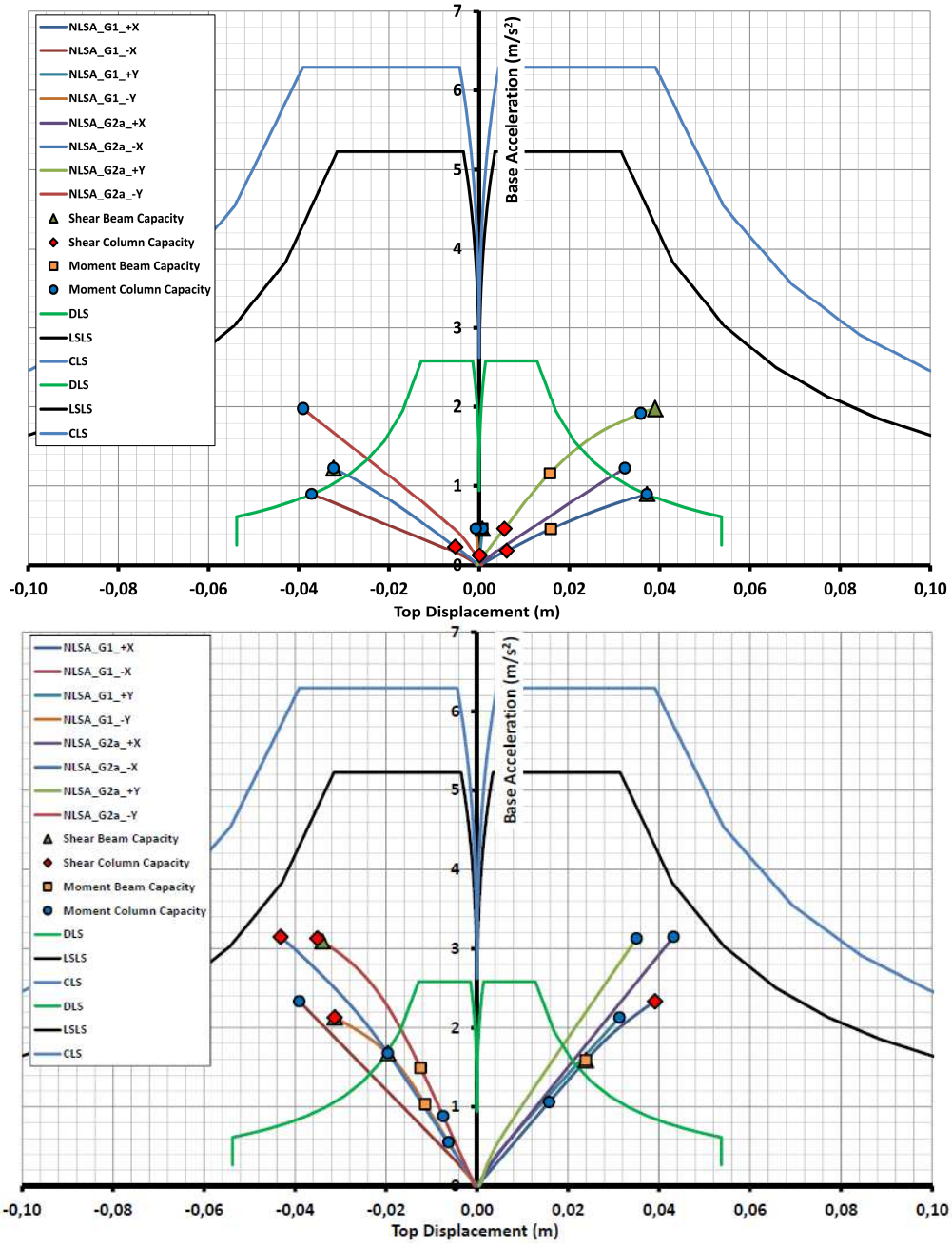


Figure 7. - Acceleration Displacement Response Spectrum (ADRS) of the as-built (*top*) and retrofitted (*bottom*) structure.

Fragility analyses of the as-built and retrofitted framed structure was also carried out. Additionally, a parametric analyses was performed to assess the influence of the angle of incidence of the earthquake ground motions on the structural response. Preliminary analysis results show that the angle of incidence may have a significant influence on the earthquake performance of a structure. For bare RC frames, the interstorey drifts (d/h) for weak storeys may be influenced by such an angle as shown in Figure 8 where the d/h has been plotted for the last floor (diagrams on the left side of Figure 8). However, when the BRBs are employed the systems tends to stabilize its response and, in turn, the effects of the angle of incidence of the earthquake input may be neglected. The latter response was also observed for the lower stories of the as-built structure, ie. the storeys with adequate lateral stiffness.

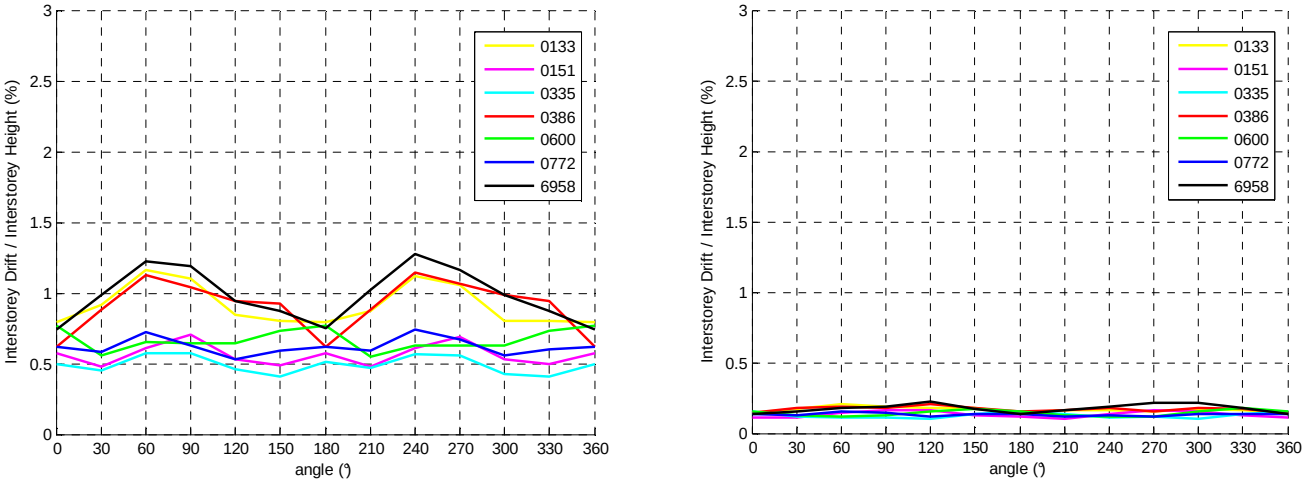


Figure 8. Effects of angle of incidence of the earthquake input on the structural response: response of the bare RC frame at the upper (*left*) and lower (*right*) floors.

The outcomes of the numerical investigations carried out on the inelastic response of the BRBs emphasize the effectiveness of such devices for seismic retrofitting of existing RC frames.

5. CONCLUSIONS

The present study has investigated the effectiveness of using buckling restrained braces (BRBs) to enhance the earthquake-induced energy absorption and dissipation of existing RC non-ductile framed buildings. The BRBs were placed along the perimeter frames of the structural systems, thus the dynamic response of the as-built RC frames was augmented and the seismic demand lowered. A displacement-based damage-controlled design procedure was employed to force the inelasticity within the added braces thus preventing the onset of the inelasticity within the existing RC frames. A numerical model has been calibrated on experimental test results of full-scale RC buildings retrofitted with BRBs. Such model was then applied to assess the earthquake response of two case study structures comprising existing non-compliant buildings located in regions with different seismic hazards. The results of the numerical investigation carried out demonstrate the effectiness of using BRBs to retrofit existing RC framed buildings. The hysteretic response of the BRBs remain stable even at large deformations and for a large number of cycles. The interstorey drifts of the retrofitted structures do not exceed 0.5%, which is generally employed as threshold values at serviceability limit state

(or damage prevention). The maximum ductility demand on the diagonal dissipative braces is equal to 10 for both first and second floors.
There is an urgent need to further investigate the response of RC frames retrofitted with BRBs including also the effects of masonry infills. The presence of such infills may alter significantly the lateral stiffness and strength, especially at serviceability, thus endangering the onset of the yielding in the braces.

6. ACKNOWLEDGMENTS

This work was financially supported by the Italian Consortium of Laboratories RELUIS (Project 2010-2013 - Task 1.1.2 – Reinforced and Precast Concrete Structures). Any opinions, findings and conclusions or recommendations expressed in this paper are those of the author and do not necessarily reflect those of the Consortium RELUIS.

REFERENCES

[1] Di Sarno, L. Elnashai, A.S. and Manfredi, G. (2011). Assessment of RC columns subjected to horizontal and vertical ground motions recorded during the 2009 L'Aquila (Italy) earthquake. *Engineering Structures*, 33(5), 1514-1535.

[2] Ricci, P. , De Luca, F. and Verderame, G.M. (2011). 6th April 2009 L'Aquila earthquake, Italy: reinforced concrete building performance. *Bulletin of Earthquake Engineering*, 9(1), 285-305.

[3] Di Sarno, L., Yenidogan, C. and Erdik, M. (2013). Field evidence and numerical investigation of the Mw = 7.1 October 23 Van, Tabanli and the Mw>5.7 November Earthquakes of 2011. *Bulletin of Earthquake Engineering*, DOI: 10.1007/s10518-012-9417-0;

[4] Di Sarno, L. and Elnashai, A.S. (2005). Innovative strategies for seismic retrofitting of steel and composite frames. *Journal of Progress in Structural Engineering and Materials*, 7(3), 115-135.

[5] Christopoulos, C. and Filiatrault, A. (2006). Principles of Passive Supplemental Damping and Seismic Isolation. IUSS Press: Pavia, Italy.

[6] Calvi, G.M. (2012). Alternative Choices and Criteria for Seismic Strengthening. *Procedings of the 15th World Conference on Earthquake Engineering*, Lisbon, Portugal, CD-ROM.

[7] Di Sarno, L. and Manfredi, G. (2010). Seismic Retrofitting with Buckling Restrained Braces: Application to An Existing Non-Ductile RC Framed Building. *Soil Dynamics and Earthquake Engineering*, 30(11), 1279-1297.

[8] Ragni, L., Zona, A. and Dall'Asta, A. (2011). Analytical expressions for preliminary design of dissipative bracing systems in steel frames. *Journal of Constructional Steel Research*; 67(1), 102–113.

[9] Di Sarno, L. and Manfredi, G. (2012). Experimental tests on full-scale RC unretrofitted frame and retrofitted with buckling restrained braces. *Earthquake Engineering and Structural Dynamics*, 41(2), 315-333.

[10] Freddi, F., Tubaldi, E., Ragni, L. and Dall'Asta, A. (2012). Probabilistic performance assessment of low-ductility reinforced concrete frames retrofitted with dissipative braces. *Earthquake Engineering & Structural Dynamics*, DOI: 10.1002/eqe.2255.

[11] Güneyisi, E.M. (2012). Seismic reliability of steel moment resisting framed buildings retrofitted with buckling restrained braces. *Earthquake Engineering & Structural Dynamics*; 41 (5), 853–874..

[12] Iwata, M., Kato, T., & Wada, A. (2000). Buckling-restrained braces as hysteretic dampers. *Proceedings of the 3rd International Conference on Behavior of Steel Structures in Seismic Areas* (STESSA 2000), Montreal, Canada, 33-38.

[13] Kim, J. and Seo, Y. (2004). Seismic design of low-rise steel frames with buckling-restrained braces. *Engineering Structures*, 26(5), 643-651

[14] Kim, J. and Choi, H. (2004). Behavior and design of structures with buckling-restrained braces. *Engineering Structures*, 26(6), 693-706.

[15] Sabelli, R., Mahin, S. and Chang, C. (2003). Seismic demands on steel braced frame buildings with buckling-restrained braces. *Engineering Structures*, 25(5), 655-666.

[16] Computers & Structures. (2012) . Integrated Solution for Structural Analysis and Design. Structural Analysis Program - SAP2000 Advanced vers 14.2.0; Berkeley, California, USA.

[17] Pinho, R. and Antoniou, S. (2012) . SeismoStruct Computer Program (http://www.seismosoft.com).

[18] Chiodi, R., Prota, A., Manfredi, G. e Di Sarno, L. (2012). Nonlinear seismic behavior of an existing RC building retrofitted with BRBs. *Proceedings of the 15th World Conference on Earthquake Engineering*, Lisbon, Portugal, CD-ROM.

[19] DD.MM.LL.PP. (2008). Norme tecniche per le costruzioni NTC (in Italian).

COMPDYN 2013
4th ECCOMAS Thematic Conference on
Computational Methods in Structural Dynamics and Earthquake Engineering
M. Papadrakakis, V. Papadopoulos, V. Plevris (eds.)
Kos Island, Greece, 12–14 June 2013

INFLUENCE OF STRUCTURAL AND FRAGILITY MODELLING DECISIONS IN THE LOSS ASSESSMENT OF RC FRAME BUILDINGS

David P. Welch[1], **Timothy J. Sullivan**[2]

[1] ROSE Programme, UME School, IUSS Pavia
1 Via Ferrata, Pavia, PV, Italy, 27100
david.welch@umeschool.it

[2] Department of Civil Engineering & Architecture, University of Pavia
1 Via Ferrata, Pavia, PV, Italy, 27100
timothy.sullivan@unipv.it

Keywords: Building Specific Assessment, Expected Annual Loss, RC Frames

Abstract. *Much advancement in structural modelling, seismic hazard analysis, and component fragility estimation techniques has been made in recent years; all of which have contributed to the feasibility of conducting building-specific loss estimates. This paper investigates the impact that certain modelling decisions can have on the outcome of loss estimates using a probabilistic performance-based earthquake engineering approach. These variations include assumptions on initial member stiffness, treatment of elastic damping, and the hysteretic properties of RC members. Further, the effect of the choice of component fragilities and decision variable formulation is investigated by implementing two loss models adopted in previous research efforts. Analyses are conducted for a benchmark four-story RC frame building that was previously assessed to allow a comparison with previous results and thereby confirm the reliability of the implemented methodology.*

The use of the expected annual loss to convey performance is shown to be the most sensitive to modelling decisions given the high contribution of lower intensity seismic excitations and initial accumulation of damage. Scenario-based loss assessments show a more consistent result between model variations that adopted the same loss model formulation. Finally, the two different loss models utilized in this study are shown to provide the largest source of deviation in loss estimates. This highlights the need for additional research, to more accurately define loss models for seismic assessment purposes.

1 INTRODUCTION

Modern seismic code provisions have presented, as a majority, their effectiveness to prevent collapse and loss of life following recent earthquakes. Conversely, many of these events have revealed a common and concerning situation of severe component damage and even pre-collapse replacement decisions that have led to an increasing focus on the development of Performance-Based Earthquake Engineering (PBEE). Much advancement in structural modelling, seismic hazard analysis, and component fragility estimation techniques has been made in recent years; all of which have contributed to the feasibility of conducting building-specific loss estimates. Most notably, the development of the Pacific Earthquake Engineering Research (PEER) center's PBEE methodology represents the pioneering compilation of these advances within a four stage approach which considers initial site through the expected repair costs and post-event conditions.

The current research is aimed to investigate how building-specific loss estimates are affected by variations in structural modelling decisions as well as differences within the loss model approach adopted. The investigation is carried out through the analysis of a four-storey reinforced concrete (RC) case study building that was previously assessed using two different loss model approaches which allows for an additional comparison to be made with respect to the reliability (repeatability) of the PEER PBEE methodology. Variations of structural modelling decisions addressed herein reflect some of the decisions that are typically left to the intuition of the analyst, including: initial member stiffness, treatment of elastic damping, and post-yield behaviour of structural elements. Notably, the current study aims to simply address the possible variations in loss estimates without any attempt to quantify the actual uncertainty associated with these variations; producing a platform to discuss the implications of structural modelling decisions combined with different adopted loss models.

The loss metrics or decision variables considered within the study consider only the losses associated with repairing damage and the costs associated with the total collapse of the building, termed here as direct losses. The additional decision variables that can be involved are numerous [4], yet the current study focuses solely on this type of loss.

2 OVERVIEW OF CASE STUDY BUILDING

2.1 Building details

The case study building is a four-storey RC frame building realized with a space frame design featuring special moment-resisting frames (SMRFs) on each column line. The building is assumed to be located within the Los Angeles basin in California on a site with deep soil conditions (NEHRP class D) possessing an average shear wave velocity of 285 m/s [1]. A probabilistic seismic hazard assessment (PSHA) for the site was conducted by [2]. The building is regular in plan and elevation with four 30 ft (9.1m) and six 30 ft (9.1m) bays in the North-South and East-West directions respectively. The storey heights of the building are 15 ft (4.6m) and 13 ft (4.0m) for the bottom storey and the upper stories respectively. The design of the building was taken from [1] that produced a simplified three-bay representation of the building as shown in Figure 1.

The reinforcement scheduling conforms to the 2003 International Building Code. Member dimensioning and detailing was controlled by joint shear requirements and columns are designed to Strong-Column Weak-Beam (SCWB) provisions. The target SCWB factor was 1.2, but it is noted that the resulting SCWB factors from assessment strengths are on the order of 1.3 for the first three stories and less than unity (< 1.0) for the roof level. More in depth information about the design of the frame building can be found within [1].

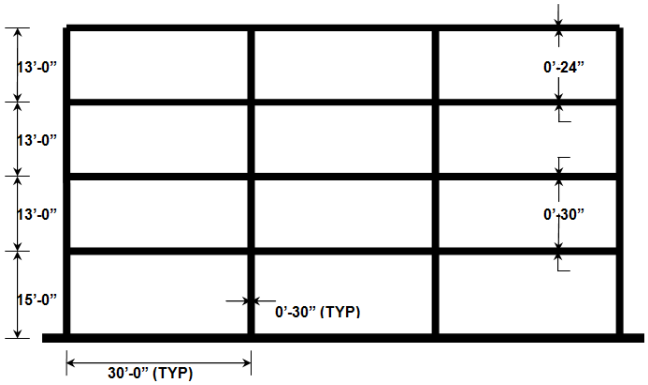


Figure 1: Elevation view of case study building (reproduced from [14])

2.2 Building occupancy and contents

The four storey case study building is a standard building with office occupancy. The building possesses lightweight gypsum drywall partitions with 3 5/8 inch (92 mm) deep studs with 5/8 inch (16 mm) thick wallboards, and are assumed to have fully attached top plate connections as opposed to free "slip-track" connections. The exterior of the building is comprised of single glazing assemblies with 5ft x 6ft (1.5m x 1.8m) panes within an aluminium frame. The ceiling system utilizes 2ft x 4ft (0.6m x 1.2m) lightweight ceiling tiles set in aluminium framing suspended by splay wires with vertical compression struts. The mechanical items, such as electrical, HVAC and fire suppression (sprinklers), are assumed to be properly anchored according to modern seismic design requirements mandated by the component's respective industry standard [3]. The general architectural layout within the building has more open space at the ground floor while a more heavily partitioned layout is assumed for the remaining levels. For more detailed information on the architectural layout, contents, and take-off quantities the reader is referred to [3].

3 IMPLEMENTED LOSS ANALYSIS PROCEDURES

3.1 Overview of the probabilistic PBEE framework

The assessment of the case study building is carried out by following the analysis procedure outlined within the Pacific Earthquake Engineering Research (PEER) Center's Performance-Based Earthquake Engineering (PBEE) framework as described within [4]. The framework consists of four analysis stages: site hazard definition, structural analysis, damage calculation, and decision variable calculation as shown in Figure 4. The framework begins with the structure definition, *D*, including both structural and non-structural configurations and the geotechnical properties of the proposed site. For a given site, the hazard analysis stage is carried out typically in the form of a Probabilistic Seismic Hazard Assessment (PSHA) which provides the mean annual frequency, λ, of an intensity measure, IM, of interest as well as uniform hazard spectra and disaggregation information in order to guide accelerogram selection for the structural analysis stage. Notably, the PSHA conducted by [2] provides mean uniform hazard spectra at eight intensities and a complete hazard curve at periods of 0.2, 1.0, and 2.0 seconds.

The structural analysis stage requires that a structural model is created in order to perform non-linear time history simulations of the site and structure from which the probability density of engineering demand parameters (EDP's) conditioned on a given intensity measure, $p[EDP|IM]$, can be evaluated. Using the EDP distributions, the likely damage of the structural and non-structural contents can be evaluated usually through the assignment of log-

normally distributed fragility functions that represent the probability of a given damage measure, DM, of a component conditioned on a given EDP such as peak inter-storey drift. Using the results from damage analysis the repair quantities for the building components are estimated by repair cost functions from which a decision variable, DV, can be quantified and the overall performance of a given site and design combination, D, can be assessed. Notably, the expected total repair cost of a given structure conditioned on IM is a common DV to be quantified but other DV's may address the probability of collapse and the expected external impact (e.g. downtime or business disruption) from a given level of seismic intensity [4].

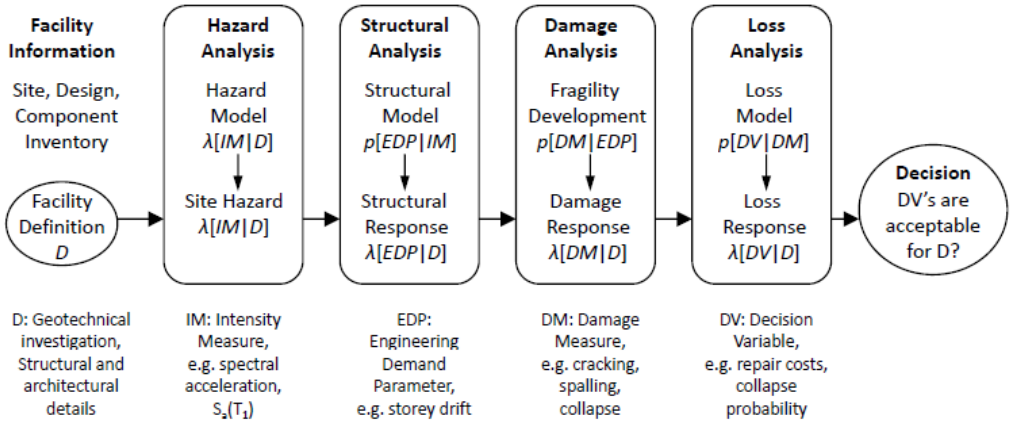


Figure 4: Overview of the PEER PBEE framework (after [4]).

The mathematical representation of the methodology is illustrated in Eq. (1) where the annual occurrence frequency of a given DV, say repair cost, is represented by $\lambda[DV|D]$ and is calculated through the evaluation of the triple integral shown, where all the terms are conditioned on the particular structure D.

$$\lambda[DV \mid D] = \iiint p[DV \mid DM]\,p[DM \mid EDP]\,p[EDP \mid IM]\,\lambda[IM]\,dIM\,dEDP\,dDM \qquad (1)$$

As an objective of this paper is to investigate the sensitivity of decision variables to a given loss model, two different loss models are considered in this work.

3.2 Component-based loss model

The first of the two loss models considered is a component-based (CB) loss model previously developed and implemented within [3]. The term component-based is used as repair costs of the structure are estimated by considering individual damageable assemblies by assigning independent fragility and repair cost functions for the last two stages of the PEER PBEE framework described in section 3.1. The damageable assemblies considered in this work (after [3]) are beams, columns, partition walls, interior paint, exterior glazing, acoustical ceilings, fire suppression systems (sprinklers), and conveying systems (elevators).

Two pertinent aspects of the CB loss model adopted herein is that the structural damage is quantified using a curvature based damage index that requires the estimation of the recoverable curvature of members and the total replacement cost of the structure is calculated based on the replacement cost of every component assigned a damage and repair fragility. Notably the results of [3] show that the replacement cost of the building is taken as $9,000,000 expressed in 2007 USD. This value will be used to express the loss estimates in terms of a mean damage factor (MDF) which represents the percentage of replacement cost of the structure.

3.3 Storey-based loss model

The second of the two loss models considered is a storey-based (SB) loss model developed within [5]. As the name suggests, the SB loss model assumes the combined fragilities of a single storey content through the development of engineering parameter to decision variable (EDP-DV) functions that allow for the direct estimation of direct losses from structural analysis results. The EDP-DV functions are developed based on expected occupancy, structural system, and building height [5]. The EDP-DV functions utilize only inter-storey drift ratio (IDR) and peak diaphragm acceleration (PDA) as EDP's and discretize the damageable assemblies into three performance groups: structural, non-structural drift sensitive, and non-structural acceleration sensitive. The set of EDP-DV functions implemented for the current study were constructed to represent a low-rise ($\leq$ 5 stories), ductile, reinforced concrete space frame with office occupancy (refer [5]). The functions relate expected contents based on the first, typical, and roof levels where an example of the EDP-DV functions assumed for the first floor are shown in Figure 5.

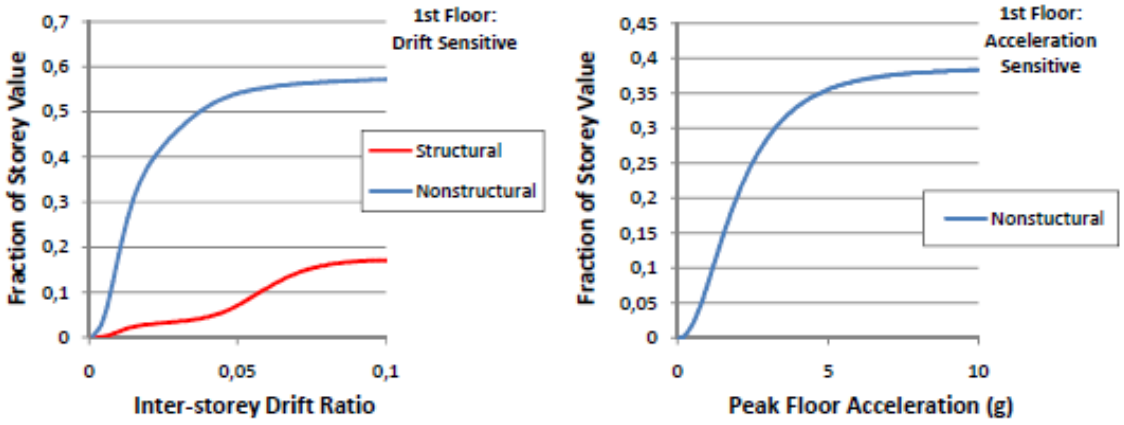


Figure 5: EDP-DV functions assumed for the first floor of the case study building (after [5]).

For the current study, it is assumed that the stories have an equal value of 25% of the replacement cost. The replacement cost of the case study building was calculated by [5] to be $12,500,000 in USD from construction estimating references however the loss models are best compared by reporting losses expressed in MDF.

3.4 Considered loss metrics

In order to gauge the seismic performance of the case study building a series of loss metrics are considered: expected loss for a design basis earthquake (DBE) scenario, and expected loss for a maximum credible earthquake (MCE) scenario, expected annual loss, and net present value of loss over 50 years.

The first two loss metrics are termed scenario-based assessments as the resulting estimate corresponds to a single event occurring based on return period, magnitude-distance couple, or other measure [7]. In much of the Western United States the DBE and MCE events correspond to a 10% and 2% probability of exceedence in 50 years respectively.

Expected annual loss (EAL) represents a time-based assessment of the likely losses a building can be expected to endure in any given year from a probabilistic standpoint [7]. The EAL considers the entire range of seismic intensities expected at a site in combination with the corresponding mean annual frequency and expected losses at each intensity.

The use of EAL as a loss metric is a valuable parameter as it allows for an estimate of what annual insurance premiums would be reasonable for a given building [7,8]. Additionally, it can be useful in order to convey loss estimates in terms of the net present value over the life-time of the building, taken here as 50 years. For example, the net present value (NPV_{50}) of losses may assist in a seismic retrofitting decision where NPV_{50} would represent the amount a risk-neutral owner would be willing to invest [8]. The NPV_{50} is calculated from the EAL using an assumed discount rate, $r_{discount}$, of 3% as shown in Eq. (2).

$$NPV_{50} = \sum_{t=1}^{50} \frac{EAL}{\left(1+r_{discount}\right)^{t}} \tag{2}$$

Although the choice of discount rate can significantly change NPV estimates [8], the main purpose for addressing NPV of loss is to illustrate EAL estimates at a similar order of magnitude as the two aforementioned scenario-based assessments.

4 STRUCTURAL ANALYSIS MODEL

The structural model utilized for the current study is developed in the finite element program RUAUMOKO [9]. The building is modeled as a three bay representation as shown in Figure 1. The base columns are assumed fixed at the base and the effects of soil structure interaction are neglected based on the previous findings of [10] using similar site and structure characteristics. The lateral mass is modeled assuming 1.34 kip-s^2/in (235 T) at each floor level with tributary masses lumped at the beam-column nodes. Second order effects (P-Delta) are accounted for during analysis using the "P-Delta" option in RUAUMOKO (refer [9]). During non-linear time history (NLTH) analyses Newmark constant average acceleration integration is implemented with an analysis time step of 0.001 or 0.002 seconds depending on the accelerogram. The treatment of structural collapse assumes a collapse fragility reported in [1] as collapse probabilities are not expected to significantly affect loss results for the modern 2003 IBC conforming design (refer [1,6] for details).

4.1 Modelling structural elements

The columns of the case study building are modelled as concrete beam-column frame elements while the beams are modelled as two point Giberson beam elements within the program Ruaumoko [9]. Both types of structural members assume lumped plasticity at the member ends with an elastic element spanning between plastic hinges. As a main objective of the current study is to compare the results of repeating the probabilistic loss assessment procedure to previous studies, the structural elements should ideally be modelled (reasonably) in the same manner as the benchmark study. As such, much information about the structural elements was taken from [1] in order to remain consistent.

Using material properties defined in [1], moment-curvature analyses of the RC beam and column sections were conducted using the program CUMBIA [11]. The resulting beam-column section properties were found to be in good agreement with those reported in [1] with nominal moment strengths (the definition of nominal moment strength and yield curvature is illustrated in Figure 6) and first yield moment strengths that encompassed the expected yield moment reported in [1]. Similarly, the ultimate moment strength, M_u, values had a maximum deviation of +12% and were within 2% of previously reported values on average. Finally, the program CUMBIA returned estimates of rotational capacity based on ultimate failure (reinforcement rupture or core crushing) and the onset of reinforcement buckling that bounded the reported rotational capacities within [1]. Therefore the assumption was made to assume that the previously reported rotational capacities would be adopted for the current study. The

beam-column elements are calibrated for monotonic loading according to a tri-linear backbone curve based on the findings of [1] in terms of peak rotational capacity and the post peak failure slope while the yield moment was taken as the nominal moment strength and the peak moment was taken as the lesser of the $1.2M_n$, M_u, and the moment corresponding to reinforcement buckling. Beam elements assume the average rotational capacity of 0.06 radians and assume yield and peak moment strengths of $M_{y,exp}$ and $1.2M_{y,exp}$ as provided in [1]. An example of the backbone curve is illustrated for a first storey interior column in Figure 6 noting that the calibration was performed before the consideration of 2nd order effects as per recommendations in [1].

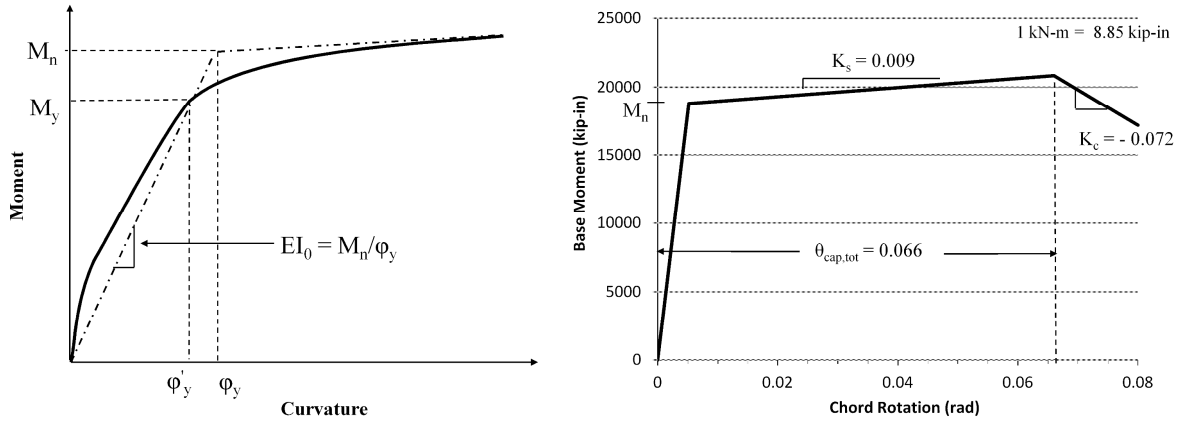


Figure 6: Nominal flexural strength and yield curvature (left), Illustration of monotonic calibration (right).

The hysteretic properties of the structural members assume a modified Takeda hysteresis as shown in Figure 7 which illustrates that in addition to the initial stiffness, k_0, and post-yielding stiffness factor, r, parameters must be defined to determine the rate, α, at which the displacement ductility dependent unloading stiffness decreases and the reloading stiffness factor, β, that relates the point on the backbone curve a current excursion will intercept with respect to the previous excursion. The selection of input parameters is based on assuming "Takeda Fat" (TF) hysteresis for beam members and "Takeda Thin" (TT) hysteresis for beam-columns. Typically, TT hysteresis assumes $\alpha = 0.5$ and $\beta = 0$ to represent the energy dissipation expected for members with high axial load (e.g. - columns) while using a TF hysteresis with $\alpha = 0.3$ and $\beta = 0.6$ is representative of modern code conforming RC beam members [12]. These parameters are adopted for the members within the four storey space frame building.

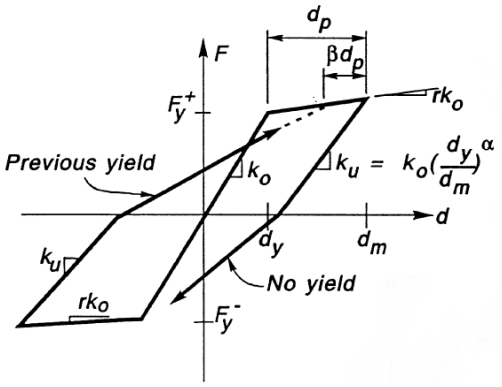


Figure 7: Modified Takeda hysteresis model (after [9])

4.2 Strength degradation and post-yield stiffness of structural members

The current study considers two general assumptions on the modelling of strength degradation of structural elements. The first considers only in-cycle degradation using the maximum ductility of the member to reduce the strength according to the monotonic backbone curve. This calibration produced a post-yielding stiffness equal to 1% of initial on average. Since the recommendations of [1] suggest that the post yielding stiffness should be 4%, a second hysteretic model allowed the member to be loaded along the 4% post-yield slope until reaching $1.2M_n$ and $1.2M_{y,exp}$ for columns and beams respectively and then including both ductility dependent in-cycle and cycle-based cycle-to-cycle degradation such that the peak response would be below calibrated monotonic curve. Examples of the two simplified hysteretic models are shown in Figure 8.

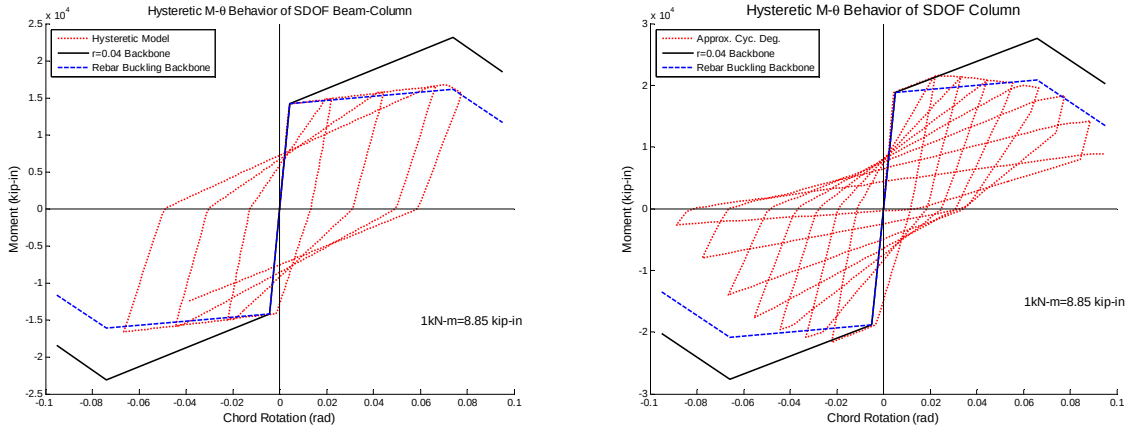


Figure 8: Ductility-based strength degradation (left), Cyclic and ductility-based strength degradation (right).

Referring to Figure 8, the black lines represent the suggested monotonic backbone by [1] and the dashed blue lines represent the reduced monotonic curve by considering the reduced peak moment in the case of reinforcement buckling. The difference in the two curves shows that although simplified strength degradation is implemented, the general response is not reproducing a calibration based on purely monotonic considerations and is assumed as a reasonable approximation in lieu of an experimental calibration study.

4.3 Initial member stiffness

The initial stiffness of beam-column members was varied between taking the effective stiffness corresponding to the nominal moment strength and using a relation from [1] that is based on approximating the initial stiffness as the secant stiffness through 40% of the expected yield moment, $M_{y,exp}$. The stiffness corresponding to nominal moment strength is shown by Eq. (3) based on recommendations of [12]:

$$EI_{eff} = \frac{M_n}{\phi_y} \tag{3}$$

where all parameters have been previously defined (refer Figure 6). For brevity, the relation proposed within [1] for the secant stiffness to 40% of the yield moment resulted in the lower bound value of 35% of the gross member stiffness ($0.35EI_{gross}$) for all beam-columns. As the relation using secant stiffness through a fraction of the yield force was shown to replicate fibre element models (distributed plasticity) with the tensile strength of the concrete modelled

this initial stiffness comparison represents the case of a new construction situation and the case of a modern, "undamaged", building that may have been subjected to a previous lateral loading (seismic or wind). Notably, the change in assumed initial stiffness returned the same nominal first mode period of 0.8s (0.01s tolerance) which suggests that very little difference will be witnessed in the loss estimates. However, as the relation of Eq. (3) gives values that range from 42% to 25% of the gross stiffness the difference in dynamic behavior cannot be expected to be negligible. Further, the difference in the initial stiffness of individual members will produce variations in the assumed recoverable curvature (for the CB model) as the unloading stiffness of each member is related to the assumed initial stiffness as shown in Figure 7. The effective stiffness of beam elements assumes the values reported in [1].

4.4 Elastic damping

The current study will consider two values of initial stiffness proportional Rayleigh damping (ISRD). A value of 6.5% of critical has been implemented in the works of researchers that have assessed the current case-study building [1,10]. Conversely, the typical value assumed for reinforced concrete buildings can safely be set to 5.0% initial stiffness damping. These two values are implemented into the loss assessment models in order to display a single comparison of one analyst's opinion versus another with respect to the treatment of elastic damping. Additionally, a brief investigation into the impact of assigning tangent stiffness proportional Rayleigh damping (TSRD) and the effect of beam-column joint stiffness is addressed within [6] yet these findings are omitted from the current discussion.

5 RECORD SELECTION FOR NON-LINEAR TIME HISTORY ANALYSIS

The selection of accelerograms for non-linear time history (NLTH) analysis was carried out following the disaggregation of the site hazard from PSHA results by [2], using accelerograms provided in the NGA database [13]. The intensity levels selected to represent the range of seismic intensity at the site is consistent with [3] where eight intensity levels are considered. A total of 20 records (2 horizontal components) are chosen for each hazard level.

One major simplifying assumption that was made for the record selection process was the selection of two suites of records. The first low intensity suite was selected based on the disaggregation of the three lowest hazard levels with respect to magnitude, *M*, distance, *r*, and the spectral shape parameter epsilon, ε. The maximum and minimum record properties were taken as the bounds defined within the range of intensities considered forming the low intensity bins (e.g. LA) as shown in Table 3.

Hazard Level	**S_a (T=1s)** (g)	**Bin**	**M_{min}**	**M_{max}**	**r_{min}** (km)	**r_{max}** (km)	**ε_{min}**	**ε_{max}**
Low-Intensity Suite								
50% PE in 5 yr	0.1	LA	5.9	7.1	5	35	-0.5	1
20% PE in 5 yr	0.19	LB	6.9	8.0	40	80	-2	0.5
10% PE in 5 yr	0.26	LC*	6.4	7.6	100	∞	0	∞
High-Intensity Suite								
50% PE in 50 yr	0.3							
20% PE in 50 yr	0.44	HA	5.9	7.1	5	35	0	2
10% PE in 50 yr	0.55							
2% PE in 50 yr	0.82	HB	6.9	8	40	80	0	∞
0.3% PE in 50 yr	1.20							

*Only three records selected from bin C representing the lowest hazard level within the low intensity suite

Table 3: Hazard disaggregation used for record selection (after [10]).

Similarly for the higher intensity hazard levels the record properties were combined to form the high intensity suite (refer Table 3). The partitioning of the hazard levels was based on the presence of negative ε and similar M and r ranges between the first three hazard levels and the remaining higher intensity hazard levels. More information about the nominal disaggregation of the site can be found within [2].

Accelerograms are scaled to the spectral acceleration at a period of 0.8 seconds using the geometric mean of the two orthogonal components. More detailed information regarding the selected records, selection criteria, and scaling approach can be found within [6].

6 LOSS RESULTS

6.1 Initial comparison using baseline parameters

The structural models representing the input parameters assumed by the parent studies conducted with the component-based (CB) loss model [3] and the storey-based (SB) loss model [5] are compared in order to represent the case of repeating the same loss assessment in order to verify the repeatability. This model assumes a post-yield slope of 4.0%, 6.5% initial stiffness proportional Rayleigh damping (ISRD) at the first and third modes, and the initial stiffness of beam-column elements assumes secant through 0.4 times the yield force. This model is referred to as model D5 (refer Table 5). The expected annual loss results for the baseline comparison are shown in Figure 10 showing a very reasonable agreement to previous studies with the CB model EAL with a deviation of +2.2% (+0.012% MDF) and the CB model showing a deviation of -4.6% (-0.042% MDF). This initial comparison illustrates the reliability of the PEER PBEE approach when considering the differences in input motion selection and analysis assumptions.

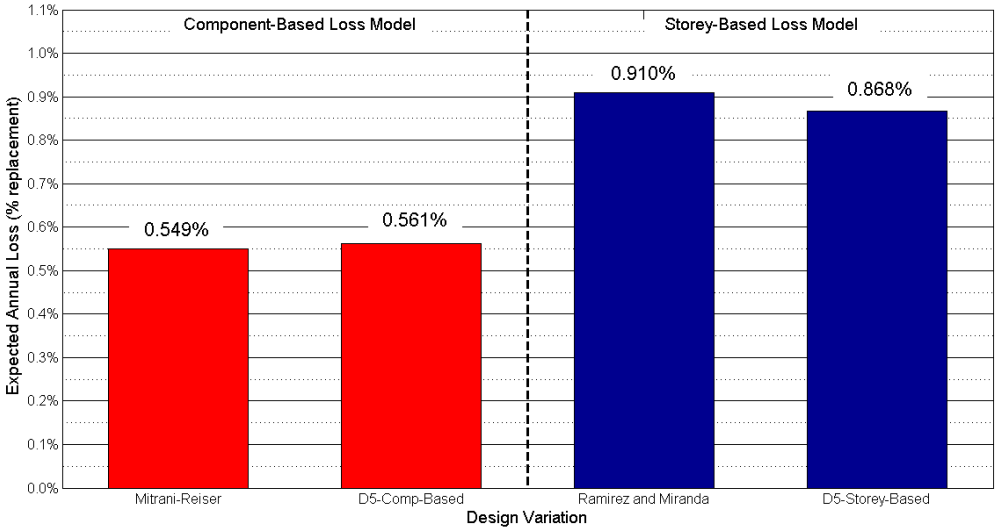


Figure 10: Comparison expected annual loss of baseline models to parent studies.

In order to give the reader a better concept of how deviations in loss estimates may affect decision making, the actual loss values for all loss metrics considered (refer section 3.4) are shown both in MDF (% replacement cost) and the corresponding dollar values in Table 4. However, it is noted that the remaining comparisons will be discussed in terms of MDF representing the percentage of the replacement cost. The results in Table 4 illustrate that the expected annual loss could produce drastically different risk management decisions based on slight deviations in terms of the magnitude of EAL. For instance, consider that the two values

from the parent studies (0.55% and 0.91%) are assumed as equally valid results using the replacement cost from the component-based loss model ($9M total cost) then the annualized losses for the structure would range from approximately $49,000 to $82,000.

	Component-Based (CB)				**Storey-Based** (SB)			
	[3] (parent)		**D5** (this study)		**[5]** (parent)		**D5** (this study)	
Loss Metric	MDF	$*	MDF	$*	MDF	$**	MDF	$**
EAL	0.549%	49410	0.561%	50490	0.910%	113750	0.87%	108500
NPV_{50}	14.1%	1269000	14.4%	1296000	23.4%	2925000	22.3%	2787500
MDF_{DBE}	26.2%	2358000	22.5%	2025000	23.5%	2937500	23.6%	2950000
MDF_{MCE}	47.7%	4293000	42.8%	3852000	39.0%	4875000	37.9%	4737500

*2007 USD, Total cost = $9M (sum of damageable assemblies) **2009 USD, Total cost = $12.5M

Table 4: Loss results for baseline comparisons illustrating magnitude of loss metrics.

Conversely, taking the MDF_{DBE} values from the two parent studies (26.2% and 23.5%) and again assuming a total cost of $9M, the loss estimates for a design level event would range from $2.12M to $2.36M which would give a much larger range in monetary costs when compared to the EAL case yet would, arguably, not drastically affect decisions based on this metric given the differences in probabilistic considerations (annual vs. 10% in 50y). This point is furthered when considering the implications of estimating total replacement costs.

Now in order to briefly illustrate the difference in the adopted loss models the disaggregation of direct losses conditioned on no collapse for model D5 is plotted versus seismic intensity in Figure 11. The figure displays the direct loss values conditioned on no collapse in terms of structural, non-structural drift sensitive and non-structural acceleration sensitive repair costs (further disaggregation is limited by the performance groups of the storey-based model).

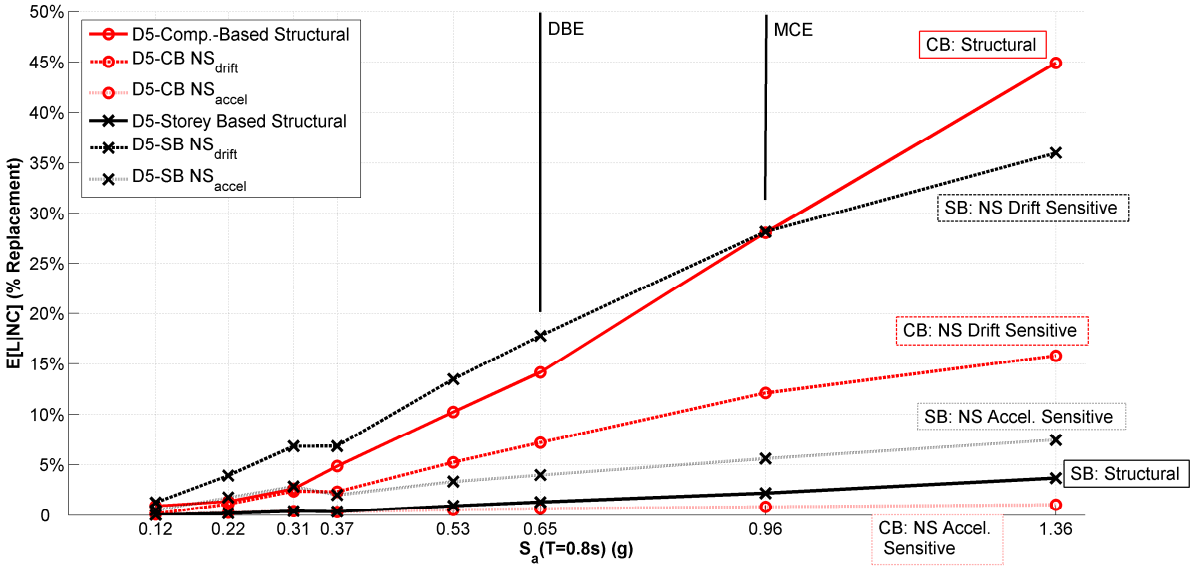


Figure 11: Direct loss disaggregation for baseline model D5.

The main differences in the two loss models are highlighted by simply comparing the governing disaggregated curve from each model; showing structural damage governing the CB

model and non-structural drift sensitive damage governing the SB model. This highlights that the CB model assumes the total repair cost of the structure is equal to the replacement cost of each damageable element considered where the repair costs for the replacement of structural elements is weighted most heavily[3,6]. Conversely, the SB model assumes much more repair cost coming from non-structural drift sensitive, NS_{drift}, elements than structural elements since total cost is based on the entire inventory of the structure as shown in Figure 5 and discussed in [5,6]. Additionally, referring to the three lowest intensity levels it is shown that the rate (slope) of the accumulation of losses in NS_{drift} components is much larger for the SB model and this can be attributed to the use of a partition fragility with a drift of 0.21% representing the onset of damage (at 50% confidence) while the CB model assumes that partition damage of 0.39% which is nearly double this value (refer [3,5]). In lieu of a full cross-examination of the two loss models, these points are deemed necessary to highlight some important differences within them.

6.2 Results comparing variation of modelling parameters and loss models

The loss estimates for all model variations are presented in Table 5. The table shows that the mean of the structural model variations considered tend toward the respective parent loss models. The component-based (CB) loss model shows that the EAL estimates are all above the value reported in the parent study (0.549% MDF) with a range of 0.561% to 0.712% MDF. The storey-based (SB) loss model shows a range that encompasses the parent study value of 0.910% MDF with a range of 0.860% to 0.988% MDF. Interestingly, both loss models return MDF_{DBE} values on the order of 25%, yet the CB loss model estimates the NPV_{50} to be significantly below 25% replacement while the SB loss model estimates NPV_{50} close to the MDF_{DBE}, noting that this deviation between NPV_{50} and MDF_{DBE} could be an important factor when considering seismic strengthening or other risk mitigation options. This last point serves to illustrate how sensitive the EAL metric could be for decision making and the trends witnessed could vary significantly based on the structure under consideration and the assumed discount rate for the calculation of NPV_{50} (refer Eq. (2)).

The influence of the individual structural modelling parameters is presented in Table 6. The influence is expressed as simply the mean percent difference (in magnitude) in a particular loss metric estimation between parameter to another. For example the initial stiffness comparison shows the percent difference between the mean values of structural models D5, D6, D7, and D8 to structural models D1, D2, D3, and D4. The assumption of initial elastic damping is clearly shown to be the most influential with differences on the order of 13%, 8%, and 6 % for EAL, MDF_{DBE}, and MDF_{MCE} respectively. Interestingly, the initial effective stiffness shows a much more significant impact on the CB loss model which is directly accounted for by two factors: the structural damage is estimated by a damage index requiring an estimation of the recoverable curvature (a function of the individual stiffness of the member) and the heavy weighting given to structural repairs (refer Figure 11). Conversely, the SB loss model is not affected significantly by the initial stiffness assumption where, in this case, the global stiffness (fundamental period) of the structure was not witnessed to change drastically (refer Section 4.3) which highlights the sensitivity to this assumption when utilizing a damage index based on recoverable curvature. The hysteretic and post-yielding assumptions were not shown to be significant which gives further reliability in performing loss assessments using the PEER PBEE approach given the numerous variations and decisions that can be associated with structural element calibration.

MODEL	Hysteresis* (post-yield factor)	Initial Effective Stiffness $EI_{0,eff}$**	Elastic Damping ξ_{el}***	Expected Annual Loss EAL	Net Present Value NPV_{50}	Design Intensity Scenario MDF_{DBE}	Maximum Credible Scenario MDF_{MCE}
Component-Based Loss Model [3]				**0.549%**	**14.1%**	**26.2%**	**47.7%**
Mean-CB (this study)				0.641%	16.5%	24.4%	45.4%
D1-CB	DBC (r = 0.04)	M_n/φ_y	6.5%	0.643%	16.3%	23.7%	43.1%
D2-CB	DBC (r = 0.04)	M_n/φ_y	5.0%	0.703%	18.1%	25.6%	45.9%
D3-CB	DB (r = 0.01)	M_n/φ_y	6.5%	0.635%	16.3%	24.3%	45.1%
D4-CB	DB (r = 0.01)	M_n/φ_y	5.0%	0.712%	18.3%	26.0%	48.2%
D5-CB	DBC (r = 0.04)	$0.35EI_g$	6.5%	0.561%	14.4%	22.5%	42.8%
D6-CB	DBC (r = 0.04)	$0.35EI_g$	5.0%	0.646%	16.6%	24.5%	45.6%
D7-CB	DB (r = 0.01)	$0.35EI_g$	6.5%	0.571%	14.7%	23.2%	44.7%
D8-CB	DB (r = 0.01)	$0.35EI_g$	5.0%	0.656%	16.9%	25.2%	47.6%
Storey-Based Loss Model [5]				**0.910%**	**23.4%**	**23.5%**	**39.0%**
Mean-SB (this study)				0.927%	23.9%	24.6%	39.1%
D1-SB	DBC (r = 0.04)	M_n/φ_y	6.5%	0.860%	22.2%	23.9%	38.5%
D2-SB	DBC (r = 0.04)	M_n/φ_y	5.0%	0.988%	25.4%	25.8%	40.4%
D3-SB	DB (r = 0.01)	M_n/φ_y	6.5%	0.877%	22.6%	23.5%	38.2%
D4-SB	DB (r = 0.01)	M_n/φ_y	5.0%	0.983%	25.3%	25.4%	40.4%
D5-SB	DBC (r = 0.04)	$0.35EI_g$	6.5%	0.868%	22.3%	23.6%	37.9%
D6-SB	DBC (r = 0.04)	$0.35EI_g$	5.0%	0.985%	25.4%	25.4%	39.6%
D7-SB	DB (r = 0.01)	$0.35EI_g$	6.5%	0.865%	22.3%	23.5%	37.8%
D8-SB	DB (r = 0.01)	$0.35EI_g$	5.0%	0.987%	25.4%	25.3%	39.8%

*DB-Ductility Based, DBC-Ductility Based Cyclic -All values reported as a percentage of replacement cost
**M_n/φ_y : secant stiffness to nominal yield, $0.35EI_{gross}$: corresponds to secant through 40% of yield after [1]
***Initial stiffness proportional Rayleigh damping ratio (% critical) applied at the first and third fundamental modes

Table 5: Loss results for nominal model variations in comparison with parent studies.

Parameter		Description	Loss Model	Expected Annual Loss EAL	Design Intensity Scenario MDF_{DBE}	Maximum Credible Scenario MDF_{MCE}
Elastic Damping	$\xi_{elastic}$*	6.5% to 5%	Component-Based [3]	+ 12.7%	+ 8.2%	+ 6.6%
			Storey-Based [5]	+ 13.6%	+ 7.9%	+ 5.2%
Initial Effective Stiffness	$EI_{0,eff}$	$0.35EI_{gross}$ to M_n/φ_y	Component-Based [3]	+ 10.7%	+ 4.3%	+ 0.9%
			Storey-Based [5]	+ 0.1%	+ 0.9%	+ 1.5%
Hysteresis and Post-Yield Factor	r	0.04 to 0.01	Component-Based [3]	+ 0.1%	+ 2.4%	+ 4.6%
			Storey-Based [5]	+ 0.3%	- 1.0%	- 0.1%

*Initial stiffness proportional Rayleigh damping at the first and third modes
**post-yield stiffness factor -Values expressed as % difference

Table 6: Comparison of mean magnitudes of deviations between modelling parameters.

7 CONCLUSIONS

- The recreation of the PEER PBEE methodology for a four-storey case study building returned similar results to parent studies highlighting the reliability in the method despite differences in analysis assumptions in order to conduct the loss assessment.
- The impact of structural modelling parameters that could represent a small set of analyst decisions showed reasonable reliability with respect to the overall deviations from the previous values reported in previous studies
- The treatment of elastic damping was shown to be the most significant of the parameters addressed which suggests that a probabilistic consideration of this parameter may be necessary in an optimized case. Conversely, in a more practical case where a deterministic value would be utilized the analyst should be aware of the implications of assigning elastic damping by rule of thumb or intuition.
- The two loss models considered varied considerably in formulation and philosophy. The component-based model provides a greater sense of accuracy as the actual take-off quantities of damageable components are considered for damage analysis rather than typical expected contents as in the storey-based model. Conversely, the storey-based model considers the entire value of the building which is more conceptually sound than the component-based model that only attributes the entire cost to the full replacement cost of components assigned fragilities which leads to a much higher weighting of structural damage. Further loss model developments should aim to combine both of the beneficial aspects of the two models, yet the feasibility of this within a real assessment will be governed by available information and time constraints where the loss model approach will rely heavily on the decisions of the analyst.
- The expected annual loss (EAL) was shown to be the most sensitive loss metric to variations in the loss model adopted, where the simulations of different modelling parameters tended toward the respective parent study. The importance of the deviations of EAL is founded in the implications of its use as a decision variable (insurance, annual improvements) highlights the need for careful formulation of the damage analysis and repair cost stages of the PEER PBEE approach as well as continued research into the development of component fragilities and repair cost functions.

ACKNOWLEDGEMENT

This research is developed as part of research line AT1-2 of the 2010-2013 RELUIS project. As such, the authors gratefully acknowledge the financial support of the RELUIS consortium (www.reluis.it) for this research.

REFERENCES

[1] C.B. Haselton, G.G. Deierlein, Assessing seismic collapse safety of modern reinforced concrete moment frame buildings. *John A. Blume Earthquake Engineering Center, Technical Report No. 156,* Stanford University, 2007.

[2] C. Goulet, C. Haselton, J. Mitrani-Reiser, J.P. Stewart, E. Taciroglu, G. Deierlein, Evaluation of the seismic performance of a code-conforming reinforced concrete frame building – Part 1: Ground motion selection and structural collapse simulation. *Proceed-*

ings of 8th National Conference on Earthquake Engineering, San Francisco, California, 2006.

[3] J. Mitrani-Reiser, J.L. Beck, An ounce of prevention: Probabilistic loss estimation for performance-based earthquake engineering. *PhD Dissertation*, California Institute of Technology (Caltech), Pasadena, California, 2007.

[4] K.A. Porter, An Overview of PEER's Performance-Based Earthquake Engineering Methodology. *Proceedings of Ninth International Conference on Applications of Statistics and Probability in Engineering*, San Francisco, California, 2003.

[5] C.M. Ramirez, E. Miranda, Building specific loss estimation methods & tools for simplified performance-based earthquake engineering. *John A. Blume Earthquake Engineering Center, Technical Report No. 171*, Stanford University, 2009.

[6] D.P. Welch, T.J. Sullivan, G.M. Calvi, Developing Direct Displacement-Based Design and Assessment Procedures for Performance-Based Earthquake Engineering. *ROSE Report 2012/03*, IUSS Press, Pavia, Italy, 2012.

[7] Applied Technology Council, Guidelines for Seismic Performance Assessment of Buildings. *ATC-58: 75% Complete Draft*, Redwood City, California, 2011.

[8] A.B. Liel, G.G. Deierlein, Assessing the Collapse Risk of California's Existing Reinforced Concrete Frame Structures: Metrics for Seismic Safety Decisions. *John A. Blume Earthquake Engineering Center, Technical Report No. 166* , Stanford University, 2008.

[9] A.J. Carr, RUAUMOKO-Users Manual, Theory, and Appendices. *Vol. 2, User manual for the 2-Dimensional version*, University of Canterbury, Christchurch, New Zealand, 2007.

[10] C.B. Haselton, C.A. Goulet, J.L. Beck, G.G. Deierlein, K.A. Porter, J.P. Stewart, E. Taciroglu, An assessment to benchmark the seismic performance of a code-conforming reinforced concrete moment-frame building. Pacific Earthquake Engineering Research Center (PEER), *Report No. PEER 2007/12*, University of California, Berkeley, 2007.

[11] L.A. Montejo, M.J. Kowalsky, CUMBIA: Set of codes for the analysis of reinforced concrete members. *Technical report No. IS-07-01*, Prepared for Alaska Department of Transportation, Constructed Facilities Laboratory, North Carolina State University, Raleigh, North Carolina, 2007.

[12] M.J.N. Priestley, G.M. Calvi, M.J. Kowalsky, *Displacement-Based Seismic Design of Structures*, IUSS Press, Pavia, Italy, 2007.

[13] PEER, Pacific Earthquake Engineering Research Center: Strong Motion Database, University of California, Berkeley, http://peer.berkeley.edu, 2011.

[14] D.P. Welch, T.J. Sullivan, G.M. Calvi, Towards a Direct Displacement-Based Loss Assessment Methodology for RC Frame Buildings. *Proceedings of the 15th World Conference on Earthquake Engineering*, Lisbon, Portugal, September 24-28, 2012.

COMPDYN 2013
4th ECCOMAS Thematic Conference on
Computational Methods in Structural Dynamics and Earthquake Engineering
M. Papadrakakis, V. Papadopoulos, V. Plevris (eds.)
Kos Island, Greece, 12–14 June 2013

DESIGN AND ASSESSMENT OF STEEL AND STEEL-CONCRETE COMPOSITE STRUCTURES: EFFICACY OF EN1998 DESIGN PROCEDURE.

A. Braconi[1], S. Caprili[2], H. Degee[3], M. Guendel[4], M. Hjaij[5], B. Hoffmeister[4], S. Karmanos[6], V. Rinaldi[7], W. Salvatore[2]

[1] RIVA FIRE S.p.A., Viale Certosa, Milano, Italy
aurelio.braconi@gmail.com

[2] Department of Civil and Industrial Engineering University of Pisa, Italy
silvia.caprili@ing.unipi.it, walter@ing.unipi.it

[3] Département ArGEnCo, Universitè de Liege, Belgique
h.degee@ulg.ac.be

[4] RWTH Aachen University, Institut für Stahlbau, Aachen, Germany
guendel@stb.rwth-aachen.de, hoff@stb.rwth-aachen.de

[5] Institut National des Sciences Appliquées de Rennes, France
Mohammed.Hjiaj@insa-rennes.fr

[6] University of Thessaly, Volos, Greece
skara@mie.uth.gr

[7] Arcelor Mittal S.A.
valerie.rinaldi@arcelormittal.com

Keywords: Behaviour factor, Incremental Dynamic Analysis, Pushover analysis

Abstract. *Design codes for seismic constructions allow the realization of structures able to dissipate energy through cyclic plastic deformations localized in specific zones, selected to involve the largest number of structural elements. The capacity design approach requires an opportune selection of the design forces and an accurate definition of structural details in the plastic hinges. The structural elements in which plastic hinges are located are over-sized with respect to the seismic actions obtained by the use of the design spectrum, while the elements that shall remain elastic are over-sized with respect to dissipative elements. The capacity design methodology requires an accurate control of the localization of plastic hinges, strongly influenced by the actual mechanical properties of materials. In the present work, developed inside the research project OPUS, different case studies were designed according to Eurocodes and subjected to a deep structural analysis, aiming to evaluate the effective allowable ductility (behaviour factor) with respect to what imposed during the design phase.*

1 INTRODUCTION

Design codes for seismic constructions nowadays allow to exploit plastic resources by realizing ductile structures able to dissipate energy by means of cyclic plastic deformations localized in the suitably chosen dissipative zones. Plastic deformations have to be located within the structures in such a way to guarantee the involvement of the largest number of structural elements. The larger is the number of the plastic hinges, the larger is the attainable global ductility and the smaller is the deformation demand at local level.

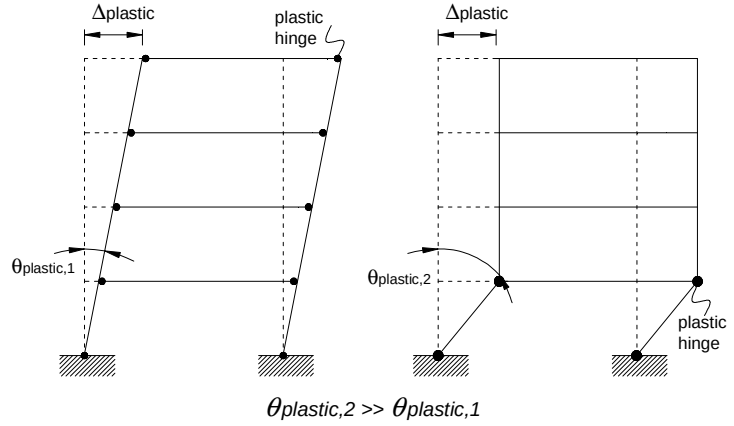


Figure 1: Global ductility vs. local rotation demand for moment resisting frames.

The design of plastic hinges in desired elements and the development of an efficient energetic dissipation, without any significant decrease in terms of resistance or stiffness, are obtained through a proper design methodology called *capacity design* and an accurate definition of structural details of elements, joints and connections. Obviously, the choice of dissipative elements depends on the structural typology; for steel structures, the most diffused are Moment Resisting Frames (MRF), Concentrically Braced Frames (CBF) and Eccentrically Braced Frames (EBF).

In multi-storey buildings, for example, to allow the development of the largest number of plastic hinges and to dissipate as much as possible seismic energy, the condition $\sum M_{Rc} \geq 1.3 \times \sum M_{Rb}$ [1] has to be checked in correspondence of each beam-to-column joint of the structure, being ΣM_{Rc} and ΣM_{Rb} the sums of the design values of the moment resistance of columns and beams, respectively, framing at a joint (figure 2). This condition aims at avoiding the formation of poor dissipative mechanisms as soft-storey, furnishing to the column sufficient overstrength with respect to the beams. The 1.3 factor, in particular, takes into account possible overstrength phenomena of materials used in beams with respect to the ones adopted for columns.

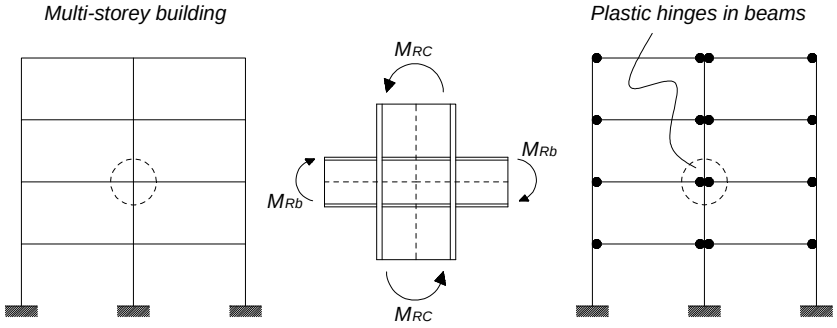


Figure 2: Distribution of plastic hinges to allow the maximum dissipation of seismic energy.

In the modal analysis procedure, commonly used in the engineering practice, the possibility to exploit plastic resources is translated in lower values of design seismic actions. To obtain the design spectrum, the elastic response one is divided by a reduction factor, summarizing the parameters that govern the structural response, the available inelastic resources and the sensibility to the second-order effects.

The aforementioned reduction factor is already introduced by several modern standards such as Eurocode 8 [1], in which it is identified as the behavior factor "q", or the US standards, Uniform Building Code, UBC [2] NEHRP provisions [3], American Seismic Provisions for Structural Steel Buildings [4], in which the reduction factor "R" is defined. The larger the reduction factor is, the larger shall be the structural ductility and the lower can be the seismic design actions. In such a way it seems possible to obtain systematically structural solutions characterized by a reduced overall weight.

However, the exploitation of the plastic capacity can be limited by other criteria adopted in the design process: for example, in the assessment at serviceability limit state, the limitation of second order effects as well as the assessments of limit states associated to static load combinations shall be considered. The fulfilment of such conditions can limit the benefits of ductile design, leading to a structure whose seismic response can be far from the one supposed at design stage. The structural elements in correspondence of dissipative zones are over-dimensioned with respect to the seismic actions obtained by the design spectrum so that, in practice, only a small percentage of ductile resources will be exploited. At the same time, as the capacity design rules are applied, the protected elastic elements are further over-dimensioned with respect to dissipative elements [5, 6].

Moreover, according to previous concepts, the seismic ductile design foresees an accurate control of plastic hinge's formation that mainly depends on the distribution of plastic resistances of structural elements. It is so clear that the *capacity design* method strongly depends on the actual mechanical properties of materials.

On the other hand, European production standards [7] do not provide adequate limitations on mechanical material properties for steel products either there is not a good agreement among provisions of different standards. For these reasons, the adoption of aforementioned design approaches is allowed by Eurocode 8 [1], for steel and composite steel-concrete structures, on the conditions that adequate safety factors are introduced and that actual values of the mechanical properties do not modify the location of plastic hinges. These conditions limit the adoption in design practice of the steel and steel-concrete composite structures, potentially a very interesting option in seismic zone because of the intrinsic ductility and dissipative capacity of the steel.

Eurocode 8, in particular, imposes additional checks on material properties in dissipative zones as, for example, in steel members where the yielding stress shall be upper limited by the overstrength coefficient, γ_{OV} fixed equal to 1.25 (1.25 times the nominal yielding value f_y).

Some first evaluations on seismic reliability of steel structures taking into account variability of steel properties were executed on concentrically braced frames [8], and eccentrically braced frames [9] but a well comprehensive study, aiming at clarifying aforementioned open problems, is still missing.

The OPUS research project, *Optimizing the seismic Performance of steel and steel-composite concrete strUctures by Standardizing material quality control*, funded by European Commission through Research Fund for Coal and Steel, contract RFCR-CT-2007-00039 [10], aimed at assessing the influence of material properties' scattering on final structural performance of steel and steel concrete composite structures designed in earthquake-prone areas. In particular, in the framework of this project, a representative set of case studies, including MRFs, EBFs and CBFs, was designed according to the Eurocode design provisions

and afterwards subjected to a deep analysis of their structural performance. A suitably developed probabilistic procedure then allowed to estimate the failure probability associated to all relevant collapse modes previously identified.

In the present paper the main results obtained by aforementioned performance analysis of the case studies are illustrated and discussed while [11] includes the main results on influence of material properties' scattering on final structural performance.

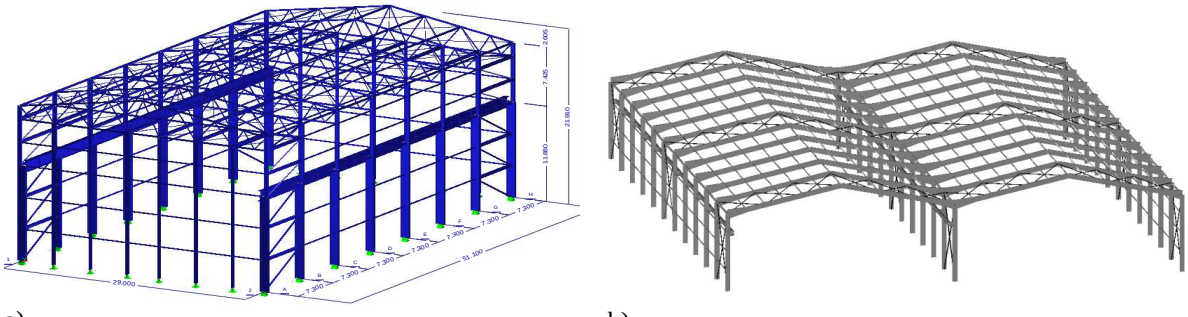
The assessment of seismic performance of all structures was executed developing plain non-linear models of the main resisting frames: about 40 models were elaborated and calibrated through a complete benchmarking process devoted to the simulations of three structural typologies. The models were analyzed employing Push-Over analysis (PO) and Incremental Dynamic Analysis (IDA) in order to characterize the structural behavior of case studies and to individuate the relevant collapse modalities.

The analysis on structural case studies was further pushed in more refined details in order to assess the real behavior factor (q) of all models and to individuate the level of Peak Ground Acceleration (PGA) able to activate the collapse modes previously identified. In particular, IDA technique was applied and, once identified the PGA able to activate relevant collapse modes, the Ballio-Setti procedure [12, 13] was used to determine the q factor.

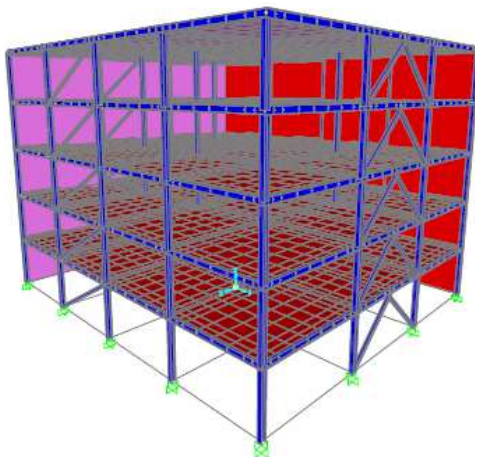
Moreover, the Ballio-Setti procedure was slightly modified for taking into account the discrepancy at first mode frequency between the target spectra and real spectra of earthquake time-histories. Such procedure allowed to compare for each considered case-study actual value of q-factor with the one used in the design process.

2 DESIGN OF THE CASE STUDIES

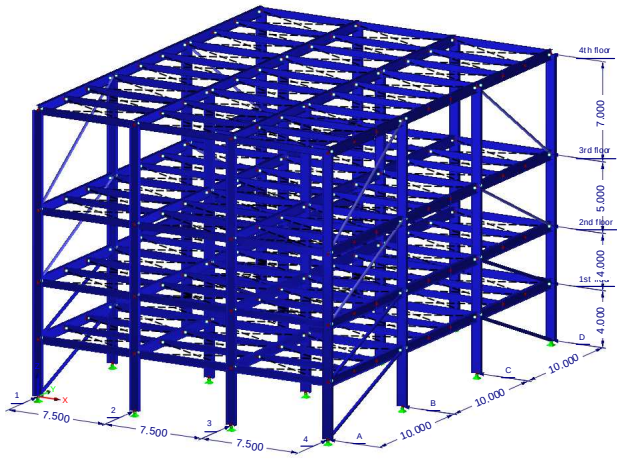
A fully representative set of case studies, including MRFs, CBFs and EBFs was designed according to Eurocode prescriptions: the geometries and the morphologies were suitably chosen in order to house offices, car parks, industrial storages, electrical power plants or ware house/light industrial activities; some examples of the designed buildings are reported in the figure 3. Two levels of seismic actions were selected in order to represent low and high seismic hazard areas; the static loads were chosen on the basis of housed activities according to EN1991 [14] and the wind action was selected fixing a unique parameters for all structures. In the table 1 all the information related to use category, live loads, environmental loads (snow, wind and earthquake) are presented, while geometry, chosen resisting systems for vertical and horizontal loads and floor system scheme are listed in the table 2.



a) b)



c)



d)

Figure 3: a) Industrial building for electrical power plant activities; b) industrial building for warehouse/light activities; c) EBF and CBF configurations for offices; d) MRF and CBF configurations for industrial storage

Building n°	Building type	Material	Live Load kN/m²	Snow kN/m²	Wind kN/m² (m/s)	Seismic action PGA [g]
1	Office	Steel	3,00	0,85	0,39	0,10
2	Office	Steel	3,00	0,85	0,39	0,10
3	Office	Steel	3,00	1,00	1,10	0,25
4	Office	Steel	3,00	1,00	1,10	0,15
5	Office	Steel	3,00	1,40	(30 m/s)	0,25
6	Office	Composite beams/ Steel columns	3,00	1,11	1,40	0,10
7	Office	Composite beams and columns	3,00	1,11	1,40	0,10
8	Office	Composite beams/ Steel columns	3,00	1,11	1,40	0,25
9	Office	Composite beams and columns	3,00	1,11	1,40	0,25
10	Office	Composite beams/ Steel columns	3,00	1,11	1,40	0,10
11	Office	Composite beams and columns	3,00	1,11	1,40	0,25
12	Industrial	Steel	5,00	1,40	(30 m/s)	0,25
13	Industrial	Steel	Crane load (10 tons)	1,40	(30 m/s)	0,25
14	Industrial	Steel	Crane load (370+140 tons)	0,85	0,39	0,25
15	Industrial	Steel	5,00 kN/m² + add. dead loads (6,8 kN/m²)	0,85	0,39	0,10
16	Car Park	Steel	2,50	1,00	1,10	0,25

Table 1:Structural typologies and design loads used for case studies.

Building ID	N°of storeys	X – direction				Y – direction			
		Resisting System	Span [m]	Secondary beam	Storey height [m]	Resisting system	Span [m]	Secondary beam	Storey height [m]
1	5	MRF	3x7m	Yes	3,5	CBF	6x6m	No	3,5
2	5	CBF	3x7m	Yes	3,5	CBF	6x6m	No	3,5
3	5	EBF shear	3x7m	No	3,5	EBF shear	4x6m	Yes	3,5
4	5	EBF bending	3x7m	No	3,5	EBF bending	4x6m	Yes	3,5
5	5	MRF	3x7,5m	Yes	3,5	CBF	4x6m	Yes	3,5
6	5	MRF	3x7m	Yes	3,5	Not designed	4x6m	No	3,5
7	5	MRF	3x7m	Yes	3,5	Not designed	4x6m	No	3,5
8	5	MRF	3x7m	Yes	3,5	Not designed	4x6m	No	3,5
9	5	MRF	3x7m	Yes	3,5	Not designed	4x6m	No	3,5
10	5	EBF shear	3x7m	No	3,5	CBF	4x6m	No	3,5
11	5	EBF shear	3x7m	No	3,5	CBF	4x6m	No	3,5
12	4	MRF	3x7,5m	Yes	4+4+5+7	CBF	3x10m	No	4+4+5+7
13	1	MRF	2x25m	Yes (purlins)	10,5	CBF	12x6m	Yes (purlins)	10,5
14	1	MRF truss girder	1x29m	No	21,9	CBF	7,30m	No	17,6
15	4	MRF	3x7,5m	No	4+4+5+7	CBF	3x10m	Yes	4 +4 + 5+7
16	2	EBF shear	5x8m 2x10m	No	4+4	EBF shear	6x10.5m	Yes	4+4

Table 2: Structural and geometrical characteristics of designed case studies.

The design procedure followed actual European and international standards [1, 14, 15, 16, 17]; in particular, the design process was repeated for all structures adopting different strategies or techniques, in order to optimize the cross sections' size and to avoid the over-sizing of structural members, a relevant aspect especially for low seismicity areas in which seismic forces can be lower than wind ones. The optimal design was not reached in all cases because of design procedures, checks and limitations imposed by Eurocodes.

In the case of MRFs, it was noted that the contemporary assessment of design checks both for static and seismic combinations obliged to over-size beams respect to seismic strength requirements. In addition, capacity design approach, beam-to-column resistance hierarchy, drift limitations and sensitivity to second order effects, following respectively equations (1), (2), (3) and (4), strongly conditioned the final sizing of the elements:

$$E_i^{c.d.} = E_i^{gravity} + 1.1 \cdot \gamma_{OV} \cdot \min(\Omega_j) \cdot E_i^{seismic} \quad (1)$$

$$\sum M_{Rd,PL}^{column} \geq 1.3 \cdot \sum M_{Rd,PL}^{beam} \quad (2)$$

$$\nu \cdot q_d \cdot d_e = \nu \cdot d_r \leq d_{\lim it} \quad (3)$$

$$\vartheta = \frac{P_{tot} \cdot d_r}{V_{tot} \cdot h} \leq \beta \tag{4}$$

where E_i is the solicitation acting on the i-th member, γ_{ov} is the material over-strength (equal to 1.25), $M_{Rd,PL}$ is the design resistant bending moment, d_e is the elastic drift coming from analyses, q_d is the displacement behaviour factor taken equal to q, P_{tot} and V_{tot} are respectively total vertical actions and horizontal action on the i-th floor.

Ω factor represents the structural over-strength, i.e. how higher is the resistance of the more solicited dissipative member respect to the maximum level of solicitations in the seismic combination, expressed by equation (5):

$$\Omega_i = \alpha \cdot \frac{R_{d,i}}{E_{i,dissipative}^{seismic}} \tag{5}$$

where α coefficient is equal to 1 for MRFs and CBFs and 1.5 for EBFs.

The over-sizing of dissipative members and the adoption of limitations for interstorey drift ratio notably increased the size of columns and of beams leading, at the end of the design process, to structures with a large amount of strength and ductility resources, higher than the ones effectively required by seismic loads.

In order to cope with these problems, in the case of MRFs it was followed an appropriate design process devoted to the selection of an optimized behaviour factor, harmonized with strength requirements coming from static load combinations. According to this procedure, in many cases, it was found more convenient to design structural configurations adopting medium ductility behaviour rather than high ductility behaviour both in high and low seismicity areas.

In the case of EBF configurations (buildings 3, 4 and 16), a similar problem for sizing seismic links was revealed, since the interaction between static and seismic combinations played an important influence and obliged to over-size seismic link sections; in addition, the control of links over-sizing inside EBF configuration was completed checking that difference between Ω_i of links was not more than 25% (table 4):

$$\frac{\Omega_{\max}}{\Omega_{\min}} \leq 1.25 \tag{6}$$

In buildings n°3 and 4, characterized by a similar geometrical scheme but designed for different levels of PGA and with a different behaviour of link elements (table 2), in order to reduce the over-strength influence on the final design, a suitable technical solution of the floor system was used in order to decuple static effects from seismic effects on the seismic links: beams contained seismic links were coupled with other beams (i.e. beam duplication) devoted to carry vertical loads only. It was so possible to optimize some structural solutions to an utilization ratio of the links (e.g. solicitation/resistance, S/R) equal to 1 arriving so to an over-strength coefficient Ω equal to 1.5. This, anyway, produced an increment of bracing sections. As for the case of MRFs, the design of EBFs was strongly influenced by second order effects and by the respect of drift limitation: as an example, the sizing of braces in frame 3x (building n°3, frame in xz plane) was determined in relation to the satisfaction of the limitation of the maximum drift limit equal to 0.05%, leading to an oversizing of bracing elements; in building 4, on the other side, the most critical condition imposed in the desing was the fulfilment of buckling in members in compression, in which, consequently, the ratio between solicitation and strenght was nearly about 1 (optimization in the design of braces).

Concerning CBF solutions, the design process proposed by EN1998-1 [1] obliged to perform several repetitive designing in order to fulfil problems related to slenderness ratio:

$$1.3 \leq \lambda \leq 2.0 \tag{7}$$

and the assessment of equations (1), (3) and (4).

Only in some cases the optimization was reached arriving to a solicitation/strength ratio near to 1; for other solutions, different steel qualities were adopted for steel bracings at different floor levels in order to optimize design checks and to satisfy all the prescriptions for seismic design (tables 4 and 6).

Obviously, the adoption of several different braces' or beams' sections, different steel grades for braced configurations and the selection of behaviour factors for MRF optimized solutions are not commonly adopted in the current engineering design practice; as a consequence, it can be argued that the design procedure proposed by EN1998-1 [1], without a complete and long conceptual preliminary phase, leads to structures with performance rather higher than the ones strictly required by seismic load combination.

What already presented confirms that EN1998-1 design procedure [1] generally allows the realization of safe structures, evidencing, at the same time, that the impossibility of reaching a full optimized structural solution represents a limit that can endanger the competitiveness of these structural typologies.

ID	*Structural Typology*		*Material*	*Floor*	*Beams*		*Columns*	*Bracing system*	
	x-dir	*y-dir*			*x- dir*	*y- dir*		*x- dir*	*y- dir*
1	MRF	CBF	Steel S235	1	IPE 400	IPE 500	HEB 400	-	CHS 139.7x12.5
				2	IPE 400	IPE 500		-	CHS 139.7x10.0
				3	IPE 400	IPE 500		-	CHS 139.7x8.0
				4	IPE 400	IPE 500		-	CHS 114.3x8.0
				5	IPE 400	IPE 500		-	CHS 114.3x4.0
12	MRF	CBF	Steel S355	1	HEB 360	HEB 400	HEB 450	-	C273,0×8.0
				2	HEB 360	HEB 400		-	C273,0×8.0
				3	HEB 360	HEB 400		-	C273,0×7.1
				4	HEB 360	HEB 400		-	C273,0×7.1
	MRF	CBF	Steel S460	1	HEB 320	HEB 340	HEB 400	-	C273,0×7.1
				2	HEB 320	HEB 340		-	C273,0×7.1
				3	HEB 320	HEB 340		-	C244,5×7.1
				4	HEB 320	HEB 340		-	C244,5×7.1
13	MRF	CBF	Steel S235	1	IPE 500	IPE 120	HEA 500	-	2L120x120x20
	MRF	CBF	Steel S275	1	IPE 450	IPE 120	HEA 500	-	2L120x120x20
15	MRF	CBF	Steel	1	IPE 550	HEA 700	HEB 700	-	CHS 244.5x8.0
				2	IPE 500	HEA 700		-	CHS 244.5x6.0
				3	IPE 500	HEA 700		-	CHS 193.7x10
				4	IPE 500	HEA 700		-	CHS 193.7x4

ID/System		*Lev. n°*	*Beams x- dir*	*y- dir*	*Braces y-dir dissipative*	*non diss.*	*Col.*
14	Steel beams and columns	1 2	Truss girder as part of MRFs	Simply supported purlins: HEA200	CHS193.7x8 CHS193.7x8	2HEA240 2HEA240	main col.: HEB1000

	X dir. MRF with truss girder Y dir. CBF	3 4 5	chords: HEA180 diag.: CHS139.7x4	fully rigid connectors HEA140	CHS193.7x8 *CHS168.3x6.3 *CHS168.3x6.3	2HEA240 2HEA240 2HEA240	roof col.: HEA450

ID/System		*Lev.* *n°*	*Beams* *x- dir*	*y- dir*	*Braces Y* *dissipative*	*Column* *x- dir*	*y- dir*
5	Steel S355 X-dir: MRF Y-dir: CBF	1	IPE330*/IPE450**	IPE270*/IPE330**	S100x8	1° floor: HEA360* HEA400**	1° floor: HEA360* HEB300**
		2	IPE330*/IPE450**	IPE270*/IPE330**	S90x8		
		3	IPE330*/IPE450**	IPE270*/IPE330**	S80x8	HEB300+ HEB360++	HEA400+ HEB360++
		4	IPE330*/IPE450**	IPE270*/IPE330**	S75x6	HEA360* HEA360**	HEA360* HEB300**
		5	IPE300*/IPE450**	IPE330*/IPE400**	S60x4	HEB300+ HEB360++	HEA360+ HEB360++

Table 3: Steel buildings with MRF and MRF-CBF structure: characteristics of structural elements (more details related to building n°5 are presented in [10]).

ID/System/Floor n°			*Beams* *x*	*y*	*Col.*	*Braces* *x- dir*	*y- dir*	*Links* *x*	*y*	*Ωi* *x*	*y*
2	CBF Steel	1	IPE 400	IPE 500	HEB 340	CHS139.7x12.5	CHS139.7x12.5	-	-	1.14	1.28
		2				CHS139.7x10	CHS139.7x10	-	-	1.11	1.19
		3				CHS139.7x8	CHS139.7x8	-	-	1.11	1.11
		4				CHS139.7x8	CHS114.3x8	-	-	1.32	1.20
		5				CHS139.7x4	CHS114.3x4	-	-	1.37	1.18
3	EBF Steel S355	1	IPE 500	IPE 360	HEB 300 HEB 320	HEB 220	HEB 280	HEB 200	HEB 200	1.66	2.12
		2				HEB 220	HEB 280	HEB 180	HEB 200	1.54	2.47
		3				HEB 220	HEB 260	HEB 160	HEB 160	1.53	2.00
		4				HEB 200	HEB 260	HEB 140	HEB 140	1.62	2.03
		5				HEB 200	HEB 260	HEB 120	HEB 100	1.86	2.24
4	EBF Steel S355	1	IPE 500	IPE 360	HEB 240 HEB 260	HEB 200	HEB 200	IPE 270	IPE 270	1.68	1.99
		2						IPE 270	IPE 270	1.87	1.74
		3						IPE 240	IPE 240	1.63	1.78
		4						IPE 220	IPE 220	1.66	1.76
		5						IPE 160	IPE 160	1.51	1.61
16	EBF Steel S275	1	-	IPE 600	HEB 240	HEB 280	HEB 260	HEB 320	HEB 300	1.53	1.57
		2	-					HEB 360	HEB 280	1.88	1.91

Table 4: Steel buildings with EBF and CBF structure: characteristics of structural elements.

ID	*Typology*	*Lev. n°*	*Beams (x-direction)*					*Column*
6	Composite beams/ Steel columns X dir: MRF Y dir: not des.	1 2 3 4 5	Fully rigid IPE 360	Concrete effective width [mm]	EC4	Mid. End.	1225 875	HEA 450
					Elastic EC8	M^- M^+	700 525	
					plastic EC8	M^- M^+	1400 1050	
		Materials: S235 – C25/35						
7	Composite beams/ Composite columns X dir: MRF Y dir: not des.	1 2 3 4 5	Fully rigid IPE 360	Concrete effective width [mm]	EC4	Mid. End	1225 875	HEA 400 Reinfor. steel 4Φ24 mm
					Elastic EC8	M^- M^+	700 525	
					plastic EC8	M^- M^+	1400 1050	
		Materials: S235 – C25/35						
8	Composite beams/ Steel columns X dir: MRF Y dir: not des.	1 2 3 4 5	Fully rigid IPE 360	Concrete effective width [mm]	EC4	Mid. End	1225 875	HEA 400
					Elastic EC8	M^- M^+	700 525	
					plastic EC8	M^- M^+	1400 1050	
		Materials: S355 – C30/37						
9	Composite beams/ Composite columns X dir: MRF Y dir: not des.	1 2 3 4 5	Fully rigid IPE 360	Concrete effective width [mm]	EC4	Mid. End	1225 875	HEA 360 Reinfor. steel 4Φ 24mm
					Elastic EC8	M^- M^+	700 525	
					plastic EC8	M^- M^+	1400 1050	
		Materials: S355 – C30/37						

Table 5: Composite structures with MRF system (no braces).

ID	*Structural system*	*Lev. n°*	*Beams x- dir*	*y- dir*	*Braces Y dissipative*	*non diss.*	*Braces Y dissipative*	*Column*
10	Composite beams/ Steel columns X dir: EBF (shear) Y dir: CBF	1	IPE 270 + slab 0,18 m	IPE 270 + slab 0,18m	HEB 260	HEB 180	UPE 160	HEB 300 strong axis X
		2			HEB 260		UPE 200	
		3			HEB 220		UPE 160	
		4			HEB 200		UPE 120	
		5			HEB 160		UPE 80	
11	Composite beams/ Steel columns X dir: EBF (shear) Y dir: CBF	1	IPE 270 + slab 0,18 m	IPE 270 + slab 0,18m	HEB 450	HEB 240	UPE 180	HEB260 strong axis X (except for ground storey – HEB 280)
		2			HEB 450		UPE 200	
		3			HEB 400		UPE 180	
		4			HEB 340		UPE 140	
		5			HEB 280		UPE 100	

Table 6: Composite structures with bracing systems.

3 DEVELOPMENT OF STRUCTURAL MODELS

The presented case studies were deeply analyzed adopting sophisticated models able to capture all relevant non-linear phenomena at structural and material level. The main aims of the present work consisted in the individuation, for each structure, of the relevant collapse criteria and of the corresponding PGA activation level and, moreover, in the evaluation of the seismic structural performance in terms of behaviour factor q. To these purposes, suitable numerical models were developed.

Given that the numerical simulations were carried out by different partners of OPUS project [10] using different software like Abaqus [21], FineLG [22], Dynacs [23] and OpenSees [24], a calibration process was executed comparing simulated capacities on simple benchmarks. Three different structures (a bracing element, a portal frame and a concentrically braced frame) were modelled and used as calibration case studies: modelling parameters employed for the definition of numerical models of the structures previously design were consequently fixed [10].

The structural behaviour of buildings n° 1, 2, 14 and 15 was investigated by using the finite element program Dynacs [23]. The structures were modelled using bi-dimensional frames with fibre beam elements, with increasing element density in dissipative regions of the MRFs (e.g. column base, beam-column connections). The non-linear material behaviour was considered adopting a bi-linear model with kinematic hardening described by yield stress, tensile stress and ultimate elongation. Braces were modelled using special developed non-linear springs elements, representing the elastic-plastic cyclic behaviour under tension, global buckling under compression and cyclic degradation. The analyses included large deformations to consider the influence of the P-Δ-effect.

Buildings n° 6, 7, 8, 9, 10 and 11 were assessed using the non linear finite element software FineLG [22]. Composite elements were modelled using fibre beam element including a steel and a concrete part. The concrete part was assumed to be a rectangular beam element with width equal to the effective one evaluated according to Eurocode 4. Diagonal members of EBF and CBF structures were modelled using steel beam element directly taking into account the possible lateral buckling under compression. The seismic links in EBF needed to include the yielding in shear, generally not possible with the adoption of classical fibre models: as a consequence, the link elements were modelled by a classical non linear beam element describing properly the bending behaviour, coupled with a non linear spring calibrated versus a shell model and accounting for the shear deformation and yielding, as briefly schematized in the figure 4.

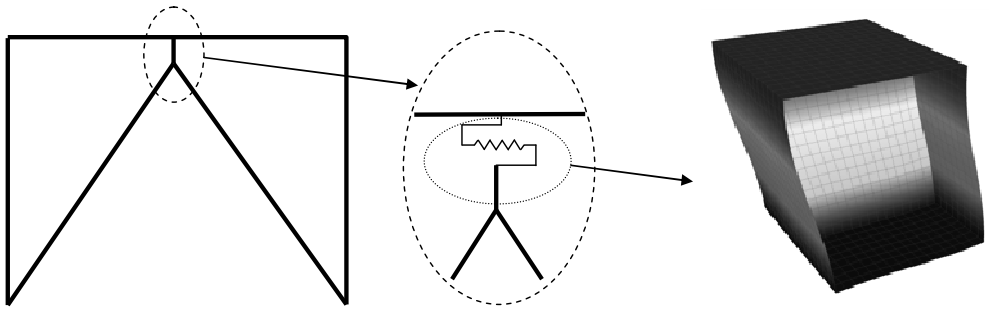


Figure 4: Modelling of the seismic shear link

Buildings n° 5, 12 and 13 were modeled by Abaqus software [22]: beams and columns were modeled using 3-node quadratic beams in plane for MRF and 3-node quadratic beams in space for concentrically braced frames.

Buildings n° 3, 4 and 16 were modeled using the numerical software OpenSees [24]. The dissipative behavior of link elements and the combined effect of shear forces and bending moments were directly taken into account modeling all the elements as fiber section elements (figure 5a). Inelastic fiber elements were used for representing columns, beams without links and short shear links; two elements were used for modeling each long bending link and four elements were employed for each brace. Buckling phenomena of braces were directly taken into account giving an initial imperfection equal to 1/500 of the brace length to the middle point of the brace itself, as represented in figure 5b; a similar imperfection was also assigned to the top of columns in order to include in the analysis P-Δ effect (figure 5b). The value adopted for the imperfection was evaluated from the calibration with literature results.

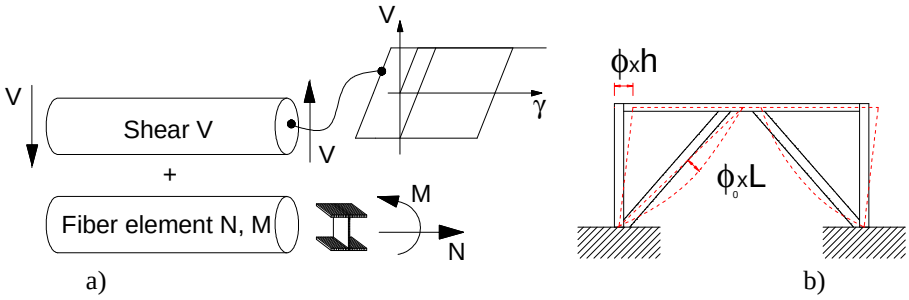


Figure 5: a) General scheme of fiber elements and b) model of imperfections of braces and columns.

For modeling the flexural behavior of steel members (beams, braces and columns), the Menegotto-Pinto law [25], characterized by bilinear elastic-plastic stress-strain curve with kinematic hardening, accurately calibrated in order to agree with literature results, was used (figure 6a); moreover, as regards the force-distortion law used for representing the shear behavior of elements, a bilinear elastic-plastic law with kinematic hardening was used for links (figure 6b).

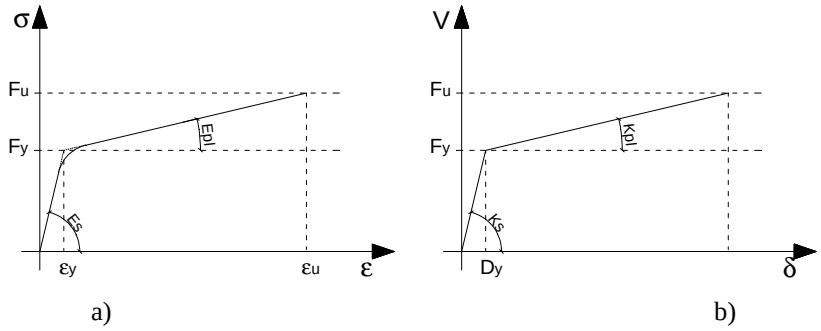


Figure 6: Constitutive law adopted for a) flexural behaviour, b) shear behaviour of dissipative elements.

4 ANALYSIS OF STRUCTURAL PERFORMANCE

4.1 Definition of collapse criteria

Seismic demand levels are usually defined in relation to performance levels as Damage Limitation (DL), Severe Damage (SD) and Near Collapse (NC). The investigations hereafter presented were carried out for the SD performance level, according to EN1998-3 [18] and corresponding to an earthquake hazard level with a medium return period of 475 years.

A crucial point in the assessment of structures using non-linear static and dynamic analysis is the definition of limit states, not exactly defined in European seismic standards. The seismic performance of structures can be evaluated by general deformation criteria (i.e. for example the over-passing of the interstorey drift limit) or local ductility criteria. Furthermore,

non seismic-specific verifications as shear capacity, global buckling, and others shall be also carried out.

Global deformation criteria as roof and storey drift defined according to FEMA356 [19] were only used as indicative values. Additionally, maximum connection forces and foundation forces were recorded for further investigations. All verifications were carried out for each structural element with regard to the maximum value obtained during a time history analysis automatically by user-defined subroutines. Only global buckling and lateral torsional buckling were checked manually in the relevant time step.

The limit axial load for the buckling of steel members in compression (columns and braces) was evaluated according to Eurocode 3 with expression (8), and was consequently strongly influenced by the mechanical properties of materials (yielding strength f_y):

$$N_{b,Rd} = \frac{\chi \cdot A \cdot f_y}{\gamma_{M1}} \tag{8}$$

All limit states considered in the case studies with moment-resisting (MRF) and concentrically braced steel frames (CBF) are presented respectively in tables 7 and 8.

For eccentrically braced frames (EBF) one of the most conditioning collapse criteria was obviously the failure of link elements, in which plastic deformation are concentrated according to the design principles. The plastic rotation was calculated as the ratio between the relative vertical displacement (δ) and the link length (e):

$$\frac{v_1 - v_2}{e} = \frac{\delta}{e} = \gamma_{LINK} \tag{9}$$

where for shear short link δ was evaluated as the relative vertical displacement between the two ends of the link (figure 6a) and for long bending links δ referred to the mid length of the element (figure 6b). The limits assumed for EBF are presented in the table 9.

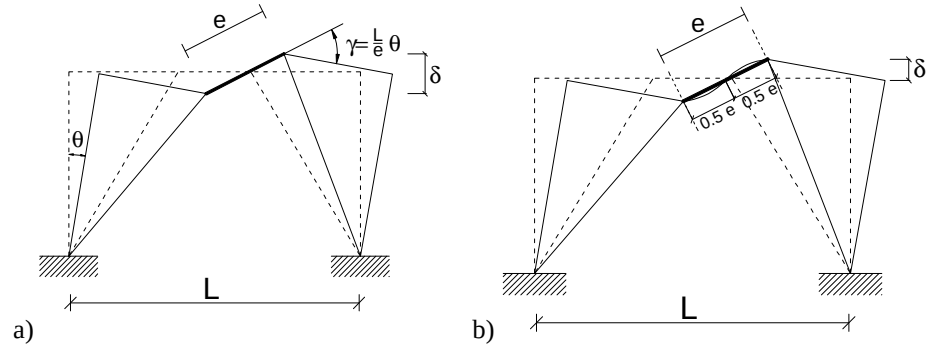


Figure 7: Evaluation of link plastic rotation a) for short shear links, b) for long bending links.

	Type	Reference	Criteria
A	Dynamic instability (Global)	-	Limit
B	Maximum roof drift ratio (Global)	FEMA 356	Indicative
C	Inter-storey drift ratio (Global)	FEMA 356	Indicative
D	Ultimate rotation of plastic hinges (Local) *	EN1998-3	Limit
E	Shear capacity (Local)	EN1993-1	Limit
F	Lateral torsional buckling (Local) **	EN1993-1	Limit
G	Global buckling (Local)	EN1993-1	Limit
H	Joint forces	-	Evaluation
I	Foundation forces	-	Evaluation

Table 7: Failure criteria for buildings with MRF. (*) for axial load ration $0.3 < n \leq 0.5$ linear reduction of rotation capacity in acc. to FEMA356; (**) Lateral torsional buckling of beams is prevented by RC-floor (no composite action)

	Type	Reference Code	Criteria
A	Dynamic instability (Global)	-	Limit
B	Maximum roof drift ratio (Global)	FEMA 356	Indicative
C	Inter-storey drift ratio (Global)	FEMA 356	Indicative
L	Ultimate deformation, tension (Local)	EN1998-3	Limit
M	Ultimate deformation, compression (Local)	EN1998-3	Limit
E	Shear capacity (Local)	EN1993-1	Limit
F	Lateral torsional buckling (Local) **	EN1993-1	Limit
G	Global buckling (Local)	EN1993-1	Limit
H	Joint forces	-	Evaluation
I	Foundation forces	-	Evaluation

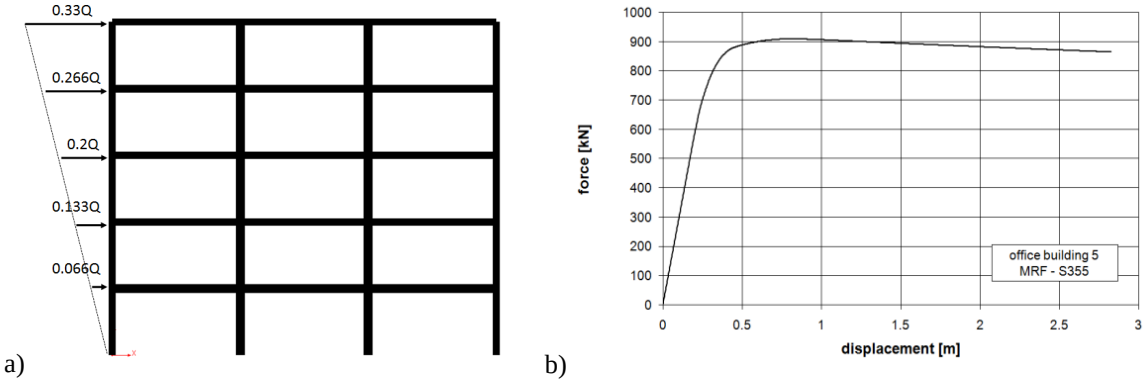
Table 8: Failure criteria for buildings with CBF. (**) Lateral torsional buckling of beams is prevented by RC-floor (no composite action).

	Type	Reference code	Criteria
A	Dynamic instability (Global)	-	Limit
B	Maximum roof drift ratio (Global)	FEMA 356	Indicative
C	Inter-story drift ratio (Global)	FEMA 356	Indicative
N	Ultimate rotation of link (Local)	FEMA 356	Limit
E	Shear capacity (Local)	EN1993-1	Limit
G	Global buckling (Local)	EN1993-1	Limit
H	Joints forces	-	Evaluation
I	Foundation forces	-	Evaluation

Table 9: Failure criteria for buildings with EBF.

4.2 Pushover analysis

In push-over (PO) analysis the non-linear behaviour, the relevant collapse criteria and the available q-factor of each structure were evaluated. Pushover analyses were performed on each structure using a monotonically increasing triangular pattern of lateral loads, applying, at the same time, the vertical loads ($G+0.3Q$), being G the sum of the self weight and the slab weight and Q the live load. The lateral loads were applied monotonically in a step-by-step nonlinear static analysis, as simply represented in the figure 7 in the case of building 2.



a) b)

Figure 8: a) Pushover analysis in Abaqus for 2D MRF (X-direction) of Office Building 5, b) Diagram Q versus δ, for pushover analysis in Abaqus, for MRF and S355

The behaviour factor was determined on the basis of the base shear-displacement curve using the following formula:

$$q_{stat} = \frac{d_u}{d_y} \cdot \frac{V_y}{V_u}, \tag{10}$$

where d_y is the displacement at the first plastic hinge, V_y the corresponding base shear, d_u the displacement when the first failure criteria is reached and V_u the corresponding base shear [26].

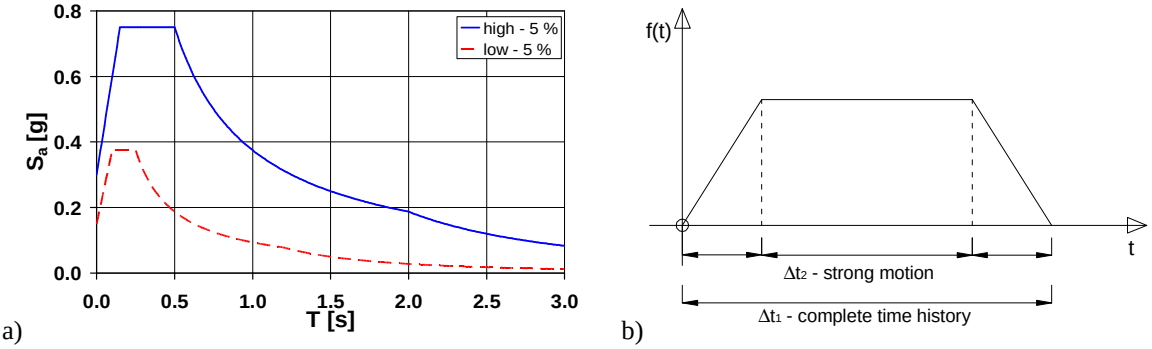
4.3 Incremental dynamic analysis

In the second step the structures were analyzed by Incremental Dynamic Analysis (IDA), using the original accelerograms multiplied for a gradually increasing factor until the collapse of the structure was reached. According to EN1998-1-1 [1] prescriptions, seven earthquake time-histories of natural or artificially generated earthquakes can be used for the analyses. In order to obtain representative results for any seismic area in Europe, artificial accelerograms meeting the elastic response spectra presented in EN 1998-1 and consistent with chosen hazard model were adopted for numerical simulations. The program SIMQKE, developed by Gasparini and Vanmarcke [20] was used for the artificial generation of time histories.

Two types of seismic intensities were considered: for high seismicity areas the PGA level was equal to 0.25 g and the type 1 spectrum for soil category B was used; for low seismicity areas, on the other hand, the PGA was fixed to 0.10 g and the type 2 spectrum for soil type C was applied (figure 8a). The filter function was defined by a trapezoidal shape, where the time intervals for the initial and ending ramps were equal to 5.0 s and the strong motion duration was 10 or 5 s respectively for high and low seismicity (figure 8b). The relevant Eigen-periods were assumed to be in a range between 0.1 s and 3.0 s. The chosen sampling interval of Δt = 0.01 s allowed a sufficient accurate calculation for Eigen-frequencies up to 20 Hz (5 points for each period).

The verification of the accelerograms by determining the velocity and displacement time histories showed that the displacements were running out (figure 9), evidencing the necessity of the application of a baseline correction in order to obtain a sufficient small displacement at the end of the record. The adequacy of the accelerograms was checked by determination of their elastic response spectra (figure 10): for periods lower than T_B the spectral acceleration S_a was slightly too high (figure 11). Anyway, the target spectrum was sufficiently met and the requirements defined in EN1998-1 [1] were pursued.

The COV of the spectral values for the 7 accelerograms varied between 0.04 and 0.12 (figure 12). It should be noted that the energy density of artificial accelerograms is generally higher than the one of natural accelerograms, since all interesting frequencies are included.



a) b)

Figure 9: Target spectra (a) and filter function (b) for the generation of artificial time histories

Seismicity	PGA	Spectrum	Soil	Total duration	Strong motion duration
Low	0.10 g	Type 2	Type C	15 s	5 s
High	0.25 g	Type 1	Type B	20 s	10 s

Table 10: Parameters of target spectra and filter function for low and high seismicity

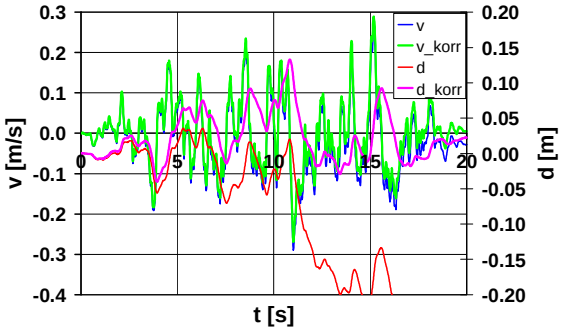
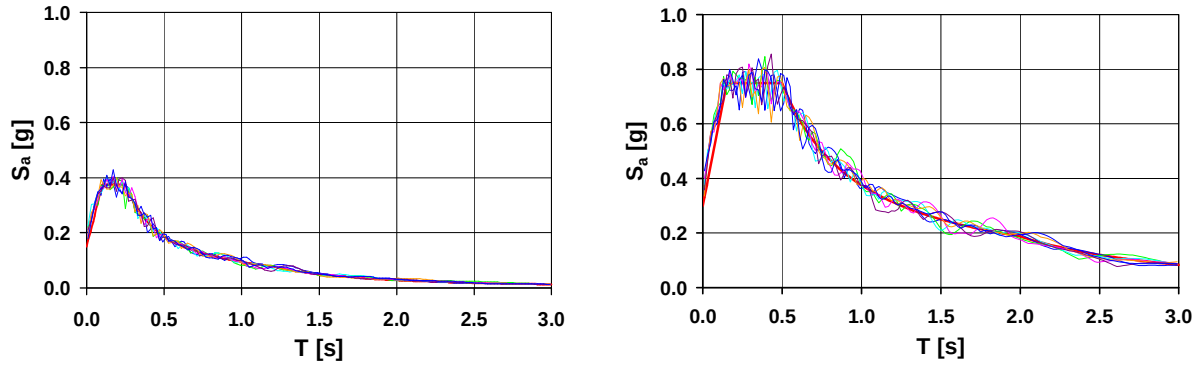


Figure 10: Baseline correction for an artificial accelerogram (high seismicity)



a) b)

Figure 11: Target spectrum and elastic response spectra of 7 artificial accelerograms: a) low seismicity and b) high seismicity.

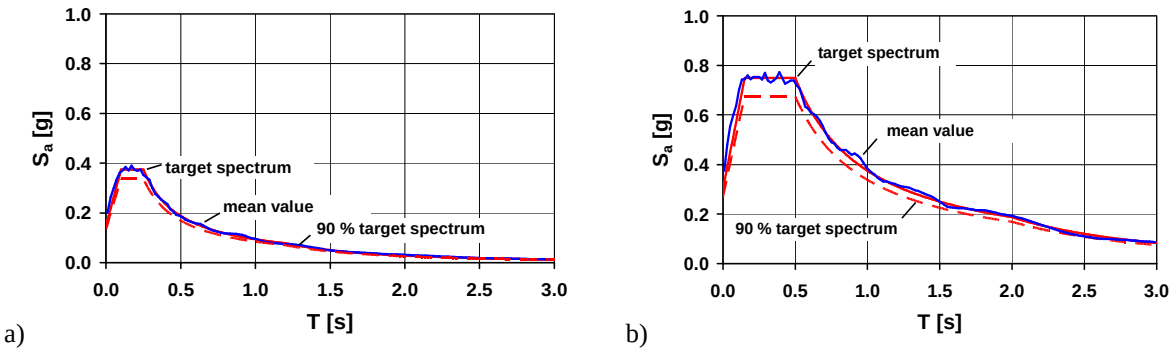


Figure 12: Target spectrum and mean value of the elastic response spectra of 7 artificial accelerograms: a) low and b) high seismicity

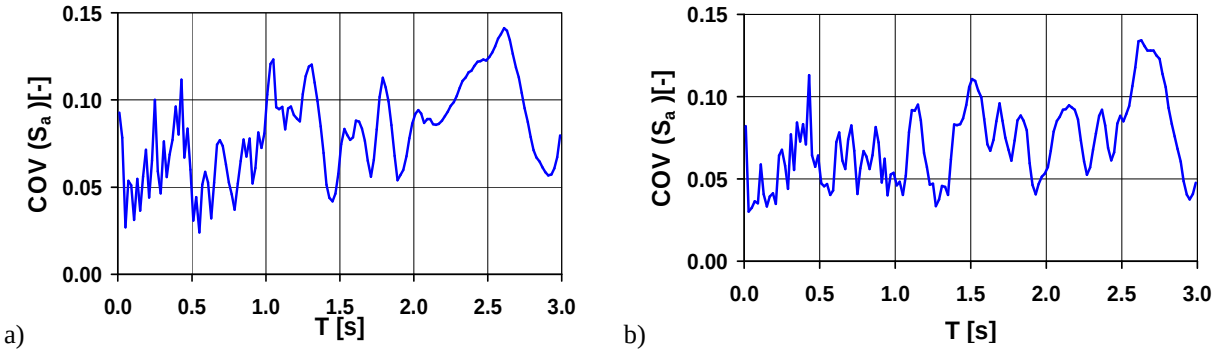


Figure 13: COV of the elastic response spectra of 7 artificial accelerograms: a) low and b) high seismicity.

Once identified the PGA able to activate relevant collapse modes, a modified Ballio-Setti procedure was used to determine the behaviour factor (q). The Ballio-Setti procedure was slightly modified for taking into account the discrepancy at first mode frequency between the target spectra and real spectra of earthquake time-histories (figure 13).

The available q-factors evaluated on the basis of IDAs' results were determined according to equation (11):

$$q = \frac{\lambda_u}{\lambda_{e,static}} \cdot \frac{a_{s,art}}{a_{sd}} \tag{11}$$

where λ_u is the accelerogram multiplier at the first limit state, $\lambda_{e,static}$ is the equivalent static seismic forces' multiplier corresponding to the first attainment of the plastic hinge in an elastic geometrically non linear pushover analysis, $a_{s,art}$ is the acceleration of the spectrum of the current accelerogram and a_{sd} the acceleration of the design spectrum, both corresponding to the fundamental period of the structure.

In the classic Ballio-Setti approach [12, 13], the second term, defined by the ratio between design spectrum PGA and artificial earthquake spectrum PGA, was not considered and the discrepancy between two PGA levels could strongly influence seismic behaviour assessment and the evaluation of the behaviour factor.

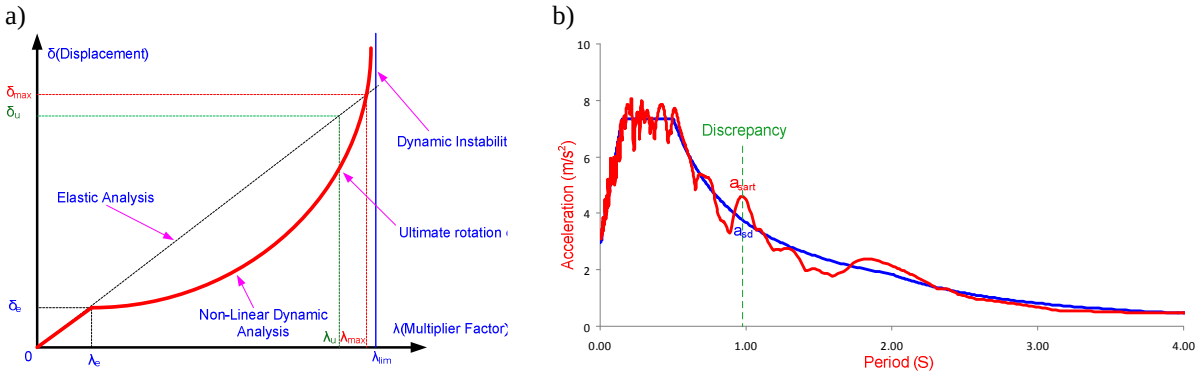


Figure 14: a) Scheme of the Ballio-Setti procedure, b) discrepancy between target spectrum and real spectrum.

4.4 Analysis of results and evaluation of q-factor

In the following paragraph, the evaluation of behaviour factors is presented considering buildings in relation to their structural typology, as well as described in the tables 3, 4 and 5.

Buildings n°1, 2, 14 and 15

The results of numerical simulations evidenced that MRF structures resisted PGA levels higher than the ones adopted in the initial design process executed using the lateral force method (table 9) The high resistance of those structures was related to the fact that seismic design requirements leaded to a general overstrength of the structure, compared to the resistance effectively required for the applied seismic design loads. Such effects were more considerable in the case of structures designed for moderate seismic actions (buildings n°1, 2 and 14), since the seismic design requirements were applied to ensure a sufficient performance of structures not only for low but also for high seismic actions characterized by longer strong motion periods.

In the MRF structures the ultimate rotation ratio was the controlling failure criterion. In the offices, as well as in the industrial buildings, the columns were the critical elements, whose ultimate rotation capacity was often reduced as a consequence of the applied axial loads. The scattering of the ultimate rotation ratio between accelerograms was considerably high (80 – 140 % and 80 – 130 %); the other failure criteria were not dominant, except for the interstorey drift ratio.

In the buildings characterized by CBF structure, the ultimate deformation of the bracings in compression was the governing failure criterion, but this criterion was neglected (since directly considered in the non linear models) and the investigations were focused on the deformation in tension criterion. The capacity ratios of the other failure criteria were rather low; the scattering of the results between different accelerograms was lower than the one evaluated for the MRFs, especially in the case of industrial buildings.

The values obtained for the behaviour factor using static non linear analysis are presented in table 11, while table 12 presents the values coming from the adoption of IDAs.

Building	1-xdir	2-xdir	14-xdir	15-xdir	15-ydir
d_y [m]	0,12	0,11	0,37	0,11	0,13
d_u [m]	0,28	0,27	0,96	0,40	0,28
V_y [kN]	709	1295	800	862	1204
V_u [kN]	830	1332	816	1164	1255
q	1,96	2,36	2,55	2,81	2,07

Table 11: Behaviour factors of case study 1, 2, 14 and 15 based on a non-linear static analysis.

Building	1-xdir	2-xdir	14-xdir	15-xdir	15-ydir
$\lambda_{e,static}$	1,54	1,28	1,32	1,27	0,85
λ_u	9,84	6,88	6,04	8,44	7,66
a_{sd} [g]*	0,07	0,046	0,477	0,034	0,055
$a_{s,art}$ [g]*	0,072	0,046	0,335	0,037	0,057
q**	6,66	5,37	3,24	7,04	9,23

Table 12: Limit states of steel structures with moment-resisting (MRF) and concentrically braced frames (CBF). (*) mean value of 7 accelerograms; (**) mean value of q-factors determined individually for 7 accelerograms.

Building n°10

As already presented, structures were assessed following the modified Ballio-Setti method, according to the improvement previously proposed. Results are presented considering the building as designed both in low and in high seismicity (design PGA respectively equal to 0.10 and 0.25g). IDA curves corresponding to EBF frame in high seismicity (PGA 0.25g, redesigned building n°10) are presented in figure 14b in terms of maximum displacement versus acceleration multiplier considering the 7 different artificial accelerograms, while figure 14a presents the same results expressed in terms of maximum base shear versus maximum top displacement. In general, due to the rather stiff behaviour of the braced structure, non linear geometrical effects did not lead to the dynamic instability of the structure, and the non linear behaviour was essentially governed by material non linearities. This situation was observed for all the four bi-dimensional frames studied, although less pronounced for CBF frame in high seismicity. The values of the behaviour factor based strictly on the modified Ballio-Setti method previously described are presented in table 13 for the cases where an intersection is identified.

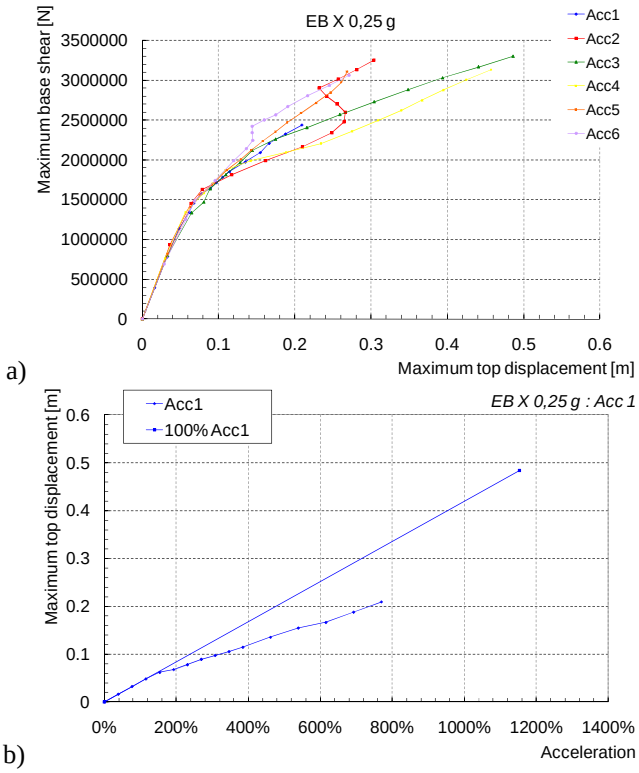


Figure 15: a) IDA curves for EBF, b) PO curve in term of maximum displacement vs acceleration multiplier for accelerogram n°1 (EBF building n°10, x direction).

Building n°10	Behaviour factor						
	Acc. 1	Acc. 2	Acc. 3	Acc. 4	Acc. 5	Acc. 6	Acc. 7
EB X 0,10 g	7,5	--	--	--	--	--	--
CB Y 0,10 g	--	--	--	--	--	--	--
EB X 0,25 g	--	5	--	6,5	--	--	--
CB Y 0,25 g	--	6,5	--	2	--	2,75	3

Table 13: Behavior factors based on IDA curves.

The values of the behaviour factor so obtained were very high (table 14), as a consequence of the fact that the presented evaluations were based on the assumption of an infinite deformation capacity of the structure. It is thus necessary to check to what extent the structural ductility can effectively be used. For EBF/CBF composite structures, the premature failure was triggered by an excessive demand on the ductile zones: i.e. excessive rotation of links for EBFs and excessive axial deformation of braces for CBFs, with limit values assumed in agreement to FEMA 356 prescriptions.

Accelerogram	q- factor for CBFs				q- factor for EBFs			
	PGA 0.1g		PGA 0.25g		PGA 0.1g		PGA 0.25g	
	SL	CP	SL	CP	SL	CP	SL	CP
1	4.6	--	--	--	7.5	7.5	5.4	6.9
2	5.4	--	6.2	6.5	--	--	3.5	3.8
3	6.2	--	--	--	--	--	6.2	6.9
4	5.4	--	2.0	2.0	--	--	4.6	4.6
5	6.2	--	--	--	--	--	6.2	--
6	5.4	--	2.75	2.75	--	--	--	8.5
7	6.2	--	3.0	3.0	--	--	5.4	6.9
Mean Values	*5.6*	*-- (*)*	*3.5*	*3.6*	*7.5 (**)*	*7.5 (**)*	*5.2*	*5.8*

Table 14: Behaviour factors. (*) CP level of the criterion is never reach by any of the 7 accelerograms even for a multiplier equal to 15; (**) Only one out of the 7 ground motion time-history is able to trigger the collapse criterion. For all other six, collapse is not reach even for an accelerogram multiplier equal to 15.

According to what presented in the table 14, EBFs were characterized by values of the allowable q-factor higher than the ones adopted in the design, also in the case of CP limit state. In the particular case of an EBF designed for low seismicity, the homogeneity rules on the over-strength factor of the joints provided an inherent global over-strength of the building, leading to q-factors higher than 7.5.

Regarding CBFs, results strongly varied if the limit state was considered as governed by compression or tension collapse of the diagonal. If the limit state was assumed to be governed by the compression limit, the behaviour factors obtained in average for the seven accelerograms were in the range between 1.7 and 3.3.

A deeper insight in the analysis of results showed that the rather poor ductility of the system obtained under these assumptions was related to a deformation concentration at the top storey of the building, due to the high slenderness of the diagonal. In the design of presented case studies, the upper limit on the diagonal slenderness was released for the 2 upper levels due the quasi-impossibility to fulfil simultaneously all the design criteria and arguing that according to Eurocode 8, the limit was not mandatory for 2-storeys building: if the potential collapse of the 5^{th} storey was assumed to be governed by tension only, results became, on the other hand, very close to the ones obtained considering tension only at all levels. Under this assumption, allowable q-factors became higher than the ones considered in

the design for low-seismicity conditions and slightly lower for high-seismicity.

Buildings n° 6, 7, 8 and 9

Building n° 6 was designed for low seismicity hazard and presented bare steel columns (table 5). The most conditioning criteria in the assessment of the building were related to beams' and columns' ductility and to the intensity of applied axial loads.

The q factor evaluated according to what previously presented was around 7 using the modified Ballio-Setti method, and around 8 using the classic method; the design behaviour factor, on the other hand, was equal to 4 [1]. As a consequence, the adoption of Medium Ductility Class (DCM) behaviour in low seismicity areas provided structural solutions not completely optimized, in which the structural capacity, in terms of q factor, was twice the design values (table 15).

Despite the high values of obtained q-factors for low seismicity, it's important to underline that, in these cases, the design was not guided by seismic action but by wind action: as a consequence, overstrength criteria to ensure the weak beam-strong column condition made the structure overdesigned.

Building n° 7 was designed for high seismicity hazard and presented partially encased composite columns (table 5); the design was executed assuming a design q factor equal to 4 for DCM behaviour. The estimated q factor was around 8.5 adopting the classical procedure and around 8 using the modified Ballio-Setti method (table 15), evidencing, also in this case, a significative overstrengthening of the elements' size.

Building n° 8 was designed for high seismicity using bare steel columns; in this case, the significant collapse criteria were related to the reaching of the ultimate rotation of plastic hinges located at the ends of beams and at the base of columns. The values of ultimate rotations were fixed according to the limit values indicated by FEMA356 [19].

The minimal rotation capacity, equal to 20 mrad according to Eurocode 8, leaded to values of the allowable ductility in terms of q-factor equal to 2.5 or 2.6 respectively adopting the modified and the classical method, differently from what imposed in the design process (behaviour factor equal to 4.0).

The values of the evaluated behaviour factors for selected case studies are presented in the table 15: as visible, in high seismic hazard q factor obtained from numerical analyses were lower than the ones adopted in the design (i.e. assuming DCM condition). On the contrary for the structures designed with a low seismic hazard, the q factor obtained from numerical simulations was systematically higher (at least 2 times) than the values adopted for the design.

Building	Modified Ballio-Setti method	Classic method	Design q factor
6	7.0	8.0	4.0
7	8.0	8.5	4.0
8	3.0	3.75	4.0
9	Not evaluated	Not evaluated	4.0

Table 15: q factor of the different buildings calculated using different methods.

Buildings n° 5, 12 and 13

Buildings n° 5, 12 and 13 (respectively, five-storey office building, four-storey industrial building and single-storey industrial building) were designed adopting two different steel grades qualities for each building considering a design PGA equal to 0.25 g.

The collapse criteria assumed for the execution of IDAs were the ones defined by FEMA356 [19], EN1993 [16] and EN1998 [1, 18]. IDAs were executed considering the 7

artificial accelerograms: original accelerograms were multiplied by factors varying between 0.5 and 20, in order to individuate the significant collapse criteria for each structural typology. As example, in the figure 16 the results coming from IDA simulations were gathered in order to trace IDA curves and to individuate the PGA levels corresponding to collapse criteria activation. The values of q-factors coming from PO (q_{PO}) and IDA (q_{IDA}) are presented in the table 16: as visible, a strong variability was revealed considering the two different methods of analysis. In general, the results of PO analyses leaded to lower values of behaviour factors, especially if compared to the ones provided by IDAs' results: for example in the case of building n°5 (y direction) q-factors varied between 3.11 and 6.28 (steel grade S355), or in the case of building n°12 (x direction) between 1.71 and 9.97 (steel grade S355).

Building n°	5 (S355 X)	5 (S460 X)	5 (S355 Y)	5 (S460 Y)	12 (S355 X)	12 (S460 X)
q_{PO}	1.98	1.98	3.11	2.55	1.71	1.63
q_{IDA}	2.80	2.68	6.28	6.04	9.97	9.56
Building	12 (S355 Y)	12 (S460 Y)	13 (S235 X)	13 (S275 X)	13 (S235 Y)	13 (S275Y)
q_{PO}	2.33	1.63	2.02	2.13	4.05	3.87
q_{IDA}	2.54	2.31	3.74	2.83	6.45	5.98

Table 16: Results for q-factor using pushover analysis and IDA.

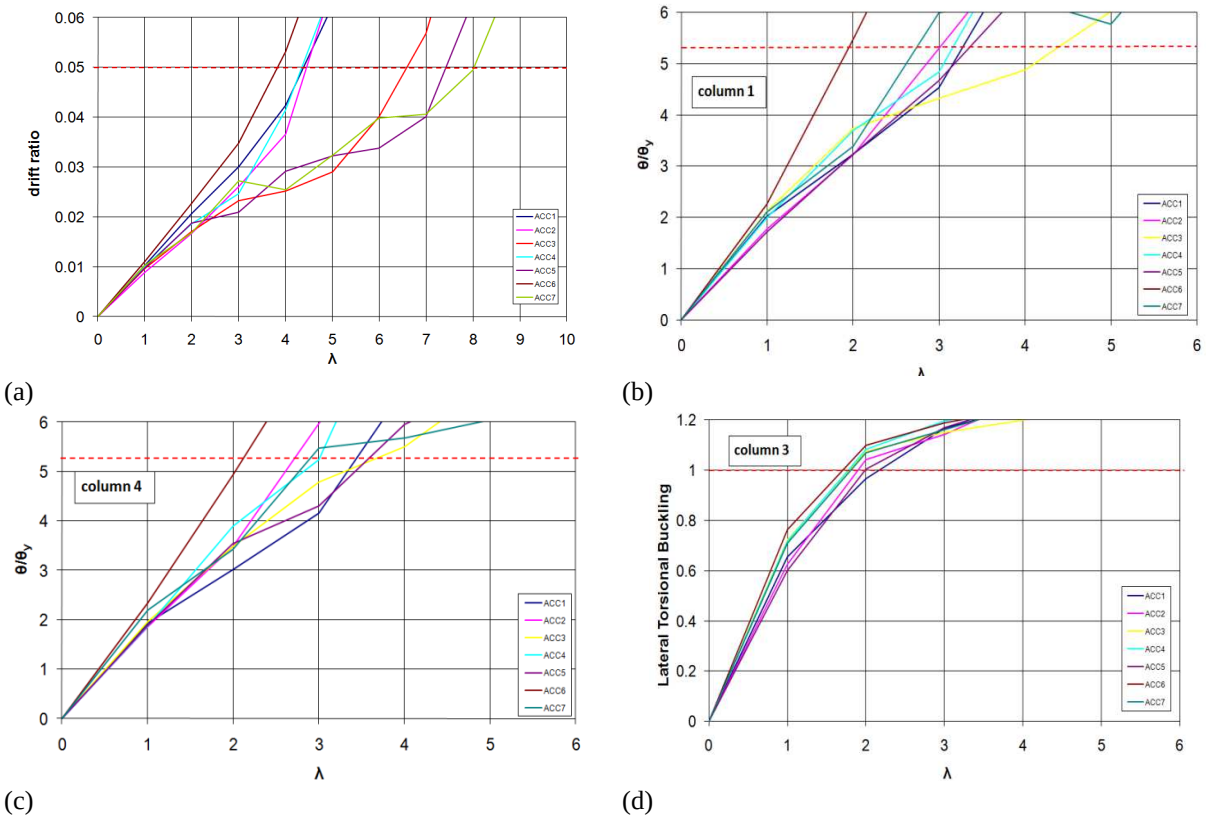


Figure 16: IDA curves for different time-histories and individuation of collapse levels: (a) drift ratio; (b) ultimate plastic hinge rotation; (c) ultimate plastic hinge rotation; (d) column buckling.

Buildings n° 3, 4 and 16

Buildings were designed considering the adoption of High Ductility Class (DCH) in high seismicity (design PGA 0.25g) for buildings n°3 and n°16, using shear link, and DCM in low seismicity for building 4 (design PGA 0.15g). The design behavior factor were equal to 6 (buildings 3 and 16) and 4 (building 4), while PO and IDAs were adopted for the evaluation of the effective allowable ductility.

Frames in medium – low seismicity area (frames 4x and 4y, table 18) were characterized by very low values of the effective q-factor, especially if the Modified Ballio – Setti method was considered; on the other hand, taking into account the traditional evaluation of q-factor, the difference between the numerical and the design behaviour factor became smaller, leading to values very close to the design one (i.e. frame 4x). This fact was mainly due to the factor $a_{s,art}/a_{s,d}$: the local difference between the accelerogram and the spectrum was higher than 5% (medium value considered by Eurocode for the definition of spectrum compatibility).

The execution of all numerical simulations clearly showed the impossibility of activating the collapse criteria related to columns; at the same time, in the case of braces (buckling of members in compression) the equivalent q factors were so high to make the exploration of the corresponding PGA level without technical meaning. PGA activation levels were determined for each relevant collapse criteria; moreover, preliminary IDA pilot simulations were carried out considering the real mechanical properties values (i.e. mean values of production data) and evaluating the following modification of activation PGA for the selected collapse criteria.

Such pilot simulations evidenced that the insertion of real mechanical properties moved PGA level to activate bracing collapse, neglecting, once again, columns' criteria.

Acc n°	q- factor for 3 EBF X				q- factor for 3 EBF Y			
	Link	Column	Brace	Drift	Link	Column	Brace	Drift
1	11,80	Not sig.	Not sig.	7,90	8,30	Not sig.	13,80	9,20
2	9,30	Not sig.	Not sig.	9,30	8,30	Not sig.	11,60	9,10
3	9,80	Not sig.	Not sig.	11,80	8,50	Not sig.	11,00	9,30
4	7,40	Not sig.	Not sig.	7,40	7,00	Not sig.	10,10	7,70
5	10,90	Not sig.	Not sig.	7,90	6,60	Not sig.	9,90	6,60
6	7,00	Not sig.	Not sig.	7,70	9,50	Not sig.	11,20	10,30
7	9,10	Not sig.	Not sig.	10,90	8,80	Not sig.	11,20	8,80

Table 17: q factor estimation using IDA simulations – Building 3.

Acc n°	q- factor for 4 EBF X				q- factor for 4 EBF Y			
	Link	Column	Brace	Drift	Link	Column	Brace	Drift
1	2,57	12,90	3,90	5,80	2,60	13,10	13,10	7,80
2	2,27	9,10	3,60	6,40	2,70	10,80	10,80	4,90
3	2,71	10,80	3,30	5,40	2,40	9,70	9,20	4,60
4	2,13	9,50	2,40	4,50	2,70	11,80	9,50	4,20
5	2,67	10,70	3,20	5,90	1,90	10,90	10,90	6,30
6	2,40	10,60	2,70	6,40	2,20	11,10	10,60	4,40
7	2,34	9,40	2,60	5,60	2,90	11,60	11,60	7,00

Table 18: q factor estimation using IDA simulations – Building 4.

Acc n°	q- factor for 16 EBF X				q- factor for 16 EBF Y			
	Link	Column	Brace	Drift	Link	Column	Brace	Drift
1	12,00	Not sig.	11,00	13,90	15,30	Not sig.	18,50	17,40
2	12,00	Not sig.	11,00	13,90	12,30	Not sig.	15,00	13,20
3	12,70	Not sig.	11,60	14,80	11,20	Not sig.	16,00	12,80
4	9,90	Not sig.	9,90	10,90	9,60	Not sig.	13,10	12,30
5	11,80	Not sig.	9,90	12,80	10,30	Not sig.	12,90	12,90
6	10,40	Not sig.	10,40	12,20	9,40	Not sig.	12,80	12,80
7	12,70	Not sig.	10,90	14,50	12,40	Not sig.	17,70	14,20

Table 19: q factor estimation using IDA simulations – Building 16.

5 COMPARISON AND CONCLUSIONS

Table 20 briefly summarizes what already presented as regards the q-factor values obtained from pushover and IDA analyses with respect to the values adopted in the design according to actual standards and to what specified in the previous paragraphs.

As visible, in the majority of cases for both the two considered main directions of the designed buildings, the values of the q-factor obtained using IDAs were higher than the ones adopted in the design, evidencing a substantial overstrength of buildings designed in high seismicity areas.

Looking at the results presented in table 20, buildings realized in low seismicity areas (characterized by a design PGA equal to 0.10g like buildings 1, 2, 6, 7, 10 and 15) were associated to higher values of the behaviour factor (evaluated adopting IDA procedure) respect to the ones adopted during the design process, leading consequently to the oversizing of structural members. As an example, in the case of building n°1, the q-factor adopted in the design was equal to 3.99 while the one obtained from the evaluation using IDA was equal to 6.66. A similar condition was revealed also for building n°2 (frame in x direction) with design value of 4.00 towards an evaluated one up to 5.37, and in the case of building n°7 with design value 4.00 versus an obtained q_{IDA} equal to 7.00.

On the other hand, considering the case of EBF structure with long bending link (building n°4) the behaviour factor evaluated according to EN 1998-1:2005 [1] seems to be over-estimated, with assumed values in the design process equal to 4.00 for both the two main directions of the building and obtained values from IDAs respectively equal to 2.45 and 2.48 for x and y directions. Otherwise, considering the structural behaviour of buildings designed for high seismicity (PGA equal to 0.25g), the q-factors assumed in the design are generally lower (or at least equal) than the ones evaluated using the modified Ballio-Setti method before presented, evidencing the correct approach of EN1998-1:2005 for the design.

Finally, table 20 presents the results obtained from buildings (indicated by the adoption of the asterisk) that were re-designed using lower q-factor values according to a preliminary evaluation using the presented Ballio-Setti procedure. In this sense, the above mentioned procedure can be used in order to optimize the design of structures.

N°	X – direction			Y – direction			q Design		PGA
	system	q_{static}	q_{IDA}	system	q_{static}	q_{IDA}	x	y	[g]
1	MRF	$1,96^{(**)}$	6,66	Not des.	-	-	2,35	3,99	0,10
2	CBF	$2,36^{(**)}$	5,37	Not des.	-	-	3,68	4,00	0,10
3	EBF shear	5,78	8,32	EBF shear	7,66	8,11	6,00	6,00	0,25

4	EBF bending	3,18	2,45	EBF bending	3,90	2,48	4,00	4,00	0,15
5	MRF S355	1,98	2,80	CBF S355	3,11	6,28	4,00	4,00	0,25
	MRF S460	1,98	2,68	CBF S460	2,55	6,04			
6	MRF	2,65(**)	7,00	Not des.	-	-	4,00	4,00	0,10
7	MRF	2,60(**)	8,00	Not des.	-	-	4,00	4,00	0,10
8	MRF	1,80(**)	3,00	Not des.	-	-	4,00	4,00	0,25
9	MRF	1,75(**)	-	Not des.	-	-	4,00	4,00	0,25
10	EBF vertical shear link	6,78	7,50(*)	CBF	4,30	5,60	4,00	4,00	0,10
11	EBF vertical shear link	6,62	5,20	CBF	4,00	3,50	4,00	4,00	0,25
12	MRF S355	1,71	9,97	CBF S355	2,33	2,54	4,00	4,00	0,25
	MRF S460	1,63	9,56	CBF S460	1,63	2,31			
13	MRF S235	2,02	3,74	CBF S235	4,05	6,45	4,00	4,00	0,25
	MRF S275	2,13	2,83	CBF S275	3,87	5,98			
14	MRF truss girder	2,55	3,24	CBF	-	-	1,55	3,80	0,25
15	MRF	11,5	12,32	CBF	4,66	7,47	1,96	2,64	0,10
16	EBF shear	2,81	7,04	EBF (shear)	2,07	9,23	6,00	6,00	0,25

Table 20: Summarizing table of q factors obtained from pushover and IDA with respect to design values. (*) frames re-designed lower q factor - values under re-evaluation (**) no material over-strength ($V_{y,real}/V_{y,design}$)

Acknowledgements The present work was developed inside the European Research Project OPUS (RFSR-CT-2007-00039), funded by the Research Fund for Coal and Steel (RFCS). It was also part of the Italian research project RELUIS, funded by Italian Department for Civil Protection.

REFERENCES

[1] UNI-EN1998-1-1: Eurocode 8 - Design of structures for earthquake resistance. Part 1: General rules, seismic actions and rules for buildings. Technical Commission 250/SC8, Brussels, 2005.
[2] ICBO – International Conference of Building Officials, (1997). Uniform building code – vol.2: structural engineering design provisions. California: Whittier.
[3] FEMA, (1995). NEHRP recommended provisions for seimsic regulations for new buildings, part I – provisions; part 2 – commentary. Washington DC: BSSC.
[4] AISC – American Institute of Steel Construction (2005). Seismic Provisions for Structural Steel Buildings. ANSI/AISC 341-05, AISC INC. Chicago, Illinois.
[5] A.Y. Elghazouli, Assessment of European seismic design procedures for steel framed structures. *Bullettin of Earthquake Engineering*, **8**(1), 65-89, 2010.
[6] M. Bosco, P.P. Rossi, Seismic behaviour of eccentrically braced frames. *Engineering Structures*, **31**, 664-674, 2009.
[7] EN10025-1÷6 General technical delivery conditions for: non-alloy, normalized/normalized rolled weldable fine grain, thermomechanical rolled weldable fine grain, improved atmospheric corrosion resistance, flat products of high yield strength in the quenched and tempered condition. European Committee for Standardization, Brussels, 2004.

[8] A. Longo, R. Montuori, V. Piluso, Influence of Design Criteria on the Seismic Reliability of X-braced Frames. *Journal of Earthquake Engineering*, **12**(3), 406- 431, 2008.
[9] P.P. Rossi, A. Lombardo, Influence of the link overstrength factor on the seismic behaviour of eccentrically braced frames. *Journal of Constructional Steel Research*, **63**, 1529–1545, 2007.
[10] AA.VV., (2011). Optimizing the seismic Performance of steel and steel-composite concrete strUctures by Standardizing material quality control, Research Fund for Coal and Steel, contract RFCR-CT-2007-00039, final report, Technical Steel Research Series, European Commission.
[11] M. Badalassi, A. Braconi, S. Caprili, W. Salvatore, Influence of steel mechanical properties on EBF seismic behaviour. *Bulletin of Earthquake Engineering*, under review, 2013.
[12] G. Ballio, F. Perotti, L. Rampazzo, P. Setti, Determinazione del fattore di struttura per costruzioni metalliche soggette a carichi assiali. *II Convegno nazionale ANIDIS, L'ingegneria Sismica in Italia*, Rapallo, 1984.
[13] P. Setti, Un metodo per la determinazione del coefficiente di struttura per le costruzioni metalliche in zona sismica. *Costruzioni Metalliche*, **3**, 1985.
[14] UNI-EN1991-1-1: Eurocode 1 – Actions on structures. Part 1-1: General actions - Densities, self-weight, imposed loads for buildings, Technical Commission 250, Brussels, 2005.
[15] UNI-EN1990: Eurocode Basis of structural design. Technical Commission 250, Brussels, 2005.
[16] UNI-EN1993-1-1: Eurocode 3 – Design of steel structures. Part 1-1: General rules and rules for buildings. Technical Commission 250/SC3, Brussels.
[17] UNI-EN1994-1-1: Eurocode 4 – Design of composite steel and concrete structures. Part 1-1: General rules and rules for buildings. Technical Commission 250/SC4, Brussels.
[18] UNI-EN1998-3: Eurocode 8: Design of structures for earthquake resistance - Part 3: Assessment and retrofitting of buildings, 2005.
[19] FEMA 356, ASCE - Prestandard and commentary for the seismic rehabilitation of buildings, 2000.
[20] E.H. Vanmarcke EH, G.A. Gordon, E. Heredia-Zavoni, SIMQKE-II, conditioned earthquake ground motion simulator: user's manual, version 2.1, Princeton University, U.S.A, 1999.
[21] Abaqus, Users' manual. Hibbitt, Karlsson, and Sorensen, Inc., 2005.
[22] FineLg User's Manual, V9.2. Greisch Info – Department ArGEnCo – ULg, 2003.
[23] J. Kuck, B. Hoffmeister, User manual for DYNACS - A Program for DYnamic Nonlinear Analysis of Composite and Steel structures (unpublished), 1993.
[24] S. Mazzoni, F. McKenna, M.H. Scott et al., Opensees command Language Manual, 2007.
[25] M. Menegotto, P. Pinto, Method of analysis for cyclically loaded reinforced concrete plane frame including changes of geometry and non elastic behavior of elements under combined normal force and bending, *IABSE Symposium on resistance and ultimate deformability of structures acted on by well defined repeated loads*, Lisbon, 1973.
[26] M. Bruneau, C. Uang, A. Whittaker A., Ductile design of steel structures, McGraw Hill, 1998.

COMPDYN 2013
4th ECCOMAS Thematic Conference on
Computational Methods in Structural Dynamics and Earthquake Engineering
M. Papadrakakis, V. Papadopoulos, V. Plevris (eds.)
Kos Island, Greece, 12–14 June 2013

MODIFICATION OF MODAL PROPERTIES OF A SYSTEM WITH NON-PROPORTIONAL DAMPING DUE TO VIBRATION ABSORBERS AND SUB-SOIL INTERACTION

Jiří Náprstek[1] **and Stanislav Hračov**[1]

[1] Institute of Theoretical and Applied Mechanics AS CR, v.v.i.
Prosecká 76, CZ-19000, Prague, Czech Republic
e-mail: {naprstek,hracov}@itam.cas.cz

Keywords: Non-proportional damping, perturbation method, modal properties.

Abstract. *The paper deals with a complex linear dynamic system with proportional damping, which is completed by various elements making the final system non-proportionally damped. Such effects emerge due to vibration absorbers, soil-structure interaction and other components and details. Influence of subsequently attached elements being a source of the non-proportional damping are reflected using perturbation method on the level of the first degree of a small parameter. This parameter characterizes the damping non-proportionality as the relevant perturbation. In the role of the first step the proportionally damped system is adopted. The basic system includes such a part of individual supplements to keep the proportional damping. Eigen-functions of the basic system are then used as a certain variational basis for approximate analysis of eigen-values and eigen-modes of the original system respecting non-proportionality.*

Wide numerical experiments have been carried out investigating interaction of eigen-modes between resonance domains. Applicability and shortcomings of proposed analytical-numerical procedures are commented. A few hints to improve the dynamic model fidelity and to reduce an effort of numerical evaluation are given. A couple of recommendations for engineering application of supplementary elements concerning their dynamic properties are indicated. Some open problems and perspectives of further development are outlined.

1 INTRODUCTION

Slender structures like TV towers, guyed masts, industrial chimneys and others are subdued to wind excitation, seismic attacks and other dynamic loading types. Therefore these structures as a rule are fitted with passive vibration absorbers of various types. Structure itself can be mostly considered as proportionally damped whether it is realized of one (e.g. mast: steel) or several materials (e.g. tower: concrete-steel-composite). However internal damping of the absorber is always significantly higher than that of the structure and so the dynamic character of the system as a whole becomes also non-proportional, see e.g. [1],[2]. Analogously dynamic interaction of the structure with the subsoil leads obviously to non-proportional damping. Some more structural details of the structure contribute to the non-proportionality as well.

In principle such a system should be investigated in a complex domain which means that the number of response components would be as twice as higher in comparison with a classical proportional approach. However the character of the system combining structure with a vibration absorber, usually enables combine the modal parameters (eigen-values and eigen-modes) of the basic "nearly proportional" system with subsequently attached strongly non-proportional supplements. Indeed such a synthesis is approximately exerting to obtain modal characteristics of the whole on a basis of modal characteristics of individual parts. This strategy enables a good insight to internal character of the structure, to optimize transparently vibration absorbers in a particular case and assess the system in a very wide extent of parameters. The reason is, that a great part of the analysis is based on analytical procedures having always more general effect than merely a numerical analysis.

To analyze the structure itself independently is inherent as it is rather geometrically large having many degrees of freedom or being modeled with continuously distributed stiffness and mass. Its effect within the system can be respected using a limited number of modal parameters only, so the transparency of the final analysis remains still obvious. On the other hand the vibration absorber is usually well examined subsystem with one or slightly more degrees of freedom well discussed independently. The same holds regarding influence of the subsoil.

Let us mention that problems of nonproportional damping has been defined and dealt in detail in classical monographs as well as in a number of papers throughout several decades, see e.g. [3], [4], [5], [6]. The dynamic response of non-proportionally damped structures is usually solved excluding the very time consuming direct method using state-space method, see e.g.[7]. The dimension of the original system is doubled and its complex eigen-modes are subsequently used for uncoupling of differential equations. The high numerical demand especially on the calculation of the complex eigen-modes has motivated many authors to define criterions for neglecting of mechanical interaction between real eigen-modes, see e.g. [8], [9], [10]. These criteria asses errors introduced when solving the problem using classical modal superposition. Another efficient approach is based on the decomposition of the modal damping matrix into the diagonal and non-diagonal parts. Then the problem is solved using an iterative method, see e.g. [11], [12]. Advantage of this strategy consists in application of matrices of the original dimension, however it doesn't provide full insight into the physics of the problem.

During last years the authors have focused on study of the complex modal properties and reductions of numerical problems of their evaluation. Adhikari [13] analyzed the sensitivity of modal properties on changes in damping, stiffness and mass of the system. Based on the assumption of small damping Woodhouse [14] and later Adhikari [15] expressed the complex eigen-modes as a combination of real undamped modes. Hračov et al. [16] has performed parametric analysis of an over-damping of individual eigen-values of double degree of freedom

system. Garvey et al. [17] determined the relation between the real and complex parts of eigen-modes for the system with symmetrical structural matrices. The new methods of eigen-problem based on e.g. Lanczos method [18] or complex sub-space iteration method [19] have been evaluated. Main and Krenk [20] proposed an approximate eigen-problem solution of a structure with viscous dampers, being obtained as a result of interpolation between the undamped and constrained eigen-problems. Finally also the widely used perturbation theory has been applied to eigen-solution of the nonproportionally damped structures, see e.g. [21], [22], [23], [24].

In this paper the modal properties of the slender structure equipped with the absorber have been evaluated using the perturbation method of the first order. The accuracy of proposed method has been verified and their results compared with the exact solution. The recommendations and limitations for application to certain types of structures are given and discussed.

2 THEORETICAL BACKGROUND

Eigen vibration of a slender console shaped structure approached as a linear one dimensional system with continuously distributed mass and stiffness completed by a linear vibration absorber can be described as follows:

$$\begin{aligned} (EJu'')'' + (Nu')' + 2b\,\dot{u} + \mu\,\ddot{u} + \delta_q[C(u_q - u_d) + 2b_d(\dot{u}_q - \dot{u}_d)] = 0\ , \quad \text{(a)} \\ m\ddot{u}_d - C(u_q - u_d) - 2b_d(\dot{u}_q - \dot{u}_d) = 0\ . \quad \text{(b)} \end{aligned} \tag{1}$$

$EJ = EJ(x), N = N(x), b = b(x), \mu = \mu(x)$ - bending stiffness, static axial force, total damping (internal viscosity, aerodynamic dissipation), mass; they are characterized by piecewise continuous positive integrable functions of the length coordinate x;

C, b_d, m - characteristics of the absorber; $b_d = \zeta_d \cdot \sqrt{C \cdot m}$, where ζ_d is the damping ratio;

$u = u(x,t), u_q = u(x_q,t), u_d = u_d(t)$ - shaft deviation, shaft deviation in point of the absorber attachment, absorber deviation;

$\delta_q = \mathrm{dir}(x - x_q)$ - x_q is the point of the absorber attachment;

The construction should be kinematically stable with respect to main boundary conditions in order to ensure the solution uniqueness.

To investigate modal characteristics of the system Eq. (1) the exponential time history of the response should be expected, namely:

$$u(x,t) = v(x)\exp(\mathrm{i}\omega t), \quad u(x_q,t) = v_q\exp(\mathrm{i}\omega t), \quad u_d(t) = v_d\exp(\mathrm{i}\omega t). \tag{2}$$

Substituting expressions Eq. (2) into Eqs (1) one obtains for amplitudes:

$$\begin{aligned} (EJv''(x))'' + (Nv'(x))' + 2\mathrm{i}\omega bv(x) - \mu\omega^2 v(x) + \\ +\delta_q[C(v_q - v_d) + 2\mathrm{i}\omega b_d(v_q - v_d)] = 0\ , \quad \text{(a)} \\ -m\omega^2 v_d - C(v_q - v_d) - 2\mathrm{i}\omega b_d(v_q - v_d) = 0\ . \quad \text{(b)} \end{aligned} \tag{3}$$

The definition domain of the above operator is finite. The relevant operator is symmetric and boundary conditions make the body fixed. Then the solution of the system Eq. (3) is an eigen-value problem. In other words there exist an infinite set of eigen-values and eigen-modes which satisfies Eq. (3) together with respective boundary conditions. Let us assume, that all eigen-modes are simple and that mutual assigning of eigen-values and eigen-modes is single-valued.

According with the previous paragraph we concentrate in the first step to solve the eigen-value problem of the system Eq. (3) with canceled damping. The reduced operator obviously reads:

$$\begin{aligned} \mathbf{L}\{v_{j,0}(x)\} + \delta_q C(v_{qj,0} - v_{dj,0}) &= \omega_{j,0}^2\, \mu(x) \cdot v_{j,0}(x)\ , \\ -C(v_{qj,0} - v_{dj,0}) &= \omega_{j,0}^2\, m \cdot v_{dj,0}\ , \end{aligned} \tag{4}$$

$$\text{where:} \qquad \mathbf{L}\{v(x)\} \equiv (EJ(x)v''(x))'' + (N(x)v'(x))'\ , \tag{5}$$

together with boundary conditions:

$$\text{- top of the structure:} v''_{j,0}(l) = 0\ , \quad \left(EJ(x)v''_{j,0}(x)\right)' + N(x)v'_{j,0}(x)\Big|_{x=l} = 0\ , \tag{6}$$

$$\text{- foot of the structure:} v_{j,0}(0) = v'_{j,0}(0) = 0\ . \tag{7}$$

Existence of the discrete spectrum of eigen-values $\omega_{j,0}$ is guaranteed by positive definiteness (including symmetry) of the operator Eqs (4)-(7). Each eigen-value $\omega_{j,0}$ is simple, so only one eigen-mode $(v_{j,0}(x), v_{dj,0})$ is assigned to it. It can be shown that eigen-modes are orthogonal in the meaning:

$$\int_S v_{k,0}(x)\mathbf{L}\{v_{j,0}(x)\}\mathrm{d}x + C \cdot (v_{qk,0} - v_{dk,0})(v_{qj,0} - v_{dj,0}) = \begin{cases} K_{jj}, & j = k \\ 0. & j \neq k \end{cases} \tag{8}$$

$$\int_S \mu(x)v_{k,0}(x)v_{j,0}(x)\mathrm{d}x + m v_{dk,0}v_{dj,0} = \begin{cases} M_{jj}, & j = k \\ 0. & j \neq k \end{cases} \tag{9}$$

Using results of lengthy reasoning which is based on a general functional form of coefficients, it can be shown, that the solution of Eq. (3) without damping can be written in a form of a convergent series in generalized coordinates a_{ij}:

$$v_{j,0}(x) = \sum_{i=1}^{n} a_{ij} w_i(x)\ , \quad v_{q,0} = \sum_{i=1}^{n} a_{ij} w_{qi}\ , \quad v_{d,0} = \sum_{i=1}^{n} a_{ij} w_{di}\ , \tag{10}$$

a_{ij} - generalized coordinates which are to be determined,

$w_i(x)$ - functions making the basis for Galerkin procedure of the variational analysis,

$w_{qi} = w_i(x_q)$ - value of w_i in place of the absorber attachment,

w_{di} - component of the absorber mass deviation.

The operator Eqs (4)-(7) is similar to the operator which is encountered in original system Eq. (1) or (3). Hence eigen-modes $(v_j(x), v_{dj})$ fulfill a priori both main as well as natural boundary conditions. Therefore also functions $w_i(x)$ are recommended to be selected as eigen-modes of the operator similar to (3). In principle the choice could be wide. For instance the final eigen-modes of the operator Eqs (4)-(7) can be adopted whatever method of their determination has been used (slope deflection method, see e.g. [25], FEM, experiment, etc.). Another possibility represent eigen-modes of the operator Eqs (4)-(7) with constant coefficients in the length coordinate (keeping the boundary conditions). All intermediate selection is allowed as well. It can be shown, that any arbitrary choice of eigen-modes mentioned here represent a complete set in $n-$dimensional space of functions continuous almost everywhere along the length coordinate.

Therefore the set of eigen-modes either $(v_{j,0}(x), v_{dj,0})$ or $(w_j(x), w_{dj})$ can be used as the Galerkin basis for a variational analysis of the system (1), see e.g. [26]. Application of such a basis enables to eliminate beforehand many problems of numerical instability namely regarding components with higher space derivatives in the area of the free edge where natural boundary condition are applied.

Let us substitute series Eqs (10) into the system Eq. (3) and evaluate the scalar product with the function $(v_k(x), v_{dk})$. Some manipulations result in a new eigen value problem for values $\omega_{j,g}$ and vectors $\mathbf{a}_{j,g} = [a_{j1,g}, .., a_{jn,g}]^T,\ j = 1, .., n$:

$$\mathbf{K} \cdot \mathbf{a}_{j,g} + 2\mathrm{i}\mathbf{B} \cdot \omega_{j,g}\, \mathbf{a}_{j,g} - \mathbf{M} \cdot \omega_{j,g}^2\, \mathbf{a}_{j,g} \ = \ 0\ , \tag{11}$$

where the square symmetric matrices $\mathbf{K}, \mathbf{B}, \mathbf{M} \in \mathbb{R}^{n\times n}$ read:

$$\begin{aligned}
\mathbf{K} &= \left[\int_S EJ(x) w_k''(x) w_j''(x)\ \mathrm{d}x + C(w_{qk} - w_{dk})(w_{qj} - w_{dj}) \right], && \text{(a)} \\
\mathbf{B} &= \left[\int_S b(x) w_k(x) w_j(x)\ \mathrm{d}x + b_d(w_{qk} - w_{dk})(w_{qj} - w_{dj}) \right], && \text{(b)} \\
\mathbf{M} &= \left[\int_S \mu(x)(x) w_k(x) w_j(x)\ \mathrm{d}x + m(w_{qk} - w_{dk})(w_{qj} - w_{dj}) \right]. && \text{(c)}
\end{aligned} \tag{12}$$

The eigen vibration of a continuous system with a concentrated supplement is now defined in generalized coordinates $\mathbf{a}_{j,g}$ which can be regarded as columns of the square matrix: $\mathbf{a}_g = [\mathbf{a}_{1,g}, ..., \mathbf{a}_{n,g}]$, where $\mathbf{a}_g \in \mathbb{R}^{n\times n}$. The mathematical model has a form which comply with that representing a system of n concentrated masses. Individual degrees of freedom, however, are ordered in way corresponding with well separated increasing eigen-values. So the convergence can be controlled quite easily limiting appropriately the number of eigen-modes taken into account or simply selecting the upper limit of n parameter.

In general matrices $\mathbf{K}, \mathbf{B}, \mathbf{M}$ are full. If the basis $w_j(x)$ is selected as to be eigen-modes of operator Eqs (4)-(7), i.e. $v_{j,0}(x) = w_j(x)$, then matrices $\mathbf{K}, \mathbf{M}$ become diagonal with elements corresponding to Eqs (8), (9). At last if the damping is proportional also $\mathbf{B}$ degenerates to diagonal form and movement proceeds independently in individual eigen-forms.

3 MODIFICATION OF MODAL PROPERTIES

Matrices $\mathbf{K}, \mathbf{M}$ in Eq. (11) can be diagonalized through pre-multiplication by the vector $\mathbf{a}_{j,g}^T$. The same operation doesn't diagonalize the matrix $\mathbf{B}$, unless the damping is proportional. When the $\mathbf{B}$ becomes diagonal, eigen-modes behave independently. Therefore Eq. (11) obviously implicates, that an interaction of eigen-modes $\mathbf{a}_{j,g}$ is given by non-proportional damping. Therefore when $\mathbf{K}, \mathbf{M}$ are already diagonalized, then a successive vanishing of the absolute value of the $\mathbf{B}$ matrix off-diagonal elements can be approximately regarded as an indicator of a justifiability of neglecting of the damping non-proportionality. Commonly known towers or chimneys even if designed using several materials (concrete, steel, composites) can be approximately considered as proportional. Provided the vibration absorber is installed, effect of non-proportionality should be taken into account. However the fact that the structure itself remains proportionally damped and the only component introducing the non-proportionality is the absorber can be reflected as a special type of perturbation. Moreover the tuning of the absorber

is always related with one of eigen-values. So that the frequency portrait of the system differs predominantly from the basic configuration in the domain of the absorber eigen frequency. With increasing difference of structure eigen-values and that of the damper, the influence of effective non-proportionality decreases. This effect is markedly visible assessing changes of modal properties due to non-proportional component of the damping.

Let us cancel matrix $\mathbf{B}$ from Eq. (11) and evaluate eigen-values and eigen-modes of the non-damped system:

$$\mathbf{K}\cdot\mathbf{a}_{j,0}-\mathbf{M}\cdot\omega_{j,0}^2\,\mathbf{a}_{j,0}\;=\;0\quad\text{or}\quad\mathbf{K}\cdot\mathbf{a}_0-\mathbf{M}\cdot\boldsymbol{\omega}_0^2\,\mathbf{a}_0\;=\;0 \tag{13}$$

and suppose that eigen-modes are normalized. Then pre-multiplication by the matrix $\mathbf{a}_0^T$ produces diagonal matrices:

$$\mathbf{a}_0^T\mathbf{K}\mathbf{a}_0=\boldsymbol{\omega}_0^2=\mathrm{diag}[\omega_{1,0}^2,..,\omega_{n,0}^2]\;,\quad\mathbf{a}_0^T\mathbf{M}\mathbf{a}_0=\mathbf{I}. \tag{14}$$

Adopting the first order approximation of perturbation, we can write:

$$\mathbf{B}\;=\;\mathbf{B}_p\;+\;\Delta\mathbf{B}, \tag{15}$$

where matrix $\mathbf{B}_p$ corresponds to proportional part of the damping. Employing the same multiplications as above, one obtains:

$$\mathbf{a}_0^T\mathbf{B}\mathbf{a}_0\;=\;\mathbf{D}_p\;+\;\Delta\mathbf{D}\;,\quad\text{where:}\quad\mathbf{D}_p\;=\;\mathbf{a}_0^T\mathbf{B}_p\mathbf{a}_0\;,\quad\Delta\mathbf{D}\;=\;\mathbf{a}_0^T\Delta\mathbf{B}\mathbf{a}_0. \tag{16}$$

Matrix $\mathbf{D}_p$ is diagonal with elements $D_{jj,p}$ and represents influence of the proportional part of the damping. Matrix $\Delta\mathbf{D}$ is symmetric with zero diagonal: $\Delta D_{jj}=0$.

The inverse assignment can be easily deduced. Indeed, one can write:

$$(\mathbf{a}_0^T)^{-1}\mathbf{D}_p\mathbf{a}_0^{-1}\;=\;\mathbf{B}_p\;,\quad(\mathbf{a}_0^T)^{-1}\Delta\mathbf{D}\mathbf{a}_0^{-1}\;=\;\Delta\mathbf{B}. \tag{17}$$

Regarding the second relation in Eqs (14) it is obvious: $(\mathbf{a}_0^T)^{-1}=\mathbf{M}\mathbf{a}_0$ and $\mathbf{a}_0^{-1}=\mathbf{a}_0^T\mathbf{M}\mathbf{a}_0$ and so can be received:

$$\mathbf{B}_p\;=\;\mathbf{M}\mathbf{a}_0\mathbf{D}_p\mathbf{a}_0^T\mathbf{M}\;,\quad\Delta\mathbf{B}\;=\;\mathbf{M}\mathbf{a}_0\Delta\mathbf{D}\mathbf{a}_0^T\mathbf{M}\;. \tag{18}$$

Reducing matrix $\mathbf{B}$ to $\mathbf{B}_P$, the equation Eq. (11) reads:

$$\mathbf{K}\cdot\mathbf{a}_{j,p}+2\mathrm{i}\mathbf{B}_p\cdot\omega_{j,p}\,\mathbf{a}_{j,p}-\mathbf{M}\cdot\omega_{j,p}^2\,\mathbf{a}_{j,p}\;=\;0\;. \tag{19}$$

Equation can be diagonalized and therefore it represents n independent scalar equations for unknown eigen-values $\omega_{j,p}$ of the proportionally damped system:

$$\omega_{j,0}^2+2\mathrm{i}D_{jj,p}\omega_{j,p}-\omega_{j,p}^2\;=\;0, \tag{20}$$

which yields immediately:

$$\omega_{j,p}\;=\;\mathrm{i}D_{jj,p}\pm\sqrt{\omega_{j,0}^2-D_{jj,p}^2}, \tag{21}$$

as it corresponds with classical literature. It should be reminded, that the damping in general is considered to be small, in order to fulfill the condition $\omega_{j,0}^2\gg D_{jj,p}^2$.

Eigen-vectors of undamped and proportionally damped systems are identical, so that it holds:

$$\mathbf{a}_p \;=\; \mathbf{a}_0 \;. \tag{22}$$

In accordance with the first order approximation of perturbation, see Eq. (15), analogously the eigen-values and eigen-modes of the real structure can be approximated:

$$\omega_{j,g} \;=\; \omega_{j,p} \;+\; \Delta\omega_j \;, \quad \mathbf{a}_{j,g} \;=\; \mathbf{a}_{j,p} \;+\; \Delta\mathbf{a}_j \;. \tag{23}$$

Revisiting Eq. (11) and taking into account Eqs (15) and (23), modified equation appears:

$$\left[\mathbf{K} + 2\mathrm{i}(\mathbf{B}_p + \Delta\mathbf{B})(\omega_{j,p} + \Delta\omega_j) \;- \mathbf{M}(\omega_{j,p} + \Delta\omega_j)^2\right] \cdot (\mathbf{a}_{j,0} + \Delta\mathbf{a}_j) \;=\; 0 \;. \tag{24}$$

Let us pre-multiply Eq. (24) by the vector $\mathbf{a}_{j,0}^T$. Making use the orthonormality of eigen-modes $\mathbf{a}_{j,0}$ following Eqs (14), canceling identity Eq. (19) and keeping only terms of the first degree of perturbation, we obtain after some manipulation:

$$\Delta\omega_j \;=\; -\frac{\omega_{j,p} \cdot \mathbf{a}_{j,0}^T \cdot \Delta\mathbf{B} \cdot \mathbf{a}_{j,0}}{\mathbf{a}_{j,0}^T \,(\mathbf{B}_p + \mathrm{i}\omega_{j,p}\mathbf{M})\, \mathbf{a}_{j,0}} \;. \tag{25}$$

Regarding the last relation Eq. (16), we learn that only diagonal elements of matrix $\Delta\mathbf{D}$ are referenced. As they are zeroes by definition, the increment $\Delta\omega_j$ vanishes. Hence it can be concluded that on the level of the first degree of perturbation the eigen-values of proportionally and non-proportionally damped system are identical. Therefore it holds:

$$\Delta\omega_j \;=\; 0 \quad \Longrightarrow \quad \omega_{j,g} \;=\; \omega_{j,p} \;. \tag{26}$$

Let us pay attention now to interaction of eigen-modes of the non-proportionally damped system. Eigen-vectors of proportional (or non-damped) system make up a complete set in $\mathbb{R}^n$. Consequently a perturbation $\Delta\mathbf{a}_j$ of the eigen-mode can be approximated with any arbitrary accuracy by a linear combination of eigen-modes of the proportional or non-damped system:

$$\Delta\mathbf{a}_j \;=\; \sum_{k=1}^{n} \alpha_{kj}\mathbf{a}_{k,0} \;\;, \tag{27}$$

where α_{kj} are coefficients to be determined.

We recall Eq. (24). After canceling identity Eq. (19), omitting terms of higher order of perturbation than the first, one obtains at first:

$$\left[\mathbf{K} + 2\mathrm{i}\mathbf{B}_p\,\omega_{j,p} - \mathbf{M}\,\omega_{j,p}^2\right] \cdot \Delta\mathbf{a}_j + \left[2\mathrm{i}(\mathbf{B}_p\Delta\omega_j + \Delta\mathbf{B}\omega_{j,p}) - 2\omega_{j,p}\Delta\omega_j\,\mathbf{M}\right] \cdot \mathbf{a}_{j,0} \;=\; 0 \;. \tag{28}$$

Subsequently the series Eq. (27) is to be substituted into Eq. (28) and then the result pre-multiplied by $\mathbf{a}_{i,0}^T$. Also consider Eq. (26). We read now:

$$\mathbf{a}_{i,0}^T \cdot (\mathbf{K} + 2\mathrm{i}\mathbf{B}_p\,\omega_{j,p} - \mathbf{M}\,\omega_{j,p}^2) \cdot \sum_{k=1}^{n} \alpha_{kj}\mathbf{a}_{k,0} \;+\; 2\mathrm{i}\omega_{j,p}\mathbf{a}_{i,0}^T \cdot \Delta\mathbf{B} \cdot \mathbf{a}_{j,0} \;=\; 0 \;. \tag{29}$$

Some manipulation respecting to Eq. (14) provides coefficients α_{kj}:

$$\alpha_{kj} \;=\; -\,\frac{2\mathrm{i}\omega_{j,p}\;\Delta B_{kj}}{\omega_{j,0}^2 + 2\mathrm{i}\omega_{j,p}\;B_{kk,p} - \omega_{j,p}^2} \;, \quad \alpha_{kk} = 0 \;. \tag{30}$$

Assembling Eqs (23), (27) and (30) together, final expression for perturbed eigen-modes can be written:

$$\mathbf{a}_{j,g} \;=\; \mathbf{a}_{j,0} \;-\; \sum_{k=1}^{n} \frac{2\mathrm{i}\omega_{j,p}\;\Delta B_{kj}\cdot \mathbf{a}_{k,0}}{\omega_{j,0}^2 + 2\mathrm{i}\omega_{j,p}\;B_{kk,p} - \omega_{j,p}^2}\;. \tag{31}$$

Take a note that the $j-$th member of summation above vanishes and doesn't influence the basic term $\mathbf{a}_{j,p}$. Coefficients Eq. (30) demonstrate the rate of other eigen-modes modifying the shape of the $j-$th eigen-mode. It is obvious that this phenomenon decays with vanishing $\Delta\mathbf{B}$ matrix.

Let us get back to series Eqs (10). They have been introduced dealing with non-damped system. However actual vectors $\mathbf{a}_{j,g}$ corresponds with the initial system Eq. 3. Consequently the eigen-modes of the initial problem can be formulated as follows:

$$v_{j,g}(x) \;=\; \sum_{i=1}^{n} a_{ij,g} w_i(x)\;, \quad v_{q,g} \;=\; \sum_{i=1}^{n} a_{ij,g} w_{qi}\;, \quad v_{d,g} \;=\; \sum_{i=1}^{n} a_{ij,g} w_{di}\;. \tag{32}$$

Regarding the time coordinate of individual eigen-modes, it is given by exponential $\exp(\mathrm{i}\omega t)$ introduced in Eqs (2), where ω should be replaced by $\omega_{j,p}$, see Eq. (21).

4 NUMERICAL EXPERIMENTS

The accuracy of approximate solutions of modal properties has been investigated for a linear discrete numerical model of the existing TV tower equipped with a tuned mass damper. The tower height is 185 m. It consists of the lower part made of reinforced concrete (square cross-section with a side length 7,8 m, thickness 0,6 m and length 51,1 m) followed by a variable cross-section steel cylinders with diameters of 6 m (thickness 25 mm, length 19,5 m), 4,5 m (thickness 25 mm, length 41,8 m), 3 m (thickness 22 mm, length 24 m) and 1,9 m (thickness 20 mm, length 28 m). The top of the tower creates a laminate extension with a diameter of 1,9 m (thickness 14 mm, length 22,6 m). The tower is in the heel fully clamped into subsoil. The pendulum absorber supplemented with viscous dampers has been installed into a laminate extension at a top of the tower to suppress excessive vibrations induced by a vortex-shedding and other aero-elastic effects. The absorber significantly eliminates unacceptable stresses in the structure, which are dangerous from the point of view of a material fatigue and a life-time of the structure. The absorber has been designed and tuned to be the most effective at vibrations related with the second eigen-mode, i.e. second eigen-value of the tower. The mass of the absorber is 1 tone, which is roughly 1/10 of a generalized mass of the second eigen-mode. A part of a vibration energy of the structure is transformed into heat due to viscous dampers of the absorber. In order to reach the most effective behavior of the absorber, its damping is intentionally higher than damping properties of the structure itself. In our case the damping ratio of the structure has been experimentally determined by low value equal 0,5 %, while the ideal damping ratio of absorber has been calculated and set equal to 20%. This difference could generate the significant source of non-proportionality of the damping.

The analyzed two dimensional discrete numerical model of the tower has been created in CALFEM (MATLAB toolbox intended for FEM analysis). The model without tuned mass damper has been built using beam elements and consisted of 15 nodes. Each node had 2 degrees of freedom, e.g. horizontal displacement and rotation around horizontal axis. The absorber has been subsequently modeled as a concentrated mass connected to the top of the tower with Kelvin-Voigt damping term having one degree of freedom in horizontal direction. Supplementing one degree of freedom due to absorber, a total number of eigen-modes of the whole system raised by one.

The new eigen-mode is associated with the second eigen-mode of the tower with respect to tuning of the absorber. The completed structure has now two eigen-modes which are similar in shape but completely different in phase shift between the tower top and absorber, see Figure 1.

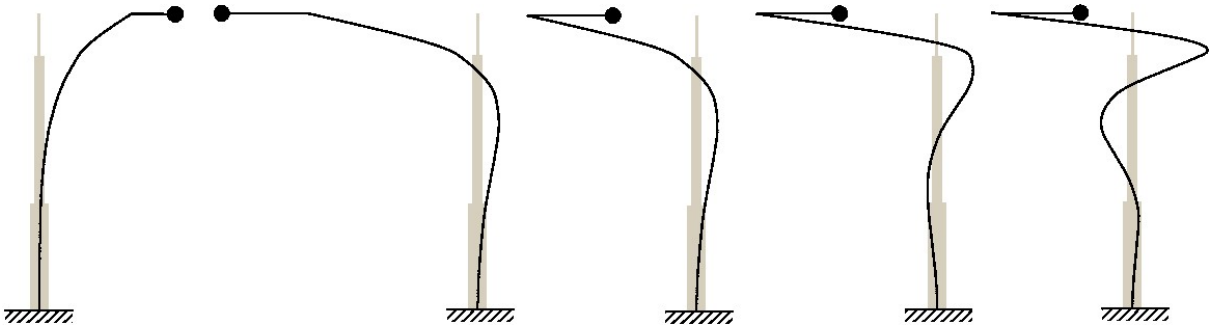


Figure 1: The first five eigen-modes of the tower with absorber; eigen-frequencies of the tower with and without absorber (f_i and $f_{i,t}$) are below corresponding eigen-modes.

The numerical model has been analyzed in order to determine a suitability of proposed perturbation method for the calculation of eigen-values and eigen-modes of the non-proportionally damped slender structure with the absorber. The damping matrix of the tower itself has been set to be proportional to a combination of the mass and the stiffness matrix. Multiplicative coefficients related to these stiffness and mass matrices have been calculated from the given structural damping ratio (ζ= 0,005) for the first two eigen-values. Factor of the damping non-proportionality of the system has been examined as follows: a set of various damping ratios of the absorber has been used ($\zeta_d = 0 \div 0{,}8$), while constant damping matrix of the tower has been kept. The first six eigen-modes of undamped tower with absorber have been used as a Galerkin base $(w_j(x), w_{dj})$ for a reduction of the matrix system Eq. (1) using transformation (10). After the reduction the modal properties have been evaluated according Eqs (26 or 21) and (32). The results have been subsequently compared with the exact solution obtained using the complex subspace iteration method, see [19].

In Figure 2 the exact eigen-values and approximate eigen-values of the tower with the absorber as a function of ζ_d are depicted in the complex plane. The solid curves represent the exact solution, while the dashed curves the approximate one. The identical markers on both curves correspond to the identical damping ratios of the absorber. Changes of eigen-value positions indicate obviously, that the damping of the absorber strongly influences the second, third and fourth eigen-values. On the other hand the first and sixth eigen-values are affected imperceptibly. The influence of the absorber on higher eigen-values significantly decreases with the increasing distance between eigen-value of the absorber and respective eigen-value of the structure. To quantify an accuracy of the perturbation method the relative error in the determination of eigen-values $\omega_{j,g}$ has been calculated separately for imaginary and real parts as follows:

$$\begin{aligned} \delta_{\mathrm{Re}}(\omega_{j,g}) &= \frac{\mathrm{Re}(\omega_{j,p}) - \mathrm{Re}(\omega_{j,g(ex)})}{\mathrm{Re}(\omega_{j,g(ex)})} \cdot 100\ [\%], \\ \delta_{\mathrm{Im}}(\omega_{j,g}) &= \frac{\mathrm{Im}(\omega_{j,p}) - \mathrm{Im}(\omega_{j,g(ex)})}{\mathrm{Im}(\omega_{j,g(ex)})} \cdot 100\ [\%]. \end{aligned} \tag{33}$$

where $\omega_{j,g(ex)}$ is an exact eigen-value of the non-proportionally damped tower with absorber.

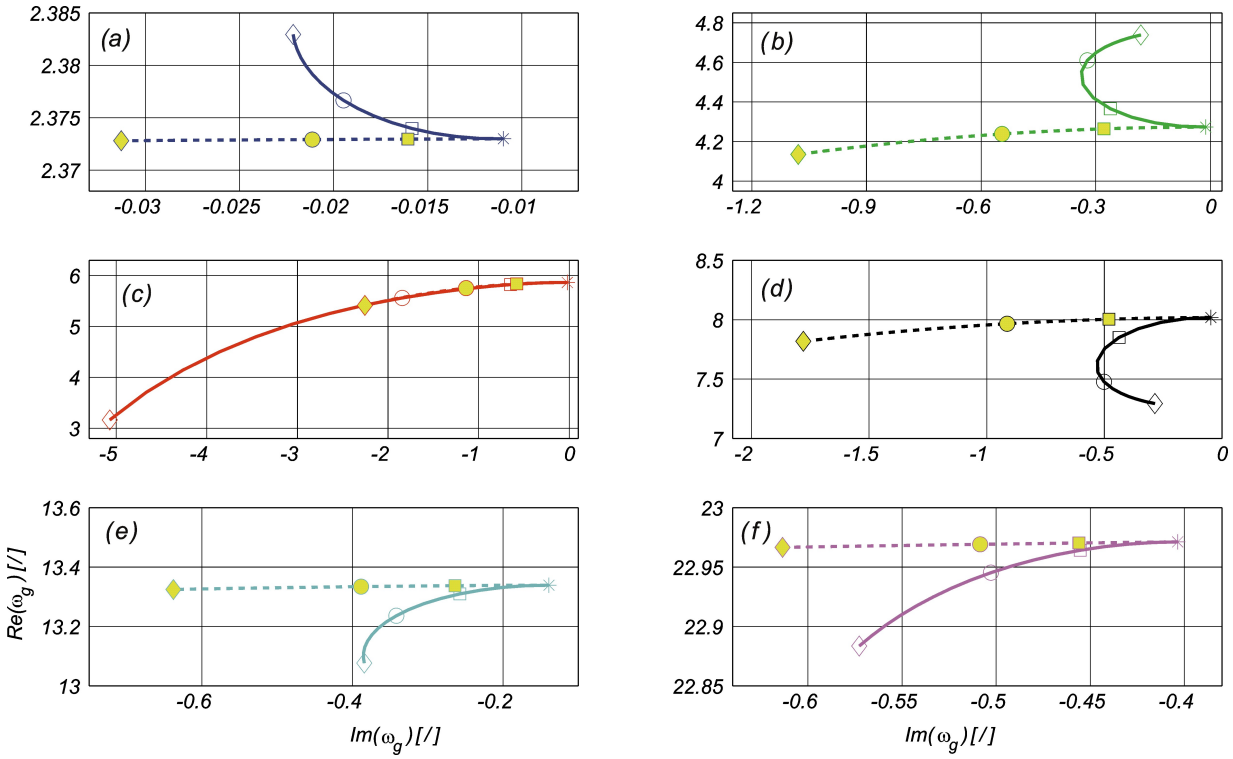


Figure 2: The first six eigen-values $\omega_{j,g}$ as a function of damping ratio ζ_d
(solid line - exact solution; dashed line and marker with yellow fill - approximate solution)
($*$ - $\zeta_d = 0$; $\square$ - $\zeta_d = 0{,}2$; $\circ$ - $\zeta_d = 0{,}4$; $\diamond$ - $\zeta_d = 0{,}8$).

The calculated relative errors for the selected damping ratio ζ_d are summarized in Tables 1 and 2. The errors in both the imaginary and the real parts of eigen-values are increasing with increase in ζ_d. They emerge due to rising difference between structural damping ratios and damping ratio ζ_d. The error of the real part representing the "frequency" component of an eigen-value, is substantially lower than that of the imaginary part representing the eigen-value "damping" component. The substantial errors came up for eigen-values which are close to eigen-value of the absorber, in particular for the second to fourth eigen-value. For the realistic damping ratio ζ_d being 20% the relative errors in determination of the real parts are at most 2% and 11% concerning the imaginary part. This accuracy is acceptable and consequently the perturbation strategy outlined in the second and third chapters is entitled to assess dynamic behavior of existing structures provided with one passive damping element. In our case a limiting value of ζ_d for which the errors are reasonable is equal 30%. Beyond this value the errors notably of the imaginary part could be higher than 25% and more sophisticated approach should be employed.

The mechanical interaction between real eigen-modes of the tower is reflected by non-zero off-diagonal elements of the matrix, where columns comprise approximate complex eigen-modes $\mathbf{a}_{j,g}$ of reduced model, Eq. 11. The complex element $a_{ij,g}$ represents the contribution of the i-th real eigen-mode to the complex and real part of the j-th eigen-mode of the non-proportionally damped system. Similarly to the analysis of complex eigen-values also the vectors $\mathbf{a}_{j,g}$ have been evaluated for several damping ratios ζ_d, see Tables 3, 4, 5 and 6. For zero ζ_d the complex eigen-modes of the whole system $v_{j,g}(x)$ are almost identical with the real

ζ_d	$\omega_{j,g}$					
[/]	j = 1	2	3	4	5	6
0	-0,0001	-0,0015	0,0006	0,0010	0,0001	1,04e-5
0,1	-0,0099	-0,5409	0,0219	0,4617	0,0514	0,0064
0,2	-0,0427	-2,3201	0,2202	1,9590	0,2071	0,0265
0,3	-0,0939	-5,2247	1,0639	4,3440	0,4468	0,0595
0,4	-0,1574	-8,0590	3,4599	6,5392	0,7406	0,1041
0,8	-0,4255	-12,7311	71,1439	7,1908	1,8949	0,3632

Table 1: Percentage relative error $\delta_{\mathrm{Re}}(\omega_{j,g})$.

ζ_d	$\omega_{j,g}$					
[/]	j = 1	2	3	4	5	6
0	-0,0004	-0,0015	0,0035	-0,0009	-3.7e-5	-1.3e-6
0,1	0,1770	1,1026	-2,3494	1,7488	0,3832	0,0199
0,2	1,3776	6,4283	-10,6109	9,7805	2,4708	0,1583
0,3	4,1112	23,5600	-24,3681	31,6932	6,8460	0,5099
0,4	8,5116	69,2541	-38,2283	82,1212	13,7089	1,1419
0,8	41,2246	491,9443	-55,5150	524,4971	66,0251	7,1132

Table 2: Percentage relative error $\delta_{\mathrm{Im}}(\omega_{j,g})$.

eigen-modes $v_{j,0}(x)$ and the contributions of other eigen-modes i.e. elements $a_{ij,g}$ are nearly vanishing, see Table 3. For higher values of ζ_d the interaction in particular of the second, third and fourth eigen-modes are important and not negligible, see Tables 4, 5 and 6, where the significant values are typed in bold. It comes from the fact, that these eigen-modes are very close in their eigen-frequencies and also regarding the tuning frequency of the absorber. The shapes of complex eigen-modes for realistic $\zeta_d = 0,2$ and $\zeta_d = 0,8$ are depicted in Figures 3 and 4 respectively. Only the perturbed solution is presented in Figure 3 due to weak graphic resolution of exact and approximate solutions, which implies a good accuracy of the latter one. However the accuracy is dropping with increasing damping ratio. Finally the approximate process fails when the damping ratio falls into the interval $\zeta_d \in (0.4 - 0.8)$, as it is notably visible referring particularly the fourth eigen-mode, see Figure 4.

In case of realistic ζ_d the considerable out of phase character of the second to fourth complex eigen-modes reflects the mechanical interaction of their corresponding undamped real counterparts. Consequently the zero nodes moving along the vertical axis of the structure emerge and vanish during their eigen-vibration process. On the other hand the first, fifth and sixth complex eigen-modes are very close to their undamped real eigen-modes and thus each one is almost synchronous. The mechanical interaction is in our case more evident and strong with increasing of the damping ratio ζ_d above the structural damping ratios. However for high value $\zeta_d = 0,8$ it appears that although the interaction is significant, some eigen-modes such as the second and the third are much closer to the corresponding real modes than in case of lower ζ_d. So we can ascertain that there exists a ratio $\zeta_{d,extr}$ leading to the highest phase shift variability within the eigen-modes, which is dropping with ζ_d approaching 0 or 1.

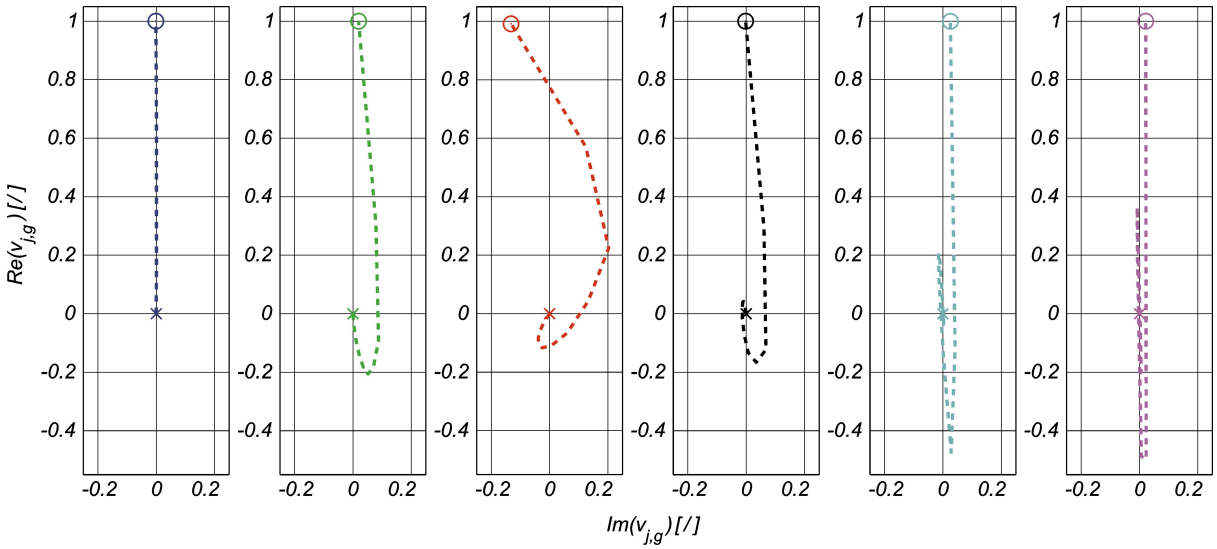


Figure 3: The first six eigen-mode of the shaft of the tower in the complex plane ($\zeta_d = 0{,}2$)
(Approximate solution; x - heel of the tower, ○ - approximate coordinate of the tower top).

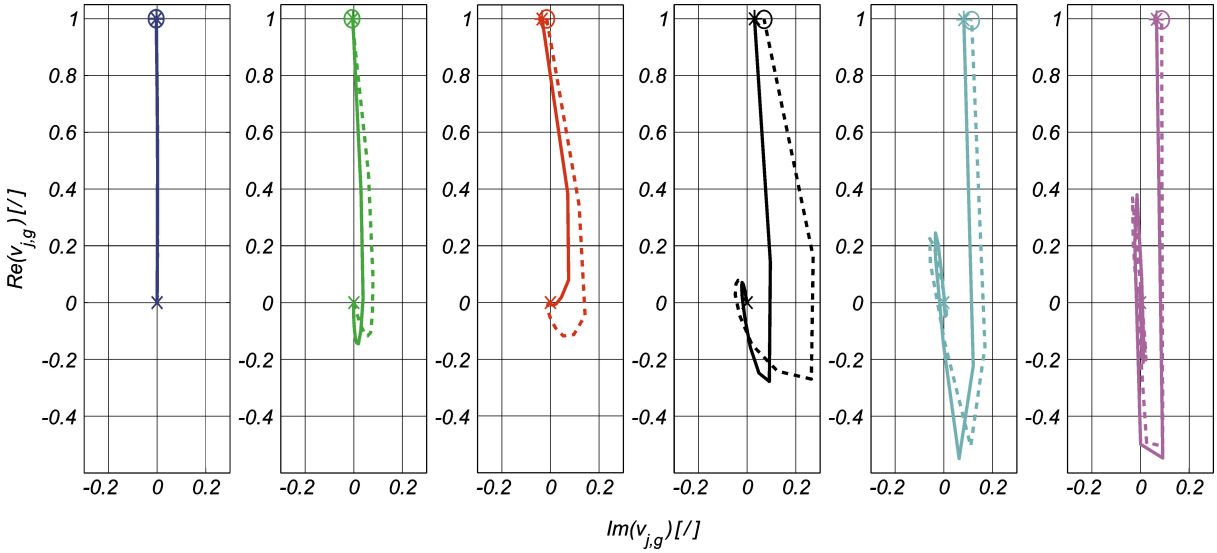


Figure 4: The first six eigen-mode of the shaft of the tower in the complex plane ($\zeta_d = 0{,}8$)
(solid line - exact solution; dashed line - approximate solution;
x - heel of the tower, ○ and ⋆ - approximate and exact coordinate of the tower top).

The important aspect from the point of view of complex eigen-modes is the moment when the real part of the third eigen-value vanishes and respective transformation of the corresponding eigen-mode from the complex to the real domain takes place.

i	$a_{ij,g}$					
	j = 1	2	3	4	5	6
1	1	-3e-6 +2e-3i	4e-7+1e-3i	2e-6 +4e-4i	9e-7 +9e-5i	5e-7 +3e-5i
2	4e-6 -9e-4i	1	-2e-5 -8e-3i	-2e-5 -3e-3i	-7e-6 -6e-4i	-4e-6 -2e-4i
3	1e-6 -4e-4i	8e-6 +6e-3i	1	-5e-5 -6e-3i	-1e-5 -10e-3i	-6e-6 -3e-4i
4	2e-7 -1e-4i	5e-6 +2e-3i	3e-5 +4e-3i	1	-1e-5 -1e-3i	-5e-6 -3e-4i
5	2e-8 -2e-5i	8e-7 +2.e-4i	3e-6 +4e-4i	5e-6 +6e-4i	1	-4e-6 -2.e-4i
6	3e-9 -3e-6i	1e-7 +4e-5i	4e-7 +8e-5i	6e-7 +1e-4i	1e-6 +1e-4i	1

Table 3: Contribution $a_{ij,g}$ of real eigen-modes to individual complex eigen-modes for ζ_d = 0.

i	$a_{ij,g}$					
	j = 1	2	3	4	5	6
1	1	-3-e3 -0,02i	-3e-3 -0,02i	-8e-4 -0,01i	-7e-5 -4e-3i	-3e-5 -1e-3i
2	+1e-3 +0,01i	1	**0,03 +0,27i**	**1e-3 +0,12i**	-7e-4 +0,03i	-4 e-5 +0,01i
3	+7e-4 +8e-3i	**-0,02 -0,20i**	1	**-0,03 +0,26i**	-4e-3 +0,05i	-5e-4 +0,02i
4	1e-4 +4e-3i	2e-3 -0,06i	**0,03 -0,19i**	1	-4e-3 +0,05i	-3e-4 +0,01i
5	4e-8 +7e-4i	6e-4 -0,01i	3e-3 -0,02i	3e-3 -0,03i	1	6e-5 +0,01i
6	-4e-7 +1e-4i	1e-4 -2e-3i	4e-4 -4e-3i	3e-4 -5e-3i	3e-5 -6e-3i	1

Table 4: Contribution $a_{ij,g}$ of real eigen-modes to individual complex eigen-modes for ζ_d = 0,2.

i	$a_{ij,g}$					
	j =1	2	3	4	5	6
1	1	-0,01 -0,05i	-0,01 -0,04i	-3e-3 -0,03i	-2e-4 -8e-3i	-6e-5 -3e-3i
2	5e-3 +0,03i	1	**0,13 +0,53i**	**3e-3 +0,24i**	-3e-3 +0,06i	-5e-4 +0,02i
3	3e-3 +0,02i	**-0,07 -0,39i**	1	**-0,12 +0,50i**	-0,02 +0,09i	-3e-3 +0,03i
4	5e-4 +7e-3i	7e-3 -0,13i	**0,10 -0,36i**	1	-0,02 +0,11i	-2e-3 +0,03i
5	2e-6 +1e-3i	3e-3 -0,02i	0,01 -0,04i	0,01 -0,06i	1	-1e-4 +0,02i
6	-1e-6 +3e-4i	5e-4 -4e-3i	2e-3 -8e-3i	1e-3 -0,01i	2e-4 -0,01i	1

Table 5: Contribution $a_{ij,g}$ of real eigen-modes to individual complex eigen-modes for ζ_d = 0,4.

i	$a_{ij,g}$					
	j = 1	2	3	4	5	6
1	1	0,04-0,08i	-0,04-0,07i	-0,01-0,05i	-7e-4 -0,02i	-1e-4 -6e-3i
2	0,02+0,05i	1	**0,49 +0,96i**	**0,01+0,48i**	-0,01+0,12i	-3e-3 +0,04i
3	0,01+0,03i	**-0,28 -0,73i**	1	**-0,43 +0,87i**	-0,06 +0,17i	-0,01 +0,06i
4	2e-3+0,01i	0,03 -0,25i	**0,37 -0,60i**	1	-0,06 +0,20i	-8e-3 +0,06i
5	1e-5+3e-3i	0,01 -0,04i	0,04 -0,07i	0,05 -0,12i	1	-1e-3 +0,04i
6	-5e-6+6e-4i	2e-3 -8e-3i	7e-3 -0,01i	5e-3 -0,02i	1e-3 -0,02i	1

Table 6: Contribution $a_{ij,g}$ of real eigen-modes to individual complex eigen-modes for ζ_d = 0,8.

The complexity or phase shift variability in length coordinate of the eigen-modes could be assessed using a modal phase co-linearity criterion defined in [27] as follows:

$$\mathrm{MPC}(v_{j,g}(x)) = \left(\frac{\lambda_1 - \lambda_2}{\lambda_1 + \lambda_2}\right)^2. \tag{34}$$

where

$$\lambda_{1,2} = \frac{S_{xx} + S_{yy}}{2} \pm S_{xy}\sqrt{\eta^2 + 1}. \tag{35}$$

$$\eta = \frac{S_{yy} - S_{xx}}{2S_{xy}}. \tag{36}$$

$$\begin{aligned} S_{xx} &= \mathrm{Re}(v_{j,g}(x))^T \cdot \mathrm{Re}(v_{j,g}(x)), \\ S_{yy} &= \mathrm{Im}(v_{j,g}(x))^T \cdot \mathrm{Im}(v_{j,g}(x)), \\ S_{xy} &= \mathrm{Re}(v_{j,g}(x))^T \cdot \mathrm{Im}(v_{j,g}(x)). \end{aligned} \tag{37}$$

It uses the variance and covariance of the real and imaginary part of the vector Eq. (37). Parameter MPC ranges from 0 to 1. The unity holds for fully phased vector (no phase shift), whereas the zero for totally dispersed vector in the complex plane. The MPC parameter has been evaluated for each complex eigen-mode and ratio ζ_d and written out in Tables 7 or 8 regarding exact or approximate solutions respectively.

ζ_d	$1 - \mathrm{MPC}_{ex}(v_{j,g}(x))$					
[/]	j = 1	2	3	4	5	6
0	3e-7	0,0001	0,0003	2e-5	4e-6	9e-7
0,1	1e-6	0,0207	0,1014	0,0087	0,0026	0,0006
0,2	7e-6	0,0589	0,2493	0,0359	0,0104	0,0024
0,3	2e-5	0,0682	0,2754	0,0771	0,0221	0,0054
0,4	2e-5	0,0496	0,2364	0,1102	0,0355	0,0093
0,8	5e-5	0,0121	0,0493	0,0734	0,0728	0,0294

Table 7: Reverse value of modal phase co-linearity criterion for exact complex eigen-modes.

ζ_d	$1 - \mathrm{MPC}_{app}(v_{j,g}(x))$					
[/]	j = 1	2	3	4	5	6
0	3e-7	0,0001	0,0003	2e-5	4e-6	1e-6
0,1	1e-6	0,0218	0,0984	0,0084	0,0027	0,0007
0,2	9e-6	0,0737	0,2483	0,0348	0,0111	0,0027
0,3	2e-5	0,1188	0,2989	0,0784	0,0250	0,0062
0,4	3e-5	0,1390	0,2805	0,1372	0,0442	0,0111
0,8	0,0001	0,0840	0,1514	0,4396	0,1624	0,0434

Table 8: Reverse value of modal phase co-linearity criterion for approximate complex eigen-modes.

To compare the approximate and the exact solution of complex eigen-modes the relative error using this criterion has been evaluated. The error has been assumed in a form:

$$\Delta\text{MPC}(v_{j,g}(x)) = \frac{\text{MPC}_{app}(v_{j,g}(x)) - \text{MPC}_{ex}(v_{j,g}(x))}{\text{MPC}_{ex}(v_{j,g}(x))} \cdot 100\ [\%]. \tag{38}$$

ζ_d	$\Delta\text{MPC}(v_{j,g}(x))$					
[/]	j =1	2	3	4	5	6
0	-6e-7	-2e-5	0,0006	5e-5	-5e-6	-1e-5
0,1	-3e-5	-0,1163	0,3322	0,0298	-0,0061	-0,0067
0,2	-0,0002	-1,5777	0,1338	0,1064	-0,0662	-0,0309
0,3	-0,0005	-5,4287	-3,2327	-0,1394	-0,3048	-0,0826
0,4	-0,0010	-9,4044	-5,7762	-3,0365	-0,9048	-0,1782
0,8	-0,0024	-7,2739	-10,7403	-39,5282	-9,6623	-1,4354

Table 9: Relative error in determination of MPC criterion using approximate eigen-modes.

Results of numerical evaluation of ΔMPC are obvious from Table 9. The range of the method applicability referring ζ_d has been confirmed once again. Another parameter worthy to be evaluated can be defined according to paper [28] as follows:

$$\begin{aligned}\text{MACX}(v_{j,g(ex)}, v_{j,g(app)}) \ &= \\ = \ &\frac{\left(\left|v^*_{j,g(ex)} \cdot v_{j,g(app)}\right| + \left|v^T_{j,g(ex)} \cdot v_{j,g(app)}\right|\right)^2}{\left(v^*_{j,g(ex)} \cdot v_{j,g(ex)} + \left|v^T_{j,g(ex)} \cdot v_{j,g(ex)}\right|\right)\left(v^*_{j,g(app)} \cdot v_{j,g(app)} + \left|v^T_{j,g(app)} \cdot v_{j,g(app)}\right|\right)}.\end{aligned} \tag{39}$$

The argument x of eigen-modes $v_{j,g}(x)$ has been omitted due to excessive equation length. The asterisk * in Eq. (39) means the complex conjugate value. The MACX parameter is equal unity for identical eigen-modes and zero for absolutely different eigen-modes. The reverse values of MACX parameter, which compare the exact and approximate solution of complex eigen-modes, are given in Table 10. The MACX criterion showed very good accuracy in determination of eigen-modes although the phase shift differences are for some ζ_d significant, see e.g. Figure 4. Therefore MACX criterion could be recommended as a tool for a general identification and pairing of corresponding eigen-modes obtained from a couple of experiments rather than for the detailed analysis of differences between them.

ζ_d	$1 - \text{MACX}(v_{j,g(ex)}, v_{j,g(app)})$					
[/]	j = 1	2	3	4	5	6
0	9e-14	4 e-10	3e-10	3e-11	8e-12	7e-12
0,1	4e-10	4e-5	2e-5	7e-6	2e-6	2e-7
0,2	8e-9	0,0004	0,0004	0,0001	4e-5	4e-6
0,3	5e-8	0,0007	0,0014	0,0010	0,0002	2e-5
0,4	2e-7	0,0002	0,0038	0,0037	0,0006	0,0001
0,8	7e-6	0,0120	0,0479	0,0008	0,0037	0,0008

Table 10: Reverse values of MACX criterion of corresponding complex eigen-modes as functions of ζ_d.

5 CONCLUSIONS

Approximate analysis of modal characteristics of one dimensional non-proportionally damped system with continuously distributed mass, stiffness and damping has been outlined. The basic structure is considered proportionally damped. Subsequently attached parts, e.g. vibration absorber, with strongly different damping are sources of the non-proportional damping of the system as a whole. The core of the study consists in extension of applicability of modal characteristics acquired for a system with proportional or zero damping into a system non-proportionally damped. As a basic tool the first order perturbation procedure has been applied.

It can be concluded that the proposed procedure is flexible and easily applicable for practical purposes. It enables wide choice of generalized coordinates when keeping their character of eigen-modes of the similar operator. Concerning final eigen-modes, the structure of results is very transparent with a possibility of detailed analysis of individual components. The approach used enabled to show an equivalence of the eigen-value of the proportionally and relevant non-proportionally damped systems. On the other hand certain limits of the approach developed should be respected. In particular the system eigen-frequencies should be well separated in order to ensure a good convergence increasing number of basis functions being taken into account. Only simple eigen-values are admitted and so effect of double (or multiple) frequency splitting cannot be analyzed. The damping itself should be small and far enough from the critical damping.

Wide numerical experiments of the model of existing slender structure equipped with absorber have been carried out investigating interaction of eigen-modes between resonance domains. Numerical experiments approved a good convergence on the level of eigen-modes of the operator with continuously distributed parameters as well as on the level of eigen-modes transforming the problem to the system of generalized coordinates. First six undamped eigen-modes being close to eigen-value of the absorber revealed to be satisfactory as Galerkin base for reduction of the original problem without any impact on the accuracy of all subsequently obtained results.

The accuracy of the perturbation method applied for estimation of complex modal properties has been investigated for several damping ratios of the absorber. The comparison of approximate and exact solutions has showed increasing errors in eigen-values with an increase in damping ratio of the absorber. The error of the real part representing the ”frequency” component of an eigen-value was substantially lower than that of the imaginary part representing the eigen-value ”damping” component. The significant errors came up for eigen-values which were close to eigen-value of the absorber. Similarly to eigen-values, the accuracy of approximate solution of complex eigen-modes dropped with increasing absorber damping ratio as well. The complex eigen-modes have been for very low damping ratio of the absorber almost identical with real undamped eigen-modes and the mechanical interaction has been negligible. For higher values of ratio the interaction of eigen-modes, especially those that are very close in their eigen-frequencies to the tuning frequency of the absorber, has been substantial. Hence there exist a certain limit of the damping ratio, which leads to the highest phase shift variability within the eigen-modes, beyond of which the complexity of the eigen-modes is dropping although the interaction of those is increasing.

The comparison with the exact eigen-solution reveals that the approximate perturbation strategy is entitled to assess dynamic behavior of existing structures provided with one passive damping element for realistic damping ratio. In our case a limiting value of the damping ratio of the absorber for which the errors were reasonable was equal 30%. Beyond this value the

errors could be significant and more sophisticated approach should be employed.

ACKNOWLEDGEMENT

The kind support of the Czech Science Foundation project No. 103/09/0094 and No. 13-41574P, Grant Agency of the ASCR project No. IAA200710902 and of the RVO 68378297 institutional support are gratefully acknowledged.

REFERENCES

[1] J. Náprstek, S. Pospíšil, S. Hračov, Random response of one-dimensional structure with non-proportional damping due to wind excitation. I. Zolotarev et al. eds. *Proc. Engineering Mechanics 2007* , Svratka, Czech Republic, 2007.

[2] S. Hračov, J. Náprstek, S. Pospíšil, Non-proportional damping effect on dynamic response of footbridges. J.Náprstek, C.Fischer eds. *Proc. Engineering Mechanics 2009*, Svratka, Czech Republic, 2009.

[3] W. C. Hurty, M. F. Rubinstein, *Dynamics of Structures.* Prentice-Hall,Inc., 1964.

[4] A. S. Veletsos, C. E. Ventura, Modal analysis of non-classically damped linear systems *Earthquake Engineering and Structural Dynamics.* **14**, 217-243, 1986.

[5] I.W. Park, J.S. Kim, F. Ma, Characteristics of modal coupling in non-classically damped systems under harmonic excitation. *Journal of Applied Mechanics*, **61**, 77-83, 1994.

[6] H. N. Özgüven, Twenty Years of Computational Methods for Harmonic Response Analysis of Non-Proportionally Damped Systems. *Proceedings of the 20th International Modal Analysis Conference*, Los Angeles, CA, USA, 2002.

[7] D. E. Newland, *Mechanical Vibration Analysis and Computation.* Longman, Harlow and John Wiley, New York, 1989.

[8] G. B. Warburton, S. R. Soni, Errors in response calculations for non-classically damped structures. *Earthquake Engineering and Structural Dynamics*, **5**, 365-376, 1977.

[9] G. Prater Jr., R. Singh, Quantification of the extent of non-proportional viscous damping in discrete vibratory systems. *Journal of Sound and Vibration*, **104(1)**, 109-125, 1986.

[10] W. Gawronski, J.T. Sawicki, Response errors of non-proportionally lightly damped structures. *Journal of Sound and Vibration*, **200(4)**, 543-550, 1997.

[11] A. Ibrahimbegovic, E. L. Wilson, Simple numerical algorithms for the mode superposition analysis of linear structural systems with non-proportional damping. *Computer and Structures*, **33 (2)**, 523-531, 1989.

[12] F. E. Udwadia, R. Kumar, Iterative methods for non-classically damped dynamic system. *Earthquake Eng. And Structural Dynamics*, **23** , 137-159,1994.

[13] S. Adhikari, Rates of change of eigenvalues and eigenvectors in damped dynamic system. *AIAA Journal*, **39(11)**, 1452-1457, 1999.

[14] J. Woodhouse, Linear damping models for structural vibration, *Journal of Sound and Vibration*, **215 (3)**, 547-569, 1998.

[15] S. Adhikari, Calculation of derivative of complex modes modes using classical normal modes. *Computers & Structures*, **77**, 625-633, 2000.

[16] S. Hračov, J. Náprstek, S. Pospíšil, Analysis of eigen-values of viscously damped two degrees of freedom system due to changes of parameters of secondary subsystem. F. Soukup et al. eds. *Proc. Dynamics of Rigid and deformable bodies 2011*, Ústí nad Labem, Czech Republic, 2011.

[17] S. D. Garvey, J. E. T. Penny, M. I. Friswell, The relationship between the real and imaginary parts of complex modes. *Journal of Sound and Vibration*, **212 (1)**, 75-83, 1995.

[18] C. Rajakumar, Lanczos Algorithm for the Quadratic Eigenvalue Problem in Engineering Applications. *International Jornal of Numerical Methods in Engineering*, **105**, 1-22, 1993.

[19] P. Fischer, Eigensolution of nonclassically damped structures by complex subspace iteration. *Computer Methods in Applied Mechanics and Engineering*, **189 (1)**, 149-166, 2000.

[20] J.A. Main, S. Krenk, Efficiency and tuning of viscous dampers on discrete systems. *Journal of Sound and Vibration*, **286**, 97-122, 2005.

[21] F. Perotti, Analytical and numerical techniques for the dynamic analysis of non-classically damped linear systems. *Soil Dynamics and Earthquake Engineering*, **13**, 197-212, 1994.

[22] J. Tang, W. L. Wang, Perturbation method for determining eigensolutions of weakly damped systems. *Journal of Sound and Vibration*, **187 (4)**, 671-681, 1995.

[23] P. D. Cha, Approximate eigensolutions for arbitrarily damped nearly proportional systems. *Journal of Sound and Vibration*, **288**, 813-827, 2005.

[24] Y. Zhou, On the eigenvalues of specially low-rank perturbed matrices. *Applied Mathematics and Computation*, **217**, 10267-10270, 2011.

[25] V. Koloušek, M. Pirner, O. Fischer, J. Náprstek, *Wind Effects on Civil Engineering Structures*. Academia-Elsevier, Prague, 1983.

[26] S.G. Michlin, *Variational Methods in Mathematical Physics* (in Russian). GITTL, Moscow, 1975.

[27] R. S. Pappa, K. B. Elliot, A. Schenk, Consistent-mode indicator for the eigensystem realization algorithm. *Journal of Guidance, Control and Dynamics*, **16(5)**, 852-858, 1993.

[28] P. Vacher, B. Jacquier, A. Bucharles, Extensions of the MAC Criterion to Complex Modes. *Proceedings of ISMA International Conference on Noise and Vibration Engineering*, Leuven, Belgium, 2010.

COMPDYN 2013
4th ECCOMAS Thematic Conference on
Computational Methods in Structural Dynamics and Earthquake Engineering
M. Papadrakakis, V. Papadopoulos, V. Plevris (eds.)
Kos Island, Greece, 12–14 June 2013

COMPARISONS OF A TALL LATTICE WIND TOWER RESPONSE WITH AND WITHOUT A TMD

Jorge M. Henriques[1], **Rui C. Barros**[1]

[1] Faculty of Engineering of the University of Porto
Rua Dr. Roberto Frias, s/n 4200-465 Porto, Portugal
{jfmh,rcb}@fe.up.pt

Keywords: Lattice tower, Eurocodes, Wind response, Vibration control, TMD.

Abstract. *This paper addresses basic concepts regarding the wind effects on a lattice wind tower with 150 m of height and the subsequent wind responses. The methodology presented for simulating series of natural wind is the method of Shinozuka. A simplified method for quantifying the dynamic action on these structures is adopted, with the purpose of studying techniques for vibration control of the along-wind response in terms of displacements and accelerations. It was also accomplished a comparative study of response of lattice wind tower when subjected to natural winds without and with a TMD.*

1 INTRODUCTION

With fossil fuels becoming increasingly scarce and expensive, the world seeks solutions to serve the interest of economic development and the preservation of nature. Wind energy plays a very important role in the global panorama of energy, as it is a source of renewable energy that has the least impact on nature [1]. Therefore the rising demand on wind energy caused the development of related technologies, for example on the type of tower.

This new idea of developing lattice towers of great height, since they have significantly lower construction costs [2][3], poses new challenges for the structural engineers with regard to dynamic effects. Lattice towers are sensitive to the dynamic environments generated by wind, ice, earthquakes, impact, blast, explosions and mechanical failures of some of their components. The vibrations induced in the tall lattice tower structures by these environmental and mechanical causes cover an ample spectrum of frequencies, which affect the towers in different ways ranging from serviceability problems to fatigue and collapse [4].

To mitigate the dynamic effects can be installed several types of damping devices, one of which is a tuned mass damper (TMD). A TMD consisting of a mass, damping and a spring, is an effective and reliable structural vibration control device commonly attached to a vibrating primary system for suppressing undesirable vibrations induced by machinery as well as by wind and earthquake loads. The natural frequency of the TMD is tuned in resonance with the fundamental mode of the primary structure, so that a large amount of the structural vibrating energy is transferred to the TMD and then dissipated by the damping as the primary structure is subjected to external disturbances. Consequently, the safety and comfort characteristics of the structure are greatly enhanced. The TMD system has been successfully installed in slender skyscrapers and slender towers to suppress the wind-induced structural dynamic responses [5]. In the following Figure 1 can be seen the scheme of a TMD

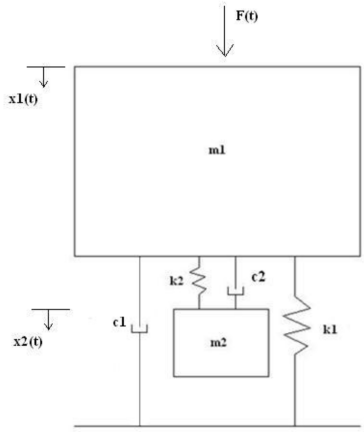


Figure 1: Theoretical scheme of a TMD [6]

2 NUMERICAL MODELING OF A TOWER AND ITS DYNAMIC WIND ACTION

This chapter begins by describing the structure and how it was modeled computationally. The program used for structural calculations associated with analysis and design was the "*Autodesk Robot Structural Analysis Professional 2012*".

The dynamic wind action was modeled to obtain the structural response of the tower. Mathematical modeling of turbulent flow is rather complex and the possibility of interaction between the flow and the tower may lead to changes in dynamic pressure and in the response of the tower along time. This chapter also addresses the simplifications used to consider this dynamic action [7].

2.1 Structural Description of the Lattice Wind Tower

The structure chosen was a tall lattice wind tower, whose design resulted from academic studies of the authors of this paper [2] [3] and is represented in Figure 2. The tower has 150 m of height and the turbine used is FL2500 of 2,5 MW with rotor diameter of 100m.

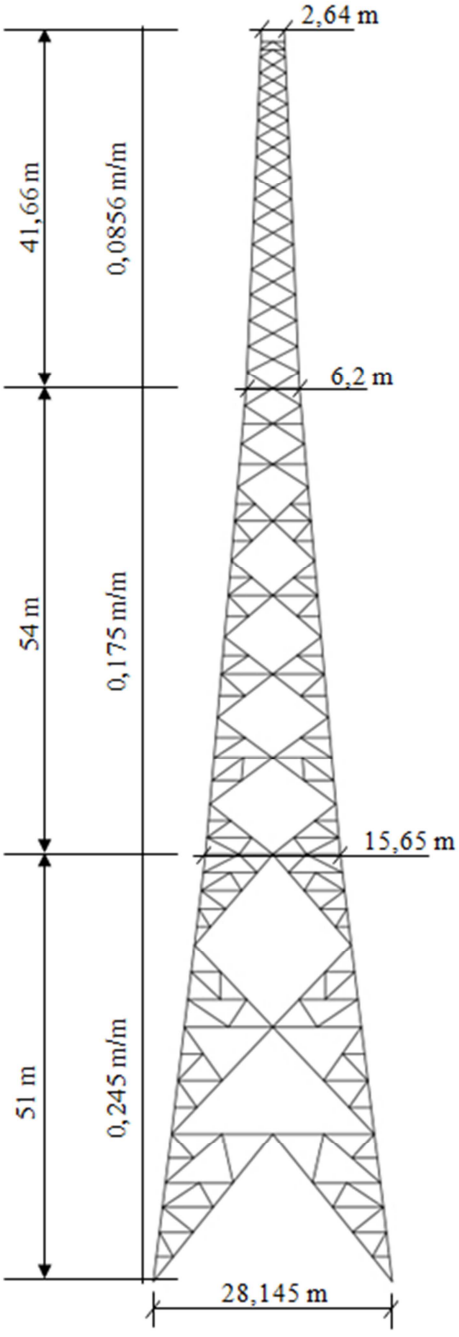


Figure 2: Tower Geometry [3]

The elements of the structure were disposed based on rules of triangles so as to shorten the lengths of buckling of the structural system. The construction of the geometry of the beams and diagonals was based on the Eurocode 3 (EN 1993-3-1) [8] and on dispositions of existing towers [3]. The sections of the bars used in the tower are angles and association of angles (Figure 3). The steel used in the design is S235 and S355.



Figure 3: Association of angles

The design follows the rules disposed in the Eurocode 1 (EC 1) EN 1991-1-4 [9] and also Eurocode 3 (EC 3) given in EN 1993-3-1 [8] and EN 1993-1-1 [10].

2.2 Modeling a Latticed Wind Tower

The model of the tower was introduced in Autodesk Robot Structural Analysis Professional 2012, using model bars linked through rigid connections; the foundations were modeled with supports that restrict all displacements and rotations.

The non-structural elements (stairs, cables) were not modeled, however were introduced two additional nodes in the bar elements of support to non-structural elements, so as to introduce the forces resulting from the actions on the non-structural elements.

The modeling of the wind turbine (by itself) was not performed. However were introduced bars with great rigidity and null weight to simulate the rigidity of the wind turbine on the top of the lattice tower structure. The weight of the wind turbine was considered at the top the tower by adding four vertical forces in the top of the tower with 362.60 kN each.

In this work it was considered that during the dynamic action the rotor is stopped in its most unfavorable position.

The mass of the structure is lumped at the structure nodal points; the masses are assumed to have only one degree of freedom (translation in X-direction).

One final aspect of the analytical model development that requires discussion is damping. Damping is the property that allows decreasing the amplitude of free vibration and is always present in structural systems. Several damping mechanisms may act simultaneously allowing dissipation of vibration energy. Due to the difficulty in identifying the damping mechanisms that may be present at a particular time, damping is cumbersome to evaluate [4]. The damping of similar towers has been calculated by other authors and researchers [3] by means of the logarithmic decrement, and the value of the viscous damping ratio used is $\xi = 5\% \xi = 5\ \%$.

Autodesk Robot Structural Analysis includes damping in its dynamic time history analysis application, through the classic formulation of Rayleigh damping with user-defined quantities. A target damping ratio equal to $\xi = 5\ \%$ was used for every mode of vibration.

In the modal analysis only the response from the first three modes were considered. The vibration modes are shown in Figure 4 and the values of the natural frequencies and of the percentage of modal mass (from the total) for each vibration mode are presented in Table 1.

Mode	f (Hz)	M_x=450161,80 kg
1	0,47	53,57 %
2	2,25	25,44 %
3	3,95	14,62 %

Table 1: Natural frequencies and percentage of modal mass, from the modal analysis

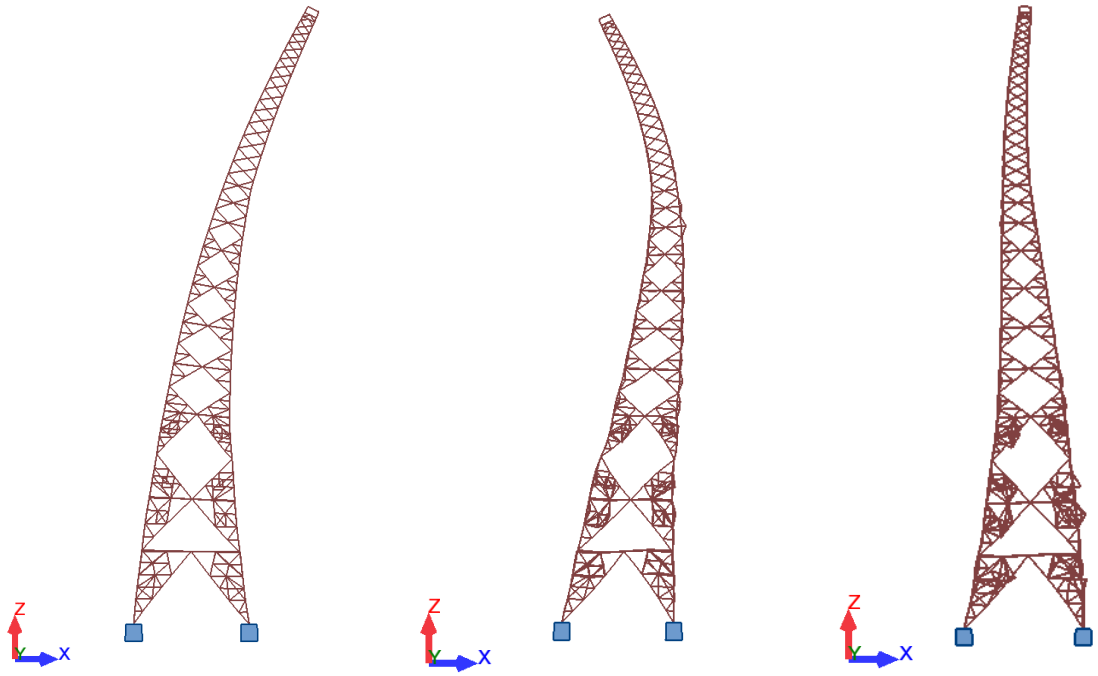


Figure 4: First, second and third modes of vibration (from left to right) from the numerical model

2.3 Modeling Wind Dynamic Action

Research has been done in the past in order to develop a spectrum that would accurately predict the dynamic characteristic of wind. Although it is recognized the great complexity in modeling turbulent flow around lattice towers, even with scaled physical models in a wind tunnel, some simplifications will be considered herein with regards to the quantification of dynamic pressures and generalized forces due to wind action along the time. For that, the fluid structure interaction (FSI) is considered negligible and also the correlations of the velocity fluctuations along the height of tower are considered in a simplified manner.

Firstly it is addressed the methodology for generating time series of wind to be used latter in the calculation of the instantaneous dynamic pressures and therefore in the quantification of the generalized wind forces acting at every floor level of the tower (diaphragms of the tower).

The methodology used to generate synthetic time series is usually referred as the Method of Shinozuka, which bases the generation of time series in calculating the inverse function of the Fourier Transform of the amplitude of the random process (given by a spectral density function of the energy of a process) [7].

Such generation of synthetic series of wind occurs in the range of wavelengths corresponding to fluctuations of wind velocity with an approximate Gaussian distribution of the atmospheric wind flow [11]. The purpose of such method is to obtain a realization of a stochastic process (for example: a time series of the fluctuations of the longitudinal component of wind velocity) from the spectral density function of the random process [7].

The method uses this function to perform a weighted sum of sinusoidal functions (in this case of cosines). The contribution of each of the N waves is given by the amplitude of the spectrum $S_L(z,n)$ (real function) for each corresponding natural frequency (n). The phases are obtained (for the case of one-dimensional spectrum of simple non correlated series) by a pseudo-random number generation in the interval $[0, 2\pi]$.

According to the Method of Shinozuka, in the simplest case of one-dimensional univariate stochastic processes, a realization of the random process may be obtained [11] [12] by the equations (1)-(2). This method has been evaluated by Ianuzzi and Spinelli [13], and it has been found to generate accurate fluctuations of longitudinal wind velocity histories *u(t)* when compared to measured wind records.

$$u(t) = \sqrt{2}\sum_{k=1}^{N} A_k.\cos(2\pi n_k t + \phi_k) \tag{1}$$

with

$$A_k = \sqrt{S_v(z, n_k)\Delta n} \tag{2}$$

and

$$\Delta n = \frac{n_{max} - n_{min}}{N} \tag{3}$$

In the previous expression *N* is the number of frequencies of the discretization of the spectrum, and *n* is frequency. To generate the synthetic time series of wind velocity it is necessary to define a spectral density function of the fluctuations of longitudinal velocity of the wind; the wind spectral density function S_L given in Eurocode 1 (EN 1991-1-4) [9] is used herein in the general dimensionless form of equation:

$$S_L(z, n_k) = \frac{n_k S_v(z, n_k)}{\sigma_v^2} = \frac{6{,}8 f_L(z, n_k)}{(1 + 10{,}2 f_L(z, n_k))^{5/3}} \tag{4}$$

with

$$f_L(z, n_k) = \frac{n_k L(z)}{v_m(z)} \;\; and \;\; L(z) = L_t\left(\frac{z}{z_t}\right)^{\alpha} \tag{5}$$

where:

L(z) is turbulent length scale represents the average gust size for natural winds. With a reference height of z_t = *200 m* and a reference length scale of L_t = *300 m*, the power α = *0,67+ 0,05 ln(z_0)* where z_0 is the roughness length.

$S_v(z,n_k)$ is the one-sided variance spectrum.

$f_L(z,n_k)$ is a non-dimensional frequency.

σ_v is standard deviation of the turbulence.

For the generation of the synthetic series to be considered an ergodic process, according to [11] the number *N* of frequencies for discretization of the spectrum should be sufficiently high. However, not having an indication of the number of discrete frequencies to use, a study of the generation of wind series was made discretizing the wind spectrum into different number of frequency ranges. Herein four processes, corresponding to four frequency intervals chosen, were studied for the division of the wind spectral density function in 100, 500, 1000 and 5000 intervals respectively; for each case, fluctuations of longitudinal wind velocity were obtained according with the process described.

These fluctuations were calculated for an elevation *H*=90 m, and considering that the tower was located on a terrain of class I according to EC 1. The base velocity assumed for a return period of 50 years was 30 m/s (Zone B in EC1) and under these conditions, according to EC1, standard deviation of the turbulent component of wind velocity was σ_v = 5,7.

The frequencies n_{min} and n_{max} must be determined accordingly with the f_L limits of power spectral density function of the EN 1991-1-4 [9], that finally allow the wind turbulence effect to be clearly characterized. Figure 5 represents the spectral density functions S_L (given in a dimensionless form) and S_v, for the previously mentioned conditions.

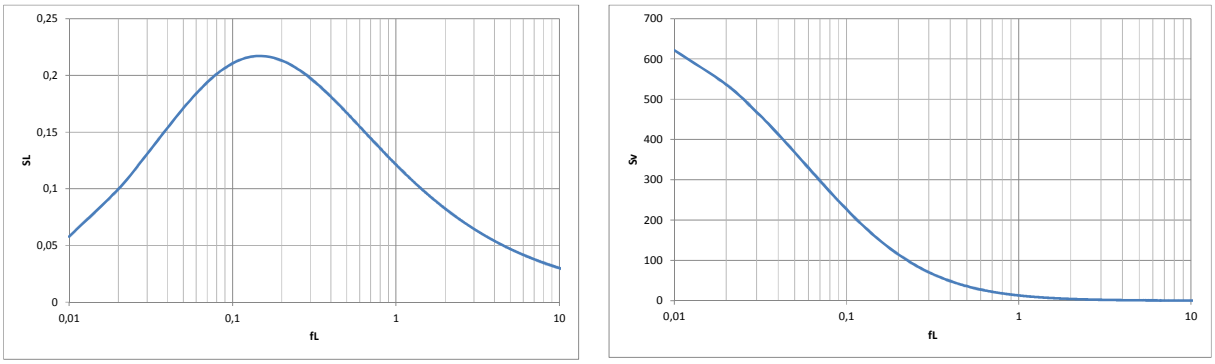


Figure 5: Wind spectral density functions

Figure 6 represents the time series of the fluctuations of wind velocity, evaluated with the previous data, for the four successively higher discretizations.

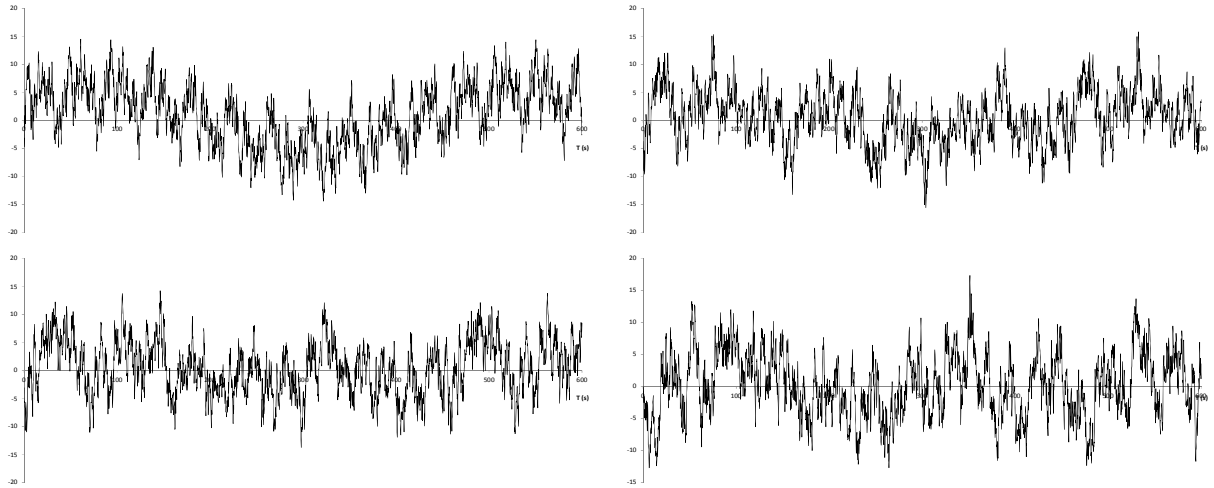


Figure 6: Time series of fluctuations of wind velocity for wind spectrum with 100-500-1000-5000 intervals

The spectral density function has high values for low frequencies but reduces rapidly with increasing frequency (Figure 5). Thus, from the analysis of the previous figures, it is noted that when choosing a lower number of frequencies of discretization (lower *N*) for generation of the synthetic time series of wind, these are clearly more affected by the low frequency components (where the spectrum has more energy) resulting in a value numerically higher.

The series chosen for resolving the problem was the one of N=1000, for which it is no longer noticeable the influence of low frequency components. The results in [6] [7] also show that the value of N=1000 is a good compromise.

For the instantaneous wind velocity *U(t)* at any height given as the sum of a constant mean component $\bar{U}$ with a dynamic fluctuation component *u(t)* (Barros [14]), the instantaneous wind force *F(t)* on any surface *A* is given by equations (6) and (7).

$$F(t) = \frac{1}{2}.\rho.c_f.A.\left[(\overline{U} + u(t)\right]^2 \tag{6}$$

$$F(t) = \frac{1}{2}.\rho.c_f.A.\overline{U}^2 + \rho.c_f.A.\overline{U}^2.u(t) + \frac{1}{2}.\rho.c_f.A.u(t)^2 \quad (7)$$

The fluctuations of wind velocity along time also have a spatial variability, which for a first approximation is herein neglected. For the case tall slender tower under study, whereas the response is majorly due to the contribution of the first mode of vibration (which is also a condition imposed by EC 1 for the calculation of the structural factor), modeled as a structural system with one degree of freedom, the passage or conversion of the power spectrum of the wind velocity fluctuations into structural response spectrum is given by:

$$S_X(n) = \frac{4\overline{X}}{\overline{U}^2}.[H(n)]^2.\chi^2(n).S_u(n) \quad (8)$$

where $[H(n)]^2$ represents the mechanical admittance and $\chi^2(n)$ represents an aerodynamic admittance function [15] given approximately by equation (9).

$$\chi(n) = \frac{1}{1 + \left(\frac{2.n.\sqrt{A}}{\overline{U}}\right)^{4/3}} \quad (9)$$

According to Holmes [16], in a frequency domain analysis for very tall tower structures, it is this latter function that takes into account the non-simultaneous occurrence of fluctuations of wind velocity. It is explicitly stated that: "*For larger structures, the velocity fluctuations do not occur simultaneously over the windward face and their correlation over the whole area must be considered. To allow for this effect, an aerodynamic admittance* $\chi^2(n)$ *is introduced*".

According to EC 1 for tall tower structures with the shape and conditions equivalent to the case study under consideration, the parameters of the spectral density function for calculating the structural factor should be determined for a reference height of approximately 0.6 of the height of the structure. Given this indication, for generating different sets of time series the height chosen was 90 meters that is about 60% of the height of lattice wind tower.

The applied wind generated forces were obtained through equation (6) taking into account the acting dynamic pressures and the influence area for each floor, considering the mean wind velocity depending on the height (given by the equation (10) below, taken from EC 1) and the fluctuation velocities given by the random series generated [6] [7]. Supporting the procedure used in Ferreira [6] and Ferreira *et al.* [7], appropriate simplifications were performed so that the wind power spectrum was multiplied by the aerodynamic admittance; it was with this new spectrum that the turbulent velocities were calculated.

$$v_m(z) = c_r(z).c_0(z).v_b \quad (10)$$

As an example, Figure 7 presents one series for the fluctuations of wind velocity generated in these conditions at a height of 90 m and using wind power spectrum of EC 1. Figure 8 shows the same series, that is adopting the same phase angles for the harmonics, but generated from the wind power spectrum multiplied by the mentioned aerodynamic admittance function.

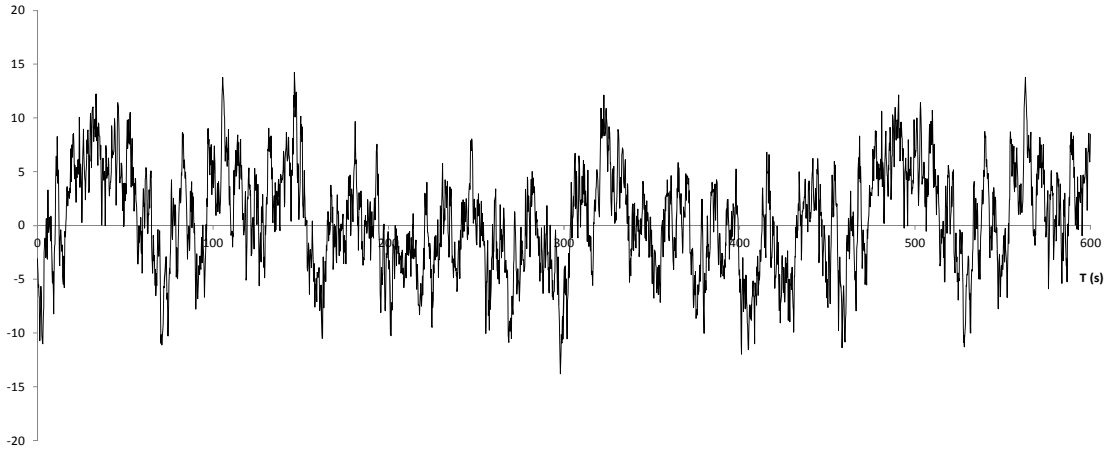


Figure 7: Fluctuation velocity time series (for height of 90 m, base velocity 30 m/s, terrain category I) using EC1 wind power spectrum (wind power spectrum not multiplied by the aerodynamic admittance function)

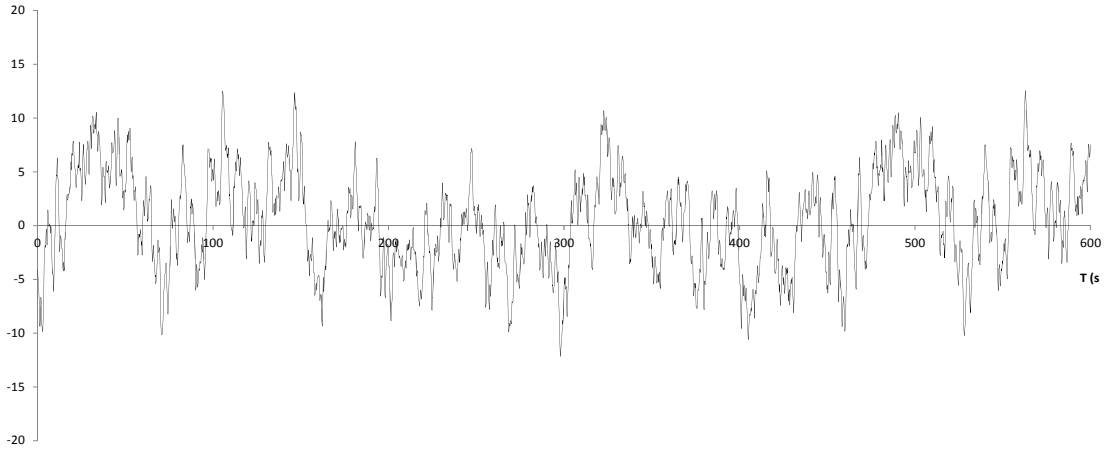


Figure 8: Fluctuation velocity time series (for height of 90 m, base velocity 30 m/s, terrain category I) using EC1 wind power spectrum multiplied by the aerodynamic admittance function

3 MODELING A TMD FOR PASSIVE CONTROL OF VIBRATIONS

The tuned mass dampers (TMD) can be used to control one or more vibration modes of structures excited by external actions. However, in many cases, control of the first mode is sufficient to reduce significantly the level of vibrations recorded. Except for cases in which it is intended to simultaneously monitor the contribution of more than one mode of vibration, the use of a single TMD may be satisfactory [7].

The design of a TMD for application to structures without damping is universally based on two parameters – mass ratio μ and frequency ratio q – as detailed in Kelly [17]. The optimum frequency ratio q_{opt} (corresponding to locating the fixed points at the same level or with the same displacement amplitude), the maximum amplitude of the controlled principal system, and the inherent optimal damping $\xi_{2,opt}$ of the TMD, are given by the set of equations (11).

$$q_{opt} = \frac{1}{1+\mu} \quad , \quad \frac{X_1}{X_{1,static}} = \sqrt{\frac{2+\mu}{\mu}} \quad , \text{ and } \quad \xi_{2,opt} = \sqrt{\frac{3\mu}{8(1+\mu)^3}} \tag{11}$$

For the design of a TMD tuned for the application to structures with damping, it is still possible to use these equations provided that the damping of the principal primary system is less or equal to 1%. For higher damping of the primary system, the use of such equations will lead to a non-optimized tuning of the TMD. For such cases, the design of the TMD can be done with design graphs (Figure 9) associated with the numerical solution of the expression giving the maximum amplitude of the controlled principal system (as used successfully in [6] [18] [19]).

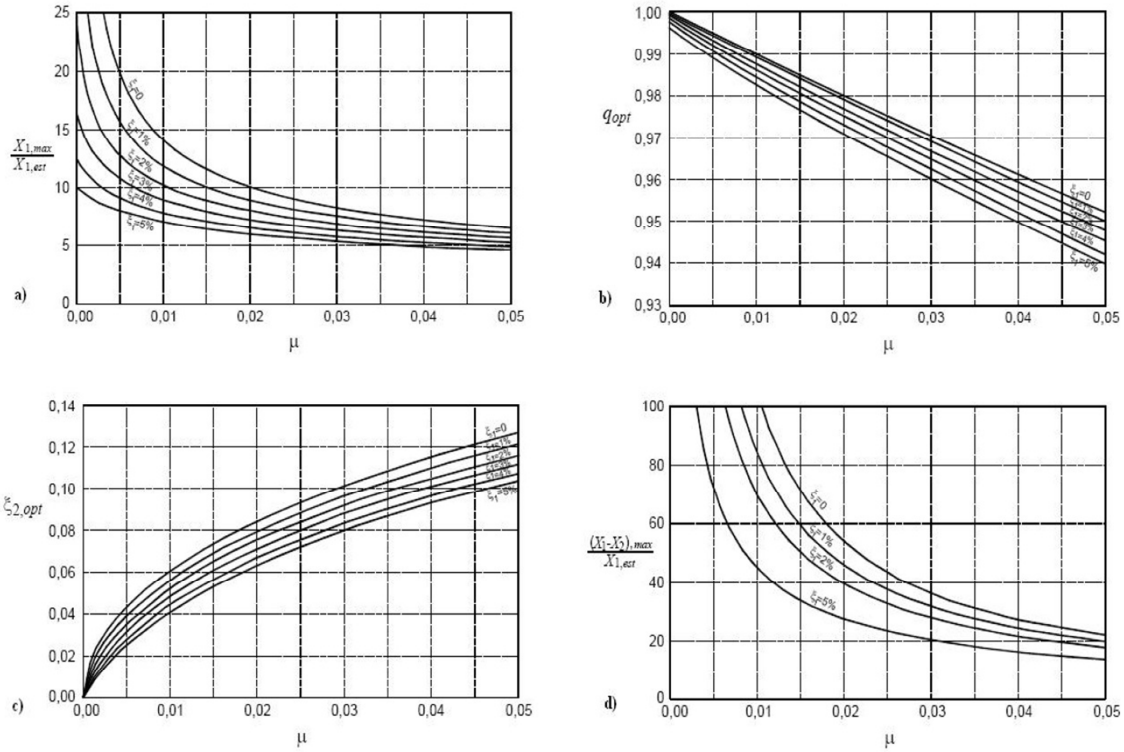


Figure 9: Design graphs of TMD ($\boldsymbol{\xi_1 \neq 0}$) [6] [18] [19]

Kwok and Samali [20] also studied the behavior of a TMD in tall buildings subjected to the action of wind and, according to them, the considerations presented about the effectiveness of a TMD in response of a system of one degree of freedom can also be extended to other solid structures – such as in the case of tall buildings – leading to a modal analysis. Kwok and Samali [20] indicated that occurred large decreases in response for the modes controlled by the TMD's installed, while the higher order modes were not affected. For such higher modes to be also less contributive to the structural response, would require implementing new TMD's tuned according to their frequency. Thus, using modal analysis, for each vibration mode whose contribution to the overall response of the structure is important, and that one wishes to control, it is necessary to determine the corresponding values of stiffness, of mass and of modal damping [7].

Since the fundamental frequency of the tall wind tower under study is very low (0.47 Hz) and because the wind action has a spectral density function with strong content for low frequencies, it is possible that the response is conditioned by the harmonic of the fundamental frequency. For control of vibrations purposes it is assumed herein that the response is only dependent on the first vibration mode, with which the TMD solutions were designed with the expressions available for harmonic vibration with the frequency equal to the first vibration frequency of the overall structure.

Accordingly, the value of the modal mass corresponding to the first mode of vibration was determined as 126,25 ton. For the case study wind tower structure with the deployment of a TMD, only one mass ratio is herein considered $\mu=0.01$, for which with the design charts (Figure 9) it was possible to determine the optimal parameters to be adopted for each TMD situation. In Table 2 the values adopted are systematized.

TMD mass ratio μ	q_{opt}	$\xi_{TMD,opt}$	m_{TMD} (ton)	ω_{TMD} (rad/s)	k_{TMD} (kN/m)	Size (cm) of square section steel bar, L=2 m
0.01	0,987	0,046	1,7626	2,915	14,974	3,89

Table 2: Optimal parameters of a TMD for the tall wind tower

Since the structural software used does not have an intrinsic function that allows the direct introduction of dampers, herein for the simulation of a TMD were determined the dimensions of a square section bar with a lateral stiffness equivalent to that required for the damper placed on top. Acting as a vibrating bar (built in end – free end) with a concentrated mass that would give the frequency obtained for the sizing of the TMD with the damping introduced in the material parameters constitutive of the bar [7].

Assuming a bar length L=2 m, made of steel with elasticity module $E=210\ GPa$, from the bar stiffness $3EI/L^3$ is obtained the equivalent inertia I of the square section bar. Table 2 also indicates the dimensions required for such bar, for the mass ratio considered in the design of the TMD. Table 3 shows the first four natural frequencies of the vibration modes of the case-study wind tower structure incorporating the TMD solution.

Mode	1	2	3	4
f (Hz)	0,45	0,49	2,25	3,95

Table 3: Natural Frequencies of the first four modes of wind tower with TMD

4 ANALYSIS OF RESULTS FOR THE TOWER WITHOUT AND WITH TMD

Based on the methodology adopted for consideration of the dynamic wind action (using a set of 4 time series and for frequencies in the wind spectral density function evaluated with 1000 frequency intervals), the results in terms of top displacements and accelerations were evaluated and compared for the computational structural model, without and with an installed TMD vibrating bar (with an hypothetical vibrating mass with the appropriate stiffness and damping properties). Using the mentioned structural software with modal superposition, a damping ratio of 5 % and an integration time step of $\Delta t = 0.2$ seconds, the four series of wind dynamic loads were applied and their average results obtained in terms of top displacements and accelerations. As an example, Figure 10 and Figure 11 show the time variations of top acceleration and displacement of the wind tower for the wind loads evaluated using equation (6), with velocity fluctuations corresponding to wind series 1. Table 4 presents a summary of maximum values of tower top displacements and accelerations, for each of the time series.

Series	1	2	3	4	Average
Maximum displacement (cm)	70,39	66,07	68,99	65,77	67,80
Maximum acceleration (cm/s^2)	184,15	179,49	179,89	222,36	191,47

Table 4: Maximum displacements and accelerations on node 3, for each of the wind time series (without TMD)

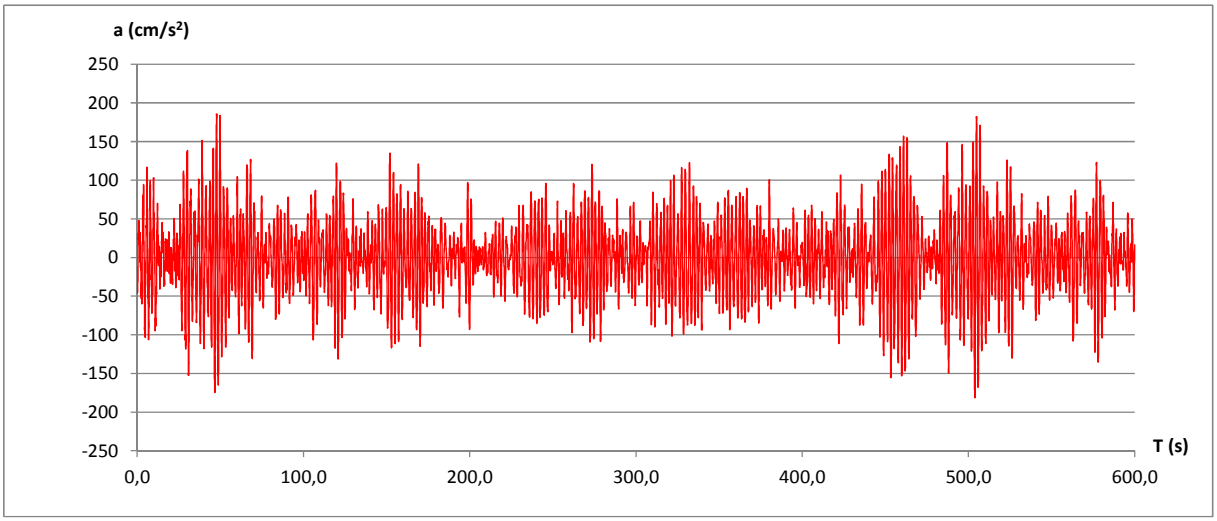


Figure 10: Accelerations on top of tower, for wind loads corresponding to wind series 1

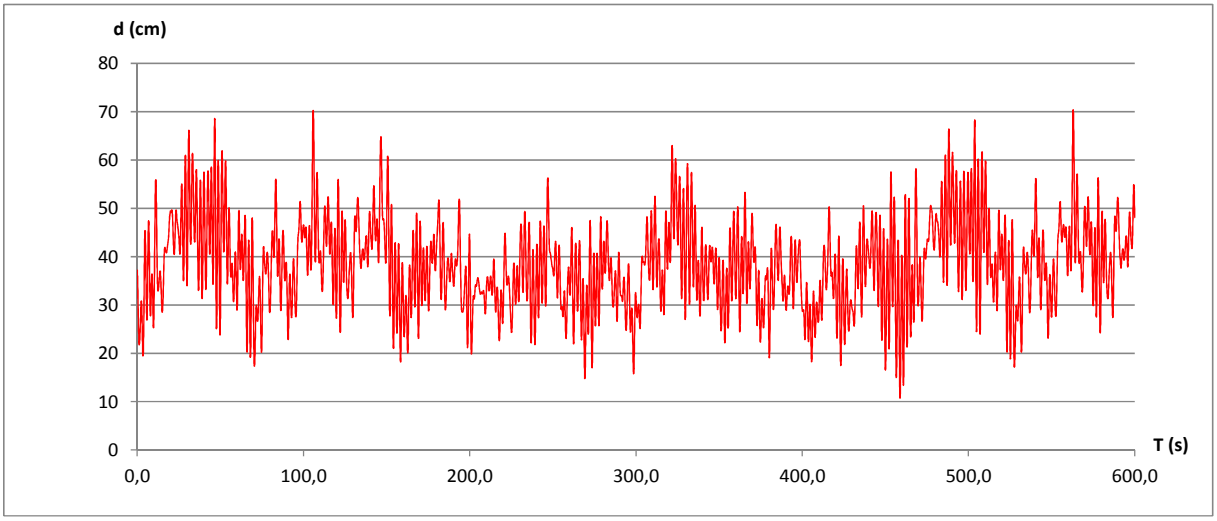


Figure 11: Displacements on top of tower, for wind loads corresponding to wind series 1

As regards to the use of a TMD on the top of the wind tower, as used in [6] [7] in an earlier comparison associated with a tall structure subjected to harmonic excitation in resonance with the fundamental frequency, the Figures 12 and 13 show such comparison of top displacements and accelerations of the given tall wind tower along the time, without and with TMD with mass ratio of 1 %. As can be seen in Figure 12 and 13, if the structure is acted upon by a harmonic action in resonance with fundamental frequency, the implementation of the TMD can considerably attenuate the response of the wind tower structure.

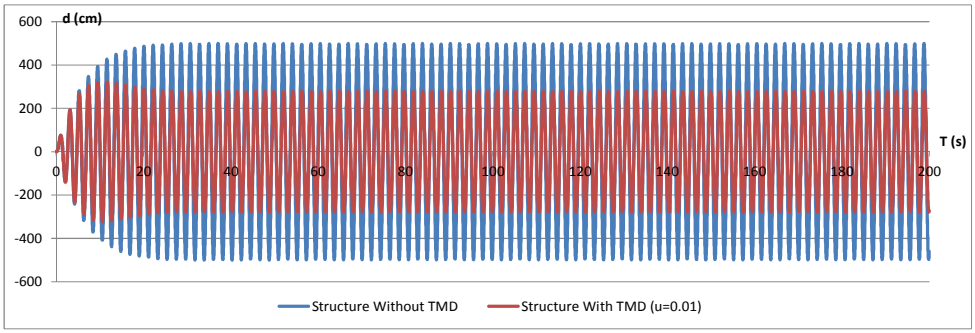


Figure 12: Top displacements, under a harmonic fundamental resonant excitation, without and with TMD

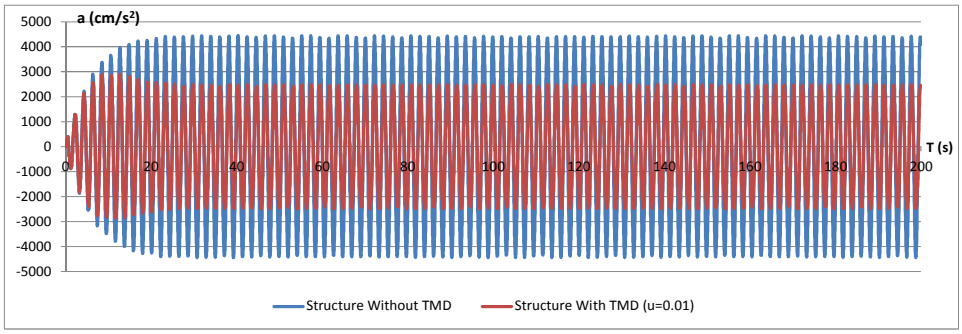


Figure 13: Top accelerations, under a harmonic fundamental resonant excitation, without and with TMD

Figure 14 and Figure 15 show the time variations of top acceleration and displacement of the wind tower, equipped with the TMD modeled before with a 1% mass ratio, for the wind loads evaluated using equation (7), with velocity fluctuations corresponding to wind series 1. Table 5 presents a summary of maximum values of top displacements and accelerations of the tower, for each of the time series. It also presents the average of such maximum values.

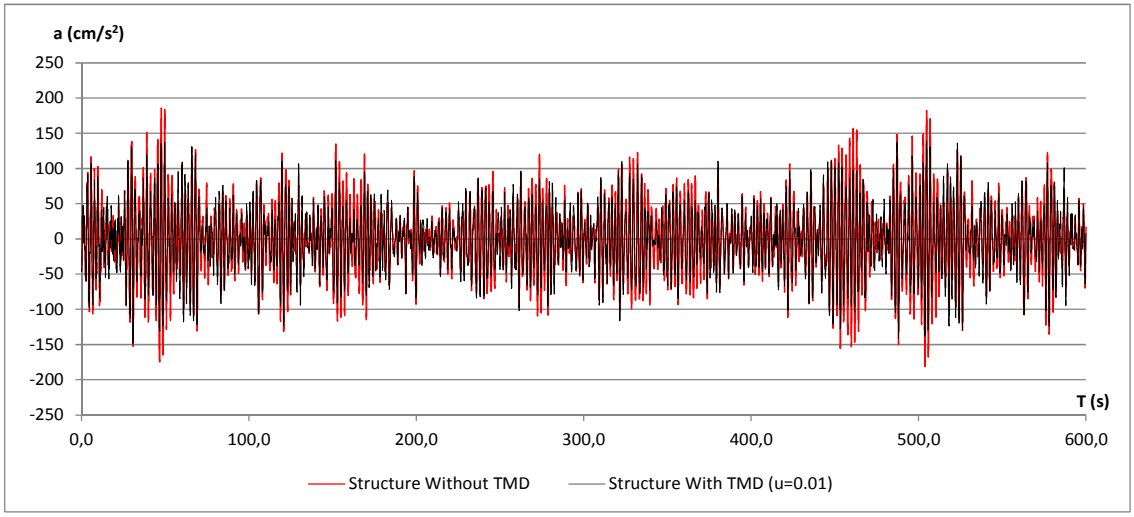


Figure 14: Acceleration on the top of tower, equipped with the TMD modeled with mass ratio of 1 % for the wind loads corresponding to wind series 1

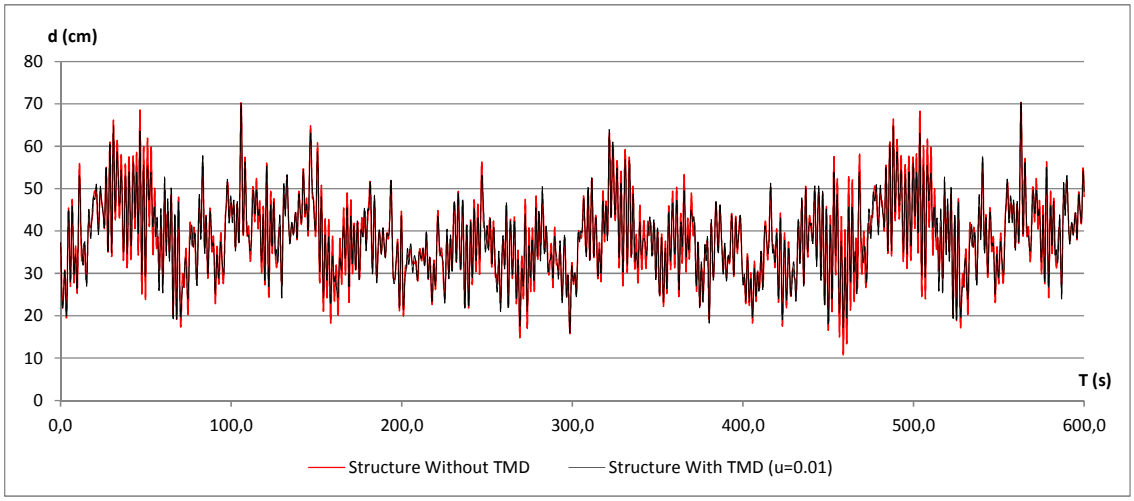


Figure 15: Displacement on the top of tower, equipped with the TMD modeled with mass ratio of 1 % for the wind loads corresponding to wind series 1

Series	1	2	3	4	Average
Maximum displacement (cm)	70,30	63,42	70,62	63,96	67,07
Maximum acceleration (cm/s^2)	139,35	151,72	156,57	180,69	157,08

Table 5: Maximum displacements and accelerations on node 3, for each of the wind time series (with TMD)

The efficiency on the use of the modeled TMD in the tower structure can be interpreted by the results of Table 6, here associated with a mass ratio of 1% : reduction of top maximum displacements and accelerations on the order of 1% and 18%, respectively.

	Structure without TMD	Structure with TMD (u=0.01)	Reduction (%) in relation to the structure without TMD
Maximum displacement (cm)	67,80	67,07	1 %
Maximum acceleration (cm/s^2)	191,47	157,08	18 %

Table 6: Efficiency of using the modeled top TMD for mass ratio of 1%

5 CONCLUSIONS

For modeling the dynamic wind action reference is made to a method of generating sets of synthetic wind – called the method of Shinozuka – and for which the number of discretization intervals to adopt is discussed; the greater the number of frequency intervals to adopt, the better the process, but with divisions over 1000 intervals results are already quite acceptable.

The simplified methodology adopted for the evaluation of the effects of the dynamic wind action, consisted of varying forces over time at each stiffening floor, following the same law of variation. This law is obtained, for each generated time series, from the Eurocode 1 wind power spectrum multiplied by the aerodynamic admittance function.

As regards to the implementation of the TMD in the tall wind tower structure under study, it was concluded that it proved to be very effective in terms of both top displacements and top accelerations, when the tower is subject to a harmonic action in resonance with fundamental frequency of vibration of the tower.

The application of this TMD passive device on top of the tower for vibration control of the designed wind tower, subjected to natural wind actions based on the generated wind series, is not as effective as for controlling harmonic resonant phenomena. With the implementation of the TMD it was concluded that this device is considerably more effective in controlling top accelerations (rather than top displacements), when the structure is subjected to the artificially generated natural wind. For the TMD modeled with the parameters calculated, were observed maximum accelerations reductions of the order of 18%, while the achieved reduction of maximum displacements was only of the order of 1%.

ACKNOWLEDGEMENTS

This work was co-participated by funds from the project “VHSSPOLES-Very High Strength Steel Poles” (Faculty of Engineering of the University of Porto, reference 21518) sponsored by the European Fund for Regional Development (FEDER) through COMPETE (Operational Program Competitiveness Factors - POFC). The Authors acknowledge herein the financial support and the opportunity to contribute to the development of the transmission towers testing site of Metalogalva (Trofa, Portugal).

REFERENCES

[1] J.R. Ferreira, F.R. Martins. *Ventos de mudança. A energia eólica em Portugal*. Centro de Estudos de Geografia e Planeamento Regional, Faculdade de Ciências Sociais e Humanas, Universidade Nova de Lisboa, Portugal, 2009.

[2] J.M. Henriques. *Projecto de torres eólicas reticuladas de grande altura (150m): Modelação e análise comparativa com estruturas tubulares auto-suportadas*. M.Sc. Thesis in Structural Engineering, Faculdade de Engenharia da Universidade do Porto (FEUP), Porto, Portugal, 2012.

[3] J. Henriques, R.C. Barros. *Design of Lattice Wind Towers and Comparison with the Typical Self-Supported Tubular Towers*. 4th International Conference on Integrity, Reliability & Failure, Funchal, 23-27 June, 2013 (*in-press*, to be published).

[4] M.K.S. Madugula (editor). *Dynamic Response of Lattice Towers and Guyed Masts*. Task Committee Report, Structural Engineering Institute, American Society of Civil Engineers (ASCE), Reston VA, 2002.

[5] C.L. Lee, Y.T. Chen, L.L. Chung, Y.P. Wang. *Optimal design theories and applications of tuned mass dampers*. Engineering Structures, 28 (1), 43-53, 2006.

[6] N.A.C. Ferreira. *Efeito do Vento em Edifícios Altos: aplicação a um caso concreto*. Dissertação de Mestrado (Especialização em Estruturas), Faculdade de Engenharia da Universidade do Porto (FEUP), Porto, Portugal, 2008.

[7] N.A.C. Ferreira, R.C. Barros, R. Delgado. *Comparisons of a tall building wind response with and without a TMD*. 3rd ECCOMAS Thematic Conference on Computational Methods in Structural Dynamics and Earthquake Engineering (COMPDYN 2011), Corfu, Greece, 25-28 May, 2011.

[8] EN 1993-3-1. *Eurocode 3: Design of steel structures - Part 3-1: Towers, masts and chimneys*. CEN, Brussels.2006

[9] EN 1991-1-4. *Eurocode 1: Actions on structures, general actions. Part 1-4: Wind actions*. CEN, Brussels, 2005.

[10] EN 1993-1-1. *Eurocode 3: Design of steel structures – Part 1-1: General rules and rules for buildings*. CEN, Brussels, 2005.

[11] J. Saraiva, F. Silva. *A Interacção do Vento com Grandes Estruturas*. Conferência Internacional sobre Métodos Computacionais em Engenharia, Lisbon, Portugal, 2004.

[12] A. Barbat, J. Canet. *Estructuras Sometidas a Acciones Sísmicas – Cálculo por Ordenador*. CIMNE, Barcelona, 1994.

[13] A. Iannuzzi, P. Spinelli. *Artificial Generation and Structural Response*. Journal of Structural Engineering, 113(12), 2382–2398, 1987.

[14] R.C. Barros. *Dimensionamento estrutural de mastros metálicos*. Revista Internacional de Métodos Numéricos para Cálculo y Diseño en Inginiería, pp: 351-365, Spain, 2002.

[15] B.J. Vickery, K.H. Kao. *Drag of Along-Wind Response of Slender Structures*. Journal of Structural Division, ASCE, 98, ST1, Proc. Paper 8635, 21-36, New York, 1972.

[16] J.D. Holmes. *Wind Loading of Structures*. Spon Press, London, 2001.

[17] S. Kelly. *Fundamentals of Mechanical Vibrations*, McGraw-Hill International Editions, Singapore, 1993.

[18] J.E. Barros, C. Moutinho, R.C. Barros. *Utilização de TMD's de Grandes Dimensões na Atenuação da Resposta Sísmica de Estruturas*, Sismica 2010 - 8º Congresso Nacional de Sismologia e Engenharia Sísmica, Universidade de Aveiro, Sociedade Portuguesa de Engenharia Sísmica, Portugal, 2010.

[19] J.E. Barros, C. Moutinho, R.C. Barros. *The use of TMD's with heavy mass to mitigate the seismic response of structures*. 3rd ECCOMAS Thematic Conference on Computational Methods in Structural Dynamics and Earthquake Engineering (COMPDYN 2011), Corfu, Greece, 25-28 May, 2011.

[20] K. Kwok, B. Samali. *Performance of tuned mass dampers under wind loads*. Engineering Structures, Vol. 17, Issue 9, pp. 655-667, Elsevier Science Ltd., Great Britain, 1995.

COMPDYN 2013
4th ECCOMAS Thematic Conference on
Computational Methods in Structural Dynamics and Earthquake Engineering
M. Papadrakakis, V. Papadopoulos, V. Plevris (eds.)
Kos Island, Greece, 12–14 June 2013

METHODS TO DESIGN A GUIDED TOWER CONCERNING DYNAMIC BEHAVIOUR

Cecília Mendonça[1] **and Rui Carneiro de Barros**[2]

[1] Faculdade de Engenharia da Universidade do Porto
Rua Dr. Roberto Frias, s/n 4200-465 Porto, Portugal
e-mail: ceciliamen@gmail.com

[2] Faculdade de Engenharia da Universidade do Porto
Rua Dr. Roberto Frias, s/n 4200-465 Porto, Portugal
e-mail: rcb@fe.up.pt

Keywords: Guyed tower, design, dynamic action, P-Δ effect, geometric non-linearity.

Abstract. *The work presented in this paper pretends to structure the main concepts associated with the design of a guyed tower. In this context, are presented the theoretical foundations and the essential steps for the various methods of analysis.*

This topic is therefore of major interest for Metalogalva (Trofa, Portugal), with which the authors collaborate and interact, since this industry complex of metallic constructions is also involved in the design and construction of tall telecommunication towers and pole structures.

Two dynamic actions are essential for the guyed tower design: The gust effect of wind and the action of earthquakes.

Therefore this paper presents various considerations and topics involved in the modeling of a 185 m height guyed tower, that enable to characterize their structural response. Since this is a slender structure it is was necessary to take into account the effects of second-order P-Δ analysis and also the nonlinear behavior of cables.

1 INTRODUCTION

Guyed towers are comprised of a very slender mast supported laterally by inclined and in tension cables, which are anchored in concrete foundations. This setting appears as an economical option to self-supporting towers. However, its behavior is generally nonlinear and therefore is complicated to study and describe. The simplifications made and the approximate models used in their design over the years, often unjustified, led to the collapse of many structures.

For the study of the dynamic behavior of the guyed tower it is really important to understand how it reacts to the wind and to an earthquake. Figure 1 shows typical normalized spectral densities of wind and earthquake actions, where average frequencies of concern for wind and earthquake actions are also emphasized. As described, these two dynamic actions excite quite differently any type of tall (and low) structures.

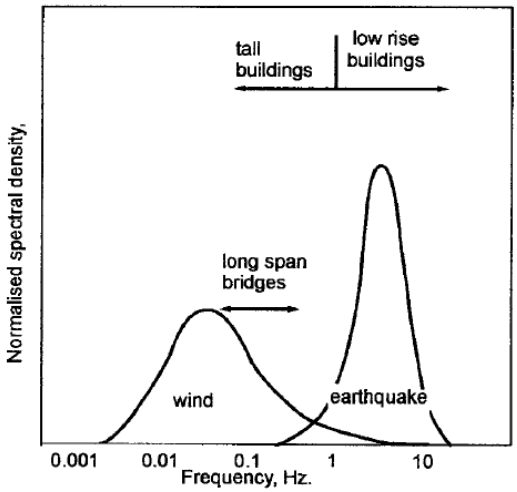


Figure 1: Dynamic excitation frequencies of structures by wind and earthquake. HOLMES [1]

The natural frequencies of truss structures are between 0,5 a 3 Hz. When the masts are very flexible it is essential to study the dynamic behaviour in the first mode response due wind action, as well as the contribution of the second degree P-Δ effect related to structural instability.

The resonant response of slender structures becomes important when the natural frequency of the structure is below 1 Hz as Carril [2]. Between the two dynamic actions considered for this study on guyed towers, the wind is generally the controlling design action in this kind of structures.

2 DYNAMIC ACTIONS

2.1 Wind

The wind speed varies with height and its variation in time varies with the type of ground where it is deployed. The wind action is represented by a simplified set of pressures or forces whose effects are equivalent to the effects of turbulent wind. Ferreira et al.[3]

The generalized forces of wind on the masts can be characterized by quasi-static and dynamic components. Both forces and the displacements associated depend primarily on the fundamental mode and frequency and its damping.

The quasi-static behavior and the time-varying behavior of these pole masts structures occurs along-the-wind (that is, in the direction of propagation of the wind) and is due to the addition of a constant wind pressure with a non-permanent gust pressure. The purely dynamic vibratory behavior of the pole-masts occurs in the transverse direction of propagation of wind (across-the-wind) and is due to the aerodynamic phenomenon of vortex shedding at the critical wind speed.

2.2. Standards

The reference standards used in the study of the behaviour of lattice towers (fixed or guyed) subjected to wind are the British Standard BS 8100 [4] American Standard ASCE [5] the German standard DIN 4131 [6] and European standard EN1991-1-4 [7].

The purely dynamic behaviour of masts occurs mainly in the transverse direction of the wind. Based on Annex E of the standard [7] and Barros[8]. One may check the elements of the structure to vortex shedding and ovalling.

The force applied to the model was obtained following the steps described in [7].

The characteristic values of the wind actions calculated in EN 1991-1-4 present an annual probability of being exceeded (2%) equivalent to an average recurrence period of 50 years. The purely dynamic behavior of masts occurs mainly in the transverse direction of the wind (across-the-wind).

The mast structure under analysis and design verifications is a 185 m height tall guyed tower, with structure and cables layout detailed in Fig. 2, located in Lisbon area of soil type D Mendonça, C.[9]

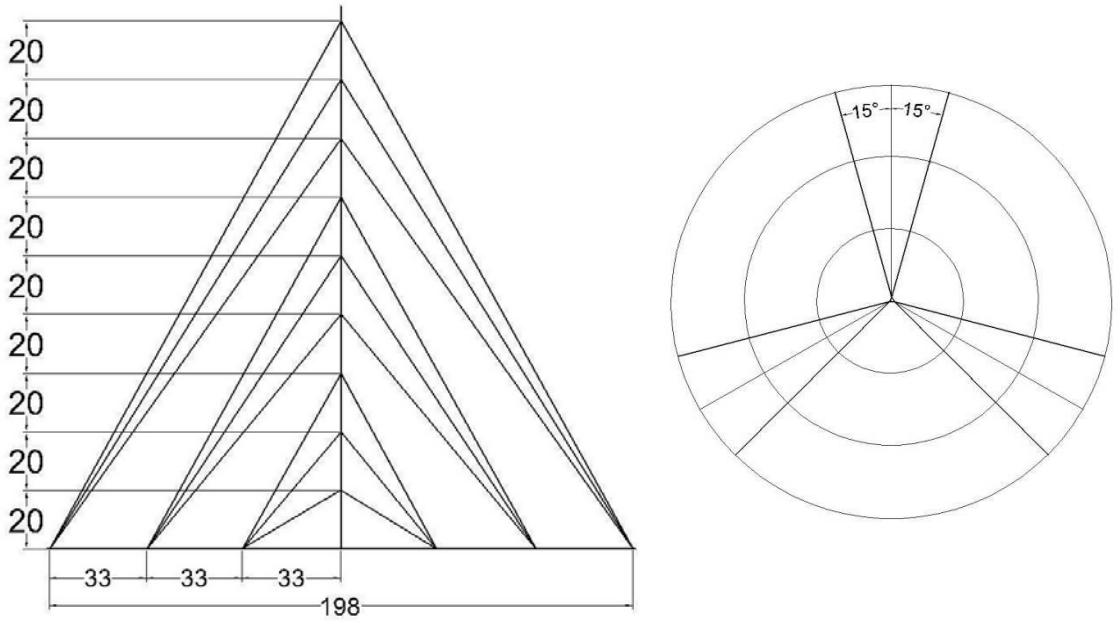


Fig. 2 – Layout (elevation and plan) of the guyed tower 185 m height

Based on Annex E of EN 1991-1-4, equation (1) and on details in [7], it is possible to evaluate the forces acting on a specific guyed tower model (Fig. 3) and access the mast structural response to vortex shedding as well as ovalization, Zar and Chu[10].

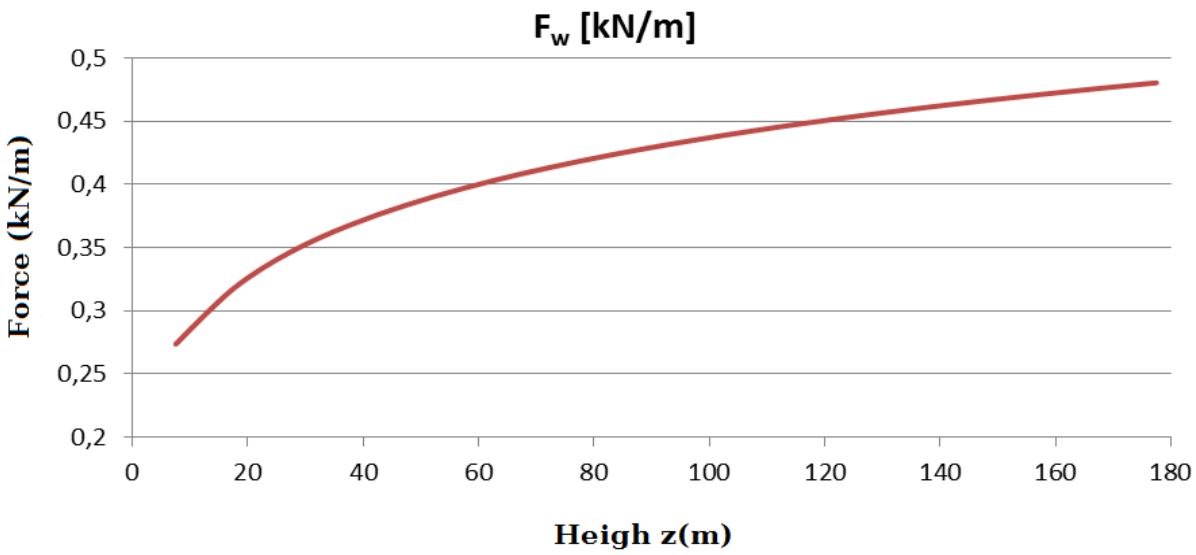


Fig. 3 – Force of the wind o the 185 m guyed tower mast (kN/m)

2.2 Earthquakes

2.2.1. Spectral Analyses

According to Chopra [11] when analyzing the response of a general structure to seismic action, the equation of motion of the multi-degree-of-freedom structure is:

$$m\,\ddot{u}_{total} + c\,\dot{u} + k\,u = 0 \tag{1}$$

Where m is the mass, c is damping, u is the displacement and k is the stiffness of the structure. The total displacement $u_{total} = u^t$ is equal to the displacement of soil $u_g(t)$, plus the relative displacement of the structure u(t).

$$u^t = u + u_g \tag{2}$$

The seismic movement only causes a dynamic response because the inertia forces depend on the total displacement of the structure (in fact they are expressed in terms of the total acceleration), while the elastic forces and damping depend only on the relative motion.

$$m\ddot{u}^t + c\dot{u} + ku = 0 \leftrightarrow m\left(\ddot{u} + \ddot{u}_g\right) + c\dot{u} + ku = 0 \leftrightarrow m\ddot{u} + c\dot{u} + ku = -m\ddot{u}_g \tag{3}$$

From equation (3), it may be inferred that the structure is acted upon by the seismic force that is defined as $F(t) = m\,\ddot{u}_g(t)$.

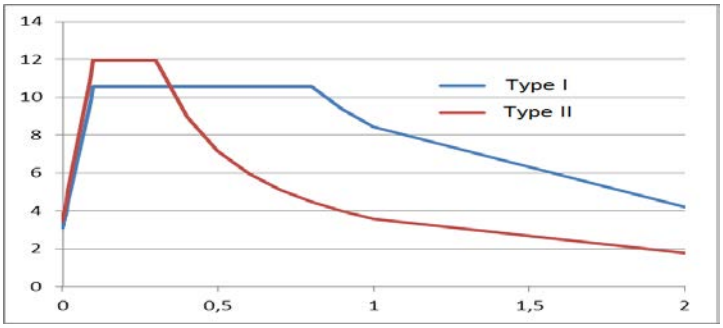


Fig. 4 – Acceleration response spectra for ξ =0.05 (Lisbon area, soil type D)

To design the structure to seismic action two norms were used: the Portuguese regulation RSA [12] and Eurocode 8.[13,14]

2.2.2 Time domain analysis for a given earthquake

The use of a time domain analysis is interesting since it allows the input of scaled ground accelerations based upon time-histories of several earthquakes (recorded or synthetically generated). Since earthquakes occur with different frequencies, it is possible that a given earthquake has the ability to excite a given structure much more than others.

When using the information of past recorded earthquakes of certain frequency content, these accelerations can be applied at the structure ground-site after normalizing the information of these earthquakes by the PGA (Peak Ground Acceleration) at the site; the later is associated with a certain recurrence period and statistical distribution of earthquakes.

The time histories and associated data of earthquakes used in the time domain analyses of the guyed tower were taken from the site of the Pacific Earthquake Engineering Research Center , PEERC [15]. The present design study used data from four earthquakes: Çaldiran (Turkey, 1976), Loma Prieta (USA, 1989), Kobe (Japan, 1995) and Chi-Chi (Taiwan, 1999). It is also noticeable that the frequency band of these earthquakes is mainly 1 Hz to 10 Hz (Fig. 6).

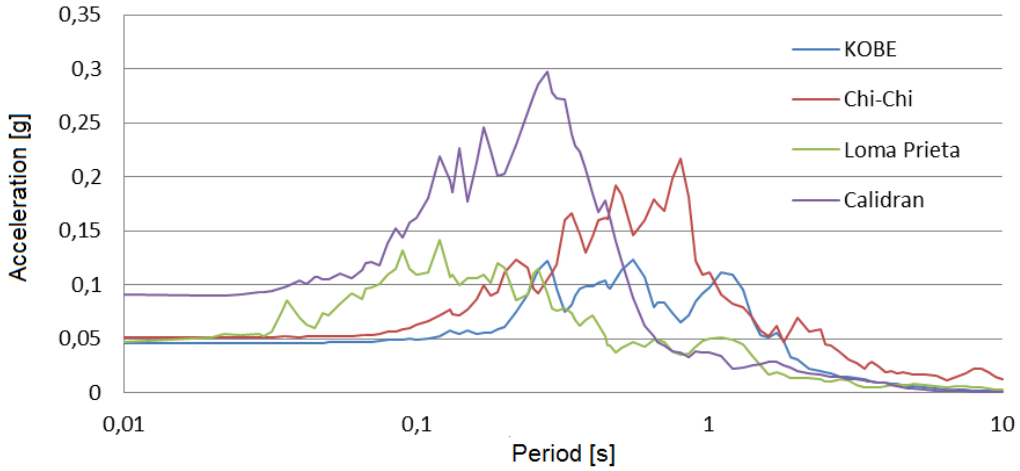


Fig. 5 – Band of frequencies of the four earthquakes

3 MODELING

As a first approach to the design of a guyed tower, Gantes [16] suggest a simplified equivalent beam model with springs to simulate the cables that constitute an interesting initial assessment. It should be used to frame the initial structural characteristics of the guyed tower so that it is possible to model it in any finite element program.

3.1 Requirements

The guyed towers designed for telecommunication have to meet service requirements of the telecommunication devices themselves, since a slight misalignment of the satellites may result in loss of signal, which may lead to poor quality of service for thousands of customers.

Section 3.8.2 of the American standard TIA 222 [17,18] specifies a maximum horizontal displacement of 3% of the height of the guyed tower structure; wherefore for lattice structures the limiting value of the horizontal displacement is only 1.5% of the tower height.

TIA 222 also specifies a maximum value for the rotation of the antennas of 4º 00' 00", which is also the limit imposed by Telebrás for VHF antennas. When it comes to broadcasting on UHF antennas Telebrás is more restrictive and imposes a maximum rotation of 1º 40' 00".

3.2 Mast

The analysis of more traditional tower masts proposes the modeling as a simple truss structure. As the links are not rigid, the structure appears more flexible than it actually is. To partially solve this problem, it resorts to the use of dummy bars. These prevent the occurrence of undesired degrees of freedom leading to the occurrence of mechanisms. The use of these bars, with very little axial stiffness, allows the structure to be stable nevertheless flexible and therefore enables analyses of the tower under design study using some software based upon the finite element method. Many manufacturers still rely on full-scale tests to verify that the results are as expected using a simpler truss model for design of the guyed tower.

Oliveira et al. [19] proposes a less conservative analysis method which combines three-dimensional framed members with horizontal and diagonal lattice members, so it is not necessary to use dummy bars. It constitutes a better and more real approximation of the structural behavior.

3.3 Cables

The cables were modeled by existing cable element in SAP 2000 v15 [20]. The program models the cable as a catenary to represent the elastic behavior of a cable subjected to its own weight. Its behavior is nonlinear and takes into account the P-Δ effects as large displacements and large deformations are accounted for.

A cable without tension is not stable and has not an unique position, so all cables should be loaded. The Canadian standard CSA S37-01 [21] requires that the values of the initial tension in the cables should be between 8% and 15% of the final cable capacity.

The environmental temperature and the applied loads (namely due to wind and earthquake) can change the cable length. The effect of these changes is similar to changes of length of the undeformed cable with the exception that there is no change in self-weight.

An alternative model that can be programmed for the dynamic study of the cables was given by Desai and Punde [22] which obtained values very close to the analytical values available, and is very quick to apply. Also Bertero [23] and Naguib and El-Saad [24] state that one can not disregard the initial deflection, or the pressure exerted by the wind on the cable itself, which otherwise would reach different values in the order of 10% to 15%.

Menin [25] also used the initial tension as 10% of the ultimate stress, designing the guyed tower from such hypothesis. As expected, and also as it can be seen by the results obtained by Naguib and El-Saad [24], the higher the value of the initial tension employed in the cables, the smaller the tower displacements would generally be. Naguib and El-Saad [24] program allows initial tensions up to 40% of the ultimate strength, which is beyond the control parameters adopted in this work and taken from the Canadian standard CSA S37-01 [21]. In this design study it was used an initial tension close to 10% of the ultimate stress. But if it would be needed an expeditious manner, without recourse to a FEM software or specific program, the one proposed by Bertero [23] is advised.

3.4 Load Cases Combinations

The combinations used for the verification of the stress in the guyed tower structure were:

$$\begin{cases} Q1: \ S = (1.35 \ ou \ 1) \times G + 1.5 \times Q_1 + 0.9 \times Q_2 \\ Q2: \ S = (1.35 \ ou \ 1) \times G + 0.9 \times Q_1 + 1.5 \times Q_2 \\ CA: \ S = G + F_{acidental} + 0.4 \times (Q_1 + Q_2) \end{cases} \quad (4)$$

Where Q1 is a variable action based on wind overload, Q2 is the variable action based on temperature variation and CA is the accidental combination.

4 ULTIMATE LIMIT STATES VERIFICATIONS

For a structure the ultimate limit states that need to be considered are: loss of static equilibrium, internal failure of the structure, excessive deformation of the ground and fatigue. In a steel structure as the guyed tower the limit state referring to internal failure involves the resistance of cross sections, the resistance of the structure to instability.

The recommended values in EC3 for the partial safety factors are the following:

$$\gamma_{M0} = 1.00, \gamma_{M1} = 1.00, \gamma_{M2} = 1.25$$

The resistance of cross sections depends on the class of the section. The verification made using the elastic resistance is valid for all classes of sections, although for class 4 only the effective area is taken into account. For classes 1 and 2 the use of the plastic resistance is advisable, so that the solution achieved is economical.

4.1 Axial Force

Replacing the axial force N of expression (5) for the maximal axial force $N_{máx}$ obtained from the load combinations one gets the minimal area needed Amin to support those actions.

$$A_{min} = \frac{N}{f_y} \quad (5)$$

4.2 Bending Moment

Replacing the bending moment M of expression (6) for the maximal bending moment $M_{máx}$ obtained from the load combinations, one gets $W_{pl,min}$ so that the section verifies for those actions.

$$W_{pl,y-min} = \frac{M}{f_y} \quad (6)$$

4.3 Bending Moment and Axial Force interaction

$$\frac{M_y}{M_{pl,y}} + \left(\frac{N}{N_{pl}}\right)^2 = 1 \quad (7)$$

4.4 Bending Moment and Shear Force interaction

$$V_{pl,rd} = \frac{A_{vz}}{\gamma_{M0}} \frac{f_y}{\sqrt{3}} \quad (8)$$

4.5 Asymmetrical bending

$$\left[\frac{M_{y,sd}}{M_{pl,y,rd}}\right]^{\alpha} + \left[\frac{M_{z,sd}}{M_{pl,z,rd}}\right]^{\beta} \leq 1 \quad (9)$$

4.6 Buckling effect

Guyed Towers are a very slender structure so it's very important to avoid the loss of stiffness in the structure when it is subjected to high compressive stresses. This effect, known as tower global buckling leads to sudden failure of the structure by progressive and excessive lateral deformations.

Guyed towers are very slender structures, so it is very important to avoid the loss of stiffness in the structure when it is subjected to high compressive stresses. This effect, known as (tower global) buckling, leads to sudden failure of the structure The evaluation of all the Euler critical loads of each individual structural member (member buckling) is not a good approach to access the buckling capacity of the tower, when trying to describe what happens with more complex structures instead than the behavior a single column. The critical load of the guyed tower – Ncr – can be determined by a series of tests, simulating the degradation of the stiffness of the tower mast.

It is known that the general equilibrium equation of a structure analyzed by the displacement method is $F = F_0 + K_T D$ where K_T is the total stiffness (elastic stiffness, geometric stiffness contribution – positive for tensile members, negative for compressed members – and decrease in stiffness due to material non-linearity). In the vicinity of a previous state of stable equilibrium, the incremental equilibrium insures that:

$$\Delta F = K_T \, \Delta D \qquad \Rightarrow \qquad K_T = \Delta F / \Delta D \tag{5}$$

Generalizing this tangent total stiffness concept to the tower structure, and labeling Fx as a disturbing horizontal load applied on the top of the tower mast and dx as the tower resulting horizontal displacement in the same point, then the ratio Fx/dx is an index or a measure of the transversal stiffness of the tower mast for each axial compressive load N applied to the mast.

A total of 15 individual computational load tests were performed in the tower model, with different vertical and horizontal forces, and the corresponding top lateral displacements were evaluated by tower structural analyses. A linear regression on the computational results obtained permits to determine computationally when the stiffness of the structure would vanish; in fact:

$$\frac{F_x}{d_x} \approx a\,\lambda + b \; = 0 \quad \rightarrow \quad \lambda = -\frac{b}{a} \tag{6}$$

where λ is the buckling load factor insuring null total stiffness of the tower at the onset of elastic instability.

5 RESULTS

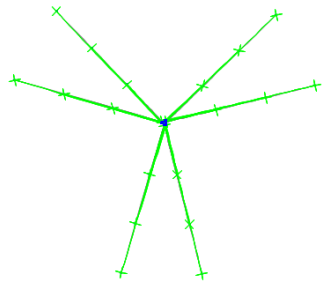
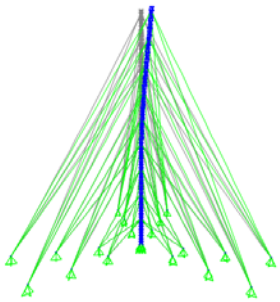
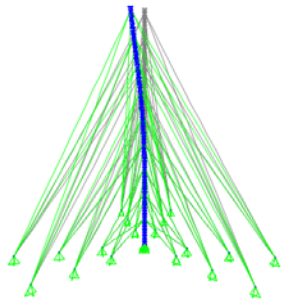
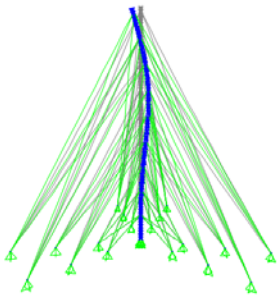
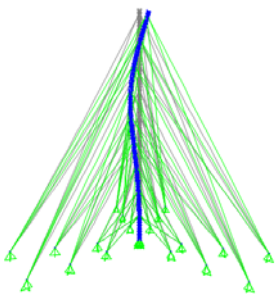
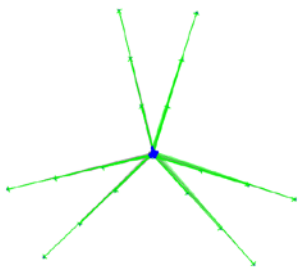
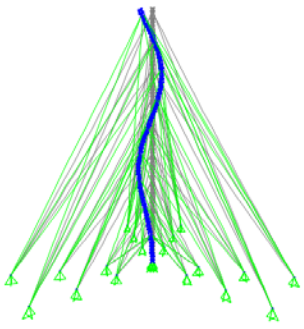
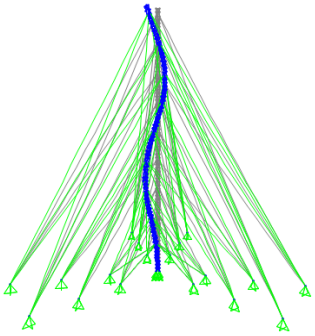
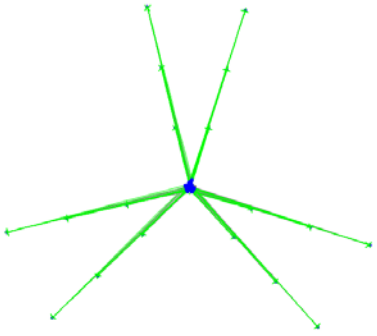
5.1 Natural vibration frequencies and vibrations modes

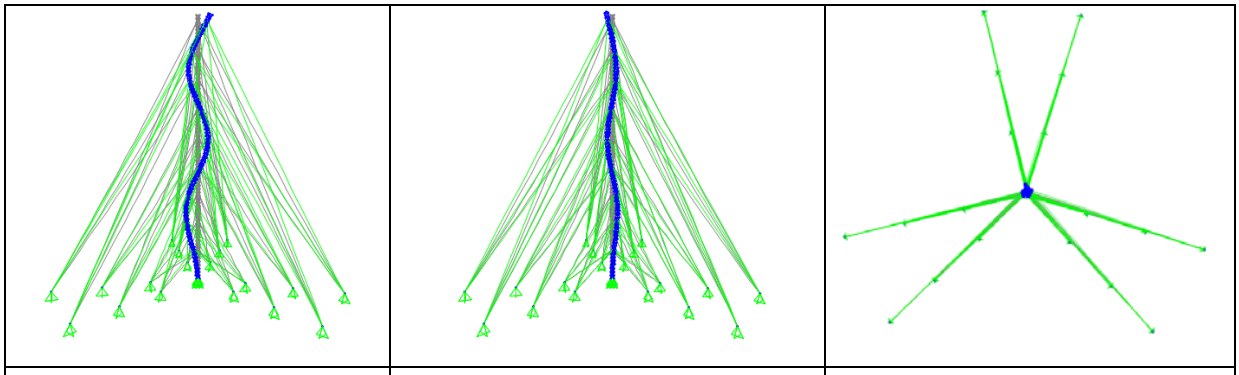
The analyses of the natural vibration frequencies and mode shapes are very important for understanding the dynamic behavior of the structure, as well as for evaluating the effective modal masses and the percentage of these needed to access the response with desired accuracy. Even though the first mode of the 185 m height guyed tower under analysis has a very low frequency (0.625 Hz), it has almost no mass associated with that torsion mode. So it is expected that the next two natural frequencies of the guyed tower (2nd and 3rd, equal by sym-

metry) of 1st (and 2nd) longitudinal bending mode along 2 perpendicular directions, would have significant effective modal masses vibrating close to 1 Hz natural frequencies.

Table 1 indicates the values and shapes of the natural frequencies (Hz) and vibration mode shapes of the considered design case study of the guyed tower.

Table 1 – Vibration frequencies and mode shapes

		
mode 1 – Torsion - f=0.625 Hz	mode 2 - f=1.011 Hz	mode 3 - Perpendicular to 2 - f=1.011 Hz
		
mode 4 - f=1.358 Hz	mode 5 – Perpendicular to 4 - f=1.358 Hz	mode 6 – Torsion - f=1.498 Hz
		
mode 7 - f=1.983 Hz	mode 8 – Perpendicular to 7 - f=1.983 Hz	mode 9 – Torsion - f=2.379 Hz



mode 10 - f=2.840 Hz	mode 11 – Perpendicular to 10 - f=2.840 Hz	mode 12 – Torsion - f=3.261 Hz

5.2 Load Cases Combinations

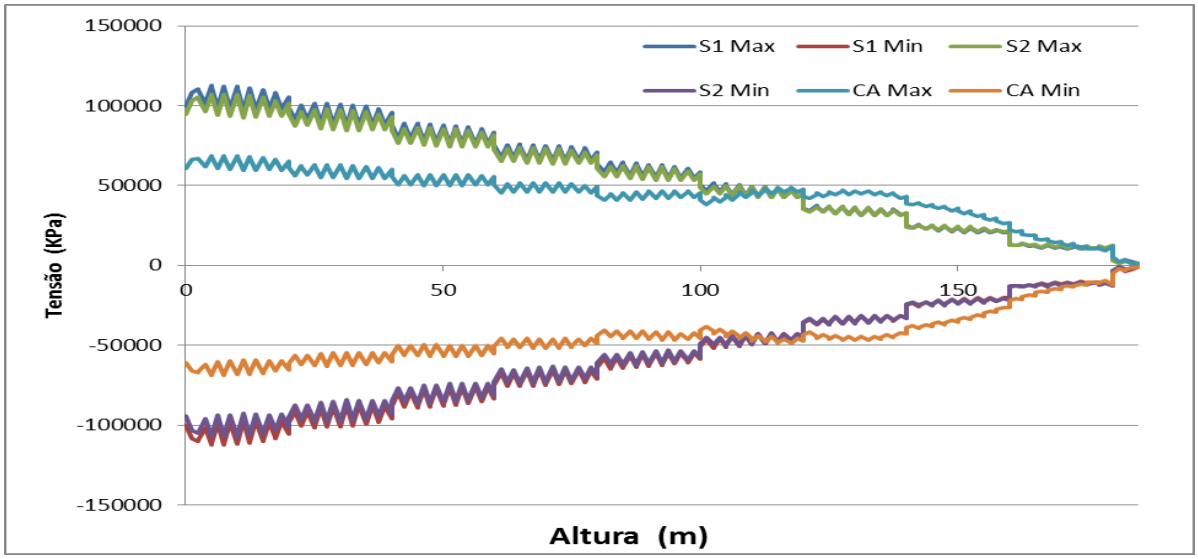


Fig. 6 – Load case combinations

One can see from this analysis that the most onerous load case combination is that of accidental earthquake load using spectrum given by Eurocode 8 for earthquake type 1; followed by the case of earthquake type 2. The load case S1 appears in 3rd place.

However when individually examined (without load combinations) the wind load would undoubtedly be more demanding for the structure than the earthquake load alone.

5.3 Overall Global Buckling

The 15 load cases applied and the displacements resulting from such load disturbances are detailed in Table 5. As it can be seen, the stiffness index F_x/d_x is getting closer and closer to zero. It can never hit zero, since the analysis program would return an error for having become unstable.

From a linear regression on the computational data (Fig. 8) the following equation is obtained:

$$\frac{Fx}{dx} = -12.789\lambda + 75.618 \quad (7)$$

For vanishing stiffness $F_x/d_x \rightarrow 0$, from which λ_{cr} = 75.618 / 12.789 = 5.912738 .

Multiplying the initial axial force (for axial load factor λ=1) by λ_{cr} , the value of N_{cr} would be:

$$N_{cr} = 5.912738 \times 600 \text{ kN} = 3547.643 \text{ kN} \quad (8)$$

Table 5 – Determination of N_{cr} of the guyed tower

	1 Column		3 Columns				
Load Case	F_x'	P'	F_x	P	d_x	F_x/d_x	λ
-	kN	kN	kN	kN	M	kN/m	-
1	4	200	12	600	0,1952	61,48	1,00
2	2	200	6	600	0,0945	63,49	1,33
3	4	250	12	750	0,2139	56,10	1,67
4	4	270	12	810	0,2223	53,98	1,80
5	4	300	6	900	0,2361	25,41	2,00
6	2	300	6	900	0,1145	52,40	2,00
7	4	350	12	1050	0,263	45,63	2,33
8	4	400	12	1200	0,1903	63,06	2,67
9	2	400	6	1200	0,1441	41,64	2,67
10	4	500	12	1500	0,3883	30,90	3,33
11	4	600	12	1800	0,5434	22,08	4,00
12	4	700	12	2100	0,8306	14,45	4,67
13	4	800	12	2400	1,5091	7,95	5,33
14	2	800	6	2400	0,9853	6,09	5,33
15	4	820	12	2460	1,8657	6,43	5,47

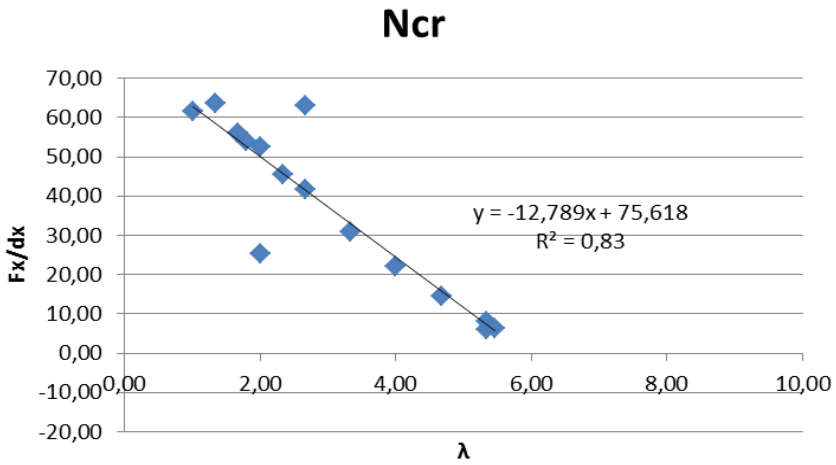


Fig.7 – Determination of N_{cr} through linear regression of stiffness indexes from a numerical simulation

6 CONCLUSIONS

Some relevant concepts and steps to design tall guyed towers were addressed, particularly those related to wind and seismic actions. The wind pressures were evaluated according to Eurocode 1 (EN 1991-1-4). The seismic actions were evaluated using RSA and also by Eurocode 8 (EN 1998-1-1 , EN 1998-6); for the design study case of the guyed tower mast, the seismic actions evaluated by EC8 are more severe than those evaluated by RSA, or even those evaluated by a time domain analysis of four historic earthquake records scaled by the PGA at the site (Lisbon area). The natural vibration frequencies and mode shapes were obtained using SAP 2000 v15. The ultimate limit states verifications were address. A general methodology for calculating the tower mast buckling load, also applicable to general complex structures, is applied.

ACKNOWLEDGMENTS

This work was co-participated by funds from the project “VHSSPOLES-Very High Strength Steel Poles” (Faculty of Engineering of the University of Porto, reference 21518) sponsored by the European Fund for Regional Development (FEDER) through COMPETE (Operational Program Competitiveness Factors - POFC). The Authors acknowledge the financial support and the opportunity to contribute to the development of the transmission towers testing site of Metalogalva (Trofa, Portugal).

REFERENCES

[1] Holmes, J.D. – *Wind Loading of Structures*. Spon Press, Taylor & Francis Group, 2001.

[2] Carril JR., C. Análise Numérica e experimental do efeito dinâmico do vento em torres metálicas treliçadas para telecomunicaçõess. Dissertação de Doutoramento, Escola Politécnica da Universidade de São Paulo, 2000.

[3] Ferreira, N.A., Barros, R.C., Delgado, R. – Comparisons of a tall building wind response with and without a TMD. 3rd International Conf on Computational Methods in Structural Dynamics and Earthquake Engng (CompDyn 2011: # 654), Corfu, 2011.

[4] BS 8100-3 – Lattice towers and masts. Code of practice for strength assessment of members of lattice towers and masts. British Standards Institute, London, 1999.

[5] ASCE Standard – Guide for the Dynamic Response of Lattice Towers. American Society of Civil Engineers, New York, 2000.

[6] DIN V 4131 – Steel Radio Towers and Masts. German Standard, 2008.

[7] EN 1991-1-4 – Ações em estruturas: Ações gerais – Ações do vento. LNEC, Lisboa, 2010.

[8] Barros, R. – Dimensionamento estrutural de mastros metálicos. Revista Internacional de Métodos Numéricos para Cálculo y Diseño en Inginiería, pp: 351-365, Spain, 2002.

[9] Mendonça, C.M.A. – Dimensionamento de torres espiadas de grande altura. Dissertação de Mestrado Integrado em Engenharia Civil, Faculdade de Engenharia da Universidade do Porto (FEUP), Porto, 2012.

[10] Zar, M. e Chu, S. – Chimneys. In: E.H. Gaylord and C. N. Gaylord, Structural Engineering Handbook. McGraw-Hill Book Company, New York, 1979.

[11] Chopra, A. – Dynamics of Structures: Theory and applications to Earthquake Engineering. Pearson Education Inc., New Jersey, 2007.

[12] RSA – Regulamento de Segurança e Ações para Estruturas de Edifícios e Pontes, Diário da Républica, 1ª Série nº 125, p. 1991, INCM, Lisboa, 1983.

[13] EN 1998-1-1 – Projecto de estruturas para resistência aos sismos – Parte 1: Regras gerais, acções sismicas e regras para edifícios. Eurocódigo 8, Norma Europeia, Bruxelas, 2010.

[14] EN 1998-6 – Design provisions for earthquake resistance of structures – Part 6: Towers, masts and chimneys. Eurocode 8, European Norm, Brussels, 2003.

[15] PEERC - Pacific Earthquake Engineering Research Center. Ground motion database, http://peer.berkeley.edu/peer_ground_motion_database , 2012.

[16] Gantes, C., Khoury, R., Connor, J.J., Pouangare, C. – *Modeling Loading and Preliminary Design Considerations* for *Tall Guyed Towers*. Computers and Structures, Vol. 49, No 5, pp: 797-805, 1993.

[17] TIA 222-F – Structural Standards for Steel Antenna Towers and Antenna Supporting Structures. Telecommunications Industry Association, American National Standard, Arlington VA, 1996.

[18] TIA 222-G – Structural Standard for Antenna: Supporting Structures and Antennas. Telecommunications Industry Association, American National Standard, Arlington VA, 2006.

[19] Oliveira, M.I.R., Silva, J.G.S., Vellasco, P.C.G.S., Andrade, S.A.L., Lima, L.R.O. – Structural Analysis of Guyed Steel Telecommunication Towers for Radio Antenna, Journal of the Brazilian Society of Mechanical Sciences and Engineering, Vol XXIX, nº 2, pp: 185-195, Rio de Janeiro, 2007.

[20] SAP 2000 v15 – Integrated Software for Structural Analysis & Design. Computers & Structures Inc. (CSI), http://www.comp-engineering.com/products/SAP2000/sap2000.html Berkeley CA, 2012.

[21] CSA S37-01 – Antennas, towers and antenna-supporting structures. CSA Group, 2011.

[22] Desai, Y.M., Punde, S. – Simple model for dynamic analysis of cable supported structures. Engineering Structures, 23, pp: 271-279. Elsevier Science, Mumbai, 2001.

[23] Bertero, V – Amplification of stress and displacement in guyed towers. Journal of the Structural Division, ASCE, Vol 85 nº ST5, pp: 89-101, 1959.

[24] Naguib, M., El-Saad, A. – Effect of Initial Sag and Tension in Cables on Outcome Responses in Cable Structures. 2006

[25] Menin, R. – Análise Estática e Dinâmica de torres metálicas estaiadas. Dissertação de Mestrado, Faculdade de Tecnologia – Universidade de Brasília, 2002.

COMPDYN 2013
4th ECCOMAS Thematic Conference on
Computational Methods in Structural Dynamics and Earthquake Engineering
M. Papadrakakis, V. Papadopoulos, V. Plevris (eds.)
Kos Island, Greece, 12–14 June 2013

EFFICIENT CALCULATION OF THE RESPONSE OF A STRUCTURAL ACOUSTIC SYSTEM UNDER AERODYNAMIC EXCITATIONS

D. Chronopoulos[1,2], M. Ichchou[2], and B. Troclet[1]

[1]EADS Astrium ST
66 Route de Verneuil, BP3002, 78133 Les Mureaux Cedex, France
e-mail: chronopoulos.dimitri@gmail.com

[2] Ecole Centrale de Lyon
36 Avenue Guy de Collongue, 69134 Ecully Cedex, France

Keywords: Fluid-structure interaction, Composite structures, Krylov-subspace methods, Random excitations

Abstract. *The problem of the dynamic response of a structural-acoustic system in the mid-frequency range is hereby considered. The system is initially modelled using finite elements, and is subsequently reduced using the Second Order Arnoldi Reduction method (SOAR) resulting in radical reduction of calculation times. The fully coupled system is modelled using a Statistical Energy Analysis like (SEA-like) approach, and the energetic characteristics for each subsystem are computed and compared to the direct FEM solution. The error with respect to the full FE solution is presented and the limits of the reliability of the reduction are explored. The loading applied to the model comprises typical random aeroacoustic excitations, such as a diffused sound field and a Turbulent Boundary Layer (TBL) excitation.*

1 INTRODUCTION

Structural acoustic interactions in a broadband frequency range are a regular problem in modern aerospace and automotive industry. The level of noise induced by structural vibration in a cavity has to be predicted, in order to optimize the acoustic transparency of a system, such as a payload cavity of a launch vehicle, or a passenger cavity for a car. The structural loading usually includes random, distributed excitations, such as diffused acoustic fields and aerodynamic excitations. The structures are often made of composite non-isotropic materials, complicating the modelling of the structural response. Moreover, the size of the cavities is often too large, which makes deterministic techniques such as Finite Elements (FE) excessively expensive in terms of computational time at higher frequencies [1]. Statistical methods such as Statistical Energy Analysis (SEA) are often considered more suitable for the medium frequency range but have limited accuracy, particularly when the modal overlap of the system is low [2]. It is therefore a vital task, the development of a robust approach for the calculation of the response of large systems, in that range where deterministic methods are too costly and statistical methods too inaccurate.

Numerous authors have investigated the fluid-structure interaction in the broadband frequency domain. In the low-frequency range, the system is typically modelled using FE or Boundary Elements (BE) as in [3]. A Component Mode Synthesis (CMS) was used in [4] in order to predict the low-frequency one-dimension fluid-structure interaction. The authors in [5] gave an energetic description of a panel-cavity coupled system in the mid-frequency range, by considering the modes of each uncoupled subsystem. The work was extended by Rochambeau et al. using an SEA-like approach in [6], in order to give an accurate description of the fluid-structure interaction problem in the mid-frequency range. The method was initially introduced and studied by the authors in [2, 7, 8, 9]. The impact of the strength of coupling between the structure and the fluid on the accuracy of the prediction is investigated in [6]. Strong coupling means that taking into account for the uncoupled modes of the subsystems will lead to inaccurate results especially for the low frequency range. Furthermore the assumption of analytical expressions of the modal data of the subsystems used in [6] restricts the applicability of the method to rectangular thin isotropic structures and rectangular cavities.

In order to reduce the computational effort required to resolve a structural-acoustic system, several reduction methods have been introduced. Modal reduction techniques have been successfully applied in [6, 10, 11], but they usually require analytical expressions of the modal data of the subsystems which are not always available (e.g for composite structures of arbitrary geometry). Recently, the moment matching approaches for the reduction of large scale second order systems have received much attention [12, 13, 14, 15]. The method consists in finding a reduced Krylov subspace to project the initial system and was successfully applied to a fully coupled structural-acoustic system in the low-frequency range in [15]. Bai and Su in [16] introduced the second-order Krylov subspace and the Second Order Arnoldi procedure (SOAR) in order for the reduced system to maintain the second order form of the initial one.

The modelling of pragmatic aerodynamic loads have been a long-term challenge. The author in [17] presented one of the first models for a Turbulent Boundary Layer (TBL) excitation. Other models derived from Corcos expression were then suggested by Chase and Efimstov in order to improve the predictions for the low-frequency range [18, 19]. In order for such loads to be integrated in an SEA type method, δ-correlated equivalent expressions for the excitations are required. Maidanik was the first to give such an expression, with the spatial-extent approach in [20]. Recently, equivalent approaches were suggested based on a wavenumber expression of

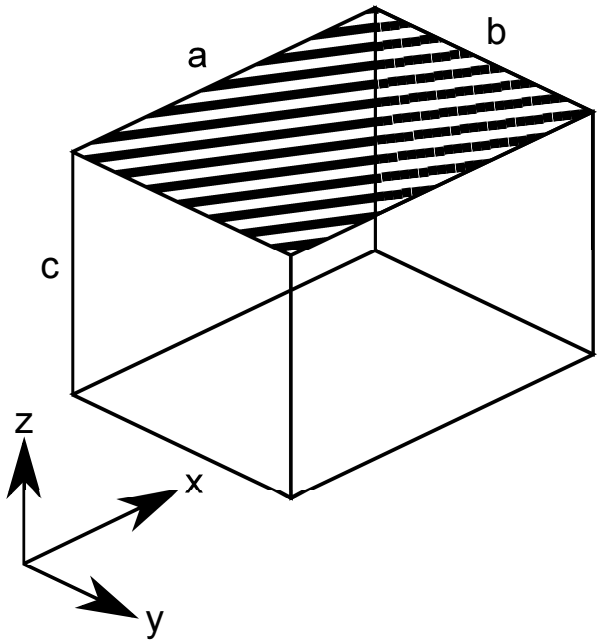


Figure 1: View of the modelled configuration

the excitation. The author in [21] modelled a TBL excitation using an asymptotic approach for the wavenumber transform of the spatial coherence function. In [22], the authors applied the equivalent δ-correlated excitation method on a rectangular panel and proposed an equivalent model for a TBL excitation.

In this work the use of a second order moment matching method in order to reduce a fully coupled structural-acoustic system, subject to realistic aerodynamic distributed excitations in a broadband frequency range is presented. An expression for the TBL equivalent coherence function when applied on an orthotropic plate is also given. The approach proves to be generic and robust. It drastically reduces the computation times. Moreover the advantages of an FE modelling are maintained. This implies that the system can be of arbitrary geometry and the structure can be made of composite nature. The coupling between the subsystems can also be of arbitrary nature.

2 Modelling a structural-acoustic system with a hybrid FE/SEA method

A vibroacoustic system as the one presented in fig.1 is to be modelled. In the mid-frequency domain FE modelling becomes greatly costly in terms of computational times. On the other hand, the conditions for forming a proper SEA matrix are not always satisfied, mainly because of the fact that the weak coupling condition between the subsystems is not satisfied and because of the indirect coupling between substructures that cannot be neglected. Moreover, in the mid-frequency range the intrinsic damping of the substructures has a great role on energetic transfer between them. Consequently, damping cannot be separated from the Coupling Loss Factors (CLF), as it is in SEA equations.

The Energy Influence Coefficient (EIC) method was presented in [23]. As in SEA, the system is discretized in distinct n interconnected subsystems. Assuming that the loads applied to different subsystems are uncorrelated, and that the loads applied to each subsystem are δ-correlated, the column matrix of subsystems kinetic energies can be written as the product of the EIC matrix with the matrix of Power Spectral Densities (PSD) of the loads applied to the subsystems:

$$\left\{ \begin{array}{c} E_1 \\ E_2 \\ ... \\ E_n \end{array} \right\} = \left[\begin{array}{cccc} A_{11} & A_{12} & ... & A_{1n} \\ A_{21} & A_{22} & ... & A_{2n} \\ ... & ... & ... & ... \\ A_{n1} & A_{n2} & ... & A_{nn} \end{array} \right] \left\{ \begin{array}{c} P_1 \\ P_2 \\ ... \\ P_n \end{array} \right\} \tag{1}$$

The SEA-like method used in [7, 8, 9], is very similar to the EIC method, with the sole difference being that the kinetic energy of the subsystems is replaced by their total energy. By exciting the subsystems one by one, the above relation can be written as:

$$\left[\begin{array}{cccc} \langle E_{11} \rangle & \langle E_{12} \rangle & ... & \langle E_{1n} \rangle \\ \langle E_{21} \rangle & \langle E_{22} \rangle & ... & \langle E_{2n} \rangle \\ ... & ... & ... & ... \\ \langle E_{n1} \rangle & \langle E_{n2} \rangle & ... & \langle E_{nn} \rangle \end{array} \right] = \left[\begin{array}{cccc} A_{11} & A_{12} & ... & A_{1n} \\ A_{21} & A_{22} & ... & A_{2n} \\ ... & ... & ... & ... \\ A_{n1} & A_{n2} & ... & A_{nn} \end{array} \right] \mathbf{I} \tag{2}$$

where

$$\langle E_{ij} \rangle = \frac{E_{ij}}{P_j} \tag{3}$$

with E_{ij} the total energy of subsystem i when subsystem j is excited and P_j the PSD injected in subsystem j. Finally, the EIC matrix can be written as:

$$\left[\begin{array}{cccc} A_{11} & A_{12} & ... & A_{1n} \\ A_{21} & A_{22} & ... & A_{2n} \\ ... & ... & ... & ... \\ A_{n1} & A_{n2} & ... & A_{nn} \end{array} \right] = \left[\begin{array}{cccc} \langle E_{11} \rangle & \langle E_{12} \rangle & ... & \langle E_{1n} \rangle \\ \langle E_{21} \rangle & \langle E_{22} \rangle & ... & \langle E_{2n} \rangle \\ ... & ... & ... & ... \\ \langle E_{n1} \rangle & \langle E_{n2} \rangle & ... & \langle E_{nn} \rangle \end{array} \right] \tag{4}$$

The injected power as well as the subsystem energies can be computed, by an FE modelling. The spatially averaged calculated values will then be used to estimate the energy of each subsystem and the energy exchange between them. Classic FE models as in [24] will be used for the structural acoustic coupling. The total energy of an acoustic subsystem comprising N nodes can be written as:

$$E_{ac}(\omega) = \frac{\langle p_i^2 \rangle V}{\rho_0 c_0^2} \tag{5}$$

with $\langle p_i^2 \rangle$ the mean-square sound pressure of subsystem i, V the volume of the cavity, ρ_0 the density of the acoustic medium and c_0 the celerity of the medium. The total energy of a structural subsystem can be written as:

$$E_{str}(\omega) = \rho_s S \left\langle \tilde{v}_i^2 \right\rangle \tag{6}$$

assuming that the potential and kinetic energies in both types of subsystems are equal. In eq.(6), $\langle \tilde{v}_i^2 \rangle$ is the mean-square velocity of subsystem i, ρ_s is the surface density of the structure and S is the total area of the structural component.

3 Random distributed excitations

As mentioned in sec.2, in order to calculate the EIC of a system using the SEA-like method, a δ-correlated 'Rain-On-the-Roof' (ROR) excitation has to be applied on the subsystems. Moreover, the excitations applied to different subsystems have to be uncorrelated. Unluckily however, ROR does not represent real world excitations.

The most commonly encountered random aeroacoustic excitations in the aerospace and automotive fields are either diffused acoustic fields, or TBL excited vibration during high speed cruising. In [6] it is shown that the following relationships between an aeroacoustic excitation and a ROR one are valid:

$$\begin{array}{l} E_{s,s}^{aer}(\omega) \approx \frac{C_{eq}(\omega)}{\rho_s} E_{s,s}^{ror}(\omega) \\ E_{a,s}^{aer}(\omega) \approx \frac{C_{eq}(\omega)}{\rho_s} E_{a,s}^{ror}(\omega) \\ P_{s}^{aer}(\omega) \approx \frac{C_{eq}(\omega)}{\rho_s} P_{s}^{ror}(\omega) \end{array} \tag{7}$$

in which s stands for the structure and a for the acoustic medium. Therefore:

$$\begin{array}{l} A_{s,s}^{aer} \approx A_{s,s}^{ror} \\ A_{a,s}^{aer} \approx A_{a,s}^{ror} \end{array} \tag{8}$$

Where $C_{eq}(\omega)$ is the equivalent coherence function of the aeroacoustic excitation. The great advantage of this formulation, is based on the fact that by calculating the energy exchange properties of the system under a ROR excitation, an aeroacoustic excitation can be simulated through its equivalent coherence function. Therefore only one simulation is needed for the prediction of the response of a system, under several simultaneously applied aerodynamic excitations.

3.1 Equivalent function for a diffused sound field

An incident diffused sound field comprises an infinite number of uncorrelated plane waves with incidence angles uniformly distributed over a half space. The equivalence correlation function of a diffused sound field can be written as in [6]:

$$C_{diff}(\omega) = \left(\frac{\pi}{k_0}\right)^2 \sigma_{rad}(\omega) \tag{9}$$

Where k_0 is the acoustic wavenumber given by $k_0 = \omega/c_0$. The radiation efficiency $\sigma_{rad}(\omega)$ for an orthotropic panel having finite dimensions can be calculated using expressions such as the set of asymptotic formulas given in [25].

3.2 Equivalent function for a TBL excitation

Following the wavenumber space equivalence approach presented in [22], an equivalent ROR excitation can be calculated. The equivalent correlation function can be expressed in the wavenumber space as:

$$C_{eq}(k_x, k_y, \omega) = \frac{C_{eq}(\omega)}{4\pi^2} \tag{10}$$

Comparing the wavenumber-frequency spectrum of the studied excitation with the one of the equivalent ROR excitation, C_{eq} can be written in cartesian coordinates as:

$$\int_{k_{x1}}^{k_{x2}} \int_{k_{y1}}^{k_{y2}} C_{eq}\left(k_x, k_y, \omega\right) dk_y dk_x = \int_{k_{x1}}^{k_{x2}} \int_{k_{y1}}^{k_{y2}} C\left(k_x, k_y, \omega\right) dk_y dk_x \tag{11}$$

Substituting eq.(10) in eq.(11) implies that for an orthotropic panel C_{eq} can be written as:

$$C_{eq}\left(\omega\right) = \frac{4\pi^2}{(k_{x2}-k_{x1})(k_{y2}-k_{y1})} \int_{k_{x1}}^{k_{x2}} \int_{k_{y1}}^{k_{y2}} C\left(k_x, k_y, \omega\right) dk_y dk_x \tag{12}$$

A classic model presented in [17] will be used hereby, according to which the coherence function for a TBL excitation propagating in the x direction is given as:

$$C_{TBL}\left(\zeta, \eta, \omega\right) = e^{-\alpha_x \frac{\omega|\zeta|}{U_c}} e^{-\alpha_y \frac{\omega|\eta|}{U_c}} e^{\frac{i\omega\zeta}{U_c}} \tag{13}$$

where $\zeta = x - x'$ and $\eta = y - y'$. The above expression can be written in the wavenumber space (see [6]) as:

$$C_{TBL}\left(k_x, k_y, \omega\right) = \frac{\alpha_x \alpha_y k_c^2}{\pi^2(\alpha_x^2 k_c^2 + (k_x - k_c)^2)(a_y^2 k_c^2 + k_y^2)} \tag{14}$$

Eventually, substituting eq.(14) in eq.(12) the equivalent coherence function of the TBL excitation can be obtained:

$$C_{eq}\left(\omega\right) = \frac{4\pi^2}{(k_{x2}-k_{x1})(k_{y2}-k_{y1})} \int_{k_{x1}}^{k_{x2}} \int_{k_{y1}}^{k_{y2}} \frac{\alpha_x \alpha_y k_c^2}{\pi^2(\alpha_x^2 k_c^2 + (k_x - k_c)^2)(a_y^2 k_c^2 + k_y^2)} dk_y dk_x \tag{15}$$

In the above equations a_x,a_y are empirical coefficients depending on the nature of the TBL excitation, U_c is the convection velocity and $k_c = \omega / U_c$ is the convection wavenumber.

4 Reduction using a second order moment matching method

Following classical FE formulation for structural-acoustic coupled subsystems [24, 26], the discretized system can be written as a system of second order ordinary differential equations as:

$$\begin{gathered} \mathbf{M} \left\{ \begin{array}{c} \ddot{\tilde{x}}(t) \\ \ddot{\tilde{p}}(t) \end{array} \right\} + \mathbf{C} \left\{ \begin{array}{c} \dot{\tilde{x}}(t) \\ \dot{\tilde{p}}(t) \end{array} \right\} + \mathbf{K} \left\{ \begin{array}{c} \tilde{x}(t) \\ \tilde{p}(t) \end{array} \right\} = \mathbf{F_{sa}} \tilde{u}(t) \\ \tilde{y}(t) = \ell^t \left\{ \begin{array}{c} \tilde{x}(t) \\ \tilde{p}(t) \end{array} \right\} \end{gathered} \tag{16}$$

For a system with N DoF, $\mathbf{M}$, $\mathbf{C}$, $\mathbf{K} \in \Re^{N \times N}$ are the non-symmetric mass, damping and stiffness matrices, $\tilde{x}(t)$ stands for the structural displacement vector, $\tilde{p}(t)$ denotes the nodal pressure vector in the acoustic fluid, $\mathbf{F_{sa}}$ is the input matrix, $\tilde{u}(t)$ signifies the load vector of the system and ℓ^t is the transposed output matrix.

4.1 The Second Order ARnoldi (SOAR) process

The objective of a model order reduction process is the calculation of a subspace $\mathbf{S} \in \mathbb{C}^{N \times m}$ with m the size of the reduced model, for which the solution of the original system is written as:

$$\left\{ \begin{array}{c} \tilde{x} \\ \tilde{p} \end{array} \right\} = \mathbf{S}\tilde{b} + \tilde{\epsilon} \tag{17}$$

with $\tilde{b} \in \Re^m$ and $\tilde{\epsilon}$ the error of the approximation process. Both m and $\tilde{\epsilon}$ have to be minimized, for the computational cost and the error of the reduced solution to be acceptable. Assuming harmonic excitation, the system of equations can be written after a Laplace transform as:

$$\begin{array}{c} s^2\mathbf{M}\left\{\begin{array}{c}\tilde{x}\\ \tilde{p}\end{array}\right\} + s\mathbf{C}\left\{\begin{array}{c}\tilde{x}\\ \tilde{p}\end{array}\right\} + \mathbf{K}\left\{\begin{array}{c}\tilde{x}\\ \tilde{p}\end{array}\right\} = \tilde{F} \\ \tilde{y} = \ell^t\left\{\begin{array}{c}\tilde{x}\\ \tilde{p}\end{array}\right\} \end{array} \tag{18}$$

After some algebraic manipulation of the above system the variable vector is eliminated and the transfer function can be written as:

$$\tilde{h}(s) = \ell^t\left(s^2\mathbf{M} + s\mathbf{C} + \mathbf{K}\right)^{-1}\tilde{F} \tag{19}$$

With $s = i\omega$, $\omega > 0$. Assuming $\mathbf{K}$ non-singular the system has a Taylor series expansion which around $s = 0$ can be written as in [27]:

$$\tilde{h}(s) = \tilde{m}_0 + \tilde{m}_1 s + \tilde{m}_2 s^2 + ... = \sum_{i=1}^{\infty}\tilde{m}_i s^i \tag{20}$$

with $\tilde{m}_i$ the leading moments. The idea of a moment matching method is to find a reduced system of dimension m, whose transfer function matches as many leading moments of the original system as possible. The second order Krylov subspace was introduced for this reason in [28]. It is defined as the subspace, spanned by the vector sequence $\tilde{q}_i$, denoted as:

$$\mathcal{K}_m\left(\mathbf{A}, \mathbf{B}, \tilde{q_0}\right) = span\left(\tilde{q_0}, \tilde{q}_1, ..., \tilde{q}_{m-1}\right) \tag{21}$$

with the vector sequence $\tilde{q}_i$:

$$\tilde{q}_i = \left\{\begin{array}{c} \tilde{q_0} \\ \mathbf{A}\tilde{q_0} \\ \mathbf{A}\tilde{q}_{i-1} + \mathbf{B}\tilde{q}_{i-2} \quad for\ i \geq 2 \end{array}\right. \tag{22}$$

Vector $\tilde{q_0}$ is called the starting vector, while vectors $\tilde{q}_i$ for $i > 0$ are called basic vectors. It is shown, [29] that for $\mathbf{A} = -\mathbf{K}^{-1}\mathbf{C}$, $\mathbf{B} = -\mathbf{K}^{-1}\mathbf{M}$, and $\tilde{q_0} = \mathbf{K}^{-1}\tilde{F}$, the moments of the system can be written with respect to the above vector sequence as:

$$\tilde{m}_i = \ell^t\tilde{q}_i \tag{23}$$

Assuming an orthogonal basis $\mathbf{S}$ of $\mathcal{K}_m$ and projecting the initial system on this basis we get the reduced second order system:

$$\begin{array}{c} s^2\mathbf{M_r}\tilde{b} + s\mathbf{C_r}\tilde{b} + \mathbf{K_r}\tilde{b} = \tilde{F}_r \\ \tilde{y}_r = \ell_r^t\tilde{b} \end{array} \tag{24}$$

with

$$\mathbf{M_r} = \mathbf{S}^t\mathbf{M}\mathbf{S},\ \mathbf{C_r} = \mathbf{S}^t\mathbf{C}\mathbf{S},\ \mathbf{K_r} = \mathbf{S}^t\mathbf{K}\mathbf{S},\ \tilde{F}_r = \mathbf{S}^t\tilde{F},\ \ell_r^t = \ell^t\mathbf{S} \tag{25}$$

In [30] it is shown that if a matrix $\mathbf{S}$ is a basis of the second-order Krylov subspace

$$\mathcal{K}_m\left(-\mathbf{K}^{-1}\mathbf{C}, -\mathbf{K}^{-1}\mathbf{M}, \mathbf{K}^{-1}\tilde{F}\right) \tag{26}$$

and $\mathbf{K_r}$ is non-singular, then the first m leading moments of the original and the reduced-order models are matched. The iterative process followed for finding an orthogonal basis $\mathbf{S}$ of the second order Krylov matrix was presented in [16], and is called a Second Order ARnoldi reduction (SOAR). The main advantage of SOAR compared to the Arnoldi reduction is the preservation of the nature of a second order system. It is therefore expected to be at least as accurate as the first order Arnoldi process [31].

4.2 Expansion about $s_0 \neq 0$

If the expansion series of the system's transfer function is to be calculated around a point $s_0 \neq 0$, eq.(19) can be written as:

$$\begin{aligned}\tilde{h}(s) &= \ell^t\left((s+s_0)^2\mathbf{M} + (s+s_0)\mathbf{C} + \mathbf{K}\right)^{-1}\tilde{F} \\ &= \ell^t\left(s^2\mathbf{M} + s(\mathbf{C}+2s_0\mathbf{M}) + (\mathbf{K}+s_0\mathbf{C}+s_0^2\mathbf{M})\right)^{-1}\tilde{F}\end{aligned} \tag{27}$$

By comparing eq.(19) to eq.(27), it can be seen that we can calculate the transfer function of a system around s_0 by substituting $\mathbf{K}$ with $\mathbf{K}+s_0\mathbf{C}+s_0^2\mathbf{M}$ and $\mathbf{C}$ with $\mathbf{C}+2s_0\mathbf{M}$ in eq.(19). The modified Krylov subspace can therefore be written as:

$$\mathcal{K}_m^{s_0} = \mathcal{K}_m\left((\mathbf{K}+s_0\mathbf{C}+s_0^2\mathbf{M})^{-1}(\mathbf{C}+2s_0\mathbf{M}), (\mathbf{K}+s_0\mathbf{C}+s_0^2\mathbf{M})^{-1}\mathbf{M}, (\mathbf{K}+s_0\mathbf{C}+s_0^2\mathbf{M})^{-1}\tilde{F}\right) \tag{28}$$

and the modified reduced system matrices will be calculated by projecting the initial system's matrices to an orthogonal basis of the modified Krylov subspace.

5 Numerical examples

In this section, numerical applications for the models presented in sec.2 to sec.4 are exhibited.

The configuration shown in fig.1 is to be modelled. The dimensions a, b and c are 0.7m, 0.6m and 0.5m respectively. The structure is a layered, highly orthotropic panel made of Material I (see Table 1), with a thickness of 0.5mm . The damping of the system is considered to be Rayleigh proportional.

The structural-acoustic system is modelled by coupling Mindlin-Reissner type two-dimensional finite elements for the panel, to three-dimensional acoustic elements for the cavity. The resulting FE model comprises 3186 structural DOF and 17832 acoustic pressure DoF. A ROR excitation is initially applied to the structural panel, using loads of equal magnitude and of random phase and position. In order to excite the entirety of the subsystem modes in each frequency band (necessary condition for a ROR excitation), the Influence Circle approach exhibited in [9] will be used to decide the number of applied loads. The error $\epsilon(\omega)$ between the FE direct solution and the estimation of the reduced model is computed as:

$$\tilde{\epsilon}(\omega) = \frac{\left|\tilde{h}_r(\omega) - \tilde{h}(\omega)\right|}{\left|\tilde{h}(\omega)\right|} \tag{29}$$

Table 1: Mechanical properties of materials

Material I	Material II	Material III
$\rho = 9740$ kg/m^3	$\rho = 1410$ kg/m^3	$\rho = 48$ kg/m^3
$E_x = 2023.7$ GPa	$E_c = 54$ GPa	$E_c = 85$ MPa
$E_y = 31375$ GPa	$E_a = 54$ GPa	$E_a = 85$ MPa
$v_{xy} = 0.028$	$v_{ca} = 0.09$	$v_{ca} = 0.23$
$v_{xz} = 0$	$v_{cr} = 0.09$	$v_{cr} = 0.23$
$v_{yz} = 0.434$	$v_{ar} = 0.09$	$v_{ar} = 0.23$
$G_{xy} = 888.79$ GPa	$G_{ca} = 8.5$ GPa	$G_{ca} = 49$ MPa
$G_{yz} = 888.79$ GPa	$G_{ar} = 8.5$ GPa	$G_{ar} = 44$ MPa
$G_{xz} = 888.79$ GPa	$G_{cr} = 8.5$ GPa	$G_{cr} = 24$ MPa

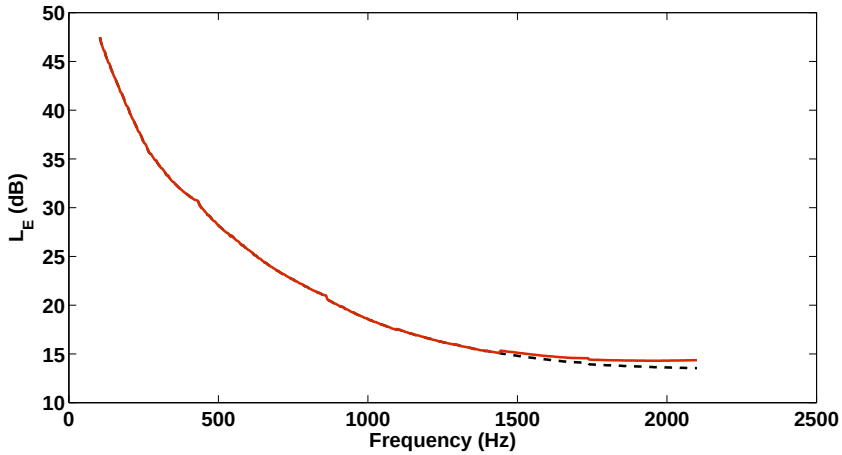


Figure 2: Steady-state energy for the structural subsystem under a reverberant field excitation: FE direct solution (- -), SOAR method (–)

5.1 Diffused field excitation

The results of an SEA-like analysis with the panel excited by a reverberant field on its dry side are presented hereby. As stated in sec.3, a new FE simulation is not needed for the response of the system to be predicted. The energy quantities of the subsystems under a diffused field excitation, are directly related to the ones for a ROR (of an equal Power Spectral Density (PSD)) through the equivalence function presented in eq.(9). The radiation efficiency of the panel is computed using the Leppington's set of asymptotic formulas, accounting for the finite dimensions, as well as the orthotropy of the panel. The resulting levels of energy L_E for the subsystems are presented in fig.2,3.

The comparison between the FE and SOAR methods are in very good agreement for the entire frequency range. The maximum difference between the predictions occurs at the end of the analysis range for both subsystems and is equal to 0.9dB for the panel's and 0.7dB for the cavity's energy level.

5.2 TBL excitation

A TBL excitation with empirical values corresponding to U_c =0.9 Mach which is a typical convection velocity for an aerospace structure, will be modelled using its equivalent coherence function presented in eq.(15). A stream propagating in x, as well as in y direction is hereby

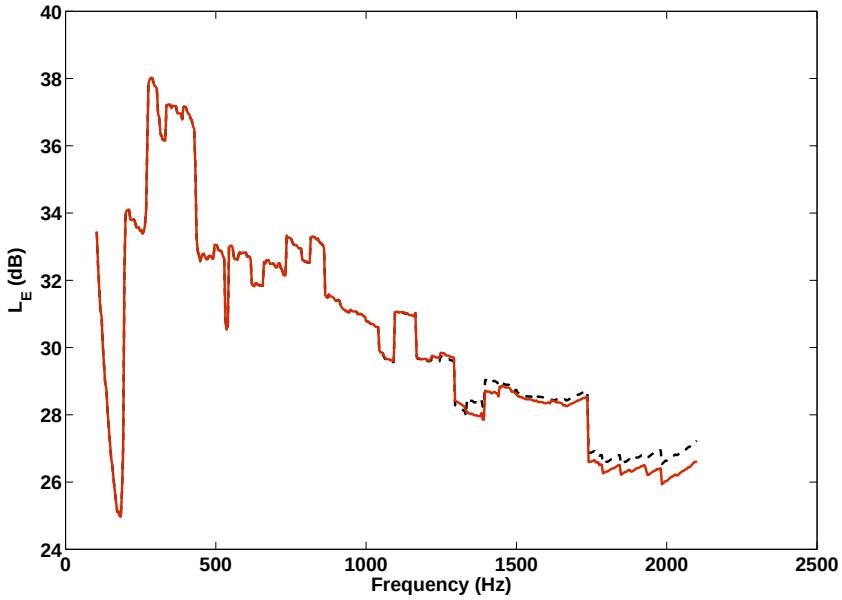


Figure 3: Steady-state energy for the acoustic subsystem under a reverberant field excitation: FE direct solution (- -), SOAR method (–)

modelled. The resulting acoustic energy inside the cavity subsystem is shown in fig.4.

It is shown that the FE results are in a very good agreement with the ones obtained after the SOAR reduction. The largest discrepancy for both results is 0.6dB at $f = 2100$Hz. The different resulting energies for the two propagation directions are due to the orthotropic characteristics of the panel. The higher induced energy for the stream propagating towards y direction implies that the convective wavenumber is closer to the panel's structural wavenumber in this direction, resulting in better coupling and more efficient energy transmission.

5.3 Predicting the sound level within a spacecraft's payload cavity

In this section the sound level within an empty payload cavity of the Ariane 5 spacecraft is to be predicted under a ROR and a TBL excitation. The configuration to be vibroacoustically computed is the SYLDA structure; its name standing for the french acronym of SYstéme de Lancement Double d'Ariane 5. The SYLDA is located inside the launcher fairing (see fig.5) and allows for multiple payloads to be simultaneously launched. A 1/4 scale of the real system is to be computed. The dimensions of the modelled acoustic cavity surrounded by the structure are shown in fig.6.

The SYLDA comprises three main substructures, two conical and a cylindrical one all made of an orthotropic sandwich material. The sandwich structure has 1mm thick facesheets made of Material II (see Table 1) and a 12.7mm thick core made of Material III. In Table 1 coordinate a coincides with the axial direction of the shell, c with the circumferential direction and r with the radial one. The structure is modelled by coupling Mindlin-Reissner type shell FE for the facesheets to 3D solid elements for modelling the core. The FE model comprises 22710 structural DoF and 35465 pressure DoF in total (see fig.7).

A δ-correlated (ROR) excitation is initially applied on the dry side of the cylindrical subsystem, using loads of equal magnitude and of random phase and position. A TBL excitation towards the axial direction of the structure is then modelled using the equivalent coherence function presented in sec.3. Firstly, the pressure level for a central cavity node is calculated in order to validate the ability of the SOAR to accurately predict the response of a single DoF. The

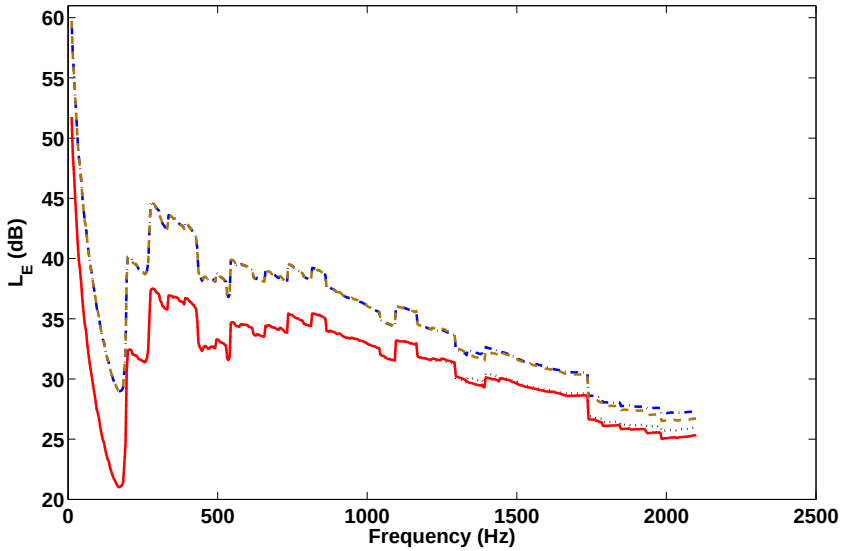


Figure 4: Energy of the cavity subsystem under a TBL excitation of 0.9 Mach applied on the panel: Layer propagating towards x: FE direct solution ($\cdots$), SOAR method (–), Layer propagating towards y: FE direct solution ($\cdot - -\cdot$), SOAR method (- -)

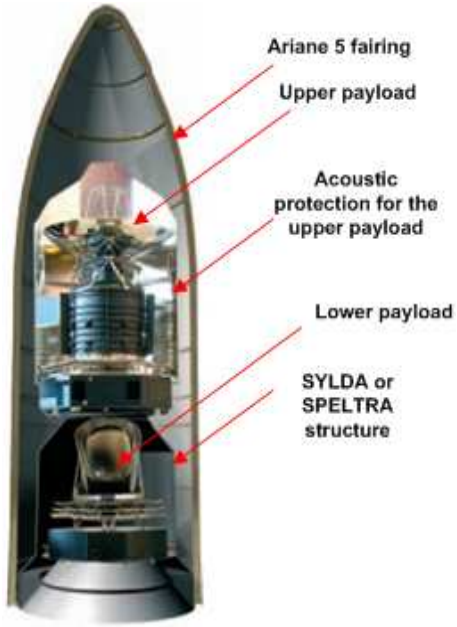


Figure 5: An illustration of the Ariane 5 spacecraft

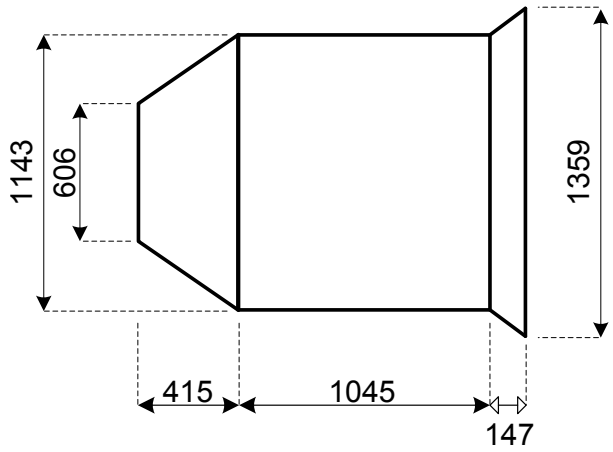


Figure 6: Dimensions of the modelled SYLDA configuration



Figure 7: Caption of the FE SYLDA (black) and cavity (blue) subsystems

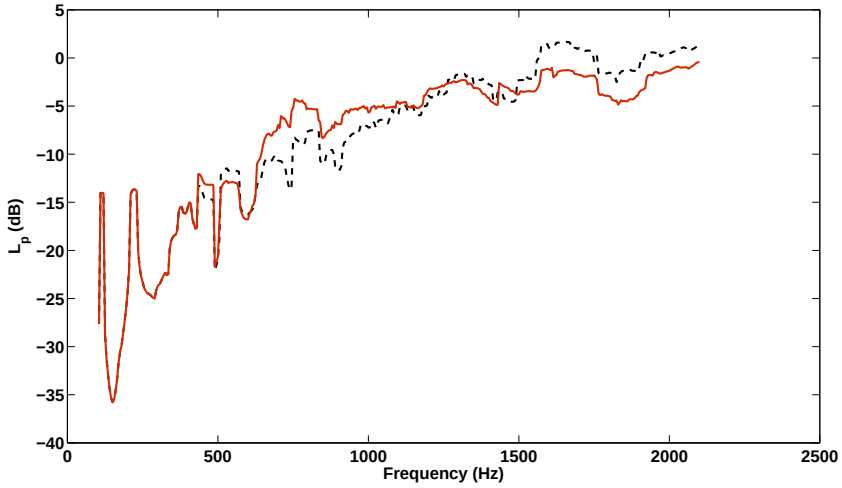


Figure 8: Acoustic pressure level at 0,0,0.7m of the payload cavity when a ROR excitation is applied on the cylindrical subsystem: FE direct solution (- -), SOAR reduction (–)

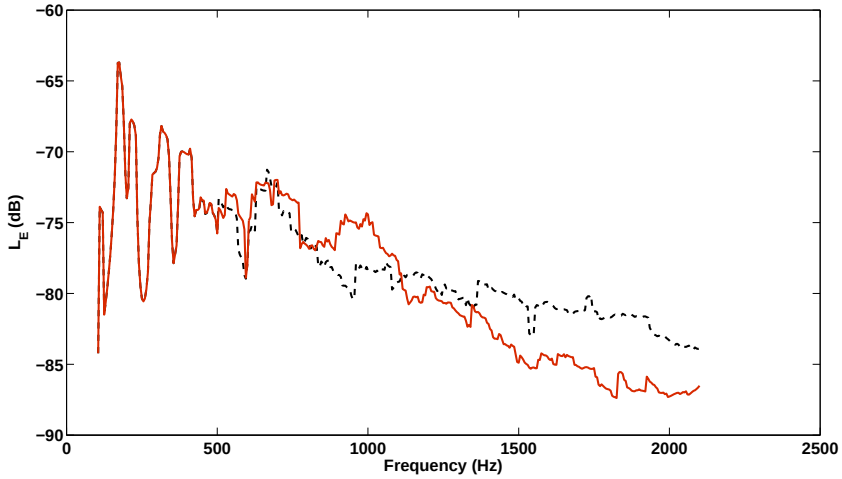


Figure 9: Acoustic energy level inside the payload cavity when a TBL excitation is applied on the cylindrical subsystem: FE direct solution (- -), SOAR reduction (–)

DoF coordinates are (0m, 0m, 0.7m). The reference pressure is pref=20μPa. The calculated SPL is shown in fig.8. The size of the reduced model is m=500 and the expansion point of the computation is s_0 = 2100Hz for all the results shown below. The results are averaged over one-twelfth octave frequency bands. Excellent agreement is observed in the low and medium frequency ranges between the FE solution and the SOAR prediction. The largest divergence of the approximation occurs at higher frequencies (f = 1650) and is equal to 3.5dB.

The acoustic energy level within the cavity when a TBL excitation is applied on the cylindrical subsystem is eventually computed. The result is presented in fig.9. As expected, the results are in a very good agreement up until 500 Hz. The largest divergence is observed at 1900 Hz, and is equal to 5.3dB. Higher accuracy can be obtained in the high frequency range by increasing m.

6 Discussion on the resulting computational efficiency of the approach

The ability of the SOAR reduction method to accurately model a structural acoustic system was exhibited in the above presented results. The calculation time for each of the above ex-

Table 2: Calculation times

	Orthotropic panel (m=2000)	SYLDA (m=500)
Full FE solution	204 min	934 min
Calculation of the Krylov subspace + solution	28 min	54 min
Calculation of the Krylov subspace + solution + 10% sampling over acoustic DoF	23 min	-

hibited calculations is presented in Table 2. It can therefore be concluded that the approach can drastically reduce the computation time while not having an important impact on the accuracy of the prediction. The total number of computed frequencies is 523. All calculations were done using a server of two, quadruple core Xeon E5343 processors, with 8Gb of RAM memory available. The direct FEM solution was done using a Lanczos algorithm within the software ANSYS 12.1, while the calculation of the Krylov subspace and the reduced solution was done using MATLAB 7.9.0. A total reduction of 88.7% was observed for the orthotropic panel system, while the reduction was equal to 94.2% in the case of the SYLDA structure. This time reduction is expected to be greater for larger industrial systems.

7 Conclusions

Concluding on the presented work, a structural acoustic system modelled with FE was reduced using the SOAR approach, and its broadband response to distributed aeroacoustic loads was calculated. The energy levels of the subsystems were calculated within an SEA-like approach. Summarizing the most important concluding points: 1) The approach can be used independently of the geometry and the structural acoustic coupling nature of the system as there is no need for analytical expressions of the dynamic characteristics of the subsystems. The structure may be composite and complex. The advantages of a FE modelling are therefore preserved. 2) Excellent agreement is observed in the low-frequency range for the SOAR estimation and the direct FE solution. The error of the approximation generally increases with respect to frequency. More vectors should therefore be added in the Krylov subspace in order to retain the error in a given level. 3) A cut-off frequency range was observed, during which the error of the reduced system approximation raises by several orders of magnitude. Increasing the dimension of the reduced model can delay the appearance of this cut-off frequency. 4) The calculation times are drastically reduced when the reduction is applied. Moreover, further reduction can be achieved by sampling over the acoustic DoF that are calculated for the application of the SEA-like approach.

Acknowledgements

The authors would like to gratefully acknowledge the ITN Marie Curie project GA-214909 'MID-FREQUENCY: CAE Methodologies for Mid-Frequency Analysis in Vibration and Acoustics' for the financial support.

REFERENCES

[1] W. Desmet, "Mid-frequency vibro-acoustic modelling: Challenges and potential solutions," in *Proceedings of the 2002 International Conference on Noise and Vibration Engi-*

neering, ISMA, pp. 835–862, 2002.

[2] B. Mace, "Statistical energy analysis, energy distribution models and system modes," *Journal of Sound and Vibration*, vol. 264, no. 2, pp. 391–409, 2003.

[3] S. P. S. Maluski and B. M. Gibbs, "Application of a finite-element model to low-frequency sound insulation in dwellings," *Journal of the Acoustical Society of America*, vol. 108, no. 4, pp. 1741–1751, 2000.

[4] M. D. C. Magalhaes and N. S. Ferguson, "Acoustic-structural interaction analysis using the component mode synthesis method," *Applied Acoustics*, vol. 64, no. 11, pp. 1049–1067, 2003.

[5] J. Pan and D. A. Bies, "The effect of fluid-structural coupling on sound waves in an enclosure - Theoretical part," *Journal of the Acoustical Society of America*, vol. 87, no. 2, pp. 691–707, 1990.

[6] M. de Rochambeau, M. Ichchou, and B. Troclet, "Modeling of random aerodynamic loads applied on fluid-structure coupled systems using rain-on-the-roof equivalent excitation," *Engineering Computations (Swansea, Wales)*, vol. 28, no. 4, pp. 472–491, 2011.

[7] B. R. Mace, "Statistical energy analysis: Coupling loss factors, indirect coupling and system modes," *Journal of Sound and Vibration*, vol. 279, no. 1-2, pp. 141–170, 2005.

[8] C. Fredö, "A SEA-like approach for the derivation of energy flow coefficients with a finite element model," *Journal of Sound and Vibration*, vol. 199, no. 4, pp. 645–666, 1997.

[9] B. Troclet, B. Hiverniau, M. N. Ichchou, L. Jezequel, K. Kayvantash, and T. Bekkour, "FEM / SEA hybrid method for predicting mid and high frequency structure-borne transmission," *The Open Acoustics Journal,*, vol. 2, pp. 45–60, 2009.

[10] L. Peretti and E. Dowell, "Asymptotic modal analysis of a rectangular acoustic cavity excited by wall vibration," *AIAA Journal*, vol. 30, no. 5, pp. 1191–1198, 1992.

[11] M. D. C. Magalhaes and N. S. Ferguson, "The development of a component mode synthesis (cms) model for three-dimensional fluid-structure interaction," *Journal of the Acoustical Society of America*, vol. 118, no. 6, pp. 3679–3690, 2005.

[12] A. C. Antoulas, "Approximation of large-scale dynamical systems," 2005.

[13] K. Willcox, J. Peraire, and J. White, "An Arnoldi approach for generation of reduced-order models for turbomachinery," *Computers and Fluids*, vol. 31, no. 3, pp. 369–389, 2001.

[14] J. S. Han, E. B. Rudnyi, and J. G. Korvink, "Efficient optimization of transient dynamic problems in MEMS devices using model order reduction," *Journal of Micromechanics and Microengineering*, vol. 15, no. 4, pp. 822–832, 2005.

[15] R. Srinivasan Puri, D. Morrey, A. J. Bell, J. F. Durodola, E. B. Rudnyi, and J. G. Korvink, "Reduced order fully coupled structural-acoustic analysis via implicit moment matching," *Applied Mathematical Modelling*, vol. 33, no. 11, pp. 4097–4119, 2009.

[16] Z. Bai and Y. Su, "SOAR: A second-order Arnoldi method for the solution of the quadratic eigenvalue problem," *SIAM Journal on Matrix Analysis and Applications*, vol. 26, no. 3, pp. 640–659, 2005.

[17] G. M. Corcos, "Resolution of pressure in turbulence," *Journal of the Acoustical Society of America*, vol. 35, no. 2, pp. 192–199, 1963.

[18] D. M. Chase, "Modeling the wavevector-frequency spectrum of turbulent boundary layer wall pressure," *Journal of Sound and Vibration*, vol. 70, no. 1, pp. 29–67, 1980.

[19] B. M. Efimtsov, "Characteristics of the field of turbulent wall pressure fluctuations at large Reynolds numbers," *Soviet Physics Acoustics*, vol. 28, no. 4, pp. 289–292, 1982.

[20] G. Maidanik, "Use of delta function for the correlations of pressure fields," *Journal of the Acoustical Society of America*, vol. 33, no. 11, pp. 1598–1609, 1961.

[21] F. Birgersson and S. Finnveden, "A spectral super element for modelling of plate vibration. part 2: Turbulence excitation," *Journal of Sound and Vibration*, vol. 287, no. 1-2, pp. 315–328, 2005.

[22] M. Ichchou, B. Hiverniau, and B. Troclet, "Equivalent 'rain on the roof' loads for random spatially correlated excitations in the mid-high frequency range," *Journal of Sound and Vibration*, vol. 322, no. 4-5, pp. 926 – 940, 2009.

[23] J. Guyader, C. Boisson, and C. Lesueur, "Energy transmission in finite coupled plates, part I: Theory," *Journal of Sound and Vibration*, vol. 81, no. 1, pp. 81–92, 1982.

[24] G. C. Everstine, "Finite element formulatons of structural acoustics problems," *Computers and Structures*, vol. 65, no. 3, pp. 307–321, 1997.

[25] F. G. Leppington, E. G. Broadbent, and K. H. Heron, "Acoustic radiation efficiency of rectangular panels," in *Proceedings of The Royal Society of London, Series A: Mathematical and Physical Sciences*, vol. 382, pp. 245–271, 1982.

[26] A. Craggs, "The transient response of a coupled plate-acoustic system using plate and acoustic finite elements," *Journal of Sound and Vibration*, vol. 15, no. 4, pp. 509–528, 1971.

[27] C. de Villemagne and R. E. Skelton, "Model reductions using a projection formulation.," *International Journal of Control*, vol. 46, no. 6, pp. 2141–2169, 1987.

[28] T.-J. Su and R. R. Craig Jr., "Model reduction and control of flexible structures using Krylov vectors," *Journal of Guidance, Control, and Dynamics*, vol. 14, no. 2, pp. 260–267, 1991.

[29] J. Lampe and H. Voss, "Second-order Arnoldi: Reduction application to some engineering problems," *Proceedings of the XVI-th Summer School on Software and Algorithms of Numerical Mathematics*, pp. 153–173, 2005.

[30] B. Salimbahrami and B. Lohmann, "Order reduction of large scale second-order systems using Krylov subspace methods," *Linear Algebra and Its Applications*, vol. 415, no. 2-3, pp. 385–405, 2006.

[31] Y. Yue and K. Meerbergen, “Using model order reduction for design optimization of structures and vibrations,” *TW Reports TW566, Department of Computer Science*, 2010.

COMPDYN 2013
4th ECCOMAS Thematic Conference on
Computational Methods in Structural Dynamics and Earthquake Engineering
S. Zghal, M-L Bouazizi, R.Nasri, N. Bouhaddi (eds.)
Kos Island, Greece, 12–14 June 2013

REDUCTION METHOD APPLIED TO VISCOELASTICALLY DAMPED FINITE ELEMENT MODELS

S. Zghal[1, 2], M-L. Bouazizi[2], R. Nasri[1], N. Bouhaddi[3]

[1] Ecole Nationale d'Ingénieurs de Tunis, Université de Tunis El Manar, Tunisie
BP 37,1002 Tunis Belvédère, Tunisie

souhirzghal@yahoo.fr;Rachid.Nasri@enit.rnu.tn
[2] Institut Préparatoire aux Etudes d'Ingénieurs de Nabeul, Université de Carthage, Tunisie
8000 M'rezga, Nabeul-Tunisie
lamjed.bouazizi@ipein.rnu.tn
[3] Institut FEMTO ST UMR 6174, Département Mécanique Appliquée, Université de Franche-Comté, Besançon-France
24 chemin de l'épitaphe 25000 Besançon-France
noureddine.bouhaddi@univ.fcomte.fr

Keywords: Sandwich, Viscoelastic Materials, Finite Element Modeling, Guyan condensation, Dynamic Condensation.

Abstract. *We propose in this paper to combine the GHM (Golla-Hughes-Mc Tavish) method with model reduction technique, especially direct condensation methods to resolve the problem of increased model order of viscoelastically structures. In fact, modeling structures using the GHM method leads to global systems of equation of motion whose numbers of degrees-of-freedom largely exceeds the order of the associated undamped system. As result, the numerical resolution of such equations can require prohibitive computational (CPU) time. So, to overcome this problem, both Static and Dynamic methods are used to reduce the order of finite elements matrices while preserving its capability to represent the dynamic behavior of viscoelastically damped structures. This paper intends to compare these two methods in direct reduction. Numerical example applied to cantilever beam structure is presented. This example will highlight the domain of validity of the studied methods. Results obtained from these two reduction methods are compared with the full model in order to illustrate its performances and its practical interest in the dynamic analysis of viscoelastically damped structures.*

1 INTRODUCTION

In the design of large industrial structures, the use of viscoelastic sandwich structures [1, 2] can provide an effective means of vibration control. However, these structures are highly dependent on the viscoelastic materials properties, which depend strongly on the excitation frequency. Therefore, a correct modeling of the viscoelastic behavior is required for the analysis of such structures. One effective approach used to model the viscoelastic behavior is the Golla-Hughes Mc Tavish [3, 4] model (GHM) which is based on the addition of internal or dissipative variables. This approach leads generally to largely dimension systems. Therefore, a model reduction should be applied to the augmented GHM model.

The present work presents an alternative two reduction methods for this problem. The first one is the Guyan condensation method [5, 6] which is applied to the structures through a partition of the equation of motion in term of master and slave coordinates leading to a static transformation whose coordinates are a subset of the original coordinates system. The second reduction is the dynamic condensation method [7] in which some slave modes are retained and added to the Guyan static transformation leading to enriched basis. The reduced order models are compared in terms of accuracy, performance and computational efficiency for the cantilever beam structure.

2 GHM FINITE ELEMENT MODEL

The viscoelastic shear modulus is represented, in the GHM model, by a series of functions in the Laplace domain such that:

$$G(s) = G_0\left(1 + \sum_{i=1}^{N_G} \alpha_i \frac{s^2 + 2\xi_i\omega_i s}{s^2 + 2\xi_i\omega_i s + \omega_i^2}\right) \tag{1}$$

Where: G_0 is the static modulus; s is the Laplace complex variable; $\alpha_i, \xi_i, \omega_i$ are the parameters of the i mini-oscillator, and N_G is the number of mini-oscillators. This leads to derive the equation of motion in term of structural dofs $\{q\}$ and dissipative dofs $\{z_i\}$ which are defined as follows:

$$\{z_i(s)\} = \left\{\frac{\omega_i^2}{s^2 + 2\xi_i\omega_i s + \omega_i^2}\right\}\{q(s)\} \tag{2}$$

After some manipulations and back to time domain, the following equation of motion in the Laplace domain is obtained:

$$\left\{s^2\begin{bmatrix}[M] & 0\\ 0 & [M_z]\end{bmatrix} + s\begin{bmatrix}0 & 0\\ 0 & [D_z]\end{bmatrix} + \begin{bmatrix}[K_q] & [K_{qz}]\\ [K_{qz}^T] & [K_z]\end{bmatrix}\right\}\begin{Bmatrix}q(s)\\ z_i(s)\end{Bmatrix} = \begin{Bmatrix}f(s)\\ 0\end{Bmatrix} \tag{3}$$

Or in compact form:

$$\left\{s^2[M_G] + s[D_G] + [K_G]\right\}\{q_G(s)\} = \{F_G(s)\} \tag{4}$$

Where: $[M_G]$; $[D_G]$ and $[K_G] \epsilon \mathbb{R}^{t_G, t_G}$ are respectively the mass, damping and stiffness matrices of viscoelastic GHM model with $t_G = N \times (1 + N_G)$ and N is the dimension of structural dofs (size of $\{q\}$).

$$\left[M_G\right]=\begin{bmatrix}[M] & 0 & \cdots & 0\\ 0 & \frac{\alpha_1}{\omega_1^2}\left[K_v^0\right] & 0 & \vdots\\ \vdots & 0 & \ddots & 0\\ 0 & \cdots & 0 & \frac{\alpha_{N_G}}{\omega_{N_G}^2}\left[K_v^0\right]\end{bmatrix};\quad \left[D_G\right]=\begin{bmatrix}0 & 0 & \cdots & 0\\ 0 & \frac{2\alpha_1\xi_1}{\omega_1}\left[K_v^0\right] & 0 & \vdots\\ \vdots & 0 & \ddots & 0\\ 0 & \cdots & 0 & \frac{2\alpha_{N_G}\xi_{N_G}}{\omega_{N_G}}\left[K_v^0\right]\end{bmatrix};$$

$$\left[K_G\right]=\begin{bmatrix}[K_e]+\left[K_v^\infty\right] & -\alpha_1\left[K_v^0\right] & \cdots & -\alpha_{N_G}\left[K_v^0\right]\\ -\alpha_1\left[K_v^0\right]^T & \alpha_1\left[K_v^0\right] & 0 & \vdots\\ \vdots & 0 & \ddots & 0\\ -\alpha_{N_G}\left[K_v^0\right]^T & \cdots & 0 & \alpha_{N_G}\left[K_v^0\right]\end{bmatrix};\ \left\{F_G\right\}=\begin{Bmatrix}f\\0\end{Bmatrix};\ \left\{q_G\right\}=\begin{Bmatrix}q\\z_i\end{Bmatrix}; \tag{5}$$

With: $\left[K_v^0\right]=G_0\left[\bar{K}_v\right]$; $\left[K_v^\infty\right]=\left[K_v^0\right]\left(1+\sum_{i=1}^{N_G}\alpha_i\right)$ are respectively, the static or low frequency stiffness matrix and the dynamic or high frequency stiffness matrix.

Consequently, the inclusion of dissipative coordinates increases the order of the differential equation of motion such that the structural degrees-of-freedom are least doubled. This increases the computational time of the system and motivates the use of reduction methods.

3 CONDENSATION METHODS

Models reduction procedures are used in order to reduce the GHM model dimension and his associated large computational times. This can be done based on the assumption that the exact responses given by the resolution of equation (4) can be approached by projections on a reduced vector basis as follows:

$$\{q_G\} = [T]\{q_C\} \tag{6}$$

Where: $[T]$ $\epsilon \mathbb{R}^{\mathbf{t_G,NR}}$is the transformation matrix formed column wise by a vector basis, $\{q_C\}$ $\epsilon \mathbb{R}^{\mathbf{NR,1}}$ are the generalized coordinates, and NR$\ll$ $\mathbf{t_G}$is the number of reduced vectors in the basis. The generalized coordinates representing the contribution of each column of $[T]$ are chosen arbitrary in which the reduced model provides a reasonable predictive into the frequency bandwidth.

The reduced equation of motion can be written as follows:

$$[M_C]\{\ddot{q}_C\} + [D_C]\{\dot{q}_C\} + [K_C]\{q_C\} = \{f_C\} \tag{7}$$

Where: $[M_C]$; $[D_C]$ and $[K_C]$ $\epsilon \mathbb{R}^{\boldsymbol{NR,NR}}$ are respectively the reduced mass, stiffness and damping matrices expressed as follows: $[M_C] = [T]^T [M_G][T]$; $[D_C] = [T]^T [D_G][T]$ $[K_C] = [T]^T [K_G][T]$; $\{f_C\} = [T]^T \{f_G\}$

Two reduction methods are adopted regarding the computation of reduction basis: Guyan condensation and Dynamic condensation.

3.1 Guyan condensation method

Guyan condensation method [5, 6] is based to divide the displacements vector of structural dofs $\{q\}$ into two subvectors:

$\{q^m\}$ $\epsilon \mathbb{R}^{\mathbf{m,1}}$: Subvector of master dofs.

$\{q^s\}$ $\epsilon \mathbb{R}^{\mathbf{s,1}}$: Subvector of slave dofs.

With $m + s = N$ being the order of the physical dofs of the viscoelastic structure and m$\ll$ $\boldsymbol{s}$.

By neglecting the inertia and the external load associated to the first equation of motion (3), partitioning it into master and slave coordinates (or dofs), the reduced model is obtained with the Guyan transformation which can be expressed as: $[T]=\begin{bmatrix} I_1 & 0 \\ t_1 & t_2 \\ 0 & I_2 \end{bmatrix} \epsilon \mathbb{R}^{t_G, m+NN_G}$

$$\left[t_1\right] = -\left[K_q^{ss}\right]^{-1}\left[K_q^{sm}\right] \epsilon \mathbb{R}^{s,m}$$

$$\left[t_2\right] = -\left[K_q^{ss}\right]^{-1}\left[K_{qz}^{sm} \quad K_{qz}^{ss}\right] \epsilon \mathbb{R}^{s,NN_G}$$

In this case, the size of reduced mass, stiffness and damping matrices is $NR= \boldsymbol{m + NN_G}$. Consequently, the reduced model have the follows dimension $[M_C]$; $[D_C]$ and $[K_C]$ $\epsilon \mathbb{R}^{m+NN_G, m+NN_G}$.

3.2 Dynamic condensation method

This method [7] consists to enrich the Guyan matrix transformation of some slaves modes obtained by the resolution of the slave eigenfrequencies problem as follows:

$$\left(\left[K_q^{ss}\right] - \lambda_i \left[M^{ss}\right]\right)\{\phi_i\} = 0 \quad i=1,\ldots..,s \tag{8}$$

Where: $\left[K_q^{ss}\right]$ and $\left[M^{ss}\right]$ are respectively the slaves' structural stiffness and mass matrices.

$$\phi_i = [\phi_1 \quad \phi_2 \quad \phi_s]; \ \lambda_i = diag(\lambda_1, \ldots\ldots\ldots, \lambda_s)$$

This base is trounced to p first slave modes $\phi_{sp} = \left[\phi_1 \quad \phi_2 \quad \phi_p\right] \epsilon \mathbb{R}^{s,p} (p \ll \boldsymbol{s})$ which are retained and added to the static basis to enrich it. Thereby, the dynamic transformation can be expressed as follows:

$$[T]=\begin{bmatrix} I_1 & 0 & 0 \\ t_1 & t_2 & \phi_{sp} \\ 0 & I_2 & 0 \end{bmatrix} \epsilon \mathbb{R}^{t_G, m+NN_G+p} \tag{9}$$

In this case, the size of reduced mass, stiffness and damping matrices is $NR= \boldsymbol{m + NN_G + p}$. Consequently, the reduced model have the follows dimension $[M_C]$; $[D_C]$ and $[K_C]$ $\epsilon \mathbb{R}^{m+NN_G+p, m+NN_G+p}$

4 NUMERICAL APPLICATION

In this section, numerical application is presented to illustrate the main features of the used condensation strategy of viscoelastic sandwich structures. We consider one mini-oscillator ($\mathbf{N_G}$=1) of viscoelastic cantilever beam which is constituted by two elastic layers (faces) in Aluminum and a viscoelastic layer (core) of the nuance ISD112. All the calculations are developed using the software MATLAB®. The material and geometrical characteristics of the used structure are shown in Table1. The values of the parameters of the viscoelastic commercially available ISD112, manufactured by3M™ used at 27°C for one mini-oscillator are presented in Table 2.

Elastic layers (Aluminum)	Shear modulus: $G_f = 9{,}6 \times 10^{10}$Pa
	Poisson ratio: $\upsilon_f = 0{,}3$
	Density :$\rho_f = 2766\text{Kg.m}^{-3}$
	Thickness: $h_f = 1{,}524\text{mm}$
Viscoelastic layer (ISD112)	Shear modulus: GHM modulus (1)
	Poisson ratio: $\upsilon_c = 0{,}49$
	Density :$\rho_c = 1600\text{Kg.m}^{-3}$
	Thickness: $h_c = 0{,}127\text{mm}$
Beam	Length: L=177,8mm Width: l=12,7mm

Table 1: Material and geometrical properties of the used sandwich structures [8]

Model GHM (i=1)	Value
α_i	4.8278
ω_i	28045
ξ_i	22.013
G_0 [MPa]	0.1633

Table2. Parameters of the GHM viscoelastic model identified for material ISD112 3M™ for one mini-oscillator

The used FE mesh of the beam involves one element through the width and 20 elements along the length, containing in total 1000 dofs. The excitation point and the response point are selected at the extremity of the beam as shown in figure 1.

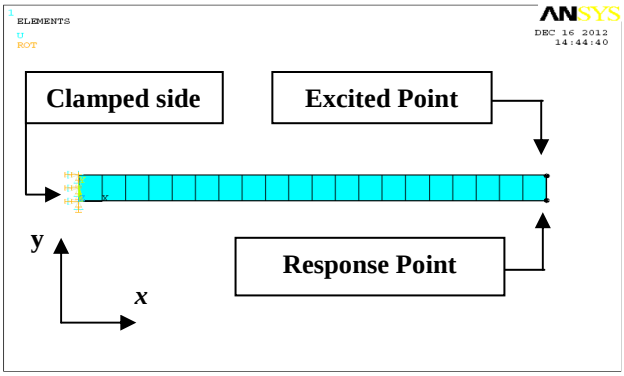


Figure1: Illustration of the FE model implemented for the Clamped-Free (C-F) viscoelastic beam

The response of the damped GHM model (described by rational fraction) and his associated undamped model of the beam under a harmonic excitation are presented in figure 2.

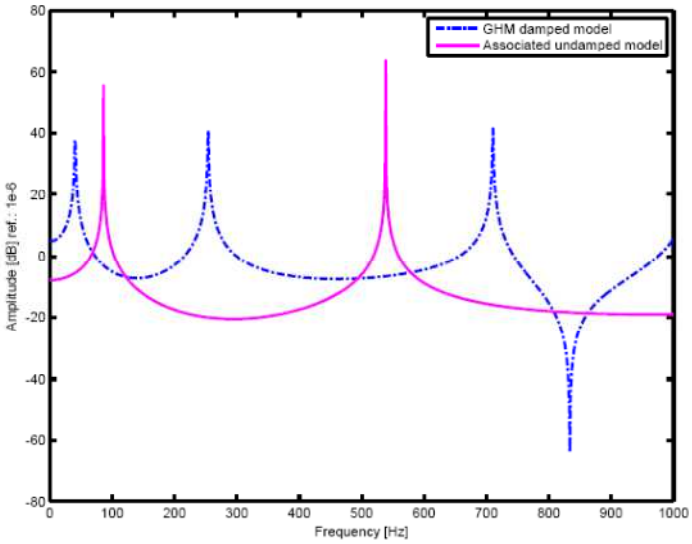


Figure2: FRFs of GHM damped model and his associated undamped model of the viscoelastic sandwich beam

The « blue » curve corresponds to the frequency response of the viscoelastic beam described by the frequency dependent GHM model and the « Magenta » curve is his associated undamped model in the frequency range of [0-1000] Hz. Indeed, these curves show a shift of both amplitudes and frequencies between the GHM rational model and his associated undamped model. This resulting first in dimuniation of amplitudes of 40% of the viscoelastic damped structure compared to his associated undamped structure.

This is explained by the damping effect introduced by the GHM model form (1) as a series of mini-oscillators while the associated undamped model is described by a static modulus $G(\omega = 0) = G_0$ which does not take account this effect. In second time, the shift of frequencies between the two models allows to determine the natural frequencies (which cannot determine

them by the classical method such as eigenvalues standard problem or MSE method) and the damped frequencies of the viscoelastic sandwich beam described by rational GHM model.

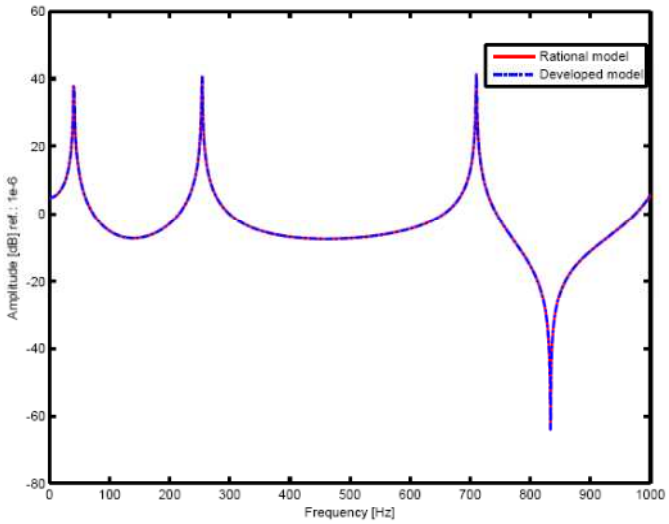


Figure3: FRFs for the rational and the developed GHM model of the viscoelastic sandwich beam

The frequency response of the rational model (1) and the developed model (3) are confused. This leads to conclude that these two models are equivalent. They are used as reference in the modeling of the viscoelastic sandwich beam.

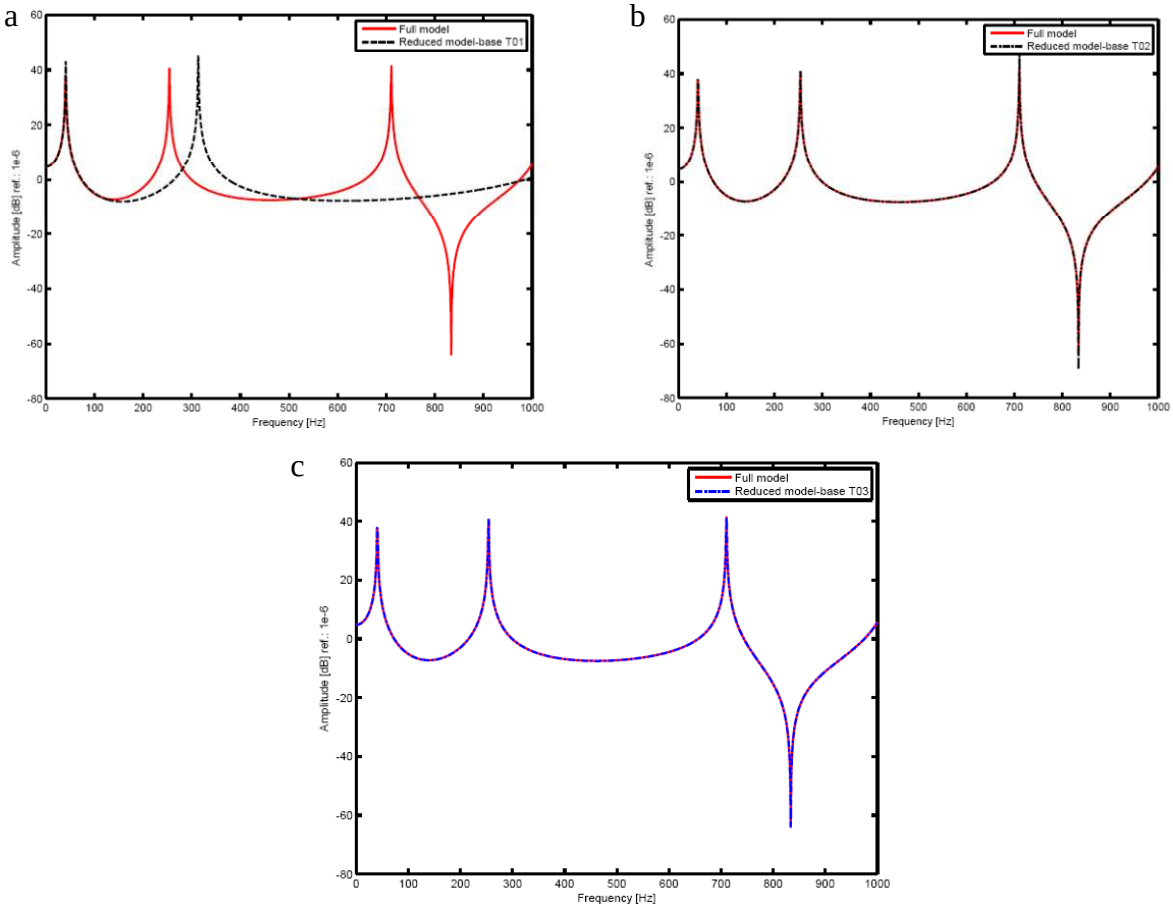


Figure4: FRFs for the full and the reduced systems by using T_{01}(a), T_{02}(b), T_{03}(c)

The interest here is to verify the accuracy and the performance of the direct condensation methods applied to viscoelastically damped structure by comparing both Guyan static condensation and Dynamic condensation methods.

The first test is intended to evaluate the Guyan condensation method by using T_{01} base which contains the static modes; $T_{01} = \left[\Theta_0\right]$ (1000×520), with m=20 dofs and s=480 dofs. Then, the dynamic condensation method is tested by using T_{02} and T_{03} bases which are obtained by enriched the static base by some slave modes. For $T_{02} = \left[\Theta_0 \quad \phi_{sp1}\right]$ (1000×530), static Guyan transformation is enriched by T_{sp_1} of 10 slave modes and for $T_{03} = \left[\Theta_0 \quad \phi_{sp2}\right]$ (1000×570), the static Guyan transformation is enriched by T_{sp_2} of 50 slave modes.

Figure 4 (a), (b) and (c) shows the frequency responses computed by using three reduction bases $T_{01}; T_{02}; T_{03}$ and compared to the amplitude of the response of the reference full model in the frequency band of interest [0-1000] Hz. As can be clearly seen, the accuracy is continuously improved upon successive enrichment of the reduction basis by the inclusion of 10 slave modes and 50 slave modes for $T_{02}; T_{03}$ respectively. This leads to confirm that the use of dynamic condensation is sufficient to represent with good accuracy the dynamic behavior of viscoelastic sandwich structure.

Table 3 provides the comparison between the time computation of full model and Guyan and dynamic condensation methods using $T_{01}; T_{02}; T_{03}$. It shows that the use of enrichment basis $T_{02}; T_{03}$ take a little bit more time of computing FRF than the use of static base T_{01} but make a drastic reduction which up to 90% with T_{02} and 87% with T_{03} compared to full model.

Moreover, one can take advantage of dynamic condensation method which combines the compromise of accuracy and time performance leading to a drastic reduction for the structures incorporating viscoelastic materials.

Model	Full	T_{01}	T_{02}	T_{03}
Computing FRF (s)	100	6	10	12
% of reduction	-	94	90	87

Table 3: Times evaluations of full and reduced methods.

The interest now is to compare the performance and the accuracy of the Guyan condensation method and the dynamic condensation method for the same order of both transformations. Indeed, we construct a Guyan transformation matrix with master dofs and slave dofs, having the same size with the dynamic transformation base T_{03}. We consider T_{Guyan}=T_{03} (1000×570), in the frequency band of interest [0-1200] Hz.

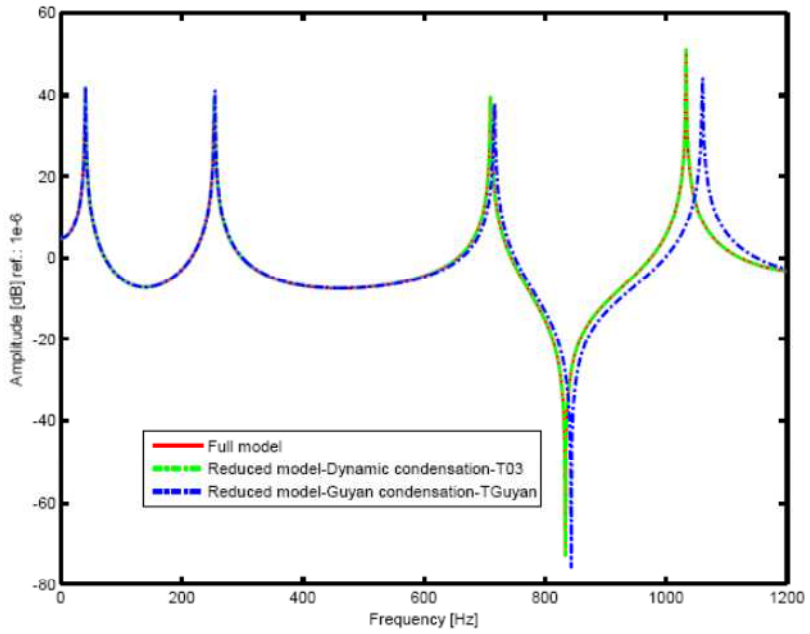


Figure5: FRFs for the full and the reduced systems-Guyan condensation/Dynamic condensation

Figure 5 shows the FRFs responses of the viscoelastic sandwich beam for the Guyan condensation method and the dynamic condensation method compared with those of full model. It can be seen that the frequency response of the dynamic condensation stick with of full model more than which is derived from Guyan condensation. The observed differences between the two direct condensation method lead to conclude that the Guyan condensation basis is not capable of overall accurately representing of the dynamic behavior of viscoelastic sandwich structures compared to the dynamic condensation method which gives satisfactory significant more accurate prediction. In fact, the static method is limited by a certain frequency called cutoff frequency which defines the domain of validity of the method and from which the results are not acceptable. For this example the cutoff frequency is around 1000 Hz. This result confirms that the use of dynamic condensation method is more efficient to represent with good accuracy the dynamic behavior of viscoelastic sandwich structures.

5 CONCLUSIONS

Finite element modeling procedures of structures incorporating viscoelastic materials are able to reproduce the FRFs responses before and after reduction was implemented, with emphasis placed on the GHM model and the implementation of two model order reduction methods: the Guyan condensation method and the dynamic condensation method.

An academic example derived from the industrial interest for the viscoelastic sandwich structures was used to illustrate the efficiency and the performance of these methods for predicting the dynamic behavior of these structures. The obtained results demonstrated the effectiveness of the two condensation strategy mainly in terms of the drastic reduction of the whole number of dofs and CPU time's computations.

REFERENCES

[1] J. Salençon, *Viscoélasticité*, Presse des ponts et chaussés, Paris, 1983.

[2] J.D. Ferry, *Viscoelastic properties of polymers*. John Wiley and Sons, New York, 1980.

[3] D.J. Mc-Tavish, P.C. Hughes, Dynamics of viscoelastic structure-a time domain, finite element formulation. *ASME, Int. J. applied mechanics*, **52**, 897-906, 1985.

[4] D.J. Mc-Tavish, P.C. Hughes, Modeling of linear viscoelastic space structures, *ASME, Int. J. vibration and acoustics of applied mechanics*, **52**, 103–113, 1993.

[5] R.J. Guyan, Reduction of Stiffness and Mass Matrices, *AIAA Journal,* Vol. **3(2),** 38, 1965.

[6] C.H. Park, D.J. Inman, M.J. Lam, Model reduction of Viscoelastic finite element models. *Int. J. Sound and Vibration*, 219, 619-637, 1999.

[7] R. R, Jr. Craig., M.C.C.Bampton, Coupling of substructures for dynamic analyses, *AIAA Journal*, 6(7):1313-1319, 1968.

[8] B. Bilasse, EM. Daya, Modélisation numérique des vibrations linéaires et non linéaires des structures sandwiches à âme viscoélastique. Thèse présentée à l'université de Metz France, 2010.

COMPDYN 2013
4th ECCOMAS Thematic Conference on
Computational Methods in Structural Dynamics and Earthquake Engineering
M. Papadrakakis, V. Papadopoulos, V. Plevris (eds.)
Kos Island, Greece, 12–14 June 2013

EFFICIENT DYNAMIC INTERACTION ANALYSIS OF HIGH-SPEED TRAIN AND RAILWAY STRUCTURE DURING AN EARTHQUAKE

M. Tanabe[1], M. Sogabe[2-1], H. Wakui[2-2], N. Matsumoto[2-3] and Y. Tanabe[3]

[1]Kanagawa Institute of Technology
Atsugi, Kanagawa, 243-0292, Japan
e-mail: tanabe@sd.kanagawa-it.ac.jp

[2] Railway Technical Research Institute
Kokubunji, Tokyo, 185-8540, Japan
e-mail: [2-1]sogabe@rtri.or.jp, [2-2]wakui@rtri.or.jp, [2-3]nobel@rtri.or.jp

[3] Laboratory for Computational Mechanics Inc.
3-14-18 Kurihara-chuo, Zama, 252-0014, Japan

Keywords: Dynamic interaction, Train, Railway structure, Derailment, Contact-impact, Earthquake.

Abstract. *An efficient computational method to solve the dynamic interaction between a high-speed train and the railway structure including derailment during an earthquake is given. The motion of the train is expressed in multibody dynamics. Efficient mechanical models to express contact-impact behaviors between wheel and the track structure including derailment during an earthquake are given. Rail and track elements with multibody dynamics and FEM combined are described. The motion of a railway structure is modeled with various finite elements and rail and track elements. A modal reduction is applied to solve the problem effectively. An exact time integration scheme has been developed that is free from the round-off error for very small time increments needed to solve the interaction between wheel and railway structure including derailment during an earthquake. Numerical examples are demonstrated.*

1 INTRODUCTION

There is a very sophisicated interaction between a high-speed train and railway structure anticipated during an earthquake. The impact force between the wheel and rail may leads to a radical dynamic phenomenon such as lifting of wheel, derailing, touching down on the track surface and the impact on surface creating a high-frequency response higher than several hundred Hz mixed with the foundamental low-frequency response of railway structure and train. This is so called a multiscale phenomenon of the frequency and is hard to get the numerical solution as the time increment needed to solve the nonlinear problem becomes very small for the convergency during each time increment that causes a round-off error in the numerical integration. To avoid the round-off error for the very small time increment in the numerical integration, the scaling techniquie has been developed [1]. It is very important to develop an efficient method to solve the dynamic interaction between the train and railway structure including derailment and post-derailment behaviors during an earthquake to build an earthquake-safe railway system.

Computational methods to solve the dynamic interaction of a high-speed train and railway structure have been developed by using mutibody dynamics together with finite element method, and various mechanical models for the car, the railway structure and the interaction between wheel and rail have been developed based on the purposes and applications to design railways [2-5]. However, very little work related to derailment and post-dearilment behaviors of the train on the railway structure during an earthquake has been reported so far [6-7].

In this paper, a simple and efficient computational method to solve the dynamic interaction of a Shinkansen train (high-speed train in Japan) and railway structure including derailment behavior during an earthquake is given.

The motion of the train is modeled in multibody dynamics with nonlinear springs and dampers to connect all components. Efficient mechanical models to express contact-impact behaviors between wheel and rail before derailment and also between wheel and the track structure after derailment are given to solve the interaction during an earthquake effectively. Rail and track elements have been developed using multibody dynamics and finite element method combined to solve the interaction between wheel and long railway components such as rail and track effectively.

The motion of railway structure is modeled with various finite elements such as truss, beam, shell, solid, and nonlinear spring and damper elements, and also with rail and track elements. The nonlinear dynamic response during an earthquake is obtained by solving equations of motions of the train and railway structure subjected to interactions between wheel and the track structure including derailment and post-derailment behaviors. A modal reduction to equations of motions is made to solve the large-scale nonlinear problems effectively. The response calculation for the nonlinear equations of the train and railway structure during an earthquake requires very small time increments due to the high-frequency impact behavior between wheel and railway structure. An exact time integration scheme has been developed that is free from the round-off error for very small time increments needed to solve the radical interaction between wheel and railway structure in derailment and post-deralment during an earthquake.

Based on the present method a computer program, DIASTARS, has been developed for the simulation of a Shinkansen train running at high speed on the railway structure including de-railment during an earthquake. Numerical examples are demonstrated.

2 MECHANICAL MODEL OF A SHINKANSEN TRAIN

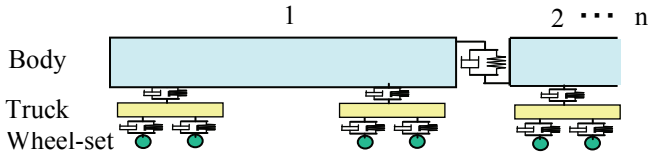


Fig. 1 Mechanical model of a Shinkansen train

A Shinkansen train is modeled with rigid components of car body, truck and wheel-set connected by nonlinear springs and dampers as shown in Fig. 1. Assuming that the train runs at a constant speed, the equation of 3D motion of the train with n cars connected is derived with 31n degrees of freedom and written in a familiar matrix form as [8]

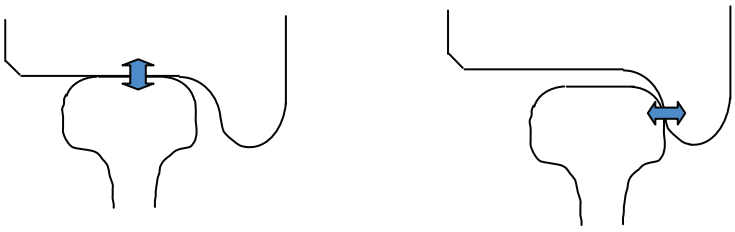
$$M^V \ddot{X}^V + D^V \dot{X}^V + K^V X^V = F^V \tag{1}$$

where X^V and F^V are displacement and load vectors of the train, and M^V , D^V and K^V are the mass, damping and stiffness matrices, respectively.

3 INTERACTION BETWEEN WHEEL AND TRACK

3.1 Contact between wheel and rail before derailment

Assuming that the yawing and rolling of wheel-set are relatively small for the contact behavior between wheel and rail considered here, two dimensional geometries of the cross sections of wheel and rail are considered, and the contact-impact behavior in the normal direction on the contact surface between wheel and rail is modeled simply in two modes of the contact in the vertical and transverse directions as shown in Fig. 2.



(a) Vertical direction (b) Transverse direction

Fig. 2 Contact modes between wheel and rail

Assuming that wheel and rail are stiff enough, regarding the vertical mode of the contact the contact displacement between wheel and rail in the vertical direction, δ_Z , is expressed as a function of displacements of the rail z_R and the wheel z_w in the vertical direction and also the relative displacement on the contact surface between wheel and rail in the transverse direction d_y depending on the geometry of the rail and wheel as follows

$$\delta_Z = \delta_Z(z_R, z_W, d_y) . \tag{2}$$

However, assuming the rolling and yawing of wheel set is relatively small, geometries of rail and wheel are defined by the cross-section, where the curve to define the cross-section is expressed by arcs and straight lines connected so that the slope of the curve is continuous at any places.

The contact displacement δ in the normal direction on the contact surface between wheel and rail is obtained from the contact angle at the contact position. When wheel contacts on rail, there is a contact force created on the contact surface. The contact force on the contact surface between wheel and rail in the normal direction, H, is expressed as a function of δ and d_y as follows

$$H = H(\delta, d_y) . \tag{3}$$

Regarding the transverse mode of the contact between wheel and rail, the contact displacement in the transverse direction δ_y is also expressed as a function of d_y and δ_Z depending on the geometry of the cross sections of wheel and rail as

$$\delta_y = \delta_y(d_y, \delta_Z) . \tag{4}$$

When a wheel contacts on the rail in the transverse direction, the contact force is obtained in the same manner as the contact mode in the vertical direction described above.

Regarding the tangential and longitudinal directions on the contact surface between wheel and rail, constitutive equations to describe the relationship between creep forces and slipping rates of wheel are given [9]. The creep force in the tangential direction Q_c and yaw moment T_c due to the creep force in the longitudinal direction on the contact surface between wheel and rail are described mathematically here as functions of slipping rates of wheel in the longitudinal and tangential directions, S_x and S_t, and also of the spin rate around the normal vector on the contact surface, S_n, as [10]

$$Q_c = Q_c(S_x, S_t, S_n) \tag{5}$$

$$T_c = T_c(S_x) . \tag{6}$$

When a wheel lifts on the rail, there is no impact and creep forces created between the wheel and the rail.

3.2 Derailment Criterion

When the relative displacement between wheel and rail in the transverse direction, d_y, exceeds derailment criterions u_{d1} or u_{d2}, it is detected that the derailment in the field side or gauge side is initiated, respectively as shown in Fig. 3 that leads to post-derailment behaviors of the wheel on the track structure. Once derailment of a wheel occurs, it is assumed here that



(a) Field-side derailment (b) Gauge-side derailment

Fig. 3 Derailment criterion of left wheel

the wheel never returns to the normal running on the rail. After derailment of wheel from rail during an earthquake the wheel touches down on the track structure and there is the

interaction between wheel and the track structure.

3.3 Contact between wheel and guard after derailment

Guards are attached on the track structure to prevent wheel deviating from the track after derailment during an earthquake to build an earthquake-safe railway system as shown in Fig. 4. After the derailment of a wheel, it contacts on the guard of the track structure in the transverse direction. The contact force Q_{Gy} is expressed here as a function of the embedded area A_{Gy} between the wheel and the guard as

$$Q_{Gy} = Q_{Gy}(A_{Gy}). \tag{7}$$

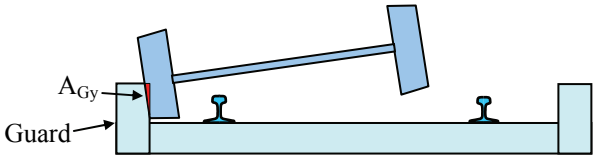


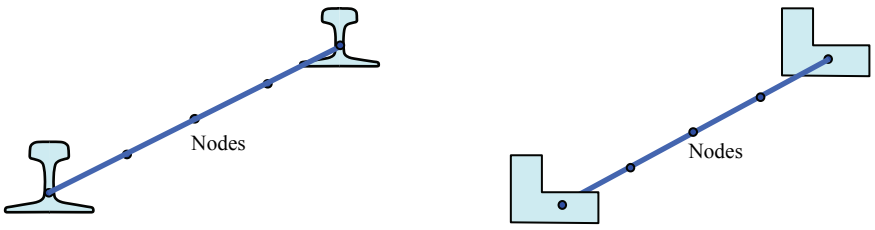
Fig. 4 Contact between wheel and guard on the track structure in the transverse direction

If the guard has an enough height and strength for the impact force between wheel and guard, the wheel is guided well between left and right guards in the rail direction after the derailment preventing wheel deviating from the track during an earthquake.

4. MECHANICAL MODEL OF RAILWAY STRUCTURE

4.1 Rail and track elements

Long railway components in the rail direction such as rail and track are considered to move as rigid bodies of the motion in plane of the cross-section. Rail and track elements have been developed to solve contact-impact behaviors between wheel and rail in the pre-derailment and between wheel and the track structure in the post-derailment effectively for the actual railway structure. Fig. 5 shows rail and track elements where motions in plane of cross-sections are expressed by multibody dynamics (MD) and motions in out-of-plane are expressed by beam elements given along the rail. The elements mixed with MD and FEM are very effective to solve contact-impact problems between wheel and a long track structure in the rail direction including derailment with a small numbers of DOFs.



(a) Rail element (b) Track element

Fig. 5 Rail and track elements

5 NUMERICAL METHOD

A railway structure is modeled with various finite elements such as truss, beam, shell, solid, mass, and nonlinear spring and damper elements, and also with rail and track elements for long railway components such as rail and track. Assembling all elements in the model, the equation of motion of a railway structure is obtained in a familiar matrix form as

$$M^b \ddot{X}^b + D^b \dot{X}^b + K^b X^b = F^b \tag{8}$$

where X^b and F^b are the displacement and load vectors of the railway structure, and M^b, D^b and K^b are the mass, damping and stiffness matrices, respectively. Note that F^b includes nonlinear forces, and is a nonlinear function of X^b, $\dot{X}^b$, X^v and $\dot{X}^v$.

5.1 Modal reduction

A modal reduction is applied to displacement vectors of the train and the railway structure to solve the practical problem with a long railway structure to allow the train to run at high speed during an earthquake effectively as

$$X^v = \Phi^v Z^v \tag{9}$$
$$X^b = \Phi^b Z^b \tag{10}$$

where Φ^v and Φ^b are rectangular matrices made of the mode vectors of the train and railway structure, and Z^v and Z^b are the modal coordinates, respectively. Moving the nonlinear terms in eqs. (1) and (8) to the right sides of equations, and operating the modal transformation by Φ^v and Φ^b respectively, equations of motions of the train and the railway structure are derived in the modal coordinates as

$$\ddot{Z}^V + \tilde{C}^V \dot{Z}^V + [(\omega_i^V)^2] Z^V = \tilde{F}^V \tag{11}$$
$$\ddot{Z}^B + \tilde{C}^B \dot{Z}^B + [(\omega_i^B)^2] Z^B = \tilde{F}^B \tag{12}$$

where ω_i^V and ω_i^B are angular frequencies of i-th mode in the train and railway structure, respectively, and $[(\omega_i^V)^2]$ denotes a diagonal matrix with i-th diagonal element of $(\omega_i^V)^2$. However

$$\tilde{C}^V = (\Phi^V)^T C^V \Phi^V \tag{13}$$
$$\tilde{C}^B = (\Phi^B)^T C^B \Phi^B \tag{14}$$
$$\tilde{F}^V = (\Phi^V)^T F^V \tag{15}$$
$$\tilde{F}^B = (\Phi^B)^T F^B \tag{16}$$

where the superscript T denotes the transpose of the matrix. Note that the nonlinear terms for the train and railway structure are included in $\tilde{F}^V$ in eq. (11) and $\tilde{F}^B$ in eq.(12), respectively.

5.2 Exact time integration

Equations of motions of the train and the structure are solved in the modal coordinates for each time increment by the exact time integration scheme by approximating the right side term with m-th degree of polynomial and applying the exact time integration for each small time increment as the numerical time integration may cause the round-off error for very small time increments needed to solve the radical dynamic interaction in the derailment during an earthquake. However, since the equations are strongly nonlinear, iterative calculations are

needed during each time increment until the unbalanced force between the train and railway structure becomes small enough within a tolerance specified.

Based on the present method, a computer program DIASTARS has been developed for the simulation of a Shinkansen train at high speed on the railway structure including derailment during an earthquake.

6 NUMERICAL EXAMPLES

6.1 One dimensional nonlinear dynamic problem

Fig. 6 shows a simple one dimensional nonlinear dynamic problem with the natural frequency of ω, damping constant of h, the gravity force of g due to the unit mass where a contact element with the gap G and the spring constant K is attached.

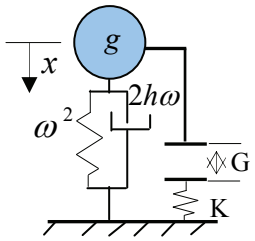


Fig. 6 One dimensional nonlinear dynamic problem

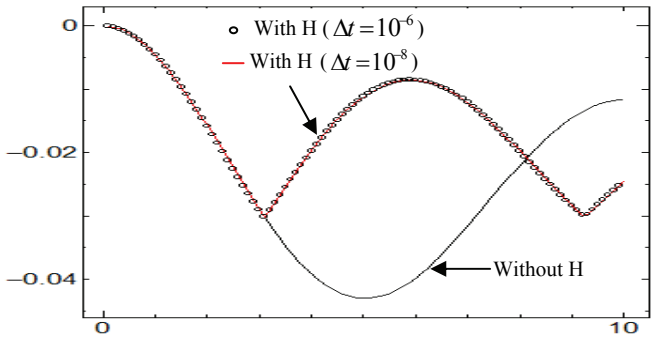


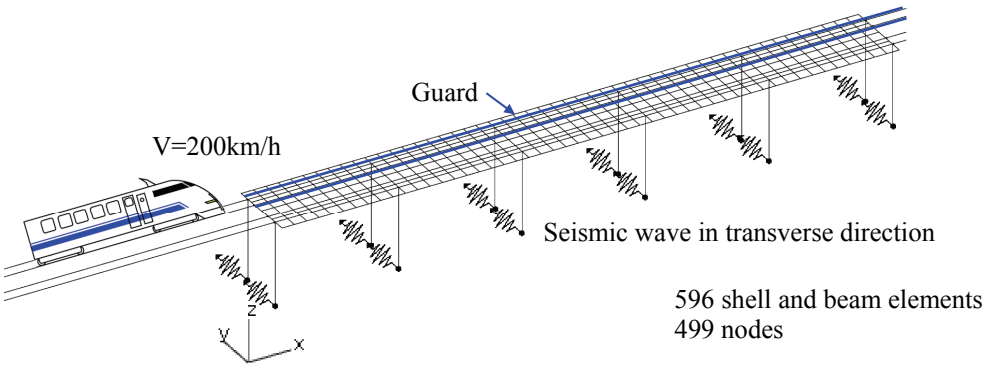
Fig. 7 Displacement response by the exact time integration

For the problem of $\omega=2\pi/10$ rad/sec, h=0.1, $K=5\times10^3$ N/m, G=0.03m and g=9.8N, the response was obtained by the exact time integration scheme mentioned in the section 5.2 where the linear approximation to the right side terms of equations is made. Fig. 7 shows the displacement response for very small time increments of $\Delta t=10^{-6}$ and 10^{-8} for the case with the contact force H and also for the case without the contact force. For very small time increments, the exact time integration scheme gives the exact solution. On the other hand, the numerical time integration by Newmark method failed due to the round-off error for both cases with H and without H for very small time increments of both $\Delta t=10^{-6}$ and 10^{-8}.

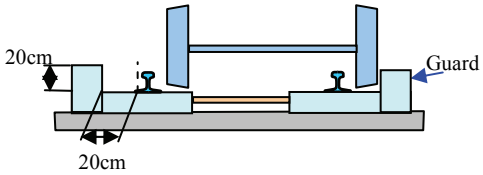
6.2 Simulation of a Shinkansen car running on the viaduct with guards attached during an earthquake

The simulation of a Shinkansen car running at a speed of 200km/h on the ladder track with guards attached on the five spanned viaduct with the height of 10m, the span-length of 8m and the width of 11.6m during an earthquake as shown in Fig. 8 has been conducted. The lad-

der track is made of ladder-shaped composite concrete beams to support rails tied with steel pipes where guards are attached to prevent wheel deviating from the track even after derailment during a strong earthquake [11-12].



(a) Railway structure modeled with shell and beam elements



(b) Cross section of the ladder track with guards

Fig. 8 Simulation of a Shinkansen car on the five spanned viaduct during an earthquake

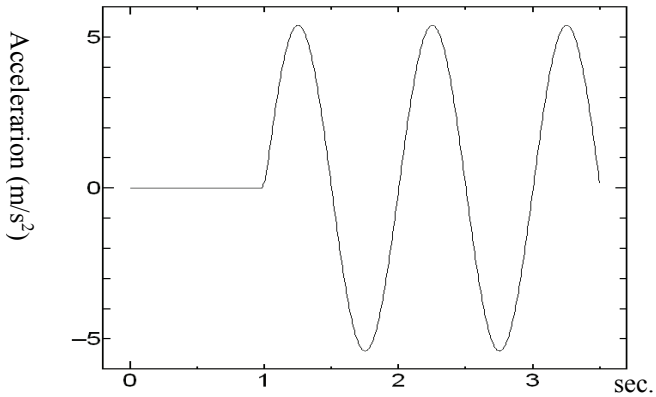


Fig. 9 Transverse acceleration at the base of the 3rd pier

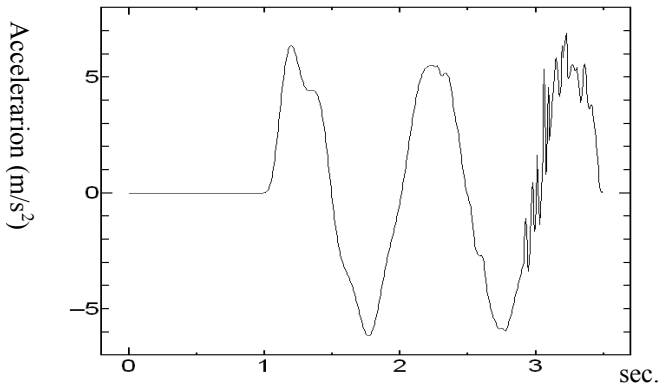


Fig.10 Transverse acceleration at the top of the 3rd pier

A sinusoidal seismic wave with the maximum acceleration of 5.4 m/sec^2, the wave number of five, and the frequency of 1Hz was given from the basis of all piers in the transverse direction. The frequency of 1Hz is close to the resonance frequency of rolling motion of the car body, truck and wheelset leading to derailment of wheel from the rail. The frame structure of the viaduct is modeled with beam elements and the concrete slab with shell elements. The rail and the ladder track with guards attached were modeled with rail and track elements mentioned earlier, respectively.

Fig. 9 and 10 show transverse acceleration at the base and top of the 3rd pier, respectively. The maximum acceleration at the top of the pier is amplified about 30% to the maximum acceleration of 5.4 m/s^2 given from the base. Fig. 11 shows the vertical displacement response of the right wheel at the 1st wheel-set. It is shown that the wheel runs onto the rail about 7 cm in height due to the impact between wheel and rail in the vertical direction, derails, touches down on the track, and lifts on the track surface during the earthquake. Fig. 12 shows the relative displacement response between right wheel and rail in the transverse direction, δ_y, at the 1st wheel-set. When δ_y exceeds u_{dl} (7cm), the derailment to the field side is initiated, the wheel touches down on the surface of the ladder track in the vertical direction, impact on the guard of the track in the transverse direction, rebounds and gets back to the rail without deviating from the track. The track with the guards attached was shown to be effective to prevent the wheel deviating from the track even after derailment during the earthquake.

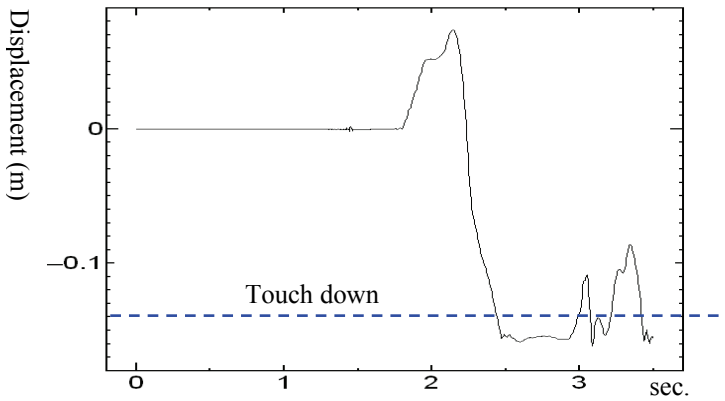


Fig. 11 Vertical displacement of the right wheel of the 1st wheel-set

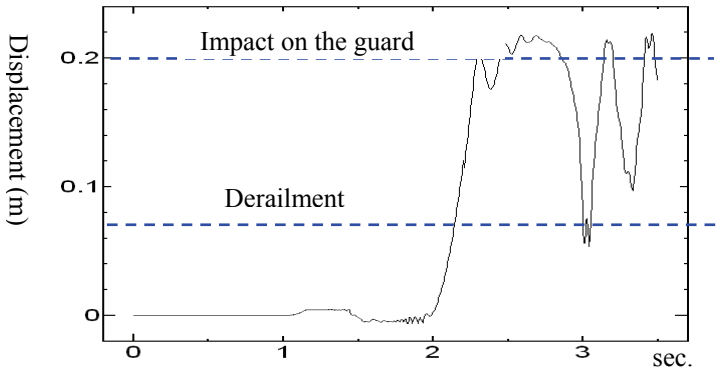


Fig. 12 Relative displacement between the right wheel and rail in the transverse direction

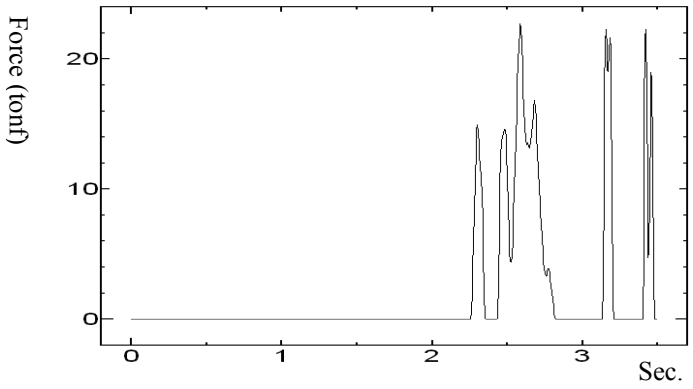


Fig. 13 Impact force of the right wheel on the guard in the transverse direction

Fig.13 shows the impact force of the right wheel on the guard. The maximum impact force of the wheel on the guard is shown to be about 22.5 tonf.

7 CONCLUSIONS

A simple and efficient computational method to solve the combined dynamic response of a high-speed train and railway structure including derailment during an earthquake was given. Efficient mechanical models to solve contact-impact behaviors between wheel and the track structure including derailment were described. Modal reduction was applied to equations of motions of train and railway structures to solve practical problems effectively. The exact time integration scheme has been developed to avoid the numerical error for very small time increments needed to solve the radical dynamic interaction between wheel and track structure during an earthquake. Simulation of a Shinkansen car on the five spanned viaduct during an earthquake was demonstrated. The computational method developed here would be effective to design an earthquake-safe railway system.

REFERENCES

[1] O. A. Bauchau, A. Epple and C. L. Bottasso, Who's afraid of high index DAES? Scaled and augmented Lagrangian formulations in multibody dynamics, *8th World Congress on Computational Mechanics*, Venice, Italy, 2008.

[2] M. Tanabe, H. Wakui and N. Matsumoto, The finite element analysis of dynamic interactions of high-speed Shinkansen, rail, and bridge, *Computers in Engineering,* Book No. G0813A, 17-22, ASME, 1993.

[3] A. Jaschinski, G. Schupp and H. Netter, Demonstration of simulation potentials in railway vehicle system dynamics through selected examples, *Proceedings of World Congress on Railway Research*, vol. D, 15-23, 1997.

[4] S. Bruni, A. Collina, R. Corradi and G. Diana, Numerical simulation of train-track-structure interaction for high speed railway systems, *Proceedings of Structures for High-Speed Railway Transportation*, *IABSE Symposium*, Antwerp, Belgium, 2003.

[5] R. Simoes, R. Calcada and R. Delgado, Track-bridge interaction in railway lines: Numerical modelling and application, *Track-Bridge Interaction on High-Speed Railways*, 205-216, FEUP Porto Portugal, 2007.

[6] M. Tanabe, N. Matsumoto, H. Wakui, M. Sogabe, H. Okuda and Y. Tanabe, A simple and efficient numerical method for dynamic interaction analysis of a high-speed train and railway structure during an earthquake, J. Computational and Nonlinear Dynamics, Vo.3/ 041002, ASME, 2008.
[7] M. Tanabe, N. Matsumoto, H. Wakui, M. Sogabe, Simulation of a Shinkansen train on the railway structure during an earthquake, *Japan J. Indust. Appl. Math.,* 28, 223-236, 2011.
[8] M. Tanabe, S. Komiya, H. Wakui, N. Matsumoto and M. Sogabe, Simulation and visualization of a high-speed Shinkansen train on the railway structure, *Japan J. Indust. Appl. Math.* vol.17, 309-320, 2000.
[9] J. J. Kalker, *Three-dimensional elastic bodies in rolling contact,* Kluwer, 1990.
[10] *Dynamics of railway vehicle,* JSME, 1994.
[11] H. Wakui, Technological innovation in railway structure system with ladder sleeper, *Concrete Journal,* Vol.36, No.5, 8-16, 1998.
[12] K. Asanuma, M. Sogabe, T. Watanabe, J. Okayama and H. Wakui, Development of a Ballasted ladder track equipped with a vehicle guide device, *RTRI Report* Vol.23, No.2, 27-32, 2009.

COMPDYN 2013
4th ECCOMAS Thematic Conference on
Computational Methods in Structural Dynamics and Earthquake Engineering
M. Papadrakakis, V. Papadopoulos, V. Plevris (eds.)
Kos Island, Greece, 12–14 June 2013

HOW TO QUANTIFY THE VIBRATION REDUCTION OF RAILWAY TRACKS

L. Auersch
[1] Federal Institute of Material Research and Testing
12200 Berlin, Germany
e-mail: Lutz.auersch-saworski@bam.de

Keywords: Railway induced ground vibration, mitigation measures, railway tracks, finite-element boundary-element method, wavenumber integrals, 1-D insertion loss.

Abstract. *Railway tracks, which reduce the ground vibration, are necessary if the trains are passing near to building. Today the reduction effect of railway tracks is often determined by the complex (time domain) simulation of the passage of a complete train. This method of evaluating the reduction is very time consuming and the results include some arbitrary scatter. It is worth to look for simpler methods which yield clearer results in shorter time. This contribution presents the combined finite-element boundary-element method as a detailed method for the track-soil interaction and, on the other hand, some possible simplifications. One important idea for the reduction assessment is to split the reduction in a vehicle-track interaction part and a track transfer part. The track transfer is not influenced by the vehicle and by single axle loads and it can be calculated as a homogeneous problem along the track. The reduction of some tracks (for example of floating slab tracks) can be dominated by this track transfer function whereas other tracks (for example tracks with soft rail pads) are completely determined by the vehicle-track-interaction part. The different force transfer functions and the ground vibration ratios of tracks with elastic rail pads or elastic sleeper pads are shown as a result of the FEBEM model under a fixed harmonic axle load. The force transfer proves to be a useful quantity for to assess the vibration reduction of railway tracks.*

1 INTRODUCTION

Trains are passing over tracks, and the irregularities of the wheel and the track yield dynamic loads on the track and the soil. Waves are generated and are propagating through the soil. The ground vibration excites buildings in the vicinity and can annoy persons who live or work inside them. Nuisance problems must be solved by countermeasures at the vehicle, the track or the transmission path. This contribution deals with special countermeasures at the track, elastic rail pads and sleeper pads.

The contribution describes different methods for the analysis of the track-soil system and, in the third section the method of vehicle-track interaction. Results are presented firstly for the track and vehicle-track system and, secondly, for the ground vibration.

2 METHODS FOR THE ANALYSIS OF THE TRACK

Four different methods will be presented which allow a dynamic analysis of the track. The most rigorous method is the combined 3-dimensional finite-element boundary-element method. The second method for a multi beam on a continuous soil can be applied for a continuous slab tracks. Whereas Fourier wavenumber integrals must be used for the continuous soil, the solution for a multi beam on a Winkler soil can be solved in space domain. Some simplifications are valid for the force transfer of the track which can be exploited by insertion loss formula.

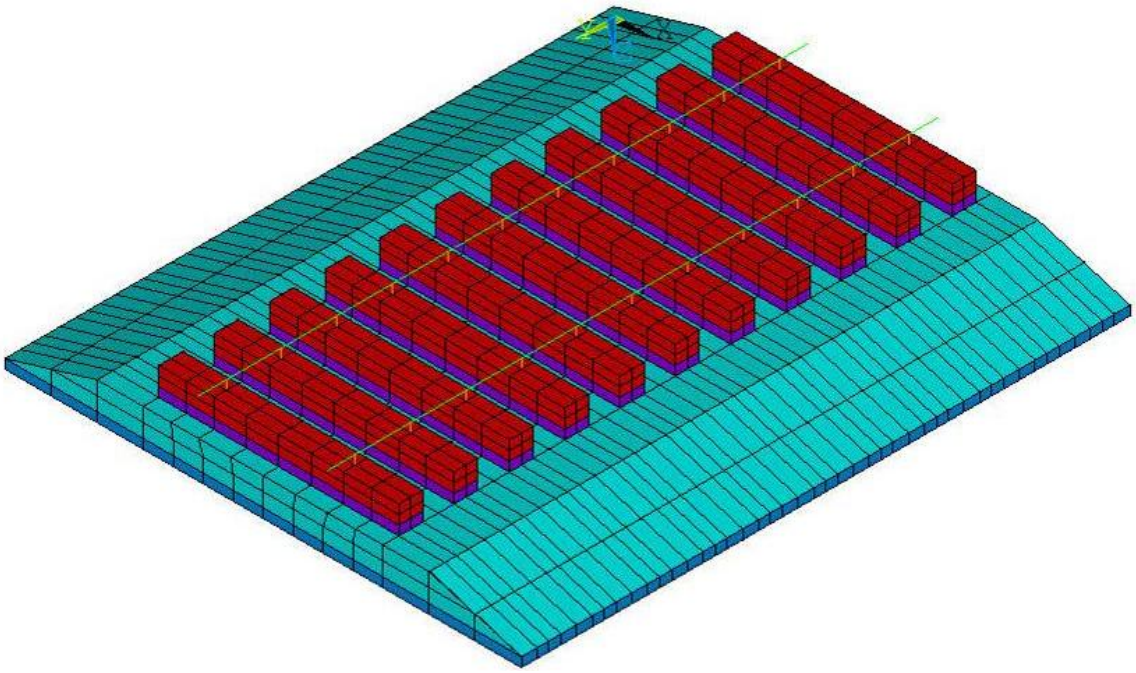


Figure 1: Finite element model of the ballasted track with elastic rail pads, sleeper pads and ballast mat.

2.1 3-dimensional finite-element boundary-element method (FEBEM)

The track-soil systems are calculated most detailed by the combined finite-element boundary-element method [1]. The track including the rails, rail pads, sleepers, under sleeper pads, and ballast is modeled by the finite element method (Fig. 1) whereas the homogeneous or layered soil is modeled by the boundary element method. The dynamic stiffness matrix of the soil is established by using the Green's functions of an elastic layered half-space [2]. All calculations (Green's functions, boundary matrix and finite element matrices) are performed in frequency domain. Special additional methods (within the FEBEM) have been developed

for infinite tracks [3] which are also applied to this study. The track displacement u_R and the total force F_S that is acting on the soil are evaluated from the results. As the Green's function of the homogeneous or layered soil are available, the ground vibration v_i at distances x_i away from the track can also be calculated.

wheelset mass	m_W = 1000, <u>1500</u>, 2000, 3000 kg
bending stiffness of the rails (UIC60)	EI = 12.6 10^6 Nm^2,
mass per length of the rails	m'_R = 2 x 60 kg/m,
distance of the rail pads	d = 0.6 m,
stiffness of the rail pads	k_P = 5, 10, 20, 40, 80, 150, <u>300</u> 10^6 N/m,
modulus of elasticity of the sleepers	E_S = 3 10^{10} N/m^2,
mass density of the sleepers	ρ_S = 0.63, 1.25, <u>2.5</u>, 5 10^3 kg/m^3,
length of the sleepers	a_S = 2.6 m,
height of the sleepers	h_S = 0.2 m,
width of the sleepers	b_S = <u>0.26</u>, 0.52 m ,
stiffness of the sleeper pads	k_S = 12.5, 25, <u>50</u>, 100, 200 10^6 N/m,
shear modulus of the ballast	G_B = 2, 4.5, 8, <u>18</u> 10^7 N/m^2,
shear wave velocity of the ballast	v_{SB} = 100, 150, 200, <u>300</u> m/s
smaller width of the ballast	a_{B1} = 3.6 m,
larger width of the ballast	a_{B2} = 5.6 m,
height of the ballast	h_B = 0.3 m,
shear modulus of the soil	G = 2, 4.5, <u>8</u>, 18, 50 10^7 N/m^2,
shear wave velocity of the soil	v_S = 100, 150, <u>200</u>, 300, 500 m/s,
mass density of the soil and ballast	ρ = 2 10^3 kg/m^3,
Poisson's ratio of the soil and ballast	ν = 0.33,
hysteretic damping of the soil and ballast	D = 2.5 %,
hysteretic damping of the elastic elements	$D_P = D_S$ = 10 %.

Table 1: Parameters of the vehicle-track-soil systems (standard parameters are underlined).

2.2 Multi beam on continuous soil

The multi beam on continuous soil is solved in frequency-wavenumber domain [4]. Each beam is described by the bending stiffness EI_j and the mass per length m_j' which are assembled in a diagonal stiffness matrix **EI** and a diagonal mass matrix **m'**. The global stiffness matrix **K'** is a nxn matrix assembled from the 2x2 dynamic stiffness matrices of each support section. The multi-beam system fulfils the set of differential equations for the beam displacements **u** under the track load $\mathbf{F_T'}$

$$\mathbf{EIu}''''+\mathbf{m'}\ddot{\mathbf{u}}+\mathbf{K'u}=\mathbf{F_T'} \tag{1}$$

The contact force F'_S between the lowest beam and the soil is distributed uniformly across the width. The average displacement of the soil across the width is equal to the displacement of the lowest beam.

The dynamic stiffness of the multi-beam track model in the frequency-wavenumber domain reads as

$$\mathbf{K_T}=k_y^4\mathbf{EI}-\omega^2\mathbf{m'}+\mathbf{K'} \tag{2}$$

where k_y is the wavenumber along the track axis. In order to couple the track and the soil, the dynamic soil stiffness $\mathbf{K_S}$ for harmonic waves along the track [4] is added to the track stiffness

(2) at the last diagonal element and the dynamic stiffness matrix of the track-soil system is established

$$\mathbf{K}_{TS} = \mathbf{K}_T + \mathbf{K}_S \tag{3}$$

The displacements in the frequency-wavenumber domain are calculated by the inversion of this matrix

$$\mathbf{u} = \mathbf{K}_{TS}^{-1}\, \mathbf{F_T}' \tag{4}$$

The wavenumber transform of the vertical point load $\mathbf{F_T}'(y) = \mathbf{F_T}\, \delta(y)$ is the constant force $\mathbf{F_T}$. The displacements along the track can be calculated by the inverse Fourier transformation as

$$\mathbf{u}(y,\omega) = \frac{1}{2\pi} \int_{-\infty}^{+\infty} \mathbf{K}_{TS}{}^{-1}(k_y,\omega)\mathbf{F_T} e^{ik_y y} dk_y \tag{5}$$

The force distribution on the track-soil interface can then be calculated by a similar Fourier integral

$$F'_S(y,\omega) = \frac{1}{2\pi} \int_{-\infty}^{+\infty} K_S(k_y,\omega) u_S(k_y,\omega) e^{ik_y y} dk_y \tag{6}$$

using the displacements of the track-soil interface $u_S(k_y, \omega)$ and the soil stiffness $K_S(k_y, \omega)$.

Finally, the total force that acts on the track-soil interface is calculated as the integral over the infinite track length

$$F_S(\omega) = \int_{-\infty}^{+\infty} F'_S(y,\omega) dy = F'_S(k_y = 0,\omega) = K_S(k_y = 0,\omega) u_S(k_y = 0,\omega) \tag{7}$$

This soil force can easily be obtained as the transformed integrand at $k_y = 0$ without any integration. Moreover, the total force computation corresponds to a two-dimensional analysis across the track.

The ground vibration, however, needs the most laborious calculation. A double Fourier transform along k_x and k_y must be performed

$$u(x,y,\omega) = \frac{1}{(2\pi)^2} \int_{-\infty}^{+\infty} \int_{-\infty}^{+\infty} H(k_x,k_y,\omega) K_S(k_y,\omega) u_S(k_y,\omega)\, p_1(k_x) e^{i(k_x x + k_y y)} dk_x dk_y \tag{8}$$

to obtain the soil displacements at any position away from the track.

2.3 Multi beam on Winkler soil

In general, the Winkler soil is not an adequate model of the real soil [1], but for certain conditions a rough approximation has been achieved [5]. In case of a Winkler soil, the soil stiffness does not depend on the wavenumber and can be expressed as a spring and a damper force so that the solution can be obtained in space domain.

The displacement solution **u** for this track system is found as

$$\mathbf{u}(y) = \sum_{j=1}^{2n} A_j \mathbf{v}_j e^{k_j y} \tag{9}$$

where the k_i are the solution of the eigenvalue problem

$$(\mathbf{EI}k^4 - \mathbf{m'}\omega^2 + \mathbf{K'})\mathbf{u} = \mathbf{0} \tag{10}$$

and $\mathbf{v}_j$ the corresponding eigenvectors, see [6] for more details. In case of a single beam on Winkler soil, the compliance solution can be expressed as

$$\frac{u_R}{F_T} = \frac{1}{2\sqrt{2}EI^{0.25}(k'-m'\omega^2)^{0.75}}. \tag{11}$$

For the force transfer F_S/F_T of the track, the following general relation holds

$$F_S = \int_{-\infty}^{\infty} F_S'\,dy = \int_{-\infty}^{\infty} \frac{F_S'}{F_T'} F_T'\,dy = \frac{F_S'}{F_T'} \int_{-\infty}^{\infty} F_T'\,dy = \frac{F_S'}{F_T'} F_T \tag{12}$$

and that means

$$\frac{F_S}{F_T} = \frac{F_S'}{F_T'} \tag{13}$$

that the ratio between the soil force F_S (the sum of all soil forces distributed along the track) and the force F_T that is acting on the track (the dynamic axle load) is the same as the ratio F_S'/F_T' for each support element independent of the load distribution by the bending stiffness of the beams.

2.4 1-dimensional insertion loss formula for the force transfer of the track

As the force transfer of the track can be analysed by the 1-dimensional support chains, the insertion loss formula

$$\frac{F_{S,without}}{F_{S,with}} = \frac{\frac{1}{K_Q} + \frac{1}{K_R} + \frac{1}{k_I}}{\frac{1}{K_Q} + \frac{1}{K_R}} = 1 + \frac{1}{k_I}\frac{K_Q K_R}{K_Q + K_R} \tag{14}$$

can be applied to get the effect of the insertion of an elastic element with a spring stiffness k_I, where K_Q and K_R are the dynamic stiffnesses of the source and the receiver, see the Appendix for the derivation.

This formula is valid for the force transfer of the track. To apply the formula also to the whole vehicle-track system as in [7] and [8], a track- and frequency-dependent track length must be used to get the same results as for the beam on Winkler soil [6]. The 2-dimensional beam-on-Winkler-soil model is almost as simple as the 1-dimensional model and the determination of realistic parameters is more straightforward. Generally, the simple 1-dimensional and 2-dimenional results must be checked by more detailed methods for the track and the soil.

3 METHODS FOR THE VEHICLE-TRACK INTERACTION

The influence of the vehicle on the track and ground vibration can be calculated in a second step. The compliance of the track is inverted to the track stiffness $K_T = (u_R/F_T)^{-1}$. A corresponding dynamic stiffness K_V of the vehicle can be calculated by multi-body dynamics [9]. It can be approximated by the inertia of the wheelset $K_V = -m_W\omega^2$ in the frequency range of interest. The vehicle is excited by the irregularities s of the track (alignment and rail roughness) and the vehicle (out-of-roundness and roughness of the wheel).

The transfer function between the irregularities s and the force F_T on the track can be calulated from these two dynamic stiffnesses as [1, 3]

$$\frac{F_T}{s} = -\frac{K_T K_V}{K_T + K_V} \tag{15}$$

The vehicle-track interaction can also be expressed as

$$\frac{F_T}{F_V} = \frac{K_T}{K_T + K_V} \tag{16}$$

if the equivalent excitation force $F_V = -K_V s$ is used. This is a second force transfer function which has to be multiplied with the force transfer function F_S/F_T of the track to get the total force transfer function

$$\frac{F_S}{F_V} = \frac{F_S}{F_T}\frac{F_T}{F_V} . \tag{17}$$

4 FORCE TRANSFER OF THE TRACK AND VEHICLE-TRACK SYSTEM

Two types of elastic elements are considered, elastic rail pads between rail and sleeper and elastic sleeper pads between sleeper and ballast. The stiffness of these elements is varied in a wide range, the rail pad stiffness as k_P = 5, 10, 20, 40, 80, 150 10^6 N/m and the sleeper pad stiffness as k_S = 12.5, 25, 50, 100, 200 10^6 N/m. By this choice, the stiffness per sleeper is approximately the same for rail and sleeper pads. As a reference, a ballasted track without sleeper pad and with a stiff rail pad of k_P = 300 10^6 N/m is used.

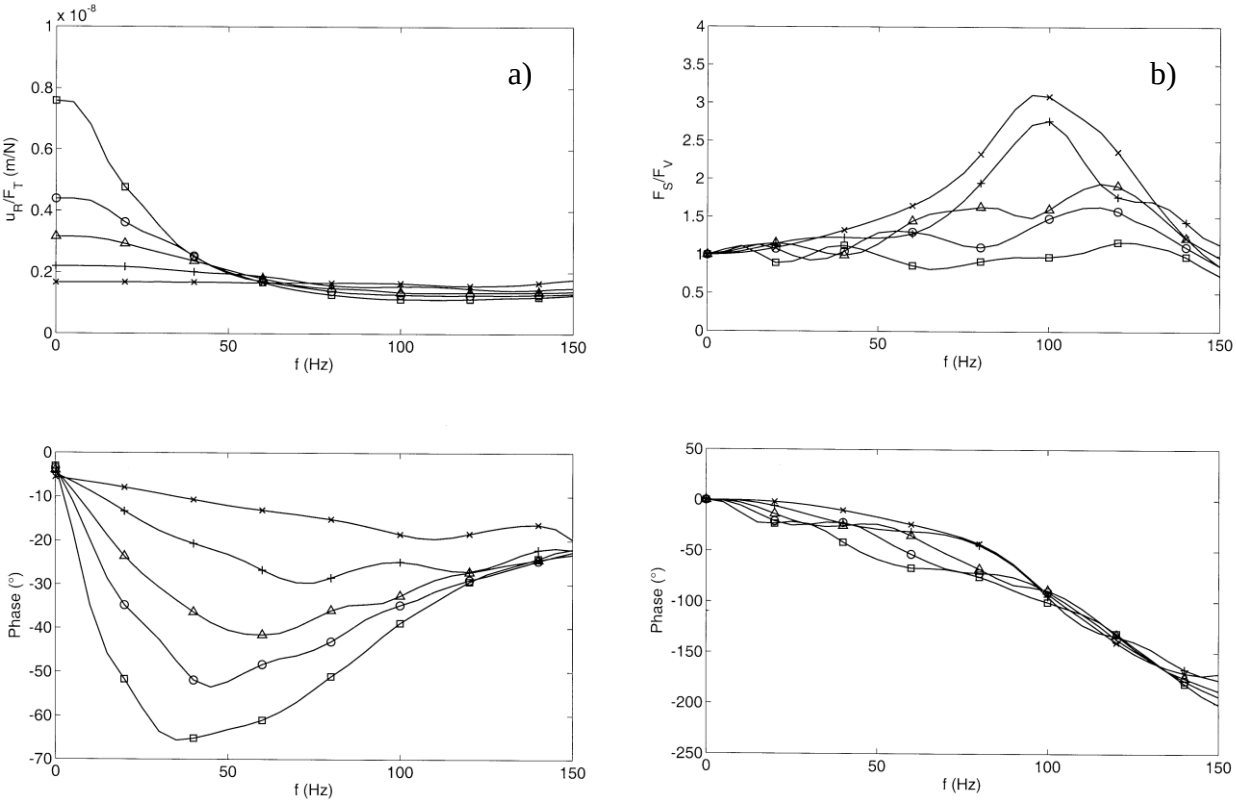


Figure 2: Compliance (a) and total force transfer (b) (amplitude and phase) of a ballasted track on different soils, v_S = □ 100, ○ 150, △ 200, + 300, × 500 m/s

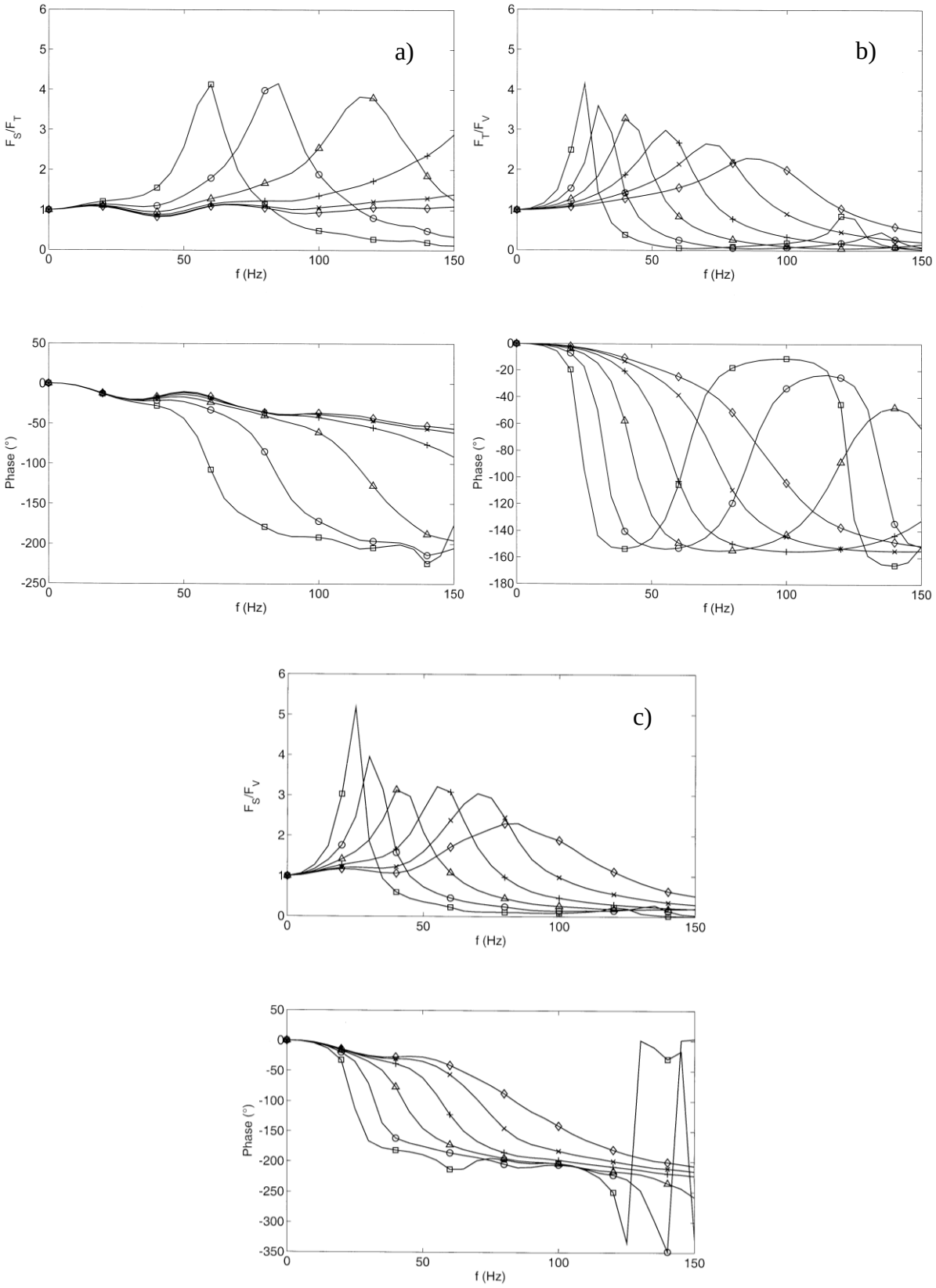


Figure 3: Tracks on different elastic rail pads k_P = □ 5, ○ 10, △ 20, + 40, × 80, ◇ 150 kN/mm, force transfer of the track (a), of the vehicle-track interaction (b) and the total force transfer (c) as amplitude and phase.

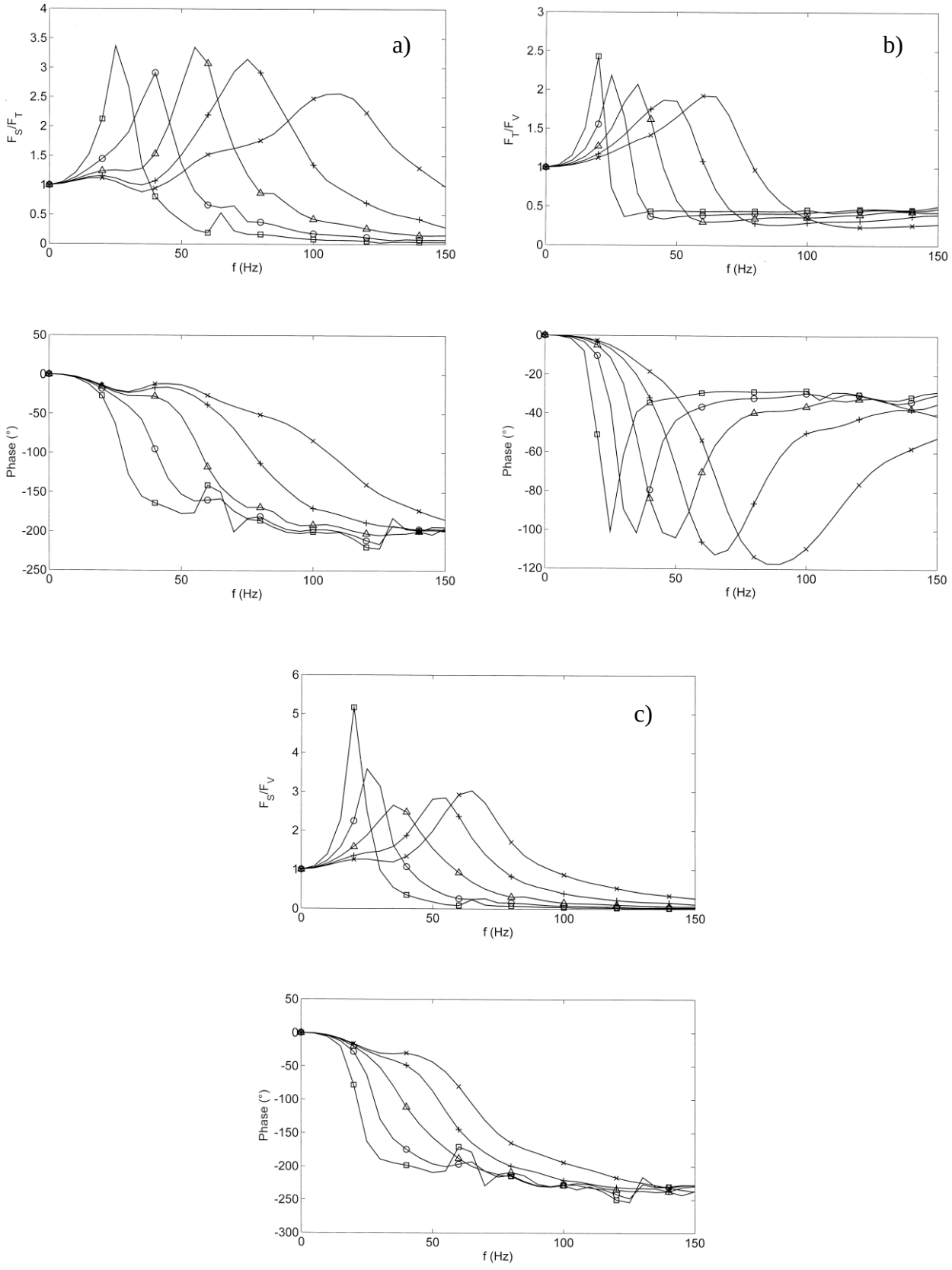


Figure 4: Tracks on different elastic sleeper pads k_S = □ 12.5, ○ 25, △ 50, + 100, × 200 kN/mm, force transfer of the track (a), of the vehicle-track interaction (b) and the total force transfer (c) as amplitude and phase.

The reference ballasted track is analysed for the track compliance u_R/F_T (Fig. 2a) and the total force transfer F_S/F_V (Fig. 2b). All results are presented as frequency dependent amplitude and phase. The influence of different soils characterized by their shear wave velocities v_S is demonstrated. A strong influence of the soil on the low-frequency compliance can be observed. At higher frequencies, the compliances are almost the same for the different soils. Therefore, similar resonance frequencies of the vehicle-track-soil systems are found at about 100-120 Hz. In general, the force transfer of a track without any elastic element is close to the value 1, and the resonance amplifications are weak due to the radiation damping into the infinite soil, except for the two stiffest soils.

The track with elastic rail pads is analysed for the three different force transfers of the track (Fig. 3a), the vehicle-track interaction (Fig. 3b), and the total force transfer (Fig. 3c). The resonance frequencies of a track with elastic rail pads are relatively high due to the small rail mass. The resonances are observed for the three softest rail pads at 60 to 150 Hz, whereas no track resonance can be found below 150 Hz for normal pad stiffnesses. The reduction effect of the rail pads is based on the greater wheelset mass and the vehicle-track interaction. Compared to the track system without wheelset mass (Fig. 3a), the complete vehicle-track system yields considerably lower resonance frequencies (Fig. 3b,c). The resonance frequencies for the whole vehicle-track system are in the range of 25 to 90 Hz for the different rail pads which means an increase according to $f_0 \sim k_P^{0.35}$. For frequencies higher than the resonance frequency, a clear reduction can be found. The reduction due to the elastic rail pads is $F_S/F_V = 0.1$ to 1.8 at 100 Hz. That means that the two stiffest rail pads do not yield a reduction at 100 Hz, only at 150 Hz with values of 0.5 and 0.3. The transfer function F_T/F_V of the vehicle-track interaction and the total force transfer F_S/F_V are close together in case of normal rail pads. The reduction effects of the rail pads are dominated by the vehicle-track interaction. For other track systems such as floating slab track it is quite opposite. The reduction effect of floating slab tracks is completely determined by the force transfer of the track [4].

The track with elastic sleeper pads is analysed in Figures 4a,b,c for the same three force transfer functions as the track with rail pads. The force transfer of the track shows the resonance frequencies of the track (Fig. 4a). All under sleeper pads yield track-pad resonances below 150 Hz, starting at 25 Hz for the softest and ending at 110 Hz for the stiffest sleeper pad. Including the wheelset mass yields a somewhat lower vehicle-track resonance between 20 and 60 Hz (Fig. 4b). The vehicle-track transfer function F_T/F_V drops down at the vehicle-track resonance frequencies and keeps an almost constant value of $F_T/F_V = 0.35$ for higher frequencies. The total force transfer function, however, has a continuous decrease after the resonance which is determined by the track transfer function F_S/F_T. The vehicle-track interaction yields the reduction just after the vehicle-track resonance and contributes a constant reduction at high frequencies. The total force transfer owing to the elastic sleeper pads can be quantified as $F_S/F_V = 0.016$ to 0.9 at 100 Hz and $F_S/F_V = 0.07$ to 0.27 at 150 Hz where the softest pads yield the strongest reduction. Below 100 Hz, only softer under sleeper pads yield considerable reductions. Around the vehicle-track resonance, all sleeper and rail pads yield resonance amplifications of $F_S/F_V = 2$ to 5, the highest amplifications for the softest pads. The force transfer functions for the different sleeper pads are also presented as the results of the beam-on-Winkler-soil model in Fig. 5 which are quite similar as in Fig. 4.

The influence of the mass of the sleeper is studied in Figures 6a,b,c: The sleeper-on-pad resonance is shifted from 80 Hz, via 60 and 50 Hz to less than 40 Hz if the mass is doubled three times. The strong reduction above this resonance frequency can clearly be seen in Figure 6a where the lowest amplitudes are found for the lowest resonance frequency. If the vehicle-track interaction is considered (Fig. 6b), the vehicle-track resonance frequencies are lower and

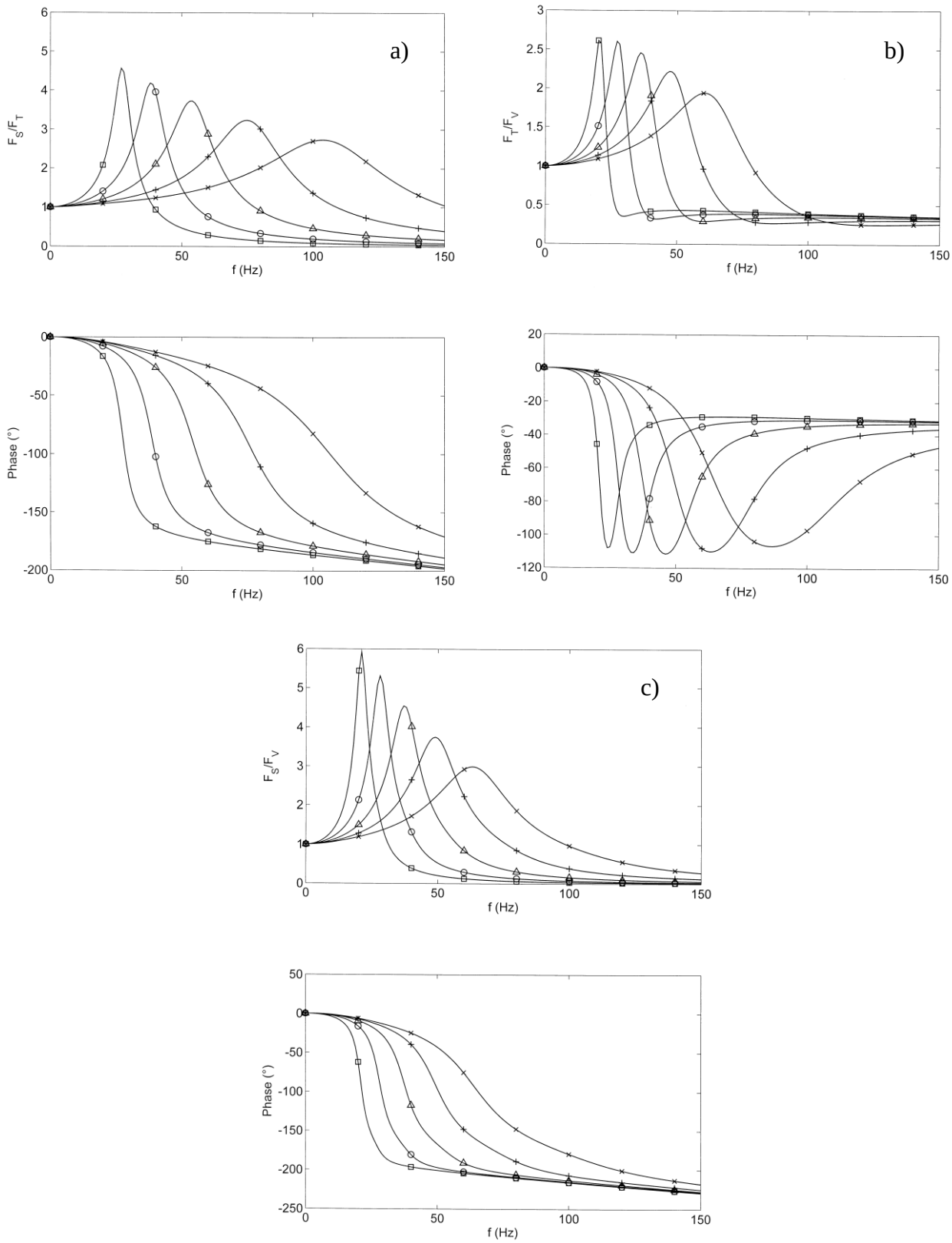


Figure 5: Tracks on different elastic sleeper pads k_S = □ 12.5, ○ 25, △ 50, + 100, × 200 kN/mm, force transfer of the track (a), of the vehicle-track interaction (b) and the total force transfer (c) calculated for the beam-on-Winkler-soil model.

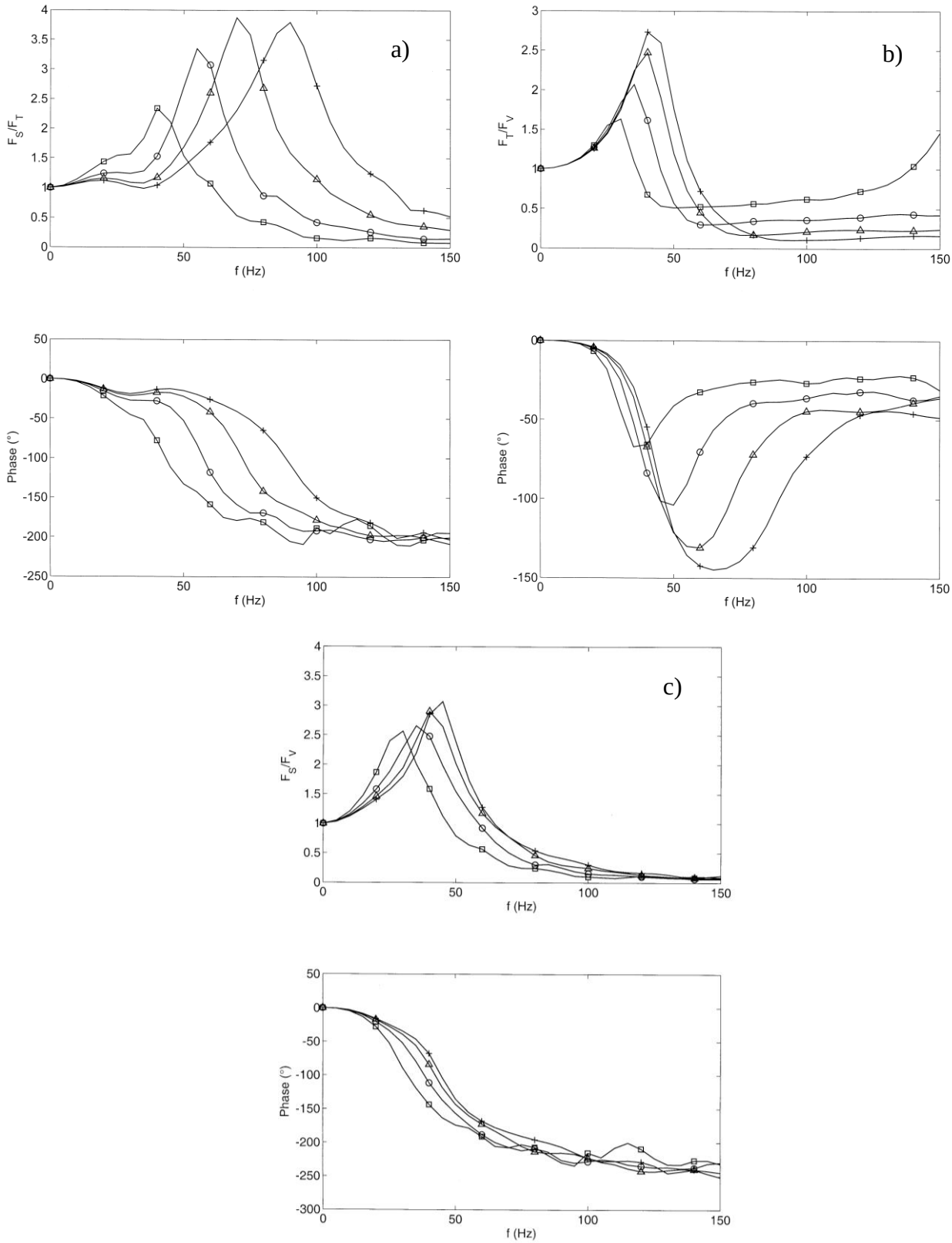


Figure 6: Track on elastic sleeper pads k_S = 50 kN/mm, different sleeper masses m_S = □ 1/4 m_{S0}, ○ 1/2 m_{S0}, △ m_{S0}, + 2 m_{S0}, force transfer of the track (a), of the vehicle-track interaction (b) and the total force transfer (c) as amplitude and phase.

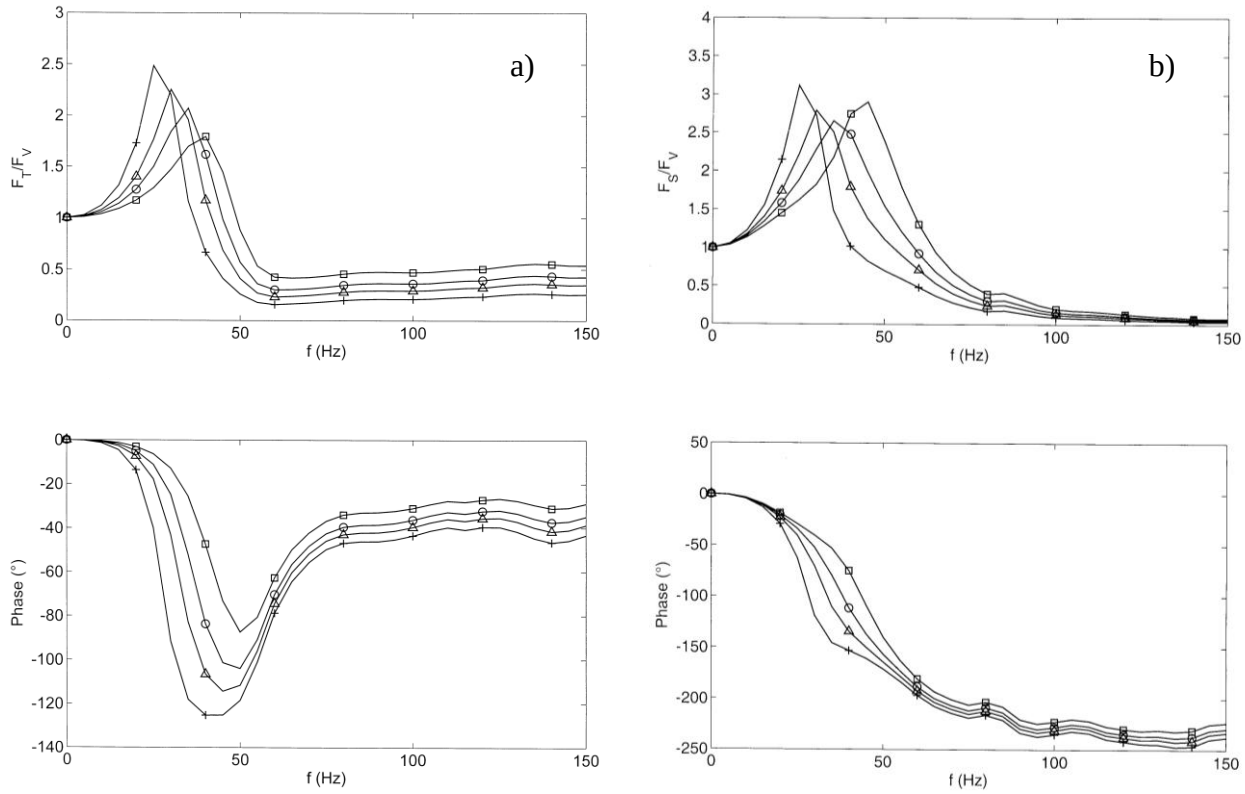


Figure 7: Track on elastic sleeper pads k_S = 50 kN/mm, force transfer of the vehicle-track interaction (a) and the total force transfer (b) for different wheelset masses m_W = □ 1000, ○ 1500, △ 2000, + 3000 kg.

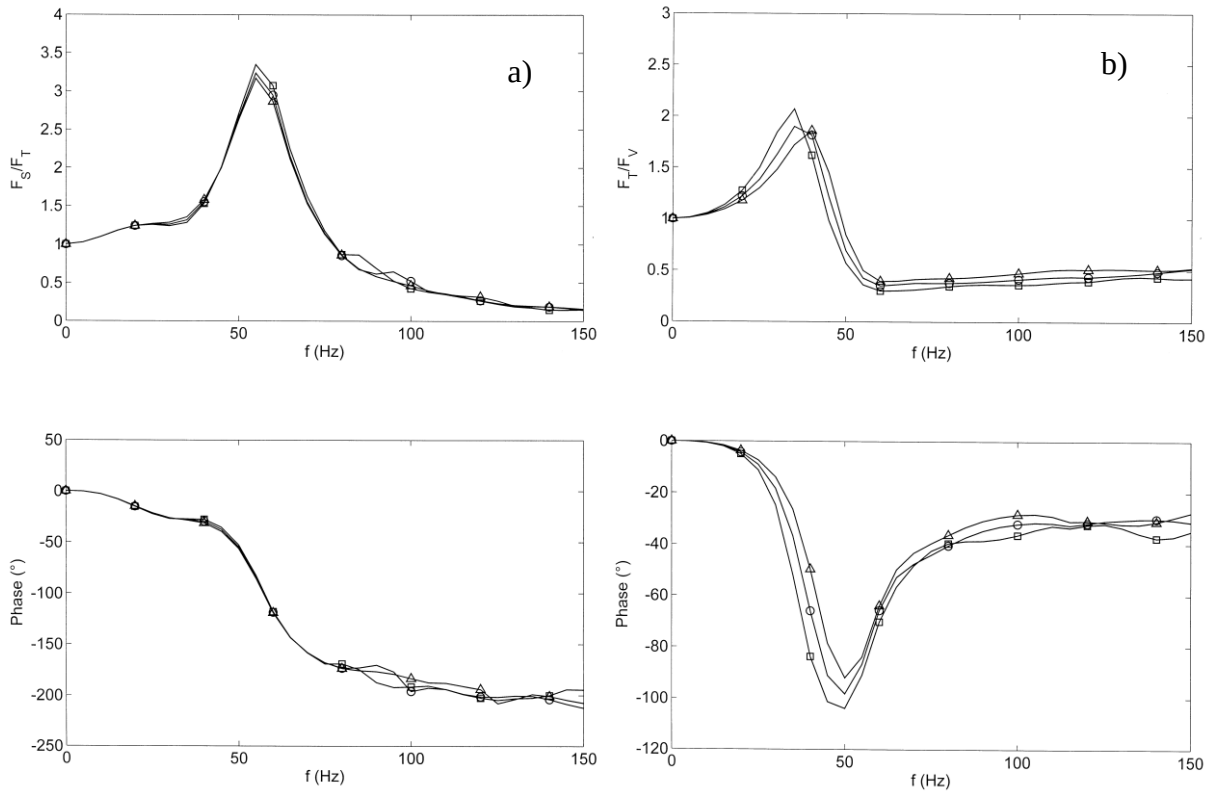


Figure 8: Tracks on elastic sleeper pads k_S = 50 kN/mm with different bending stiffnesses of the rails, EI = □ EI_0, ○ $2EI_0$, △ $4EI_0$,, force transfer of the track (a), of the vehicle-track interaction (b) and the total force transfer (c) as amplitude and phase.

closer together. That means that the influence of the track mass on the whole system is weaker. The vehicle-track force transfer functions are almost constant at high frequencies, but with different reduction values which are lower for lower masses. The total transfer function in Figure 6c shows the vehicle-track resonances close together and also the high-frequency amplitudes close together what is due to the opposite effects of the track transfer and the vehicle-track transfer. Whereas the force reduction is similar for the small sleeper masses, a better reduction can be found for the double sleeper mass compared to the reference track for most frequencies above 32 Hz.

The influence of the wheelset mass is presented in Figures 7a and b. For higher wheelset masses the force reduction of the elastic sleeper pads can be improved. The force transfer of the track remains unchanged when the wheelset mass is varied. Therefore the additional effect is caused by the vehicle-track force transfer (Fig. 7b). The vehicle-track resonance frequency is shifted down to 25 Hz for a heavy wheelset of $m_W = 3000$ kg. The transfer function drops down and keeps constant above the track resonance at 55 Hz. The additional reduction depends on the mass of the wheelset and is in the range of $F_T/F_V = 0.2$ to 0.55 for $m_W = 3000$ to 1000 kg. The continuous decrease of the total force transfer (Fig. 7b) at higher frequencies is due to the force transfer of the track with sleeper pads.

The minor influence of the bending stiffness of the track is demonstrated on Figure 8. As stated in the methods sections, the bending stiffness has no influence on the force transfer of the track (Fig. 8a). The influence on the track stiffness and the vehicle-track interaction (Fig. 8b) is weak. Although the bending stiffness is increased by a factor of 4, the changes of the force transfer are less than 20 per cent.

Due to the higher track mass, the track with sleeper pads has lower resonance frequencies and stronger high-frequency reductions compared to the track with elastic rail pads.

5 GROUND VIBRATION AND GROUND VIBRATION RATIOS

So far, only the track behaviour has been considered. Now, the ground vibrations which are propagating away from the track are examined. The velocity amplitudes of the soil are calculated at the distances $x = 5$, 10, 15, 20, 25, 30 m from the exciting force and are shown in Figures 9a,b as admittance spectra $v/F(f)$ for the standard track and the track with sleeper pads of $k_S = 50$ kN/mm. All admittance functions start with similar increasing amplitudes at low frequencies. The curves of the point load would continue to increase for almost all frequencies. Only the high-frequency far-field amplitudes are reduced due to the material damping. The standard track load yields almost constant ground vibration amplitudes at frequencies higher than 40 Hz what is due to the distribution of the load across the track width (see Auersch, 2005b for details). The distribution of the force leads also to a marked minimum of amplitudes at 63 and 80 Hz if one wavelength of the soil fits into the sleeper length. The isolated track (Fig. 9b) has decreasing ground vibration amplitudes (admittance functions) at higher frequencies due to the additional reduction effect of the resiliently supported track mass.

To determine the effectiveness of the mitigation measure, the soil response (including the vehicle track interaction) of the isolated track is compared with the soil response of the un-isolated track. The amplitude ratios between the isolated and un-isolated slab tracks of different sleeper pads are shown in Figures 9f,g for a near-field ($x = 5$ m) and a far-field point ($x = 30$ m). The amplitude ratios of the ground vibrations typically present the resonance of the vehicle and track on the sleeper pads and the reduction at higher frequencies. The ground vibration ratios under the track (Fig. 9e) are somewhat smaller than those of the near and far field. The vibration ratios for the track start with values smaller than 1, and the resonance amplifications are also smaller.

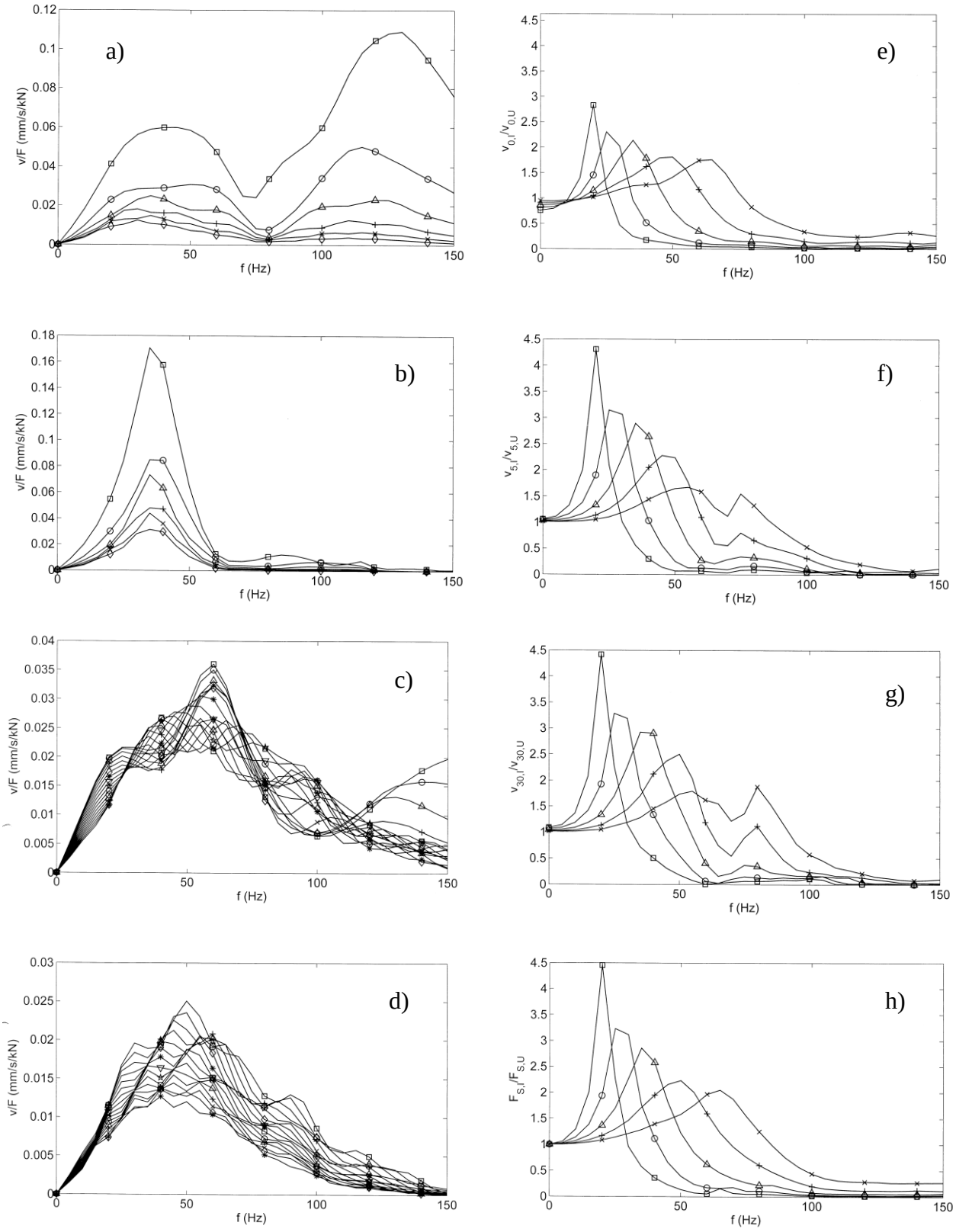


Figure 9: a, b) Ground vibration amplitudes at x = □ 5, ○ 10, △ 15, + 20, × 25, ◇ 30 m distance from the load on the reference ballasted track (a) and the track with elastic sleeper pad of k_S = 50 kN/mm. c, d) Ground vibration at x = 8 m from the reference ballasted track, variation of the longitudinal distance from the load y = 0 to 15 m (c) and y = 16 to 31 m. e, f, g, h) ratios between isolated and un-isolated tracks, rail pads of k_S = □ 12.5, ○ 25, △ 50, +100, × 200, ground vibration at x = 0 m (e), 5 m (f) and 30 m (g), total soil force (h).

These are effects of the load distribution along the track. The effects of the load distribution across the track yield some irregularities of the ground vibration ratios at 60 to 80 Hz.

In Figure 9h, also the ratio of the soil forces for isolated and un-isolated tracks are presented. These force ratios are in good agreement with the ground vibration ratios. As the force ratios are very similar to the total force transfer F_S/F_V in Figure 4c, both force functions (force ratios and force transfer function) are good quantities to assess the mitigation potential of elastic elements of the track such as rail and sleeper pads. The force functions are smoother than the ground vibrations which depend on the specific load distribution under the track. Another method to get smoother results is to average the ground responses for different load positions which have less frequency-dependent variations for longitudinal distances $y > 4$ m as shown in Figures 9c,d.

6 CONCLUSION

Methods to assess the reduction of railway tracks have been presented. Detailed 3-dimenional track-soil models are calculated by the combined finite-element boundary-element method (FEBEM). The force transfer is established as two parts, the force transfer of the track and the force transfer of the vehicle-track system. Simplifications are possible for the force transfer of the track where 2-dimensional beam-on-support models or 1-dimensional insertion loss formula are applicable if the track parameters are calibrated by detailed models.

Results have been shown for a track with rail pads, a track with sleeper pads and a track without any elastic element. Track resonances, vehicle-track resonances, and reduction effects at higher frequencies are found for the tracks with elastic elements. The best reduction values at 100 Hz for elastic rail and sleeper pads are 0.1and 0.016. These strong effects can only be achieved with very soft elements which, on the other hand, yield undesirable great displacements under the static train load. With constrained static displacements, the reductions of 0.27 and 0.18 at 100 Hz are more realistic. The mitigation effect is better for the sleeper pads owing to the higher track mass supported on the elastic element. Some parameter variations (pad stiffness, sleeper mass, wheelset mass, bending stiffness) are presented for the sleeper pads showing the vanishing influence of the bending stiffness on the track transfer and the possible improvement by heavier sleepers.

It has been found that the force reduction of the rail pads is almost completely determined by the vehicle-track interaction. The vehicle-track interaction has a considerable influence on the reduction of the sleeper pads, but the total reduction is also influenced by the force reduction of the track, which can be improved by heavier sleepers. For other track systems as ballasted tracks on ballast mats or floating slab tracks, the reduction effect is almost completely determined by the force reduction of the track.

The total soil force ratio is very close to the ground vibration ratio. Therefore, it may be concluded that the total force is the track quantity which is best suited to predict the reduction of the ground vibration by elastic track elements.

7 APPENDIX: EFFECTIVENESS OR INSERTION LOSS OF A MITIGATION MEASURE

The system is divided into a part close to the source (index Q) and a part close to the receiver (index R). The following dynamic stiffness relations hold for the two divided parts of the system

$$\begin{aligned} K_Q u_1 &= -F_1 + F \\ K_R u_2 &= -F_2 \end{aligned} \tag{18}$$

where an exciting force F has been introduced at the source side.

These formula yield directly the transfer function of the force for the case without any mitigation measure ($u_1 = u_2$, $F_1 = -F_2$)

$$\frac{F_2}{F}\Big|_{without} = \frac{K_R}{K_Q + K_R} \tag{19}$$

which means that the force transfer F_2/F is the ratio of the dynamic stiffness of the receiver to the dynamic stiffness of the parallel source and receiver.

The mitigation can be done by inserting a soft element to reduce the stiffness K_R of the receiver to K_R*. Thus the force transfer is reduced

$$\frac{F_2}{F}\Big|_{with} = \frac{K_R^*}{K_Q + K_R^*} \ . \tag{20}$$

The ratio E of the force transfer function with and without the mitigation measure is called the effectiveness of the mitigation measure

$$E = \frac{\frac{F_2}{F}\Big|_{without}}{\frac{F_2}{F}\Big|_{with}} = \frac{K_R}{K_Q + K_R}\frac{K_Q + K_R^*}{K_R^*} = \frac{K_R}{K_R^*}\frac{K_Q + K_R^*}{K_Q + K_R} \ . \tag{21}$$

In special situations, namely for 1-dimensional systems, the effectiveness of a mitigation measure can be calculated by simpler formulas without specifying the excitation and the output quantity. If the mitigation measure is specified by the following stiffness relation

$$\begin{aligned} F_1 &= K_{11} u_1 + K_{12} u_2 \\ F_2 &= K_{21} u_1 + K_{22} u_2 \end{aligned} \tag{22}$$

where the index 1 holds for the source side and index 2 for the receiver side. These two equations and the two equations (21) can be solved to get the transfer function of the force

$$\begin{aligned} F_0 &= (K_{11} + K_Q) u_1 + K_{12} u_2 \\ 0 &= K_{21} u_1 + (K_{22} + K_R) u_2 \end{aligned} \tag{23}$$

which yields

$$\begin{aligned} u_1 &= -\frac{K_{22} + K_R}{K_{21}} u_2 \\ F &= \left(-\frac{(K_{11} + K_Q)(K_{22} + K_R)}{K_{21}} + K_{12} \right) u_2 \end{aligned} \tag{24}$$

The ratio of the transfer functions without and with mitigation system yields the effectiveness or insertion loss

$$E = \frac{\left.\frac{F_2}{F}\right|_{without}}{\left.\frac{F_2}{F}\right|_{with}} = \frac{(K_{11}+K_Q)(K_{22}+K_R)-K_{12}K_{21}}{-K_{21}K_R}\frac{K_R}{K_Q+K_R} = \frac{(K_{11}+K_Q)(K_{22}+K_R)-K_{12}K_{21}}{-K_{21}(K_Q+K_R)} \quad (25)$$

The insertion loss is independent of the excitation load and the output quantity.

This formula can be specialised to the most simple mitigation measure. A single spring of stiffness k_I has a stiffness matrix

$$K = \begin{bmatrix} k_I & -k_I \\ -k_I & k_I \end{bmatrix} \quad (26)$$

and therefore an effectiveness of

$$E = \frac{(k_I+K_Q)(k_I+K_R)-k_I^{\,2}}{k_I(K_Q+K_R)} = \frac{\frac{1}{K_Q}+\frac{1}{K_R}+\frac{1}{k_I}}{\frac{1}{K_Q}+\frac{1}{K_R}} = 1+\frac{1}{k_I}\frac{K_Q K_R}{K_Q+K_R} \quad (27)$$

The insertion loss of a spring is the ratio of the total compliance of all elements to the compliance of source and receiver.

If the mitigation measure is described by a transfer matrix T as

$$\begin{aligned} F_1 &= T_{11}F_2 + T_{12}u_2 \\ u_1 &= T_{21}F_2 + T_{22}u_2 \end{aligned} \quad (28)$$

these two and the source and receiver equations (note the opposite sign convention of F_2 in the transfer matrix approach)

$$\begin{aligned} K_Q u_1 &= -F_1 + F \\ K_R u_2 &= +F_2 \end{aligned} \quad (29)$$

can be solved as

$$\begin{aligned} F - K_Q u_1 = T_{11}F_2 + T_{12}u_2 &= T_{11}F_2 + \frac{T_{12}}{K_R}F_2 \\ u_1 = T_{21}F_2 + T_{22}u_2 &= T_{21}F_2 + \frac{T_{22}}{K_R}F_2 \end{aligned} \quad (30)$$

and finally

$$F = \left(T_{11} + \frac{T_{12}}{K_R} + K_Q T_{21} + \frac{K_Q T_{22}}{K_R}\right)F_2 . \quad (31)$$

The effectiveness E can be given as

$$E = \frac{\left.\frac{F_2}{F}\right|_{without}}{\left.\frac{F_2}{F}\right|_{with}} = \frac{K_R T_{11} + T_{12} + K_R K_Q T_{21} + K_Q T_{22}}{K_Q + K_R} \tag{32}$$

As an example for a mitigation element described by a transfer matrix, a single mass is considered. A single mass m has a transfer matrix

$$T = \begin{bmatrix} 1 & -m\omega^2 \\ 0 & 1 \end{bmatrix} \tag{33}$$

and the following effectiveness as a mitigation measure

$$E = \frac{K_R T_{11} + T_{12} + K_R K_Q T_{21} + K_Q T_{22}}{K_Q + K_R} = \frac{K_R - m\omega^2 + K_Q}{K_Q + K_R} = 1 - \frac{m\omega^2}{K_Q + K_R} \tag{34}$$

For this case, the insertion loss is the ratio of the total dynamic stiffness of all elements to the dynamic stiffness of source and receiver. According to these formula, the mass must be dynamically stiff compared to the source and receiver, to yield a high effectiveness, whereas the spring k_I in equation (27) must be soft compared to the source and the receiver.

REFERENCES

[1] L. Auersch, Dynamics of the railway track and the underlying soil: the boundary-element solution, theoretical results and their experimental verification. *Vehicle System Dynamics* **43**, 671-695, 2005.

[2] L. Auersch, Wave propagation in the elastic half-space due to an interior load and its application to ground vibration problems and buildings on pile foundations. *Soil Dynamics and Earthquake Engineering* **30**, 925 – 936, 2010.

[3] L. Auersch, Dynamic axle loads on tracks with and without ballast mats – numerical results of three-dimensional vehicle-track-soil models. *Journal of Rail and Rapid Transit* **220**, 169-183, 2006.

[4] L. Auersch, The dynamic behaviour of slab tracks on homogeneous and layered soils and the reduction of ground vibration by floating slab tracks. *Journal of Engineering Mechanics* **138**, 923-933, 2012.

[5] L. Auersch, Simplified methods for wave propagation and soil-structure interaction: The dispersion of layered soil and the approximation of FEBEM results. C. Soize, G. Schuëller eds. *Proc. 6th Int. Conf. on Structural Dynamics (EURODYN 2005)*, Paris, France, 2005, 1303-1309

[6] L. Auersch, 2- and 3-dimensional methods for the assessment of ballast mats, ballast plates and other isolators of railway vibration. *International Journal of Acoustic and Vibration* **11**, 167-176, 2006.

[7] R. Wettschureck, U. Kurze, Einfügungsdämmaß von Unterschottermatten. *Acustica* **58**, 177-182, 1985.

[8] DIN V45673-4, *Mechanische Schwingungen – Elastische Elemente des Oberbaus von Schienenfahrwegen – Teil 4: Rechnerische Ermittlung der Einfügungsdämmung im eingebauten Zustand*. Beuth Verlag, Berlin, 2008.

[9] L. Auersch, Zur Parametererregung des Rad-Schiene-Systems: Berechnung der Fahrzeug-Fahrweg-Untergrund-Dynamik und experimentelle Verifikation am Hochgeschwindigkeitszug Intercity Experimental. *Ingenieur-Archiv* **60**, 141-156, 1990.

[10] L. Auersch, The excitation of ground vibration by rail traffic: Theory of vehicle-track-soil interaction and measurements on high-speed lines. *Journal of Sound and Vibration* **284**, 103-132, 2005.

COMPDYN 2013
4th ECCOMAS Thematic Conference on
Computational Methods in Structural Dynamics and Earthquake Engineering
M. Papadrakakis, V. Papadopoulos, V. Plevris (eds.)
Kos Island, Greece, 12–14 June 2013

HIGH-SPEED TRAIN PASSAGE EFFECTS IN BUILDINGS: VIBRATION ASSESSMENT AND ISOLATION

A. Romero[1], **M. Solís**[2], **P. Galvín**[3]

Escuela Técnica Superior de Ingeniería. Universidad de Sevilla
Camino de los Descubrimientos s/n, 41092 Sevilla, Spain
e-mail: {aro[1],msolis[2],pedrogalvin[3]}@us.es

Keywords: Dynamic soil-structure interaction, Resonant response, BEM-FEM model, High Speed Train, Isolation system

Abstract. *This paper analyses train induced vibration in buildings. Emission, transmission and immission mechanisms are considered rigorously. Track-ground-building interaction have been studied, concluding that maximum vibration levels are achieved in the floors of the structure. Building induced vibration due to an impulsive load applied at the track have been analysed. The results show an amplification of the structure response around the natural frequencies. Also, an attenuation in the medium-high range frequency is found. Finally, the effects produced by the high speed trains have been investigated. The conclusions show that vibration levels could exceed the limits set by the standards. In theses cases, corrective actions are required. Effectiveness of isolated track systems is evaluated*

1 INTRODUCTION

Induced vibration and radiated noise in buildings due to railway traffic are two of the most important tasks in the design of the new high-speed lines (HSL). This problem (Figure 1) consists of the emission of vibration, wave propagation in soil and the building immission of incident wave field. Vibration levels on attached buildings to HSL depend on the distance to the road, the transmitted load by the train, the train speed, the characteristics of the track and the dynamic properties of the soil. Moreover, structural characteristics of the building and the foundation determine the dynamic response. Taking into account that vibrations produced by train passages may induced high levels, it is necessary to analyse those points on the track where buildings are close and, if necessary, get mitigation actions.

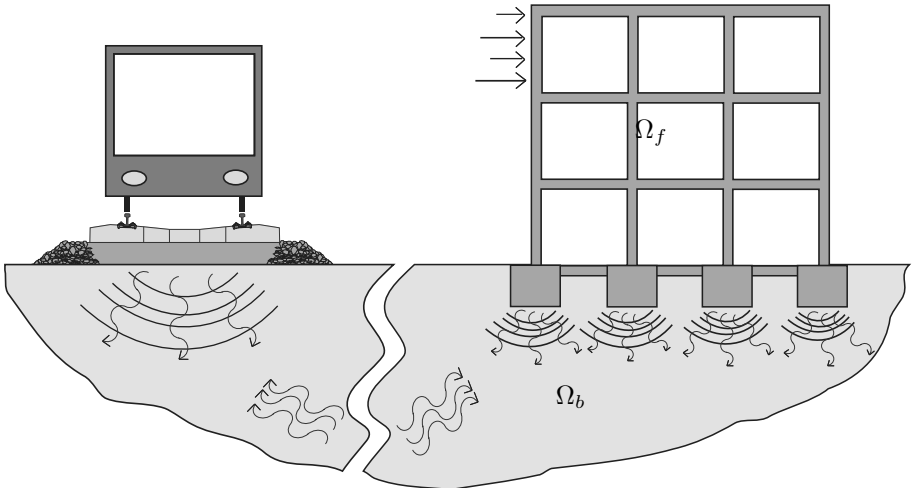


Figure 1: Emission, transmission and immision of train induced vibrations on buildings.

Building vibration analysis requires numerical models which allow to represent adequately generation and propagation mechanisms, as well as the dynamic effects on the structure. Numerical models based on the Boundary Element Method (BEM) and the Finite Element Method (FEM) allow to study soil-structure interaction (SSI) problems rigorously. The BEM [1] is especially suited for the analysis of wave propagation in soils. Sommerfeld radiation condition [2] is satisfied implicitly and the semi-infinite character of soils is well considered. The FEM is very useful to analyse the dynamic behaviour of structures taking into account nonlinear effects [3].

Number of works on the dynamic effects in buildings produced by trains is not very extensive. Numerical models differ in the modelization of the mechanisms involved in this problem, and the formulation can be simplified if some mechanisms are decoupled. Auersch [4, 5, 6] presented a simplified model to predict vibration in buildings. This model allows to take into account the effect of the SSI and the dynamic behaviour of buildings. In these works, Auersch concluded that resonance effects are moderate and decrease at high frequency when SSI is considered.

Simplified models present limitations related to the real geometry of the structure and the building foundation excitation. If these constraints are not acceptable, three dimensional (3D) numerical models are required. Pyl et al. [7, 8] presented one of the first works in which a 3D BEM-FEM model was used. In theses works, the authors analysed the response of a detached house considering that the immission mechanism were decoupled. Similarly, François

et al. [9] presented an analysis of the SSI influence in the road traffic induced vibrations on buildings, and they concluded that the vibration levels depend on the relative stiffness between the foundation and the soil. Fiala et al.[10] analysed the effectiveness of different mitigation system in buildings, using a numerical model developed in two dimensions and a half (2.5D) and based in the substructure method. Mitigation system consisted in the complete or partial isolation room, and also in the use of dampers at the building foundation. Authors concluded that the latter measure was the most effective of those studied.

However, the isolation of buildings using mitigation elements in the structure is limited to the construction of new buildings or the modification of existing ones. Alternatively, isolated railway track systems are studied in this paper. A numerical model has been used to study this problem. The model is formulated in time domain and it is based on the boundary element method and on the finite element method. This model considers the dynamic interaction between vehicle, track, soil and other structures that break the uniformity of the track, such as buildings and underpasses. The proposed model allows to study the actual geometry of the problem and represents the quasi-static and the dynamic excitation mechanisms.

This work was done using SSIFiBo 1.0 MATLAB toolbox for studying Soil-Structure Interaction (SSI) problems in time domain. SSIFiBo is a general purpose package of functions for mechanical and civil engineering research. The package is based on the BEM and FEM elastodynamic formulations in time domain, on the FEM-BEM coupled formulation, and on nonlinear SSI methodology. The SSIFiBo functioning is briefly described in this paper.

2 NUMERICAL MODEL

The boundary element system of equations can be solved step-by-step to obtain the time variation of the boundary unknowns, i.e. displacements and tractions. Piecewise constant time interpolation functions are used for tractions and piecewise linear functions for displacements. The fundamental displacement and traction solutions are evaluated analytically without much difficulty, and nine node rectangular and six node triangular quadratic elements are used for spatial discretization. Explicit expressions of the fundamental displacement and traction solutions corresponding to an impulse point load in a three-dimensional elastic full space can be seen in reference [11]. An approach based on the idea of using a linear combination of equations for several time steps in order to advance one step is used to ensure that the stepping procedure is stable in time. Details of this stabilization approach can be found in [12].

Once the integral equation is discretized one obtains the following equation for each time step:

$$\mathbf{H}^{nn}\mathbf{u}^{n} = \mathbf{G}^{nn}\mathbf{p}^{n} + \sum_{m=1}^{n-1}(\mathbf{G}^{nm}\mathbf{p}^{m} - \mathbf{H}^{nm}\mathbf{u}^{m})\exp\left[-2\pi\alpha(n-m)\Delta t\right] \tag{1}$$

where $\mathbf{u}^{n}$ is the displacement vector and $\mathbf{p}^{n}$ is the traction vector at the end of the time interval n, and $\mathbf{H}^{nn}$ and $\mathbf{G}^{nn}$ are the full unsymmetrical boundary element system matrices, in the time interval n, α is the soil attenuation coefficient and Δt is the time step. The right hand side term derived from previous steps is damped by an exponential coefficient using a linearly increasing exponent with time [13].

Usually, the Spectral Analysis of Surface Waves (SASW) is used to determinate the dynamic soil properties at the studied site. In this test, ground vibrations are generated by means of hammer impacts on a foundations. The response is measured at several points at the soil's surface. The soil's damping coefficient α can be estimated from these measurements solving an inverse problem (a minimization procedure where the variable is α).

The equation which results from the finite element method can be expressed symbolically as follows if an implicit time integration Newmark method is applied [14]:

$$\mathbf{D}^{nn}\mathbf{u}^{n} = \mathbf{f}^{n} + \mathbf{f}^{n-1} \tag{2}$$

where $\mathbf{D}^{nn}$ is the dynamic stiffness matrix, $\mathbf{u}^{n}$ the displacement vector and $\mathbf{f}^{n}$ the equivalent force vector, in the time interval n.

A multi-body model is used to represent the train-track dynamic interaction due to an axle passage [15]. The primary and secondary suspensions isolate the carriages from the track vibrations. The axles and the car body are considered as rigid parts and the primary and secondary suspensions are represented by spring and damper elements [16].

Coupling boundary element and finite element sub-regions entails satisfying equilibrium and compatibility conditions at the interface between both regions.

3 COMPUTATIONAL BACKGROUND

This paper uses the SSIFiBo 1.0 MATLAB toolbox[1] devoloped to study SSI problems in time domain. SSIFiBo is a general purpose package of functions for mechanical and civil engineering research. The package is based on the visco-elastodynamic formulation in time domain proposed by Galvín and Domínguez [11], on the FEM-BEM coupled formulation presented by Galvín et al. [15] to study train induced vibrations, and on the work by Romero et al. [17] for analysing nonlinear SSI problems.

SSIFiBo 1.0 MATLAB toolbox is based on the three dimensional boundary element and finite element formulation in time domain. BEM functions include elemental subdivision and constant velocity approach in order to improve the stability and the accuracy of the method. Computational effort has been reduced with truncation techniques and interpolation procedures. Two different FEM formulations have been used: the nonlinear Newmark GN22 scheme proposed by Chang [18], and the implicit Green's function approach presented by Soares and Mansur [19].

The numerical model allows domain decomposition into subdomains represented by BEM and FEM. Coupling of the equations of the subdomains requires that equilibrium of forces and compatibility of displacements at the interface are satisfied. SSIFiBo 1.0 toolbox includes two different coupling algorithms: a direct coupling procedure, and a nonlinear coupling algorithm to analyse contact effects at the soil-structure interfaces. It is also available a numerical model to study train induced vibrations.

This package has not a FEM preprocessor. Instead of, commercial or freeware FEM distributions are used to made the discretization and to compute mass, damping and stiffness matrices.

FEM and BEM algorithms require large computing resources (CPU and memory storage). The package allows running parallel tasks using several CPUs on a computer. The workload is distributed among the available processors with high performance. The package modularity allows simple and efficient implementation of new enhancements. Therefore, it could be a powerful tool for researching.

4 TRAIN INDUCED VIBRATION ON A THREE STORY BUILDING

This section concerns with the evaluation of building vibrations induced by an AVE S100 High-Speed Train (HST) passage at $v = 300\,\text{km/h}$. The building is located at $20\,\text{m}$ from the track.

[1] http://personal.us.es/pedrogalvin/ssifibo.en.html

The building consists of three floors ($14.4\,\text{m} \times 10.8\,\text{m}$) with height equal to $3\,\text{m}$. Each floor is supported by 8 concrete columns with cross section of $0.3\,\text{m} \times 0.3\,\text{m}$. The structure is reinforced by a concrete core of $0.15\,\text{m}$ thick and was built on a continuous slab with thickness $0.3\,\text{m}$. A damping $\xi = 2\,\%$ is estimated for the structure in the frequency range up to 80 Hz.

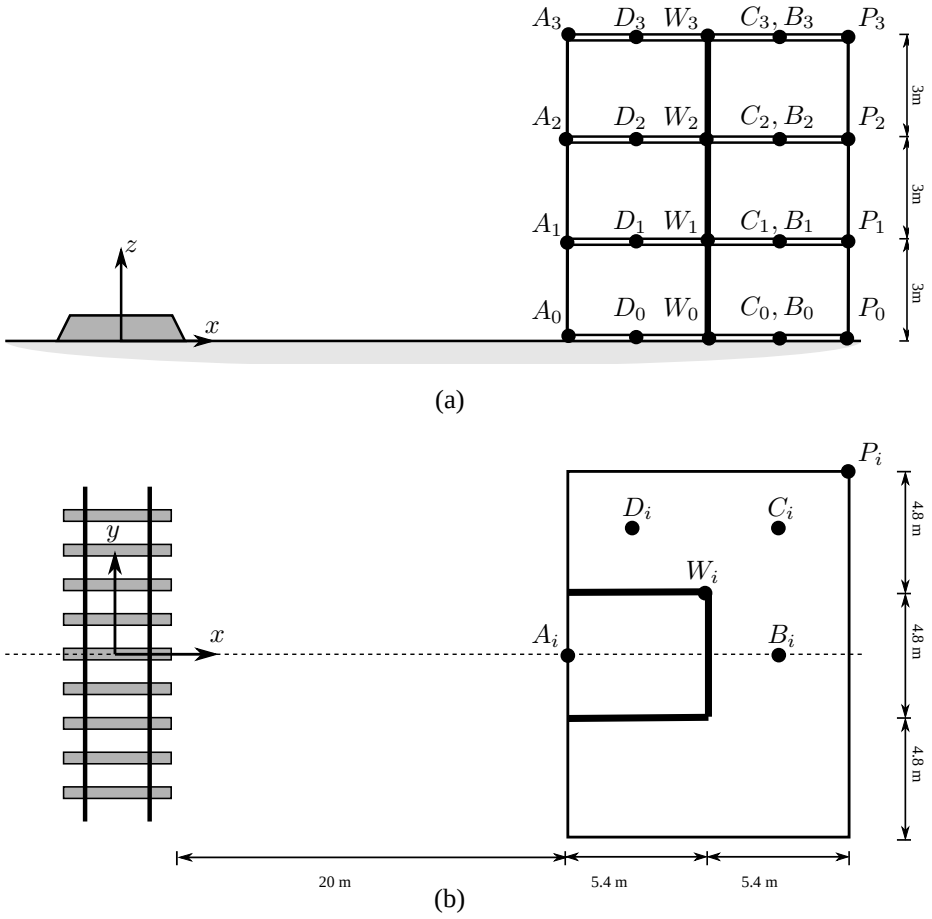


Figure 2: Three story building geometry: (a) frontal and (b) plan view.

The structure was modelled with finite elements. The element size was selected to obtain precise results for a maximum frequency 80 Hz, according to the minimum bending wave wavelengths.

All the track systems considered in this paper are composed of two UIC60 rails with a bending stiffness $E_r I_r = 6.45 \times 10^6$ Nm^2 and a mass per unit length $m_r = 60.3$ kg/m for each rail. The rail-pads are 10 mm thick and their stiffness and damping values are $k_{rp} = 150 \times 10^6$ N/m and $c_{rp} = 13.5 \times 10^3$ Ns/m, respectively. The prestressed concrete monoblock sleepers have a length $l_{sl} = 2.60$ m, a width $w_{sl} = 0.235$ m, a height $h_{sl} = 0.205$ m (under the rail) and a mass $m_{sl} = 300$ kg. A distance $d_{sl} = 0.6$ m between sleepers is considered. The rails and the sleepers are modelled as Bernoulli-Euler beam elements and the rail-pads are modelled as spring-damper elements.

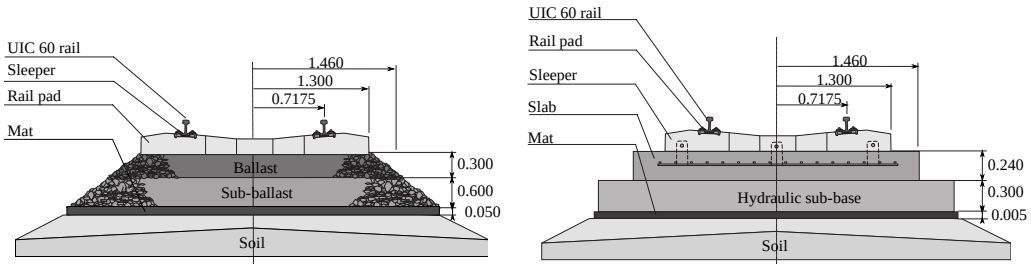
The resilience of the ballast tracks is due to two layers: a ballast layer on a subballast layer. The ballast has a Young's modulus $E_b = 280 \times 10^6$ N/m^2, a shear modulus $G_b = 116 \times 10^6$ N/m^2 and a density $\rho_b = 1500$ kg/m^3. The subballast layer has a Young's modulus $E_{sb} = 140 \times 10^6$ N/m^2, a shear modulus $G_{sb} = 58 \times 10^6$ N/m^2 and a density $\rho_{sb} = 1500$ kg/m^3. The damping value in both layers is $c_b = 24 \times 10^3$ Ns/m^2. The width of the ballast equals 2.92 m and the

height $h_b = 0.7$ m. The ballast and the subballast layers are represented by solid elements.

The slab track systems are composed of a concrete slab on a hydraulic subbase. The concrete slab has a Young's modulus $E_s = 34 \times 10^9$ N/m^2, a shear modulus $G_s = 14.2 \times 10^9$ N/m^2 and a density $\rho_s = 2500$ kg/m^3. The hydraulic subbase has a Young's modulus $E_{hs} = 10 \times 10^9$ N/m^2, a shear modulus $G_{hs} = 4.2 \times 10^9$ N/m^2, a density $\rho_{hs} = 2500$ kg/m^3 and the same width as the concrete slab. The slab and the subbase are represented by solid elements.

In the case of the isolated tracks, a slab mat is considered under the subballast layer (Figure 3.(a)) or the hydraulic subbase (Figure 3.(b)). For a isolated track, the isolation frequency is defined as the resonance frequency of a single-degree-of-freedom system with a mass equal to the track's mass per unit length, m_s, and stiffness equal to the vertical stiffness of the mat bearings, k_f:

$$f_m = \frac{1}{2\pi}\sqrt{\frac{k_f}{m_s}} \tag{3}$$



(a) (b)

Figure 3: Isolated track systems: (a) ballast track and (b) slab track.

The tracks are located at the surface of a homogeneous half-space that represents a soft soil, with a S–wave velocity $c_s = 150$ m/s, a P–wave velocity $c_p = 300$ m/s, and density $\rho = 1850$ m/s. These soil properties coincide with those obtained for the upper soil layer from experimental measurements in the HSL between Córdoba and Málaga [20].

Listing 1 shows the SSIFiBo input file, including soil properties, the structural damping, train type and track unevenness.

Figure 4 shows track, soil and structure wave field induced by an impulsive load acting at both rails. Displacements are normalized to soil properties, load amplitude and distance to the point load ($\tilde{u} = \pi c_s^2 \rho u r / p_0$). The incident wave field induced large vertical deformations on the floors.

Next, train induced vibrations by an AVE S100 HST travelling at $v = 300$ km/h are studied. Figure 6 shows the vertical acceleration time histories and frequency contents at the top floor and the ground floor of the structure, considering an unisolated ballast track. Frequency content shows peaks at bogie passage frequency, $f_b = 4.41$ Hz, and at the building resonance frequencies. A clear amplification between both floors is detected. Also, medium range frequency due to the dynamic contribution can be observed.

Figure 6 shows the running RMS value and the one-third octave band spectra of the vertical acceleration at ground floor and third floor. Again, clear amplification can be observed at the third floor response regarding to the ground floor. One-third octave band spectra shows local maximum at frequency bands related with the bogie passing frequency ($f_b = 4.41$ Hz) and building resonance frequencies close to 20 Hz.

```
% JOB TITLE
JOB='EXAMPLE3'

% SOIL PROPERTIES
CP=300          % P-wave propagation velocity [m/s]
CS=150          % S-wave propagation velocity [m/s]
RO=1850         % Density [kg/m^3]
DAMP=0.09       % Damping

% STRUCTURAL DAMPING (C=alpha*M+beta*K)
ALPHA=2.35      % [s^-1]
BETA=1.18e-4    % [s]

% TIME STEP OPTIONS
NSTEP=173       % Number of time steps
AT=0.006        % Time interval [s]

% TRAIN AND TRACK PROPERTIES
TRAIN='S100'    % Train type
SPEED=83        % Train speed [m/s]
UNEVENNESS='A'  % ISO 8608 road classification (range from 'A' to 'H')

% CALL SSIFIBO
ssifibo(JOB,CP,CS,RO,DAMP,ALPHA,BETA,NSTEP,AT,TRAIN,SPEED,UNEVENNESS)
```

Listing 1: Input file to compute train induced vibration on a three story building.

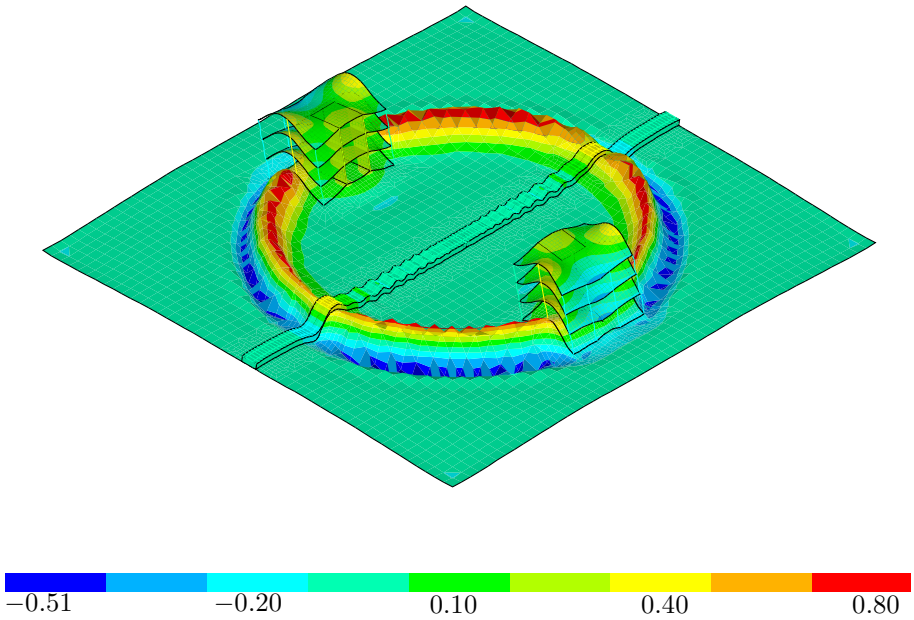
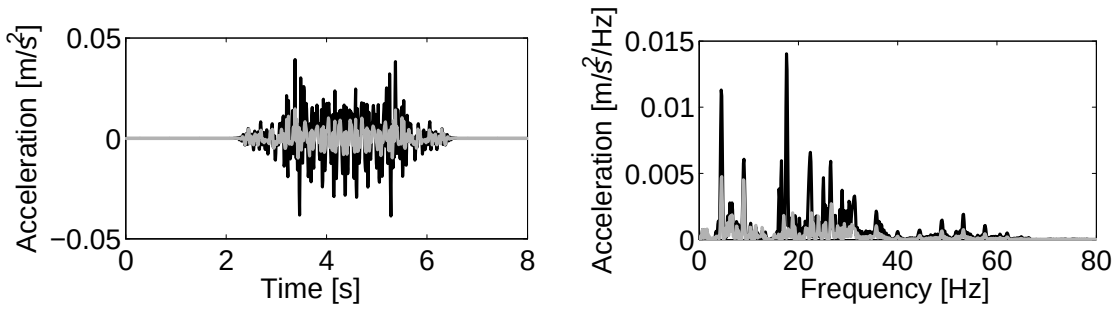
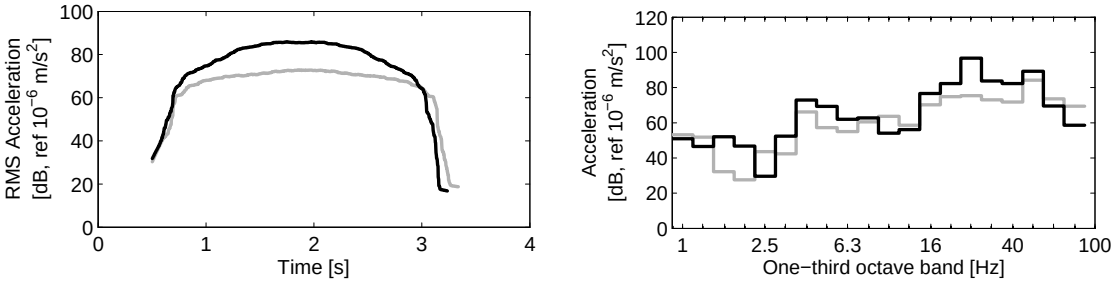


Figure 4: Dimensionless wave field due to an impulsive load acting at the track.



(a) (b)

Figure 5: (a) Time history and (b) frequency content of vertical acceleration at the ground floor (grey line) and the top floor (black line), during the passage of an AVE S100 HST at a speed $v = 300$ km/h.



(a) (b)

Figure 6: (a) Running RMS value and (b) one-third octave band spectra of the vertical acceleration at ground floor (grey line) and third floor (black line) during the passage of an AVE S100 HST at a speed $v = 300$ km/h.

5 VIBRATION ASSESSMENT AND ISOLATION

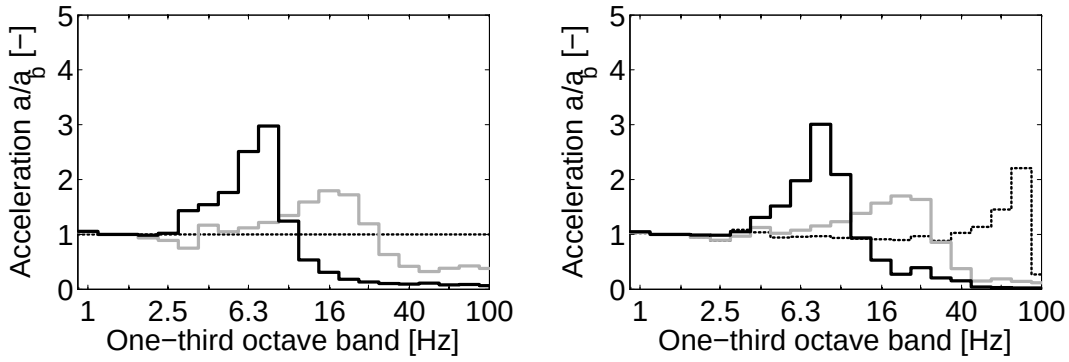
In this section, the assessment of track isolation is evaluated. That solution gives a effective control of ground borne vibration after the cut-off track isolation frequency f_0. However,

response amplification occurs around the track isolation frequency f_m. Efficiency of isolated track systems depends on insertion loss, IL, and cut off frequency of the mat [21]. In this work, two different mats are studied. Table 1 shows the track isolation frequency f_m and the cut-off frequency f_0 for the isolated ballast and slab track.

Track system	E_m [N/m^2]	ρ_m [kg/m^3]	ζ_m [-]	f_m [Hz]	f_0 [Hz]
Isolated ballast track I	0.26×10^6	100	0.1	8.8	12.4
Isolated ballast track II	2.15×10^6	100	0.3	23.8	33.0
Floating slab track I	0.26×10^6	100	0.1	8.9	12.5
Floating slab track II	2.15×10^6	100	0.3	25.1	36.4

Table 1: Properties of isolated track systems: mat Young's modulus (E_m), density (ρ_m) and damping (ζ_m); isolation (f_m) and cut off (f_0) frequencies.

Figure 7 presents the ground borne vibration for a point located at 28 m from the track, due to an impulsive load $p(t) = p_0 H(t - 0.025\,\text{s})$ acting in both rails. Results show an amplification around the isolation track frequency f_m and a mitigation for higher frequencies. Maximum isolation is reached for floating slab track when soft mat is used and for frequencies above 10 Hz.

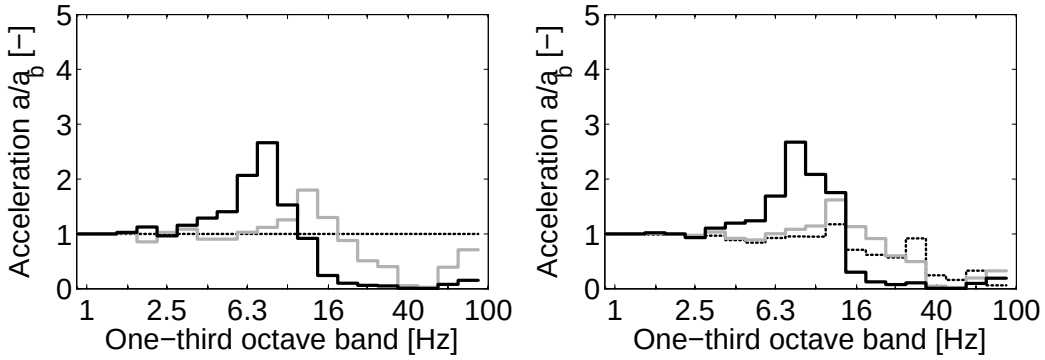


(a) Ballast track. (b) Slab track.

Figure 7: Ground borne amplification at a point located at 28.1 m from the track due to impulsive load acting at the rails, considering unisolated track system (dotted black line), isolated system I (solid black line) and isolated system II (solid grey line).

Having examined the response at the free field, building response due to the incident wave field is presented in Figure 8. There is an amplification around the resonant frequency of the track, that is close to the natural frequencies of the structure. After, building response is mitigated and a maximum isolation level is reached for a ballast track with soft mat for frequencies above 25 Hz. Unisolated slab track does not allow an effectiveness ground borne vibration control, as can be seen in Figure 7.(b). That figure shows an amplification at high frequency. However, this effect occurs for frequencies higher than building resonant frequencies and does not affect to the structure response (Figure 8.(b)).

Finally, Figures 9 and 10 show running RMS value and the insertion loss of the vertical acceleration at the third floor, for a HST passage at $v = 300$ km/h travelling on the different tracks. The insertion loss is obtained from the relation between the vibration levels for unisolated ballas track, a_b, and the others track systems:

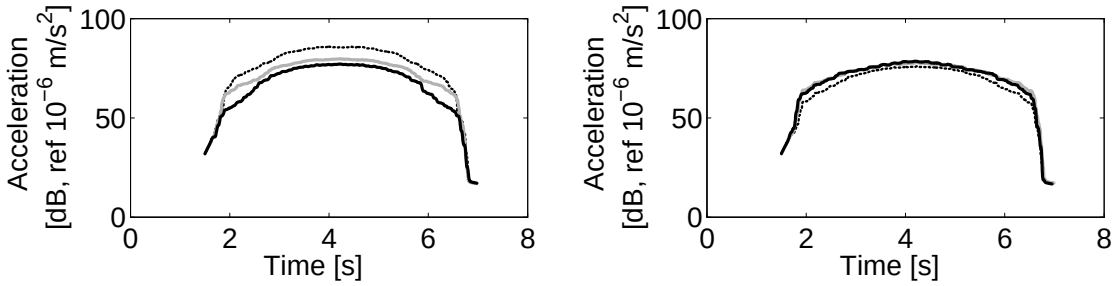


(a) Ballas track. (b) Slab track.

Figure 8: Building amplification at the top floor due to impulsive load acting at the rails, considering unisolated track system (dotted black line), isolated system I (solid black line) and isolated system II (solid grey line).

$$IL = 20 \log_{10} \left(\frac{a}{a_b} \right) \tag{4}$$

Isolated ballast tracks exhibit a maximum mitigation of $9\,$dB and an insertion loss of $-35\,$dB. Floating slab tracks produce an increase of the running RMS value of $2.5\,$dB and a decrease of $-29\,$dB. Both track systems induced an amplification around the track resonant frequency.

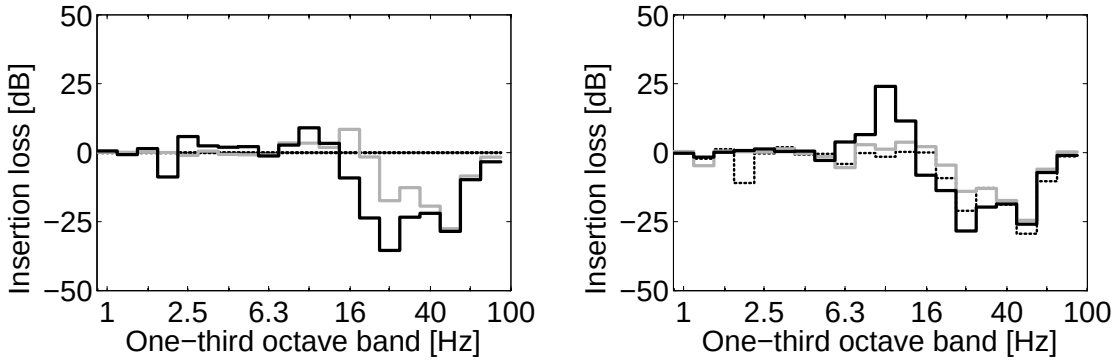


(a) Ballast track. (b) Slab track.

Figure 9: Running RMS value of the vertical acceleration at the top floor during the passage of an AVE S100 HST at a speed $v = 300\,$km/h, considering unisolated track system (dotted black line), isolated system I (solid black line) and isolated system II (solid grey line).

6 CONCLUSIONS

In this paper, HST induced vibration in buildings has been presented. A numerical model based on time domain three-dimensional finite element and boundary element formulations was used. This model allows to take into account local soil discontinuities, underground constructions, and nearby structures that break the uniformity of the geometry along the track line. Track and other structures are modelled using the finite element method and their non-linear behaviour could be considered because a time domain formulation is employed. The soil was represented using the boundary element method, where a full space fundamental solution was used in combination with quadratic boundary elements. The train vehicle was modelled as a multi-body and, therefore, the quasi-static and the dynamic excitation mechanisms can be considered, taking into account the dynamic effects due to discrete sleeper support and the wheel and rail irregularities.



(a) Ballast track.

(b) Slab track.

Figure 10: Insertion loss of the vertical acceleration at the top floor during the passage of an AVE S100 HST at a speed $v = 300$ km/h, considering unisolated track system (dotted black line), isolated system I (solid black line) and isolated system II (solid grey line).

Results show that induced vibrations by HST are amplified around building resonance frequencies. Efficiency of isolation mats has been evaluated. Choice of mats characteristics are related to track properties, soil behaviour and building resonance frequencies. Building response could be amplified if the isolation frequency is close to the natural frequencies of the structure. Ballasted track with low stiffness mat allows to reduce vibration levels and, therefore, that system becomes an effective and alternative system to floating slab tracks.

7 ACKNOWLEDGEMENT

This research was funded by the Spanish Ministry of Economy and Competitiveness (Ministerio de Economía y Competitividad) through research project BIA2010-14843. Financial support is gratefully acknowledged. The authors also wish to acknowledge the support provided by the Andalusian Scientific Computing Centre (CICA)

REFERENCES

[1] J. Domínguez. *Boundary elements in dynamics*. Computational Mechanics Publications and Elsevier Aplied Science, Southampton, 1993.

[2] A.C. Eringen and E.S. Suhubi. *Elastodynamics, Volume 2, Linear theory*. Academic Press, New York, USA, 1975.

[3] O.C. Zienkiewicz. *The finite element method*. McGraw-Hill, third edition, 1986.

[4] L. Auersch. Simplified methods for waves propagation and soil-structure interaction: The dispersion of layered soil and the aproximation of FEBEM results. *Procedings of 6th International Conference on Structural Dynamics (EURODYN 2005), Millpress, Rotterdam*, pages 101–112, 2005.

[5] L. Auersch. Two- and three-dimensional methods for the assessment of ballast mats, ballast plates and other isolators of railway vibrations. *International Journal of Acoustics and Vibration*, 11(3):167–176, 2006.

[6] L. Auersch. Building response due to ground vibration – Simple prediction model based on experience with detailed model and measurements. *International Journal of Acoustics and Vibration*, 15(3):101–112, 2010.

[7] L. Pyl, G. Degrande, and D. Clouteau. Validation of a source–receiver model for road traffic induced vibrations in buildings. II: Receiver model. *Journal of Engineering Mechanics, Procedings of the ASCE*, 130(12):1394–1406, 2004.

[8] L. Pyl, G. Degrande, G. Lombaert, and W. Haegeman. Validation of a source–receiver model for road traffic induced vibrations in buildings. I: Source model. *Journal of Engineering Mechanics, Procedings of the ASCE*, 130(12):1377–1393, 2004.

[9] S. François, L. Pyl, H.R. Masoumi, and G. Degrande. The influence of dynamic soil–structure interaction on traffic induced vibrations in buildings. *Soil Dynamics and Earthquake Engineering*, 31416(27):655–674, 2007.

[10] P. Fiala, G. Degrande, and F. Augusztinovicz. Numerical modelling of ground-borne noise and vibration in buildings due to surface rail traffic. *Journal of Sound and Vibration*, 301(31416):718–738, 2007.

[11] P. Galvín and J. Domínguez. Analysis of ground motion due to moving surface loads induced by high-speed trains. *Engineering Analysis with Boundary Elements*, 31(11):931–941, 2007.

[12] M. Marrero and J. Domínguez. Numerical behavior of time domain BEM for three-dimensional transient elastodynamic problems. *Engineering Analysis with Boundary Elements*, 27(1):39–48, 2003.

[13] P. Galvín and J. Domínguez. High-speed train-induced ground motion and interaction with structures. *Journal of Sound and Vibration*, 307(3-5):755–777, 2007.

[14] N.M. Newmark. A method of computation for structural dynamics. *ASCE Journal of the Engineering Mechanics Division*, 85(1):67–94, 1959.

[15] P. Galvín, A. Romero, and J. Domínguez. Fully three-dimensional analysis of high-speed train-track-soil-structure dynamic interaction. *Journal of Sound and Vibration*, 329(24):5147–5163, 2010.

[16] X. Sheng, C.J.C. Jones, and D.J. Thompson. A theoretical model for ground vibration from trains generated by vertical track irregularities. *Journal of Sound and Vibration*, 272(3-5):937–965, 2004.

[17] A. Romero, P. Galvín, and J. Domínguez. 3D non-linear time domain FEM-BEM approach to soil-structure interaction problems. *Engineering Analysis with Boundary Elements*, DOI: 10.1016/j.enganabound.2013.01.001, 2012.

[18] S.Y. Chang. Nonlinear error propagation analysis for explicit pseudodynamics algorithm. *Journal of Engineering Mechanics ASCE*, 123:841–850, 2003.

[19] D. Soares and W.J. Mansur. A time domain FEM approach based on implicit Green's functions for non-linear dynamic analysis. *International Journal for Numerical Methods in Engineering*, 62(5):664–681, 2005.

[20] P. Galvín and J. Domínguez. Experimental and numerical analyses of vibrations induced by high-speed trains on the Córdoba-Málaga line. *Soil Dynamics and Earthquake Engineering*, 29(4):641–657, 2009.

[21] R. G. Wettschureck. Measures to reduce structure-borne noise emissions induced by above-ground, open railway lines. *Rail Engineering International*, 31416(2):12–16, 1997.

COMPDYN 2013
4th ECCOMAS Thematic Conference on
Computational Methods in Structural Dynamics and Earthquake Engineering
M. Papadrakakis, N.D.Lagaros, V. Plevris (eds.)
Kos Island, Greece, 12–14 June 2013

A NONLINEAR VEHICLE-STRUCTURE INTERACTION METHODOLOGY WITH WHEEL-RAIL DETACHMENT AND REATTACHMENT

P. A. Montenegro[1], S.G.M. Neves[2], A.F.M. Azevedo[4] and R. Calçada[3]

[1,2,3,4] University of Porto, Faculty of Engineering
Rua Dr. Roberto Frias s/n, 4200-465 Porto, Portugal

[2] Polytechnic Institute of Porto, ISEP
Rua Dr. António Bernardino de Almeida, 431, 4200-072 Porto, Portugal

[1] pedro.montenegro@fe.up.pt
[2] sgm.neves@fe.up.pt
[3] alvaro@fe.up.pt
[4] ruiabc@fe.up.pt

Keywords: Vehicle-Structure Interaction, Dynamic Analysis, Nonlinear Contact, Lagrange Multipliers, Bridge.

Abstract. *A vehicle-structure interaction methodology with a nonlinear contact formulation based on contact and target elements has been developed. To solve the dynamic equations of motion, an incremental formulation has been used due to the nonlinear nature of the contact mechanics, while a procedure based on the Lagrange multiplier method imposes the contact constraint equations when contact occurs. The system of nonlinear equations is solved by an efficient block factorization solver that reorders the system matrix and isolates the nonlinear terms that belong to the contact elements or to other nonlinear elements that may be incorporated in the model. Such procedure avoids multiple unnecessary factorizations of the linear terms during each Newton iteration, making the formulation efficient and computationally attractive. A numerical example has been carried out to validate the accuracy and efficiency of the present methodology. The obtained results have shown a good agreement with the results obtained with the commercial finite element software ANSYS.*

1 INTRODUCTION

The dynamic interaction between vehicles and structure has attracted much attention during the last three decades due to the increase of the loads and speed of the vehicles. Such factors strongly influence the interaction between both systems. In the particular case of railways, the maintenance of the existing high-speed rail networks and the construction of new lines urge the development of new algorithms that can accurately and efficiently analyze the interaction between both systems.

With the increase of the running speed, the probability of incidents such has track instability or derailments also increases. Therefore, the development of more complex train-bridge interaction models that can accurately evaluate the train running safety is a major topic of research.

A significant number of studies have been conducted in the last decades to better understand this phenomenon. In a problem of this type, the model has to guarantee the coupling between the independent systems by establishing the dynamic equilibrium through two sets of equations of motion, one for the vehicle and one for the structure. One way to solve these equations is through an iterative procedure which ensures the coupling between the two systems [1-3]. Such methods, despite being simpler to implement, may require a large computational effort and can lead to convergence problems.

Yang et al. [4] proposed another approach to solve the coupled equations which consisted on condensing the degrees of freedom (d.o.f.) of the vehicle to those of the bridge elements in contact. With such approach, the system matrix is time-dependent and has to be factorized at each time step.

Most finite element programs are able to handle contact problems using either the penalty method or the Lagrange Multiplier method [5]. However, these methods are mostly used in multibody dynamic simulations that do not take into account the track flexibility [6-7]. Antolin et al. [8] proposed an hybrid finite element/multibody formulation that used the penalty method to introduce geometrical constraints in the equilibrium equations. These constraints are formulated based on lookup tables that establish the geometrical compatibility between the wheels and rails. Unlike other multibody formulations, this approach takes into consideration the flexibility of the track and structure, but cannot deal with situations where the wheel and rail lose contact.

Tanabe et al. [9] developed a train-structure interaction software, DIASTARS, in which the train is modeled as a multibody system, while the bridge is modeled with finite elements to take the structure flexibility into account. This methodology divides the wheel-rail contact in two modes, one vertical and one lateral, that are simulated with nonlinear contact springs to represent the wheel-rail contact stiffness. Hence, no specific contact methods are used in this approach.

Neves et al. [10] developed a simple methodology based on the Lagrange multipliers method in which the dynamic equilibrium equations of both systems are complemented with additional displacement compatibility equations, forming a single system of equations that can be directly solved. However, this method did not take into account the nonlinearities presented in a wheel-rail contact problem such as the bodies separation or deformations.

In the present paper, a contact search algorithm based on contact and target elements is used to detect which elements are in contact. When contact occurs, contact constraints equations are imposed using a procedure based on the Lagrange multipliers method, while the dynamic equations of motion are solved through an incremental formulation due to the nonlinear nature of the contact mechanics. These two types of nonlinear equations form a single system with displacements and contact forces as unknowns. In order to solve the problem efficiently,

a block factorization solver that reorders the system matrix is also presented. This solver avoids multiple factorizations of the linear terms during each Newton iteration, making the formulation computationally attractive

The proposed methodology is referred to as the direct method and has been implemented in MATLAB [11] which import and manipulate the structural matrices extracted from ANSYS [12], a commercial finite element software used to model the vehicle and structure. A numerical example is presented to evaluate the efficiency and accuracy of the proposed vehicle-structure interaction methodology.

2 GENERAL CONCEPT OF THE ALGORITHM

2.1 Contact algorithm concept

The vehicle-structure interaction problem can be solved by a direct method [10], based on the Lagrange multiplier method, that avoids an iterative procedure to ensure the coupling between the two systems. This method complements the dynamic equilibrium equations of both systems with additional constraint equations, forming a single system of equations that can be directly and efficiently solved. However, when the contact nonlinearities are taken into account an iterative algorithm has to be added to the formulation in order to solve the nonlinear equations. The iterative schemes most widely used for the solution of nonlinear finite element equations are based on the Newton method [13-14].

When studying the contact between two bodies, the surface of one body is conventionally taken as a contact surface and the surface of the other body as a target surface (see Figure 1). This contact pair concept is widely used in computational contact mechanics. A two-dimensional node-to-segment contact element is used in the present paper but the extension of the formulation to other types of finite elements and to three-dimensional problems is straightforward. The algorithm used does not account for the surface profiles of the contact and target elements.

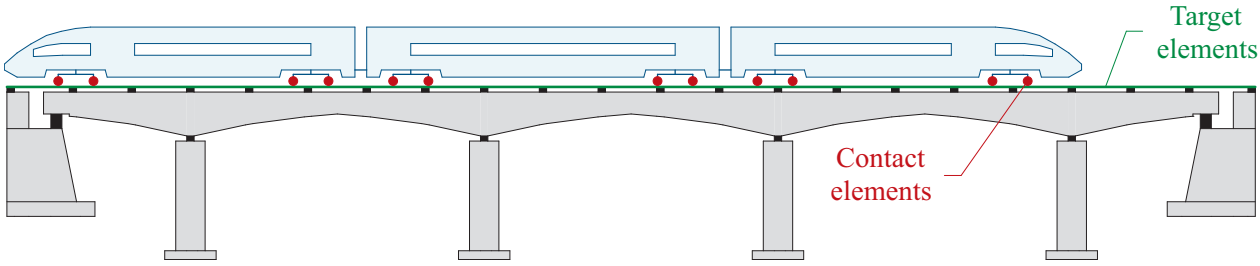


Figure 1: Contact pair concept.

In the present paper, a contact search algorithm is used to detect which elements are in contact, being the contact constraints only imposed when contact occurs. Since only the frictionless contact is considered herein, the contact constraint equations are purely geometrical constraints that relate the displacements of the contact node to the displacements of the corresponding target element.

2.2 Classification of the degrees of freedom

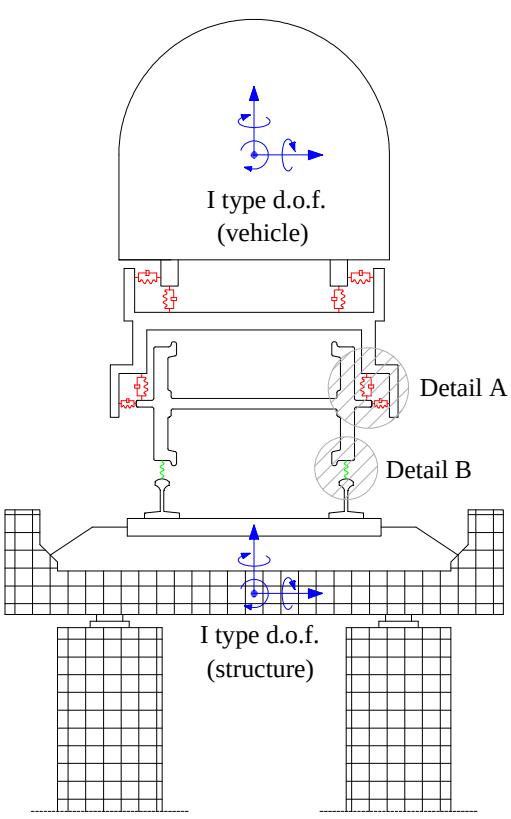
Since the main nonlinearities of the system are concentrated on the d.o.f. of the contact elements, the corresponding terms of these elements in the system matrix can be reordered and manipulated to avoid multiple factorizations of the entire matrix in each Newton iteration (see section 4). This procedure is also valid for other nonlinear elements, such as nonlinear sus-

pension in the vehicles or nonlinear bearings in the structure. Table 1 shows the d.o.f. classification adopted in the present algorithm.

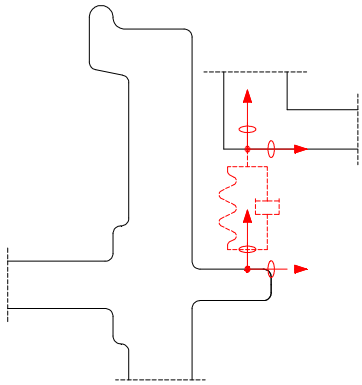
I	Unconstrained nodal d.o.f. (linear terms)
R	Reordered nodal d.o.f. (nonlinear terms)
Y	Contact nodal d.o.f.
F	Free nodal d.o.f. (includes *I*, *R* and *Y* type d.o.f.)
P	Prescribed nodal d.o.f.

Table 1: Classification of the d.o.f.

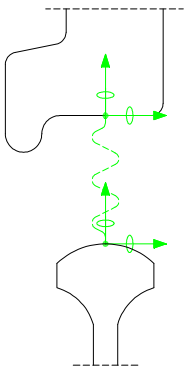
The *I* type d.o.f. correspond to all unconstrained d.o.f. without any nonlinear property, the *R* type d.o.f. correspond to the nonlinear terms that are reordered for efficiency (material nonlinearities), *Y* type d.o.f. correspond to the nonlinear terms from the contact elements and the *P* type d.o.f. are the prescribed d.o.f. Note that, despite both *R* and *Y* type d.o.f. correspond to the same type of d.o.f. (nonlinear unconstrained d.o.f.), the algorithm separate them, since the dimension of the *Y* type d.o.f. can vary due to the changes of the contact status (the *Y* type d.o.f. exists only if contact occurs). The above mentioned d.o.f. classification is illustrated in Figure 2.



a) Vehicle-structure interaction scheme



b) Detail A - *R* type d.o.f. in a nonlinear suspension



c) Detail B - *Y* type d.o.f. in the contact element

Figure 2: Schematic representation of the d.o.f. classification

3 VEHICLE-STRUCTURE INTERACTION FORMULATION

3.1 Formulation of the nonlinear dynamic equations

In a nonlinear dynamic analysis, the nodal point forces corresponding to the internal element stresses may depend nonlinearly on the nodal point displacements [13]. Based on the

α method [15] and assuming that the applied loads are deformation-independent, the equations of motion of the vehicle-structure system can be expressed as

$$\mathbf{M}\,\ddot{\mathbf{a}}^{c} + \mathbf{C}\left[(1+\alpha)\,\dot{\mathbf{a}}^{c} - \alpha\,\dot{\mathbf{a}}^{p}\right] + (1+\alpha)\,\mathbf{R}^{c} - \alpha\,\mathbf{R}^{p} = (1+\alpha)\,\mathbf{F}^{c} - \alpha\,\mathbf{F}^{p} \tag{1}$$

where **M** is the mass matrix, **C** is the viscous damping matrix, **R** is nodal point forces corresponding to the internal element stresses, **F** is the externally applied nodal loads vector and **a** are the nodal displacements. The superscript *c* indicates the current time step ($t + \Delta t$) and the superscript *p* indicates the previous one (t).

To solve Eq. (1) let the *F* type d.o.f. represent the free nodal d.o.f., whose values are unknown, and the *P* type d.o.f. represent the prescribed nodal d.o.f., whose values are known. Thus, the load vector can be expressed as

$$\mathbf{F}_{F} = \mathbf{P}_{F} + \mathbf{D}_{FX}^{CE}\ \mathbf{X}^{CE} + \mathbf{D}_{FX}^{TE}\ \mathbf{X}^{TE} \tag{2}$$

$$\mathbf{F}_{P} = \mathbf{P}_{P} + \mathbf{D}_{PX}^{CE}\ \mathbf{X}^{CE} + \mathbf{D}_{PX}^{TE}\ \mathbf{X}^{TE} + \mathbf{S} \tag{3}$$

where **P** corresponds to the externally applied nodal loads whose values are known and **S** are the support reactions. The matrices **D** relate the contact forces defined in the local coordinate system of each contact pair to the nodal point forces in the global coordinate system. The superscripts *CE* and *TE* denote contact and target element respectively.

The equilibrium between the two bodies is guaranteed only if the forces acting in the contact interface respect the following equation

$$\mathbf{X}^{CE} + \mathbf{X}^{TE} = 0 \tag{4}$$

Thus, Substituting Eq. (4) into Eqs. (2) and (3) leads to

$$\mathbf{F}_{F} = \mathbf{P}_{F} + \mathbf{D}_{FX}\ \mathbf{X} \tag{5}$$

$$\mathbf{F}_{P} = \mathbf{P}_{P} + \mathbf{D}_{PX}\ \mathbf{X} + \mathbf{S} \tag{6}$$

where

$$\mathbf{X} = \mathbf{X}^{CE} \tag{7}$$

$$\mathbf{D}_{FX} = \mathbf{D}_{FX}^{CE} - \mathbf{D}_{FX}^{TE} \tag{8}$$

$$\mathbf{D}_{PX} = \mathbf{D}_{PX}^{CE} - \mathbf{D}_{PX}^{TE} \tag{9}$$

Substituting Eqs. (5) and (6) into Eq. (1) and partitioning into *F* and *P* type d.o.f. gives

$$\begin{bmatrix} \mathbf{M}_{FF} & \mathbf{M}_{FP} \\ \mathbf{M}_{PF} & \mathbf{M}_{PP} \end{bmatrix} \begin{bmatrix} \ddot{\mathbf{a}}_{F}^{c} \\ \ddot{\mathbf{a}}_{P}^{c} \end{bmatrix} + \begin{bmatrix} \mathbf{C}_{FF} & \mathbf{C}_{FP} \\ \mathbf{C}_{PF} & \mathbf{C}_{PP} \end{bmatrix} \left[(1+\alpha) \begin{bmatrix} \dot{\mathbf{a}}_{F}^{c} \\ \dot{\mathbf{a}}_{P}^{c} \end{bmatrix} - \alpha \begin{bmatrix} \dot{\mathbf{a}}_{F}^{p} \\ \dot{\mathbf{a}}_{P}^{p} \end{bmatrix} \right] + (1+\alpha) \begin{bmatrix} \mathbf{R}_{F}^{c} \\ \mathbf{R}_{P}^{c} \end{bmatrix} - \alpha \begin{bmatrix} \mathbf{R}_{F}^{p} \\ \mathbf{R}_{P}^{p} \end{bmatrix}$$
$$= (1+\alpha) \begin{bmatrix} \mathbf{P}_{F}^{c} + \mathbf{D}_{FX}\ \mathbf{X}^{c} \\ \mathbf{P}_{P}^{c} + \mathbf{D}_{PX}\ \mathbf{X}^{c} + \mathbf{S}^{c} \end{bmatrix} - \alpha \begin{bmatrix} \mathbf{P}_{F}^{p} + \mathbf{D}_{FX}\ \mathbf{X}^{p} \\ \mathbf{P}_{P}^{p} + \mathbf{D}_{PX}\ \mathbf{X}^{p} + \mathbf{S}^{p} \end{bmatrix} \tag{10}$$

The first line of blocks in Eq. (10) represents the system of nonlinear equations that has to be solved in order to calculate the unknowns of the problem (displacements and contact forces). Rearranging the first line of blocks leads to

$$\mathbf{M}_{FF}\,\ddot{\mathbf{a}}_{F}^{c} + (1+\alpha)\mathbf{C}_{FF}\,\dot{\mathbf{a}}_{F}^{c} + (1+\alpha)\mathbf{R}_{F}^{c} - (1+\alpha)\,\mathbf{D}_{FX}\ \mathbf{X}^{c} = \overline{\mathbf{F}}_{F} \tag{11}$$

where

$$\begin{aligned}\overline{\mathbf{F}}_F = &(1+\alpha)\mathbf{P}_F^c - \alpha\,\mathbf{P}_F^p - \mathbf{M}_{FP}\,\ddot{\mathbf{a}}_P^c - (1+\alpha)\mathbf{C}_{FP}\,\dot{\mathbf{a}}_P^c \\ &+\alpha\left[\mathbf{C}_{FF}\,\dot{\mathbf{a}}_F^p + \mathbf{C}_{FP}\,\dot{\mathbf{a}}_P^p\right] + \alpha\,\mathbf{R}_F^p - \alpha\,\mathbf{D}_{FX}\,\mathbf{X}^p\end{aligned} \tag{12}$$

The second line of blocks is used to calculate de support reactions after solving the system of nonlinear equations given by Eq. (11).

3.2 Incremental formulation for the solution of the nonlinear dynamic equations

Since the coefficients of the vector of the internal element stresses in Eq. (10) depend on the current displacements, an iterative scheme must be adopted to obtain the solution of the equilibrium equations at the current time step. The iterative schemes most widely used for the solution of nonlinear finite element equations are based on the Newton method [13-14].

Alternatively, the nonlinear Eq. (11) can be written in the form

$$\boldsymbol{\psi}\left(\mathbf{a}_F^*, \mathbf{X}_X^*\right) = \mathbf{0} \tag{13}$$

where $\boldsymbol{\psi}$ is the vector of residual which have to be null in order to satisfy the dynamic equilibrium. For the solution $\left(\mathbf{a}_F^*, \mathbf{X}_X^*\right)$, the residual vector is given by

$$\boldsymbol{\psi}\left(\mathbf{a}_F^*, \mathbf{X}^*\right) = \overline{\mathbf{F}}_F - \mathbf{M}_{FF}\,\ddot{\mathbf{a}}_F\left(\mathbf{a}_F^*\right) - (1+\alpha)\mathbf{C}_{FF}\,\dot{\mathbf{a}}_F\left(\mathbf{a}_F^*\right) - (1+\alpha)\mathbf{R}_F\left(\mathbf{a}_F^*\right) + (1+\alpha)\,\mathbf{D}_{FX}\,\mathbf{X}^* \tag{14}$$

The nodal velocities and accelerations depend on the nodal displacements and thus are not unknowns in the equation. In the α method, the velocity and displacement at the current time step are approximated with

$$\dot{a}^c = \dot{a}^p + \left[(1-\gamma)\,\ddot{a}^p + \gamma\,\ddot{a}^c\right]\Delta t \tag{15}$$

$$a^c = a^p + \dot{a}^p\,\Delta t + \left[\left(\frac{1}{2}-\beta\right)\ddot{a}^p + \beta\,\ddot{a}^c\right]\Delta t^2 \tag{16}$$

where β and γ are parameters that control the stability and accuracy of the method. Solving Eq. (16) for $\ddot{a}^c$ gives

$$\ddot{a}^c = \frac{1}{\beta\Delta t^2}a^c - \frac{1}{\beta\Delta t^2}a^p - \frac{1}{\beta\Delta t}\dot{a}^p - \left(\frac{1}{2\beta}-1\right)\ddot{a}^p \tag{17}$$

Substituting Eq. (17) into Eq. (15) yields

$$\dot{a}^c = \frac{\gamma}{\beta\Delta t}a^c - \frac{\gamma}{\beta\Delta t}a^p + \left(1-\frac{\gamma}{\beta}\right)\dot{a}^p + \Delta t\left(1-\frac{\gamma}{2\beta}\right)\ddot{a}^p \tag{18}$$

Assuming that $\mathbf{a}_F^{c,i}$ and $\mathbf{X}^{c,i}$ have already been evaluated, the function $\boldsymbol{\psi}$ can be expanded using a Taylor series [16] about the solution $\left(\mathbf{a}_F^*, \mathbf{X}^*\right)$. Neglecting the second and higher order terms leads to

$$\boldsymbol{\psi}\left(\mathbf{a}_F^*, \mathbf{X}^*\right) = \boldsymbol{\psi}\left(\mathbf{a}_F^{c,i}, \mathbf{X}^{c,i}\right) + \frac{\partial\,\boldsymbol{\psi}}{\partial\,\mathbf{a}_F^*}\left(\mathbf{a}_F^{c,i}, \mathbf{X}^{c,i}\right)\times\left(\mathbf{a}_F^* - \mathbf{a}_F^{c,i}\right) + \frac{\partial\,\boldsymbol{\psi}}{\partial\,\mathbf{X}^*}\left(\mathbf{a}_F^{c,i}, \mathbf{X}^{c,i}\right)\times\left(\mathbf{X}^* - \mathbf{X}^{c,i}\right) \tag{19}$$

where the superscript *i* denotes variables that were evaluated in the *i*th Newton iteration. Substituting Eqs. (13), (14), (17) and (18) into Eq. (19) and differentiating the function $\boldsymbol{\psi}$ with respect to the variables leads to

$$\mathbf{0} = \boldsymbol{\psi}\left(\mathbf{a}_F^{c,i}, \mathbf{X}^{c,i}\right) + \left[-\frac{1}{\beta \Delta t^2}\mathbf{M}_{FF} - (1+\alpha)\frac{\gamma}{\beta \Delta t}\mathbf{C}_{FF} - (1+\alpha)\frac{\partial \mathbf{R}_F}{\partial \mathbf{a}_F^*}\left(\mathbf{a}_F^{c,i}\right)\right]\left(\mathbf{a}_F^* - \mathbf{a}_F^{c,i}\right) + (1+\alpha)\mathbf{D}_{FX}\left(\mathbf{X}^* - \mathbf{X}^{c,i}\right) \tag{20}$$

Eq. (20) can be rearranged into the following incremental form

$$\overline{\mathbf{K}}_{FF}^{c,i}\ \Delta \mathbf{a}_F^{i+1} - (1+\alpha)\mathbf{D}_{FX}\ \Delta \mathbf{X}^{i+1} = \boldsymbol{\psi}\left(\mathbf{a}_F^{c,i}, \mathbf{X}^{c,i}\right) \tag{21}$$

where $\overline{\mathbf{K}}_{FF}^{c,i}$ is the current effective stiffness matrix defined by

$$\overline{\mathbf{K}}_{FF}^{c,i} = \frac{1}{\beta \Delta t^2}\mathbf{M}_{FF} + (1+\alpha)\frac{\gamma}{\beta \Delta t}\mathbf{C}_{FF} + (1+\alpha)\frac{\partial \mathbf{R}_F}{\partial \mathbf{a}_F^*}\left(\mathbf{a}_F^{c,i}\right) \tag{22}$$

with

$$\Delta \mathbf{a}_F^{i+1} = \mathbf{a}_F^* - \mathbf{a}_F^{c,i} \tag{23}$$

$$\Delta \mathbf{X}^{i+1} = \mathbf{X}^* - \mathbf{X}^{c,i} \tag{24}$$

Since Eq. (19) represents only a Taylor series approximation about $\left(\mathbf{a}_F^*, \mathbf{X}^*\right)$, the incremental nodal displacements and contact forces given by Eqs. (23) and (24) are used to obtain the next approximations

$$\mathbf{a}_F^{c,i+1} = \mathbf{a}_F^{c,i} + \Delta \mathbf{a}_F^{i+1} \tag{25}$$

$$\mathbf{X}^{c,i+1} = \mathbf{X}^{c,i} + \Delta \mathbf{X}^{i+1} \tag{26}$$

In matrix notation, Eq. (21) may be expressed as

$$\left[\overline{\mathbf{K}}_{FF}^{c,i} \quad \overline{\mathbf{D}}_{FX}\right]\begin{bmatrix} \Delta \mathbf{a}_F^{i+1} \\ \Delta \mathbf{X}_X^{i+1} \end{bmatrix} = \boldsymbol{\psi}\left(\mathbf{a}_F^{c,i}, \mathbf{X}^{c,i}\right) \tag{27}$$

in which

$$\overline{\mathbf{D}}_{FX} = -(1+\alpha)\mathbf{D}_{FX} \tag{28}$$

3.3 Formulation of the constraint equations

When contact occurs, a constraint equation as to be added to the system of nonlinear equations defined in Eq. (27) to avoid penetrations between the two bodies. Thus, the non-penetration condition for the normal direction is given by

$$\mathbf{v}^{CE} - \mathbf{v}^{TE} \geq -\mathbf{g} + \mathbf{r} \tag{29}$$

where $\mathbf{v}^{CE}$ are the displacements in the node of the contact element, $\mathbf{v}^{TE}$ the displacements in the auxiliary point of the target element, $\mathbf{r}$ are eventual irregularities between the contact and target elements and $\mathbf{g}$ an initial gap that separates the two elements.

The displacements of the contact nodes belonging to the contact elements are given by

$$\mathbf{v}^{CE} = \mathbf{H}_{XF}^{CE}\ \mathbf{a}_F^{c,i+1} + \mathbf{H}_{XP}^{CE}\ \mathbf{a}_P^c \tag{30}$$

where the displacement transformation matrices **H** relate the displacements of the contact nodes, defined in the local coordinate system, to the nodal displacements defined in the global coordinate system. Also, by analogy, the displacements of the auxiliary points of the target elements are given by

$$\mathbf{v}^{TE} = \mathbf{H}_{XF}^{TE}\ \mathbf{a}_F^{c,i+1} + \mathbf{H}_{XP}^{TE}\ \mathbf{a}_P^{c} \tag{31}$$

Substituting Eqs. (30) and (31) into Eq. (29) and taking into account eventual irregularities **r** between the contact and target elements yields

$$\mathbf{H}_{XF}\ \mathbf{a}_F^{c,i+1} = -\mathbf{g} + \mathbf{r} - \mathbf{H}_{XP}\ \mathbf{a}_P^{c} \tag{32}$$

where

$$\mathbf{H}_{XF} = \mathbf{H}_{XF}^{CE} - \mathbf{H}_{XF}^{TE} \tag{33}$$

$$\mathbf{H}_{XP} = \mathbf{H}_{XP}^{CE} - \mathbf{H}_{XP}^{TE} \tag{34}$$

Since only the active constraints are considered in Eq. (32) the inequality (29) becomes an equality. Substituting Eq. (25) into Eq. (32) leads to

$$\mathbf{H}_{XF}\ \Delta\mathbf{a}_F^{i+1} = -\mathbf{g} + \mathbf{r} - \mathbf{H}_{XP}\ \mathbf{a}_P^{c} - \mathbf{H}_{XF}\ \mathbf{a}_F^{c,i} \tag{35}$$

Multiplying Eq. (35) by $-(1+\alpha)$ gives

$$\overline{\mathbf{H}}_{XF}\ \Delta\mathbf{a}_F^{i+1} = \overline{\mathbf{g}} \tag{36}$$

where

$$\overline{\mathbf{H}}_{XF} = -(1+\alpha)\,\mathbf{H}_{XF} \tag{37}$$

$$\overline{\mathbf{g}} = -(1+\alpha)\left(-\mathbf{g} + \mathbf{r} - \mathbf{H}_{XP}\ \mathbf{a}_P^{c} - \mathbf{H}_{XF}\ \mathbf{a}_F^{c,i}\right) \tag{38}$$

3.4 Complete system of equations

The incremental formulation of the equilibrium equations of motion of the vehicle-structure system presented in Section 3.2 together with the contact constraint equations presented in Section 3.3 form a complete system of equations whose unknowns are incremental nodal displacements and contact forces. Eqs. (27) and (36) can be expressed in matrix form leading to the following complete system of linear equations

$$\begin{bmatrix} \overline{\mathbf{K}}_{FF}^{c,i} & \overline{\mathbf{D}}_{FX} \\ \overline{\mathbf{H}}_{XF} & \mathbf{0} \end{bmatrix} \begin{bmatrix} \Delta\mathbf{a}_F^{i+1} \\ \Delta\mathbf{X}^{i+1} \end{bmatrix} = \begin{bmatrix} \boldsymbol{\psi}\left(\mathbf{a}_F^{c,i}, \mathbf{X}^{c,i}\right) \\ \overline{\mathbf{g}} \end{bmatrix} \tag{39}$$

The symmetry of the coefficient matrix presented in Eq. (39) was demonstrated using the Betti's theorem but is not presented here due to space limitations.

The efficiency of the algorithm used for solving the system of equations (39) is very important. Thus, an efficient and stable block factorization algorithm is shown in Section 4 that takes into account the specific properties of each block, namely, symmetry, positive definiteness (if exists) and bandwidth.

4 BLOCK FACTORIZATION SOLVER ALGORTIGM

The time required to solve the system of nonlinear equations (39) represents, in the majority of the problems, the largest percentage of the total solution time. In a dynamic nonlinear analysis the effective stiffness matrix is time-dependent, which implies its factorization in each iteration. Generally, this is a major drawback since the factorization of large matrices is time consuming. However, in the present problem, the nonlinear terms are substantially smaller that the linear terms, since the material nonlinearities are concentrated only in the contact elements (Hertz contact model [5] or creep models [17]) and on nonlinear elements of the model, like vehicle suspensions or structure bearings. Hence, in order to take advantage of this situation, the effective stiffness matrix given by Eq. (22) is reordered according to the adopted d.o.f. classification presented in Section 2

$$\begin{bmatrix} \overline{\mathbf{K}}_{II}^{c,i} & \overline{\mathbf{K}}_{IR}^{c,i} & \overline{\mathbf{K}}_{IY}^{c,i} & \overline{\mathbf{D}}_{IX} \\ \overline{\mathbf{K}}_{RI}^{c,i} & \overline{\mathbf{K}}_{RR}^{c,i} & \overline{\mathbf{K}}_{RY}^{c,i} & \overline{\mathbf{D}}_{RX} \\ \overline{\mathbf{K}}_{YI}^{c,i} & \overline{\mathbf{K}}_{YR}^{c,i} & \overline{\mathbf{K}}_{YY}^{c,i} & \overline{\mathbf{D}}_{YX} \\ \overline{\mathbf{H}}_{XI} & \overline{\mathbf{H}}_{XR} & \overline{\mathbf{H}}_{XY} & \mathbf{0} \end{bmatrix} \begin{bmatrix} \Delta\mathbf{a}_I^{i+1} \\ \Delta\mathbf{a}_R^{i+1} \\ \Delta\mathbf{a}_Y^{i+1} \\ \Delta\mathbf{X}^{i+1} \end{bmatrix} = \begin{bmatrix} \boldsymbol{\psi}\left(\mathbf{a}_I^{c,i}, \mathbf{X}^{c,i}\right) \\ \boldsymbol{\psi}\left(\mathbf{a}_R^{c,i}, \mathbf{X}^{c,i}\right) \\ \boldsymbol{\psi}\left(\mathbf{a}_Y^{c,i}, \mathbf{X}^{c,i}\right) \\ \overline{\mathbf{g}} \end{bmatrix} \tag{40}$$

With this reordering, only the nonlinear terms, *R* and *Y* type d.o.f., have to be factorized in each iteration, while the largest block $\overline{\mathbf{K}}_{II}$ is factorized only once in the beginning of the dynamic analysis.

The coefficient matrix presented in Eq. (40) can be factorized as following

$$\begin{bmatrix} \overline{\mathbf{K}}_{II} & \overline{\mathbf{K}}_{IR} & \overline{\mathbf{K}}_{IY} & \overline{\mathbf{D}}_{IX} \\ \overline{\mathbf{K}}_{RI} & \overline{\mathbf{K}}_{RR} & \overline{\mathbf{K}}_{RY} & \overline{\mathbf{D}}_{RX} \\ \overline{\mathbf{K}}_{YI} & \overline{\mathbf{K}}_{YR} & \overline{\mathbf{K}}_{YY} & \overline{\mathbf{D}}_{YX} \\ \overline{\mathbf{H}}_{XI} & \overline{\mathbf{H}}_{XR} & \overline{\mathbf{H}}_{XY} & \mathbf{0} \end{bmatrix} = \begin{bmatrix} \mathbf{L}_{11} & \mathbf{0} & \mathbf{0} & \mathbf{0} \\ \mathbf{L}_{21} & \mathbf{L}_{22} & \mathbf{0} & \mathbf{0} \\ \mathbf{L}_{31} & \mathbf{L}_{32} & \mathbf{L}_{33} & \mathbf{0} \\ \mathbf{L}_{41} & \mathbf{L}_{42} & \mathbf{L}_{43} & \mathbf{L}_{44} \end{bmatrix} \times \begin{bmatrix} \mathbf{U}_{11} & \mathbf{U}_{12} & \mathbf{U}_{13} & \mathbf{U}_{14} \\ \mathbf{0} & \mathbf{U}_{22} & \mathbf{U}_{23} & \mathbf{U}_{24} \\ \mathbf{0} & \mathbf{0} & \mathbf{U}_{33} & \mathbf{U}_{34} \\ \mathbf{0} & \mathbf{0} & \mathbf{0} & \mathbf{U}_{44} \end{bmatrix} \tag{41}$$

where $\mathbf{L}_{ij}$ and $\mathbf{U}_{ij}$ are lower and upper triangle submatrices, respectively. The superscripts presented in Eq. (40) are neglected for simplification in the present section.

The first step of the solver consists on factorizing block $\overline{\mathbf{K}}_{II}$ and on calculating the upper triangle submatrix $\mathbf{U}_{12}$.

$$\overline{\mathbf{K}}_{II} = \mathbf{L}_{11}\,\mathbf{L}_{11}^{T} \tag{42}$$

$$\overline{\mathbf{K}}_{IR} = \mathbf{L}_{11}\,\mathbf{U}_{12} \tag{43}$$

Due to the positive-definiteness property of matrix $\overline{\mathbf{K}}_{II}$, a Cholesky factorization [18] has been used in the operation (42). Since the submatrices $\overline{\mathbf{K}}_{II}$ and $\overline{\mathbf{K}}_{IR}$ are time-independent, Eqs. (42) and (43) have to be solved only once in the beginning of the analysis.

The second step consists on calculating the remaining upper triangle submatrices. In the coefficient matrix presented in Eq. (40), the blocks $\overline{\mathbf{K}}_{RR}$ and $\overline{\mathbf{K}}_{YY}$ represent the effective stiffness matrices with the nonlinear terms, while the blocks $\overline{\mathbf{H}}_{ij}$ and $\overline{\mathbf{D}}_{ij}$ depend on the train position and on the contact status of each contact pair. Therefore, both types of blocks are time-dependent and have to be factorized in each iteration. However, the dimensions of the previous mentioned blocks are small when compared to the linear block $\overline{\mathbf{K}}_{II}$, making the next operations less expensive in terms of computational effort.

Thus, the remaining upper triangle submatrices are given by

$$\overline{\mathbf{K}}_{IY} = \mathbf{L}_{11}\,\mathbf{U}_{13} \tag{44}$$

$$\overline{\mathbf{D}}_{IX} = \mathbf{L}_{11}\,\mathbf{U}_{14} \tag{45}$$

$$\overline{\mathbf{K}}_{RR} = \mathbf{L}_{21}\,\mathbf{U}_{12} + \mathbf{L}_{22}\,\mathbf{U}_{22} \tag{46}$$

$$\overline{\mathbf{K}}_{RY} = \mathbf{L}_{21}\,\mathbf{U}_{13} + \mathbf{L}_{22}\,\mathbf{U}_{23} \tag{47}$$

$$\overline{\mathbf{D}}_{RX} = \mathbf{L}_{21}\,\mathbf{U}_{14} + \mathbf{L}_{22}\,\mathbf{U}_{24} \tag{48}$$

As mentioned before, the nonlinear contact elements make the connection between the two systems, vehicle and structure. Depending of the problem, the stiffness matrix of these elements can assume other properties other than positive definiteness, thus it cannot be solved with factorization methods without pivoting, like Cholesky or $\mathbf{L}\,\mathbf{D}\,\mathbf{L}^T$ [18]. Therefore, the proposed block factorization algorithm evaluates the positive definiteness of the block $\overline{\mathbf{K}}_{YY}$ and solves it with pivoting if needed, as explained below.

The third part of the solver consists on solving the following intermediate system of equations

$$\begin{bmatrix} \mathbf{L}_{11} & \mathbf{0} & \mathbf{0} & \mathbf{0} \\ \mathbf{L}_{21} & \mathbf{L}_{22} & \mathbf{0} & \mathbf{0} \\ \mathbf{L}_{31} & \mathbf{L}_{32} & \mathbf{L}_{33} & \mathbf{0} \\ \mathbf{L}_{41} & \mathbf{L}_{42} & \mathbf{L}_{43} & \mathbf{L}_{44} \end{bmatrix} \begin{bmatrix} \mathbf{y}_1 \\ \mathbf{y}_2 \\ \mathbf{y}_3 \\ \mathbf{y}_4 \end{bmatrix} = \begin{bmatrix} \boldsymbol{\psi}(\mathbf{a}_I, \mathbf{X}) \\ \boldsymbol{\psi}(\mathbf{a}_R, \mathbf{X}) \\ \boldsymbol{\psi}(\mathbf{a}_Y, \mathbf{X}) \\ \overline{\mathbf{g}} \end{bmatrix} \tag{49}$$

in which the vectors $\mathbf{y}_1$ to $\mathbf{y}_4$ are obtained by forward substitution

$$\mathbf{L}_{11}\,\mathbf{y}_1 = \boldsymbol{\psi}(\mathbf{a}_I, \mathbf{X}) \tag{50}$$

$$\mathbf{L}_{22}\,\mathbf{y}_2 = \boldsymbol{\psi}(\mathbf{a}_R, \mathbf{X}) - \mathbf{L}_{21}\,\mathbf{y}_1 \tag{51}$$

$$\overline{\mathbf{y}}_3 = \mathbf{L}_{33}\,\mathbf{y}_3 \tag{52}$$

$$\overline{\mathbf{y}}_4 = \mathbf{L}_{43}\,\mathbf{y}_3 + \mathbf{L}_{44}\,\mathbf{y}_4 \tag{53}$$

where

$$\overline{\mathbf{y}}_3 = \boldsymbol{\psi}(\mathbf{a}_Y, \mathbf{X}) - \mathbf{L}_{31}\,\mathbf{y}_1 - \mathbf{L}_{32}\,\mathbf{y}_2 \tag{54}$$

$$\overline{\mathbf{y}}_4 = \overline{\mathbf{g}} - \mathbf{L}_{41}\,\mathbf{y}_1 - \mathbf{L}_{42}\,\mathbf{y}_2 \tag{55}$$

Finally, the solution of the system equations is given by

$$\begin{bmatrix} \mathbf{U}_{11} & \mathbf{U}_{12} & \mathbf{U}_{13} & \mathbf{U}_{14} \\ \mathbf{0} & \mathbf{U}_{22} & \mathbf{U}_{23} & \mathbf{U}_{24} \\ \mathbf{0} & \mathbf{0} & \overline{\mathbf{A}}_{33} & \overline{\mathbf{A}}_{43}^T \\ \mathbf{0} & \mathbf{0} & \overline{\mathbf{A}}_{43} & \overline{\mathbf{A}}_{44} \end{bmatrix} \begin{bmatrix} \Delta\mathbf{a}_I \\ \Delta\mathbf{a}_R \\ \Delta\mathbf{a}_Y \\ \Delta\mathbf{X} \end{bmatrix} = \begin{bmatrix} \mathbf{y}_1 \\ \mathbf{y}_2 \\ \overline{\mathbf{y}}_3 \\ \overline{\mathbf{y}}_4 \end{bmatrix} \tag{56}$$

where the first part of the solution of the system, $\Delta\mathbf{a}_Y$ and $\Delta\mathbf{X}$, is obtained by factorizing and solving the two last lines of blocks with pivoting

$$\begin{bmatrix} \overline{\mathbf{A}}_{33} & \overline{\mathbf{A}}_{43}^{T} \\ \overline{\mathbf{A}}_{43} & \overline{\mathbf{A}}_{44} \end{bmatrix} \begin{bmatrix} \Delta\mathbf{a}_Y \\ \Delta\mathbf{X} \end{bmatrix} = \begin{bmatrix} \overline{\mathbf{y}}_3 \\ \overline{\mathbf{y}}_4 \end{bmatrix} \tag{57}$$

in which

$$\overline{\mathbf{A}}_{33} = \overline{\mathbf{K}}_{YY} - \mathbf{L}_{31}\mathbf{L}_{31}^{T} - \mathbf{L}_{32}\mathbf{L}_{32}^{T} \tag{58}$$

$$\overline{\mathbf{A}}_{43} = \overline{\mathbf{H}}_{XY} - \mathbf{L}_{41}\mathbf{L}_{31}^{T} - \mathbf{L}_{42}\mathbf{L}_{32}^{T} \tag{59}$$

$$\overline{\mathbf{A}}_{44} = -\mathbf{L}_{41}\mathbf{L}_{41}^{T} - \mathbf{L}_{42}\mathbf{L}_{42}^{T} \tag{60}$$

and the last part of the solution, $\Delta\mathbf{a}_I$ and $\Delta\mathbf{a}_R$, is obtained by back substitution

$$\mathbf{L}_{22}^{T}\Delta\mathbf{a}_R = \mathbf{y}_2 - \mathbf{L}_{32}^{T}\Delta\mathbf{a}_Y - \mathbf{L}_{42}^{T}\Delta\mathbf{X} \tag{61}$$

$$\mathbf{L}_{11}^{T}\Delta\mathbf{a}_I = \mathbf{y}_1 - \mathbf{L}_{21}^{T}\Delta\mathbf{a}_R - \mathbf{L}_{31}^{T}\Delta\mathbf{a}_Y - \mathbf{L}_{41}^{T}\Delta\mathbf{X} \tag{62}$$

5 NUMERICAL VALIDATION

In order to validate the accuracy of the proposed methodology a numeric examples is presented in this section. The example consists of two simply supported spans subjected to four moving sprung masses (see Figure 3). The spans are modeled with solid elements in order to test not only the accuracy, but also the efficiency of the algorithm. The two simply supported spans are discretized with sixteen thousand 8-node solid elements ($2\times80\times10\times10$) and have a total of 58696 unconstrained d.o.f. The geometrical and mechanical properties of the system are the following: length of each span $L = 20\,\text{m}$, width of the square cross section b = 2.45 m, Young's modulus $E = 25\,\text{GPa}$, Poisson's ratio $\nu = 0.2$, moment of inertia $I = 3\,\text{m}^4$, mass per unit length $m = 30000\ \text{kg/m}$, suspended mass $M_v = 30000\,\text{kg}$ and spring stiffness $k_v = 156550\ \text{kN/m}$. The distance between each sprung mass is $d = 20\,\text{m}$.

The results obtained using the direct method are compared with the results obtained by the commercial software ANSYS [12], using the Lagrange multiplier method [5].

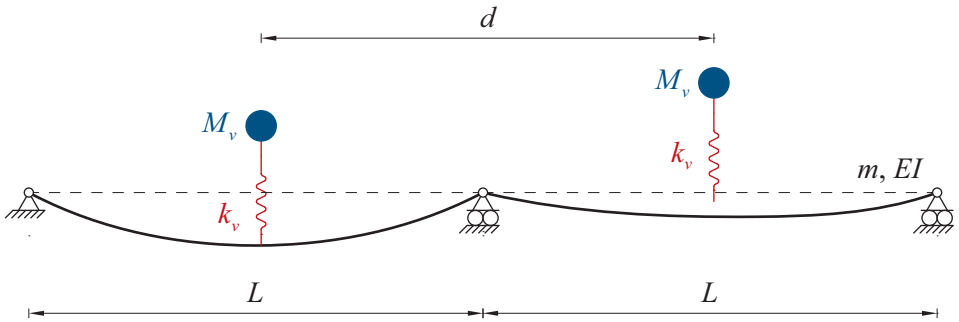


Figure 3: Two simply supported spans subjected to four moving sprung masses.

The sprung masses move at a constant speed $\text{v} = 115\,\text{m/s}$. The following parameters for the α method are considered: $\alpha = 0$, $\beta = 0.25$ and $\gamma = 0.5$, which correspond to the constant average acceleration method. The time step is $\Delta t = 0.001\text{s}$ and the total number of time steps is 900.

The vertical displacement at the midpoint of the first span, obtained using the direct method and ANSYS, is plotted in Figure 4. The vertical displacements of the first and last sprung masses, SM1 and SM4 respectively, are compared in Figure 5. The results obtained using the proposed methodology and ANSYS show a very good agreement.

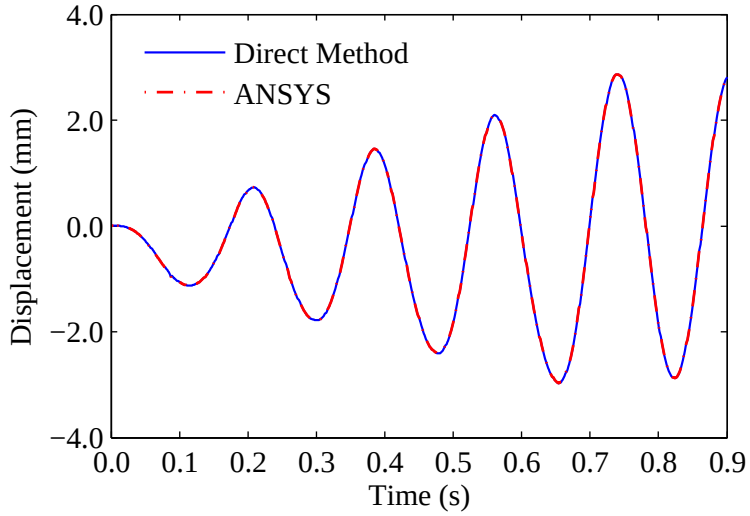


Figure 4: Vertical displacement at the midpoint of the first span.

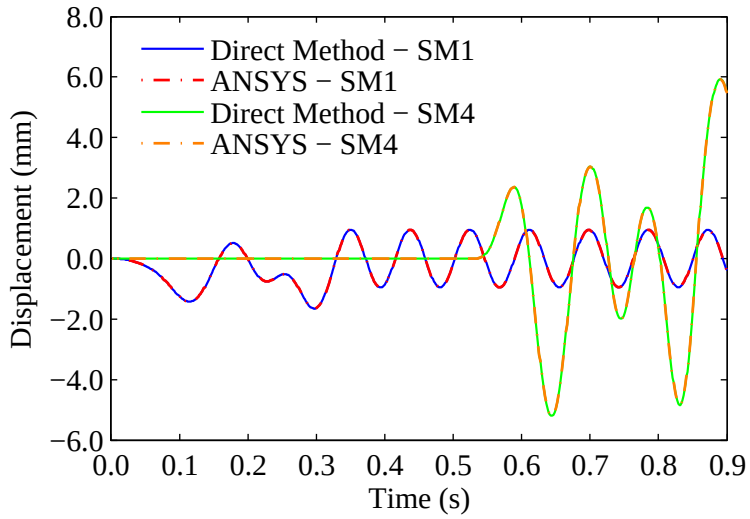


Figure 5: Vertical displacement of the first and last suspended masses.

Finally, the comparisons between the contact forces of the first and last sprung masses are plotted in Figure 6. The results obtained using the direct method perfectly match the corresponding ANSYS solutions obtained using the well-known Lagrange multiplier method. As was expected, the first sprung mass is in permanent contact during all the analysis, since the excitation of the beam is not enough to cause the sprung mass separation. However, the last sprung mass loses contact with the beam a significant number of times as can be observed in Figure 6 when the contact force is zero. This is due to the fact that the excitation of the beam is considerably higher during the passage of the last sprung mass. Therefore, the present methodology demonstrates good accuracy both when the vehicle detaches from the structure and when reattaches.

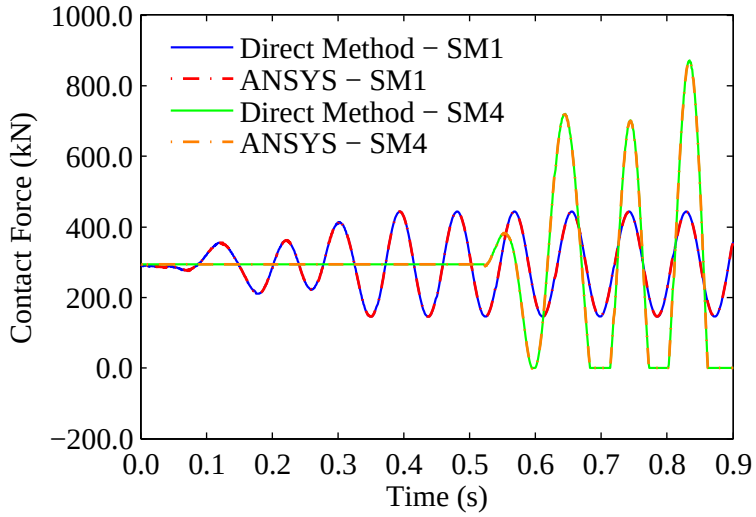


Figure 6: Vertical contact force of the first and last suspended masses.

The calculations of the present example were performed using a workstation with an Intel Xeon E5620 dual core processor running at 2.40 GHz. For a more accurate comparison the calculations in ANSYS and MATLAB were performed using a single thread. The execution time was 16608 seconds using ANSYS and 264 seconds using the direct method with the optimized block factorization algorithm, which is about 63 times faster. Hence, in terms of computational speed, the direct method has proven to be very efficient.

6 CONCLUSIONS

An accurate and efficient methodology for analyzing the vehicle-structure interaction problem has been developed. The nonlinear equations of motion of the vehicle and structure are complemented with additional constraint equations, forming a single system of equations that can be directly and efficiently solved. Due to the nonlinear nature of the contact mechanics, an incremental formulation has been used to solve the equations of motion, while a procedure based on the Lagrange multiplier method imposes the contact constraint equations when contact occurs. The system of nonlinear equations is solved by block factorization solver that reorders the system matrix and isolates the nonlinear terms, thus avoiding multiple unnecessary factorizations of the linear terms during each Newton iteration.

The accuracy and efficiency of the proposed methodology has been confirmed with a numerical example. The example consisted of two simply supported spans modeled with 8-node solid elements subjected to four moving sprung masses, totalizing 58684 unconstrained d.o.f. The responses of the structure, vehicles as well as the contact forces obtained with the proposed methodology have been compared with the results obtained with the commercial software ANSYS using the Lagrange multiplier method. A good agreement between the proposed methodology and ANSYS has been observed. In terms of efficiency, the proposed methodology has also showed very good results, since it is about 63 times faster than ANSYS.

ACKNOWLEDGMENTS

The authors wish to thank Professor Rui Manuel Faria of the University of Porto for the helpful discussions during the preparation of this manuscript, especially regarding the incremental formulation used in this work. This article reports research developed under financial support provided by "FCT - Fundação para a Ciência e Tecnologia", Portugal, under grant number SFRH/BD/39190/2007 and SFRH/BD/48320/2008.

REFERENCES

[1] Delgado, R., Santos, S.M. - Modelling of railway bridge-vehicle interaction on high speed tracks, *Computers & Structures*, **63**, 511-523, 1997.

[2] Lei, X., Noda, N.A. - Analyses of dynamic response of vehicle and track coupling system with random irregularity of track vertical profile, *Journal of Sound and Vibration*, **258**, 147-165, 2002.

[3] Yang, F., Fonder, G. - An iterative solution method for dynamic response of bridge-vehicles systems, *Earthquake Engineering and Structural Dynamics*, **25**, 195-215, 1996.

[4] Yang, Y.B., Wu, Y.S. - A versatile element for analyzing vehicle-bridge interaction response, *Engineering Structures*, **23**, 452-469, 2001.

[5] Wriggers, P. - *Computational Contact Mechanics*, John Wiley & Sons Ltd, Chichester, UK, 2002.

[6] Pombo, J., Ambrosio, J., Silva, M. - A new wheel-rail contact model for railway dynamics, *Vehicle System Dynamics*, **45**, 165-189, 2007.

[7] Shabana, A., Zaazaa, K.E., Escalona, J.L., Sany, J.R. - Development of elastic force model for wheel/rail contact problems, *Journal of Sound and Vibration*, **269**, 295-325, 2004.

[8] Antolín, P., Goicolea, J.M., Oliva, J., Astiz, M.A. - Nonlinear train-bridge lateral interaction using a simplified wheel-rail contact method within a finite element framework, *Journal of Computational and Nonlinear Dynamics*, **7**, art. no. 041014, 2012.

[9] Tanabe, M., Matsumoto, N., Wakui, H., Sogabe, M., Okuda, H., Tanabe, Y. - A simple and efficient numerical method for dynamic interaction analysis of a high-speed train and railway structure during an earthquake, *Journal of Computational and Nonlinear Dynamics*, **3**, art. no. 041002, 2008.

[10] Neves, S.G.M., Azevedo, A.F.M., Calçada, R. - A direct method for analyzing the vertical vehicle–structure interaction, *Engineering Structures*, **34**, 414-420, 2012.

[11] MATLAB® - R2011b, The MathWorks Inc., Natick, MA, 2011.

[12] ANSYS® - Academic Research, Release 13.0, ANSYS Inc., Canonsburg, PA, 2010.

[13] Bathe, K.J. - *Finite element procedures*, Upper Saddle River, NJ: Prentice-Hall, 1996.

[14] Owen, D.R.J., Hinton, E. - *Finite Elements in Plasticity: Theory and Practice*, Swansea, UK: Pineridge Press Limited, 1980.

[15] Hughes, T.J.R. - *The finite element method: Linear static and dynamic finite element analysis*, Dover Publications, New York, 2000.

[16] Arfken, G. - *Mathematical methods for physicists*, Orlando, FL: Academic Press, 1985.

[17] Kalker, J.J. - *Three-dimensional elastic bodies in rolling contact*, Kluwer Academic Publishers, Dordrecht, The Netherlands, 1990.

[18] Burden, R.L., Faires, J.D. - *Numerical analysis*, ITP, Pacific Grove, CA, 1997.

COMPDYN 2013
4th ECCOMAS Thematic Conference on
Computational Methods in Structural Dynamics and Earthquake Engineering
M. Papadrakakis, V. Papadopoulos, V. Plevris (eds.)
Kos Island, Greece, 12–14 June 2013

A SHEET PILING WALL AS A WAVE BARRIER FOR TRAIN INDUCED VIBRATIONS

A. Dijckmans[1], A. Ekblad[2], A. Smekal[2], G. Degrande[1] and G. Lombaert[1]

[1]KU Leuven Department of Civil Engineering
Kasteelpark Arenberg 40, B-3001 Leuven, Belgium
e-mail: {arne.dijckmans,geert.degrande,geert.lombaert}@bwk.kuleuven.be

[2] Trafikverket
405 33 Göteborg, Sweden
e-mail: {alf.ekblad,alexander.smekal}@trafikverket.se

Keywords: ground borne vibration, buried wall barrier, 2.5D, finite element, boundary element

Abstract. *Numerical simulations have been carried out with a two-and-a-half dimensional coupled finite element - boundary element methodology to assess the effectiveness of a sheet piling wall to reduce railway induced vibrations. In the method, the geometry of the problem is assumed invariant in the longitudinal direction along the track.*

The sheet piling wall acts as a stiff wave barrier of which the effectiveness is determined by the depth and the contrast in stiffness between the barrier and the soil. It is important to take into account the orthotropic behavior of the sheet piling wall, as the bending stiffness in the vertical direction (along the profiles) is much larger than the bending stiffness in the longitudinal direction (perpendicular to the profiles). Calculations show that the reduction of vibration levels is entirely due to the relatively high axial stiffness and vertical bending stiffness, while the longitudinal bending stiffness is too low to affect the transmission of vibrations.

At Furet, Sweden, a sheet piling wall has been installed next to the track to reduce train induced vibrations in several buildings close to the track. The vibration levels caused by train passages have been measured before and after the construction of wall. Furthermore, the Rolling Stiffness Measurement Vehicle (RSMV) has been used to perform measurements with stationary track excitation. A preliminary comparison is made of the experimental results and predicted insertion loss values.

1 INTRODUCTION

At Furet vibration problems occur in several buildings close to a railway track (Figure 1a). The site of Furet is located in the southwest of Sweden in the city of Halmstad along the West Coast Line between Gothenburg and Lund. The buildings in Furet have two to three floors and are mostly built around 1950, along $750\,\mathrm{m}$ at the west side of the track, $700\,\mathrm{m}$ north of Halmstad station. The track consists of a classical ballasted track.

In 2002 an Environmental court decided that residents should have less than $1.0\,\mathrm{mm/s}$ frequency weighted RMS at night (10pm-07am). Measurements indicate that in at least eight buildings the vibration levels exceed this value. The highest vibration levels were measured in the frequency range $4 - 5\,\mathrm{Hz}$.

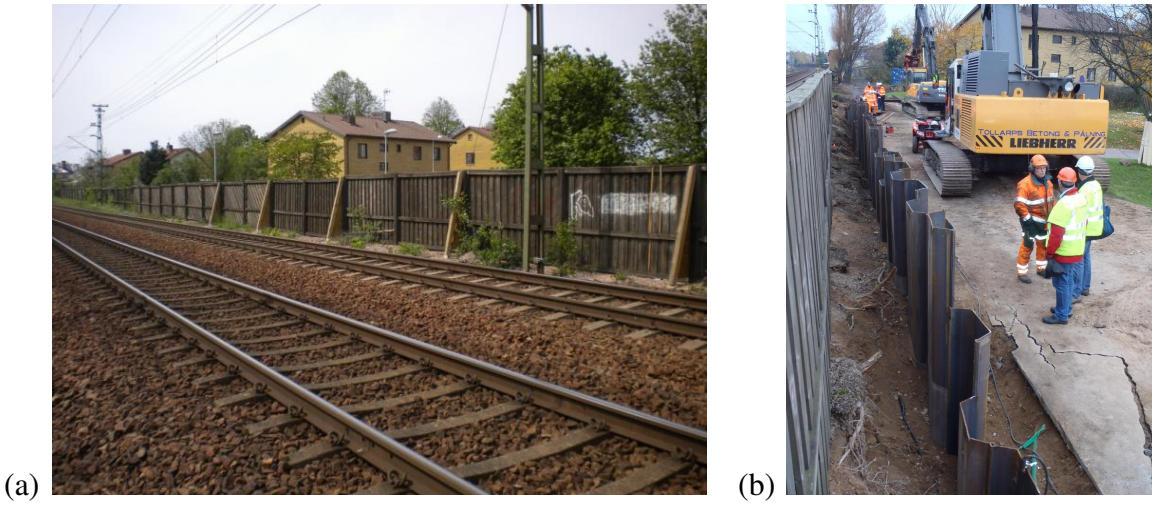


Figure 1: Site of Furet: (a) track, noise barrier and buildings close to the track, and (b) installation of the sheet piling wall.

The first attempt to mitigate vibration has been done in 2006. Sleepers at the track close to the noise barrier have been replaced and substituted by sleepers with under sleeper pads (USP). At the same time the ballast has been exchanged and leveling of the track has been carried out. Unfortunately measurements performed after these measures showed insufficient vibration mitigation. Therefore it was decided to use a sheet piling wall as a method to further reduce the train induced vibrations at the site. A sheet piling wall with a length of $100\,\mathrm{m}$ was installed next to the track in November 2011 (Figure 1b).

The sheet piling wall is a VL 603-K profile (Figure 2). The depth of the sheet piles is $12\,\mathrm{m}$ with every fourth pile extended to $18\,\mathrm{m}$. Adjacent sheet piles were welded together over the top $30\,\mathrm{cm}$. The distance from the center of the nearest track to the center of the sheet piling wall is approximately $5.60\,\mathrm{m}$. The properties of the VL 603-K profile are given in Table 1.

Measurements after installation of the sheet pile wall have showed sufficient reduction of vibration levels, except for a small house with wooden structure at approximately $40\,\mathrm{m}$ distance from the track.

The sheet piling wall designed and constructed by Trafikverket is subjected to a program of measurements and theoretical analysis within the frame of the EU FP7 project RIVAS (Railway Induced Vibration Abatement Solutions). First simulation results and experimental results are presented in this paper.

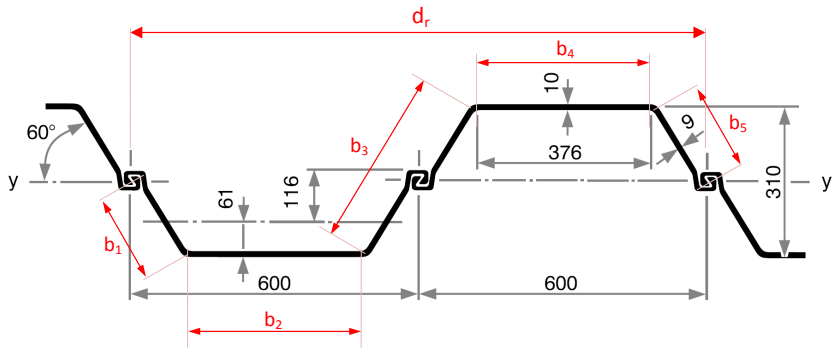


Figure 2: Cross section of the sheet piling wall (VL 603-K profile)

Mass m_{w} $[\mathrm{kg/m^2}]$	Sectional area A_{w} $[\mathrm{cm^2/m}]$	Moment of inertia I_{w} $[\mathrm{cm^4/m}]$	Width t_{w} $[\mathrm{m}]$
113.5	144.8	18900	0.310

Table 1: Characteristics of the sheet piling wall (VL 603-K profile)

2 MEASUREMENTS

2.1 Dynamic soil characteristics

Geotechnical and geophysical surveys performed by the consulting company Tyréns in the area include cone penetration tests (CPT), seismic cone penetration tests (SCPT), standard piston sampling, sampling by Helical auger and weight sounding. The undrained shear strength is $20-35\,\mathrm{kPa}$ to $13\,\mathrm{m}$ depth and $50-70\,\mathrm{kPa}$ deeper than $13\,\mathrm{m}$, investigation done in 4 boreholes with depth to at least $18\,\mathrm{m}$.

The soil profile consists of a relatively firm layer of sand up to $2-3\,\mathrm{m}$ depth underlain by clayey silt up to a depth of $5-10\,\mathrm{m}$ (layers of clay), underlain by silty clay. The silt has a density of $1850\,\mathrm{kg/m^3}$ and the clay $1710\,\mathrm{kg/m^3}$. These densities are determined as average values from three samples per meter from one of the boreholes.

The shear wave velocity C_{s} has been measured by means of a SCPT and multichannel analysis of surface waves (MASW) test. The SCPT test indicated a shear wave velocity of $110\,\mathrm{m/s}$ between $3-14\,\mathrm{m}$, and $150\,\mathrm{m/s}$ between $15-18\,\mathrm{m}$. Two setups were used for the MASW test. The first setup employed 24 geophones in a straight line perpendicular to the track, equally spaced between $10\,\mathrm{m}$ and $56\,\mathrm{m}$ from the hand-held hammer impact aluminium plate. The second setup used 24 geophones in a straight line perpendicular to the track, equally spaced between $10\,\mathrm{m}$ and $33\,\mathrm{m}$ from the hand-held hammer impact aluminium plate. The analysis shows a $2\,\mathrm{m}$ thick top layer with a shear wave velocity of $160\,\mathrm{m/s}$, a $10\,\mathrm{m}$ thick mid layer with a shear wave velocity of $115\,\mathrm{m/s}$ and a halfspace with a shear wave velocity of about $200\,\mathrm{m/s}$.

The results from the different in situ tests are in good agreement. The SCPT results showed a shear wave velocity of $110\,\mathrm{m/s}$ for the mid layer and a shear wave velocity of $150\,\mathrm{m/s}$ for the halfspace. The MASW results showed a slightly higher shear wave velocity, $119\,\mathrm{m/s}$ and $200\,\mathrm{m/s}$. The presence of the stiffer top layer impedes the determination of the dilatational wave velocity C_{p} from a seismic refraction test, the values for C_{p} have been estimated from the results for C_{s} assuming a Poisson's ratio of 0.40. Table 2 provides a summary of the soil

parameters for each layer.

Layer	Thickness h [m]	Shear wave velocity C_s [m/s]	Dilatational wave velocity C_p [m/s]	Damping ratio β [-]	Density ρ [kg/m^3]	Poisson's ratio ν [-]
1	2	154	375	0.025	1800	0.40
2	10	119	290	0.025	1850	0.40
3	∞	200	490	0.025	1710	0.40

Table 2: Dynamic soil characteristics for the Furet test site.

2.2 Vibration measurements

Vibration measurements were performed according to the RIVAS measurement protocol [1]. In the protocol, the combination of two procedures is recommended to determine the efficiency of vibration mitigation measures. In the first procedure, the vibration levels obtained at adjacent track sections with and without mitigation measure are compared to determine the insertion loss. In the second procedure, vibration levels before and after installation of the mitigation measure are compared.

At Furet, vibration measurements were performed both before and after installation of the sheet pile wall on two measurement lines perpendicular to the track, one at the test section with sheet pile wall and one at a reference section. Measurement line A was close to the middle of the sheet pile wall (Figure 3). Geophones were placed at $8\,\mathrm{m}$, $16\,\mathrm{m}$, $32\,\mathrm{m}$ and $64\,\mathrm{m}$ from the center of the track. Geophones were also placed at $8\,\mathrm{m}$ and $16\,\mathrm{m}$ at the opposite side of the track to verify whether there is no increase in vibration levels. Two geophones were placed on the sleepers to measure the track stiffness. A second, reference measurement line was placed a couple of hundred meters south of the sheet piling wall. Here, measurements were performed on the sleepers and at $8\,\mathrm{m}$ and $16\,\mathrm{m}$ from the track center.

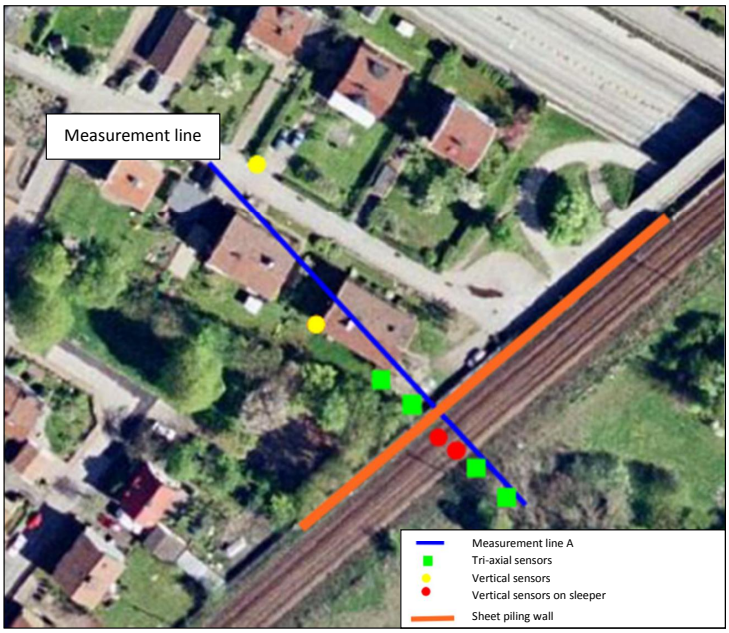


Figure 3: Measurement setup for the vibration measurements at the test site.

Vibration measurements during train passages have been performed during an entire week to include all types of traffic and to cover differences between working days and weekend days. At the test site, a total of 112 train passages occur per 24 hours, of which 29 are freight trains.

Preliminary comparison between the results at the test section before and after installation of the sheet pile wall indicate a significant reduction in vertical vibration levels behind the sheet pile wall at $8\,\mathrm{m}$, $16\,\mathrm{m}$, and $32\,\mathrm{m}$ from the track center. The effectiveness is higher closer to the wall where the maximum vibration levels are reduced by about 50%. At $32\,\mathrm{m}$ the maximum levels are reduced by about 30%. At $64\,\mathrm{m}$ from the track center, no reduction in maximum vibration levels is seen. Measurements at the other side of the track show no increase in vertical vibration levels.

Furthermore, vibration measurements have been carried out with the Rolling Stiffness Measurement Vehicle (RSMV). In this case stationary excitation of the track has been applied. The excitation has been performed before and after installation of the sheet pile wall at both the test site and the reference site. The excitation duration was 30 seconds at each operating frequency ($3\,\mathrm{Hz}$, $4\,\mathrm{Hz}$, $5\,\mathrm{Hz}$, $6\,\mathrm{Hz}$, $7\,\mathrm{Hz}$, $8\,\mathrm{Hz}$, $9\,\mathrm{Hz}$, $10\,\mathrm{Hz}$, $15\,\mathrm{Hz}$ and $20\,\mathrm{Hz}$). Figure 4 shows preliminary results for the measured insertion loss for the excitation frequencies of $5\,\mathrm{Hz}$ and $20\,\mathrm{Hz}$, as determined from the measurements at the test site before and after installation of the sheet pile wall. These results indicate that a considerable reduction is already obtained at $5\,\mathrm{Hz}$. Furthermore, the reduction generally decreases with increasing distance from the sheet piling wall.

Further processing of the measurements is needed for a more detailed assessment of the effectiveness.

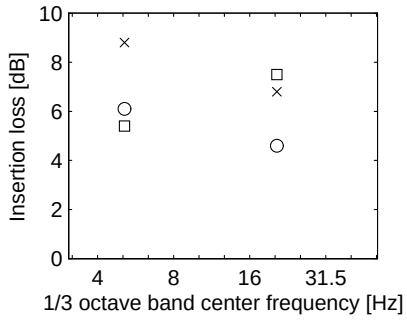


Figure 4: Vertical insertion loss measured at $8\,\mathrm{m}$ ($\times$), $16\,\mathrm{m}$ ($\square$) and $32\,\mathrm{m}$ ($\circ$) with stationary track excitation (RSMV) at $5\,\mathrm{Hz}$ and $20\,\mathrm{Hz}$.

3 SIMULATIONS

3.1 Methodology

For the prediction of railway induced vibrations, the geometry of the track-soil system is often assumed to be invariant in the longitudinal direction. The loading due to a point force or train introduces a dependence on the longitudinal dimension. By assuming homogeneity of the geometry and material properties in the track direction, a Fourier transform of the longitudinal coordinate allows for a two-and-half-dimensional (2.5D) approach [2, 3, 4]. This method is computationally more efficient than a full 3D approach. Andersen and Nielsen [5] have applied the methodology to study the effect of vibration isolating screens along a railway track.

For the computation of the dynamic interaction between a layered soil and structures with a longitudinally invariant geometry, a coupled finite element - boundary element (FE–BE)

methodology formulated in the frequency domain is used [6]. The classical 2.5D FE method is combined with the 2.5D BE method using 2.5D Green's functions of a horizontally layered halfspace [7, 8]. In this way, the free surface and the layer interfaces of the halfspace don't have to be discretized with boundary elements, avoiding spurious reflections at mesh truncations. The BE mesh can be limited to the interface between the structure and the soil, significantly reducing the size of the BE mesh.

Solving the set op coupled FE–BE equations provides the structural response in the frequency-wavenumber domain. The radiated wavefield in the soil is obtained by means of the wavenumber domain formulation of the integral representation theorem [6]. Finally, an inverse Fourier transform is used to recover the three-dimensional response in the frequency-spatial domain.

3.2 Sheet piling wall model

The sheet piling wall was analyzed by means of 2.5D calculations. Since this requires assuming the geometry of the sheet piling wall to be longitudinally invariant, separate calculations have been made for depths d of 12 m and 18 m. The actual sheet piles have a depth of 12 m, with every fourth sheet pile extended to 18 m. To reduce the computational cost, the presence of the track was disregarded in the models. A vertical unit harmonic point force is applied directly at the surface at a distance $R = 5.60\,\mathrm{m}$ from the sheet pile wall (Figure 5). This corresponds with the distance from the center of the nearest track to the center of the sheet piling wall at the test site in Furet.

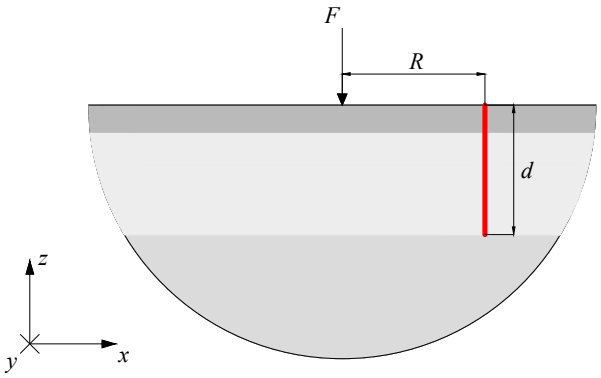


Figure 5: 2.5D plate model of the sheet piling wall

An equivalent orthotropic plate model of the sheet piling wall was adopted in the calculations to account for the fact that the stiffness is much larger for bending with respect to the horizontal axis than for the vertical axis. In the frequency range of interest (0-100 Hz), the bending wavelength λ_b in the sheet piling wall is much larger than the repetition distance $d_\mathrm{r} = 1200\,\mathrm{mm}$ of the sheet piling wall. Therefore, the profiling of the plate can be disregarded and the sheet piling wall can be modeled as an equivalent orthotropic plate.

The thickness $\bar{t}$, moduli of elasticity $\bar{E}_y$ and $\bar{E}_z$, and Poisson's ratios $\bar{\nu}_{yz}$ and $\bar{\nu}_{zy}$ of the equivalent orthotropic plate are chosen such that the plate has approximately the same bending stiffness as well as axial stiffness as the VL 603-K profile. The axial stiffness and bending stiffness in the vertical direction can be determined from the characteristics of the VL 603-K profile (Table 1).

$$\frac{\bar{E}_z \bar{t}}{1 - \bar{\nu}_{yz}\bar{\nu}_{zy}} = E_\mathrm{s} A_\mathrm{w} = 3.041 \times 10^9\,\mathrm{N/m} \tag{1}$$

$$\frac{\bar{E}_z \bar{t}^3}{12(1-\bar{\nu}_{yz}\bar{\nu}_{zy})} = E_\mathrm{s} I_\mathrm{w} = 3.97 \times 10^7 \,\mathrm{Nm^2/m} \tag{2}$$

with $E_\mathrm{s} = 210\,\mathrm{GPa}$ the modulus of elasticity of steel. Solving equations (1) and (2) yields $\bar{t} = 0.396\,\mathrm{m}$ and $\frac{\bar{E}_z}{1-\bar{\nu}_{zy}\bar{\nu}_{yz}} = 7.68\,\mathrm{GPa}$. Due to the profiling of the sheet piling wall, the Poisson's ratios $\bar{\nu}_{yz}$ and $\bar{\nu}_{zy}$ can be assumed zero. This eventually gives a modulus of elasticity $\bar{E}_z = 7.68\,\mathrm{GPa}$.

The bending stiffness in the longitudinal direction is approximately the same as this of a flat steel plate with the same thickness, but taking into account the effective increase in plate width due to the profiles [9].

$$\frac{\bar{E}_y \bar{t}^3}{12(1-\bar{\nu}_{yz}\bar{\nu}_{zy})} = \frac{E_\mathrm{s} h^3}{12(1-\nu_\mathrm{s}^2)} \frac{d_\mathrm{r}}{\sum b_n} = 1.27 \times 10^4 \,\mathrm{Nm^2/m} \tag{3}$$

with $\nu_\mathrm{s} = 0.30$ the Poisson's ratio of steel, $h = 9\,\mathrm{mm}$ the thickness of the steel plate and $\sum b_n = 1320\,\mathrm{mm}$ the total length of the sheet piling wall profile along the length $d_\mathrm{r} = 1200\,\mathrm{mm}$ (Figure 2). Solving for the longitudinal modulus of elasticity yields a value $\bar{E}_y = 2.47\,\mathrm{MPa}$, which is approximately 3100 times smaller than $\bar{E}_z$.

The shear modulus $\bar{\mu}_{yz}$ of the equivalent orthotropic plate is taken equal to the geometric mean of the Young's moduli in the two orthogonal directions [9].

$$\bar{\mu}_{yz} = \frac{\sqrt{\bar{E}_y \bar{E}_z}}{2} = 6.89 \times 10^7 \,\mathrm{N/m^2} \tag{4}$$

For the mass density $\bar{\rho}$, a value of $286.6\,\mathrm{kg/m^3}$ is chosen such that the equivalent plate has the same mass as the VL 603-K profile.

$$\bar{\rho}\bar{t} = m_\mathrm{w} = 113.5\,\mathrm{kg/m^2} \tag{5}$$

An overview of the model parameters can be found in Table 3.

	R [m]	d [m]	$\bar{t}$ [m]	$\bar{E}_y$ [N/m^2]	$\bar{E}_z$ [N/m^2]	$\bar{\mu}_{yz}$ [N/m^2]	$\bar{\nu}_{yz}$ [-]	$\bar{\nu}_{zy}$ [-]	$\bar{\rho}$ [kg/m^3]
Model 1	5.60	12	0.396	2.47×10^6	7.68×10^9	6.89×10^7	0.0	0.0	286.6
Model 2	5.60	18	0.396	2.47×10^6	7.68×10^9	6.89×10^7	0.0	0.0	286.6

Table 3: Geometric parameters and properties of the sheet piling wall used in the models

The sheet piling wall was modeled with 2-noded 2.5D orthotropic shell elements. These elements were coupled to a conforming BE mesh for the surrounding soil. The element dimensions were chosen to ensure at least eight elements per minimal shear wavelength.

3.3 Results for homogeneous halfspace

First, the effectiveness of a sheet piling wall as a mitigation measure and the influence of the orthotropic behavior is investigated. To facilitate the physical interpretation, the soil is assumed to be homogeneous in this section. The site at Horstwalde (Germany) with homogeneous soil conditions, which is one of the reference sites considered in the RIVAS project, is used. The soil characteristics of the Horstwalde site are given in Table 4.

Layer	Thickness h	Shear wave velocity C_s	Dilatational wave velocity C_p	Damping ratio β	Density ρ	Poisson's ratio ν
	$[\mathrm{m}]$	$[\mathrm{m/s}]$	$[\mathrm{m/s}]$	[-]	$[\mathrm{kg/m^3}]$	[-]
1	∞	250	1470	0.025	1945	0.485

Table 4: Dynamic soil characteristics of the homogeneous halfspace (Horstwalde)

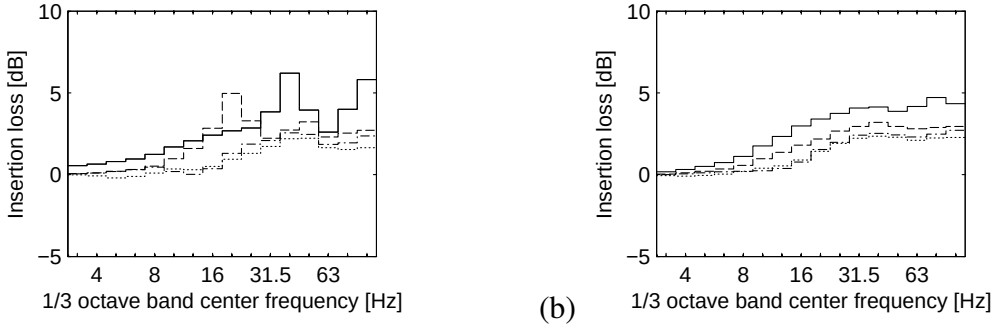


Figure 6: Vertical insertion loss at $8\,\mathrm{m}$ (solid line), $16\,\mathrm{m}$ (dashed line), $32\,\mathrm{m}$ (dash-dotted line) and $64\,\mathrm{m}$ (dotted line) for the $12\,\mathrm{m}$ deep sheet piling wall installed in the homogeneous halfspace. Excitation by (a) a point load and (b) a line load.

Figure 6 shows the vertical insertion loss in 1/3 octave bands for the $12\,\mathrm{m}$ deep sheet piling wall installed in the homogeneous halfspace, for several receiver points at the other side of the wall. The vertical insertion loss $\mathrm{IL_z}$ is the difference in vertical vibration levels in the case with and without vibration mitigation measure,

$$\mathrm{IL_z} = 20 \log_{10} \frac{|\hat{u}^{\mathrm{ref}}|}{|\hat{u}|},$$

where $\hat{u}$ is the vertical displacement in the case with mitigation measure and $\hat{u}^{\mathrm{ref}}$ is the vertical displacement in the reference case without mitigation measure. The hat denotes the representation in the frequency domain.

Figure 6a shows the insertion loss values when a vertical harmonic point force is applied to the soil at the surface at position $(x, y) = (0\,\mathrm{m}, 0\,\mathrm{m})$.

To simulate the efficiency of the sheet piling wall for train induced vibrations, the velocity response due to a number of uncorrelated forces applied at the line $x = 0\,\mathrm{m}$ (referred to as a line load in the following) and the corresponding insertion loss are also calculated. For the line load, the positions of the point forces are determined from the positions of the axles of an InterCity train, when the middle of the train is located at $y = 0\,\mathrm{m}$. The InterCity train consists of a locomotive HLE13, seven standard central HVI11 coaches and one back coach HV I11 BDx. It has a total length of $230.31\,\mathrm{m}$. The carriage length L_t, the distance L_b between bogies and the axle distance L_a of all carriages are summarized in Table 5. The 1/3 octave band insertion loss values when the line load is applied, are shown in Figure 6b.

For the homogeneous halfspace, very little vibration reduction is seen below $12\,\mathrm{Hz}$. The frequency above which a reduction in vibration levels can be expected, is in the first place determined by the depth of the wall, relative to the Rayleigh wavelength. As a rule of thumb, it is stated that an open trench could reduce surface vibration propagation significantly at frequencies for which the ratio of the depth of the trench to the Rayleigh wave length of propagating vibration is larger than about 0.6 [10]. As the Rayleigh wave velocity is $233\,\mathrm{m/s}$, a significant

	Axles [-]	L_t [m]	L_b [m]	L_a [m]
Locomotive HLE13	4	19.11	10.40	3.00
Central coach HVI11 A	4	26.40	18.40	2.56
Central coach HVI11 B	4	26.40	18.40	2.56
End coach HV I11 BDx	4	26.40	18.40	2.56

Table 5: The InterCity train

reduction can only be expected from $12\,\mathrm{Hz}$ on for an open trench with depth $12\,\mathrm{Hz}$. Therefore, the insertion loss for a sheet piling wall with the same depth will also be negligible below this frequency. Above $12\,\mathrm{Hz}$, the insertion loss of the sheet piling wall increases slowly to a plateau value which is reached at $30\,\mathrm{Hz}$. This plateau value depends on the distance from the point load. At the receiver position $x = 8\,\mathrm{m}$, which is located $2.4\,\mathrm{m}$ behind the wall, a value of $4\,\mathrm{dB}$ is reached. At $64\,\mathrm{m}$, the insertion loss at high frequencies is limited to $2\,\mathrm{dB}$.

At frequencies where the depth of the wall is large compared to the Rayleigh wavelength, the insertion loss will be determined by the reflection and transmission properties of the sheet pile wall. The difference in stiffness between the sheet piling wall and the soil will strongly determine the possible reduction in vibration levels. For the sheet piling wall, the bending stiffness along the vertical direction (z) is much larger than the bending stiffness along the longitudinal direction (y). Here, the influence of the orthotropy and the relative influence of the vertical and longitudinal stiffness is investigated by considering two cases (Table 6). In the first case, the sheet piling wall is modeled as an equivalent isotropic plate having the same bending stiffness in the longitudinal as in the vertical direction. In the second case, the longitudinal stiffness and mass of the sheet piling wall are set to zero.

	R [m]	d [m]	$\bar{t}$ [m]	$\bar{E}_y$ [$\mathrm{N/m^2}$]	$\bar{E}_z$ [$\mathrm{N/m^2}$]	$\bar{\mu}_{yz}$ [$\mathrm{N/m^2}$]	$\bar{\nu}_{yz}$ [-]	$\bar{\nu}_{zy}$ [-]	$\bar{\rho}$ [$\mathrm{kg/m^3}$]
Case 1	5.60	12	0.396	6.99×10^9	6.99×10^9	2.69×10^9	0.3	0.3	286.6
Case 2	5.60	12	0.396	0.0	7.68×10^9	0.0	0.0	0.0	0.0

Table 6: Geometric parameters and properties of the walls used to investigate the influence of the orthotropy and the relative influence of the vertical and longitudinal stiffness

Figure 7 shows the vertical insertion loss at $25\,\mathrm{Hz}$ for the sheet piling wall and the isotropic wall (case 1). At $25\,\mathrm{Hz}$, the sheet piling wall reduces the vibration levels at the surface with insertion loss values around $3\,\mathrm{dB}$. The reduction in vibration levels is fairly homogeneous at the surface behind the sheet piling wall. For the isotropic wall, the insertion loss at $25\,\mathrm{Hz}$ is larger than for the sheet piling wall in certain areas. On a line perpendicular to the wall, the insertion loss is similar as in the case of the sheet piling wall. Here, the longitudinal bending stiffness does not influence the vibration levels. The longitudinal bending stiffness does, however, influence the insertion loss noticeably for points further away from this line.

The wave impeding effect depends on the relationship between the Rayleigh wavelength in the soil and the free bending wavelength in the sheet piling wall [11]. The transmission of plane waves in the soil with a longitudinal wavelength smaller than the longitudinal bending wavelength is hindered. This is clear from Figure 8b which shows the insertion loss for case 1 in function of frequency and dimensional longitudinal wavenumber $\bar{k}_y = k_y C_s/\omega$. Superimposed

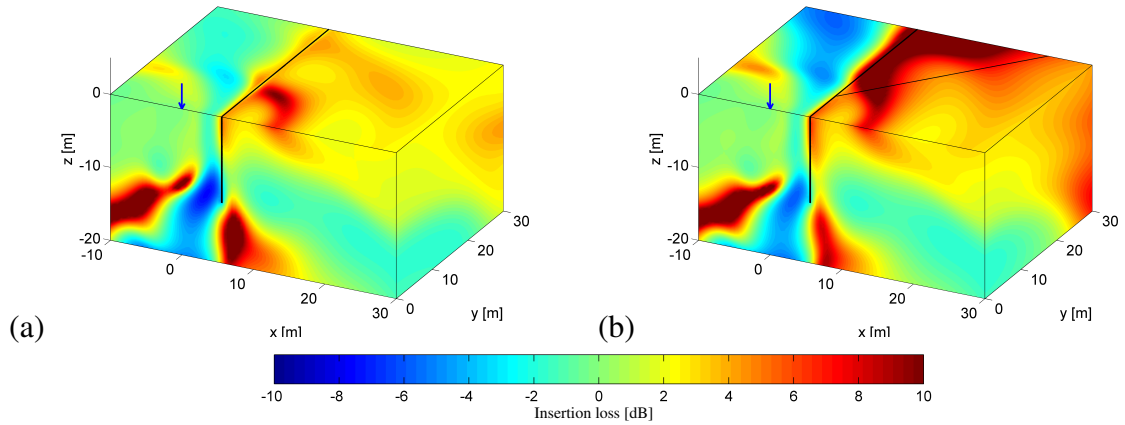


Figure 7: Vertical insertion loss for the sheet piling wall in the homogeneous halfspace at 25 Hz. (a) sheet piling wall and (b) case 1.

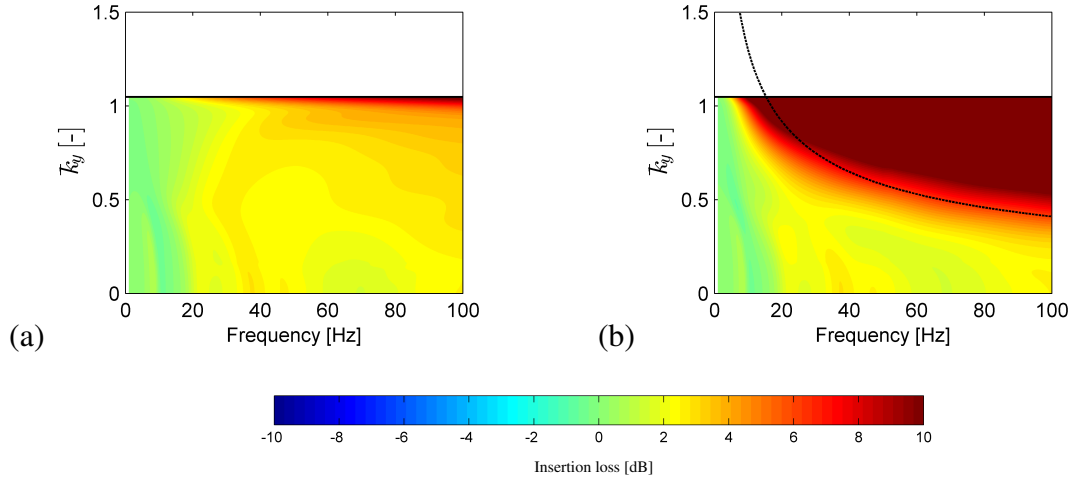


Figure 8: Vertical insertion loss IL_z ($x = 32\,\mathrm{m}$, $\overline{k}_y$, ω, $z = 0\,\mathrm{m}$) for (a) the sheet piling wall and (b) case 1. Superimposed are the Rayleigh wave dispersion curve (solid black line) and the dispersion curve of a free bending wave in the wall in the longitudinal direction (dotted line).

is the dispersion curve of a Rayleigh wave propagating in the y-direction and the dispersion curve of a free bending wave in the longitudinal direction. Above a critical frequency, at which the Rayleigh wavelength in the soil is equal to the free bending wavelength in the wall, the isotropic wall starts to be effective as a wave impeding barrier. The critical frequency f_c can be calculated from [9, 11]:

$$f_c = \frac{C_\mathrm{R}^2}{2\pi}\sqrt{\frac{\rho_\mathrm{w} A_\mathrm{w}}{E_{\mathrm{w},y} I_{\mathrm{w},y}}} \tag{6}$$

where C_R is the Rayleigh wave velocity of the soil. ρ_w, A_w, $E_{\mathrm{w},y}$ and $I_{\mathrm{w},y}$ are the density, the cross section area, the Young's modulus in the y-direction and the moment of inertia in the y-direction of the wall, respectively. For the isotropic wall (case 1), the critical frequency is equal to 15 Hz. This wave impeding effect caused by the longitudinal bending stiffness is not seen for the sheet piling wall (Figure 8a). The longitudinal bending stiffness is far too low, leading to a critical frequency of approximately 850 Hz.

The area for which a significant reduction of vibration levels is obtained above the critical

frequency, is determined by a critical angle θ_c. The critical angle depends on the ratio between the free bending wavelength $\lambda_{\mathrm{b},y}$ in the wave barrier in the y-direction and the Rayleigh wavelength λ_{R} in the soil,

$$\theta_c = \sin^{-1}\left(\frac{\lambda_{\mathrm{R}}}{\lambda_{\mathrm{b},y}}\right) = \sin^{-1}\left(C_{\mathrm{R}}\sqrt[4]{\frac{\rho_{\mathrm{w}}A_{\mathrm{w}}}{E_{\mathrm{w},y}I_{\mathrm{w},y}\omega^2}}\right) \tag{7}$$

For the isotropic wall (case 1), the critical angle is equal to 51° at $25\,\mathrm{Hz}$. This angle is also indicated on Figure 7b.

Figure 9 compares the 1/3 octave band insertion loss results of the sheet piling wall with the results for case 1 and case 2. The results are identical for the sheet piling wall model and case 2. This indicates that the reduction in vibration levels by the sheet piling wall is entirely due to the relatively high axial stiffness and vertical bending stiffness of the sheet piling wall. The effect of the longitudinal bending stiffness and the inertia of the sheet piling wall are negligible in the frequency range considered.

The vertical insertion loss values for a point load are similar for the orthotropic and isotropic wall model (case 1), especially at larger distances from the point load. For a point load, the vibration levels at a line perpendicular to the track are determined by Rayleigh waves which impinge perpendicularly on the sheet piling wall. At normal incidence, the longitudinal bending stiffness does not influence the vibrations in the sheet piling wall.

The insertion loss values for a line load differ strongly for the orthotropic and isotropic wall model. For the orthotropic sheet piling wall, the insertion loss for a line load is similar to the insertion loss for a point load. For the isotropic wall, the insertion loss for a line load is significantly larger than for a point load. The difference is larger for higher frequencies and for smaller distances from the sheet piling wall. This can be understood when looking at the results in Figure 7. For a line load, contributions from different point loads are added, which complies with a spatial averaging over the longitudinal direction.

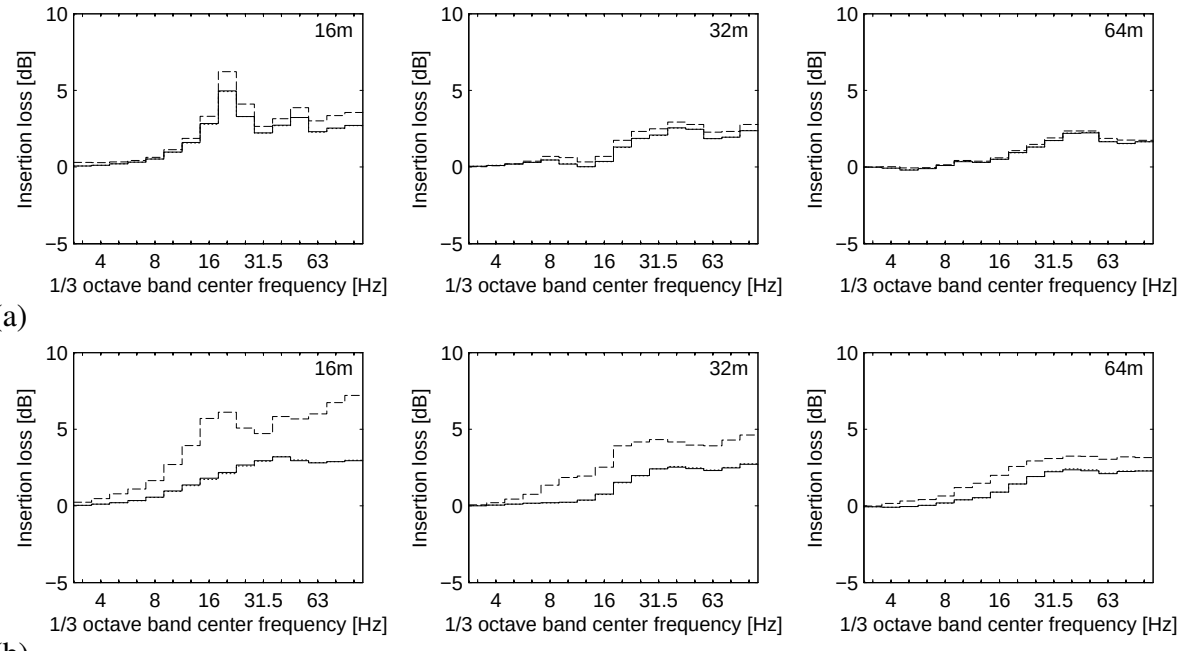


Figure 9: (a) Vertical insertion loss for a point load and (b) vertical insertion loss for a line load for the orthotropic sheet piling wall (solid lines), case 1 (dashed lines) and case 2 (dotted lines).

These results indicate that it is important to take into account the orthotropic behaviour of the sheet piling wall in the model. By use of an isotropic model for the sheet piling wall, the bending stiffness in the longitudinal direction is strongly overestimated. This will not affect the results for a point load at a line perpendicular to the track. The actual insertion loss for a train passage, here represented in a simplified way by a line load, will, however, be strongly overestimated.

3.4 Results for Furet test site

In this section, the efficiency of the sheet piling wall installed at the test site in Furet is analyzed. Separate 2.5D calculations have been made for depths of $12\,\mathrm{m}$ and $18\,\mathrm{m}$. In both models, the sheet pile wall is modeled as an equivalent orthotropic plate (Table 3). Calculations have been performed up to $50\,\mathrm{Hz}$ and $30\,\mathrm{Hz}$ for the $12\,\mathrm{m}$ and $18\,\mathrm{m}$ deep sheet pile wall, respectively.

Figure 10 shows the insertion loss at $5\,\mathrm{Hz}$ and $25\,\mathrm{Hz}$ for a vertical point load for the $12\,\mathrm{m}$ and $18\,\mathrm{m}$ deep sheet piling wall. At 5 Hz, the $12\,\mathrm{m}$ deep sheet piling wall only reduces the vibration levels significantly immediately behind the wall. At larger distances, the insertion loss is very limited. At $25\,\mathrm{Hz}$, the sheet piling wall reduces the vibration at the surface with more than $6\,\mathrm{dB}$. This reduction is reasonably homogeneous over the entire surface behind the sheet piling wall. It can be noticed, however, that the reduction in vibration levels is restricted to the top five meters of soil. Lines of constructive and destructive interference between direct and reflected Rayleigh waves can be observed at the other side of the sheet piling wall. For the $18\,\mathrm{m}$ deep sheet piling wall, a significant reduction is obtained at $5\,\mathrm{Hz}$ in the entire region behind the wall, although

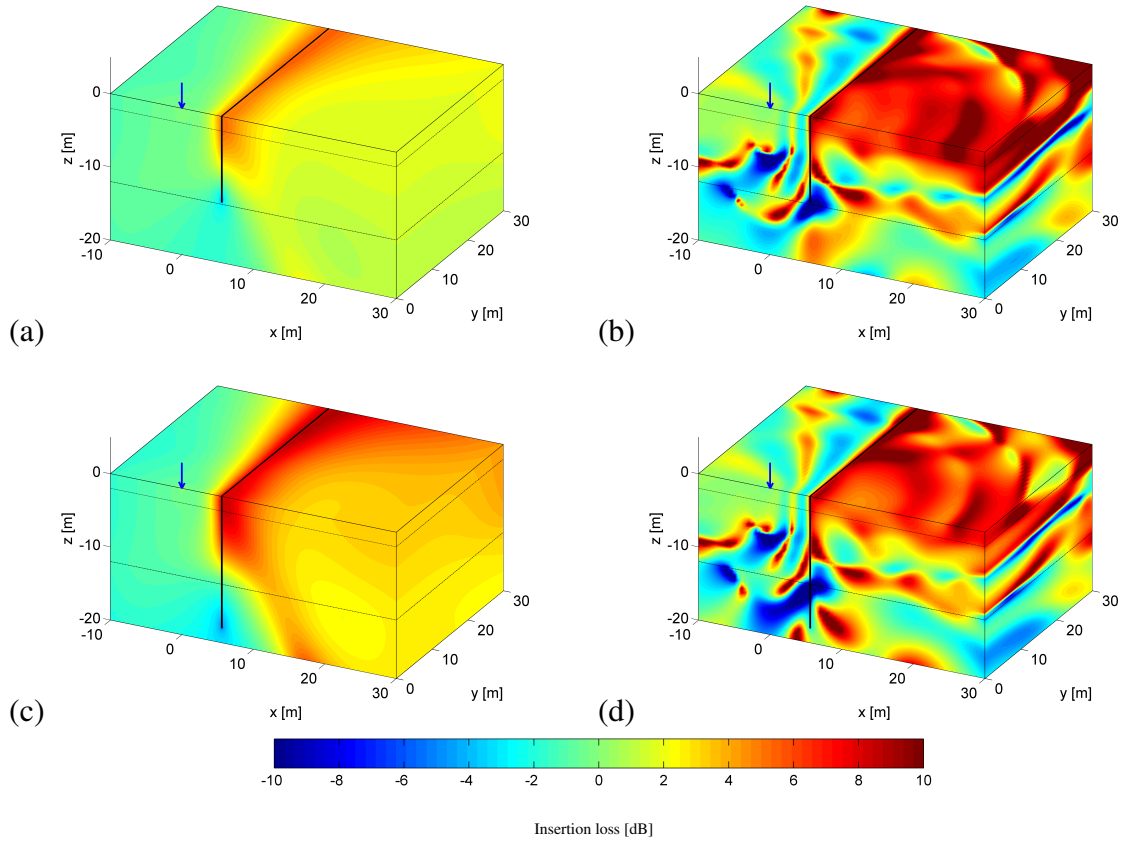


Figure 10: Vertical insertion loss for a vertical point load (a) at $5\,\mathrm{Hz}$, depth $12\,\mathrm{m}$, (b) at $25\,\mathrm{Hz}$, depth $12\,\mathrm{m}$, (c) at $5\,\mathrm{Hz}$, depth $18\,\mathrm{m}$ and (d) at $25\,\mathrm{Hz}$, depth $18\,\mathrm{m}$.

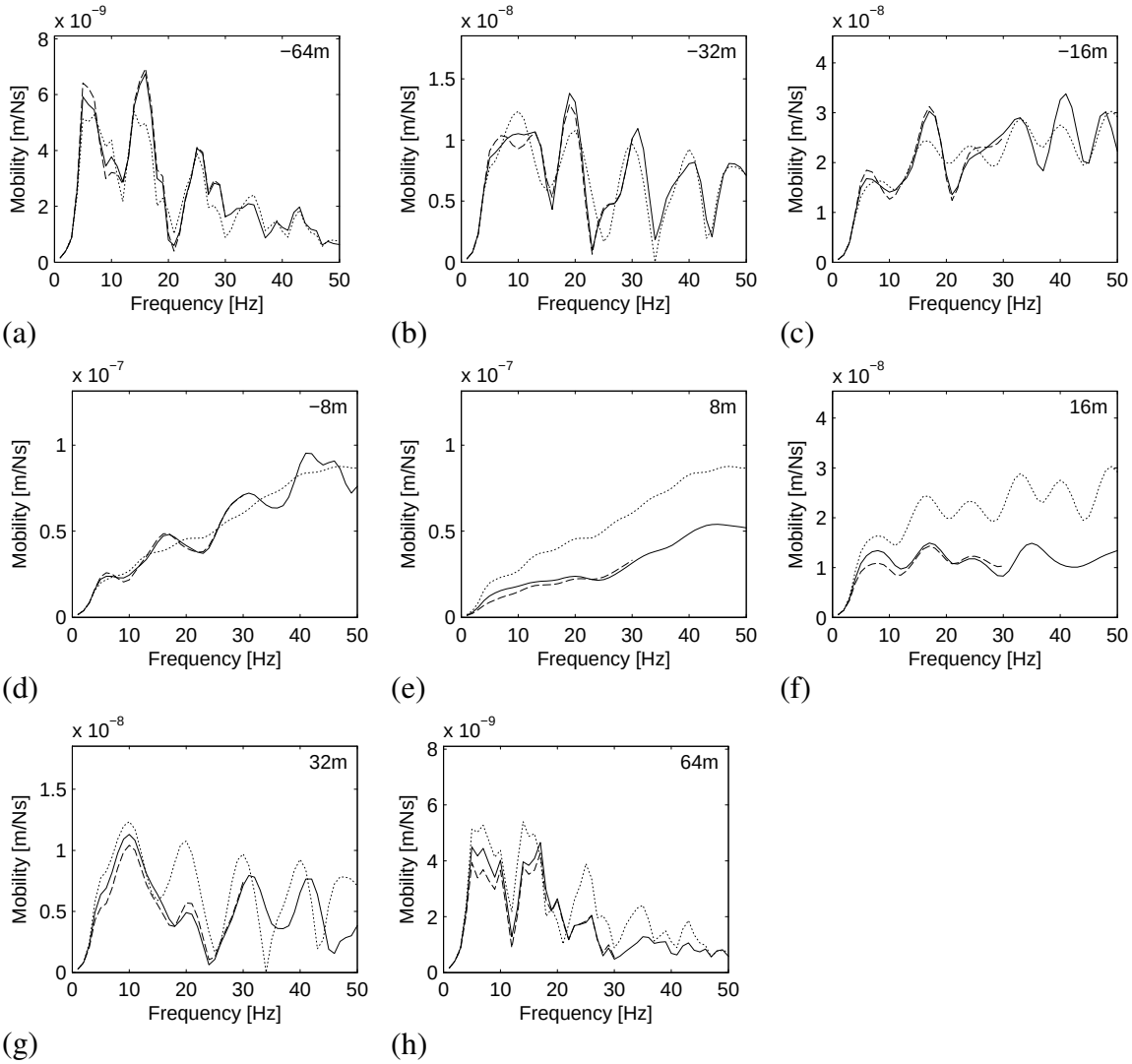


Figure 11: Transfer mobility at a distance of (a) $-64\,\mathrm{m}$, (b) $-32\,\mathrm{m}$, (c) $-16\,\mathrm{m}$, (d) $-8\,\mathrm{m}$, (e) $8\,\mathrm{m}$, (f) $16\,\mathrm{m}$, (g) $32\,\mathrm{m}$, and (h) $64\,\mathrm{m}$ from the point load in the reference case (dotted lines), for the $12\,\mathrm{m}$ deep (solid lines) and $18\,\mathrm{m}$ deep (dashed lines) sheet piling wall at the Furet test site.

the effectiveness decreases with increasing distance. The higher effectiveness compared with the $12\,\mathrm{m}$ deep sheet piling wall indicates that a significant amount of the vibrational energy passes underneath the $12\,\mathrm{m}$ deep wall at $5\,\mathrm{Hz}$. At $25\,\mathrm{Hz}$, the increased depth of the sheet piling wall does not significantly change the insertion loss. This may be explained by the fact that the motion of the Rayleigh waves is mainly limited to the top two layers at this frequency. Therefore, the insertion loss is largely determined by the transmission of vibrations through the sheet pile wall.

Figure 11 shows the transfer mobilities from a vertical harmonic point load applied to the soil at position $(x, y) = (0\,\mathrm{m}, 0\,\mathrm{m})$ to several positions in the free field for the Furet test site without mitigation measure, when the $12\,\mathrm{m}$ deep sheet piling wall is installed and when the $18\,\mathrm{m}$ deep sheet piling wall is installed. Figure 12 shows the corresponding insertion loss in 1/3 octave bands for the $12\,\mathrm{m}$ and $18\,\mathrm{m}$ deep sheet piling wall. Insertion loss values as measured with the RSMV at the test site are indicated with circles. The 1/3 octave band insertion loss values for the $12\,\mathrm{m}$ and $18\,\mathrm{m}$ deep sheet piling wall when the line load is applied, are shown in

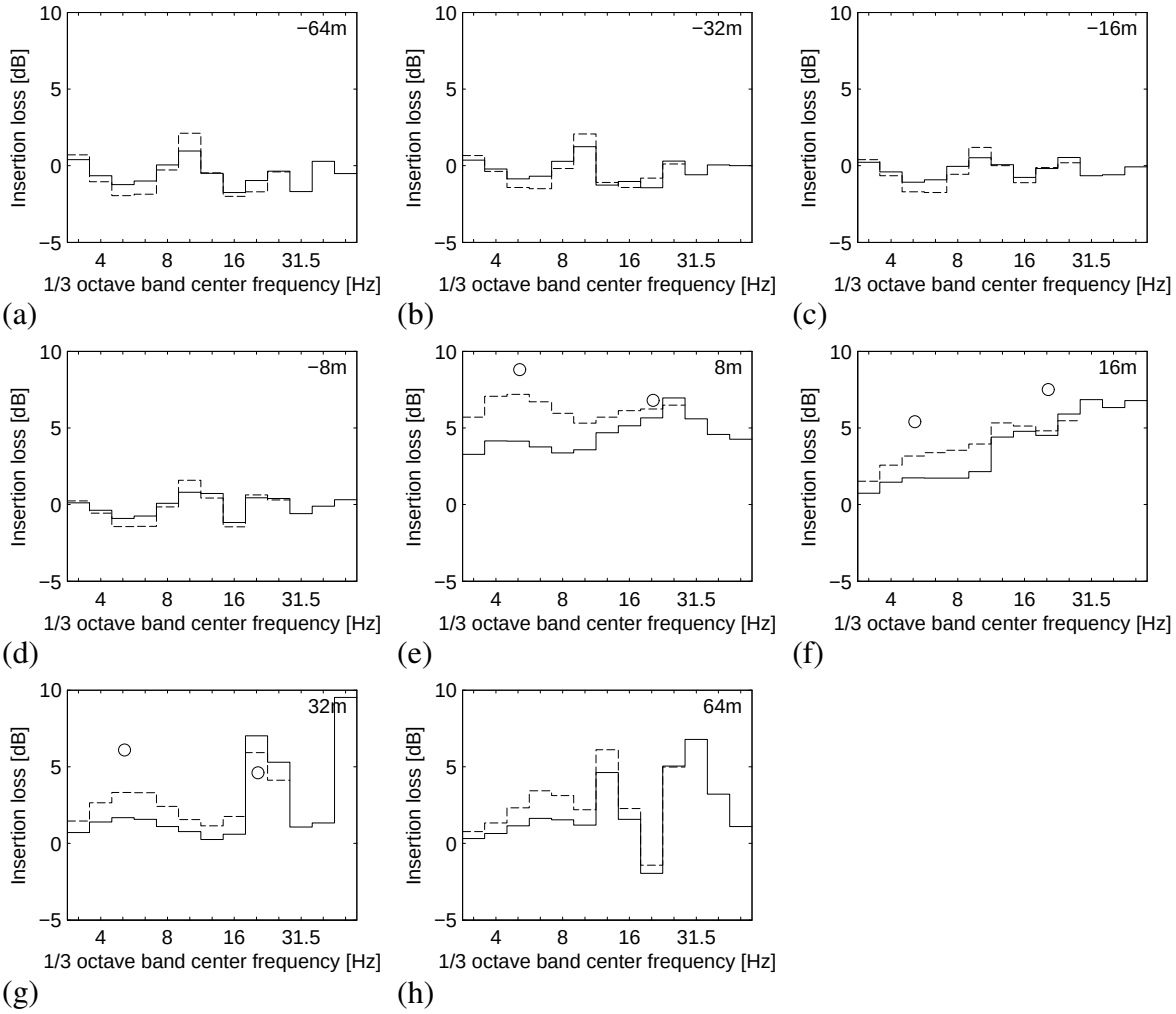


Figure 12: Vertical insertion loss at a distance of (a) $-64\,\mathrm{m}$, (b) $-32\,\mathrm{m}$, (c) $-16\,\mathrm{m}$, (d) $-8\,\mathrm{m}$, (e) $8\,\mathrm{m}$, (f) $16\,\mathrm{m}$, (g) $32\,\mathrm{m}$, and (h) $64\,\mathrm{m}$ in the case of a point load for the $12\,\mathrm{m}$ deep (solid lines) and $18\,\mathrm{m}$ deep (dashed lines) sheet piling wall at the Furet test site. Measured values with the RSMV are indicated with circles.

Figure 13.

For positions at the same side of the sheet piling wall as the point load ($-64\,\mathrm{m}$, $-32\,\mathrm{m}$, $-16\,\mathrm{m}$, $-8\,\mathrm{m}$), the vibration levels are either increased or reduced due to constructive or destructive interference of the direct and reflected waves (Figure 11). As a result, the insertion loss for the point load varies on average between plus and minus $2\,\mathrm{dB}$ (Figure 12). The insertion loss for a line load is smoothed (Figure 13), as the calculation involves a spatial averaging of the vibration field. For the line load, the vibration levels are on average increased by $2\,\mathrm{dB}$ at these positions due to the presence of the sheet pile of wall. For the $18\,\mathrm{m}$ deep sheet piling wall, the increase in vibration levels is about $1\,\mathrm{dB}$ larger at frequencies below $10\,\mathrm{Hz}$.

The results for receiver points at the other side of the sheet piling wall ($8\,\mathrm{m}$, $16\,\mathrm{m}$, $32\,\mathrm{m}$, $64\,\mathrm{m}$) indicate that the sheet piling wall can effectively reduce the vibration levels. For a point load, insertion loss values of $5\,\mathrm{dB}$ and more are predicted above $20\,\mathrm{Hz}$ for the $12\,\mathrm{m}$ deep sheet piling wall (Figure 12). It must be reminded, however, that the frequency range $4-5\,\mathrm{Hz}$ is targeted. Below $20\,\mathrm{Hz}$, the insertion loss is limited to $2\,\mathrm{dB}$ for the $12\,\mathrm{m}$ deep wall. Only for small distances behind the wall ($8\,\mathrm{m}$), the insertion loss can reach up to $4\,\mathrm{dB}$ below $10\,\mathrm{Hz}$. For a line load, the insertion loss is on average 1 to $2\,\mathrm{dB}$ larger (Figure 13). The results indicate

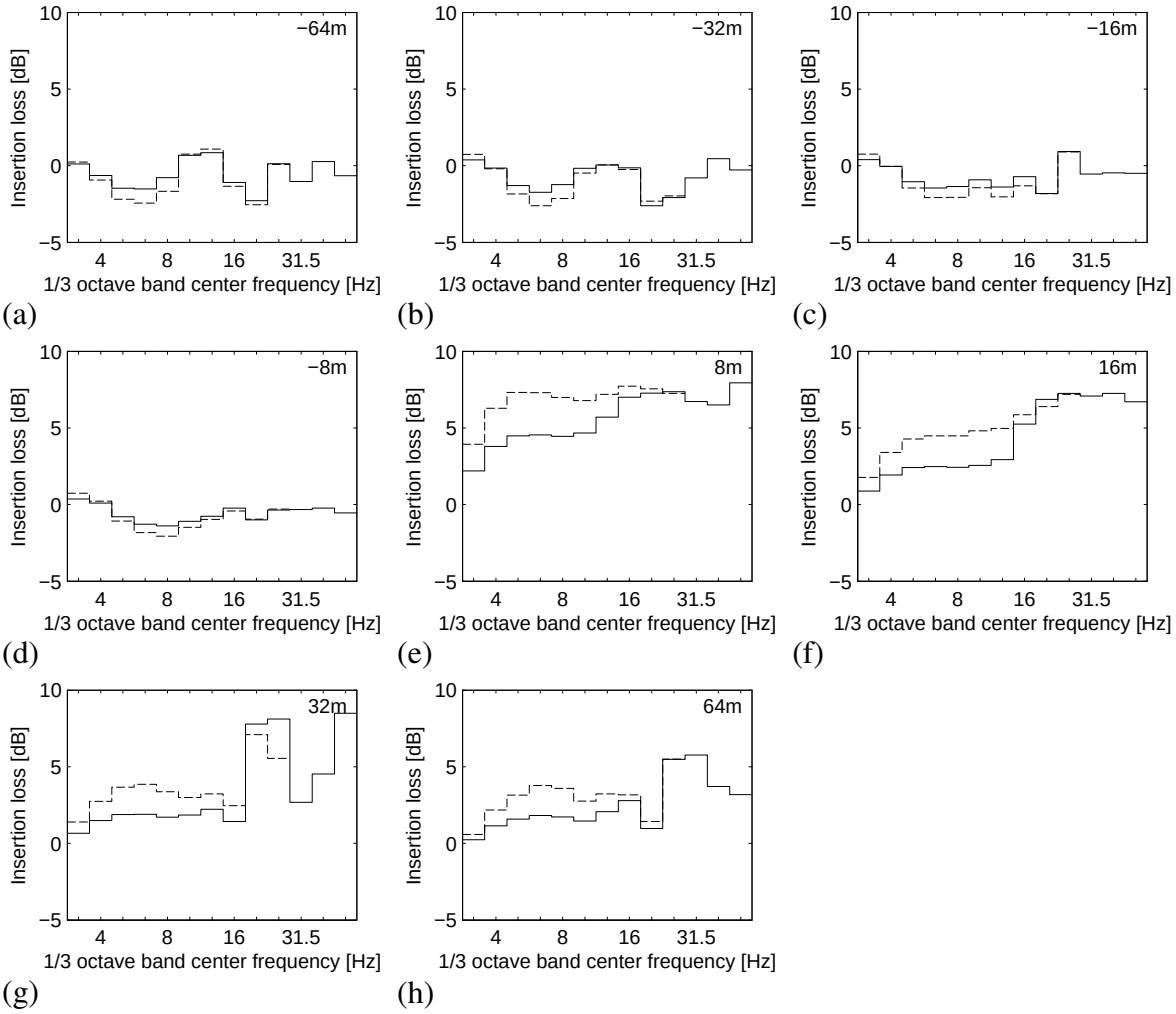


Figure 13: Vertical insertion loss at a distance of (a) $-64\,\mathrm{m}$, (b) $-32\,\mathrm{m}$, (c) $-16\,\mathrm{m}$, (d) $-8\,\mathrm{m}$, (e) $8\,\mathrm{m}$, (f) $16\,\mathrm{m}$, (g) $32\,\mathrm{m}$, and (h) $64\,\mathrm{m}$ in the case of a line load for the $12\,\mathrm{m}$ deep (solid lines) and $18\,\mathrm{m}$ deep (dashed lines) sheet piling wall at the Furet test site.

that the increase in depth to $18\,\mathrm{m}$ has a favorable effect at low frequencies. The insertion loss is increased by $2\,\mathrm{dB}$ in the 1/3 octave bands between $4\,\mathrm{Hz}$ and $16\,\mathrm{Hz}$, both for a point load and a line load. Above $20\,\mathrm{Hz}$, the insertion loss is not improved. Prediction results even indicate a slight reduction in efficiency for the deeper wall. For the actually constructed sheet piling wall with alternating depth, the insertion loss is expected to lie in between the values for a $12\,\mathrm{m}$ deep and an $18\,\mathrm{m}$ deep sheet piling wall.

A preliminary comparison with the experimental results is made in Figure 12. Although the order of magnitude of the insertion loss is reasonably well predicted, further processing of the measurements is needed before a detailed comparison can be made and possible reasons for discrepancies can be investigated.

4 CONCLUSIONS

To reduce the train induced vibrations at the site of Furet, a sheet piling wall was installed next to the track. The depth of the sheet piles is 12 m with every fourth pile extended to $18\,\mathrm{m}$. The effectiveness of the sheet pile wall was analyzed by means of 2.5D calculations for a $12\,\mathrm{m}$

and $18\,\mathrm{m}$ deep wall. An equivalent orthotropic plate model of the sheet pile wall was adopted.

The sheet piling wall acts as a stiff wave barrier, of which the effectiveness is determined by the depth and the contrast in stiffness between the barrier and the soil. The sheet piling wall only starts to act when the depth of the sheet piling wall is sufficiently large compared to the Rayleigh wavelength in the soil. Increasing the depth from 12 m to 18 m consequently results in an increased reduction at low frequencies.

It is important to take into account the orthotropic behavior of the sheet piling wall, as the bending stiffness in the vertical direction (along the profiles) is much larger than the bending stiffness in the longitudinal direction (perpendicular to the profiles). Calculations show that the reduction of vibration levels is entirely due to the relatively high axial stiffness and vertical bending stiffness, while the longitudinal bending stiffness is too low to affect the transmission of vibrations. A simplified isotropic model does not allow accounting accurately for the transmission of waves at grazing incidence.

Calculation results for the site of Furet show that at $8\,\mathrm{m}$ from the track, a reduction in transmitted ground vibration is already obtained at frequencies above $4\,\mathrm{Hz}$. The performance decreases with increasing distance from the track as observed in the vibration measurements carried out for train passages and with the RSMV. Further processing of the measurements is needed before a detailed comparison to the numerical results can be made.

5 ACKNOWLEDGEMENTS

The results presented in this paper have been obtained within the frame of the EU FP 7 project RIVAS (Railway Induced Vibration Abatement Solutions).

REFERENCES

[1] D. Stiebel, B. Nelain, and N. Vincent. How to measure and transfer efficiencies of vibration-mitigation measures: results of the European project RIVAS, P. Sas, D. Moens, and S. Jonckheere eds. *Proceedings of ISMA 2012 International Conference on Noise and Vibration Engineering*, pages 2959–2971, Leuven, Belgium, September 2012. CD-ROM.

[2] D. Aubry, D. Clouteau, and G. Bonnet, Modelling of wave propagation due to fixed or mobile dynamic sources. N. Chouw and G. Schmid eds. *Workshop Wave '94, Wave propagation and Reduction of Vibrations*, pages 109–121, Ruhr Universität Bochum, Germany, December 1994.

[3] X. Sheng, C.J.C. Jones, and M. Petyt, Ground vibration generated by a harmonic load acting on a railway track. *Journal of Sound and Vibration*, **225**(1), 3–28, 1999.

[4] G. Lombaert, G. Degrande, and D. Clouteau, Numerical modelling of free field traffic induced vibrations. *Soil Dynamics and Earthquake Engineering*, **19**(7), 473–488, 2000.

[5] L. Andersen and S.R.K. Nielsen, Reduction of ground vibration by means of barriers or soil improvement along a railway track. *Soil Dynamics and Earthquake Engineering*, **25**, 701–716, 2005.

[6] S. François, M. Schevenels, G. Lombaert, P. Galvín, and G. Degrande, A 2.5D coupled FE-BE methodology for the dynamic interaction between longitudinally invariant structures and a layered halfspace. *Computer Methods in Applied Mechanics and Engineering*, **199**(23-24), 1536–1548, 2010.

[7] M. Schevenels, G. Degrande, and S. François, EDT: an ElastoDynamics Toolbox for Matlab. *Book of Abstracts of the Inaugural International Conference of the Engineering Mechanics Institute (EM08)*, page 82, Minneapolis, Minnesota, U.S.A., May 2008.

[8] M. Schevenels, S. François, and G. Degrande, EDT: An ElastoDynamics Toolbox for MATLAB. *Computers & Geosciences*, **35**(8), 1752–1754, 2009.

[9] C. Hopkins, *Sound insulation*, Elsevier Ltd., Oxford, 2007.

[10] C.J.C. Jones, D.J. Thompson, and J.I. Andreu-Medina, Initial theoretical study of reducing surface-propagating vibration from trains using earthworks close to the track. *Proceedings of the 8th International Conference on Structural Dynamics, EURODYN 2011*, pages 684–691, Leuven, Belgium, July 2011.

[11] P. Coulier, S. François, G. Degrande, and G. Lombaert, Subgrade stiffening next to the track as a wave impeding barrier for railway induced vibrations. *Soil Dynamics and Earthquake Engineering*, 2013. http://dx.doi.org/10.1016/j.soildyn.2012.12.009i. In press.

COMPDYN 2013
4th ECCOMAS Thematic Conference on
Computational Methods in Structural Dynamics and Earthquake Engineering
M. Papadrakakis, V. Papadopoulos, V. Plevris (eds.)
Kos Island, Greece, 12–14 June 2013

A NUMERICAL STUDY OF SUBGRADE STIFFENING AS A MITIGATION MEASURE FOR RAILWAY INDUCED VIBRATIONS THROUGH 2.5D AND 3D FE–BE MODELS

Pieter Coulier, Stijn François, Geert Degrande, and Geert Lombaert

KU Leuven, Department of Civil Engineering
Kasteelpark Arenberg 40, 3001 Leuven, Belgium
e-mail: {pieter.coulier,stijn.francois,geert.degrande,geert.lombaert}@bwk.kuleuven.be

Keywords: Railway induced vibrations, dynamic soil–structure interaction, elastodynamic wave propgation, finite element–boundary element coupling.

Abstract. *This paper studies the efficiency of subgrade stiffening next to the track as a mitigation measure for railway induced vibrations. A computationally efficient two-and-a-half-dimensional (2.5D) methodology is first employed, assuming invariance of the geometry in the longitudinal direction. An analysis in the frequency–wavenumber domain reveals that an infinitely long block of stiffened soil next to the track can act as a wave impeding barrier. It is demonstrated that the wave impeding effect depends on the relation between the Rayleigh wavelength in the soil and the free bending wavelength in the block of stiffened soil, as the transmission of plane waves in the soil with a longitudinal wavelength smaller than the bending wavelength is hindered. This leads to a critical frequency from which this mitigation measure starts to be effective, depending on the stiffness contrast between the soil and the block of stiffened soil. The existence of a critical angle delimiting an area where vibration levels are reduced in case of harmonic excitation on the rail is also demonstrated. Fully three–dimensional (3D) calculations are finally performed to assess the vibration reduction efficiency if subgrade stiffening is only implemented along a finite length, indicating that the length of the block should be approximately two times the free bending wavelength of an infinitely long beam in order to ensure that a finite block can act as a wave impeding barrier.*

1 INTRODUCTION

Railway induced vibrations are an important source of annoyance in the built environment. Vibrations in buildings (1–80 Hz) can disturb sensitive equipment and cause discomfort to inhabitants, while re–radiated noise (16–250 Hz) may be perceived when bending resonances of floors and walls are excited.

During the last decades, a lot of research has been performed to obtain efficient and cost-effective vibration countermeasures [1, 2]. Three categories of vibration reduction methods can generally be distinguished. The most effective way is to tackle the problem at the source as this affects all nearby structures. These methods include the use of ballast mats [3], soft railpads [4], under–sleeper pads [5] and floating slab tracks [6] and are frequently used for new railway infrastructure. Interventions on the propagation path between source and receiver, such as an open trench in the soil [7], form a second category of methods to reduce the vibration levels. Their main advantage is that no modifications of the track are required, but their implementation may, however, be infeasible due to practical limitations. The third category of vibration reduction methods consists of measures taken at the receiver side, such as base isolation [8]; these are only effective for the structure where the mitigation measure is applied to.

Renewed attention has recently been paid to vibration reduction technologies on the transmission path, but installed close to the track as part of the railway infrastructure [9]. These measures include vibration isolation screens [10, 11], buried wall barriers [12], subgrade stiffening [13, 14], wave impeding blocks [15, 16] and wave reflectors [17]. Subgrade stiffening is often applied under railway tracks on soft soils with the aim of reducing settlements or track displacements [18]. Common techniques to obtain the desired stiffening include deep vibro compaction, deep soil mixing, gravel or cement columns, hydraulic fracture injection with stable cement-bentonite mixtures, and vacuum consolidation [19]. Subgrade stiffening is also known to lead to reduced ground-borne vibration levels due to the increase of the effective stiffness of the soil beneath the railway track. Vibrations are therefore expected to be reduced in the lower frequency range for all vehicle speeds and at all distances from the track. Subgrade stiffening seems to be a good solution for sites with an originally soft soil [13].

Although subgrade stiffening under the track is expected to be the most efficient way to reduce vibration levels, its practical implementation often requires interruption of train traffic and might cause uplifting of the track. This paper therefore focuses on subgrade stiffening next to the track, where a block of stiffened soil next to the track acts as a wave impeding vibration barrier. The effectiveness of the proposed mitigation measure is analyzed in section 2 assuming invariance of the geometry in the longitudinal direction, which allows for the application of a computationally efficient two-and-a-half-dimensional (2.5D) approach. The reduction of vibration levels is studied in case of harmonic excitation on the rail, as well as during the passage of a train, using a coupled finite element – boundary element (FE–BE) methodology. The construction of a jet grouting wall is in practice limited to finite dimensions, however, and the assumption of longitudinal invariance is therefore not fulfilled. A fast BE method based on hierarchical matrices [20] is employed in section 3 to solve the fully three–dimensional (3D) dynamic soil–structure interaction problem, allowing for the assessment of the vibration reduction efficiency if subgrade stiffening is only implemented along a finite length.

2 TWO–AND–A–HALF–DIMENSIONAL ANALYSIS

2.1 Dynamic properties of the track, the soil and the stiffened soil

Within the framework of the EU FP7 project RIVAS (Railway Induced Vibration Abatement Solutions) [9], a field test is planned in Spain to demonstrate the vibration reduction efficiency of subgrade stiffening next to the track. A conventional railway line on the Spanish network of ADIF between Barcelona and Gerona is therefore considered throughout this section; the track cross section is shown in figure 1. Although the soil properties at the site under consideration in reality vary with depth, the soil is assumed to be homogeneous in this paper in order to facilitate physical interpretation of the results. A halfspace with a shear wave velocity $C_\mathrm{s} = 200\,\mathrm{m/s}$, a dilatational wave velocity $C_\mathrm{p} = 400\,\mathrm{m/s}$, a density $\rho = 2000\,\mathrm{kg/m^3}$ and a material damping ratio $\beta_\mathrm{s} = \beta_\mathrm{p} = 0.025$ in both deviatoric and volumetric deformation is considered. The phase velocity C_R of the Rayleigh waves is equal to $186\,\mathrm{m/s}$ [21].

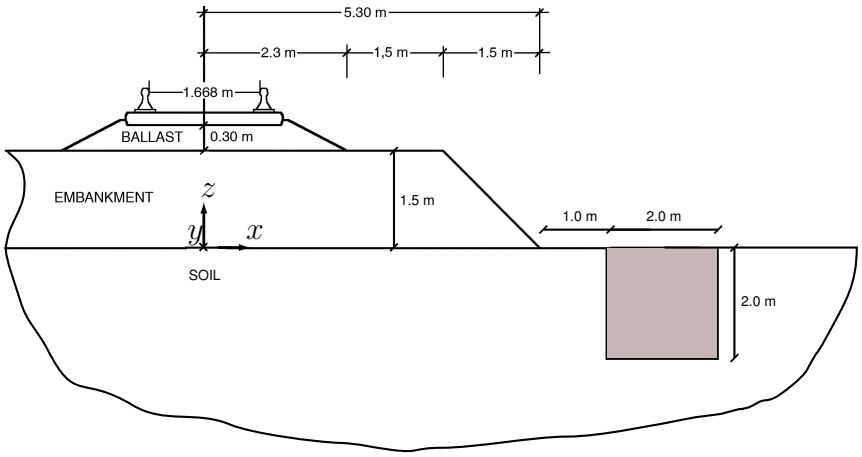


Figure 1: Track cross section.

The track consists of UIC 54 rails supported by rail pads on concrete sleepers, which are founded on a ballast layer and the embankment. The rails are modelled as Euler-Bernoulli beams with a bending stiffness $E_\mathrm{r}I_\mathrm{r} = 4.83 \times 10^6\ \mathrm{Nm^2}$ and a mass per unit length $\rho_\mathrm{r}A_\mathrm{r} = 54.4\,\mathrm{kg/m}$ for each rail. A wide track gauge of $1.668\,\mathrm{m}$ is used on this conventional Spanish track. The rail pads have a stiffness $k_\mathrm{rp} = 153.4 \times 10^6\,\mathrm{N/m}$ and a damping coefficient $c_\mathrm{rp} = 13.5 \times 10^3\,\mathrm{Ns/m}$. The following sleeper characteristics are considered: a length $l_\mathrm{sl} = 2.60\,\mathrm{m}$, a width $b_\mathrm{sl} = 0.250\,\mathrm{m}$, a height $h_\mathrm{sl} = 0.230\,\mathrm{m}$ (under the rail), a centre-to-centre distance $d_\mathrm{sl} = 0.60\,\mathrm{m}$ and a mass $m_\mathrm{sl} = 315\,\mathrm{kg}$.

A ballast layer with a thickness $t = 0.30$ m (under the sleepers) is also included in the track model. The ballast has a shear wave velocity $C_\mathrm{s} = 340\,\mathrm{m/s}$, a dilatational wave velocity $C_\mathrm{p} = 635\,\mathrm{m/s}$, a density $\rho = 1700\,\mathrm{kg/m^3}$ and a material damping ratio $\beta_\mathrm{s} = \beta_\mathrm{p} = 0.020$ in both deviatoric and volumetric deformation. The embankment has a thickness $t = 1.50\,\mathrm{m}$, a shear wave velocity $C_\mathrm{s} = 140\,\mathrm{m/s}$, a dilatational wave velocity $C_\mathrm{p} = 290\,\mathrm{m/s}$ and a density $\rho = 1700\ \mathrm{kg/m^3}$. The same material damping ratios as for the ballast are used. The remaining geometric dimensions of the ballast and embankment are indicated on figure 1.

The reference case outlined above is compared to the case where a block of soil with a width and depth of $2\,\mathrm{m}$ located at $1\,\mathrm{m}$ from the tail of the embankment is stiffened (figure 1). The block of stiffened soil has a shear wave velocity $C_\mathrm{s} = 550\,\mathrm{m/s}$, a dilatational wave velocity $C_\mathrm{p} = 950\,\mathrm{m/s}$, a density $\rho = 2000\,\mathrm{kg/m^3}$ and a material damping ratio $\beta_\mathrm{s} = \beta_\mathrm{p} = 0.050$ in both deviatoric and volumetric deformation.

2.2 The numerical model

Several subproblems have to be addressed in order to investigate the vibration reduction efficiency of subgrade stiffening next to the track, such as the train–track interaction problem which allows for the determination of the dynamic axle loads, the track–soil interaction problem for the calculation of the transfer functions, and the computation of the response to moving loads [22, 23].

The response in the free field at distances sufficiently far from the track is dominated by dynamic axle loads if the train speed is small compared to the Rayleigh wave velocity C_{R}. Although several mechanisms contribute to the generation of these dynamic axle loads, often only those originating from the track unevenness are taken into account [22]. This kind of dynamic excitation can be calculated based on a compliance formulation in a moving frame of reference, which requires the vehicle and track compliance. The interaction forces are subsequently combined with the transfer functions between the track and the free field, which are determined from the track–soil interaction problem.

The track–soil interaction problem is solved by means of a coupled FE–BE methodology formulated in the frequency domain [24]. The domains Ω_1 and Ω_2 are modelled by means of finite elements, while boundary elements on the soil–structure interfaces Σ_1 and Σ_2 are used to model the soil domain Ω_{s} (figure 2). Green's functions for a horizontally layered halfspace are used as fundamental solutions in the BE formulation [25, 26]. By assuming invariance of the geometry in the longitudinal direction, a computationally efficient two-and-a-half-dimensional (2.5D) approach can be applied. The longitudinal coordinate y is transformed to the wavenumber k_y by means of a forward Fourier transform, and all calculations can be performed in the frequency–wavenumber domain. Although the track has a periodic layout due to the discrete support of the sleepers, an equivalent continuous model is employed. An equivalent rail pad stiffness $\overline{k}_{\mathrm{rp}} = k_{\mathrm{rp}}/d_{\mathrm{sl}}$, damping coefficient $\overline{c}_{\mathrm{rp}} = c_{\mathrm{rp}}/d_{\mathrm{sl}}$ and a uniformly distributed sleeper mass $\overline{m}_{\mathrm{sl}} = m_{\mathrm{sl}}/d_{\mathrm{sl}}$ per unit length are calculated. The sleepers are assumed to be rigid in the plane of the track cross section and not to contribute to the longitudinal stiffness of the track. A detailed description of the governing equations of the equivalent continuous rails/rail pads/sleepers–system can be found in [22].

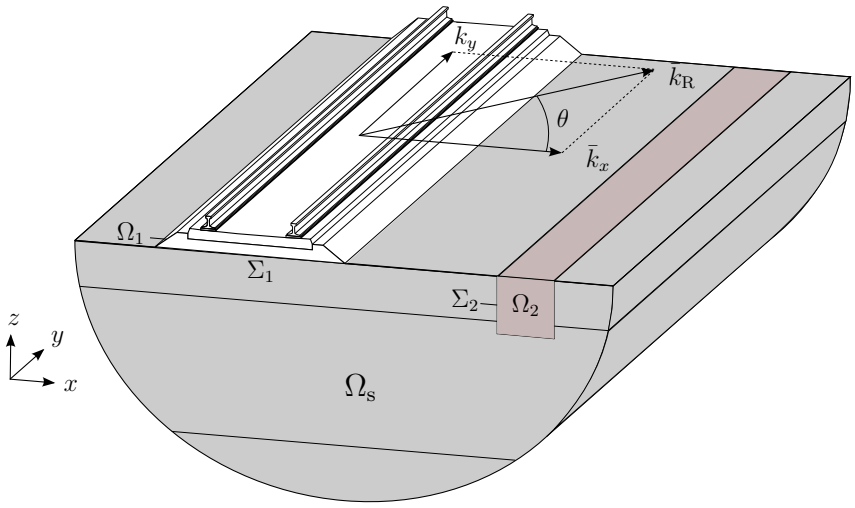


Figure 2: The 2.5D dynamic soil–structure interaction problem.

If N structures are considered, a weak variational formulation of the equilibrium of structure j ($j = 1, \ldots, N$) results in the following set of coupled FE–BE equations [24]:

$$\left[\tilde{\mathbf{K}}_j(k_y,\omega) - \omega^2 \mathbf{M}_j\right] \underline{\tilde{\mathbf{u}}}_j(k_y,\omega) + \sum_{k=1}^{N} \tilde{\mathbf{K}}^{\mathrm{s}}_{jk}(k_y,\omega)\underline{\tilde{\mathbf{u}}}_k(k_y,\omega) = \underline{\tilde{\mathbf{f}}}_j(k_y,\omega) \tag{1}$$

where a tilde above a variable denotes its representation in the frequency–wavenumber domain. $\underline{\tilde{\mathbf{u}}}_j(k_y,\omega)$ collects the nodal degrees of freedom of structure j, while $\tilde{\mathbf{K}}_j(k_y,\omega)$ and $\mathbf{M}_j$ are the finite element stiffness and mass matrix of this structure. $\tilde{\mathbf{K}}^{\mathrm{s}}_{jk}(k_y,\omega)$ is a dynamic soil stiffness matrix, representing the through–soil coupling of structures j and k for $j \neq k$, and is computed by means of the BE method. The force vector $\underline{\tilde{\mathbf{f}}}_j(k_y,\omega)$ results from the external forces on structure j [24]. In this paper, the number of structures N will be limited to $N = 1$ in the reference case (where only the track is considered) or $N = 2$ in the case a block of stiffened soil is introduced next to the track.

Figure 3 shows the finite element discretization. Eight–node quadrilateral finite elements are used to model the ballast, the embankment and the block of stiffened soil, which are coupled to a conforming BE mesh for the surrounding soil. The element dimensions are limited in order to ensure that at least 10 elements per minimal shear wavelength $\lambda_{\mathrm{s}} = 2\pi C_{\mathrm{s}}/\omega$ are used up to $100\,\mathrm{Hz}$ (determined by the shear wave velocity of the embankment), resulting in a maximum element size $l_e = 0.13\,\mathrm{m}$.

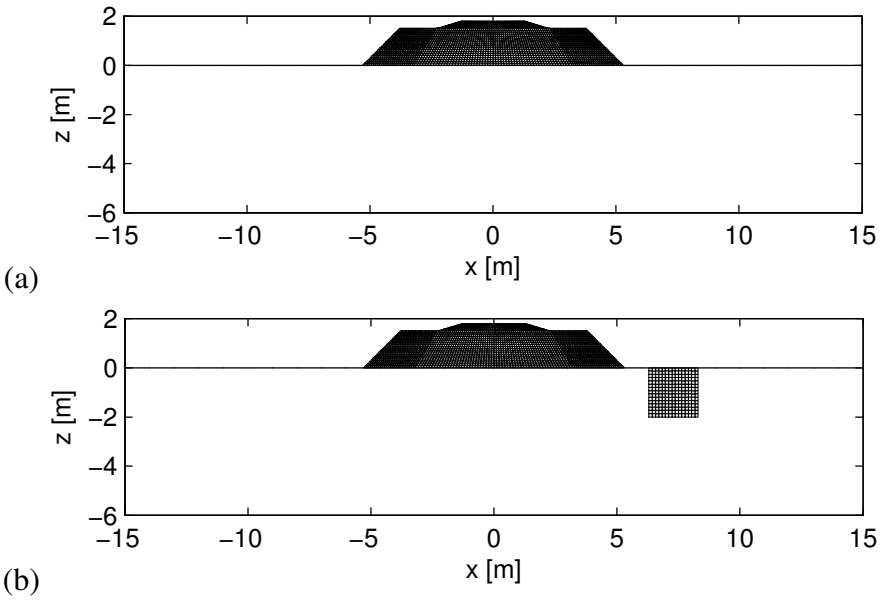


Figure 3: Finite element discretization (a) in the reference case and (b) in the case of stiffening next to the track.

Solving the set of coupled FE–BE equations (1) provides the structural response in the frequency–wavenumber domain. The wavenumber domain formulation of the integral representation theorem [24] subsequently allows for the calculation of the radiated wavefield in the soil. The response in the frequency–spatial domain can finally be found by means of an inverse Fourier transform.

The influence of subgrade stiffening on each of the aforementioned subproblems is investigated separately in the next subsections. The train–track and the track–soil interaction problems will be addressed in subsections 2.3 and 2.4, respectively, while the overall efficiency of

subgrade stiffening during the passage of a Renfe S599 train will finally be evaluated in subsection 2.6.

2.3 The track compliance in the frequency domain

The dynamic axle loads are computed by means of a compliance formulation in a moving frame of reference based on the vehicle compliance, the track compliance, and the track unevenness. It can be anticipated, however, that subgrade stiffening next to the track will only have a minor impact on the track compliance, so that the dynamic axle loads will not be affected. In order to verify this, the track compliance is computed by applying a unit harmonic vertical point load to the right rail at $y = 0\,\mathrm{m}$ in both cases. The response in the frequency–wavenumber domain is found from the solution of equation (1), and an inverse Fourier transform provides the response in the frequency–spatial domain.

Figure 4 shows that the rail receptance $\hat{u}_\mathrm{r}(y = 0\,\mathrm{m}, \omega)$ is not significantly modified by the presence of the block of stiffened soil next to the track, in the frequency range considered. The track compliance, and hence the dynamic axle loads, will remain unaffected, which implies that the efficiency of subgrade stiffening can be assessed by investigating the transfer functions only.

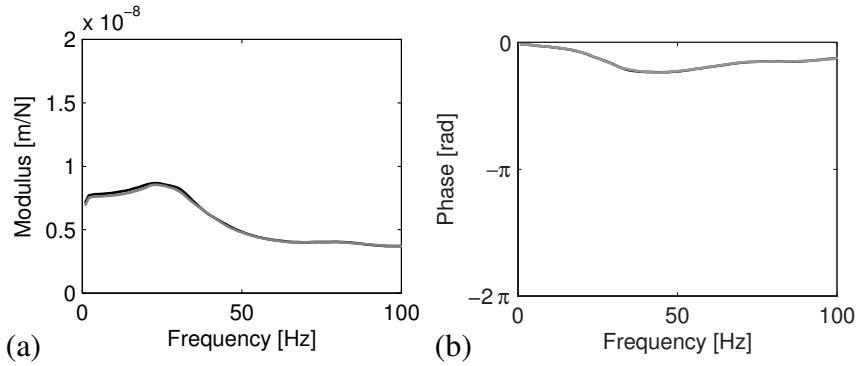


Figure 4: (a) Modulus and (b) phase of the rail receptance $\hat{u}_\mathrm{r}(y = 0\,\mathrm{m}, \omega)$ in the reference case (black line) and in the case of stiffening next to the track (grey line).

2.4 The free field impulse response in the frequency–wavenumber domain

As indicated in subsection 2.2, the radiated wavefield in the soil in the frequency–wavenumber domain can be obtained by application of the integral representation theorem [24]. The logarithm of the modulus of the vertical free field velocity $i\omega\tilde{u}_z\left(x = 64\,\mathrm{m}, \bar{k}_y, z = 0\,\mathrm{m}, \omega\right)$ is shown in figures 5a and 5b as a function of the dimensionless longitudinal wavenumber $\bar{k}_y$ and the frequency $\omega/2\pi$ in the reference case and in the case of stiffening next to the track, respectively. The dimensionless wavenumber $\bar{k}_y$ is defined as $\bar{k}_y = k_y C_\mathrm{s}/\omega = C_\mathrm{s}/C_y$, where C_s is the shear wave velocity of the halfspace and C_y is the phase velocity of the waves. Superimposed on both figures is the dispersion curve $\bar{k}_y = \bar{k}_\mathrm{R} = C_\mathrm{s}/C_\mathrm{R}$ of a Rayleigh wave propagating in the y-direction. This dispersion curve is a horizontal line $\bar{k}_\mathrm{R} = 1.073$ (as the halfspace has a Poisson's ratio $\nu = 1/3$) due to the non-dispersive character of the Rayleigh wave in a homogeneous halfspace.

The contribution of longitudinal wavenumbers $\bar{k}_y$ larger than $\bar{k}_\mathrm{R}$ to the free field response is very limited, as can be seen in figures 5a and 5b. This is due to the fact that the lateral

wavenumber $\bar{k}_x = -i\sqrt{\bar{k}_y^2 - \bar{k}_\mathrm{R}^2}$ is imaginary for $\bar{k}_y > \bar{k}_\mathrm{R}$, and the wave in the x-direction hence becomes evanescent.

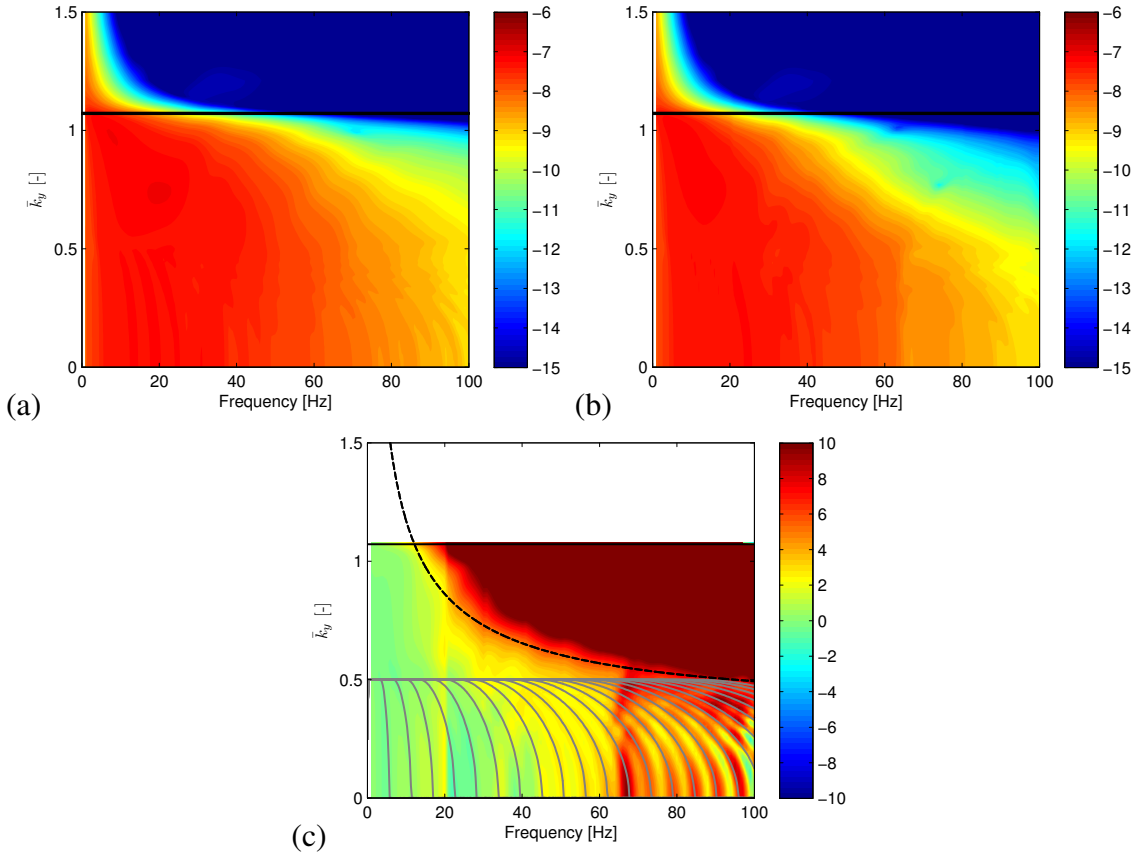


Figure 5: Logarithm of the modulus of the vertical free field velocity $i\omega\tilde{u}_z\left(x = 64\,\mathrm{m}, \bar{k}_y, z = 0\,\mathrm{m}, \omega\right)$ (a) in the reference case and (b) in the case of subgrade stiffening next to the track. The corresponding insertion loss $\widetilde{\mathrm{IL}}_z\left(x = 64\,\mathrm{m}, \bar{k}_y, z = 0\,\mathrm{m}, \omega\right)$ is shown in (c). Superimposed are the dispersion curve of a Rayleigh wave in the y-direction (solid black line), the free bending wave dispersion curve in an infinitely long beam (dashed black line) and the relation between $\bar{k}_y$ and ω given by equation (9) (solid grey lines).

The efficiency of a mitigation measure can be quantified in the frequency–wavenumber domain through the vertical insertion loss $\widetilde{\mathrm{IL}}_z(x, \bar{k}_y, z, \omega)$:

$$\widetilde{\mathrm{IL}}_z(x, \bar{k}_y, z, \omega) = 20\log_{10}\frac{|\tilde{u}_z^{\mathrm{ref}}(x, \bar{k}_y, z, \omega)|}{|\tilde{u}_z(x, \bar{k}_y, z, \omega)|} \qquad [\mathrm{dB}] \tag{2}$$

Positive values of the insertion loss indicate a reduction of the vertical free field vibrations. Figure 5c shows the insertion loss $\widetilde{\mathrm{IL}}_z\left(x = 64\,\mathrm{m}, \bar{k}_y, z = 0\,\mathrm{m}, \omega\right)$. The insertion loss is only shown in a range $0 \leq \bar{k}_y \leq \bar{k}_\mathrm{R}$, as propagating waves only exist in this range. A clearly delimited area in the $(\bar{k}_y, \omega)$–domain corresponding to a significant insertion loss can be distinguished in this figure.

Figure 5c can physically be explained by regarding the block of stiffened soil as an infinitely long beam. The partial differential equation describing the transverse displacement $u_z(y, t)$ of a Timoshenko beam can be transformed to the frequency–wavenumber domain and reads as

follows [27]:

$$\left(-\rho A\omega^2 + EIk_y^4 - \rho I\left(1+\frac{E}{\kappa\mu}\right)\omega^2 k_y^2 + \frac{\rho^2 I}{\kappa\mu}\omega^4\right)\tilde{u}_z(k_y,\omega) = \tilde{f}(k_y,\omega) \tag{3}$$

where E is the Young's modulus, μ the shear modulus, ρ the density, A the cross sectional area, I the moment of inertia for bending with respect to the horizontal axis and κ the shear coefficient of the beam. Figure 6 shows the normalized admittance $|\tilde{Y}(\bar{k}_y,\omega)/\tilde{Y}(\bar{k}_y=0,\omega)|$, where the admittance $\tilde{Y}(k_y,\omega)$ is defined as the ratio of the transverse velocity $i\omega\tilde{u}_z(k_y,\omega)$ and the external loading $\tilde{f}(k_y,\omega)$. The dimensionless wavenumber $\bar{k}_y$ is defined as above.

The dispersion relation follows from equation (3) and can be written as:

$$\left(-\frac{E}{\rho}k_y^2+\omega^2\right)\left(-\frac{\kappa\mu}{\rho}k_y^2+\omega^2\right) - \frac{\kappa\mu A}{\rho I}\omega^2 = 0 \tag{4}$$

The dispersion relation (4) comprises two branches of the dispersion curve, corresponding to a bending and shear mode, respectively [27]. Below a certain radial cut-on frequency equal to $\sqrt{\frac{\kappa\mu A}{\rho I}}$, there is a single branch which corresponds to real wavenumbers, and thus a propagating (bending) mode. The cut-on frequency equals $2\pi \times 138\,\mathrm{Hz}$ in the present case, which implies that only the bending mode is of importance in the frequency range considered.

Superimposed on figure 6 is the dispersion curve $\bar{k}_y = \bar{k}_\mathrm{b}$ of a free bending wave in the beam which satisfies the dispersion relation (4). This figure clearly illustrates that the amplitude of propagating bending waves in a beam becomes very small for wavenumbers $\bar{k}_y$ larger than $\bar{k}_\mathrm{b}$, which equivalently corresponds to wavelengths λ_y smaller than the free bending wavelength λ_b. The response is then dominated by the bending stiffness of the beam and the amplitude decreases proportionally to k_y^{-4} at a given radial frequency ω (cfr. equation (3)).

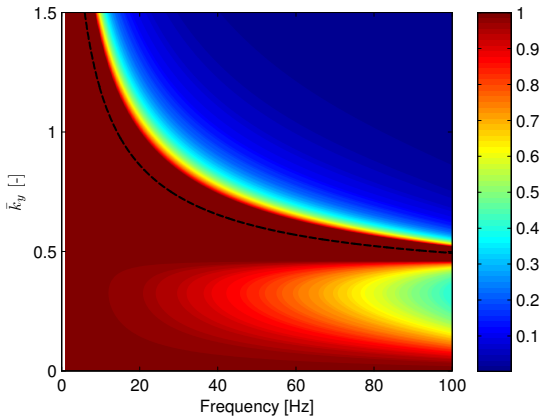


Figure 6: Normalized admittance $|\tilde{Y}(\bar{k}_y,\omega)/\tilde{Y}(\bar{k}_y=0,\omega)|$ of a beam with the dynamic properties of the block of stiffened soil next to the track. Superimposed is the free bending wave dispersion curve (dashed black line).

Figure 5c can now be interpreted based on the interaction of the Rayleigh wave in the soil and bending waves in the block of stiffened soil. At low frequencies, the wavenumber $\bar{k}_\mathrm{b}$ is larger than the wavenumber $\bar{k}_\mathrm{R}$, and the Rayleigh wave propagates through the block of stiffened soil. From a critical frequency on, the wavefield contains propagating plane waves ($\bar{k}_y \leq \bar{k}_\mathrm{R}$) with a wavenumber $\bar{k}_y$ larger than $\bar{k}_\mathrm{b}$ (i.e. with a wavelength λ_y smaller than λ_b). The transmission

of these plane waves is impeded by the block of stiffened soil as soon as $\bar{k}_y$ is slightly larger than $\bar{k}_\mathrm{b}$ (cfr. figure 6). This explains why the zone of significant insertion loss in figure 5c is clearly delimited by the free bending wave dispersion curve. The critical radial frequency ω_c from which the block of stiffened soil can act as a wave impeding barrier is determined by the intersection of the Rayleigh wave and the free bending wave dispersion curves:

$$\omega_\mathrm{c} = C_\mathrm{R}^2 \sqrt{\frac{\rho A}{EI}} \sqrt{\frac{E\mu\kappa}{\left(E - \rho C_\mathrm{R}^2\right)\left(\mu\kappa - \rho C_\mathrm{R}^2\right)}} \tag{5}$$

which equals $2\pi \times 12\,\mathrm{Hz}$ in the actual case. If the shear deformation and rotational inertia of the block of stiffened soil are neglected, equation (3) reduces to the Euler–Bernoulli beam equation, and the critical frequency can be approximated as:

$$\omega_\mathrm{c} \simeq C_\mathrm{R}^2 \sqrt{\frac{\rho A}{EI}} = \frac{C_\mathrm{R}^2}{h} \sqrt{\frac{12\rho}{E}} \tag{6}$$

where h is the depth of the block of stiffened soil, if bending with respect to the horizontal axis is considered. It is clear from the discussion above that the mitigation measure can only be effective for frequencies above ω_c. Equations (5) and (6) reveal that the critical frequency strongly depends on the stiffness contrast between the soil and the block of stiffened soil, indicating that this mitigation measure will be more effective at sites with a soft soil. These expressions furthermore illustrate that increasing the depth h of the stiffened block is beneficial, as this results in a reduction of the critical frequency. A minimal width is also required, however, in order to ensure that the block of stiffened soil behaves as a beam. Equation (6) is of great practical importance, as it provides a simple design guideline to assess the expected vibration reduction efficiency of soil stiffening next to the track, without the need of an extensive FE–BE calculation.

The physical mechanism outlined above closely resembles the phenomenon of coincidence in acoustics [28], where sound waves impinging on an infinite plate are freely transmitted if the wavelength of bending waves in the plate equals the trace wavelength of the acoustic waves in the air. In acoustics, the transmission loss below coincidence is predominantly related to the so-called mass law [28]. At the coincidence frequency, a prominent dip occurs in the transmission loss. At higher frequencies, the transmission loss increases significantly due to the increased bending stiffness. In the present case, a reduction of vibration levels is only seen above coincidence, attributed to the bending stiffness of the block of stiffened soil next to the track, while the inertia effect is negligible. An increase of the density with respect to the original soil is, however, also expected to be beneficial.

The propagating plane waves ($\bar{k}_y \leq \bar{k}_\mathrm{R}$) are characterized by a wave propagation direction $\theta = \sin^{-1}\left(\bar{k}_y / \bar{k}_\mathrm{R}\right)$ (figure 2). As a result, a reduction of vibration levels will only be obtained in an area delimited by a critical angle $\theta_\mathrm{c}(\omega) = \sin^{-1}\left(\bar{k}_\mathrm{b} / \bar{k}_\mathrm{R}\right)$, defined as:

$$\sin\theta_\mathrm{c}(\omega) = C_\mathrm{R} \sqrt{\rho \frac{E + \mu\kappa \pm \sqrt{\left(E - \mu\kappa\right)^2 + \frac{4E(\mu\kappa)^2 A}{\rho I \omega^2}}}{2E\mu\kappa}} \tag{7}$$

where the plus and minus signs correspond to the first and second branch of the beam dispersion curve, respectively. As indicated above, only the first branch is of interest in the frequency

range considered. At limiting high frequencies, the critical angle related to this branch can be approximated as:

$$\sin\theta_{\mathrm{c}} = C_{\mathrm{R}}\sqrt{\frac{\rho}{\mu\kappa}} \tag{8}$$

Figure 5c furthermore exhibits a regular pattern of regions where an increased insertion loss can be observed, for $0 < \bar{k}_y < s$, where $s = C_{\mathrm{s}}/C_{\mathrm{p}} = 0.5$ in the present case. This can be explained by the fact that the P-wave travels faster through the block of stiffened soil than in the halfspace, which introduces a phase shift between the wave fronts in the reference case and in the case where stiffening next to the track is included. The following expression gives the relation between wavenumbers $\bar{k}_y$ and radial frequencies ω which result in a phase shift equal to a multiple of 2π:

$$\left(\sqrt{\left(\frac{\omega}{C_{\mathrm{R}}}\right)^2 - \left(\frac{\bar{k}_y\omega}{C_{\mathrm{s}}}\right)^2} - \sqrt{\left(\frac{\omega}{C_{\mathrm{p}}}\right)^2 - \left(\frac{\bar{k}_y\omega}{C_{\mathrm{s}}}\right)^2}\right) x - \omega\frac{w}{\Delta C_{\mathrm{p}}} = 2\pi n \quad \text{for} \quad n = 0, 1, 2, \ldots \tag{9}$$

with $x = 64\,\mathrm{m}$ the location under consideration, $w = 2\,\mathrm{m}$ the width of the block of stiffened soil and $\Delta C_{\mathrm{p}} = 550\,\mathrm{m/s}$ the difference in dilatational wave velocities between the halfspace and the stiffened block. The square roots between brackets are the dimensionless lateral wavenumbers $\bar{k}_{x\mathrm{R}}$ for the Rayleigh wave and $\bar{k}_{x\mathrm{p}}$ for the P-wave, respectively, while the term $\omega w/\Delta C_{\mathrm{p}}$ denotes the phase shift. Lines corresponding to the relation given by equation (9) are superimposed on figure 5c. These lines coincide almost perfectly with the regions where an increased insertion loss is observed, especially at frequencies above $50\,\mathrm{Hz}$, as the wavelength in the soil then becomes comparable to the dimensions of the block of stiffened soil.

The physical mechanism that determines the effectiveness of subgrade stiffening next to the track has been interpreted in the frequency–wavenumber domain. In the following, it is shown how this mechanism becomes apparent in the frequency–spatial domain.

2.5 The free field impulse response in the frequency–spatial domain

The track and soil response in the frequency–spatial domain can be found by means of an inverse Fourier transform. Figures 7a and 7b show the real part of the vertical displacement $\hat{u}_z(\mathbf{x},\omega)$ at $5\,\mathrm{Hz}$ in the reference case and in the case of stiffening next to the track, respectively, due to a unit harmonic vertical point load applied to the right rail at $y = 0\,\mathrm{m}$. The Rayleigh wavelength $\lambda_{\mathrm{R}} = 2\pi C_{\mathrm{R}}/\omega$ in the soil is much larger than the width of the track, resulting in a wave field characterized by nearly cylindrical wave fronts. The corresponding insertion loss $\widehat{\mathrm{IL}}_z(\mathbf{x},\omega)$ is shown in figure 7c. As the considered frequency is smaller than the critical frequency $\omega_{\mathrm{c}}/2\pi$, the block of stiffened soil is unable to impede the propagation of the Rayleigh wave, and the insertion loss is zero almost everywhere in the soil domain.

Figure 8 shows the real part of the vertical displacement $\hat{u}_z(\mathbf{x},\omega)$ at a frequency of $30\,\mathrm{Hz}$, which is above the critical frequency $\omega_{\mathrm{c}}/2\pi$. The wave fronts at the surface of the soil are no longer cylindrical due to the dynamic interaction between the track and the halfspace. The critical angle at the considered frequency equals $\theta_{\mathrm{c}} = \sin^{-1}(0.73/1.073) = 43°$. This angle is indicated on figure 8c, which confirms that a significant reduction of vibration levels is obtained for $\theta > \theta_{\mathrm{c}}$. The insertion loss reaches values of $10\,\mathrm{dB}$ and more in this region. The reduction is not only obtained at the surface of the halfspace, but also at depth, although some localized areas

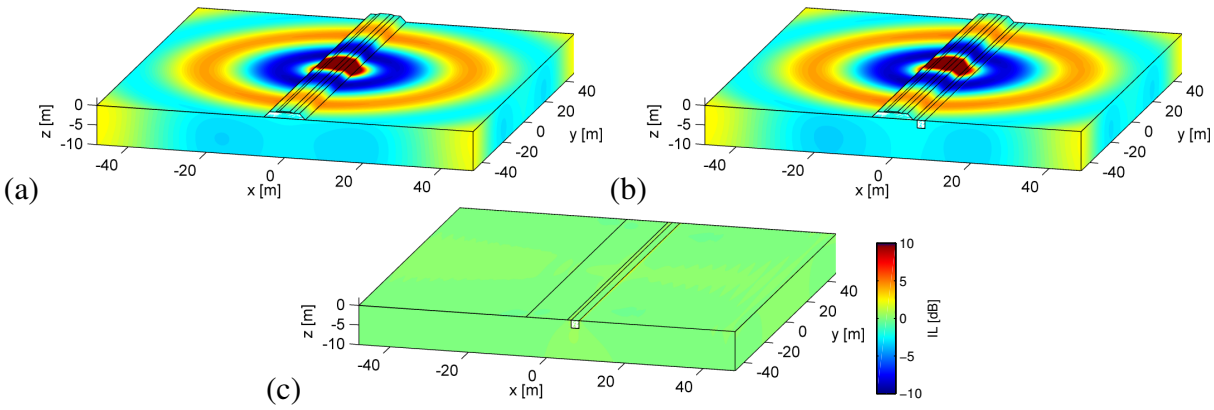


Figure 7: Real part of the vertical displacement $\hat{u}_z(\mathbf{x},\omega)$ due to harmonic excitation on the right rail at $5\,\mathrm{Hz}$ (a) in the reference case and (b) in the case of stiffening next to the track, and (c) the corresponding insertion loss $\widehat{\mathrm{IL}}_z(\mathbf{x},\omega)$.

can be identified with increased vibration levels with respect to the reference case. The angle $\sin^{-1}\left(s/\bar{k}_\mathrm{R}\right) = \sin^{-1}\left(0.50/1.073\right) = 28°$ is also indicated on figure 8c, which delimits the area where an interference pattern as considered in equation (9) is visible. Lines of constructive and destructive interference between direct and reflected Rayleigh waves can furthermore be observed at the opposite side of the track (i.e. where no soil stiffening is applied).

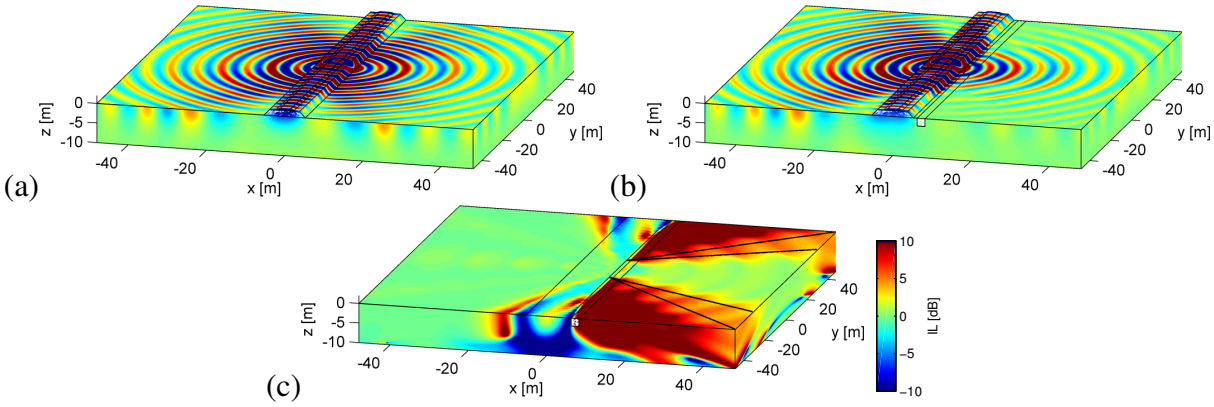


Figure 8: Real part of the vertical displacement $\hat{u}_z(\mathbf{x},\omega)$ due to harmonic excitation on the right rail at $30\,\mathrm{Hz}$ (a) in the reference case and (b) in the case of stiffening next to the track, and (c) the corresponding insertion loss $\widehat{\mathrm{IL}}_z(\mathbf{x},\omega)$.

Figure 9 shows the real part of the vertical displacement $\hat{u}_z(\mathbf{x},\omega)$ at a frequency of $60\,\mathrm{Hz}$. As in figure 8, the wave fronts are not cylindrical. The critical angle at this frequency is $\theta_\mathrm{c} = \sin^{-1}(0.57/1.073) = 32°$, and is clearly visible in figure 9c. The interference pattern in the area bounded by the angle $\sin^{-1}\left(s/\bar{k}_\mathrm{R}\right)$ is even more clear than in figure 8. Lines of constructive and destructive interference at the opposite side of the track can be observed as well.

It follows from the previous discussion that a reduction of vibration levels is only obtained above the critical frequency $\omega_\mathrm{c}/2\pi$, predominantly in the area delimited by the critical angle $\theta_\mathrm{c}(\omega)$. The reduction on a line perpendicular to the track at the position where the load is applied is less than in other points. This is confirmed in figure 10, which shows the free field mobility at a lateral distance of $24\,\mathrm{m}$ from the center of the track, at $y = 0\,\mathrm{m}$ and at $y = 24\,\mathrm{m}$. This implies

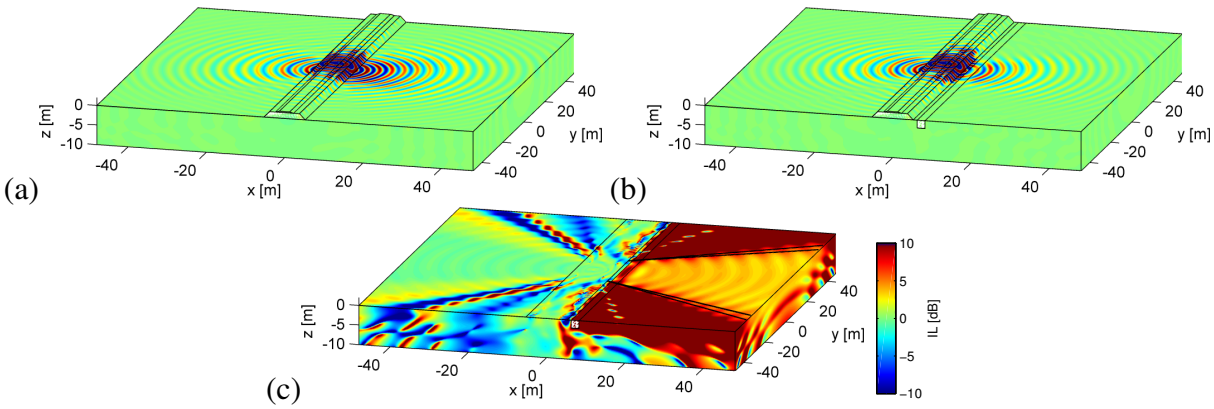


Figure 9: Real part of the vertical displacement $\hat{u}_z(\mathbf{x},\omega)$ due to harmonic excitation on the right rail at $60\,\mathrm{Hz}$ (a) in the reference case and (b) in the case of stiffening next to the track, and (c) the corresponding insertion loss $\widehat{\mathrm{IL}}_z(\mathbf{x},\omega)$.

that, if the passage of a train is considered, the contribution of the dynamic axle loads moving towards or away from a receiver will be mitigated more effectively than the contribution of the dynamic axle loads located close to the receiver. The passage of a train is discussed in more detail in the next subsection.

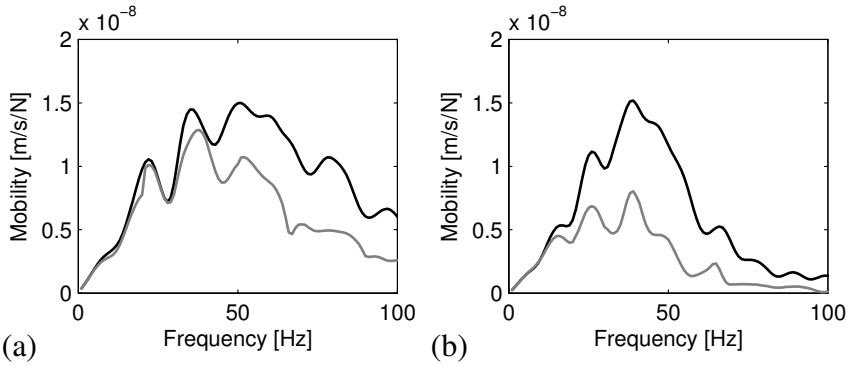


Figure 10: Free field mobility at $x = 24\,\mathrm{m}$ and (a) $y = 0\,\mathrm{m}$ and (b) $y = 24\,\mathrm{m}$ in the reference case (black line) and in the case of stiffening next to the track (grey line).

2.6 The free field response during the passage of a Renfe S599 train

Finally, the vibration reduction efficiency of the proposed mitigation measure during the passage of a Renfe S599 train at a speed of $160\,\mathrm{km/h}$ is investigated. This type of train consists of two motor coaches and a central carriage and has a total length of $75.98\,\mathrm{m}$. Each carriage is supported by two bogies and has four axles. The number of axles N_a, the carriage length L_t, the distance L_b between bogies, the axle distance L_a, and the unsprung axle mass M_u of the carriages are summarized in table 1. Only these unsprung masses are taken into account, as the carriage's primary and secondary suspension isolate the body and the bogie from the wheelset at frequencies above a few Hertz [29].

As indicated in subsection 2.2, only the dynamic axle loads originating from the track unevenness are taken into account. A track with an unevenness profile according to the FRA class 3 [30] is assumed. The free field velocity due to a train passage is characterized by an in-

	N_a $[-]$	L_t $[\mathrm{m}]$	L_b $[\mathrm{m}]$	L_a $[\mathrm{m}]$	M_u $[\mathrm{kg}]$
Two motor coaches	4	25.85	17.73	2.50	1940
One central carriage	4	24.28	18.00	2.50	1704

Table 1: Characteristics of the Renfe S599 train.

creasing vibration level when the train is approaching, a nearly stationary vibration level during the passage of the train and a decreasing vibration level when the train is moving away. It has been shown that the dominating stationary part of the free field velocity can be well approximated by a prediction in which the dynamic axle loads are applied at fixed positions [31]. This approach is employed throughout this section.

Figure 11 shows the one–third octave band RMS spectra of the vertical free field vibration velocity during the passage of a Renfe S599 train at a speed of $160\,\mathrm{km/h}$. In the reference case, the frequency content of the free field vibrations close to the track is mainly situated in a frequency range between $20\,\mathrm{Hz}$ and $100\,\mathrm{Hz}$, while at larger distances from the track, material damping in the soil results in a strong attenuation of the response at high frequencies. In the case of subgrade stiffening next to the track, a reduction of vibration levels is obtained above the critical frequency of $12\,\mathrm{Hz}$. Superimposed on figure 11 are ISO vibration criterion curves for the effect of vibrations on people in buildings [32], indicating that subgrade stiffening can be used as an effective mitigation measure in order to comply with vibration criteria. Subgrade stiffening has furthermore a negligible effect on the vibration levels at the opposite side of the track, as the interference patterns observable in case of harmonic excitation (cfr. figures 8c and 9c) cancel each other out during the passage of a train.

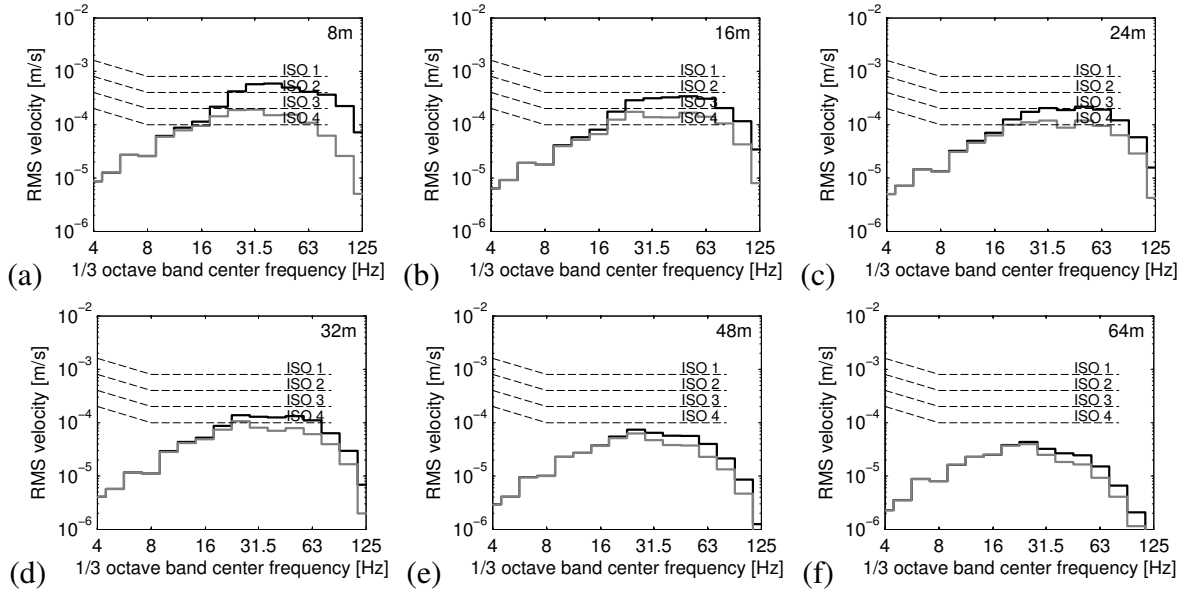


Figure 11: One–third octave band RMS spectra of the vertical free field vibrations in the reference case (black line) and in the case of stiffening next to the track (grey line) at a distance of (a) $8\,\mathrm{m}$, (b) $16\,\mathrm{m}$, (c) $24\,\mathrm{m}$, (d) $32\,\mathrm{m}$, (e) $48\,\mathrm{m}$ and (f) $64\,\mathrm{m}$ from the center of the track due to the passage of a Renfe S599 train at a speed of $160\,\mathrm{km/h}$.

The efficiency of the mitigation measure is investigated in more detail in figure 12, which shows the vertical insertion loss $\widehat{\mathrm{IL}}_z(\mathbf{x},\omega)$ for several locations at increasing distance from the

track. The insertion loss is defined in a similar way as in equation (2), but now for the one–third octave band RMS spectra of the vertical free field vibration velocity. This figure clearly confirms that a reduction can be obtained above the critical frequency $\omega_c/2\pi$. Generally speaking, the insertion loss is higher at locations closer to the track, while an increase of insertion loss with frequency can be observed at a particular location.

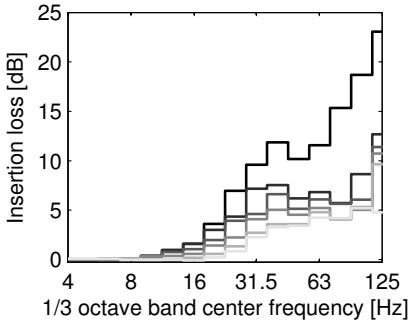


Figure 12: Vertical insertion loss $\widehat{\mathrm{IL}}_z(\mathbf{x},\omega)$ at $8\,\mathrm{m}$, $16\,\mathrm{m}$, $24\,\mathrm{m}$, $32\,\mathrm{m}$, $48\,\mathrm{m}$ and $64\,\mathrm{m}$ from the center of the track (black to light grey lines) due to the passage of a Renfe S599 train at a speed of $160\,\mathrm{km/h}$.

The results in figure 12 can be understood by considering figure 13, which shows a top view of the track, the block of stiffened soil next to the track and the free field. The fixed positions of the dynamic axle loads $\hat{\mathbf{g}}_k(\omega)$ are indicated, as well as two receiver locations $\mathbf{x}_1 = \{x_1, 0, 0\}^{\mathrm{T}}$ and $\mathbf{x}_2 = \{x_2, 0, 0\}^{\mathrm{T}}$ in the free field, with $x_1 < x_2$. At each axle load position, thin grey lines indicate the critical angle $\theta_c(\omega)$, delimiting the area in which the free field vibrations resulting from excitation at the considered position are significantly reduced. Figure 13a illustrates that, at a particular radial frequency $\omega_1 > \omega_c$, the contribution of all axle loads to the free field vibration at the location $\mathbf{x}_1$ is significantly reduced, except for the axle loads $\hat{\mathbf{g}}_{i-1}(\omega)$ to $\hat{\mathbf{g}}_{i+1}(\omega)$ (as $\mathbf{x}_1$ is not situated within the area where a significant reduction can be expected for these axle loads). At the location $\mathbf{x}_2$ further away from the track, however, the transfer of a smaller number of axle loads is effectively mitigated by the block of stiffened soil, as the contribution of the axle loads $\hat{\mathbf{g}}_{i-3}(\omega)$ to $\hat{\mathbf{g}}_{i+3}(\omega)$ will not be reduced. This indicates that subgrade stiffening next to the track is less efficient at locations further away from the track. At a higher radial frequency ω_2 ($\omega_c < \omega_1 < \omega_2$), the critical angle $\theta_c(\omega_2)$ decreases corresponding to equation (7), which implies that the area in which the transfer to the free field is reduced, enlarges. As illustrated in figure 13b, the contribution of all axle loads to the free field vibrations at $\mathbf{x}_1$ will be reduced at this frequency except for $\hat{\mathbf{g}}_i(\omega)$, while the contribution of all axle loads, except $\hat{\mathbf{g}}_{i-1}(\omega)$ to $\hat{\mathbf{g}}_{i+1}(\omega)$, will be reduced at $\mathbf{x}_2$.

The previous discussion reveals that the contribution to the free field vibration of a larger number of axle loads is significantly reduced if a receiver location closer to the track is considered, and for increasing frequencies. These trends are confirmed in figure 12. The free field vibration in the near field is dominated by the closest axle loads (whose contribution will not be reduced), while all axle loads contribute almost equally to the response in the far field. The actual value of the insertion loss $\widehat{\mathrm{IL}}_z(\mathbf{x},\omega)$ obtained at a particular receiver location $\mathbf{x}$ is therefore determined by a trade–off between the relative importance of each axle load and the possibility to mitigate the transfer from the axle load to the free field.

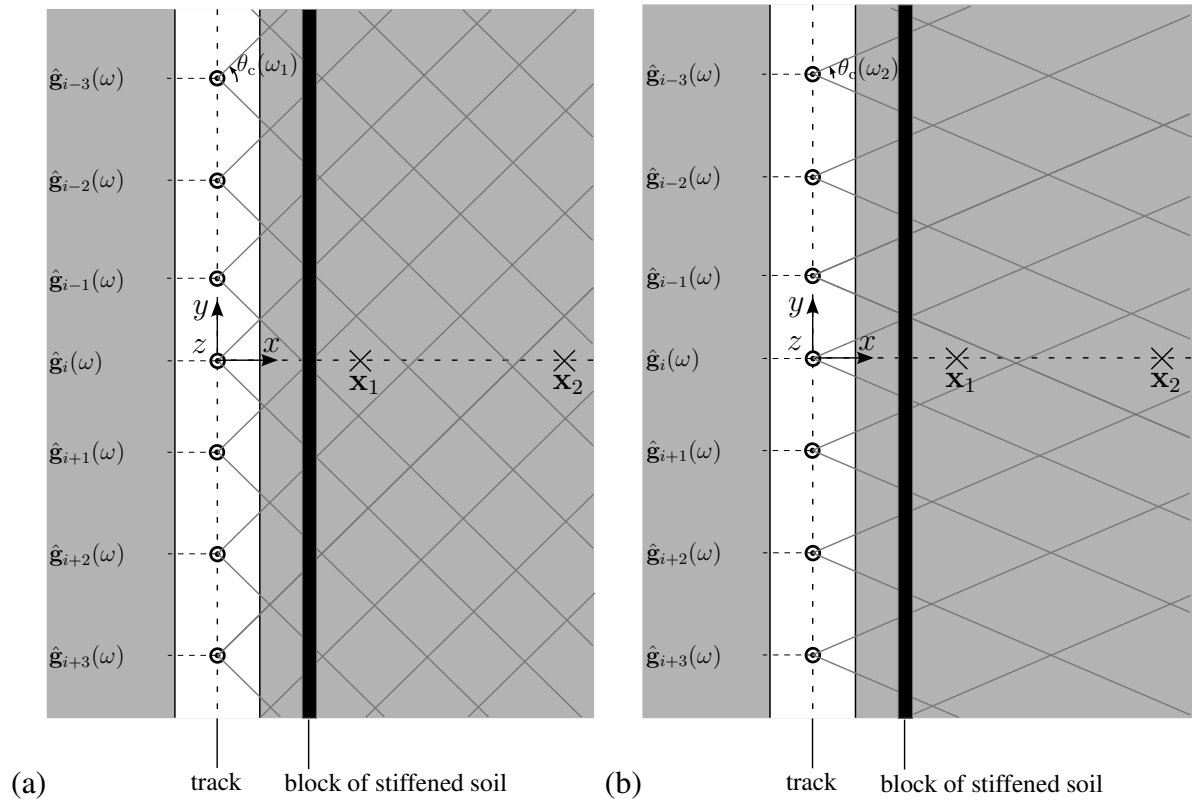


Figure 13: Top view of the track (white), the block of stiffened soil next to the track (black) and the free field (grey). The fixed positions of the dynamic axle loads $\hat{\mathbf{g}}_{i-3}(\omega)$ to $\hat{\mathbf{g}}_{i+3}(\omega)$ are indicated with circles. Superimposed at each axle load position are thin grey lines indicating the critical angle $\theta_{\mathrm{c}}(\omega)$ at a radial frequency (a) ω_1 and (b) ω_2, with $\omega_{\mathrm{c}} < \omega_1 < \omega_2$.

2.7 Influence of the soil stratification

For a layered halfspace, the propagation of Rayleigh waves is dispersive due to the variation of the soil properties with depth, and multiple modes with associated cut-on frequencies exist. The physical mechanism outlined above is still identified in the case of a layered halfspace [33], however, and the region in the $(\overline{k}_y, \omega)$–domain where a significant insertion loss is obtained is bounded by the fundamental Rayleigh wave dispersion curve and the free bending wave dispersion curve. Equations (5) and (7) for the critical frequency and angle, respectively, are still valid, demonstrating their usefulness as a design tool even in the case of a layered halfspace, although C_{R} has to be replaced by $C_{\mathrm{R}}(\omega)$ due to the dispersive nature of the Rayleigh wave. A detailed investigation of case studies involving a layered halfspace can be found in [33].

2.8 Comparison with results from literature

It is instructive to compare the results outlined in this section with previous studies [12, 13, 15, 34, 35]. The current results confirm that subgrade stiffening is more efficient at sites with a soft soil and that increasing the stiffness of the block of soil next to the track is beneficial. It has also been observed in [13] that trenches backfilled with concrete serve as 'concave lenses', where a reduction of the vibration levels is predominantly achieved behind and in front of the source. This can be related to the existence of a critical angle, as outlined in subsection 2.4. A more comprehensive explanation of the underlying physics is, however, formulated in the present paper. This study furthermore demonstrates the necessity of 2.5D/3D models to

correctly reveal the underlying physical mechanism and indicates that the use of 2D models is not sufficient.

The proposed mitigation measure can also be compared to alternative methods such as vibration isolation screens. Open trenches aim at reflecting the impinging waves and are effective for trench depths of about one Rayleigh wavelength [10]. The construction of open trenches is, however, for stability reasons limited to shallow depths; the use of in–fill materials allows to increase the depth. If a soft in–fill material is used, the behaviour of a filled trench resembles that of an open trench. The use of a stiff in–fill material, however, results in a wave impeding effect closely related to the physical mechanism outlined in the present paper, and the vibration reduction of such a trench is no longer based on the reflection of incident waves [36].

3 THREE–DIMENSIONAL ANALYSIS

The implementation of subgrade stiffening next to the track is in practice limited to finite dimensions, and the assumption of longitudinal invariance adopted in section 2 is therefore not fulfilled. Accounting for the finite length requires the solution of a fully 3D dynamic soil–structure interaction problem, which is computationally very demanding due to the fact that fully populated unsymmetric matrices arise from classical BE formulations. In order to circumvent the stringent memory and CPU requirements, a fast BE method based on hierarchical matrices ($\mathscr{H}$–matrices) [20] is therefore employed in this section.

3.1 The numerical model

The use of $\mathscr{H}$–matrices provides an elegant way to treat the fully populated matrices arising from the BE method with almost linear complexity [37], as they approximate the original matrices (with an arbitrary prescribed accuracy) by means of data–sparse, memory–efficient representations. The construction of $\mathscr{H}$–matrices is based on the identification of admissible and inadmissible hierarchical cluster pairs in the BE mesh; the partially pivoted adaptive cross approximation (ACA) algorithm [38, 39] is employed to compute low rank approximations of matrix blocks corresponding to admissible cluster pairs. A major advantage of ACA is its purely algebraic character, avoiding the need for (semi–)analytical expressions of the Green's functions employed in the BE formulation (e.g. allowing for the incorporation of Green's functions for a horizontally layered halfspace [20]). The reader is referred to the literature [37, 40, 41] for a detailed description of the methodology regarding $\mathscr{H}$–matrices.

The conventional FE–BE coupling strategy outlined in subsection 2.2 is not well suited to provide an efficient solution of the dynamic soil–structure interaction problem in case $\mathscr{H}$-BE models are employed [42]. An alternative iterative procedure is therefore applied, in which the governing equations of each subdomain are solved separately, while the boundary conditions at the soil–structure interface are updated until convergence is achieved. As demonstrated in [42], a sequential Neumann–Dirichlet algorithm is preferred due to the strong stiffness contrast between the FE and $\mathscr{H}$-BE subdomain (with Neumann boundary conditions imposed on the most stiff subdomain, i.c. the block of stiffened soil).

3.2 The free field impulse response in the frequency–spatial domain

A block of stiffened soil with dimensions $2\,\mathrm{m} \times L_y \times 2\,\mathrm{m}$ and aligned along $x = 5\,\mathrm{m}$ (figure 2) is considered in this subsection. The same dynamic characteristics for the halfspace and the block of stiffened soil as defined in subsection 2.1 are employed. A track is not included in the model, however, as it is inconvenient to combine a 2.5D model for the track with a 3D

model for the block of stiffened soil. This limits the investigation to transfer functions between a unit vertical harmonic point load applied at the origin of the coordinate system and the free field response.

Eight–node solid finite elements are employed for the discretization of the block of stiffened soil, which are coupled to a conforming mesh of four–node quadrilateral boundary elements for the surrounding soil domain. Halfspace Green's functions are employed in the $\mathscr{H}$-BE formulation [20]. The numerical analysis is performed for a block of stiffened soil with a longitudinal length L_y of $15\,\mathrm{m}$, $30\,\mathrm{m}$, and $60\,\mathrm{m}$; the properties of the resulting FE and BE discretizations are listed in table 2.

L_y [m]	# FE elements [−]	# FE nodes [−]	# FE DOFs [−]	# BE elements [−]	# BE nodes [−]	# BE DOFs [−]
15	3840	4941	14823	1568	1637	4911
30	7680	9801	29403	3008	3137	9411
60	15360	19521	58563	5888	6137	18411

Table 2: Properties of the FE and BE discretizations of a block of stiffened soil with a length of $15\,\mathrm{m}$, $30\,\mathrm{m}$, and $60\,\mathrm{m}$.

Figures 14a and 14b–d show the real part of the vertical displacement $\hat{u}_z(\mathbf{x},\omega)$ at a frequency of $15\,\mathrm{Hz}$ in the reference case and in case a block of stiffened soil is included over a finite length L_y, respectively, while the result of a 2.5D calculation based on the assumption of longitudinal invariance is shown in figure 14e. The corresponding vertical insertion loss $\widehat{\mathrm{IL}}_z(\mathbf{x},\omega)$ is also included. The real part of the vertical displacement $\hat{u}_z(\mathbf{x},\omega)$ and the insertion loss $\widehat{\mathrm{IL}}_z(\mathbf{x},\omega)$ at $30\,\mathrm{Hz}$ and $60\,\mathrm{Hz}$ are shown in figures 15 and 16, respectively. The wave impeding effect and the existence of a critical angle can clearly be observed in the invariant cases (figures 14–16e); the area where vibration levels are significantly reduced is enlarged at higher frequencies. It is also evident, however, that stiffening of the soil considering a finite length of $15\,\mathrm{m}$ does not suffice to mimic the dynamic behaviour of an infinitely long block of stiffened soil at $15\,\mathrm{Hz}$ and $30\,\mathrm{Hz}$; a much better correspondence is obtained at $60\,\mathrm{Hz}$. The wavefield in the soil and the insertion loss in the cases where subgrade stiffening is applied over a length of $30\,\mathrm{m}$ or $60\,\mathrm{m}$ agree reasonably well with the result of a 2.5D calculation, at all frequencies under concern.

The observations in figures 14–16 can be interpreted by comparing the length L_y of the block to the free bending wavelength $\lambda_\mathrm{b}(\omega)$ of an infinitely long beam. The latter yields $\lambda_\mathrm{b}(\omega) = 2\pi\left(\frac{Eh^2}{12\rho\omega^2}\right)^{1/4}$ for an Euler–Bernoulli beam, where h is the depth of the block of stiffened soil, and is equal to $14.50\,\mathrm{m}$, $10.25\,\mathrm{m}$, and $7.25\,\mathrm{m}$ at $15\,\mathrm{Hz}$, $30\,\mathrm{Hz}$, and $60\,\mathrm{Hz}$, respectively. This indicates that the length L_y should be approximately two times the free bending wavelength $\lambda_\mathrm{b}(\omega)$ in order to ensure that a finite block can act as a wave impeding barrier and to achieve a vibration reduction efficiency comparable to the invariant case. Even then, however, a finite block is unable to impede the direct transmission of waves from the point of excitation to the free field due to its limited length; this is clearly apparent for a block with a length of $15\,\mathrm{m}$ (figures 14–16b). Furthermore, diffraction occurs at the extremities of the block, and the modal behaviour also affects the wavefield in the soil.

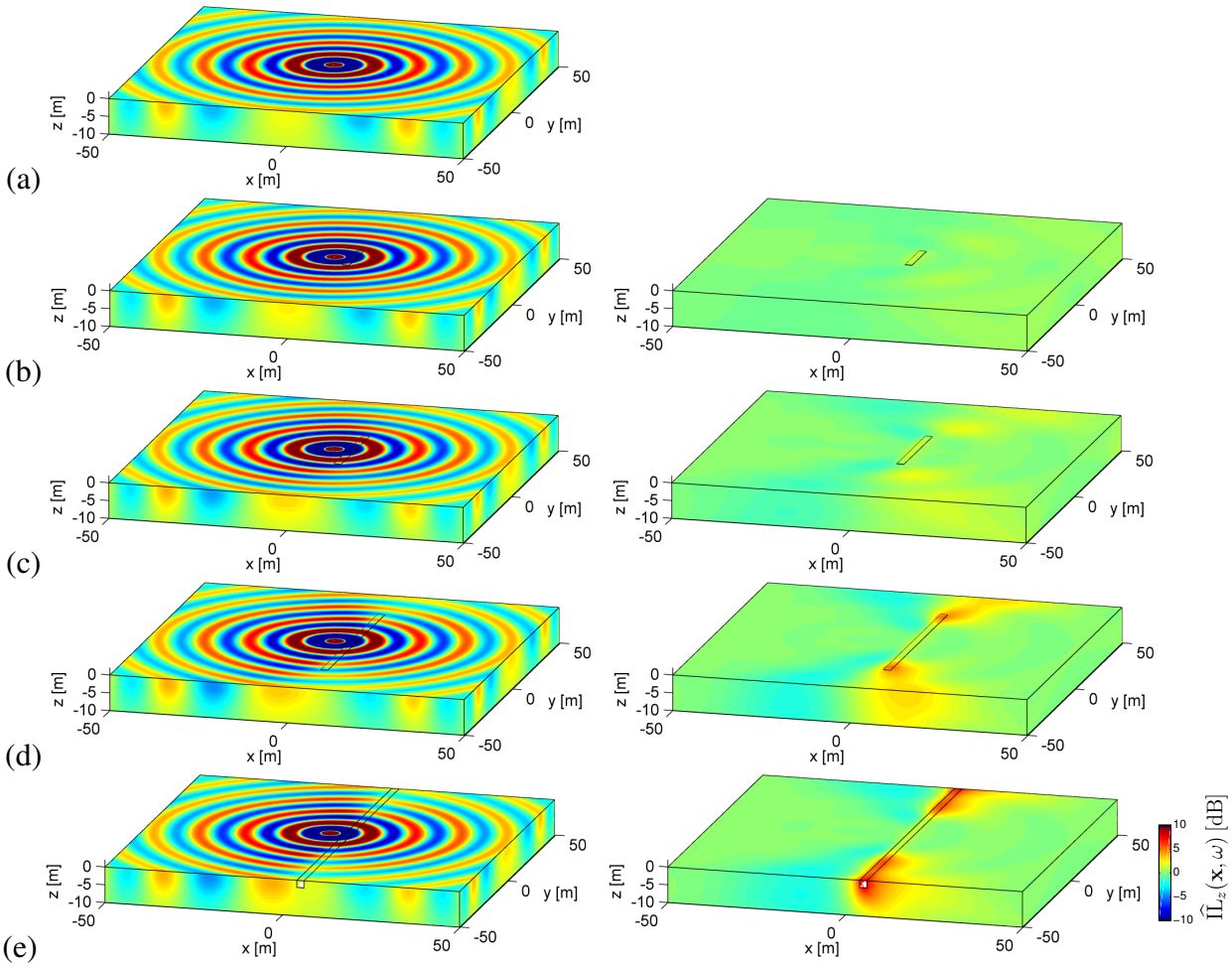


Figure 14: Real part of the vertical displacement $\hat{u}_z(\mathbf{x},\omega)$ due to harmonic excitation at 15 Hz (a) in the reference case and in case a block of stiffened soil is included with a length (b) $L_y = 15\,\mathrm{m}$, (c) $L_y = 30\,\mathrm{m}$, (d) $L_y = 60\,\mathrm{m}$, and (e) $L_y = \infty$ (left hand side). The corresponding insertion loss $\widehat{\mathrm{IL}}_z(\mathbf{x},\omega)$ is shown at the right hand side.

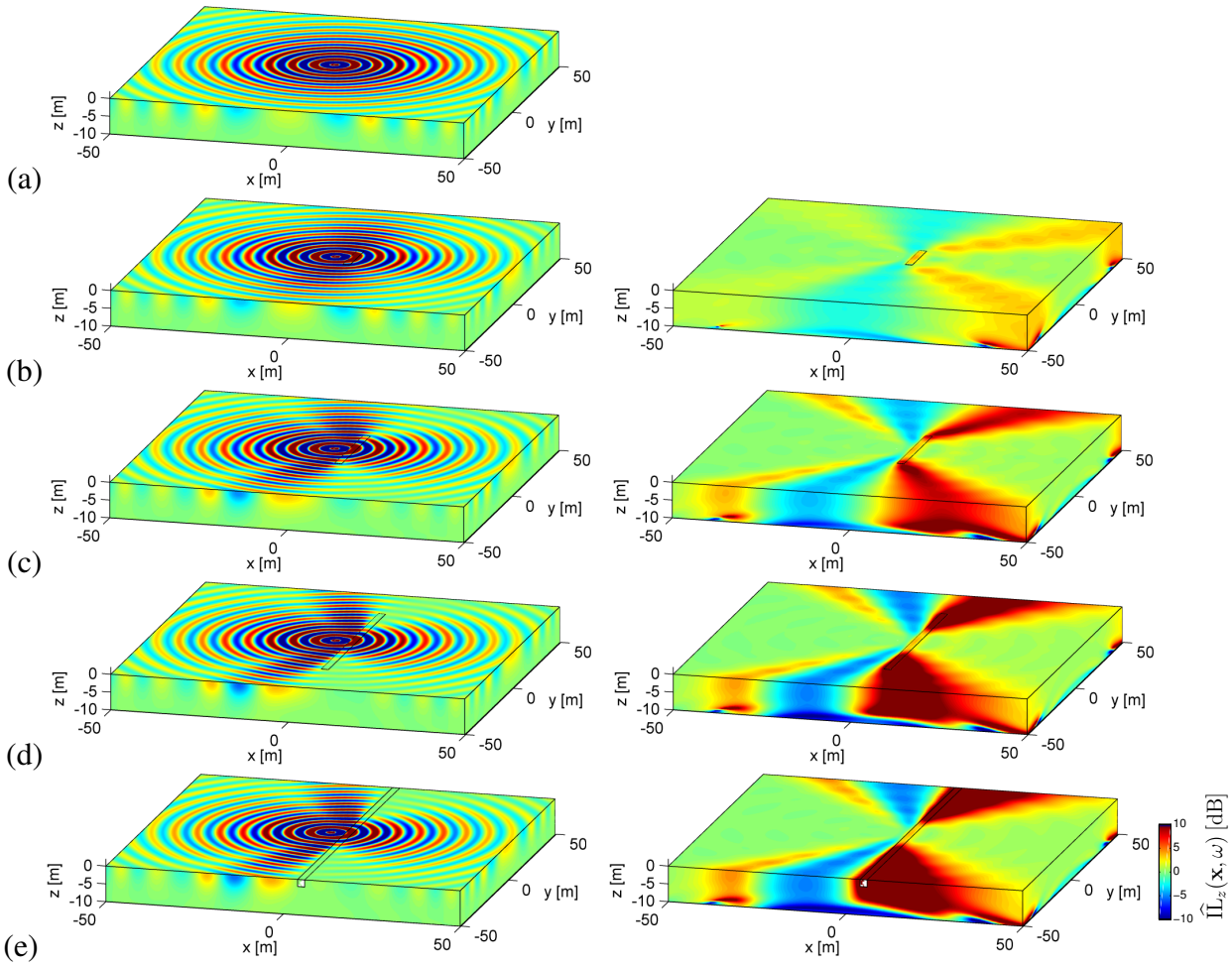


Figure 15: Real part of the vertical displacement $\hat{u}_z(\mathbf{x},\omega)$ due to harmonic excitation at 30 Hz (a) in the reference case and in case a block of stiffened soil is included with a length (b) $L_y = 15\,\mathrm{m}$, (c) $L_y = 30\,\mathrm{m}$, (d) $L_y = 60\,\mathrm{m}$, and (e) $L_y = \infty$ (left hand side). The corresponding insertion loss $\widehat{\mathrm{IL}}_z(\mathbf{x},\omega)$ is shown at the right hand side.

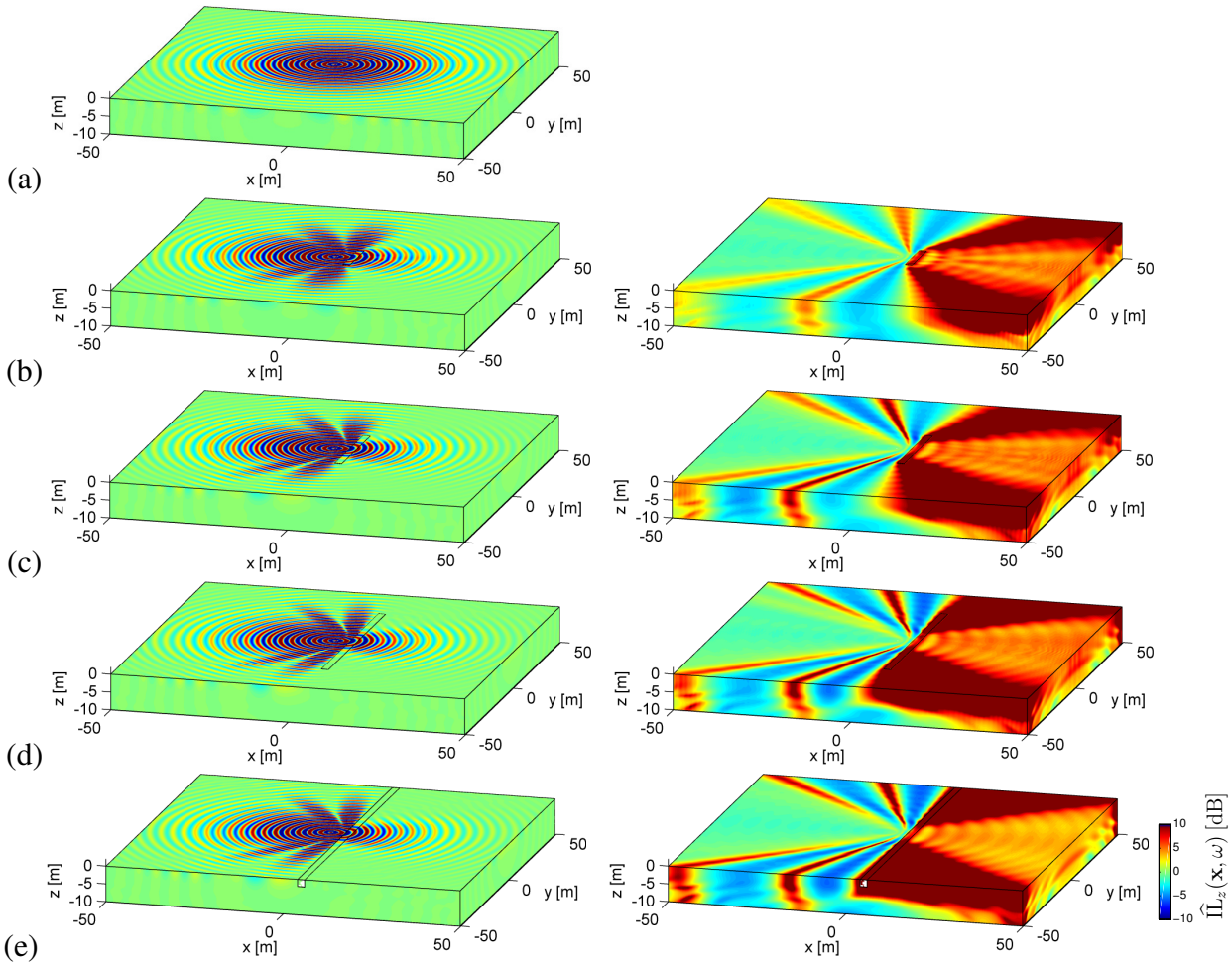


Figure 16: Real part of the vertical displacement $\hat{u}_z(\mathbf{x},\omega)$ due to harmonic excitation at 60 Hz (a) in the reference case and in case a block of stiffened soil is included with a length (b) $L_y = 15\,\mathrm{m}$, (c) $L_y = 30\,\mathrm{m}$, (d) $L_y = 60\,\mathrm{m}$, and (e) $L_y = \infty$ (left hand side). The corresponding insertion loss $\widehat{\mathrm{IL}}_z(\mathbf{x},\omega)$ is shown at the right hand side.

4 CONCLUSIONS

In this paper, the efficiency of subgrade stiffening as a mitigation measure for railway induced vibrations has been investigated. Under the assumption of longitudinal invariance of the geometry, a 2.5D analysis in the frequency–wavenumber domain has clearly illustrated that an infinitely long block of stiffened soil next to the track can act as a wave impeding barrier. The wave impeding effect does, however, critically depend on the relation between the Rayleigh wavelength in the soil and the free bending wavelength in the block of stiffened soil next to the track. This leads to the existence of a critical radial frequency ω_{c} from which this mitigation measure starts to be effective, as well as a critical angle $\theta_{\mathrm{c}}(\omega)$ delimiting the area where the vibration levels are reduced. The expressions for ω_{c} and $\theta_{\mathrm{c}}(\omega)$ have a practical implication, as they allow to assess the expected efficiency of soil stiffening in an early design stage, avoiding an extensive FE–BE calculation. The passage of a train has been investigated as well, revealing that the free field vibration levels can significantly be reduced. It was shown that the number of axle loads of which the contribution to the free field vibration at a certain location is reduced, decreases with the distance from the track and increases with the frequency.

The vibration reduction efficiency in case subgrade stiffening is only implemented along a finite length has finally been assessed through 3D calculations, using a fast BE method based on $\mathscr{H}$–matrices. These calculations indicate that the length of the block should be approximately two times the free bending wavelength of an infinitely long beam in order to ensure that a finite block can act as a wave impeding barrier.

ACKNOWLEDGEMENTS

The results presented in this paper have been obtained within the frame of the EU FP7 project RIVAS (Railway Induced Vibration Abatement Solutions) [9]. The first author is a doctoral fellow and the second author is a postdoctoral fellow of the Research Foundation Flanders (FWO). The financial support is gratefully acknowledged.

REFERENCES

[1] C.J.C. Jones. Use of numerical-models to determine the effectiveness of anti-vibration systems for railways. *Proceedings of the Institution of Civil Engineers-Transport*, 105(1):43–51, 1994.

[2] A.M. Kaynia, C. Madshus, and P. Zackrisson. Ground vibration from high speed trains: prediction and countermeasure. *Journal of Geotechnical and Geoenvironmental Engineering, Proceedings of the ASCE*, 126(6):531–537, 2000.

[3] R. Müller. Mitigation measures for open lines against vibration and ground-borne noise: a Swiss overview. In Burkhard Schulte-Werning, David Thompson, Pierre-Etienne Gautier, Carl Hanson, Brian Hemsworth, James Nelson, Tatsuo Maeda, and Paul de Vos, editors, *Noise and Vibration Mitigation for Rail Transportation Systems*, volume 99 of *Notes on Numerical Fluid Mechanics and Multidisciplinary Design*, pages 264–270. Springer Berlin / Heidelberg, 2008.

[4] R. Hildebrand. Effect of soil stabilization on audible band railway ground vibration. *Soil Dynamics and Earthquake Engineering*, 24:411–424, 2004.

[5] H. Loy. Mitigating vibration using under-sleeper pads. *Railway Gazette International*, 168(4):40–43, 2012.

[6] G. Lombaert, G. Degrande, B. Vanhauwere, B. Vandeborght, and S. François. The control of ground borne vibrations from railway traffic by means of continuous floating slabs. *Journal of Sound and Vibration*, 297(3-5):946–961, 2006.

[7] A. Karlström and A. Boström. Efficiency of trenches along railways for trains moving at sub- or supersonic speeds. *Soil Dynamics and Earthquake Engineering*, 27:625–641, 2007.

[8] J.P. Talbot and H.E.M. Hunt. A generic model for evaluating the performance of base-isolated buildings. *Journal of Low Frequency Noise, Vibration and Active Control*, 22(3):149–160, 2003.

[9] http://www.rivas-project.eu, 2011.

[10] R.D. Woods. Screening of surface waves in soils. *Journal of the Soil Mechanics and Foundation Division, Proceedings of the ASCE*, 94(SM4):951–979, 1968.

[11] K.R. Massarsch. Vibration isolation using gas-filled cushions. In *Proceedings of the Geo-Frontiers 2005 Congress*, Austin, Texas, January 2005. American Society of Civil Engineers.

[12] C.J.C. Jones, D.J. Thompson, and J.I. Andreu-Medina. Initial theoretical study of reducing surface-propagating vibration from trains using earthworks close to the track. In *Proceedings of the 8th International Conference on Structural Dynamics, EURODYN 2011*, pages 684–691, Leuven, Belgium, July 2011.

[13] L. Andersen and S.R.K. Nielsen. Reduction of ground vibration by means of barriers or soil improvement along a railway track. *Soil Dynamics and Earthquake Engineering*, 25:701–716, 2005.

[14] A.T. Peplow and A.M. Kaynia. Prediction and validation of traffic vibration reduction due to cement column stabilization. *Soil Dynamics and Earthquake Engineering*, 27:793–802, 2007.

[15] H.H. Hung, Y.B. Yang, and D.W. Chang. Wave barriers for reduction of train-induced vibrations in soils. *Journal of Geotechnical Engineering, Proceedings of the ASCE*, 130(12):1283–1291, 2004.

[16] X. Sheng, C.J.C. Jones, and D.J. Thompson. Prediction of ground vibration from trains using the wavenumber finite and boundary element methods. *Journal of Sound and Vibration*, 293:575–586, 2006.

[17] V.V. Krylov. Scattering of Rayleigh waves by heavy masses as method of protection against traffic-induced ground vibrations. In H. Takemiya, editor, *Environmental vibrations. Prediction, Monitoring, Mitigation and Evaluation*, pages 393–398. Taylor and Francis Group, London, 2005.

[18] D. Adam, A. Vogel, and A. Zimmermann. Ground improvement techniques beneath existing rail tracks. *Ground Improvement*, 11(4):229–235, 2007.

[19] B.O. Skipp, editor. *Ground dynamics and man made processes*. Thomas Telford, 1998.

[20] P. Coulier, S. François, G. Lombaert, and G. Degrande. A hierarchical boundary element method for elastodynamics based on Green's functions for a horizontally layered halfspace. *Engineering Analysis with Boundary Elements*. Submitted for publication.

[21] J.W.S. Rayleigh. On waves propagated along the plane surface of an elastic solid. *Proceedings of the London Mathematical Society*, 17:4–11, 1887.

[22] G. Lombaert, G. Degrande, J. Kogut, and S. François. The experimental validation of a numerical model for the prediction of railway induced vibrations. *Journal of Sound and Vibration*, 297(3-5):512–535, 2006.

[23] X. Sheng, C.J.C. Jones, and D.J. Thompson. A theoretical model for ground vibration from trains generated by vertical track irregularities. *Journal of Sound and Vibration*, 272(3-5):937–965, 2004.

[24] S. François, M. Schevenels, G. Lombaert, P. Galvín, and G. Degrande. A 2.5D coupled FE-BE methodology for the dynamic interaction between longitudinally invariant structures and a layered halfspace. *Computer Methods in Applied Mechanics and Engineering*, 199(23-24):1536–1548, 2010.

[25] E. Kausel and J.M. Roësset. Stiffness matrices for layered soils. *Bulletin of the Seismological Society of America*, 71(6):1743–1761, 1981.

[26] M. Schevenels, S. François, and G. Degrande. EDT: An ElastoDynamics Toolbox for MATLAB. *Computers & Geosciences*, 35(8):1752–1754, 2009.

[27] P. Hagedorn and A. DasGupta. *Vibrations and Waves in Continuous Mechanical Systems*. John Wiley & Sons, Chichester, United Kingdom, 2007.

[28] L. Cremer, M. Heckl, and B.A.T. Petersson. *Structure-borne sound: Structural vibrations and sound radiation at audio frequencies*. Springer, Berlin, 3rd edition, 2005.

[29] K. Knothe and S.L. Grassie. Modelling of railway track and vehicle/track interaction at high frequencies. *Vehicle Systems Dynamics*, 22: 209–262, 1993.

[30] V.K. Garg and R.V. Dukkipati. *Dynamics of railway vehicle systems*. Academic Press, Canada, 1984.

[31] H. Verbraken, G. Lombaert, and G. Degrande. Verification of an empirical prediction method for railway induced vibrations by means of numerical simulations. *Journal of Sound and Vibration*, 330(8):1692–1703, 2011.

[32] International Organization for Standardization. *ISO 2631-2:1989: Evaluation of human body exposure to whole-body vibration - Part 2: Continuous and shock-induced vibration in buildings (1 to 80 Hz)*, 1989.

[33] P. Coulier, S. François, G. Degrande, and G. Lombaert. Subgrade stiffening next to the track as a wave impeding barrier for railway induced vibrations. *Soil Dynamics and Earthquake Engineering*, 48:119–131, 2013.

[34] S. Ahmad and T.M. Al-Hussaini. Simplified design for vibration screening by open and in-filled trenches. *Journal of Geotechnical Engineering, Proceedings of the ASCE*, 117(1): 67–88, 1991.

[35] R.K. Shrivastava and N.S.V. Kameswara Rao. Response of soil media due to impulse loads and isolation using trenches. *Soil Dynamics and Earthquake Engineering*, 22(6): 695–702, 2002.

[36] S. François, M. Schevenels, B. Thyssen, J. Borgions, and G. Degrande. Design and efficiency of a vibration isolating screen in the soil. *Soil Dynamics and Earthquake Engineering*, 39:113–127, 2012.

[37] L. Grasedyck and W. Hackbusch. Construction and arithmetics of $\mathscr{H}$-matrices. *Computing*, 70:295–334, 2003.

[38] S. Rjasanow and O. Steinbach. *The Fast Solution of Boundary Integral Equations (Mathematical and Analytical Techniques with Applications to Engineering)*. Springer-Verlag New York, 2007.

[39] M. Bebendorf and S. Rjasanow. Adaptive low–rank approximation of collocation matrices. *Computing*, 70:1–24, 2003.

[40] W. Hackbusch. A sparse matrix arithmetic based on $\mathscr{H}$-matrices. Part I: Introduction to $\mathscr{H}$-matrices. *Computing*, 62(2):89–108, 1999.

[41] M. Bebendorf. *Hierarchical Matrices: A Means to Efficiently Solve Elliptic Boundary Value Problems*. Springer Publishing Company, 1st edition, 2008.

[42] P. Coulier, S. François, G. Lombaert, and G. Degrande. A coupled finite element – hierarchical boundary element method based on Green's functions for a horizontally layered halfspace. In N. Heuer and C. Jerez-Hanckes, editors, *Proceedings of the Symposium of the International Association for Boundary Element Methods IABEM 2013*, pages 23–30, Santiago, Chile, January 2013. CD-ROM.

COMPDYN 2013
4th ECCOMAS Thematic Conference on
Computational Methods in Structural Dynamics and Earthquake Engineering
M. Papadrakakis, V. Papadopoulos, V. Plevris (eds.)
Kos Island, Greece, 12–14 June 2013

A COMPREHENSIVE METHODOLOGY FOR THE EVALUATION OF INFRASTRUCTURE INTERDEPENDENCIES

D. Solari[1], **G.P. Cimellaro**[1]

[1] Department of Structural, Building and Geotechnical Engineering, (DISEG)
Politecnico di Torino
Corso Duca degli Abruzzi 24, 10129, Turin, Italy

gianpaolo.cimellaro@polito.it

Keywords: Lifeline interdependencies, Natural disasters, Community resilience.

Abstract. *Nowadays infrastructure networks are the basis of life and economy of every community, large or small. These infrastructures have always a certain degree of interdependency among them. This means that when the community is subjected to a shock (earthquake, terrorism, hurricanes, floods, etc.) it is more vulnerable when the degree of interdependency among infrastructures is higher. In this article, after defining a reference nomenclature based on the analysis of the literature in the field and after identifying a total of sixteen type of infrastructures that compose each community: seven core infrastructures (Electricity, Oil delivery, Transportation, Telecommunication, Natural Gas delivery, Water supply, Wastewater treatment) and nine no-core infrastructures (Financial system, Building services, Business, Emergency services, Food supply, Government, Health care, Education, Commodities), we propose a method of analysis of the degree of interdependency among the various members of the community infrastructure. Using a matrix approach, an index is evaluated that takes into account the effect that any infrastructure can induce on another subordinated to it. This index depends on the type of failure that an infrastructure may cause to another one (coupled and uncoupled) and on the number of systems affected. From the matrix display is then possible understanding what are the most important infrastructures for the community and then focus all the efforts to reduce wherever possible the degree of interdependency and/or restore them as quickly as possible in the case of a partial or total disruption.*

1 INTRODUCTION

In literature there are many definitions about the interdependencies that exist among the lifelines of a community. According to President's Commission on Critical Infrastructure Protection (PCCIP) 1997 [1], the *infrastructure* "is a network of interdependent, mostly privately-owned, manmade systems and processes that function collaboratively and synergistically to produce and distribute a continuous flow of essential goods and services". *Infrastructure* is also defined as the framework of interdependent networks and systems comprising identifiable industries, institutions (including people and procedures), and distribution capabilities that provide a reliable flow of products and services essential to the defense and economic security, the smooth functioning of governments at all levels, and society as a whole (The Clinton Administration's Policy on Critical Infrastructure Protection: Presidential Decision Directive 63)[2].

In the fundamental work of Rinaldi et al.[3], *dependency* is defined as a linkage or connection between two infrastructures, through which the state of one infrastructure influences or is correlated to the state of the other (unidirectional relationship). A distinction of dependencies is also made for different periods in respect to the occurrence of the perturbation (normal operating conditions, which can vary from peak to off-peak conditions, times of severe stress or disruption, or times when repair and restoration activities are under way), as well as between supported and supporting infrastructures. *Interdependency* is defined as a bidirectional relationship between two infrastructures through which the state of each infrastructure influences or is correlated to the state of the other. In other words, two infrastructures are interdependent when each is dependent on the other, and interdependencies are connections among components in different infrastructures in a general system of systems. Consequently, the risk of failure or deviation from normal operating conditions in one infrastructure can be a function of risk in a second infrastructure if the two are interdependent [4]. The knowledge of the degree of interdependency is necessary to plan a resilient community.

The resilience of a community is a very important parameter. Increasing the resilience of systems is fundamental to ensure the sustainability condition for a community over time. For Mileti [6] "disaster resilient community is a community that can withstand an extreme event, natural or man-made event, with a tolerable level of losses and can take mitigation action consistent with achieving that level of protection". Into 2005 the Multidisciplinary Center for Earthquake Engineering Research (MCEER) provides a comprehensive definition that is particularly useful for assessing resilience of infrastructure systems [7]. Community resilience to hazards is defined as the ability of social units (organizations, communities) to mitigate hazards, contain the effects of hazard-related disasters when they occur, and carry out recovery activities in ways that minimize social disruption and mitigate the effects of future hazards. The objectives of enhancing disaster resilience are to minimize loss of life, injuries, and economic impacts in short, to minimize any reduction in quality of life due to these hazards. According to Bruneau et al. [7], resilience has been defined as the ability of a system to reduce the chances of a shock, to absorb such a shock if it occurs and to recover quickly after a shock. Resilience of a lifeline can be conceptualized with four dimensions: *Robustness* which is the inherent strength or resistance in a system to withstand external demands without degradation or loss of functionality; *Redundancy* that is the system properties that allow for alternate options, choices, and substitutions under stress; *Resourcefulness* which is the capacity to mobilize needed resources and services in emergencies; *Rapidity* that is the speed with which disruption can be overcome and safety, services, and financial stability restored. In Cimellaro et al. [8][9][10] resilience is defined as a normalized function indicating capability to sustain a level of functionality or performance for a given building, bridge, lifeline, networks or com-

munity over a period of time T_{LC} (life cycle, life span etc. etc) including the recovery period after damage in an extreme event. The time T_{LC} includes the building recovery time T_{RE} and the business interruption time that is usually smaller compared to the other one. Resilience can be achieved by enhancing the ability of a community's infrastructure, (lifelines and structures), to perform during and after a hazard, as well as through emergency response and strategies that effectively cope with and contain losses and recovery strategies that enable communities to return to levels of pre-disaster functioning (or other acceptable levels) as rapidly as possible [11]. In October 2009, the National Infrastructure Advisory Council [12] defines Infrastructure resilience as "the ability to reduce the magnitude and/or duration of disruptive events. The effectiveness of a resilient infrastructure or enterprise depends upon its ability to anticipate, absorb, adapt to, and/or rapidly recover from a potentially disruptive event." The NIAC establish resilience as a fundamental concept for sustaining and enhancing infrastructure capability. According to this study, resilience is one of three core concepts within this framework to provide a comprehensive approach to homeland security. Resilience helps to mitigate risk to communities, enhance recovery capabilities, and ensure continuity of essential services and functions. This study also established two core resilience objectives: *Broad-based resilience* which is the "improve capabilities of families, communities, private-sector organizations, and all levels of government to sustain essential services and functions", and *Infrastructure resilience* which "increases the ability of critical infrastructure systems, networks, and functions to withstand and rapidly recover from damage and disruption and adapt to changing conditions".

In this paper, a reference nomenclature based on the analysis of the literature in this field (definition of community, infrastructure, systems, subsystems, units and parts) is proposed. Sixteen types of infrastructures which compose each community are identified: seven core infrastructures (Electricity, Oil delivery, Transportation, Telecommunication, Natural Gas delivery, Water supply, Wastewater treatment) and nine no-core infrastructures (Financial system, Building services, Business, Emergency services, Food supply, Government, Health care, Education, Commodities). Finally a method for the analysis of the degree of interdependency among the infrastructures (lifelines) of a community is proposed.

2 INTERDEPENDENCY

Many authors have tried to clarify the taxonomy in this branch of scientific research [4], but nowadays a unique nomenclature, when it talks about interdependency within a community, does not exist. In this paper, for clearness, will be used the following definitions, as shown in Figure 1:

Community: All of the social and physical infrastructures (or lifelines) which contribute and help to the normal daily life of an organized group of people who live in a given area. (i.e. a nation like Italy).

Infrastructure (lifeline): The set of all the systems that contribute to the creation and operation of a physical or social network within a community. (i.e. national power delivery).

System: A set of sub-systems placed together with a specific order and a specific behavior. (i.e. wind power plant).

Sub-system: A combinations of units which create a machinery or equipment or procedure that have defined and specific characteristics and properties (i.e. wind turbine).

Unit: The set of all components (or parts) assembled with a certain order. A unit is an object or a procedure that, by itself, does not have a unique goal (i.e. the gearbox of the wind turbine).

Part: Is the fundamental element with which you can build a unit (i.e. the ball bearing of the gearbox of the wind turbine).

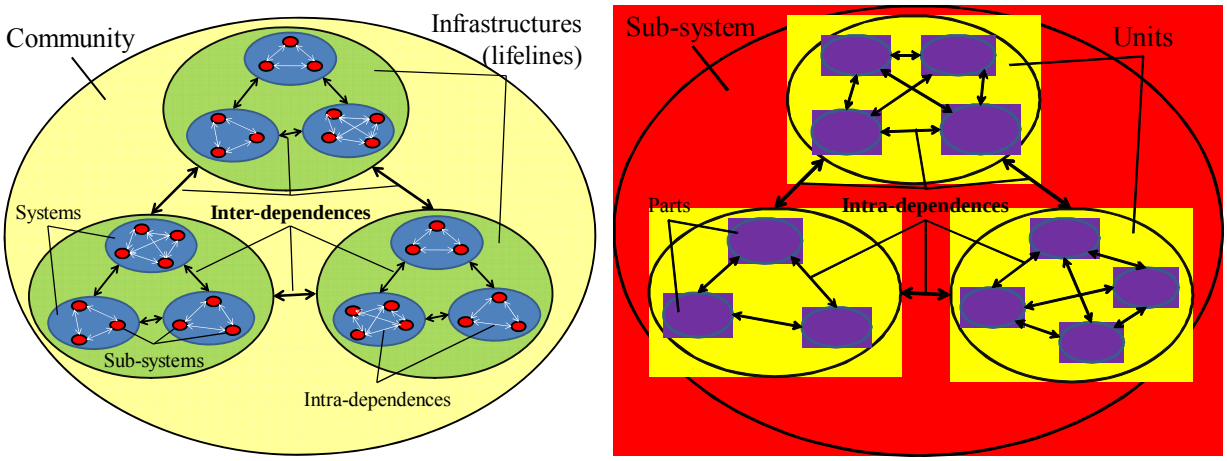


Figure 1. Taxonomy used in this paper.

Also the relationships between the various elements that make up a community does not have a unique definition. In this paper, as shown in Figure 1, is proposed and it is uses the following nomenclature for these internal relationships:

Interdependencies: Bidirectional relationship between the different infrastructures (lifelines) that make up a community and between the different systems that compose an infrastructure (lifeline).
Intradependencies: Bidirectional relationship between the different sub-systems that compose a system, between the different units that make up a sub-system and between the different parts that compose up a unit.

Starting from the literature review proposed by Kongar and Rossetto [13], it has been divided a typical community into sixteen infrastructures (lifelines), which are: *Electricity (Power delivery), Oil delivery, Transportation, Telecommunication, Natural Gas delivery, Water supply, Wastewater treatment, Financial system, Building services, Business, Emergency services, Food supply, Government, Health care, Education, Commodities*. For Kongar and Rossetto [13] there is a core group of infrastructure that are widely recognized as being lifelines: power delivery, telecommunications, transportation, water supply, wastewater treatment, oil delivery and natural gas delivery. The common factor amongst these infrastructure is that although there is some human interfacing to support their operation, they are largely physical systems. In this paper, according to Kongar and Rossetto [13], it has been divided the sixteen infrastructures (lifelines) into two main groups: the *core lifelines* (Electricity, Oil delivery, Transportation, Telecommunication, Natural Gas delivery, Water supply, Wastewater treatment) and the *no-core lifelines* (Financial system, Building services, Business, Emergency services, Food supply, Government, Health care, Education, Commodities).

3 RESILIENCE

Resilience is defined as a normalized function indicating capability to sustain a level of functionality or performance for a given building, bridge, lifeline, networks or community

over a period of time T_{LC} (life cycle, life span etc. etc) including the recovery period after damage in an extreme event [8]. In this thesis the resilience of a community will be calculated starting from the restoration curves (or curves of functionality) of lifelines of the community damaged by a natural disaster.

4 TYPE AND EFFECT OF INTERDEPENDENCY

Nowadays there is not a clear classification about the type of interdependencies between infrastructures. Many authors over the years have tried to give their contribution to this problem. Rinaldi et al. [3] and Peerenboom et al. [14] describes four general categories of infrastructure interdependencies: *Physical, Cyber, Geographic* and *Logical interdependency*. For Pederson et al. [15] there are six general categories of infrastructure interdependencies: *Physical, Cyber, Geographic, Logical, Policy/Procedural* and *Societal interdependency*. In the article of Zhang and Peeta [17] the classification of interdependencies among the infrastructure systems is as follows: *Functional*, *Physical*, *Budgetary*, and *Market and Economic interdependency*.

In this paper, as shown in Figure 2, it has chosen the following classification, identifying seven different types of interdependencies [4]:

Physical interdependency: a physical reliance on material flow from one infrastructure to another. Physical dependencies include the reliance on road and rail networks to move crews and equipment.

Cyber interdependency: a reliance on information transfer between infrastructures. Cyber dependencies include the reliance on telecommunications for supervisory control and data acquisition (SCADA) systems and information technology for ecommerce and business systems.

Geographical interdependency: a local environmental event affects components across multiple infrastructures due to physical proximity. Geographical dependencies include, for example, common corridors that natural gas pipelines share with electric power lines and/or telecommunications lines.

Policy/Procedural: An interdependency that exists due to policy or procedure that relates a state or event change in one infrastructure sector component to a subsequent effect on another component. Note that the impact of this event may still exist given the recovery of an asset.

Societal interdependency: The interdependencies or influences that an infrastructure component event may have on societal factors such as public opinion, public confidence, fear, and cultural issues. Even if no physical linkage or relationship exists, consequences from events in one infrastructure may impact other infrastructures. This influence may also be time sensitive and decay over time from the original event grows.

Budgetary interdependency. “Many infrastructure systems involve some level of public financing, especially under a centrally-controlled economy or during disaster recovery, leading to resource allocation budget interdependencies.”

Market & Economy interdependency. “Shared market resources imply that all systems are interacting sectors in the same economic system. Another manifestation of this interdependency is that these infrastructure systems serve the same end users who determine the final demand for each commodity/service subject to budget constraints. Further interdependencies

exist due to the shared regulatory environment where the government agencies may control and impact the individual systems through policy, legislation or financial means such as taxation or investment. An example is how fuel prices can affect both the supply and demand sides of transportation, which in turn can affect the supply and demand for fuel."

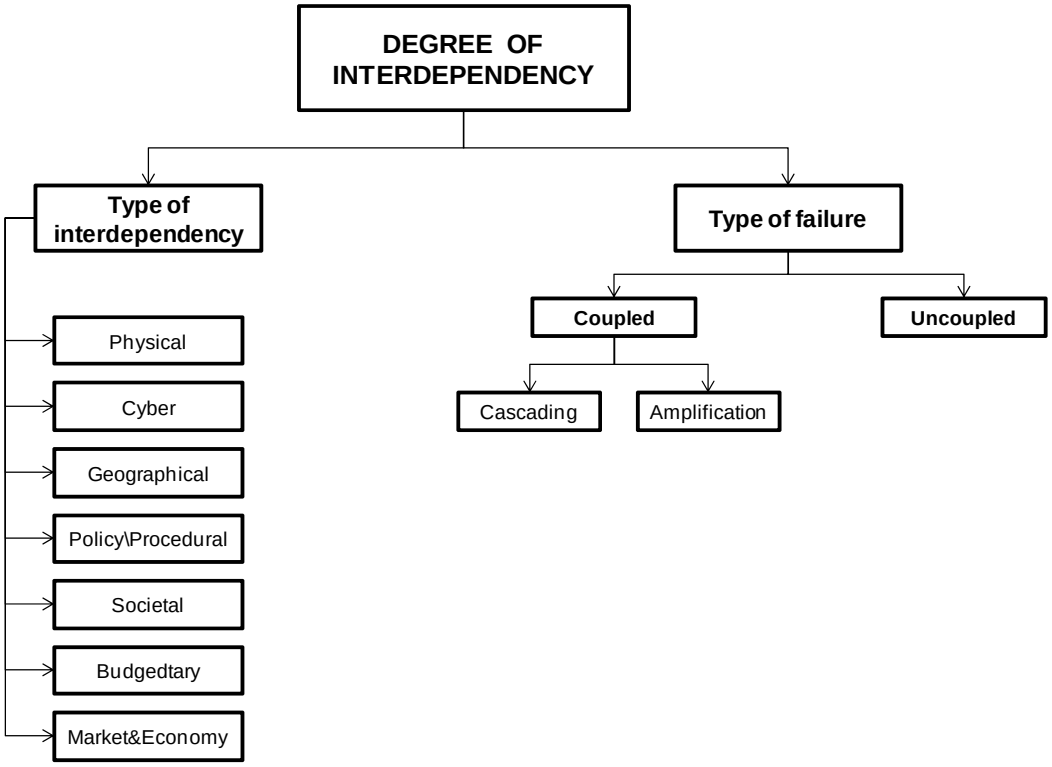


Figure 2. Interdependency index: dependencies on type of interdependency and on type of failure.

In addition to the type of interdependency is useful to understand which is the type of failure that undergoes a lifeline. As shown in Figure 2, the type of failure is classified as follows:

Coupled failure: A drop of functionality of an infrastructure, due to a single perturbation (damaging event) on the community, causes the fall of functionality in at least one other lifeline. If this drop of functionality takes place at the same time for both lifelines, this failure is called *Cascading failure* (Figure 3), while if this drop of functionality takes place in this two lifelines (at least) with a certain time-delay, this failure is called *Amplification failure* (Figure 4)

Uncoupled failure: A drop of functionality of one infrastructure, due to a single perturbation (damaging event) on the community, do not cause any failure in other infrastructures. There is no propagation of failure among infrastructures (Figure 5).

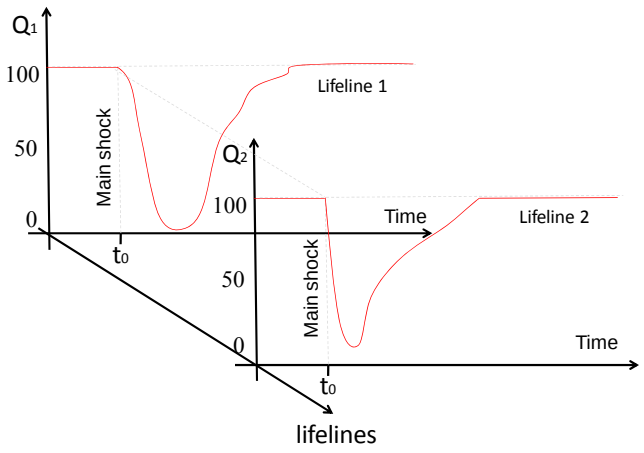


Figure 3. *Coupled failure*: example of *Cascading failure*

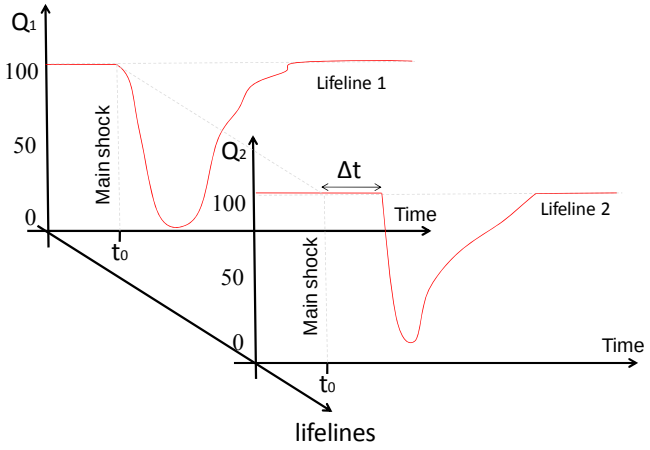


Figure 4. *Coupled failure*: example of *Amplification failure.* The failure in the second lifeline occurs with a time-delay Δt.

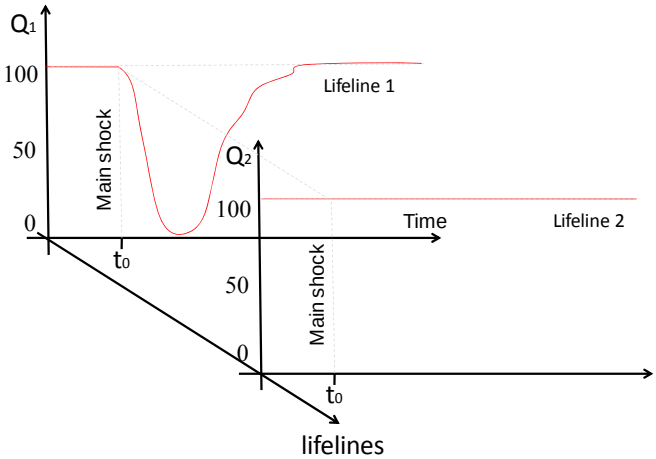


Figure 5. Example of *Uncoupled failure*.

The degree of interdependency is a function, as well as the *type of interdependence* and the *type of failure*, also of the *importance factor* of each lifeline's system (which depends on the degree of interconnection and the degree of importance that has the system with respect to the other lifelines in the community). If the *importance factor* is wide [small], the degree of interdependency must be high [low]. This classification has been carried out so that the degree of interdependency results hazard-uncorrelated and damage-uncorrelated, so that it can be used as a basis for any kind of scenario arising from any damaging event (earthquake, hurricane, flood, fire, tsunami, Electromagnetic pulse attack (EMP), etc.).

5 FRAMEWORK FOR THE EVALUATION OF THE DEGREE OF INTERDEPENDENCY AMONG LIFELINES

For the evaluation of the degree of interdependency, it is necessary to calculate, at first, the degree of dependence which has the first lifeline on the second and the degree of dependence which has the second lifeline on the first. To do this, it is necessary to analyze the dependencies at systems level, subdividing each lifeline in systems and assigning a value of dependence of each system of the lifeline under consideration, on all the sixteen lifelines that make up the community [5]. The degree of dependency of each system of a lifeline with respect to another lifeline can be evaluated using the procedure proposed below. This procedure is a framework useful to focus on the interdependencies that are presents in a community, analyzing it at the level of systems.

- Divide each lifeline in systems, according to the definition of *system* given previously (Figure 1).
- Divide the systems into seven groups correspondents on the seven types of interdependency as defined in Figure 2 (*Physical, Cyber, Geographic, Policy/Procedural*, *Societal, Budgetary*, *Market & Economy interdependency).*
- For each system and for each group defined at the point above, is assigned a degree of interdependency with respect to the sixteen lifelines of the community. This degree of interdependency is a function of two values assigned at every system of the lifeline. The first value is assigned as a function of the type of failure (*Cascading, Amplification, Uncoupled*); the second value is assigned as a function of the *importance factor* that has each lifeline's system.
- The values obtained at the end of the third point are combined into a single value which is the degree of interdependency among the two lifelines under examination. The result is one degree of interdependency for each group defined in the second point of this procedure (seven values for each pair of lifelines). So, finally there are seven matrices of the degree of interdependency, one for each type of interdependency.
- The seven matrices obtained at point 4 are assembled together using different weight coefficients for different types of interdependency (Figure 6) [15]. Further studies will be able to address the problem of the determination of the weight coefficients to be assigned at each type of interdependency.

The matrix thus obtained is the interdependency index matrix of lifelines (S) which is a 16x16 matrix in which each row and each column represents a lifeline. The values are arranged such that the interdependence value *S* at row i and column j ($S_{i,j}$) is the value of interdependence of the lifeline on the column j with respect to the lifeline on the row i. By placing the interdependencies in this way, it can find additional information from the matrix just been built; according to Paton and Johnston [18], adding the data per row in the matrix $S_{i,j}$ it can

obtain a number that indicates the level of leadership (*Leadership index* in Figure 6) that the lifeline of that row has respect to the other fifteen lifelines of the community; adding the data per column in the matrix $S_{i,j}$ it can obtain a number that indicates the level of subordination (*Subordination index* in Figure 6) that the lifeline of that column has respect to the other fifteen lifelines of the community.

	can affects ↓ in this points:															
the ↓	Electricity	Oil delivery	Transportation	Telecomunication	Natural Gas delivery	Water supply	Wastewater tratment	Financial system	Building services	Business	Emergency services	Food supply	Government	Health care	Education	Commodities	Leadership index
Electricity	1	1	0,6	1	1	0,6	0,6	0,6	0,6	1	0,6	1	1	0,6	0,3	0,6	12,1
Oil delivery	0,6	1	0,6	0,3	0,3	0,3	0,3	0,6	0,6	0,6	0,6	0,6	0,6			0,6	7,6
Transportation	0,3	0,6	1		0,6			0,6	0,6	1	1	1	0,6	0,6	0,3	1	9,2
Telecomunication	0,3	0,3	0,3	1	0,3	0,3	0,3	1		1	1	0,6	1	0,3		0,3	8
Natural Gas delivery	0,6		0,3		1			0,6	0,3	0,6	0,6	0,6	0,6	0,3	0,3	0,3	6,1
Water supply	0,6	0,3		0,3	0,3	1		0,3	1	0,6	0,6	1	0,6	0,6	0,6	0,6	8,4
Wastewater tratment		0,3			0,3	0,6	1		0,3	0,6	0,3	0,3	0,3	0,6		0,3	4,9
Financial system	0,3	0,3	0,6	0,3	0,3	0,3	0,3	1	0,6	1	0,3	0,6	1	0,3		1	8,2
Building services	0,3	0,3	0,6	0,3	0,3	0,3	0,3	0,6	1	0,6	0,6		0,3			0,6	6,1
Business	0,3	0,6	1	0,6	0,6	0,3	0,3	1	0,6	1		0,6	1			1	8,9
Emergency services	0,6	0,6	0,6	0,6	0,6	0,6		1	0,3	1	1	1	1	1	0,6		10,5
Food supply	0,3	0,3	0,6		0,3	1	0,3	1	0,3	1	0,6	1	1	0,6	0,6	0,3	9,2
Government	0,6	0,6	0,6	0,6	0,6	0,6	0,6	1	0,6	1	1	1	1	1	1	0,6	12,4
Health care			0,3					0,3	0,3	0,3	1	0,6	1	1	0,3	0,3	5,4
Education	0,3	0,3	0,3	0,3	0,3	0,3	0,3	1	0,3	0,6	1	0,3	1	0,6	1	0,3	8,2
Commodities	0,3	0,3	1	0,3	0,3	0,3	0,3	1	0,6	1	0,3	0,3	1	0,3		1	8,3
Index of subordination (dependence)	6,4	6,8	8,4	5,6	7,1	6,5	4,6	11,6	8,0	12,9	10,5	10,5	13,0	7,8	5,0	8,8	

Figure 6. Community interdependency matrix. In yellow are highlighted the core lifelines interdependency matrix

The lifeline that has the highest value of *Leadership index* is the one on which pay the greatest attention, because if its functionality falls, the functionality of the community decreases dramatically. To increase the resilience of the community, this lifeline must have the lowest vulnerability to any kind of hazard. Available resources must be concentrated for the improvement of this lifeline or for the reduction of the degree of dependence of other lifelines of the one in question, (for example using redundant networks, accumulators, etc..). The lifeline that has the highest value of *Subordination index* is the one that has the greatest dependence on other lifelines within the community. If the community suffers damage, this lifeline is the first that suffer the effects of propagation of the damage due to the interdependencies, even if, at first, it does not suffer damages. To increase the resilience of the community, available resources must be concentrated for the improvement of this lifeline. This improvement must be a reduction of the dependencies of this lifeline on the others (for example using redundant networks, accumulators, etc.). Every effort must be aimed to achieve that the interdependencies between lifelines of the community are the lowest possible. To do this it defines three situations, in which the community can be found, using the matrix of interdependency index $S_{i,j}$ previously defined. Is defined as (Figure 7):

Very vulnerable community (VVC) the community in which the matrix of interdependency (S) is a matrix in which every values is equal to 1.

Ideal community (IC) the community in which the matrix of interdependency (*S*) is a matrix in which the values on the diagonal are 1, while the other values are 0. In this community there is only self-dependence, while the interdependence between the different lifelines disappears.

Typical community (TC) all of the others situations between VVC and IC.

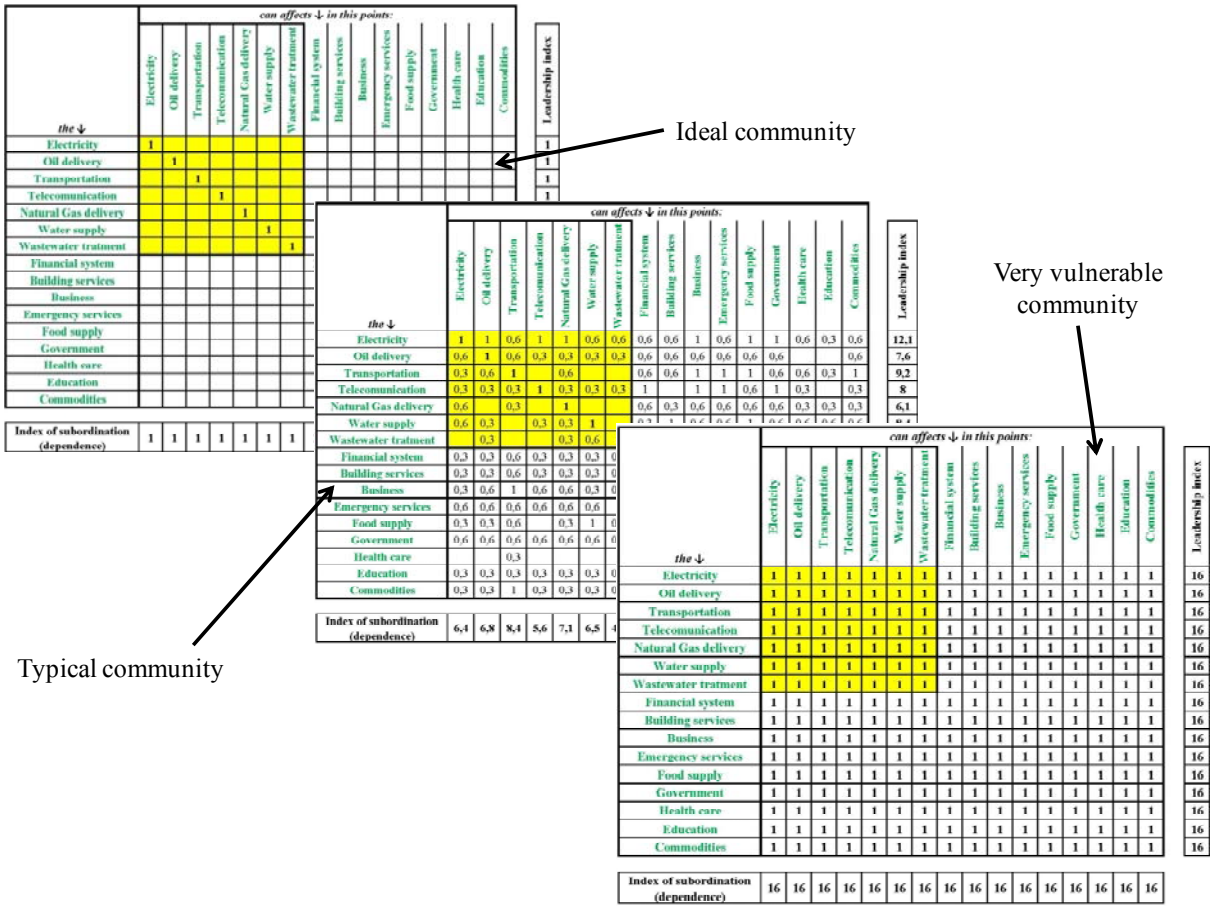


Figure 7. Infrastructures interdependencies matrix. In yellow are highlighted the core lifelines interdependency matrix

If it is necessary, the evaluation of the interdependency can be more detailed with the decomposition of the systems that make up a lifeline, into different sub-systems. The interdependency index matrix can be evaluate with the same procedure shown previously, but now the result is the interdependency index matrix of the systems of two specific lifelines. In Figure 8 is shown how a single value into the interdependency index matrix of the community can be exploded into a matrix of interdependency among two specific lifelines, thus reaching a higher level of detail . This type of analysis is much more expensive, both in terms of time and in terms of cost but it can be more realistic, because going into detail, it is easier to find the interdependencies and it is also possible to compute in a more realistic way. The level of detail for the calculation of the interdependency index matrix can be chosen based on the

knowledge that one can about the community and its lifelines, systems, sub-system, units and parts.

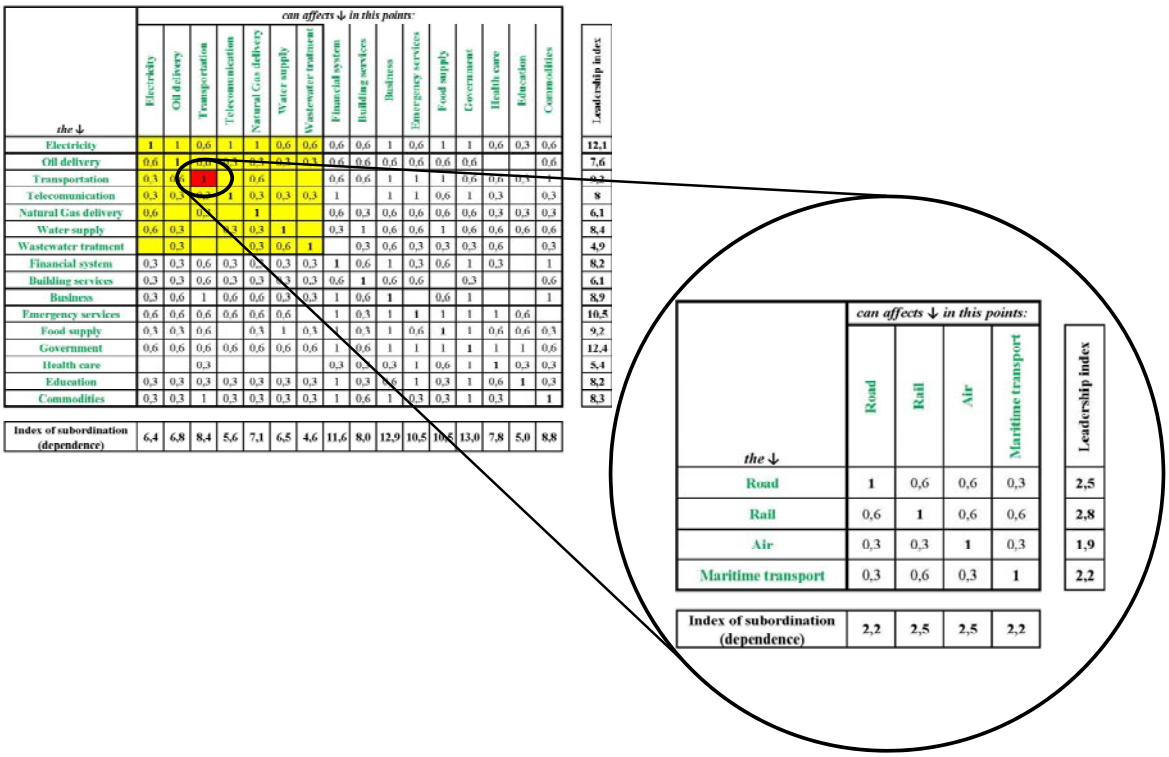


Figure 8. Interdependency matrix of systems. In yellow are highlighted the core lifelines interdependency matrix.

Each number into the interdependency index matrix can change over time. These variations can be positive or negative and, often, may be due to the normal management of the community; some of these reasons are listed below:

- Improving of the lifelines functionality (positive variation)
- Reduction of lifelines vulnerability (positive variation)
- Creation of a certain redundancy degree among lifelines (positive variation)
- Creation of stocks and emergency systems (positive variation)
- Aging (negative variation)
- Negative human intervention on the lifeline (negative variation)
- etc.

Positive [negative] variation is referred to an improving [worsening] of the global response of the community, reducing [increasing] the degree of interdependency for at least one lifeline.

The degree of interdependency can change through the time when human interventions are performed or because of aging effects, but they are not dependent on the magnitude or type of disaster faced. If the magnitude of an extreme event increases only the "effects" of interdependency increase, but the degree of interdependency which is a property of the community remains the same.

6 A CASE STUDY: FUKUSHIMA DAIICHI NUCLEAR POWER PLANT DISASTER

Fukushima Daiichi (Daiichi means "first"), was a multi-reactor nuclear power plant in the prefecture of Fukushima of Japan (Figure 9a). The Fukushima I Nuclear Power Plant consists of six, boiling water reactors (BWR, Figure 12) designed by General Electric driving electrical generators with a combined power of 4700 MW, making Fukushima I one of the 25 largest nuclear power stations in the world.



(a)



(b)

Figure 9. Fukushima Daiichi Nuclear Power Plant before (a) and after (b) the disaster

When the earthquake occurred on March 11th, 2011, the reactors on Units 1, 2, and 3 were operating, but those on Units 4, 5, and 6 had already been shut down for periodic inspection. Units 1, 2 and 3 underwent an automatic shutdown, called "SCRAM", when the earthquake struck. When the reactors are shutdown, the plant does not to generate electricity anymore. TEPCO reported that one of the two connections to off-site power for reactors 3 also failed so 13 on-site emergency diesel generators began to powered the plant's cooling and control systems.

The earthquake was followed by a tsunami with waves between (13÷15)m maximum height which arrived arriving approximately 50 minutes after the earthquake. The waves topped the 5.70m plant's seawall, flood the basement of the turbine buildings and disabled the emergency diesel generators located there at approximately 15:41 local time. At this point, TEPCO notified authorities, as required by law, of a "First level emergency".

The Fukushima Daini plant (Daini means “second”), which was also struck by the tsunami, incorporated design changes which improved its resistance to flooding and it sustained less damage. Generators and related electrical distribution equipment were located in the water-tight reactor building, so that power from the grid was used by midnight. Seawater pumps for cooling were protected from flooding, and although 3 of 4 failed in the tsunami, they were able to be restored in service. Furthermore they were three additional backup generators for Unit 2 and 4 that were placed in new buildings located on the hillside.

All six reactors were connected to these generators, but the switching stations that sent power from these backup generators to the reactors' cooling systems for Units 1 through 5 were still in the poorly protected turbine buildings. The three generators on the hillside were operational after the tsunami. If the switching stations had been moved to inside the reactor buildings or to other flood-proof locations, power would have been provided by these generators to the reactors' cooling systems. After the diesel generators located in the turbine buildings failed, emergency power for control systems was supplied by batteries that were designed to last about eight hours. Further batteries and mobile generators were dispatched to the site, delayed by poor road conditions, therefore the first did not arrived at the site until 21:00 JST of March 11th , almost six hours after the tsunami struck. The attempts to connect the mobile generators to the water pumps were eventually interrupted after numerous attempts, as the connection point in the Turbine Hall basement was flooded and because of difficulties in finding suitable cables. Below is reported the time schedule of the events that arise after the main shock (until five days after the event). The time is given in Japan Standard Time (JST) which is UTC plus nine hours:

2011, March 11th

- 14:46: A 9.0 magnitude earthquake strikes off the coast of Honshu Island at a depth of about 24 kilometers. The Fukushima I power plant's nuclear reactors 1, 2, and 3 are automatically shut down by the vibrations. Nuclear reactors 4, 5, and 6 were undergoing routine maintenance and were not operating, (reactor 4 was defueled in November 2010). The vibration has the additional effect of causing the power plant to be cut off from the Japanese electricity grid, however, backup diesel generators activated to continue cooling the reactors. Tokyo Electric Power Company (TEPCO), the plant's operator, finds that units 1 and 2 are not operating correctly and notifies the proper officials.
- 14:52: Emergency cooling system of reactor 1, which is capable of running without external power, turns on automatically.
- 15:03: Emergency cooling system of reactor 1 is manually shut down.
- 15:27: The first tsunami strikes the plant (Figure 10).



(a)



(b)

Figure 10. The first tsunami strikes the seawalls (a). Flooding of the plant (b) the tsunami had a height of about 14 meters

- 15:30: The emergency condenser designed to cool the steam inside the pressure vessel of the reactor 1 fails.
- 15:46: A 14 meters tsunami, unleashed by the earthquake, overtops the seawall designed to protect the plant from a tsunami of 5.7 meters, inundating the Fukushima facility and disabling the backup diesel generators (all but one of which were housed underground) and washing away their fuel tanks. With the loss of all electrical power supply, the low-pressure core spray, the residual heat removal and low-pressure coolant injection system main pumps, and the automatic depressurization systems all failed (most of the emergency core cooling system). Only the steam-powered pump systems (isolation condenser in reactor 1, high-pressure coolant injection and reactor core isolation cooling system in reactors 2 and 3 remained available. Later, as the temperature rose, a system started that used steam-powered pumps and battery-powered valves.

- 16:00: The Nuclear and Industrial Safety Agency of Japan (NISA) initiates an emergency headquarters in an attempt to gather information on the 55 nuclear reactors in Japan. There is no report that radiation was detected outside power-plant borders.
- 18:00: The falling water level in reactor 1 reaches the top of the fuel, and the core temperature starts climbing.
- 18:18: Emergency cooling system of reactor 1 is once again back on.
- 19:03: Prime Minister Naoto Kan declares a nuclear emergency status announced by Yukio Edano, Chief Cabinet officer in Japan. Japanese government officials try to comfort the people of Japan by telling them that the proper procedures are being undertaken. They also announce that no radioactive leaks have been detected.
- 19:30: The fuel in reactor 1 becomes fully exposed above the water surface, and fuel damage in the central core begins soon after.
- 21:00: An evacuation order is issued by the government to persons within a radius of 3 kilometers from the Fukushima I station. Those within a radius of 10 kilometers are told that they can remain in their homes, and carry on with regular activities, until told otherwise. TEPCO announces that the pressure inside reactor unit 1 of Fukushima I is more than twice normal levels.

2011, March 12th

- 02:44: Emergency battery power for the high pressure core-flooder system (HPCFS) for reactor 3 runs out.
- 04:15: Fuel rods in reactor 3 are exposed.
- 05:30: Despite the high risk of hydrogen (produced from the water in the containment vessel) igniting after combining with oxygen from water or in the atmosphere, and in order to release some of the pressure inside the reactor at Fukushima I unit 1, the decision is taken to vent some of the steam (which contained a small amount of radioactive material) into the air within the metal container building surrounding the unit.
- 05:50: Fresh water injection into reactor 1 is started.
- 06:50: Although unknown at the time, the core of reactor 1 has now completely melted and falls to the bottom of the reactor pressure vessel.
- 10:09: TEPCO confirms that a small amount of vapor has been released into the air to release pressure in reactor unit 1 at Fukushima I.
- 10:58: Pressure still remains too high inside reactor unit 2 at Fukushima I. In order to alleviate some of this pressure, a consensus is reached to once more vent radioactive vapor into the air.
- 14:50: Fresh water injection into reactor 1 is stopped.
- 15:30: Evacuation of residents within 3 km of Fukushima II and within 10 km of Fukushima I are underway.
- 15:36: There is a massive explosion in the outer structure of unit 1. The concrete building surrounding the steel reactor vessel collapses as a result of the explosion; however no damage is believed to have been sustained to the reactor itself. Four workers are injured(Figure 11).
- 19:00: Sea water injection into reactor 1 is started. TEPCO orders Daiichi to stop seawater injection at 19:25, but Daiichi plant boss Masao Yoshida orders workers to continue with the seawater injection.
- 21:40: The evacuation zone around Fukushima I is extended to 20 km, while the evacuation zone around Fukushima II is extended to 10 km.



Figure 11. Massive explosion of Unit 1

To release pressure within reactor unit 1 at Fukushima I, steam is released out of the unit into the air. This steam contains water vapor, hydrogen, oxygen and some radioactive material, mostly tritium and nitrogen-16. TEPCO engineers decided to directly inject sea water inside the pressure vessel of the reactors by means of the mobile trucks of the firemen. The pressure relief was also necessary to allow the firemen to inject seawater into the reactors vessels.

2011, March 13th

- 02:42: The high pressure coolant injection system for reactor 3 stops and, shortly thereafter, the water level within the reactor starts falling.
- 07:00: The water level in reactor 3 reaches the top of the fuel.
- 09:00: Core damage starts occurring in reactor 3.

A partial meltdown was reported to be possible at unit 3. At 13:00 JST reactors 1 and 3 are vented to release overpressure and then re-filled with water and boric acid for cooling, and to inhibit further nuclear reactions. Unit 2 was possibly suffering a lower than normal water level, but was thought to be stable; although pressure inside the containment vessel was high. The Japan Atomic Energy Agency announced that it was rating the situation at unit 1 as level 4 (an accident with local consequences) on the International Nuclear and Radiological Event Scale.

2011, March 14th

- 11:01: The unit 3 reactor building explodes, injuring six workers. According to TEPCO there was no release of radioactive material beyond that already being vented, but total damage affected the water supply to unit 2.
- 13:15: The reactor core isolation cooling system for reactor 2 stops and, shortly afterwards, the water level within the reactor starts falling.
- 15:00: A major part of the fuel in reactor 3 drops to the bottom of the reactor pressure vessel.
- 18:00: The water level in reactor 2 reaches the top of the fuel.
- 20:00: Core damage starts occurring in reactor 2.

The president of the French nuclear safety authority (ASN), said that the accident should be rated as a 5 (an accident with wider consequences) or even a 6 (a serious accident) on INES.

2011, March 15th

- 06:00 An explosion damaged the 4th floor rooftop area of the Unit 4 reactor as well as part of the adjacent Unit 3.
- 11:00: A second explosion of reactor 3
- 20:00: A majority of the fuel in reactor 2 drops to the bottom of the reactor pressure vessel.

Damage to the temporary cooling systems on unit 2 from the explosion in unit 3, plus problems with its venting system, meant that water could not be added to the extent that unit 2 was in the most severe condition of the three reactors. An explosion in the "pressure suppression room" causes some damage to containment system of unit 2. A fire breaks out at unit 4. Radiation levels at the plant rise significantly but subsequently fall. Radiation equivalent dose rates of 400 milli Sieverts per hour (400 mSv/h) are observed at one location in the vicinity of Unit 3.

To operate safely, a nuclear power plant needs to be cooled continuously, especially when the reactor is shut down, because reactors continues to generate heat also when the chain reaction is stopped because of the radioactive decay of unstable isotopes and fission products created by this process. The decay heat in the reactor core decreases over several days. Nuclear fuel rods that have reached cold shutdown temperatures typically require another several years of water cooling in a spent fuel pool.

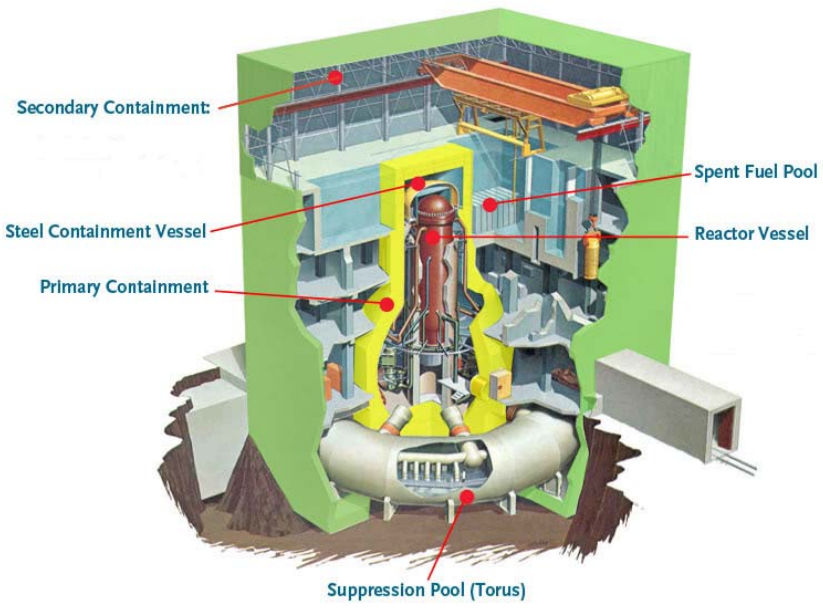


Figure 12. Design of a Boiling Water Reactor (BWR)

The reason that cooling is so essential for a nuclear reactor, is that many of the internal components and fuel assembly cladding is made from zircaloy[1] [[1]Zirconium alloys are solid solutions of zirconium or other metals, a common subgroup having the trade mark Zircaloy.

Zirconium has very low absorption cross-section of thermal neutron, high hardness, ductility and corrosion resistance]. At normal operating temperatures (of approximately 300 degrees Celsius), zircaloy is inert. However, when heated to above 500 degrees celsius in the presence of steam, zircaloy undergoes an exothermic reaction where the zircaloy oxidizes, and produces free hydrogen gas. The reaction between the zirconium cladding and the fuel can also lower the melting point of the fuel and thus speed up a core melt. The result of this problem is shown in Figure 9b.

To circulate cooling water when the reactor is shut down and not producing electricity, cooling pumps can be powered by other units on-site, by other units off-site through the grid, or by diesel generators. In addition, boiling water reactors have steam-turbine driven emergency core cooling systems that can be directly operated by steam still being produced after a reactor shutdown, which can inject water directly into the reactor. Steam turbines results in less dependence on emergency generators, but steam turbines only operate so long as the reactor is producing steam. Some electrical power, provided by batteries, is needed to operate the valves and monitoring systems. Is the fail of the cooling system that had lead to the nuclear disaster in the Fukushima Daiichi nuclear power plant.

6.1 Interdependency that occurred

To analyze the interdependencies it is necessary to frame the Fukushima Daiichi nuclear power plant in the model presented in the previous paragraphs. In this case the community is *Japan*, The infrastructure (lifeline) on which the power plant are insert is *Electricity* (Power delivery) and the Fukushima Daiichi nuclear power plant is a *system* of this lifeline.

From the time line listed above, it is clear that the *system* "Fukushima Daiichi nuclear power plant" is interdependent with the *Electricity* (for the external power supply when the reactor are shout down in order to guarantee the operability of cooling system) and the *Transportation* (more precisely with the *system* "road network" for the emergency supply of materials) lifelines. Going into details, in order to use the information on the nuclear disaster that are mentioned above to evaluate a certain degree of interdependency, it is necessary to subdivide the system "Fukushima Daiichi nuclear power plant") into the following main subsystems and list which interdependency appeared after the tsunami: The main sub-systems are: *Reactors*, *Cooling system of Reactors*, *Emergency generator for the cooling system of Reactors*, *Control room of the power plant*, *Tsunami barriers*, *Automatically shutdown system of Reactors*.

Based on the time line listed above, are appeared the following physical intradependencies:

- *Amplifying failure* of reactors if the cooling systems fail
- *Amplifying failure* of reactors if the emergency generators fail
- *Cascading failure* of cooling systems if the emergency generators fail
- *Amplifying failure* of reactors if the tsunami barriers fail
- *Cascading failure* of cooling systems if the tsunami barriers fail
- *Cascading failure* of emergency generators if the tsunami barriers fail
- *Cascading failure* of reactors caused by the automatically shutdown system of reactors

The matrix of physical intradependency among this sub-systems can made in the following way (Table 1), where R = reactors, CS = cooling systems, EG = emergency generators for the cooling system, CR = control room, TB = tsunami barriers, ASS = automatically shutdown systems.

	R	CS	EG	TB	ASS
R	1	-	-	-	-
CS	A	1	-	-	-
EG	A	C	1	-	-
TB	A	C	C	1	-
ASS	C	-	-	-	1

Table 1. Physical intradependency index matrix among the sub-systems of the Fukushima Daiichi power plant system.

where A = Amplifying failure and C = Cascading failure. 1 is the maximum possible degree of intradependency. Based on the same time line, the following cyber intradependencies are appearing:

- *Cascading failure* of automatically shutdown system of reactors if the control room fail;
- *Cascading failure* of emergency generators if the control room fail;
- *Cascading failure* of emergency generators if the automatically shutdown system fail;

The matrix of cyber intradependency among these sub-systems is shown in Table 2:

	CR	ASS	EG
CR	1	C	C
ASS	-	1	C
EG	-	-	1

Table 2. Cyber intradependency index matrix among the sub-systems of the Fukushima Daiichi power plant system.

Give an univocal numerical value at every intradependencies can not be possible, because of the complexity of the examined system. However a complex system like the Fukushima Daiichi nuclear power plant can be easy framed into the method proposed in this paper.

Recently Cimellaro et al. [19] have proposed a method based on the use of the restoration curves of some lifelines. The authors developed an equation based on the cross correlation function among two restoration curved (after a normalization, logarithmically transformation and second differentiation of the restoration curves) with which they calculate the interdependency index *S*. This kind of method lead to a simplified evaluation of the interdependency index, because the index *S* come from two restoration curves that contain, without distinction, information derived from the single systems of which they are composed. The method proposed in this paper is more detailed respect to the one proposed Cimellaro et al. [19], because

the evaluation of the interdependency index are based on the interdependency that arise among different systems (or sub-systems). Every system contribute to the final value of interdependency and it is possible to identify which are the systems that cause more problems of interdependency into a lifeline in order to adequate or improve only that systems, focusing only the available resources in order to maximize the ratio between invested money and reduction of interdependency. However the method proposed by Cimellaro et al. [19] can give a numerical quantification (although simplified, because all the information about systems interdependencies are into a single restoration curve) of the interdependency index. The method proposed in this paper can be a useful framework to analyze the interdependency that arises among different lifelines and different systems into a community.

7 CONCLUSIONS

In this paper, it is proposed a framework to evaluate the degree of interdependency between infrastructures (lifelines) of a community. A reference nomenclature is defined while sixteen infrastructures that compose each community are identified: seven core infrastructure (*Electricity, Oil delivery, Transportation, Telecommunication, Natural Gas delivery, Water supply, Wastewater treatment*) and nine no-core infrastructure (*Financial system, Building services, Business, Emergency services, Food supply, Government, Health care, Education, Commodities*). Each lifeline is divided in *systems*, while interdependencies are subdivided in seven types (*Physical, Cyber, Geographic, Policy/Procedural*, *Societal, Budgetary*, *Market & Economy interdependency*).

For each system and for each type of interdependency, it is assigned a degree of interdependency, which is function of two values assigned at every type of lifeline. The first value is function of the type of failure (*Cascading, Amplification, Uncoupled*). The second value is function of the *importance factor* that each lifeline's system has. Lifeline interdependencies are evaluated combining the values of interdependency of systems in which the different lifelines have been divided.

Finally there are seven types of interdependencies for each lifeline's pair, which are organized in seven interdependencies matrices. The degree of interdependency (or interdependency index) can assume values between 0 and 1, where 0 represents the absence of interdependency, while 1 represents maximum interdependency between the two infrastructures. For each matrix, it can be evaluate the *Leadership index* that the lifeline of a given row has with respect to the other fifteen lifelines identified in the community (obtained adding per row the data in the interdependency matrix $S_{i,j}$) and the *Subordination index* that the lifeline of a given column has with respect to the other fifteen lifelines in the community (obtained adding per column the data in the interdependency matrix $S_{i,j}$). The lifeline that has the highest value of *Leadership index* is the most important lifeline in the community which requires a higher level of attention, because if its functionality fails, the performances of the community decrease dramatically. The lifeline that has the highest value of *Subordination index* is the one that has the greatest dependency on the other lifelines within the community. If the community suffers damage, this lifeline is the first that suffers the effects of propagation of the damage due to the interdependencies, even if, it does not suffer damages. It is important to know which the lifeline with the maximum Leadership index is, and which the lifeline with the maximum *Subordination index* is, in order to focus all the available resources of the community on these two lifelines, in order to do not waste resources and optimizing the global response of the community in terms of interdependency and sustainability. Finally as case study, it is analyzed the 2011, March 11th, Fukushima Daiichi nuclear power plant disaster. Some sub-system intradependencies are highlighted and are placed into the proposed frame-

work. Further studies are necessary in order to give a numerical quantification of interdependencies at the *system* level (local level), in the same manner which is proposed at a global level when infrastructures are considered as global entities.

ACKNOWLEDGEMENTS

The research leading to these results has also received funding from the European Community's Seventh Framework Programme - Marie Curie International Reintegration Actions - FP7/2007-2013 under the Grant Agreement n° PIRG06-GA-2009-256316 of the project ICRED - Integrated European Disaster Community Resilience.

REFERENCES

[1] PCCIP. "Critical foundations: Protecting America's infrastructures: The report of the President's Commission on Critical Infrastructure Protection." U.S. Government Printing Office, Washington, D.C., 1997.

[2] President. "The Clinton Administration's Policy on Critical Infrastructure Protection: Presidential Decision Directive 63 [Online]. Available: http://www.ciao.gov." White Paper, 1998.

[3] S.A. Rinaldi, J.P. Peerenboom, and T.K. Kelly. Identifying, understanding, and analyzing critical infrastructure interdependencies. *Ieee Control Systems Magazine*, **21**(6), 11-25, 2001

[4] K. Kakderi, S. Argyroudis, and K. Pitilakis. State-of-the-art literature review of methodologies to assess the vulnerability of a "system of systems". *D2.9*, Aristotle University of Thessaloniki, 2011.

[5] G.P. Cimellaro, D. Solari, C. Renschler, A.M. Reinhorn, and M. Bruneau. "Community resilience index integrating network interdependencies." *Proceedings of the 2013 Structures Congress (SEI 2013)* Pittsburgh, Pennsylvania, May 2-4, 2013, Year.

[6] D. Mileti. Disasters by design: A reassessment of Natural Hazards in the United States, Washington, D.C., 351., 1999.

[7] M. Bruneau, S.E. Chang, R.T. Eguchi, G.C. Lee, T.D. O'Rourke, A.M. Reinhorn, M. Shinozuka, K. Tierney, W.A. Wallace, and D. Von Winterfeldt. A Framework to Quantitatively Assess and Enhance the Seismic Resilience of Communities. *Earthquake Spectra*, **19**(4), 733-752, 2003

[8] G.P. Cimellaro, A.M. Reinhorn, and M. Bruneau. "Quantification of Seismic Resilience." 8th U.S. National Conference on Earthquake Engineering, San Francisco, California, USA, April 18-22,, 2006.

[9] G.P. Cimellaro, A.M. Reinhorn, and M. Bruneau. Framework for analytical quantification of disaster resilience. *Engineering Structures*, **32**(11), 3639–3649, 2010

[10] G.P. Cimellaro, A.M. Reinhorn, and M. Bruneau. Seismic resilience of a hospital system. *Structure and Infrastructure Engineering*, **6**(1-2), 127-144, 2010

[11] T. McDaniels, S. Chang, D. Cole, J. Mikawoz, and H. Longstaff. Fostering resilience to extreme events within infrastructure systems: Characterizing decision contexts for mitigation and adaptation. *Global Environmental Change*, **18**(2), 310-318, 2008

[12] NIAC. A Framework for Establishing Critical Infrastructure Resilience Goals. Final Report and Recommendations by the Council. 2010.

[13] I. Kongar, and T. Rossetto. "A framework to assess the impact of seismic shocks on complex urban critical infrastructure networks." 15th World Conference on Earthquake Engineering (15WCEE), Lisbon, Portugal, September 24-28, 2012, 2012.

[14] J. Peerenboom, Fisher, R., Whitfield, R. "Recovering from disruptions of interdependent critical infrastructures." Workshop on Mitigating the Vulnerability of Critical Infrastructures to Catastrophic Failures, Lyceum, Alexandria, Virginia., 2001.

[15] G.P. Cimellaro, and D. Solari. Considerations about the optimal period range to evaluate the weight coefficient of coupled resilience index. *Engineering Structures*, in review, 2013

[16] P. Pederson, D. Dudenhoeffer, S. Hartley, and M. Permann. "Critical Infrastructure Interdependency Modeling: A Survey of U.S. and International Research." D. o. E. N. Laboratory, ed., Idaho National Laboratory, 2006.

[17] P. Zhang, and S. Peeta. A generalized modeling framework to analyze interdependencies among infrastructure systems. *Transportation Research Part B: Methodological*, **45**(3), 553-579, 2011

[18] D. Paton, and D. Johnston. *Disaster resilience an integrated approach*, Charles C Thomas publisher LTD, 2006.

[19] G.P. Cimellaro, D. Solari, and M. Bruneau. Interdependency and Regional Resilience Index after 2011 Tohoku Earthquake in Japan. *Earthquake Engineering & Structural Dynamics*, in review, 2013

COMPDYN 2013
4th ECCOMAS Thematic Conference on
Computational Methods in Structural Dynamics and Earthquake Engineering
M. Papadrakakis, V. Papadopoulos, V. Plevris (eds.)
Kos Island, Greece, 12–14 June 2013

EVALUATING THE POST-EARTHQUAKE ACCESSIBILITY OF HOSPITALS FOR MITIGATION STRATEGY DECISION SUPPORT BY FRAGILITY AND CONNECTIVITY MODELLING

Indranil Kongar[1], Enrica Verrucci[1,2], Tiziana Rossetto[1], and John Bevington[2]

[1]University College London,
Department of Civil, Environmental & Geomatic Engineering, Gower Street, London, WC1E 6LT.
e-mail: {indranil.kongar.10,e.verrucci,t.rossetto}@ucl.ac.uk

[2]ImageCat Ltd.
Centrepoint House, 2 Denmark Road, Guildford, Surrey, GU1 4DA.
e-mail: {ev,jb}@imagecatinc.com

Keywords: Lifelines, Fragility, Connectivity, Earthquake Engineering, Mitigation.

Abstract. *The aim of this paper is to present a trivial proof of concept for analysing the impact of post-earthquake damage to lifelines on indicators of social resilience. The conceptual methodology is demonstrated by carrying out a GIS-based analysis of the impact of damage to highways bridges on accessibility to emergency healthcare facilities in the Santa Clarita suburb ofLos Angeles. A magnitude 6.9 earthquake from the Santa Susana fault zone was used as a scenario event with bridge damage predicted using the HAZUS methodology to calculate exceedance probabilities and uniform random sampling to assign damage states. Moderate damage state was used as the threshold for bridge closure. The system performance was measured as the mean travel time between neighbourhoods and the local hospital, weighted to account for population. The distribution of delay amongst the population has also been derived. The analysis was repeated for three further scenarios to identify the critical node for prioritisation of mitigation works by comparing the impacts with the post-earthquake scenario. The analysis was based on the Los Angeles County disaster route network with straight-line approximations for travel distance on local roads. Results were compared to those obtained using the actual path distance on local roads and this showed that interpretation of the results could vary depending on the measurement method and the decision variable used. Therefore straight-line distance is not a safe approximation. The methodology proposed here will be expanded in the future for a more detailed study assessing the riskfrom damage to multiple lifelines and using a wider range of indicators.*

1 INTRODUCTION

In the emerging philosophy of resilience, focus moves away from vulnerability and emphasises instead the inherent structural capacities of physical systems and the social capital of communities [1]. Therefore resilience can be classified as having a 'hard' component, associated to land-use and to urban development and a 'soft' component, referring to communities and their social-capital. As represented in the framework of resilience proposed by Verrucci [2], lifelines are at the intersection between these two components. Lifelines are socio-technical systems whose efficiency has direct impact on the ability of the community to perform both routine and emergency response activities. This lifeline efficiency is particularly vulnerable to the impact of natural hazards such as earthquakes since the structural components of lifeline systems are vulnerable to ground shaking and ground displacements. Damage to lifelines can be caused directly due to ground motion or indirectly due to disruption caused by damage to other associated lifelines. This has two impacts, firstly the cost associated with repair or reconstruction and secondly the impact on people, businesses and emergency response activities due to service interruption. Lifeline damage therefore has an effect on the functioning of a community and it is important to understand their level of connection, interdependency and inter-linkages with social systems.

Strategies for assessing and mitigating lifelines risk are commonly based on repair costs and system performance. However, lifelines are socio-technical systems and so it is not the system performance itself which matters, but the impact that reductions in performance have on the community, in terms of both routine and emergency operation. Appraisal of disaster mitigation strategies should therefore use decision variables that account for these social impacts on local communities. Previous studies have developed disaster mitigation decision support tools based on lifelines and community impacts but either focus on a single lifeline only or measure impacts qualitatively [3, 4]. The EPICentre group at University College London have recently started a project, in conjunction with ImageCat (Guildford, UK, Long Beach, CA.) and the Willis Research Network, which aims to produce a more quantitative and holistic decision support tool. As a first step in this exercise, a simplified proof of concept has been produced to demonstrate the concept and the strategy of the proposed tool using a single lifeline. This case study investigates the impact of highway network damage on emergency healthcare accessibility in the Santa Clarita suburb of Los Angeles with decision variables based on travel time, but does not account for decision-making processes. This paper presents the methodology used in this case study and the results obtained from assessing the impacts of a single scenario event. It goes on to discuss the inference of those results and the role that the selection of decision variable plays in how the results are interpreted.

2 METHODOLOGY

2.1 Data acquisition

An evaluation of the spatial connectivity and interdependency of the highway system and health care facilities in Santa Clarita, Los Angeles, has been performed by means of GIS spatial analysis. Spatial overlay, proximity and network analyses have been applied. The study required the acquisition of data on the spatial distribution of the highways network and healthcare facilities as well as the identification of preferred routes between neighbourhoods and healthcare facilities, defined by the shortest travel time. The study has required the acquisition, cleansing and enhancement of several spatial datasets. For data rich case studies, like Santa Clarita, spatial data information were easily obtainable and so several data sources have been investigated. When potentially useful datasets were available from more than one

source, the most recent and up-to date layer was adopted or a final layer was produced based on the spatial comparison of same feature raw layers.

Spatial overlay and proximity analysis have been used in conjunction with each other in order to derive preliminary information about the spatial relationship between the street layer, the healthcare facilities and the neighbourhoods. Network analysis has then been applied to identify the most efficient routes based on travel-time. A simplified road network has been used in the model based on the primary disaster routes designated by the Los Angeles County Department of Public Works (LADPW) [5]. The exclusion of local roads from the analysis is justified since observation shows that the local road network exhibits a high degree of redundancy. Furthermore, where redundancy is high, complete routing analysis becomes computationally intensive.

The road network layer has been obtained by comparing the Census TIGER 2010 [6] road layer with the most recent acquisition of Google Earth satellite imagery [7] and with the disaster route maps produced by LADPW [5]. In some cases the disaster route followed the path of two roads, e.g. a local main road adjacent to an elevated highway. In these cases it was assumed that the disaster route would follow the highway since these have higher traffic carrying capacity. For this proof of concept only ground shaking hazard was considered and so it has been assumed that bridges are the only vulnerable component in the highways network, since roads are more vulnerable to ground deformation. The distribution of highway bridges was extracted as a subset of the California-wide spatial database in the HAZUS software [8] and was compared against the bridge layout of the Caltrans web-GIS platform [9]. The data extracted from HAZUS included structural characteristics allowing for evaluation of fragility. In the cases where bridges were missing from the HAZUS database but included within the Caltrans database, structural typology information has been acquired by querying tabular data published alongside the Caltrans web-GIS platform.

The layer of health facilities has been produced by comparing the subset extracted from HAZUS [8] with tabular data available on the American Hospital Association (AHA) website [10]. The information from the HAZUS layer has been enhanced by adding the number of beds and medical personnel information for each of the medical facilities located in the study area and also entry points to the hospitals. The layers have been integrated into a single geo-spatial database. In this case study, the Santa Clarita suburb was assumed to be a boundary-constrained region with the condition that no flow was possible between Santa Clarita and neighbouring suburbs. This condition consequently meant that the neighbourhoods within Santa Clarita had access to only one hospital.

Based on visual interpretation of the Google Earth satellite image [7], access points to/from the disaster route network have been added to the geo-spatial database to produce the final layer. These include access points between local neighbourhoods and the disaster route network (neighbourhood access points) and access points between the hospitals and the disaster route network (hospital access points).

The Santa Clarita suburb is made up of a number of smaller neighbourhoods and one of the decision variable selected for this analysis accounted for the mean travel time between these neighbourhoods and local hospitals, weighted by neighbourhood population. For the definition of the spatial extent of the neighbourhoods, a simplistic procedure was adopted of visually identifying and manually digitising polygons using Google Earth satellite imagery [7], which were subsequently converted into an ArcGIS shapefile. The layer was validated against the road network, where small neighbourhoods were identified as built-up clusters with a single access main road feeding into a network of local roads. In total 55 neighbourhoods were identified. The complete dataset is shown in Figure 1.

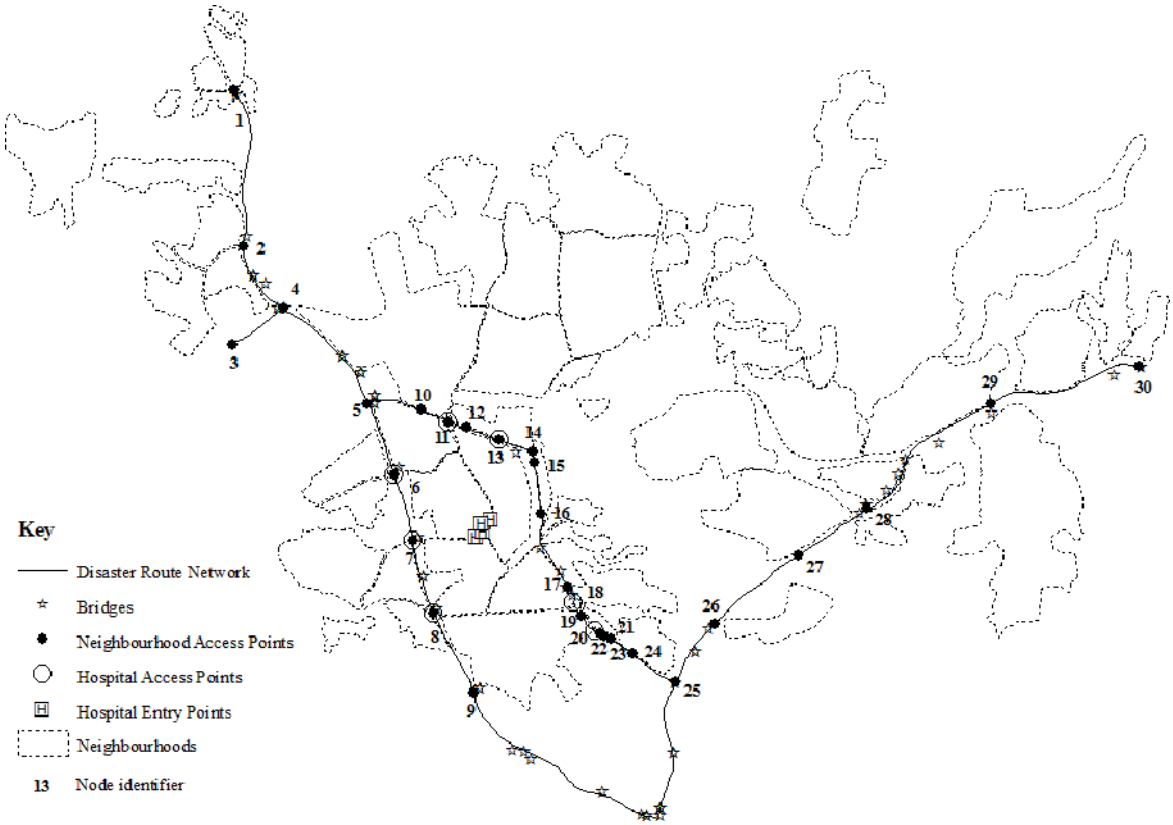


Figure 1: Final dataset of Santa Clarita suburb for GIS analysis including neighbourhood, hospital and highways data

2.2 Hazard

Probabilistic seismic hazard assessment (PSHA) is a common approach to defining hazard for risk assessment exercises. The process identifies the intensity measures (IM) values that will occur with defined return period based on multiple earthquake sources. However this procedure is not appropriate for the risk assessment of lifelines. Firstly, lifelines are spatially distributed and so one cannot assume the same value of IM at all component sites. Secondly, hazard maps display PSHA outputs as fields of IMs but whilst these IMs are predicted to occur at each location within the specified return period, they are not necessarily predicted to occur at the same time. The performance of a system following an earthquake will depend on its fragility and the redundancy it exhibits. System redundancy can only be assessed by understanding the behaviour of components simultaneously in response to a shock. Consequently alternative approaches must be used for spatially distributed systems, which model simultaneous IM values.

It is possible to assess the lifelines risk by selecting a single deterministic event, such an important historic earthquake or a defined maximum credible earthquake from a particular source, then calculating the decision variable for this event. Such an approach has benefits with respect to public engagement of risk but accounts for neither the uncertainty in predicting the location and magnitude of earthquakes, nor the natural variation in strong motion resulting from them. A more robust alternative is to run a Monte Carlo simulation (MCS), using historic earthquake data to generate a stochastic set of deterministic events. These events can be from a single source or from different sources and the MCS approach can account for this locational uncertainty, as well as uncertainty in magnitude, depth and fault characteristics. The decision variable can then be calculated for each event and subsequently

predicted probabilistically from the distribution of these results. This methodology is analogous to the way that the insurance sector estimates building losses for spatially distributed portfolios.

The MCS methodology is proposed for the next stage study, but for this proof of concept a single scenario earthquake has been used for simplicity. Shiraki et al. [11] identified maximum credible earthquakes (MCE) for fifteen fault sources in the Los Angeles area based on an earlier study by Petersen et al. [12]. The scenario selected for the case study was the MCE for the Santa Susana fault zone, the closest fault zone to the Santa Clarita study area. This MCE was attributed with a moment magnitude of 6.9. Other characteristics were unspecified, but not required to calculate peak ground acceleration (PGA) using the selected ground-motion prediction equation (GMPE) developed by Boore & Atkinson [13], which was appropriate for the shallow crustal environment in California. The GMPE also required input values for $V_{s\,30}$, the average shear-wave velocity to 30m depth, which were obtained from the USGS Global $V_{s\,30}$ Map Server [14].

This GMPE includes two residual terms representing inter-event and intra-event variability. The inter-event term is constant at all sites for a single earthquake while the intra-event term varies across all sites. Both residuals are normally distributed with zero mean and specified standard deviations. Thus both residual terms could be estimated by randomly sampling from this distribution. However, the random sampling of the intra-event residual does not account for correlation between IMs at sites close together. A local model for spatial correlation can be applied to resolve this. Whilst this detailed approach is proposed for the next stage of the study, for the proof of concept, this variability was not considered and median values were calculated from the GMPE.

2.3 Lifeline fragility

The damage scenario of a lifeline system identifies the damage state of all components in that system following a single earthquake scenario. The predicted damage state experienced by a lifeline component was related to the IM using fragility functions, which evaluate the exceedance probabilities of pre-defined damage states. To assign a damage state to the component based on these probabilities, a uniformly distributed variable, u, was randomly sampled such that $0 \leq u \leq 1$. The sampled value was then compared to the exceedance probabilities and the damage state was assigned as described in Equation 1. For a fragility function with m damage states, d_0 represents the 'no damage' state and d_m represents the 'complete damage' state. Component i of a lifelines system was assigned to the nth damage state if the condition in Equation 1 was satisfied, where n is an integer between 0 and m, u_i is the sampled random variable for component i and $P_{n,i}$ is the exceedance probability of damage state n for component i at the assessed IM value.

$$P_{n+1,i} < u_i \leq P_{n,i} \tag{1}$$

By repeating for all components, a damage scenario for the system was generated. However, since damage state exceedance is probabilistic, this damage scenario represented just one possible expression of the system response. System performance and subsequent decision variable calculations will change depending on which components are damaged and how severely, as some components will have more importance than others. To account for this uncertainty and reflect the full distribution of possible system responses, a damage scenario MCS should be run for each earthquake. The decision variable could then be calculated for each earthquake and damage scenario pair to produce the exceedance curve. It is proposed that this simulation approach is adopted for the next stage of work, but for this proof of concept, only one damage scenario has been generated for the scenario earthquake.

For the Santa Clarita study, it has been assumed that bridges were the only vulnerable component in the highways network. Damage to roads due to geotechnical effects and displacements were not considered. The bridge data was extracted directly from HAZUS with appropriate structural classification and the HAZUS methodology was used to calculate exceedance probabilities based on local PGA values.

This case study was interested in the performance of emergency services in the immediate aftermath of an earthquake. On this basis it was assumed that damage states of moderate or higher would result in precautionary bridge closure [15]. It may be expected that minor damage could reduce the capacity and hence average speed across a bridge might reduce, but this assumption does not take into account reductions in demand and that the travel times of emergency vehicles are likely to be less affected by such changes. Therefore, it was assumed that a minor damage state has no impact on travel time.

For the assessment of the highways system performance, the highways network was modelled as a graph made up of links (roads) and nodes (junctions). The nodes coincided with either neighbourhood access points or hospital access points or junctions between disaster routes. Bridges were attributed to either a node (e.g. a grade-separated junction) or a link (e.g. an overpass without connection to another link). It was assumed that bridge failure at a node would cause failure of that node and all links connected to that node and bridge failure at a link would cause failure of that link. In some cases, more than one bridge was attributed to a link, in which case failure of at least one bridge would result in link failure. From the identification of failed links and nodes, a post-earthquake highways network was generated.

2.4 Spatial analysis

The calculation of travel time between a neighbourhood and the hospital consisted of three parts. Firstly, the travel time between the neighbourhood and a neighbourhood access point on the disaster route network; secondly, the travel time along the disaster route network and finally, the travel time between a hospital access point on the disaster route network and the hospital itself. To calculate the travel time between the neighbourhoods and the disaster route network, the point (straight-line) distance between the neighbourhood polygon centroid and the nearest neighbourhood access point was measured in ArcGIS. To ensure this scenario was realistic, the assigned access points were checked against a local street map to ensure that they were accessible from the neighbourhood. Where this was not the case, the nearest access points were re-assigned manually and re-measured in ArcGIS. An average speed of 50km/h was assumed for this section. This conservative estimate accounts for delays at intersections and due to congestion. It was then assumed that a vehicle will leave the disaster route network at the closest hospital access point. The disaster route network in this area consisted of two types of road. Most of the network is made up of highways (Interstate 5 and State Route 14), along which an average speed of 130km/h was assumed. A small section of the disaster route network is made up of local main roads (Magic Mountain Parkway and Railroad Avenue), along which an average speed of 80km/h was assumed. Finally between the disaster route network and the hospital, an average speed of 50km/h was assumed since this section returned to the local street network. The hospital had four entry points and point distance was used to measure the distance between the hospital access point on the disaster route network and the nearest entry point.

Two decision variables were evaluated for this study. The first was a mean travel time for all neighbourhoods, weighted according to the residential population of each neighbourhood, from which a mean delay can be inferred. This is designed to ensure that the travel time for more populous areas is attributed greater significance. The population was estimated by examining building occupancy and unit count. The analysis required the acquisition of tax

assessor parcel data, purchased through the LA County GIS portal [16]. This consists of a series of polygons for each taxable unit in a building. This implies that for multi-unit buildings, the parcel data layer presents overlapping polygons of same shape and size.

All buildings are identified by a four-digit use code. The first digit provides information about the occupancy (e.g. "0" identifies residential properties). The second and third digit provide information about the unit count ("01" – single unit; "02" – duplex unit, etc.) for all the residential units, except for condominiums. The last digit helps with the identification of vacant proprieties and condominiums (e.g. "V" – Vacant; "C" – condominiums). The first step of the analysis required the identification of non-vacant residential units and the creation of a "unit count" field based on the second and third digits of the use code. Since for condominiums the unit count cannot be derived from the use code, a "points-in-polygon" analysis was applied to obtain the exact number of units. For this purpose, the co-ordinates of the centroid of the each condominium polygon were calculated. The co-ordinates were used to create a point layer and to automatically delete the overlapping polygons in the original parcel layer. The spatial correlation of all the points falling into the modified polygon parcel layer automatically creates a second unit count field for the condominiums. The population count was then obtained by multiplying the final unit count by the average occupancy per residential unit, derived from the 2010 Census [17] for each zip code.

The populations of each neighbourhood were assigned weights as set out in Equation 2 and the weighted mean travel time, $\bar{t}$, was calculated using Equation 3, where pop_j is the population of neighbourhood j, w_j is the weight attributed to neighbourhood j in a study area with k neighbourhood and t_j is the travel time from neighbourhood j.

$$w_j = \frac{pop_j}{\sum_{j=1}^{k} pop_j} \tag{2}$$

$$\bar{t} = \sum_{j=1}^{k} w_j \times t_j \tag{3}$$

However whilst the mean can provide a trivial and objective statistic for comparison, the compromise from this simplicity is loss of information on the distribution of delay amongst neighbourhoods, e.g. a similar mean delay can result from a few people experiencing a large delay or many people experiencing a short delay. To account for the distribution, the second decision variable measured the number of people experiencing delays greater than a series threshold values using the neighbourhood population estimates. The thresholds ranged from 0%-100% with 10% intervals and the variable was evaluated cumulatively. This variable provides more information than just the mean but subsequently requires more subjective interpretation.

3 ANALYSIS AND DISCUSSION

The mean travel time analysis has been carried out for two scenarios, a baseline scenario with a functioning highways network and a post-earthquake scenario with the highways network modified following fragility analysis. The scenario earthquake used was the 6.9-magnitude MCE centred at the Santa Susana fault area.

The fragility analysis of the earthquake scenario predicted that four bridges would experience extensive damage, two bridges would experience moderate damage and two bridges would experience minor damage. This would result in the closure of six bridges. Figure 2 shows the locations of the closed bridges and the impact this had on the highways

network in terms of links and nodes. This also represented the highways network that was used for post-earthquake network analysis. Four of the bridge closures occurred at nodes. This resulted in the failure of three nodes (5, 6 and 8) and indirectly the six links that connect to these nodes. The other two bridge closures occurred along links and resulted in the closure of these two links: between nodes 2 and 4 and between nodes 9 and 25. In terms of routing, the closures resulted in the loss of three neighbourhood access points and two hospital access points, although both of the closed hospital access points were co-located with closed neighbourhood access points.

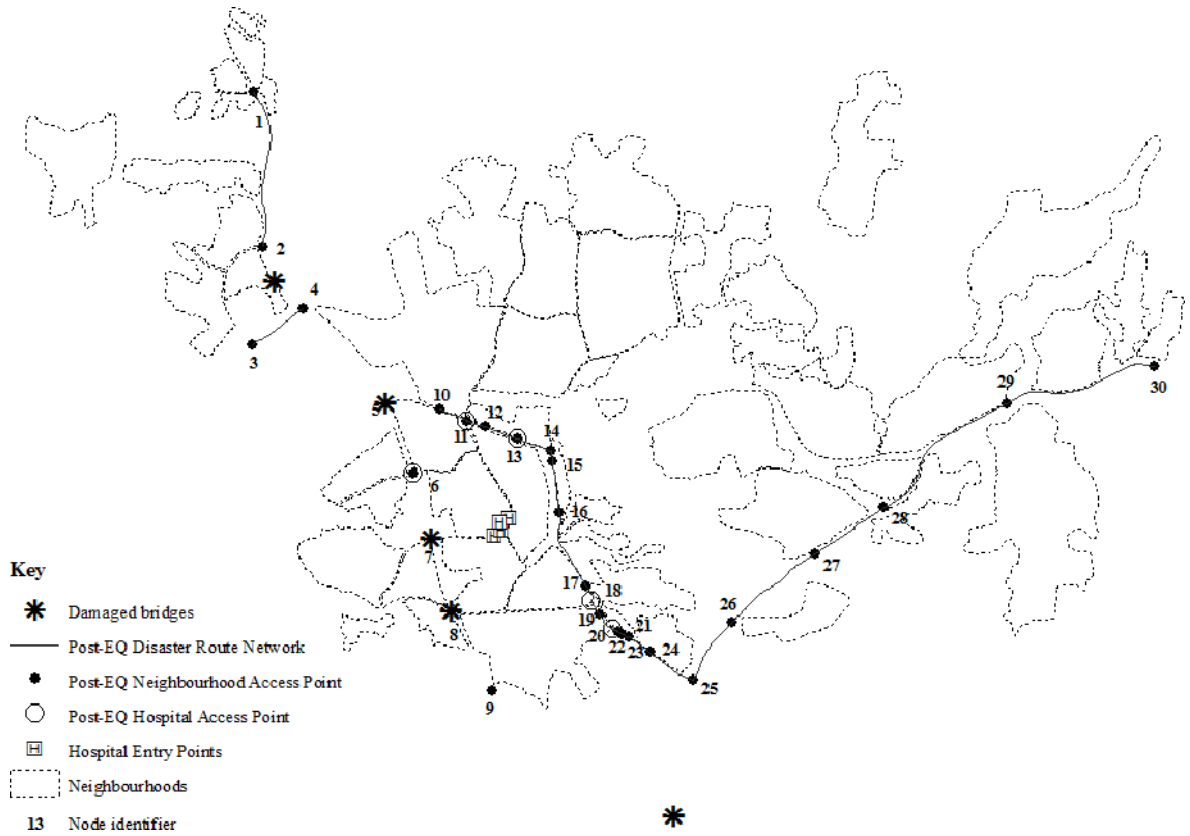


Figure 2: Post-earthquake dataset showing damaged bridges and removal of links from the disaster route network

In the baseline scenario, the weighted mean travel time was calculated at 7m58s. In the post-earthquake scenario, 15 neighbourhoods required re-routing onto the disaster route network, all to the west and northwest of the study area. For the re-routing, it was assumed that a vehicle would travel to the nearest neighbourhood access point that had an unbroken route to a hospital access point, i.e. routes which required vehicles to leave the disaster network at a damaged component and re-join downstream were excluded. Because of redundancy in the local street network, no neighbourhoods became isolated as a result of the predicted bridge damage. For the post-earthquake scenario, the weighted mean travel time was computed as 8m36s. However, because of the approximations and assumptions used in the routing exercise, these absolute travel time values are not in themselves useful. Rather it is the relative performance that is informative and here the earthquake scenario results in a travel time increase of 7.9%. This delay appears small indicating that there is a high degree of resilience in the local disaster route network.

One approach for mitigation planning is to use risk assessment analyses to compare the impact of alternative mitigation strategies. This concept has been demonstrated in this case study by measuring the weighted mean travel time for three further scenarios. In each scenario, one of the failed nodes (5, 7 or 8) was restored to the post-earthquake highways network, simulating the case where the bridge at that node was strengthened prior to the earthquake and therefore did not experience a level of damage requiring necessitating its closure. The fragility analysis was not re-run for these scenarios, which have been designed to identify the most critical node and thus the priority for mitigation interventions. The cases of the two direct link failures were not considered in the sensitivity analysis since neither would improve travel time if restored, due to their location. Table 1 shows the impact on mean travel times in these scenarios. The analysis shows that restoration of node 5 results in the largest reduction in delay. Hence, it is the most critical node and the bridge at node 5 should be prioritised for mitigation. This result was expected from observation since this node is essential to service the neighbourhoods to the northwest of the study area.

Scenario	Weighted mean travel time	% Delay
Baseline	7m58s	-
Post-earthquake	8m36s	7.9
Post-earthquake Node 5 restored	8m17s	3.8
Post-earthquake Node 7 restored	8m28s	6.1
Post-earthquake Node 8 restored	8m33s	7.2

Table 1: Post-earthquake travel time impacts using point distance analysis. The candidate restoration nodes are shown in Figure 2. The % Delay relates to the increase in weighted mean travel time compared to the baseline scenario.

The distribution of the delay amongst the population for each scenario is shown in Figure 3. The results show why the interpretation of this data is more difficult than the mean. The analysis of mean travel time is clear in its identification of the most critical node, albeit at the expense of completeness in terms of information. The distribution is more informative but the results are less clear and more open to subjective interpretation. With the restoration of Node 5, very few people experience delays greater than 50%, and significantly fewer than the other mitigation scenarios. However, in the Node 5 restoration scenario, there are more people who experience an 80% delay than the other two scenarios. Also the Node 7 restoration scenario is clearly the best for minimising the number of people who experience any kind of delay, i.e. total number of people affected. A planner would therefore have to decide which is more important, the total number of people affected or the frequency of large delays only. If the latter, then another decision needs to be made on what the threshold of a large delay should be, i.e. at what point does a delay become unacceptable. This is irrespective of whether delay is presented in percentage or absolute terms. However, Figure 3 also highlights the usefulness of the distribution. In the initial post-earthquake scenario, nearly 35,000 people (approximately one sixth of the total population), experience a delay of over 40%. Also in terms of mean delay, the Node 5 restoration scenario more than halves the delay caused by the earthquake, yet in terms of total number of people affected (delay> 0%), the benefit of restoring Node 5 is not nearly as great.

It is worth noting that, as a decision variable, delay also excludes information. Delay, whether measured in percentage terms or absolutely, does not take into account whether the post-earthquake travel time is actually significant. For example, compare two neighbourhoods, one of which has a baseline travel time of 1 minute and post-earthquake travel time of 6

minutes and another which has a baseline travel time of 10 minutes and a post-earthquake travel time of 15 minutes. Both have the same numerical delay and the former has a much greater percentage delay yet for emergency treatment, the latter neighbourhood has a more significant delay, since its post-earthquake travel time is now quite high. Therefore, it is not that the delay that is important but the actual travel time, which can be compared to a target threshold. One then needs to decide what an acceptable travel time for a vehicle to travel to an emergency medical facility is. It is likely that this will vary from place to place as the acceptable travel time will increase as the extents of the area served by the hospital widen. Where the area is large, the acceptable travel time might also need to be tiered, i.e. for some neighbourhoods a higher travel time is tolerated because of the distance from the hospital. This highlights the importance of including societal and community considerations in infrastructure performance evaluation. Wholly physical system performance metrics, such as delay, only measure vulnerability. It is only by including societal considerations that the emphasis can shift to capacity, as prescribed by the resilience philosophy. This approach was not used in this proof of concept since it requires dialogue with local healthcare providers and planners, but will be considered in the next stage of the study.

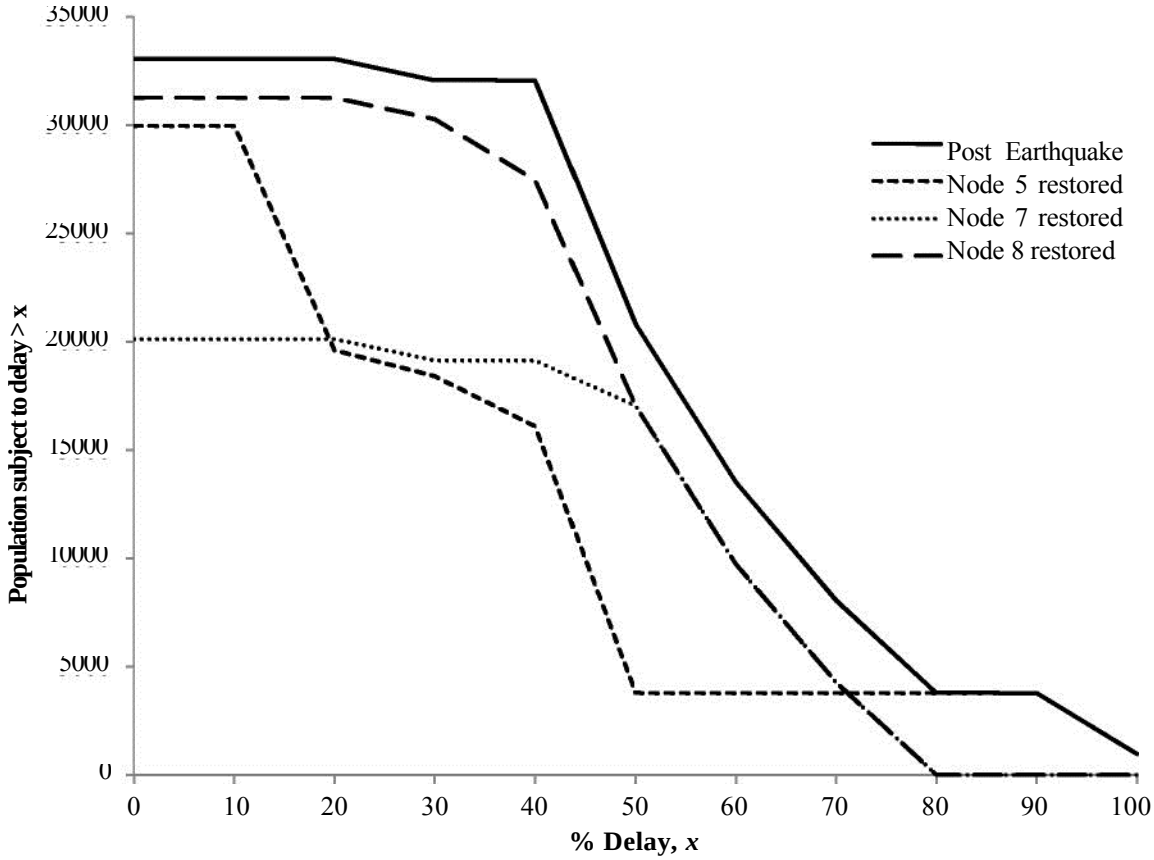


Figure 3: Cumulative distribution of population against the percentage delay in travel time using point distance analysis. The cumulative frequency is measured at 10% intervals.

One of the approximations used in the analysis was the use of point distance between the neighbourhoods and the disaster route network, and also between the hospital and the disaster route network. In most cases road networks are unlikely to follow a straight-line path and so the distance measured is underestimated. The nature and complexity of road networks is such

that the difference between point distance and path distance (measured along roads) can itself vary significantly between neighbourhoods and so the relationship between the two cannot be generalised. The use of point distance could therefore skew the results in certain scenarios where one or more neighbourhoods exhibit a large difference between their point distance and path distance measurements.

As a sensitivity test, the whole analysis, including node restoration was repeated using the actual road distance between neighbourhood centroids and the neighbourhood access points and between the hospital access points and the hospital. This was done by overlaying the shapefile of the final dataset onto a Bing street layout base map embedded within ArcGIS [18] and using the functionality of ArcGIS to trace and measure a path along the local roads, using a heuristic approach for routing based on observed street hierarchy. This heuristic method was only practical for this case study due to the network being small. For a larger network, the local roads would need to be digitised in ArcGIS and the routing analysis undertaken computationally using a shortest-path algorithm. Nevertheless, the heuristic approach provides an approximate indication of how the point distance and path distance methods compare. The new path distance results are shown in Table 2 and Figure 4.

Scenario	Weighted mean travel time	% Delay
Baseline	9m19s	-
Post-earthquake	10m07s	8.6
Post-earthquake Node 5 restored	9m50s	5.5
Post-earthquake Node 7 restored	9m52s	5.8
Post-earthquake Node 8 restored	10m03s	7.8

Table 2: Post-earthquake travel time impacts using path distance.

The comparison shows that the mean delay caused by the earthquake is slightly higher in percentage terms when using the path distance for all post-earthquake scenarios except the Node 7 restoration scenario. The differences are small except for the Node 5 restoration scenario. Since the baseline travel time is higher when using path distance, one might expect the delays to decrease in percentage terms. However this is probably offset since damage to bridges increases the travel time spent on local roads, which is the component of total travel time underestimated by using point distance. Table 2 shows similar values for percentage delay compared to Table 1 and if this method was used for identification of critical node, the result is the same (Node 5), indicating that point distance is a useful approximation. Figure 4 shows that the Node 5 restoration scenario is the worst of the mitigation scenarios for total number of people affected. It also has the highest number of people experiencing delays above 60%. When using the full distribution of information like this, the selection of threshold values for decision making is critical. The results show that depending on the threshold chosen, the two methods, point distance and path distance, would provide different solutions for the identification of critical node. Therefore the validity of using point distance is dependent on the decision variable being used. Since individual networks are unique and complex, there is no way of confirming the validity of using point distance without undertaking full analysis with both distance measurement methods, so there is no actual reduction in computation. Consequently, it is proposed in the next stage of the study to use path distance from the outset.

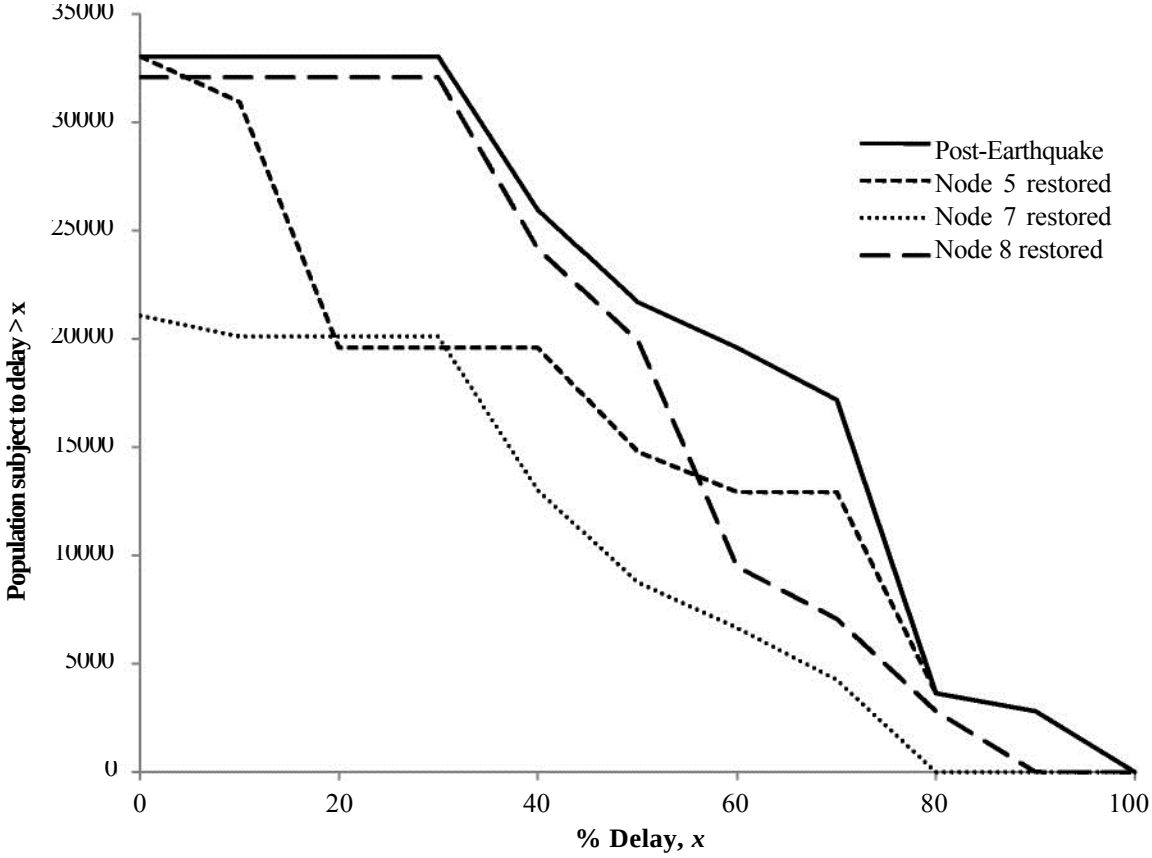


Figure 4: Cumulative distribution of population against the percentage delay in travel time using path distance analysis. The cumulative frequency is measured at 10% intervals.

4 CONCLUSIONS

The analysis described in this paper has demonstrated a simple GIS-based method for assessing highways system performance and the consequent impact on access to healthcare facilities using the Santa Clarita suburb of Los Angeles as a case study. It has also shown how outputs from risk assessment can be used to appraise disaster mitigation strategies. The simplicity of the method allows it to be used and understood by those without expert knowledge in programming and can thus play an important role in making the public and local officials more aware of risk assessment and increasing the perception of risk. Whilst it is possible to undertake more complex analysis using more powerful platforms, a simplified approach is appropriate in certain circumstances such as community engagement and prioritisation of mitigation.

However this case study has been undertaken only as a proof of concept for a larger more detailed study, involving a wider range of lifelines and impacts, and its purpose has been to demonstrate the strategy rather than the detailed methodology, aspects of which will be specific to the case study location. The next stage of the project is to upscale the proof of concept. In particular the methodology described here requires revision to more robustly account for uncertainty. It has already been proposed that Monte Carlo simulation (MCS) should be used to account for uncertainty in hazard and assignment of damage states to components, but these are not the only sources of uncertainty. There is also uncertainty in the selection of GMPE, the inter-event and intra-event variability in GMPE and the relationship between component performance and damage state. One possibility could be to carry out a

MCS for each of these variables too, but that would make the computation prohibitively large. The issue of uncertainty needs to be explored further and is critical in developing a robust tool for interdependent lifelines risk assessment.

Finally, there are also aspirations in the forthcoming stages of the project to investigate a wider range of performance indicators. Current practice in risk assessment focuses on loss estimation and, to a lesser degree, casualties. However, the impacts of an earthquake extend beyond this. The impacts can also be measured in terms of the effect on critical services and the resilience of communities. Building on the work by Verrucci [1], it is proposed to establish a series of key social indicators that can be used to characterise both risk and resilience in relation to lifelines.

REFERENCES

[1] S.C. Moser, *Resilience in the Face of Global Environmental Change*. CARRI Research Report 2. Oak Ridge National Laboratory, US Department of Energy, Tennessee, 2008.

[2] E. Verrucci, *Multi-disciplinary Indicators to Measure and Monitor Earthquake Resilience by using Remote sensing and GIS*. MPhil Report. University College London, London, 2010.

[3] N. Basoz, A.S. Kiremidjian, *Risk Assessment for Highway Transportation Systems*. Blume Report No. 118, Stanford University, California, 1996.

[4] C.A. Bana e Costa, C.S. Oliveira, V. Vieira, Prioritization of bridges and tunnels in earthquake risk mitigation using multicriteria decision analysis: application to Lisbon. *The International Journal ofManagement Science*, **36**, 442-450, 2008.

[5] Los Angeles County Department of Public Works, *Disaster Routes: Los Angeles County Operational Area*. http://dpw.lacounty.gov/dsg/DisasterRoutes (accessed 20 January 2013).

[6] United States Census Bureau (Department of Commerce), *2010 Census TIGER/Line® Shapefiles*. http://www.census.gov/geo/www/tiger/tgrshp2010/tgrshp2010.htm (accessed 20 January 2013).

[7] Google Earth 6.2.2.6613, *Santa Clarita, Los Angeles*. Satellite Image Data Layer. Available through http://www.google.co.uk/intl/en_uk/earth/index.html/ (accessed 20 January 2013).

[8] National Institute of Building Sciences, *HAZUS MR4 Technical Manual*, Washington D.C., 2003.

[9] Calfornia Department of Transport, *Caltrans Earth*. http://earth.dot.ca.gov/ (accessed 29 January 2013).

[10] American Hospital Association, *AHA Health Care Data Viewer*. http://www.ahadataviewer.com/ (accessed 29 January 2013).

[11] N. Shiraki, M. Shinozuka, J.E. Moore, S.E. Chang, H. Kameda, S. Tanaka, System risk curves: probabilistic performance for highway networks subject to earthquake damage. *Journal ofInfrastructure Systems*, **13**, 43-54, 2007.

[12] M.D. Petersen, W.A. Bryant, C.H. Cramer, T. Cao, M. Reichle, A.D. Frankel, J.J Lienkaemper, P.A. McCrory, D.P. Schwartz, *Probabilistic Seismic Hazard Assessment*

for the State of California. Open-File Rep. No. 96-08, California Department of Conservation, Division of Mines and Geology, Sacramento, California, 1996.

[13] D.M. Boore, G.M. Atkinson, Ground-motion prediction equations for the average horizontal component of PGA, PGV and 5%-damped PSA at spectral periods between 0.01s and 10.0s. *Earthquake Spectra*, **24(1)**, 99-138, 2008.

[14] United States Geological Survey, *Global V_S^{30} Map Server*. http://earthquake.usgs.gov/hazards/apps/vs30/ (accessed 30 January 2013).

[15] J.E. Padgett, R. DesRoches, Bridge functionality relationships for improved seismic risk assessment of transportation networks. *Earthquake Spectra*, **23(1)**, 115-130, 2007.

[16] Los Angeles County, *Los Angeles County GIS Data Portal – Assessor Parcels*. http://egis3.lacounty.gov/dataportal/?s=tax+assessor&submit.x=0&submit.y=0&submit=Search (accessed 30 January 2013).

[17] United States Census Bureau (Department of Commerce), *American Fact Finder*. http://factfinder2.census.gov/faces/nav/jsf/pages/searchresults.xhtml?refresh=t/ (accessed 30 January 2013).

[18] ESRI ArcMap 10.0, *Bing Maps Road Layer*. Available through http://www.esri.com/ (accessed 30 January 2013).

COMPDYN 2013
4th ECCOMAS Thematic Conference on
Computational Methods in Structural Dynamics and Earthquake Engineering
M. Papadrakakis, V. Papadopoulos, V. Plevris (eds.)
Kos Island, Greece, 12–14 June 2013

SECURING COMMUNITY RESILIENCE BY MODERN INFRASTRUCTURE DESIGN

Thomas Pickering[1], Sarah Dunn[2], Dr Sean Wilkinson[2]

[1]School of Civil Engineering and Geosciences, Newcastle University
Newcastle University, Newcastle Upon Tyne NE1 7RU, UK
thomas.pickering@ncl.ac.uk

[2]School of Civil Engineering and Geosciences, Newcastle University
Newcastle University, Newcastle Upon Tyne NE1 7RU, UK
sarah.dunn@ncl.ac.uk, s.m.wilkinson@ncl.ac.uk

Keywords: Infrastructure, Disaster Engineering, Resilience, Fragility

Abstract: *In the National Security Strategy and Strategic Defence and Security Review, the UK Government prioritised the need to improve security and resilience against attack, damage or destruction of infrastructure critical to keeping the country running. In response to this a guide (Keeping the Country Running: Natural Hazards & Infrastructure) was produced to focus on one of these threats, natural hazards.*

The purpose of the guide is outlined as "to encourage infrastructure owners and operators, emergency responders, industry groups, regulators, and government departments to work together to improve the resilience of critical infrastructure and essential services" [1]. "To share best practice and advice to enable organisations to continuously improve their infrastructure's resilience to natural hazards." And to "supplement existing guidance and fills gaps identified during the consultation on the Strategic Framework and Policy Statement in March 2010".

The guide suggests that resilience can be secured through a combination of four main elements; namely: resistance, reliability, redundancy, and response and recovery. In this paper we demonstrate how these components all contribute to achieving resilient communities. We analyse the resilience of a simple network which is augmented and subjected to events of different magnitudes to quantify the performance of the degraded systems. In our examples, the first network has a greater resistance (which incorporates reliability) to the disruption, whilst the second network has a greater redundancy and the third network has a superior response. We demonstrate that for each disruption the three networks have different resilience and that the most resilient network changes for each level of disruption. The examples presented in this paper illustrate a methodology for designing resilient critical infrastructure networks and demonstrate how all elements of resilience must be considered to achieve communities that can resist natural hazards.

INTRODUCTION

In the National Security Strategy and Strategic Defence and Security Review the UK government prioritises the need to improve security and resilience of critical infrastructure [1]. The review identifies that natural hazards are a large risk to the UK's security interest, as a result the "Keeping the Country Running: Natural Hazards & Infrastructure" document was developed as a guide to "*encourage infrastructure owners and operators, emergency responders, industry groups, regulators, and government departments to work together to improve the resilience of critical infrastructure and essential services*" [1]. This document presents a methodology to assess the resilience of critical infrastructure to natural hazards and to test potential mitigation strategies prior to deployment.

The Cabinet Office [1] defines Resilience as, "*the ability of assets, networks and systems to anticipate, absorb, adapt to and / or rapidly recover from a disruptive event*", the guide then progresses to define four key principles which contribute to infrastructure resilience (Table 1).

Resistance	"*to prevent damage or disruption by providing the strength or protection to resist the hazard"*
Reliability	"*ensuring that the infrastructure components are inherently designed to operate under a range of conditions"*
Redundancy	"*availability of backup installations or spare capacity will enable operations to be switched or diverted to alternative parts of the network"*
Response and Recovery	"*enable a fast and effective response to and recovery from disruptive events"*

Table 1 – Captions of definitions from the "Keeping the Country Running" document

These four principles are important in achieving community resilience because unlike other forms of the built environment these systems form complex networks which provide essential services to the community. The design emphasis therefore is to provide systems capable of delivering critical services even when the design hazard is exceeded and not simply providing infrastructure components with sufficient resistance to withstand particular hazard intensities. For example the power network supplies electricity across the country and a small physical disruption to the infrastructure of this system can have a devastating effect on the service it provides and in turn the citizens who rely on it.

The work presented in this study examines each of these principles to determine the influence each has on network resilience. This is achieved by subjecting three simple six node power networks to a simulated wind hazards and then relating post event performance to each of the four principles.

RESISTANCE, REDUNDANCY AND RESPONSE OF A SIMPLE NETWORK

So how do we incorporate all of these into our critical infrastructure networks? We do this by adapting a methodology used in earthquake engineering. Seismic design is unusual in that there is increased emphasis on scenarios where the system is overloaded. This started as a dual design approach, which is still what is used in the majority of cases, but has moved to performance based design - at least theoretically. In this approach we are trying to minimise the cost due to earthquake induced damage by integrating all of the costs resulting from all likely earthquakes during the life of a structure. This is achieved by using a hazard model to generate earthquakes which are then fed into a computer simulation that predicts building damage, the cost of which is then estimated by a damage model. One approach to this type of methodology is the discussion presented by Bruneau [2]. In the discussion Bruneau outlines

the aspects involved in securing community resilience for earthquake hazards and confers a framework, which enables the assessment and evaluation of the contributions of various activities to resilience. In a similar way this study aims to evaluate the aspects of infrastructure design which contribute to resilience, however the objective of this study is to demonstrate a methodology which can assess the performance of a network at system level by evaluating resilience to hazard at a component level.

To demonstrate this methodology and how the four principles of infrastructure resilience contribute to system resilience a simple network model is analysed, where an electricity Control Network (Figure 1a) with a single generation source (node 1), supplies surrounding demand nodes (substations). To demonstrate the concepts of resistance, redundancy and response, the resistance of the network is modelled using a fragility curve (a curve which relates probability of failure for a component to an event magnitude [3]) (Figure 2), enhanced with additional links for redundancy (Figure 1c) and a simulated crisis management plan for response (which does not alter the network's physical properties) (Figure 1d). The fragility curve for each network is used to determine random failures, and the resulting network connectivity's are analysed to determine which network performs best for each hazard.

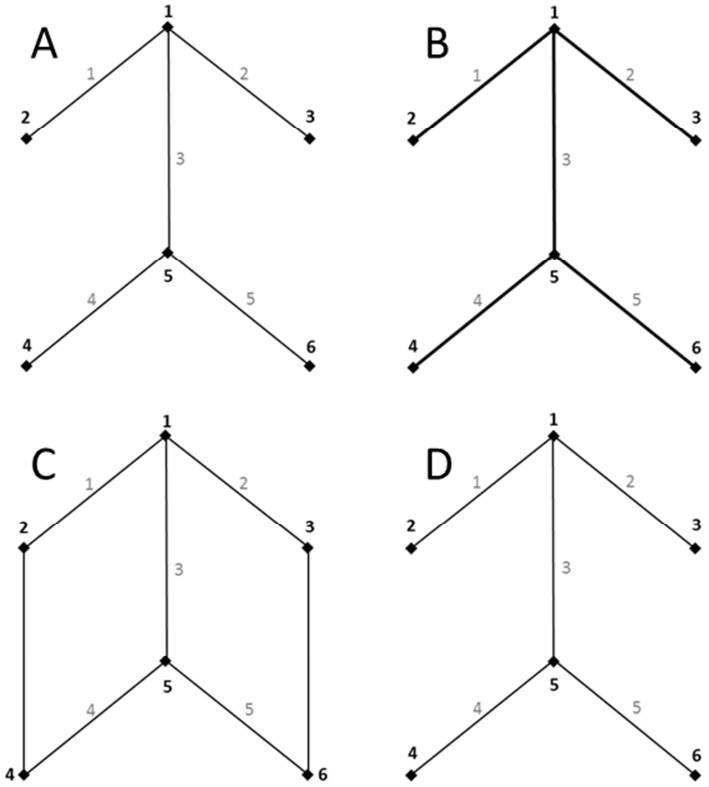


Figure 1 - Network Maps – Control (A), Resistant (B), Redundant (C), Response (D).

The networks are subjected to hypothetical windstorm events which vary in magnitude; however for demonstration purposes the intensity on each element within each network is considered equal (i.e. the hazard that each element is exposed to is identical.) This technique reflects the properties of a desired system in which each element with the same physical properties has the same fragility. In a real system however variations may exist in some characteristics, which could affect this (for example, lack of maintenance at one of the substations, or a transmission tower being located in a coastal environment resulting in increased corrosion) but for now we will ignore this.

Resistance is represented by fragility curves [3, 4, 5], where the probability of failure of the population of elements is defined as a function of hazard intensity, in this case wind speed (Figure 2). The Resistance Network has greater strength (a result of the network being constructed with stronger materials for example), and therefore its components have a correspondingly smaller probability of failure. The fragility of the Redundant and Response Networks are identical to the Control Network, the resilience of the Redundant Network originates from additional network links, and the Response Network from a better crisis management plan, which enables repair of damaged links to be made more quickly.

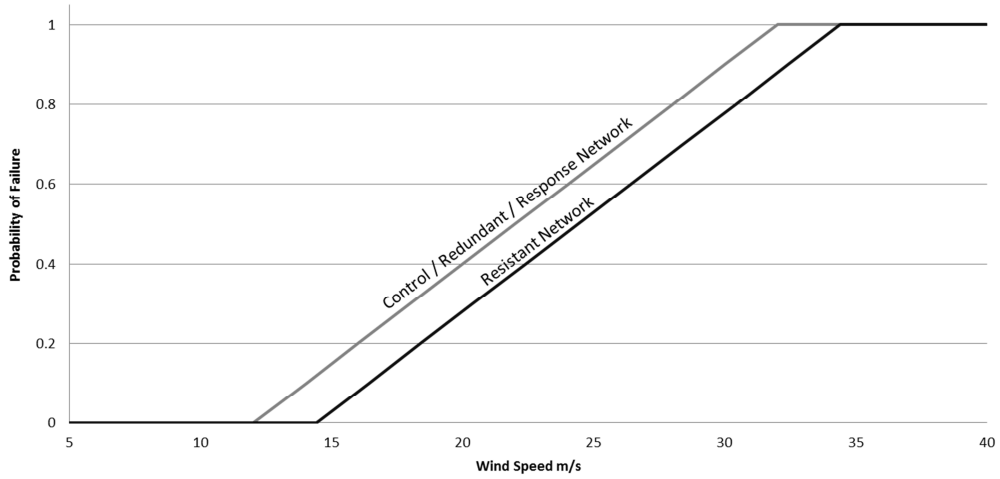


Figure 2 - Network resistances are depicted as conceptual fragility curves. As the event magnitude increases, the probability of failure increases linearly, until it equals 1 (where complete failure of the network occurs).

$$P(F_i|v)\ \epsilon_i = 1,2,3 \quad (1)$$
$$P(F_i|v)\ \epsilon_i = 4 \quad (2)$$

By introducing additional links into the Control Network we create resilience through redundancy. Therefore, in the event of failure, the network has an increased chance of staying connected (i.e. each of the substations maintain a connection to the supply), even if it may be at a reduced efficiency. Figure 1 Network C shows the augmentation introduced to the Control Network to create this redundancy.

To determine which network is more resilient, the process adopted has been to conduct a Monte Carlo simulation where events of a given magnitude are used to generate failure probabilities for each component in the various networks and then to assess the performance of the degraded networks. The results of many simulations are then averaged and compared to determine their relative resilience. Three intensity scales have been investigated; low magnitude, medium magnitude and high magnitude.

Low magnitude event

The first scenario considered is a low magnitude event at $14ms^{-1}$, which results in a probability of failure of 10% for each link in the Control Network (as well as the Redundant and Response Networks), and correspondingly a 0% of failure on the Resistant Network.

In this simulation the result of 100 trials of the Monte Carlo simulation, the Control Network sustained 48 node disconnections out of a possible total of 500; similarly the Redundant Network sustained 11 out of 500 disconnections. In the case of the Resistant Network however, the increased strength of the elements results in no links failing (Table 2),

as the Response Network is identical to the Control Network, the result for the Control Network is representative of both networks.

	Control Network	Resistant Network	Redundant Network
Total nodes analysed	500	500	500
Number of isolated nodes	68	0	11
Percentage of failed nodes	13.6%	0%	2.2%
Degraded performance ratio	-	0	0.16

Table 2 – Summary of 100 trials comparing the control, resistant and redundant networks for a low magnitude event

The key value from Table 2 is the degraded performance ratio; this indicates the comparative difference in the number of disconnections between a network and the Control Network. For this low magnitude event it can therefore be seen that the degraded performance of the Redundant Network compared to the Control Network is 0.16, (i.e. an 84% decrease in the number of isolated nodes). For the Resistant Network this value is 0, this indicates that for the low magnitude scenario it is the most resilient as the closer the degraded performance is to zero the better the network has performed in relation to the Control Network.

Consequently for low magnitude events, Table 2 indicates that the Resistant Network is the most resilient as there are no repair costs associated with replacing any failed links (i.e. the least number of failures), nor is there any associated cost with service losses. Both the Control and the Response networks have the greatest number of node disconnections; however the Control Network is the least resilient as the Response Network will be repaired more quickly and this is demonstrated in greater detail in the next example.

Medium magnitude event

In the second event, the magnitude is increased to $20ms^{-1}$. Figure 2 now indicates corresponding failure probabilities of 40% and 28% for the Control and Resistant Network elements respectively. The simulation is repeated and new performance ratios are obtained. The results of the simulation are displayed in Table 3.

	Control Network	Resistant Network	Redundant Network
Total nodes analysed	500	500	500
Number of isolated nodes	224	157	126
Percentage of failed nodes	44.8%	31.4%	25.2%
Degraded performance ratio		0.70	0.56

Table 3 – Summary of 100 trials comparing the control network to the resistant network for a medium magnitude event

What can be seen from **Error! Reference source not found.** is that for the medium magnitude event the degraded performance ratios are 0.7 and 0.56 for the Resistant and Redundant Networks respectively, which indicates that the Redundant Network has outperformed the Resistant Network by 6%. For the medium magnitude event it can therefore be concluded that Redundant Network is the most resilient, as it results in less disruption to consumers.

Medium magnitude event - Response

Keeping the Country Running, outlines response as "*the effectiveness of this element is determined by the thoroughness of efforts to plan, prepare and exercise in advance of events*"[1], because of this, resilience cannot be quantified through the methods previously investigated. Instead, resilience is obtained through planning and event management; by incorporating these additional preparations network restoration time after a failure is reduced. To demonstrate this response planning each of the networks is first subjected to a medium magnitude event, and the restoration of the network is then plotted as available capacity against time (Figure 3). In the example shown by Figure 3, response planning allows the reconstruction of failed links to begin in 50% of the time it takes the other networks; only one link per time step can be restored in this model, regardless of network type.

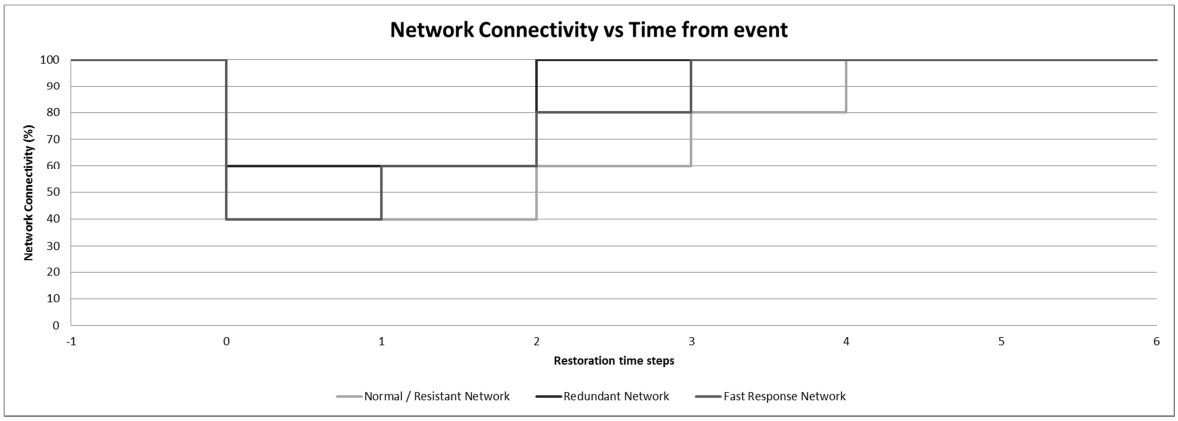


Figure 3 - Graphical representation or restoration time for each network after an event

Figure 3 displays the effect of a medium magnitude event on each of the network types. The event has disrupted links 1, 2 and 5 on all networks. This reduces the functioning capacity of the Control Network group to 40% (2 connected nodes) and 60% on the Redundant Network (3 connected nodes). Progressively one time step allows the Response Network to have its first link repaired increasing its connectivity to 60%, a result of the better event planning. At the second time step the Response Network increases to 80% connectivity, the Control and Resistant Network increase to 60% connectivity (first repair); however the Redundant Network reconnects all nodes to the network, a result of the additional links which did not fail. This makes the Redundant Network the most resilient as the other networks at the end of the second time step each have one node disconnected. In time step 3 the Response Network is restored, and in time step four the Control and Resistant Networks are restored.

Large magnitude event

In this event, a large magnitude of wind speed ($36ms^{-1}$) is chosen, this wind speed results in failure of all the links in all the networks. The advanced planning associated with the Response Network returns it to full capacity in the shortest time making it the most resilient, (Figure 4) resulting in fewer overall losses. The Control, Resistant and Redundant Networks are returned to operating capacity in the same amount of time after the Response Network (note the redundant network has the same resilience as it will be initially repaired in a form that is identical to the other networks. Subsequent to this it will continue to be restored to its original configuration and there would be an extra cost associated with this. The Resistant

and Redundant Networks are the least resilient for a high magnitude event because of the additional cost associated with the stronger elements and additional links (transmission lines) in each respective network.

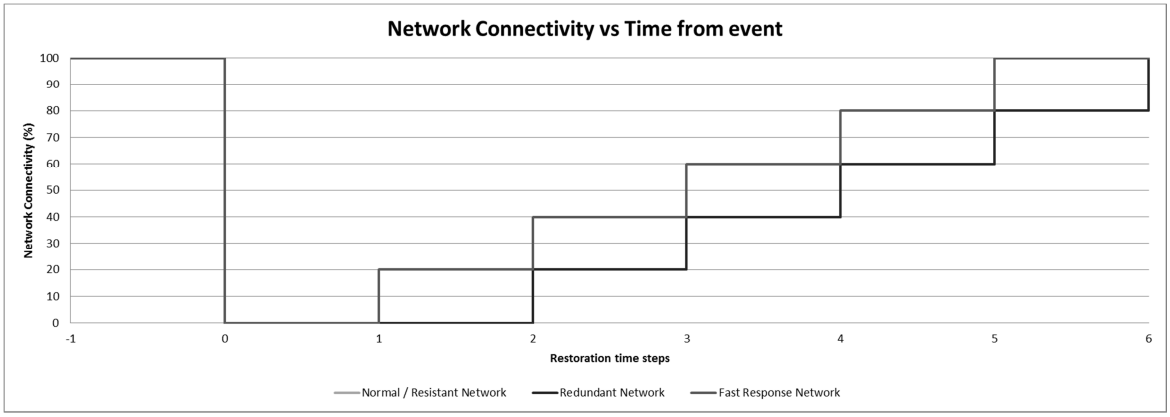


Figure 4 - Large magnitude event network restoration

RELIABILITY OF NETWORKS

"The Reliability component is concerned with ensuring that the infrastructure components are inherently designed to operate under a range of conditions and hence mitigate damage or loss from an event. The tendency of a reliability strategy is to focus only on the events within the specified range, and not events that exceed the range. This can lead to insufficient awareness or preparation for events outside of the range, and hence significant wider and prolonged impacts can occur. Reliability cannot therefore be guaranteed, but deterioration can sometimes be managed at a tolerable level until full services can be restored after the event" [1]

Put simply this definition of reliability is concerned with both the infrastructure having sufficient resistance for events that can be considered reasonable design events but also to have some capacity after exposed to events greater than this.

One interpretation of reliability is therefore; for the expected range of events, components are designed to be strong enough they operate efficiently during normal conditions, which is the resistance procedure already analysed. For events that are not designed for, i.e. events which cause loads above the design threshold; reliability idealises some operational capacity to remain after a failure occurs, which can be interpreted as a form of redundancy. This can be imagined using a transmission line. The line operates within tolerances until it is subjected to an event greater than the design strength of the system and its components, which for example causes the failure of a conductor, hence failure of one circuit of the transmission line. The line can then be considered failed, however the tower may support a second circuit which remains operational and hence the line in the network still holds some capacity after the failure event, unlike the redundancy study investigated earlier where a failure was complete interruption of the line. It can also be considered that additional power capacity may also exist in the second circuit if it was not operating at its maximum when the event occurred (redundancy in the cables). During a higher magnitude event the tower may experience a collapse failure, in this case complete failure would be observed. True redundancy is therefore a combination of the number of circuits in a line, the amount of power flow in these circuits as a percentage of their peak power flow, and the number of lines which can supply power from site A to site B.

Reliability is then formed from the resistance of these components, some amount of spare capacity and the redundancy of the system that these components create.

In regards to deterioration effects, which are highlighted in the definition for reliability [1], a traditional approach can be used. Deterioration can be considered at component and system levels. In the previously examined cases, component resistance has been described through use of a fragility curve. When we consider deterioration in component resistance, this fragility curve shifts leftwards along the magnitude axis, a result which could for example be caused by corrosion. The result of this is that probability of failure increases for lower magnitude events; maintenance closely returns the fragility curve to its initial position (Figure 5).

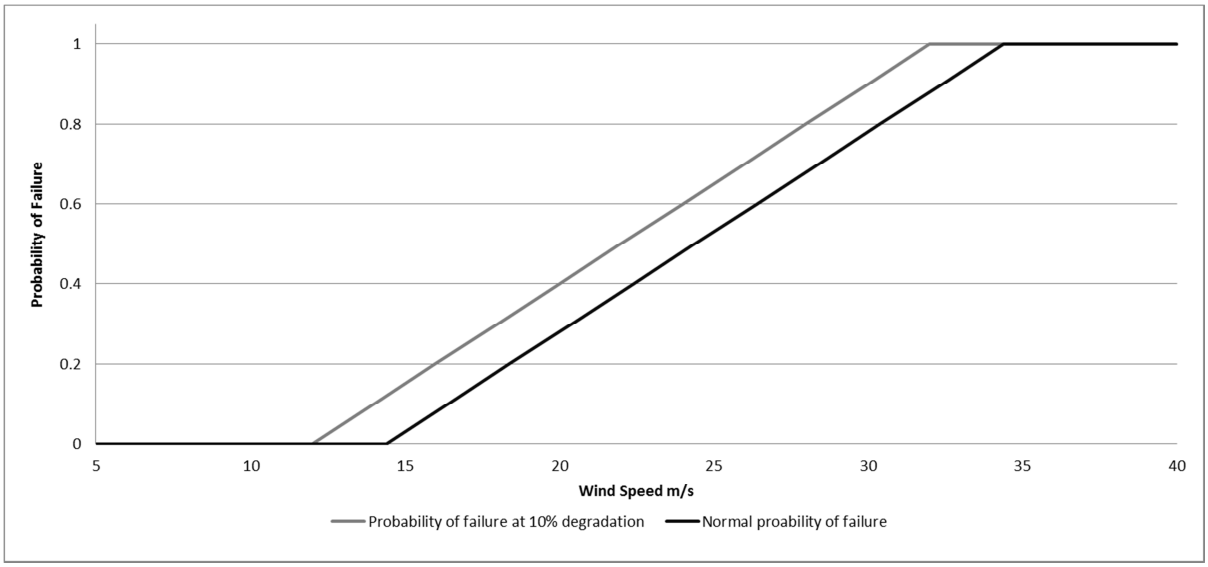


Figure 5 – Probability of failure comparison showing the normal curve and the deteriorated curves

System level deterioration is determined through simulations such as those previously presented. It can be determined that the longer a component is left without a maintenance check and repairs if necessary, the more likely it is that the component in question would have an increased vulnerability; leading to a potential reduction in system reliability which could be quantified by ascribing costs to repair components and costs of system level disruption.

CONCLUDING REMARKS

This paper outlines a methodology for assessing resilience of infrastructure networks that is consistent with The Keeping the Country Running: Natural Hazards & Infrastructure document. It demonstrates the method by analysing three simple networks that have different levels of resistance, redundancy and response. In our first event the networks suffer a relatively small magnitude event that only causes minor damage to the Control, Redundant and Response Networks, and no damage to the Resistant Network. By the time all networks are repaired and the total costs are calculated it can be seen that the Resistant Network has the least cost associated with it (as it suffers no damage). Running the event again but this time with a greater magnitude and therefore greater intensities at the component level, more widespread damage occurs. Here the greater resilience of the Redundant Network allows all components to keep functioning (all be it at a reduced rate) and therefore end up incurring the lowest cost due to disruption, whereas failure of the individual components of the Control, Resistant and Response Networks result in a greater loss of service. Finally a high magnitude

event results in total network outage and so the time to recover is the most important factor in reducing the cost due to losses, resulting in the Response Network having the greatest resilience even though it loses the ability to provide service the easiest.

Providing robustness (in the form of resistance) to individual components of a network may not always be the cheapest solution as a similar result can be obtained by increasing the redundancy of the network, as this provides an alternative route to supply services and therefore capacity may still be present when a link is severed. This has been shown by the networks presented, as the degraded performance ratio (relative number of link failures compared to the Control Network) decreases from the Resistant Network (0.7) to the Redundant Network (0.56) (Table 3) based on maintaining connections.

These examples could be considered as measures of reliability in the context in which the definition is written by the Cabinet office (although cost due to service disruption and repairs to components should be included). It has been determined that reliability is simply the combination of resistance for event magnitudes (load conditions) which are forecasted for in the design of the system under consideration, and redundancy for events which are beyond the scope of the design. In conclusion the components of infrastructure networks (for example electricity transmission towers) are designed with particular resistances. Whereas the failure of individual components is important, it is the provision of services that they enable that is the major design consideration. Maximising the resilience of this service to the widest range of hazards requires consideration of the resistance, robustness and reliability of the individual components as well as ensuring the network has sufficient redundancy so that the redistributed services can still reach the intended recipients.

For utility owners to adopt this methodology for real Infrastructure networks, development of fragility curves and recovery curves are required. Reliable forms of fragility curves are not presently available; however the RESNET project [6] is attempting to produce them for the UK electricity transmission network. Recovery curves may exist for relatively small disruptions, but these are not in a form that can be readily used in a risk assessment as they are usually the uncorrelated repair records of utility owners and in the case of large scale disruption are likely to be absent.

Reference

[1] UK Cabinet Office, *Keeping the Country Running: Natural Hazards and Infrastructure*. UK Cabinet Office, 2011.

[2] Bruneau, M., Chang, S.E., Eguchi, R.T., Lee, G.C., O'Rourke, T.D., Reinhorn, A.M., Shinozuka, M., Tierney, K., Wallace, W.A. and Winterfeldt, D. *A Framework to Quantitatively Assess and Enhance the Seismic Resilience of Communities,* Earthquake Spectra, Volume 19, No. 4, pages 733–752, Earthquake Engineering Research Institute, 2003.

[3] Zentner, I., Nadjarian, A., Humbert, N. and Viallet, E. *Numerical Calculation of Fragility Curves for Probabilistic Seismic Risk Assessment,* The 14th World Conference on Earthquake Engineering, 2008

[4] Applied Technology Council, *Seismic Performance Assesment of Buildings Volume 1 – Methodology, ATC-58-1 75% Draft*, Applied Technology Council, 2011.

[5] Ahmed, A., Arthur, C. and Edwards, M. *Collapse and pull – down analysis of high voltage electricity transmission towers subjected to cyclonic wind*. IOP Conference Series: Materials Science and Engineering **10**: 012004. 2010

[6] RESNET – Resilient Electricity Networks for Great Britain. 2012. http://www.tyndall.manchester.ac.uk/projects/resnet/index.html

COMPDYN 2013
4th ECCOMAS Thematic Conference on
Computational Methods in Structural Dynamics and Earthquake Engineering
M. Papadrakakis, V. Papadopoulos, V. Plevris (eds.)
Kos Island, Greece, 12–14 June 2013

DAMAGE REPORT WITH SMARTPHONES DURING EMILIA EARTHQUAKE, 2012

V. Arcidiacono[1] **and G.P. Cimellaro**[1]

[1] Politecnico di Torino
Corso Duca degli Abruzzi 24, Torino, Italy
e-mail: vincenzo.arcidiacono@polito.it, gianpaolo.cimellaro@polito.it

Keywords: Damage Assessment, Emilia Earthquake, Recovery Plan, Damage Report, and Smartphone Application.

Abstract. *On May 20th and 29th 2012, two earthquakes of 5.9Mw and 5.8Mw have struck the Emilia Romagna region of Italy, causing 27 deaths and widespread damage. The epicentres were between Finale Emilia and Medolla. The damage report during the emergency response was managed from the Italian Civil Protection and volunteers, using AEDES hardcopy forms. Since the use of smart phones is spreading among citizens our team decided to develop a smartphone application, which works on Android technology, to record the damage state of residential buildings. This was tested during the emergency response of Emilia earthquake to help the Piedmont Civil Protection on recording the damage report and, moreover, it was compared with the standard procedure based on the use of AEDES hardcopy forms.*

1 INTRODUCTION

The increasing capabilities of mobile communication and computing of handheld devices [1][2][3][4][5][6] are very helpful to provide a damage report after a natural disaster such as a earthquake. Emergency managers have to receive and record the data related to damages of physical infrastructure (e.g. buildings, etc.) and then they have to develop and transmit emergency plans as fast as possible [7]. The acquisition of damage reports starts from the citizens that require a first-level damage report – i.e. certificates of usability made with the AeDES survey form. Then the operative centre organizes many technical teams to evaluate and perform the damage reports that are processed and organized according to their importance. Much of damage reports of physical infrastructure are currently done by the use of hardcopy forms. These are processed step by step and not in real time – i.e. the emergency managers wait for the slow uploading of the data blocks that are acquired in hardcopy forms from the Di.Coma.C. (Operative centre) – loosing the overall view of the emergency. Moreover, the communication system can break off due to the fragility of telecommunication networks, which makes the damage report more difficult. Therefore, the rapid changing of information during a disaster suggests developing a procedure that can acquire in real time the damage reports using a robust telecommunication network.

In the paper, it is proposed a smartphone application *D.A.S.* – Damage Assessment with Smartphones, which works on Android technology, which acquires citizens' requests and assess the damage state of buildings, providing efficient real-time information for the evaluation of emergency plans required after a natural disaster [8]. The smartphone application was tested during the emergency response in Emilia – that was affected by two strong earthquakes on the 20th and 29th of May 2012 – to help the Piedmont Civil Protection with recording the damage reports. Moreover, the proposed procedure was compared with the standard procedure, evidencing the strengths of using handheld devices.

2 EMILIA EARTHQUAKE

A series of important seismic events occurred in Italy in the Po valley, starting from Sunday morning of May 20th, 2012, when at 04:03:53 local time (02:03:53 UTC) a strong earthquake whit magnitude Mw 5.9 struck. The epicentre was located in Finale Emilia (44°50'N 11°17'E) in the province of Modena. On Tuesday May 29th, at 09:00:03 local time (07:00:03 UTC) a new strong earthquake whit magnitude Mw 5.8 occurred in the same seismic region of the previous event (44°85'N 11°09'E) and even this time it was felt throughout northern Italy. The shock of the nine followed three other mayor shocks again on May 29th: one at 12:55 with magnitude Mw 5.4, another one at 13:00 whit magnitude Mw 4.9 and a further one at the same time with magnitude Mw 5.2. The main earthquake of May 20th was anticipated by a first event with magnitude M_w 4.1 in the same place at 01:13 local time on Saturday May 19th. The strong earthquake of 4:03 has begun with a long seismic sequence, which was continued in the following weeks with more than 2200 shocks; seven were with M_w >5 (Table 1).

Date	UTC (local time)	Latitude	Longitude	Depth	Magnitude	Source
20/05/12	02:03:52 (04:03:52)	44.889	11.228	6.3	5.9	iside.rm.ingv.it
20/05/12	02:07:31 (04:07:31)	44.863	11.370	5.0	5.1	iside.rm.ingv.it
20/05/12	13:18:02 (15:18:02)	44.831	11.490	4.7	5.1	iside.rm.ingv.it
29/05/12	07:00:03 (09:00:03)	44.851	11.086	10.2	5.8	iside.rm.ingv.it
29/05/12	10:55:57 (12:55:57)	44.888	11.008	6.8	5.3	iside.rm.ingv.it
29/05/12	11:00:25 (13:00:25)	44.879	10.947	5.4	5.2	iside.rm.ingv.it
03/05/12	19:20:43 (21:20:43)	44.899	10.943	9.2	5.1	iside.rm.ingv.it

Table 1 Main earthquakes with M_w >5 (updated on July 13, 2012).

All of these earthquakes had a devastating effect on the towns near the epicentre, resulting in 27 fatalities. The collapse of industrial structures was the major contributor to life hazard, because most people were working when the second earthquake struck. The most affected town centres by earthquakes were: *Alberone, Camurano (Meddola), Canaletto, Finale Emilia, Galeazza, Mirandola, San Felice sul Panaro, and San Carlo (INGV)*. Many low-rise unreinforced masonry construction and the most vulnerable buildings have suffered major damage that made them unusable. Some monuments have been damaged with huge losses for the historical heritage. Frequently, the fall of chimneys from the roofs occurred in residential buildings, but generally the new buildings have not been damaged, while many abandoned houses in the countryside collapsed.

3 MANAGEMENT OF THE EMERGENCY RESPONSE IN EMILIA

The earthquakes, which have struck the Emilia Romagna region, can be classified as an inter-regional disaster [10][11] – that required coordination at the national level – because it involved more than 80,000 people distributed across 40 municipalities (16 in the Province of Modena, 7 in Mantua, 7 in Bologna, 6 in Ferrara, and 4 in Reggio Emilia) and it damaged historic buildings in the largest towns (Ferrara, Mantua, Modena and Bologna). The civil protection of the Emilia-Romagna region is one of the best-equipped and organised in Italy, with a big headquartered in Bologna and huge number of vehicles, manpower, equipment, and supplies. Moreover, it was one of the first Italian regions to introduce TETRA system (TErrestrial Trunked RAdio, Figure 1), which creates an alternative emergency communication network if the previous one is damaged.

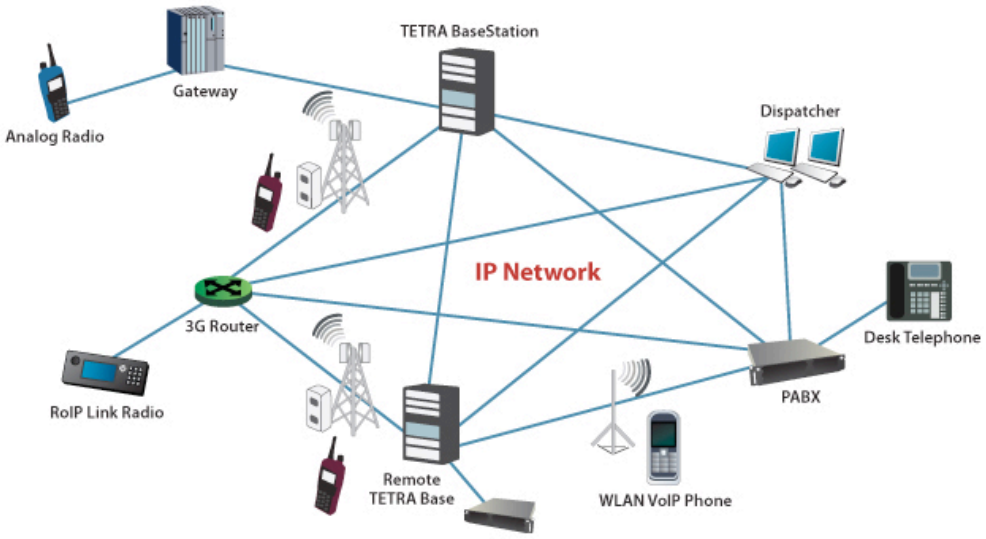


Figure 1 TETRA system (TErrestrial Trunked RAdio).

The Emilia emergency issue was the regeneration of industry and employment. The evacuations were limited to brief exits at the time of the tremors, but anyway, the earthquakes left about 20,000 people in need of shelters (62% in Modena, 30% in Ferrara, 5% in Bologna, and 3% in Mantua). The damage to housing was slight, but the undamaged houses inside the red zones – areas such as the city centres, which were cordoned off in order to maintain public safety – were inaccessible. These buildings needed anyway a first-level damage report to be realised.

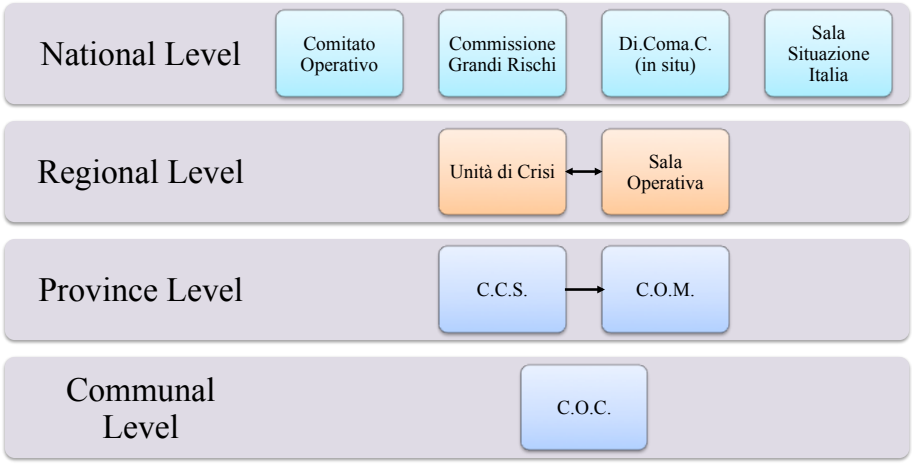


Figure 2 Italian system of coordination.

Figure 2 shows the Italian system of coordination in which resources are managed by sectors from national level (Di.Coma.C.), through regional level (Unità di Crisi) to the larger (C.O.M.) and then smaller local settlements (C.O.C.). One of the competencies managed by the national Department of Civil Protection is to coordinate technical assessments of the stability and usability of residential buildings.



Figure 3 Volunteer technician of Politecnico di Torino.

Volunteer technicians from various regions (Figure 3) have performed the surveys for assessing the damage of residential buildings during the emergency response with the AeDES survey forms (certificates of usability) making 38,726 surveys (3,665 in Bologna, 8,827 in Ferrara, 24,144 in Modena, and 2,090 in Reggio Emilia) from 21st of May until 30th of August (101 days). Also our group of the Department of Structural, Geotechnical & Building Engineering (DISEG) of Politecnico di Torino have participated collaborating with the Piedmont Civil Protection making about 500 surveys.

Figure 4 shows the certificate of usability (i.e., AeDES survey form) that was used in Emilia, which defines six outcomes of building usability: (A) usable building, (B) UNUSABLE building (totally or partially), but USABLE after short-term countermeasures, (C) PARTIALLY UNUSABLE building, (D) TEMPORARILY UNUSABLE building requiring a more detailed investigation, (E) UNUSABLE building, and (F) UNUSABLE building due to

external risk. Moreover, it is composed by nine sections: (1) building identification, (2) building description, (3) typology, (4) damage to structural elements and short term countermeasures carried out, (5) damage to non structural elements and short term countermeasures carried out, (6) external damage due to other constructions and short term countermeasures carried out, (7) soil and foundations, (8) usability judgment, and (9) other observations.

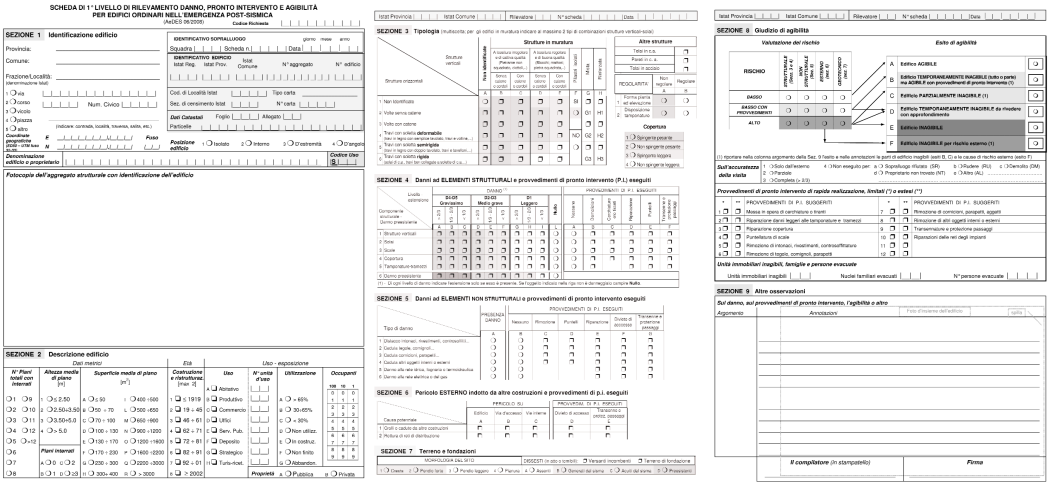


Figure 4 AeDES survey form.

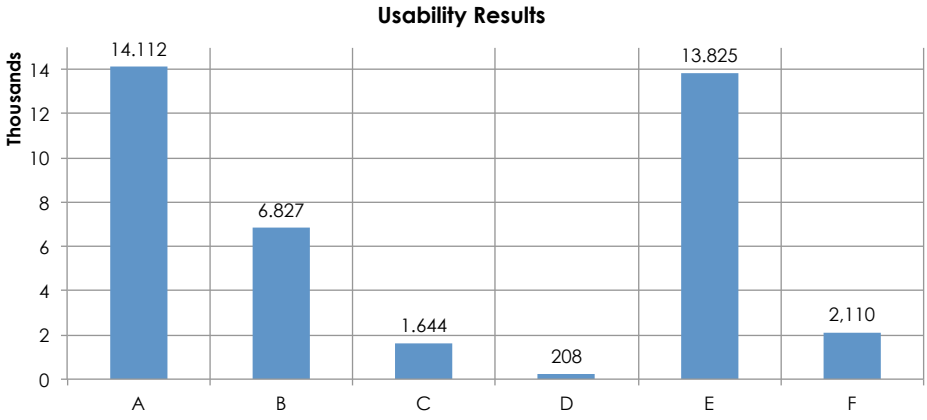


Figure 5 Usability results after 101 days from 20th of May.

Figure 5 shows the results of certificates of usability at the national level, until the 29th of August, which were: 14,112 (36.4%) of A, 6,827 (17.6%) of B, 1,644 (4.2%) of C, 208 (0.5%) of D, 13,825 (35.7%) of E, and 2,110 (5.4%) of F.

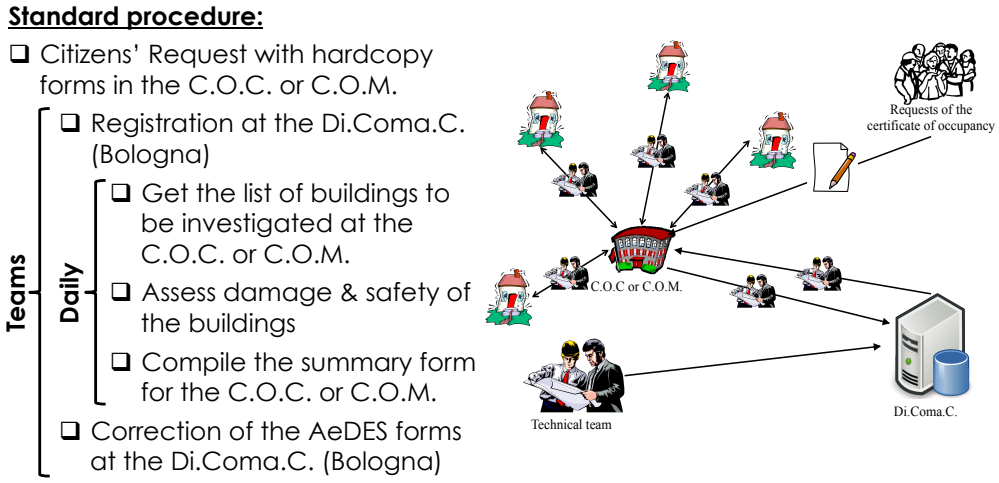


Figure 6 Standard procedure for the certificates of usability during the Emilia earthquake.

As mentioned above, the surveys were made by several technical teams. The standard procedure (Figure 6) for the certificates of usability during the emergency was:

- Citizens' request of certificates of usability with hardcopy forms in the C.O.C. or C.O.M.
- Organization of technical teams

  Then for each technical team:
  - Registration of the technical team at the Di.Coma.C. (Bologna)

    For each day:
    - Get the list of buildings to be investigated at the C.O.C. or C.O.M.

      For each building:
      - Reach the building to be investigated
      - Fill the AeDES survey form (certificate of usability)
    - Compile the summary form for the C.O.C. or C.O.M.
    - Reach the accommodation
  - Correction of the AeDES forms at the Di.Coma.C. (Bologna).

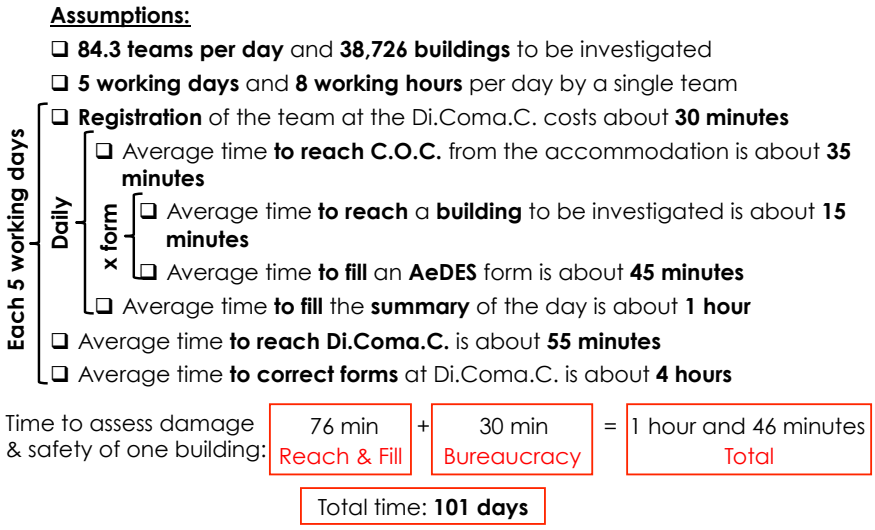


Figure 7 Assumptions and times for the standard procedure.

With the assumptions shown in Figure 7, each certificate of usability has cost 1 hour and 46 minutes, where 30 minutes were lost for bureaucratic procedures. This means that 28% (29

days) of the total time (101 days) for performing the certificates of usability of damaged residential buildings was lost only for the bureaucratic procedures, without considering of the lost time to get the list of buildings to be investigated at the C.O.C. or C.O.M..

4 SMARTPHONE APPLICATIONS DURING EMERGENCY RESPONSE

Since the use of smartphones is gaining interest in people, our team decided to implement the smartphone technology into the standard procedure for making certificates of usability of the damaged residential buildings. During the emergency response, for helping the Piedmont Civil Protection, a smartphone application was developed. This was tested during the emergency response of Emilia earthquake to acquire 24 citizens' requests (Figure 8a) and 70 AeDES survey forms.



Figure 8 (a) Citizens' requests made with application, and (b) graphical interface

The application shown in Figure 8 is a user-friendly and reduces the bureaucratic procedures and simplifies the evaluation and the acquisition of the certificates of usability. The application provides:

1. Registration of the technical team requiring the identification data of technical team – i.e. identification team number, names and signatures of technicians – that are using the handheld device, reducing the time of the registration.
2. Prefilled AeDES survey form, speeding up the acquisition process.
3. Geo-referencing of the forms trough the GPS localization of the device.
4. Sketches and photos of the investigated building that are attached to the certificate of usability.
5. Auto-correction of the survey form, deleting any error.
6. Creation of the certificate of usability in PDF format.
7. Sending of the certificate, photos, and sketches to the operative centre (in our case the Politecnico di Torino), reducing and optimizing the time to perform the damage report.

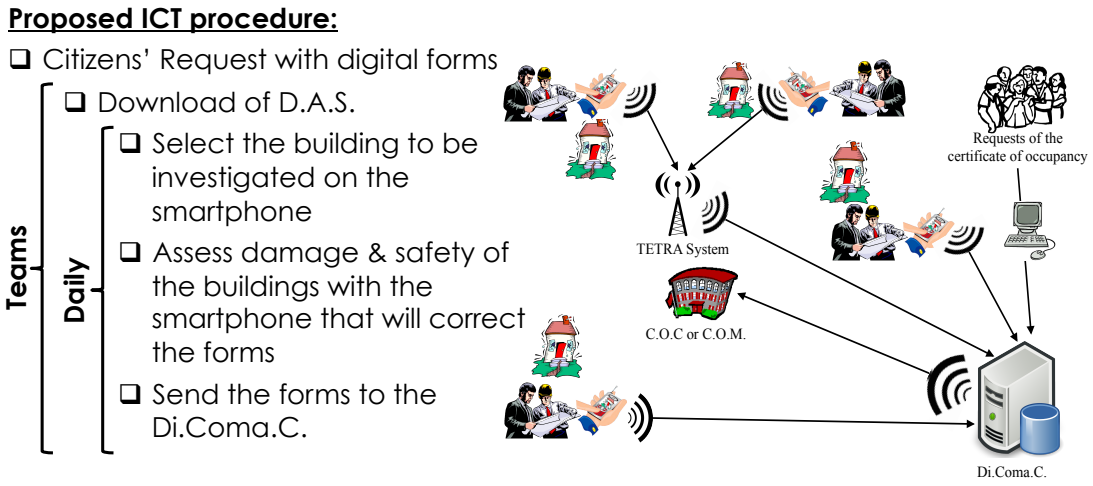


Figure 9 Proposed procedure to make the certificates of usability.

Therefore, our research intends to propose a new procedure (i.e., ICT procedure, Figure 9) to make efficiently the certificates of usability during emergencies: integrating the TETRA system (robust network that permits the use of ICTs), removing all bureaucratic procedures, and reducing detours and missing appointments (giving the routing to the closer and available residential building to be investigated). The proposed ICT procedure is defined as follows:

- Citizens' request of certificates of usability in digital format
- Organization of technical teams

  Then for each technical team:
  - Download of D.A.S. application and registration of the technical team

    For each day and each building:
    - Select the building to be investigated on the application
    - Reach the building to be investigated
    - Fill the AeDES form with the smartphone, which is corrected by the application
    - Send the AeDES form to the Di.Coma.C. by internet connection (TETRA system)
    - Reach the accommodation.

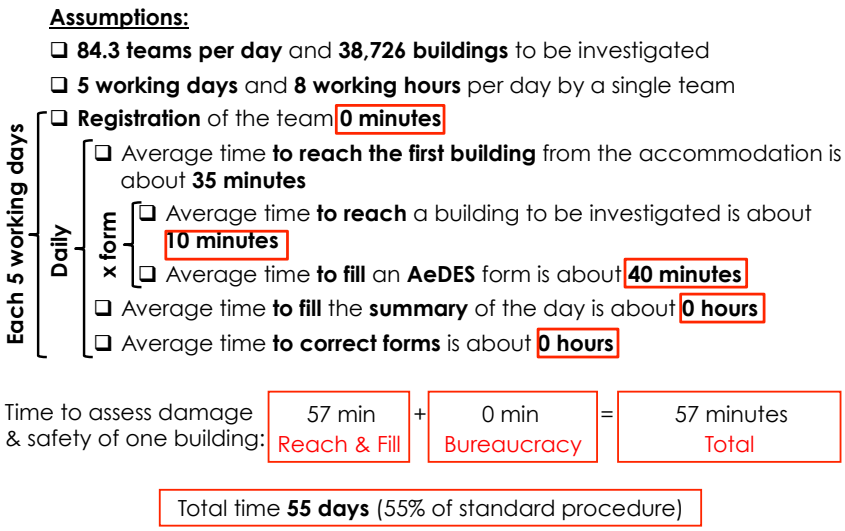


Figure 10 Assumptions and times for the proposed ICT procedure.

In conclusion, with the assumptions shown in Figure 10, each certificate of usability costs 57 minutes. In particular, it doesn't waste time in bureaucratic procedures. This means that the ICT procedure would permit to save 45% (i.e., 46 days) compared to the total time of the standard procedure.

5 CONCLUSIONS

Two earthquakes of 5.9Mw and 5.8Mw, on the 20th and 29th of May 2012, have struck the Emilia Romagna region of Italy, involving more than 80,000 people distributed across 40 municipalities and damaged historic buildings in the larger towns. The Emilia emergency issue was the regeneration of industry and employment.

The Politecnico di Torino helps the Piedmont Civil Protection, with a series of volunteer technical teams, to assess the damage status of the residential buildings and produce the damage report during the emergency. Hence, an application for assisting technicians and engineers was developed in order to improve the speed of producing damage reports for buildings during catastrophic events. The procedure uses a robust telecommunication network (i.e. TETRA system), it reduces the bureaucratic procedures and simplifies the compilation of the first-level damage reports required to assess the stability and the usability of the investigated residential buildings. The smartphone application was tested, during the emergency response of Emilia earthquake, to acquire 24 citizens' requests and 70 AeDES survey forms. The proposed ICT procedure, which works more efficiently during emergencies, was simulated and applied to the case of Emilia earthquake, showing the advantages with respect to the hardcopy standard procedure.

ACKNOWLEDGEMENTS

The research leading to these results has also received funding from the European Community's Seventh Framework Programme - Marie Curie International Reintegration Actions - FP7/2007-2013 under the Grant Agreement n° PIRG06-GA-2009-256316 of the project ICRED - Integrated European Disaster Community Resilience. The research was also sponsored by the Israel-Italy Joint Innovation Program for Industrial, Scientific and Technological Cooperation in R&D, EUREKA Label under the Grant agreement no.: 3435777CDC of the project ECRIS - European Communities resilient integrated through Smart Phones.

REFERENCES

[1] E. Aoki, T. Kikuchi, K. Korida, N. Yoshiyama, Y. Shibata, M. Takahashi, M. Takenaka, Study on the Social Networking System of Disaster Prevention using Smart Phones. *International Conference on Complex, Intelligent, and Software Intensive Systems,* 2011.

[2] J.T.B. Fajardo, C.M. Oppus, A Mobile Disaster Management System Using the Android Technology, *INTERNATIONAL JOURNAL OF COMMUNICATIONS Issue 3, Volume 3*, 2009.

[3] C.B. Hare, Redefining user input on handheld devices, *Third International Conference on 3G Mobile Communication Technologies, pp. 388-393*, 2002.

[4] H.Y. Kung, H.H. Ku, A Real-time Mobile Multimedia Communication System for the Prevention and Alert of Debris-Flow Disaster, *Proceeding of: Vehicular Technology Conference*, 2003.

[5] J. Lee, D.L. Niko, H. Hwang, M.G. Park, C. Kim, A GIS-based Design for a Smartphone Disaster Information Service Application, *First ACIS/JNU International Conference on Computers, Networks, Systems, and Industrial Engineering*, 2011.

[6] H.S. Shim, G.Y. Min, D.H. Jeong, A Study on the Development of Disaster Information Reporting and Status Transmission System based on Smart Phone, *ICTC 2011*, 2011.

[7] V. Arcidiacono, G.P. Cimellaro, A.M. Reinhorn, and M. Bruneau. "Community Resilience Evaluation including interdependencies." *15th World Conference on Earthquake Engineering (15WCEE)*, Lisbon, Portugal, September 24-28th, 2012.

[8] G.P. Cimellaro, V. Arcidiacono, A.M. Reinhorn, and M. Bruneau. "Resilience of ambulance service during emergency." *11th International Conference on Structural Safety & Reliability (ICOSSAR2013)*, June16-20, 2013, Columbia University, New York, Year.

[9] INGV strong motion data. http://www.mi.ingv.it/ISMD/ismd.html (accessed October 2012).

[10] Regione Emilia-Romagna 2012. Aggiornamento del 17.09.2012 Emergenza sisma maggio 2012.

[11] T. Rossetto, D. Alexander, E. Verrucci, I. Ioannou, R. Borg, J. Melo, B. Cahill, I. Kongar, The Emilia (Italy) Earthquake of 20th May 2012, EPICentre Field Observation Report No. EPI-FO-200512, 2012.

[12] G.P. Cimellaro, A.M. Reinhorn, and M. Bruneau. Framework for analytical quantification of disaster resilience. *Engineering Structures, 32(11), 3639-3649*, 2010.

[13] G.P. Cimellaro, A.M. Reinhorn, and M. Bruneau. Seismic resilience of a hospital system. *Structure and Infrastructure Engineering, 6(1-2), 127-144*, 2010.

[14] G. Scura, V. Arcidiacono, G.P. Cimellaro, C. Renschler, and A.M. Reinhorn. "Integrated Damage Assessment Communication system using smartphone network during 2012 Emilia earthquake." Vienna Congress on Recent Advances in Earthquake Engineering and Structural Dynamics & 13. D-A-CH Tagung (VEESD2013), Vienna, Austria, August 28-30, 2013.

[15] V. Arcidiacono, G.P. Cimellaro, and A.M. Reinhorn. "A software for measuring disaster community resilience according to the PEOPLES methodology." *Proceedings of the 3rd International Conference on Computational Methods in Structural Dynamics and Earthquake Engineering (COMPDYN 2011)*, Corfu`, Greece, May 26-28, 2011, Year.

COMPDYN 2013
4th ECCOMAS Thematic Conference on
Computational Methods in Structural Dynamics and Earthquake Engineering
M. Papadrakakis, V. Papadopoulos, V. Plevris (eds.)
Kos Island, Greece, 12–14 June 2013

NUMERICAL INVESTIGATION OF WIND INDUCED OVALLING VIBRATIONS IN SILO GROUPS

Jeroen Hillewaere[1], Joris Degroote[2], Ali Rezayat[3], Steve Vanlanduit[3], Geert Lombaert[1], Jan Vierendeels[2], and Geert Degrande[1]

[1]Department of Civil Engineering, KU Leuven
Kasteelpark Arenberg 40, B-3001 Heverlee, Belgium
e-mail: {jeroen.hillewaere,geert.lombaert,geert.degrande}@bwk.kuleuven.be

[2]Department of Flow, Heat and Combustion Mechanics, Ghent University
St. Pietersnieuwstraat 41, B-9000 Gent, Belgium
e-mail: {joris.degroote,jan.vierendeels}@ugent.be

[3]Department of Mechanical Engineering, Vrije Universiteit Brussel
Pleinlaan 2, B-1050 Brussels, Belgium
e-mail: {arezayat,svanlandui}@vub.ac.be

Keywords: Wind-structure interaction, ovalling vibrations, wind tunnel validation, silo structure.

Abstract. *Wind induced ovalling vibrations were observed during a storm in October 2002 on several empty silos of a closely spaced group consisting of 8 by 5 thin-walled silos in the port of Antwerp (Belgium). In the present study, it is investigated if the observed ovalling oscillations can be numerically predicted. To this end, the silo structures are modeled using a finite element (FE) model and the wind flow around a single silo is investigated using 3D computational fluid dynamics (CFD) simulations. A wind tunnel experiment was set up to validate the CFD simulations. To explain the onset of the wind induced ovalling vibrations, the interaction of the wind field with the structural vibrations has to be taken into account. Therefore, the complex interplay of both fields is investigated with both one-way and two-way coupling simulations. It is interesting to compare the results of both coupling approaches to assess the necessity of performing the computationally much more time-consuming two-way coupling simulations. It is found in both coupling approaches that the mode shapes with the lowest natural frequencies are excited dynamically. The results in the one-way coupling simulations differ however from those in the two-way coupling, demonstrating the importance of performing fully coupled simulations for suchlike aeroelastic problems.*

1 INTRODUCTION

Wind induced ovalling vibrations were observed during a storm in October 2002 on several empty silos of a closely spaced group consisting of 8 by 5 thin-walled silos in the port of Antwerp (Belgium) (figure 1). Numerical techniques are a valuable alternative to wind tunnel tests or full scale measurements to study the onset of these aeroelastic structural vibrations. For this purpose, the coupled wind-structure interaction (WSI) problem as a whole should be considered numerically. This implies that the 3D computational fluid dynamics (CFD) simulations of the wind flow and the structural vibrations, calculated with a finite element (FE) model should be considered as one coupled problem.



Figure 1: The 8 by 5 silo group in Antwerp.

Due to the complexity of this coupled problem when the entire 8 by 5 silo group is considered, it is advisable to first study a more simple subproblem to verify and validate the numerical procedures. Therefore, in the present paper, the case of a single 3D silo in cross flow is considered.

The outline of the paper is as follows. The dynamic properties of the silo structures will be presented first. Finite element modeling is used to determine natural frequencies and ovalling mode shapes of a silo. The 3D CFD simulation of the highly turbulent flow around a single silo is presented in the third section. In addition to the description of the applied numerical procedures and the approach to apply realistic inlet conditions a separate section is dedicated to the validation of the numerical results in a wind tunnel experiment. In the last section, the wind-structure interaction problem is considered where the numerical model for the structure and for the wind flow are coupled. The first and easiest approach investigated is the one-way coupling simulation, where the aerodynamic surface pressures on the silo surface are applied as external transient loads on the FE model of the structure. Finally, a two-way coupled simulation is performed where feedback is given in each time step from the structure to the flow field. It takes approximately five times longer to compute a single time step in the two-way coupling simulations when compared to the one-way coupling.The results of both coupling simulations are compared to assess the necessity of performing the computationally much more time-consuming two-way coupling simulations to investigate such aeroelastic phenomenon.

2 STRUCTURAL MODEL

Ovalling deformations of a thin-walled shell structure are defined as a deformation of the cross section of the structure without bending deformation with respect to the longitudinal axis of symmetry [11]. The ovalling mode shapes for the thin-walled empty silos (diameter $D =$

$5.5\,\mathrm{m}$ and wall thickness $t_\mathrm{s} = 0.07\,\mathrm{m} - 0.10\,\mathrm{m}$ varying along the height of the silo) are referred to by a couple (m, n) where m denotes the half wave number in the axial direction and n is the number of circumferential waves (figure 2).

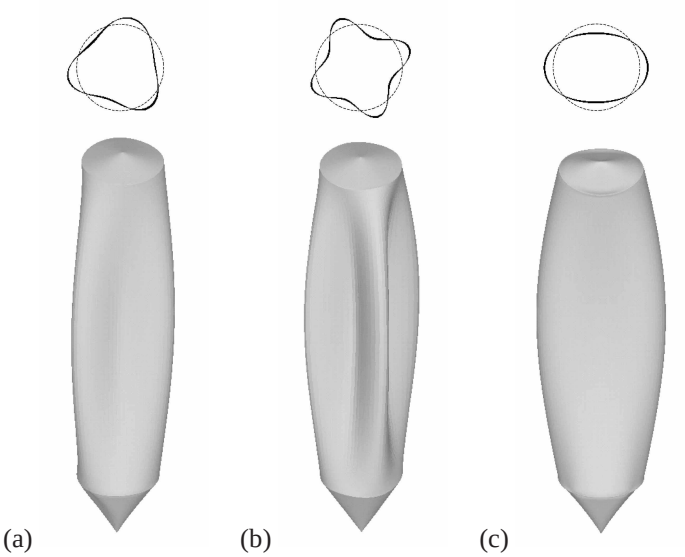


Figure 2: Selected ovalling eigenmodes of a single silo: (a) mode $\mathbf{\Phi}_1 = (1, 3)$ at 3.93 Hz, (b) mode $\mathbf{\Phi}_3 = (1, 4)$ also at 3.93 Hz and (c) mode $\mathbf{\Phi}_{11} = (1, 2)$ at 7.76 Hz [3].

The governing equations for the structural problem are defined as follows:

$$\mathbf{M}\ddot{\mathbf{U}}(t) + \mathbf{C}\dot{\mathbf{U}}(t) + \mathbf{K}\mathbf{U}(t) = \mathbf{P}(t) \tag{1}$$

where $\mathbf{M}$, $\mathbf{C}$ and $\mathbf{K}$ are the mass, damping and stiffness matrix respectively, $\mathbf{U}(t)$ represents the structural displacements and $\mathbf{P}(t)$ are the external loads on the structure. Rayleigh damping is assumed for the damping matrix $\mathbf{C} = \alpha_\mathrm{R}\mathbf{M} + \beta_\mathrm{R}\mathbf{K}$ with $\alpha_\mathrm{R} = 0.186\,\mathrm{s}^{-1}$ and $\beta_\mathrm{R} = 3.03\times10^{-4}\,\mathrm{s}$, based on a constant damping ratio $\xi = 0.75\%$ for the two lowest eigenmodes. This is a realistic approximation since modal damping ratios ξ for this specific structure, determined during on site measurements by Dooms et al. [6], were found to vary between 0.07% and 1.32%. These low values of modal damping are typical for a welded aluminium structure.

A FE approach is used to discretize the governing structural equations in the Abaqus software package [3]. To accommodate an easy transfer of the aerodynamic pressures on the silo walls to the mesh of the structural model in the coupled simulations (section 4), the mesh of the FE model was chosen conforming to the mesh on the silo walls in the 3D CFD simulations (figure 4). Since the cone at the bottom of the silo structures is covered by a prismatic building below the silo, this part of the structure is not exposed to the wind flow. A separate mesh was defined for this part of the structure, compatible with that of the superstructure. Shell elements with linear FE interpolation functions are used for all silo elements and the following material properties for aluminium are used: density $\rho = 2700\,\mathrm{kg/m^3}$, Young's modulus $E = 67.6\,\mathrm{GPa}$ and Poisson's ratio $\nu = 0.35$. The silo structures are connected to a steel framework, covered by the prismatic building below, at 4 discrete points along the circumference of the cylindrical part of the silo. The mode shapes and natural frequencies of the silo structure are then found by solving the following generalized eigenvalue problem:

$$\mathbf{K}\mathbf{\Phi} = \omega^2\mathbf{M}\mathbf{\Phi} \tag{2}$$

where $\omega = 2\pi f_{\text{eig}}$ with f_{eig} the eigenfrequencies of the structure. The mass normalized eigenmodes $\mathbf{\Phi}$ of this eigenvalue problem with the lowest corresponding eigenfrequencies are summarized in table 1. Note that most of the mode shapes come in pairs: e.g. $\mathbf{\Phi}_1$ and $\mathbf{\Phi}_2$ are both classified as mode shapes $(1,3)$ but are mutually orthogonal.

$\mathbf{\Phi}_j$	(m,n)	f_{eig} [Hz]
$\mathbf{\Phi}_{1,2}$	$(1,3)$	3.93
$\mathbf{\Phi}_{3,4}$	$(1,4)$	3.93
$\mathbf{\Phi}_{5,6}$	$(1,5)$	5.28
$\mathbf{\Phi}_{7,8}$	$(1,5)$	5.59
$\mathbf{\Phi}_{9,10}$	$(1,6)$	7.38
$\mathbf{\Phi}_{11}$	$(1,2)$	7.76

Table 1: Structural natural frequencies f_{eig} of ovalling mode shapes of the silo structure.

The visually detected pattern of vibrations at the lee side of the silo group during the 2002 storm are believed to have been ovalling mode shapes $(1,3)$ and $(1,4)$, with the lowest natural frequencies of the silo structure. Measurements during normal wind loading have also shown that eigenmodes with 3 or 4 circumferential wavelengths have the highest contribution to the response of the silos [6].

3 WIND FLOW SIMULATIONS

The highly turbulent wind flow around a single silo is investigated by performing 3D CFD simulations. The numerical procedure, computational domain and issues concerning the boundary conditions are discussed first. For validation purposes, a comparative study of the aerodynamic pressures determined in the simulations and measured in a wind tunnel experiment is performed. Finally, the flow pattern around the single silo is discussed and qualitatively compared with available literature.

3.1 Numerical procedure

The governing incompressible Navier-Stokes equations are discretized by means of the finite volume method in the CFD simulations. Since the focus in this analysis is on the structural response, it is unnecessary to resolve all details of turbulent fluctuations in the flow. Instead of resolving all turbulent scales in a direct numerical simulation (DNS), other numerical techniques were developped for the treatment of turbulence in the simulations, e.g. Reynolds averaged Navier-Stokes (RANS) simulations or large eddy simulations (LES).

For the highly turbulent, external aerodynamic flow of the present case ($\mathrm{Re} = 1.24 \times 10^7$), DNS or LES simulations are computationally too demanding, especially since accurate near-wall flows are required to get a good prediction of the aerodynamic pressures on the silo walls. It is therefore advisable to use the near-wall modeling of the RANS techniques. In this light, delayed detached eddy simulations (DDES) are performed in Ansys Fluent [1].

DES models are refered to as hybrid LES/RANS models because the URANS modeling of the boundary layer flow in the near-wall region is combined with the LES approach in the separated regions, where large unsteady turbulence scales are dominant. In the delayed DES approach, a shielding function is used to ensure that RANS is applied in the entire boundary layer since a sole geometrical separation of RANS and LES regions based on mesh size has been shown to be insufficient. For the shielding function, the blending functions of the SST

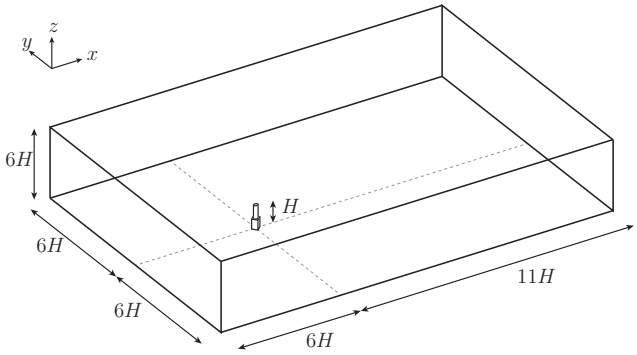


Figure 3: Dimensions of the 3D computational domain and global coordinate system , with origin at the bottom of the domain at the center of the structure.

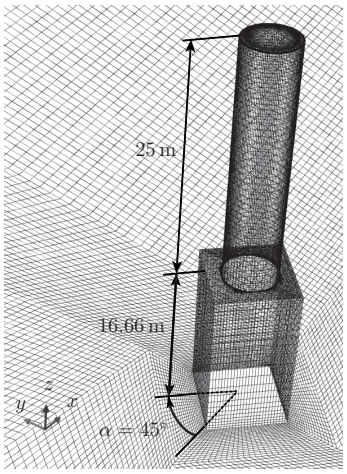


Figure 4: Detail of the mesh for 3D DDES of a single silo structure with the wind at an angle of incidence $\alpha = 45°$.

turbulence model are used [10]. Coupled pressure-based simulations with a second-order interpolation of the pressure, a second-order upwind interpolation of the turbulent kinetic energy k and the specific dissipation rate ω and a second-order implicit, unconditionally stable, time stepping method are performed. For the discretization of the momentum equations a bounded central differencing scheme is used in DDES.

3.2 Computational domain and boundary conditions

The boundaries of the computational domain should be sufficiently far from the zone of interest in the centre of the domain (i.e. where the silo structures are located). Several guidelines are available in the literature with rules of thumb for the size of the computational domain and the boundary conditions.

Based on wind tunnel experiments, guidelines have been set up by the Architectural Institute of Japan (AIJ) for the size of the computational domain in 3D wind simulations [18]. For a single building model, the lateral and the top boundaries should be set $5H$ or more away from the building and the outflow boundary should be located at least $10H$ behind the building where H is the height of the building. Furthermore, the blocking ratio (i.e. building cross section/domain section) should be below 3%. As shown in figure 3, slightly larger values of $6H$ and $11H$ are used, resulting in a blocking ratio of 1.7%. The outflow boundary is modeled as a pressure outlet while symmetry is imposed on lateral and top boundaries. The walls of the structure are considered smooth and no-slip boundary conditions are applied.

Since the specific atmospheric conditions near the silo group were not monitored during the storm, approximative wind conditions have to be set up, based on the location of the group and mean wind velocities for storm conditions in design codes. Based on the Eurocode 1 design guidelines for wind loading [5], a mean wind velocity $v_\infty = 31.8\,\mathrm{m/s}$ is determined at half the height of the silos (approx. $z = 30\,\mathrm{m}$), resulting in a post-critical wind flow at Reynolds number $\mathrm{Re} = v_\infty D/\nu = 1.24 \times 10^7$. Furthermore, the logarithmic velocity profile and realistic turbulence profiles of the atmospheric boundary layer (ABL) have to be imposed at the inlet of the 3D computational domain. As recommended by AIJ [18], a power law is used in the

simulations:

$$v_x(z) = v_{\mathrm{R}}(z/z_{\mathrm{R}})^{\alpha} \quad (3)$$

$$\mathrm{Tu}(z) = 0.1(z/z_{\mathrm{G}})^{-\alpha-0.05} \quad (4)$$

where $v_{\mathrm{R}} = v_{\infty} = 31.8\,\mathrm{m/s}$ is the reference velocity at a reference height $z_{\mathrm{R}} = 30\,\mathrm{m}$. The exponent $\alpha = 0.14$ and gradient height $z_{\mathrm{G}} = 300\,\mathrm{m}$ are determined for terrain category 2 (open country) according to the AIJ guidelines [18]. Based on these inlet boundary conditions and standard relations in fluid mechanics, inlet profiles for turbulent kinetic energy k and specific dissipation rate ω can be derived and imposed at the inlet. To simulate time dependent fluctuations superimposed on these mean profiles, a spectral synthesizer method is used [16].

3.3 Experimental validation

Apart from the verification of the numerical procedure (grid size refinement and time step refinement), which is not discussed in detail in this paper, it is very important that the simulation results are also validated with some experimental data or full-scale measurements. Because of the high Reynolds number and the particular geometry of this single silo case (figure 4), no such data are available in the literature. An experimental set-up of the present geometry was therefore prepared in a wind tunnel.

In view of the present purposes, the experimental validation is primarily aimed at a comparison of the aerodynamic pressure distribution on the silo surface. Pressures on the square prismatic building below the silo stucture and other parameters of interest (e.g. velocities in the wake flow etc.) are not considered in this paper.

3.3.1 Experimental apparatus and techniques

The experiments were carried out in the fluid mechanics laboratory at the Department of Mechanical Engineering at the Vrije Universiteit Brussel (VUB), using the wind tunnel 1 facility. This open circuit wind tunnel is mainly designed for civil engineering experimental setups and the relatively high testing chamber ($2\,\mathrm{m}$ wide, $1\,\mathrm{m}$ high and $12\,\mathrm{m}$ long) allows conducting measurements with different geometry shapes. The dimensions of the scaled model are calculated by optimizing the cross section area of the model inside the wind tunnel. This method leads to a compromise between blockage effect reduction and Reynolds number increase. The resulting scale factor is 1:50 and the model geometry is rotated 45° with respect to the flow direction, similarly as in the CFD simulations of the single silo. No roughness elements were placed in the wind tunnel section to simulate a natural boundary layer.

The scaled model consists of two different compartments: the building part where no probes are installed (wooden box), and a cylindrical PVC tube including the pressure sensor system (figure 5a). The free end of the PVC tube is finished with a conical PVC top to match the silo geometry. The measurement points in the cylindrical part are distributed uniformly along the height of the tube (figure 6). At each point, a pressure tap (metallic needle) is installed through the tube shell in order to capture the (unsteady) static pressure on its surface (figure 5b). The installation of these pressure taps is particularly critical. The silo surface should have the smallest possible discontinuities and the needles need to be installed perpendicular to the surface to minimize the effect of dynamic pressure contribution.

A Scanivalve pressure measurement device [2] is installed in the wooden building compartment of the model and is connected to all pressure taps via flexible tubes. For this set of experiments a 64-channel valve-less piezoelectric device is used that communicates the unsteady

(a)  (b) 

Figure 5: Set up of the wind tunnel experiments: (a) downstream view of the scale model of the silo structure in the wind tunnel and (b) pressure tabs installed in the interior of the PVC tube.

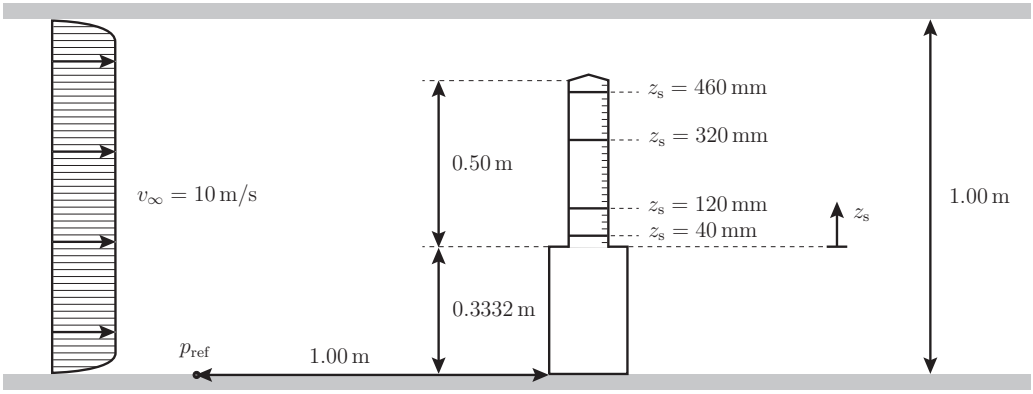


Figure 6: Schematic representation of wind tunnel test section.

pressure data to a computer, using a channel-multiplexing method. The ability to measure multiple channels at high frequencies up to $2\,\mathrm{kHz}$ is one of the main advantages of this device. A set of 24 pressure taps is installed, aligned and equally distributed along the vertical axis of the cylinder (figure 5). The cylindrical tube is installed in such a way that the complete pressure distribution on the surface can be measured by rotating the entire cylinder around its axis of symmetry in 16 rotational steps ($22.5°$).

The experiments are carried out in the ambient conditions of the lab. The Scanivalve device measures the differential pressure with respect to a reference point. In this case, the static pressure is measured in a reference point situated $1\,\mathrm{m}$ upstream of the model at the bottom of the wind tunnel test section (figure 6). All possible fluctuations of air humidity and temperature are neglected during the measurements.

3.3.2 Experimental and numerical set-up

For a good comparison of experimental and numerical results, the wind tunnel flow should have similar characteristics as the numerically simulated natural wind around the structure or vice versa. Furthermore, reduced geometric scales are typically used in wind tunnel experiments for obvious reasons of economy and convenience. Such scaling operation introduces the question of physical simulitude for which a set of dimensionless numbers and/or similarity criteria are applicable to both flow and structure. Numerous works have been published describing these similarity requirements, e.g. [15].

In the present study, however, dimensional analysis and difficulties to achieve similarity between wind tunnel and real atmospheric flows have been avoided by adapting the wind tunnel experiments and the simulations to each other. On the experimental side, a model was constructed corresponding to the geometry of the single silo. The size of this model had to be small enough in order to fit the wind tunnel section and large enough so that it could be instrumented with the pressure tabs. The numerical simulations in their turn were scaled down to the exact size of the wind tunnel experiment (i.e. scaling of 1:50) but leaving the dimensions of the computational domain (cfr. figure 3) and the mesh refinement unchanged with respect to the structure size. These operations have several important consequences for the validation:

- The wind velocities that can be reached in the wind tunnel are not nearly large enough to simulate a wind flow at a Reynolds number similar to that in the full scale numerical simulations ($\mathrm{Re} = 1.24 \times 10^7$), described in section 3.2 . Instead, a velocity of $10\,\mathrm{m/s}$ is applied at the inlet of the wind tunnel and also in the numerical simulations. The resulting Reynolds number ($\mathrm{Re} = 6.25 \times 10^4$) categorizes the wind flow in the subcritical flow regime (transition in the shear layer) as opposed to the post-critical regime (fully turbulent shear layer and wake) in the real-scale simulations at higher wind velocities and Reynolds number [15, 19]. This should be taken into account for the interpretation of the simulation results because different physical phenomena are to be expected in the transitional and post-critical regime, especially in the behaviour of the attached shear layer.

- Due to the vicinity of the top wall of the wind tunnel (figure 6), some blockage effects are to be expected in the pressure measurements in the upper part of the silo structure. In the simulations, the top of the computational domain is much more distant from the free end of the silo structure and pressures might differ.

These discrepancies make the present comparison not entirely representative as validation for the single silo in cross flow. However, taking into account the above mentioned considerations in the comparison of the results, this validation is nevertheless a valuable asset to increase the confidence in the numerical simulations.

3.3.3 Comparison of experimental and numerical results

As mentioned, only the pressure distribution on the silo structure will be reviewed in the validation study. Both mean pressures and root-mean square (RMS) values of the surface pressures are shown in figure 7 at four locations along the height of the cylinder surface.

At the windward side of the cylinder, the mean pressures agree very well in the attached flow from the stagnation point until separation is reached. In the simulations, separation occurs later than in the experiments, leading to lower negative base pressures at the lee side of the cylinder. This difference between simulations and experiments in the prediction of the separation point and consequently the base pressures at the lee side, can be explained by considering the applied turbulence model in the simulations.

In the DDES simulations, the SST turbulence model [9] is used for the RANS solution in the near-wall regions. This turbulence model is typically very efficient for fully turbulent boundary layers at high Reynolds numbers but switches to turbulent modelling of the boundary layer flow too quickly at lower Reynolds numbers. The separation point is consequently not captured accurately in the simulation for subcritical flow in the experiments and a narrower

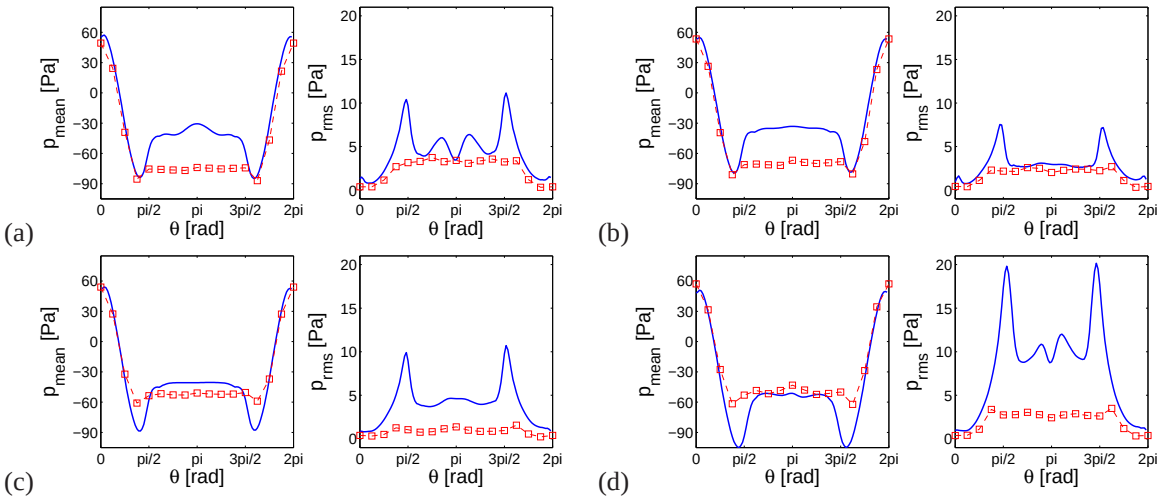


Figure 7: Experimental (□, dashed line) and numerical (full line) mean pressure and RMS pressure distribution along the circumference of the cylindrical silo structure for four different locations along the height of the silo: (a) $z_s = 40\,\mathrm{mm}$, (b) $z_s = 120\,\mathrm{mm}$, (c) $z_s = 320\,\mathrm{mm}$, and (d) $z_s = 460\,\mathrm{mm}$.

wake is formed at the lee side of the cylinder, typical for post-critical flows. Unfortunately, no DES simulations can be performed with a more suitable transitional turbulence model in the RANS part and on the other hand, no wind tunnel simulations can be performed up to Reynolds numbers high enough to capture a fully turbulent boundary layer on the cylinder surface. Nevertheless, for the present full-scale application with post-critical wind flow, the applied numerical turbulence model is believed to yield accurate results.

Furthermore, although experiments and simulations seem to generate comparable pressure profiles near the bottom part of the cylinder surface (figure 7a, b), the agreement seems to decrease moving towards the free end of the cylinder (figure 7c, d). This discrepancy is attributed to blockage effects due to the vicinity of the top wall of the wind tunnel near the free end of the structure (figure 6).

The conclusions for the mean pressures can be extended to the fluctuating pressures (RMS) as well. The agreement is good at the windward side of the structure while the separation point is delayed in the simulations, resulting in higher fluctuating pressure peaks. However, the agreement of the fluctuating pressures at the leeward side of the cylinder seems to be better than for the mean pressures. The leeward pressure fluctuations are of the same order of magnitude in experiments and simulations, although the agreement deteriorates when moving upwards. This is in agreement with the observations for the mean pressures.

3.4 Flow pattern around the single silo

To gain physical insight in the flow pattern around the present single silo structure in the natural wind conditions ($\mathrm{Re} = 1.24 \times 10^7$), it is instructive to compare the simulated flow pattern with that around similar surface-mounted bluff bodies in cross flow. Furthermore, apart from the quantitative validation discussed in section 3.3, such qualititave comparison increases the confidence in the simulation results.

The present geometry can be considered as the combination of two different types of bluff bodies: a cylinder is placed on top of a square prism. A reasonable amount of literature can be found where the flow around cantilevered cylinders [4, 12, 13] and prismatic obstacles [7, 14,

17] is investigated experimentally. However, as for the wind tunnel experiment in this paper, Reynolds numbers in the experimental set-ups in the literature are typically in the order of magnitude of $10^4 - 10^5$. Great care should therefore been taken when comparing the present flow pattern with experimental flow visualization studies in the literature.

Due to the highly 3D nature of the flows, different flow patterns coexist over different spanwise positions of the silo structure. For this purpose the streamlines of the flow are shown along a vertical plane in figure 8 and in 5 horizontal planes across the height of the silo structure in figure 9.

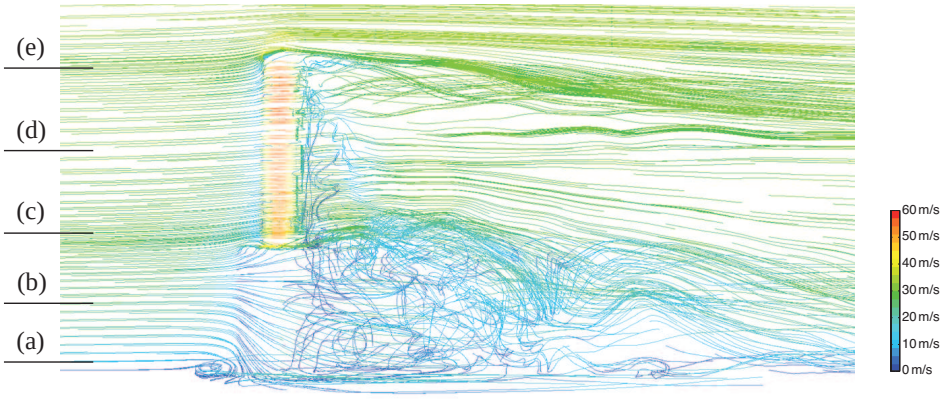


Figure 8: Velocity streamlines of the wind flow around a single silo structure at $t = 70\,\mathrm{s}$, colored according to the velocity magnitude, in a vertical plane $y = 0\,\mathrm{m}$. Reference is made to the 5 horizontal planes shown in figure 9.

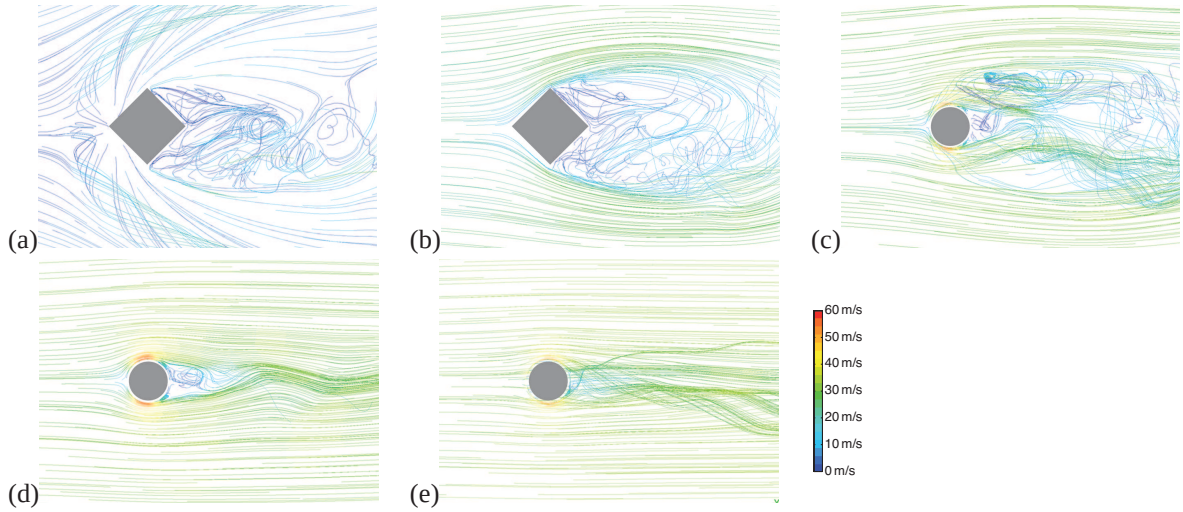


Figure 9: Velocity streamlines of the wind flow around a single silo structure at $t = 70\,\mathrm{s}$, colored according to the velocity magnitude, in horizontal planes at (a) $z = 0.5\,\mathrm{m}$, (b) $z = 8\,\mathrm{m}$, (c) $z = 17.16\,\mathrm{m}$, (d) $z = 29.16\,\mathrm{m}$, and (e) $z = 41.16\,\mathrm{m}$.

At the base of the silo structure, the wind flow is forced around the square prismatic building which is rotated at an angle of $45°$ with respect to the incident wind flow. As observed in the literature [4], upstream of an isolated surface-mounted structure, the natural turbulent boundary layer on the surface undergoes a three-dimensional separation and the lower regions of the

separated boundary layer roll up to form a vortex system upstream of the building (figure 8). The ends of this vortex system are swept downstream and the typical horseshoe (or necklace) vortex is formed. This behaviour is observed for both prismatic [14, 17] and cylindrical [4] cantilevered structures. In figure 9a, the formation of a horseshoe vortex upstream of the obstacle is also observed in the present simulations at much higher Reynolds number.

At mid-span of the square prismatic building below the silo structure, the flow near the lateral upstream faces of the structure are mainly stable and no flow separation is observed (figure 9b). The attached flow separates at the transverse corners of the square prism. At the lee side, a turbulent wake is produced between the separated shear layers.

At the connection of the square prismatic building to the cylindrical silo structure, the flow is slightly accelerated and deflected upwards along the upper corners of the lateral upstream sides (figure 8). The flow separates and is simultaneously deflected sideways, parried by the cylindrical silo structure (figure 9c).

The flow pattern around the upper silo structure resembles that around a cantilevered cylinder in cross flow. In this part of the structure, 3D flow effects are mainly attributed to the flow separation and resulting downwash flow near the free end of the cylinder. Nonetheless, a suppressed 2D region can exist along the cylinder height, even with vortex shedding resembling the von Kármán vortex street at lower Reynolds numbers [8]. In figure 9d, the streamlines at mid-span of the cylindrical structure are shown. The flow is separated at the lee side of the cylindrical silo surface, generating a highly turbulent and narrow wake region, typical for high Reynolds number cross flows around cylinders [15, 19].

Near the top of the cylinder (figures 8 and 9e), the approaching flow moves upward, accelerates and then separates from the cylinder circumference at the free end to form a trailing vortex. No large recirculation zones are observed at the top of the cylindrical silo and the separated trailing vortex is mainly dragged downstream and only slightly deflected downwards. The limited downwash at the lee side of the cylinder also results in minor interaction with the flow at midspan of the silo.

For lower Reynolds number flows (e.g. 2×10^4 in [12]), two counter-rotating vortices are formed above the free end of the cylinder which subsequently descend along the central section of the wake. The vortices expand laterally, move slightly downwards and interact with the vortices shed from the two sides of the cylinder in the upper half of the near-wake region of the cylinder [12]. Finally, Park et al. [13] found that a modification of the free end geometry of the cylinder (e.g. a bevelled or radiussed free end) can reduce the width of the wake formed behind the finite cylinder. This narrow wake region is also observed in the present simulations (figures 9d and 9e) but is of course also related to the higher Reynolds number flow in the present application.

4 WIND-STRUCTURE INTERACTION SIMULATIONS FOR A SINGLE SILO

With a numerical model available for both the structure and the wind flow, it is now possible to consider the coupled numerical problem as a whole. In the wind-structure interaction simulations, the solvers remain separated and the interaction between both domains is only active at the interface between structure and wind flow. The structural solver can be denoted as follows:

$$\boldsymbol{\mathcal{S}}\left[\mathbf{P}(t)\right] = \mathbf{U}(t) \tag{5}$$

where $\mathbf{U}(t)$ are the displacements of the structure and $\mathbf{P}(t)$ are the aerodynamic pressures acting on the structure. This expression corresponds with the numerical solution of the structural

governing equation (equation 1). Similary, the numerical solver of the Navier-Stokes equations of the wind flow can be denoted as:

$$\boldsymbol{\mathcal{F}}\left[\mathbf{U}(t)\right] = \mathbf{P}(t) \tag{6}$$

As mentioned in the introduction, two different coupling approaches are considered as schematically represented in figure 10. Only partitioned techniques are being considered here, implying that both the structural and flow solver are maintained as separated solvers (e.g. two black-box solvers) with only interaction at the wind-structure interface.

In the one-way coupling approach (figure 10a), the structure is considered as a rigid body in the wind flow simulations: $\mathbf{U}(t_i) = \mathbf{0}$. In every time step, the aerodynamic surface pressures on the rigid body structure can be determined in the flow solver: $\boldsymbol{\mathcal{F}}\left[\mathbf{0}\right] = \mathbf{P}(t_i)$. Subsequently, the resulting time history of surface pressures $\mathbf{P}(t)$ is applied as an external transient load on the structure and the resulting structural displacements can be computed: $\boldsymbol{\mathcal{S}}\left[\mathbf{P}(t)\right] = \mathbf{U}(t)$. To avoid interpolation of surface pressures on the interface, the computational grid of the silo surface was made identical in flow and structural solver. This way, the aerodynamic pressures and structural displacements on the wind-structure interface can be transferred between solvers with a node-to-node algorithm, without further need of approximations through interpolation.

In the two-way coupling approach, on the contrary, the structural and flow solver are coupled in every time step (figure 10b). To ensure equilibrium at the fluid-structure interface in every time step, several Gauss-Seidel coupling iterations between solvers are performed. In the first coupling iteration (superscript ^{1}) the aerodynamic surface pressures are calculated in the flow solver $\boldsymbol{\mathcal{F}}\left[\mathbf{U}^*(t_i)\right] = \mathbf{P}^1(t_i)$ from an extrapolation of the structural displacements from previous time steps, denoted $\mathbf{U}^*(t_i)$. Subsequently, the structural response to these aerodynamic pressures is calculated $\boldsymbol{\mathcal{S}}\left[\mathbf{P}^1(t_i)\right] = \mathbf{U}^1(t_i)$. In the second coupling iteration, feedback is given from the structural to the flow solver where the fluid mesh deforms, the wind flow is slightly modified and new surface pressures can be calculated: $\boldsymbol{\mathcal{F}}\left[\mathbf{U}^1(t_i)\right] = \mathbf{P}^2(t_i)$. The updated surface pressures in their turn give rise to new structural displacements: $\boldsymbol{\mathcal{S}}\left[\mathbf{P}^2(t_i)\right] = \mathbf{U}^2(t_i)$. This iterative procedure is repeated until convergence of aerodynamic surface pressures and structural displacements. In the present simulations, five Gauss-Seidel iterations per time step are needed to reach convergence on the wind-structure interface.

It is self-evident that the computational effort to perform a two-way coupled simulation is larger. Although it is difficult to compare the exact amount of computation time required to simulate a single time step in the one-way coupling (where the flow solver and the structural solver have to be set-up separately and the one precedes the other) and the two-way coupling, it takes approximately 5 times longer to execute a two-way coupling simulation. It is therefore interesting to assess the necessity of performing these computationally much more imposing simulations.

4.1 One-way coupling simulations

In the one-way coupling simulations, the structural response $\mathbf{U}(t)$ is calculated by applying the previously determined time history of aerodynamic pressures $\mathbf{P}(t)$ on the FE model of the silo. A direct time integration scheme, the unconditionally stable and second order accurate Hilbert-Hughes-Taylor method as implemented in the Abaqus FE solver [3], is used to solve the governing system of dynamic structural equations (equation 1).

To avoid a long period of transitional effects in the structural response, a static calculation

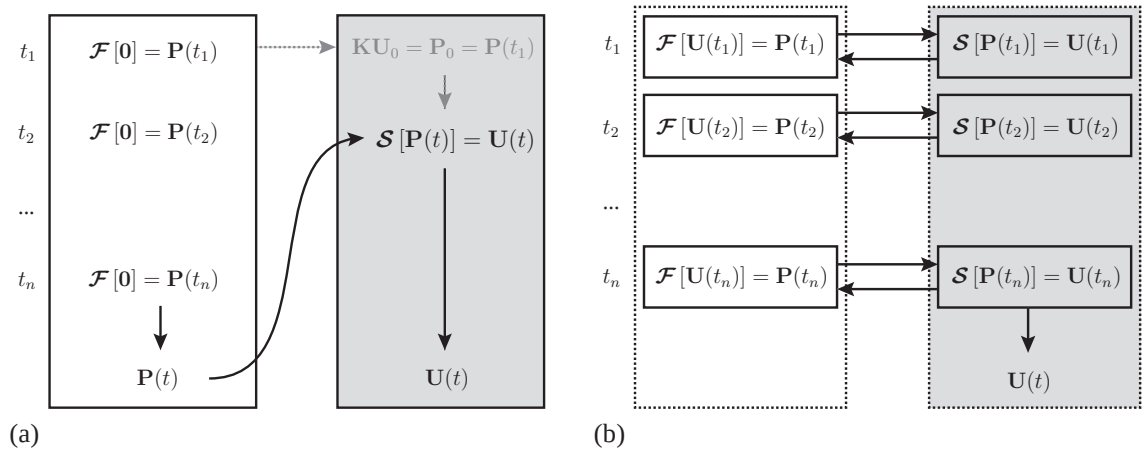


Figure 10: Schematic representation of the interaction between flow solver (white) and structural solver (grey) in the (a) one-way and (b) two-way partitioned coupling approaches.

precedes the dynamic calculation (cfr. figure 10a):

$$\mathbf{K}\mathbf{U}_0 = \mathbf{P}_0 \tag{7}$$

The applied pressures in this stationary step are taken equal to those of the first dynamic time step: $\mathbf{P}_0 = \mathbf{P}(t_1)$. The structural response $\mathbf{U}_0$ can subsequently be used as an initial condition for the dynamic calculations. The effect of this preliminary static calculation has been verified for the present simulations and found to be very effective.

The calculated structural response $\mathbf{U}(t)$ to the aerodynamic surface pressures, shows peak displacements of about $0.03\,\mathrm{m}$. This value is realistic but relatively high considering the estimated $0.05 - 0.10\,\mathrm{m}$ of the observed vibrations during the 2002 storm in the Antwerp silo group, based on video footage.

In order to distinguish the contribution of the different mode shapes to the response, modal decomposition techniques are used to determine the kinetic and deformation energy in the structural response. Both the deformation energy $E_\mathrm{d}(t)$ and the kinetic energy $E_\mathrm{k}(t)$ can be easily calculated from the known structural displacements $\mathbf{U}(t)$ and velocities $\dot{\mathbf{U}}(t)$:

$$E_\mathrm{d}(t) = \frac{1}{2}\,\mathbf{U}^\mathrm{T}(t)\,\mathbf{K}\,\mathbf{U}(t) \qquad\qquad E_\mathrm{k}(t) = \frac{1}{2}\,\dot{\mathbf{U}}^\mathrm{T}(t)\,\mathbf{M}\,\dot{\mathbf{U}}(t) \tag{8}$$

By applying modal decomposition of the structural deformations $\mathbf{U}(t) = \mathbf{\Phi}\boldsymbol{\alpha}(t)$ and velocities $\dot{\mathbf{U}}(t) = \mathbf{\Phi}\dot{\boldsymbol{\alpha}}(t)$ where $\boldsymbol{\alpha}(t)$ represent the modal coordinates, the energy content of each structural mode shape in the response can be quantified:

$$\begin{aligned} E_\mathrm{d}(t) &= \frac{1}{2}\,\mathbf{U}^\mathrm{T}(t)\,\mathbf{K}\,\mathbf{U}(t) \\ &= \frac{1}{2}\,\boldsymbol{\alpha}^\mathrm{T}(t)\mathbf{\Phi}^\mathrm{T}\,\mathbf{K}\,\mathbf{\Phi}\boldsymbol{\alpha}(t) \\ &= \frac{1}{2}\sum_{j=1}^{N}\omega_j^2\alpha_j^2(t) \\ &= \sum_{j=1}^{N}E_{\mathrm{d},j}(t) \end{aligned} \qquad\qquad \begin{aligned} E_\mathrm{k}(t) &= \frac{1}{2}\,\dot{\mathbf{U}}^\mathrm{T}(t)\,\mathbf{M}\,\dot{\mathbf{U}}(t) \\ &= \frac{1}{2}\,\dot{\boldsymbol{\alpha}}^\mathrm{T}(t)\mathbf{\Phi}^\mathrm{T}\,\mathbf{M}\,\mathbf{\Phi}\dot{\boldsymbol{\alpha}}(t) \\ &= \frac{1}{2}\sum_{j=1}^{N}\dot{\alpha}_j^2(t) \\ &= \sum_{j=1}^{N}E_{\mathrm{k},j}(t) \end{aligned} \tag{9}$$

Based on these scalar energy expressions where N represents the total number of mode shapes, the energy contribution $E_{\mathrm{d},j}(t)$ and $E_{\mathrm{k},j}(t)$ of every seperate mode shape j to the structural response can be determined using only the modal coordinates $\boldsymbol{\alpha}(t)$ and $\dot{\boldsymbol{\alpha}}(t)$.

However, in the present form of equations 9, the entire basis of N mode shapes $\boldsymbol{\Phi}$ would have to be determined to extract the modal coordinates $\boldsymbol{\alpha}(t)$ from the known structural displacements $\mathbf{U}(t)$. It is however computationally very inefficient to solve the entire eigenvalue problem (equation 2) for the determination of $\boldsymbol{\Phi}$. Furthermore, only the lowest eigenmodes are relevant in the dynamic response of the structure for a typical low frequency wind excitation. It is therefore desirable to use only a subset $\boldsymbol{\Phi}_{\mathrm{s}}$ with corresponding modal coordinates $\boldsymbol{\alpha}_{\mathrm{s}}(t)$ to determine the deformation and kinetic energy, where $\boldsymbol{\Phi} = \left[\, \boldsymbol{\Phi}_{\mathrm{s}} \,|\, \boldsymbol{\Phi}' \,\right]$ and $\boldsymbol{\alpha}(t) = \begin{Bmatrix} \boldsymbol{\alpha}_{\mathrm{s}}(t) \\ \boldsymbol{\alpha}'(t) \end{Bmatrix}$.

Of course, while $\mathbf{U}(t) = \boldsymbol{\Phi}\boldsymbol{\alpha}(t)$ is always true, an alternative projection $\hat{\boldsymbol{\alpha}}_{\mathrm{s}}(t)$ has to be proposed to approximate $\boldsymbol{\alpha}_{\mathrm{s}}(t)$ so that $\mathbf{U}(t) = \boldsymbol{\Phi}_{\mathrm{s}}\hat{\boldsymbol{\alpha}}_{\mathrm{s}}(t)$. It can easily be shown by relying on the orthogonality property of the structural mass matrix that the modal coordinates $\boldsymbol{\alpha}_{\mathrm{s}}(t)$ can be exactly calculated by using the following projection method:

$$\boldsymbol{\alpha}_{\mathrm{s}}(t) \equiv \hat{\boldsymbol{\alpha}}_{\mathrm{s}}(t) = \boldsymbol{\Phi}_{\mathrm{s}}^{\mathrm{T}}\mathbf{M}\mathbf{U}(t) \tag{10}$$

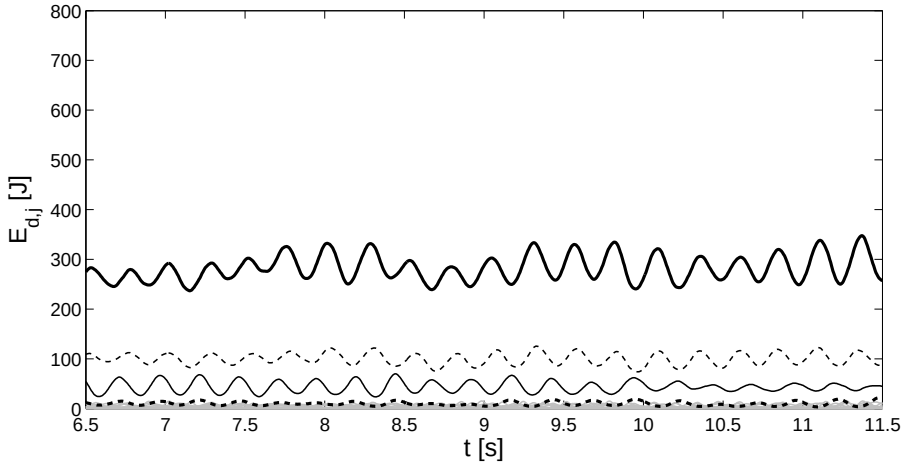


Figure 11: Modal deformation energy $E_{\mathrm{d},j}$ for the first 20 mode shapes, based on the structural response in the one-way coupling simulation: $\boldsymbol{\Phi}_1 = (1,3)$ (dashed bold black line), $\boldsymbol{\Phi}_2 = (1,3)$ (solid bold black line), $\boldsymbol{\Phi}_3 = (1,4)$ (dashed thin black line), $\boldsymbol{\Phi}_4 = (1,4)$ (solid thin black line), and the remaining mode shapes $\boldsymbol{\Phi}_j$ (solid light grey lines, with small energy content).

Figure 11 shows the modal deformation energy $E_{\mathrm{d},j}(t)$ for the first 20 mode shapes. Only mode shapes $\boldsymbol{\Phi}_1 = (1,3)$, $\boldsymbol{\Phi}_2 = (1,3)$, $\boldsymbol{\Phi}_3 = (1,4)$ and $\boldsymbol{\Phi}_4 = (1,4)$ have a significant contribution to the structural response of the silo. The contribution of other mode shapes is distinctly smaller. The deformation energy of the first three mode shapes mentioned has an important static (time averaged) component indicating that these mode shapes contribute significantly to the static deformation of the silo structure. The deformation energy of all these excited mode shapes is oscillating at about $4\,\mathrm{Hz}$, coinciding with their natural frequencies and hence indicating a dynamic response in mode shapes $(1,3)$ and $(1,4)$. After transformation to the frequency domain of the modal deformation energy $E_{\mathrm{d},j}(f)$, the excitation at the natural frequencies is

clearly confirmed (figure 12). However, smaller and irregular low frequency fluctuations can be observed as well, especially for the mode shapes with the largest static excitation. These low frequency oscillations are also visible in figure 11 and are inherent to the simulated low frequency content wind turbulence. These oscillations can be seen as a 'quasi-static' sway about the mean static response, depending on and following the turbulent fluctuations of the incoming wind flow.

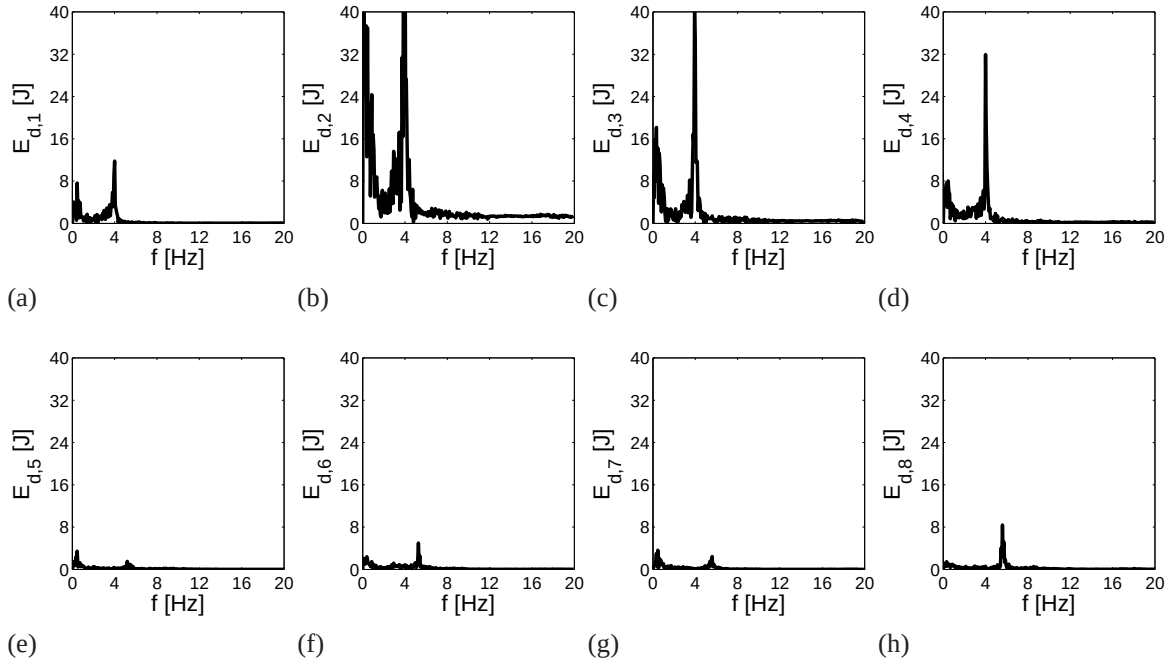


Figure 12: Modal deformation energy $E_{d,j}(f)$ in the frequency domain for the first eight mode shapes, based on the structural response in the one-way coupling simulation: (a) $\mathbf{\Phi}_1 = (1,3)$, (b) $\mathbf{\Phi}_2 = (1,3)$, (c) $\mathbf{\Phi}_3 = (1,4)$, (d) $\mathbf{\Phi}_4 = (1,4)$, (e) $\mathbf{\Phi}_5 = (1,5)$, (f) $\mathbf{\Phi}_6 = (1,5)$, (g) $\mathbf{\Phi}_7 = (1,5)$, and (h) $\mathbf{\Phi}_8 = (1,5)$.

Although these results are based on one-way coupling simulations of only a single silo, the computationally predicted vibrations correspond well with the observed ovalling vibrations during the 2002 Antwerp storm. While vibration levels are probably still smaller than for the entire silo group arrangement, the simulations already seem to confirm that the mode shapes with the lowest natural frequencies are excited by the aerodynamic pressures.

4.2 Two-way coupling simulations

In the two-way coupling simulations, several additional computational issues arise. The first concerns possible interpolation issues at the interface of structural and flow solver. As mentioned, this problem is bypassed by using identical meshes for the wind-structure interface (i.e. the silo surface) in both structural and flow solver. The second concerns the choice and implementation of an implicit coupling scheme to ensure equilibrium at the interface in every time step. In this application, Gauss-Seidel iterations are performed and are found to be stable. Thirdly and finally, the mesh movement of the computational grid in the flow solver is made possible using the arbitrarian Lagrangian-Eulerian (ALE) description as implemented in Ansys Fluent [1].

The analysis of the structural response in the two-way coupling simulation is identical to that in the one-way coupling simulation. Based on the structural displacements, the modal deformation energy $E_{\mathrm{d},j}(t)$ and kinetic energy $E_{\mathrm{k},j}(t)$ can be determined to investigate the excitation of the different mode shapes in the structural response.

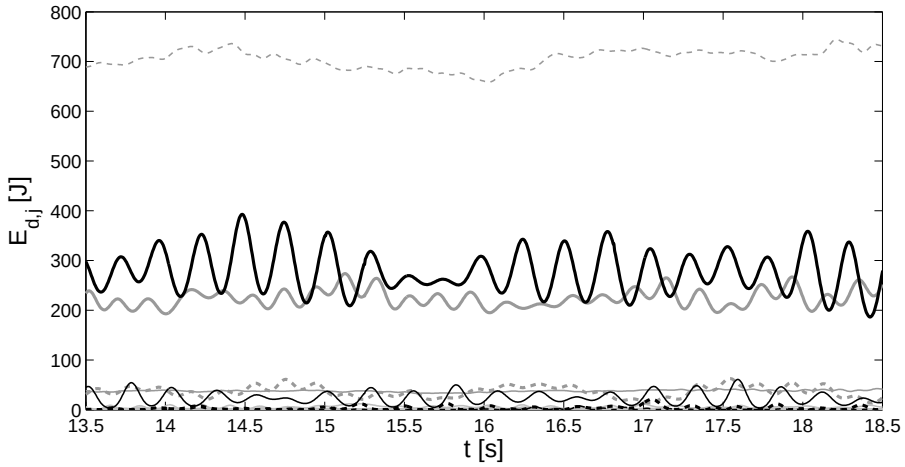


Figure 13: Modal deformation energy $E_{\mathrm{d},j}$ for the first 20 mode shapes, based on the structural response in the two-way coupling simulation: $\mathbf{\Phi}_1 = (1,3)$ (dashed bold black line), $\mathbf{\Phi}_2 = (1,3)$ (solid bold black line), $\mathbf{\Phi}_3 = (1,4)$ (dashed thin black line), $\mathbf{\Phi}_4 = (1,4)$ (solid thin black line), $\mathbf{\Phi}_5 = (1,5)$ (dashed bold grey line), $\mathbf{\Phi}_6 = (1,5)$ (solid bold grey line), $\mathbf{\Phi}_{14} = (2,6)^*$ (dashed thin grey line), $\mathbf{\Phi}_{18} = (2,6)$ (solid thin grey line), and the remaining mode shapes $\mathbf{\Phi}_j$ (solid thin light grey lines, with small energy content).

Figure 13 shows the modal deformation energy $E_{\mathrm{d},j}(t)$ for the first 20 mode shapes, similarly as in figure 11 but now based on the structural response in the two-way coupling simulation. Similarly as for the one-way coupling simulation, mode shape $\mathbf{\Phi}_2 = (1,3)$ has a significant contribution to the deformation energy in the range of approximately $300\,\mathrm{J}$. The 'quasi-static' low-frequency variation of the static component and oscillations at the natural frequency are also observed.

The other mode shapes that were significantly contributing to the structural response in the one-way coupling simulation, namely $\mathbf{\Phi}_1 = (1,3)$, $\mathbf{\Phi}_3 = (1,4)$ and $\mathbf{\Phi}_4 = (1,4)$, now represent only very small to negligible energy variations. Instead, mode shape $\mathbf{\Phi}_6 = (1,5)$ has a significant contribution in the structural displacements, with a large 'quasi-static' part and less pronounced dynamic oscillations. The contribution of mode shape $\mathbf{\Phi}_5 = (1,5)$ is still small in the two-way coupling simulations but has become more important than the contribution of e.g. mode shape $\mathbf{\Phi}_1 = (1,3)$ and $\mathbf{\Phi}_3 = (1,4)$ whose contribution is close to negligible when compared to the one-way coupling results.

A major difference compared to the results of the one-way coupling, is the contribution of mode shape $\mathbf{\Phi}_{14} = (2,6)^*$ and, although less pronounced, mode shape $\mathbf{\Phi}_{18} = (2,6)$ to the deformation energy. The notation $(2,6)^*$ is used to characterize the hybrid mode shape combining $(2,6)$ and $(1,2)$. Both mode shapes $\mathbf{\Phi}_{14}$ and $\mathbf{\Phi}_{18}$ have a mainly 'quasi-static' component and are only little excited dynamically.

Finally, the peak displacements of the structural response in the two-way coupling simulations has doubled compared to the one-way results. The present maximum of $0.06\,\mathrm{m}$ is very high, certainly when considering that the silo is isolated. It is likely but difficult to predict

how the vicinity of the neighbouring silo structures in the group arrangement will influence the displacement of the silo structure.

From these results, it is clear that the results in the one-way coupling simulations differ from those in the two-way coupling. Both simulations confirm that mode shape $\Phi_2 = (1, 3)$ contributes most to the structural dynamic response, or hence the ovalling vibrations. The secondary mode shapes differ slightly in the one-way and two-way coupling simulations. Nevertheless, the mode shapes with the lowest natural frequencies remain those to be preferentially excited dynamically. An important mismatch between the two coupling approaches is found concerning the 'quasi-static' response of the silo structure: in the two way coupling, two mode shapes with higher natural frequencies are found to contribute significantly to the 'quasi-static' swaying deformation of the silo structure.

These simulations demonstrate the importance of performing fully coupled, two-way simulations for suchlike aeroelastic problems. For the case of the entire 8 by 5 silo group, it is plausible that the two-way coupling simulations will yield even more different results compared to the one-way coupling simulations.

5 CONCLUSIONS

To investigate the occurence of wind induced ovalling vibrations in a silo group, the present study proposes a numerical approach. Presently, a single silo in natural wind flow is considered. The silo structure is numerically calculated using a finite element (FE) model and the wind flow around a single silo is investigated using 3D computational fluid dynamics (CFD) simulations. For the validation of the numerical wind flow simulation, a wind tunnel experiment around a rigid structure was set up. Despite several modifications (e.g. scale, inlet conditions, etc.) the experimental results show reasonably good agreement with the numerical results. Because the turbulence model used in the CFD simulations is not adequate for the lower Reynolds number wind flow in the experiments, the separation point is not predicted correctly. Nevertheless good agreement is found for the mean pressures at the windward side of the cylinder surface until separation and also for the fluctuating pressures at the lee side of the cylinder surface. The wind flow pattern is also compared qualitatively to similar cases of finite surface-mounted structures in cross flow. Several similarities can be observed that increase the confidence in the present CFD simulation results.

The coupled wind-structure interaction problem is subsequently simulated using two different coupling approaches. In the one-way coupling simulation, the aerodynamic surface pressures are applied to the FE model of the silo structure as external transient loads without deformation of the flow domain while in the two-way coupling simulation, the interaction of the structural deformation with the wind flow field is taken into account in every time step. Modal decomposition techniques are applied in both simulations to calculate the modal deformation energy for the determination of the excited mode shapes in the structural response. It is found in both coupling approaches that the mode shapes with the lowest natural frequencies are excited dynamically. The results in the one-way coupling simulations differ however from those in the two-way coupling, demonstrating the importance of performing fully coupled simulations for suchlike aeroelastic problems.

REFERENCES

[1] FLUENT 14.0. *User's Guide*. Ansys Inc., 2011.

[2] Scanivalve ZOC 33/64Px Electronic Pressure Scanning Module. *Instruction and Service Manual*. Scanivalve Corp., July 2010.

[3] Abaqus 6.10. *User's Manual*. Dassault Systèmes Simulia Corp., 2010.

[4] C.J. Baker. The turbulent horseshoe vortex. *Journal of Wind Engineering and Industrial Aerodynamics*, 6:9–23, 1980.

[5] BIN. *NBN EN 1991-1-4:2005/AC Eurocode 1: Actions on structures - Part 1-4: General actions - Wind actions (+ AC:2010)*. Belgisch Instituut voor Normalisatie, December 2010.

[6] D. Dooms, G. Degrande, G. De Roeck, and E. Reynders. Finite element modelling of a silo based on experimental modal analysis. *Engineering Structures*, 28(4):532–542, 2006.

[7] Y. Gai and W.K. Chow. Numerical studies on air flow around a cube. *Journal of Wind Engineering and Industrial Aerodynamics*, 93:115–135, 2005.

[8] Y. Liu, R.M.C. So, and Z.X. Cui. A finite cantilevered cylinder in a cross-flow. *Journal of Fluids and Structures*, 20(4):589–609, 2005.

[9] F.R. Menter. Two-Equation Eddy-Viscosity Turbulence Models for Engineering Applications. *AIAA Journal*, 32(8):1598–1605, 1994.

[10] F.R. Menter, M. Kuntz, and R. Langtry. Ten Years of Industrial Experience with the SST Turbulence Model. In K. Hanjalić, Y. Nagano, and M. Tummers, editors, *Proceedings of the Fourth International Symposium on Turbulence, Heat and Mass Transfer*, pages 625–632, Antalya, Turkey, October 2003. Begell House, Inc.

[11] M.P. Païdoussis, S.J. Price, and H.C. Suen. Ovalling oscillations of cantilevered and clamped-clamped cylindrical-shells in cross flow: An experimental-study. *Journal of Sound and Vibration*, 83(4):533–553, 1982.

[12] C.-W. Park and S.-J. Lee. Free end effects on the near wake flow structure behind a finite circular cylinder. *Journal of Wind Engineering and Industrial Aerodynamics*, 88:231–246, 2000.

[13] C.-W. Park and S.-J. Lee. Effects of free-end corner shape on flow structure around a finite cylinder. *Journal of Fluids and Structures*, 19:141–158, 2004.

[14] Martinuzzi R. and C. Tropea. The flow around surface-mounted, prismatic obstacles placed in a fully developed channel flow. *Journal of Fluids Engineering, Transactions of the ASME*, 115:85–92, 1993.

[15] E. Simiu and R. H. Scanlan. *Wind Effects on Structures*. John Wiley & Sons, 1986.

[16] A. Smirnov, S. Shi, and I. Celik. Random Flow Generation Technique for Large Eddy Simulations and Particle-Dynamics Modeling. *Journal of Fluids Engineering, Transactions of the ASME*, 123:359–371, 2001.

[17] V.I. Terekhov, A.I. Gnyrya, and S.V. Korobkov. Vortex pattern of the turbulent flow around a single cube on a flat surface and its heat transfer at different attack angles. *Journal of Wind Engineering and Industrial Aerodynamics*, 96:1749–1761, 2008.

[18] Y. Tominaga, A. Mochida, R. Yoshie, H. Kataoka, T. Nozu, M Yoshikawa, and T. Shirisawa. AIJ guidelines for practical applications of CFD to pedestrian wind environment around buildings. *Journal of Wind Engineering and Industrial Aerodynamics*, 96:1749–1761, 2008.

[19] M.M. Zdravkovich. *Flow Around Circular Cylinders, Volume 1: Fundamentals*. Oxford University Press, Oxford, England, 1997.

COMPDYN 2013
4th ECCOMAS Thematic Conference on
Computational Methods in Structural Dynamics and Earthquake Engineering
M. Papadrakakis, V. Papadopoulos, V. Plevris (eds.)
Kos Island, Greece, 12–14 June 2013

CHARACTERISATION OF THE AERODYNAMIC BEHAVIOUR OF THE GRANDE RAVINE VIADUCT FROM PROTOTYPE MONITORING

Fernando Bastos[1], Elsa Caetano[1], Álvaro Cunha[1], Xavier Cespedes[2], Mathieu Arquier[2], Olivier Flamand[3]

[1] ViBest, Faculty of Engineering, University of Porto
R. Dr. Roberto Frias, 4200-465 Porto, Portugal
ecaetano@fe.up.pt

[2] SETEC Tpi
Paris 42/52, quai de la Rapée, 7, 75 583 Paris cedex12
cespedes@tpi.setec.fr

[3]Centre Scientifique et Technique du Bâtiment
11 rue Henri Picherit- 44300 Nantes- France
olivier.flamand@cstm.fr

Keywords: Wind monitoring; Full-scale measurements; Bridge Aerodynamics.

Abstract. *The Grande Ravine Viaduct, at the Reunion Island, is a girder bridge crossing an abrupt volcanic breach conceived and designed by Alain Spielmann and the design office SETEC TPI [1]. The location in a zone frequently affected by typhoons and the typology of the bridge, for which limited experience existed previously in terms of description of the wind behaviour, motivated the installation of a monitoring system, in order to characterise the wind loads acting on the bridge, the corresponding aerodynamic behaviour and the structure dynamic response. The monitoring system comprehends various anemometers distributed along and outside the bridge, pressure and temperature sensors and accelerometers.*

In the context of a collaboration established between the Designer, ViBest/FEUP and CSTB, the data recorded by the monitoring system for a period of 3 years has been analysed, allowing the comparison between the characteristics of the wind model based on site measurements and the wind parameters defined at design stage based on numerical computational fluid dynamics and wind tunnel tests studies.

In this context, it is the purpose of this paper to present and discuss preliminary results of the prototype monitoring during a 2-year period, describing in particular numerical tools implemented with the purpose of selecting relevant data, processing signals and extracting relevant effects in terms of the wind response.

1 INTRODUCTION

Crossing an abrupt breach 320 m in width and 170 m in depth, the Grande Ravine Viaduct, at the Reunion Island, is a girder bridge with a total length of 288 m (Figure 1) located in a zone frequently affected by typhoons.

The characteristics of this structure [1], which lead to a classification as stiff when compared to well studied cable-stayed and suspension bridges, although flexible when compared with typical girder bridges, point to a limited experience in terms of the aerodynamic characterisation. In particular, some hypotheses required by the typical wind tunnel tests of physical models, by the numerical computational fluid dynamic studies and by the wind formulations of the structural response require validation.

At the same time, the availability at the present moment of robust technology for full scale monitoring of structures, combined with the evolution in data communication, which allow the storage and remote transfer of significant volumes of data, suggest the characterisation of local wind by means of "in situ" monitoring, based on an adequate spatial distribution of anemometers in order to validate and improve consolidated design methodologies, and permit also the monitoring of the response for establishment of correlations with the wind loads.

Having these aspects into consideration, SETEC promoted the installation of an aerodynamic monitoring system on the bridge [2]. This system comprehends various anemometers, pressure and temperature sensors and accelerometers, and has been operating for a period of 3 years. Collaboration with ViBest/ FEUP and with CSTB has been established, with the purpose of processing and interpreting the prototype data and validating design hypotheses and studies.

This paper presents and discusses preliminary results of the prototype monitoring based on the data collected during a 2-year period. Some aspects of the management of the huge database and of the tools implemented with the purpose of selecting relevant data, processing signals and extracting relevant effects in terms of the wind response are described.



Figure 1: Grande Ravine viaduct, site image.

2 BRIDGE CHARACTERISTICS AND MONITORING SYSTEM

The Grande Ravine viaduct is a motorway bridge formed by a steel orthotropic deck 22.7 m in width and 4 m in height continuous over the 288 m length (Figure 2). The deck is supported by inclined cantilevered struts made of high resistance concrete, at angles of 20° to the horizontal, fitted in a counter balancing concrete abutment founded in solid rock.

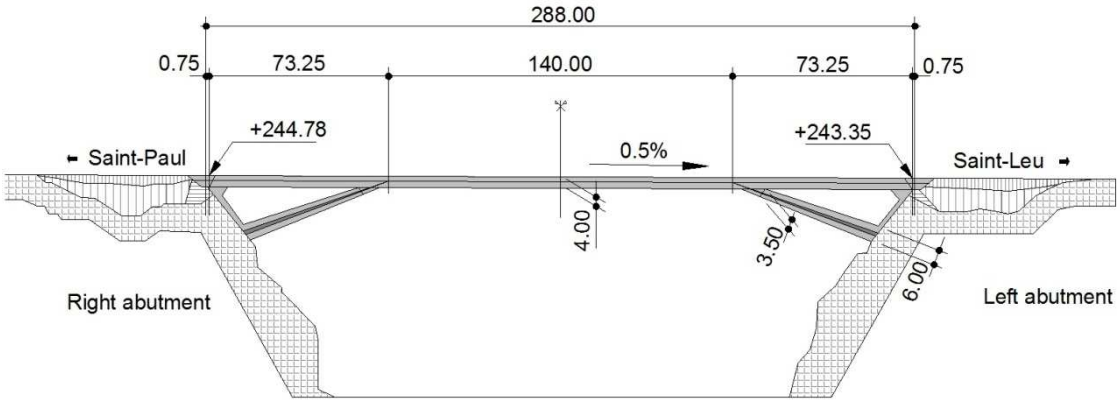
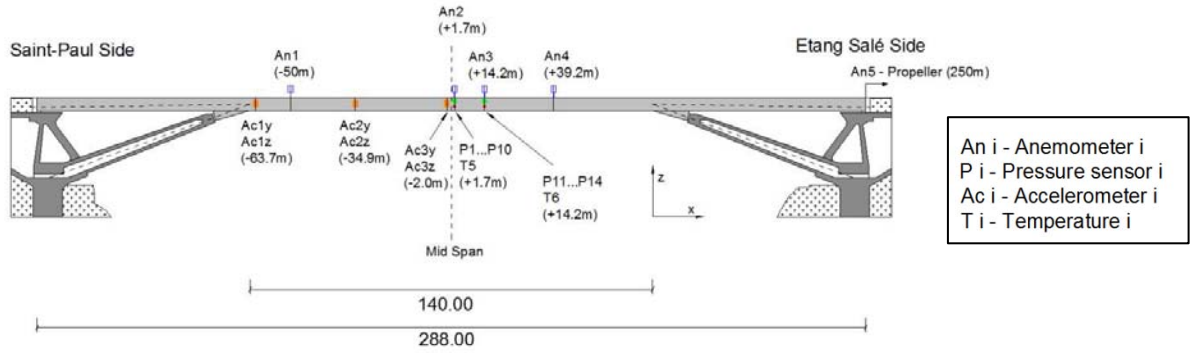
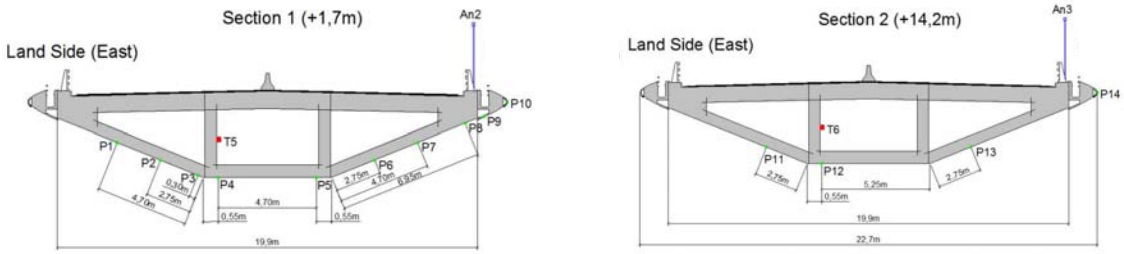


Figure 2: Profile of the Grande Ravine Viaduct.

The monitoring system installed by ADVITAM [3], whose instrumentation layout is represented in Figure 3, comprehends the following devices: 4 sonic anemometers, distributed along the bridge and mounted on 3.5 m high masts; one propeller anemometer, mounted on a 10 m high mast positioned outside the viaduct at a distance of 250 m from one of the abutments; 14 pressure transducers, distributed in two sections close to the mid-span; external temperature sensors coupled with the anemometers, and internal temperature sensors placed in the same cross sections of the pressure sensors; and 6 accelerometers mounted in vertical and transversal direction in three sections along the deck.



a)



c)

Figure 3: Layout of instrumentation: (a) distribution of sensors along the viaduct profile; (b) pressure sensors in section 1, +1,7m from mid-span; (c) pressure sensors in section 2, +14,2m from mid-span.

The acquisition system is based on a MOXA card, that groups the signals from the sonic anemometers, and on a 16-bit National Instruments acquisition card that digitises the signals from the accelerometers, temperature and pressure sensors. The propeller anemometer signals are conditioned by a ICP converter connected by serial port to the acquisition computer. Data acquisition is made by a software developed by ADVITAM [3] in the LABVIEW platform and has been programmed to sample for continuous periods of 13 minutes using different sampling frequencies for the different sensors: sonic and propeller anemometers are sampled at 32Hz and 5Hz, respectively; accelerometers are sampled at 1000Hz; pressure sensors, at 300Hz, and temperature sensors, at 10Hz. Implemented in the acquisition software is a routine to filter, re-sample at 40Hz and record data into text files. Each file stores 32321 lines of the 40 channel data (14 from the anemometers, 14 from the pressure sensors, 6 from temperature sensors and 6 from the accelerometers). Text records are saved in a computer located inside the bridge deck and then transferred to a computer in FEUP by a management routine that comprises the download via FTP, storage and backup of files.

The monitoring system has been operating continuously since December 2009, with occasional interruptions due to power failure and maintenance activities.

The raw data stored in the computer at FEUP are processed by a code developed in the MATLAB platform. This code was developed aiming at: characterising the wind model in the Grande Ravine bridge site; characterising the bridge behaviour in operational conditions; and, particularly, characterising the structural behaviour under the local wind excitation.

The methodology adopted in the development of this code follows the diagram presented in Figure 4. The Preliminary Processing routine comprehends an initial check of data by inspecting the text files for irregular situation, detecting for example, breaks in acquisition, correcting and packing valid records into MATLAB binary format files (.mat). Subsequently, the signals are re-sampled, de-spiked and finally decimated to 20Hz.

The Global Processing routine provides a global statistic analysis of the records. Mean, maximum, standard-deviation estimates are computed for all signal sensors. Wind records are processed in order to characterise the global atmospheric pattern and the acceleration records are treated with the objective of identification of the dynamic structural properties (natural frequencies, modal configurations and modal damping).

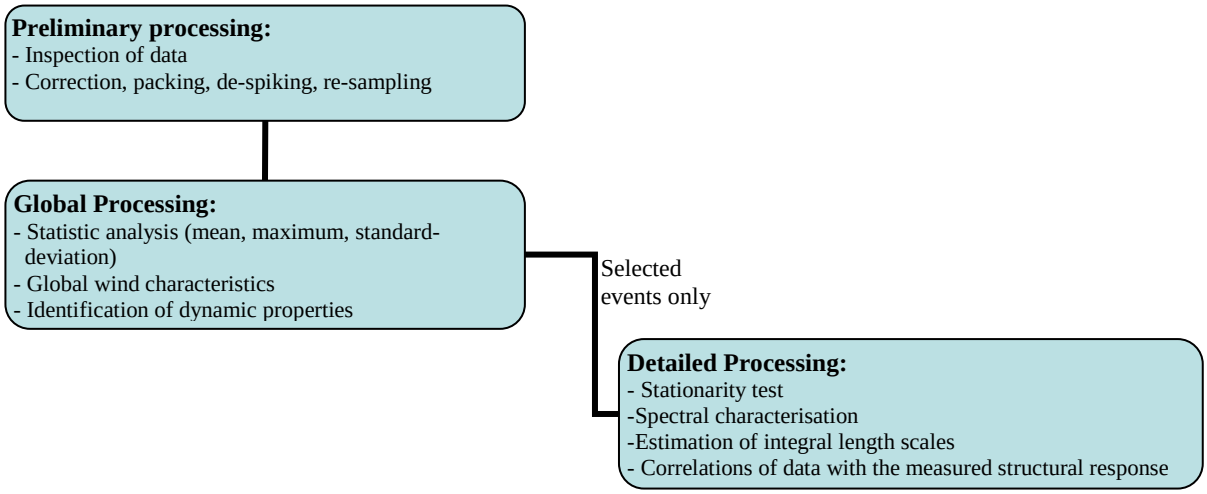


Figure 4: Methodology for data processing.

The Detailed Processing routine is applied only to selected events, for example to the records exceeding some wind velocity threshold. The wind data is sorted by 10-minute mean

wind events higher than a defined threshold and subjected to a stationarity test. The detailed processing of wind records comprehends a spectral characterisation, with estimation of correlation and integral length scales. Correlations of these quantities with pressure data and with the structural response captured by the accelerometers are then established.

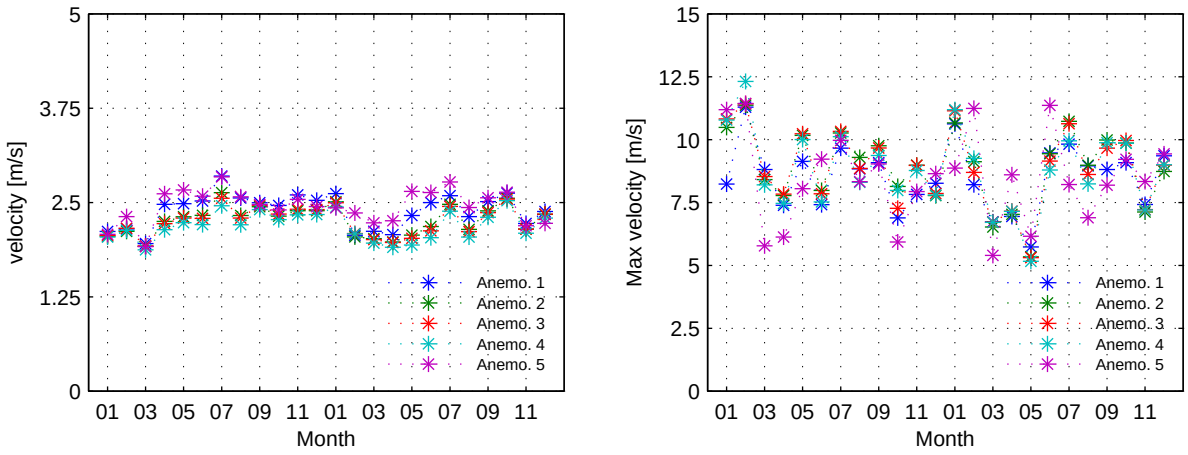
3 ANALYSIS OF FULL-SCALE DATA

The diversity of the sensors integrating the monitoring system demands different, although articulated strategies in the processing of data. These respect specifically the wind records, the pressure and the acceleration measurements. The following sections will focus only on the wind data analysis.

The results presented in this section respect a period of 24 months, from January 1st to 31st December 2012.

The wind signals are acquired in the anemometer referential, in the form of a horizontal direction, a horizontal velocity and vertical velocity. After packaging and preliminary processing, the data are transformed into the referential of mean wind velocity and treated on the basis of 10-minute intervals.

The global analysis of mean velocity data during the studied period, shows that the 10-minute mean wind velocity is quite low (Figure 5a)), of the order of 2.5 m/s, reaching in very few situations mean velocities above 11 m/s (Figure 5b)). Despite the location in an area of high cyclonic risk, in the period under analysis no significant event of such nature occurred.



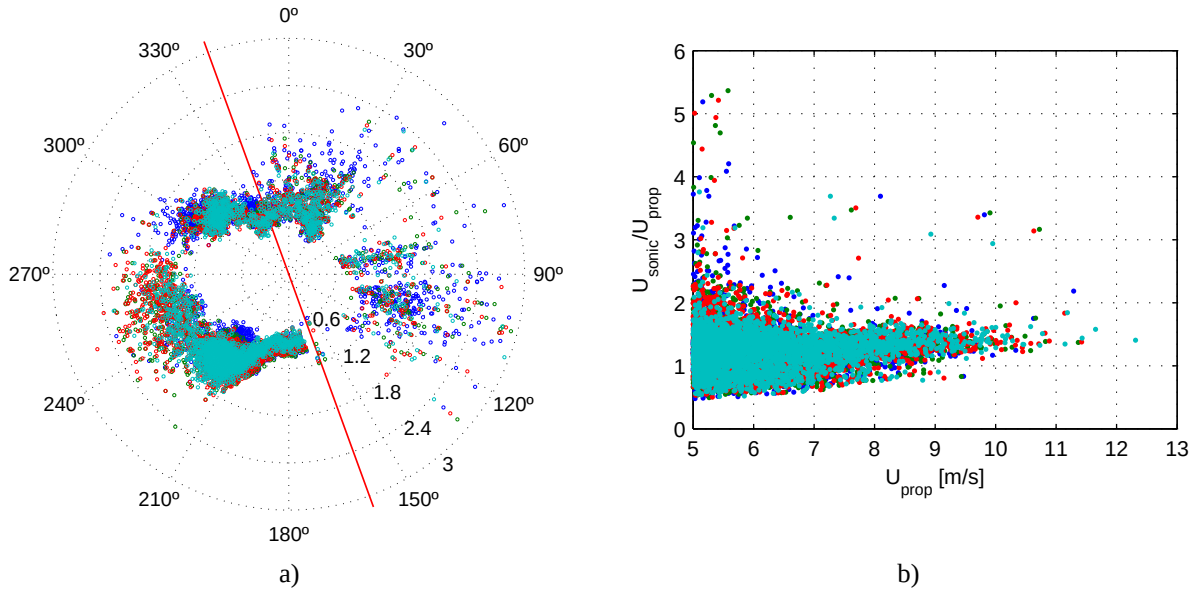
a) b)

Figure 5: (a) Monthly averaged 10-minute mean wind velocity and (b) monthly maximum 10-minute mean wind velocity.

For detailed processing, only time series with 10-minute mean velocity higher than 5m/s were selected. The time series satisfying this criterion were further screened through stationarity tests. From the two-year period in analysis, it was concluded that only about 3% of the records have 10-minute mean velocity exceeding 5m/s and less than 2.45% of the data exhibit stationary properties [4].

In order to understand particular characteristics of the wind at the bridge site, the ratio between the mean velocity recorded by each of the sonic anemometers U and the reference propeller anemometers U_{prop} has been calculated and is represented in the "rose" of Figure 6a). This figure evidences higher values of U/U_{prop} for directions [50,135] and [200,315], which coincide with the ravine and are almost perpendicular to the viaduct, whose axis is marked by the line in the rose representation. Figure 6b) shows also that U/U_{prop} grows with the mean

wind velocity. It is concluded that the wind aligned with the ravine is higher than the reference propeller velocity.



a) b)

Figure 6: Ratio U/U_{prop} as function of direction (a) and reference velocity (b).

Another aspect to analyse refers to the understanding of how the presence of a ravine with very abrupt walls influences the wind along the bridge.

A comparison of synchronous directions registered by the sonic anemometers with the reference propeller can be observed in Figure 7. The analysis of this figure evidences generally a linear relationship between site and reference propeller directions. Exception is made to the direction intervals [60,150] and [215,285] in which sonic anemometers register a quasi constant direction defined in the ranges [85,105] and [260,275], respectively. These constant directions reflect the alignment of the wind with the ravine.

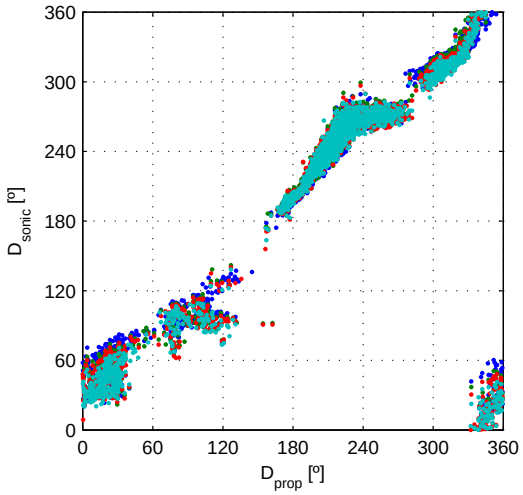


Figure 7: 10-minute mean direction of sonic anemometers vs mean direction of reference propeller.

Figure 8 represents the viaduct location and the critical wind directions according to full-scale measurements.

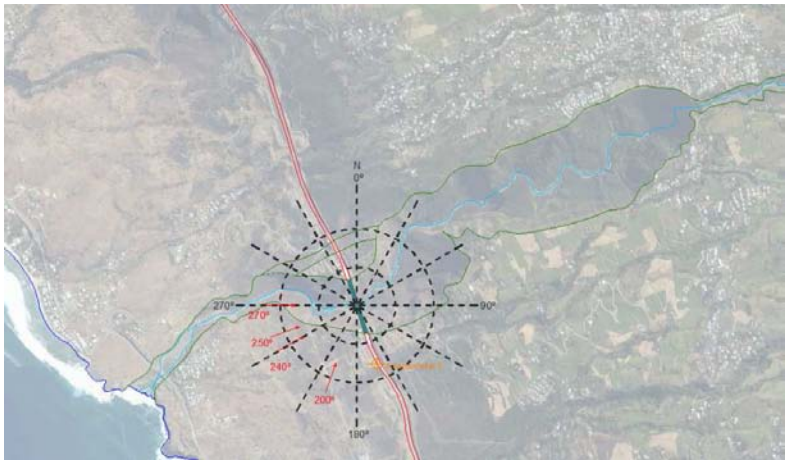
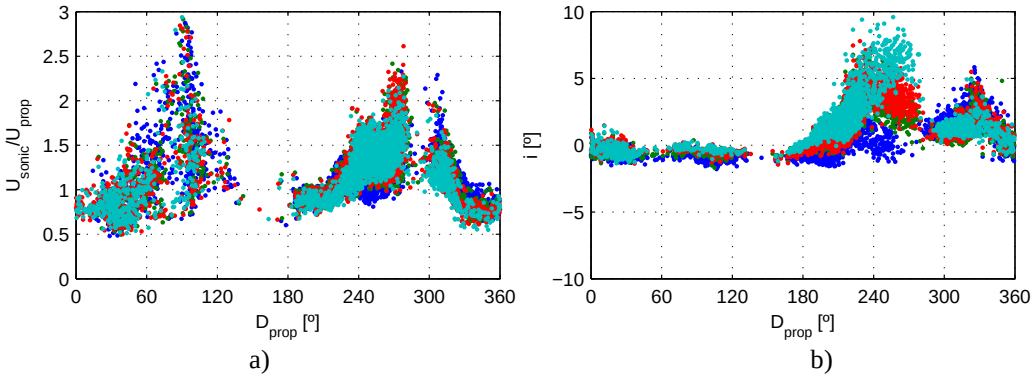


Figure 8: Scheme presenting the most critical directions observed in Grande Ravine site.

Associated with the representation in Figure 9 of the ratio U/U_{prop} with the wind direction, the plot of the incidence with the mean wind direction evidences a range [20°,190°], related with the wind from the interior of the island, in which the wind has a downward direction, with maximum angle to the vertical of -1.5°. In the range [190°,20°], wind has an ascending direction characterised by two peaks: one with an average value reaching 8°, occurs for directions [215°,275°]; and the other, with an average value of 5°, occurs for directions [315°,355°].



a) b)

Figure 9: Representation of (a) U/U_{prop} and of (b) 10-min mean incidence with mean wind reference direction.

The gust factor, obtained from the ratio between the maximum wind velocity, calculated from a 3-s averaging period, and the mean value of velocity estimated for a 10-minute interval, is represented in Figure 10(a) as a function of the wind direction. This figure shows that the gust factor values vary in the range [1.3, 2.5]. For lower values of mean wind velocity, the average gust factor has an average value of 2, decreasing to approximately 1.5 for higher values of mean wind velocity (Figure 10b).

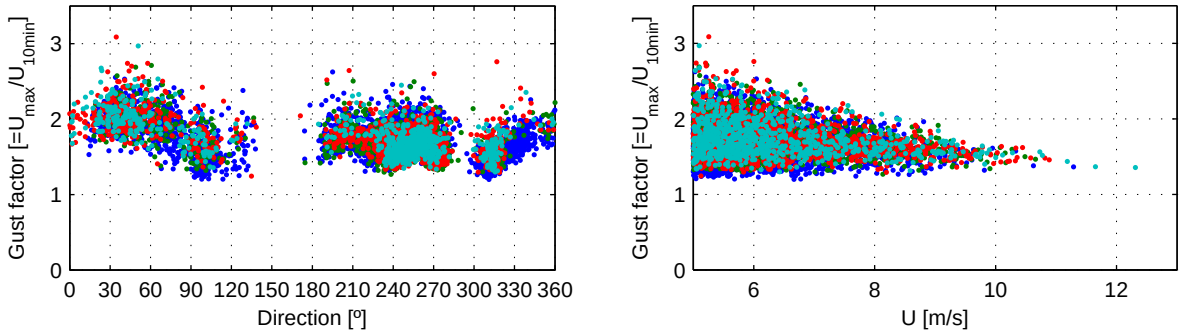


Figure 10: Gust factor variation with (a) mean wind direction and (b) mean wind velocity.

The turbulence intensity provides a measure of the variability of local turbulence, associated with each velocity component u, v and w, and is represented by the ratio between the estimate of the standard-deviation for each velocity component and the estimated mean velocity, for a 10-minute interval.

Figure 11 presents the variation of the turbulence intensity for each wind fluctuating component u, v and w with direction (a) and mean velocity (b). The average turbulence intensity of each component u, v and w of velocity tends to 0.21, 0.20 and 0.11, respectively, as the mean velocity increases. The turbulence strongly varies with the mean direction of wind. This variation is mainly due to the variation of roughness upstream the bridge site. The proximity to the walls of the ravine is evident by the strong variation of the transverse turbulence intensity.

The scales of turbulence constitute some of the parameters of highest interest in the characterisation of turbulent flows, representing the dimension of the average eddies of a turbulent flow. The turbulence length scales in longitudinal direction can be calculated directly from the integral of correlation estimates of the wind time histories or from the curve fitting of theoretical functions to the spectral estimates of wind records.

Average mean spectral estimates based on 10-minute wind turbulent component records have been obtained and are exemplified in Figure 12 for one particular wind record. Curve fitting of these data points is done using a von Karman spectral model from which parameters the longitudinal length scales $l_{[u,v,w]x}$ of u, v and w wind components are obtained.

Figure 13 presents the variation with mean wind direction and intensity of turbulence length scales of the fluctuating wind components u, v and w, obtained from spectral estimates. The analysis of this figure denotes the presence of a high level of variation with direction, which is essentially due to the upstream roughness. This variation diminishes as the mean wind velocity increases, stabilising for values around 50m, 20m e 10m in the case of u, v and w wind component, respectively. The turbulence length scale for w wind component has very low values when direction is associated with wind coming from the interior of the island (ie, in the range [40, 160]).

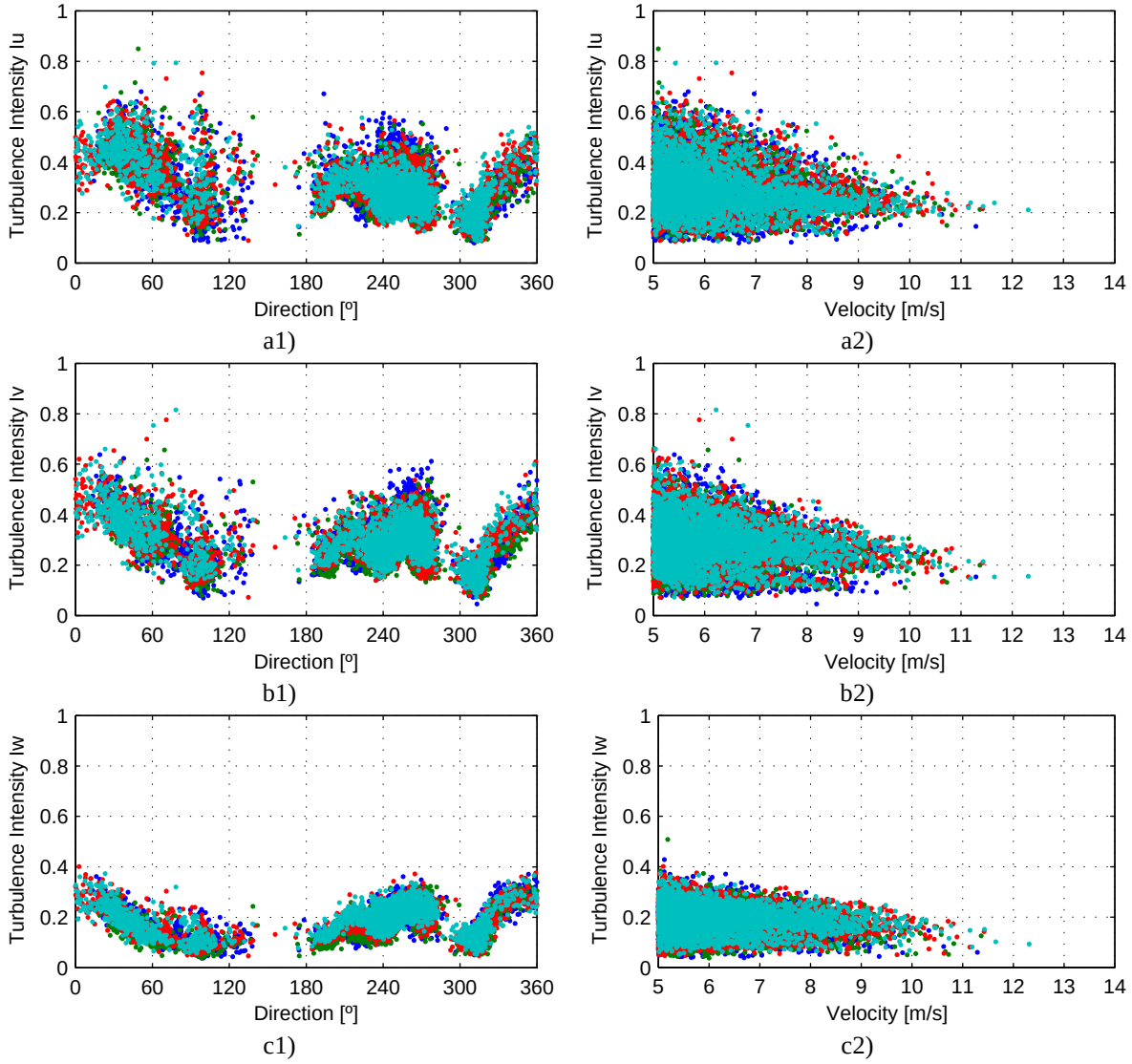


Figure 11: Turbulence intensity of wind components u, v and w variation with mean wind (a) direction and (b) velocity.

The coherence function allows the description of spatial correlation of wind turbulence in the frequency domain. This function is estimated from the ratio between the square of the modulus of the cross spectral estimates and the spectral estimates, at different points, and has been approximated, according to Davenport [5], by an exponential decay function. The fitting of experimental data by this exponential decay function provided the exponential decay coefficients presented in Figure 14, varying with mean wind direction (a) and intensity (b).

The identified exponential decay coefficients exhibit high variation with the direction, essentially due to the turbulence intensity variation for lower wind speed. From the observation of Figure 14(b), it can be concluded that exponential decay coefficients increase as the mean wind velocity grows, stabilising around 8, 4.5 and 7.5 for u, v and w wind turbulent component, respectively, ie, the coherence between wind time histories raises as the mean wind velocity increases and consequently as the turbulence intensity decreases.

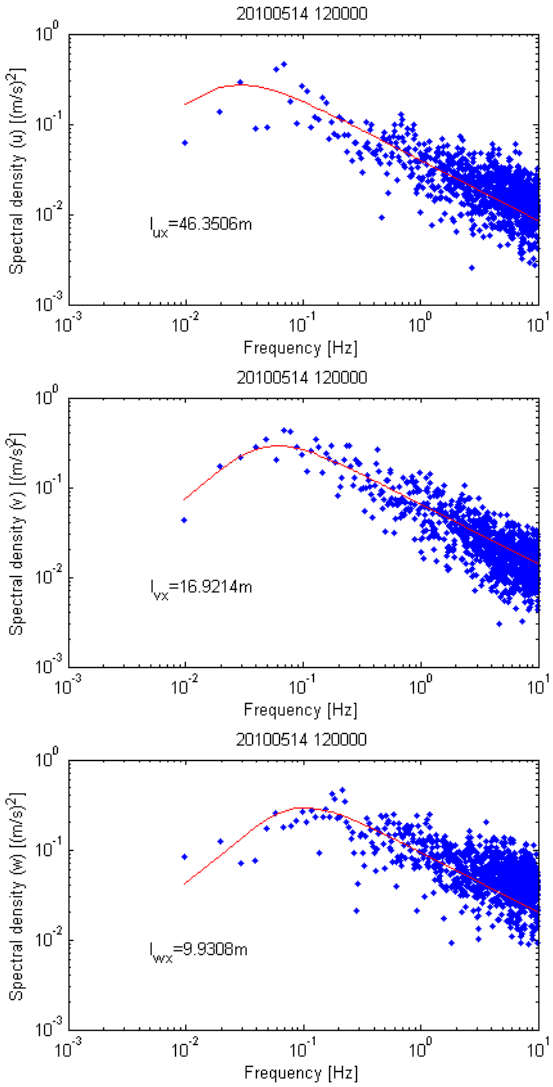


Figure 12: Fitting of von Karman curve to mean spectral estimates.

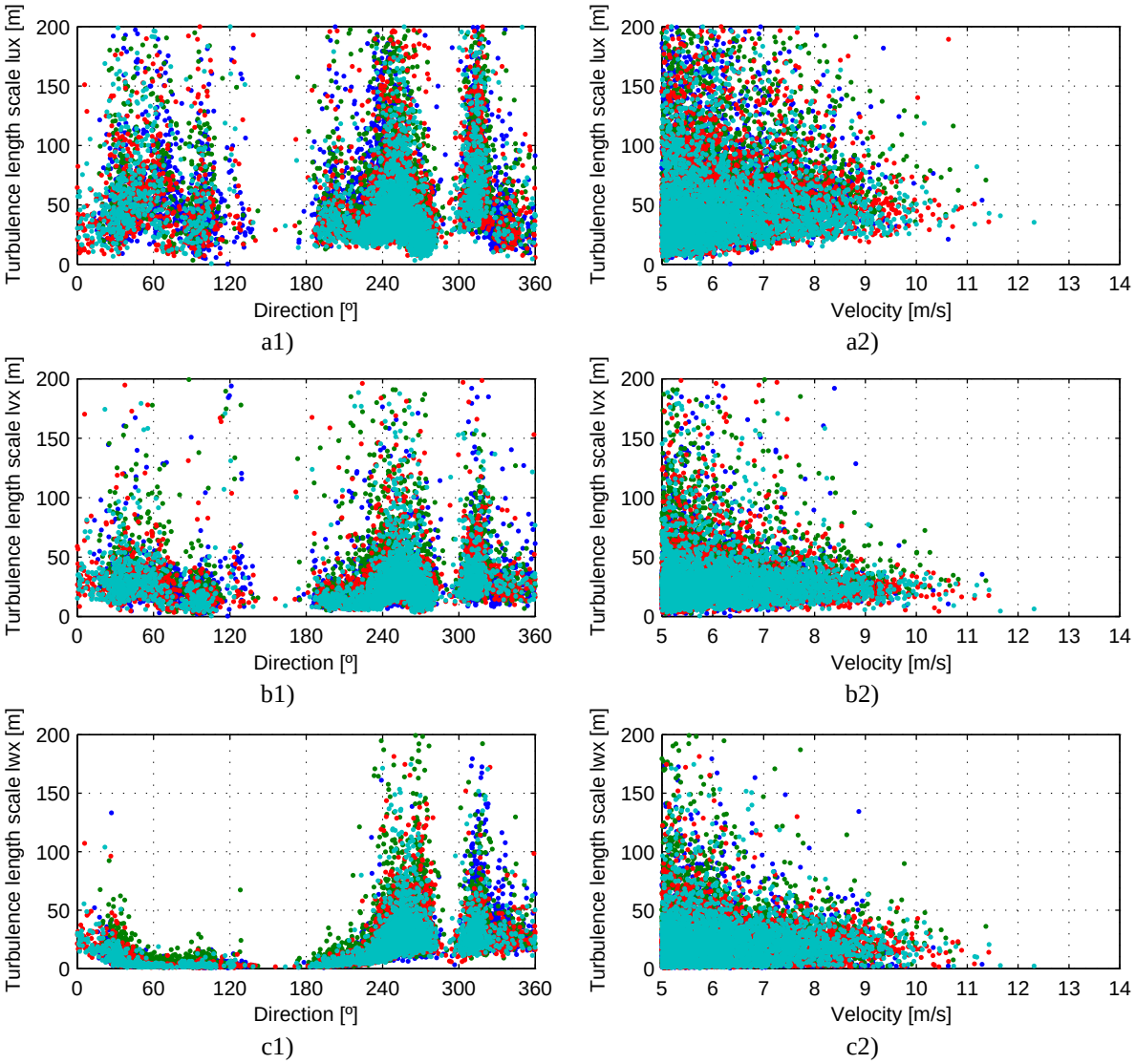


Figure 13: Variation of longitudinal turbulence length scales of wind fluctuating components u (a), v (b) and w (c), with mean wind direction (1) and intensity (2).

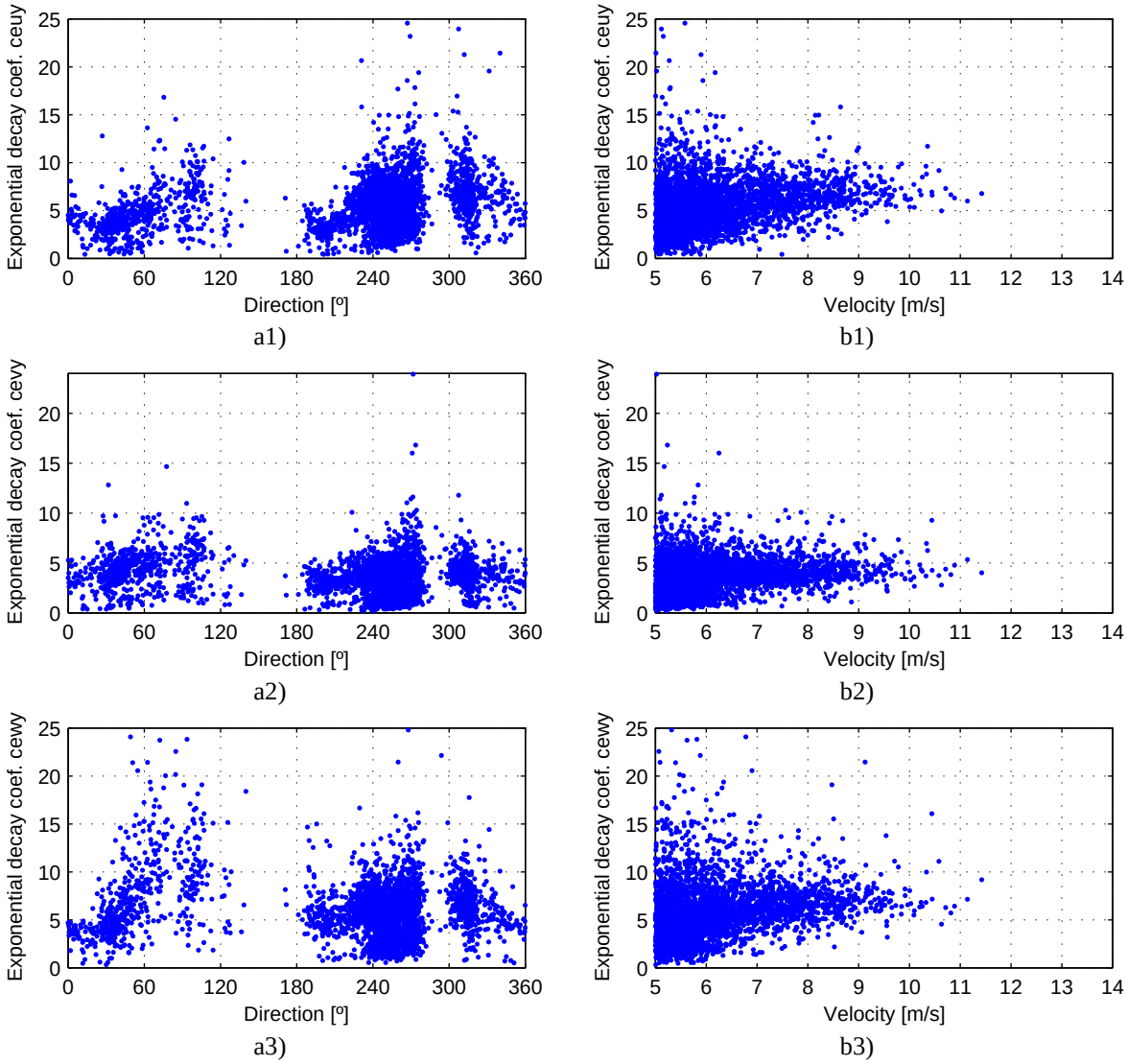


Figure 14:Variation with mean wind direction (a) and intensity (b) of exponential decay coefficients of wind turbulent component u, v and w.

4 WIND MODEL

Based on the results from full-scale measurements during the 2-year monitoring period above described, a wind model for the Grande Ravine site is proposed in this section, and a comparison is made with parameters defined at design stage on the basis of numerical CFD and wind tunnel studies.

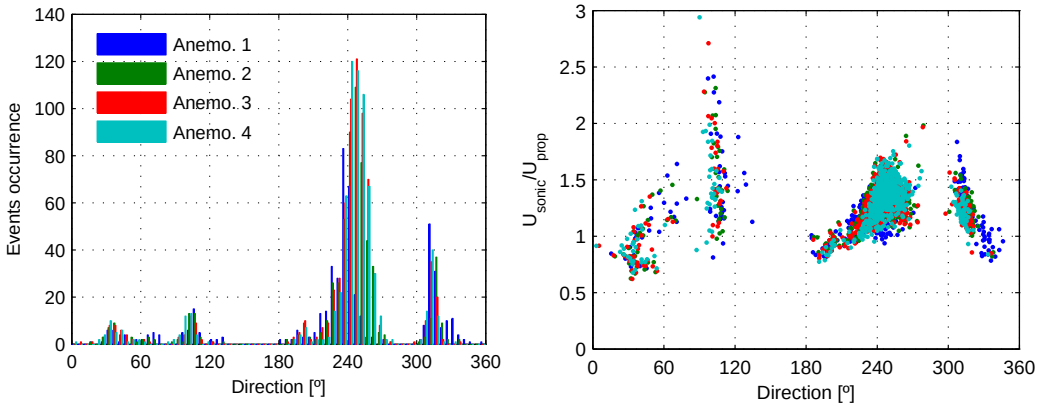
4.1 Critical wind directions

The analysis of collected wind records with mean wind velocity greater than 7.5m/s allowed the identification of the prevalent wind directions. According to the representation of Figure 15(a), it can be concluded that the most common directions are in the range [200°, 360°], corresponding to wind perpendicular to the viaduct axis. Moreover, it could be observed that the ravine causes a “bottleneck” effect (see Figure 7).

Figure 15(b) represents the coefficients defined by the ratio between the mean wind velocity collected at the bridge site (anemometers 1 to 4) and the mean wind velocity measured by

the anemometer located outside the bridge (propeller anemometer no. 5). For the prevailing wind direction, the ratio U/U_{prop} varies in the range [0.9, 1.8].

Table 1 presents the qualitative representation of the results obtained from Figure 15(a) and the average value of U/U_{prop} ratio estimated from Figure 15(b) with angular amplitude of 15° (±7.5°). The analysis of Figure 15 and of this table evidences that the direction 250°, normal to the viaduct axis, presents the highest occurrence and the highest intensity winds, therefore being selected as the most critical in the present study. Furthermore, Figure 15 shows that above 280° the wind presents low occurrence and intensity. Based on this information, the following directions were taken as critical for analysis: 200°, 240°, 240° and 270°. These are indicated in Figure 8.



(a) (b)

Figure 15: (a) Mean wind prevalence and (b) U_{sonic}/U_{prop} variation with wind direction.

Directions	Angle with normal to deck	Full-scale measurements	
		Prev. direction	U/U_{prop}
200°	-50°	++	1.05
240°	-10°	+++	1.44
250°	0°	+++	1.59
270°	20°	++	1.55
300°	50°	+	1.32
360°	110°	+	0.98

Table 1: Wind parameters for most prevalent directions.

4.2 Wind velocity

In the design study [7], the reference velocity of 34m/s was considered, according to the proposal by Eurocode 1 [8] for the Reunion Island territory. This velocity represents a mean wind velocity at 10m height on a flat field terrain type associated with a 50-year return period.

To assess the mean wind velocity at the Grande Ravine site for a 50-year return period on the basis of full-scale measurements, the reference velocity is affected by the roughness coefficient obtained from meteorological data [7] and by transfer coefficients calculated by averaging the values of the ratio between the 10-minute mean velocity measured by sonic anemometers at the viaduct and the 10-minute mean velocity measured, synchronously, by the propeller anemometer positioned at 10m height.

Table 2 summarises the obtained mean wind velocity values for the most critical directions, together with the values adopted in design [7]. It can be observed that the mean wind velocity derived from full-scale measurements is generally smaller than the one adopted in design.

This difference is even more relevant for the direction 200°, meaning that the effect of the ravine is not felt in this direction.

Directions	Full-scale [m/s]	Adopted in design [m/s]
200°	30.64	49.7
240°	42.24	51.13
250°	46.48	-
270°	45.46	56.5

Table 2: Mean wind design velocity definition for most critical directions: full-scale measurements and adopted design model.

4.3 Wind incidence

Table 3 presents the comparison between mean incidences registered for the most penalising directions and the ones adopted in design. Significant differences with regard to the design hypotheses are found, fact that may be explained by the very complex topography of the bridge site. In effect, the abrupt walls of the ravine and the presence of a small hill reflect the influence of upstream topography and roughness in the flow at the measuring site. Full-scale incidence values exhibit always positive value (ascending direction), growing as the direction moves from 200 to 270°.

Direction	Full-scale	Adopted in design
200°	0.02	6.00
240°	0.76	0.00
250°	1.61	-
270°	3.54	6.00

Table 3: Mean wind incidence for most penalising directions: full-scale measurements and adopted in design.

4.4 Turbulence intensity

Table 4 presents the comparison, for the most penalising directions, of turbulence intensity of the wind fluctuating components u, v and w, obtained from full-scale measurements with the values adopted in design. The analysis of this table shows that the values obtained from full-scale measurements are higher than the design values. The values of lateral and vertical turbulence intensity tend to grow for directions in the range [240°, 270°] due to the influence of the walls of the ravine upstream the viaduct site.

Turbulence intensity	Direction	200°	240°	250°	270°
Iu	Full-scale	0.2597	0.2336	0.2497	0.2481
	Adopted in design	0.1690	0.0931	-	0.0920
Iv	Full-scale	0.2317	0.2331	0.2605	0.2993
	Adopted in design	0.1352	0.1117	-	0.1012
Iw	Full-scale	0.1147	0.1454	0.2134	0.2395
	Adopted in design	0.1183	0.0465	-	0.0460

Table 4: Turbulence intensity for most penalising directions: full-scale measurements and adopted in design.

The influence of the local roughness in the fluctuating wind components is also notorious. For a wind direction of 200°, the turbulence intensity ratios Iv/Iu and Iw/Iu, presented in Table 5, are 0.892 and 0.442, respectively. Although turbulence conditions are higher, these ratios are comparable to the ratios presented in [10, 11] for flat surrounding conditions,

confirming that for this direction the effect of the ravine is not significantly felt. When the wind direction tends to 270°, the effect of the ravine topography and wall roughness on wind turbulence components tend to increase, reaching for this particular direction of 270° almost equal turbulence intensities in the three wind components (see Table 5).

Direction	Full-scale		Adopted in design	
	Iv/lu	lw/lu	lv/lu	lw/lu
200°	0.892	0.442	0.800	0.700
240°	0.998	0.622	1.200	0.500
250°	1.043	0.855	-	-
270°	1.166	0.965	1.100	0.500

Table 5: Ratios lv/lu and lw/lu: full-scale measurements and adopted in design.

4.5 Gust factor

Table 6 presents the mean gust factor for the most penalising directions obtained from the full-scale measurements, as well as the values adopted in design. It is shown that the gust factors obtained from full-scale measurements are higher than the design values and are coherent with the values registered for the turbulence intensity presented in Table 4.

Direction	Full-scale	Adopted in design
200°	1.67	1.48
240°	1.59	1.26
250°	1.61	-
270°	1.64	1.26

Table 6: Gust factor for most penalising directions: full-scale measurements and adopted in design.

4.6 Turbulence length scales

Turbulence length scales for the most penalising directions obtained from full-scale measurements are summarised in Table 7 and the ratios to the longitudinal turbulence length scales presented in Table 8. The analysis of these tables shows that the turbulence length scale ratios associated with the wind direction 200° are coherent with the ones shown in the extensive review made in [11] and also similar to the ratios presented in [12]. As the direction increases from 240° to 270°, the longitudinal length scale tends to slightly decrease and the lateral and vertical ratios tend to increase.

Turbulence length scales	200°	240°	250°	270°
lux	50.14	44.42	47.92	40.11
lvx	15.39	19.44	21.41	17.15
lwx	3.97	10.87	15.93	16.61

Table 7: Turbulence length scales for most penalising direction.

Direction	Full-scale		Adopted in design	
	lvx/lux	lwx/lux	lvx/lux	lwx/lux
200°	0.307	0.079	0.300	0.250
240°	0.438	0.245	0.200	0.250
250°	0.447	0.332	-	-
270°	0.428	0.414	0.150	0.125

Table 8: Ratio between turbulence length scales of lateral and vertical wind component and turbulence scale of longitudinal wind component: full-scale measurements and adopted in design.

Table 9 shows the turbulence length scales measured for the transversal direction (y direction) for the most penalising directions. Table 10 presents the values registered from full-scale measurements of the relations between turbulence length scales, together with the reference values based on the theory of homogeneous and isotropic turbulence [13]. It can be concluded that the values from full-scale measurements tend to be similar to the literature values as the wind direction tends to 270°. The values registered for wind direction 200° illustrate the elongated character of the eddies within the flow.

Transversal length scale	200°	240°	250°	270°
Luy	120.80	50.96	54.09	43.67
Lvy	77.45	65.37	61.08	42.75
Lwy	29.98	35.78	40.36	33.01

Table 9: Transversal length scale for most penalising directions.

	Lux/Lvy	Luy/Lux	Lvx/Lvy	Lwy/Lwx
Theory [13]	1	0.5	0.5	1
200°	0.757	2.060	0.434	4.114
240°	0.823	0.947	0.444	2.144
250°	0.926	0.956	0.537	1.837
270°	1.010	1.011	0.726	1.086

Table 10: Ratio between turbulence length scales of wind turbulence component u, v and w, in longitudinal and transversal directions.

4.7 Coherence coefficients

Table 11 systematises the coherence coefficients for the most conditioning directions obtained from full-scale measurements.

The data presented in Figure 11 demonstrate that when the wind velocity increases, the turbulence intensity tends to stabilise around a value which corresponds to the stationary pattern of atmospheric conditions. The same trend is observed for the coherence coefficients. However, the dispersion of coherence coefficients is lower, starting from a lower value at low wind velocity and increasing till stabilisation for higher wind velocity. As a consequence, the values of the coherence coefficients for each direction were obtained by adjusting a curve, to the higher values of wind velocity in the limit of the coherence coefficients registered values.

Coherence coefficients	200°	240°	250°	270°
ceuy	4.75	8.27	9.45	8.19
cevy	4.23	5.25	6.19	7.84
cewy	6.28	8.23	8.72	7.77

Table 11: Coherence coefficients for most penalising directions.

4.8 Wind model from full-scale measurements

Table 12 summarises the Grande Ravine wind model extracted on the basis of the full-scale measurements systematised in the previous sections. Comparing the proposed wind model with the one adopted in design, it can be concluded that the mean wind component of full-scale wind model is less severe, while turbulence intensities are much higher and turbulence length scales much lower and with dimensions close to the viaduct dimensions. The transversal length scales and coherence coefficients are similar to the values adopted in design.

Direction [°]	200	240	250	270
Mean wind velocity [m/s]	30.64	42.24	46.48	45.46
Incidence [°]	0.02	0.76	1.41	3.54
Turbulence Intensity				
u	0.2597	0.2336	0.2497	0.2481
v	0.2317	0.2331	0.2605	0.2993
w	0.1147	0.1454	0.2134	0.2395
Turbulence length scales [m]				
lux	50.14	44.42	47.92	40.11
lvx	15.39	19.44	21.41	17.15
lwx	3.97	10.87	15.93	16.61
Luy	120.80	50.96	54.09	43.67
Lvy	77.45	65.37	61.08	42.75
Lwy	29.98	35.78	40.36	33.01
Coherence coefficients				
ceuy	4.75	8.27	9.45	8.19
cevy	4.23	5.25	6.19	7.84
cewy	6.28	8.23	8.72	7.77

Table 12: Grande Ravine wind model based on full-scale measurements.

5 CONCLUSIONS

This paper presents a comprehensive study of the wind characteristics at the Grande Ravine viaduct site, crossing a deep ravine. The research is based on the analysis of wind collected by means of a monitoring system installed in the structure over a 2-year period.

The parameters extracted from the treatment of the data recorded by the four sonic anemometers located along the bridge deck and the propeller anemometer placed 250m outside the viaduct were compared with those defined in the context of the viaduct design, based on a CFD numerical study and on wind tunnel test.

Based on the full-scale measurements, a wind model is proposed, whose parameters have been summarised in Table 12. The comparison between this model and the one adopted in design evidences that the mean wind component of the full-scale wind model is less severe than the one adopted in design, while turbulence intensities are much higher. These characteristics are not necessarily conservative, as they can lead to higher structural dynamic response. This wind model will now be used to validate the calculations conducted at design stage.

ACKNOWLEDGEMENTS

The present work has been developed in the sequence of a collaboration established between the University of Porto and the design office SETEC.tpi, responsible for the design and installation of the monitoring system at the viaduct site. Additional cooperation has been established with CSTB. The first author acknowledges the PhD scholarship (SFRH/BD/46126/2008) funded by FCT.

REFERENCES

[1] Croiset J-E, Ryckaert J, Spielmann A, Viel G. 2005. *Le viaduc de la Grande Ravine: Un pont à effet d'arc limité et contrôlé*. Travaux, No.823:110-6.

[2] Viel, G., Boileau, C., Ryckaert, J. 2008. *Viaduc de la Grande Ravine, Tranche conditionnelle 1 : Instrumentation en service de l'ouvrage*. Report 18353/S/T/E2051, SETEC.

[3] Callewaert F, Laurent E. 2009. *La Grande Ravine. Manuel d'utilisation du logiciel*. Paris: ADVITAM; 2009.

[4] Bastos, F., Caetano, E., Cunha, A., Cespedes, X. and Flamand, O. 2000. *Characterisation of the wind properties in the Grande Ravine Viaduct*. Paper submitted to Engineering Structures.

[5] Simiu E, Scanlan RH. 1996. *Wind Effects on Structures: Fundamental and Applications to Design*. Third Edition ed: John Wiley & Sons.

[6] Barré C. *EN-CAPE 02.141 C-V0 - Caractérisation du vent sur 4 sites de la route des Tamarins à la Réunion - Étude en soufflerie atmosphérique sur maquettes topographiques.* Nantes: CSTB; 2002.

[7] Delaunay D, Sabre M. *EN-CAPE 02.109 C-V1 - Calcul numérique du vent sur quatre sites de la route des Tamarins à la Réunion*. Nantes: CSTB; 2002.

[8] Delaunay D. *EN-AEC 99.1 - Chartographie des vents cyclonics dans les departments d'Outre mer*. Nantes: CSTB; 1999.

[9] ENV1991-2-4. *Eurocode 1: Basis of design and actions on structures - Part 2-4: Actions on structures - Wind actions*. Brussels, Belgium ed: Comité Europeen de Normalisation; 1995.

[10] Hui MCH, Larsen A, Xiang HF. Wind turbulence characteristics study at the Stonecutters Bridge site: Part I - Mean wind and turbulence intensities. Journal of Wind Engineering and Industrial Aerodynamics. 2009;97:22-36.

[11] Solari G, Piccardo G. Probabilistic 3-D turbulence modeling for gust buffeting of structures. Probabilistic Engineering Mechanics. 2001;16:73-86.

[12] Cremona C, Foucriat J-C. Comportement au vent des ponts. Paris - France: Presses de l'école nationale des Ponts et Chaussées; 2002.

[13] Baloche C, Barnaud G, Bietry J, Chevalier J-L, Delaunay D, Duforestel T et al. Traité de Physique du Batiment - Tome 1 : Connaissances de base. Paris, France: Centre Scientifique et Technique du Bâtiment (CSTB); 1995.

COMPDYN 2013
4th ECCOMAS Thematic Conference on
Computational Methods in Structural Dynamics and Earthquake Engineering
M. Papadrakakis, V. Papadopoulos, V. Plevris (eds.)
Kos Island, Greece, 12–14 June 2013

CHARACTERISATION OF THE AERODYNAMIC BEHAVIOUR OF THE BRAGA STADIUM SUSPENSION ROOF FROM PROTOTYPE MONITORING

Elsa Caetano[1], Nuno Martins[1] and Álvaro Cunha[1]

[1] ViBest, Faculty of Engineering, University of Porto
R. Dr. Roberto Frias, 4200-465 Porto, Portugal
e-mail: ecaetano@fe.up.pt

Keywords: Suspension roof, Dynamic monitoring, Wind monitoring, Wind, Temperature, Modal variability.

Abstract. *The Laboratory of Vibrations and Structural Monitoring (ViBest) of the Faculty of Engineering of the University of Porto has installed dynamic and wind monitoring systems at the Braga Stadium suspension roof, including two sonic anemometers and various accelerometers operating continuously since 2009, aiming at providing a characterisation of the wind loads on the roof and establishing correlations with the response. This paper presents the most relevant properties of the wind measured on the prototype, establishing correlations with the measured accelerations, in order to validate numerical design studies, and analyses the influence of wind and temperature on the natural frequencies and modal damping ratios.*

1 INTRODUCTION

Designed by Eduardo Souto Moura in conjunction with Afassociados, the Braga Municipal Stadium was built for the 2004 European Football Championship that took place in Portugal [1].

A particular aspect of this structure is the suspension roof structure, formed by 34 pairs of cables spanning 202 m and supporting two composite slabs 0.245 m thick over the stands, in extensions of 57 m from the anchorages.

This very slender structure was object of various design studies, which comprehended numerical studies for dynamic assessment and wind tunnel tests on rigid and flexible physical models, to determine pressure coefficients, identify potential aeroelastic instabilities and assess the response to turbulent wind. These studies pointed in general to a risk of high vibrations due to resonant effects and of high local vortex shedding stresses.

These factors motivated extensive tests conducted on the constructed structure to assess damping, and the installation of a monitoring system in order to monitor the roof response under wind excitation.

In the context of the research activity of the Laboratory of Vibrations and Structural Monitoring (ViBest) of the Faculty of Engineering of the University of Porto, a complementary monitoring system was installed, including two sonic anemometers and various accelerometers, aiming at providing a characterisation of the wind loads on the roof and establishing correlations with the response.

The present paper aims at presenting the most relevant properties of the wind measured on prototype, establishing correlations with the measured accelerations, in order to validate numerical design studies, and analyses the influence of wind and temperature on the natural frequencies and modal damping ratios**.**

2 DESCRIPTION OF BRAGA STADIUM SUSPENSION ROOF

The present study is focused on the roof structure of the Braga Municipal Stadium, located in Braga, in the north west of Portugal (Figure 1). This infrastructure was built for the 2004 European Football Championship that took place in Portugal.



(a) (b)

Figure 1: (a) Top view and (b) perspective of the Braga Municipal Sports Stadium.

The stadium was constructed on the mountainside of Monte Castro, where one of the tribunes was built into the hill itself, and the second was erected on the other side of the pitch. While the north-west side of the stadium is wide open to the valley, a great granite massif stretches along the south-east side (Figures 1 and 2).

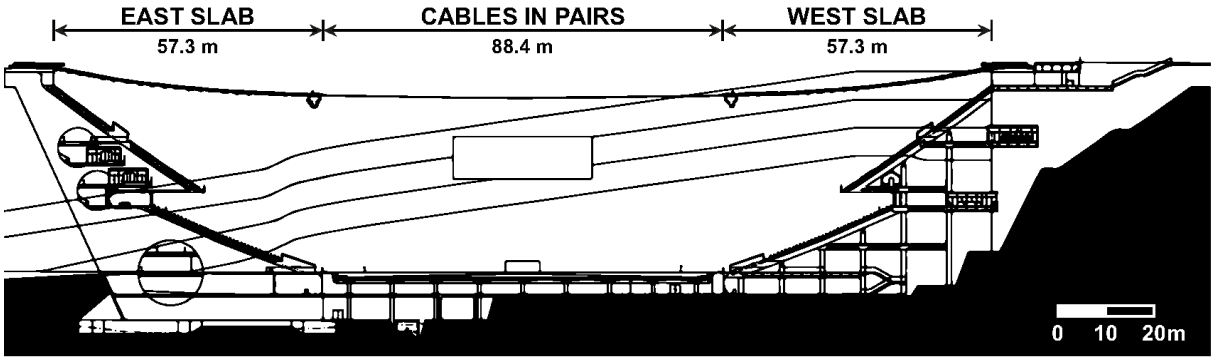


Figure 2: Longitudinal section of the stadium suspension roof.

The highlight of the stadium is its suspension roof shown also in Figures 1 and 2. The roof is composed by 34 pairs of full locked coil cables with diameters varying between 80 and 86 mm, spaced 3.75 m apart from each other. The cables span 202 m between the tops of both tribunes, supporting the two slabs on the first 57.3 m in each end, the central 88.4 m being free. The slender concrete slabs, only 0.245 m thick, are supported by the cables only in their normal direction, allowing for relative tangential movements between the two types of elements. A slight slope towards the south east side is achieved by a variation of the cables length, which allows the efficient drainage of the rainwater. A transversal triangular truss is suspended from the inner border of each slab acting as a stiffness beam and simultaneously accommodating the floodlights and loudspeakers. The roof cables are anchored in two large beams at the top of both tribunes – east and west. The east tribune (seen on the left in Figure 1(b) and in Figure 2) is structurally formed by 50 m high concrete walls, whose geometry was defined in order to minimise, at the level of the foundation, the unbalanced moments motivated by the combination of the gravitational action of the tribune and the high forces transmitted by the roof cables. In the west stand (seen on the right in Figure 1(b) and Figure 2), the concrete walls are anchored in the rock and the roof cable forces are transmitted to the foundation by prestressing tendons embedded in the concrete. The particular characteristics of the structure and the expected proneness to dynamic effects induced by the wind have motivated extensive studies developed during the design phase by various independent entities, with the purpose of adequately defining design loads and evaluating the corresponding static and dynamic behaviour [2-5]. The results provided by such studies as well as those obtained from numerical simulations and wind tunnel tests have demonstrated that the structure could be vulnerable to aeroelastic instabilities [5].

3 CONTINUOUS MONITORING OF THE ROOF STRUCTURE

The need of a strict control of the influence of environmental factors on the structural behaviour and geometry led to the installation of a static, dynamic and wind monitoring system during the construction of the structure [1]. The static monitoring system was essential during the construction and is based on a series of load cells installed in the cable anchorages, on embedded instrumentation of the concrete structure (strain gauges, tiltmeters and thermometers) and on instrumentation of the rock massifs and foundations with load cells installed in the anchors to the earth and in-place inclinometers. The dynamic monitoring system is important to observe the response of the roof to the wind excitation and is composed by 6 accelerometers, installed in the inner edges of the concrete slabs, and by cells to measure the wind pressure at various points on the underside and top of the roof slabs.

With the purpose of investigating the sensitivity of the structure to ambient effects and wind, ViBest/FEUP has installed two complementary monitoring systems on the west con-

crete slab: one to measure the dynamic response [6] and other to collect wind and temperature data [7]. The dynamic monitoring system has been active since March 2009 and has allowed the characterisation of the amplitudes of vibration of the slab, as well as the permanent identification of natural frequencies, modal shapes and modal damping ratios. The wind monitoring system was installed in December 2011, and is composed by two three-dimensional ultrasonic anemometers, suitable to measure wind velocities and directions, as well as sonic temperatures, at high sampling frequencies. The synchronisation of both measuring systems is enabled by accurate internal clocks set by GPS.

The installation of the two monitoring systems followed the layout represented in Figure 3 [7].

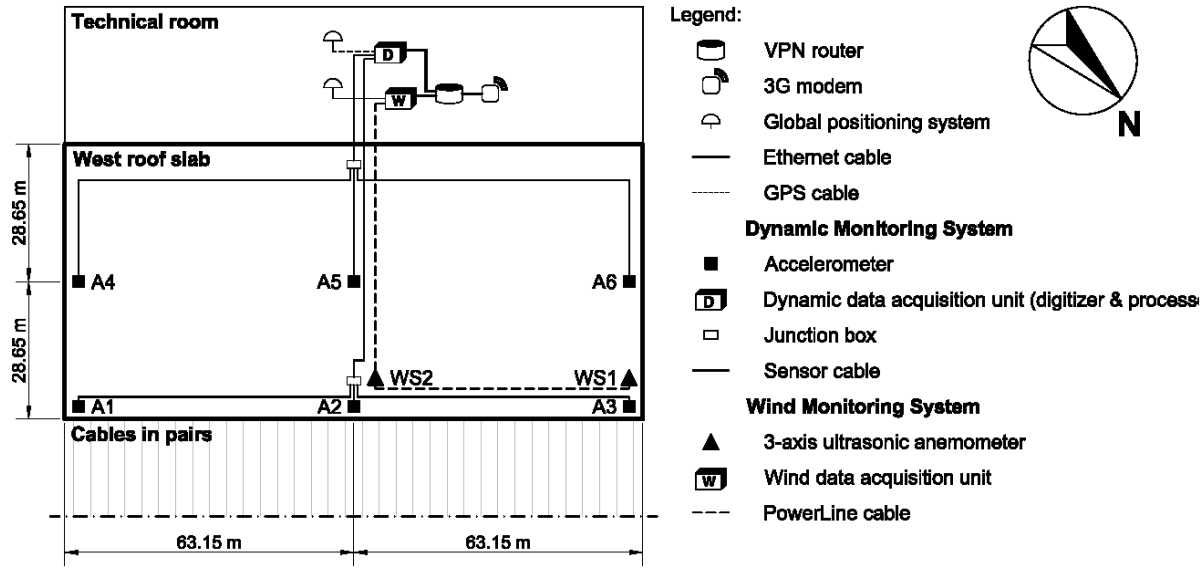


Figure 3: Partial plan of the Braga stadium roof (west roof slab) showing the location of the two monitoring systems installed for wind measurements and acquisition of vertical accelerations.

3.1 Dynamic monitoring system

The dynamic monitoring system is essentially composed by six force balance accelerometers, a digitizer and a robust field processor. The six accelerometers are distributed on the top of the west slab according to the scheme shown in Figure 3. The spatial distribution was defined with the goal of reasonably characterising at least the 10 first mode shapes identified in previous experimental and numerical works [8]. Two junction boxes group the signals of three sensors each in a single cable that is then linked to the acquisition system. The acquired acceleration records are then transmitted to the field processor through an Ethernet cable.

The field processor organises the acceleration time series sampled at 20 Hz in consecutive text files with a time duration of 60 minutes. The selection of this length for the time records resulted from a compromise between the goals of obtaining reliable estimates of modal damping ratios and a characterisation of the daily variations of the model parameters [6].

3.2 Wind measurement system

This system comprehends two three-dimensional ultrasonic anemometers which allow the characterisation of the wind through time averaged statistics of speed, direction and incidence angles, spectra and co-spectra of velocity components and temperature. These quantities can be subsequently used to assess the influence of the wind loading on the dynamic behaviour of the roof structure. According to the scheme and picture presented in Figure 3, the two ane-

mometers were placed on the top of the west slab, both along its inner edge, WS1 in the northernmost point, and WS2 in the middle of the slab [7], just next to accelerometers A3 and A2 from the dynamic monitoring system, respectively. Both sensors are mounted on masts 3 m high in order to reduce the interferences from the structure with the flow. A sampling rate of 10 Hz was chosen in order to efficiently measure the turbulent component of the wind flow [9]. The collected wind time series are then stored in text files with a length of 10 minutes.

4 FIELD MEASUREMENT OF WIND PARAMETERS

The three-dimensional ultrasonic anemometers were configured to record the wind speed as three wind speed components, each along one of the sonic orthogonal axes *x*, *y* or *z*. A coordinate rotation must be applied in order to obtain the mean wind speed, direction and elevation angles, as well as the turbulent component time series for the longitudinal, lateral and vertical directions. In this study, a double coordinate rotation scheme was used, described in some detail in [9, 10]. According to this approach, the streamline referential is redefined every block-averaging period. The block time series are averaged, from which results a mean wind speed vector defined in the sonic coordinate system *x*, *y*, *z* with sonic components ($\overline{u}_m$, $\overline{v}_m$, $\overline{w}_m$). The objective of the double rotation method is to impose $\overline{v} = \overline{w} = 0$, so that the total velocity vector is expressed by a streamline mean speed plus three orthogonal turbulent speed components (($\bar{U} + u'$), v', w'), a mean direction angle (γ) and a mean elevation angle (β).

The data presented herein corresponds to approximately eight months of continuous measurements, between mid-December 2011 and the first days of August 2012.

4.1 Mean wind speed, direction and elevation angles

Figure 4 shows the variation of the 10-min mean wind speed measured by the two sonic anemometers since the installation of the wind measurement system. From this representation, one can verify that the evolution of the mean wind speed is generally coherent through the entire time between the two instruments, the values measured by WS1 being commonly higher. The observed mean wind speed shows maximum values of 9.37 m/s and 7.22 m/s for ultrasonic anemometers WS1 and WS2, respectively. Nevertheless, it is possible to conclude that the mean wind speed measured is generally low, with most of the measurements below 4 m/s. Henceforward just the data points with a significant wind speed will be considered and all measurements with 10-min mean wind speed below 4 m/s will be discarded.

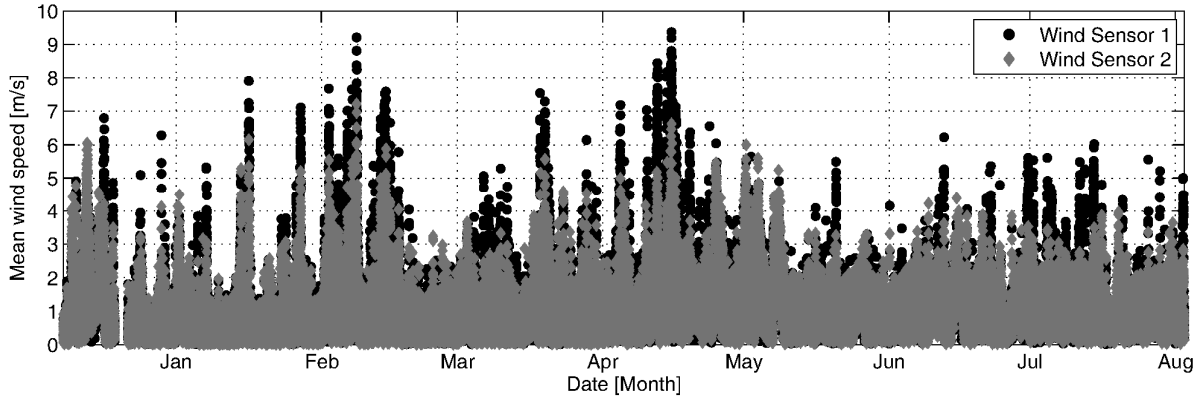
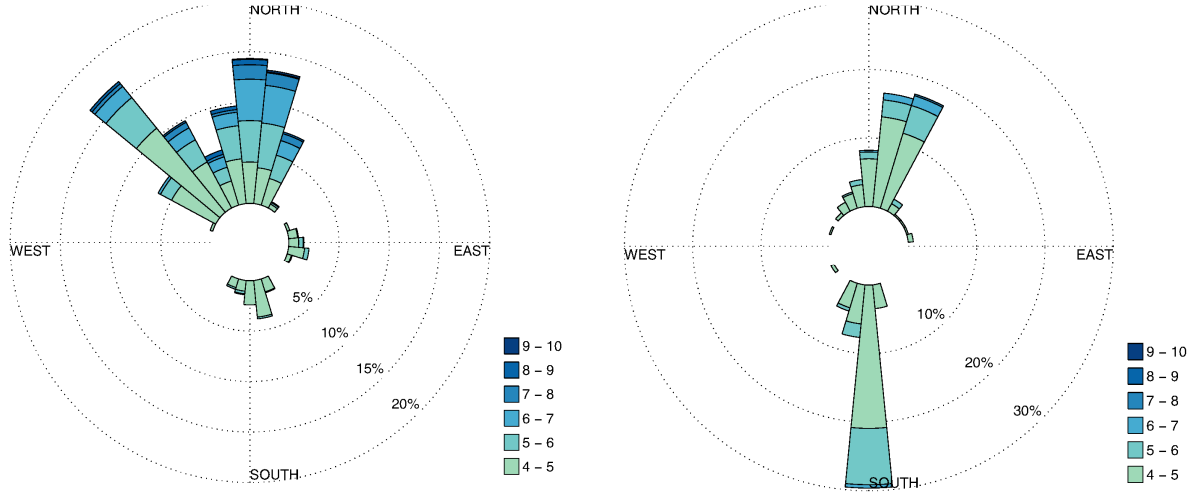


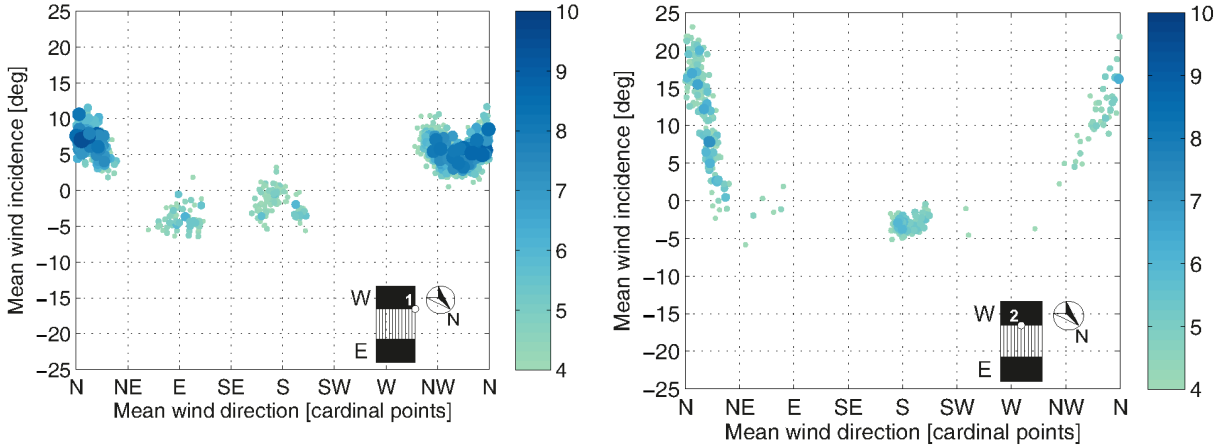
Figure 4: Time-history of 10-min mean wind speed measured by the two sonic anemometers over the period of 8 months.

Wind direction distribution is shown in the wind rose histograms of Figure 5. These illustrations show, by means of a polar histogram, the dominant directions categorised by wind speed magnitude.



(a) (b)

Figure 5: Wind rose histograms of 10-min mean speed and corresponding direction for sonic anemometers: (a) WS1 and (b) WS2.



(a) (b)

Figure 6: Distribution of 10-min mean wind speed with direction and incidence angles measured by sonic anemometers: (a) WS1 and (b) WS2.

Besides the horizontal direction, Figure 6 depicts the distribution of the incidence angle and respective wind speed with the orientation. The negative and positive values of incidence account for descending and ascending angles respectively, while the size and shade of each point evidence the measured mean speed.

The presented results are in agreement with the expected wind behaviour for the structure's implantation in the terrain and the sensors position on the structure. As previously seen, the stadium is positioned approximately along the north-east – north-west axis (see Figure 1(a)) and the anemometers located on the west roof slab (see Figure 3). In both cases, the wind measured from south comes from the top of the west slab, accordingly it must have descending incidence angle, while the wind from the north-west - north-east sector flows from the stadium open side, reaching the anemometers with ascending incidence. The most unusual

results observed were the high incidence angles measured by the sonic anemometer WS2 (Figure 6(b)). These observations can be explained by the north and north-west winds that reach this sensor (located in the middle of the west slab as seen in Figure 3) being strongly influenced by the stadium structure.

4.2 Turbulence intensity

The turbulence intensity describes the characteristics of the fluctuating wind speed. The longitudinal, *u*, lateral, *v*, and vertical, *w*, turbulence intensities can be determined by the following equations:

$$I_u = \frac{\sigma_u}{\overline{U}}, \quad I_v = \frac{\sigma_v}{\overline{U}}, \quad I_w = \frac{\sigma_w}{\overline{U}} \tag{1}$$

where σ_u, σ_v and σ_w are the standard deviation or the RMS value of each fluctuating velocity component and $\overline{U}$ is the wind mean speed for the same time period. In this study, the same 10-minute period used before was adopted for the calculation of these parameters.

Figure 7 shows the variations of the longitudinal, lateral and vertical turbulence intensities as a function of the mean wind speed, independent of direction and incidence angles, for the anemometers WS1 and WS2. A general trend for $I_u > I_v > I_w$ is noticed across both sensors data.

The turbulence intensity is simply related to the surface roughness [11], and therefore to the wind incoming direction. In Figure 8 turbulence intensities from all incoming directions are represented, leading to a widespread distribution, especially in the case of WS2. Shown in Figure 8 are longitudinal, lateral and vertical turbulence intensities as a function of the 10-min mean wind direction, and the respective mean wind speed. From these, characteristic turbulence intensities can be identified by direction and a consistent evolution through direction is perceived.

Figure 9 shows the variation of the averaged longitudinal, lateral and vertical turbulence intensities as a function of the 10-min mean wind direction, categorised in sixteen 22.5º directional sectors. It is noted from Figure 9(a), corresponding to sensor WS1, that the three component turbulent intensities are rather homogeneous across all directions, with the exception of the two upward trends: one between SE and SSW; and other between N and WNW. On the other hand, measurements from wind sensor WS2 (see Figure(b)) reveal two rather distinct clusters: one, centred on the south direction, with an upward trend from SSE to SSW and a very narrow spread in direction; and another, centred on the north direction, with turbulence intensities generally greater than the first.

The variation of the averaged turbulence intensity ratios σ_v/σ_u and σ_w/σ_u as a function of mean direction, categorised in 16 directional sectors, is translated by Figure 10. Overlaid is the number of data points measured for each direction sector, expressed by a histogram.

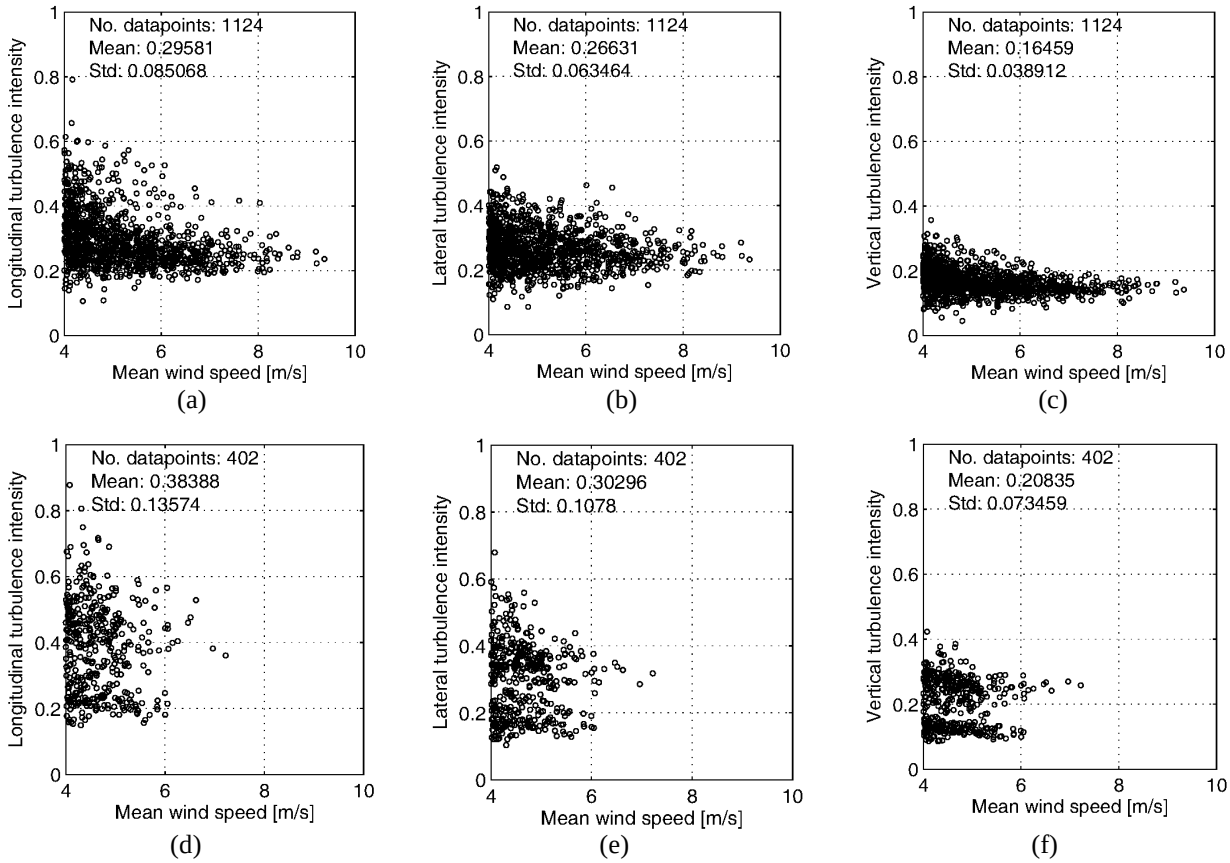


Figure 7: Variation of the turbulence intensity with the mean wind speed: (a) WS1 Longitudinal I_u; (b) WS1 Lateral I_v; (c) WS1 Vertical I_w; (d) WS2 Longitudinal I_u; (e) WS2 Lateral I_v; and (f) WS2 Vertical I_w.

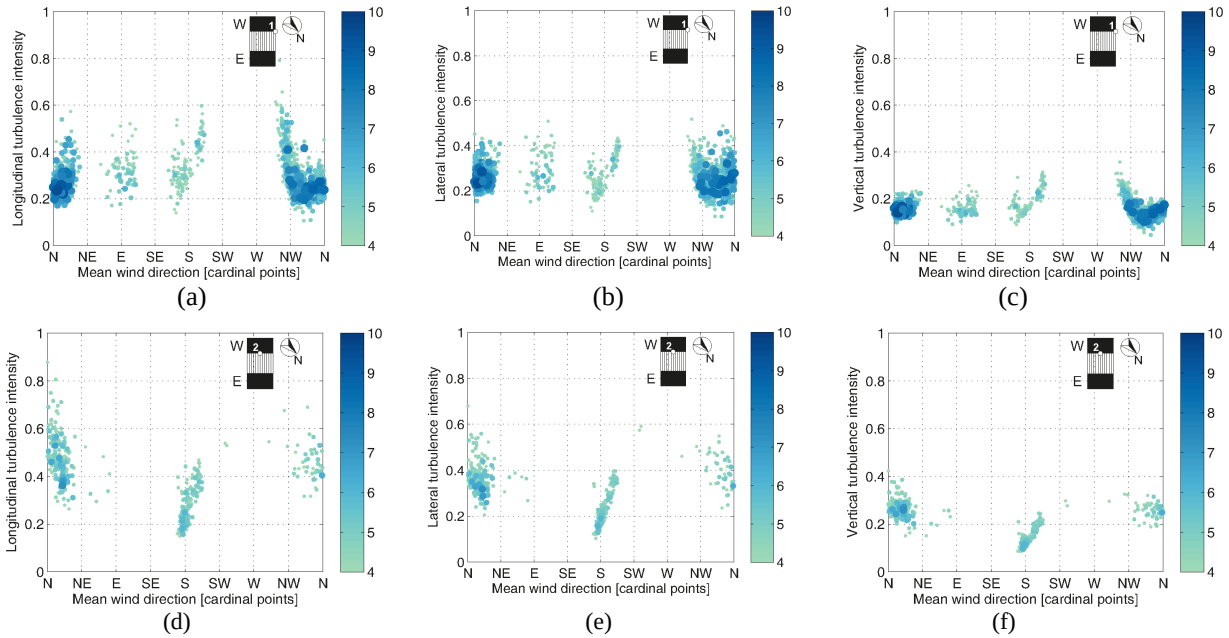
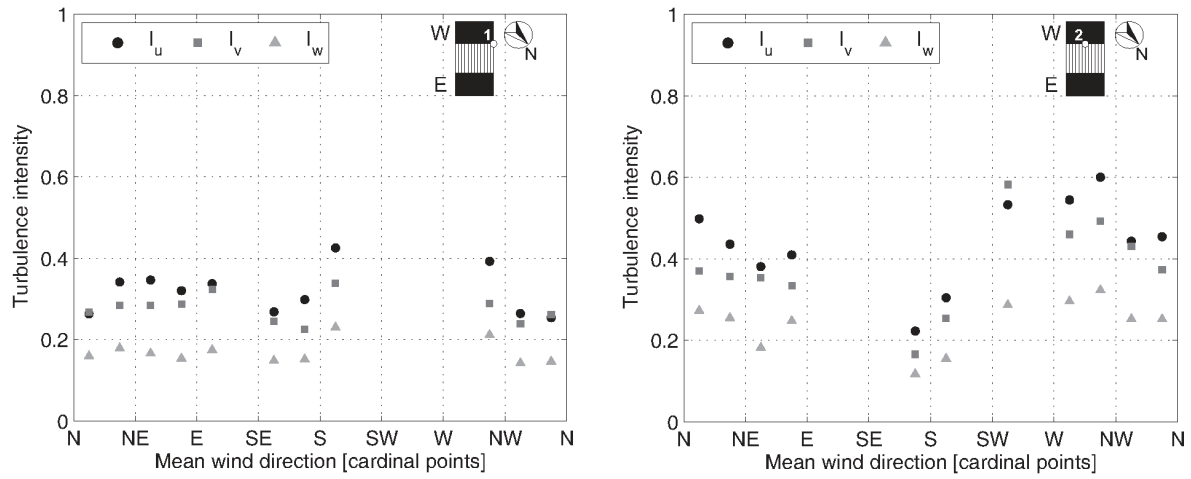
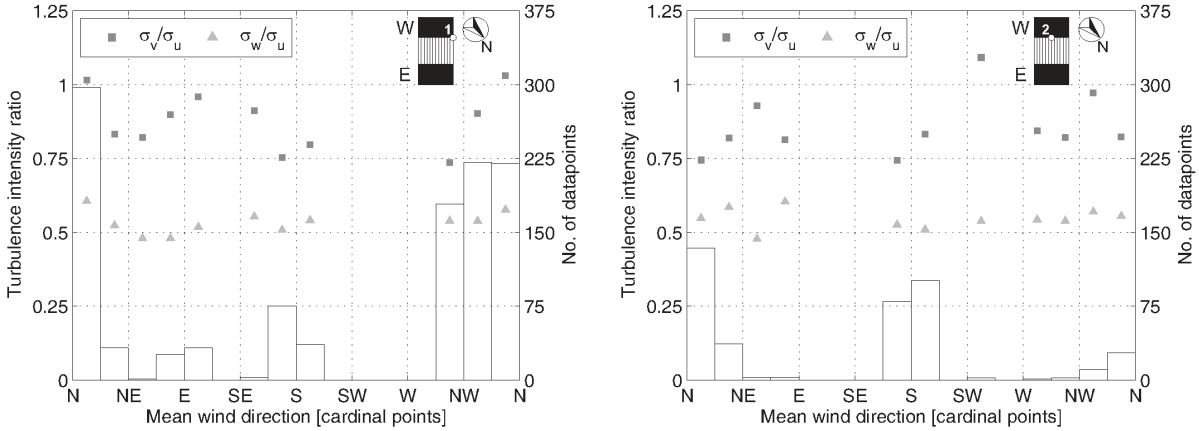


Figure 8: Variation of the turbulence intensity with the mean wind direction: (a) WS1 Longitudinal I_u; (b) WS1 Lateral I_v; (c) WS1 Vertical I_w; (d) WS2 Longitudinal I_u; (e) WS2 Lateral I_v; and (f) WS2 Vertical I_w.



(a) (b)

Figure 9: Variation of averaged longitudinal, lateral and vertical turbulence intensities with 10-min mean wind direction measured by sonic anemometers: (a) WS1 and (b) WS2.



(a) (b)

Figure 10: Variation of averaged turbulence intensities ratios σ_v/σ_u and σ_w/σ_u as a function of 10-min mean wind direction: (a) WS1 and (b) WS2.

4.3 Power spectra of wind speed

Two samples of wind data with very distinct characteristics were selected for spectral analysis, both measured by sonic anemometer WS1. The criterion for this selection was the extraction of two-hour records with relatively high mean wind speed, but with opposite mean direction and incidence angles. Also, the wind sample should exhibit stationary characteristics, i.e., the mean wind speed from each segment should not differ more than 25 % from the wind speed mean of the full time series and, additionally, the corresponding direction angle must not vary by more than 15 deg [12].

The first sample chosen, with a north direction (15.9 deg) and an upward incidence (6.85 deg) was collected on 8 February 2012 between 11:50 and 13:50, and shows a mean wind speed of 7.73 m/s. The second sample, measured on the 25 April 2012 between 13:30 and 15:30, is characterised by a south direction (193 deg), a downward incidence (-2.94 deg) and a mean wind speed of 4.69 m/s.

The reduced auto power spectra computed for both wind samples for each turbulent component are depicted in Figure 11.

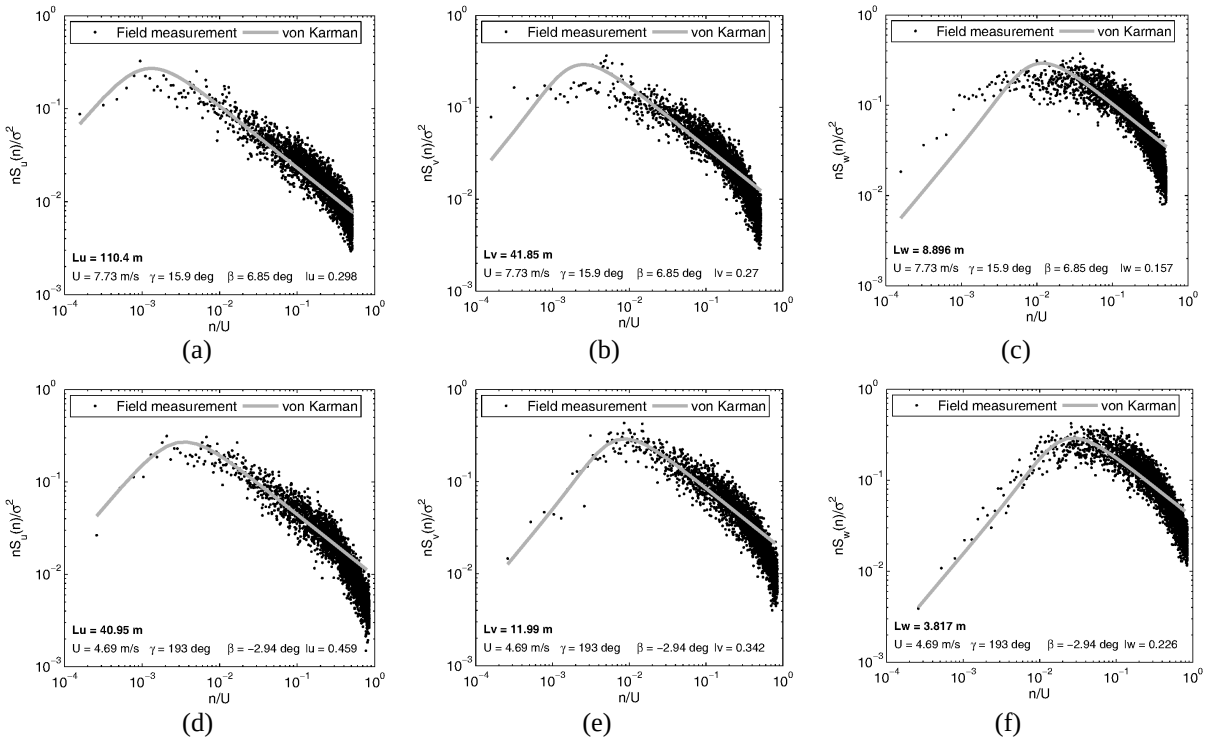


Figure 11: Power spectral density of wind measured by ultrasonic anemometer WS1. north – 8/2/2012: (a) along-wind; (b) cross-wind; (c) vertical wind; south – 25/4/2012 (d) along-wind ; (e) cross-wind; (f) vertical wind.

4.4 Turbulence integral length scales

The turbulence length scales define the average size of the turbulent eddies of the flow. The von Kármán spectra fitted to the power spectra density functions are represented in Figure 11, together with the resulting integral length scale. The values of the turbulence integral length scale obtained for the along-wind, cross-wind and vertical wind directions are, respectively, 110.4 m, 41.85 m and 8.896 m for northern winds and 40.45 m, 11.99 m and 3.817 m for southern winds. A prominent distinction is found between the parameters obtained for the two opposite prevailing directions. Turbulence integral length scales from northern winds present values 2-3.5 times greater than those measured from southern winds.

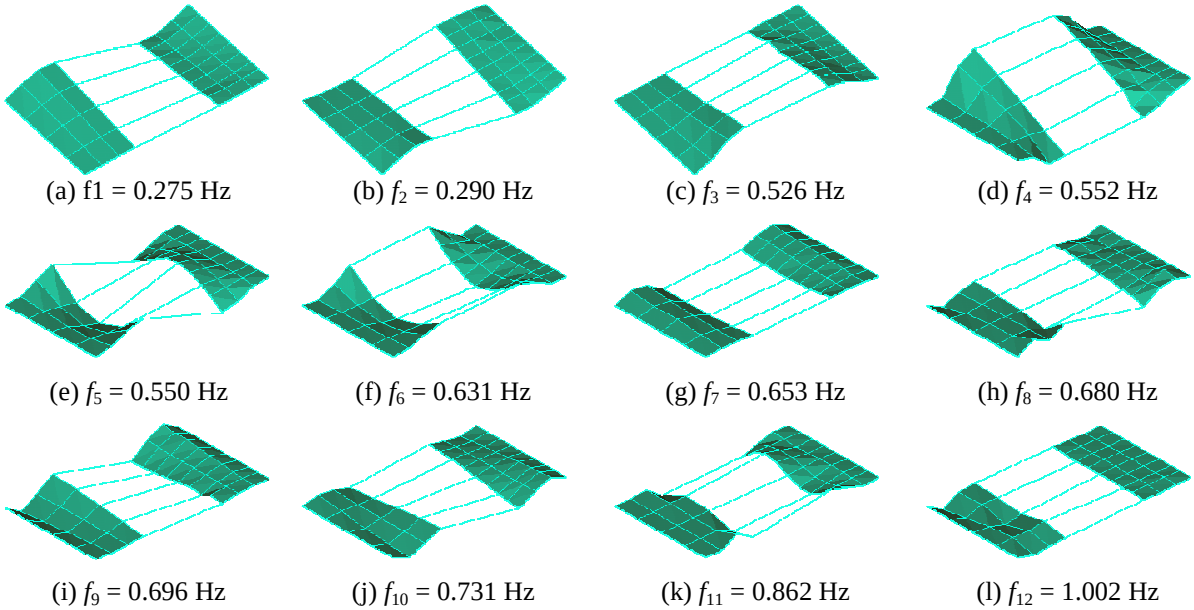
5 MODAL PARAMETERS

The automatic identification of the modal parameters (natural frequencies, mode shapes and damping ratios) is performed based on the ambient vibration response continuously measured by the dynamic monitoring system. For this purpose, developed algorithms process 60-minute acceleration files using the Covariance driven Stochastic Subspace Identification method (SSI-COV) complemented with a methodology based on the hierarchical clustering algorithm to automatically interpret stabilisation diagrams [13].

Table 1 summarises the mean and standard deviation values obtained for the analysis of the natural frequencies and damping ratios identified between December 2011 and August 2012. Representation of the corresponding modal configurations is shown in Figure 12.

Mode	Frequency [Hz]		Damping [%]	
	mean	std	mean	std
1	0.275	0.001	0.21	0.12
2	0.290	0.001	0.19	0.11
3	0.526	0.002	0.21	0.08
4	0.542	0.001	0.17	0.07
5	0.555	0.004	0.38	0.13
6	0.631	0.002	0.27	0.09
7	0.653	0.001	0.21	0.06
8	0.680	0.004	0.15	0.06
9	0.696	0.002	0.14	0.05
10	0.731	0.003	0.14	0.06
11	0.862	0.004	0.33	0.12
12	1.002	0.005	0.40	0.10

Table1: Mean and standard deviation values of the natural frequencies and damping ratios identified in the period between December 2011 and August 2012.



(a) f1 = 0.275 Hz (b) f_2 = 0.290 Hz (c) f_3 = 0.526 Hz (d) f_4 = 0.552 Hz

(e) f_5 = 0.550 Hz (f) f_6 = 0.631 Hz (g) f_7 = 0.653 Hz (h) f_8 = 0.680 Hz

(i) f_9 = 0.696 Hz (j) f_{10} = 0.731 Hz (k) f_{11} = 0.862 Hz (l) f_{12} = 1.002 Hz

Figure 12: Identified modal configurations associated with the first twelve modes [3].

6 INFLUENCE OF WIND ON THE STRUCTURAL RESPONSE

In this section, the influence of wind speed on structural response is described by the relationship between the 10-min root-mean-square (RMS) acceleration response and the mean wind speed and direction for the same period of time. The vertical acceleration response measured by the six accelerometers of the monitoring system was analysed for periods of time in which the 10-min mean wind speed measured by WS1 (Figure 3) were greater than 4 m/s. Furthermore, the analysis took into account the 10-min mean wind direction, dividing acceleration responses according to sixteen 22.5º directional sectors.

Figure 13 shows the relationship between the mean wind speed measured by WS1 and the vertical RMS accelerations measured by each accelerometer according to the three dominant

wind directions. From the performed analysis only the three directional sectors between 315º (NW) and 22.5º (NNE) showed a reasonable amount of observations.

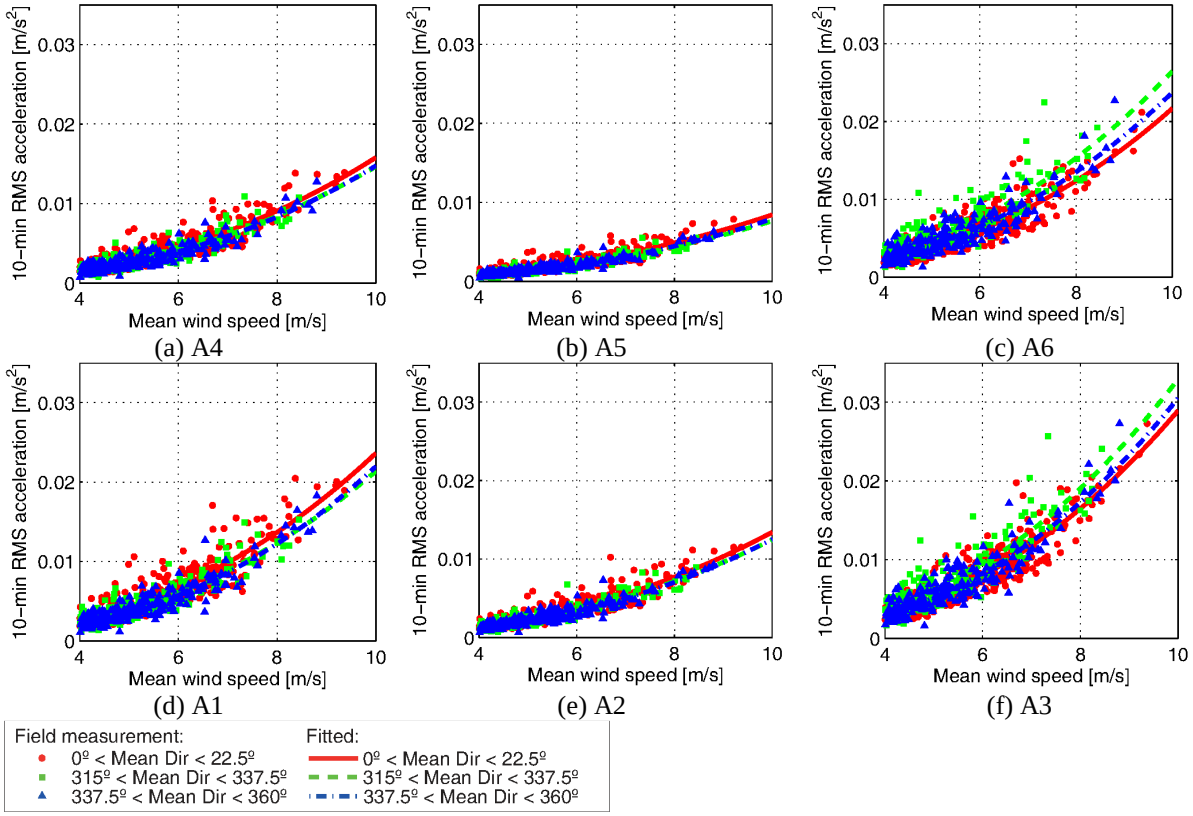


Figure 13: Relationship between mean wind speed from 3 dominant wind directions and 10-min RMS acceleration (see Figure 3).

The analysis of Figure 13 clearly shows the similarities in acceleration magnitude between accelerometers in the same suspension roof longitudinal direction (A1-A4, A2-A5 and A3-A6) (see Figure). It is also noticeable that sensors placed near the slab inner edge (A1, A2 and A3) show higher RMS accelerations than the corresponding sensors placed along the middle of the slab (A4, A5 and A6). The acceleration levels observed for each of the six accelerometers, and the relation between them, reflect the modal shapes of the first vibration modes (see Figure 12). The accelerometers placed on the north-west border of the slab (A3 and A6) show the highest magnitudes of acceleration, with nearly 0.03 m/s^2 RMS and 0.13 m/s^2 maximum for the higher wind speeds.

7 INFLUENCE OF WIND SPEED AND TEMPERATURE ON THE NATURAL FREQUENCIES AND MODAL DAMPING RATIOS

The modal parameters identified by the dynamic monitoring system reflect the influence of environmental and operational factors. In order to analyse the dependence between the mean wind speed, the ambient temperature variation and the value of the identified natural frequencies, the Pearson correlation coefficients were computed. Table 2 summarises the measures of correlation found between the identified natural frequencies and the mean wind speed and temperature.

	Natural frequency of mode:											
	1	2	3	4	5	6	7	8	9	10	11	12
$\overline{U}$	-0.28	-0.27	0.03	0.08	-0.26	-0.34	-0.37	-0.30	-0.21	-0.18	-0.46	-0.38
$\overline{T}$	-0.60	-0.69	0.76	0.62	-0.36	-0.04	-0.44	-0.59	-0.66	-0.61	-0.41	-0.34

Table 2: Pearson correlation coefficients between the natural frequency values and the mean wind speed and mean sonic temperature.

It is evident from the analysis of Table 2 that, apart from modes 3 and 4, the value of natural frequencies tends to vary inversely with both the mean wind speed and the mean temperature. The correlation with the mean wind speed in modes 3 (Figure 14(a,d)) and 4 is the smallest observed, with values close to zero, and contrary to the general trend, the value of the natural frequency tends to increase with higher ambient temperatures. An overall trend for a greater correlation between the natural frequencies and the mean temperature than with the mean wind speed is observed across Table 3. Exceptions are found for mode 6 (Figure 14 (b,e)), where the correlation with mean temperature is approximately zero, and modes 11 (Figure 14(c,f)) and 12, that show a similar degree of correlation with both variables.

To further investigate the effect of mean wind speed and mean temperature variation on the value of natural frequencies, the following linear regression was applied:

$$f_i = \beta_0 \overline{T} + \beta_1 \overline{U} + \beta_2 \tag{2}$$

where f_i is the natural frequency, $\overline{T}$ is the mean temperature, $\overline{U}$ is the mean wind speed, and β_0, β_1 and β_2 are fitting parameters.

Table 3 lists the regression parameters and the R^2 value for each mode.

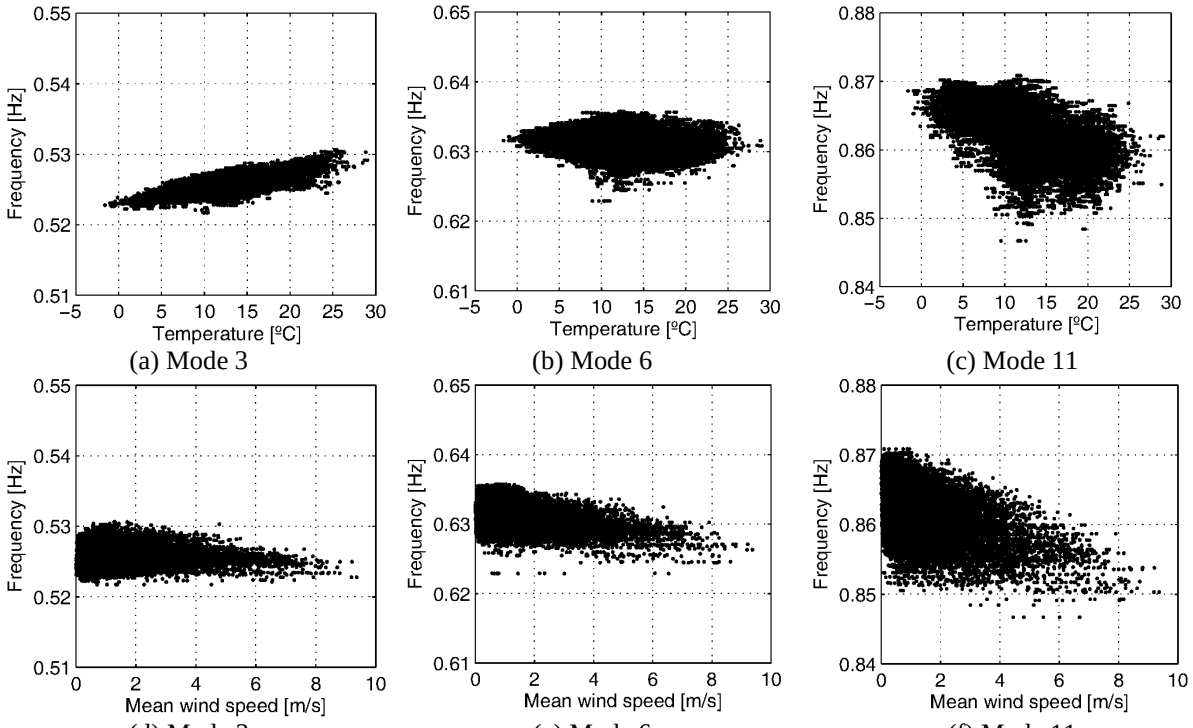


Figure 14: Correlation between the identified natural frequencies and: (a,b,c) mean sonic temperature; and (c,d,e) mean wind speed; for modes 3, 6 and 11.

Mode	β_0 [x10^{-4} Hz $^oC^{-1}$]	β_1 [x10^{-4} Hz $(m/s)^{-1}$]	β_2 [Hz]	R^2
1	-0.65	-0.99	0.275	0.53
2	-1.19	-1.47	0.292	0.64
3	2.08	-0.49	0.523	0.58
4	1.35	0.46	0.540	0.30
5	-2.51	-7.00	0.554	0.19
6	-0.53	-4.46	0.632	0.14
7	-0.93	-3.38	0.654	0.35
8	-2.17	-5.29	0.683	0.14
9	-2.48	-1.87	0.699	0.48
10	-3.54	-2.23	0.736	0.35
11	-3.62	-13.25	0.868	0.45
12	-2.71	-17.12	1.007	0.29

Table 3: Regression parameters between the identified natural frequencies, the mean sonic temperature and the mean wind speed measured by WS1.

It is worth noting that the natural frequencies of modes 10 and 11 show a greater sensibility to temperature change, while values from modes 1 and 6 are the least sensitive to this variable. Frequencies from modes 11 and 12 show higher variations with mean wind speed change. On the other hand, values corresponding to modes 3 and 4 show the smallest influence.

To study the relationship between damping ratios and the mean temperature and mean wind speed, the Pearson correlation coefficients between these variables were calculated. Table 4 summarises the most important results of the correlation analysis. The analysis of this table shows a trend for the identified damping ratios to vary proportionally with both the mean wind speed and the mean temperature, the only exception being the almost null correlation coefficient with temperature of the damping ratio associated with mode 11. The main conclusion is that for all investigated modes the variation of the damping ratio is more associated with the change of mean wind speed than of mean temperature. For this reason, only the relationship between damping ratios and mean wind speed has been considered in subsequent analyses.

	Damping ratio of mode:											
	1	2	3	4	5	6	7	8	9	10	11	12
$\bar{U}$	0.49	0.48	0.46	0.41	0.34	0.36	0.40	0.50	0.37	0.43	0.35	0.46
$\bar{T}$	0.17	0.18	0.17	0.13	0.27	0.19	0.13	0.18	0.14	0.21	-0.05	0.27

Table 4: Pearson correlation coefficients between identified damping ratios and the mean wind speed and mean sonic temperature.

Figure 15 represents the relation with mean wind speed of the identified damping ratios for modes 1, 3 and 9. The approximately linear relationship observed in the range of measured mean wind speed is common to all identified modes and reflects the wind induced added damping to the total identified damping ratio.

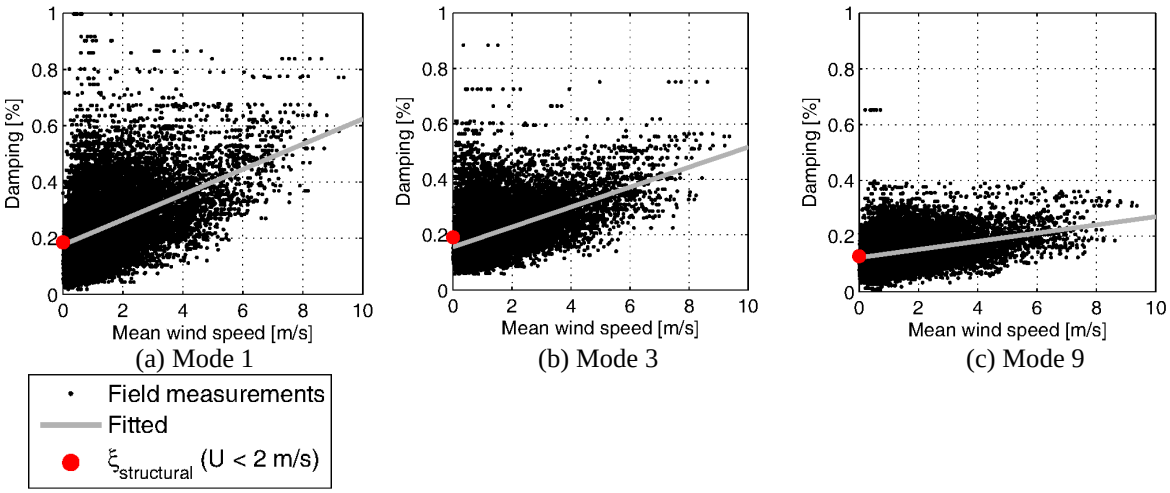


Figure 15: Correlation between the identified damping ratio and the mean wind speed; for modes (a) 1, (b) 3 and (c) 9, including the least-square fit and structural damping computed from low wind speeds.

The damping measurements corresponding to periods of very low wind speeds (lower than 2 m/s) were averaged for each mode in order to obtain an estimate of the structural damping ($\xi_{structural}$). In a different approach, least-squares linear fit was applied to the identified damping points associated with mean wind speed higher than 2 m/s. The constant term of the fitted line provides alternatively an estimate of the structural damping, while the slope parameter expresses the wind induced added damping gradient ($\Delta\xi_{aerodynamic}$) [14].

A great resemblance for the estimated structural damping values is found across all modes, with a general trend for greater values obtained by the averaging approach at low wind speed. The computed values for wind induced added damping range from 0.015 % $(m/s)^{-1}$, for mode 9, to 0.060 % $(m/s)^{-1}$, for mode 11, and correspond to an average of 20 % of the structural damping per m/s. The quality of the least-square linear fits is generally low, due to the significant scatter of the identified damping ratios.

8 CONCLUSIONS

Combining recent developments in terms of sensors, data communicating systems, computational power and identification algorithms, the continuous monitoring program established around the suspension roof of the Braga stadium has allowed the continuous measurement of wind, temperature and acceleration. The variation of such quantities during a period of 8 months has been investigated, with the purpose of obtaining a characterisation of the wind action based on field tests, establishing correlations with the structural response and finally analysing the influence of wind and temperature on the variation of modal parameters.

The measurement of wind using two sonic anemometers mounted on one of the slabs has permitted the identification of dominant directions, incidences and intensity of the typical wind speed, as well as allowed the characterisation of the intensity of turbulence and the spectral content, for the purpose of future verification of the design wind model.

The measurement of acceleration at 6 points along one of the slabs has allowed the establishment of response correlations with the wind velocity, which will be used as well to verify corresponding information obtained from wind tunnel tests at design stage.

Finally, the continuous identification of modal parameters together with wind and temperature measurements have allowed the investigation of the latter parameters on their variation.

Despite the low wind velocity generally measured and considering the corresponding interval of variation, it has been shown that most natural frequencies are simultaneously influ-

enced by temperature and wind, although temperature generally plays a dominant role, even if having a varying importance according to the vibration mode.

As for damping ratios, whose estimates typically exhibit higher scatter, and again despite the low wind velocity, it was possible to evidence the dominant influence of wind and, using two different approaches, separate the structural from the aerodynamic damping components, with very satisfying agreement, also confirmed by previous estimates based on free and forced vibration methods.

ACKOWLEDGEMENTS

The authors would like to acknowledge: (1) all the supports provided by the Portuguese Foundation for Science and Technology (FCT) to ViBest / FEUP, particularly in the context of Projects "Wind analysis of special structures from full scale measurements" and "DYNAMO_DEMO - Advanced Tools for Dynamic Structural Health Monitoring of Bridges and Special Structures" (2) the support of AFA Consult (Engº Carlos Quinaz) and Câmara Municipal de Braga; (3) the Ph.D. Scholarship (SFRH/BD/44291/2008) provided by FCT to the third author.

REFERENCES

[1] R. Furtado, C. Quinaz, R. Bastos, "New Braga Municipal Stadium, Braga," *Structural Engineering International*, vol. 2, pp. 72–76, 2005.

[2] E. Caetano, "Numerical modeling of the structural behaviour of the new Braga Stadium roof," Porto, Portugal, Technical Report, 2001.

[3] E. Caetano, Á. Cunha, F. Magalhães, "Numerical and experimental studies of the Braga Sports Stadium suspended roof," *Structure and Infrastructure Engineering*, vol. 6, no. 6, 2010, pp. 715–724.

[4] F. Magalhães, E. Caetano, Á. Cunha, "Operational modal analysis and finite element model correlation of the Braga Stadium suspended roof," *Engineering Structures*, vol. 30, no. 6, 2008, pp. 1688–1698.

[5] M. Majowiecki, N. Cosentino, "Dynamic aspects of the New Braga Stadium large span roof," *Proceedings of IASS Symposium*, 2007.

[6] F. Magalhães, Á. Cunha, E. Caetano, "Installation of a Continuous Dynamic Monitoring system at Braga Stadium Suspended Roof: initial results from automated modal analysis," in *EVACES 2009, Wroclaw, Poland*, 2009.

[7] N. Martins, A. Cardoso, E. Caetano, "Development of an observation system based on anemometry to characterize the wind action over a suspension roof," in *YIC2012*, 2012.

[8] F. Magalhães, E. Caetano, Á. Cunha, "Operational modal analysis of the Braga sports stadium suspended roof," in *IMAC XXIV, St. Louis, MO*, 2006.

[9] J. C. Kaimal, J. J. Finnigan, *Atmospheric boundary layer flows: their structure and measurement*. Oxford University Press, USA, 1994.

[10] J. M. Wilczak, S. P. Oncley, S. A. Stage, "Sonic anemometer tilt correction algorithms," *Boundary-Layer Meteorology*, vol. 99, no. 1, 2001, pp. 127–150.

[11] J.D. Holmes, "*Wind Loading of Structures*", Spon Press, 2001.

[12] C. Cremona, J.-C. Foucriat, "*Comportement au Vent des Ponts*", Presses de l'École Nationale des Ponts et Chaussées, 2002.

[13] F. Magalhães, Á. Cunha, E. Caetano, "Online automatic identification of the modal parameters of a long span arch bridge," *Mechanical Systems and Signal Processing*, vol. 23, no. 2, 2009, pp. 316–329.

[14] J. H. G. Macdonald, "Separation of the contributions of aerodynamic and structural damping in vibrations of inclined cables," *Journal of Wind Engineering and Industrial Aerodynamics*, vol. 90, no. 1, 2002, pp. 19–39.

COMPDYN 2013
4th ECCOMAS Thematic Conference on
Computational Methods in Structural Dynamics and Earthquake Engineering
M. Papadrakakis, N.D.Lagaros, V. Plevris (eds.)
Kos Island, Greece, 12–14 June 2013

WIND CHARACTERISTICS AROUND AND EFFECTS ON A SEA-CROSSING BRIDGE BASED ON MONITORING DATA

Limin SUN[1], Yi ZHOU[1], and Zhihua MIN[2]

[1] State Key Laboratory for Disaster Reduction of Civil Engineering, Tongji University
Siping Rd. 1239, Shanghai, 200092, P.R.China
lmsun@tongji.edu.cn

[2] College of Civil Engineering, Shanghai Normal University
Haisi Rd. 100, Fengxian, Shanghai, 201418, P.R.China
zhmin_tj@hotmail.com

Keywords: Wind Environment, Wind Induced Vibration, Structural Health Monitoring, Cable-Stayed Bridge.

Abstract. *Wind loading is critical for a long-span and flexible bridge under operation. This paper studied the wind loading on a sea-crossing bridge, namely the Main Navigational Channel Bridge (MNCB) of Donghai Bridge at Shanghai, utilizing the field measurement data from its Structural Health Monitoring System (SHMS). Located at the typhoon prone area off the eastern coast of China, the instrumented bridge is a five-span cable-stayed bridge arranged as 73+132+420+132+73m, with a three-cell steel-concrete composite box girder. In this paper, first of all, based on the data of wind speed and direction monitored by two anemometers, one on the mid-span of girder and the other on one tower's tip, the wind environment at the bridge site during the period from January 2007 to December 2012 is summarized in terms of the 10-min mean wind speed, mean wind direction, turbulence intensities and so on. Then, the extreme wind environment during strong winds, e.g. typhoons, and the strong-wind-induced structural responses, such as accelerations, are investigated by statistical analysis. Finally, the influence of strong winds on the variation of the bridge's modal frequency and damping ratio is discussed. During the high winds, modal frequencies become more scattered while damping ratios have an increasing trend. This research could serve as a field measurement basis for wind-resistance design and evaluation of long-span bridges in similar environments.*

1 INTRODUCTION

Wind is one of dominant loads for the large-span, light-weighted and flexible structures. Focused on the cable supported long-span bridges, the wind resistant evaluation, whether in the design stage or in the operation stage, is desired in the view of safety, serviceability and durability. As is quite well known, on the other hand, full-scale measurement of civil structures becomes more and more common, especially with the booming of Structural Health Monitoring campaigns around the world. [1-12] A well-developed SHM system could provide a huge database of recorded environmental conditions and structural responses, which has two attractive features, say, on-site and full-scale, compared with the results from numerical simulation and wind tunnel experiments. Although field measurement inevitably suffers from both the large uncertainty from unknown/uncontrolled factors and the limited measurement points due to the budgets, long-term and even continuously recorded data are still invaluable and much suitable to perform statistical analysis for the validation of or feed-back to the design theories and assumptions. As a result, more and more researches have been conducted about the wind characteristics and its effects on the stay cables, bridge girders and so on, based on the field measurements. [13-17]

The current paper presents two topics, i.e. wind environment and wind's effects, in summary form, processing the data from SHMS installed on the MNCB of Donghai Bridge over a period of 6 years. The former topic explores the statistical characteristics of the overall wind field on-site from 2007 to 2012 and during the strong wind events, which could serve as a field measurement basis for the verification of the wind-resistance design and the subsequent bridge condition evaluation. The latter topic discusses the bridge's acceleration responses and modal parameters' variation during high winds, with an attempt to better understand the responding mechanism of the long-span bridges to wind, as well as to better control the daily traffic conditions.

2 DONGHAI BRIDGE AND ITS SHMS

Located off the China's eastern coast and open to the traffic in Dec. 2005, Donghai Bridge is a vital sea-crossing linkage between Luchao Port at Shanghai City and the Yangshan Deepwater Port with a total length of over 32.5km (Figure 1). One of the key portions of this transport artery is the Main Navigational Channel Bridge (MNCB), a five-span cable-stayed bridge arranged as 73+132+420+132+73m. Its girder is a three-cell composite box girder, consisting of steel bottom flange and webs, and prestressed high-performance concrete top flange, with a width/depth ratio of 33m/4m=8.25. Twinned stays are arranged in a single plane and the two towers have an inverted Y shape with the designed elevation at top 159m. The MNCB's axis goes with a slightly rotation, about 1°, from the north-south direction in anticlockwise.

In order to optimize the bridge maintenance and ensure the service standard, a Structural Health Monitoring System (SHMS) has come into use since Sep. 2006, which includes 8 monitoring regions and 478 sensors of various kinds measuring the structural static and dynamic responses as well as environmental conditions. [18] The MNCB is the 5th monitoring region and totally 181 sensors were distributed on the girder, pylons and cables (Figures 2 and 3). For example, to accurately measure the horizontal wind on site, the instrumentation system includes two anemometers, one at the top of the northern tower PM335 denoted as 5WS001, the other at the center span of the girder denoted as 5WS002 with 6m away from the midpoint to the north. Both of anemometers have a sampling frequency of 1Hz and a range of wind speed of 0.4m/s ~ 75m/s. The elevations of 5WS001 and 5WS002 are, respectively, 159.50m and 58.15m above the sea level incorporating the sensor's masts.

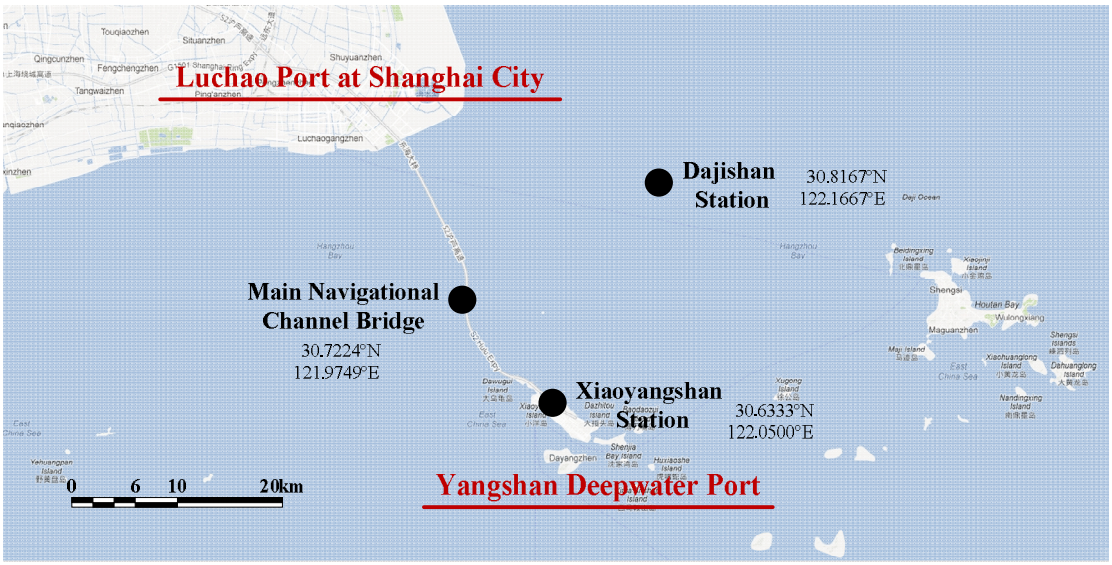


Figure 1: Locations of Measurement Stations and MNCB

In the design stage, this region's wind condition was determined according to the following two meteorological stations nearby, i.e. Dajishan Station (DJS for short) and Xiaoyangshan Station (XYS for short) as shown in Figure 1. DJS is about 21km away from the MNCB at the altitude of 81.00m, while XYS is nearly 12km away from the MNCB at the altitude of 32.90m. [19, 20]

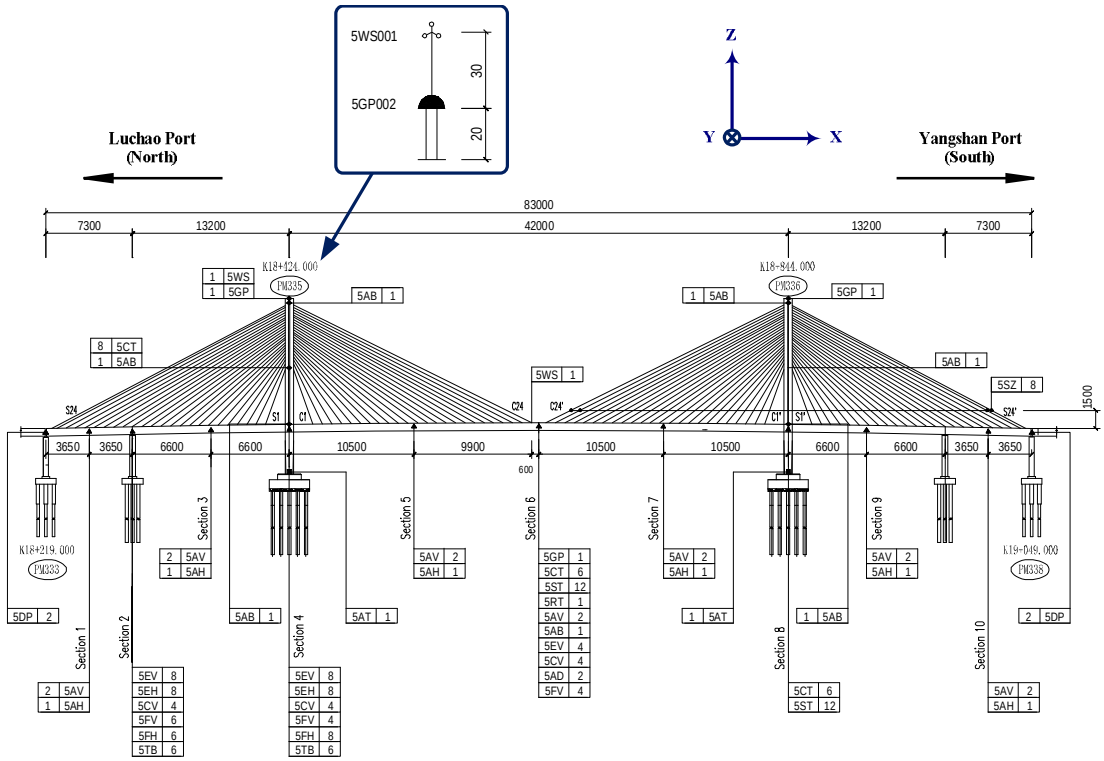


Figure 2: Elevation of the Main Navigational Channel Bridge (Unit: cm; 5EV/5CV/5EH-Strain Gauge; 5SZ-Cable Force; 5GP-GPS Station; 5AV/5AH/5AB/5AT/5AD-Accelerometer; 5FV/5FH-Fatigue Sensor; 5WS-Weather Station; 5DP-Extensometer; 5ST/5RT/5CT/5TB-Thermometer)

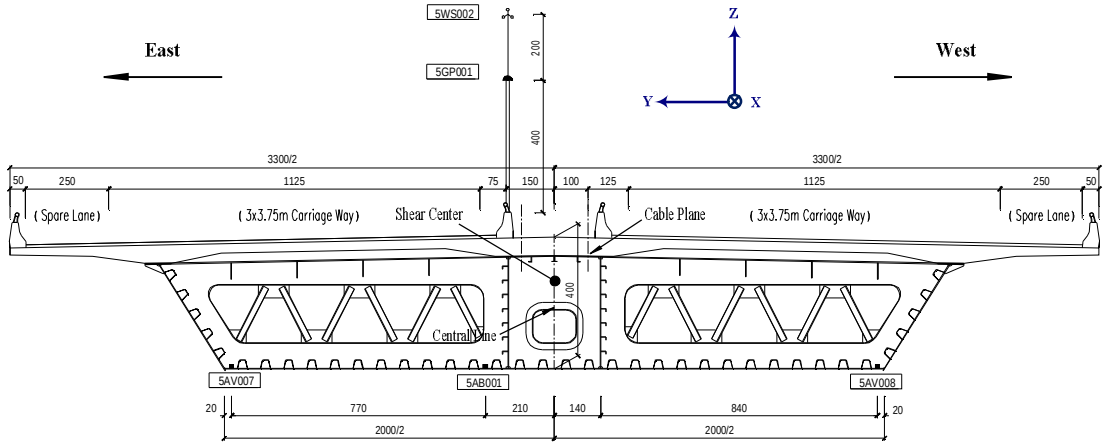
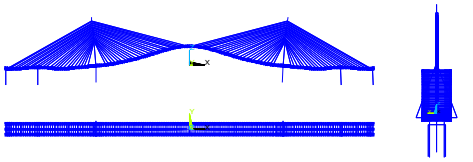
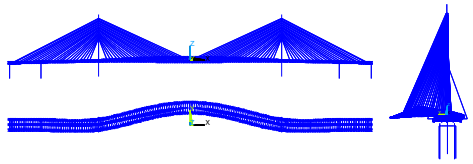


Figure 3: Section View of the MNCB (Unit: cm)

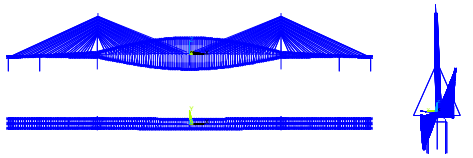
The MNCB's modes regarding the center span of the girder within 0~5 Hz are listed in Table 1, and the 1st vertical bending mode, the 1st lateral bending mode and the 1st torsional mode of the MNCB are plotted in Figure 4.



(a) 1st Vertical Bending Mode



(b) 1st Lateral Bending Mode



(c) 1st Torsional Mode

Figure 4: 1st Vert./Lat./Tor. Modes

Mode (Description)	Freq. (Hz)	Mode (Description)	Freq. (Hz)
Mode # (Vert. #)		**Mode # (Lat. #)**	
2 (Ver. 1)	0.361	3 (Lat. 1)	0.434
4 (Ver. 2)	0.513	13 (Lat. 2)	1.245
8 (Ver. 3)	0.778	26 (Lat. 3)	2.282
9 (Ver. 4)	1.013	54 (Lat. 4)	3.919
14 (Ver. 5)	1.378	77 (Lat. 5)	5.425
17 (Ver. 6)	1.694	**Mode # (Tor. #)**	
22 (Ver. 7)	2.042	5 (Tor. 1)	0.635
31 (Ver. 8)	2.662	12 (Tor. 2)	1.186
40 (Ver. 9)	3.113	21 (Tor. 3)	2.030
49 (Ver. 10)	3.593	30 (Tor. 4)	2.497
57 (Ver. 11)	4.145	38 (Tor. 5)	3.013
65 (Ver. 12)	4.602	53 (Tor. 6)	3.890
71 (Ver. 13)	4.954	58 (Tor. 7)	4.243
Mode # (Long. #)		64 (Tor. 8)	4.593
1 (Long. 1)	0.206	70 (Tor. 9)	4.857
29 (Long. 2)	2.497		
61 (Long. 3)	4.416		

Table 1: Modes of Center Span within 0~5Hz

3 OVERALL WIND CHARACTERISTICS DURING 6 YEARS

The records of wind speed and wind direction from 2007-1-1 to 2012-12-31 are retrieved and processed through the conventionally vector-decomposition based method [21] with the averaging period 10 minutes, thus obtaining the 10-min mean wind speed $\overline{U}$ and the fluctuating components at longitudinal and lateral direction, u and v. After excluding the data over the periods when the monitoring system failed, the statistics of the 6 years wind field are computed from approximately 270000 10-min records at the deck level, and about 230000 10-min records at the tower-top level.

3.1 Wind frequency during 6 years

Figure 5 displays the wind roses of the mean wind speeds from both tower-top and deck measurements for a comparison with the assumed wind roses in the design stage. The radial distances in the plot represent the percentage of the total number of the 10-min segments from a particular direction. It can be seen that wind directions at tower-top and deck level are dramatically different, which might reflect the Ekman spiral. However more probably, it comes from the interference from the bridge. Furthermore, the wind frequency at the bridge site is significantly different from those at DJS and XYS, which indicates the weak correlation between two spots separated about 20km in this region.

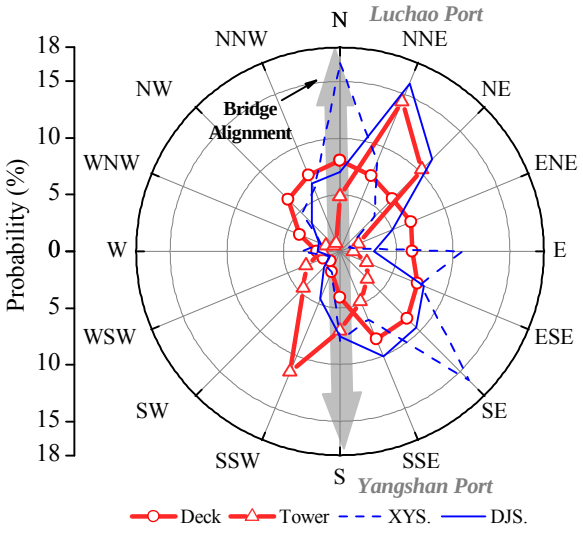


Figure 5: Wind Frequency Compared with Design

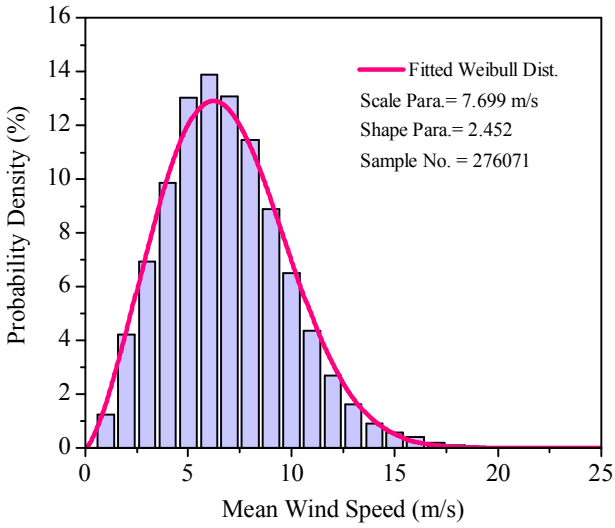


Figure 6: 10-min Mean Wind Speed Histogram

3.2 Mean wind profile

According to the power-law profile, recommended by China's Wind-resistant Design Specification for Highway Bridges [22], the exponent α in (1) is estimated from the 10-min records over the periods when both 5WS001 and 5WS002 are normal.

$$\frac{U_t}{U_d} = \left(\frac{Z_t}{Z_d}\right)^{\alpha} \tag{1}$$

In (1)(2), U and Z respectively represent the 10-min mean wind speed and measurement point's height, while the subscripts t and d denotes tower-top and deck. Given Z_d =58.15m and Z_t =159.50m, then the mean of α is 0.15, which is close to the value corresponding to terrain category B in [22] but larger than α =0.10 in the design manual.

Considering the deck is of more interest in the design and evaluation, only the deck measurement is considered in the following for brevity.

3.3 Mean wind speed distribution

The histogram of 10-min mean wind speed at the deck level is shown in Figure 6, which is in good agreement with the Weibull distribution [23] whose p.d.f. is formulated as (2), and the fitted parameters are 2.452 for the shape parameter k, and 7.699m/s for the scale parameter c.

$$f(x) = \left(\frac{kx^{k-1}}{c^k}\right) \exp\left[-\left(\frac{x}{c}\right)^k\right] \tag{2}$$

3.4 Recurrence of wind field

Figure 7 and 8 are the wind roses of 10-min mean wind and daily maximum mean wind for each year. The style of wind rose here are different from that in Figure 5 in that a tangential length, which is meaningless, is added just for visualization enhancement. The wind speed intervals in Figure 7 and 8 are based on the Beaufort Wind Scale [24] without the height modification. In Figure 7, 0~7.9m/s, 8.0~13.8m/s, ⩾13.8m/s correspond to scale 0~4, scale 5~6, and greater or equal than scale 7; likewise, in Figure 8, 0~13.8m/s, 13.9~17.1m/s, ⩾ 17.2m/s correspond to scale 0~6, scale 7 and greater or equal than scale 8. These two figures show an obvious one-year cycle, which indicates a particular wind distribution pattern does exist at the location of the MNCB and it could be modeled by joint probability density function of wind speed and wind direction. [25]

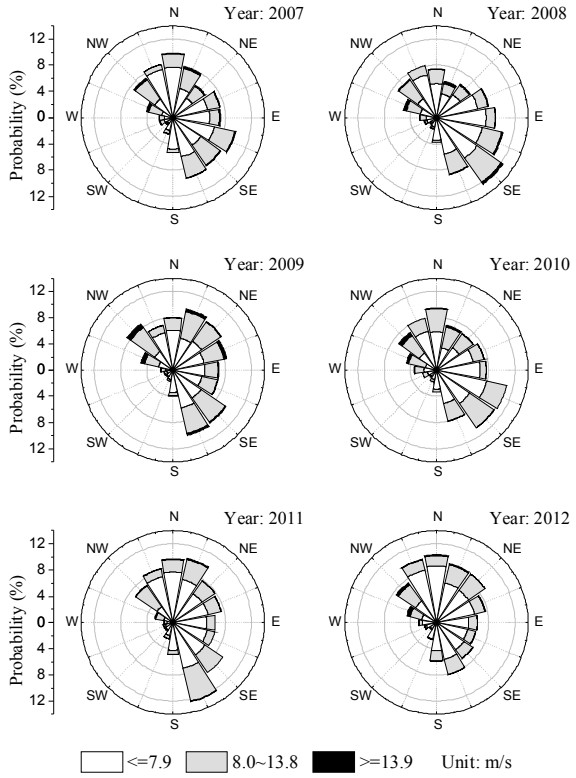


Figure 7: Mean Wind for Each Year

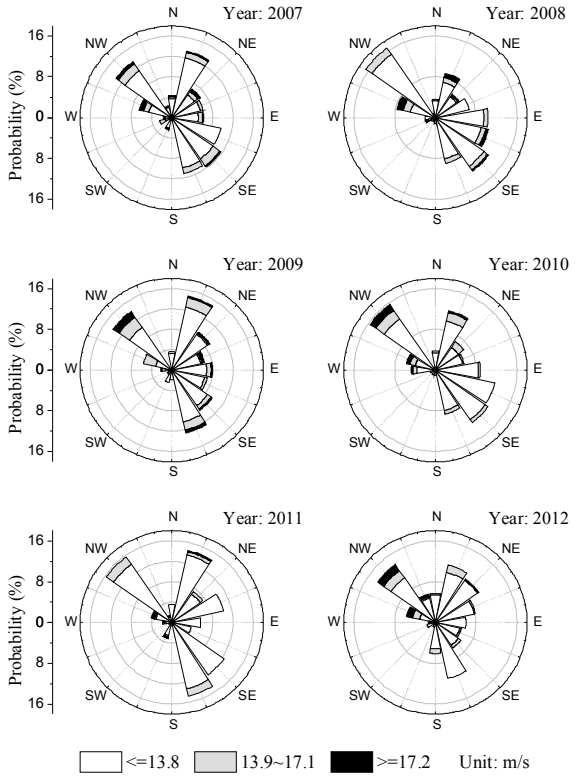


Figure 8: Daily Maximum Wind for Each Year

Further examination on the wind frequency for each season is also performed, which exhibits the characteristics of a subtropical monsoon climate, i.e. wind mainly blowing from southeast in summer and from northwest in winter.

3.5 Characteristics of turbulence components

The variance, turbulence intensity, integral length scale are calculated to characterize the fluctuating components u and v, as listed in the 4th column of Table 2. It is important to point out that in the current paper, all the quantities are computed from 10-min averaging duration following the conventional method, which assumes the wind is stationary in each 10-min segment. The actual wind field during some periods, however, are far from the stationarity,

e.g. during the typhoon Haikui the wind direction changed fiercely (Figure 12). Therefore, the turbulent characteristics are generally overestimated in Table 2, and a more appropriate average time duration is needed for the subsequent research in the near future.

	Formula	Design Value	6 Years	8-22 Gale	Wipha	Krosa	Muifa	Haikui	Bolaven
Time Interval Time1	From ~ To		2007/1/1 0:00 ~ 2013/1/1 0:00	2008/8/22 17:30 ~ 2008/8/22 18:30	2007/9/19 0:00 ~ 2007/9/19 16:00	2007/10/7 14:00 ~ 2007/10/9 8:00	2011/8/6 13:00 ~ 2011/8/7 17:00	2012/8/7 11:00 ~ 2012/8/9 5:00	2012/8/27 0:00 ~ 2012/8/28 0:00
Max. Gust m/s	$\max(U(t))$	–	–	46.40	25.50	33.00	37.00	35.20	30.10
Max. Mean Wind m/s	$\max(\overline{U})$	–	–	23.38	20.38	24.96	26.38	23.81	22.87
Mean Wind $\overline{U}$ (m/s)	$\frac{1}{T}\int_0^T U(t)\,dt$	51	6.828	11.29	16.28	17.14	18.06	10.46	11.30
Variance σ_u^2 (m/s)^2	$\frac{1}{T}\int_0^T u^2(t)\,dt$	–	0.876	40.54	1.73	3.39	5.99	65.77	1.82
Variance σ_v^2 (m/s)^2	$\frac{1}{T}\int_0^T v^2(t)\,dt$	–	0.943	17.21	1.79	3.06	3.55	60.94	1.09
Turb. Int. I_u (%)	$\frac{\sigma_u}{\overline{U}}$	10	13.78	35.35	7.91	10.89	12.53	161.42	14.00
Turb. Int. I_v (%)	$\frac{\sigma_v}{\overline{U}}$	9	14.58	26.50	8.13	10.50	10.48	157.16	12.90
Gust Factor $G_u(t_g)$	$1+\max(u(t_g))/\overline{U}$	1.38	1.299	1.75	1.17	1.23	1.29	3.71	1.34
Gust Factor $G_v(t_g)$	$\max(v(t_g))/\overline{U}$	–	0.295	0.43	0.18	0.22	0.23	3.01	0.29
Integ. Len. L_u^x (m)	$\frac{\overline{U}}{\sigma_u^2}\int_0^{0.05\sigma_u^2} R_u(\tau)\,d\tau$	120	89.079	630.57	154.53	274.30	194.58	159.40	154.98
Integ. Len. L_v^x (m)	$\frac{\overline{U}}{\sigma_v^2}\int_0^{0.05\sigma_v^2} R_v(\tau)\,d\tau$	60	53.093	492.36	48.63	178.70	134.44	204.56	96.48

*Note: u and v denote longitudinal and lateral characteristics respectively; and t_g in Gust Factor is 3s.

Table 2: Wind Characteristics on site

Figure 9 and 10 show the polar plots of the mean values of the turbulence intensities I_u, I_v and integral length scales L_u, L_v versus directions ranging from 0~360° in 22.5° increments at the deck level. It is interesting to note that I_u, I_v on the north and south are greater than those on the other directions, while L_u, L_v on the north and south are smaller than other directions. Both of the above results indicate the wind has stronger turbulence along the bridge axis, which most likely results from the disturbance from the bridge.

4 WIND CHARACTERISTICS DURING STRONG WIND

In this section, wind characteristics during strong wind at the MNCB's site are explored. According to the website [26], there is in total 17 typhoon processes entering the circle with the center at the MNCB and the radius 400km from Jan. 2007 to Dec. 2012, and 5 of them

have an instantaneous wind speed exceeding 25m/s at the deck level, whose tracks were shown in Figure 11. Additionally, the measured highest wind speed at the deck level over 6 years comes from a strong localized gale process occurred on 2008-8-22, which is also picked out for a further discussion.

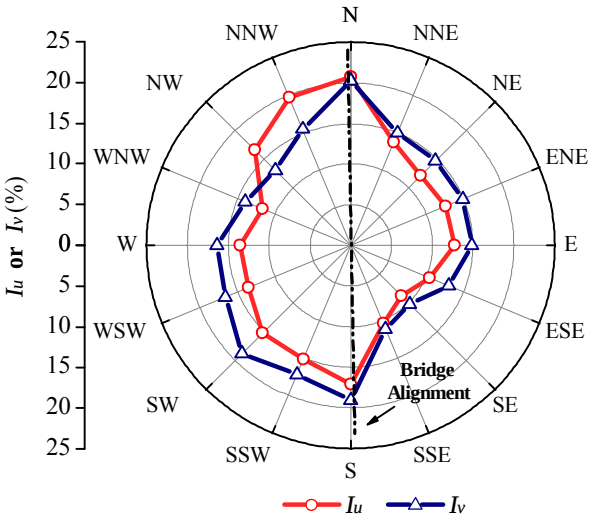


Figure 9: I_u and I_v for Each Direction

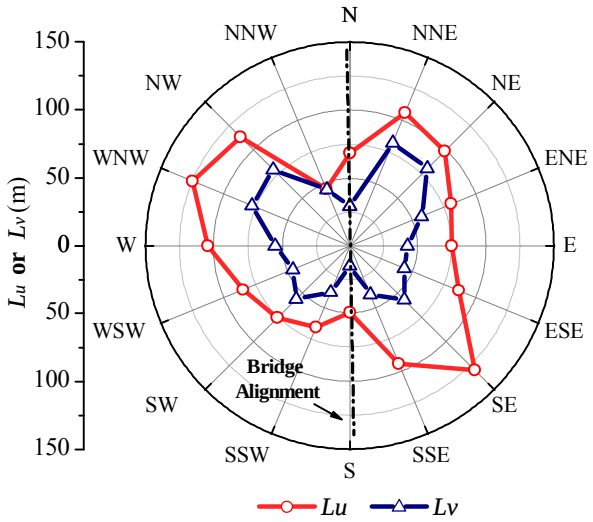


Figure 10: L_u and L_v for Each Direction

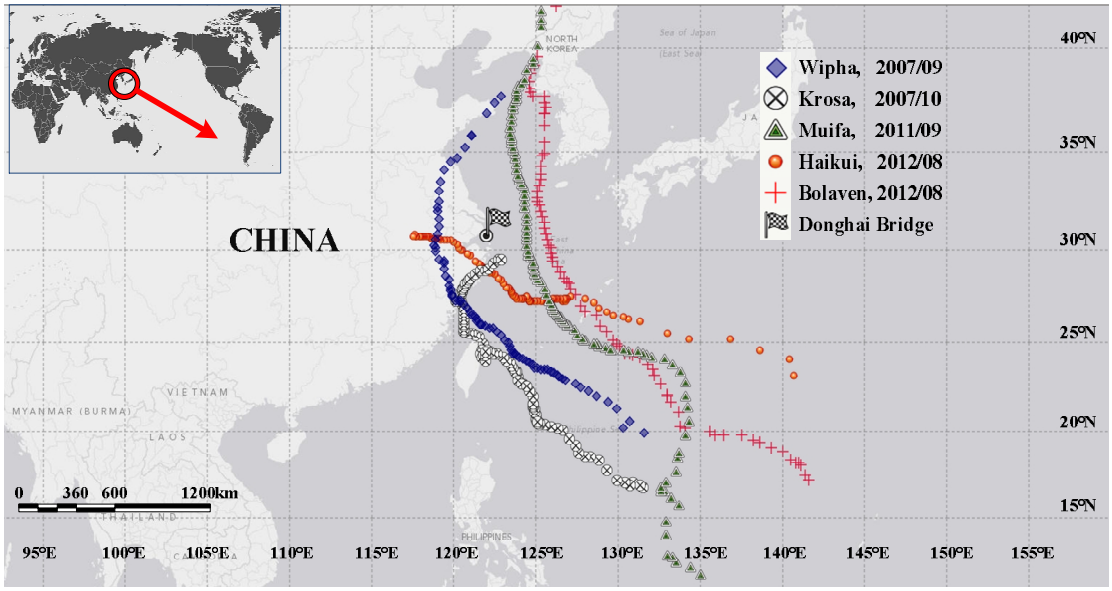


Figure 11: Typhoon Tracks

The measured wind speeds and directions during these 6 strong wind processes are plotted in Figure 12, where the dashed lines indicates the periods when the MNCB is within the typhoon circle with the radius of 15.4m/s for the 5 typhoon processes. Typhoon Haikui is unique because the MNCB is even within the typhoon circle with the radius of 25.7m/s as indicated by the dot and dash lines in Figure 12 (e). Table 2 lists the characteristics of each strong wind which is calculated based on the 10-min average time duration. By comparison with the statistics over 6 years, it can be seen that the turbulent variance σ^2 and the mean wind speed during strong wind processes are consistently larger than those in the ordinary wind field, but the gust factors G, turbulence intensities I and integral length scales L does not ex-

hibit obviously qualitative trend. It should be noted that usually the wind field is non-stationary during strong winds, so the calculated statistics in Table 2 may not reflect the physical characteristics as mentioned above. Preferable are either shorter averaging duration or other methods suitable to model the non-stationary wind field like in [27].

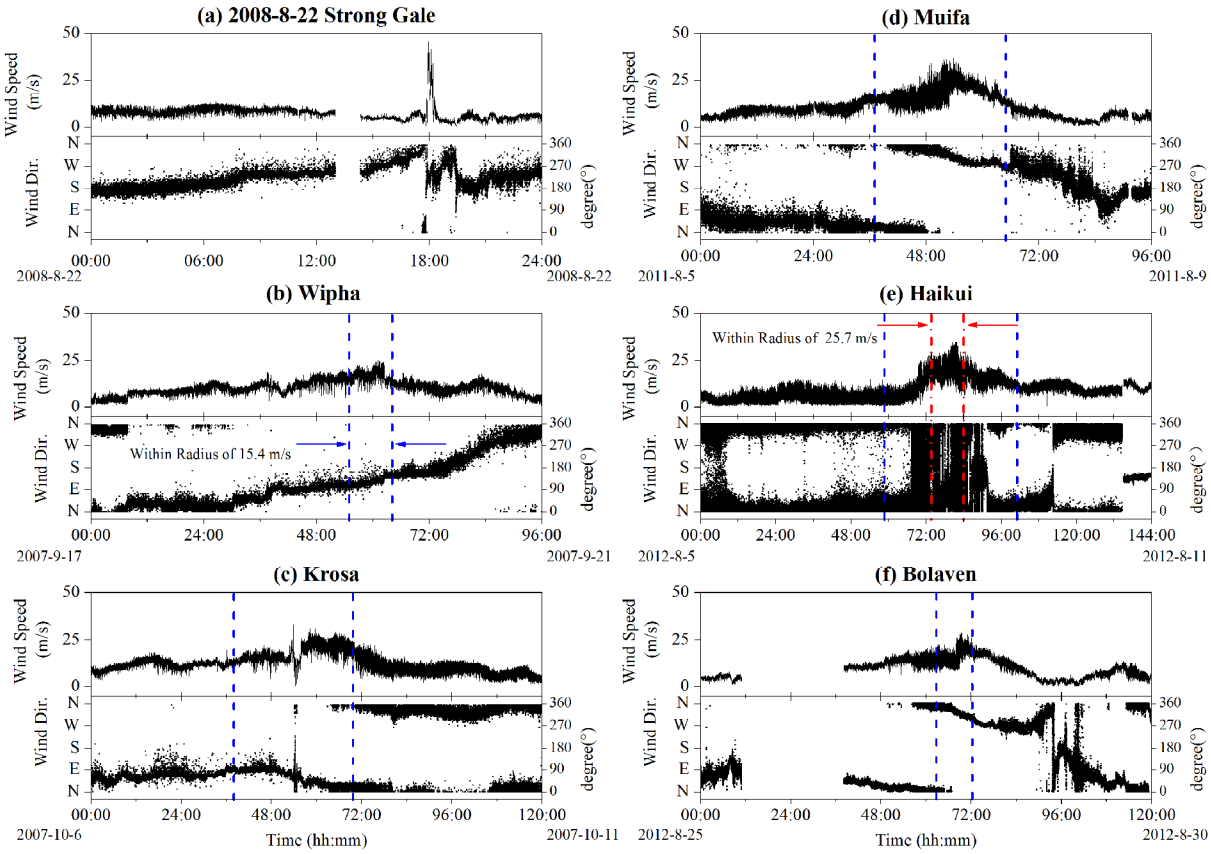


Figure 12: Time Histories of Each Strong Wind

5 STRUCTURAL RESPONSE DURING STRONG WINDS

This paper focuses on the acceleration responses during strong winds at the mid span of girder. As shown in Figure 3, the accelerometers don't reside on the centroid of the cross-section, so the first step is to transform the measured acceleration responses to the vertical, lateral, torsional accelerations $\ddot{V}$、$\ddot{H}$、$\ddot{\alpha}$ regarding to the centroid. Note that the centroid and shear center of the standard cross-section of the MNCB are 1.29m and 1.34m below the top surface, respectively; thus it is acceptable not to distinguish them strictly. The measurement points for the vertical acceleration are $AV007$ and $AV008$, which are 19.6m apart from each other; and for the horizontal acceleration is $AB001$, which is 2.71m below the centroid. The measurement data could be related to $\ddot{V}$、$\ddot{H}$、$\ddot{\alpha}$ as

$$\begin{cases} \ddot{\alpha} \times 9.8 + \ddot{V} = AV007 \\ -\ddot{\alpha} \times 9.8 + \ddot{V} = AV008 \\ \ddot{\alpha} \times 2.71 + \ddot{H} = AB001 \end{cases} \tag{3}$$

Hence,

$$\begin{cases} \ddot{\alpha} = (AV007 - AV008) / (2 \times 9.8) \\ \ddot{V} = (AV007 + AV008) / 2 \\ \ddot{H} = AB001 - 2.71 \times \ddot{\alpha} \end{cases} \tag{4}$$

Figures 13 and 14 are the acceleration time histories at the midspan of the girder during 2008-8-22 gale and Typhoon Haikui. When Haikui hit the MNCB, the bridge was closed to traffic for about 35 hours and this period could be readily identified from Figure 14, indicating the traffic has great impact on the bridge's dynamic response. With closer observation, it is possible to compare the effects of wind and traffic on the acceleration amplitude. For the vertical and torsional acceleration, the traffic loading seems to take more advantages than the wind. Because only the super strong winds like 8-22 Gale and Typhoon Haikui could excite these two accelerations to the same order of magnitude as the traffic loading. However, for the lateral acceleration, the wind loading is so dominant that the maximum magnitude during high wind is many times as that in the normal traffic condition, which is also listed in Table 3.

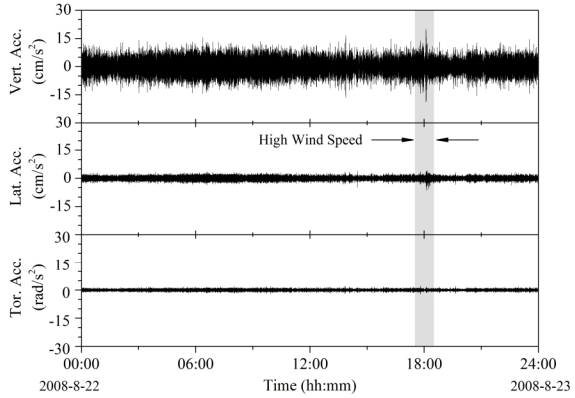


Figure 13: Acceleration on 2008-8-22

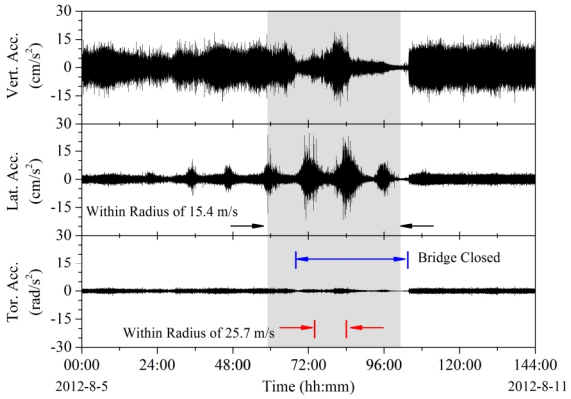


Figure 14: Acceleration during Typhoon Haikui

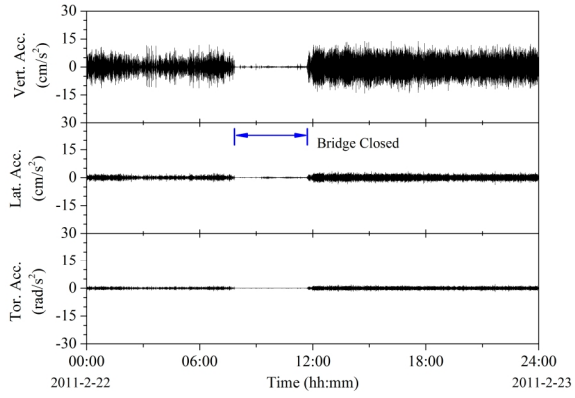


Figure 15: Acceleration on 2011-2-22

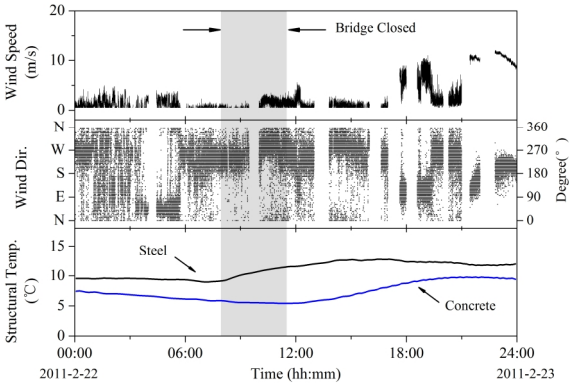


Figure 16: Temp. and Wind Condition on 2011-2-22

In order to investigate the relationship among wind, traffic loading and girder's accelerations, the following four "one-hour" records are selected out, which correspond to four typical cases:

- CASE I: without high wind and without traffic, i.e. 2011-2-22 9:00~10:00;
- CASE II: without high wind but with traffic, i.e. 2011-2-22 5:00~6:00;
- CASE III: with high wind but without traffic, i.e. 2012-8-8 11:00~12:00 during Haikui;

- CASE IV: with high wind and with traffic, i.e. 2008-8-22 17:30~18:30.

On the morning of 2011-2-22, a severe traffic accident happened on the Donghai Bridge, causing the bridge closed for about 4 hours. Figures 15 and 16 present the deck acceleration responses, structural temperatures and wind condition at the tower top (the deck's anemometer is out of work). Fortunately, during the bridge closure the wind is small and temperature is stable, so CASE I could serve as a base-line. By comparing other cases with it, the strong wind and traffic loading's effects could be clear.

			1/2 of the Middle Span				Tower Bot. of PM335		
	Time Interval Time2	Statistics	Vert. Acc. cm/s^2	Lat. Acc. cm/s^2	Tor. Acc. rad/s^2	Long. Acc. cm/s^2	Lat. Acc. cm/s^2	Long. Acc. cm/s^2	Vert. Acc. cm/s^2
8・22 Gale	2008/8/22 17:30 ~ 2008/8/22 18:30	Max	19.92	4.14	2.03	2.14	0.39	2.33	1.24
		RMS1*	2.66	0.57	0.27	0.36	0.05	0.21	0.12
	Other	RMS2*	1.91	0.46	0.23	0.30	0.05	0.07	0.05
Typhoon Haikui	2012/8/7 21:00 ~ 2012/8/9 7:00	Max	19.02	24.55	2.18	3.78	1.78	5.24	34.52
		RMS1*	1.81	0.81	0.19	0.24	0.07	0.42	0.42
	Other	RMS2*	2.12	0.56	0.25	0.35	0.06	0.16	0.07
Traffic Accident	2011/2/22 8:00 ~ 2011/2/22 11:00	Max	1.76	0.59	0.22	0.35	0.06	0.22	0.06
		RMS1*	0.07	0.05	0.01	0.02	0.00	0.01	0.00
	Other	RMS2**	1.85	0.42	0.22	0.31	0.05	0.07	0.05

*RMS1 is Acc. RMS during "Time2" in the left column, while RMS2 corresponds to "Time1" in Table 2 excluded "Time2" here.

** RMS2 here corresponds to other times on 2011-2-22

Table 3: Structural Acc. Responses for Diff. Cases

Figure 17~Figure 19 are the power spectral density (PSD) plots of the vertical, lateral and torsional accelerations at the midspan, and CASE I is replotted in every subplot in each figure. For acceleration's sampling frequency is set to 50Hz, thus the cut-off frequency is 25Hz. Concentrating on the frequency range of 0~5Hz, some interesting phenomena could be seen from these figures. Firstly, the PSD of the acceleration induced only by the traffic loading increase by a larger amount in the frequency range of 2~5Hz than in the 0~2Hz by comparing CASE II with CASE I; secondly, acceleration's PSD induced only by the strong wind increased more obviously in the frequency range of 0~2Hz than 2~5Hz by comparing CASE III with CASE I, which is also found in [12]; and finally when acceleration is excited by both traffic and high winds, i.e. CASE IV, the frequency intervals 0~2Hz and 2~5Hz have similar increments in the acceleration PSD. It could be inferred that the exciting frequency of strong winds is lower than that of traffic.

The accelerations on the tower top and tower bottom have also been investigated. Figure 20 gives the PSD of acceleration response at the bottom of PM335, and the results also support the above inference on the frequency contents of high winds and traffic. In terms of CASE II, i.e. without high winds but with traffic, the traffic loading is only directly on the girder, the PSD in the upper subplot of Figure 20 demonstrates the vibration of the girder did affect the tower bottom. Although the vibration intensity caused by traffic is much lower than that in an earthquake, it is obviously different between CASE I and CASE II for the tower bottom vibration. Hence, it might not be appropriate to model the tower bottom as a fixed boundary when conducting dynamic analysis. Tabulated in Table 3 are the statistics of acceleration responses related to CASE I ~ CASE IV for a further comparison.

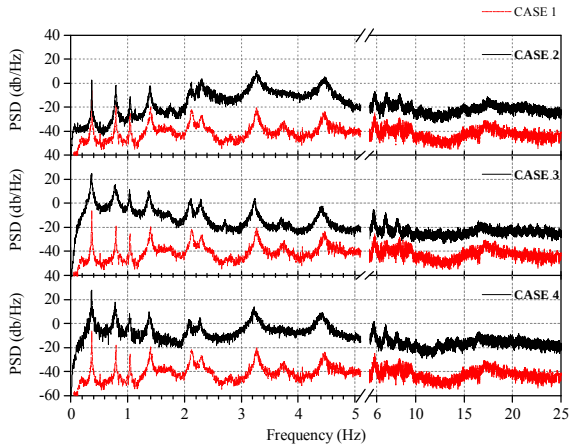


Figure 17: PSD of Vert. Acc. at the Midpoint

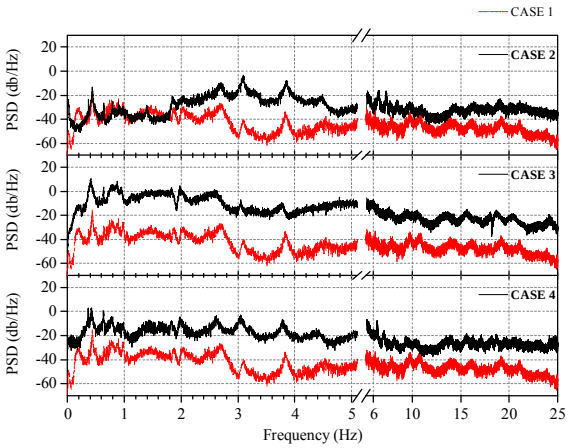


Figure 18: PSD of Lat. Acc. at the Midpoint

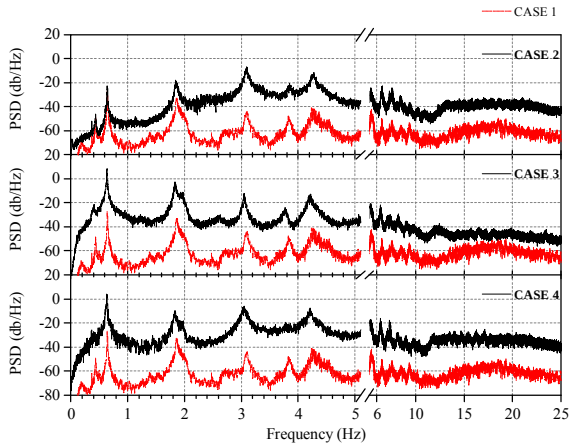


Figure 19: PSD of Tor. Acc. at the Midpoint

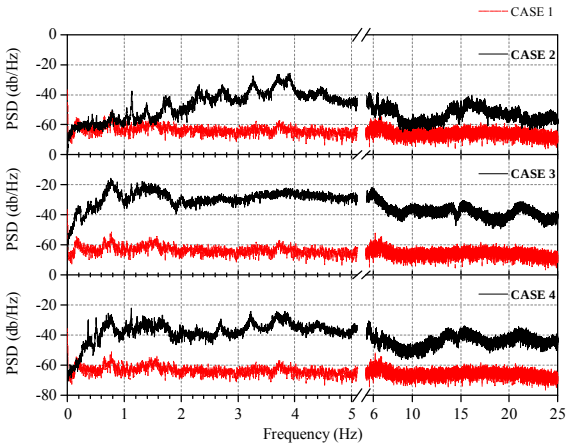


Figure 20: PSD of Lat. Acc. at Bot. of PM335

6 VARIATION OF MODAL PARAMETER DURING STRONG WINDS

Here, only the lower modes are considered. The frequencies and damping ratios of the 1st vertical bending, 1st lateral bending and 1st torsional modes are identified using Eigensystem Realization Algorithm (ERA) based on each of the 10-min acceleration data at the midspan. Figure 21~Figure 24 show the variation of modal parameters during 8-22 Gale and Typhoon Haikui, with the gray background meaning the high wind periods. Generally speaking, the modal frequencies become more scattered and in the meanwhile the damping ratios have an increasing tendency during high winds. The reason why the dynamic properties of the MNCB during high winds are so scattered might have something to do with the following facts:

- Structural stiffness, damping properties are not stable in high winds influenced by aero-dynamic effects;
- With exception of wind, modal parameters may also be affected by vibration intensity, structural temperature and so on;
- Measurement noise and algorithm errors coming from parameter identification process may also increase the uncertainty of the results.

Figures 25 and 26 are scatters of modal parameters versus wind speed, acceleration RMS and deck temperature during the bridge closure in Typhoon Haikui, where all the quantities are mapped to the interval [0, 1] and the wind speed is the component normal to the bridge axis. It appears that the modal parameters have a closer relation with the acceleration RMS, but other clear relations among these quantities are hard to be found. From the previous researches like [6, 9], the variation of modal parameters with regard to wind properties is also not so obvious, and the corresponding authors were cautious with their results as here.

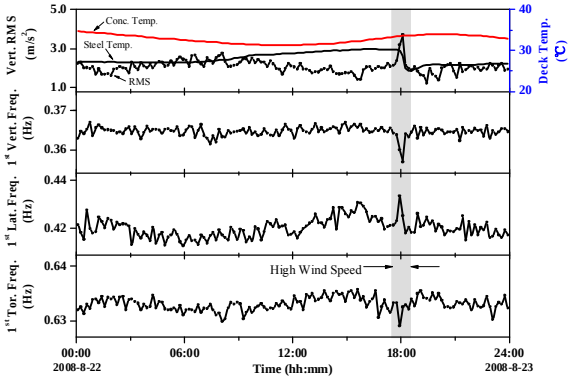


Figure 21: Modal Freq. on 2008-8-22 (1/2L)

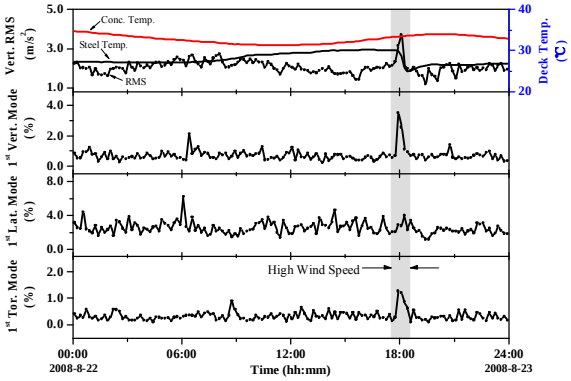


Figure 22: Damping Ratio on 2008-8-22 (1/2L)

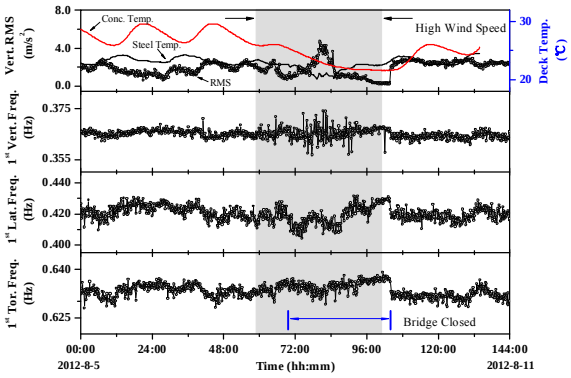


Figure 23: Modal Freq. during Haikui (1/2L)

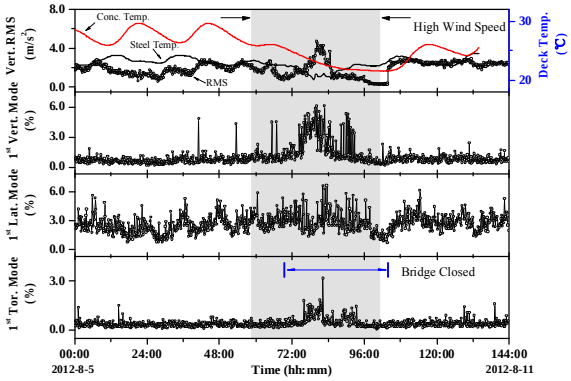


Figure 24: Damping Ratio during Haikui (1/2L)

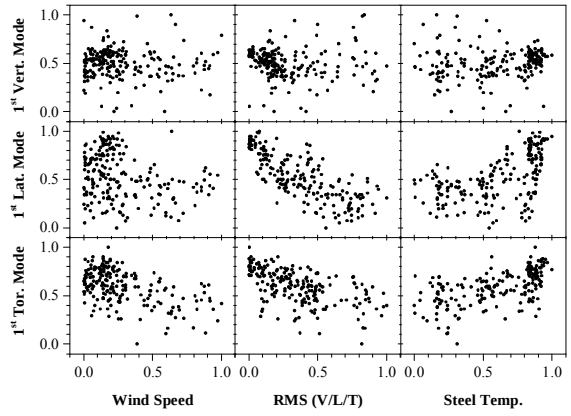


Figure 25: Freq. Vs Wind/RMS/Temp. during Haikui (1/2L)

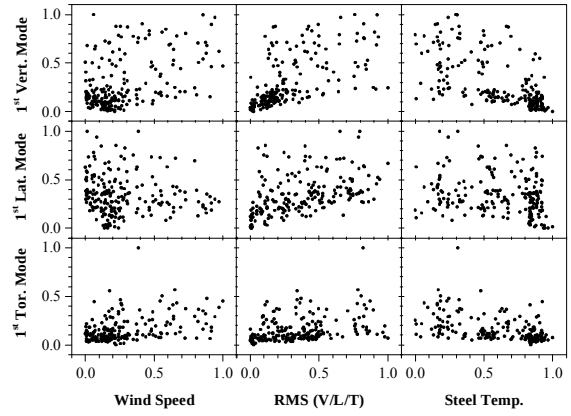


Figure 26: Damping Vs Wind/RMS/Temp. during Haikui (1/2L)

Additionally, there are two interesting phenomena that should be put forward. One comes from Figure 23, where modal frequencies drop by a relatively large amount at the end of bridge closure. This phenomenon demonstrates the influence of traffic loading on the modal frequency. The other phenomenon comes from Figure 17~Figure 19, where the higher modal frequencies also shift clearly to the lower side during CASE III and CASE IV. It should be kept in mind that CASE I and CASE II happened in the February, thus at low temperature, while CASE III and CASE IV happened in the August, with high temperature. Hence, the frequencies' decrease here may be attributed to the temperature's increase.

7 SUMMARY

Based on the field monitoring data from SHMS on the MNCB of Donghai Bridge, this paper investigates the wind field on site, and the wind effects in terms of structural acceleration responses and modal parameter's variation. Here some conclusions could be drawn as following:

1) About the Wind Environment: firstly, learned from the measurements, the wind field on the MNCB's site has a good repetition by one-year, and it is reasonable and possible to obtain the wind's probability density function by statistic approach; secondly, the measured wind characteristics could not be well represented by the assumption during the design stage, which indicates the importance and necessity of the feed-back from the field measurement to the design; thirdly, when the wind field is non-stationary, e.g. the wind direction changes dramatically, it is better to adopt a shorter average time duration than 10 minutes, or use a time-varying mean wind speed model; last but not least, the measured wind records on site might be disturbed by the structure. When making use of wind data from SHMS, it is necessary to consider the interference from the structure, e.g. directional effects;
2) About the Wind Effects on Structural Dynamic Responses: first of all, the strong winds and the traffic loading have different effects on the girder's vibration, at least for the MNCB of Donghai Bridge: the vertical and torsional vibrations depend more on the traffic loading while the lateral vibration are more sensible to the wind. In addition, wind loading has lower frequency contents than the traffic loading; secondly, under the operational conditions for a cable-stayed bridge, the vibration of the girder could be transferred to the bottom of the tower considerably, so it seems not to be so appropriate to take the bottom of the tower as a fixed point when performing dynamic analysis;
3) About the Wind Effects on Structural Modal Parameters: during high winds, the structural damping ratios have an increasing trend, and the modal frequencies become scattered, which might be caused by the structure's instability, other environmental or operational conditions, measurement noise and algorithm errors, etc... After each strong wind, the modal parameters of the MNCB could return to the stable and normal values, suggesting its good condition.

As a preliminary work, this paper inevitably has some shortcomings; and a further research concerning wind's effects on structures is required. Comments and suggestions would be welcome.

ACKNOWLEDGEMENT

The authors would extend great thanks to the financial support by the Research Program of State Key Laboratory of Disaster Reduction in Civil Engineering, Tongji University (Grand No. SLDRCE084-A-05), and the help from Shanghai Donghai Bridge Management Co., LTD as well as Shanghai Just One Technology Development Co., LTD.

REFERENCES

[1] Cross E J, Koo K Y, Brownjohn J M W, et al, Long-term monitoring and data analysis of the Tamar Bridge. *Mechanical Systems and Signal Processing*, 35(1–2), 16-34, 2013.

[2] Sohn H, Effects of environmental and operational variability on structural health monitoring. *Philosophical Transactions of the Royal Society A-Mathematical Physical and Engineering Sciences*, 365(1851), 539-560, 2007.

[3] Cury A, Cremona C, Dumoulin J, Long-term monitoring of a PSC box girder bridge: Operational modal analysis, data normalization and structural modification assessment. *Mechanical Systems and Signal Processing*, 33(0), 13-37, 2012.

[4] Joseph A M, Nicholas P J, A Comparison of Full-Scale Measurements of Stay Cable Vibration. Advanced Technology in Structural Engineering, Elgaaly M eds. *Structures Congress 2000-ASCE*, Philadelphia, USA, May, 2000.

[5] Fujino Y, Vibration, control and monitoring of long-span bridges—recent research, developments and practice in Japan. *Journal of Constructional Steel Research*, 58(1), 71-97, 2002.

[6] Abe M, Fujino Y, Yanagihara M, et al, Monitoring of Hakucho Suspension Bridge by ambient vibration measurement. Nondestructive Evaluation of Highways, Utilities, and Pipelines IV, Aktan A E, Gosselin S R eds. *SPIE 3995*, Newport Beach, CA, USA, March, 2000.

[7] Xu Y L, Zhu L D, Buffeting response of long-span cable-supported bridges under skew winds. Part 2: case study. *Journal of Sound and Vibration*, 281(3–5), 675-697, 2005.

[8] Xu Y L, Guo W W, Chen J, et al, Dynamic Response of Suspension Bridge to Typhoon and Trains. I: Field Measurement Results. *Journal of Structural Engineering*, 133(1), 3-11, 2007.

[9] Chen J, Xu Y L, Zhang R C, Modal parameter identification of Tsing Ma suspension bridge under Typhoon Victor: EMD-HT method. *Journal of Wind Engineering and Industrial Aerodynamics*, 92(10), 805-827, 2004.

[10] Wang H, Li A, Guo T, et al, Comparable study on typhoon and strong northern wind characteristics of the Runyang Suspension Bridge based on field tests. *Journal of Southeast University (English Edition)*, 25(01), 99-103, 2009.

[11] Min Z, Probabilistic analysis of condition properties of cable-stayed bridge based on long-term structural health monitoring. *Doctoral Dissertation of Tongji Univ.*, Shanghai, P.R.China, 2009.

[12] Min Z, Sun L, Dan D, Analysis of Wind-induced Response and Dynamic Properties of Cable-stayed Bridge Under Typhoon. *Journal of Tongji University (Natural Science)*, 37(9), 1139-1145, 2009.

[13] Brownjohn J M W, Zasso A, Stephen G A, et al, Analysis of experimental data from wind-induced response of a long span bridge. *Journal of Wind Engineering and Industrial Aerodynamics*, 54 – 55(0), 13-24, 1995.

[14] Miyata T, Yamada H, Katsuchi H, et al, Full-scale measurement of Akashi – Kaikyo Bridge during typhoon. *Journal of Wind Engineering and Industrial Aerodynamics*, 90(12 – 15), 1517-1527, 2002.

[15] Zuo D, Jones N P, Interpretation of field observations of wind- and rain-wind-induced stay cable vibrations. *Journal of Wind Engineering and Industrial Aerodynamics*, 98(2), 73-87, 2010.

[16] Ni Y Q, Wang X Y, Chen Z Q, et al, Field observations of rain-wind-induced cable vibration in cable-stayed Dongting Lake Bridge. *Journal of Wind Engineering and Industrial Aerodynamics*, 95(5), 303-328, 2007.

[17] Delaunay D, Grillaud G, Field measurements of the wind-induced response of a cable stayed bridge: Validation of previsional studies. *Journal of Wind Engineering and Industrial Aerodynamics*, 74 – 76(0), 883-890, 1998.

[18] Sun L, Sun Z, Dan D, et al, Large-span bridge and their health monitoring systems in China. In *Proceedings of 2007 International Symposium on Integrated Life-Cycle Design and Management of Infrastructure*, Shanghai, China, 2007.

[19] Zhu Z, Wind-induced responses research on main navigational channel bridge of Donghai Bridge. *Master's Thesis of Tongji Univ.*, Shanghai, P.R.China, 2007.

[20] Huang R, A Sea-Crossing's Design and Construction: Donghai Bridge, 1st Edition. China Communications Press, 2009.

[21] Xu Y L, Zhan S, Field measurements of Di Wang Tower during Typhoon York. *Journal of Wind Engineering and Industrial Aerodynamics*, 89(1), 73-93, 2001.

[22] Ministry of Transport of the People's Republic of China, *Wind-resistent Design Specification for Highway Bridges (JTG/T D60-01—2004)*. Beijing: China Communications Press, 2004.

[23] Holmes J D, *Wind Loading of Structures*, 1st Edition. Spon Press, 2001.

[24] Zhang X, Structural Wind Engineering: Theory, Code and Practice, 1st Edition. China Architecture & Building Press, 2006.

[25] Xu, Y, Chen J, et al, Occurrence probability of Wind-Rain-Induced stay cable vibration. *Advances in Structural Engineering*, 11(1), 53-69, 2008.

[26] The Water Resources Department of Fujian Province of P.R.China, Website of the water resource information system of Fujian Province, http://www.fjwater.gov.cn:8089, Nov, 2012.

[27] Xu Y, Chen J, Characterizing nonstationary wind speed using empirical mode decomposition. *Journal of Structural Engineering*, 130(6), 912-920, 2004.

COMPDYN 2013
4th ECCOMAS Thematic Conference on
Computational Methods in Structural Dynamics and Earthquake Engineering
M. Papadrakakis, V. Papadopoulos, V. Plevris (eds.)
Kos Island, Greece, 12–14 June 2013

RELIABILITY ASSESSMENT OF PIPE NETWORKS UNDER SEISMIC LOADS

Michalis Fragiadakis[1,2], **Symeon Christodoulou**[1,3]

[1]Department of Civil and Environmental Engineering, University of Cyprus
[2] School of Civil Engineering, National Technical University of Athens, Greece
e-mail: mfrag@mail.ntua.gr

[3] Nireas International Water Research Center, Nicosia, Cyprus
e-mail: schristo@ucy.ac.cy

Keywords: Water distribution networks (WDN), Lifelines, Graph theory, Survival analysis, Reliability assessment.

Abstract. *Piping systems are a key component of industrial structures. Most research on structures of industrial facilities is targeted to individual structures such as atmospheric tanks, pressure vessels, etc. Piping systems are considered of secondary importance and thus the research on their risk assessment is limited despite the significant consequences of their possible failure. We propose a methodology for assessing the reliability of pipe networks and is able to combine data from past nonseismic damage with the seismic vulnerability of network components. The fragility of the network components is assessed using the approach suggested in the guidelines of the American Lifeline Association (ALA), but the methodology presented is open to any fragility data. The network reliability is assessed using Graph Theory, while the system reliability is calculated using Monte Carlo simulation. Of particular importance is the degradation of the piping components due to repeated loading in the plastic range under strain-controlled conditions or due to failure of the supporing structure. The methodology proposed is demonstrated both on a simple, small-scale, network and also on a real-scale piping system. The proposed approach allows the estimation of the probability that the network fails and of capacity-upgrade actions pertaining to existing pipe networks.*

1 INTRODUCTION

Water distribution networks deliver the water from its sources to the customers of the network. Being able to assess the reliability of the network against different hazards, helps water distribution agencies to prioritize their interventions and ensure a minimum reliability level of the network. Therefore, water distribution agencies are required to develop and implement new methods for monitoring, repairing (or replacing) ageing WDN infrastructures, as well as modelling deteriorating WDN conditions and proactively devising strategies to keep the networks in operation. In essence, water distribution agencies are faced with the increasingly more complex task of intelligently and efficiently assessing (or modelling) the condition of a pipe network, while managing the network in ways that maximize its reliability and minimize its operational and management costs. The question that usually arises is whether an organization should repair or replace deteriorating water mains and, in either case, what should be the sequence of any such repairs as part of a long-term network rehabilitation strategy.

The seismic risk assessment of critical infrastructures has been the subject of extensive past research. For example, Nuti *et al.* [1] propose a methodology for the reliability assessment of electric power, water and road systems, neglecting the interdependence between the networks, while Poljnašek *et al.* [2] propose a method for gas and electricity transmission networks considering the increased vulnerability due to interdependency. Cimellaro [3] proposed a performance index for evaluating the functionality of a road network during extreme events such as earthquakes that can be utilized within the general PEOPLES framework for measuring disaster resilience indices for a community at various scales. Regarding water supply networks, Romero *et al.* [4] discuss the possible seismic hazards and present results that correspond to a severe event in California, while Esposito [5] worked on the seismic performance evaluation of gas distribution networks and produced fragility curves for these systems. Moreover, Wang *et al.* [6] propose a methodology for the seismic risk assessment and identification of critical links of water supply systems. The U.S. Federal Emergency Management Agency has also developed the nationally applicable standardized methodology and software program HAZUS-MH MR3 [7], which estimates potential losses from earthquakes, hurricane winds, and floods.

The reliability of a water pipe network can be calculated if the vulnerability (also termed fragility) of every element of the water network is known. Although water pipe networks consist of several elements (pipes, house connections, tanks, pumps, etc.), focus is given on the pipes, which are, not only the most important component in a piping network but they are also the most difficult component to inspect and replace. Many possible risk-of-failure parameters can be identified [4]. Our methodology takes into consideration the fragility that corresponds to pipe failures that occur frequently during the everyday operation of the water network and also more severe, but less often, failures due to earthquakes. The pipe vulnerability due to nonseismic causes is assessed using survival analysis techniques on available everyday measurements. Survival analysis considers a number of parameters, e.g. number of observed previous breaks (NOPB), pipe material, diameter or age that affect the pipe survival curves [8] in order to develop survival/hazard rates and time-to-failure curves for system components based on a multitude of risk-of-failure factors and data stratifications. To account for the vulnerability due to seismic hazard, we rely on the procedure described in the American Lifelines Alliance (ALA) [9] guidelines and we propose a rational approach for combining it with the results of survival analysis in order to consider the effect of previously observed breaks in the network.

Even though the procedure proposed herein is presented based on performance data from urban water networks of the island of Cyprus, it is general in scope and applicable to any locale

with historical records of pipe-break incidents in its water distribution network. Being a South European island, Cyprus has suffered during the last years from low rainfalls and shortage in its water reserves. Under such conditions, a common practice followed by water distribution agencies has been to periodically interrupt the water flow in different areas of the city network for variable time intervals, e.g. 12 hours of water supply every 48 hours. This practice offers a more rational treatment of the water resources, but is also considered responsible for an increasing the failure rate of the network pipes. The worsening failure rate in the water pipe networks of all major cities of the island prompted the initiation of an extensive program of monitoring and keeping track of the every damage incident, in order to be able to assess the network conditions and assist its proper maintenance. The post-processing of the vast amount of available data is performed using survival analysis tools and producing pipe survival curves that allow considering the effect of different parameters (e.g. material, age, diameter) on the failure rate. In fact, although the island is located in a moderate seismicity environment, the seismic vulnerability of its water distribution networks increases to considerable levels due to the deterioration of the pipe properties.

2 SURVIVAL ANALYSIS

Survival analysis is a branch of statistics dealing with deterioration and failure over time and involves the modelling of the elapsed time between an initiating event and a terminal event [10]. In the case of piping networks such initiating events can be the installation of a pipe, a water-leak observation or the start of a pipe treatment. Cases of terminal events can be a relapse of a previous leak, a fix or a failure. The method is based on estimating the reliability of a system and its lifetime subject to multiple risk factors. The aim is to provide answers on the population fraction (pipes) that survives past an expected lifetime, on the effect of the various risk factors on the systems lifetime, and on the probability of survival and the expected mean time to failure [10, 11]. The data values used in the analysis are a mixture of both complete and censored observations. In the former case, a terminal event is thought to have occurred, while in the latter case a terminal event has not occurred. A terminal event is assumed to occur just once for every subject.

A pipe's survival function, S, for elapsed time, T, until the occurrence of a pipe failure is given by the expression:

$$S\left(t\right) = \int_{T}^{\infty} p\left(x\right) dx = 1 - P\left(t\right) \tag{1}$$

Thus, the survival function is the probability that the time to failure is longer than some specified time t. Moreover, $P(t)$ is the cumulative distribution function that denotes the probability that a pipe survives until time t and $p(t)$ is the corresponding probability density function. the rate of the survival function is denoted as $h(T)$ and provides the probability that a pipe at time T experiences the event in the next time instant. The cumulative hazard function $H(T)$ is the integral of $h(t)$ from 0 to T, and therefore:

$$S(t) = \exp\left[-\int_{0}^{T} h(x)dx\right] = \exp\left[-H(T)\right] \tag{2}$$

and

$$h\left(T\right) = p(T)\,/S\left(T\right) \tag{3}$$

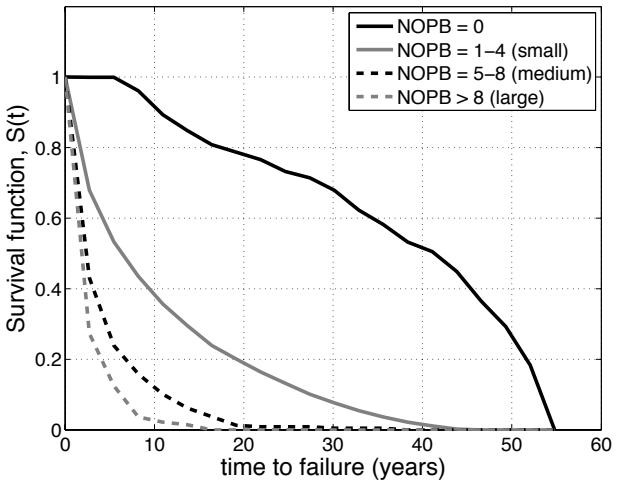


Figure 1: Survival curves for Asbestos Cement (AC) pipes as function of the number of previous breaks (NOPB).

The survival function S is usually the primary quantity of interest and is numerically calculated using kernels, such as the Epanechnikov kernel and the Kaplan-Meier estimator [12]. The Kaplan-Meier estimator is of particular importance because it is non-parametric and therefore relies on data rather than analytical equations and probability density functions in order to produce the survival curves. A plot of the Kaplan-Meier estimate of the survival function is a series of horizontal steps of declining magnitude which approaches the true survival function for the population in study and whose values between successive distinct sampled observations are assumed to be constant. Another important advantage of the Kaplan-Meier curve is that the method can take into account both left and right-censored data. When no truncation or censoring occurs, the Kaplan-Meier curve is equivalent to the empirical distribution function.

In terms of piping networks, the survival function has been shown to be dependent on several factors, the most important of which are the 'number of observed previous breaks' (NOPB), the age and the material of the pipes [13]. These risk factors have been studied extensively [13, 8] both when acting separately or together. The non-parametric survival analysis produces the effects of such risk-of-failure actions on the network, clustered by risk factor and its subgroups, and enables us a deeper insight into the behaviour of the piping network. For example, a survival analysis reported by Christodoulou and Ellinas [8] of an urban water distribution network under abnormal operating conditions, revealed almost identical survival curves for the network mains and its house connections, but when clustered by the 'number of previous breaks' (NOPB) the survival curves varied substantially.

A typical set of survival curves is shown in Figure 1. The curves have been derived from real data and refer to asbestos cement (AC) pipes. The data have been clustered according to the 'number of observed previous breaks' (NOPB) and four survival curves are derived. The four curves correspond to 0, 1-4, 5-8 and more than 8 previous breaks and are denoted as 'zero', 'small', 'medium' and 'large' NOPB clusters. According to Figure 1, even in the 'NOPB = 0' case, the pipe will have to be eventually replaced after approximately fifty-five (55) years, while a pipe that has already broken more than 8 times is not expected to survive more than eighteen (18) years. Moreover, a pipe that has broken at least once, is considerably more vulnerable compared to an intact pipe that has never been damaged.

3 SEISMIC VULNERABILITY ANALYSIS OF WATER PIPES

3.1 Pipe vulnerabilities according to the ALA guidelines

The seismic vulnerability (or fragility) of buried pipelines is discussed in the ALA (American Lifelines Association) document [9]. The ALA document provides vulnerability curves for water pipes, using observations from past disruptive earthquakes. The failure parameters that affect buried pipes are identified and vulnerability functions are proposed. The vulnerability functions are defined as functions of the peak ground velocity (PGV) and the permanent ground deformation (PGD). PGV is related with strong ground shaking caused by seismic wave propagation, while PGD is used to measure factors that include landslides, liquefaction, ground settlement and fault crossing. Parameters that also affect the vulnerability of a pipe are also the diameter, the age, the year of construction and possible discontinuities along the pipe. The pipe vulnerability functions of the ALA document [9], provide the repair rate (*RR*) per 1000 ft of pipe length and have the form:

$$\begin{aligned} RR_{PGV} &= K_1 \cdot 0.00187 \cdot PGV \\ RR_{PGD} &= K_2 \cdot 1.06 \cdot PGD^{0.319} \end{aligned} \tag{4}$$

The units for PGV and PGD are in/s and in, respectively. Tabulated values are provided for K_1 and K_2 depending on the material of the pipe. $K_1 = K_2 = 1$ refers to pipes made from cast iron (CI) or asbestos cement (AC). The pipe repair rates of Eq. 4 can be due to a complete fracture, a leak or a damage to an appurtenance of the pipe, or any other reason that requires the water agency to intervene. For typical water pipe networks, a rule-of-thumb is that for failure due to wave propagation 15-20% of failures are breaks and the rest are leaks, while for failures due to PGD 80-85% are breaks that result to the loss of pipeline hydraulic continuity [14].

Once the repair rate (*RR*) is known, i.e. the number of leaks/breaks per pipe length, the failure probability of the pipe can be easily calculated. The failure probability of a pipe is equal to one minus the probability of zero breaks along the pipe. Using the well-known exponential distribution CDF formula, the pipe failure probability $\bar{P}_{\mathrm{f}}$ is therefore calculated as [9]:

$$\bar{P}_{\mathrm{f}} = 1 - e^{-RR \cdot L} \tag{5}$$

where $RR = max(RR_{PGV}, RR_{PGD})$, with RR_{PGV} and RR_{PGD} calculated by use of Eq. 4. Note that Eq. 5 is a Poisson process and thus is "memoryless" disregarding any failures that may have occurred along the pipe in the past. Also note that the bar ('-') above P_{f} (e.g. Eq. 5) is used to distinguish the failure probability of a single pipe/edge from the failure probability in the network level, which in the remaining of the paper will be denoted as P_{f}.

3.2 Proposed strategy for pipe vulnerability assessment

As aforementioned, the study's goal is to propose a seismic vulnerability assessment methodology for water pipe networks, exploiting available data of everyday network failures due to sources other than seismic. This methodology is useful in the case of networks under abnormal operating conditions, as in the case of intermittent water supply. Previous research has shown that survival analysis is a valuable tool for implementing methods for monitoring, repairing or replacing ageing infrastructures and proactively devising strategies to keep the network in operation. Compared to failures caused by earthquakes, failures from non-seismic causes are more frequent and well distributed in time, while failures due to seismic effects occur intermittently and only when a major earthquake strikes. Thus, it is convenient to compile separately

the data from the two failure causes. This approach is also close to the current practice, since usually it is the water agencies that maintain records of the everyday failure causes, while the seismic effects on the lifelines are usually given a more high-level attention by the civil protection agencies. Moreover, the approaches followed for seismic and non-seismic effects have distinct differences and therefore it is not straightforward to post-process the data in a manner that allows to combine consistently pipe survival curves and vulnerability curves.

In our study we combine the vulnerability curves suggested in the ALA [9] guidelines with available survival curves that were compiled using network data available from the Water Boards. To this cause we adopt a simplified engineering approach that allows us to quickly combine data that are not similar. Having in our disposal the pipe survival curves (e.g. Figure 1) of *S*(*t*) versus time we know the survival probability of a pipe, depending on the number of previous breaks (NOPB) and the pipe type (e.g. material, age, diameter). We thus penalize the pipe vulnerability function of Eq. 4 by the ratio of the survival curve of the damaged case (NOPB≠0) over the undamaged pipe (NOPB=0). Therefore, after t days, we define the ratio:

$$k(t) = S_{UD}(t)/S_D(t) \geq 1 \tag{6}$$

where subscripts "UD" and "D" stand for "undamaged" and "damaged", respectively. The modified pipe failure probability that now includes memory of past nonseismic failures is obtained after modifying Eq. 5 as follows:

$$\bar{P}_{\mathrm{f}}(t) = 1 - e^{-k(t)\cdot RR\cdot L} \tag{7}$$

Therefore, Eq. 7 allows calculating the failure probability $\bar{P}_f$ of the pipe after t days given its NOPB metric, which is usually available from historical records.

4 RELIABILITY ASSESSMENT OF A WATER SYSTEM

Once the failure probability, $\bar{P}_{\mathrm{f}}$, of every pipe is known, the performance of the network and its failure probability P_{f} can be assessed. Depending on the problem at hand, different approaches can be preferred. Perhaps the most significant parameter that affects the selection of the strategy to follow is how the network performance is measured and thus how the failure probability of the network is defined. In the simplest case, the network fails when it is not able to deliver water from its sources (inflow vertices) to every house connection (outflow vertices). Another, approach would consider the number of customers that are left without water. If such, rather simplified, network performance definitions are adopted, the performance of the network can be quickly evaluated using methods based on Graph Theory [15].

We consider as failure of the network its inability to provide water to a consumer/house connection. Therefore, we define the failure probability as the probability of the network being unable to provide water from an inflow source vertex *i* to an outflow (e.g. house connection) vertex *j*. If the failure probability to deliver water between *i* and *j* is $P_{\mathrm{f,ij}}$, the network reliability $R_{\mathrm{f,ij}}$ is defined as:

$$R_{ij} = 1 - P_{f,ij} \tag{8}$$

For water networks with more than one inflow sources, we consider as failure probability the smallest probability of all possible sources and the outflow vertex j examined. This definition refers to the probability that the outflow node j is left without water.

The Monte Carlo Simulation (MCS) method is often employed when the analytical solution is not attainable and the failure domain can not be expressed or approximated analytically. This

is mainly the case in problems of complex nature with a large number of basic variables where other reliability methods are not applicable. When Monte Carlo simulation (MCS) is adopted on pipe networks, the calculation is based on reducing the network topology, i.e. removing pipe segments which are assumed as failed. Successful applications of MCS on networks can be found in [16] and [17]. For every simulation a state vector is produced. In this vector, two states can be considered for every pipe: *0-state*, which refers to a failed state with probability of $P_{\mathrm{f,ij}}(t)$ Eq. 7) and *1-state* that corresponds to non-failure with probability $1 - P_{\mathrm{f,ij}}(t)$. Once a state vector is obtained, the failed pipes are removed from the network. Using common graph algorithms we can determine whether a path between vertices *i* and *j* exists , thus allowing water flow delivery from node i to node i. In all our applications, a standard Dijkstra algorithm [15] gave quick and robust calculations. If at least one path exists the simulation is successful, otherwise it has failed. The network reliability $R_{\mathrm{f,ij}}$ can then be evaluated by dividing the number of successes with the total number of simulations performed. MCS can easily accommodate both pipe and node failures.

5 CASE STUDY

The case study considered, is a district metered area (DMA) of the water network of the city of Limassol, Cyprus (Figure 2). The city network is clustered into DMAs, which are areas with one inflow vertex. This practice allows the Water Board to isolate damage in the network within finite domains (DMAs) and then handle any problem that may occur within a DMA without affecting the rest of the city network. Fig. 2a shows the aerial view of the city together with the graph model used for simulating the network, which has been produced using available GIS data.

In total, the water network consists of 337 pipes/edges and 259 vertices/nodes. The total pipe length is 23,724 m, and according to the records of the Water Board, the number of consumers served by the DMA studied is 6,585 people. The pipe material is asbestos cement (AC) and is the same for every pipe. Since the elevation is practically constant throughout the network, we assume that the network is bi-directional. Figure 2b shows the topology of the network and the number of previous breaks of every network pipe/edge. The pipe survival curves were those of Figure 1, which were based on real data obtained from the Water Board of Limassol.

Based on the above observations, we consider two seismic scenaria. In the first scenario, damage is only due to wave propagation. Being consistent with the seismic hazard in the island of Cyprus which is mainly controlled by distant and moderate magnitude events, it is valid to assume uniform seismic intensity throughout the DMA. Here we measure seismic intensity with the aid of peak ground velocity (PGV). In the second scenario both PGV and PGD occur, but PGD is isolated in a small part of the network. For both scenaria, we produce fragility curves for every outflow node j.

Figure 3 shows the fragility curve of every vertex with respect to peak ground velocity (PGV) for four time instances measured from the installation of the network. As PGV increases we calculate the pipe failure probability $\bar{P}_{\mathrm{f,ij}}$ using Eq. 4 and the corresponding node probability $P_{\mathrm{f,ij}}$ using Eq. 5. Therefore, the gray lines correspond to the probability of water being able to reach the corresponding valve, while the black lines are the median (50% percentile) and the 16% and 85% percentile curves, which are shown to provide a measure of the overall condition of the network.

Figure 3a shows the fragility curves after 10 years of network operation. Since the network would be of 'young age', the mean fragilities lie below 0.1, even for considerably high PGV values, e.g. PGV$\geq$200 cm/s. Still, some house connections are vulnerable and their failure



(a) (b)

Figure 2: (a) Aerial view of the city of Limassol, Cyprus and the DMA considered, (b) topology of the graph network and number of previous breaks (NOPB) of every pipe.

probability may exceed 20%. Moreover, in Fig. 3a, there is one node whose failure probability is very high. This is due to the fact that this node is connected with the inflow source through pipes that are connected in series, thus if any of the connecting pipes fails the water will not be able to reach this node. In this case, the remedy will be to create conditions of redundancy by forming alternative water paths. Figures 3b,c,d have the well-known form of fragility curves, showing that the system vulnerability increased as the time passes and PGV increases. Note that since the construction of the pipes is made at a present time, the NOPB values are kept constant. Actually, NOPB will also vary as time passes, probably increasing the system vulnerability, but the prediction of survival analysis is based on the data available at the present time and therefore this effect is not considered in our analyses. Again in Fig. 3b,c there are stray lines away from the average, indicating that the vulnerability of some house connections may considerably differ from the average and thus the interpretation of the analysis should also be done on a node by node basis and not rely purely on global metrics on the DMA level. After forty years of operation (Fig. 3d), even a relatively moderate PGV ($\simeq$ 50 cm/s) will lead to high failure probabilities and therefore extensive damage on the network.

In the second scenario considered, we assume a permanent ground deformation (PGD) due to a random cause. The PGD affects a wide area of radius equal to 200m around a point shown in Fig. 4 with a red square. The deformation is assumed to be constant and equal to 12.6 cm (5 in). In Fig. 4 we also show with a thick red line the pipes that are affected by the imposed PGD. The fragility curves of every vertex for $t = 20$ years and $t = 30$ years are shown in Fig. 5. It is evident from the plot, that there are nodes whose vulnerability is considerably higher that the rest. More specifically, looking and PGV$= 0\ cm/s$ there are nodes whose probability $\bar{P}_{\mathrm{f,ij}}$ is larger than zero. The vulnerability of these nodes is governed by PGD and for visual purposes we show them with solid black lines and in the legend of Fig. 5 are denoted as "PGD-sensitive". In a similar manner, the grey lines correspond to vertices whose vulnerability is "PGV-sensitive". For the t=30 years case, the "PGD-sensitive" curves start from high probability values, and quickly approach 1, while for t=20 years a larger dispersion is observed. In any case, the "PGD-sensitive" curves are also affected by the increase of PGV (although with a smaller rate), since they operate within a network that combines PGV and

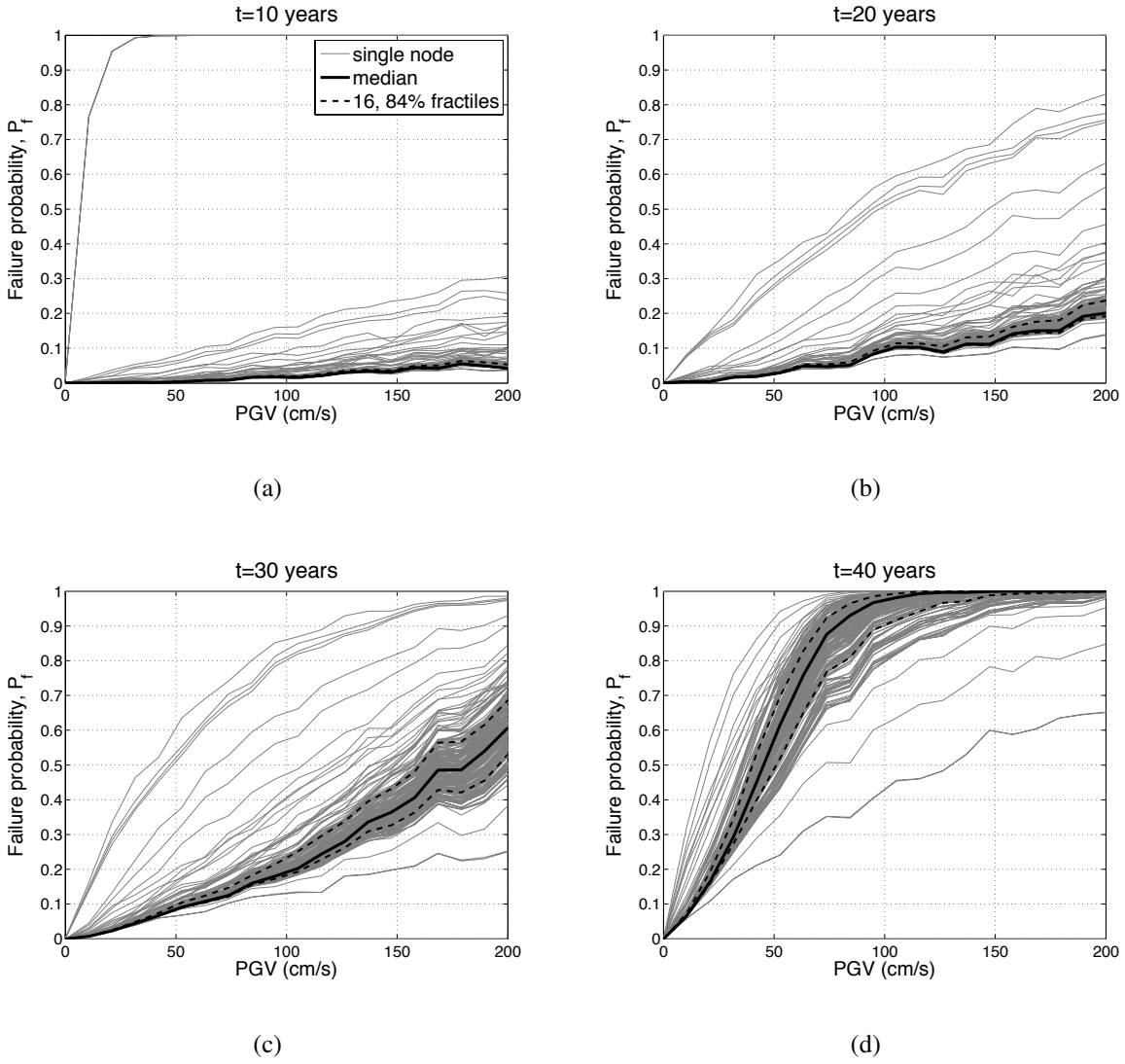


Figure 3: Fragility curves of every house connection versus the peak ground deformation (PGV), after: (a) t=10 years, (b) t=20 days, (c) t=30 days, and (d) t=40 years.

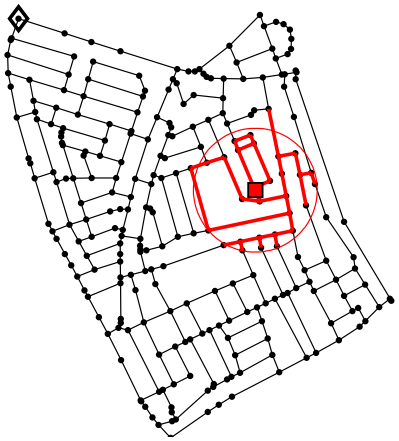
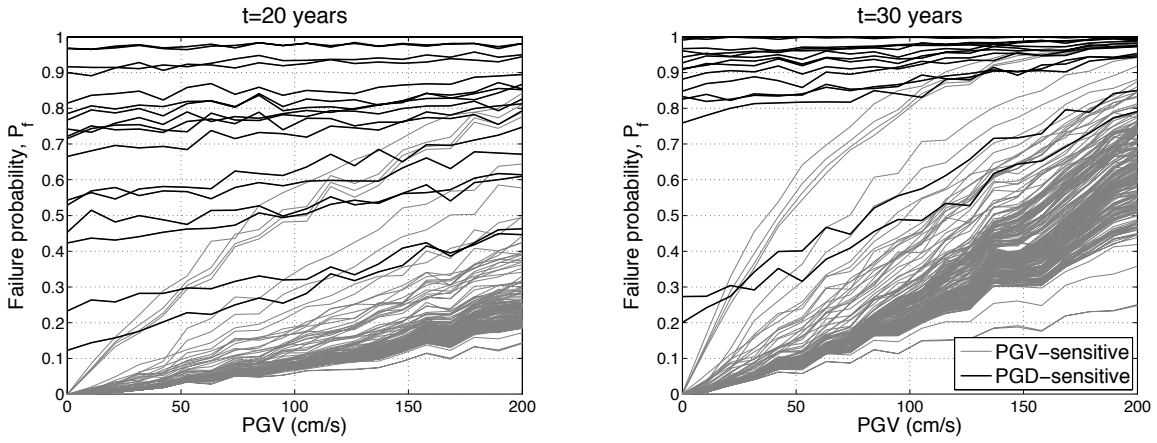


Figure 4: Water distribution network and the area where a PGD equal to 12.6 cm (5in) is imposed. The circle shows the affected area and the square is its center.

PGD-sensitive components. Moreover, when considering both PGV and PGD the practice of producing average curves (e.g. Fig. 3) is not useful, since the probabilities vary considerably and depend on the location of the node with respect to where the permanent ground formation occurred.



(a) (b)

Figure 5: Fragility curves versus peak ground velocity (PGV) when PGD is imposed, after: (a) t=20 years (b) t=40years.

6 CONCLUSIONS

A general-purpose methodology for the reliability assessment of water pipe distribution networks has been presented. The proposed methodology efficiently combines the general ALA guidelines with localized information on failures caused by seismic and non-seismic sources. The more frequent non-seismic failures are typically repaired immediately after the damage is reported to the water agency and result to increasing the future vulnerability of the damaged pipe. This sort of information is often available by water agencies and can be post-processed to provide the pipe survival curves.

7 ACKNOWLEDGEMENT

This research has been co-financed by the European Union (European Social Fund - ESF) and Greek national funds through the Operational Program "Education and Lifelong Learning" of the National Strategic Reference Framework (NSRF) Research Funding Program: **THALES**. Investing in knowledge society through the European Social Fund. The second author would like to acknowledge the NIREAS-IWRC research project, which is co-financed by the European Regional Development Fund and the Republic of Cyprus through the Cyprus Research Promotion Foundation (Grants No. NEA YPODOMI/STRAT/0308/09).

REFERENCES

[1] Nuti, C., Rasulo, A., Vanzi, I., Seismic safety of network structures and infrastructures, *Structure and Infrastructure Engineering*, **6**, 95-110, 2010.

[2] Poljanšek, K., Bono, F., Gutièrrez, E, Seismic risk assessment of interdependent critical infrastructure systems: The case of European gas and electricity networks, *Earthquake Engng Struct. Dyn.*, **41**, 61-79, 2012.

[3] Cimellaro, G.P., Renschler, C., Arendt, L., Bruneau, M., Reinhorn, A.M., Community resilience index for road network systems, *EURODYN 2011: 8th International Conference on Structural Dynamics*, Leuven, Belgium, 4-6 July, 2011.

[4] Romero, N., O'Rourke, T.D., Nozick, L.K., Davis, C.A.,Seismic hazards and water supply performance, *Journal of Earthquake Engineering*, **14**(7), 1022-1043, 2010.

[5] Esposito, S., Seismic Risk Analysis of Gas Distribution Networks. *PhD Thesis, University of Naples Fegerico II, Ph.D. Porgramme in Seismic Risk*, Naples, Italy, 2010.

[6] Wang, Y. Au, S.-K., Fu, Q., Seismic Risk Assessment and Mitigation of Water Supply Systems, *Earthquake Spectra*, **26**(1), 257-273, 2010.

[7] FEMA, HAZUS-MH technical manual: earthquake model. *Multi Hazard Loss Estimation Methodology. United States Department of Homeland Security, Federal Emergency Management Agency*, Washington, DC, 2003.

[8] Christodoulou, S.E., Water Network Assessment and Reliability Analysis by Use of Survival Analysis, *Water Resources Management*, **25**, 1229-1238, 2011.

[9] ALA, American Lifelines Alliance: Seismic Fragility Formulations for Water Systems-Guideline and Appendices, 2001.

[10] Hintze, J., *NCSS and PASS. Number Cruncher Statistical Systems*, Kaysville, Utah, 2001.

[11] Hosmer, D.W., Lemeshow, S., May, S. *Applied survival analysis: regression modeling of time to event data*, Wiley, Hoboken, 2008.

[12] Kaplan, E.L., Meier, P., Nonparametric estimation from incomplete observations. *J. Am. Stat. Assoc.*, **53**, 457-481, 1958.

[13] Christodoulou, S.E. and Deligianni, A., A Neurofuzzy Decision Framework for the Management of Water Distribution Networks, *Water Resources Management*, **24**(1), 139-156, 2010.

[14] Ballantyne, D., Earthquake Loss Estimation Modelling of the Seattle Water System, *Report N. 886005, supported by U.S. Geological Survey Project Number 14-08-0001-G1526*, Kennedy/Jenks Consultants, 1990.

[15] Gibbons, A., *Algorithmic Graph Theory*, Cambridge University Press, 1985.

[16] Javanbarg, M.B., Scawthorn, C., Kiyono, J. and Ono, Y., Minimal Path Sets Seismic Reliability Evaluation of Lifeline Networks with Link and Node Failures, *In Proc. Lifeline Earthquake Engineering in a Multihazard Environment*, ASCE Technical Council on Lifeline Earthquake Engineering, June-July, Oakland, CA, 2009.

[17] Ramirez-Marquez, J.E., Coit, D.W., A Monte-Carlo simulation approach for approximating multi-state two-terminal reliability, *Reliability Engineering and System Safety*, **87**, 235-264, 2005.

COMPDYN 2013
4th ECCOMAS Thematic Conference on
Computational Methods in Structural Dynamics and Earthquake Engineering
M. Papadrakakis, V. Papadopoulos, V. Plevris (eds.)
Kos Island, Greece, 12–14 June 2013
Paper # 1134

SEISMIC BEHAVIOR OF DAMAGED BUILDINGS: A COMPARISON OF STATIC AND DYNAMIC NONLINEAR APPROACH

Maria Polese[1], Marco Gaetani d'Aragona[1], Andrea Prota[1] and Gaetano Manfredi[1]

[1] Department of Structures for Engineering and Architecture, University of Naples Federico II
via Claudio 21, 80125 Naples, Italy

e-mail: maria.polese@unina.it; marco.gaetanidaragona@unina.it; andrea.prota@unina.it; gaetano.manfredi@unina.it

Keywords: residual capacity, damaged building, pushover analysis, nonlinear time history analysis, post-earthquake assessment, reinforced concrete frame.

Abstract. *Seismic behavior of damaged buildings may be expressed as a function of their REsidual Capacity (REC_{ag}), that is a measure of seismic capacity "reduced" due to damage and represented in terms of peak ground acceleration a_g. REC_{ag} may be estimated through pushover analyses. In fact, adopting a lumped plasticity model, the plastic hinges may be suitably modified to account for the damage level of the single elements [1]; as shown in [2] nonlinear static analyses of the modified damaged models yield pushover curves that, depending on the number of elements involved in the damaged mechanism and on their damage level, may differ significantly with respect to original ones. The applicability of Pushover Analyses (PA) has been demonstrated for regular structures [3, 4], with their significance being generally supported by the comparison of the results obtained by these "simplified" analyses with Nonlinear dynamic Time-History (NTH) analyses. However, the usability of pushover analysis for the assessment of the behavior of damaged buildings has not been verified yet, and the study presented in this paper aims at contributing in the evaluation of this issue. The results of PA are confronted with those of NTH for Multi Degree Of Freedom (MDOF) systems representative of existing R.C. building typologies in the Mediterranean regions. In particular, the response (and damage) of each one of the original "intact" MDOF systems for earthquakes of increasing intensity is studied with either the PA and NTH. Next, applying the methodology described in [2], damage dependent behavior is estimated for varying levels of initial seismic (damaging) intensity. The maximum inter-storey drift and shape along the height, as well as the "modified" REC_{ag} are compared to the ones that could be obtained with NTH by subsequent application of suitably scaled pairs of accelerograms. The results of this study suggest that degree of approximation that is obtained by PA applied to damaged structures with respect to NTH does not vary with respect to the approximation of standard PA compared to NTH.*

1 INTRODUCTION

Seismic behavior of damaged buildings, and their relative seismic safety, may be suitably represented by their seismic capacity modified due to damage, the so-called REsidual Capacity (*REC*). Indeed, in the guidelines for seismic assessment of damaged buildings [5], the building tagging is based on the likelihood that an aftershock will exceed a specific (reduced) capacity associated with each damage state representing the quantitative measure of degradation. In [2] REC is defined as a parameter aimed at representing the building seismic capacity (up to collapse) in terms of a spectral quantity; in particular, REC_{Sa} of a building is defined as the smallest ground motion spectral acceleration (at period T_{eq}, of the Single Degree Of Freedom SDOF system equivalent to the real structure) corresponding to collapse state of the building. Considering the seismic demand and the local damage that the elements in a Multi Degree of Freedom (MDOF) system may be forced to sustain due to a mainshock earthquake, the system's capacity may be considerably reduced, as evidenced in [2]. Because of the convenience of direct estimation of peak ground acceleration, a_g, as a damaging intensity parameter, the residual capacity is evaluated also in terms of a_g: given the spectral shape, REC_{ag} is the minimum anchoring peak ground acceleration such as to determine building collapse and corresponds to REC_{Sa} scaled by the spectral amplification factor for T_{eq}. By way of example, with reference to an EC8 spectral shape [6] and considering a system with $T_C<T_{eq}<T_D$, the following relation applies:

$$REC_{ag} = \frac{REC_{Sa}}{(S \cdot \eta \cdot 2.5)} \cdot \left(\frac{T_{eq}}{T_C} \right) \tag{1}$$

As explained in [2], and briefly summarized in [7], *REC* (REC_{Sa} and/or REC_{ag}) may be evaluated based on Pushover Analyses (PA) obtained for the structure in different (initial) damage state configurations, where the behavior of the damaged building is simulated with modification of plastic hinges for damaged elements. Ideally, Nonlinear dynamic Time-History (NTH) analyses, that predicts the forces and cumulative deformation (damage) demands in every element of the structural system, would be the best solution for capturing building's seismic performance. In fact, the use of structural models with appropriate stiffness/strength deterioration mechanisms would allow the simulation of response taking into account the cyclic accumulation of damage. However, NTH is a quite complex and time consuming analysis, hardly suitable for practical design/assessment by engineering professionals. In addition, in order to overcome the sensitivity of dynamic response to the characteristics of the input motions, a suite of representative accelerograms has to be carefully selected, greatly increasing the computational effort.

For the above reasons, it was preferred to rely on pushover based procedure for the assessment of the behavior of damaged buildings. PA represent an optimal compromise between the need to investigate building's nonlinear behavior and to perform a relatively simple static analysis, applicable for design/assessment purposes by practitioners. Indeed, under the limitation of applying it mainly to building structures oscillating predominantly in a single (fundamental) mode, standard PA allows a sound evaluation of damage progression for increasing levels of seismic demand and investigation of damage distribution within the MDOF systems [8].

The applicability of PA has been evaluated in several previous studies [3, 4, 9-12]. The first studies followed the approach of comparing the results of PA with those of NTH only at

certain loading levels, e.g. design level, or at equal top displacement (roof displacement from pushover equal to the maximum dynamic roof displacement). For example, in [10, 11] a set of 10 and 7 ground motions, respectively, were selected so to be compatible with given spectral shapes, and comparison of PA results with those of NTH analyses were performed, for a single scaling of those ground motions, in terms of displacements (or deflection profiles), inter-storey drifts and plastic hinge rotations. More recently, [4, 12] presented more exhaustive comparisons, developing complete pushover-like load–displacement curves from incremental dynamic analysis up to collapse for different structural configurations. They compared the pushover curves obtained for different lateral load distributions with the dynamic envelops (maximum absolute drifts and base shear) obtained for increasing levels of ground motion intensity.

Despite the availability of several validation examples for PA, the usability of pushover analysis for the assessment of the behavior of damaged buildings [2] has not been verified yet, and the study presented in this paper aims at contributing in the evaluation of this issue.

Two MDOF frame systems, representative of mid and high rise existing RC buildings in the Mediterranean region, are analyzed and results obtained with pushover based procedure and NTH compared.

Section 2 of this paper presents the geometry and nonlinear (static and dynamic) modeling of the two studied frames, also explaining the use of plastic hinge modification factors for PA of damaged building.

Adopting REC_0 ($REC_{Sa,0}$ and/or $REC_{ag,0}$) and REC_i ($REC_{Sa,i}$ and/or $REC_{ag,i}$) as representative parameter for the seismic capacity of a building in its intact and generic i^{th} damaged state, we follow the approach of comparing the REC that can be obtained via PA with the one that may be evaluated via NTH. In addition, also the lateral maximum inter-storey drift profiles are compared.

Section 3 describes the assessment of REC_0 and REC_i with the pushover based approach. In particular, REC_0 is evaluated with PA adopting a lumped plasticity model. Next, as described in [2], based on the damage level D_i that is attained due to an hypothetical main-shock, the inelastic model is modified and PA re-executed, so that REC_i can be obtained.

Next, section 4 describes the evaluation via NTH analysis, with PA-NTH comparisons being presented and discussed in section 5.

2 DESCRIPTION OF THE BUILDING AND MODELING ASSUMPTIONS

The comparison of PA with NTH analysis is performed with reference to two bare Reinforced Concrete Frames (RCF), of 4 and 8 storeys respectively (see Figure 1), that have been designed to be representative of existing under-designed buildings in the Mediterranean area. In particular, the RCF were designed with a simulated design procedure as suggested in [13] and in the first seismicity class with reference to old seismic codes [14] in force in the beginning of age '60s, not applying principles of capacity design or proper reinforcement detailing and based on allowable stress method. The structure of the RCFs, that represent the perimeter frames of buildings with planar dimensions of 18m x10m, is formed by two bays of 5 m length, while the inter-storey height is of 3 m. As explained in [7], the simulated design is performed with allowable stresses for concrete of σ_c = 6 MPa for columns and 7.5 MPa for beams, while the allowable stress for steel, that considering the design period is assumed to be a smooth type Aq50 [14], is σ_s = 180 MPa [15].

The columns dimensions are represented in Figure 1. For what concern the beams, their dimension for the 4 storey RCF vary from 30x60 at the first two storeys to 30x50 at the upper ones, while for 8 storey building the beams at the first three storeys have section 35x65, 30x60 at fifth and sixth storeys, and 30x50 at the upper ones.

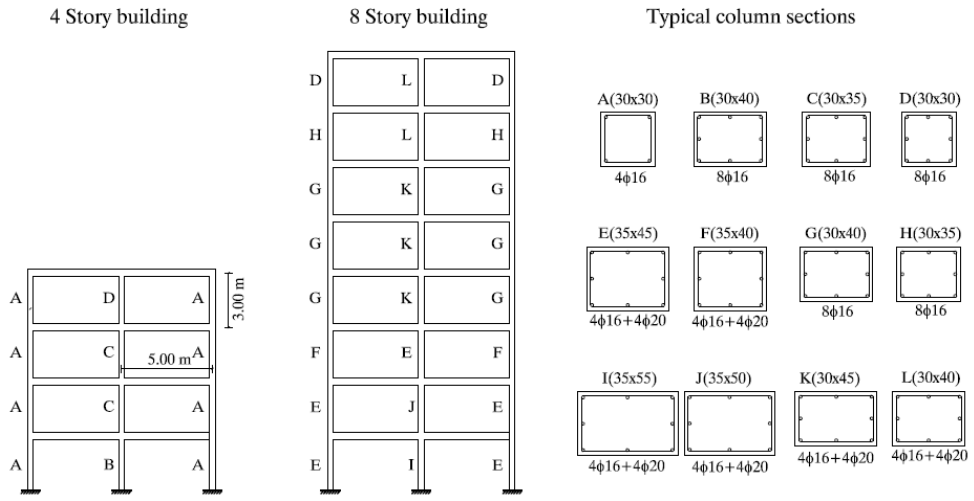


Figure 1: Model geometry and typical columns section and reinforcement.

2.1 Modeling issues for Pushover Analysis

Structural modeling, numerical analyses and post-processing of damage data, including the 3D graphic visualization of the deformed shape, are performed through the "PBEE toolbox" [16], which allows rapid generation of simple nonlinear models and the analysis of RC frames combining MATLAB® with OpenSees [17]. The toolbox was suitably modified in order to allow definition of bilinear plastic hinges according to ASCE-SEI/41 [18] and in order to allow the plastic hinge modification for the analyses of damaged buildings, as described later.

A lumped plasticity model was adopted for the two-dimensional MDOF Reinforced Concrete Frame buildings. The model is very simplified, not including geometric nonlinearity (i.e. P-Δ effects). In addition, although brittle shear failures in columns or beams may be expected in existing under-designed buildings [19, 20] and brittle behavior of beam-columns joints [21] is an additional vulnerability factor, these aspects are not considered in this study. Indeed, the main aim of this study is to test the capability of PA to capture, after suitable modification of flexural type plastic hinges, the post-seismic behavior of a damaged building. Therefore, in order to avoid introducing further complexity in the model the sole flexural behavior is explicitly investigated.

For RCF buildings, element flexural behavior is conveniently characterized by a bilinear moment–rotation relationship in the plastic hinges of the beams and columns, described by means of two characteristic points, i.e. the yielding (M_y and θ_y) and ultimate (M_y and θ_u) moment and rotation. The moment M_y can be determined by moment–curvature analyses for the element's extreme sections. In particular, a mean concrete strength of f_c =26.7 MPa and a steel yield stress of f_y=370 MPa are assumed. The latter corresponds to mean yielding value for smooth type steel Aq50 [15] that, considering an hypothesized construction age of 1960, was one of the most used type of steel. Yielding and ultimate rotations are derived from the ASCE-SEI41 [17] approach, with updated limit values as suggested in ACI 369R-11 [22]. In particular, yielding rotation θ_y is calculated accounting for a reduced effective stiffness, EI_{eff}, with respect to that of the un-cracked gross section [23], while ultimate rotation θ_{CP} is obtained by summing a plastic rotation a to the yielding one, depending on section characteristics.

As noted in [24], the frame members in Opensees are modeled as an elastic element connected in series with rotational springs at either end, and the stiffness of these components must be modified so that the equivalent stiffness of this assembly is equivalent to the stiffness

of the actual frame member. Following the approach proposed in [24], the rotational springs are made "n" times stiffer than the rotational stiffness of the elastic element in order to avoid numerical problems. To ensure the equivalent stiffness of the assembly is equal to the stiffness of the actual frame member, the stiffness of the elastic element must be "(n+1)/n" times greater than the stiffness of the actual frame member.

2.2 Modification of plastic hinges for damaged elements in PA

For Nonlinear Time History analyses, the seismic behavior of intact buildings may be studied by performing nonlinear static Pushover Analyses (PA). In the same manner, the seismic behavior of damaged buildings may be studied with PA performed on a suitably modified nonlinear model that conveniently account for damage. In fact, given the local damage level in each of the structural elements caused by a hypothetical main-shock, the moment-rotation relationships describing the plastic hinges of the elements that have entered the plastic range are modified as suggested in [2, 25], and a new PA for the structure in its damaged state may be performed.

The flowchart in Figure 2, referring to framed structures, illustrates the basic steps needed to determine the variation in building behavior from the intact to the different damage states.

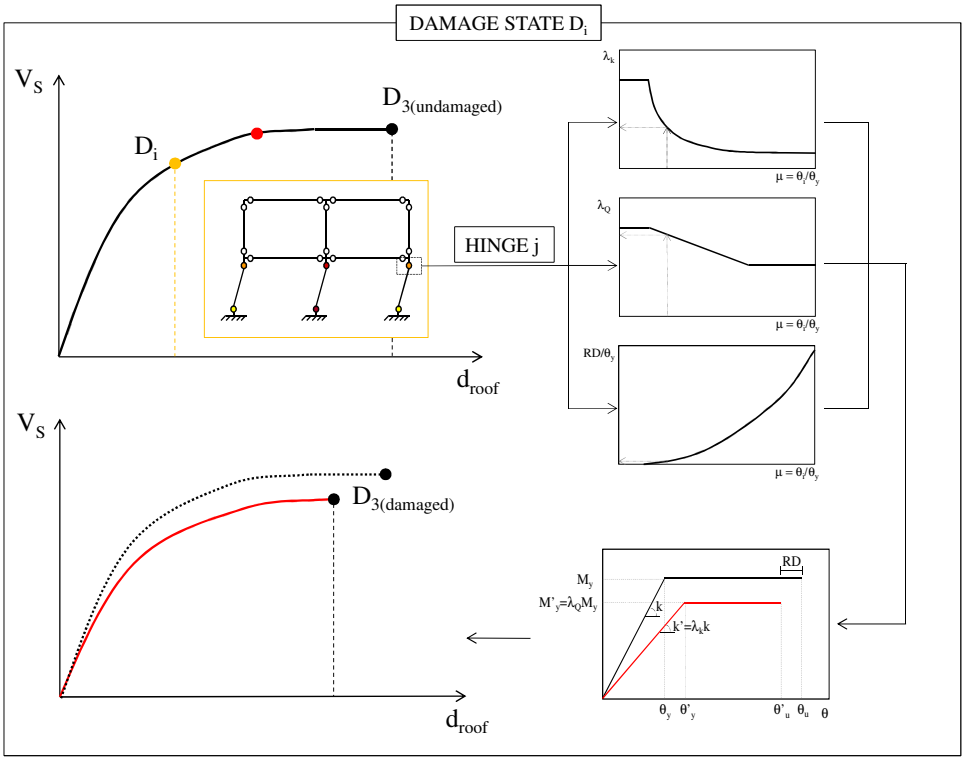


Figure 2: Assessment procedure for a framed structure.

In particular, each global damage level for the structure corresponds to a local distribution of damage for the structural elements, that may be represented by the local ductility demand for the plastic hinges that have entered the plastic range (see left-top panel in Figure 2). Based on the local ductility demand for the elements, the relative plastic hinges are modified (see right panel in Figure 2) applying a suitable variation in the relative stiffness ($K'=\lambda_k K$), strength ($M_y'=\lambda_Q M_y$) and plastic rotation capacity ($a'= a-a_d = a-(\theta'_y - \theta_y) - RD = a-(\theta_y(\lambda_Q/\lambda_k - 1)-RD$), with λ stiffness or strength modification factors and RD residual drift of the element (for further details see [2, 25]). The PBEE toolbox has been conveniently modified in order to

allow, after computation of the elements ductility demand for the generic step of PA analysis, the modification of plastic hinges with the formulations proposed in [25].
Nonlinear static analysis of the modified damaged models yields pushover curves that, depending on the number of elements involved in the damaged mechanism and on their damage level, may differ significantly with respect to the original ones.

2.3 Modeling issues for Nonlinear Time-History Analysis

The plastic hinges for beam-column elements are modeled with pinching4 material [26] in Opensees [17], that allows to simulate their degrading hysteresis behavior with damage progression. Figure 3 represents the backbone curve of the pinching4 material, evidencing pinched Moment-rotation response and cyclic degradation of strength and stiffness in three ways: unloading stiffness degradation, reloading stiffness degradation, strength degradation. Degradation due to damage is assumed to be a function of displacement history and energy accumulation.

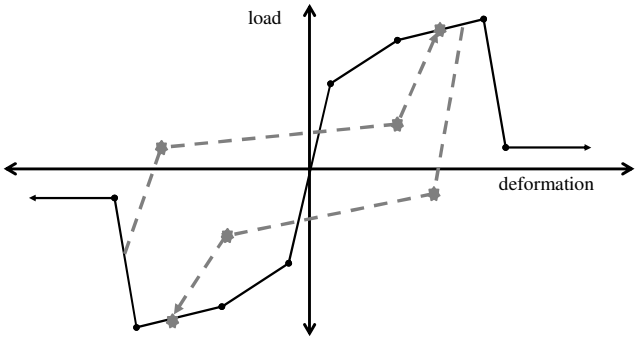


Figure 3: Pinching4 hysteretic material (after [26])

Bilinear backbone has been adopted in order to be consistent with the bilinear model adopted in static PA, furthermore, a slight hardening (0.1% of the Young's modulus) has been considered in plastic phase in order to avoid convergence problems.

For NTH analyses, 5% critical damping was assigned [27]; mass proportional damping was assumed. During the analysis, local P-delta effects were not included.

3 PUSHOVER ANALYSIS FOR INTACT AND DAMAGED BUILDINGS

In order to describe the progression of damage due to a hypothetical mainshock, four global damage states [2] were assumed as reference for the assessment for the case-study buildings:

- D_0 (no damage) in this state the building is still in its intact, or pre-mainshock, condition.
- D_1 (limited damage) corresponds to the onset of non-linear behavior, it is assumed as the Yield Displacement on the Idealized (*YDI*) bilinear pushover curve.
- D_2 (moderate damage) corresponds to the first attainment of the 50% of the Collapse Prevention (*CP*) limit state for an element [2];
- D_3 (collapse) corresponding to the first attainment of the Collapse Prevention limit state (*CP*), that is conventional collapse.

3.1 Analysis of the intact structure

Pushover analysis for the 'intact' building was performed applying two different horizontal force distributions (proportional to the main vibration mode MO and proportional to masses MA), as required by modern seismic codes (e.g., [28]). The resulting pushover curves are shown as gray dashed line in Figure 4(a), and 4(b), respectively, referring to 4 and 8 storey RCF under MA forces , and in Figure 4(c) and 4(d) referring to 4 and 8 storey RCF under MO forces, respectively.

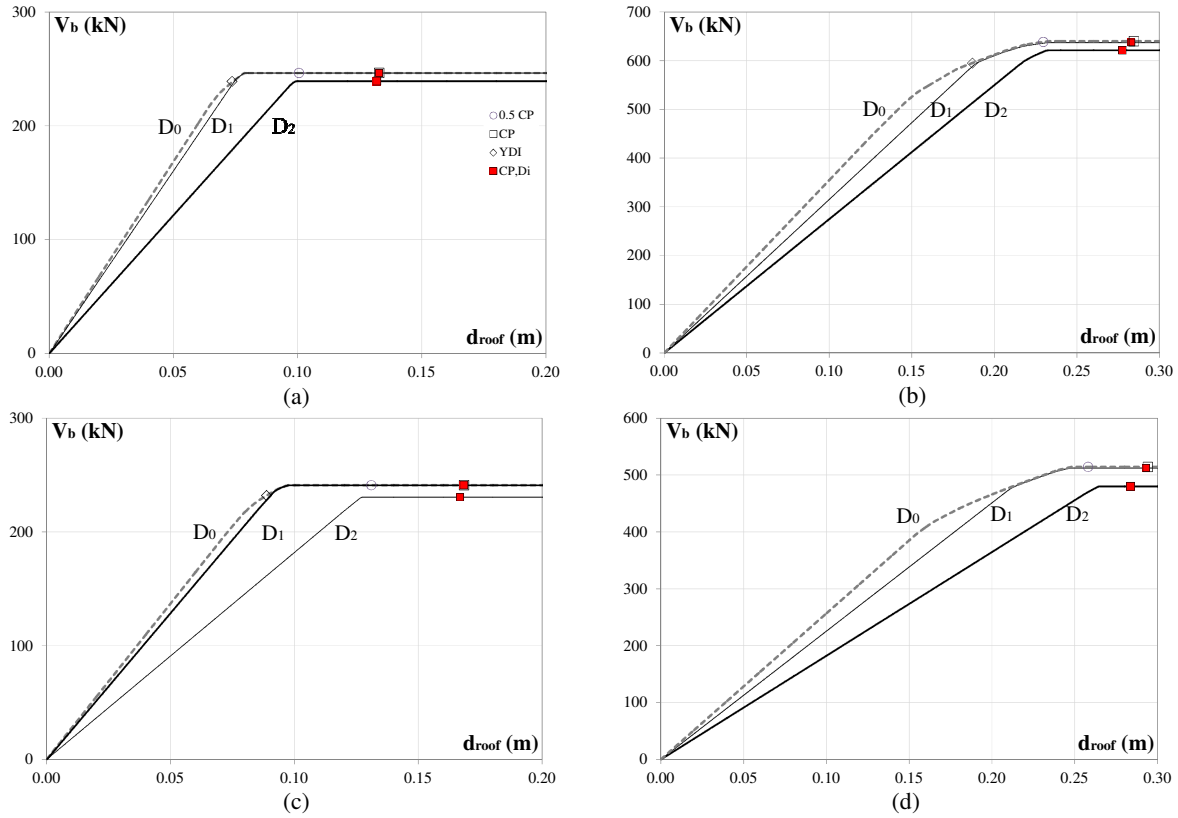


Figure 4: Pushover curves for the 4 and 8 RCFs obtained under MA and MO horizontal forces distribution and for intact (D_0), and D_1 or D_2 damaged states. (a, c) 4 storey MA or MO; (b, d) 8 storey MA or MO

The points marked on the curves in Figure 4, that is, *CP*, 0.5*CP* and *YDI*, represent the global damage states D_3, D_2, and D_1 that will be considered for further analysis of the 'damaged' structure.

The collapse mechanism type for the 4 storey building is the soft storey type at the 1st and 2nd storey, for MA and MO horizontal load distributions, respectively. For the 8 storey building and MA distribution of forces, a two-storey mechanism, involving mainly the columns of the 1st and 2nd storey, is observed, while for 8 storey building with MO a soft-storey mechanism, involving mainly the columns of the 5th level, is formed.

3.2 Analysis of the damaged structure

We study the behavior of the two RCFs for the damage states D_1 and D_2. For each of the global damage states a separate analysis of the 'damaged' structure is performed. Each pushover analysis performed for the "intact" structure is stopped in the deformed configuration at D_k (for k = 1, 2) and the plastic hinge state (ductility demand) is recorded. Next, the plastic hinges of the elements that have entered the plastic range are modified as a function of their

ductility demand. Figure 4 shows the pushover curves obtained for each of the considered damaged models. The grey dashed line represent the pushover curves for the intact structure, indicated as D_0, together with the points corresponding to D_1 and D_2; the black thin line represents the Pushover curve obtained for a structure that has attained damage state D_1 and the black bold line for the damage state D_2. On each of the curves corresponding to the analysis of the damaged building the points corresponding to the first attainment of the (reduced) CP for an element are also shown as small red squares.

The building residual capacity for the intact and damaged states was computed applying the IN2 method [29] on the equivalent SDOF obtained based on the relative PA, as explained in [2]. Tables 1 e 2 summarize the results in terms of REC_{Sa} and REC_{ag}, together with the representative parameters of the equivalent SDOF, obtained after bi-linearization of the capacity curve, T_{eq}, C_b, and μ_{cap}, for the 4 storey and 8 storey building respectively.

ID	Damage	T_{eq} [s]	μ_{cap}	C_b [g]	REC_{Sa} [g]	REC_{ag} [g]	PL
MA	D_0	1.42	1.81	0.15	0.26	0.26	0%
	D_1	1.45	1.73	0.15	0.25	0.26	1%
	D_2	1.67	1.34	0.14	0.19	0.19	26%
MO	D_0	1.24	1.89	0.17	0.33	0.27	0%
	D_1	1.47	1.79	0.17	0.31	0.26	2%
	D_2	1.52	1.31	0.17	0.22	0.24	11%

Table 1. Representative parameters of the equivalent SDOF system for the structure in different configurations (intact and damaged) and *REC* in terms of spectral acceleration and anchoring (peak) ground acceleration, for the 4 storey building

ID	Damage	T_{eq} [s]	μ_{cap}	C_b [g]	REC_{Sa} [g]	REC_{ag} [g]	PL
MA	D_0	1.98	1.52	0.19	0.29	0.53	0%
	D_1	2.07	1.39	0.19	0.27	0.52	2%
	D_2	2.21	1.23	0.19	0.23	0.50	5%
MO	D_0	1.68	1.41	0.21	0.30	0.39	0%
	D_1	1.77	1.28	0.27	0.27	0.39	1%
	D_2	1.88	1.15	0.24	0.24	0.38	3%

Table 2. Representative parameters of the equivalent SDOF system for the structure in different configurations (intact and damaged) and *REC* in terms of spectral acceleration and anchoring (peak) ground acceleration, for the 8 storey building

It is here noted that, in order to allow appropriate comparison with NTH, the spectrum assumed to determine REC_{ag} from REC_{Sa} is the mean spectrum built from the accelerograms in NTH (see § 4.1). The mean spectrum is close to Eurocode 8 [6], soil type B, spectral shape.

Further important information that may be inferred by Table 1 and 2 is the *PL* for each of the damaged configurations. *PL*, which represents a measure of the loss of lateral capacity, is defined as:

$$PL = 1 - \frac{REC_{ag,k}}{REC_{ag,0}} \tag{2}$$

where $REC_{ag,k}$ is residual capacity in terms of peak ground acceleration of the structure in the D_k damage configuration and $REC_{ag,0}$ for the intact structure.

4 ASSESSMENT OF DAMAGED BUILDING VIA NTH ANALYSIS

We want to check if the PA, performed on a suitably modified building model accounting for damage experienced during an earthquake, is able to capture the effective variation of building *REC* and the relative *PL*.

To this end, the REC_{ag} obtained with the methodology described above, relying on modified building model for two considered damage states, namely D_1 and D_2, is compared to the REC_{ag} that can be obtained via NTH.

Similarly to the approach adopted in [30], in order to study the behavior of the MDOF system after the attainment of the same damage level D_i, as considered for the PA assessment, multiple earthquake sequences are built through suitable scaling of selected accelerograms. In particular, each nonlinear time history analysis is performed applying sequences of two suitably scaled earthquakes. The first one has to be scaled at the intensity able to "damage" the MDOF system to the same damage level considered on the initial pushover (D_1 or D_2). In order to find this damaging intensity, Incremental Dynamic Analysis (IDA) [31], with the aid of PBEE toolbox [16], is performed and the intensities determining the attainment of D_1 and D_2 and D_3 on the initially intact structures, $a_{g,D1}$, $a_{g,D2}$ and $a_{g,D3}$ are retrieved. In particular, $a_{g,D3}$ and $a_{g,D2}$ correspond to the first attainment on IDA curve of CP and CP/2 rotation for a structural element, and $a_{g,D1}$ corresponds to the identification on IDA curve of the maximum Interstorey Drift Ratio (IDR_{max}) corresponding to the YDI evaluated with PA analysis. $a_{g,D3}$ is, by definition, the REC_{ag} for the intact structure computed based on NTH for a single earthquake.

The second earthquake (applied after the first one scaled at $a_{g,Di}$) is the sole one that is successively scaled, performing IDA analysis on a structure that has already attained a given damage state (see Figure 5). This way the $REC_{ag,i}$, varied with respect to the initial one determined on the intact structure, may be determined as the a_g (to which the second accelerogram has to be scaled) corresponding to building collapse (D_3 state, as defined above).

The PBEE has been modified in order to allow scaling only second record in the sequence, while the first record one is scaled to a fixed IM, namely $a_{g,D1}$ or $a_{g,D2}$, that corresponds to the reaching of a given damage state. A time gap of 20 seconds between first earthquake and second earthquake is added between multiple earthquake events (see Figure 5).

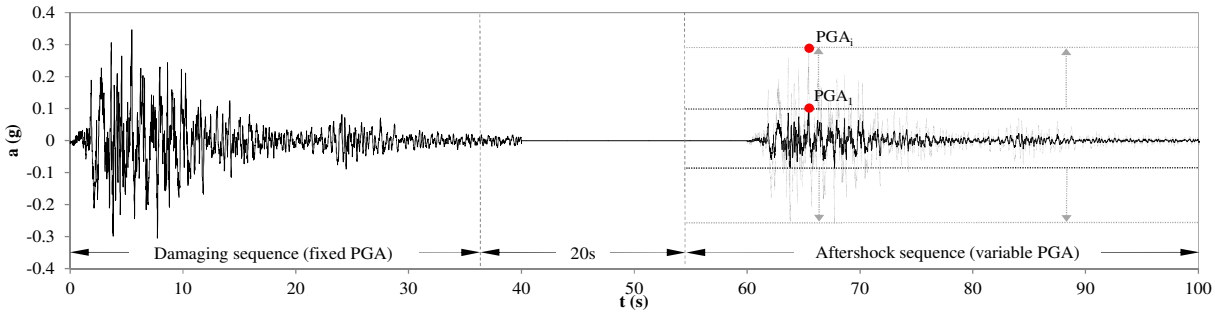


Figure 5: Example seismic sequence.

After the excitation of the first record, the vibration of structure will cease gradually due to damping, so that when the second earthquakes arrives it may be considered as a new one; on the other hand, the structural elements and plastic hinges had been previously damaged by the

first record and this shall be properly accounted for by application of the earthquakes in such a "continuous" sequence.

Dynamic analysis of the sequence is repeated with increasing scale factors applied to the second records in the series until the structure collapses, providing incremental dynamic analysis results for structures having attained a given damage level due to the first earthquake.

For what concerns the NTH evaluation, a set of 8 representative ground motions (16 accelerograms, considering the x and y directions of the recorded signals) is selected in order to be compatible with EC 8 spectrum for Soil Type B (stiff soil) [6]. To account for the effect of record-to-record variability on structural response, IDA is repeated for each of 16 ground motions in the set.

By combining each of the 16 "damaging" ground motions with the same 16 ground motions applied as subsequent earthquakes, a set of 256 record sequences are created for each damage state and structure model.

4.1 Seismic action

A set of 8 couples of response spectrum compatible natural accelerograms has been used to perform Incremental dynamic analyses (see Table 3). Different combinations of first record-second record have been performed in order to simulate damaging earthquake and a subsequent variation in residual capacity in a more realistic way. These records are earthquakes with M_w between 5.4 and 6.9 and sites with epicentral distance 2.9 to 72.0 km. The unscaled records have peak ground accelerations from 0.11 to 0.40 g.

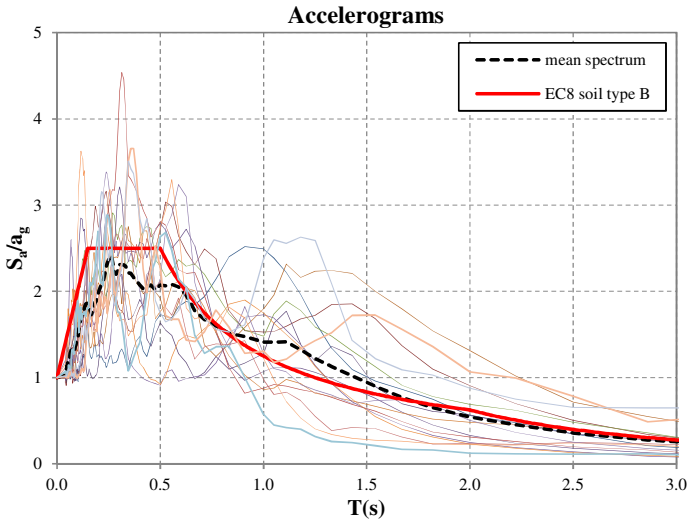


Figure 6: Acceleration spectra for accelerograms recorded on stiff soil.

Single earthquakes were selected from *European Strong-Motion Database* [32], according to the following criteria: a) magnitude of event equal to or greater than 4.0; b) available information about the soil condition, which correspond to Soil Type B [6]; c) seismic sequences having peak ground acceleration (a_g) of the mainshock horizontal component greater than 100 cm/s^2; d) significant duration smaller than 35 s; e) Cosenza and Manfredi Index smaller than 12 [33, 34]. Under these criteria 8 seismic earthquakes with two orthogonal horizontal components were selected for this investigation. Table 3 lists the selected earthquakes and significant seismological parameters.

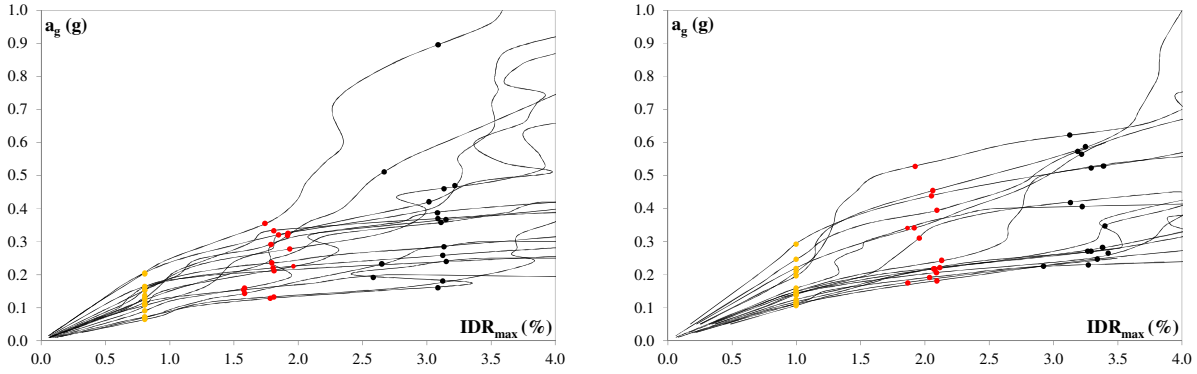
Earthquake Name	Station	Code	M_w	a_g (g)	I_D	Significant duration [35] (s)	Epicentral distance (km)
Montenegro -15/4/1979	Ulcinj-Hotel Olimpic, NS	197x	6.9	0.29	10.6	20.9	24
Montenegro -15/4/1979	Ulcinj-Hotel Olimpic, EW	197y	6.9	0.24	7.2	21.7	24
Montenegro -15/4/1979	Bar-Skupstina Opstine, NS	199x	6.9	0.38	8.4	17.9	16
Montenegro -15/4/1979	Bar-Skupstina Opstine, EW	199y	6.9	0.36	10.4	15.7	16
Kalamata -13/9/1986	D2.7 Kalamata-Prefecture, N265	413x	5.9	0.21	5.4	5.5	5.9
Kalamata -13/9/1986	Kalamata-Prefecture, N355	413y	5.9	0.30	5.8	7.1	5.9
Kalamata -13/9/1986	Kalamata-OTE Building, N80E	414x	5.9	0.24	4.6	5.1	2.9
Kalamata -13/9/1986	Kalamata-OTE Building, N10W	414y	5.9	0.27	7.4	6.3	2.9
Umbria-Marche - 06/10/97	Colfiorito, NS	622x	5.5	0.12	5.2	8.4	5.5
Umbria-Marche - 06/10/97	Colfiorito, EW	622y	5.5	0.11	6.7	7.2	5.5
Filippias - 16/06/90	Vasiliki town-Hall, NS	1981x	5.5	0.14	8.7	12.0	59
Filippias - 16/06/90	Vasiliki town-Hall, EW	1981y	5.5	0.12	10.2	12.0	59
Mt. Hengill Area - 04/06/98	Thorlakshofn, NS	5081x	5.4	0.20	9.3	10.9	21
Mt. Hengill Area - 04/06/98	Thorlakshofn, EW	5081y	5.4	0.37	8.3	10.9	21
Kozani - 13/05/95	Katerini-Agriculture Institute, NS	6101x	6.5	0.40	9.2	32.2	72
Kozani - 13/05/95	Katerini-Agriculture Institute, SW	6101y	6.5	0.34	10.4	32.2	72

Table 3. Accelerograms used in the study

Figure 6 shows the elastic 5% damped spectra for the selected earthquakes as well as their mean acceleration spectrum. The mean spectrum is quite similar and even higher for periods around 1.0 to 2.5s as EC 8 spectrum for Soil Type B [6].

4.2 Study of damaging sequences

As explained in § 4.1, for each record initially applied on the structure the intensity measure (in terms of a_g) corresponding to the attainment of damage level D_i is estimated via IDA.



(a) (b)

Figure 7: IDA curves for 'intact' buildings subjected to each mainshock. (a) 4 storey, (b) 8 storey building.

In Figure 7 the IDA results for the 4-storey intact building are shown, where x-axis represents the Maximum experienced Inter-storey Drift Ratio (IDR_{max}) and the y-axis the peak ground acceleration (a_g). The dot points marked on each IDA curve, that is, *CP* (black), 0.5*CP* (red) and that corresponding to the yield displacement of the idealized pushover curve (orange), represent the attainment of global damage states D_3, D_2, and D_1 that will be considered for further analysis of the 'damaged' structure, respectively. Due to differences in frequency content, duration and other ground motion characteristics, each ground motion have to be scaled to a different intensity before a particular damage level occurs.

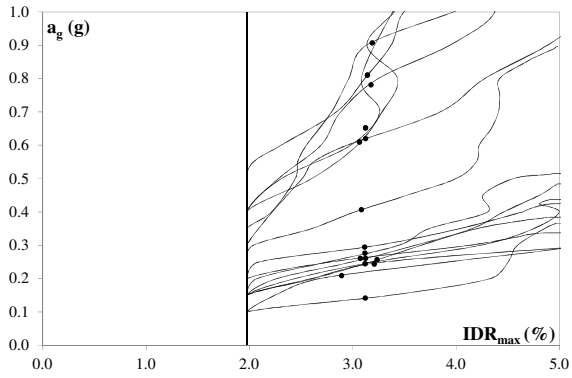


Figure 8: IDA curves for 4 storey building in D_2, subjected to record 197x

Once the $a_{g,D1}$ (or $a_{g,D2}$) is found for each damaging earthquake (first record), the (first record-second record) sequence may be built; the first record is scaled to $a_{g,D1}$ (or $a_{g,D2}$) while the second record has to be scaled in order to perform IDA on D_1 or (D_2) damaged structure. The results for the 4 storey RCF obtained from those IDA sequences are shown in Figure 8 that refers to the record 197x as (first record) damaging earthquake, scaled to $a_{g,D2} = 0.22$. Each point on those curves represent IDR_{max} (maximum interstorey drift ratio) that is attained in correspondence of each intensity level a_g (of the second ground motion in the sequence). Black dots in Figure represent the MDOF response when $D_3|D_2$ damage state is obtained.

Results are shown for 4-storey building that has reached damage state D_2 due to the first record. The black bold line indicates the threshold after which the interstorey drifts undergone during the second record are greater than those experienced during the first record. Indeed, when applying the earthquake sequence, the IDR_{max} that is registered in each analysis will be always the IDR_{max} corresponding to the first earthquake until the second earthquake has an IM such as to let the maximum inter-storey drift increase. The Figure shows significant scatter in the intensity levels at which a particular damage state occurs for different records after the same damaging (first) record.

5 COMPARISON OF PA AND NTH RESULTS

In this paragraph a comparison between PA and NTH results for the two considered MDOF RCFs is performed. In particular, with the aim of assessing the ability of PA to evaluate the behavior of damaged buildings, we make reference to systems that have attained varying damage levels due to hypothetical main-shocks.

First comparison is performed in terms of the IDR_{max}. Initially, the IDR_{max} distribution along the height for buildings in the undamaged state are compared. In particular, making reference to increasing levels of earthquake demand, i.e. such as to determine the attainment of D_2 or D_3 damage states on the RCFs, the IDR_{max} shapes obtained through pushover analyses with MA or MO forces distribution (indicated as PA-MA and PA-MO, respectively), are compared with the median values (and 16^{th} and 84^{th} fractiles) obtained with the NTH approach. Figure 9 (a, c) shows the diagrams obtained for the initially intact 4 storey RCF at D_2 and at D_3, respectively. It may be noted, that PA satisfactorily captures the median IDR_{max} shape and value that is obtained through NTH approach; indeed, the plastic mechanism type does not change relevantly for increasing levels of seismic intensity and the MA forces distribution in this case better simulates earthquake response.

Figure 9 (b, d) shows similar diagrams for the 8 storey initially undamaged RCF. Although the storey where maximum IDR_{max} is not suitably identified with PA approach, its value com-

pared with median results obtained with NTH approach is satisfactorily captured by the PA-MO.

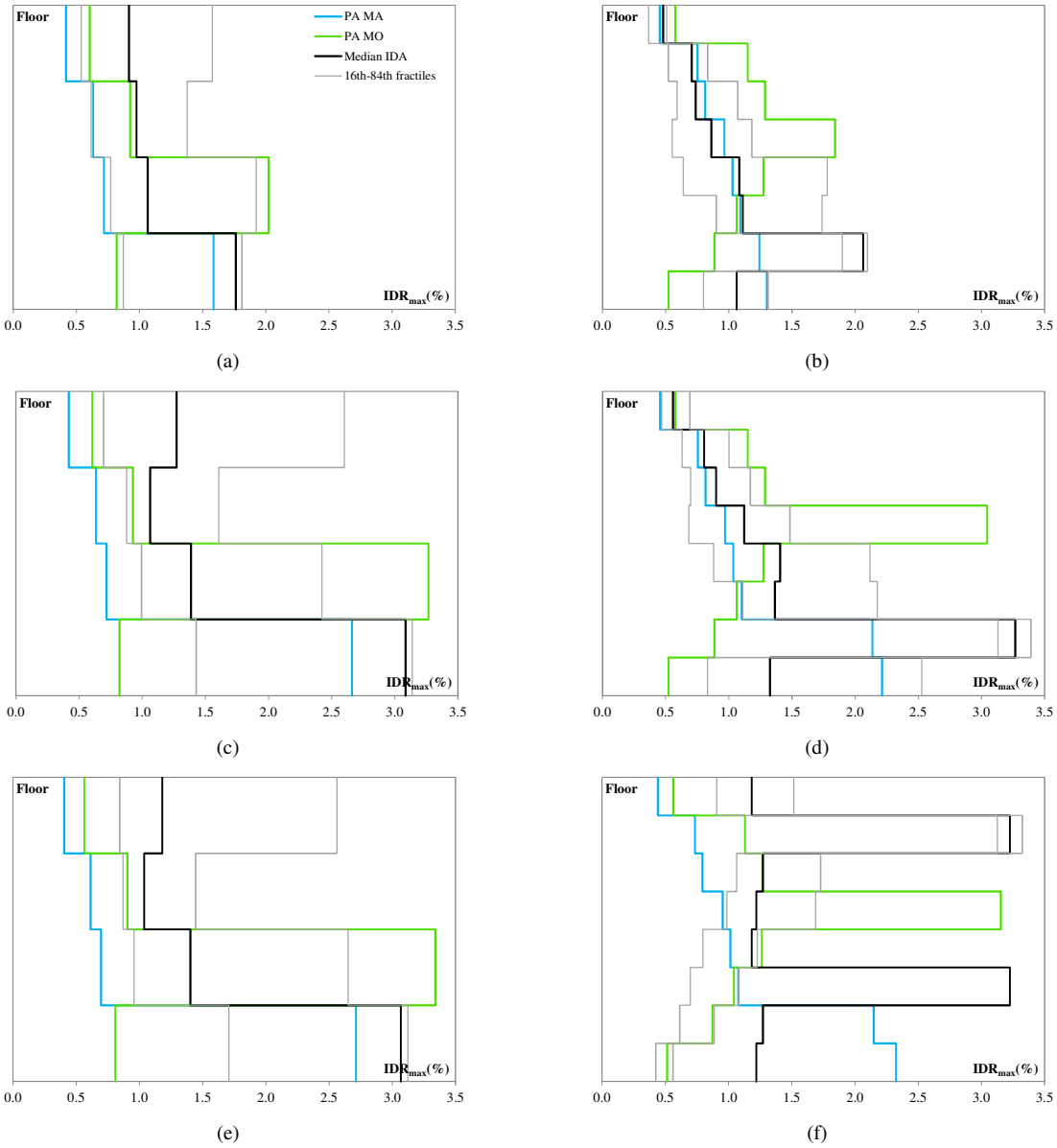


Figure 9: IDR_{max} for 4 storey (a, c, e) and 8 storey building (b, d, f), for 'intact' building with respect to D_2 (a, b) and D_3 (c, d), and for D_2 damaged structure with respect to D_3, i.e. IDR_{max} shape at $D_3|D_2$ (e, f), respectively.

Figure 9 (e, f), referring to 4 and 8 RCFs respectively, show the IDR_{max} distribution along the height at $D_3|D_2$, i.e. derived for systems that had initially sustained D_2 damage state due to the first earthquakes and that arrive at D_3 for the second earthquake (or are are pushed to D_3 damage state after modification of the MDOF model for PA analysis).

With reference to the 4 storey RCF (Figure 9 (e)), it can be seen the maximum inter-storey drifts obtained via PA-MA, and the relative distribution, satisfactorily represent the results that may be obtained via NTH analysis approach. Considering the 8 storey RCF (Figure 9 (f)), it is, again, noted that the maximum inter-storey drifts value is captured with reasonable approximation with PA-MO, while the storey where the concentration of damage occurs is the 5th, differently from NTH analysis evidencing a most probable formation of soft storey at level 7. Such discrepancy could be possibly reduced using an adaptive pushover approach.

Second comparison is performed in terms of the $REC_{ag.}$ Figure 10 (a, b, c, d) shows the comparison in terms of $REC_{ag,i}$ for the two considered MDOF systems and two considered damage level. More in detail, Figure 10 (a) refers to the 4 storey RCF, displaying the $REC_{ag,1}$ for the D_1 damaged system. The single $REC_{ag,1}$ values corresponding to each first record (damaging earthquakes) are represented by a number of points aligned along vertical lines (identified by the same ID). Each group of points with the same ID represent the $REC_{ag,1}$ obtained varying the second record in the relative ID sequence (i.e. the sequence with ID record as the first damaging earthquake).

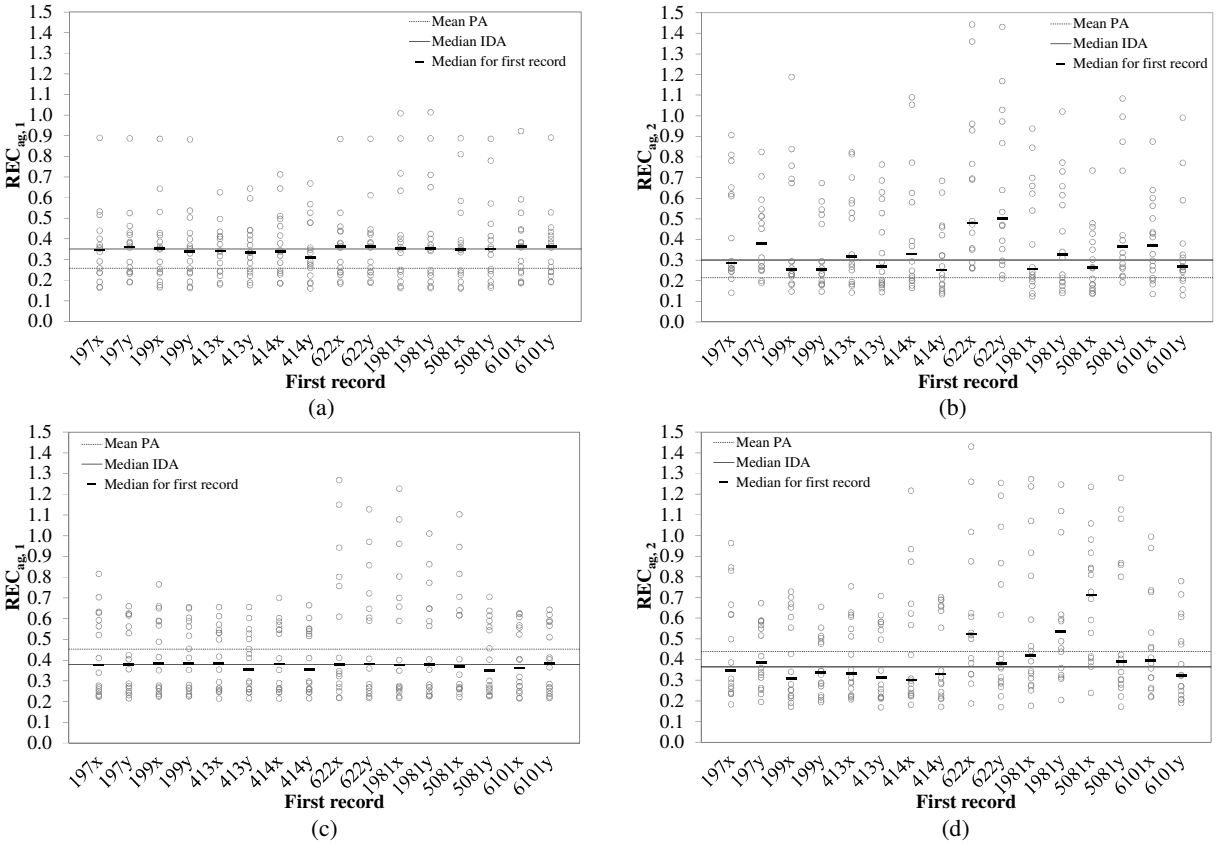


Figure 10: Comparison between PA and NTH computations of $REC_{ag,i}$ for 4 storey (a, c) and 8 storey (b, d) buildings, in damage states D_1 and D_2 respectively.

For each group of first record-second record sequence, the median of $REC_{ag,1}$ is represented by black square, while the horizontal continuous line in figure represents the median obtained as the median of those medians. For comparison, the median value of $REC_{ag,1}$ obtained with PA considering the MO and MA distribution is represented as horizontal dashed line in Figure. Figure 10(b), (c) and (d) show similar results with respect to $REC_{ag,1}$ for the 8 storey RCF, for $REC_{ag,2}$ for the 4 storey RCF and for $REC_{ag,2}$ for the 8 storey RCF.

Observing the Figure 10 a relatively good agreement between the results in terms of $REC_{ag,i}$ obtained with PA, performed on suitably modified model for D_i damaged structure , and those obtained through the consecutive records sequences, suitably scaled as described in § 4, is noted. Table 3 resumes the median $REC_{ag,i}$ that are obtained on the intact structures ($REC_{ag,0}$), as well as those obtained for the structures that had been damaged to D_1 or D_2 damage states ($REC_{ag,1}$ or $REC_{ag,2}$), for both PA and NTH based analyses.

It has to be noted that it may (rarely) happen that, for the single first record-second record sequences, the REC_{ag} computed after the entire sequence is larger than the REC_{ag} computed for the sole first record. This may happen because of different polarity (i.e direction) of the

second earthquake with respect to the first one; indeed if earthquakes have different polarity the second record may beneficially act in reducing residual displacements attained after the first one. It has been shown [30] that the polarity of second record with respect to first one may impact the post-earthquake fragilities for extensively damaged buildings. This issue was not investigated in the present study and has to be properly taken into account in future works.

It is interesting to observe that median Performance Loss (Eq.(1)) that may be expected considering the results of NTH based analyses, i.e. referring to the ratio of the median $REC_{ag,i}$ versus the median $REC_{ag,0}$, is quite close to the median *PL* that is computed with pushover based approach. In fact, a *PL* equal to 3.0% or 17.1% is obtained for 4 storey RCF with NTH based analyses for the D_1 or D_2 damaged structures, while *PL* equal to 1.4% or 18.5% for the same cases is obtained via pushover based analyses. For the 8 storey RCF, a *PL* of 1.2% or 4.1% is obtained for PA. Analyzing the D_1 or D_2 damaged structures with the NTH approach a slightly negative *PL* is found in the former case, probably due to the polarity issue evidenced before, while a *PL* equal to 3.1% is obtained for the latter case. However, in absolute terms those median *PL* values retrieved with NTH analysis approach are very close to the PA based results.

	4 storey			8 storey		
	$REC_{ag,0}$	$REC_{ag,1}$	$REC_{ag,2}$	$REC_{ag,0}$	$REC_{ag,1}$	$REC_{ag,2}$
NTH (median (g))	0.36	0.35	0.30	0.38	0.38	0.37
PA (median (g))	0.26	0.26	0.22	0.46	0.45	0.44

Table 4. Comparison between PA and NTH analysis at damage state D_i

6 CONCLUSIONS

The study presented in this paper aims at contributing in the evaluation of the usability of pushover analysis for the assessment of the behavior of damaged buildings.

In particular, the efficiency of Pushover analysis PA to capture the variation of buildings Residual Capacity *REC* after they have sustained varying damage levels due to hypothetical main-shock is checked by comparison of the PA results with those of Nonlinear Time-History analysis NTH.

Two case study Reinforced Concrete Frames (RCF) are considered, namely a 4 storey and an 8 storey RCFs that have been designed in 1st seismicity class according to old seismic codes in force in the early '60s.

The first PA-NTH comparison is performed for the initially undamaged structures. Concerning the 4 storey building, the PA satisfactorily captures the median IDR_{max} shape and value that is obtained through NTH approach for increasing level of earthquake intensity. For the 8 storey RCF the maximum inter-storey drifts value is captured with reasonable approximation by PA, while the storey where the concentration of damage occurs is not the same as evidenced with NTH approach.

For what concerns the REC_{ag} for the undamaged structure, $REC_{ag,0}$, i.e. the initial residual capacity in terms of a_g, it is noted that PA yields a value that is approximately 30% lower than NTH for the 4 storey building and approximately 20% higher for the 8 storey one.

Next PA-NTH comparison is performed for damaged structures. Concerning IDR_{max} the maximum value and distribution along the height obtained at D_3/D_2 (i.e. at D_3 for structures that were previously damaged to D_2) are, again, well captured for the 4 storey RCF, while for the 8 storey only the maximum value is compliant.

For what concerns the REC variation, it is observed that the same PA-NTH scatter obtained for intact structures is obtained for D_i damaged MDOF (with i=1, 2). Indeed, $REC_{ag1,PA}$/ $REC_{ag1,NTH}$ ratio for the 4 storey building is 0.74 and for the 8 storey one is 1.18, while the $REC_{ag2,PA}$/ $REC_{ag2,NTH}$ ratio for 4 and 8 storey RCF are 0.73 and 1.19, respectively.

These results suggest that, although applying a pushover based procedure for the assessment of damaged buildings the results will be inevitably affected by a certain degree of approximation with respect to Nonlinear Time History analyses executed on a set of seismic sequences, such approximation does not vary significantly with respect to the one that is obtained with standard Pushover Analyses applied to intact structures.

The study do not pretend to be exhaustive, having compared the results of PA with NTH for only two case study frame building. Moreover, a number of assumptions were applied (e.g. brittle failures and P-Δ effect neglected, varying earthquake polarity not considered).

Further studies will have to address these issues.

ACKNOWLEDGEMENTS

This study was performed in the framework of PE 2010–2013; joint program DPC-Reluis Task 1.1.2: Ordinary and Precast Reinforced Concrete Structures.

REFERENCES

[1] FEMA. "FEMA 306: Evaluation of earthquake damaged concrete and masonry wall buildings – basic procedures manual". *Federal Emergency Management Agency*, 1998. Washington D.C

[2] M. Polese, M. Di Ludovico, A. Prota, G. Manfredi, Damage-dependent vulnerability curves for existing buildings. *Earthquake Engineering and Structural Dynamics,* (in press), DOI: 10.1002/eqe.2249, 2012.

[3] P. Fajfar, P. Gašperšič, The N2 method for the seismic damage analysis of RC buildings. *Earthquake Engineering and Structural Dynamics*, **25**, 31–46, 1996

[4] A.M. Mwafy, A.S. Elnashai. Static pushover versus dynamic collapse analysis of RC buildings. *Engineering Structures*, **23**, 407–424, 2001

[5] P. Bazzurro, C.A. Cornell, C. Menun, M. Motahari, Guidelines for seismic assessment of damaged buildings, Proceeding of the 13thWCEE, Paper No. 1708, Vancouver, Canada, August 1-6, 2004.

[6] Comitée Européen de Normalisation, European Standard EN 1998-1: Eurocode8. Design of structures for earthquake resistance. Part 1. General rules, seismic actions and rules for buildings, Brussels, 2005.

[7] M. Polese, M. Marcolini, A. Prota, G. Zuccaro, Mechanism based assessment of damaged building's residual capacity. *Computational Methods in Structural Dynamics and Earthquake Engineering, Compdyn 2013*, Paper No. 1524, Kos, Greece, 2013.

[8] M. Polese, G.M. Verderame, C. Mariniello, I. Iervolino, G. Manfredi, Vulnerability analysis for gravity load designed RC buildings in Naples – Italy, *Journal of Earthquake Engineering,* **12** (S2), 234-245, 2008.

[9] H. Krawinkler, GDPK. Seneviratna, Pros and cons of a pushover analysis of seismic performance evaluation. *Engineering Structures*, **20**(4-6), 452–64, 1998.

[10] WK. Tso, AS. Moghadam, Pushover procedure for seismic analysis of buildings. *Progress in Structural Engineering and Materials*, **1**(3), 337–44, 1998.

[11] RS. Lawson, V. Vance, H. Krawinkler, Nonlinear static push-over analysis — why, when, and how? In: *Proceedings 5th US NCEE*, vol. 1. IL, USA: Chicago; 283–92, 1994.

[12] S. Antoniou, A. Rovithakis, R. Pinho, Development and verification of a fully adaptive pushover procedure, *12th European Conference on Earthquake Engineering*, paper # 822, London, 2002.

[13] G. M. Verderame, M. Polese, C. Mariniello, G. Manfredi, A simulated design procedure for the assessment of seismic capacity of existing reinforced concrete buildings, *Advances in Engineering Software*, **41** (2), 323-335, 2010.

[14] R.D.L. no. 2229/1939. Regulations for the execution of simple and reinforced concrete constructions; 1939 [in Italian].

[15] G.M. Verderame, P. Ricci, M. Esposito, G. Manfredi, 2012. STIL v1.0 – Software per la caratterizzazione delle proprietà meccaniche degli acciai da c.a. tra il 1950 e il 2000. ReLUIS. http://www.reluis.it/ (in Italian)

[16] M. Dolšek, Development of computing environment for the seismic performance assessment of reinforced concrete frames by using simplified nonlinear models. *Bulletin of Earthquake Engineering*, **8(6)**, 1309-329, 2010.

[17] F. McKenna, G.L. Fenves, M.H.Scott, OpenSees: Open system for earthquake engineering simulation, Pacific Earthquake Engineering Research Center, University of California, Berkeley, California, USA, 2004. http://opensees.berkeley.edu

[18] ASCE-SEI 41–06. Seismic Rehabilitation of Existing Buildings, ASCE Standard, American Society of Civil Engineers, Reston, Virginia, 2007.

[19] G.M. Verderame, M. Polese, E. Cosenza, Vulnerability of existing R.C. buildings under gravity loads: A simplified approach for non sway structures, *Engineering Structures,* **31** (9), 2141-2151, 2009.

[20] M. Polese, G.M. Verderame, G. Manfredi, Static vulnerability of existing R.C. buildings in Italy: a case study, *Structural Engineering and Mechanics,* Techno-Press, **39** (4), 599-620, 2011.

[21] C.A. Pagni, L.N. Lowes, Fragility Functions for older reinforced concrete beam-column joints, *Earthquake Spectra*, **22** (1), 215–238, 2006.

[22] ACI 369R-11. Guide for Seismic Rehabilitation of Existing Concrete Frame Buildings and Commentary. Reported by ACI committee 369, American Concrete Institute, 2011. ISBN: 978-0-87031-419-3

[23] K.J. Elwood and M.O. Eberhard, Effective stiffness of reinforced concrete columns, *ACI Structural Journal*, **106** (3), 476-484, 2009.

[24] L.F. Ibarra, H. Krawinkler, Global collapse of frame structures under seismic excitations, Technical Report 152, The John A. Blume Earthquake Engineering Research Center, Department of Civil Engineering, Stanford University, Stanford, CA, 2005.

[25] M. Di Ludovico, M. Polese, M. Gaetani d'Aragona, A. Prota, G. Manfredi, Modeling of damaged RC columns in nonlinear static analyses: a proposal for plastic hinges modification factors. Engineering Structures, **51**, 99–112, 2013.

[26] L.N. Lowes, M. Nilanjan, A. Altoontash, A beam-column joint model for simulating the earthquake response of reinforced concrete frames, PEER Report 2003/10, Pacific Earthquake Engineering Research Center, University of California, Berkeley, February, 2004.

[27] F.A. Charney, Unintended consequences of modeling damping in structures, Journal of Structural Engineering, **134**(4), 581–592, April 1, 2008.

[28] Comitée Européen de Normalisation, European Standard EN 1998–3: Eurocode8. Design of structures for earthquake resistance. Part 3. Assessment and retrofitting of buildings, Brussels, 2004.

[29] M. Dolsek, P. Fajfar, IN2- A simple alternative for IDA, 13th World Conference on Earthquake Engineering, Paper No. 3353, Vancouver, B.C., Canada, 2004.

[30] M. Rahunandan, A.B. Liel, H. Ryu, N. Luco, S.R. Uma, Aftershock fragility curves and tagging assessments for a mainshock-damaged building, Proceeding of the 15thWCEE, Paper No. 1708, Lisboa, Portugal, August 1-6, 2004

[31] D. Vamvatsikos, A. Cornell, Incremental dynamic analysis. *Earthquake Engng Struct. Dyn*., **31** (3), 491-514, 2002.

[32] N. Ambraseys, P. Smit, R. Sigbjornsson, P. Suhadolc, and B. Margaris, Internet-site for european strong-motion data, European Commission, Research-Directorate General, Environment and Climate Programme, 2002.

[33] E. Cosenza, G. Manfredi, Damage indices and damage measures, *Progress in Structural Engineering and Materials,* **2**(1) 50–59, 2000.

[34] Cosenza E., Manfredi G., Polese M., A simplified method to include cumulative damage in the seismic response of SDOF systems, *Journal of Engineering Mechanics*, ASCE, **135**(10), 1081-1088, 2009.

[35] M.D., Trifunac and A.G., Brady, A study on the duration of strong earthquake ground motion. Bulletin of the Seismological Society of America, **65**, 581-626, 1975.

COMPDYN 2013
4th ECCOMAS Thematic Conference on
Computational Methods in Structural Dynamics and Earthquake Engineering
M. Papadrakakis, V. Papadopoulos, V. Plevris (eds.)
Kos Island, Greece, 12–14 June 2013

INVESTIGATION INTO ANALYTICAL VULNERABILITY CURVES DERIVATION ASPECTS CONSIDERING MODELLING UNCERTAINTY FOR INFILLED RC BUILDINGS

A. Meslem[1], and D. D'Ayala[2]

[1] University College London
a.meslem@ucl.ac.uk

[2] University College London
d.d'ayala@ucl.ac.uk

Keywords: Fragility curves, Vulnerability Assessment, Modelling Uncertainty, Infilled RC building.

Abstract. *Reinforced concrete (RC) buildings represent the dominant type of construction in several earthquake prone countries and in the rest of the world. These structures are usually characterized by the presence of partition walls commonly made of unreinforced masonry bricks infill. To reduce the computational effort required to derive fragility functions, numerous researchers have attempted to use simplified assumptions, such as, the use of default values to model structural characteristics-related parameters (i.e., mechanical properties, geometric configuration, and dimensions), ignoring the contribution of infills in the seismic response by modelling infilled RC building as bare frame,...etc.,. However, such simplifications may highly decrease the reliability and accuracy of the obtained results introducing important epistemic uncertainty in the fragility function construction process. This paper investigates the different aspects of uncertainties resulting in adopting simplification in structural and mathematical modelling, and the resulting fragility curves. In the first section, the paper presents the results of sensitivity analysis that has been conducted examining the influence of the variation in structural characteristics-related parameters. The second section is devoted to a comparative analysis of different fragility curves developed with and without considering the contribution of infill panels (i.e. influence of numerical model completeness). The present study was conducted within the framework of the research project "Global Vulnerability Estimation Methods" funded by the Global Earthquake Model (GEM) foundation.*

1 INTRODUCTION

In order to reduce the calculation efforts, many researchers have attempted to use simplified assumptions in seismic vulnerability studies [28]. Indeed, it has been widely observed in literature [55, 31] that default nonlinear properties values (e.g. a default value of concrete strength, or steel strength, or an estimate of transverse reinforcement spacing...etc.), provided in existing guidelines/codes and implemented in commonly used structural programs, are assigned to represent mechanical, geometric configuration, and dimension characteristics. Usually, this is due either to lack of information, especially, for the case of older structures where design documents are generally not available, or to expedience.

Moreover, fragility curves of buildings located anywhere in the world have been generated using, for instance, HAZUS capacity curves derived for buildings in the US [36, 60]. This is particularly common when studies are conducted for large portions of the building stock and resources for direct survey and data acquisition are modest. Typically, differences in construction techniques and detailing between different countries are significant, even when buildings are nominally designed to the same code clauses. Furthermore, regarding the numerical modelling extensive literature review has shown that often vulnerability functions for infilled RC buildings are generated from analysis of bare frames structures [26, 32]. As a consequence, such assumptions and simplifications may highly decrease the reliability and accuracy of the obtained results due to the increase of epistemic uncertainty in modelling.

Apart from Liel et al (2008) very few studies have consistently analyzed the effect of the variability of several structural characteristics or of the simplified modelling assumptions on the generated fragility curves, with the scope of estimating the level of uncertainties that should be taken into account. In general practice, the aleatoric uncertainties associated to the structural characteristics-related parameters are accounted for by considering the probabilistic variability in their values [6, 8, 27, 29, 47, 50, 53, 54, 59]. In some others vulnerability studies [12, 13, 14, 33] the effect of dispersion in structural characteristics-related parameters were accounted for by survey of a large number of existing buildings and definition of a median and standard deviation of the sample of buildings, after calculation of the capacity and damage threshold for each building in the sample.

This paper presents the result of investigation on the sensitivity of fragility functions to variation in structural characteristics-related parameters' values and to numerical modelling completeness. The classes of structures considered are low-ductility RC buildings designed according to earlier seismic codes, and which are in general characterized by poor quality of materials, workmanship and detailing. To best identify the expected mean and range for the various parameter analysed a real frame in Turkey, is the reference prototype, however the methodology and results obtained are applicable to other typologies and locations, once the basic data is available. The sensitivity study is based on 3D nonlinear adaptive pushover analysis. The observations of the influence of variability of the selected parameters are conducted in terms of deformation capacity, considering different damage thresholds. The effect of model completeness is investigated by performing a comparative analysis of fragility curves derived with and without considering the contribution of masonry infill panels.

2 ADOPTED PROCEDURE

2.1 Selected capacity-related parameters

With regards to the effort by Liel and Deierlein [35], which has been also considered in the ATC-63 [3], the sensitivity study was conducted by considering height and framing system as variable parameters. In the present study, the investigated structural characteristics-related

parameters are those associated to mechanical characteristics, dimension characteristics, and geometrical characteristics, as shown by Table 1. The mechanical characteristics parameters that have been considered are: compressive strength of concrete, yield strength of reinforcement, and strength of infill walls (in terms of compressive strength and thickness). Floor-to-floor story height was selected as dimensional parameter. In terms of geometrical characteristics, the examined associated parameter is transverse reinforcement spacing. The completeness of model is also taken into account by considering the effect of the contribution of infill walls. The structural characteristics-related parameters that have been considered are those associated to mechanical properties, geometric configuration, and structural details: compressive strength of concrete, yield strength of reinforcement, strength of infill walls (in terms of compressive strength and thickness), story height, and transverse reinforcement spacing. The reason for the choice of these parameters is to fill the gap regarding the availability of details on their effects with regard to the expected uncertainties that might result in deriving fragility functions. The choice of expected mean and range for each parameter, as shown in Table 1, is based on the results of structural characteristics assessment [7, 9], post-earthquakes surveys [18, 19, 21], on the requirement from different versions of earlier seismic codes, e.g. TS500 [58], and other references [22, 25, 30].

Parameters	Mean Value	Range of Value
Strength of reinforced concrete (fc)	17 MPa	14MPa ~ 20MPa
Tensile strength of steel (fy)	260 MPa	200MPa ~ 320MPa
Transverse reinforcement spacing (S)	200 mm	150mm ~ 250mm
floor-to-floor Story height (h)	2.8 MPa	2.5m ~ 3.2m
Thickness of infill walls (tw)	16 cm	13cm ~ 19cm
Compressive strength of infill walls (fw)	1.25 MPa	1.0MPa ~ 1.5MPa

Table 1: Expected mean and range of value for the structural characteristics-related parameters

2.2 Selected analysis type and numerical modelling

The accuracy of any selected procedure for the sensitivity analyses might depends on the type of the selected analysis approach, and the adopted mathematical model that must be consistent with the chosen numerical procedure. Different approaches, varying from nonlinear static to nonlinear dynamic analyses, might be used to conduct a sensitivity study, and estimate the performance of the structure. The sensitivity analyses conducted by Liel and Deierlein [35] were based on the implementation of Incremental Dynamic Analysis [61], using 2-D bare frame structures as numerical model.

Analysis type

In the present study, the sensitivity analyses have been based on the implementation of Adaptive Pushover Analysis, using 3-D bare frames and infilled frames structures as numerical models. One of the advantages in using this type of analysis is its relative simplicity in evaluating the response of inelastic structures, and can provide reasonable estimates of vulnerability functions and fragility curves. Furthermore, when using this type of analysis the variation in the structural stiffness at different deformation levels, and consequently the system degradation can be better accounted for [44].

	Model	Concrete Compressive Strength [MPa]	Steel Yield Strength [MPa]	Transverse Reinforcement Spacing [mm]	Story height [m]	Compressive Strength of Infill [MPa]	Thickness of Infill Panel [cm]
Infilled Frame Structures	M-01	**14**	260	200	2.8	16	1.25
	M-02	**15**	260	200	2.8	16	1.25
	M-03	**16**	260	200	2.8	16	1.25
	M-04	**17**	**260**	**200**	**2.8**	**16**	**1.25**
	M-05	**18**	260	200	2.8	16	1.25
	M-06	**19**	260	200	2.8	16	1.25
	M-07	**20**	260	200	2.8	16	1.25
	M-08	17	**200**	200	2.8	16	1.25
	M-09	17	**220**	200	2.8	16	1.25
	M-10	17	**240**	200	2.8	16	1.25
	M-11	17	**280**	200	2.8	16	1.25
	M-12	17	**300**	200	2.8	16	1.25
	M-13	17	**320**	200	2.8	16	1.25
	M-14	17	260	**150**	2.8	16	1.25
	M-15	17	260	**175**	2.8	16	1.25
	M-16	17	260	**225**	2.8	16	1.25
	M-17	17	260	**250**	2.8	16	1.25
	M-18	17	260	200	**2.5**	16	1.25
	M-19	17	260	200	**3.2**	16	1.25
	M-39	17	260	200	2.8	**13**	1.25
	M-40	17	260	200	2.8	**19**	1.25
	M-41	17	260	200	2.8	16	**1.00**
	M-42	17	260	200	2.8	16	**1.50**
Bare Frame Structure	M-20	**14**	260	200	2.8	---	---
	M-21	**15**	260	200	2.8	---	---
	M-22	**16**	260	200	2.8	---	---
	M-23	**17**	**260**	**200**	**2.8**	---	---
	M-24	**18**	260	200	2.8	---	---
	M-25	**19**	260	200	2.8	---	---
	M-26	**20**	260	200	2.8	---	---
	M-27	17	**200**	200	2.8	---	---
	M-28	17	**220**	200	2.8	---	---
	M-29	17	**240**	200	2.8	---	---
	M-30	17	**280**	200	2.8	---	---
	M-31	17	**300**	200	2.8	---	---
	M-32	17	**320**	200	2.8	---	---
	M-33	17	260	**150**	2.8	---	---
	M-34	17	260	**175**	2.8	---	---
	M-35	17	260	**225**	2.8	---	---
	M-36	17	260	**250**	2.8	---	---
	M-37	17	260	200	**2.5**	---	---
	M-38	16	220	100	**3.2**	---	---

Table 2: Infilled and Bare frames structures considered for the sensitivity analysis

Numerical modelling

A reinforced concrete member can be modeled with three constitutive material models: unconfined concrete (corresponding to the cover), confined concrete (corresponding to the core concrete) and reinforcing steel. Fiber-based structural modelling, which allows to discretize the cross section of the member to account for the different behaviour of cover and core concrete and steel, was adopted to model reinforced concrete members. By modelling separately the three constitutive material and their distribution over the cross-section the progression of

nonlinear phenomena in the concrete member are more accurately simulated and hence one can capture more accurately response effects on such elements.

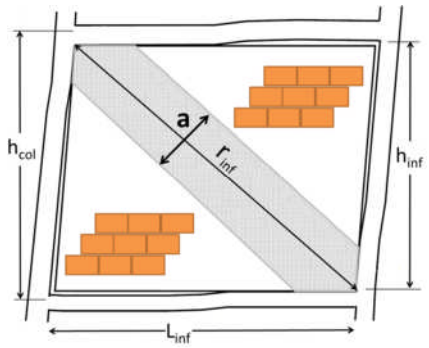


Figure 1: Equivalent diagonal strut representation of an infill panel

For infill panels, the buildings were modeled considering 50% of masonry infills [46]. Diagonal strut model, which has been the most frequently used by researchers and adopted in many documents and guidelines [1, 10, 40, 43], was implemented in this study (Figure 1). Each infill panel is simulated with a pair of compression struts. The equivalent strut "*a*" is computed using the formula based on the work of Mainstone and Weeks [39] and Mainstone [38]:

$$a = 0.175\left(\lambda_I\ h_{col}\right)^{-0.4} r_{\text{inf}} \quad , \quad \lambda_I = \left[\frac{E_m t_{inf} sin2\theta}{4E_f\ I_{col} h_{inf}}\right]^{\frac{1}{4}} \tag{1}$$

Global threshold damage states

With regard to the global threshold damage states, three global limit states: Slight Damage, Moderate Damage, and Near Collapse have been estimated from the analysis as a progression of local damage through several structural and non-structural elements. This is done by calculating for each element geometry and material characteristics, the ultimate concrete compressive strain [48], considering also the limit of curvature corresponding to the condition of yielding curvature and ultimate curvature, as indicated in Eurocode-8 [20] and FEMA-356 [2].

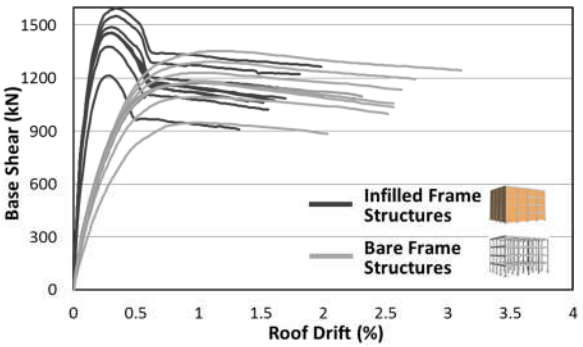


Figure 2: Resulted adaptive pushover curves for infilled frame and bare frame structures.

2.3 Selected models

Forty-two 3-D models, infilled frames and bare frames structures, were analyzed as shown in Table 2. For the considered structural characteristics-related parameters, the values were changed slightly representing the range the most probable for the case of existing low-

ductility buildings constructed with respect to earlier seismic codes. The influence of these variations in the parameters' values has been observed in terms of deformation capacity for different damage conditions, obtained from adaptive pushover analysis. The response of each frame in terms of capacity curve is shown in Figure 2.

3 EFFECT OF STRUCTURAL CHARACTERISTICS-RELATED PARAMETERS

Figure 3 shows the influence of the variation in the structural characteristics-related parameters' values on the structure response, for different damage condition in terms of roof drift. Table 3 summarizes the level of sensitivity of the response to the change for each parameter in terms of Coefficient of Variation (CV), defined as ratio of standard deviation by mean value, and the percentage of difference (Diff) in deformation capacity for different damage condition.

The result of sensitivity analysis has shown that structural characteristics-related parameters are found to have a significant effect on the structural response, for different damage condition. Indeed, at the highest level of damage a remarkable variation (CV reaches a value up to 38%) in terms of deformation capacity (roof drift) has been observed even for a modest variation (CV = 12.7%) in compressive strength of concrete, as seen in Figure 3a (see Table 3); however, no difference in structure response has been found at the lowest level of damage, i.e. Slight Damage.

For tensile strength of steel, the effect has been found to be pretty different comparing to the compressive strength (Figure 3b). The effect is almost insignificant. For a CV= 16.1% of tensile strength, the CV in deformation capacity increase very slight-ly from Slight Damage to Moderate Damage and attained a value of only 9.2%, and then decrease to 7% at near collapse.

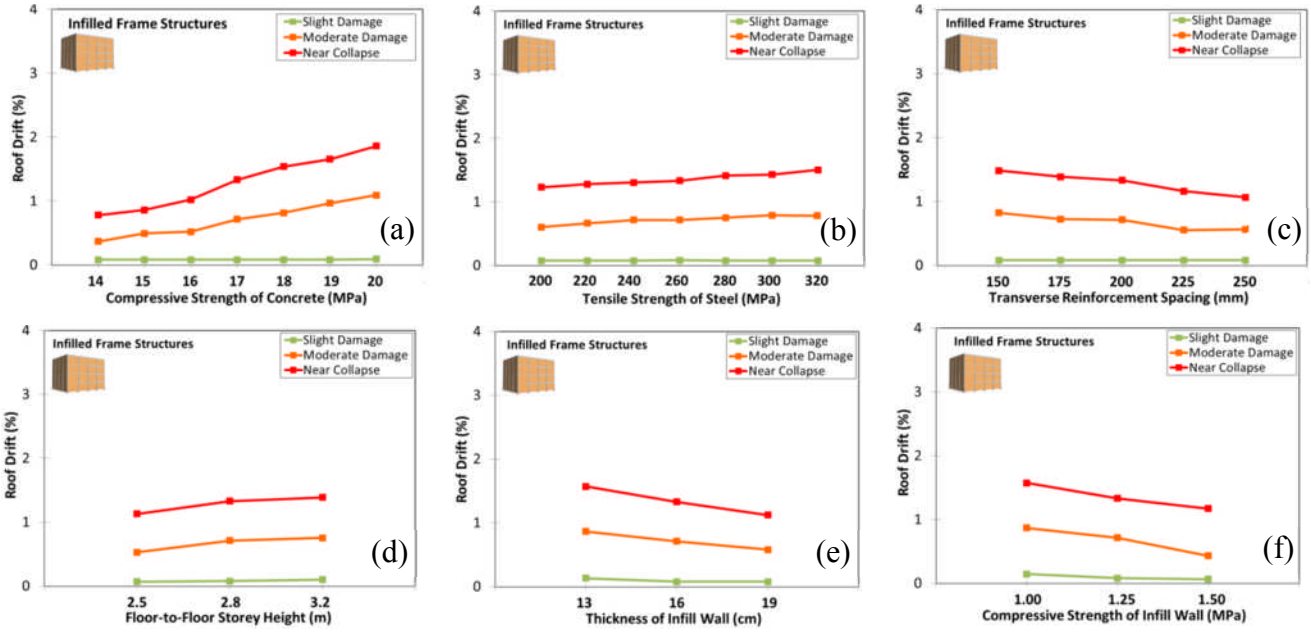


Figure 3: Sensitivity of the structure response to the variation in structural characteristics-related parameters' values. (a) Variation in compressive strength of concrete. (b) Variation in tensile strength of steel. (c) Variation in transverse reinforcement spacing. (d) Variation in storey height. (e) Variation in thickness of infill wall. (f) Variation in compressive strength of infill wall.

Parameters	Parameters' values		Slight Damage		Moderate Damage		Near Collapse	
	Range of Value	CV [%]	CV [%]	Diff. [%]	CV [%]	Diff. [%]	CV [%]	Diff. [%]
Strength of reinforced concrete	14MPa ~ 20MPa	12.71	4.13	11.11	37.47	197.56	32.28	139.08
Tensile strength of steel	200MPa ~ 320MPa	16.62	6.24	12.50	9.22	30.80	7.12	22.27
Transverse reinforcement spacing	150mm ~ 250mm	19.76	0.00	0.00	17.01	48.39	13.24	39.50
floor-to-floor Story height	2.5m ~ 3.2m	12.39	19.16	45.09	17.96	42.32	10.59	22.93
Thickness of infill walls	13cm ~ 19cm	18.75	31.49	66.67	19.85	49.23	16.65	39.68
Compressive strength of infill walls	1.0MPa ~ 1.5MPa	20.00	44.30	128.57	33.17	102.08	14.90	34.35

Table 3: Effect of the variation in the structural characteristics-related parameters' values on the structure response

In terms of ductility, the transverse reinforcement spacing was accounted for by adopting a certain range of values that are with respect to the result of structural characteristics assessment in existing buildings [19, 28]. Ac-cording to the result of sensitivity analysis, the structural response has been found to be moderately affected to the full range of variation in transversal reinforcement spacing (s=150 to 250mm), as shown in Figure 3c. For a variation of spacing CV = 19.76%, the CV in structural response attained a value of 18% and 10.6% for Moderate damage and near collapse, respectively. At Slight Damage level, no difference was observed in the structural response.

Floor-to-floor story height also shows a moderate effect on the seismic performance of the structure (see Figure 3d). The full range of variation CV = 12.4% leads to a remarkable difference in the de-formation capacity at different damage condition (CV in deformation capacity reaches value from 10.6 to 19.2%).

The effect of variation in the characteristics of in-fill walls was examined in terms of compressive strength and the thickness of infill walls. The sensitivity analysis was conducted for values range from 13cm to 19cm for thickness and 1.0MPa to 1.5MPa for compressive strength and of masonry infill walls, as shown in Figures 3e and 3f, respectively. According to the result of analyses, the two parameters have shown significance effect on the structure performance, at Slight to Moderate Damage condition. For the full range of variation of the thickness of infill walls, 18.75%, the structure response has been found to be CV=31.5% at Slight Damage and decrease to 19.85% at Moderate Damage. For CV=20% in the compressive strength of infill walls, the variation in structure response has been found to be CV=44.3% at Slight Damage and decrease to 33.2% at Moderate Damage. Both parameters show a significantly reduced effect on the structural response at Near Collapse. The variation in structure response has been found to be CV=16.65% for the full range of variation of compressive strength and 14.9% for the full range of variation of thickness of infills. This can be explained by the fact that the damage in infills in general occur at the early stage comparing to the RC members (see Figure 2, softening branch of the curve); hence, the infills will start to have less effect with the increase of damage.

Taking into consideration the class of buildings used in the analyses (which is low-ductility buildings characterized by poor quality of materials, workmanship and detailing), the different results shown above clearly reveal the significant effect that structural characteristics-related parameters variation might have on estimating structural response. It is to note that in the literature there have been some re-searchers who believe that the uncertainty in structural characteristics-related parameter such as mechanical properties, for instance, might be considered as not important as much as the uncertainty in the seismic record [45].

4 EFFECT OF NUMERICAL MODEL COMPLETNESS

Aiming to investigate the effect of numerical model completeness, a comparative analysis is performed between the two types of modelling frames systems, infilled frame with bare frame systems (Figure 4). For the same structural characteristics configuration, the infilled frame and bare frame models lead to a remarkable difference in estimating/capturing the response of the building (bias in deformation capacity), as shown in the Figure 4, and in Table 4. By considering the entire structural characteristics con-figuration, the computed mean value of deformation capacities from bare frame models has been found to be 6 times greater than the one calculated from in-filled frame models, at Slight Damage level. At the Moderate Damage level, the difference in the structural response between infilled frame and bare frame structures is also observed. The resulted mean value from bare frame models is found to be 2.2 times greater than the value from infilled frame models. For Near Collapse, this factor, in terms of mean value, is estimated to have a value of 1.8.

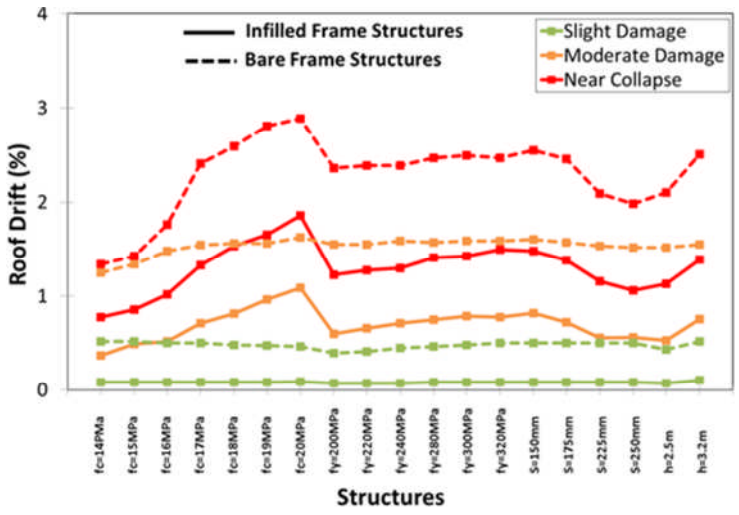


Figure 4: Comparison between the use of infilled frame and bare frame models for different structural characteristics configuration.

	Roof Drift					
	Slight Damage		Moderate Damage		Near Collapse	
	Mean [%]	CV [%]	Mean [%]	CV [%]	Mean [%]	CV [%]
Infilled Frame	0.08	8.71	0.69	24.88	1.30	20.35
Bare Frame	0.48	7.54	1.53	5.96	2.29	18.10
Factor	6		2.2		1.8	

Table 4: Sensitivity of structural response to the contribution of masonry infill panels.

Regarding the above outcomes (i.e. the observed differences in deformation capacity between infilled frame and bare frame systems), it is worth to mention that modelling of infill is also associated to many other complex parameters that can be a source of significant uncertainty, such as, reduced strut width, strain at maximum stress, ultimate strain [41]. These parameters are in general calibrated directly from experiment. On the other hand, it should be recalled that in this study the masonry infills were modeled using equivalent diagonal strut

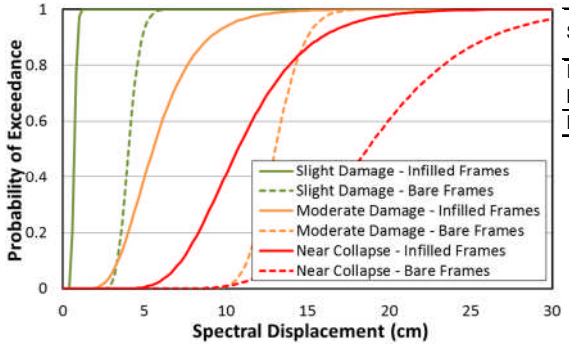
model which is belonging to the macro model approach. In general, models from this approach are considered as simple, involving relatively modest calculations effort and computing time. However, there also numerous models which have been proposed in the literature and which are classified as belonging to the micro model approach. Models from this later approach are based on a finite element representation [24, 51, 52].

In order to derive fragility curves, the transformation of adaptive pushovers curves, defined in terms of base shear vs. top displacement, into capacity curves, defined in terms of pseudo spectral acceleration vs. spectral displacement, was carried out using the standard approach documented in many codes of practice, e.g. ATC-40 [4]; HAZUS-MH MR3 [23]. Fragility curves have been derived by selecting thirteen (13) infilled frame models, and thirteen (13) bare frame models (see Figure 4 for the selected models). Assuming a lognormal distribution (common assumption in seismic studies), fragility curves are defined as the conditional probability of being in or exceeding, a particular damage state ds_i, given the spectral displacement, S_d:

$$P[ds \geq ds_i \mid S_d] = \Phi\left[\frac{1}{\beta_{ds_i}} ln\left(\frac{S_d}{\overline{S}_{d,ds_i}}\right)\right] \quad (3)$$

where, $\overline{S}_{d,ds_i}$ is the median value of spectral displacement at which the building reaches the threshold of damage state ds_i ; β_{ds_i} is the standard deviation of the natural logarithm of spectral displacement for damage state ds_i ; Φ is the standard normal cumulative distribution function.

Using the aforementioned procedure, Figure 5 shows the fragility curves that have been derived for each system, i.e., infilled frame and bare frame structures. Each fragility curve is defined by a median value of spectral displacement that corresponds to the threshold of that damage state, and by the variability (β) associated with that damage state. These two parameters are estimated using the First-Order Second-Moment (FOSM) method. Detailed information about the models can be found in D'Ayala and Meslem [63].



System	Slight Damage		Moderate Damage		Near Collapse	
	Median [mm]	β	Median [mm]	β	Median [mm]	β
Infilled Frames	7	0.18	55	0.38	107	0.30
Bare Frames	40	0.15	130	0.11	187	0.26
Factor	5.8		2.4		1.7	

Figure 5: Comparisons of fragility curves of the structures with and without considering the contribution of masonry infill walls.

It is evident form Figure 5 the role played by the inclusion or exclusion of the masonry infill in the modelling. The exclusion of infills' contribution leads to a significant bias in fragility curves. The median capacity varies by a factor of 5.8, 2.4, and 1.7 for Slight Damage, Moderate Damage, and Near Collapse, respectively. Moreover, when the infilled RC building

is modeled as bare frame structure, the resulted fragility curves show greater lateral displacement capacity for all damage levels; whereas, the building is found to be more vulnerable when the infilled frame model is used. Indeed, the result of pushover analysis has shown (either for infilled frame or bare frame structures) that the first-storey mechanism was the most observed, and the presence of infills leads to the occurrence of this mechanism at earlier stage comparing to the case of bare frame structures. It should be noted that difficulties have been encountered to predict shear failure which is still not fully understood despite much experimental research and analysis. In fact, the shear column failure might have a significant effect on the structure performance, especially for infilled building designed without considering horizontal actions, or building with low concrete strength.

With regards to the dispersion, β, a simplification has been used in the literature in the expression of the uncertainty in the structure capacity. For instance, Kappos et al. [30] constructed fragility curves by adopting value of 0.3 and 0.25 for the uncertainty in the capacity for low and high code buildings, respectively, assuming that these values are for all damage states. These values have been suggested by FEMA-NIBS [23]. Throughout the study by Shahzada et al. [57] a same value of 0.3 was assigned for the uncertainty associated with the capacity curve of buildings for all damage states, as it is proposed in Wen et al. [62]. Satter and Liel [56] and Raghunandan et al. [49] have used a value of 0.5, which has been suggested based on previous research work by Liel et al. [34], to account for uncertainty due to the structural modelling, for Collapse level only. However, the results of present study have clearly shown that the value of dispersion, β, is not the same for all damage states and that the trends from one state of damage to next not necessarily linear, and not systematic. For the case of building that has been investigated in this study, the value of β is found to be bigger at the Moderate Damage for the case of infilled frame model ($\beta = 0.38$), while for bare frame the biggest value is found to be at Near Collapse ($\beta = 0.26$). On the other hand, β is found to be smaller at the Slight Damage for the two modelling option ($\beta = 0.18$ for infilled frame, and 0.15 for bare frame model).

5 CONCLUSIONS

- This present study was devoted to examine the influence in modelling the building capacity-related parameters in aim to probe the issue of their associated uncertainty in predicting the seismic performance and derivation of fragility functions.
- It was clearly observed that special care should be given when assigning values to represent the structural details, especially, material characteristics-related values. Reinforced concrete strength-related variation values have shown a significant effect on the building capacity, and this effect increase with the progress of damage condition.
- The comparison of fragility curves between the two modelling types, infilled and bare frames, indicate a significant difference in predicting the seismic performance of the building. Modelling building as bare frame structure lead to lowest risk of damage, however, the building is found to be more vulnerable if the infilled frame system is adopted.
- Trends in dispersion from one state of damage to next and from one modelling option to next might not necessarily be linear, and monotonic.
- For the masonry infills, the two parameters considered in the sensitivity analysis are compressive strength and thickness of infills. However, this element is also associated to many other complex parameters that can be a source of significant uncertainty, such as,

reduced strut width, strain at maximum stress, ultimate strain. These parameters are in general calibrated directly from experiment.

- Difficulties that might be encountered to predict shear failure which is still not fully understood despite much experimental research and analysis.
- The sensitivity analyses was conducted for low-ductility RC buildings designed according to earlier seismic codes and which are, in general, characterized by poor quality of material. Hence, more investigation should be conducted for building with high compressive strength in aim to analyse the sensitivity of different capacity-related parameters on seismic performance prediction and derivation of vulnerability curves.

REFERENCES

[1] American Society of Civil Engineers (ASCE), *Seismic rehabilitation of existing buildings.* ASCE Standard ASCE/SEI 41-06, Southpointe, Canonsburg, PA., 2006.

[2] American Society of Civil Engineers (ASCE), *FEMA-356: Prestandard and commentary for the seismic rehabilitation of buildings.* Federal Emergency Management Agency, Washington, DC, 2000.

[3] Applied Technology Council (ATC), *Recommended methodology for quantification of building system performance and response parameters*, ATC-63 90% Draft. Redwood City, CA, 2007.

[4] Applied Technology Council (ATC), *Seismic evaluation and retrofit of concrete buildings*, ATC-40. Redwood City, CA, 1996.

[5] Applied Technology Council (ATC), *Seismic performance assessment of buildings, Volume 1 - Methodology*, ATC-58-1 75% Draft. Redwood City, CA, 2011.

[6] B.O. Ay, and A. Erberik, Vulnerability of Turkish low-rise and mid-rise reinforced concrete frame structures. *Journal of Earthquake Engineering*, 12, 2-11, 2008.

[7] B.O. Ay, *Fragility based assessment of low-rise and mid-rise reinforced concrete frame buildings in Turkey*, Middle East Technical University, MSc. Thesis, 2006.

[8] A. Bakhshi, and K. Karimi, Method of developing fragility curves a case study for seismic assessment of masonry buildings in Iran. *7th International Congress in Civil Engineering*, Tehran, Iran, 2006.

[9] I.E. Bal, H. Crowley, and R. Pinho, Detail assessment of structural characteristics of Turkish RC buildings stock for loss assessment models. Soil Dynamic and Earthquake Engineering, 28, 914-932, 2008.

[10] Canadian Standards Association (CSA), *Design of masonry structures CSA-S304.1-04*, Ontario, Canada, 2004.

[11] F. Colangelo, Pseudo-dynamic seismic response of reinforced concrete frames in lled with non-structural brick masonry. *Earthquake Engineering and Structural Dynamics*, 34,1219-1241, 2005.

[12] D.F. D'Ayala, Force and displacement based vulnerability assessment for traditional buildings. *Bulletin of Earthquake Engineering*, 3, 235-265, 2005.

[13] D.F. D'Ayala, R. Spence, C. Oliveira, and A. Pomonis, Earthquake loss estimation for Europe's historic town centres. *Earthquake Spectra*, 13, 773-793, 1997.

[14] D.F. D'Ayala, and S. Paganoni, Assessment and analysis of damage in L'Aquila historic city center after 6th April 2009. *Bulletin of Earthquake Engineering*, 9, 81-104, 2010.

[15] M. Dolsek, Incremental dynamic analysis with consideration of modelling uncertainties, *Earthquake Engineering and Structural Dynamics*, 38, 805-825, 2009.

[16] M. Dolsek, and P. Fajfar, The effect of masonry infills on the seismic response of a four storey reinforced concrete frame-a probabilistic assessment, *Engineering Structures*, 30, 1991-2001.

[17] C. Dymiotis, A. Kappos, and M. Chryssanthopoulos, Seismic reliability of masonry-infilled rc frames. *Journal of Structural Engineering*, 127, 296-305.

[18] Earthquake Engineering Field Investigation Team (EEFIT), *The Kocaeli, Turkey earthquake of 17 August 1999*. Institution of Structural Engineers, a Field Report by EEFIT, 2003.

[19] Earthquake Engineering Research Institute (EERI), *Kocaeli. Tyurkey, earthquake of August 17, 1999: reconnaissance report*. Earthquake Spectra, 2000.

[20] European Committee for Standardization (CEN), *Design of structures for earthquake resistance, Part 1: General rules, seismic actions and rules for buildings*, Eurocode-8, ENV 1998-1-1, Brussels, Belgium, 2004.

[21] F.L. Ellul, *Static nonlinear finite element analysis of low engineered masonry infilled reinforced concrete frames for seismic assessment*, PhD Thesis, University of Bath, 2006.

[22] G. Erol, E. Yuksel, H. Saruhan, G. Sagbas, P.T. Tuga, and H.F. Karadogan, A complementary experimental work on brittle portioning walls and strengthening by carbon fibers. Proceeding of the 13th World Conference on Earthquake Engineering, Vancouver, Canada, 2004.

[23] Federal Emergency Management Agency – National Institute of Building Sciences (FEMA-NIBS), Multi-hazard loss estimation methodology – earthquake model: HAZUS®MH Advanced engineering building module - Technical and user's manual, Washington DC., 2003.

[24] A.K. Ghosh, and A.M. Made, Finite element analysis of infilled frames. *Journal of Structural Engineering*, 128, 881-889, 2002.

[25] P. Gulkan, M. Aschhein, and R. Spence, *Reinforced concrete frame building with masonry infills*, World Housing Encyclopedia, Report No. 64, 2002.

[26] H.A. Howary, and S.S.F. Mehanny, Seismic vulnerability evaluation of RC moment frame buildings in moderate seismic zones. *Earthquake Engineering and Structural Dynamics*, 40, 215-235, 2011.

[27] I. Iervolino, G. Manfredi, M. Polese, G.M. Verderame, and G. Fabbrocino, Seismic risk of RC building classes. *Engineering Structures*, 29, 813-820, 2007.

[28] M. Inel, and H.B. Ozmen, Effects of plastic hinge properties in nonlinear analysis of reinforced concrete buildings. *Engineering Structures*, 28, 1494-1502, 2006.

[29] H. Jiang, H. Lu, and L. Chen, Seismic fragility assessment of RC moment-resisting frames designed according to the current Chinese seismic design code. *Journal of Asian Architecture and Building Engineering*, 11, 153-160, 2012.

[30] A.J. Kappos, G. Panagopoulos, and G. Penelis, A hybrid method for the vulnerability assessment of R/C and URM buildings. *Bulletin of Earthquake Engineering*, 4 , 391-413, 2006.

[31] R.A. Khan, and T. Naqvi, Reliability analysis of steel building frame under earthquake forces. *International Journal of Emerging Technology and Advanced Engineering*, 2, 356-361, 2012.

[32] M.S. Kircil, and Z. Polat, Fragility analysis of mid-rise R/C frame buildings. *Engineering Structures*, 28, 1335-1345, 2006.

[33] K. Lang, and H. Bachmann, On the seismic vulnerability of existing buildings: A case study of the city of Basel. *Earthquake Spectra*, 20, 43-66, 2004.

[34] A.B. Liel, C.B. Haselton, G.G. Deierlein, J.W. Baker, Incorporating modelling uncertainties in the assessment of seismic collapse risk of buildings. *Structural Safety*, 31, 197-211, 2009.

[35] A.B. Liel, and G.G. Deierlein, *Assessment the collapse risk of California's existing reinforced concrete frame structures: Metrics for seismic safety decisions*. Blume Center Technical Report No. 166, 2008.

[36] L.A. Lourdes, R.R. Lopez, A. Saffar, Development of fragility curves for medium rise reinforced concrete shear wall residential buildings in Puerto Rico. S.A. Elaskar, E.A. Pilotta, G.A. Torres eds. *Mecanica Computacional Vol XXVI,* Cordoba, Argentina, October, 2007.

[37] A. Madan, and A. Hashmi, Analytical prediction of the seismic performance of masonry infilled reinforced concrete frames subjected to near-field earthquakes. *Journal of Structural Engineering*, 134, 1569-1581.

[38] R.J, Mainstone, *On the stiffness and strengths of infilled frame*. Proceedings Institution of Civil Engineers, Supplement IV, 57–90, 1971.

[39] R.J. Mainstone, G.A. and Weeks, *The influence of bounding frame on the racking stiffness and strength of brick walls*. 2nd International Brick Masonry Conference, Stoke-on-Trent, UK, 1970.

[40] Masonry Standards Joint Committee (MSJC), *Building code requirements for masonry structures, ACI 530-02/ASCE 5-02/TMS 402-02*, American Concrete Institute, Structural Engineering Institute of the American Society of Civil Engineers, The Masonry Society, Detroit, 2002.

[41] A. Meslem, and D. D'Ayala, *Toward worldwide guidelines for the development of analytical vulnerability functions and fragility curves at regional level*. 15th World Conference on Earthquake Engineering, Lisbon, Portugal, 2012.

[42] G.V. Mulgund, and A.B. Kulkarni, Seismic assessment of rc frame buildings with brick masonry infills. *International Journal of Advanced Engineering Sciences and Technologies*, 2, 140-147, 2011.

[43] New Zealand Society for Earthquake Engineering (NZSEE), *Assessment and Improvement of the Structural Performance of Buildings in Earthquakes*, 2006.

[44] V.K. Papanikolaou, and A.S. Elnashai, Evaluation of conventional and adaptive pushover analysis I: methodology. *Journal of Earthquake Engineering*, 10, 923-941, 2005.

[45] L. Pasticier, C. Amadio, and M. Fragiacomo, Non-linear seismic analysis and vulnerability evaluation of a masonry building by means of the SAP2000 V.10 code. *Earthquake Engineering and Structural Dynamics*, 37, 467-485, 2008.

[46] T. Paulay, and M.J.N. Priestley, *Seismic Design of Reinforced Concrete and Masonry Buildings*. John Wiley & Sons, Inc, 1992.

[47] M. Polese, G.M. Verderame, C. Mariniello, I. Iervolino, and G. Manferedi, Vulnerability analysis for gravity load designed RC buildings in Naples – Italy. *Journal of Earthquake Engineering*, 12, 234-245, 2008.

[48] M.J.N. Priestley, F. Seible, and G.M.S. Calvi, *Seismic design and retrofit of bridges*. New York: John Wiley & Sons, 1996.

[49] M. Raghunandan, A.B. Liel, H. Ryu, N. Luco, and S.R. Uma, *Aftershock fragility curves and tagging assessment for a mainshock-damaged building*. 15th World Conference on Earthquake Engineering, Lisbon, Portugal, 2012.

[50] P. Rajeev and S. Tesfamariam, Effect of construction quality variability on seismic fragility of reinforced concrete building. *Proceedings of the Ninth Pacific Conference on Earthquake Engineering Building and Earthquake-Resilient Society*, Auckland, New Zealand, April 14-16, 2011.

[51] J.R. Riddington, and B. Stafford-Smith, Analysis of infilled frames subject to racking with design recommendations. *The Structural Engineer*, 55, 263-268, 1977.

[52] C.E. Rivero, and W.H. Walker, *An analytical study on the interaction of frames and infill masonry walls*. 8th World Conference on Earthquake Engineering, Proceddings, Vol. IV, 591-598, 1984.

[53] T. Rossetto, and A. Elnashai, A new analytical procedure for the derivation of displacement-based vulnerability curves for populations of RC structures. *Engineering Structures*, 27, 397-409, 2005.

[54] H. Ryu, N. Luco, H.R. Uma, and A.B. Liel, Developing fragilities for mainshock-damaged structures through incremental dynamic analysis. *Proceedings of the Ninth Pacific Conference on Earthquake Engineering Building and Earthquake-Resilient Society*, Auckland, New Zealand, April 14-16, 2011.

[55] S. Salvador, A. Monica, S. Michael, J. Cristian, and E. Luis, Seismic response of reinforced concrete buildings in Caracas, Venezuela. *The 14th World Conference on Earthquake Engineering*, Beijin, China, October 12-17, 2008.

[56] S. Sattar, and A.B. Liel, *Seismic performance of reinforced concrete frame structures with and without masonry infill walls*. 9th U.S. National and 10th Canadian Conference on Earthquake Engineering, Toronto, Canada, 2010.

[57] K. Shahzada, B. Gencturk, A.N. Khan, A. Naseer, M. Javed, and M. Fahad, Vulnerability assessment of typical buildings in Pakistan. *International Journal of Earth Sciences and Engineering*, 4, 208-211, 2011.

[58] Turkish Standards Institute (TSE), *TS-500, Building code requirements for reinforced concrete*. Ankara, Turkey, 1985.

[59] S.R. Uma, H. Ryu, N. Luco, A.B. Liel, and M. Raghunandan, Comparison of main-shock and aftershock fragility curves developed for New Zealand and US buildings. *Proceedings of the Ninth Pacific Conference on Earthquake Engineering Building and Earthquake-Resilient Society*, Auckland, New Zealand, April 14-16, 2011.

[60] R. Vacareanu, A.B. Chesca, B. Georgescu, M. Seki, Case study on the expected seismic losses of soft and weak groundfloor buildings. *International Symposium on Strong Vrancea Earthquake and Risk Mitigation*, Bucharest, Romania, October, 2007.

[61] D. Vamvatsikos, and C.A. Cornell, Incremental dynamic *analysis. Earthquake Engineering and Structural Dynamics*, 3, 491-514, 2002.

[62] Y.K. Wen, B.R. Ellingwood, and J. Bracci, *Vulnerability function framework for consequence-based engineering*. Mid-America Earthquake (MAE) Center, Project DS-4 Report, 2004.

[63] D'Ayala, D. and Meslem. A. Derivation of analytical vulnerability functions considering modeling uncertainties. *Proceeding of the 11th International Conference on Structural Safety & Reliability*, New York, 2013.

COMPDYN 2013
4th ECCOMAS Thematic Conference on
Computational Methods in Structural Dynamics and Earthquake Engineering
M. Papadrakakis, V. Papadopoulos, V. Plevris (eds.)
Kos Island, Greece, 12–14 June 2013

DEAGGREGATION OF SEISMIC SAFETY IN THE DESIGN OF REINFORCED CONCRETE BUILDINGS USING EUROCODE 8

J. Žižmond[1]and M. Dolšek[2]

[1] University of Ljubljana, Faculty of Civil and Geodetic Engineering
Jamova 2, 1000 Ljubljana, Slovenia
jzizmond@fgg.uni-lj.si

[2] University of Ljubljana, Faculty of Civil and Geodetic Engineering
Jamova 2, 1000 Ljubljana, Slovenia
mdolsek@fgg.uni-lj.si

Keywords: Factor of Safety, Earthquake-resistant Design, Eurocode, Behavior Factor, Push-over Analysis, Reliability of Structures

Abstract. *Design of earthquake-resistant structures according to Eurocod 8 is not based on the concept of acceptable/tolerable probability of exceedance of the near collapse limit state. Rather than that standard introduces fundamental non-collapse and damage limitation requirements, which are associated with the design seismic action. It is foreseen that the non-collapse requirement is satisfied when the regular structure does not collapse in the case of an earthquake with a return period of 475 years. Probability of such an even in 50 years is 10%. Therefore it is obvious that probability of failure of structures, which would be designed strictly according to the fundamental non-collapse requirement, would be unacceptable for society. Due to factors of safety involved in design the structures withstand much stronger earthquakes in comparison to an earthquake with a period of 475 years. In order to assess which factor of safety have the greatest impact on the overall safety of code-conforming buildings, two multi-storey reinforced concrete buildings were investigated. The strength and the system ductility of the six variants of the structures were evaluated on the basis of the pushover analysis gradually taking into account the requirements of the Eurocode 2 and 8, as well as gradually excluding the design assumptions. Safety in design of the buildings was evaluated by the difference between the calculated and prescribed behaviour factor, by the ratio between the design ground acceleration and that associated with the near collapse limit state, which was assessed using the N2 method, and by the escalation of safety in terms of probability of exceedance of the near collapse limit state. The results of this analysis are discussed in the paper. For the investigated buildings it is shown that the design seismic action has the greatest impact on the yield strength of the structure and the peak ground acceleration, which cause the near-collapse limit state. On the other hand, the partial factors of material strength contribute around 50% to the return period of the near-collapse limit state, whereas the contribution of the capacity design principles to overall safety is minor.*

1 INTRODUCTION

Current standard for earthquake design of buildings Eurocode 8 [1] which is used in Slovenia prescribes that buildings should be design to withstand two fundamental requirements: no-collapse requirement and damage limitation requirement. It is assumed that the non-collapse requirement is satisfied when the structure is designed according to Eurocode 8 provisions taking into account an earthquake with a return period of 475 years. Usually design procedures involve factors of safety since the design is based on simplified elastic analysis method and design acceleration spectrum, which implicitly takes into account the ability of inelastic energy absorption of the structural system. Thus, seismic risk of newly designed structures is only implicitly controlled through the concept of reduction (behavior) factor and capacity design procedure.

In ATC 19 [2] it is discussed based on ATC-3-06 that the reduction factors were intended to reflect reduction in design force vales that were justified on the basis of risk assessment, economics, and nonlinear behavior. Therefore determination of the reduction factors is not trivial. In the basic formulation of the reduction factor it can be shown that it can be defined as the product of equivalent global ductility factor and overstrength factor [3]. However, some other authors, as discussed in ATC 19 [2], defined the reduction factor as the product of period-dependent strength factor, the period-dependent ductility factor, the redundancy factor and in some cases also as the product of the viscous damping factor. A comprehensive evaluation of proposals for strength reduction factors (R_μ) for earthquake-resistant design was done by Miranda and Bertero [4]. They concluded that the ductility-, period- and site-dependent strength reduction factors, together with estimates of the overstrength of the structure, can lead to a more rational and transparent seismic design approach.

However, current building code involves different factors of safety which affect structural configuration (dimensions of structural elements and corresponding reinforcement). In order to identify, which factors have the greatest impact on the seismic safety of code-conforming buildings, seismic safety deaggregation was performed for two reinforced concrete frame buildings which are located in the region with moderate seismicity and designed for ductility class medium. In the paper, the pushover-based method for estimation of the failure probability, which were used in the analysis, are briefly described. Then the factor of safety are defined and assessed for two investigated buildings.

2 SUMMERY OF PUSHOVER-BASED METHOD FOR ESTIMATION OF FAILURE PROBABILITY OF BUILDING STRUCTURES

The basic pushover-based methods are often used to approximately assess risk of near-collapse state of the building (e.g. [5, 6]), which is expressed by the mean annual frequency of exceedance as follows:

$$P_{NC} = \int_0^\infty P\left[NC \mid A_g = a_g \right] \cdot \left| \frac{dH\left(a_g\right)}{da_g} \right| da_g \tag{1}$$

where $P\left[NC \mid A_g = a_g \right]$ is the fragility, i.e. the conditional probability of violating the near-collapse limit state for a given level of ground motion intensity a_g, $H\left(a_g\right)$ is the hazard function approximately representing the probability of exeedance of a_g per year, and NC stands for the near collapse limit state, which can be defined in various manners. The fragility is often defined by assuming lognormal distribution of ground motion intensity which causes the near-

collapse limit state. In this case the fragility can be expressed by using standard normal probability integral $\Phi(\cdot)$:

$$P\left(NC\middle|A_g = a_g\right) = \Phi\left(\frac{\ln\left(a_g\right) - \ln\left(\tilde{a}_{g,NC}\right)}{\beta_{NC}}\right) \tag{2}$$

where $a_{g,NC}$ is the median value of ground motion intensity causing the violation of NC limit state and β_{NC} is the logarithmic standard deviation of $a_{g,NC}$. In the case if the fragility is defined by means of Eq.(2) and if the hazard is assumed linear in log-log domain, the Eq.(1) can be solved in closed-form [7, 8]:

$$P_{NC} \approx H\left(a_{g,NC}\right) \cdot e^{\frac{1}{2} \cdot k_{NC}^2 \cdot \beta_{NC}^2} \tag{3}$$

where k_{NC} is the slope of the hazard curve associated with the near-collapse limit state.

In general case the fragility parameters ($a_{g,NC}$, β_{NC}) are estimated by using nonlinear response history analysis. Such approach is computationally demanding, especially if used in the designs process, which requires several iterations in order to obtain the final structural configuration. Therefore approximate methods are often employed for estimation of the fragility parameters [5, 6, 9]. In the simplest approach, the $a_{g,NC}$ is determined according to the N2 method [10], which involves pushover analysis, often performed by assuming the invariant distribution of lateral forces corresponding to first vibration mode. Based on the results of pushover analysis, the equivalent SDOF model is defined utilizing the transformation factor Γ and the mass of the equivalent SDOF model m^* [10]:

$$\Gamma = \frac{m^*}{\sum_{j=1}^{n} m_j \phi_{1,j}^2}, \quad m^* = \sum_{j=1}^{n} m_j \phi_{1,j} \tag{4}$$

where m_j is the jth storey mass of the structure and $\phi_{1,j}$ is the jth component of the first natural vibration mode, which is normalized to a roof displacement equal to 1. In order to determine the force-displacement relationship of the equivalent SDOF model, the pushover curve has to be idealized. There are many options how the pushover curve is idealized. Recently a web-based application was developed, which enables quadrilateral idealization of the pushover curve and prediction of the approximate relationship between the ground motion intensity measure and the displacement of the equivalent SDOF model [11]. In the most basic case, the pushover curve is idealized by elasto-plastic force-displacement relationship. This approach enables use of inelastic spectra. Consequently the reduction factor due to ductility $R_{\mu,NC}$, i.e. due to the hysteretic energy dissipation of ductile structures [10], corresponding to the near-collapse ductility μ_{NC} can be rapidly estimated as follows [10]:

$$R_{\mu,NC} = \begin{cases} \left(\mu_{NC} - 1\right)\dfrac{T^*}{T_C} + 1 & \cdots \quad T^* < T_C \\ \mu_{NC} & \cdots \quad T^* \geq T_C \end{cases}, \quad \mu_{NC} = \frac{D_{NC}}{D_y} \tag{5}$$

where D_{NC} and D_y are, respectively, the displacement corresponding to the near-collapse limit state and displacement at yielding of the idealized pushover curve, T^* is the period of the equivalent SDOF model and T_C the period between the range of the constant acceleration and

constant velocity of the acceleration spectrum. The reduction factor $R_{\mu,NC}$ and the period T^* are defined as follows [10]:

$$R_{\mu,NC} = \frac{S_{a,NC}}{S_{ay}}, \quad S_{ay} = \frac{F_y}{\Gamma \cdot m^*}, \quad T^* = 2\pi\sqrt{\frac{m^* \cdot D_y}{F_y}} \tag{6}$$

where $S_{a,y}$, $S_{a,NC}$, F_y are, respectively, the spectral acceleration causing 'yielding' of the equivalent SDOF model, the spectral acceleration causing the near-collapse limit state, and the yield displacement of the idealized force-displacement relationship.

When fragility parameters are assessed by using the above-described procedure, the β_{NC} has to be predetermined according to previous studies (e.g. [6, 9, 11]). However, the $a_{g,NC}$ can be calculated based on the shape of the elastic acceleration spectrum used for the assessment of the $S_{a,NC}$, which is determined for the known μ_{NC} and by employing Eq.(5) and Eq.(6).

3 FACTORS OF SAFETY ASSOCIATED WITH EARTHQUAKE-RESISTANT DESIGN OF BUILDINGS

The objective of this study is deaggregation of the seismic safety against near-collapse performance of buildings designed according the Eurocode 8 [1]. It is worth to emphasize that discussion regarding the adequacy of seismic safety of code-conforming buildings is not the topic of this study. Therefore it is assumed that the reinforced concrete buildings designed in compliance with all provisions of Eurocode 2 [12] and Eurocode 8 are safe, although this is a subject for debate.

Standards for earthquake-resistant design of structures involve several provisions, which have an impact on the seismic safety of the structure. Additionally, the actual amount of reinforcement in structural elements is larger than that obtained from design. However, it has been assumed that the following factors have a direct or indirect impact on the seismic safety of the facility:

a) seismic design action
b) minimum requirements of Eurocode 2 for detailing and dimensioning of structural elements
c) minimum requirements of Eurocode 8 for detailing and dimensioning of structural elements
d) ratio between the actual (mean) and design strength of material
e) ratio between the actual and required amount of reinforcement in structural elements
f) capacity design principles prescribed in Eurocode 8.

In order to quantify how the above-mentioned factors affect the seismic safety of the code-conforming building, the overall factor of safety and so-called partial factor of safety are defined as follows:

$$FS = \frac{y_{all}}{y_0} \tag{7}$$

$$\delta FS_k = \frac{y_k}{y_{k-1}} \tag{8}$$

where y_{all} is the parameter of the code-conforming structure or its seismic performance, y_0 is the same parameter but assessed for the case when the seismic design action is the only con-

sidered factor which affects structural configuration, and the y_i corresponds to the case when first *k*th number of factors from the list above are considered in the design of a building. According to this definition the overall factor of safety is defined as the product of the partial factor of safety:

$$FS = \prod_{k=1}^{n} \frac{y_k}{y_{k-1}} \tag{9}$$

where *n* is number of all factors which affect the seismic safety of the code-conforming buildings.

For simplicity reasons, the above-defined factors of safety are assessed for the global structural parameters (F_y, μ_{NC}), which are obtained from the idealized pushover curves, and for factors of safety associated with structural performance, such as $a_{g,NC}$, P_{NC} (or $T_{R,NC} = 1/P_{NC}$) and q_{NC}, which can be understood as actual (realized) behaviour factor (Eurocode 8). The q_{NC} is herein defined according to Fischinger and Fajfar [3] as follows:

$$q_{NC} = R_s \cdot R_{\mu,NC} \tag{10}$$

where R_s is the reduction factor due to overstrength and $R_{\mu,NC}$ the reduction factor due to the hysteretic energy dissipation of ductile structures (Eq.(6)). Note that a value of a global structural parameter and a value of performance parameter depend on the safety measures, which are considered in the design. However, the overstrength reduction factor is defined as ratio between actual F_y and design lateral strength F_d:

$$R_s = \frac{F_y}{F_d} \tag{11}$$

Design lateral strength F_d is herein determined according to the modal analysis taking into account the effect of first vibration mode $\{\phi_1\}$ and corresponding spectral acceleration $S_a(T_1)$:

$$F_d = [M] \cdot \{\phi_1\} \cdot \Gamma \cdot S_a(T_1) \tag{12}$$

4 VARIANTS OF PARTIALLY CODE-CONFORMING STRUCTURES

Six variants of partially code-conforming structures were defined (Table 1) in order to gradually take into account some of factors, which have an impact on the seismic safety of buildings designed according to Eurocodes. The variant 0 ideally satisfy only the fundamental 'non-collapse' requirement associated with the design seismic action. This is actually artificial variant of the structure, since it is assumed that it does not have redundancy and overstrength, but only the available ductility, which is equal to the behaviour factor assumed in the design. Consequently, this structure meet the near-collapse limit state in the case of the reference seismic action associated with a reference probability of exceedance, which is herein assumed 10% in 50 years.

All additional structural variants were indeed designed and its performance was assessed with the N2 method (Section 1). Therefore the effect of redundancy is automatically considered in the assessment of factors of safety. Note that each subsequent structural variant takes into account the additional design safety measure, as presented in Table 1. Such escalation of safety measures was defined in order to achieve gradual increase of buildings strength and near-collapse ductility between most of structural variants.

The largest difference between the reinforcement in the columns and beams was observed for variants 1 and 2 due to significantly greater requirements of the Eurocode 8 for minimum amount of longitudinal and transverse reinforcement in the columns and beams. The difference in the reinforcement of columns due to capacity design principles was observed only for transverse reinforcement in bottom stories of the building, since the minimum amount of the reinforcement was adequate for most parts of columns of the 8-storey and 11-storey building. This was not the case of the beams, as expected, since consideration of the capacity design principles caused larger amount transverse reinforcement in all stories. Additional observation was made for variants 3 and 4. In this case the difference in the amount of reinforcement in the columns of the structural variants is practically negligible since the utilization rate (i.e. the ratio between the actual and calculated amount of reinforcement) of the columns was almost equal to 1. However, utilization ratio for the beams was slightly smaller. Therefore actual amount of reinforcement in the beams slightly exceeded the amount of required reinforcement.

Variant of structure	Design safety measures					
	a) design seismic action	b) minimum requirements Eurocode2	c) minimum requirements Eurocode 8	d) actual material strength	e) actual amount of reinforcement	f) capacity design principles
0	x					
1	x	x				
2	x	x	x			
3	x	x	x	x		
4	x	x	x	x	x	
5	x	x	x	x	x	x

Table 1: Description of structural variants associated with gradual consideration of design safety measures.

5 EXAMPLES

5.1 Description of buildings and structural models

The 11-storey and 8-storey reinforced concrete frames (Figures 1 and 2) were designed according to provisions of Eurocode 2 and 8. Both buildings were designed for ductility class M and reference peak ground acceleration of 0.25 g. It was assumed that the 11-storey and the 8-storey building are located on soil type B and C, respectively. The behaviour factor was assumed 3.9. The quality of reinforcing steel was S500B, whereas the concrete C35/45 and C30/37 was used, respectively, for the 11- and 8-storey building. Some global characteristics of structures and design parameters are presented in Table 2.

The structural model in general follows the Eurocode 8 requirements for the modelling of structures as discussed elsewhere [13]. The beam and column flexural behaviour is therefore modelled by one-component lumped plasticity elements, composed of an elastic beam and two inelastic rotational hinges (defined by a moment-rotation relationship). The element formulation is based on the assumption of an inflexion point at the midpoint of the element. The gravity load is represented by the uniformly distributed load on the beams, and by the concentrated loads at the top of the columns. For the beams, the plastic hinge is used for major axis bending only. For the columns, two independent plastic hinges for bending about the two principal axes are used. The moment-rotation relationship before strength deterioration is

modelled by a bi-linear relationship. A linear negative post-capping stiffness is assumed after the maximum moment is achieved. The axial force due to gravity loads is taken into account when determining the moment-rotation relationship for the columns, while in the case of the beams zero axial force and the rectangular cross-sections were assumed. The ultimate rotation Θ_u in the columns and beams at the near collapse (NC) limit state, which corresponds to a 20% reduction in the maximum moment, was estimated by means the EC8-3 formulas [14]. The parameter γ_{el} was assumed to be equal to 1.5. For the structural variant 1 (no seismic detailing), the ultimate rotations were multiplied by a factor of 0.825 [14]. Post-capping negative stiffness was calculated by assuming the ratio between the rotation at zero strength and the rotation corresponding to the maximum moment equal to 3.5. For structural variants No. 3, 4 and 5, the seismic performance assessment based on actual (mean) strength of material. For these variants the mean concrete strength was assumed 8 MPa greater than the characteristic compressive strength, whereas for the steel, the mean strength (570 MPa) was assumed 14 % greater than the characteristic steel strength.

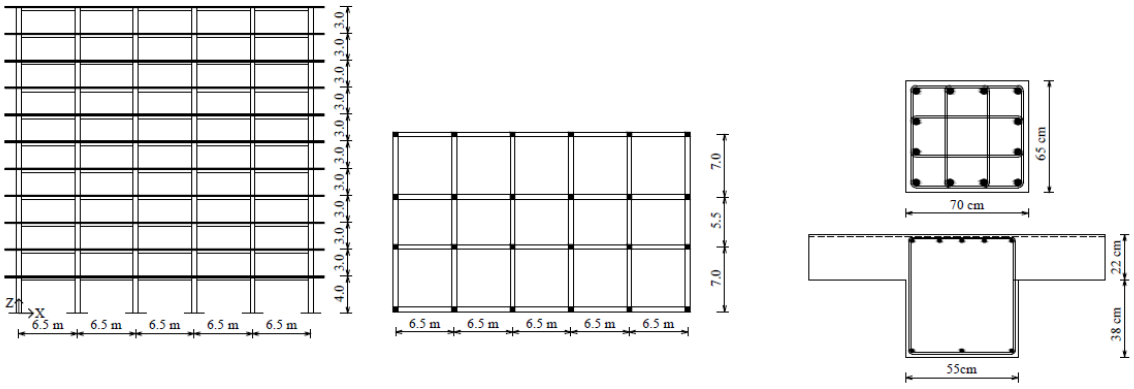


Figure 1: The elevation, plan view and reinforcement in typical columns and beams of code-conformed 11-storey buildings (variant 5).

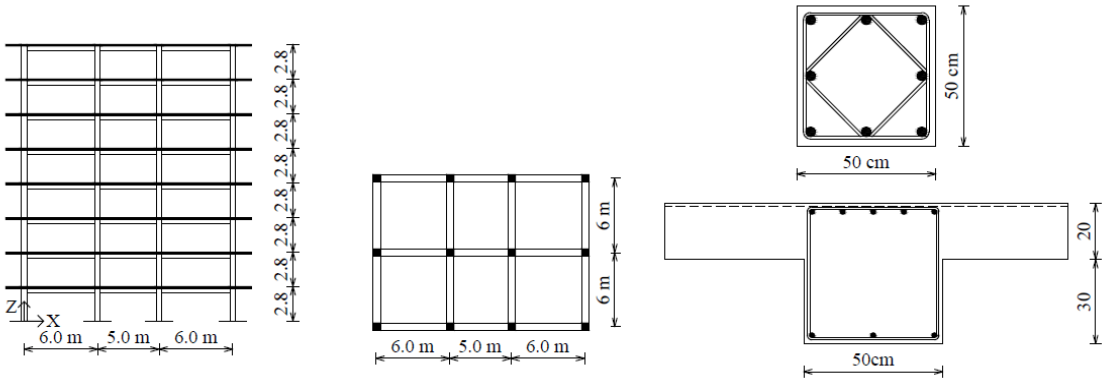


Figure 2: The elevation, plan view and reinforcement in typical columns and beams of code-conformed 8-storey buildings (variant 5).

	Total mass [t]	Period [s]	$a_{g,d,R}$	Soil factor	F_b/W	$F_{b,1}/W$
8-storey	2326	1.45	0.25	1.15	6.5%	6.0%
11-storey	10218	1.92	0.25	1.2	4.6%	3.9%

Table 2: The mass, the first vibration period, the reference peak ground acceleration of on type A ground, the soil factor S, the ratio between the design base shear and the weight and the ratio between the 'first-mode' base shear and the weight of 8-storey and 11-storey buildings.

All the analyses were performed with OpenSees [15], using the PBEE toolbox [13], which is a simple yet effective tool for the seismic performance assessment of reinforced concrete frames by using simplified nonlinear models. The PBEE toolbox includes different functions for the calculation of the moment-rotation relationship of the plastic hinges in the columns and beams, functions for the generation of the tcl input code for OpenSees, functions for the post-processing of the analysis results, and functions for structural performance assessment. More details regarding the PBEE toolbox can be found elsewhere [13].

It should be emphasized that the ultimate rotations in the beams and columns as modelled in this comparative study are lower than the mean values since γ_{el} was assumed to be equal to 1.5. Consequently, the deformation capacity is also underestimated. Additionally, the strength and the stiffness of the beams are also underestimated since the slab effective width was neglected (rectangular sections). Therefore, the expected strength, deformation capacity and the $a_{g,NC}$ of the investigated buildings are likely to be greater than those obtained in this study.

5.2 Pushover analyses

The pushover analyses were performed for X (longitudinal) direction (Figure 1 and 2) using the invariant force vector were which corresponded to product of the storey masses and the first vibration mode ($\Phi_{1,X,11\text{-storey}}$=[0.12 0.24 0.37 0.49 0.60 0.70 0.79 0.86 0.92 0.96 1], $\Phi_{1,X,8\text{-storey}}$=[0.11 0.28 0.44 0.60 0.73 0.84 0.91 1]). The pushover curves and corresponding idealized force-displacement relationship are presented in Figures 3 and 4. Note that the idealized force-displacement relationship ends at displacement which corresponds to the near-collapse limit state, which is obtained when all the rotation in all the columns or beams in one storey exceeds the corresponding ultimate rotation. It should be emphasized that the pushover curve for variant 0 is not available, since it is assumed that variant 0 does not have redundancy and the overstrength, but only the 'available' ductility, which is equal to the behaviour factor assumed in the design.

For the investigated buildings it can be observed that the capacity design principles do not have the impact on the buildings' strength and just small influence on the deformation capacity. On the other hand, it seems that the greatest factor-of-safety can be associated with the material safety factors (see difference between pushover curve corresponding to variant 2 and 3). Moderate impact on the buildings' strength is observed due to the minimum requirements for reinforcement according to Eurocode 8 (variants 1 and 2) and the ratio between the actual (selected) and required (calculated) amount of reinforcements (variants 3 and 4).

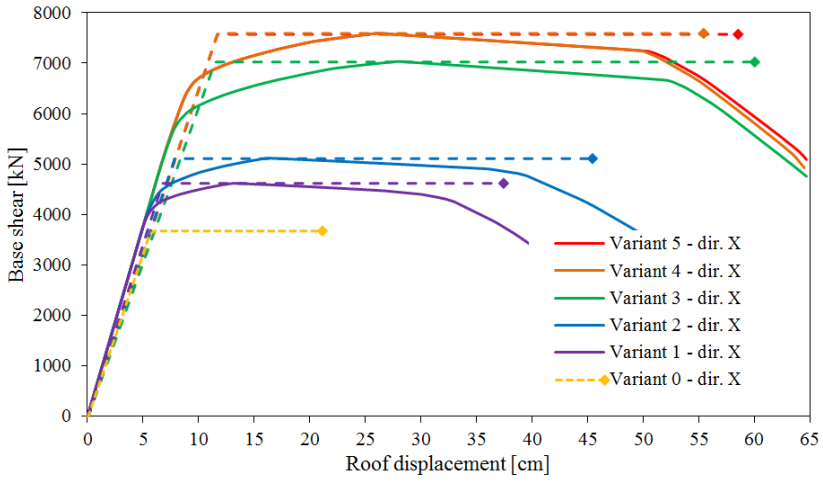


Figure 3: The pushover curves and corresponding idealized force-displacement relationship of the six variants of the 11-storey building.

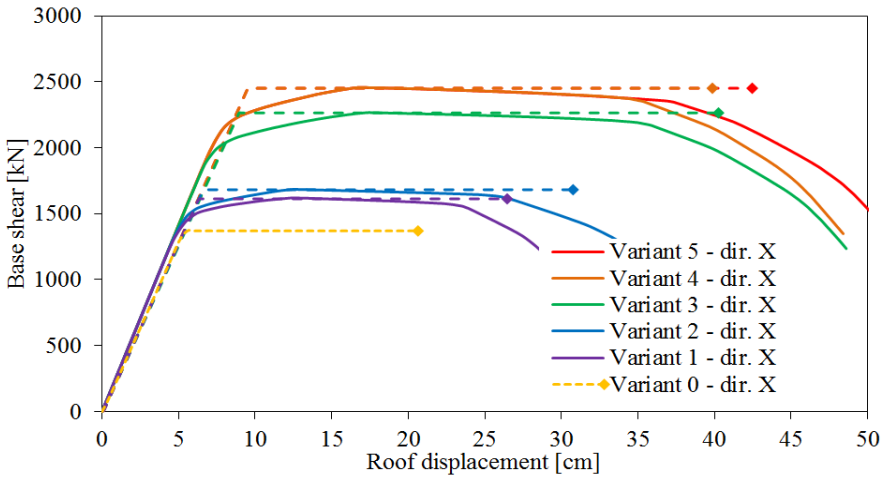


Figure 4: The pushover curves and corresponding idealized force-displacement relationship of the six variants of the 8-storey building.

5.3 Seismic hazard and risk calculation

The seismic hazard at the location of buildings was assessed according to EZ-FRISK [16, 17], which is well-known software for conducting the probabilistic seismic hazard analysis. However, it includes only simplified seismicity model for the central European region (Europe III). This is not consistent with the seismicity models used for the calculation of the seismic hazard maps [18] prescribed by Eurocode 8. Note, that the EZ-FRISK provided greater exceedance rate in this range of peak ground accelerations, whereas the peak ground acceleration associated with the 475-year return period were almost equal to that prescribed for design, which is consistent with the hazard map for 475-year return period. However, since the objective of this study is deaggregation of the seismic safety, the discussion regarding the absolute values of hazard and risk will be omitted.

In addition to the hazard curve, the logarithmic standard deviation β_{NC} of the $a_{g,NC}$ and the slope of the hazard curve k_{NC} associated with the near-collapse limit state has to be assumed.

In this study the standard deviation β_{NC} was assumed equal to 0.6 [9], whereas the the hazard parameter k_{NC}=2.9 was obtained by fitting the hazard curve in log-log coordinates using the method of least.

5.4 Results and discussion

The structural parameters and the performance parameters of the variants of the investigated buildings are presented in Tables 3 and 4, while the corresponding overall factor of safety and the partial factor of safety are presented in Tables 5. The strengths of the structure and the yield displacements gradually increase with respect to the number of safety measures excluded in the performance assessment. However, the gradual increase of structural parameters between the two variants is not general. For example, the available ductility μ_{NC} reduces between the variant 3 and 4, since the increment of the yield displacement is greater as the increment of displacement corresponding to the near-collapse limit state (Figures 3 and 4). However, the effect of the ratio between the actual and the required reinforcement causes positive effect on the strength of the structure and slightly negative effect on the deformation capacity, since the storey drifts associated with the near-collapse limit states of variant 3 (required amount of reinforcement) are more uniformly distributed along the building's height that those corresponding to variant 4. The greatest difference in storey drifts occurred in the central part of the building between 3th and 8th storey and 6th and 7th storey, respectively, for 11-storey and 8-storey building.

The variation of $S_{a,NC}$ and the $a_{g,NC}$ is the consequence of the variation of the overstrength factor and ductility at the near-collapse limit state, since the variation of the estimated period due to the six variants of the structure is almost negligible, and the vibration period exceed T_C. Consequently, the overall factor of safety, if expressed as the ratio between the ground-motion intensity which causes the near-collapse limit state and the intensity associated with the design seismic action, can be determined as the product of the FS_{Rs} and $FS_{R\mu}$, which amounted to 2.47 and 2.07, respectively, for the 11-storey and the 8-storey building.

y	Variant					
	0	1	2	3	4	5
F_y [kN]	3961	4620	5119	7036	7592	7591
D_y [cm]	6.1	6.7	7.8	11.4	11.7	11.7
T^* [s]	2.02	1.96	2.01	2.08	2.02	2.02
$R_{\mu,NC}=\mu_{,NC}$	3.90	5.59	5.83	5.26	4.97	5.03
R_s	1.00	1.17	1.29	1.78	1.92	1.92
q_{NC}	3.9	6.5	7.5	9.3	9.5	9.6
$S_{ae,NC}$ [m/s^2]	1.80	3.01	3.49	4.32	4.40	4.46
$a_{g,NC}$ [g]	0.30	0.48	0.58	0.76	0.73	0.74
P_{NC} [10^{-4}]	95.7	24.1	14.5	6.4	7.2	6.9
$T_{R,NC}$	105	416	692	1550	1392	1441

Table 3: The global structural parameters and performance parameters of the six variants of the 11-storey building.

y	Variant					
	0	1	2	3	4	5
F_y [kN]	1370	1620	1685	2267	2458	2458
D_y [cm]	5.3	6.3	6.5	8.9	9.5	9.5
T^* [s]	1.50	1.50	1.51	1.52	1.50	1.50
$R_{\mu,NC}=\mu_{,NC}$	3.90	4.24	4.71	4.53	4.22	4.49
R_s	1.00	1.18	1.23	1.65	1.79	1.79
q_{NC}	3.9	5.0	5.8	7.5	7.6	8.1
$S_{ae,NC}$ [m/s^2]	2.82	3.62	4.18	5.41	5.46	5.82
$a_{g,NC}$ [g]	0.29	0.37	0.43	0.56	0.56	0.59
P_{NC} [10^{-4}]	95.7	46.1	30.1	14.0	14.0	11.7
$T_{R,NC}$	105	217	333	715	714	857

Table 4: The global structural parameters and performance parameters of the six variants of the 8-storey building.

According to definition of the variants, the FS_{Rs} significantly exceeded the $FS_{R\mu}$. The FS_{Rs} was estimated equal to 1.92 and 1.79 for the 11-storey and 8-storey building, whereas corresponding $FS_{R\mu}$ amounted 1.29 and 1.15, respectively. The overall factors of safety can be further decomposed due to the effect of each safety measure. In this case the effect of each safety measure is assessed by the partial factor of safety. Based on results presented in Table 5, it can be concluded that the partial safety factor due to the redundancy and the minimum design requirements according to Eurocode 2 $\delta FS_{1,Rs}$ is around 1.18, whereas the greatest impact on the partially safety factor was observed due to the effect of the ratio between the mean and design strength of material ($\delta FS_{3,Rs} \approx 1.35$). However, it should be emphasized that the values of partial factors of safety can be different if sequence of safety measures corresponding to the variants of structure would be changed.

The factors of safety, which are incorporated in the design process in addition to that corresponding the design seismic action, actually reduces the probability of exceednace of the near-collapse limit state for a factor of around 10 (i.e. $FS_{TR,NC}$ is 13.8 in the case of 11-storey building and 8.2 in the case of 8-storey building). The major increment of safety is the consequence of the redundancy, minimum requirements for reinforcement and the partial material factors.

Deaggregation of yield strength, ground acceleration causing near-collapse limit state and the return period of the near-collapse limit state, are presented in Figure 5 and 6. It is obvious that the major contribution to the strength of the building is the consequence of the design seismic action, follows the contribution of the mean material strength in conjunction with the ratio between the actual and required amount of reinforcement or the contribution of the redundancy in conjunction with minimum requirements of Eurocode 2, whereas the capacity design principles practically does not contribute to the yield strength or the $a_{g,NC}$. However, deaggregation of $T_{R,NC}$ shows different image, since around 50% of safety is controlled by the the partial factors of strength of material and the other 50% is the consequence of other factors of safety.

11-storey building	δFS_i					FS
	1	2	3	4	5	
$R_{\mu,NC}=\mu_{NC}$	1.43	1.04	0.90	0.94	1.01	1.29
R_s	1.17	1.11	1.37	1.08	1.00	1.92
q_{NC}	1.67	1.16	1.24	1.02	1.01	2.47
$a_{g,NC}$ [g]	1.61	1.19	1.32	0.96	1.01	2.47
P_{NC} [10^{-4}]	0.3	0.6	0.4	1.1	1.0	0.07
$T_{R,NC}$	3.98	1.66	2.24	0.90	1.04	13.78

8-storey building	δFS_i					FS
	1	2	3	4	5	
$R_{\mu,NC}=\mu_{NC}$	1.09	1.11	0.96	0.93	1.06	1.15
R_s	1.18	1.04	1.35	1.08	1.00	1.79
q_{NC}	1.29	1.15	1.30	1.01	1.06	2.07
$a_{g,NC}$ [g]	1.29	1.16	1.30	1.00	1.07	2.07
P_{NC} [10^{-4}]	0.5	0.7	0.5	1.0	0.8	0.12
$T_{R,NC}$	2.08	1.53	2.15	1.00	1.20	8.20

Table 5: The partial safety factors and the overall safety factor for the global structural parameters and performance parameters of the variants of the 11-storey and 8-storey building.

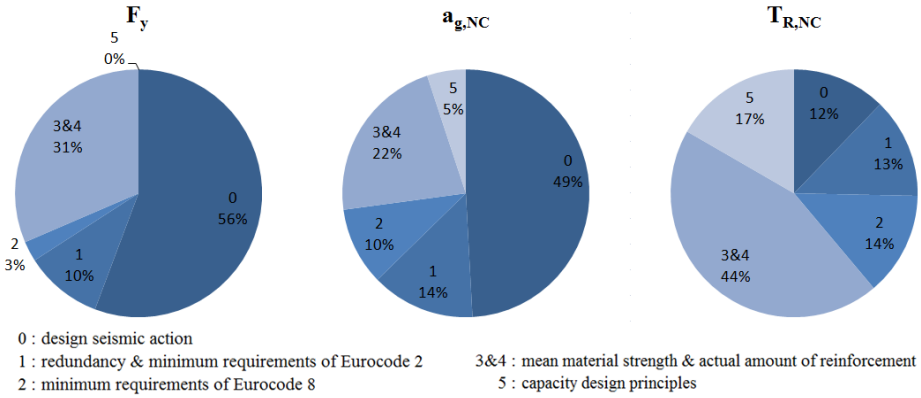


Figure 5: Deaggregation of yield strength, ground acceleration causing near-collapse limit state and the return period of the near-collapse limit state of the 8-storey reinforced concrete building.

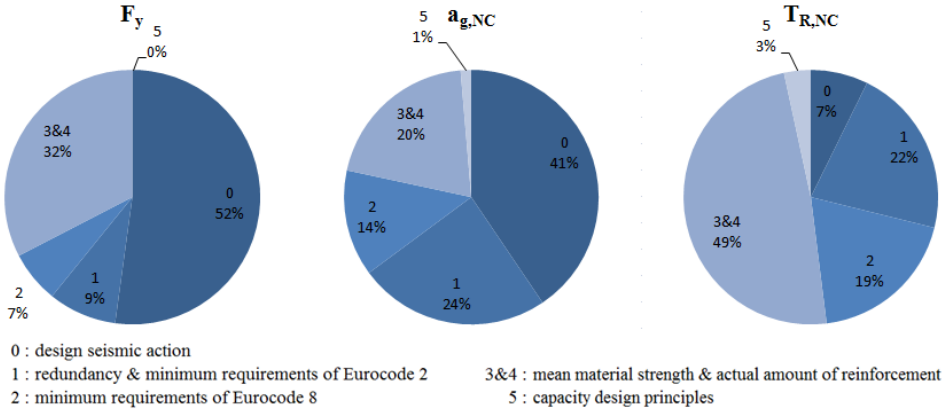


Figure 6: Deaggregation of yield strength, ground acceleration causing near-collapse limit state and the return period of the near-collapse limit state of the 11-storey reinforced concrete building.

6 CONCLUSIONS

Deaggregation of seismic safety in design of two reinforced concrete frame building is investigated in this study on the basis of the pushover analysis gradually taking into account the requirements of the Eurocode 2 and 8, as well as gradually excluding the design assumptions. For these buildings it was shown that the design seismic action has the greatest impact on the yield strength of the structure and the peak ground acceleration which causes the near-collapse limit state. On the other hand, the partial factors of material strength contribute around 50% to the return period of the near-collapse limit state, whereas the contribution of the capacity design principles and the design seismic safety to overall safety is minor. Based on this observation it is argued that it would be better to make the nonlinear model of the building and explicitly design the building for tolerable risk based on several iterations rather to use current standards for earthquake-resistant design, which based on capacity design approach in conjunction with elastic intensity-based assessment.

ACKNOWLEDGMENT

The results presented in this paper are based on work supported by the Slovenian Research Agency. This support is gratefully acknowledged

REFERENCES

[1] Eurocode 8: Design of structures for earthquake resistance. Part 1: General rules, seismic actions and rules for buildings.

[2] Applied Technology Council. ATC-19: structural response modification factors. ATC report, Redwood City, CA, 1995.

[3] M. Fischinger, P. Fajfar, On the response modification factors for reinforced concrete buildings. *Proceedings of Fourth U.S. National Conference on Earthquake Engineering*, Palm Springs, California, May 20-24, 1990.

[4] E. Miranda, V.V. Bertero, Evaluation of strength reduction factors for earthquake resistent design, *Earthquake Spectra*, vol. 10, no. 2, 357–379, 1994.

[5] M. Dolšek, P. Fajfar, Simplified probabilistic seismic performance assessment of plan-asymmetric buildings. *Earthquake Engineering & structural dynamics*, vol. 36, no. 13, 2021-2041, 2007.

[6] P. Fajfar, M. Dolšek, A practice-oriented estimation of the failure probability of building structures. *Earthquake Engineering & structural dynamics*, vol. 41, no. 3, 531-547, 2012.

[7] C.A. Cornell, Calculating building seismic performance reliability: a basis for multi-level design norms. *Proceedings of 11th World Conference on Earthquake Engineering*, New York: Elsevier, Acapulco, Mexico, 1996.

[8] R.K. McGuire, Seismic hazard and risk analysis. Earthquake Engineering Research Institute, MNO-10, 2004.

[9] M. Dolšek, Simplified method for seismic risk assessment of buildings with consideration of aleatory and epistemic uncertainty. *Structure and infrastructure engineering*, vol. 8, no. 10, 939-953, 2012.

[10] P. Fajfar, Nonlinear analysis method for performance-based seismic design. *Earthquake Spectra* 16:3, 573-592, 2000.

[11] I. Peruš, R. Klinc, M. Dolenc, M. Dolsek, A web-based methodology for the prediction of approximate IDA curves. *Earthquake Engineering & structural dynamics*, vol. 42, no. 1, 43-60, 2013.

[12] Eurocode 2: Design of concrete structures – Part 1-1: General – Common rules for building and civil engineering structures.

[13] M. Dolšek, Development of computing environment for the seismic performance assessment of reinforced concrete frames by using simplified nonlinear models. *Bulletin of earthquake engineering*, vol. 8, no. 6, 1309-1329, 2010.

[14] Eurocode 8: Design of structures for earthquake resistance. Part 3: Assessment and retrofitting of buildings.

[15] Open system for earthquake engineering simulation (OpenSEES). Pacific Earthquake Engineering Research Center (PEER), University of California, Berkeley, CA. http://opensees.berkeley.edu

[16] EZ-FRISK, Software for Earthquake Ground Motion Estimation, version 7.62, Risk Engineering, Inc., Louisville, Colorado, USA, 2012.

[17] J.W. Baker, Seismic hazard assessment for Ljubljana using EZ-FRISK. Personal communication, July 2011.

[18] J. Lapajne, B. Šket Motnikar, P. Zupančič, Probabilistic seismic Hazard assessment methodology for distributed seismicity. *Bulletin of the Seismological Society of America*, vol. 93, no. 6, 2502–2515, 2003.

COMPDYN 2013
4th ECCOMAS Thematic Conference on
Computational Methods in Structural Dynamics and Earthquake Engineering
M. Papadrakakis, V. Papadopoulos, V. Plevris (eds.)
Kos Island, Greece, 12–14 June 2013

APPLICATION OF THE RISK-BASED SEISMIC DESIGN PROCEDURE TO A REINFORCED CONCRETE FRAME BUILDING

Nuša Lazar[1] **and Matjaž Dolšek**[2]

[1] University of Ljubljana, Faculty of Civil and Geodetic Engineering
nlazar@fgg.uni-lj.si

[2] University of Ljubljana, Faculty of Civil and Geodetic Engineering
mdolsek@fgg.uni-lj.si

Keywords: seismic risk, risk-based design, envelope-based pushover analysis, reinforced concrete frame.

Abstract. *Usually seismic design procedures are based on elastic analysis by using design acceleration spectrum, which implicitly takes into account the ability of inelastic energy absorption of the structural system, and capacity design principles. Thus, current standards for earthquake-resistant design of buildings do not control seismic risk to such an extent that would be acceptable for all types of structures and for all investors. Development is therefore oriented towards advanced design methods, which can be used to achieve well informed decision-making based on target reliability. In this paper, the risk-based seismic design procedure is applied in order to design a reinforced concrete building for a tolerable seismic risk. The procedure is based on the use of nonlinear methods of analysis (pushover-based method and nonlinear time history analysis). Herein the procedure for risk assessment is briefly described. It involves envelope-based pushover analysis procedure and the new closed-form solution for estimating the annual probability of exceeding selected limit states, which provide less conservative results as that proposed by Cornell. The procedure is demonstrated by designing an eight-storey RC frame building for tolerable risk. It is shown that several iterations were needed in order to fulfill the requirement of tolerated seismic risk. However, the final configuration of the structure was checked using nonlinear response history analysis, where it is shown that the envelope-based pushover analysis procedure provided a slightly conservative estimate of collapse risk. The proposed design procedure enables explicit estimation of the seismic risk and verification of the collapse mechanism, which is an advantage in comparison to the design procedure prescribed by Eurocode 8.*

1 INTRODUCTION

Seismic risk of newly designed structures is usually not calculated, since it is assumed that current standards for earthquake-resistant design of buildings (e.g. Eurocode 8 [1], ACI-318-11 [2]), which involve elastic analysis and design acceleration spectrum, guarantee that buildings designed according to their provisions are safe against collapse due to earthquakes. Therefore current standards for earthquake-resistant design of buildings do not control seismic risk to such an extent that would be acceptable for all types of structures and for all stakeholders.

Incorporation of seismic risk assessment in the process of design is difficult since assessment of risk is a complex problem which links seismic hazard analysis, vulnerability analysis of the building and socio-economic consequences that result from strong earthquakes. However, several simplified procedures have been proposed. In the simplest case, seismic risk can be communicated by means of the mean annual frequency of exceedance of a selected limit state, such as the near-collapse limit state. This information incorporates effects of all possible earthquakes that could affect the structure at a defined location and not only the design earthquake, which is the case when the structure is designed according to current standards. By comparing estimated seismic risk with an acceptable risk we can eventually decide whether the newly designed structure meets all safety requirements or not. The simplest, practice-oriented approach, combines probability assessment in closed form [3] with the pushover-based methods (e.g. [4, 5]). Herein a new pushover analysis procedure, called envelope-based pushover analysis procedure [6], is used in order to assess the building's performance. Additionally, the collapse risk is assessed by using a new closed-form formula, which takes into account the lower and the upper ground–motion intensity. It is assumed that the limit state can be exceeded only for the ground-motion intensity which is greater than the minimum ground motion intensity causing the near-collapse limit state. On the other hand it is assumed that the ground-motion intensity cannot exceed the upper-bound intensity, which can be estimated using the results of the hazard analysis. Recently it was observed by the authors of this paper that such an approach provides less conservative estimates of probability of failure as that obtained by assuming integration of the risk equation on the interval $[0,\infty)$.

Several quite comprehensive reliability-based frameworks for the design of structures were already developed. Among others, Wen [7] proposed a design procedure based on minimum lifecycle cost criteria. He concluded that there are capabilities which allow development of risk-based, comprehensive, and yet practical design procedures familiar to engineers. Similar methods for risk-based design were proposed and applied to steel frames by Liu, Wen and Burns [8] and Rojas, Pezeshk and Foley [9]. They used genetic algorithms for determination of an optimal structural configuration. Recently, a procedure for seismic design of reinforced concrete frames based on the observation of the response of structures was proposed [10]. Optimal structural behavior is achieved through redistribution of longitudinal reinforcement with the goal of uniform deformations through the height of the structure. An attempt has been made recently in order to incorporate the basic pushover-based method for risk-based seismic design of building [11]. The proposed process is iterative. The first step involves preliminary design of the structure. Then the seismic risk is estimated for the initial structural configuration and compared to an acceptable risk. If the seismic risk is too high, measures are taken to reduce it. The seismic risk is then re-evaluated for a new and improved structure.

In this paper the iterative risk-based design procedure is demonstrated by means of an example of an eight-storey reinforced concrete building. Since system failure modes of such buildings vary due to ground motions, envelope-based pushover analysis procedure was used for the estimation of the peak ground acceleration associated with the collapse of the building.

2 RISK-BASED DESIGN PROCEDURE

In this paper an iterative risk-based design procedure [11] was used to design an 8-storey building. This design procedure involves definition of the acceptable risk, which is discussed later in the paper (Section 4). The next step involves determination of an initial structural configuration, which can be achieved by using standards for earthquake-resistant design of buildings or by engineering judgment, which is also often used by experienced structural engineers. In the example presented in Section 5, a simple initial structural configuration was determined based on design of reinforcement for vertical loads with consideration of the maximum allowable axial force in columns and the design criteria associated with the minimum allowable size of elements and the amount of reinforcement. For the initial structural configuration seismic risk is estimated and compared to the predefined acceptable risk. If the seismic risk which corresponds to the initial structural configuration exceeds the acceptable risk, measures are taken to reduce it and the seismic risk is re-evaluated for a new and improved structure. In the proposed design procedure (see Fig. 1) the last three steps are repeated until the estimated seismic risk is less than the acceptable risk. As opposed to current standards, e.g. Eurocode 8, the proposed process does not involve the design earthquake. The main advantages of the proposed design procedure in comparison to that prescribed in Eurocode 8 are explicit simulation of structural damage due to earthquakes and explicit estimation of seismic risk.

In the simplest case, measures for the reduction of collapse probability ("improvements") can be based on trial and error procedure. However, guidelines can be specified for different types of buildings in order to assess the impact of variation of input parameters, such as the amount of reinforcement in columns and/or beams, on the most basic global parameters of the building (e.g. maximum base shear, global ductility, collapse mechanism), which can be used for the estimation of variation in the probability of collapse.

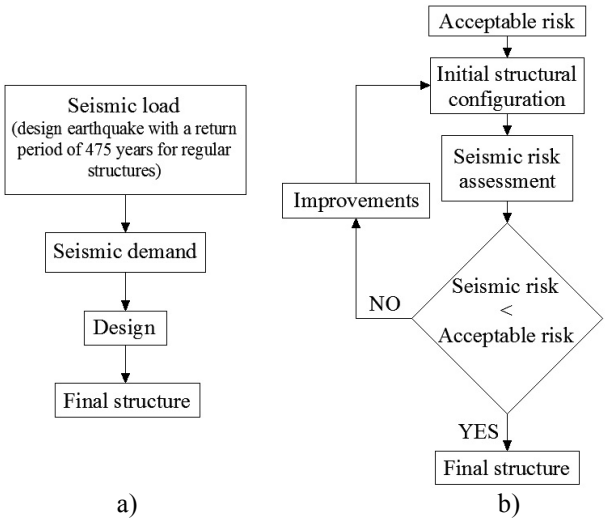


Figure 1: Flowchart showing the process of seismic design according to a) Eurocode 8 and b) proposed risk-based design procedure [11].

3 SEISMIC RISK ASSESSMENT

In the simplified approach seismic risk assessment provides estimates of the mean annual frequency (MAF) of limit-state exceedance. For the most severe limit states such as collapse, the MAF of limit state exceedance is almost equal to the annual probability of exceeding a selected limit state (*LS*), and can be determined as follows

$$P_{LS} \approx \lambda_{LS} = \int_0^{\infty} P\left(LS \middle| IM = im\right) \cdot \left| \frac{\mathrm{d}H(im)}{\mathrm{d}im} \right| \cdot \mathrm{d}im \,, \tag{1}$$

where $P(LS|IM = im)$ is the fragility or probability of exceeding the limit state LS given the intensity measure (im) and $H(im)$ is the hazard, i.e. the mean annual frequency that the ground motion intensity exceeds im. If the hazard is assumed to be linear in log-log coordinates ($H=k_0 \cdot im^{-k}$) and if the fragility is expressed by means of the standard normal probability integral $\Phi[(\ln im - \ln im_{LS,50})/\beta_{LS}]$, Eq. (1) can be approximated by the simple formula 3:

$$P_{LS} \approx H\left(im_{LS,50}\right) \cdot e^{\frac{1}{2} \cdot k_{LS}^2 \beta_{LS}^2} \,, \tag{2}$$

where P_{LS} is the mean annual frequency of exceeding a given limit state, $im_{LS,50}$ is the median value of the IM -based capacity (i.e. the median ground-motion intensity which causes the given limit state), β_{LS} is its logarithmic standard deviation and k_{LS} is the slope of the hazard curve close to $im_{LS,50}$.

The MAF of limit-state exceedance according to Eq. (2) is a result of integrating the risk equation (Eq.(1)) in the range from 0 to ∞. However, this is not physically-consistent since all structures designed according to standards have a quite large collapse capacity. Therefore, there is no ground motion which would cause collapse of a structure and have the intensity measure lower than im_1. The upper integration limit im_2 also exists, since ground motions are constrained with several physical phenomena [12]. Due to these facts, the MAF assessed according to Eq.(2) can become quite conservative. Authors of this paper recently derived the closed-form solution of Eq.(1) if it is integrated in the interval [im_1, im_2]. If a lower-bound truncated lognormal distribution is assumed for the fragility function $P(LS|IM = im)$, Eq.(1) can be expressed as follows:

$$P_{LS,im12} = P_{LS} \cdot \frac{\mathrm{erf}\left[\frac{1}{\sqrt{2}\beta_{LS}} \left(k_{LS}\beta_{LS}^{\,2} + \ln \frac{im_2}{im_{LS,50}} \right) \right] - \mathrm{erf}\left[\frac{1}{\sqrt{2}\beta_{LS}} \left(k_{LS}\beta_{LS}^{\,2} + \ln \frac{im_1}{im_{LS,50}} \right) \right]}{1 + \mathrm{erf}\left[\frac{1}{\sqrt{2}\beta_{LS}} \ln \frac{im_{LS,50}}{im_1} \right]} \,, \tag{3}$$

where erf[x] is the error function and is determined as follows:

$$\mathrm{erf}\left[x\right] = \frac{2}{\sqrt{\pi}} \int_0^x \exp\left[-\tau^2\right] d\tau \,. \tag{4}$$

The fragility parameters $im_{LS,50}$ and β_{LS} can be assessed by means of different methods. The theoretically most accurate approach for assessment of fragility parameters would be based on nonlinear response history analysis. However, this type of analysis is computationally demanding. As an alternative it is possible to use pushover-based procedures which involve pushover analysis of an entire structure and seismic demand analysis using an equivalent single degree of freedom (SDOF) model, e.g. the N2 method [13]. However, this basic procedure does not take into account the impact of higher modes of vibration, which makes it less accurate for taller buildings. Several procedures [14, 15] were proposed in order to overcome this shortcoming including the extended N2 method [16]. In this study an envelope-based pushover analysis procedure (EPA) [6] was used in order to assess the fragility parameters.

The EPA procedure utilizes several pushover analyses, which are performed for invariant horizontal force distributions corresponding to the first three vibration modes, and the inelastic response history analysis of a modal-based and so-called failure based SDOF models. Each

engineering demand is then obtained by enveloping results associated with the three system failure modes. Such approach enables approximate simulation of system failure modes caused by ground motions. More details about the method can be found elsewhere [6]. An overview of the method is also given in the paper No. 1451 presented at this conference.

4 ACCEPTABLE COLLAPSE PROBABILITY

In this paper the acceptable risk or target reliability is defined by the probability of collapse. Several models can be used to estimate the target reliability, but there is no consensus regarding the most appropriate model. It should be noted that in this study we distinguish between the acceptable and tolerated risk. Tolerated risk is associated with loss of human life, whereas the acceptable risk is associated with the remaining types of consequences, for example, with the collapse of the structure. Tolerated risk can be estimated by multiplying the acceptable risk with the fatality rate, which is the conditional probability of loss of life given the collapse of the structure. For ductile reinforced concrete frames, which were investigated in this study, the fatality rate amounted to 0.15 [17].

When an acceptable risk is based on the acceptable collapse probability P_C, then the acceptable probability is often expressed by the reliability index β [18]. The relationship between these quantities [18] is as follows

$$P_C = \Phi(-\beta), \tag{5}$$

where Φ is the cumulative distribution function of a standardized normal variable. The acceptable collapse probability P_C or reliability index β can obtained from codes and guidelines (e.g. [1, 19, 20]) or from other models of acceptable/tolerated risk, such as equations proposed by Allen and CIRIA [21] or by Helm's model [22] of tolerable risk. These models and corresponding equations of acceptable risk have been described elsewhere [11]. Herein Helm's model will be used to define acceptable risk (Section 5).

Helm [22] divided risk into four regions; negligible, ALARP (as low as reasonably possible) region, possibly unjustifiable and unacceptable risk, as shown in Fig. 2. If the possible number of fatalities or the number of occupants N is known and if the acceptable region of risk is chosen, the frequency of N or more fatalities, herein equated to the tolerable risk, can be obtained. The acceptable risk (probability of collapse), as defined in this study, is obtained by dividing the tolerated risk with the fatality rate.

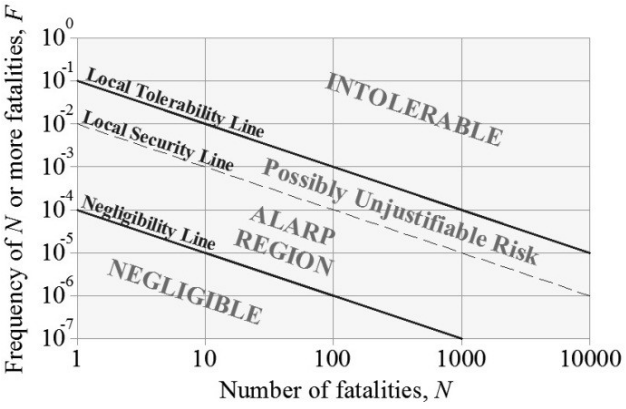


Figure 2: Helm's Frequency – Fatality curve according to [22].

5 EXAMPLE

The proposed design procedure is demonstrated by means of an 8-storey reinforced concrete building. It is assumed that the building is located in Ljubljana, i.e. in a moderate seismic region on soil type B. For illustration, the peak ground acceleration for a 475-year return period amounted 0.24 g. The initial structural configuration is based on Eurocode's provisions for minimum/maximum reinforcement ratio of the primary beams and columns corresponding to the ductility class medium. Additionally, the beams were rapidly designed for gravity loads only and the strong-column weak-beam concept was checked using the input results of the nonlinear structural model. For comparison reasons, the MAF of collapse was determined according to Eqs. (2) and (3), whereas the median peak ground acceleration at collapse $a_{g,C,50}$ and the corresponding standard deviation β_C was obtained by fitting a lognormal distribution to the sample of the $a_{g,C}$ (i.e. capacity points) determined based on the EPA procedure.

5.1 Description of the initial structure and structural model

The observed eight-storey frame building is a parking garage (Fig. 3). The height of the first and second storey is 5 m, whereas the height of other storeys is only 3.1 m, which makes this building irregular in elevation. The slab thickness is 20 cm. Concrete C30/37 and reinforcing steel S500, class B, were adopted. All columns and beams of the initial structural configuration have the same dimensions and amount of reinforcement. The only exceptions are the beams in the first and second storey, which have a greater amount of the top longitudinal reinforcement (6ϕ20) in comparison to that initially designed for other beams (4ϕ20) (see Fig. 3c and 3d). The longitudinal reinforcement in all columns amounted to 1% of the cross-section area. Stirrups were based on the criteria of the minimum concrete confinement. The exception was the columns at the base, where a greater amount of confinement is required according to Eurocode 8. In this case a 5 cm distance between the stirrups was prescribed, whereas for all other elements the distance between stirrups was 15 cm. The total mass of the building was 3856 t and the fundamental period amounted to 1.76 s.

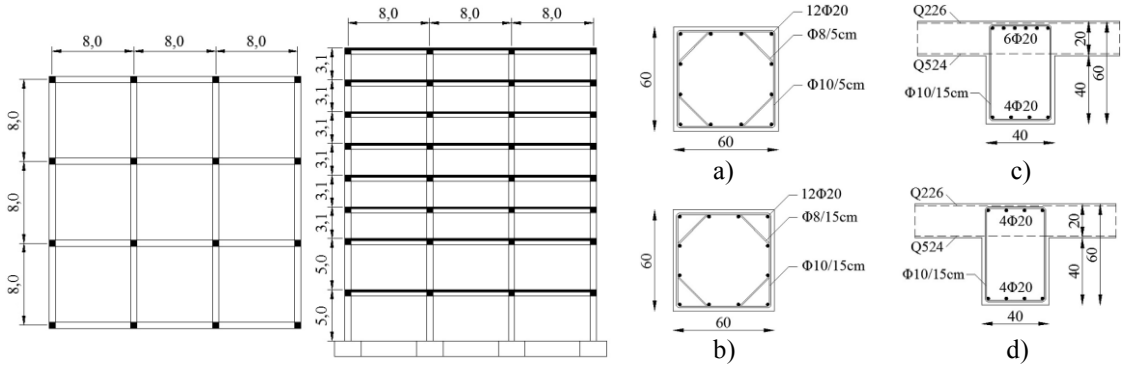


Figure 3: Plan, elevation view and reinforcement of beams and columns for the initial structural configuration of the eight-storey building.

It should be noted that the so determined initial structural configuration of the 8-storey building is practically equal to the structural configuration obtained by designing the building for the seismic action associated with a 475-year return period and behavior factor q=3.9, since the internal forces in the beams due to gravity loads are greater than those corresponding to the seismic action and since the minimum amount of longitudinal reinforcement in the columns is sufficient. Therefore a direct comparison between the structural configuration obtained by Eurocode 8 provisions and the proposed preliminary design procedure is possible.

A simplified nonlinear structural model was used, which in general follows the Eurocode 8 requirements for the modeling of structures. The beam and column flexural behaviour was therefore modelled by one-component lumped plasticity elements, composed of an elastic beam and two inelastic rotational hinges (defined by a moment–rotation relationship). The element formulation is based on the assumption of an inflexion point at the midpoint of the element. The gravity load is represented by the uniformly distributed load on the beams and by the concentrated loads at the top of the columns. For the beams, the plastic hinge is used for major axis bending only. For the columns, two independent plastic hinges for bending about the two principal axes are used. The moment–rotation relationship before strength deterioration is modelled by a bilinear relationship. A linear negative post-capping stiffness is assumed after the maximum moment is achieved. The PBEE Toolbox [23] in conjunction with OpenSees [24] was used to generate the simplified nonlinear models and to perform the nonlinear analyses, i.e. the pushover analyses of the entire building and the nonlinear response history of the equivalent SDOF models in the design phase, and the response history analysis in order to verify the final structural configuration.

5.2 Seismic hazard and ground motions

The risk-based design procedure requires the seismic hazard curve, which was obtained by using EZ-FRISK [25, 26]. This software contains a seismicity model for the central European region (Europe III). It should be noted that the seismicity model built in EZ-FRISK is not consistent with the seismicity models used for determination of the seismic hazard maps for Slovenia [27], which are used to define the seismic action according to Eurocode 8. However, according to results of the probabilistic seismic hazard analysis, the hazard parameter k=2.9 was obtained by fitting a straight line to the hazard curve in log-log coordinates with the method of least squares.

The ground-motion records were selected using an algorithm proposed by Jayaram et al. [28], which involves generation of the response spectra based on target spectrum and its variance by utilizing the Monte Carlo simulation and then selection of the records from the NGA database [29]. The minimum difference between the target spectrum and the spectrum corresponding to the selected ground motions is achieved by a greedy optimization. The target response spectrum for the response history analysis was assumed as the uniform hazard spectrum used for the design of the building, although it should be noted that hazard-consistent procedures (e.g. [30, 31]) exists, but were not applied in this study for simplicity reasons and due to the lack of the data (detailed hazard deaggregation is not available for the region of Slovenia). The ground motions were selected based on the magnitude between 5.5 and 7.5, fault distance between 5 and 50 km and shear wave velocity in the upper 30 m higher than 180 m/s.

The target uniform hazard spectrum, median response spectrum conditioned to the fundamental period of the analyzed structure and the corresponding 16th and 84th percentiles are presented in Fig. 4. In addition to the spectral acceleration at first period of the building ($S_a(T_1)$), the ground motions were conditioned also on the peak ground acceleration (a_g). In this case the median spectral acceleration of the selected ground motion records was also similar to the target spectrum. Therefore it was herein assumed that this set of ground motions is also appropriate for the case when the peak ground acceleration is selected for an intensity measure.

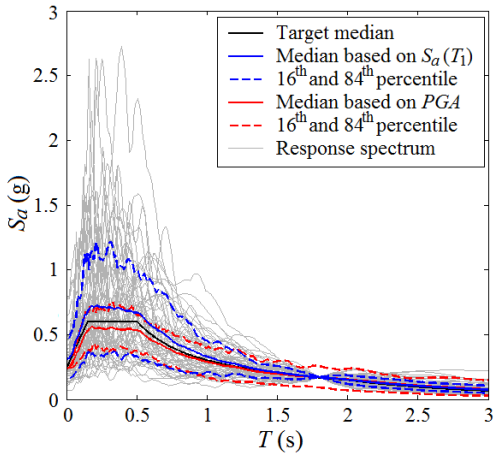


Figure 4: The target uniform hazard spectrum, spectra for each selected ground motion, the median spectrum of the selected ground motions and the corresponding 16th and 84th percentiles.

5.3 Definition of acceptable risk

Firstly, an acceptable risk was assessed using the models of ISO [19], EC0 [1], JCSS [20], CIRIA [21], Allen [21] and Helm [22]. Some models of acceptable risk (e.g. ISO, CIRIA and Allen) take into account the number of people exposed to danger. In this case we assumed that 10 people are exposed in the building at the time of an event. Additionally, a moderate cost of safety measures and small consequences were taken into account. Based on these decisions the social criterion factor K_s according to CIRIA's model was assumed equal to 0.5. For the case of Allen's model, the activity and warning factors were set, respectively, to 3.0 and 1.0. Acceptable risk according to Helm's model was evaluated based on the negligibility line (Fig. 3).

The acceptable risk according to the six models was calculated based on the above-described decisions and expressed in terms of acceptable collapse probability P_C or reliability index β (Table 1). Since the ISO standard ignores differentiation of the acceptable risk based on activities and the number of people in the building if it is lower than 100, the estimated acceptable risk in comparison to other models is quite low. Eurocode 0 does not prescribe that its model of acceptable risk should be used in the case of seismic hazard. This could be a reason that it provides a relatively low value of acceptable risk. The acceptable risk according to the model of CIRIA and Allen provided a similar value of acceptable risk as that assessed according to Eurocode 0, whereas the acceptable risk according to the JCSS model is too high according to our opinion.

Finally it was decided to design the building for the acceptable risk determined by Helm's model. The target reliability index amounted to 3.8 and the acceptable P_C for a period of 50 years was 0.33%.

It should be noted that the probability of failure, as it is defined in the various models, is often associated with the ultimate limit state, which in our study corresponded to the collapse of the building. Thus we assumed that the acceptable risk is associated to structural collapse and will be hereafter referred to as probability of collapse.

Method	ISO	EC 0	JCSS	CIRIA	Allen	Helm
β	4.4	4.2	3.7	4.0	4.3	**3.8**
P_C	$6.7\cdot10^{-6}$	$1.3\cdot10^{-5}$	$1.1\cdot10^{-4}$	$3.3\cdot10^{-5}$	$1.0\cdot10^{-5}$	$\mathbf{6.7\cdot10^{-5}}$

Table 1: The acceptable P_C and reliability index β defined with different models of acceptable risk.

5.4 Description of the design procedure

The initial structural configuration was analyzed with envelope-based pushover analysis (EPA) procedure. The estimated collapse probability amounted to $2.9 \cdot 10^{-4}$ if calculated with Eq.(2), which exceeded the acceptable collapse probability by a factor of 4.3. In order to assess the probability of collapse using Eq.(3), the maximum intensity a_{g2} has to be estimated. From a theoretical point of view, the maximum peak ground acceleration can be estimated based on the seismicity model used in hazard analysis and the ground motion prediction model, which are both uncertain, especially in regions of moderate and low seismicity, where the recorded ground motions are rare. Additionally, the truncation of the ground-motion probability is required in order to theoretically assess the upper bound ground-motion intensity. Therefore it is suggested to use different ground-motion prediction (GMP) equations for a given truncation level (e.g. 2 or 3 standard deviations above the mean value) in order to assess the a_{g2}. For the purpose of this study it was assumed that the worst-case scenario is an earthquake with magnitude 7, which is consistent with the seismic hazard analysis for Slovenia [27], and the source-to-site distance R_{jb}=0 km. The truncation level was assumed equal to 2.5. Based on these assumptions, the a_{g2} was calculated for the GMP models proposed by Sabetta and Pugliese [32], Bindi et al. [33], Akkar and Bommer [34] and Peruš and Fajfar [35]. Finally, the a_{g2} was assessed by assuming equal weights for the four GMP models, and amounted to 2.4 g. This is a very large level of peak ground acceleration for moderate seismicity. However, the collapse probability of the initial structural configuration estimated according to Eq.(3) amounted to $2.1 \cdot 10^{-4}$, which is around 40% smaller than that calculated according to Eq.(2), but it still exceeds the acceptable collapse probability by a factor of 3.1. This result indicates that the difference between the collapse probabilities calculated with both equations is not negligible, although the a_{g2} is very high. This confirms that the assessment of the probability of collapse according to Eq.(2) is most probably too conservative.

The initial (first) structural configuration was modified, since the probability of collapse for the initial structural configuration exceeded the acceptable probability of collapse. Decision regarding the improvement of the structural configurations was based on knowledge obtained from a previously performed sensitivity study on similar reinforced concrete frame buildings [11]. Based on this study it was decided that for the 'second' structural configuration the amount of longitudinal reinforcement of the columns in the first four stories was increased for 0.2% of the columns cross-section area. However, additional iterations were needed as presented in Table 2, since the system failure modes observed in the pushover analysis did not provide sufficient system ductility. Note that the label AsC (AsB) refers to the increase of the amount of reinforcement in columns (beams) and the label AcC (AcB) refers to the increase of the cross-section area of columns (beams) for a certain percentage. T_1 is the fundamental period of vibration, $a_{g,C,50}$ is the median ground acceleration causing the collapse of the structure obtained by the EPA procedure, β_C is the lognormal standard deviation and a_{g1} is the minimum observed ground acceleration causing collapse.

In Table 3 the probability of collapse calculated according to Eqs. (2) and (3) is presented for all iterations within the design process. It can be observed that Helm's condition of acceptable risk was satisfied with the fifth iteration. In this specific case the use of Eq.(3) for the determination of the probability of collapse did not affect the final structural configuration.

The pushover curves and the approximate median IDA curves based on EPA procedure are presented in Fig. 5 in order to better understand how the adopted structural modifications affected the strength and the system ductility of the building and eventually how this affected the $a_{g,C,50}$. It can be seen that the base shear, system ductility and the $a_{g,C,50}$ are increased after each structural modification. The largest increment in base shear and ductility can be ob-

served for the fifth iteration, which corresponds to an increase of the beams' height in the most damaged storeys. A significant increase of ductility can also be observed in the fourth step of the design procedure, where the area of the cross-section of columns was increased. Consequently the largest increment of the a_{g1} and $a_{g,C,50}$ was also observed for the 4th and 5th iteration. In these cases the system failure mode provided significantly largest system ductility in comparison to that observed for the initial structural configuration. In Fig. 6 the deformation shape and damage pattern corresponding to the near-collapse limit state is presented for the structure designed according to Eurocode 8 (i.e. initial structural configuration) and for the final structural configuration obtained with the proposed design procedure. It can be seen that for the structure designed according to Eurocode 8 storey drifts are concentrated in the first and second storey, which was prevented with the proposed design process.

Iteration	Modification	T_1 (s)	$a_{g,C,50}$ (g)	β_C	a_{g1} (g)
1	Initial structural configuration	1.76	1.13	0.68	0.20
2	0.2% AsC first 4 storeys	1.76	1.17	0.68	0.21
3	0.2% AsC first 4 storeys	1.76	1.20	0.67	0.23
4	10% AcC first 4 storeys	1.69	1.44	0.64	0.31
5	5% AcB first storey	1.73	1.56	0.59	0.38

Table 2: Brief description of the safety measures for the five structural configurations, the corresponding first vibration period, parameters of the fragility function and the minimum intensity a_{g1} which causes collapse of the structure.

Iteration	$P_C \cdot 10^{-4}$	$P_{C,1}/P_{C,i}$	$P_{C,im12} \cdot 10^{-4}$	$P_{C,im12,1}/P_{C,im12,i}$
1	2.92	1.0	2.09	1.0
2	2.59	1.1	1.85	1.1
3	2.30	1.3	1.63	1.3
4	1.11	2.6	0.78	2.7
5	**0.65**	4.5	**0.49**	4.2

Table 3: Probability of collapse assessed according to Eqs.(2) and (3) for each structural configuration within the design process.

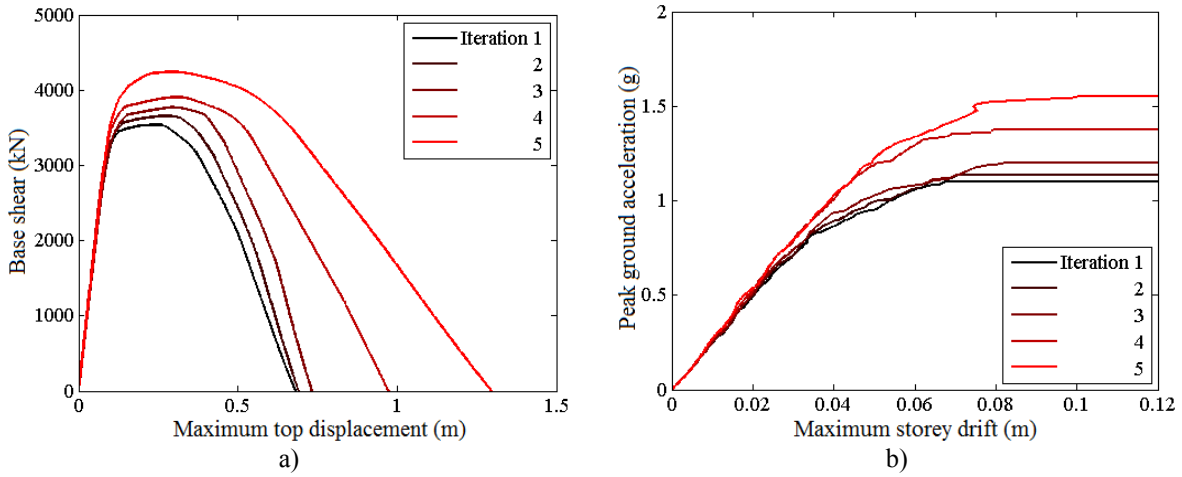


Figure 5: a) Pushover curves for each structural configuration and b) the corresponding approximate median IDA curves based on EPA procedure.

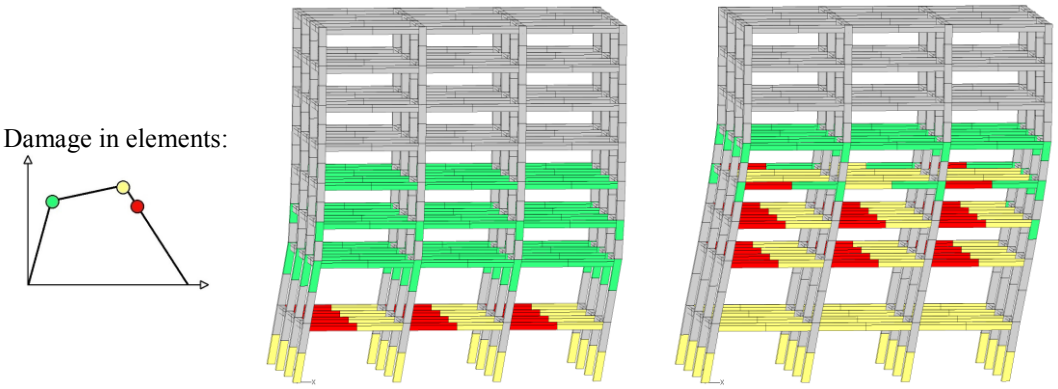


Figure 6: Deformation shape and damage pattern corresponding to the near-collapse limit state for the building designed according to a) Eurocode 8 provisions (i.e. initial structural configuration) and b) the final structural configuration (iteration 5).

In order to check the adequacy of the final structural configuration the collapse capacity was assessed using response history analysis for a set of ground motions. The median collapse capacity based on the response history analysis was similar to that provided by the envelope-based pushover analysis procedure (Fig. 7). However, the result obtained by the EPA procedure was slightly conservative. For comparison reasons, the median maximum storey drift ration obtained by taking into account only the modal-based SDOF model corresponding to the first-mode pushover analysis (PA1) is presented in Fig. 7. It can be observed that for the first three iterations higher modes (EPA) have no impact $a_{g,C,50}$ due to the predominant impact of soft storey mechanism that causes collapse. However, for the final structural configuration, where the soft story mechanism is prevented (Fig. 6), a greater impact of the higher modes of vibration can be observed since the difference between the response based on EPA and PA1 gradually increases. From Fig. 7 it can be observed that the median collapse capacity $a_{g,C,50}$ based on the basic pushover-based method is significantly overestimated.

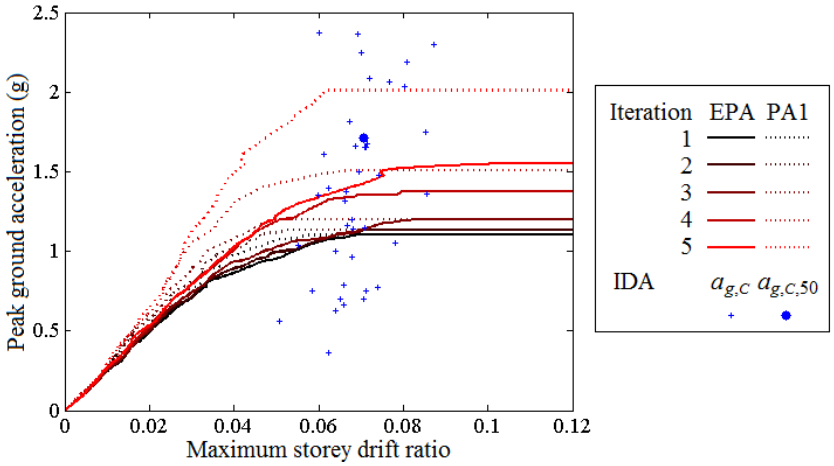


Figure 7: The relationship between the peak ground acceleration and the median value of the maximum storey drift obtained with EPA and the basic pushover-based method (PA1) for all five structural configurations, and the collapse capacity for the final structural configuration obtained by response history analysis.

6 CONCLUSIONS

In the paper an iterative design procedure based on acceptable risk was described and demonstrated by means of an example of a reinforced concrete frame building. The procedure was first presented in [11], where the basic pushover-based method was used to assess structural performance. In this paper structural performance was assessed by using the recently introduced EPA procedure, whereas the probability of collapse was calculated with consideration of the lower and the upper integration limit of the risk equation. Such an approach provided more accurate estimation of the collapse risk due to less conservative assessment of risk and due to more accurate estimation of the $a_{g,C,50}$, since the EPA procedure enables approximate simulation of system failure modes, which are significantly different to that corresponding to the first-mode pushover analysis.

The risk-based design offers the possibility to overcome shortcomings of the standards for earthquake resistant design of structures in order to achieve well-informed decision-making, which is a key element for the future protection of the built environment against earthquakes. However, further research is needed in order to adequately address some underdeveloped components of the proposed design process. Additionally, development of software is also required, which would eventually enable practical applications of the proposed design process.

ACKNOWLEDGEMENT

The results presented in this paper are based on work supported by the Slovenian Research Agency. This support is gratefully acknowledged.

REFERENCES

[1] CEN, Eurocode 8: design of structures for earthquake resistance. Part 1: general rules, seismic actions and rules for buildings, 2004.

[2] American Concrete Institute (ACI), Building code requirements for structural concrete and commentary. *ACI 318-11*, Farmington Hills, MI, 2011.

[3] C.A. Cornell, Calculating building seismic performance reliability: a basis for multi-level design norms. *Eleventh World Conference on Earthquake Engineering, Mexico City, Mexico*, Paper No.2122, 1996.

[4] M. Dolšek, P. Fajfar, Simplified probabilistic seismic performance assessment of plan-asymmetric buildings. *Earthquake Engineering and Structural Dynamics*, **36**(13), 2021–2041, 2007.

[5] P. Fajfar, M. Dolšek, A practice-oriented estimation of the failure probability of building structures. *Earthquake Engineering and Structural Dynamics*, **41**(3), 531-547, 2012

[6] M. Brozovič, M. Dolšek, Envelope-based pushover analysis procedure for seismic performance assessment of buildings. *Earthquake Engineering & Structural Dynamics* (in review), 2013.

[7] J.K. Wen, Reliability and performance-based design. *Structural Safety*, **23**(4), 407-428, 2001.

[8] M. Liu, Y.K. Wen, S.A. Burns, Life cycle cost oriented seismic design optimization of steel moment frame structures with risk-taking preference. *Engineering Structures*, **26**(10), 1207-1421, 2004.

[9] H.A. Rojas, C. Foley, S. Pezeshk, Risk-Based Seismic Design for Optimal Structural and Nonstructural System Performance. *Earthquake Spectra*, **27**(3), 857-880, 2011.

[10] I. Hajirasouliha, P. Asadi, K. Pilakoutas, An efficient performance-based seismic design method for reinforced concrete frames. *Earthquake Engineering and Structural Dynamics*, **41**(4), 663-679, 2012.

[11] N. Lazar, M. Dolšek, Risk-based seismic design – An alternative to current standards for earthquake-resistant design of buildings. *15th World Conference on Earthquake Engineering (15WCEE)*, Lisbon, Portugal, September 24-28, 2012.

[12] J.J. Bommer, N.A. Abrahamson, F.O. Strasser, A. Pecker, P.-Y. Bard, H. Bungum, F. Cotton, D. Fäh, F. Sabetta, F. Scherbaum, J. Studer, The challenge of defining upper bounds on earthquake ground motions. *Seismological Research Letters*, **75**(2), 82-95, 2004.

[13] P. Fajfar, Nonlinear analysis method for performance-based seismic design. *Earthquake Spectra,* **16**(3), 573-592, 2000.

[14] A.K. Chopra, R.K. Goel, A modal pushover analysis procedure for estimating seismic demands for buildings. *Earthquake Engineering and Structural Dynamics*, **31**(3), 561-582, 2002.

[15] H. Sucuoglu, M.S. Günay, Generalized force vectors for multi-mode pushover analysis. *Earthquake Engineering and Structural Dynamics*, **40**(1), 55-74, 2011

[16] M. Kreslin, P. Fajfar, The extended N2 method taking into account higher mode effectd in elevation. *Earthquake Engineering and Structural Dynamics*, **40**(14), 1571-1589, 2011.

[17] K.S. Jaiswal, D.J. Wald, Development of a semi-empirical loss model within the USGS Prompt Assessment of Global Earthquakes for Response (PAGER) System. *9th US and 10th Canadian Conference on Earthquake Engineering: Reaching Beyond Borders,* 2010.

[18] R.E. Melchers, *Structural Reliability Analysis and Prediction, 2nd Edition*. John Wiley & Sons, 1999.

[19] International Organization for Standardization (ISO), ISO 2394:1998(E) – General principles on reliability for structures, 1998.

[20] Joint Committee on Structural Safety, Probabilistic model code – Part 1: Basis of Design, 2000.

[21] B. Bhattacharya, R. Basu, K. Ma, Developing target reliability for novel structures: the case of the Mobile Offshore Base. *Marine structures*, **14**, 37-58, 2001.

[22] P. Helm, Integrated Risk Management for Natural and Technological Disasters. *Tephra*, **15**(1), 5-19, 1996.

[23] M. Dolšek, Development of computing environment for the seismic performance assessment of reinforced concrete frames by using simplified nonlinear models. *Bulletin of Earthquake Engineering*, **8**(6), 1309-1329, 2010.

[24] Open System for Earthquake Engineering Simulation (OpenSEES). Pacific Earthquake Engineering Research Center (PEER), Univ. of California, Berkeley, CA, 2004. (http://opensees.berkeley.edu/).

[25] EZ-FRISK, Software for Earthquake Ground Motion Estimation, version 7.62. Risk Engineering, Inc., Louisville, Colorado, USA, 2012.

[26] J.W. Baker, Seismic hazard assessment for Ljubljana using EZ-FRISK. *Personal communication*, July 2011.

[27] J. Lapajne, B. Šket Motnikar, P. Zupančič, Probabilistic Seismic Hazard Assessment Methodology for Distributed Seismicity. *Bulletin of the Seismological Society of America*, **93**(6), 2502-2515, 2003.

[28] N. Jayaram, T. Lin, J.W. Baker, A Computationally Efficient Ground-Motion Selection Algorithm for Matching a Target Response Spectrum Mean and Variance. *Earthquake spectra*, **27**(3), 797-815, 2011.

[29] B.S.J. Chiou, R.B. Darragh, N.J. Gregor, W.J. Silva, NGA project strong-motion database. *Earthquake Spectra*, **24**(1), 23-44, 2008.

[30] J.W. Baker, Conditional Mean Spectrum: Tool for ground motion selection. *Journal of Structural Engineering*, **137**(3), 322-331, 2011

[31] B.A. Bradley, A ground motion selection algorithm based on the generalized conditional intensity measure approach. *Soil Dynamics and Earthquake Engineering*, **40**, 48-61, 2012.

[32] F. Sabetta, A. Pugliese, Estimation of Response Spectra and Simulation of Nonstationary Earthquake Ground Motions. *Bulletin of Seismological Society of America*, **86**(2), 337-352, 1996

[33] D. Bindi, F. Pacor, L. Luzi, R. Puglia, M. Massa, G. Ameri, R. Paolucci, Ground motion prediction equations derived from the Italian strong motion database, *Bulletin of Earthquake Engineering*, **9**(6), 1899-1920, 2011

[34] S. Akkar, J.J. Bommer, J.J, Empirical Equations for the Prediction of PGA, PGV, and SpectralAccelerations in Europe, the Mediterranean Region, and the Middle East. *Seismological Research Letters*, **81**(2), 195-206, 2010

[35] I. Peruš, P. Fajfar, Ground-motion prediction by a non-parametric approach. *Earthquake engineering and structural dynamics*, **39**(12), 1395-1416, 2010.

COMPDYN 2013
4th ECCOMAS Thematic Conference on
Computational Methods in Structural Dynamics and Earthquake Engineering
M. Papadrakakis, V. Papadopoulos, V. Plevris (eds.)
Kos Island, Greece, 12–14 June 2013

ISSUES ON THE USE OF TIME-HISTORY ANALYSIS FOR THE DESIGN AND ASSESSMENT OF MASONRY STRUCTURES

A. Penna[1,2], M. Rota[2], A. Mouyiannou[3] and G. Magenes[1,2]

[1] Department of Civil Engineering and Architecture, University of Pavia
Via Ferrata 3, I-27100 Pavia
andrea.penna@unipv.it, guido.magenes@unipv.it

[2] European Centre for Training and Research in Earthquake Engineering
Via Ferrata 1, I-27100 Pavia
maria.rota@eucentre.it

[3] ROSE Programme, UME School, Institute for Advanced Studies Pavia
Via Ferrata 1, I-27100 Pavia
amaryllis.mouyiannou@umeschool.it

Keywords: Time-history analysis, Masonry, TREMURI, Limit states, Record selection.

Abstract. *Nonlinear dynamic analysis is widely recognized as the most accurate analysis technique for the design and assessment of structures. However, its use is still not common in the everyday engineering practice, mainly due to various issues concerning its performance and the interpretation of its results. A first issue includes the limited availability of computer programs that allow the performance of time history analysis, especially for the case of masonry structures, although some software are currently available to this aim. Another difficulty is related with the selection of appropriate input ground motion records to be used for the analysis. Real records are well known to be a preferable choice with respect to artificial or synthetic ground motions, but the limited availability of real records often requires scaling them, with all the concerns associated with this operation. Also, a proper selection of seismic input requires some level of expertise, which is not so common in the professional field. A third problem regards the difficulty in the interpretation of the results of nonlinear dynamic analysis in terms of performance limits. The definition of significant limit states in relation to the results of nonlinear dynamic analyses is still indeed a very open problem and it is related to the fact that the achievement of a local limit condition (e.g. failure of a pier element) would not adequately represent the overall damage state of the building. Therefore there is the need to find a definition of limit states describing the global building performance, i.e. taking into account not only the peak concentrated damage in a single element, but also the diffusion of damage through the different structural elements and the evolution of the global collapse mechanism. This would also allow for a rational implementation of the qualitative definition of damage states commonly adopted in performance-based earthquake engineering.*

1 INTRODUCTION

As reported in EC8 (clause 4.3.3.1(5) of EN 1998-1 [1]) "Non-linear analyses should be properly substantiated with respect to the seismic input, the constitutive model used, the method of interpreting the results of the analysis and the requirements to be met."

This basic statement well identifies the main issues related to the use of nonlinear analysis and, in particular, of nonlinear time-history analysis, which is indubitably the most accurate method for assessing the seismic response of structures provided that these critical issues are properly tackled and suitable tools are used.

Nonlinear dynamic analysis requires the seismic input to be represented in terms of properly defined time-series (e.g. accelerograms), which need to be consistent with the seismic hazard at the site. In many building codes, this idea is associated with the concept of "spectrum-compatibility", that will be discussed in more detail in section 3.

A suitable modeling strategy for the analysis of the dynamic seismic response of complete masonry buildings is presented and discussed in section 2.

Finally, an extended discussion on the definition and identification of appropriate limit states for the interpretation of the results of nonlinear time-history analysis of masonry buildings is presented in section 4. Different criteria are compared and some suggestions are given based on their application to five building models.

2 A NONLINEAR MODEL FOR DYNAMIC ANALYSIS OF URM STRUCTURES

The need for nonlinear analysis tools for complete masonry buildings arose in the late 1970s in Italy and in Slovenia, where simplified modeling techniques and analysis methods were developed and adopted in practice [2]. In the following decades several other nonlinear models were developed and some of them are already available to practitioners and make now possible to carry out reliable nonlinear pushover analysis of masonry structures [3][4]. These methods, generally based on the equivalent frame approach [5][6][7] and the macro-element discretization (single 2-node elements modeling structural members such as piers and spandrel beams), require a limited computational burden since the number of degrees of freedom and elements in the structural model is limited.

An effective equivalent-frame formulation allowing the dynamic global analysis of whole buildings, when only in-plane response of walls is considered, is available in the TREMURI model [8][9].

The nonlinear macro-element model representative of a whole masonry panel described in Penna et al. [10] permits, with a limited number of degrees of freedom (8), to represent the two main in-plane masonry failure modes, i.e. bending-rocking and shear-sliding (with friction) mechanisms (and their interaction), on the basis of mechanical assumptions. This model was explicitly formulated [11] to simulate the cyclic behavior of masonry piers, considering, by means of internal variables, the shear damage evolution, which controls the strength deterioration (softening) and the stiffness degradation. The macro-element also accounts for the effect (especially in bending-rocking mechanisms) of the limited compressive strength of masonry: toe crushing effect is modeled by means of a phenomenological non-linear constitutive law with stiffness degradation in compression. Recent developments [12] have also extended the macro-element capabilities including second order effects which can be important in case of large displacements or for other applications of the model (e.g. simulation of local/out-of-plane failure modes).

A frame-type representation of the in-plane behavior of masonry walls is adopted: each wall of the building is subdivided into piers and spandrel beams (2-node macro-elements)

connected by rigid areas (nodes). Post-earthquake damage observation shows, in fact, that only rarely (very irregular geometry or very small openings) cracks appear in these areas of the wall. Hence, the deformation of these regions is assumed to be negligible, relatively to the macro-element non-linear deformations governing the seismic response. The presence of ring beams, tie-rods (non-compressive truss elements), previous damage, heterogeneous masonry portions, gaps and irregularities can be easily included in the structural model (Figure 1).

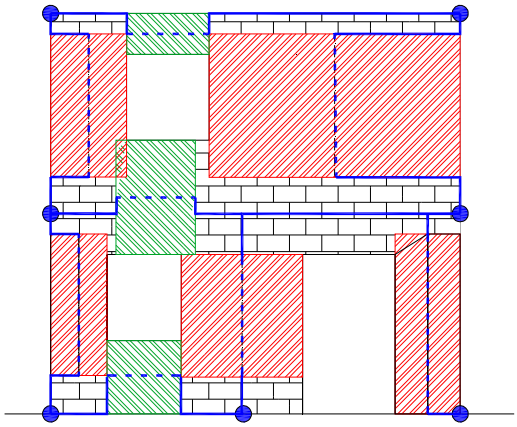


Figure 1 Example of macro-element modeling of a masonry wall (piers in red and spandrels in green).

The presence of reinforced concrete elements (e.g. ring beams, internal columns and walls in mixed structures) can be also modeled by 2-node elements with simplified Takeda nonlinear behavior (Figure 2).

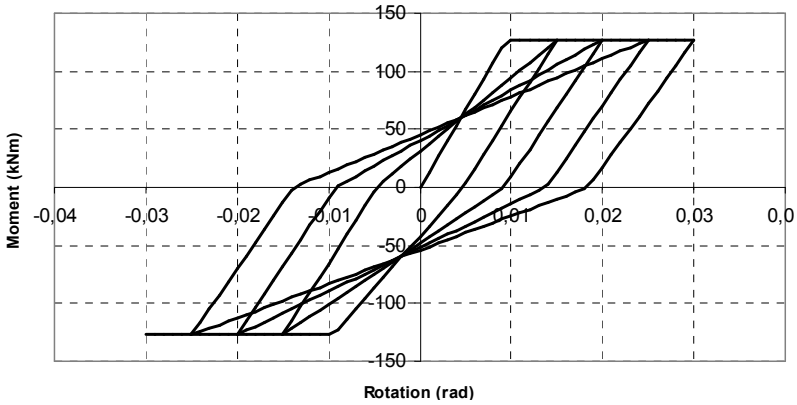


Figure 2 Bilinear simplified Takeda model for simulating the cyclic response of RC members [13].

As described in [9], three-dimensional modeling of whole URM buildings starts from some hypotheses on their structural and seismic behavior: the bearing structure, both referring to vertical and horizontal loads, is identified, inside the construction, with walls and floors (or vaults); the walls are the bearing elements, while the floors, apart from sharing vertical loads to the walls, are considered as planar stiffening elements (orthotropic 3-4 nodes membrane elements) governing the distribution of the horizontal actions between the walls. The local flexural behavior of the floors and the wall out-of-plane response are not computed because they are considered negligible with respect to the global building response, which is governed

by their in-plane behavior (a global seismic response is possible only if vertical and horizontal elements are properly connected).

In order to perform non-linear seismic analyses of URM buildings a set of analysis procedures has been implemented: incremental static (Newton-Raphson) with force or displacement control, 3D pushover analysis with fixed and adaptive load pattern ([14]) as well as 3D time-history dynamic analysis (Newmark integration method; Rayleigh viscous damping).

The results of the simulation of the response of the quasi-static tests performed on a full-scale two-story clay brick masonry building ([15]) reported in Figure 3 show the capability of the equivalent-frame macro-element model in reproducing the experimental hysteretic behavior [4].

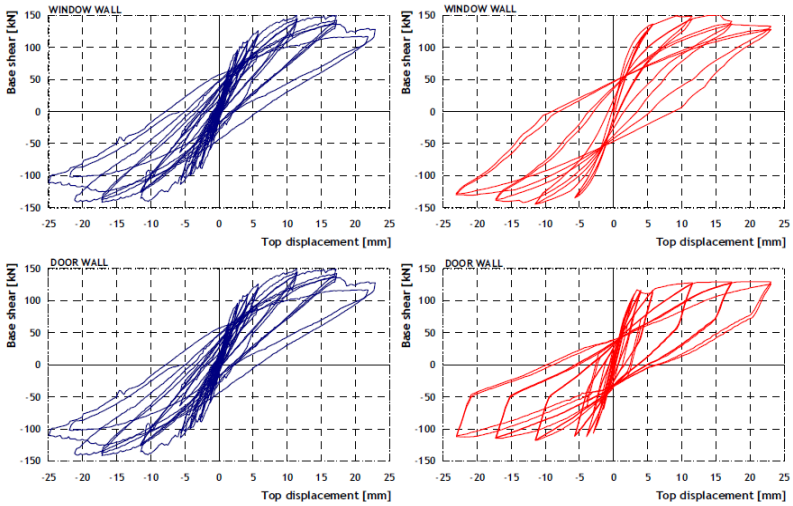


Figure 3 Comparison of experimental (left) and numerical (right) force-displacement curves for the two main walls of the clay brick masonry building tested by [15].

3 SELECTION OF INPUT GROUND MOTIONS FOR TIME HISTORY ANALYSIS

As already mentioned, the execution of time history analyses requires the definition of the seismic action in terms of appropriately selected time-series.

As discussed in more detail in other works (e.g. [18],[19]), accelerograms are typically subdivided in three categories: real (or natural) records selected from accredited strong-motion databases, synthetic accelerograms generated through complex mathematical models of the seismic source and wave propagation phenomena, and artificial accelerograms generated by stochastic algorithms and constrained to be spectrum-compatible to a target response spectrum. Although the choice of the type of record to be used for defining the seismic input for time history analyses depends on the problem under study, in many cases real accelerograms are the best choice, since they are more realistic than spectrum-compatible artificial records and easier to obtain than synthetic seismograms generated from seismological source models. Since they are genuine records of ground shaking produced by real earthquakes, they retain all the ground motion characteristics (e.g. amplitude, frequency, energy content, duration, number of cycles, and phase) and reflect all the factors that influence the seismic motion (i.e., source, path, and site). Moreover they correctly reflect the correlation between the vertical and horizontal components of motion.

As the definition of seismic hazard at the site is usually performed in probabilistic terms, which also account for maximum effects potentially caused by different events, the selection of real records compatible with the expected seismic demand, usually represented in terms of response spectra, necessarily requires the selection of multiple records. Each selected record contributes in a different way to this envisaged compatibility. It is then not surprising that a significant record-to-record variability is commonly found in the selected sets and that it can be particularly relevant in case of nonlinear analysis of degrading systems like masonry structures. Hence, the outcome of the analysis implies a dispersion of the results, normally increasing as the nonlinear component of the structural response increases. This dispersion in the assessed response has to be properly coped with when interpreting the analysis results, as discussed in the following sections.

As also required by several building codes, the consistency of the selected time-series with the seismic hazard is often associated with the idea of "spectrum-compatibility", normally consisting in imposing that the difference between the average response spectrum of the selected accelerograms and the target response spectrum is smaller than a predefined tolerance in a specified interval of structural periods (based on the fundamental period of the system to be analyzed). In most cases, to satisfy spectrum-compatibility, records need to be linearly scaled to a predefined value, which can be the PGA or another selected ordinate of the target spectrum. It is important to emphasize however that the selected records also need to satisfy the requirement of "seismo-compatibility" which means that they must be consistent with the regional seismotectonic and seismogenic setting, as discussed for example in [19].

The rapidly increasing number of good quality strong-motion records seems to make the use of real records a natural and easier choice for practitioners. Moreover, in recent years, several international strong-motion accelerometric databases have been developed, most of which are available over the web, which allow to interactively search events and retrieve waveforms in digital form with prescribed characteristics. Searches can be generally performed using parameters such as magnitude, epicenter distance (or some other definition of distance from the source), site classification, rupture mechanism, peak ground acceleration (PGA), peak ground velocity (PGV), and peak ground displacement (PGD). Specific tools have been developed for the selection of spectrum-compatible suites of real accelerograms, both limited to research purpose (e.g. ASCONA [19]) or available to the general public (e.g. REXEL [20]). Both ASCONA and REXEL-DISP [21] allow for imposing spectrum compatibility either to the acceleration or the displacement response spectrum, being the second option preferable in case of nonlinear analysis.

Despite this, the selection of the appropriate input for time history analysis still requires some skills that are not common for practitioners. For this reason, Rota et al. [22] proposed a web application named SEISM-HOME (SElection of Input Strong-Motion for HOmogeneous MEsozones), available at the internet site www.eucentre.it/seismhome.html, which allows an automatic and prompt definition, at any location of the Italian territory, of the seismic input represented by suites of real spectrum- and seismo-compatible accelerograms recorded at outcropping rock sites with flat topographic surface. However, these records are currently available for the 475 years return period only.

4 IDENTIFICATION OF SUITABLE LIMIT STATES FROM NONLINEAR DYNAMIC ANALYSES OF MASONRY STRUCTURES

The need of identifying suitable performance limit states was early recognized and a rather vague and qualitative definition of the desired performance was described by socio-economic terms. Expressions like "collapse", "near collapse", "collapse prevention", "life safety",

"operational", "fully operational", "immediate occupancy", "damage control" and "serviceability" are used to describe the performance limit states in various documents (e.g. [23]). Nevertheless, as already realized by many authors, these definitions are not appropriate for direct application in numerical analyses and the quantitative translation of the limit states is not straightforward,. For example, Tomaževič [24] observed that it is not possible to quantify the limit states on the basis of the observed damage or of damage indices, which measure the damage occurring to the walls and/or buildings as a whole. Therefore, he tried to establish a correlation between this qualitative definition and the results of experimental studies. Along the same ways, several examples of experimental studies can be found in the literature, where cyclic in-plane tests were performed on masonry piers aiming to describe the different deformation limits at the structural element level for the two damage modes (flexural/rocking and shear failure mode) of the in-plane response of masonry structures (e.g. [25],[26],[27],[16]).

To interpret the results of numerical analyses a quantitative definition of performance levels is necessary, consisting of a proper damage indicator, able to represent the global seismic performance, and adequate damage thresholds expressed in terms of the selected damage indicator.

A quantitative measure of structural performance can be realized with the use of drift/deformation quantities. Such drift thresholds are influenced by the masonry typology, the level of axial loading, the effective boundary conditions and other construction details (e.g. [28]). As discussed for example in [29], displacements and deformations are better indicators of damage than forces and therefore the identification of structural performance levels should be better based on these quantities. In addition to the previous, it is necessary to find significant thresholds of each limit state, that should be expressed in terms of the aforementioned drift quantities and derived from some other measures of structural performance extracted from the results of nonlinear dynamic analyses. Examples of the latter could be some parameter expressing the extension of damage within the different structural elements, or the degradation of the structural response (i.e. in terms of stiffness, lateral strength, etc…) due to progressive damage.

Since a quantitative definition of limit states based on the results of nonlinear static analysis has been proposed by many authors, once the indicators and the thresholds are defined, the results in terms of the selected limit state indicators could be compared to limit state thresholds defined from results of nonlinear static analyses. Examples of some of the adopted definitions of limit states are based on the following quantitative parameters:

1. Significant displacements from the global pushover curve (i.e. the base shear-top displacement curve), as proposed for example in [17]. Specifically, in that work, LS2 was defined as the global displacement corresponding to the attainment of the maximum base shear and LS3 as the displacement corresponding to a shear strength degradation up to 80% of its maximum value (as also suggested in several building codes).
2. Global displacement thresholds corresponding to the attainment of inter-story drift limits. For example, Calvi [30] defined LS2 as the displacement corresponding to the attainment of a maximum inter-story drift of 0.3% and LS3 as the displacement corresponding to the attainment of an inter-story drift of 0.5%.
3. Some indicator of the diffusion of damage, identified for example in [28] by monitoring the level of damage reached in each wall panel.

For the assessment of masonry structures the limit states of interest can be described as:

- LS1-immediate occupancy,
- LS2-damage limitation,

- LS3-life safety,
- LS4-near collapse.

An analytical study with the objective of proposing a suitable definition of significant limit states for masonry buildings, applicable to the results of incremental dynamic analyses (IDA, [31]) was conducted recently by the authors [32].

The study concentrated on the investigation of possible limit state definitions corresponding to the two intermediate limit states (LS2 and LS3) as their identification appears more uncertain and somehow more critical than that of the first and last limits. The identification of LS4 was not addressed, because the definition of the near collapse limit state from the results of numerical analyses is really a difficult task. With reference to nonlinear dynamic analyses, this limit state could be identified by monitoring the IDA curve for each earthquake record and identifying the point for which the slope of the curve approaches zero, as suggested by Ibarra and Krawinkler [33]. However this definition is really vague and it does not easily allow a univocal identification of this limit state. Moreover, as also discussed by Zareian and Krawinkler [34], evaluation of near collapse structural response parameters is strongly related to issues such as assumptions in the structural model, computer program used for the analysis, numerical convergence and stability of the solution. Therefore, the evaluation of LS4 was left aside.

The identification of limit state indicators was approached by applying some proposed criteria to five building models of existing stone masonry buildings. The methodology included the identification of performance limit states from both the results of nonlinear static and dynamic analysis and the comparison of the results obtained in the two cases.

4.1 Drift quantities selected to describe and compare performance levels

To be able to compare alternative definitions of the significant thresholds of structural performance, the significant thresholds derived from different damage quantities need to be expressed by the same drift/displacement quantities. For this reason, in the analytical work of Mouyiannou et al. [32] all the analysis results were interpreted according to two drift quantities, namely the maximum inter-storey drift δ_{max} and a weighted average drift δ_w $\boldsymbol{\delta_w}$, which were derived from nodal displacements and from element drifts respectively.

The maximum inter-storey drift δ_{max} is the maximum value of pier drift δ_i, derived by the absolute difference of nodal displacements divided by the inter-story height as:

$$\delta_{max} = \max\{\delta_i\} = \frac{\max|d_{N_j} - d_{N_i}|}{h} \quad (1)$$

where: d_{Nj} and d_{Ni} are the displacements of nodes N_j (top node of the pier) and N_i (bottom node of the pier), respectively, and h is the inter-story height.

The weighted average drift δ_w is calculated as the average of the drifts of all the elements of the critical story, weighted on their area, according to the formula:

$$\bar{\delta}_w = \frac{\sum_{i=1}^{n}[(A]_i \delta_i)}{\sum_{i=1}^{n} A_i} \quad (2)$$

where A_i is the area of the pier i, δ_i is the drift of the pier i and n is the total number of piers of the critical storey, identified as the storey where damage concentrates. The values of δ_i are the element shear drifts, which only account for the shear element deformation, i.e. they are computed by removing the flexural deformation and rigid rotation components from the element drift. This shear drift is an output of the macro-element model, to which the shear behavior with stiffness degradation and strength deterioration is directly related and hence it is

considered a suitable indicator of the level of damage in the element. The criteria proposed in [32] for the identification of each limit state are described in the following sections.

4.2 Identification of LS1 (one criterion)

The first limit state can be identified as the displacement that corresponds to the first pier reaching its maximum shear resistance.

4.3 Identification of LS2 and LS3 (3 criteria)

The application of three different criteria was investigated in order to identify limit states which are not directly based on drift quantities, but also described by means of some parameter, representative of the evolution of the structural condition during the nonlinear dynamic analysis. Therefore, each criterion is based on consideration of different damage indicators, all of them trying to synthesize the overall structural behavior, such as for example the extension of damage to the structural elements (criterion 2) or the degradation of the structural response with progressive damage (criterion 1).

As explained in the previous section, the drift quantities corresponding to the attainment of the limit states according to the different criteria were evaluated and compared among each other, to verify whether these definitions of the limit states provide stable and reasonable results in terms of the deformation conditions reached by the structure during the dynamic response. The drifts were also compared to the results of similar criteria applied to pushover analysis.

Regarding the damage limitation state, an extra limitation to the maximum inter-story drift, which should not exceed the value of 0.2% was also adopted.

The criteria proposed to define the damage limitation limit state (LS2) and life safety limit state (LS3) from the results of incremental dynamic analyses (IDA) are discussed in the following.

Criterion 1: identification of LS2 and LS3 from total base shear

The methodology considered for criterion 1 is similar to the definition of limit states from the pushover curve reported in [17], where LS2 and LS3 were identified as corresponding to the attainment of the maximum lateral strength and to its degradation to 80% of the maximum value, respectively. Similarly, for the case of time-history analysis, for each earthquake record analyzed, LS2 is attained at the analysis step for which the shear resistance is reaching its maximum value and LS3 at the step where it drops to 80% of its maximum value. Then the drifts corresponding to the two limit states are derived and their average values among the earthquake records used for the analyses can be calculated. This criterion is very fast and easy to apply and it does not require any engineering judgment or subjectivity, as the definition of the corresponding limit states is quantitative and objective.

Criterion 2: identification of LS2 and LS3 based on the percentage of pier area failing

According to criterion 2, LS2 and LS3 are identified based on the number and percentage of piers achieving the maximum shear drift (predefined value). A reasonable value for maximum shear drift could be 0.4%, as suggested in the EC8-3 [35], although it makes reference to a different definition of element drift. The drift mentioned in the codes is the total element drift, including both shear and flexural components and eventually excluding rigid motions, whilst in the described analytical work the flexural component is removed. The use of the limit of 0.4% indicated in the codes was considered appropriate, because it is derived

from experimental evidence of in-plane cyclic tests on mainly squat masonry panels, in which it can be assumed that, when shear failure occurs, the shear deformation component is the one representative of the degradation of the structural response and it is prevailing over the flexural one.

LS2 (damage limitation) is assumed to occur when the first pier reaches the predefined value of shear drift. In order to provide results meaningful for comparison to the results from other criteria, the results are expressed in terms of the average drift values (as defined in section 4.1) calculated from all the earthquake motions used for the analysis.

LS3 is instead corresponding to an appropriately defined level of damage extension, which is expressed in terms of the percentage of the area of the piers that have attained the maximum shear drift with respect to the total pier area, i.e.:

$$A_{fp}[\%] = \frac{\sum_i^m A_{pi}}{\sum_j^n A_{pj}} \cdot 100 \tag{3}$$

where m is the number of the piers attained the maximum shear drift and n is the total number of piers. For each PGA level considered for the analyses, and for each earthquake record, the percentage of the pier area failing is calculated and compared with a predefined target percentage. For each considered building, LS3 is then attained when the average (among all the earthquake records used) percentage area reaches the predefined drift limit.

Attention should be taken when evaluating the appropriate target percentage area for LS3 since the procedure is strongly dependent on its definition which needs to be identified case by case and whose value cannot be considered as general. The value needs to be selected based on engineering judgment and should be associated with drift values which are in accordance with those derived from nonlinear static analyses. In addition, this percentage should guarantee collapse prevention, i.e. limited lateral strength degradation, since the criterion is applied to identify the life safety condition. A reasonable percentage, representative of the results, was considered to be 50% of the total pier area in the direction of analysis.

Criterion 3: identification of LS2 and LS3 from PGA-drift curves

The third criterion is applied to the so-called IDA curves which form an alternative representation of the results of incremental dynamic analyses, reporting the level of PGA versus an appropriately defined drift quantity. Each curve is a multi-linear curve obtained by joining the drift values calculated for subsequent levels of PGA examined. The average PGA-drift curve for the critical story of each building can be evaluated by plotting the average drifts among the earthquake records for each PGA.

LS2 can be identified at the first significant change of slope in the average curve. This change of slope is related to an increased rate of drift variation as a function of PGA, which can be seen as representative of an increase of structural damage.

LS3 can be identified as the range of drifts between which the slope of the curve degrades reaching a predefined percentage of the initial slope. This percentage is selected according to engineering judgment in order to represent a damage level adequate for the life safety limit state and should provide drift values in agreement with the results of nonlinear static analysis. Based on the results obtained in the considered analytical study and specifically on the comparison of the corresponding drift values with those derived from the results of nonlinear dynamic analyses by applying the other criteria and the results of nonlinear static analyses, a percentage equal to 7% of the initial slope was selected (after having tried different values up to 10%).

4.4 Application of limit state identification criteria to the results of nonlinear dynamic analysis of existing masonry buildings

The identification criteria for the three limit states discussed above were applied to 5 building prototypes, which are briefly presented in the following. The main outcomes obtained from the application of the criteria are then discussed.

4.4.1 Building prototypes, modeling assumptions and selected ground motions

Five building configurations were selected as representative of different structural typologies of unreinforced stone masonry structures. Their models are shown in Figure 4. All the analyses were performed is the x-direction indicated in the figure.

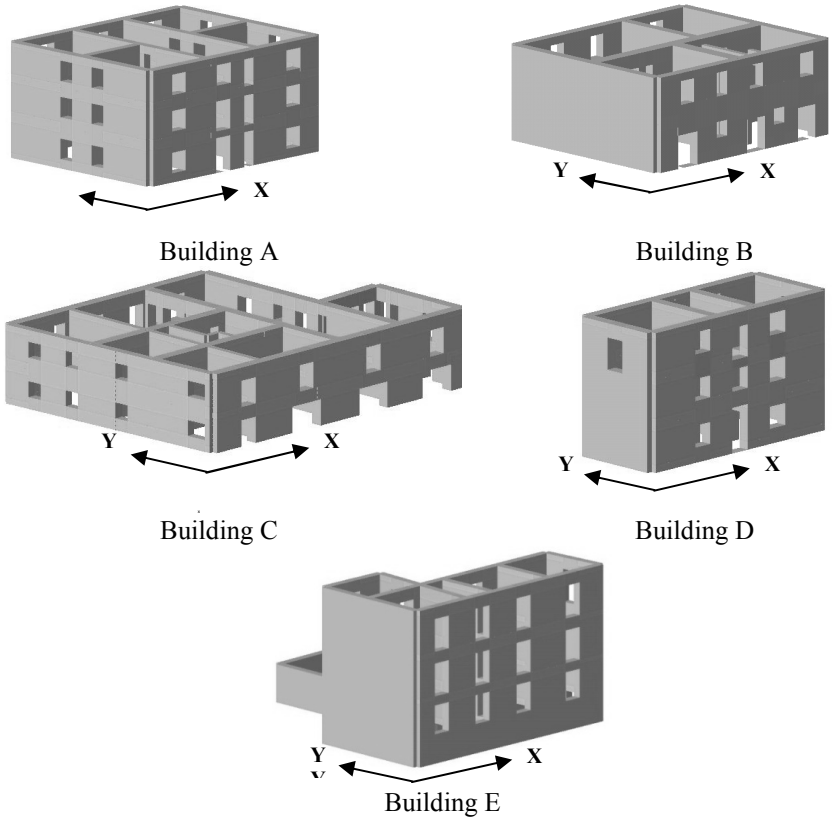


Figure 4 Analyzed structural configurations (after [32]).

All buildings were assumed to have stiff diaphragms, an assumption consistent with the adopted modeling approach which only considers a global type of response, which is not governed by the out-of-plane behavior of walls. Out-of-plane failure mechanisms are assumed to be prevented by proper connections and detailing.

The mechanical properties of stone masonry adopted in the model were defined according to the specimens of an extended experimental campaign carried out in Pavia in the last years ([36][37]), consisting of a wide characterization campaign (including tests on mortar, vertical compression and diagonal compression tests on wallettes, cyclic shear compression tests on walls), followed by full-scale shaking table tests on three prototype buildings [38][39]. The average experimental values of the elastic modulus, E, the shear modulus, G, the masonry density, ρ, and the compressive strength of masonry, f_m have been used. The values used for the initial shear resistance for zero compression, f_{v0} and the friction coefficient, μ were instead

obtained from the calibration of the macro-element model on the results of cyclic in-plane tests of masonry piers [26].

Incremental dynamic analyses were performed using seven real earthquake records, scaled to increasing values of PGA (from 0.05g to 0.60g) to represent different levels of seismic severity. The selection of the real spectrum-compatible accelerograms was made using the algorithm of the ASCONA program [19]. The real records were selected to be compatible in the mean with the EC8-1 [1] type 1 acceleration response spectrum. The spectrum was anchored to a PGA of 0.2g, selected to be approximately a central value of the seismic intensities considered for the analyses. This choice was based on the attempt of limiting the scale factors applied to the records, as these seven records were then scaled to the different levels of PGA for which nonlinear dynamic analyses were carried out.

4.4.2 Resulting drift thresholds for LS1, LS2 and LS3

LS1 was identified as the state corresponding to the first pier reaching its maximum shear strength as reported in section 4.2. The average values (between the 7 earthquake records analyzed) of maximum element drifts corresponding to LS1, are presented in Figure 5.

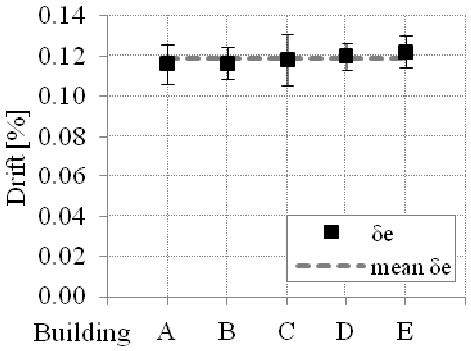
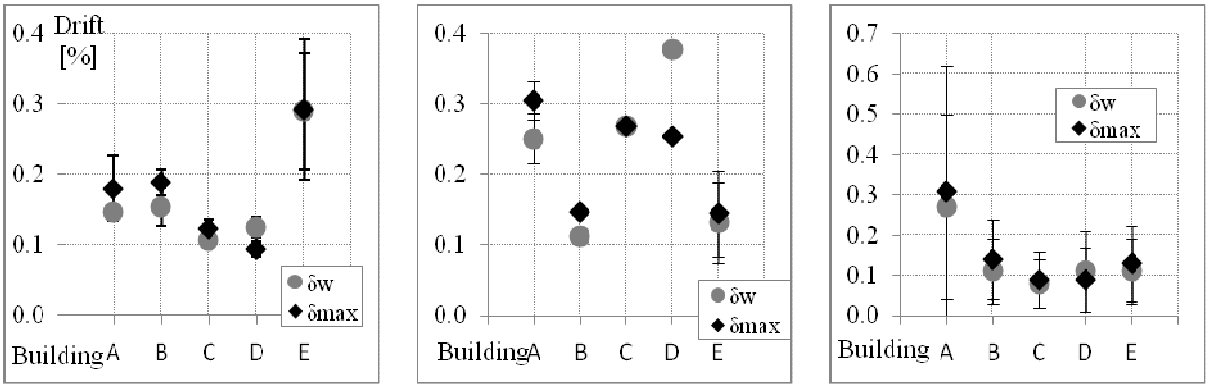


Figure 5 Maximum element drifts corresponding to the attainment of LS1 (average of 7 earthquake records)

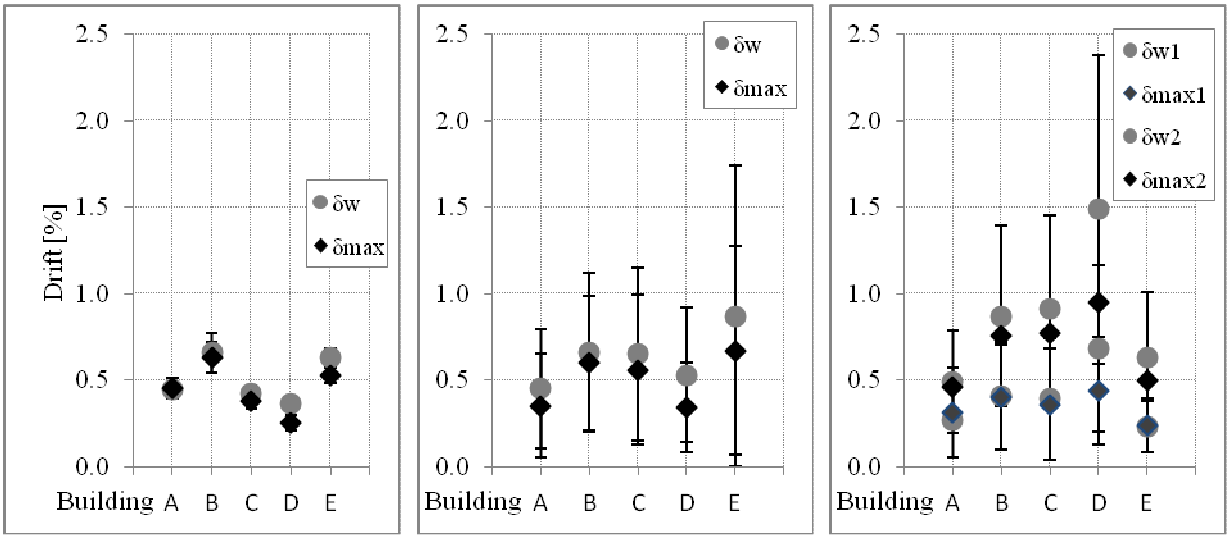
The average value derived from all buildings is 0.12%, in agreement with the experimental results obtained in [27], according to which the maximum shear resistance of a stone masonry element is reached for a maximum element drift in the range of 0.10-0.15%. The results confirm that the drifts corresponding to LS1 are not depending on the building typology or on the earthquake records, as they are only a property of the numerical model and of the masonry typology.

The drift values corresponding to the attainment of the damage limitation limit state and life safety limit state were identified by applying the three identification criteria as described previously. The derived drift quantities, namely the average (between the earthquake records used) maximum inter-story drift (δ_{max}) and weighted average story drift (δ_w), resulted by the application of the criteria for the identification of LS2 and LS3 are presented in Figure 6 and Figure 7 respectively for all the buildings analyzed. The drift values noted with black diamonds correspond to δ_{max} and grey circles to δ_w. The error bars represent the coefficient of variation (C.o.V) resulting from record-to-record variability.



a) Criterion 1 b) Criterion 2 c) Criterion 3

Figure 6 Average drift quantities resulting from the application of criteria for the identification of LS2



a) Criterion 1 b) Criterion 2 c) Criterion 3

Figure 7 Average drift quantities resulting from the application of criteria for LS3

As observed in Figure 6.a), the application of criterion 1 for LS2 identification, results in values of both the drift quantities between 0.1 and 0.2%, with the only exception of the drifts for building E. In this case, both drifts are equal to 0.29%, which in case of δ_{max} exceeds the limit value of 0.2%. However the limits for building E are characterized by the largest coefficient of variation. Apart from the case of building B, the C.o.V. of the values of δ_w is always lower than that of δ_{max}, although their values vary significantly from building to building.

The range of drift values obtained by the application of criterion 2 is larger than the range of drift values of LS2 resulting from the application of criterion 1, with values between 0.1 and 0.38%, as shown in Figure 6b. Nevertheless the values of C.o.V are lower than the values resulting from the other criteria, indicating a small dependence of the application of criterion 2 to the record-to-record variability.

Regarding the average drift values obtained by the application of criterion 3 for LS2 (Figure 6.c), similar values around 0.1% are observed for all buildings except for building A, which attained a significantly higher value. It has to be underlined that the C.o.V has very

large values for the application of criterion 3, showing a high dependency of the results of the criterion on the record-to-record variability.

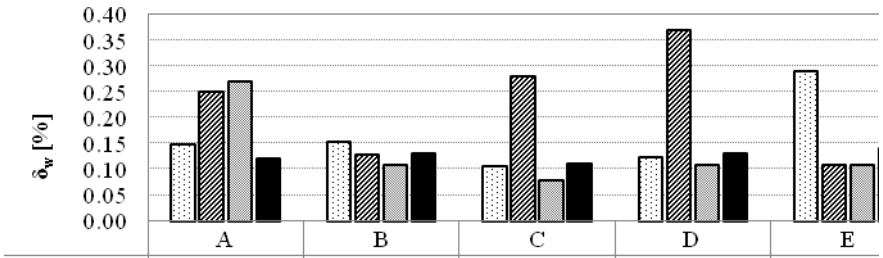
The drift values corresponding to LS3, derived by the application of criterion 1 are ranging between 0.25% and 0.65%. The maximum C.o.V.is found for the case of δ_w for building B, and it is equal to 17.5%, which is small compared to the values of C.o.V resulting from the application of the other criteria for the derivation of LS3. It can be noted that, as observed from the application of criterion 1, the average values of the two drift quantities for LS3 are quite similar to each other, with the exception of building D.

The drift values of LS3 obtained by the application of criterion 2 (shown in Figure 7.b.) correspond to the level of PGA for which the average percentage (among the results from seven earthquakes) of piers reaching the maximum shear drift exceeds the 50% of the total pier area. From the values obtained, a rather wide range of drift is noticed, with buildings A and D having similar drift values at the lower bound of the range and buildings B, C and E having similar values at the higher bound of the range. It is important to notice the very large C.o.V. resulting for all buildings, indicating the significant dependence of the results of this criterion on the record-to-record variability.

As previously explained the results of criterion 3 are expressed by two values of drift corresponding to the upper and lower value of the drift range for which the slope of the IDA curve drops below a predetermined percentage of the initial slope. The results (reported in Figure 7.c) show a significant variability from building to building both in terms of the range width and of the values corresponding to the upper and lower bound drift values. This is related to the level of discretization of the PGA values used for the analyses and to the slope of the curve in the drift range of interest. Also, the very large values of C.o.V. indicate the strong dependency of the results on the record-to-record variability.

4.5 Comparison of the applied criteria and selection of the optimal criteria for LS2 and LS3 identification

A comparison between the results derived by the application of different criteria to the results of nonlinear dynamic analysis and also to the results of nonlinear static analysis is visualized with the histograms from Figure 8 to Figure 11. The first two histograms correspond to the results for LS2 and represent the values of weighted average story drift and its C.o.V due to the record-to-record variability. The choice of reporting only the results for LS2 in terms of weighted average story drift is based on the fact that it provided a better match with the results of pushover analyses than the maximum inter-story drift.



	A	B	C	D	E
Crit. 1 [TH]	0.15	0.15	0.11	0.13	0.29
Crit. 2 [TH]	0.25	0.13	0.28	0.37	0.11
Crit. 3 [TH]	0.27	0.11	0.08	0.11	0.11
Cyclic PO	0.12	0.13	0.11	0.13	0.14

Figure 8 Weighted average drift limits for LS2 derived from the results of nonlinear dynamic analysis by applying the three identification criteria and from the results of nonlinear static analysis.

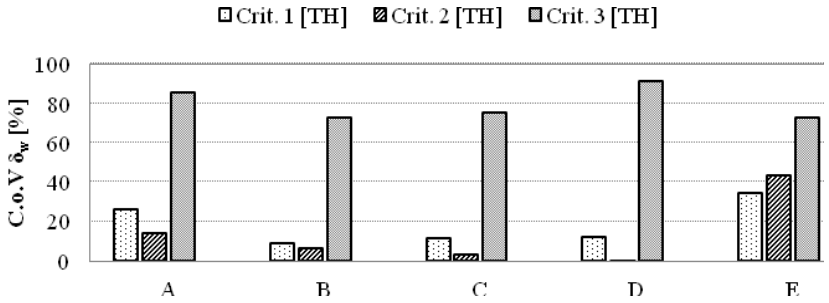
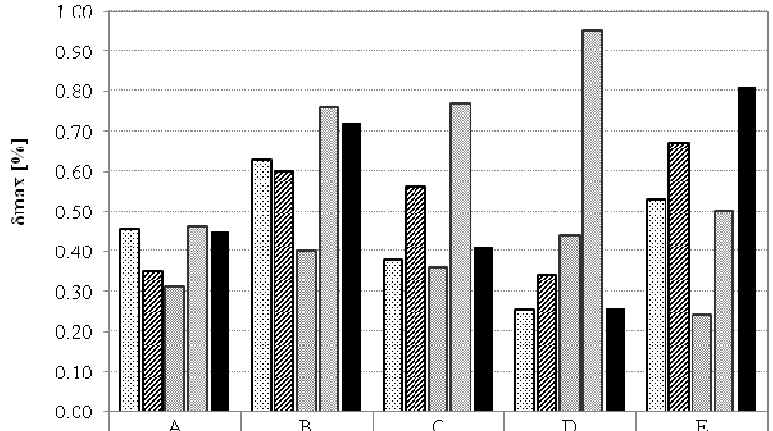


Figure 9 Coefficient of variation of the values of weighted average story drift limits of LS2, due to record-to-record variability.

Looking at the results obtained for LS2 in terms of weighted average drift as presented in Figure 8, it can be noted that criterion 1 and criterion 3 are reproducing quite well the results obtained from pushover analysis, with the exception of building E and A, respectively for the two criteria. Criterion 2 provides higher values of drift than all other criteria for buildings C and D and, in general, a good agreement with the results obtained from pushover analysis cannot be found.

As can be observed by Figure 9 criterion 3 has a significantly higher value of C.o.V. with respect to the others. For both criteria 1 and 2, building E has significantly higher values of C.o.V., which may be related to the marked structural irregularity of the building. Consequently both criterion 1 and criterion 2 appear to be suitable for the identification of LS2, always combined with the limitation of the maximum inter-story drift to the value of 0.2%.

A comparison of the drift limits provided by the different criteria for LS3 is shown in Figure 10 and Figure 11 in terms of the average value of maximum inter-story drift and its C.o.V due to record-to-record variability respectively. For this limit state, results are presentedin terms of maximum inter-story drift, since this drift shows a better agreement with the results of nonlinear static analysis.



	A	B	C	D	E
Crit. 1 [TH]	0.45	0.63	0.38	0.26	0.53
Crit. 2 [TH]	0.35	0.60	0.56	0.34	0.67
Crit. 3-min[TH]	0.31	0.40	0.36	0.44	0.24
Crit. 3-max[TH]	0.46	0.76	0.77	0.95	0.50
Cyclic PO	0.45	0.72	0.41	0.26	0.81

Figure 10 Maximum inter-story drift values for LS3 derived from the results of nonlinear dynamic analysis by applying the three identification criteria and from the results of nonlinear static analysis.

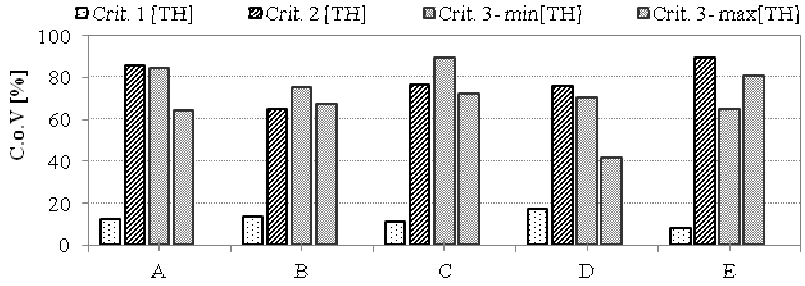


Figure 11 Coefficient of variation of the values of maximum inter-story drift for LS3, due to record-to-record variability.

The histogram of Figure 10 shows that the different criteria provide different results in terms of attained drifts, as expected since each criterion is based on consideration of different quantities. In order to apply criteria 2 and 3, some reasonable target values has been assumed for the percentage of pier area failing and the percentage of the initial slope, respectively. It is generally noticed that there is no unique value of percentage to be set for criteria 2 and 3 to guarantee that the requirements of the other criteria will be met for all buildings. For the application of criterion 3 to identify LS3, the considered target value of the slope reduction with respect to the initial slope (7%) leads to drift ranges which are not always in agreement with the results of criterion 1 and 2. In case of the maximum inter-story drift, even for building E the value produced by criterion 1 is outside the range of criterion 3. Criterion 2 provides instead results within the range defined by criterion 3 only for buildings A, B and C.

The results obtained from pushover analyses are in general more consistent with the results from criterion 1 rather than with those obtained from the other two criteria, with the only exception of building E. This similarity of the results could be expected as criterion 1 is analogous to the definition of limit states used for pushover analyses. Regarding building E it should be noted that the structure is irregular in plan and in elevation and therefore the application of nonlinear static analysis is questionable and the validity of its results is not guaranteed.

Finally by observing Figure 11 it is obvious that the drifts derived from criterion 1 for LS3 have a coefficient of variation much smaller than that corresponding to the other criteria.

The aforementioned difficulties in the application of criteria 2 and 3, in addition to the significantly larger coefficient of variation of the drifts obtained by these criteria, led to the selection of criterion 1 as the optimum for the identification of LS2 and LS3 from the results of nonlinear dynamic analysis. Criterion 1 is indeed the criterion providing the most stable and consistent results and it is the least dependent on the record-to-record variability. Moreover, it is equivalent to the definition of LS2 and LS3 based on the results of nonlinear static analyses and it is the most straightforward to apply, as it does not require any particular engineering judgment or the definition of target values. (i.e. the percentage of pier area failing for criterion 2 and the percentage of slope reduction for the PGA-drift curves for criterion 3).

5 CONCLUDING REMARKS

As stated in the introduction, the use of nonlinear time-history analysis for masonry structures requires suitable modeling approaches and an appropriate selection of input ground-motion records. The latter is an issue common to all structural types and several solutions are available.

The TREMURI computer program, concisely presented in section 2, includes modeling and analysis features specifically developed for the dynamic analysis of entire masonry buildings.

What is still missing is a well-defined method for identifying the structural performance levels based on damage and/or displacement/deformation indicators, which would help in the interpretation of the results of dynamic analyses and may support a broader application of the performance-based procedure with incremental time-history analysis of masonry buildings.

A procedure for the identification of limit states has been presented in this paper. The first limit state considered, i.e. immediate occupancy (LS1), was identified as corresponding to the first pier reaching its maximum shear strength. The definition of LS2 (damage limitation) and LS3 (life safety) from the results of time-history analyses was more problematic and therefore three different criteria were proposed and tested, each one concerning requirements on different quantities. The first criterion was based on global lateral strength evolution, the second criterion on damage diffusion and the third criterion on the degradation of the structural response for increasing levels of ground motion. Each of these parameters was considered to be a good descriptor of the global structural performance, taking into account the overall behavior of the considered buildings. In order to compare the results of the different criteria (which are based on completely different quantities) and to make sure that they provide reasonable results in terms of deformation capacity, conveniently defined drift quantities were associated with the limit states identified with the different criteria

For each limit state, the best criterion was selected together with the associated drift quantity providing the most stable (and the least dependent on the record-to-record variability) and consistent results, i.e.:

- LS1 identified as corresponding to the first pier attaining its maximum shear resistance;
- LS2 defined as the average weighted story drift corresponding to the attainment of the maximum base shear;
- LS3 identified as the maximum inter-story drift corresponding to a 20% degradation from the maximum value of base shear.

The reported study was limited to a small number of building configurations and a specific masonry typology. Other important parameters should also be explored in order to verify the adequacy of the proposed criteria for the identification of relevant limit states. In addition to the previous, the consistency of the proposed approach with experimental results and empirical observations should be verified.

ACKNOWLEDGEMENTS

This work was carried out with the partial financial support of the EUCENTRE Executive Project 2012-2014 e3 “Seismic vulnerability of masonry buildings”, funded by the Italian Department of Civil Protection, and the PRIN Project 2009 “Analysis and modeling of multi-leaf masonry structures for the protection of built heritage”, funded by the Italian Ministry of Instruction, University and Research.

REFERENCES

[1] EN 1998-1. Eurocode 8: Design of structures for earthquake resistance - Part 1: General rules, seismic actions and rules for buildings. CEN, Bruxelles, 2004.

[2] M. Tomaževič, The computer program POR, Report ZRMK, Ljubljana, 1978 (in Slovenian).

[3] G. Magenes and A. Della Fontana, Simplified non-linear seismic analysis of masonry buildings, *Proc. of the British Masonry Society*, No. 8, 190-195, 1998.

[4] A. Galasco, S. Lagomarsino, A. Penna and S. Resemini, Non-Linear Seismic Analysis of Masonry Structures, *Proc. 13th World Conference on Earthquake Engineering*, Vancouver, Canada, 2004.

[5] G. Magenes, A Method for Pushover Analysis in Seismic assessment of Masonry Buildings, *Proc. 12th World Conference on Earthquake Engineering*, CD-ROM, Auckland, New Zealand, 2000.

[6] A.J. Kappos, G.G. Penelis and C.G. Drakopoulos, Evaluation of simplified models for lateral load analysis of unreinforced masonry buildings, *Journ. of Struct. Engineering*, ASCE, 128(7): 890-897, 2002.

[7] Y. Belmouden and P. Lestuzzi, An equivalent frame model for seismic analysis of masonry and reinforced concrete buildings, *Construction and Building Materials*, 23(1): 40-53, 2009.

[8] S. Lagomarsino, A. Galasco and A. Penna, Non Linear Macro-Element Dynamic Analysis of Masonry Buildings, *Proc. ECCOMAS Thematic Conference on Computational Methods in Structural Dynamics and Earthquake Engineering*, Rethymno, Crete, Greece, 2007.

[9] S. Lagomarsino, A. Penna, A. Galasco and S. Cattari, TREMURI program: an equivalent frame model for the nonlinear seismic analysis of masonry buildings. *Submitted to Engineering Structures*, 2013.

[10] A. Penna, S. Lagomarsino and A. Galasco, A nonlinear macro-element model for the seismic analysis of masonry buildings. S*ubmitted to Earthquake Engineering and Structural Dynamics*, 2013.

[11] L. Gambarotta and S. Lagomarsino, On the dynamic response of masonry panels, *Proc. of the National Conference "Masonry Mechanics Between Theory and Practice"*, Messina, Italy, 1996 (in Italian).

[12] A. Penna and A. Galasco, A macro-element model for the nonlinear analysis of masonry members including second order effects, *4th International Conference on Computational Methods in Structural Dynamics and Earthquake Engineering (COMPDYN)*, Kos Island, Greece, 2013.

[13] A. Penna, 3D frame-type macro-element modeling for seismic analysis of masonry buildings, in G. De Roeck, G. Degrande, G. Lombaert, G. Muller (eds.), *Proc. 8th Intl. Conf. Struct. Dyn*., Leuven, Belgium, 2011.

[14] A. Galasco, S. Lagomarsino and A. Penna, On the use of pushover analysis for existing masonry buildings, *Proc. 1st ECEES*, Ginevra 2006

[15] G. Magenes, G.M. Calvi and G.R. Kingsley, Seismic Testing of a Full-Scale, Two-Story Masonry Building: Test Procedure and Measured Experimental Response. University of Pavia, Department of Structural Mechanics, Italy, 1995.

[16] A.A. Costa, A. Penna and G. Magenes (2011) Seismic performance of Autoclaved Aerated Concrete (AAC) masonry: from experimental testing of the in-plane capacity of walls to building response simulation, *Journal of Earthquake Engineering*, 15(1): 1-31

[17] M. Rota, A. Penna and G. Magenes (2010) A methodology for deriving analytical fragility curves for masonry buildings based on stochastic nonlinear analyses, *Engineering Structures*, 32(5): 1312-1323.

[18] J.J. Bommer and A.B. Acevedo, The use of real earthquake accelerograms as input to dynamic analysis, *Journal of Earthquake Engineering*, 8(SI1), 43-91, 2004.

[19] M. Corigliano, C.G. Lai, M. Rota and C.L. Strobbia, ASCONA: Automated Selection of COmpatible Natural Accelerograms. *Earthquake Spectra*, 28(3), 965-987, 2012.

[20] I. Iervolino, C. Galasso, and E. Cosenza, REXEL: computer aided record selection for code-based seismic structural analysis, *Bulletin of Earthquake Engineering* 8, 339-362, 2010.
[21] C. Smerzini, C. Galasso, I. Iervolino and R. Paolucci, Ground motion record selection based on broadband spectral compatibility, Earthquake Spectra (in press), 2013.
[22] M. Rota, E. Zuccolo, L. Taverna, M. Corigliano, C.G. Lai, A. Penna, Mesozonation of the Italian territory for the definition of real spectrum-compatible accelerograms. *Bulletin of Earthquake Engineering*, 10(5), 1357-1375, 2012.
[23] H. Krawinkler, Challenges and progress in Performance-Based Earthquake Engineering, *Proc. of Intl. Seminar on Seismic Engineering for Tomorrow- in Honor of Professor Hiroshi Akiyama*, Tokyo, Japan, 1999.
[24] M. Tomaževič, Earthquake-resistant design of masonry buildings, Imperial College Press, Series on innovation in structures and constructions, 1999.
[25] M. Tomaževič, M. Lutman, and M. Petković, Seismic behaviour of masonry walls: experimental simulation, *J. of Structural Engineering*, ASCE, 122(9): 1040-1047, 1996.
[26] G. Magenes, P. Morandi, and A. Penna, In-plane cyclic tests of calcium silicate masonry walls, *Proc. of the 14th Intl. Brick/Block Masonry Conference*, Sydney, Australia, 2008.
[27] A. Galasco, G. Magenes, A. Penna, and M. Da Paré, In-plane cyclic shear tests of undressed double leaf stone masonry panels" *Proceedings of the 14th European Conference on Earthquake Engineering*, paper N. 1435, Ohrid, Macedonia, 2010.
[28] A. Penna, Tools and strategies for the performance based seismic assessment of masonry buildings, Protection of Built Environment Against Earthquakes, ed. Dolšek, M., Springler Science, 2011.
[29] M.J.N. Priestley, G.M. Calvi and M.J. Kowalsky, Direct Displacement-based Seismic Design of Structures. IUSS Press, Pavia, 2007.
[30] G.M. Calvi, A displacement-based approach for vulnerability evaluation of classes of buildings, *Journal of Earthquake Engineering* 3(3), 411-438, 1999.
[31] D. Vamvatsikos and C.A. Cornell, Incremental dynamic analysis, *Earthquake Engineering & Structural Dynamics*, 31(3): 491-514, 2002.
[32] A. Mouyiannou, M. Rota, A. Penna and G. Magenes, Identification of suitable limit states from nonlinear dynamic analyses of masonry structures. *Journal of Earthquake Engineering*, 2013 (submitted).
[33] L.F. Ibarra and H. Krawinkler, Global collapse of frame structures under seismic excitations, Report No. 152, J. A. Blume Earthquake Engineering Center, Stanford, 2005.
[34] F. Zareian and H. Krawinkler, Simplified performance based earthquake engineering, Report No. 169, J. A. Blume Earthquake Engineering Center, Stanford University, 1999.
[35] EN 1998-3. Eurocode 8: Design of structures for earthquake resistance - Part 3: Assessment and retrofitting of buildings. CEN, Bruxelles, 2005.
[36] G. Magenes, A. Penna and A. Galasco, A full-scale shaking table test on a two-storey masonry building, *Proc. of the 14th European Conference on Earthquake Engineering*, Ohrid, Macedonia, 2010.
[37] G. Magenes, A. Penna, A. Galasco and M. Rota, Experimental characterisation of stone masonry mechanical properties, *Proc. 8th Intl. Masonry Conference*, Dresden, 2010.
[38] G. Magenes, A. Penna, I. Senaldi, M. Rota and A. Galasco, Shaking table test of a strengthened full scale stone masonry building with flexible diaphragms. *International Journal of Architectural Heritage*, 2013 (submitted).
[39] I. Senaldi, G. Magenes, A. Penna, A. Galasco and M. Rota, The effect of stiffened floor and roof diaphragms on the experimental seismic response of a full scale unreinforced stone masonry building, *Journal of Earthquake Engineering*, 2013 (submitted).

COMPDYN 2013
4th ECCOMAS Thematic Conference on
Computational Methods in Structural Dynamics and Earthquake Engineering
M. Papadrakakis, V. Papadopoulos, V. Plevris (eds.)
Kos Island, Greece, 12–14 June 2013

NEW DAMAGE MODELS FOR PERFORMANCE-BASED EARTHQUAKE ENGINEERING

Terje Haukaas[1] **and Abbas Javaherian Yazdi**[1]

[1] Department of Civil Engineering, University of British Columbia
6250 Applied Science Lane, Vancouver, BC, V6T 1Z4, Canada
{terje, abbas}@civil.ubc.ca

Keywords: Damage Models, Performance-based Earthquake Engineering, Logistic Regression, Probabilistic Methods.

Abstract. *This paper suggests two improvements to the modeling of damage in contemporary performance-based earthquake engineering. Prior to describing these developments, a review of existing performance-based engineering approaches is provided. The review describes three approaches and is accompanied by worked examples to expose the detailed steps. Particular attention is given to the modeling of damage. Subsequently, logistic regression is described for the modeling of discrete damage, followed by a description of Bayesian linear regression for the modeling of continuous visual damage. These two improvements of the state-of-the-art in damage modeling are demonstrated by application to reinforced concrete shear walls.*

1 INTRODUCTION

This paper recommends two improvements to the damage models that are presently employed in performance-based earthquake engineering (PBEE). The work is motivated by the central role that damage modeling plays in PBEE. The prediction of damage and ensuing costs is the key novelty in PBEE compared with traditional force-based and displacement-based seismic design approaches. As such, PBEE represents a crucial step forward because it allows design decisions to be based on cost-benefit considerations that weigh the cost of damage against the cost of construction to prevent such damage. However, cost predictions require a host of models for hazards and structural performance. Furthermore, significant shortcomings remain in our understanding of structural behavior and damage. As a result, this paper stresses the importance of probabilistic modeling and the gathering of data for steady improvement of the models over time.

The point of departure for the two improvements suggested in this paper is the groundbreaking work conducted by the Pacific Earthquake Engineering Research Center (PEER) and the Applied Technology Council 58 project (ATC-58). Conditional probability models form the basis for these efforts, as exemplified by the utilization of fragility functions as damage models in the ATC-58 project. The use of fragility functions has important implications for the damage modeling. Although these functions fit into an appealing analytical framework, they impose several restrictions on the damage modeling that are discussed and relaxed in this paper. The first improvement is to employ logistic regression to create multinomial and multivariate damage models that fit directly into the ATC-58 analysis procedure.

In contrast, the second improvement represents a departure from the ATC-58 analysis procedure. Instead of conditional probability models, which yield probability values, this paper advocates the development of models that predict visual damage, such as crack widths. This approach retains the advantages of the first improvement, namely multivariate modeling, and provides additional advantages in the downstream use of the damage predictions. Specifically, the prediction of visual damage facilitates the prediction of repair actions, which in turn facilitates better predictions of the cost and time of repair.

A challenge associated with the two improvements suggested in this paper is the lack of data to calibrate the new models. In traditional testing of structural components it is common to record force-deformation results, but not visual damage that can be linked to repair actions. This lack of data is a general phenomenon that hampers all damage modeling and this highlights a pressing research need. This paper argues that the solution is not to revert to simple fragility functions based on expert opinion. Rather, the solution is a commitment by the research community to increase the focus on data gathering and steady improvement of probabilistic models. The PEER and ATC-58 projects offer a substantial step in the right direction, and this paper suggests two additional steps.

2 COMPARISON OF METHODOLOGIES

The approach selected for damage modeling is naturally influenced by the methodology selected for the overall PBEE analysis. At present, several PBEE approaches are under development, and all aim to predict the monetary costs associated with earthquakes. To provide context for the damage models put forward in this paper, three PBEE approaches are reviewed. The first is the total-probability-based framing equation established by PEER [1]; the second is the sampling-based analysis approach adopted by ATC-58 [2]; the third is the reliability-based approach employed in the authors' research group [3]. The following exposure stresses the different approaches for damage modeling, and employs worked examples with artificial data to explain the details of each step in the different PBEE approaches.

2.1 PEER framing equation

To understand the PEER approach, consider the four continuous random variables *IM*, *EDP*, *DM*, and *DV*. These represent, respectively, the earthquake intensity measure, the engineering demand parameter that measures the structural response, the damage measure, and the decision variable that measures the repair cost. In the following, random variables are denoted by uppercase letters, while the same lowercase letters represent their realizations. The PEER framing equation employs the theorem of total probability to express the sought probability distribution for DV [1, 4]

$$\begin{aligned} G(dv) &= \int_0^\infty \int_0^\infty \int_0^\infty G(dv \mid dm) \cdot \left| \frac{\mathrm{d}G(dm \mid edp)}{\mathrm{d}dm} \right| \cdot \left| \frac{\mathrm{d}G(edp \mid im)}{\mathrm{d}edp} \right| \cdot \left| \frac{\mathrm{d}G(im)}{\mathrm{d}im} \right| \cdot \mathrm{d}dm \cdot \mathrm{d}edp \cdot \mathrm{d}im \\ &= \int_0^\infty \int_0^\infty \int_0^\infty G(dv \mid dm) \cdot f(dm \mid edp) \cdot f(edp \mid im) \cdot f(im) \cdot \mathrm{d}dm \cdot \mathrm{d}edp \cdot \mathrm{d}im \end{aligned} \tag{1}$$

where G denotes the complementary cumulative distribution function (complementary CDF) and f denotes the probability density function (PDF). $G(\ |\ )$ and $f(\ |\ )$ denote conditional probability distributions. In the original formulation [1] the exceedance probabilities $G(dv)$ and $G(im)$ were replaced by the annual exceedance rates $\lambda(im)$ and $\lambda(dv)$. This is not a principal difference, but to understand the meaning of G it is helpful to note that

$$G(dv) \equiv P(DV \geq dv) \tag{2}$$

and

$$G(dm \mid edp) \equiv P(DM \geq dm \mid EDP = edp) \tag{3}$$

An important purpose of Eq. (1) is its compartmentalization of intensity modeling, structural modeling, damage modeling, and cost modeling. For example, researchers charged with the task of developing damage models for the PEER formulation are asked to develop conditional probability models of the type in Eq. (3). To understand the details of the PEER approach, which is the foundation for the ATC-58 approach described later, Eq. (1) is evaluated in the following for a set of artificial data and models. Figure 1 displays the assumed hazard function, $G(im)$, which is selected to be the lognormal distribution with mean 0.8 and 20% coefficient of variation. For the sake of clarity, the variable *IM* can here be thought of as a unidirectional horizontal pseudo-spectral acceleration, measured in units of acceleration of gravity.

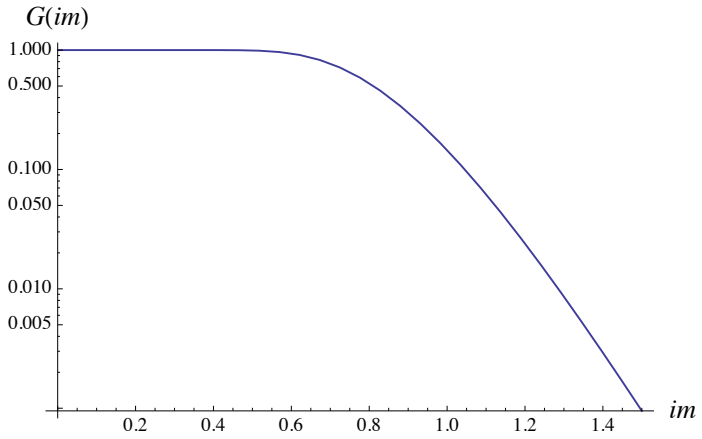


Figure 1. Hazard function.

Figure 2 displays the structural model, $G(edp|im)$ namely the conditional probability distribution for *EDP* given *IM*. Assuming that *EDP* is an inter-storey drift in percent, i.e., the ratio of peak displacement to storey height multiplied by 100, the distribution for *EDP* is here selected to be the lognormal distribution with mean $\mu_{EDP}=2im$ and 20% coefficient of variation. This means that drift realizations will be greater than zero, while drift realizations greater than 5% are unlikely. Naturally, Figure 2 shows that the probability for a high *edp*-value increases with increasing *im*-value.

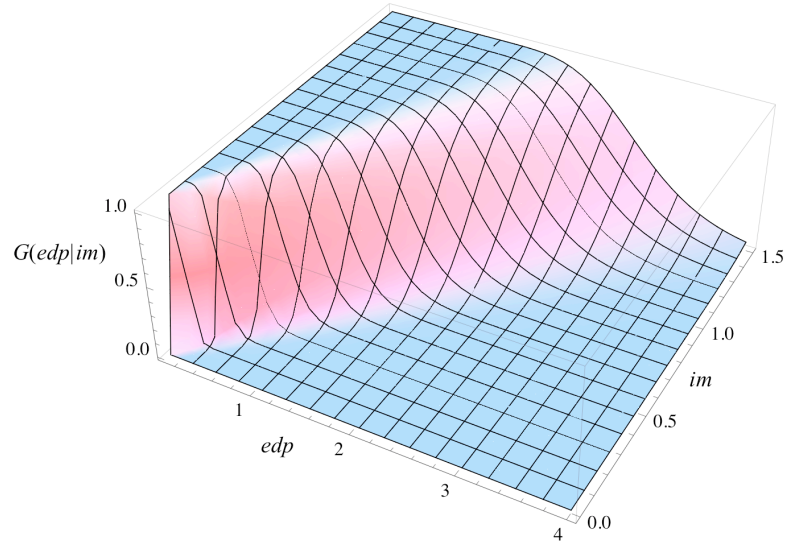


Figure 2. Structural model.

Figure 3 displays the damage model, $G(dm|edp)$, i.e., the conditional probability distribution for *DM* given *EDP*. Assuming that *DM* is a damage index that takes on values in the range from zero to around unity, the distribution for *DM* is here selected to be the lognormal distribution with mean $\mu_{DM}=0.25edp$ and 20% coefficient of variation. Figure 3 shows that the probability for high damage increases with increasing *edp*-value.

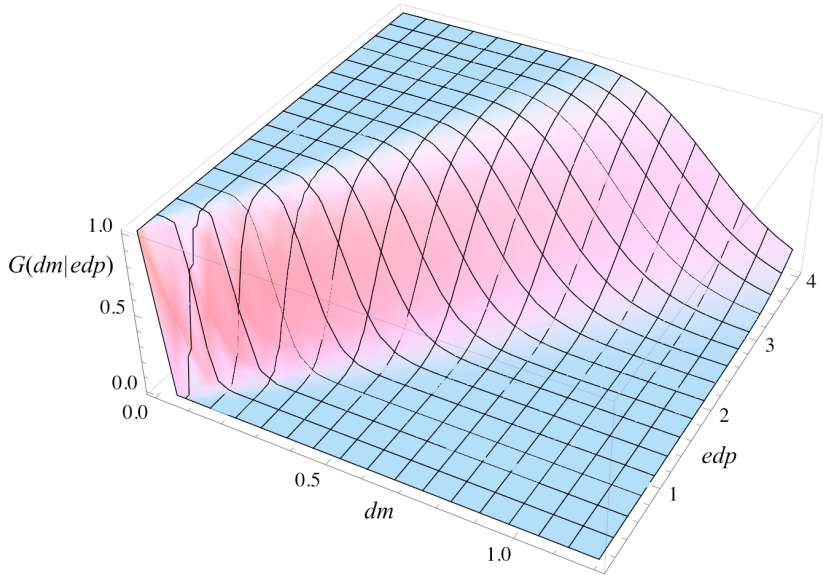


Figure 3. Damage model.

Under the assumption that *DV* represents the cost of repair of damage, $G(dv|dm)$, is selected to be a lognormal distribution with mean μ_{DV}=\$10,000+\$20,000*dm* and 20% coefficient of variation. Figure 4 shows how the probability for high cost increases with increasing damage.

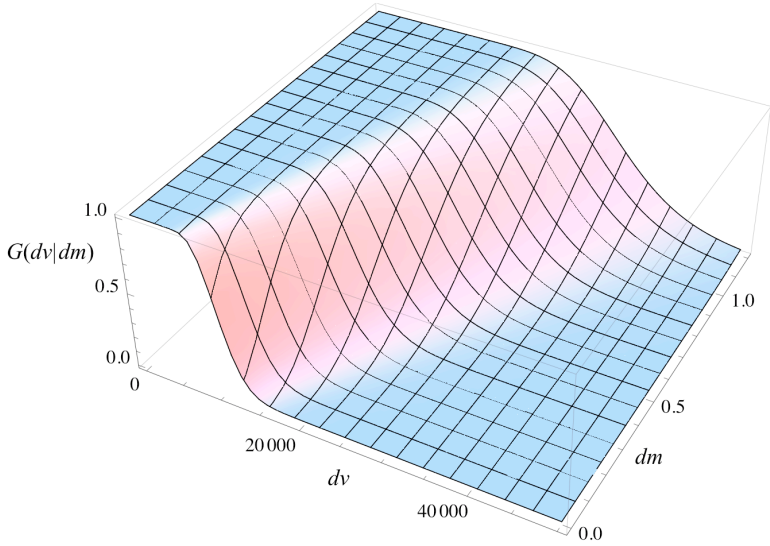


Figure 4. Cost model.

The analytical evaluation of the triple-integral in Eq. (1) is cumbersome. A robust and appealing alternative is to evaluate it numerically as a matrix-vector product. This is achieved by evaluating the probability distributions $G(dv|dm)$, $G(dm|edp)$, $G(edp|im)$, and $f(im)$ at a grid of points along the axes *dv*, *dm*, *edp*, and *im*. Employing index notation, these points are denoted by dv_l, dm_k, edp_j, im_i. Figures 1 through 4 display $f(im_i)$, $G(edp_j|im_i)$, $G(dm_k|edp_j)$, $G(dv_l|dm_k)$ evaluated at those points. This discretization strategy means that $f(im_i)$ is a vector and that the conditional PDFs $f(edp_j|im_i)$, $f(dm_k|edp_j)$, and $f(dv_l|dm_k)$ in Eq. (1) are matrices. As a result, Eq. (1) is evaluated by the matrix-vector product

$$G(dv_l) = G(dv_l \mid dm_k) \cdot f(dm_k \mid edp_j) \cdot f(edp_j \mid im_i) \cdot f(im_i) \tag{4}$$

where summation over repeated indices is implied. From the index notation it is understood that the left-hand side is a vector, and evaluating Eq. (4) with the values displayed in Figures 1 through 4 yields the function $G(dv_l)$ that is plotted in Figure 5. In other words, Figure 5 displays the probability of exceedance of a range of cost values. It is observed that the mean is around \$20,000 and that it is likely that the cost will be greater than \$10,000. Conversely, it is unlikely that the cost will be greater than \$40,000.

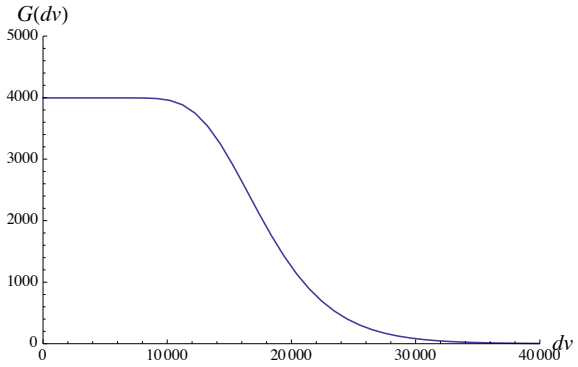


Figure 5. Exceedance probability curve for the decision variable.

The models and results presented above are intended to illustrate the key concepts of the PEER approach. In particular, it is observed that damage is modeled by a conditional probability distribution, as the one visualized in Figure 3. This is a model with significant limitations. Most importantly, neither the model nor the evaluation of Eq. (1) maintains the above simplicity when *EDP* and *DM* are vector-valued. This has been recognized in PEER because Eq. (1) is primarily employed to coordinate the research among researchers who address different components of the PBEE problem.

2.2 ATC-58 approach

The ATC-58 project originated with efforts to extend the PEER approach to comprehensive and realistic building analysis [5]. A key aspect of the framing equation is retained in the ATC-58 formulation, namely the use of conditional probability functions. In particular, damage is modeled by "fragility functions." However, these fragility functions should not be confused with the conditional probability model $G(dm|edp)$ that appears in the PEER framing equation. As illustrated shortly, the ATC-58 project employs discrete random variables to characterize damage, while *DM*, introduced earlier, is a continuous random variable.

An ATC-58 analysis commences with the creation of a detailed finite element model of the structure under consideration. This model is subjected to a suite of recorded ground motions that are scaled to specific hazard levels. For example, the ground motions may be scaled so that they match the pseudo-spectral acceleration that has 50%, 10%, and 5% probability of being exceeded in 50 years. For the sake of this demonstration, suppose Table 1 is obtained by recording the peak inter-storey drifts of a three-storey building at those three hazard levels. Typically, finite element analyses are conducted to obtain these results, but Table 1 is here created with artificial data. The first-, second-, and third-storey drift realizations are denoted edp_1, edp_2, and edp_3, respectively and these three variables are collected in the vector **edp**. A comprehensive analysis would of course include additional EDPs that may affect the damage, such as peak inter-storey acceleration values.

	50% in 50 years			10% in 50 years			5% in 50 years		
	edp_1	edp_2	edp_3	edp_1	edp_2	edp_3	edp_1	edp_2	edp_3
GM#1	1.10	0.76	1.19	1.76	2.14	2.46	2.71	2.93	2.96
GM#2	1.29	0.91	0.91	1.87	1.23	2.38	2.98	3.23	3.61
GM#3	1.11	0.97	0.74	2.15	1.85	2.09	3.55	2.60	3.37
GM#4	0.80	1.01	1.20	1.57	1.68	1.79	2.89	2.86	3.83
GM#5	0.89	0.75	0.94	1.68	1.48	1.58	2.71	3.16	3.07
GM#6	0.94	0.66	0.96	1.56	2.38	1.68	3.98	3.14	3.41
GM#7	1.09	1.01	0.99	2.29	3.16	1.55	2.77	3.42	3.00
GM#8	0.86	0.95	1.03	2.16	2.40	2.20	2.36	2.90	2.88
GM#9	0.87	0.76	1.36	1.40	2.33	2.26	3.76	2.42	3.81
GM#10	0.69	0.91	0.90	1.99	1.90	1.54	3.11	2.54	3.04

Table 1: EDP values, drift in percent (GM=ground motion).

The ATC-58 approach proceeds by fitting a joint lognormal distribution to the EDPs to facilitate computationally efficient generation of many more realizations of the EDPs. In accordance with [5] this is accomplished by first taking the natural logarithm of all values in Table 1. The result is shown in Table 2, where the notation $\mathbf{Y}=\{Y_1, Y_2, Y_3\}$ is employed to de-

note these variables, whose realizations are denoted $\mathbf{y}=\{y_1, y_2, y_3\}$. According to the lognormality assumption for **edp**, the variables **Y** have the joint normal distribution.

50% in 50 years			10% in 50 years			5% in 50 years		
y_1	y_2	y_3	y_1	y_2	y_3	y_1	y_2	y_3
0.09	-0.28	0.18	0.56	0.76	0.90	1.00	1.08	1.09
0.25	-0.09	-0.09	0.62	0.21	0.87	1.09	1.17	1.28
0.10	-0.03	-0.31	0.76	0.62	0.74	1.27	0.95	1.21
-0.22	0.01	0.18	0.45	0.52	0.58	1.06	1.05	1.34
-0.12	-0.28	-0.06	0.52	0.39	0.46	1.00	1.15	1.12
-0.06	-0.42	-0.04	0.45	0.87	0.52	1.38	1.14	1.23
0.09	0.01	-0.01	0.83	1.15	0.44	1.02	1.23	1.10
-0.16	-0.05	0.03	0.77	0.87	0.79	0.86	1.06	1.06
-0.14	-0.27	0.31	0.34	0.85	0.81	1.33	0.88	1.34
-0.37	-0.09	-0.10	0.69	0.64	0.43	1.14	0.93	1.11

Table 2: The natural logarithm of the values in Table 1.

Next, considering one hazard level at a time, the second-moment statistical information for the variables **Y** is computed. For the values shown in Table 2, the second-moment results are shown in Table 3. Following common statistical notation, the second-moment statistics for **Y** at each hazard level are collected in the mean vector, $\mathbf{M_Y}$, the diagonal matrix of standard deviations, $\mathbf{D_Y}$, and the correlation matrix $\mathbf{R_{YY}}$. This information, shown in Table 3, essentially defines the probability distribution for the inter-storey drifts and represents the uncertainty in the peak structural responses due to the varying characteristics of the ground motions. It will shortly be demonstrated how inter-storey drift realizations are generated from the information in Table 3.

50% in 50 years			10% in 50 years			5% in 50 years		
y_1	y_2	y_3	y_1	y_2	y_3	y_1	y_2	y_3
-0.0533	-0.1485	0.0081	0.5989	0.6871	0.6534	1.1139	1.0653	1.1881
0.1859	0.1507	0.1749	0.1632	0.2716	0.1866	0.1648	0.1128	0.1069
1	0.0398	-0.2548	1	0.2215	-0.1162	1	-0.3891	0.5990
	1	-0.2538		1	-0.1844		1	-0.2742
		1			1			1

Table 3: Second-moment information for the random variables **Y**. First row of numbers are mean values. Second row of numbers are standard deviations. The three last rows are symmetric correlation matrices.

Having established the probability distribution for the structural responses, attention is turned to the damage and repair-cost models. As mentioned earlier, the ATC-58 approach stands apart from the PEER formulation by adopting a discrete variable, *DS*, to denote the damage state of a component. This random variable typically has two to four damage states, denoted by ds_1, ds_2, etc. In ATC-58 parlance, models that describe the probability that a component is in a particular damage state or greater are referred to as fragility functions [2]. This terminology is adopted in this paper although, formally, a fragility function should represent the probability of failure for a component or building for given values of an intensity measure, including uncertainty in both demand and capacity. In the ATC-58 methodology, the generic fragility function is written [2]

$$\mathrm{P}(DS \geq ds_j \mid EDP = edp) = \Phi\left(\frac{1}{\sigma_j} \cdot \ln\left(\frac{edp}{\mu_j}\right)\right) \tag{5}$$

where j is the damage state number, Φ is the standard normal cumulative distribution function, and μ_j and σ_j are parameters of the distribution function. However, it is strongly emphasized that Φ does *not* represent a probability distribution in this equation. It is reiterated that the function Φ has no connection with the function $G(dm|edp)$ employed earlier because DM is continuous while DS is discrete. Rather, the distribution function Φ is employed because it is an appealing two-parameter function that varies smoothly between zero and unity as edp increases. As a result, it is understood that there is no principal reason to prefer Φ in place of, say, a one-parameter trigonometric function or a multi-parameter polynomial function. Φ is simply a well-behaved two-parameter function that is employed in the ATC-58 project to model the probability that a component is in a specific damage state or greater.

Figure 6 shows the fragility functions that are employed in this demonstration. Each curve displays the probability that the damage state is equal to or greater than the associated state. Hence, this example includes four damage states. The left-most curve in the figure displays the probability that the component is in damage state 1 or greater; the next curve displays the probability that the component is in damage state 2 or greater, and so forth. As a result, the probability that a component is in damage state number j for a given EDP value is:

$$\mathrm{P}(DS = ds_j) = \mathrm{P}(DS \geq ds_j) - \mathrm{P}(DS \geq ds_{j+1}) \tag{6}$$

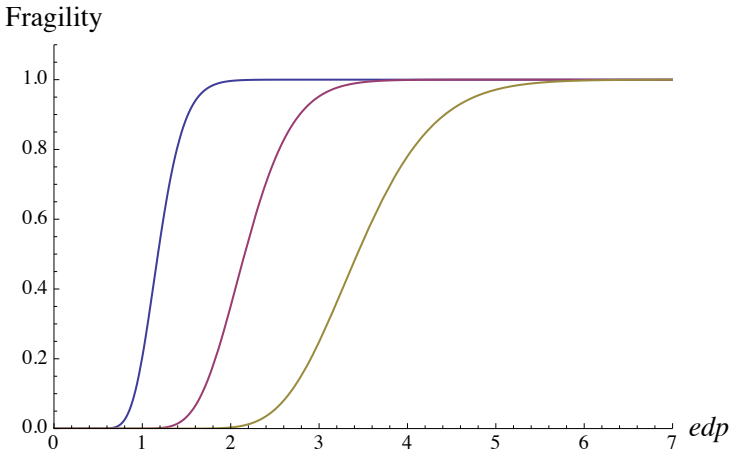


Figure 6. Fragility functions.

In the ATC-58 approach, the damage state determines the surface area to be repaired, which directly determines the repair cost. Economy-of-scale is included by reducing the repair cost for large repair jobs. In this simple demonstration example it is assumed that the repair cost, dv, per storey is \$0, \$10,000, \$20,000, and \$40,000 for damage states 1, 2, 3, and 4, respectively. Having established the damage and repair-cost models, the sampling analysis that is at the heart of the ATC-58 is conducted by executing the following algorithm, at each hazard level:

1. For each sample:
    a. Generate the realization of three independent standard normal random variables, collected in the vector **u**
    b. Transform the realization **u** into a realization of **y** by the well-known probability transformation [6]

$$\mathbf{y} = \mathbf{D}_{\mathbf{Y}}\mathbf{L}_{\mathbf{Y}}\mathbf{u} + \mathbf{M}_{\mathbf{Y}} \tag{7}$$

    where $\mathbf{L}_{\mathbf{Y}}$ is the lower-triangular Cholesky decomposition of $\mathbf{R}_{\mathbf{YY}}$.

    c. Transform the realization of **y** into a realization of **edp** by taking the exponent of each element of the vector **y**
    d. For each edp_i:
        i. Generate a realization, q, of a random variable that is uniformly distributed between 0 and 1
        ii. If $q>\mathrm{P}(DS\geq ds_1|EDP=edp_i)$, that is, if q lies above the left-most fragility function at the given edp, then the damage state is 1
        iii. Otherwise, if $q>\mathrm{P}(DS\geq ds_2|EDP=edp_i)$, then the damage state is 2
        iv. Otherwise, if $q>\mathrm{P}(DS\geq ds_3|EDP=edp_i)$, then the damage state is 3
        v. Otherwise the damage state is 4
        vi. Compute the cost of repair, dv, which is directly determined by the damage state
    e. Append the total cost, i.e., the sum of the repair cost in each storey, to an array that contains the total cost value for each sample

Figure 7 shows the complementary cumulative frequency diagram for DV obtained by 10,000 samples at each hazard level. Because the damage and ensuing loss is discrete, the diagrams that are produced from the sampling results are jagged. The smooth functions in Figure 7 are lognormal distributions that are fitted to the jagged distributions.

Each curve in Figure 7 is a conditional distribution $G(dv|im)$, where the cost is denoted dv. The final loss curve is obtained, in theory, by the integral

$$G(dv) = \int_0^\infty G(dv|im)\cdot f(im)\,\mathrm{d}\,im \tag{8}$$

In practice, this integral must be evaluated by summation instead of integration because $G(dv|im)$ is evaluated only at three hazard levels. The rule of total probability yields

$$G(dv) = \sum_{i=1}^{3} G(dv|im_i)\cdot p_i \tag{9}$$

where p_i represents the relative probability of occurrence of hazard level i, obtained by differentiation of the hazard curve and scaled to satisfy the constraint $p_1+p_2+p_3=1$. The values $p_1=0.2$, $p_2=0.6$, and $p_3=0.2$ yield the combined loss curve, $G(dv)$, in Figure 8.

In this simple demonstration example, one repair cost is associated with each EDP. This is a substantial simplification of the ATC-58 approach, although the difference is not conceptual.

The complete methodology developed by ATC-58 divides the structural and non-structural components into a host of "performance groups." For example, one performance group may be reinforced concrete columns of a certain type, while another may be internal partition walls of a specific type. Each performance group is associated with an *EDP*, such as inter-storey drift or inter-storey acceleration.

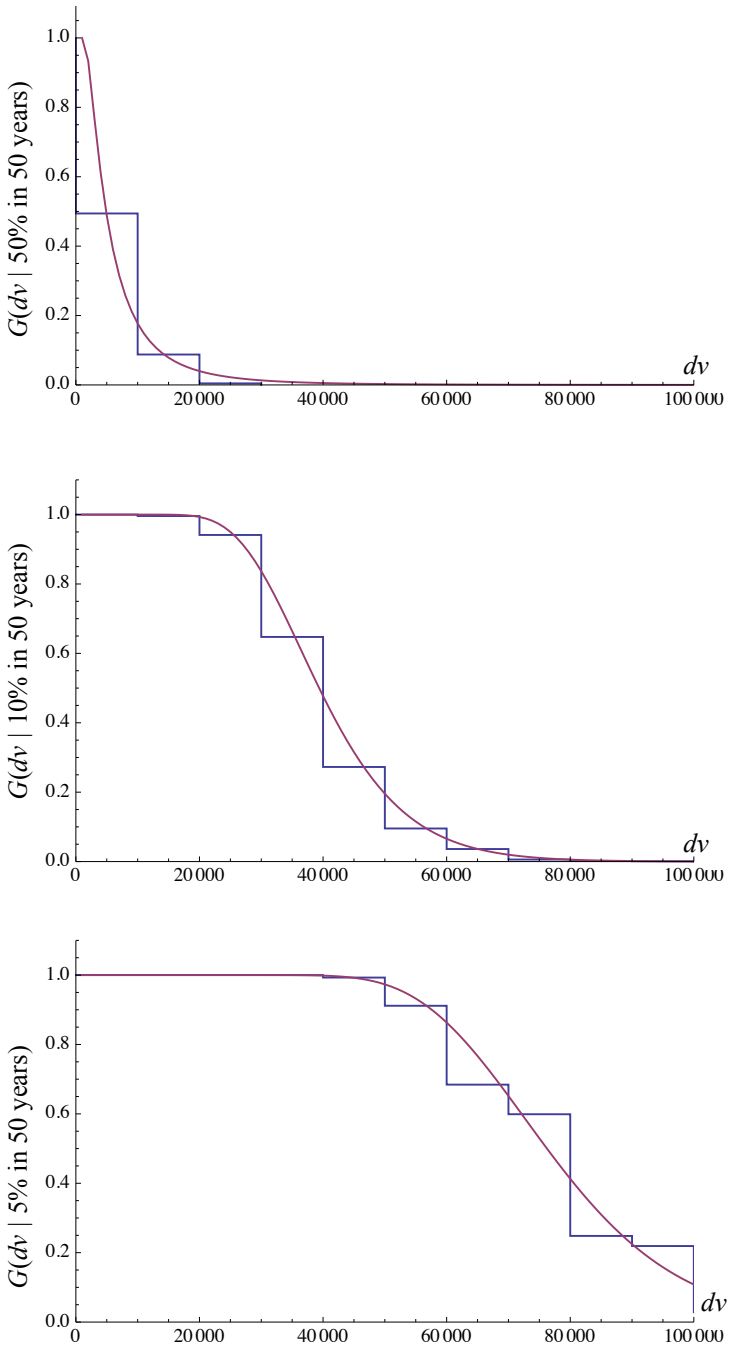


Figure 7. Loss curves at the three hazard levels.

The damage within each performance group is governed by fragility functions of the type in Eq. (5). This type of damage modeling is omnipresent in contemporary performance-based earthquake engineering. The reason for this is, in part, the appealing analytical form, which renders possible total probability integration. Another reason is that damage modeling is in-

herently challenging, and it is often difficult to justify more complex models. On the other hand, several disadvantages are associated with the use of Eq. (5). First, it may be argued that a better approach would be to model the actual visual damage rather than the probability of damage. It is also observed that the damage in Eq. (5) is solely determined by the value of one structural response. Neither the influence of material and geometry parameters, nor the influence of boundary conditions and other structural responses are accounted for. As a result, an entire "phonebook" of fragility functions are needed to cover the range of building components encountered in practice. Therefore, although the ATC-58 project represents a comprehensive and commendable effort to create a library of univariate fragility functions, the potential for improvements exists.

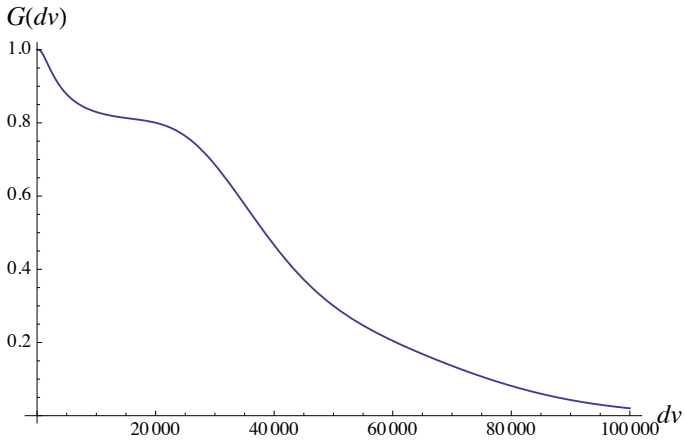


Figure 8. Combined loss curve.

2.3 Reliability-based approach

It is understood from the previous examples that the key result of a PBEE analysis is the probability distribution for the repair cost, *DV*. Figure 5 shows this result obtained by the PEER approach and Figure 8 shows the result obtained by the ATC-58 approach. An alternative analysis approach, based on reliability methods, is now demonstrated. This approach has been referred to as unified reliability analysis [3] because of the flexible but unified format of the models employed in this approach.

To understand the reliability-based methodology it is helpful to recall that reliability problems have two ingredients: random variables and limit-state functions. The random variables describe the uncertainty and the limit-state functions define the response events for which the probability is sought. In the following, one limit-state function, $g(\mathbf{x})$, is employed, where $\mathbf{x}$ is the vector of random variables. Following classical reliability theory [7], g is defined so that the event of interest yields negative realizations of g. Conversely; the complement of that event yields positive realizations of g. In the context of PBEE, the limit-state function is

$$g(\mathbf{x}) = dv_o - dv(\mathbf{x}) \tag{10}$$

where dv_o is a cost value selected by the analyst. A reliability analysis with the limit-state function in Eq. (10) yields the probability that dv exceeds the threshold dv_o. In other words, it yields one point on the function $G(dv)$.

A key strength of the reliability-based approach is the flexibility it offers in the choice of models. In a plug-and-play fashion, advanced finite-element-based damage models can be replaced with a simple regression-based damage model. This flexibility is available for all mod-

els, from earthquake characteristics to repair cost. In fact, it is straightforward to add costs related to construction and cost of environmental impacts, without any changes in the analysis framework. This is a substantial advantage in the quest to continuously improve probabilistic models in PBEE.

To illustrate the reliability-based approach, consider the following simple example. Suppose the ground motion intensity, *IM*, is modeled by the same random variable as the one visualized in Figure 1, namely a lognormal random variable with mean 0.8 and 20% coefficient of variation. It is here stressed that a reliability-based analysis would often aim to model the physical phenomena behind the ground motion intensity, i.e., the magnitude, location, and attenuation of the earthquake [8]. However, this is not pursued in this paper.

Next, the ground motion intensity is translated into forces applied to the structural model shown in Figure 9. This structural model is created in the computer program St, which is freely available from the website that belongs to the authors' research group, www.inrisk.ubc.ca. The loads are applied as three point loads with value F_1 at the first storey and two point loads with value F_2 at the second storey. These loads are modeled as $F_1=\alpha_1 \cdot IM$ and $F_2=\alpha_2 \cdot IM$ where α_1 and α_2 are lognormal random variables with means 500kN and 600kN, respectively, and 20% coefficient of variation. These models are selected simply to demonstrate the flexibility in introducing random variables in each model. The structural model in Figure 9 has linear material properties and consists of frame, truss, and plane continuum elements. It is unnecessary to describe the structural model in detail here, but it is noted that the model takes many material and geometry random variables as input and gives displacements and other responses as output. Of course the use of a nonlinear structural model instead of a linear model poses no conceptual problems for the reliability-based methodology. The results employed in the following are the inter-storey displacement of the two storeys.

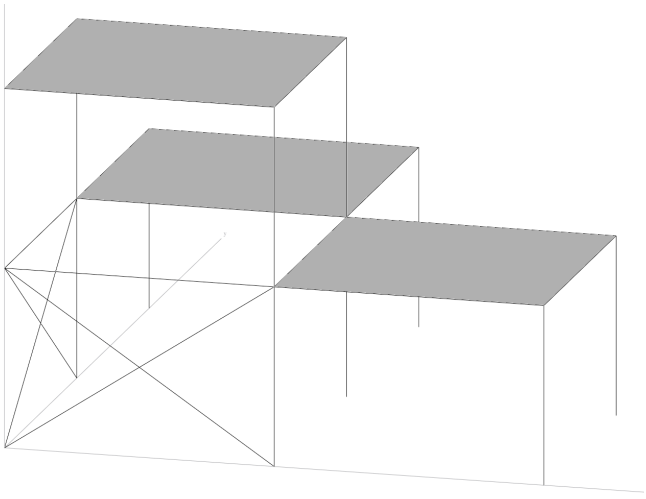


Figure 9. Structural model.

Denoting inter-storey drift by δ, the structural responses are input to the damage model

$$\eta = \begin{cases} 0 & \delta < \delta_{max} \\ \frac{1}{2} \cdot \left(\sin\left(\frac{\pi}{\varepsilon \cdot \delta_{max}} \cdot \delta - \frac{\pi}{2} \right) + 1 \right) & 0 < \delta < \delta_{max} \\ 1 & \delta > \delta_{max} \end{cases} \tag{11}$$

where η is a damage indicator, here referred to as a damage ratio, ε is a normally distributed random variable with unit mean and standard deviation 0.1, and δ_{max} is set equal to 6% drift. As shown in Figure 10, this model is a function that describes a smooth increase in damage as the drift increases.

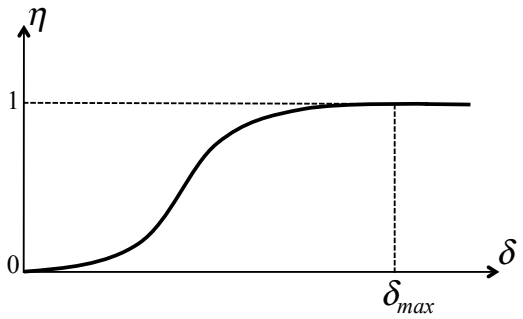


Figure 10. Visualization of the damage model in Eq. (11).

Finally, the cost is computed with the model

$$dv = \left(\eta_1 \cdot A_1 \cdot C \cdot \varepsilon\right) + \left(\eta_2 \cdot A_2 \cdot C \cdot \varepsilon\right) \tag{12}$$

where dv is the repair cost, η_1 and η_2 are the damage ratios from the damage model. A_1=108m^2 and A_2=36m^2 are floor areas of the first and second storeys, respectively. C is a random variable that represents the cost of repair per unit area, which is modeled as a lognormal random variable with mean \$2,000/m^2 and standard deviation \$400/m^2. ε is a normal random variable with unit mean and standard deviation 0.3.

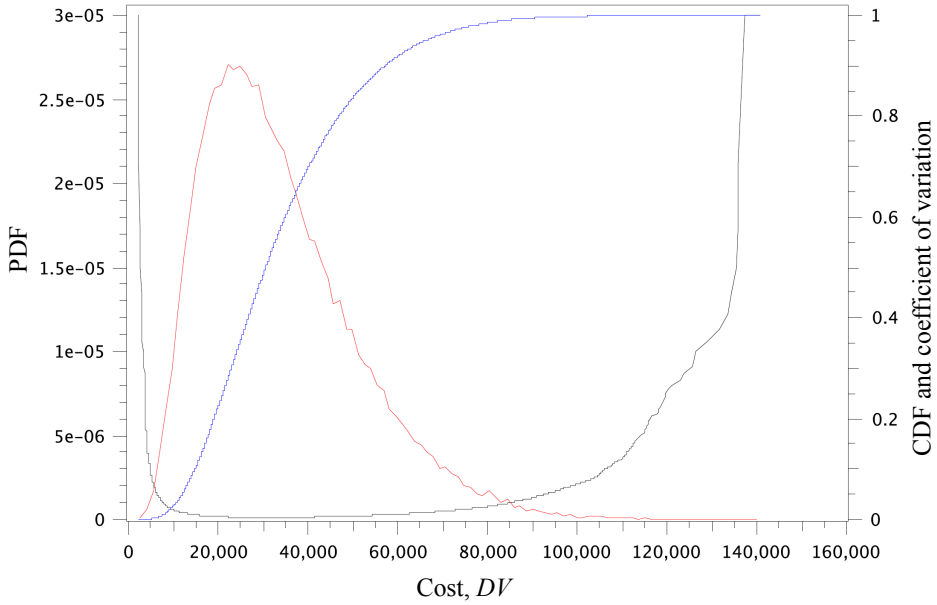


Figure 11. Visualization of $f(dv)$ and $F(dv)$ by sampling.

The reliability analysis with the above models is conduced with the computer program Rt [9], which is freely available from the website www.inrisk.ubc.ca. Rt has many analysis options and two of them are employed in the following. It is noted that the models described above take the realization of an array of random variables as input and ultimately give a realization of dv as output. For this reason, Monte Carlo sampling can be utilized to get a rough

sense of the probability distribution for *DV*. The red line in Figure 11 shows the relative frequency diagram, which is comparable to a PDF, and the blue line shows the cumulative frequency diagram, which is comparable to a CDF. It is emphasized that Monte Carlo sampling is a computationally costly approach that does not yield high accuracy in the probability estimates in the tails of the distribution. In fact, the black line in Figure 11 shows the coefficient of variation of the cumulative frequency diagram at various cost thresholds. The black line shows that the uncertainty in the sampling result is highest in the distribution tails.

To obtain the loss curve with better accuracy in the tails of the distribution, FORM analysis is carried out with the limit-state function in Eq. (10) at different cost thresholds. The accuracy of these results can be further improved by computationally effective importance sampling about the design point from FORM, but this is not done here. Figure 12 shows the resulting loss curve, $G(dv)$, obtained by FORM analysis at ten cost thresholds.

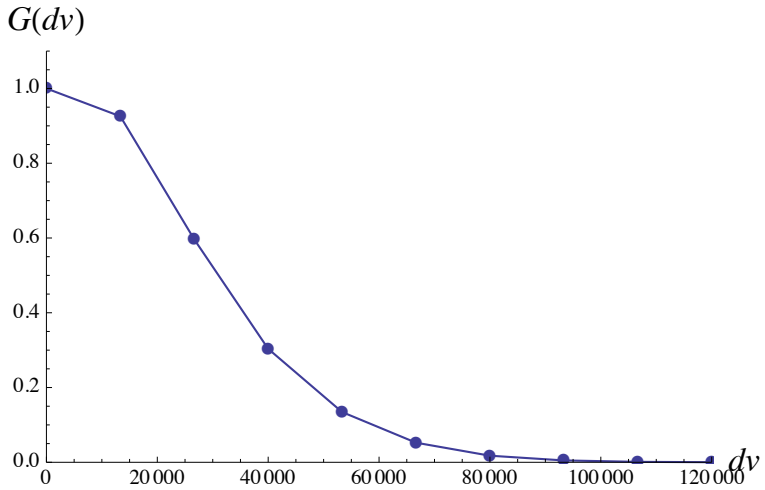


Figure 12. Points on the $G(dv)$ curve obtained by FORM and sampling reliability analysis.

It is not meaningful to compare the loss curves in Figure 5, Figure 8, and Figure 12, because the models employed in the three examples are different. Instead, the purpose has been to expose the steps of the analysis methods, and to compare the types of models that can be employed. In the reliability-based approach demonstrated in this section, none of the models are conditional probability models. Instead, all the models take random variable realizations as input and give corresponding response realizations as output. Ultimately, the response of the last model in the chain is input to the limit-state function. This modeling concept is sometimes not well understood, and the following overview of characteristics is provided to emphasize the format of models employed in the reliability-based approach.

A model, in the reliability-based PBEE approach, is an equation or algorithm, that essentially simulates possible scenarios of physical phenomena without conservative bias. This type of model discretizes all uncertainty in terms of random variables, and it takes as input the realization of continuous random variables. Ideally, it has random model parameters whose probability distribution is updated when new data emerge; i.e., it includes epistemic uncertainty. It may also take constants and design variables as input. The model returns one or more physical responses, not probabilities, and it returns a unique response for each unique realization of the random variables. It returns a response that is "continuously differentiable," i.e., smooth, with respect to the random variables, which is necessary for gradient-based reliability methods, such as FORM. It permits the simulation of all possible realizations of the outcome

space, and finally, it is modularized in the sense that it can take input from "upstream" models and/or return output to "downstream" models.

In the introduction to the seminal textbook on structural reliability methods [7], Ditlevsen and Madsen argue that probabilistic analysis is an extension of deterministic analysis because deterministic quantities can be interpreted as particularly trivial random variables. This philosophy is adopted in the above definition of a probabilistic model; the starting point is always a deterministic model in which random variables are substituted for the deterministic ones. This is the format for the collection of models that are implemented in the computer program Rt.

3 MODELING DISCRETE DAMAGE BY LOGISTIC REGRESSION

In contemporary PBEE, the ATC-58 project is an important initiative that provides context for this paper. As seen above, the ATC-58 employs fragility functions to model damage. In particular, the fragility curve represents P(*DS*≥*ds*|*EDP*=*edp*).The idea in this paper is to utilize logistic regression to develop multivariate models for P(*DS*≥*ds*), where any number of EDPs and material and geometry parameters influence the damage. For readers unfamiliar with logistic regression, an introduction is provided in the following. Additional details are provided in many textbooks, including [10, 11]. As the starting point, a generic regression model is written

$$r = h(\mathbf{x}, \boldsymbol{\theta}) \tag{13}$$

where r is a continuous response variable, h is a linear or nonlinear function, $\mathbf{x}$ is a vector of explanatory variables, such as material, geometry, and structural response parameters, and $\boldsymbol{\theta}$ is a vector of model parameters. The arctypical example of Eq. (13) is the linear regression model

$$r = \theta_1 + \theta_2 \cdot x_2 + \cdots + \theta_m \cdot x_m + \varepsilon \tag{14}$$

where ε is the model error and the model is said to be linear because it is linear in the model parameters. Conversely, nonlinear regression employs a right-hand side that is nonlinear in the model parameters. Regression models of the form in Eq. (14) have been employed in a variety of engineering disciplines. For example, [12] employed models of the form

$$r = \theta_1 + \theta_2 \cdot h_2(\mathbf{x}) + \cdots + \theta_m \cdot h_m(\mathbf{x}) + \varepsilon \tag{15}$$

where h_i are explanatory functions that consist of individual or combined explanatory variables, to model the capacity of reinforced concrete columns.

Logistic regression differs from ordinary regression in two aspects: The model error, ε, is removed from the right-hand side and the left-hand side is reformulated. Specifically, in logistic regression the right-hand side is the logit function:

$$\underbrace{\ln\left(\frac{p}{1-p}\right)}_{r} = \theta_1 + \theta_2 \cdot h_2(\mathbf{x}) + \cdots + \theta_m \cdot h_m(\mathbf{x}) \tag{16}$$

where p=P(*DS*≤*ds*)=probability of a certain damage *or less*. That is, the probability in Eq. (16) is the *complement* of the fragility function presented in Eq. (5). The logit function is sketched in Figure 13 to emphasize that p varies from zero to unity while r varies from minus to plus infinity. As a result, a regression model of the form in Eq. (16) can be employed to model

probability values, which vary between 0 and 1, such as the probability that a structural component is in a specific damage state. More precisely, Eq. (16) is employed in this paper to model the probability that a component is in damage state *j* or less. The two key advantages of logistic regression in this context are that it is readily implemented in the ATC-58 analysis procedure, and that it facilitates the development of multivariate damage models.

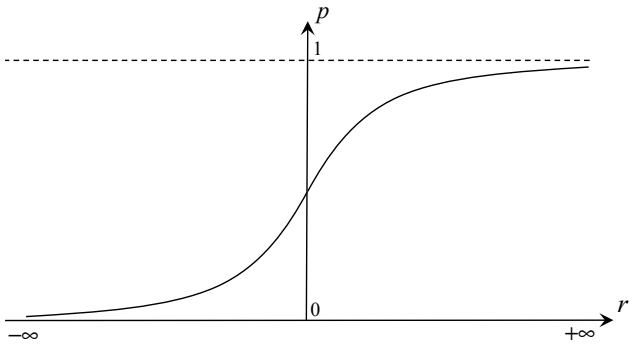


Figure 13. The logit function.

3.1 Binomial logistic regression

In order to explain how to develop multivariate models for P(*DS*≥*ds*) by means of Eq. (16) it is useful to start with binomial logistic regression, where only two damage states are considered. Suppose *n* observations are made, and that regressor values and the corresponding damage state have been recorded in each experiment. Furthermore, let the binary variable *b*={0,1} denote the damage state.

One technique for determining point estimates for the model parameters, $\boldsymbol{\theta}$, is the maximum likelihood method. The likelihood function represents the probability of observing the observed data. Provided independent observations, the likelihood function is the following product:

$$L(\boldsymbol{\theta}) = \prod_{i=1}^{n} p_i^{b_i} \cdot (1 - p_i)^{1-b_i} \tag{17}$$

The validity of Eq. (17) as a likelihood function is understood by first considering the case with one observation with *b*=1, in which case the likelihood function correctly evaluates to *p*, namely the probability of observing *b*=1. Conversely, for an observation with *b*=0 the likelihood function correctly evaluates to 1–*p*, namely the probability of observing *b*=0. The maximization of Eq. (17), or its logarithm, implies that the following equation must be solved:

$$\frac{\partial \ln\left(L(\boldsymbol{\theta})\right)}{\partial \boldsymbol{\theta}} = \mathbf{0} \tag{18}$$

This is a popular and straightforward approach for the determination of point estimates for the model parameters. Additional techniques are available in the literature for the determination of the variances and covariances of the model parameters [13]. Once the statistics for the model parameters, $\boldsymbol{\theta}$, in Eq. (16) are determined, "fragilities" of the type employed in the ATC-58 project are determined from the formula

$$\mathrm{P}(DS \geq ds_j) = 1 - p = 1 - \frac{e^r}{1 + e^r} \tag{19}$$

3.2 Multinomial logistic regression

The difference between binomial and multinomial regression is that the latter allows more than two damage states. The following notation is employed:

$$p_j = P(DS \le ds_j) \tag{20}$$

where j=1, 2,…, k–1, where k is the number of damage states. This implies that the sought fragility model for the ATC-58 analysis format is

$$P(DS \ge ds_{j+1}) = 1 - p_j \tag{21}$$

where the above definition of j is maintained because caution must be exercised to ensure consistent numbering of the damage states. The generic format of the multinomial regression model that are adopted in this paper is [14]

$$\ln\left(\frac{p_j}{1-p_j}\right) = \theta_{ds_j} + \theta_2 \cdot h_2(\mathbf{x}) + \theta_3 \cdot h_3(\mathbf{x}) + \cdots + \theta_m \cdot h_m(\mathbf{x}) \tag{22}$$

Importantly, the first model parameter in the right-hand-side, namely the intercept parameter, is the only model parameter that changes from the model for one damage state to the model for another. As a result, the following constraint is employed:

$$\theta_{ds_1} \le \theta_{ds_2} \le \cdots \le \theta_{ds_{k-1}} \tag{23}$$

In short, each model is a shifted version of the model for the first damage state, and the shift is incorporated in the intercept parameter. As a result, for a situation with *four* damage states the complete set of model parameters for the *three* logistic regression models is:

$$\boldsymbol{\theta} = \left(\theta_{ds_1}, \theta_{ds_2}, \theta_{ds_3}, \theta_2, \theta_3, \ldots, \theta_m\right) \tag{24}$$

In accordance with the maximum likelihood approach, point estimates for the model parameters are obtained by solving Eq. (18), where

$$L(\boldsymbol{\theta}) = \prod_{i=1}^{n}\left(\prod_{j=1}^{k} p_{ij}^{b_{ij}}\right) \tag{25}$$

where b_{ij}=1 if observation i is in damage state j, otherwise b_{ij}=0. Analogous to Eq. (6), the probability of a particular damage state is now

$$\mathrm{P}(DS = ds_j) = p_{j+1} - p_j \tag{26}$$

where the above definition of j and k are maintained. An application of logistic regression to damage modeling for reinforced concrete shear walls is provided later in this paper.

4 MODELING VISUAL DAMAGE BY BAYESIAN LINEAR REGRESSION

The second suggested improvement to damage modeling is modeling of measurable damage and use of the reliability-based analysis procedure. This contrasts with the use of fragility curves, which gives the probability of a damage state as output instead of a physical measurable quantity. The advantage of predicting the physical damage, hereafter called visual damage, is twofold. First, it allows direct use of recorded damage data, such as crack widths, without the need for an intermediate and subjective step to characterize the damage as being in a cer-

tain damage state. Second, the prediction of visual damage makes it easier to predict the time and cost of repair. This is because the contractor will invariably use the visual damage as the primary basis for selection of repair actions, which in turn determines the time and cost of the repair.

Several techniques are available for developing models for visual damage. One approach is detailed finite element modeling of each structural component. Another approach is suggested here, namely the use of Bayesian linear regression. This is an appealing approach for two reasons. First, the Bayesian approach implies that epistemic uncertainty, i.e., model uncertainty, is explicitly addressed by probability distributions for the model parameters. Second, the use of a multivariate regression technique means that any number of EDPs, material properties, and geometry parameters can be included in the model. In the past, this type of linear regression has been employed in a variety of applications, including the development of capacity models for structural components [12].

Echoing the previous description of logistic regression, a brief description of Bayesian linear regression is provided in the following. The reader is referred to standard statistics textbooks for further details, including [15]. The generic model form is that of Eq. (15), where the model parameters are collected in the vector $\boldsymbol{\theta}=\{\theta_1, \theta_2, \ldots\}$ and the model error, ε, is assumed to be normally distributed. The observations that are employed to calibrate the model in Eq. (15) are organized in a vector $\mathbf{r}$ and a matrix $\mathbf{X}$. The matrix contains observed values of the explanatory functions, $\mathbf{x}$. One observation occupies one component of $\mathbf{r}$ and the correspond row of $\mathbf{X}$. The mean of the model parameters is the point estimate from ordinary least squares regression:

$$\mathbf{M}_{\boldsymbol{\theta}} = \left(\mathbf{X}^T\mathbf{X}\right)^{-1}\mathbf{X}^T\mathbf{r} \tag{27}$$

The standard error from classical linear regression

$$s^2 = \frac{1}{n-m}\cdot\left(\mathbf{r}-\mathbf{X}\mathbf{M}_{\boldsymbol{\theta}}\right)^T\left(\mathbf{r}-\mathbf{X}\mathbf{M}_{\boldsymbol{\theta}}\right) \tag{28}$$

also plays a role in Bayesian regression, where n is the number of observations and m is the number of explanatory variables. Assuming non-informative priors, the model parameters have the multivariate t-distribution and the standard deviation of the model error has the inverse chi-squared distribution with ν is the degrees of freedom, where $\nu=n-m$. In summary, when ν is sufficiently large, the covariance matrix for the model parameters is

$$\boldsymbol{\Sigma}_{\boldsymbol{\theta}\boldsymbol{\theta}} = s^2\left(\mathbf{X}^T\mathbf{X}\right)^{-1} \tag{29}$$

The mean of the standard deviation of the model error is

$$\mu_\sigma = s \tag{30}$$

The variance of the standard deviation of the model error is

$$\sigma_\sigma^2 = \frac{s^2}{2(\nu-4)} \tag{31}$$

Although the above formulas for the second-moment statistics of the model parameters appear simple, it is critical that sufficient efforts are devoted to model diagnostics and potential remedial actions. A host of potential issues exist, including collinearity among the explanato-

ry variables, heteroskedasticity in the model error, correlation between observed errors, non-normality in the observed errors, outliers, and model nonlinearity.

5 APPLICATIONS TO REINFORCED CONCRETE SHEAR WALLS

The two proposed improvements to damage modeling are demonstrated in the following for concrete walls. In the first application, logistic regression is employed to develop models based on actual observations. Thereafter, Bayesian regression is employed to model the amount of repairable cracks, based on data generated by an advanced numerical simulation software.

5.1 Logistic regression models for shear wall damage

The authors have been given access to data for reinforced concrete walls of the type illustrated in Figure 14. A number of researchers have conducted laboratory experiments for such shear walls, and the data have been merged into a unified database. The shear walls were subjected to cyclic testing, and load-displacement curves like those shown in Figure 15 were recorded. From such hysteresis curves, the "backbone curve," shown as solid straight lines in Figure 15, was extracted for each test specimen. In this paper, the lateral displacement is measured by the dimensionless quantity drift ratio rather than displacement, where the drift ratio is defined as

$$\delta = \frac{u}{h_w} \tag{32}$$

where u and h_w are defined in Figure 14. The data that is available for this study have the format shown in Table 4, and includes the axial load ratio, $P/A_g f'_c$, the wall height, h_w, horizontal wall length, l_w, concrete compressive strength, f'_c,yield strength of flexural reinforcement in web, f_{yl}, yield strength of flexural reinforcement in boundary zone, f_{ylb}, flexural reinforcement ratio in web zone, ρ_{lw}, flexural reinforcement ratio in boundary zone, ρ_{lb}, transverse reinforcement ratio in both web, ρ_{hw}, transverse reinforcement ratio in boundary zone, ρ_{hb}, and the drift ratio at three key points on the backbone curve.

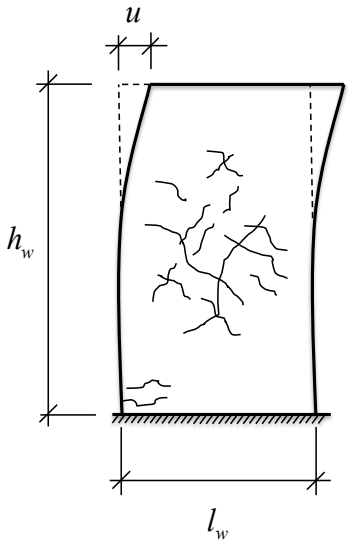


Figure 14. Reinforced concrete shear wall.

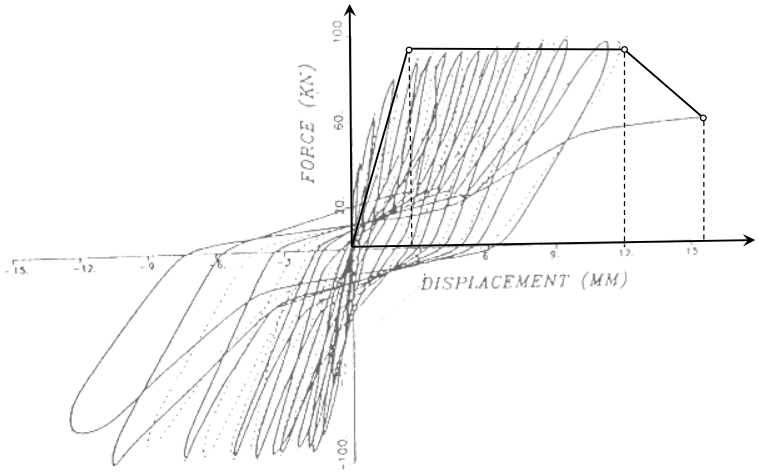


Figure 15. Backbone curve from cyclic testing.

Table 4. Excerpt from the shear wall database.

Test No.	$P/A_g f'_c$	h_w/l_w	$f'c$ [MPa]	f_{yl} [MPa]	f_{ylb} [MPa]	ρ_{lw} [%]	ρ_{lb} [%]	ρ_{hw} [%]	ρ_{hb} [%]	δ [%]
										0.61
1	0.07	2.0	47	400	471	0.27	3.17	0.26	1.5	2.17
										2.87
										0.73
2	0.07	2.0	48	448	477	0.61	7.14	0.61	1.5	3.03
										3.03
										0.49
3	0.07	1.5	48.7	399	471	0.32	3.17	0.36	1.5	3.06
										3.94
										.
.	.	.	.	.	.	.	.	.	.	.
										.

In lieu of more information about damage from the tests, it is hypothesized in this study that the characteristic points on the backbone curve are indicative of damage. Specifically, it is assumed that the drift-values δ_y, δ_u, and δ_c identify the transition from one damage state to another. Figure 16 illustrates this assumption by showing the drift-ranges where the wall is assumed to be in Damage State 1 (ds_1), Damage State 2 (ds_2), etc. Even after identifying damage states for each shear wall, another step is necessary before the data can be employed in logistic regression. This is because the observed values for δ_y, δ_u, and δ_c cannot serve as observations for developing logistic regression model. The reason is that δ_y, δ_u, and δ_c identify the *transition* between damage states, rather than regressor values within damage states. Figure 16 illustrates one way of making the data amenable to logistic regression. Instead of directly using the values for δ_y, δ_u, and δ_c, drift-values that belong to specific damage states are recorded. In Figure 16, the points on the abscissa axis that are marked by asterisk show a strategy where two drift-values are employed for each damage state. In contrast, the drift values marked my lines show an alternative strategy, where five drift-values are employed in

each damage state. Results presented shortly show that the results are not highly sensitive to the number of selected drift-values.

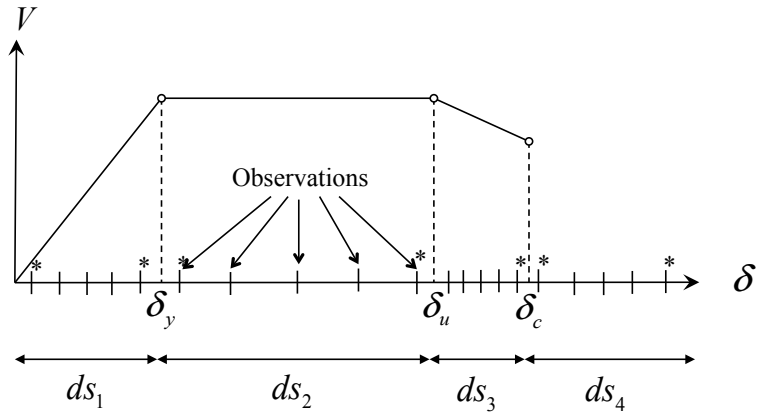


Figure 16. Damage states relative to the backbone curve.

Table 5 enumerates the explanatory functions that are used in the multinomial logistic regression models. It is noted that the natural logarithm of δ is employed rather than δ itself, to ensure zero probability of damage at zero drift.

Table 5. List of explanatory functions, $h_i(\mathbf{x})$.

h_2	Axial load ratio	$P/A_g f'_c$
h_3	Aspect ratio	h_w/l_w
h_4	Concrete compressive strength	f'_c
h_5	Yield strength of flexural reinforcement (web)	f_{yl}
h_6	Yield strength of flexural reinforcement (boundary)	f_{yb}
h_7	Flexural reinforcement (web)	ρ_{lw}
h_8	Flexural reinforcement (boundary)	ρ_{lb}
h_9	Horizontal reinforcement (web)	ρ_{hw}
h_{10}	Horizontal reinforcement (boundary)	ρ_{hb}
h_{11}	Drift ratio	$\ln(\delta)$

For the sake of simplicity of notation, let **h** denote an n-by-10 dimensional matrix whose rows contain the value of the 10 explanatory functions shown in Table 5 for each of the n observations. The n-dimensional vector **y** is also defined, to collect the damage state for each observation. Following the methodology described earlier, the MATLAB® subroutine "mnrfit" for multinomial logistic regression is utilized to estimate model parameters. Specifically, the model parameters are computed by the command $\boldsymbol{\theta}$=mnrfit(**h**,**y**,'model','ordinal'), where $\boldsymbol{\theta}$ are point estimates for the model parameters and the options 'model' and 'ordinal" are employed to obtain multinomial logistic regression models of the form described earlier. For the considered shear wall data, which includes four damage states, the models read

$$\ln\left(\frac{p_1}{1-p_1}\right) = \theta_{ds_1} + \theta_2 \cdot h_2(\mathbf{x}) + \theta_3 \cdot h_3(\mathbf{x}) + \cdots + \theta_{11} \cdot h_{11}(\mathbf{x}) \tag{33}$$

$$\ln\left(\frac{p_2}{1-p_2}\right) = \theta_{ds_2} + \theta_2 \cdot h_2(\mathbf{x}) + \theta_3 \cdot h_3(\mathbf{x}) + \cdots + \theta_{11} \cdot h_{11}(\mathbf{x}) \tag{34}$$

$$\ln\left(\frac{p_3}{1-p_3}\right) = \theta_{ds_3} + \theta_2 \cdot h_2(\mathbf{x}) + \theta_3 \cdot h_3(\mathbf{x}) + \cdots + \theta_{11} \cdot h_{11}(\mathbf{x}) \tag{35}$$

where Table 6 provides the point estimates for the model parameters, given two or five drift-observations in each damage state, as explained earlier.

Table 6. Model parameters for the models in Eqs. (33) to (35).

Model parameter	2 recorded observations in each damage state	5 recorded observations in each damage state
θ_{ds1}	-6.2815	-7.8127
θ_{ds2}	-3.5362	-4.4351
θ_{ds3}	-1.5746	-2.2594
θ_2	-2.8518	-3.818
θ_3	0.8837	1.1815
θ_4	0.0021	0.003
θ_5	0.0013	0.0016
θ_6	0.0011	0.0015
θ_7	-0.2861	-0.3224
θ_8	0.0078	0.0039
θ_9	1.5821	2.0884
θ_{10}	-0.1604	-0.2148
θ_{11}	-2.7209	-3.5176

It is observed in Table 6 that the results for two drift-observations in each damage state are correlated with the results for with five observations. In other words, the results are not highly dependent on the choice of drift-observations. This point will be further discussed shortly. Table 6 also provides information about the relative influence of each explanatory function. However, caution must be exercised, because the θ-values in Table 6 have different units. Nonetheless, by accounting for the practical range of variation of each explanatory function, it can be concluded the yield strengths of reinforcement and the compressive strength of concrete are relatively insignificant in comparion with h_w/l_w and P/Agf'_c.

To demonstrate that the models in Eqs. (33) to (35) can be employed to produce the same results as a fragility function, Figure 17 shows the fragility functions for a wall with $P/A_g f'_c$=0.5, h_w/l_w=2, f'_c=30MPa, f_{yl}=450MPA, f_{ylb}=500MPA, ρ_{lw}=0.25% ρ_{lb}=4%, ρ_{hw}=2%, and ρ_{hb}=1.5%. It is observed in Figure 17 that the models developed with two drift-observations are quite similar to those with five dift-observations. Furthermore, from the slope of the fragility curves in Figure 17 it is concluded that the drift at which the wall transitions into damage state 4 is far more uncertain than the drift at which the wall enters into damage state 1. It is also stressed that the models in Eqs. (33) to (35) are far more versatile than the impression given in Figure 17. In fact, Figure 17 is provided only to show that results similar to the ATC-58 fragility functions can be obtained when values are given for all the explanatory functions that influence damage.

At present, the models in Eqs. (33) to (35) are intended primarily for demonstration purposes. In ongoing research, more parsimonious models are developed by various model selection procedures [16].

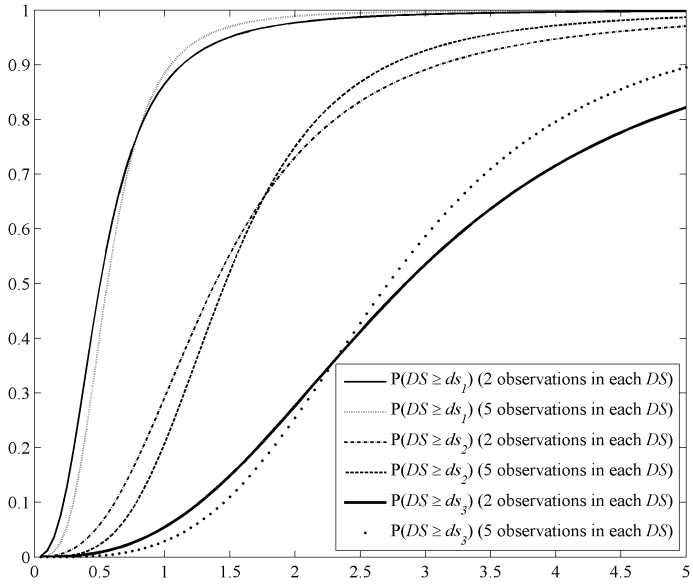


Figure 17. Variation of fragility probabilities with δ for a specific wall from multinomial logistic regression.

5.2 Linear regression models for shear wall damage

A probabilistic model for visual damage is now presented, based on work in [17]. This model aims at predicting a physical measure of damage, rather than the probability of different damage states. In particular, wall damage is formulated as a continuous variable. As mentioned earlier, once the visual damage is determined, the repair action and the associated direct and indirect costs can be estimated. Here, the physical quantity of damage is the length of cracks in the wall. In lieu of data from experiments, data is generated by detailed finite element analysis, as described shortly. To this end, 32 reinforced concrete shear walls are designed based on the Canadian Standard Association code requirements. Table 7 shows an excerpt of the properties of the walls; further details are provided in [17].

Table 7. Design details of walls.

Wall No.	f'_c [MPa]	$\sqrt{f'_c}$	$P/A_g f'_c$	ρ_{lw}	ρ_{lb}	ρ_h	f_y [MPa]	h_w/l_w
1	35	5.92	5%	0.78%	1.20%	1.00%	455	3.02
2	25	5.00	5%	0.78%	1.20%	1.00%	455	3.02
…	…	…	…	…	…	…	…	…
31	35	5.92	5%	0.79%	1.40%	1.00%	455	3.02
32	35	5.92	5%	0.81%	1.30%	1.00%	455	3.02

Each wall is subjected to a cyclic loading history in the computer program VecTor2 [18]. VecTor2 is a two-dimensional non-linear program for analysis of reinforced concrete elements. A screenshot of a wall modeled in VecTor2 is shown in Figure 18. The load cycles have steadily increasing amplitude, and after each load cycle the repairable residual cracks corresponding to the zero-force position of the wall are determined. Conducting this type of

analysis for all 32 walls yields a database of results that are employed in linear regression analysis. This data is not given in this paper, where focus is on the modeling procedure and the resulting model.

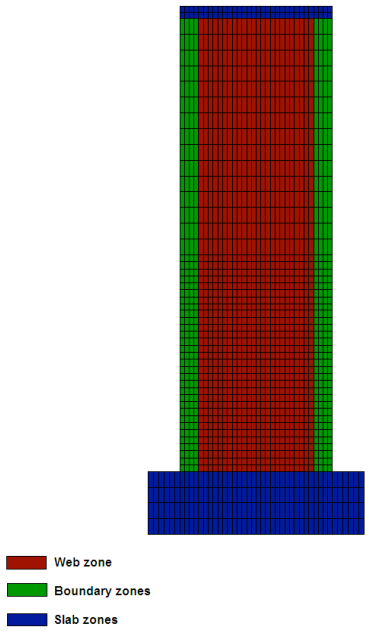


Figure 18. A screenshot of a wall modeled in VecTor2.

Once the data is available, the first step in the modeling procedure is to select a comprehensive set of explanatory functions. These are shown in Table 8. The generic model form is that of Eq. (15) and the model response is l_c/l_w, where l_c is the total crack length and l_w is the horizontal length of the wall.

Table 8. List of explanatory functions.

h_1	Drift ratio	δ
h_2	Concrete tensile strength	$\sqrt{f'_c}$
h_3	Concrete compressive strength	f'_c
h_4	Axial load ratio	$P/A_g f'_c$
h_5	Flexural reinforcement (web)	ρ_{lw}
h_6	Flexural reinforcement (boundary)	ρ_{lb}
h_7	Horizontal reinforcement (web & boundary)	ρ_h
h_8	Yield strength of flexural reinforcement	f_y
h_9	Slenderness ratio	h_w/l_w

The next step is to employ the Bayesian inference presented earlier to assess the model parameters. Furthermore, an iterative procedure is utilized to remove explanatory functions that do not influence the crack length [12]. At each iteration, the second-moment statistics of $\boldsymbol{\theta}$

and σ are calculated and the explanatory function with largest coefficient of variation of the corresponding model parameter is deemed to have the least influence on the crack length. By trial and error, explanatory functions are removed and reinserted while monitoring the standard deviation of the model error, σ. In this manner, the "optimal" model is achieved, which balances parsimoniousness with model accuracy [12]. The first iteration includes all the nine explanatory functions, where the least significant explanatory function is the ratio of flexural reinforcement in the boundary region, ρ_{lb}. In subsequent iterations, the ratio of horizontal reinforcement is removed followed by the compressive and tensile strength of concrete. The final model form, which is achieved in the sixth iteration, after which any further reduction deteriorates the model drastically, is

$$\frac{l_c}{l_w} = \theta_1 \cdot \delta + \theta_4 \cdot \frac{h_w}{l_w} + \theta_5 \cdot \frac{P}{A_g \cdot f'_c} + \theta_6 \cdot \rho_{hw} + \sigma \cdot \varepsilon \tag{36}$$

where the second-moment statistics for the model parameters is shown in Table 9.

Table 9. Statistics of model parameters.

Coefficients	Mean	COV	Correlation coefficient			
			θ_1	θ_4	θ_5	θ_6
θ_1	7.1	0.023	1.00	-0.52	-0.02	-0.16
θ_4	-0.72	0.16	-0.52	1.00	-0.70	-0.18
θ_5	-0.31	0.19	-0.02	-0.70	1.00	-0.20
θ_6	0.86	0.21	-0.16	-0.18	-0.20	1.00
σ	0.95	0.06	-	-	-	-

6 ACKNOWLEDGEMENTS

This work is supported by the first author's Discovery Grant from the National Science and Engineering Research Council of Canada (NSERC). The authors also gratefully acknowledge Ms. Shahrzad Talachian who conducted the VecTor2 analyses during her Master's studies in 2010.

7 CONCLUSIONS

The context for this paper is uncertainty analysis in contemporary performance-based earthquake engineering. In performance-based engineering the prediction of damage is a central ingredient, and this paper suggests two improvements to current damage assessment procedures. These advances are presented with the "ATC-58 approach" as a benchmark, in which fragility functions are employed to model damage probabilities. Specifically, lognormal cumulative distribution functions, which are univariate functions of a demand variable, provide the probability that a component is damaged beyond a pre-defined damage state. Each fragility function is uniquely defined by two parameters, which essentially represent the mean and standard deviation of the lognormal distribution. In the early stages of the ATC-58 project these two parameters are often based on expert opinion, but this is improving as more test data is becoming available.

The first contribution in this paper is the use of logistic regression to develop fragility functions. Logistic regression is similar to ordinary regression in the sense that any number of explanatory variables can be included to describe the phenomena. However, it differs from

ordinary regression in an important way; the output of a logistic regression model is a probability. As a result, logistic regression can be employed to develop damage fragility functions. This is a powerful extension of the ATC-58 approach because it avoids several difficulties in the current approach and it facilitates the inclusion of any number of variables that may influence the damage. In existing models, only one demand variable, for example displacement, is input to the fragility function to obtain the damage probability. With logistic regression it is possible to add any number of geometry and material variables, as well as model uncertainty variables, thus merging many fragility functions into one robust model. This paper provides a detailed description of logistic regression, together with an example and a demonstration of how such models fit within the ATC-58 analysis framework.

The analysis framework adopted by ATC-58 employs Monte Carlo sampling to obtain the key result, namely the loss exceedance probability curve. As an alternative, this paper puts forward a second extension of the ATC-58 approach, in which any reliability method can be used to obtain such results. Importantly, this paper describes how damage is modeled in the alternative approach. While logistic regression models fit directly into the ATC-58 framework, this second extension requires a reformulation of the damage models, whereby the visual damage is explicitly modeled, followed by models that predict repair action(s), in turn followed by models that predict the cost and time of the repair. None of these new models produce a probability as output. Instead, each model produces realizations of physical measurable parameters. On one hand this approach is even more flexible than the use of logistic regression above and points to a future with simulation models, but on the other hand it entails a substantial reformulation of the ATC-58 approach. Several examples are provided in this paper to compare the approaches, in order to highlight advantages and disadvantages.

REFERENCES

[1] C. Cornell and H. Krawinkler, Progress and challenges in seismic performance assessment. *PEER Center News*, http://peer.berkeley.edu/news/2000spring/index.html, 2000.

[2] Applied Technology Council, *Development of next generation performance-based seismic design procedures for new and existing buildings*. Applied Technology Council Report 58, 2008.

[3] T. Haukaas, Unified reliability and design optimization for earthquake engineering, *Probabilistic Engineering Mechanics*, **23**, 471-481, 2008.

[4] A. Der Kiureghian, Non-ergodicity and PEER's framework formula. *Earthquake Engineering and Structural Dynamics*, **34**, 1643-1652, 2005.

[5] T. Y. Yang, J. Moehle, B. Stojadinovic and A. Der Kiureghian, Seismic performance evaluation of facilities: Methodology and implementation. *Journal of Structural Engineering*, **135**, 1146-1154, 2009.

[6] A. H. Ang and W. H. Tang, *Probability Concepts in Engineering, Vol I*. Wiley, 2007.

[7] O. Ditlevson and H. O. Madsen, *Structural Reliability Methods*. Wiley, 1996.

[8] M. Mahsuli and T. Haukaas, Seismic risk analysis with reliability methods, part I: Models. *Structural Safety*, **42**, 54-62, 2013.

[9] M. Mahsuli and T. Haukaas, Computer program for multimodel reliability and optimization analysis. *Journal of Computing in Civil Engineering*, **27**, 87-98, 2013.

[10] T. P. Ryan, *Modern Regression Methods*. Wiley-Interscience, 2008.

[11] A. Agresti, *An Introduction to Categorical Data Analysis*. Wiley, 1996.

[12] P. Gardoni, A. Der Kiureghian and K. M. Mosalam, Probabilistic capacity models and fragility estimates for reinforced concrete columns based on experimental observations. *Journal of Engineering Mechanics,* **128**, 1024-1038, 2002.

[13] D. Hosmer and S. Lemeshow, *Applied Logistic Regression*. Wiley, 2000.

[14] P. McCullagh and J. A. Nelder, *Generalized linear models, Monographs on statistics and applied probability 37*. Chapman Hall, 1989.

[15] G. E. P. Box and G. C. Tiao, *Bayesian Inference in Statistical Analysis*. Addison–Wesley, 1992.

[16] A. Javaherian Yazdi and T. Haukaas, Multivariate probabilistic damage models for performance-based earthquake engineering. *Proceedings of the 11th International Conference on Structural Safety and Reliability, ICOSSAR 2013*.

[17] S. Talachian, *Probabilistic models for damage and repair cost for reinforced concrete structural members*. MASc thesis, Department of Civil Engineering, University of British Columbia, 2010.

[18] P. S. Wong and F. J. Vecchio, *Vector2 and formworks user's manual*. Department of Civil Engineering, University of Toronto, 2002.

COMPDYN 2013
4th ECCOMAS Thematic Conference on
Computational Methods in Structural Dynamics and Earthquake Engineering
M. Papadrakakis, V. Papadopoulos, V. Plevris (eds.)
Kos Island, Greece, 12–14 June 2013

RISK ASSESSMENT OF REINFORCED CONCRETE BUILDINGS CONSIDERING THE EARTHQUAKE DIRECTIONALITY EFFECTS

Yeudy F. Vargas[1], Lluis G. Pujades[1], Alex H. Barbat[2], Jorge E. Hurtado[3]

[1]Universidad Politécnica de Cataluña
Department of Geotechnical Engineering and Geosciences, Jordi Girona 1-3, Building D2, Campus Norte UPC, 08034 Barcelona Spain
(yeudy.felipe.vargas, lluis.pujades,)@upc.edu

[2]Universidad Politécnica de Cataluña
Department of Structural Mechanics, Jordi Girona 1-3, Building C1, Campus Norte UPC, 08034 Barcelona Spain
alex.barbat@upc.edu

[3]Universidad Nacional de Colombia
Universidad Nacional de Colombia, Apartado 127, Manizales, Colombia
jehurtadog@unal.edu.co

Keywords: Seismic risk assessment, non-linear dynamic analysis, uncertainties, earthquake directionality effects

Abstract. *In order to assess the seismic risk of structures, several methods based on pushover analysis have been developed. These methods are very useful in the case of symmetric structures because they can be easily approximated by means of a 2D model. In the case of asymmetric structures several improvements to the pushover analysis procedure have been proposed for considering the effect of asymmetry on the global response. However, such methods, in some cases, can be more expensive, from computational point of view, than the nonlinear dynamic analysis. In this article, we propose to assess the effect of the directionality of the earthquake by using non-linear dynamic analysis and considering uncertainties in the mechanical properties of the materials and in the seismic action. We use as a case study a group of reinforced concrete buildings located in Lorca, Spain, damaged by the earthquake of May 2011. The results show a good agreement between the observed and the calculated damage.*

1 INTRODUCTION

In the seismic risk assessment of buildings are involved two main random variables, the vulnerability of the structure and the intensity of the seismic action. The uncertainty related to the former one depends on the mechanical properties of the materials, the weight supported by the structure or the participation of the non-structural elements, among others. The uncertainty of the second one depends on the fault mechanism and the soil conditions, among many others. Even if the seismic action is known, for instance in the case that the earthquake has occurred and an acceleration record is available, there is another source of uncertainty related to the directionality effect. It means that, due to topographical and geological conditions, among others, it is difficult to establish the incidence of the acceleration upon the buildings of the studied area. If data associated with the observed seismic damage are available, one can validate the computational method used for calculating the seismic damage. Several methodologies based on static procedures have been developed for assessing the expected seismic damage of buildings [1, 2, 3, 4, 5]. These methodologies are based on the assumption that the behaviour of the building is governed by the first mode of vibration. For tall or asymmetric buildings, further consideration should be made by taking into account the effects of higher modes in elevation [6, 7], in plan [8, 9, 10] or in both, plan and elevation [11, 12, 13, 14]. But, in some cases, due to the high irregularity of a building, it is very difficult to perform a reliable pushover analysis, which is the base of the procedures based on nonlinear static methods. In these cases, from our point of view, it is necessary to assess seismic damage by performing non-linear dynamic analysis (NLDA) instead of pushover analysis. However, ignoring particular cases, simplified static methodologies were applied in several previous studies in order to calculate the seismic risk of urban areas [15, 16, 17, 18, 19] obtaining successful results. In this article we propose to calculate the seismic damage of a group of buildings located in the San Fernando neighborhood of the city of Lorca, Spain, which was affected by the earthquake occurred in May 2011, by considering as numerical tool the NLDA. We include the uncertainties related to the mechanical properties of the materials and the directionality of the earthquake.

2 DESCRIPTION OF THE STUDIED BUILDING

In this article we calculate the expected seismic damage of a group of buildings located in the San Fernando neighborhood of the city of Lorca, Spain, after the earthquake in May 2011. These buildings have 5 stories, reinforced concrete structure, and are configured with columns and waffle slabs. Some of these buildings have been strongly affected by the earthquake. One important fact is that all the buildings have been built using the same structural blueprints. However, the difference between their damage levels was considerable: some of them were damaged beyond repair limit and others had no damage. A picture of one of these buildings can be seen in Figure 1. This figure also shows some damaged columns at the ground floor. . This fact can be explained if we consider the uncertainties associated with the mechanical properties of the materials and the effect of the directionality of the earthquake. In order to prepare the structural model, we have used the blueprints of the building which contains information not only on the geometry but also on the strength of the materials. Figure 2a shows a blueprint of the analyzed building. Figure 2b shows a plan view of the structural model used as a reference to define the angle of rotation in the calculations which have been carried out. From this figure, it can be concluded that the building is weaker in the x direction (the axes are indicated in the figure).



Figure 1: Buildings located in the San Fernando neighborhood of the city of Lorca, Spain, affected by the earthquake occurred on May 2011

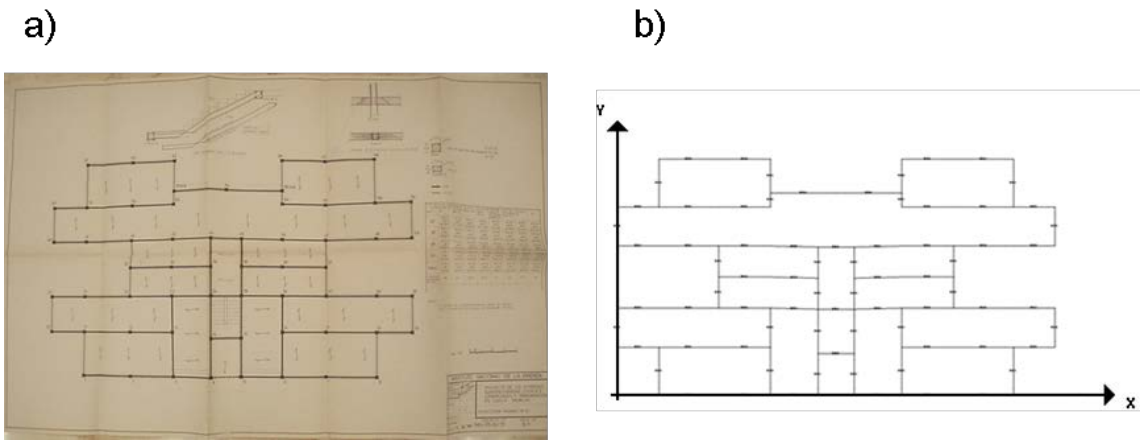


Figure 2: a) Blueprint of the building b) Plan view of the structural model

Figure 3 shows an aerial photo of the buildings of the San Fernando neighborhood, scored according to the damage caused by the earthquake. Green indicates that the building was not damaged; yellow indicates that the damage is reparable; and red shows that there is an imminent risk of collapse and, therefore, the building has been recommended for demolition. It is important to note that some buildings form aggregates up to 3 units, but the 2 units aggregate is the more common. . It can be seen that the buildings whose *x* axis makes an angle of approximately 20° or 200° with the EW component (using as reference the axes shown in Figure 2b) have a tendency to suffer less damage. The opposite happens with the buildings which make an angle with *x* axis of about 110° or 290°. However, the San Fernando neighborhood is

located far away from the seismological station where the earthquake was recorded and, therefore, due to topographical and geological conditions, among others, it is difficult to determine the angle with which the record should be rotated according to the position of the neighborhood. For this reason, the seismic action is treated as a random variable whose source of uncertainty is due to the directionality.



Figure 3: Plan view of the buildings located in San Fernando neighborhood affected by the Lorca earthquake. Green indicates that the building was not damaged; yellow indicates that the damage is reparable; red indicates that there is an imminent risk of collapse

A 3D structural model used in the structural analysis of the buildings is shown in Figure 4. The software to perform the analyses was RUAUMOKO [20]. The modified Takeda model [21] was chosen among the hysteretic models available in the RUAUMOKO program to describe the mechanical behaviour of reinforced concrete. In order to define the yield surfaces of the material of the columns and beams, it was necessary to create interaction diagrams between the bending moment and the axial force, and between the bending moment and the angular deformation, respectively. The non-linear behaviour in shear has not been considered. Programs have been developed in MATLAB in order to calculate the yielding points necessary when defining the behaviour of the structural elements used in the dynamic analyses of the structures. The tangent-stiffness proportional Rayleigh damping model was used.

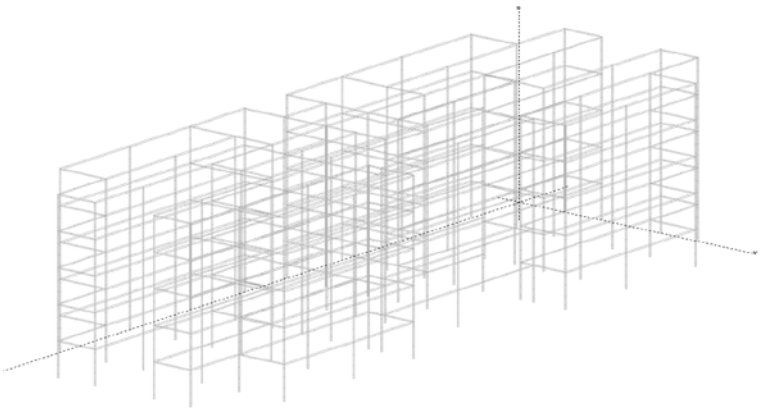


Figure 4: 3D structural model of the building

3 LORCA, MAY 2011 EARTHQUAKE

The magnitude of the Lorca earthquake was 5.1, that is, a moderated earthquake. But, this earthquake caused 9 casualties and great economic losses. This fact highlights the high seismic vulnerability of the buildings located in that area, but which is similar in other regions of Spain. The horizontal components of the earthquake are shown in Figure 5.

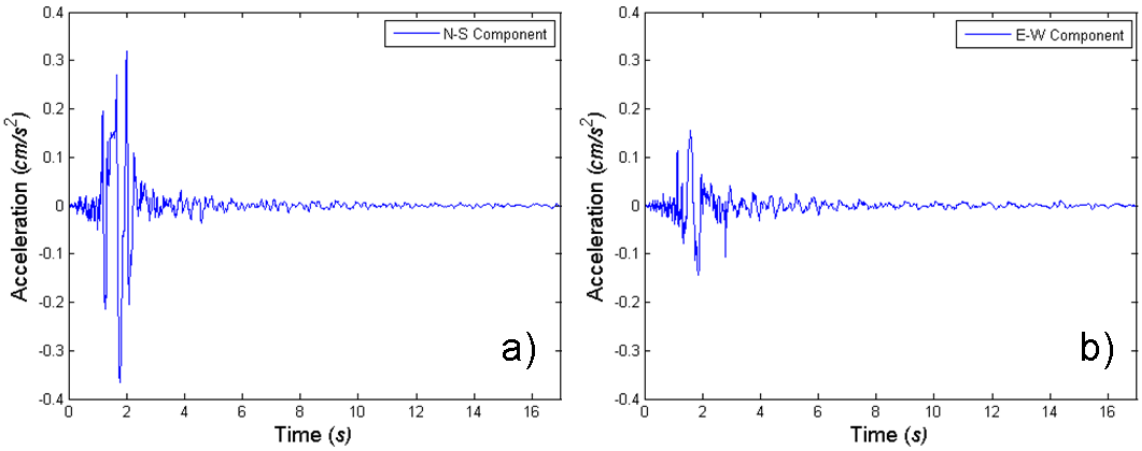


Figure 5: Horizontal components of the May 2011 Lorca earthquake

The uncertainties in the seismic hazard are considered by rotating the horizontal components of the record by an angle θ [22]

$$\begin{pmatrix} \ddot{u}_{x(\theta)}(t) \\ \ddot{u}_{y(\theta)}(t) \end{pmatrix} = \begin{bmatrix} \cos(\theta) & sen(\theta) \\ -sen(\theta) & \cos(\theta) \end{bmatrix} \begin{pmatrix} \ddot{u}_{x}(t) \\ \ddot{u}_{y}(t) \end{pmatrix} \tag{1}$$

where $a_{x(\theta)}(t)$ and $a_{y(\theta)}(t)$ are the horizontal components of the accelerogram when rotated anti-clockwise by an angle θ, while $a_x(t)$ and $a_y(t)$ are the original components of the record. In order to consider the directionality effect, we rotated the horizontal components of the earthquake with an angle θ varying from 0° to 180° with increments of 1° and, then, for each angle, we calculated the response spectra of the rotated record $\ddot{u}_{x(\theta)}(t)$. Figure 6 shows the acceleration response spectra obtained after rotating the horizontal components. It can be seen that the variation in terms of spectral acceleration is very high in the range of the considered. It indicates that the seismic behavior of a building located in Lorca, when subjected to the Lorca earthquake, strongly depends on its azimuth. For this reason, it is necessary to include the directionality as a random variable in order to get reliable and accurate results. For instance, the fundamental period of the studied buildings is about 0.8 seconds and, for this value, the spectral accelerations vary from 0.072 *g* to 0.3748 *g*.

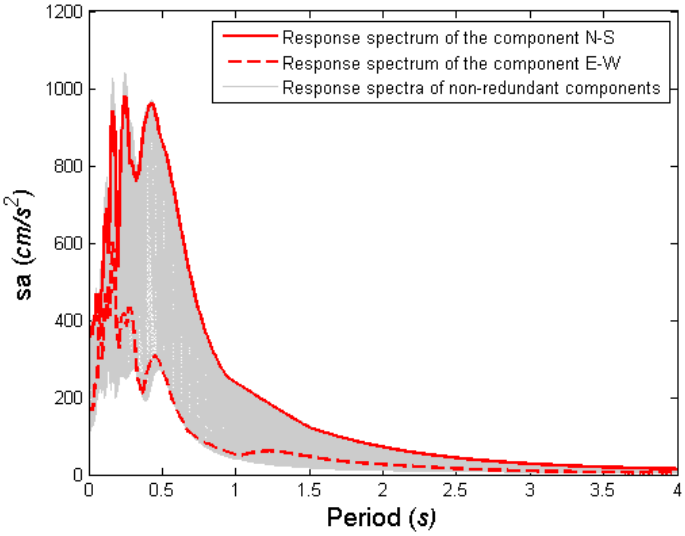


Figure 6: Acceleration response spectra obtained after rotating the acceleration record registered during Lorca earthquake

4 PROBABILISTIC NON-LINEAR DYNAMIC ANALYSIS

In the case of the studied building, the system of axes is given in Figure 2b. A series of nonlinear dynamic analysis has been performed considering not only the variation of the angle of incidence of the seismic action with the building but also the uncertainties associated to the mechanical properties of the materials. Thus, 3600 nonlinear dynamic analyses have been performed, in which the angle of rotation of the earthquake is treated as a random variable with a uniform probability distribution in the interval (0°, 180°). The compressive strength of concrete, *fc*, and the tensile strength of steel, *fy*, are also considered as random variables, following a Gaussian probability distribution whose characteristics are shown in Table 1. These values are taken from the original blueprints. The spatial variability of these variables has been also considered as shown by Vargas et al. [23].

Variable	μ_x (kPa)	σ_x (kPa)
fc	21000	2100
fy	500000	50000

Table 1: Statistical moments of the mechanical properties of the materials considered herein

It can be expected that the seismic damage depends strongly on the angle of rotation and that even the effect of the uncertainties associated with the materials properties could be negligible. After performing the dynamic analysis, we calculated the damage index of Park and Ang [24]

$$DI_{\mathrm{E}} = \frac{\mu_m}{\mu_u} + \frac{\beta E_h}{F_y \mu_u \delta_y} \tag{2}$$

where μ_m and μ_u are the maximum and ultimate ductilities, respectively, and the subscript E stays for the element level damage index; β is a non-negative parameter which considers the effect of cyclic loading on the structural damage; E_h is the dissipated hysteretic energy; F_y is the yield load; and δ_y is the yield displacement. The global damage index of the structure, *DI*,

is a weighted mean of the element damages, in which the weights are the ratio of the hysteretic energy dissipated by each element to the total hysteretic energy dissipated by the structure:

$$DI = \sum_i \lambda_i DI_{\mathrm{E}} \tag{3}$$

In this equation, *DI* is the dynamic analysis based global damage index of the structure, λ_i is the ratio of the dissipated hysteretic energy of an element E to the dissipated hysteretic energy of the entire structure. Vargas et al. [25] have used the damage index of Park and Ang to get damage curves by considering uncertainties. Figure 5 shows the variation of damage as a function of the incidence angle of the action and also shows the uncertainty associated with the mechanical properties of materials. To evaluate the distribution of damage, it is convenient to group the results shown in Figure 5 in the histogram shown in Figure 6.

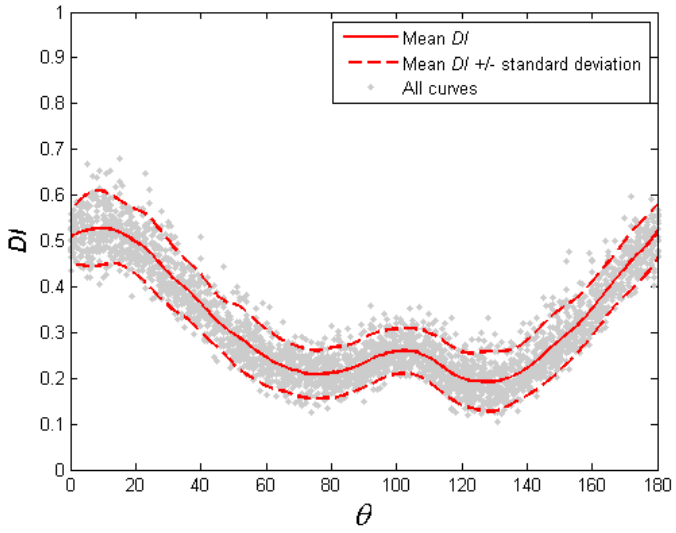


Figure 5: Variation of the damage index considering the angle of rotation of the earthquake and the uncertainties associated with the mechanical properties of materials

This histogram shows that the resultant distribution function has a bimodal shape. This is due to the fact that the expected damage, when the seismic action is maximum in the *y* direction, is greater than when the seismic action is maximum in the *x* direction. This may explain why some buildings suffered more damage in one direction than the others. On the other hand, Park et al. [26] assigned a qualitative description of the damage depending on the calculated value of the damage index. For example, they state that, if the damage index of a building is greater than 0.4, the repair cost exceeds the construction cost of the building; for lower damage repair is economically viable. If the calculated damage index is less than 0.2, Park et al [26] consider that damage is slight, corresponding to '*sporadic occurrence of cracking*'. These thresholds are important in the analysis of the results because, as is shown in Figure 3, some buildings were not damaged and others were recommended for demolition. If we analyze the histogram of Figure 6 according to the limits of damage described previously (see the red lines) we can establish the percentages of buildings that suffer slight, moderate and extensive damage, assuming that extensive damage is not repairable and, therefore, the building should be demolished. This can be done by counting the number of samples contained in each interval. This count shows that 511 samples presents a *DI*<0.2, 2109 samples are in the range 0.2>*DI*<0.4 and for 980 samples *DI*>0.4. Whereas the number of samples is 3600, the proba-

bilities of occurrence of each damage state are 14.19%, 58.86% and 26.95% for slight, moderate and extensive damage, respectively. The damage observed indicated that 13.33% of the buildings had damage slight, 60% had moderate damage and 26.67% had extensive damage, for these last cases, demolition was recommended.

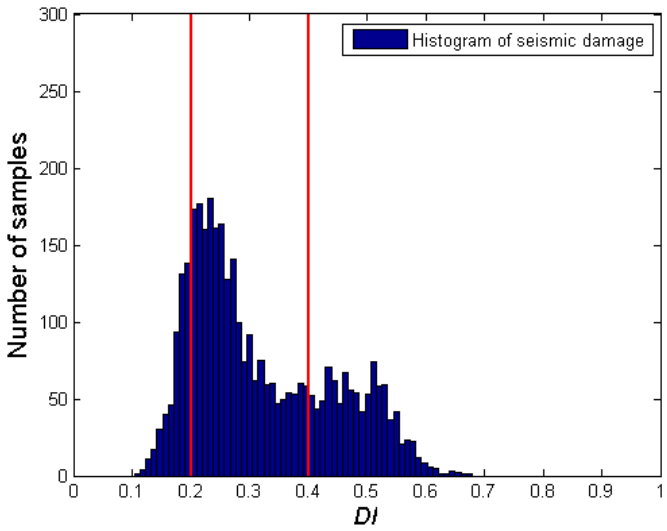


Figure 6: Histogram of the expected damage of Park and Ang

These results are plotted in the histogram shown in Figure 7 in which a good agreement between calculated and observed damage can be appreciated which highlights the importance of considering the uncertainties in the risk and vulnerability analysis of structures.

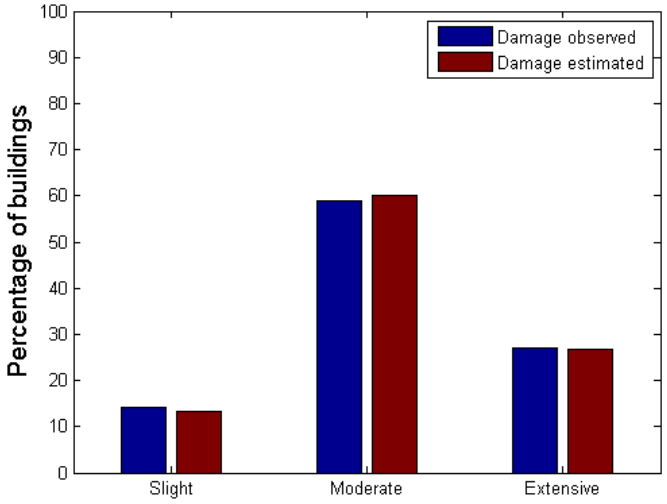


Figure 7: Comparison of observed and calculated damage

It is complicated to establish, from the available data, which is the angle at which the acceleration record should be rotated to simulate the acceleration occurred in the San Fernando neighborhood. Figure 5 shows the specific damage distributions for any angle of rotation, reducing uncertainty. That is, if damage probability distributions are analyzed for two orthogonal angles, e.g. 40° and 130°, we obtain the probability density functions shown in Figure 8.

The principal moments of these probability density functions are shown in Table 2. It might be supposed that 40° coincides with the more damaged direction and 130° coincides with the less damaged direction. Note that this assumption could explain quite well the variation between the observed damage. However, this is a hypothesis and the theoretical basis on which it is established is beyond the scope of this paper.

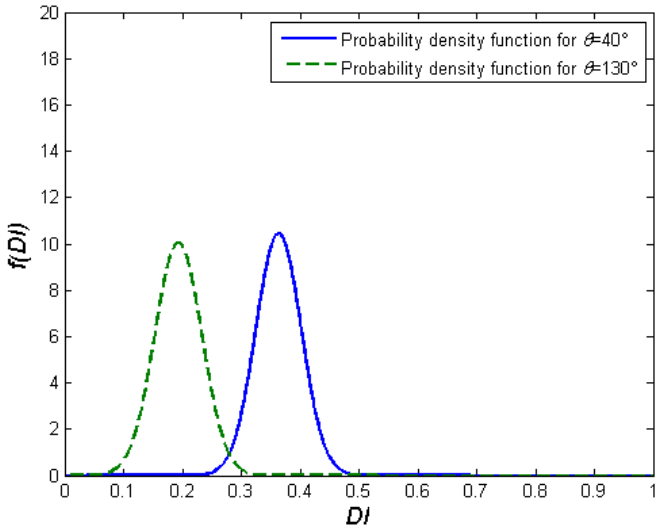


Figure 8: Probability density functions of damage for $\theta = 40°$ and $\theta = 130°$

$\theta°$	μ_{ID}	σ_{ID}
40°	0.3634	0.0382
130°	0.1930	0.0397

Table 2: Statistical moments of damage for $\theta = 40°$ and $\theta = 130°$

5 CONCLUSIONS

This article shows how the methodology of seismic risk assessment based on the nonlinear dynamic analysis considering uncertainties, is an excellent alternative for studying the directionality effect of the seismic action on asymmetric buildings. We modeled the expected seismic damage of a group of buildings affected by an earthquake occurred in May 2011 in Lorca, Spain. Thus, the objective was to assess the damage in buildings due to a specific action and it was not been necessary to consider the uncertainties due to the earthquake-to-earthquake variation. The computational cost to obtain the results presented in this paper is relatively high. However, the results are in good correspondence with the observed damage. Due to the treatment of the uncertainties related to the seismic action and to the mechanical properties of the materials, the results obtained in this article can be extended for assessing the behavior of others buildings of similar typology affected by the earthquake of Lorca. It is important to note that, if the angle with which the acceleration record should be rotated in order to simulate its effect in a given area is known, the results obtained can be extended to predict the distribution of the seismic damage with less uncertainty.

Acknowledgements

This work has been partially funded by the Geologic Institute of Catalonia (IGC) and FEDER funds. The funding of the Spanish government and of the European Commission through research projects CGL2008-00869/BTE, CGL2011-23621, INTERREG: POCTEFA 2007-2013/ 73/08 and MOVE—FT7-ENV-2007-1-211590 is also acknowledged. Yeudy F. Vargas has a scholarship from an IGC-UPC joint agreement.

REFERENCES

[1] S.A. Freeman, J.P. Nicoletti, J.V. Tyrell, Evaluations of existing buildings for seismic risk. A case study of Puget Sound Naval Shipyard, Bremerton, Washington. *Proc. 1st U.S. National Conference of Earthquake Engineering*, EERI, Berkeley, 113-122, 1975.

[2] S.A. Freeman, *Development and use of capacity spectrum method*. Proc. 6th U.S. National Conference of Earthquake Engineering. EERI, Seattle CD-ROM, 1998.

[3] P. Fajfar, P. Gaspersic, The N2 method for the seismic damage analysis of RC buildings. *Earthquake Engineering and Structural Dynamics*, 25(1), 31-46, 1996.

[4] A.K. Chopra, R.K. Goel, Capacity-demand-diagram methods for estimating seismic deformation of inelastic structures: SDOF systems. *PEER Report 1999/02 Berkeley: Pacific Earthquake Engineering Research Center, University of California*, 1999.

[5] P. Fajfar, Capacity spectrum based on inelastic demand spectra. *Earthquake Engineering and Structural Dynamics*, 28(9): 979-993, 1999.

[6] A.K Chopra, R.K. Goel, C. Chintanapakdee, Evaluation of a modified MPA procedure assuming higher modes as elastic to estimate seismic demands. *Earthquake Spectra*, 20(3), 757-778, 2004.

[7] M. Poursha, F. Khoshnoudian, A.S. Moghadam, A consecutive modal pushover procedure for estimating the seismic demands of tall buildings. *Engineering Structures*, 31(2), 591-599, 2009.

[8] A.K Chopra, R.K. Goel, A modal pushover analysis procedure to estimate seismic demand for unsymmetric-plan buildings. *Earthquake Engineering and Structural Dynamics*, 33(8), 903-927, 2004.

[9] R. Bento, C. Bhatt, R. Pinho, Using nonlinear static procedures for seismic assessment of the 3D irregular SPEAR building. *Earthquake and structures*, 1(2), 177-195, 2010.

[10] C. Bhatt, R. Bento, Assessing the torsional response of existing RC building using the extended N2 method. *Bulletin of Earthquake Engineering*, doi: 10.1007/s10518-011-9258-8, 2011.

[11] M. Kreslin, P. Fajfar, The extended N2 method considering higher mode effects in both plan and elevation. *Bulletin of Earthquake Engineering*, 10(2), 695-715, 2012.

[12] J.C. Reyes, A.K. Chopra, Three-dimensional modal pushover analysis of building subjected to two components of ground motions, including its evaluation for tall buildings. *Earthquake Engineering and Structural Dynamics*, doi: 10/1002/eqe.1060, 2010.

[13] J.C. Reyes, A.K. Chopra, Evaluation of three-dimensional modal pushover analysis for unsymmetric-plan buildings subjected to two components of ground motion. *Earthquake Engineering and Structural Dynamics*, doi: 10/1002/eqe.1100, 2011.

[14] K. Fujii, Nonlinear static procedure for multi-story asymmetric building considering bi-directional excitation. *Journal of Earthquake Engineering*, 15(2), 245-273, 2011.

[15] A.H. Barbat, L.G. Pujades, N. Lantada, R. Moreno, Seismic damage evaluation in urban areas using the capacity spectrum method: application to Barcelona. *Soil Dynamics and Earthquake Engineering*, 28(10-11), 851–865, 2008.

[16] N. Lantada, L.G. Pujades, A.H. Barbat, Vulnerability index and capacity spectrum based methods for urban seismic risk evaluation. A comparison. *Natural Hazards*, 51(3), 501-524, 2009.

[17] L.G. Pujades, A.H. Barbat, R. González-Drigo, J. Avila, S. Lagomarsino, Seismic performance of a block of buildings representative of the typical construction in the Eixample district in Barcelona (Spain). *Bulletin of Earthquake Engineering*, 10(1), 331–349, 2012.

[18] Y.F. Vargas, L.G. Pujades, A.H. Barbat, J.E. Hurtado, Evaluación probabilista de la capacidad, fragilidad y daño sísmico en edificios de hormigón armado. *Métodos numéricos para cálculo y diseño en ingeniería*, 2013. (in press).

[19] R. Gonzalez-Drigo, J.A. Avila-Haro, A.H. Barbat, L.G. Pujades, Y.F. Vargas, S. Lagomarsino, S. Cattari, Modernist URM buildings of Barcelona. Seismic vulnerability and risk assessment. *International Journal of Architectural Heritage: Conservation, Analysis, and Restoration,* doi: 10.1080/15583058.2013.766779, 2013.

[20] A.J. Carr, Ruaumoko-Inelastic Dynamic Analisys Program. *Department of Civil Engineering, University of Canterbury, Christchurch, New Zealand*, 2000.

[21] S. Otani, Inelastic analysis of RC frame structures. *J. Struct. Div. ASCE*, 100(7), 1433–1449, 1974.

[22] K. Beyer, J.J. Bommer, Relationships between median values and between aleatory variabilities for different definitions of the horizontal component of motion. *Bulletin of Seismological Society of America*, 96(4), 1512–1522, 2006.

[23] Y.F. Vargas, L.G. Pujades, A.H. Barbat, J.E. Hurtado, Probabilistic seismic risk evaluation of RC buildings. *Structures and buildings*, 2013 (in press)

[24] Y.J. Park, A.H.S. Ang, Mechanistic seismic damage Model for Reinforced Concrete. *Journal of Structural Engineering ASCE*, 111(4), 722-739, 1985.

[25] Y.F. Vargas, L.G. Pujades, A.H. Barbat, J.E. Hurtado, *Computational methods in stochastic dynamics, Vol II*. Springer, 2012.

[26] Y.J. Park, A.H.S. Ang Y. Kwei-Wen, Seismic damage analysis of reinforced concrete buildings. *Journal of Structural Engineering ASCE*, 111(4), 740-757, 1985.

COMPDYN 2013
4th ECCOMAS Thematic Conference on
Computational Methods in Structural Dynamics and Earthquake Engineering
M. Papadrakakis, V. Papadopoulos, V. Plevris (eds.)
Kos Island, Greece, 12–14 June 2013

SEISMIC FRAGILITY AND VULNERABILITY ASSESSMENT USING SIMPLIFIED METHODS FOR THE GLOBAL EARTHQUAKE MODEL

Dimitrios Vamvatsikos, and Athanasia K. Kazantzi

National Technical University of Athens
9 Heroon Polytechneiou, 157 80 Athens, Greece
{divamva,kazantzi}@mail.ntua.gr

Keywords: Fragility, Vulnerability, Earthquake, Probabilistic, Static Pushover, Structural Model.

Abstract. *The Global Earthquake Model (GEM) has commissioned the preparation of analytical vulnerability guidelines for general use. Within this framework, a distinct modeling and analysis method hierarchy has been proposed, whereby both detailed and reduced-order models can be analyzed using nonlinear static or dynamic methods. Each subsequent reduction in complexity increases the speed of application, yet generates additional error that needs to be considered in the form of epistemic uncertainty. The available choices represent different levels of compromise between the accuracy achieved and the associated effort needed, meant to suit users having different levels of expertise and resource availability. Our particular focus will be on the middle path that is expected to become the most popular choice, combining (a) a simplified stick model of the structure with (b) a static pushover analysis with accurate record-to-record dispersion information. The entire procedure is cast within an appropriate probabilistic framework that can effortlessly incorporate all the epistemic and aleatory uncertainty sources to become a viable path for evaluating structural fragility for a building class.*

1 INTRODUCTION

The Global Earthquake Model (GEM) is a grand effort to offer a comprehensive open-source tool for loss assessment on a large scale. A vital component of it is the definition of physical vulnerability for different classes of buildings (Figure 1), a task that has been undertaken by an international consortium of researchers. Separate thrusts of the project are geared towards defining building vulnerability functions based on (a) empirical data (b) expert opinion and (c) structural analysis. Our focus will be on the latter part with emphasis on low- and mid-rise structures and specifically on the development of guideline documents for estimating analytical fragility functions for assessing structural damage.

The analytical vulnerability guidelines are being developed as a hierarchy of approaches that can accommodate different levels of expertise. Our proposal thus accommodates several paths towards reasonable approximations that strike different compromises between the time committed and the accuracy achieved. The present work deals with the case where the analyst has the skills and time to perform nonlinear static analysis. The minimum target is for a structural engineer with Master's level training and the ability to create simplified nonlinear structural models, to be able to determine the vulnerability functions pertaining to structural response, damage or loss with reasonable effort. This has been defined as 20-40 man-hours for any single structure, and 80-160 man-hours for a class of buildings.

Estimating vulnerability for a class of buildings involves a number of steps that need to be undertaken in series. First and foremost, a set of "index" buildings needs to be selected to represent the class. These are typically 3 to 7 distinct structures having different macro-characteristics, such as number of stories, level of construction quality and degree of vertical or plan asymmetry. Subsequently, appropriate structural models need to be generated and structural analysis undertaken to determine their response to seismic loads. Fragility curves, i.e., probability-valued functions of the seismic intensity for exceeding specified damage states for each story or an entire building, are then estimated. The final step is the estimation of losses. At each step all sources of uncertainty need to be quantified and propagated to the final result, taking into account the variability of ground motions, single building properties, population diversity and our own methodological errors.

Our focus will be on the modeling and analysis stages, with particular emphasis on providing a solid basis for evaluating fragility curves for a single building without loss of any probabilistic information. Among a wealth of offered paths to achieve this, we are only going to discuss the option of applying nonlinear static analysis on simplified stick models of the structures, representing an excellent compromise between accuracy and simplicity.

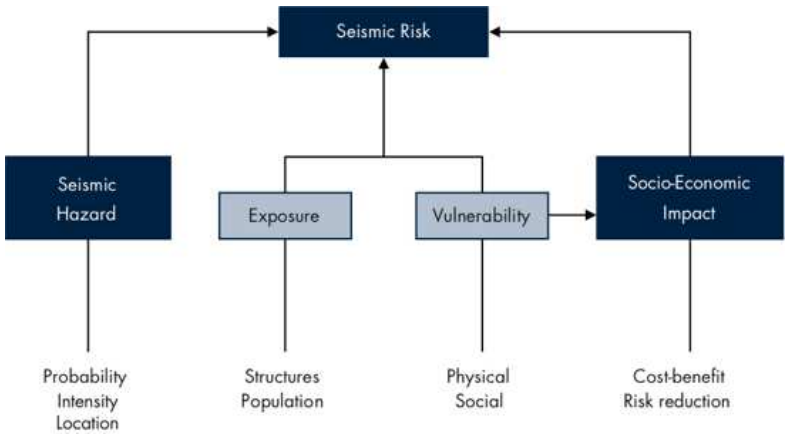


Figure 1: Conceptual framework for seismic risk assessment adopted by GEM (source: http://en.wikipedia.org/wiki/Global_Earthquake_Model).

2 SIMPLIFIED STICK MODELS

The development of structural models for each index building is an important issue when deriving analytical vulnerability functions. The complexity of detailed modeling offers undeniable accuracy, yet it often absorbs most of the effort due to the multiple representative buildings employed. Typically, a detailed 2D or 3D multi-degree-of-freedom model would be required for each index building. Appropriate representation of the nonlinear behavior of all identified lateral-load resisting components in the building (columns, beams, walls, braces etc.) is essential. Significant global or local geometric nonlinearities (e.g., P-Δ effects, brace buckling) also need to be included. In short, this is a modeling level that is roughly equivalent to the detail needed for assessing an individual building according to current seismic guidelines. Despite the inherent accuracy and reliability of such detailed models, their use in loss estimation for an entire class may not always be practical. The broad variability within the class means that individual details that have been painstakingly modeled will eventually disappear and only some macro-characteristics may dominate. Then, the simplicity of a 2D stick representation of a building becomes a cost-effective alternative.

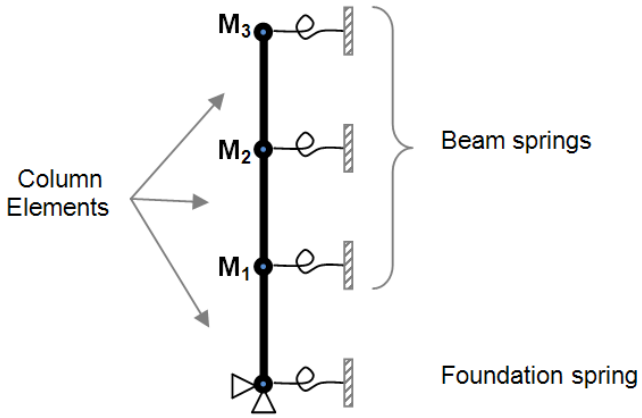


Figure 2: A three-story stick model, showing column elements, floor masses M_1 – M_3 and rotational springs to represent beam and foundation stiffness.

Our proposal for a simplified macro-model is based on the concept of "fishbone" models pioneered by Luco et al. [1] to represent moment-resisting frame buildings. This would reduce a frame to a single column-line, each story rotationally restricted by two half-beams that are roller-supported at their opposing ends. This idea has been further simplified and generalized to represent both flexural and shear buildings as shown in Figure 2. It retains the column-line, comprising *N* columns and *N* nodes (plus the foundation node) for *N* stories, each with 3 degrees of freedom (horizontal, vertical, rotational) in 2D space. The nodes are further restrained by *N* rotational springs representing the strength and stiffness of beams at each floor. All elements are nonlinear, at the very minimum having a capped elastoplastic behavior, i.e., an elastic perfectly-plastic relationship of force-deformation, moment-rotation or stress-strain that contains a hard-coded ultimate ductility to simulate component failure (Figure 3). Element characteristics can be easily derived using the aggregate stiffness of the columns, piers, walls or beams in each story together with the corresponding yield and ultimate displacements or rotations. Only translational story masses need be assigned to each node, while global P-Δ effects are explicitly taken into account.

By thus condensing the characteristics of each story into one column and one rotational spring, the stick model achieves remarkable economy. While it can capture many of the sali-

ent features of modern buildings, especially height, vertical irregularities and flexural versus shear behavior, it cannot take into account any effects related to the two neglected horizontal dimensions. For example, the effect of column compression/tension due to the overturning moment, or any shear lag effects within a single beam-line are not captured. In addition, as with any 2D structure, 3D interaction effects are not modeled. This is of little importance for plan-symmetric structures with distinct lateral load-resisting systems in the two horizontal directions. It becomes an issue for plan-asymmetric structures or wherever the appearance of mass/shear center eccentricity causes torsion. It may also introduce bias in the results if the system strength in the two horizontal directions is strongly interacting, thus making biaxial shaking significantly more detrimental than uniaxial.

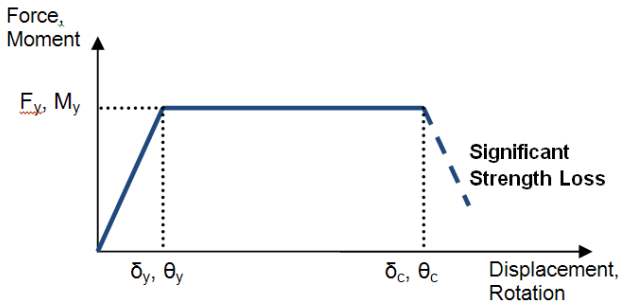


Figure 3: The capped elastic-plastic backbone is the simplest recommended force-deformation or moment-rotation backbone relationship for elements.

Such 3D effects can still be taken into account approximately by using theoretical or regression expressions to relate, e.g., the index of plan asymmetry to a reduction in the column and beam ductility capacities incorporated in the model. This is considered a far superior approach than using a direct “damage modifier”, where the modification is applied on the EDP displacement (or acceleration) response of the model rather than its properties, leading to considerable difficulties in properly defining collapse. In other words, it is not easy to make such modifications influence the seismic intensity level causing collapse when applying them only in post-processing. By including them in the model properties, though, their integration becomes more natural. For example, for square-plan multi-bay space-frames with ductile members, it can be shown that a normalized plan eccentricity of e leads to an increase of elastic base shear in any of the two directions by a factor of $1+1.5e$. Reducing the yield and ultimate ductility of both the beam spring and the column element in the corresponding eccentric stories yields a simple method to roughly account for this effect.

3 EVALUATION OF FRAGILITY CURVES USING NSP

While nonlinear dynamic analysis is steadily gaining ground as the standard method of analysis, at present its use largely remains within the academic community. The mainstay of current practical guidelines for seismic assessment is currently the nonlinear static procedure (NSP). There are several methodologies for estimating fragility curves for a structure that are based on NSP, using a pushover analysis to evaluate system performance. They are generally simple and relatively easy-to-use methods that are intuitive for engineers that have worked with nonlinear static analysis. Apart from any inaccuracies incurred by the well-known approximating nature of the pushover, they do share one major drawback: Despite trying to capture an inherently probabilistic quantity such as the fragility curve, they are in essence deterministic approaches, simply because of their root in classic pushover analysis.

Typical NSP approaches determine a single demand value for any structural response variable (or engineering demand parameter, EDP) that corresponds to a given level of the seismic intensity measure (IM), as measured in terms of the spectral acceleration $S_a(T)$ at period T. This is summarized in the so-called performance point, situated on the capacity curve at an estimated target displacement (typically of the roof). This single demand value can be estimated via two possible methods, namely displacement modification/coefficient method (Veletsos and Newmark [2]) or the equivalent linearization approach (Jacobsen [3]). In the first case, an R-μ-T relationship is employed to provide an approximation to the mean or median value of ductility, μ, of a nonlinear single-degree-of-freedom oscillator with period T that is subjected to a given level of intensity, defined by the strength ratio R. The latter is the ratio of the seismic force over the oscillator yield strength, or simply the seismic intensity in S_a terms over its value that causes yield. This method is the basis of most current US and EU guidelines, namely ASCE/SEI 41-06 [4] and EN1998-Part III [5]. The equivalent linearization method, instead, utilizes a lengthened period and an increased damping value to define a linear oscillator that can provide the needed (mean/median) displacement response. It has been popularized by the ATC-40 document and it was later shown to be able to deliver mean or median results of similar accuracy to the displacement modification approach (FEMA 440 [6]), as long as a direct physical interpretation is not a constraint when deriving the equivalent period and damping. Still, it remains an indirect approach that has not seen much use beyond ATC-40 [7]. Therefore it will not be the focus of our proposed approach.

Summing up, the constraints placed upon NSPs by the target displacement approximation method essentially limit its ability to provide a full distribution of response for a given level of intensity and hence capture the seismic input randomness. As a result, the static pushover itself is only used as a method to determine the central value (median or mean) of intensity measure (IM) capacity that anchors the fragility curve, while the dispersion around it is typically an assumed constant value, regardless of period or deformation. This has the undesirable effect of providing only a rough approximation of the considerable record-to-record variability, while not offering any insight into the additional dispersion due to aleatory and epistemic sources inherent in modeling, analysis and threshold values of EDP capacity.

Recent advances in R-μ-T relationships have offered at least two viable options for introducing record-to-record variability back into NSP estimates. The first is the work of Vamvatsikos and Cornell [8] on SPO2IDA, a spreadsheet-level tool that allows estimating the median and dispersion of ductility for complex quadrilinear capacity curves that may incorporate a negative stiffness segment, e.g. due to P-Δ or material in-cycle degradation and a residual strength branch, similar to the post-peak response of a braced or infilled frame. The second approach comes from Ruiz-Garcia and Miranda [9] that have offered R-μ-T (or, more precisely C_R-μ-T, where $C_R = \mu(R)/R$) expressions with dispersion information for elasto-plastic oscillators. Such tools offer substantially improved information that can be used to inject probability back into traditional NSPs.

3.1 Probabilistic basis of fragility

Fragility curves have been around for a long time, dating back to the early work in the nuclear industry, e.g., Kennedy and Ravindra [10]. In our case, the probabilistic formulation that will be adopted to represent the fragility curve goes back to at least the concepts forming the backbone of the SAC/FEMA framework (Cornell et al [11]) that have also appeared in the earlier or later work of many researchers, for example Shinozuka et al [12], Choi et al [13] and Kazantzi et al. [14]. Following in their footsteps, the fragility function is defined as the probability function of the limit-state capacity C being exceeded by the demand D for a given intensity level (i.e. IM-value), s. It may be defined for an entire building or for any of its sto-

ries. In both cases, if demand and capacity are expressed in terms of intensity levels, then we get the simplest representation of fragility:

$$P_{LS}(s) = P(C < D \mid s) = P(s_c < s \mid s) = F(s_c \mid s) \tag{1}$$

where s_c is the (random) IM-value of capacity that when exceeded signals violation of the limit-state and F[·] is the cumulative distribution function (CDF) of its arguments. Essentially, the fragility curve then becomes the CDF of s_c evaluated at the intensity level s. It is usually assumed that s_c is lognormal, leading to the simple expression of:

$$P_{LS}(s) = \Phi\left(\frac{\ln s - \ln \hat{s}_c}{\beta_{Sc}}\right) \tag{2}$$

where $\hat{s}_c$ is the median IM-value of capacity and β_{Sc} the corresponding dispersion (standard deviation of the log-data). While conceptually simple, these two parameters may become difficult to evaluate as the results of structural analysis are in terms of EDP given the level of IM, rather than vice-versa.

Therefore, a more intuitive format is based on the expression of both demand and capacity in terms of the engineering demand parameter that is used to test for limit-state violation. If θ_c is the corresponding EDP capacity and θ the structural demand (both random variables), then

$$P_{LS}(s) = P(C < D \mid s) = P(\theta_c < \theta \mid s) \tag{3}$$

Again, it is assumed that both demand and capacity are lognormal with medians $\hat{\theta}(s)$, $\hat{\theta}_c$ and dispersions $\beta_{\theta d}$, $\beta_{\theta c}$, respectively.

Then, considering that the sum (or difference) of two normal variables is also normal, and assuming that demand and capacity are independent (see also the relevant discussion in Cornell et al. [11]) the following well-known result comes up (e.g., Kennedy and Ravindra [10]):

$$P_{LS}(s) = \Phi\left(\frac{\ln \hat{\theta}(s) - \ln \hat{\theta}_c}{\sqrt{\beta_{\theta d}^2 + \beta_{\theta c}^2}}\right) \tag{4}$$

Following the work of Cornell et al. [11], a power law approximation is assumed for the median EDP demand given IM, which is valid as long as the structure has not approached the global instability region:

$$\theta(s) \approx a \cdot s^b \tag{5}$$

Then, by introducing the above into Eq. (4) a simpler approximation may be derived for fragility that resembles the earlier IM formulation:

$$P_{LS}(s) = \Phi\left(\frac{\ln a + b \ln s - \ln \hat{\theta}_c}{\sqrt{\beta_{\theta d}^2 + \beta_{\theta c}^2}}\right) = \Phi\left[\frac{\ln s - \left(\ln \hat{\theta}_c - \ln a\right)/b}{\sqrt{\beta_{\theta d}^2 + \beta_{\theta c}^2}/b}\right] \tag{6}$$

Now, it becomes obvious by comparing Eq. (2) and (6) that the median and dispersion of the IM value of capacity, s_c, may be estimated as:

$$\hat{s}_c = \left(\frac{\hat{\theta}_c}{a}\right)^{1/b} \tag{7}$$

$$\beta_{Sc} = \frac{1}{b}\sqrt{\beta_{\theta d}^2 + \beta_{\theta c}^2} \tag{8}$$

In order to introduce the effect of epistemic uncertainty, it is assumed that demand and capacity maintain their medians but acquire additional dispersion of $\beta_{U\theta d}$ and $\beta_{U\theta c}$, respectively. This is typically referred to as the "first-order assumption" and it causes the overall dispersion of Eq. (8) to become instead:

$$\beta_{TSc} = \frac{1}{b}\sqrt{\beta_{\theta d}^2 + \beta_{\theta c}^2 + \beta_{U\theta d}^2 + \beta_{U\theta c}^2} \tag{9}$$

The dispersions $\beta_{\theta c}$, $\beta_{U\theta d}$ and $\beta_{U\theta c}$ are essentially parameters of the problem that need to be provided and cannot be easily determined by a simple computational analysis. For example, Kazantzi et al. [15], Liel et al [16], Dolsek [17], Vamvatsikos and Fragiadakis [18] offer a number of computational methods for estimating $\beta_{U\theta d}$ when dealing with models having uncertain parameters. Similarly, the median EDP capacity is best determined by experimental data, post-earthquake surveys or expert judgment. On the other hand, a, b and $\beta_{\theta d}$ can be reasonably approximated, ideally by multiple dynamic analyses (e.g. incremental dynamic analysis, IDA, Vamvatsikos and Cornell [19]) or, in many cases, with a simple static pushover. The latter will be the focus of the proposed method.

3.2 Estimation in a pushover setting without global collapse

The "central value" of roof (or generally control node) displacement response corresponding to any level of spectral acceleration intensity, $S_a = s$ can be estimated as follows (e.g. EN1998 [5], ASCE/SEI 41-06 [4]):

$$\hat{\delta}_{roof} = \Gamma \hat{C}_R \frac{T^2}{4\pi^2} \cdot s \tag{10}$$

where Γ is the first-mode participation factor (estimated for the first-mode shape normalized by the roof displacement), T is the equivalent SDOF system period and $\hat{C}_R$ is the median inelastic displacement ratio for the given strength ratio R. Considering that the pushover results offer practically a one-to-one mapping between any local EDP and the roof displacement, with the possible exception of isolated spots in the negative stiffness region, we can represent the median roof drift as a function of the corresponding median EDP, i.e. $\hat{\delta}_{roof} = \delta_{roof}(\hat{\theta})$. Then we can use the pushover results to easily estimate the δ_{roof} corresponding to the median capacity value, θ_c, and solve for the corresponding median seismic intensity:

$$\hat{s}_c = \frac{4\pi^2}{\Gamma \hat{C}_R \mathrm{T}^2} \cdot \delta_{roof}\left(\hat{\theta}_c\right) \tag{11}$$

For the median C_R, one can use SPO2IDA for practically any shape of capacity curve, or resort to the simpler relationships provided by Ruiz-Garcia and Miranda [9], valid for elastoplastic systems:

$$\hat{C}_R = \frac{\hat{\mu}(R)}{R} = 1 + \frac{R-1}{79.12\, T^{1.98}} \tag{12}$$

An appropriate value for R for use with Eq. (12) should generally correspond to a value of seismic intensity close to the region of interest, or, in other words, close to the median EDP-

value of capacity. In terms of ductility, this maps to the value of $\mu_{lim} = \delta_{roof}\left(\hat{\theta}_c\right)/\delta_y$. A potential solution would be to prescribe $R_{lim} = \mu_{lim}$ in the sense of the equal displacement rule, but this would grossly overestimate both b and $\beta_{\theta d}$ for shorter periods. A much better solution is to set $\mu = \mu_{lim}$ in Eq. (12) and solve the resulting quadratic expression for R. Since b and the dispersion $\beta_{\theta d}$ tend to increase with R (rather than remain constant), it is best to take a point estimate (a form of biased fitting) at a reduced value, say at 85% of the resulting R-value

$$R_{lim} = \max\left\{0.425\left(1 - c + \sqrt{c^2 + 2c(2\mu_{lim} - 1) + 1}\right),\ 1.0\right\}, \text{ where } c = 79.12\,T^{1.98} \tag{13}$$

A lower limit of 1.0 has been imposed for performance points close to yielding as the 85% reduction taken above may make R_{lim} become less than 1.0.

Thanks to the proportionality between C_R and d_{roof}/s_c, a useful local b can be estimated through Eq. (12) by interpolating in log-space between the yield point at $(\mu,R) = (1,1)$ and the value of the median μ at R_{lim}. This is equivalent to the ratio of the logs of the latter two values, which can be easily estimated from Eq. (12) above, by taking the log of both sides and then dividing by $\ln R_{lim}$:

$$b \cong \frac{\ln \hat{\mu}(R_{lim})}{\ln R_{lim}} = 1 + \frac{\ln\left(1 + \dfrac{R_{lim} - 1}{79.12\,T^{1.98}}\right)}{\ln R_{lim}} \tag{14}$$

In the limiting case of $R_{lim} = 1$, signifying elastic response, the slope b is always set to 1.0. Strictly speaking, this is the b-slope corresponding to the roof displacement. In the case of inelastic response, proportionality should be locally valid between δ_{roof} and θ for the above b to be usable for the latter. Otherwise more careful interpolation will need to be performed close to the median value of θ_c.

Finally, the needed conditional demand dispersion can also be estimated from either SPO2IDA [8], or the work of Ruiz-Garcia and Miranda [9]. Then, the dispersion of δ_{roof} is the same as the dispersion of C_R, as they are proportional:

$$\sigma_{\ln \delta_{roof}} = \sigma_{\ln C_R} = 1.957\left[\frac{1}{5.876} + \frac{1}{11.749(T + 0.1)}\right]\left\{1 - \exp\left[-0.739(R_{lim} - 1)\right]\right\} \tag{15}$$

If proportionality holds in the vicinity of s_c between δ_{roof} and θ, then they both share the same dispersion. This is a reasonable assumption that generally makes sense for most situations. Otherwise, it is best to estimate $\beta_{\theta d}$ as one half of the difference between the 16 and 84 percentiles of θ at the given intensity level:

$$\beta_{\theta d} = \frac{\ln\theta_{84} - \ln\theta_{16}}{2} = \frac{\ln\theta\left[\hat{\delta}_{roof}\exp\left(\sigma_{\ln\delta_{roof}}\right)\right] - \ln\theta\left[\hat{\delta}_{roof}\exp\left(-\sigma_{\ln\delta_{roof}}\right)\right]}{2} \tag{16}$$

where $\theta[\cdot]$ represents the inverse mapping offered by the pushover between roof drift and the EDP of choice.

Note that when multiple EDPs are used to define a limit-state, where exceeding any one of them signals violation, the above framework shows that they will generally offer the same $\beta_{\theta d}$ dispersion to the fragility curve. As long as no significant differences are introduced by the other aleatory and epistemic contributions to the dispersion between the different EDPs, then we only need to define the appropriate median intensity capacity that corresponds to the EDP that governs, i.e., use the one whose θ_c median capacity corresponds to the lowest roof displacement. This is for example the case of using the story drifts to determine the limit-state:

Separate checks for each story can be conveniently replaced by a single check of the maximum drift over all stories, as long as all stories have about the same drift capacity and the limit-state is considered to be violated if any story drift exceeds it (which is the usual choice). Even if the dispersions corresponding to each EDP differ significantly, the above statements are still true as long as the dispersion corresponding to the governing EDP is the highest. Otherwise, all EDPs may need to be taken into account, for example via the formulation discussed in Choi et al [13], to incorporate issues of correlation. It is noted however that such considerations are mostly an issue for tagging applications, where assigning a single damage-state to an entire building makes sense. Seismic loss assessment is best performed through a fine-grained application of fragility, at the story or even component level that allows a more accurate calculation of cost. Furthermore, structural, non-structural and content damage is best considered separately rather than through a common damage-state. Thus, it is not envisioned that multiple EDPs will become important when defining such localized damage-states.

In summary, a simple algorithm for estimating fragility curves for an elastoplastic system and for any limit-state defined by a single scalar EDP under the assumptions presented above can be cast as follows:

1. Run a static pushover analysis in order to obtain the capacity curve and the corresponding results for the EDP needed for limit-state definition.
2. Fit the pushover curve via an elastoplastic idealization
3. From the pushover results estimate $\delta_{roof}(\hat{\theta}_c)$, i.e., the median roof displacement corresponding to the median EDP capacity.
4. Estimate the median IM capacity, $\hat{s}_c$ from Eq. (11) and (12)
5. Estimate b from Eq. (14)
6. Estimate $\beta_{\theta d}$ from Eq. (15) or (16)
7. Evaluate the fragility dispersion according to Eq. (8) or (9).

Use of SPO2IDA only changes steps 4-6, where instead of Eq. (12), (14) and (15) to estimate C_R, b and $\beta_{\theta d}$, respectively, direct numerical results are taken from the SPO2IDA tool.

In any case, the overall fragility curve is defined by the median IM capacity and the corresponding total dispersion, according to Eq. (2) in this very simple scheme that needs no iterations and no assumptions about record-to-record variability. Moreover, it is fully compatible with nonlinear dynamic analysis results, as long as the assumptions of the pushover analysis hold, the R-μ-T relationship is accurate enough for the capacity curve employed (see also De Luca et al. [20] on fitting) and the limit-state is not close to the region of global dynamic instability.

3.3 Introducing global collapse information

The phenomenon of global dynamic instability may only appear if adequate modeling of P-Δ and/or material in-cycle degradation has been employed, or, at the very least, some ultimate ductility capacity has been imposed a posteriori on the pushover results. Such modeling options generate a distinctive plateau on the IDA curves in IM versus EDP co-ordinates (for example the region beyond the ductility of 5 in Figure 4a). This corresponds to an explicit simulation of the results of global collapse. Then, estimation of the fragility for limit-states that occur close to this region cannot be reliably performed with the aforementioned proce-

dure. To be more precise, if the corresponding median intensity capacity $\hat{s}_c$ is higher than the 16% spectral acceleration collapse capacity (i.e., an *R*-value of about 2.3 in Figure 4b), the power-law approximation of Eq. (5) is no longer accurate. Thus, additional steps need to be taken when defining the fragility curve to ensure that collapse (which by default violates all limit-states) is taken into account.

First, the values of C_R, b and $\beta_{\theta d}$ should only be based on intensities that directly precede the 16% value of capacity. In other words, they should be based on non-collapse responses (ideally, higher intensities should also be included by taking into account only non-collapse data points but this definition is only usable when discrete dynamic analyses are available). Then, the probability of collapse needs to be directly incorporated by conditioning on collapse and non-collapse (Jalayer and Cornell [21]):

$$P_{LS}(s) = P\big(C < D \mid s, NC\big)\cdot\big(1 - P_C(s)\big) + P_C(s) \tag{17}$$

where $P_C(s)$ is the probability of collapse, or simply, the fragility of the global collapse limit-state and $P(C<D|s, NC)$ is the fragility curve determined with the procedure presented earlier.

Note that due to the nature of global instability, simplified assumptions fail to deliver the desired fidelity if an EDP basis is chosen for evaluating the collapse fragility $P_C(s)$. The appearance of multiple "infinite" values of EDP due to individual collapses (Figure 4a) means that the distribution of EDP at a given intensity cannot be characterized by a lognormal. On the contrary, an IM basis is perfectly adequate, as lognormality still holds. Thus, the collapse fragility can only be defined via Eq. (1), whose parameters are directly provided by SPO2IDA. Note here that this is different from other definitions of collapse where the model happily goes on forever (i.e., the IDA curves never flatline in Figure 4a) and collapse is retro-actively defined by some EDP capacity. Such cases may not offer the fidelity and accuracy of the above formulation, yet they have the advantage of being conveniently handled with the originally presented approach, without needing to separately account for global instability.

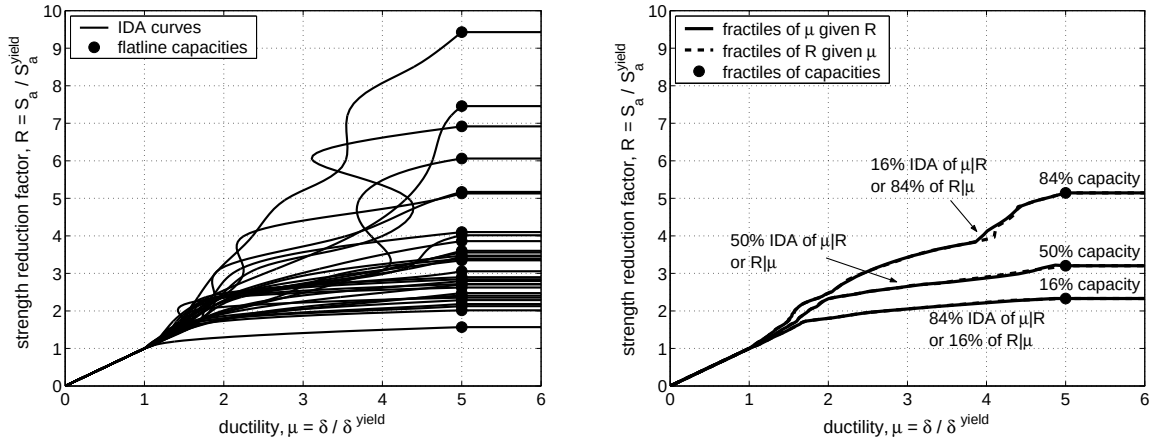


Figure 4: (a) Forty IDA curves and (b) their summarization into 16/50/84% fractiles for an SDOF system. The EDP is ductility and the IM is $S_a(T_1)$ normalized by its yield-level value. The *x*% fractiles EDP|IM curves are practically identical to the (1-*x*)% IM|EDP curves (Vamvatsikos and Cornell [19]).

4 CONCLUSIONS

A simplified method has been presented for extracting fragility curves via the static pushover method preferentially coupled with simplified stick models for optimal application to large sets of buildings. The methodology allows the accurate estimation of the record-to-

record variability and the introduction of any additional source of uncertainty, without needing to resort to ad hoc assumptions. It is thus simple and reliable enough to be applicable to a large number of buildings and become useable for estimating fragility not just for a single but for an entire class of structures, as required for application with the Global Earthquake Model.

ACKNOWLEDGEMENT

The authors gratefully acknowledge the support of the GEM Foundation through the GEM Vulnerability Consortium.

REFERENCES

[1] N. Luco, Y. Mori, Y. Funahashi, C.A. Cornell, M. Nakashima, Evaluation of predictors of non-linear seismic demands using 'fishbone'models of SMRF buildings. Earthquake Engineering and Structural Dynamics, 32(14), 2267–2288, 2003.

[2] A.S. Veletsos, N.M. Newmark, Effect of inelastic behavior on the response of simple systems to earthquake motions. *Proceedings of the 2nd World Conference on Earthquake Engineering*, Vol. 2, Tokyo and Kyoto, Japan, 895–912, 1960.

[3] L.S. Jacobsen, Damping in composite structures. *Proceedings of the 2nd World Conference on Earthquake Engineering*, Vol. 2, Tokyo and Kyoto, Japan, 1029–1044, 1960.

[4] ASCE/SEI, Minimum design loads for buildings and other structures, *ASCE/SEI Standard 07-10*, American Society of Civil Engineers, Reston, VA, 2010.

[5] CEN, Eurocode 8: Design of structures for earthquake resistance. *EN 1998*, European Committee for Standardisation, Brussels, 2005.

[6] FEMA, Improvement of Nonlinear Static Seismic Analysis Procedures. *Report FEMA 440*, prepared by the Applied Technology Council for the Federal Emergency Management Agency, Washington, D.C., 2005.

[7] ATC, Seismic evaluation and retrofit of concrete buildings. *Report No. ATC-40*, Volume 1-2, Applied Technology Council, Redwood City, CA, 1996.

[8] D. Vamvatsikos, C.A. Cornell, Direct estimation of the seismic demand and capacity of oscillators with multi-linear static pushovers through Incremental Dynamic Analysis, *Earthquake Engineering and Structural Dynamics*, **35**(9), 1097–1117, 2006.

[9] J. Ruiz-Garcia, E. Miranda, Probabilistic estimation of maximum inelastic displacement demands for performance-based design. *Earthquake Engineering and Structural Dynamics*, **36**, 1235–1254, 2007.

[10] R.P. Kennedy, M.K. Ravindra, Seismic fragilities for nuclear power plant risk studies. *Nuclear Engineering and Design*, **79**(1): 47–68, 1984.

[11] C.A. Cornell, F. Jalayer, R.O. Hamburger, D.A. Foutch, Probabilistic basis for 2000 SAC Federal Emergency Management Agency Steel Moment Frame Guidelines, ASCE Journal of Structural Engineering, **128**(4), 526–533, 2002.

[12] M. Shinozuka, M.Q. Feng, H.-K. Kim, S.-H. Kim, Nonlinear static procedure for fragility curve development. *Journal of Engineering Mechanics ASCE*, **126**(12), 1287–1295, 2000.

[13] E. Choi, R. DesRoches, B. Nielson. Seismic fragility of typical bridges in moderate seismic zones. *Engineering Structures* **26**, 187–199, 2004.

[14] A.K. Kazantzi, T.D. Righiniotis, M.K. Chryssanthopoulos, Fragility and hazard analysis of a welded steel moment resisting frame. *Journal of Earthquake Engineering*, **12**(4), 596–615, 2008.

[15] A.K. Kazantzi, T.D. Righiniotis, M.K. Chryssanthopoulos, A Simplified Fragility Methodology for Regular Steel MRFs. *Journal of Earthquake Engineering*, **15**(3), 390–403, 2011.

[16] A.B. Liel, C.B. Haselton, G.G. Deierlein, J.W. Baker, Incorporating modeling uncertainties in the assessment of seismic collapse risk of buildings. *Structural Safety*, **31**(2), 197–211, 2009.

[17] M. Dolsek, Incremental dynamic analysis with consideration of modelling uncertainties. *Earthquake Engineering and Structural Dynamics*, **38**(6), 805–825, 2009.

[18] D. Vamvatsikos, M. Fragiadakis, Incremental dynamic analysis for estimating seismic performance uncertainty and sensitivity. *Earthquake Engineering and Structural Dynamics*, **39**(2), 141–163, 2010.

[19] D. Vamvatsikos, C.A. Cornell, Incremental Dynamic Analysis. *Earthquake Engineering and Structural Dynamics*, **31**(3), 491–514, 2002.

[20] F.D. De Luca, D. Vamvatsikos, I. Iervolino, Near-optimal piecewise linear fits of static pushover capacity curves for equivalent SDOF analysis. *Earthquake Engineering and Structural Dynamics*, **42**(4): 523–543, 2013.

[21] F. Jalayer, C.A. Cornell, Alternative non-linear demand estimation methods for probability-based seismic assessments. *Earthquake Engineering and Structural Dynamics*, **38**(8) 951–1052, 2009.

COMPDYN 2013
4th ECCOMAS Thematic Conference on
Computational Methods in Structural Dynamics and Earthquake Engineering
M. Papadrakakis, V. Papadopoulos, V. Plevris (eds.)
Kos Island, Greece, 12–14 June 2013

MEASURING BIAS IN INCREMENTAL DYNAMIC ANALYSIS USING BOOTSTRAP

Athanasia E. Zacharenaki[1*], Michalis Fragiadakis[2], and Manolis Papadrakakis[1]

[1] Institute of Structural Analysis and Antiseismic Research, National Technical University of Athens,
Iroon Polytecheiou Str., Zografou Campus, 15780, Athens, Greece
azachare@mail.ntua.gr, mpapadra@central.ntua.gr

[2] Department of Civil and Environmental Engineering, University of Cyprus
P.O. Box 20537, 1678 Nicosia, Cyprus
mfrag@ucy.ac.cy

Keywords: Incremental Dynamic Analysis, Cloud Analysis, Record Scaling, Bias, Bootstrap.

Abstract. *We present a methodology for the evaluation of the effect of scaling when Incremental Dynamic Analysis (IDA) is performed. The median capacity curve of IDA is compared to the capacity curve obtained using cloud analysis. Cloud analysis data contain results obtained using unscaled natural and synthetic ground motion records. Synthetic records were used due to the lack of a statistically significant number of natural records for large intensities. Nonlinear regression is performed with the aid of the Local Regression Smoothing Algorithm (LOESS) in order to post-process the results of cloud analysis. The primary difference between the two methods is that cloud analysis allows obtaining capacity curves without scaling the ground motion records, as opposed to the IDA algorithm. To investigate the statistical significance of this comparison, the bootstrap method is used. The bootstrap method is a powerful and easy-to-implement tool that allows calculating confidence intervals. Using bootstrap we are able to measure the bias introduced by record scaling when IDA is adopted. Thus, the bias is examined quantitatively and qualitatively for the full range of limit-states, yielding useful conclusions regarding scaling and its legitimacy in the context of IDA. A three-storey and a nine-storey steel moment resisting frames are used as testbeds for our investigations.*

1 INTRODUCTION

Incremental Dynamic Analysis (IDA) [1] is a method where the mathematical model of the structure is subjected to a number of ground motion records. Every record is scaled to several levels of intensity, producing the structure's capacity curve in terms of an Engineering Demand Parameter (EDP) versus an Intensity Measure (IM). IDA provides a powerful performance estimation framework, which, however, is often questioned due to the scaling of records with factors that considerably differ from one. This practice leads to ground motions that may not represent a realistic physical process and may under or over estimate the demand, or in other words, may introduce bias in the capacity estimation. This study investigates in a systematic manner the effect of record scaling providing an approach for measuring the bias introduced when IDA analysis is performed.

In Shome et al. [2] it is shown that small-to-moderate scaling factors do not introduce bias in the response estimation. It was also shown that there are structures for which scaling does not introduce bias, e.g. moderate period buildings in sites with no directivity. Vamvatsikos and Cornell [1] discuss how accurate the scaling practice is within the frameworks of IDA. They say that the problem depends on the EDP, the IM, the structure and the record population. They conclude that scaling is legitimate when the choice of the IM is such that the IM values, conditional on the EDP, are effectively independent of the magnitude and the distance scenario. Moreover, Iervolino and Cornell [3] observed that scaling arbitrarily selected records to match the strength of stronger records does not introduce bias in the seismic demand estimations. Luco and Bazzuro [4] suggest biased responses when the mean scale factor of a bin was larger than one. Furthermore, according to Baker [5] when the number of records that are scaled up is approximately equal to the number of records that are scaled down unbiased median interstory drift ratios are obtained.

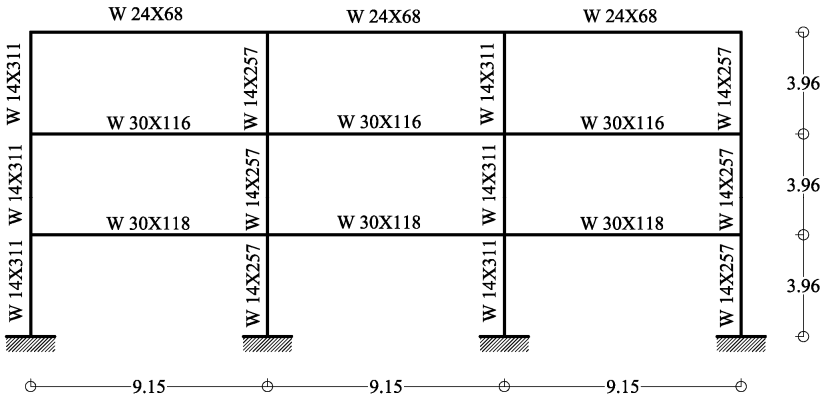
The issue of selecting and scaling records without biasing the response has been investigated by several other researches. Katsanos et al. [6] discuss the different record selection procedures for seismic design. Watson-Lamprey and Abrahamson [7] show that a proper selection of records does not lead to biased results. Baker and Cornell [8] proposed selecting seismic records using the epsilon 'ε'-method in order to reduce the bias. Iervolino et al. [9] compared different procedures in terms of inelastic seismic response that led to obtain sets of spectral matching accelerograms for nonlinear dynamic analysis of structures. The outcome of the analysis leads to the fact that artificial or adjusted accelerograms may underestimate the displacement response when compared to original natural records which are considered as a benchmark. Kayhan et al. [10] propose a model to obtain input ground motion datasets compatible with given design spectra using a meta-heuristic harmony search algorithm.

The above studies discuss the selection and scaling of ground motion records. They, also discuss the bias introduced in the response estimation when nonlinear response history analysis is performed. In this study the issue of scaling records within Incremental Dynamic Analysis (IDA) is investigated. To assess IDA, the response statistics of an Engineering Demand Parameter (EDP) are obtained using a large number of natural and synthetic records that are left unscaled. The structures considered, are two steel moment-resisting frame buildings. The bias introduced due to record scaling is assessed both qualitatively and quantitatively for the full range of limit-states.

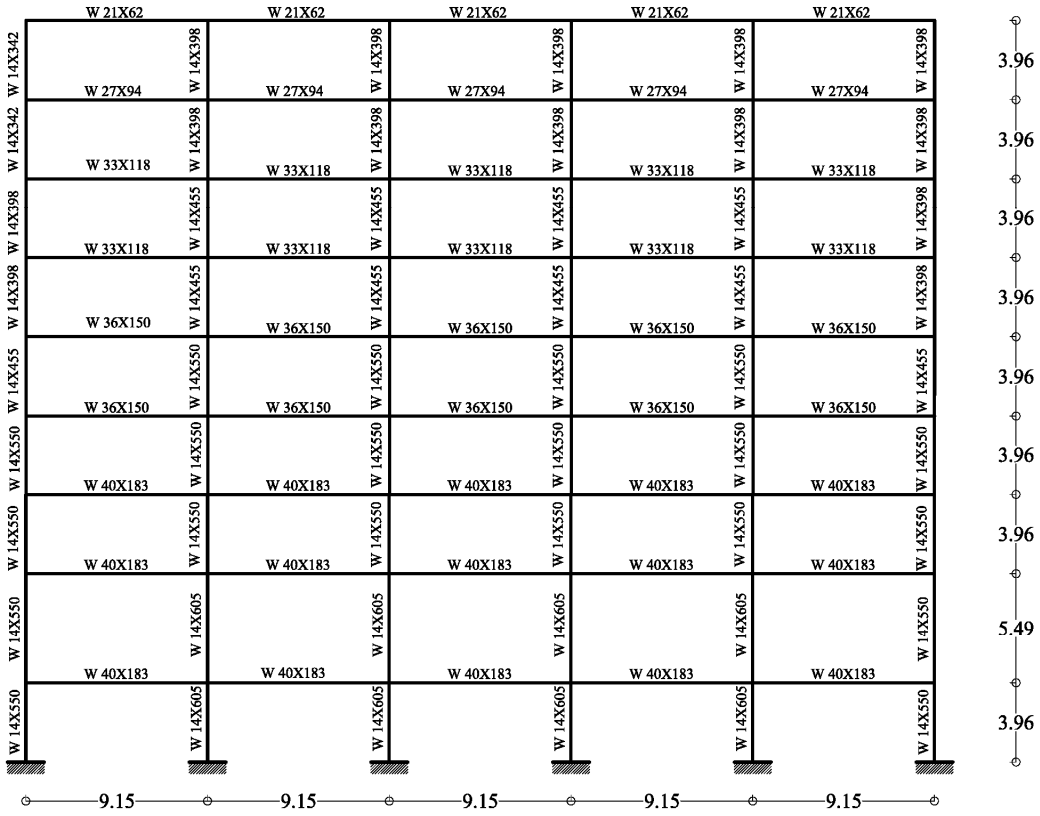
2 BUILDINGS CONSIDERED

The multi-degree of freedom (MDOF) structures used in this study are two steel moment-resisting frames that have been designed for a Los Angeles site according to the 1997 NEHRP (National Earthquake Hazard Reduction Program) provisions. More specifically we study a

three-storey and a nine-storey steel moment resisting frame, denoted as LA3 and LA9, respectively. Both buildings have been designed according to the strong-column, weak-beam design philosophy [11], while all analyses were conducted using the Opensees program [12]. Centerline models are used to model the two-dimensional exterior moment-resisting frame of each building. The fundamental periods of the frames are T_1=0.93sec and T_1=2.34sec, respectively. Therefore both moment-resisting frames are in essence first-mode dominated, while the LA9 building has some sensitivity also to higher modes.



(a)



(b)

Figure 1: Geometry and cross-sections of steel moment resisting frames: (a) LA3 building, (b) LA9 building.

3 GROUND MOTION RECORDS

For IDA analysis a set of 30 records was used. These records correspond to relatively large magnitudes of 6.5-6.9 that have been recorded on dense soil and bear no marks of directivity. Details about these records are given elsewhere [13].

For cloud analysis 1480 natural and synthetic ground motions are used. 1015 natural records were chosen randomly from the PEER NGA database [14] ensuring uniform processing. These records were selected giving no regard to a certain Intensity Measure (IM) and assuming dense soil. A large number of these records correspond to low magnitudes and when left unscaled give low $S_a(T_1,5\%)$ intensities and thus are not capable of causing yielding or collapsing of our structures.

For cloud analysis we have also used 465 synthetic records. The synthetic records were obtained following the procedure discussed in [15]. Assimaki et al. [15] combine regional velocity and attenuation structures that have been initially compiled using near-surface geotechnical data with the crustal velocity structure at three downhole arrays in Southern California. Broadband ground motion simulations were next conducted for rupture scenaria of weak, medium and large magnitude events (M_w=5÷7.5) and three component seismograms were computed on a surface station grid at distances 2-75km from the surface projection of the fault [16]. In this study we used horizontal components with magnitudes 6, 6.5, 7.5 each within a PGA range of 0.1~2.0g. Approximately 465 out of 3150 ground motions fulfilled the latter restriction.

4 METHODOLOGY

4.1 Incremental Dynamic Analysis and Cloud Analysis

In performance-based earthquake engineering (PBEE), the capacity curve of a building can be formed in the plane of an Engineering Demand Parameter (EDP) versus an Intensity Measure (IM). The Intensity Measure may be any of the record's characteristic parameters, such as peak ground acceleration (PGA), Arias Intensity or the five-percent damped, first-mode spectral acceleration, $S_a(T_1,5\%)$. The latter parameter takes into account the structure's first mode and is considered as an efficient, sufficient and practical IM which reflects the nonlinear response of the structure. The EDP considered here is the maximum interstorey drift over all the stories and is denoted as θ_{max}.

Incremental Dynamic Analysis (IDA) and Cloud Analysis (CA) are two popular seismic performance estimation methods. In IDA the mathematical model of the structure is subjected to a suite of ground motion records with increasing scaling factors offering thorough seismic demand and capacity prediction capability. Figure 2 shows, as an example, a 30-record IDA curves and the corresponding median curve of a nine-storey steel frame. To perform IDA several algorithms are available with the hunt-and-fill algorithm to be the most efficient [1]. According to Figure 2, IDA has to be repeated using different ground motion records in order to obtain meaningful statistical averages of the response, usually expressed as the median capacity curve and the 16^{th} and 84^{th} fractiles of the response.

In CA the mathematical model of the structure is subjected to a suite of ground motion records with a common scale factor, usually equal to one. The EDP-IM dataset which is formed from the nonlinear response history analysis is called "cloud".Once the cloud is formed a capacity curve can be obtained by nonlinear regression. When the scale factor is one the CA is called "single CA" since a single cloud in the EDP-IM plane has been formed. When several increasing scale factors are considered it is called "multiple CA".

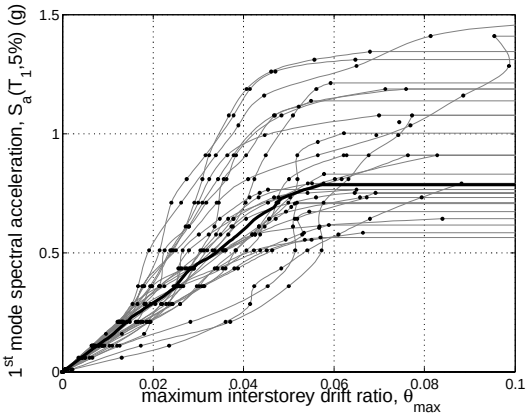
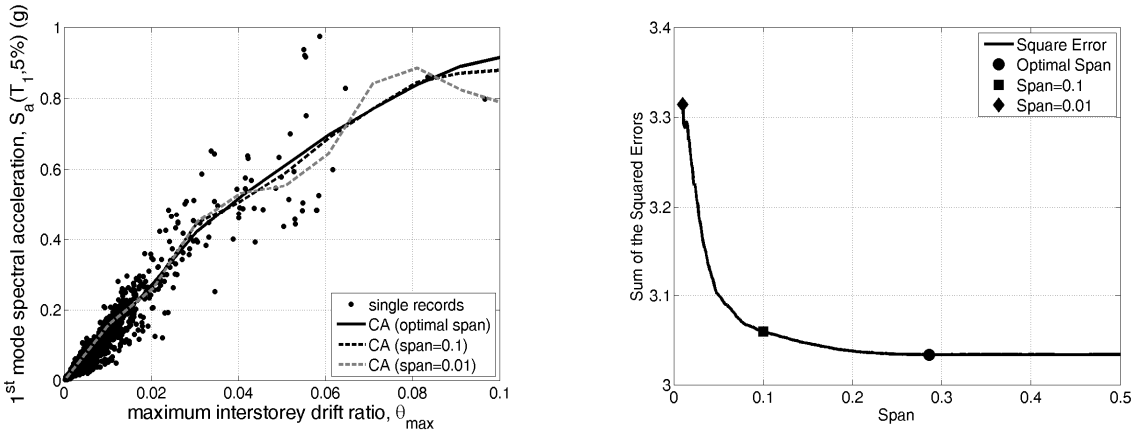


Figure 2: 30-record IDA curves and the corresponding median curve of a nine-story steel frame.

The LOESS (Locally Weighted Scatterplot Smoothing) algorithm [17] is used to perform nonlinear regression on the cloud of EDP-IM data when cloud analysis is adopted. This is a nonlinear regression algorithm that uses second degree polynomials and least square fitting to fit a polynomial curve on the data. A span of the moving average is needed for this algorithm in order to define a window of neighboring points that will be included in our estimations. The effect of the span value chosen can be seen in Figure 3. A large span of the moving average leads to increased smoothness, while a small span decreases the smoothness giving a curve that is more sensitive to the data (Figure 3a).

Nonlinear regression and the span value of the moving average are sources of additional bias on the seismic performance estimation. To decrease this outcome we chose the *k*-fold cross validation algorithm to obtain an optimal span value [17]. This algorithm has the following steps: i) the cloud is randomly partitioned to *k* subsamples, ii) a single subsample is retained as the validation cloud set, and iii) the remaining *k*-1 subsamples are used as training set to generate the LOESS curve. The mean squared error is the square of the distance between the LOESS curve of the training set and the curve produced by the testing set. The mean squared error with the span value is presented in Figure 3b. In this way the goodness-of-fit as function of the span value is evaluated. As optimal span value we take the one that minimizes the sum of the squared errors, i.e. the minimum value of the curve of Figure 3b.



(a) (b)

Figure 3: (a) Capacity curves for different span values of the LOESS fit and (b) square error of the LOESS fitting as function of the span.

4.2 Bootstrap analysis

Bootstrap [18] is used in order to investigate the statistical significance of our response statistics. The confidence interval of a quantity, here the IM values can be obtained with the aid of bootstrap. Bootstrap is an easy-to-implement tool which entails sampling with replacement from the initial population in order to generate a new population which we use to calculate the confidence intervals.

Bootstrap confidence intervals can be calculated for both IDA and CA. The process followed for both methods is the same. In both methods, the data is scattered on the EDP-IM plane. For both cases the bootstrap method resamples with replacement to obtain 1000 samples. Sampling with replacement means that after we have randomly drawn an observation from the original sample, we put it back before drawing the next observation. In IDA analysis this is repeated for the whole range of EDP values, since as samples we consider the θ_{max} and $S_a(T_1,5\%)$ values of every single record IDA curve. When cloud analysis is performed, every sample produces a new population of EDP-IM pairs on which nonlinear regression is performed, with the optimal span value as discussed in paragraph 4.1.

In Figure 4 the derivation of the bootstrap confidence intervals of the nine-storey steel moment-resisting frame is shown. In Figure 4a cloud analysis is performed on the scattered data, while in Figure 4b the bootstrap curves are shown. The dashed bold lines show the 95% bootstrap confidence interval while the solid bold lines the median curve obtained with LOESS. According to Figure 4a for $\theta_{\max}$ over 0.06 the original data are becoming scarce. However, this occurs for large drift values not affecting the early limit-states that usually are of interest. Moreover, due to limitation of cloud analysis to provide the dispersion, we are limited to study only the bias of the median $S_a(T_1,5\%)$ capacities.

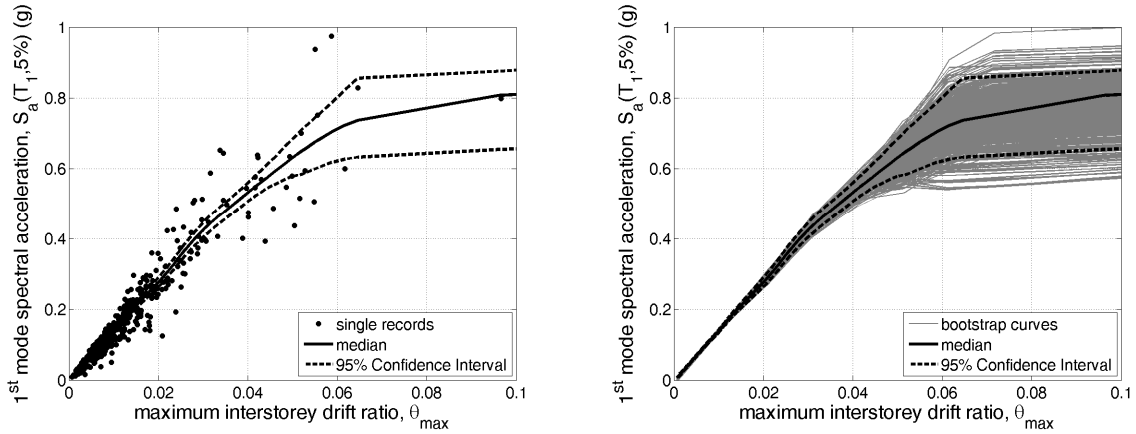
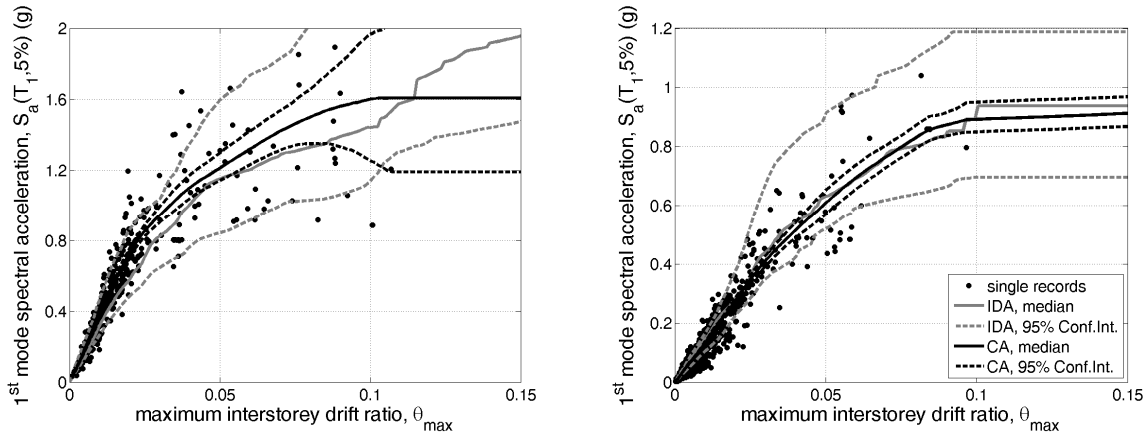


Figure 4: Estimate of the median and 95% Confidence Intervals, versus: (a) the initial scattered data, and (b) 1000 capacity curves generated after bootstrapping the results of cloud analysis.

5 NUMERICAL RESULTS

Figure 5 presents the capacity curves and their 95% confidence intervals for the three-storey and the nine-storey building. For the LA3 frame the median IDA and CA curves coincide until $\theta_{\max}$=0.03. Beyond this value there is a slowly increasing deviation until $\theta_{\max}$=0.15. IDA underestimates the demand until $\theta_{\max}$=0.12 and beyond this value it overestimates it. The maximum difference between both curves is 0.4g in $\theta_{\max}$=0.15. For the nine-storey building, the IDA curve is entirely included within the confidence intervals of the CA curve as can be

seen in Figure 5b. Therefore, IDA and CA analysis produce estimates of the capacity very close thus indicating that the bias in IDA is not significant.



(a) (b)

Figure 5: Median capacity curves and their 95% confidence intervals: (a) three-storey building (LA3), and (b) nine-storey building (LA9).

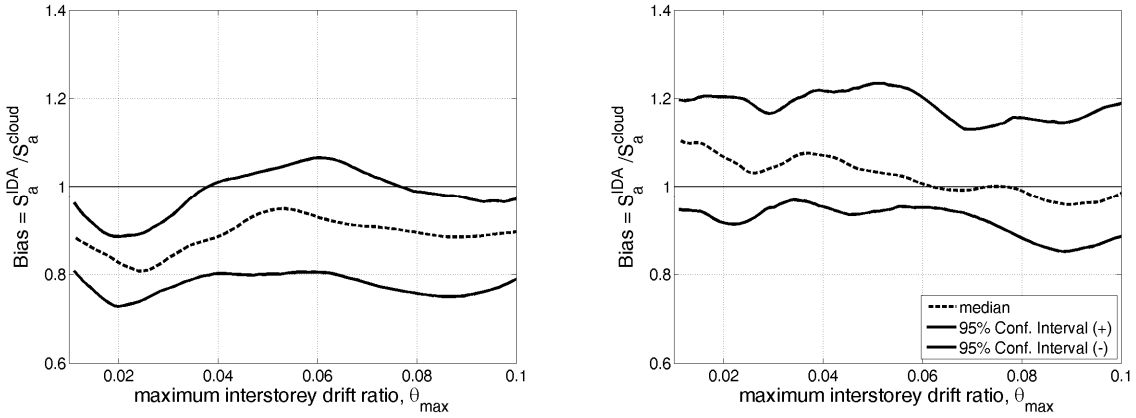
Bias is the systematic over or under-estimation of the $S_a(T_1,5\%)$ capacity conditional on the limit state $\theta_{\max}$ demand. The measure of the bias here adopted is based on cloud analysis which is considered as unbiased. Therefore, the bias is quantified as:

$$bias = \frac{\left(\overline{S}_a\left(T_1,5\%\right)|\,\theta_{\max}\right)_{IDA}}{\left(\overline{S}_a\left(T_1,5\%\right)|\,\theta_{\max}\right)_{cloud}} \tag{1}$$

where $\overline{S}_a\left(T_1,5\%\right)|\,\theta_{\max}$ is the bootstrap $S_a(T_1,5\%)$ capacities conditional on maximum interstorey drift, $\theta_{\max}$. To quantify the bias and calculate the corresponding confidence intervals we perform bootstrap on the bias values as estimated using Eq.(1). Therefore, the confidence intervals of the bias show the effect of scaling the ground motion records within IDA.

The confidence intervals of the bias give an estimate whether the scaling practice biases the response. The bias quantification can be realized by observation of the width of the confidence intervals, the position of the unity line and their symmetry. If the unity line is not entailed in the confidence interval, then we assume that, at the 95% level, scaling is not the cause of the difference. Still, if the interval contains the unity line, we have reasonable evidence reinforcing the previous assumption that when the unity line is close to one bound there is some bias induced by scaling. Little evidence exists if the unity line is in the middle of the interval. In this case, scaling has doubtful effect in the estimation of bias. The width of the confidence interval, also provide an indication of the variability of the parameter studied.

Figure 6 presents the results of the bias for the three-storey and the nine-storey steel moment resisting frames as function of $\theta_{\max}$. As Figure 6 shows, the bias in the overall nonlinear structural response is more prominent in the three-storey than in the nine-storey building as the state of collapse is approached. According to Figure 6a for the three-storey building a slight bias is observed, since both bounds of the interval are below the unit line, while the distance of the bounds starts to increase from $\theta_{\max}$=0.02 until 0.05 and decreases from $\theta_{\max}$=0.05 until $\theta_{\max}$=0.1. For the nine-storey building where the IDA and CA curves were close (Figure 5b), the confidence intervals are symmetric with respect to the unity line, as shown in Figure 6b, thus indicating that the effect of bias is small for this building.



(a) (b)

Figure 6: Bootstrap 95% confidence intervals on the ratio of the median $S_a(T_1,5\%)$-capacities given θ_{max} of the IDA case over the cloud case (Eq. 2) for: (a) three storey building, (b) the nine storey building.

6 CONCLUSIONS

This study presents an approach for approximately assessing the effect of scaling in Incremental Dynamic Analysis. We perform nonlinear regression on cloud analysis containing building responses from unscaled natural and synthetic ground motion records. On this basis the influence of the scaling is enabled with the aid of the bootstrap method, which allows to quantify the bias. For the three-storey steel moment resisting frame the IDA curve does not induce significant bias in the seismic capacity assessment, where a small effect is observed from θ_{max}= 0.02 until 0.1. For the nine-storey building the bias was not significant for the whole range of limit states. In conclusion, for both buildings the bias introduced by IDA is small and within limits acceptable in the engineering practice.

REFERENCES

[1] D. Vamvatsikos, C.A. Cornell, Incremental dynamic analysis. *Earthquake Engineering & Structural Dynamics*, **31**, 491–514, 2002.

[2] N. Shome, C.A. Cornell, P. Bazzurro, J.E. Carballo, Earthquakes, records, and nonlinear MDOF responses. *Earthquake Spectra*, **14**, 469–500, 1998.

[3] I. Iervolino, C.A Cornell, Record selection for nonlinear seismic analysis of structures. *Earthquake Spectra*, **21,** 685–713, 2005.

[4] N. Luco, P. Bazzurro, Does amplitude scaling of ground motion records result in biased nonlinear structural drift responses? *Earthquake Engineering & Structural Dynamics*, **36**, 1813-1835, 2007.

[5] J.W. Baker, Measuring bias in Structural Response caused by ground motion scaling. *8th Pacific Conference on Earthquake Engineering*, December 5-7, 2007.

[6] E.I. Katsanos, A.G. Sextos, G.D. Manolis, Selection of earthquake ground motion records: A state-of-the-art review from a structural engineering perspective. *Soil Dynamics and Earthquake Engineering*, **30**, 157-169, 2010.

[7] J. Watson-Lamprey, N. Abrahamson, Selection of ground motion time series and limits on scaling. *Soil Dynamics and Earthquake Engineering*, **26,** 477-482, 2006.

[8] J.W. Baker, C.A. Cornell, Vector-Valued Ground Motion Intensity Measures for Probabilistic Seismic Demand Analysis. *John A. Blume Earthquake Engineering Center. Report No. 150, Stanford, CA*, 2006.

[9] I. Iervolino, F. De Luca, E. Cosenza, Spectral shape-based assessment of SDOF nonlinear response to real, adjusted and artificial accelerograms. *Engineering Structures*, **32**, 2776-2792 , 2010.
[10] A.H. Kayhan, K.A. Korkmaz, A. Irfanoglu, Selecting and scaling real ground motion records using harmony search algorithm. *Soil Dynamics and Earthquake Engineering*, **31,** 941-953, 2011.
[11] FEMA-350, Recommended seismic design criteria for new steel moment-frame buildings. Report No. FEMA-350, *SAC Joint Venture, Federal Emergency Management Agency*, Washington DC, 2000.
[12] F. McKenna, G.L Fenves, The OpenSees Command Language Manual -Version 1.2. *Pacific Earthquake Engineering Research Centre, University of California*, *Berkeley*, 2001.
[13] D. Vamvatsikos, C.A. Cornell, Developing efficient scalar and vector intensity measures for IDA capacity estimation by incorporating elastic spectral shape information, *Earthquake Engineering & Structural Dynamics*, **34**, 1573-1600, 2005.
[14] PEER. PEER NGA Database. Pacific Earthquake Engineering Research Center. Available from http://peer.berkeley.edu/smcat/, last accessed on 2008.
[15] D. Assimaki, J. H Steidl, P.-C Liu, Attenuation and Velocity Structure for Site Response Analyses via Downhole Seismogram Inversion. *Pure and applied geophysics*, **163**, 81-118, 2006.
[16] D. Assimaki, W. Li, M. Fragiadakis, Site Effects in Structural Performance Estimation, *Earthquake Spectra*, **28**, 859-883, 2012.
[17] W.S. Cleveland, S.J. Delvin, Locally-weighted Regression: An approach to Regression Analysis by local fitting. *Journal of American Statistical Association*, **83**, 596-610, 1988.
[18] B. Efron, R. Tibshirani, *An introduction to the Bootstrap*. New York, Chapman & Hall, 1993.

COMPDYN 2013
4th ECCOMAS Thematic Conference on
Computational Methods in Structural Dynamics and Earthquake Engineering
M. Papadrakakis, V. Papadopoulos, V. Plevris (eds.)
Kos Island, Greece, 12–14 June 2013

EXTERNAL COUPLING OF FE CODES FOR STRUCTURAL DYNAMICS

M. Brun[1]*, A. Gravouil[2], A. Combescure[2], A. Limam[1]

[1]INSA-Lyon, Laboratoire de Génie Civil en Ingénierie Environnementale, Bât. Coulomb, 34 avenue des Arts, 69621, Villeurbanne, France; Michael.brun@insa-lyon.fr

[2] INSA-Lyon, Laboratoire de Mécanique des Contacts et des Structures, Bât. Jean d'Alembert, 18-20 rue des Science, 69621, Villeurbanne, France

Keywords: Subdomain decomposition, Structural Dynamics, Coupling software, multi-time step explicit/implicit co-computations.

Abstract. *Two external coupling software, whose purpose is enabling to conduct multi-time step explicit/implicit co-computations for structural dynamics problems, are set up. They are based on the coupling algorithms proposed by Gravouil and Combescure (GC method) and Prakash and Hjelmstad (PH method). The salient features of the multi-time step partitioning methods are presented: they involve non-overlapping partitions, follow a dual Schur approach by ensuring the velocity continuity at the interface with Lagrange multipliers. The main difference between the two methods lies in the time scale at which the interface problem is solved: micro time scale for the GC-algorithm and macro time scale for the PH-algorithm. During the multi-time step co-computations involving two Finite Element codes (explicit and implicit FE codes), the tasks carried out by the coupling software PH-CPL, based on a variant of the PH algorithm, are illustrated and compared to the coupling software GC-CPL based on the GC-algorithm. The advantage of the new coupling software PH-CPL is highlighted in terms of parallel capabilities. In addition, the coupling software PH-CPL alleviates the dissipative drawback of the GC method at the interface between the subdomains. Academic cases are investigated to check the accuracy order for the GC and PH algorithms. Finally, explicit/implicit multi-time step co-computations with GC-CPL and PH-CPL software are conducted under the assumption of linear elastic material for a reinforced concrete frame structure under blast loading striking its front face.*

1 INTRODUCTION

The increasing complexity of numerical models for engineering systems, seeking to account for an ever finer mesh, accurate material models and multiphysics phenomena with very different space and time scales, boosted the development of partitioning approaches. In structural dynamics such as a structure subjected to localised impact loads, a small part of the structure is expected to experience strong non linear phenomena on a short duration with high frequency features, whereas the remaining of the structure would be mainly concerned with linear low-frequency vibration on a much longer duration. In this case, the choice of the subdomain decomposition of the whole mesh is driven by computational consideration: taking different time-step and time-integration schemes (explicit or implicit) depending on the parts of the structure is much more interesting in terms of computation times than a unique time-step imposed by the smallest element of the mesh in the case of conditionally stable time-integration schemes (explicit).

The GC method proposed by Combescure and Gravouil [1] has been built in the framework of the FETI method proposed by Farhat and Roux [2-3] in the beginning of the nineties. The kinematic continuity of quantities at the interface is prescribed by means of Lagrange multipliers. The GC method requires a three step resolution: one solves first the free solution on each subdomain, then one ensures the velocity continuity at the interface of the subdomains through the resolution of a small interface problem at the fine time scale, and finally one computes a linked solution on each subdomain resulting from the interface forces expressed in terms of the previous Lagrange multipliers. The authors showed that the stability of the subdivided problem is ensured for any Newmark time-integration schemes by prescribing the velocity continuity at the interface: using the energy method (Hughes [4]), the authors also proved that the multi-time heterogeneous partitioning solution is stable as soon as the time step size satisfies the stability criterion of each subdomain. Nonetheless, a small amount of energy is dissipated at the interface when very different time steps are considered. As a result, when using Newmark time-integration schemes of the second order accuracy, the accuracy order of the coupling method is equal to two in the case of the same time step, and is reduced by one order in the case of different time steps. Furthermore, the GC method proposed for Newmark schemes in linear dynamics has been extended to non linear dynamics (Gravouil and Combescure [5]), explicit non linear dynamics with non matching meshes at the interface (Herry *et al.* [6]), and coupling of subdomains described according to a modal approach (Faucher *et al.* [7]).

More recently, Prakash and Hjelmstad [8] dealt with the energy dissipation problem at the interface by improving the GC method. The main difference lies in the time scale at which the interface problem is solved: contrary to the GC method whose interface problem is solved at the fine time scale, the interface problem is considered at the large time scale. The coupling scheme turned out to be stable and non dissipative at the interface in the sense that the interface pseudo-energy involved in the energy method remains equal to zero. The partitioning method remains of second order accuracy when Newmark second order accurate time integration schemes are considered. A comparison of coupling GC and PH algorithms with heterogeneous time integration schemes has been conducted by Mahjoubi *et al.* [9]. One must mention here that the kinematic continuity is not ensured in this case for each small time step.

The heterogeneous time integrators multi-time step algorithm, labelled as the GC method proposed by Gravouil and Combescure, is first reminded before presenting the Prakash and Hjelmstad method. A coupling software is set up on the basis of the PH algorithm and is validated for a split oscillator and a reinforced structure under blast loading.

2 COUPLING CONTINUOUS IN TIME SUBDOMAINS

Both GC and PH coupling methods are based on a Dual Schur complement approach by imposing the continuity of velocities across the interface between subdomains by means of Lagrange multipliers. The Lagrange multipliers represent the interface forces between the two subdomains Ω_A and Ω_B. The continuous in time kinematic constraint related to the velocity continuity across the interface is expressed as:

$$L_A \dot{u}^A(t) + L_B \dot{u}^B(t) = 0 \tag{1}$$

where L_A and L_B are Boolean connectivity matrices for matching meshes at the interface. Velocity constraint at the interface is ensured by means of Lagrange multipliers $\Lambda(t)$. Therefore, the semi-discretized equilibrium equation (discrete in space and continuous in time) in the case of linear elastic material can be written as:

$$\begin{cases} M_A \ddot{u}^A(t) + K_A u^A(t) = f_{ext}^A(t) - L_A^T \Lambda(t) \\ M_B \ddot{u}^B(t) + K_B u^B(t) = f_{ext}^B(t) - L_B^T \Lambda(t) \end{cases} \tag{1.1}$$

where M is the symmetric definite-positive mass matrix, K is the semi-definite positive stiffness matrix and $u(t)$ denotes the nodal displacements. A superposed dot over a quantity denotes its time derivative. The subscripts A and B are used for denoting the subdomains for the matrix quantities, whereas the superscripts A and B are used for vector quantities.
On the right side of the above equations, the interface forces, $-L_A^T \Lambda(t)$ and $-L_B^T \Lambda(t)$, acting on subdomains Ω_A and Ω_B, are defined by the product of the transpose of the connectivity matrices with the Lagrange multipliers $\Lambda(t)$. It can be noted that they act on a given subdomain as a field of external forces.

3 COUPLING DISCRETE IN TIME SUBDOMAINS ACCORDING TO THE GC METHOD

Let us now consider two time integration schemes for the subdomains Ω_A and Ω_B from the Newmark family, characterised by the parameters γ_A , γ_B and β_A , β_B. One of the main interests of the subdomain decomposition method is to deal with a problem exhibiting very different time scales, by choosing appropriate time steps depending on subdomains. Thus, two time scales are considered, a macro time scale with the size $h_A = [t_0, t_m]$ for the subdomain Ω_A and a micro time scale with the size $h_B = [t_{j-1}, t_j]$ for the subdomain Ω_B. The discretized equilibrium equation becomes at the end of the macro time-step and at the end of the micro time-steps:

$$\begin{cases} M_A a_m^A + K_A u_m^A = f_{ext,m}^A - L_A^T \Lambda_m \\ M_B a_j^B + K_B u_j^B = f_{ext,j}^B - L_B^T \Lambda_j \ , \ j = 1, \ldots, m \end{cases} \tag{1.2}$$

The discrete continuity on velocities is imposed at each micro time t_j :

$$L_A v_j^A + L_B v_j^B = 0 \ , \ \ j = 1, \ldots, m \tag{1.3}$$

where velocities v_j^A at the micro times t_j are linearly interpolated from the velocities at the beginning and at the end of the macro time step $h_A = [t_0, t_m]$, namely v_0^A and v_m^A.
By introducing the approximate formula for Newmark schemes, the system of equilibrium equations over the macro time step can be rewritten as:

$$\begin{cases} \tilde{M}_A \, a_m^A = f_{ext,m}^A - K_A \, {}^p u_0^A - L_A^T \Lambda_m \\ \tilde{M}_B \, a_j^B = f_{ext,j}^B - K_B \, {}^p u_{j-1}^B - L_B^T \Lambda_j \ , \ j = 1, \ldots, m \end{cases} \tag{1.4}$$

where the predictors ${}^p u_0^A$ and ${}^p u_{j-1}^B$ depending only on quantities known at the beginning of the macro and micro time steps, respectively. The dynamic operators at the left hand side are defined by:

$$\begin{cases} \tilde{M}_A = M_A + \beta_A h_A^2 K_A \\ \tilde{M}_B = M_B + \beta_B h_B^2 K_B \end{cases} \tag{1.5}$$

The splitting procedure proposed by Combescure and Gravouil for Newmark time integration schemes consists in splitting the kinematic quantities (displacements, velocities, and accelerations) into free and linked quantities. A linear assumption over the macro time step for the velocities in the subdomain Ω_A is required in order to express the velocity continuity at the micro times t_j as a small-size symmetric dual problem in the form:

$$H_{GC} \, \Lambda_j = b_j \tag{1.6}$$

where the left hand side matrix H_{GC} denotes the interface operator for the GC method, and the right hand side vector b_j is only dependent on free velocities in subdomains Ω_A and Ω_B. They are defined by:

$$\begin{cases} H_{GC} = \gamma_A h_A L_A \tilde{M}_A^{-1} L_A^T + \gamma_B h_B L_B \tilde{M}_B^{-1} L_B^T \\ b_j = L_A v_{free,j}^A + L_B v_{free,j}^B \end{cases} \tag{1.7}$$

The above interface problem in (1.6) has to be solved at all the micro times t_j so as to derive the Lagrange multipliers Λ_j and then the linked quantities at the micro time scale.
It has to be underlined that the GC method is completely staggered: macro subdomain first for free quantities followed by micro subdomain for free quantities and again, macro subdomain first for linked quantities followed by micro subdomain for linked quantities. Thus, the free and link computations cannot be done in a concurrent way for both subdomains. The Prakash and Hjelmstad algorithm provides an improvement in terms of parallel capabilities with respect to its GC progenitor method.

4 COUPLING DISCRETE IN TIME SUBDOMAINS ACCORDING TO THE PH METHOD

The method proposed by Prakash and Hjelmstad [8] permits to eliminate the interface pseudo-energy in the sense of the energy method (Hughes, [4]). The key difference from the GC method is the enforcement of the velocity continuity by Lagrange multipliers at the macro-time scale rather than at the micro-time scale as done in the GC method. The discrete velocity continuity at the end of the macro time step (at time t_m) becomes:

$$L_A v_m^A + L_B v_m^B = \mathbf{0} \tag{1.8}$$

As for the GC method, the system of equilibrium equations for both subdomains is decomposed into free and linked quantities as follows:

- the free problem:

$$\begin{cases} M_A a_{free,m}^A + K_A u_{free,m}^A = f_{ext,m}^A \\ M_B a_{free,j}^B + K_B u_{free,j}^B = f_{ext,j}^B \ , \ j = 1,\ldots,m \end{cases} \tag{1.9}$$

- the link problem:

$$\begin{cases} M_A a_{link,m}^A + K_A u_{link,m}^A = -L_A^T \Lambda_m \\ M_B a_{link,j}^B + K_B u_{link,j}^B = -L_B^T \Lambda_j \ , \ j = 1,\ldots,m \end{cases} \tag{1.10}$$

In order to express the interface problem, the interpolated quantities in subdomain Ω_A are required at the micro time t_j, written above as:

$$\begin{cases} w_{free,j}^A = \left(\mathbf{1} - \dfrac{j}{m}\right) w_0^A + \left(\dfrac{j}{m}\right) w_{free,m}^A \\ w_{link,j}^A = \left(\dfrac{j}{m}\right) w_{link,m}^A \end{cases} \tag{1.11}$$

where the quantities *w* denote for the displacements, velocities and accelerations in the subdomain Ω_A.

Then, the authors introduced an unbalanced free interface reaction and an unbalanced linked interface reaction defined by:

$$\begin{cases} S_j = L_A \left(f_{ext,j}^A - M_A a_{free,j}^A - K_A u_{free,j}^A \right) \\ T_j = L_A \left(-M_A a_{link,j}^A - K_A u_{link,j}^A \right) - \Lambda_j \end{cases} \tag{1.12}$$

The above interface forces can be viewed as the disequilibrium of the free and link problem for the macro subdomain Ω_A expressed at the micro time scale. This disequilibrium comes from the assumed interpolated quantities from the Eq. (1.11), projected to the interface of the

subdomain Ω_A.

The two disequilibrium terms must be counterbalanced at each micro time t_j as:

$$T_j + S_j = L_A\left(f_{ext,j}^A - M_A a_j^A - K_A u_j^A - L_A^T \Lambda_j \right) = \mathbf{0} \tag{1.13}$$

Using the second equation of (1.11), the projected disequilibrium of the linked quantities can be expressed as:

$$T_j = -\left(\frac{j}{m}\right) L_A \left(M_A a_{link,m}^A + K_A u_{link,m}^A \right) - \Lambda_j \tag{1.14}$$

In addition, incorporating the expression (1.10) for subdomain Ω_A into the above equation, the projected disequilibrium of the linked quantities can be written as:

$$T_j = \left(\frac{j}{m}\right) L_A \left(L_A^T \Lambda_m \right) - \Lambda_j \tag{1.15}$$

And finally, by using Eq. (1.13) at the micro time, a relationship linking the Lagrange multipliers at the micro time scale to the unbalanced free interface forces and to the Lagrange multipliers at the macro time step, is derived as:

$$\Lambda_j = S_j + \left(\frac{j}{m}\right) \Lambda_m \tag{1.16}$$

The above relationship permits to express the Lagrange multipliers Λ_j at the micro time scale as a function of the unbalanced free interface reactions S_j and the Lagrange multipliers Λ_m at the end of the macro-time step. The unbalanced term S_j are first computed by solving the system of free equilibrium equations. Then, the relationship (1.16) is incorporating into the equilibrium equations for the subdomain Ω_B given in Eq. (1.2):

$$M_B a_j^B + K_B u_j^B = f_{ext,j}^B - L_B^T S_j - \frac{j}{m} L_B^T \Lambda_m \ , \ j = 1, \ldots, m \tag{1.17}$$

Without entering in further details, it can be shown that the global system composed of the equilibrium equation in subdomain Ω_A and the m equilibrium equations (1.17), can be solved in three stages by splitting the equations into free and link problems:

- Solve the global free problem only accounting for the external forces $f_{ext,j}^B$ and the unbalanced terms $-L_B^T S_j$ at each micro time t_j (from $j = \mathbf{1}$ to $j = m$).

- Solve the interface problem derived from the velocity continuity given in (1.8) at the macro-time scale. As showed by the authors [8], the interface problem takes the form:

$$H_{PH} \Lambda_m = b_m \tag{1.18}$$

H_{PH} denoting the interface operator at the macro time scale, and the right hand side vector b_m

being only dependent on free velocities at the end of the macro time step:

$$\begin{cases} H_{PH} = L_A y_m^A + L_B y_m^B \\ b_m = L_A v_{free,m}^A + L_B v_{free,m}^B \end{cases} \tag{1.19}$$

The algorithm for building the PH interface operator is shown in Table 1. It depends on the matrices y_m^A and y_m^B, iteratively computed by looping from micro time step to micro time step.

(2A) Macro subdomain SD*A*

$$y_0^A = 0, \dot{y}_0^A = 0, \ddot{y}_0^A = 0$$

$${}^p y_0^A = y_0^A + h_A \dot{y}_0^A + \left(\frac{1}{2} - \beta_A\right) h_A^2 \ddot{y}_0^A$$

$${}^p \dot{y}_0^A = \dot{y}_0^A + (1-\gamma_A) h_A \ddot{y}_0^A$$

$$\ddot{y}_m^A = \tilde{M}_A^{-1} \left(L_A^T - K_A \, {}^p y_0^A\right)$$

$$\dot{y}_m^A = {}^p \dot{y}_0^A + \gamma_A h_A \ddot{y}_m^A$$

$$y_m^A = {}^p y_0^A + \beta_A h_A^2 \ddot{y}_m^A$$

(2B) Micro subdomain *SDB*

$$y_0^B = 0, \dot{y}_0^B = 0, \ddot{y}_0^B = 0$$

Loop for j=1…m

$${}^p y_{j-1}^B = y_{j-1}^B + h_B \dot{y}_{j-1}^B + \left(\frac{1}{2} - \beta_B\right) h_B^2 \ddot{y}_{j-1}^B$$

$${}^p \dot{y}_{j-1}^B = \dot{y}_{j-1}^B + (1-\gamma_B) h_B \ddot{y}_{j-1}^B$$

$$\ddot{y}_j^B = \tilde{M}_B^{-1} \left(\frac{j}{m} L_B^T - K_B \, {}^p y_{j-1}^B\right)$$

$$\dot{y}_j^B = {}^p \dot{y}_{j-1}^B + \gamma_B h_B \ddot{y}_j^B$$

$$y_j^B = {}^p y_{j-1}^B + \beta_B h_B^2 \ddot{y}_j^B$$

(2') Computation of the interface operator

$$H_{PH} = L_A \dot{y}_m^A + L_B \dot{y}_m^B$$

Table 1: Computation of the interface operator for the PH method.

- Finally, once obtained the Lagrange multipliers Λ_m at the macro time scale, the linked quantities are obtained by solving the link problem only accounting for the terms $-\frac{j}{m} L_B^T \Lambda_m$ in Eq. (1.17).

It is interesting to note that the resolution of the free problem is staggered in the PH method. Indeed, the free quantities of the macro subdomain are first computed, then the unbalanced free interface forces S_j can be derived, and finally, the free quantities of the micro subdomain are obtained, from the first micro time step (end time t_1) to the last micro time step (end time t_m). Contrary to the free problem, the linked quantities for the two subdomains can be computed in parallel. Indeed, as soon as the Lagrange multipliers at the end of the macro time step are known, the linked quantities of both subdomains can be determined in a concurrent way. In comparison to the progenitor GC method which is completely staggered (in free and link computations), the parallelised features of the PH algorithm represent an improvement with respect to the GC method.

5 TWO EXTERNAL COUPLING SOFTWARE FOR EXPLICIT/IMPLICIT CO-COMPUTATIONS

Two external code coupling software have been set up in order to make a first finite element (FE) code based on an implicit time integration interact with a second FE code based on an explicit time integration.

In the following, we focus on the building of the PH coupling software, developed in C language, whereas the GC coupling software, presented in previous papers (Brun *et al.* [10,11]), is briefly reminded for comparison purpose. Two finite element codes are connected to the coupling software: CAST3M (implicit or explicit, [12]) and Europlexus (explicit, [13]).
Communications between processors use the pipe technology, enabling to send or receive data from one process to another process. The data exchange by means of pipes is very fast and does not require memory space in comparison to the classical writing and reading in classical files. Another important advantage in view of synchronizing the computations between the FE codes and the coupling software is the blocking feature of the reading function through a pipe.
The co-computation is carried out between the actors (the coupling software and the two FE codes for subdomains SDA and SDB) over the macro time step h_A. The tasks undertaken by the GC-CPL, that is the GC-based coupling software, are compared with the PH-CPL, that is the PH-based coupling software in Figure 1.

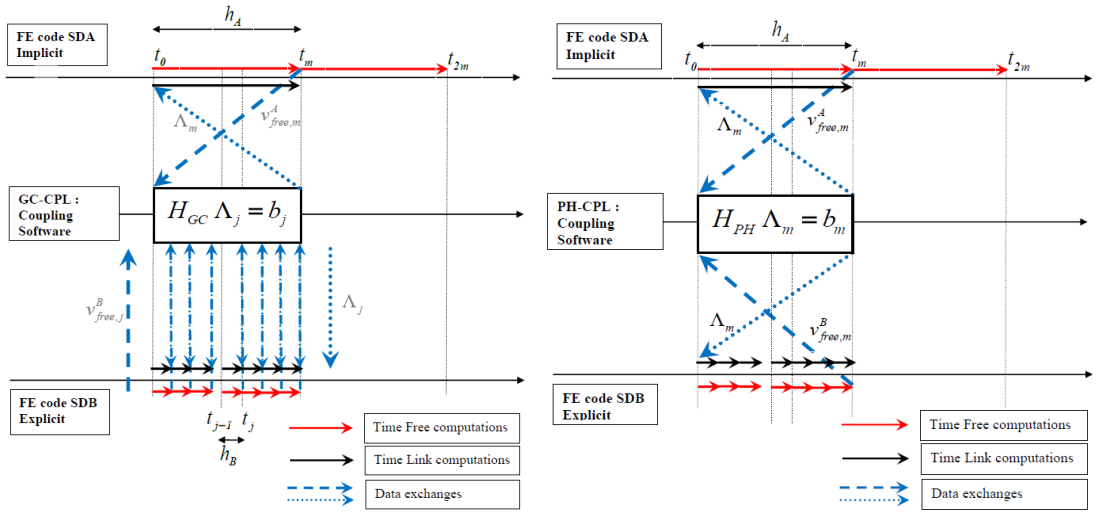


Figure 1: Time-computations and data exchanges over a macro time step between FE codes (subdomains SDA and SDB) and the external coupling software according to the GC algorithm (on left side) and to the PH algorithm (on the right side).

Over a given macro time step associated with the subdomain Ω_A, the following tasks undertaken by the PH-CPL are detailed below:

- Computing the free quantities by the FE code SDA over the macro-time step h_A and sending the free velocities $v^A_{free,m}$ to the PH-CPL.
- Solving the series of free problems in the subdomain Ω_B at the micro time scale by the FE code SDB, by looping over the macro-time step h_A, composed of m micro-time step h_B (for $j = 1,\ldots,m$). The last free velocities $v^B_{free,m}$ in subdomain Ω_B is sent from the FE code SDB to the PH-CPL.

- The interface problem can be set up. The PH interface operator has been previously built in the PH-CPL. The right hand side b_m is composed of the free velocities at the end of macro time step coming from both FE codes SDA and SDB.
- Solving the interface problem by computing the Lagrange multipliers Λ_m at the end of the macro-time step and sending the Lagrange multipliers to the FE codes SDA and SDB.
- Computing the linked quantities by the FE code SDA on the macro-time step h_A and updating the quantities (free+linked)
- Solving the series of linked problems in the subdomain Ω_B at the micro time scale by the FE code SDB, by looping over the macro-time step h_A, composed of m micro-time step h_B (for $j = \mathbf{1},\ldots,m$) and updating all the quantities at the micro time scale.

From Figure 1, it can be checked that no data exchange occurs directly between the two FE codes. Apart from the initial building of the PH interface operator, the mission of the PH-CPL exclusively consists in receiving free velocities from the FE codes and sending back the computed Lagrange multipliers. The coupling software completely ensures the interface between the two FE codes. In addition, the co-computations can be conducted without interfering in the parallel computing strategies employed by both the FE codes.
Contrary to the building of the interface operator which is much time consuming in the case of the PH algorithm, the requirements in terms of data exchanges in comparison to the GC algorithm, depicted on the left side of Figure 1, are clearly alleviated. Indeed, the GC coupling software has to communicate $\mathbf{2}m$ times over the macro-time step to solve the quantities in subdomain Ω_B: at each micro time step, one way for reading the free velocities $v^B_{free,j}$ from the FE code SDB, and one way for sending back the computed Lagrange multipliers Λ_j at the fine time scale. In the PH algorithm, only $\mathbf{2}$ data exchanges are involved concerning the computation in the FE code SDB: the PH-CPL reads the last free velocities $v^B_{free,m}$ from the FE code SDB and sends back the computed Lagrange multipliers Λ_m at the end of the macro-time step. It can be concluded that the PH algorithm is far more effective than the GC algorithm in terms of exchange data.

6 NUMERICAL EXAMPLES

6.1 Split oscillator

The first academic example is a single degree of freedom problem involving an oscillator with a mass and a stiffness split into two masses and two springs linked together through a Lagrange multiplier. Accuracy order will be checked for the GC and PH algorithms.
The equation of motion, continuous in time, of the undamped oscillator characterised by the angular frequency ω, under free vibrations is:

$$a(t) + \omega^2 u(t) = \mathbf{0} \tag{1.20}$$

The oscillator angular frequency is defined by the mass m and the stiffness k as: $\omega = \sqrt{\frac{k}{m}}$. Initial conditions are noted as: $u(t=0)=u_0$, $v(t=0)=v_0$. In the following, the analytical solution of the undamped oscillator under free vibration will be used as reference results so as to assess the accuracy order of the multi-time step algorithms.

The mass and the stiffness are split as follows: $m = m_A + m_B$ and $k = k_A + k_B$. The following values for the split system have been adopted: $m_A = 1.10^{-6}$, $k_A = 1.10^4$, $m_B = 1.10^{-6}$, $k_B = 1.10^4$ An initial displacement problem is considered: $u_0 = 1$, $v_0 = 0$. The macro subdomain Ω_A with a large time step Δt_A is integrated in time using the average acceleration scheme ($\gamma_A = \frac{1}{2}, \beta_A = \frac{1}{4}$), whereas the micro subdomain Ω_B with a fine time step Δt_B is integrated using the central difference scheme ($\gamma_B = \frac{1}{2}, \beta_B = 0$). The time step ratio between the two time steps is noted as m and is set to 100. The final time of the free vibration simulation is: $T_f = 2.10^{-4} s$.

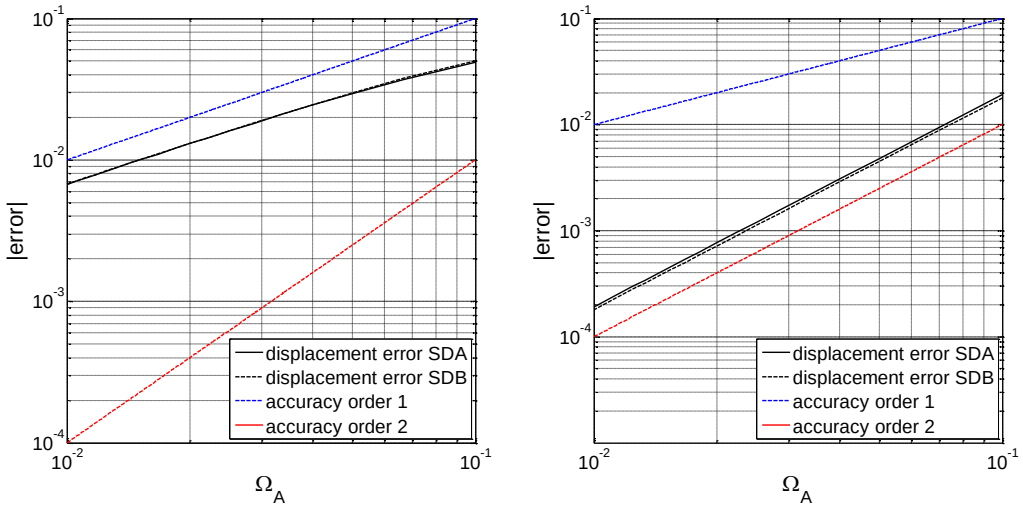


Figure 2: Convergence rate for the displacements of the multi-time step GC (on the left side) and PH (on the right side) algorithm for a time step ratio equal to 100.

In the case of the multi-time step GC algorithm, the errors in terms of displacements are plotted versus the reduced angular frequency of the subdomain SDA in Figure 2, along with slopes corresponding to the accuracy order equal to 1 or 2. It is shown that the convergence rate is reduced by one order when different time step sizes are involved as already highlighted in previous works (Mahjoubi *et al.* [9]). In the case of the multi-time step PH algorithm, the convergence rate remains equal to 2 for multi-time scales as shown on the right side of the Figure 6. The PH algorithm achieves a second order of accuracy, corresponding to the minimum of the orders of accuracy for the time integrators involved in the partitioned simulation.

6.2 Reinforced concrete frame structure under blast loading

The case of a non-earthquake resistant reinforced structure under blast loading is considered. The model of the structure has already been presented in previous works (Brun *et al.* [11]).

Briefly, the model of the frame structure is composed of multi-fibre Timoshenko beam elements, whose cross-section is discretised into material fibres for concrete and longitudinal reinforcement. The purpose is to assess the advantages of the PH-CPL coupling software in terms of energy dissipation at the interface in comparison to the GC-CPL coupling software. In Figure 3, the complete mesh of the structure is illustrated (3D visualisation for exhibiting the cross-section of the beam elements) as well as the partitioning assumed in the following co-computations: beam elements for columns and column-beam joints are gathered into the explicit partition, whereas the remaining of the mesh (the FE beams without the joints) are included in the implicit partition with the macro time step. Linear elastic behaviour is assumed for all the concrete and steel fibres with Young modulus equal to 25000 MPa and 200000 MPa, respectively. Dead and live loads are taken into account as well as the blast loads applied to the front face of the structure.

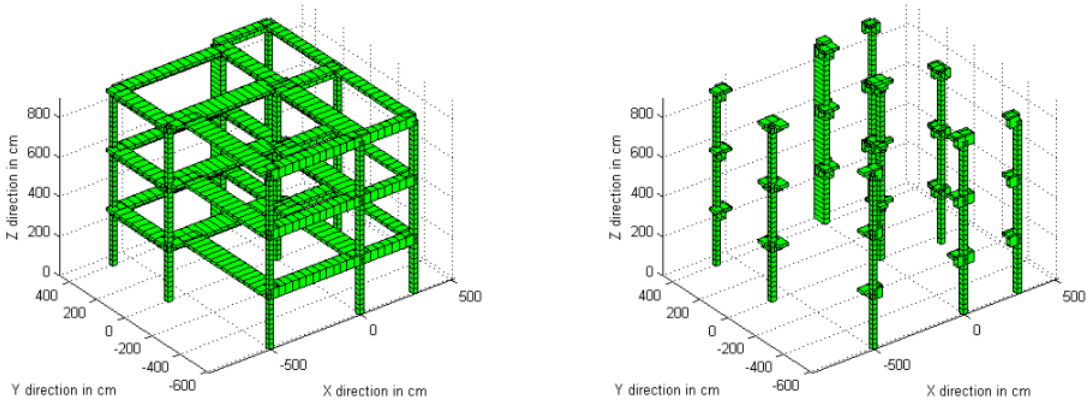


Figure 3: Mesh of the reinforced concrete beam-column structure and its partitioning (on the right side, the explicit subdomain)

Co-computations are carried out with both coupling software, the GC-CPL and the PH-CPL, by making interact two CAST3M processes, dealing with either the implicit or explicit partitions. The time-step ratio adopted between the macro time step and the micro time step is equal to 40. The reference results are provided by a full-explicit computation using the CAST3M code. Figure 4 shows the comparison of the investigated co-computations and the reference results in terms of displacements and velocities in the direction of the blast (axis Y) at the top of a column C5 of the structure. The almost perfect agreement between the results is highlighted.

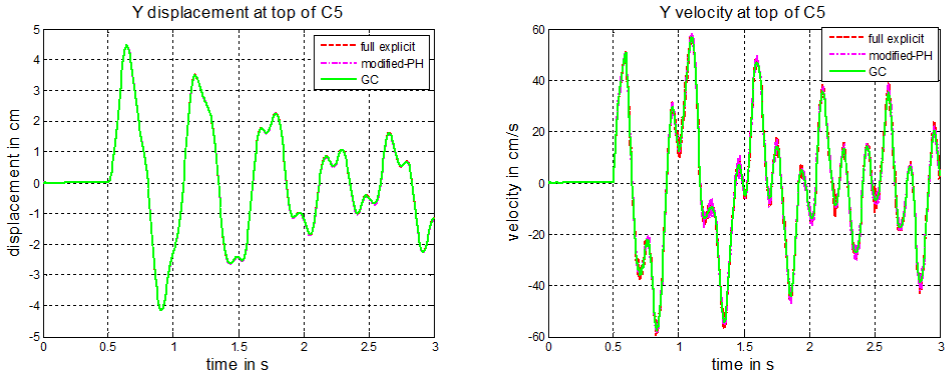


Figure 4: Time history Y-displacements (top graph) and Y-velocities (bottom graph) at the top of the C5 column predicted by full-explicit computation and co-computations according to the GC and PH algorithms

The unbalanced energy $W_{unbalanced}$, corresponding to the sum of the kinetic W_{kin}, internal W_{int}, complementary W_{comp} energies minus the external energy W_{ext} for both subdomains, are checked for the both coupling approaches. Note that the complementary energy is equal to zero when considered the implicit Newmark scheme with parameters $\gamma = \frac{1}{2}$ and $\beta = \frac{1}{4}$ and appears in the case of explicit Newmark subdomain with $\gamma = \frac{1}{2}$ and $\beta = 0$ (Hughes, [4]). This additional term with respect to the mechanical energy $W_{tot} = W_{kin} + W_{\text{int}}$ appearing in the balance energy equation is generated by the Newmark time discretization (Krenk, [14]). The interface energy coming from the coupling algorithms corresponds to the unbalanced energy when considered only energy conserving schemes. On the left of Figure 5, the dissipated energy created at the interface by the GC algorithm is highlighted as proved by the authors as soon as different time steps are adopted. As shown on the right of Figure 5, this spurious dissipative energy at the interface between subdomains is almost cancelled using the PH-based coupling software.

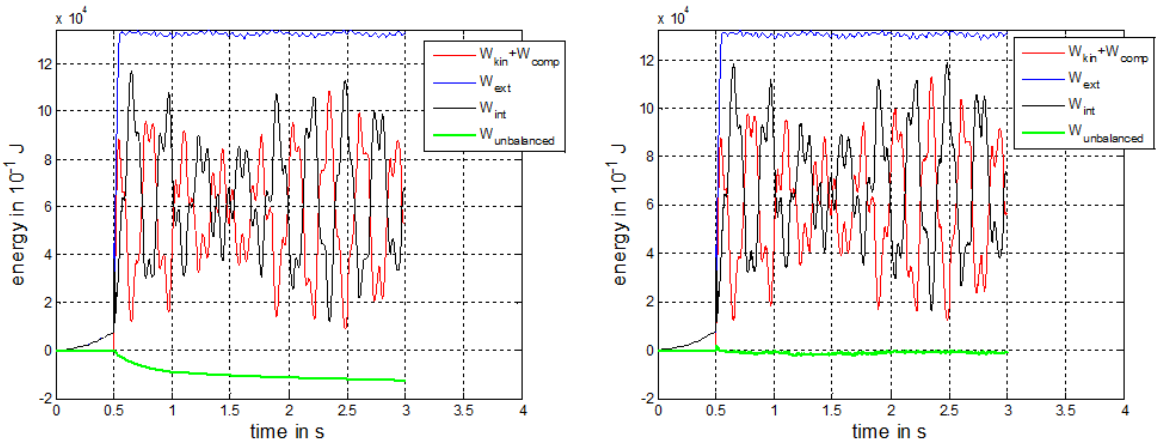


Figure 5: Time histories of kinetic (+complementary), internal, external energies and unbalanced energy from co-computations with GC-CPL (on the left) and PH-CPL (on the right) coupling software (time step ratio equal to 40).

7 CONCLUSIONS

This paper presents the set up of coupling software for structural dynamics. The coupling software makes interact in time Finite Element codes based on explicit and implicit time integration schemes. Two multi time step coupling algorithms are investigated: the GC algorithm, proposed by Gravouil and Combescure, and the PH algorithm, proposed by Prakash and Hjelmstad. The main difference between the two algorithms lies in the time scale at which the interface problem is solved: at the micro-scale for the GC algorithm and at the macro-scale for the PH-algorithm. The coupling software based on the PH algorithm, noted as PH-CPL, provides enhanced parallel capabilities and alleviates the energy dissipation drawback at the interface between subdomains.

The first numerical example is a simple split oscillator: using the modified-PH algorithm, the second-order of accuracy is achieved, whereas the GC algorithm only leads to first-order of accuracy when different time steps are considered depending on the subdomains.

The following application makes use of both coupling software GC-CPL and PH-CPL. It

deals with a reinforced concrete frame structure under blast loading striking its front face. Multi time step explicit/implicit co-computations with GC-CPL and PH-CPL software have been validated with respect to the full explicit computations. The two algorithms predict very close displacements and damage states. Nevertheless, the PH-CPL performs better with respect to the GC-CPL when one compares the spurious energy coming from the algorithms at the interface.

REFERENCES

[1] Combescure A, Gravouil A. A numerical scheme to couple subdomains with different time-steps for predominantly linear transient analysis. *Computer methods in applied mechanics and engineering* 2002; **191**:1129-1157.
[2] Farhat C, Roux F.X. A method of finite element tearing and interconnecting and its parallel solution algorithm. *International Journal for Numerical Methods in Engineering* 1991; **32**:1205-1227.
[3] Farhat C, Crivelli L, Roux F.X. Transient FETI methodology for large-scale parallel implicit computations in structural mechanics. *International Journal for Numerical Methods in Engineering* 1994; **37**:1945-1975.
[4] Hughes T.J.R. The Finite Element Method: Linear Static and Dynamic Finite Element Analysis. Prentice-Hall, Englewood Cliffs, NJ, 1987.
[5] Gravouil A, Combescure A. A multi-time-step explicit-implicit method for non-linear structural dynamics. *International Journal for Numerical Methods in Engineering* 2001; **50**:199-225.
[6] Herry B, Di Valentin L, Combescure A. An approach to the connection between subdomains with non-matching meshes for transient mechanical analysis. *International Journal for Numerical Methods in Engineering* 2002; **55**:973-1003.
[7] Faucher V, Combescure A. Local modal reduction in explicit dynamics with domain decomposition. Part 1: extension to sub-domains undergoing finite rigid rotations *International Journal for Numerical Methods in Engineering* 2004; **60**:2531-2560.
[8] Prakash A, Hjelmstad KD. A FETI-based multi-time-step coupling method for Newmark schemes in structural dynamics *International Journal for Numerical Methods in Engineering* 2004; **61**:2183-2204.
[9] Mahjoubi N, Gravouil A, Combescure A. Coupling subdomains with heterogeneous time integrators and incompatible time steps. *Computational mechanics* 2009; DOI 10.1007/s00466-009-0413-4.
[10] Brun M., Batti A., Limam A. and Combescure A. Implicit/Explicit multi-time step co-computations for predicting reinforced concrete structure response under earthquake loading. *Soil dynamics and Earthquake Engineering*;**33(1)**:19-37.
[11] Brun M., Batti A., Limam A., Gravouil A. Explicit/implicit multi-time step co-computations for blast analyses on a reinforced concrete frame structure. *Finite Elements in Analysis & Design 2012*;**52**:41-59.
[12] Verpeaux P, Charras T, Millard A, CASTEM 2000 une approche moderne du calcul de structures. In *Calcul de structure et intelligence artificielle*. Pluralis , Fouet JM, Ladeveze P., Ohayon R. (ed.), 1988, 261-271.
[13] EuroPlexus, A computer program for the finite element simulation of fluid-structure systems under dynamic loading, *User's manual*, CEA Saclay, CEA/DEN/SEMT/DYN, 2002.
[14] Krenk S. Energy conservation in Newmark based time integration algorithm. *Computer methods in applied mechanics and engineering* 2006; **195**:6110-6124.

COMPDYN 2013
4th ECCOMAS Thematic Conference on
Computational Methods in Structural Dynamics and Earthquake Engineering
M. Papadrakakis, V. Papadopoulos, V. Plevris (eds.)
Kos Island, Greece, 12–14 June 2013

FINITE ELEMENT MODELING OF LINEAR ELASTODYNAMICS PROBLEMS WITH EXPLICIT TIME-INTEGRATION METHODS AND LINEAR ELEMENTS WITH REDUCED DISPERSION. COMPARATIVE STUDY OF DIFFERENT FINITE ELEMENT TECHNIQUES USED FOR ELASTODYNAMICS.

Alexander V. Idesman

Texas Tech University
Box 41021, Lubbock, TX 79409, USA
e-mail: alexander.idesman@coe.ttu.edu

Keywords: elastic waves, numerical dispersion, explicit time integration, finite elements.

Abstract. *We have developed two finite element techniques with reduced dispersion for linear elastodynamics that are used with explicit time-integration methods. These techniques are based on the modified integration rule for the mass and stiffness matrices and on the averaged mass matrix approaches that lead to the numerical dispersion reduction for linear finite elements. The analytical study of numerical dispersion for the new techniques is carried out in the 1-D, 2-D and 3-D cases. The numerical study of the effectiveness of the dispersion reduction techniques includes two-stage time-integration approach with the filtering stage (developed in our previous papers) that quantifies and removes spurious high-frequency oscillations from numerical results. We have found that in contrast to the standard linear elements with explicit time-integration methods and the lumped mass matrix, the finite element techniques with reduced dispersion yield more accurate results at small time increments (smaller than the stability limit) in the 2D and 3-D cases. The advantages of the new technique are illustrated by the solution of the 1-D and 2-D impact problems. The new approaches with reduced dispersion can be easily implemented into existing finite element codes and lead to significant reduction in computation time at the same accuracy compared with the standard finite element formulations. Finally, we compare the accuracy of the linear elements with reduced dispersion, the spectral low- and high-order elements as well as the isogeometric elements by the solution of the 1-D impact problem. For all these solutions we use two-stage time integration technique with the filtering stage that removes spurious oscillations and allows an accurate comparison of different space discretization techniques used for elastodynamics. It is also interesting to mention that the amount of numerical dissipation at the filtering stage can be used as a quantitative measure for the comparison of accuracy of the different numerical formulations used for elastodynamics.*

1 INTRODUCTION

The application of the space discretization to transient acoustics or transient linear elastodynamics problems leads to a system of ordinary differential equations in time

$$\boldsymbol{M}\ddot{\boldsymbol{U}} + \boldsymbol{C}\dot{\boldsymbol{U}} + \boldsymbol{K}\boldsymbol{U} = \boldsymbol{R}, \tag{1}$$

where $\boldsymbol{M}$, $\boldsymbol{C}$, $\boldsymbol{K}$ are the mass, damping, and stiffness matrices, respectively, $\boldsymbol{U}$ is the vector of the nodal displacement, $\boldsymbol{R}$ is the vector of the nodal load. Zero viscosity, $\mathbf{C} = \mathbf{0}$, is considered in the paper. Due to the space discretization, the exact solution to Eq. (1) contains the numerical dispersion error; e.g., see [7, 9, 11, 26, 27, 28, 30, 31, 32, 14, 12] and others. The space discretization error can be decreased by the use of mesh refinement. However, this procedure significantly increases computational costs. Therefore, special techniques have been developed for the reduction in the numerical dispersion error which is also related to "the pollution effect" (e.g., see [1, 2, 10] and others for the study of the pollution error). One simple and effective technique for acoustic and elastic wave propagation problems is based on the calculation of the mass matrix $\boldsymbol{M}$ in Eq. (1) as a weighted average of the consistent and lumped mass matrices $\boldsymbol{M}$; see [26, 27, 28, 30] and others. For the 1-D case and linear finite elements, this approach reduces the error in the wave velocity for harmonic waves from the second order to the fourth order of accuracy. However, for harmonic wave propagation in the 2-D and 3-D cases, these results are not valid (nevertheless, in the multidimensional case, the averaged mass matrix yields more accurate results compared with the standard mass matrix; e.g., see the numerical results in Section 3). We should also mention that the known publications on the techniques with the averaged mass matrix do not include the effect of finite time increments on the dispersion error and on the accuracy of the numerical results. As shown in the current paper, if we use the weighting coefficients for the averaged mass matrix that are independent of time increments (as in the known approaches) and if the time increments for explicit time-integration methods are close to the stability limit then there is no advantages in the use of the averaged mass matrix compared with the lumped mass matrix.

An interesting technique with implicit and explicit time-integration methods is suggested in [32] for acoustic waves in the 2-D case. It is based on the modified integration rule for the calculation of the mass and stiffness matrices for linear finite elements. In contrast to the averaged mass matrix, the use of the modified integration rule increases the accuracy for the phase velocity from the second order to the fourth order in the general multi-dimensional case of acoustic waves. However, the applicability of this technique to elastodynamics problems has not been studied. The technique in [32] has not treated spurious oscillations that may significantly destroy the accuracy of numerical results.

We should mention that the analysis of numerical dispersion estimates the numerical error for propagation of harmonic waves. In the general case of loading (boundary conditions), the estimation of the accuracy of numerical techniques with reduced dispersion is difficult due to the presence of spurious high-frequency oscillations in numerical solutions; e.g., see [11, 26].

In our paper [17], we have described the finite element techniques with reduced dispersion for elastodynamics that are based on implicit time-integration methods with very small time increments. These techniques significantly reduce the computation time at the same accuracy compared with the standard finite element formulations with the consistent mass matrix. However, one of the disadvantages of the use of implicit time-integration methods is the necessity to solve a system of algebraic equations that can require large computational resources for a large number of degrees of freedom. In this paper we have extended the finite element techniques

with reduced dispersion that can be used with explicit time-integration methods. We have considered two techniques: one of them is based on the use of averaged mass matrix; another is based on the modified integration rule for the mass and stiffness matrices. In contrast to our paper [17], in the present paper we have also studied the effect of time increments on the accuracy of the numerical results.

2 THE FINITE ELEMENT TECHNIQUES WITH REDUCED DISPERSION FOR EXPLICIT TIME-INTEGRATION METHODS

Here we will present the averaged mass matrix technique and the modified integration rule technique that are used with explicit time-integration methods. These two techniques significantly reduce the numerical dispersion error and the computation time compared with the standard finite element formulations for linear elastodynamics. In contrast to the study of the averaged mass matrix technique and the modified integration rule technique for the scalar wave equation considered in [26, 32], the analytical study of these techniques for elastodynamics problems is much more complicated due to a greater number of non-linear terms in the dispersion equation for elastodynamics and the presence of two different types of waves (compressional and shear waves). For the use explicit time-integration methods (for simplicity we assume that the damping matrix is zero, $\boldsymbol{C} = \boldsymbol{0}$), we will first modify Eq. (1) similar to the paper [26]. Let's rewrite Eq. (1) with the diagonal (lumped) mass matrix $\boldsymbol{D}$ as follows

$$\boldsymbol{D}\dot{\boldsymbol{V}} + \boldsymbol{K}\boldsymbol{U} = \boldsymbol{R}, \tag{2}$$

where $\boldsymbol{V}$ is the vector of nodal velocity. Relationships between the nodal displacements and velocities can be written down as (similar to those in [26, 32])

$$\boldsymbol{D}\dot{\boldsymbol{U}} = \boldsymbol{M}\boldsymbol{V} \qquad \text{or} \qquad \boldsymbol{D}\ddot{\boldsymbol{U}} = \boldsymbol{M}\dot{\boldsymbol{V}} \tag{3}$$

where $\boldsymbol{M}$ is the non-diagonal mass matrix calculated by the averaged mass matrix technique (see Eq. (6) below) or by the modified integration rule technique (see Eqs. (7), (9) and (11) below). Inserting Eq. (3) into Eq. (2) we will get

$$\boldsymbol{D}\ddot{\boldsymbol{U}} + \boldsymbol{M}\boldsymbol{D}^{-1}\boldsymbol{K}\boldsymbol{U} = \boldsymbol{M}\boldsymbol{D}^{-1}\boldsymbol{R}. \tag{4}$$

Eq. (4) differs from the standard finite element equations with the lumped mass matrix by the stiffness matrix and the load vector which are multiplied by the term $\boldsymbol{M}\boldsymbol{D}^{-1}$. For the time integration of Eq. (4) we will use the standard explicit central-difference method (the most popular explicit method); e.g., see [20, 13, 3]. Replacing the second time derivative in Eq. (4) by the corresponding finite difference approximation used in the central-difference method, we obtain

$$\boldsymbol{D}\,[\boldsymbol{U}(t+\Delta t) - 2\boldsymbol{U}(t) + \boldsymbol{U}(t-\Delta t)]/\Delta t^2 + \boldsymbol{M}\boldsymbol{D}^{-1}\boldsymbol{K}\boldsymbol{U}(t) = \boldsymbol{M}\boldsymbol{D}^{-1}\boldsymbol{R}(t)\,, \tag{5}$$

where Δt is the time increment. Eq. (5) is used for the analysis of the numerical dispersion of the finite element formulations with the averaged mass matrix and modified integration rule techniques.

In order to decrease the numerical dispersion of finite element results, we consider the following two possibilities for the calculation of the mass and stiffness matrices: the mass matrix $\boldsymbol{M}$ is calculated as a weighted average of the consistent $\boldsymbol{M}^{cons}$ and lumped $\boldsymbol{D}$ mass matrices with the weighting factor γ (similar to that used in [26, 27, 30])

$$\boldsymbol{M}(\gamma) = \boldsymbol{D}\gamma + \boldsymbol{M}^{cons}(1-\gamma) \tag{6}$$

or the mass and stiffness matrices of each finite element are calculated with the modified integration rule (similar to those used in [32])

$$\boldsymbol{M}^e(\alpha_M) \,=\, \rho A \int\limits_{-1}^{1} \boldsymbol{N}^T(s)\boldsymbol{N}(s) det(\boldsymbol{J}) ds \,\approx \rho A \sum_{m=1}^{2} \boldsymbol{N}^T((-1)^m \alpha_M)\, \boldsymbol{N}((-1)^m \alpha_M) det(\boldsymbol{J})\,, \quad (7)$$

$$\boldsymbol{K}^e(\alpha_K) \,=\, \int\limits_{-1}^{1} E\boldsymbol{B}^T(s)\boldsymbol{B}(s) det(\boldsymbol{J}) ds \approx \sum_{m=1}^{2} E\boldsymbol{B}^T((-1)^m \alpha_K)\, \boldsymbol{B}((-1)^m \alpha_K) det(\boldsymbol{J}) \quad (8)$$

in the 1-D case,

$$\boldsymbol{M}^e(\alpha_M) \,=\, \rho b \int\limits_{-1}^{1}\int\limits_{-1}^{1} \boldsymbol{N}^T(s,t)\boldsymbol{N}(s,t) det(\boldsymbol{J}) ds dt$$

$$\approx \rho b \sum_{m=1}^{2}\sum_{j=1}^{2} \boldsymbol{N}^T((-1)^m \alpha_M, (-1)^j \alpha_M)\, \boldsymbol{N}((-1)^m \alpha_M, (-1)^j \alpha_M) det(\boldsymbol{J})\,, \quad (9)$$

$$\boldsymbol{K}^e(\alpha_K) \,=\, \int\limits_{-1}^{1}\int\limits_{-1}^{1} \boldsymbol{B}^T(s,t)\bar{\boldsymbol{C}}\boldsymbol{B}(s,t) det(\boldsymbol{J}) ds dt$$

$$\approx \sum_{m=1}^{2}\sum_{j=1}^{2} \boldsymbol{B}^T((-1)^m \alpha_K, (-1)^j \alpha_K)\, \bar{\boldsymbol{C}}\boldsymbol{B}((-1)^m \alpha_K, (-1)^j \alpha_K) det(\boldsymbol{J}) \quad (10)$$

in the 2-D case,

$$\boldsymbol{M}^e(\alpha_M) \,=\, \rho \int\limits_{-1}^{1}\int\limits_{-1}^{1}\int\limits_{-1}^{1} \boldsymbol{N}^T(s,t,q)\boldsymbol{N}(s,t,q) det(\boldsymbol{J}) ds dt dq$$

$$\approx \rho \sum_{m=1}^{2}\sum_{j=1}^{2}\sum_{p=1}^{2} \boldsymbol{N}^T((-1)^m \alpha_M, (-1)^j \alpha_M, (-1)^p \alpha_M)\, \boldsymbol{N}((-1)^m \alpha_M, (-1)^j \alpha_M, (-1)^p \alpha_M) det(\boldsymbol{J})\,, \quad (11)$$

$$\boldsymbol{K}^e(\alpha_K) \,=\, \int\limits_{-1}^{1}\int\limits_{-1}^{1}\int\limits_{-1}^{1} \boldsymbol{B}^T(s,t,q)\bar{\boldsymbol{C}}\boldsymbol{B}(s,t,q) det(\boldsymbol{J}) ds dt dq$$

$$\approx \sum_{m=1}^{2}\sum_{j=1}^{2}\sum_{p=1}^{2} \boldsymbol{B}^T((-1)^m \alpha_K, (-1)^j \alpha_K, (-1)^p \alpha_K)\, \bar{\boldsymbol{C}}\boldsymbol{B}((-1)^m \alpha_K, (-1)^j \alpha_K, (-1)^p \alpha_K) det(\boldsymbol{J}) \quad (12)$$

in the 3-D case. Here, $\boldsymbol{N}$ and $\boldsymbol{B}$ are the standard finite element shape and B matrices; $\bar{\boldsymbol{C}}$ is the matrix of elastic coefficients:

$$\bar{\boldsymbol{C}} \,=\, \frac{E(1-\nu)}{(1+\nu)(1-2\nu)} \begin{pmatrix} 1 & \frac{\nu}{1-\nu} & 0 \\ \frac{\nu}{1-\nu} & 1 & 0 \\ 0 & 0 & \frac{1-2\nu}{2(1-\nu)} \end{pmatrix}$$

in the 2-D case of plane strain and

$$\bar{\boldsymbol{C}} \,=\, \frac{E(1-\nu)}{(1+\nu)(1-2\nu)} \begin{pmatrix} 1 & \frac{\nu}{1-\nu} & \frac{\nu}{1-\nu} & 0 & 0 & 0 \\ \frac{\nu}{1-\nu} & 1 & \frac{\nu}{1-\nu} & 0 & 0 & 0 \\ \frac{\nu}{1-\nu} & \frac{\nu}{1-\nu} & 1 & 0 & 0 & 0 \\ 0 & 0 & 0 & \frac{1-2\nu}{2(1-\nu)} & 0 & 0 \\ 0 & 0 & 0 & 0 & \frac{1-2\nu}{2(1-\nu)} & 0 \\ 0 & 0 & 0 & 0 & 0 & \frac{1-2\nu}{2(1-\nu)} \end{pmatrix}$$

in the 3-D case; the diagonal terms of the lumped mass matrix $\boldsymbol{D}$ (except those for the boundary nodes) for the linear elements are dx; dx^2; dx^3 in the 1-D case, in the 2-D case for square elements and in the 3-D case for cubic elements, respectively; $\boldsymbol{J}$ is the Jacobian matrix ($det(\boldsymbol{J}) = dx/2$; $dx^2/4$; $dx^3/8$ in the 1-D case, in the 2-D case for square elements and in the 3-D case for cubic elements, respectively; dx is the length of a finite element); A is the cross sectional area in the 1-D case; b is the thickness in the 2-D case of plane strain; s, t, q are the isoparametric coordinates; α_M and α_K are the coordinates of the integration points for the mass and stiffness matrices to be determined (2, $2 \times 2 = 4$ and $2 \times 2 \times 2 = 8$ integration points are used for linear elements in the 1-D, 2-D and 3-D cases, respectively); e.g., see [13, 3] for the derivation of finite element matrices. The integration error due to the application of the modified integration rule for the mass and stiffness matrices does not change the convergence rate of finite element solutions; see [32].

We use the dispersion analysis in order to find such γ, α_M and α_K that reduce the numerical dispersion error. The results of the dispersion analysis considered in detail in our paper [21] are summarized below. In the 1-D case, the numerical dispersion error decreases at $\gamma = \gamma^{opt} = \frac{3-\bar{\tau}^2}{2}$ and at $\alpha_M = \alpha_M^{opt} = \sqrt{\frac{4-\bar{\tau}^2}{3}}$ where $\bar{\tau} = \frac{c_o \Delta t}{dx}$ is the Courant number, dx is the size of a finite element, Δt is the size of a time increment, c_o is $c_o = \sqrt{E/\rho}$ is the wave velocity in the 1-D case, ρ is the density, E is Young's modulus. We should mention that at $\bar{\tau} \approx 0$ (for very small time increments), the optimal value of $\gamma^{opt} = \frac{3}{2}$ coincides with the results obtained in [26] for the 1-D case. However, the size of time increments may significantly affect γ^{opt}. For example, the stability limit for the time integration of Eq. (5) on uniform meshes with linear elements equals $\Delta t^{st} = \frac{dx}{c_o}$ or $\bar{\tau} = 1$. In this case, $\gamma^{opt} = 1$ and $\boldsymbol{M} = \boldsymbol{D}$ (see Eq. (6)); i.e., for this particular case, Eq. (5) reduces to the standard finite element formulation with the lumped mass matrix (it is known that in the 1-D case, the standard linear finite elements and the explicit central difference method yields the exact solution to the 1-D impact problem at $\bar{\tau} = 1$; e.g., see [13]). It can be also shown that for linear elements with the averaged mass matrix and 1-D uniform meshes, the dispersion error increases with the decrease in the size of time increments Δt for time increments smaller than the stability limit. At $\gamma = (3\alpha_M^2 - 1)/2$ (with the optimal value of $\alpha_M^{opt} = \sqrt{\frac{4-\bar{\tau}^2}{3}}$ or the same as in [32]), the modified integration rule and the average mass matrix techniques yield the same results and are completely equivalent in the 1-D case.

In the multi-dimensional case, the numerical dispersion error decreases at $\alpha_M = \sqrt{\frac{4-\tau^2}{3}}$ and $\alpha_K = \sqrt{\frac{4(2\nu-1)}{3(4\nu-3)}}$ for the modified integration rule and $\gamma = \frac{3-\tau^2}{2}$ for the averaged mass matrix technique where $\tau = \frac{c_2 \Delta t}{dx}$, $c_2 = \sqrt{\frac{E}{2\rho(1+\nu)}}$ is the phase velocity of the shear waves and ν is Poisson's ratio. In contrast to the 1-D case, the dispersion error decreases with the decrease in time increments; see [21].

3 NUMERICAL MODELING

The new finite element techniques with reduced dispersion are implemented into the finite element code FEAP [33]. Below they are applied to 1-D and 2-D impact linear elastodynamics problems for which all low and high frequencies are excited. Due to spurious high-frequency oscillations, these problems cannot be accurately solved by existing time-integration methods based on the introduction of artificial viscosity (or numerical dissipation) at each time increment, especially in the case of long-term integration. Therefore, the two-stage time integration technique developed in our previous papers [22, 18, 20] (see also the Appendix) is used. The filtering stage of this technique includes the time-continuous Galerkin (TCG) method with

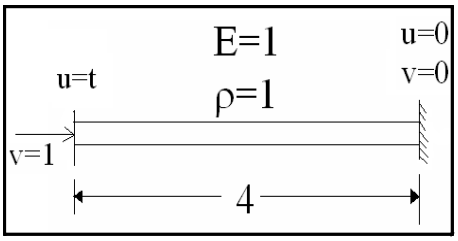


Figure 1: Impact of an elastic bar of length $L = 4$ against a rigid wall.

$N = 10$ time increments (5 positive plus 5 negative time increments) the size of which is calculated according to Eqs. (13) - (15) (see [22, 18, 20] and the Appendix below). We also compare the numerical results obtained by the linear elements with reduced dispersion (see Section 2), by the spectral low- and high-order elements (e.g., see [6, 23, 24, 25, 29] and others) and by the isogeometric elements (e.g., see [4, 5, 8, 14] and others).

3.1 1-D impact of an elastic bar against a rigid wall

The impact of an elastic bar of the length $L = 4$ and the cross section $A = 1$ against a rigid wall is considered in the 1-D case (see Fig. 1). Young's modulus is chosen to be $E = 1$ and the density to be $\rho = 1$. The following boundary conditions are applied: the displacement $u(0, t) = t$ (which corresponds to the velocity $v(0, t) = v_0 = 1$) and $u(4, t) = 0$ (which corresponds to the velocity $v(4, t) = 0$). Initial displacements and velocities are zero; i.e., $u(x, 0) = v(x, 0) = 0$. The analytical solution to this problem for time $0 \le t \le L\sqrt{\rho/E} = 4$ includes the continuous variation of displacements $u_a(x, t) = t - x$ for $t \ge x$ and $u_a(x, t) = 0$ for $t \le x$, and the piecewise constant variation of velocities and stresses $v_a(x, t) = -\sigma^a(x, t) = 1$ for $t \ge x$ and $v_a(x, t) = \sigma^a(x, t) = 0$ for $t \le x$ (at the interface $x = t$, jumps in stresses and velocities occur). For time $4 \le t \le 8$ the solution is similar to that for $0 \le t \le 4$ with the difference that the elastic wave reflects from the right end and propagates to the left. For time $8 \le t \le 12$ the solution is the same as for time $0 \le t \le 4$ and so on. In order to compare the results at short- and long-term integrations, the observation times are chosen to be $T = 2; 18; 98; 194$. The exact distributions of the velocities and stresses along the bar are the same at these observation times and correspond to the location of the wave front in the middle of the bar.

Along with the linear elements with reduced dispersion described in Section 2, we will solve the 1-D impact problem using the spectral low- and high-order elements (up to the 10th-order). For these space-discretization methods, the diagonal mass matrices and the explicit central-difference method with very small time increments are used. We should also mention that the spectral 1st- and 2nd-order elements coincide with the standard finite elements of the same orders. For the comparison of accuracy, we will also present the results obtained by the isogeometric 3rd-order elements with the consistent (non-diagonal) mass matrix and the implicit time-integration method with very small time increments. Uniform meshes with 101 degrees of freedom (dof) are used for all types of elements; see Figs. 2 - 6. In addition to these meshes, we also use uniform meshes with 201, 301 and 401 dof for the linear elements with reduced dispersion; see Fig. 5. Figs. 2 - 4 show the numerical solutions for the velocity at different observation times. All space-discretization methods yield spurious oscillations after basic computations and the amplitudes of these oscillations increase with the increase in the observation time; see Figs. 2a,b - 4a,b. The slope of the wave front in the basic computations is steeper for short observation times and is more diffusive for large observation times. The filtering stage

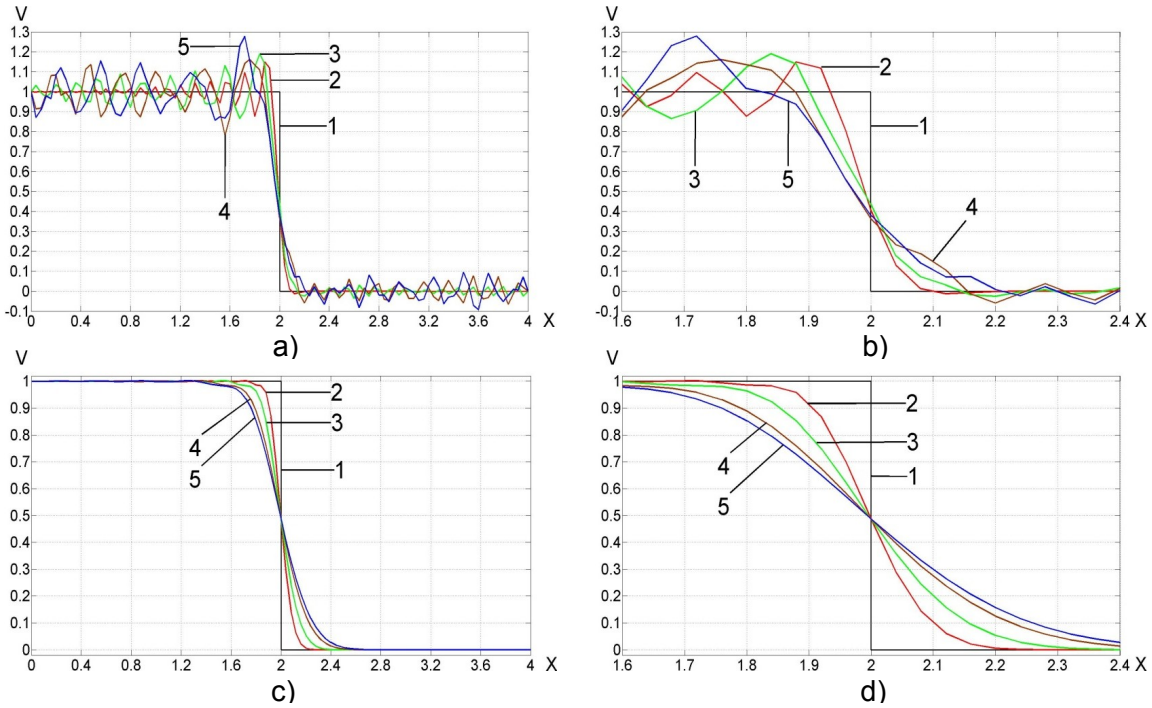


Figure 2: The velocity distribution along the bar after (a, b) basic computations (the lumped mass matrix and small time increments) and after (c, d) post-processing. A uniform mesh with the linear elements with reduced dispersion and 101 dof is used. Curves 1 correspond to the analytical solutions. Curves 2, 3, 4 and 5 correspond to the observation times $T = 2,\ 18,\ 98$ and 194, respectively. b) and d) show the zoomed graphs a) and c) in the range $1.6 < x < 2.4$.

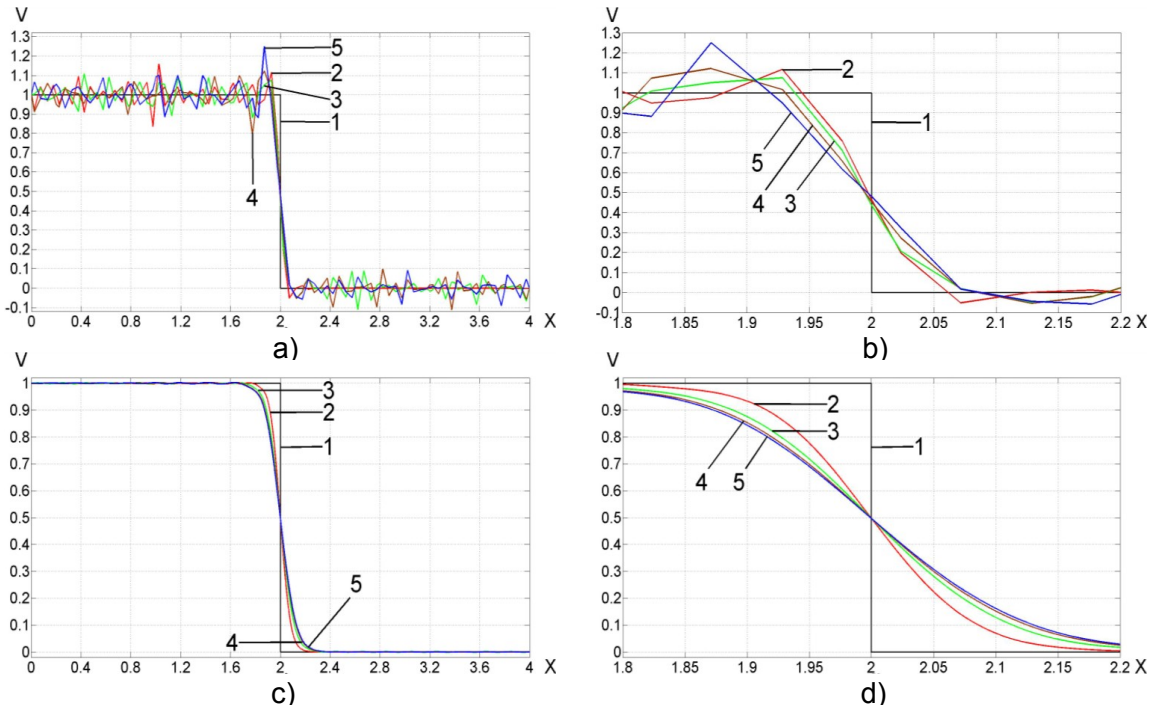


Figure 3: The velocity distribution along the bar after (a, b) basic computations (the lumped mass matrix and small time increments) and after (c, d) post-processing. A uniform mesh with the spectral 5th-order elements and 101 dof is used. Curves 1 correspond to the analytical solutions. Curves 2, 3, 4 and 5 correspond to the observation times $T = 2,\ 18,\ 98$ and 194, respectively. b) and d) show the zoomed graphs a) and c) in the range $1.8 < x < 2.2$.

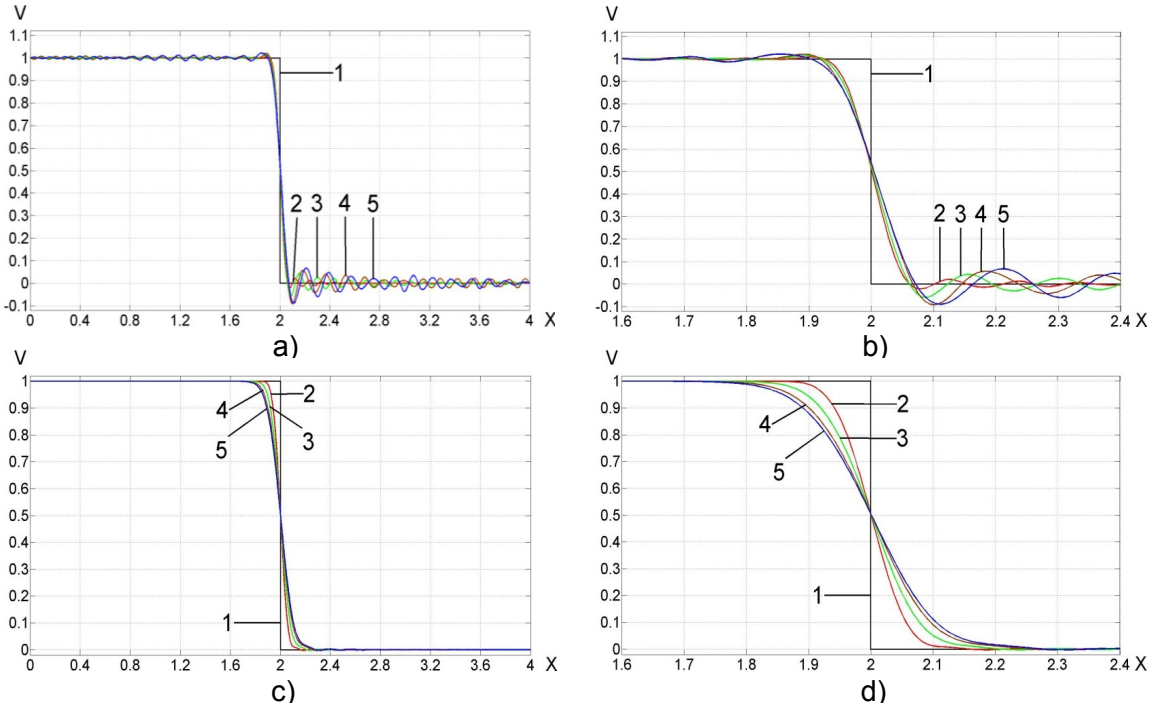


Figure 4: The velocity distribution along the bar after (a, b) basic computations (the consistent mass matrix and small time increments) and after (c, d) post-processing. A uniform mesh with the isogeometric 3rd-order elements and 101 dof is used. Curves 1 correspond to the analytical solutions. Curves 2, 3, 4 and 5 correspond to the observation times $T = 2,\ 18,\ 98$ and 194, respectively. b) and d) show the zoomed graphs a) and c) in the range $1.6 < x < 2.4$.

removes the spurious oscillations. However, despite the same analytical solutions at the selected observation times, the numerical results after the filtering stage are more accurate for short observation times than those for large observation times; see Figs. 2c,d - 4c,d. Because the error in time is very small in these calculations and can be neglected, the difference in the numerical results for different observation times is due to the space-discretization error (which is also related to the dispersion error). This difference is also smaller for higher-order elements compared with lower-order elements (the dispersion error for higher-order elements is smaller).

Fig. 5a,b shows that at the same number 101 of dof, the increase in the order of the spectral elements improves the accuracy; see curves 3-7. At the same number of dof, the linear elements with reduced dispersion are slightly more accurate than the standard 2nd-order elements with the lumped mass matrix; see curves 2 and 4 in Fig. 5a,b. Fig. 5c,d also shows that the linear elements with reduced dispersion and 201 dof are more accurate than the spectral 5th-order elements with 101 dof at time $T = 18$ and are slightly less accurate than the spectral 5th-order elements with 101 dof at the large observation time $T = 194$; see curves 2 and 6. Similarly, the linear elements with reduced dispersion and 301 dof are more accurate than the spectral 10th-order elements with 101 dof at time $T = 18$ and yield practically the same accuracy as the spectral 10th-order elements with 101 dof at the large observation time $T = 194$; see curves 3 and 7.

For the explicit time integration, the computations are very often implemented on the level of elements without the calculation of the global mass and stiffness matrices. Therefore, the computation cost in this case is related to the multiplication of the local effective stiffness matrix by a non-zero vector and is proportional to $n_{dof}^2 n_{el}$ where n_{dof} is the the number of dof for one element and n_{el} is the number of elements. For example, $n_{dof}^2 n_{el} = 11^2 \cdot 10 = 1210$ for the

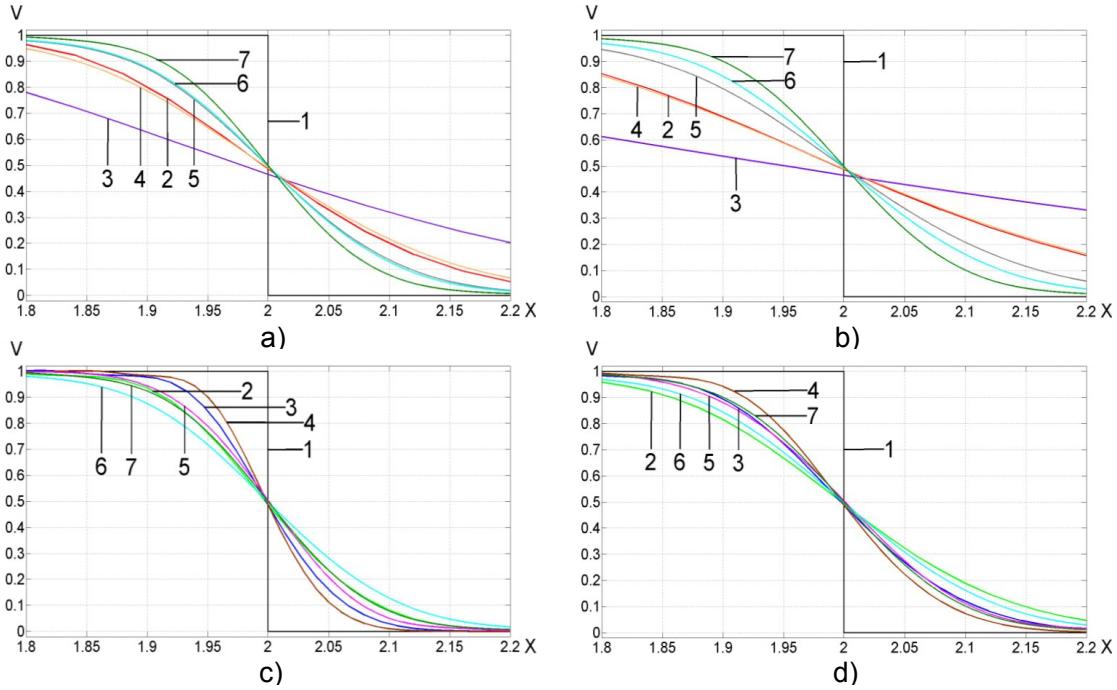


Figure 5: The velocity distribution along the bar in the range $1.8 < x < 2.2$ at the observation times $T = 18$ (a, c) and $T = 194$ (b, d) after post-processing. Curves 1 correspond to the analytical solutions. Curves 2 in (a, b), 2 in (c, d), 3 in (c, d) and 4 in (c, d) correspond to the linear elements with reduced dispersion (the lumped mass matrix) with 101, 201, 301 and 401 dof, respectively. Curves 3 in (a, b), 4 in (a, b), 5 in (a, b), 6 and 7 correspond to the spectral linear, quadratic, 4th-order, 5th-order and 10th-order elements with 101 dof. Curves 5 in (c, d) correspond to the isogeometric 3rd-order elements with 101 dof.

spectral 10th-order elements with 101 dof and $n_{dof}^2 n_{el} = 2^2 \cdot 300 = 1200$ for the linear elements with reduced dispersion and 301 dof; i.e., the computational costs are approximately the same in this case. However, we can also reduce the computational cost for the linear elements with reduced dispersion by the use of the following procedure. Let us combine every 30 linear elements (e.g., staring from the left end of the bar) into one superelement. In this case we will obtain $n_{el} = 10$ superelements. The computation cost for $n_{el} = 10$ superelements is $n_{dof} b n_{el} = 31 \cdot 2 \cdot 10 = 620$ where $n_{dof} = 31$ is the number of dof of one superelement and $b = 2$ is the bandwidth of the effective stiffness matrix of one superelement consisting of 30 linear elements with reduced dispersion. This means that at the same or better accuracy (e.g, see curves 3 and 7 in Fig. 5c,d at the observation times $T = 18$ and $T = 194$), the linear elements with reduced dispersion and 301 dof require less computation time and are more computationally effective compared with the spectral 10th-order elements with 101 dof at times $T = 18$ and $T = 194$.

In order to compare the accuracy of the numerical results obtained with the different space-discretization techniques as well as with the diagonal and non-diagonal mass matrices, Fig. 5c,d also includes the numerical solutions obtained by the isogeometric 3rd-order elements (the non-diagonal mass matrix) with 101 dof. As can be seen, the accuracy of the isogeometric 3rd-order elements at time $T = 18$ and $T = 194$ is close to that of the spectral 10th-order elements at the same number of dof; see curves 5 and 7.

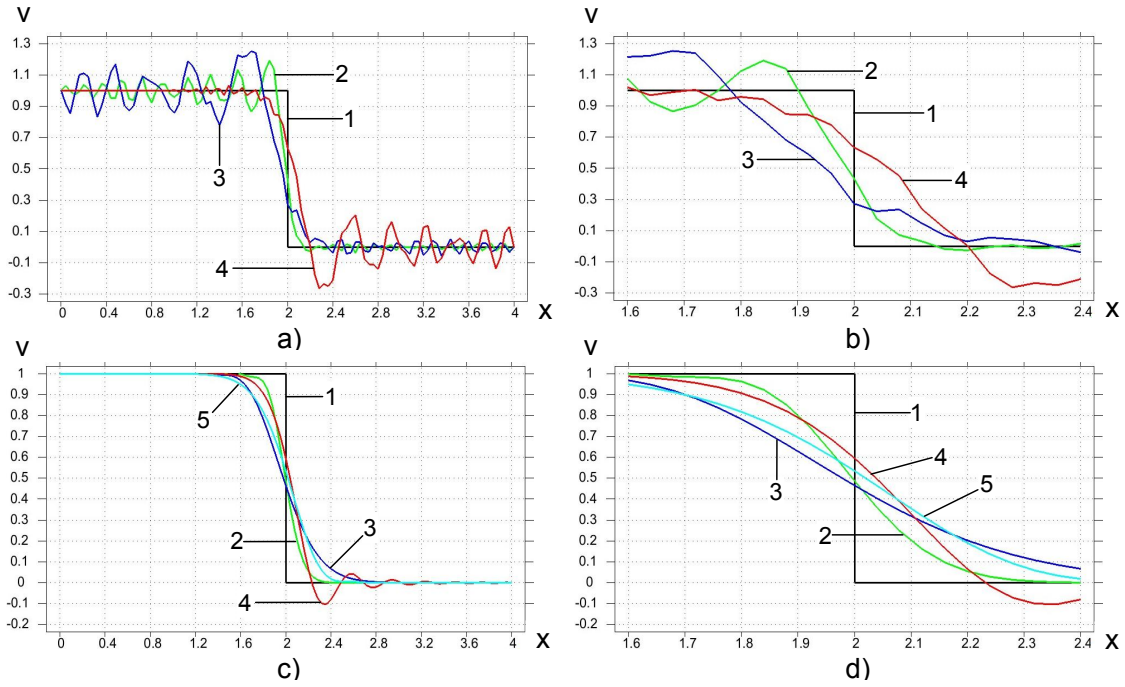


Figure 6: The velocity distribution along the bar at observation time $T = 18$ after basic computations (a, b) and after post-processing (c, d). A uniform mesh with 100 linear 2-node finite elements is used. Curves 1 correspond to the analytical solution. Curves 2 and 3 correspond to the numerical solutions with the averaged ($\gamma = \frac{3-\tau^2}{2}$) and lumped mass matrices (with small time increments $\Delta t = \Delta t^{st}/20$ in basic computations). Curves 4 correspond to the numerical solutions for the averaged ($\gamma = 1.5$) mass matrix and the time increments in basic computations close to the stability limit. b) and d) show the zoomed graphs a) and c) in the range $1.6 < x < 2.4$. Curves 4 and 5 in c) and d) differ by the amount of numerical dissipation used at the filtering stage; see the text.

It is interesting to note that the size of time increments at the filtering stage calculated according to the formulas Eqs. (13) - (14) from the Appendix indirectly defines the range of actual frequencies used in numerical solutions and can be used for the comparison of the accuracy of different space-discretization techniques; see our papers [17, 20, 21]. If at the selected observation time T the time increment at the filtering stage for one space-discretization technique is smaller than that for another space-discretization technique then the former technique yields more accurate results at time T than the latter technique (if time increments are close to each other then the techniques yield approximately the same results). This means that Eqs. (13) - (14) allow the quantitative comparison of the accuracy of different space-discretization techniques. For example, according to Eqs. (13) - (14), we use the following time increments for the filtering stage at time $T = 18$: $\Delta t_1 = 0.0405$, $\Delta t_2 = 0.0235$, $\Delta t_3 = 0.0171$ and $\Delta t_4 = 0.0137$ for the linear elements with reduced dispersion (the diagonal mass matrix) with 101 dof, 201 dof, 301 dof and 410 dof, respectively; $\Delta t_5 = 0.0448$ for the standard quadratic elements (the diagonal mass matrix) with 101 dof; $\Delta t_6 = 0.0222$ for the spectral 10th-order elements (the diagonal mass matrix) with 101 dof; $\Delta t_7 = 0.0188$ for the isogeometric 3rd-order elements (the consistent mass matrix) with 101 dof. At the large observation time $T = 194$, we have the following time increments for the filtering stage: $\Delta t_1 = 0.0679$, $\Delta t_2 = 0.0395$, $\Delta t_3 = 0.0288$ and $\Delta t_4 = 0.0230$ for the linear elements with reduced dispersion (the diagonal mass matrix) with 101 dof, 201 dof, 301 dof and 410 dof, respectively; $\Delta t_5 = 0.0695$ for the standard quadratic elements (the diagonal mass matrix) with 101 dof; $\Delta t_6 = 0.0266$ for the spectral 10th-order elements (the diagonal mass matrix) with 101 dof; $\Delta t_7 = 0.0269$ for the isogeometric 3rd-order

elements (the consistent mass matrix) with 101 dof. Comparing these time increments at the same observation time, we can describe the accuracy of the numerical results discussed above. For example, at times $T = 18$ and $T = 194$, the time increments Δt_6 and Δt_7 are close to each other and the corresponding space-discretization techniques yield approximately the same accuracy; see curves 5 and 7 in Fig. 5c,d (similar results we have for the time increments Δt_1 and Δt_5; see curves 2 and 4 in Fig. 5a,b). We also have that $\Delta t_3 < \Delta t_6$ at time $T = 18$ and $\Delta t_3 > \Delta t_6$ at time $T = 18$ (see curves 3 and 7 in Fig. 5c,d and the comparison of the spectral elements and the elements with reduced dispersion described above in this section). It can be also seen that Δt_4 has the smallest value among all presented time increments and the corresponding linear elements with reduced dispersion and 401 dof yield the most accurate results; see curves 4 in Fig. 5c,d.

In Fig. 6, we have also analyzed the numerical results for the averaged mass matrix with $\gamma = \frac{3}{2}$ (as suggested in [26]) and the explicit central difference method with time increments close to the stability limit Δt^{st} at basic computations. As we can see, in this case the results after basic computations (curve 4 in Fig. 6a,b) are less accurate than those described by curve 2 in Fig. 6a,b. If we filter these results (curve 4 in Fig. 6a,b) with the amount of numerical dissipation (time increments) used for curve 2 in Fig. 6a,b, then spurious oscillations remain after the filtering stage (curve 4 in Fig. 6c,d). If we use a sufficient amount of numerical dissipation at the filtering stage then the results (curve 5 in Fig. 6c,d) are close to curve 3 in Fig. 6c,d. This means that the approach suggested in [26]) for the averaged mass matrix does not improve the dispersion error and the accuracy of numerical results if relative large time increments (close to the stability limit) are used in calculations. However, at small time increments $\Delta t \approx 0$, parameter $\tau \approx 0$ is also small and $\gamma = \frac{3-\tau^2}{2} \approx \frac{3}{2}$; i.e., the results for $\gamma = \frac{3}{2}$ will coincide with curve 2 in Fig. 6 at small time increments in basic computations.

3.2 2-D impact of an elastic bar against a rigid wall (plane strain)

This problem is a more general plane strain formulation of the 1-D impact problem considered in Section 3.1; see Fig. 7a. In contrast to the 1-D impact problem, compressional and shear elastic waves propagate in the 2-D case.

A bar of length $L = 4$ and height $2H = 2$ is considered. Due to symmetry, the problem is solved for a half of the bar $ABCD$ where AD is the axis of symmetry. Young's modulus is chosen to be $E = 1$, the density to be $\rho = 1$ and Poisson's ratio to be $\nu = 0.3$. The following boundary conditions are applied: along boundary AB $u_n = t$ (it corresponds to velocity $v_n = v_0 = 1$) and $\tau_n = 0$; along boundaries BC and CD $\sigma_n = 0$ and $\tau_n = 0$; along boundary AD $u_n = 0$ and $\tau_n = 0$, where u_n, v_n, and σ_n are the normal displacements, velocities and the tractive forces, respectively; τ_n are the tangential tractive forces. Initial displacements and velocities are zero; i.e., $u(x, y, 0) = v(x, y, 0) = 0$. The observation time is chosen to be $T = 13$. During this time the velocity pulse travels within the bar with multiple reflections from the ends of the bar and from the external surface BC.

The problem is solved on uniform meshes with $40 \times 160 = 6400$ and $120 \times 480 = 57600$ linear four-node quadrilateral finite elements with the modified integration rule for the mass and stiffness matrices ($\alpha_M = \sqrt{\frac{4-\tau^2}{3}}$ and $\alpha_K = \sqrt{\frac{4(2\nu-1)}{3(4\nu-3)}}$) and with the lumped and averaged ($\gamma = \frac{3-\tau^2}{2}$) mass matrices. In order to study the effect of time increments at basic calculations on the accuracy of numerical results, we will use time increments $\Delta t \approx \Delta t^{st}$ close to the stability limit Δt^{st} and very small time increments $\Delta t = \Delta t^{st}/20$).

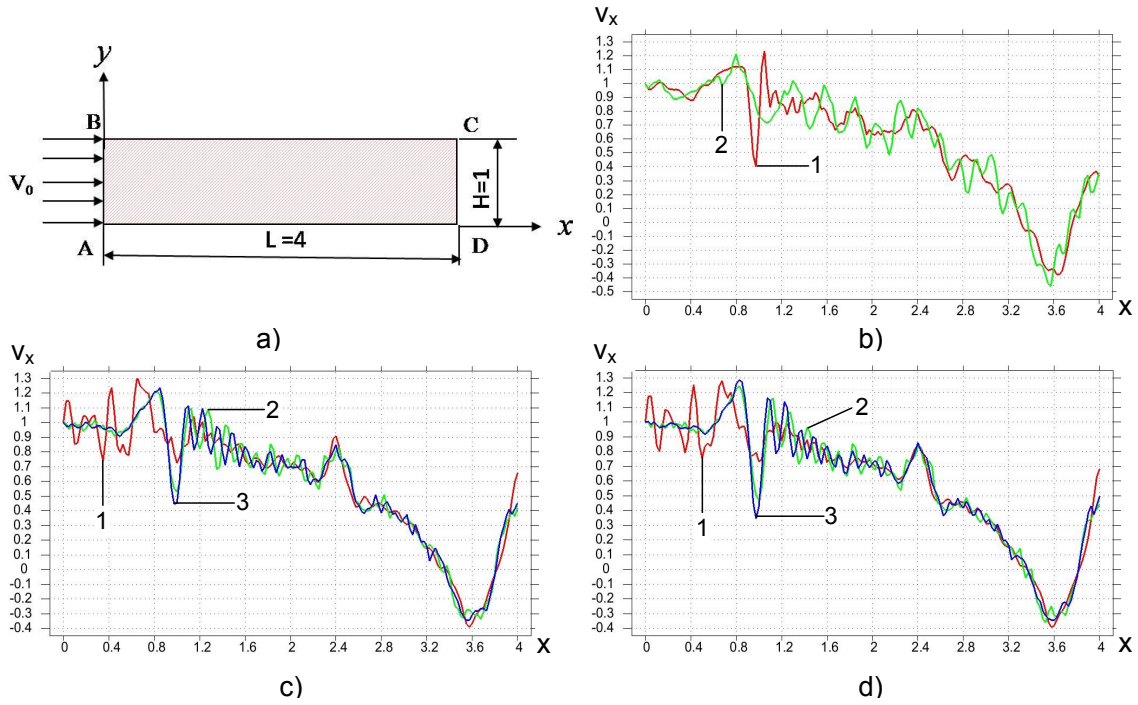


Figure 7: A 2-D plane strain impact problem (a). The axial velocity distribution along the axis of symmetry AD at observation time $T = 13$. The results are shown after basic computations obtained by the explicit central difference method with the lumped mass matrix (b), with the modified integration rule (c), and with the averaged mass matrix (d). Curves 1 and 2 correspond to the numerical solutions obtained with the time increments Δt^{st} and $\Delta t^{st}/20$, respectively. Curves 3 correspond to the numerical solutions (from our paper [20]) obtained by the implicit time-integration method with the modified integration rule (c) and the averaged mass matrix (d). A uniform mesh with $40 \times 160 = 6400$ linear 4-node finite elements is used.

Figs. 7 - 8 show the distribution of the axial velocity along the axis of symmetry AD at observation time $T = 13$ after basic computations (Fig. 7) and after the filtering stage (Fig. 8). Similar to the previous 1-D impact problem, the numerical results after basic computations with the lumped stiffness matrix and the formulations with reduced numerical dispersion contain spurious oscillations at very small time increments $\Delta t = \Delta t^{st}/20 = \frac{dx}{20c_1}$; see curves 2 in Fig. 7. However, in contrast to the 1-D impact problem, the spurious oscillations and the dispersion error at basic computations do not disappear at the time increments close to the stability limit; see curves 1 in Fig. 7. It also can be seen from Fig. 7 (see curves 1 and 2) that the results after basic computation for the time increments close to the stability limit and for very small time increments are different for all methods. We should also note that at very small time increments, the numerical solutions for the linear elements with reduced dispersion obtained with the explicit central difference method (curves 2 in Fig. 7c,d) and with the implicit trapezoidal rule (see our paper [17] as well as curves 3 in Fig. 7c,d) are close to each other. However, it is difficult to compare the accuracy of different approaches after basic computations due to large spurious oscillations.

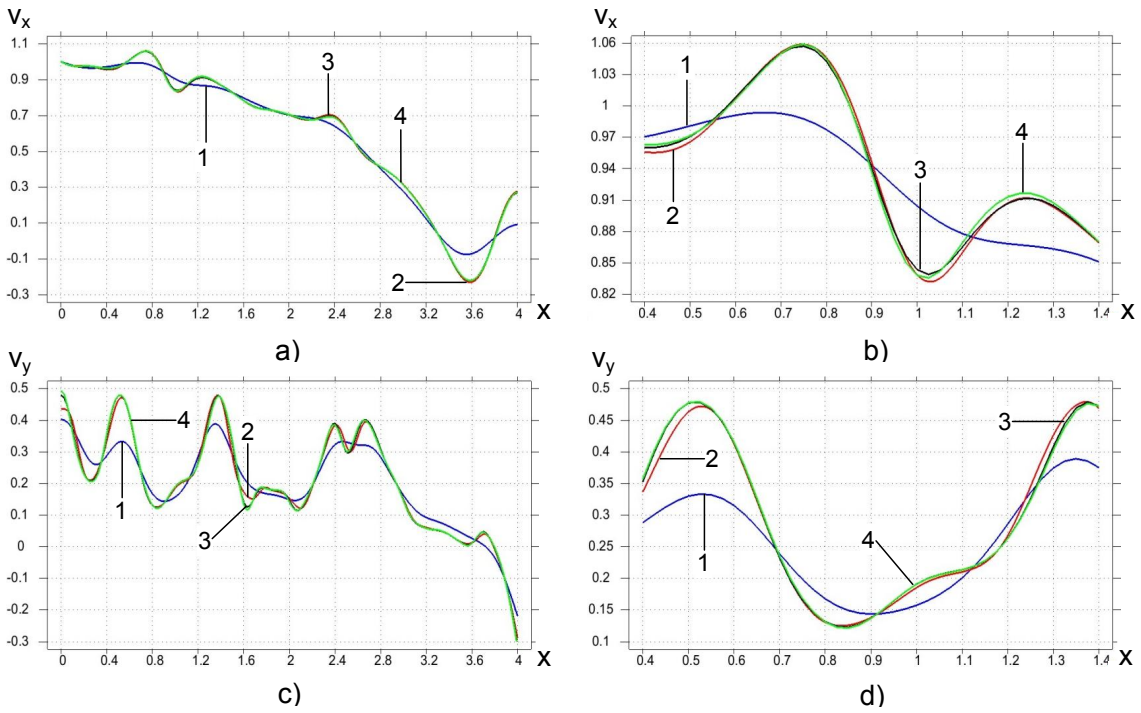


Figure 8: The axial velocity distribution v_x along the axis of symmetry AD (a, b) and the transverse velocity distribution v_y along the external surface BC (c, d) at observation time $T = 13$ for the Poisson's ratio $\nu = 0.3$. The results are shown after the filtering of the solutions at basic computations obtained by the explicit central difference method with the lumped mass matrix (curves 1 and 2), with the modified integration rule (curve 3), and with the averaged mass matrix (curve 4). Small time increments $\Delta t^{st}/20$ are used at basic computations (see Fig. 7). Uniform meshes with $40 \times 160 = 6400$ (curves 1, 3 and 4) and $120 \times 480 = 57600$ (curve 2) linear elements are used. b) and d) show the zoomed graphs a) and c) in the range $0.4 < x < 1.4$.

After filtering spurious oscillations at the filtering stage, the solutions at basic computations obtained by the explicit central difference method at very small time increments $\Delta t^{st}/20$ with the modified integration rule (curves 3 in Fig. 8) and with the averaged mass matrix (curves 4 in Fig. 8) are close to each other. The results in Fig. 8 show that despite the impact along the x-axis elastic waves propagate in all directions and the magnitudes of the transverse velocity v_y are comparable with those for the axial velocity v_x; i.e., a general case of propagation of elastic waves occurs for the considered problem. As can be seen from Fig. 8, after the filtering stage the results obtained by the explicit central difference method at very small time increments $\Delta t^{st}/20$ and the lumped mass matrix (curves 1) are much less accurate than those obtained with the elements with reduced dispersion (curves 3 and 4). The results obtained by the standard approach with the explicit central difference method on a fine mesh with $120 \times 480 = 57600$ linear elements (curves 2 in Fig. 8) show that at the selected observation time, the elements with reduced dispersion reduce the number of degrees of freedom by a factor of 9 compared with those for the standard approach at the same accuracy (compare curves 3 or 4 for a mesh with $40 \times 160 = 6400$ linear elements and curves 2 for a mesh with $120 \times 480 = 57600$ linear elements in Fig. 8).

Remark. Similar to the 1-D case in Section 3.1 and the results reported in our paper [17] for implicit time-integration methods, the size of the time increments calculated by Eqs. (13) - (15) for the filtering stage allows the quantitative estimation of the advantage of the modified integration rule (or the averaged mass matrix) technique compared with the standard lumped mass matrix. For example, for a uniform mesh with $40 \times 160 = 6400$ linear finite elements and

the modified integration rule (or the averaged mass matrix), the size of the time increments at the filtering stage is $\Delta t_1 = 0.038204$ according to Eqs. (13) - (15). For a uniform mesh with $120 \times 480 = 57600$ linear finite elements and the lumped mass matrix, the size of the time increments at the filtering stage is $\Delta t_2 = 0.036717$ according to Eqs. (13) - (15). Because Δt_2 is close to Δt_1, then curves 2 and 3 (or 4) in Fig. 8 are close to each other. We should also mention that with the increase in the observation time, the effectiveness of the elements with reduced dispersion increases compared with that for the standard approach; i.e., according to Eqs. (13) - (15), for the same accuracy of numerical results, the ratio $\frac{N_{FE}^{lump}}{N_{FE}^{red}}$ is an increasing function of the observation time (N_{FE}^{lump} and N_{FE}^{red} are the numbers of finite elements used with the standard formulation and with the formulations with reduced dispersion).

4 CONCLUSIONS

- The numerical techniques with reduced dispersion based on explicit time-integration methods significantly reduce the number of degrees of freedom compared with the standard finite elements at the same accuracy (e.g., by a factor of 3 in the 1-D case and 9 in the 2-D case and 27 in the 3-D case. This leads to a huge reduction in the computation time;

- The two-stage time-integration technique recently suggested in our papers [19, 20, 22] yields accurate numerical results for elastodynamics problems solved with different space-discretization approaches such as the linear elements with reduced dispersion, the spectral low- and high-order elements, the isogeometric elements;

- Except the known case of of the linear elements with the lumped mass matrix, all other space-discretization techniques considered in the paper require small time-increments for time integration at the stage of basic computations;

- The comparison of the space-discretization techniques based on the diagonal mass matrices (used with explicit time-integration methods) show that at the same number of dof, the spectral high-oder elements yield more accurate results compared with the standard linear and quadratic finite elements and the linear elements with reduced dispersion. However, when we compare the computational costs at the same accuracy, the numerical results show the the linear elements with reduced dispersion are more computationally effective than the spectral high-order elements. We should also mention that compared with the spectral 10th-order elements,the computational effectiveness of the linear elements with reduced dispersion decreases with the increase in the observation time;

- It is interesting to note that the size of time increments at the filtering stage of the two-stage time-integration technique (this size is calculated according to Eqs. (13) - (15) from the Appendix) defines the range of actual frequencies used in numerical solutions and can serve as a quantitative measure for the comparison and prediction of the accuracy and the computational effectiveness of different space-discretization techniques.

ACKNOWLEDGMENTS

The research has been supported in part by the Air Force Office of Scientific Research (contract FA9550-12-1-0324) and by Texas Tech University. The technical assistance of P. Duc is appreciated.

APPENDIX. THE TWO-STAGE TIME-INTEGRATION TECHNIQUE WITH FILTERING SPURIOUS OSCILLATIONS (see [19, 22, 20])

In order to filter spurious high-frequency oscillations, numerical dissipation (or artificial damping) is usually introduced for the time integration of Eq. (1). As we showed in our paper [20], the use of a time-integration method with numerical dissipation (or artificial damping) at each time increment leads to inaccurate numerical results for low frequencies as well, especially for a long-term integration. It is also unclear in this case how to select the amount numerical dissipation and the range of high frequencies to be filtered.

To resolve these issues, we have developed the two-stage time-integration technique (see [19, 22, 20]) with the stage of basic computations and the filtering stage. This technique is based on the fact that for linear elastodynamics problems, there is no necessity to filter spurious oscillations at each time increment because the errors in high frequencies do not affect the accuracy of low frequencies during time integration; see [20]. In the current paper, we use the standard explicit central-difference time-integration method (without numerical dissipation or artificial viscosity) at basic computations in order to obtain an accurate solution of the semi-discrete elastodynamics problem, Eq. (1) (this solution contains spurious high-frequency oscillations). We should mention that other known explicit time-integration methods can be also used for basic computations (however, in this case the dispersion analysis should be modified for the corresponding explicit time-integration method). For the filtering of spurious oscillations, the implicit TCG method with large numerical dissipation developed in [20] is used at the filtering stage. For all elastodynamics problem, we use $N = 10$ uniform time increments (5 positive plus 5 negative time increments) at the filtering stage. This means that there is no real time integration at the filtering stage (the sum of 10 time increments used at the filtering stage is zero). As shown in [20], this procedure is equivalent to the multiplication of each velocity and displacement of the uncoupled system of the semi-discrete equations by a factor of $\left(\frac{(3+m)^2+\Omega^2}{(3+m)^2+(2+m)^2\Omega^2}\right)^5$ (where $\Omega = \omega_j \Delta t$ and ω_j are the eigen-frequencies of the semi-discrete system, Δt is the time increment as well as $m = 15$ is used) and does not require the modal decomposition and the calculation of eigen-frequencies. As can be seen, this factor is close to zero for large Ω and is close to unity for small Ω. The size Δt of time increments at the filtering stage indirectly defines the amount of numerical dissipation and the range of spurious oscillations and is calculated according to the following formulas (for uniform meshes)

$$\Delta t = \alpha(\frac{c_o T}{dx}) \frac{dx \Omega_{0.1}(N)}{c_o}\,, \tag{13}$$

with

$$\alpha(\frac{c_o T}{dx}) = a_1 \left(\frac{c_o T}{dx}\right)^{a_2} \tag{14}$$

in the 1-D case and

$$\Delta t = \max_{m,j} \left[\alpha(\frac{c_m T}{dx_j}) \frac{dx_j}{c_m}\right] \Omega_{0.1}(N) = \max_{m,j} \left[\frac{dx_j}{c_m}\right]^{1-a_2} a_1\, T^{a_2}\, \Omega_{0.1}(N)$$
$$= \left[\frac{\max\limits_j dx_j}{\min\limits_m c_m}\right]^{1-a_2} a_1\, T^{a_2}\, \Omega_{0.1}(N) = \left[\frac{dx_{max}}{c_2}\right]^{1-a_2} a_1\, T^{a_2}\, \Omega_{0.1}(N)\,, \tag{15}$$

in the 2-D and 3-D cases (see our papers [22, 20]). Here, $c_o = \sqrt{\frac{E}{\rho}}$ is the wave velocity; dx is the size of a finite element in the 1-D case; T is the observation time; $c_2 = \min\limits_m c_m$ $(i = 1, 2)$

is the minimum value between the velocities of the compressional wave c_1 and the shear wave c_2; $dx_{max} = \max\limits_j dx_j$ is the maximum dimension of finite elements along the axes x_j ($j = 1, 2$ for 2-D problems and $j = 1, 2, 3$ for 3-D problems); $\Omega_{0.1}(N = 10) = 0.81$ for the TCG method with $N = 10$ time increments. Eq. (15) is based on Eqs. (13) and (14) with the selection of the maximum size of a time increment with respect to the compressional and shear waves, and the maximum size of a finite element along the coordinate axes. Using the calibration procedure described in [22], we found the following coefficients a_1 and a_2 for linear elements with the averaged ($\gamma = \frac{3-\tau^2}{2}$) mass matrix or the modified integration rule: $a_1 = 0.3296$ and $a_2 = 0.218$ for the explicit time-integration method as in the current paper and $a_1 = 0.2942$ and $a_2 = 0.2104$ for the implicit time-integration method as in our paper [17]; for the standard explicit time integration with linear elements and the lumped mass matrix: $a_1 = 0.3342$ and $a_2 = 0.3363$ (see our paper [16]). The coefficients a_1 and a_2 for the spectral and isogeometric elements are presented in our paper [15]. These coefficients a_1 and a_2 are calibrated in the 1-D case for the filtering of numerical results obtained at basic computations with very small time increments. In order to use the same coefficients a_1 and a_2 in the 2-D and 3-D cases, small time increments should be used at basic computations for the 2-D and 3-D problems. We should also mention that the filtering stage can be applied in the beginning of calculations as a pre-processor, in the end of calculations as a post-processor or at some intermediate time (see [17, 18, 20, 16] for numerous examples of the application of the two-stage time-integration technique).

REFERENCES

[1] I. Babuska, F. Ihlenburg, T. Strouboulis, and S. K. Gangaraj. Posteriori error estimation for finite element solutions of helmholtz' equation - part ii: estimation of the pollution error. *International Journal for Numerical Methods in Engineering*, 40(21):3883–3900, 1997.

[2] I. Babuska, T. Strouboulis, S. K. Gangaraj, and C. S. Upadhyay. Pollution error in the h-version of the finite element method and the local quality of the recovered derivatives. *Computer Methods in Applied Mechanics and Engineering*, 140(1-2):1–37, 1997.

[3] K. J. Bathe. *Finite element procedures*. Prentice-Hall Inc., Upper Saddle River, New Jersey, 1996.

[4] D. J. Benson, Y. Bazilevs, E. De Luycker, M.-C. Hsu, M. Scott, T. J. R. Hughes, and T. Belytschko. A generalized finite element formulation for arbitrary basis functions: From isogeometric analysis to xfem. *International Journal for Numerical Methods in Engineering*, 83(6):765–785, 2010.

[5] D.J. Benson, Y. Bazilevs, M.-C. Hsu, and T.J.R. Hughes. A large deformation, rotation-free, isogeometric shell. *Computer Methods in Applied Mechanics and Engineering*, 200(1316):1367 – 1378, 2011.

[6] F. Casadei, E. Gabellini, G. Fotia, F. Maggio, and A. Quarteroni. A mortar spectral/finite element method for complex 2d and 3d elastodynamic problems. *Computer Methods in Applied Mechanics and Engineering*, 191(45):5119–5148, 2002.

[7] H. P. Cherukuri. Dispersion analysis of numerical approximations to plane wave motions in an isotropic elastic solid. *Computational Mechanics*, 25(4):317–328, 2000.

[8] J.A. Cottrell, A. Reali, Y. Bazilevs, and T.J.R. Hughes. Isogeometric analysis of structural vibrations. *Computer Methods in Applied Mechanics and Engineering*, 195(41-43):5257 – 5296, 2006.

[9] W. Dauksher and A. F. Emery. Solution of elastostatic and elastodynamic problems with chebyshev spectral finite elements. *Computer Methods in Applied Mechanics and Engineering*, 188(1):217–233, 2000.

[10] A. Deraemaeker, I. Babuska, and P. Bouillard. Dispersion and pollution of the fem solution for the helmholtz equation in one, two and three dimensions. *International Journal for Numerical Methods in Engineering*, 46(4):471–499, 1999.

[11] D. Gabriel, J. Plesek, R. Kolman, , and F. Vales. Dispersion of elastic waves in the contactimpact problem of a long cylinder. *Journal of Computational and Applied Mathematics*, 234:1930–1936, 2010.

[12] Z. C. He, A. G. Cheng, G. Y. Zhang, Z. H. Zhong, and G. R. Liu. Dispersion error reduction for acoustic problems using the edge-based smoothed finite element method (esfem). *International Journal for Numerical Methods in Engineering*, 86(11):1322–1338, 2011.

[13] T. J. R Hughes. *The Finite Element Method: Linear Static and Dynamic Finite Element Analysis*. Prentice- Hall, Englewood Cliffs, NJ,, 1987.

[14] T.J.R. Hughes, A. Reali, and G. Sangalli. Duality and unified analysis of discrete approximations in structural dynamics and wave propagation: Comparison of p-method finite elements with k-method nurbs. *Computer Methods in Applied Mechanics and Engineering*, 197(49-50):4104 – 4124, 2008.

[15] A. Idesman, P. Duc, J. R. Foley, and M. Schmidt. The comparative study of different orders of the standard, spectral and isogeometric finite elements as well as the linear elements with reduced dispersion used for the solution of elastodynamics problems. *Computational Mechanics*, 2013 (submitted).

[16] A. Idesman, M. Schmidt, and J. R. Foley. Accurate 3-d finite element simulation of elastic wave propagation with the combination of explicit and implicit time-integration methods. *Wave Motion*, 48:625–633, 2011.

[17] A. Idesman, M. Schmidt, and J. R. Foley. Accurate finite element modeling of linear elastodynamics problems with the reduced dispersion error. *Computational Mechanics*, 47:555–572, 2011.

[18] A. Idesman, K. Subramanian, M. Schmidt, J. R. Foley, Y. Tu, and R. L. Sierakowski. Finite element simulation of wave propagation in an axisymmetric bar. *Journal of Sound and Vibration*, 329:2851–2872, 2010.

[19] A. V. Idesman. A new high-order accurate continuous galerkin method for linear elastodynamics problems. *Computational Mechanics*, 40:261–279, 2007.

[20] A. V. Idesman. Accurate time integration of linear elastodynamics problems. *Computer Modeling in Engineering & Sciences*, 71(2):111–148, 2011.

[21] A. V. Idesman and D. Pham. Finite element modeling of linear elastodynamics problems with explicit time-integration methods and linear elements with the reduced dispersion error. *Computer Methods in Applied Mechanics and Engineering*, pages 1–33, 2013 (submitted).

[22] A. V. Idesman, H. Samajder, E. Aulisa, and P. Seshaiyer. Benchmark problems for wave propagation in elastic materials. *Computational Mechanics*, 43(6):797–814, 2009.

[23] D. Komatitsch, C. Barnes, and J. Tromp. Simulation of anisotropic wave propagation based upon a spectral element method. *Geophysics*, 65(4):1251–1260, 2000.

[24] Dimitri Komatitsch and Jean-Pierre Vilotte. Spectral element method: an efficient tool to simulate the seismic response of 2d and 3d geological structures. *Bulletin of the Seismological Society of America*, 88(2):368 – 392, 1998.

[25] Dimitri Komatitsch, Jean-Pierre Vilotte, Rossana Vai, JOSE M. Castillo-Covarrubias, and Francisco J. Sanchez-Sesma. The spectral element method for elastic wave equations - application to 2-d and 3-d seismic problems. *International Journal for Numerical Methods in Engineering*, 45(9):1139 – 1164, 1999.

[26] S. Krenk. Dispersion-corrected explicit integration of the wave equation. *Computer Methods in Applied Mechanics and Engineering*, 191:975–987, 2001.

[27] K. J. Marfurt. Accuracy of finite difference and finite element modeling of the scalar and elastic wave equation. *Geophysics*, 49:533–549, 1984.

[28] R. Mullen and T. Belytschko. Dispersion analysis of finite element semidiscretizations of the two-dimensional wave equation. *International Journal for Numerical Methods in Engineering*, 18:11–29, 1982.

[29] C. Pozrikidis. *Introduction to Finite and Spectral Element Methods Using MATLAB*. CRC Press, 2005.

[30] G. Seriani and S. P. Oliveira. Optimal blended spectral-element operators for acoustic wave modeling. *Geophysics*, 72(5):95–106, 2007.

[31] G. Seriani and S. P. Oliveira. Dispersion analysis of spectral element methods for elastic wave propagation. *Wave Motion*, 45(6):729–744, 2008.

[32] B. Yue and M. N. Guddati. Dispersion-reducing finite elements for transient acoustics. *Journal of the Acoustical Society of America*, 118(4):2132–2141, 2005.

[33] O. C. Zienkiewicz and R. L. Taylor. *The Finite Element Method*. Butterworth-Heinemann, Oxford, UK, 2000.

COMPDYN 2013
4th ECCOMAS Thematic Conference on
Computational Methods in Structural Dynamics and Earthquake Engineering
M. Papadrakakis, V. Papadopoulos, V. Plevris (eds.)
Kos Island, Greece, 12–14 June 2013

APPLICATIONS OF VARIATIONALLY CONSISTENT SELECTIVE MASS SCALING IN EXPLICIT DYNAMICS

Anton Tkachuk[1], **Manfred Bischoff**

[1] Institute of Structural Mechanics, University of Stuttgart
Pfaffenwaldring 7, 70569 Stuttgart, Germany
e-mail: {tkachuk,bischoff}@ibb.uni-stuttgart.de

Keywords: Selective mass scaling, Hamilton's principle, explicit dynamics, hybrid-mixed.

Abstract. *The aim of Selective Mass Scaling (SMS) in context of non-linear structural mechanics is to increase the critical time-step for explicit time integration without substantial loss in accuracy in the lower modes. The Conventional Mass Scaling (CMS) adds artificial mass only to diagonal terms of the lumped mass matrix and thus preserves diagonal format of mass matrix. It is usually applied in little number of small or stiff elements, like spot-welds in car crash, whose high eigenfrequencies limit time-step. However, translational and rotational inertia of the structure increases, which may cause non-physical phenomena. SMS technique adds artificial terms both to diagonal and non-diagonal terms, which results in non-diagonal mass matrix, but at least allows preservation of translational mass. Thus SMS can be used uniformly in domain with less non-physical artifacts. The previous works on SMS rely on algebraically constructed mass scaling matrices or stiffness proportional mass scaling. These approaches provide very small choice of mass scaling templates and they lack rigorous variational formulation. The goal of this paper is to develop variational basis for SMS with consistent discretization of inertial term and to assess efficiency of the proposed approach.*

1 INTRODUCTION

Scaling of inertia for explicit time integration is a common procedure since 70s. For beam and shell elements diagonal terms of rotational inertia are scaled using formulas given in [6, 2]. This allows to increase the critical step of these elements up to corresponding critical step of rod or membrane element. The Conventional Mass Scaling for translational degrees of freedom is described in manuals of *LS-Dyna*, *Radioss* etc. Application of CMS is limited to little number of small or stiff elements with overall increase of mass of model up to 1-3%.

Selective mass scaling was proposed by group of Lars Olovsson [8, 10] and it aimed increasing of stable time-step for explicit integration of solid-based shells and eight-node hexahedral elements. In combination with an iterative solver for acceleration (see [9]) it proved to be efficient for some applications such as deep drawing of metal sheets and drop tests [3], dynamics of solid-shell modeled structures [4].

The original idea of paper [10] relies on following *algebraic* construction of scaled mass matrix of individual element $\mathbf{m}^\circ$

$$\begin{aligned} \mathbf{m}^\circ &= \mathbf{m}_e + \boldsymbol{\lambda}^\circ \\ \boldsymbol{\lambda}^\circ &= \triangle m \left(\mathbf{I} - \sum_i \mathbf{e}_i^T \mathbf{e}_i \right) \end{aligned} \tag{1}$$

where $\mathbf{m}_e$ and $\boldsymbol{\lambda}^\circ$ are lumped mass matrix (LMM) and mass augmentation (MA), $\triangle m$ is artificially added mass and $\mathbf{e}_i$ is some set of *rigid body modes*. Initially it was proposed to include only translational rigid body modes [10]. Later implementation also included rigid body rotation [3]. Hence, the properties of the algebraic SMS are defined by linear hull of vectors $\mathbf{e}_i$.

SMS has following effect on structural behavior. The critical time-step roughly increases by factor $\sqrt{1+\beta}$ with β being ratio of added mass to element mass $\triangle m/m$, see [9]. The eigenmodes of the structure are distorted and the order of the modes is changed. If only translational rigid body modes are taken then rotary inertia of the structure is excessive. If all rigid body modes are taken then the rotary inertia is preserved, but the scaled mass matrix obtains coupled terms between inertia in x-, y- and z-directions [3]. Condition number of the global mass matrix $\mathbf{M}^\circ$ increases by factor approximately $1+2\beta$ and number of iterations needed for solution of the system $\mathbf{Ma} = \mathbf{f}$ grows proportionally to $\sqrt{1+2\beta}$.

Variationally based method for SMS was proposed recently in [11]. The starting point of the proposed approach is a new parametrized variational principle of elasto-dynamics, which can be interpreted as penalized Hamiltons principle. It uses independent variables for displacement, velocity and momentum (three-field formulation). The penalized Hamiltons principle imposes relations between velocity, momenta and displacements via penalty method. Consistent discretization of the latter principle results in a parametric family of mass matrices. In this way the translational inertia, center of gravity and polar momenta of individual elements may be preserved, which guarantees convergence of the method with mesh refinement. Thus, the distinctive feature of the method is variational rigorousness, mass augmentation is prescribed via ansatz spaces and more accurate results for bending dominated problems can be obtained.

Variational mass scaling in paper [11] considered general three-field formulation for linear elasto-dynamics and only three-node triangle, four-node quadrilateral and eight-node hexahedral elements. Here, variational mass scaling based on simplified two-field formulation is discussed. The examples are focused on nine-node and eight-node quadrilateral elements. For the eight-node quadrilateral element no good LMM is available [12, 7], which makes SMS for the

element very promising. Results for transient and eigenfrequency benchmarks are given and discussed.

2 TWO-FIELD VARIATIONAL FORMULATION OF ELASTO-DYNAMICS

In this section the modified variational formulation is derived. Consider the strong form of initial value problem for finite strain dynamics

$$\begin{cases} \rho_0 \ddot{\mathbf{u}} = \mathrm{DIV}\,\mathbf{P} + \rho_0 \hat{\mathbf{b}} & \text{in } (0, t_{\mathrm{end}}] \times \mathcal{B} \\ \mathbf{F} = \mathbf{I} + \dfrac{\partial \mathbf{u}}{\partial \mathbf{X}} & \text{in } (0, t_{\mathrm{end}}] \times \mathcal{B} \\ \mathbf{P} = \mathbf{P}(\mathbf{F}) & \text{in } (0, t_{\mathrm{end}}] \times \mathcal{B} \\ \mathbf{u}(t=0) = \mathbf{u}_0 & \text{in } \mathcal{B} \\ \dot{\mathbf{u}}(t=0) = \mathbf{v}_0 & \text{in } \mathcal{B} \\ \mathbf{u} = \mathbf{0} & \text{in } (0, t_{\mathrm{end}}] \times \partial\mathcal{B}_u \\ \mathbf{P}\mathbf{n} = \hat{\mathbf{t}} & \text{in } (0, t_{\mathrm{end}}] \times \partial\mathcal{B}_\sigma, \end{cases} \tag{2}$$

where $\mathbf{u}$ and $\mathbf{F}$ are displacements vector and deformation gradient, $\mathbf{P}$ is 1^{st} Piola-Kirchhoff stress tensor, which can be found from a given constitutive equation $\mathbf{P}(\mathbf{F})$, ρ_0 and $\hat{\mathbf{b}}$ are an initial material density and a body load, respectively, $\mathbf{u}_0$ and $\mathbf{v}_0$ are initial displacement and velocity, $\partial\mathcal{B}_u$ is part of surface with prescribed zero displacement and $\hat{\mathbf{t}}$ is prescribed traction on part of surface $\partial\mathcal{B}_\sigma$. The problem is stated with respect to the actual configuration of the body $\mathcal{B}$ within a given time interval $(0, t_{\mathrm{end}}]$.

Following the standard derivation (see [2]), the virtual work principle can be written as

$$\begin{aligned} &\delta W^{\mathrm{int}}(\mathbf{u}, \delta u) - \delta W^{\mathrm{ext}}(\mathbf{u}, \delta u) + \delta W^{\mathrm{kin}}(\mathbf{u}, \delta u) = 0 \\ &\delta W^{\mathrm{int}}(\mathbf{u}, \delta u) = \int_{\mathcal{B}_0} \delta\mathbf{F} : \mathbf{P}\, \mathrm{d}V \\ &\delta W^{\mathrm{ext}}(\mathbf{u}, \delta u) = \int_{\mathcal{B}_0} \delta\mathbf{u} \cdot \rho_0 \hat{\mathbf{b}}\, \mathrm{d}V + \int_{\partial\mathcal{B}_{\sigma,0}} \delta\mathbf{u} \cdot \hat{\mathbf{t}}\, \mathrm{d}A \\ &\delta W^{\mathrm{kin}}(\mathbf{u}, \delta u) = \int_{\mathcal{B}_0} \delta\mathbf{u} \cdot \rho_0 \ddot{\mathbf{u}}\, \mathrm{d}V, \end{aligned} \tag{3}$$

where $\delta\mathbf{u}$ is kinematically admissible displacement, $\mathcal{B}_0$ and $\partial\mathcal{B}_{\sigma,0}$ are reference domain and pull-back to reference configuration of traction boundary.

We propose to modify the weak statement(3) by introduction of independent variable for velocity $\mathbf{v}$. The kinematic equation between velocity and displacement $\dot{\mathbf{u}} = \mathbf{v}$ can be imposed weakly in modified expression for work of d'Alembert forces

$$\delta W^{\mathrm{kin},\circ}(\mathbf{u}, \delta\mathbf{u}, \mathbf{v}, \delta\mathbf{v}) = \int_{\mathcal{B}_0} \delta\mathbf{u} \cdot \left[(1 + C_1)\rho_0 \ddot{\mathbf{u}} - C_1 \dot{\mathbf{v}}\right] \mathrm{d}V - \int_{\mathcal{B}_0} \delta\mathbf{v} \cdot \left[\rho_0 C_1 (\dot{\mathbf{u}} - \mathbf{v})\right] \mathrm{d}V. \tag{4}$$

Here constant C_1 plays a role of penalty factor, see [11].

Substitution of the latter expression in (3) instead of δW^{kin} leads to formulation used herein. Note, that if internal and external forces possess potentials $\delta\Pi = \delta W^{\mathrm{int}} - \delta W^{\mathrm{ext}}$, then the

modified formulation is equivalent to penalized Hamiltonian formulation

$$\begin{aligned} \delta H^{\circ}(\mathbf{u},\mathbf{v}) &= \delta \int_0^{t_{\mathrm{end}}} (T^{\circ} - \Pi)\,\mathrm{d}t \\ T^{\circ} &= \int_{\mathcal{B}_0} \left[\frac{1}{2}\rho_0 \dot{\mathbf{u}}\cdot\dot{\mathbf{u}} + \frac{C_1}{2}\rho_0(\mathbf{v}-\dot{\mathbf{u}})\cdot(\mathbf{v}-\dot{\mathbf{u}})\right]\mathrm{d}V. \end{aligned} \tag{5}$$

3 DISCRETIZATION

Here a standard total Lagrangian formulation of weak form (3) with modified inertia term (4) is used. Displacements are discretized with time-independent shape function matrix $\mathbf{N}$. Shape functions for velocity field $\boldsymbol{\psi}$ may depend on time see for reasons Section 4. Thus, the approximations of fields reads as follows

$$\begin{aligned} \mathbf{u}^h &= \mathbf{N}\mathbf{U} & \mathbf{v}^h &= \boldsymbol{\psi}\mathbf{V} \\ \delta\mathbf{u}^h &= \mathbf{N}\delta\mathbf{U} & \delta\mathbf{v}^h &= \boldsymbol{\psi}\delta\mathbf{V} \\ \dot{\mathbf{u}}^h &= \mathbf{N}\dot{\mathbf{U}} & \dot{\mathbf{v}}^h &= \boldsymbol{\psi}\dot{\mathbf{V}} + \dot{\boldsymbol{\psi}}\mathbf{V} \\ \ddot{\mathbf{u}}^h &= \mathbf{N}\ddot{\mathbf{U}} \end{aligned} \tag{6}$$

Substitution of the latter ansatz in the virtual work expression yields

$$\begin{aligned} \delta W^{\mathrm{int},h} &= \delta\mathbf{U}^{\mathrm{T}} \int_{\mathcal{B}_0} \mathbf{B}^{\mathrm{T}}\mathbf{P}\,\mathrm{d}V = \delta\mathbf{U}^{\mathrm{T}}\mathbf{f}^{\mathrm{int}} \\ \delta W^{\mathrm{ext},h} &= \delta\mathbf{U}^{\mathrm{T}} \int_{\mathcal{B}_0} \mathbf{N}^{\mathrm{T}}\rho_0\hat{\mathbf{b}}\,\mathrm{d}V + \delta\mathbf{U}^{\mathrm{T}} \int_{\partial\mathcal{B}_{\sigma,0}} \mathbf{N}\hat{\mathbf{t}}\,\mathrm{d}A = \delta\mathbf{U}\mathbf{f}^{\mathrm{ext}} \\ \delta W^{\mathrm{kin},\circ,h} &= \delta\mathbf{U}^{\mathrm{T}} \int_{\mathcal{B}_0} \mathbf{N}^{\mathrm{T}}\left[(1+C_1)\rho_0\mathbf{N}\ddot{\mathbf{U}} - C_1(\boldsymbol{\psi}\dot{\mathbf{V}} - \dot{\boldsymbol{\psi}}\mathbf{V})\right]\mathrm{d}V - \\ &\quad \delta\mathbf{V}^{\mathrm{T}} \int_{\mathcal{B}_0} \boldsymbol{\psi}^{\mathrm{T}}\left[(1+C_1)\rho_0(\mathbf{N}\dot{\mathbf{U}} - \boldsymbol{\psi}\mathbf{V})\right]\mathrm{d}V = \\ &\quad \delta\mathbf{U}^{\mathrm{T}}\left[(1+C_1)\mathbf{M} - C_1\mathcal{A}\dot{\mathbf{V}} - C_1\dot{\mathcal{A}}\mathbf{V}\right] - C_1\delta\mathbf{V}^{\mathrm{T}}\left[\mathcal{A}^{\mathrm{T}}\dot{\mathbf{U}} - \mathcal{Y}\mathbf{V}\right], \end{aligned} \tag{7}$$

where $\mathbf{f}^{\mathrm{int}}$ and $\mathbf{f}^{\mathrm{ext}}$ are internal and external nodal force vectors, $\mathbf{M} = \int_{\mathcal{B}_0}\rho_0\mathbf{N}^{\mathrm{T}}\mathbf{N}\,\mathrm{d}V$ is CMM, $\mathcal{A} = \int_{\mathcal{B}_0}\rho_0\mathbf{N}^{\mathrm{T}}\boldsymbol{\psi}\,\mathrm{d}V$ is projection matrix $\mathbf{V}\to\mathbf{U}$ and $\mathcal{Y} = \int_{\mathcal{B}_0}\rho_0\boldsymbol{\psi}^{\mathrm{T}}\boldsymbol{\psi}\,\mathrm{d}V$ is a mass matrix computed for discrete velocity vector $\mathbf{V}$. For the actual motion the sum of the virtual work terms vanishes, thus leading to equations of motion with kinematic constrains

$$\begin{aligned} \left[(1+C_1)\mathbf{M}\ddot{\mathbf{U}} - C_1\mathcal{A}\dot{\mathbf{V}} - C_1\dot{\mathcal{A}}\mathbf{V}\right] + \mathbf{f}^{\mathrm{int}} &= \mathbf{f}^{\mathrm{ext}} \\ \mathcal{A}^{\mathrm{T}}\dot{\mathbf{U}} &= \mathcal{Y}\mathbf{V}. \end{aligned} \tag{8}$$

Elimination of vector $\mathbf{V}$ from equation (8_1) using equation (8_2) leads to final expression of equation of motion, scaled mass and mass augmentation

$$\begin{aligned} \mathbf{M}^{\circ}\ddot{\mathbf{U}} + \mathbf{f}^{\mathrm{int}} &= \mathbf{f}^{\mathrm{ext}} - \frac{\mathrm{d}\boldsymbol{\lambda}^{\circ}}{\mathrm{d}\,t}\dot{\mathbf{U}} \\ \mathbf{M}^{\circ} &= \mathbf{M} + \boldsymbol{\lambda}^{\circ} \\ \boldsymbol{\lambda}^{\circ} &= C_1\left[\mathbf{M} - \mathcal{A}\mathcal{Y}^{-1}\mathcal{A}^{\mathrm{T}}\right]. \end{aligned} \tag{9}$$

4 Good ansatz spaces

Efficiency of the proposed mass scaling technique significantly depends on the ansatz spaces for velocity [11]. The mass scaling works only if the ansatz space for velocity is poorer than the ansatz space for displacement. In order to provide high accuracy even for high values of scaling C_1, the ansatz should exactly represent all rigid body modes. Here for eight- and nine-node elements it is proposed to use following time-independent basis functions

$$\boldsymbol{\psi}_{=} \left[\begin{array}{cccccc} 1 & 0 & X^h & 0 & Y^h & 0 \\ 0 & 1 & 0 & X^h & 0 & Y^h \end{array} \right], \tag{10}$$

with X^h and Y^h being the reference position of points in element. In this case the rotary inertia of individual elements is accurately approximated for moderate distortions of elements. In addition, the term $\frac{\mathrm{d}\boldsymbol{\lambda}^\circ}{\mathrm{d}t}\dot{\mathbf{U}}$ in (9) vanishes. Another advantage of the basis is that the mass augmentation is invariant under rotation of reference configuration. This also means that the mass augmentation works efficiently even after finite rotations in actual configuration, which makes the approach very attractive for non-linear structural problems where finite rotations occur often. Note, that efficiency of this basis was tested for 4-node quadrilateral element in [11] and it was found inapplicable for the element.

Alternatively a time-dependent basis may also be considered, which allows exact preservation of the rotary inertia of individual elements. It reads as follows

$$\boldsymbol{\psi}_{=} \left[\begin{array}{cccccc} 1 & 0 & x^h & 0 & y^h & 0 \\ 0 & 1 & 0 & x^h & 0 & y^h \end{array} \right], \tag{11}$$

with x^h and y^h being the actual positions of material points. This ansatz requires update of the mass augmentation $\boldsymbol{\lambda}^\circ$ each time-step, which increases overhead on SMS. This basis is not examined in the examples below because of space limitations.

5 EXAMPLES

Performance of the proposed formulation is evaluated on two examples. The first example is a standard eigenfrequency benchmark for a tapered membrane from NAFEMS. The second example is a transient dynamics of simplistic 2D model of arch bridge.

For these examples LMM is computed in two different ways. For nine-node quadrilateral element standard row sum lumping is applied. For eight-node quadrilateral element Hilton-Rock-Zienkiewicz method is used [5]. Standard displacement formulation is used for stiffness calculation. Both the mass and stiffness matrices are computed using 3x3 Gauss quadrature rules. Eigenvalue benchmark is computed in computer algebra program *Maple*. The transient example is computed using in-house finite element code *NumPro*. In both cases hardware double precision numbers are taken for floating point operations.

5.1 FV32 eigenfrequency benchmark

The eigenfrequency benchmark FV32 of NAFEMS [1] considers a modal problem for a tapered membrane. Geometry, mesh and material properties of the membrane are presented in Figure 1. Clamping $u_x = u_y = 0$ is imposed along the y-axis.

Results of the benchmark are presented in Figures 2 and Tables 1 and 2. The ratio of frequencies for initial and mass scaled systems have expected form, i.e. several lower modes are almost unaffected for the variational mass scaling. The algebraic mass scaling changes the lowest modes much more, see Table 1. However, for the same increase of critical time-step dt,

the variational mass scaling yields higher conditioning of the mass matrix. This means that the variational mass scaling is more accurate but expensive method.

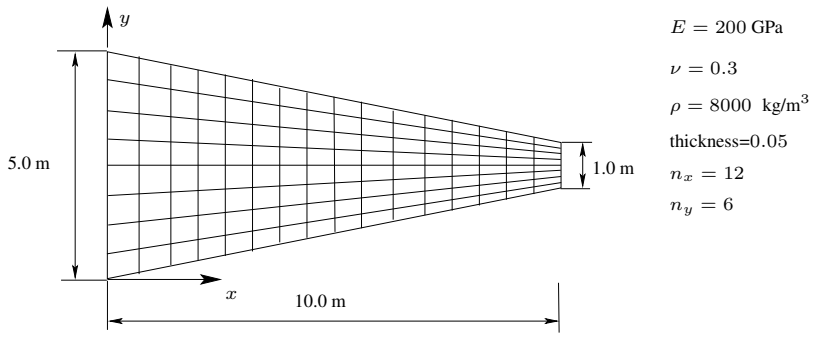


Figure 1: Setup of NAFEMS FV32 benchmark.

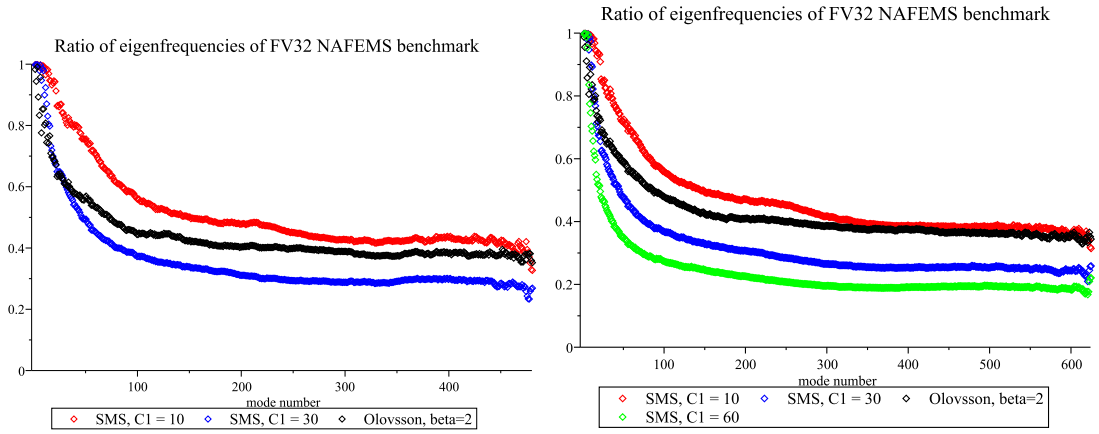


Figure 2: Ratio of eigenfrequencies for eight-node element (left) and nine-node element (right).

5.2 A model of an arch bridge

The model for a transient problem is shown in Figure 3. Initial zero displacements and velocities are assumed. The model is loaded in the middle of left arch by an abrupt point load F. Structural response is compared using history of the vertical displacement w under the load, Figures 4 and 5.

Computation with lumped mass matrices required 3691 and 2634 time-steps for eight- and nine-node element, respectively. For eight-node element following observations can be made. Application of small variational mass scaling factor $C_1 = 10$ with 1693 steps leads to very accurate results. Larger values of mass scaling result in larger conditioning of mass matrix without substantial reduction of time-step and are not recommended. Usage of algebraic mass scaling $\beta = 10$ with 832 steps increases inertia and results in phase shift of the displacement. For nine-node element similar behavior is observed. However, the conditioning of mass matrix for variational mass scaling is better.

The conditioning of mass matrix reflects on the number of necessary iterations for computation of the acceleration vector. The preconditioned conjugate gradient method with Jacobi

	f_1, [Hz]	f_1, [Hz]	f_3, [Hz]	f_4, [Hz]	f_5, [Hz]	f_6, [Hz]
reference	44.623	130.03	162.70	246.05	379.90	391.44
CMM	44.626	130.06	162.70	246.15	380.23	391.46
$C_1 = 10$	44.625	130.01	162.70	245.72	378.04	391.30
$C_1 = 30$	44.622	129.93	162.69	244.83	373.05	390.95
$C_1 = 60$	44.618	129.79	162.68	243.36	363.58	390.31
$\beta = 2$	43.943	122.99	161.50	220.18	317.47	375.50

Table 1: Six lowest eigenfrequencies f_{1-6} for FV32 benchmark with eight-node elements [1]

	eight-node		nine-node	
Mass type	dt_{crit}, [μs]	cond $\mathbf{M}$	dt_{crit}, [μs]	cond $\mathbf{M}$
LMM	8.7	49	8.4	79
CMM	14.8	219	13.4	128
$\beta = 10$	34.5	184	38.5	72
$\beta = 30$	50.1	236	64.8	153
$\beta = 60$	61.0	348	91.0	247
$C_1 = 30$	31.4	299	31.7	149
$C_1 = 60$	36.7	537	37.1	275
$C_1 = 100$	41.9	857	42.4	444

Table 2: Critical time-step and conditioning of mass matrix for FV32 benchmark

preconditioner is used for the numerical experiments. The relative error of residual norm is taken as 10^{-6}. For the nine-node element with values of algebraic mass scaling factor $\beta = 10$, 30 and 100, the average number of iterations is 25, 41 and 60, respectively. For values of variational mass scaling factors $C_1 = 30$, 100 and 300, the average number of iterations is 37, 65 and 111. This numbers perfectly correlate with the expected number of iterations, which is proportional to square root of condition number.

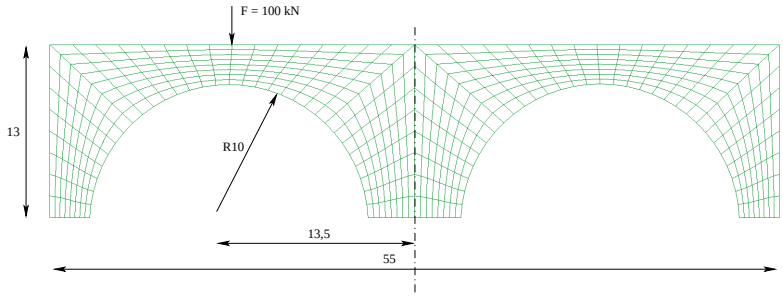


Figure 3: A model of an arch bridge. Material properties: $E = 30$ GPa, $\nu = 0.2$, $\rho = 2400$ kg/m^3, plane stress, thickness $= 1$ m. Mesh: 512 elements (eight- or nine-node quadrilaterals). Load: point force $F = 100$ kN applied in the middle of left arch. Duration: $t_{\text{end}} = 0.1$ s.

It was found that critical time-step and conditioning of mass matrix grow with C_1, see Table 3. Least square fit of the data yields following approximated relations

$$\begin{aligned} \text{eight-node:} \quad & \frac{dt^{\circ}_{\text{crit}}}{dt_{\text{crit}}} \approx 1 + \frac{2}{3}\sqrt[4]{C_1} \quad \text{cond}\,\mathbf{M}^{\circ} \approx \text{cond}\,\mathbf{M}_{\text{CMM}} + 3C_1 \\ \text{nine-node:} \quad & \frac{dt^{\circ}_{\text{crit}}}{dt_{\text{crit}}} \approx 1 + \frac{2}{3}\sqrt[4]{C_1} \quad \text{cond}\,\mathbf{M}^{\circ} \approx \text{cond}\,\mathbf{M}_{\text{CMM}} + \frac{4}{3}C_1. \end{aligned} \tag{12}$$

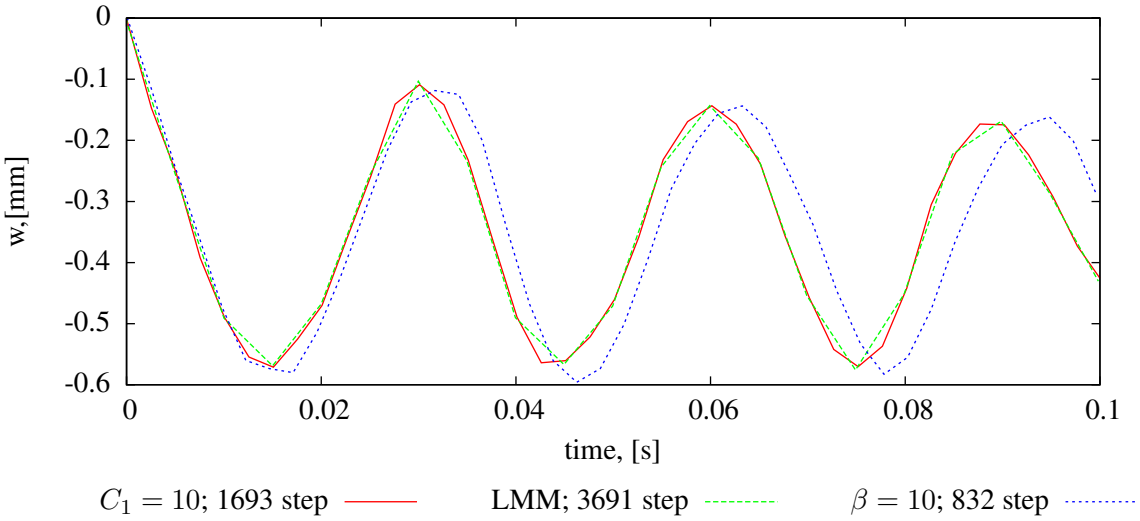


Figure 4: Displacement under external load. Results for eight-node element.

	eight-node		nine-node	
Mass type	dt_{crit}, [μs]	cond $\mathbf{M}$	dt_{crit}, [μs]	cond $\mathbf{M}^\circ$
LMM	26.8	19	42.0	29
CMM	42.4	93	26.5	62
$\beta = 10$	134.9	43	115.5	51
$\beta = 30$	227.1	98	194.5	115
$\beta = 100$	410.3	190	351.7	303
$C_1 = 30$	71.8	159	71.5	77
$C_1 = 100$	85.2	372	84.7	191
$C_1 = 300$	103.6	903	103.0	470

Table 3: Critical time-step and conditioning of mass matrix for the bridge model.

The quality of this fit is illustrated in Figure 6. On can see that rise of critical time-step is the same for eight- and nine-node elements. At the same time conditioning of scaled mass matrix $\mathbf{M}^\circ$ for eight-node element is much larger. Thus, it can prohibit its usage for large values of mass scaling C_1.

6 CONCLUSIONS

The main results of this contribution is extension of penalized Hamiltonian formulation to finite deformations with independent fields for displacement and velocity. Here it is proposed to use the new formulation for eight- and nine-node quadrilateral elements. Choice of ansatz spaces for velocity in form (10) allows an efficient implementation for selective mass scaling. This selective mass scaling works efficiently even after finite rotations.

The proposed mass scaling is tested for one eigenvalue and one transient benchmark. The eigenvalue benchmark showed better preservation of the lowest eigenfrequencies with the proposed method in comparison to algebraic mass scaling [10]. More accurate results with the proposed method are obtained for the transient benchmark. The phase error in oscillations is much lower. In addition the rules for growth of the conditioning of mass matrix $\operatorname{cond} \mathbf{M}^\circ$ and the critical time-step $dt^\circ_{\text{crit}}/dt_{\text{crit}}$ for discussed elements are found. This result can be used for

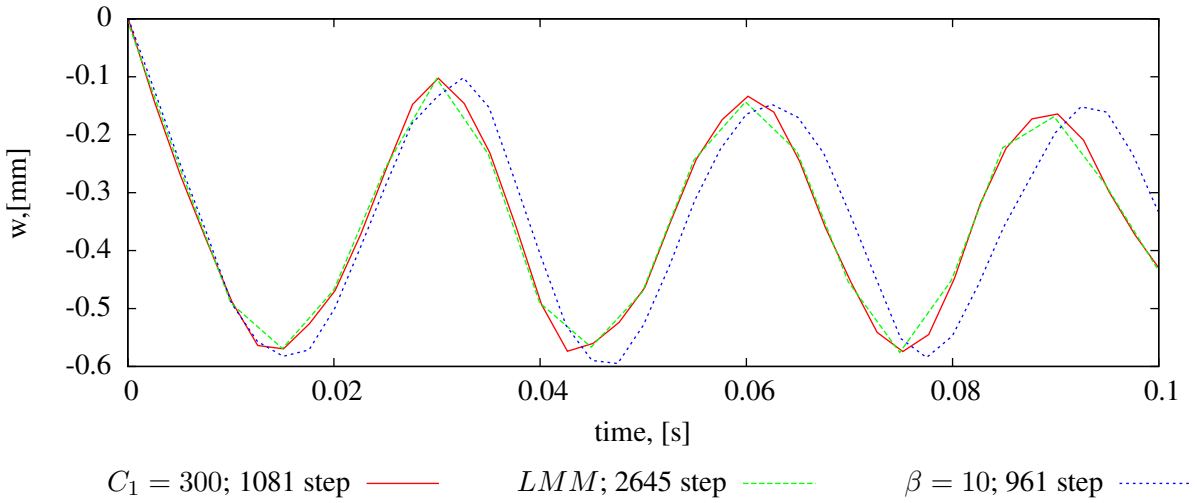


Figure 5: Displacement under external load. Results for nine-node element.

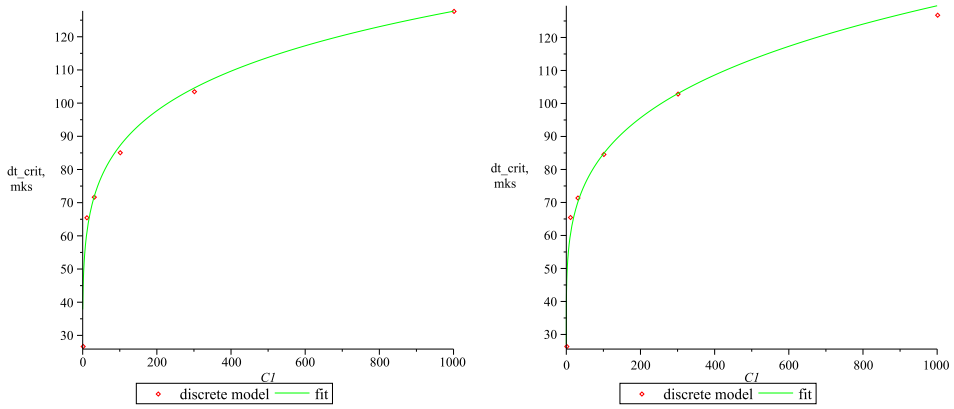


Figure 6: Dependence of the critical time-step on C_1 for eight-node (left) and nine-node (right) element. Computed values vs. fitted curve.

other structures for estimation of computational cost of selective mass scaling.

A possible directions of future work are extension of the variational mass scaling for 10-node tetrahedral elements, 20- and 27-node hexahedral elements and development of more efficient preconditioners for the scaled mass matrix.

The main conclusion is that variational selective mass scaling provides more accurate results than algebraic mass scaling. Application of variational selective mass scaling for quadratic elements reduce their computational cost in explicit codes and broad their usage.

Acknowledgements

Acknowledgements to Baden-Württemberg Stiftung gGmbH, Grant HPC-10, and Deutsche Forschungsgemeinschaft, Grant BI 722 7.1.

REFERENCES

[1] National Agency for Finite Element Methods & Standards (Great Britain). *The standard NAFEMS benchmarks*. NAFEMS, 1990.

[2] Ted Belytschko, W.K. Liu, and B. Moran. *Nonlinear finite elements for continua and structures*. Wiley, Chichester, 2000.

[3] T Borrval. Selective mass scaling in ls-dyna to reduce non-physical inertia effects. In *Developers' forum, DYNAMORE, Stuttgart, Germany, 2011*, 2011.

[4] Giuseppe Cocchetti, Mara Pagani, and Umberto Perego. Selective mass scaling and critical time-step estimate for explicit dynamics analyses with solid-shell elements. *Computers & Structures*, (0):–, 2012.

[5] E. Hinton, T. Rock, and O. C. Zienkiewicz. A note on mass lumping and related processes in the finite element method. *Earthquake Engineering & Structural Dynamics*, 4(3):245–249, 1976.

[6] S. W. Key and Z. E. Beisinger. The transient dynamic analysis of thin shells by the finite element method. In *Proc. of the Third Conference on Matrix Methods in Structural Mechanics*, 1971.

[7] R. Kolman, J. Plešek, D. Gabriel, and M. Okrouhlk. Optimization of lumping schemes for plane square quadratic finite element in elastodynamics. *Applied and Computational Mechanics*, 1:105 – 114.

[8] L. Olovsson, M. Unosson, and K. Simonsson. Selective mass scaling for thin walled structures modeled with tri-linear solid elements. *Comput Mech*, 34:134–136, 2004.

[9] Lars Olovsson and Kjell Simonsson. Iterative solution technique in selective mass scaling. *Comm Num Methods Engrg*, 22(1):77–82, 2006.

[10] Lars Olovsson, Kjell Simonsson, and Mattias Unosson. Selective mass scaling for explicit finite element analyses. *Int J Numer Methods Engrg*, 63(10):1436–1445, 2005.

[11] Anton Tkachuk and Manfred Bischoff. Variational methods for selective mass scaling. *Comput Mech*. in print.

[12] O.C. Zienkiewicz and R.L. Taylor. *The Finite Element Method Set*. Elsevier Science, 6 edition, 2006.

COMPDYN 2013
4th ECCOMAS Thematic Conference on
Computational Methods in Structural Dynamics and Earthquake Engineering
M. Papadrakakis, V. Papadopoulos, V. Plevris (eds.)
Kos Island, Greece, 12–14 June 2013

STUDIES IN NUMERICAL STABILITY OF EXPLICIT CONTACT-IMPACT ALGORITHM TO THE FINITE ELEMENT SOLUTION OF WAVE PROPAGATION PROBLEMS

Ján Kopačka[1], Dušan Gabriel[1], Radek Kolman[1], Jiří Plešek[1] and Miran Ulbin[2]

[1]Institute of Thermomechanics, Academy of Sciences
Dolejškova 5, 182 00 Prague 8, Czech Republic
e-mail: {gabriel,kopacka,kolman,plesek}@it.cas.cz

[2] Faculty of Mechanical Engineering, University of Maribor
Smetanova 17, 2000 Maribor, Slovenia
e-mail: ulbin@uni-mb.si

Keywords: Contact-impact, central difference method, stability, penalty method, bipenalty method.

Abstract.

In dynamic transient analysis, recent comprehensive studies have shown that using mass penalty together with standard stiffness penalty, the so-called bipenalty technique, preserves the critical time step in conditionally stable time integration schemes. In this paper, the bipenalty approach is applied in the explicit contact-impact algorithm based on the pre-discretization penalty formulation. The attention is focused on the stability of this algorithm. Specifically, the upper estimation of the stable Courant number on the stiffness and mass penalty is derived based on the simple dynamic system with two degrees-of-freedom. The results are verified by means of the dynamic Signorini problem, which is represented by the motion of a bar that comes into contact with a rigid obstacle.

1 INTRODUCTION

In contact problems the contact constraints can be enforced either by the Lagrange multiplier method or by the stiffness penalty method. In practise the latter approach has gained in substantial popularity, because its implementation is easy, straightforward and has a clear physical meaning. On the other hand, the choice of the penalty parameter influences the accuracy of the approximate solution. In addition, in contact-impact applications the stiffness penalty method tends to decrease the critical time step in conditionally stable time integration schemes. This is due to the fact that the stiffness-type penalty can greatly enlarge the maximum eigenfrequency of a system.

In dynamic transient analysis, the penalty method can also be applied to the mass matrix. This technique is known as the mass penalty or the inertia penalty method. In contrast to the stiffness penalty approach, it significantly reduces one or more eigenfrequencies. In Reference [1] the bipenalty technique was introduced, where the both penalty formulations were used simultaneously. The goal of this method is to find the optimum of the so-called critical penalty ratio (CPR) defined as the ratio of stiffness and mass penalty parameters so that the maximum eigenfrequency and the critical time step are preserved. The calculation of CPR requires an analysis of the full bipenalised problem. Owing to mathematical difficulty, it limits the classes of elements that can be taken into account. In order to overcome this problem, a simple relationship between the CPR of an element and its maximum unpenalised eigenfrequency was derived in [2]. Thus, the multiple constraints and more complex element formulations can be directly accounted for [3].

In this paper, the bipenalty approach is applied in the explicit contact-impact algorithm based on the pre-discretization penalty formulation [4]. The attention is focused on the stability properties of this algorithm. In Section 2.1 the formulation of contact initial/boundary value problem is presented, followed by the variational formulation in Section 2.2. The idea of the bipenalty approach for imposing the contact constraints is described in Section 2.3. Finite element discretization is outlined in Section 2.4. The numerical stability of explicit time integration scheme is discussed in Section 2.5. Based on the behaviour of the simple dynamic system with two degrees-of-freedom the upper estimation of the stable Courant number on the stiffness and mass penalty is derived. In Section 3, the stability of the algorithm is tested on the dynamic Signorini problem, followed by concluding remarks in Section 4.

2 PROBLEM DESCRIPTION

2.1 Contact initial/boundary value problem

The problem of linear elastodynamics is governed by the balance of linear momentum

$$\boldsymbol{\nabla} \cdot \boldsymbol{\sigma}(\mathbf{u}) + \mathbf{b} = \rho \ddot{\mathbf{u}}(\mathbf{x}, t) \quad \text{in } \Omega \times \mathbb{I} \tag{1}$$

where $\Omega = \bigcup_i \Omega_i, i = 1, 2$ is n-dimensional set of spatial points, $\mathbf{x} \in \mathbb{R}^n$, defining the contacting bodies, $\mathbb{I} = (0, T)$ is the time domain, $\mathbf{u}$ is the displacement field, $\boldsymbol{b}$ are the body forces and $\boldsymbol{\sigma}$ is the stress field (see Figure 1). The superimposed dots denote the time derivatives. In linear elasticity the stress can be computed from the linear strain field

$$\boldsymbol{\varepsilon} = \frac{1}{2}\left((\boldsymbol{\nabla}\mathbf{u})^{\mathrm{T}} + \boldsymbol{\nabla}\mathbf{u}\right) \tag{2}$$

via Hooke's law

$$\boldsymbol{\sigma} = \mathbf{c} : \boldsymbol{\varepsilon} \tag{3}$$

where $\mathbf{c}$ is the tensor of elastic constants given as

$$\mathbf{c} = \lambda \mathbf{I} \otimes \mathbf{I} + 2\mu \mathbf{I} \tag{4}$$

where $\mathbf{I}$ is the second-order identity tensor and λ, μ are the Lamé constants. The problem is in general subject to certain initial and boundary conditions as well. The initial conditions

$$\mathbf{u}(\mathbf{x}, 0) = \mathbf{u}_0 \quad \text{in } \bar{\Omega} \tag{5}$$
$$\dot{\mathbf{u}}(\mathbf{x}, 0) = \mathbf{v}_0 \quad \text{in } \bar{\Omega} \tag{6}$$

are prescribed in the closure of domain $\bar{\Omega}$. The displacement and traction boundary conditions

$$\mathbf{u} = \bar{\mathbf{u}} \quad \text{on } \Gamma_{\mathrm{u}} \tag{7}$$
$$\boldsymbol{\sigma} \cdot \mathbf{n} = \bar{\mathbf{t}} \quad \text{on } \Gamma_{\sigma} \tag{8}$$

are prescribed on the $\Gamma_{\mathrm{u}} \subset \Gamma$ and $\Gamma_{\sigma} \subset \Gamma$, respectively; Γ denotes the boundary of the domain Ω; $\bar{\mathbf{u}}$ and $\bar{\mathbf{t}}$ are the prescribed displacements and the prescribed tractions, respectively; the vector $\mathbf{n}$ stands for the outward normal vector to Γ_{σ}. Further, the contact constraints are described on the contact boundary $\Gamma_{\mathrm{c}} \subset \Gamma$ by the Signorini-Hertz-Moreau conditions

$$g_{\mathrm{N}} \geq 0 \quad t_{\mathrm{N}} = \boldsymbol{\sigma} \cdot \mathbf{n} \leq 0 \quad g_{\mathrm{N}} t_{\mathrm{N}} = 0 \quad \text{on } \Gamma_{\mathrm{c}} \tag{9}$$

also known as the Karush-Kuhn-Tucker (KKT) conditions. Here, the normal gap function g_{N} has been introduced, which is defined as

$$g_{\mathrm{N}} = \begin{cases} (\mathbf{x}_2 - \bar{\mathbf{x}}_1) \cdot \bar{\mathbf{n}}_1 & \text{if } (\mathbf{x}_2 - \bar{\mathbf{x}}_1) \cdot \bar{\mathbf{n}}_1 < 0 \\ 0 & \text{otherwise} \end{cases} \tag{10}$$

The definition is apparent from Figure 1, where $\bar{\mathbf{x}}_1$ is the closest point projection of the point $\mathbf{x}_2$, lying on the contact boundary of body Ω_2, onto the contact boundary of body Ω_1. The vector $\bar{\mathbf{n}}$ denotes the contact normal vector.

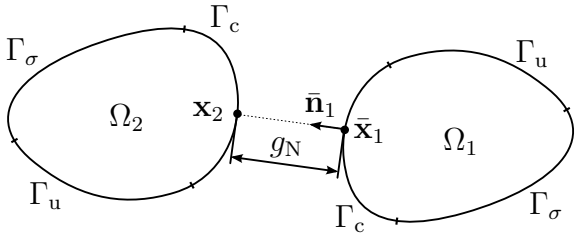


Figure 1: Definition of the normal gap function.

The first inequality $(9)_1$ is called the impenetrability condition. The second condition $(9)_2$ asserts the negative traction vector on the contact boundary. And finally, the third equality $(9)_3$ is called the complementarity condition ensuring the complementarity between the gap function and the contact traction vector.

2.2 Variational formulation

In order to be able to perform the finite element discretization, it is necessary to reformulate the strong form of the contact initial/boundary value problem presented in the preceding section in a weak sense. Hamilton's principle is a simple and powerful tool that can be utilised to derive discretized dynamic system of equations. It states that of all admissible time histories of displacement field the solution is one which minimizes the action functional

$$\mathbf{u} = \arg\min \left(\int_0^T \mathcal{L}\left(\mathbf{u}, \dot{\mathbf{u}}\right) \, \mathrm{d}t \right) \quad \text{subjected to } g_{\mathrm{N}} \geq 0 \text{ on } \Gamma_{\mathrm{c}} \tag{11}$$

where the Lagrangian functional, $\mathcal{L}(\mathbf{u}, \dot{\mathbf{u}})$, is defined as

$$\mathcal{L}\left(\mathbf{u}, \dot{\mathbf{u}}\right) = \mathcal{T}\left(\dot{\mathbf{u}}\right) - \left(\mathcal{U}\left(\mathbf{u}\right) - \mathcal{W}\left(\mathbf{u}\right)\right) \tag{12}$$

where

$$\mathcal{T}\left(\dot{\mathbf{u}}\right) = \int_\Omega \frac{1}{2} \rho \dot{\mathbf{u}} \cdot \dot{\mathbf{u}} \, \mathrm{d}V \tag{13}$$

$$\mathcal{U}\left(\mathbf{u}\right) = \int_\Omega \frac{1}{2} \boldsymbol{\sigma} : \boldsymbol{\varepsilon} \, \mathrm{d}V \tag{14}$$

$$\mathcal{W}\left(\mathbf{u}\right) = \int_\Omega \mathbf{u} \cdot \mathbf{b} \, \mathrm{d}V + \int_{\Gamma_\sigma} \mathbf{u} \cdot \bar{\mathbf{t}} \, \mathrm{d}S \tag{15}$$

are the kinetic energy, the strain energy, and the work done by external forces, respectively.

2.3 Bipenalty method

In dynamics, the simultaneous use of the stiffness penalties and inertia/mass penalties, called the bipenalty method, was originally proposed in [1]. There was defined the penalty ratio as

$$R = \frac{\epsilon_{\mathrm{s}}}{\epsilon_{\mathrm{m}}} \left[\mathrm{s}^{-2}\right] \tag{16}$$

where ϵ_{s} and ϵ_{m} are the stiffness and mass penalty parameter, respectively. There were also derived optimum values of the penalty ratios–the so-called critical penalty ratios (CPR)–for a number of finite elements such that the critical time step of the penalised system remains unaffected. A new method of calculating the CPR associated with a finite element formulation was developed in [2]. Recently, this finding was extended to include systems with an arbitrary set of multipoint constraints [3].

Now, a brief description of the bipenalty method follows. Let us assume that the contact boundary Γ_{c} is known. The standard stiffness penalty method adds an extra term to the strain energy (14) to enforce the zero gap on the contact boundary

$$\mathcal{U}_{\mathrm{p}}\left(\mathbf{u}\right) = \int_\Omega \frac{1}{2} \boldsymbol{\sigma} : \boldsymbol{\varepsilon} \, \mathrm{d}V + \int_{\Gamma_{\mathrm{c}}} \frac{1}{2} \epsilon_{\mathrm{s}} g_{\mathrm{N}}^2 \, \mathrm{d}S \tag{17}$$

Further, the inertia penalty term can also be added to the kinetic energy (13) to enforce the zero gap rate on the contact interface

$$\mathcal{T}_{\mathrm{p}}\left(\dot{\mathbf{u}}\right) = \int_\Omega \frac{1}{2} \rho \dot{\mathbf{u}} \cdot \dot{\mathbf{u}} \, \mathrm{d}V + \int_{\Gamma_{\mathrm{c}}} \frac{1}{2} \epsilon_{\mathrm{m}} \dot{g}_{\mathrm{N}}^2 \, \mathrm{d}S \tag{18}$$

Now, a new penalised Lagrangian functional can be defined as

$$\mathcal{L}_{\mathrm{p}}(\mathbf{u}, \dot{\mathbf{u}}) = \mathcal{T}_{\mathrm{p}}(\dot{\mathbf{u}}) - (\mathcal{U}_{\mathrm{p}}(\mathbf{u}) - \mathcal{W}(\mathbf{u})) \tag{19}$$

The unknown displacement field can be found as one which renders the penalised action functional stationary

$$\delta \int_0^T \mathcal{L}_{\mathrm{p}}\left(\mathbf{u}, \dot{\mathbf{u}}\right)\, \mathrm{d}t = 0 \tag{20}$$

where δ denotes the first variation or the directional derivative in the direction of virtual displacement $\delta\mathbf{u}$. Using the standard procedures one arrives to the principle of virtual displacement

$$\int_\Omega \rho\delta\mathbf{u}\cdot\ddot{\mathbf{u}}\,\mathrm{d}V + \int_\Omega \delta\boldsymbol{\varepsilon} : \boldsymbol{\sigma}\,\mathrm{d}V + \int_{\Gamma_{\mathrm{c}}} \delta g_{\mathrm{N}}(\epsilon_{\mathrm{m}}\ddot{g}_{\mathrm{N}} + \epsilon_{\mathrm{s}} g_{\mathrm{N}})\,\mathrm{d}S = \int_\Omega \delta\mathbf{u}\cdot\mathbf{b}\,\mathrm{d}V + \int_{\Gamma_\sigma} \delta\mathbf{u}\cdot\mathbf{t}\,\mathrm{d}S \tag{21}$$

which serves the base for the finite element discretization. The integrals in Equation (21) represent the virtual work of the inertia forces, internal forces, contact forces, body forces, and traction forces, respectively. It is worth noting that the integral of the virtual contact work are expressed with the aid of the inertia and the stiffness penalty.

2.4 Finite element method

Applying the finite element discretization to the variational formulation (21) introduces the system of nonlinear ordinary differential equations

$$\mathbf{M}\ddot{\mathbf{u}} + \mathbf{K}\mathbf{u} + \mathbf{R}_{\mathrm{c}}(\mathbf{u}, \ddot{\mathbf{u}}) = \mathbf{R} \tag{22}$$

Here, $\mathbf{M}$ is the mass matrix, $\mathbf{K}$ is the stiffness matrix, $\mathbf{R}_{\mathrm{c}}$ is the contact residual vector, which is the source of the nonlinearity. Further, $\mathbf{R}$ is the time-dependent load vector, and $\mathbf{u}$ and $\ddot{\mathbf{u}}$ contain nodal displacements and accelerations, respectively. The element mass and stiffness matrices are given by

$$\mathbf{M}_e = \int_{\Omega_e} \rho\mathbf{H}^{\mathrm{T}}\mathbf{H}\,\mathrm{d}V \qquad \mathbf{K}_e = \int_{\Omega_e} \mathbf{B}^{\mathrm{T}}\mathbf{C}\mathbf{B}\,\mathrm{d}V \tag{23}$$

where $\mathbf{C}$ it the elasticity matrix, $\mathbf{B}$ is the strain-displacement matrix, and $\mathbf{H}$ stores the shape functions. Note that the integration is carried over the element domain Ω_e. Global matrices are assembled in the usual fashion.

In the case of geometrically linear kinematics, the contact residual vector can be written as

$$\mathbf{R}_{\mathrm{c}}(\mathbf{u}, \ddot{\mathbf{u}}) = \mathbf{M}_{\mathrm{p}}\ddot{\mathbf{u}} + \mathbf{K}_{\mathrm{p}}\mathbf{u} + \mathbf{f}_{\mathrm{p}} \tag{24}$$

where

$$\mathbf{M}_{\mathrm{p}} = \int_{\Gamma_{\mathrm{c}}} \epsilon_{\mathrm{m}}\mathbf{N}\mathbf{N}^{\mathrm{T}}\,\mathrm{d}S \qquad \mathbf{K}_{\mathrm{p}} = \int_{\Gamma_{\mathrm{c}}} \epsilon_{\mathrm{s}}\mathbf{N}\mathbf{N}^{\mathrm{T}}\,\mathrm{d}S \qquad \mathbf{f}_{\mathrm{p}} = \int_{\Gamma_{\mathrm{c}}} \epsilon_{\mathrm{s}}\mathbf{N} g_0\,\mathrm{d}S \tag{25}$$

Here, $\mathbf{M}_{\mathrm{p}}$ is the additional mass matrix due to inertia penalty, $\mathbf{K}_{\mathrm{p}}$ is the additional stiffness matrix due to stiffness penalty, and $\mathbf{f}_{\mathrm{p}}$ is the part of the contact force due to the initial gap g_0. The matrix $\mathbf{N}$ represents an operator from the displacement field $\mathbf{u}$ to the gap function g_{N}

$$g_{\mathrm{N}} = \mathbf{N}^{\mathrm{T}}\mathbf{u} + g_0 \tag{26}$$

The particular form of the matrix $\mathbf{N}$ follows from the used contact discretization. A comprehensive overview can be found in [5].

2.5 Explicit time integration and numerical stability

We now consider the time integration of the semi-discretized system (22) by the central difference method (CDM) [7]

$$(\mathbf{M}+\mathbf{M}_{\mathrm{p}}^{t})\frac{\mathbf{u}^{t+\Delta t}-2\mathbf{u}^{t}+\mathbf{u}^{t-\Delta t}}{\Delta t^{2}}+(\mathbf{K}+\mathbf{K}_{\mathrm{p}}^{t})\mathbf{u}^{t}+\mathbf{f}_{\mathrm{p}}^{t}-\mathbf{R}^{t}=\mathbf{0} \tag{27}$$

Assuming that displacements are known at time $t-\Delta t$ and t, one can resolve unknown displacements at time $t+\Delta t$. Note that the matrices $\mathbf{M}_{\mathrm{p}}^{t}$ and $\mathbf{K}_{\mathrm{p}}^{t}$ are time-dependent because they are associated with active contact constraints. This fact causes the system to be nonlinear.

It is well known that the CDM for a linear system is conditionally stable. The linear stability theory establishes the upper bound of the time step as

$$\Delta t \leq \frac{2}{\omega_{\max}} \tag{28}$$

where $\omega_{\max}$ is the maximum eigenfrequency of the finite element mesh. Indeed, the computation of even a single eigenvalue of a large systems may be expensive. Therefore, it would be advantageous to have an estimate on the maximum eigenvalue that is easy to compute. Such an estimate is provided by the element eigenvalue inequality [7]

$$\omega_{\max} < \max_{e} \omega_{\max}^{e} \tag{29}$$

Note that the element eigenvalue inequality is not limited only to element level submatrices. The submatrices may be also an assemblage of elements.

Unfortunately, there are no stability theorems for contact-impact problems [7]. In this case the linear stability theory can be applied carefully. In practise, for example, the stability may be preserved by checking the energy balance during a nonlinear computation. In Reference [8] an upper bound for the stiffness penalty was derived. Moreover, it was shown that the stiffness penalty always decreases the stable time step. In this work, we generalize this estimate for the bipenalty approach following the Belytschko approach [8].

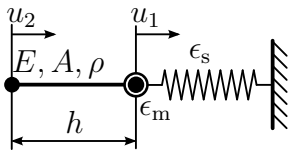


Figure 2: A simple dynamic system with two degrees-of-freedom.

Let us consider a simple dynamic system, depicted in Figure 2, with two degrees-of-freedom. The system consists of one 1D constant strain truss element with lumped mass matrix. The active contact constraint is set in node 1. The aim is to determine the maximum eigenfrequency of this system to estimate the stable time step in the form (28). To this end, the eigenvalue problem can be formulated as

$$\frac{EA}{h}\begin{bmatrix} 1+\beta_{\mathrm{s}} & -1 \\ -1 & 1 \end{bmatrix}\mathbf{u}=\omega^{2}\frac{\rho Ah}{2}\begin{bmatrix} 1+\beta_{\mathrm{m}} & 0 \\ 0 & 1 \end{bmatrix}\mathbf{u} \tag{30}$$

where the dimensionless mass and stiffness penalty have been introduced as

$$\beta_{\mathrm{m}} = \frac{2}{\rho A h}\epsilon_{\mathrm{m}} \quad \beta_{\mathrm{s}} = \frac{h}{EA}\epsilon_{\mathrm{s}} \tag{31}$$

The maximum eigenfrequency of the problem (30) is given by

$$\omega_{\max} = \frac{c_0}{h}\sqrt{1 + \frac{(1+\beta_{\mathrm{s}})}{(1+\beta_{\mathrm{m}})} + \sqrt{1 + \frac{(1+\beta_{\mathrm{s}})^2}{(1+\beta_{\mathrm{m}})^2} + \frac{2(1-\beta_{\mathrm{s}})}{(1+\beta_{\mathrm{m}})}}} \tag{32}$$

The Courant dimensionless number is defined as

$$C_{\mathrm{r}} = \frac{c_0 \Delta t}{h} \tag{33}$$

Substituting (32) into (28) using (33) the upper bound of the stable Courant number for the bipenalty method is obtained

$$C_{\mathrm{r}} = \frac{2}{\sqrt{1 + \frac{(1+\beta_{\mathrm{s}})}{(1+\beta_{\mathrm{m}})} + \sqrt{1 + \frac{2(1-\beta_{\mathrm{s}})}{(1+\beta_{\mathrm{m}})} + \frac{(1+\beta_{\mathrm{s}})^2}{(1+\beta_{\mathrm{m}})^2}}}} \tag{34}$$

Now, it is useful to introduce a new dimensionless penalty ratio r as

$$r = \frac{1}{2}\frac{\beta_{\mathrm{s}}}{\beta_{\mathrm{m}}} = \frac{h^2}{4c_0^2}R \tag{35}$$

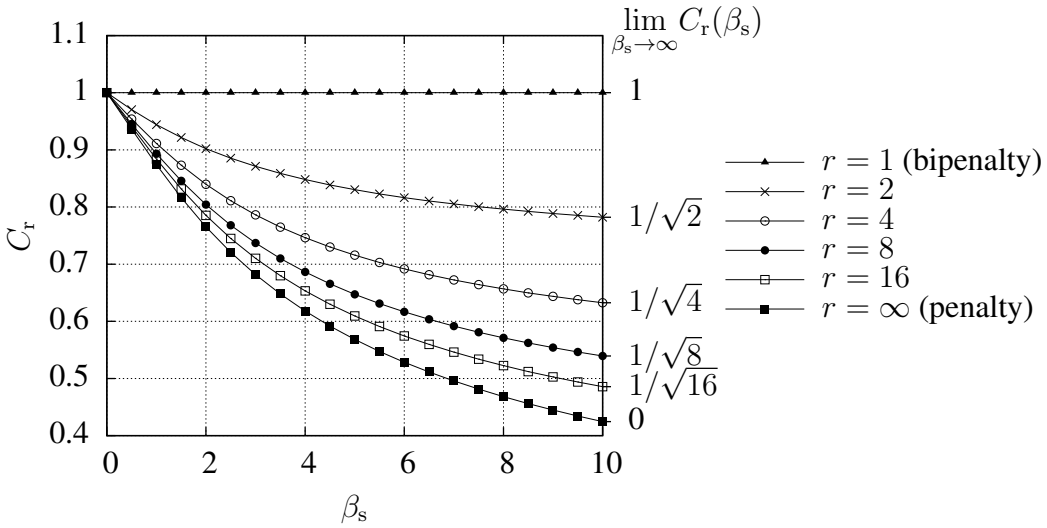


Figure 3: The dependence of the Courant number C_{r} on the dimensionless stiffness penalty β_{s} for selected dimensionless penalty ratios r.

The dependence of the Courant number C_{r} on the dimensionless stiffness penalty β_{s} is plotted in Figure 3, where the dimensionless penalty ratio r is employed as the parameter. The curve

for $r \to \infty$ (i.e. $\beta_{\mathrm{m}} \to 0$) corresponds to the standard stiffness penalty method. It illustrates the main disadvantages of the standard stiffness penalty method: the Courant number C_{r} rapidly decrease with increasing dimensionless stiffness penalty β_{s}. On the other hand, the curve for $r = 1$ confirms the existence of the CPR, for which the stable time step remains unchanged for an arbitrary value of the dimensionless stiffness penalty β_{s}. In addition, there are more curves in Figure 3 for dimensionless penalty ratios $r = 2, 4, 8,$ and 16. For each of them, there are limits of the Courant number for $\beta_{\mathrm{s}} \to \infty$ on the right edge of the picture. It is clear that the bipenalty method with the penalty ratio equal to the CPR is superior over the standard stiffness penalty method.

3 NUMERICAL EXAMPLE

In this section, the stability of explicit contact-impact algorithm using bipenalty technique was studied on the dynamic Signorini problem, which was represented by the motion of a bar that comes into contact with a rigid obstacle (see Figure 4). The bar of length $L = 1\,[\mathrm{m}]$ with the initial velocity $v_0 = 1\,[\mathrm{m} \cdot \mathrm{s}^{-1}]$ is situated at distance of $g_0 = 0\,[\mathrm{m}]$ in front of the obstacle. The area of the bar section $A\,[\mathrm{m}^2]$, Young's modulus $E\,[\mathrm{MPa}]$ and density $\rho\,[\mathrm{kg} \cdot \mathrm{m}^{-3}]$ were chosen to be unit.

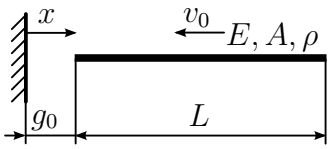


Figure 4: 1D dynamic Signorini problem.

The bar was discretized by a regular finite element mesh containing one hundred 1D constant strain truss elements. For the effective integration of equilibrium equations by the CDM method the consistent mass matrix was diagonalized by the row sum technique. The maximum eigenvalue of the mesh was $\lambda_{\max} = 4e4\,[\mathrm{s}^{-2}]$ and the corresponding eigenfrequency was $\omega_{\max} = 200\,[\mathrm{s}^{-1}]$.

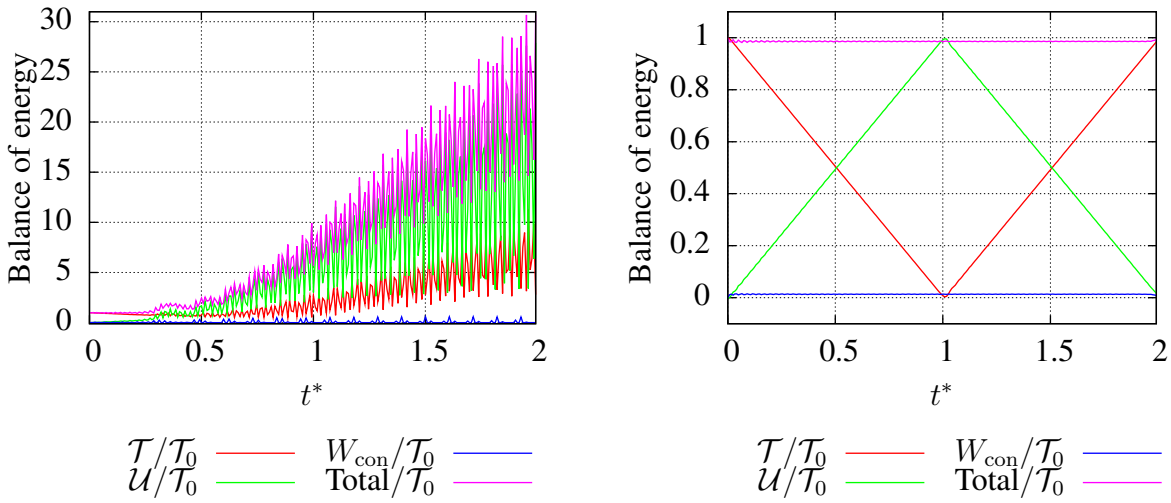
Let us introduce following dimensionless quantities

$$t^* = \frac{c_0 t}{L} \qquad x^* = \frac{x}{L} \qquad u^* = \frac{u(0,t)}{L} \qquad F_{\mathrm{c}}^* = \frac{c_0 F_{\mathrm{c}}}{v_0 E A} \qquad \sigma^* = \frac{\sigma A}{F_{\mathrm{c}}} \tag{36}$$

where $t^*, x^*, u^*, F_{\mathrm{c}}^*, \sigma^*$ is the dimensionless time, coordinate, contact displacement, contact force, stress, respectively. In the following figures, the results for the standard penalty method (left) and the bipenalty method (right) are plotted.

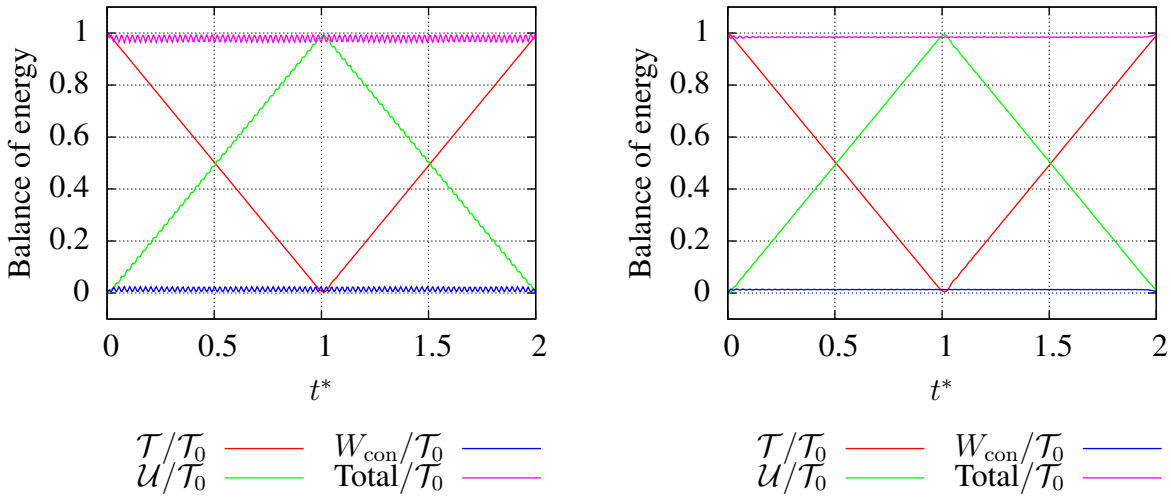
The dimensionless stiffness penalty β_{s} was chosen to 1.5. In order to verify derived formula of the stability (34) the Courant number C_{r} was set to 0.82, which was slightly higher than the critical value $C_{\mathrm{r}} = 0.81649658$ for the penalty method. The results are shown in Figure 5a, where time distributions of the kinetic energy, the potential energy, the total energy, the work done by contact forces are plotted. It was confirmed that the stability of the CDM was lost for the penalty method, whereas the solution obtained by the bipenalty method still perfectly conserved the total energy. When the Courant number C_{r} was set to 0.5 both methods were stable (see Figure 6).

Note that the work of contact force W_{c} is almost zero. In fact, it should be exactly zero because the displacement of the contact force was restricted by the rigid obstacle. However, in



(a) $r = \infty$ (penalty method) (b) $r = 1$ (bipenalty method)

Figure 5: Time distribution of the balance of energy for $\beta_{\text{s}} = 1.5$ and $C_{\text{r}} = 0.82$.

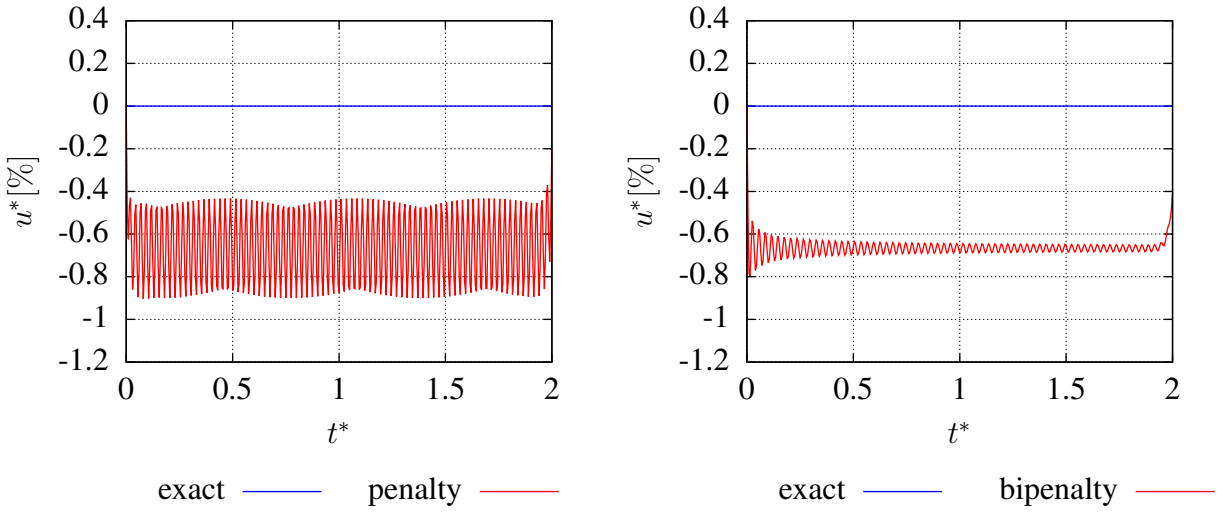


(a) $r = \infty$ (penalty method) (b) $r = 1$ (bipenalty method)

Figure 6: Time distribution of the balance of energy for $\beta_{\text{s}} = 1.5$ and $C_{\text{r}} = 0.5$.

the penalty-like methods, contact forces perform a spurious work on penetrations. This work converges to zero as β_{s} tends to infinity. Nevertheless, a finite value of the stiffness penalty parameter always results in a non-zero work of contact force. One can also notice the presence of oscillations in the distributions of the potential energy and the work of contact forces, which result in oscillations in the distributions of the total energy. This phenomenon is primarily caused by the oscillations in the gap function, which will be discussed further.

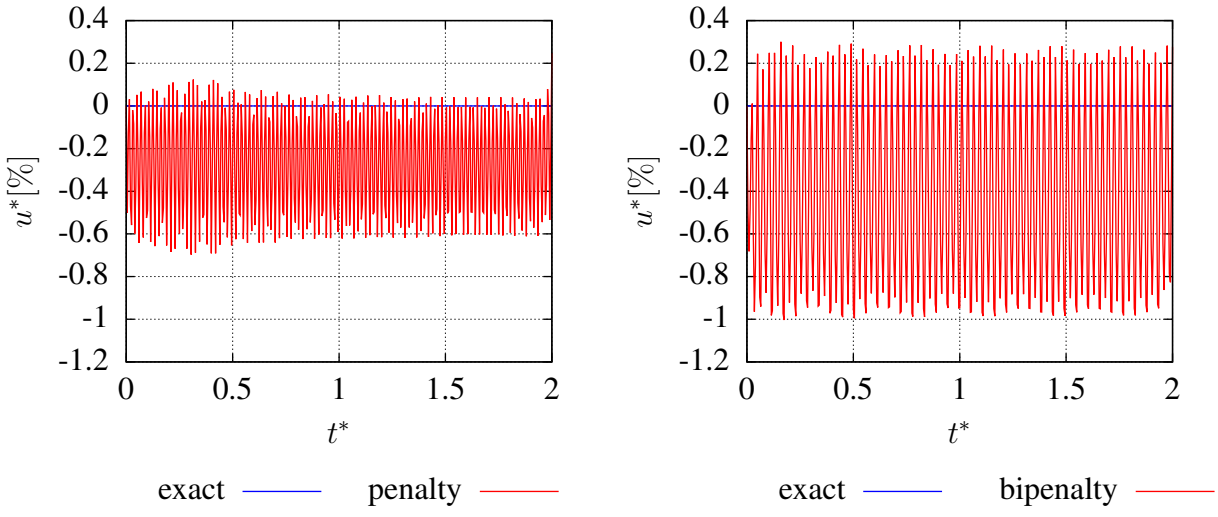
Figure 7 shows time distribution of the dimensionless contact displacement for $\beta_{\text{s}} = 1.5$ and $C_{\text{r}} = 0.5$. The gap should be equal to zero during the impact, which is indicated by the exact solution in the Figure 7. It is well known that penalty-like methods allow certain



(a) $r = \infty$ (penalty method)

(b) $r = 1$ (bipenalty method)

Figure 7: Time distribution of the dimensionless contact displacement for $\beta_s = 1.5$ and $C_r = 0.5$.



(a) $r = \infty$ (penalty method)

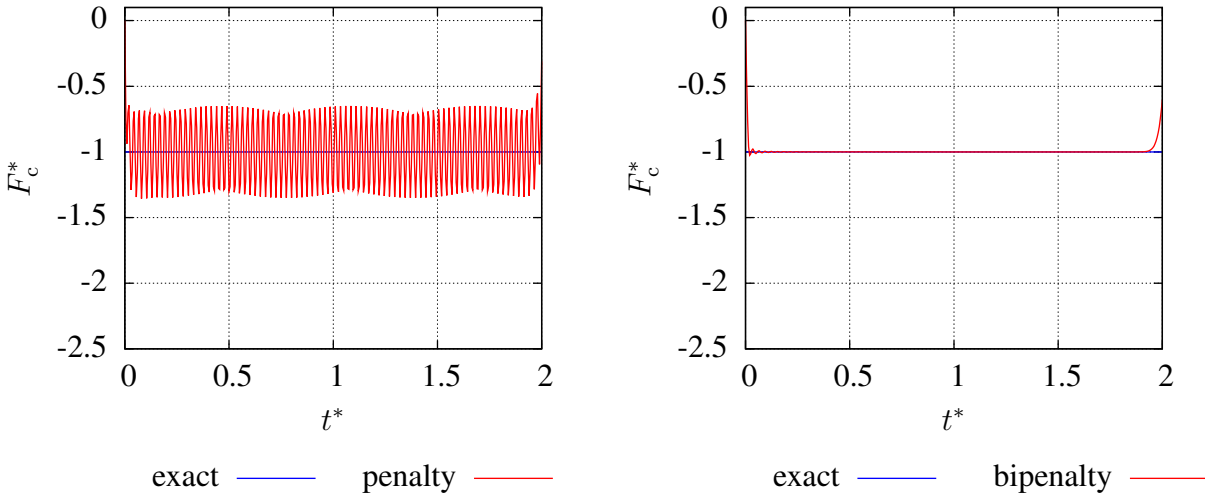
(b) $r = 1$ (bipenalty method)

Figure 8: Time distribution of the dimensionless contact displacement for $\beta_s = 3.5$ and $C_r = 0.5$.

penetration of contact interfaces. As a result, the oscillations of kinematic and stress quantities can occur in impact problems. Figure 7b displays an attenuation of the oscillations for the bipenalty approach in comparison with the penalty method. However, from a certain value of the dimensionless stiffness penalty β_s it was observed that the amplitude of oscillations were even higher for the bipenalty method than for the penalty method. An example is shown in Figure 8, where $\beta_s = 3.5$ was considered. The reason probably is that the oscillation of the contact displacement overshot zero value. Thus, the contact constraint was deactivated and the

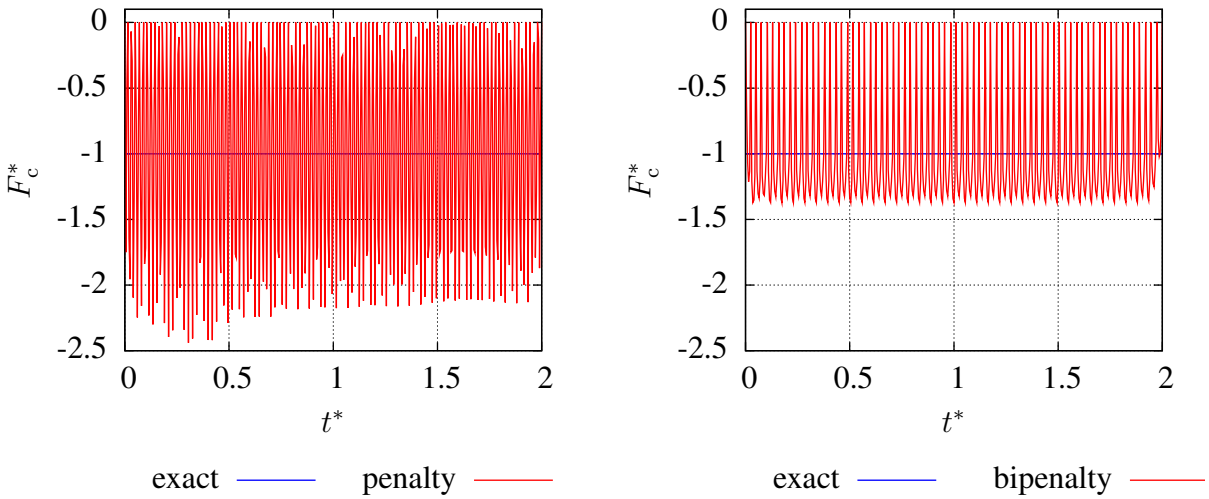
contact force disappeared. In consequent iterations, the contact constraint was again activated. Therefore, the system was switching between two states which generated the oscillations.

This phenomenon can also be observed in Figure 10, where time distribution of the dimensionless contact force is plotted. Both distributions are bounded by zero value. On the other hand, for the previously chosen value of dimensionless stiffness penalty $\beta_s = 1.5$ time dependence of of the dimensionless contact force oscillated around the exact solution as indicated in Figure 9. Similarly to distribution of the contact displacement in Figure 7b the bipenalty method dumped oscillations in the distribution of contact force depicted in Figure 9b.



(a) $r = \infty$ (penalty method) (b) $r = 1$ (bipenalty method)

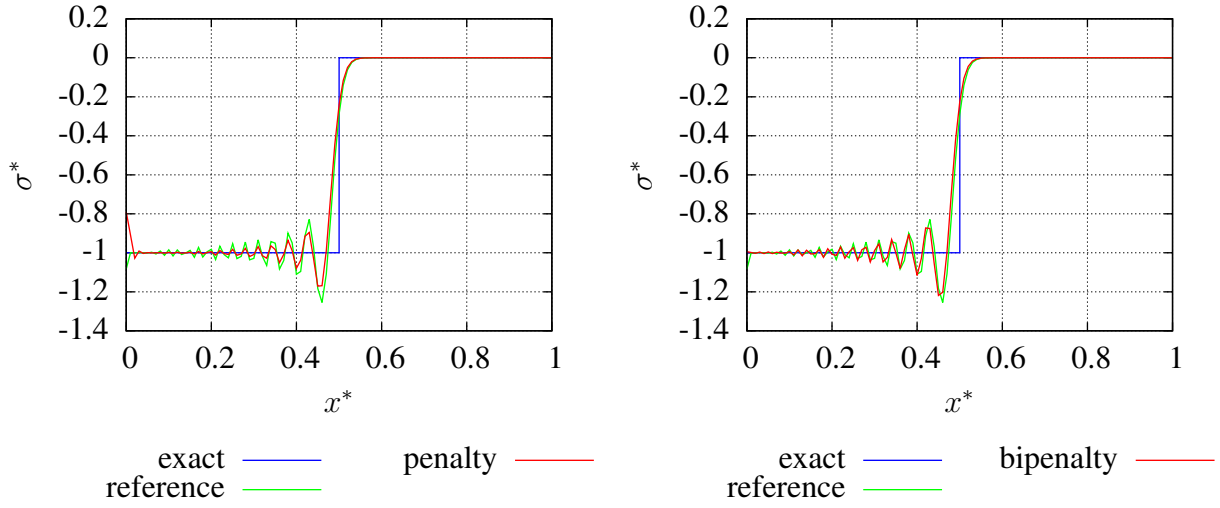
Figure 9: Time distribution of the dimensionless contact force for $\beta_s = 1.5$ and $C_r = 0.5$.



(a) $r = \infty$ (penalty method) (b) $r = 1$ (bipenalty method)

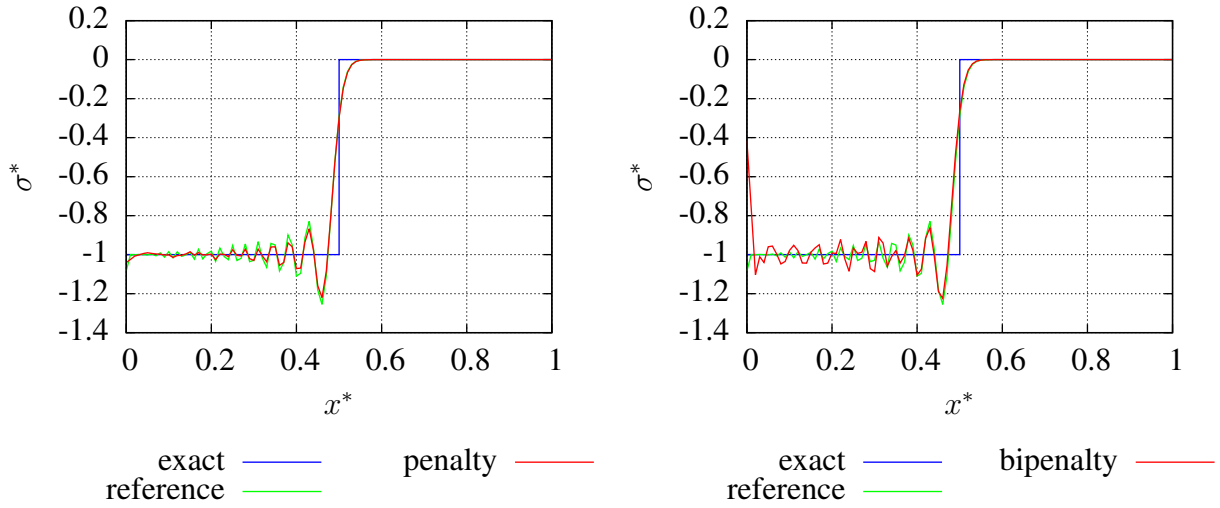
Figure 10: Time distribution of the dimensionless contact force for $\beta_s = 3.5$ and $C_r = 0.5$.

Figure 11 shows spatial distribution stress along the bar when the wavefront reached a half of the bar. In addition to contact analysis, a reference calculation was performed, where the axial displacement of the contact node was fixed.



(a) $r = \infty$ (penalty method) (b) $r = 1$ (bipenalty method)

Figure 11: Spatial distribution of the dimensionless stress for $\beta_s = 1.5$ and $C_r = 0.5$.



(a) $r = \infty$ (penalty method) (b) $r = 1$ (bipenalty method)

Figure 12: Spatial distribution of the dimensionless stress for $\beta_s = 3.5$ and $C_r = 0.5$.

Stress distributions for both the penalty and the bipenalty method was in a good agreement with the reference solution (see Figures 11 and 12). The reason probably is that the finite element mesh behaves as a low-pass filter [9] and therefore high frequency oscillations introduced by the penalty-like methods do not affect the solution.

4 CONCLUSIONS

In this paper, the stability of explicit contact-impact algorithm [4] using the bipenalty approach was studied. The upper bound of the stable Courant number on the stiffness penalty and mass penalty was derived based on the simple dynamic system with two degrees-of-freedom. It was shown that the critical Courant number tend towards zero for the stiffness penalty approaching infinity whereas the mass penalty was considered to be zero. On the other hand, when the penalty ratio was set to the critical value CPR, which corresponded to the maximum eigenvalue of the unpenalised system, the critical Courant number was equal to one for the arbitrary value of the stiffness penalty.

The derived upper bound of the stability was verified by means of the simple 1D dynamic Signorini problem. It was demonstrated decreasing the critical time step for the standard penalty method and its preserving for the bipenalty method. The example also revealed that both methods caused spurious oscillations in the distributions of displacement and the contact force. This effect was especially obvious for higher values of stiffness penalty parameters. The estimation of the penalty parameter ensuring non-oscillated behaviour of both methods will be investigated in further work.

5 ACKNOWLEDGEMENTS

Support by ME10114, GAP101/12/2315 and GA101/09/1630 with institutional support RVO:61388998 is acknowledged.

REFERENCES

[1] H. Askes, M. Caramés-Saddler, A. Rodriguez-Ferran, Bipenalty method for time domain computational dynamics. *Proceedings of the Royal Society A: Mathematical, Physical and Engineering Sciences*, **466**, 1389–1408, 2010.

[2] J. Hetherington, A. Rodriguez-Ferran, H. Askes, A new bipenalty formulation for ensuring time step stability in time domain computational dynamics. *International Journal for Numerical Methods in Engineering*, **90**, 269–286, 2012.

[3] J. Hetherington, A. Rodriguez-Ferran, H. Askes, The bipenalty method for arbitrary multipoint constraints. *International Journal for Numerical Methods in Engineering*, **93**, 465–482, 2013.

[4] D. Gabriel, J. Plešek, M. Ulbin, Symmetry preserving algorithm for large displacement frictionless contact by the pre-discretization penalty method. *International Journal for Numerical Methods in Engineering*, **61**, 2615–2638, 2004.

[5] P. Wriggers, *Computational contact mechanics, 2nd Eddition*. Springer, 2006.

[6] T.R. Hughes, *The finite element method: Linear static and dynamic finite element analysis*. Prentice-Hall, 1987.

[7] T. Belytschko, W.K. Liu, B. Moran, *Nonlinear finite elements for continua and structures*. John Wiley & sons, 2000.

[8] T. Belytschko, M.O. Neal, Contact-impact by the pinball algorithm with penalty and lagrangian methods. *International Journal for Numerical Methods in Engineering*, **31**, 547–572, 1991.

[9] L. Jiang, R.J. Rogers, Effects of spatial discretization on dispersion and spurious oscillations in elastic wave propagation. *International Journal for Numerical Methods in Engineering*, **29**, 1205–1218, 1990.

COMPDYN 2013
4th ECCOMAS Thematic Conference on
Computational Methods in Structural Dynamics and Earthquake Engineering
M. Papadrakakis, V. Papadopoulos, V. Plevris (eds.)
Kos Island, Greece, 12–14 June 2013

EFFECT OF NEAR-FAULT GROUND MOTIONS ON SEISMIC RESPONSE OF DEEP BASEMENT WALLS

E. Amirzehni[1], M. Taiebat[1], W.D.L. Finn[1], and Ronald H. Devall[2]

[1]Department of Civil Engineering, University of British Columbia, Vancouver, BC, Canada
e-mail: {elnazam,mtaiebat,finn}@civil.ubc.ca

[2] Read Jones Christoffersen Ltd., Vancouver, BC, Canada
e-mail: rdevall@rjc.ca

Keywords: Basement Wall, Seismic Response, Near-Fault Motions, Dynamic Analysis

Abstract. *The current state of practice for seismic design of basement walls in British Columbia is using the Mononobe-Okabe (M-O) method, which is based on the Peak Ground Acceleration (PGA). Preliminary results from a recent study of the authors show that the designed walls based on the M-O method with the code mandated PGA for Vancouver are too conservative. This conclusion was achieved by designing the basement wall for the earth pressures derived from the M-O method with different fraction of the code PGA, then subjecting the designed walls to ground motions matched to the UHS of Vancouver in a series of dynamic analyses, and monitoring the performance of the walls from results of the analyses. It was found that walls designed for the M-O pressures based on 50-60% PGA in Vancouver result in satisfactory performance in terms of moment, shear capacity, and drift ratio along the height of the wall, when subjected to ground motions with a 2% exceedance rate in 50 years. This conclusion was based on the use of far-fault motions for analysis. The objective of the present study is to check whether such walls would be safe when subjected to near-fault motions of approximately similar intensity.*

1 INTRODUCTION

Ground motions close to a ruptured fault can be significantly different than those observed further away from the seismic source. The near-fault zone is typically assumed to be restricted to within a distance of about 10 km from the ruptured fault. In the near-fault zone, ground motions contain large velocity pulses, typically with periods of $T = 2^+$ seconds, which impart concentrated energy input at the longer periods [1]. Pulse-type motions have been identified as critical in the design of buildings in the near-fault zone and their effect is to increase the long-period portion of the acceleration response spectrum which leads to larger displacements [2].

The current state of practice for seismic design of basement walls in British Columbia is using the Mononobe-Okabe (M-O) method [3, 4], which is based on the Peak Ground Acceleration (PGA). In 2005 the National Building Code of Canada (NBCC) changed the seismic hazard level from 10% in 50 years in NBCC 1995 to 2% in 50 years in NBCC 2005, which leads to doubling the PGA in Vancouver from 0.24g to 0.46g [5, 6]. This new hazard level remained the same in NBCC 2010 [7]. The new PGA leads to very large seismic forces that make the resulting structures much more expensive. Since there is a little evidence of any significant damage to basement walls during major earthquakes, the Structural Engineers Association of British Columbia (SEABC) considered that current design procedures must be overly conservative and initiated a task force to review the current design procedures for seismic design of basement walls. The authors have the task to evaluate the current design procedure.

A series of nonlinear two-dimensional dynamic analyses have been conducted to model the seismic behavior of the basement walls designed for various fractions of the NBCC 2010 PGA for Vancouver. Preliminary results in recent studies of the authors indicate that walls designed for M-O pressures based on 50-60% PGA in Vancouver are safe for the ground motions with a 2% exceedance rate in 50 years [8, 9]. These conclusions are based on the use of far-fault motions for analysis. This paper describes an extension of the previous study to evaluate the performance of basement walls subjected to near-fault motions with approximately similar intensities. These motions differ from near-fault motions in having large velocity pulses.

2 DESCRIPTION OF COMPUTATIONAL MODEL

A basement wall was designed by Structural Engineering Association of British Columbia (SEABC) specifically for this study based on the current state of practice but using the earth pressure derived from the M-O method with 50% of the code mandated PGA for Vancouver. The design PGA for Vancouver in the current code NBCC 2010 is 0.46g which corresponds to the probability of exceedence of 2% in 50 years. Taiebat et al. [8, 9] analyzed the nonlinear seismic response of this basement wall by using the two–dimensional finite difference computer program FLAC 7.00 [10]. In their simulations the response of the soil was modeled by a Mohr-Coulomb elastic-perfectly

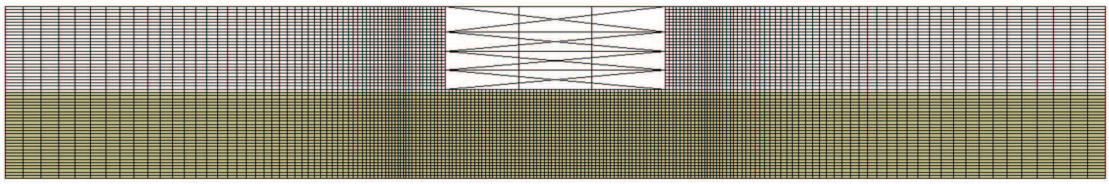
(d) 

Figure 1: Basement wall model in FLAC [8, 9]

plastic constitutive model with degraded elastic moduli. The required model parameters were elastic shear modulus, Poisson's ratio, cohesion, friction, and dilation angles of soil. Similar numerical model has been employed in the present study to explore the effect of near fault ground motions on the seismic response of the designed basement wall. The properties used in conjunction with the Mohr-Coulomb model for the two layers of soil shown in Figure 1 are the same as used by Taiebat et al. [8, 9] in their analyses of the same wall under far-fault motions. Predominant period of the system under the damped free vibration conditions was calculated to be $T = 0.4$ seconds.

3 SELECTING GROUND MOTIONS

The ground motion database compiled for studying the effects of near-fault ground motions constitutes a representative number of far-fault and near-fault ground motions. Eigth far-fault ground motions, listed in Table 1, were selected from the Pacific Earthquake Engineering Research Center (PEER) strong ground motion database [11]. The candidate input motions are in the magnitude range of 6.5 to 7.5, within 30 km of the causative fault plane from earthquake sites with average shear wave velocities, Vs30, in the range of 360 and 760 m/s which is consistent with the reference site class in NBCC 2010. Each of the selected motions has two components, fault normal and fault parallel; the component of the motion which has a higher PGA was selected for the analysis and reported in Table 1.

A total of nine near-fault records with forward directivity were also chosen from the PEER database and are shown in Table 3. They cover a range of PGA, PGV, pulse periods, and distances from the fault. Only the effect of forward directivity is considered; the fling step effect is not studied. The records are from earthquakes having moment magnitudes range of 6.5 to 7.5, and were recorded at closest fault distances of 0 to 20 km. The records are again taken from site class C soils. In the case of near-fault motions, for each record, the component of the motion which leads to the higher drift ratio, after conducting the dynamics analyses (next section), is reported in Table 3 as the selected component.

Table 1: Earthquakes included in the study of far-fault ground motions

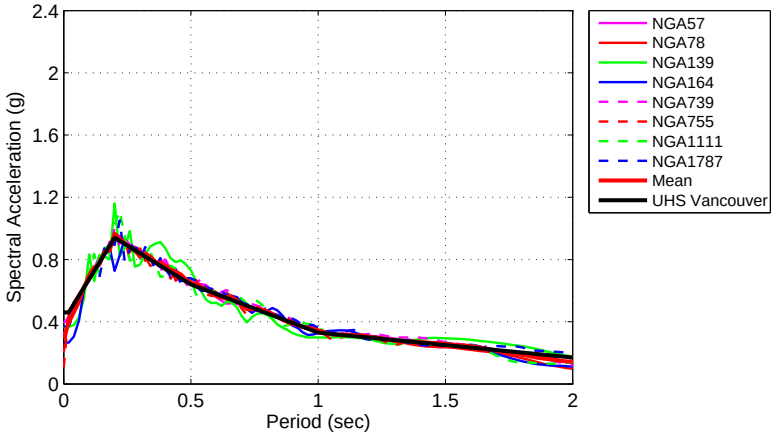
NGA	Event	Year	Station	Mag	Mechanism	R_{jb}(km)[a]	R_{rup}(km)[b]	Vs30(m/s)	Selected Comp.
57	San Fernando	1971	Castaic - Old Ridge Route	6.61	Reverse	19.3	22.6	450.3	FN
78	San Fernando	1971	Palmdale Fire Station	6.61	Reverse	24.2	29	452.9	FP
139	Tabas- Iran	1978	Dayhook	7.35	Reverse	0	13.9	659.6	FN
164	Imperial Valley-06	1979	Cerro Prieto	6.53	Strike-Slip	15.2	15.2	659.6	FN
739	Loma Prieta	1989	Anderson Dam (Downstream)	6.93	Reverse-Oblique	19.9	20.3	488.8	FN
755	Loma Prieta	1989	Coyote Lake Dam (SW Abut)	6.93	Reverse-Oblique	20	20.3	597.1	FP
1111	Kobe- Japan	1995	Nishi-Akashi	6.9	Strike-Slip	7.1	7.1	609	FN
1787	Hector Mine	1999	Hector	7.13	Strike-Slip	10.3	11.7	684.9	FN

(a) Joyner-Boore distance to rupture plane.
(b) Closest distance to rupture plane.

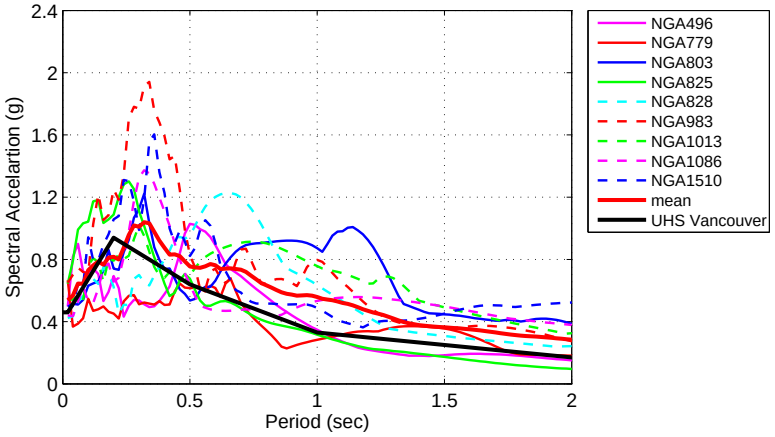
Table 2: Earthquakes included in the study of near-fault ground motions

NGA	Event	Year	Station	Mag	Mechanism	R_{jb}(km)	R_{rup}(km)	Vs30(m/s)	Selected Comp.
496	Nahanni- Canada	1985	Site 2	6.76	Reverse	0	4.9	659.6	FP
779	Loma Prieta	1989	LGPC	6.93	Reverse-Oblique	0	3.9	477.7	FP
803	Loma Prieta	1989	Saratoga - W Valley Coll.	6.93	Reverse-Oblique	8.5	9.3	370.8	FN
825	Cape Mendocino	1992	Cape Mendocino	7.01	Reverse	0	7	513.7	FP
828	Cape Mendocino	1992	Petrolia	7.01	Reverse	0	8.2	712.8	FN
983	Northridge-01	1994	Jensen Filter Plant Generator	6.69	Reverse	0	5.4	525.8	FP
1013	Northridge-01	1994	LA Dam	6.69	Reverse	0	5.9	629	FN
1086	Northridge-01	1994	Sylmar - Olive View Med FF	6.69	Reverse	1.7	5.3	440.5	FN
1510	Chi-Chi- Taiwan	1999	TCU075	7.62	Reverse-Oblique	0.9	0.9	573	FN

The selected far-fault ground motions were spectrally matched to the NBCC 2010 Uniform Hazard Spectra (UHS) of Vancouver, in the period range of 0.02–1.7 seconds using computer program SeismoMatch [12]. The mean acceleration spectrum of these scaled records is shown in Figure 2(a) together with the NBCC 2010 UHS for Vancouver. Thus, on average, the nine time histories reasonably represent the NBCC 2010 UHS design level for Vancouver. On the other hand, the near-fault motions were lin-



(a) Spectrally matched far-fault records



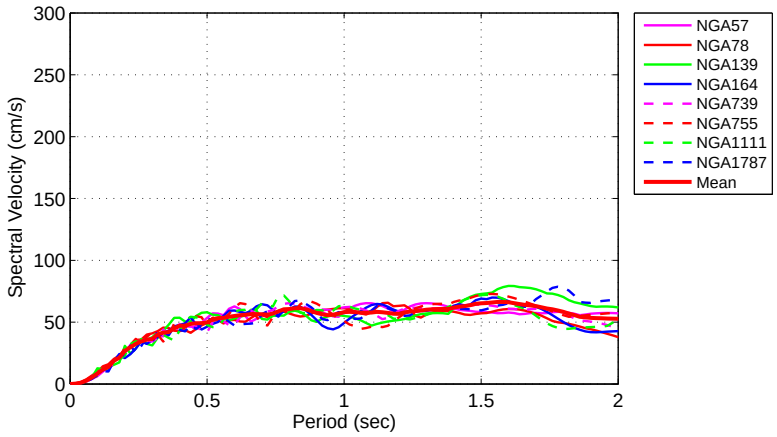
(b) Linearly matched near–fault records

Figure 2: Design spectrum and acceleration response spectra of (a) spectrally matched far fault motions, and (b) linearly matched near-fault motions with forward directivity.

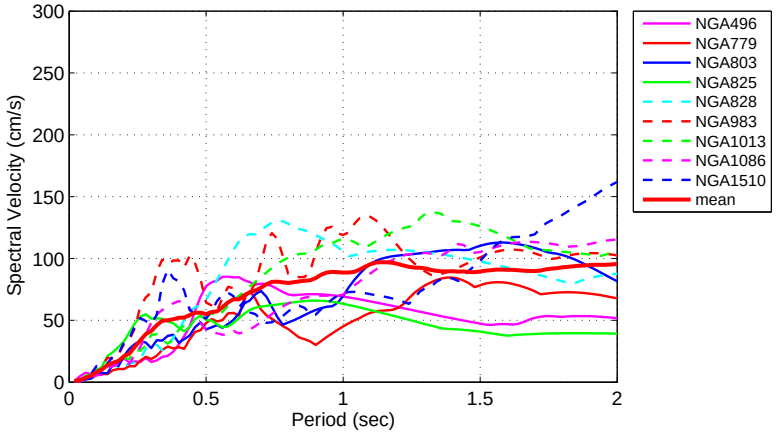
early matched to UHS of Vancouver in the period range of 0.02–1.7 seconds to provide a basis for comparison of results from near-fault and far-fault ground motions. The acceleration response spectra of the scaled near-fault ground motions together with the

response spectrum defined for NBCC 2010 site class C are illustrated in Figure 2(b).

Figure 3 illustrates the velocity spectra of the far-fault and near-fault and records. This figure shows a great variability in near-fault response spectra especially in the longer periods. The figure demonstrates that near-fault records can impose very larger demands in the longer periods that should be taken into account in the design process.



(a) Spectrally matched far-fault records



(b) Linearly matched near-fault records

Figure 3: Velocity response spectra of (a) spectrally matched far fault motions, and (b) linearly matched near-fault motions with forward directivity.

An important observation from the near-fault velocity spectrum is the existence of a predominant peak in most of the near-fault records. The predominant peak of the velocity spectrum is used to estimate the pulse periods in the near-fault records which are reported in Table 4.

4 RESULTS OF ANALYSIS AND DISCUSSION

Drift ratio is usually defined as the relative displacement between floor levels divided by story height. The deformation or the relative displacement of the wall at the middle of each basement is calculated as the difference between the displacement of the wall at that level and the displacement of the wall at its base. Drift ratio for each story is calculated as shown in Figure 4. The resulting drift ratio from this figure is a useful indicator to determine the amount of damage to the wall. In this figure h is the floor height, $u_{\text{floor,top}}$ and $u_{\text{floor,bottom}}$ are the wall deformations at the floor levels and u_{wall} is the deformation at the mid height of the wall (between two floors).

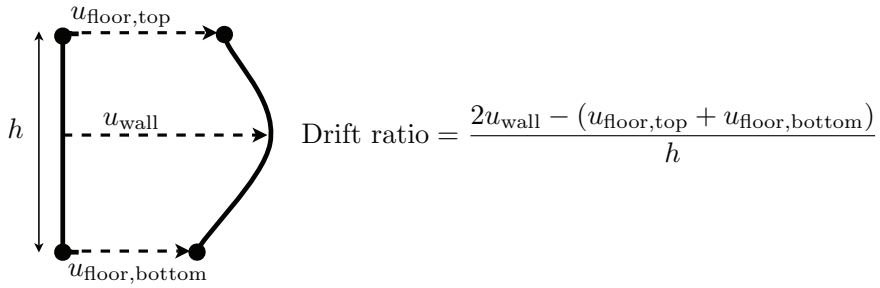


Figure 4: Definition of drift ratio for each story of the basement wall [8, 9].

This definition is consistent with the definition of hinge rotation used by Task Committee on Blast Resistance Design [13]. This committee related hinge rotation to structural performance. They specified two performance categories which may apply to basement walls; low and medium response categories. The Low Response Category is defined as 3.5% drift ratio: "localized building/component damage. Building can be used; however repairs are required to restore integrity of structural envelope. Total cost of repairs is moderate". The Medium Response Category is defined as 7% drift ratio: "widespread building/component damage. Building cannot be used until repaired. Total cost of repairs is significant". Tentatively a drift ratio of 3.5% or less is taken as an index of satisfactory performance in this study, consistent with the performance criterion in the previous studies of the authors on this subject [8, 9].

Calculated drift ratios for the far-fault and near-fault motions are presented in Tables 3 and 4, respectively, and are illustrated in Figure 5. The orientation of the structure with respect to the fault direction may determine the severity of the ground motion that the structure will experience in the near-fault region of a fault rupture. So regarding to the current selection of the near-fault motions, in some cases the fault-normal component causes the higher drift ratio in the basement wall and in other cases, the fault-parallel component. As mentioned previously, the component of the near-fault motion that causes the more severe deformation is reported in the tables.

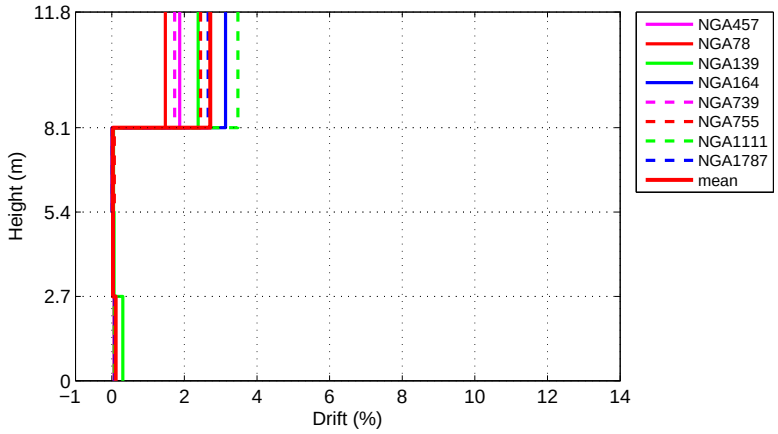
Table 3: Spectral values of the selected component of the far-fault records and the corresponding maximum resultant drift ratios

NGA	Event	Selected Comp.	PGA (g)	PGV (cm/s)	PGD (cm)	Max. Drift Ratio (%)
57	San Fernando	FN	0.36	24.82	5.36	1.94
78	San Fernando	FP	0.34	18.11	4.25	1.49
139	Tabas- Iran	FN	0.36	24.98	8.79	2.58
164	Imperial Valley-06	FN	0.26	19.51	4.94	3.21
739	Loma Prieta	FN	0.32	21.21	7.19	1.92
755	Loma Prieta	FP	0.45	34.60	10.68	2.44
1111	Kobe- Japan	FN	0.36	34.91	8.70	3.47
1787	Hector Mine	FN	0.37	32.02	11.45	2.65

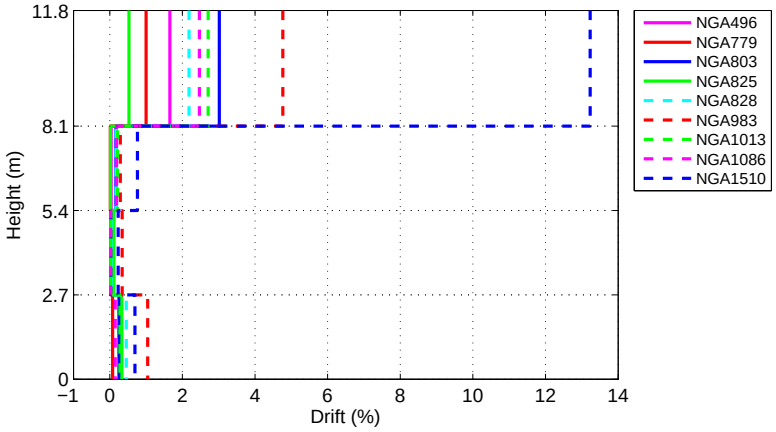
Table 4: Spectral values of the selected component of the near-fault records and the corresponding maximum resultant drift ratios

NGA	Event	Selected Comp.	PGA (g)	PGV (cm/s)	PGD (cm)	Pulse Period (sec)	Max. Drift Ratio (%)
496	Nahanni-Canada	FP	0.41	41.81	9.30	0.81	1.72
779	Loma Prieta	FP	0.28	38.34	16.24	3	1.02
803	Loma Prieta	FN	0.49	73.60	36.54	1.9	3.01
825	Cape Mendocino	FP	0.62	51.32	16.55	4.9	1.22
828	Cape Mendocino	FN	0.42	41.33	17.81	0.95	2.18
983	Northridge-01	FP	0.63	38.38	13.70	3.5	5.49
1013	Northridge-01	FN	0.53	37.75	14.83	1.7	2.7
1086	Northridge-01	FN	0.43	32.27	6.39	2.44	2.46
1510	Chi-Chi-Taiwan	FN	0.47	53.73	45.32	5.1	13.22

In both far-fault and near-fault motions, the maximum drift ratio is concentrated at the top story of the basement wall. There is no significant difference between the behavior of the wall excited by far-fault or near-fault motions. In both cases the amount of maximum drift ratio occurs at the top story is around 2.5%, except for the Chi-Chi record NGA 1510, which produced 13% inter-story drift ratio at the top story. This is related to the high PGV of this motion compared with the other near-fault records and the fact that the Chi-Chi record has a peak in its ARS at the fundamental period of the system (0.4 sec) (Figures 2 and 3). The Northridge record NGA 983 leads to a higher drift (5.5%) compared with the rest of the near-fault records for the same reason.



(a) Analysis results for far-fault motions



(b) Analysis results for near-fault motions

Figure 5: Result of the analysis for the model excited by (a) far-fault motions (b) near-fault motions.

5 CONCLUSIONS

The key conclusions of the study are as follows:

- According to the low fundamental period of the system, 0.4 second, generally there is not any significant difference in the drift ratio profiles along the basement wall due to near-fault and far-fault motions.
- For both near-fault and far-fault motions the highest drift ratio occurs at the top story of the basement wall. This level is taller and less confined than the lower levels.
- A peak in the spectral acceleration and velocity plots at the predominant period of the system, will cause more drift at the top story level of the basement wall.

Acknowledgements

The materials presented in this paper are part of an ongoing study conducted by the authors as members of a task force committee for evaluation of seismic pressure on basement walls; struck by the Structural Engineers Association of British Columbia (SEABC). The authors are grateful for many constructive discussions with committee members: Ali Amini, Don Anderson, Peter Byrne, Mat Kokan, Jim Mutrie, Ernest Naesgaard, Rob Simpson, and Doug Wallis. Support to conduct this study is provided in part by the Natural Sciences and Engineering Research Council of Canada (NSERC).

REFERENCES

[1] J. D. Bray and A. Rodriguez-Marek, "Characterization of forward-directivity ground motions in the near-fault region," *Soil Dynamics and Earthquake Engineering*, vol. 24, no. 11, pp. 815–828, 2004.

[2] E. Kalkan and S. K. Kunnath, "Effects of fling step and forward directivity on seismic response of buildings," *Earthquake Spectra*, vol. 22, no. 2, pp. 367–390, 2006.

[3] S. Okabe, "General theory of earth pressure," *Proceedings of the Japan Society of Civil Engineers*, vol. 12, no. 1, pp. 123–134, 1926.

[4] N. Mononobe and H. Matsuo, "On the determination of earth pressures during earthquakes," in *Proceedings of World Engineering Conference*, pp. 176–182, 1929.

[5] National Building Code of Canada, *NBCC*. Institute for Research in Construction, National Research Council of Canada, Ottawa, ON, Canada, 1995.

[6] National Building Code of Canada, *NBCC*. Institute for Research in Construction, National Research Council of Canada, Ottawa, ON, Canada, 2005.

[7] National Building Code of Canada, *NBCC*. Institute for Research in Construction, National Research Council of Canada, Ottawa, ON, Canada, 2010.

[8] M. Taiebat, A. Ahmadnia, W. D. L. Finn, C. E. Ventura, E. Naesgaard, and R. H. Devall, "Seismic assessment of basement walls for different design criteria," in *Proceedings of the 4th Pan-American and 64th CGS conference*, (Toronto, ON, Canada), pp. Paper ID: 1069, 7 pages, 2011.

[9] M. Taiebat, W. Finn, A. Ahmadnia, E. Amirzehni, and C. Ventura, "Seismic evaluation of existing basement walls," in *Computational Methods in Earthquake Engineering* (M. Papadrakakis, M. Fragiadakis, and V. Plevris, eds.), vol. 2 of *Computational Methods in Applied Sciences*, p. 20 pages, Springer, 2013.

[10] Itasca Consulting Group, Inc., Minneapolis, Minnesota, *FLAC: Fast Lagrangian Analysis of Continua, Version 7.0*, 2012.

[11] PEER, "Pacific Earthquake Engineering Research Center strong motion database." `http://peer.berkeley.edu/peer_ground_motion_database`, accessed on 7 January 2013.

[12] Seismosoft, "SeismoMatch version 1.0.3." `http://www.seismosoft.com/`, 2009.

[13] TC-ASCE, "Design of blast-resistant buildings in petrochemical facilities," tech. rep., Task Committee on Blast-Resistant Design of the Petrochemical Committee of the Energy Division of ASCE, 1997.

COMPDYN 2013
4th ECCOMAS Thematic Conference on
Computational Methods in Structural Dynamics and Earthquake Engineering
M. Papadrakakis, V. Papadopoulos, V. Plevris (eds.)
Kos Island, Greece, 12–14 June 2013

EARTHQUAKE RESPONSE ANALYSES OF SOIL-STRUCTURE INTERACTION SYSTEM USING NONLINEAR ENERGY TRANSMITTING BOUNDARY

Naohiro NAKAMURA[1]
[1]Research & Development Institute, Takenaka Corporation,
1-5-1, Ohtsuka, Inzai, Chiba, Japan, 270-1395
nakamura.naohiro@takenaka.co.jp

Keywords: Transmitting boundary, Frequency Dependency, Nonlinear, Soil Impedance, Time History Response Analysis.

Abstract. *The energy-transmitting boundary, which is used in the well-known FEM program FLUSH, is a quite efficient technique for the earthquake response analysis of buildings considering soil-structure interaction. However, it is applicable only in the frequency domain. The author has studied and proposed methods for transforming frequency dependent soil impedance into the time domain.*

In the previous paper, the author proposed an earthquake response analysis method using the energy transmitting boundary in the time domain using the transform method, because the kernel of the boundary is the frequency dependent impedance full matrix. Then, an earthquake response analysis with a nonlinear building using the boundary was carried out, and the accuracy and the efficiency of the boundary were confirmed. In that analysis, the inner field (the region inside the boundary) could be treated as the nonlinear system, but the free field (the region outside the boundary) and the boundary were treated as the linear system.

Contrary to this, in this paper, the nonlinear transmitting boundary is proposed. By using it, all of the inner field, the free field and the boundary itself can be treated as the nonlinear system. The boundary impedance matrix is calculated in the frequency domain corresponding to the condition of the free field at the specific times. Then, these impedance matrices are transformed to the impulse response matrices in the time domain. In the nonlinear response analysis of the total system, the transmitting boundary at each time step is obtained by interpolation of these impulse response matrices between the specific times. Then, example earthquake response analyses were performed using a practical soil and building model to evaluate the soil-structure interaction effect. The response accuracy was compared with the cases of viscous boundary, which is the most common and representative boundary in the time domain. It was shown that the area of the inner field can be greatly reduced by using the proposed method because the accuracy of the boundary is quite high. Therefore, it was confirmed that the proposed method is effective.

1 INTRODUCTION

The energy transmitting boundary (hereinafter referred to as TB), which is used in FLUSH [1] and ALUSH [2], is a side wave boundary that is highly accurate and is highly effective. These programs developed in the 1970s are still utilized today as powerful tools in design study for architecture and civil engineering. However, TB has been formulated in the frequency domain, and can only perform linear analysis and equivalent linear analysis within the frequency domain. During a severe earthquake the building and its surrounding soil exhibit nonlinear behaviour. It is thus desirable to be able to use this boundary in the time domain also.

The author has previously studied how to transform TB to the time domain with high accuracy and ease in cases where the dynamic stiffness has a strong frequency dependency [3, 4]. As part of these efforts, the author transformed TB of the 2-dimensional in-plane problem, which is equivalent to FLUSH, into the time domain, and showed that high-accuracy analysis is possible in the same manner as with the frequency domain. In addition, the author applied a nonlinear characteristic to an inner field building, conducted response analysis, and demonstrated the effectiveness of this method for nonlinear problems [5] (hereinafter referred to as "the previous study").

In the above study, it was possible to consider the nonlinear characteristic for the inner field, but it was necessary to treat the outer field (free field) and TB as linear or equivalent linear. In this paper, the author makes it possible to consider the nonlinear characteristic for outer field objects as well as TB, and proposes a seismic response analysis method that considers the entire analysis model as nonlinear (See Table 1). The analysis target is a 2-dimensional in-plane problem, in the same manner as the previous study.

First, the author outlines the evaluation method for the nonlinear characteristic of outer field, inner field, and TB. Due to the nonlinear characteristics of the material, the physical properties of the outer field changes at each time step. TB also changes at each time step based on the outer field change. However, if we constantly recalculate TB, the computational load will likely become significant. Therefore, in this paper the author proposes a method to interpolate TB which was calculated at representative time. Furthermore, as an example study, the author conduct a seismic response analysis of a soil-structure interaction system (hereafter referred to as SSI system) using these nonlinear analysis methods, thus demonstrating the effectiveness of the nonlinear TB. For comparison, the viscous boundary [6] (hereafter referred to as VB), which is the conventional representative method, and linear TB used in the previous study are used.

	Outer field	TB	Inner field
Frequency Domain TB	L	L	L
Time Domain TB	L	L	N
Proposed Method	N	N	N

*) L: linear or equivalent linear, N: nonlinear

Table 1 Method proposed in this paper

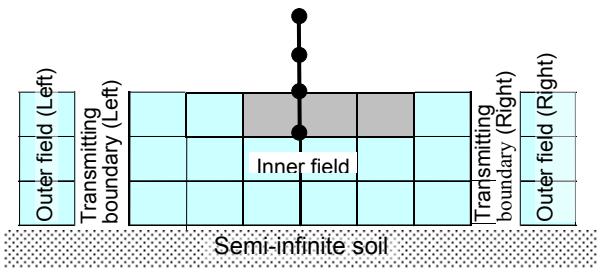


Figure 1 Image of analysis model studied in this paper

2 ANALYSIS METHOD USING NONLINEAR TB

In seismic response analysis which uses TB, the analysis region can be divided into three sections, as shown in Figure 1: (1) outer field, (2) inner field, (3) TB. In this chapter, the au-

thor outlines the method of nonlinear response analysis used in this paper for each of these three sections.

2.1 Outer field

The outer field is distant from the inner field and represents parallel layered soil (free field) which has sufficient spread. In order to be consistent with the analysis result of the inner field, a 1-dimensional wave propagation analysis is performed using a vertical column soil model in which the depth direction is split and soil physical properties the same as the outermost edge of the inner field. This is achieved by constraining the vertical degrees of freedom such that only horizontal shear deformation is allowed.

In the previous study, linear analysis was performed for the analysis of the outer field using 1-dimensional wave theory (SHAKE [7]). In this paper, nonlinear analysis is performed using the same plane strain elements as the outermost edge of the inner field. Physical properties of each element are considered to change based on the given dynamic deformation characteristics (G-γ, h-γ relationship). Here, G is the shear modulus, h is the damping ratio, and γ is the shear strain.

In this paper, nonlinear causal hysteretic damping model [8] is used for the soil analysis. This is a model where the stiffness and damping changes at each time step under the condition that the damping ratio is almost constant in a certain frequency range. Shear modulus and damping ratio changes at each time step depending on the maximum shear strain of the previous 1 second. It should be noted that while Reference [8] uses the lumped mass model with shear element, this paper uses the plane strain element. However, there is no essential difference in the analysis.

2.2 Inner Field

The inner field consists of the building, the foundation, and soil in the vicinity thereof. In this paper, the building is represented by a lumped mass model with shear element. The restoring force characteristics are set for each member, and time history nonlinear responses analysis is performed.

The soil, as with the outer field, is modeled using plane strain elements, and the nonlinear characteristic of every moment is evaluated by the nonlinear causal hysteretic damping model, based on the given G-γ, h-γ relationship. For the shear strain, in the same manner as FLUSH, the main shear strain (γ_1) of Equation (1) is used, and the shear modulus and damping ratio are varied according to the maximum principal shear strain (γ_{1max}) of the previous 1 second. In addition, in Equation (1), ε_x, ε_y, γ_{xy} are respectively x direction axis strain, y direction axis strain, xy direction shear strain.

$$\gamma_1 = \sqrt{(\varepsilon_x - \varepsilon_y)^2 + \gamma_{xy}{}^2} \tag{1}$$

For this analysis, as with FLUSH, the Poisson's ratio does not change even after nonlinear deformation. As a result, the Young's modulus of each element changes with the same ratio as the shear modulus.

2.3 TB

TB is also changed depending on the change of the physical properties of outer field. However, calculating the impedance matrix of TB for each ΔT (analysis time step) is likely to incur a large computational load. Therefore, for a certain time interval (hereinafter referred to as

ΔT_b), TB is calculated using the physical properties of that time, and is also interpolated during that time. More specifically, the calculation is performed as follows (see Figure 2):

(1) First the outer field is calculated, the soil physical properties are determined for each time ΔT_b (0, ΔT_b, $2\Delta T_b$, $3\Delta T_b$, ...).
(2) Using this soil physical property, the impedance matrix of TB for each ΔT_b is calculated.
(3) The components of the matrix for each ΔTb are transformed to the time domain, and the impulse response matrix is calculated. In addition, the time domain transform method is C method, which is the same as the previous study.
(4) The parameters that control the interpolation of TB are selected. In this paper, the element which has the maximum shear strain in the outer field is selected, and the shear strain value of that element at each time is used as the control parameter (hereinafter, $\gamma_{Emax}(t)$).
(5) Let us assume, current time (hereinafter referred to as t) is between j ΔT_b and (j+1) ΔT_b. First, we solve the ratio that $\gamma_{Emax}(t)$, and internally divide γ_{Emax} ($j\Delta T_b$) and γ_{Emax} ((j+1) ΔT_b). The impulse response matrix at time t has the same ratio as above, and is used to internally divide the impulse response matrices of $j\Delta T_b$ and (j+1) ΔT_b. The impulse response matrices for all analysis times are thereby calculated.

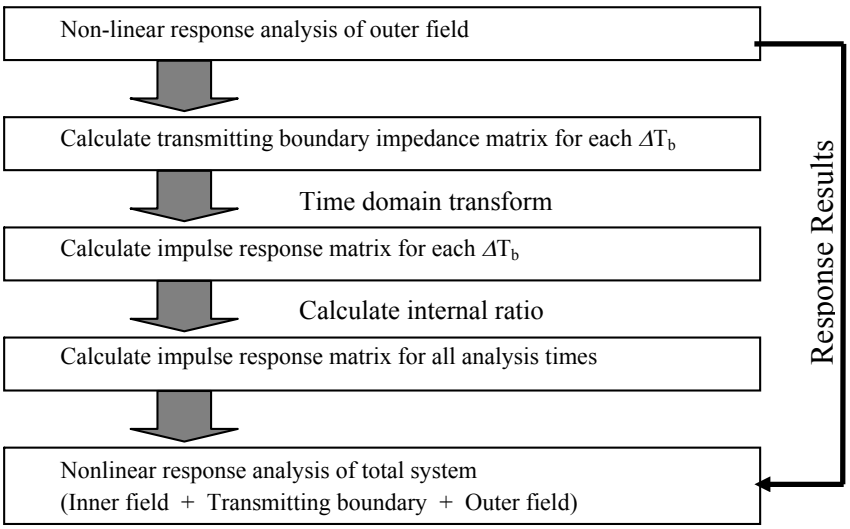


Figure 2 Flow chart of earthquake response analysis using non-linear transmitting

In this paper, ΔT_b is set to 1 second and ΔT is set to 0.01 seconds. If ΔT_b is decreased to ΔT, it becomes the same as calculating TB matrix at each analysis time.

2.4 Equation of motion of the time domain

Equation of motion of the time domain basically is the same as in the previous study. However, in the study, the equation of motion was formulated as a 1/2 model, using inverse-symmetry conditions. In this paper, however, it is formulated as a full model without using an inverse symmetry condition to account for nonlinear characteristics, and a TB and free field are provided to the left and right of the model. In addition, the material of the inner field and TB are nonlinear.

Considering these factors, the equation of motion is given by equation (2). Here {u(t)} is the displacement vector, $[M_I]$, $[K_I(t)]$ are a mass matrix and a stiffness matrix of the inner field, respectively. Also [L(t)], [R(t)] are TB matrix on the left and right sides, and $\{F_L(t)\}$,

$\{F_R(t)\}$ are the boundary force vectors on the left and right sides. The stiffness matrix and TB matrix are nonlinear, so (t) is attached to indicate change with time.

$$[M_I]\{\ddot{u}(t)\}+([K_I(t)]+[L(t)]+[R(t)])\{u(t)\}=-\ddot{y}(t)[M_I]\{1\}+\{F_L(t)\}+\{F_R(t)\} \tag{2}$$

$$\{F_L(t)\}=([L(t)]-[D_L(t)])\{u_L{}^*(t)\},\quad \{F_R(t)\}=([R(t)]-[D_R(t)])\{u_R{}^*(t)\} \tag{3}$$

Where:

$$[D_R]_j=-[D_L]_j=\frac{1}{2}\begin{bmatrix} 0 & \lambda(t)_j & 0 & -\lambda(t)_j \\ G(t)_j & 0 & -G(t)_j & 0 \\ 0 & \lambda(t)_j & 0 & -\lambda(t)_j \\ G(t)_j & 0 & -G(t)_j & 0 \end{bmatrix} \tag{4}$$

$\{u_L{}^*(t)\}$ and $\{u_R{}^*(t)\}$ of the Equation (3) are the response displacement of the right and left side free field which are calculated by nonlinear analysis of the outer field. In addition, $-[D_L(t)]\{u_L{}^*(t)\}$ and $-[D_R(t)]\{u_R{}^*(t)\}$ are the correction force vector (also known as excavation force) acting on the left boundary and right boundary when the earthquake motion is propagated from downward in the vertical direction.

$[D_L(t)]$ and $[D_R(t)]$ are represented by the superposition of sub-matrix $[D_L(t)]_j$ and $[D_R(t)]_j$ which are given by Equation (4), using the Lame constant (G(t)j, λ(t)j) of each element of the free field. Since the Lame constants of each element change over time, $[D_L(t)]$ and $[D_R(t)]$ also change over time. In addition, when performing the equivalent linear analysis, [L(t)], [R(t)], $[D_L(t)]$, $[D_R(t)]$ are constant values which do not change over time.

Among these, [L(t)], [R(t)] are time domain transformed values of the impedance which has a frequency dependency. For this reason, for the calculation of $[L(t)]\{u(t)\}$, in addition to the current displacement vector, the current velocity and acceleration vectors and the past displacement and velocity vectors are needed. The same is true for the calculation of $[R(t)]\{u(t)\}$, $[L(t)]\{u_L{}^*(t)\}$, $[R(t)]\{u_R{}^*(t)\}$. For more information please refer to the previous study.

2.5 Nonlinear causal hysteretic damping model

In time history earthquake response analysis of the inner field and outer field, the causal hysteretic damping model is used in the same manner as in the previous study, as a way to represent the frequency-independence of the material damping. The applicability of causal hysteretic damping model to the nonlinear element has been confirmed in Reference 13. In the example analysis of the next chapter, it is used for the quadrilateral plane strain elements representing the soil, and shear spring elements representing the building.

Equation (5) shows the relational expression of element displacement - element force of the time domain using the nonlinear causal hysteretic damping model. It is almost the same as the previous study. In this paper, however, to take into account the nonlinear characteristics of the element, time change is represented by (t) attached to the element stiffness matrix $[K_e(t)]$ and element damping ratio $h_e(t)$.

$$\{F_e(t)\}=[K_e(t)\ ]\left[\{u_e(t)\}+2h_e(t)\left(c_0\{\dot{u}_e(t)\}+\sum_{j=1}^{n}k_j\{u_e(t-t_j)\}\right)\right] \tag{5}$$

Also $\{F_e\}, \{u_e\}$ are the element force vector and the element displacement vector, respectively. Damping force is calculated by the damping term simultaneous component (c_0) and the stiffness term time delay component ($k_1, k_2, \ldots k_n$), where $k_j = k(j\Delta t)$). As indicated in the previous study, the study frequency range is set as 0-10Hz, Δt =0.05 s, and the 18 term model [9] is used.

3. EXAMPLE STUDY

In this chapter, an example problem is studied to evaluate the applicability and effectiveness of the proposed nonlinear TB.

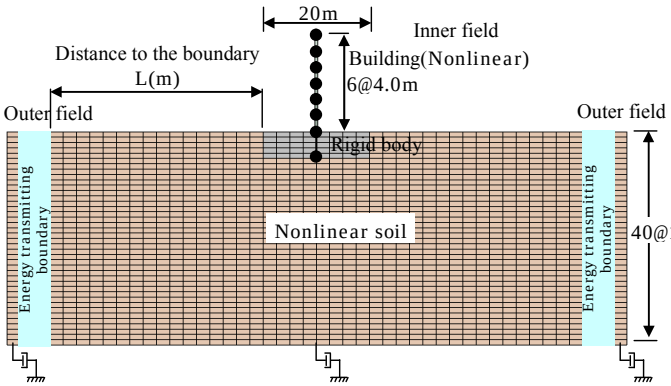


Figure 3 SSI system analysis model

	Inner field	Outer field	Boundary
Case NT	N	N	Transmitting (N)
Case LT	N	N	Transmitting (L)
Case V	N	N	Viscous (L)

*) L: linear, or equivalent-linear, N: nonlinear

Table 2 Case analysis

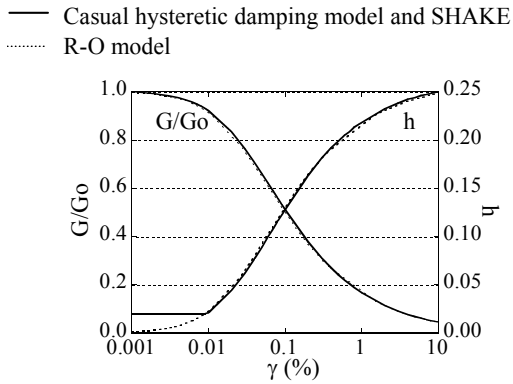


Figure 4 Dynamic deformation characteristics of soil

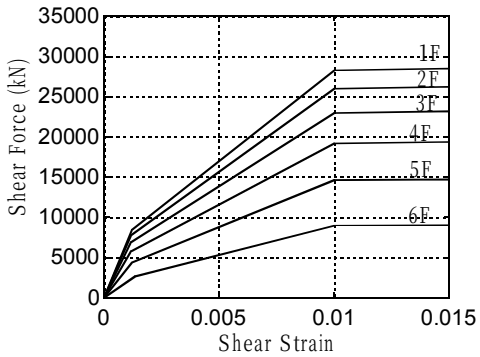


Figure 5 Building skeleton curves

3.1 Analysis model and analysis condition

The analysis model is shown in Figure 3. Both the soil and building have nonlinear characteristics. Soil consists of the surface layer and the base rock. In the surface layer, the thickness is 40 m, the shear velocity is 300 m/s, and the nonlinear characteristics are considered based on the G-γ, h-γ relationship shown in Figure 4. As for the base rock, shear velocity is 500m/s, and the effect is considered as the bottom VB. Figure 5 shows the skeleton curve of each floor of the building. The shear force of the first folding point and second folding point of each curve have been set to correspond to the static seismic intensity 0.3, 1.0respectively.

Input earthquake motion is defined as 2E (twice the upward wave) using maximum acceleration 500Gal of El Centro 1940 NS wave (duration: 10 seconds, time step ΔT=0.01 se-

conds). Time integration is carried out using the Newmark-β method and the average acceleration method (β=1/4).

3.2 Calculation of the outer field

First, the time history nonlinear analysis of the outer field was performed. In this paper, the nonlinear causal hysteretic damping model (F_{max}=10Hz, 18 term model) is used. For each soil element, calculation is performed using the shear modulus and damping ratio determined from the given G-γ, h-γ relationship, for the maximum shear strain amplitude absolute value of the past Δt_m seconds. Hereinafter, Δt_m is called the maximum strain memory time.

First, we look at the impact the difference of Δt_m has on response. The distribution of the maximum response values of acceleration, shear strain, and shear stress when Δtm is 0.1s, 0.5s, 1.0s, 2.0s are shown in Figure 6. From these figures, the result of Δt_m =0.1s shows a difference from others, but the other results roughly correspond. Thus, the result of Δt_m=1.0 s is used in the subsequent study.

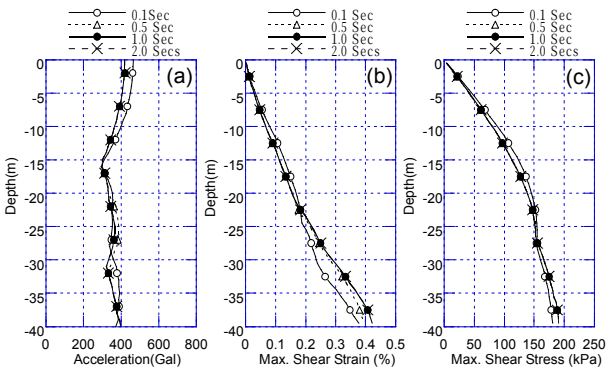


Figure 6 Distribution of maximum response of outer field (Effect of differences in Δt_m on response), (a) Maximum acceleration, (b) Maximum shear strain, and (c) Maximum shear stress.

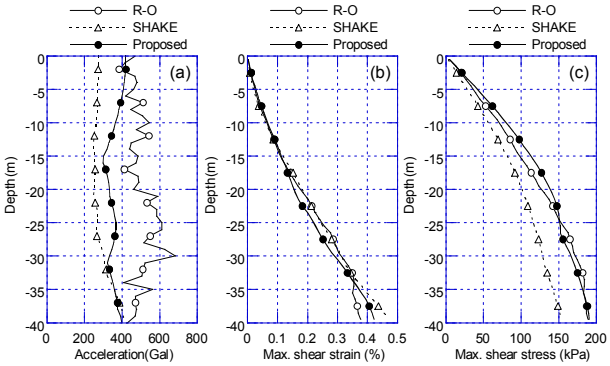


Figure 7 Distribution of maximum response of outer field （Comparison of R-O and SHAKE） (a) Maximum acceleration, (b) Maximum shear strain, and (c) Maximum shear stress.

Next, nonlinear analysis using the R-O model, and equivalent linear analysis using SHAKE is performed, and compared with the causal hysteretic damping model (Δt_m=1.0 s). Figure 7 shows the maximum response value distribution of acceleration, shear strain, and shear stress. The shear strain reaches a maximum at the lowest element and was 0.42% in the causal hysteretic damping model, 0.38% in the R-O model, and 0.47% in SHAKE. The results of each model corresponds well overall, However, results of the R-O model for maximum acceleration has a discontinuous change and has some difference with others. This behavior is similar to the results shown in reference [9].

In this analysis, the shear wave velocity (Vs) and damping ratio (h) of each element is needed for each time for the later calculation of TB. For this reason, the later study is performed using the nonlinear causal hysteretic damping model in which these values are explicitly output.

3.3 Calculation of TB

The calculation of the nonlinear TB is performed based on the response results of the outer field by the causal hysteretic damping model. The number of DOF (degrees of freedom) of TB becomes 82 (41 nodes × 2, i.e., horizontal and vertical degrees of freedom). In addition, using the results of the equivalent linear analysis of the outer field according to SHAKE, VB

and linear TB of the time domain are also calculated (see Table 2). Calculation of the nonlinear TB is performed as follows in accordance with the flowchart in Figure 2.

Figure 8 indicates the shear strain time history waveform of the representative position of the outer field. As shown in the previous section, Δt_m=1.0 s is used. According to γ of Δt_m=1.0 s, the shear modulus G and the damping ratio h changes based on the G-γ, h-γ relationship. TB matrix of the frequency domain is calculated using the physical properties at each ΔT_b. In this paper, ΔT_b=1 s is used.

Figure 9 shows the distribution of the shear strain, Vs (shear wave velocity), and h (damping ratio) calculated from the G-γ, h-γ relationship at representative times (1 s, 3 s, 8 s),. Accordingly, TB matrix of the frequency domain corresponding to the soil physical properties is calculated for each time. Frequency analysis carried out over the range of 0.5Hz to 20Hz in 0.5Hz increments. From here, TB matrix is obtained as a frequency-dependent complex matrix of 82×82 components, for each time.

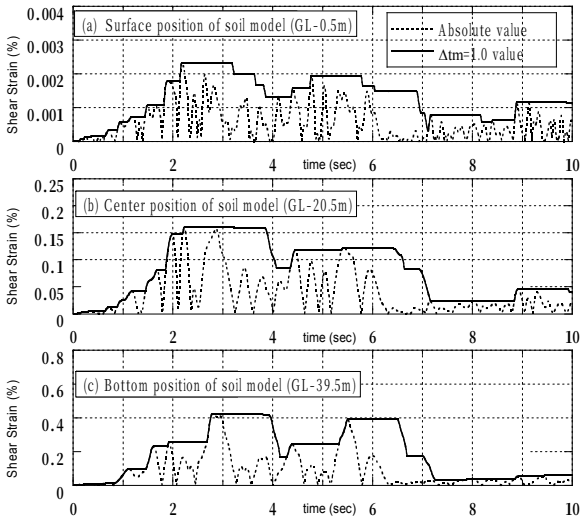


Figure 8 Shear strain time history waveform of the representative position of the outer field

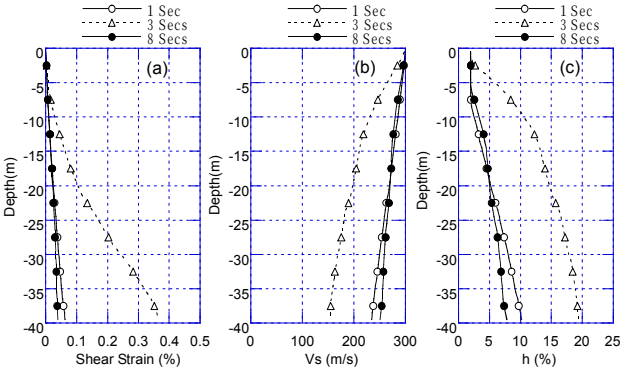


Figure 9 Representative time distribution, (a) Shear Strain, (b) Shear wave velocity, and (c) damping ratio

These impedance matrices are transformed to the time domain, and TB impulse response matrix for each ΔT_b is obtained. The method to transform time domain, is the C method, and the analysis conditions are the same as in the previous study.

By interpolating TB impulse response matrix for each ΔT_b from the previous section, the impulse response matrix for each analysis time step (ΔT: 0.01 seconds in this study) is calculated. The control point used for interpolation is the shear strain of the element of the bottom layer that produces maximum strain.

3.4 SSI system response analysis

The nonlinear soil and building are set in the inner field, and a SSI system response analysis is performed. To clarify the impact that the differences in the boundary have on response, the outer fields are all unified in nonlinear analysis.

The study is performed for the three cases indicated in Table 2. Case NT uses the nonlinear TB proposed in this paper. Case LT uses the equivalent linear TB proposed in the previous study. Case V uses a VB representative of a conventional method. In Case LT and Case V, equivalent linear analysis of the outer field using SHAKE was performed, and TB and VB

calculated from the equivalent physical properties obtained. Furthermore, the effect of the width of the inner field (L) on the accuracy is investigated for each case.

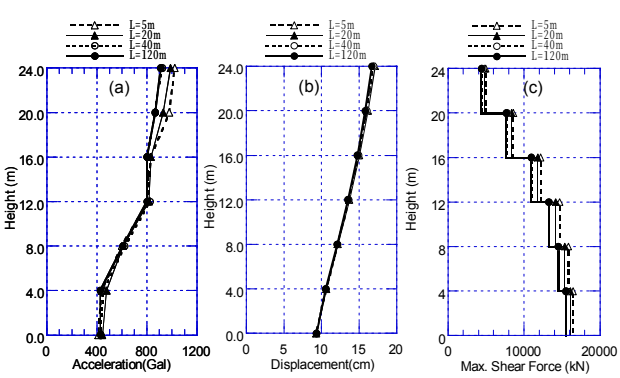


Figure 10 Comparison of maximum response value of the building (case NT: with nonlinear TB), (a) Maximum response acceleration, (b) Maximum response displacement, and (c) Maximum shear force.

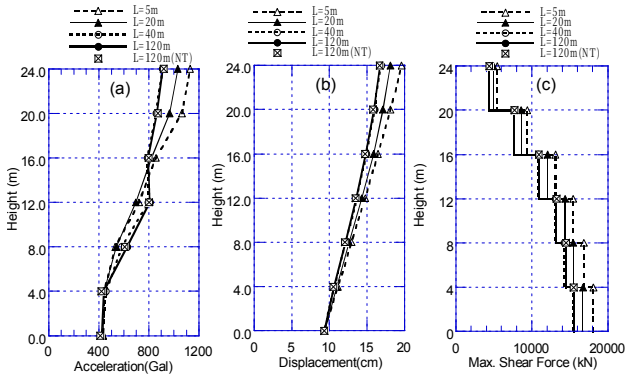


Figure 11 Comparison of maximum response value of the building (case LT: with linear TB), (a) Maximum response acceleration, (b) Maximum response displacement, and (c) Maximum shear force

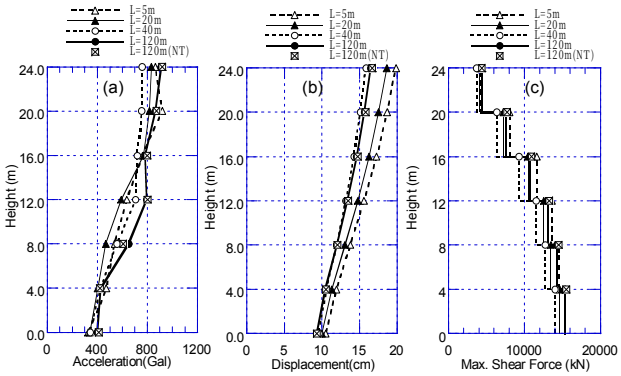


Figure 12 Comparison of maximum response value of the building (case V: with VB), (a) Maximum response acceleration, (b) Maximum response displacement, and (c) Maximum shear force.

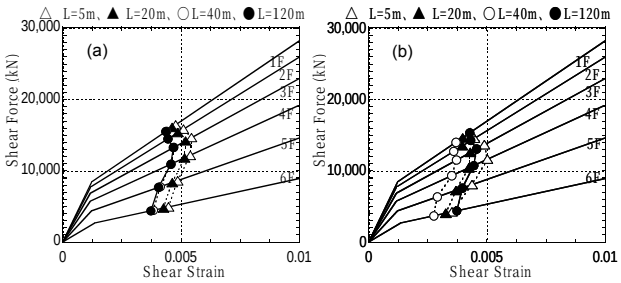


Figure 13 Comparison of the maximum response value on the skeleton curve, (a) Case NT: with nonlinear TB, and (b) Case V: with VB

3.5 Maximum response value of the building

First, the results of the building response in each case are shown below. The response results using the nonlinear TB proposed in this paper are shown below. Figure 10 shows a comparison of the maximum response values (acceleration, displacement, and shear force) of the building for representative models (L=5m, 20m, 40m, 120m). The line with black circles indicates the response result of L=120m where the inner field is at a maximum and likely to be the most accurate. For all figures it can be said that all models correspond well with the most accurate result. This shows that the accuracy of the response results was good even if L is small. Accordingly, it can be said that the response results of this model have good accuracy even for a small model region.

Next, the response results using the equivalent linear TB proposed in the previous study are shown. Figure 11 shows a comparison of the maximum response values. The response re-

sults of L=120m for Case NT are also shown in the figure. In all the figures, the results of L=120m for this case and are generally similar to the results of Case NT. Accordingly, the result of this case has slightly lower accuracy than Case NT, and it is necessary to make L greater than 40m in order to make the differences less than ±10%.

Finally, the response results when using VB is shown, which is a representative method of conventional methods. Figure 12 shows a comparison of the maximum values of the building for each model. In all figures, the results of L=120m are generally similar for Case V and Case NT. The results of each model have some differences with the results of L=120m, and the variation is even greater compared to Figure 10 and Figure 11. In this case, unlike the Case LT, the increase of L does not improve the accuracy except when L is sufficiently large.

3.6 Maximum response value on the skeleton curve

Figure 13 compares the maximum response value on the skeleton curve of each floor, in the cases using the nonlinear TB (Case NT) and VB (Case V). The analysis results of L=5m, 20m, 40m, and 120m are plotted. Results of L=120m (line with black circles) are almost the same at the nonlinear TB and VB. Response value of L=5-40m correspond relatively well to L=120m at the nonlinear TB, but the difference is large in VB. Both of these results show a similar trend to that of the previous section.

3.7 Comparison of calculation load

All the analyses in this chapter were calculated using IBM Power5+ (2.2GHz). Compared to VB, there are a lot of calculation procedures for calculation of TB, so computation time is longer for the same model. However, as shown in the previous chapters, analysis accuracy is high so reduction of the inner field becomes possible.

In figures 10 to 12, when the differences in response is under 10%, L=30m is minimum in the nonlinear TB cases, L=40m is minimum in the equivalent linear TB cases, and L=100m in the VB cases. Computation times including pre-processing are 17.4 minutes (13.8 +3.6 minutes), 16.6 minutes (16.3 +0.3 minutes), and 17.2 minutes respectively. There are no significant differences in this problem. However, in 3-dimensional problems, due to the reduction of the analysis region, the reduction of computational load becomes noticeable, so this proposed method is considered to have a significant advantage.

4. SUMMARY

In the previous study, the author proposed the time history response analysis using the time domain energy TB while it was conventionally possible to apply to only the frequency domain. Accordingly, it became possible to consider nonlinear characteristics for the inner field. However, the outer field and TB were dealt as linear or equivalent linear. In this paper, by providing a method that enable to consider the nonlinear characteristic of TB, a seismic response analysis method that considers the entire analysis model as nonlinear was proposed.

First, the analysis method used in this paper was outlined. Particularly, TB may change every time step, so the computational load becomes significant when recalculations are continually made. Therefore, the author demonstrated a method to interpolate TB calculated at a representative time.

As a further example study, using these nonlinear characteristic evaluation methods, the seismic response analysis of the SSI system was conducted and the effectiveness of using the nonlinear TB was shown. By comparison with VB, which is a representative conventional method, it was shown that there was a big advantage in accuracy when using the nonlinear TB, especially in 3-dimensional problems.

REFERENCES

[1] J. Lysmer, T. Udaka, H. B. Seed, R. N. Hwang, FLUSH a Computer Program for Approximate 3-D Analysis of Soil-structure Interaction Problems, *Report No.EERC75-30, University of California, Berkeley*, 1975

[2] J. Lysmer, T. Udaka, C.-F. Tsai, H. B. Seed, , ALUSH a Computer Program for Seismic Response Analysis of Axisymmetric Soil-structure Systems, *Report No.EERC75-31, University of California, Berkeley*, 1975

[3] N. Nakamura, A Practical Method to Transform Frequency Dependent Impedance to Time Domain, *Earthquake Engineering and Structural Dynamics*, **35**, 217-231, 2006

[4] N. Nakamura, Improved Methods to Transform Frequency Dependent Complex Stiffness to Time Domain, *Earthquake Engineering and Structural Dynamics*, **35**, 1037-1050, 2006

[5] N. Nakamura, Nonlinear Response Analysis of Soil-Structure Interaction System Using Transformed Energy Transmitting Boundary in the Time Domain, *Soil Dynamics and Earthquake Engineering*, **29**, 799-808, 2009

[6] J. Lysmer, R.L. Kuhlelameyer, Finite Dynamic Model for Infinite Area, *J. Eng. Mech. Div., ASCE*, **95**, EM3, 859-877, 1969

[7] P. B. Schnabel, J. Lysmer, H. B. Seed, SHAKE A Computer Program for Earthquake Response Analysis of Horizontally Layered Sites, *Report No.EERC72-12, University of California, Berkeley*, 1972

[8] N. Nakamura, Practical Causal Hysteretic Damping, *Earthquake Engineering and Structural Dynamics*, **36**, 597-617, 2007

[9] N. Nakamura, A Study on Application of Nonlinear Causal Hysteretic Damping Model to Multi-node System Soil Model, Response Analysis of Soil Deposit Considering Both Frequency and Strain Amplitude Dependencies Using Nonlinear Causal Hysteretic Damping Model, *J. of Structural and Construction Engineering (Transaction of AIJ)*,, **662**, 107-114 (In Japanese), 2007

COMPDYN 2013
4th ECCOMAS Thematic Conference on
Computational Methods in Structural Dynamics and Earthquake Engineering
M. Papadrakakis, V. Papadopoulos, V. Plevris (eds.)
Kos Island, Greece, 12–14 June 2013

EMULATIVE COLUMN-FOOTING CONNECTIONS FOR SEISMIC DESIGN IN ACCELERATED BRIDGE CONSTRUCTION

Zachary B. Haber[1], M. Saiid Saiidi[2], and David Sanders[3]

University of Nevada, Reno
1664 N. Virginia St. MS. 258, Reno, NV 89512
[1]e-mail: zhaber@unr.edu
[2]e-mail: saiidi@unr.edu
[3]e-mail: sanders@unr.edu

Keywords: Mechanical splice, ductility, precast, cyclic loading, damage

Abstract. *Accelerated bridge construction (ABC) is gaining substantial momentum in the US because of its many advantages. Extensive use of precast members is necessary for ABC to succeed. Some of the key advantages of ABC are: (1) higher quality of construction for structural elements because of fabrication in plants, (2) more durable materials because of more appropriate curing in plants, (3) concurrent execution of different tasks, (4) reduced traffic interruption and less risk to the traveling public and construction crew, and (5) reduced direct and indirect effect on the environment due to expedited construction and the use of more efficient technologies that require less energy. Despite their numerous advantages prefabricated columns have rarely been used in areas of high seismicity because of high uncertainty about their seismic performance.*

Extensive effort has been in progress at the University of Nevada, Reno to develop and evaluate earthquake resistant connections for use in accelerated bridge construction. This effort included the study of five half-scale bridge column models that were constructed and tested under reversed slow cyclic loading. The study focused on developing four new moment connections at column-footing joints for accelerated bridge construction in regions of high seismicity. The new connections were employed in precast columns each utilizing mechanical splices to create connectivity with reinforcing bars in a cast-in-place footing. Two different mechanical splices were studied; an upset headed coupler and grout-filled sleeve coupler. Along with the splice type, the location of splices within the plastic hinge zone was also a test variable. All precast models were designed to emulate conventional cast-in-place construction thus were compared to a conventional cast-in-place test model. Results indicate that the new connections are promising and duplicate conventional cast-in-place construction with respect to key response parameters although the plastic hinge mechanism could be significantly affected by the presence of splices.

1 INTRODUCTION

Accelerated bridge construction (ABC) has become increasingly popular throughout the United States because of its numerous advantages. In many cases, ABC methodologies have been shown to decrease bridge construction time and reduce the overall project cost. To effectively execute ABC projects, designers use prefabricated structural elements that can be manufactured offsite in parallel with on-site construction, which can result in improved element quality. These members are then delivered to the site and can be quickly assembled to form a functional structural system. It is advantageous to the bridge designer if ABC systems emulate conventional cast-in-place construction systems because this would allow typical analysis and design procedures to be used. The difficulty with developing emulative systems is usually encountered in designing connections because of their critical role in transferring forces from the superstructure to the foundation. Substructure connections are particularly critical in high seismic zones because they must dissipate energy through significant cyclic nonlinear deformations while maintaining capacity and stability of the structural system.

There have been a limited number of studies conducted on substructure connections for ABC projects in seismic zones. A summary of different connection details for moderate-to-high seismic zones is presented in the work by Marsh et al., 2011. Many of the connections mentioned in this literature survey were evaluated experimentally and include grouted duct connections (Restrepo et al., 2011), pocket-type connections (Restrepo et al., 2011), and column-in-socket connections (Motaref et al., 2011). The performance of these connections were comparable to cast-in-place baseline models but may require unconventional design procedures or detailing requirements. Mechanically spliced connections could provide emulative behavior without deviating substantially from conventional design procedures and details. There are only a limited number of studies that have been conducted on using these devices in plastic hinge zones (Hironobu et al., 2005; Huang et al., 1997; Lehman et al., 2001; and Reetz et al., 2004)

These previous studies do not provide information as to how mechanical splices can be used to design and construct precast bridge columns that conform to US standards. An experimental study was conducted at the University of Nevada, Reno to investigate the performance of these devices in moment connections between precast columns and cast-in-place (CIP) footings by testing five large-scale models under cyclic loading. This paper highlights the key aspects of study and the results. A detailed description of this study can be found in Haber et al., 2013.

2 HALF-SCALE BRIDGE COLUMN MODELS

Five half-scale reinforced concrete bridge column models with circular sections were investigated in this study: one conventional cast-in-place (CIP) benchmark column and four precast columns. The models were identical except for the details in the plastic hinge connection region. The benchmark column was designed using the California Department of Transportation (Caltrans) Seismic Design Criteria (SDC) (Caltrans, 2010) for a target design displacement ductility of $\mu_D = 7.0$ to achieve large inelastic deformations prior to failure. The geometry and reinforcement details of CIP were selected to be representative of flexural-dominate columns commonly used in California with modern seismic detailing. CIP was reinforced with eleven evenly-distributed D25 [No. 8] bars in the longitudinal direction and a D10 [No. 3] spiral with a 51 mm [2 in] pitch. These reinforcement details correspond to reinforcement ratios of approximately 2% and 1% in the longitudinal and transverse directions, respectively. The design axial load was taken as 10% the nominal axial load capacity of the

gross concrete area of the column, which was 1005 kN [226 kips]. CIP was half-scale, with a 610-mm [24-in] diameter, assuming a 1220-mm [48-in] diameter prototype, and was 2743 mm [108 in] in height from the surface of the footing to lateral loading point. A rectangular reinforced concrete head atop each column was used to transfer lateral load from the actuator. The footings were designed to remain elastic and were post-tensioned to the strong floor to prevent sliding and over-turning under lateral loads. Figure 1-a depicts the general geometry and reinforcement configuration for the column cage of CIP.

The remaining four models were precast and utilized a hollow concrete shell that contained the same longitudinal and transverse reinforcement as CIP. Once the precast column shells were connected to the footing, the core was filled with self-consolidating concrete (SCC). The connection of the precast column shell to the footing was achieved by using mechanical bar couplers. Two different connection details were developed using two different mechanical reinforcing bar splices. The first detail (Figure 1-b) employed the use of upset headed couplers to make the connection between the longitudinal steel in the precast column shell and that embedded within the footing. This connection was made by lowering the column shell onto the footing then joining the two elements with transition reinforcing bars. Once the transition bars were locked in place, the transverse steel spiral was tied into place. Finally, formwork was constructed and the connection was completed by pumping cementitious grout to cover the connection region area. The second connection detail (Figure 1-c) utilized ductile cast-iron grout filled sleeves to connect the column shell to the footing. The connection between the shell and footing was achieved by lowering the shell onto bar dowels that protruded from the footing. Once the shell was lowered onto the dowels, each sleeve was pressure grouted through plastic ducts that protruded from the column shell. The grout used was a high strength (100+ MPa) proprietary mix that was supplied by the grout sleeve manufacturer. Two column models were tested for each connection detail; one where the connection was made directly to the footing and the second where the column was mounted on a 305-mm [12-in] precast pedestal (Figure 1-d), which was used to reduce the moment demand over the connection location. Longitudinal reinforcing bar passed though the pedestals via grout-filled corrugated steel ducts. Column models were denoted by the type of coupler ("HC" for headed coupler and "GC" for grouted coupler) and whether the model included a pedestal ("NP" for no pedestal and "PP" for precast pedestal).



(a) (b) (c) (d)

Figure 1: Experimental models: (a) Details of the benchmark column (CIP); (b) Connection region of HCNP; (c) Connection region of GCNP; (d) Precast pedestal for GCPP

3 EXPERIMENTAL METHODS

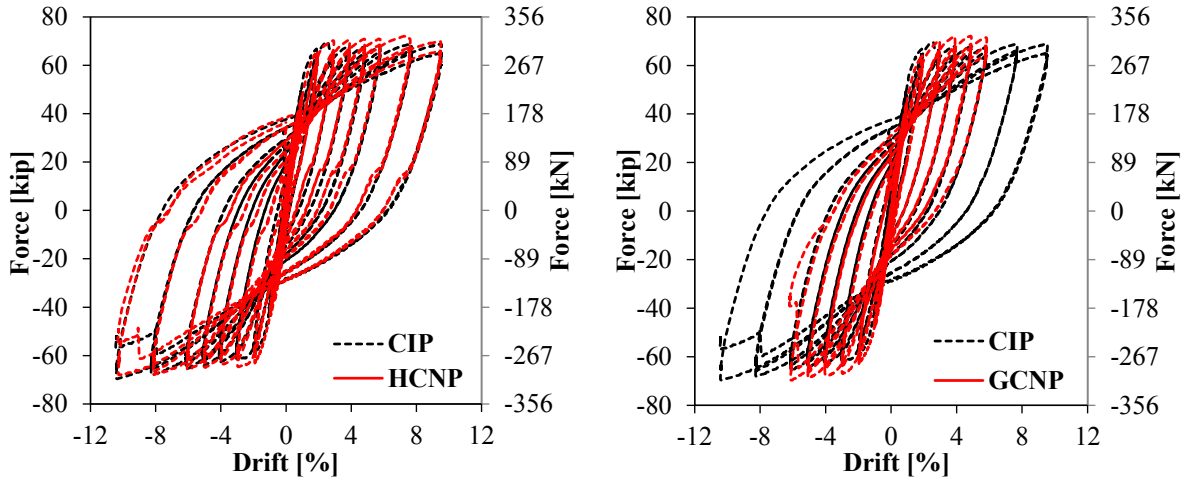
Each column model was instrumented with several layers of foil-backed resistive strain gages installed on the longitudinal and transverse reinforcing bars. String pot and linear variable displacement transducers (LVDT) were used to record the column head displacement, plastic hinge curvatures, bond-slip at the base of the column, and rotations at the column-to-pedestal joint. Tests were conducted at the Large-scale Structures Laboratory at the University of Nevada, Reno using a single cantilever loading configuration. Lateral load was applied with a 978 kN [220 kip] servo-controlled hydraulic actuator that was mounted to a reaction pylon. Column models were subjected to slow cyclic loading using a drift-based displacement-control loading protocol. Two full push and pull cycles were completed at drift levels of 0.25, 0.5, 0.75, 1, 2, 3, 4, 5, 6, 8, and 10% until failure, defined to be a drop in lateral. A nominally constant axial load of 890 kN [200 kip] was applied to each column model using two hydraulic rams and a spreader beam.

3.1 Force-Deformation Behavior

The measured force-displacement relationships for the precast models HCNP and GCNP are plotted along with that of CIP in Figure 2; models with precast pedestals behavior similar to the counterparts without pedestals. CIP exhibited wide loops, stable post-yield regions, and minimal strength degradation, as expected for a column with modern seismic detailing. The measured response of HCNP was approximately the same as that of CIP except for slight differences in peak load per drift level and pinching during unloading. The reason for the pinching is as follows: when longitudinal bars are under tension, the headed ends within the threaded splice collars separate and a gap is formed. Upon reversal of the load, these bars move toward each other, but a compressive force is developed only after the gap is closed. The column displaces slightly to close this gap, which leads to a pinch. Although this behavior is clearly observable, the path of the hysteresis loop varies only slightly from that of CIP. The first abrupt drop in lateral load occurred during the second cycle of -10% drift in both models. The same pinching behavior was seen in the response of HCPP but did not cause significant deviation in the loops when compared to CIP. The measured response of GC models was also similar to that of CIP. Figure 2-b shows a comparison between the GCNP and CIP. The primary difference between CIP and the GC models was the drift capacity. CIP completed one full cycle at the 10% drift ratio prior to loss of lateral load capacity while GCNP and GCPP experienced abrupt loss during the 6% drift cycles.

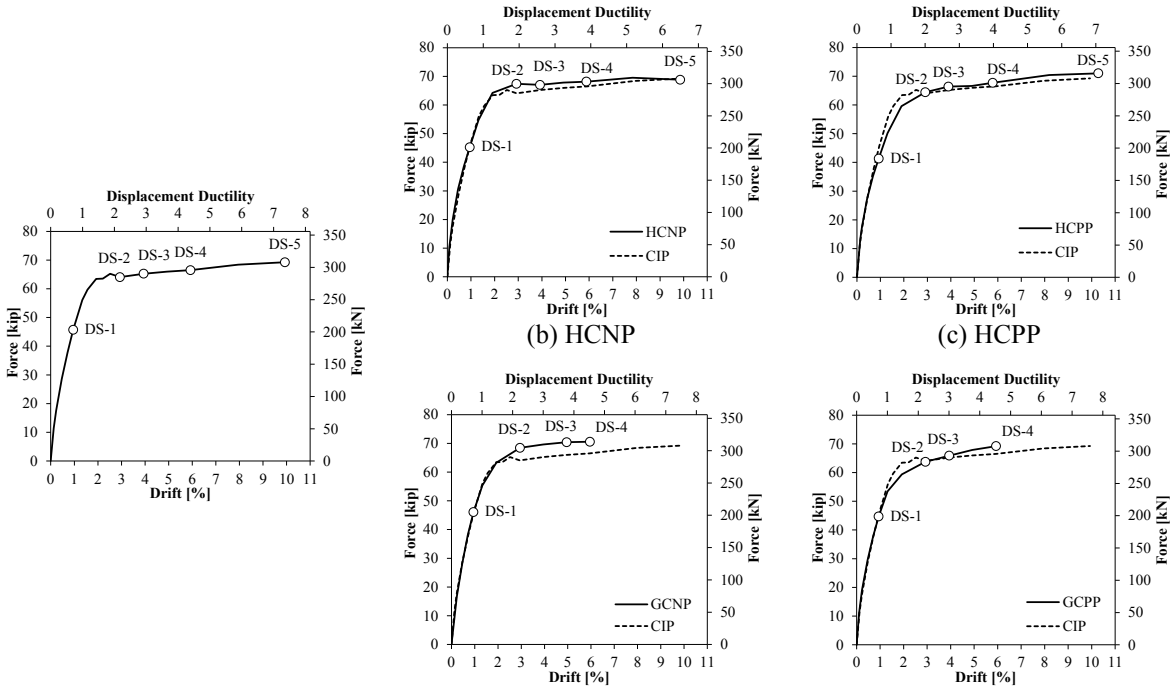
The envelopes of the measured force-displacement relationships are shown in Figure 3. The curves represent the average envelope from the first cycle of the push-pull loadings. In all cases, the envelope curves for the precast models were comparable with CIP. The initial stiffness up to a lateral load of 156 kN [35 kips] was the same among the five models at which point the stiffness of HCPP decreased slightly. At a lateral load of 236 kN [53 kips], GCPP began to soften due to yielding and subsequently followed a path similar to that of HCPP. The paths of HCNP and GCNP did not deviate from CIP until approximately 2.5% drift which corresponded to spalling of cover concrete. Despite these subtle differences, all five curves exhibited similar ascending braches, stable post-yield plateaus, and achieved approximately that same lateral load capacity.

Figure 3 also shows the displacement ductility achieved by each model. In all cases the displacement ductility capacity was satisfactory. That is, CIP and the HC models achieved ductility within 0.5 of the target design ductility of 7.0. The GC models both failed at displacement ductility 4.5. Although this was 35% lower than the target design ductility it would be sufficient in regions with moderate to high seismicity.



(a) Comparison between CIP and HCNP (b) Comparison between CIP and GCNP

Figure 2: Hysteretic force-displacement relationships



(a) Cast-in-place (CIP) (b) HCNP (c) HCPP (d) GCNP (e) GCPP

Figure 3: Average envelope curves

3.2 Apparent Damage and Failure

The progression of damage in the precast models was similar to that of CIP. The damage progression of each model was evaluated by first defining five distinct damage states (DS). The damage state corresponded to presence of flexural cracks (DS-1), first spall and development of shear cracks (DS-2), extensive cracking and spalling of concrete (DS-3), visible longitudinal and/or transverse reinforcement (DS-4), and on-set of confined concrete core damage (DS-5: imminent failure). Figure 4 illustrates each damage state as observed in CIP. The progression of damage for each model is depicted on the average envelope curves shown in Figure 3. The HC models reached all five damages, which occurred at approximately the same point in the force-displacement history as CIP. The GC models achieved damages states DS-1 through DS-4 prior to failure, which occurred at 6% drift. The progression of damage

for the GC models was the same as CIP except for DS-3 in GCNP, which occurred at a later drift ratio.

All five models exhibited cracking and delamination of concrete at the footing surface due to strain penetration of the longitudinal bar. Yet, the extent of this damage was much greater in the GC models compared to CIP and the HC models. By 6% drift, severe damage to the footing was observed in both GCNP and GCPP, which included extensive cracking and delamination of concrete. The loss of the surrounding concrete in the footing resulted in buckling of longitudinal bars and their eventual fracture. This level of damage in the footing was not observed the HC models or CIP until 8.0% drift.

To determine the failure mechanism and location, concrete was removed from the plastic hinge region and footing of each model. It was determined that the dominant failure mode in all models was longitudinal bar fracture. Ruptured bars where found 76-254 mm [3-10 in] above the footing in CIP and HCNP, and approximately 102-127 mm [4-5 in] below the surface of the footing in the other models. It was concluded that bar rupture below the footing surface was caused by strain concentrations that developed as a results of the presence of the grouted pedestal ducts and cast-iron grouted coupler sleeves.

In order to assess possible damage, mechanical splices were removed from HCNP and GCNP because they were subjected to the highest moment demand and inelastic deformations. The upset-headed splice did not display any indication of distress or damage. However there was slack between the deformed heads within the threaded splice collar, which is likely associated with permanent localized deformations within the splice collar. The grouted-sleeves removed from GCNP did not exhibit any damage and the bond between the high-strength grout and reinforcing bar was sound. There was, however, evidence of strain penetration into the coupler sleeve as shallow grout-cone pull-out was observed at both ends.



(a) DS-1 (b) DS-2 (c) DS-3 (d) DS-4 (e) DS-5

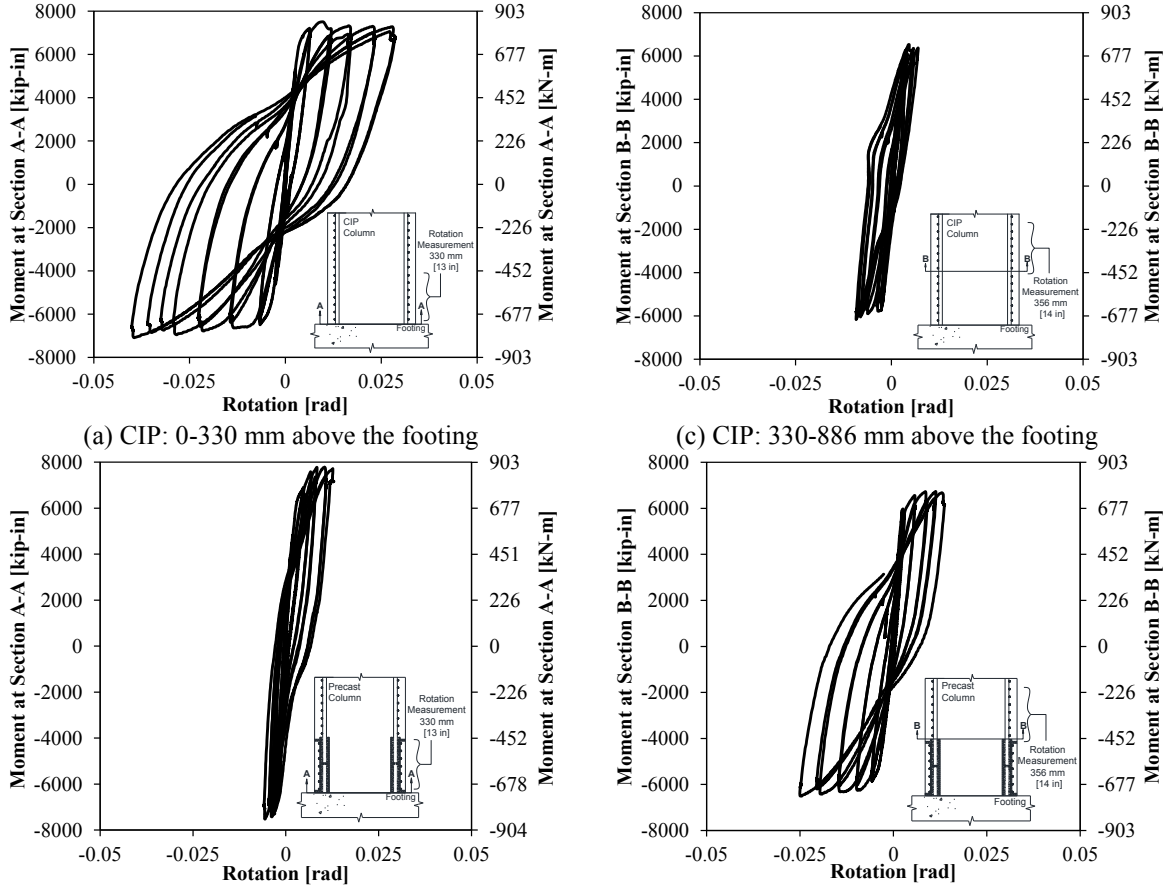
Figure 4: Apparent damage states

3.3 Plastic Hinge Behavior

The plastic hinge behavior of each model was evaluated using longitudinal reinforcing bar strains and rotations measured within the first 1.5 column diameters above the footing. CIP exhibited well distributed strain throughout the plastic hinge, which resulted in a large region where plastic rotation occurred. HCNP also displayed well distributed strains throughout the plastic hinge region and the magnitude of the strains were approximately the same as CIP. Conversely, the measured distributions of strain for the HCPP and the GC models were not as uniform as those for CIP and HCNP. For HCPP and the GC models, maximum tensile strains occurred within the footing, which was consistent with the observed longitudinal bar rupture locations. Furthermore, large plastic strains were also measured at the column-pedestal interface for HCPP and GCPP. For these models, the tensile strains occurring within the pedestal were not as substantial as those occurring at the joints due to the additional stiffness provided

by the grout-filled corrugated steel ducts. These observations indicate that the plastic hinge behavior of the columns was altered by presence of the grouted coupler and the precast pedestals.

The change in plastic hinge behavior can be further quantified by comparing the moment-rotation relationships for CIP and GCNP, which represents the most extreme difference. Figure 5 depicts the moment-rotation relationships that were measured for CIP and GCNP. It can be observed that within the first half column diameter (approximately) above the footing, CIP (Fig. 5-a) exhibits significantly more plastic rotation than GCNP (Fig. 5-b). The presence of the grouted coupler sleeves increased the section stiffness within this region resulting in reduced plastic rotation. It can be observed in Figures 5-c and –d, which depict the moment-rotation relationships for the region within the second half column diameter, that the plastic rotation for GCNP exceeds that of CIP. This further confirms that hinge shifting is occurring.



(a) CIP: 0-330 mm above the footing

(c) CIP: 330-886 mm above the footing

(b) GCNP: 0-330 mm above the footing

(d) GCNP: 330-886 mm above the footing

Figure 5: Hinge rotation comparison between CIP and GCNP

4 SUMMARY AND CONCLUSIONS

The study presented in this paper focused on evaluating the seismic performance of four emulative precast column-to-footing connections which utilized mechanical reinforcing bar. A set of geometric and reinforcement details were developed using a half-scale benchmark column such that two different mechanical splices could be incorporated into the plastic hinge zone reinforcement details. The benchmark design details were also used to construct conventional cast-in-place (CIP) column model that served as the baseline for evaluating the performance of precast models. Four precast column models were constructed with different

plastic hinge connection details: Two were connected directly to the footing (HCNP and GCNP), and two were connected atop a precast pedestal one-half column diameter in height (HCPP and GCPP).

A number of similarities were found between the behavior of CIP and the precast models. All models exhibited hysteresis loops that were wide and stable, similar average force-displacement envelope curves, and all three models had approximately the same ultimate lateral load capacity. The damage accumulated by each model at the various drift level was also similar. The main difference between the CIP and the precast models was observed in GCNP and models with precast pedestals; a distinct difference in the plastic hinge behavior was observed. The hinge region in CIP allowed for plastic deformation to occur evenly throughout the section whereas HCPP, GCNP, and GCPP forced this deformation to occur at pedetsal joints and within the footing.

It can be concluded that the behavior of the connections tested in this study are emulative of conventional cast-in-place construction except there where some difference in displacement ductility capacity. The presence of the grouted couplers and precast pedestals in the plastic hinge forced a large amount of plastic deformations within the footing, which ultimately resulted in longitudinal bar fracture. Nevertheless, the displacement ductility achieved by each of the precast models was sufficient for construction in moderate and high seismic zones.

REFERENCES

[1] Marsh, M. L., Wernli, M., Garrett, B. E.; Stanton, J. F.; Eberhard, M. O.; and Weinert, M. D., "Application of Accelerated Bridge Construction Connections in Moderate-to-High Seismic Region," *NCHRP Report 698*, pp. 65, 2011.

[2] Restrepo, J. I., Tobolski, M. J., and Matsumoto, E. E., "Development of a Precast Bent Cap System for Seismic Regions," *NCHRP Report 681*, pp. 116, 2011.

[3] Motaref, S., Saiidi, M., and Sanders, D. H., "Seismic Response of Precast Bridge Columns with Energy Dissipating Joints," *Report No. CCEER-11-01*, Center for Civil Engineering Earthquake Research, pp. 760, 2011.

[4] Hironobu, A. et al., "Cyclic Loading Experiment of Precast Columns of Railway Rigid-Frame Viaduct Installed with NMB Splice Sleeves," *Proceedings of the Japan Concrete Institute*, V. 27, No. 2, 2005.

[5] Huang, S .W., Yu, J. T., Chiou, H. D., Asakawa, T., and Tsai, K. C., "Final report of experiment on precast reinforced concrete beam-column assemblage," *Chinese Society of Structural Engineering*. 2011.

[6] Lehman, D. E., Gookin, S. E., Nacamuli, A. M., and Moehle, J. P., "Repair of Earthquake-Damaged Bridge Columns," *ACI Structural Journal*, V. 98, No. 2, 2001.

[7] Reetz, R. J., Ramin, M. V., and Matamoros, A., "Performance of Mechanical Splices within the Plastic Hinge Region of Beams Subject to Cyclic Loading," *Proceeding of the 13th World Conference on Earthquake Engineering*, August 1-6, 2004.

[8] Haber, Z. B., Saiidi, M., and Sanders, D. H., "Precast Column-Footing Connection for Accelerated Bridge Construction in Seismic Zones," Center for Civil Engineering Earthquake Research, Department of Civil and Environmental Engineering, University of Nevada, Reno, Nevada, *Report No. CCEER-##-13*, In Preparation, 2013.

[9] California Department of Transportation, "*Seismic Design Criteria (SDC) Version 1.6*," Division of Engineering Services, Sacramento, Calif., pp. 160, 2010.

COMPDYN 2013
4th ECCOMAS Thematic Conference on
Computational Methods in Structural Dynamics and Earthquake Engineering
M. Papadrakakis, V. Papadopoulos, V. Plevris (eds.)
Kos Island, Greece, 12–14 June 2013

SPECTRUM RESPONSE AND CODES EVOLUTION CASE STUDY – POST-COMPRESSED GIRDER BRIDGE

Carmen BUCUR[1], **Victor Mircea BUCUR**[2]

[1] Technical University of Civil Engineering
Member of IABSE - WG7
Bucharest, Romania
e-mail: vmb51@yahoo.com

[2] External Collaborator -Technical University of Civil Engineering
Bucharest, Romania
e-mail: vmb51@yahoo.com

Keywords: Earthquake Engineering, Technical Regulations, Spectral response, Evolution, Reinforced concrete

Abstract. *The object of this study is a bridge structure with sectioned, prefabricated, post-compressed, reinforced concrete girders, to be used as a foot-walk. The bridge has two 32.25 m spans. The utilised 33.0 m girders are the longest in the Romanian Prefab Girders Catalogue. Later on, the bridge function was extended, it being used for the road vehicles traffic as well. The bridge, still in use, was checked two times, according to different technical codes. The article is built up on three plans, namely: (i) a brief presentation of Vrancea seismic epicentre, Romania, (ii) a brief presentation of the evolution of the Romanian technical codes for designing the building - and bridge type structures under the seismic action, (iii) application of these codes on this existing bridge type structure and comparing its spectrum response under the seismic action, modelled according to various codes. The analysis of the bridge was carried out taking into consideration the hypothesis of two ductility classes: limited ductility and ductile.*

.

1 INTRODUCTION

During 1988 – 1989 a foot-walk was built to cross-over a hydro-power station off-take. The bridge having two 32.25 m-long spans has sectioned, prefabricated, and post-compressed, simply supported reinforced concrete girders. The utilised 33.0 m long girders are the longest in the Romanian Prefab Girders Catalogue.

In 1995 – 1996 they thought of opening this bridge for the road vehicles traffic as well. Consequently, a general bridge overhaul was carried out, also implying a spectrum analysis according to a new technical code ("Norm for seismic design of the road and railway bridges and of the road over-or under-crossing passages made out of reinforced and pre-stressed concrete") being under technical debate at that time.

Presently, the bridge is to be rehabilitated and shall be checked for the earthquake resistance, being modelled complying with the Romanian codes in force (i) *Design of structures for earthquake resistance. Part 2: Bridges* – Romanian Standards Association, SR EN 1998-2:2006; (ii) *Design of structures for earthquake resistance. Part 2: Bridges. National Annexe* - Romanian Standards Association, SR EN 1998-2:2006/NA:2010; (iii) *Seismic Design Code, Part 1 - P100-1/2006, Earthquake Resistant Design of buildings* - Ministry of Transports, Construction and Tourism, 2007.

From seismic point of view, the area where the bridge is built on is affected by the earthquakes in Vrancea Region, but with reduced exposure (figures 3 and 4). No earth accelerations were registered, and, consequently no "time history" study was drawn up.

The article is structured on three plans, namely: (i) a brief presentation of Vrancea seismic epicenter, Romania, (ii) a brief presentation of the evolution of the Romanian technical codes for designing the building and bridge type structures under the seismic action, and (iii) the application of these regulations on this existing bridge type structure and comparing its spectrum response under the seismic action, modelled according to various codes. The analysis of the bridge was carried out taking into consideration the hypothesis of two ductility classes: limited ductility and ductile.

2 BRIEF PRESENTATION OF VRANCEA SEISMIC EPICENTRE

Romania is highly vulnerable to earthquakes and flood. It is also one of the most seismically active countries in Europe [7]

According to the number of people lost in earthquakes during the XX^{th} century (1574 people as well as those lost in the earthquake on March 4, 1977, 1424 in Bucharest), Romania can be ranked as the 3rd country in Europe, after Italy and Turkey. Romania is followed by the former Yugoslavia and by Greece.

The Vrancea region, located where the Carpathians Mountains Arch bends, at about 135 ± 35 km epicentre distance from Bucharest, is a source of sub-crustal seismic activity, affecting the Romania's territory and an important part of the territories of Republic of Moldova, Bulgaria and Ukraine. The seismic areas cover about 65% of the territory of Romania, fig. 1, [4].

Vrancea region, which is Romania's main seismogenic zone, is characterized by the following main remarkable features [6]: (i) Its shallow seismic activity is located mainly in the lower crust (h>15km), and consists of small and moderate magnitude earthquakes; (ii) The sub-crustal seismicity represents the main feature of Vrancea region; (iii) The recurrence times estimated from the available catalogues are the following: 10 years for Mw > 6.5, 25 years for Mw > 7.0 and 50 years for Mw > 7.4; (iv) The large instrumentally recorded earthquakes show a remarkably similar fault plane solution. They typically strike SW-NE (220°), dip 60° to 70° to the NW, and the slip angle is roughly 80° to 90°.



Figure 1: Vrancea sub-custral (60-180 km) seismic source in the Carpathian Mountains of Romania [4]

3 BRIEF PRESENTATION AND EVOLUTION OF THE ROMANIAN EARTHQUAKE - CODES

- ***Seismic Design Code, Part 1 - P100-1/2006-Earthquake Resistant Design of buildings,***
- ***SR EN 1998-2:2006-Design of structures for earthquake resistance. Part 2: Bridges***
- ***SR EN 1998-2:2006/NA: 2010- Design of structures for earthquake resistance. Part 2: Bridges. National Annexe***

3.1 Historical evolution

In 1941 the first national seismic code (after the 1940 earthquake) named "Draft Instructions" took effect. It's followed in 1945 by "Instructions for preventing the damage of buildings due to earthquakes". Between 1963 – 1977 there are two successive versions of the code with the indicative P13.

In figure 2 it is presented the evolution of the values of the normalized acceleration spectrum (β) for T_C=1.5 sec, [3].

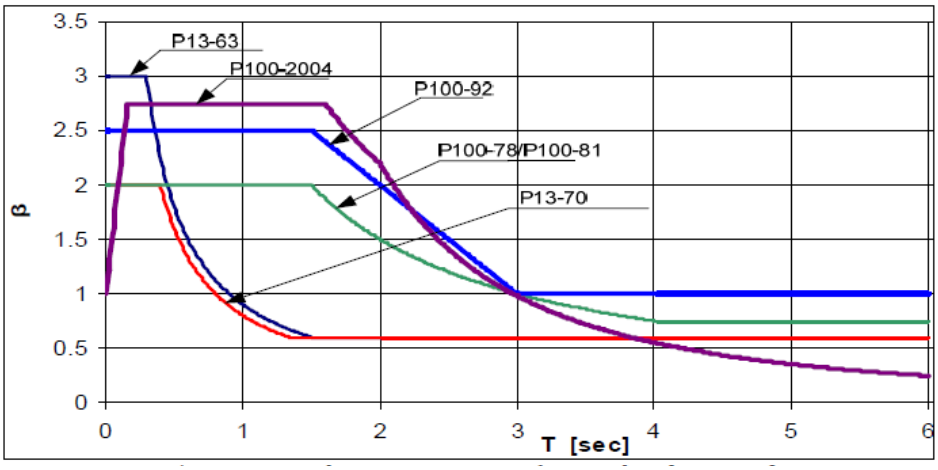


Figure 2: Evolution of the normalized acceleration spectrum values (β) for T_C=1.5 sec [3]

From 1977, after the great earthquake, a series of versions for the code with the indicative

P 100 took effect. They were permanently tweaked by the last researches. The actual version of the code "P100-1:2006 Code for earthquake resistance of buildings and structure" is in accord with EUROCODE 8.

The first code for bridges took effect in 1978. In Table 1 there is a synthesis of the evolution of the earthquake resistance codes for bridges in Romania.

STAS 10101 (1978)	Actions on structures – Classification and combination of Actions for Railway Bridges and Viaducts - *National Committee for Science and Technology – National Institute for Standardization*
PD 197 (1980)	„Design Provisions for Earthquake Resistance of Transportation and Telecommunications Constructions" - *National Committee for Science and Technology – National Institute for Standardization*
DRAFT (1997) Inspired by EUROCODE 8	„Design Provisions for Earthquake Resistance of Road, Railway Bridges and Overpasses Made of Reinforced and Prestressed Concrete" - *Ministry of Public Works and Territorial Administration*
Actual - EUROCODE 8	1. EUROCODE 8 – Design of structures for earthquake resistance. Part 2: Bridges 2. National Annex – may 2010 *Ministry of Transports, Construction and Tourism*

Table 1: The evolution of the codes for earthquake resistance of bridges in Romania

3.2 The presentation of actual norms

In Romania the value of P_{NCR} (probability – within the next 50 years - to exceed the reference seismic action for no-collapse requirement - life safety) is 39% in 50 years, and T_{NCR} (reference return period of the reference seismic action for no-collapse requirement - life safety) is 100 years. The value of P_{DLR} (in 10 years, the probability of exceeding the seismic action for damage limitation requirement) is 28% in 10 years, and T_{DLR} (reference return period of the seismic action for damage limitation requirement) is of 30 years. The ground classification scheme (A, B, C, D, E, S1 and S2) is not applicable in present. For design, the local site conditions are classified in 3 zones/sites, Z_1, Z_2, Z_3, based on accelerograms recorded during 1977, 1986 and 1990 Vrancea earthquakes, zones characterized by the values of the control period of the response spectra, T_C, fig. 3, [10].

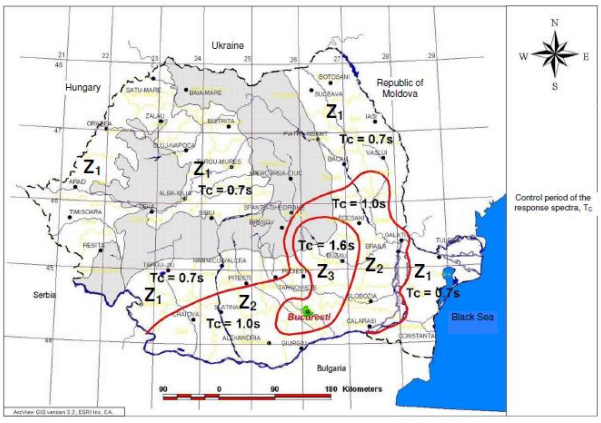


Figure 3: Zone/site in the Romanian territory in terms of control period T_C, [10]

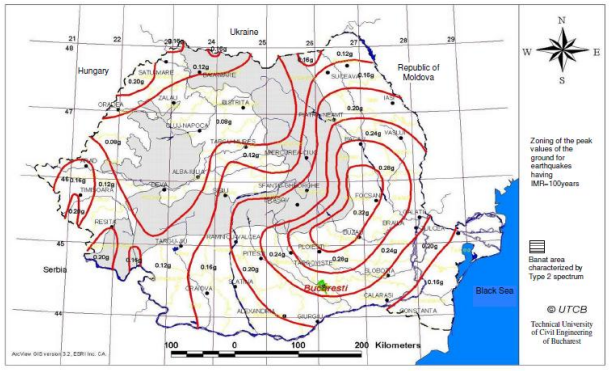


Figure 4: Zoning map of the Romanian territory of the peak values of the ground, [10]

The zoning design ground acceleration a_{gR} in Romania, for seismic events having the mean recurrence interval for the no-collapse requirement – life safety (of the magnitude) T_{NCR} = 100 years, is indicated in the figure 4 and is used for the design of buildings in the ultimate limit state for all zones/sites (country territory), [10].

The procedures for low seismicity are not applicable in Romania.

On Romanian territory three importance classes for bridges are defined, table 2, [9].

Importance classes	Description
III	Road and railway bridges of critical importance for maintaining communications, especially in the immediate post-earthquake period (the bridges supporting the emergency traffic after a major seismic event).
II	Road and railway bridges located on lines of communications of average importance.
I	All the bridges, except those of III and II class as well as road or railway bridges located on small lines of communications. For example, temporary bridges sited on industrial lines of communication - but only with beneficiary agreement and the bridges do not serve important economical or social objectives where they have to maintain communications after a major seismically event.

Table 2: The importance classes for bridges on Romanian territory, [9]

The regulations provide that both the ductile structures and the limited ductile ones shall be designed based on the linear analysis using a modified spectrum response, called designed spectrum.

The limit value of the displacement along the bridge of the abutment rigidly connected to the deck depends on the bridge importance class, namely for Class III - d_{lim}=60 mm; and for Class I – there is no limitation.

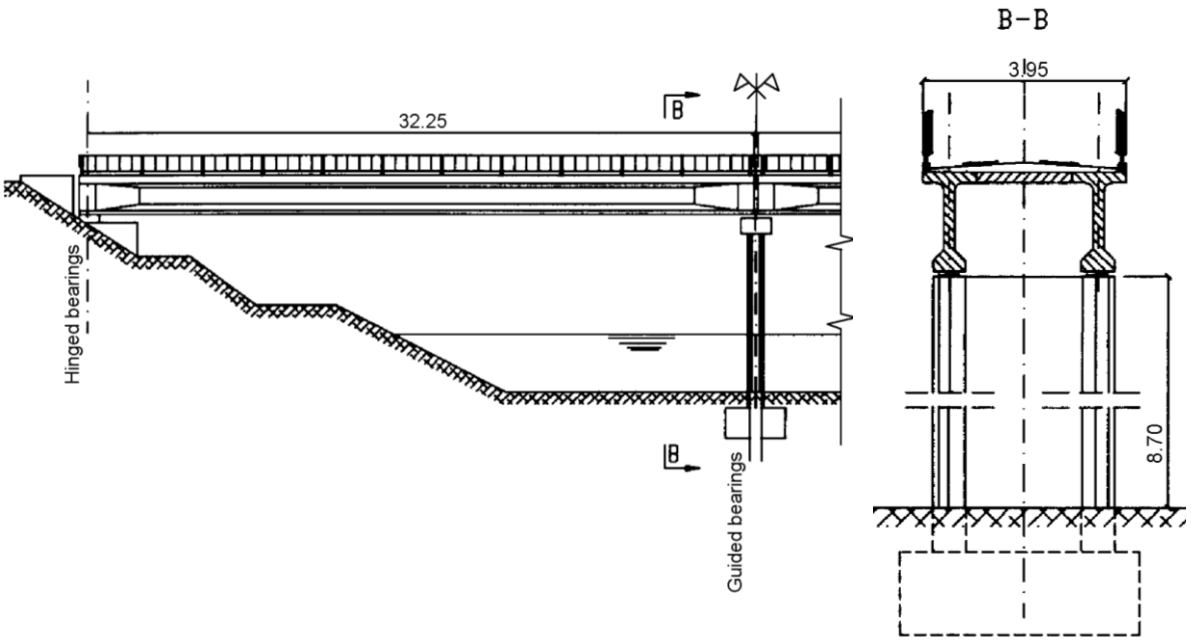
In case of ultimate limit state, after appearing the design seismic action, the bridge shall preserve its structural and residual integrity, although damages may appear in certain areas of the bridge. So, it is allow some plastic areas to appear in the piers due to their bending. These plastic areas (hinges) act as energy dissipation primary elements. The bridge deck shall remain in the elastic domain.

4 THE ANALYSIS OF THE BRIDGE

4.1 Structure description

The bridge was built in 1988 – 1989 to be a foot-walk having two 32.25 m long spans, simply supported girders, fig. 5.a, [2].

The abutments are massive. The reinforced concrete pier has a lamellar elevation and a foundation is made out of a marl-embedded concrete block, fig.5.b. The deck is made up of two sectioned, prefab, reinforced concrete girders, post-compressed on site, being 33.0 m long and 1.80 m high. This prefab 33.0 m girder is the longest in the Romanian Catalogue for road bridges girders. The girders have 2.70 m inter-axe distance, with a 1.95 m wide and 0.18 m thick monolith plate (equal with the thickness of the girders upper plate). The link between the two girders is ensured by three cross-bars (two marginal and a central one). The girders bearings are of hinged-type out of neoprene on the abutments and simple ones on the pier.



a. Elevation b: Cross section

Figer 5: The structure

The bridge belongs to the Importance Class II.

4.2 Design model

This structure is space modelled with finite elements. The abutments and the pier foundation were eliminated out of the structure. The axes system was chosen in the following way**:** the Ox axis is along the bridge, the Oy axis is transversal on the bridge, the Oz axis is vertical; the xOy plan is at the level of the supports of the superstructure girders.
The model, fig. 6, is made up in the following way:

Superstructure:

- In one of the spans, the concrete girders were modelled using one-dimensional finite elements with equivalent geometrical characteristics. The cross-girders were also modelled with one-dimensional elements. The surface-concreting plate was modelled with bi-dimensional elements. This span will be called FRAME in the article.
- In the second span, all the elements making up the superstructure were modelled using bi-dimensional elements having combined the behaviours of the membrane and the plate. This span will be called SHELL.

Pier:

- The finite elements used for the pier elevation are the three-dimensional ones. The pier is considered to be fixed into the foundation.

Girders bearings:

- On the abutments, the hinge type neoprene bearings were modelled using three simple translation-type connections on the three axes of the coordinates, as follows: vertical and transversal on the bridge with rigid ties; longitudinally with a constant elastic spring, equivalent to the used neoprene bearing.
- On the pier, the simple type neoprene bearings were modelled as follows: vertically and transversally on the bridge identical displacement conditions were imposed between the girders and the pier; longitudinally one-dimensional finite elements (double-hinged bar) of known

length were introduced, having geometric and elastic characteristics equivalent to the used bearing type, linking the girders to the pier.
- The rotations are free.

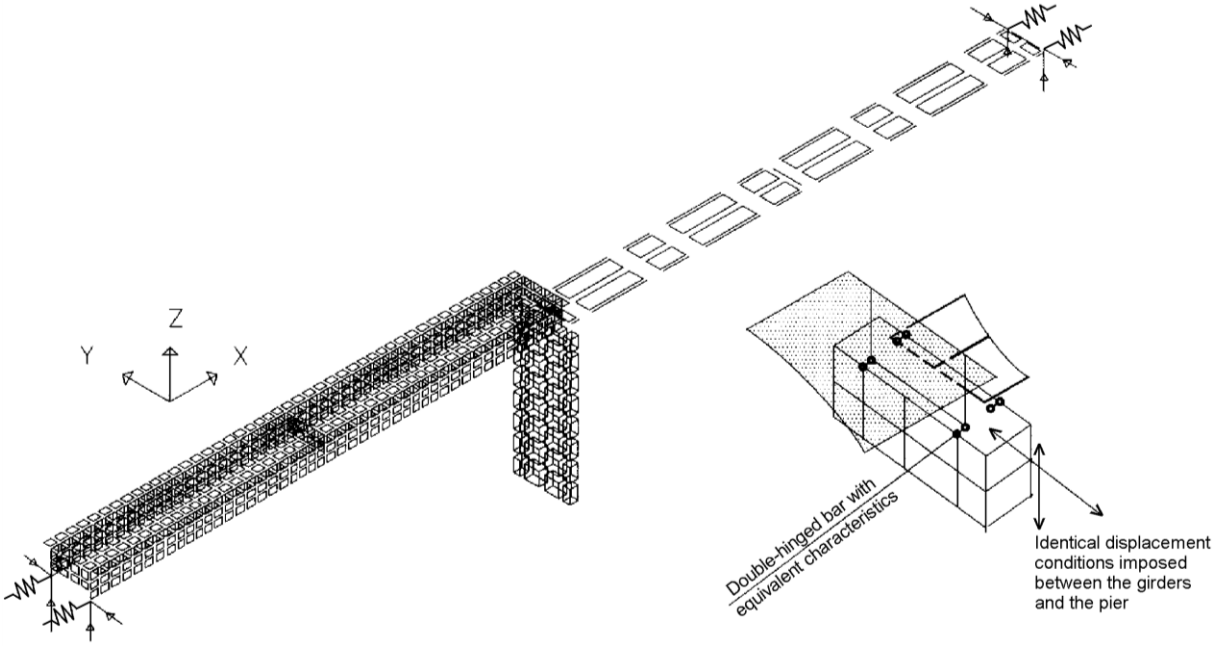


Figure 6: Design model

For design, they took into consideration the masses of the resistance structure for every sub-assembly, as well as the masses of non-structural elements and the masses of the live load, concentrated on the girders. The masses of the live load are considered to be 20%. The live load taken into consideration was the maximum allowed one, as found out when transforming the foot walk into a bridge.

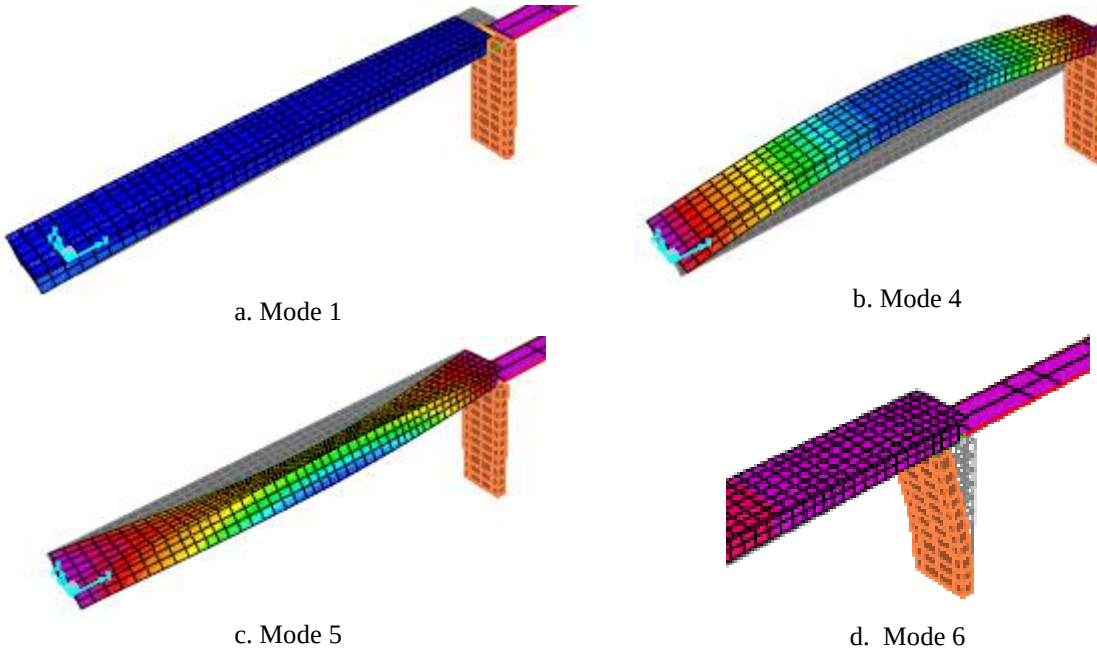
4.3 Proper dynamic response

Results

21 proper vibration modes were considered whose summed up effective modal mass represents about 97% in the longitudinal direction, 90% in the transversal direction and 87% on the vertical one.

- *Modes 1 and 2* (T1=0.558s, T2=0.548s) are vibrations along the bridge, first those of the discrete deck with bi-dimensional elements (SHELL), fig. 7a, and then the discrete one with one-dimensional elements (FRAME). The value of the fundamental period shows that the structure places itself at the upper part of the rigid behaviour. The form of the proper vectors of the modes 1 and 2 presents a rigid body movement (translation) of the two decks along the bridge.
- *Modes 3 and 4* (T3=0.348 and T4=0.323s) are vertical vibrations, bending with a single half-wave, first of the FRAME deck and then of the SHELL deck. The pier has also a slight vibration along the bridge, as if it would be mobilized by the vibrating deck, fig. 7b.
- *Mode* 5 (T5=0.317s) is the torsion vibration mode of SHELL deck, fig. 7c.
- *Mode 6* (T6=0.267) is the bending vibration mode of the pier compared to the bridge transversal axis, fig. 7d.
- *Mode 7* (T7=0.247s) is the FRAME deck torsion in rated by the bridge longitudinal axis – corresponding to mode 5 of SHELL deck.

- In *mode 8* (T8=0.208s) the two decks have different vibrations. The SHELL deck has torsion while the FRAME deck has a lateral vibration. The pier has also a lateral vibration.



a. Mode 1 b. Mode 4

c. Mode 5 d. Mode 6

Figure 7: Particular vibration modes

Comments

1. The value of the fundamental periods places the structure at the limit between the rigid and half-rigid behaviour.

2. The minor differences of the vibrations periods (longitudinal – 1.8% and bending – 7.7%), obtained for modelled SHELL and FRAME decks show that the modelling based on equivalence with FRAME elements is acceptable for these types of vibrations.

3. The first pier vibration mode intercalates between the torsion type vibrations of the two decks.

4. The high difference between the torsion vibration periods – 28.3%, of the two decks, shows that for this type of vibration the FRAME modelling is not advisable. The vertical development of the SHELL modelled deck (which is lost at FRAME deck) allows it to simulate a more complete dynamic response.

5. For the span modelled with elements bi-dimensional (SHELL) the torsion accompanies more or less the majority of the vibrations.

4.4 Spectrum response. Comparisons

The spectrum analysis was carried out according to the recommendations in several technical codes grouped as follows:

(1) (i) Norm for the design of the earthquake-resistant road and railway bridges and of the road under-and over-crossing passages out of reinforced and pre-stressed concrete – under technical debate in 1997;
(ii) R 11100/1-1993 - Macro-seismic zoning of Romania's territory;

(2) (i) Design of structures for earthquake resistance. Part 2: Bridges;
(ii) Design of structures for earthquake resistance. Part 2: Bridges. National Annex;
(iii) Seismic Design Code, Part 1 - P100-1/2006, Earthquake Resistant Design of buildings.

In the article, the study situation according to regulations (1) is named **Code 1997** and that for the study situation according to regulations (2) is named **Code 2006.**

The bridge location in the context of the Romania's seismic map leads, for the case study **Code 1997** to ratio $a_g/g=0.1$ and $T_c \leq 0.8s$ and for the case study **Code 2006** at $a_g=0.12g$ and $T_C=0.7$ respectively. For **Code 2006,** beside the situation of the seismic action modelled under the form of the elastic spectrum - called **Code 2006-Se**, there are also considered two other situations of the design spectrum referring to the structural ductility, namely a limited ductile structure ($q_{duct.limit}=1.5$) - called **Code 2006-Sd(q=1.5)** and ductile structure ($q_{duct.}=3.5$) - called **Code 2006-Sd(q=3.5)**.

In figure 8 acceleration spectra for all study situations are presented graphically.

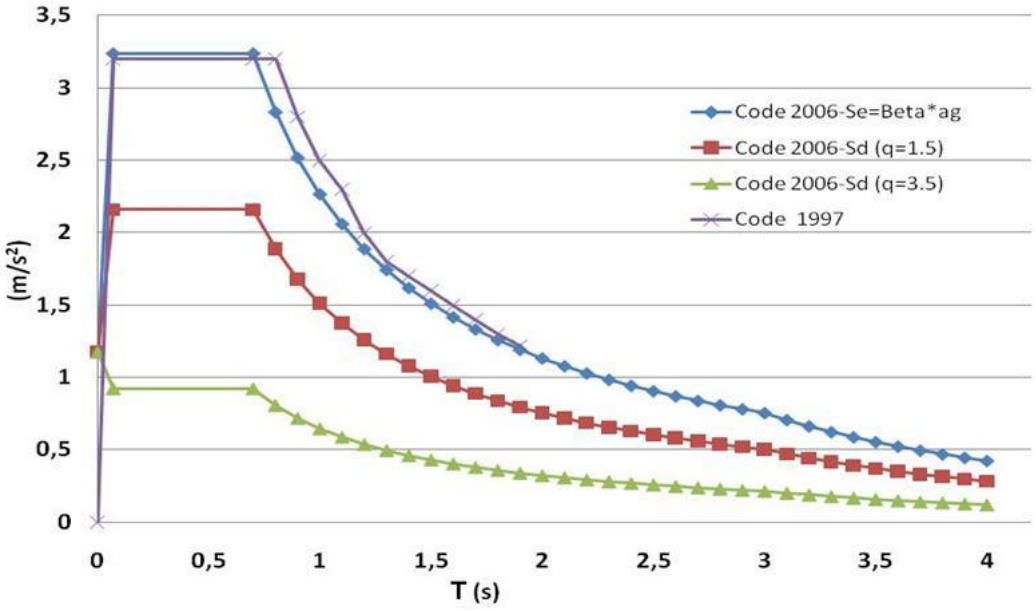


Figure 8: Acceleration spectra for all study situations

Studying the spectrum values one can find out that in the case **Code 1997** starts from the zero value but for the horizontal zone the coordinates are practically equal with those for the situation **Code 2006-Se**. For all cases **Code 2006 (Se, Sd)** the first coordinate has the same value. The other spectrum coordinates differ one from the other in inverse ratio to the considered ductility coefficient – 1.5 and 3.5 respectively.

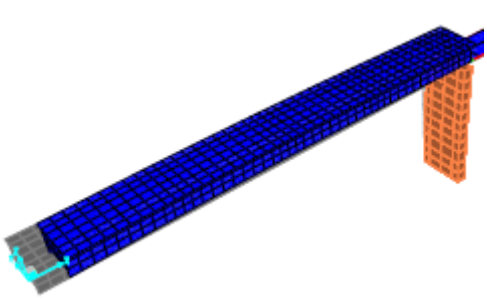
The cases of spectrum loading – twelve in number – are as follows: **Code 1997** with three directions of spectrum action, x-longitudinal, y-transversal and z-vertical; **Code 2006-Se, Code 2006-Sd(q1.5), Code 2006-Sd(q=3.5)** each with three directions.

The horizontal spectrum action is described by two orthogonal components considered independent between them and represented by the same response spectrum. For the vertical component the same response spectrum may be considered, but with reduced coordinates depending on the magnitude of the bridge vibration periods. The fraction from the critical amortization was considered 5%. The total maximum effects are defined based on the maximum values produced by the spectral action applied separately on the three directions according to rule SRSS.

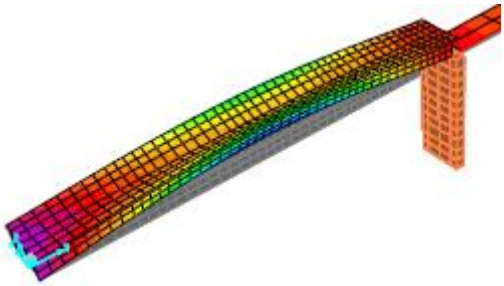
Spectrum displacements. Results, comments

Spectrum displacements follow the bridge „sensible" vibration forms. The maximum value is that in the bridge longitudinal direction, followed by the transversal and the vertical ones. The examples are given in figure 9. The figure 10 presents a synthesis of the spectrum displacements maximum values in the 12 loading situations.

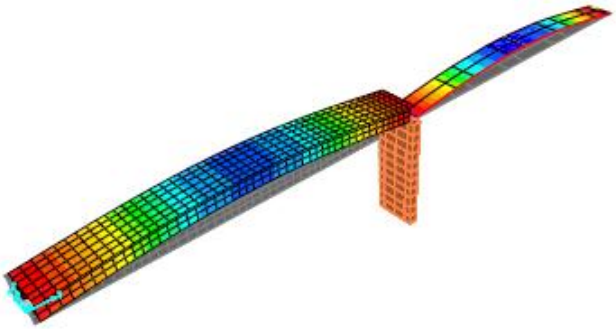
The obtained displacements for the spectrum loading **Code 1997** and **Code 2006-Se** (elastic spectrum) are practically equal, namely 0.0301 m and 0.0305 m respectively. Decrease of the displacements values for the cases considering the limited ductile structure and ductile as compared the cases considering the elastic structure - 1.5 and 3.46 respectively - is practically proportional with the ductility coefficient.



Spectrum displacements for loading
Code 1997 –longitudinal direction



Spectrum displacements for loading
Code 2006-Se – transversal direction



Spectrum displacements for loading
Code 2006-Sd (q=1.5) –vertical direction

Figure 9: Spectrum displacements

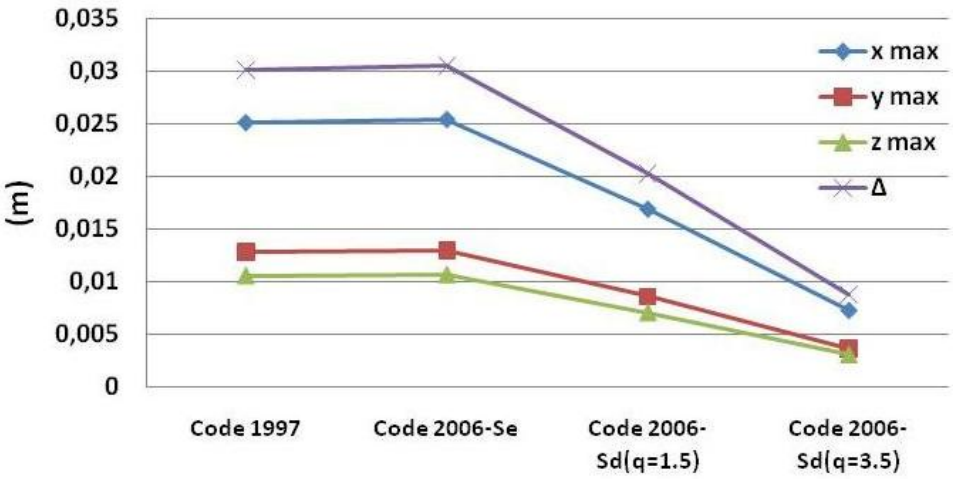


Figure 10: Systematization of spectrum displacements values

It is found out that the influence of the first spectrum coordinate (that does not comply with the right proportion rule) is much reduced. It happens because in the acceleration spectrum the first zone – between 0 and T_B=0.07s – is narrow and then the influence of this zone is reduced.

The displacements along the bridge for the spectrum loading **Code 1997** and **Code 2006-Se** are 0.0251 m and 0.0254 m respectively. These values represent about 42% from the limit displacement at the ultimate limit state for class II where the bridge belongs from (d_{lim}=60 mm)

The displacements values on the bridge transversal direction resulted from the spectrum loading in the same direction, (transversal), represents about 50% from the values of the longitudinal displacements for the longitudinal spectrum loading.

The displacements values on the bridge vertical direction resulted from the spectrum loading in the same direction, (vertical), represents about 42% from the values of the longitudinal displacements for the longitudinal spectrum loading.

Spectrum efforts. Results, comments

Studying the obtained values one can find out the same variation ratio as for the spectrum displacements, namely:

(1) Values of the spectrum efforts obtained for the loading situation in **Code 1997** are practically equal with those in the loading situation in **Code 2006-Se** – Elastic spectrum.

(2) Values of the spectrum efforts obtained for the loading situation with the design spectrum are practically divided by the ductility coefficients that are 1.5 and 3.5, with some exceptions – stresses in the bi-dimensional type elements – where the values have decreased with 1.6 and 3.7 respectively.

Consequently, bellow, we'll comment the values obtained for the loading situation in **Code 2006-Se** – Elastic spectrum.

* *In the deck modelled with one-dimensional elements*, fig. 11:

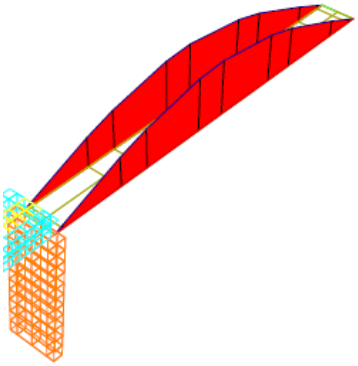
- the maximum dynamic moment develops in the field at the spectrum action on the vertical direction (M=1109 kNm), fig. 11.a;
- the maximum dynamic axial force develops in the field from the transversal spectrum action (N=725 kN), fig. 11.b;
- at the longitudinal seismic action the area where the deck rests on the abutment is stressed where the axial force represents about 30% from the maximum one, fig.11.c.

* *In the deck modelled with bi-dimensional elements*, fig. 12:

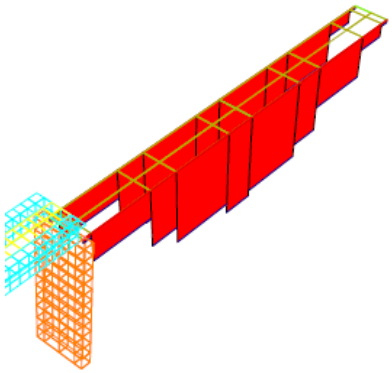
- force in the plan of bi-dimensional elements, on the bridge longitudinal direction has the maximum value (1526 kN(/m)) of the seismic action on vertical direction; position on the deck is in the center and on the flange, fig. 12.a;
- from the seismic action on the bridge transversal direction one can obtain: (i) the maximum value for the force on the transversal direction (607 kN(/m)) located in the area where it rests on the pier, (ii) for the moment after the longitudinal axis, fig. 12.b, the maximum value is in the area where it rests on the abutment (157 kNm(/m)), (iii) for the moment on the direction of the transversal axis, the maximum value (87 kNm(/m)) is also in the area where it rests on the abutment;
- values of the moments resulted from the seismic action on longitudinal and vertical directions are not significant.

* *In the pier*, fig. 13:

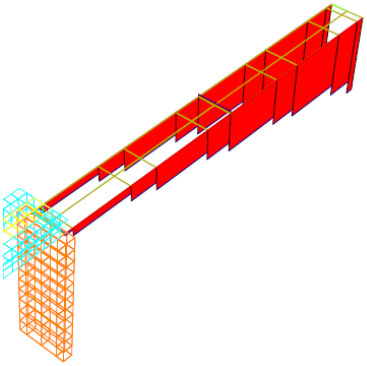
- from the dynamic action on the longitudinal direction, the maximum values are obtained for the stresses on longitudinal (758 kN/m^2) and vertical (2951 kN/m^2) directions, fig. 13.a;



a: Maximum moment in the seismic action on the vertical direction

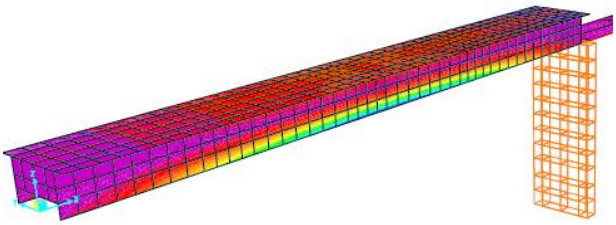


.b: Maximum axial force in the seismic action on the transversal direction

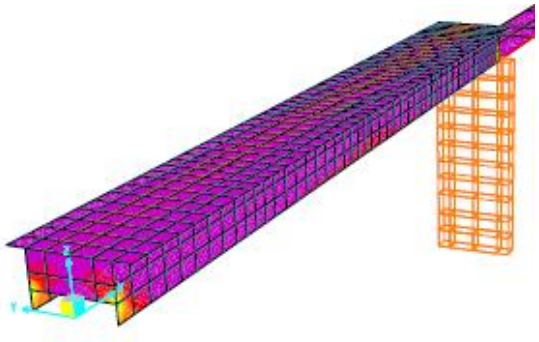


c: Maximum axial force in the seismic action on the longitudinal direction

Figure 11

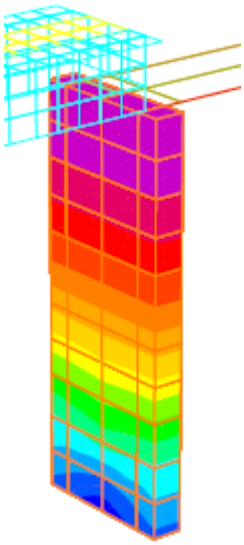


a: Force on the bridge longitudinal direction from the seismic action on the vertical direction

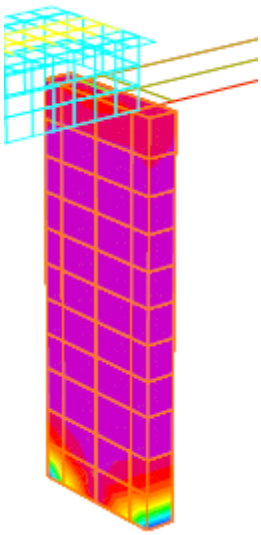


b: Moment on the bridge longitudinal axis resulted from the seismic action on the transversal direction.

Figure 12



a: Stresses on the vertical direction resulted from the seismic action on the longitudinal direction



b: Stresses on the transversal direction from the dynamic action on the transversal direction.

Figure 13

- the maximum value of the stress on transversal direction is obtained from the seismic action on the same direction (2660 kN/m^2), fig. 13.b;
- the lowest stress on the three directions results out of the seismic action on the vertical direction.

5. FINALE COMMENTS

1. Modelling the two decks (SHELL and FRAME) with different finite elements leads to the following observations: (i) it is find out a decoupling of the proper dynamic response of the two decks, they entering the vibration by turns – SHELL span first for the longitudinal and torsion type vibrations, FRAME span first for the vertical and transversal type vibrations; (ii) the periods differences vary from 2% for the longitudinal vibration and 28% for the torsion vibration; (iii) in case of the bi-dimensional span modelled with SHELL elements torsion accompanies more or less the majority of the vibrations.
In conclusion, to obtain a dynamic response as complete as possible the deck design model shall preserve its development along is three directions.

2. From the spectrum loading **Code 1997** and **Code 2006-Se** one can obtain practically the same dynamic response. The values of the dynamic response for the design spectra, **Code 2006-Sd(q1.5)** and **Code 2006-Sd(q=3.5)** are lower proportionally with the ductility coefficients - 1.5 and 3.5 respectively. This is due to the fact that in the acceleration spectrum, the first zone – between 0 and T_B=0.07s where, generally, the coordinates do not comply with the proportional rule with the ductility coefficients – is narrow and its influence reduced.

3. From the spectrum action on the bridge longitudinal direction one can find out that: (i) the dynamic displacement has the maximum value; (ii) the decks have the displacement of a rigid body so that the dynamic efforts appear only in the supporting areas; (iii) the stress on the pier is maximum.

4. In case of the spectrum action on the transversal direction one can find out the following: (i) the displacements on the transversal direction are 50% from the longitudinal displacement for the case of the spectrum action on the longitudinal direction; (ii) the maximum dynamic efforts are in the center of the decks.

5. From the spectrum action on the vertical direction one can find out that: (i) the displacements on the represent about 42% from the longitudinal displacement for the case of the spectrum action in the longitudinal direction; (ii) the maximum dynamic efforts are in the center of the deck.

REFERENCES

[1] Avram C., Bob C., Friedrich R., Stoian V. - *Reinforced Concrete Structures. Finite Element Method. Theory of Equivalences*, Ed. Academiei Republicii Socialiste România, 1984

[2] C. Bucur, A. Rus, A. Ghiţă - *Răspuns dinamic - studiu de caz. Pasarela peste canalul de fugă de la Săcădat* -A1 X-lea Congres Naţional de drumuri şi poduri, Iaşi 1998 Referate şi comunicări Vol. III pag.314-321

[3] Creţu D., Demetriu S. - *Metode pentru calculul răspunsului seismic în codurile româneşti de proiectare. Comparaţii şi comentarii* - Revista AICPS, Nr. 3/2006

[4] Lungu D., Văcăreanu R., Arion C., Aldea A. - *Building inventory data for seismic risk mitigation* – NERO European Building Inventory Workshop, Pavia 2011

[5] Negoescu E., Fierbinþeanu V. - *Proiectarea şi protecţia antiseismică a podurilor şi construcţiilor pentru transporturi*, Editura Tehnicã, 1985

[6] Moldoveanu C.L., Radulian M., Mărmureanu Gh., Panza G.F. – *Outlines of seismic Microzoning of Bucharest, Romania* - United Nations Educational Scientific and Cultural Organization and International Atomic Energy Agency, The ABDUS SALAM International Centre for Theoretical Physics, MIRAMARE – TRIESTE March 2002

[7] *** United Nations, International Strategy for Disaster Reduction (The World Bank) – *South eastern Europe Disaster Risk mitigation and adaptation Initiative* - Geneva 2002

[8] *** SR EN 1998-1/NA November 2008 - Eurocode 8: Design of structures for earthquake resistance – *Part 1: General rules, seismic actions and rules for building, National Annex*

[9] *** SR EN 1998 2/NA May 2010 - Eurocode 8: Design of structures for earthquake resistance - *Part 2: Bridges, National Annex*

[10] *** Seismic Design Code, *Part 1 - P100-1/2006, Earthquake Resistant Design of buildings*

[11] *** SR EN 1998-2/ 2006, *Eurocode 8: design of structure for earthquake resistance. Part 2: bridges*

[12] *** Technical University of Civil Engineering, Bucharest, Building Research Institute, International Institute for Seismology and Earthquake Engineering (Japan) – *Study on early Earthquake Damage evaluation of existing Buildings in Bucharest, Romania* – march 2006

[13] *** *Norm for the anti-seismic designing of the road, railway bridges as well as of the under path of reinforced and prestressed concrete*, 1997 (draft - in Romanian)

COMPDYN 2013
4th ECCOMAS Thematic Conference on
Computational Methods in Structural Dynamics and Earthquake Engineering
M. Papadrakakis, V. Papadopoulos, V. Plevris (eds.)
Kos Island, Greece, 12–14 June 2013

BRIDGES WITH FIXITIES AND BEARINGS VS ISOLATED SYSTEMS

Stergios A. Mitoulis[1]

[1] Civil and Environmental Engineering, Surrey University
e-mail: s.mitoulis@surrey.ac.uk
http://www.surrey.ac.uk/cee/people/dr_stergios_mitoulis

Keywords: Bridge, Isolation, Bearing, Shear key, Hybrid design.

Abstract. *Seismic isolation exhibits a breakthrough in contemporary bridge engineering. The principal of isolation is to protect the bridge piers, by either reducing their seismic actions or through the increase in the damping of the structure. However, there are bridges in which the seismic loading of piers is not effectively reduced when using seismic isolation, and hence the use of expensive and expendable isolators can be avoided. The ineffectiveness of seismic isolation with typical elastomeric bearings was observed in bridges with tall piers. As such the piers can be connected with the deck through rotation-free connections, such as fixed bearings or stoppers, while their seismic loading is not significantly increased. A parametric study is conducted with alternative isolated bridge-models to identify the necessity of piers' isolation against longitudinal seismic actions. Bridge-models with bents of variable heights ranging from 5m to 30m and cross sections ranging from flexible to stiff bent-types were analyzed. All bridge-models were re-analyzed considering that shear keys placed on the piers restrict the longitudinal deck displacements. The adequacy of the piers was checked against longitudinal and transverse seismic actions. The analyses for two levels of the seismic action indicated specific bridge design cases that can utilize both rotation-free pier-to-deck fixities and bearings, while the bridge remains essentially elastic.*

1 INTRODUCTION

A breakthrough of seismic isolation in bridge engineering is established during the last decades. To date there are several hundred bridges in New Zealand, Japan, Italy and the United States using seismic isolation principles and technology for their seismic design. [1]. An isolation system placed between the bridge superstructure and its supporting substructure lengthens the fundamental period of the bridge structure such that the bridge does not respond to the most damaging energy content of the earthquake input [2], while offering damping to the bridge. During the bridge service, bearings accommodate the constraint movements of the deck that are the changes in the length of the bridge due to thermal effects, creep, shrinkage and prestressing. There are bridge construction methods, such as the precast and the incremental launching method, which lead to the compulsory use of bearings, because the deck is not connected rigidly to the piers. According to Calvi et al. [3] seismic isolation practice and technology went farther than research and codes. At the same time, conceptual design of bridges, which is strongly related to the selection of an appropriate earthquake resisting system (ERS) for the bridge, has been disregarded or is given far too little attention by bridge engineers [4] [5]. Conceptual design is fundamental to achieving adequate seismic performance and low, as possible, structural costs [6]. The correct identification of the lateral-force-resisting concept and the selection of the necessary elements to facilitate the concept are essential, while earthquake resistance is enhanced by systems with regular configurations and evenly distributed stiffness and strength according to MCEER/ATC-49 [7] and Imbsen [8].

Isolation bearings and dampers were proved to perform well even during the tremendous seismic loading of the late Tohoku 2011 earthquake according to Kawashima [9]. However, seismic isolation is not always efficient. Liao et al. [10] compared the response of regular and LRB isolated 3-span continuous RC box girder bridges subjected to the near and far records of the Chi Chi Taiwan earthquake and concluded that the PGA is the most important factor in determining the response of isolated bridges, and that during near-field earthquakes the base shear reduction from the use of bridge isolation is limited. Nearly two hundred highway bridges and numerous rail bridges were damaged during earthquake by effects including span unseating and ruptured bearings [11]. Damaged bearings, following severe earthquakes, is a quite frequent bridge failure mode as observed by Chang et al. [12]. According to Lin et al. [13] the lift-off failure of the bearings was one of the significant reasons for the collapse of Baihwa bridge. Similarly, the Dong Feng bridge girders were dislodged and fallen due to the failure of the supporting bearings, while Ji-lu bridge suffered similar span unseating (Chang et al. 2000). Ruptures of bearings were also observed in the last Tohoku earthquake. On the other side, isolated bridges are expected to remain essentially elastic during an earthquake that is reflected by the use of a q-factor of Eurocode 8-2 [14] and R-factors as prescribed by AASHTO's Tables 3.10.7.1-1 and section 3.10.9.5 [15] and also stated by Constantinou et al. [16]. This implies that the ductility based portion of the R-factor is unity or close to unity [17], while bearings burden significantly bridge's initial and final costs. Isolation devices should be inspected and replaced every 5 to 20 years according to the Chinese [18] and the Australian [19] code respectively, as the reliability of the ERS of the bridge relies heavily on the integrity and the response of the bearings. Large seismic displacements of flexible isolated bridge systems increase the requirements of the expansion joints movement capacities and their cost, induce P-D effects and increase the likelihood of span unseating. To reduce these effects, supplementary damping with dampers is attempted to reduce deck's movements, expansion joints are designed with limited gap clearances, i.e. 80% of the seismic design action according to AASHTO's section 9 [17] and 40% according to Eurocode 8-2 (2005), or no consideration for seismic displacements [20] [21] and bridges are equipped with cable restrainers, span

unseating devices, shear keys and a vast of new innovative and emerging technology devices. It is questionable though whether these devices will respond as prescribed or if bridges will require retrofitting in the near future.

During the last years many bridge engineers and academics have shed light on alternative bridge ERS. Rigid pier to deck connections have been achieved through accelerated bridge construction (ABC) methods [22] [23] as means to reduce maintenance costs supporting the philosophy of "get in, get out, stay out". An experimental study of a highway bridge with shape memory alloy restrainers have been conducting by Anxin [24] to enhance the seismic performance of isolated bridges. Xu et al [25] have studied different earthquake resisting systems for high-pier continuous bridges to decide on the most appropriate and efficient system to receive lateral seismic actions. A partial bridge isolation scheme is proposed, which is a combination of fixed and sliding supports. Their analytical results showed that the correct selection of fixed and isolated bents can significantly reduce the force of piers the displacements of the bridge. The need for a technically sound selection of the bearings, expansion joints and shock transmission units (STU) for an effective control of the seismic loading of the substructures was studied by Bandyopadhyay [26]. Monzon et al. [27] have also studied hybrid isolation schemes to reduce deck displacements, while their research concluded that both full isolation and partial isolation are successful at protecting the columns, even during the maximum considered earthquake that is 150% the design earthquake. In particular, an efficient structural concept was demonstrated by the so-called "hybrid system", which combined the self-centering properties of unbonded posttensioning together with energy dissipation characteristics being provided by internal mild steel or other means of energy dissipaters [28]. Hybrid seismic isolation has been found to offer lower levels of damage and negligible residual deformations. The development of alternative solutions for precast concrete buildings based on jointed ductile connections has introduced innovative concepts in the design of lateral-load resisting frame and wall systems [29]. Palermo [30] compared hybrid bridge isolation schemes with traditional monolithic solutions and found that hybrid is a viable and efficient solution for an improved seismic performance of bridge systems. Concept of hybrid system offers self-centering and energy dissipation capacity are adequately combined [31]. Dicleli [32] found that the hybrid seismic isolation system provided a structure with a fundamental period long enough to attract smaller seismic forces, while controlling the magnitude of bearings' displacements. It also resulted in a more uniform distribution of seismic forces among substructure elements, while the piers may provide a restoring force to re-center the structure in such circumstances. The aim of the new design configuration was to allow the designer to pre-assign, to some extent, the seismic characteristics of the bridge, as done in the study of Saiidi et al. [33]. This is related to the even distribution of seismic actions that is based on the regularity criteria set in codes for bridges that are expected to dissipate energy through hysteretic behavior. The resulting configuration is in contrast to the case that existing topography dictates the bridge geometry. Eurocode 8-2 allows the design of the isolation system without taking into account the flexibility of the piers. However, the abutment bearing displacements may be underestimated if the flexibility of the piers is ignored [2] [34].

A viable and efficient solution for an improved seismic performance of bridges is the use of shear keys that restrict longitudinal deck displacements at piers. Use of shear keys is a mature and reliable technology covered extensively by both the current state-of the-art and codes. External shear keys have been proposed in bridges to minimize longitudinal movements [35]. Hindi and Dicleli [36], studied the modification of the seismic response of bridges when modifying the fixity conditions of bearings. Bridge systems were modified to obtain different configurations of bridge earthquake resisting systems. Their research yielded that changing the fixities of the bearings may be an effective response modification technique to mitigate the

effect of seismic forces on vulnerable substructures of the bridge under consideration. AASHTO and Caltrans [37] require the use of shear keys to minimize the possibility of span unseating. Accordingly, Eurocode 8-2 [14] requires the use of seismically inactive shear keys that reduce the deck dislodgment potential, while additional to this the Japanese code [38] [39] requires that stoppers should provide means to dissipate the seismic energy. The Chinese code specifies that, except for displacement limiting and dissipation, shear keys can be used for two levels of resistance [18].

Toward this end an extended parametric study is performed in this paper. The study aims to identify which piers can be connected through rotation-free connections to the deck, under the criterion that the piers remain elastic, while being reinforced with the minimum flexural and shear reinforcements. The study included eight different pier heights, six different pier sections and two levels of the seismic action. More than one hundred realistic bridge-models were analyzed and the study illustrates conclusions that can be useful for future design of hybrid bridge systems that combine shear keys and bearings as means to enhance both seismic resistance and cost-effectiveness. Alternative bridge models were compared on the basis of the aforementioned parameters. Maximum piers' capacity against bending moments was designed to be the same to all the models, while piers were considered to have the same reinforcement ratios, i.e. equal to 1% that is the minimum requirements for columns according to Eurocode 2-1 and Eurocode 2-2 [40] [41]. An extended parametric study was performed to identify whether the seismic isolation with elastomeric bearings is more efficient and cost effective or if bridge systems with fixed connections of the piers to the deck result in a more economical bridge designs**.**

2 THE BENCHMARK BRIDGE

A simplified version of a real bridge was used as a benchmark. The bridge is described in detail by Manos et al. [34]. The simplified bridge system consists of four spans as opposed to the six spans of the real structure, and a total length equal to 154.0 m. Figure 1 shows the longitudinal section of the bridge, as well as the deck and pier cross sections. The finite element model of the isolated bridge system is given in Figure 2.

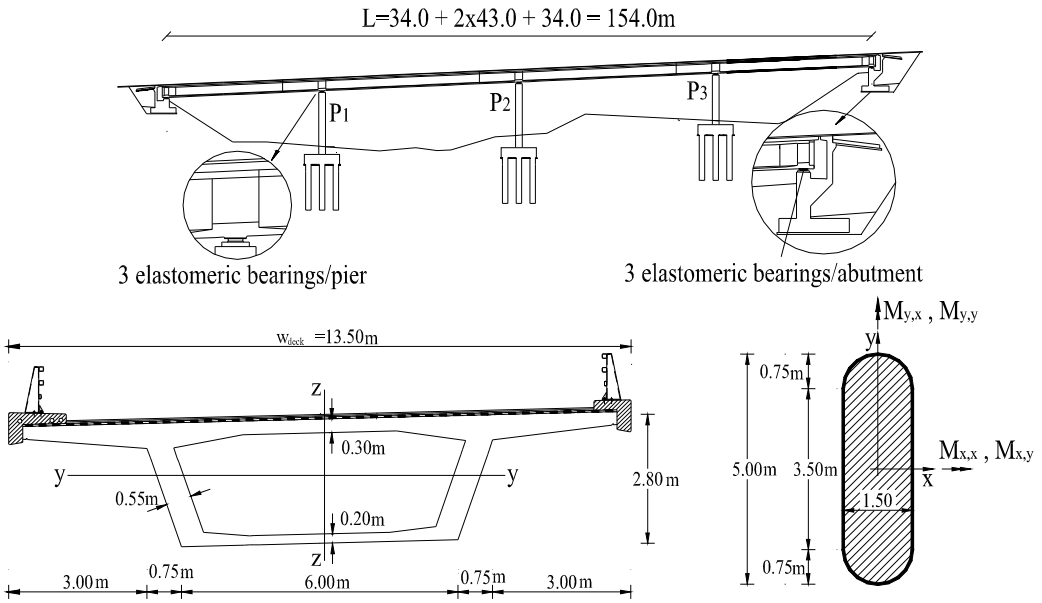


Figure 1: Geometry of the benchmark bridge.

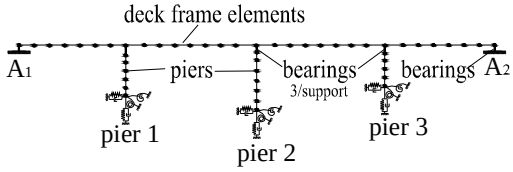


Figure 2: Simplified model of the benchmark bridge with frame elements.

Three bearings were selected for supporting the deck on each abutment and pier in order. The length of the central spans is 43m, the lengths of the end spans are 34m, the shape of the bearings is rectangular, soil type was taken corresponding to class B according to the Eurocode 8, the design ground acceleration was taken equal to 0.16g, the importance factor was assumed to be γ_I=1.30. The bearings were considered to have shear modulus G=1MPa for all the alternative bridge models that were generated based on the benchmark bridge. The deck mass was estimated equal to 308.4kN/m and took into account the dead, the additional permanent and 20% of the live vertical load of the bridge according to Eurocodes.

3 PARAMETRIC STUDY ON ARAHTHOS-PERISTERI BENCHMARK BRIDGE

The bridge of Arachthos-Peristeri that belongs to Egnatia Odos was used to generate realistic bridge-models that were parameterised to account for the following different seismic input motions corresponding to EC8-2 elastic spectrums and to two different Eurocode's 8-1 [14] ground types i.e. ground type B ($v_{s,30}$≈580m/s, N_{SPT}>50 and c_u>250kPa) and C ($v_{s,30}$≈270m/s, N_{SPT}≈32 and c_u≈160kPa) were used. Elastic spectra were calculated by considering the critical damping equal to 5% of the critical one, as the isolators are low damping bearings. Potential different designs that may by adopted by the bridge engineer during the conceptual design process were examined as follows: (a) different pier heights, all bridge models were considered to have variable pier heights ranging from 5m to 30m, (b) different pier cross sections, the piers were considered to be either wall-type columns, circular square, hollow circular, hollow rectangular or multi-column bents, (c) fully isolated bridge-models, i.e. bridges whose deck rests on the piers through low damping elastomeric bearings and bridge models with pier-to-deck connections through shear keys, namely through rotation-free connections that allow for the free relative rotations of adjacent spans and accommodate the constraint movements of the deck during the bridge service (creep, shrinkage, thermal movements). Table 1 illustrates the parameters of the study.

The efficiency of seismic isolation was assessed in all bridge-models. Seismic isolation is considered to be efficient in case the piers actions are effectively reduced by the seismic isolation. The following ratios were considered to be significant in assessing the efficiency of the seismic isolation: (a) the longitudinal pier cap displacement versus the deck's displacement, (b) the bearings' shear displacement versus the deck's displacement, (c) the piers' bending moments versus the piers' bending capacity at yielding (elastic capacity) and (d) the shear displacement of the bearings versus the total thickness of their elastomer that reflects the bearings' shear strain, which is the most important check against failures.

Parameter	pier heights (m)	pier cross section	seismic action PGA (g)	Soil type (Eurocode 8-1)	direction of the bridge	pier-to-deck connection
range of parameter or description	5,10,15,20, 25,30,35,40	wall-type (3.0x5.0m) circular (d=2.5m) square (2.0x2.0m) hollow circular (d_{ex}=3.0m, d_{in}=2.0m, t=0.5m) hollow rectangular (5.0mx3.0m, t=0.5m) multi column (5 columns with diameter 1.0m transverse distance between columns: 2.0m)	0.16 or 0.24	**B** ($v_{s,30}$≈580m/s, N_{SPT}>50 and c_u>250kPa) or **C** ($v_{s,30}$≈270m/s, N_{SPT}≈32 and c_u≈160kPa)	longitudinal (x) or transverse (y)	through bearings or through shear keys (rotation-free)

Table 1: The parameters of the study.

	bearing used					
pier height: **pier type**	**5m**	**10m**	**15m**	**20m**	**25m**	**30m**
multi-column	B1*	B2**	B2	B2	B2	B2
wall-type	B1	B1	B1	B2	B2	B2
square	B1	B1	B1	B2	B2	B2
circular	B1	B1	B1	B2	B2	B2
hollow circular	B1	B1	B1	B1	B2	B2
hollow rectangular	B1	B1	B1	B1	B2	B2

*B1: 800x700x70(50) 3 layers of 16.67mm each

**B2: 800x800x79(59) 3 layers of 19.67mm each

Table 2: The bearings used at the isolated bridge-models for a_g=0.16g.

	bearing used					
pier height **pier type**	**5m**	**10m**	**15m**	**20m**	**25m**	**30m**
multi-column	B5	B6	B4	B4	B4	B4
wall-type	B2	B5	B6	B3	B4	B4
square	B2	B5	B6	B3	B4	B4
circular	B2	B5	B6	B6	B7	B4
hollow circular	B2	B5	B5	B6	B3	B4
hollow rectangular	B2	B2	B5	B5	B6	B6

B3: 800x700x150(110) 7 layers of 15.7mm

B4:800x700x270(200) 13 layers of 15.4mm

B5: 800x800x102(77) 4 layers of 19.3mm

B6: 800x800x125(95) 5 layers of 19mm

B7: 800x800x148(113) 6 layers of 18.8mm

Table 3: The bearings used at the isolated bridge-models for a_g=0.24g.

4 RESULTS

4.1 Comparison of isolated and hybrid solutions

It was considered to be essential to choose pier-deck fixed-hinged connections to piers that are not subjected to significant constraint movements during the bridge service, i.e. due to creep, shrinkage and thermal effects. The displacements of the bearings and the bending moments of the piers under the longitudinal seismic action were considered to be the significant design parameters. Based on the study of Manos et al. the isolation schemes of all isolated bridge-cases were re-designed. Tables 2 and 3 show the dimensions of the elastomeric bearings used at alternative bridge-models under different levels of the seismic action. It is stressed that the area of the isolators was not significantly changed due to the fact that the vertical compressive load of the bearings is not altered significantly, as vertical loading of the isolators is mostly dependent on the dead load plus the live load of the deck [14].

Based on Figures 3 and 4 (continuous black lines indicated by letter b) it is evident that the shear capacity of the bearings, in terms of maximum allowable shear strain of the bearings, is not fully developed in any case. Hence, the displacements that are received by the isolators is lower than the Eurocode's 8-2 [14] maximum allowable shear strain that equals ε_s=200%. The bearings shear deflection is maximum when the stiff piers (i.e. hollow circular and rectangular) were used and when the height of the piers was the minimum, namely when the bridge's ERS is quite stiff. The opposite was found to be valid when the flexible pier was considered (i.e. the multi column bent) and when the heights of the pier was increased. Bearings were found to receive relatively small shear displacements, corresponding to less than ε_s=100% of the maximum allowable shear strain, when the bridge models with multi-column, wall-type, square, circular, hollow circular and hollow rectangular bents were used with heights greater than 6m, 10m, 11m, 12m, 14m and 19m respectively (as shown by the black discontinuous lines). Correspondingly, the multi-column, wall-type, square, circular, hollow circular and hollow rectangular bents were found to receive 40%, 40%, 45%, 40%, 45% and 43% of the maximum deck's longitudinal displacement. The piers were found to develop 76%, 40%, 72% 62%, 75% and 25% of their bending moment at yielding (elastic capacity), that was estimated based on the minimum longitudinal reinforcement ratio of ρ=1% [40] [41]. Hence, piers' elastic capacity redundancy is not developed, while the role of the bearings is reduced effectively when the bridge systems became more flexible, i.e. when more flexible bents were used and when taller piers were used. Figures 3 and 4 show that the piers' elastic capacity was not developed in any bridge-case under the transverse seismic action (figures on the right). It is stressed that transverse seismic displacements of the deck were restricted by shear keys placed on the bents.

When the higher seismic action 0.24g was considered, the bearings were found to receive relatively small shear displacements, corresponding to less than 50% of the the maximum allowable shear strain (i.e. ε_s=100%), when the bridge models with multi-column, wall-type, square, circular, hollow circular and hollow rectangular bents were used with heights greater than 8m, 12m, 14m, 15m, 17m and 23m respectively, as shown by the black discontinuous lines of Figure 4. Correspondingly, the multi-column, wall-type, square, circular, hollow circular and hollow rectangular bents were found to receive 50%, 50%, 55%, 44%, 50% and 47% of the maximum deck's longitudinal displacement. The multi-column, the square, and the hollow-circular cross sections of the piers were found to receive bending moments greater than their elastic capacity, when considering a longitudinal reinforcement ratio ρ=1%, while the wall-type, the circular and the hollow rectangular bents were found to develop 57%, 92% and 37% of their elastic capacity. The multi-column, the square, and the hollow-circular piers

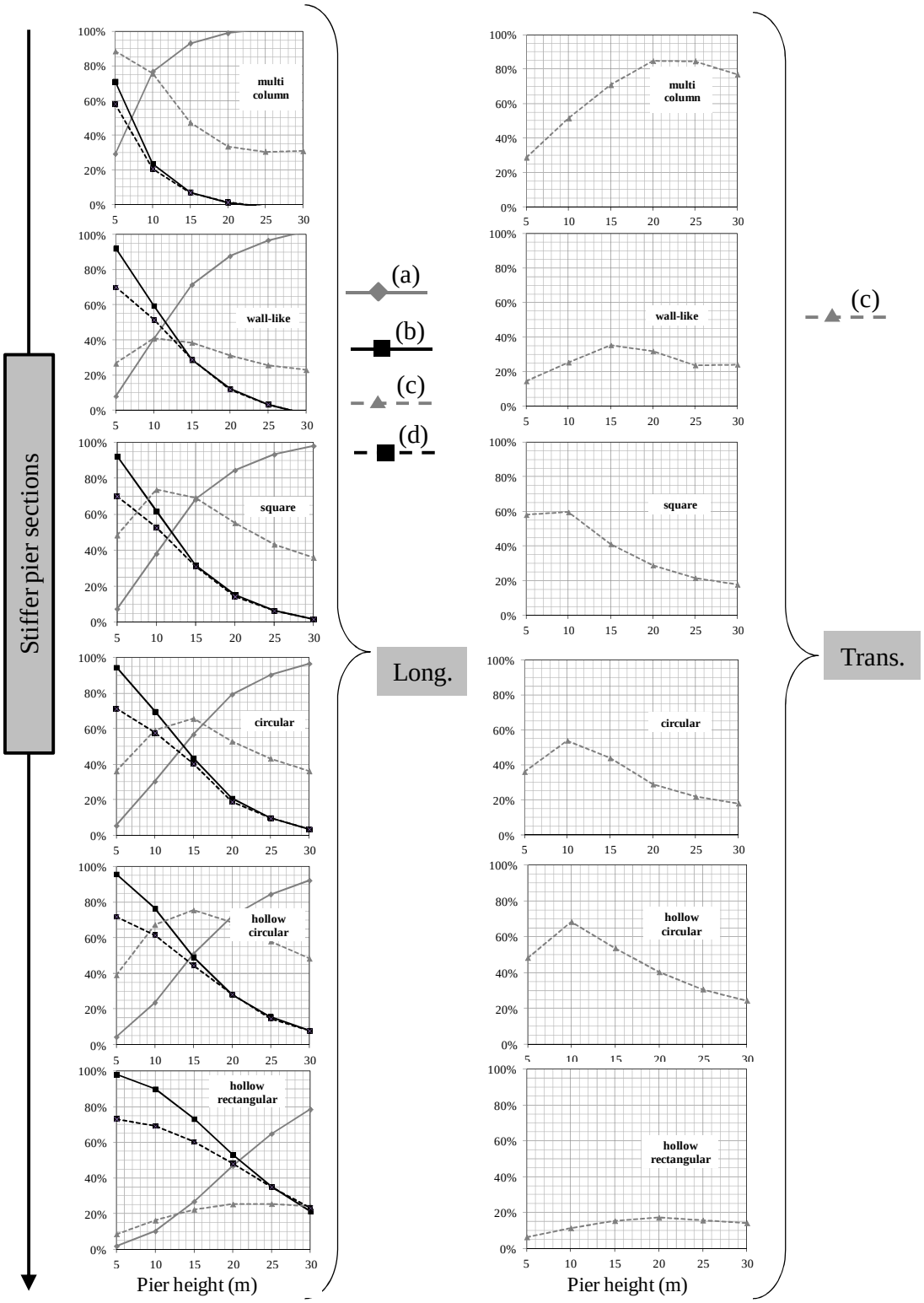


Figure 3: The ratios of (a) the longitudinal pier cap displacement versus the deck displacement (continuous gray line), (b) the bearings' shear displacement versus the deck displacement (continuous black line), (c) the piers' flexural loading versus the piers' bending moment at yielding (elastic capacity) (discontinuous gray line) and (d) the shear displacement of the bearings versus the total thickness of their elastomer (discontinuous black line) (a_g=0.16g).

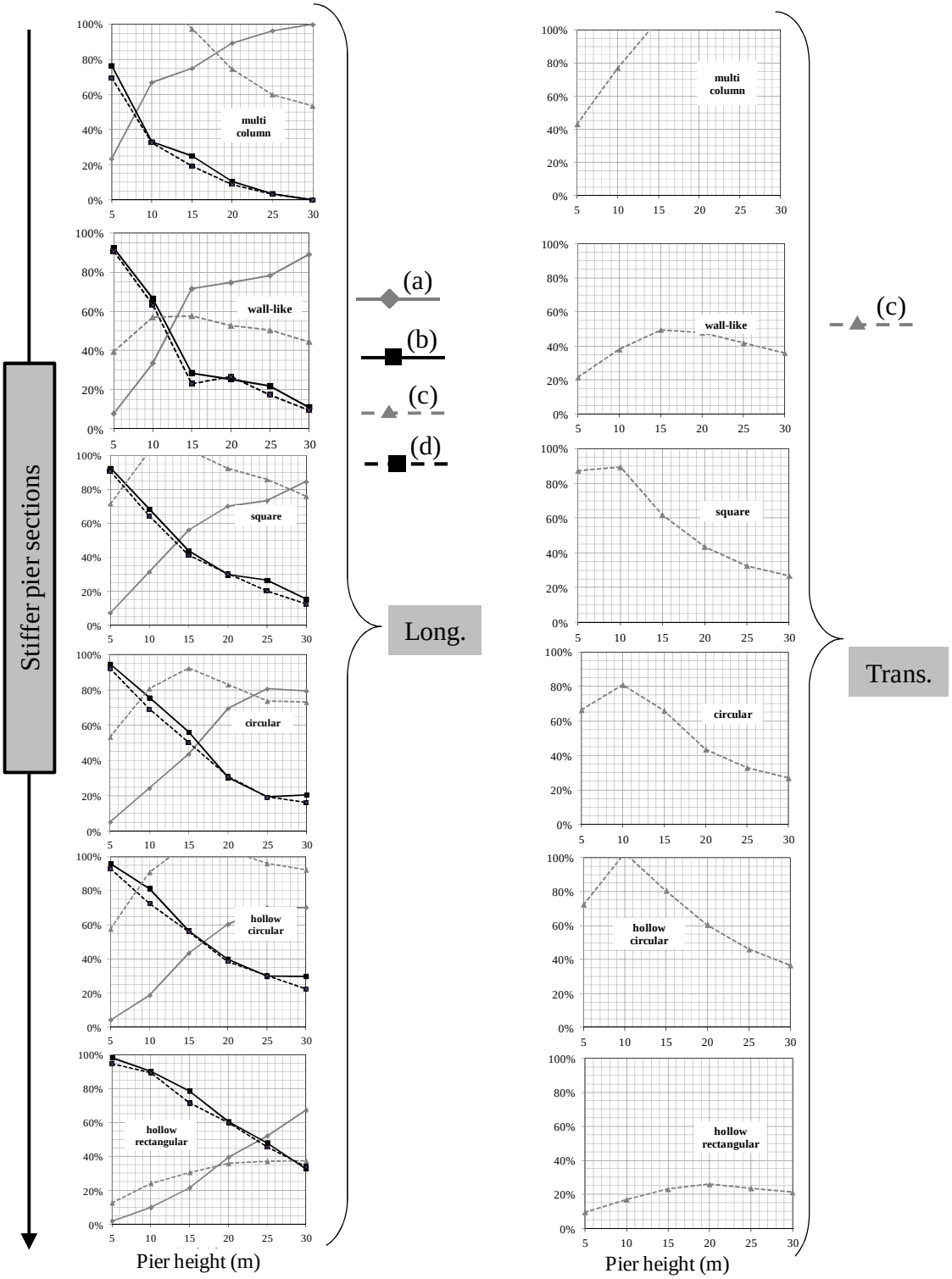


Figure 4: The ratios of (a) the longitudinal pier cap displacement versus the deck displacement (continuous gray line), (b) the bearings' shear displacement versus the deck displacement (continuous black line), (c) the piers' flexural loading versus the piers' bending moment at yielding (elastic capacity) (discontinuous gray line) and (d) the shear displacement of the bearings versus the total thickness of their elastomer (discontinuous black line) (a_g=0.24g).

were found to remain within the elastic range in case their heights were greater than 14m, 16m and 23m correspondingly. The check of the piers, when the bridge-models were subjected to the transverse seismic action, showed that the multi column pier yield, i.e. the bending moment action is greater than the elastic capacity. For the other bent types, the elastic capacity was greater than the one developed during an earthquake with a PGA equal to 0.24g.

Hence, it seems that there are bridge-designs in which seismic isolation may not be used to safeguard the piers against seismic actions, due to the fact that on the one hand the bearings receive small part of the deck's displacements, while on the other hand the piers can receive safely the seismic actions without exhibiting yielding, while using only the minimum longitudinal reinforcements, i.e. 1%. Hence, the piers can be connected to the deck through rotation free connections, such as shear keys, to provide a cost-effective bridge design, while the seismic safety of the bridge can be relied on both isolation devices, namely on the bearings, and on the resistance of the piers. The selection of the piers, which can be connected to the deck through rotation-free connections, have been studied in a previous paper [42]. Table 4 summarizes the results of this parametric study showing what the minimum required height of the piers is in case a rotation-free connection is used for the design of the ERS of the bridge. The results are based on the parametric study that was conducted on isolated bridge-models.

All the analyses were repeated considering that all the piers are connected to the deck through rotation-free connections, i.e. shear keys that restrict both the relative pier-deck displacements in the longitudinal and the transverse direction of the structure. This case was considered to be the "stiff" version of the bridge-model, while the bridge-models with seismic isolation that was studied above were considered to be the "flexible" versions of the bridge-models. Table 5 shows the minimum pier heights that can utilize rotation-free connection, under the assumption that the piers will not require additional reinforcements than the ones required in the benchmark bridge-model (i.e. 1%).

	pier section					
pier type:	multi-column	wall-type	square	circular	hollow circular	hollow rectangular
seismic action						
0.16g	6	10	11	12	14	19
0.24g	-	12	16	15	23	23

Table 4: The minimum pier heights in isolated bridge-models that were found to have ineffective isolation (flexural reinforcement of the piers 1%).

	pier section					
pier type:	multi-column	wall-type	square	circular	hollow circular	hollow rectangular
seismic action						
0.16g	10	all heights	14	15	19	all heights
0.24g	-	12	20	20	25	20

Table 5: The minimum pier height that can utilize rotation-free connection (flexural reinforcement of the piers 1%).

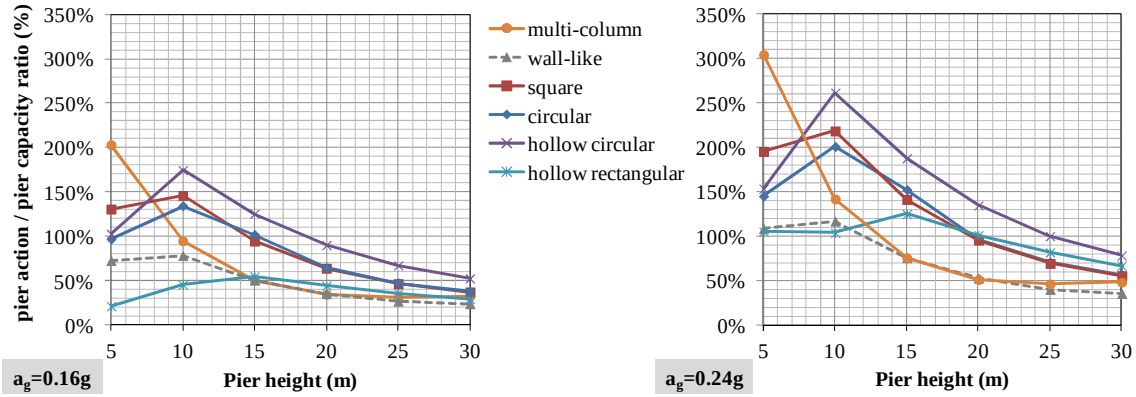


Figure 5: The pier action (bending moment) vs the pier elastic capacity ratio when all the piers of the bridge models are connected to the deck with rotation-free connections (figure's results summarized in Table 5).

The two tables reveal that there are bridge-models that can combine both seismic isolation and rotation-free pier-to-deck connections. The pier heights given in Table 4 show what is the maximum pier height after which the benefits of seismic isolation are fading, while the pier heights shown in Table 5 are the minimum pier heights that are required in case all the piers are connected to the deck through rotation-free connections. Intermediate values of piers' heights indicate the bridge design case in which some piers may be connected to the deck, whereas the rest of the bents may be isolated.

4.2 Modification of the dynamic system of the bridge

The parametric study that was conducted for this paper emphasized on the modification of the dynamic response of bridges that is strongly related to the period of the bridge-models in both the longitudinal and the transverse direction of the bridge. For this reason the fundamental periods in both the longitudinal and the transverse directions of the bridge-models were estimated. The analyses of the bridge-models with and without pier-to-deck rotation-free connections revealed that the modal periods are only slightly altered when the piers are connected to the deck under the condition that the piers have heights greater than the ones shown in Table 4. More specifically, the bridge-models with the 10m long multi-column, the 15m long wall-type, the 15m long square, the 15m long circular, the 25m long hollow circular and the 25m long hollow rectangular bents revealed a decrease in their longitudinal periods of the order of 4%, 5%, 7%, 12%, 2% and 7% when the piers were connected to the deck instead of isolating them. The above period reductions corresponded to the following increases in the seismic action: 4%, 5%, 6%, 12%, 2% and 8%. It follows that no significant increase in the induced seismic action took place in case the piers were connected to the deck through shear keys. At the same time, the piers remained elastic despite the use of minimum flexural reinforcements (1%), while the initial and final cost of the bridge is effectively reduced, due to the use of smaller bearing sections and smaller expansion clearances.

5 CONCLUSIONS

An extended parametric study was conducted to compare the seismic response of conventional seismically isolated bridge-models to the hybrid bridge alternative, which combines the use of isolation and rotation-free connections, i.e. shear keys. Towards this comparison the minimum required piers' flexural reinforcement ratio of 1% was considered, while the piers were considered to remain essentially elastic. The parametric study included different pier

heights, pier sections and different levels of the seismic action. The study came to the following conclusions:

There are bridge designs, with flexible pier sections that is either bents with relatively small sections or tall piers, in which seismic isolation benefits fading. This is due to the fact that the piers receive a large portion of the deck's longitudinal and transverse seismic displacements. Hence, bearings are considered to be superfluous in that case and as such can be avoided by utilizing common shear keys.

The study showed that isolation became ineffective in bridges having flexible piers. The analyses indicated what were the maximum pier heights for the different pier sections that isolation is effective in reducing their loading. Isolation was considered to be ineffective when the bearings' movement capacity is not developed, namely when the shear strains ε_s are smaller than 100% and when the piers loading is smaller than their elastic flexural capacity. The above consideration was found to be valid when the bridge-models with the multi-column, wall-type, square, circular, hollow circular and hollow rectangular bents were used with heights greater than 6m, 10m, 11m, 12m, 14m and 19m respectively. The results refer to the case that a seismic action equal to 0.16g was considered, while in case a PGA equal to 0.24g was considered the corresponding pier heights of the bridge-models with multi-column, wall-type, square, circular, hollow circular and hollow rectangular bents were used with heights greater than 8m, 12m, 14m, 15m, 17m and 23m respectively. However, when 0.24g was considered the transverse seismic action required additional flexural reinforcements for the piers (i.e. a ratio greater than 1%). This was found to affect the multi-column bents which required an increase in their reinforcements in all cases. In case the square and the hollow-circular piers were considered the piers' loading was found to be smaller than their elastic capacity if the piers have heights greater than 16m and 23m.

Re-analyses of all bridge-models considering that all the piers are connected to the deck through rotation-free connections were conducted to indicate what are the minimum piers' heights for different bent sections that can be connected to the deck. The analyses yielded that the multi-column, square, circular, and hollow circular piers can be connected to the deck when their heights are greater than 10m, 14m, 15m, 19m correspondingly. If the pier have a wall-type or a hollow rectangular section then all the piers may be connected to the deck independently from their heights. The former results refers to the case that the bridge-models were subjected to a seismic action of 0.16g, while in case a PGA equal to 0.24g was considered then the wall-type, square, circular, hollow circular and hollow rectangular piers should have at least heights 12m, 20m, 20m, 25m and 20m respectively. The multi-column piers having a flexural reinforcement ratio 1% were found to be inadequate to receive the 0.24g seismic action.

REFERENCES

[1] I.G. Buckle, M.C. Constantinou, M. Dicleli, and H. Ghasemi, Seismic Isolation of Highway Bridges. *Special Report MCEER-06-SP07*, Multidisciplinary Center for Earthquake Engineering Research, Buffalo, NY, 171pp, 2006.

[2] M.C. Kunde and R.S. Jangid, Effects of Pier and Deck Flexibility on the Seismic Response of Isolated Bridges. *Journal of Bridge Engineering*, **11**, No 1, 2006.

[3] G.M. Calvi, P.E. Pinto, Assessment of EC8 provisions for reinforced concrete bridges, *In proc. 11th World Conference of Earthquake Engineering (WCEE) Acapulco*, Mexico, No. 2052, 1996.

[4] C. Menn, An approach to bridge design. *Engineering Structures*, **13**(2) 106-112, 1991.

[5] A. Palermo, S. Pampanin and D. Marriott, Design, Modeling, and Experimental Response of Seismic Resistant Bridge Piers with Posttensioned Dissipating Connections. *Journal of Structural Engineering*, **133**(11), 2007.

[6] S.A. Mitoulis, I.A. Tegos, K.-C. Stylianidis, Cost-effectiveness related to the earthquake resisting system of multi-span bridges, *Engineering Structures*, **32**(9), Pp. 2658-2671, 2010.

[7] MCEER/ATC-49, Recommended LRFD Guidelines for the Seismic Design of Highway Bridges Part I: Specifications, *Based on NCHRP Project 12-49*, FY '98, 2003.

[8] R.A. Imbsen, Proposed AASHTO Guide Specifications for LRFD. *Seismic Bridge Design Subcommittee for Seismic Effects on Bridges T-3*, 2007.

[9] K. Kawashima, Damage of bridges due to the 2011 great east japan earthquake, In Proceedings, *International Symposium on Engineering Lessons Learned from the 2011 Great East Japan Earthquake*, March 1-4, 2012, Tokyo, Japan, 2012.

[10] W.I. Liao, C.H. Loh and B.H. Lee, Comparison of dynamic response of isolated and non-isolated continuous girder bridges subjected to near-fault ground motions, *Engineering Structures*, **26**(14), 2173- 2183, 2004.

[11] Earthquake Engineering Research Institute (EERI), *Learning from Earthquakes Bridge Performance in the Mw 9.0 Tohoku*, Japan, Earthquake of March 11, 2011.

[12] K.-C. Chang, D.-W. Chang, M.-H. Tsai and Y.-C. Sung, Seismic performance of highway bridges. *Earthquake Engineering and Engineering Seismology*, **2(**1) 55-77, 2000.

[13] L. Chu-Chieh, J.H.-H. Hung, K.-Y. Liu and J.-F. Chai, Reconnaissance Observation on Bridge Damage Caused by the 2008 Wenchuan (China) Earthquake Chu-Chieh. *Earthquake Spectra*. **26(**4), 1057-1083, 2010.

[14] EN 1998-2 Eurocode 8: Design of structures for earthquake resistance, Part 2: Bridges, 2005

[15] AASHTO LRFD *Bridge Design Specifications SI Units 4th Edition*, 2007.

[16] MCEER-99-0012, *Property Modification Factors for Seismic Isolation Bearings*, by M.C. Constantinou, P. Tsopelas, A. Kasalanati and E. Wolff, 7/20/99, (PB2000-103387, A11, MF-A03).

[17] American Association of State Highway and Transportation Officials (AASHTO). *Guide specifications for seismic isolation design*, 3rd Edition, Washington, D.C, 2010.

[18] K. Wang, H.Wei and Q. Li, Philosophies on seismic design of highway bridge with small or medium span. Research Institute of Highway, the Ministry of Transport, Beijing, In Proceedings, *15th WCEE - World Conference on Earthquake Engineering*, Lisbon, Portugal, paper No. 550, 2012.

[19] AS 5100.4-2004 Supplementary to the Australian standard and commentary, *Design of deck joints for road bridges*. Bridge design-bearings and deck joints. 1999/002.

[20] C.S. Gloyd, Seismic movement at bridge abutments. *ACI Spec Publ.***164**, 273-288. SP164-15, 1996.

[21] S.A. Mitoulis, Seismic design of bridges with the participation of seat-type abutments, *Engineering Structures*. **44**, 222-233, 2012.

[22] M.L. Marsh, M. Wernli, B.E. Garrett, J.F. Stanton, M.O. Eberhard, M.D. Weinert, application of accelerated bridge construction connections in moderate-to-high seismic regions, *NCHRP Report 698*, 2011.

[23] J.I. Restrepo, C.A. Matthew, J. Tobolski, CA Eric, E. Matsumoto, Development of a precast bent cap system for seismic regions. *NCHRP Report 681*, 2011

[24] G. Anxin, Z. Qingjie and L. Hui, Experimental study of a highway bridge with shape memory alloy restrainers focusing on the mitigation of unseating and pounding, *Earthquake Engineering and Engineering Vibration*. **11**, 195-204, 2012

[25] X. L. Xu, X. Xu, X. H. Li, Z. J. Li, K. R. Wang & D. Zhou, Study on Seismic Constraint System of High-Pier Continuous Bridges. In proc. *World Conference of Earthquake Engineering (WCEE)*, Lisbon, Portugal, No. 3868, 2012.

[26] N. Bandyopadhyay, A. Ghoshal and A. Sengupta, Relevance of bearings and expansion joints-case studies for indeterminate bridges. *IABSE-JSCE Joint Conference on Advances in Bridge Engineering-II*, Dhaka, Bangladesh. ISBN: 978-984-33-1893-0 Amin, Okui, Bhuiyan (eds.), 2010.

[27] E.V. Monzon, C.Wei, I.G. Buckle and A. Itani, Seismic response of full and hybrid isolated curved bridges structures. *American Society of Civil Engineers Congress*, Chicago, Illinois, United States, 2012

[28] J.F. Stanton, W.C. Stone and G.S. Cheok, A hybrid reinforced precast frame for seismic regions. PCI Journal, **42**(2), 20-32, 1997.

[29] A. Palermo, S. Pampanin G.M. Calvi, Concept and development of hybrid solutions for seismic resistant bridge systems, *Journal of Earthquake Engineering*, **9**(6), 899-921, 2005.

[30] A. Palermo, Enhanced seismic performance of hybrid bridge systems: Comparison with traditional monolithic solutions, *Journal of Earthquake Engineering*, **12**,1267-1295, 2008.

[31] W.F. Chen, L. Duan, *Bridge engineering handbook*. Boca Raton (London, New York, Washington, DC): CRC Press, 1999.

[32] M. Dicleli, Seismic design of lifeline bridge using hybrid seismic isolation, Journal of Bridge Engineering. **7**(2), 94-103, 2002.

[33] S.M. Saiidi, R.. Moore, A. Itani, Seismic performance of reinforced concrete bridges with unconventional configurations, *ACI Structural Journal*, **98**(5), 717-726, 2001.

[34] G.C. Manos, S.A. Mitoulis, A.G. Sextos, A knowledge-based software for the preliminary design of seismically isolated bridges, *Bulletin of Earthquake Engineering*, **10**(3),1029-1047, 2012.

[35] S.A. Mitoulis, I.A. Tegos, Restrain of a seismically isolated bridge by external stoppers, *Bulletin of Earthquake Engineering*, **8**(4), 973-993, 2010.

[36] R. Hindi and M. Dicleli, Effect of modifying bearing fixities on the seismic response of short- to medium-length bridges with heavy substructures, *Earthquake Spectra*, **22**(1) 65-84, 2006.

[37] California Department of Transportation (CalTrans), *Bridge Memo to Designers* (20-1). Seismic Design Methodology, California Department of Transportation, Sacramento, CA. 1999.

[38] Japan Road Association (JRA), *Manual for seismic design of highway bridges*, Tokyo, Japan. 1997

[39] Japan Road Association (JRA), Chapter 1 *Seismic design specifications for highway bridges*, International Institute of Seismology and Earthquake Engineering, Tokyo, Japan, 2002.

[40] EN 1992-1-1, Eurocode 2: Design of concrete structures, Part 1: General rules and rules for buildings, 2004.

[41] EN 1992-2, Eurocode 2: Design of concrete structures, Part 2: Concrete bridges, 2004.

[42] S.A. Mitoulis The inefficacy of seismic isolation in bridges with tall piers", In Proc., *15th WCEE - World Conference on Earthquake Engineering*, Lisbon, Portugal, 2012, pp. No 3944.

COMPDYN 2013
4th ECCOMAS Thematic Conference on
Computational Methods in Structural Dynamics and Earthquake Engineering
M. Papadrakakis, V. Papadopoulos, V. Plevris (eds.)
Kos Island, Greece, 12–14 June 2013

SEISMIC RESPONSE OF BRIDGE ABUTMENTS ON SURFACE FOUNDATION SUBJECTED TO COLLISION FORCES

Sotiris A. Argyroudis[1], Stergios A. Mitoulis[2], and Kyriazis D. Pitilakis[3]

[1] Aristotle University of Thessaloniki
Department of Civil Engineering, P.O.B. 424, 54124, Thessaloniki, GREECE
sarg@civil.auth.gr

[2] University of Surrey
Department of Civil and Environmental Engineering, 21AA02, Guildford, GU2 7XH, Surrey, UK
s.mitoulis@surrey.ac.uk

[3] Aristotle University of Thessaloniki
Department of Civil Engineering, P.O.B. 424, 54124, Thessaloniki, GREECE
kpitilak@civil.auth.gr

Keywords: Bridge; abutment; embankment; collision force; modeling; Plaxis; SAP 2000; abutment failure modes.

Abstract. *Bridges are important components of the roadway and railway networks, as they must remain operational in the aftermath of the seismic event. Permanent movements of the backwall and the backfill soil and rotational deformations of the abutment-backfill system are well known failure modes that potentially may incite deck unseating mechanisms. However, only a few studies dealt with the modeling of deck-abutment-backfill pounding effect. In this framework, an extended parametric study was conducted on a simplified abutment-backfill analytical model. A typical seat-type abutment was analyzed using 2D nonlinear FE model in Plaxis. Simultaneously, a refined abutment-backfill model was built in commercial software SAP2000 in view to highlight significant parameters of the interaction aiming at identifying the effect of collisions on anticipated damages of the abutment. The assessment of the deck-abutment-backfill response was performed on the basis of longitudinal maximum and residual movements and rotations of the abutment that may affect both the integrity and the post-earthquake accessibility of the bridge. SSI effects due to the interaction of the deck with the abutment and the backfill soil were considered; analyses showed that large seismic movements during an earthquake and permanent movements of the abutment are deemed to put in danger the abutment itself, the integrity of the end spans and finally the accessibility of the bridge. Comparison of different seat-type abutment models in Plaxis and SAP2000 revealed that modeling of bridge abutments with emphasis on the geotechnical design should be properly made. Poor design assumptions may have a serious impact in the assessment of the response of the abutment-backfill-bridge system.*

1 INTRODUCTION

The earthquake resisting system of bridges mostly relies on the piers and foundations, the isolators and the shear keys. During an earthquake, plastic hinges are expected to be developed at the piers; properly designed isolators intend to increase the fundamental period of the system and dissipate energy through hysteretic behavior. Shear keys are typically used against span unseating. This philosophy seems to be adequately covered by current codes for most of bridge structural elements except the abutments.

However, abutment response, soil-structure interaction and backfill flexibility have been found by post-earthquake reconnaissance reports to significantly influence the response of an entire bridge system under moderate to strong intensity ground motions [1, 2, 3, 4, 5, 6, 7, 8]. The influence of soil-structure-interaction on the dynamic response of bridges has been recognized [2, 9] and has been widely addressed the following years in instrumented bridge overpasses [10, 11]. The known backfill-abutment-deck interaction constitutes a wide field of study in integral abutment bridges [12] and in bridges with seat-type abutments like the one shown in Figure 1. In the latter case, the backwall of the abutment is typically designed to break free of its base support when is struck by a bridge deck [13, 14] mobilizing high values of the passive resistance of the backfill soil [15, 16, 17, 18]. The seismic demand and therefore the cost of bridges are strongly influenced by the resistance of the abutment. Hence, refined modelling approaches are necessary in order to reveal the potential mechanisms triggered in the seismic assessment of bridges [4, 5].

Dynamic analysis of highway bridges and modelling of the abutment's capacity is prescribed by various agencies [13, 14, 19]. However, current design practice varies considerably on the use of the abutments as part of the bridge's earthquake resisting system ERS [20]. Simplified force-deflection relationships for modelling embankment-abutment systems were proposed by Sextos et al. [21]. Shamsabadi et al. [22] used mobilized logarithmic-spiral failure surfaces coupled with a modified hyperbolic soil stress-strain behavior -known as LSH soil model- to estimate abutment nonlinear force-displacement capacity as a function of wall displacement and backfill soil properties. The analytical force-displacement expressions were also validated by experimental studies [23].

The seismic response of seat-type abutments and their effect on the integrity of bridges depend on the dynamic resistance and response of the backfill soil and on the capacity and mass of the abutment's structural members (backwall, footing, wingwalls and the approach slab) [7, 24]. The openings at the expansion joints [25, 26, 7, 24] influence strongly the pounding effects [27] and in turn affect the seismic response of the bridge. However, the post-earthquake condition of abutments has not been studied or evaluated adequately although it is considered to be of vital importance for the bridge to maintain operational and to avoid permanent rotations [24], that would trigger potential primarily damages of the backwall and hence widening of the expansion joints or unfavorable span-unseating mechanisms. In that case, different abutment's design parameters are important: (a) the gap between the deck and the backwall, (b) the mass, the stiffness and the post-earthquake condition of the backwall, (c) the possible overall rotation of the abutment which has been revealed in past earthquakes (Figure 2a), (d) the pre- and post-earthquake condition of the backwall and the backfill (see Figure 2b) and its relation to the backfilling material. The latter is also influenced by the serviceability and seismic induced settlements, the condition of the approach slab and the wing walls. All these parameters are affecting the performance indicators of the bridge and the selection of appropriate damage states indices (and values) for the construction of fragility curves.

Recent studies on the seismic fragility of bridges consider the contribution of abutments to the overall bridge system fragility following the common seismic design practices taking into account the activation of the abutment-backfill system due to the gap closure between the deck and the abutments [28, 29]. Argyroudis et al. [30] proposed numerical fragility curves for cantilever bridge abutments on surface foundation considering different soil types, abutment heights and seismic input motions. The performance of the abutment is defined based on the range of the backfill settlement. However, the effect of collision force due to the pounding of the deck to the abutment in the overall system fragility is not considered in these studies.

In this framework, an extended parametric study was conducted and a typical seat-type abutment was modeled and analyzed using 2D nonlinear FE model in Plaxis. Simultaneously, a refined non-linear abutment-backfill model was built in SAP 2000 (ver. 15.0.0) using the validated p-y curves of Plaxis. Modeling accounted for the construction stages of the abutment that modify the initial states of stresses within the backfill soil and the soil pressures on the abutment. A step-by-step analysis-validation procedure was followed, starting from simple static to complex non-linear dynamic models. Comparisons was mainly performed on the basis of horizontal displacement of the abutment's stem and base rotation The properties of the backfill employed in the analyses are based on typical design cases and literature. We selected representative input to cover typical magnitudes, frequency content and duration. SSI effects and the post-impact response of the abutment-backfill were evaluated on the basis of permanent movements and rotations that may affect the bridge's integrity in terms of available seating widths. Potential failure modes of typical seat-type abutments were recognized and qualitatively described when strongly non-linear SSI effects are mobilized due to the interaction of the deck with the abutment and the backfill.

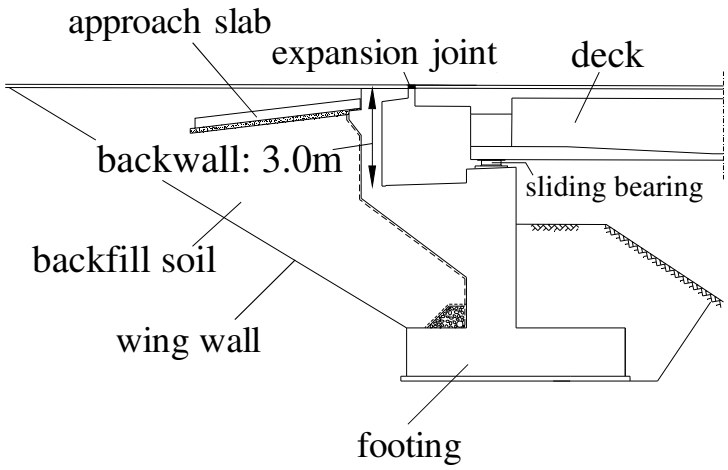


Figure 1: A typical seat type abutment.



(a) (b)

Figure 2: (a) Rotation of the entire abutment-backfill substructure due to pounding effects (Rio Banano bridge, Costa Rica, 25/3/1990, M_w=7.0). (b) Light pounding-induced failure, the expansion joint is damaged but no evidence of large permanent lateral movements is shown.

2 MODELLING OF ABUTMENT-BACKFILL

2.1 Modelling in Plaxis

The coupled soil-wall interaction analyses were performed with the 2D (plane strain) finite element code Plaxis (ver. 9.02). Figure 3 describes the model used with a width properly selected to avoid boundary effects. A set of initial analyses is performed to simulate initial geostatic stresses as well as the construction of the wall and the backfill. Then, depending on the validation case, the static or dynamic analyses followed, where the pounding forces are applied at the top of the abutment and the seismic input is applied uniformly at the basis of the model.

Elastic or elasto-plastic soil behavior (i.e. Mohr-Coulomb criterion) is used depending on each case. Proper interface elements with a realistic friction coefficient of R_{inter}=0.70 were used to model the interface behavior between the backfill and foundation soil with the wall, allowing the relative movement between the soil and the abutment. The soil material damping is introduced numerically in the form of Rayleigh damping in case of dynamic analysis.

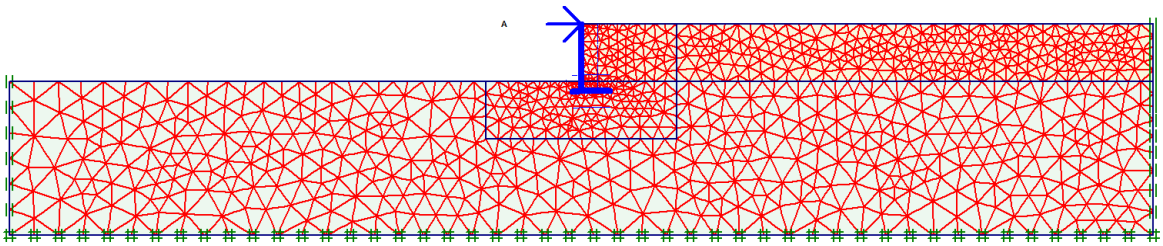


Figure 3: Example of the modeling mesh in Plaxis.

2.2 Modelling in SAP2000

Simplified to more complex bridge abutment models were built in SAP 2000 using stick models for the frames and linear or non-linear links for the backfill soil depending on the validation case. Frame sections were used to model the 1-m width of the analyzed abutment-

backfill system. The objective of this simplified modelling was to provide a step-by-step analysis-validation procedure from simplest to more complex models. This procedure facilitated the validation of the abutment response parameters between the two different simulation approaches employed in the study (SAP 2000 structural model and Plaxis model). This comparison was deemed to be essential as the complex and non-linear response of the abutment under pounding loads is not yet recognized or assessed before. Both models were subjected to longitudinal loading that was compatible to the pounding forces [7]. The time history of the collision forces was induced at the stem (top) of the backwall by the colliding deck. Modeling followed the technique that is described in detail by Mitoulis [7].

Pilot analyses included initially static loading and simulation of backfill's resistance with only linear spring elements attached at both the web of the abutment and the surface foundation of the abutment. Static analyses (Cases 3, 4, 5a, 5b) were performed using linear spring elements that were estimated by the force-displacement diagrams calculated in the Plaxis model. A 0.5m at backfill's height discretization was used at this stage to identify both the accuracy offered by potential coarse and dense discretization grids and to estimate the critical height of the backfill soil that participated strongly to the modeled impacts, as it was evident that not the entire height of the backfill soil resists to this effect. Linear and non-linear link elements with hysteretic behavior were used to model the response of the backfill soil under dynamic deck-to-abutment collision force that was introduced in models 6 and 7 (see Figures 6 and 9). The multi-linear plastic with kinematic hysteretic model of SAP2000 was used (case 7, Figure 9). The model was chosen to match the response of the SAP model with the Plaxis-produced hysteresis loops of the backfill soil under pounding loading. The procedure introduced the analysis of Plaxis' abutment-backfill model and the outcomes were utilized to decide on the load-dependent non-linear p-y curves with zero tension resistance and a hysteretic response under compression for the SAP-model. Modelling of the backfill soil was performed at the upper 3m due to two reasons. Firstly, it was recognized that the accuracy of the model is not influenced strongly by the abutment-backfill translational resistance of the lower part. Secondly, the p-y relations at very low backfill's deflections that were observed at lower soil layers are not reliable to be used for the estimation of non-linear properties of links used at SAP 2000. Besides, the comparison of the two models showed a good agreement between SAP and Plaxis, namely the simplified and the rigorous model. Thus, modelling of the abutment was made by frame elements that are properly account for the stiffness of the backwall. The observed discrepancy in the computed longitudinal movements (U_x) between the two models was deemed satisfactory in case of linear soil behavior. However, when a non-linear behavior is introduced (case 7) the results present considerable differences which are attributed to particular differences of the two models.

3 COMPARISON OF THE TWO MODELS (SAP2000 AND PLAXIS)

3.1 Collision force as a static loading

The following cases (1 to 5) are examined (Figure 4). The analysis was performed assuming an elastic behavior of the soil. We compare the results of the two models on the basis of the computed horizontal displacement on the top of the abutment and the developed stresses of the abutment (M, N, Q diagrams).

Case 1

The foundation of the abutment is assumed on rock and is considered as restrained. The rock has volumetric weight γ= 24 kN/m^3, Young's modulus E = 2.0E+08 kN/m^2 and Poisson's ratio v= 0.3. A horizontal force equal to 1000 kN is applied on the top of the abutment. Initially, the structural response of the abutment was compared to the one of the SAP2000

model. The comparison incorporated the concrete part of the abutment-system only (i.e. a zero resistance backfill was used) to represent the first stage of construction. A very good agreement between Plaxis (27 mm) and SAP (26 mm) models is observed. The theoretical value is 28.85 mm accounting for both the flexural and shear deflection at fixed based cantilever.

Case 2

Same as case 1; however rotation is now allowed at the abutment base. The comparison of the two models is again satisfactory. In case of Plaxis model, rock exhibited slight base rotations that were translated into longitudinal abutment movements at its top. Hence, the SAP model responded with smaller rotations.

Case 3

The foundation of the abutment is assumed again on rock and the backfill soil is considered with volumetric weight γ= 18kN/m^3, Young's modulus E= 2.5E+05 kN/m^2 and Poisson's ratio v= 0.499. As previously a horizontal force equal to 1000 kN is applied on the top of the abutment. The backfill in SAP is modeled through static springs, which are estimated based on the response of the backfill in the Plaxis model. In particular, the variation of static stiffness (k_x) with depth is estimated based on the variation of horizontal displacements and stresses in the interface between the abutment wall and the backfill. The corresponding spring constants are calculated every 0.5m of the wall by fitting a polynomial function in the displacements' and stresses' profiles.

A good agreement between Plaxis (9.3 mm) and SAP (10.3 mm) models is observed when the horizontal displacements on the top of the abutment are compared. As expected the displacement is lower than case 2 due to the resistance of the backfill. If a fixed base is considered, the SAP model gives a displacement equal to 9.9 mm, which is even closer to the Plaxis results.

Case 4

The same model as in case 3, but the force here has different direction towards the deck and is again equal to 100 kN/m. The comparison of the two models is satisfactory. The response of the wall is almost the same with a free cantilever. In case of Plaxis model, the backfill abutment resistance due to friction reduces up to 4.5% the movement of the wall. If a restrained base is considered, then the displacement on the top is equal to -2.29 mm and -2.94 mm in Plaxis and SAP model respectively.

Case 5

The abutment is now founded on soil with volumetric weight γ= 18 kN/m^3, Young's modulus E= 5.0E+05 kN/m^2 and Poisson's ratio v= 0.499. The spring constants are evaluated for the backfill and the foundation soil, following the same procedure as described in case 3. Depending on the type of loading, different parts of the foundation soil are activated. Two types of forces are applied, 1000 kN/m towards the backfill (case 5a) and 100 kN/m in the opposite deck direction (case 5b).

In case 5a the comparison is satisfactory; a displacement of 13 mm was calculated with the Plaxis model, while 12.2 mm movement was calculated with SAP model.

In case of a compliant foundation (case 5b), the outward displacement at the top of the wall (~5 mm) is due to the bending motion of the wall (3 mm) and the rotation of the foundation (another 2 mm). In Plaxis model the effect of the friction between the backfill and the wall results to lower total displacement (about 20% of difference). When a fixed base model was considered for the abutment for case 5b, then the displacement at abutment's top was found equal to 2.60 mm and 2.94 mm in Plaxis and SAP model respectively.

Differences between the two models in terms of M_{max} and U_x reflect the fact that the SAP FEM model cannot capture completely the developed soil pressures on the abutment wall, compared to Plaxis were obviously active and passive pressures were better captured.

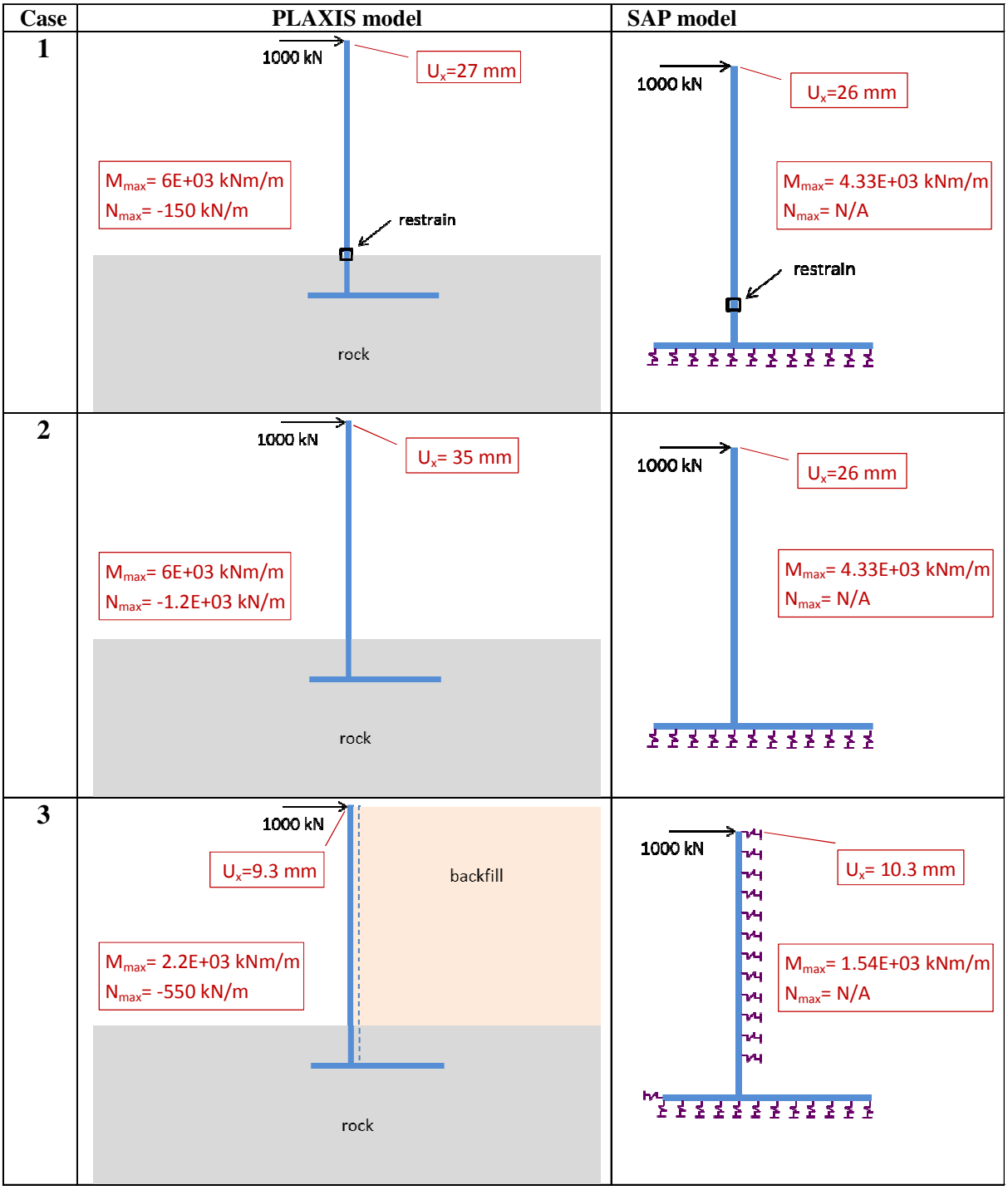


Figure 4: Cases 1 to 5: Static horizontal loading on top of the abutment. Comparison between Plaxis and SAP. Displacement at the top of the abutment, bending moments and axial forces.

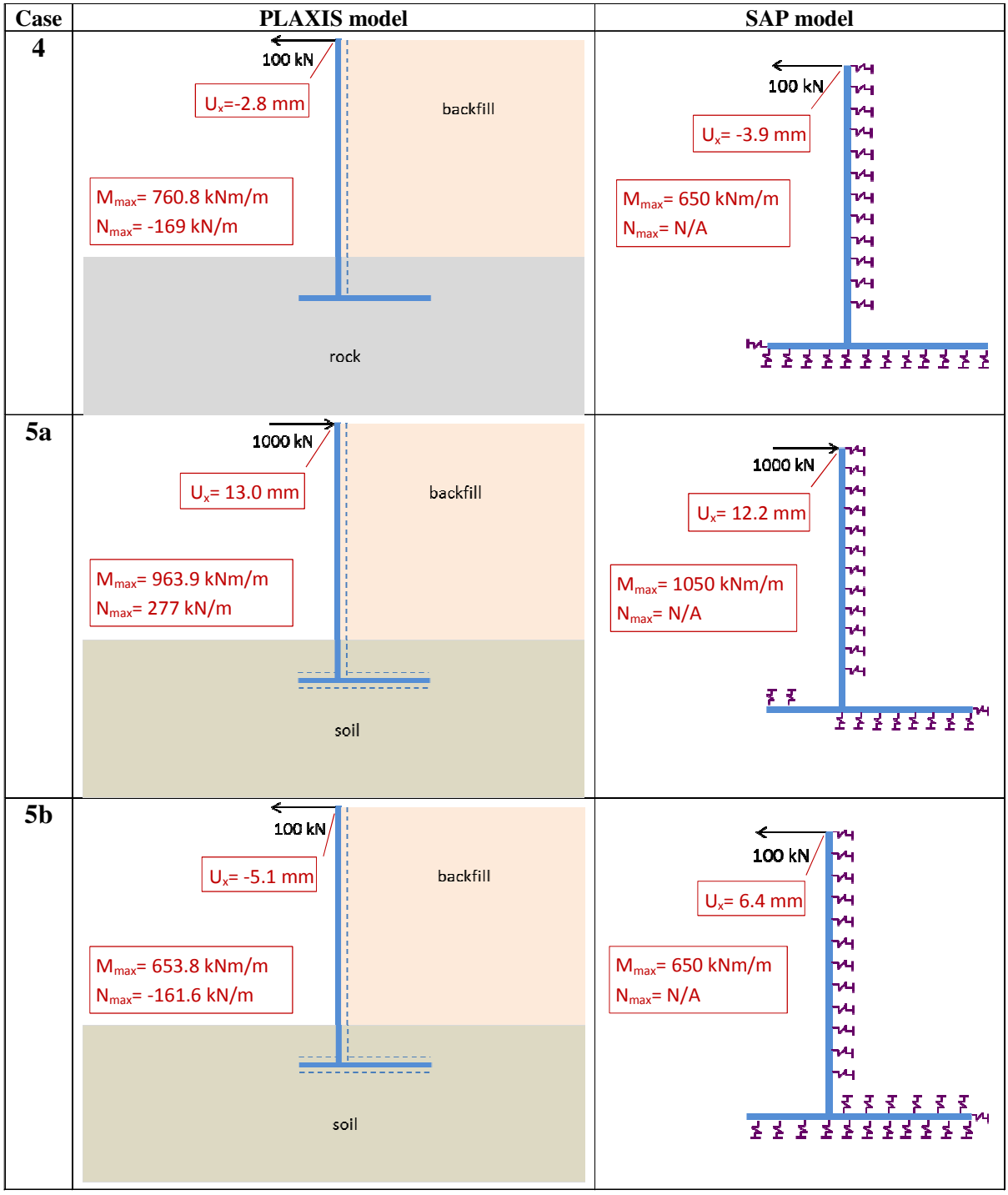


Figure 4: Cases 1 -5: Static horizontal loading on top of the abutment. Comparison between Plaxis and SAP. Displacement at the top of the abutment, bending moments and axial forces (continued).

3.2 Collision force as a simplified dynamic loading

Pounding is a geometrically non-linear dynamic effect. Most of bridge engineers are familiar with the effect mostly by identifying post-earthquake local damages to bridge deck slabs and abutments, rather than from analytical and theoretical approaches [25, 27]. Current state of practice introduced several structural schemes to mitigate pounding effects and its consequences on bridges, such as elastomeric pads interjecting between colliding elements. Such measures are expected to reduce effectively pounding force magnitudes [31]. In the following

cases (Figures 5, 6, 8), the deck-to-abutment collision is modeled through 4 different simplified input motions with variable durations ranging from 0.35s to 3.5s and frequencies ranging from 1 to 10 Hz. Based on analytical results [7], the maximum positive force towards the abutment-backfill was up to 1000 kN/m, i.e. 1000 kN per meter in the transverse direction of the abutment. The negative force (towards the deck) reaches 150 kN/m, based on typical bearings' resistance that is activated when the deck is drawn away from the abutment. The frequencies of the input motion have been selected in accordance to the fundamental period of the abutment-backfill system that was found to be at the order of 0.25 s.

The following periods (T) and durations (t) of the motion are considered: a) T=0.10 s, t=0.35 s; b) T=0.25 s, t=0.875 s; c) T=0.50 s, t=1.75 s; d) T=1.00 s, t=3.50 s.

Case 6

Analyses were performed considering that the soil behavior is linear (Figures 5, 6). The stiffness values estimated in previous case 5 were applied to model the foundation soil. The spring values for the backfill are estimated from the Plaxis model results. In particular, using two values of the resulting Plaxis p-y curve, linearization of the p-y curve was performed. The two p-y set of values were obtained as follows: one at the time when the abutment is at its original position (i.e. when displacement equals zero) and one at the moment when the abutment reaches its maximum displacement, i.e. when the force towards the backfill equals 1000 kN/m.

As an example, Figure 7 illustrates the response of the abutment for case 6c (T=0.50s). The time window captured abutment's response between t=0.82s (U_x=0mm) and t=1.26s (U_x=13.3mm). The same figure shows the displacement computed with SAP model. In this model the springs that have been estimated from the Plaxis model as described before are applied. A good agreement is observed for the peak values of positive displacements, which corresponds to the maximum applied forces towards the backfill. The difference between the two models for t=0.70-1.0s, and beyond t=1.45s is due to the resistance of the backfill to the lower part of the abutment in Plaxis model, when the force towards the deck is applied.

In Table 1 the displacements at the top of the abutment at the end of the analysis and the maximum values of M, N, Q are reported, showing a good agreement between the two models.

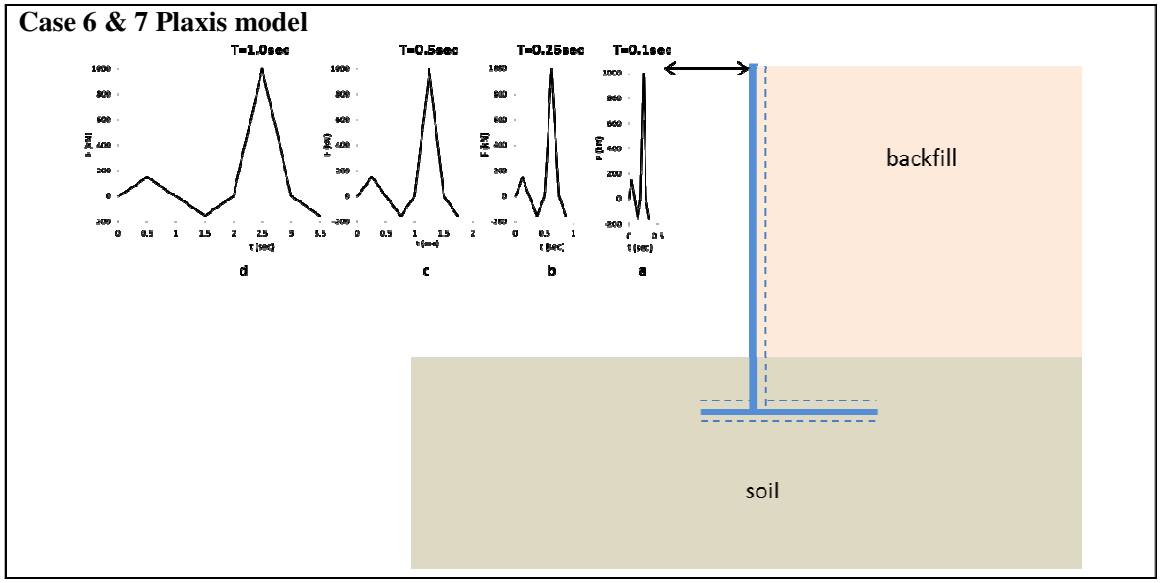


Figure 5: Case 6 and 7 in Plaxis model. The deck-to-abutment collision is applied as time history with different frequency and duration. The soil behavior is assumed to be elastic (Case 6) or elasto-plastic (Case 7).

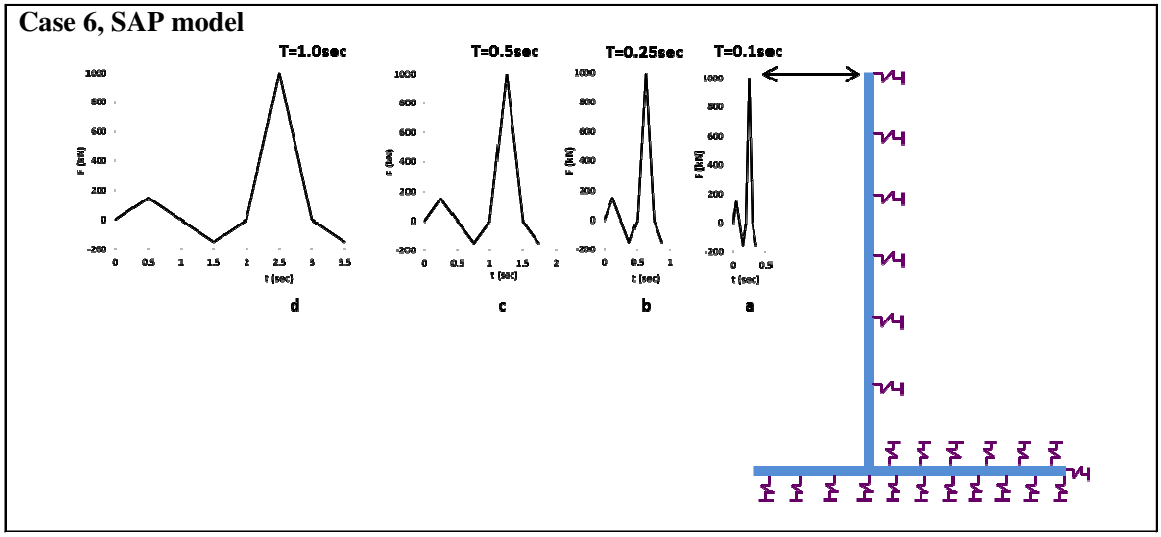


Figure 6: Case 6 in SAP model. The deck-to-abutment collision is applied as time history with different frequency and duration. The backfill and foundation soil is modeled with static springs.

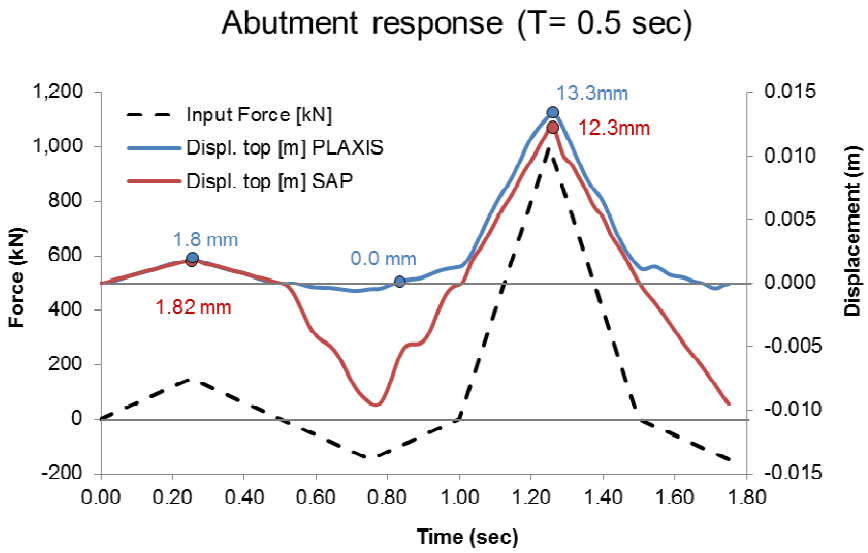


Figure 7: Comparison of estimated displacement at the top of the abutment from Plaxis and SAP models for case 6c (T=0.5s).

Case 7

Following the modeling process in case 6, the backfill soil now is modeled by an elasto-plastic soil behavior obeying the Mohr-Coulomb criterion. In this case, the springs on the wall of SAP model follow a bi-linear behavior (Figure 9) with the upper 3.0 m of the backfill considered as crucial for the abutment behavior (see §2.2). The bi-linear behavior is defined based on the relation between force (F_x) and displacement (U_x) for the loading between F_x= 0 and F_x= 1000 kN of the previously (case 6) applied input motions.

The variation of displacement is estimated from the Plaxis model in the interface between the 6m high wall and the backfill for the corresponding force steps and for the upper 3.0 m of the structure (i.e. from depth -3m up to the surface of the backfill soil). Figure 8 shows an example of the deformed abutment-backfill model and the variation of displacement in the interface with applied force at the surface of backfill (i.e. top of the abutment). A bi-linear curve is

then fitted to each F_x-U_x curves in order to describe the behavior of the springs in SAP model (Figure 9).

The frequency (period) of the applied collision force has an important effect as it is shown in Figure 8. In particular, the estimated displacements are increasing when the frequency of the input force is decreasing. In Table 1 the displacements at the top of the abutment at the end of the analysis (residual) and the maximum values of M, N, Q during the analysis are reported for the input force with T= 0.1s (10Hz) and T= 0.5s (2Hz). The observed differences are attributed to the non-linear soil behavior and SSI effects, which are not modeled in the same way in the two models. In particular, in SAP only the upper 3 m of the backfill are modeled through the corresponding springs while the mass of the backfill is not considered and the pressure of the backfill towards the wall and the friction between the wall and the backfill are also not accounted as it happens in Plaxis. Finally, in case 7, the foundation soil is modeled through linear springs, while an elasto-plastic behavior is assumed in Plaxis model.

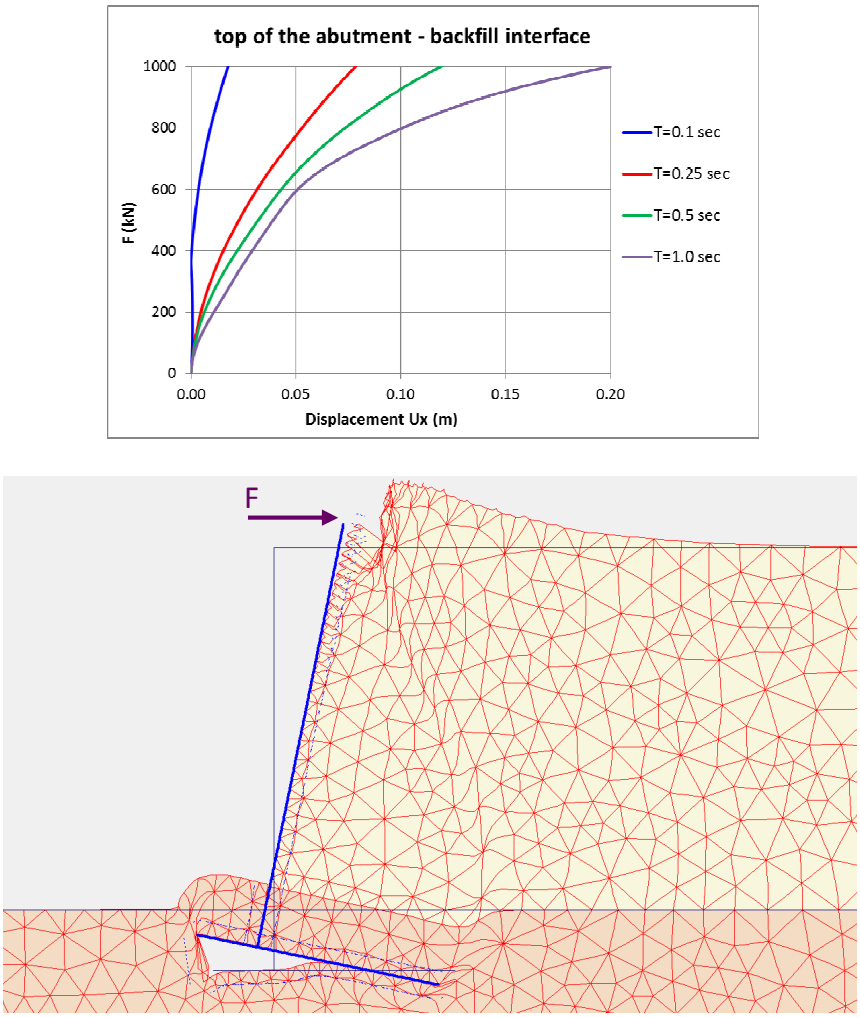


Figure 8: Deformed abutment-backfill model and computed displacements at the top of the abutment-backfill interface for applied collision force F (from 0 to 1000 kN) with different periods (frequencies).

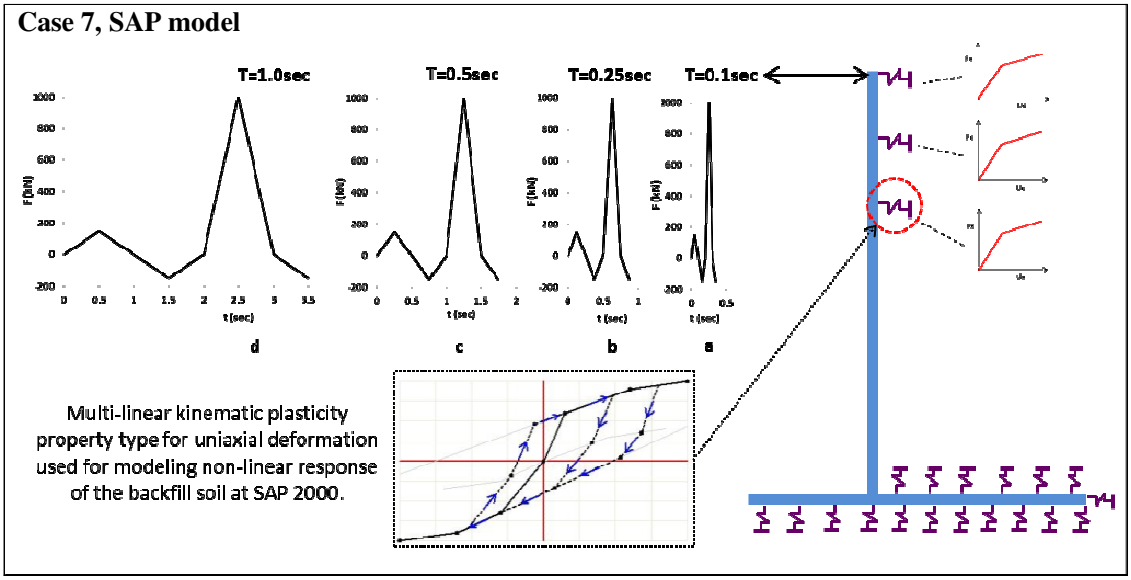


Figure 9: Case 7 in SAP model. Time histories of the deck-to-abutment collision for different frequency, duration and non-linear soil behavior. The backfill is modeled with bi-linear springs.

model	max U_x (top) (mm)	max M (kNm/m)	max N (kN/m)	max Q (kN/m)
case 6, T=0.1sec (Plaxis)	11.6	-1440	391.6	998.5
case 6, T=0.1sec (SAP)	9.6	-1199	N/A	232.4
case 6, T=0.5sec (Plaxis)	8.5	-1010	350	998.5
case 6, T=0.5sec (SAP)	9.5	-968.8	N/A	157
case 7, T=0.1sec (Plaxis)	27.5	-1850	364.6	999.8
case 7, T=0.1sec (SAP)	1.0	-582.6	N/A	86.6
case 7, T=0.5sec (Plaxis)	383.7	-2070	279.8	999.8
case 7, T=0.5sec (SAP)	268.5	-2929	N/A	385.1

Table 1: Displacement at the top of abutment at the end of analysis and maximum values of M, N, Q during the analysis.

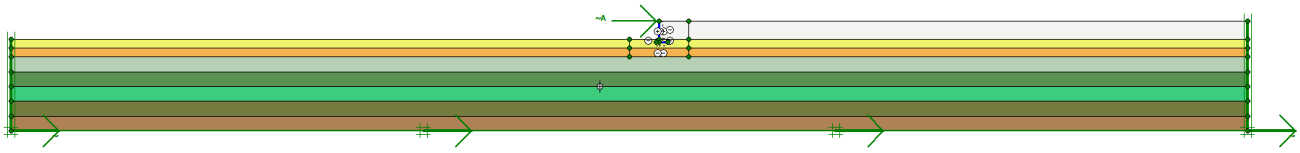
4 DYNAMIC MODELLING OF SEISMIC INPUT AND COLLISION FORCE

Case 8

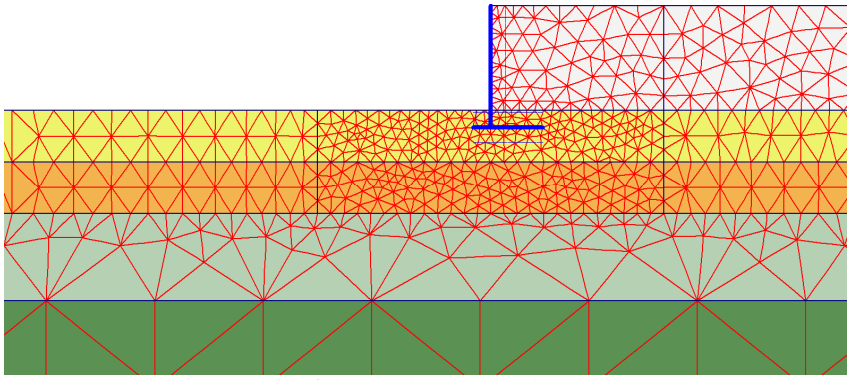
A full dynamic analysis is performed in Plaxis, considering both the deck-to-abutment collision and the seismic motion at the bedrock with real time histories (Figure 10). In particular, the deck-to-abutment pounding time history is applied on the top of the abutment wall (Figure 11b). Further details can be found in a previous analytical study [7] that was conducted utilizing real bridges with seat-type abutments. The seismic input is applied uniformly at the basis of the model using the record of Figure 11a. The properties of the soil and backfill are given in Table 2.

The basis of the model was assumed to be rigid. The total width of the model is 420m, which is sufficient to avoid boundary effects considering that absorbent boundaries were also used at the lateral boundaries. The domain was discretised with 3822 15-node plain strain triangular elements. In the area around the abutment wall the mesh was refined as shown in Fig-

ure 10. The soil behavior follows the Mohr-Coulomb criterion. Proper interface elements with a realistic friction coefficient of R_{inter}=0.70 were again used to model the interface between the backfill and foundation soil with the wall.

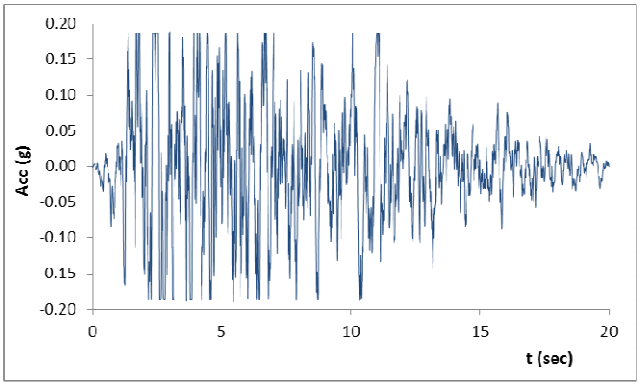


soil-abutment-backfill model

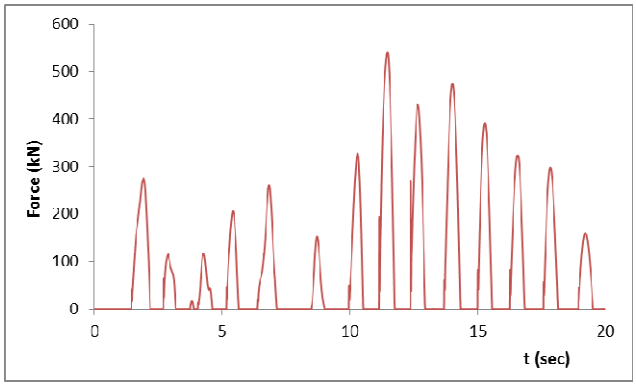


detail of the mesh near the abutment

Figure 10: Case 8 in Plaxis model. The deck-to-abutment collision is given as time history and a seismic input motion is applied in the basis of the model.



(a)



(b)

Figure 11: Seismic input (a) and collision force (b) applied in the full dynamic analysis with Plaxis.

Layer	Depth (m)	γ	E (kN/m^2)	c (kN/m^2)	φ (^{0})	v
backfill	0-6	18.0	3.260E+04	0.01	36	0.30
1	0-3	19.0	9.378E+04	50.0	0	0.35
2	3-6	19.0	9.378E+04	73.8	0	0.35
3	6-11	19.0	1.825E+05	92.0	0	0.35
4	11-16	19.0	2.269E+05	115.0	0	0.35
5	16-21	19.0	2.722E+05	139.0	0	0.35
6	21-26	19.0	3.173E+05	168.8	0	0.35
7	26-31	19.5	3.708E+05	192.5	0	0.35

Table 2: Properties of soil and backfill

An example of the analysis output is given in Figures 12 and 13 where the vertical and horizontal displacements of the backfill as well as the deformed mesh are illustrated. The maximum permanent displacements reach about 34.2 cm in the horizontal and 4.3 cm in the vertical direction of the backfill. It is noted that the approach slab and the wing walls of the abutment, which would improve the overall performance of the abutment-backfill system, are not considered in the analysis, as the objective of the present study is the preliminary estimation of the abutment performance considering the soil-abutment-backfill interaction under collision forces and seismic motion. The role of this interaction is important for the identification of failure modes and therefore for the vulnerability assessment of bridges.

Despite the simplifications considered in this study, it can be underlined that the calculated response of the abutment-backfill system is found to be significant in both the response and the post-impact and post-earthquake performance of the bridge. Firstly, the computed abutment maximum lateral displacement in the longitudinal direction of the bridge is large enough to put in question the support of the deck. Seating width of the order of 450mm to 600mm required in Eurocode [32] (referred to as overlap length) and Caltrans [14] respectively may not be sufficient. Moreover, we must notice that the permanent deflection of the backwall, which may occur when the deck pounds onto the backwall, is not considered in these provisions. Additionally, the post-earthquake residual displacements of the abutment, which was found equal to 262mm in our case (see Figure 13) is deemed to be critical, as bridges are expected to be accessible for emergency transportation. Hence, adequate measures must be taken for the abutment and the backfill to ensure the post-earthquake emergency traffic. Last but not least, the computed vertical movement of the abutment (43mm, Figure 12a) is considered quite large at least for box girder bridges, constructed by either the incremental launching method or the balanced cantilever method. Prestressed box-girder decks are not allowed to be cracked under seismic loading. This is required in order to preserve the durability of the tendons. Hence, a 43mm vertical movement of the abutment may trigger secondary effects that will reflect on the durability of the bridge. Such issues should not be overlooked under the seismic design philosophy that introduces the “controllable failure mode” philosophy.

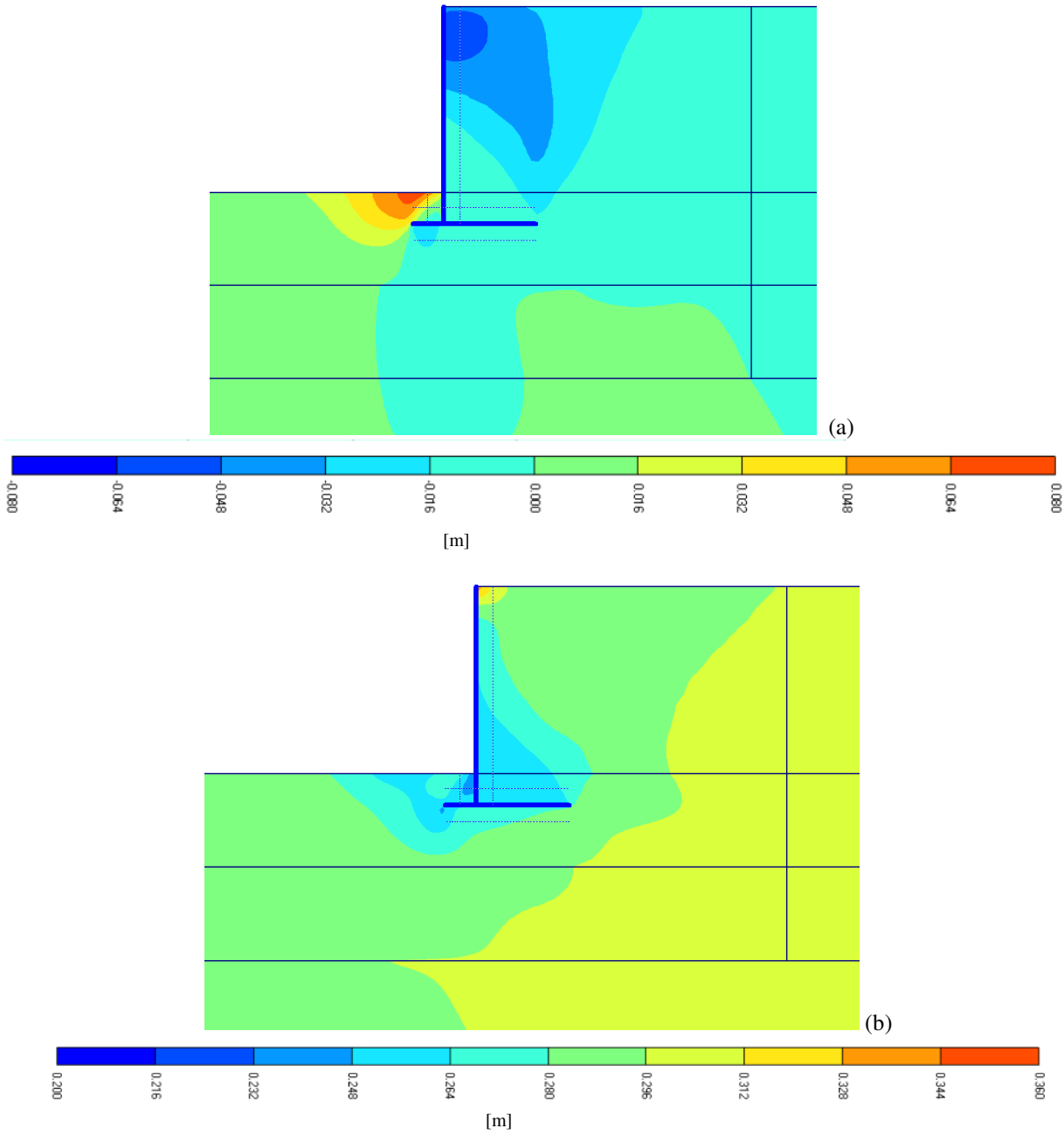


Figure 12: Distribution of the backfill permanent (a) vertical (max 43mm) and (b) horizontal (max 342mm) displacements

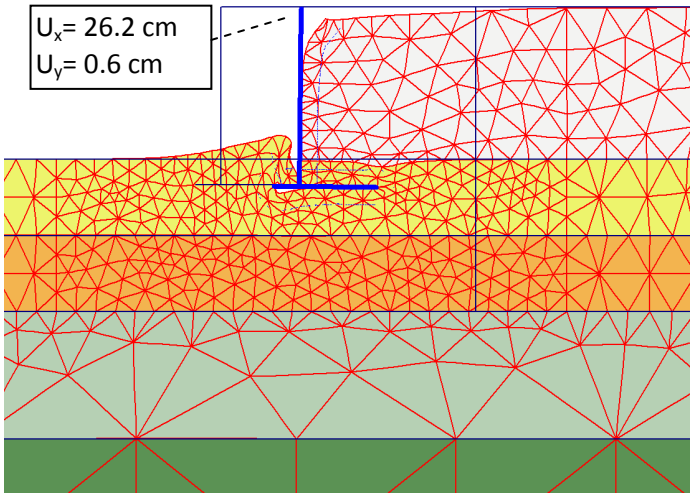


Figure 13: Deformed mesh of the abutment-backfill model and maximum permenant displacements of the abutment

5 CONCLUSIONS

A typical seat-type abutment was analyzed using 2D FE model in Plaxis and SAP2000. The SAP model is compared to the Plaxis results considering the interaction between abutment and backfill under static and dynamic deck-to-abutment collision forces. In particular, the variation of estimated displacements in the abutment-backfill interface with Plaxis model is used for the definition of spring properties that are used to model the backfill behavior in the SAP model.

In case of elastic soil behavior and static input forces the agreement between the two models is satisfactory. When a simplified dynamic loading is imposed under the assumption of linear soil behavior the agreement between the two models is good in terms of peak values of displacements. When a non-linear soil behavior is introduced, the soil springs follow a bi-linear behavior. Observed differences between the two models are attributed to the fact that the SAP model cannot capture the "passive" soil pressures towards the abutment, while both active and passive pressures were captured with the Plaxis FEM model.

Finally, a full dynamic analysis is performed under both real collision and seismic motion. A preliminary identification of failure modes considering the collision forces as well as the seismic motion is made. The residual horizontal and vertical displacements of the backfill together with the inward or outward rotation of the abutment are critical features for the accessibility of the bridge in the emergency period just after the earthquake event. Therefore these failure modes should be clearly identified and quantified for the definition of damage states in an integrated vulnerability analysis of bridges and abutments. It is pointed out that both the maximum and the permanent post-earthquake longitudinal abutment movement may trigger unseating mechanisms and emergency traffic disruption respectively. Observed vertical abutment seismic movements may cause cracking to the deck, especially for bridges with stiffer box-girder prestressed continuous superstructures, in which cracking may reduce rapidly the life of the tendons and therefore to cause significant long term effects.

To generalize this observation through a comprehensive parametric analyses it is necessary to accurately model the non-linear soil behavior and most important, to capture the SSI effects, and to model the structure-backfill interface behavior in a way the soil pressures and gap phenomena could be reproduced accurately

REFERENCES

[1] A. Aviram, K.R. Mackie, B. Stojadinovic, Effect of abutment modeling on the seismic response of bridge structures. *Earthquake Engineering and Engineering Vibration*; 7 (4): 395-402, 2008.

[2] R.K. Goel, A. Chopra. Evaluation of bridge abutment capacity and stiffness during earthquakes. *Earthquake Spectra*; 13(1): 1-23, 1997.

[3] M. Inel, M.A. Aschheim, Seismic Design of Columns of Short Bridges Accounting for Embankment Flexibility. *ASCE Journal of Structural Engineering*; 130(10): 1515-1528, 2004.

[4] A.J. Kappos, P. Potikas, A.G. Sextos. Seismic assessment of an overpass bridge accounting for non-linear material and soil response and varying boundary conditions, *ECCOMAS Thematic Conference on Computational Methods in Structural Dynamics and Earthquake Engineering*, Crete, Greece, 2007.

[5] A.J. Kappos, A.G. Sextos, Seismic assessment of bridges accounting for nonlinear material and soil response, and varying boundary conditions. *NATO Science for Peace and Security Series C: Environmental Security*, 2009, III, 195-208, DOI: 10.1007/978-90-481-2697-2_15, 2009.

[6] A. Kotsoglou, S. Pantazopoulou, Response simulation and seismic assessment of highway overcrossings. *Earthquake Engineering & Structural Dynamics*; 39 (9): 991-1013, 2010.

[7] S.A. Mitoulis, Seismic design of bridges with the participation of seat-type abutments, *Engineering Structures*, 44: 222-233, 2012.

[8] A. Mwafy, A. Elnashai, W.H. Yen, Implications of Design Assumptions on Capacity Estimates and Demand Predictions of Multispan Curved Bridges. *ASCE Journal of Bridge Engineering*; 12 (6): 710-726, 2007.

[9] K. Mackie, B. Stojadinovic. Bridge Abutment Model Sensitivity for Probabilistic Seismic demand evaluation, *Proceedings of the 3rd National Seismic Conference & Workshop on Bridges & Highways*, April 28-May 1, 2002. Portland, 2002.

[10] J. Zhang, N. Makris, Kinematic response functions and dynamic stiffnesses of bridge embankments. *Earthquake Engineering and Structural Dynamics*; 31 (11): 1933-1966, 2002.

[11] M. Inel, M.A. Aschheim, Seismic Design of Columns of Short Bridges Accounting for Embankment Flexibility. *ASCE Journal of Structural Engineering*; 130(10): 1515-1528, 2004.

[12] M. Dicleli, Integral Abutment-Backfill Behavior on Sand Soil-Pushover Analysis Approach. *ASCE Journal of Bridge Engineering*; 10(3), 354-364, 2005.

[13] AASHTO HB-17, *Standard Specifications for Highway Bridges*, 17th Edition American Association of State and Highway Transportation Officials, 2002.

[14] CalTrans, *Seismic Design Criteria, Version 1.6*. California Department of Transportation, Sacremento, CA, 2010.

[15] A. Lemnitzer, E.R. Ahlberg, R.L. Nigbor, A. Shamsabadi, J.W. Wallace, J.P. Stewart. Lateral Performance of Full-Scale Bridge Abutment Wall with Granular Backfill. *ASCE Journal of Geotechnical and Geoenvironmental Engineering*; 135(4), 2009.

[16] R. Siddharthan, M. El-Gamal, E.A. Maragakis, Nonlinear bridge abutment stiffnesses: Formulation verification and design curves. *NDOT Research Report: RDT95-012*, 2001.

[17] P. Wilson and A. Elgamal, Bridge-abutment-backfill dynamic interaction modeling based on full scale tests. Proceedings of the *9th U.S. National and 10th Canadian Conference on Earthquake Engineering*; Paper No 777, Toronto, Canada, 2010.

[18] P. Wilson and A. Elgamal, Full-Scale Bridge Abutment Passive Earth Pressure Experiment and Simulation. *ASCE Journal of Geotechnical and Geoenvironmental Engineering*, 136(12): 1634-1643, (2010).

[19] EN 1997-1 Eurocode 7: *Geotechnical design* - Part 1: *General rules*, 2004.

[20] NCHRP 472, *Comprehensive Specification for the Seismic Design of Bridges, National Cooperative Highway Research Program*, Transportation Research Board, ATC/MCEER Joint Venture Redwood City, CA and Buffalo, NY, 2002.

[21] A. Sextos, K. Mackie, B. Stojadinovic, O. Taskari, Simplified P-y relationships for modelling embankment abutment systems of typical California bridges, *14th World Conference on Earthquake Engineering*, Beijing, China, 2008.

[22] A. Shamsabadi, K.M. Rollins, M. Kapuskar, Nonlinear Soil-Abutment-Bridge Structure Interaction for Seismic Performance-Based Design. *ASCE Journal of Geotechnical and Geoenvironmental Engineering*; 133 (6): 707-720, 2007.

[23] A. Shamsabadi, P.K. Tehrani, J.P. Stewart, E. Taciroglu, Validated Simulation Models for Lateral Response of Bridge Abutments with Typical Backfills. *ASCE Journal of Bridge Engineering*; 15 (3): 302-311, 2010.

[24] J.P. Moehle, M.O. Eberhard, Earthquake damage to bridges. *Bridge Engineering Handbook. Ed*. Wai-Fah Chen and Lian Duan Boca Raton: CRC Press, 2000.

[25] R. Jankowski, K. Wilde and Y. Fujino. Pounding of superstructure segments in isolated elevated bridge during earthquakes. *Earthquake Engineering & Structural Dynamics*; 27(5): 487-502, 1998.

[26] R. Jankowski, K. Wilde and Y. Fujino. Reduction of pounding effects in elevated bridges during earthquakes. *Earthquake Engineering & Structural Dynamics*; 29(2): 195-212, 2000.

[27] S.A. Anagnostopoulos, Equivalent viscous damping for modeling inelastic impacts in earthquake pounding problems. *Earthquake Engineering and Structural Dynamics*; 33 (8): 897-902, 2004.

[28] B.G. Nielson, R. DesRoches, Seismic fragility methodology for highway bridges using a component level approach. *Earthquake Engineering Structural Dynamics* 36(6), 823-839, 2007.

[29] I.F. Moschonas, A.J. Kappos, P. Panetsos, V. Papadopoulos, T. Makarios, P. Thanopoulos, Seismic fragility curves for greek bridges: methodology and case studies. *Bulletin of Earthquake Engineering* 7(2), 439-468, 2009.

[30] S. Argyroudis, A.M. Kaynia, K. Pitilakis, Development of fragility functions for geotechnical constructions: application to cantilever retaining walls. *Soil Dynamics and Earthquake Engineering*, http://dx.doi.org/10.1016/j.soildyn.2013.02.014, 50, 2013.

[31] S.A. Mitoulis, I.A. Tegos, Reduction of inertial seismic forces in bridges by using the abutment backwall as a "yielding" stopper" *Proc., Earthquake Resistant Engineering Structures (ERES)*, Skiathos, Greece, Chapter V, 507-520, 2005.

[32] EN 1998-2:2005. *Eurocode 8: Design of structures for earthquake resistance, Part 2: Bridges*, 2005.

COMPDYN 2013
4th ECCOMAS Thematic Conference on
Computational Methods in Structural Dynamics and Earthquake Engineering
M. Papadrakakis, V. Papadopoulos, V. Plevris (eds.)
Kos Island, Greece, 12–14 June 2013

PARAMETRIC INVESTIGATION FOR THE OPTIMIZATION OF A LONGITUDINAL SEISMIC RESTRAINING SYSTEM CONSISTING OF STRUTS-TIES FOR CONCRETE BRIDGES

Olga G. Markogiannaki[1], **Ioannis A. Tegos**[2]

[1] Department of Civil Engineering, Aristotle University of Thessaloniki
e-mail: omarkogiannaki@civil.auth.gr

[2] Department of Civil Engineering, Aristotle University of Thessaloniki
e-mail: itegos@civil.auth.gr

Keywords: Concrete Bridge, Steel Restrainer, Abutment, Earthquake, Displacement Reduction, Parametric Analysis, Compliance Criteria

Abstract. *Seismic response of R/C bridges is an issue that has been investigated thoroughly the last decades. Many efforts have been conducted towards the enhancement of bridges seismic response and two categories of seismic design practices can be identified; seismic isolated systems and ductile systems. This paper focuses on a seismic restraining system, consisting of steel bundles, that aims on improving R/C bridges seismic response. The restraining system limits the longitudinal displacements of continuous integral concrete bridges under lateral earthquake loading. The targeted reduction of the longitudinal seismic displacements is achieved with four bundles of steel bars that act in tension and compression, as well. The steel bars of the four bundles are installed in post-tension ducts, in the superstructure of the bridge longitudinally, without bonding with the bridge's deck concrete. The forces of the steel bundles are transferred to properly designed abutments. The study includes a parametric investigation on the area, the number and length of the steel bars for optimum results in the seismic response of a concrete bridge. A six-span concrete bridge was used as the benchmark bridge and a corresponding nonlinear finite element model was developed according to the analyses' demands. Nonlinear analyses were performed for variable parameters, i.e. material and geometrical properties, number of spans, ground motion etc., after proper sampling. The analyses results have shown how the seismic performance of bridges varies when the area, number and length of steel bars (as restrainers) applied in each analysis case change and how the optimization for the dimensioning of the proposed system can be achieved. The parametric investigation can be the basis for a more general guideline for the design of the system. An optimized selection is found to reduce the longitudinal displacements efficiently and improve the seismic performance of bridges without introducing any structural capacity issues to the rest of the structural members of the bridge.*

1 INTRODUCTION

Concrete bridges in seismic regions are designed for lateral forces induced by strong earthquake motions. Bridge's seismic resistance can be achieved through several design practices that can be divided into two main categories. The first corresponds to the design of bridges as seismic isolated structures. In seismic isolation the means of seismic resistance consist of devices, such as bearings (i.e. elastomeric, lead) or dampers (i.e. hydraulic, viscous), that are installed on the bridge. Another common design practice is the design of bridges as ductile structures that aim on the contribution of the post-elastic behavior of the structural components of the bridge, i.e. more often the piers. Except from the contribution of piers, international seismic design codes, i.e. Eurocode [1] and researchers suggest the participation of other structural members of bridges such as the abutments that can participate in the seismic resistance of bridges. More specifically, integral abutments, [2][3], or abutments equipped with seismic links, such as shear key arrangements, buffers, can receive the seismic forces of the bridge according to Eurocode [1].

The ongoing research has shown that except the traditional seismic links there are further effective systems that can activate the participation of abutments. Such examples include the design of the approach slab for the connection of the bridge with the abutment [4], the design of integral abutments with transversely directed R/C walls [5] and the design of sidewalks connected with the abutments as restrainers [6]. Furthermore, steel or cables restrainers [7] can be used for limiting the longitudinal displacements between the abutments and the deck of the bridge. Recently, shape memory alloys [8] that are introduced as a more effective restrainer system for bridges than the steel restrainer have been suggested for limiting the longitudinal drift as well. Nevertheless, steel cable systems are applied more often for retrofit purposes and mainly on simply supported bridges, [9].

The authors have presented in previous research work, [10] [11], a restraining system with steel bundles that can be installed on R/C bridges and can increase the contribution of the abutments to the seismic resistance of bridges. The steel bundles act as a struts-ties system, applied longitudinally in the outer spans of the deck of the bridge through the abutments. The restraining system limits the longitudinal movements of the bridge and transfers part of the seismic forces to the abutments. It is noted that the restraining system of struts-ties can be applied with some modifications, regarding its installation, in the superstructure of the bridge for the seismic retrofit of concrete bridges, as well [12]. The key objective of this paper is to investigate the performance of the struts-ties restraining system through a comprehensive parametric analysis and to derive some guidelines that can be applied on the design of in multi-span continuous R/C bridges.

2 RESTRAINING SYSTEM OF STRUTS-TIES

The restraining system can be described as a mechanism that reduces bridge seismic displacements through the activation of its components that act in tension and compression, as well (act like struts-ties). The mechanism can be applied in different bridge classes. This paper focuses on the application of the mechanism in multi-span continuous concrete box girder bridges that is shown in an indicative representation in Figure 1. The restraining system involves the installation of four bundles of steel bars in the cross section of the deck of the bridge. The bundles are installed towards the longitudinal direction of the bridge and each two bundles are placed in the outer spans of the bridge extending through the abutments' wing walls. The bars are placed in plastic ducts, similar to prestressed concrete practices,in order to avoid bonding between the steel bars and the concrete of the bridge. The steel bars are only bonded with the concrete at their ends to ensure sufficient anchorages. Each of the four bundles consists of groups of steel bars that are anchored at different points

so that the anchorage forces are not developed in the same positions. The bundles of the steel bars are not only activated as tension members but also as members that receive compression, since the installation of the steel bars inside the deck protects them from buckling issues. The steel bars have common steel strength (i.e. S500) and medium diameters of 14mm or 16mm that are available in steel market in lengths up to 200m.

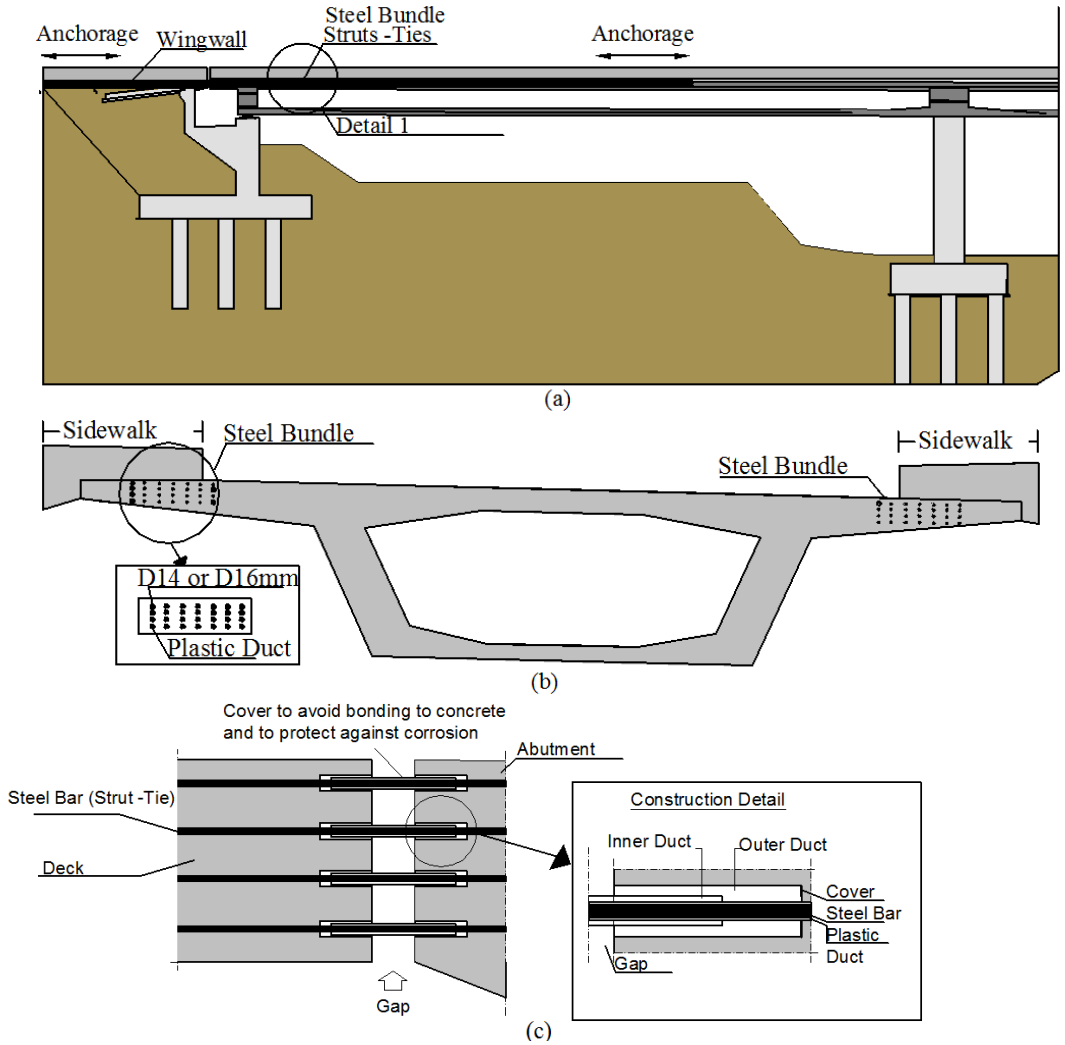


Figure 1: Restraining System. a. Longitudinal view of the bridge, b. Detail 1: cross section of the deck of the bridge, c. Detail at the Expansion Joint between Deck and Abutment

3 DESIGN OBJECTIVES IDENTIFICATION AND SEISMIC COMPLIANCE CRITERIA

The identification of the design objectives and the criteria that shall be fulfilled in a bridge seismic design is necessary for the investigation of the performance of the seismic restraining system. Structural design focuses on reaching a solution at which the bridge components satisfy the design criteria, defined as the design constraints, and is the optimum one that minimizes the cost of the bridge, which is defined generally as the design objective.

For a better understanding of the compliance criteria for the design of R/C Bridges that are equipped with the restraining system, it is necessary to take into consideration the distribution of forces in the structural system of the bridge. The service loads as defined by Eurocode, [1], activate the struts-ties system. The steel bundles are in tension during deck contraction and are compressed during deck expansion. One design compliance criterion for the steel bundles regarding the in-service loads is to have elastic behavior in the serviceability limit state. This

criterion corresponds to a minimum acceptable steel bar length that can be calculated by Equation (1) and Equation(2), [11]. The term Δl is the deformation of a steel bar of the struts-ties system, a is the coefficient of thermal expansion, $\Delta T_{N,tot}$ is the sum of the maximum variation of the uniform bridge temperature contraction component $\Delta T_{N,con}$ and the equivalent uniform bridge contraction temperature $\Delta T_{N,per}$ due to prestressing, creep and shrinkage [13]. L_{tot} is the total length of the superstructure, l is the length of the steel bar., l_{eff} is the effective length of the bar from the expansion joint to the anchorage point in the deck; $l_{eff}=l-2l_b-l_w$, where l_b is the anchorage length and l_w is the length of the bar in the wingwall. ε_{smax} is the maximum allowable deformation for steel bars corresponding to 85% of the maximum steel deformation *esy*=0.001 due to low cycle fatigue.

$$\Delta l = a \cdot \Delta T_{N,tot} \cdot \left\lfloor \frac{L_{tot}}{2} - l_{eff} \right\rfloor + a \cdot \Delta T_{N,per} \cdot (l - 2l_b) \quad (1) \qquad \frac{\Delta l}{l - 2l_b} = \varepsilon_{s\max} \quad (2)$$

Earthquake loads induce lateral forces in bridges that are accommodated by the structural components of the bridge. Continuous box girder R/C bridges are designed as ductile systems. The bridge components that are highly activated under seismic loading in common design practice are the piers that are designed to respond in an inelastic manner. With the presence of the restraining system the longitudinal seismic displacements of the bridge are reduced [11] and the seismic forces are redistributed to the structural members of the bridge. A part of the seismic forces is transferred through the steel bundles to the abutments and the piers receive the rest of the seismic forces. In this manner, the abutments are activated and contribute to the seismic resistance of the bridge. The compliance criteria regarding the abutments induced in the design of bridges with the restraining mechanism include: the fulfillment of increased seismic resistance requirements of the abutments and the accommodation of stability issues. Although part of the seismic forces is transferred to the abutments, the piers continue to play a significant role in the seismic resistance. The compliance criterion regarding the design of piers in bridges that have the restraining system of struts-ties is to ensure that the piers continue to high contribute highly to the seismic resistance. In this manner, the ductility of the system can be utilized. The criterion is determined according to the concept of the formation of plastic hinges at the bottom and top of the piers. More specifically, it is preferable that the seismic demand pier moments approach or exceed the piers' yielding moments.

The transverse seismic resistance is addressed with the use of rectangular cross-sections of the piers (the long side in the transverse direction) and with shear keys at the abutments.

Optimum Solution		Cost Minimization (Piers & Abutments Dimensions)
Compliance Criteria	Service Loads:	Steel bundles Elastic Behavior
	Seismic Loads	Abutment Capacity
		Abutment Stability
		Creation of Plastic hinges in Piers

Table1: Design Objective and Compliance Criteria for bridges with the restraining system

Except from the determination of the compliance criteria, the design objective shall be determined, as well, in order to reach optimum design solutions. In design practice the minimization of the bridge cost is defined as the design objective. The design of bridges equipped with the restraining mechanism follows the same concept. The selection of minimum cross-sections and reinforcement ratios of the piers and the abutments that fulfill the compliance criteria is crucial for the minimization of the total bridge cost. The cost of

steel bundles, which includes four bundles of steel bars, has minor contribution to the total cost. Hence, the minimization of the cross-section of the steel bars in the bundles is not included in the design objective. The size and length of steel bundles can be derived from the evaluation seismic performance of the bridge and the compliance with the aforementioned criteria. In Table 1 the design objective and compliance criteria are summarized.

For the configuration of a more general guideline that could be incorporated in the design of R/C bridges with the suggested steel bundles requires an extensive parametric analysis in order to observe the influence of various parameters on the response of the mechanism. The present study investigates various bridge and restraining system properties in combination with different earthquake intensities in order to screen the effect of each parameter on the seismic performance of the bridge.

4 BRIDGE 3-D ANALYTICAL MODEL

The parametric analysis was performed on 3-D bridge models. The models were generated in the finite element analysis software *O*penSees, [14].

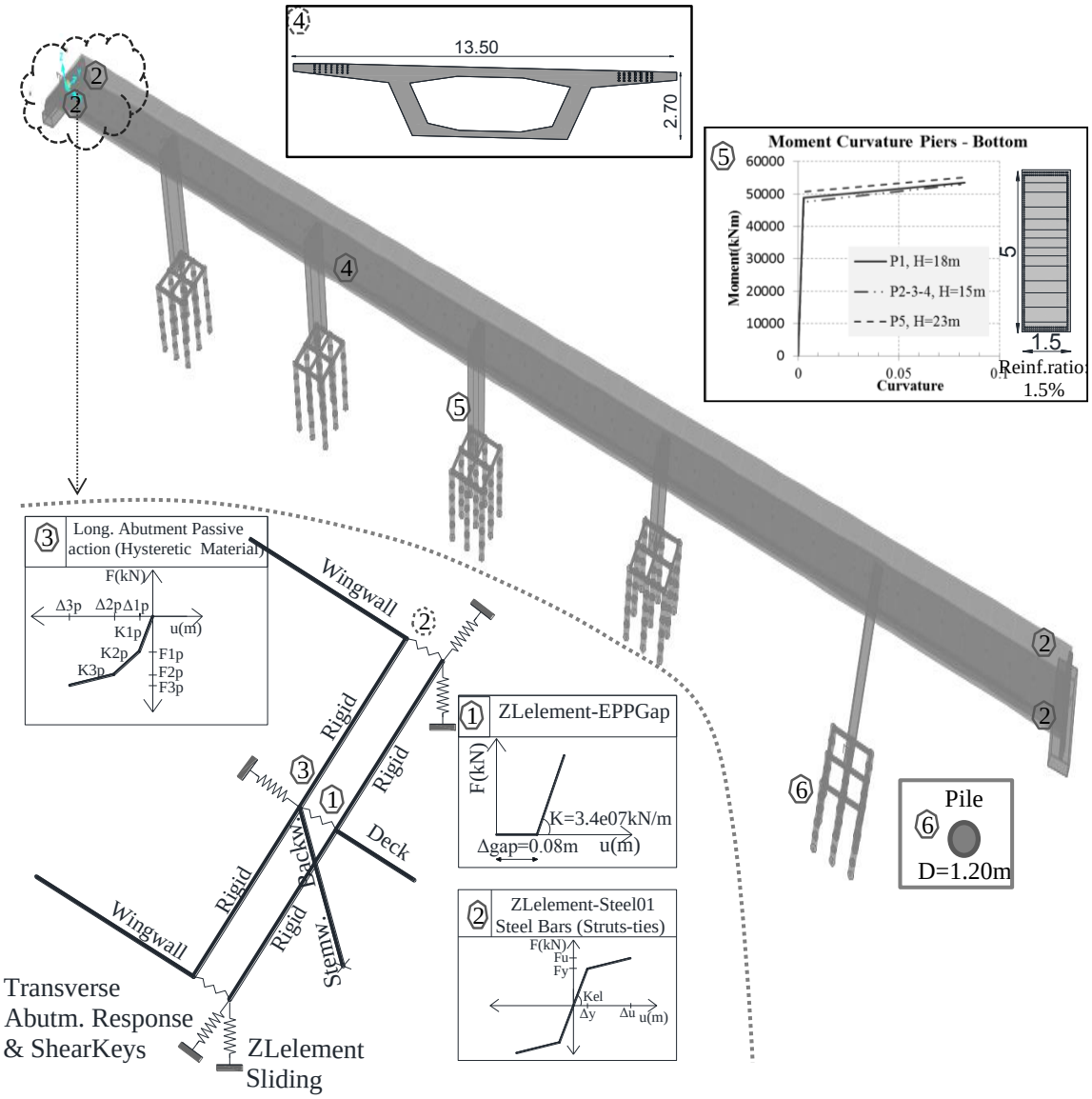


Figure 2: 3-D Bridge Model

Figure 2 demonstrates the properties of one of the models created for a typical six span concrete box girder bridge, based on the characteristics of an Egnatia Highway bridge, T5. The total length of the bridge is 240m and the deck is monolithically connected to the piers, while sliding bearings on the abutments support the two outer spans of the deck. The bridge components are modeled with frame elements taking into consideration material nonlinearities. The section analysis for the assignment of concentrated plasticity at the top and bottom of piers was performed with Bomber Biaxial v3.8.2,[15]. The foundation springs were provided by the geotechnical report of the bridge. For the passive resistance of the abutments, the stiffness values from Caltrans, [16], and the procedure demonstrated by Nielson, [17], were used. The derived values are shown in Table 2. The steel bars of the restraining system (in 4 bundles) were modeled as nonlinear springs, as shown in Figure 2 and Table 3 (*AsBars* refers to the Steel area of each of the four bundles and *lbar* to the length of each steel bar without accounting for the anchorage length). Time-history nonlinear dynamic analyses were carried out with 7 independent pairs of recorded events taking the average of the individual responses as the design seismic demand. The records were selected with REXEL 3.5 Beta [18] and they are compatible, their average spectra, to Eurocode design spectra for 0.16g, 0.24g and 0.36g and for soil type B.

Habtm (mm)	3200	Ae(m2)	10.24
	Longitudinal		Longitudinal
K1p (kN/m)	91840.00	F1p (kN)	2351.10
Δ3p (m)	0.26	F2p (kN)	4980.52
Δ2p (m)	0.09	F3p (kN)	7131.86
Δ1p (m)	0.03		

Table 2: Abutment Passive Action

STEEL BUNDLE PROPERTIES			
fy	AsBars x σy (500MPa)	fu	AsBars x σu (600MPa)
Δy	esy(0.001) x lbar	Δu	esu x lbar
Kel	E x Area of Bars / lbar	Kinel	0.8% x Kel

Table 3: Steel bundle properties (applicable to each of the 4 steel bundles applied in deck

5 PARAMETRIC ANALYSIS AND RESULTS

5.1 Variation of Parameters

A number of parameters are utilized to screen the effects of the application of the proposed mechanism on the seismic response of continuous concrete box girder bridges. The parameters considered involve the structural system of the bridge, the mechanism characteristics and the earthquake intensity.

Starting from the geometry, the first parameter considered is the number of spans. It is determined by local site conditions and defines the nature of the bridge. The various resulting bridge configurations (1 span, 2 spans, 6spans etc.) are characterized by heterogeneity and, the overall bridge length differentiation plays significant role in the determination of the appropriate restraining mechanism characteristics. Hence, in the analysis bridges with different number of spans are treated separately and the rest of the parameters are screened for each bridge configuration. The second parameter is the height of the piers which depends on the topography of the bridge site. Because of the participation of the piers in the seismic response of continuous concrete bridges it is necessary to study the influence of the mechanism and the redistribution of forces on the response of bridges with variable pier heights. A subsequent pair of parameters includes the dimensioning of the piers, the width of

the cross-section and the longitudinal reinforcement of the piers. The investigation of the performance of various pier dimensions and reinforcement ratios is crucial for the implementation of optimized solutions for bridge design with the restraining system of steel bundles.

PARAMETERS	VALUES
No. of Spans	1-6
Height of piers (m)	13 18 23
Width of piers (m)	1.2 1.5
Long. Steel Reinforcement (%)	0.1 0.15 0.2 0.3
Length of Restrain. Bars ('factor'xLmin)	1.25 1.5 1.75 2
Diameter of Restrain. Bars (mm)	D14 D16
No. of Restrain.Bars/Bundle	7 14 21 28 35
Seismicity	0.16g 0.24g 0.36g

Table 4: Parameter Values

Another set of parameters consists of the mechanism characteristics. In particular, the effect of the *length* and *cross-section of the steel bars* of each bundle that are installed in the outer spans of the bridge is screened for different bridge configurations and pier geometries. The variable characteristics correspond to various effective stiffness values of the mechanism that influence the seismic response and the distribution of forces of the bridge. Regarding seismicity, all parameters are screened for the three seismic design intensity levels according to Eurocode 8, [1]. The parameter values used in the study are presented in Table 4. The selection of the geometrical parameter values is based on typical values of R/C bridges in Greece.

5.2 Results Discussion

In the paper the authors have selected to include a part of the total investigation in order to highlight the important results of the study and to satisfy clarity purposes. The analysis discussion for the effect of each parameter is sorted by the various bridge configurations that were created based on the number of spans.

a. Analysis Results for Single-Span Continuous Concrete Bridge

The main characteristic of single-span bridges is the absence of piers. Generally these bridges have elastomeric bearings. The restraining system of struts-ties aims on limiting the longitudinal displacements which leads to the use of sliding bearings, as a more preferable solution.

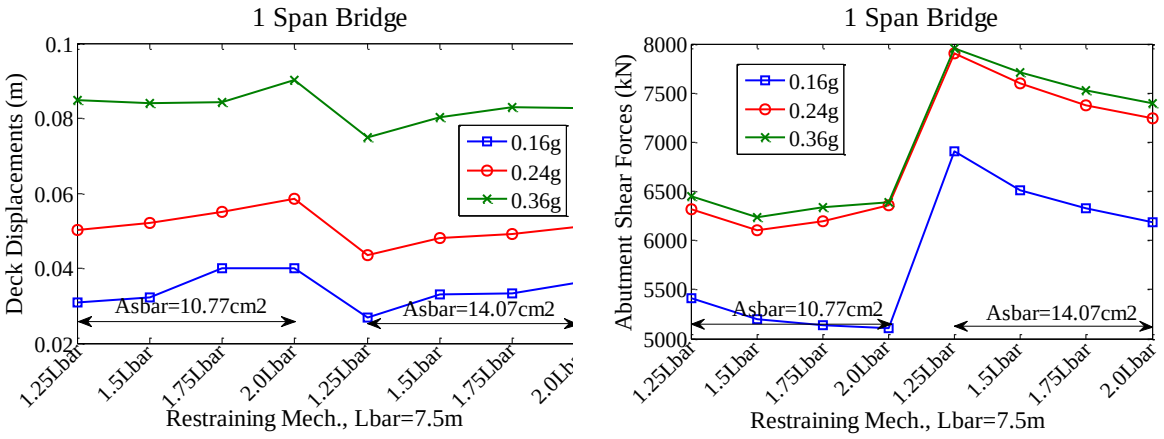


Figure 3: Analysis results for a Single - Span Bridge – varying restraining system characteristics

In Figure 3, a 34m long single-span bridge was investigated with two different sizes of steel bundles (Asbar/bundle, 4 bundles-one bundle at each wingwall) and various lengths. The lengths are determined by applying variable factors to the minimum required steel bar length (Lbar) derived by Eq(1) and Eq(2), Lbar=7.5m. The movements of the bridge are lower for the larger bundle cross-section while the total abutment (values for both the abutments) shear forces are increased respectively. Additionally, it appears that the various lengths affect more the value of the abutment forces with the larger lengths leading to lower abutment shear forces.

b. Analysis of Multi-span Bridges

The bridge configurations presented in the following figures include: a. 2-span bridge 64m long b. 6-span bridge 240m long. The piers in both bridges have 1.5mx5m rectangular cross section and longitudinal reinforcement of 1.5%. Although the reference bridge had variable pier heights, the authors selected three different height values that were applied to total number of piers in the six and two spans bridges in each case study.

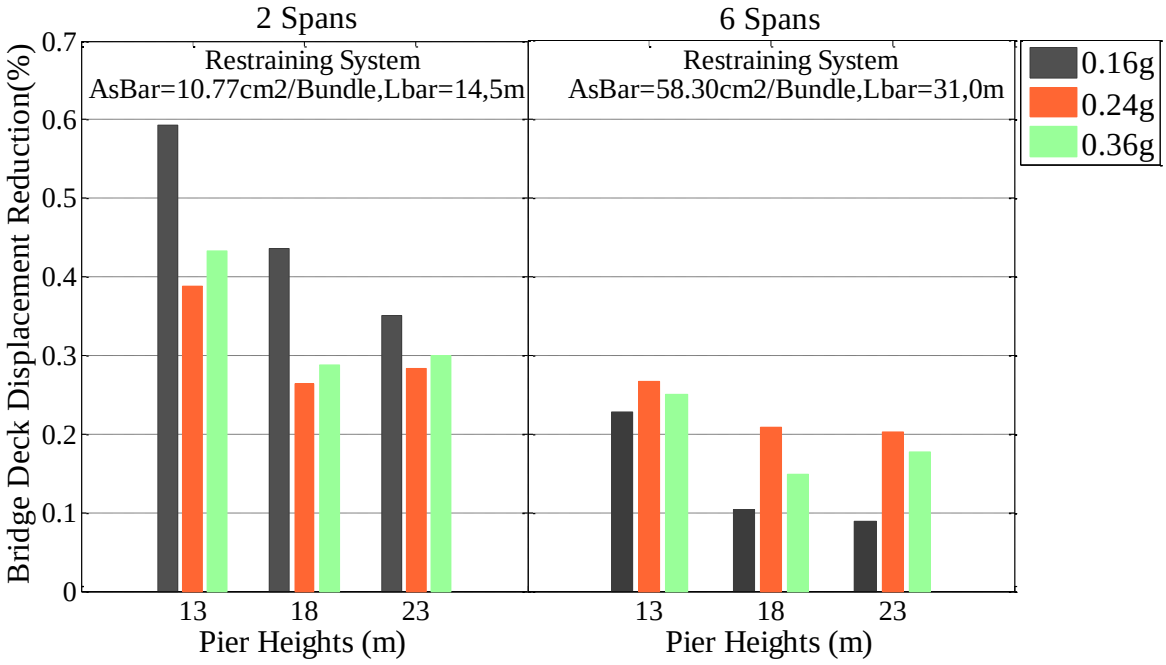


Figure 4: Reduction of Bridge Displacements for variable pier heights

Figures 4 and 5, demonstrate the effect of the pier height variation. The length for the steel bundle bars is determined by the minimum required length (Eq.(1),Eq.(2)) increased with a 1.25 factor. Since the minimum length requirement depends on the total length of the bridge the required lengths derived for the bridges of two and six spans vary significantly. The selection of the size of the steel bars in each bundle is based on the size of the bridge, as well. The short bridge requires smaller steel bundle sizes, i.e. 7 bars of 14mm diameter = 10.77cm2/Bundle, in contrast to the longer six spans bridge that requires for instance 28 bars of 16mm = 58.30cm2/Bundle. It can be noted that bridge deck movement reduction is higher for bridges with shorter piers. In bridges with six spans the contribution of piers to the seismic resistance is higher (considering the number and higher stiffness of piers). As a result the redistribution of shear forces with the presence of the restraining mechanism increases largely the abutment participation. The higher contribution of the abutments is more evident in bridges with shorter piers.

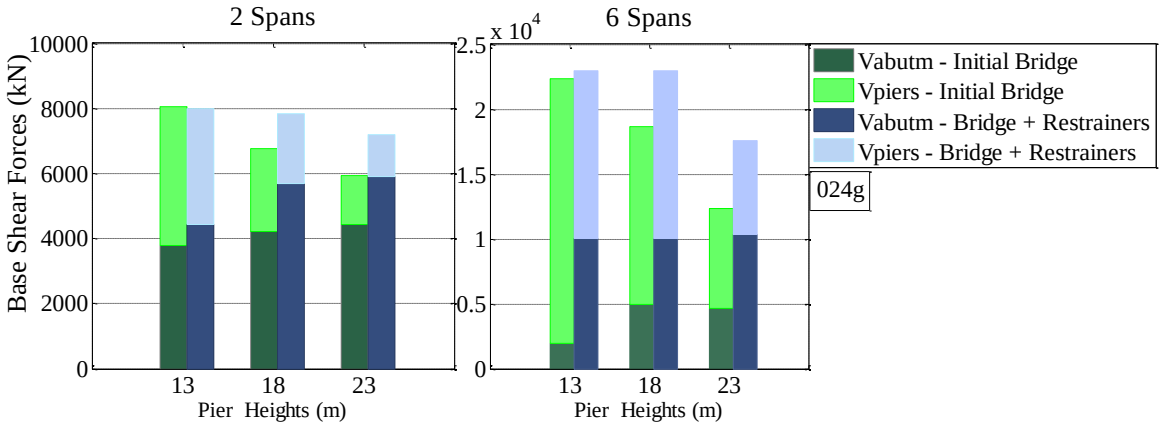


Figure 5: Distribution of Bridge Shear Forces for variable pier heights

Regarding the effect of the mechanisms' characteristics on the seismic response of bridges, the data shown in Figure 6 indicates the trend of the response. In Figure 6, it is observed that the increase in the reduction of bridge displacements follows the increase of the size of steel bundles. This trend has been also observed for bridges with a single-span (Figure 3).

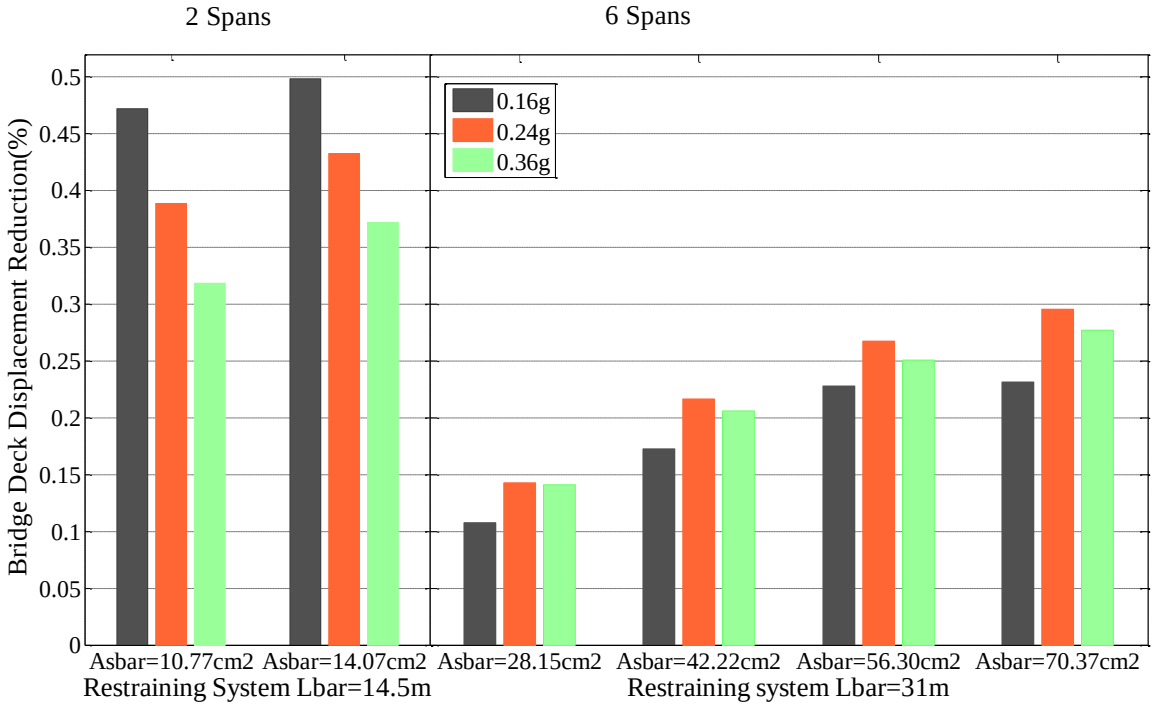


Figure 6: Reduction of Bridge Displacements for variable bundle cross section, Asbar/bundle

Similar plots are presented in Figures 7-8, for the effect of the length variability on the seismic response of the bridge. The increase of the steel bundle length results in a reduction in the effectiveness of the struts-ties system, as shown in Figure 7, which can be characterized as minor (~10%). However, the increase in the steel bundle length is advantageous for the abutments, since it reduces the seismic forces received by the abutments, Figure 8. This reduction can compromise the reduction in the efficiency of the restraining system in limiting the seismic displacements.

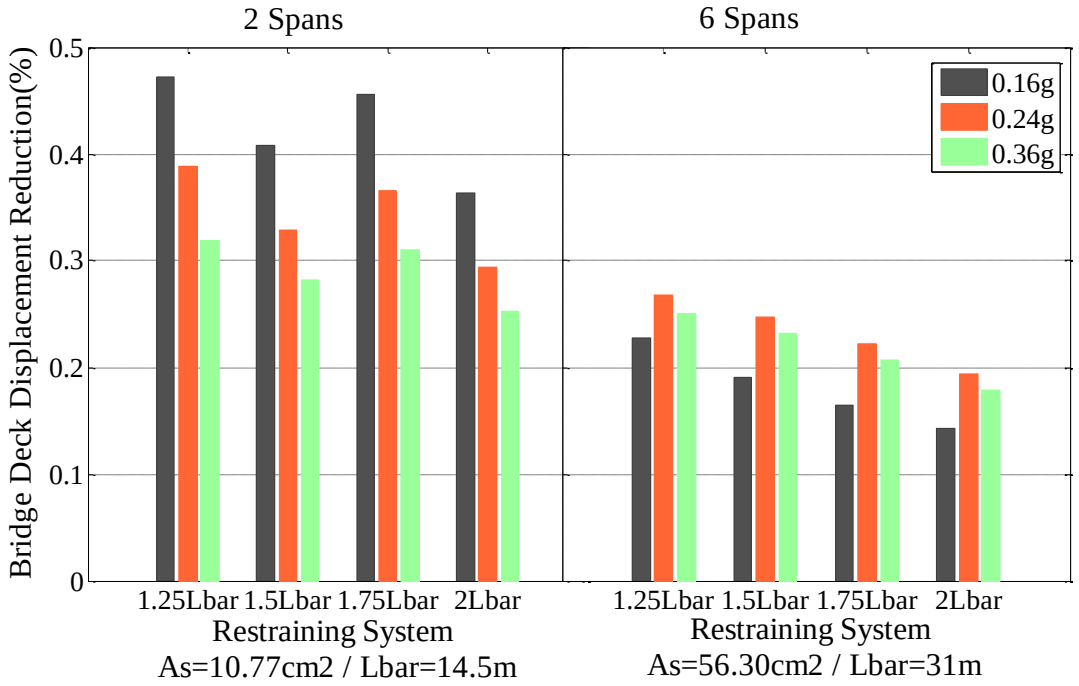


Figure 7: Reduction of Bridge Displacements for variable steel bundle lengths

The influence of the steel bar length on both the abutment seismic contribution and the seismic displacements allows for length modifications of the steel bundles that can lead to lower seismic forces to the abutments capacity level.

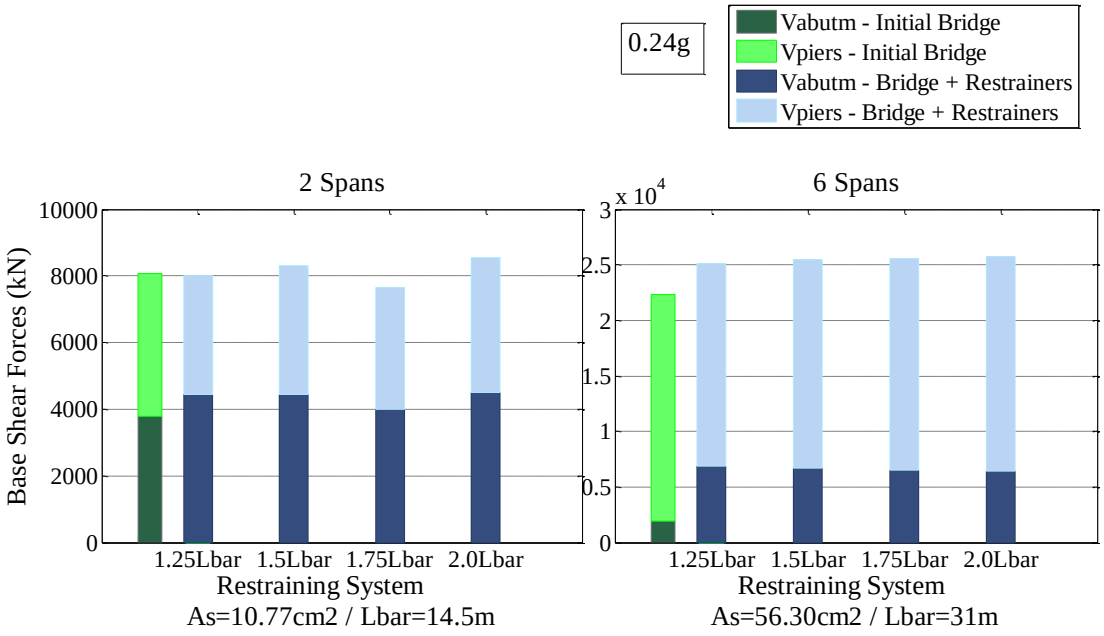
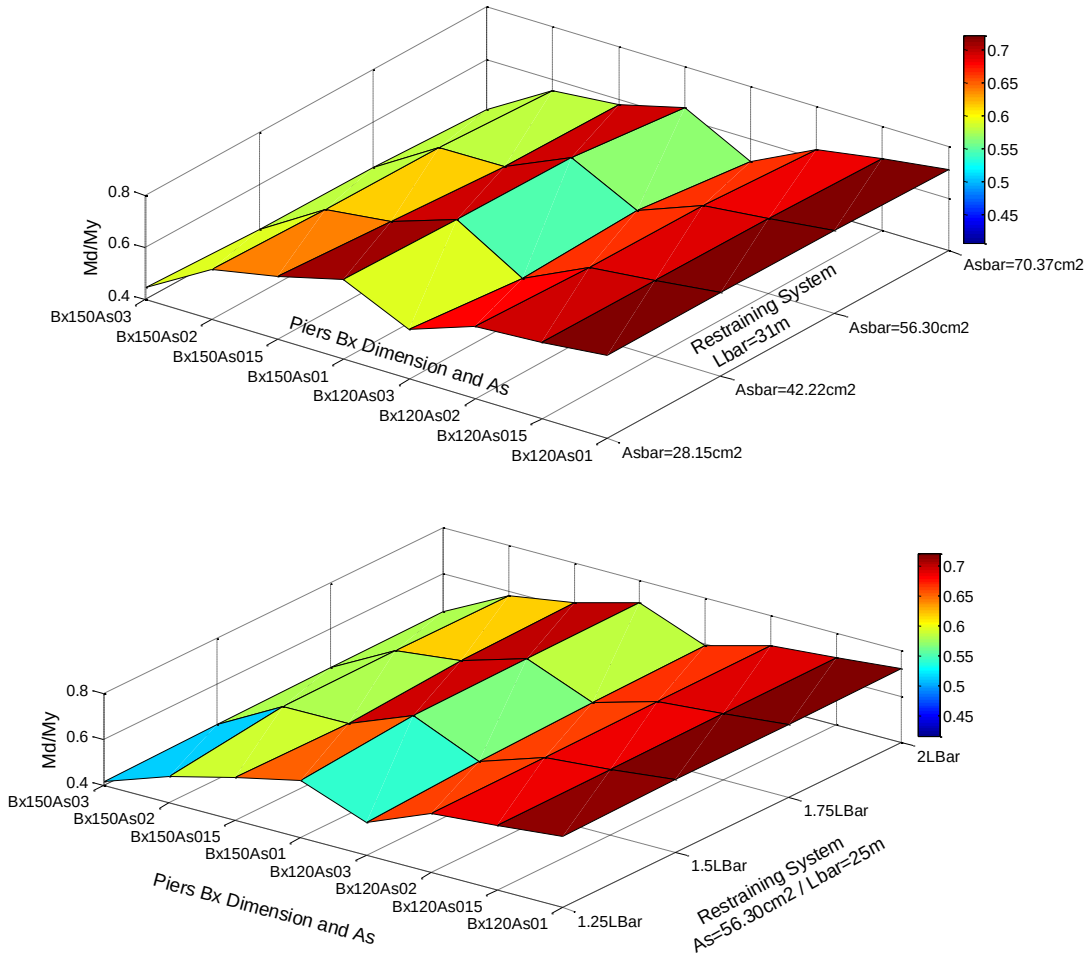


Figure 8: Distribution of Bridge Shear Forces for variable bundle lengths

The effect of the variation of piers' cross-sections and the reinforcement ratios has been analyzed in combination with the variation of the steel bundle size and length. Regarding the cross-section of the piers the variation refers to the width (short side) of the rectangular cross section, since the long side addresses the transverse seismic requirements.

In Figure 9 it is worth highlighting that with the presence of the restraining system design seismic demand moments that reach pier yielding moments (higher pier contribution) are

developed in the case of shorter piers (Bx120) with higher reinforcement ratios in comparison to larger piers (Bx150) with the minimum reinforcement ratio of 1%. Figure 10 indicates that larger sizes of piers lower the participation of the abutments-mechanism. Hence, the use of the restraining system is more preferable to be combined with small pier dimensions that have higher longitudinal reinforcement ratios.



(b)

Figure 9:a. Piers & Length of Bars b. Piers & Length of Bars – ratio of M/My on Middle Pier (6-span, 024g).

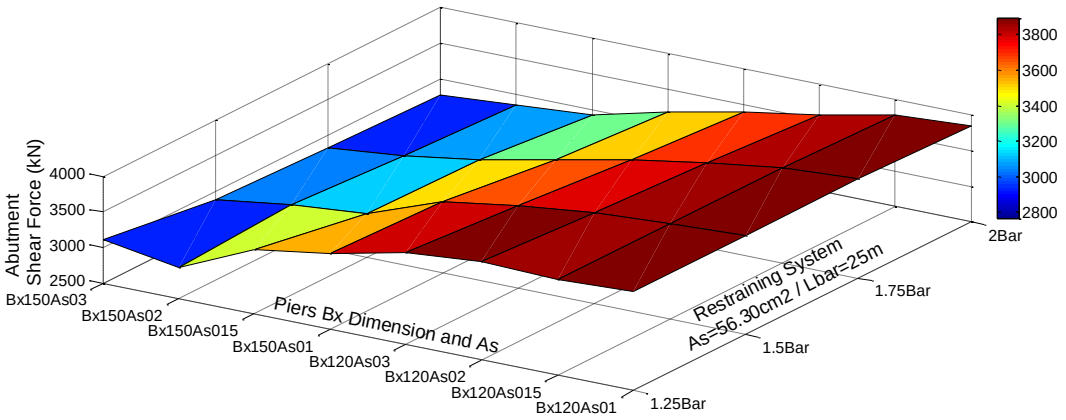


Figure 10: Piers & Length of Bars Forces developed at the abutments (6-span, 024g)

6 GUIDELINES FOR OPTIMUM DESIGN SOLUTIONS FOR BRIDGES WITH THE RESTRAINING SYSTEM

Useful concepts for the design of bridges with the restraining system can be derived from the observations and conclusions from the parametric analysis. Herein these concepts are presented in a guideline form in order to address the issue of optimum design solutions for bridge structural systems - restraining system properties. These concepts can be incorporated in the design process of a bridge under Eurocode Provisions and the guideline form includes an iterative design procedure, Figure 13.

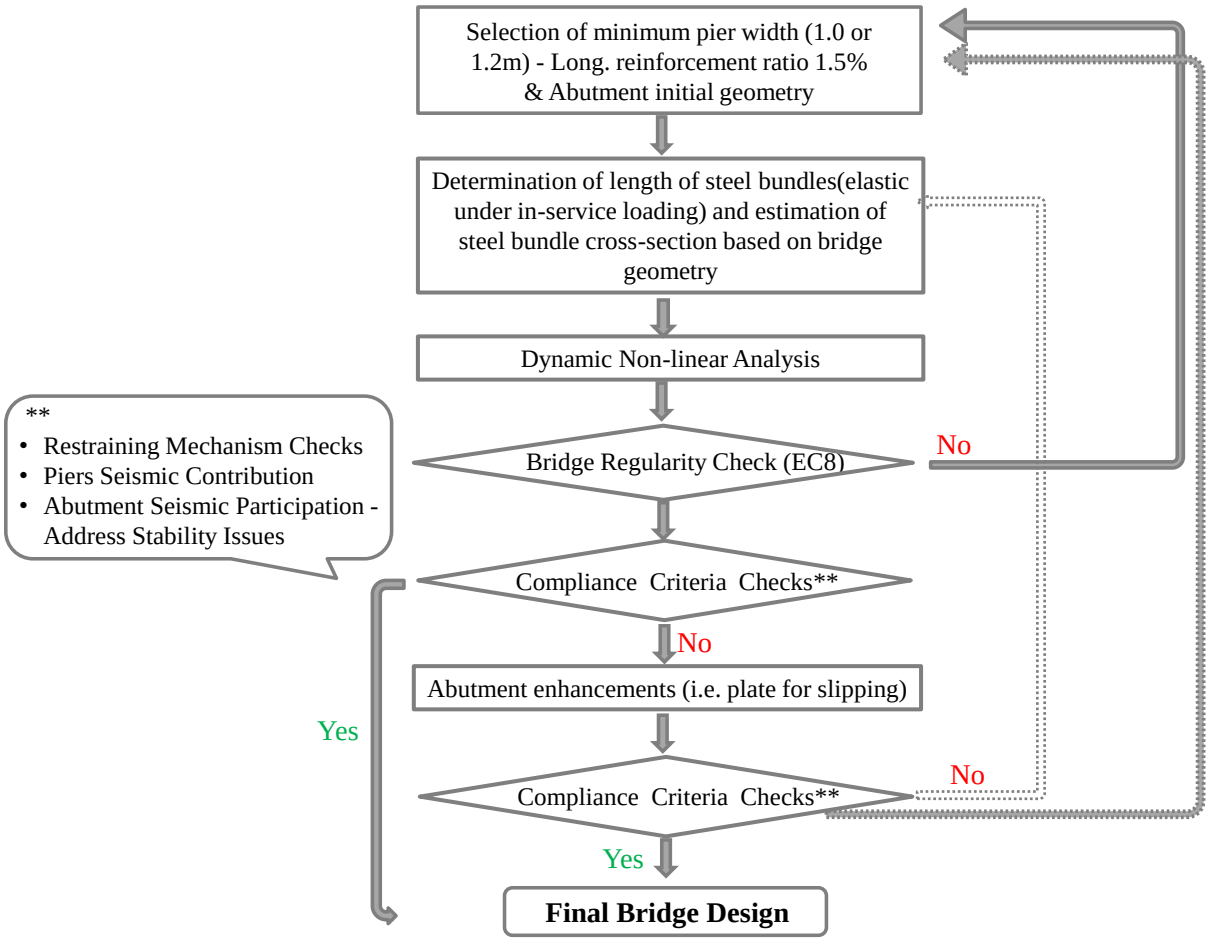


Figure 13: Guideline for optimum design solutions for bridges with the restraining system of struts-ties

The key points are described in the following paragraphs.

- The procedure starts with the selection of piers cross-section and reinforcement ratio. The piers are the most crucial bridge component regarding the minimization of the design objective (cost of bridge) and the response of the bridge; as shown in Figures 9-11 the cross-section of piers determines the range of seismic forces distributed to the structural components.
- After the determination of the restraining systems' properties and the seismic analysis of the bridge, the first check that shall be performed corresponds to the check of regularity of the bridge, [1]. It is expected that the design will result in regular bridge

solutions. Thus, if a bridge is found irregular the cross section of the pier is revised before continuing to the next design steps.

- The compliance criteria to be checked include: a. the response of the mechanism; forces on the steel bundles shall be lower than the ultimate values, b. the distribution of the seismic forces between the abutment and the piers. The piers shall contribute highly to the seismic resistance. The abutments are designed for the additional forces transferred from the steel bundles that may cause stability problems as well. If stability issues are not accommodated with the geometry determined in the initial design, abutment enhancement solutions are investigated,[19]. Indicative examples are slabs that protrude towards the embankment, under the weight of which the slipping of abutment is prevented by developing friction or the use of piles for the overturning moments. If the criteria requirements are not fulfilled a revised deisgn solution is saught.
- After the iterative design procedure has established the optimum dimensions for piers and abutments, the bridge design is continued with the remaining comprehensive design checks.

7 CONCLUSIONS

The influence of various parameters on the seismic response of continuous integral concrete box girder bridges with the struts-ties restraining system (bundles of steel bars in the superstructure of the bridge) has been investigated. The objective of the parametric analysis has been to present the observations acquired and to configure a suggestion for the optimization of the bridge design for the struts-ties mechanism. The main conclusions derived are:

- It has been identified that compliance criteria for R/C bridges designed with the restraining mechanism related to the ratio of the distribution of seismic forces between the piers and the abutments of the bridge are necessary. The criteria refer to a balanced participation of the bridge components in the seismic response so that the compliance criteria of stability, regarding the abutments and the criteria of regularity, economy and aesthetics, regarding the piers are satisfied.
- Because of the minor cost of steel bundles, the economy criterion regarding the size of the steel bars is not included in the optimum design selection.
- The abutments have higher contribution to the seismic resistance of bridges with the presence of struts-ties system. It is noted that before revising their dimensions, the designer can use low cost design solutions, like a friction slab, in order to address the increased seismic demand.
- The parametric analysis has shown the influence of different bridge geometries and steel bundle properties on the effectiveness of the mechanism and the response of bridges
- The guidelines presented include a simple iterative procedure for the optimum design of bridges with the struts-ties that could be incorporated in the bridge design process

Future research work has already been initiated for the poly-parametric investigation of other bridge classes (i.e. cantilever bridges) aiming on highlighting the effectiveness of the struts-ties restraining system in a wide range of bridges.

ACKNOWLEDGEMENTS

The authors would like to acknowledge the assistance of METESYSM Company and EGNATIA ODOS A.E, since they provided all the necessary data and drawings for the investigated reference bridge.

REFERENCES

[1] CEN[Comité Européen de Normalisation], Eurocode 8: Design of structures for earthquake resistance - Part 2: Bridges. 2003.

[2] M. Arockiasamy, N. Butrieng, and M. Sivakumar, Discussion of " State-of-the-Art of Integral Abutment Bridges : Design and Practice ", no. February, pp. 135–136, *2006*.

[3] S. A. Mitoulis, I. A. Tegos, and M. A. Tsitotas, Integral Abutments Configurations for Arahthos-Peristeri Bridge (Bridge T5 , Length 240.0m) of Egnatia Highway, in *A seismic design and construction in Egnatia Odos, the highway connecting Epirous through Macedonia to Thrace and the eastern border of Greece*, Thessaloniki: Ziti Publications, 2010, pp. 1–11.

[4] S. A. Mitoulis and I. A. Tegos, Connection of Bridges with Neighborhooding Tunnels, Journal of Earthquake Engineering, *Journal of Earthquake Engineering*, vol. *14*, no. *3*, pp. 331–350, Mar. 2010.

[5] S. D. Tegou, S. a. Mitoulis, and I. a. Tegos, An unconventional earthquake resistant abutment with transversely directed R/C walls, *Engineering Structures*, vol. *32*, no. *11*, pp. 3801–3816, Nov. 2010.

[6] I. A Tegos, Michail A Tsitotas, S. D. Tegou, and S. A. Mitoulis, Reduction in seismic actions of bridges by utilizing the sidewalks as restrainers, pp. 1–16, *16th Hellenic Concrete Conference*, Pafos

[7] R. DesRoches and G. L. Fenves, Simplified Restrainer Design Procedure for Multiple-Frame Bridges, *Earthquake Spectra*, vol. *17*, no. *4*, pp. 551–567, *Nov. 2001*.

[8] R. DesRoches and M. Delemont, Seismic retrofit of simply supported bridges using shape memory alloys, *Engineering Structures*, vol. 24, no. *3*, pp. 325–332, Mar. 2002.

[9] E. Choi, J. Park, S.-J. Yoon, D.-H. Choi, and C. Park, Comparison of seismic performance of three restrainers for multiple-span bridges using fragility analysis, *Nonlinear Dynamics*, vol. 61, no. 1–2, pp. 83–99, Dec. 2009.

[10] I. Tegos and O. Markogiannaki, A Seismic Restraining System For Bridges : Analytical study of a strut-ties mechanism, 2011, *IBSBI Conference*, Athens.

[11] O. Markogiannaki and I. Tegos, A smart and costless solution for upgrading the seismic resistance of bridges Description of the proposed struts-ties system, *in IABSE Conference*, 2012.

[12] O. Markogiannaki and I. Tegos, Seismic retrofit of bridges through the external installation of a new type restraining system, *in 15WCEE*, 2012.

[13] J. A. Rhodes, H. G. Geymayer, B. B. Hope, W. R. Lorman, J. A. Means, M. A. Ward, C. Members, J. W. Dougill, H. K. Hilsdorf, D. J. Carreira, and S. K. Hirata, Prediction of Creep , Shrinkage , and Temperature Effects in Concrete Structures Reported by *ACI Committee* 209, vol. *92*, *1997*.

[14] McKenna, F. and Fenves, G. L. ,2005. "Open System for Earthquake Engineering Simulation" Pacific Earthquake Engineering Research Center, Version 1.6.2.

[15] V. K. Papanikolaou, Analysis of arbitrary composite sections in biaxial bending and axial load, *Computers & Structures*, vol. *98–99*, pp. 33–54, *May 2012*.

[16] Caltrans, SEISMIC DESIGN CRITERIA VERSION 1 . 6, no. November, *2010*.

[17] B. G. Nielson, Analytical Fragility Curves for Highway Bridges in Moderate Seismic Zones Analytical Fragility Curves for Highway Bridges in Moderate Seismic Zones, no. December, 2005.

[18] I. Iervolino, C. Galasso, and E. Cosenza, REXEL: computer aided record selection for code-based seismic structural analysis, *Bulletin of Earthquake Engineering*, vol. 8, no. 2, pp. 339–362, Aug. 2009.

[19] Caltrans, MEMO TO DESIGNERS 5-1, October 1992

COMPDYN 2013
4th ECCOMAS Thematic Conference on
Computational Methods in Structural Dynamics and Earthquake Engineering
M. Papadrakakis, V. Papadopoulos, V. Plevris (eds.)
Kos Island, Greece, 12–14 June 2013

OPTIMUM SELECTION OF RETROFIT MEASURES FOR R/C BRIDGES USING FRAGILITY CURVES

Sotiria P. Stefanidou[1], **Andreas J. Kappos**[2]

[1] Department of Civil Engineering, Aristotle University of Thessaloniki
54124 Thessaloniki, Greece
e-mail: ssotiria@civil.auth.gr

[2] Department of Civil Engineering, City University London
London EC1V OHB, UK
Andreas.Kappos.1@city.ac.uk

Keywords: Bridge Retrofit, Pier Jackets, Bearing Replacement, Global and Local Engineering Demand Parameters, Fragility curves

Abstract. *The key objective of this paper is to present a methodology for the selection of the appropriate retrofit scheme for bridges, based on the performance of different components (piers, bearings, abutments) with a view to upgrading the seismic performance of the system. The methodology is applied to a common bridge type, with monolithic pier-to-deck connections. Threshold values for global and local parameters are properly defined based on performance criteria, for different damage states. The correlation of local and global threshold values calculated on the basis of member and system capacity, respectively, reveals the structural system's robustness and identifies the most critical member with respect to the seismic performance of the system. Alternative retrofit measures, i.e. reinforced concrete (R/C) and fibre-reinforced polymer (FRP) jackets, and bearing replacement, are applied to critical members of the structure.*

Fragility curves are generated for the resulting retrofitted bridges using a probabilistic seismic demand model based on the results of inelastic dynamic response history analysis for appropriately selected earthquake ground motions, while bridge capacity is estimated through pushover analysis. The engineering demand parameter used for the quantification of the limit state threshold values for the retrofitted bridge is the bridge displacement (global parameter), related to the most critical component's displacement for every limit state and to local parameters (such as the pier curvature ductility). Alternative sets of retrofit properties are considered, and material uncertainties are treated in a probabilistic way in the bridge model (Latin Hypercube Sampling Method). The alternative retrofit schemes are finally evaluated and the optimum retrofit solution is identified on the basis of its efficiency, emerging from the comparison of fragility curves (as-built and retrofitted case) for different levels of seismic action.

1 INTRODUCTION

Damage due to recent earthquakes worldwide, albeit minor in several cases, highlights the role of bridges as the most vulnerable component of the transportation network. Bridge damage (Fig. 1) can cause significant disruption to the transportation system, resulting in substantial direct and indirect losses. The Loma Prieta 1989 earthquake resulting in more than 40 deaths due to bridge damage and $1.8 billion direct losses due to damage to the transportation system [1] has shown the need for retrofit of older bridges in order to reduce their vulnerability and withstand a future seismic event with controlled damage. Retrofit measures used for the enhancement of the bridges' seismic performance were tested during the 1994 Northridge earthquake, where significant damage occurred to older as well as retrofitted bridges, resulting in questioning the effectiveness of several retrofit measures and strategies used.



Figure 1: Bridge damage due to recent earthquakes.

Pre-earthquake retrofit decision making should best be based on the results of probabilistic assessment of the bridges' seismic performance for different levels of seismic hazard. The use of fragility curves for assessing the vulnerability of bridges became a common practice during the last two decades. Numerous methodologies for the derivation of empirical [2], as well as analytical fragility curves [3,4,5,6,7,8,9] have been developed. The differences among the existing methodologies mainly lie in the quantitative definition of limit states (engineering demand parameter used, threshold values of limit states considered), the type of analysis, and the probabilistic model used for the fragility analysis. The probability of reaching or exceeding a specific limit state is calculated on the basis of exceeding threshold values of an engineering demand parameter, correlated to damage in the system. The engineering demand parameter may be either a global parameter (bridge displacement) [5,8] or a local one (material strains, column ductility, bearing deformation) [3,4,9], whereas the damage index is also commonly used [6]. The bridge fragility may be defined considering one bridge component as the most critical for the bridges' seismic performance [6,7] or a combination of different bridge components [3,4,10] in a series or parallel system [10,11].

Recent methodologies [3,4,5,9] propose the combination of component fragility curves for the derivation of the system fragility. Bridge piers, abutments, and bearings are considered to be the most critical components regarding the bridge seismic performance. The probabilities of the demand exceeding the capacity are calculated separately for each component and every limit state, based on local engineering demand parameters, and the derived component fragilities are subsequently synthesised in order to derive the overall system's fragility.

Since fragility curves can be used for retrofit prioritization and decision-making, system fragility should preferably highlight the most vulnerable component for every limit state, so that it can guide the designer to the most effective intervention for the enhancement of the system's performance to the desired level. The latter requires mapping between component (local) and system (global) capacities for the limit state definition and only recently [12] the research interest moved towards this direction.

Retrofit measures for the enhancement of bridge seismic performance can be categorized into those that target strength, stiffness, or ductility, enhancement (R/C, steel, or FRP pier jackets), the increase of energy dissipation (elastomeric or lead bearings, isolation systems), or control of displacements (restrainer cables, shear keys, seat extenders). Steel and FRP jackets are arguably the most popular retrofit measures for bridge piers [13,14], since they increase the flexural and shear strength as well as the member's ductility without significant change to the member stiffness that will typically result to increased seismic forces. The behaviour of FRP jackets has been investigated experimentally as well as analytically [15,16]; nevertheless, their implementation requires qualified staff that might not be locally available, as FRPs are not as widely used as R/C jackets. Replacement of existing bearings with elastomeric and lead rubber bearings, and addition of energy dissipation devices were found to be very effective for the pre-earthquake retrofit since they reduce the seismic input to the structure [17]. Their effectiveness has been evaluated and optimum properties for the system's vulnerability reduction have been defined [11]. Finally, various retrofit measures concerning the structure's displacement control (including unseating), namely restrainer cables, shape memory alloys, shear keys and seat extenders were evaluated experimentally as well as analytically with regard to both component and system vulnerability reduction [18].



Figure 2: Retrofit measures for R/C bridges.

The most efficient retrofit measures and retrofit strategies for the enhancement of the bridge seismic performance are not always apparent, and use of advanced computational tools is necessary for their proper selection and comparative evaluation. Fragility curves of retrofitted bridges quantify the efficiency of retrofit measures, when compared to the as-built ones. Limited studies concerning various retrofit measures applied to a single bridge component [19,20] or a number of components [10] reveal the retrofit impact and the performance of the retrofitted structures under various seismic intensities. Another important issue apart from the efficiency of the retrofit measures is the efficiency of retrofit strategies [1] that can emerge from the combination of different retrofit measures applied to the system components.

The key objective of this paper is the presentation of a methodology for the derivation of fragility curves using a component-level approach, relating the component (local) to system (global) limit state capacities (threshold values for each limit state) in order to identify the most critical component for each limit state. A parametric study is carried out to assess the sensitivity of the system capacity to different geometric, reinforcement, and soil-foundation

properties of the components. To enhance the seismic performance, different retrofit measures might be appropriate for different performance levels; R/C and FRP pier jackets as well as bearing replacement, are evaluated here through fragility analysis of the retrofitted bridges and the optimum selection of retrofit measure is discussed.

2 METHODOLOGY FOR THE DERIVATION OF FRAGILITY CURVES CORRELATING COMPONENT TO SYSTEM PERFORMANCE

A new methodology for the derivation of bridge fragility curves is presented, focusing on the correlation between system (global) and component (local) seismic performance and associated guidelines for the most effective retrofit intervention for the selected performance level(s). The methodology consists of three distinct steps and is described in the next sections.

2.1 Component Subsystems – Correlation between local and global engineering demand parameters for the definition of limit state threshold values

A critical issue for the derivation of fragility curves is the definition of limit states. Limit states are typically related to damage observed to the structural system or member by means of an engineering demand parameter, which can either refer to the whole system (displacement) [5,8] or to a bridge member [7] or section [4,21]. Threshold values of engineering demand parameters reflect the bounds of the system's capacity for each limit state.

The first step of the proposed methodology refers to the definition of subsystems, critical for the seismic performance of the bridge system. Bridge piers, abutments and bearings were found to be the most important bridge components as far as performance under seismic actions is concerned [4,9,10,11]. The importance of the foundation is also recognized, though it is not considered as a different subsystem at this stage of development of the method.

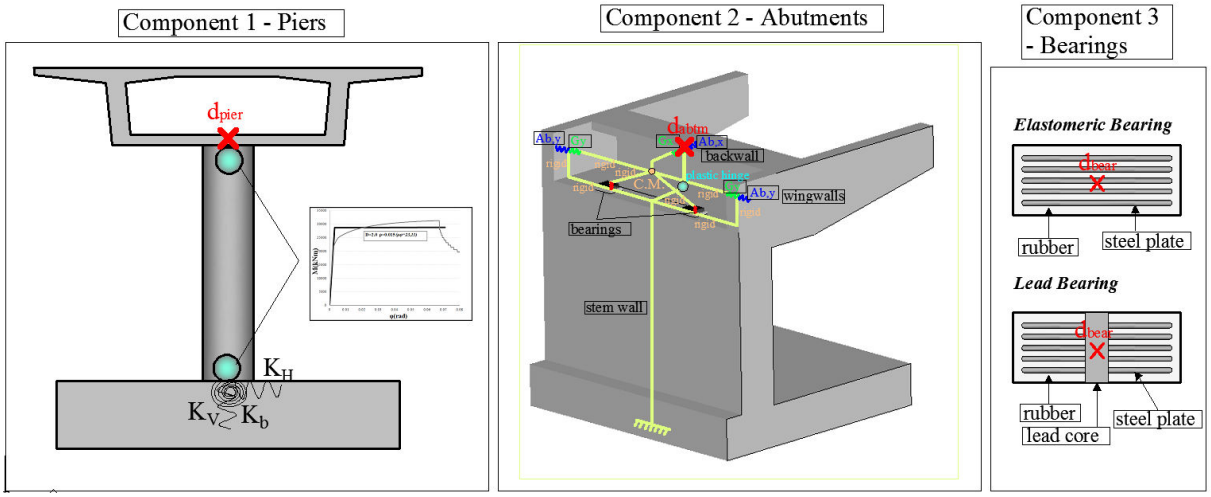


Figure 3: Subsystems consisting of bridge critical components.

According to the proposed methodology the aforementioned subsystems are individually analysed. Boundary conditions are introduced through equivalent translational and rotational springs at connection points with the deck, calculated through static condensation of the full model, while equivalent mass is also estimated and introduced. Foundation translational and rotational springs are defined here for the case of shallow foundation. Threshold values for engineering demand parameters are defined based on local parameters and are correlated to global ones (component control point displacement) with the aid of pushover analysis.

The bridge piers considered are monolithically connected to the deck, hence having two potential plastic hinge formation regions located at the top and bottom of the pier. The piers are modelled using beam-column elements with concentrated plastic hinges at the top and bottom. Cross section analysis is performed [23] using appropriate stress-strain curves for concrete and steel [24] in order to obtain moment-curvature diagrams, while the plastic hinge length L_p is also calculated [25]. The engineering demand parameter used for the definition of limit states threshold values is the curvature (Table 1), related to material strain limits [25,26] that correspond to experimentally observed member damage (cover spalling, buckling of longitudinal reinforcement, first hoop fracture) and crack widths [26]. It is noted that in the present study only flexural failure modes are taken under consideration.

Limit State	Threshold values of curvature (φ)	Quantitative Performance Description
LS 1 – Minor/Slight damage	φ_y	Quasi-elastic behaviour – Cracks barely visible.
LS 2 – Moderate damage	min (φ: $\varepsilon_c \leq 0.004$, φ: $\varepsilon_s \geq 0.015$)	Spalling of the cover concrete , strength may continue to increase – Crack width 1-2mm.
LS 3 – Major/Extensive damage	min (φ: $\varepsilon_c \leq 0.004 + 1.4\rho_w \cdot \frac{f_{yw}}{f_{cc}}$, φ: $\varepsilon_s \geq 0.06$)	First hoop fracture, buckling of longitudinal reinforcement, initiation of crushing of concrete core – Crack width>2mm.
LS 4 – Failure/Collapse	min (φ: $M_{res} < 0.85 \cdot M_{max}$ φ: $\varepsilon_s \geq 0.075$)	Loss of load-carrying capacity - Collapse

Table 1: Limit states for component 1: Bridge Piers.

For the threshold values of limit states to be quantified, inelastic static pushover analysis is performed to the subsystem and the component's control point displacement corresponding to each threshold local engineering demand parameter (φ) value is monitored. Hence, limit states in terms of deformation (global parameter) are directly mapped to limit states in terms of curvature (local parameter) for the component under consideration.

Limit State	Threshold values	Quantitative Performance Description
LS 1 – Minor/Slight damage	$\mu_{\varphi,backwall}$=1.5	Cracking and significant damage to the backwall
LS 2 – Moderate damage	$d = 0.01 \cdot h_{backwall}$	First yield of the abutment soil
LS 3 – Major/Extensive damage	$d = 0.035 \cdot h_{backwall}$	Excessive deformation of abutment soil
LS 4 – Failure/Collapse	$d = 0.1 \cdot h_{backwall}$	Ultimate deformation of abutment soil (cohessionless soil)

Table 2: Limit states for component 2: Abutments.

Limit state threshold displacement values are defined in a similar way for the abutment. The abutment was modelled using beam column elements with potential hinges in the backwall as shown in Figure 3. Cross section analysis was performed for the backwall [23] in or-

der to obtain moment-curvature diagrams, and the plastic hinge length L_p is calculated as before [25]. The embankment-abutment interaction (passive action) after gap closure was considered [22] taking under consideration the Caltrans provisions. Limit state definitions for the abutments are given in Table 2. Subsequently, inelastic static (pushover) analysis is performed for the abutment subsystem in order to define the threshold value in terms of displacement of the control point for the first limit state (the other three LSs are directly expressed in terms of fractions of the backwall height).

Except from the piers and abutments another critical bridge component, namely the bearings, is considered. The bearing stiffness is properly defined [27] and modelled using an elastoplastic hysteresis model. The engineering demand parameter used to define the component's threshold limit state values is the shear strain (γ=d/t,$_{rubber}$) [28]; threshold values based on information from the literature are given in Table 3.

Limit State	Threshold values of shear strain (γ)	Quantitative Performance Description
LS 1 – Minor/Slight damage	100%	Initiation of nonlinear behaviour, potential yielding of anchor bolts and cracking of pedestals.
LS 2 – Moderate damage	150%	Visible damage to the bearing. Yield of steel shims.
LS 3 – Major/Extensive damage	200%	Lift off at the edge of the bearing, uplift and rocking. May cause delamination, bonding failure between rubber layers and steel shim plates.
LS 4 – Failure/Collapse	250%	Lift-off, rotation. Unseating, failure of bearings.

Table 3: Limit states for component 3: Bearings.

2.2 Bridge system capacity – Definition of limit states for the system in terms of global parameters

Since the combination of components may influence the seismic performance of the system differently, formulation of the whole system bridge model is necessary to relate the bridge control point displacement to the displacement of the control (monitoring) point of individual components and define the threshold limit state values (capacity) for the system.

Pushover analysis of the bridge system is performed for the longitudinal and transverse direction. Displacement of the control point is recorded when each one of the components considered enters a specific limit state as depicted in Figure 4; the bridge centre of mass is taken as the control point for the longitudinal direction, whereas the bridge end is taken for the transverse direction, since in the studied bridge this is the point of maximum displacement. The threshold value for the limit state considered is taken as the minimum of the displacements obtained, assuming a series connection between the components (conservative approach). Therefore the threshold values for every limit state are defined for the system in terms of the displacement of the control point (global parameter), hence being directly correlated to local performance of the components.

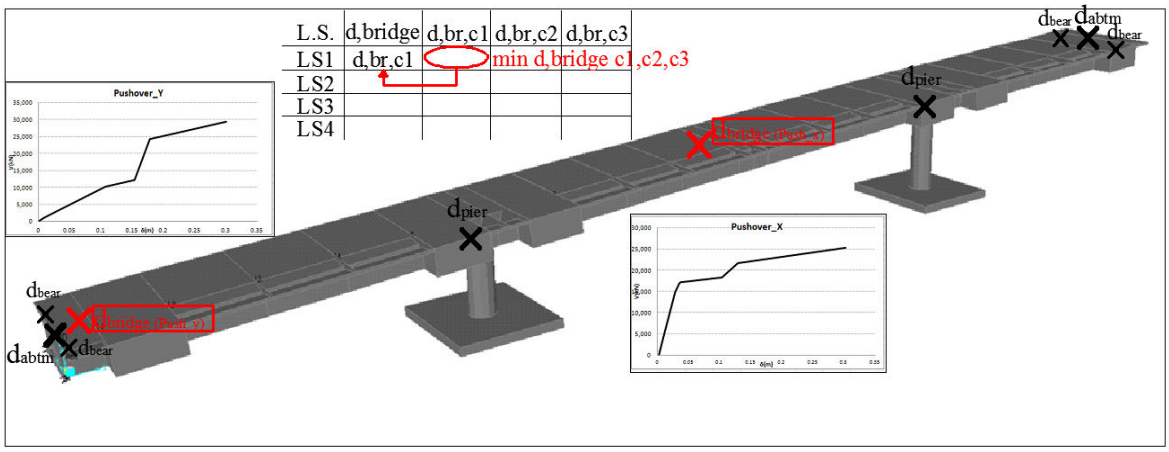


Figure 4: Bridge system limit state definition.

2.3 Uncertainties in capacity and demand

Aleatory and epistemic uncertainties should be considered during the demand and capacity estimation regarding the material and geometric properties, whereas other type of uncertainties, such as the uncertainty in the limit state definition are also deemed to be important.

Different bridge realizations, statistically different, yet nominally identical, are considered for the probabilistic treatment of fragility curves and Latin Hypercube sampling (LHS) is implemented to reduce the computational effort. LHS is as a stratified sampling procedure, that provides an efficient way of sampling variables from their distributions while limiting the required sample size compared to Monte Carlo sampling methods. The algorithm suggested by Iman and Conover [29] was implemented in the frames of the proposed methodology for the treatment of uncertainty in capacity and demand .

2.4 Fragility Curves

Fragility curves represent the conditional probability of reaching or exceeding a limit state as a function of a ground motion intensity parameter.

$$P_F = P[D \geq C] \tag{1}$$

where P_F= probability of failure, D=structural demand and C=structural capacity. Various intensity measures (PGA, S_a, S_v) were evaluated based on their efficiency, practicality, sufficiency and hazard computability, with the PGA considered as the optimum choice for the derivation of fragility curves [18].

Having defined the capacity of the bridge from step 2, the Probabilistic Seismic Demand Model (PSDM) is employed to derive analytical fragility functions using nonlinear response history analysis of the bridge. There are two approaches regarding the implementation of the PSDM, namely the “cloud” (Probabilistic Seismic Demand Analysis) and the “scaling” (Incremental Dynamic Analysis) approach, with the latter having the advantage of not requiring an a priori assumption for the probabilistic distribution of seismic demands in order to derive fragility curves [11].

The one implemented herein is the IDA approach for different levels of seismic action ranging from 0.4 to 4 times the A_d. The limit state probability of exceedance at a specific IM level equals the occurrence ratio of the specific limit state, defined as the ratio of the number of damage cases n_i, for the damage state I over the number of simulations *N*, as noted in equation 2.

$$P[\langle D \geq DS_i | I_M \rangle = \frac{n_i}{N} \quad (i = 1 \; to \; 4) \tag{2}$$

Fragility curves are commonly fitted with a log-normal cumulative distribution function [8,11] (equation 3) and if normalized to A_d become independent of the design seismic action [30].

$$P[\langle DI \geq LS | I_M \rangle = \int_{-\infty}^{I_M} \frac{1}{I_M \sqrt{2\pi \cdot \hat{\beta}}} e^{\left\{ -\frac{[\ln(I_M) - \hat{\mu}]}{2\hat{\beta}^2} \right\}} d(I_M) \tag{3}$$

The median value of A_g for every limit state and the standard deviation are calculated based on the results of nonlinear response-history analysis of all the realizations and different levels of A_g. Their values are obtained from equation 4, where M is the number of realizations and a_i is associated with the onset of collapse for the i^{th} realization [31].

$$\hat{\mu} = \frac{1}{M} \sum_{i=1}^{M} ln(a_i) \tag{4}$$

$$\hat{\beta} = \sqrt{\frac{1}{(M-1)} \sum_{i=1}^{M} (ln(a_i) - \hat{\mu})^2}$$

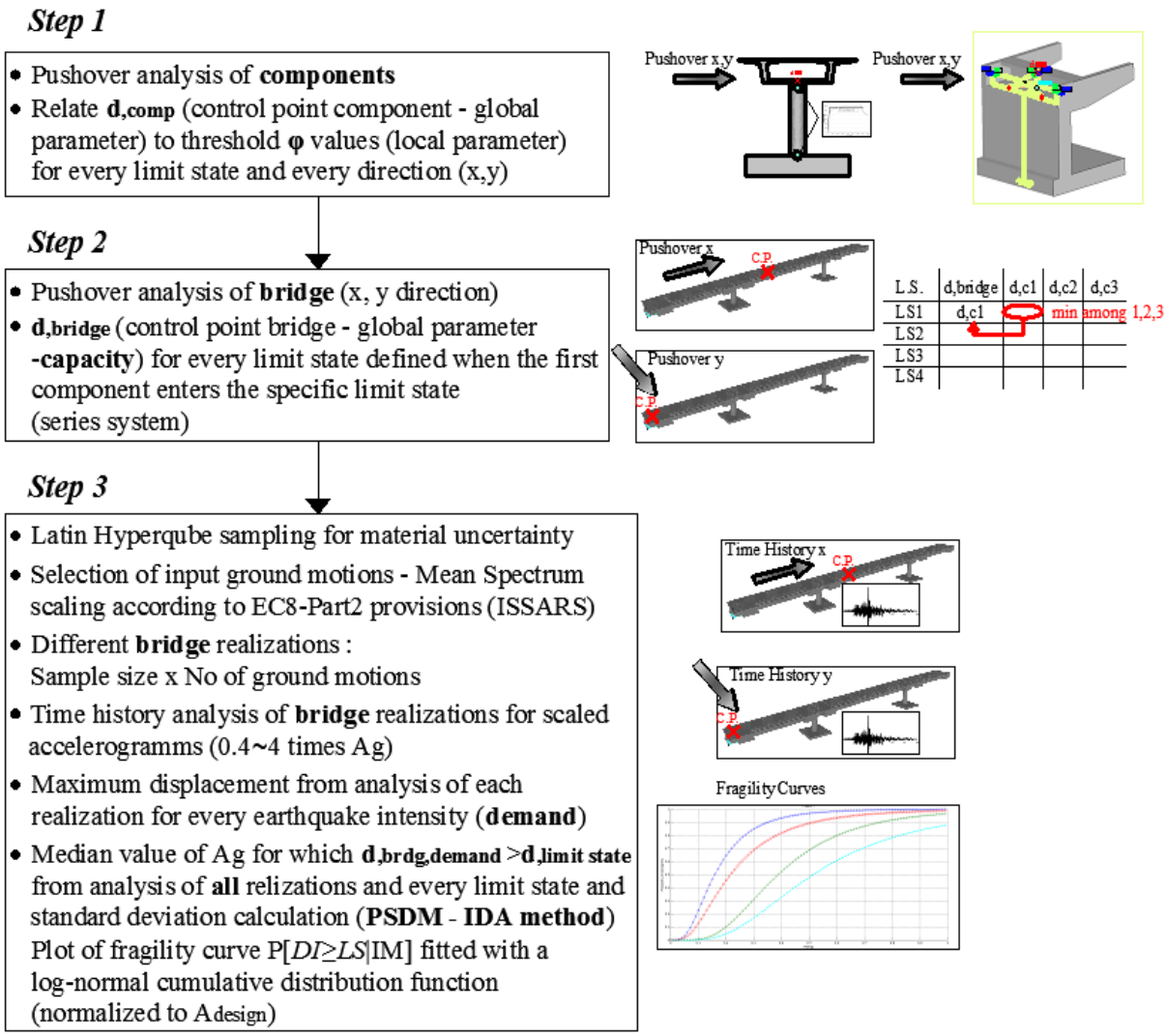


Figure 5: Outline of the proposed methodology.

The methodology presented herein is briefly outlined in Figure 5. It is clear that since, according to the proposed methodology the global capacity is directly related to component performance, it is straightforward to identify the most effective retrofit scheme using the fragility curves for selected performance level(s). A Matlab-code was written for the implementation of the different steps of the methodology.

3 FRAGILITY CURVES OF T7 BRIDGE (AS-BUILT) ACCORDING TO THE PROPOSED METHODOLOGY

The methodology described above is used for the derivation of fragility curves of a case study bridge, a typical overpass of Egnatia Motorway, depicted in Figure 6 and the investigation of the optimum retrofit strategy according to the performance level selected for various seismic events. The two piers having 5.94 m and 7.94 m heights are circular (D=2.0m) and monolithically connected to the deck consisting of a box section. Both piers and abutments have shallow foundations. The deck is connected to the abutment through elastomeric bearings, having a gap in the longitudinal (10 cm) as well as the transverse direction (15 cm).

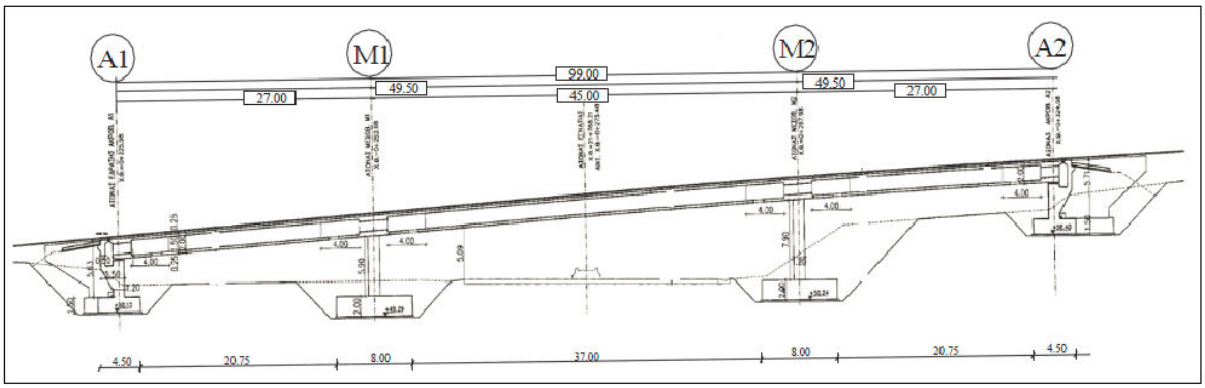


Figure 6: Geometry of T7 Bridge.

3.1 Modelling assumptions

The structure is modelled and analysed using OpenSees [32]. For the formulation of the 3D model as depicted in Figure 7, elastic beam-column elements are used for the deck and beam-column with hinges (lumped plasticity) elements for the piers. Cross section analysis was performed for the piers [23] in order to obtain moment-curvature diagrams for the potential plastic hinges (pier top and bottom), while the plastic hinge length L_p is calculated according to [25]. The abutment-backfill interaction (passive action) after gap closure was considered [22] taking under consideration the relevant Caltrans provisions [33].

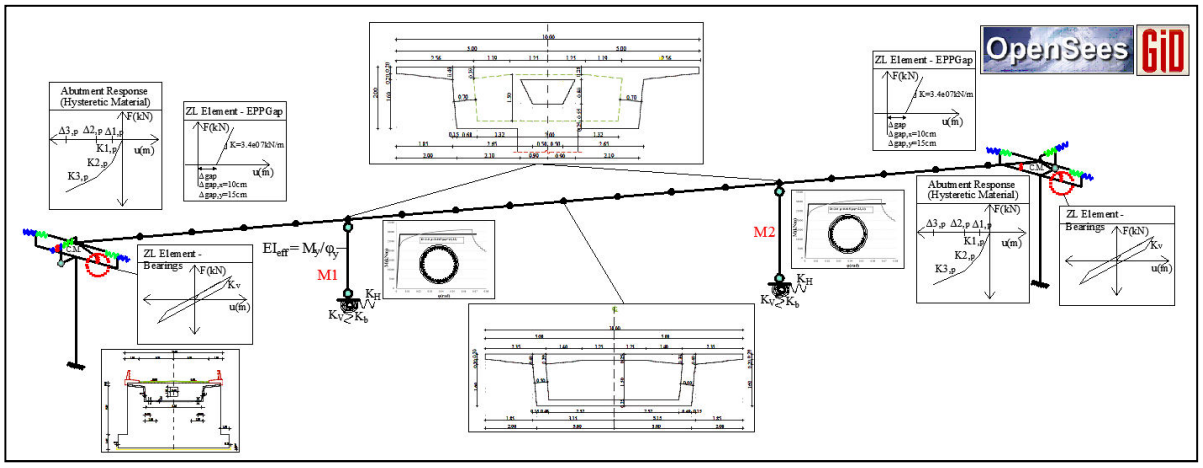


Figure 7: 3D model of T7 overpass bridge.

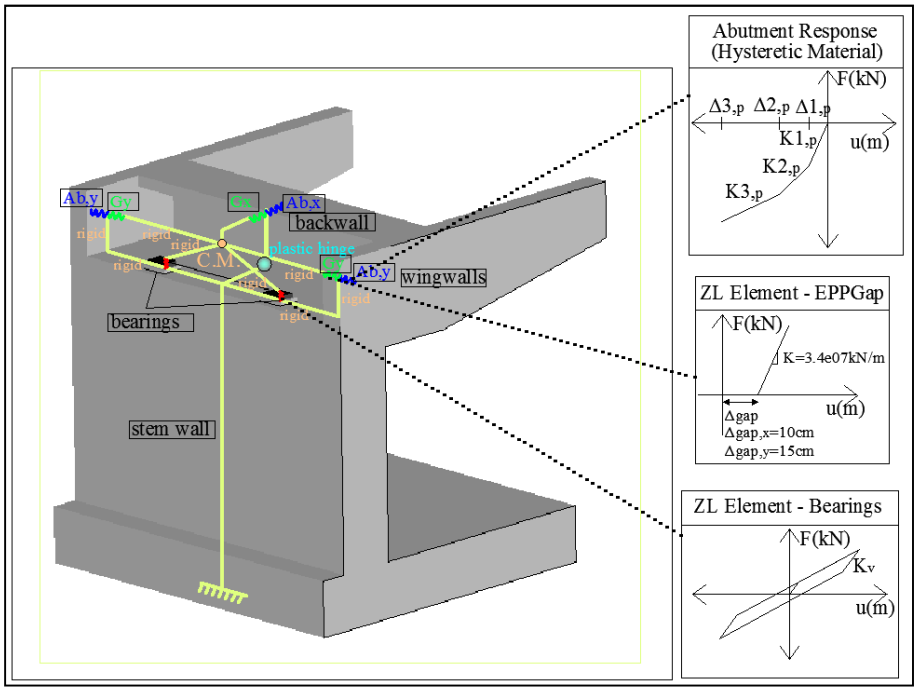


Figure 8: Details of the abutment model.

3.2 Uncertainty treatment

Uncertainty in material properties is considered for the probabilistic assessment of the bridge, regarding concrete compressive strength (f_c) and yield strength of steel (f_y). Concrete and steel strengths are assumed to be a normally distributed random variables, with mean and standard deviation values as shown in Table 4 [9]. The LHS algorithm was employed for N=10 statistically different, yet nominally identical, realizations (resulting to a total number of 700 analyses for the derivation of fragility curves)

Random Variable	Distribution	Mean	Standard deviation
f_c	normal	35.5	3.9
f_y	normal	550	6.13

Table 4: Assumed distributions for random variables.

3.3 Implementation of the methodology (Steps 1 and 2 – System Capacity)

The methodology described is implemented, for the different realizations of the bridge model considered. Pushover analyses (a total of 20) of the components are performed for their longitudinal and the transverse direction (Figure 8), as well as pushover analyses (20) of the bridge system for the two directions.

The most critical component (among piers, abutments, and bearings) defines the threshold value for which the system reaches the specific limit state; this component is generally different for each limit state considered. More specifically, the piers were found to define the first two limit states of the system in both the longitudinal and transverse direction, whereas the bearings through which the bridge deck sits on the abutment the third and fourth ones (corresponding to unseating of the bridge deck). For the bridge type studied here the abutment was not found to define any threshold value for the system, as expected, since gaps of 10 and 15 cm exist between the bridge deck and the abutment in the longitudinal and transverse direction, respectively. However, the abutment interacts with the other components and exceeds the component's threshold limit state values (first and second as depicted in figure 9); this occurs for larger system displacements (subsequent to gap closure), when the other components have already developed excessive deformations and the bridge system is considered to enter a higher limit state.

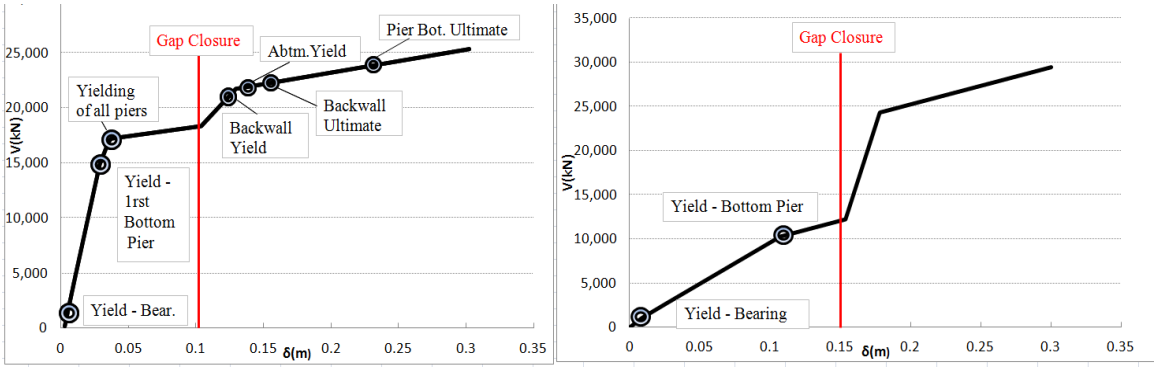


Figure 9: Pushover curves for the bridge's longitudinal (left) and transverse directions.

According to the above, to enhance the system capacity with respect to the first two limit states, retrofit interventions should primarily reduce the vulnerability of the piers, whereas for the last two limit states retrofit measures should focus on increasing the deformation capacity of the bearings and/or reducing the demand to bearings by additional damping. The most efficient retrofit scheme for various seismic intensities according to the prescribed performance level will emerge with the aid of fragility curves, more specifically the comparison between as-built and post-retrofit curves.

3.4 Parametric study of components

In order to investigate the effect of member geometry and reinforcement on the system capacity, a parametric study was carried out for its components, as summarised in Figure 10. The combinations were implemented keeping one parameter constant at a time. Steps 1 and 2 of the proposed methodology were applied, the most critical component for the system derived and subsequently compared with the results for the bridge.

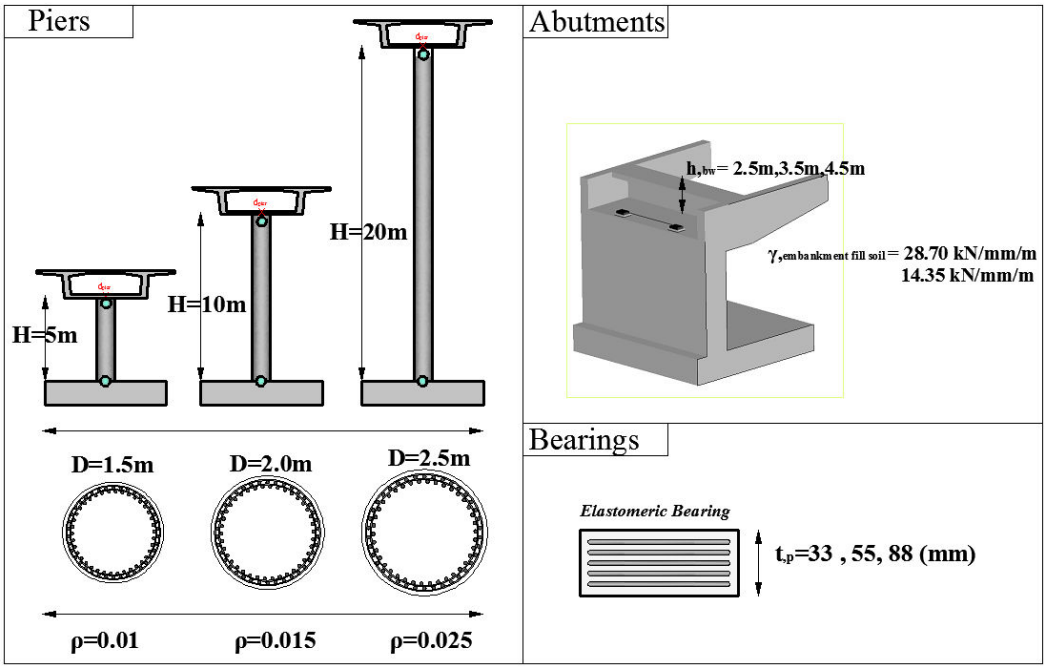


Figure 10: Parametric study of the components of the bridge.

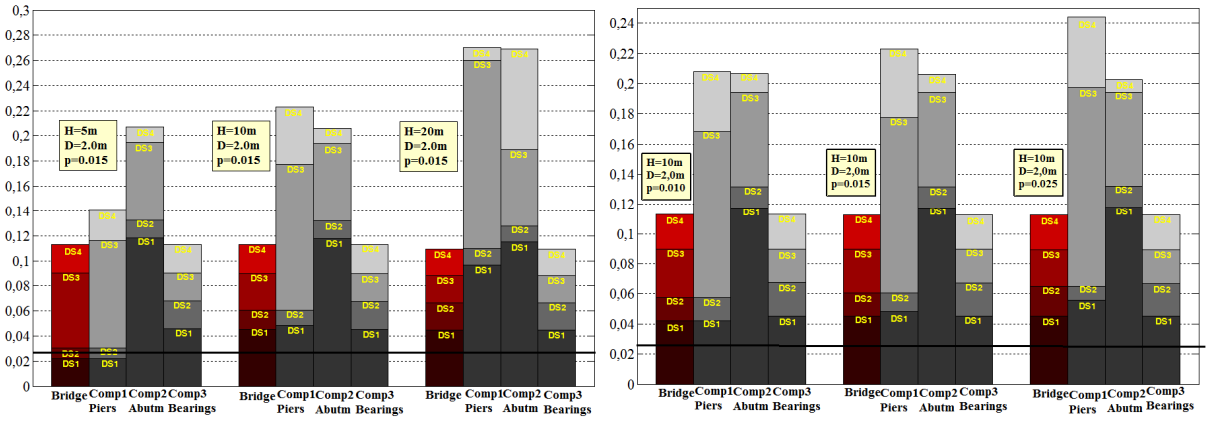


Figure 11: System limit state definition (varying pier height, H, and reinforcement ratio, ρ).

Comparison of the bridge control point displacement when each component exceeds the threshold limit state value is depicted in Figure 11. Threshold values for the system, assuming series connection between the components, are estimated, while the target displacement for the design earthquake is also noted (black line). Therefore the target displacement for the bridge system, calculated for various earthquake intensities, when correlated to the performance level required for the structure (determined by the designer and/or owner) can be directly mapped to the component local performance and guide towards the most efficient retrofit intervention to enhance the seismic performance of the system.

The bridge piers were found to be the most critical component regarding the first two limit states for the majority of cases considered, for both directions (longitudinal and transverse), while the bearings for the two last ones. It is noted that in a few cases, when cohesionless backfill soil was considered, the abutment emerged as more critical than the bearings with regard to the major and collapse limit states. Additionally, when bearings with greater rubber thickness were considered, the piers emerged as the most critical component for all limit states, hence defining the threshold values for the system.

3.5 Derivation of fragility curves (Step 3)

Fragility curves for the T7 bridge (as-built case) are estimated according to the methodology proposed. The 7 accelerograms used for time-history analysis were selected according to Katsanos and Sextos [34] for soil type B and PGA 0.24 and were appropriately scaled according to the EC8-Part 2 provisions [35]. Longitudinal and transverse directions were treated separately (1400 time history analyses – all realizations considered).

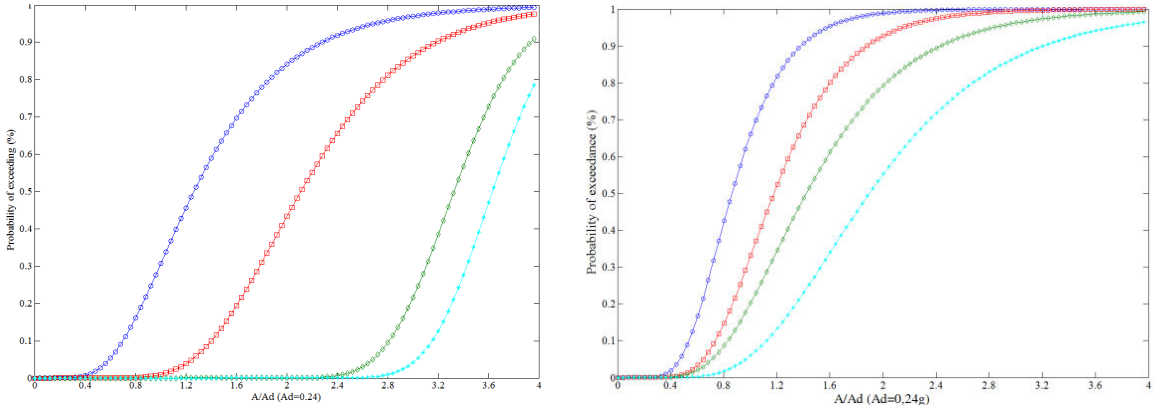


Figure 12: Fragility curves of the as-built bridge: longitudinal (left) and transverse direction.

4 FRAGILITY CURVES OF RETROFITTED BRIDGES AND OPTIMUM SELECTION OF RETROFIT MEASURE

According to the proposed methodology, the most critical member was identified, whose retrofit will efficiently improve the seismic performance of the bridge for the selected performance objective (seismic intensity and associated performance level). However, the most efficient retrofit measures and retrofit strategies for the enhancement of the bridges' seismic performance are not always apparent. In view of this, different retrofit measures and strategies are tested and the optimum strategy solution for the bridge is determined, comparing the as-built and post-retrofit fragility curves.

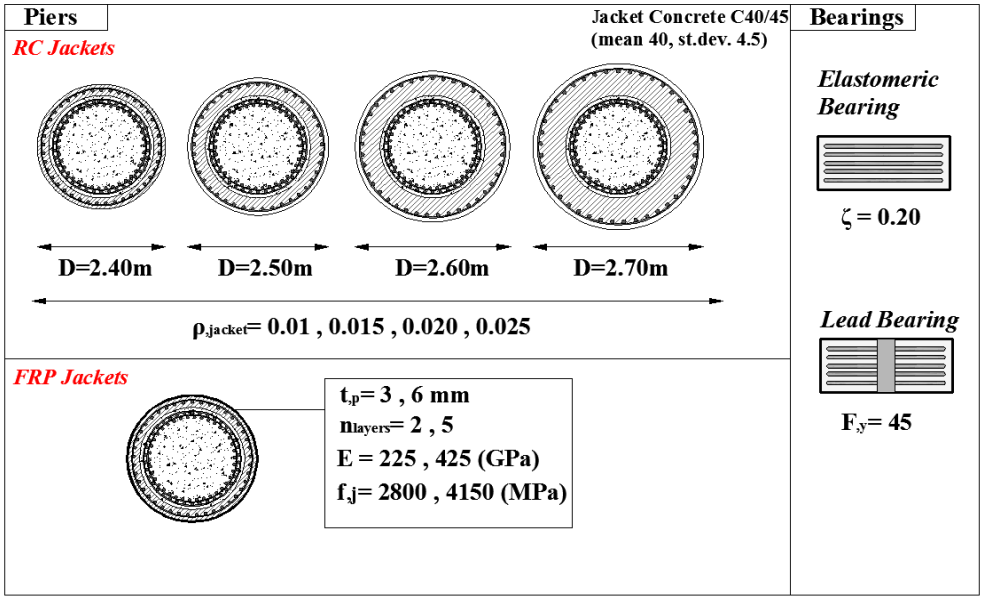


Figure 13: Properties of the retrofit measures considered.

Four different retrofit strategies are examined including R/C and FRP jacketing of the piers and upgrading of the bearings, i.e. use of elastomeric bearings with higher damping, or lead rubber bearings (LRB); different geometric and material properties are considered as depicted in Figure 13.

The proposed methodology is implemented in order to define the retrofitted systems' threshold limit state values and derive the fragility curves. Section analysis for all parameter combinations (16 for the case of R/C jackets and 16 for FRP jackets) are performed in order to derive component threshold values, using appropriate material laws [24, 36].

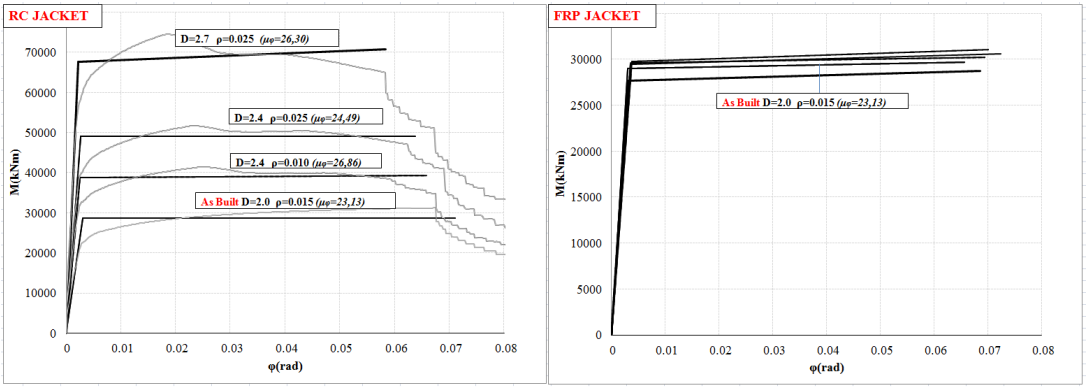


Figure 14: Section analysis of retrofitted structures.

Material uncertainty for the demand and capacity is considered and response-history analyses for the same accelerograms used for fragility analysis of the as-built bridge are performed for all retrofit cases and realizations derived (total number of analyses: 35,000). It is noted that as far as pier retrofit of the as-built bridge is concerned, the same retrofit measure was considered to be implemented to both piers at a time.

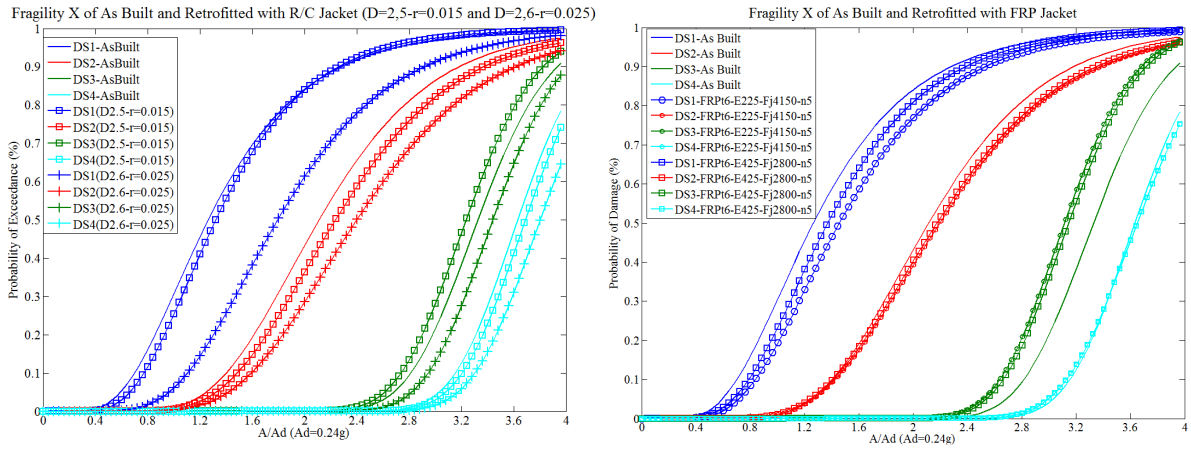


Figure 15: Fragility curves for bridge retrofitted with R/C and FRP jackets compared to as-built case (long.).

Fragility curves for the as-built and retrofitted bridge are compared in Figures 15 and 16 with a view to defining the most effective retrofit measure of the bridge type studied for different performance levels. As shown in Figure 15, retrofitting with R/C jacket obviously enhances the bridge seismic performance as far as the probability of exceedance of the first two limit states (that depend on the pier strength) is concerned, while it has negligible effect on the major and collapse limit state that are mainly controlled by the bearings' performance (recall

the series system assumption). Strengthening of the piers increases the bridge bearing capacity, however it results in higher input seismic forces (increase of stiffness - decrease of the fundamental period) and does not necessarily improve the bridge behaviour. Since the bearings are not replaced or retrofitted, despite the increase in stiffness and strength, the major and collapse limit state are not affected by this retrofit measure. As observed in Figure 15, the effectiveness of this retrofit measure increases for higher reinforcement ratio in the jacket, i.e. as the relative increase in strength exceeds the increase in stiffness, the retrofit measure becomes more effective. Similar conclusions are drawn from the transverse direction assessment (Figure 16-right).

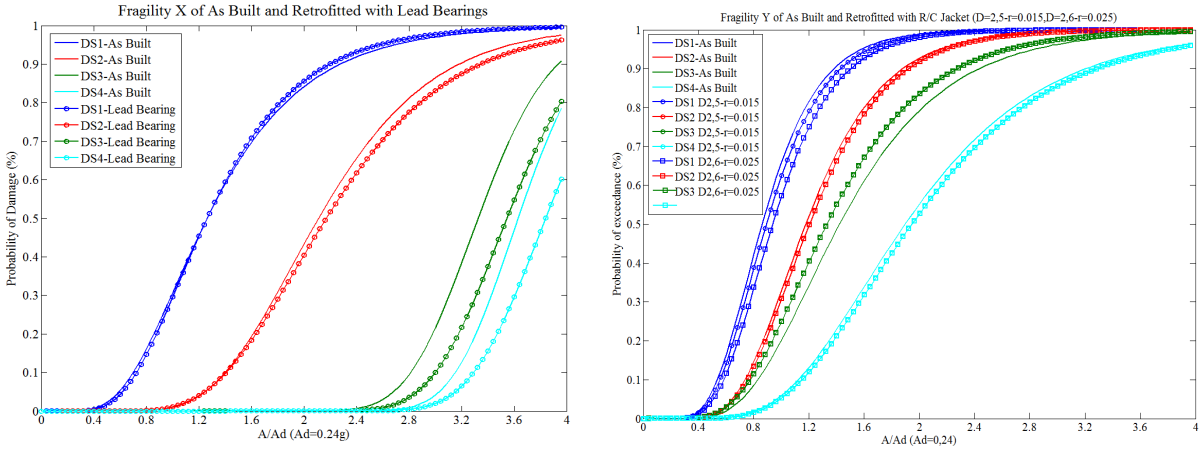


Figure 16: Fragility curves for bridge retrofitted with lead rubber bearings (long) and R/C jackets (trans.) compared to the as-built case.

Retrofitting with FRP jackets also improves the seismic performance for the first two limit states, while it does not affect the performance for the other two. FRP jackets increase pier ductility, nevertheless reaching the last two limit states are controlled by the bearings' performance. Compared to the R/C jacket retrofit, FRPs were found to be less effective for the improvement of the seismic performance for the first two limit states.

Replacement of elastomeric bearings with LRBs with larger rubber thickness was found to be the most effective retrofit measure with respect to major and collapse limit states, while using bearings with higher damping (20%) but the same thickness as the existing bearings was found to have negligible effect on the system's performance.

The aforementioned results refer to the studied bridge type, i.e. bridges with piers monolithically connected to the deck. The different components considered were assumed to be connected in series, a conservative approach that affects the results. It is noted that the studied bridge is a rather recently constructed structure, compliant with existing seismic code provisions; more unfavourable results are expected for non-seismically designed bridges.

5 CONCLUSIONS

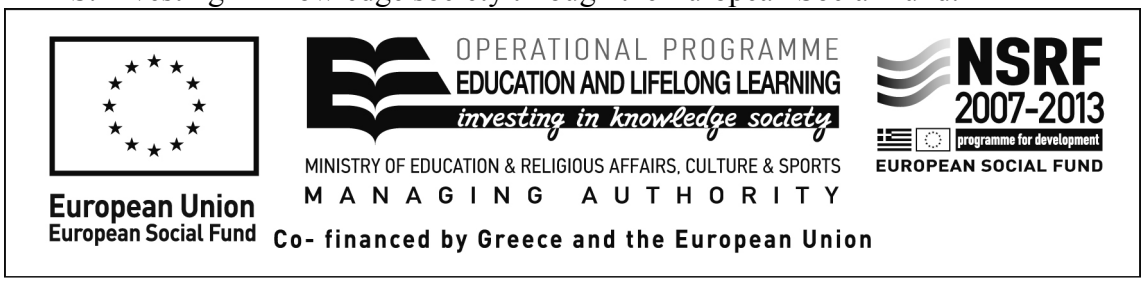
In the present study a new methodology for the derivation of fragility curves is presented and implemented to a common type of bridge. The basic aspects of the methodology are the correlation of component limit state threshold values to global ones referring to the whole bridge system and the identification of the most efficient retrofit measure with regard to the selected performance objective(s). Bridge systems with monolithic pier-to-deck connection were assessed for various levels of seismic action and four different retrofit measures were implemented with a view to identifying the most effective one for every limit state, comparing

as-built and post-retrofit fragility curves. An important finding was that different retrofit solutions are the most effective ones, depending on the selected performance level; increasing pier strength (especially by R/C jacketing) improves damage-related performance, whereas increasing the thickness of bearings improves performance related to failure-collapse.

Although combinations of retrofit measures are often used in practice, this study did not evaluate the effect of combinations of retrofit measures on the overall system fragility. Finally, it is noted that for the final selection of the optimum retrofit measure and strategy, the cost of the interventions should also be taken into consideration.

Acknowledgement

This research has been co-financed by the European Union (European Social Fund – ESF) and Greek national funds through the Operational Program "Education and Lifelong Learning" of the National Strategic Reference Framework (NSRF) –Research Funding Program: THALES. Investing in knowledge society through the European Social Fund.



REFERENCES

[1] Y. Zhang, W.F. Cofer, D.I. McLean, Analytical Evaluation of Retrofit Strategies for Multicolumn Bridges, *Journal of Bridge Engineering,* 4(2), 143-150, 1999.

[2] N. Basöz, A.S. Kiremidjian, Evaluation of Bridge Damage Data from the Loma Prieta and Northridge, CA, Earthquakes. *Technical Report* MCEER-98-004, Buffalo, NY, 1998.

[3] Ö. Avşar, A. Yakut, A. Caner, Analytical Fragility Curves for Ordinary Highway Bridges in Turkey. *Earthquake Spectra*, 27(4), 971-996, 2011.

[4] E. Choi, R. DesRoches, B. Nielson, Seismic fragility of typical bridges in moderate seismic zones. *Engineering Structures*, 26(2), 187-199, 2004.

[5] A.S. Elnashai, Borzi B., Vlachos S., Deformation-based vulnerability functions for R/C bridges. *Structural Engineering and Mechanics,* 17(2), 215-244, 2004.

[6] K. R. Karim, F. Yamazaki, F, A simplified method of constructing fragility curves for highway bridges. *Earthquake Engineering & Structural Dynamics*, 32(10), 1603-1626, 2003.

[7] K.R. Mackie, B. Stojadinović, R-Factor Parameterized Bridge Damage Fragility Curves. *Journal of Bridge Engineering*, 12(4), 2007.

[8] I. F. Moschonas, A. J. Kappos, P. Panetsos, V. Papadopoulos, T. Makarios, P. Thanopoulos. Seismic fragility curves for greek bridges: methodology and case studies. *Bulletin of Earthquake Engineering*, 7(2), 439-468, 2008.

[9] B.G. Nielson, R. DesRoches, Seismic fragility methodology for highway bridges using a component level approach, *Earthquake Engineering and Structural Dynamics,* 36, 823-839, 2007.

[10] J.E. Padgett, R. DesRoches, Methodology for the development of analytical fragility curves for retrofitted bridges. *Earthquake Engineering and Structural Dynamics,* 37, 1157-1174, 2008.

[11] J. Zhang, Y. Huo, Evaluating effectiveness and optimum design of isolation devices for highway bridges using the fragility function method. *Engineering Structures,* 31, 1648-1660, 2009.

[12] N. Ataei, J.E. Padgett, Limit state capacities for global performance assessment of bridges exposed to hurricane surge and wave. *Structural Safety,* 41, 73-81, 2013.

[13] K.J. Fridley, Z. Ma, Reliability-based design of seismic retrofit for bridges. *The Washington State Department of Transportation,* Report No. WA-RD 664.1, 2007.

[14] K. Kawashima, Seismic Design and Retrofit of Bridges. *12 World Conference on Earthquake Engineering*, Auckland, New Zealand, Jan. 30-Feb .4, 2000.

[15] B. Binici, Design of FRPs in circular bridge column retrofits for ductility enhancement. *Engineering Structures*, 30(3), 766-776, 2008.

[16] M.F.M. Fahmy, Z. Wu, G. Wu, Post-earthquake recoverability of existing R/C bridge piers retrofitted with FRP composites. *Construction and Building Materials*, 24(6), 980-998, 2009.

[17] R.S. Jangid, Seismic Response of Isolated Bridges. *Journal of Bridge Engineering*, 9(2), 156-166,2004.

[18] J.E. Padgett, Seismic Vulnerability Assessment of Retrofitted Bridges Using Probabilistic Methods, *Ph.D. Thesis,* Georgia Institute of Technology, 2007.

[19] S.-H. Kim, M. Shinozuka, Development of fragility curves of bridges retrofitted by column jacketing. *Probabilistic Engineering Mechanics*, 19(1-2), 105-112, 2004.

[20] V. Bisadi, M. Head, P. Gardoni, Seismic Fragility Estimates and Optimization of Retrofitting Strategies for Reinforced Concrete Bridges: Case Study of the Fabela Bridge in Toluca, Mexico. ASCE *Structures Congress 2011*, 13-22.

[21] B.G. Nielson, Analytical Fragility Curves for Highway Bridges in Moderate Seismic Zones, *Ph.D. Thesis,* Georgia Institute of Technology, 2005.

[22] G. Mylonakis, S. Nikolaou, G. Gazetas, Footings under seismic loading : Analysis and design issues with emphasis on bridge foundations. *Soil Dynamics and Earthquake Engineering*, 26(9), 824-853, 2006.

[23] V.K. Papanikolaou, Analysis of arbitrary composite sections in biaxial bending and axial load. *Computers and Structures*, 98-99, 33-54, 2012.

[24] J.B. Mander, M.J.N. Priestley, R. Park, Theoretical Stress-Strain Model for Confined Concrete. *Journal of Structural Engineering*, 114(8), 1804-1826,1988.

[25] M.J.N. Priestley, G.M. Calvi, M.J. Kowalsky, Displacement-Based Seismic Design of Structures. *IUSS Press, Pavia, Italy*, 2007.

[26] M.N. Sheikh, F. Legeron, Seismic performance-based design of bridges with quantitative local performance criteria, *2nd International Structures Specialty Conference,* June 9-12, Winnipeg, Manitoba, 2010.

[27] F. Naeim, J.M. Kelly, *Design of Seismic Isolated Structures: From Theory to Practice.* John Wiley & Sons, Inc., 1999.

[28] A. Mori, P.J. Moss, N. Cooke, A.J. Carr, The Behavior of Bearings Used for Seismic Isolation under Shear and Axial Load. *Earthquake Spectra,* 15(2), 199-224, 1999.

[29] R.L. Iman, W.J. Conover, A distribution-free approach to inducing rank correlation among input variables. *Communication in Statistics – Simulation and Computation*, 11(3), 311-334, 1982.

[30] C. Dymiotis, A.J. Kappos, M.K. Chryssanthopoulos, Seismic Reliability of R/C Frames with Uncertain Drift and Member Capacity. *Journal of Structural Engineering*, 125(9), 1038-1047 ,1999.

[31] K. Porter, R. Kennedy, R. Bachman, Creating Fragility Functions for Performance-Based Earthquake Engineering. *Earthquake Spectra*, 23(2), 471-489, 2007.

[32] F. McKenna, G.L. Fenves, Open System for Earthquake Engineering Simulation Pacific Earthquake Engineering Research Center, Version 2.4.0., *Pacific Earthquake Research Center,* 2005.

[33] Caltrans, *Caltrans Seismic Design Criteria (2nd end),* California Department of Transportation: Sacramento, CA, 1999.

[34] E.I. Katsanos, A.G. Sextos, ISSARS: An intergrated software environment for structure-specific earthquake ground motion selection. *Advances in Engineering Software*, 58, 70-85, 2013.

[35] CEN (Comité Européen de Normalisation) Eurocode 8 : Design provisions of structures for earthquake resistance - Part 2: Bridges (EN1998-2), CEN Brussels, 2005.

[36] M.R. Spoelstra, G. Monti, FRP-Confined Concrete Model, *Journal of Composites for Construction,* 3, 143-150, 1999.

COMPDYN 2013
4th ECCOMAS Thematic Conference on
Computational Methods in Structural Dynamics and Earthquake Engineering
M. Papadrakakis, V. Papadopoulos, V. Plevris (eds.)
Kos Island, Greece, 12–14 June 2013

ASSESSMENT OF EC8 PROCEDURES FOR THE ASYNCHRONOUS EXCITATION OF BRIDGES BASED ON NUMERICAL ANALYSES AND RECORDED DATA

Savvas Papadopoulos[1], Vassilios Lekidis[2], Anastasios Sextos[1] and Christos Karakostas[2]

[1] Department of Civil Engineering
Aristotle University of Thessaloniki, Greece
e-mail: savvaspp@civil.auth.gr, asextos@civil.auth.gr

[2] Earthquake Planning and Protection Organization (EPPO- ITSAK)
Thessaloniki, Greece
e-mail: lekidis@itsak.gr, christos@itsak.gr

Keywords: spatial variability of earthquake ground motion, bridges, seismic response, incoherency patterns, system identification, Evripos bridge

Abstract. *The significance of the spatial variability of earthquake ground motion SVEGM is recognized by all modern seismic codes (EC8, AASHTO, ATC, JRA) but it is only EC8 that provides a clear, though simplified, methodology to account for asynchronous motion for design purposes. Currently, two amendments of the EC8 methodology have been proposed by Sextos & Kappos (2009) and Nuti & Vanzi (2009) both aiming to improve the applicability and robustness of the EC8 simplified procedure. In the present study, the above EC8 framework is comparatively assessed in the light of actual, low-amplitude measurements obtained along the Evripos cable stayed bridge. A permanent accelerometer special array of 43 sensors was installed on the bridge in 1994 by the Institute of Engineering Seismology and Earthquake Engineering. Since then, the bridge's behavior to seismic excitations has been continuously monitored. A reliable numerical model was first developed and was updated to match the monitored response given the available free-field recordings. Subsequently, various (synchronous and asynchronous) seismic scenarios were developed to identify the impact of ground motion spatial variation on the action effects of the bridge using the 7/9/1999, Athens earthquake (Ms=5.9) records. The results indicate that spatial variability of earthquake ground motion has generally a favorable effect on the Evripos bridge response, primarily due to the significant flexibility of its deck. It is also concluded that the Eurocode 8 simplified method, being essentially a pseudo-static loading is inable to capture the salient features of dynamic response under multiple-support excitation.*

1 INTRODUCTION

Asynchronous motion, typically referred to as Spatial Variability of Earthquake Ground Motion (SVEGM), denotes the differences in amplitude, phase and frequency content among ground motions recorded over extended areas [1–3]. It is true that the critical question is not whether seismic motion is indeed different along an extended structure; this is almost self-evident [4], physically justified [5] and the sources of spatial and temporal variations of seismic motion have been well identified [6] as: (a) waves that travel at a finite velocity, so that their arrival at each support point is out of phase (b) wave coherency loss in terms of gradual reduction of their statistical dependence with distance and frequency, due to multiple reflections, refractions and superpositioning during propagation and (c) local site effects. As a result of all the above sources, both peak ground acceleration and frequency content of the motion may be significantly different among the various foundation points. Moreover, although often neglected, the potential filtering at the foundation level that results from the relative flexibility of the foundation-soil system components, is an additional source of seismic motion variability [7]. In addition to the above theoretical justification, Spatial Variability of Earthquake Ground Motion (SVEGM) has also been recorded in various densely instrumented arrays all over the world (SMART-1 and LSST-Lotung in Taiwan, Chiba in Tokyo, USGS-Parkfield and Imperial Valley in California, as well as Euroseis-Test in Greece among others), hence the fact that a long structure is expected to be excited with asynchronous and partially uncorrelated seismic forces is evident and well documented.

Although many methods have been proposed during the last 40 years in order to consider the consequences of SVEGM on bridges, asynchronous motion is an aspect not accounted for in the vast majority of the design cases irrespectively of piers' distance and bridge length [8]. This tendency may be attributed to the simplicity of synchronous excitation analysis and to the false perception that SVEGM has a generally favorable effect on bridge dynamic response [4]. However, the potential effects of SVEGM on bridge response cannot be deterministically approached especially in cases where local soil conditions exhibit significant variation with length [4]. Indeed, the uncertainty related to the definition of the appropriate seismic motion at each support and the conditions under which asynchronous motion could be detrimental for a structure is fundamental. Numerous studies have been performed investigating the effects of changes in various parameters regulating the ground motion field as well as the impact of field characteristics on different bridge configuration [7], [9–11]. The results of these studies, though, do not indicate a clear trend regarding the beneficial or detrimental effect of asynchronous excitation on bridge response. It is also recognized that even in cases where the SVEGM effect could be important, the definition of some reasonable input motions and relative motions to resemble the expected ones at bridge supports is by far the most difficult process. Nevertheless, in each case, bridge supports' soil conditions provide an indication about the structure's sensitivity to the phenomenon or not; SVEGM's importance arises when local soil conditions vary significantly with length increasing in this way the probability of failure for even relatively short bridges.

The main question therefore, is how the designer may produce 'reasonable' spatially varying suites of ground motion, what the response of a structure would be under such an asynchronous excitation, whether the final response is detrimental compared to the prediction made assuming a structure uniformly excited in the time domain, and especially whether it can be indeed predictable in advance during the design process. The answer to this question is difficult not only due to the complexity in predicting incoherency patterns but also, due to the significant coupling between earthquake input, dynamic characteristics of the soil-structure system (particularly in terms of foundation compliance and energy dissipation) at the soil-

foundation interface. To deal with this problem, modern seismic codes (such as the US Standard Specifications for Highways and Transportation Bridges, ATC-32, Japanese Design Specifications for Highway Bridges) prescribe increased seating lengths for the deck.

A more practically-oriented approach is prescribed in EC8, currently the only seismic code worldwide providing a clear and detailed framework for considering the effect of SVEGM in bridge design, through a simplified and an analytical methodology, the latter in the form of an informative annex. An improvement to EC8 simplified methodology has also been proposed by Sextos & Kappos [12] and Nuti & Vanzi [2], [13].

However, with the exception of the latter studies [2], [13], neither the EC8 simplified method nor the numerically-derived suggested improvements have been compared or calibrated to free-field or on-structure recordings. In this context, a comparative assessment between analytical solutions, numerical predictions and actual recordings has been undertaken for the case of Evripos cable-stayed bridge in Greece, a cable-stayed structure that has been permanently monitored by an accelerometer network since 1994. A valuable set of motions is provided, recorded both in bridge vicinity and on specific locations on the structure and its foundation. Based on these data, an effort is made to:

(a) develop a reliable finite element model after appropriate system identification and model updating procedures and
(b) assess the bridge sensitivity to SVEGM effects using the free field (asynchronopus) ground motion excitations in the light of the aforementioned EC8 suggested amendments.

A brief description of the bridge structure, its monitoring system and the recorded response under various asynchronous ground motion cases is provided in the following.

2 SIMPLIFIED METHODOLOGIES EXAMINED

2.1 EC8-part2 provisions

EC8-Part 2 recognizes the importance of multi-support excitation in case that (a) soil properties along the bridge vary in such a way that the soil at the various supports may be considered to belong to more than one category (as specified in Eurocode 8-Part 1), or (b) soil properties along the bridge are approximately uniform, but the length of the continuous deck exceeds a pre-specified limit, L_{lim}. The recommended value of L_{lim} equals L_g/1.5, where L_g is given in Table1 as a function of ground conditions and corresponds to the distance beyond which, motions may be regarded as completely uncorrelated.

For the general case, the potential maximum values of the considered seismic action effect (i.e. member force or deformation) can be estimated through an adequate (albeit simplified) procedure. This method should be followed, unless a more accurate analysis is carried out. To this end, the more detailed procedure for the assessment of the asynchronous motion effects in the frequency domain [6] is proposed in an informative annex to the Code, while guidance on the generation of artificial spatially variable ground motions is also provided. The idea (put forward by the EC8-2 drafting panel) to compute in a simplified way the necessary stress or displacement increase due to SVEGM effects is simple, practical, and physically-motivated: Since motion is different between support points, the various bridge supports are subjected to different values of (location-dependent) earthquake accelerations, which are partially correlated; as a result, pseudo-static internal forces develop [14], [15]. From the numerous possible combinations of relative support vibration, two cases are identified as the most critical: a) all piers are subjected to ground displacements of the same sign (but varying magnitude) and b) the two piers in each pair of two successive piers are displaced in opposite directions. More details about this methodology are presented in **Figure 1**.

Ground Type	A	B	C	D	E
L_g (m)	600	500	400	300	500
L_{lim} (m)	400	333	266	200	333

Table 1: Limiting length to consider spatial variability effects, as a function of ground type

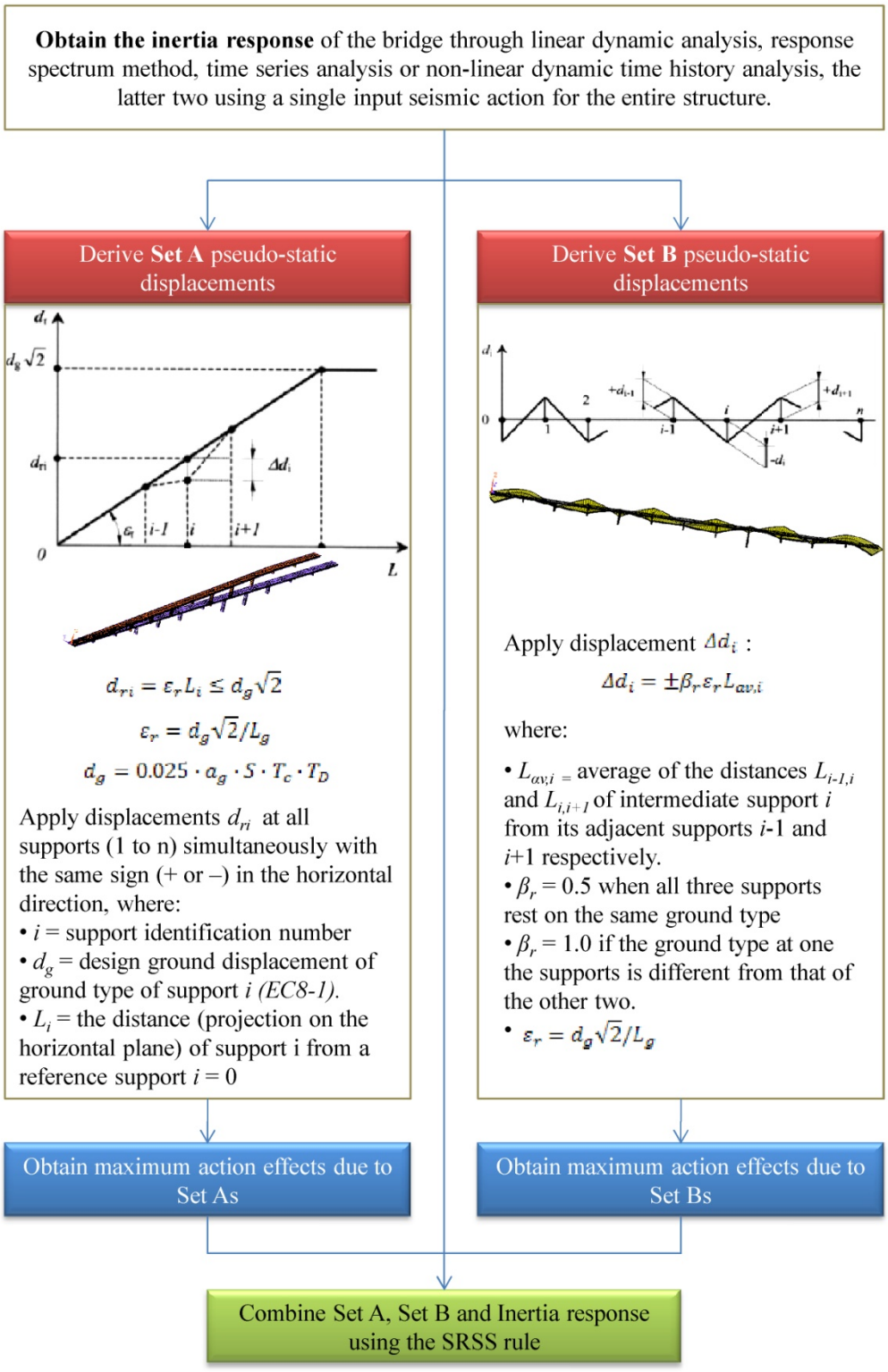


Figure 1: The simplified methodology proposed by EC8 to account for SVEGM effects [12].

2.2 EC8-Part 2 suggested amendments

Numerous parametric analyses have been performed assessing the effect of asynchronous input motion on different bridge types and configurations based on the simplified EC8 method. It is concluded [12] that provisions adopted by EC8-2 are clearly a step forward not only compared to the previous version of the code, but also with respect to modern seismic codes worldwide. The limits for considering asynchronous excitation (i.e., 400m to 200m for ground categories A to D according to EC8 classification) are in line with other research findings [16] while SVEGM effects should be considered even for shorter bridges in cases wherein ground conditions vary significantly among supports, a fact that is verified in the literature as well [17–19]. On the other hand, the simplified approach proposed by Eurocode 8 systematically leads to negligible seismic demand increase even in cases where the effect of multiple-support excitation is apparent. Furthermore, it has been shown that the pseudo-static nature of the EC8 simplified method is inevitably unable to capture dynamic effects triggered by multiple-support earthquake input, such as excitation of higher modes of vibration. In case that the application of the simplified method is the only available option, an amendment has been proposed [12] that results in higher values of Set A and Set B imposed displacements as a means to implicitly compensate for the increased structural demand. In particular, displacements are calculated from the following modified EC8 expressions:

$$d_{ri} = e_r L_i < 8 d_g \tag{1}$$

where

$$e_r = 8 d_g / L_g \tag{2}$$

Application of both the original and the amended Set A and Set B imposed support displacement profile for the case of Evripos bridge is illustrated in Figure 2 for a PGA equal to 0.24g and different soil classes.

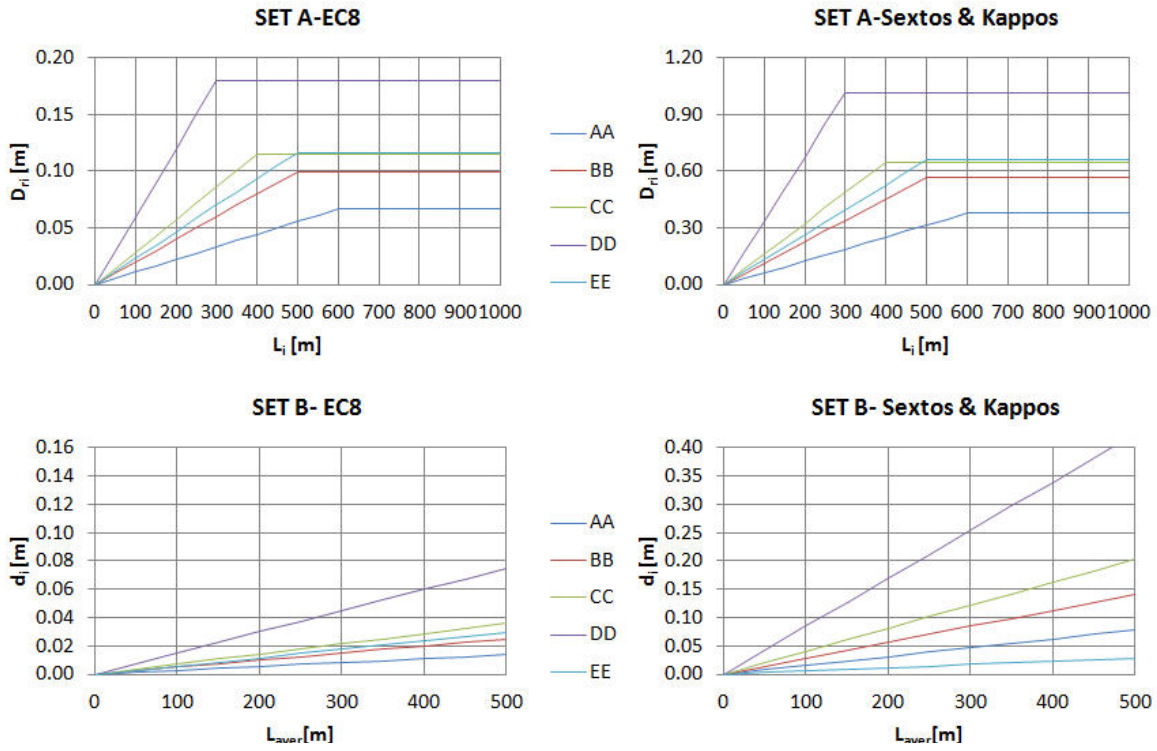


Figure 2: Comparison between the pseudo-static displacements imposed at the supports of the structure according to the EC8 provisions (left) and the suggested approach of Sextos and Kappos [12].

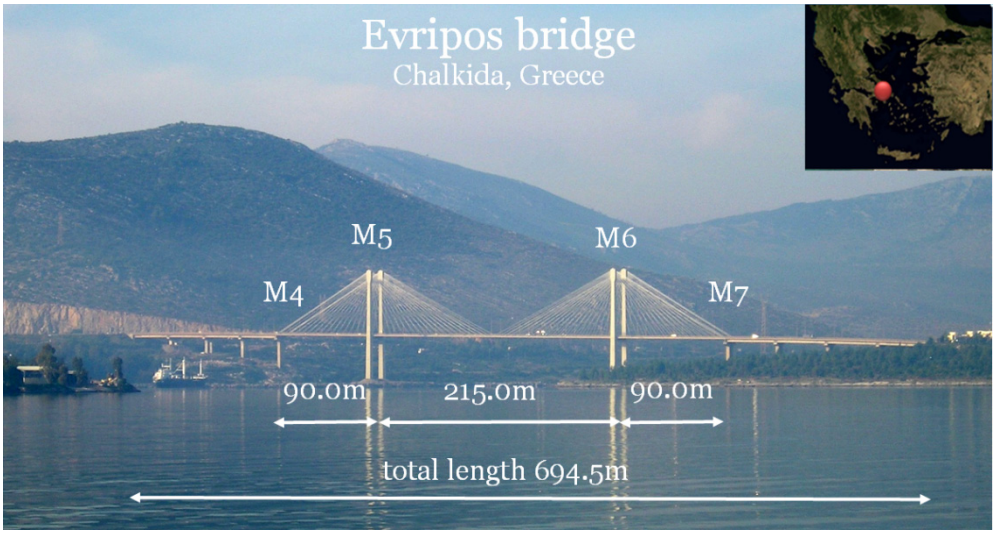


Figure 3: The Evripos cable stayed bridge in the central Greece.

2.3 Italian Seismic code

The same critical rationale lies behind the work of Nuti and Vanzi [20], [21], later reported in the new Italian Seismic Code [22], aiming at improving the simplified EC8 method by inducing a modified set of differential displacements d_{ij} between successive support points after appropriate consideration of soil conditions:

$$d_{ij}(x) = 1.25\left|d_{gi} - d_{gj}\right| + 1.25\left(\sqrt{d_{gi}^2 + d_{gj}^2} - \left|d_{gi} - d_{gj}\right|\right)\left[1 - e^{-1.25(x/v_s)^{0.7}}\right] \quad (3)$$

where v_s is the velocity of shear waves, d_{gi} and d_{gj} are the maximum design ground displacements at the supports i and j, respectively, x is the distance between these two successive piers. It is also noted that the relative displacement between the adjacent pairs (i-1, i) and (i, i+1) is taken equal to $d_{ij}/2$, while d_{ij} is assumed zero at all other support pairs.

3 THE EVRIPOS CABLE-STAYED BRIDGE

3.1 Description of the bridge

The Evripos bridge is a reinforced concrete roadway bridge that crosses Evripos channel, connecting the Euboean coast on the island of Evia to the Boeotean coast in continental central Greece (Figure 3). It has an overall length of 694.5m and it is formed by three parts; a central cable-stayed section 395 m long and two side parts made of pre-stressed beams that rest on elastomeric bearings. The central cable-stayed section is formed by a central span of 215 m and two side spans of 90 m length each, while both side parts of the bridge have four spans of 39 m (Euboean coast) and 35.875 m (Boeotean coast) length respectively. The deck in the central part of the bridge, about 13.00 m wide and only 0.45 m thick, is 40 m above sea level, suspended from 72 pairs of cables arranged in a semi-fan pattern, is monolithically connected to the two H shaped concrete towers (piers M5 and M6) of a total height of 90 m. A special mechanism at the deck's edges (piers M4 and M7) allows displacements along the longitudinal direction while those in the transverse direction are blocked [23–25]. At the present study, only the cable-stayed section is examined.

As already mentioned, the Evripos cable-stayed bridge has been constantly monitored since 1994 by EPPO-ITSAK. Since then, a series of small earthquakes at a distance range of 20-70 km have been recorded. Sensor positions are carefully selected, for the dynamic behav-

ior of the bridge to be fully described. In particular, there are four triaxial sensors, two located at the pilegroup cap and two free-field. Furthermore, twenty-four sensors (six vertical and two transverse in the central span, four longitudinal, two of them at the level of the deck and the others at the pylons' top, two transverse at both pylons and two vertical at each side-span) are permanently monitoring the response of the superstructure. The solid-state accelerometers are interconnected to provide common triggering, common timing and common sampling, the latter at a rate of 200 sps.

In a hypothetical scenario, if the bridge were to be designed today, EC8 provisions would dictate consideration of spatial variability aspects of earthquake ground motion. As a result, this bridge seems to provide an excellent opportunity for the simplified methodologies mentioned above to be compared with real data recorded on-site.

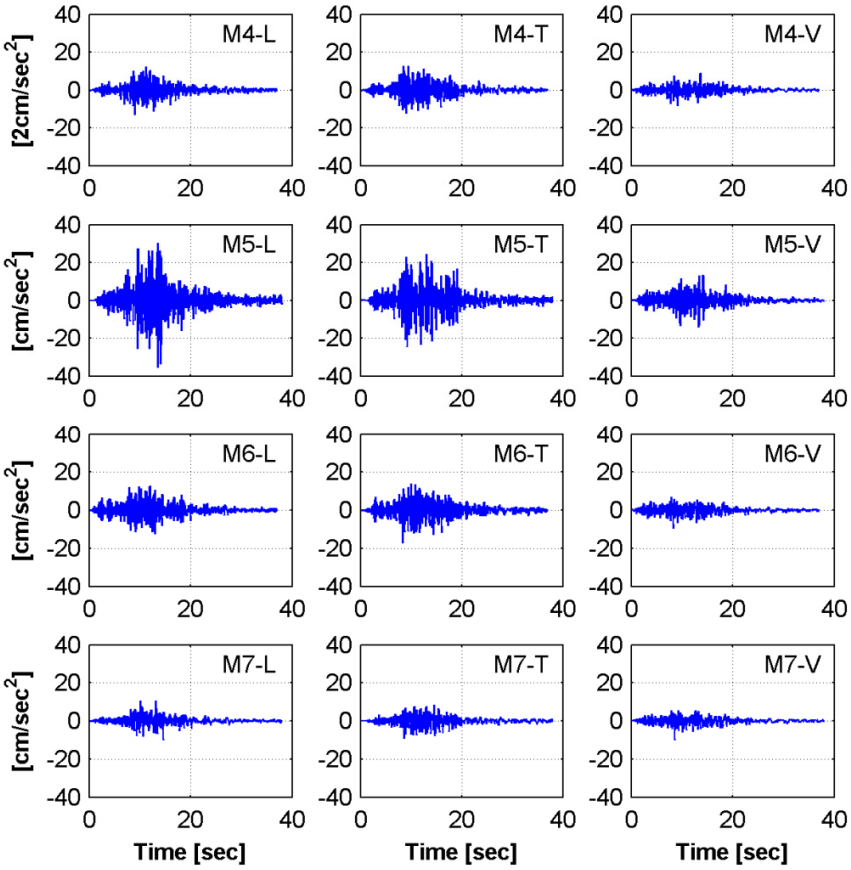


Figure 4: Time histories recorded at the base of piers M4-M7 during the Athens earthquake (7/9/1999, M_s=5.9)

3.2 Free-field measurements

Due to the significant overall length (395m) of the central section of the bridge, an effort is made to process specific groups of records available on-site in order to investigate the impact of SVEGM. For this purpose, a set of four ground motions was used, as recorded during the Athens earthquake, that occurred on 7/9/1999 at a source-to-site distance of approximately 43km with a surface Magnitude M_s=5.9. The recorded time histories are presented in Figure 4 where the longitudinal and transverse component is illustrated in different rows for each location (i.e., M4, M5, M6, M7 as defined in Figure 3).

Having ensured that the common time and common trigger condition was fulfilled, the records were first filtered in the frequency range of 0.65-25Hz in order to remove the influence of the vibration of the superstructure which was transmitting waves back to the soil due to inertial soil-structure interaction. Then, the coherency between all pairs of records was computed using a GUI-based, Matlab script written for this purpose. For each individual record, the power spectrum was computed after appropriate smoothing using an 11-point Hamming window [26] for 5% structural damping.

The diagrams of lagged coherency were computed separately for each component of all pairs of records and the spatially variable nature of ground motion was confirmed. As expected, at low frequencies and short separation distances the lagged coherency tends to unity, while it decreases with an increasing separation distance and frequency. Some of these diagrams are illustrated in Figure 5 and are compared with some of the most popular models for coherency loss prediction [27–32].

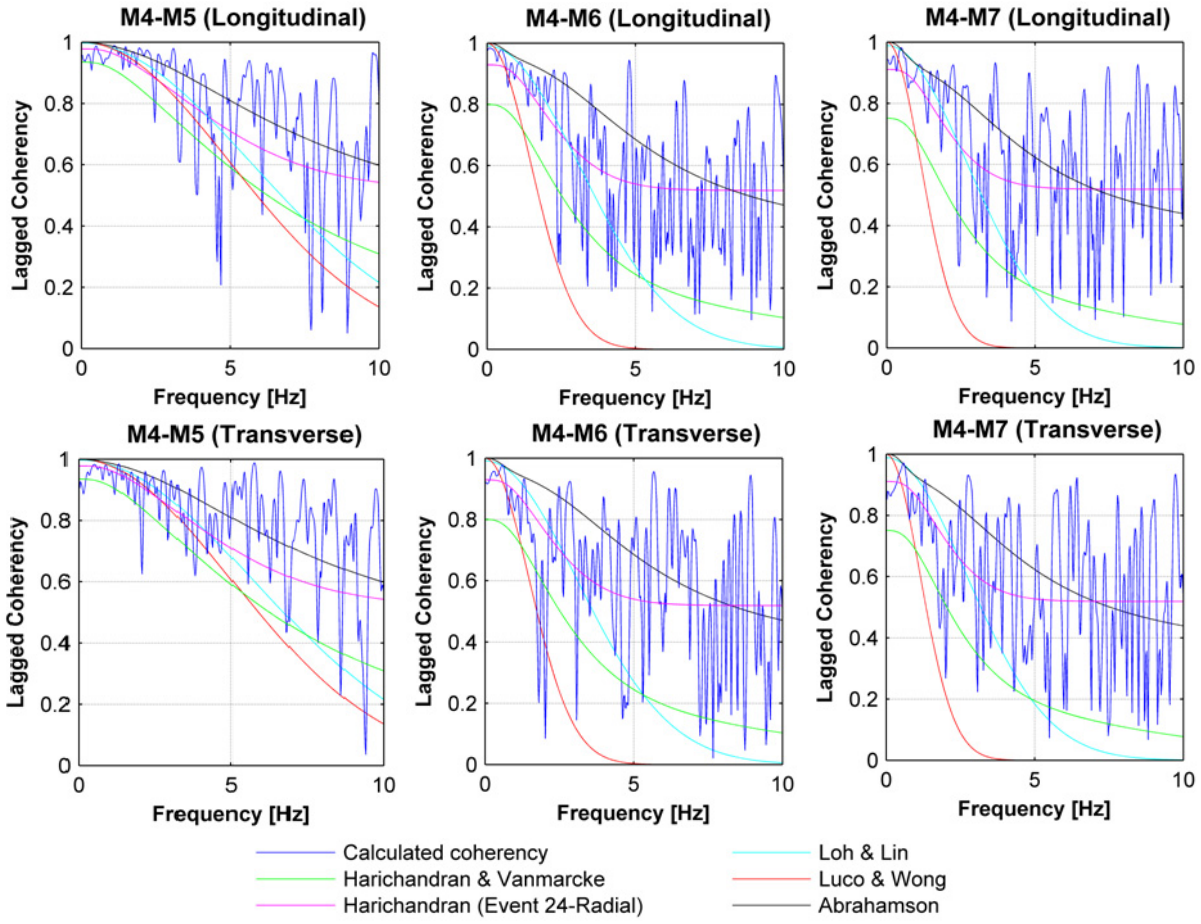


Figure 4: Computed lagged coherencies for the pairs of motions recorded during the Athens earthquake (7/9/1999,M_s=5.9)

4 FINITE ELEMENT MODEL UPDATING

The availability of bridge excitation data and the respective response records generally enables the development of reliable numerical models through the optimization of specific parameters whose response is in good agreement with the monitored ones. However, optimization methods cannot guarantee a univocal solution as the parameters' combinations for which the optimization process could actually result in a model with satisfactory response

are numerous. Moreover, the parameters considered ought to be continuous functions for their values to be optimized. In the present study, parameters such as the supports' stiffness, especially at the two edges, cannot be considered as continuous functions as they heavily depend on other parameters like earthquake intensity, different soil layers' properties etc. Keeping in mind the scope of the present study, namely the investigation of the dynamic response of an existing bridge under asynchronous excitation and the comparison of the actual response to the ones stemming from simplified methodologies, it is obvious that the use of an optimization method does not serve its objectives. The provided data, therefore, proved to be a good opportunity to try to build up a more reliable model through an iterative process aiming to minimize, to an acceptable level, the differences between the recorded and the computed Fourier spectra of the accelerations at specific points on the structure.

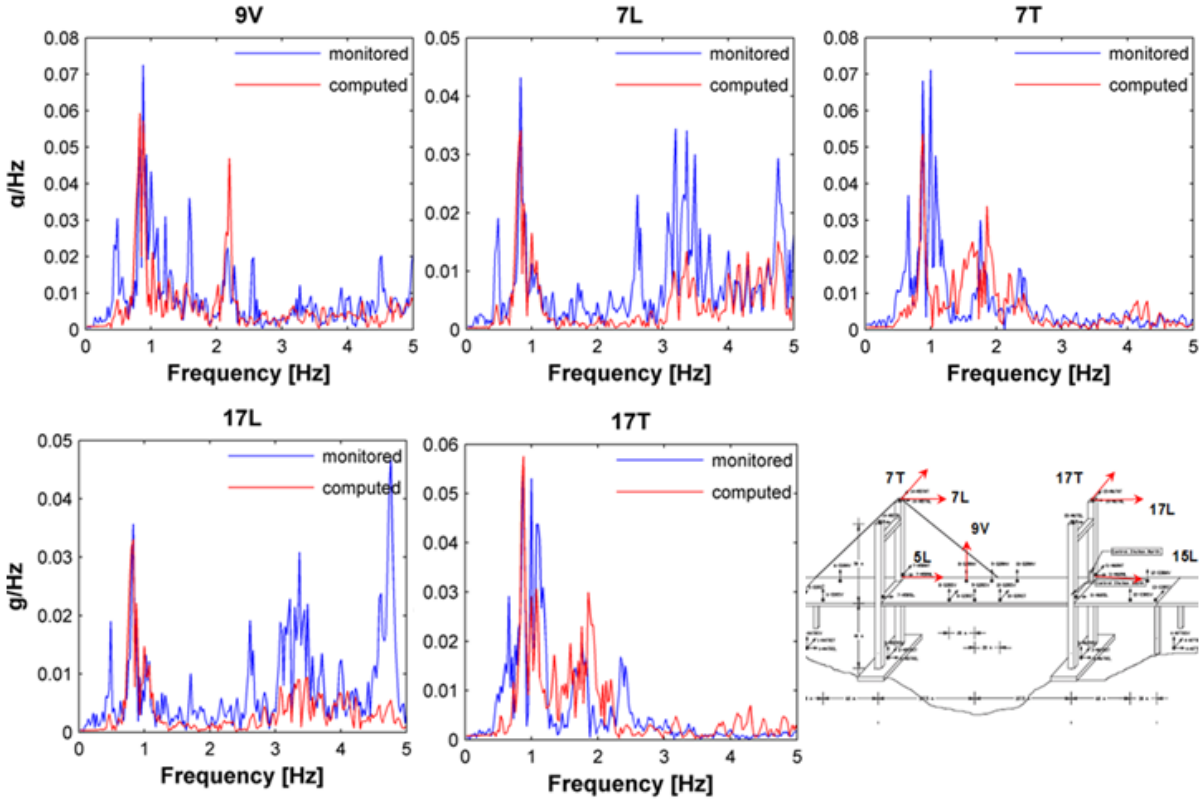


Figure 5: Comparison between the Fourier spectra of monitored and computed accelerograms at specific points of the superstructure.

The deck and the piers were modeled through shell and beam elements respectively, while the geometrical non-linearity induced by the bridge cables was taken into account assuming tension-only capabilities. Soil stiffness at the two edges and at the two pylons' foundation level, as well as the load combination factor ψ_{21} for traffic loads (according to EC8) were the parameters selected for optimization. The comparison was based on the sum of squared error between all the computed and monitored Fourier spectra at the location of the sensors within a frequency range of 0-5 Hz leading to a reasonably reliable finite element model that acceptably matches the observed response. Figure 6 illustrates the graphic comparison between the acceleration Fourier spectra of the recorded and the predicted transverse response at the top of pylons M5 and M6, as well as the vertical response of the deck (20m left from the middle of the central span). Matching was also optimized at 25 different superstructure locations.

5 COMPARATIVE ASSESSMENT OF PREDICTIVE MODELS AND RECORDED STRUCTURAL RESPONSE

The effect of SVEGM on structural response is investigated on the basis of the ratio ρ of the developed bending moment at the base of the main pylons M5 and M6 (Table 2) for the asynchronous case over the synchronous one, for all predictive models studied (i.e., EC8, EC8 modification and new Italian Code). Absolute values of seismic bending moments are also summarized in Table 3. A note that has to be made is that, for the case of the Athens earthquake records, the asynchronous over synchronous ratio ρ cannot be defined unless the "synchronous" idealization is decided first. To this end, the reference case of "synchronous" excitation is defined by uniformly applying each one of the four free-field recordings obtained at the base of pylons M4-M6 after appropriate scaling to match the same average spectral acceleration at the frequency of the first natural mode [33]. Naturally, this assumption led to four different asynchronous over synchronous ratios depicted as ρ synch M4-M7 in Table 2 below.

	Pier M5		Pier M6	
	M3	M2	M3	M2
ρ EC8	1.000	1.001	1.000	1.001
ρ EC8-Sextos& Kappos	1.008	1.024	1.008	1.024
ρ Nuti & Vanzi	1.003	1.039	1.000	1.015
ρ synch. M4	1.030	1.114	1.078	0.988
ρ synch. M5	0.755	0.685	0.767	0.608
ρ synch. M6	0.739	0.909	0.760	0.806
ρ synch. M7	0.700	0.820	0.703	0.729

Table 2: Ratios of seismic bending moments' ratios (asynchronous over synchronous response) resulting from the application of various predictive models.

		Pier M5		Pier M6	
		M3 [kNm]	M2 [kNm]	M3 [kNm]	M2 [kNm]
	Response Spectrum	71296.8	123375.9	71296.8	123375.9
	Set A	-1539.2	-1998.3	-1536.9	1992.5
EC8	Set B	391.6	4508.3	391.6	-4508.3
	Combination	71314.5	123474.4	71314.4	123474.3
EC8	Set A	-8704.3	-11310.1	-8704.3	11310.1
Sextos &	Set B	2216.3	25499.6	2216.3	-25499.6
Kappos	Combination	71860.4	126490.2	71860.3	126490.2
	1-2	3081.3	13979.6	-765.7	-4670.4
Nuti &	2-3	-4213.3	-31649.3	305.7	20604.9
Vanzi	3-4	-197.1	11578.1	2367.5	-17783.9
	Combination	71487.6	128135.5	71301.8	125171.8

Table 3: Absolute values of seismic bending moments at the base of pylons M5 and M6 resulting from the application of various predictive models.

From Table 2 it is seen that the effect of spatial variability for the case of Evripos bridge and the Athens earthquake records, is in general beneficial (ρ varying between 0.60-0.90). It is only when record M4 is used as the uniform excitation where the effect of SVEGM exceeds unity and leads to an increase of 11%. On the other hand, it is clear that all simplified predic-

tive models share the same two distinct features: (a) they result to only minor increase of pylon base moments (i.e., avoiding excessive and unrealistic predictions), which in general is in agreement with the observed SVEGM effect and (b) lead to values of ρ that are, by definition, higher than unity as they are derived by the application of the SRSS rule. The latter essentially suppresses the fact that asynchronous excitation can be beneficial in case of specific structural configurations as the one studied herein.

This is a key issue for understanding the mechanism of multiple-support excitation and the subsequent relative contribution of the pseudo-static and dynamic component of motion. In fact, it is seen that the extremely thin deck of this cable-stayed bridge coupled with the significant length of the central span between the two pylons allows the structure to conform to the pseudo-static imposed displacements without any substantial distress (i.e., increase in the bending moments at the base of the pylons). This is indeed anticipated, as it has long been shown that the pseudo-static effects under asynchronous motion are more critical in the case of stiff structures [15], [17], [34]. To further illustrate this phenomenon, a simplified configuration, in terms of number of spans, of the Evripos bridge has been examined (Figure 7) under multiple-support excitation after appropriate variation of deck stiffness.

Figure 8 depicts the variation of pseudo-static component contribution (expressed as the ratio between the pseudo-static and the dynamic components of structural response) as a function of the deck stiffness for the case of the simplified bridge. It is clear that pseudo-static response (and subsequently, the potential impact of all the simplified EC8 and Italian Code predictive methodologies) is only minor (i.e., less than 10% for flexible deck structures) but it can greatly increase with increasing deck stiffness. Most importantly, the same trend is observed for the actual case of Evripos bridge when subject to non-uniform excitation for various levels of deck stiffness, illustrated in Figure 9. Again, should the deck had been stiffer, the contribution of the pseudo-static component of structural response would have been significantly higher.

Clearly, the above observation refers to the anticipated impact and outcome of the (essentially static) simplified methods proposed in seismic codes and does not imply that the actual overall response of the bridge would be always beneficial or detrimental for any bridge under every earthquake scenario. Indeed, most flexible structures are more tolerant to multiple-support earthquake input but the potential excitation of higher modes and the increase of specific critical engineering demand parameters should by no means be underestimated.

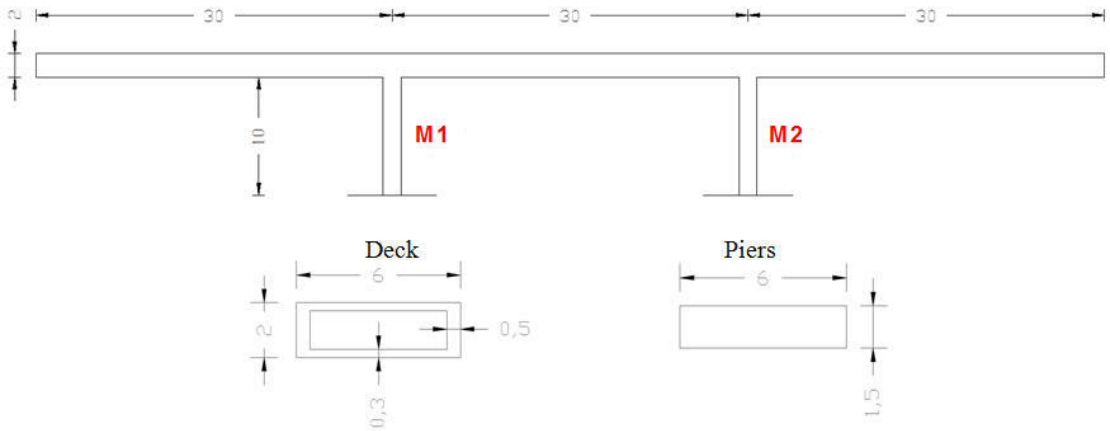


Figure 7:Simplified version of the Evripos bridge configuration for the investigation of the relative pseudo-static and dynamic component contribution to the overall response under asynchronous excitation.

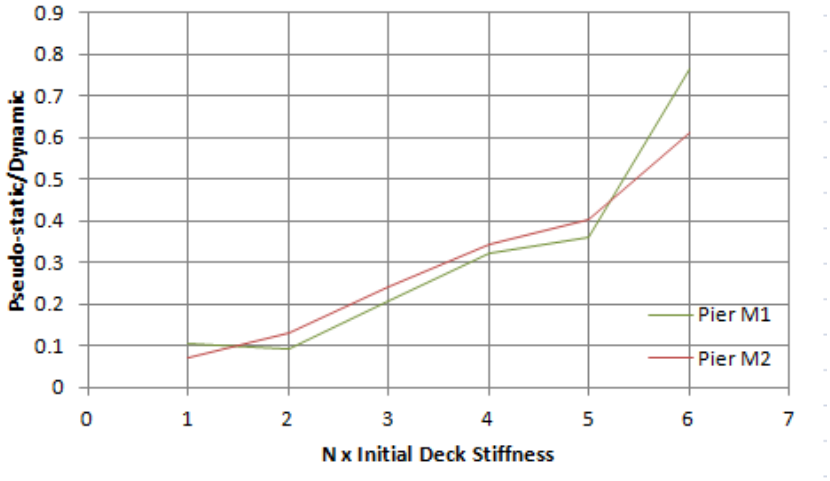


Figure 8: Variation of pseudo-static component contribution as a function of the deck stiffness (for the case of the simplified bridge).

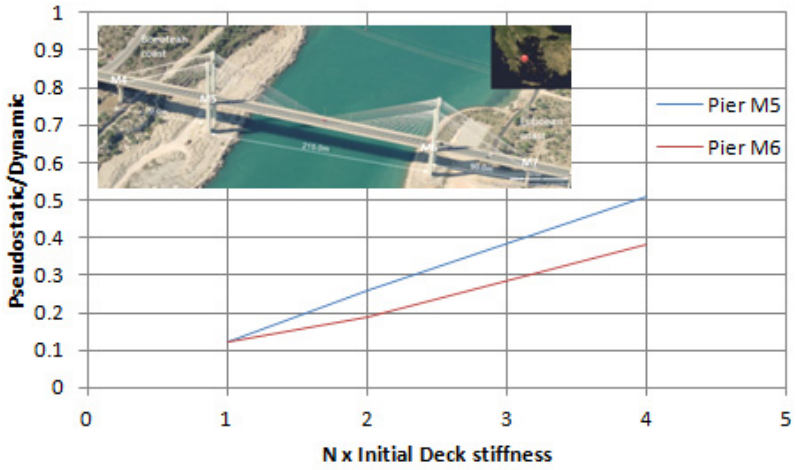


Figure 9: Variation of pseudo-static component contribution as a function of the deck stiffness (for the case of the Evripos cable-stayed bridge).

6 CONCLUSIONS

In this paper, the applicability of three simplified methods (EC8-Part 2 provisions and the improved by Sextos & Kappos and Nuti & Vanzi EC8-based methods) to capture the effects of spatial variability of earthquake ground motion is investigated through the case study of the Evripos cable-stayed bridge in Greece. The predicted, according to the simplified methodologies, structural response of the bridge is compared with the actually monitored behavior based on four free-field recording during the M_s=5.9, 7/9/1999 Athens earthquake. The coherency of these motions was computed for all the available pairs and incoherency patterns were duly identified. A detailed finite element model of the cable-stayed bridge was also updated based on the available measurements, until reasonable matching was achieved between the numerically predicted and the measured response. The results of the comparative assessment indicate that, the spatial variability of earthquake ground motion had a generally beneficial effect on the response of Evripos bridge with the exception of specific critical response components, a fact that is mainly due to the significant flexibility of the bridge deck. It was also shown however, that the impact of pseudo-static displacements depends heavily on the deck stiffness,

hence the above observation can by no means be generalized. Specific concerns were also expressed with respect to the applicability of all the simplified code-based predictive models, as their inherent static nature essentially suppresses the dynamic impact of asynchronous excitation. When the application of such methods is inevitable, engineering judgment has to be exercised based on the whole range of results available in the literature.

REFERENCES

[1] A. Zerva, "Spatial Variation of Seismic Ground Motions: Modelling and Engineering Applications," *Nonlinear Dynamics*. CRC Press, Taylor & Francis Group, LLC, p. 460, 2009.

[2] S. Biondi, G. Leoni, C. Nuti, G. Tropeano, and I. Vanzi, "Non synchronous earthquake motion in bridges design," in *15th World Conference on Earthquake Engineering*, 2012, no. 2004.

[3] T. Albanesi, C. Nuti, and I. Vanzi, "Site specific spectrum-compatible non-synchronous motion," in *1st US-Italy Seismic Bridge Workshop*, 2007.

[4] P. E. Pinto and P. Franchin, "Open Issues in the Seismic Design and Assessment of Bridges," vol. 17, M. Garevski and A. Ansal, Eds. Dordrecht: Springer Netherlands, 2010.

[5] S. Liao and A. Zerva, "Physically compliant, conditionally simulated spatially variable seismic ground motions for performance-based design," *Earthquake Engineering & Structural Dynamics*, vol. 35, no. 7, pp. 891–919, Jun. 2006.

[6] A. Der Kiureghian and A. Neuenhofer, "Response spectrum method for multi-support seismic excitations," *Earthquake Engineering and Structural Dynamics*, vol. 21, no. September 1991, pp. 713–740, 1992.

[7] A. G. Sextos, K. D. Pitilakis, and A. J. Kappos, "Inelastic dynamic analysis of RC bridges accounting for spatial variability of ground motion, site effects and soil-structure interaction phenomena. Part 2: Parametric study," *Earthquake Engineering & Structural Dynamics*, vol. 32, no. 4, pp. 629–652, 2003.

[8] A. J. Kappos, *Seismic Design and Assessment of Bridges*, vol. 21. Dordrecht: Springer Netherlands, 2012.

[9] fib [fédération international du béton], "Structural solutions for bridge seismic design and retrofit—a state of the art," 2007.

[10] A. Lupoi, P. Franchin, P. E. Pinto, and G. Monti, "Seismic design of bridges accounting for spatial variability of ground motion," *Earthquake Engineering and Structural Dynamics*, vol. 34, no. 4–5, pp. 327–348, 2005.

[11] A. G. Sextos, K. D. Pitilakis, and A. J. Kappos, "Inelastic dynamic analysis of RC bridges accounting for spatial variability of ground motion, site effects and soil-structure interaction phenomena. Part 1: Methodology and analytical tools," *Earthquake Engineering & Structural Dynamics*, vol. 32, no. 4, pp. 607–627, 2003.

[12] A. G. Sextos and A. J. Kappos, "Evaluation of seismic response of bridges under asynchronous excitation and comparisons with Eurocode 8-2 provisions," *Bulletin of Earthquake Engineering*, vol. 7, no. 2, pp. 519–545, 2009.

[13] L. Carnevale, S. Imperatore, D. Lavorato, C. Nuti, G. Leoni, and G. Tropeano, "Assessment of Seismic Behavior of R.C. Bridges under Asynchronous Motion and Comparison with Simplified Approaches," in *15th World Conference on Earthquake Engineering*, 2012.

[14] A. Zerva and V. Zervas, "Spatial variation of seismic ground motions: An overview," *Applied Mechanics Reviews*, vol. 55, no. 3, p. 271, 2002.
[15] A. Zerva and M. Shinozuka, "Stochastic differential ground motion," *Structural Safety*, vol. 10, pp. 129–143, 1991.
[16] M. Shinozuka, V. Saxena, and G. Deodatis, "Effect of spatial variability of ground motion on bridge fragility curves," in *8th ASCE Specialty Conference on Probabilistic Mechanics and Structural Reliability*, 2000.
[17] A. G. Sextos, A. J. Kappos, and K. D. Pitilakis, "Inelastic dynamic analysis of RC bridges accounting for spatial variability of ground motion, site effects and soil-structure interaction phenomena. Part 2: Parametric study," *Earthquake Engineering & Structural Dynamics*, vol. 32, no. 4, pp. 629–652, 2003.
[18] L. Lou and A. Zerva, "Sensitivity of the Nonlinear Seismic Response of a Short RC Bridge to Numerical Modeling," in *15th World Conference on Earthquake Engineering*, 2012.
[19] L. Lou and A. Zerva, "Effects of spatially variable ground motions on the seismic response of a skewed, multi-span, RC highway bridge," *Soil Dynamics and Earthquake Engineering*, vol. 25, no. 7–10, pp. 729–740, 2005.
[20] C. Nuti and I. Vanzi, "Influence of earthquake spatial variability on differential soil displacements and SDF system response," *Earthquake Engineering & Structural Dynamics*, vol. 34, no. 11, pp. 1353–1374, 2005.
[21] C. Nuti and I. Vanzi, "Design Of Bridges For Non Synchronous Seismic Motion," in *Seismic Engineering Conference Commemorating the 1908 Messina and Reggio Calabria Earthquake*, 2008.
[22] Ministero Infrastrutture, "Norme Tecniche per le Costruzioni. Gazzetta Ufficiale. 29:(S.O. 30) (in Italian)." 2008.
[23] V. Lekidis, M. Tsakiri, K. Makra, C. Karakostas, N. Klimis, and I. Sous, "Evaluation of dynamic response and local soil effects of the Evripos cable-stayed bridge using multi-sensor monitoring systems," *Engineering Geology*, vol. 79, no. 1–2, pp. 43–59, 2005.
[24] V. Lekidis, C. Karakostas, and D. Talaslidis, "Instrumentation, measurements and numerical analysis of bridges: an example of the cable-stayed bridge on Evripos channel, Greece," *Strong Motion instrumentation for Civil Engineering*, pp. 481–493, 2001.
[25] C. Karakostas, A. Sextos, V. Lekidis, and S. Papadopoulos, "Investigation of the Cable-Stayed Bridge in Greece , under Asynchronous Ground Motion Records," in *COMPDYN 2011, 3rd ECCOMAS Thematic Conference on Computational Methods in Structural Dynamics and Earthquake Engineering*, 2011.
[26] N. A. Abrahamson, J. F. Schneider, and J. C. Stepp, "Empirical spatial coherency functions for applications to soil-structure interaction analyses," *Earthquake Spectra*, vol. 7, no. 1, pp. 1–27, 1991.
[27] R. S. Harichandran, "Estimating the spatial variation of earthquake ground motion from dense array recordings," *Structural Safety*, vol. 10, pp. 219–233, 1991.
[28] R. S. Harichandran, A. Hawwari, and B. N. Sweidan, "Response of Long-Span Bridges to Spatially Varying Ground Motion," *Journal of Structural Engineering*, vol. 122, no. 5, pp. 476–484, 1996.
[29] R. S. Harichandran and E. H. Vanmarcke, "Stochastic variation of earthquake ground motion in space and time," *Journal of Engineering Mechanics*, vol. 112, no. 2, pp. 154–174, 1986.

[30] J. E. Luco and H. L. Wong, "Response of a rigid foundation to a spatially random ground motion," *Earthquake Engineering and Structural Dynamics*, vol. 14, pp. 891–908, 1986.
[31] C. H. Loh and S. G. Lin, "Directionality and simulation in spatial variation of seismic waves," *Engineering Structures*, vol. 12, pp. 134–143, 1990.
[32] N. A. Abrahamson, "Spatial variation of multiple support inputs," in *Proceedings of the 1st U.S. Seminar on Seismic Evaluation and Retrofit of Steel Bridges. A Caltrans and University of California at Berkeley Seminar*, 1993.
[33] C. Karakostas, A. G. Sextos, V. Lekidis, and S. Papadopoulos, "Investigation of the dynamic response of the Evripos cable-stayed bridge in Greece, under asynchronous ground motion records," in *3rd ECCOMAS Thematic Conference on Computational Methods in Structural Dynamics and Earthquake Engineering*, 2011.
[34] J. P. Nicoletti, M. J. N. Priestley, F. Seible, and G. M. Calvi, *Seismic design and retrofit of bridges*, vol. 12, no. 3. New York: Wiley, 1996.

COMPDYN 2013
4th ECCOMAS Thematic Conference on
Computational Methods in Structural Dynamics and Earthquake Engineering
M. Papadrakakis, V. Papadopoulos, V. Plevris (eds.)
Kos Island, Greece, 12–14 June 2013

SHEAR STRENGTH ASSESSMENT OF REINFORCED CONCRETE COLUMNS

Stamatina G. Chasioti[1], Konstantinos G. Megalooikonomou[2], and Stavroula J. Pantazopoulou[2,3]

[1] IWB, University of Stuttgart
Pfaffenwaldring 4, 70569 Stuttgart, Germany
e-mail: stamatina.chasioti@iwb.uni-stuttgart.de

[2] Department of Civil and Environmental Engineering, University of Cyprus
P.O. Box 20537, 1687 Nicosia, Cyprus
kmegal01@ucy.ac.cy
pantazopoulou.stavroula@ucy.ac.cy

[3] on leave of absence from Democritus University of Thrace, Greece

Keywords: seismic assessment, shear strength, the modified compression field theory, inclination of the compression strut, columns, concrete web crushing.

Abstract. *Seismic assessment of reinforced concrete structures depends on strength values that can be estimated with sufficient accuracy only when the modes of failure are ductile. The level of accuracy degrades when considering brittle mechanisms of resistance, particularly when focusing on shear transfer and the associated deformation capacity. In this paper, it has been found that an important factor affecting the primary estimation of the shear strength is the inclination of the plane of sliding failure θ, identified as 45^o by the Mörsch truss, an assumption that does not comply with experimental results on columns. Using basic mechanics, the proposed model improves the correlation of the estimations, regarding both the concrete and transverse reinforcement contributions, V_c and V_s, presenting a new method for estimating θ, in particular in cases where applicability of the MCFT is limited by sparse stirrup spacing (i.e., assumptions about smearing of reinforcement are inappropriate). The concrete contribution component is established from first principles having as point of departure the fact that concrete directly supports shear only over the compression zone of the member, where cracks may be assumed to have closed. Conditions of concrete diagonal tension cracking and compressive crushing are both considered. Published experiments are used to guide and verify the development of the analytical model.*

1 INTRODUCTION

Explicit description of the load-deformation performance of structural elements is an essential ingredient of displacement-based seismic assessment procedures. Column elements are the most critical components for the safety of structure when the structure undergoes lateral sway as they carry the overbearing structure. The load-displacement curve is the envelope of the lateral shear – drift relationship; this follows the relationship of the characteristic Moment Rotation relationship of the element (since $V=M/L_s$), but apart from the basic flexural action, a number of premature phenomena may terminate the deformation capacity of the member. Syntzirma and Pantazopoulou (2010) used capacity based prioritizing of the modes of failure in order to identify the weakest mechanism of resistance so as to calculate the available deformation capacity of the member.

As a first step in seismic assessment of columns, flexural behavior is calculated from established procedures. The effect of shear is not taken into account in the approach but as an external acceptance criteria, in comparing the flexural force demand with the shear strength. The latter may be reduced for comparisons beyond flexural yielding, depending on displacement ductility (see EC8-III(2005), as an example). A great degree of uncertainty still dominates the shear strength response. Figure 1 compares the parametric sensitivity of the dominant equations for shear strength adopted by EC8-III (2005) and the ASCE/SEI 41 (2007) assessment guidelines for a simple case example. The greater source of discrepancy is the angle of the truss model that interprets the response of the member after diagonal web cracking. In the presence of densely detailed reinforcement the Modified Compression Field Theory (MCFT) could be used to calculate moment-shear-axial load interaction and to derive shear strength and response to deformation. However, an essential condition is smearing of reinforcement and stress and strain, which is not possible if reinforcement is sparse, as occurs in older construction. An alternative approach for lightly reinforced members, where the MCFT cannot be directly applied, has been pursued by Chasioti et al. (2012) whereby the plane of sliding failure after web cracking is associated with the principal tensile direction in the compression zone at the critical column cross section.

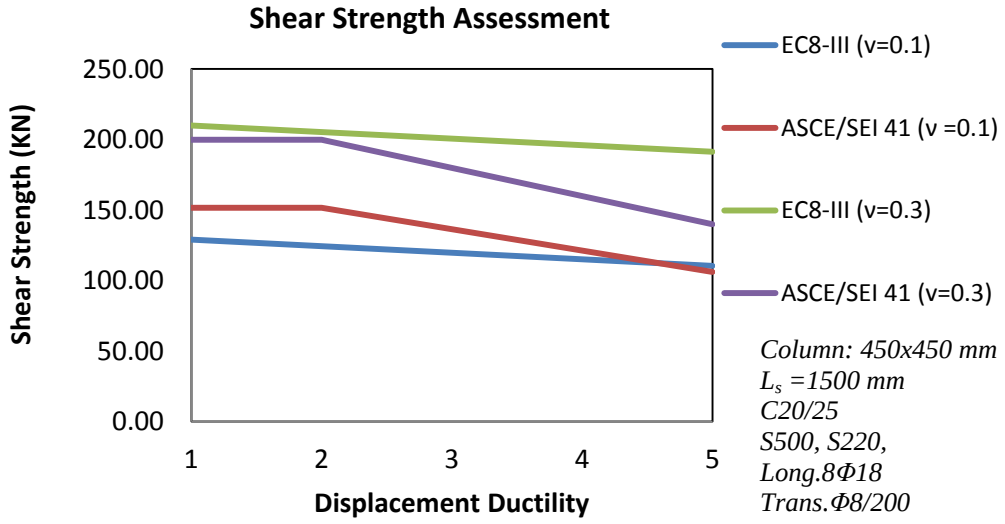


Figure 1: Shear Strength Assessment Example according to EC8-III and ASCE/SEI 41.

2 THE SHEAR TRANSFER MECHANISM

Traditionally, post cracking shear strength was estimated from summation of various separate contributions, attributed to concrete V_c (comprising shear transfer over the compression zone V_{cc}, and aggregate interlock and dowel action over the tension zone V_{ct}), to web reinforcement V_s and to axial load (Figure 2). It is a point of contention as to whether these mechanisms can actually be separated and independently estimated; it may be more honest to admit that these may be viewed as successive refinements to the underlying basic truss model that was inspired by Mörsch more than 100 years ago, so as to improve its correlation with the test data. Despite the departure of modern expressions from the original truss model, its origin should stay in focus: the concrete contribution was meant to be a correction over the truss term (web reinforcement) so as to match the test results. So the concrete contribution cannot be a significant portion of the strength (as it sometimes occurs in practical calculations when using the code expressions to severely undereinforced elements); this concern is only mentioned in the ASCE/SEI 41 (2007) where it is postulated that conforming elements are those where more than 75% of the available shear strength is owing to the web reinforcement term. Oddly enough, no particular attention is paid to the relative magnitude of the V_c and the V_s components of shear strength in EC8-III (2005).

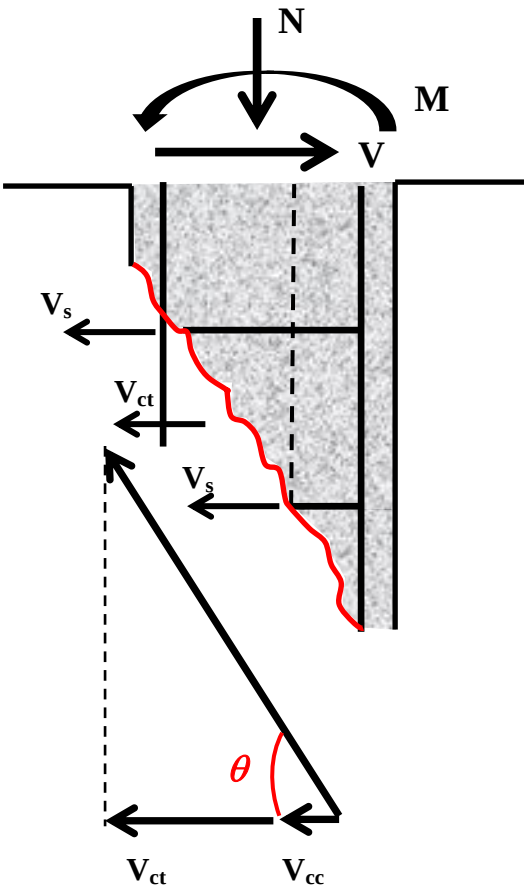


Figure 2: Free body diagram across a diagonal shear crack.

The presence of axial load in reinforced concrete columns (contrary to RC beams) is an important parameter which affects occurrence of diagonal cracking. This influence can be assessed both qualitatively and quantitatively. For example, compressive axial force delays di-

agonal tension cracking, increases the height of the compression zone of the member and increases the amount of shear force required to render the principal tensile stress of the web equal to the tensile strength of concrete.

Thus shear resistance to cracking increases with the axial load ratio whereas the value of the angle θ forming between the primary diagonal crack at tension failure, with the longitudinal axis of the member departs from the 45^o postulate. Actually, this particular variable has a critical influence on the determined strength since the inclination of the major sliding plane (i.e. the angle θ) determines the number of stirrup layers mobilized in shear, i.e., the V_s term in Eqn. 1. Several other variables appear to have a stronger influence, namely, the axial load magnitude, the aspect ratio of the member on shear strength and the effective area of the concrete section mobilized in the "concrete" shear contribution. In this paper these issues are explored from first principles and with particular reference to older type columns with non-ductile details under lateral sway.

$$V_n = V_c + V_s \tag{1}$$

3 THE STATE OF STRESS IN THE COMPRESSION ZONE

Both code procedures cited in the preceding refer to the effective web cross sectional area, ($0.8A_g$) in the estimation of concrete contribution to shear strength. It is believed that this assumption may be problematic, since open cracks prevent shear transfer under cyclic loads. To amend this counterintuitive argument, Syntzirma and Pantazopoulou (2006) introduced a requirement that the axial load ratio exceeds the difference between tension and compression reinforcement (ρ_{s1}-ρ_{s2}) as pre-requisite for consideration of the concrete contribution component. Recently, an alternative expression for the V_c term was considered, whereby it was postulated that only the part of the cross section that bears normal compression may be able to directly support shear stress in the presence of bending moment. So the effective area A_v, contributing to shear resistance is taken equal to $b_w \times c$. While is it generally acceptable that limited shear stress can also be developed in the tension zone of the cross section due to aggregate interlock , the statement above is on the safe side for the assessment phase. The depth of compression zone c and its location varies along the height of a column bent in double curvature and carrying a constant axial load N: consider the state of stress at the end cross-sections (terms with subscript e) as well as that at the column midheight (terms with subscript m) in Figure 3. Clearly, in the latter case, c_m extends over the entire depth of the cross section with the normal compressive stresses at the cross section being moderated as $\nu_o f_c$, where ν_o the axial load ratio in the column. To the contrary, in the end cross section normal stresses are localized within the depth of compression zone c_e, which supports a compressive force that is much higher than the net axial load, as illustrated in Fig. 3. Thus, the compressive stress resultant, F_{ce}, may be obtained from equilibrium as:

$$F_{ce}+\rho_{s2} b_w d f_{s2,e}-\rho_{s1} b d f_{s1,e}-N=0, \text{ thus, } F_{ce} = N+(\rho_{s1} f_{s1,e}-\rho_{s2} f_{s2,e}) b_w d \tag{2}$$

where the local compressive stress is,

$$\sigma_e=F_{ce}/b_w c_e, \text{ and } \nu_e=F_{ce}/b_w c f_c \quad i.e., \ \nu_e=\sigma_e/f_c \tag{3}$$

It is evident that the local stress intensity far exceeds the mean value, $\sigma_m = \nu_o f_c$ (where ν_o the normalized axial load ratio defined as, $\nu_o = N/(b_w d f_c)$) which occurs at the mid-height cross section.

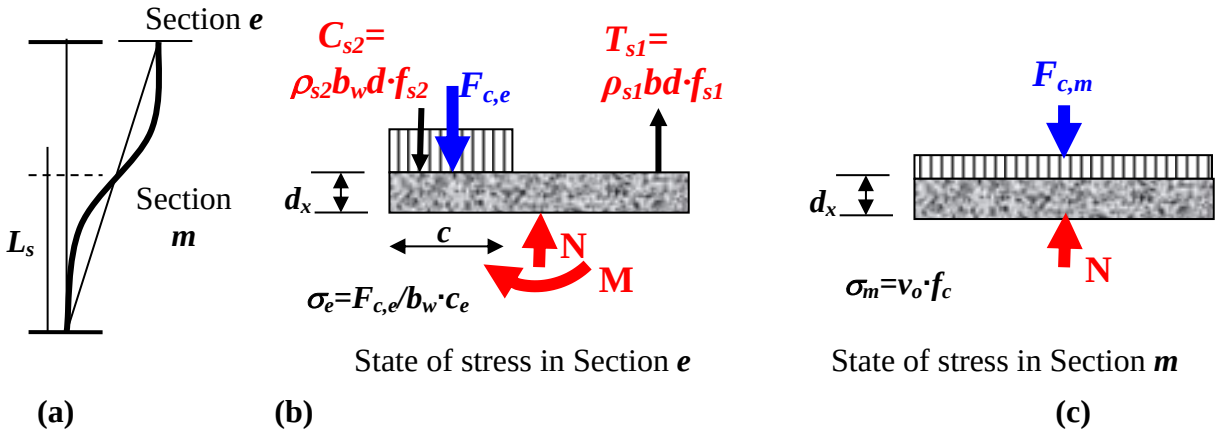


Figure 3: (a) Column under lateral sway, (b) Equilibrium of normal forces at section *e*, (c) Nominal normal forces at section *m*.

4 SHEAR FAILURE UNDER COMBINED LATERAL AND AXIAL LOAD

Members with non-ductile detailing are symptomatic of the older construction practices used in concrete structures up to only few years ago. In this context, a frequent example is the occurrence of high axial load ratios and large longitudinal reinforcement ratios. In these cases a brittle shear failure is often anticipated prior to the occurrence of flexural yielding. In order to evaluate the member's shear strength, the local state of stress depicted in Figure 3 need be considered as a point of reference for the calculation of the shear sliding plane. An assumption of this approach is that the sliding plane occurs along the main diagonal crack thereby defining the number of stirrups mobilized in tension and the geometry of the so-called variable angle truss model. Conditions of cracking considered refer to the state of stress in the compression zone where it is believed that the major concrete resistance to shear originates. In this direction, principal stress directions are considered for two possible events, namely: (a) diagonal tension failure in the compression zone, orthogonal to the compressive strut, (b) diagonal strut crushing failure due to excessive compression; a third mode of failure, which determines the basic strength of the variable angle truss model is associated to yielding of transverse reinforcement (case c). In each one of the first two modes the occurrence of cracking, either due to tensile stress or due to tensile strain (Poisson's effects) respectively, determines the sliding failure prior to flexural yielding at different stress levels and therefore they would result in different truss geometry. In this paper these two cases are referred to as two extreme conditions under which cracking may occur in the compression zone.

CASE A: Strength at Diagonal Tension Failure

With reference to Figure 3, for the end cross section *e* subjected to shear stress τ and normal stresses $\nu'_e = \nu_e f_c$, and $\sigma_{yy}=0$, the direction of principal tension may be determined by setting the associated principal tensile stress value equal to the tensile strength of concrete

f_{ctk}=0.5$\sqrt{f_c}$ at the onset of diagonal cracking of the web. This is evaluated from the following equation (considering the least – i.e., tensile – principal stress):

$$\underline{\sigma} = \begin{bmatrix} \sigma & \tau \\ \tau & 0 \end{bmatrix} \Rightarrow \sigma_{1,2} = \frac{v'_e}{2} \pm \sqrt{\tau^2 + \left(\frac{v'_e}{2}\right)^2} \Rightarrow -f_{ctk} = \frac{v'_e}{2} - \sqrt{\tau^2 + \left(\frac{v'_e}{2}\right)^2} \Rightarrow$$

$$\Rightarrow \tau^2 + \left(\frac{v'_e}{2}\right)^2 = \left(f_{ctk} + \frac{v'_e}{2}\right)^2 \Rightarrow \tau = \sqrt{f_{ctk} \cdot (f_{ctk} + v'_e)} = f_{ctk} \cdot \sqrt{1 + \frac{v'_e}{f_{ctk}}} \qquad (4)$$

The shear stress τ is related to the flexural moment at the end cross section when considering that $V=M/L_s$ where L_s is the member's shear-span:

$$\tau = \frac{V}{b_w \cdot c} = \frac{M}{b_w \cdot c \cdot L_s} \qquad (5)$$

Upon substitution to Eqn. 4, Eqn. 6 is obtained for ν'_e.

$$\tau = \frac{M}{b_w \cdot c \cdot L_s} = f_{ctk}\sqrt{1 + \frac{v'_e}{f_{ctk}}} \Rightarrow v'_e = \left[\left(\frac{M}{c \cdot b_w \cdot L_s \cdot f_{ctk}}\right)^2 - 1\right] \cdot f_{ctk} \qquad (6)$$

Parameter ν'_e represents the normal stress in the concrete compression zone of the member's end critical section for the case where cracking occurs due to diagonal tension i.e., when direct tension is transferred to the concrete compression zone via the lateral load (note that the value of the normalized longitudinal stress ν_e is much higher than $\nu_o = N/ f_c b_w d$ which represents the nominal axial load ratio reported in tests, a value that occurs at the point of inflection in the absence of flexural moment).

CASE B: Concrete Web Crushing (Axial Load Prevailing)

Consistently with Figure 3 and with the calculations above for the end cross section *e*, at the onset of concrete web crushing the principal compressive stress may be set equal to the compressive strength of concrete f_c. Solving accordingly the Eqn. 4 of the stress tensor for the plus sign (+) and substituting τ from the Eqn. 5, will result in ν''_e (Eqn. 7), which represents the normal stress at the end cross section at which concrete web crushing may occur. In this case, the combination of lateral load and high axial load is taken in consideration, with the axial load to be controlling failure and the inclination of the principal compression to be influenced by flexural and shear-stress combination. The result is a steeply inclined shear crack.

$$v''_e = \left[1 - \left(\frac{M}{c \cdot b_w \cdot L_s \cdot f_{ctk}}\right)^2\right] \cdot f_c \qquad (7)$$

Equations 6 and 7, estimate the normal stress in the cross section which will result in shear cracking owing to direct tension induced by the lateral load (case A), ν'_e, and owing to the concrete web crushing (case B), ν''_e. Both values depend on the values of the flexural moment *M*. Cases A and B both represent two extreme modes of failure, associating the flexural moment *M* in terms of forces acting to the member (stress resultant), to the cross section's normal stresses in the compression zone, ν'_e, and ν''_e respectively.

To facilitate immediate solution to this problem, values ν'_e, and ν''_e (from Eq. 6 and 7) are plotted against the compressive stress $\sigma_e=F_{ce}/b_w c_e$ (Eqn. 3) as a function of the bending moment *M*. Thus, the point of intersection of the resistance curve M- σ_e, to the either two potential failure curves will result in a critical combination of acting shear $V=M/L_s$, which determines the point of the shear crack initiation. Juxtaposition of the curves covers the com-

plete range of the member's response, starting with the uncracked cross section response in phase I all the way to flexural failure (here associated with 20% postpeak loss of the maximum carrying load).

CASE C: Cracking Due To Indirect Tension Induced From Compression Load

If the resistance curve M- σ_e does not intersect any of the two potential failure curves of the two failure modes referred to as cases A and B above, a check for cracking is performed in terms of strain. This is in recognition of the fact that diagonal tension failure may also occur indirectly due to lateral expansion in consideration of the Poisson's phenomenon. In such a situation, the point of shear crack initiation corresponds to a value of the moment M with a certain combination of τ and σ_e, where the longitudinal strain ε_{long} in the fiber where the concrete resultant F_c is applied, derives from a value of lateral strain ε_{lat} which is equal to the concrete tensile strain capacity. This is calculated from the ratio of concrete's tensile strength f_{ctk} divided by the concrete's modulus of elasticity E_c (Eqn. 8). Here, F_c is considered to be applied at the centroid of the compression zone, i.e. $0.4 \cdot c$ from the extreme compression fiber, where c the compression zone depth (on grounds of the established practice to represent the concrete stresses with a rectangular stress block extending over 80% of the depth of compression zone).

$$v \cdot \varepsilon_{long} = \varepsilon_{lat} = f_{ctk}/E_c \tag{8}$$

In Eq. (8), v is the Poisson's ratio, taken here equal to -0.25. For normal concrete strength class C20/25, $f_{ctk}=0.5\sqrt{f_c}$, and E_c=25000 MPa, the ε_{lat} is estimated as -0.00010 to -0.00015. Therefore, the point of shear crack in the resistance curve corresponds to a moment M in the end cross section with a longitudinal strain in the critical fiber in the direction of principal tension of $\varepsilon_{long,}$= (0.0001/0.25 = 0.0004) to (0.00015/0.25 = 0.0006).

The controlling case, A or B or C will define the point of initiation of shear cracking in the resistance curve with a specific combination of flexural moment $M_{cr,support}$, shear stress τ and normal stress σ_e. For a linear moment diagram (constant shear) along the shear span of the column, the flexural moment at distance d from the support, is equal to: $M_d=(L_s-d)\cdot M_{cr,support} / L_s$ when the moment at the face of the support equals $M_{cr,support}$. With reference to Eqn. 3 for the moment M_d the compression stress acting on the compression block is σ_d, while the shear stress τ remains approximately constant (assuming that the depth of compression zone is nearly the same as at the face of the support). The orientation of principal axes, ϑ, at the centroid of the compression zone a distance d from the support is obtained with reference to the longitudinal member axis, using basic mechanics according with Eqn. 9:

$$\tan 2\vartheta = \frac{2\tau}{\sigma_x - \sigma_y} = \frac{2\tau}{\sigma_d} \tag{9}$$

The number of the stirrups intersected by the shear plane is:

$$\frac{d-c}{s \cdot \tan\vartheta} \tag{10}$$

whereas the corresponding steel contribution, V_s, is obtained from the sum of forces of the total number of stirrup legs parallel to the plane of action and intersected by the inclined crack plane:

$$V_s = A_{s,tr} \cdot f_{y,tr} \cdot \frac{d-c}{s \cdot \tan\vartheta} \tag{11}$$

In Eq. (11), $A_{s,tr}$ is the total area of stirrups layers parallel to the plane of action, $f_{y,tr}$ the yield strength of the transverse steel, d the effective depth of the cross section, c the compression zone depth and s, the stirrup spacing.

The concrete contribution, is given by the shear stress resultant τ over the compression zone area of the critical section, $V_c = \tau \cdot 0.8 b_w \cdot c$

5 EXPERMENTAL CORROBORATION

Test specimens used in this paper in order to derive and calibrate the shear model were selected from among the available experimental literature with particular interest to the case of lightly reinforced members under constant axial load and cyclic displacement reversals simulating earthquake effects, where shear failure occurred prior to or immediately after flexural yielding. These are listed in Table 1. The cross section stirrup patterns are presented in Fig. 4; note that all the specimens considered had 90^0 hooks for anchorage of transverse reinforcement.

Tests No.1 to 4, failed in shear prior to flexural yielding and their experimental values regarding the shear strength serve as reference for comparison with the derived analytical values, since no degradation phenomena took place. Note that significant axial stresses are imposed on these columns, $P/f_c'A_g \approx 0.2\text{-}0.6$, which are raised substantially with increasing moment magnitude due to bending. In order to widen the range of possible axial load/implied moment combinations and to concentrate on the significance of the magnitude of the axial load on the column's shear performance, one more column was added to the database. Specimen No. 5 with a normalized axial load of 0.07 fails in shear immediately after the attainment of yielding.

Specimen ID; Serial No		**Mode of failure**	**angle** θ	**Geometry**				$P/f_c'A_g$	f_c' MPa	**Long. Reinf.**		**Transverse Reinf.**		
				b mm	h mm	L_s/d	a			D_{bl} mm	f_{yl} MPa	d_t mm	f_{yh} MPa	s mm
Spec. 1 [1]	1	S	28	457	457	3.75	1	0.32	33.0	8Ø28.7	445	9.5	372	457
Spec. 2 [1]	2	S	14	457	457	3.75	1	0.21	33.0	8Ø28.7	445	9.5	372	457
Spec. 3 [1]	3	S	13	457	457	3.75	1	0.62	17.0	8Ø32.3	445	9.5	372	457
X−9 [2]	4	S	18	267	267	1.60	2	0.50	28.6	12Ø12+4Ø16	395	6.0	270	100
2CLH18 [3]	5	FS	NA	457	457	3.83	1	0.07	33.1	8Ø25.4	331	9.5	400	457

[1]Woods and Matamoros (2010);[2] Lam et al (2003); [3]Lynn at al (1996); mode of failure, S: shear prior to flexural yielding, FS: shear after yielding ; angleθ: test value of the inclination of the sliding plane with respect to the longitudinal member's axis; b, h: cross section width and height, respectively; L_s/d: aspect ratio; P: axial load as % of $f_c'A_g$; f_c': concrete strength; D_{bl},f_{yl}: diameter and yield stress of longitudinal Reinf.; d_t,f_{yh}: diameter and yield stress of stirrups; s: spacing of stirrups.

Table 1: Test specimen materials and details (a is a cross section index with reference to Fig. 4)

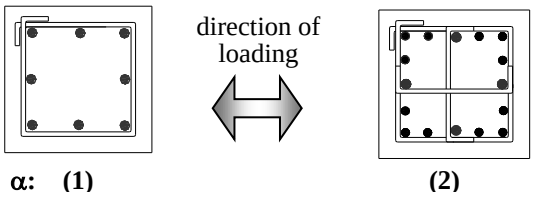


Figure 4: Cross section patterns of the specimens considered – in accordance with Table 1.

The theory presented in Chapter 4 was applied in the above specimens. For the specimens No 1 to 4 (Figures 6 to 9), the stress resultants were plotted versus only the moment values till

the point of flexural yielding (since these specimens failed prior to flexural yielding) whereas for the specimen No. 5 moment values were plotted for the entire range till the point of flexural failure while corresponds to the moment value M_u. The analysis for each specimen includes three diagrams. In the first one the values of normal stresses mentioned in Chapter 4 are plotted versus the moment M. In the second diagram, the blue curve corresponds to the lateral strain induced by the longitudinal of the third diagram as shown in Eqn. 8, while the red dashed line is the limiting value for the concrete's ultimate strain in tension. The curve of the third diagram shows the longitudinal strain of the fiber where the concrete resultant F_c is applied in the compression zone center of gravity in a distance of $0.4 \cdot c$ from the extreme compression fiber.

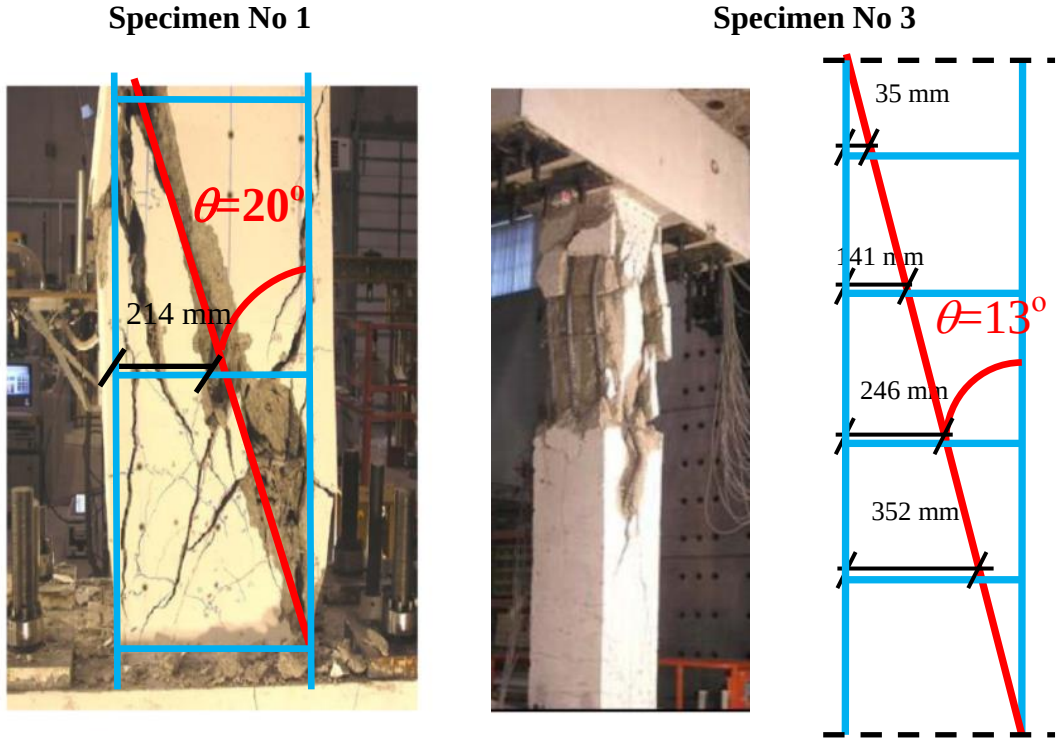


Figure 5: Truss geometry for the specimens 1 and 3.

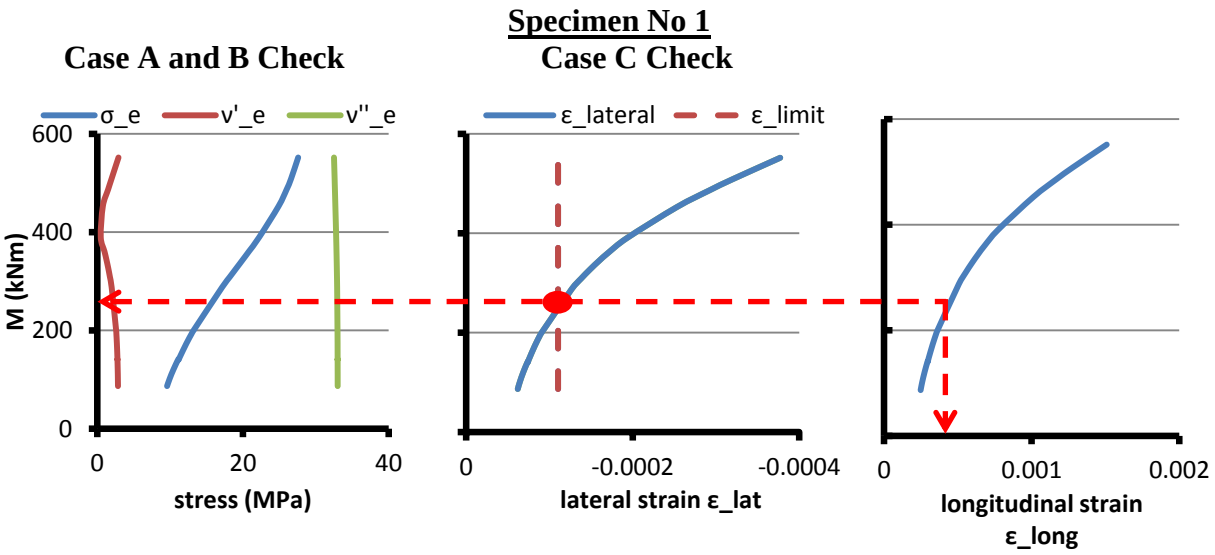


Figure 6: Analysis for the specimen No.1.

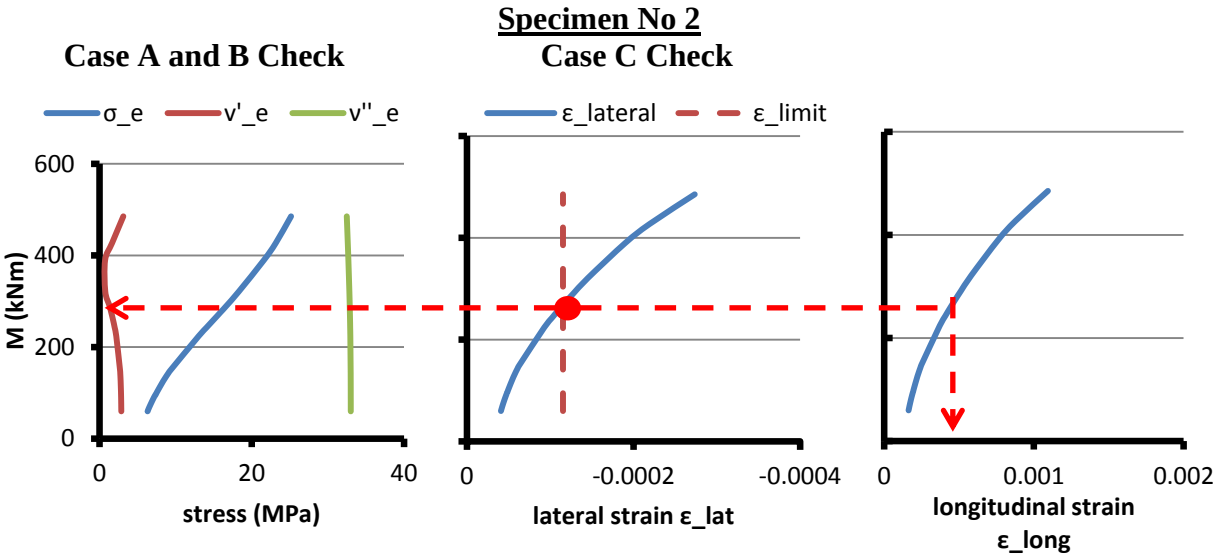


Figure 7: Analysis for the specimen No.2

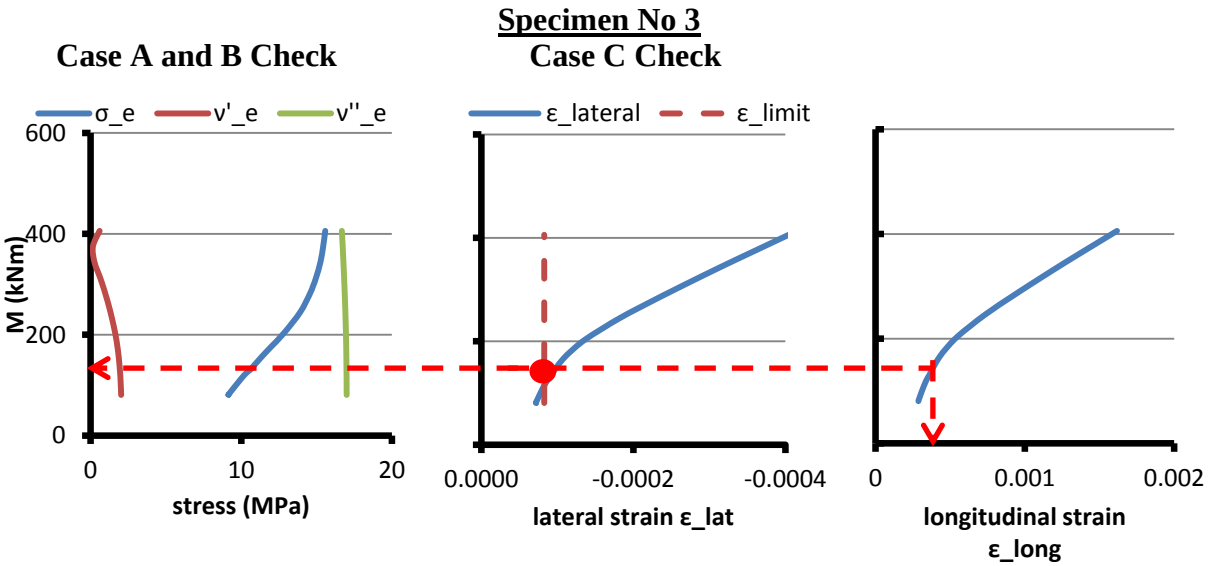


Figure 8: Analysis for the specimen No.3

Note that for the first four columns the point of the shear crack initiation comes from Case C as described in Chapter 4, i.e. lateral strain of the compression zone fiber where the concrete resultant is applied exceeds the concrete's ultimate tensile strain. Excessive axial load in all first four columns induces increased compression stresses in the compression block and delays cracking avoiding the case of diagonal tension failure. Specimen No. 5 has similar geometry and material properties to specimen No.1 as shown in Table 1, with the only difference the low axial load. Shear crack initiation is controlled in this case from Check A, i.e. diagonal tension failure is the prevailing mode, and the point of intersection of the blue and red curve precedes the point of cracking from criterion C as depicted by the second diagram of Figure 10.

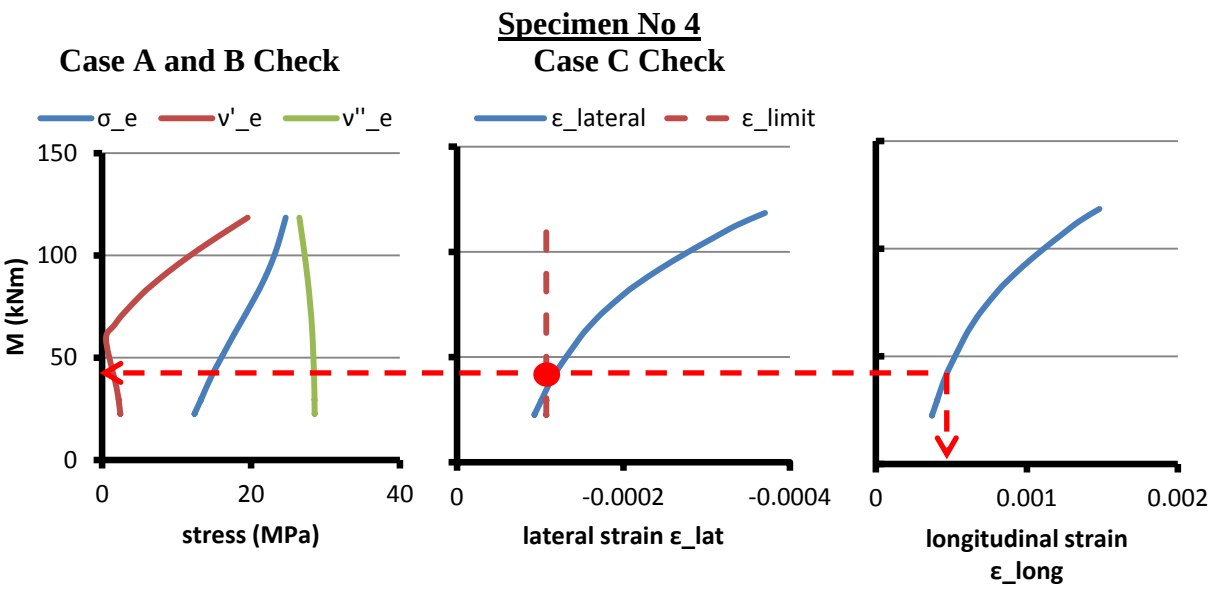


Figure 9: Analysis for the specimen No.4.

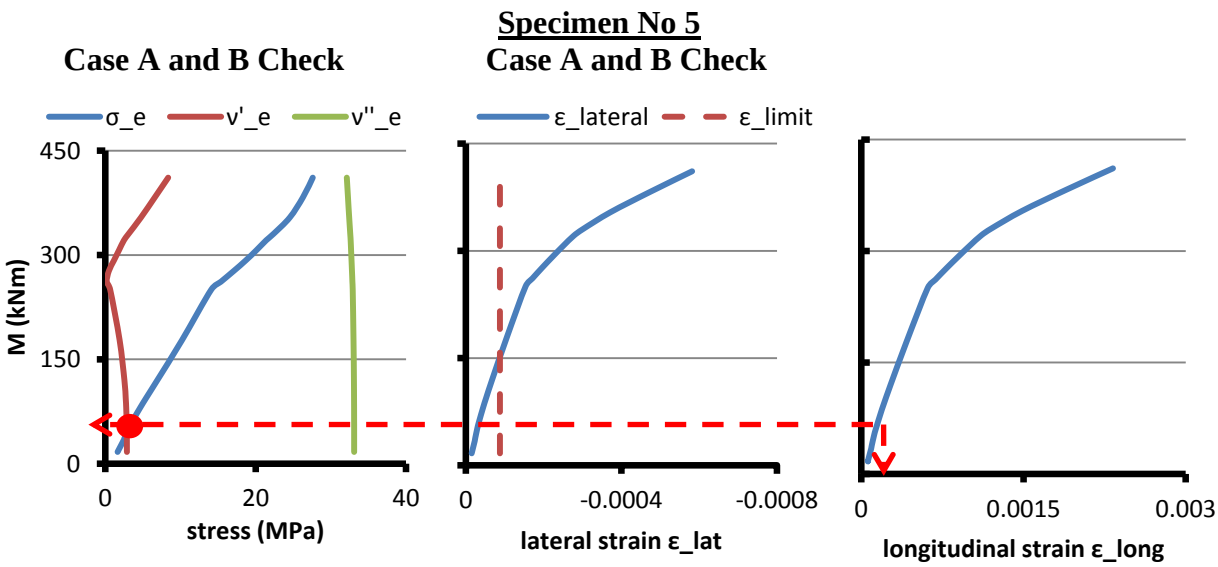


Figure 10: Analysis for the specimen No.5.

After assessment of the states of stress and strain as described above, the moment values which correspond to face of the support at shear failure for specimens No 1 to 5 are: 288, 276, 124, 37 and 52 kNm, whereas the corresponding values at d from the support are, 211, 202, 91, 14 and 38 respectively. The inclination of the angle θ is estimated for the second set of moment values for all five columns, as follows: 9^o, 10^o, 3^o, 8^o and 5^o respectively. Figure 11 shows the correlation between the shear strength values as obtained from the test data versus the estimated values according to the proposed model. Furthermore, the proposed procedure seems consistent with the basic inception of concrete contribution as a minor correction to the estimations of the truss model for shear strength (i.e. that the concrete contribution V_c is ought to be a significantly smaller component than V_s, Figure 12).

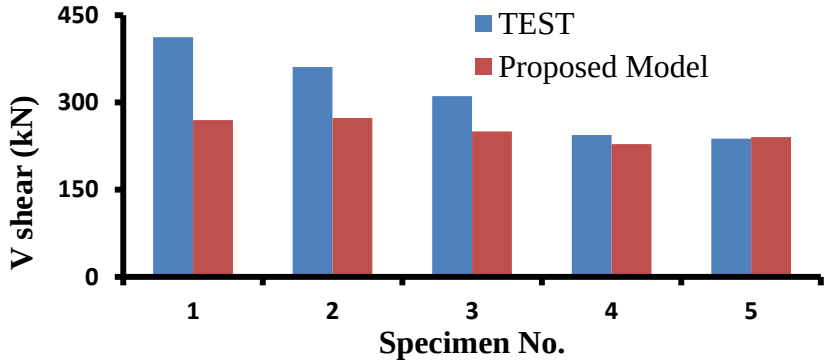


Figure 11: Shear strength test values vs. predicted values as calculated according to the proposed model.

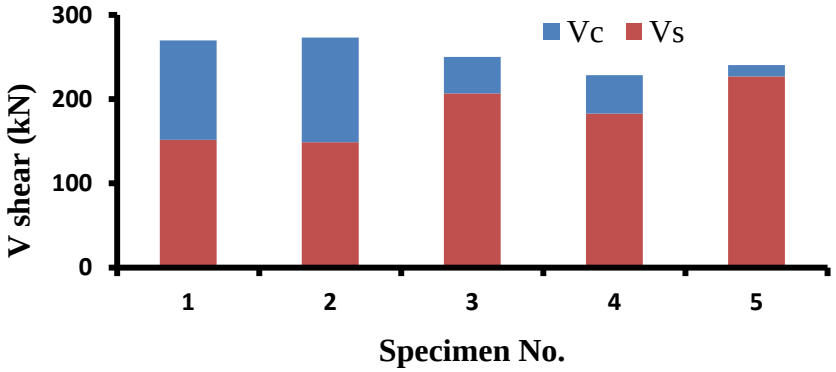


Figure 12: Concrete *Vc* and steel *Vs* contribution indices proportional to the total shear strength estimate.

6 CONCLUSIONS

This paper presents results of an analytical investigation aiming to establish shear strength in lightly reinforced columns where shear failure is driven by sparsely spaced stirrups. In such situations the assumptions of the MCFT theory about smearing of reinforcement are not appropriate, and the state of stress is primarily established with reference to the concrete cross section. To quantify the participation of web reinforcement and concrete to shear strength at the occurrence of the primary plane of failure, it is postulated that this is defined by diagonal tension cracking in the compression zone of the member owing to the combined action of shear stresses and axial stresses in that part of the cross section. Diagonal tension cracking is determined either from exceedance of tensile stress (due to combined shear action) or tensile lateral (expansion) strain due to Poisson's effects. This enables definition not only of the effective shear stress that may be carried in the compression zone but also the flexural moment associated with the onset of shear failure, as well as the number of stirrups intersected by the sliding plane (and therefore contributing to shear resistance). The methodology is tested against the available tests in the literature which are marked by shear failure in sparsely reinforced columns with either high or low axial load, in all cases producing good correlation with reported modes of failure and attained lateral load strength.

REFERENCES

[1] B. Martin-Perez, S. J. Pantazopoulou, Mechanics of Concrete Participation in Cyclic Shear Resistance of RC. *Journal of Structural Engineering*, ASCE, **124 (6)**, 633-641, 1998.

[2] M.J.N. Priestley, R. Verma, Y. Xiao, Seismic Shear Strength of Reinforced Concrete Columns. *Journal of Structural Engineering*, ASCE, **120 (8)**, 2310-2329, 1994.

[3] Tureyen, A.K. and Frosch, R.J. (2003). Concrete shear strength: Another perspective. *ACI Structural Journal **10:5***,609-615.

[4] Lam, S.S.E., Wu, B., Wong, Y.L., Wang, Z.Y., Liu, Z.Q. and Li, C.S. (2003), Drift capacity of rectangular reinforced concrete columns with low lateral confinement and high-axial load. *ASCE Journal of Structural Engineering **129:6***,733-742.

[5] Sezen, H. and Moehle, J. (2004). Strength and deformation capacity of R.C. columns with limited ductility. *13thWorld Conference on Earthquake Engineering*. No 279.

[6] Woods, C. and Matamoros, A.B. (2010). Effect of longitudinal reinforcement ratio on the failure mechanism of R/C columns most vulnerable to collapse. *9thU.S. National and 10th Canadian Conference on Earthquake Engineering*. No 1636.

[7] ASCE/SEI 41 (2007). Seismic Rehabilitation of Existing Buildings, American Society of Civil Engineers.

[8] CEB-FIP Model Code (2010). Chapter 6:Interface Characteristics; Chapter 7:Design.

[9] Elwood, K., Matamoros, A., Wallace, J., Lehman, D., Heintz, J., Mitchell, A., Moore, M., Valley, M., Lowes, L., Comartin, C., and Moehle, J. (2007), Update to ASCE/SEI 41 Concrete Provisions. *Earthquake Spectra* **23:3**,493-523.

[10] Eurocode 8 (2005). Design of structures for earthquake resistance – Part.3: Assessment and retrofitting of buildings, European Committee for Standardisation.

[11] FEMA 356 (2000). Prestandard and commentary for the seismic rehabilitation of buildings, Federal Emergency Management Agency.

[12] Pantazopoulou, V. and Syntzirma, D. (2009). Code expressions for deformation capacity of lightly reinforced concrete members – a comparative study. *ACES Workshop: Advances in Performance-Based earthquake Engineering.*

[13] Syntzirma, D.V., and Pantazopoulou, S.J. (2006), Deformation capacity of R.C. members with brittle details under cyclic loads. ACI Special Publication **Vol. 236:** 1-22.

[14] ACI 318-99 (1999), Building Code Requirements for Structural Concrete, American Concrete Institute.

[15] Syntzirma, D.V., and Pantazopoulou, S.J. (2010), Deformation capacity of lightly reinforced concrete members – comparative evaluation. *ACES Workshop: Advances in Performance-Based earthquake Engineering*, Series Geotechnical, Geological, and Earthquake Engineering, Vol. 13, Springer.

[16] Chasioti S.G., Pantazopoulou S.J. and Syntzirma D.V. (2012), "Seismic Assessment of Lightly Reinforced Buildings: A Study of Shear Demand VS. Supply", *15th World Conference on Earthquake Engineering*, Lisbon, Portugal, September 24-28, 2012.

[17] Lynn, A., Moehle, J.P., Mahin, S., and Holmes, W. (1996), Seismic evaluation of existing R.C. building columns. *Earthquake Spectra* ***12:4***, 715-739.

COMPDYN 2013
4th ECCOMAS Thematic Conference on
Computational Methods in Structural Dynamics and Earthquake Engineering
M. Papadrakakis, V. Papadopoulos, V. Plevris (eds.)
Kos Island, Greece, 12–14 June 2013

NUMERICAL MODELLING OF A FOUR-SPAN BRIDGE, BI-AXIALLY TESTED ON THREE SHAKE TABLES

Tatjana Isakovic[1], Saiid M. Saiidi[2], and Matej Fischinger[3]

[1,3] University of Ljubljana, Faculty of Civil and Geodetic Engineering
Jamova 2, 1000 Ljubljana, Slovenia
[1] tisak@ikpir.fgg.uni-lj.si
[3] matej.fischinger@ikpir.fgg.uni-lj.si

[2] Department of Civil and Environmental Engineering, University of Nevada, Reno
Mail Stop 258, University of Nevada, Reno, NV 89557, USA
saiidi@unr.edu

Keywords: seismic response of bridges, bi-axial excitation, numerical modelling, abutments, impact, experiment on shake tables.

Abstract. *Most of existing experimental investigations of bridges were under slow cyclic loading. Data about the dynamic response of bridge components are relatively rare. The experiments investigating the response of the whole bridge are only few. One of these very rare (dynamic) tests of the whole bridges was recently performed at the University of Nevada, Reno. Large scale model (scale 1:4) of an asymmetric, four-span, torsionally sensitive bridge was bi-axially tested on three shake tables. Additionally, the influence of the abutments to the seismic response of the whole bridge was also investigated, exciting the bridge in the longitudinal direction simultaneously with actuators attached to the abutment seats. The response of the bridge was very complex, exhibiting large in-plane deck (torsional) rotations.*

The results of this test were used to evaluate the existing numerical models of different bridge components, and their interaction. The 3D analytical study of the bridge was performed using the OpenSees programme platform. Beside the standard existing fibre models of columns, different models of less investigated bridge components were evaluated. The crucial elements, having the significant influence on the overall response were the abutments. Two types of elements (zeroLengthContact3D and zeroLengthImpact3D), which were capable of modelling the impact as well as the friction between the superstructure and the abutments, were tested. It was found that the impact between the abutments and the superstructure was one the most important parameters influencing the response. Although the bridge was straight, the centre of its rotations was significantly changing, due to the impact between the abutments and the superstructure, substantially amplifying its in-plane rotations.

1 INTRODUCTION

There are many different numerical models available, which are commonly used to model various structural components of reinforced concrete bridges. The evaluation of these models has been commonly performed using the experimental data, which were obtained within the test of individual structural components. In most of the cases these experiments were under slow cyclic loading. Data about the dynamic response of bridge components are relatively rare. The experiments investigating the response of the whole bridge are only few.

One of these very rare (dynamic) tests of the whole bridges was recently performed at the University of Nevada, Reno [1]. Large scale model (scale 1:4) of an asymmetric, four-span, torsionally sensitive bridge was bi-axially tested on three shake tables (see Figure 1). Additionally, the influence of the abutments to the seismic response of the whole bridge was also investigated, exciting the bridge in the longitudinal direction simultaneously with actuators attached to the abutment seats. The response of the bridge was very complex, exhibiting large in-plane deck (torsional) rotations, which were importantly influenced by the impact of the abutments and superstructure. The short overview of the experiment and the main findings are presented in Section 2.

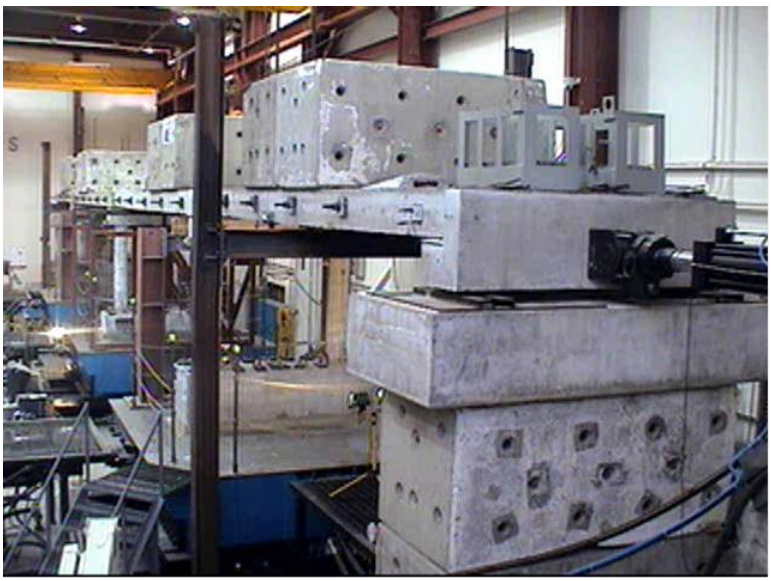


Figure 1: The investigated bridge was bi-axially tested on three shake tables (courtesy of UNR)

The results of this test were used to evaluate the existing numerical models of different bridge components, and their interaction. The 3D analyses of the bridge were performed using the OpenSees [2] programme platform. The numerical model is briefly introduced in Section 3.

Beside the standard existing fibre models of columns, different models of less investigated bridge components were evaluated. The crucial elements, having the significant influence on the overall response were the abutments. Two types of elements (zeroLengthContact3D [2] and zeroLengthImpact3D [3]), which were capable of modelling the impact as well as the friction between the superstructure and the abutments, were tested. Only zeroLengthImpact3D element is briefly described in Section 3, since it was included into the final numerical model of the analysed bridge.

The analytical and experimental results are compared in section 4. The main findings of the analysis are summarized in Section 5.

2 BRIEF OVERVIEW OF THE EXPERIMENT

The bridge was tested in a large scale 1:4. The main dimensions of the specimen are presented in Figure 2a. It is a four span bridge, supported by three two-column bents. The length of the end and inner spans was 7.47 m and 8.84 m, respectively. The deck was prestressed. The bridge was supported by circular columns of diameter 30.5 cm. The length of the columns was 1.52 m, 2.44 m and 1.83 m in bents: B1, B2 and B3, respectively. The geometry of the typical bent is presented in Figure 2b. The columns were reinforced by 16 bars of diameter 9.5 mm. The transverse reinforcement consisted of spiral reinforcement, with a diameter 4.9 mm. The space between the transverse bars was 32 mm.

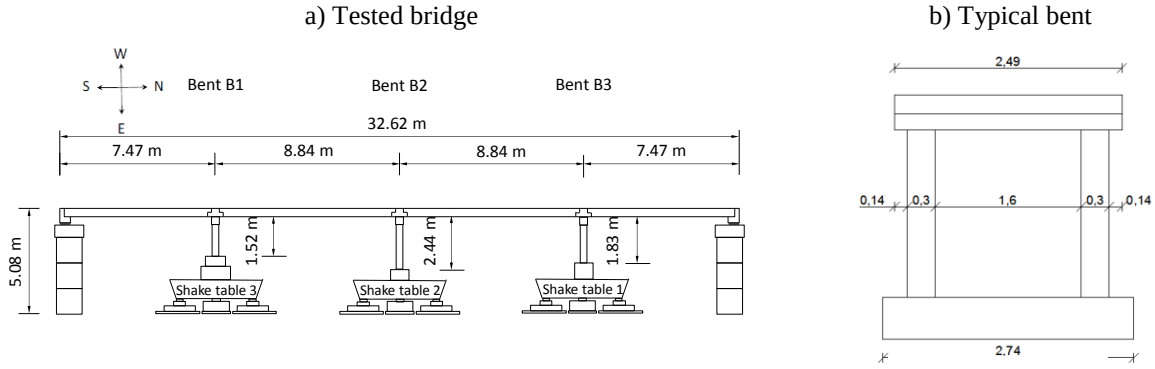


Figure 2: Scheme of the tested structure

At both ends of the bridge an additional mass of 40.8 t was applied (for more details see [1]). Consequently, in the analysis, an axial force of 183 kN and 175 kN was taken into account in columns of the side and central bent, respectively.

The bridge was tested bi-axially on three shake tables. It was subjected to different seismic intensity levels. The main investigation consisted of 7 high amplitude tests, denoted as tests T1D – T7 (see Table 1). All these tests were included in the analytical studies. In between the main tests, additional white-noise tests and test of the abutments were performed. They were not considered in the analytical investigation of the bridge.

Direction	Test T1D	Test T2	Test T3	Test T4D	Test T5	Test T6	Test T7
Transverse	0.075	0.15	0.25	0.50	0.75	1.00	1.00
Longitudinal	0.09	0.18	0.30	0.60	0.90	1.20	1.20

Table 1: Target maximum accelerations expressed as a percentage of the acceleration due to gravity

In the transverse direction of the bridge, the target intensity of the table accelerations was varied between 0,075 g (T1D) and 1.00 g (T7) (see Table 1). In the longitudinal direction the maximum target accelerations were between 0.09 g and 1.20 g. According to [1] most of the damage was observed in the columns of the side bents (B1 and B3). The damage of the columns of the central bents was significantly smaller. Even during the strongest tests T6 and T7 these columns were exposed to very limited yielding. Response of the side bents was essentially elastic during the initial three tests (T1D – T3). Their yielding was firstly observed during the tests T4D and T3 for bent B1 and B3, respectively. The significant damage of the side bents was observed during the test T5, when the significant permanent displacements in the transverse direction were noticed, on the east and west side of bent B1 and B3, respectively. Some of the longitudinal bars were ruptured and the majority of them buckled in the columns of the bent B1 during the test T7. Damage in bent B3 was similar, however smaller number of

the longitudinal bars were buckled. Some damage of the superstructure and abutments was observed during the last three tests, particularly at the north abutment.

3 NUMERICAL MODEL OF THE BRIDGE AND THE INPUT MOTIONS

Numerical model of bents and their connections to the superstructure is presented in Figure 3. Columns were modelled using nonlinear "Beam with Hinges" force based fiber model [4]. The length of the plastic hinges was determined based on the standard formulas [5], which were proved to be accurate enough in the previous investigations of the similar bridge [6]. The cross section of the columns was divided to 16 radial segments. The cover concrete was defined with three segments, and the core of the cross section was divided onto 12 segments. For the cover concrete the properties of the unconfined concrete, reported in [1] were taken into account. The core concrete was modelled taking into account the confinement, using the standard Mander's model. In both cases the Concrete04 [2] was used.

Each longitudinal bar was represented with one corresponding fiber having the properties of the steel reported in the [1]. Steel02 model was used [2].

Superstructure and beams were modelled with elastic elements. Connection of the beams and the superstructure were pinned in the longitudinal direction of the bridge and fixed in the transverse direction.

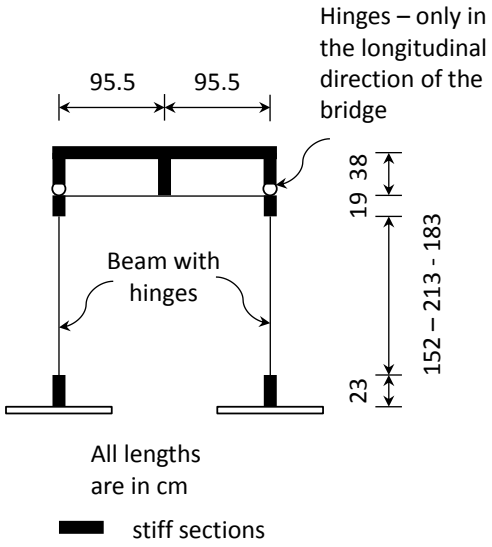


Figure 3: Numerical model of bents

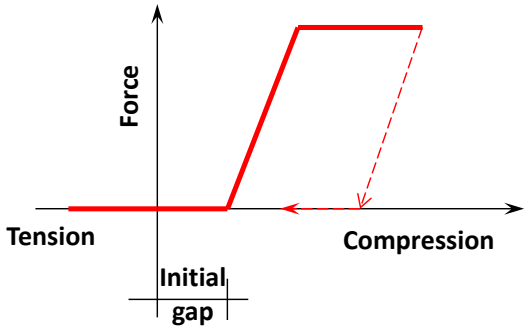


Figure 4: ZeroLengthImpact3D element: Force-displacement relationship in the direction of the element

In the presented analysis the main point of interest was the influence of the impact between the superstructure and the abutments to the overall response of the bridge. Therefore a special attention was devoted to this problem. Several numerical models, available in OpenSees programme [2] were taken into consideration. The zeroLengthImpact3D element [3], which was recently included into the OpenSees programme, was included into the final model. This element was able to take into account the initial gap between the abutments and the superstructure as well as its changes. This is a quite new feature comparing to the other elements.

The envelope force-displacement relationship corresponding to the used element is presented in Figure 4. This relationship defines the response in the longitudinal direction of the bridge. When there is no contact between the superstructure and the abutment, there is no

force in the longitudinal direction and the superstructure can move freely. When the gap (which is variable) is closed at the moment of the impact between the superstructure and the abutment, the superstructure is not subjected only to the force acting in the longitudinal direction of the bridge, but also in its transverse direction. The force in the transverse direction is a friction force between the superstructure and the abutment. It is limited by the product of the friction coefficient and the impact force in the longitudinal direction. Note that the friction reduces the displacements of the bridge in the transverse direction (particularly the residual displacements) and has no influence to the rotations of the bridge (similarly to other types of elements available in OpenSees that can be used to model the impact between superstructure and the abutments).

Due to the significant rotations of the superstructure and certain rotations of the abutments, the impact between the superstructure and the abutment occurred close to their corners, Therefore, two elements at each abutment were used to model the impact. Their position is presented in Figure 5.

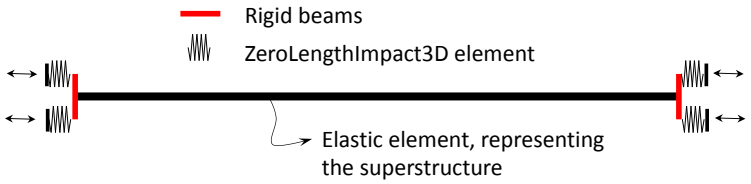


Figure 5: In-plane model of the superstructure

Note that the impact between the superstructure and the abutments did not occur exactly at the abutments' and superstructure's corners, however the position of the impact was not significantly distant from these points.

When the gap was closed, the stiffness of the springs was modelled to be large (10^6 kN/cm). The initial gaps were defined based on the measured relative displacements between the superstructure and the abutments: 2.0, 1.45, 1.90, 2.15 cm for the NE, NW, SE and SW abutments' corners, respectively.

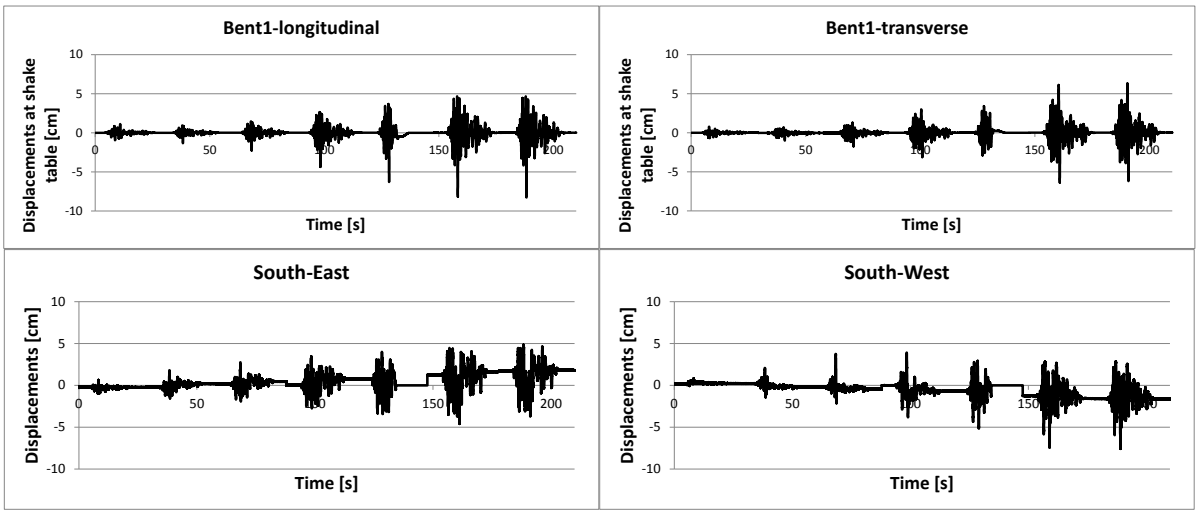


Figure 6: Input displacements at the shake table below bent B1 and longitudinal displacements at the corners of the south abutment (for all tests, that were considered in the analysis)

Since some friction between the abutments and the superstructure occurred at the moment of the impact, it was also taken into account. The best match with experimental data was ob-

tained when the friction of 0.03 was considered and the stiffness of the abutments in the transverse direction of $5x10^3$ was taken into account.

The structure was subjected simultaneously in the longitudinal and transverse direction at the positions corresponding to the shake tables. The input displacements, which were registered during the experiment, were taken into account. At the abutments, displacements, which were measured at their corners, were applied simultaneously with the excitations of the shake tables. The input motions at the shake table below Bent 1 and at the corners of the south abutment are presented in Figure 6 as an example.

4 COMPARISON OF THE EXPERIMENT AND THE ANALYSIS

During the experiment absolute transverse displacements of the east edge of the superstructure were measured at stations, presented in Figure 7. Absolute longitudinal displacements were measured at the centre of the deck and corners of the abutments (DS1 – DS4). The relative displacements of the abutments and the superstructure were measured at the corners of the abutments (DS5 – DS8, presented in Figure 7).

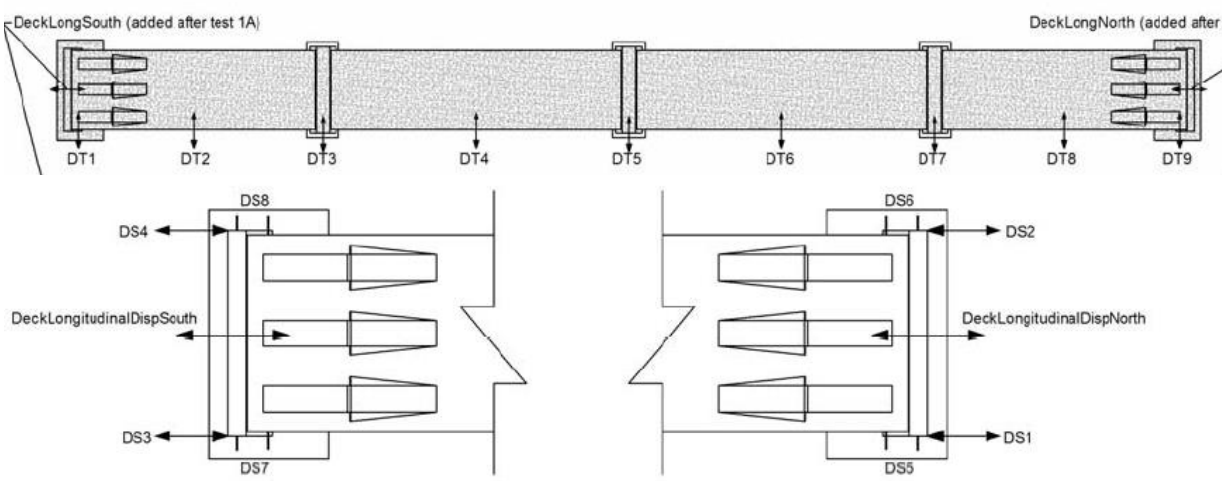


Figure 7: Scheme of the measured displacements (courtesy of UNR [1])

Measured and calculated displacements are compared in Figures 8 – 10. Displacements, which were observed during the tests T1D (essentially elastic response of bents), T4D (yielding of the side bents) and T6 (significant damage of the side bents) are presented. Since the longitudinal displacements of the centre of the deck at the south and north abutment are almost the same, only the displacements at the south abutment are presented in Figure 8. Transverse displacements of the deck above bents B1 and B3 are presented in Figures 9 - 10.

Quite a good agreement of the deck longitudinal displacements was obtained for tests T1D and Test T4D. At test T6 certain noise can be observed in some time intervals. This noise occurred for two reasons: a) all the moments of the impact were not perfectly captured in the analytical model; b) there is a certain noise in the input data. In the analytical model the impact between the superstructure and the abutments depends on several parameters such as: model of the columns, models of beams and superstructure, model of connection between beams and superstructure, model of the impact and input data.

Based on the discrepancy between the analysis and experiment in certain intervals of the test T6, considering the transverse displacements, presented in Figures 9 and 10, it can be concluded, that the model of the columns and the model of the superstructure need to be somewhat revised, particularly at the north side of the bridge.

Comparing Figures 9 and 10, it can be observed that the match between experiment and analysis is quite good above bent B1 (including test T6). Discrepancy between the analysis and experiment is somewhat larger above the bent B3, where the maximum displacements were different. This is an indication that the numerical model needs certain changes.

After the analysis of the measurements reported in [1] it was concluded that both, model of the bent B3 as well as model of the superstructure should be revised, since certain notable damage of the superstructure was observed near the north abutment. This will be done in further studies of the bridge.

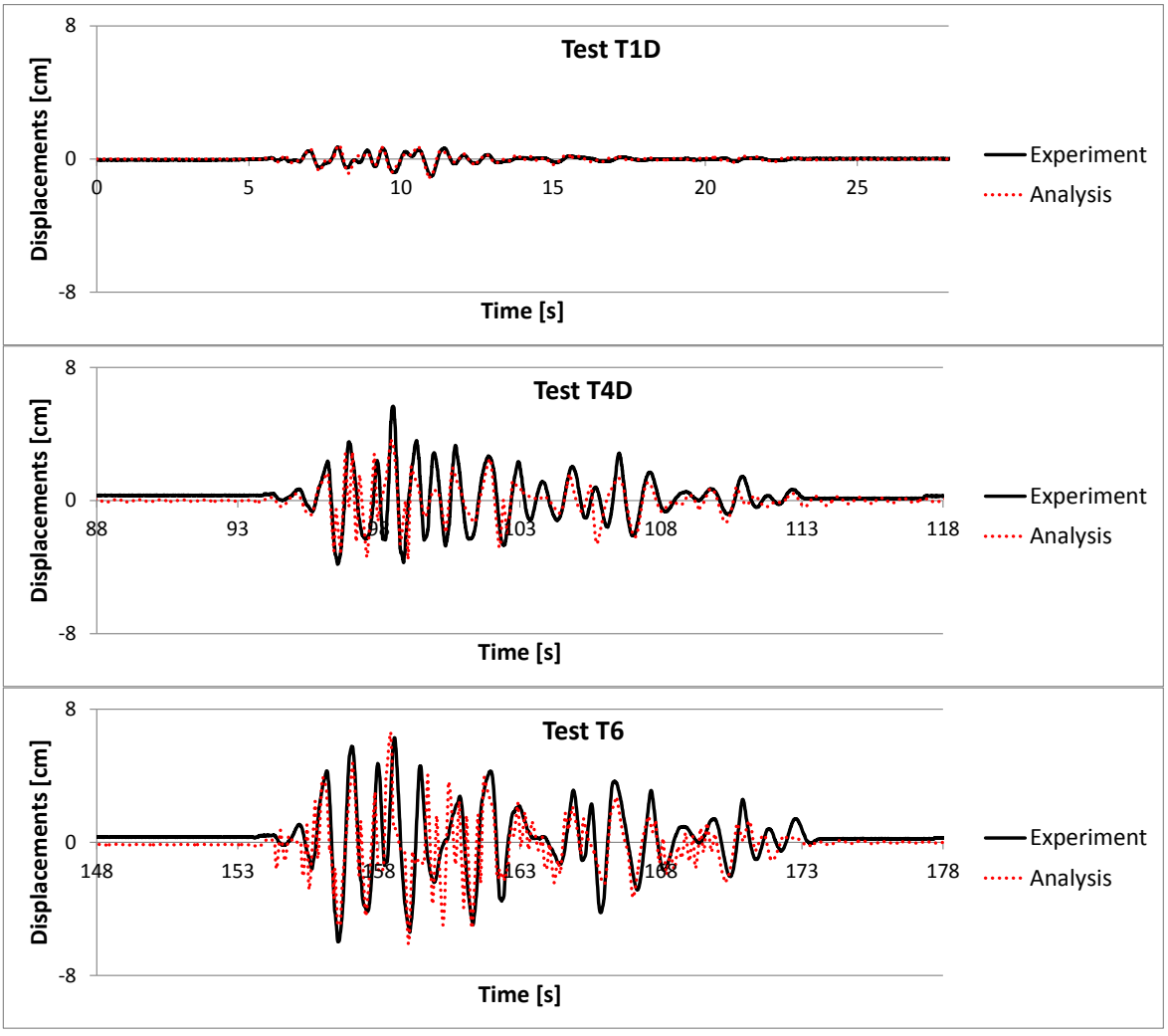


Figure 8: Longitudinal displacements of the centre of the deck

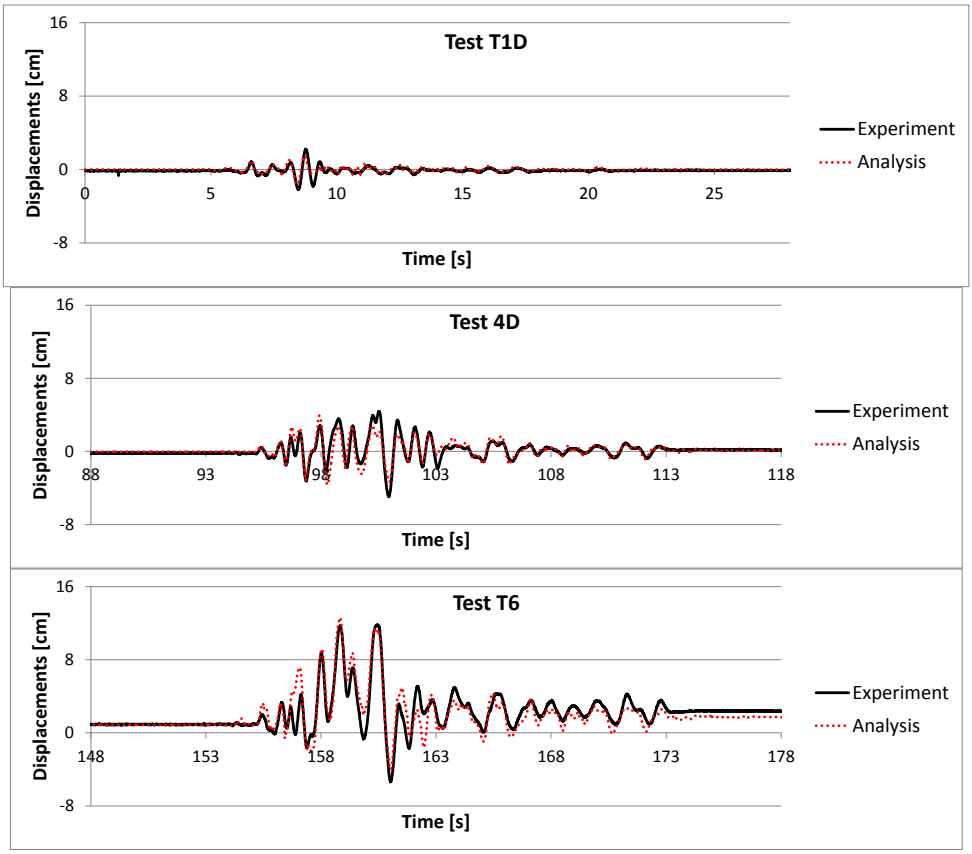


Figure 9: Transverse displacements of the deck above bent B1

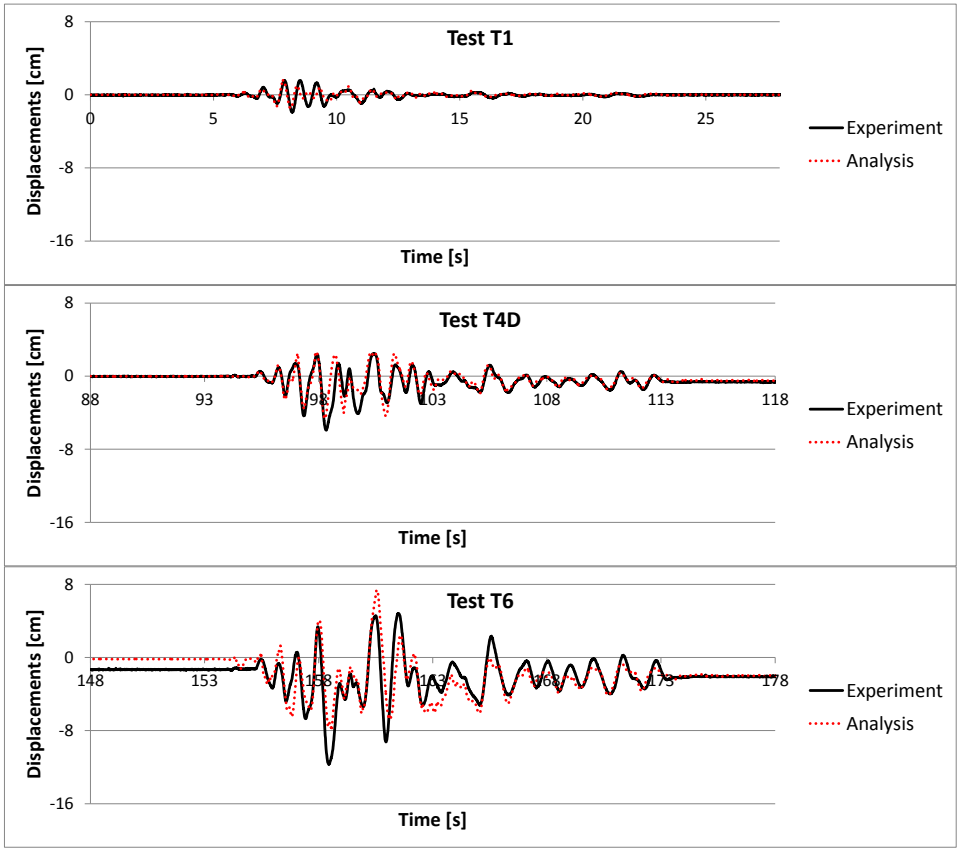


Figure 10: Transverse displacements of the deck above bent B3

5 MAIN FINDINGS OF THE ANALYSIS

The most important parameters that predominantly influenced the response of the analysed bridge are:

1) The impact between the superstructure and the abutments occurred close to the abutments' corners. This considerably changed the centre of the in-plane rotations of the bridge. The impact occurred due to different rotations of the superstructure and the abutments.
2) The initial gap size, which was not the same at all abutments' corners,
3) The excitations of the abutments,
4) The damage of bents.

1) The initial eccentricity or the centre of the stiffness (rotations) was defined by different stiffness of the side bents. If the bents were uncracked and supposing that they were 100% fixed at the bottom and at the top in the transverse direction of the bridge, the initial eccentricity was 1.95 m in the longitudinal direction of the bridge and 0 m in the transverse direction (due to the symmetry of bents in the transverse direction) .

When the impact between the superstructure and the abutment occurred, the centre of rotation was shifted. Since both, the superstructure and the abutment were rotated, and these rotations were different, the impact of the superstructure and the abutments occurred close to the abutment's corner. The centre of the rotation was, therefore, shifted almost for the half of the abutment width, because the stiffness of the abutment was considerably larger than the stiffness of the bents. Since the width of the abutment was about 2.4 m, the shift of the centre of the rotation was considerable. The shift in the transverse direction was about 1.2m, which was comparable with the initial eccentricity in the longitudinal direction. Due to the shift of the centre of the rotation, the bridge rotated around the corner of the abutment as long as the impact between the superstructure and the abutment was provided (see Figure 11).

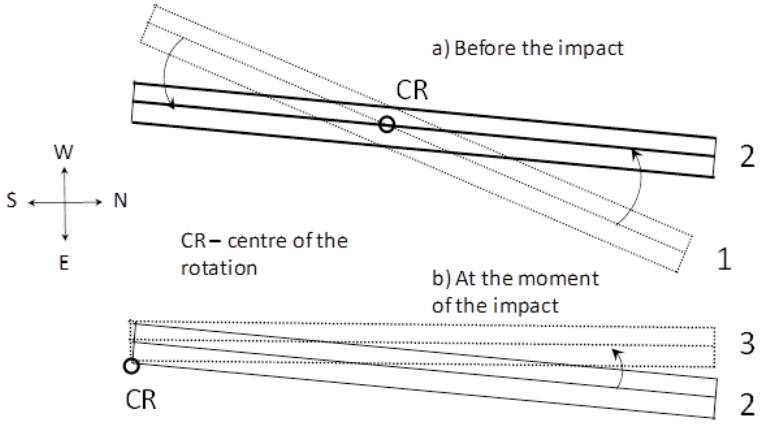


Figure 11: In-plane rotations of the superstructure: a) when there is no impact (at the moment before the impact); b) during the impact

For an illustration, an instance of the in-plane rotations of the superstructure, defined based on its measured displacements (during the experiment) in the transverse direction, is presented in Figure 12. The rotations before the impact (Figure 12a) and during the impact (Figure 12b) are illustrated. Note that rotations of the east edge of the superstructure (for which the experimental data are available) are presented (not the central line of the superstructure).

It can be observed from Figure 12 that the situation was even more complex than that presented in Figure 11. The superstructure was not infinitely rigid (it did not rotate as the perfectly rigid beam) and the centre of the rotation at the moment of the impact was slightly changing in the transverse direction of the bridge, due to the transverse displacements of the superstructure (for about 0.5 cm). However, the general trend was the same as that presented in Figure 11.

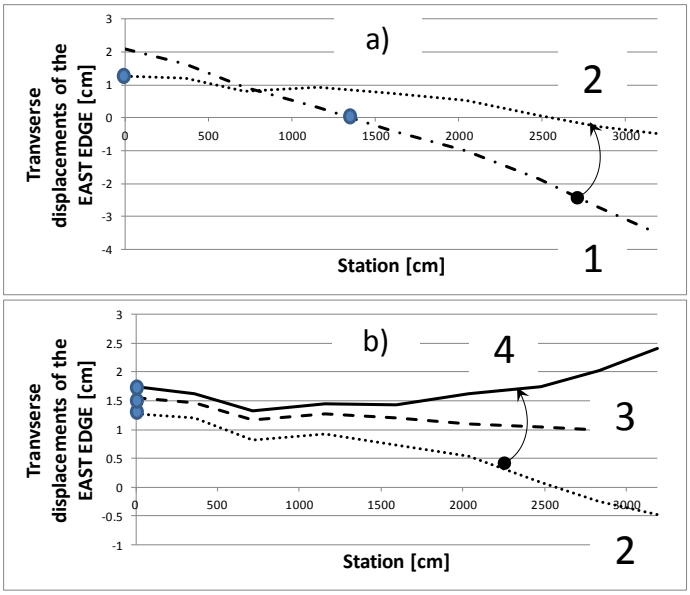


Figure 12: In-plane rotations of the superstructure before and at the moment of the impact, observed during the experiment

The main conclusion that can be obtained from the previously described response of the bridge is that the centre of the rotation will be shifted in all cases where the rotations of the superstructure and/or the abutments occurred during the impact and these rotations are different. The observed response can be expected also in straight bridges which are supported asymmetrically by columns of different heights, and where the considerable in-plane rotations of the superstructure can be expected – torsionally sensitive structures; in other words in structures, where the torsional stiffness is less than its translational stiffness, as it is the case in the investigated bridge. Note that the torsional sensitivity of the bridge is caused by relatively long side spans, which were not supported in the transverse direction. If the bridge were supported by strong shear keys, the response would be considerably different.

Based on the results of the experiment, and previous analytical observations, it can be concluded that in all cases, where considerable rotations of the superstructure and/or abutments are expected, their impact should be modelled by more than one element (as it was common in the past practice). The elements, which are used to model the impact, should be provided at the corners of the superstructure/abutments. This is particularly important in short bridges, which are supported by few bents. In longer structures the impact between the superstructure and the abutments would be important only locally.

2) If the gap between the superstructure and the abutment is large enough to accommodate relative rotations between the superstructure and the abutment, the contact between the superstructure and the abutment will not occur. That is why the size of the gap importantly influences the response. In the investigated case the gap size was not the same at both ends (abutments) of the bridge. Moreover the gaps at the corners of one abutment were also different, due to the different rotations of the abutments and the deck. That is why the rotations of

the abutments were important in the investigated case, since they influence the size of the gap and consequently the moment of the impact.

The gap size was important, since it defined the moment (time) of the impact and considerable changes of the dynamic properties of the bridge at the moment of impact. Small changes of the gap had considerable influence to the response, since the stiffness of the abutments was large and the gap size was small. Therefore the problem was poorly constrained and very challenging for numerical modelling.

3) To obtain the impact at the abutment's corner, the relative rotations between the superstructure and abutments are needed. The rotations of the abutments occurred due to the different motions of the abutments' corners. These rotations, combined with the relatively small size of the gaps, had considerable influence to the position as well as the moment (the time) of the impact between the superstructure and the abutment. The size of the gap and the rotations of the abutments had considerable influence to the residual transverse displacements observed during the tests T5 – T7 (see Figures 9 and 10).

4) The damage of the bents had a considerable influence to the torsional and the translational stiffness of the bridge, and consequently also to the eccentricity (centre of the rotations) and the rotations of the bridge in-between the impacts of the superstructure and the abutments.

6 CONCLUSIONS

The numerical analysis of the bridge which was bi-axially tested on the three shake table has been performed. This was a great opportunity to test some common numerical models of RC columns and new zeroLengthImpact3D model, which was used to take into account the impact between the abutments and the superstructure. It has been found that the accuracy of these models was quite good.

Since the tested bridge was torsionally flexible structure, substantial in-plane (torsional) rotations were observed. These rotations were significantly amplified at the moment of the impact between superstructure and the abutments, because the centre of the stiffness (rotation) of the bridge was shifted close to the abutments' corners. Based on this observation, it can be concluded that in all cases, where considerable relative rotations of the superstructure and/or abutments are expected, their impact should be modelled by more than one element (as it was common in the past practice).

Elements, which are used to model the impact, should be provided at the corners of the superstructure/abutments. This model should be used in all torsionally sensitive structures, even if they are straight. This is particularly important in short bridges, which are supported by few bents. In longer structures the impact between the superstructure and the abutments would be important only locally.

Certain friction was observed between the abutments and superstructure at the moment of the impact. It reduced the displacements in the transverse direction of the bridge (particularly the residual displacements). The new zeroLengthImpact3D element was able to model the friction in an appropriate manner. However, like the other similar elements, it did not increase the rotations of the superstructure when the friction occurred. This did not have significant influence to the analysis and the results.

The response of the bridge was significantly influenced by the size of the gap between the superstructure and abutments. When it is large enough to accommodate relative rotations between the superstructure and the abutment, there will be no impact and the amplifications of the superstructure in-plane rotations.

In the investigated bridge, small changes of the gap size had considerable influence to the response, since the stiffness of the abutments was large and the gap size was relatively small.

Therefore the problem was quite challenging from the numerical point of view, since it was poorly constrained.

The damage of the bents had a considerable influence to the torsional and the translational stiffness of the bridge, and consequently also to the eccentricity (centre of the rotations) and the rotations of the bridge in-between the impacts of the superstructure and the abutments.

REFERENCES

[1] R.B. Nelson, M. Saiidi, S. Zadeh. *Experimental Evaluation of Performance of Conventional Bridge Systems*, Center for Civil Engineering Earthquake Research, Department of Civil Engineering, University of Nevada, Reno, Nevada, Report No. CCEER-07-04, October 2007.

[2] S. Mazzoni, F. McKenna, M. H. Scott, G.L. Fenves et al. *Open system for Earthquake Engineering Simulation User Command-Language Manual*, PEER, University of California Berkeley, version 1.7.3., 2006.

[3] A.E. Zaghi, *ZeroLengthImpact3D element*, personal communication, 2012.

[4] M.H. Scott and G.L. Fenves. "Plastic Hinge Integration Methods for Force-Based Beam-Column Elements", *Journal of Structural Engineering, ASCE,* 132(2):244-252, February 2006.

[5] M.J.N. Priestley, F. Seible & G.M. Calvi, *Seismic Design and Retrofit of Bridges*, John Wiley &Sons. 1996.

[6] T. Isakovic and M. Fischinger. Applicability of pushover methods to the seismic analyses of an RC bridge, experimentally tested on three shake tables. *Journal of Earthquake Engineering* 15(2):303–320, 2011.

COMPDYN 2013
4th ECCOMAS Thematic Conference on
Computational Methods in Structural Dynamics and Earthquake Engineering
M. Papadrakakis, V. Papadopoulos, V. Plevris (eds.)
Kos Island, Greece, 12–14 June 2013

ASSESSMENT AND DESIGN OF SEISMICALLY ISOLATED BRIDGES IN PROXIMITY OF MAJOR FAULTS AND LOCATED ON LIQUEFIABLE SOILS

C. Ozkaya[1], **M. Gercek**[2]

[1] Yuksel Proje Uluslararası AS
Birlik Mah. 450. Cad. No:23 ANKARA-TURKEY
e-mail: cozkaya@yukselproje.com.tr

[2] Mete Gercek Consulting Engineer
Sumbul Sok. No:19 Levent ISTANBUL-TURKEY
e-mail: meteger@gmail.com

Keywords: Seismic Isolation, Seismic Assessment, Near-Field, Liquefaction, Viaduct

Abstract. *In this paper, seismic isolation design of one highway viaduct and one high-speed railway viaduct located within few hundred meters of North Anatolian fault in Turkey is studied. Strong near-field characteristics such as directivity and liquefaction are expected due to soft soil conditions under the scenario earthquake. Seismic assessments of viaducts are performed considering these unfavorable effects.*

For the highway viaduct, a hybrid seismic isolation system is chosen for the bridge consisting of four natural and two lead-rubber bearings supporting the six steel-girders at each substructure. Lead cores in the lead-rubber bearings are designed to have an overall characteristic strength equal to 10% of the superstructure weight. This large characteristic strength is intentionally chosen to limit the isolator displacements under near-field effects. Furthermore, the supplementary four natural rubber bearings over each substructure provided additional stiffness to achieve a small post elastic period.

For the railway viaduct, the same design philosophy was followed with considering the serviceability issues related to high-speed railway bridges. Since yield displacement of lead-rubber bearings are about 2-3 cm, which is unsatisfactory for stringent displacement limits specified in international railway codes, in this case curved surface slider bearings having a dynamic friction coefficient of 12% with 2.54 mm yield displacement are selected.

1 INTRODUCTION

Bozuyuk-Mekece state highway is connecting the cities in the Mediterranean region and internal Anatolia to Istanbul, Turkey. Upgrading the highway was planned due to heavy traffic and accidents. Total length of the project is about 85 km and the project includes many tunnels, bridges and overpasses. Sakarya-II viaduct is the most important structure of this project since half of the project is at one side of Sakarya river and other half at the other side. Sakarya-II viaduct is the key element connecting the halves. Highspeed railway line between Ankara and Istanbul follows almost the same route with Bozuyuk-Mekece highway.

Turkey is an earthquake prone country and about 95% of the population is susceptible to earthquakes. Most of the earthquakes in Turkey take place on North Anatolian fault. North Anatolian fault is about 1500 km long and crosses the country from east to west. The fault is a strike-slip fault having characteristics similar to San Andreas fault. Destructive earthquakes up to Mw= 7.5 occurred on the fault-line resulting in many life and economical losses. Recent earthquakes on the North Anatolian fault are 17 August 1999 Izmit (Mw=7.4) and 12 November 1999 Duzce (Mw=7.2) earthquakes.

The Sakarya-2 viaduct and highspeed railway viaduct VK-14A is very close to each other as shown in Figure 1.

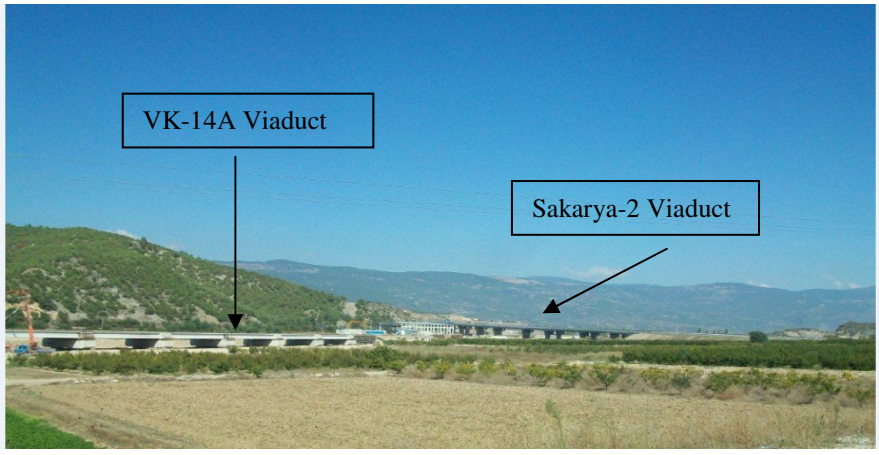


Figure 1: General View of the Highway and Railway Viaducts at Pamukova – Turkey

2 SEISMICITY AND GOETCHNICAL PROPERTIES OF THE SITE

North Anatolian fault has two branches at Marmara region. The northern branch is more active compared to southern one and 17 August earthquake occurred on this branch. Northern branch is very close to TEM highway and Istanbul. On the other hand, part of the southern branch between Geyve-Iznik is not active for centuries. Therefore, this portion of the fault may be classified as seismic gap. Sakarya-II Viaduct is about 300 meters far from the southern branch of the North Anatolian fault. Historical seismicity of the region and bridge site is presented in Figure 2. In Figure 2, earthquakes with magnitudes larger than 4.0 are highlighted.

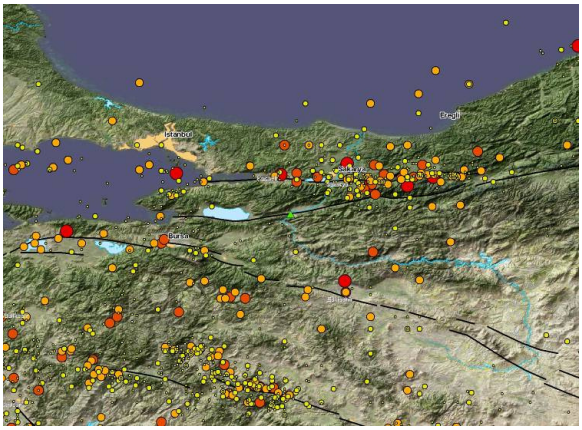


Figure 2: Seismicity of the Marmara Region and Bridge Site (1900-2006) [1]

Site specific studies have indicated that scenario earthquake having a magnitude of Mw=7.5 may be expected at the site during the economic life of the bridge. Return period of the maximum credible earthquake was selected as 1000 years. By using the attenuation relationships, peak ground acceleration at the bedrock level is calculated as 0.96g [1]. However, there is little seismic data for sites that are closer than 3 km to a major fault line.

Due to close proximity of the bridge to the fault, strong directivity effects are expected at the bridge site during a major earthquake. Near-fault earthquakes contain significant wave pulses. For strike-slip faults, they dominate the horizontal motion and may appear as single or double pulses with single or double-sided amplitudes. The period of the main pulse is in between 0.5sec-5 sec [2]. These pulses result in very high displacements and forces.

Elastic response spectrum analysis cannot capture strong nonlinear characteristics of near-field earthquakes. Therefore, nonlinear time history analyses were utilized in design of the bridge. Seven near-field earthquake records were selected and scaled according to AASHTO Guide Spec [3]. Records [1] are presented in Table-1.

Earthquake	Station Code	M_w	PGA_{EW}	PGA_{NS}	PGV_{EW}	PGV_{NS}
1976-Gazli-Uzbekistan	Karakyr	6.8	1.74	2.05	187	205
1994- Northridge-USA	Jensen	6.7	1.01	1.82	135	119
1994- Northridge-USA	La Sepulveda	6.7	2.74	3.41	285	277
1995 – Kobe, Japan	Takatori	6.9	0.49	0.50	103	98
1999- Duzce, Turkey	Bolu	7.2	2.05	2.31	158	175
Northridge -01	Sylmar	6.69	0.76	1.11	146	126
1999- Chi Chi, Taiwan	TCU 065	7.62	1.00	0.74	155	97

Table 1: Earthquake Record Utilized In Analysis [1]

Conformance of ensemble spectrum formed by taking the average of the SRSS spectra for the individual earthquakes and 1.3×Code spectra is presented in Figure 3. It is observed from the figure that average of the earthquakes match the code spectrum at intermediate periods corresponding to isolation period. Scaling factors are selected for each record so as to match the code spectra in between 1.5sec-2 sec. On the other hand, as presented in Figure 4, at short periods, spectra of some records do not fit well to the code spectra. Since short periods represent vibration periods of the substructure, this unfit may result in overestimation or underestimation of substructure forces.

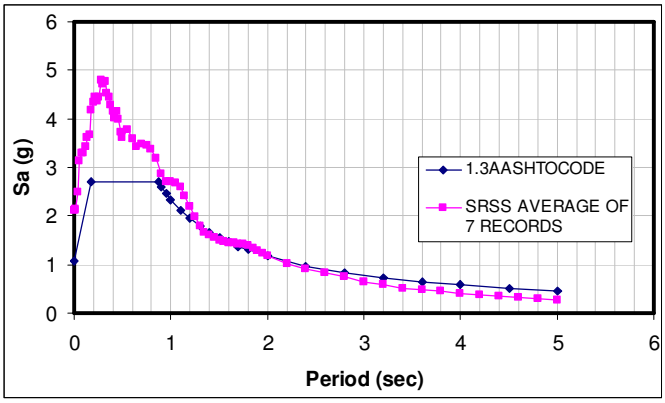


Figure 3: Code Spectrum and Average Spectrum of 7 Earthquakes

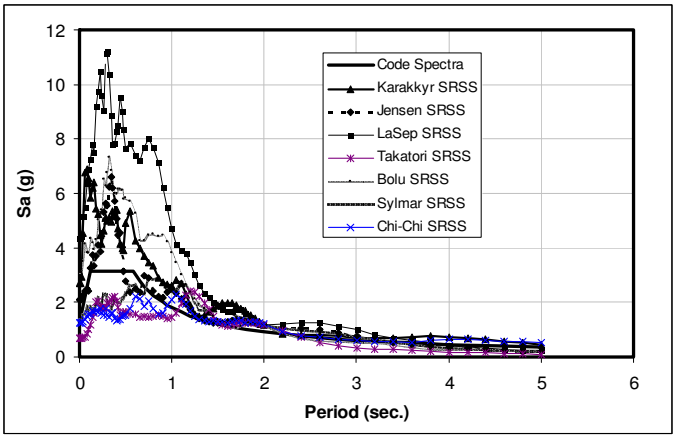


Figure 4: Code Spectrum and SRSS of Selected Earthquake Records

Upper 30 meters of the soil at the bridge site consists of sand, gravel and silt. SPT values increase as depth increases. SPT values ($N_{1,60}$) in between 15-30 are common at the upper 15-20 meters. Moreover, level of water table is close to the free field since the viaducts are on Sakarya river. Liquefaction triggering is a function of ground motion intensity and characteristics as well as geotechnical parameters [4]. Procedure proposed by Seed et al. [4] was utilized for establishing the liquefaction susceptibility of the site. Results have revealed that the site is susceptible to liquefaction during a major earthquake due to high level of seismic input.

In order to verify susceptibility of the bridge site to liquefaction, equivalent linear dynamic analyses were performed by using software Proshake [5]. Scaled earthquake records and geotechnical parameters of the site were set as input. Analyses results have indicated that lateral stiffness of the soil strata between 0-10 meters from the top decreases to almost zero during a major earthquake as presented in Figure 5.

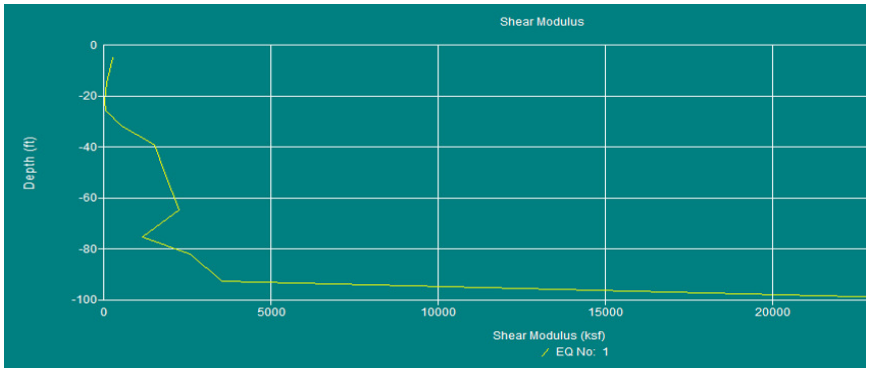


Figure 5: Equivalent Shear Modulus during Expected Earthquake

3 SAKARYA-2 VIADUCT

Sakarya-II viaduct consists of two twin bridges. Two bridges have very similar span lengths and substructures. The bridges have nine spans with a total length of 384 meters for the longer one and 365 meters for the shorter one. Longest span length is 52 meters and shortest span length is 32 meters. The viaduct has a horizontal curvature near one of the abutments as presented in Figure 6.



Figure 6: View of the Sakarya-2 Viaduct

3.1 Superstructure

The superstructure is slab on steel girder with six continuous steel girders. Steel girders are selected in order to provide a lighter superstructure compared to reinforced concrete superstructure. A view of the superstructure cross-section is presented in Figure 7.

The depths of the girders are variable with minimum depth of 1.75 meters and maximum depth of 2.75 meters. Center-to-center spacing between steel girders is 2.30 meters. Expan-

sion joints are only present at abutments. By selecting a continuous superstructure, risk of unseating due to rotation of the substructure and unexpected displacements is eliminated to an important extent.

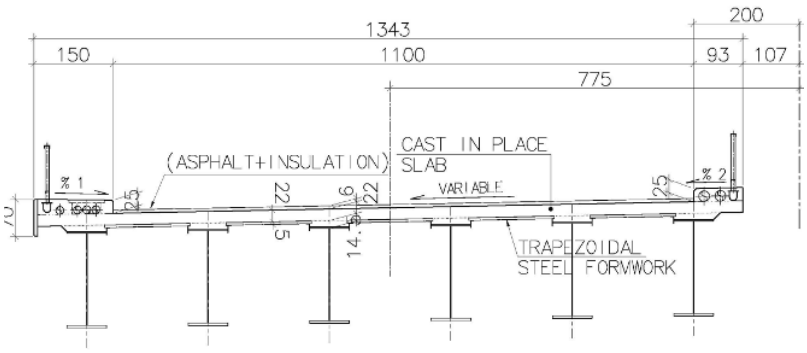


Figure 7: Cross-Section of Superstructure

3.2 Substructure

Piers are hammerhead type with an oblong shaped column. Past experience has indicated that seismic performance of bridges with piers having multiple columns is better compared to those having only one column. In case of piers with single column, stability problems in the transverse direction and large vertical accelerations at the cap beam level due to transverse displacement may be the reasons of such an advantage. Unfortunately, a pier with double column could not be selected for this bridge due to space problems since the bridge crosses the present railway line, highway line and the highspeed railway line that is recently in construction. The bridge has 20° skew angle. The dimensions of the oblong shaped column are 6.00 meters×2.00 meters.

Cast in place reinforced concrete piles with a diameter of 120 cm were utilized in the bridge foundations. There are 20 piles at a pier and 25 at an abutment. The piles are embedded to the bedrock. One pier at each bridge has a spread footing since a very hard rock (conglomerate) was encountered at the surface during construction.

3.3 Seismic Isolation Bearings

A hybrid seismic isolation system consisting of natural rubber bearings and lead rubber bearings were selected for this viaduct. At each substructure, four natural rubber bearings and two lead rubber bearings support six steel I girders.

The four natural rubber bearings over each substructure was intended to provide additional stiffness to achieve a small post elastic period to deflect the earthquake input energy transferred through the underlying soft soil and to limit the isolator displacements under near-field effects.

Lead core in lead rubber bearings increases damping of the system by its elasto-plastic behavior under lateral loads. Structural deformations and forces diminish with energy dissipation capacity. Overall characteristic strength of lead rubber bearings is selected as 10% of the superstructure weight in order to limit the isolator displacements. On the other hand, higher characteristic strength may result in high heat generation at lead core. Therefore, heating up of

the lead core may result in reduced energy dissipation capacities under repeating loading cycles.

3.4 Structural Model

A 3D model of the viaduct is built and analyzed using the software Larsa 4D [6]. The structural model is capable of simulating the non-linear behavior of piers, seismic isolation bearings and soil-structure interaction effects.

Lead rubber bearings are modeled using hysteretic translational springs. An equivalent pile diameter was found by performing a non-linear static analysis on the foundation system. Equivalent single pile has nearly identical lateral response with that of the foundation system. Utilizing a single pile in analyses drastically reduced computation time. Soil-structure interaction is modeled using linear viscous dampers representing effects of soil damping and radiation damping. P-y curves are utilized in analyses. Dimensions of the soil column should be selected sufficiently large in order to be able to change vibration characteristic of pile group. Shear moduli of the soil layers are taken from dynamic analyses results of the soil site.

3.5 Analysis Results

Non-linear analyses with near-field earthquake records resulted in very high substructure forces and isolator displacements. Effective isolation period is found out to be around 1.5 sec. This relatively short isolation period was intentionally selected in order to reduce the sensitivity of the bridge to long-period velocity pulses and high dominant site period due to soft soil and liquefaction. Lateral design displacement for the lead rubber bearings and elastomeric bearings are ±850 mm which resulted in very large isolation bearings. Maximum isolator displacements for each record are presented in Table 2 (in cm).

Earthquake	Long Disp	Trans Disp
Karakyr	50	100
Jensen	40	58
La Sepulveda	117	89
Takatori	24	60
Bolu	41	80
Sylmar	32	80

Table-2: Isolator displacements (in cm)

3.6 Tests of Seismic Isolation Bearings

Natural rubber bearings and lead rubber bearings at 9 of 10 axes have a diameter of 1100 mm. Overall heights of the bearings are 580 mm. Diameter of the bearings utilized in the pier with spread footing is 1400 mm with an overall height of 912 mm. Shear moduli of the rubber bearings is in between 0.42 MPa-0.915 MPa. Bearings with 1400 mm diameter were manufactured in two parts and then connected by using pins and welding.

Test velocity of the lead rubber bearings was calculated as 2.2 m/sec. Combined with lateral design displacement of ±850 mm, testing became the critical issue since there are few laboratories in the world capable of performing such tests. Bearing manufacturer Alga Spa selected EUCenter Laboratory for prototype tests. However, lateral stroke capacity of the testing equipment in EUCenter is limited to ±580 mm. Therefore, prototype tests were divided into two parts as static prototype tests and dynamic prototype tests.

Static prototype tests were performed at Alga spa laboratory with a velocity of 1.6 mm/s and maximum lateral displacement of approximately 1060 mm. Lateral displacement capacity and stability of the bearings were verified during static prototype tests. Nevertheless, no heating in the lead core was observed due to very low testing velocity.

Dynamic prototype tests started with a velocity of 2.2 m/s. However, lateral accelerations in the movable base plate increased to 4g at tests having low displacement amplitudes [7]. Lateral inertial force at the base plate accounted for approximately 50% of the total force. Moreover, stability of the equipment was endangered due to very low axial load levels. For these reasons, tests with 1.4 m/sec, 1.6 m/sec and 1.8 m/sec were performed as confirmation tests. Unfortunately, heating-up of the hydraulic oil did not allow successive cycles without interruption. On the other hand, tested bearings were not damaged during tests as presented in Figure 8.

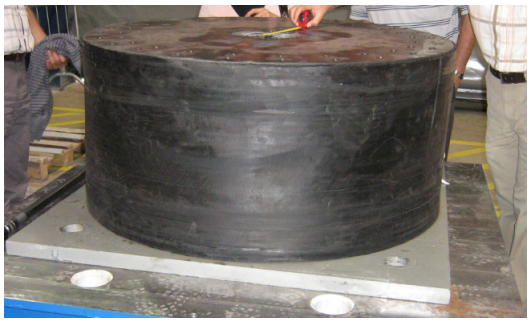


Figure 8: Lead Rubber Bearing After Dynamic Prototype Test

4 VK14A VIADUCT

VK14A viaduct is a 1020 meter long structure with 33 meter spans. There is a gentle horizontal curvature on the viaduct. The viaduct is a part of Ankara-Istanbul highspeed railway line. A general view of the viaduct is presented in Figure 9.



Figure 9:View of VK14A Viaduct

4.1 Superstructure

The superstructure consists of 10 precast prestressed I girders with a 30 cm cast-in-place R/C slab. The view of the superstructure is presented in Figure 10. Superstructure is made continuous by cast in place diaphragm beams connected with I girders by means of U bars emerging from I girders, as presented in Figure 11.

The rails are continuous UIC 60 type rails. In the superstructure, expansion joints are present at every 3 or 4 spans in order to limit additional rail stresses due to train acceleration, deceleration and temperature changes.

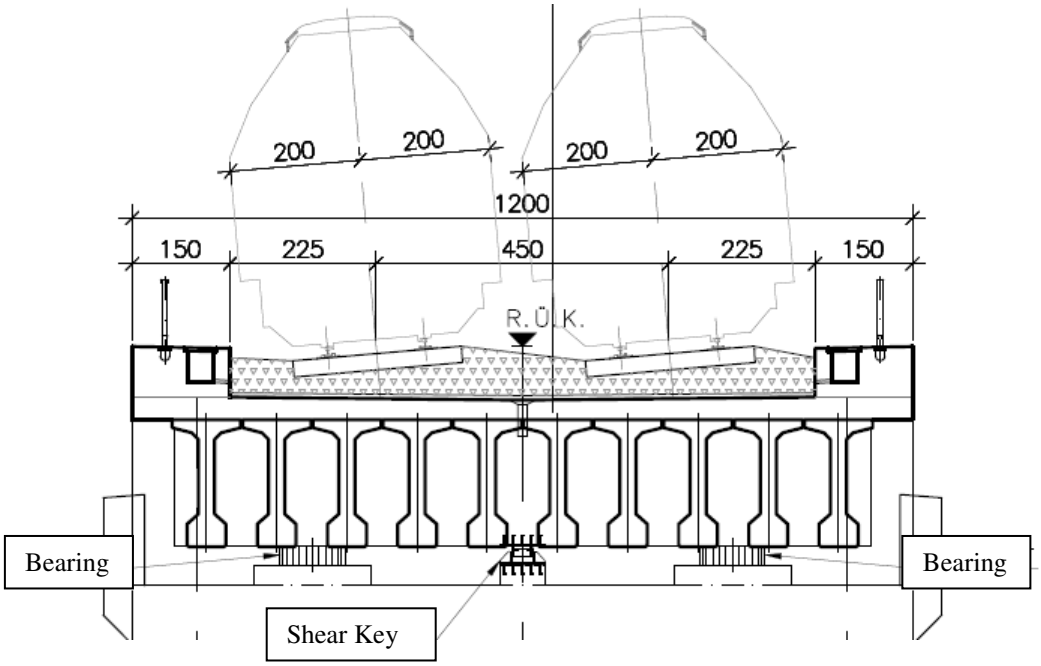


Figure 10:Cross-Section of VK14A Viaduct



Figure 11:Reinforcement Cage of I Girders

4.2 Substructure and Seismic Isolation System

The selected bearing system consists of curved surface sliding bearings with 12% dynamic friction coefficient. There are two bearings at each pier located on diaphragm beams. View of a curved surface sliding bearing during installation is presented in Figure 12. Relatively high friction coefficient is selected in order to fulfill stringent service load requirements of railway bridges. Radius of curvature of the bearings is selected as 2000 mm in order to limit post-elastic period of the structure, which is critical for near-field structures. The bearing supplier is Alga Spa.



Figure 12: Curved Surface Sliding Bearing Installation

At intermediate expansion joints, steel shear keys allowing free longitudinal movement and restraining transverse movement during service load conditions are selected in order to prevent differential transverse movement between modules which can damage rails. During an earthquake, the connection of the steel pipe to its anchorage plate fails and the seismic isolation system becomes fully active. Configuration of a shear key is presented in Figure 13.

In the longitudinal direction, viscous lock-up devices were utilized in order to connect modules to provide continuity. The devices are force-limiting type, meaning that after a force threshold the control valves open and the device acts as a viscous damper. Total stroke of the device is ±200 mm.

Double column piers are utilized with a pile foundation. Pile diameter is 165 cm. Since, piers heights are low and they are mostly embedded in soil, the substructure is designed to behave essentially elastic during a major earthquake.

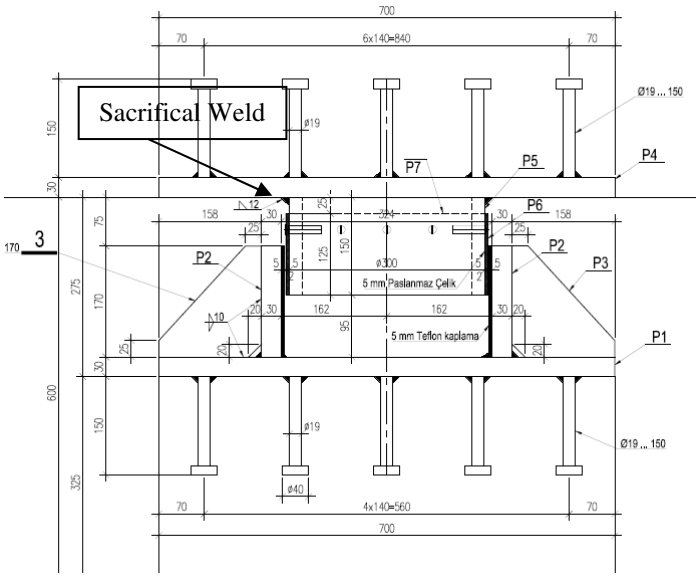


Figure 13: Shear Key Detail

4.3 Structural Model and Analysis Results

The structural model of this viaduct is similar to that of Sakarya-2 viaduct. Design isolator displacement is selected as 500 mm. According to Eurocode 15129 [8], restraining rings should not be utilized at sliding bearings so as to prevent seismic pounding, which may result in bearing damage and transmission of very high pounding forces to substructure. Sectional view of the utilized bearing is presented in Figure 14.

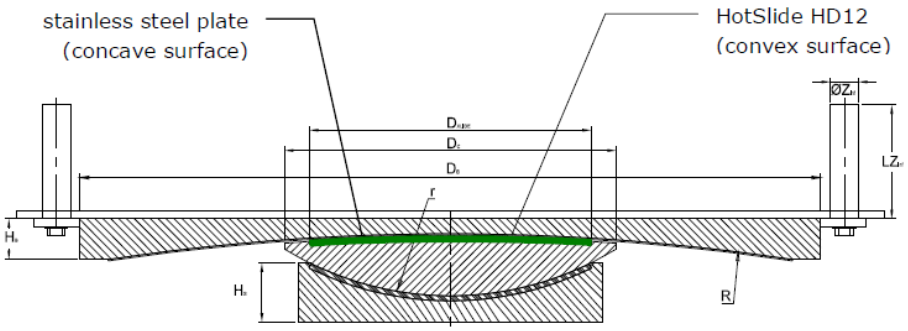


Figure 14: Sectional View of the Selected Curved Surface Sliding Bearings

4.4 Tests of Seismic Isolation Bearings

Tests of seismic isolation systems for railway viaducts is more severe compared to other structures due to stringent service load requirements for these structures in addition to seismic load requirements. Wearing is an important issue for sliding bearings and as expected the effect of wearing increases as the friction coefficient increases.

Wearing resistance of sliding material utilized for this viaduct should be very high since selected friction coefficient is 12% and the superstructure is located directly on bearings. Wearing tests are performed for a total travel path of 1.5 miles. Results of wearing tests are presented in Figure 15.

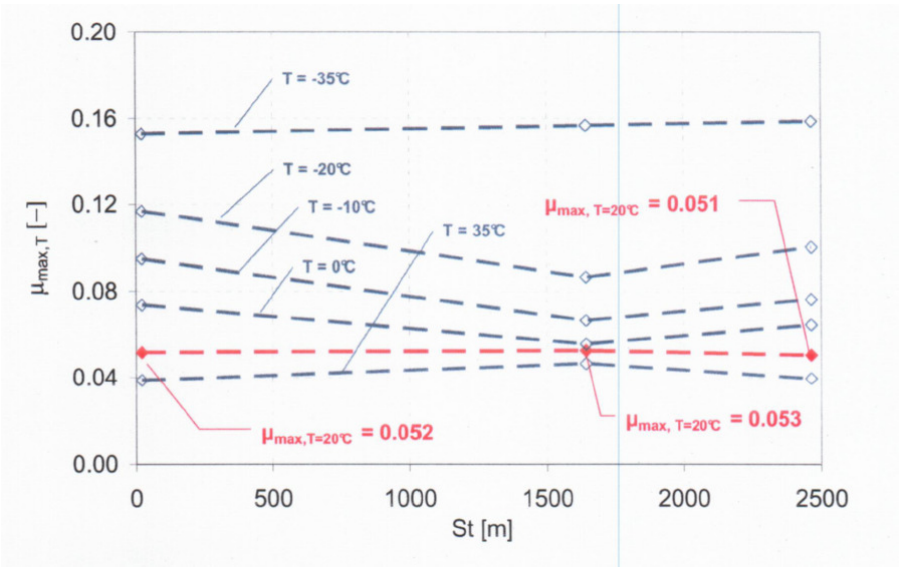


Figure 15: Results of Wearing Tests [9]

As seen in Figure 15, wearing resistance of the sliding material is quite high which has a favorable effect on rail-structure interaction. Temperature sensitiveness of friction coefficient implies that friction coefficient shall not be considered as a definite value but its variation with temperature and wearing shall be considered during structural design.

Behavior of the bearings during dynamic prototype tests was quite satisfactory and degradation in energy dissipation capacity was quite low under repeating load cycles, as presented in Figure 16.

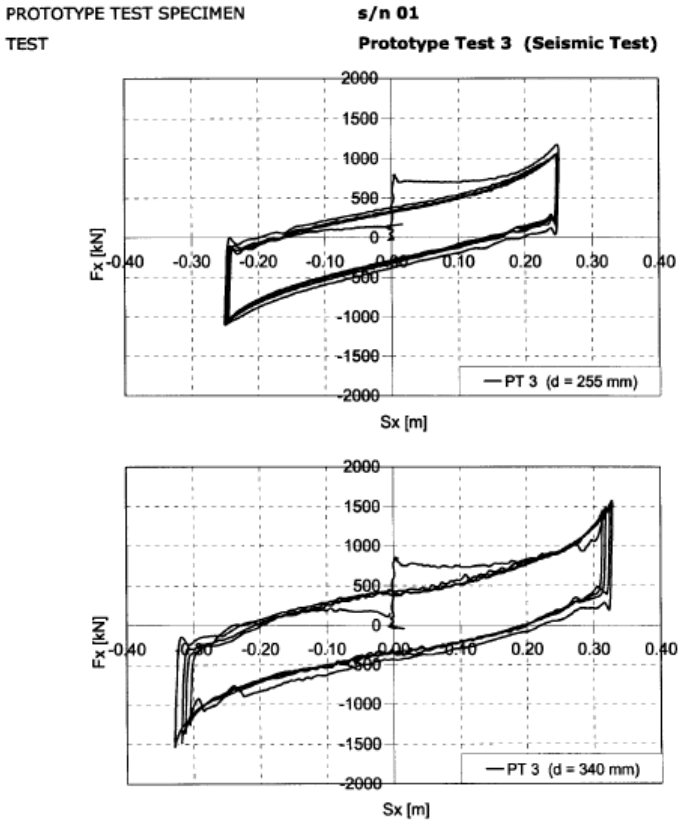


Figure 16: Results of Dynamic Prototype Tests [10]

5 CONCLUSIONS

- The two seismically isolated viaducts were designed to withstand an MCE Mw=7.5 earthquake.
- Seismic isolation period in near-field structures can be kept relatively small in order to provide high restoring force and shift isolation period from that of high intensity velocity pulses.
- Soil structure interaction shall be considered for structures on soft soils.
- Testing of seismic isolation systems for near-field structures require special attention.
- For railway bridges, requirements for bearing systems during service load conditions are as important as seismic load conditions.

REFERENCES

[1] K.O. Cetin, Probabilistic Seismic Risk Report For Sakarya-II Viaduct. *Middle East Technical University*, 2008.

[2] B.A. Bolt, Seismic Input Motions for Nonlinear Structural Analysis. *ISET Journal of Earthquake Technology* , Paper No:448, Vol:41, June-December 2004.

[3] AASHTO, *Guide Specifications for Seismic Isolation Design. USA,* 1999.

[4] S.L. Kramer, Geotechnical Earthquake Engineering. *Prentice Hall*, 1996.

[5] EduPro Civil Systems Inc, Proshake. March 2003.

[6] Larsa Inc., Larsa 2000 4D. New York.

[7] EUCentre, Pre-Characterization and Characterization Tests of LRB Algasism 1100×580. *Pavia-Italy*, October 2009.

[8] Eurocode, *EN 15129:Anti-Seismic Devices. Brussels,* 2009.

[9] Politecnico Di Milano, Wear Test on Special Sliding Material Used In Friction Pendulum Bearings for VK12&VK14A Viaducts At Eskişehir-Kosekoy Highspeed Railway Bridges. *Milano-Italy*, March 2011.

[10] Politecnico Di Milano, Qualification Tests On Anti-seismic Sliding Isolators for VK12&VK14A Viaducts. *Milano-Italy*, July 2011.

COMPDYN 2013
4th ECCOMAS Thematic Conference on
Computational Methods in Structural Dynamics and Earthquake Engineering
M. Papadrakakis, V. Papadopoulos, V. Plevris (eds.)
Kos Island, Greece, 12–14 June 2013

RESTRAINED CONCRETE SHRINKAGE IN CASE OF STRENGTHENED BRIDGE PIERS BY CONCRETE JACKETING

Andreas P. Lampropoulos[1], Ourania T. Tsioulou[2], and Stephanos E. Dritsos[2]

[1]School of Environment and Technology, University of Brighton
Lewes Road, Brighton, BN2 4GJ, UK
a.lampropoulos@brighton.ac.uk

[2]Department of Civil Engineering, University of Patras
Patras 26500, Greece
tsioulou@upatras.gr, dritsos@upatras.gr

Keywords: bridge piers, concrete jackets, finite elements, restrained shrinkage.

Abstract. *Reinforced concrete (RC) jacketing of weak bridge pier columns is an effective retrofitting technique, particularly in seismic regions. The effect of restrained concrete shrinkage on the strength of concrete jackets is investigated in this study. A series of compressive tests are performed on square prism concrete specimens where steel plates are placed to represent the restrained shrinkage effect on the concrete of the jacket. Then, a numerical procedure to simulate the concrete shrinkage effect using the finite element method is proposed and results are justified and validated using the experimental data. The results indicate that restrained concrete shrinkage considerably reduces the stiffness and the maximum load of the strengthened elements.*

1 INTRODUCTION

Reinforced concrete (RC) jacketing of weak bridge pier columns is an effective retrofitting technique, particularly in seismic regions. Much experimental work has been performed in the area of strengthening existing structures using additional reinforced concrete layers and jackets [1–7] and it has been proved that a critical parameter for the performance of strengthened elements is the connection procedure between the jacket and the original column. An additional critical parameter for the response of the strengthened elements is the restrained concrete shrinkage. Experimental work has been conducted and it has been found that the compressive strength of concrete elements under restrained shrinkage can be considerably reduced due to a biaxial stress state [8].

In the present paper the findings of this experimental work have been used and finite element analyses have been conducted in monolithic and strengthened reinforced concrete columns with and without concrete shrinkage. The reliability of the numerical model has been examined in a previous study and it was found that the numerical model can accurately predict the response of strengthened elements when the interface between the old and the new concrete is simulated using two-dimensional contact elements and when concrete shrinkage is simulated using a volumetric strain [9]. The results of this study indicate that when jacket's shrinkage is simulated, strength and stiffness are reduced while the deflection at yield and failure is increased.

2 EXPERIMENTAL INVESTIGATION

The experimental investigation of the effect of restrained concrete shrinkage will be presented in this section. Fourteen identical specimens were examined. Seven were cast with steel plates (A_r, B_r, C_r, D_u, E_r, F_r, G_u) representing the restraint shrinkage condition, and seven were cast with pieces of expanded polystyrene (A_f, B_f, C_f, D_f, E_f, F_f, G_f) representing the free shrinkage condition [8]. Specimens' geometry is presented in figure 1.

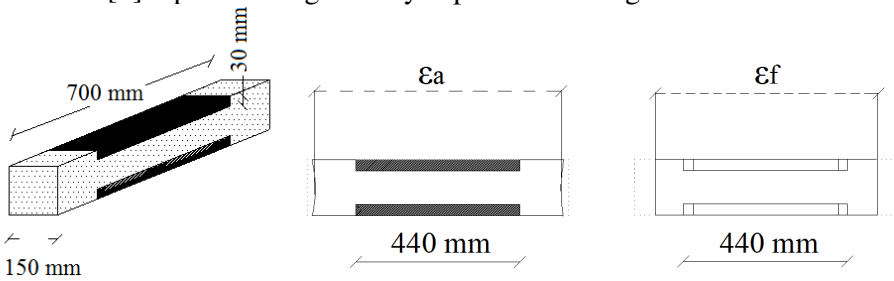
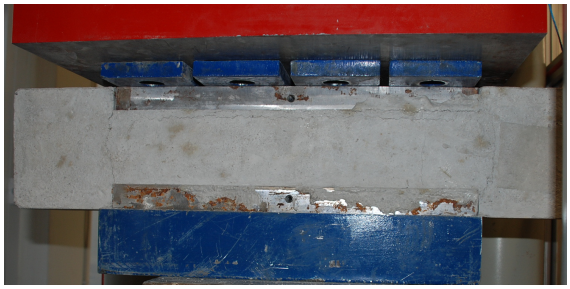


Figure 1: Specimens' geometry.

These specimens were stored until testing in a room with a constant temperature of 25 ^{o}C and a relative humidity of 50%. Dial gauges were placed at the ends of the specimens to measure concrete shrinkage strain (figure 2a) [8]. Then the specimens were tested under compression (figure 2b). The specimens with the steel plates were tested first and then the steel plates were removed from the broken specimen and used to replace the expanded polystyrene in the other specimens before testing. For two pairs of specimens, D and G, the steel plates were removed from the specimens in order to unload the tensile stresses due to restrained shrinkage. Then the steel plates were reattached to the specimens to perform the compressive tests [8].



(a)



(b)

Figure 2: Experimental setup a) for the measurement of shrinkage strain and b) for the compressive testing.

The maximum load for each specimen and the strength reduction due to restrained concrete shrinkage are presented in table 1.

Specimens		Description	Maximum load (kN)	Strength reduction (%)
A (14 days)	A_f	Free concrete shrinkage	1577.6	20
	A_r	Restrained concrete shrinkage	1261.9	
B (28 days)	B_f	Free concrete shrinkage	1976.5	26
	B_r	Restrained concrete shrinkage	1471.9	
C (112 days)	C_f	Free concrete shrinkage	2092.2	24
	C_r	Restrained concrete shrinkage	1579.9	
D (112 days)	D_f	Free concrete shrinkage	2399.5	6
	D_u	Restrained concrete shrinkage and unloading	2244.3	
E (14 days)	E_f	Free concrete shrinkage	2132.3	21
	E_r	Restrained concrete shrinkage	1688.9	
F (28 days)	F_f	Free concrete shrinkage	2444.8	28
	F_r	Restrained concrete shrinkage	1770	
G (28 days)	G_f	Free concrete shrinkage	2444.8	6
	G_u	Restrained concrete shrinkage and unloading	2308.7	

Table 1: Experimental results of maximum load and strength reduction due to restrained concrete shrinkage.

Equation 1 was used for the calculation of the tensile stress values perpendicular to the direction of the compressive loading.

$$\sigma = E_{ct} \cdot \varepsilon_{r,el} \tag{1}$$

where:

E_{ct} is the reduced modulus of elasticity taking into account the stress relief due to creep.

The following equations were used to calculate E_{ct} [10]:

$$E_{ct} = \frac{E_c}{1 + x * C_t}, \; E_c = 9500(f_{cm})^{1/3} \tag{2}$$

where:

E_c is the modulus of elasticity of concrete. This was calculated using compressive test results of standard 150 mm concrete cubes;

x is a coefficient that depends on the concrete age and can be considered to equal 0.8;

$$C_t = 2.35 * \left(\frac{t^{0.6}}{10 + t^{0.6}} \right);$$

t is the age in days; and
f_{cm} is the concrete compressive strength.

The difference between the free (ε_f) and the actual shrinkage (ε_a) of the specimens with restrained concrete shrinkage defines the restrained shrinkage strain (ε_r). This strain comprises of the elastic ($\varepsilon_{r,el}$) and the plastic restrained shrinkage strain ($\varepsilon_{r,pl}$). The elastic strain ($\varepsilon_{r,el}$) was used for the calculation of the tensile stresses (equation 1). To estimate $\varepsilon_{r,el}$, the strain was measured when unloading the tensile stresses by removing the steel plates.
The tensile stress (σ), the ratio of the tensile stress over the tensile strength (σ/f_t), and the respective strength reduction ($f_{c,shrink}/f_{c,free}$) are presented in table 2.

Specimen	E (MPa)	E_{ct} (MPa)	$\varepsilon_{r,el}$ (microstrains)	σ (MPa)	σ/f_t	$f_{c,shrink}/f_{c,free}$
A	22500	13925	46	0.64	0.38	0.80
B	24200	13455	58	0.78	0.41	0.74
C	24200	11086	58	0.64	0.33	0.76
E	25800	15967	46	0.73	0.33	0.79
F	26600	14790	58	0.86	0.37	0.72

Table 2: Tensile stresses due to restrained concrete shrinkage and the respective strength reduction.

The compressive concrete strength reduction with the tensile stress due to restrained concrete shrinkage is presented in figure 3 together with the model proposed by Kupfer et al. [11] for concrete under biaxial stress state.

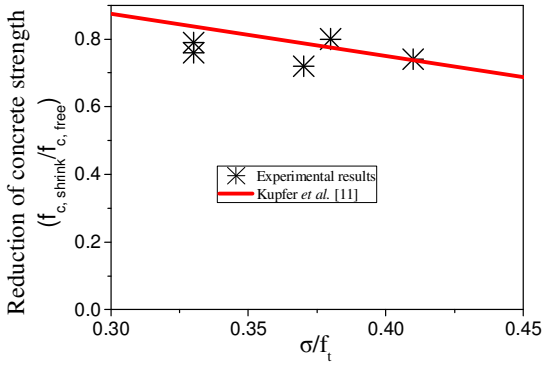


Figure 3**:** Concrete compressive strength reduction with the perpendicular tensile stress values.

From figure 3, it can be observed that the experimental results are in a very good agreement with the model proposed by Kupfer et al. [11] for biaxial stress state. This model was adopted for the numerical simulation of this study.

3 NUMERICAL SIMULATION

3.1 Numerical Assumptions

ATENA software [12] was used for the numerical simulation. To simulate the concrete, an eight-node element was used with nonlinear stress versus strain behaviour in compression and softening branches in both compression and tension. To simulate the steel, linear elements were used with a bilinear stress versus strain behaviour including strain hardening. These elements are capable of including the relative slip of the reinforcement in relation to the surrounding concrete.

The interface between the old and the new column was simulated using special contact elements with coefficients of friction and cohesion of 1.0 and 0.0 MPa, respectively. These values were used to model a well roughened interface as it has been demonstrated [9] that using low and constant values, strength degradation at the interface due to earthquake cyclic loading can be effectively simulated [9, 13].

The geometry and the material properties of the examined specimens were based on a previous work where the reliability of the numerical model was examined [9]. The cross sectional dimensions of the original columns were 250 mm by 250 mm and their height was 1800 mm, while jacket thickness was 75 mm and placed to a height of 1300 mm. The longitudinal reinforcement of the initial columns was 4 bars of 14 mm diameter with a yield stress of 313 MPa and a rupture stress of 442 MPa. Stirrups were 8 mm diameter spaced at every 200 mm with a yield stress of 425 MPa and a rupture stress of 596 MPa. The longitudinal reinforcement of the jacket was 4 bars of 20 mm diameter with a yield stress of 487 MPa and a rupture stress of 657 MPa. Jacket stirrups were 10 mm diameter spaced at every 100 mm with a yield stress of 599 MPa and a rupture stress of 677 MPa. The concrete cover of the longitudinal reinforcement of the original column was 15 mm. For the jacket, the cover was 25 mm when a 75 or 150 mm thick jacket was examined and it was 10 mm when a 25 mm thick jacket was considered. The concrete strengths of the initial columns and jackets were 27.0 MPa and 55.8 MPa, respectively. An axial load was applied to the top of the specimens and a horizontal displacement was applied to the columns at a height of 1600 mm above the footing [13]. The cross section of the examined model and the finite element model are presented in cross section of the examined columns are presented in figure 4.

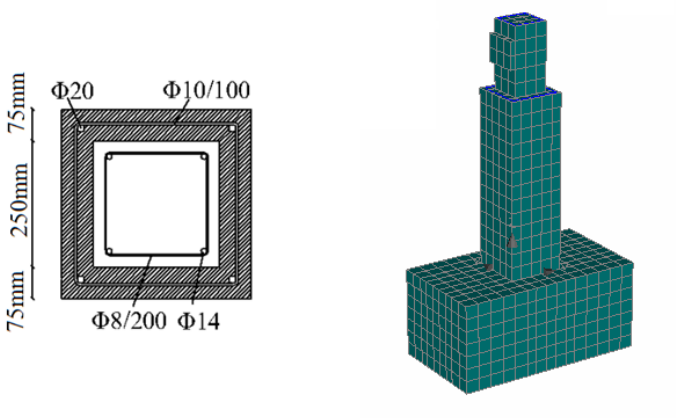


Figure 4: Cross section of the strengthened column and finite element model.

Concrete shrinkage was simulated with a volumetric strain to the concrete elements of the jacket. In the present study, an ultimate free concrete shrinkage value of 800 microstrains was used. This value was considered to be reduced to half (400 microstrains) in order to include the stress relaxation due to creep [13, 14]. The stress distribution in the column and the jacket is presented in the following figure (figure 5).

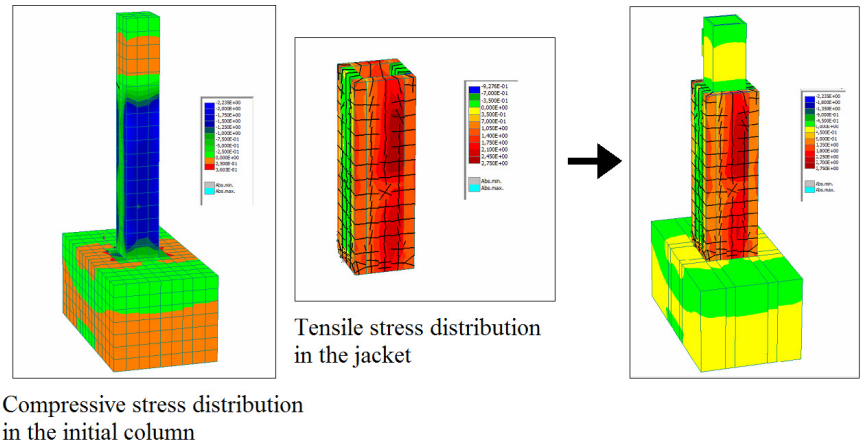


Figure 5: Stress distribution in the column and the jacket due to concrete shrinkage.

In figure 5, the tensile stresses of concrete jacket and the equivalent compressive stress distribution to the concrete of the initial column are presented. It can be observed that the tensile stress of the jacket exceeds the tensile strength and the concrete cracks due to restrained concrete shrinkage.

The results of the analyses of the strengthened columns with and without concrete shrinkage are compared to the experimental results. The numerical results of the respective monolithic specimen, where perfect bond between the old and the new concrete was assumed, are also presented (figure 6) [9].

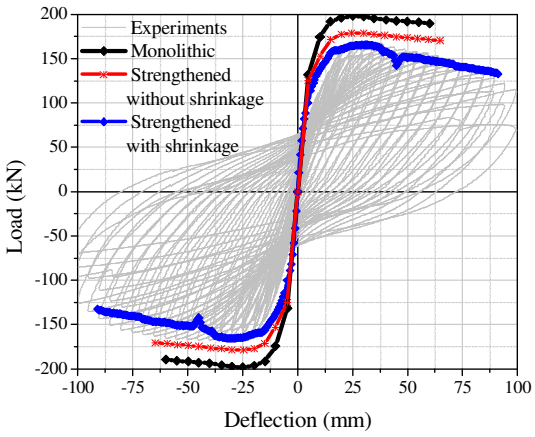


Figure 6: Load-deflection results of the analyses with and without concrete shrinkage together with available experimental results [9].

The simulation of concrete shrinkage considerably improved the accuracy of the numerical predictions. The analysis of the monolithic specimens overestimated the strength and the stiffness of the columns. The deviation between the numerical and the experimental results was reduced when the interface between the old and the new concrete was simulated ('Strengthened without shrinkage'). The results were found to be in a very good agreement with the experimental results when concrete shrinkage was also simulated.

3.2 Parametric Study

A parametric study was conducted in order to investigate the effect of the normalized axial load on the response of strengthened piers with RC jackets.

For the calculation of normalized axial load (v) values, equation 3 was used.

$$v = \frac{N}{A_{co} \cdot f_{co} + A_{cj} \cdot f_{cj}}, \tag{3}$$

where:

N is the applied axial load value;

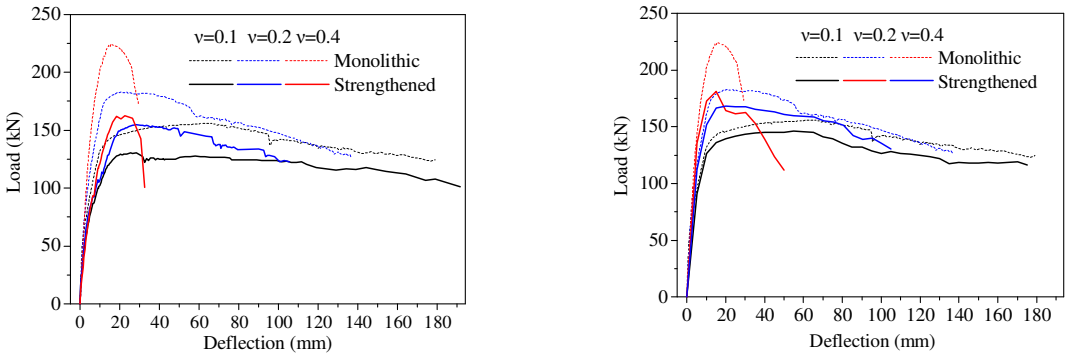
A_{co} is the cross sectional area of the original column;

f_{co} is the concrete strength of the original column;

A_{cj} is the cross sectional area of the concrete jacket; and

f_{cj} is the concrete strength of the jacket.

Analyses were performed with and without concrete shrinkage for strengthened piers where the interface between the old and the new concrete was simulated. Respective monolithic specimens were also examined where perfect bond between the old and the new concrete was assumed. The results of the analyses with and without the simulation of concrete jacket's shrinkage are presented in figures 7a and 7b.



(a) (b)

Figure 7: Load-deflection results of the analyses a) with and b) without concrete shrinkage for different values of normalized axial load values.

Monolithic coefficients for the strength, stiffness, and deflection (δ) or rotation angle (θ) at yield and failure were calculated using equation 4. These coefficients correlate the behaviour of the strengthened specimens with the respective monolithic.

$$K_F = \frac{[F_{max}]_{STR}}{[F_{max}]_{MON}}, \quad K_k = \frac{\left[F_y / \delta_Y\right]_{STR}}{\left[F_y / \delta_Y\right]_{MON}}, \quad K_{\delta,\theta_y} = \frac{[\delta_y]_{STR}}{[\delta_y]_{MON}}, \quad K_{\delta,\theta_u} = \frac{[\delta_u]_{STR}}{[\delta_u]_{MON}}, \tag{4}$$

where:

K_F, K_k, and $K_{\delta,\theta_{y,u}}$ are monolithic coefficients for the strength, stiffness, and deflection or rotation angle, respectively;

F_y and F_{max} are the yield and maximum load; and

δ_y and δ_u are the deflections at yield and failure.

Subscripts *STR* and *MON* indicate strengthened and monolithic specimens, respectively [13].

To estimate the load and the deflection at yield point, the load versus deflection curve up to the maximum load was converted to an equivalent bilinear approximation according to the procedure proposed in ATC 40 [15]. Failure was considered to occur when the load capacity was reduced to 80% of the maximum load value. Using this procedure, the load versus deflection curve was converted to an equivalent tri–linear distribution based on the characteristic points of yield, maximum load and failure of the specimen. These equivalent points were then used to calculate monolithic coefficient values (equation 4) [13].

The tri-linear load deflection curves of monolithic and strengthened columns with and without concrete shrinkage have been calculated and the results are presented in figure 8.

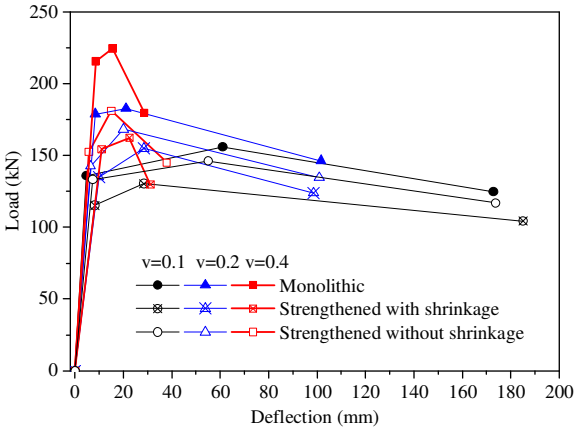


Figure 8: Tri-linear load-deflection results of the analyses with and without the simulation of concrete shrinkage.

Using the results of figure 8 and equation 4, the monolithic coefficient values for strength, stiffness, and deflection or rotation angle at yield and failure were calculated. Figure 9 shows the distribution of these values with the normalized axial load.

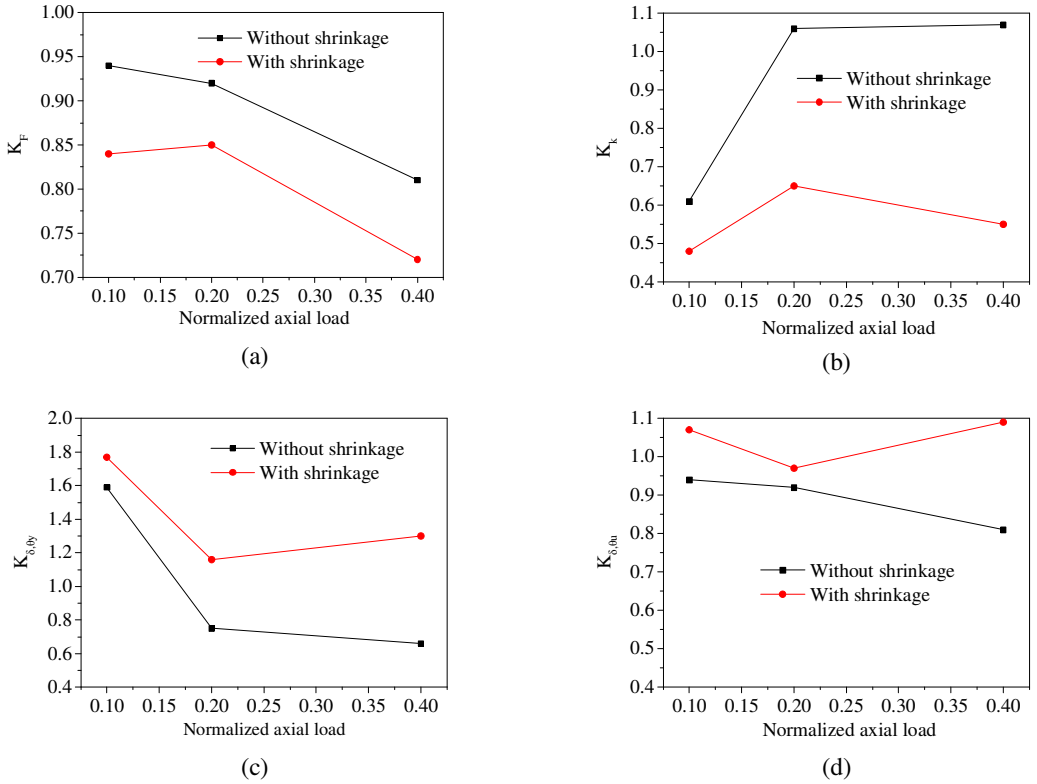


Figure 9: Monolithic coefficient value distribution with the normalized axial load values for the a) strength, b) stiffness, and c,d) deflection/ rotation angle at yield and at failure.

From the results of figure 9, it can be observed that the strength and the stiffness are reduced when concrete shrinkage is simulated, while the deflection/rotation angle at yield and failure is increased. The effect of concrete shrinkage is summarized in table 3.

		Shrinkage effect			
	ν	Strength reduction (%)	Stiffness reduction (%)	Deflection/ rotation angle increment (%)	
				at yield	at failure
Numerical investigation	0.1	11	21	11	14
	0.2	8	39	55	5
	0.4	11	49	97	35

Table 3: Shrinkage effect on strength, stiffness and deflection/rotation angle at yield and failure.

The results indicate that there is a reduction of strength and stiffness due to concrete shrinkage. The reduction of strength is 8-11% depending on the normalized axial load value. A significant reduction of the stiffness was observed. The reduction was considerably affected by the normalized axial load value. For large values of the normalized axial load the stiffness was considerably reduced when concrete shrinkage was simulated. A significant increment of deflection (or rotation angle) at yield and failure for high values of the normalized axial load can also be observed.

4 CONCLUSIONS

The effect of restrained concrete shrinkage on the response of strengthened elements was investigated in this study. The results of an experimental investigation were presented and it was found that the compressive strength of the specimens is considerably reduced when there are tensile stresses due to restrained concrete shrinkage. Concrete shrinkage effect was also simulated using finite element method and jacketed columns were examined using different values of jacket's thickness and normalized axial load. Analyses were performed with and without the simulation of concrete shrinkage. Respective monolith columns were also examined and monolithic coefficient values were calculated. From the monolithic coefficient values the following conclusions can be drawn:

- The strength of the jacketed columns is reduced when the shrinkage of the jacket is simulated and the reduction was found to be in the range of 8-11% for all the examined specimens.
- The stiffness of the jacketed columns was also reduced and the reduction was higher as the normalized axial load was increased.
- The deflection/rotation angle of the columns at yield and failure was considerably increased. This increment was higher for the deflection/rotation angle at yield and for high values of the normalized axial load.

The effect of restrained concrete shrinkage is highlighted in this paper. It can be observed that restrained concrete shrinkage can reduce the concrete compressive strength and this can considerably reduce the strength and the stiffness of strengthened bridge pier columns. It is not conservative to neglect concrete shrinkage effect when strengthened elements with RC jackets are examined.

5 REFERENCES

[1] B.J. Bett, R.E. Klingner, J.O. Jirsa, Lateral load response of strengthened and repaired reinforced concrete columns, *ACI Structural Journal* 1988; **85**(5), 499-508, 1988.

[2] U. Ersoy, A.T. Tankut, R. Suleiman, Behaviour of jacketed columns. *ACI Structural Journal*, **90**(3), 288-293, 1993.

[3] M. Rodriguez, R. Park, Seismic load tests of reinforced concrete columns strengthened by jacketing, *ACI Structural Journal,* **91**(2), 150-159, 1994.

[4] E.S. Julio, F. Branco, V.D. Silva, Structural rehabilitation of columns with reinforced concrete jacketing, *Progress in Structural Engineering and Materials Journal***, 5,** 29-37**,** 2003**.**

[5] K.G. Vandoros, S.E. Dritsos, Interface treatment in shotcrete jacketing of reinforced concrete columns to improve seismic performance, *Structural Engineering and Mechanics Journal*, **23**, 43-61, 2006.

[6] K.G. Vandoros, S.E. Dritsos, Concrete jacket construction detail effectiveness when strengthening RC columns. *Construction and Building Materials Journal*, **22**(3), 264-276, 2008.

[7] S. Bousias, D. Biskinis, M. Fardis, A.L. Spathis, Strength, stiffness and cyclic deformation capacity of concrete jacketed members, *ACI Structural Journal,* **104**(5), 521-531, 2007.

[8] A.P. Lampropoulos, O.T. Tsioulou, S.E. Dritsos, Biaxial Stress due to Shrinkage in Concrete Jackets of Strengthened Columns, *ACI Materials Journal*, **109**(3), 331-340, 2012.

[9] A.P. Lampropoulos, S.E. Dritsos, Modelling of RC columns strengthened with RC jackets, *Journal of Earthquake Engineering and Structural Dynamics*, **40**(15), 1689–1705, 2011.

[10] ACI 209R-92, *Prediction of Creep, Shrinkage and Temperature Effects in Concrete Structures*, American Concrete Institute, Farmington Hills, 1997.

[11] H. Kupfer, H. Hilsdorf, H. Rusch, Behavior of Concrete under Biaxial Stresses, *American Concrete Institute Journal*, **66**(8), 656-666, 1969.

[12] V. Cervenka, L. Jendele, J. Cervenka, *ATENA Program Documentation 2005*, Cervenka Consulting, Prague, 2005.

[13] A.P. Lampropoulos, O.T. Tsioulou, S.E. Dritsos, Monolithic Coefficient Values for Design when Seismically Strengthening RC Columns with Jackets, *Journal of Earthquake Engineering*, **16**(7), 1023-1042, 2012.

[14] A.P. Lampropoulos, S.E. Dritsos, Concrete Shrinkage Effect on Columns Strengthened With Concrete Jackets**,** *Structural Engineering International*, **20**(3), 234-239, 2010.

[15] ATC 40, *Seismic Evaluation and Retrofit of Concrete Buildings*, Applied Technology Council, California, Vol. 1, 1996.

COMPDYN 2013
4th ECCOMAS Thematic Conference on
Computational Methods in Structural Dynamics and Earthquake Engineering
M. Papadrakakis, V. Papadopoulos, V. Plevris (eds.)
Kos Island, Greece, 12–14 June 2013

STUDY OF THE IN-PLANE BEHAVIOUR OF GROUND FLOOR REINFORCED CONCRETE (R/C) FRAMES RETROFITTED WITH JACKETING AND AN ENCASED R/C PANEL IN ORDER TO WITHSTAND SEISMIC FORCES

George C. Manos[1], V. Soulis[1], K. Katakalos[1]*, G. Koidis[1]

[1] Laboratory of Strength of Materials and Structures, Dept. Civil Engineering, Aristotle University, Thessaloniki, GREECE
gcmanos@civil.auth.gr

Keywords: Retrofitting, Reinforced Concrete Frames, Encasement R/C Panels, Jacketing, Soft Ground Floor

Abstract. *The in-plane behaviour of one-bay single-storey reinforced concrete (R/C) frames was numerically examined when they were subjected to cyclic seismic-type horizontal loading and their retrofitting scheme included jacketing of their columns together with a cast-in-place infill R/C panel as an encasement. This numerical study examined the influence of the presence of such an encased R/C panel, being connected with the surrounding frame with or without steel ties, on the overall behaviour of such a system. From the preliminary numerical analysis results it can be concluded that such an encasement results in a considerable increase of the stiffness and the bearing capacity of the studied system, especially when steel ties are present at the interface. Moreover, the placement of steel ties also moderates the amplitude of the forces that are transferred at the narrow column-to-beam joint regions in a direction normal to the interface through the contact/gap mechanism, and consequently, mitigate the possibility of crushing the encased panel and/or parts of the columns or beams at these regions. Consequently, it can be concluded that the presence an encased R/C panel being connected by the appropriate steel ties with the surrounding R/C frame, has an overall beneficial effect on the behaviour of this type of structural system subjected to seismic type loading An experimental sequence was also performed in order to quantify the behaviour of such steel tie connections at the interface under a stress field that is expected to develop at this part of the encasement during seismic type loading. Such measured behaviour is in agreement with the assumptions made concerning the behavioural characteristics of these steel ties in the preliminary numerical analysis*

1 INTRODUCTION

Many multi-storey reinforced concrete (R/C) structures, built in seismic regions, have their ground floor designed to function as a parking space. Therefore, the bays of the R/C frames at this level are left without masonry infills whereas all the stories above have their corresponding bays of the R/C frames infilled with external masonry walls (with or without door and window openings) or with internal masonry partitions. It was demonstrated by extensive past research that the dynamic and earthquake behaviour of such structures, having a relatively flexible (soft) ground floor and stiff upper stories, results in increased demands on the structural elements of the ground floor, due to the interaction of the masonry infills with the surrounding R/C frames. This, in turn, leads to structural damage, unless the structural R/C elements at the ground floor are properly designed ([1], [3], [5], [6], [7]). As this behaviour was not well understood in the past, there are many structures with such a soft storey that were designed and constructed with their R/C structural elements now in need of upgrading their capacity in order to meet such increased demands imposed on them from potential future seismic actions.

The objective of this paper is to investigate the performance of a retrofitting scheme that can be easily applied to such a soft ground floor of multi-storey reinforced concrete (R/C) structures ([2], [4], [8], [9], [10]). A common retrofitting scheme usually consists of:

- R/C jacketing of the existing R/C columns at the ground floor level.
- R/C jacketing of the existing R/C beams at the ground floor level.

The jacketing at this level is considered as feasible due to fewer construction constraints than a similar jacketing scheme at the upper stories, which will be prevented from various obstacles such as: the existing partitions, the floors and many other non-structural features.

With the jacketing of the main ground floor structural elements, a certain increase in their strength and ductility is expected to be achieved. The current Greek guidelines for retrofitting reinforced concrete buildings [4], also provides for the addition of an R/C panel that can be added as an encasement, filling the space between the jacketed columns and beams. This can be done for a number of bays at such a soft ground floor in need of being strengthened. The placement of such infilling R/C encasement panels will provide additional stiffness and possible strength at this level, thus balancing the initial abrupt change of stiffness between this floor and the rest of the upper stories, that initiates its unfavourable performance.

In the relevant provisions of these guidelines [4] the designer is provided with a number of distinct choices. In the present investigation the following choices will be studied:

a. The encasement of the R/C panel is done without any connection with the surrounding R/C structural elements within a bay (columns or beam). The provisions describe a limited connection of the R/C panel to the upper and lower horizontal boundaries (beams) of the bay.

b. The encasement of the R/C panel is constructed together with a connection with the surrounding R/C structural elements strengthened by jacketing within a bay (columns or beam), utilizing steel ties. In this case, the thickness of the encasing R/C panel is smaller than the width of the beams that form the encased bay.

c. The previous case is differentiated by a third type of encasement, where the added R/C panel has a thickness larger than the width of the beams of the bay. This is envisaged as a construction of an additional shear wall rather than an encasement and should be treated differently. This last case is not investigated here. Therefore, the present study is limited to cases a and b described above.

2 PRELIMINARY NUMERICAL SIMULATION

The numerical study was limited to examining a single storey one bay R/C frame formed by two columns (left and right) and two beams (top and bottom), as shown in figure 1. The overall dimensions of this frame were chosen, arbitrarily, as follows: The length between the mid axes of the two columns equal to 6m. The height between the mid-axes of the top and bottom beams equal to 3m. The cross section of the columns 340mm x 340mm; that of the top beam 300mm x 600mm and that of the bottom beam with large flexural stiffness representing a rather stiff foundation beam, to be specially constructed for this purpose. The numerical model included three non-linear springs located at all the interconnections between the columns and the beams either at the top and bottom of each column or at the left and right side of each beam, whereas the region representing the actual beam-column joint was considered as non-deformable. These non-linear springs were provided with tri-linear moment-rotation properties thus representing the possibility of plastic hinges forming at these locations. The properties of these moment-rotation springs were derived considering typical reinforcing details for the columns and beams for such structural elements at the ground floor as well as an axial force level for the columns equal to 510 KN, representing the axial force level for a building with three more stories above the ground floor where the examined single-storey one bay R/C sub-assembly is assumed to be located. In this way, only the scenario of non-linear behaviour from flexure, by the formation of the plastic hinges is considered, excluding any shear non-linear behaviour of the R/C structural members.

In this preliminary numerical simulation, the behaviour of the encased R/C panel itself was considered to be elastic. A subsequent numerical simulation considered the possibility of non-linear behaviour of the encased R/C panel itself.

The properties of these moment-rotation springs were derived considering typical reinforcing details for the columns and beams for such structural elements at the ground floor as well as an axial force level for the columns equal to 510 KN, representing the axial force level for a building with three more stories above the ground floor where the examined single-storey one bay R/C sub-assembly is assumed to be located. The thickness of the encased R/C panel was assumed to be equal to 150mm constructed with a material having Young's modulus equal to E=7GPa to account for a level of cracking.

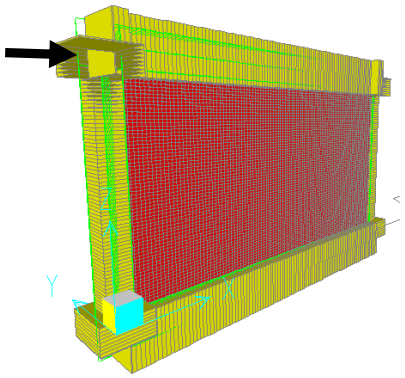


Figure 1. The studied single-storey one bay R/C frame with the encased R/C panel

The following distinct models were considered:

1. *bare frame*" model. This first model was that without any encasement.

All the other models, which were studied and are described briefly below, included an encased R/C panel (with a 150mm thickness) which was connected to the surrounding frame in a variety of ways, as will be explained below. The connection of the encased R/C panel with the surrounding frame was numerically simulated with two distinct types of non-linear link

elements each one representing a distinct force transfer mechanism ([1], [7]). The first type of link represents the contact/gap mechanism between the R/C panel and the surrounding frame. As such, this link can transfer only compressive forces with a direction normal to the interface without any limitation, transferring at the same time forces with a direction tangent to the interface, considering an acceptable friction transfer mechanism. However, when the stress field at the interface between the encased R/C panel and the structural member of the surrounding frame becomes tensile then this transfer of forces either in the normal or in the tangent to the interface direction through the first type of link becomes neutralized. The second type of connection between the R/C encasement panel and the surrounding frame represents an additional force transfer mechanism that simulates the presence of a steel metal tie. These metal ties are embedded at both the R/C panel and the structural elements (columns or beams) of the surrounding frame at certain intervals on the interface. They are placed in a direction normal to the interface and can thus transfer tensile forces normal to the interface (the compressive forces being transferred mainly by the contact/gap mechanism) or tangential forces in addition to the contact transfer mechanism. This second type of link was assumed to have an elasto-plastic behaviour in its longitudinal direction, representative of a steel reinforcing bar with a diameter of 12mm and a yield stress of 500MPa. A similar elasto-plastic behaviour was also assumed in the tangential direction representing such tangential behaviour of a 12mm diameter tie. Towards the quantification of such tangential behaviour of a steel tie, a sequence of tests was conducted that will be briefly described in section 4. These metal ties were assumed to be spaced at 180mm intervals along the interface of the numerical models

The behaviour of the following three distinct models were studied that included an encasement of an R/C panel within the one-storey one bay R/C frame.

2. *Encased model a***.** This model was provided with only the first type of links all around the interface of the R/C encased panel with the surrounding frame, thus representing a connection between the R/C encased panel and the surrounding frame that could transfer forces at their interface only through the contact/gap mechanism.
*3. Encased model b***.** In this model, the previous contact/gap transfer mechanism was retained through the first type of links. In addition to that the second type of links were added only at the interface of the encased R/C panel with the top and bottom beams of the surrounding R/C frame, as provided by the relevant guidelines, representing 12mm steel ties spaced at 150mm intervals.
*4. Encased model c***.** In this model, the contact/gap transfer mechanism was again retained through the first type of links. The second type of links were added both at the interface of the encased R/C panel with the top and bottom beams of the surrounding R/C frame as well as at the interface of the encased R/C panel with the left and right columns of the surrounding R/C frame, representing 12mm steel ties spaced at 150mm intervals.

3 NUMERICAL RESULTS

All the previous numerical models were subjected to a horizontal incremental force in a direction coinciding with the mid-axis of the top beam, This was done in a “push - over” type of loading with sufficient increment so that equilibrium could be established through an iteration process, taking into account all the non-linear mechanisms that were included in these models. These were the following:

- The possibility of developing plastic hinges at the top and bottom of the columns as well as at the left and right edge of the top beam.

- The possibility to triggering the contact/gap mechanism at the interface between the encased panel and the surrounding R/C frame
- The possibility of the steel ties connecting the encased panel with the top and bottom beam and the left and right column behaving in an elasto-plastic way both in a direction normal as well as tangential to the interface.
- The non-linear mechanisms were not extended to include the R/C panel itself at this preliminary numerical analysis. This non-linear behaviour of the encased R/C panel was included in a subsequent simulation that is not presented here.

In the subsequent figures the obtained numerical results include: a) The variation of the applied horizontal force at the axis of the top beam against the corresponding displacement. b) The deformed shape of the single-storey one bay frame with or without the encasement at the maximum deformation level at the end of the "push – over" loading sequence. c) The variation of the forces that developed at the interface between the encased panel and the surrounding R/C frame.

3.1 Behaviour of the "bare frame' model

The non-linear trend in the curve representing the variation of the applied horizontal force at the axis of the top beam against the corresponding displacement, as depicted in figure 2a, is quite evident when the horizontal displacement level exceeds the value of 15mm. When the top beam horizontal displacement level reaches the maximum amplitude of 24.5mm, plastic hinges develop at the critical locations of the beams and columns, as depicted in figure 2b. The maximum amplitude of the horizontal force at that level is 174KN which represents the bearing capacity of the bare frame whereas its initial stiffness is approximately 10KN/mm

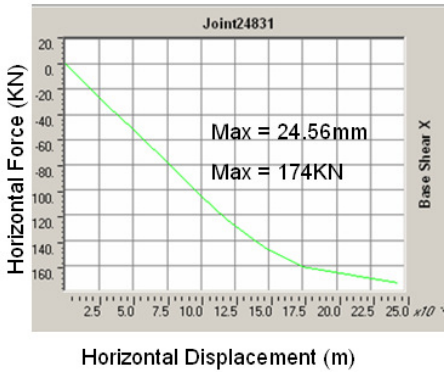


Figure 2a. The Horizontal force - Horizontal displacement "bare frame response

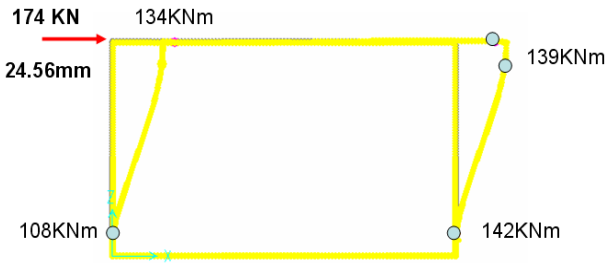


Figure 2b. The studied "bare frame" single-storey one bay R/C frame without the encased R/C panel

3.2 Behaviour of the "encased model a"

The non-linear trend in the curve representing the variation of the a applied horizontal force at the axis of the top beam against the corresponding displacement, as depicted in figure 3a, is quite evident when the horizontal displacement level exceeds the value of 10mm. These non-linear trends are less pronounced than what can be observed in the corresponding curve for the bare frame model. When the top beam horizontal displacement level reaches the maximum amplitude of 19.92mm, the corresponding maximum amplitude of the horizontal force at that level is 1950KN (figure 3b). If this force level is compared to the bearing capacity of

the bare frame it, represents an increase of 800%. A similar increase can also be observed in the stiffness that reaches the level of 150KN/mm.

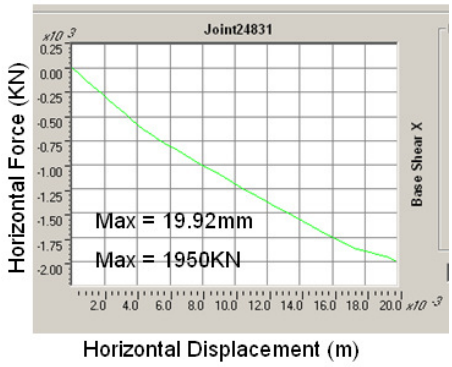


Figure 3a. The Horizontal force - Horizontal displacement "encased model a" response

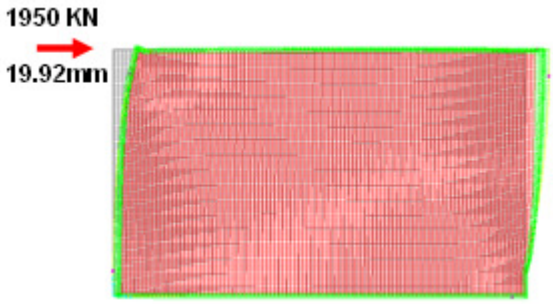


Figure 3b. The studied "encased model a" single-storey one bay R/C frame with the encased R/C panel

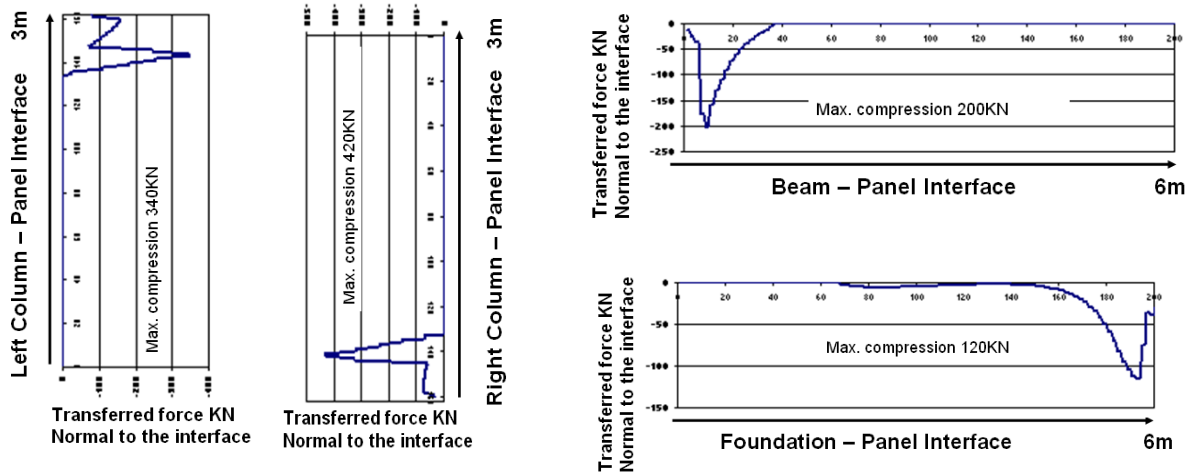


Figure 4. Transfer of forces at the interface between the encased panel and the top and bottom beams as well as between the left and right columns for the simulation of the encased model a

Figures 4 represent the transfer of forces at the interface between the encased panel and the surrounding frame through the contact/gap mechanism alone ([1], [7]). As can be seen, this transfer takes place at the corners of the encased panel where it contacts the columns and the beam near the region of column-to-beam joints whereas a large part of the interface is free of forces due to the gap that forms at the interface at these locations. It can also be seen that these contact forces in a direction normal to the interface reach a relatively large amplitude in these narrow column-to-beam joints regions. Such high amplitude forces are expected to introduce additional non-linear mechanisms such as crushing of the encased panel and/or parts of the columns or beams at these regions. These additional mechanisms are not included in this preliminary numerical simulation.

3.3 Behaviour of the "encased model b"

The non-linear trend in the curve representing the variation of the applied horizontal force at the axis of the top beam against the corresponding displacement, as depicted in figure 5a, is quite evident when the horizontal displacement level exceeds the value of 8mm.

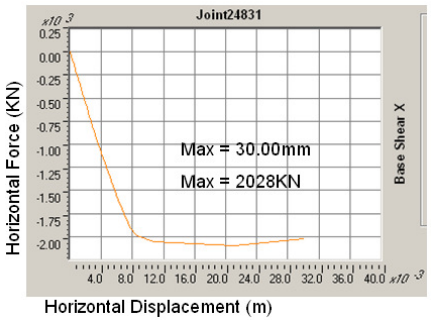


Figure 5a. The Horizontal force - Horizontal displacement "encased model b" response

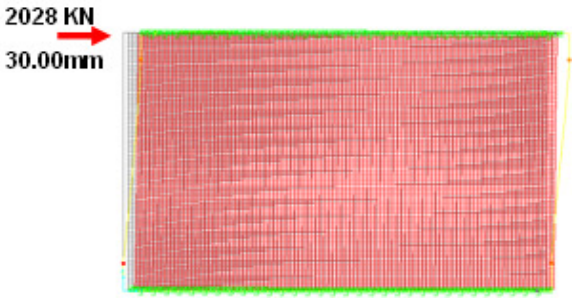


Figure 5b. The studied "encased model b" single-storey one bay R/C frame with the encased R/C panel

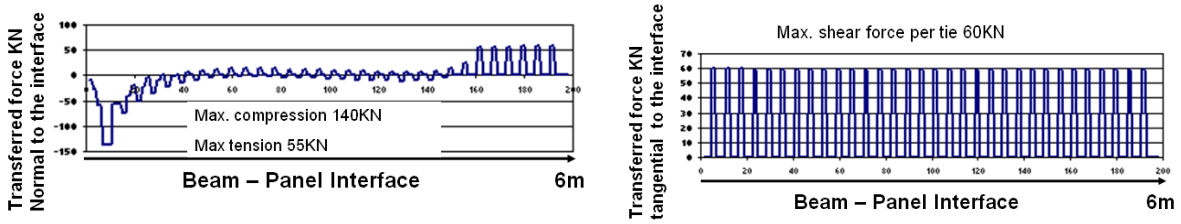


Figure 6. Transfer of forces at the interface between the encased panel and the top beam from the simulation of the encased model b

When the top beam horizontal displacement level reaches the maximum amplitude of 30.00mm, the corresponding maximum amplitude of the horizontal force at that level is 2028KN (figures 5a and 5b). The presence of steel ties between the encased panel and the surrounding frame retained the increase in the bearing capacity and the stiffness that was observed in the *encased model a* before. The stiffness reaches the value of 250KN/mm. Figure 6 represent the transfer of forces at the interface between the encased panel and the surrounding frame through the steel ties. As can be seen, the transfer takes place partly through the steel ties that are located at the interface between the encased panel and the top beam in the tangential direction. This transfer mechanism also results in moderating the amplitude of the forces that are transferred at the narrow column-to-beam joints regions in a direction normal to the interface through the contact/gap mechanism. Such transfer of forces at the interface will mitigate the possibility of crushing of the encased panel and/or parts of the columns or beams at these regions.

3.4 Behaviour of the "encased model c"

The non-linear trend in the curve representing the variation of the a applied horizontal force at the axis of the top beam against the corresponding displacement, as depicted in figure 7a, is quite evident when the horizontal displacement level exceeds the value of 7.5mm. When

the top beam horizontal displacement level reaches the maximum amplitude of 24.95mm the corresponding maximum amplitude of the horizontal force at that level is 4880KN. The presence of steel ties between the encased panel and the surrounding frame both at the top and bottom beam as well as the left and right columns further augments the increase in the bearing capacity and the stiffness that was observed in the *encased model b* before (figures 7a and 7b). The stiffness reaches the value of 300KN/mm.

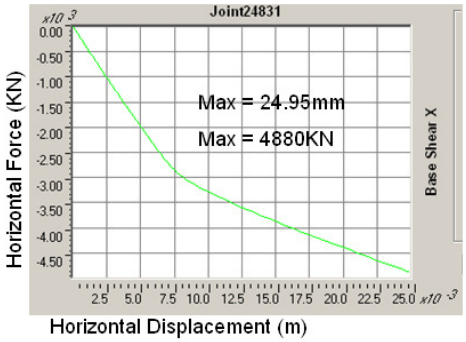


Figure 7a. The Horizontal force - Horizontal displacement "encased model c" response

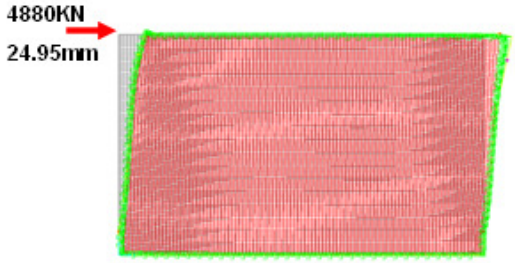


Figure 7b. The studied "encased model c" single-storey one bay R/C frame with the encased R/C panel

Figures 8 represent the transfer of forces at the interface between the encased panel and the surrounding frame through the top beam steel ties whereas figures 9 depict the transfer of forces through the ties that are located at the left and right columns.

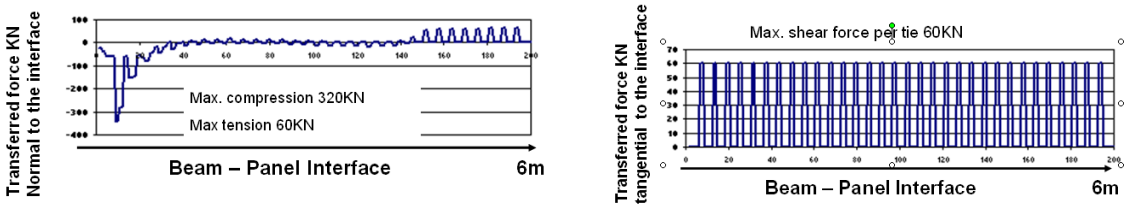


Figure 8. Transfer of forces at the interface between the encased panel and the top beam from the simulation of the encased model c

As can be seen, the transfer takes place partly through the steel ties that are located at the interface between the encased panel and the surrounding frame in the tangential direction.

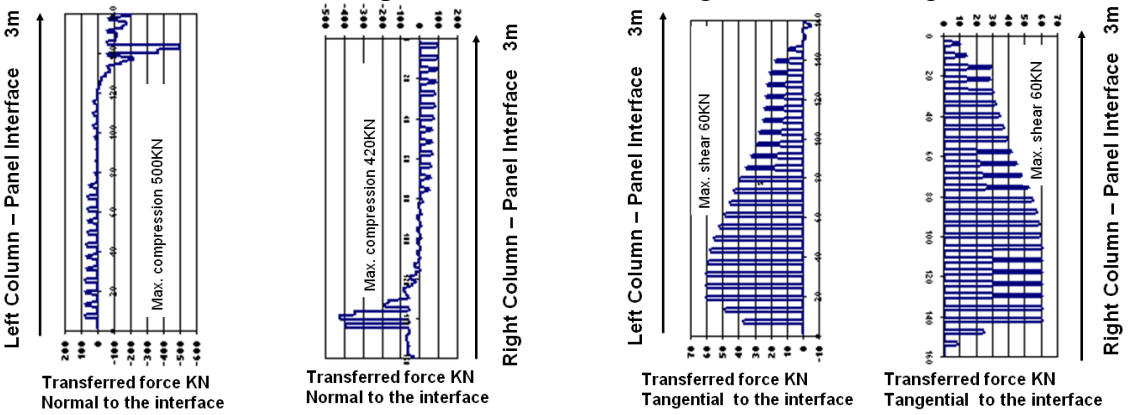


Figure 9. Transfer of forces at the interface between the encased panel and the left and right columns from the simulation of the encased model c

This transfer mechanism also results in moderating the amplitude of the forces that are transferred at the narrow column-to-beam joints regions in a direction normal to the interface through the contact/gap mechanism. Such transfer of forces at the interface will mitigate the possibility of crushing of the encased panel and/or parts of the columns or beams at these regions.

3.5 Conclusive observations of the influence of the encased R/C panel and its connection with steel ties to the surrounding R/C framer

As could be observed from the preceded preliminary numerical analysis, the encasement of the R/C panel within the single-storey one bay R/C frame resulted in a significant increase of the stiffness and the bearing capacity of the studied system. Moreover, the placement of steel ties apart from increasing the stiffness and the bearing capacity also resulted in moderating the amplitude of the forces that are transferred at the narrow column-to-beam joints regions in a direction normal to the interface through the contact/gap mechanism. Such moderation in the amplitude of the transferred forces at the interface will mitigate the possibility of crushing of the encased panel and/or parts of the columns or beams at these regions. As a final observation, it can be concluded that the presence of steel ties in the interface between the encased R/C panel and the surrounding R/C frame has an overall beneficial effect on the behaviour of this type of structural system to seismic type loading. Figure 10 depicts typical horizontal and vertical cross-sections that include part of either the beam or the column together with the corresponding part of the encased panel. As shown in the preliminary numerical study when there are steel ties in such an interface these ties will transfer forces in a direction normal and tangential to the interface simultaneously. The level of these forces may vary in amplitude as well as in direction during the loading of the structure in a cyclic seismic type of loading. An experimental investigation was carried out with its main objective to study the mechanism of the transfer of such forces at the interface in such a way that this mechanism can be described both in terms of bearing capacity at a limit-state level linked with failure modes that are expected to appear. A summary of this study is presented in the next section.

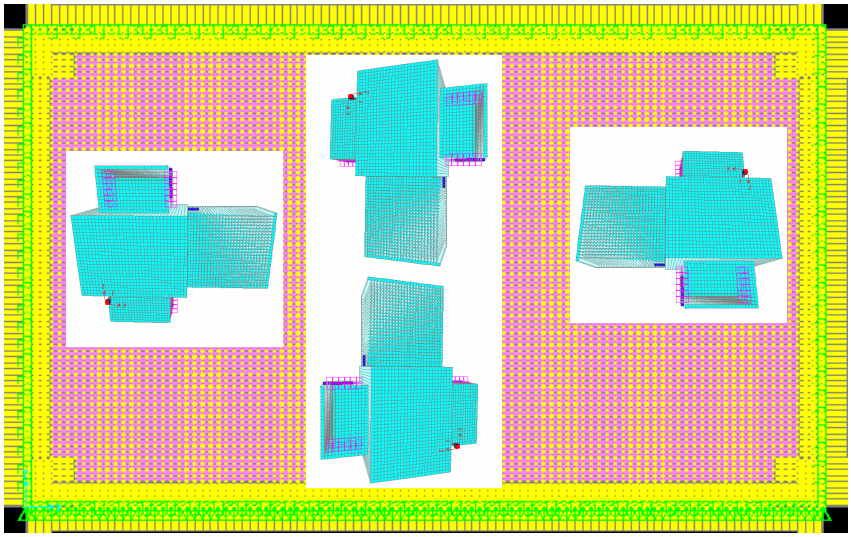


Figure 10. Cross sections that include part of the R/C encased panel and part of either column or beam of the surrounding frame together with the embedded steel ties.

4 SUMMARY OF THE EXPERIMENTAL SEQUENCE

4.1 Description of the studied specimens

Figure 11 depicts the dimensions of the studied specimens. As already explained, such a specimen represented a portion of an R/C encased panel connected with a portion of a column of the surrounding frame with the use of steel ties, which are embedded at the mid-plane of the panel and are anchored to the mass of the old concrete of the column, which is also retrofitted with a jacket. Both the jacket and the R/C encased panel are indicated in a different color in figure 11 in order to signify the new concrete as compared to the existing column (old concrete). If this detail is rotated 90^{o} clockwise it represents a similar connection between part of the R/C panel and the top beam (see figure 10).

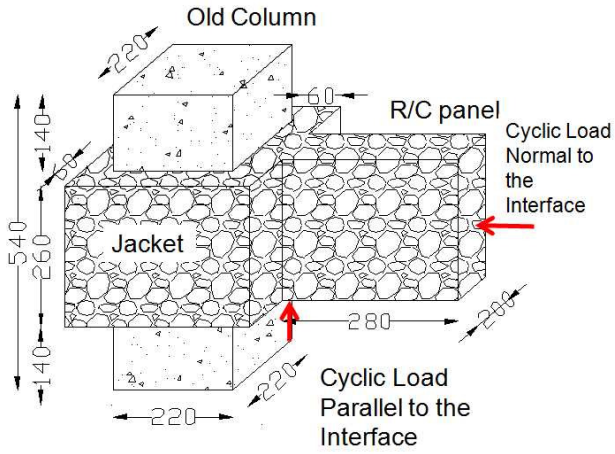


Figure 11. Specimen representing portion of encased R/C panel and the jacketed column

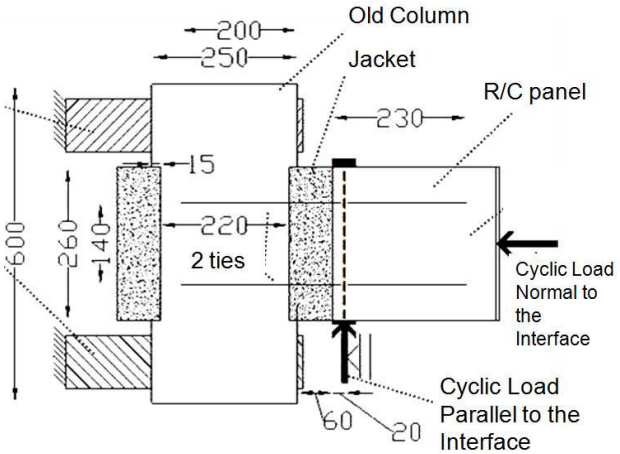


Figure 12a. Loading arrangement of the specimen representing portion of encased R/C panel and the jacketed column

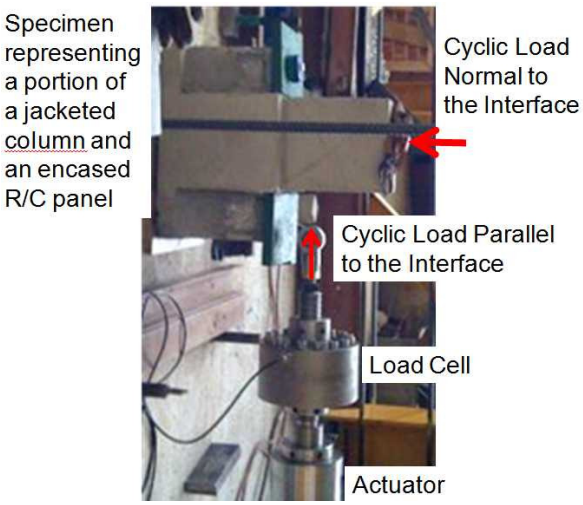


Figure 12b. Loading arrangement of the specimen representing portion of encased R/C panel and the jacketed column

This specimen was loaded as indicated in figure 12a and 12b. A load was applied normal to the interface (horizontal in figures 12a and 12b) whereas at the same time an additional load was applied in a direction parallel to the interface (vertical in figures 12a and 12b). The load that was applied parallel to the interface was varied in time in a manner consisting of

three sinusoidal cycles of constant amplitude with a frequency 0.1Hz. The load that was applied normal to the interface was either kept constant at a predetermined level (tension or compression) or it was also varied in the same way as the load applied parallel to the interface. This type of load was expected to represent the transfer of forces at such an interface with the presence of steel ties, as was found by the preliminary numerical analysis described in a summary form in section 3 and shown schematically in figure 10. The total loading sequence per specimen consisted of a series of such cycles with continuously increasing amplitude till the failure of the specimen. This type of combined cyclic loading is believed to be adequately representative of the stress field that is expected to develop at this part of the encasement from the transfer of forces between the R/C panel and the surrounding frame arising from the seismic type of loading of the single-storey one bay frame, as was indicated by the preliminary numerical analysis results. The increase in the amplitude in such a gradual cyclic way is consistent with a similar variation of the horizontal force at the level of mid-axis of the top beam (figure 1), representing in this way the variation of a seismic type load.

Instrumentation was provided to measure the variation of the applied loads as well as the deformation of the specimen during the loading sequence. Figure 13 depicts such measured response for one of the specimens, namely specimen bare21 with 4 steel ties of 12mm diameter. The applied load in a direction parallel to the interface is measured in the ordinates whereas the measured sliding displacement at the interface between the portion of the panel and the jacketed column is measured at the abscissa. It was expected that due to the stress field that would arise in the vicinity of the interface when the combined loading was applied, the expected modes of failure would include a shearing pattern for the concrete accompanied by a local deformation of the steel ties. As can be seen in this figure, the measured response reveals three stages in the performance of such a steel-tie connection. Up to a relatively small cyclic displacement level, in this case of the order of 1.0mm, the measured response is almost linear elastic. Then, when the maximum capacity of the connection is reached there are small amplitude plastic deformations. Finally, the plastic deformations increase substantially accompanied by a significant drop in the bearing capacity. At this final stage, excessive cracking of the interface occurs that reveals the deformed shape of the steel ties, as they are shown in figure 14.

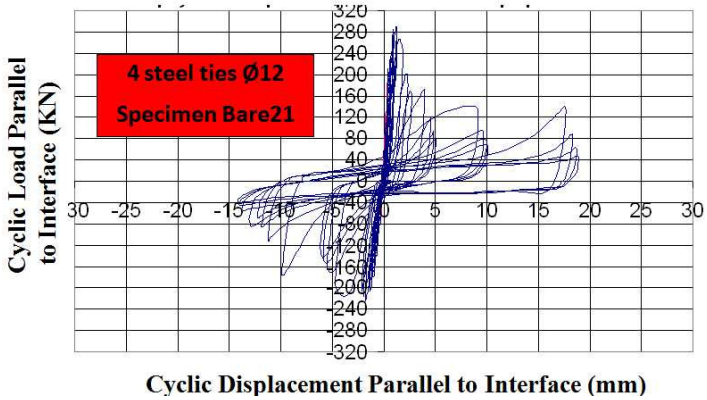


Figure 13. Measured Load-displacement cyclic response in direction parallel to the interface



Figure 14. Deformed shape of the steel ties at the final stage of the loading sequence. They are still anchored to the old column

The measured response of this steel tie connection at the interface, in a direction parallel to the interface, under a combined loading representative of the stress field that is expected to develop at this part of the encasement, is in agreement with the assumptions made concerning the behavioural characteristics of the these steel ties in the preliminary numerical analysis de-

scribed in section 3. Therefore, the main observations made on the performance of the encasement, as derived from this preliminary numerical analysis, are expected to be in general valid, especially concerning the performance of the interface.

5 CONCLUSIONS

- The in-plane behaviour of one-bay single-storey reinforced concrete (R/C) frames was numerically examined when they were subjected to cyclic seismic-type horizontal loading and their retrofitting scheme included jacketing of their columns together with a cast-in-place infill R/C panel as an encasement. This numerical study examined the influence of the presence of such an encased R/C panel, being connected with the surrounding frame with or without steel ties, on the overall behaviour of such a system.
- From the preliminary numerical analysis results it can be concluded that such an encasement results in a considerable increase of the stiffness and the bearing capacity of the studied system, especially when steel ties are present at the interface. Moreover, the placement of steel ties also moderates the amplitude of the forces that are transferred at the narrow column-to-beam joints regions in a direction normal to the interface through the contact/gap mechanism, and consequently, mitigate the possibility of crushing of the encased panel and/or parts of the columns or beams at these regions.
- Consequently, it can be concluded that the presence of encased R/C panel being connected with the appropriate steel ties with the surrounding R/C frame, has an overall beneficial effect on the behaviour of this type of structural system to seismic type loading
- An experimental sequence was also performed in order to quantify the behaviour of such steel tie connections at the interface under a stress field that is expected to develop at this part of the encasement during seismic type loading. Such measured behaviour, is in agreement with the assumptions made concerning the behavioural characteristics of the these steel ties in the preliminary numerical analysis

ACKNOWLEDGEMENTS

- Partial financial support for this investigation was provided by the Hellenic Earthquake Planning and Protection Organization (EPPO)

REFERENCES

[1] G.C. Manos, V. J. Soulis, J. Thauampteh "*The behaviour of masonry assemblages and masonry-infilled R/C frames subjected to combined vertical and cyclic horizontal seismic-type loading*", J. Advances in Engineering Software, 45 (2012) 213-231.

[2] G.C. Manos (2012) "*Cyclic In-plane Behaviour of R/C Frames Retrofitted with Jacketing and an Encased R/C Panel*" Report to Hellenic Earthquake Planning and Protection Organization (EPPO) in Greek

[3] [Organization of Earthquake Planning and Protection of Greece (OASP), Guidelines for Level—An earthquake performance checking of buildings of public occupancy, published by OASP, Athens, 2001.

[4] Organization of Earthquake Planning and Protection of Greece (OASP), Guidelines for Retrofitting in Reinforced Concrete Buildings, Government Gazette, Δ17α /04/5/ΦΝ 429-1, No 42, Athens, 20 Jan. 2012.

[5] Provisions of Greek Seismic Code 2000, Organization of Earthquake Planning and Protection of Greece OASP, Dec. 1999 published by OASP. Revisions of seismic zonation introduced in 2003, Government Gazette, Δ17α /115/9/ΦΝ275, No. 1154, Athens, 12 Aug. 2003.

[6] G.C. Manos, Consequences on the urban environment in Greece related to the recent intense earthquake activity, Int. Journal of Civil Eng. and Architecture 5 (12) (2011) 1065-1090.

[7] G.C. Manos, V. J. Soulis and J. Thauampteh. "A Nonlinear Numerical Model and its Utilization in Simulating the In-Plane Behaviour of Multi-Storey R/C frames with Masonry Infills", *The Open Construction and Building Technology Journal,6,* (Suppl. 1-M16) 254-277,2012.

[8] Klingner R. E. and Bertero V.V." Infilled Frames in Earthquake-Resistance Construction", EERC Report No.76-32, Dec. 1976.

[9] Klingner R. E. and Bertero V.V. " Earthquake Resistance of Infilled Frames", ASCE Journal of Structural Engineering. Vol 116, pp. 973-989, 1978.

[10] T. Sugiyama, Y. Matsuzaki, K. Nakano, "Design for Structural Performances of R/C Frame with Cast in Place Non-Structural R/C Walls", 13th World Conference on Earthquake Engineering Vancouver, B.C., Canada August 1-6, 2004, Paper No. 1277

COMPDYN 2013
4th ECCOMAS Thematic Conference on
Computational Methods in Structural Dynamics and Earthquake Engineering
G.C.Manos, V.Soulis, J.Thauampteh (eds.)
Kos Island, Greece, 12–14 June 2013

IN-PLANE BEHAVIOUR OF MASONRY INFILLS WITHIN MULTI-STOREY R/C FRAMES SUBJECTED TO SEISMIC TYPE LOADS AND THEIR UTILIZATION IN RETROFITTING

G.C. Manos[1], V. Soulis[1], J. Thauampteh[1]

[1]ILaboratory of Strength of Materials and Structures, Dept. Civil Engineering, Aristotle University, Thessaloniki, GREECE

e-mail: gcmanos@civil.auth.gr

Keywords: Numerical simulation, Masonry-infilled R/C frames, Equivalent step-by-step analysis

Abstract. *Observations from past strong earthquake activity have shown that masonry infill panels can be damaged to a substantial degree.Under certain circumstances this interaction of masonry infills with the surrounding R/C frame during the seismic response may result in either beneficial effects, by increasing the stiffness, strength and seismic energy absorption of the structure, or in adverse consequences (damage) to the main R/C structural elements. Consequently, there is need first to understand this behavior resulting from the masonry infill to R/C frame interaction and next to have reliable tools to predict it in order to prohibit adverse consequences. These tools can then be utilized in the retrofitting of R/C multistorey structures designed and constructed according to old earthquake resistant design provisions. This paper presents first a valid, fully non-linear 2-D numerical model that can capture realistically the in-plane hysteretic behaviour of reinforced concrete (R/C) frames with masonry infills when they are subjected to combined vertical and cyclic horizontal load. The effectiveness of this simulation was validated by comparing the numerically predicted behaviour with results from an experimental sequence whereby a number of 1:3 scale, one-bay, one-storey R/C frame specimens, including weak and strengthened masonry infills, were subjected to combined vertical and cyclic horizontal seismic-type loads. Next, this paper deals with the applicability of this successful non-linear masonry-infill concrete-frame numerical simulation to predict realistically the seismic behaviour of a prototype multi-storey R/C frame structural formations with masonry infills. Further more the proposed numerical simulation of the same multi-storey R/C frame structural formation was utilized in an application of a retrofitting scheme. In order to overcome the obstace of computational time and computer memory requirements, use was made of an equivalent post-elastic "pushover" type of analysis that draws information on the stiffness and strength variation from one-bay, one-storey R/C masonry infilled unit frames that compose a given multistorey structural formation.*

1 INTRODUCTION

Many researchers in the past were involved in the effort to propose valid numerical simulation to capture the behaviour observed experimentally of multi-storey 2-D frames. The numerical simulation proposed by Soulis [1] was used to simulate the behaviour of three-storey structural formations including masonry infills; in particular a multi-storey planar R/C frame structure, that was constructed and tested at the University of California, Berkeley by Klingner and Bertero [2] was examined. Reasonably good agreement was observed between the numerical results and the experimental measurements regarding the hysteretic behaviour of the "bare", and infilled three-storey specimens. Next, a "pushover" analysis was performed for a planar 6-storey infilled RC building. This analysis was accomplished to a satisfactory degree despite the significant number of finite elements utilized in the numerical simulation and the high computational requirements. In order to overcome this difficulty a new equivalent analysis is proposed and validated, aiming to incorporate the influence of the masonry infills for multi-storey structural formations. For this purpose, the previously mentioned planar 6-storey structural formation is selected for the validation of the proposed equivalent method of analysis. More specifically, as will be described in section 3 of this paper, the masonry infills of this planar 6-storey, R/C structure are modeled as diagonal strut members as proposed by Holmes [3], [4]; however, these are modeled with multi-linear properties. The numerical response obtained from a "pushover" analysis employing these "multi-linear" diagonal struts is compared with the corresponding predictions employing the fully non-linear approach presented in the first part of this paper.

Previous studies by Mainstone and Liauw [5],[6] as well as the extensive experimental and numerical investigation conducted before by the authors [1],[7],[8] and briefly reported here, demonstrated that the stiffness and strength added in single-storey R/C frames through the use of masonry infills can be affected by various non-linear mechanisms such as:

a) The non-linear behaviour of the R/C frame.

b) The non-linear mechanisms that develop at the interface between the R/C frame and the masonry infill with the individual mechanical properties and their interactions.

c) The level of shear deformation that develops in the masonry infill and consequently its non-linear behaviour for that level of shear deformation.

Consequently, the development of all these non-linear mechanisms dictates the total behaviour of masonry infill frames and renders an elastic type of analysis a crude approximation. In the first part of this paper (section 2) it is shown that all these (a to c) non-linear mechanisms are quite successfully simulated numerically by the proposed "fully non-linear" numerical treatment (Type A simulation). This type A simulation assumes that: a) the masonry infills are simulated with plane stress elements, having non-linear mechanical characteristics, b) the infill to frame interface is simulated by sets of non-linear joint element, whereas the R/C structural members have the capability of developing plastic hinges at their ends, as described in section 2.1. The major obstacle in extending this type of full non-linear numerical treatment to a multi–storey masonry-infilled R/C frame structure, in order to simulate separately all these non-linear mechanisms for the R/C frame members, the masonry infills, and the interfaces between the R/C frames and masonry infills, is the computational time and computer memory requirements needed for the completion of such numerical analysis. It is believed that all these dominant non-linear mechanisms that develop in a single-storey masonry infilled R/C frame, as described in the first part of this paper, can also develop in the same way in a multi-storey R/C frame structure with masonry infills when subjected to "seismic type" loading. In the second part of this paper, presented in section 3, the non-linear response of masonry infilled multi-storey framed R/C planar structural formations is

addressed through an equivalent post-elastic *"pushover"* analysis to confront the obstacle of the high computational requirements of the fully non-linear approach; this is done by utilizing the full non-linear response of a number of "single-storey" infilled frame units that such a multi-storey structure can be decomposed to. It must be stressed that only in-plane stiffness and strength variation of these masonry infilled units is considered in this approximation whereas the out-of-plane behaviour and its possible effects, although important, are not addressed.

Pushover analysis is a nonlinear static procedure which validity and applicability have been extensively studied in literature. According to Eurocode 8 Part 3 (EN 1998-3)[9]: paragraph 4.4.4 (1) Nonlinear static ("pushover") analysis is a non-linear static analysis under constant gravity loads and monotonically increasing horizontal loads. (2) Buildings not complying with the criteria for regularity in plan shall be analysed using a spatial model. (3) For buildings complying with the regularity criteria the analysis may be performed using two planar models, one for each main direction.

According to Eurocode 8 Part 1 (EN 1998-1):4.3.3.4.2.3[9] (1), the relation between base shear force and the control displacement (the "capacity curve") should be determined by "pushover" analysis for values of the control displacement ranging between zero and the value corresponding to 150% of the target displacement. (2) The control displacement may be taken at the centre of mass of the roof of the building. The top of a penthouse should not be considered as the roof.

This approximate *"pushover"* analysis, outlined in the following steps a to h and summarized in Table 1, deals with the non-linear behaviour of masonry infilled multi-storey R/C frames, with respect to their in-plane stiffness and strength variation, utilising the findings of the in-depth research in the behaviour of the single-storey masonry infill R/C frame units; this was presented in the first part of this paper (section 2) and is also included in the work reported by Manos, Soulis and Thaumpteh ([8]). The objective of this section is to approximate the complex behaviour of multi-storey R/C infilled frames and retrofitted multi-storey R/C infilled frames by applying the simplified equivalent diagonal strut simulation briefly presented in section 3, so that a realistic solution of such practical problems becomes attainable in terms of computer time and computer memory requirements.

An equivalent post-elastic numerical simulation is proposed (Type B simulation) for multi-storey R/C frame structural formations that include masonry infills and retrofitted multi-storey R/C frame structural formations with strengthened masonry infills. This type B simulation is built assuming that the masonry infills are simulated with diagonal strut members, having multi-linear mechanical characteristics, whereas the R/C structural members have the capability of developing plastic hinges at their ends, as described in section 2.1. The steps that describe the methodology are extensively outlined by Manos et.al [8]. These steps are briefly outlined in Table 1 presented below:

Step a:	*Multi-storey frame.* Decompose the multi-storey structural formation to individual single-storey one-bay masonry infilled R/C frame units. Group these units according to their common geometric and mechanical characteristics of the R/C elements and masonry infills, in order to minimize the number of different units to be analysed in the next steps.
Step b:	*Single-storey units.* Prepare simulation type A for each one of these single-storey units in order to obtain their full non-linear response.
Step c:	*Single-storey units.* Perform a "pushover" analysis with simulation type A for each single-storey unit and obtain its full non-linear response together with the accumulation of damage of the masonry infills that can be linked to the increase of the shear strain

	levels.
Step d:	*Single-storey units.* Prepare a number of simulations type B for each one of these single-storey units by replacing the masonry infill with an equivalent multi-linear diagonal strut member whereas retaining the capability of the R/C members to develop plastic hinges at their ends.
Step e:	*Single-storey units.* For each single-storey unit obtain horizontal load (H) versus horizontal displacement (δ) or shear strain (γ) response curve from "pushover" analyses employing simulation type B. Adjust the diagonal strut properties in such a way that both type A and type B simulations result in approximately the same stiffness and strength variation for the chosen shear strain levels for the masonry infill (e.g. 0.1%, 0.15%, 0.2%, 0.25%, 0.3%, etc.).
Step f:	*Multi-storey frame.* Perform a "pushover" analysis with simulation type B for the multistorey structural formation having replaced the masonry infills with the equivalent multi-linear diagonal struts found from step e. For every interval (i+1) of this analysis a target top storey displacement is set. Each time the target displacement value is such that corresponds approximately to shear strain levels already examined in steps d) and e) (e.g. 0.1%, 0.15%, 0.2%, 0.25%, 0.3%, etc.)
Step g:	*Multi-storey frame* Record at pre-selected intervals (i+1) of step f) and for target top storey displacement that corresponds to shear strain levels (e.g. 0.1%, 0.15%, 0.2%, 0.25%, 0.3%) the actual storey displacements and forces as well as the shear-strain levels γ_{i+1} for each masonry infill as they result from the type B analysis.
Step h:	*Multi-storey frame* Assess the performance of each masonry infill of the multi-storey structure by using the corresponding full non-linear response type A simulation (step c) and the obtained shear strains γ_{i+1} values in the previous step (g) for each masonry infill of the multi-storey structure at interval i+1.

Table 1: Steps of equivalent post-elastic analysis for the examination of the ultimate state of masonry infills.

2 THE NUMERICAL SIMULATION OF THE BEHAVIOUR OF MASONRY-INFILLED R/C FRAMES EMPLOYING THE SIMULATION TYPE A AND SIMULATION TYPE B FOR THE MASONRY INFILL

In order to verify the degree of approximation of both the simulation types A and B, two scaled models that have been tested in the experimental study of Thauampteh [10] were utilized. Namely specimen F3N(R1f,0w)*s and specimen F3N(R1f,R1w)s will be simulated. In this case the results from the simplified approach utilizing a tri-linear diagonal strut model (Simulation type B) will be compared to the corresponding numerical results of the more explicit numerical simulation (fully non-linear, Simulation type A), as well as with the corresponding experimental results.

The single-storey one-bay R/C frame scaled specimens F3N(R1f,0w)*s and specimen F3N(R1f,R1w)s with masonry infills were constructed and tested at the strong reaction frame of the Laboratory of Strength of Materials of Aristotle University of Thessaloniki (Thauampteh [10]). These specimens include one-bay one-storey 1/3-scale models with overall external dimensions 1720mm (length) x 1000mm (height) and a length over height ratio equal to 1.7 (l/h=1.7, figure 1). The cross-section of the columns was 110mmx110mm and that of the beam 100mmx155mmm. These two scale masonry infilled frame models incorporate two different types of infills the one with relatively weak infill and one with reinforced infill.

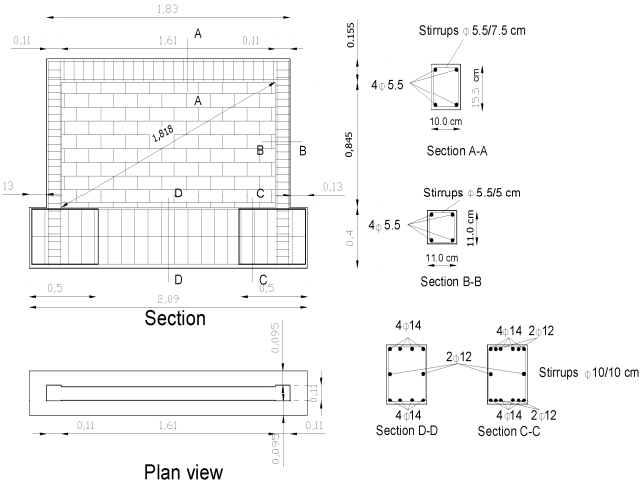


Figure 1a: Masonry infilled R/C frame specimen F3N(R1f,0w)*s and design details [10].

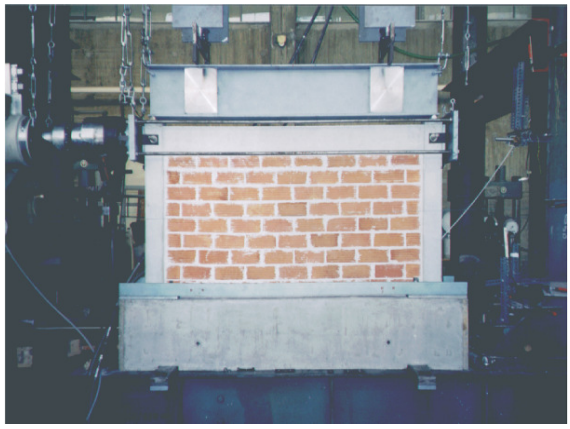


Figure 1b: Test set up of frame with repaired masonry infill F3N(R1f,0w)*s.

Brief information on the selected masonry infilled R/C specimens is listed in table 2 and described extensively by Thauampteh [10] and Soulis [1].

Frame Code name	Length over Height ratio	Vertical load on Columns (KN)	Technical description of masonry infill	Masonry Infill thickness (mm)	Technical description of the interface between frame and infill
F3N(R1f,0w)*s (**Repaired**) [10]	1.7	50	mortar **V1**	58.5	mortar **H** thickness **15mm** (without plaster)
F3N(R1f,R1w)s (**Repaired**) [10]	1.7	50	Infill with mortar **V1**, reinforced with reinforced plaster, and transverse reinforcement type **II**	78.5	mortar **H** thickness **15mm**. The reinforced plaster is not in contact with the surrounding frame

Table 2: Outline of all specimens for the 1st and 2nd group of specimen.

As already mentioned, the influence exerted by the interface between the masonry infill and the surrounding frame was also examined in both studies by Thauampteh [10] and by Soulis[1]. Tables 3, 4 and 5 list the mechanical properties of the materials used in the construction of the specimens.

Masonry infill	Masonry Infill thickness (mm)	Compressive strength of masonry (N/mm^2)	Shear strength of masonry diagonal compression (N/mm^2)	Compressive strength of masonry units (N/mm^2)	Compressive strength of concrete (N/mm^2)	Compressive strength of mortar cylinders (N/mm^2)
Virgin infill [10]						
V1	58,5	2,765	0.180	6.50	25.9	1.125
Reinforced infill[10]						
Infill with mortar **V1**, reinforced with reinforced plaster	78,5	3,75	0.44	6.50	25.9	1.125

Table 3**:** Strengths of masonry infills and concrete used in the specimens [10].

A/α	Yield stress f_{sy} (N/mm^2)	Ultimate strength f_{su} (N/mm^2)	Strain at yield ε_{sy} (%)	Strain at ultimate stress ε_{su} (%)	Young Modulus (N/mm^2)
Φ5.5	311	425	0.8	22.0	$6.5X10^4$
Φ5.5 stirrups	360	542	0.6	20.0	$6.5X10^4$

Table 4**:** Tensile strength of the reinforcement used in the specimens [10].

A/a	Simulation of joint interface between frame and infill	**E** Young Modulus (N/mm^2)	**G** Shear Modulus (N/mm^2)	$\mathbf{f_k}$ Measured Compressive Strength of mortar (N/mm^2)	$\mathbf{f_{tn}}$ Assumed Tensile Strength of mortar (N/mm^2) (as % of f_c)	**τo** Local bond shear strength of mortar (N/mm^2)	**μ** friction coefficient
1	**H** mortar	60	26	0.60	0.06(10%)	0.078	0.58

Table 5**:** Mechanical properties of the mortar joint located between the infill and the surrounding frame (mortar type H).

2.1 Simulation type A

Extensive comparison of various numerical simulations with the behaviour observed by Thauampteh [10], as well as by Stylianides [11], Valiasis [12], and Yasin [13] for the masonry infilled R/C frames is included in the work of Soulis[1] where the conclusions of the corresponding extensive validation, utilizing the results of all these experimental studies [10], [11], [12], [13] are presented. In the recent publications by Manos, V. J. Soulis, J. Thauampteh [7], [8] the numerical simulation of the behaviour of masonry-infilled R/C

frames using plane stress elements for the simulation of the masonry infill (Simulation type A) is presented. This type of simulation is shown in figure 2.

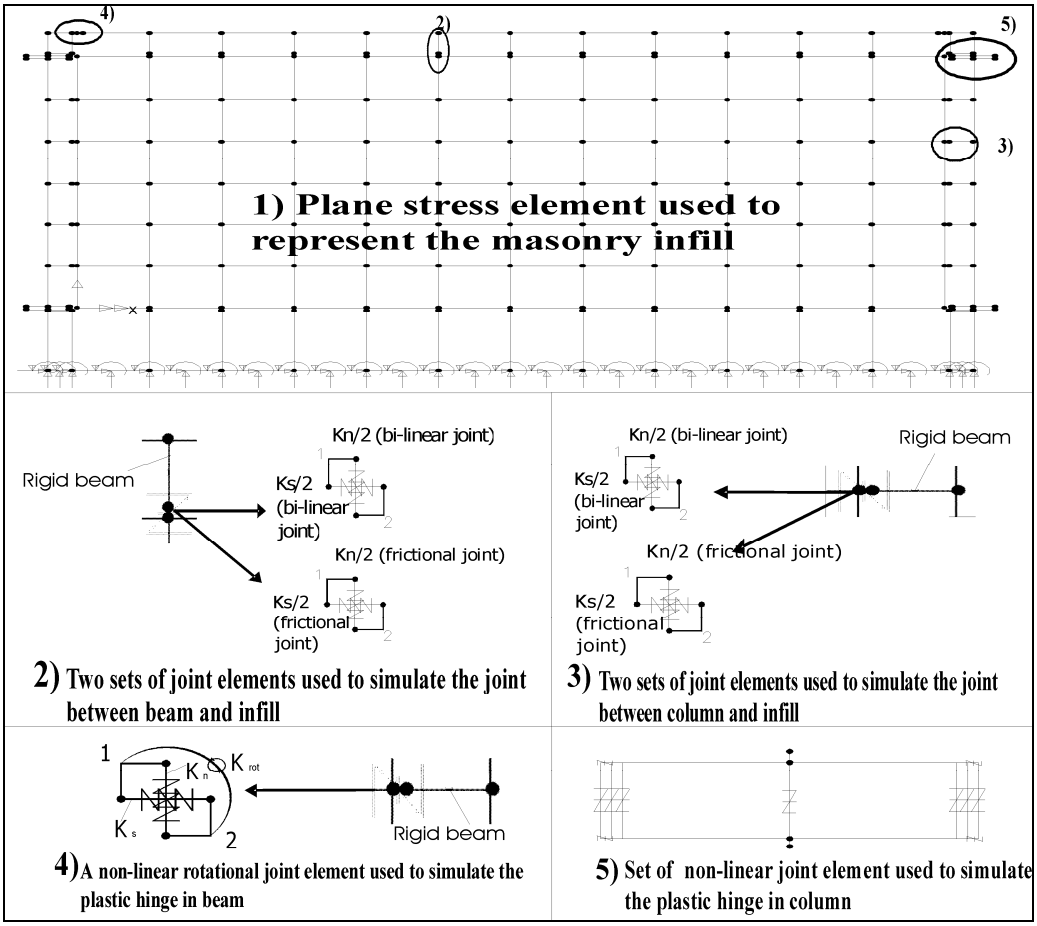


Figure 2: Finite element simulation of masonry infilled R/C model.

In this numerical model of the surrounding R/C frame the beam and the two columns are simulated, together with the locations of possible plastic hinge formation at the ends of each element (figure 2 detail No 4 and 5). Thick beam elements, able to deform and rotate in plane, were employed for both the columns and the beam. Rigid beam elements were also employed to simulate the corner connection between the beam and the column (figure 2, detail No. 4). A number of non-linear 2-D joint elements were also employed at the ends of each column (figure 2, detail No. 5). The selected numerical simulation showed that the non-linear moment-rotation relationships for the beam and column cross-sections could be simulated successfully. Plane stress elements are used for simulating the masonry infill (figure 2 detail No 1); they are connected to the surrounding frame by a different series of 2-D joint elements that simulate the masonry infill to R/C frame interface (peripheral mortar joint). Two sets of non-linear 2-D joint elements are used to simulate the separation and slip between frame and infill as well as the transfer of compression and shear for the specific type of interface that is simulated. The first set of these 2-D joint elements (figure 2 details No 2 and No 3) is active in the direction transverse to the interface; it is of a frictional type, while the second set of non-linear joint elements (figure 2 details No 2 and No 3) is active in both the transverse and the normal to the interface directions. In the current study the mechanical properties of the joint interface between the masonry infill and the surrounding frame can be depicted in table

5.The mechanical elastic and post-elastic properties of the unreinforced and reinforced masonry panels that are utilized in this numerical simulation are presented in the study of Soulis [1], and Manos et.al [7].

2.2 Simulation type B

The implementation of the simulation type B described in the previous section demands the simplification of the masonry infill frame response for a single-bay one storey infilled frame adopting an equivalent diagonal strut model. This simplification will have the following characteristics:

1. The contact interface of the masonry with the surrounding frame will not be represented in the direct way employed before in section 2.1 As a result, the masonry infill 2-D representation, as outlined in section 2.1 will also be replaced by the well known equivalent diagonal strut model (figure 3). On the contrary, all the aspects of the reinforced concrete frame representation, described in section 2.1, will be retained.

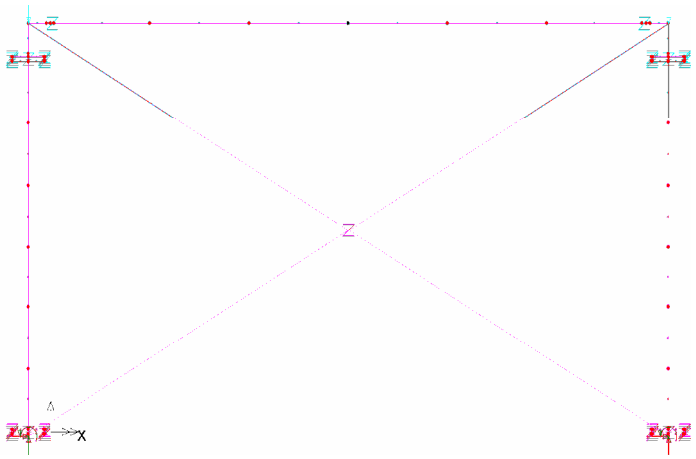


Figure 3: Equivalent diagonal strut model.

2. The equivalent diagonal strut will be a multi-linear model, active in compression only. Its force – displacement properties are defined by a "pushover" type of analysis in such a way that the total force – displacement response of the R/C infill frame, with the diagonal strut in-place, in terms of envelope curve, is as close as possible to the envelope curve of the numerical simulation of the same problem whereby the contact interface and the masonry infill were simulated separately (sections 2.1 respectively).

3. Because the non-linear mechanisms and its properties of the R/C frame standing alone remain the same the non-linear response that arises at either the interface or at the masonry infill, which were addressed separately by the simulation of sections 2.1 is approximated this time in a combined way, utilizing the multi-linear equivalent diagonal strut approximation. It is obvious that through this simplified numerical treatment one loses the directness of treating this problem with a clear representation of the various non-linear mechanisms as they physically occur at either the contact interface or the masonry infill. Moreover, the degree of approximation of the masonry infill – contact interface – R/C frame interaction by the equivalent diagonal strut is based on the validity of the full non-linear treatment of the masonry infill – contact interface – R/C frame problem, which was demonstrated in section 2.1.

2.3 Validation of the proposed equivalent diagonal strut model proposed by Simulation type B

Figures 4a and 4b depict the comparison of the predicted behavior, in terms of envelope curves resulting from a "pushover" type of loading, whereby the infill was simulated with a tri-linear equivalent diagonal strut(Simulation type B) with the corresponding behavior of the same infill frame that was simulated according to the fully non-linear treatment (Simulation type A). The envelope curves as resulted from the experiments are also plotted in these figures for masonry infilled model frames F3N(R1f,0w)*s and F3N(R1f,R1w)s. The tri-linear equivalent strut behaviour was obtained by a relatively small number of trials for the properties of the diagonal strut retaining the same numerical simulation for the surrounding R/C frame for both numerical simulations as the one described in section 2.1.

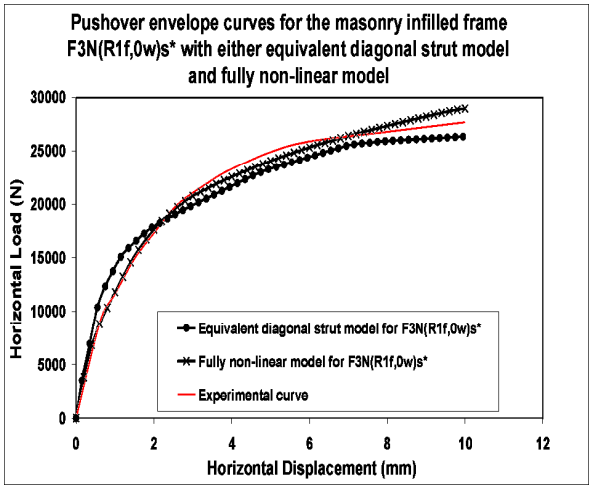


Figure 4a: Comparison of envelope curves for masonry infilled model frame F3N(R1f,0w)*s.

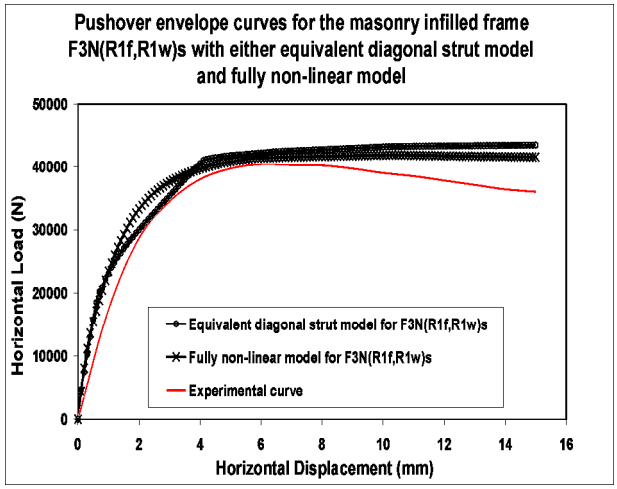


Figure 4b: Comparison of envelope curves for masonry infilled model frame F3N(R1f,R1w)s.

As can be seen, the envelope curve predicted with the tri-linear diagonal strut (Simulation type B) compares quite well to both the experimental envelope curve as well as to the one resulting from the fully non-linear treatment (Simulation type A). This comparison is extended for the case of cycling loading that was utilized during the experiments. The properties of the tri-linear diagonal strut model defined before were kept unaltered. The numerical results obtained this time by employing either the tri-linear diagonal strut simulation for the masonry infill or the fully non-linear treatment are compared in figures 5a and 5b for specimens F3N(R1f,0w)*s and F3N(R1f,R1w)s, respectively. As can be seen in figures 5a,b, the (P-δ) cycling curves predicted with the tri-linear diagonal strut compare quite well to both the corresponding (P-δ) curves obtained from the experiments as well as with the ones resulting from the fully non-linear treatment (sections 2.1. to 2.2).

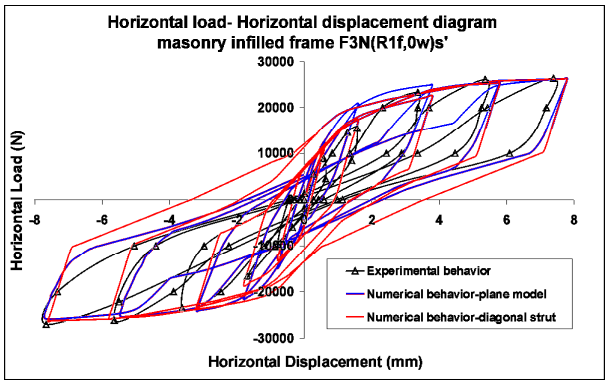


Figure 5a: Comparison of cyclic response for specimen F3N(R1f,0w)*s.

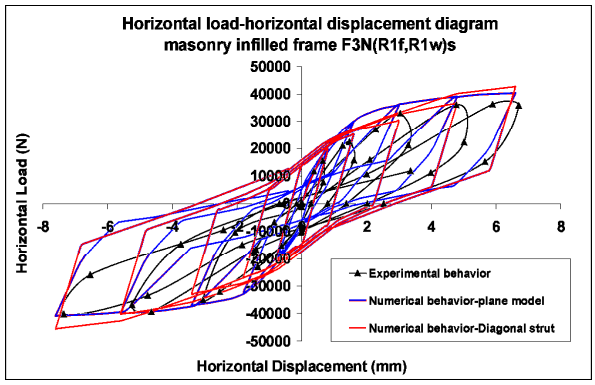


Figure 5b: Comparison of cyclic response for specimen F3N(R1f,R1w)s.

It must also be underlined again that the degree of approximation of the masonry infill – contact interface – R/C frame interaction by the equivalent diagonal strut is based on the validity of the full non-linear treatment of the masonry infill – contact interface – R/C frame problem, which was demonstrated in sections 2.1. Considerable gains in terms of computer time as well as computer memory requirements results from adopting the multi-linear diagonal strut approximation together with a "pushover" type of analysis. The application of such a simplification for multi-storey R/C infilled frames is outlined in section 3.

3 APPLICATION OF THE PROPOSED EQUIVALENT STEP-BY-STEP ANALYSIS

A 6-storey masonry infilled planar frame structural formation is selected for the validation of the proposed method of analysis when this structure is subjected to seismic-type horizontal loading. More specifically an outer planar section of a 6-storey masonry infilled R/C building is studied. The results from the application of the proposed equivalent "pushover" type B analysis for this 6-storey R/C frame with masonry infills will be compared with the results from a "pushover" fully non-linear type A numerical simulation of the same structure. Additionally the proposed equivalent post-elastic analysis will be applied in the case of a retrofitted 6-storey jacked R/C frame with reinforced masonry infills.

3.1 Description of the 6- storey R/C building numerical simulation

A characteristic plan view of the 6-storey masonry infilled R/C building is shown in figure 6.The outer facade of this 6-storey building is shown in the figures 7. Only a section in the large dimension of the structure will be utilized for the application of the proposed analysis (figure 7). The retrofitted scheme for a typical base storey frame unit that was utilized in the current study includes both the jacketing of columns and the strengthening of the masonry infill panels with reinforced plaster(figure 8). The reinforced masonry infill panel was connected to the surrounding frame with weak mortar (type H) similar to the one used in the construction of F3N(R1f,R1w)s specimen.

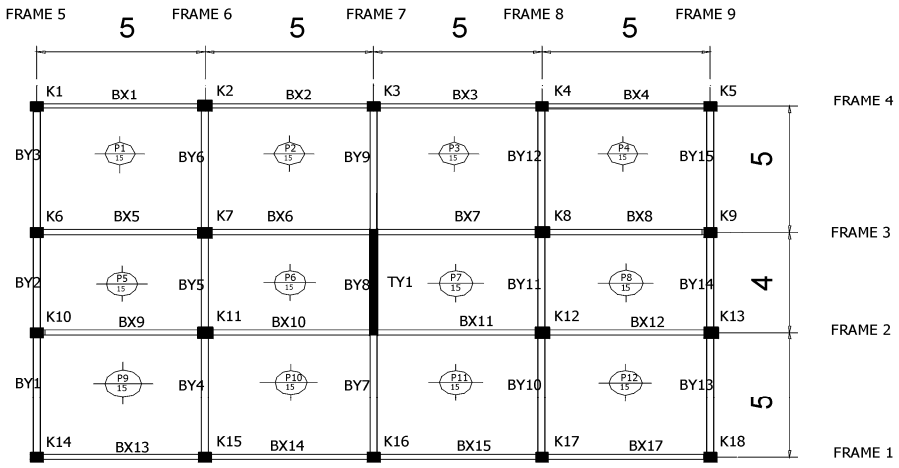


Figure 6: Plan of a typical floor level

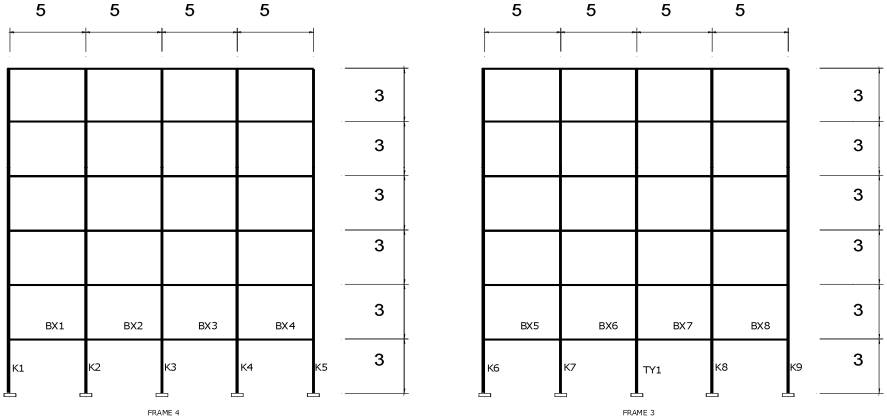


Figure 7: Typical section of structure, frames 4-3

The height of the structure is 18m. Table 6, lists the cross section areas of the columns and beams of the 6-storey structure. In the same table the cross section areas of the retrofitted elements are also shown.

The following vertical loads are imposed apart from the self-weight:

The self-weight of the masonry infills (3,6KN/m^2), applied at the perimeter of the structure

The marble coating of each floor 1,3kN/m^2

The imposed vertical liveload is assumed to be Q=2kN/m^2

	Storey	Columns K1-K5, K14-K18, K6,K9,K10,K13	Columns K7-K8-K11-K12	Shear Wall TYi	Beam $BXi_{(1,17)}$	Beam $BYi_{(1,7,9,15)}$	Beam BY8
Initial	$1^{o\varsigma} – 5^{o\varsigma}$	40/40	45/45	400/25	20/60	20/60	30/90
Retrofitted	$1^{o\varsigma} – 5^{o\varsigma}$	55/55	60/60	400/25	20/60	20/60	30/90

Table 6: Cross sections of columns, beams and wall of the 6-storey structure.

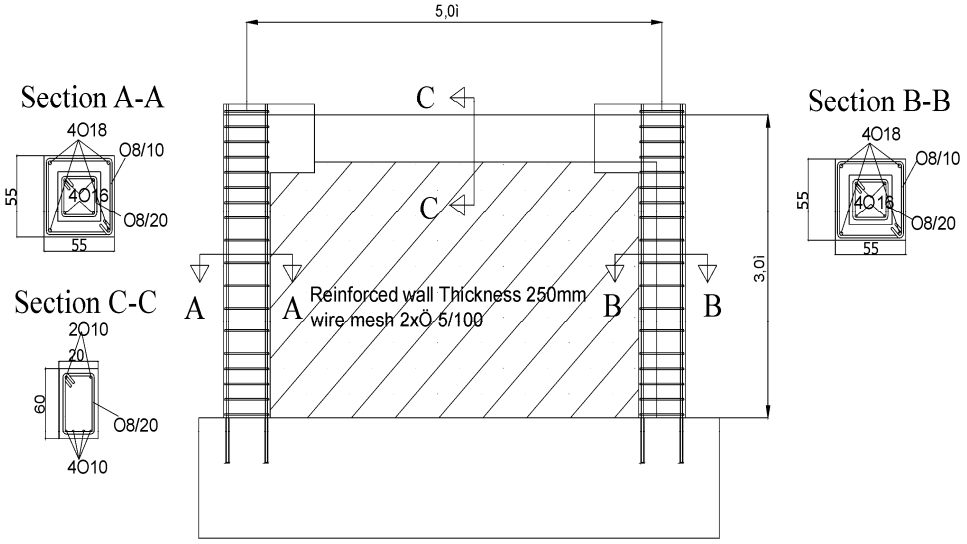


Figure 8: Typical base storey retrofitted frame with the columns' jackets and strengthened infill panel with reinforced plaster.

The validation of the proposed equivalent type B "pushover" analysis for frame No. 4 of the 6-storey structure will proceed according to the steps outlined in the table 1 provided in the introduction. Figure 9a depicts the numerical simulation of frame No. 4 whereby the masonry infills are simulated as nonlinear plane stress elements with their contact interfaces (simulation type A), whereas figure 9b depicts the simulation of frame No. 4 where the masonry infills are simulated as multi-linear diagonal strut members (Simulation type B).

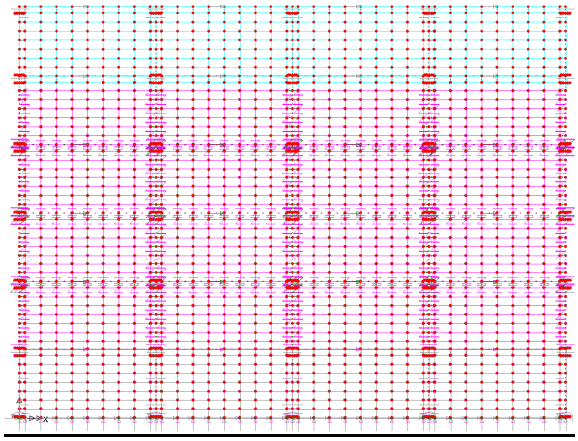


Figure 9a: Type B numerical simulation of 6-storey plane structure with masonry infills simulated as diagonal struts.

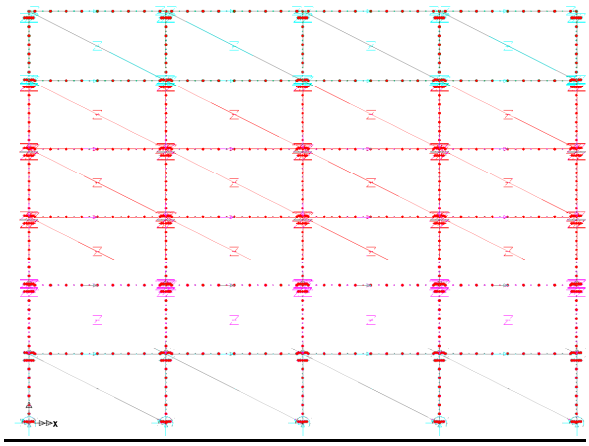


Figure 9b: Type A numerical simulation of 6-storey plane structure with masonry infills simulated as plane stress elements.

For the fully non-linear "pushover" type A analysis of the 6-storey structure, the maximum target displacement at the top was set equal to 54mm, with the displacement profile along the height of the building assumed to be triangular. The resulting in this way displacement was imposed at each floor level in a gradual increasing fashion. The corresponding lateral forces at each floor level resulting from this fully non-linear analysis were recorded especially for horizontal maximum top displacement levels of 18mm, 27mm, 36mm, 45mm, 54mm, 57,6mm. Both type A and type B simulations predicted the corresponding deformation pattern of the whole structure at each floor level. By comparing the load-deformation obtained

through either the type A (fully non-linear approach) or the type B (equivalent post-elastic with multi-linear struts approach) the validity of the type B approximation of the masonry infill response will be assessed.

3.2 Numerical simulation of the single storey unit

The equivalent post-elastic analysis that was described in table 1 determines the decomposition of the multi-storey structural formation to individual single-storey one-bay masonry infilled R/C frame units. The numerical simulations of the fully non-linear masonry infilled R/C frame unit (simulation type A), and the non-linear R/C frame unit that utilizes the diagonal strut for the simulation of masonry infill (Simulation type B) is described below.

A) Fully non-linear masonry infilled R/C frame response (simulation type A): The successful numerical simulation that has been proposed in section 2 will be applied first for the whole 6-storey structure. The horizontal load-horizontal displacement fully non-linear response curve resulting from this simulation will include non-linear mechanisms for the masonry infill, the surrounding R/C frame, the interface between the masonry infill and the surrounding prototype frame. Described briefly in what follows is the numerical simulation of the masonry infill, that of the R/C frame and of the interface between the R/C frame and the masonry infill (figures 10a, 10b and 10c).

a) Simulation of the masonry infill. The simulation of the masonry infill, utilizing non-linear plane stress finite elements, was described extensively in section 2. This is also followed here (figure 10b). The isotropic nonlinear material law of Modified Von Mises was utilized. The adopted mechanical properties of the initial and the strengthened masonry infill panels are listed in Table 7.

Mechanical properties	**Initial**	**Strengthened**
Young Modulus (N/mm^2)	2500	3500
Poisson Ratio	0,20	0,20
Tensile strength (N/mm^2)	0,20	0,80
Compressive strength (N/mm^2)	2,50	4,50
Softening Modulus under compression (N/mm^2)	0	0
Softening Modulus under tension(N/mm^2)	0	0

Table 7: Mechanical properties used for the description of Von Mises failure criterion of the initial and strengthened masonry infills for the 6-storey structure.

b) *Simulation of the beam/column R/C elements and the plastic hinge formation.*The simulation of the surrounding R/C frame is done with linear elastic beam and column members together with predetermined locations of possible plastic hinge formation at the ends of each element the same way as described in section 2.1.

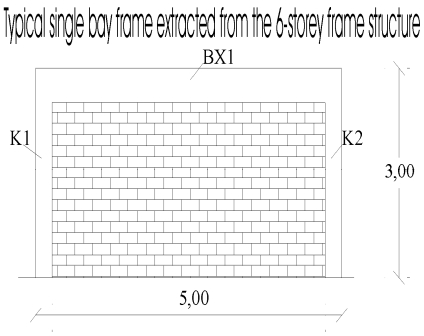


Figure 10a: Typical masonry infilled frame unit of the 6-storey building.

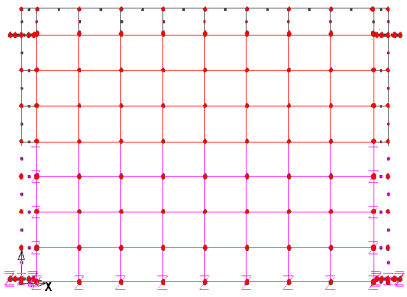


Figure 10b: Fully non-linear masonry infilled R/C frame simulation (type A).

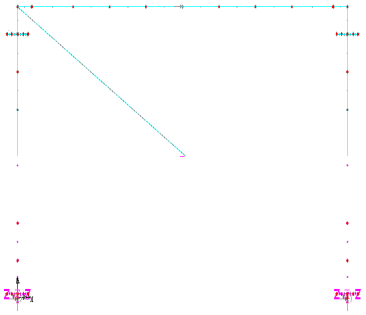


Figure 10c: Non-linear surrounding R/C frame- with multi-linear diagonal for masonry infill (type B).

c) *Simulation of interface between the R/C frame and the masonry infill* The numerical simulation of the interface between the prototype R/C frame and the masonry infill is done in the same way as described in section 2.1, utilizing non-linear joint elements in the axial and transverse direction. This interface is assumed that was built with mortar type H (see Thauampteh [10] and Table 5) with mechanical properties typical to the ones used in the Greek building practice.

B) Non-linear surrounding R/C frame with multi-linear diagonal struts (Simulation type B): Next, the proposed equivalent type B numerical simulation that has been proposed in section 2.2. will also be applied for the whole 6-storey structure. As was done in simulation type A here too the numerical simulation of R/C members will be done with linear elastic beam and column elements together with predetermined locations of possible plastic hinge formation at the ends of each element (figure 10c). The properties of each equivalent diagonal struts are determined with successive approximations as described in step e of Table 1.

For each one of these single-stories masonry infilled R/C frame units a "pushover" type A analysis is performed and the horizontal load (H) versus horizontal displacement (δ) or shear strain (γ) response curve is obtained, as indicated by figure 11. The accumulation of damage to the masonry infills is also obtained linked to the increase of the shear strain levels as it results from this fully non-linear type A simulation (as indicated in figure 11). This is done for preselected shear strain values (e.g. 0.1%, 0.15%, 0.2%, 0.25%, 0.30% and >0.35%). For each one of these single-storey masonry infilled R/C frame units a number of type B simulations are next prepared. A "pushover" type B analysis is now performed. The properties of a multi-linear diagonal strut are found approximating for each single-storey infilled frame the stiffness and strength variation as obtained from its fully non-linear A type simulation. In figure 12, a comparison between push over curves obtained from simulation type A and simulation type B of a retrofitted single storey R/C masonry infilled frame unit can also be depicted. For the predicted shear strain value of 3,2‰ the expected performance (development and propagation of damage) can be deduced for each masonry infill (initial and retrofitted) of the multi-storey structure, as shown in the figures 13a and 13b.

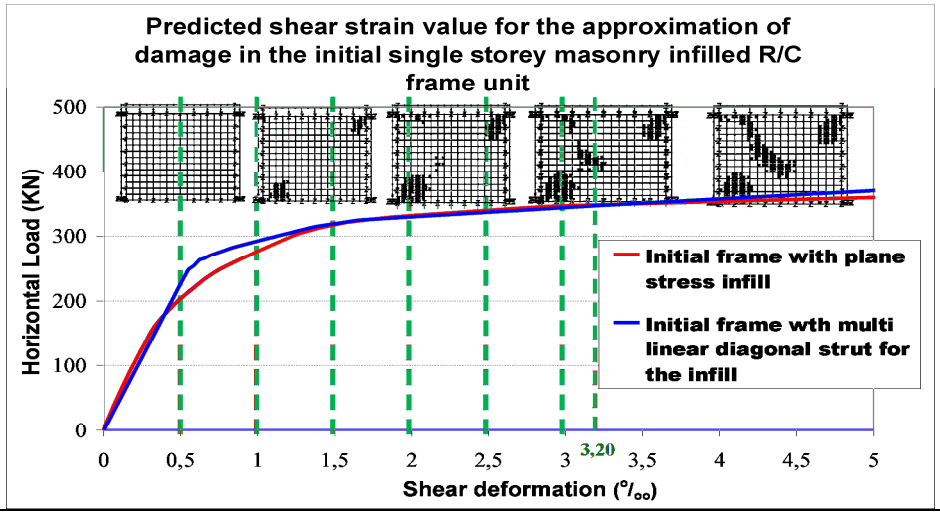


Figure 11: Comparison between push over curves obtained from simulation type A and simulation type B of a single storey R/C masonry infilled frame unit.

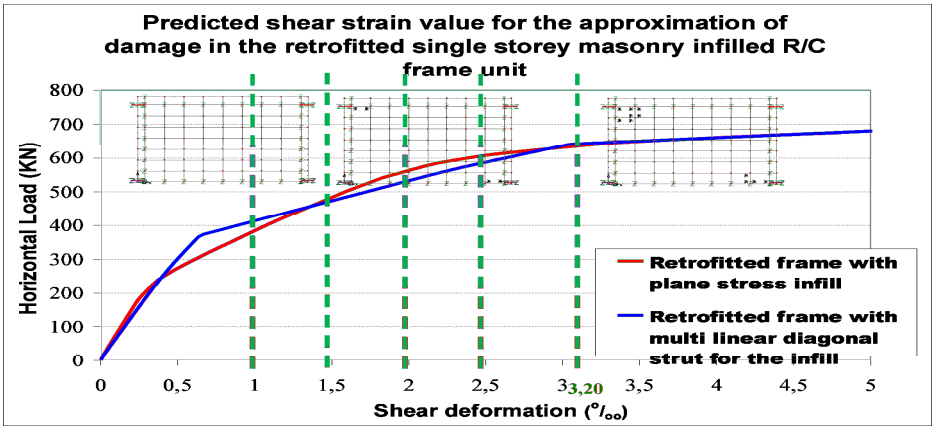


Figure 12: Comparison between push over curves obtained from simulation type A and simulation type B of a retrofitted single storey R/C masonry infilled frame unit.

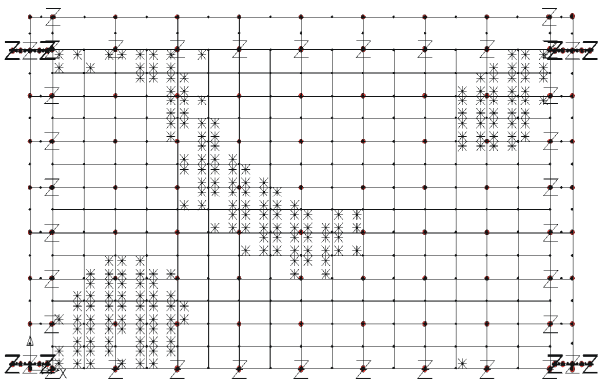


Figure 13a: Damage pattern of the infill, as predicted from the full non-linear analysis (type A) for the shear strain level 3,2°/oo.

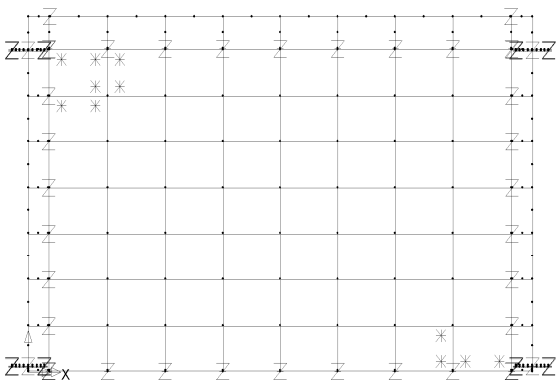


Figure 13b:Damage pattern of the strengthened infill, as predicted from the full non-linear analysis (type A) for the shear strain level 3,2°/oo.

3.3 Numerical simulation of the Multi-storey frame and Predicted damage "Pushover" curves

Figure 14 depicts the base shear – top deformation curve obtained either by the fully non-linear "pushover" type A analysis for an initial masonry infilled 6-storey structure, when the top displacement reached the target value of 54mm, or the proposed equivalent type B analysis with the multi-linear diagonal struts. In the same figure the behaviour curve of a retrofitted 6-storey structure with strengthened masonry infills is also presented. The target displacement corresponds to approximately 0.3% shear strain level for the masonry infills. The employed type B simulation is also depicted in the top left of figure 14 together with the horizontal storey displacements at this maximum shear strain level (0.3%). As can be seen, the load-displacement response obtained by the equivalent post-elastic analysis is in good agreement with that predicted by the fully non-linear analysis. Using the procedure of step h of Table 1, the predicted masonry damage along the height of this structure was also obtained. Figure 15a,b depicts in more detail the predicted damage of the masonry infills of the 6-storey structural formation as it resulted from either the fully non-linear type A or the equivalent type B numerical simulations, respectively. As can be seen, good agreement is obtained between the masonry infill damage predictions of the equivalent type analysis with those resulting from the fully non-linear type A approach for the whole 6-storey structure. In figure 16a,b the predicted damage patterns are also presented for the retrofitted masonry infilled R/C frame that utilizes strengthened infills.

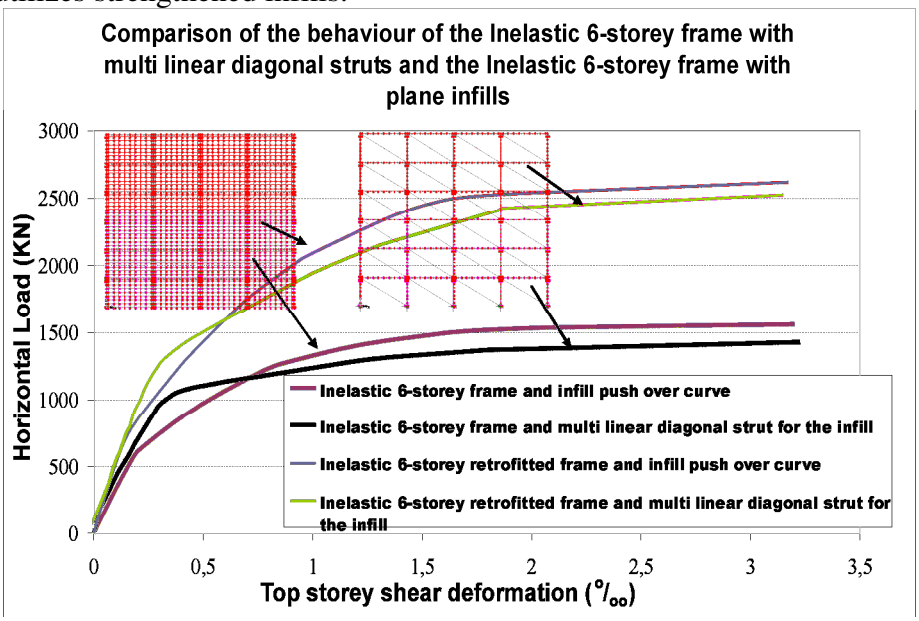
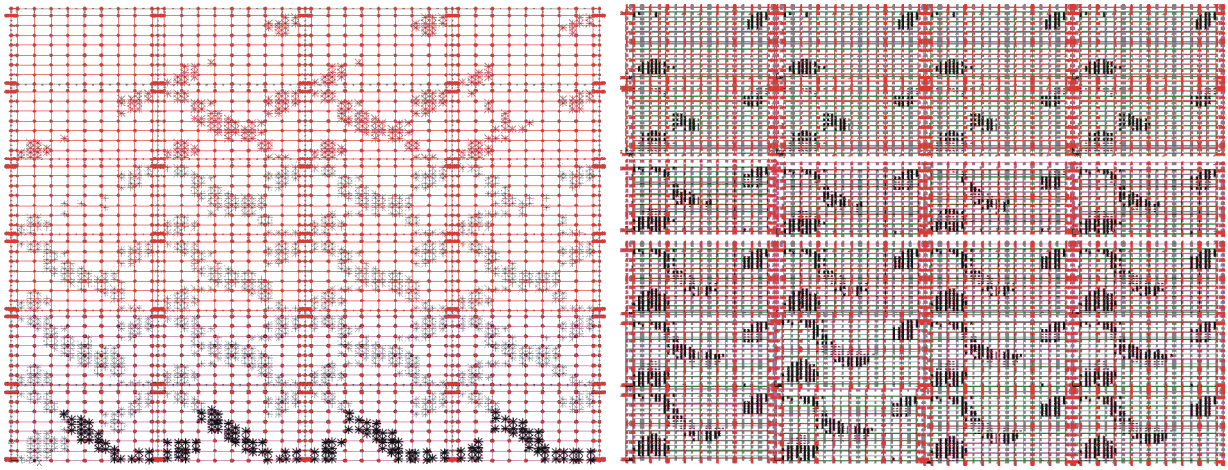


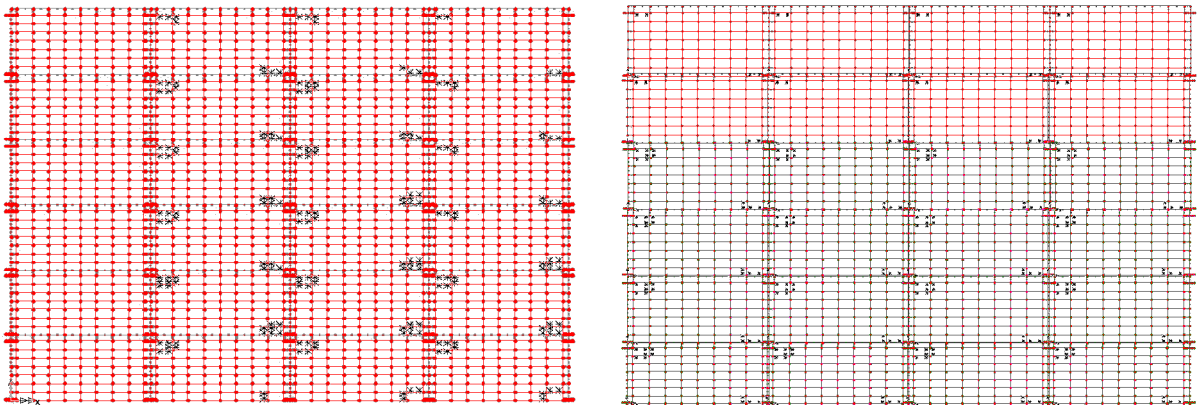
Figure 14: Base shear – top storey deformation "pushover" response as predicted by either type A or type B ($\gamma = 0.3\%$).



a) Masonry damage prediction type A

b)Masonry damage prediction type B

Figure 15: Detail of masonry infill damage patterns, as predicted for top storey target displacement equal to 0.3% of the building height by a) type A or b) type B simulations.



a)Masonry damage prediction type A

b)Masonry damage prediction type B

Figure 16: Detail of strengthened masonry infill damage patterns, as predicted for top storey target displacement equal to 0.3% of the building height by a) type A or b) type B simulations.

As can be seen from these figures there is reasonably good agreement in the pushover "top storey versus base shear" response of the 6-storey structural formation predicted by the equivalent type B analysis with that predicted with the considered more accurate fully non-linear type A analysis. Moreover, there is also reasonably good agreement between the damage patterns of the masonry infills predicted by the type B simulation as explained in step h) of the outlined methodology in Table 1 with the corresponding damage patterns of the masonry infills, as predicted by the more accurate fully non-linear type A analysis.

The corresponding "pushover" analysis for this strain level when employing the fully non-linear simulation of the masonry infilled frames lasted 50 minutes whereas the "pushover" analysis with diagonal struts lasted 2 minutes and 30 seconds. Thus, considerable gains in terms of computer time as well as computer memory requirements results from adopting the multi-linear diagonal strut approximation together with a "pushover" type of analysis.

4 CONCLUDING OBSERVATIONS

1. The strength and load-displacement hysteretic behaviour observed during the experiments of single-storey one-bay masonry-infilled R/C frames examined in this study is successfully predicted of by the proposed numerical simulation.
2. The development of plastic hinges at the predetermined positions of columns and beam of the surrounding R/C frame observed during the experiments as well as the damage patterns for the masonry infill, in terms of crack propagation is also successfully predicted.
3. Finally, the dissipated energy during the experimental "seismic-type" cyclic-loading sequence is in good agreement with that resulting from the proposed numerical simulation.
4. The employed numerical simulation of masonry-infilled R/C frames having their infill repaired with reinforced plaster, predicts successfully the observed during testing increase in stiffness, strength and energy dissipation due to this presence of the partially reinforced masonry infill.
5. The proposed numerical simulations of masonry infills incorporates influences arising from the interface between the masonry infill and the surrounding R/C frame, as these are found to be important in obtaining realistic predictions of the masonry infill to frame interaction. Thus, the proposed numerical simulation seems to represent in a reasonable way the most important influences that the interface between masonry infill and the surrounding frame could exert on the cyclic behaviour of such structural assemblies in terms of stiffness, strength modes of failure, as demonstrated from the observed behaviour.
6. The proposed numerical simulation can accommodate the use of an interface provided that the mechanical properties of the constituents of such an interface are known.
7. The damage patterns of the masonry infill observed during testing were well approximated by the proposed numerical simulation. The well known damage patterns for relatively weak "Greek" type masonry in the form of either diagonal cracking or compression failure in the regions where the masonry infill corners meet the R/C column to beam joint, are reproduced quite well by the proposed simulation.
8. Based on the successful validation of the proposed numerical simulation of the non-linear response of single-storey one-bay masonry-infilled R/C frames an equivalent "pushover" analysis is proposed next for predicting the behaviour of masonry infills from their interaction with the surrounding R/C structural elements when these masonry infills are incorporated within multi-storey frame structural formations.
9. By comparing the response of a planar multi-storey R/C masonry-infilled frame, as predicted by the fully-nonlinear simulation type A validated in the first part of this paper and the proposed equivalent "pushover" type B analysis, it can be demonstrated that this proposed "equivalent pushover analysis" is quite successful in predicting reasonably well the *"top storey versus base shear"* response of the 6-storey structure used for validation purposes.
10. By comparing the response of a planar multi-storey R/C masonry-infilled frame, as predicted by the fully-nonlinear simulation type A validated in the first part of this paper and the proposed "equivalent pushover" type B analysis, it can be demonstrated that this proposed "equivalent pushover" analysis is quite successful in predicting reasonably well the *propagation of the masonry infills damage* along the height of the 6-storey structure used for validation purposes.

11. The computational time needed for this "equivalent pushover" analysis is considerably less than the computational time needed for the fully non-linear analysis of multi-storey masonry infilled R/C frames when all the non-linear mechanisms of structural members are included, presented in the first part of this paper. Thus, it can be used as a useful design tool in order to assess the state of masonry infills within complex multi-storey structural formations. The proposed approach can also be utilized in the seismic- design for assessing the state of masonry infills and their potential damage for either newly designed or for an existing structures as part of a potential damage screening process.
12. It must be stressed that the proposed "equivalent pushover" analysis is an approximation. It approximates part of the non-linear bahavior and the masonry-infill to surrounding frame interaction utilizing the stiffness and strength variation of masonry infilled single-storey one bay frame units that the multi-storey structure is decomposed to. In this framework, given the computer time and computer memory gains that can be achieved by the proposed approximations it can be utilized in practical applications following the procedures that are generally recommended for such "pushover" type of analyses in the relevant codes of practice for earthquake design .

REFERENCES

[1] Soulis V.J. "Investigation of the Numerical Simulation of Masonry Infilled R/C Frame Structures under Seismic-type Loading", Ph.D. Thesis, Department of Civil Engineering, Aristotle University of Thessaloniki, 2009.

[2] R.E. Klingner and V.V. Bertero, "Infilled Frames in Earthquake - Resistant Construction", EERC, Report No. 76-32, University of California, Berkeley, California, USA, Dec. 1976.

[3] M. Holmes," Steel Frames with Brickwork and Concrete Infilling" Proceedings of the Institution of Civil Engineers (ICE), Vol. 19, 1961.

[4] M. Holmes, "Combined Loading on Infilled Frames " Proceedings of the Institution of Civil Engineers (ICE), Vol. 25, 1963.

[5] Mainstone R.J., "On the stiffnesses and strengths of infilled frames", Proceedings of the Institution of Civil Engineers, Supplement (V), pp. 57-90, 1971.

[6] Liauw T.C., and Kwan K., "Non-linear behavior of non-Integral infilled frames", Computers and Structures, Vol.18, No.3, pp.551-560, 1984.

[7] G.C. Manos, V.J. Soulis and J. Thauampteh, "The Behaviour of Masonry Assemblages and Masonry-infilled R/C Frames Subjected to Combined Vertical and Cyclic Horizontal Seismic-type Loading", Journal of Advances in Engineering Software, Vol. 45, pp. 213-231, 2011.

[8] G.C. Manos, V. J. Soulis and J. Thauampteh. "A Nonlinear Numerical Model and its Utilization in Simulating the In-Plane Behaviour of Multi-Storey R/C frames with Masonry Infills", *The Open Construction and Building Technology Journal,6,* (Suppl 1-M16) 254-277,2012.

[9] Eurocode 8: Design of structures for earthquake resistance EN 1998, European Committee for Standardization, December 2004.

[10] J. Thauampteh, "Experimental Investigation of the Behaviour of Single-storey R/C Frames with Masonry Infills, Virgin and Repaired, under Cyclic Horizontal Loading", Ph.D. Thesis, Department of Civil Engineering, Aristotle University of Thessaloniki, 2009.

[11] K. Stylianides, "Experimental Investigation of the Behaviour of Single-storey Infilled R/C Frames under Cyclic Quasi-static Horizontal Loading (Parametric Analysis", Ph.D. Thesis, Department of Civil Engineering, Aristotle University of Thessaloniki, 1985.

[12] Th. Valiasis, "Experimental Investigation of the Behavior of R.C. Frames Filled with Masonry Panels and Subjected to Cyclic Horizontal Load - Analytical Modelling of the Masonry Panel", Ph.D. Thesis, Department of Civil Engineering, Aristotle University of Thessaloniki, 1989.

[13] B. Yasin, "Experimental Investigation of the Influence of Infills on the Dynamic Response of Building Structures Through the Study of Scaled Physical Models", Ph.D. Thesis, Department of Civil Engineering, Aristotle University of Thessaloniki, 1999.

COMPDYN 2013
4th ECCOMAS Thematic Conference on
Computational Methods in Structural Dynamics and Earthquake Engineering
M. Papadrakakis, V. Papadopoulos, V. Plevris (eds.)
Kos Island, Greece, 12–14 June 2013

NUMERICAL AND EXPERIMENTAL STUDY OF THE ROCKING RESPONSE OF UNANCHORED BODY TO HORIZONTAL BASE EXCITATION

G.C. Manos[1]*, A. Petalas[1], M. Demosthenous[1]

[1]Laboratory of Strength of Materials and Structures
Dept. Civil Engineering. Aristotle University of Thessaloniki
University Campus, Egnatia street, Thessaloniki, 54006
gcmanos@civil.auth.gr

Keywords: Rocking, Rigid Body, Numerical Simulation Experimental Verification, Ancient Monuments

Abstract. *Ancient Greek and Roman structures composed of large heavy members that simply lie on top of each other in a perfect-fit construction without the use of connecting mortar, are distinctly different from relatively flexible contemporary structures. The colonnade (including free standing monolithic columns or columns with drums) is the typical structural form of ancient Greek or Roman temples. The seismic response mechanisms that develop on this solid block structural system during strong ground motions can include sliding and rocking, thus dissipating the seismic energy in a different way from that of conventional contemporary buildings. This paper presents results and conclusions from an experimental study that examines the dynamic response of rigid bodies, representing simple models of ancient columns. These models are subjected to various types of horizontal base motions (including sinusoidal as well as earthquake base motions), reproduced by the Earthquake Simulator Facility of Aristotle University. The employed rigid bodies were made of steel and are assumed to be models of prototype structures 20 times larger. In addition to the experimental study, numerical simulations of the observed dynamic and earthquake rocking response of the free standing steel rigid block specimens were also carried out. These numerical simulations were performed in two different ways. At first, a specific software was developed based on analytical expressions of the equations of motion for this problem together with numerical integration techniques that yielded predictions of the rocking response. Next, the numerical simulation employed a commercial finite element software package (Abaqus) and utilized the capabilities of this software to obtain predictions of the rocking response of the tested in the laboratory free standing steel rigid block specimens. The numerical results obtained from these two different numerical simulations are presented and compared with the experimental response measurements as well as among each other. From this comparison the reliability of these two distinct numerical simulations is presented and discussed.*

1 INTRODUCTION

Ancient Greek and Roman structures composed of large heavy members that simply lie on top of each other in a perfect-fit construction without the use of connecting mortar, are distinctly different from relatively flexible contemporary structures. The colonnade (including free standing monolithic columns or columns with drums) is the typical structural form of ancient Greek or Roman temples ([7], [8], [9]). The columns are connected at the top with the epistyle (entablature), also composed of monolithic orthogonal blocks, spanning the distance between two columns (figure 1a).

The seismic response mechanisms that develop on this solid block structural system during strong ground motions can include sliding and rocking, thus dissipating the seismic energy in a different way from that of conventional contemporary buildings ([4], [6]). This paper presents results and conclusions from an extensive experimental study that examines the dynamic response of rigid bodies, representing simple models of ancient columns or colonnades. These models are subjected to various types of horizontal base motions (including sinusoidal as well as earthquake base motions), reproduced by the Earthquake Simulator Facility of Aristotle University. The rigid bodies employed in this study were made of steel and are assumed to be models of prototype structures 20 times larger ([6]). The basic configuration that is examined here is that of a single steel prismatic model. Apart from this model, additional models of cylindrical as well as of a truncate cone form were also studied (see figure 1b) but not reported here. Dynamic and simulated earthquake rocking response results are presented in a summary form, mainly in section 2, obtained from an extensive investigation employing these monolithic free-standing rigid models [6]. The measured response is next compared with predictions from numerical simulations that employed software developed at Aristotle University (termed analytical results, [4], [6], section 3). Finally, numerical predictions of the dynamic and simulated earthquake rocking response of the prismatic model, as obtained by applying the commercial software abaqus are also presented and compared with the experimental and analytical results.



Figure 1a. The Temple of Zeus, Ancient Corinth

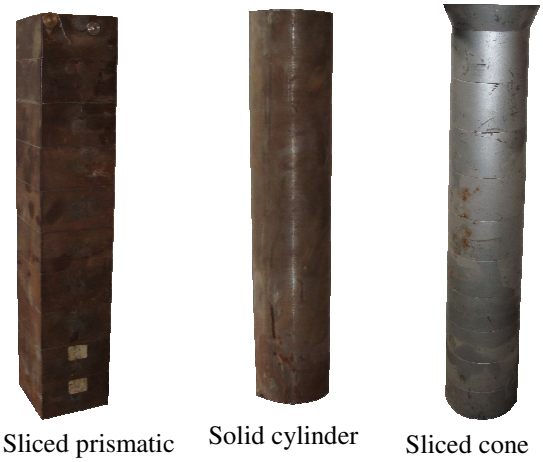
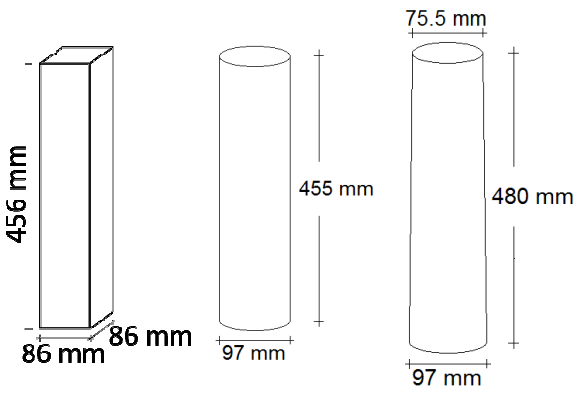


Figure 1a. The characteristics of the three specimens



Sliced/solid Prismatic | Sliced/ solid Cylinder | Sliced/ solid Truncate cone



Rigid Body Steel Specimens: Sliced Cylinder, Sliced Cone, Solid Cylinder, Sliced Prismatic

Figure 2. Dimensions of the three specimens

Specimen	Mass (kg)	Side length / diameter (mm)	Height (mm)	Distance center of mass from rocking pole (mm)	Critical Rocking Angle (rad)	Mass Moment of Inertia-rocking pole kg m^2	Natural Rocking Frequency (rad/sec)
Prismatic	26.10	86	456	232	0.1886	1.873	5.631
Cylindrical	26.30	97	455	227	0.2132	1.883	5.631
Truncate cone	21.94	75.5 / 97	480	220	0.2203	1.527	5.631

Table 1. Basic parameters for the rocking response of the three specimens.

2 INVESTIGATION OF THE DYNAMIC RESPONSE OF A SOLID RIGID BODY

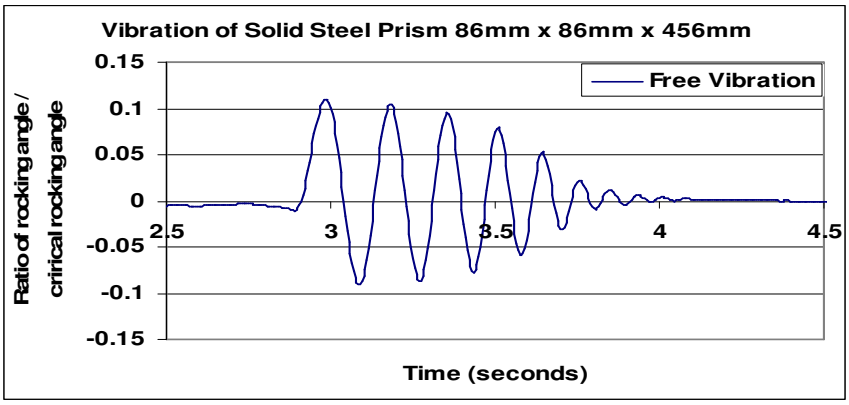
The dimensions of the examined rigid models, are shown in figure 2. These specimens were placed on the earthquake simulator simply free-standing on the horizontal moving platform of the shaking table. A very stiff, light metal frame was built around each studied model in order to carry the displacement transducers that measured the rocking angle; this metal frame also provided temporary support to the specimen during excessive rocking displacements indicating overturning.

The dynamic behaviour of each specimen was governed by its rocking response. The experimental investigation of its rocking response included periodic sine-wave tests with a chosen range of frequencies and amplitudes as well as earthquake simulated tests using the El Centro 1940 record. A simple way to estimate the dissipation of energy during rocking is to obtain the value of the coefficient of restitution by comparing free vibration rocking response measurements with those predicted numerically. From such comparisons the coefficient of restitution was obtained with the value that yields the best agreement between measured response parameters and results from a numerical solution outlined in section 3.

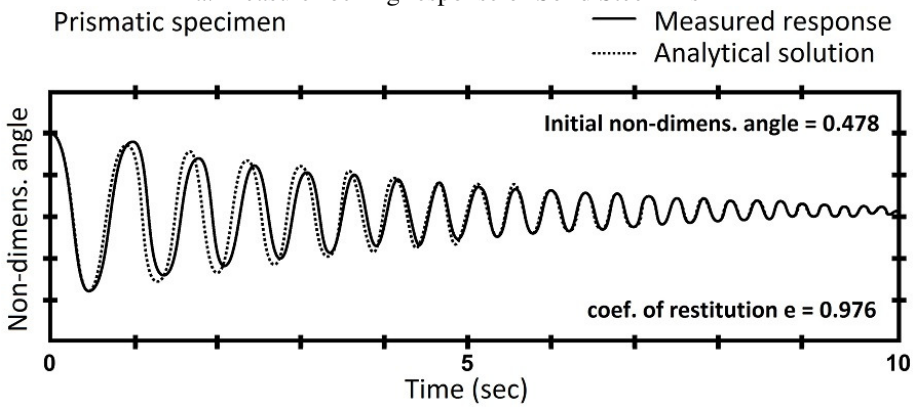
The numerical solutions employed were verified for their stability and convergence through an extensive parametric study that examined various methods of numerical integration and time step. This correlation was next extended with measurements from sinusoidal as well as earthquake simulated tests (section 3). The numerical studies in this case employed the same base excitations recorded at the Earthquake Simulator during the tests and used as values for the coefficient of restitution the ones determined from the same experimental sequence and the best numerical solution that was found from the above mentioned study ([4], [5], [6]).

2.1. Free Vibration Tests.

The sequence of tests for the solid truncate cone included free vibrations tests, with the objective of assessing the coefficient of restitution of the test structure. The following figure (figure 3) depicts the rocking angle response (solid line) from such a free vibration test. Superimposed on this graph with a dash line is the numerically predicted rocking response, with a coefficient of restitution value that gave the best fit to the experimental measurements. The predicted rocking response was derived from the linearised equations of the rocking motion ([1], [6]). Certain discrepancies are apparent at the initial large amplitude rocking stages. This must be attributed to three-dimensional (3-D) rocking ([3]), since rocking in a perfect plane for a 3-D model requires exacting initial conditions and the slightest out-of-plane disturbance will cause rocking to be 3-D. When the specimen tested is prismatic instead of truncate cone the 3-D response during rocking is minimized and good correlation can be obtained between observed and predicted behaviour thus assessing more accurately the coefficient of restitution ([4], [6]). A summary of the "analytical solution" is given in section 3.



a. Measure rocking response of Solid Steel Prism



b. Measured and predicted free vibration rocking response of Solid Steel Prism

Figure 3. Free vibration response of the prismatic specimen and comparison with analytical predictions

2.2. Sinusoidal Tests

During these tests the frequency of motion was varied from 1Hz to 7Hz in steps of 1Hz from test to test. This resulted in groups of tests with constant frequency for the horizontal sinusoidal motion for each test. In the various tests belonging to the same group of constant frequency, the amplitude of the excitation was varied progressively from test to test. Figures 4a, 4b and 4c depict the rocking response of the solid specimen during this sequence of tests

for three different excitation cases for the same non-dimensional frequency Ω having a value equal to 3.35 (see equation 1).

$$\mathrm{A} = \frac{x}{\theta_{cr} \cdot g}, \qquad \Omega = \frac{\omega}{p}, \qquad p = \sqrt{\frac{W \cdot R_c}{I_o}} \tag{1}$$

A = Non-dimensional base acceleration amplitude
x = Actual horizontal peak base acceleration of the sinusoidal motion
θ_{cr} = Critical angle (rad) indicating overturning of the specimen
g = The gravitational acceleration
Ω = Non-dimensional frequency
ω = Actual sinusoidal frequency (rad/sec)
p = The natural rocking frequency of the specimen (rad/sec)
W = The weight of the block
R_c = The distance of the center of gravity from the rocking pole
I_o = The mass moment of inertia with respect to the rocking pole

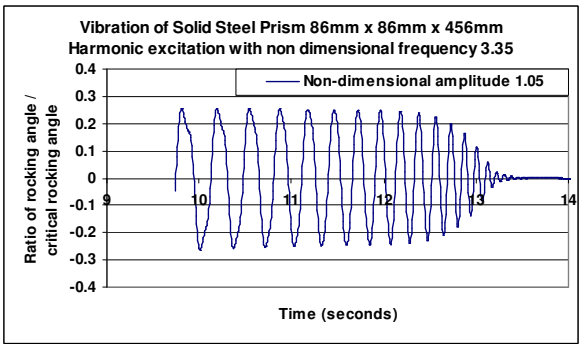


Figure 4b. Rocking response of prismatic specimen for Ω=3.35, A=1.05

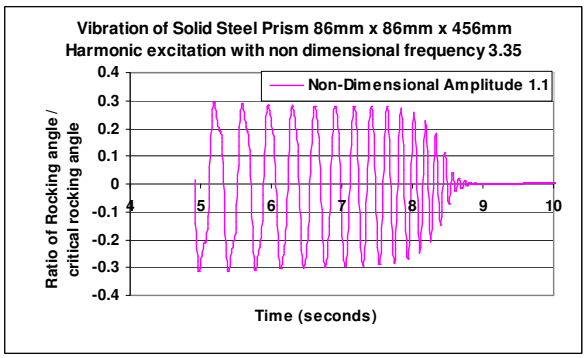


Figure 4b. Rocking response of prismatic specimen for Ω=3.35, A=1.1

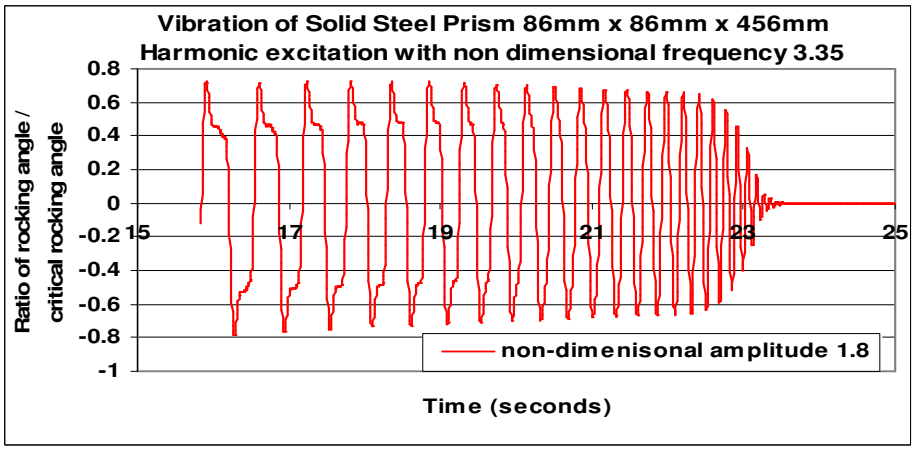


Figure 4c. Rocking response of prismatic specimen for Ω=3.35, A=1.80

The response parameter that is plotted in figures 4a to 4c is the ratio of the rocking angle over the critical angle. For the case of the prismatic specimen the critical angle is equal to 0.1886rad. Moreover, the intensity of the excitation, as expressed by the value of the non-

dimensional amplitude A, keeps increasing from the value of 1.05 to the value of 3.35.

The following points can be made from the observed behaviour during these tests:

- For small amplitude tests the rocking behaviour is not present; the motion of the specimen in this case follows that of the base.
- As the horizontal base motion is increased in amplitude, rocking is initiated. This rocking appears to be sub-harmonic in the initial stages and becomes harmonic at the later stages.
- Further increase in the amplitude of the base motion results in excessive rocking response, which after certain buildup leads to the overturning of the specimen. At this stage, the rocking response is also accompanied by some significant sliding at the base as well as by rotation and rocking response out-of-plane of the excitation axis.

The above observations have been noted when the sinusoidal excitations were performed keeping the non-dimensional frequency value constant and equal to Ω_1 varying at the same time the non-dimensional amplitude A_j of the excitation. Each observation is termed in three distinct ways; that is: a)no-rocking, b) stable rocking, and c) unstable rocking which leads to overturning of the rigid specimen. Moreover, each of these observations corresponds to a set of non-dimensional frequency value Ω_1 and non-dimensional amplitude A_j of the excitation. If the above experiments are repeated with a new constant value of the non-dimensional frequency equal to Ω_i varying again only the non-dimensional amplitude A_k of the excitation a new set of observations (Ω_i , A_k) will be obtained. For the new set of observations the comments made before will again be valid. All these sets of observations (Ω_i , A_k) can be depicted on a plot having as abscissa the non-dimensional frequency value Ω_i and as ordinates the non dimensional amplitude of the base motion A_k.

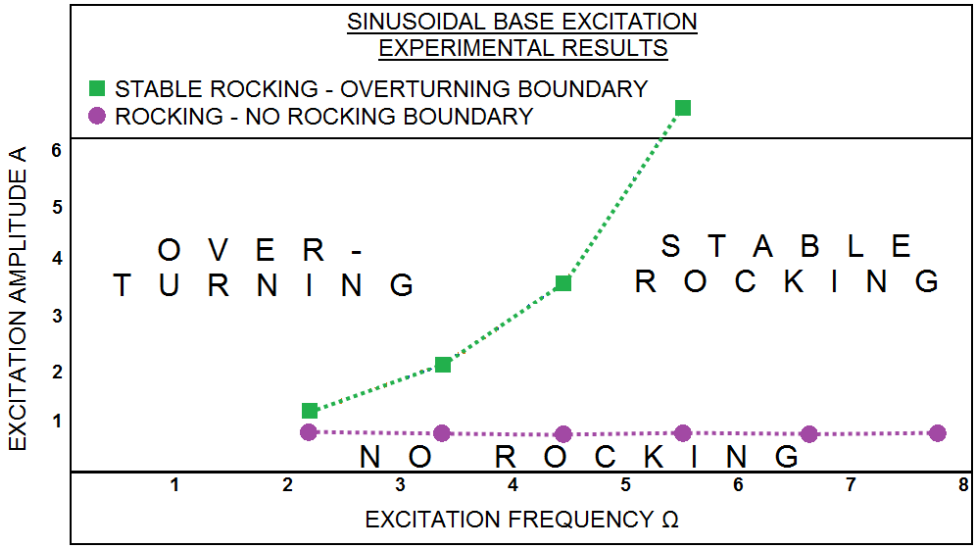


Figure 5. Mapping the stable-unstable rocking response

The above stages are graphically portrayed in the plot of figure 5 (together with the numerical results as is explained below). In this figure, the two boundaries, as established from consecutive experiments of sinusoidal vibrations of constant non-dimensional frequency Ω_i and amplitude A_k of increasing intensity are marked. The first is the rocking-no rocking boundary, which is marked with circles; it indicates the limit state of sinusoidal vibrations that changes from no-rocking to stable rocking when the non-dimensional amplitude takes a

value that places this motion above this boundary. The second is the stable rocking-unstable rocking boundary, which is marked with squares; it indicates the limit state of sinusoidal vibrations that changes from stable rocking to overturning when the non-dimensional amplitude takes a value that places this motion above this boundary the. These two boundaries have been obtained from a large number of experiments whereby the prismatic specimen has been subjected to sinusoidal base motions each time with the different value of non-dimensional frequency Ω_i and non-dimensional amplitude A_k. The following observations summarize the main points of these two boundary lines of figure 5:

- The non-dimensional stable-unstable limit rocking amplitude values A_k increases rapidly with the non-dimensional frequency.
- For small values of the non-dimensional frequency Ω_i the transition stage from no-rocking to overturning, in terms of non-dimensional amplitude value A_k, is very small and it occurs with minor amplitude increase.
- The no-rocking stable rocking non-dimensional amplitude values A_k remain almost constant and equal approximately to one (1) for all non-dimensional frequency values Ω_i.

3 NUMERICAL SIMULATION BASED ON AN ANALYTICAL SOLUTION OF ROCKING

Initially, the numerical simulation was based on a software that was developed at the Laboratory of Strength of Materials and Structures ([4], [6]). This software was based on the integration in the time domain of the equations of motion for the rocking response of a rigid body. This solution investigated two alternative time step integration schemes that will be described in a summary in the following.

First, the simple time step integration scheme was employed whereby the equation of motion was expressed for a time step (t_i) through the values of the unknown parameters at the previous step (t_{i-1}). Thus, for finding the value of a function Θi(t) the values of this function and its derivatives must be known at the previous time step $\Theta(t_{i-1})$ τηζ $\Theta'(t_{i-1})$ (see figure 6a).

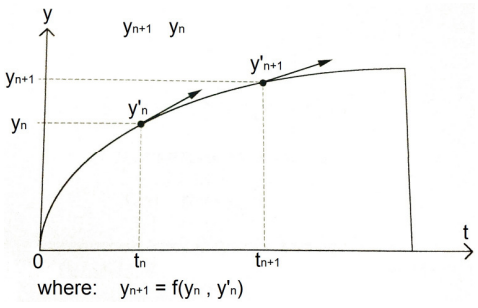


Figure 6a. Simple time step integration scheme

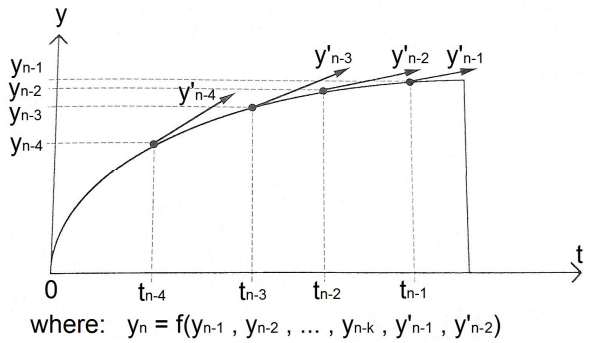


Figure 6b. Multiple time step integration scheme

Alternatively, a multiple time step integration scheme was employed, whereby for finding the value of a function Θi(t) the values of this function and its derivatives must be known at a number of previous time steps $\Theta(t_{i-1})$ and $\Theta'(t_{i-1})$, $\Theta(t_{i-2})$ and $\Theta'(t_{i-2})$, $\Theta(t_{i-3})$ and $\Theta'(t_{i-3})$, etc. (see figure 6b). In the framework of this investigation, the Hamming approximation was utilized whereby the value at a time step Θi(t) was based on the values of four previous time steps. The first four values for every rocking cycle are obtained applying the method Runge Kutta according to Runge.

3.1. Sinusoidal Tests

A numerical study has been performed, aimed to simulate the dynamic response of the solid prismatic specimen, using the non-dimensional linear equations for sinusoidal excitation as given by Spanos and Koh ([2]) and with a value for the coefficient of restitution as obtained from the free vibration tests presented before. The numerical analyses have been performed for various combinations of amplitude A_k and frequency Ω_i as was done for the experiments previously described. Figure 7 presents these results in a summary form using the same way to portray the response as was done to describe the rocking response in figure 5, observed during the experimental sequence with the horizontal sinusoidal base motion. These boundaries, that is the no-rocking stable rocking boundary and the stable-rocking-overturning boundary, are also plotted in figure 7, as predicted from the results of this numerical analysis, based on the integration of the analytical equations of rocking motion. As can be seen in figure 7, the stable rocking-overturning boundary is depicted with two boundary lines; one corresponds to smaller amplitude values A_k (lower limit, plotted with a solid line) and a second that corresponds to larger amplitude values A_k (upper limit, plotted with a dashed line). This signifies that the results of this type of numerical analysis do not define a single stable rocking - overturning boundary line as was defined by the experimental sequence.

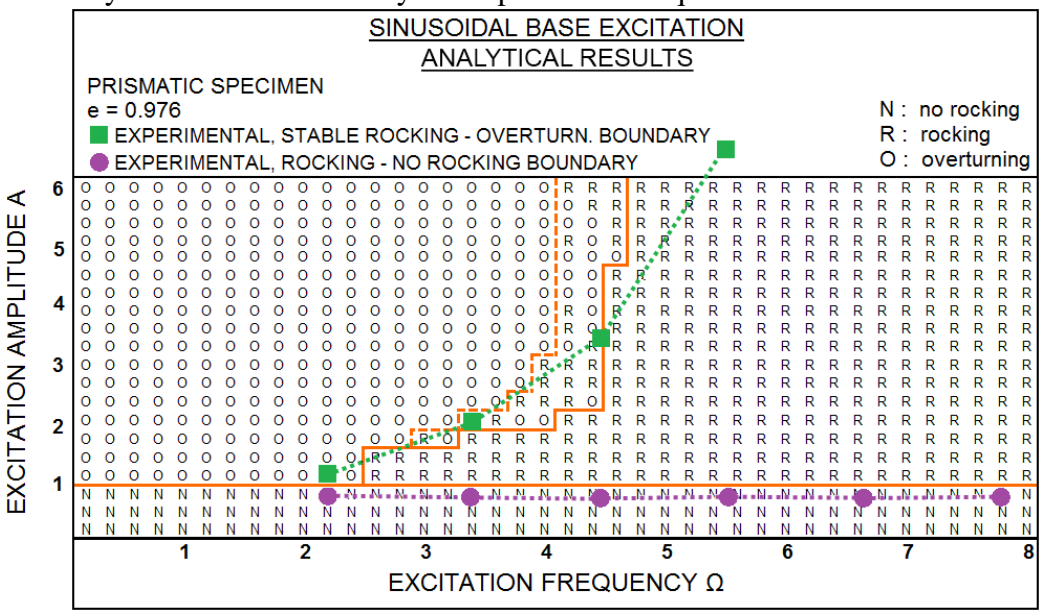


Figure 7. Mapping the stable-unstable rocking response. Analytical predictions and experimental measurements

The experimentally defined boundaries are superimposed on the analytical results in the plot of figure 7. Fairly good agreement can be seen between numerical predictions and the corresponding experimental measurements in terms of defining the two boundaries.

3.2. Simulated Earthquake tests

A number of tests were performed during this sequence with progressively increasing intensity, based on the 1940 El Centro Earthquake record. The intensity is measured with the indicator Span (figures 8a to 8c); higher intensity of the simulated earthquake motion corresponds to a larger value for the indicator Span. The base acceleration and displacement response was measured together with the rocking response of the tested specimen. The principal objective of these tests was to observe again the stable-unstable behaviour of the model. The

base excitations recorded at the Earthquake Simulator were used in the numerical simulation of the earthquake response; the value for the coefficient of restitution was taken from the free vibration tests. The full time history of the predicted rocking angle response is compared with the corresponding measured rocking angle in figures 8a to 8c. The measured response in these plots is compared with numerical solutions obtained utilizing a software developed for this purpose based on the analytical equations of rocking, as described before. These results are termed in these plots as analytical results. The time step that was adopted was DT=0.0001 sec; this time step was divided by ten (DT1=DT/10) just before and after each time the rocking specimen was making full contact with its supporting base.

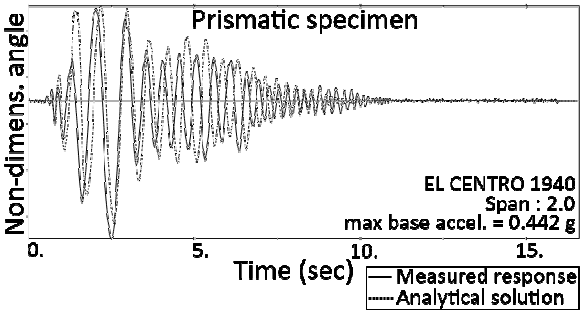


Figure 8a. Measured and analytically predicted rocking response of prismatic specimen Earthquake simulated test Span 2.0

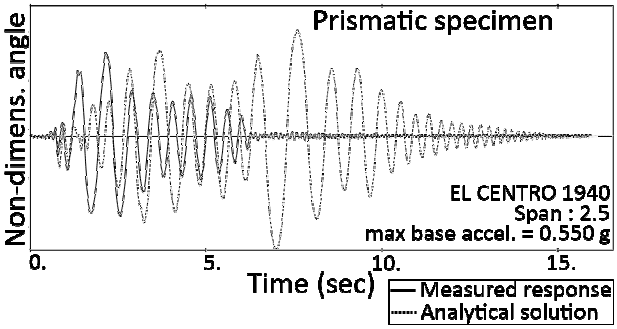


Figure 8b. Measured and analytically predicted rocking response of prismatic specimen Earthquake simulated test Span 2.5

For the tests with intensity Span 2 and Span 3 (figures 8a and 8c) good agreement was achieved between the numerical results based on the analytical equations of rocking and the measured rocking response. However, for the test with simulated earthquake intensity indicator Span 2.5 (figure 8b), the numerical rocking response exhibits large amplification at a time (approximately 6sec.) when the measured response has subsided.

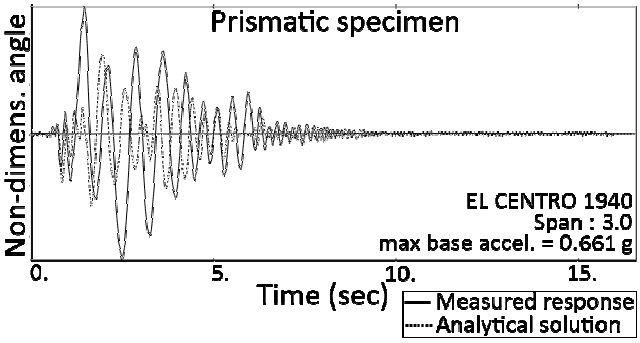


Figure 8c. Measured and analytically predicted rocking response of prismatic specimen Earthquake simulated test Span 3.0

4 NUMERICAL SIMULATION BASED ON A COMMERCIAL SOFTWARE

Initially, the free vibration response of the prismatic specimen, presented in section 2.1., was numerically simulated with the F.E. Abaqus software. At this initial numerical simulation, the influence of the input parameter of the critical damping fraction (CDF) was investigated. This was done by simulating the rocking response of the prismatic specimens with three different discretizations denoted as coarse mesh (1224 DOF) medium mesh (5478 DOF) and fine mesh (20332 DOF). For each one of these three discretizations, the free vibration rocking response of the prismatic specimen was examined, performing for each one of these numerical models (coarse, medium, fine mesh) simulations of the rocking response varying the time step of the non-linear integration scheme. This was done setting the time step equal to one of the following three specific values; that is 100μseconds, 10μseconds and 1μsecond. For each one of these nine basic numerical simulations (with different mesh and different time step) the CDF value was found that results in the best agreement between the Abaqus rocking

predictions of the free vibration rocking behaviour of the prismatic specimen with that obtained by the software based on the analytical equations. This CDF value was found by performing a considerable number of solutions with the Abaqus model through a trial and error process. These values of CDF, that result in the best agreement between the numerical Abaqus results and the analytical results of the free vibration rocking response are included in table 2. It was shown in section 2.1. that the analytically predicted free vibration rocking is in good agreement with the corresponding experimental measurements ([6]), defining indirectly in this way the value of the coefficient of restitution (e=0.976 in the case of the prismatic specimen). As can be seen from the variation of the values of CDF in table 2, when a medium or fine mesh is adopted, with a time step equal or less than 10μseconds, the numerical Abaqus results are in agreement with the analytical results, provided that the parameter CDF is set at a constant value equal to 0.40. Based on this preliminary investigation of the free vibration rocking response of the prismatic model, all the subsequent numerical simulations of the dynamic or simulated earthquake rocking response employed a value for the parameter CDF equal to 0.40. This was done employing at the same time the medium discretization mesh (figure 9) and a time step equal to 10μseconds. As can be seen in figure 10, good agreement could be obtained between the analytical results and the F.E. Abaqus simulation numerical results regarding the free vibration rocking response of the prismatic model.

Mesh	DOF	dt = 100 μs		dt = 10 μs		dt = 1 μs	
		CDF	cost (sec)	CDF	cost (sec)	CDF	cost (sec)
Coarse	1224	1.70	25	0.25	200	0.25	2000
Medium	5478	2.20	70	0.40	600	0.40	6000
Fine	20322	2.60	300	0.40	2700	-	-

Table 2. Values of the critical damping fraction for various mesh schemes and time steps (dt).

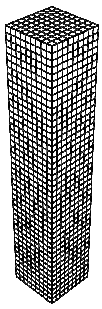


Figure 9. Utilized F.E. mesh

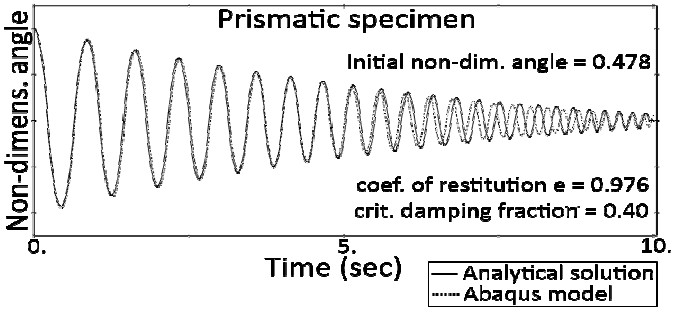


Figure 10. Comparison of numerical results obtained by either the analytical solution or the Abaqus software

4.1. Simulation of Sinusoidal Tests.

A series of numerical simulations with the Abaqus model were performed next using a horizontal base excitation of a sinusoidal type, prescribed by the non-dimensional frequency value Ω1 and the non-dimensional amplitude Aj (see equation 1), as was done in sections 2.2 and 3.1. This sinusoidal base motion is depicted in figure 11, as reproduced by the earthquake simulator of the Laboratory of Strength of Materials and Structures at Aristotle University. The same sinusoidal input motion was also used in the numerical simulations. The obtained results are depicted in figure 12, in the same way as plotted in sections 2 and 3 before, establishing the no rocking-stable rocking boundary as well as the stable rocking-overturning boundary.

These boundary lines are plotted in figure 12 using solid and dashed lines. As was observed in section 3.1. before, the stable rocking-overturning behaviour is depicted with two boundary lines; one corresponds to smaller amplitude values A_k (lower limit, plotted with a solid line) and a second that corresponds to larger amplitude values A_k (upper limit, plotted with a dashed line). This again signifies that the results of this type of numerical analysis do not define a single stable rocking - overturning boundary line as was defined by the experimental sequence

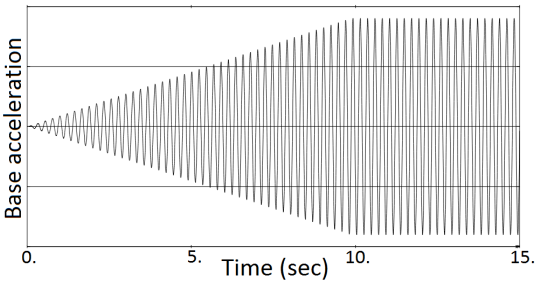


Figure 11. Sinusoidal horizontal base motion used in both the experimental sequence and in the numerical solutions

The no-rocking-stable rocking boundary is indicated with a solid line that corresponds to non-dimensional amplitude (A_k) approximately equal to 1, irrespective of the non-dimensional frequency value (Ω). In the plot of figure 12, the corresponding boundary lines as found from the experimental sequence described in section 2.2 are also plotted. As can be seen very good agreement was obtained between the experimental observations for the stable rocking – overturning boundary (points indicated with the squares) and the corresponding lower limit boundary line predicted by the Abaqus model (plotted with a solid line in figure 12). The very good agreement is also observed between the numerically predicted and the no rocking – stable rocking boundary line established by measurements established by measurements.

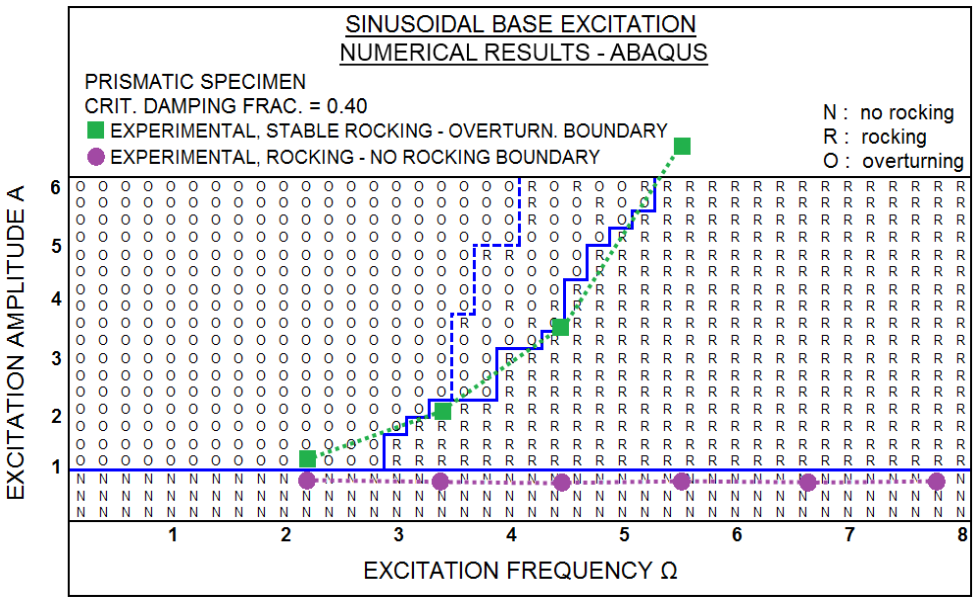


Figure 12. Mapping the stable-unstable rocking response. Numerical predictions with the Abaqus model and experimental measurements

The same comparison is presented in figure 13. This time, apart from the measured (designated as experimental) and the predicted by the Abaqus model boundaries (designated as numerical), the ones obtained by the integration of the analytical equations of rocking, presented in section 3.1. (designated as analytical) are also included. As can be seen, the numerical predictions (lower limit) obtained by the Abaqus model are in better agreement to the observed stable rocking-overturning boundary than the corresponding boundary established by the integration of the analytical equations of rocking

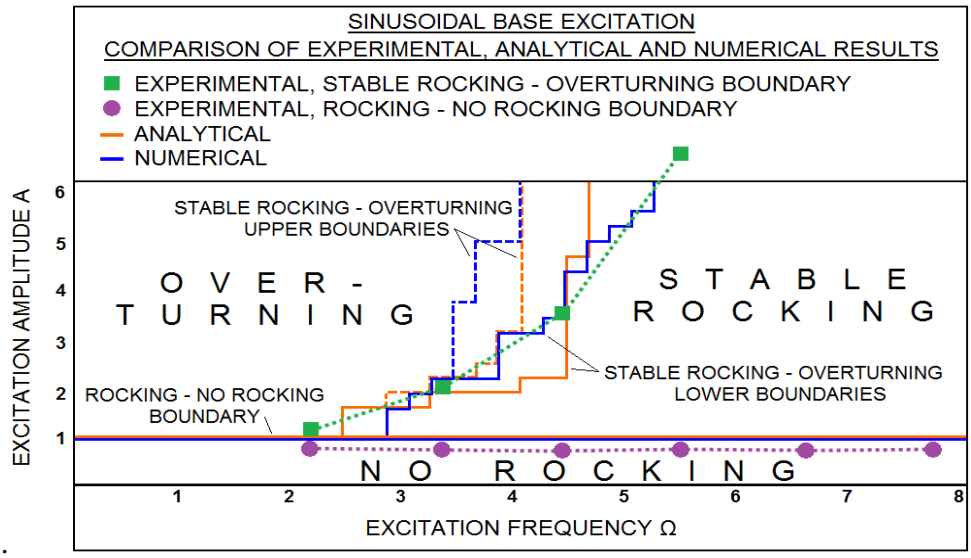


Figure 13. Mapping the stable-unstable rocking response. Numerical predictions with the Abaqus model, the analytical solution and the experimental measurements

4.2 Simulated Earthquake tests

A number of numerical simulations were obtained with the Abaqus model and were compared with the rocking response results obtained during the sequence of simulated earthquake tests presented in section3.2. The intensity of the horizontal base motion is described, as before, by the indicator Span (figures 14).

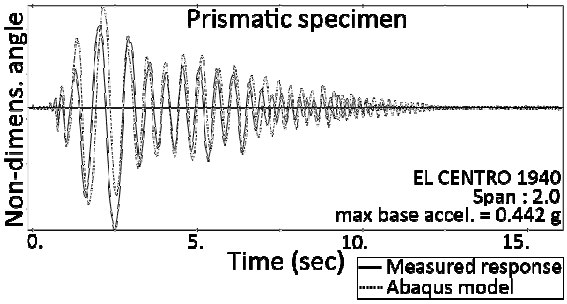


Figure 14a. Measured and numerically predicted rocking response of prismatic specimen Earthquake simulated test Span 2.0

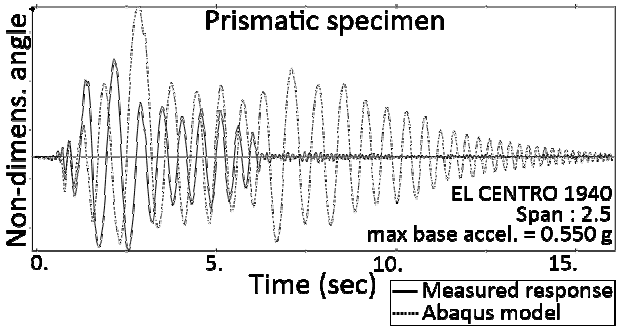


Figure 14b. Measured and numerically predicted rocking response of prismatic specimen Earthquake simulated test Span 2.5

Higher intensity of the simulated earthquake motion corresponds to a larger value for the indicator Span. For the tests with intensity Span 2 and Span 3 (figures 14a and 14c) good agreement was achieved between the numerical results based on the Abaqus model and the measured rocking response. However, for the test with intensity Span 2.5 (figure14b), the numerical rocking response exhibits large amplification at a time (approximately 6sec.) when the measured response has subsided.

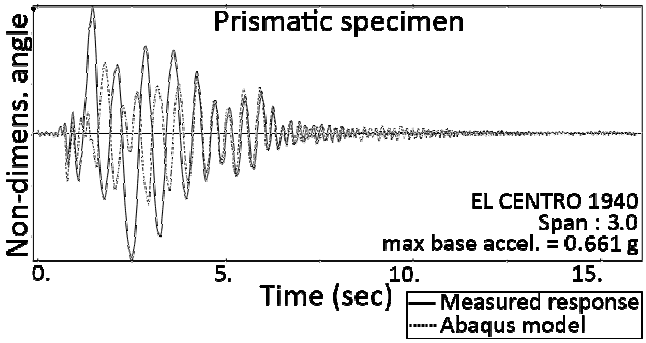


Figure 14c. Measured and numerically predicted rocking response of prismatic specimen Earthquake simulated test Span 3.0

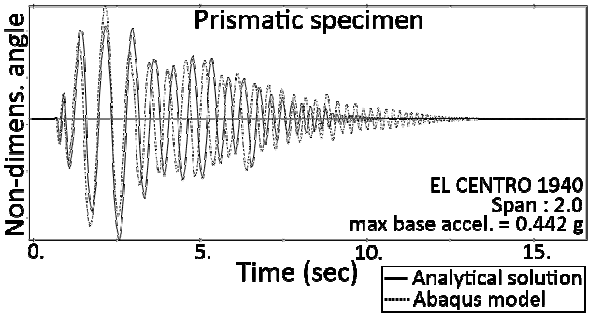


Figure 15a. predicted rocking response (Abaqus model or analytical solution) of prismatic specimen Earthquake simulated test Span 2.0

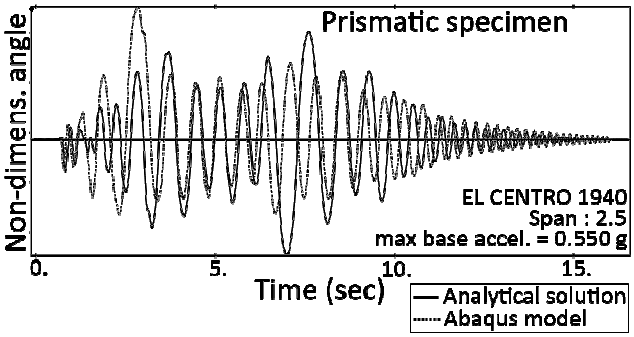


Figure 15b. predicted rocking response (Abaqus model or analytical solution) of prismatic specimen Earthquake simulated test Span 2.5

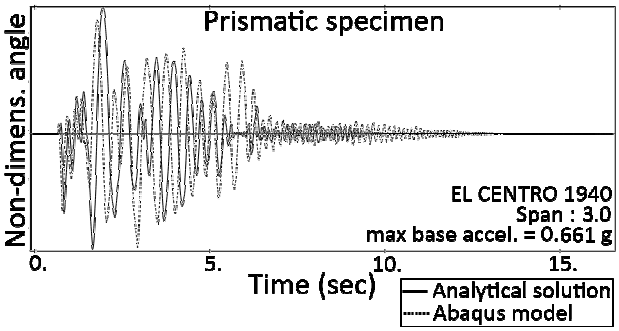


Figure 15c. predicted rocking response (Abaqus model or analytical solution) of prismatic specimen Earthquake simulated test Span 3.0

The same comparison shown in figures 14 is again made in figures 15a to 15c. However, this time instead of the measured rocking response of the prismatic specimen at the shaking table the numerical results obtained either by the Abaqus model or by the analytical equations of motion are shown. The predictions of the rocking response for the prismatic specimen, when subjected to simulated horizontal earthquake excitation, obtained by either the Abaqus model or by the integration of the analytical equations of rocking, exhibit reasonably good agreement.

5 CONCLUSIONS

The predicted dynamic rocking performance of a prismatic steel model column was obtained in two different ways. First, through a software that was developed for this purpose, which is based on the integration of the equations of motion that govern the rocking response. Second, utilizing the capabilities of a commercial general purpose software.

The predicted rocking performance, by either the developed software or the commercial software dynamic performance, in terms of stability of the examined prismatic steel model, exhibited similar trends with regard to the influence that the excitation frequency and amplitude of the horizontal sinusoidal base motion exert on its rocking amplitude and its subsequent overturning to the corresponding performance that was observed at the laboratory.

The earthquake rocking response of the examined model prismatic steel column, predicted by either the developed software or the commercial software, in terms of stability and maximum rocking amplitude, exhibited, in general, similar trends to the corresponding performance that was observed at the laboratory.

REFERENCES

[1] Aslam , M.M., et.all. 1978. Rocking and Overturning response of rigid bodies to earthquake motions, Report No. LBL-7539, Lawrence Berkeley Lab. Univ. Of California, Berkeley.

[2] Spanos, P.D. and Koh A.S., 1984. Rocking of rigid blocks due to harmonic shaking. J. of Engin. Mech., ASCE 110 (11), pp. 1627-1642

[3] Koh, A.S. and Mustafa G. 1990. Free rocking of cylindrical structures, J. of Eng. Mechanics, Vol. 116, N0 1, pp.35-54.

[4] M. Demosthenous and G.C. Manos : "Dynamic Response of Models of Ancient Monuments Subjected to Horizontal Base motions", IABSE, Struct. Preservation of Archit. Heritage, Italy, 1993, pp. 361-368.

[5] G.C. Manos and M. Demosthenous : "Comparative Study of the Global Dynamic behaviour of Solid and Sliced Rigid Bodies", 10ECEE, Vienna, Austria, 1994.

[6] Demosthenous M, 1994. Experimental and numerical study of the dynamic response of solid or sliced rigid bodies, Ph. D. Thesis, Dept. of Civil Engineering, Aristotle University of Thessaloniki.

[7] Manos, G.C. Reports on Task 1, Task 2 and Task 8, 1998. ISTECH project, Program Environment and Climate, European Commission, Contract No. ENV4-CT95-0106.

[8] G.C. Manos, M. Demosthenous, V. Kourtides, A. Hatzigeorgiou “The Dynamic and Earthquake Behaviour of Ancient Columns and Colonnades with and without Shape Memory Alloy Devices”, STREMAH 2001, Florence, Italy, 2001.

[9] G.C. Manos et.al “Study of the Dynamic and Earthquake Behaviour of Rigid Bodies with or without the Inclusion of Shape Memory Alloy Devices” , 16SMIRT, Washington D.C. 2001.

COMPDYN 2013
4th ECCOMAS Thematic Conference on
Computational Methods in Structural Dynamics and Earthquake Engineering
M. Papadrakakis, V. Papadopoulos, V. Plevris (eds.)
Kos Island, Greece, 12–14 June 2013

EXPERIMENTAL RESEARCH ON THE CAPACITY OF BRIDGE SHEAR KEYS

Stergios A. Mitoulis[1*], Ioannis A. Tegos[2], Andreas Malekakis[3]

[1]Civil and Environmental Engineering, Surrey University
e-mail: s.mitoulis@surrey.ac.uk

[2,3]Aristotle University of Thessaloniki, Laboratory of Reinforced Concrete and Masonry Structures,
email: itegos@civil.auth.gr

Keywords: Bridge, Shear key, Design, experiment, effective width.

Abstract. *Conceptual design of bridges has evolved rapidly during the last ten years and new, efficient and cost effective design schemes have been introduced in practice. Use of shear keys, as an active seismic link, is not prohibited in current codes. However, the major concern of having the shear keys damaged one-by-one due to their asynchronous participation still remains an open issue. As such, shear keys are typically used to prevent potential span unseating. Shear keys, also known in European literature as seismic links or stoppers, are stub RC structural elements. A capacity design procedure is provided for these elements, to safeguard the support of the deck. Design of shear keys engineering is an open issue in contemporary bridge. Current state-of-the-art deals with the efficient use of reinforcements, while practitioner engineers dealt with the seismic role of these elements and have proposed different materials for the design of stoppers and/or different reinforcement materials, since sacrificial shear keys can respond as structural fuses to limit the demand of the piers. Shear keys, whether they receive seismic actions or not -the last referring to the case in which keys are utilized to avoid the common unseating of the spans- have peculiar response and unconventional reinforcement requirements due to their loading. Simultaneously, their geometry and size is restricted due to bridge's esthetics. Hence, stoppers are relatively small and stub concrete "blocks", which are expected to receive reliably and safely large pounding forces. In this framework, two alternative reinforcement layouts with transverse hairpin bars were assessed. The efficiency of the proposed reinforcement was assessed by comparing the above rebar with the state-of-practice shear key reinforcements. The required hairpin reinforcement ratio was then evaluated through an analytical procedure that accounted for the relation between the reinforcement hairpin ratio vs the capacity of the shear keys. The procedure indicated the most appropriate reinforcement ratio for a required capacity of the stopper. The study proposes the reinforcement of the stoppers with additional diagonal rebar. Conclusions are drawn based on the analytical models and the experimental campaign.*

1 INTRODUCTION

Conceptual design of earthquake resistant bridges has evolved rapidly during the last ten years. New design concepts based on hybrid earthquake resisting concepts [1][2][3][4][5], seismic isolation [6][7], integral and semi-integral lateral resisting systems [8][9] have been introduced in modern bridge designs. Within this evolution, a noiseless but practically sustainable philosophy has been established. The philosophy is based on the design of bridges in which serviceability movements of the deck are tackled with isolation bearings, while central piers that are less susceptible to constraint movements due to creep and shrinkage, are expected to receive seismic loading and provide ductility to the structure. This concept is deemed to be enhanced by the use of seismically active shear keys, in the sense that appropriate gaps may be left between the superstructure and the bents to provide space for deck's "breath" (i.e. contraction and expansion), while in case of large longitudinal loading, the shear keys may restrain movements.

Shear keys serve to restrain the deck displacements in either the longitudinal or transverse direction of the bridge. These devices are typically reinforced concrete blocks provided at each bearing location. They have found to be more effective in protecting bearing vulnerability in the transverse direction of the bridge [10]. However, Eurocode 8-2 (2005) [11] allows the use of the so-called seismic links (shear keys) also in the longitudinal direction, as means to reduce the seismic displacements of the deck and to minimize the potential of span unseating in case insufficient seat lengths are used [12]. Many different designs have been proposed in the past for the shear keys. Ghosh et al [13] have tested rigid stopper devices, yielding stoppers, steel restrainers, and superelastic shape memory alloy (SMA) shear keys. A study on the seismic performance of girder bridges equipped with bi-directional energy-dissipating sacrificial devices have been performed by Kwang et al. [14]. Different design approaches of these elements have been proposed in the past by other researchers [15] [16] [17]. Current codes [11] [18] [19] [20] place the focus on the prevention of falling off the superstructure and no attention is given to the prevention of the failure and the reinforcements of the stoppers itself. However, further advances on appropriate methods and devices of preventing 'dislodgement' or 'unseating' of the superstructure in the event of severe ground shaking have been established. These ideas can be used in economical earthquake resistant design of bridges as stated by [21][22]. In that case stoppers must be appropriately designed. Correct design of stoppers should include not only reinforcements, as shear keys shall be designed for the axial and shear forces associated with the column's overstrength moment including the effects of overturning, but also a correct estimation of the effective width that should be taken into account when calculating the capacity of the pier cap beam especially in bridges with hammerhead piers.

In this framework, two alternative reinforcement layouts with transverse hairpin bars were assessed. The efficiency of the proposed reinforcement was assessed by comparing the above rebar with the current/state-of-practice shear keys reinforcements based on Eurocode 8-2 [11] and other researchers [23][24] that is based on the sliding shear and the diagonal tension. The required hairpin reinforcement ratio was then evaluated through an analytical procedure that accounted for the relation between the reinforcement hairpin ratio vs the capacity of the shear keys. The procedure indicated the most appropriate reinforcement ratio for a required capacity of the stopper. The study proposes the reinforcement of the stoppers with additional diagonal rebar. Conclusions are drawn based on the analytical models and the experimental campaign.

2 TYPICAL EXAMPLES OF SHORT AND VERY SHORT STRUCTURAL ELEMENTS-THE PROBLEM OF EFFECTIVE WIDTH

Figure 1 shows different typical cases of short cantilevers used in practice. Such structural elements are met in most bridge structures either in end supports (Figure 1a), longitudinal stoppers installed at the abutments (Figure 1b) or intermediate supports of beams above the piers (Figure 1c). In that case the effective width of the structural elements should be determined, as the calculation of the effective width based on codes does not cover such cases for two distinct reasons: (a) the loads imposed at the short elements illustrated at Figures 1a, b and c are concentrated and as such the typical calculation of the effective width that correspond to distributed loads is not considered to be appropriate and (b) loading of the these elements is either static, dynamic or pounding-type (extremely dynamic) loading that may lead to different effective widths. For example the imposition of load on the shear keys is extremely dynamic.

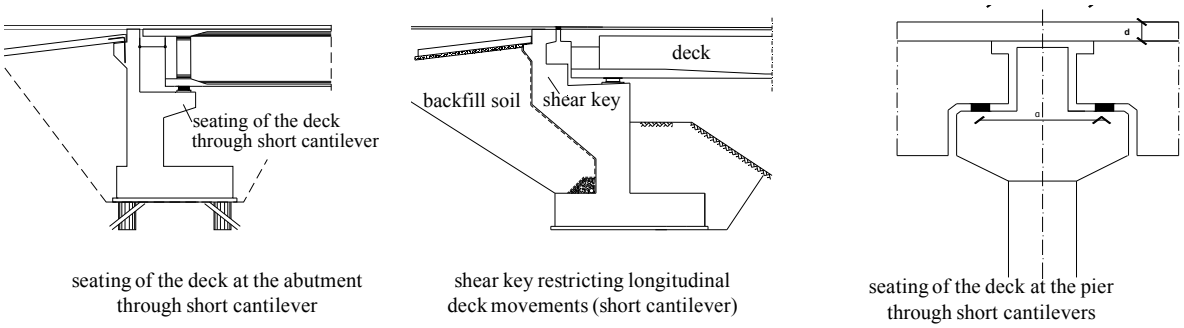


Figure 1: Three typical cases where short cantilevers are used in practice and their effective width should be calculated, (examples of short and very short cantilevers).

Figure 2 illustrates shear keys at the abutments and at the piers. Use of shear keys is common at the abutments. Figure 2a shows the a typical shear key that restrains transverse movements at the abutments, while Figure 2b shows in detail the reinforcements used at such shear keys. An elastomeric bearing is interjected between the deck and the shear keys in order to increase the duration of pounding and hence to reduce effectively the magnitude of potential pounding forces during an earthquake. High reinforcement ratios, including both longitudinal and transverse-hairpin bars, cause congestion of steel within the shear keys. Another issue is the structural joint left between the shear key and the cap-beam, as the cap beam is casted prior to the construction of the shear keys.

Figure 2c, d and e show the use of shear keys at bridge piers. Two different types of shear keys can be found in contemporary bridges: (a) seismically inactive shear keys shown in Figures 2c and d having a large gap between the superstructure and the piers. Seismically inactive shear keys are typically used to prevent span unseating of the deck. (b) Seismically active shear keys shown in Figure 2e. Active shear keys are designed to allow for serviceability deck movements, due to creep, shrinkage and thermal effects, while during an earthquake shear keys transmit the seismic actions to the piers.

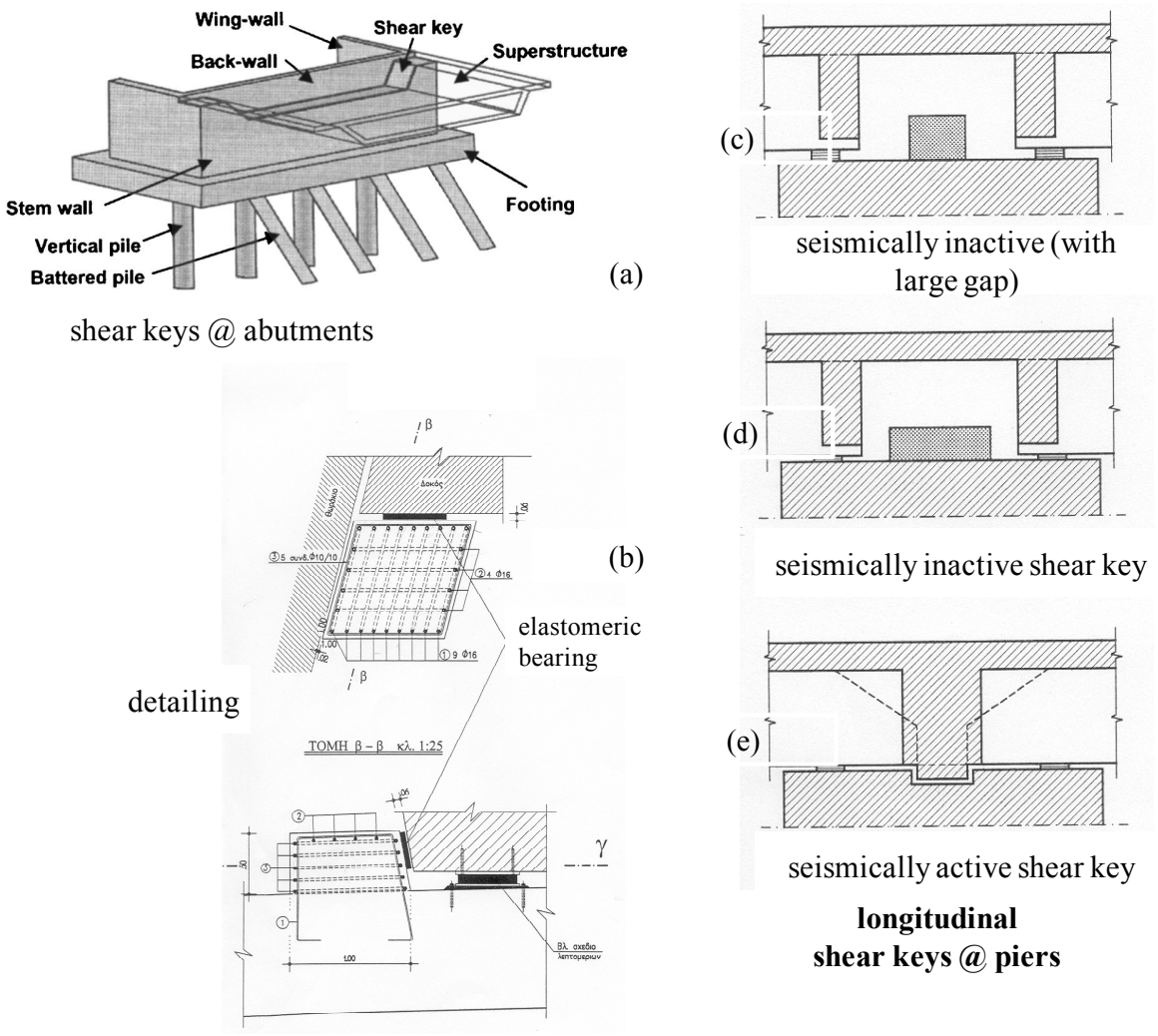


Figure 2: Typical shear keys at the abutment and at the pier.

3 EXPERIMENTAL CAMPAIGN

3.1 The specimens

An extended experimental campaign was had taken place in the Laboratory of Reinforced Concrete Structures. Both the rebar's requirements and its efficiency in enhancing the capacity of the shear keys were considered to be significant for the seismic response of the shear keys. Effective widths of the shear keys was calculated based on the experiments and compared to the ones given in current code design [25]. Shear key's reinforcements and loading pattern influences strongly their effective width that in turns reflects on their design, i.e. the selection of their cross section and reinforcements. It is noted that the integrity of these elements is essential as on the one hand the seating beams illustrated at the Figure 1c above (short seating cantilevers) are required to resist to vertical and lateral loading of the deck so that span unseating is prevented. On the other hand, the stoppers should be designed to restrict large deck movements and they should block primarily deck's fall-off and dislodgment during severe seismic motions. Figure 3 illustrates the two different specimen types that were experimentally tested. The first type of specimen corresponds to flexible elements, having a shear ratio a_s=1, while on the right side of Figure 3 a specimen having predominantly shear response (a_s=0.4) is illustrated. Figure 3 shows the cross section of the specimen, while longitu-

dinal dimension of the specimens was 600mm. This paper emphasized on the second type of shear keys, which are the most common ones met in bridge structures.

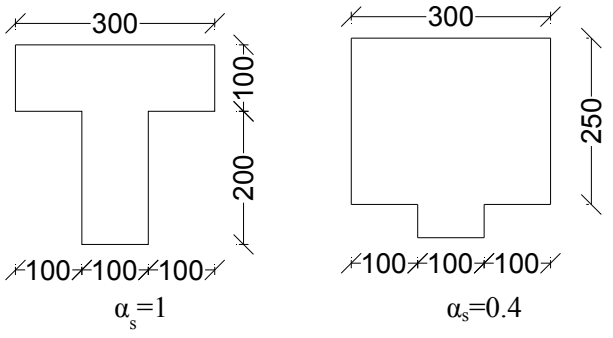


Figure 3: Cross sections of the specimen (a) short cantilever with shear ratio αs=1 and (b) very short cantilever with αs=0.4 referring to shear keys.

3.2 Loading

Loading is shown in Figure 4. The shear keys are considered to be extended along the total transverse width of the seating beam. Different types of loading were imposed to the specimen. The specimens were initially being loaded to the total length that is 600mm. This case represented the total capacity of the shear key and corresponds to the maximum load that the shear key can receive. This loading represents the ideal case that a bridge is subjected to longitudinal seismic motion, i.e. no out of plane rotations of the deck are expected. Then different lengths (see dimension **α** in Figure 4c) of the shear key were tested to identify different effective widths of the shear key. Additionally, different loading areas we also tested, as on the one hand the total load was applied in the central part of the specimen, as shown in Figure 4c and 4d, while specimens having been loaded at their ends were also tested (as shown in Figure 4e). Short cantilevers having shear ratio α_s=0.4 as well as flexural shear keys having shear ratio α_s=1 were tested. To take into account the fact that not all of the height of the shear key is loaded, the load was applied along different widths (distance b in Figure 4c) ranging from 50mm to 100mm. Loading of the shear keys is not applied to all of its height due to the fact that between the pier cap and the superstructure a bearing with a considerable height (typically between 50 to 200mm including the preparatory concrete slabs) is interjected and raises the level of the superstructure with respect the pier-cap. Hence, the shear key, which is fixed at the pier cap, receives at its upper part the loading of the superstructure. To model this effect, i.e. the potential loading of the shear keys at different heights, different widths of loading were applied to the specimen (width of loading **b** is shown in Figure 4c). Part of the results of the extended experimental campaign is shown in this paper. Emphasis was placed on the case where α=150mm and b=50mm, while both the outcomes of the central (Figure 4c and 4d) and end loading (shown in Figure 4e) are given.

Effective width was calculated by comparing the capacity of the shear keys when the total length (600mm) of the shear was loaded to the one that was experimentally extracted when a smaller loading width α=150mm was adopted. The latter case, i.e. the loading of 150mm of the specimen, yielded a capacity that was smaller than the one found for the α=600mm loading width. However, the first load, which corresponds to α=150mm was not 600/150=4 times smaller due to the development of the effective width of the shear keys. Hence, additional loading was deemed to be due to the effective width. The loading shown in Figure 4c and d are expected to reveal what is the effective width of the stoppers when both sides of the shear key are activated, while the loading shown in Figure 4e corresponds to the case that the shear

key is expected to be assisted by one-side effective widths and corresponds to the case where end sacrificial keys are used, i.e. shear keys installed at the ends of the cap-beams.

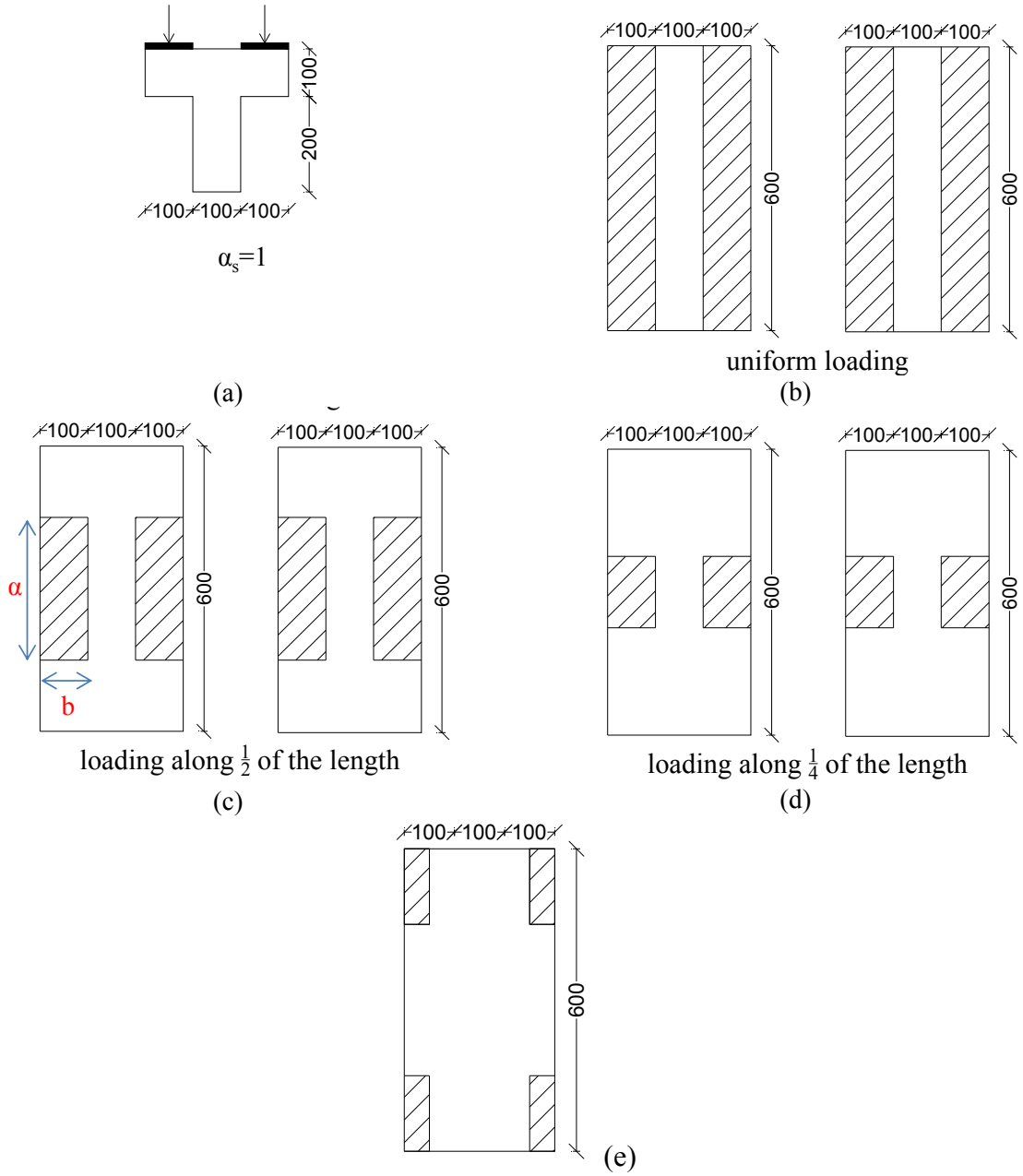


Figure 4: The loading of the specimens: (a) cross section of the specimen and loading; (b) uniform loading to obtain the maximum shear key capacity, (c) loading at half (1/2) of the specimen's length, distances α and b of the loading are shown in this figure, (d) loading at a quarter (1/4) of the specimen's length; (e) loading at the quarters (1/4+1/4) ends of the specimen.

Figures 5 to 10 illustrate different designs attempted for the shear keys. Different tests were aimed at identifying what are the most efficient reinforcements in enhancing both the capacity and the effective width of the shear key. A total of twelve different tests are illustrated in this paper. Figure 5 shows a picture of the specimen reinforcements. Thirteen hairpin shear reinforcements having a diameter 8mm (13Ø8) were used in this specimen, while no significant longitudinal reinforcements were used in this case. Five "floors" of reinforcements

were used in the height of the stopper to enhance the capacity of the shear key. Figure 6 illustrates the reinforcement layout of a different specimen having both hairpin reinforcements and strong longitudinal (along the 600mm length of the specimen) reinforcements. Figures 6 to 11 illustrate all the different specimens tested in the laboratory. Reinforcement layout and geometries are also given in detail.



Figure 5: Sample of the reinforcments of the shear keys.

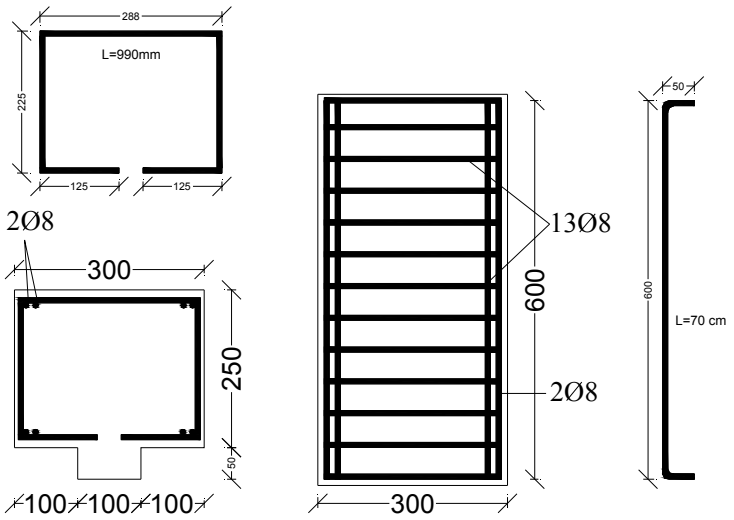


Figure 6. Reinforcement layout and geometry of specimen 1 (Specimen code 3.1 - loading at 1/4 of the length).

4 RESULTS

Figures 12 to 17 and the embedded tables illustrate the results of the experimental campaign. The maximum load recorded at all the tests was recorded. The black lines illustrate the maximum capacity of the shhear keys reached when the loading was uniform along the longitudinal 600mm length of the specimen. The gray lines illustrate the capcity of specimen with identical geometries and reinforcments, but for a loading corresponding to a part of the longitudinal dimension l=600mm of the specimen, i.e. l/4 at the mid-span (central part of the specimen) or l/4+l/4, i.e. the quarters of the specimen's ends as shown in Figure 4e.

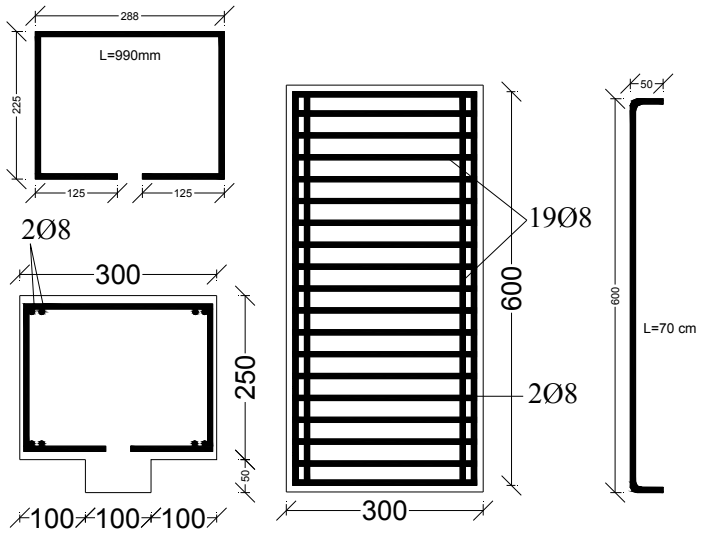


Figure 7. Reinforcement layout and geometry of specimen 2 (Specimen code 3.2 - loading at 1/4 of the length)

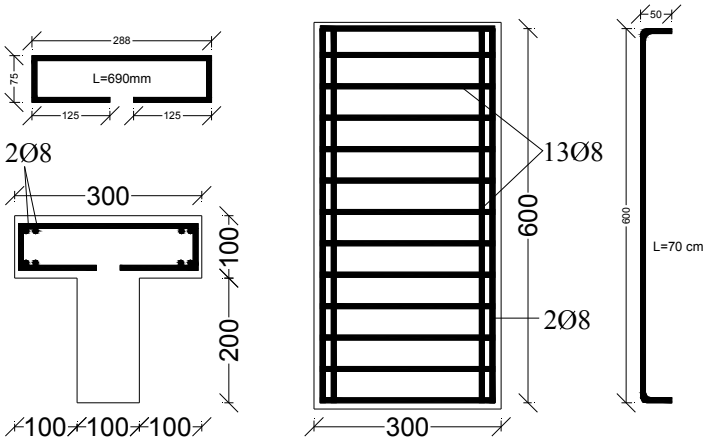


Figure 8. Reinforcement layout and geometry of specimen 3 (Specimen code 3.3 - loading at 1/4 of the length).

Figure 12 shows the recorded capacity vs displacement of the first specimen. Strong hair-pin reinforcements were used in this specimen. The first column if the table under the figure shows the loading length, which is either the total length of the specimen (black line), i.e. 600mm or a quarter of the specimen's length (gray line), i.e. 150mm. The second column of the table shows the capacity per length of the specimen, i.e. the first column divided by 0.6m. This quantity is meaningful for the first loading of the specimen, as in the second loading type both the l/4 plus the effective width of the specimen are receiving the load. The third column indicates the prospected capacity of the specimen. This capacity is meaningful only for the second loading (at l/4) of the specimen and shows what would be the prospected capacity of the specimen in case no effective width had participated in the total capacity of the specimen. Hence, this value is the outcome of the capacity per length of the specimen (column 2) multiplied by 150mm, which is the loading width. Accordingly, column 5 shows the additional effective length, which is the additional capacity (588.60 minus 370.25kN based on the results above) divided by 2468.32kN/m. Hence, the width of loading (i.e. 150mm) plus the addition

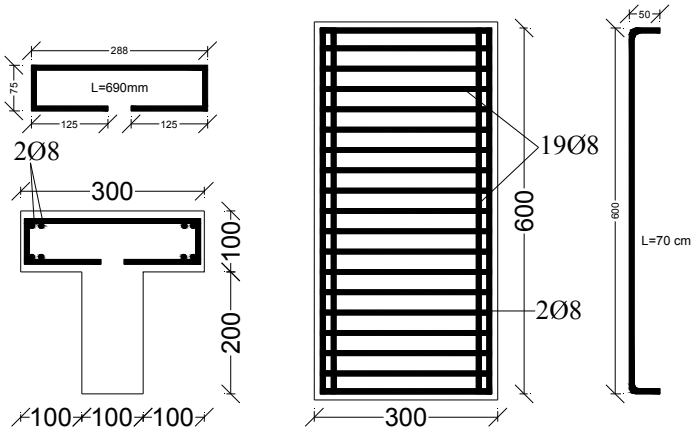


Figure 9. Reinforcement layout and geometry of specimen 4 (Specimen code 3.4 - loading at 1/4 of the length).

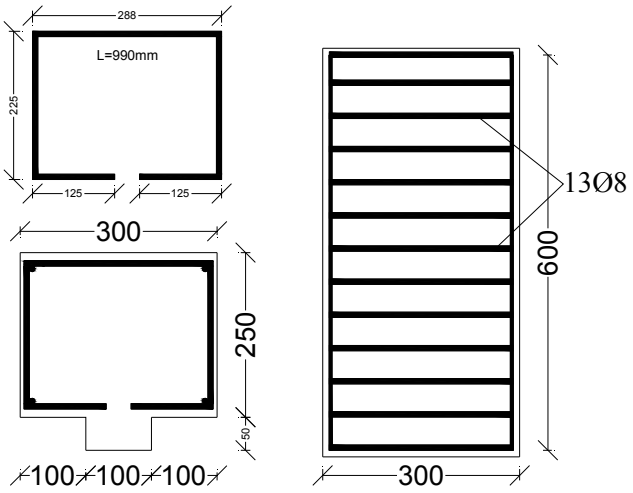


Figure 10. Reinforcement layout and geometry of specimen 5 (Specimen code 3.5 - loading at 1/4 of the length).

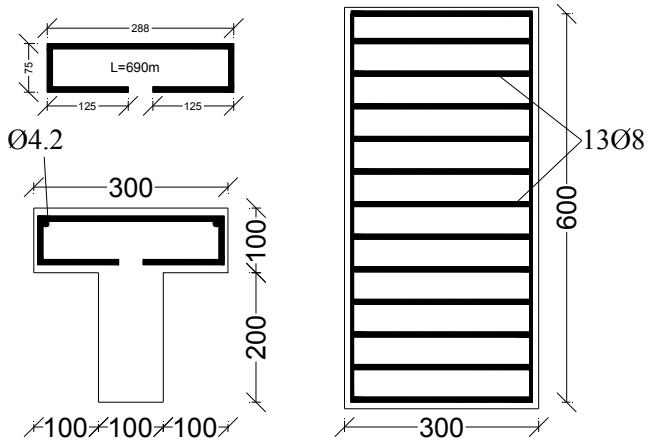
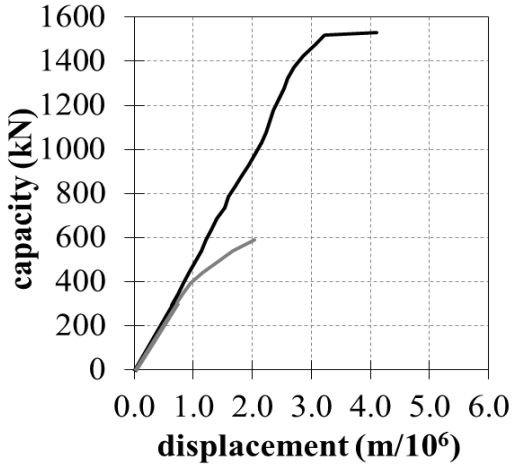
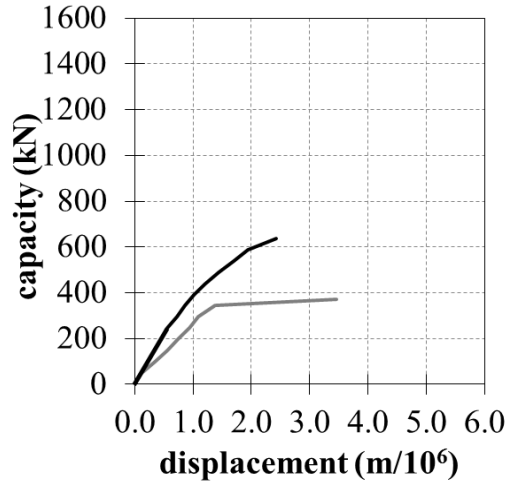


Figure 11. Reinforcement layout and geometry of specimen 6 (Specimen code 3.6 - loading at 1/4 of the length).



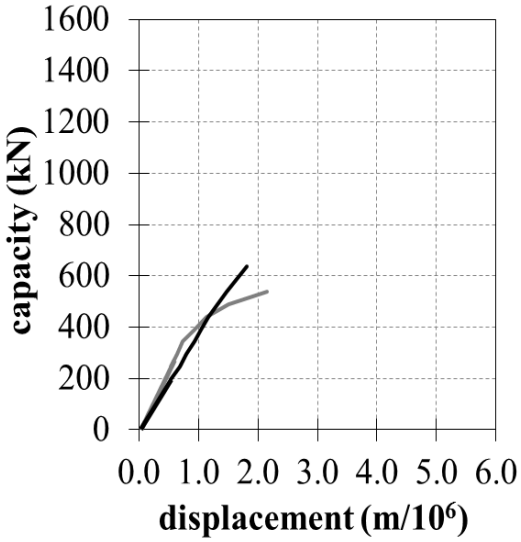
loading length α (mm)	capacity (kN)	capacity per length (kN/m)	prospected capacity (kN)	additional effective length (m)	additional effective length at each side (m)	prospected angle of distribution (deg)
600mm	1530.36	2468.32	-	-	-	-
150mm	588.60	-	370.25	0.088	0.044	41.5

Figure 12. Capacity vs displacement of the 1st specimen under loading at l and at l/4 mid-span.



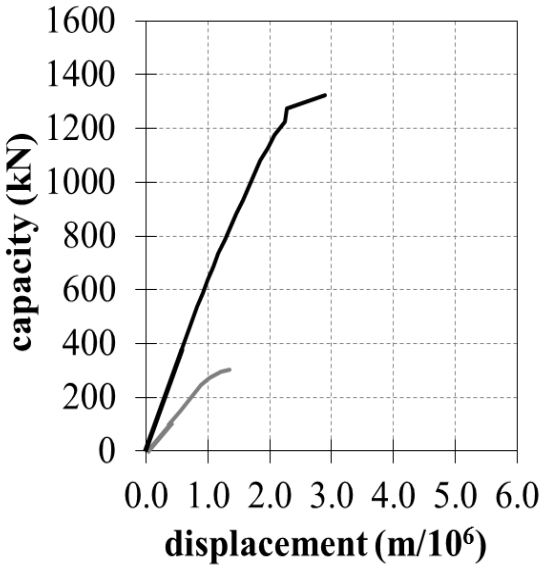
loading length α (mm)	capacity (kN)	capacity per length (kN/m)	prospected capacity (kN)	additional effective length (m)	additional effective length at each side (m)	prospected angle of distribution (deg)
600mm	637.65	1028.47	-	-	-	-
150mm	372.78	-	154.27	0.212	0.106	64.8

Figure 13. Capacity vs displacement of the 2nd specimen under loading at l and at l/4 mid-span.



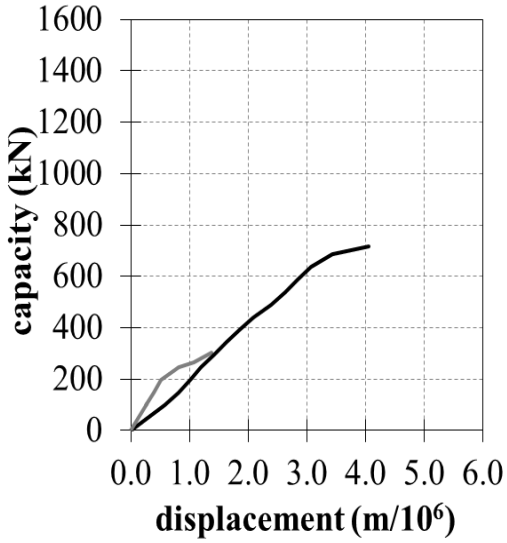
loading length α (mm)	capacity (kN)	capacity per length (kN/m)	prospected capacity (kN)	additional effective length (m)	additional effective length at each side (m)	prospected angle of distribution (deg)
600mm	637.65	1028.47	-	-	-	-
150mm	539.55	-	154.27	0.375	0.187	75.1

Figure 14. Capacity vs displacement of the 3rd specimen under loading at l and at l/4 mid-span.



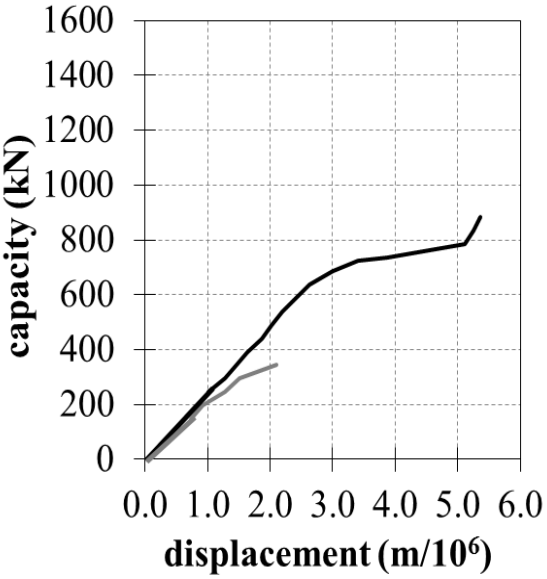
loading length α (mm)	capacity (kN)	capacity per length (kN/m)	prospected capacity (kN)	additional effective length (m)	additional effective length at each side (m)	prospected angle of distribution (deg)
600mm	1324.35	2136.05	-	-	-	-
150mm	304.11	-	320.41	-0.008	-0.004	-4.4

Figure 15. Capacity vs displacement of the 4th specimen under loading at l and at l/4 end part.



loading length α (mm)	capacity (kN)	capacity per length (kN/m)	prospected capacity (kN)	additional effective length (m)	additional effective length at each side (m)	prospected angle of distribution (deg)
600mm	0.00	0.00	-	-	-	-
150mm	716.13	-	304.11	0.000	0.000	0.8

Figure 16. Capacity vs displacement of the 5th specimen under loading at l and l/4 end part.



loading length α (mm)	capacity (kN)	capacity per length (kN/m)	prospected capacity (kN)	additional effective length (m)	additional effective length at each side (m)	prospected angle of distribution (deg)
600mm	0.00	0.00	-	-	-	-
150mm	882.90	-	343.35	0.000	0.000	0.7

Figure 17. Capacity vs displacement of the 6th specimen under loading at l and l/4 end part.

al effective length calculated in column 5 results in the effective length of the specimen that receives the loading. Since, the loading in the specimen's mid-span the additional effective length (88mm) is extended at both sides of loading width (150mm). Hence, the additional width that participates in receiving the loading at each side is is 88mm/2=44mm and this is given in column 6 of the table. Based on the result given in column 6 and taking into account the geometry of the specimen it is possible to calculate the inclination of the crack that caused the failure of the specimen. This angle also indicates the effective length of the shear key. This angle is given in codes equal to 45 deg, however, the experimental campaign revealed that this angle can vary based upon the loading type -uniform or concentrated- the geometry of the specimen, i.e the shear ratio, and the reinforcement of the shear key. Specimen 1 to 3 were found to have a clear increase in their effective width, while the angles calculated are ranging from 41.5 deg to 75.1 deg, showing that the reinforcements in that case increased the effective width of the shear keys. Additionally, the loading of the specimen at the mid-span was identified to be a favorable loading condition. Contrarily, the specimens 4 to 6 illustrate a poor distribution of action, as it seems that no additional length of the specimens is participating in receiving loading. Prospected angles of load distribution were found to be either negligible ~1deg or even negative, showing that one the one hand the loading at the end of the specimen is an unfavorable loading condition and, on the other hand, the reinforcements in these specimen failed to enhance both the capacity and the of the shear keys effective width of the shear keys.

Elaboration on the experimental outcomes, which was also complemented by past experiments, yielded similar force-displacement diagramms. The following analytical equation was derived representing the effective width of shear keys:

$$\mathbf{b_{eff} = bo + \lambda \cdot \alpha \cdot l_k} \qquad \text{eq. 1}$$

where b_o is the width of the loading, α is the shear ratio equal to l_k/d_c where l_k is the distance of the loading input with respect the fixing joint of the stopper and h_c is the height of the shear key, λ is the coefficient that was calculated based on the experimental campaign that is equal to 1.6 for cantilevers with $\alpha \geq 1$, while equals 1.4 for short and very short cantilevers, i.e. when $\alpha < 1$.

5 CONCLUSIONS

This paper aims at shedding light on the conceptual design of bridges by utilizing seismically active shear keys that restrain longitudinal seismic movements of the deck, while providing adequate gaps to let the bridge "breath" under thermal, creep and shrinkage movements. Alternative designs of shear keys with different reinforcements and different loading patterns were introduced in order to identify on the one hand the efficiency of reinforcement layouts on the capacity of the keys and the prospected effective width of the shear keys. Outcomes of an extended experimental study were illustrated with emphasis placed on keys having a low shear ratio α_s=0.4. The following conclusions were drawn:

- The capacity of the shear keys can be enhanced when utilizing main longitudinal reinforcements, additional (secondary) longitudinal reinforcements set at levels parallel to the one of the main reinforcements and long hairpin shear reinforcements.

- Secondary longitudinal reinforcements were found to increase the effective width of the shear key, which is a desirable effect as keys are typically loaded by concentrated loads.
- The distribution of the load does not follow the known 45 degrees mode, which means that a revision is needed in case shear keys are loaded under concentrated loads, especially when the load in not central.

REFERENCES

[1] S.A. Mitoulis, Seismic design of bridges with the participation of seat-type abutments, *Engineering Structures*. 44, pp. 222-233, 2012.

[2] S.A. Mitoulis, I.A. Tegos, Two new earthquake resistant integral abutments for medium to long-span bridges, *Structural Engineering International: Journal of the International Association for Bridge and Structural Engineering* (IABSE), 21 (2), pp. 157-161, 2011.

[3] S.A Mitoulis, I.A. Tegos, An unconventional restraining system for limiting the seismic movements of isolated bridges, *Engineering Structures*. 32(4), pp. 1100-1112, 2010.

[4] S.A. Mitoulis, I.A. Tegos, Connection of bridges with neighbour-hooding tunnels, *Journal of Earthquake Engineering (JEE)*, 1559-808X, 14(3), pp. 331-350, 2010.

[5] S.A. Mitoulis, I.A. Tegos, Restrain of a seismically isolated bridge by external stoppers, *Bulletin of Earthquake Engineering*, 8(4), pp. 973-993, 2010.

[6] I.G. Buckle, M.C. Constantinou, M. Dicleli, and H. Ghasemi, Seismic Isolation of Highway Bridges. *Special Report MCEER-06-SP07*, Multidisciplinary Center for Earthquake Engineering Research, Buffalo, NY, 171pp, 2006.

[7] M.C. Kunde and R.S. Jangid, Effects of Pier and Deck Flexibility on the Seismic Response of Isolated Bridges. *Journal of Bridge Engineering*, 11(1), 2006.

[8] M. Arockiasamy, N. Butrieng, M. Sivakumar, State-of-the-art of integral abutment bridges: Design and practice. *ASCE Journal of Bridge Engineering*. 9(5):497-506, 2004.

[9] S. Arsoy, J.M. Duncan, R.M. Barker. Behavior of a semiintegral bridge abutment under static and temperature-induced cyclic loading. *ASCE Journal of Bridge Engineering*, 9(2): 193-199, 2004.

[10] J.E. Padgett, R. DesRoches, Three-Dimensional Nonlinear Seismic Performance Evaluation of Retrofit Measures for Typical Steel Girder Bridges, *Engineering Structures*, 30(7), pp. 1869-1878, 2008.

[11] EN 1998-2. Eurocode 8: *Design of structures for earthquake resistance*, Part 2: *Bridges*., 2005

[12] M.T.A. Chaudhary, M. Abe, Y. Fujino, Investigation of a typical seismic response of a base-isolated bridge. Engineering Structures, 24(7), 945-953, 2002.

[13] G. Ghosh, Y. Singh, S.K. Thakkar, Seismic response of a continuous bridge with bearing protection devices, *Engineering Structures*, 33(4), pp. 1149-1156, 2011.

[14] K-I. Cho, S.-H. Kim, M.-S. Choi and J.-Y. Lim, A Study on Seismic Performance of Girder Bridges Equipped with Bi-Directional Energy-Dissipating Sacrificial Devices, *Steel Structures*, 8, pp. 59-65, 2008.

[15] M. Saiidi, E.A. Maragakis, S. Feng, An evaluation of the current Caltrans seismic restrainer design method. *Report No. CCEER-92-8*. Reno (NV): Civil Engineering Department, University of Nevada; 1992.

[16] [7] Fenves G, DesRoches R. Response of the Northwest Connector in the Landers and Big Bear earthquakes. Report No. UCB/EERC-94/12. Berkeley (CA): University of California; 1994.

[17] L.G Selena, L.J. Malvar, R.J. Zelinski, Bridge retrofit testing: hinge cable restrainers. *ASCE Journal of Structural Engineering*, 15(4), 920-934, 1989.

[18] American Association of State Highway and Transportation Officials (AASHTO), *Standard specifications for highway bridges*, 16th edition. Washington (DC), 1996.

[19] California Department of Transportation (CALTRANS). *Memo to designers*, 20-3, 20-4. Sacramento (CA), 1994.

[20] California Department of Transportation (CALTRANS). *Seismic Design Criteria*, 20-3, 20-4. Sacramento (CA): California Department of Transportation; 1999.

[21] M. Tandon, Economical design of earthquake-resistant bridges, *ISET Journal of Earthquake Technology*, pp.No 453, 42(1), pp. 13-20, 2005.

[22] J.P. Conte, Y. Zhang, Performance Based Earthquake Engineering: Application to an Actual Bridge-Foundation-Ground System, Keynote paper, *12th Italian National Conference on Earthquake Engineering*, Pisa, Italy, June 10-14, 2007.

[23] R.A. Imbsen, AASHTO Guide Specifications for LRFD Seismic Bridge Design, Subcommittee for Seismic Effects on Bridges, *T-3, Prepared by: Imbsen Consulting*, May 2007.

[24] A. Bozorgzadeh, S. Megally, J. Restrepo, and S. Ashford. Capacity Evaluation of Exterior Sacrificial Shear Keys of Bridge Abutments. *Journal of Bridge Engineering*, 11(5), pp. 555-565, 2006.

[25] ENV 1992-1-1:1992 Eurocode 2: *Design of concrete structures* - Part 1-1: *General – Common rules for building and civil engineering structures*.

COMPDYN 2013
4th ECCOMAS Thematic Conference on
Computational Methods in Structural Dynamics and Earthquake Engineering
M. Papadrakakis, V. Papadopoulos, V. Plevris (eds.)
Kos Island, Greece, 12–14 June 2013

ANALYTICAL AND EXPERIMENTAL INVESTIGATION ON THE SEISMIC EFFICIENCY OF A NEW RESTRAINING SYSTEM FOR LIMITING THE SEISMIC MOVEMENTS OF THE BRIDGE DECK

Sevasti D. Tegou[1] **and Ioannis A. Tegos**[2]

[1] Aristotle University of Thessaloniki
Department of Civil Engineering
e-mail: stegou@civil.auth.gr

[2] Aristotle University of Thessaloniki
Department of Civil Engineering
e-mail: itegos@civil.auth.gr

Keywords: Bridge, Abutment, Earthquake Resistance, Height, Length, Experimental Setup

Abstract. *The aim of this study is the analytical and experimental investigation on the seismic efficiency of an innovative restraining system. This system consists of transversely directed R/C walls, which behave as seismic stoppers. The aforementioned walls constitute part of the abutment and they are transversely directed to the longitudinal direction of the bridge. The available height of the abutment and the thickness of the walls are the main parameters affecting the serviceability level and seismic resistance of the aforementioned system. These parameters are strongly correlated, as they both influence the shear ratio of concrete walls and consequently, the seismic efficiency of the abutment. It is noted that the restraining walls of the abutment contribute not only by their own stiffness but also by dissipating energy through hysteretic behavior. In the first part of the study the investigation on the applicability of the proposed restraining system in all bridge types, independently of their length and the abutment's available height is presented. In the second part of the study the experimental investigation on the seismic efficiency of the proposed restraining system under monotonic and cyclic loading is presented. The experimental program involves three specimens. The results of the investigation showed that the proposed restraining system improves the safety, durability, serviceability, aesthetics and cost-effectiveness of bridges. Specifically, the exploitation of the proposed abutment in monolithic and floating deck bridge systems showed that, the longitudinal and transverse movements of the deck are effectively reduced. The aforementioned reductions in the seismic movements lead to reduced seismic actions of the piers. It is noted that, the reduction in the seismic actions leads to cost- effective and smaller cross-sections of the piers, which also serve aesthetics. Finally, the experimental investigation verified that the capacity of the system to dissipate energy is significant.*

1 INTRODUCTION

In-service requirements are mainly critical in the longitudinal direction of the bridge and require the free expansion and contraction of the deck due to temperature [1], creep, shrinkage [2] and prestressing effects. These requirements are in contrary to the bridge earthquake resistance requirements, as they are usually enhanced by rigid, as possible, connections. In these cases, the increase of the capacity of the structure to avoid structural damage is usually the most common solution in order to meet the ultimate lime state requirements. However it is not practical to continuously increase the strength of the structure as this also increase the structural cost. For this reason the conceptual concept of ductility is introduced by Codes [3]. According to this concept the structural elements are deformed beyond the elastic limit in a controlled manner.

An alternative to the aforementioned approach which is based on the reduction of the seismic demand is represented by seismic isolation practice. In many bridges, deck is supported on piers and abutments through bearings aiming at the shift of the vibrational period of the structure so as to avoid resonance with the excitations. These devices constitute the most used isolation system. In long bridges dampers are also used to increase the in-structure damping and to reduce the lateral movements of the bridge due to the seismic loading. The support of the deck on the piers and abutments through bearings also accommodates the in-service bridge requirements.

The use of bearings for the deck support on the piers is inevitable, especially in precast bridges and bridges constructed with the incremental launching method, as the deck construction method does not allow the monolithic connection of the deck to the piers. Bridges whose deck consist of beams or boxes, cast in place or precast, lifted or launched into place are usually protected against earthquakes by using seismic isolation devices. As a result these bridges are considered as structures with limited ductile behaviour and analyzed for values of the behaviour factor less or equal to 1.5 [3]. A recent study proposes a method based on the Code's provisions, for the conversion of these bridges to ductile systems [4-5].

It is obvious from the previous analysis that the treatment of problem of seismic safety aims at the satisfaction of the well-known inequality of safety, which includes, in its first member, resistances of critical cross-sections and in the second the loads, as these arise from the familiar loads of design earthquake. In the second case of seismic isolation, intervention in the second member of inequality is sought through the deliberate reduction of seismic action having as a final objective the alleviation of the cross-sections of load-bearing members of the system. However doubts arise about the time-related performance of seismic isolation devices. Concerns are also formulated regarding the future of these devices and questions arise if their future is going to be similar with that of bearings and expansion joints, which although they gave the perfect solution against the in-service induced movements of the deck, however the current bridge engineering seeks their expulsion.

Recent studies [6-7] showed that the reduction in the demand can also be achieved by the abutment and backfill soil participation which contribute to the enhancement of the earthquake resistance of bridges. The advantages of this seismic participation are reflected on the construction cost of the bridge [8], as smaller pier cross-sections meet Code's requirements as well as bridge aesthetics. The authors of this study have proposed an innovative seismic restraining system consisting of concrete walls which behave as seismic stoppers [9]. These walls constitute part of the abutment and they are transversely directed to the longitudinal direction of the bridge. This study presents the analytical investigation on the applicability in different bridge types, serviceability performance and seismic efficiency of the unconvention-

al abutment. The experimental investigation on the seismic efficiency of the abutment under monotonic and cyclic loading is also presented in this study.

2 PRESENTATION OF THE PROPOSED ABUTMENT-ANALYTICAL INVESTIGATION

2.1 Description and serviceability performance of the proposed abutment

The proposed restraining system consists of transversely directed R/C walls, which behave as seismic stoppers. The aforementioned walls constitute part of the abutment and they are transversely directed to the longitudinal direction of the bridge, Figure 1. In cases that the serviceability requirements of the bridge are not critical the concrete walls are rigidly connected to the extension of the deck slab. Alternatively, the R/C walls are arranged in pairs between extrusions of the extension of the deck's slab. Each pair of concrete walls is in contact with the extrusion of the slab toward the abutment's web while a clearance of some centimeters depending on the serviceability requirements of the bridge separates it from the extrusion constructed toward the embankment. The distance between the walls is achieved by the interjection of an expanded polystyrene (EPS) layer, with a small thickness, i.e. 20mm. The walls are constructed in a concrete box-shaped substructure, which replaces the conventional wing walls and retains the backfill material. The longitudinal clearance between the box-shaped wall and the transversely directed R/C walls is designed to absorb the total seismic movement of the deck. The longitudinal walls of the concrete box are used to increase the foundation's stiffness, as the abutment is designed to transmit not only the soil pressures of the backfill, but also the seismic loads of the R/C walls. The earth pressures affect only the stability of the concrete box-shaped substructure and the abutment's foundation, but not the earthquake resistance of the restraining walls.

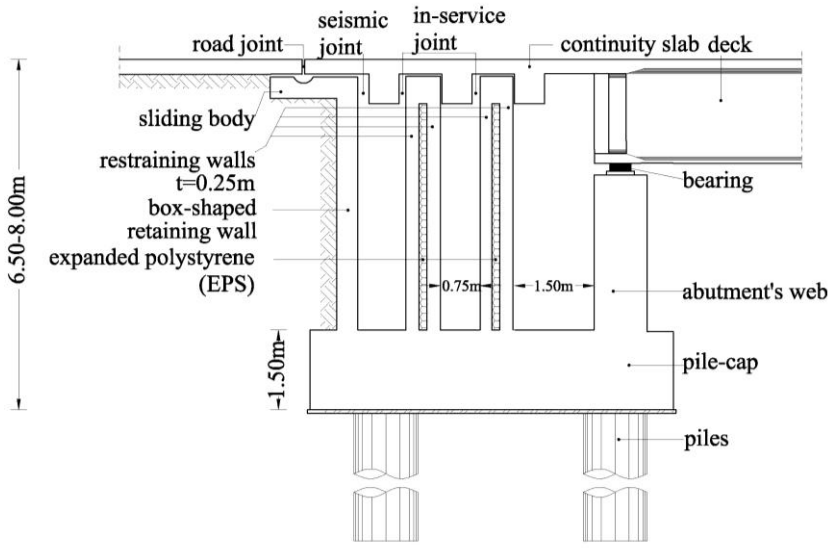


Figure 1: Longitudinal section of the proposed abutment.

In cases that the walls are rigidly connected to the extension of the deck slab the constrained-type movements of the deck due to the serviceability requirements of the bridge are restrained. The complete control the deformation of the deck due to creep, shrinkage effects, prestressing and thermal movements is quite difficult. However, additional structural

measures can be taken to minimize their influence. Specifically, the extension of the deck slab can be constructed during the final stage of the bridge construction. This measure ensures that creep and shrinkage effects have been partially or fully developed and consequently their influence is controllable and may be effectively reduced.

The selection of the height and thickness of the walls is mainly depended on the serviceability requirements of the bridge. The in-service bridge loading is increased as the length of the bridge is also increased. Figure 2 shows the minimum required height of the walls for bridges whose length is from 100m to 400m, considering that the thickness is from 25mm to 40mm and the longitudinal reinforcement D16@100mm or D16@50mm. The horizontal axis of the figure shows the equivalent total uniform bridge temperature $\Delta T_{N,tot}$ due to creep, shrinkage and thermal effects. The figure shows that for a given longitudinal reinforcement of the walls, (e.g. D16@100mm or D16@50mm) the increase of the walls' thickness also increases the minimum required height. The increase of the total bridge's length, also increases the minimum required height of the walls. The figure shows that for bridges whose total length is 400m and for $\Delta T_{N,tot.}=40^{o}C$, which is an acceptable temperature value, the minimum required height of the walls is 8.9m or 6.5m, when the longitudinal reinforcement of the walls is D16@100mm or D16@50mm respectively. However, it is well-known that the use of high walls would lead to a lower seismic efficiency of the restraining system, as the stiffness of the walls would be effectively reduced [9]. Hence, their seismic loading would not lead to the development of plastic hinges at the walls. For this reason, in long bridges, the non-rigid connection between the R/C walls-stoppers and the extension of the deck's slab is proposed. The clearances between the slab's extrusions and the wall pairs allow the partial contraction of the deck without the activation of the resistance of the walls.

2.2 Comparative analytical investigation on the seismic efficiency of the proposed abutment in different bridge types

The analytical investigation on the seismic efficiency of the proposed abutment showed that it can be implemented in all bridge types (monolithic, precast I-beam bridges, incrementally launched bridges), independently of their length by applying proper modifications imposed by serviceability requirements. It is noted that the restraining walls of the abutment contribute not only by their own stiffness but also by dissipating energy through hysteretic behavior. As a result, the proposed abutment should mainly be exploited in ductile bridge systems. In this respect, the authors of this study have proposed in previous studies a methodology for the modification of floating deck bridges to ductile systems[4-5]. It is noted that, floating deck bridges are the ones constructed using the method of segmental erection with precast prestressed I-beams and the incremental launching method.

The aim of the investigation is the comparative presentation of the seismic efficiency of the proposed abutment in different bridge types (monolithic, precast I-beam bridges, incrementally launched bridges). Three representative bridges of the major motorways in Greece are used as the "reference" cases of the investigation: The monolithic bridge of Aracthos- Peristeri (B1) with total length 240m [9], a precast I-beam bridge of P.A.TH.E Motorway (B2) with total length of 177.5m [9] and an incrementally launched bridge of Egnatia Odos Motorway (B3) with total length of 481.7m [4]. The analytical description, of the "reference" bridges is presented in detail in previous studies [4] [9] . Table 1 summarizes the main characteristics of the bridges. The "reference" bridges were analyzed for the purposes of the present study. These bridges were also re-analyzed considering the abutment proposed in the paper. Table 2 summarizes the main properties of the walls-stoppers as they are prescribed by the serviceability requirements of each bridge system.

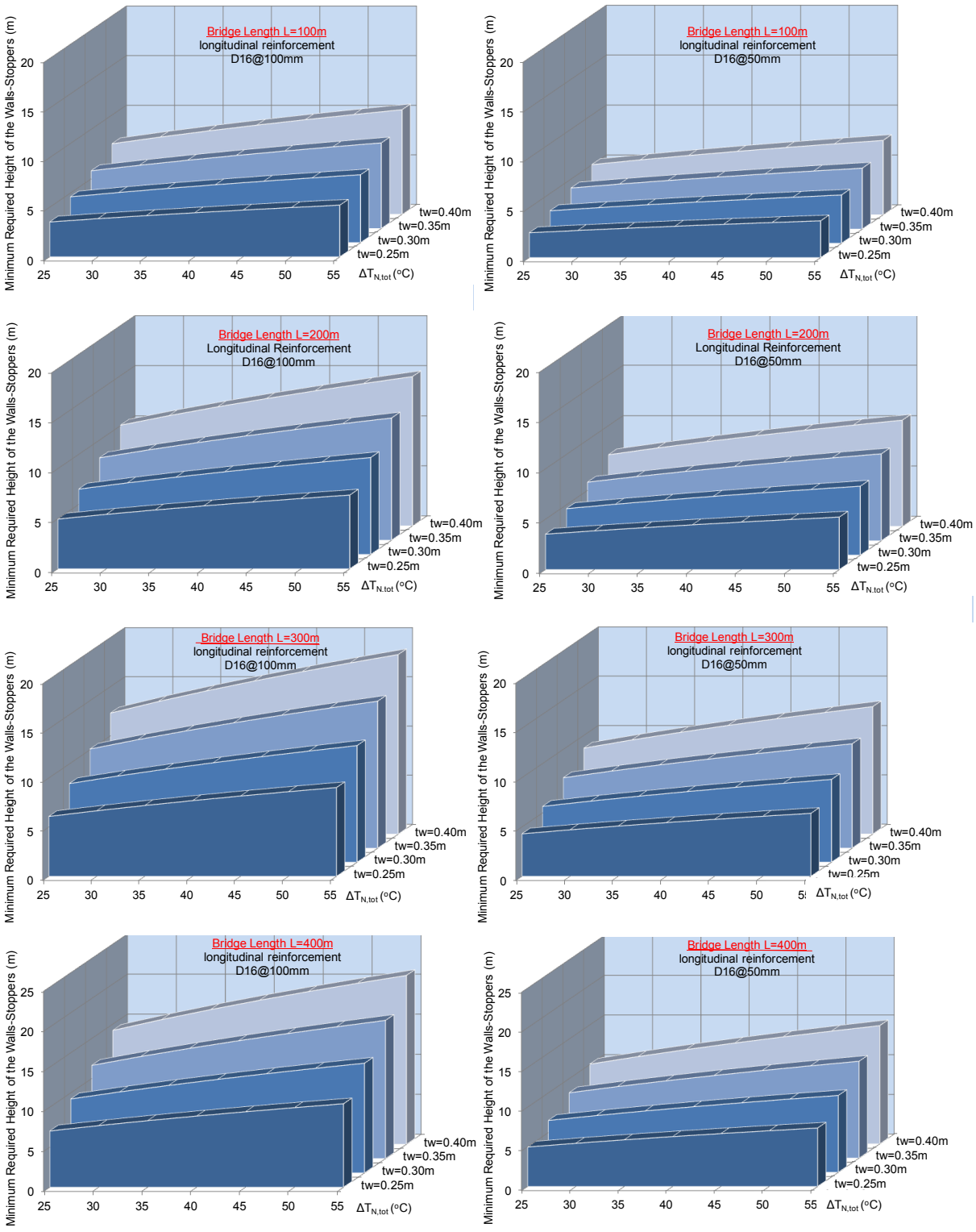


Figure 2: The minimum height of the walls required by serviceability loading for bridges whose length is 100m, 200m, 300m, 400m and for two different longitudinal reinforcement patterns, D16@100mm and D16@50mm.

The selection of the total number of walls per abutment is mainly based on economic criteria. In cases that the walls are rigidly connected to the continuity slab the use of five walls per restraining abutment seems to be a rational selection as this accommodates both cost-effectiveness and earthquake resistance of the bridge [9]. Each unconventional abutment of

bridges B1 and B2 consist of 5 walls-stoppers rigidly connected to the extension of the deck's slab. In the case of bridge B3, the walls are arranged in pairs between extrusions of the deck's slab and as a result the abutment should consist of an even number of walls (e.g. four).

Bridge	Type	Length	Cross- sections	Soil Class	Design ground acceleration
B1	Monolithic Bridge	240m (6 spans)	Deck: Single cell box girder Piers: Wall-type columns	B	0.16g
B2	Precast I-beam Bridge	177.5m (5 spans)	Deck: Precast prestressed beams Piers: Hollow circular sections	B	0.24g
B3	Incrementally Launched Bridge	481.7m (11 spans)	Deck: Single cell box girder Piers: Hollow rectangular section	B	0.16g

Table 1: The main characteristics of the "reference" bridges.

Bridge	Height/ Thickness	Number of walls per abutment	Type of connection between walls and deck's slab	Longitudinal Reinforcement pattern
Monolithic Bridge (B1)	4.5m/0.25m	5	rigid	D16@50mm
Precast I-beam Bridge (B2)	4.5m/0.25m	5	rigid	D16@50mm
Incrementally Launched Bridge (B3)	4.5m/0.25m	4	Isolated head of the pair of walls (clearance s=70mm)	D16@100mm

Table 2: The main characteristics of the abutments of the unconventional bridges.

The seismic performance of the analyzed bridge systems was assessed using nonlinear time history analysis. Analysis was carried out by using the SAP 2000 program [10]. The models and the analysis procedure are described in detail in previous studies [4] [9].

The calculation of the percentage reductions in the longitudinal movements of the bridge deck was used for the comparative assessment of the restraining effect of the proposed walls-stoppers. Figure 3 shows the percentage reductions in the average longitudinal movements of the three bridge decks for design accelerations 0.16g, 0.24g and 0.36g. It is noted that the longitudinal movement of the different joints of the deck over the piers is about constant and the calculated percentage reductions correspond to the average value of the movements of these joints. The figure shows that the abutment is more efficient in monolithic and precast I-beam bridges whose length is of the order of 200m, as the longitudinal movements are reduced from 50 to 65%. The corresponding reduction in the longitudinal movements of the long bridge constructed with the incremental launching method varies from 18% to 38%. The figure also shows that the abutment is more efficient in higher design accelerations (e.g. 0.24g and 036g) which is attributed to the inelastic response of the concrete walls.

The aforementioned results show that the proposed abutment is quite efficient even in the case that the walls are not rigidly connected to the extension of the deck's slab. The proposed configuration at the walls heads gives the opportunity to reduce the longitudinal reinforce-

ment ratio, which is mainly determined by the serviceability and not the seismic bridge requirements. Considering that the unconventional bridge is designed as a ductile system and hence the formation of plastic hinges is allowable, this leads to the yielding of the walls' longitudinal reinforcement.

Although the longitudinal earthquake is more demanding than the transverse one, the investigation showed that the restraining effect of the abutment is also significant in the transverse direction. Analytical results concerning this direction are available in previous study [9].

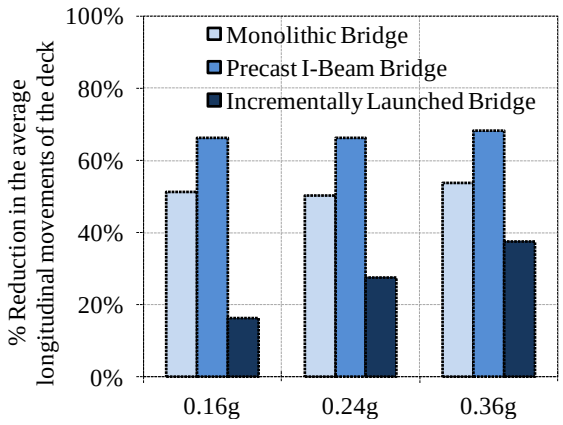


Figure 3: The percentage reduction in the average longitudinal movements of the bridge deck.

3 EXPERIMENTAL INVESTIGATION

The scope of the experimental investigation is the verification of the analytical results concerning the strength, stiffness and ductility of the walls-stoppers of the proposed abutment, Figure 1. The experimental investigation of the above properties is accomplished under monotonic and cyclic loading. The accuracy of the consideration of the complete restrain at the ends of the walls is also examined under monotonic loading.

3.1 Description of specimens

The experimental program presented in this work involves 3 specimens, denoted as SPEC1 SPEC2 and SPEC3. SPEC1 was subjected under monotonic loading while SPEC2 and SPEC3 were subjected under cycling loading. All specimens were constructed under a scale 1:2. The difficulty on the experimental investigation of members whose ends are completely restrained under monotonic loading, motivated the authors of this investigation to study a substitute symmetrical simple supported member. This member consists of three rows of walls arranged along its height. The walls are rigidly connected at their ends. Figure 4 shows the geometry and steel reinforcements of specimen 1 (SPEC1). The longitudinal reinforcement ratio of SPEC1 is 1.6% and corresponds to walls with longitudinal reinforcement D16@100mm. Steel reinforcement (longitudinal and transverse) was instrumented using strain gages.

Each of specimens 2 and 3 (SPEC2, SPEC3) consists of two walls. Figures 5 and 6 show the geometry and steel reinforcements of specimens 2 and 3 (SPEC2 and SPEC3) respectively. SPEC2 has a longitudinal reinforcement ratio equal to 1.6% (D16@100mm in the real scale) while the longitudinal reinforcement ratio of SPEC3 is 2.9% (D16@50mm in the real scale). In all specimens, the diameter of the transverse reinforcement is 4.2mm while its spacing along the length of the walls is 25mm at the possible plastic hinges regions (20cm from the ends of the walls) and 50mm at the other regions.

3.2 Overview of experimental setup

Test specimen 1 (SPEC1) was subjected to loading coming from a single load at the middle, Figure 7. A deflection measuring system was attached at the midspan of the specimen. Figure 7 also illustrates the positions of the strain gages used for the instrumentation of the reinforcement (longitudinal and transverse).

Figure 8(a) illustrates the experimental setup used for the cyclic loading of specimens 2 and 3. The setup consists of the two steel beams HEB 320, which substitute the bridge deck and pile-cap respectively. The double-acting hydraulic actuator is connected to the one steel beam, which has the ability to slip through two steel bars fixed at the laboratory's floor. It is noted that the connection between this steel beam and the specimen allows the partial rotation of the specimen's head. In cases that the serviceability requirements impose the construction of abutments' web with height greater than 4.5m (this height corresponds to the 1:2 scale of the experiment), but it is not possible, due to other parameters' limitations (i.e. construction cost, seismic efficiency etc.), these rotations accommodate part of the in-service induced movements (see Section 2). The second steel beam is fixed at the laboratory's floor. The aforementioned specimens were subjected to a number of cycles of quasi-static cyclic loading, Figure 8(b).

3.3 Discussion of Results

Figure 9 displays the variation of the deflection in the middle of SPEC1 with the increment of the load. The theoretically calculated effective stiffness of the specimen which is also displayed (red line) in the figure is very close to the experiment one. This stiffness is calculated according to Codes provisions [3] and is equal to 8043 kN/m while the experimental one is 9879 kN/m. The figure also shows that the specimen developed a displacement ductility factor equal to 11.7 which is attributed to the well –confined ends of the walls. The theoretical displacement ductility factor of the specimen is calculated according to the methodology proposed in Caltrans Seismic Design Criteria [11] and is equal to 7.2. Figure 10 displays the P-ε diagrams of steel strain gages. Specifically, Figures 10(a) and 10(b) correspond to the strain gages placed at the longitudinal bars of the external and the middle walls of SPEC1 (according to Figure 7), while Figure 10(c) corresponds to the strain gages placed at the stirrups. The figures show that the longitudinal bars of the middle walls yield and consequently they are activated more than the corresponding of the external ones. A plumb line was used at the end of the experiment as a simple but accurate tool, for determining that the edges of the specimen is perfectly vertical, Figure 11.

Hysteresis loops for the two specimens (SPEC2 and SPEC3) subjected to cycling loading are shown in Figure 12. Regardless of the large relevant displacements between the specimen's head and foot, the failure of the specimens was not reached. The noticed plastic branch has short length in both cases and consequently, a conclusion about the ductility of the specimens it is not possible to be extracted. However, the observation of the last loop indicates that, both specimens have available ductility, as the three last loops corresponding to the maximum displacement are coincided. The intended non-full impaction of the specimens' head caused rotations, which affect the results.

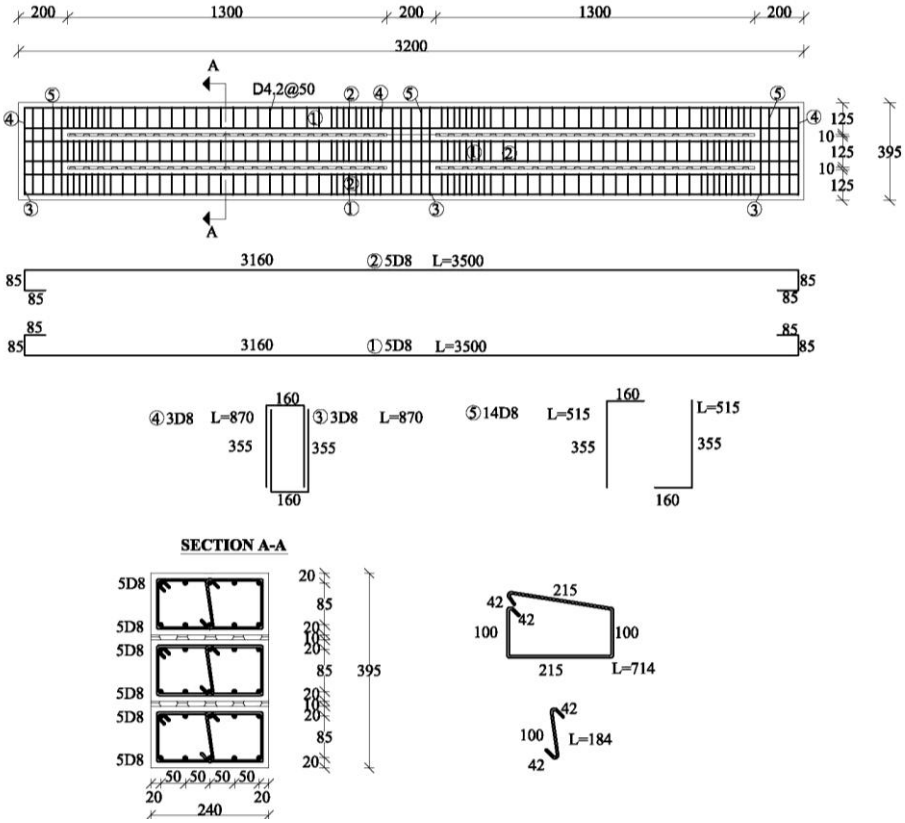


Figure 4: Geometry and steel reinforcement of specimen 1 (SPEC1).

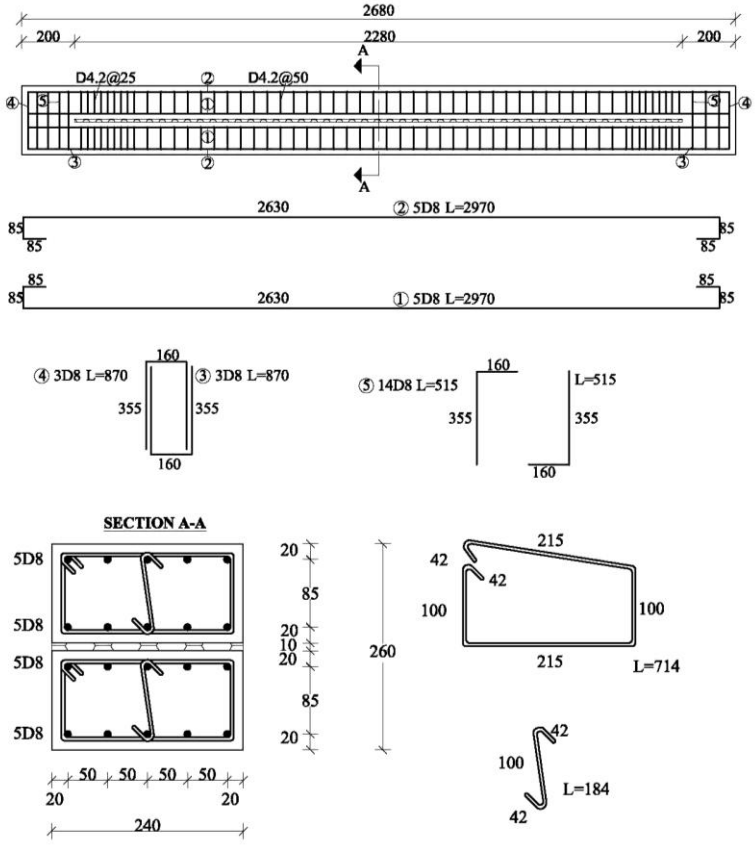


Figure 5: Geometry and steel reinforcement of specimen 2 (SPEC2).

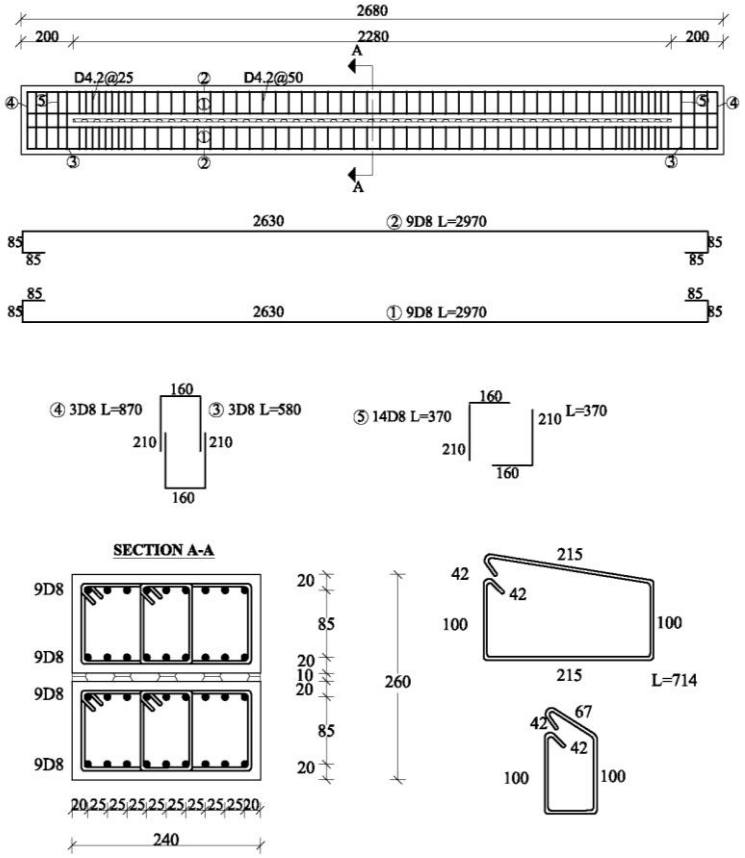


Figure 6: Geometry and steel reinforcement of specimen 3 (SPEC3).

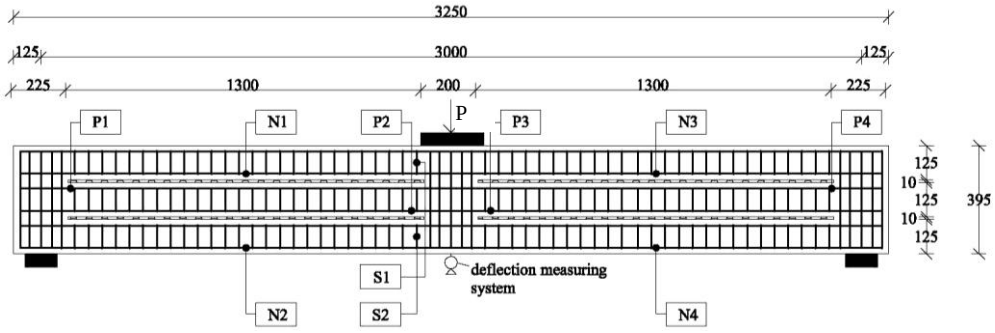


Figure 7: Experimental loading of specimen 1 (SPEC1) and positions of steel strain gages and deflection measuring system.

Any relevant movement between the specimen's head and base causes (a) linear variant bending moments along the height of the walls, (b) tension and compression axial forces corresponding to the direction of the head's movement (the presence of the tensile axial loading is confirmed by the appearance of flexural cracks in the middle of the tensile wall of the specimen during the loading) and (c) second-order effects. The described above parameters affect the loops' shape and cause the loops' pinching. In any case, the area enclosed by the envelope, which is quite large, indicates that the energy dissipation is significant in both specimens. Figure 13 shows that the energy dissipated by SPEC3 (SPEC3, ρ=2.9%) is greater than the corresponding dissipated by SPEC2 (SPEC2, ρ=1.6%). According to this figure the energy dissipation presents normal, gradually increasing progress. Finally, the experimental values of

the stiffness are smaller than the theoretical ones due to the partial restrain of the specimens' ends.

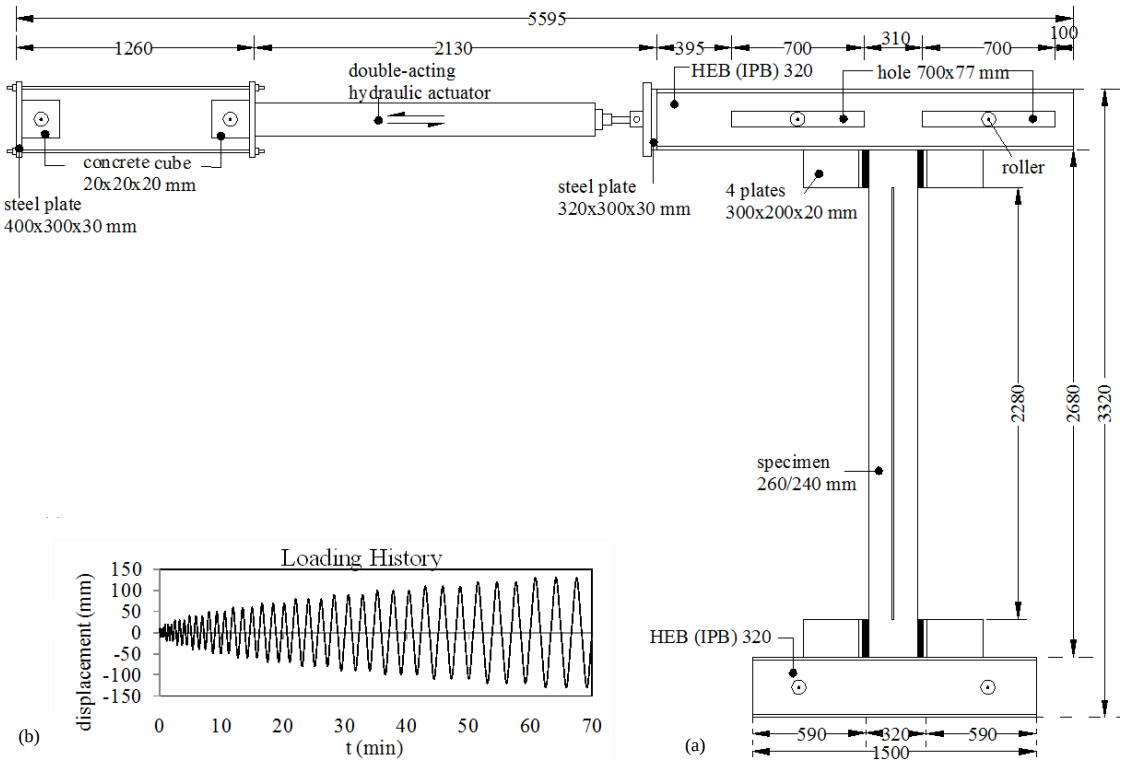


Figure 8: (a) Experimental setup for cycling loading and (b) loading history.

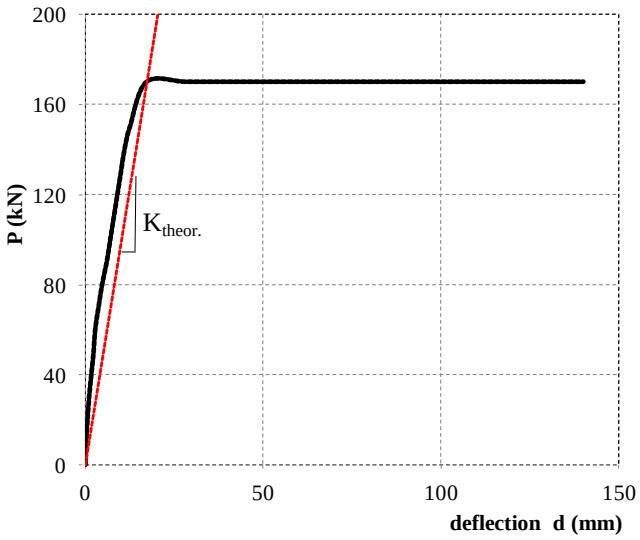


Figure 9: P-d diagram of specimen 1 (SPEC1) under monotonic loading P.

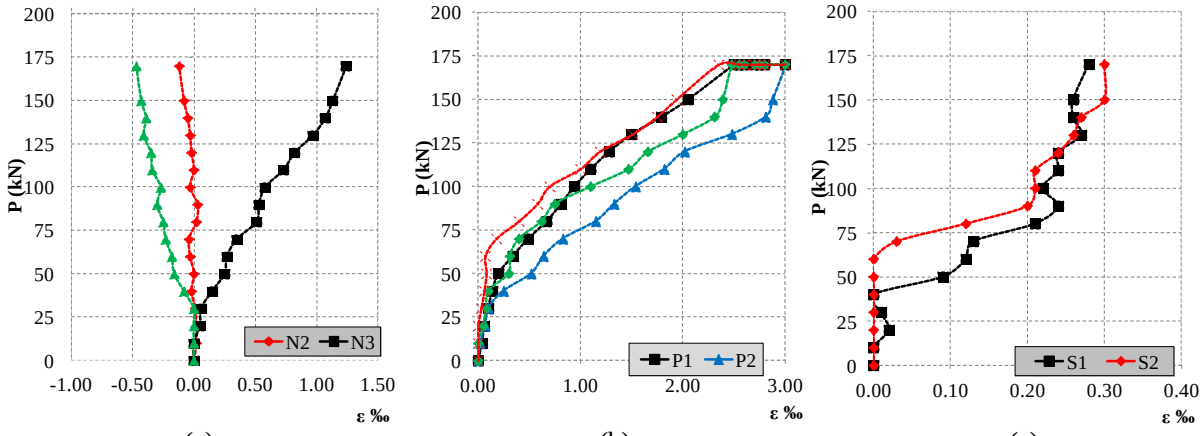


Figure 10: P-ε diagrams of strain gages placed at (a) longitudinal bars of the external walls, (b) longitudinal bars of the middle walls and (c) stirrups of specimen 1 (SPEC1).



Figure 11: Using of plumb line for determining that the edges of the specimen are perfectly vertical.

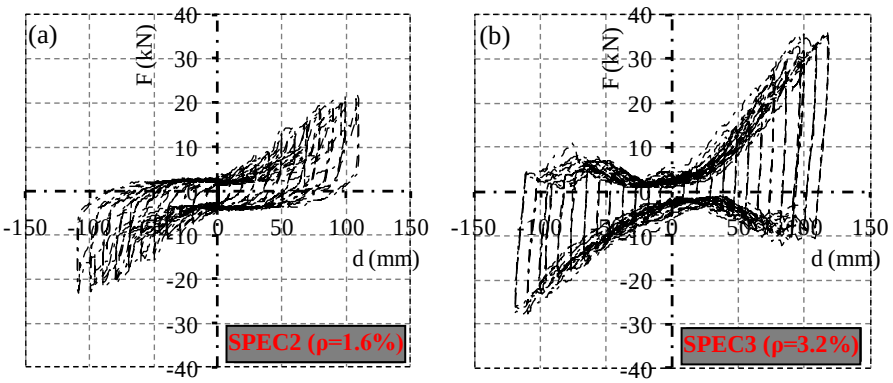


Figure 12: Hysteresis loops for (a) specimen 2 (SPEC2) and (b) specimen 3 (SPEC3).

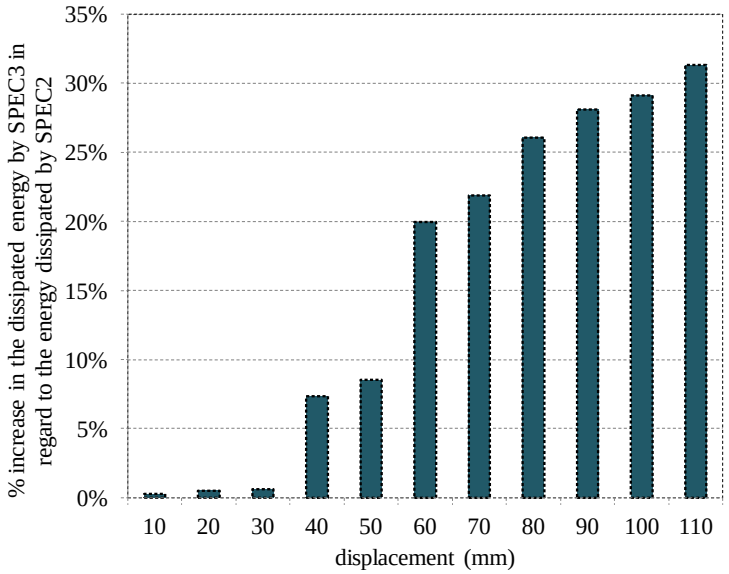


Figure 13: % Increase in the dissipated energy by SPEC3 in regard to the energy dissipated by SPEC2.

4 CONCLUSIONS

In this study the analytical and experimental investigation on the seismic efficiency of an unconventional abutment was presented. This system consists of transversely directed R/C walls, which behave as seismic stoppers. The main conclusions of the investigation are the following:

- The proposed restraining system consisting of walls-stoppers is quite efficient in both long and short bridges. The longitudinal and transverse movements of the deck are effectively reduced.
- Proper structural configuration at the walls' heads accommodates a part of the in-service constraint bridge movements. The aforementioned accommodation reduces the longitudinal reinforcement requirement of the walls as it is mainly determined by the serviceability and not the seismic bridge requirements. Considering that the unconventional bridges are designed as ductile systems and hence the formation of plastic hinges is allowable, the longitudinal reinforcement of the walls yields and consequently a great part of the induced seismic energy is dissipated through the hysteretic behaviour of the restraining walls.
- The experimental study of members whose ends are completely restrained under monotonic loading was accomplished. The plump line used at the end of the experiment determined that the edges of the specimen were perfectly vertical.
- The well-confined possible plastic hinge regions at the ends of the walls improved the ductility of the specimens under monotonic and cyclic loading.
- The experimental effective stiffness of the specimen (monotonic loading) is quite close to the theoretical one. The ductility of the specimen under monotonic loading is about two times the theoretically calculated according to Code's provisions.
- The failure of the specimens under cycling loading was not reached despite the large relevant movements between their ends. The observation of the last loop indicates that, both specimens have available ductility, as the three last loops corresponding to the maximum

displacement are coincided. The intended non-full impaction of the specimens' head caused rotations, which affect the results.

ACKNOWLEDGEMENTS

The greatest gratification for the researcher is the opportunity to express his appreciation to the people who generously helped in the different phases of the study. The authors of this study wish to express their gratitude to Dr. Salonikios Thomas, senior researcher at E.P.P.O., as well as to the staff of the Laboratory of Experimental Strength of Materials and Structures of Aristotle University of Thessaloniki for their precious help in the experimental investigation. Acknowledgements are also due to METE SYSM S.A. and EGNATIA ODOS S.A. for the kind offer of the original study of the bridges for the analytical investigation. The authors wish also to express their warmest thanks to MASOUTIS S.A. for the kind offer of the experimental setup.

REFERENCES

[1] CEN, *Eurocode 1: Actions on structures - Part 1-5: General actions -Thermal actions*. 2003.

[2] M. Arockiasamy and M. Sivakumar, Design Implications of Creep and Shrinkage in Integral Abutment Bridges. ACI Special Publication, **227**, 85-106, 2005.

[3] CEN, *Eurocode 8: Design of structures for earthquake resistance, Part 2:Bridges*. 2003.

[4] S.D. Tegou and I.A. Tegos, Improvement of the Earthquake Resistance of Incrementally Launched Bridges. *15th World Conference on Earthquake Engineering*, Lisbon, Portogual, September 24-28, 2012.

[5] S.D. Tegou and I.A. Tegos, A proposal for cost-effective design of precast I-beam bridges. *International Conference on Innovations on Bridges and Soil- Bridge Interaction.* **Vol I**, 149-156, October 13-15, 2011.

[6] T. Mikami, S. Unjoh, M. Kondoh, *The effect of abutments as displacement limiting measure on seismic performance of bridges*. www.pwri.go.jp/eng/ujnr/tc/g/pdf/19/4-1mikami.pdf, Accessed 5 April 2012, 2008.

[7] S.A. Mitoulis and I.A. Tegos, An unconventional restraining system for seismically isolated bridges. *Engineering Structures*, **32: 4**, 1100-1112, 2010.

[8] R.V. Nutt and R.L. Mayes, *Comparison of Typical Bridge Columns Seismically Designed With and Without Abutment Participation Using AASHTO Division I-A and Proposed AASHTO LRFD Provisions*, Task F3-1(a), 2000.

[9] S.D. Tegou, S.A. Mitoulis, I.A. Tegos, An unconventional earthquake resistant abutment with transversely directed R/C walls. *Engineering Structures*, **32:11**, 3801-3816, 2010.

[10] Computers and Structures Inc., *SAP 2000 Nonlinear Version 11.0.3, User's Reference Manual*. California, 2007.

[11] California Department of Transportation, *Caltrans- Seismic Design Criteria, SDC version 1.4*. 2006.

COMPDYN 2013
4th ECCOMAS Thematic Conference on
Computational Methods in Structural Dynamics and Earthquake Engineering
M. Papadrakakis, V. Papadopoulos, V. Plevris (eds.)
Kos Island, Greece, 12–14 June 2013

SHAKING TABLE STUDY OF THE SEISMIC INTERACTION OF AN ISOLATED BRIDGE DECK WITH THE ABUTMENT UTILIZING SMALL-SCALE MODELS AND NUMERICAL SIMULATIONS

Stergios A. Mitoulis[1], George C. Manos[2], and Ioannis A. Tegos [2]

[1]Civil and Environmental Engineering, University of Surrey: s.mitoulis@surrey.ac.uk

[2,3] Civil Engineering, Aristotle University of Thessaloniki

Keywords: bridge, shake table test, dynamic, pounding, SDOF, analytical.

Abstract. *It has been recognized that an isolated deck develops horizontal displacements of considerable amplitude during a strong earthquake. In this case the possibility of mobilizing the abutments in moderating such large amplitude horizontal response is beneficial for the safety of the structure. Thus, apart from lowering the seismic forces by the low-stiffness isolator units, the interaction between the deck and the abutments in the form of pounding for large horizontal deck response amplitudes aims at limiting through this mechanism excessive horizontal deck displacements. Such a problem was examined at the laboratory of Strength of Materials and Structures of Aristotle University using a small-scale physical representation that retains in a qualitative way the following important features: 1. A relatively stiff steel platform, representing the bridge deck, which is supported on a shaking table by two flexible supports, representing the isolator units; it is subjected to simulated horizontal earthquake motions developing large amplitude horizontal displacement response. 2. The possibility of bridge deck pounding on the abutment was introduced through a connector device that became active after the deck response exceeded a certain amplitude, introducing an initial gap within this connector. Despite the fact that these two basic response mechanisms, flexibility of isolator units and connector force-displacement characteristics, are crude small-scale representations of the actual mechanisms that are mobilized in a prototype bridge deck, the qualitative characteristics of this problems are retained. A number of simulated earthquake tests provided the necessary measured acceleration and displacement response of the model steel platform of the small-scale model and the force-displacement response of the connector and the flexible supports of the steel platform with the shaking table. This was next utilized to validate numerical simulations of this small-scale experimental representation of the bridge-deck pounding problem. By comparing the numerical predictions with the measured response of this small-scale experimental representation of the bridge-deck pounding problem it can be concluded that such numerical simulations can yield quite accurate predictions provided that the force-displacement characteristics of the isolator units as well as the force-displacement characteristics of the mechanism representing the bridge deck-abutment pounding are defined with reasonable accuracy for the prototype bridge.*

1 INTRODUCTION

The basic principle of conventional earthquake resistant design is to ensure an acceptable safety level, while avoiding collapse and loss of life. This approach can be considered adequate for most types of structures. However, for important structures, such as bridges, higher level of performance is required, as bridges should maintain emergency communications even after severe earthquakes. Over the last twenty years, a lot of research has been conducted in order to raise the safety level of bridges, while keeping construction costs reasonable. Seismic isolation has had numerous applications during recent decades [1] [2] [3], especially in important structures such as bridges, which should maintain the emergency communications, with appropriate reliability, after the design seismic event [4]. One of the goals of the seismic isolation is to shift the fundamental frequency of a structure away from the dominant frequencies of earthquake ground motion. The other purpose of an isolation system is to provide an additional means of energy dissipation, thereby reducing the transmitted acceleration of the deck, which represents the critical structural element of the bridges, [1].

However, large seismic displacements of flexible isolated bridge systems increase the requirement at expansion joints, which are expected to have large movement capacities. Hence, their cost is increased, while large deck displacements increase the likelihood of span unseating. To reduce these implications, supplementary damping with dampers is developed to reduce deck's movements. To minimize extra displacement-related costs at expansion joints, movement capacities are limited by sizing the gaps (clearances) with 80% of the seismic design action according to AASHTO's section 9 [5] and 40% according to Eurocode 8-2 [4]. No consideration for seismic displacements is given in expansion joints in international literature [6] under the concept that the backwall and the expansion joint are expendable non-structural elements that may be damaged and replaced after the main seismic shock thus accepting indirectly the impact between the deck and the abutments. Despite the vast of analytical [7][8]and experimental studies [9][10] involving or not SSI effects at bridge abutments [11], there are no experimental studies investigating the dynamic bridge-abutment interaction neither qualitatively nor quantitatively. However, this approach has the following implications. First, damage may result from pounding that will not be confined only to the parts of the bridge which were designed to accommodate it. Second, the dynamics of the pounding system may differ substantially from those that were taken into account in the design without considering the pounding. This change in the dynamic system introduced by the pounding was investigated without taking a-priori that it will always have beneficial consequences for the bridge deck response. Extended research has been carried out aiming to identify the fundamental characteristics of this deck-abutment interaction utilizing a series of numerical simulations.

2 DESCRIPTION OF THE BRIDGE MODEL-INSTRUMENTATION AND ANALYTICAL MODELING

Two elastomeric bearings with cross section 150x150mm and a height of 150mm (total thickness of the elastomer 120mm) were used to support on the shake table the steel platform which represented the bridge deck model, by fixing them with bolts both to the steel platform and the shaking table (see figure 1). Additional mass was rigidly attached on this steel platform so that the total model deck mass was equal to 0.988t. In this way, the fundamental frequency of the deck - elastomeric bearings model was within the 1Hz to 20Hz frequency range. In this frequency range the employed shaking table is capable of introducing horizontal motions of sufficient amplitude in terms of acceleration and displacement. The steel platform was provided with side rollers aimed to prohibit its motion at any other horizontal direction apart the longitudinal direction that coincided with the direction of the horizontal table motion.

The connector was fixed to either the shaking table or the steel platform with steel attachments of sufficient stiffness in a way that the load-displacement response of this link to be dictated by the properties of the copper connector itself and not by its attachments (see figure 1). The connector was made by a copper cylinder encased within a steel ring. A small gap between the copper cylinder and the steel ring was provided in order to simulate the gap between the bridge deck and the adjacent abutment. The amplitude of such a gap before the commencement of a strong earthquake motion cannot be exactly known as it depends on actual expansion and contraction movements of the deck prior to the seismic motion. The bridge model, with or without the copper connector in place, was subjected to a uni-direction simulated earthquake horizontal motion based on the horizontal components of the actual ground motion record of the Kern County, California 1957 earthquake. This simulated earthquake motion resulted from speeding up in the time domain the original recording in order to include sufficient energy in the above mentioned frequency range. Figure 2a depicts the frequency content of the simulated earthquake motion as it was found by the Fourier transformation of the shaking table acceleration recorded during the experimental sequence. Figure 2b depicts the fundamental frequency of the model deck - elastomeric bearings dynamic system as found from its acceleration response during one of the simulated earthquake experiments.

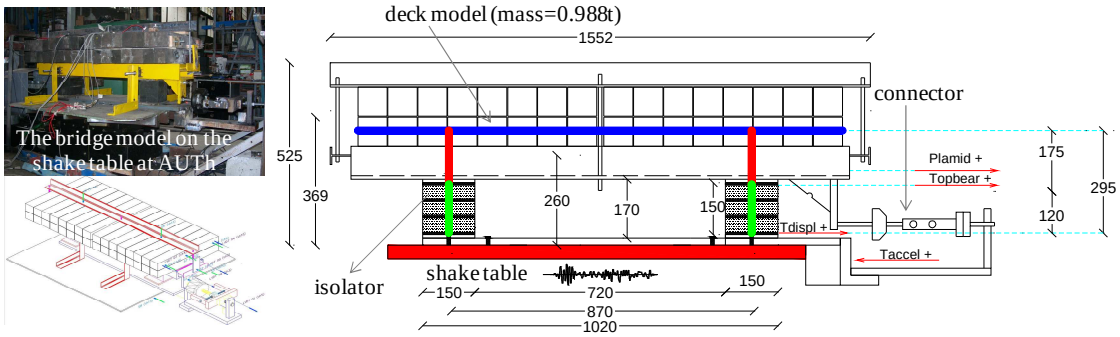
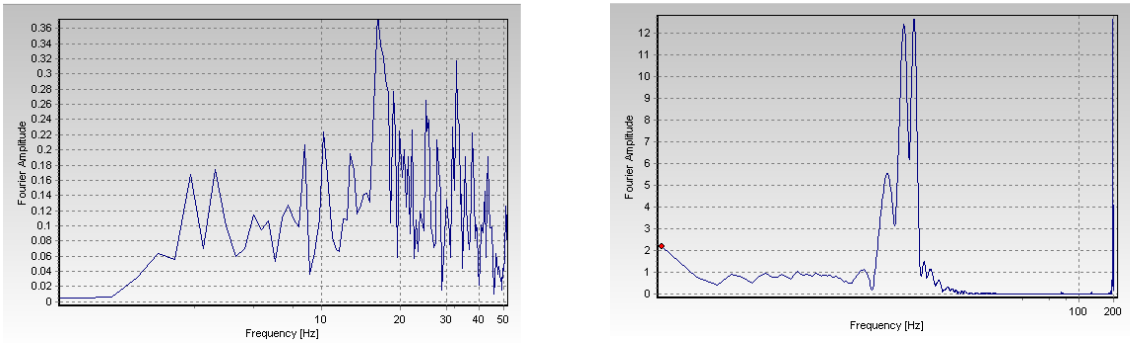


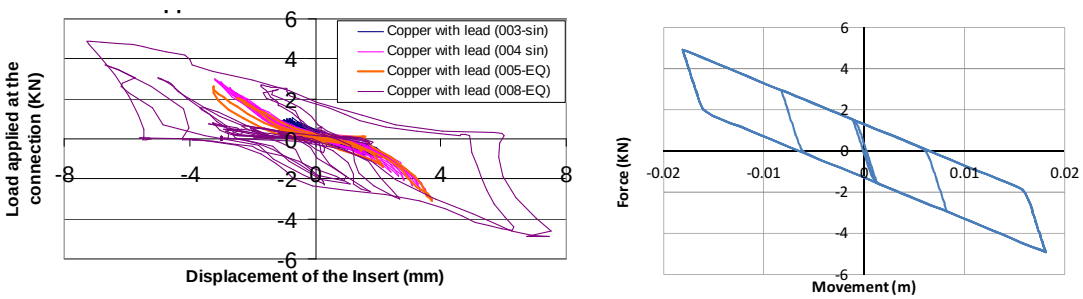
Figure 1: The geometry of the SDOF specimen as built on the shake table of the Laboratory of Strength of Materials and Structures @ AUTh and the model of the equivalent model bridge in commercial FEM code SAP 2000.



(a) (b)

Figure 2: (a) Fourier transformation of the shaking table acceleration measured during the experiments utilizing simulated earthquake motions based on the Kern county 1957 prototype earthquake recordings, (b) Acceleration response of the model deck-elastomeric bearings system with peaks at 3.052Hz and 3.711Hz.

Instrumentation was provided in order to capture the acceleration and displacement response along the longitudinal axis of motion both of the shaking table level as well as of the



(a) (b)

Figure 3: (a) Measured cyclic load-displacement response of the copper connector and (b) numerical cyclic load-displacement response of the copper connector (no gap).

steel platform representing the model deck. For the model platform this was done both at the level corresponding to the center of mass as well as at the level just above the point of fixity of the elastomeric bearings with the steel platform (see Figure 1, Plamid, Topbear). Additional instrumentation was also provided to measure the vertical acceleration of the steel platform as well as the horizontal acceleration along the transverse horizontal direction. Finally, the actual load-displacement response of the copper connector itself was monitored independently by a load cell positioned in line with the connector as well as with a displacement transducer measuring the relative displacement of the two connector ends. At the beginning of the experimental sequence a gap of 1.5mm was introduced between the copper cylinder and the steel ring of the connector. This gap became larger during the experiments due to the plastification of the copper cylinder. The plastification of the cylinder is aimed at simulating the response of the soil surrounding the abutment during deck ponding. Figure 3a shows the cyclic load-displacement connector response as was measured during one particular experiment with a simulated earthquake motion whereas Figure 3b is the numerical simulation of the copper connector load displacement response that was used in the numerical investigation, which is presented next.

3 NUMERICAL SIMULATION

The deck - elastomeric bearings model response was numerically simulated employing a commercial software package (SAP 2000) and utilizing all the relevant information from the specific constituents of the elastomeric bearings, copper connector and steel platform in terms of mass and load-displacement characteristics. The load-displacement characteristics of the elastomeric bearings in horizontal shear, vertical axial force and bending moment as well as those of the copper connector were measured by specific experiments and as such were introduced to the numerical simulation through the options provided by the software. The actual geometry of the model deck-bearings-connector system was introduced in the numerical simulation through a 2-D representation. This is shown in Figure 1a (top right) as well as in Figure 4.

The steel platform representing the model deck is simulated by rigid frame elements that have very large stiffness and the total mass (red solid line, Figure 4). These rigid frame elements are located in the horizontal plane going through the center of mass of the steel platform (see Figure 1). The elastomeric bearings are simulated with link elements that are located vertically in a way coinciding with the central axis of the model elastomeric bearings (green solid line, figures 1 and 4). These link elements were given such non-linear properties as found from tests performed with the model elastomeric bearings, as shown in figure 5. Rigid elements with very large axial, shear and flexural stiffness values are used to connect these link ele-

ments representing the elastomeric bearings with the rigid frame elements representing the steel platform. Finally, a link element with non-linear axial load-displacement response properties coinciding with those of the copper connector (see figures 3a and 3b) is used to represent numerically the connection of the steel platform with the shaking table.

Four different alternatives of the non-linear properties for the link elements representing the elastomeric bearings were examined (figure 5). These alternative non-linear properties were based on the target displacement, the damping areas and the stiffness of the loading and the unloading branch of the tested bearings. Modeling these non-linear model elastomeric bearing characteristics the option of Wen load-displacement constitutive law was adopted offered by the software. From these four alternative numerical simulations of the model elastomeric bearings cyclic response the second alternative was selected based on the comparison of the numerical predictions with the corresponding load-displacement hysteresis loops obtained during testing, as shown in Figure 4. This 2nd alternative was found to simulate in a satisfactory way the stiffness variation and the hysteretic damping of the bearing, the shear deformation at the bearing's yielding point and the effective stiffness of the bearing under the maximum target displacement measured during the experiments. It was also found to illustrate accurately the unloading branch of the hysteresis loops which was observed during testing.

The numerical response of the deck-elastomeric bearing model without the connector was validated by comparing it with the corresponding experimental measurements. Figure 6 depicts this comparison in terms of deck displacement of the center of mass. As can be seen from this figure reasonably good agreement was obtained between numerical and measured displacement response in the time domain. The maximum predicted model deck displacement agrees quite well with the measured value. Based on that, the numerical simulation was extended to the model with the connector in place.

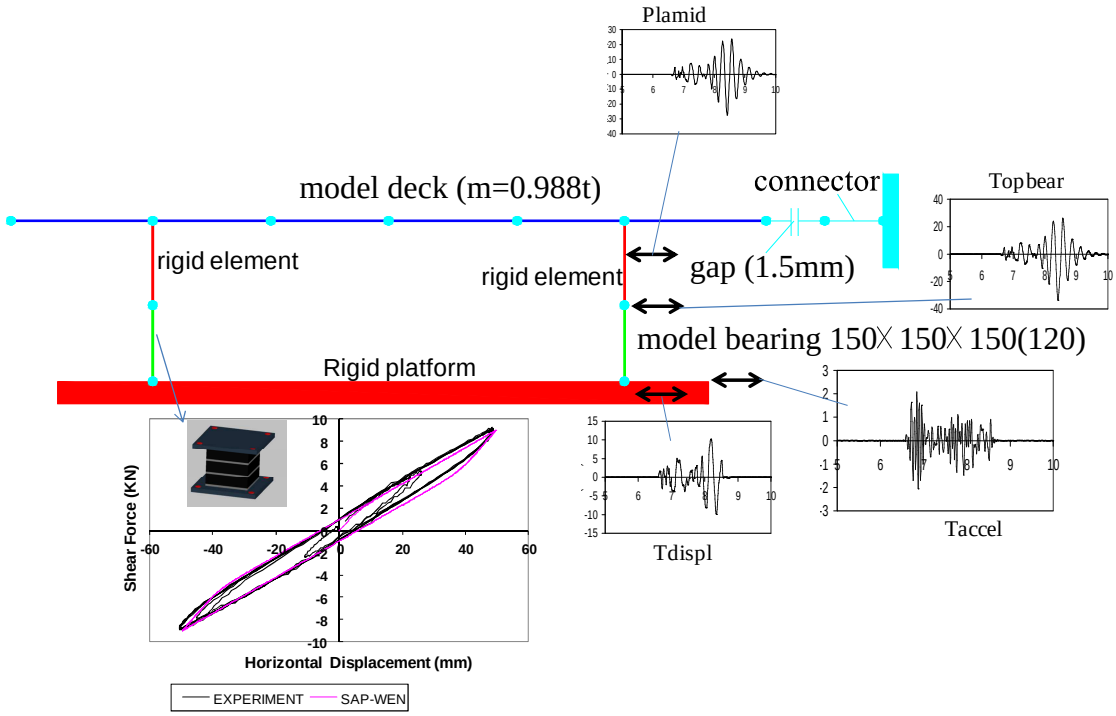


Figure 4: The idealized model deck with the bearings and the connector. The recorded time histories of the model and the hysteresis loops of the model bearing are shown.

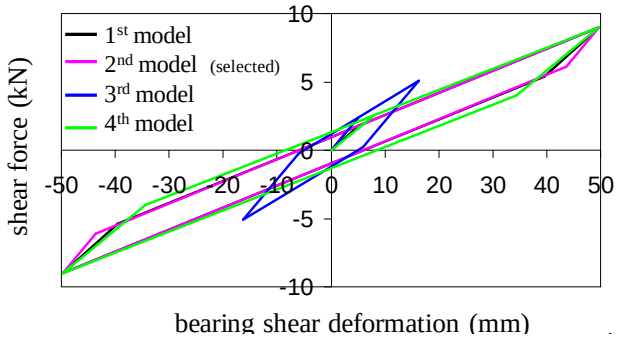


Figure 5: The alternative bearing models used in SAP 2000 for different target displacements, and unloading stiffnesses.

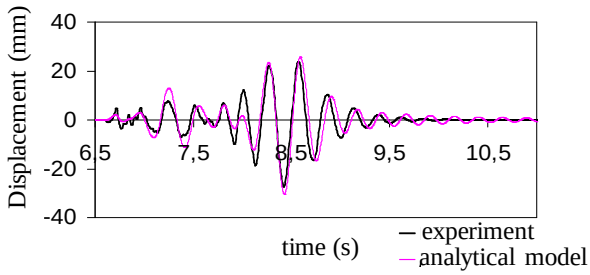


Figure 6: The time histories of the recoded response as the top of the bearing (Topbear).

4 NUMERICAL SIMULATION OF THE BRIDGE'S DECK-ABUTMNET POUNDING INTERACTION

In this part of the numerical study the bridge's deck-abutment pounding interaction will be examined by introducing in the numerical model the numerical simulation of the copper connector, which was used during the experimental sequence to physically simulated in small-scale this interaction. This has been already explained and presented in figures 3a and 3b. As can be seen, the employed copper connector possesses a non-linear force-displacement capability that is symmetric and represents in this way pounding of the deck in the two opposite abutments of the bridge. Modeling of pounding effects has been studied extensively during the last years[12] [13] [14] [15] [16]. In terms of amplitude, the maximum pounding force in a prototype bridge with total deck length equal to 100m is expected to be of the order of 12000kN [7]. The total weight was estimated approximately equal to 24800kN [17]. Thus, the maximum pounding force represents approximately 50% of the weight of the deck. Similarly, the model deck weights approximately 9.89kN and together with the maximum measured copper connector force (of the order of 5kN) form a similar ratio of maximum pounding force over deck weight as the previously mentioned prototype bridge deck. It is debatable, whether the force-displacement response that will develop between the abutment and the bridge deck during pounding will bear any similarity to the cyclic response of the copper connector depicted in figure 3a. Such a prototype deck-abutment force displacement relationship can only be defined from direct in-situ measurements and is beyond the present study. Thus, the current numerical examination is limited to demonstrate the effect of this interaction by assuming that the measured copper connector load-displacement cyclic response bears some resemblance with the deck - twin abutment pounding interaction of a prototype bridge. Moreover, when such a prototype force-displacement response becomes available from in-situ measure-

ments it can be included into a numerical simulation in a way similar to the one that is followed here.

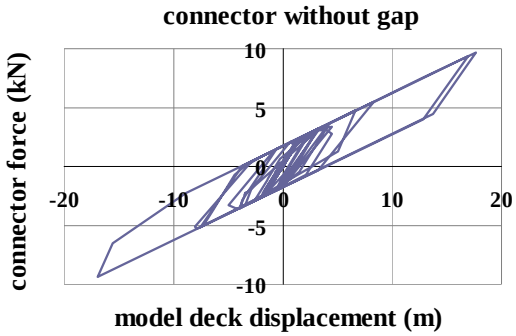


Figure 7: Connector force vs relative deck-connector displacement (no gaps)

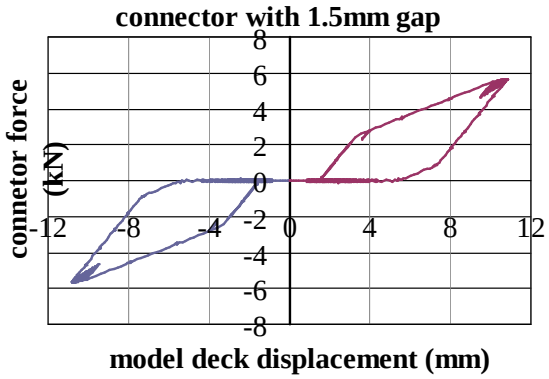


Figure 8: Connector force vs relative deck-connector displacement with 1.5mm gap

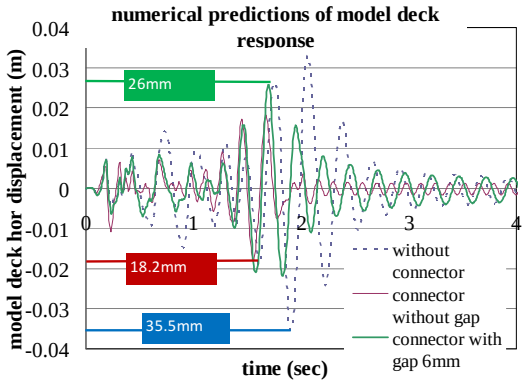


Figure 9: Comparison of the model deck displacement response without the connector or with connector in-place (with or without a gap)

Two different numerical models were utilized to simulate numerically the scale-model behavior when the copper connector was in place. The first model is a non-linear link element with an initial stiffness equal to 1500kN/m, a yielding force equal to 2.5kN and a post-yield stiffness equal to 30% of the initial stiffness (Figure 7). However, in this way it is assumed that the deck-abutment interaction starts as soon as the deck displaces horizontal. As this assumption is not realistic, a second numerical model was utilized in order to simulate the condition that a physical gap exists between the deck and the abutment. Thus, in order for the

pounding interaction to commence the horizontal deck displacement should be of such an amplitude that exceeds this gap. The second model simulates the existence of a ±1.5mm gap between the deck model and the copper connector. This is done by connecting in line the previously described non-linear link element with a gap element having as an initial gap value equal to 1.5mm (see figure 8).

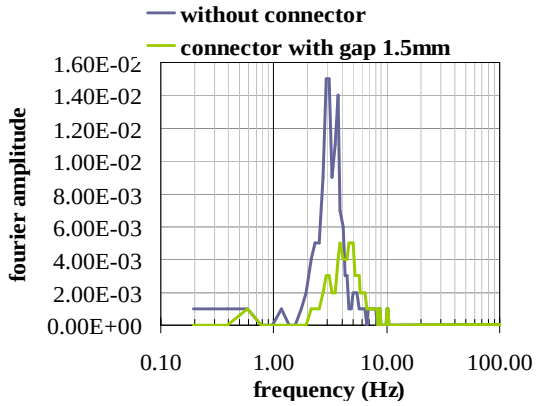


Figure 10: Comparison of the model deck displacement response without the connector or with connector in-place (with or without a gap) in terms of FFT plots

5 CONCLUSIONS

- It has been established in the past that the decks of isolated bridges interact with the abutments during strong earthquakes. This deck-abutment interaction has been evaluated in past experimental studies in scaled abutment models including their backfills.
- The influence of isolated bridge deck - abutment interaction from pounding was investigated in this paper by simple numerical tools that take into account the dynamic and non-linear nature of this interaction. The non-linearity springs from the isolator bearings themselves, but mostly from the deck to abutment interaction. This was introduced to the numerical simulation by a combination of non-linear link and gap elements
- An experimental study was also carried out utilizing a small-scale model to represent the isolated bridge deck and a copper connector to approximate qualitatively this deck-abutment interaction. A number of shaking table tests was performed without and with this connector in place. The numerical predictions of the maximum model deck displacement response are in reasonable good agreement with the measured values, when the gap element is employed.
- The presence of the connector results in a stiffer dynamic system that has a higher dominant frequency. Similarly, a prototype bridge is expected to become stiffer when the deck is pounding on the abutment and the backfill soil than in the case where a sufficient gap is provided to prohibit such an interaction.
- The force-displacement response that will develop between the abutment and the prototype bridge deck during pounding will be similar in a qualitative way to the force-displacement cyclic copper connector response utilized in this study. This can only be defined from direct in-situ measurements and is beyond the present study.
- The current numerical examination, which includes non-linear mechanisms arising from the gap between the abutment and the deck as well as from the deck-abutment interaction during pounding, is limited to demonstrate the effect of such an interaction. Despite the

inherent quantitative inaccuracies included in this study, it is believed that the most significant response mechanisms were included. Consequently, the employed numerical simulation is expected to yield reasonably accurate predictions for prototype isolated bridge decks interacting with their abutments during strong earthquakes provided that realistic estimates of prototype deck-abutment force-displacement response becomes available from in-situ measurements.

REFERENCES

[1] M.C. Kunde and R.S. Jangid, Seismic Behavior of Isolated Bridges: A-state-of-the-art review. *Electronic Journal of Structural Engineering, 3: 140-170*, 2003.

[2] K. Kawashima, Seismic isolation of highway bridges. *Journal of Japan Association for Earthquake Engineering (Special Issue); 4(3): 283-297*, 2004.

[3] American Association of State Highway and Transportation Officials (AASHTO). *Guide specifications for seismic isolation design, 3rd Edition, Washington, D.C.* 2010.

[4] Eurocode 8: Design of structures for earthquake resistance, Part 2: bridges, 2003.

[5] AASHTO (2010) Guide specifications for seismic isolation design, Third Ed..

[6] C.S. Gloyd, Seismic movement at bridge abutments. *ACI Spec Publ;164: 273-288*. SP164-15, 1996.

[7] S.A. Mitoulis, Seismic design of bridges with the participation of seat-type abutments, *Engineering Structures, Vol. 44, pp. 222-233*, 2012.

[8] A. Aviram, K. Mackie, B. Stojadinovic, Effect of abutment modeling on the seismic response of bridge structures. *Earthq Eng Vibration 7(4):395-402, 2008.*

[9] A. Elgamal and P. Wilson, Full Scale Testing and Simulation of Seismic Bridge Abutment-Backfill Interaction, *Special Topics in Earthquake Geotechnical Engineering Geotechnical, Geological and Earthquake Engineering, Volume 16, 109-127, ,* 2012.

[10] R. Siddharthan, M. El-Gamal, E.A. Margakis, Nonlinear Bridge Abutment Stiffnesses: Formulation Verification and Design Curves. Nevada Department of Transportation, Research Division, 2001.

[11] AASHTO LRFD *Bridge Design Specifications*. Washington (DC): American Association of State Highway and Transportation Officials, 2007.

[12] S.A. Anagnostopoulos and K.V.Spiliopoulos, An Investigation of Earthquake Induced Pounding Between Adjacent buildings. *Earthquake Engineering and Structural Dynamics, Vol. 21:pp. 289 - 302*, 1992.

[13] K.T. Chau and X.X. Weil, Pounding of structures modelled as non-linear impacts of two oscillators, *Earthquake Engineering and Structural Dynamics, Vol.30 633-651*, 2001.

[14] Y. Fujino, M.Abe, P.Zhu, A 3D contact friction model for pounding at bridges during earthquakes, *WG-1, Earthquake-Resisting Technologies for Civil Infrastructures, 3rd EQTAP Workshop*, Manilla, Filippines, 2000.

[15] Y.Fujino, M. Abe, P. Zhu, Modelling three-dimensional nonlinear seismic performance of elevated bridges with emphasis on pounding of girders, *Earthquake Engineering and Structural Dynamics, Vol. 31: 1891-1913*, 2002.

[16] R. Jankowski, Analytical expression between the impact damping ratio and the coefficient of restitution in the non-linear viscoelastic model of structural pounding, *Earthquake Engineering & Structural Dynamics, Volume 35, Issue 4*, 2006, Pages: 517-524.

[17] G.C.Manos, S.A. Mitoulis, A. Sextos, A knowledge-based software for the preliminary design of seismically isolated bridges. *Bulletin of Earthquake Engineering, Volume 10, Issue 3, pp 1029-1047*, 2011.

[18] Computers and Structures Inc, *SAP 2000 Nonlinear version 1.1.03 Θser's reference manual*. Berkeley, California, 2007.

COMPDYN 2013
4th ECCOMAS Thematic Conference on
Computational Methods in Structural Dynamics and Earthquake Engineering
M. Papadrakakis, V. Papadopoulos, V. Plevris (eds.)
Kos Island, Greece, 12–14 June 2013

EXPERIMENTAL AND NUMERICAL INVESTIGATION OF RECTANGULAR R/C BEAMS RETROFITTED AGAINST SHEAR UTILIZING FRP STRIPS

G.C. Manosr[1], K. Katakalos[1*], M. Theofanous[1], E. Kozikopoulos[1]

[1]Laboratory of Strength of Materials and Structures
Dept. Civil Engineering. Aristotle University of Thessaloniki
University Campus, Egnatia street, Thessaloniki, 54006
gcmanos@civil.auth.gr

Keywords: R/C beams, Shear Upgrade, CFRP, SFRP, anchorage, numerical validation

Abstract. *Reinforced concrete structures, designed and constructed according to old earthquake resistant design provisions are in need of retrofitting. This paper presents results from an investigation aiming to examine the behaviour of rectangular R/C beams in need of being retrofitted against shear. Towards this objective, ten (10) R/C beam specimens of prototype dimensions were constructed and tested under four point flexure. The retrofitted scheme which was investigated was based on fiber polymer sheets, either made of carbon (CFRP) or steel (SFRP); strips of such FRP sheets were attached externally on the R/C beam specimens as transverse reinforcement in order to upgrade their bearing capacity in shear. One potentially weak point of such a retrofitting scheme was investigated in depth; that is the debonding mode of failure of the FRP strips from the concrete surface, when these strips develop considerable stresses that cannot be transferred to the main volume of the structural element solely by the bonding surface. This mode of failure limits the potential of the high tensile strength capability of these FRP strips and inhibits the aimed increase of the shear capacity of the R/C beams. In order to confront with this limitation the effectiveness of an innovative type of anchoring device that can be incorporated together with such FRP strips was specially examined. The obtained experimental results are discussed in order to demonstrate the capability of such a retrofitting scheme, when proper anchoring of the FRP strips is utilized, to efficiently upgrade the shear capacity of such R/C beams. The experimental results were validated through a numerical simulation of the experimental set-up employing the ABAQUS finite element software. This numerical simulation took into consideration the non-linear behaviour of the concrete and steel as well as the cohesive surface zone between concrete and FRP strips in their contact area. Moreover, the presence or not of an anchoring device was also simulated numerically. From the comparison between the observed behavior, in terms of either load-displacement response or mode of failure, with the results of the numerical simulation the reliability of such a numerical simulation is demonstrated. This research was conducted in the framework of an initiative introduced by the Hellenic Earthquake Planning and Protection Organization aiming to support relevant provisions of the Greek Code for the repair and strengthening of R/C structures.*

1 INTRODUCTION

A wide range of fiber reinforced composite materials have been successfully used for the repair and strengthening of existing reinforced concrete (R/C) structures [1]. Strengthening with externally bonded FRPs is particularly common, due to the numerous advantages related with their use. These advantages include the speed and ease of installation, the low weight and their high tensile strength [4]. The most commonly used strengthening systems are glass or carbon fiber reinforced polymer (FRP) composite materials [1-5]. Lately, a new strengthening system based on high strength steel fibers known as steel reinforced polymers (SRP) [3] was introduced as an alternative having high strength and ability of inelastic deformations. The shear capacity of reinforced concrete (R/C) structural elements, with low value of the steel transverse reinforcement ratio (stirrups), can be enhanced by applying as transverse external reinforcement such materials in the form of strips [1, 3, 4].

However, the exploitation of the high tensile strength of such FRP's or SFRP's is usually rather low due to the debonding type of failure. In the case that these strips can be fully wrapped around the structural member, the degree of exploitation of these materials increases and the mode of failure can then result due to fiber fracture of the external reinforcement [2,6]. However, there are many practical applications that full wrapping cannot be practically materialized. This paper presents results from an experimental investigation that focuses on the upgrade of the shear capacity of 3m span R/C beams strengthened with either CFRP or SRP open hoop strips, placed with an anchoring device in order to avoid the debonding mode of failure and thus increase the exploitation of the CFRP / SFRP materials. This specific anchoring device is developed at the Laboratory of Strength of Materials and Structures, in Thessaloniki, Greece under the patent number WO2011073696 [6]. Finally the experimental results are validated through a numerical simulation employing the ABAQUS finite element software. This numerical simulation takes into consideration the non-linear behaviour of the concrete and steel as well as the cohesive surface zone between concrete and FRP strips in their contact area. Moreover, the presence or not of an anchoring device is also simulated numerically.

2 EXPERIMENTAL SETUP

2.1 Materials

Totally ten reinforced concrete beams were fabricated and tested at the Laboratory of Experimental Strength of Materials and Structures of Aristotle University of Thessaloniki. The compressive strength of concrete was measured equal to 22.4 MPa. The internal reinforcement yielded at f_y=527MPa and failed at a stress equal to f_{ul}=645MPa. The rectangular beams were strengthened with either CFRP or SFRP. CFRP sheets and epoxy resins were provided by SIKA Hellas. The type of CFRP is SikaWrap 230C and the two substitute epoxy is named SikaDur 330. SFRP sheets were fabricated, specifically for this project. Unidirectional tension tests were conducted on resin rich CFRP and SFRP sheets up to failure to obtain the Young's modulus (E_1) and strength (f_u) in their fibre orientation and the Poisson's ratio (ν_{12}=(E_1/E_2) ν_{21}). The remaining two material properties pertaining to the orthotropic nature of the material under the plane stress assumption, namely the transverse Young's modulus E_2 and the shear modulus G_{12}, were derived by applying the conventional rule of mixture for composites (Hashin 1983), taking into account the manufacturer's specifications for the resin (citation SIKA) and the FRP (citation SIKA) sheets and the experimentally determined volume fraction of resin and FRP sheets.

Material property	E_1 (MPa)	ν_{12}	f_{u1} (MPa)	E_2 (MPa)	G_{12} (MPa)
CFRP	41784	0.305	376	4476	1935
SRP	36350	0.312	330	4400	1900

Table 1. Material properties of CFRP and SFRP

2.2 Geometry and loading of specimens

The present research program includes the investigation of ten rectangular R/C beams under monotonic loading conditions. The cross section of the beams was 120X360 (mm). All specimens were longitudinally reinforced with 3Ø20mm bars at the top and 3Ø20mm at the bottom of the beam. (see figure1)

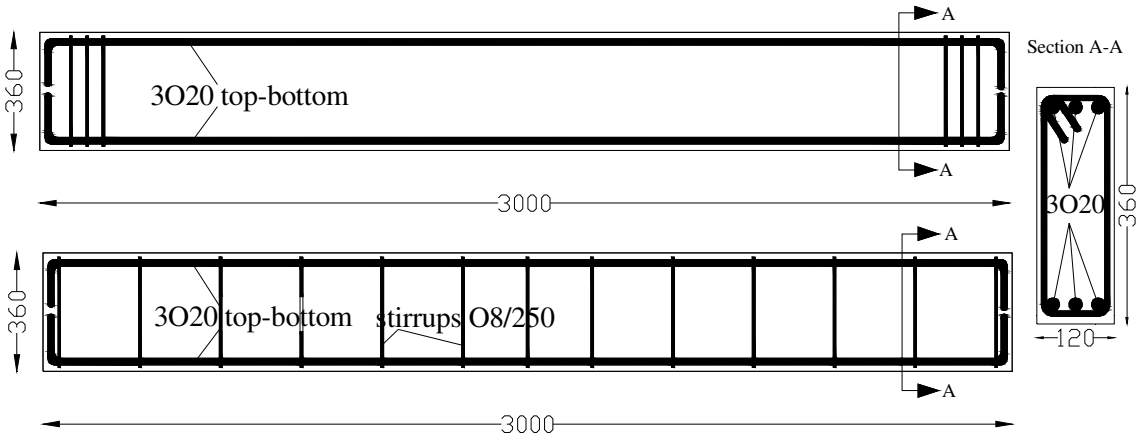


Figure 1. Mean dimensions and reinforcement details of specimens

Two control beams were tested. The first one, named as RB, had no internal shear reinforcement whereas the second, named as RBs, had Ø8/250mm as transverse reinforcement. The remaining eight beams did not have any internal transverse reinforcement, thus were strengthened with externally bonded open hoop CFRP or SFRP sheets, with or without an anchorage device. The strengthened beams were designed in such way that would be able to upgrade their shear capacity at least to the point of the RBs' strength. Table 2 that follows depicts the variables that were taken under consideration for each specimen.

BEAM NAME	SHEAR REINF/MENT	ANCHORAGE	FRP WIDTH (mm)	FRP axial DISTANCE (mm)
RB	NO	-	-	-
RBs	Ø8/ 250	-	-	-
RB200C	CFRP	NO	100	200
RB200Ca	CFRP	YES	100	200
RB200S	SFRP	NO	100	200
RB200Sa	SFRP	YES	100	200
RB150C	CFRP	NO	100	150
RB150Ca	CFRP	YES	100	150
RB150S	SFRP	NO	100	150
RB150Sa	SFRP	YES	100	150

Table 2. Experimental variables of specimens

All beams were subjected under four point monotonic loading conditions. The overall beam span was 2700mm whereas the shear span was equal to the 1/3 of the total length, thus 900mm. Figure 2 represents the experimental setup. The loads as well as the vertical displacements at two points, under the application of the load, were recorded. Strain gauges were placed to every FRP sheet in order to record the developed strains on them. Figure 2 also shows a photographic demonstration of the experimental setup.

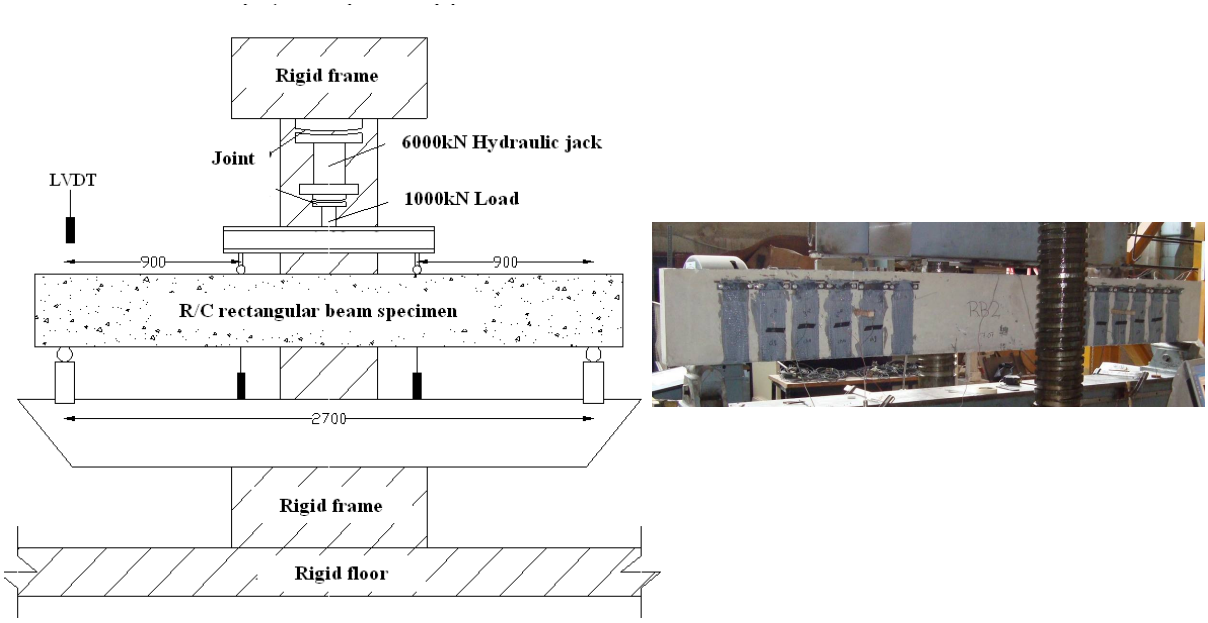


Figure 2. Experimental Setup (sketch and photo)

The present investigation also focuses on the application of a novel anchoring device which was developed and patented at the Laboratory of Experimental Strength of Materials and Structures of Aristotle University of Thessaloniki. The developed anchoring device is transforming the axial tensile forces, applied on the FRP sheet, to shear forces imposed through the bolts into the concrete mass of the beam. Figure 3 shows a front face and a section of the novel anchoring device.

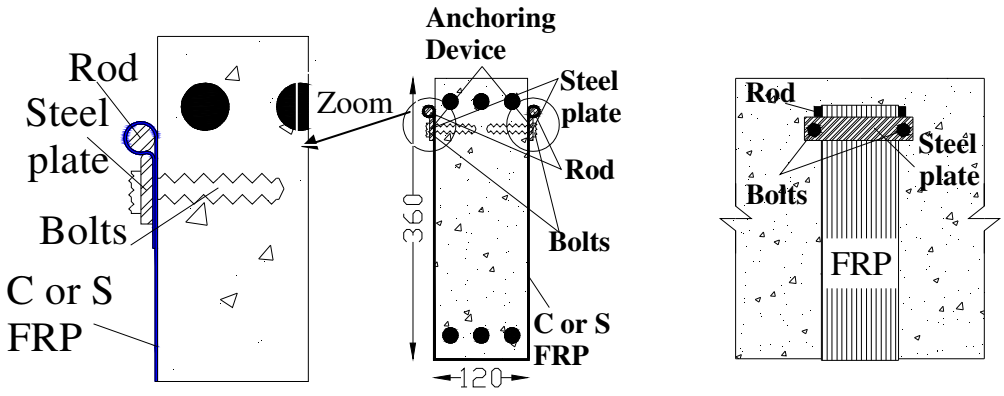


Figure 3. Patented Anchoring Device (WO2011073696) [6]

3 EXPERIMENTAL RESULTS

Totally ten R/C rectangular beams were investigated. For all beams not only load and vertical deflection were recorded but strains at each FRP sheet as well. Table 3 depicts the obtained data from the experimental investigation. The experimental measured shear force is depicted at fourth column of Table 3 whereas the measured strains of the FRP sheets that the shear crack is intersecting are mentioned at fifth and sixth columns of the same table.

BEAM NAME	ANCHORAGE	EXP. SHEAR FORCE (kN)	STRAIN of 1st STRIP (μstrain)	STRAIN of 2nd STRIP (μstrain)	CALC. SHEAR FORCE (kN)	MODE OF FAILURE
CRB	-	39.4	-	-	-	Brittle shear crack
CRBs	-	90.9	-	-	-	Yield of stirrups
RB200C	NO	97.8	7390	610	98.05	Debonding
RB200Ca	YES	115.1	4580	6590	107.77	CFRP fracture
RB200S	NO	94	5935	4620	99.77	Debonding
RB200Sa	YES	122	6115	6415	104.68	Anchorage failure
RB150C	NO	101	3820	5580	108.88	Debonding
RB150Ca	YES	123	7145	6080	120.61	CFRP fracture
RB150S	NO	103	4530	4905	103.53	Debonding
RB150Sa	YES	119	7855	6245	115.13	Anchorage failure

Table 3. Experimental results

The shear strength of the control beam (CRB) without any stirrups was recorder equal to 39.4kN, whereas the specimen CRBs with Ø8/250mm as transverse reinforcement was increased to 90.9kN. The strengthening scheme that took place to the remaining of the beams had an objective to increase the shear strength at a lower limit equal to CRBs. From the results shown in Table 3, it is evident that the maximum recorded shear load for all strengthened beams was significantly greater than that of the CRB. In Table 4 the percentage of the increase of the shear load is presented.

	CRB	CRBs	RB200C	RB200Ca	RB200S	RB200Sa	RB150C	RB150Ca	RB150S	RB150Sa
% INCREASE compared to CRB	0	130.7	148.2	192.1	138.6	209.6	156.3	212.2	161.4	202.0
% INCREASE compared to CRBs	-	0	7.6	26.6	3.4	34.2	11.1	35.3	13.3	30.9

Table 4. Experimental results

The shear load of the strengthened beams, compared to CRB, met an increase of more than 200%, but not less than 130%. The largest percentages of that increase were observed, as it was expected, for the strengthened beams that the novel anchoring device was used in combination with FRP sheet. The biggest increase of the shear load was observed for specimen RB150Ca and was equal to 212,2%. For this strengthened beam the mode of failure was located at the fracture of the CFRP sheet which demonstrates that the novel anchoring device anchored the CFRP sheet properly on the concrete beam. Specimen RB150Sa exhibit a maximum shear load equal to 119kN that resulted to a 202% increase compared to CRB. For this specimen the anchoring devised posed an upper limitation to the shear load of the beam due to the fact that the device failed it self, before the failure of SFRP sheet. Nevertheless the strains that were recorded reached 7000μstrain which is close to the maximum strain at failure of SFRP sheet (9000μstrain). This specimen reached the maximum recorded average displacement for the maximum load, fact that results to an increase of an inelastic behavior.

By comparing the beams that were strengthened with CFRP vs. SFRP it could be noted that the overall behavior was similar. SFRP sheets could be utilized as an alternative material for strengthening applications. More specifically, focusing on strengthened beams without the use of the anchoring device, RB150S exhibit the biggest shear load (103kN) which is very close to RB150C's (101kN). Figure 4 presents the shear load vs. the average displacement of all beams in two graphs. The first one shows the behavior of the strengthened beams without an anchoring device, compared with the control beams CRB and CRBs, whereas the second graph deals with those that the anchoring device was utilized for the proper attachment of FRP sheets.

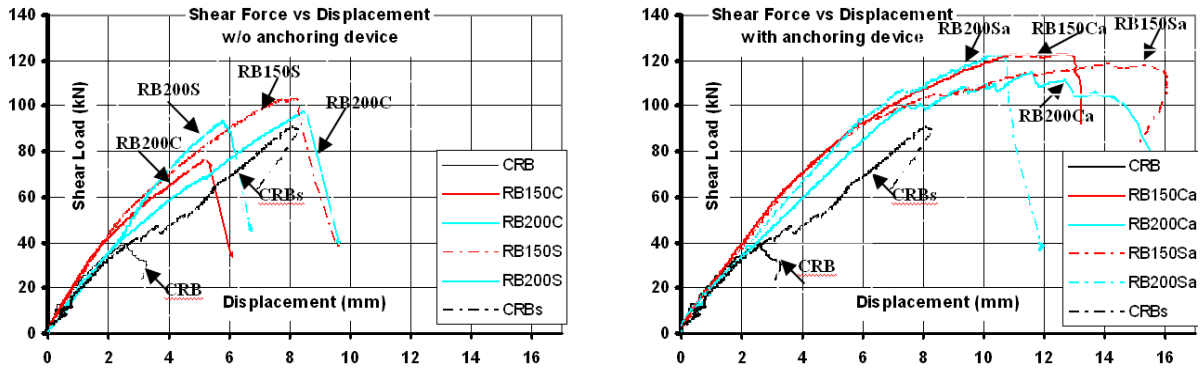


Figure 4. Shear Force vs. Displacement graphs w/o and with the novel anchoring device

Specimens, where the novel anchoring device was utilized, exhibit a clear increase of the shear load as well as of the developed average displacement. The premature mode of failure, the debonding of FRP sheet, changed to either fracture of FRPs or failure of the anchoring device, when the sheets were properly anchored. The prevention of the premature delamination resulted to an increase of the specimen's strength. However, the initial stiffness remains the same for all specimens. On the other hand after the first cracking the stiffness of the strengthened beams is greater than the stiffness of the control beams. This phenomenon is stronger for the specimens that FRP sheets were anchored. The behavior of the control beam with stirrups (CRBs) was sufficiently reached by the strengthened beams without the anchoring device, despite the fact that the premature debonding of the sheets, either CFRP or SFRP, posed an upper limitation. The rest of the strengthened beams, where the FRP sheets were properly anchored, presented a better behavior than CRBs', concerning not only the shear force but the average displacement as well. Finally, as far as the measured strains are concerned it could be said that the existence of the anchoring device is allowing the development

of greater strains on FRP sheets compared to the cases that the anchoring device was not utilized, where a limitation was posed due to the debonding.

4 NUMERICAL VERIFICATION

4.1 Assumptions of modeling

The general purpose FE software ABAQUS [7] was employed to generate FE models to simulate numerically the structural response of the previously described concrete beams strengthened with externally attached FRP sheets. The generated models were validated against all respective experimental results. The aim of this part of the study is to generate reliable FE models that can be utilized to enhance the understanding of the fundamental structural response of the FRP shear strengthening scheme of R/C beams with and without anchorage devices and hence optimize the anchorage device design. In order to reduce the computational cost, the symmetry of the structure with respect to the x-y and z-y mid-planes was exploited, by numerically simulating one quarter of the physical model and applying the appropriate boundary conditions at each of the two planes of symmetry as shown in Figure 5.

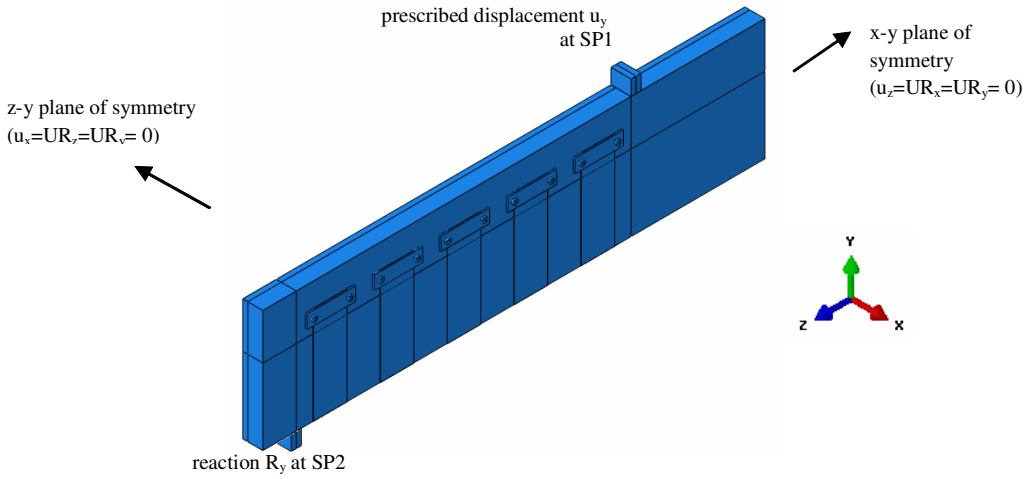


Figure 5. Modeled geometry and applied boundary conditions.

The contact between the various parts of the model (steel bolts, steel plates and concrete volume) was explicitly modeled and a friction coefficient equal to 0.3 was assumed for tangential contact behaviour except for the contact between the concrete beam and the loading reaction plates which was assumed frictionless.

Variation of the friction coefficient applied to the bolt-concrete interface between the idealized frictionless and rough contact extreme cases was attempted, but no significant effect on the overall solution was observed. Moreover, in order to reduce computational cost, the actual detail of the cylindrical rod of the anchoring device through which load is transferred from the FRP strips to the concrete beam through the steel plate was somewhat simplified (see figures 3 and 6); towards this end, the displacements of the FRP's edge were constrained to be equal to the respective displacements of the steel plate's mid plane for the numerical representation of the anchoring device. The interface between the FRP and the concrete was simulated as a cohesive zone endowed with a suitable traction separation response.

Material properties for all components were obtained from experimental measurements, as they were described previously, and used as input to model the structure.

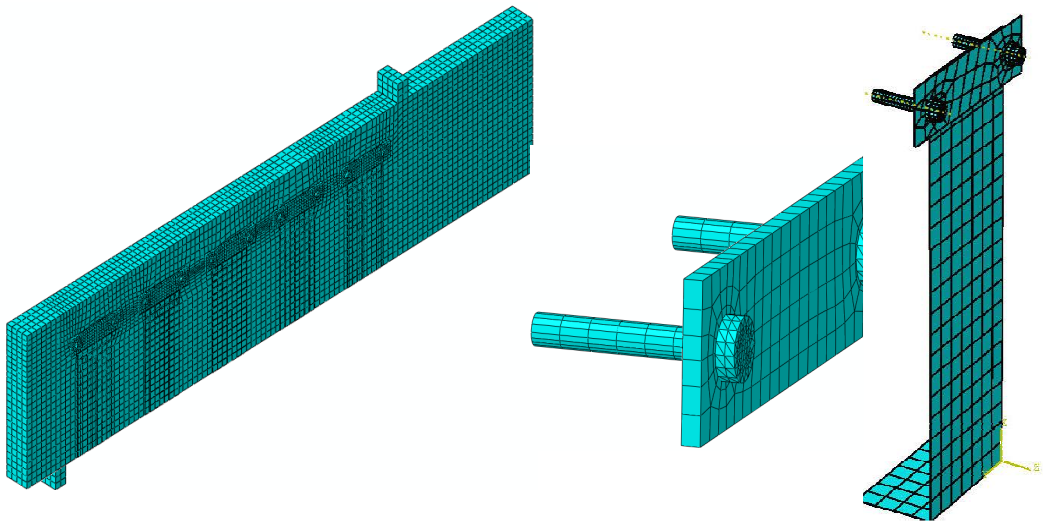


Figure 6. FE discretisation of the rectangular beam and close-ups of the discretization of the anchoring device

Linear 8-noded brick elements were adopted for the discretisation of the concrete beam, steel bolts, steel plates and loading plates, whilst the longitudinal reinforcing bars and the steel stirrups were discretised with linear truss elements embedded in the concrete region (i.e. no relative displacement between reinforcement and concrete was allowed for). Linear 4-noded shell elements were used to discretise the FRP sheets, the degrees of freedom (DOF) of which were tied to the respective DOFs of the underlying 8-noded 3D cohesive elements. The mesh size was dictated by the attempt to minimize computational time whilst maintaining accuracy and, upon extensive mesh convergence studies, a uniform mesh size of 15mm was adopted for the concrete beam, cohesive zone and FRP sheets, whilst smaller mesh sizes were adopted for the steel plates, bolts and concrete regions surrounding the bolts as shown in Figure 6.

4.2 Numerical results - Discussion

The F.E. numerical predictions regarding the ultimate shear capacity ($^{num}V_{max}$) and failure modes with the ones observed during testing (see Table 2) are summarized in Table 5.

The ratio of numerically predicted over measured ultimate shear capacity is listed in column 3 of table 4 with values very close to 1.0, which signifies a very good agreement of the numerically predicted ultimate shear capacity values with the respective experimental ones included in Table 1. Moreover, the numerically predicted modes of failure are also in very good agreement with the ones observed during testing, with the exception of specimen RB200Ca. This discrepancy can be attributed to the premature failure of the CFRP strip due to the non-ideal preparation of the concrete surface at the bottom fiber of this specimen prior to gluing this CFRP strip. Detailed discussion for each of the three types of rectangular beams considered in the present study follows.

The observed behaviour of the two control beam specimens, which were initially tested to obtain the basic structural response of the reinforced concrete rectangular beam specimens without the added complexity of the attached FRP sheets, was, in general, well-predicted by the FE numerical models with $^{num}V_{max}$ / $^{exp}V_{max}$ ratios equal to 1,0 and 0,97 respectively

BEAM NAME	Numerical ultimate shear capacity $^{num}V_{max}$ (kN)	$^{num}V_{max}$ / $^{exp}V_{max}$	Numerical failure mode	Observed failure mode
(1)	(2)	(3)	(4)	(5)
CRB	39.44	1.00	Shear cracking	Shear cracking
CRBs	87.89	0.97	Yielding of stirrups	Yielding of stirrups
RB200C	97.99	1.00	Debonding	Debonding
RB200Ca	118.79	1.03	Anchorage failure	Premature FRP rupture
RB200S	87.54	0.93	Debonding	Debonding
RB200Sa	112.47	0.92	Anchorage failure	Anchorage failure
RB150C	99.65	0.99	Debonding	Debonding
RB150Ca	120.58	0.98	FRP rupture	FRP rupture
RB150S	96.95	0.94	Debonding	Debonding
RB150Sa	123.52	1.04	Anchorage failure	Anchorage failure

Mean Value
0.98
Coef. Of Variation
0.05

Table 5. Summary of Numerical results

The experimental vs numerical comparison the concrete beam specimens strengthened with FRP sheets without the provision of additional anchoring devices resulted to an excellent agreement between the experimental and the numerical results in terms of ultimate load and mode of failure. (see table 5) The debonding of the FRP sheets commenced and propagated rapidly, leading to the formation of critical diagonal cracks and thus to failure. This observed behaviour was also accurately reproduced by the previously described numerical simulations.

The provision of additional anchorage by means of the device shown in Figure 3 allows for additional forces to be carried by the FRPs once debonding has occurred; these forces are transferred by the anchoring device finally through the bolts into the concrete thus resulting in an increased ultimate shear capacity and thus in a more efficient utilisation of the FRP material. The anchorage zone is stressed from the onset of loading but deformations and stresses remain small as long as the resin remains effective. Upon debonding, the anchorage zone experiences high localised stresses. The failure is no longer due to FRP debonding but rather localised above the anchorage zone, due to the high stresses transmitted by the bolts in the vicinity of the bolt holes. The failure mode is complex and involves a combination of local concrete cracking and crushing near the bolt holes, flexure of the compressive reinforcement due to the forces exerted by the bolts and possibly pullout of the anchoring bolts. In some cases, FRP rupture may occur prior to the failure of the anchorage device or anchorage zone.

The generated FE models were in general able to capture the sequence of failure as described above. From the input of table 5 ${}^{num}V_{max}$ / ${}^{exp}V_{max}$ ratios vary from 0,92 to 1,04 but the modes of failure are in perfect agreement.

5 CONCLUSIONS

- The present study examined both experimentally and numerically the behaviour of ten (10) full scale rectangular R/C beams in need of being retrofitted against shear, by utilizing anchored or non-anchored Carbon or Steel FRP strips.
- Steel Fiber Reinforced Polymers (SFRP) that were specially fabricated for this research program could be equally used as an alternative strengthening material.
- Reinforced Concrete beams (R/C) that were strengthened without the use of the anchoring device exhibit a limitation to the maximum shear load and displacement due to the debonding mode of failure occurred on FRP sheet. Despite that fact the limited developed shear load was greater than the control's beam with stirrups (CRBs).
- When the novel anchoring device is utilized for the proper attachment of the FRP sheets, either carbon or steel, to the R/C beams a further increase of the shear capacity of the beams is observed. At some case this increase is greater that 210% compared to the control beam without stirrups and 35% greater compared with CRBs.
- The successful numerical simulation of the application of a novel anchoring device together with open hoop FRP strips, which enhances the efficiency of these FRP sheets applied as shear reinforcement for reinforced concrete rectangular beams, was demonstrated by this study.
- The validation of the numerical simulation is based on the measured behaviour of two (2) full-scale reinforced concrete rectangular beams without or with nominal shear reinforcement as well as with eight (8) full-scale reinforced concrete rectangular beams that employed open hoop FRP strips, with or without novel anchoring devices, as a means of upgrading their shear capacity.
- The success of the deployed numerical simulation is fully demonstrated by comparing first the observed and numerically predicted ultimate shear capacity and second by comparing next the observed and numerically predicted mode of failure, for each one of the ten (10) tested specimens. The achieved accuracy of the predicted ultimate shear capacity and mode of failure is excellent.
- Based on the validated FE numerical models presented here, further research is underway to identify the key features affecting overall structural response and thus to optimise the structural arrangement of the proposed novel anchoring device in terms of strength and ductility.

ACKNOWLEDGEMENTS

- Carbon fibers and epoxy resins were provided by Sika Hellas
- Steel fibers are not commercially available and were provided for the present study by Bekaert Industries

- Partial financial support for this investigation was provided by the Hellenic Earthquake Planning and Protection Organization (EPPO)
- The employed, in this study, anchoring device is patented under the no. WO2011073696

REFERENCES

[1] G. C. Manos, K. Katakalos, V. Kourtides, "The influence of concrete surface preparation when fiber reinforced polymers with different anchoring devices are being applied for strengthening R/C structural members", Applied Mechanics and Materials, Vol, 82, 2011, Pages 600-605.

[2] C. G. Papakonstantinou, K. Katakalos, "Flexural behavior of reinforced concrete beams strengthened with a hybrid inorganic matrix - Steel fiber retrofit system", Structural Engineering and Mechanics, Vol. 31, Issue 5, March 2009, Pages 567-585.

[3] P. Casadei, A. Nanni, T. Alkhrdaji, "Steel-reinforced polymer: An innovative and promising material for strengthening infrastructures", Concrete Engineering International, Vol. 9, No. 1, 2005, pp. 54-56.

[4] N. Plevris, T. C. Triantafillou, "Time-dependent behavior of RC members strengthened with FRP laminates", Journal of Structural Engineering, Vol. 120, No. 3, 1994, pp. 1016-1042.

[5] K. Katakalos, C. G. Papakonstantinou, "Fatigue of reinforced concrete beams strengthened with steel-reinforced inorganic polymers", Journal of Composites for Construction, Vol. 13, Issue 2, 2009, Pages 103-112.

[6] G. C. Manos, K. Katakalos, V. Kourtides, "Construction structure with strengthening device and method", European Patent Office, Patent Number WO2011073696 (A1) — 2011-06-23.

[7] Hibbitt, Karlsson & Sorensen, 2010, Inc. ABAQUS user's manual volumes I-V and ABAQUS CAE manual. Version 6.10.1. (Pawtucket, USA).

COMPDYN 2013
4th ECCOMAS Thematic Conference on
Computational Methods in Structural Dynamics and Earthquake Engineering
M. Papadrakakis, V. Papadopoulos, V. Plevris (eds.)
Kos Island, Greece, 12–14 June 2013

DYNAMIC BEHAVIOUR OF GREEK POST-BYZANTINE CHURCHES WITH FOUNDATION DEFORMABILITY AND EVALUATION OF THEIR EARTHQUAKE PERFORMANCE – EXPERIMENTAL INVESTIGATION OF STONE MASONRY MATERIAL PROPERTIES

G.C. Manos[1], L. Kotoulas[1]*, V. Matsou[1], O. Felekidou[1]

[1]Laboratory of Strength of Materials and Structures
Dept. Civil Engineering. Aristotle University of Thessaloniki
University Campus, Egnatia street, Thessaloniki, 54006
gcmanos@civil.auth.gr

Keywords: Post-Byzantine Churches, Numerical Simulation, Deformable Foundation, Experimental study of stone masonry, Retrofitting.

Abstract. *The earthquake performance of stone masonry Post-Byzantine churches subjected to seismic forces is examined. The examined churches are: 1. A three-nave Basilica with a system of stone-masonry vaults and domes as a superstructure together with a wooden roof. 2. An 18th century church of the cruciform type which also utilizes a system of cylindrical vaults and spherical domes that form the superstructure together with the wooden roof. 3. A three-nave 18th century Basilica whose the wooden roof is supported directly on the peripheral masonry walls and the internal colonnades. All these churches developed structural damage to the masonry elements that is believed to arise from the amplitude of the gravitational and seismic actions combined with the deformability of the foundation, a parameter that is also part of this investigation. The numerical results together with assumed strength values are utilized to predict the behaviour of the various masonry parts in in-plane shear and normal stress as well as out-of-plane flexure. It is demonstrated that the foundation deformability explains, partly, the appearance of structural damage. When comparing the numerically predicted regions that reach limit state conditions with actual damage patterns a reasonably good agreement in a qualitative sense can be observed. The masonry walls near the foundation, the door and window openings, and the roof appear to be the most vulnerable either in out-of-plane bending or in in-plane shear for the critical combination of seismic forces and gravitational loads. Moreover, the vaults and domes of the superstructure appear to be vulnerable also. A relatively mild retrofitting scheme that utilizes special mortar injections as well as semi-temporary shoring together with wooden and metal ties is then examined. This is also investigated numerically being applied to a 16th Century Basilica with a wooden roof. The numerical investigation is supplemented with a series of limited Laboratory tests on the constituent materials represented by old stone masonry.*

1 INTRODUCTION

During the last thirty years various parts of Greece have been subjected to a number of damaging earthquakes ranging from Ms=5.2 to Ms=7.2 on the Richter scale. One of the most demanding tasks for counteracting the consequences of all these seismic events was the effort to ensure the structural integrity of old churches, that were built in periods ranging from 400 A.D. up to today; in many cases they sustained considerable damage [1]. The earthquake behavior of churches belonging to the so-called Post-Byzantine period (16th to 19th century A.D.) has been studied numerically in some detail ([2], [3], [4], [5], [6], [7], [8]. In all these cases the foundation was considered to be non-deformable. However, this is a gross approximation as in most cases these churches are founded on deformable soil. In some instances, the deformability of the soil caused considerable damage as is the case of the church of The Assumption of the Virgin Mary at Dilofo-Voio-Kozani, as will be presented in section 2. In some other cases the main cause of recent damage is the earthquake activity that is accentuated by the deformability of the soil. This will be presented in the sections 3 and 4, where the damage of the church of Agia Triada at Vithos-Kozani and of Profitis Elias at Siatista-Kozani is also included. Finally, in section 5 as a summary of retrofitting principles together with brief results from a relevant numerical and experimental investigation focusing on the behavior of St. Dimitrios of Palatitsia is also presented. It must be noted that these churches were built in a number of phases on old existing sacred sites by extending old remains, due to prohibitions by the Turkish occupation authorities imposed on the Christian population forbidding the construction of new churches but only allowing the maintenance of existing ones, after special permit [19]..

2 THE ASSUMPTION OF THE VIRGIN MARY AT DILOFO-VOIO-KOZANI

The outlay of this church is shown in figure 1 by a cross-section in the longitudinal direction. Its basic dimensions are 21.5m long (together with the apse of the East wall) 11m wide and a maximum height to the top of the wooden roof 10m. With the dashed line the hard-soil is indicated. As can be seen, the West part of this church is founded on hard soil (weathered flysch layers) whereas the East part is founded on relatively soft soil that was deposited on top of the layers to compensate for the natural slope at this location. Apart from the relatively soft soil deposits at the East part of this church the malfunction of the drainage system at this point initiated considerable settlement of these soft soil deposits.

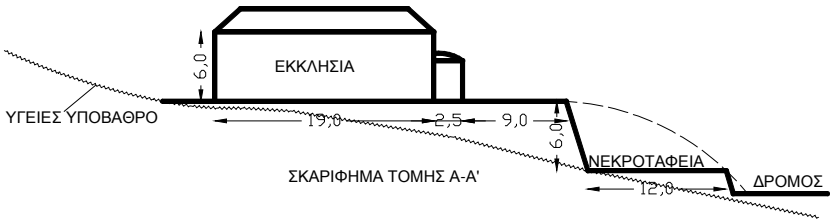


Figure 1. The layout of the church of the Assumption of Virgin Mary

The unequal settlement of the foundation of the stone masonry walls as well as of the internal columns that supported the vaulting system, which covered this church, caused considerable damage. An external view of this church from the South is shown in figure 2a whereas figure 2b depicts the extensive damage that developed at the South-East corner. A very wide crack initiates at the top of the East peripheral wall near the apse and propagates towards the bottom of this wall being inclined to the South-East corner. Furthermore, a similarly wide crack propagates through the North peripheral wall from top to bottom as is shown in figure 2c. It must be noted that the thickness of these masonry walls varies from 750mm to 800mm.

From this extensive peripheral wall damage, the vaulting system that is supported by these peripheral walls also suffered extensive cracking that eventually caused the partial collapse of a part of the central dome, as shown in figure 2d.



Figure 2a. Side view from the South



Figure 2b. Damage to the South-East corner



Figure 2c. Damage to the North wall



Figure 2d. Partial collapse of the central dome

2.1. Numerical Simulations

Initially, the numerical simulation assumed that the foundation was non-deformable [9]. Based on this assumption the 3-D numerical representation of the church, including the peripheral walls, the vaulting system of the superstructure, as shown, and the wooden roof were subjected to load combinations of either 0.9G±1.4Ex or 0.9G±1.4Ey, where G is the gravitational load and Ex, Ey the earthquake forces ([10]) along the x-x axis (longitudinal East-West direction) or the y-y axis (transverse North-South direction, respectively.

Non - Deformable Foundation

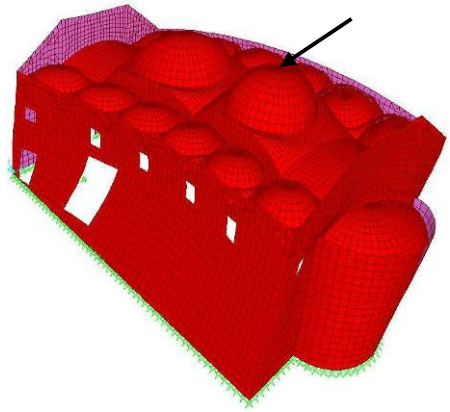


Figure 3a. Displacement Response. 0.9G+1.4(+Ex) Ux= 6.81 mm Uz= -1.51 mm

. Deformable Foundation

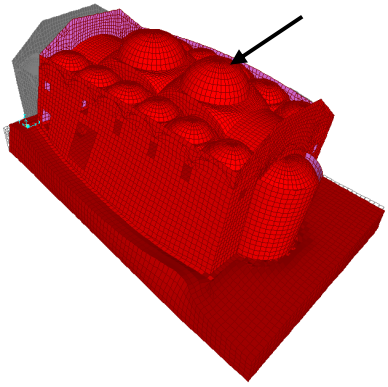
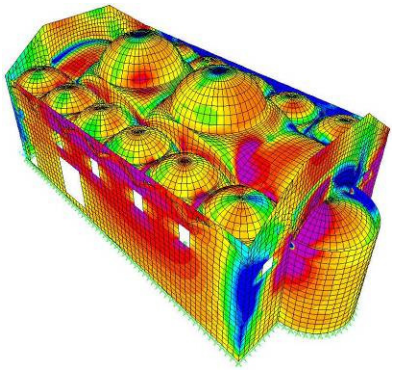


Figure 3b. Displacement Response. 0.9G+1.4(+Ex) Ux= 21.33 mm Uz= -14.80 mm

All the supports were assumed to prohibit the translations along all three axes but not to restrain the rotations. It was found from previous studies that full fixity of the masonry walls at the foundation level leads to the development of considerable bending moments that corre-

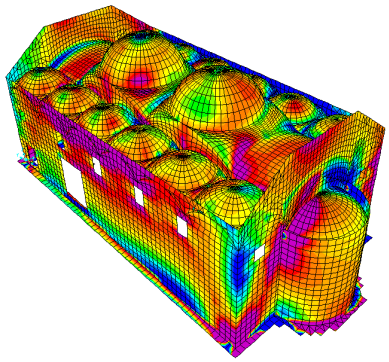
spond to tensile stresses which cannot be sustained by the weak stone masonry used to construct these churches. For the load combination 0.9G+1.4(+Ex) the maximum deformations at the top of the central dome were found equal to Ux= 6.81 mm Uz= -1.51 mm (figure 3a). For this load combination the maximum tensile stresses parallel to the bed joint $\boldsymbol{\sigma_{11}}$ were found equal to 0.51 MPa, at the bottom face of the masonry walls (figure 4a). As can be seen in this figure, high tensile stresses parallel to the bed joint develop both at the top of the North wall as well at the South-East corner of the East wall.

Non - Deformable Foundation



a) $\boldsymbol{\sigma_{11}}$ bottom face, maxσ= 0.51 MPa.

Deformable Foundation



b) $\boldsymbol{\sigma_{11}}$ bottom face maxσ= 0.64 MPa

Figure 4. Out-of-plane behavior, Load Combination 0.9G+1.4(+Ex)

2.1.1. Numerical Simulation of the state of stress arising from the foundation settlement.

Next, layers of deformable soil were introduced beneath the foundation of all the peripheral walls and internal colonnades. The stiffness of these soil layers was varied in order to simulate the relatively hard soil at the West part of the church and the relatively soft soil at the North-East part of the church (see figure 1). For quantifying the stiffness of these soil layers use was made of the data from three boreholes drilled at the vicinity of the church relevant to the constitution of the soil deposits at a depth up to 10m [9]. For the load combination 0.9G+1.4(+Ex) the maximum deformations at the top of the central dome were found equal to Ux= 21.33 mm Uz= -14.80 mm (figure 3b); these values represent a considerable increase in the deformation at the top of the church from the previous case where the soil was considered non-deformable. Figure 4b depicts the distribution of stresses $\boldsymbol{\sigma_{11}}$ parallel to the bed joint; the maximum tensile values were found equal to 0.64 MPa, at the bottom face of the masonry walls. As can also be seen in this figure, high tensile stresses parallel to the bed joint develop both at the top of the North wall and at the South-East corner of the East wall. The increase in the tensile stresses for the deformable soil is of the order of 30% to 50% when compared to the corresponding maximum tensile stresses when the soil was considered non-deformable. As could be seen from the preceding numerical study, the uneven deformability of the soil under the foundation of such structural formations, as Post-Byzantine Basilica churches, can introduce an increase in the critical tensile stresses. The regions of the masonry elements where such tensile stress concentration appear correlate reasonably well with the areas of damage that was observed in this church.

3 THE AGIA TRIADA (HOLY TRINITY) AT VITHOS-VOIO-KOZANI

This is a Post-Byzantine church of the cruciform type with three domes. There is a central dome that rises at the highest elevation to 15.75m from ground level, whereas the length of

the church in the longitudinal East-West direction is 17.60m and its width in the North-South direction is 9.85m. The construction of this stone-masonry church was completed in 1797 A.D. using the local natural stone. The plan and the East-West cross-section are shown in figures 5a and 5b.

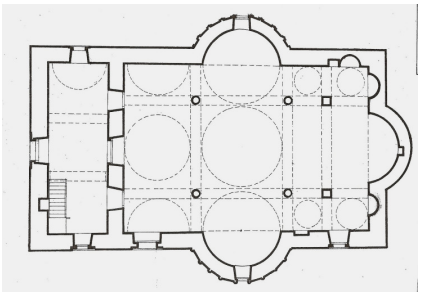


Figure 5a. Plan

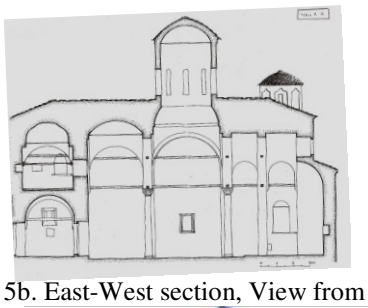


Figure 5b. East-West section, View from the South



Figure 5c. View from the South-West

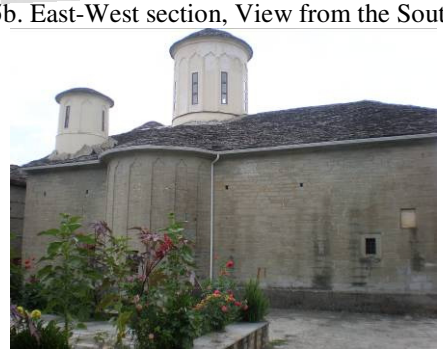


Figure 5d. View from the North

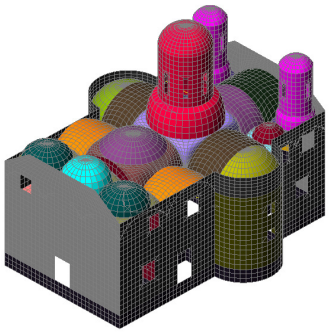


Figure 5e. View from the South-West

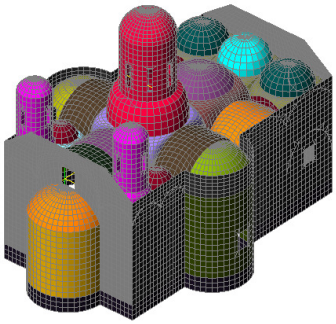


Figure 5f. View from the North-East

The vaulting system that supports the three domes is depicted in figures 5a to 5f, as can be seen from the top by removing the wooden roof. The numerical simulation considered two distinct models. The first model assumed non-deformable foundation where the translations along the three axes (x, y, z) were restrained to zero.

The second model tries to account for the deformability of the foundation by using as supports linear springs with stiffness properties that were estimated taking into consideration the quality of the underlying media (figure 6) as well as the thickness of the foundation and the discretization employed.

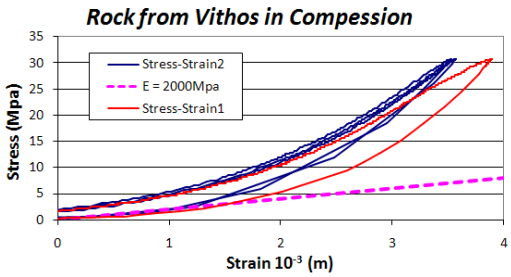
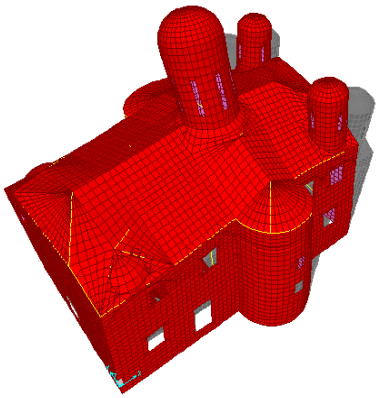
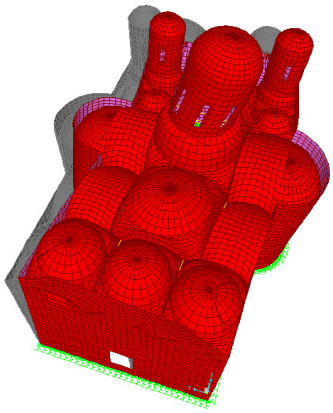


Figure 6. Compressive stress-strain behaviour of a slate sample taken from the vicinity of the church



Non-deformable foundation

Figure 7a. 1st Translational eigen-mode y-y, T_y= 0.154 sec modal mass ratio U_y = 44.67 %



Deformable foundation

Figure 7b. 1st Translational eigen-mode y-y, T_y= 0.197 sec modal mass ratio U_y = 60.26 %

The modal analysis results, depicted in figures 7a and 7b, demonstrate the first effect of the deformable foundation which is the lengthening of the eigen-periods of the most significant translational modes as well as the mobilization of larger modal mass ratios for these eigen-modes when the deformable foundation was considered as compared to the corresponding values of the non-deformable foundation.

Next, the deformations of the structural system were obtained for both the non-deformable and the deformable foundation model. These were obtained for two sets of load combination. The first is designated as 0.9G + 1.4Ex and signifies the combination of the gravitational forces (G) with the seismic actions in the East-West (x-x) longitudinal direction. The seismic action was enforced by applying the dynamic spectral method with a design spectrum specified by the current Greek Seismic Code and for seismic Zone I and soil category A [10]. The second load combination is designated as 0.9G + 1.4Ey and signifies the combination of the gravitational forces (G) with the seismic actions in the North-South (y-y) transverse direction. The results are depicted in figures 8a to 8d.

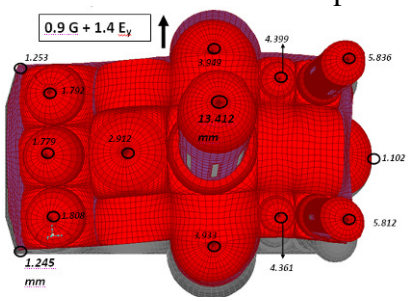


Figure 8a. 0.9G+1.4E_y Non-Deformable Foundation Max. Disp. Top central dome 13.442mm

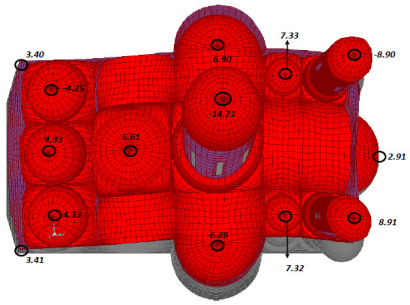


Figure 8b. 0.9G+1.4E_y Deformable Foundation Max. Disp. Top central dome 14.640mm

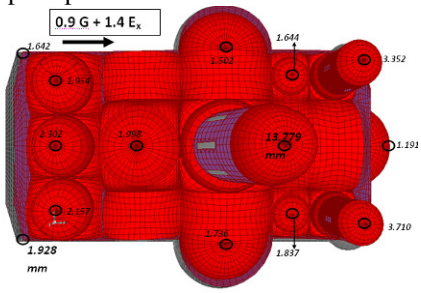


Figure 8c. 0.9G+1.4E_x Non-Deformable Foundation Max. Disp. Top central dome 13.779mm

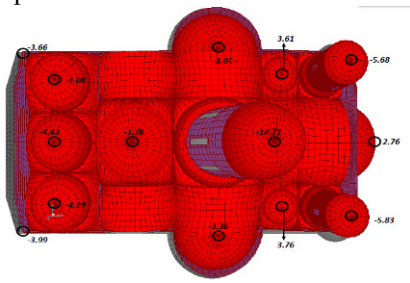


Figure 8d. 0.9G+1.4E_x Deformable Foundation Max. Disp. Top central dome 14.710mm

Due to the foundation deformability the earthquake actions combined with the gravitational forces result in a considerable increase in the horizontal displacement response. This is more pronounced at the top of the peripheral wall where the vaults of the superstructure and roof are supported than at the top of the central dome level. At that level, the maximum displacement is equal to 14.710m for the deformable foundation and 13.779mm for the non-deformable foundation for the load combination $0.9G+1.4E_{x.}$ For the load combination $0.9G+1.4E_y$ the maximum displacement at the top of the central dome level is 13.442mm for the non-deformable foundation as compared with 14.640mm for the deformable foundation. Similar influence of the foundation deformability can also be observed in the maximum stress values that develop at either the peripheral walls, the internal transverse wall or at parts of the vaulting system of the superstructure.

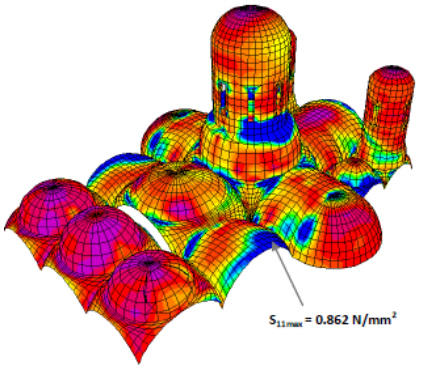


Figure 9a. $0.9G+1.4E_x$ Non-Deformable Foundation top face Max. Tensile $\boldsymbol{\sigma_{11}}$ 0.862Mpa

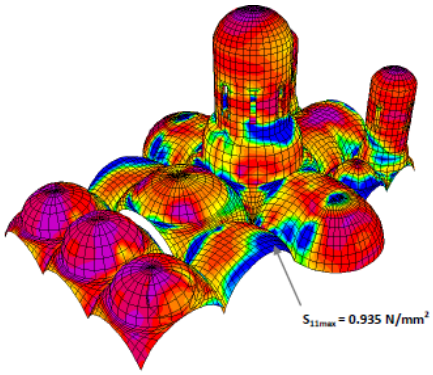


Figure 9b. $0.9G+1.4E_x$ Deformable Foundation top face Max. Tensile $\boldsymbol{\sigma_{11}}$ 0.935Mpa



Figure 9c. Damage of the vaulting system

Figures 9a and 9b depict the tensile stress concentration at the outer (top) face of the vaulting system, as it results from either load combination $0.9G+1.4E_x$ or $0.9G+1.4E_y$. As can be seen, the foundation deformability increases the tensile stress demand at critical locations for the vaulting of the superstructure. This observation, which is based on the numerical results, is also supported by in-situ evidence of damage to the masonry parts of the vaulting system, as shown in figures 9c.

Table 1 lists the assumed mechanical characteristics for the stone masonry in terms of Young's modulus and Poisson's ratio as well as compressive and tensile strength values [11]. Moreover, a Mohr-Coulomb failure envelope was adopted for the in-plane shear limit state of the stone masonry, when a $\boldsymbol{\sigma_n}$ stress is acting normal to the mortar bed joint simultaneously with the shear, that is defined through relationship (1) ([2], [3], [4], [5], [6], [7], [8], [11]).

$$f_{vk} = f_{vko} + 0.4\ \sigma_n \tag{1}$$

where: f_{vko} is the shear strength of the stone masonry when the normal stress $\boldsymbol{\sigma_n}$ is zero; f_{vko} was assumed to be equal to 0.192 N/mm2, a relatively high value.

	Young's Modulus (N/mm^2)	Poisson's Ratio	Compressive Strength (N/mm^2)	Tensile Strength normal / parallel bed-joint (N/mm^2)	shear strength f_{vko} (N/mm^2)
Limit values	2500	0.2	3.818	0.250 / 0.800	0.192

Table 1. Assumed Mechanical Characteristics of the Stone Masonry

Next, certain commonly used masonry failure criteria were adopted for either in-plane tension-compression or out-of-plane tension. All the masonry parts of the studied structures were examined in terms of in-plane and out-of-plane stress demands posed by the considered load combinations against the corresponding capacities, as these capacities were obtained by applying the Mohr-Coulomb criterion of equation 1 or the stone masonry compressive and tensile strength limits listed in Table 1. Due to space limitations such results are not shown in detail here. Selective results obtained from this evaluation process are shown in figures 10, 12 and 14. With $\mathbf{R_\sigma}$ or with $\mathbf{R_\tau}$ the ratio of the in-plane tensile or shear strength value over the corresponding demand is signified, whereas with $\mathbf{R_M}$ the ratio of the out-of-plane tensile strength value over the corresponding demand is denoted. Ratio values smaller than one ($\mathbf{R_\tau}$ $\mathbf{R_\sigma}$, $\mathbf{R_M}$ <1) predict a corresponding limit state condition. As can be seen, the followed methodology is based on combining numerical stress demands resulting from elastic analyses with limit-state strength values. A different approach is to combine these limit-state strength values with a non-linear push-over type of analyses, as was done by Manos et al. [2]. It was shown that the methodology applied here correlates quite well with the non-linear approach proposed by Manos et al. [2], in predicting regions of structural damage.

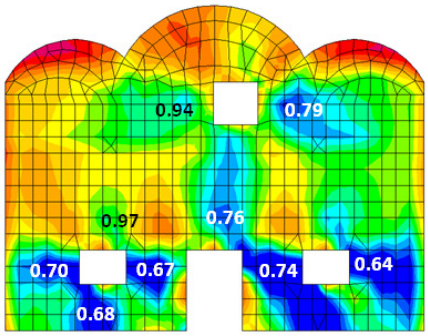


Figure 10a. Internal Transverse Wall, 0.9G+1.4Ey , Non-Deformable Foundation, Max in-plane shear stress strength / demand ratio $\mathbf{R_\tau}$

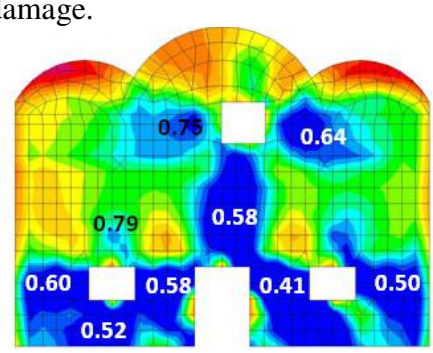


Figure 10b. Internal Transverse Wall, 0.9G+1.4Ey , Deformable Foundation, Max in-plane shear stress strength / demand ratio $\mathbf{R_\tau}$

Figures 10a and 10b depict the $\mathbf{R\tau}$ ratio values of the in-plane shear strength / shear demand for the load combination 0.9G+1.4Ey . The structural element that these ratio values belonged to is the internal transverse wall which separates the main church from the women's quarters situated at the west portion of the church (see figures 5a). This wall as well as internal faces of all the peripheral walls, vaults and domes are decorated with very valuable frescos that bear signs of extensive damage (see figures 9 and 11).



Figure 11. Damage of the Internal Transverse Wall and the adjacent arch

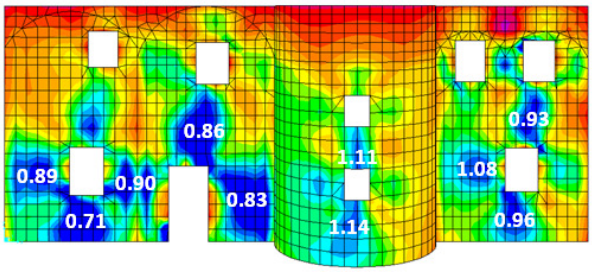


Figure 12a. Non-Deformable Foundation South Peripheral Longitudinal Wall, 0.9G+1.4Ex, Ratio values of $\mathbf{R_\tau}$ in-plane shear strength / shear demand

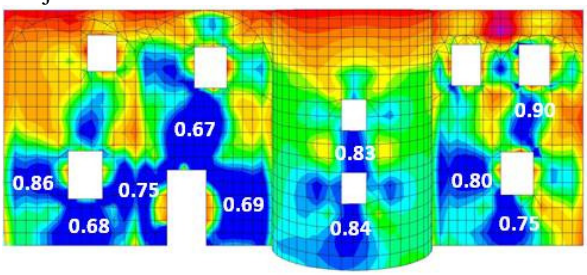


Figure 12b. Deformable Foundation South Peripheral Longitudinal Wall, 0.9G+1.4Ex, Ratio values of $\mathbf{R_\tau}$ in-plane shear strength / shear demand

This damage is also predicted by the numerical analysis results as can be seen from the strength / demand $\mathbf{R\tau}$ ratio values that are well below one ($\mathbf{R\tau}$ <1) in many locations (Figures 12a and 12b). Moreover, the deformability of the foundation leads this ratio to obtain even smaller values than for the case of the non-deformable foundation, which demonstrates the detrimental effect of the flexibility of the foundation for this church. The deformability of the foundation has such an effect in almost all peripheral walls; this can be established by either comparing the values of the in-plane shear strength / demand ratio $\mathbf{R\tau}$ (figures 12a and 12b) or the out-of-plane tensile strength / demand ratio $\mathbf{R_M}$ (see figures 13a and 13b), that is also visible at the outer face (figures 14).

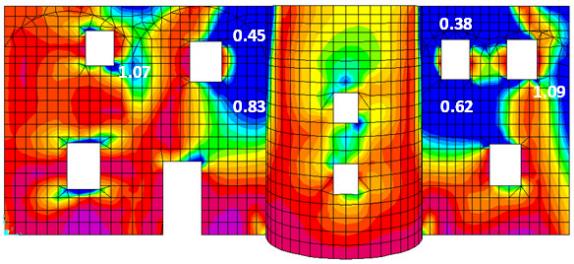


Figure 13a. Non-Deformable Foundation South Peripheral Wall, 0.9G+1.4Ey , Ratio values of $\mathbf{R_M}$ out-of-plane $\boldsymbol{\sigma_{11}}$ normal strength / demand (Top face)

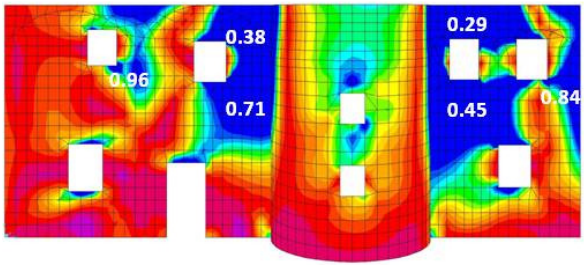


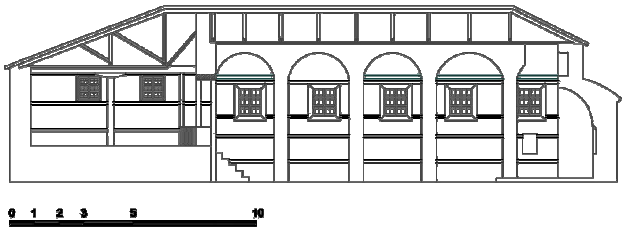
Figure 13b. Deformable Foundation South Peripheral Wall, 0.9G+1.4Ey ,Ratio values of $\mathbf{R_M}$ out-of-plane $\boldsymbol{\sigma_{11}}$ normal strength / demand (Top face)



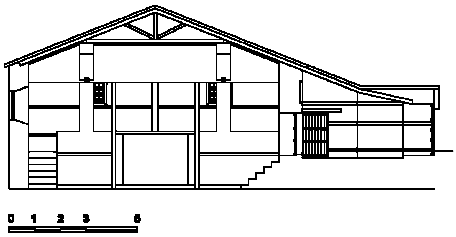
Figure 14. Damage of the peripheral masonry walls.

4 THE CHURCH OF PROFITIS ILIAS AT SIATISTA - KOZANI

This is also a Post-Byzantine three nave Basilica built in 1701 A.D. on the top of a hill in the town of Siatista of the prefecture of Kozani. It also has a wooden roof without the vaulting system of the Post-Byzantine Basilica described in section 2.



a. Longitudinal cross-section



b. Transverse cross-section



c. Wooden shoring of South longitudinal wall



d. Wooden shoring of mid-transverse wall

Figure 15. The church of Profitis Ilias at Siatista - Kozani

The horizontal dimensions of this church are 23.25m in length and 16.60m in width. The top of the roof lies at 7.1m from the floor level of the interior of this church. The naves are formed by 4-column colonnades (figures 15a and 15b) built with stone masonry. The lower part of the key of each arch of these colonnades lies at 5.25m from the floor level of the interior of this church. All the exterior walls are made of stone masonry. Apart from the main church a narthex was built at the North side at a later stage; this narthex is of a lower height than the main church. The West part of the church is allocated to the women quarters that is separated from the rest of the interior by a mid- transverse wall (figure 15d). The South longitudinal wall is supported by a system of wooden beams as is shown in figure 15c. These were installed after the Kozani-1995 earthquake sequence. Additional wooden supports are also placed at the mid-transverse wall (figure 15d) as well as at the mid-span of a longitudinal beam that spans the women quarters from East-West. According to past records, the structural system of this church showed signs of distress from soil-settlement sometime before the occurrence of this particular earthquake sequence. The records do not give information of any countermeasures being taken in the past up to the point of the earthquake occurrence. The main structural damage, as recorded after this earthquake sequence, is described below. Inclination of the South longitudinal wall outwards that is accompanied with extensive cracking at its joints with the East and West exterior masonry walls as well as with the mid-transverse wall. Extensive cracking is also evident at the East wall with the apses (figure 16a) and at the arches of the colonnades (figure 16b). Despite the fact that 18 years have passed since this earthquake damage, the counter measures so far are in the form of the temporary wooden shoring as well as the renovation of the wooden roof.



Figure 16a. Extensive cracking of the apse at the East wall



Figure 16b. Extensive cracking at the joint of the South longitudinal wall with the mid-transverse wall with its wooden shoring

4.1. Numerical Simulation including the influence of the soil deformability

The current numerical investigation of this church included the following:
- Simulation of the behavior assuming non-deformable supports at the foundation level.
- Simulation of the behavior assuming deformable supports at the foundation level, introducing at this level elastic springs with properties reflecting the actual soil deformability that was found from in-situ sampling. The soil consists of clay in its upper layers. For quantifying the stiffness of these soil layers use was made of the data from three boreholes drilled in the vicinity of the church relevant to the constitution of the soil deposits at a depth up to 15m (see figure 17)

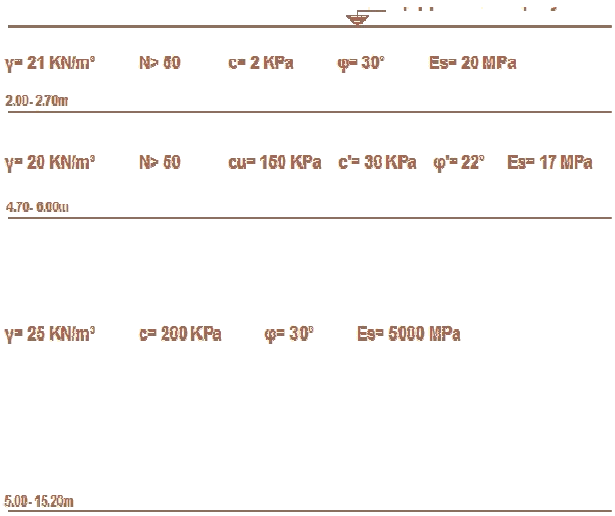
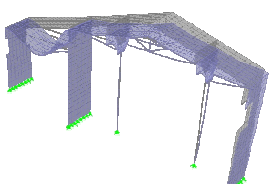
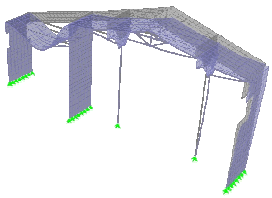


Figure 17. Properties of the Soil Profile obtained from boreholes drilled in the vicinity of the church

All the numerical simulations assumed elastic behaviour with relatively low-values of the modulus of elasticity for the stone masonry equal to E=1660MPa. The thickness of the masonry walls varied from 0.75m to 1.0m. The system of the wooden roof was modeled as well as all the wooden elements that connect the longitudinal and transverse walls with the interior colonnades and the mid-transverse wall. Figure 18 depicts the numerical predictions of the displacement response of this church when it is subjected to only gravitational loads

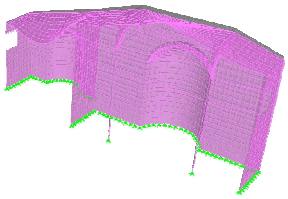


Non-deformable soil
Max Uz=1.2mm,
Ux=0.2mm

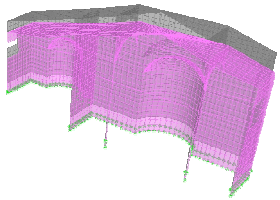


Deformable soil
Max Uz=12mm,
Ux=2mm

Mid-church Transverse cross-section



Non-Deformable soil
Max Uz=0.8mm,
Ux=0.2mm



Deformable soil
Max Uz=11.6mm,
Ux=1.9mm

East-wall cross-section

Figure 18. Deformations for gravitational forces (Non-deformable / Deformable foundation)

A small number of mortar specimens were taken from this church. Some basic properties of these mortar samples are listed in Table 2. Moreover, the type of natural stone used in the masonry elements is a type of slate with a compressive strength equal to 24MPa, as given in the literature survey.

Mortar Sample code name	Absorption %	Specific gravity KN/m3	Porous count %
K1	5.312	22.51	11.95
K2	0.51	27.22	13.89

Table 2. Characteristics of mortar samples taken from the church

Table 3 lists the assumed mechanical characteristics for the stone masonry in terms of Young's modulus and Poisson's ratio as well as compressive and tensile strength values. These values were based mainly from data included in the literature. From the comparison of the limit strength values of Table 3 with those of Table 1 it can be easily seen that the stone masonry of the church of Profitis Ilias of Siatista is much weaker than that of the church of Agia Triada at Vithos.

	Young's Modulus (N/mm^2)	Poisson's Ratio	Compressive Strength (N/mm^2)	Tensile Strength normal / parallel bed-joint (N/mm^2)	shear strength f_{vko} (N/mm^2)
Limit values	1660	0.2	1.0	0.10 / 0.25	0.10

Table 3. Assumed Mechanical Characteristics of the Stone Masonry

Moreover, a Mohr-Coulomb failure envelope was adopted for the in-plane shear limit state of the stone masonry, when a σ_n normal stress is acting simultaneously, that is defined through the following relationship that is the same as equation (1) described before in section 3 ([2], [3], [4], [5], [6], [7], [8], [11]).

$$f_{vk} = f_{vko} + 0.4\,\sigma_n \qquad (1)$$

As was done before the values of the strength over demand ratios at the most critical locations of the masonry walls and vaults were obtained by comparing the strength values listed in table 3 with the corresponding demand values as they were obtained from the numerical simulation. The ratio of the in-plane tensile or shear strength value over the corresponding demand is signified by $\mathbf{R_\sigma}$ or $\mathbf{R_\tau}$ whereas with $\mathbf{R_M}$ denotes the ratio of the out-of-plane tensile strength value over the corresponding demand. Ratio values smaller than one ($\mathbf{R_\tau}$ $\mathbf{R_\sigma}$, $\mathbf{R_M}$ <1) predict a corresponding limit state condition

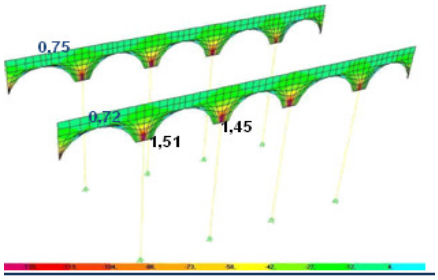


Figure 19a. G+0.3Q. Non-Deformable soil $\mathbf{R_\sigma}$ Ratio of in-plane strength / demand **F22** (KN/m) normal to bed joint

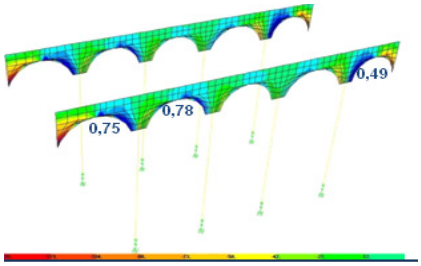


Figure 19b. G+0.3Q. Deformable soil Ratio $\mathbf{R_\sigma}$ of in-plane strength / demand **F22** (KN/m) normal to bed joint

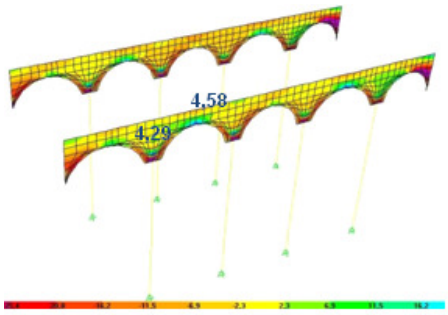


Figure 19c. G+0.3Q. Non-Deformable soil $\mathbf{R_\sigma}$ Ratio of in-plane strength / demand **F11** (KN/m) parallel to bed joint

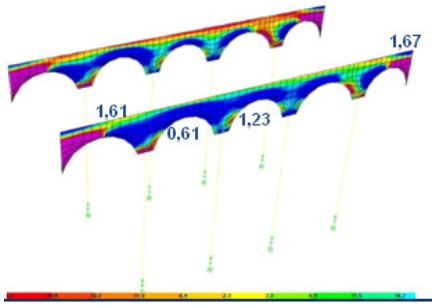


Figure 19d. G+0.3Q. Deformable soil $\mathbf{R_\sigma}$ Ratio of in-plane strength / demand **F11** (KN/m) parallel to bed joint

These $\mathbf{R_\sigma}$ ratio values of in-plane strength / demand applying the limit tensile strength scenario, either normal to bed-joint (**F22**) or parallel to bed-joint (**F11**) are depicted in figures 19a to 19d for the masonry arches above the internal colonnades. The demands in these figures were obtained for the load combination G+0.3Q. As can be seen from these figures the $\mathbf{R_\sigma}$ ratio values are smaller for the deformable than the non-deformable foundation, which demonstrates the detrimental effect of the foundation deformability for this church even only for the gravitational forces.

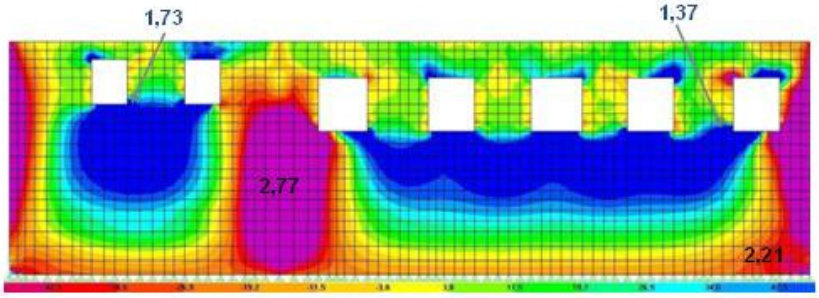


Figure 20a. Non-Deformable soil 0.9G+1.4E_y. $\mathbf{R_M}$ Ratio out-of-plane strength / demand $\boldsymbol{\sigma_{11}}$ (KN/m^2) Outer-face.

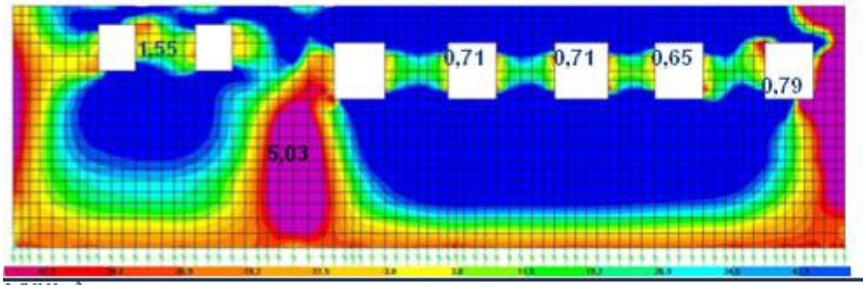


Figure 20b. Deformable soil 0.9G+1.4E_y. $\mathbf{R_M}$ Ratio out-of-plane strength / demand $\boldsymbol{\sigma_{11}}$ (KN/m^2) Outer-face.

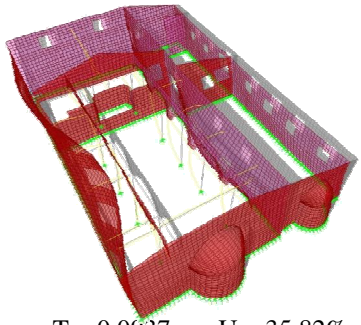
For the load combination 1.3G+1.5Q, that dictates the design for the gravitational forces under current code provisions, the above ratio values will become even smaller, which signifies that the colonnades cannot withstand the maximum gravitational forces. This is verified by the observed damage which is quite evident for these structural elements in this church as it stands today being supported after the earthquake event of 1995 by temporary wooden shoring internally as well as externally (see figure 15c, 15d, 16a and 16b). The numerical simulation was also repeated for the load combinations either 0.9G+1.4Ex or 0.9G+1.4Ey. Initially this was done with the seismic loads considered as static forces either Ex or Ey generated at the existing masses by a constant acceleration of such value that results in the same base shear value that was found when the earthquake actions were considered through a dy-

namic spectral analysis as will be explained below. In figures 20a and 20b the $\mathbf{R_M}$ ratio out-of-plane strength / demand ($\boldsymbol{\sigma_{11}}$) (KN/m^2) are depicted. The numerical simulation was repeated to include the seismic actions in the form of dynamic spectral analysis utilising the design spectrum derived by applying the provisions of the current Greek Seismic code for seismic zone I, soil category B and importance factor 1.3 [10] .

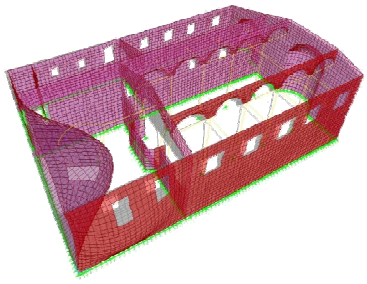
Non-Deformable Foundation



1st y-y. Ty=0,1179 sec, Uy=28,366%

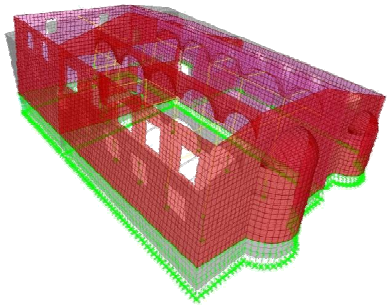


2nd y-y. Ty=0,0937sec, Uy=35,82%

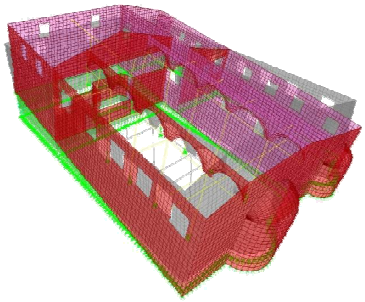


3rd x-x. Tx=0,0917sec, Ux=20,535%

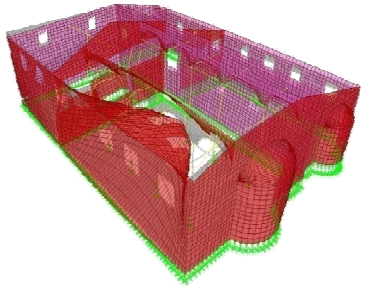
Deformable Foundation



1st y-y. Ty=0,212sec, Uy=24,707%



2nd x-x. Tx=0,2007sec, Ux=12,867%



3rd y-y. Ty=0,114sec, Uy=10,236%

Figure 21. The most significant eigen-modes for the non-deformable and the deformable foundation together with the values of the corresponding eigen-frequencies and modal mass participation ratios.

This dynamic spectral analysis was based on a sufficient number of eigen-modes capable of mobilising sums of modal mass larger than 65% of the total mass of the structure. Figures 21 depict the most significant translational x-x and y-y eigen-modes together with their corresponding eigen-period and modal mass ratio values. This is done for both the non-deformable as well as the deformable foundation numerical models. As was also observed previously, the modal analysis results demonstrate the first effect of the deformable foundation which is the lengthening of the eigen-periods of the most significant translational modes.

From the evaluation of the demands obtained from the numerical simulation as compared with the limit strength values adopted for the stone masonry of this church it can be concluded that the deformability of the foundation results in strength / demand ratio values ($\mathbf{R_\tau}$ $\mathbf{R_\sigma}$, $\mathbf{R_M}$) smaller than the corresponding ratio values for the non-deformable foundation.

These results signify the existence of critical regions for the various masonry structural elements that cannot withstand the demands, as they were quantified by the numerical analyses and the current code provisions. Such an evaluation can explain, up to a point, the development of the existing current state of structural damage. Gaining such confidence in the employed methodology, the designer also gains the advantage in evaluating with the same methodology the effectiveness of a potential retrofitting scheme. In order for such a retrofitting scheme to be effective, the resulting strength / demand ratios should attain values larger than the corresponding values without this retrofitting scheme and, if possible, larger than one ($\mathbf{R_\tau}$ $\mathbf{R_\sigma}$, $\mathbf{R_M}$ >1).



Figure 22. South Peripheral Wall. Regions with small values of the strength / demand $\mathbf{R_M}$ out-of-plane tensile behaviour (orange), $\mathbf{R_\sigma}$ in-plane tensile behaviour (blue)

Such an evaluation has been performed for the most vulnerable structural elements of this church; that is the internal colonnades, the South and North peripheral walls and the East peripheral wall with the apses. The predictions by the numerical analysis of potential damage regions is indicated with the strength / demand ratio values well below one ($\mathbf{R_\tau}$ $\mathbf{R_\sigma}$, $\mathbf{R_M}$ <1). These predictions are depicted in figure 22 through the values of ratio $\mathbf{R_\sigma}$ (in-plane tensile behaviour, blue), ratio $\mathbf{R_M}$ (out-of-plane tensile behaviour, orange). In almost all structural elements the out-of-plane tensile behaviour results in strength / demand ratios with values well below one ($\mathbf{R_M}$ <1). The smallest $\mathbf{R_M}$ ratio value appears at the South longitudinal peripheral wall and is approximately equal to $\mathbf{R_M}$ = 0.15. The average value of this $\mathbf{R_M}$ ratio obtained by averaging the corresponding values at six (6) different locations well spread over the entire length of this wall is equal to 0.245. This strongly indicates that the existing capacity of this wall in out-of-plane bending is exceeded fourfold by the corresponding demands. It is not surprising that this wall has visible signs of out-of-plane displacements that are in agreement with such a state of distress, as predicted by the followed methodology.

5 RETROFITTING - EXPERIMENTAL INVESTIGATION.

Retrofitting of heritage structures is, in general, a difficult task as it cannot employ traditional retrofitting techniques that have been developed for reinforced concrete structures ([12], [13], [14]). The latter can be termed as strong non-reversible interventions, because such retrofitting schemes usually do not respect the principles either of compatibility of the old materials with the new materials or that of reversibility of the employed intervention scheme. The latter is thought to be a necessary feature of a retrofitting scheme, intended to be applied on a heritage structure, so that it can be potentially replaced by a more efficient retrofitting scheme in the future. Such a retrofitting scheme for heritage structures can mobilize the following:

- The upgrading of the strengths of the existing masonry. This is usually achieved, up to a point, with compatible mortars that can be injected with low pressure and fill the voids of the existing weak stone masonry (see section 5.1.).

- The strengthening of the wooden parts of the roof and their connection to the masonry.
- The replacement of the wooden elements or ties and the addition of new metal ties.
- The strengthening of the foundation with various forms of external or internal encasement schemes. This was studied for the church of the Virgin Mary at Dilofo (section 2, [9]).
- Semi-temporary external shoring employing wooden, metal or reinforced concrete parts.
- The utilization of more advanced retrofitting methods, such as base isolation in an effort to lower the demands. This, although desirable, can encounter significant construction difficulties ([15], [16], [17], [18]).

Temporary wooden shoring, internal as well as external, was proposed and partly employed in the cases of the church of the Virgin Mary at Dilofo and Profitis Ilias at Siatista (see figures 15c and 16a). Such temporary wooden shoring, although erected until it is replaced by the permanent retrofitting scheme, usually remains in many applications for considerably long periods. However, the connections of such a temporary scheme to the structure and the surrounding soil become less effective with time under a variety of environmental influences that they were not designed for, rendering such a scheme ineffective



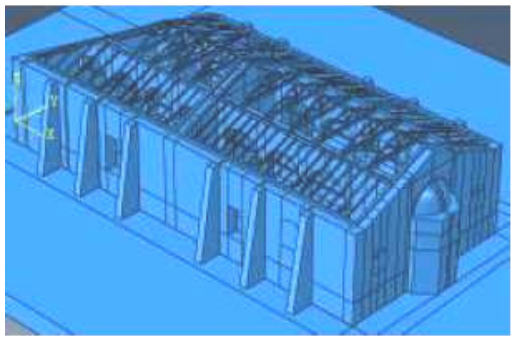


Figure 23. The church of Agios Dimitrios at Palatitsia

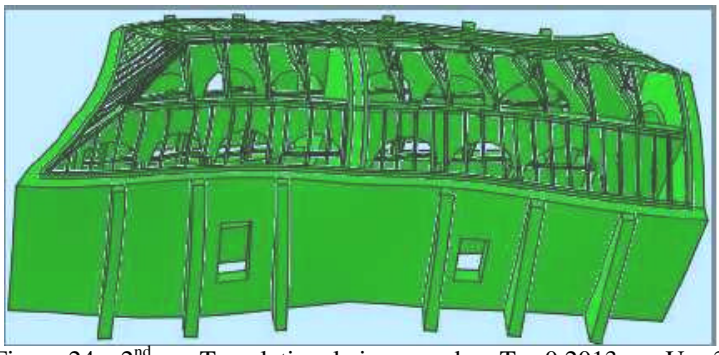


Figure 24a. 2nd x-x Translational eigen-mode. Tx=0,2013sec, Ux=38,5%

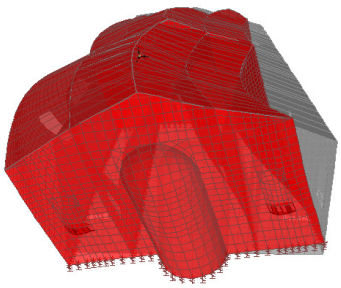


Figure 24b. Present condition, deformable foundation, Main Transversal y-y eigen-mode, T_y = 0,326sec Uy=61,62%

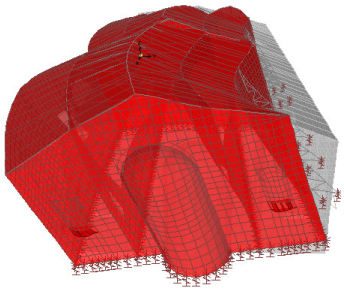


Figure 24c. Retrofitted with seimi-permanent shoring. Deformable foundation, Main Transversal y-y eigen-mode, T_y = 0,263sec Uy=68.17%

Semi-permanent shoring must be designed and constructed respecting the principle of reversibility. Moreover, it can be combined with the rest of the reversible techniques mentioned above, taking into consideration environmental influences. Such a retrofitting scheme is currently being investigated to be applied at Agios Dimitrios at Palatitsia Imathias, a 16th century three-nave Basilica. This church is 27.10m long on its South side and 22.15m long on its North side with an average width 12.625m. The height from the ground level to the top of the roof is 6.75m (figure 23). The studied retrofitting scheme consists of a system of semi-temporary external shoring of the longitudinal peripheral walls together with the upgrading of the wooden roof, the replacement of the internal wooden ties and the addition of new metal ties as well as mortar injections for all stone masonry. The performance of such a retrofitting scheme was investigated numerically by a full dynamic analysis (figures 24) employing the methodology described in sections 2, 3 and 4.

This retrofitting scheme in the current investigation takes a variety of alternative forms. The numerical results so far provide sufficient evidence that such a retrofitting scheme can be quite effective in upgrading the performance of the various stone masonry elements in such a way that the strength / demands ratio values $\mathbf{R_\tau}$ in-plane shear, $\mathbf{R_\sigma}$ in-plane tension, and $\mathbf{R_M}$ out-of-plane tensile flexure, described in sections 2, 3 and 4 before, obtain values larger than the corresponding values for the current state of stress before any intervention. The objective of the current study is for these strength / demands ratio values **t**o reach the threshold value of 1, ideally at all critical locations, thus signifying acceptable performance. Typical results are shown in figures 25 for the out-of-plane σ_{22} demands. This is done for both the existing condition (figure 25a) as well as for the condition after the previously described retrofitting scheme is applied (figure 25b). The existing state of stress includes large areas in the vicinity of the window openings with considerable tensile stress concentration exceeding the strength values, thus indicating potential structural damage regions. The introduction of the proposed retrofitting resulted in a considerable decrease of these out-of-plane σ_{22} demands. This decrease in the demands when combined with an increase in the strength values, achieved from injecting the stone masonry with compatible mortar, results in values of the strength / demands ratios ($\mathbf{R_\tau}$ in-plane shear, $\mathbf{R_\sigma}$ in-plane tension, and $\mathbf{R_M}$ out-of-plane tensile flexure) nearing the threshold value of one, thus satisfying the objective of the retrofitting scheme.

Present condition

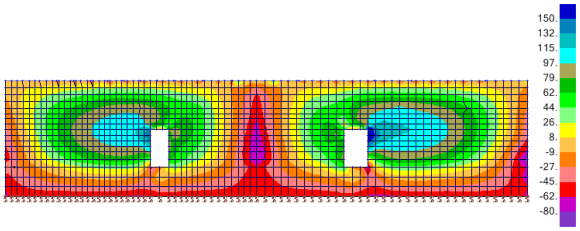


Figure 25a. South Longitudinal Wall, G+0.30Q+Ey Present comdition, deformable foundation, σ_{22} (kN/m2, Kpa)- normal stress - Bottom face.

Retrofitted with semi-temporay metal shoring

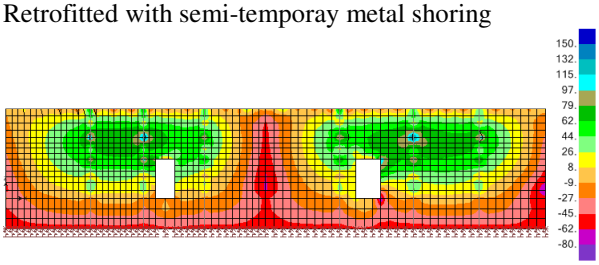


Figure 25b. South Longitudinal Wall, G+0.30Q+Ey Present comdition, deformable foundation, σ_{22} (kN/m2, Kpa)- normal stress - Bottom face.

5.1. Shear capacity of stone masonry - summary of experimental testing

A number of stone masonry specimens were built at the laboratory using lime mortar and natural stones. The lime mortar had such a composition as to be representative of old relatively weak mortars commonly used in the past. A series of such samples were tested accompanied by constant compression with variable shear as shown in figure 26b. This set-up was designed in an effort to record the shear force at a limit state which represented the failure of the mortar bed-joint as depicted in figures 26c,d. Based on these experimental results, the

the mortar bed-joint as depicted in figures 26c,d. Based on these experimental results, the Mohr-Coulomb limit state criterion (figure 26a, equation 1) can be approximately quantified.

Mohr Coulomb failure criterion $f_v = f_{vo} + 0.45\,\sigma$
$f_{vo} = 0.12$ Mpa

	Normal Stress σ (Mpa)	Predicted $f_v = f_{vo} + 0.45\,\sigma$ (Mpa)	Measured value f_v (Mpa)	Ratio Measured f_v / Predicted f_v
Sample 1	0.53	0.359	0.396	1.103
Sample 2	0.61	0.395	0.41	1.038
Sample 3	0.46	0.327	0.305	0.933
Sample 4α	0.30	0.255	0.20	0.784
Sample 4β	0.54	0.363	0.375	1.033

Figure 26a. Verification of the Mohr-Coulomb criterion

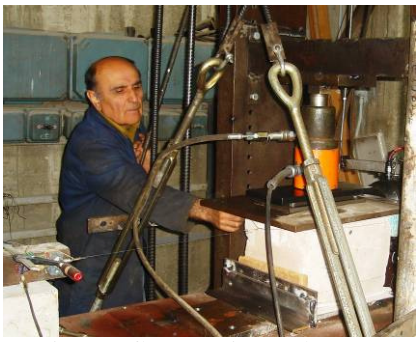


Figure 26b. Experimental set-up



Figure 26c. Sliding mode of failure



Figure 26d. Sliding mode of failure

Following these initial samples, another sequence of tests will be performed aimed at quantifying the Mohr-Coulomb failure envelope representing old stone masonry that was injected in the framework of a mild retrofitting scheme. The injected mortar should be of such a composition as: a) to be compatible with the existing materials b) to be able to fill the existing voids and c) to result in higher strength values. This experimental sequence is still under way.

6 CONCLUSIONS

1. The eigen-periods, eigen-modes, and the deformation patterns to horizontal earthquake actions of the examined churches, predicted numerically, document that the longitudinal peripheral walls develop much larger out-of-plane displacements at their top than in-plane displacements Moreover, the presence of the apses exercise a significant out-of-plane stiffening effect. The presence of stone masonry vaulting system increases the stiffening effect at the top of the peripheral wall level; however, such a vaulting system also adds considerable masses at a high level which generate seismic actions of large amplitude.

2. The numerical stress results together with assumed strength values for the various masonry elements of the examined churches predict that the regions most vulnerable to damaged are near the door and window openings for the in-plane behavior. These regions together with the regions near the foundation appear to be the most vulnerable to out-of-plane bending, particularly for the longitudinal masonry walls. Such numerical predictions of structural damage are in reasonably good agreement, in a qualitative sense, with actual observed damage. This is despite the fact that the numerical simulation is based on elastic analysis assumptions. The employed limit state criteria of strength / demands ratio values ($\mathbf{R}_\tau$ in-plane shear, $\mathbf{R}_\sigma$ in-plane

tensile, and $\mathbf{R_M}$ out-of-plane tensile behaviour) lead to successful predictions of actual distress of the peripheral walls. When the superstructure consists of vaults and domes large seismic forces are generated that lead to areas of stress concentration at the bases of the domes and vaults and at the keys of the arches. Further investigation is needed to establish appropriate limit-state criteria for these stone masonry elements.

3. The foundation deformability was also investigated by introducing linear deformable springs at the foundation level. The results of such a numerical approximation combined with the followed methodology of limit state criteria of strength / demands ratio values ($\mathbf{R_\tau}$ in-plane shear, $\mathbf{R_\sigma}$ in-plane tensile, and $\mathbf{R_M}$ out-of-plane tensile behaviour) demonstrated in all the examined cases that the foundation deformability, when combined with the gravitational forces and seismic actions, leads to $\mathbf{R_\tau}$, $\mathbf{R_\sigma}$, and $\mathbf{R_M}$ strength / demands ratio values that are considerably smaller than for the case of non-deformable foundation, thus verifying the detrimental effect of the foundation deformability in all the examined cases.

4. A retrofitting scheme, which combines mortar grouting, wooden and metal ties, external semi-temporary shoring of the longitudinal walls together with foundation encasement is being currently investigated. The numerical results so far provide sufficient evidence that such a retrofitting scheme can be quite effective in upgrading the performance of the various stone masonry elements in such a way that the $\mathbf{R_\tau}$, $\mathbf{R_\sigma}$, and $\mathbf{R_M}$ strength / demands ratio values are larger than the corresponding values for its current state before any intervention. The objective of the current study is for these strength / demands ratio values **t**o reach the threshold value of 1, ideally at all critical locations, thus signifying acceptable performance.

5. An experimental sequence is also in progress that tries to quantify combined shear and compression limit-state criteria for stone masonry specimens that represent parts of the stone masonry walls prior to any intervention with compatible mortar injections.

REFERENCES

[1] Manos George, “Consequences on the urban environment in Greece related to the recent intense earthquake activity”, Int. Journal of Civil Engineering and Architecture, Dec. 2011, Volume 5, No. 12 (Serial No. 49), pp. 1065–1090.

[2] Manos G.C., Soulis V., Diagouma A. (2008) “Numerical Investigation of the behavior of the church of Agia Triada, Drakotrypa, Greece”, Journal in Advances in Engineering Software 39 (2008) 284-300.

[3] G.C. Manos, V.J. Soulis, O. Felekidou, “The dynamic and Earthquake Behavior of Greek Post-Byzantine Churches”, 14WCEE, Beijing, CHINA, 2008.

[4] G. C. Manos, V. J. Soulis, O. Felekidou, A. Koutsianou, P. Lipiridou, «The dynamic and earthquake response of Greek Byzantine and Post-Byzantine Basilicas”, COMDYN 2009, Rhodes, Greece.

[5] G.C Manos, V. Soulis, N. Karamitsios, O. Felekidou, Numerical Simulation of the Dynamic and Earthquake Behaviour of Greek Post-Byzantine Churches with and without Base Isolation”, PROHITECH 2009, 21 to 24 June 2009, Rome, Italy.

[6] Manos George, Soulis V., Felekidou O., "Numerical Study of the Dynamic and Earthquake Behavior of Byzantine and Post-Byzantine Basilicas", 8th International Masonry Conference, 2010, Dresden, Germany.

[7] Manos George, Soulis V., Felekidou O., Matsou V. "A Numerical Investigation of the Dynamic and Earthquake Behavior of Byzantine and Post-Byzantine Basilicas", 9th U.S. National and 10th Canadian Earthquake Engineering Conference, 2010, Canada.

[8] Manos George, Soulis V., Felekidou O., Matsou V. "A Numerical Investigation of the Dynamic and Earthquake Behavior of Byzantine and Post-Byzantine Basilicas", 3rd International Workshop on Conservation of Heritage Structures Using FRM and SHM, 2010, Ottawa, Canada.

[9] G.C. Manos "The bearing capacity of the Assumption of Virgin Mary, a three-nave Basilica at Dilofo-Voio-Kozani and a retrofitting proposal", Technical Report to the Greek Ministry of Culture, April, 2011 (in Greek).

[10] Provisions of Greek Seismic Code 2000, Organization of Earthquake Planning and Protection of Greece OASP, Dec. 1999 published by OASP. Revisions of seismic zonation introduced in 2003, Government Gazette, Δ17α /115/9/ΦΝ275, No. 1154, Athens, 12 Aug. 2003.

[11] European Committee for Standardization, Euro code 6; "Design of Masonry Structures, Part 1-1:General Rules for Building. Rules for Reinforced and Un-reinforced Masonry", EN 1996-1-1:2005.

[12] Earthquake Engineering Retrofitting of Heritage Structures "Design and evaluation of strengthening techniques", Edited By: S. Syngellakis, Wessex Institute of Technology, UK, ISBN: 978-1-84564-754-4, eISBN: 978-1-84564-755-1, Published: 2013.

[13] G. C. Manos and E. Papanaoum, "Earthquake Behaviour of a R/C Building Constructed in 1933 before and after its Repair" STREMAH 2009, Tallin, 22-24 June, 2009.

[14] Organization of Earthquake Planning and Protection of Greece (OASP), Guidelines for Retrofitting in Reinforced Concrete Buildings, Government Gazette, Δ17α /04/5/ΦΝ 429-1, No 42, Athens, 20 Jan. 2012.

[15] G. C. Manos, V. Soulis, O. Felekidou, N. Karamitsios, L. Kotoulas, "Numerical Study of the Dynamic and Earthquake Response of Greek Post-Byzantine Churches with or without Base Isolation", 3rd International Workshop on Conservation of Heritage Structures Using FRM and SHM, 2010, Ottawa, Canada.

[16] G.C. Manos, N. Karamitsios, " Numerical Simulation of the Dynamic and Earthquake Behavior of Greek Post-Byzantine Churches with and without Base Isolation", COMPDYN 2011, Corfu, Greece, 26–28 May 2011.

[17] G.C. Manos, N. Karamitsios, "Study of the Dynamic and Earthquake Response of Greek Post-Byzantine Churches with and without Base Isolation" EURODYN 2011, Leuven, Belgium, 4-6 July, 2011.

[18] G. C. Manos and N. Karamitsios, "Earthquake Numerical Simulation of the Dynamic and Earthquake Behaviour of Greek Post-Byzantine Churches with and without Base Isolation", STREMAH-2011, Chianciano, Italy, Sep. 2011.

[19] V. Dimitriadis "An ordinance for the erection of the first church in Gianitsa", Mekedonika, Vol. 9, Society for Mecedonian Studies, Thessaloniki 1969.

COMPDYN 2013
4th ECCOMAS Thematic Conference on
Computational Methods in Structural Dynamics and Earthquake Engineering
M. Papadrakakis, V. Papadopoulos, V. Plevris (eds.)
Kos Island, Greece, 12–14 June 2013

THE EARTHQUAKE BEHAVIOUR OF LOW-RISE HOUSES MADE BY EITHER REINFORCED CONCRETE, PARTIALLY REINFORCED MASONRY OR A NOVEL STEEL COMPOSITE SYSTEM

G.C.Manos[1], K.Katakalos[1*], M.Theofanous[1], A.Nalmpantidou[1], V.Tsakalidis[1], C.Stathi[1]

[1]Laboratory of Strength of Materials and Structures, Dept. Civil Engineering, Aristotle University, Thessaloniki, GREECE,
gcmanos@civil.auth.gr

Keywords: low-rise houses, earthquake behaviour, light weight concrete, partially reinforced masonry, reinforced concrete, composite construction

Abstract. *This paper discusses features for the seismic design of low-rise houses made by three different construction techniques. A typical two-storey residential house with a basement is chosen for examination. This house, with the same dimensions in elevation and plan, is being built by three different construction techniques, thus resulting in three different structures. The first is that of conventional reinforced concrete construction whereas the second is that of partially reinforced masonry. The 2nd construction technique utilizes such hollow ceramic bricks that longitudinal as well as transverse reinforcement can be accommodated within the vertical walls built with these bricks. The compression, flexural and shear behaviour of such masonry walls has been documented by a series of experiments conducted for this purpose. The novel 3rd construction technique utilizes steel structural elements in the form of sheets for the slabs or cold-formed sections for the beams and columns in order to form the structure, together with a special light weight concrete mix (SLWC). The mechanical properties of the SLWC mix were found from a series of laboratory tests. This investigation is mainly numerical, making use at the same time of the mechanical properties of the materials utilized in each one of the three different construction techniques as determined through laboratory testing, especially those of the innovative Super Light Weight Concrete. The seismic design follows the provisions of the Greek seismic code or those of the Euro-Codes; it utilizes the dynamic spectral method that is incorporated in the commercial software SAP2000. The main dynamic response characteristics are first established and discussed for each one of the three different structures made by the three distinct construction techniques mentioned before. Next, the demands to be used in the earthquake design at critical sections of the various structural elements are also computed and compared with the design strengths as provided by the relevant codes. Use is made here of strength data documented during the laboratory tests. The maximum design quantities for the same two-storey structure built by the three different techniques, in terms of storey drifts, and base shear as well as in terms of slab deflections are compared and discussed.*

1 INTRODUCTION

Seismic design demands that a structure should sustain its main functions, such as its safety and serviceability, both during and after a particular earthquake exposure. A structure is considered safe if it does not endanger the lives and well-being of the occupants, by partially or completely collapsing. In general, the greater the dead load masses, the larger the seismic forces imposed on the structure. Consequently, it is desirable to possibly decrease the seismic forces through a decrease of the dead load mass for a structure. It is also desirable that this decrease in seismic loads and seismic demands on the structural members of a building may also lead to a decrease in the final construction cost.

Lightweight concrete can be defined as a type of concrete mix which includes an expanding agent which increases the volume of the mixture and decreases the dead weight while giving additional qualities such as nailibility and thermal insulation. It is lighter than the conventional concrete with its dry density ranging form 250 kg/m^3 to 1840 kg/m^3; that is 90% to 26% lighter than regular conventional concrete mixes. It was first introduced by the Romans in the second century when 'The Pantheon' was constructed using pumice, the most common type of aggregate used in that particular year [1]. From there on, the use of lightweight concrete spread widely across other countries such as the USA, the United Kingdom and Sweden. The main specialities of lightweight concrete are its low density and thermal conductivity. Its advantages are that there is a reduction of dead load, faster building rates in construction and lower haulage and handling costs.

The present study investigates features of a low-rise house incorporating, in its construction, light weight concrete together with steel structural elements in the form of sheets for the slabs or cold-formed sections for the beams and columns. The purpose of the current numerical investigation is to focus on the consequences of such an innovative construction on the dynamic response and earthquake design of low-rise houses made by such an innovative construction as compared with two other well established conventional constructions; that is conventional reinforced concrete construction or partially reinforced masonry. The properties of special light concrete mix, to be incorporated with the novel construction technique, have been documented by a series of experiments conducted for this purpose at the Laboratory of Strength of Materials and Structures of Aristotle University.

2 EXPERIMENTAL INVESTIGATION OF NOVEL LIGHT WEIGHT CONCRETE

A series of compressive and flexural tests were conducted at the Laboratory of Strength of Materials and Structures of Aristotle University in order to determine the mechanical properties of the innovative Super Light Weight Concrete (SLWC) that was intended for use in the numerically investigated building of the 3rd construction type. In total two materials were investigated; the first with density 350 kg/m^3 and the second with density 800 kg/m^3. The obtained results are listed in Table 1. SLWC with density 350 kg/m^3 has an average maximum compressive strength equal to 1,94Mpa and tensile strength (defined from four point bending tests) equal to 0,53 MPa. SLWC with density 800 kg/m^3 has an average maximum compressive strength equal to 2,54MPa and tensile strength (defined from four point bending tests) equal to 0,83 MPa. In the framework of present numerical investigation, the mechanical properties of the SLWC mix with density 800 kg/m^3 are considered for the simulation of the building made with the 3rd construction type.

Figure 1 depicts the average overall stress-strain behaviour of both 350kg/m^3 and 800kg/m^3 SLWC. Both types of SLWC are relatively soft with a modulus of elasticity equal to 150MPa. Both materials can keep their 80% strength for big deformations, especially the SLWC with density 350kg/m^3.

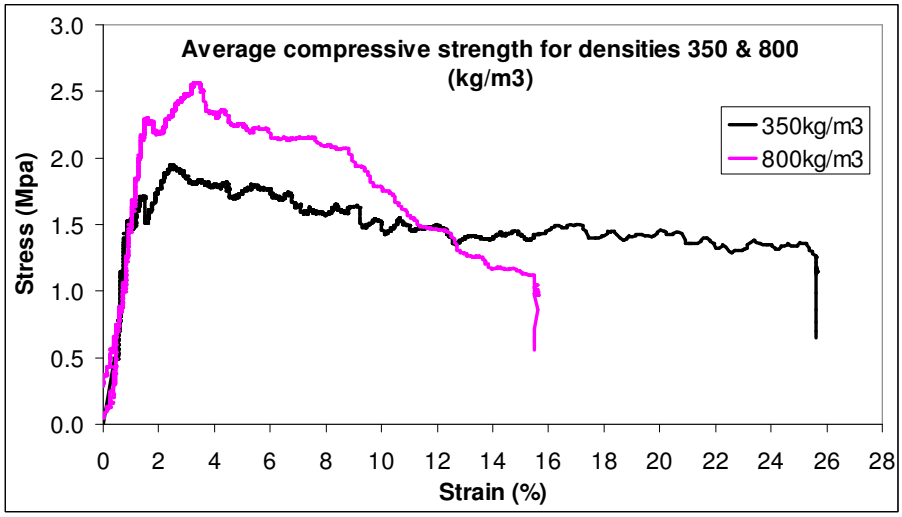


Figure 1. Average compressive strengths for SLWC 350 & 800 (kg/m^3)

test	Max tensile stress from flexural tests (N/mm^2)		Max compressive stress (N/mm^2)					
			350 kg/m^3			800 kg/m^3		
	350 kg/m^3	800 kg/m^3	max	@ strain 2%	@ strain 10%	max	@ strain 2%	@ strain 10%
1st	0,52	0,89	1,95	1,77	1,83	2,51	2,3	1,75
2nd	0,52	0,8	1,95	1,66	1,48	2,57	1,5	1,48
3rd	0,56	0,81	1,93	1,63	1,33	2,55	2,1	1,6
Average	**0,53**	**0,83**	**1,94**	1,69	1,55	**2,54**	1,97	1,61

Table 1. Tensile and compressive max stresses for SLWC 350 & 800 (kg/m^3)

3 EXPERIMENTAL INVESTIGATION OF PARTIALLY REINFORCED MASONRY

The properties of partially reinforced masonry construction, utilized in the framework of the present numerical study, were found from an extensive laboratory investigation with a considerable number of partially reinforced masonry piers. All these masonry specimens were constructed with the special "Greek" brick with vertical holes depicted in figure 2. These brick units were produced in three different types, that is A, B and C. Brick D, was the unit that was industrially produced in large quantities and was used for the majority of the specimens. The measured strength of the brick unit is given in Table 2. The partially reinforced pier specimens were subjected to horizontal cyclic seismic-type loading together with the simultaneous application of vertical load at the top (figure 3), thus simulating prototype conditions. Detailed information of this experimental sequence and the obtained results is given in [7], [8], [9], [10]. These partially reinforced piers were of the following geometry:

- Length 1330mm, height 1330mm and thickness 154mm.
- Length 660mm, height 1330mm and thickness 154mm.

Apart from the above geometry, which must be considered as ½ scaled specimens and represent the bulk of the testing sequence, a limited number of specimens near to prototype scale were also tested. These specimens were of the following geometry:

- Length 2700mm, height 2475mm and thickness 320mm.
- Length 2700mm, height 2475mm and thickness 154mm.

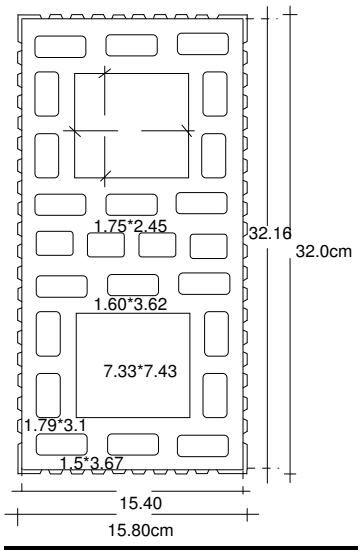


Figure 2. special "Greek" brick with vertical holes

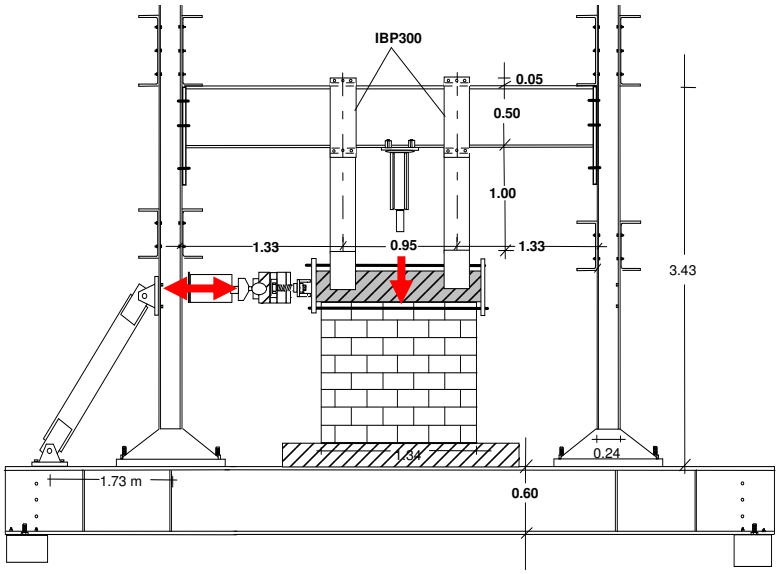


Figure 3. Partially reinforced masonry piers simultaneously loaded with a horizontal cyclic seismic-type load as well as with a vertical load

Brick Unit	Strength (Gross) fb (MPa)	Strength (Net) fb (MPa)	% of Voids
B	2.59	5.20	50%
C	8.93	17.38	49%
D	7.14	15.48	54%

Table 2. Compressive Strength of Brick Units

The average compressive strength of the mortar employed in the construction of these piers was either 2.1MPa for the relative weak mortar or 4.27MPa for the relatively strong mortar. Various longitudinal and transverse reinforcing arrangements were examined together with a variation of the level of uniform compression.

4 NUMERICAL SIMULATION OF TWO-STOREY STRUCTURE WITH BASEMENT

The present study investigates the static and dynamic response of a typical two storey building with a basement [5], [6]. The typical floor plan of the building is illustrated in figure 4. The overall dimensions of the building in plan are 13,40m x 12,70m.

Three such buildings with the same dimensions but made with three different construction techniques are studied. The maximum seismic response of these three buildings is obtained numerically and comparison is made. The seismic loading is defined following the provisions of the current Greek Seismic Code [4]. This numerical dynamic and earthquake loading study

was made by discretizing each building with finite elements (FE) and then utilizing the capabilities of the commercial software SAP2000 based on elastic analysis assumptions.

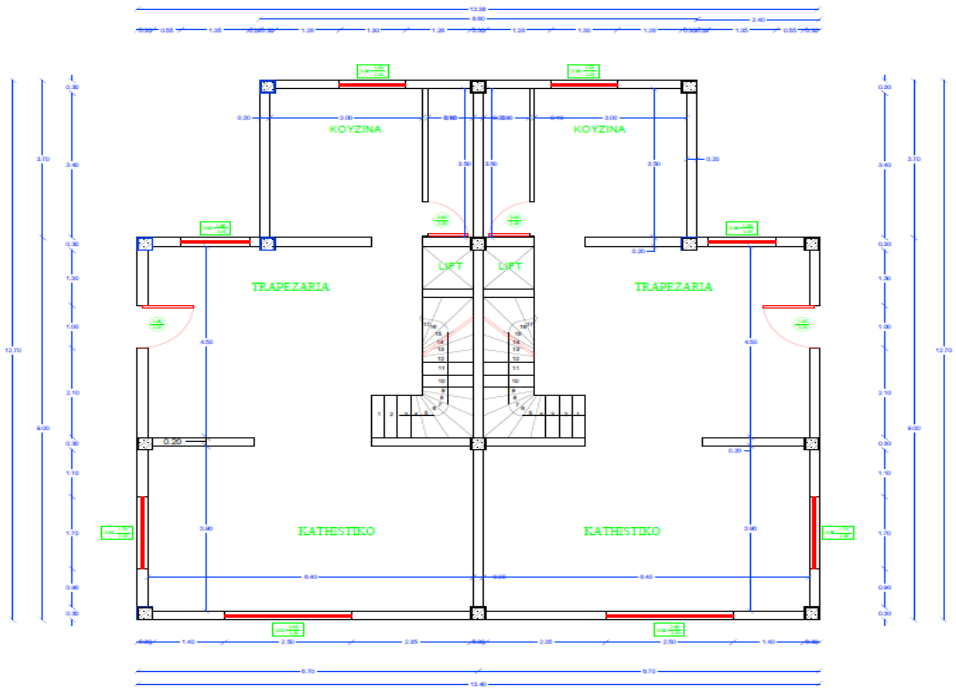


Figure 4. Typical floor plan of low-rise building (3-storey)

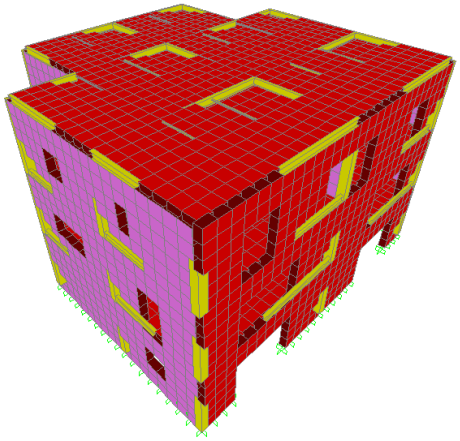


Figure 5a. F.E. Discretization a) used for the numerical simulation of the behaviour of the house built by either partially reinforced masonry (PRM) or Composite Innovatiove Technique (CIT)

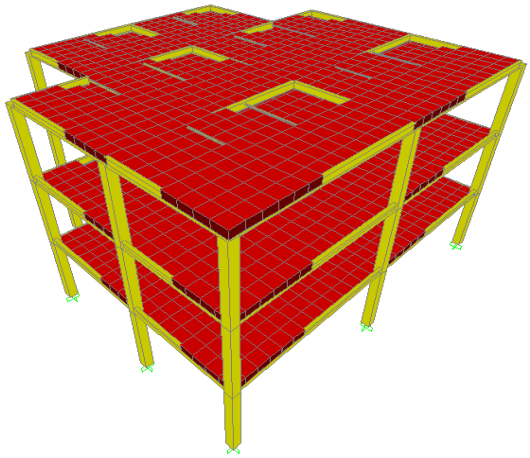


Figure 5b. F.E. Discretization b) used for the numerical simulation of the behaviour of the house built by reinforced concrete (R/C)

The considered three different construction types are:

i) Reinforced Concrete (R/C) [3]
ii) Partially Reinforced Masonry (PR/M)
iii) Composite Innovative Technique (CIT) combining SLWC (800kg/m^3) with cold formed thin-walled steel.

Figures 5a and 5b depict the employed discretizations as utilized, combined with each one of the three construction techniques mentioned before. The discretization depicted in figures

5a and 5b combined with the assumptions made according to the mass and stiffness properties of the constituent materials employed in each construction technique, resulted in a large number of numerical models. The following 4 models will be considered in the results presented in this paper:

Model CIT-II, representing the house built with the Composite Innovative Technique (CIT) combining SLWC (800kg/m^3), assuming a stiffness of SLWC equal to 500MPa for the infilled walls within the steel frames made by SLWC, employing discretization a (figure 5a)

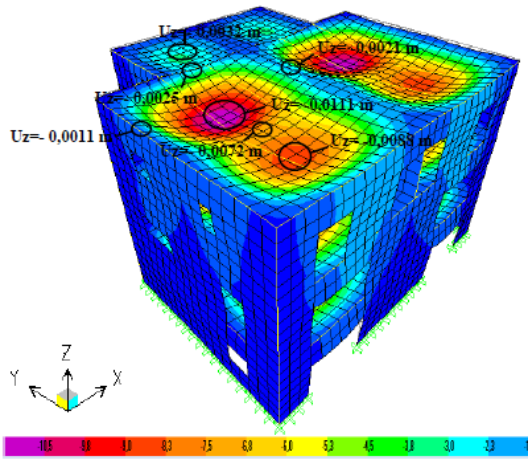
Model CIT-IV, representing the house built with the Composite Innovative Technique (CIT) combining SLWC (800kg/m^3), assuming zero stiffness of SLWC for the infilled walls within the steel frames made by SLWC, employing discretization a (figure 5b).

Model R/C, representing the house built with the Reinforced Concrete (R/C), employing discretization b (figure 5b)

Model PR/M, representing the house built with the Partially Reinforced Masonry (PR/M), employing discretization b (figure 3), employing discretization a (figure 5a).

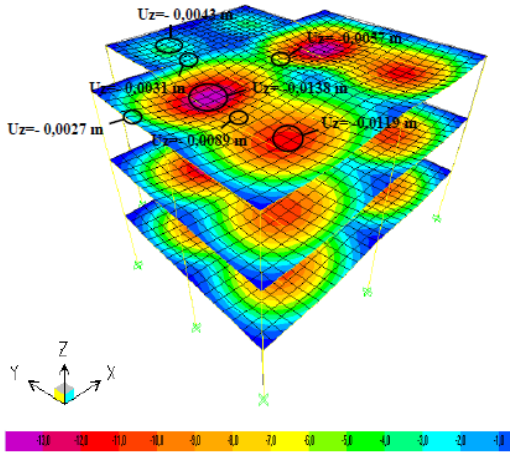
5 PERFORMANCE OF THE SLABS UNDER GRAVITATIONAL FORCES

Figures 4a and 4b depict the deflections of the slab at the top of the 2nd storey as resulting from the load combination *1,35(G1+G2) +1,5Q* whereby: G1 the dead loads, G2 additional dead loads and Q live loads. Figure 4a corresponds to the deflection patterns for *Model CIT-II* whereas figure 4b for *Model CIT-IV*.



1,35(G1+G2) +1,5Q , Model CIT-II

Figure 6a. Deflections of the slab at the top of the 2nd storey



1,35(G1+G2) +1,5Q , Model CIT-IV

Figure 6b. Deflections of the slab at the top of the 2nd storey

Name of Storey Slab	*Model CIT-II,* ***1,35(G1+G2) +1,5Q*** Slab Max. deflections Uz (mm)	*Model CIT-IV,* ***1,35(G1+G2) +1,5Q*** Slab Max. deflections Uz (mm)
Bottom of 1st storey	9.4	12.8
Top of 1st storey	9.8	12.8
Top of 2nd storey	11.1	13.8

Table 3. Slab maximum deflection values

The maximum slab deflection values predicted from these two numerical models for the slabs at all three levels are listed in Table 3. These values correspond to the two examined models, *Model CIT-II and Model CIT-IV,* and for the load combination *1,35(G1+G2) +1,5Q* (figures 6a and 6b)**.**

In order to check whether the slabs constructed in the proposed composite way, that is the utilization of corrugated thin metal steel sheets and the SLWC concrete mix, comply with the criteria of functionality the maximum deflections were also obtained for numerical models *Model CIT-II and Model CIT-IV* for the load combination*(G1+G2) +Q*. This load combination is designates as SIS. The inequality (1) describes the limit ($_{max}\boldsymbol{\delta}^{1all}$) for the maximum deflection of each slab loaded with the load combination SIS ($_{max}\boldsymbol{\delta}^{SIS}$). This maximum allowable deflection $_{max}\boldsymbol{\delta}^{1all}$ for this load combination is set equal to L_{max} / 250. L_{max} the maximum span for the slab that is checked.

$$_{max}\boldsymbol{\delta}^{1all} > _{max}\boldsymbol{\delta}^{SIS} \quad (1)$$

An additional limit was also used for ensuring the functionality of these slabs. This time the maximum deflection of the slab produced by the live loads Q ($_{max}\boldsymbol{\delta}^{Q}$) must be less than $_{max}\boldsymbol{\delta}^{2all}$, (inequality (2). This maximum allowable deflection ($_{max}\boldsymbol{\delta}^{2all}$) is set equal to L_{max} / 350. L_{max} the maximum span for the slab that is checked. This limit value is set for partitions that should have an extra degree of protection otherwise the limit for $_{max}\boldsymbol{\delta}^{2all}$ is set to a less stringent value equal to L_{max} / 300.

$$_{max}\boldsymbol{\delta}^{2all} > _{max}\boldsymbol{\delta}^{Q} \quad (2)$$

The maximum deflection values obtained from the numerical simulation models *Model CIT-II and Model CIT-IV,* representing the structures to be built with slabs with the proposed innovative construction technique, i.e. utilizing corrugated thin metal steel sheets and the novel SLWC concrete mix, comply with the criteria of functionality of their maximum deflections, as described with inequalities (1) and (2) above. These criteria are also satisfied for the reinforced concrete slabs incorporated in *Model R/C* and *Model PR/M.*

6 MODAL ANALYSIS

Table 4 lists the results of the modal analysis in terms of eigen-period values together with the modal mass participation ratio values. This is done for the most significant translational eigen-modes x-x and y-y. Due to the distribution of the mass and stiffness the modal mass participation ratios for the main two translational x-x/y-y modes attains values larger than 66.5% of the total mass. Consequently, the sufficient accuracy can be attained by a dynamic spectral analysis that includes only the first 5 modes as they can mobilize modal masses larger that 85% to 90% of the total mass.

From the values of the eigen-periods for the 4 different models it can be seen that the dynamic system with the smallest eigen-period is *Model CIT-II.* This is due to the fact that this system has relatively less mass due to the presence of the SLWC as infilling material. In addition, the infilling material was given a stiffness equal to 500MPa. When this stiffness becomes equal to zero (*Model CIT-IV*) it results in a rather flexible dynamic system that has larger eigen-period values than the previous model (*Model CIT-II.*). The structure with partially reinforced masonry is stiffer and has larger mass than *Model CIT-II.*

	Eigen-mode	Eigen-Period (sec)	Modal Participation Ratio x-x	Modal Participation Ratio y-y
Model CIT-II	Translation x-x	0.193	0.780	-
	Translation y-y	0.138	-	0.808
Model CIT-IV	Translation y-y	0.370	-	0.830
	Translation[a] x-x	0.359	0.666	-
	Translation[b] x-x	0.275	0.175	-
Model R/C	Translation[a] x-x	0.370	0.083	-
	Translation[b] x-x	0.240	0.665	-
	Translation y-y	0.187	-	0.830
Model PR/M,	Translation[a] x-x	0.203	0.741	-
	Translation y-y	0.167	-	0.751
	Translation[b] x-x	0.071	0.087	-

Table 4. Eigen period and modal mass participation values for *Model CIT-II*

The resulting eigen-period values are somewhat larger than those of *Model CIT-II* and smaller than those of *Model CIT-IV*. The main translational x-x and y-y eigen-modes for model *Model CIT-II* are depicted in figures 7a and 7b, respectively, and for *Model CIT-IV* in figures 7c and 7d.

Model CIT-II

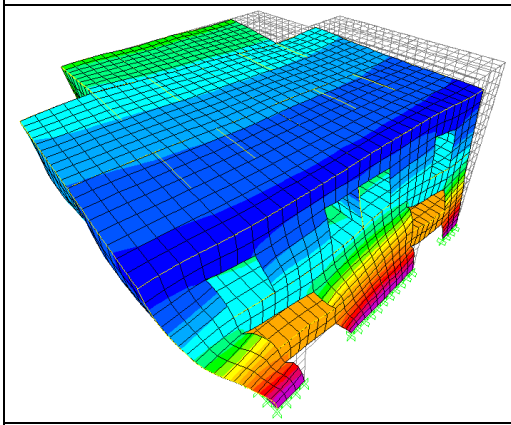


Figure 7a. Translation x-x, Eigen-Period 0.193 (sec) Modal Participation Ratio x-x 0.780

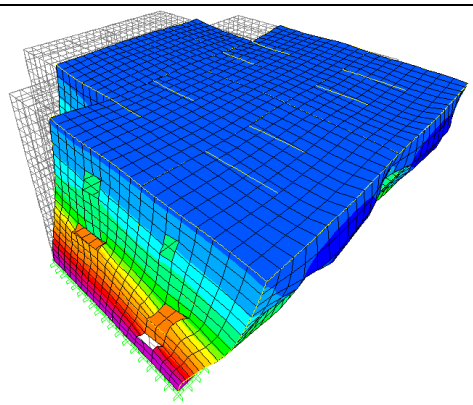


Figure 7b. Translation y-y, Eigen-Period 0.138 (sec) Modal Participation Ratio y-y 0.808

Model CIT-II

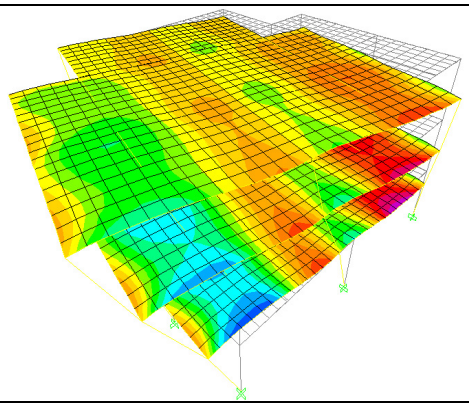


Figure 7c. Translation x-x, Eigen-Period 0.359 (sec) Modal Participation Ratio x-x 0.660

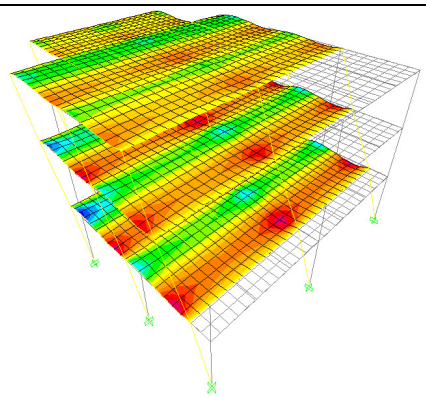
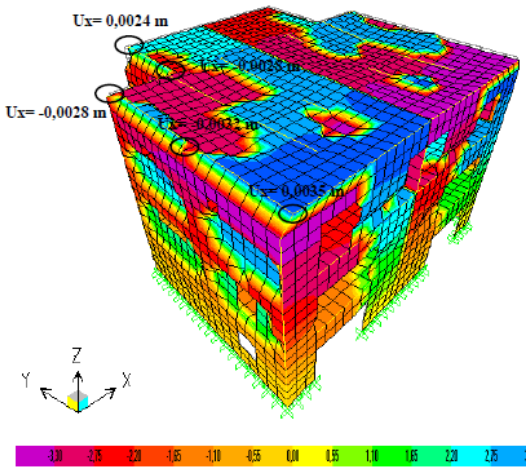


Figure 7d. Translation y-y, Eigen-Period 0.370 (sec) Modal Participation Ratio y-y 0.830

7 DYNAMIC SPECTRAL ANALYSIS

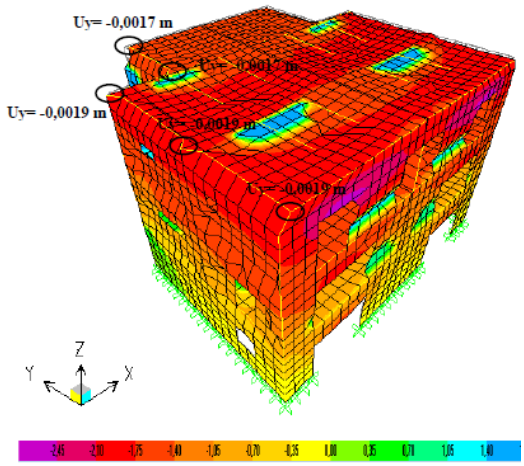
For all four models the dynamic response spectrum analyses were performed, taking into account the provisions of the Greek Seismic Code (EAK2000). As already explained in section 6, the dynamic spectral analysis could attain sufficient accuracy by including only the first 5 modes as they can mobilize modal masses larger that 85% to 90% of the total mass. The summation of the modal responses obtained from the dynamic spectral method are the results produced from the seismic loading designated as "*Seismic*" (either x-x, or y-y). Therefore the following loading combination was examined:

(G1+G2)+0,3Q + Seismic where: G1 the dead loads, G2 additional dead loads and Q live loads. (3)



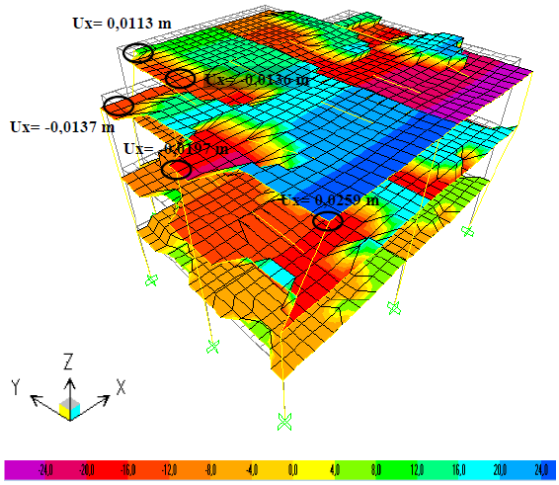
(G1+G2)+0,3Q + Seismic x-x

Figure 8a. Model CIT-II, Earthquake x-x, Maximum horizontal displacement Ux = 3.6mm at top 2nd storey slab



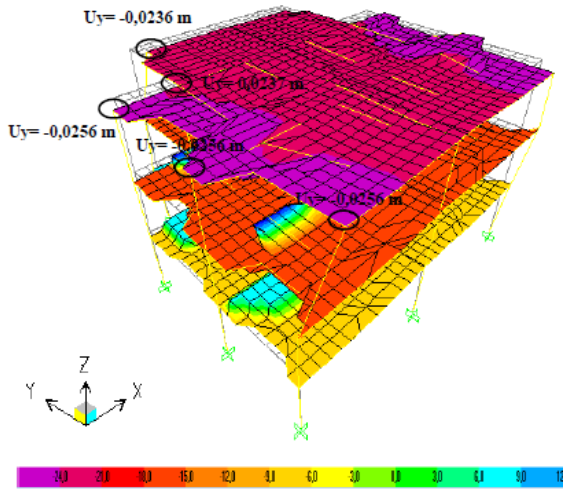
(G1+G2)+0,3Q + Seismic y-y

Figure 8b. Model CIT-II, Earthquake y-y, Maximum horizontal displacement Uy = 2.0mm at top 2nd storey slab



(G1+G2)+0,3Q + Seismic x-x

Figure 9a. Model CIT-IV, Earthquake x-x, Maximum horizontal displacement Ux = 26.0mm at top 2nd storey slab



(G1+G2)+0,3Q + Seismic y-y

Figure 9b. Model CIT-II, Earthquake y-y, Maximum horizontal displacement Uy = 25.6mm at top 2nd storey slab

Figures 8a and 8b display the horizontal displacement patterns for *Model CIT-II* and for load combination (*G1+G2)+0,3Q + Seismic*, in the direction x-x or y-y respectively. This is also depicted in figures 9a and 9b; however, this time for *Model CIT-IV* . Table 5 lists the Maximum horizontal displacement values at the three slab levels. As expected, when the SLWC panels contribute to the horizontal stiffness, as is the case for *Model CIT-II,* the horizontal displacements at the three slab levels are considerably smaller than for the case where such SLWC infill stiffness is ignored, as is the case for *Model CIT-IV.*

Name of Storey Slab	*Model CIT-II,* ***(G1+G2)+ + 0.3Q + Seismic*** Slab Max. Hor. Displacements Ux (mm) / Uy (mm)	*Model CIT-IV* ***(G1+G2)+ + 0.3Q + Seismic*** Slab Max. Hor. Displacements Ux (mm) / Uy (mm)
Bottom of 1st storey	1.4 / 0.8	7.5 / 7.3
Top of 1st storey	2.8 / 1.6	18.3 / 17.9
Top of 2nd storey	3.6 / 2.0	26.0 / 25.6

Table 5. Maximum horizontal displacement values at the three slab levels.

8 COMPARISON OF THE SEISMIC PERFORMANCE

Table 6 lists the base shear as obtained by the numerical solution of the dynamic spectral method utilizing the four models mentioned before. In the dynamic spectral method, the response modification factor was given the value of q=3.5 for *Model CIT-II, Model CIT-IV and Model R/C* and q=2.5 for *Model PR/M.* It is interesting to note that the models representing the proposed innovative construction technique resulted in significantly lower values for the base shear than either the conventional reinforced concrete construction or the construction utilizing partially reinforced masonry.

	Model CIT-II	*Model CIT-IV*	*Model R/C*	*Model PR/M*
Base Shear (KN)	608	608	1467	1720

Table 6. Base shear values as obtained by the four numerical model

In what follows two additional criteria will be employed. First, the maximum non-dimensional shear strain (γ) is obtained through equation (4) based on the maximum inter-storey drift value ($\Delta_{\varepsilon\lambda}$); where q is the response modification value and h is the storey height.

$$\gamma = \frac{q \cdot \Delta_{\varepsilon\lambda}}{2{,}50 \cdot h} \tag{4}$$

Next, a parameter (θ) is calculated, as an indicator of 2nd order effect, employing equation (5), ($N_{o\lambda}$) and ($V_{o\lambda}$) is the sum of the axial and shear forces per storey, respectively.

$$\theta = \frac{N_{o\lambda} \cdot q \cdot \Delta_{\varepsilon\lambda}}{V_{o\lambda} \cdot h} \tag{5}$$

Table 7 lists the maximum values for the parameters (γ) and (θ), as calculated from the numerical results obtained from the four numerical models, that is *Model CIT-II, Model CIT-IV, Model R/C, Model PR/M.* The maximum allowable values for these two parameters, that is γ^{max} and θ^{max} are also listed in this table. As can be seen, the house built with all four construction techniques are below the maximum allowable θ^{max} value, which indicates that they are not susceptible to 2nd order effects. This was expected for the conventional R/C or

partially reinforced masonry construction techniques but it was less obvious for the proposed innovative construction technique, especially when the stiffening effect of the infill SLWC panels is not taken into account. Furthermore, the inter-storey maximum shear strain values are just above the maximum allowable value γ^{max} for *Model CIT IV* and *Model PR/M*. This should be further investigated for the infill SLWC panels. The relatively large γ value for the model representing the partially reinforced masonry construction is due to the large value of the base shear as well as to the relatively low value of Young's modulus assumed in the analysis for this type of construction (1300MPa).

Model	γ maximum value from numerical simulation	γ^{max} maximum allowable value	θ maximum value from numerical simulation	θ^{max} maximum allowable value
Model CIT II	0,00089	< 0,005	0,00853	< 0,10
Model CIT IV	0,00546	≈ 0,005	0,0053	< 0,10
Model R/C	0,00446	< 0,005	0,0043	< 0,10
Model PR/M	0,00602	≈ 0,005	0,058	< 0,10

Table 7. Maximum values of inter-storey shear strain (γ) values and 2nd order effect indicator

9 CONCLUSIONS

1. The dynamic and earthquake behaviour of a typical two-storey residential house with a basement is examined. This structure is built either using R/C or partially reinforced masonry. It is also studied when it is built using an innovative composite construction technique employing special light weight concrete mix and steel parts. The compression, flexural and shear behaviour of such special light weight concrete mix has been documented in a series of experiments conducted for this purpose at the Laboratory of Strength of Materials and Structures of Aristotle University. Similarly, the compression, flexural and shear behaviour of partially reinforced masonry piers was determined

2. From the values of the eigen-periods for the 4 different models it can be seen that the dynamic system with the smallest eigen-period is the model representing the innovative composite construction with an assumed stiffness of 500MPa for the infilling material. This is due to the fact that this system has relatively less mass due to the presence of the SLWC as infilling material. When this stiffness of the infilling material is assumed equal to zero (*Model CIT-IV*) it results in a rather flexible dynamic system with large eigen-period values. The structure with partially reinforced masonry is relatively stiff and has larger mass than *Model CIT-II.*

3. The models representing the proposed innovative construction technique resulted in significantly lower values for the base shear than either the conventional reinforced concrete construction or the construction utilizing partially reinforced masonry. This is mainly due to the low weight of the special SLWC concrete mix. It must also be noted that in the dynamic spectral method the response modification factor was given the value of q=3.5 for the

structures made with either reinforced concrete or with the innovative construction technique and the value of q=2.5 for the structure made by partially reinforced masonry.

4. The slabs of all three construction techniques conform with the functionality requirements. Moreover, all these houses are not susceptible to 2nd order effects.

5. The inter-storey maximum shear strain values are just above the maximum allowable value γ^{max} for the structure constructed with the innovative composite construction technique, assuming zero stiffness of the infilling material. This should be further investigated for the infill SLWC panels. The relatively large γ value for the model representing the partially reinforced masonry construction is due to the large value of the base shear as well as to the relatively low value of Young's modulus assumed in the analysis for this type of construction (1300MPa).

REFERENCES

[1] Mohd Roji Samidi,(1997), First report research project on lightweight concrete, Universitiy of Teknologi Malaysia, Skudai, Johor Bahru.

[2] Eurocode 8 - Design of structures for earthquake resistance - Part 2: Bridges, DRAFT No 3, European Committee for Standardization; 2004.

[3] Greek Code for the Design of Reinforced Concrete Structures, 2000 (in Greek),

[4] Provisions of Greek Seismic Code 2000, Organization of Earthquake Planning and Protection of Greece OASP, Dec. 1999 published by OASP. Revisions of seismic zonation introduced in 2003, Government Gazette, Δ17α /115/9/ΦΝ275, No. 1154, Athens, 12 Aug. 2003.

[5] Tsakalidis V. (2012) "The dynamic and earthquake behaviour of a 2-storey house made with an innovative composite construction technique", Diploma Thesis, Aristotle University, Thessaloniki, Greece.

[6] Stathi Ch., Dimomarkou E., Trikalioti A., (2010), "The dynamic and earthquake behaviour of a 2-storey made by R/C or partially reinforced masonry",Diploma Thesis, Aristotle University, Thessaloniki, Greece.

[7] G.C. Manos, M. Yasin, J. Thawabteh, V. Kourtides. "The earthquake performance of partially reinforced masonry piers subjected to in-plane cyclic loading. G.C. Manos, M. Yasin, J. Thawabteh, V. Kourtides", 9th Canadian Conference on Masonry Structures, Univ. New Braunswick, Canada, 2001.

[8] G.C. Manos, M. Yasin, J. Thawabteh, V. Kourtides, "The performance of partially reinforced masonry walls subjected to combined horizontal cyclic and compressive loads", 6th Int. Masonry Conference, London, Nov. 2002, pp. 284-293.

[9] G.C. Manos, M. Yasin, "The Earthquake Performance of Partially Reinforced Brick Walls under horizontal in-plae cyclic loading", 12th European Earthquake Engineering Conference, London, England, 2002.

[10] G. C. Manos, M. Yasin, Thawabteh, V. Kourtides, "The Performance of Partially Reinforced Masonry Subjected to Horizontal Cyclic and Compressive Loads", 9th North American Masonry Conference, Clemson Univ., North Carolina, USA, 2003.

COMPDYN 2013
4th ECCOMAS Thematic Conference on
Computational Methods in Structural Dynamics and Earthquake Engineering
M. Papadrakakis, V. Papadopoulos, V. Plevris (eds.)
Kos Island, Greece, 12–14 June 2013

INFLUENCE OF THE LOADING RATE ON THE AXIAL COMPRESSIVE BEHAVIOR OF CONCRETE SPECIMENS CONFINED WITH SRG JACKETS

Georgia E. Thermou[1], Konstantinos Katakalos[1], and George Manos[1]

[1] Aristotle University of Thessaloniki
Dept. of Civil Engineering, 54124, Thessaloniki, Greece
gthermou@civil.auth.gr; kkatakal@civil.auth.gr; gcmanos@civil.auth.gr

Keywords: Retrofit, Strengthening, Jackets, Steel reinforcement, Axial compression, Loading rate

Abstract. *In the present paper, an experimental study was carried out where the main objective was to investigate the favorable confinement characteristics of steel reinforced grout (SRG) jackets on the compressive behavior of unreinforced concrete prisms under monotonic and cyclic axial loading. SRG jackets were made by applying steel fiber reinforced fabrics of reduced density combined with cementitious grout that serves as the connecting matrix. For this purpose, one layer of the novel jacketing system was applied to a number of unreinforced concrete prismatic specimens constructed for a moderate concrete cylindrical compressive strength of 25 MPa. The parameters of this investigation were: a) the density of the fabric used in the steel reinforced concrete jackets and b) the rate of axial loading. The density of the fabric was either medium (2 cords/cm) or relatively low (1 cord/cm). The specimens were subjected to monotonic concentric uni-axial compression load applied either in a slow rate reaching the maximum load in 400 secs or at a axial load rate ten times faster. Both the slow rate load and the fast rate load were applied in the following manner. Initially, approximately 50% of the maximum load was reached in 3 load-unload cycles that were followed by 3 load-unload cycles at approximately 75% of the maximum load before the specimen reached the maximum load and failure at a final loading cycle. The experimental sequence was carried out at the Laboratory of Strength of Materials and Structures of Aristotle University of Thessaloniki. The magnitude of the maximum load reached, as well as the mode of failure attained at the end of each loading sequence was monitored. From the obtained results, the influence of the loading rate on the ultimate compressive load and on the mode of failure in relation to the SRG jacket characteristics was studied. The whole effort intended to examine the effect on the response behavior of SRG jacketed specimens when axial load is dynamic in nature.*

1 INTRODUCTION

Reinforced concrete (RC) structures built according to older generation of codes present deficiencies related to structural integrity issues. Retrofitting is deemed necessary in order for this category of structures to survive future earthquake events by avoiding premature failure modes. When the retrofit strategy requires local intervention measures (at member level) to be taken or when the objective is the enhancement of the ductility level, then one of the most widely applied methods is wrapping with composite fabrics (carbon, glass or aramid). Although fiber reinforced polymer (FRP) jacketing is considered an efficient intervention method combining many advantages (no change in the geometry, fast in application, high-strength-to-weight ratio, corrosion resistance), issues related mainly to the high cost (due to the use of epoxy resins) and poor behavior of resins at high temperatures have led the research community to the investigation of new materials that will keep the easiness in application of the method (e.g. FRM [1], TRM [2]).

Within this framework, the last decade a new material has been introduced, the steel reinforced fabric combined with either polymer (SRP) or grout (SRG). This type of fabric consists of high strength steel cords embedded in epoxy resin or grout matrix. Most of the applications concern the use of SRP as externally bonded longitudinal reinforcement in flexural members [e.g. [3]-[13]]. The use of the steel reinforced fabric as a jacketing device was investigated experimentally to predamaged cantilever specimens of old type detailing for the first time in 2007 by Thermou and Pantazopoulou [14]. The proposed jacketing system comprised steel fiber reinforced fabrics of reduced density (this was required in order to improve impregnation of the metallic fibers in the intended matrix but also to reduce axial stiffness of the metallic fabric to the level of a carbon sheet) combined with cementitious grout that served as the connecting matrix. Recently, El-Hasha and Mashrik [15], El-Hacha and Abdelrahman [16] investigated experimentally the confinement effectiveness of resin impregnated high density steel fibre reinforced fabric (SRP) jackets applied to both cylindrical and prismatic specimens.

The SRG jacketing system proposed by Thermou and Pantazopoulou [14] was implemented in a large number of cylindrical specimens subjected to axial monotonic compression [17]. The results have shown that both strength and deformability were improved substantially for a single layer of jacket of medium to low density (The gain in compressive strength ranged between 47% and 84%, whereas the gain in ultimate strain ranged between 166% and 366%). Based on these promising results, the objective was to investigate further the potential of the SRG jackets, this time by applying the proposed retrofit scheme on prismatic specimens of square cross section subjected to both monotonic and cyclic axial compression. Despite the adverse effect of the edge sharpness increase on the confinement effectiveness, it was decided to keep a zero corner radius in order to simplify construction. Moreover, the nature of the loading was a parameter of study in order to observe the influence of the loading rate on the effectiveness of the SRG jackets.

An experimental study was carried out where the main objective was to investigate the effectiveness of SRG jackets on prismatic specimens with sharp edges subjected to both slow-rate and fast-rate axial compression up to failure. The slow-rate compression was applied in a monotonic way whereas a small number of cycles of load-unload were used in the fast-rate compression. Tests parameters were the density of the steel reinforced fabric and the nature of loading. The results have shown the SRG jacketing schemes tested herein provided a higher compressive strength compared to their unconfined counterparts. The role of the type of loading was revealed. The fast rate loading simulating dynamic loading in nature had a detri-

mental effect on the response of both unconfined and confined concrete prisms, rendering in some cases the applied confining measure ineffective.

2 CONFINEMENT OF UNREINFORCED CONCRETE PRISMATIC MEMBERS WRAPPED WITH COMPOSITE FABRICS

2.1 Edge sharpness impact on the axial compressive strength

The shape of the cross section influences in a determinant way the effectiveness of composite fabric jackets in increasing both strength and ductility of unconfined plain concrete. Experimental evidence has shown that as the edge sharpness of non-circular cross sections increases the composite wraps become less efficient [18]. This is explained by the fact that the confining internal lateral pressure is not uniformly distributed over the rectangular cross and instead confined and unconfined regions are developed (Fig. 1). The effect of the zero corner radius on the behavior of axially loaded fiber reinforced polymer (FRP) jacketed prismatic specimens has been studied experimentally by a number of researchers the majority of whom claims that a certain degree of effective confinement is provided by a jacket with sharp corners [19-21]. The experimental study of Wang and Wu [18], where 108 prismatic specimens were confined with FRP jackets with various corner radius, shed light on the influence of the corner radius on the strength and ductility increase. It was found that the strength gain of confined concrete columns, f_{cc}/f_{co} is in direct proportion to the corner radius ratio and independent of the confinement level and the concrete quality. Although no strength increase was observed in jacketed specimens with sharp corners, higher ductility levels were reached indicating the increased deformability ought to the provided confinement. Moreover, it was found that the attained ductility depends on both the concrete quality and corner of radius. Thus, for concrete quality C30/37 confinement is effective in increasing the ductility only in specimens with sharp or small corners, whereas for concrete quality C50/60 confinement is effective in increasing the ductility of all the column types.

The influence of the shape of the cross section on the effectiveness of the composite jackets is reflected through the confinement effectiveness coefficient [22]:

$$k_e = 1 - \frac{(b-2r)^2 + (h-2r)^2}{3A_g(1-\rho_l)} \tag{1}$$

where b, h are the width and height of the cross section, r is the corner radius, A_g is the cross sectional area and ρ_l is the percentage of the longitudinal reinforcement. The confinement effectiveness coefficient of the jacket becomes, k_e=1, for circular cross sections.

The lateral confining pressures induced by the FRP wrapping reinforcement on a rectangular cross section in the two principal directions are equal to [22]:

$$f_{lx} = \rho_{jx} k_e E_j \varepsilon_{ju} \text{ and } f_{ly} = \rho_{jy} k_e E_j \varepsilon_{ju} \tag{2}$$

where ρ_{jx}, ρ_{jy} are the volumetric ratios of the FRP jackets, k_e is the confinement effectiveness coefficient, E_j is the elastic modulus of the FRP wrap and ε_{ju} is the nominal deformation capacity of the jacket material. From Eqs. (1) and (2), it is evident the influence of the shape of the cross section on the provided lateral confining pressure.

All the above refer to the research that has been conducted so far on prismatic specimens wrapped with composite FRP jackets. The behavior of steel reinforced grout (SRG) jacketed prismatic specimens under compressive load is still under investigation. It is expected that the

corner radius is going influence the SRG jacketed members in the same way as in the FRP jacketed ones. In the test specimens presented herein, it was decided the sharp edges of the specimens to be left intact in order to simplify jacket construction.

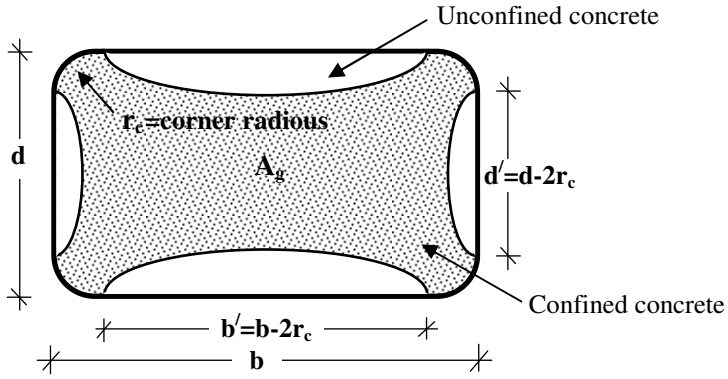


Figure 1: Confined core for rectangular cross sections.

2.2 Axial cyclic compression and its effect on confined concrete

The knowledge of the stress–strain behavior of concrete confined after wrapping with composite fabrics under cyclic compression is of particular interest in the seismic design of retrofitted structures as well as in performing nonlinear dynamic analysis. The majority of the experimental and analytical studies conducted so far focus on either FRP confined concrete cylinders or FRP confined specimens with rectangular cross section (concrete prisms) subjected to monotonic axial compression loading (e.g., [19]-[21],[23]-[25]). On contrary, the effect of axial cyclic compression on FRP confined specimens has been studied by a limited number of researchers (e.g., [26], [27]]. The research carried on FRP-confined concrete prisms is even more limited (e.g., [28]-[32]). Experimental evidence related to both unreinforced and reinforced FRP-confined specimens of various shapes and sizes subjected to different loading patterns (involving single or multiple complete unloading / reloading cycles at prescribed displacement levels, as well as partial loading / reloading cyclic loading) revealed the general trend which is that the envelope curves of cyclic stress–strain response are almost identical to the monotonic stress–strain responses of geometrically equivalent specimens.

The response of FRP-confined unreinforced prismatic specimens subjected to axial cyclic compression, was studied by Abbasnia and Ziaadiny [30], Abbasnia et al. [31, 32] with parameters of investigation the patterns of cyclic loading, the confinement level and the aspect ratio of the cross section. The main conclusions drawn are that: (i) the envelope curve of the cyclic stress-strain curve is similar to the monotonic stress-strain curve; (ii) plastic strain of FRP-confined concrete prisms is a linear function of the envelope unloading strain; (iii) unloading/reloading cycles have cumulative effect on the plastic strain and stress deterioration; (iv) the stress deterioration and plastic strain are independent of the column parameters; and (v) the unloading path is highly nonlinear and is dependant to the unconfined concrete strength. Moreover, it is commented by the authors that the effect of the sharpness of the section on the cyclic behavior of the FRP-confined prisms is an open issue that requires further research. Wang et al. [31] investigated the influence of axial cyclic compression to both reinforced and unreinforced square C-FRP confined columns. With test variables the section size, the volumetric ratio of hoop reinforcement, the number of layers of CFRP wrap and the damage level before CFRP wrapping, the square cross section columns were subjected to monotonic or cyclic axial loading. For one more time, it was observed that the envelope curves of

specimens subjected to cyclic loading were almost identical to the stress-strain responses of the monotonically loaded specimens. Other conclusions drawn are: (i) specimens subjected to cyclic axial compression attained larger axial strains compared to the monotonically loaded counterparts; (ii) failure of columns is postponed if subjected to unloading/reloading cycles; (iii) predamage had little effect on the monotonic stress-strain response; and (iv) the hoops provided influenced the ultimate axial strain capacities, the shape of the stress-strain curves and the shape of the unloading path and the plastic strains. Based on the results of their experimental campaign, Wang et al. [32] proposed an axial stress-strain model for C-FRP square reinforced confined RC columns which comprises a monotonic stress-strain model to describe the envelope curve, a polynomial expression for the unloading path and a straight line for the reloading path (Fig. 2).

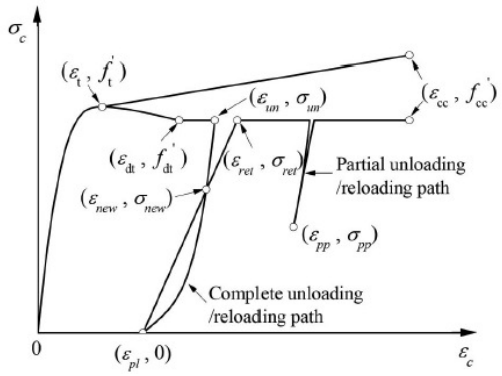


Figure 2: Schematic Cyclic stress-strain model proposed by Wang et al. [2].

3 EXPERIMENTAL PROGRAM

A number of unreinforced prismatic specimens with a 200-mm square cross section and a specimen height of 600 mm was tested in uni-axial compression (Fig. 3(a)). All specimens were wrapped with a single layer of steel fabric with the orientation of the high strength cords depicted in Fig. 3(b). The parameters considered in the investigation were: a) the density of the steel fabric and b) the rate of axial loading.

Two types of steel reinforced fabrics were used in the experimental program, the 3X2 and 12X (Fig. 3(c)). The 3X2 wire cord is made by twisting five individual wires together – three straight filaments wrapped by two filaments at a high twist angle, whereas the 12X wire cord is made by twisting two different individual wire diameters together in 12 strands with over twisting of one wire around the bundle. The density of the fabric related to the number and spacing of the steel cords was selected to be 2 cords/cm and 1 cord/cm, respectively, corresponding to medium and low density fabrics. The objective of utilizing fabrics of different type (12X and 3X2) and density (2 cords/cm, 1 cord/cm) was twofold. The different density aimed at investigating the influence of the fabric tensile strength on the provided lateral confining pressure, whereas the use of different types intended to examine whether the different surface roughness distribution has any effect on the quality of the interfacial mechanical interlock between the cords and cementitious grout matrix.

The rate of axial loading and its effect on the response of the steel grout jacketed specimens was another parameter of investigation. The specimens were subjected to monotonic concentric uni-axial compression load applied either in a slow rate reaching the maximum load in 400 sec or at a axial load rate ten times faster.

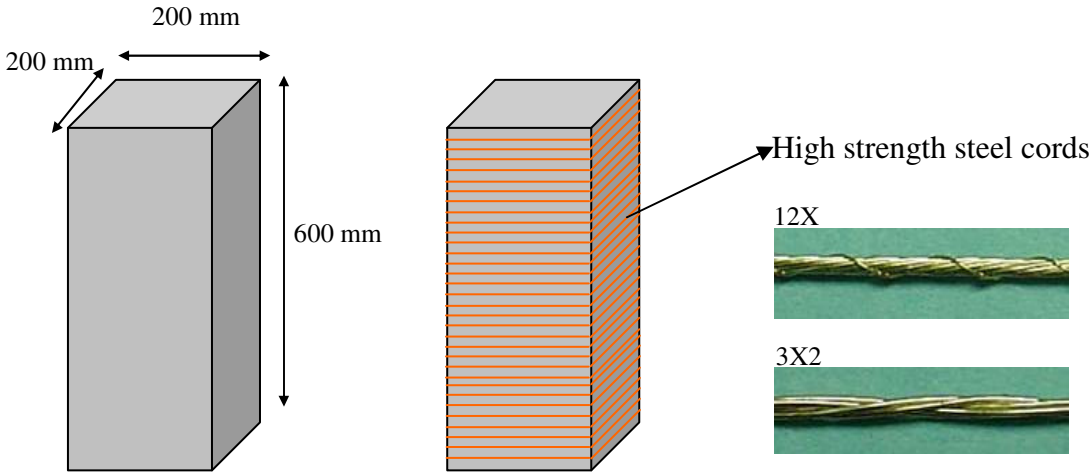


Figure 3: (a) Specimen geometry; (b) column wrapping – orientation of cords; (c) types of cords.

3.1 Test specimens

The number and characteristics of the test specimens appear in Table 1. Three prismatic specimens, No 1a, 13 and 14, were used as control specimens. With parameters the type of the steel fabric and its density four different jacket schemes are defined. Two of them were applied in the specimens of the current experimental study. The 3X2 low density steel reinforced fabric (1 cord/cm, i.e. spacing between successive cords 1 cm), named hereafter 3X2/1, was applied to specimens No 10 and No 12, whereas the 12X medium density fabric (2 cords/cm, i.e spacing between successive cords 5 mm), name hereafter 12X/0.5 cm, was applied to No 7, No 8 and No 9 specimens. In two of the jacketed specimens, No 7 and No 12, confinement was enhanced by the addition of an anchorage system placed at the end of the lap. Two load sequences were considered differentiated by the rate of the applied load and the inclusion or not of load/unload cycles. The slow rate loading, denoted as *slow* in Table 1, was applied at approximately 400 secs to specimens No 13, No 14 (unconfined) and No 9 (confined). The fast rate loading which included three load/unload cycles at two levels of the maximum axial load attained (a detailed description in provided in section 3), was applied 10 times faster to specimens No 1a (unconfined), No 7, No 8, No 10 and No 12 (confined).

Specimen ID	SRP type	Density (cords/cm)	Anchoring	Load type
1a	Control	Without confinement	No	fast
13	Control	Without confinement	No	slow
14	Control	Without confinement	No	slow
7	12X	2	Yes	fast
8	12X	2	No	fast
9	12X	2	No	slow
10	3X2	1	No	fast
12	3X2	1	Yes	fast

Table 1: Specimen details.

3.2 Material properties

The prismatic specimens were cast in one batch using concrete of moderate compressive strength classified as C25/30 (EC2, 2004). The concrete compressive strength defined by three cubes of 200 mm was 36 MPa. Both top and bottom surface of the specimens were

capped with a self-leveling high-strength mortar in order to ensure smooth surface for uniform loading.

The two types of high carbon steel cords, 3X2 and 12X, utilized in the experimental program had a micro-fine brass also known as AOBrass (adhesion optimised) coating. The tape density of the original 3X2 and 12X steel reinforced fabrics, as produced by the manufacturer, was 9.06 cords/cm considered high-density tape (Fig. 4(a)). The modified density of both the 3X2 and 12X consisted of 1 and 2 cords/cm characterized herein as low and medium density, respectively (Fig. 4(b)). Redundant cords were removed manually, paying attention not to damage the underlying net that essentially keeps the cords in position. The distance of 1.0 and 0.5 cm between successive cords in the low and medium density was considered satisfactory for uninhibited flow of the cementitious grout through the steel reinforced fabric. The mechanical properties of the steel reinforced fabrics used in the experimental study are presented in Table 2. The axial stiffness of the two types of fabric used for wrapping the prismatic specimens are: i) for 3X2/1 $K_f^{3X2/1}$=7320 N/mm and (ii) for 12X/2 $K_f^{12X/0.5}$=13158 N/mm.

Steel fabric type	Density (cords/cm)	Tape tensile load (N/cm)	Equivalent tape thickness (mm)	Tape stress (MPa)
12X	1	1250	0.062	2013.8
	2	2500	0.124	2013.8
3X2	1	1539	0.062	2479.4
	2	3078	0.124	2479.4

Table 2: Tape properties of the steel fabric types utilized in the experimental program.

A commercial cementitious grout with fibres and special additives was utilized as a binding material for the application of the SRP jackets. The mechanical characteristics at 28 days according to the manufacturer are flexural strength 6.78 MPa, compressive strength 22.1 MPa and adhesion to dry concrete 1.88 MPa.

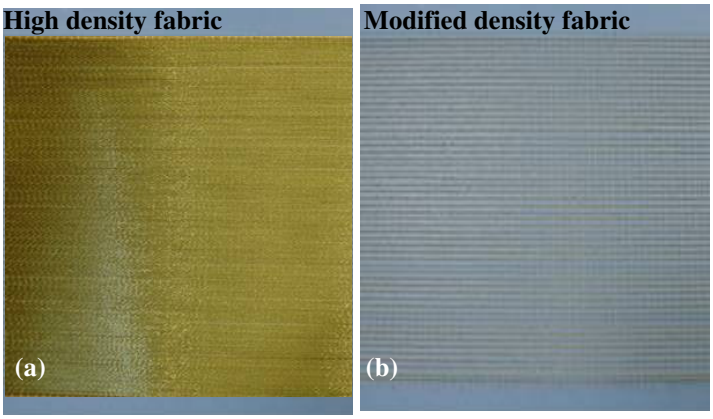


Figure 4: Steel reinforced fabric of (a) high and (b) modified density.

3.3 SRG wrapping

The first step of the proposed jacketing device comprised the application of a thin layer (≈0.5 cm) of cementitious grout placed manually with the help of a trowel directly onto the lateral surfaces of the prismatic member (Fig. 5(a)). The application of the steel fabric followed. In order for the fabric to be embedded in the connecting matrix, the grout was squeezed out between the rovings of the fabric by applying pressure manually (Fig. 5(b)). The

fabric was applied to one full-cycle with an overlapping length equal to the length of the side of the prismatic member (Fig. 5(c)). A final coat of the cementitious grout was applied to the exposed surface (Fig. 5(d)). The thickness of the grout layer including the steel fabric was only 10 mm thick.

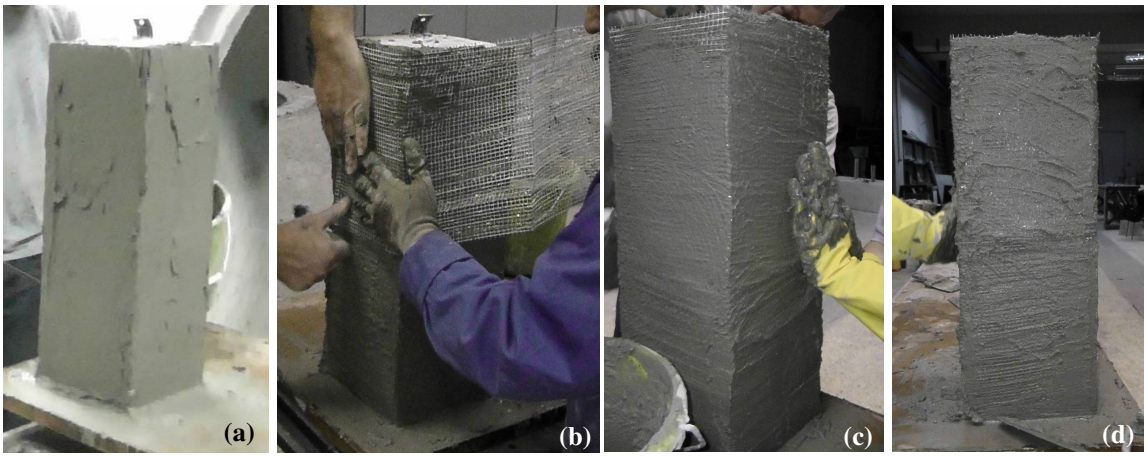


Figure 5: Application of the SRG jacket.

3.4 Confinement enhancement by the addition of an anchoring device

The previously described confinement schemes were selectively enhanced by adding the anchorage system depicted in Figs. 6(a), (b) (see Table 1). The scope behind the use of this anchoring scheme was to prevent sliding of the steel fabric from the end of the lap. Despite the fact that this was considered a probable mode of failure, it was not observed. Instead tensile fracture of the high strength steel cords at the corners of the prismatic specimens was the prevalent mode of failure . This justifies why the use of the anchorage system did no have any effect on the observed compressive strength as shown by experimental evidence (section 5).

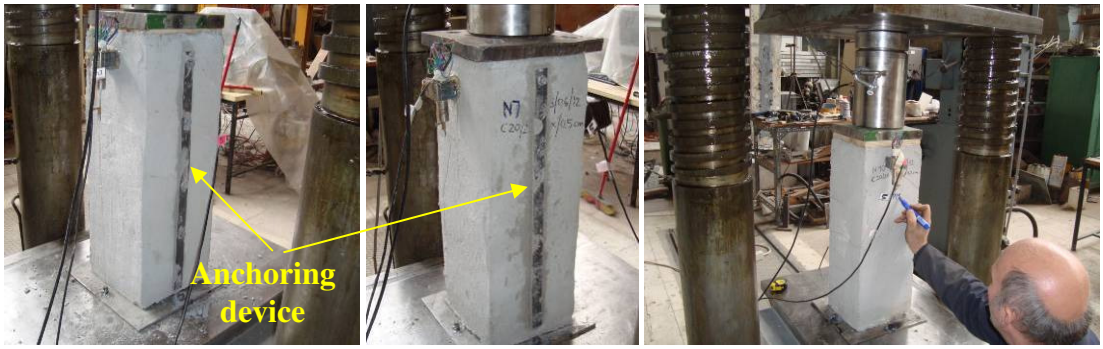


Figure 6: (a), (b) Confined specimens that include the applied anchoring; (c) Loading arrangement of the specimens placed at the loading machine.

4 INSTRUMENTATION AND LOADING ARRANGEMENT

The prismatic specimens were loaded till failure by using a compression testing machine of 6000 kN capacity. Specimens placed on the steel platform of the loading machine in such a way that the compressive load was applied along their central axis (Fig. 6(c)). The two end platforms of this loading machine are linked in a hinge manner in order to prohibit the development of moments at the end of the specimens. The applied axial compressive load was monitored by using a 5000 kN capacity load cell placed above the specimens, whereas verti-

cal deformations measured by using four linear variable displacement transducers (LVDTs) mounted at each side at the mid-height of the column. The axial compressive strain (shortening) of the specimen was found from averaging these vertical deformations and assuming a uniform distribution over the height of the specimen. The axial compressive stress value that corresponds to an axial load level was found by assuming uniform distribution of the axial compressive stress in the horizontal cross section of the specimen.

Two distinct types of loading sequences were applied. As far as the first loading sequence is concerned, the load was applied monotonically up to failure in a relatively slow rate reaching its highest value at approximately 400 seconds. In the second loading sequence an axial compressive load was again applied; however, this time three load-unload cycles were introduced in two levels of the axial load which corresponds to approximately 1/2 and 2/3 of the maximum load attained. These six load-unload cycles were followed with a final monotonic load increase up to failure of the specimen. The second loading sequence was applied at a relatively fast loading rate so that the six load-unload cycles together with the final loading up to failure took approximately 40 seconds being 10 times faster than the first loading sequence. With the available testing machine this was the fastest loading rate that could be possibly applied. This second sequence of load-unload cycles that are combined with a relatively faster rate of loading than the conventional slow-rate monotonic load termed herein as *fast* load simulates in laboratory conditions the axial compressive loads applied in a dynamic manner at vertical structural members located at the low levels of multi-story structures. Such loads resulting from the overturning mode of response due to the horizontal seismic forces are considered as additional axial loads to the axial loads resulting from other actions.

5 DISCUSSION OF OBTAINED RESULTS

In what follows the obtained results are presented in plots that depict for each tested specimen the variation of the applied load in terms of axial compressive stress together with the corresponding variation of the deformation of each specimen in terms of corresponding strain values reflecting the vertical shortening of each specimen.

The following parameters are examined:

(a) The effect of the loading rate; i.e. the effect of the two loading sequences described previously.

(b) The effect of the confinement for the two distinct schemes of confinement; namely 3x2/1 and 12X/0.5.

5.1 Effect of loading rate on unconfined concrete prisms

Figure 7 depicts the axial compressive stress – axial strain curves as obtained from three unconfined (No1a No13 and No14) concrete prismatic specimens. Two of the specimens (No13 and No14) were subjected to monotonically increasing axial load without any load-unload cycles adopting the conventional slow rate. The third specimen was subjected to the fast load sequence with the characteristics described in the previous section (i.e. the load was applied 10 times faster compared to specimens No13 and No14 and three load-unload cycles were introduced at two levels of the axial stress).

The average maximum compressive stress specimens No 13, No 14 loaded with the slow load rate was found equal to 31.1 MPa whereas the corresponding value for specimen No1b loaded with the fast load rate was found equal to 27.76 MPa, presenting a decrease of approximately 11%. Thus, it seems that the fast load sequence leads to a slight decrease in the axial

compressive strength but to an improved level of ductility. The modes of failure for the two types of loading are depicted in Fig. 8.

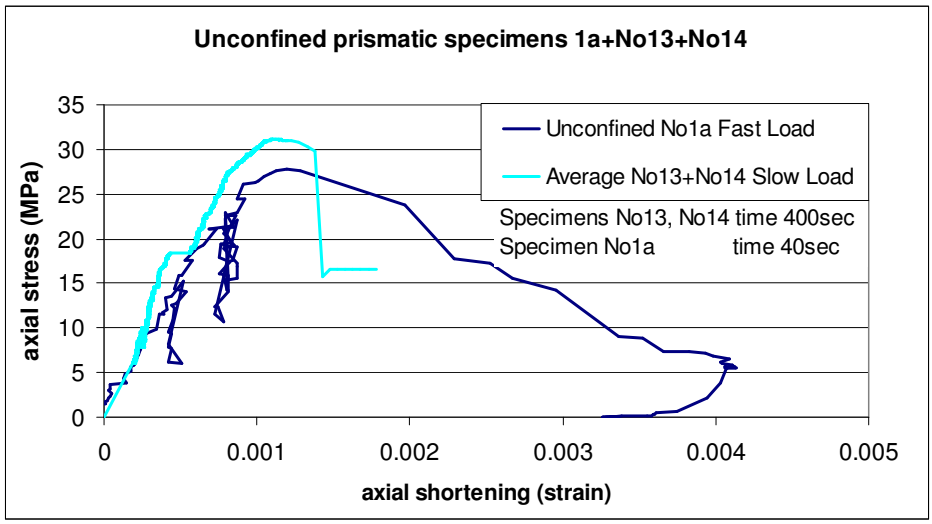


Figure 7: Comparison of axial stress – axial strain curves for the unconfined prismatic specimens subjected to the *fast* and *slow* loading sequences.



Figure 8: Mode of failure of unconfined specimens No 1a (fast loading rate) and No 13, No 14 (slow loading rate).

5.2 Effect loading rate on SRG confined concrete prisms

In Fig. 9 the response of two confined prismatic specimens (No10 and No12) subjected to the fast loading sequence are compared to the response of the unconfined prismatic specimens presented in the preceding section (No 1b, No 13, No 14). Both No 10 and No 12 specimens were confined by using the low density 3X2 steel fabric (1 cord/cm, see Table 1). The confinement of specimen No 12 was further enhanced by employing an anchoring scheme which aimed at delaying sliding of the steel fabric from the end of the lap (Fig. 4(a), (b)). The maximum axial compressive stress attained for specimen No 10 was equal to 30.85 MPa, whereas in the case of specimen No 12 a higher value was reached equal to 33.80 MPa due to the addition of the confinement device. These values represent an increase of 21.8% and 11.1% respectively, when they are compared to the corresponding maximum axial compressive stress value (27.76MPa) of the unconfined specimen No1a loaded with the same fast load rate conditions as the confined specimens.

From the above, it is evident that the steel fabric jacketing alone (without anchoring system) has a relatively small effect on the increase of the axial compressive strength when compared to that of the unconfined specimens (11.1% increase). The use of a simple anchoring scheme as in the case of specimen No 12 doubles the increase of the axial compressive strength of the jacketed specimens as compared to the corresponding one of the unconfined specimens (21.8% increase). Moreover, if the maximum compressive stress of the simple confinement specimen No 10 under fast loading rate (30.8 5MPa) is compared with that of the unconfined specimen (31.1 MPa) under slow loading rate (average of specimen No13 and No14) it is concluded that the low density steel fabric jackets (3X2, 1 cord/cm) cannot fully compensate for the loss of strength due to the relatively fast application of the load.

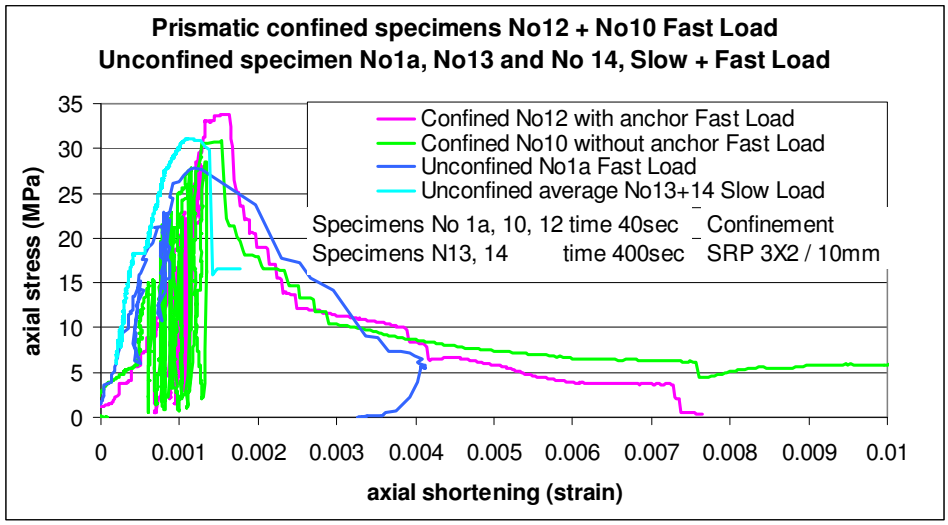


Figure 9: Comparison of axial stress – axial strain curves of the confined prismatic specimens No 10 and No12 to the unconfined prismatic specimens No 1a, No 13 and No 14 subjected to the *fast* and *slow* loading sequences.

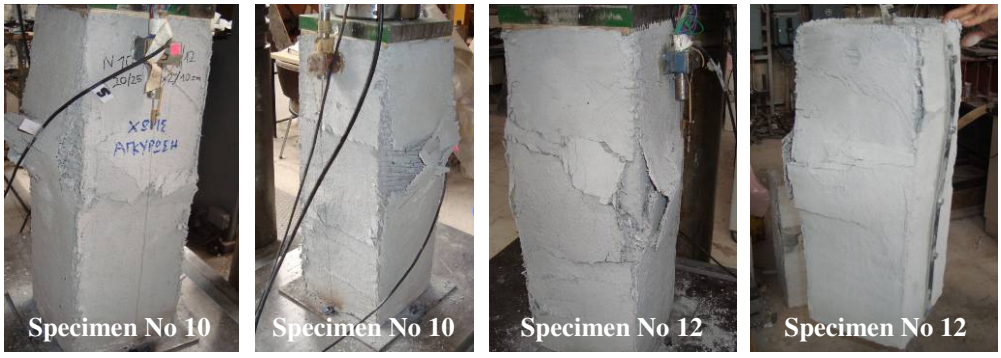


Figure 10: Mode of failure of confined specimens No 10 (without anchor, fast Load) and No 12 (with anchor, fast Load).

Figure 11 depicts the axial stress – axial strain response curves of specimens No 7, No 8 and No 9, which were all jacketed by employing the medium density 12X steel fabric (2 cords/cm, Table 1). The confinement of Specimen No 7 was further enhanced by employing the anchorage system presented in Figs. 4(a), (b). Specimens No 7 and No 8 were subjected to the fast loading rate, whereas specimen No 9 was subjected to the slow loading rate.

The comparison of the maximum axial compressive stresses attained for specimens No 7 (27.1 MPa) and No 8 (28.5 MPa) reveals that the anchorage system placed in specimen No 7 did not have any effect in increasing its maximum compressive strength (both specimens were subjected to the fast loading rate). At the same time specimen No 9 (simple confinement but loaded with the slow loading rate) reached a compressive strength equal to 36.41 MPa. Thus, for the 12X medium density jackets (2 cords/cm) a decrease of at least 21.7% of the maximum compressive strength can be attributed to the fast rate of loading (comparison between the maximum axial stresses attained by No 8 and No 9).

This decrease is twice as much as the corresponding decrease that was observed by comparing the obtained compressive strength of unconfined specimens No1b (27.76 MPa, fast load) and No13, No14 (31.1 MPa, slow load) depicted in Fig. 7. This is also shown in Fig. 13 where the obtained stress - strain response curves of confined specimens No 7, No 8 and No 9 are compared to the corresponding ones for the unconfined specimens No 1b, No 13 and No 14.

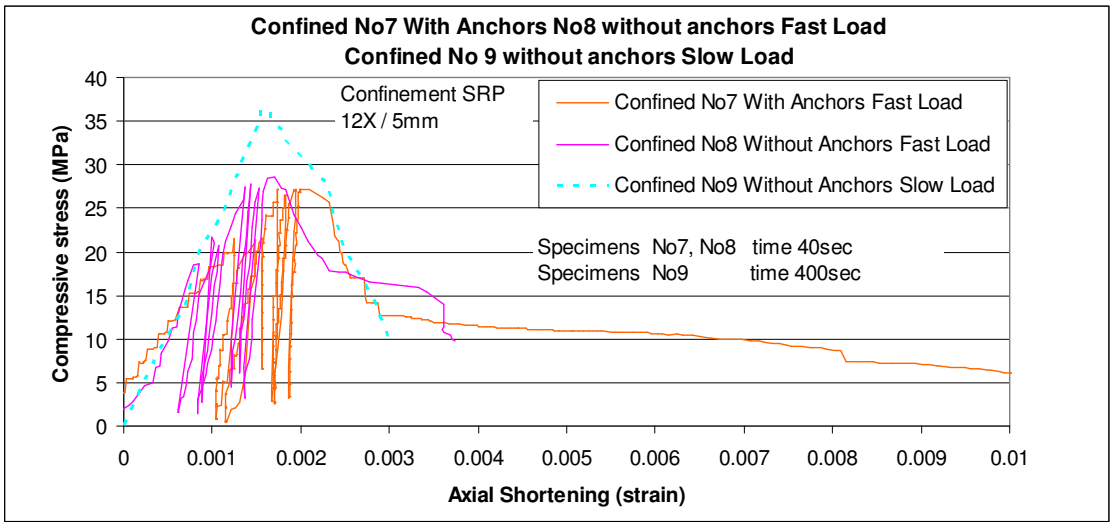


Figure 11. Comparison of axial stress – axial strain curves of the confined prismatic specimens No 7, No 8 and No 9 subjected to the *fast* and *slow* loading sequences.

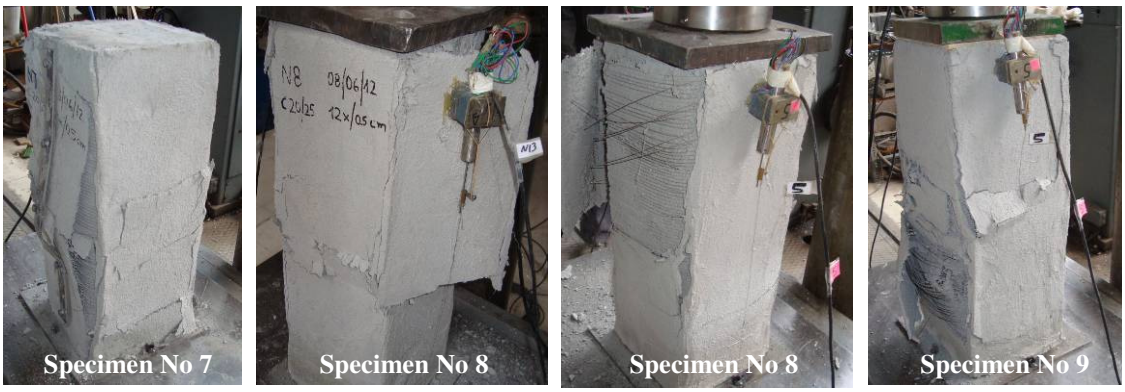


Figure 12: Mode of failure of confined specimens No 7 (with anchor, fast load), No 8 (without anchor, fast load) and No 9 (without anchor, slow load).

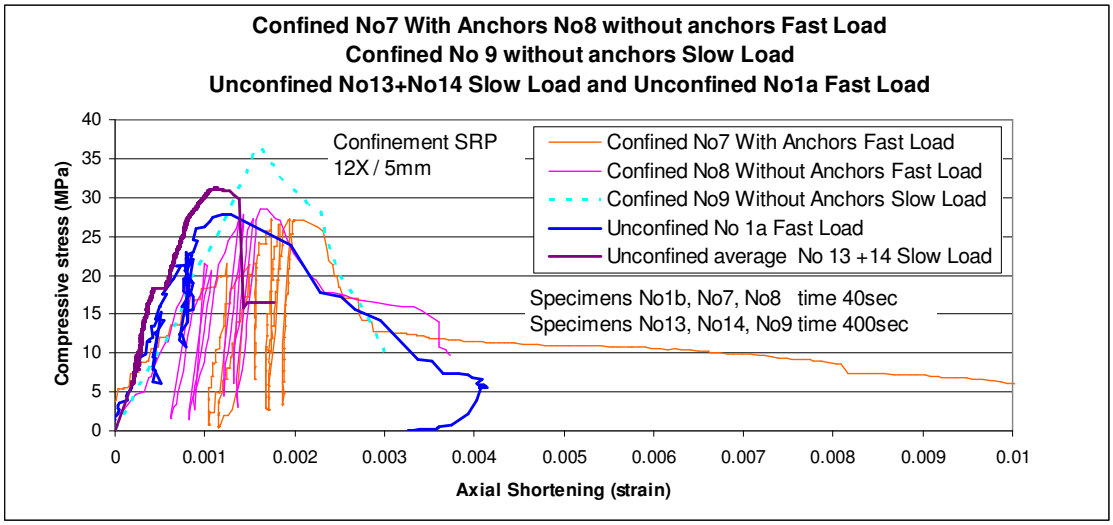


Figure 13. Comparison of axial stress – axial strain curves of the confined prismatic specimens No 7, No 8 and No 9 and the unconfined specimens No 1b, No 13 and No 14subjected to the *fast* and *slow* loading sequences.

6 CONCLUSIONS

The behavior of steel reinforced grout (SRG) jacketed concrete prisms subjected to both monotonic and cyclic axial loading was investigated experimentally. A single layer of steel reinforced fabric was applied to all specimens. Alternative jacketing schemes were applied depending on the density and the type of the fabric. The uni-axial compression load was applied to either a slow rate reaching the maximum load in 400 secs or at an axial load rate ten times faster. Despite the relatively small number of specimens used in the present investigation the following general conclusions can be drawn:

1. The fast loading rate of the applied axial compressive load results in an 11% decrease of the obtained strength of unconfined prismatic specimens.
2. In case of the medium density 12X (12x/0.5) SRG jackets, the slow rate of loading demonstrates an increase in compressive strength of 17%, whereas the fast rate load render this confinement ineffective as the obtained compressive strength of the confined specimen is almost the same as that of the unconfined specimen.
3. The recorded compressive strength of the low density (3x2/1) SRG jacketed specimens subjected to the fast loading rate considering also the favorable effect of the anchoring system is 22% larger than the unconfined strength for the same loading rate but only 9% higher compared to the slow loading rate of the unconfined strength.
4. Despite the preliminary nature of all these results it is revealed that such a dynamic application of compressive loads can lead to significant strength decrease for the tested confinement schemes that can almost render them ineffective. This does not mean that such an adverse effect can be expected to result from the dynamic application of the compressive load to any confinement scheme. However, it is a problem that should be investigated further considering also the effect of the edge sharpness and the number of fabric layers in the case of the SRG jacketing technique.

7 ACKNOWLEDGEMENTS

The authors wish to thank Dr. V. Kourtidis and Mr. T. Koukouftopoulos for their assistance in the experimental program. The program was conducted in the Laboratory of Strength of Materials and Structures and funded by the Research Committee of Aristotle University of Thessaloniki within the frame work of the program "Funding for new researchers". The materials were donated by SIKA Hellas and Interbeton.

REFERENCES

[1] S. Kurtz, P. Balaguru, Comparison of inorganic and organic matrices for strengthening of RC Beams with carbon sheets. *ASCE Journal of Structural Engineering*, **127(1)**, 35-42, 2001.

[2] T.C. Triantafillou, C.G. Papanicolaou, P. Zissimopoulos, T. Laourdekis, Concrete confinement with textile-reinforced mortar jackets, *ACI Structural Journal*, **103(1)**, 28-37, 2006.

[3] B. Barton, E. Wobbe, L.R. Dharani, P. Silva, V. Birman, A. Nanni, T. Alkhrdaji, J.Thomas, G. Tunis, Characterization of reinforced concrete beams strengthened by steel reinforced polymer and grout (SRP and SRG) composites. *Materials science and engineering A*, **412** , 129–136, 2005.

[4] P. Casadei, A. Nanni, T. Alkhrdaji, J. Thomas, Performance of double-T prestressed concrete beams strengthened with steel reinforced polymer. *7th International Symposium on Fiber Reinforced Polymer Reinforcement for concrete structures*, Kansas, USA, Paper No. SP-230-44, 2005.

[5] W. Figeys, L. Schueremans, K. Brosens, D. Van Gemert, Strengthening of concrete structures using steel wire reinforced polymer. *7th International Symposium on Fiber Reinforced Polymer Reinforcement for concrete structures*, Kansas, USA, Paper No. SP-230-43, 2005.

[6] K. Katakalos, C.G. Papakonstantinou, Fatigue of reinforced concrete beams strengthened with steel-reinforced inorganic polymers. *ASCE Journal of Composites for Construction*, **13(2)**, 103-112, 2009.

[7] Y.J. Kim, A. Fam, M.F. Green, Flexural strengthening of reinforced concrete beams with steel-reinforced polymer composites: analytical and computational investigations. *Journal of reinforced plastics and composites*, **29(14)**, 2141-2155, 2010.

[8] Y.J. Kim, A. Fam, M.F. Green, Application of SRP composite sheets for retrofitting reinforced concrete beams: Cracking and tension stiffening. *Journal of reinforced plastics and composites*, **29(17)**, 2647-2662, 2010.

[9] Y.J. Kim, A. Fan, A. Kong, R. El-Hacha, Flexural strengthening of RC beams using steel reinforced polymer (SRP) composites. *7th International Symposium on Fiber Reinforced Polymer Reinforcement for concrete structures*, Kansas, USA, Paper No. SP-230-93, 2005.

[10] A. Lopez, N. Galati, T. Alkhrdaji, A. Nanni, Strengthening of a reinforced concrete bridge with externally bonded steel reinforced polymer (SRP). *Composites: Part B*, **8**, 429–436, 2007.

[11] M. Pecce, F. Ceroni, A. Prota, G. Manfredi, Response prediction of RC beams externally bonded with steel-reinforced polymers. *ASCE Journal of Composites for Construction*, **10(3)**, 195–203, 2006.

[12] A. Prota, Tan K.-Y., A. Nanni, M. Pecce, G. Manfredi, Performance of shallow reinforced concrete beams with externally bonded steel-reinforced polymer. *ACI Structural Journal*, **163(2)**, 163-170, 2006.

[13] G.J. Mitolidis, T.N. Salonikios, A.J. Kappos, Tests on RC beams strengthened at the span with externally bonded polymers reinforced with carbon or steel fibers. *ASCE Journal of Composites for Construction*, **16(5)**, 2012.

[14] G.E. Thermou, S.J. Pantazopoulou, Metallic fabric jackets: an innovative method for seismic retrofitting of substandard RC prismatic members. *Structural Concrete Journal***,** The fib Journal, Thomas Telford, **8(1)**, 35-46, 2007.

[15] R. El-Hacha, K. Abdelrahman, Slenderness effect of circular concrete specimens confined with SFRP sheets. *Composites: Part B*, **44,** 152–166, 2013.

[16] R. El-Hacha, M.A. Mashrik, Effect of SFRP confinement on circular and square concrete columns. *Engineering Structures*, **36,** 379–393, 2012.

[17] G.E. Thermou, Concrete confinement through a novel intervention scheme, the steel reinforced grout jackets. *Workshop of the Hellenic Society of Civil Engineering* "The seismic engineering through the scientific approach of young researchers and engineers", Thessaloniki, Greece (in Greek), 2012.

[18] Y.A. Al-Salloum, Influence of edge sharpness on the strength of square concrete columns confined with FRP composite laminates. Composites: Part B, 38, 640–650, 2007.

[19] P. Rochette, P.Labossiere, Axial testing of rectangular column models confined with composites. ASCE Journal of Composites for Construction, 4(3),129–136, 2000.

[20] O. Chaallal, M. Hassan, M. Shahawy, Confinement model for axially loaded short rectangular columns strengthened with fiber-reinforced polymer wrapping. *ACI Structural Journal*, **100(2)**, 215–221, 2003.

[21] L.-M. Wang, Y.-F. Wu. Effect of corner radius on the performance of CFRP-confined square concrete columns: Test. *Engineering Structures*, **30,** 493–505, 2008.

[22] fib Bulletin 14, Externally Bonded FRP Reinforcement for R.C. Structures. *Report by Task Group 9.3*, federation international du béton (fib), Lausanne Switzerland, 130, 2001.

[23] A. Mirmiran, M. Shahawy, M. Samaan, H.E. El-Echary, J.C. Mastrapa, O. Pico, Effect of column parameters on FRP-confined concrete. *ASCE Journal of Composites for Construction*, **2(4)**, 175–185, 1998.

[24] S.T. Smith, S.J. Kim, H.W. Zhang, Behavior and effectiveness of FRP wrap in the confinement of large concrete cylinders. *ASCE Journal of Composites for Construction*, **14(5)**, 573–582, 2010.

[25] Y. Xiao, H. Wu, Compressive behavior of concrete confined by carbon fiber composite jackets. ASCE Journal of Materials in Civil Engineering, **12(2)**, 139–146, 2000.

[26] L. Lam, J.G. Teng, C.H. Cheng, Y. Xiao, FRP-confined concrete under axial cyclic compression. Cement and Concrete Research, **28(10)**, 949–958, 2006.

[27] T. Ozbakkaloglu, E. Akin, Behavior of FRP-confined normal- and high-strength concrete under cyclic axial compression. *ASCE Journal of Composites for Constr*uction, **16(4)**, 451-463, 2012.

[28] R. Abbasnia, H. Ziaadiny, Behavior of concrete prisms confined with FRP composites under axial cyclic compression. *Engineering Structures*, **32**, 648-655, 2010.

[29] R. Abbasnia, R. Ahmadi, H. Ziaadiny, Effect of confinement level, aspect ratio and concrete strength on the cyclic stress–strain behavior of FRP-confined concrete prisms. *Composites: Part B*, **43,** 825–831, 2012.

[30] R. Abbasnia, F. Hosseinpour, M. Rostamian, H. Ziaadiny, Cyclic and monotonic behavior of FRP confined concrete rectangular prisms with different aspect ratios. *Construction and Building Materials*, **40**, 118–125, 2013.

[31] Z. Wang, D. Wang, S.T. Smith, D. Lu, CFRP-confined square RC columns. I: Experimental investigation. *ASCE Journal of Composites for Construction*, **16(2)**, 150-160, 2012.

[32] Z. Wang, D. Wang, S.T. Smith, D. Lu, CFRP-confined square RC columns. II: Cyclic axial compression stress-strain model. *ASCE Journal of Composites for Construction*, **16(2)**, 161-170, 2012.

COMPDYN 2013
4th ECCOMAS Thematic Conference on
Computational Methods in Structural Dynamics and Earthquake Engineering
M. Papadrakakis, V. Papadopoulos, V. Plevris (eds.)
Kos Island, Greece, 12–14 June 2013

DESIGN AND VERIFICATION OF A DYNAMIC EXPERIMENTAL CAMPAIGN ON ANCHORING SYSTEMS THROUGH MACRO AND MICRO NUMERICAL MODELS

Nicola Mazzon[1*], Giovanni Tecchio[1], Marco Abate[2], Daniele Alì Santoro[1], Daniele Gualano[1], Claudio Modena[1]

[1] University of Padua, Department of Civil, Environmental and Architectural Engineering
via Marzolo 9, 35131, Padova
nicola.mazzon@unipd.it

[2] ITW Construction Products Italy srl
V.le Regione Veneto 5, 35127, Padova
marco.abate@itw-italy.com

Keywords: Anchorage, shaking-table test, non-structural components, macro numerical modelling, micro numerical modelling, Earthquake Engineering.

Abstract. *The seismic safety of non-structural elements especially in the case of relevant components on strategic structures, such as hospitals, fire and police stations as well as any further building for the emergency management, is often linked to the behaviour of connections with the structure [1-3].*

This paper presents the design of a dynamic experimental campaign on a whole structure on the basis of two different numerical simulations, an overall macro model and a detailed micro model. The whole experimental program involves the study of fasteners with different functioning principles, namely bond, expansion and undercut. The calibration of the numerical simulation of an anchoring system, among those considered in the laboratory campaign, is based on the results of tension and shear tests performed on the selected fastening.

This paper discusses both the design of this experimental campaign and the calibration of the local model for an anchor, comparing numerical and experimental results [4].

The first macro model considers the whole structure to be tested, in order to study the modification of the seismic input through the height of the specimen. This preliminary analysis is developed for all the considered fasteners. The design of masses, in terms of weight, is based on these global FE models. This numerical simulation is performed for all the considered anchoring systems. The second micro model, based on the results of the first one, analyses in detail the dynamic behaviour of a single anchor. The overall strength and the load-slipping behaviour is studied and compared with the experimental results. This micro model is based on a preliminary calibration obtained from quasi-static tests performed on the considered fastening system.

The comparison between numerical and experimental results confirms the good agreement of the predicted behaviour with that observed during the quasi static tests on a single anchor. This will also allow to extent the FE simulation to different loading conditions as well as to develop parametric studies for different applications, especially in the case of dynamic numerical analyses.

1 INTRODUCTION

The non-structural components normally present on buildings are those elements housed or fixed to the floors and walls such as suspended ceilings or facilities which do not contribute to the structural behaviour of the building [1]. These are generally complementary elements as electricity or mechanical devices, architectural equipment or building contents.

In case of a seismic event the non-structural components may be subject to large forces, transmitted to these elements by the anchors. Thus fastening systems should be designed to ensure the stability of the non-structural element in case of an earthquake. As an example, the collapse of a suspended ceiling or the overturning of a library represents a serious and relevant risk for the occupants of a building. Furthermore for strategic structures, such as hospitals or police or fire stations the operability of the building immediately after a seismic event should be guaranteed. In this sense the anchoring systems of non-structural elements should be designed in order to prevent the occurrence of damage to these components.

The purpose of the presented research is to predict the dynamic behaviour of different anchoring solutions, in order to design an experimental campaign aimed at verifying the strength and the failure mechanisms of some fastening methodologies. These analyses could be then compared with the experimental results [5].

2 TEST FRAME AND EXPERIMENTAL SETUP

The behaviour of different anchoring systems will be investigated by shaking table tests at the ENEA Research Center "la Casaccia" (National Agency for New Technologies, Energy and Sustainable Economic Development). The experimental campaign involves several steps for each testing setup. Anchors of different mechanical principles and with different overall strength are considered [6]. In particular three kinds of fastening methodologies are considered: expansion, undercut and bonded anchors (Figure 3).

A concrete structure was designed as a support frame [2] and this is constituted by four RC walls arranged with cross plan (Figure 4). On each concrete wall a couple of steel masses are hanged to the structure. Each of these is fixed with a single anchor in order to more easily study the overall strength and failure mechanisms of the considered fastening solution.

The input signal transmitted to the shake-table is generated according to AC156 [5].

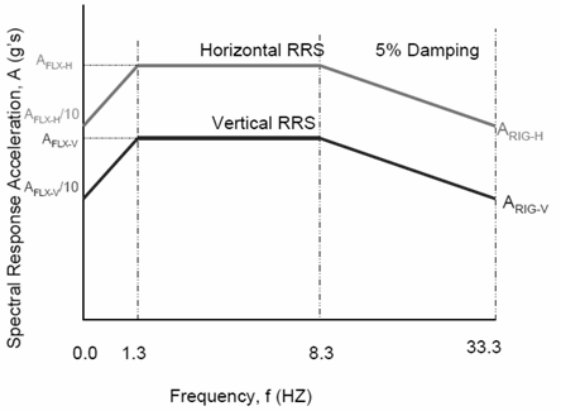


Figure 1: Required response spectrum, normalized for the component [5].

This standard imposes detailed limits to be met on both the frequency content of the signal and its elastic response spectrum. In particular, the signal should have a frequency content between 1.3Hz and 33.3Hz, a duration of at least 30s of which 20s of strong motion and an envelope profile build-hold-decay. On the basis of these parameters a dynamic signal in compliance with the operating limits of the shake-table should be generated. In this sense the lim-

its are a maximum displacement of 0.25m, a maximum velocity of 0.5m/s and a maximum acceleration related to the maximum overturning moment of 300kNm.

To generate the input and to comply with all these requirements a synthetic signal has been generated through the SIMQKE code [7]. Subsequently a band-pass filter between 0.6Hz and 33.3Hz and a spectrum matching procedure with addition of wavelets were applied to correct both the frequency content and the spectrum of generated signal [8]. The input was finally scaled to obtain the signals for the different runs of the test with increasing intensity.

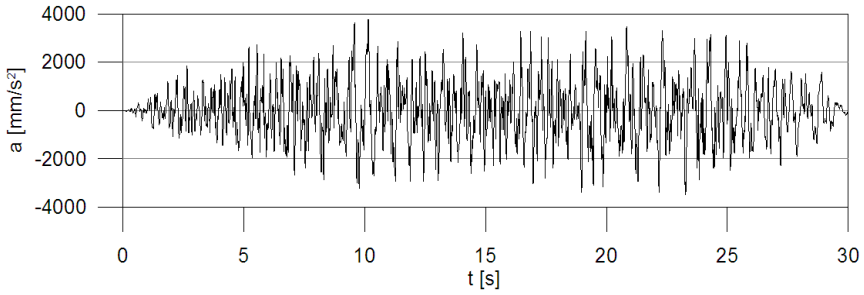


Figure 2: Acceleration time history in direction x with ZPA = 0.4 g.

For each session of tests several ground motions at increasing levels of ZPA (Zero Period Acceleration, as presented on [5]) were applied. This procedure will also allow to study the dynamic behaviour of non-structural elements installed at different floor levels if the floor spectra are considered on the analyses [9].

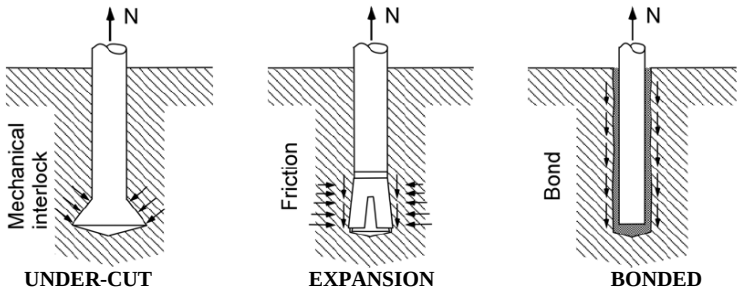


Figure 3: Different types of anchoring systems.

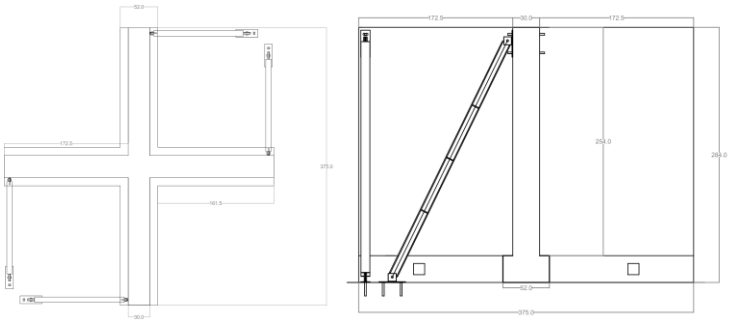


Figure 4: Design of the concrete structure.

The design of the experimental campaign was performed on the basis of two different numerical analyses. A first model of the whole structure has been used to calibrate the entity of the masses to be hanged and to study the variation of stress on the anchors increasing the intensity of the seismic input. The second model has been used to study in detail the overall behaviour of an anchoring system. In particular an expansion fastening system with plastic sleeve was considered.

3 MACRO MODELLING

3.1 Description of the Model

The use of a finite element model in order to predict the behaviour of the testing frame has imposed the need to preliminarily evaluate the reliability of the model itself [3, 10]. For this purpose, different numerical simulations with a gradually increasing complexity were developed to obtain the final model, used to design the structure considered in the experimental campaign. All the numerical analyses were performed using the software Straus7 [11]. This process allowed the reliability of the more basic models to be verified comparing the obtained results in terms of frequencies and mode shapes. The most important features of the structure are essentially the natural frequencies of vibration and the vibration modes that depends on the stiffness of the frame [6 9]. The four considered models are presented on figures from Figure 5 to Figure 8 respectively and they are characterized by an increasing complexity.

The complete FE model consists of 3608 plates to represent the walls and 4 truss elements to simulate the influence of braces. Each steel element, fixed to the structure through the selected anchors, is modelled using a nodes with an assigned mass, positioned in the centre of gravity of the steel block, and 8 beam elements to connect these nodal masses with the surface of the support. The beam elements have been preferred to the link elements since a well calibrated stiffness do not affect the behaviour of the structure and it allows the stress in the connected nodes to be investigated.

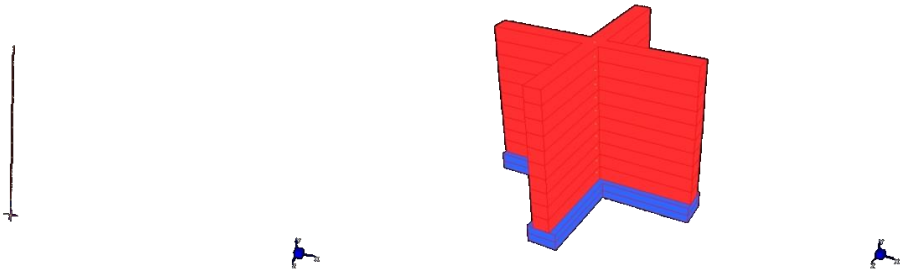


Figure 5: Single beam model, wireframe and solid views.

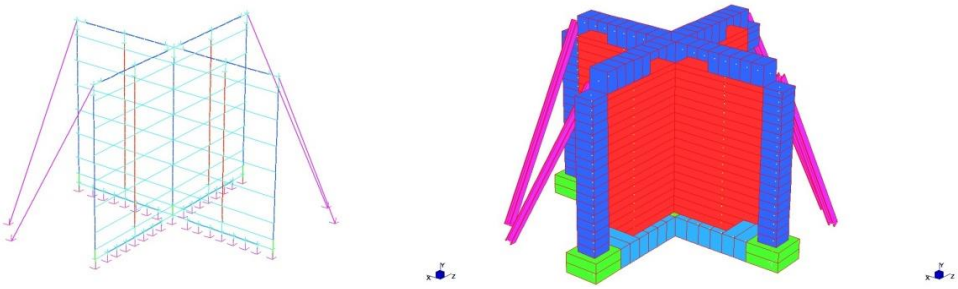


Figure 6: Multi beams model, wireframe and solid views.

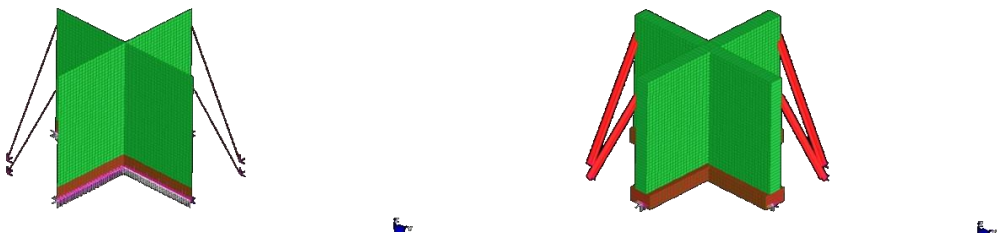


Figure 7: Plate model, wireframe and solid views.

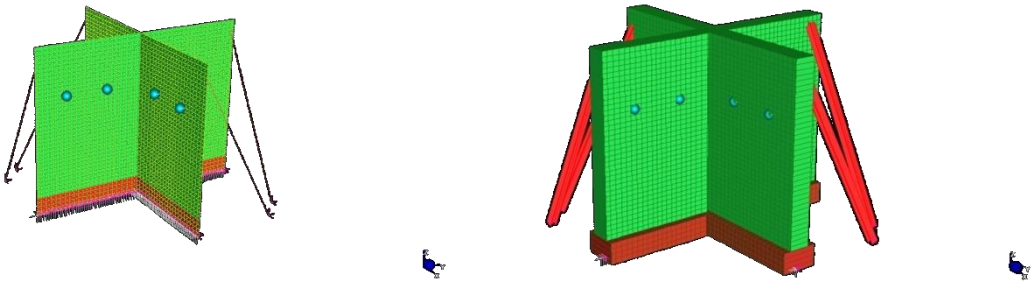


Figure 8: Plate model with adjunctive masses, wireframe and solid views.

3.2 Numerical Results

The first three models were considered to determine the stiffness of the structure. As Table 1 shows, the natural frequencies obtained from different numerical analyses are very close to each other. In this sense the more refined numerical simulation shows overall characteristics, especially in terms of stiffness, similar to those of the less complex models, so this was used for the subsequent analyses.

Mode	Single Beam Model [Hz]	Beam Model [Hz]	Plate Model [Hz]
1	35.34	58.13	59.61
2	105.19	75.49	75.38
3	125.49	77.62	78.50
4	125.49	78.89	81.01

Table 1: natural frequencies of different macro models.

The first design phase of the experimental campaign aimed at calibrating the values of mass to be anchored on the structure. This allowed the stress of the fastening systems to be maximized in compliance with the operating limits of the shaking table. The first considered approach was to fix the mass value for each anchor and to determine the maximum achievable level of acceleration. The computed load acting on each block was compared to the related anchor resistance, under dynamic conditions. These data allowed the verification of the fastening systems through the following normalized formulation:

$$F_{eq,adim} = \frac{N_{tot}}{N_R} + \frac{T_{xz}}{T_R} + \frac{T_{xy}}{T_R} \quad (1)$$

where:

- N_{tot} is the total axial force, which is the sum of: $N_{tot} = N + \frac{M_{xz}}{b_{xz}} + \frac{M_{xy}}{b_{xy}}$ with M_{xz} and M_{xy} principal moments, and b_{xz} e b_{xy} distances between the anchor and the contact point of steel block with the wall in horizontal and vertical directions;
- T_{xz} is the shear force acting on the x-z plane;
- T_{xy} is the shear force acting on the x-y plane;
- N_R is the tensile resistance for dynamic loading;
- T_R is the shear resistance for dynamic loading.

The second procedure considers the maximization of the load acting on the anchor increasing the hanged mass and allowing a reduction of the maximum attained acceleration. Comparing the results obtained from the various tests, the second approach has provided the best result.

Table 2 summarizes the value of hanged masses depending on each anchor type. The corresponding maximum normalized stresses are presented on the last column.

When the factor $F_{eq,\ adim}$, computed as presented on equation (1), attains the unit the maximum resistance in the element is achieved thus this corresponds to its failure. The maximum normalized stress on anchors of different types, evaluated with the global model, results less than the resistance. However this simplified model neglects some details to contain the computational effort of the FE models. In this case the strength of the anchoring systems was estimated applying an appropriate reduction factor to the static resistance. On these bases the anchors can be supposed to be failed also for ratios lower than the unit. In this sense the results presented on table 2 can be considered to identify the failure of the fastenings.

Subsequently to the calibration of the anchored masses, all testing steps have been numerically simulated considering increasing levels of ZPA. As an example, Figure 9 shows the results obtained for a plastic expansion anchor for a ZPA equal to 0.9 g (Figure 2).

Furthermore, this model allowed to study the effective seismic signal acting on each anchor. Indeed the structure filters the dynamic input and this could induce some modifications on the dynamic properties of the selected time history.

Anchor Typology	Steel Plate [kg]	$F_{eq,adim}$ [-]
Expansion (plastic)	300	0.98
Under-cut	500	0.75
Expansion (metallic)	700	0.86
Bond	900	0.90

Table 2: values of masses fixed to the structure and normalized load-strength ratios.

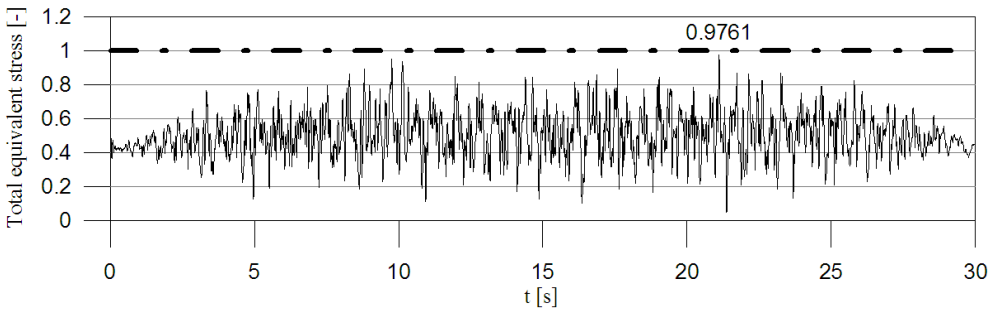


Figure 9: Total equivalent stress in the plastic expansion anchor for a test with a ZPA of 0.9 g.

4 MICRO MODELLING

4.1 Description of the Model

The local model was used to deepening the overall behaviour of an anchor system on the basis of the dynamic load actions computed using the macro model. This also allowed the hypothesis of reduction of the static resistance due to dynamic effects [4] to be validated.

The plastic expansion anchor was modelled using the software DIANA [12]. In particular the local model (Figure 10) consists of four parts: (1) a cube with the sides 10cm long to reproduce the concrete support; (2) a cylindrical hollow element to simulate the plastic sleeve; (3) a cylindrical component to model the screw; a set of 4 trusses to reproduce the overall behaviour of the steel block anchored to the testing frame.

In order to better modelling the behaviour of the whole fastening system subjected to both tensile and shear loads, two interfacial surfaces were inserted: one between the concrete and the plastic anchor and the other one between the plastic anchor and the central element reproducing the screw (Figure 11).

The concrete was modelled using the Modified Maekawa Concrete Model, while the screw was modelled using a Von-Mises criterion to define the yield surface of steel's behaviour.

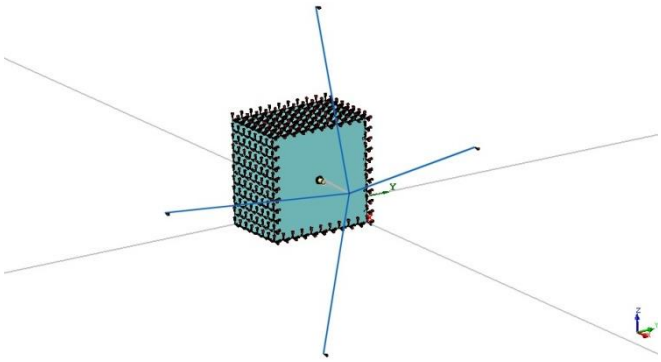


Figure 10: Detail of the adopted micro model.

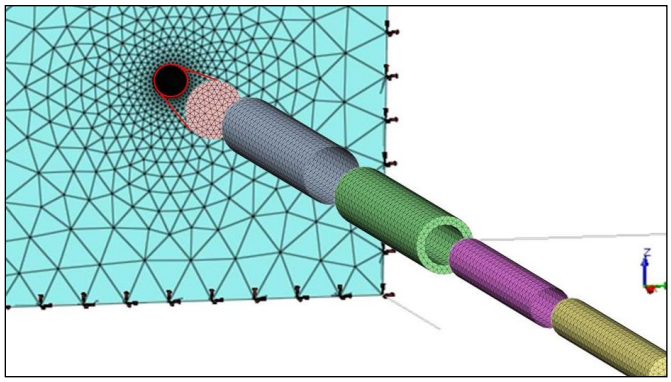


Figure 11: Micro model exploded view.

4.2 Calibration of Interface Elements

The behaviour of the whole fastening system subjected to extraction forces has been reproduced calibrating the stiffness of the plastic anchor assuming invalid the effects of mutual sliding and simulating this through the accumulation of plastic deformation in the external hollow element that represents the sleeve.

The overall behaviour of the fastening system subjected to both tensile and shear actions have been reproduced by calibrating the stiffness values of the material used for the sleeve. This calibration was based on the results of quasi-static tests (Figure 12).

Any specific constitutive model for plastic elements could not be found, thus the Modified Maekawa Concrete Model was applied. This allowed a non-linear behaviour with softening and plastic deformation to be defined. The principal parameters are presented in

Table 3.

Parameter	Unit	Value
Compressive strength	[N/mm^2]	16.00
Tensile strength	[N/mm^2]	3.96
Fracture energy	[N/mm]	1.00
Shear retention	[-]	0.20

Table 3: parameters used to perform the Modified Maekawa Concrete Model.

The results obtained from the proposed model show a good agreement with the experimental measures in terms of both tensile and shear loads.

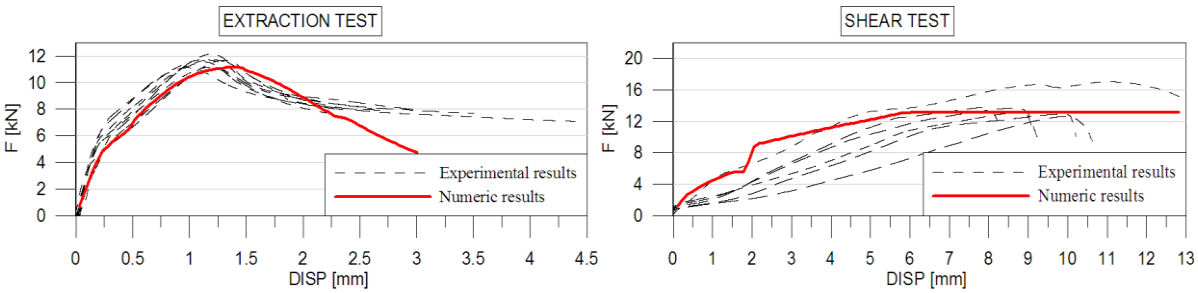


Figure 12: Calibration of micro model, numeric and experimental results.

4.3 Numerical Results

The two target-contacter surfaces were specifically inserted to simulate the progressive increasing of the shear stiffness with the crushing of the plastic anchor. This interface also guarantees the respect for the geometric limits, namely when the screw comes into contact with the support and its deformation is concentrated outside the support (Figure 13).

The calibrated mechanical law for the interface elements was included into the micro model. The acceleration time history obtained from the macro model at the exact point of application of the fastening system was then applied as input on this local numerical simulation. Figure 14 shows the results obtained for the most strong seismic input, also taking into account the effects of previous load steps.

The obtained results confirm as the dynamic analysis provides a much more heavy stress in the anchor if compared with that computed on the global model, that is based on a linear analysis. On the actual numerical analysis the failure is attained at 8.1s of the seismic input and this confirms the reliability of the considered assumptions.

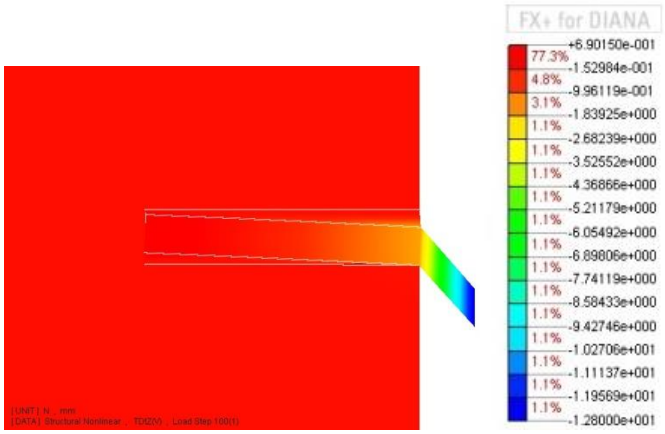


Figure 13: Shear failure of micro model, strain in "z" direction.

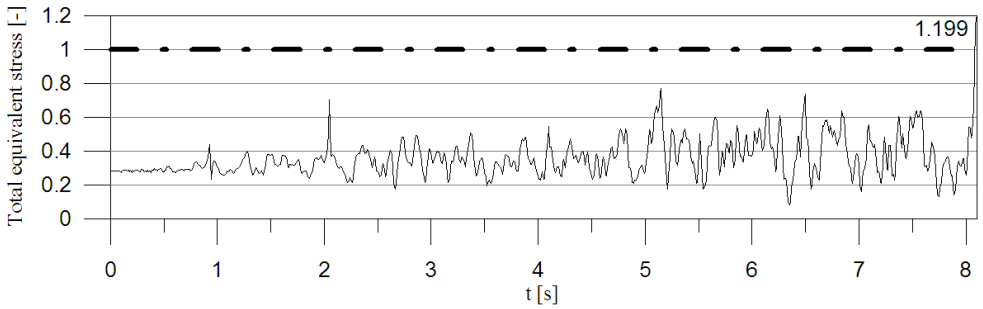


Figure 14: Micro model, simulation of run with a ZPA of 0.9 g.

5 CONCLUSIONS

The paper presents a series of numerical analyses characterized by an increasing complexity and by more refined results. On these bases an experimental campaign could be designed considering both the limits of the laboratory facilities and the mechanical characteristics of the selected anchoring methodologies.

Different macro models aimed at simulating the overall behaviour of a concrete structure upon which 8 steel masses are fixed with four different anchoring systems. These FE models allowed the calibration of the mass levels to be considered in the experimental program. Furthermore these analyses allowed to study the modification of the input signal from the base of the structure up to the fastening point, highlighting as any significant variation can be observed.

A second phase considered a micro model focused on a detailed numerical analysis of a single anchor. A preliminary calibration allowed the overall behaviour of the considered fastening solution to be reproduced by a FE simulation. The comparison of these numerical and experimental results in terms of the load-displacement curve confirmed the reliability of developed studies.

The dynamic input obtained from the macro model could then be considered as the input for the micro model, thus allowing the overall behaviour of the considered fastening solution to be studied in terms of load and displacement capacity. This second step of analysis allowed in particular to study the seismic level that induces the failure on the analysed anchor.

Finally the adopted overall process of analysis that considers two steps, a series of global models with increasing complexity and a refined local simulation, allows on one hand to limit the computational cost of the numerical study and on the other hand to obtain detailed results.

ACKNOWLEDGEMENTS

The authors are grateful to ITW C.-P. Italy for the economic and technical support provided within this research and for the experimental data supplied for the calibration of the numerical models.

REFERENCES

[1] R. Villaverde, Earthquake resistant design of secondary structures: a report on the state of the art, *Proceedings of the 11th World Conference on Earthquake Engineering*, paper n. 643, Elsevier Science Ltd., Oxford, England, 1996.

[2] A.M. Reinhorn, K P. Ryu, G. Maddaloni, Modeling and seismic evaluation of non-structural components: testing frame for experimental evaluation of suspended ceiling systems", *Technical report MCEER-10-0004*, 2010.

[3] M.S. Hoehler, M. Panagiotou, J.I. Restrepo, J.F. Silva, L. Floriani, U. Bourgund, H. Gassner, Performance of suspended pipes and their anchorages during shake table testing of a seven-story building, *Earthquake Spectra*, **25(1)**, 71-91, 2009.

[4] D.A. Watkins, Seismic Behavior and Modeling of Anchored Non-structural components Considering the Influence of Cyclic Cracks, *PhD thesis*, University of California, San Diego, 2011.

[5] AC156 - Acceptance criteria for seismic certification by shake-table testing of nonstructural components, Whittier, California, ICC-ES, 2010.

[6] N. Mazzon, M. Abate, F. da Porto, C. Modena, Shaking-Table Tests on Post-installed Anchors for Concrete and Masonry Applications, *Proceedings of the XV Italian National Association of Earthquake Engineering (ANIDIS)*. Padua, Italy, June 30th – July 4th, accepted paper.

[7] SIMQKE_GR version 2.6, –prof. Piero Gelfi, university of Brescia, Online: http://dicata.ing.unibs.it/gelfi/software/simqke/simqke_gr.htm.

[8] N.A. Abrahamson, Non-stationary spectral matching, *Seismological Research Letters* **63(1)**, 30, 1992.

[9] S.R. Chaudhuri, T.C. Hutchinson, Distribution of peak horizontal floor acceleration for estimating non-structural element vulnerability, *Proceedings of the 13th World Conference on Earthquake Engineering*, paper n. 1721, Vancouver, B.C., Canada, August 1-6, 2004.

[10] O.C. Zienkiewicz, R.C. Taylor, The finite element method, Vol. I, 4th Edition. McGraw Hill, 1989.

[11] Straus7 rel. 2.3.3, G+DComputing HSH – Padova – Italy. Online: www.straus7.com.

[12] Diana rel. 9.4.4, TNODIANA b.v. Documents Online: www.midasuser.com.

SEECCM III
3rd South-East European Conference on Computational Mechanics-
an ECCOMAS and IACM Special Interest Conference
M. Papadrakakis, M. Kojic, I. Tuncer (eds.)
Kos Island, Greece, 12–14 June 2013

SEISMIC RELIABILITY OF REINFORCED CONCRETE BRIDGE COLUMNS BASED ON DAMAGE APPROACHES

M. O. Benamer[1*], Y. T. Feng[2]

Civil and Computational Engineering Centre

Swansea University, SA2 8PP, Wales, UK

[1]474825@swansea.ac.uk [2]y.feng@swansea.ac.uk

Keywords: Seismic loads, Loading rate, Stress-based damage, Fracture-based damage, Plastic hinge, quasi-brittle, confinement, ductility, demand/capacity principle.

Abstract. *The seismic energy response of a reinforced concrete bridge column is dissipated through the initiation of plastic hinges, which represent the resulting damage in the column member. The seismic design criterion SDC that is used by many building codes employs the demand/capacity ductility principle for a performance-based design, which assumes a low damage state in the member, allowing for a better serviceability of the structure after the seismic event. The damage in the plastic hinge, according to the SDC, is limited to spalling and yielding of the longitudinal reinforcement bars, but the crack growth in the column core can lead to excessive strength degradation in the hysteresis behaviour of the structure.*

In this paper, a dynamic non-linear analysis using the Fibre Element Method is performed to obtain the hysteretic analysis for a designed column subjected to different loading rates. A stress-based method is used to determine the local damages in the core and cover of the reinforced column. Different damage states are obtained under different loading rates. The Discrete Element/Finite Element/ method, DE/FEM, with Rotating cracke model is used as a small-scale approach, to investigate the crack growth in the critical zones with softening strains and fractured elements across the concrete column's core and cover. Despite its excessive computation time, the DE/FEM model provides reliable information about the local damage state of the RC column core, which enhances understanding the seismic performance of the structural member.

In this RC column, designed according to the SDC of the California Department of Transportation (Caltrans 2001), a large area of the column core zone at the plastic hinge is damaged when subjected to Lexington Dam, Loma Prieta, 1989, and the column loses its integrity in the plastic zone, which affects the bar/concrete bond substantially. This could lead to total collapse especially if the reinforcement bars are quite exposed and start to buckle.

1 INTRODUCTION

The principle of PBSD performance-based seismic design has played a vital role in Earthquake Engineering. Its significance is to assure that the constructed buildings will resist the effects of earthquake ground motions of different severities within acceptable limiting levels of damage. This implies that the structure will not be damaged beyond certain limit states [1]. In general, the PBSE performance-based seismic engineering has a broad concept which includes the evaluation of damage in structural members, non-structural facilities and also floor contents. In terms of structural members, PBSE is concerned with all aspects of the building process, such as the design criteria, selection of a structural system, layout proportions, detailing of the structural members, construction quality control and long-term maintenance. Therefore, the majority of research work in this concern is associated with determining the different levels of reliability that a building can act under specified levels of excitations [1].

Several levels of reliability could be investigated; such as the material, section, member and the overall structure behaviour. One of the most important is the reliability of reinforced concrete RC bridge columns, which are seismically designed according to the Demand/Capacity principle of seismic design criteria, SDC.

It is a general concept in Eurocode 8 and also other codes that "the bridge should retain its structural integrity and adequate residual resistance after the seismic event"[2]. However, there are structural parts in RC bridges that are susceptible to damage by their contribution to energy dissipation during the seismic event, but the structure should still sustain emergency traffic [2].

Therefore, one of the design principles in bridge engineering is to allow local minor damages in the bridge columns, considering the initiation of PH plastic hinge zones. The concept of a plastic hinge in the design methodology presumes the loss of the concrete cover only, known as spalling, and the initiation of non-linear straining of the longitudinal bars along the PH zone. However, this may not be the case during severe earthquakes. A sever local damage may destroy the concrete core of the column section, and could lead to a total collapse of the structure, especially when the longitudinal reinforcement bars are severely deformed or buckled. The main goal of this research is to investigate the damaged plastic hinges at the core of RC bridge columns when subject to earthquake loading.

Seismic analytical models are used to perform non-linear dynamic analyses, but they may not necessarily predict the damage growth in the elements and its effect on the adjacent elements. However the damage growth mechanism in quasi-brittle 3D continuum is still a complex subject in Material Mechanics Engineering.

In relevance to damage, several earthquake records show that relatively long duration impulses with low frequency have the potential to cause further damage, more than those records having similar PGA's but with relatively short duration impulses and higher frequency. The phenomenon of long duration and low frequency is known as the Acceleration Pulse, or Fling [3], which increases the seismic hazard and brings more challenges to PBSE in the field of RC bridges design and assessment. Singh [3] considers that having PGA as an Intensity Measure IM alone is a poor parameter for evaluating the damage potential.

In addition to damage, two other important issues are also crucial to PBS design for RC bridge columns, and should be taken into consideration; the residual displacement after an earthquake, and the structure's displacement exceeding the allowable lateral displacement stated by building codes. These two issues, if not considered, can also reduce the seismic

performance of the structure, even in case of low damage levels. These issues are not within the scope of this work.

In this paper, using two different methods for non-linear analysis, the local damage of plastic hinges PH is investigated analytically in a RC bridge column under seismic loading. They are; the Fibre Element Method and the combined Discrete Element/Finite Element Method.

2 LOADING RATE

Different loading rates can have significant effects on the performance of a RC structure. The uncertainty of intensity and rate of earthquake loading increases the challenge to predict responses of high risk excitements. In general, seismic loads can be relatively classified by the acceleration rate into different acceleration pulses.

2.1 Acceleration Pulse

Two useful classifications for ground acceleration records are relevant to the expected damage in the structures. The first is the phenomenon of long duration impulses with low frequency in ground acceleration records, which is known as the Acceleration Pulse, or Fling. The second is the acceleration peak associated with short duration impulses of high frequency, and known as the Acceleration Spike [3]. It has been found that an Acceleration Spike is not as severely damaging to the RC bridge columns as an Acceleration Pulse [3].

The reason behind having such a high potential damage in a long duration impulse is that it allows for a higher velocity and thus higher displacement response. However, short duration impulses in a record of high frequencies, i.e. acceleration spikes, can also be very damaging if their high frequencies are within the range of the structure's natural frequencies. However, PGA of high frequencies can seldom initiate resonance or produce large scale damage since most structures are not within the range of high frequencies records [3]. Therefore, large PGA alone can seldom initiate resonance or produce large scale damage.

Many researchers have shown that the frequency, duration, incremental velocity and incremental displacement can have profound effects on the structural response more than the PGA, especially in the inelastic range [3]. E Cosenza and G Manfredi stated that the PGA is a basic measure of earthquake potential but is not totally reliable [4]. Examinations of recorded seismic events have shown that earthquakes with a very large PGA could not produce appreciable structural damage, while earthquakes with very low PGA's produced an unexpectedly high level of destruction [4]. Instead, the PGV seems to be a more representative measure of earthquake intensity as it is directly connected with energy demand[3].

3 DAMAGE APPROACHES

3.1 Stress-based Damage

Damage can be estimated by measuring the loss of stresses at the critical zones in a plastic hinge. In inverted pendulum problems, such as bridge column problems, most of the damage is due to excessive axial compressive and tensile strains. Thus, classified as a flexural damage. However, a very limited portion of the damage is caused by shear failure in these

problems, especially in relatively small diameter members, therefore, no shear failure is expected.

The elasto-plastic constitutive relationship for a selected element can be used to indicate the damage state at that zone approximately. The Local compressive damage index for concrete fibres is based on the ratio between axial compressive stresses $\sigma_{i,fibre}$ and the ultimate strength of concrete σ_{ult}, and can be obtained during the strain softening of the analysed fibres, as in the following equation:

$$D_i = 1 - \frac{\sigma_{i,fibre}}{\sigma_{ult}} \quad (1)$$

where *i* is the time-step, or pseudo time in case of quasi-static analysis. When D_i equals 1, the fibre has lost its strength and is not capable to resist any more axial compressive stresses, indicating a local totally damaged state under compression.

This index is sufficiently expressive, but it is mostly used for elements under compressive stresses only since that concrete elements with tensile stresses are considered fully damaged due to their very limited strength to resist tension.

Using the Fibre Element Method, the non-linear analysis for the RC columns is performed, by using the SeismoStruct dynamic solver [5], which is capable of plotting the constitutive curves of the stressed fibre elements. The fibre elements are designed to compute the non-linear axial forces with the flexible failure mode. However, shear forces are also obtained from the coupled stiffness matrix, but their corresponding shear stresses are not calculated since the shear failure mode in these problems is not dominant.

The following example for RC single-cell box-girder bridge columns, shown in figure 1, has a damping ratio of 5% and subjected to artificial ground accelerations applied at the base of the structure. The relative change in the duration of acceleration pulses of ground acceleration is conducted in 3 different slope rates; 1.414 g/s, 1.880 g/s and 2.801 g/s, where g is the gravity constant, as shown in figure 2. These loading rates have been taken based on the PGA of Lexington Dam record from the Loma Prieta earthquake 1989, which reaches approximately 6.0 m/s^2.

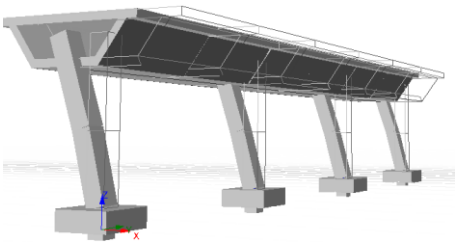


Figure 1, Displacement in RC bridge columns

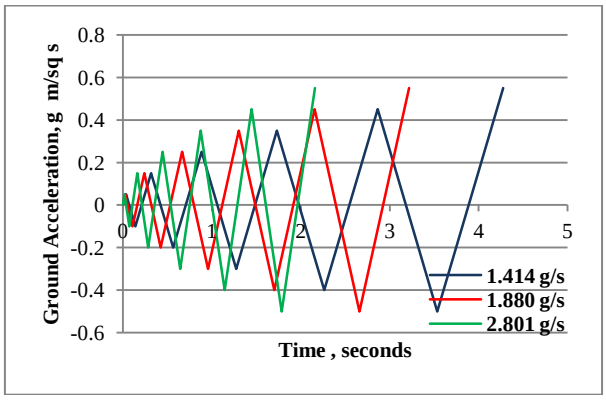
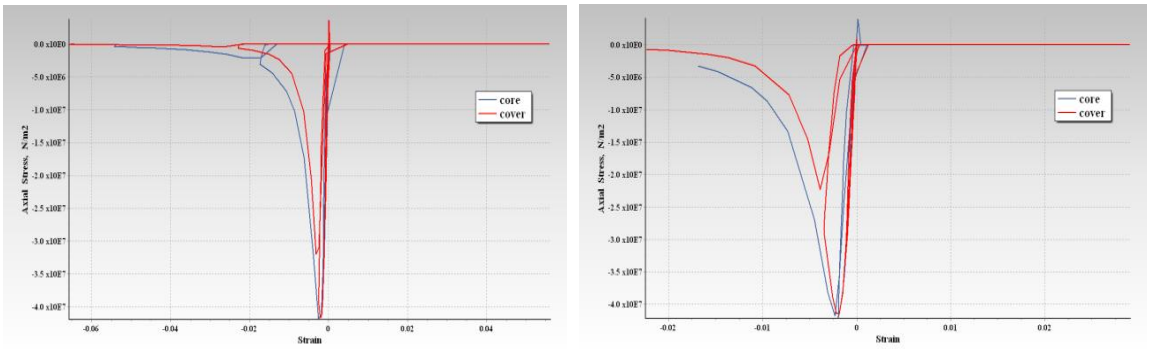


Figure 2, Loading rates

As a nonlinear response to the effect of different loading rates, the constitutive curves shown in figures 3,4 and 5 show that for longer durations of an acceleration pulse the response tend to have more plastic stresses, and for shorter durations the response tends to have less plastic stresses. The corresponding damage can be then determined for the stressed fibres at selected points on the cover and core of the column's section, using equation (1). The loading rate of 1.414 g/s, (longer duration loading), showed an extended constitutive curve

with large plastic strains and degraded strength on the core and cover in figure 3. In figure 4 less plasticity is expressed on the core and cover with 1.880 g/s loading rate, and almost linear constitutive curves are found with 2.801 g/s loading rate, (shorter duration loading).

This indicates that much less damage occurs with larger loading rates, and more damage occurs as the loading rate decreases.



Figures 3&4 stress-strain curves at 1.414 g/s and 1.88 g/s loading rates

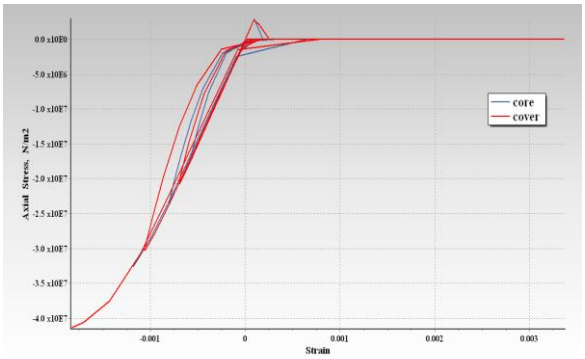


Figure 5 stress-strain curves at 2.801 g/s loading rate

3.2 Fracture-based Damage

This method is based on modelling the fractured elements of the model by using a DE/FE Explicit Dynamic solver. The Explicit-Elfen code is used to perform the non-linear dynamic analysis for a limited time of applied loading, since fracture analysis takes a relatively large computational time to attain the analysis of few seconds of loading.

3.2.1 Failure and Fracture Model

The non-linear dynamic analysis in this approach is governed by Mohr-Coulomb/Rankin with tension cut-off model, covering both tensile and shear failure modes, Mode (I) and Mode (II), respectively. The failure model is characterised by shear strength, angle of friction, angle of dilation and tensile strength. The fracture model is characterized by tensile strength and fracture energy, to simulate the tensile cracking mode Mode(I) only, and is known as the Rotating Crack model. Mode (I) is suitable to represent the cracks in the column's dynamic oscillation motion, since the fracture in the column base is mostly due to tensile cracking mode.

The applied dead load in the proposed example is 4.5MN, which is only 5% of the column's capacity for axial load, and thus, the confinement reached by the transverse reinforcement stirrups is found to be only 4.5% of the steel yield stress f_y. This leads to less confinement, and thus, the principal stresses of the concrete become closer to the failure envelope, and concrete is more vulnerable to fail.

In this FE analysis the bond effect is not simulated since that 2D steel bar elements are fully conjugated with the edges of the tetrahedral 3D concrete elements. In general, bond friction could have some effect on the fracture mechanism and crack growth, but its existence could also increase the computational effort significantly.

3.2.2 Fracture Energy

The fracture energy is defined as the amount of energy needed to create a continuous crack on a unit area, and it is the equivalent alternative to the softening law. The fracture energy for a controlled volume, often chosen to be the finite element, is the area under the softening curve, as shown in figure 6. Modelling wise, if the stresses have not dropped to zero in the softening stage, the area under the softening curve is less than the assigned fracture energy G_f, and the material is partially damaged, i.e. the Failure Factor is assigned between 0 and 1, and the controlled volume is under micro-cracks but no cracks are initiated yet. If this area is equal to the fracture energy, the material is totally damaged, i.e. Failure Factor=1, and cracks start to initiate.

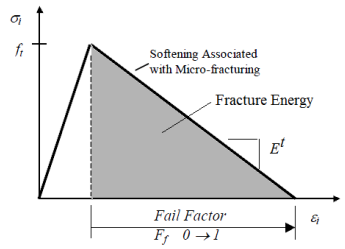


Figure 6 Fracture energy under softening curve

The release of the fracture energy rate ∂G_f is dependent on the degree of damage caused during the softening stage, which is defined as:

$$\partial G_f = \sigma . du \tag{2}$$

$$G_f = \int \sigma . du = \int \sigma . \varepsilon(s) . ds \tag{2'}$$

Where σ is the stress, u is the displacement and $\varepsilon(s) = \frac{du}{ds}$ is the softening strain in the direction s of the principal plane. Integrating over a localization band l_c for a constant slope softening model, this gives:

$$E^t = \frac{\partial \sigma}{\partial \varepsilon} = -\frac{f_t^2 \, l_c}{2G_f} \tag{3}$$

where, l_c is a function of an element area and f_t is the concrete tensile stress, and the negative sign is for the modulus slope. The fracture energy is used to define the softening curve E^t, and the resulting area under the curve is either less than or equal to the energy fracture G_f. Once the area under the curve reaches G_f, which is usually 100 to 150 N/m for concrete, the fracture energy of that point is said to be released, i.e. work of "softening strains" is completed during the softening stage at that plastic zone, and a crack initiates.

Fracture is now introduced using an algorithm that updates the topology of the mesh through insertion of discrete fractures in the "failed" regions. A visible crack is then allowed to initiate, and also propagate.

3.2.3 Problem Set-up for the FE Analysis

As equivalent to the PGA motion of Lexington Dam record, from the Loma Prieta earthquake 1989, loading is applied on the RC structure, which has a damping ratio of 5%. This force is applied at the side surface of the top mass, and its rate of loading should be similar to that of the ground acceleration. The required axial loading is due to the dead load which is modelled by having an artificial mass structure with density and volume producing an equivalent loading effect. For less computation efforts in the analysis, the following procedures have been taken:

1- Applying only half structure since both geometry and loading are symmetric about the xy vertical plane.
2- Excluding modelling of reinforcement stirrups apart from the PH zone, since the confinement of concrete core is more important in that zone.
3- Out of the total record time of 40 seconds, only partial loading with the PGA value is selected from the Lexington Dam record of Loma Prieta earthquake 1989. The maximum loading lateral force is approximately 2.2e6 N, and the corresponding time is from 3.48 seconds up to 5.48 seconds, lasting for 2.0 seconds only. This applied peak forces vary in rate, from 0.70 to 2.0g per second, as shown in figure 7.

Another dynamic loading rate is applied, with a loading rate of 2.27g per second on the same example, to compare its analysis with the previous one, and discover the influence of rate change.

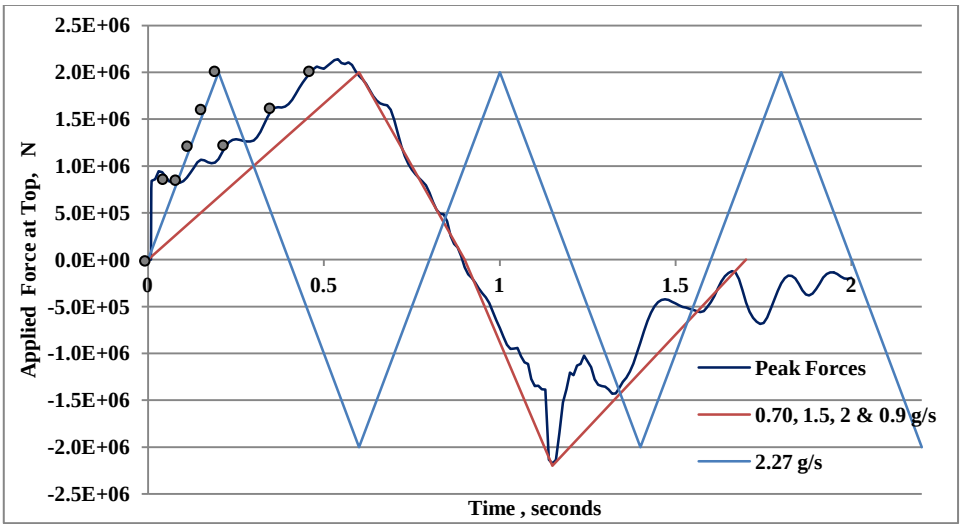


Figure 7: Different rates of applied forces at top of structure.

3.2.4 Results and Discussion

Prior to comparing between the problem responses of different loading rates, it is useful to compare the performance of the two dynamic solvers; the DE/FE fracture analysis using the Explicit-Elfen compiler and the SeismoStruct analyser. Figure 8 shows the load-deflection

curves by SeismosStruct, for the quasi-static and dynamic nonlinear analyses for the RC column problem, subjected to Lexington Dam record of the Loma Prieta earthquake 1989 in the dynamic case. It also shows the load-deflection curve by the DE/FE fracture analysis for the same problem, but subjected to only 2 seconds of the peak forces of the Loma Prieta earthquake. Due to severity of damage, the structure is deflecting towards an unstable position as the plastic hinge PH becomes severely fractured. Comparing this with the response of SeismoStruct analysis for the same problem, the linear stiffness of the SeismoStruct curves have a good agreement with the Elfen response, but differences are noticeable in the non-linear behaviour and during the hysteretic stages. This concludes that under strong ground motion, with peaks such as PGA reaching approximately 6.0 m/s^2, the damage could be very severe and leads to a total collapse of the structure.

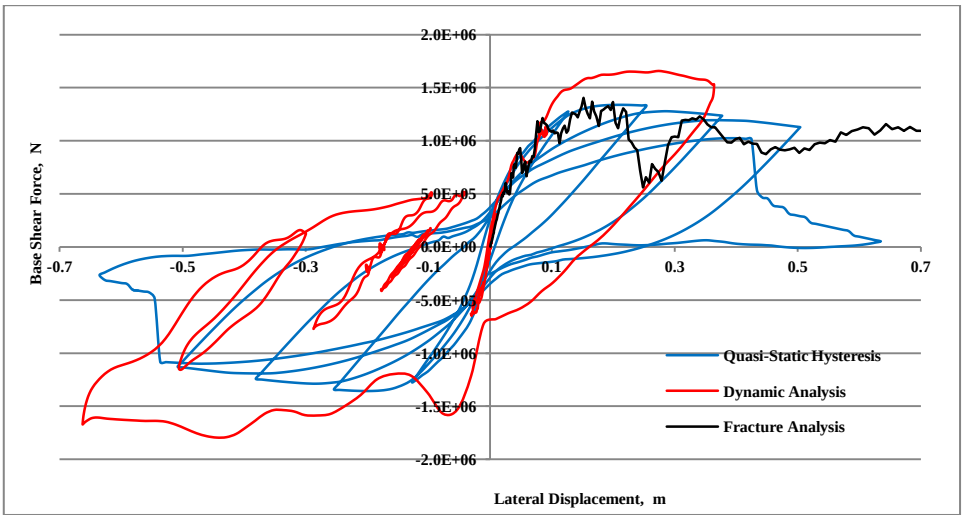
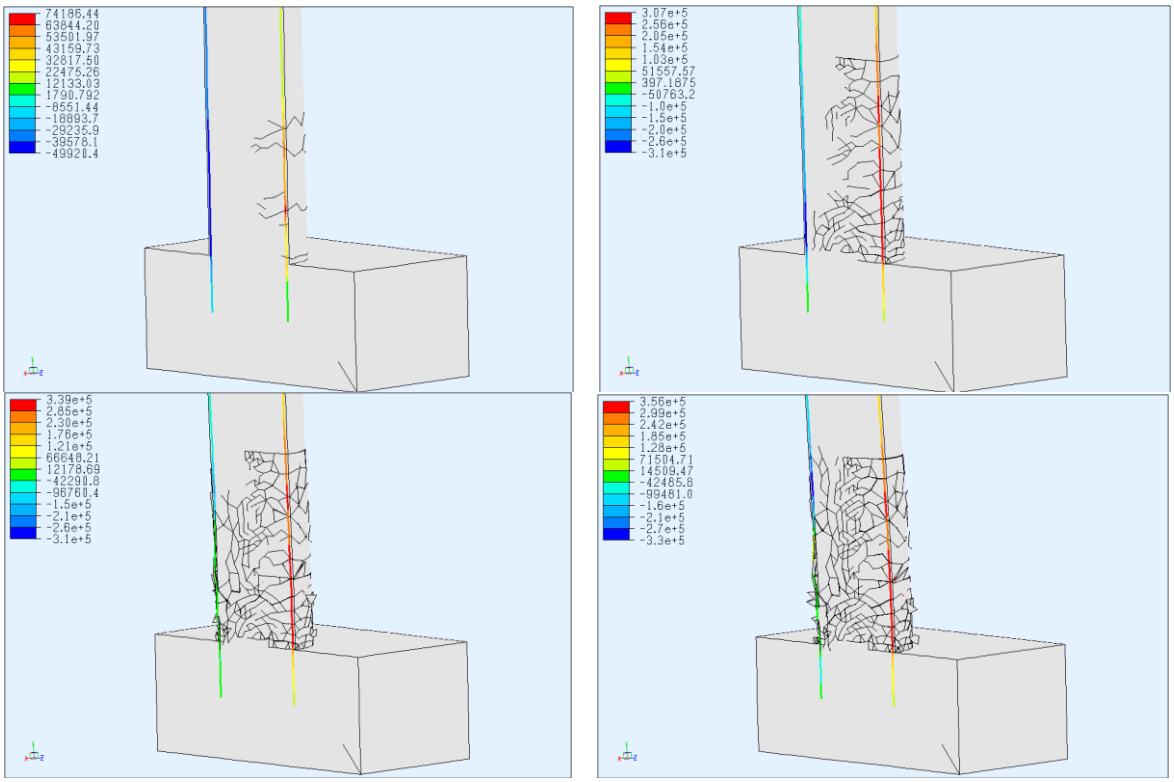


Figure 8, Load-Deflection curves by different analyses for the structure under Loma Prieta earthquake.

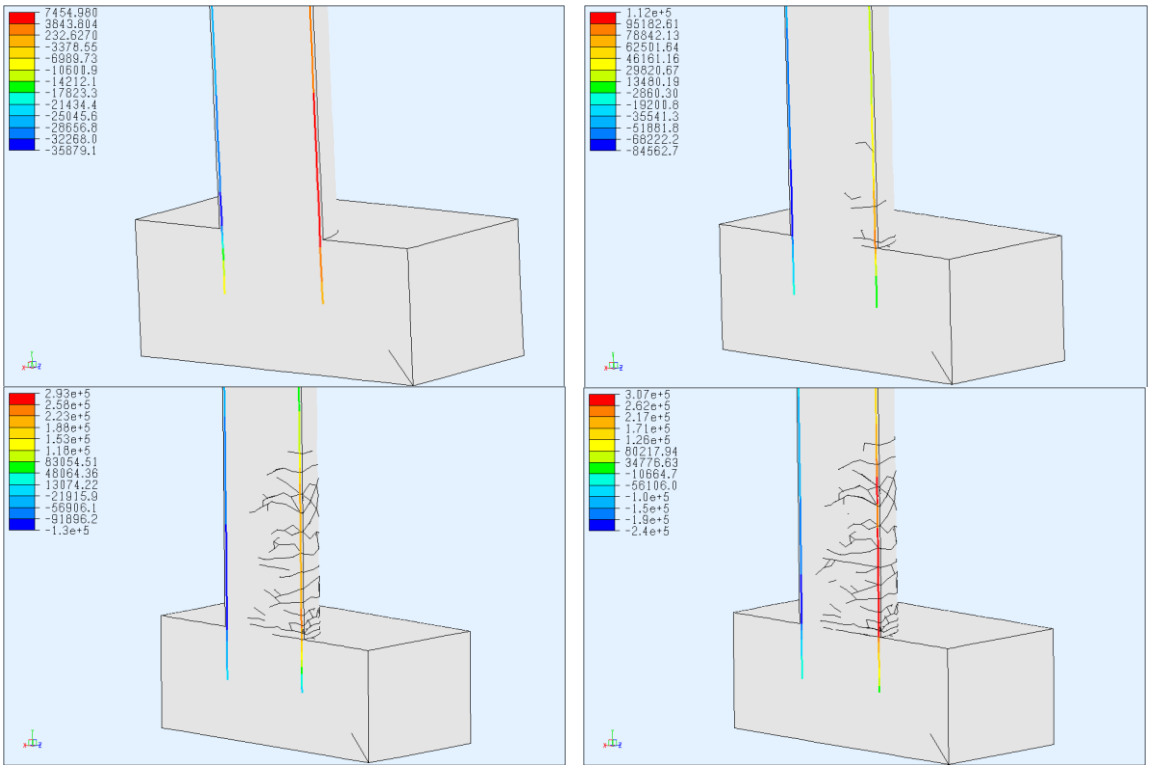
Under different rates of loading, different responses have been obtained for the same lateral loads that are applied on each problem, and marked by points on the in figure 7. Table 1 shows the responses of time, displacements, degree of damage and bar tensile stresses for long and short duration lateral loads. The 4 applied loads; 0.821, 1.208, 1.619 and 2.03 MN, care selected to show the damage that's pictured in figures 9, 10, 11 and 12 for the problem with case(A) of longer duration.

Applied Lateral Load (MN)	**Case (A): Long Duration, Low Frequency Acceleration Pulse, 0.70g per second.**			**Case (B): Short Duration, High Frequency Acceleration Spike, 2.27g per second.**		
	Time (s)	**Lateral Displacement (m)**	**Bar Tensile Stress at PH, MPa**	**Time (s)**	**Lateral Displacement (m)**	**Bar Tensile Stress at PH, MPa**
0.76	0.01	0.0163	-9.92	0.076	0.002	1.9
0.821	0.09	0.04093	98.7	0.082	0.007	11.5
1.04	0.14	0.10242	269.0	0.104	0.0141	94.7
1.208	0.22	0.24028	474.8	0.121	0.022	121.9
1.44	0.33	0.29027	491.8	0.144	0.0365	221.1
1.619	0.36	0.43260	524.3	0.162	0.0517	399.0
1.83	0.43	0.43260	524.3	0.183	0.074	475.0
2.03	0.47	0.53106	550.6	0.2	0.095	475.0

Table 1: Responses of RC column under long and short duration applied lateral loads.



Figures: 9, 10, 11 and 12; Concrete fracture and steel tensile forces due to applied loads of 0.821, 1.208, 1.619 and 2.03 MN, respectively, for longer duration case (A).



Figures: 13, 14, 15 and 16; Concrete fracture and steel tensile forces due to applied loads of 0.821, 1.208, 1.619 and 2.03 MN, respectively, for shorter duration case (B).

The states of damage caused by the same 4 applied loads but with shorter duration of loading, case (B), are pictured in figures 13, 14, 15 and 16. It is obvious that cracks tend to grow densely in the long duration case more than in the short duration case. As the structure is symmetrically modelled and loaded, the pictures show an obvious grow of cracks inside the column core itself, especially with at large loading. Such cracks are obtained for the peak loads of that record only, but more cracks could accumulate if the rest of the loads of the record are added.

Damage is the result of lateral displacements, and the maximum displacement in case (B) is approximately 20% of that in case (A) even though both are subjected to the same load value, but with different loading rates.

In respect of tensile stresses in the reinforcement bars, stresses are consequently less in case (B), and their ductility is less consumed than in case (A). However, bar tensile stresses in case (B) rise fast as loading rises, and then reach 86% of the tensile stresses in case (A). This shows that a huge part of the seismic energy is dissipated by the steel reinforcement bars, causing less damage to the concrete body. At displacement of 0.095m, the tensile stresses in case (B) reaches 475MPa, while a displacement of 0.102m, the tensile stresses in case (A) does not exceed 269MPa. This is because that less damage is found in case (B), and therefore, more concrete-steel bond exists in the context of the plastic hinge, while in case (A) more crack growth formation with less concrete-steel bond exist, and thus, less tensile stresses may produce. This indicates that ductility is affected and the member does not follow the demand/capacity principle sufficiently in the nonlinear stage. Therefore, the SDC seismic design criterion based on this principle could fail due to lack of ductility.

4 CONCLUSION

- The damage of quasi-brittle materials such as concrete is very sensitive to the rate of loading, and the inconsistency of loading rates of earthquake motion makes the damage pattern in such RC columns with low confinement unpredictable and difficult to generalize. Therefore, it is very much recommended to analyse each loading case independently for an approximated fracture simulation.
- At responses of approximately similar displacements, the bar tensile stresses reach 475MPa and 269MPa in the two nonlinear analyses; with short duration and longer duration loads, respectively. This is because that less damage is found in the short duration loading case, and therefore, more concrete-steel bond functions in the context of the plastic hinge, while in the longer duration loading case more crack growth is formed with less concrete-steel bonding, and thus, less tensile stresses is produced.
- The SDC seismic design criterion that’s used by many building codes is based on the principle of seismic demand/seismic capacity balance. This principle functions effectively in both linear and non-linear cases, but requires an effective ductility of the members to function properly during the non-linear stage. However, in quasi-brittle materials this principle lacks to sufficient ductility of the members, since concrete cracks cause less concrete/steel bond, and thus, the steel bars do not reach sufficient ductility. In such case the seismic demand/capacity principle is not sufficiently fulfilled.

- Confinement action could prevent much of crack penetration inside the concrete column core, however, the formation of confinement stresses around the core is a function of the axial load on the section, and it produces the balance between outward strains of the concrete and inward stresses of the steel hoops. If the axial loads are not sufficient, very low confinement is produced, and therefore, more cracks may penetrate inside the column core.
- RC columns supporting single-cell box-girder bridges are vulnerable to high risk damage at their plastic-hinge zones, since they have less confinement action due to low axial stresses and are subject to strong ground motion or long duration ground acceleration.

- For such structural systems to function according to a performance-based seismic design when subjected to strong ground motion, they must be provided by one of the energy dissipative devices such as seismic isolation systems or damping braces. Alternatively, they should be provided by some sufficient means that enhance their confinement action such as carbon-fibre confinement sheets.

REFERENCES

[1] Raul D. Bertero, Vitelmo V. Bertero, Performance-based seismic engineering: the need for a reliable conceptual comprehensive approach, *Earthquake Engng Struct. Dyn, 2002; 31:627 – 652* .

[2] Basil Kolias, Eurocode 8 – Part 2. Seismic Design Of Bridges.

[3] J.P.Singh. Characterization of ground motion for severity and damage potential. *http://nisee.berkeley.edu/lessons/singh.html*

[4] E. Cosenza and G. Manfredi, Damage Indices and Damage Measures, *Prog. Struct. Engineering Mater.2000*

[5] Bibliography of SeismoStruct Earthquake engineering Software, *SeismoStruct v5.2.2 Official release of 22/08/2011*.

[6] Housner GW & Jennings PC. Earthquake design criteria. *EERI Monograph Series. Berkeley, CA: Earthquake Engineering Research Institute. 1982.*

[7] Junichi Sakai, Stephen A. Mahin, Analytical investigations of new methods for reducing residual displacements of reinforced concrete bridge columns, *Pacific Earthquake Engineering Research Centre, PEER Report 2004/02*.

[8] J. Zhangh & Y. Huo, Evaluation effectiveness and optimum design of isolation devices for highway bridges using fragility function method, *Journal of Engineering Structures,1648-1660, March 2009.*

[9] Kabir Sadeghi, Energy based structural damage index based on nonlinear numerical simulation of structures subjected to oriented lateral cyclic loading, *International Journal of Civil Engineering, Vol. 9, No. 3, September 2011.*

[10] Erduran, E. and A. Yakut, *Component damage functions for reinforced concrete frame structures.* Engineering Structures, 2007. **29**(9): p. 2242-2253.

[11] Junichi Sakai, S.U., Earthquake simulation test of circular reinforced concrete bridge column under multidirectional seismic excitation. *Earthquake Engineering and Engineering Vibration, 2006. Vol. 5, No. 1.*

[12] Junichi Sakai, S.A.M., Analytical Investigations of New Methods for Reducing Residual Displacements of Reinforced Concrete Bridge Columns, 2004, *Pacific Earthquake Engineering Research Center(PEER).*

[13] Neto, E.d.S., *Computational methods for plasticity : theory and applications*, ed. D. Perić and D. Owens2008, Chichester: Wiley.

[14] Robinson, W.H., Lead-rubber Hysteretic Bearings Suitable for Protecting Structures During Earthquakes. *Earthquake Engng. & Struct. Dyn, 1982. 10(4 , Jul.-Aug. 1982).*

[15] Galindo, C.M., J.G. Belda, and T. Hayashikawa, Non-linear seismic dynamic response of curved steel bridges equipped with LRB supports. *Steel Construction, 2010. 3(1): p. 34-41.*

[16] Stewart, J.P., J.P. Conte, and I.D. Aiken, Observed behavior of seismically isolated buildings. *Journal of Structural Engineering, 1999. 125(9): p. 955-964.*

[17] Tsai, M.H., Transverse earthquake response analysis of a seismically isolated regular bridge with partial restraint. *Engineering Structures, 2008. 30(2): p. 393-403.*

[18] Wenguang Liu, F.Z., Feng Sun, Da Huo, Weiming Yan, Product Specification and Mechanical Properties of Chinese Rubber Bearings 2001.

COMPDYN 2013
4th ECCOMAS Thematic Conference on
Computational Methods in Structural Dynamics and Earthquake Engineering
M. Papadrakakis, N.D.Lagaros, V. Plevris (eds.)
Kos Island, Greece, 12–14 June 2013

APPLICABILITY OF PRINCIPLE OF SUPERPOSITION IN OBTAINING HORIZONTAL IMPEDANCE FUNCTIONS OF PILE GROUPS UNDER SOIL NONLINEARITY

Chandra S. Goit[1*], Masato Saitoh[1], and George Mylonakis[2]

[1] Department of Civil and Environmental Engineering, Saitama University
255 Shimo-Okubo, Saitama, Japan
chandra@kiban.civil.saitama-u.ac.jp *
saity@mail.saitama-u.ac.jp

[2] Department of Civil Engineering, University of Patras
256 00 Patras, Greece
mylo@upatras.gr

Keywords: Pile-to-pile interaction, horizontal impedance functions, principle of superposition, soil nonlinearity

Abstract. *The effects of soil nonlinearity on the pile-to-pile horizontal interaction factors and horizontal impedance functions of piles through model testing are investigated. Separate experiments with a solitary pile and closely spaced 3x3-pile groups with spacing to diameter ratio of 2.5 embedded in cohesionless soil, are considered. Lateral harmonic pile-head loadings in the form of accelerations with amplitudes of 0.2, 0.5, 1 and 2 m/s^2 for a wide range of frequencies are reported. Results obtained from model soil-pile systems encased in a laminar shear box show that local nonlinearity and resonant behavior of soil have a significant impact on both the interaction factors and the impedance functions. Utilizing the measured values of horizontal impedance functions of a single pile and the horizontal pile-to-pile interaction factors, Poulos' superposition method is assessed in obtaining the horizontal impedance functions of the pile group. Comparisons between computed and experimentally measured values show very good agreement, suggesting that the principle of superposition is applicable under nonlinear conditions.*

1 INTRODUCTION

Safe and efficient design of pile-supported structures depends on the reliable prediction of the response of soil-pile-structure systems, rather than that of the individual components treated separately. For such, the consideration of soil-structure interaction effects in the analysis is essential. The horizontal impedance functions (IF) of piles are an important component in the analysis of laterally loaded soil-pile-structure systems with the consideration of soil-structure interactions. These horizontal IF are complex-valued, frequency dependent quantities and are expressed by their real and imaginary parts as

$$K_{hh}^{*} = k_{hh} + iC_{hh} \tag{1}$$

where k_{hh} and C_{hh} are the real and imaginary parts of the complex pile-head horizontal IF, respectively. The real part reflects the stiffness of the soil-pile system, while the imaginary part reflects the damping in the form of material and radiation energy dissipation. It is noteworthy that the IF for a pile group is different from that of a single pile, as pile-to-pile interaction exists in a group of piles.

The superposition method initially suggested by Poulos for static loads [1] and later extended by various investigators to the dynamic regime ([2], [3], [4], [5]), where it is assumed that the interaction effects between the individual piles pairs can be superimposed, have been extensively used for the computation of pile group response once the IF of a single pile and interaction factors between pairs of piles in the distances and frequencies of interest are known. A number of elasticity-based approximate solutions for computing the pile-to-pile interaction factors are available ([2], [3]). In addition, analytical solutions for obtaining the IF of single piles are also available [1]. However, formulation of these available solutions relies upon the assumption that both the pile and soil behave elastically. It is well known that under strong excitation, soil near a pile behaves nonlinearly and has a strong influence on the response, which cannot be captured by elastic considerations.

The article at hand reports on an experimental investigation of soil-pile systems in assessing the applicability of Poulos' superposition method under strong dynamic excitation. Three distinct sets of experiment are carried out for: (a) horizontal IF's of single piles, (b) pile-to-pile interaction factors, and (c) horizontal IF's of pile groups. Fixed-head floating piles are considered, except for the testing involving pile-to-pile interaction where free head conditions were maintained. Closely spaced pile group configurations consisting of 3x3 piles with spacing-to-diameter ratio (s/d) of 2.5 are reported. Experiments consider both the effects of resonance and local nonlinearities of soil due to applied loads at the pile-head.

2 EXPERIMENTAL PROGRAM

2.1 Law of similitude

In model testing, as the response of a model differs from that of the true prototype, scaling laws are fundamental in correlating the response of the two systems. Early procedures are derived by Rocha [6] and Roscoe [7], who discuss scaling relations between model and prototype in terms of stress and strain. Additional work was carried out by Kagawa [8], Kokusho and Iwatate [9], in generalizing the theory to more general conditions. For the present investigation, scaling laws derived by Kokusho and Iwatate [9] under one-*g* testing environment are employed.

Table 1 summarizes the scaling relationship used in the present study where λ is the geometric scaling ratio of the model to the prototype and η is the density scaling ratio of the model to the prototype.

Items	Similitude		Scaling factors			Units
	Law	Factor	Prototype	Model	Attained	
Length of pile (l)	λ	0.05	18.0	0.90	0.90	m
Depth of soil (H)	λ	0.05	20.0	1.00	1.00	m
Diameter of pile (d)	λ	0.05	0.80	0.04	0.04	m
Density of pile (ρ_p)	η	0.81	2.40	1.95	1.21	t/m^3
Density of soil (ρ_s)	η	0.81	1.80	1.46	1.46	t/m^3
Young's modulus of pile (E_p)	$\eta^{1/2}\lambda^{1/2}$	0.20	25.0	5.04	3.20	GPa
Shear wave velocity (V_s)	$\eta^{-1/4}\lambda^{1/4}$	0.50	171.5	85.44	95.72	m/s
Natural frequency of soil (f_n)	$\eta^{-1/4}\lambda^{-3/4}$	9.96	2.14	21.36	23.93	Hz

Table 1: Scaling relations for model testing

2.2 Experimental setup

The experimental model consisted of soil-pile systems cased in a laminar shear box (1200 mm x 800 mm x 1000 mm) bolted on a uniaxial shaking table.

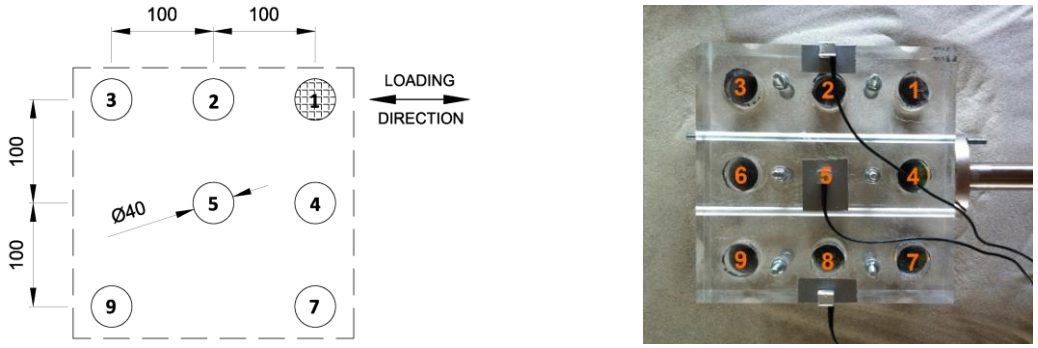
2.2.1. Soil

Homogenous dry Gifu sand was employed, the standard properties of which are available as published by Ishida et al. [10]. The desired density of sand was attained by compaction through base vibration of the shear box at frequency of 40 Hz and amplitude of 5 m/s^2.

2.2.2. Single pile

A solid cylindrical acrylic pile with the diameter d = 40 mm and length l = 900 mm having a pile-head (125 mm x 125 mm x 125 mm) was used. The pile-head was fixed with an actuating device ensuring that only horizontal displacement is applied in that elevation. No contact between pile-head and soil was allowed.

2.2.3. Pile group



(a) pile-to-pile interaction (dimensions in mm) (b) pile group

Figure 1: Layout of pile group

Nine solid acrylic piles capped by a solid acrylic pile-cap with thickness of 100 mm were used to form a 3x3 pile group with s/d = 2.5 as shown in Figure 1(b). The pile-cap was connected to the horizontal actuator as in the case of the single pile, such that only horizontal translation was allowed. In addition, no contact between pile-cap and soil was allowed.

A similar layout was used for the measurement of pile-to-pile interaction factors, but without the pile-cap. Pile 1, as shown in Figure 1(a), was fixed to the horizontal actuator while all the other piles were free head piles. Horizontal interaction factors for piles in line to the direction of loading (pile 2 and 3) and perpendicular to the direction of loading (pile 4 and 7) were measured. Horizontal interaction factors for all the other piles (i.e., 5, 6, 8 and 9) are straightforwardly computed by simple trigonometric expressions ([2], [4]), based on piles 2, 3, 4 and 7.

2.2.4. Loading

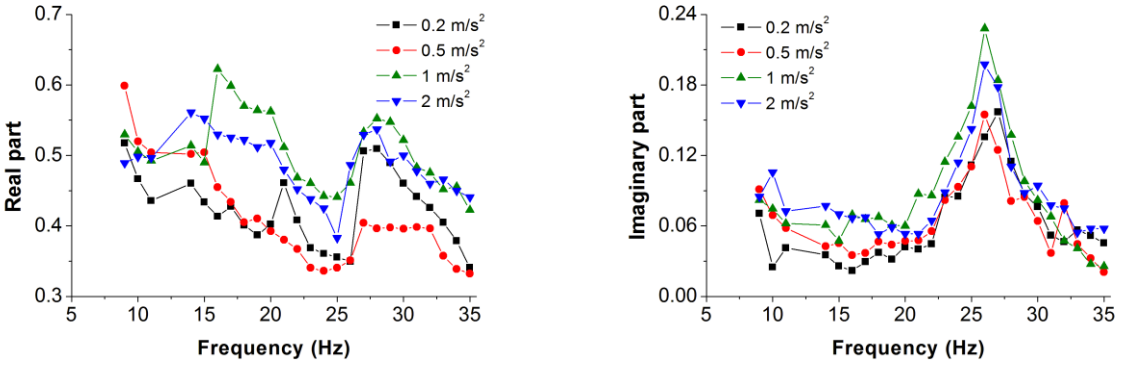
Four different amplitudes of lateral harmonic accelerations (0.2, 0.5, 1, 2 m/s^2) at the pile-head level are considered to test the system in low-to-high strain levels in soil, for the frequency range of 9 ~ 35 Hz.

3 RESULTS

The measured data from the experiments are processed in the frequency domain and are presented in this section. Resonance of the soil-pile systems is distinctly observed for all loading amplitudes within the measured range of frequencies.

3.1 Horizontal impedance functions of single pile

Horizontal IF of a single pile subjected to different amplitudes of pile-head harmonic loadings are presented in Figure 2. Real part of the IF in the measured range of frequencies does not show a definite trend among the loading amplitudes. Considering the global nonlinearity of soil, the pile-head stiffness is expected to decrease with the increase in loading amplitude, however, no clear pattern is observed. On the other hand, the imaginary part shows an increase in value with increasing loading amplitude, distinctly in the low-frequency region.



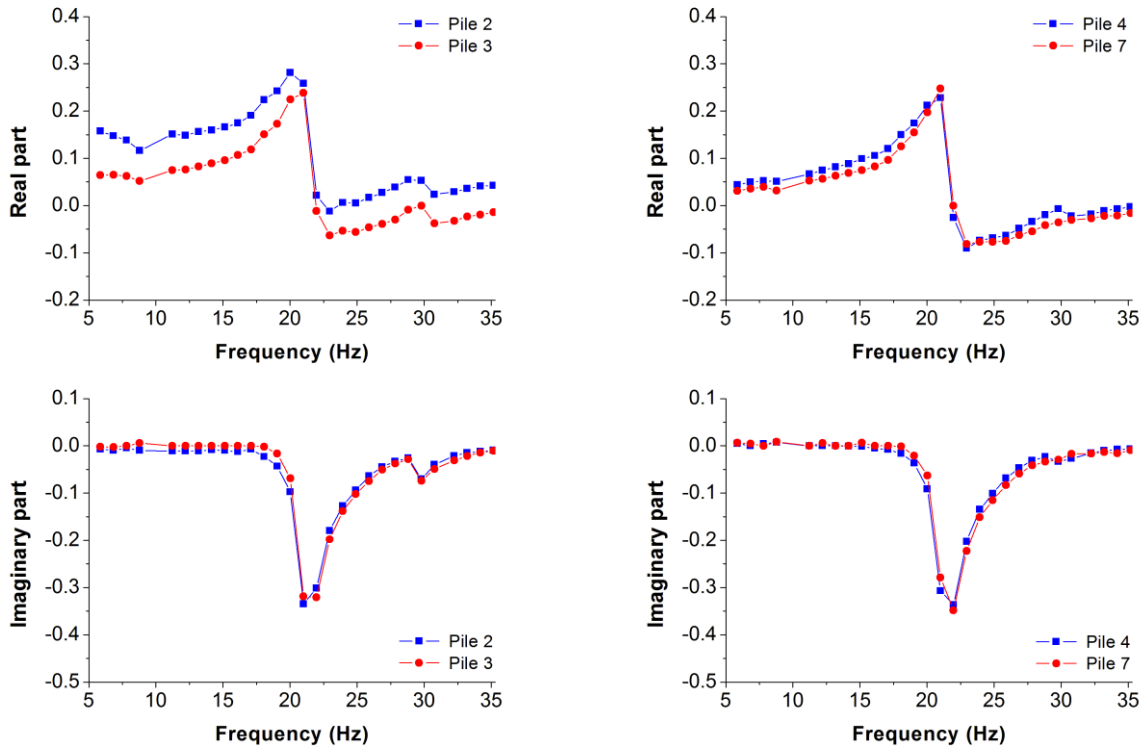
(a) real part (b) imaginary part

Figure 2: Horizontal impedance functions of a single pile (in kN/mm)

3.2 Horizontal pile-to-pile interaction factors

Measured dynamic pile-to-pile horizontal interactions for the highest amplitude of loading utilized in present work (i.e., 2 m/s^2 at the pile head) are presented in Figure 3.

In the low-frequency range, pile 2 exhibits the highest value of interaction factor. On the other hand, pile 3, which is at a distance twice that of the pile 2 shows a very small value of interaction factors, suggesting that the interaction between pile 1 and pile 3 is not so significant. High-frequency region, on the other hand, exhibits similar behavior as of the low-frequency region (i.e., pile 2 shows the higher value of interaction factors). The imaginary part shows out of phase movement with identical peak values.



(a) pile 2 and 3

(b) pile 4 and 7

Figure 3: Horizontal pile-to-pile interaction factors

Pile-to-pile interaction in the direction perpendicular to loading (i.e., pile 4 and 7) is found to be minimal. The low-frequency region shows a negligible increase in the value of the horizontal interaction factor for pile 4. Around resonant frequency, peak values of the horizontal interaction factor for both the piles 4 and 7 are nearly identical. The imaginary part also shows identical peak values.

4 PRINCIPLE OF SUPERPOSITION

Utilizing Poulos' superposition method [1], the horizontal IF for pile groups can be written as function of the corresponding IF for single piles and pile-to-pile interaction factors. Displacement of individual piles in a group based on identical load carrying capacity of a pile can be written straightforwardly as function of solitary pile stiffness and the applied force. The procedure is detailed in Dobry and Gazetas [2].

Based on the experimentally measured horizontal IF of a single pile and the horizontal interaction factors, horizontal IF of the 3x3-pile group is computed with Poulos' superposition method. Such obtained pile groups' horizontal IF are compared with the experimentally obtained horizontal IF for the 3x3-pile group. Also compared are the results with no considera-

tion for group effect, i.e., sum of individual stiffness of piles in the pile group with no account for the pile-to-pile interaction factors.

For all loading amplitudes, the comparisons between the computed and experimentally obtained results show a very good agreement, asserting that the Poulos' superposition method is applicable under nonlinear conditions. Furthermore, results indicate significant influence of group effect on the response of pile groups, as anticipated. Figures 4 and 5 show the comparisons for the lowest (0.2 m/s^2) and highest (2 m/s^2) loading amplitudes utilized in present work.

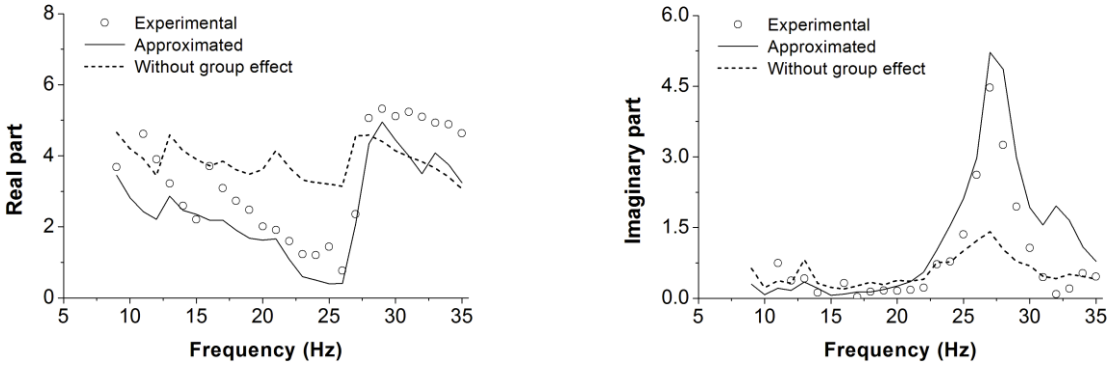


Figure 4: Horizontal impedance functions of a 3x3-pile group (in kN/mm) for 0.2 m/s^2

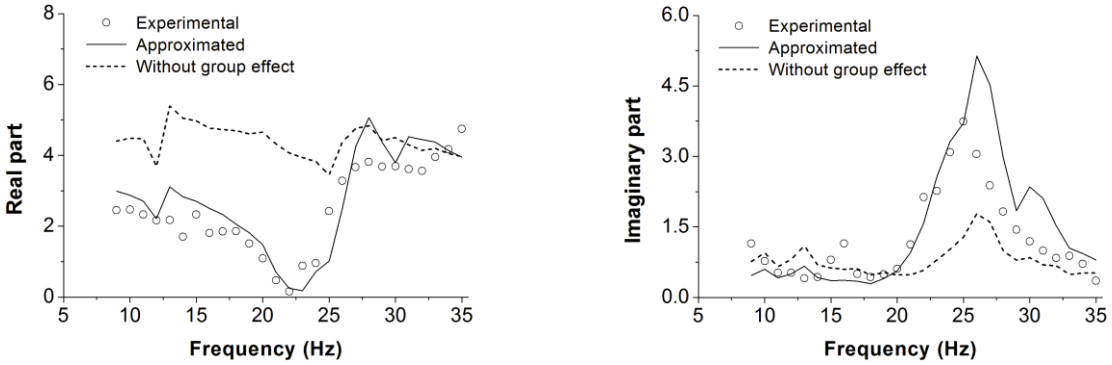


Figure 5: Horizontal impedance functions of a 3x3-pile group (in kN/mm) for 2 m/s^2

5 CONCLUSIONS

The reported experimental work was carried out for assessing the applicability of Poulos' superposition method under strong loading conditions, encompassing both the effect of soil nonlinearity and resonance of the soil-pile system. Comparisons between computed and experimentally measured values of horizontal impedance functions for the pile group show a very good agreement, suggesting that the principle of superposition can be used for practical conditions even in presence of considerable nonlinearity.

ACKNOWLEDGMENT

This paper was supported by JSPS Grant-in-Aid for Scientific Research (C) No. 23560562. Any opinions, findings, conclusions, or recommendations expressed in this material are those of the authors and do not necessarily reflect the views of the sponsors.

REFERENCES

[1] H.G. Poulos and E.H. Davis, *Pile foundation analysis and design*. John Wiley & Sons, New York, 1980.

[2] R. Dobry and G. Gazetas, Simple method for dynamic stiffness and damping of floating pile groups. *Géotechnique*, **38**(4), 557-574, 1988.

[3] G. Gazetas, K. Fan, A. Kaynia and E. Kausel, Dynamic interaction factors for floating pile groups. *Journal of Geotechnical Engineering*, ASCE, **117**(10), 1531-1548, 1991.

[4] A.M. Kaynia, and E. Kausel, Dynamic stiffness and seismic response of pile groups. Research Report, R82-03, Massachusetts Institute of Technology, 1982.

[5] G. Mylonakis, *Contribution to static and seismic analysis of piles and pile-supported bridge piers*, PhD thesis, University of New York at Buffalo.

[6] M. Rocha, The possibility of solving soil mechanics problems by the use of models. *Proceedings of the Fourth International Conference on Soil Mechanics*, London, Vol. 1, 183-188, 1957.

[7] K.H. Roscoe, Soils and model tests. *The Journal of Strain Analysis for Engineering Design*, **3**(1), 57-64, 1968.

[8] T. Kagawa, On the similitude in model vibration tests of earth-structures. *Proceedings of Japan Society of Civil Engineers* (275), 69-77, 1978. [in Japanese].

[9] T. Kokusho and T. Iwatate, Scaled model tests and numerical analyses on nonlinear dynamic response of soft grounds. *Proceedings of Japanese Society of Civil Engineers*, (285), 57-67, 1979 [in Japanese].

[10] T. Ishida, H. Watanabe, H. Ito, Y. Kitahara and M. Matsumoto, Static and dynamic mechanical properties of sandy materials for model tests of slope failure under the condition of low confining stress. *Research Report of Electrical Power Center Research Institute*, No. 380045, 1981 [in Japanese].

COMPDYN 2013
4th ECCOMAS Thematic Conference on
Computational Methods in Structural Dynamics and Earthquake Engineering
M. Papadrakakis, V. Papadopoulos, V. Plevris (eds.)
Kos Island, Greece, 12–14 June 2013

EXPERIMENTAL AND NUMERICAL INVESTIGATION OF THE SEISMIC BEHAVIOR OF RECTANGULAR TUNNELS IN SOFT SOILS

Grigorios Tsinidis[1], Kyriazis Pitilakis[1], Charles Heron[2] and Gopal Madabhushi[2]

[1] Aristotle University of Thessaloniki
Laboratory of Soil Mechanics, Foundations and Geotechnical Earthquake Engineering, POB 424, 54124, Thessaloniki, Greece
e-mail: gtsinidi@civil.auth.gr, kpitilak@civil.auth.gr

[2] University of Cambridge, Schofield Centre
High Cross, Madingley Road, Cambs CB3 0EL, Cambridge, UK
cmh78@cam.ac.uk, mspg1@cam.ac.uk

Keywords: Underground Structures, Rectangular Tunnels, Dynamic Centrifuge Tests, Dynamic Analysis

Abstract. *Underground structures constitute crucial components of the transportation networks. Considering their significance for modern societies, their proper seismic design is of great importance. However, this design may become very tricky, accounting of the lack of knowledge regarding their seismic behavior. Several issues that are significantly affecting this behavior (i.e. earth pressures on the structure, seismic shear stresses around the structure, complex deformation modes for rectangular structures during shaking etc.) are still open. The problem is wider for the non-circular (i.e. rectangular) structures, were the soil-structure interaction effects are expected to be maximized. The paper presents representative experimental results from a test case of a series of dynamic centrifuge tests that were performed on rectangular tunnels embedded in dry sand. The tests were carried out at the centrifuge facility of the University of Cambridge, within the Transnational Task of the SERIES EU research program. The presented test case is also numerically simulated and studied. Preliminary full dynamic time history analyses of the coupled soil-tunnel system are performed, using ABAQUS. Soil non-linearity and soil-structure interaction are modeled, following relevant specifications for underground structures and tunnels. Numerical predictions are compared to experimental results and discussed. Based on this comprehensive experimental and numerical study, the seismic behavior of rectangular embedded structures is better understood and modeled, consisting an important step in the development of appropriate specifications for the seismic design of rectangular shallow tunnels.*

1 INTRODUCTION

During past earthquakes, underground structures behaved generally better than near surface or aboveground structure. However, several cases of extensive damage and even collapse are reported in the literature [1], [2]. The most interesting case is that of the Daikai station in Kobe, Japan, that collapsed during the major Hyogoken-Nambu earthquake (1995) [3],[4]. This is actually, the first well-reported case of a total collapse of a large underground structure under seismic shaking. These recent failures revealed some important weaknesses in the current seismic design practices.

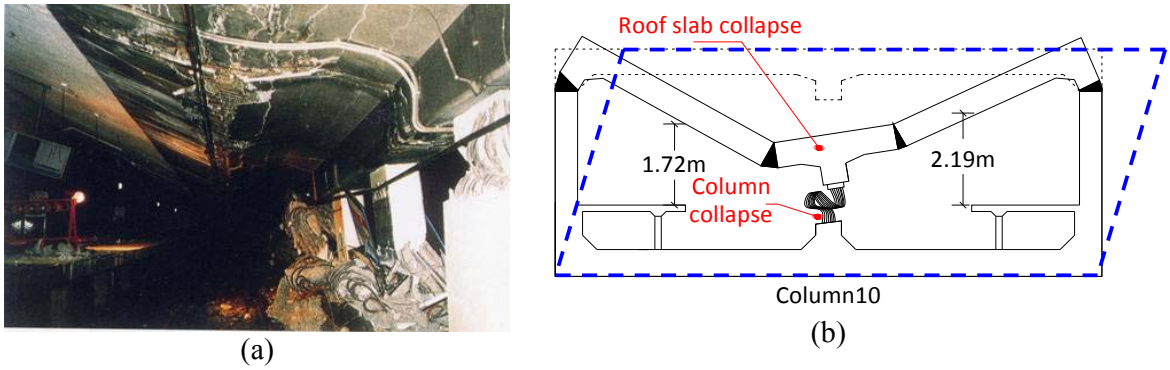


Figure 1: Daikai Station. (a) Collapse of the central columns of the station, [5], (c) Failure modes (modified after [3])

The seismic response of embedded structures to ground shaking is very distinct with respect to the aboveground structures. The kinematic loading imposed on the structure from the surrounding soil is prevailing, while the inertial effects are of secondary importance. The soil-structure interaction effects, that are expected to be increased in cases of non-circular (i.e. rectangular) embedded structures, are closely related to two crucial parameters, namely:

(i) the relative flexibility of the structure and the ground and
(ii) the interface characteristics between the structure and the surrounding soil.

The exact affection of these parameters on structural seismic response is not well known.

For the evaluation of the seismic response of underground structures, several methods may be found in the literature, ranging from uncoupled methods, simplified closed form solutions and equivalent static analysis schemes, to the most sophisticated full dynamic analysis of the coupled soil-structure system incorporating advanced numerical methods (i.e. [6-9] etc). The results of these methods may substantially deviate, even under the same assumptions, indicating the lack of knowledge regarding some very crucial issues that are significantly affecting the seismic response [10]. The lack of knowledge is even more pronounced for the non-circular structures. The seismic earth pressures on the side walls, the seismic shear stresses around the perimeter of the structure along with the soil-structure interface characteristics, the complex deformation modes during the shaking (i.e. rocking for stiff structures or inward deformations for the flexible structures) and the affection of the soil-structure relative flexibility on the seismic response are, among others, issues that need further study.

To this end, a comprehensive series of tests has been performed at the University of Cambridge (UCAM) jointly with Aristotle University of Thessaloniki (AUTH) on square tunnel models embedded in dry sand. The tests were carried out at the geotechnical centrifuge facility of the University of Cambridge, within the Transnational Access Task of the SERIES EU

research program (TA project: TUNNELSEIS). The produced experimental data are used to better understand the seismic behavior of rectangular embedded structures and also to validate advance numerical models, improving at the end the design methods. The experimental procedure and the set up for one of the tests cases is briefly presented in the ensuing paper along with the some representative experimental results. Numerical predictions, achieved by preliminary numerical simulations of the test, are also briefly presented and compared to the experimental data.

2 DYNAMIC CENTRIFUGE TESTS

2.1 Geotechnical facility

The tests were carried out on a square aluminum tunnel-model embedded in dry sand, at the "Turner beam centrifuge" of the University of Cambridge (Schofield Centre), under centrifuge acceleration of 50g.

Earthquake input motions were applied using the Stored Angular Momentum (SAM) actuator [11], which is designed to apply sinusoidal input motions at a maximum frequency up to 60Hz and at a maximum amplitude of 20g (in model scale).

A large Equivalent Shear Box (ESB) was used as the container for the models, having inside dimensions 673mm in length, 255mm in width and 427mm in depth. The box is designed to match the shear stiffness of the contained soil for the range of shear strains of interest, in order to minimize any soil-container interactions [12].

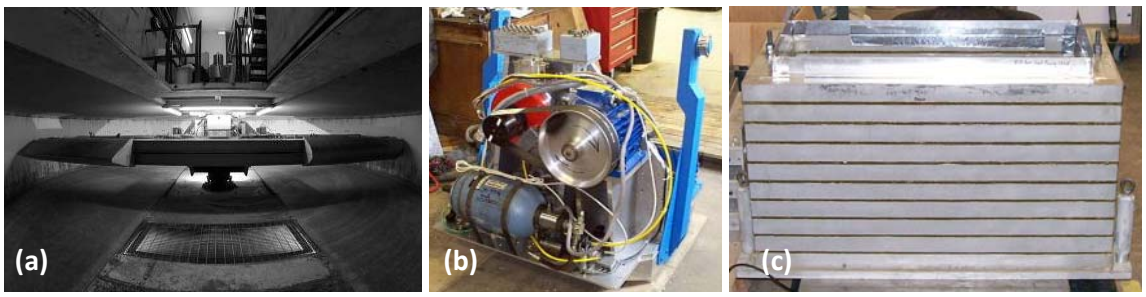


Figure 2: (a) Turner beam centrifuge, (b) SAM actuator, (c) ESB box

2.2 Materials

The model was made of dry uniform Hostun HN31 sand having a relative density of about 90%. The mechanical properties of the sand are tabulated in Table 1.

The tunnel model (Figure 3), manufactured from 6063A aluminum alloy, is 100mm wide and 220mm long, having a thickness of 2mm. The aluminum alloy mechanical properties are summarized in Table 2. According to the scale factor (N=50), the model corresponds to a 5×5×11 (m) square tunnel having an equivalent concrete lining thickness equal to 0.13m (assuming E = 30 GPa for the concrete). This thickness is obviously unrealistic in practice, as the design analysis for the static loads will result in a much thicker lining. However, this selection was necessary to achieve measurements of the lining strains. To simulate more realistically the soil-structure interface, Hostun sand was stuck on the external face of the tunnel-model, creating a rough surface.

	ρ_s (g/cm^3)	e_{max}	e_{min}	d_{10} (mm)	d_{50} (mm)	d_{60} (mm)
Hostun HN31	2.65	1.01	0.555	0.209	0.335	0.365

Table 1: Sand mechanical properties (after [13])

Unit weight, γ (kN/m^3)	Elastic modulus, E (GPa)	Poisson ratio v	Tensile strength, f_{bk} (MPa)
2.7	69.5	0.33	220

Table 2: Tunnel model mechanical properties

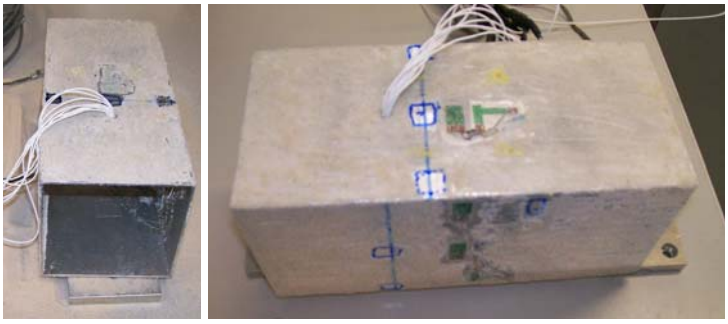


Figure 3: Tunnel model

2.3 Model preparation

The sand model was made using an automatic hopper system [14]. During the construction, the tunnel and all the embedded transducers were positioned in the model. Several phases of the model construction are presented in Figure 4. To avoid any interaction of the tunnel with the ESB box, the tunnel was shorter than the box width. Two PVC rectangular plates were placed at both the tunnel ends to avoid the sand entrance into the tunnel-model.



Figure 4: Model preparation

2.4 Model set up – instrumentation

Figure 5 presents the final model layout and the instrumentation scheme. Miniature accelerometers were used to measure the acceleration in the soil, on the tunnel and on the ESB box. To estimate the soil shear wave velocity profile before each earthquake, air hammer tests were performed [15]. For this purpose, a small air-hammer was introduced close to the base of the soil layer while a set of accelerometers were placed above it, forming an array, allowing a record of the arrival times of the waves emanating from the air-hammer. The soil surface settlements were recorded in two locations using linear variable differential transformers (LVDTs), while two position sensors were attached on the upper side of the walls of the tunnel to capture the vertical displacement and the possible rocking of the tunnel model. Both the LVDTs and the POTs were attached on gantries running above the ESB box. Two miniature total earth pressure cells were attached on the left side wall of the tunnel, allowing the measurement of the soil earth pressures on the wall.

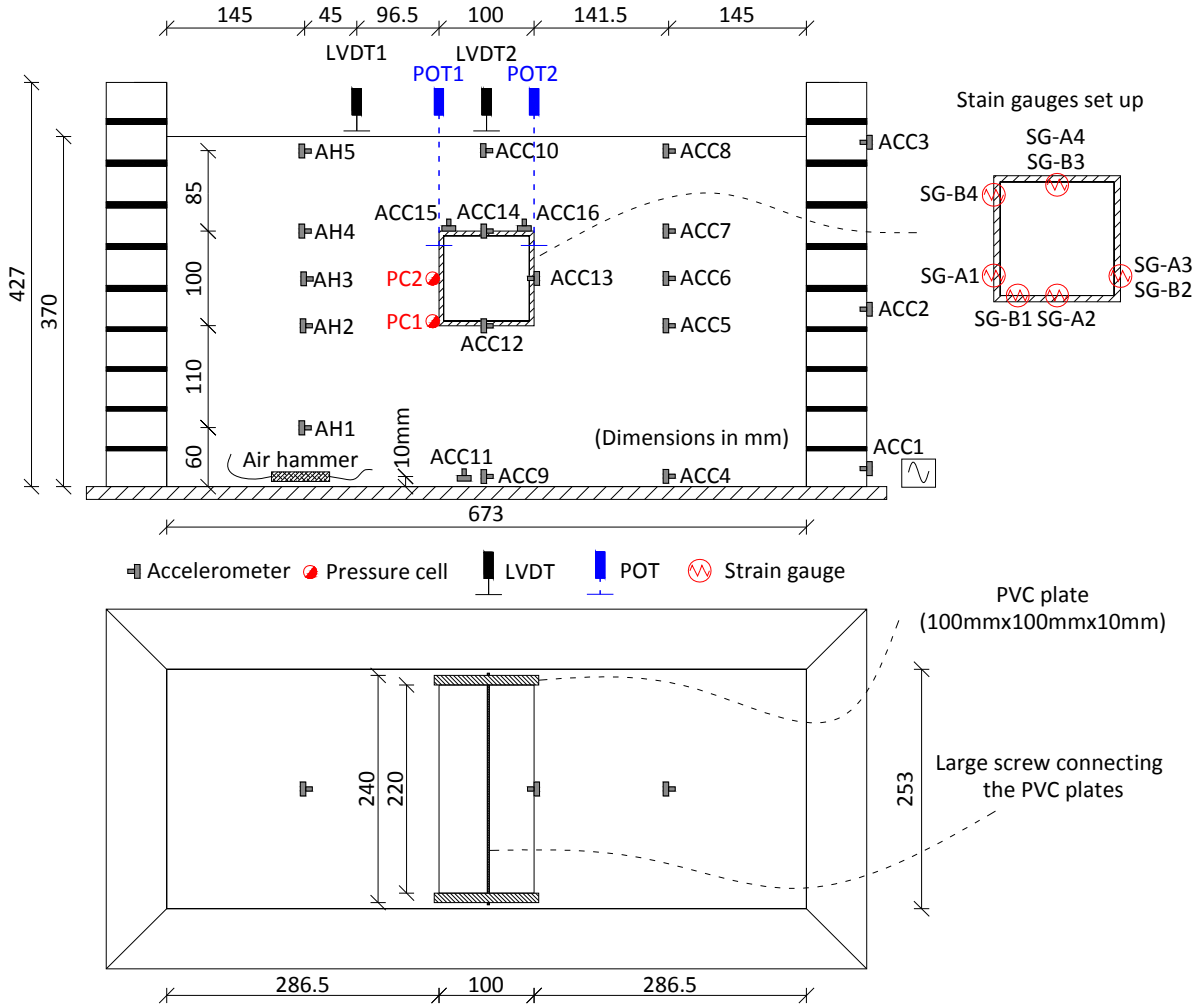


Figure 5: Model configuration – instrumentation scheme

Resistance strain gauges were glued on the inner and the outer face of the tunnel to measure the model strains at several locations. Four of them were measuring the axial strains at the walls and the slabs, while four were recording the bending moment strains near the model corners and at the middle of the roof slab. The latter strain gauge was broken during the testing procedure. In the following presented results, positive values represent bending moment with tensile stress increments for the internal lining face and tensile axial force. The gauges cables were running from the inside face of the tunnel, to avoid any interactions with the soil-tunnel interface. All the instruments were adequately calibrated before and checked after the tests, as described in detail in [16].

2.5 Experimental procedure

During each flight, the centrifuge was spun up in steps stopping at 10g, 30g and 50g and then the earthquakes were fired in a row, leaving some time between them to acquire the data. The data was recorded at sampling frequency of 4 Hz during the swing up and at 4 kHz during the earthquakes.

Before each shake, air-hammer tests were conducted to evaluate the new (modified) shear wave velocity (V_s) profile of the soil deposit. The V_s profiles were estimated based on the travel times of the waves, between accelerometers that are placed at known distances apart. These distances did not change significantly after each shake, as the recorded soil settlements were small due to the high relative density of the soil deposit. The travel times were estimated in a simplified way from the arrivals of the waves, produced by air-hammer. To make sure that the arrival times were adequately recorded, the DasyLab software was used as the acquisition system for the air-hammer array of accelerometers, allowing for a sampling frequency equal to 50 kHz.

The model was subjected to a total of eight "earthquakes" during two flights. The earthquakes were pseudo-harmonic wavelets except the last earthquake fired during the first flight that was a sine sweep. The main characteristics of the input motions are tabulated in Table 3 both in model and prototype scale (bracketed values), while the time histories are depicted in Figure 6.

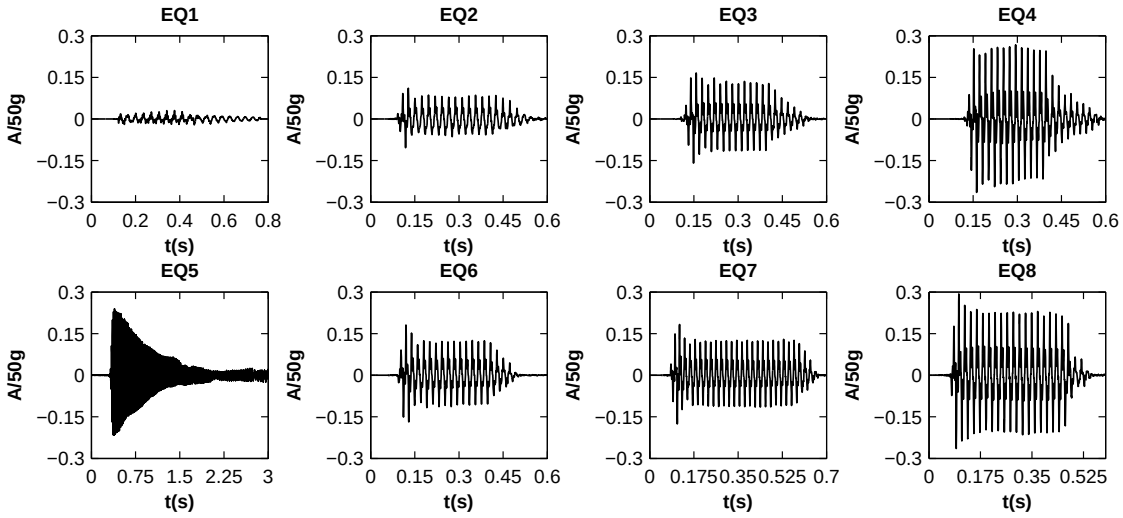


Figure 6: Input motions time histories

	Input type	Frequency	Amplitude (g)	Nominal Duration (s)
Flight 1				
EQ1	Pseudo-Harmonic	30 {0.6}	1.0 {0.02}	0.4 {20}
EQ2		45 {0.9}	4.0 {0.08}	
EQ3		50 {1}	6.5 {0.13}	
EQ4		50 {1}	12 {0.24}	
EQ5	Sine Sweep	60 {1.2}	12 {0.24}	3.0 {150}
Flight 2				
EQ6	Pseudo-Harmonic	50 {1}	5.8 {0.116}	0.4 {20}
EQ7		50 {1}	6.0 {0.12}	0.6 {30}
EQ8		50 {1}	11.0 {0.22}	0.5 {25}

Table 3: Input motions characteristics (bracketed values: values in prototype scale)

2.6 Experimental results

Representative experimental results are presented in the following sections comparatively to the numerical predictions, for EQ4. The main findings are summarized in the following:

- The horizontal acceleration recorded at several locations, is amplified towards the surface, while, the amplification ratio with respect to the base amplitude reduces with increased input motion amplitude due to the soil non-linear behavior.
- Vertical acceleration-time histories recorded on the sides of the model's roof slab were out of phase indicating a rocking mode of vibration for the tunnel.
- The tunnel's racking distortions, computed from the acceleration-time histories, indicate a rigid structure with respect to the surrounding soil.
- Small ground settlements were recorded at the soil surface during swing up and shaking, due to the high relative density of the studied soil deposit.
- During shaking the dynamic increments of the pressures were higher for the invert slab-side wall corner due to the larger rigidity of the model at this location compared to the middle of the side-wall. Residual values are observed after each shake that can be mainly attributed to the soil plastic deformations and to a small amount of soil densification during shaking that can cause stress redistribution.
- The dynamic bending moments correspond in a similar way with the recorded dynamic earth pressures. Large residual values were detected after each shake, as a result of cumulative strains during the shaking.
- Smaller residuals were observed for the dynamic axial forces after shaking. These residuals in addition to the previously mentioned ones are most probably due to an amount of sliding observed on the soil-tunnel interface.

3 NUMERICAL SIMULATION

3.1 Description of the numerical model

For the numerical simulation of the test we used the generic FE code ABAQUS [18]. Full dynamic time history analyses of the coupled soil-tunnel system were performed, under plane strain conditions, on a prototype scale model. Appropriate scaling laws were used to convert the computed quantities from prototype to model scale [17].

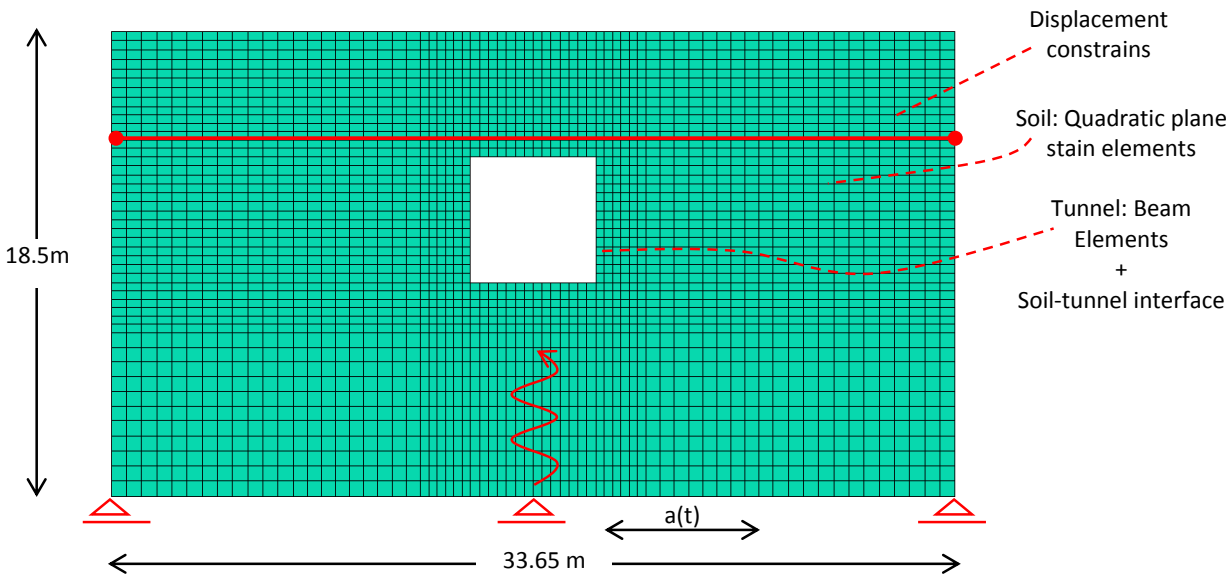


Figure 7: Numerical model in ABAQUS

More specifically, the soil was meshed with quadratic plane-strain elements, while the model tunnel was modeled with beam elements (Figure 7). Linear elastic behavior was assumed for the model tunnel (E=69.5GPa, v=0.33), while the soil behavior was modelled with (i) a linear visco-elastic material (equivalent linear approach), (ii) a combined equivalent linear-elastoplastic approximation, using a Mohr-Coulomb failure criterion and (iii) a modified kinematic hardening model combined with a Von-Mises failure criterion and an associated plastic flow rule, as presented in detail in the following. The base boundary of the model was modelled as rigid bedrock, while kinematic constrains were introduced at the vertical boundaries, forcing the opposite vertical sides to move simultaneously preventing any rotation. The soil-tunnel interface was simulated using contact algorithms available in ABAQUS [18]. More specifically, the tangential behavior was modelled using the penalty friction formulation, introducing a friction coefficient μ=0.84, considering the stack sand on the tunnel outer face. The normal surface behavior was adequately simulated, so to preclude penetration and allow separation between the two media, precluding tensile strains on the soil. The input motion was introduced at base of the model in terms of acceleration time histories, referring to the motion recorded at the reference accelerometer (see Figure 6). The analyses were performed in two steps; first the gravity loads were introduced, while in the second step the earthquake input motion was applied in a dynamic step.

Representative numerical predictions in terms of accelerations, displacements, dynamic earth pressures on the tunnel and dynamic internal forces of the tunnel lining are presented in the following sections compared to the experimental data, for the EQ4 earthquake scenario.

3.2 Soil constitutive models

- Visco-elastic analyses

For a first series of analyses, the soil non-linear behavior was modeled with a visco-elastic material, with properties (stiffness and damping) adequately selected, according to the shear deformation level, estimated for each earthquake scenario by means of 1D equivalent linear soil response analysis. The calculation was performed in the frequency domain using the code EERA [19]. The small-strain shear modulus (G_{max}) was computed according to Hardin and

Drenvich [20] that was found to give similar results, with the air-hammer tests (Figure 8a). The G-γ-D curves required for the analysis were estimated through a try and error procedure, checking different curves, so to achieve the best fitting of the numerical predictions with the experimental results (horizontal acceleration at the "free-field" array). The G_{max} and the G-γ-D, finally adopted, are presented in Figure 8, along with the maximum horizontal acceleration as computed with EERA and compared with the experimental data for EQ4 (Figure 8c).

In the 2D full dynamic analysis of the soil-tunnel system, the reduced soil shear modulus was introduced, following the distribution with depth, as computed with EERA. For this purpose, a user subroutine was encoded in ABAQUS. The damping was introduced in the Rayleigh type formulation as a mobilized value over all the soil depth. The mechanical properties of the soil as adopted for this case are summarized in Table 4.

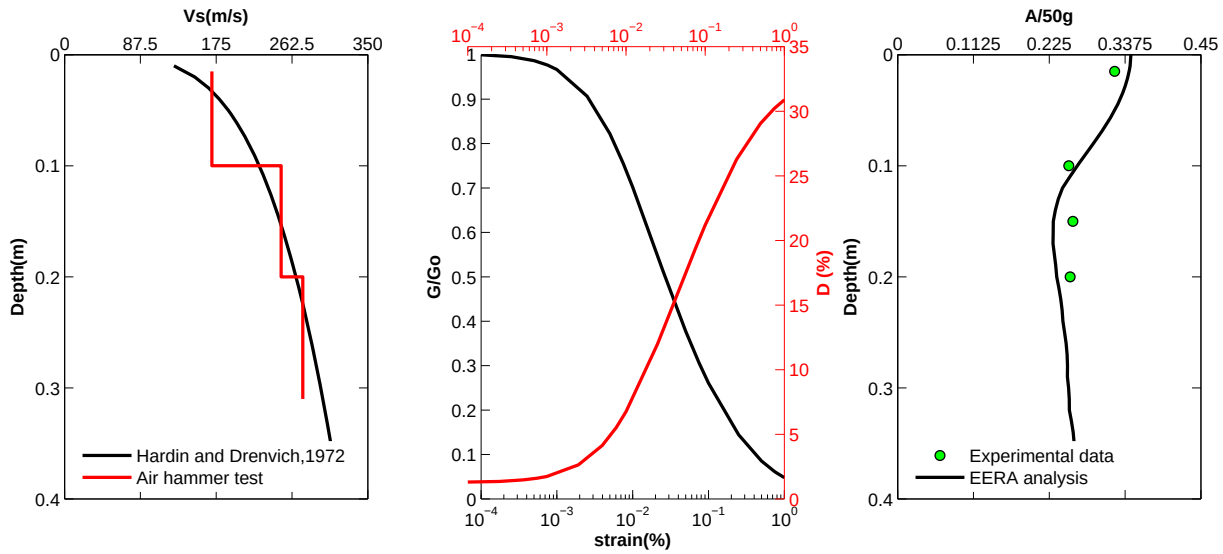


Figure 8: (a) V_{so} profile estimated from Hardin and Drenvich [20] compared to the air hammer test results, (b) G-γ-D curves adopted in the analyses, (c) Comparison of the maximum horizontal acceleration along the "free field array" as estimated from the experimental data and computed from EERA analysis for EQ4

- Combined equivalent linear-elastoplastic approximation

To account of the soil plastic response (i.e. permanent deformations, residual values for the internal forces etc), a Mohr-Coulomb failure criterion was introduced in a second series of analyses. The elastic stiffness was kept reduced with respect to small-strain elastic stiffness, corresponding to the computed, from the 1D EQL response analysis, value. Regarding the strength parameters of the sand, the values were selected according to a literature reference for the specific fraction [21].

- Modified kinematic hardening model combined with a Von-Mises failure criterion and an associated plastic flow rule

For the final series of analyses, the soil non-linear behavior was modeled using a kinematic hardening model combined with a Von-Mises failure criterion and an associated plastic flow rule. The model is embedded in ABAQUS and modified through a user subroutine, as presented by Anastasopoulos et al. [22], to be applicable also for sands.

According to the model, the evolution of stress is defined as:

$$\sigma = \sigma_0 + \alpha \tag{1}$$

where σ_0 corresponds to the stress at zero plastic strain, and α, is the responsible for the kinematic evolution of the yield surface in the stress space, backstress. This is performed through a function F which defines the yield surface, as:

$$F = f\left(\sigma - \alpha\right) - \sigma_0 \tag{2}$$

Accounting of the associated plastic flow rule, the plastic flow rule rate $\dot{\varepsilon}^{pl}$ is computed as:

$$\dot{\varepsilon}^{pl} = \dot{\bar{\varepsilon}}^{pl} \frac{\partial F}{\partial \sigma} \tag{3}$$

where $\dot{\bar{\varepsilon}}^{pl}$ is the equivalent plastic strain rate.

The evolution law comprises of an isotropic hardening component that describes the change of the equivalent stress defining the size of the yield surface σ_0 as a function of plastic deformation and a nonlinear kinematic hardening component, which describes the translation of the yield surface in the stress space. The latter is defined as an additive combination of a kinematic term and a relaxation term, which introduces the non-linearity. The evolution of the kinematic component of the yield stress is described according to the following formulation:

$$\dot{a} = C\frac{1}{\sigma_0}\left(\sigma - \alpha\right)\dot{\bar{\varepsilon}}^{pl} - \gamma\alpha\dot{\bar{\varepsilon}}^{pl} \tag{4}$$

where C is the initial kinematic hardening modulus (equal to the elastic stiffness) and γ a parameter that describes the rate at which the kinematic hardening decreases with the increasing plastic deformation.

The evolution of the two hardening components (isotropic and kinematic) is illustrated in Figure 9 for unidirectional and multiaxial loading. The evolution law for the kinematic hardening component implies that the backstress α is contained within a cylinder of radius equal to $\sqrt{2/3}\,C/\gamma$. Since the yield surface remains bounded, any stress point must lie within a cylinder of a radius $\sqrt{2/3}\sigma_y$, where σ_y is the maximum yield stress at saturation. To account of the confining pressure (i.e. for sands), σ_y is defined as a function of the octrahedral stress and the friction angle φ of the sand, as:

$$\sigma_y = \sqrt{3}\left(\frac{\sigma_1 + \sigma_2 + \sigma_3}{3}\right)\sin\varphi \tag{5}$$

where, $\sigma_1, \sigma_2, \sigma_3$ are the principles stresses. Since $\sigma_y = C/\gamma + \sigma_0$, γ can be computed for cohesionless soils as:

$$\gamma = \frac{C}{\sqrt{3}\left(\frac{\sigma_1 + \sigma_2 + \sigma_3}{3}\right)\sin\varphi - \sigma_0} \tag{6}$$

The model parameters were calibrated against the small strain shear modulus distribution and the G-γ-D curves presented before. For this purpose, numerical simulations of cyclic simple shear tests were performed, for several shear strain levels, so to compute the shear modulus degradation and the increasing damping with the increasing strain. The results of these analyses are presented in Figure 9c, comparatively to the target G-γ-D curves.

Table 4 summarizes the mechanical properties of the sand, finally adopted for all the constitutive models implemented.

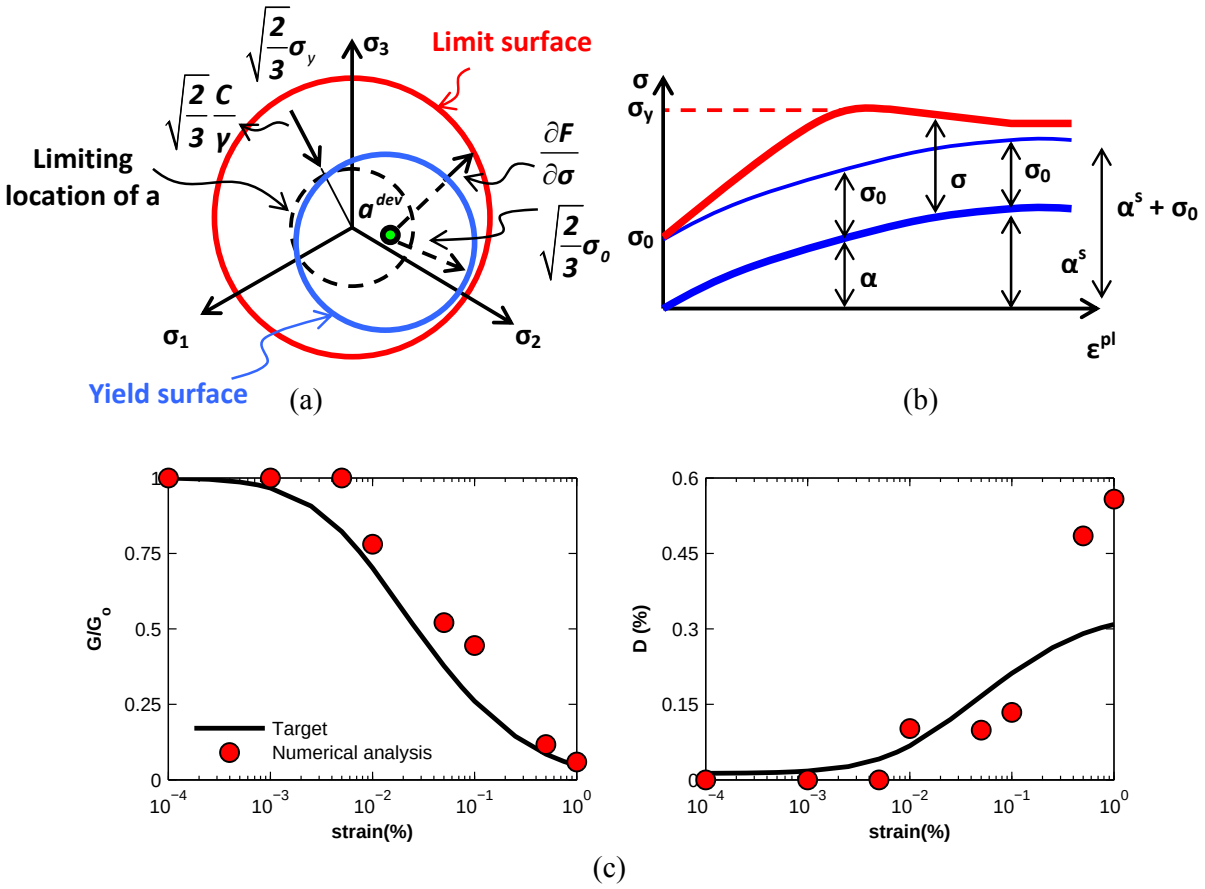


Figure 9: (a), (b) Nonlinear isotropic/kinematic hardening constitutive soil model: three-dimensional (a) and simplified one-dimensional (b) representation of the hardening law, (c) Calibration of the constitutive model against the GγD curves adopted for the specific test case

	Shear modulus G	ρ (t/m^3)	ν	Damping (%)	φ (^{o})	ψ (^{o})	c (kPa)
Visco-elastic analysis	Reduced distribution	1.63	0.333	15 (Rayleigh type)	-	-	-
Combined EQL elastoplastic analysis	Reduced distribution	1.63	0.333	15 (Rayleigh type)	40	12	2
Kinematic hardening model	G_o distribution	1.63	0.333	10 (Rayleigh type) + hysteretic	40	-	2

Table 4: Soil mechanical properties adopted for each analysis case

4 EXPERIMENTAL DATA VS. NUMERICAL PREDICTIONS

In this section we present, representative numerical results compared to the experimental data. The results are presented and discussed for EQ4 in terms of horizontal and vertical accelerations, dynamic earth pressures, dynamic internal forces of the model lining and soil surface settlements. They are shown at model scale, if not differently stated.

4.1 Horizontal acceleration

Figures 11-13 present windows of the computed and recorded acceleration time histories at several locations. The numerical predictions are in very good agreement with the records, with an exception for ACC14 (tunnel roof slab). The analysis where the kinematic hardening model is used to describe the non-linear behavior of the sand seems to slightly over predict the amplification of the horizontal acceleration with respect to the experimental data and the other analyses (Figure 10), but in general the representation of the actual behavior seems to be fair enough. The minor differences are mainly attributed to the difference between the assumed soil mechanical properties (stiffness and damping) and their actual values during the test.

The large difference between the recorded and the computed horizontal acceleration on the roof slab (ACC14) is probably attributed to a recording error, as the analyses are reproducing quite efficiently the acceleration both at the soil surface above the tunnel and on the other locations of the tunnel (middle of the right wall, invert slab).

4.2 Fundamental frequency of the soil deposit

Figure 14 presents the transfer functions (at prototype scale) as computed along the "free-field" vertical array of the accelerometers, by the experimental data and the numerical analyses. Both experimental and the numerical results are reasonable well compared indicating a fundamental frequency of about 2Hz for the soil deposit.

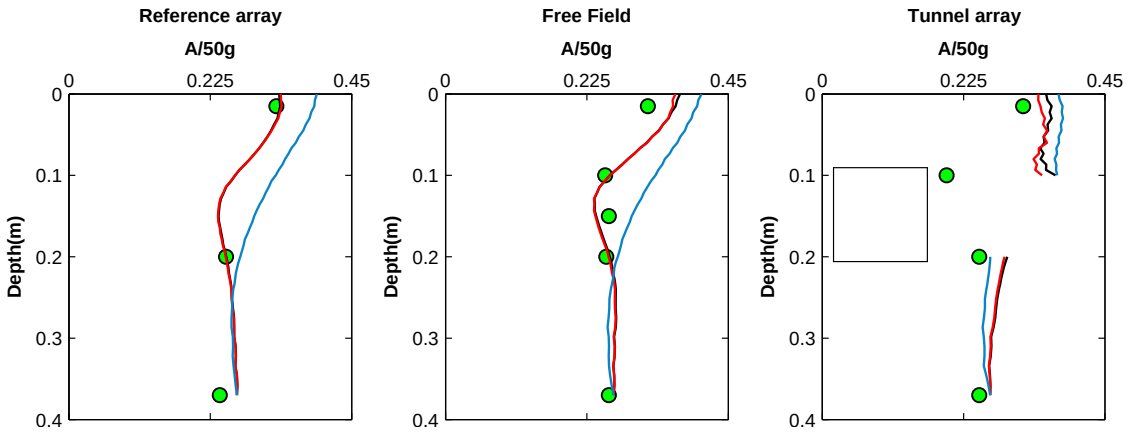


Figure 10: Maximum horizontal acceleration along vertical accelerometers arrays; Experimental data vs. numerical predictions (green circle points: experimental data, black solid line: visco-elastic analysis, red solid line: combined EQL elastoplastic analysis, blue solid-line: kinematic hardening model)

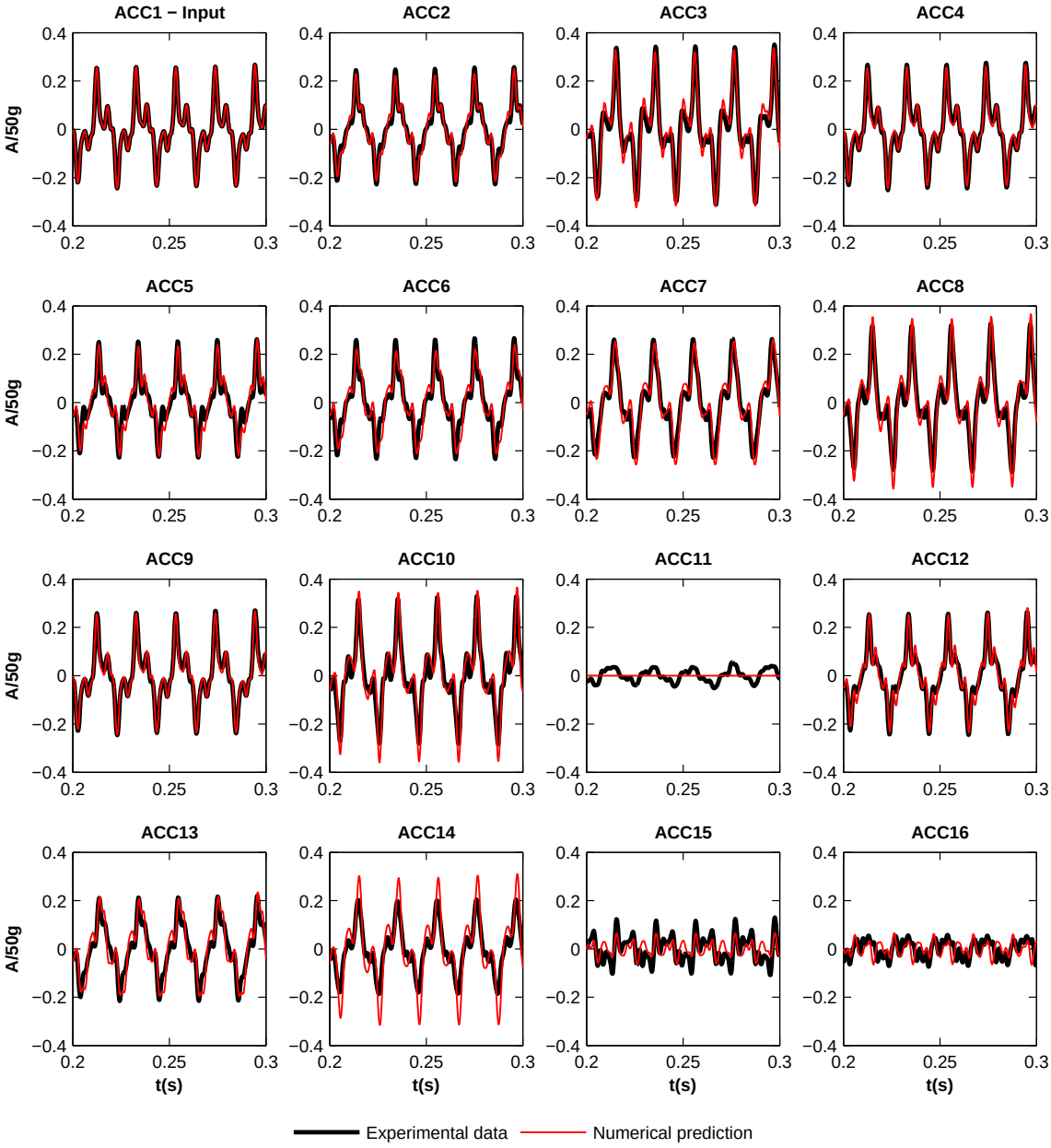


Figure 11: Windows of acceleration time histories for EQ4; Experimental records vs. visco-elastic analysis results

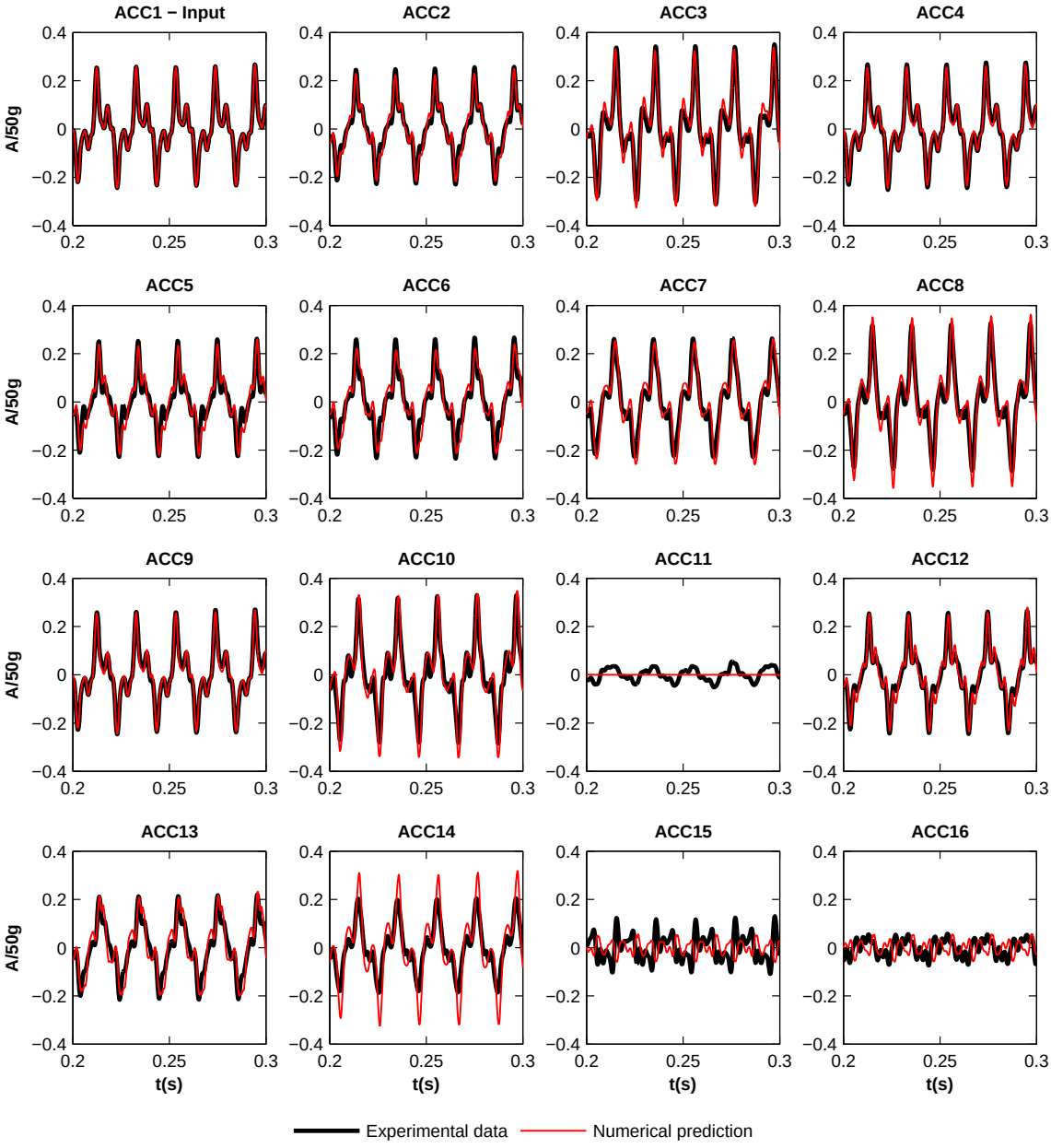


Figure 12: Windows of acceleration time histories for EQ4; Experimental records vs. combined EQL-elastoplastic analysis results

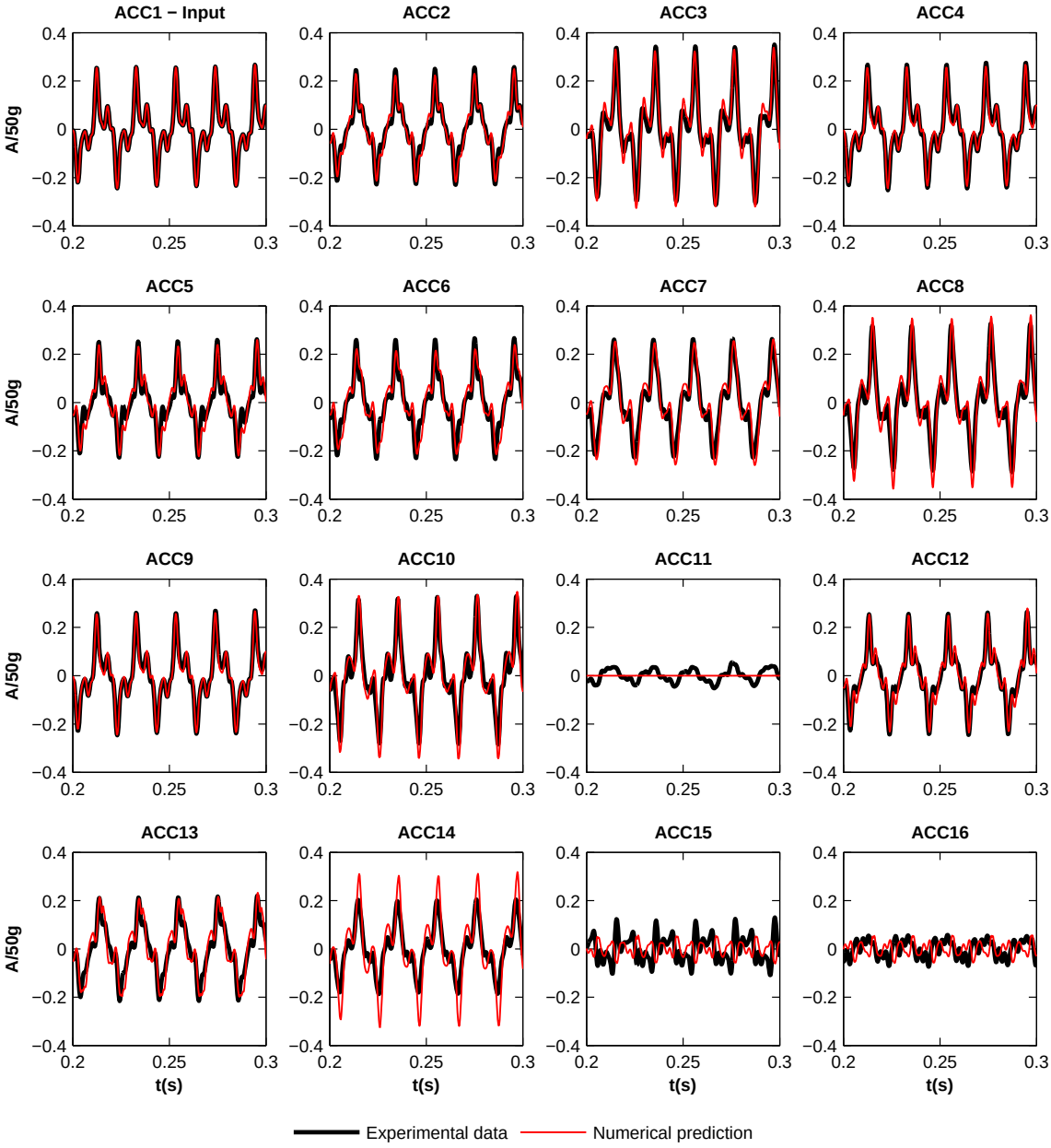


Figure 13: Windows of acceleration time histories for EQ4; Experimental records vs. kinematic hardening model results

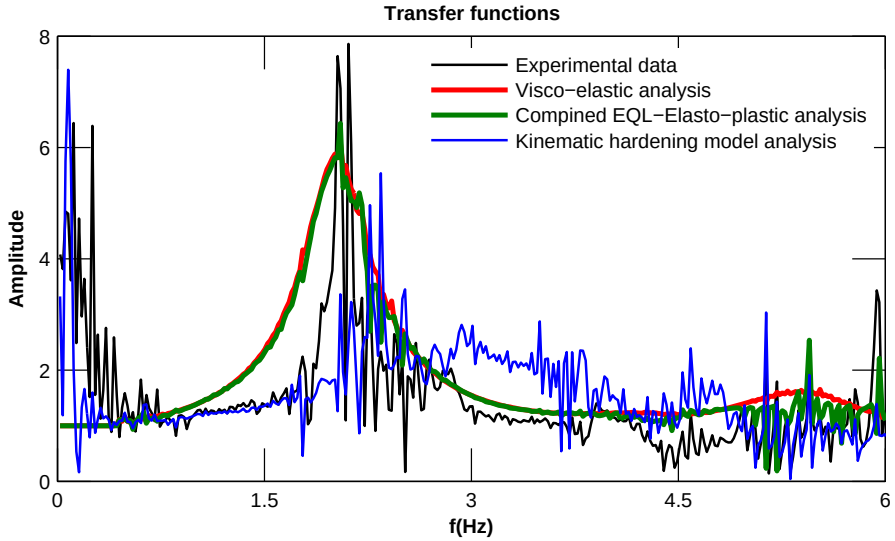


Figure 14: Transfer functions along the "free field" vertical array of accelerometers for EQ4

4.3 Vertical acceleration

Small values of vertical acceleration were recorded near the soil deposit base. This is probably attributed to the reduced parasitic yawing movement of the ESB box on the shaking table, which is not modeled in the numerical analyses. Noticeable vertical accelerations were recorded and also computed at the sides of the tunnel roof slab (Figure 15). In both recorded and computed values we observe an out of phase response indicating a rocking mode of vibration for the tunnel, except the prevailing racking distortion. The reproduction of this mode of vibration by the numerical analysis, even without the simulation of the yawing movement of the ESB box, indicates that the yawing movement probably amplifies this behavior but in any case it is present. It is noted that this mode of vibration is usually precluded from the simplified analysis methods.

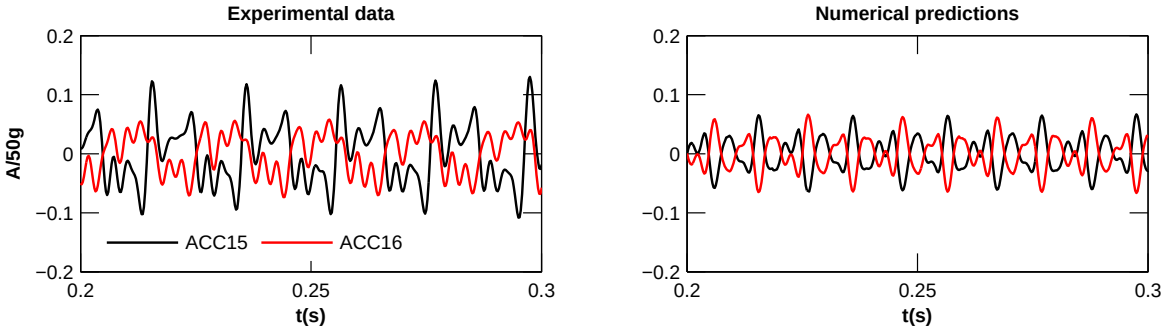


Figure 15: Windows of vertical acceleration time histories for EQ4; (a) Experimental records. (b) Visco-elastic analysis results

4.4 Soil surface settlements

Figure 16 presents the recorded and computed soil surface settlements (in model scale) during EQ4 test. The numerical analyses generally underestimate the soil settlements, which are anyway quite small (less than 0.6mm for this case), due to the high relative density of the soil deposit. However it should be noticed that the experimental results maybe biased to some

extend by the way the LVDTs are fixed to the gantries of the box and by the small bending of these gantries caused by the strong gravity forces.

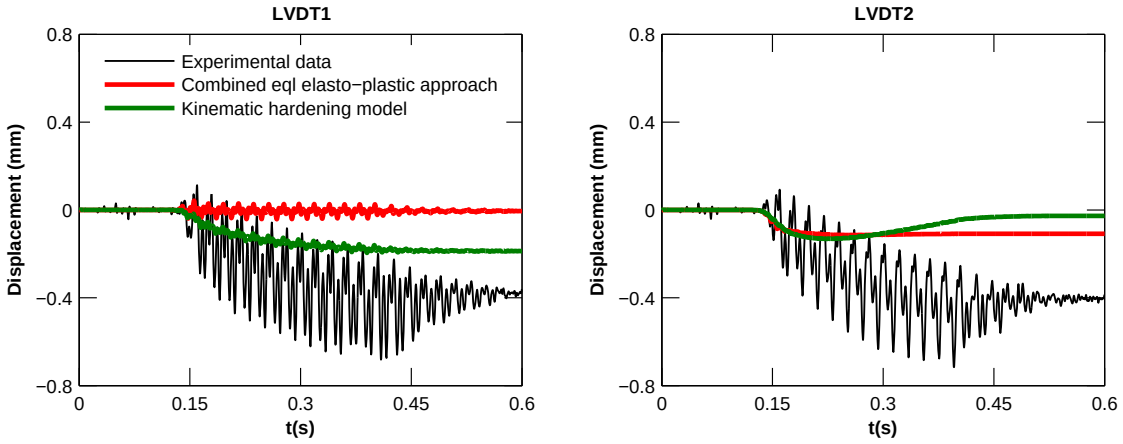


Figure 16: Soil surface settlements, EQ4; Experimental records vs. numerical predictions

4.5 Dynamic earth pressures

The computed and recorded dynamic earth pressures close to the invert slab-left wall corner and at the middle of the left side wall are presented in Figure 17.

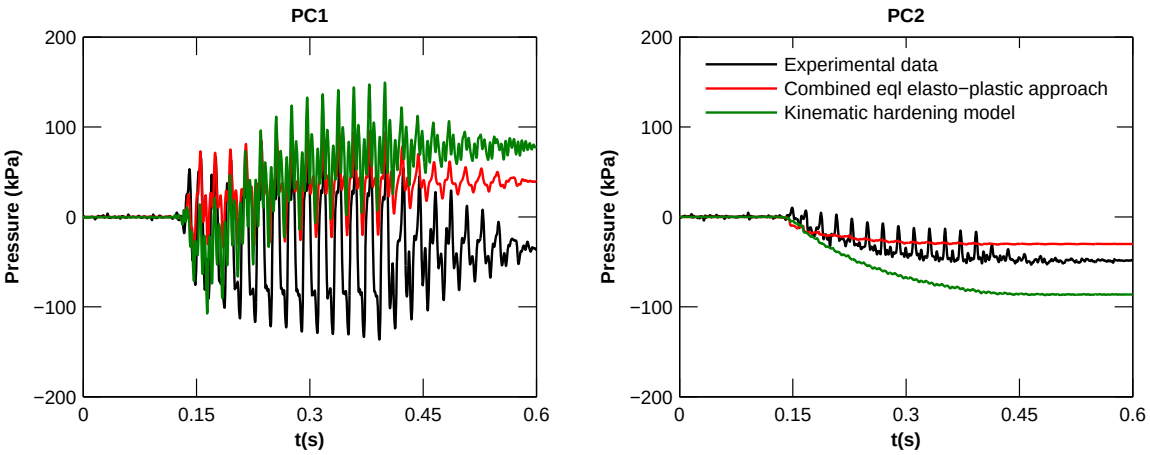


Figure 17: Dynamic earth pressures, EQ4; Experimental records vs. numerical predictions

Looking at the experimental data, three phases may be indentified, namely a transient stage, a steady state stage and finally a post-earthquake residual stage. During the first few cycles of loading, seismic earth pressures are building up. Then in the steady state stage the earth pressures are oscillating around a mean value. During this step, the pressures are shifting from active to passive state due to the tunnel oscillation. Finally, in the post-earthquake stage residual stresses are recorded on the tunnel lining. This behavior has been also reported in other similar centrifuge tests [23]. The dynamic increments of the pressures were found to be larger near the corner, while at the middle of the side wall the increments were much smaller due to the

flexibility of the wall at this location. Generally, this complex behavior is attributed to the soil plastic deformations and the soil densification during shaking.

Similar observations were drawn from the numerical analyses, as the three aforementioned stages were reproduced to some extend. The differences in terms of dynamic increments (i.e. semi-amplitude of cycles in the time histories) and residual values are mainly attributed to differences between the adopted soil and soil-tunnel interface mechanical properties (i.e. soil stiffness and strength near the tunnel, interface coefficient of friction) and the actual values. It is noted that these parameters are highly interrelated. For example, a more "rigid" connection of the tunnel with the soil (i.e. larger coefficient of friction) can affect the soil stiffness degradation near the tunnel resulting in different stress redistribution in the soil around the tunnel. To this end, proper estimation of these parameters is of major importance.

4.6 Dynamic internal forces

The recorded and computed dynamic internal forces are presented in Figures 18-19.

Regarding the bending moments records, similar behavior to the earth pressures response is observed, as the three aforementioned stages are also reported in this case. This cumulative response has also been observed during dynamic centrifuge tests performed on circular tunnel models embedded in dry sand [24]. Similar response is observed in the numerical analyses. More specifically, both the combined EQL elasto-plastic analysis and the kinematic hardening model, seem to reproduce the three stages mentioned before (transient stage, steady state stage and post-earthquake residual stage), with the latter predicting much higher residual values after shaking.

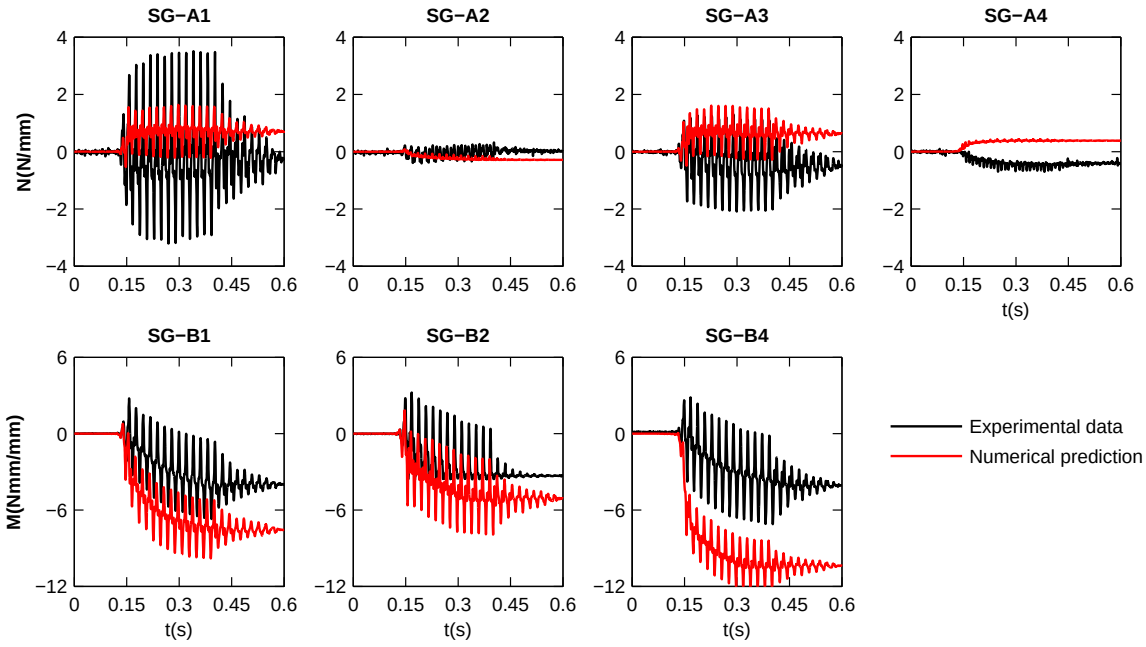


Figure 18: Dynamic internal forces, EQ4; Experimental records vs numerical predictions for the combined EQL elasto-plastic model

Residual values were also observed for the axial forces. These residuals, that were generally smaller than the bending moment ones, found to be larger at the slabs. They can be attributed to the small soil densification as well as to the possible sliding effects on the soil-tunnel interface and to some extent to the soil non-linear behavior.

It is also important to notice that the dynamic axial forces recorded and computed on the sidewalls of the model, were out of phase (Figure 20), indicating again the rocking mode of vibration for the tunnel, as also mentioned for the vertical accelerations.

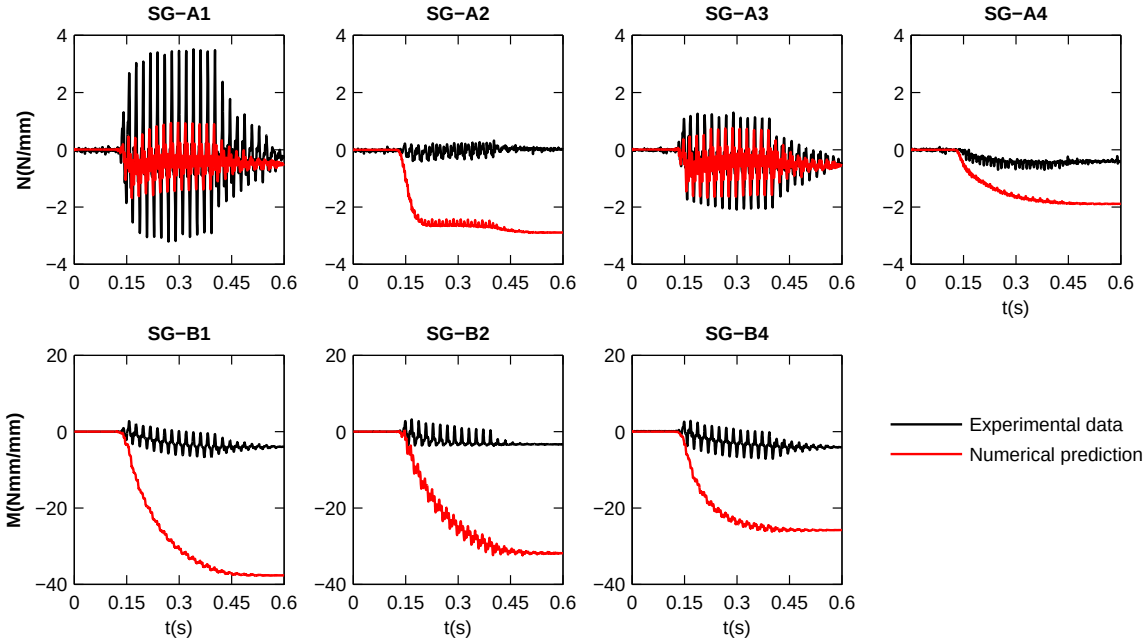


Figure 19: Dynamic internal forces, EQ4; Experimental records vs. numerical predictions for the kinematic hardening model

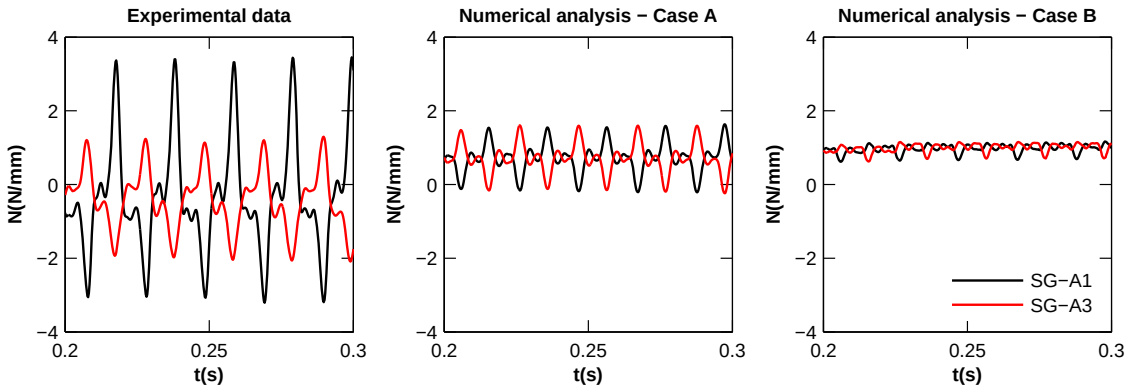


Figure 20: Time windows of the recorded and computed dynamic axial forces of the side walls; Case A: Combined EQL elasto-plastic analysis, Case B: Combined EQL elasto-plastic analysis – full slip conditions

Similar to the earth pressures, the differences between the recorded response and the numerical predictions are attributed to the differences between the adopted and the actual values of the soil and soil-tunnel interface mechanical properties and to some extend to their interre-

lation. To check this hypothesis, we run the combined EQL elastoplastic analysis assuming full slip conditions for the soil-tunnel interface (no shear stress is transferred from soil to the tunnel). Figure 21 compares the recorded internal forces with the numerical predictions for this case. It can be observed that the dynamic increments of the axial forces are highly reduced with respect to the previous case (finite slip conditions), while the computed bending moments come closer the experimental data. The interrelation of the soil non-linear behavior and the soil-tunnel interface characteristics can also be observed in Figure 22, where the soil plastic strains as computed by the non-linear analyses are presented on the deformed shaped models. Actually, we can see differences on the soil plastic deformations distributions around the tunnel for the different assumptions regarding the soil-tunnel interface. For the full-slip conditions the soil plastic deformations are smaller near the walls and larger above the tunnel, with respect to the finite slip case.

5 CONCLUSIONS

The paper presented some representative results from a test of a series of dynamic centrifuge tests that were conducted on a square tunnel model embedded in dry sand. The case was also numerically modeled using different models for the soil behavior and soil-tunnel interface properties. Numerical predictions were compared to the experimental data. The main conclusions drawn may be summarized in the following:

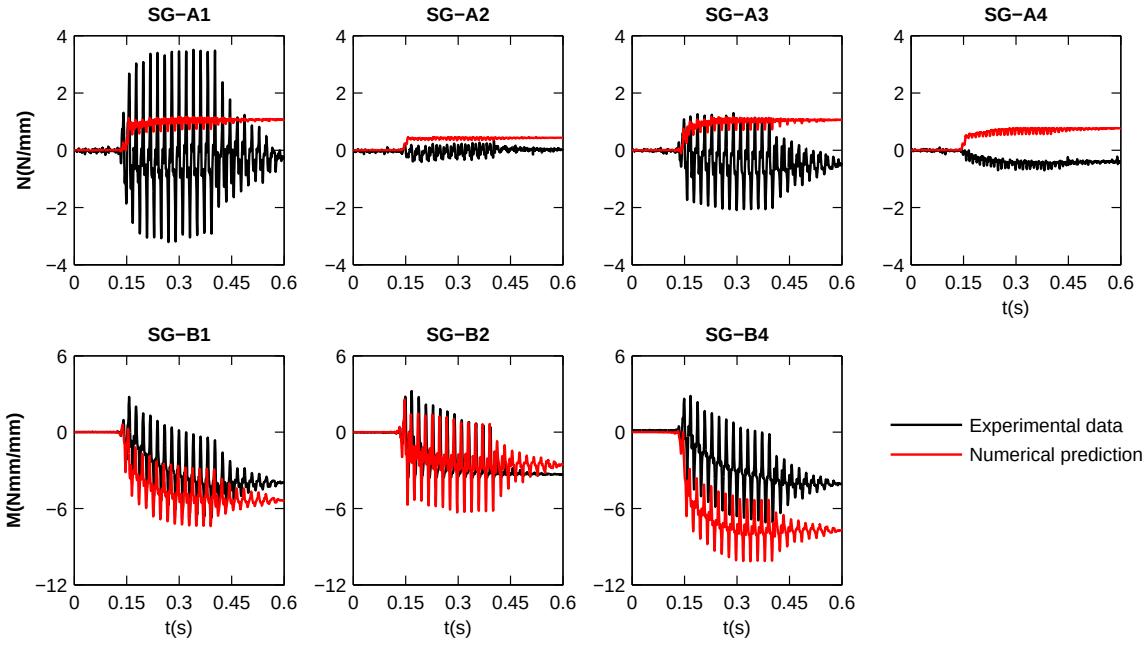


Figure 21: Dynamic internal forces, EQ4; Experimental records vs. numerical predictions for the combined eql elasto-plastic model assuming full slip conditions

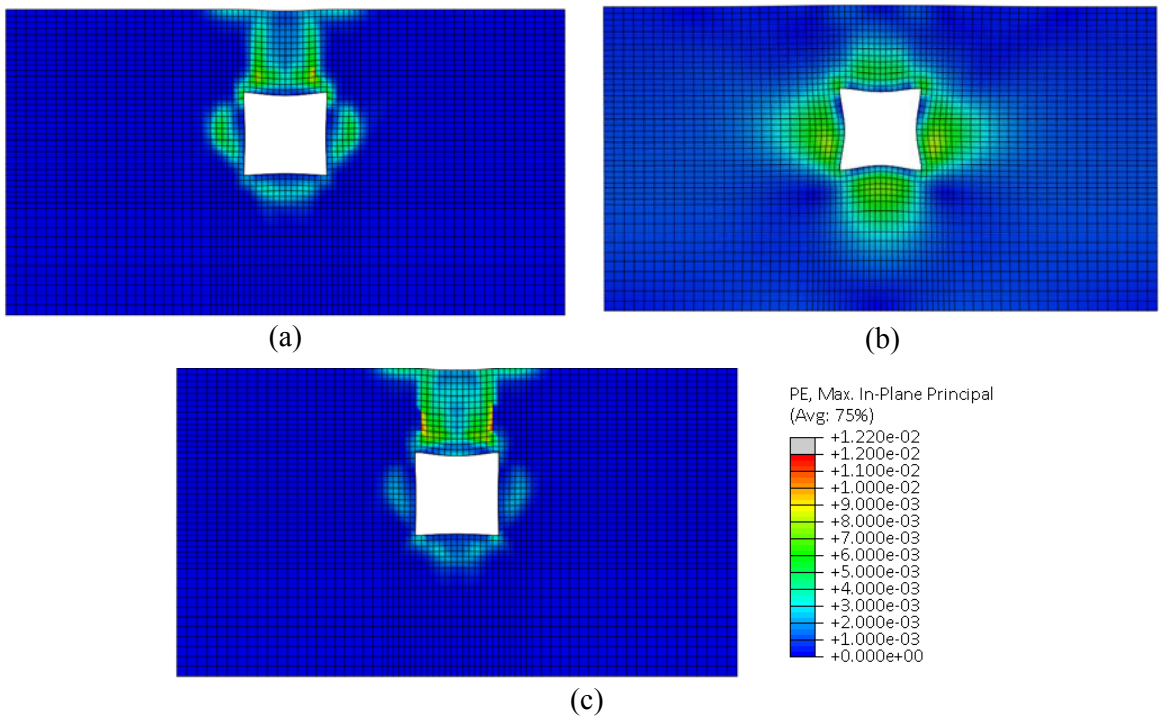


Figure 22: Soil plastic strains around the tunnel: (a) Combined EQL elasto-plastic analysis, (b) Kinematic hardening model, (c) Combined EQL elasto-plastic analysis – full slip conditions

- The horizontal accelerations recorded at several locations, are amplified towards the surface. This amplification was efficiently reproduced by the numerical analyses.
- Vertical acceleration-time histories recorded on the sides of the model's roof slab were out of phase indicating a rocking mode of vibration for the tunnel. This response was verified by the numerical analysis.
- The recorded earth pressure increments are higher at the slab-wall corner due to the larger rigidity of the model at this location compared to the middle of the wall. Residual values were observed after each shake that can be attributed to the soil plastic deformations and to a small amount of soil densification during shaking that can cause stress redistribution. This general trend was also numerically reproduced.
- The dynamic bending moments follow the same trend as for the dynamic earth pressures. Large residual values were detected after each shake, as a result of cumulative strains during the shaking.
- Smaller residuals were observed for the dynamic axial forces after shaking. In addition to the aforementioned parameters that can cause these residual values, a small amount of sliding on the soil-tunnel interface is also affecting this behavior.
- The numerical models used herein, generally reproduced the general trends observed from the recorded dynamic internal forces. The differences between the computed and the recorded values are attributed to the differences between the adopted soil and soil-tunnel interface mechanical properties compared to the actual values and to some extend to their interrelations. Errors related with the records (i.e. calibration of the instruments) can also cause differences to some extend.
- Generally, we concluded that numerical models may reproduce accurately, considering all kind of uncertainties involved, the recorded response of a rectangular tunnel in the

centrifuge. Further analysis of the recorded data and better evaluation of the soil and structure properties during shaking are expected to provide even better insight of the complex behavior of this kind of structures.

ACKNOWLEDGMENTS

The research leading to these results has received funding from the European Community's Seventh Framework Programme [FP7/2007-2013] for access to the University of Cambridge under grant agreement n° 227887 (SERIES Research Program). The technical support received by the Technicians of the Schofield Centre is gratefully acknowledged. The authors would like to acknowledge Assistant Professor Ioannis Anastasopoulos and Dr. Fani Gelagoti, for the fruitful discussions they had with for the implementation of the kinematic hardening model.

REFERENCES

[1] S. Sharma, W.R. Judd, Underground opening damage from earthquakes. *Eng Geology* **30**, 263-276, 1991.

[2] M. Power, D. Rosidi, J. Kaneshiro, S. Gilstrap, S.J. Chiou, *Summary and evaluation of procedures for the seismic design of tunnels*. Final Report for Task 112-d-5.3(c). National Center for Earthquake Engineering Research, Buffalo, New York, 1998.

[3] H. Iida, T. Hiroto, N. Yoshida, M. Iwafuji, Damage to Daikai subway station. Special issue on geotechnical aspects of the January 17 1995 Hyogoken–Nanbu earthquake. *Soils Found*, 283-300, 1996.

[4] Y.M.A. Hashash, J.J. Hook, B. Schmidt, J.I.-C. Yao, Seismic design and analysis of underground structures. *Tunneling Undergr Space Technol*, **16** (2), 247-293, 2001.

[5] Special Issue of Soil and Foundations. Selected photographs on the 1995 Hyogoken-Nambu earthquake. *Special issue on geotechnical aspects of the January 17 1995 Hyogoken-Nambu earthquake*. Japanese Geotechnical Society, 1996.

[6] J.N. Wang, *Seismic Design of Tunnels*. Parson Brinckerhoff, New York, 1993.

[7] J. Penzien, Seismically induced racking of tunnel linings. *Earthquake Eng Structural Dyn*, **29**, 683-691, 2000.

[8] ISO 23469, *Bases for design of structures - Seismic actions for designing geotechnical works*. ISO International Standard. ISO TC 98 / SC3 /WG10, 2005.

[9] F.W.H.A., *Technical manual for design and construction of road tunnels – Civil elements*. U.S. Department of transportation. Federal Highway Administration. Publication No. FHWA-NHI-09-010, 2009.

[10] K. Pitilakis K, G. Tsinidis, Performance and seismic design of underground structures. *II International Conference on Performance Based Design in Earthquake Geotechnical Engineering* (State of the art lecture), Taormina, Italy, May, 2012.

[11] S.P.G. Madabhushi, A.N. Schofield, S. Lesley, A new stored angular momentum (SAM) based actuator. T. Kimura, O. Kusakabe, J. Takemura, eds. *Centrifuge 98*, Tokyo, Japan. A.A. Balkema publishers 111-116, 1998.

[12] A.N. Schofield, X. Zeng, Design and performance of an equivalent shear beam (ESB) container for earthquake centrifuge modelling. Technical Report, CUED/D-Soils/I'R245, Cambridge University, 1992.

[13] H. Mitrani, *Liquefaction Remediation Techniques for Existing Buildings*. PhD Thesis, University of Cambridge, 2006.

[14] Y. Zhao, K. Gafar, M.Z.E.B Elshafie, A.D Deeks, J.A. Knappett, S.P.G. Madabhushi, Calibration and use of a new automatic sand pourer. Zhang, Wang eds. *Physical Modelling in Geotechnics – 6th ICPMG '06*, Taylor & Francis Group, London, 2006.

[15] B. Ghosh, S.P.G. Madabhushi, An efficient tool for measuring shear wave velocity in the centrifuge. R. Phillips, P.J. Guo, R. Popescu eds. *Int Conf on Physical Modelling in Geotechnics*, St Johns, NF, Canada. AA Balkema publishers, 119-124, 2002.

[16] G. Tsinidis, C. Heron, S.P.G. Madabhushi, K. Pitilakis, M. Stringer, SERIES TA Project: TUNNELSEIS: Investigation of several aspects affecting the seismic behaviour of shallow rectangular underground structures in soft soils, Technical Report (Under development), 2013.

[17] A.N. Schofield, Cambridge Geotechnical Centrifuge Operations. *Geotechnique* **30**, (3), 227-268, 1981.

[18] ABAQUS Analysis User's Manual – Volumes I - IV, Dassault Systèmes, SIMULIA Inc, USA {Computer code}

[19] J.P. Bardet, K. Ichii, C.H. Lin, *EERA: A computer program for equivalent-linear earthquake site response analyses of layered soil deposits*. University of California, Department of Civil Engineering, 2000.

[20] B.O. Hardin, V.P. Drnevich, Shear modulus and damping in soils: design equations and curves. *J Soil Mech Found Division* **98** (SM7), 667-692, 1972.

[21] T. Schanz, P.A. Vermeer, Angles of friction and dilatancy of Sand. Geotechnique, **46** (1), 145-151, 1996.

[22] I. Anastasopoulos, F. Gelagoti, R. Kourkoulis, G. Gazetas, Simplified constitutive model for simulation of cyclic response of shallow foundations: Validation against laboratory tests. J Geotech Geoenvironmental Eng, **137 (12),** 1154-1168, 2011.

[23] U. Cilingir, S.P.G. Madabhushi, A Model Study on the Effects of Input Motion on the Seismic Behavior of Tunnels. *J. Soil Dyn Earthquake Eng*, **31**, 452-462, 2011.

[24] G. Lanzano, E. Bilotta, G. Russo, F. Silvestri, S.P.G. Madabhushi, Centrifuge modeling of seismic loading on tunnels in sand. *Geotech Testing J*, **35**, 2012.

COMPDYN 2013
4th ECCOMAS Thematic Conference on
Computational Methods in Structural Dynamics and Earthquake Engineering
M. Papadrakakis, V. Papadopoulos, V. Plevris (eds.)
Kos Island, Greece, 12–14 June 2013

FULL-SCALE TESTING OF A MODEL STRUCTURE IN EUROSEISTEST TO STUDY SOIL-FOUNDATION-STRUCTURE INTERACTION

Kyriazis Pitilakis[1], Anastasios Anastasiadis[1], Dimitris Pitilakis[1] and Emmanuil Rovithis[2]

[1]Aristotle University Thessaloniki

Aristotle University Thessaloniki, 54124, Thessaloniki, Greece

pitilakis@civil.auth.gr

[2]Earthquake Planning and Protection Organization EPPO-ITSAK Cosmos Offices, P.O. Box 53 Finikas, 55102, Thessaloniki, Greece

Keywords: field test, real-scale experiment, prototype, free-vibration, forced-vibration, wave propagation, earthquake engineering.

Abstract. *A large experimental campaign to study soil-foundation-structure interaction and wave propagation in soil media due to structural oscillation is presented in the large-scale experimental facility of EuroSeistest in Greece, where a real-scale model structure (EuroProteas) was recently constructed. The structure was especially designed to promote soil-foundation-structure interaction taking into account the well-known foundation soil at site. Six experimental campaigns were performed: three pull-out (free-vibration) and three forced-vibration sets of tests. Pull-out was performed with a counterweight and the total pull-out force exceeded 15kN. Forced-vibration sine sweep tests were performed using an eccentric mass vibrator and total force exceeded 20kN. The vibrator was placed both on the foundation and the top of the structure. Response was recorded by a dense 3D array composed of more than 80 recording devices (accelerometers, seismometers, shape acceleration arrays). In this paper we present the recorded response from selected tests, highlighting soil-foundation-structure effects in the structure and in the soil.*

1 INTRODUCTION

Experimental investigation of soil-foundation-structure interaction is nowadays regularly investigated in small-scale by implementing experiments in shaking-table or centrifuge apparatuses. The increasing number of such experimental facilities worldwide has lead to a significant number of scientific publications [1, 2]. Nevertheless, laboratory tests present limited ability to reproduce certain field conditions, such as boundary conditions.

On the other hand, large-scale field experiments of SFSI involve inherently realistic boundary conditions that are necessary for model calibrations. Among the first SFSI field studies, Lin and Jennings (1984) [3] and Luco et al. (1988) [4] derived foundation impedance functions based on forced-vibration field tests, while de Barros and Luco (1995) [5] performed forced-vibration tests on a reduced-scale model of a nuclear reactor. Recently, Tileylioglu et al. (2011) [6] realized forced-vibration SFSI experiments on a large-scale model test structure in Garner Valley, California, focusing on dynamic impedance functions.

In this study, we present a large experimental campaign to study soil-foundation-structure interaction and wave propagation in soil media due to structural oscillation, in the full-scale experimental facility of *EuroProteas* in Greece. The tests series were performed in the framework of the on-going European project "Seismic Engineering Research Infrastructures for European Synergies, SERIES" by means of a large-scale simplified prototype structure built in *EuroSeistest* site, in the north of Thessaloniki, Greece.

2 DESCRIPTION OF EUROPROTEAS FACILITY

2.1 Foundation soil conditions

Subsoil stratigraphy and dynamic properties of the foundation soil at *EuroProteas* site are already well-documented from extended geotechnical and geophysical surveys [7, 8, 9]. However, in order to define the detailed soil stratigraphy immediately below the prototype structure, additional geotechnical and geophysical surveys were performed to measure the exact soil properties at site. The abovementioned investigation comprised of drilling boreholes, geophysical down-hole measurements and laboratory tests on selected soil samples.

Specifically, a 30m deep borehole was drilled in the geometric center of the foundation slab of the model and a 15m deep borehole was drilled at the edge of model. Standard penetration tests (S.P.T.) were conducted in the 30m deep hole and continuous samples were taken according to Eurocode 7 [10] regulations for undisturbed sampling. Split-spoon and undisturbed samples were retrieved for laboratory index testing and soil classification to establish strength and compressibility soil characteristics. In addition, resonant column tests were performed at representative soil specimens. The boreholes were cased for the execution of down-hole tests, for the installation of a down-hole accelerograph in the geometrical center of *EuroProteas'* foundation and for the installation of shape-acceleration-arrays (SAAR, Measurand, Inc.) sensors at the edge of the model. Figure 1 shows soil stratigraphy and shear wave velocity profile, as estimated from geotechnical and geophysical tests from the borehole in the geometrical center of the foundation, prior to the construction of the structure.

Soil consists of silty clay in the uppermost 15m, to silty sand at depth of 30m. In the upper 5m, shear wave velocity is estimated approximately at 130m/s, while it increases to more than 300m/s at 50m depth. The detailed sedimentary structure and the full geometry of all soil deposits, as well as, the Vs structure, of the test site is very well defined to a depth of 200 m, where the more significant impedance contrast lies between the gneissic bedrock soil and sediments [7,8,9].

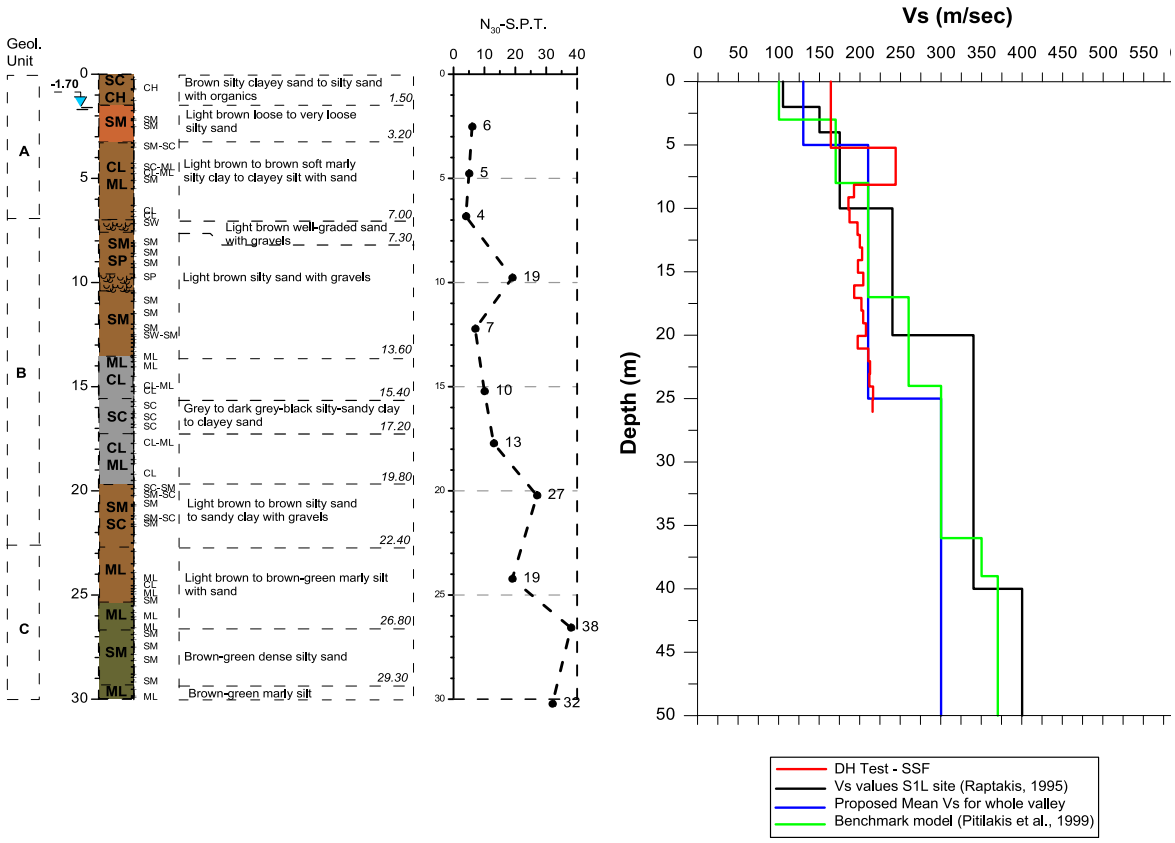


Figure 1: a) Soil stratigraphy from borehole TST-1DSM-BH-02 in the center of the foundation and b) shear wave velocity profile from down-hole tests, compared with literature

2.2 Structure

The design concept of *EuroProteas* prototype structure in *EuroSeistest* site involved a stiff, simplified structure, with reconfigurable mass and stiffness, aiming to mobilize strong SFSI. In this manner, salient effects of SFSI mechanism can be clearly attested on the superstructure and soil response. More specifically, the following requirements were envisaged during the design of the *EuroProteas*:

- Fixed-base natural frequency of the prototype adjusted with stiffness and mass modification.
- Large superstructure mass to ensure notable SFSI response, in conjunction with the soft foundation soil.
- Steel moment frame to allow flexibility and easy construction.
- Reconfigurable bracing system to allow stiffness and damping modification.
- Strong rigid reinforced concrete (RC) roof slab to allow for mass addition and eccentric mass shaker mounting.
- 50% of superstructure mass in RC foundation slab to accommodate for stability, dynamic footing response and eccentric mass shaker mounting.

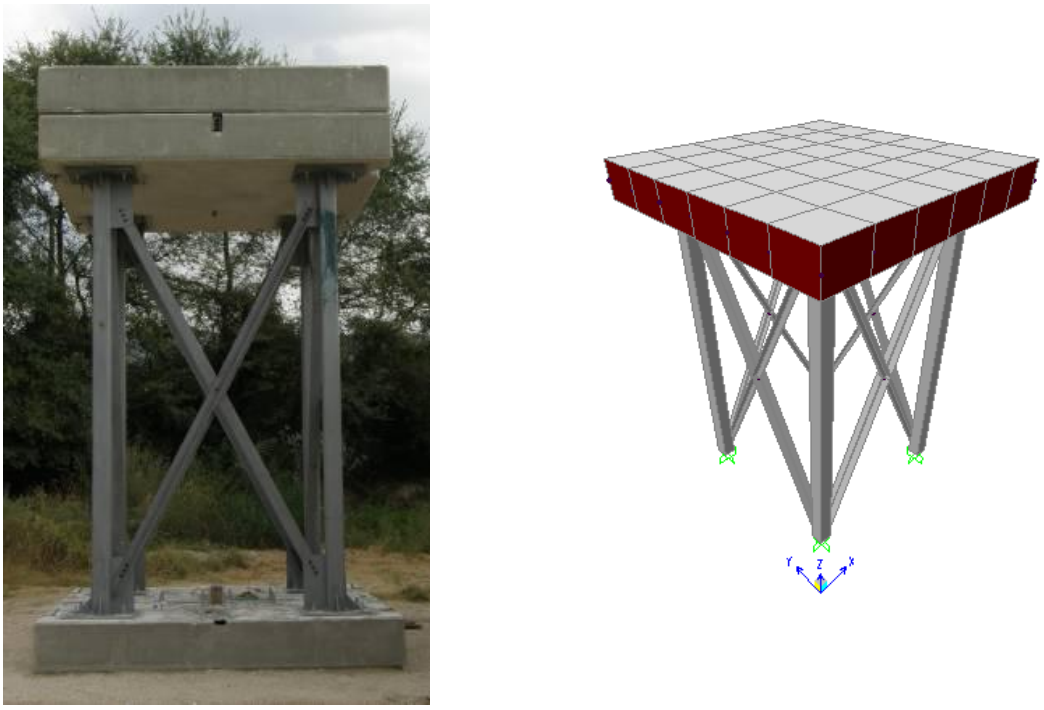


Figure 2: (a) Prototype structure (*EuroProteas*) constructed at *EuroSeistest* site (b) FE model of the structure under fixed-base conditions

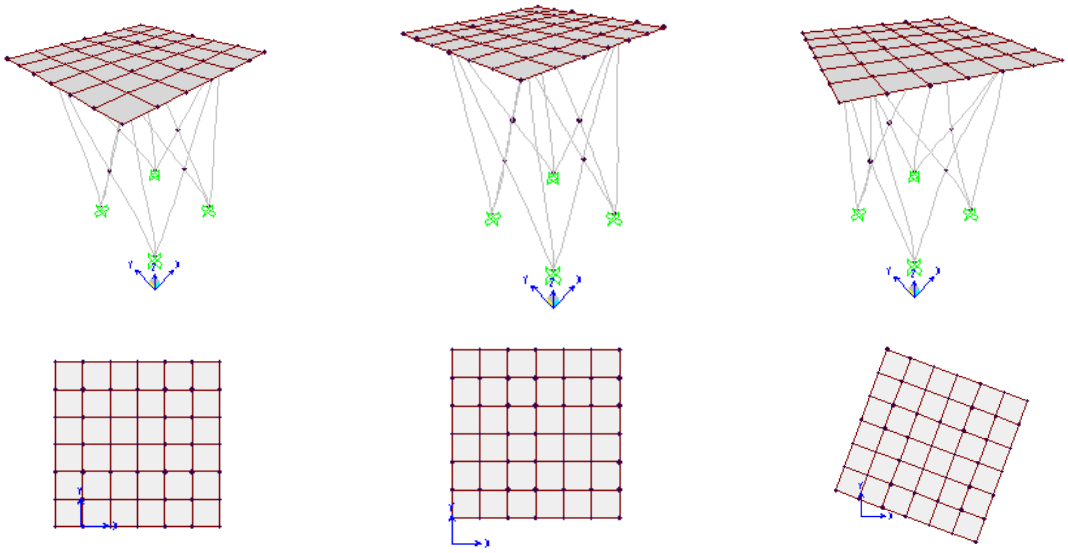


Figure 3: Modal analysis of the model structure (a) 1st uncoupled transverse mode (T_1=0.12sec) (b) 2nd uncoupled transverse mode (T_2=0.12sec) (c) 3rd torsional mode (T_3=0.093sec)

The structural design conformed to the provisions of modern codes and regulations (i.e. Eurocode 3 [11] for the design of steel members and connections, Eurocode 7 [10] and Eurocode 2 [12] for the design of the foundation, and Eurocode 8 [13] for seismic design).

Based on the above requirements, the prototype was designed to comprise of one RC foundation slab 3x3x0.4m, on top of which four steel columns with free height 3.80m are clamped,

supporting the superstructure mass of one (or two, depending on the configuration) RC slabs identical to the foundation slab. The four steel columns are connected with X-braces in both directions, forming a totally symmetric structure (Figure 2). The mass of each RC slab is 9.16Mg, assuming uniform concrete weight 25kN/m^3. The total height from the bottom of the foundation slab to the top of the upper roof slab is 5.0m. Fixed-base natural frequency can be configured between 2.1Hz and 11.5Hz, depending of the number of roof slabs and the bracing system. For the experimental campaign that will be presented herein, the natural fixed-base frequency of *EuroProteas* is configured at 8.32Hz along the horizontal axes, based on modal analysis of the test structure FE model (Figure 2b) performed by means of SAP2000 [14]. The corresponding modes of vibrations under fixed-base conditions are shown in Figure 3 revealing two uncoupled swaying modes (Figure 3a and 3b) along the horizontal axes and one torsional mode (Figure 3c) due to the symmetrical distribution of the structural stiffness.

3 EXPERIMENTAL CAMPAIGN

In the framework of the European project SERIES, six experimental campaigns took place in the *EuroProteas* test site, including three sets of free-vibration tests and three forced-vibration tests, performed at different excitation levels. Experiments are described in detail in the ensuing.

3.1 Instrumentation

A large number (more than 80) of various types of instruments were installed in every test to monitor structural, foundation and soil response. In this manner, a particularly dense three dimensional instrumentation scheme was set, recording wave propagation and SFSI due to the vibration of the structure. Instrumentation included digital broadband seismometers (CMG-6TD and CMG-40T), triaxial accelerometers (CMG-5TD), borehole accelerometers (CMG-5TB) and Shape Accelerations Arrays (SAAR). Instrumentation was made available from the Research Unit of Soil Dynamics and Geotechnical Earthquake Engineering of Aristotle University of Thessaloniki (SDGEE-AUTH) and the Earthquake Planning and Protection Organization (EPPO-ITSAK).

Figure 4 shows a typical instrumentation layout of the experiments at *EuroProteas*. The structural response is recorded by seven accelerometers, five of which are located at the top of the roof slab and two at the top of the foundation slab. Superstructure instrumentation was mostly in line with the direction of loading, whereas accelerometers were also installed at the two opposite corners of the roof slab to capture possible transverse and torsion response. Furthermore, two 1.2m-long shape-acceleration-arrays SAAR arrays are attached to a steel column of the structure to measure possible deviation of structural response along the column length.

Soil response is recorded with seismometers installed on the free soil surface in both directions, covering an area of 9x9m around the structure, as seen in Figure 4. In the direction of loading, a 12m-long shape-acceleration-array (SAAR) is placed on the soil surface. This instrument consists of an array of MEM sensors every 0.5m, making a total of 25 acceleration recording instruments. In the borehole in the center of the foundation is placed an accelerometer at depth equal to one time the foundation width. In the borehole at 0.5m from the side of the foundation is placed a second 12m-long SAAR, providing recordings every 0.5m to a depth of 12m.

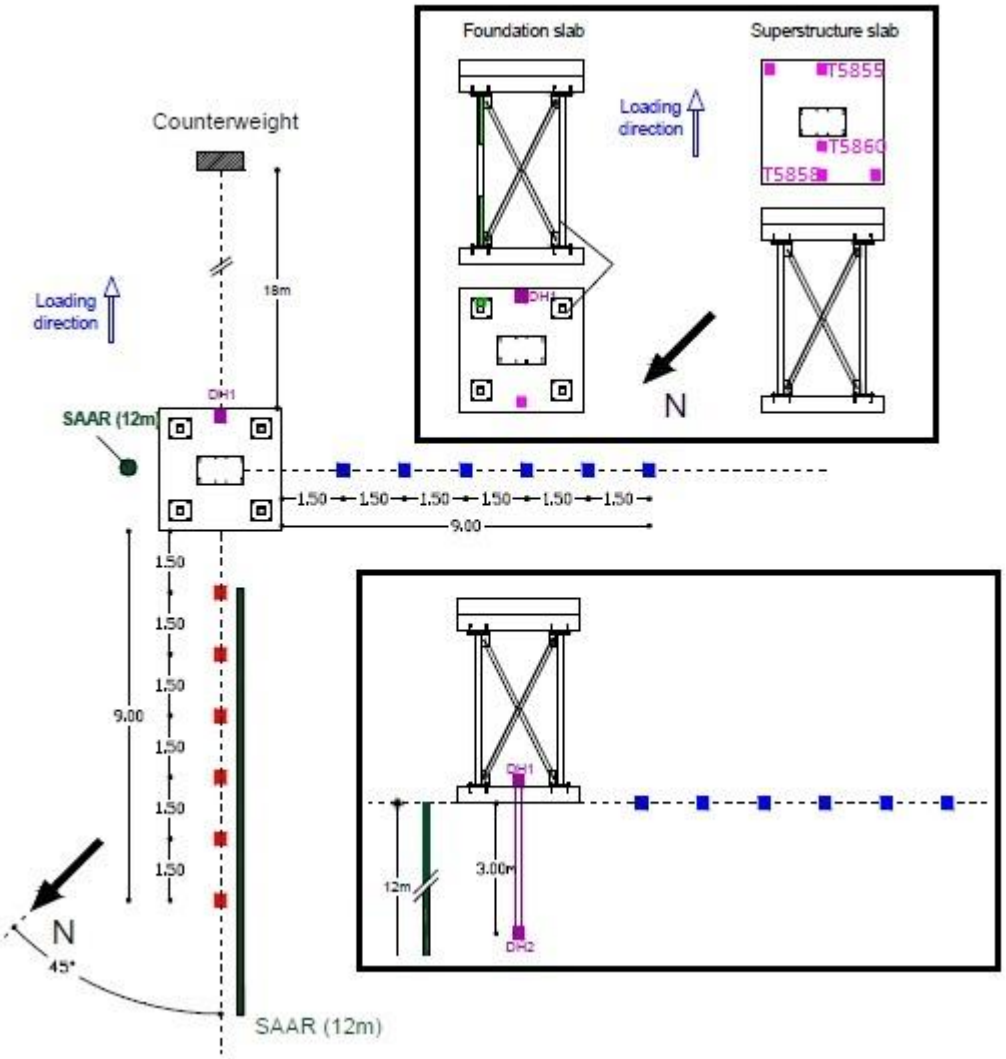


Figure 4: Instrumentation layout of the experimental campaign at *EuroProteas*

From the above, it is obvious that response due to vibration of the structure is recorded in three directions in the soil, providing a uniquely dense instrumentation scheme to study SFSI and wave propagation effects due to structural oscillation.

3.2 Free-vibration testing

In the free-vibration test series, pull-out forces were applied to the roof slab by a wire rope, clamped at a RC counterweight of 1.5t buried in the soil at 28m away from the structure. Tension was applied to the wire rope by mechanical means, and then the wire rope was cut loose to cause free oscillation of the structure until rest. Tension force was measured on the wire rope using an electronic load cell. In total, more than 25 pull-out experiments were performed on the *EuroProteas* structure, with the pull-out force varying between 2.5kN and 15kN.

Figure 5 shows indicative the recorded acceleration response at instruments T5858, T5855 and T5856 (Figure 4), all located on the roof slab along the excitation axis, T5858 and T5856 fixed close to the slab edge and T5855 close to the geometric center.

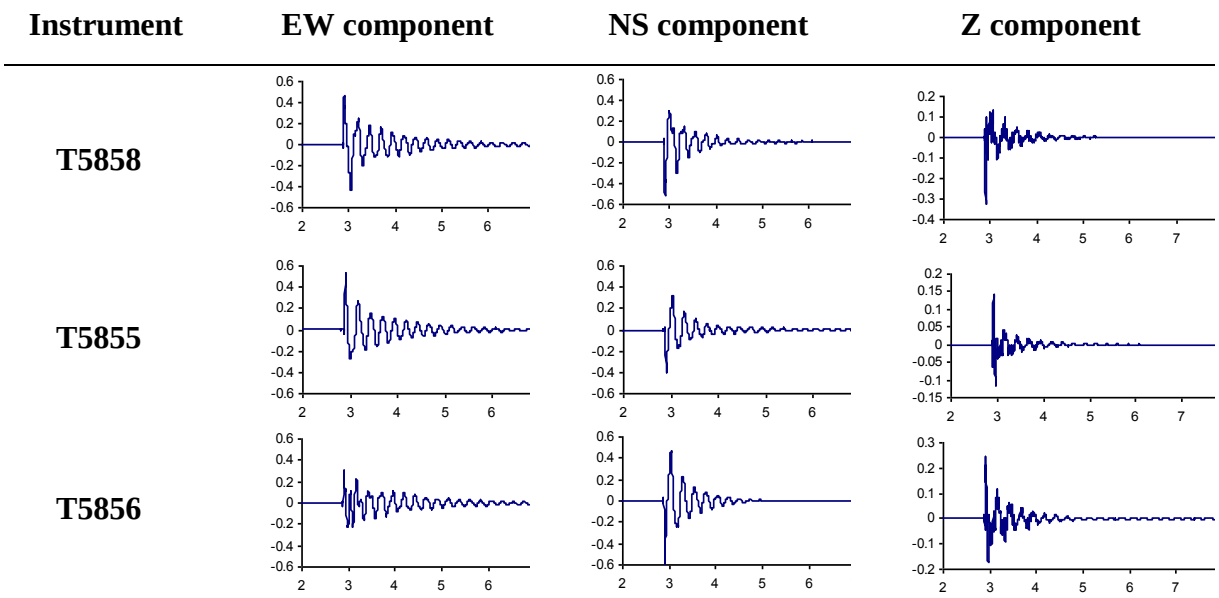


Figure 5: Free-vibration acceleration response (measured in m/s^2) at the top of the structure test at pull-out force 10.3kN

The viscously damped vibration of the structure is clear in Figure 5, caused by the pull-out force. Almost constant structural damping may be attested by the form of the recorded motion in time.

In a similar way, the recorded velocity response on the free soil surface in the direction of shaking is shown in Figure 6. Similar form of the response is apparent in the soil, due to the unit pulse excitation of the structure. Because of soil damping, the oscillation fades out after approximately two seconds. Moreover, the decay of maximum amplitude is obvious with increasing distance from the structure.

Looking at the Fourier spectra (Figure 7) of the recordings on the structure and on the soil surface, the resonant soil-foundation-structure system frequency can be estimated approximately at 4Hz.

Regarding the recordings from the shape-acceleration-arrays (SAAR) due to structural oscillation, unfortunately the pull-out force amplitude and the consequent vibration amplitude were low, within the instrument noise levels (displacement in the order of 10^{-4}m), making conclusions rather obscure even for forces around 15kN.

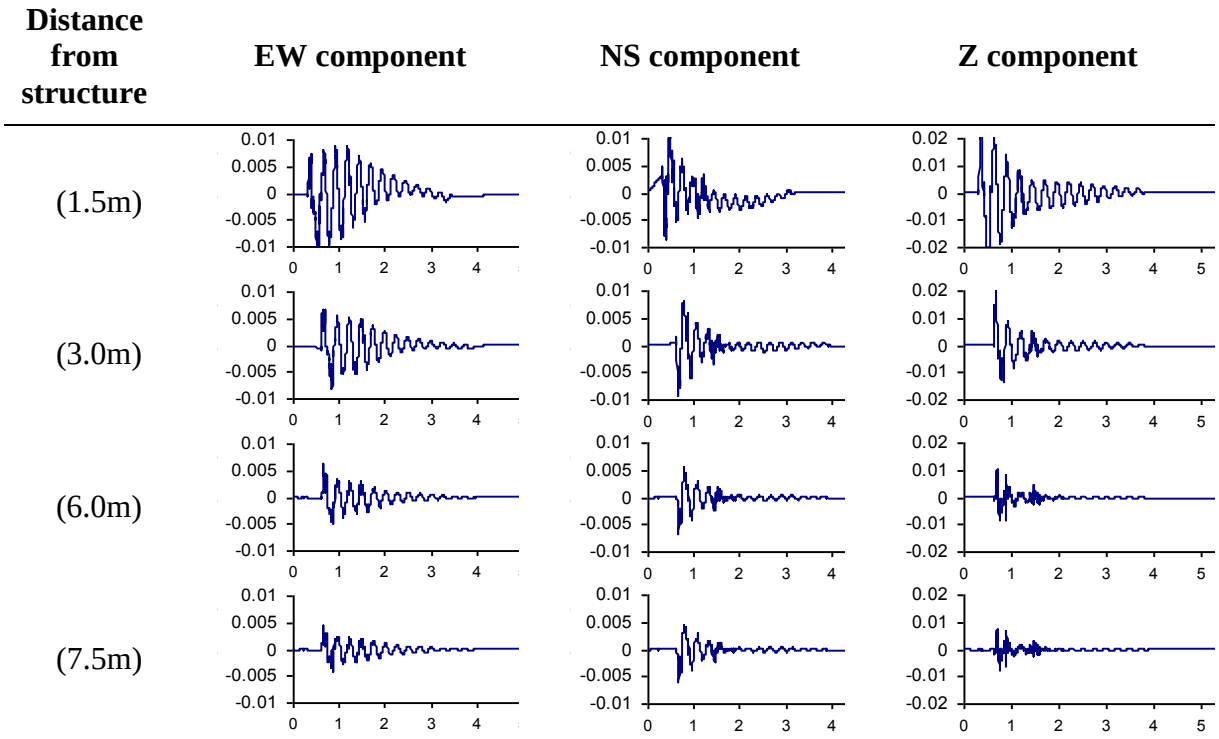


Figure 6: Velocity time histories (measured in m/s) recorded on the soil surface with increasing distance from the foundation due to pull-out force of 8.89kN.

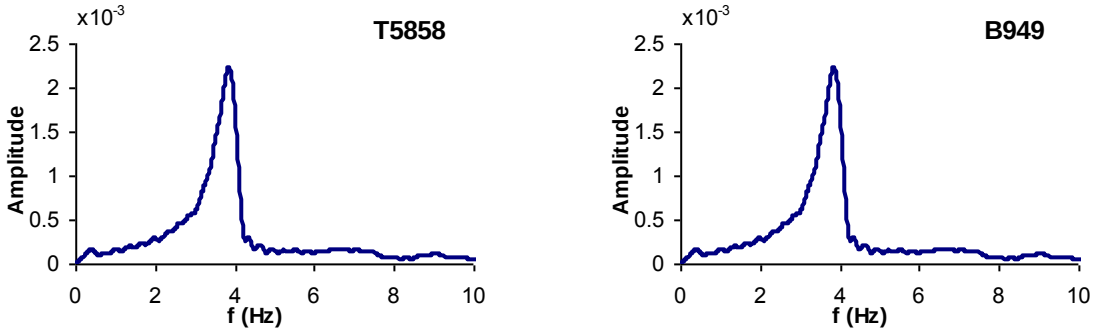
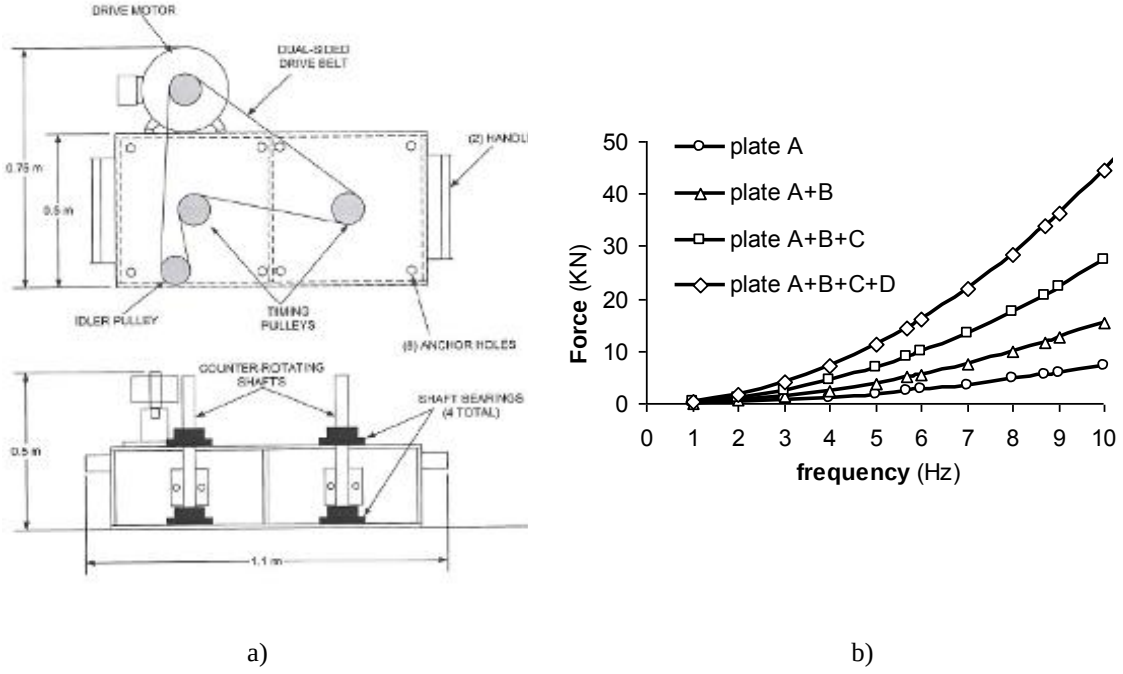


Figure 7: Fourier spectra of recording a) on the roof slab and b) on the soil surface at distance 1.5m from the foundation

3.3 Forced-vibration tests

For the forced-vibration tests, the MK-500U eccentric mass vibrator system owned by the Earthquake Planning and Protection Organization EPPO-ITSAK [15] was implemented as a source of harmonic excitation imposed on the model structure. The particular mass vibrator system is a portable, unidirectional dual counter-rotating shaker that can produce a maximum sinusoidal horizontal force of 5 tons and can be operated from 0.1 to 20Hz. The shaker's eccentricity can be varied between 0.15kgm and 11.3kgm in various increments to produce maximum horizontal force from 10.5Hz to 20Hz. The shaker is powered by a 2.2kW,



a) b)

Figure 8: (a) MK-500U schematic (b) frequency-force relationship of the MK-500U shaker [ANCO Engineers, Inc]

1200rpm electric drive motor (Figure 8) controlled by a Toshiba VF-S9 adjustable speed drive. During the forced-vibration tests at *EuroProteas*, the motor drive was operated manually adjusting the operating speed of the shaker to the desired excitation frequency.

The produced force of the vibrator is governed by the following equation:

$$F = E\ (2\pi\ f)^2 \tag{1}$$

where F is the shaker output force (in N), E is the total eccentricity of the shaker (in kg-m) and f stands for the rotational speed of the shaker (in Hz). The MK-500U shaker has a total of eight mass plates in four different sizes (A, B, C and D) that can be used to adjust the vibrator's eccentricity. One plate of each size is to be mounted to the hub on each rotating shaft in specific order and orientation. These plates allow the shaker eccentricity to be adjusted as mentioned above. Depending on the number of plates and the operating frequency, output force can be adjusted, as seen in Figure 8b.

Three series of forced-vibration tests were performed on *EuroProteas*. In the first series of tests, the eccentric mass vibrator system was clamped on the specially designed metal plate at the geometrical center of the foundation. Moreover, it was orientated so that the produced force would be on the same direction as the applied pull-out forced at the free-vibration tests. In the second and third series of forced-vibration at *EuroProteas*, the vibrator was placed both on the foundation and on the top roof slab, in order to increase rocking of the structure.

As mentioned before, the produced force of the vibrator can be adjusted by the mass of the plates and the output frequency. In all three forced-vibration experimental campaigns, the total force varies between 0.07kN and 21kN, at frequencies that range from 1Hz to 10Hz, depending on the mass shaker configuration.

Forced-vibration Series No. / Mass plate	**2 / A+B**
Instrument Series No	**T5856**
Recorded motion	**Structural response / Acc. (m/sec^2)**

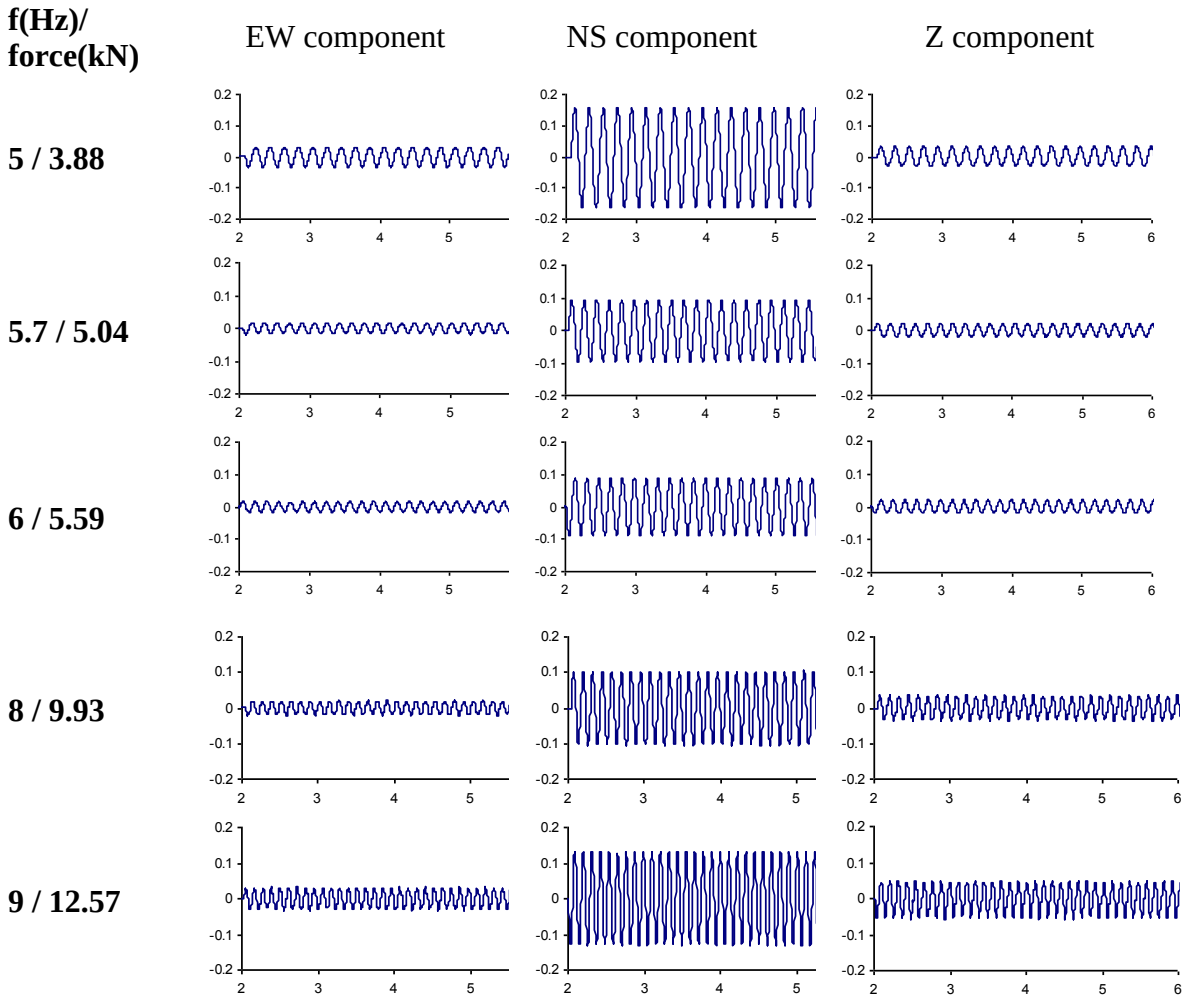


Figure 9: Acceleration time histories (measured in m/s^2) from forced-vibration tests recorded at the top of the roof slab, for different excitation frequencies and forced amplitudes

As in the case of the free-vibration tests, selected recordings at the soil and the structure are presented in the ensuing. Similarly, the three components of the recorded motion are shown for each instrument. Structural response was recorded by accelerometers and SAARs, while soil response was recorded by seismometers and SAARs.

In Figure 9, structural accelerations records from instrument T5856 located close to the edge of the roof slab are depicted along the direction of shaking. The recorded acceleration response is presented for a series of tests, according to the output frequency and the output force of the vibrator system.

As the eccentric mass vibrator is able to produce larger forces, and thus vibration amplitudes on the structure, response in the soil was also recorded in the vertical direction by the SAAR. Figure 10 presents acceleration recordings in three directions (horizontal x-x and y-y, x-x being the direction of shaking, and vertical z-z) in the soil in a vertical array up to 5m depth. Recorded motion in both in-plane (x-x) and out-of-plane (y-y) directions seems to fade out after a depth equal to one time the foundation width (3m) for horizontal shaking, something in accordance with the literature [16].

Mass plates	**A+B+C**
Output frequency (Hz) / Output force (kN)	**8 / 17.51**
Recorded motion	**Soil response (in vertical direction)**
Type of recorded motion	**Acceleration (g)**

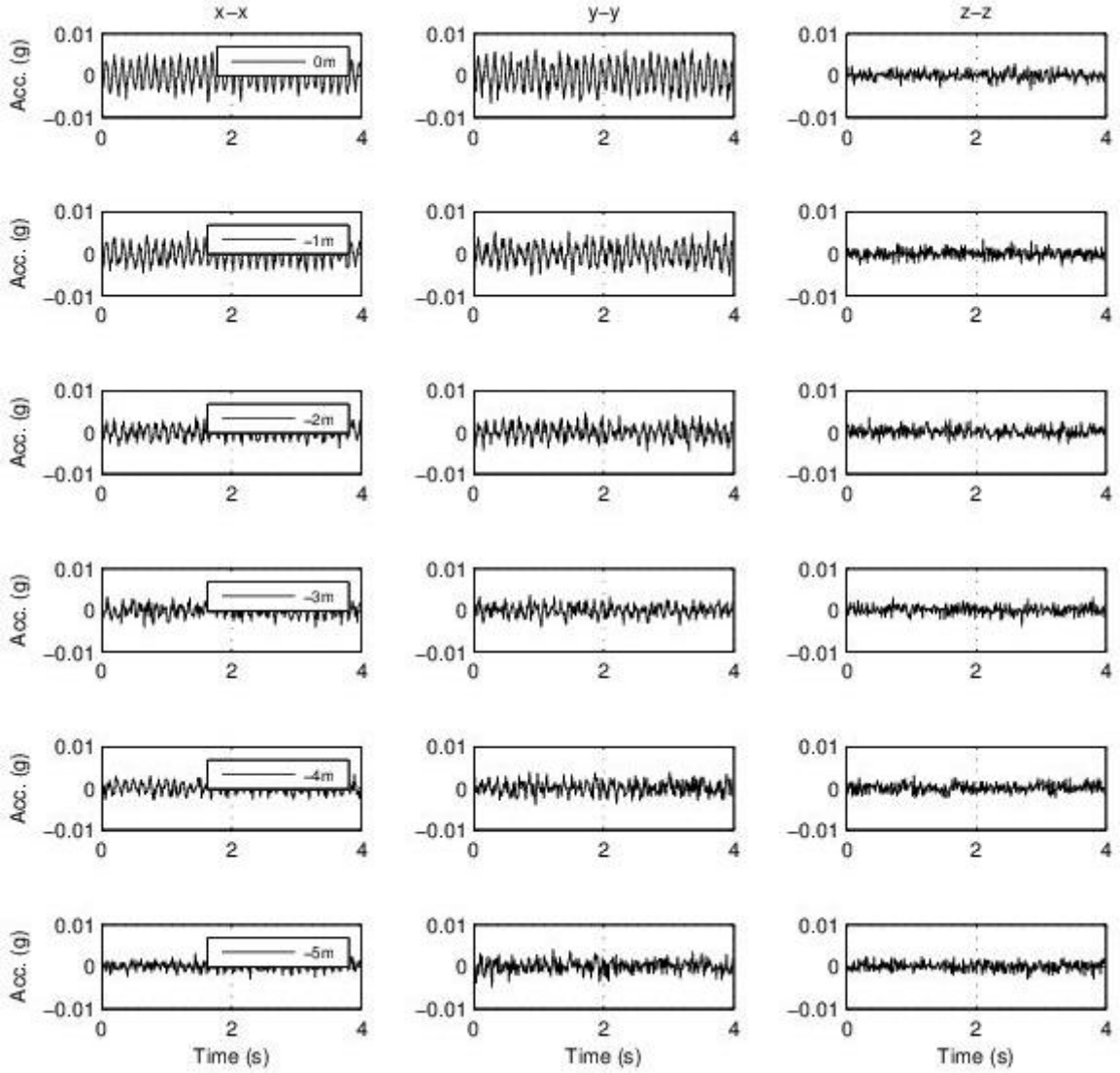
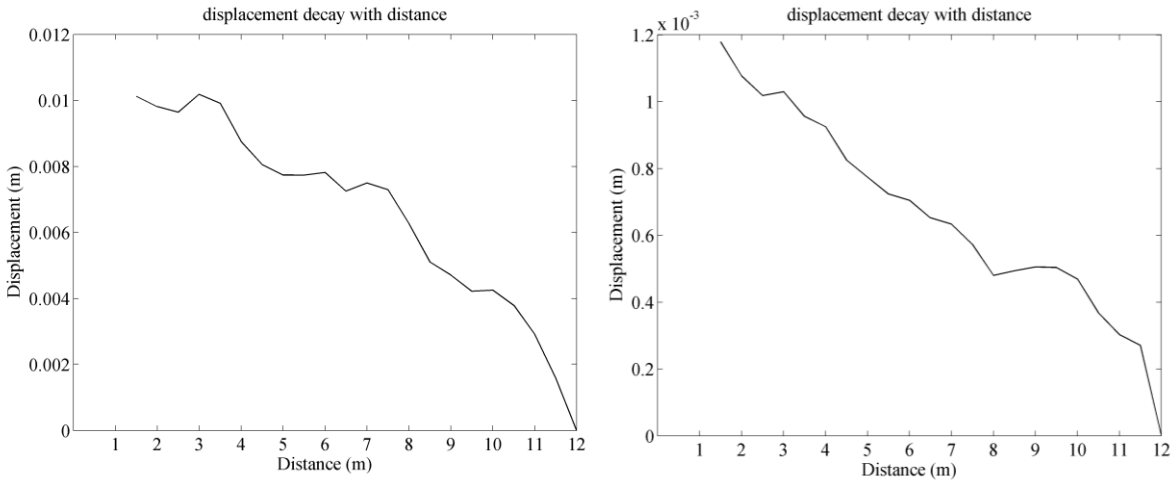


Figure 10: Recorded acceleration in the soil in the vertical array for output frequency 8Hz and output force 17.51kN of the eccentric mass vibrator. Acceleration is presented with depth, from soil surface to 5m depth

Figure 11 presents the decay of acceleration with distance from structure for forced-vibration shaking at 8Hz and output force 17.51kN. It can be seen that in the vertical array (Figure 11a), the decay of displacement response amplitude decreases at almost instant rate from distance larger than one time the foundation width (3m), while in the horizontal array (Figure 11b) the decrease of displacement amplitude is constant with distance.



a) b)

Figure 11: Decay with distance of the recorded displacement from the vertical (a) and horizontal (b) SAARs for output frequency 8Hz, and output force 17.51kN

4 DISCUSSION

A model structure (*EuroProteas*) was constructed in the *EuroSeistest* site array in order to study soil-foundation-structure interaction in large-scale. Free-vibration and forced-vibration tests were performed on the soil-foundation-structure system, using pull-out forces by a wire rope and an eccentric mass vibrator respectively. Aim of the study is to better understand and identify SFSI mechanism, as well as wave propagation effects in the coupled soil-foundation-structure system, induced by free and forced structural oscillation. In large-scale experiments we avoid all disadvantages arising from reduced-scale modeling, typically met in shaking table or centrifuge experiments.

Basic novelties of the study are:

- The very dense instrumentation of the SFS system, including more than 80 accelerometers and seismometers deployed in three directions, covering a volume of 9x9x12m around and beneath the structure. Such an instrumentation is able to capture wave propagation effects in the soil mobilized by structural oscillation, in addition to soil-foundation-structure interaction phenomenon identification.
- The easily reconfigurable mass and stiffness of *EuroProteas* structure in conjunction with the very well-known soil properties, are such to promote strong SFSI effects.
- The large number of pull-out tests performed to elucidate the so-called soil-foundation-structure system natural frequency.
- The large number of forced-vibration tests performed in the range of 1Hz to 10Hz, with exciting force amplitudes up to 20kN. The eccentric mass shaker was mounted on the foundation and on the roof slab of *EuroProteas*, enabling for different approximations of structural oscillation and foundation vibration analyses.
- The development of a *EuroSeistest* database portal (www.euroseisdb.civil.auth.gr) where all the recordings will be made available.

ACKNOWLEDGEMENTS

The construction of *EuroProteas* and the experimental study were performed in the framework of the European project "Seismic Engineering Research Infrastructures for European Synergies, SERIES", Grant agreement 227887. The authors wish to thank all members of the Research Unit of Soil Dynamics and Geotechnical Earthquake Engineering (SDGEE) of Aristotle University of Thessaloniki and the scientific and technical staff of ITSAK who contributed in the experimental campaign. The authors would like to thank Jonathan Stewart for his valuable help in the early stages of this study.

REFERENCES

[1] Pitilakis, D., Dietz, M., Muir Wood, D., Clouteau, D., & Modaressi-Farahmand-Razavi, A. (2008). Numerical simulation of dynamic soil–structure interaction in shaking table testing. *Soil Dynamics and Earthquake Engineering*, 28(6), 453–467.

[2] Gajan, S., Raychowdhury, P., Hutchinson, T. C., Kutter, B. L., & Stewart, J. P. (2010). Application and Validation of Practical Tools for Nonlinear Soil-Foundation Interaction Analysis. *Earthquake Spectra*, 26(1), 111.

[3] Lin, A. N., and Jennings, P. C. (1984). Effect of embedment on foundation-soil impedances. *ournal of Engineering mMechanics*, 110(7), 1060–1075.

[4] Luco, J. E, Trifunac, M. D., and Wong, H. L. (1988). "Isolation of soil structure interaction effects by full-scale forced vibration tests. *Earthquake Engineering and Structural Dynamics*, 16(1), 1–21.

[5] Barros, F. C. P. de P. De, & Luco, J. E. (1995). Identification of foundation impedance functions and soil properties from vibration tests of the Hualien containment model. *Soil Dynamics and Earthquake Engineering*, 14(94), 229–248.

[6] Tileylioglu, S., Stewart, J. P., & Nigbor, R. L. (2011). Dynamic Stiffness and Damping of a Shallow Foundation from Forced Vibration of a Field Test Structure. *Journal of Geotechnical and Geoenvironmental Engineering*, 137(4), 344.

[7] Raptakis, D., Chávez-Garcia, F., Makra, K., & Pitilakis, K. (2000). Site effects at *EuroSeistest*—I. Determination of the valley structure and confrontation of observations with 1D analysis. *Soil Dynamics and Earthquake Engineering*, 19, 1–22.

[8] Pitilakis K., Raptakis D., Lontzetidis K., Tika-Vasillikou T., Jongmans D. (1999). Geotechnical and geophysical description of EUROSEISTEST, using field, laboratory tests and moderate strong motion records, *Journal of Earthquake Engineering*. 3(3), 381-409.

[9] Manakou, M., Raptakis, D., Cha, F. J., Chávez-García, F. J., Apostolidis, P., & Pitilakis, K. (2010). 3D soil structure of the Mygdonian basin for site response analysis. *Soil Dynamics and Earthquake Engineering*, 30(11), 1198–1211.

[10] CEN (2004). Eurocode 7: Geotechnical design - Part 1: General rules European Committee for Standardization.

[11] CEN (1992). Eurocode 3: Design of steel structures. Part 1.1: General rules and rules for buildings, European Committee for Standardization.

[12] CEN (2004). Eurocode 2: Design of concrete structures - Part 1-1: General rules and rules for buildings. European Committee for Standardization.

[13] CEN (2004). Eurocode 8: Design of Structures for Earthquake Resistance—Part 1: general rules, seismic actions and rules for buildings. European Committee for Standardization.

[14] Computers and Structures Inc. (2007). SAP2000: Static and Dynamic Finite Element Analysis of Structures (Version 11.0.2) *Analysis Reference Manual*, Berkeley, CA, U.S.A.

[15] Salonikios, T., Makarios T., Sous, I., Lekidis V. Karakostas Ch. (2005) Design of instrumentation and vibration testing programs of structures through analytical investigations. *In Computational Methods and Experimental Measurements XII*, Brebbia and Carlomagno (eds), Malta, pp: 579-588.

[16] Gazetas, G. (1983). Analysis of machine foundation vibrations: State of the art. *Soil Dynamics and Earthquake Engineering*, 2(1), 2–42.

COMPDYN 2013
4th ECCOMAS Thematic Conference on
Computational Methods in Structural Dynamics and Earthquake Engineering
M. Papadrakakis, V. Papadopoulos, V. Plevris (eds.)
Kos Island, Greece, 12–14 June 2013

PILES-INDUCED FILTERING ACTION AND ITS EFFECT ON THE SEISMIC RESPONSE OF BUILDINGS

Nicola Caterino[1], Luca de Sanctis[1], Raffaele Di Laora[2] and Giuseppe Maddaloni[1]

[1] Department of Technology, University of Napoli Parthenope,
Centro Direzionale, isola C4, 80123 Naples, Italy
{nicola.caterino, luca.desanctis, giuseppe.maddaloni}@uniparthenope.it

[2] Department of Civil Engineering, Design, Building and Environment, Second University of Napoli,
Via Roma 29, 81031 Aversa (CE), Italy
raffaele.dilaora@unina2.it

Keywords: Pile-soil kinematic interaction, filtering effect, inertial interaction, dynamic response, earthquakes, seismic design.

Abstract. *The inertial interaction analysis of a structure founded on piles is usually performed by taking that the support motion at the foundation level is merely that of the free field, thus neglecting the filtering action exerted by piles. By contrast, the existence of frequency filtering is confirmed through works referring to theoretical studies and experimental evidence, even if this effect has not been so far taken into consideration in design practice. Based on analytical and numerical studies, the importance of the filtering effect is highlighted. This paper focuses on the seismic performance of frame buildings, excited alternatively by the filtered input motion or the free-field input motion. The results of these analyses, expressed in terms of top displacements and base shear, allowed to assess the importance of the beneficial effect coming from the piles on the inertial response of the superstructure.*

1 INTRODUCTION

The analysis of the seismic response of a structure is usually performed assuming that the support motion at the foundation level is merely that of the free-field. Contrarily to this assumption, the superstructure interacts with its foundation and the surrounding soil, creating additional soil deformation, so as the foundation motion can differ substantially from that of the free-field. Assuming a linear soil-foundation-superstructure response, the analysis of the complete system can be performed following the three consecutive steps: (i) calculate the motion of the foundation in the absence of the superstructure, i.e. the so-called foundation input motion; (ii) determine the dynamic impedance functions associated to swaying, vertical, rocking and cross swaying-rocking oscillation of the foundation; (iii) evaluate the response of the superstructure supported on the springs and dashpots and subjected to the motion of the foundation determined at the first step. This method is truly convenient as an alternative to fully 3D analyses involving the complete pile-soil-superstructure that are very complex and rarely performed in engineering practice.

The most attractive application of the substructure method is to assume that the support motion equals the free-field seismic motion. By contrast, the free-field motion is filtered out by the piles, especially in the case of soft soils, where piles are recurrently required to increase the bearing capacity of the foundation and/or to reduce settlements [1, 2]. The importance of the filtering effect has been reported in theoretical studies and works referring to experimental evidence, even if this effect has not been so far taken into consideration in engineering practice. The goal of this paper is threefold: (i) to offer an insight into the filtering effect; (ii) to propose a correction to design spectra that can be of assistance for seismic risk design strategies; (iii) to quantify the beneficial effect coming from the piles on the seismic response of structures. Pertaining to this last point, the study has focused on the response of linear reinforced concrete frame buildings excited by either the filtered input motion or the free-field input motion, to quantify the beneficial effect coming from the piles on the seismic performance of non-dissipative structures. In this respect, the results presented herein can be considered representative of the response to earthquakes that are likely to occur during the life-span of the structure.

2 LITERATURE OVERVIEW

The problem of the filtering action exerted by the piles has been examined in the seminal work by Flores-Berrones and Whitman [3]. By means of a Winkler-type model, the authors expressed the ratio of pile and soil accelerations as function of excitation frequency in a closed form solution, for the case of an infinitely-long pile in homogeneous halfspace. As an outcome, piles were found to reduce seismic motion with increasing excitation frequency and pile diameter, whereas an increase in soil stiffness lead to a decrease in the filtering effect.

Gazetas [4] carried out a parametric analysis with reference to end-bearing single piles embedded in different soil profiles. He concluded that the filtering effect is also affected by the degree of soil inhomogeneity.

Fan et al. [5] studied the kinematic behaviour of single piles and pile groups. They found that group effects, although clearly depending on pile spacing, are not relevant for lateral vibrations. By contrast, they may strongly affect the rotational component of motion which, however, lies beyond the scope of this paper.

All the studies above and further studies on the subject [6-11] demonstrate that for motions that are rich in high frequency components, even practically flexible piles may not be able to follow the wavy movements of the free-field. On the other hand, if low-frequency compo-

nents of the input motion are predominant, the scattered field is weak, and the support motion can be expected to be approximately equal to that of the free-field [12-14]. There is also some experimental evidence supporting the importance of the frequency content [4, 15-17]. The seismic response of structures founded on piles, however, is a complicated problem and it is difficult to delineate the role of pile-soil-interaction. Kawamura et al. [15] have reported the case history of a 7-storey residential building in Japan (Fig. 1). Acceleration recordings were available since 1971 at two groups of points, the 'building line' and the 'soil line'. Comparing the records at the two lines during 20 earthquakes, they found that the maximum amplification at the ground surface was about 1.5 that recorded at the base slab of the building. They also plotted the Fourier spectral ratio between the building line and the soil line at the level of the base slab pertaining to a particular earthquake event (see again Fig. 1); for structural periods smaller than 0.3 s the ratio of the two accelerations recorded during the event at hand is 0.5 as an average. For increasing structural periods the Fourier spectral ratios have a tendency to approximate unity. It is argued from this case history that the high frequency components of the free-field motion are filtered out by the pile-soil-superstructure interaction.

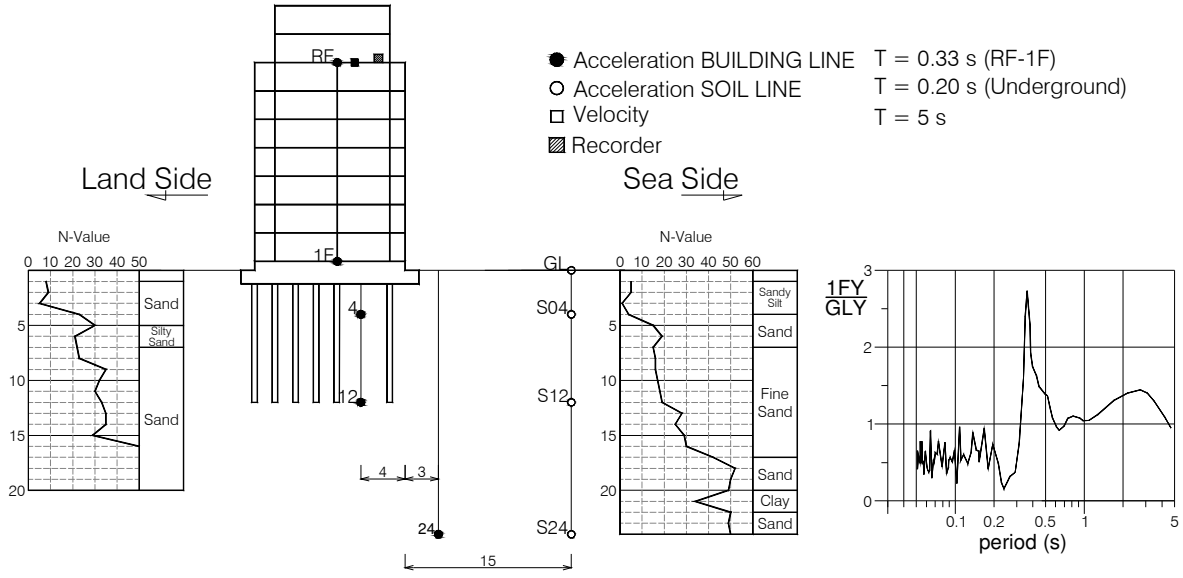


Figure 1. Case history of a 7-storey residential building in Japan (after Kawamura et al. [15])

Gazetas [4] has described an example of (large diameter) bored piles for which acceleration recordings were available at both the pile-cap and at the ground surface on a far-distant axis representing free-field conditions. By comparing the acceleration spectra of the two motions he noticed that the spectrum of the far distant motion included frequency contents higher than those at the pile cap, in agreement with the conclusion of the study by Kawamura et al. [15].

The limited amount of experimental evidence demonstrates that the frequency content of the input signal might exert a remarkable influence on the support motion.

3 THE MECHANISM OF FILTERING EFFECT

Flores-Berrones and Whitman [3] showed that in the homogenous halfspace the ratio between the acceleration atop a fixed-head infinitely long pile, a_p, and that at the soil surface, a_s, is given by:

$$I_u = \frac{a_p}{a_s} = \Gamma \tag{1}$$

where Γ is an interaction factor which may be approximately expressed as:

$$\Gamma = \frac{4\lambda^4}{4\lambda^4 + q^4} \tag{2}$$

in which q (=ω/V_s) is the wave number of the harmonic SH wave travelling in the soil, and λ is the well-known Winkler parameter:

$$\lambda = \left(\frac{k + i\omega c}{4E_p I_p} \right) \tag{3}$$

The stiffness of the springs k may be taken as proportional to soil stiffness E_s by a coefficient δ, which typically assumes values close to unity [18], whereas the dashpot coefficient is expressed as [19]:

$$c = 6\omega^{-\frac{1}{4}} \rho_s V_s^{\frac{5}{4}} d^{\frac{3}{4}} + 2\beta_s k / \omega \tag{4}$$

Compared to the original formulation, the above derivations neglect the inertia contribution due to the pile mass. Eq. (2) is plotted in Fig. 2a against the traditional dimensionless parameter $a_0 = \omega d/V_s$, accounting for excitation frequency, for different values of stiffness ratio E_p/E_s. Pile-to-soil acceleration ratio is always smaller than unity (i.e. piles play always a beneficial role in reducing the seismic motion that excites the superstructure) and decreases with frequency. This effect is physically due to the resistance that the pile offers in adapting to the short wavelengths of the soil, as the dimensionless frequency a_0 may be interpreted as the ratio of pile diameter d and soil wavelength λ_s (=V_s/ω). Moreover, at a given frequency pile-soil acceleration ratio is progressively smaller as pile-soil stiffness ratio increases. The physical interpretation of this phenomenon deserves special discussion as reported below.

The ability of the pile to follow soil displacements is well represented by the characteristic wavelength:

$$\lambda_p = d \left(\frac{E_p}{E_s} \right)^{\frac{1}{4}} \tag{5}$$

which encompasses both diameter and pile-soil stiffness ratio. Eq. (5) can be substituted into Eq. (2), to express λ as a function of E_s. Finally, assuming δ = 1, the amplitude of Γ can be expressed as:

$$\Gamma = \left[1 + \frac{1}{20} \left(\frac{\omega \lambda_p}{V_s} \right) \right]^2 \tag{6}$$

The new dimensionless parameter $\omega\lambda_p/V_s$ can be viewed as the ratio of pile characteristic wavelength and soil wavelength. Eq. (6) is plotted in Fig. 2b against such parameter. It can be

seen that the larger is the characteristic wavelength of the pile compared to the soil wavelength, the greater is the amount of the filtering effect. For comparison, results from Fan et al. [5] are plotted in the graph, according to the new normalization. Results undertaken from finite elements carried out in the frequency domain have been also added for comparison.

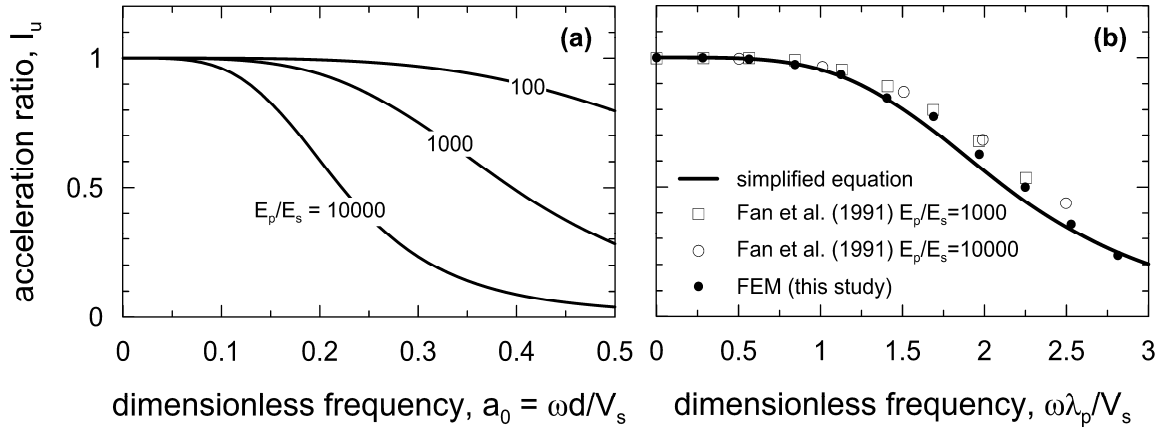


Figure 2. Pile-soil acceleration ratio as function of different dimensionless frequency parameters

4 PARAMETRIC ANALYSIS FOR FILTERING EFFECT

To investigate quantitatively the filtering effect exerted on the Foundation Input Motion by a piled foundation, a comprehensive set of Finite Element analyses has been performed. Owing to the second-order influence of group effects for lateral vibration [5], a single pile embedded in a two-layer soil has been considered, as shown in Fig. 3a. Harmonic S-waves applied at the bedrock level and propagating up and down constitute the seismic excitation.

The total height of the soil deposit, H, is set equal to 30 m, whereas the pile has diameter d = 1 m, length L = 20 m and Young's modulus Ep = 30 GPa. Soil and pile density are set to 1.75 and 2.5 Mg/m^3, respectively, whereas the value of soil Poisson's ratio is 0.4.

Although the problem is 3D, the geometry is axisymmetric whereas the load is antisymmetric. To simplify the analysis, stresses and displacements are expanded into a Fourier series in the circumferential direction, according to the technique introduced by Wilson [20]. For the example at hand, only the first-order term of the series is needed. Owing to this procedure, the original three-dimensional problem is conveniently reduced to a 2D one, as shown in Fig. 3b.

Numerical analyses were conducted using the commercial FE code ANSYS. Four-noded axisymmetric 2D elements are used to mesh soil and pile. The assumption of a line of antisymmetry implicitly implies the use of 'periodic' or 'tied' boundaries. As a consequence, the model under examination does not allow for the transmission of outgoing waves generated at the pile-soil interface, which remains trapped inside the model. A common procedure to check the amount of inaccuracy coming from this choice is that originally suggested by Zienckiewicz et al. [21] for both linear and non linear models. It consists of comparing the results of the complete model with those predicted by the free-field conditions at the location of the boundary. For the problem under examination, Di Laora et al. [22] have shown that the assumption of tied boundaries provides sufficient accuracy, provided that the width of the entire model is large enough. To this aim, the lateral boundary of the model was set at 400 d from the pile axis. Vertical displacements are restrained along the lateral boundary of the mesh, while nodes at the base of the model are restrained to both horizontal and vertical directions to represent a rigid bedrock. The vertical size of the elements is constant and set to 0.5

diameters, whereas the horizontal size is 1/8 pile diameters at pile-soil interface, thereby increasing with radial distance up to 1.5 diameters at the free-field. The analyses performed in the parametric study were carried out in the frequency domain, first extracting vibrational modes with frequency up to 25 Hz, each having a pre-specified level of viscous damping. In this way the drawbacks stemming from use of common energy loss formulations such as Rayleigh damping were avoided. An FFT algorithm was employed to transfer responses from the frequency to the time domain and vice versa. Transient response is investigated by using real signals, selected from an Italian database [23] and the European database by Ambraseyes et al. [24]. Time histories and Fourier spectra of the above events are reported in Di Laora and de Sanctis [25].

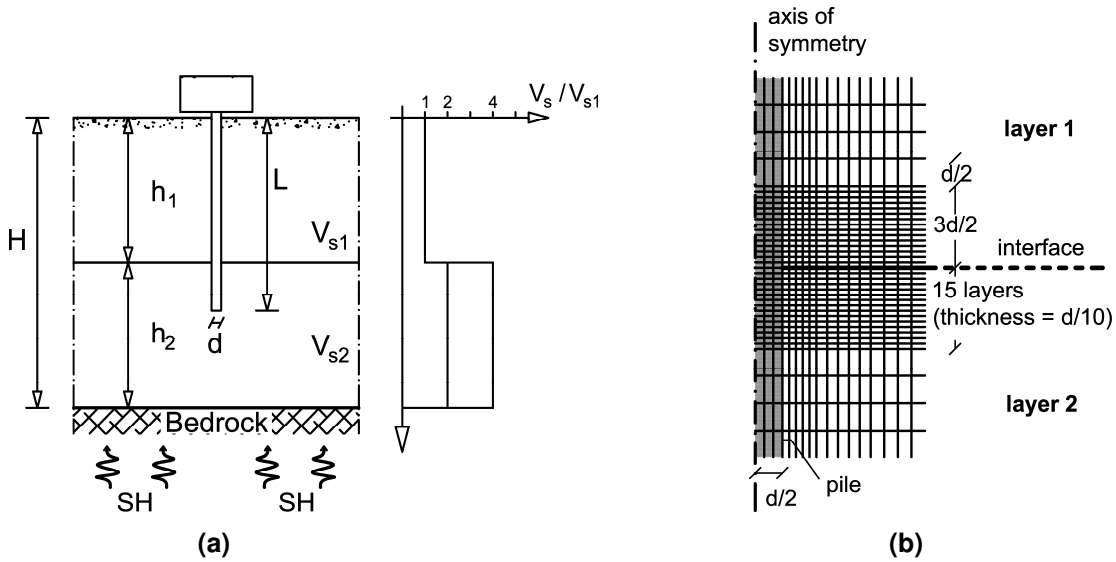


Figure 3. (a) Problem under consideration and (b) Finite Element mesh employed in the analyses.

Some results of the parametric analysis are illustrated in Fig. 5, where the ratio ξ of the spectral acceleration of the filtered motion, $S_{a,p}$, over that of the free field, $S_{a,s}$, is plotted against the structural period. For a given subsoil profile and any particular earthquake event it is possible to recognize two critical points: (i) that corresponding to the minimum value of the spectral acceleration ($T_{\min}$, $\xi_{\min}$); (ii) that pertaining to the structural period after which the filtering effect becomes negligible (T_{crit}, ξ_{crit}). The second point can be identified with the point of maximum curvature of the spectral ratio function, whose ordinate can be considered nearly coincident with unity, so that the coordinates of the second point can be assumed to be (T_{crit}, 1). The most interesting result is that for any subsoil the structural periods T_{crit} and $T_{\min}$ are practically unaffected by the earthquake event. On the other hand, the $\xi_{\min}$ is clearly dependent on the frequency content of the input signal. The spectral acceleration ratio at $T = 0$, ξ_0, is a purely kinematic interaction factor and is also strongly affected by the frequency content.

The result of the parametric analysis can be conveniently condensed in the form of mean spectral acceleration ratios, as shown in Fig. 6. It is worthy to note that for both V_{s1} = 50m/s and V_{s1} = 100 m/s, the mean spectral ratios have un upper bound, corresponding to the homogeneous soil deposit. In this case, in fact, the contribution to the filtering effect due to the kinematical restraint exerted by the lower stiffer vanishes. At the same time, the impedance contrast has only a weak effect on the structural periods $T_{\min}$ and T_{crit}. As a result, Fig. 6 can

be further synthesized by referring only the upper bound represented by the homogenous subsoil.

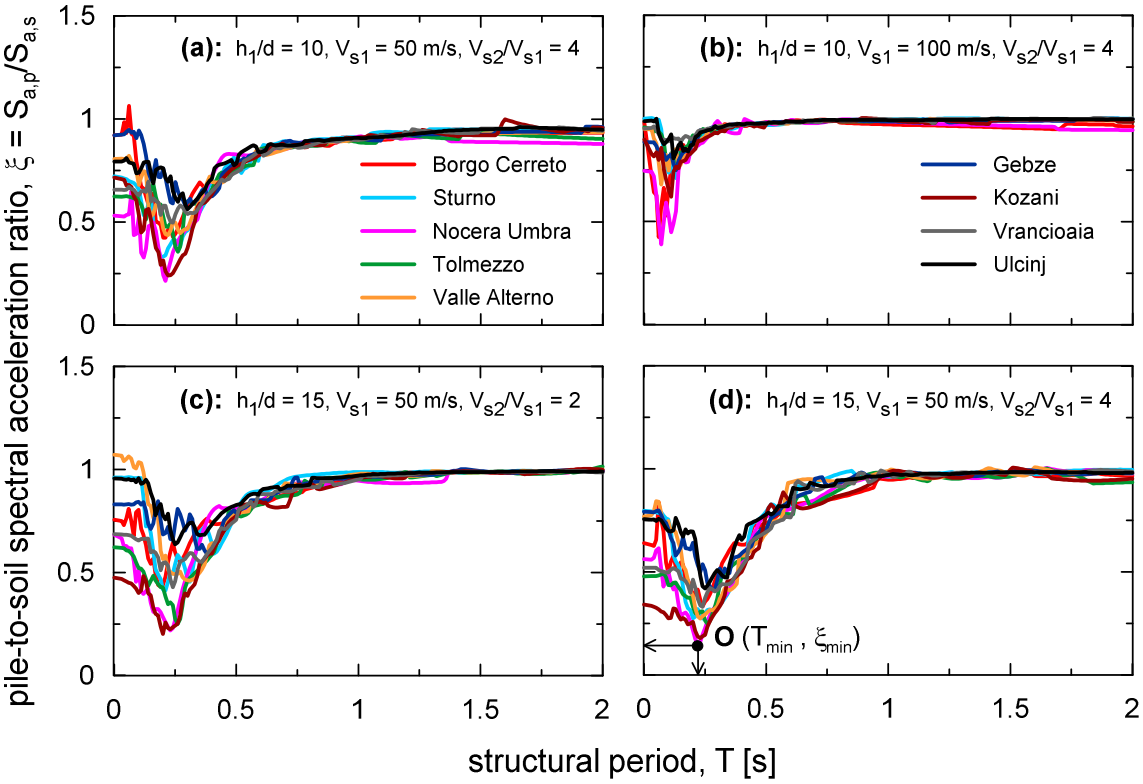


Figure 5. Pile-head spectral acceleration over that of the free-field.

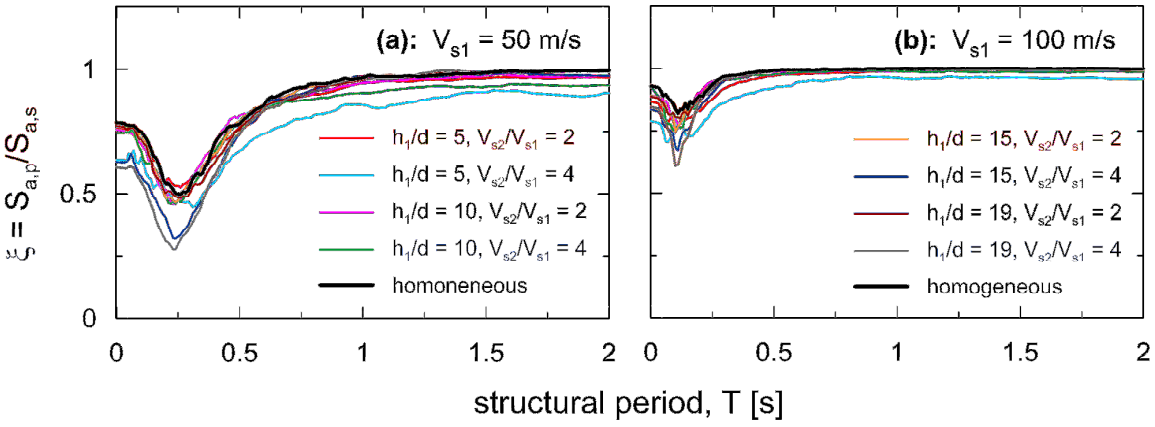


Figure 6. Mean spectral ratios for the subsoils considered in the parametric study.

It is straightforward to recognize that the structural periods T_{min} and T_{crit} can be expressed through the linear correlations:

$$T_{min} = 12\frac{d}{V_s} \tag{7}$$

$$T_{crit} = 3.5\, T_{min} \tag{8}$$

It is also easy to verify that the reduction parameters ξ_0 and ξ_{min} pertaining to the ratio between the mean spectral functions satisfy the equations:

$$\xi_0 = \left(1 + 0.15 \frac{\lambda_p}{V_{s1}} \cdot 10 rad/s \right)^{-1} \tag{9}$$

$$\xi_{min} = 2.5\, \xi_0 - 1.5 \tag{10}$$

For further details about Eqs (9, 10) the reader can refer to Di Laora & de Sanctis [25]. All the ingredients are now available to define reduced design spectra. It is suggest to adopt the reduction factor for acceleration spectra defined by the following equations:

$$\begin{cases} \xi(T) = \xi_0 - \dfrac{(\xi_0 - \xi_{min})}{T_{min}^2} T^2 = \xi_0 - (\xi_0 - \xi_{min}) \left(\dfrac{T}{T_{min}} \right)^2 ; & T \le T_{min} \\ \xi(T) = 1 - (1 - \xi_{min}) \left(\dfrac{T_{crit} - T}{T_{crit} - T_{min}} \right)^2 ; & T_{min} \le T \le T_{crit} \end{cases} \tag{11a,b}$$

Eqs (11a,b), also plotted in Fig. 6 for two different values of the shear wave velocity V_{s1}, may be conveniently adopted to evaluate the seismic vulnerability of existing structures or to evaluate efficiently the seismic response of a structure from the design standpoint. The same criterion can be also adopted within the framework of the substructure method, whatever the structure be modeled as a dissipative or a non dissipative system, to evaluate the opportunity of carrying out the computational cost associated to the pile-soil kinematic interaction analysis.

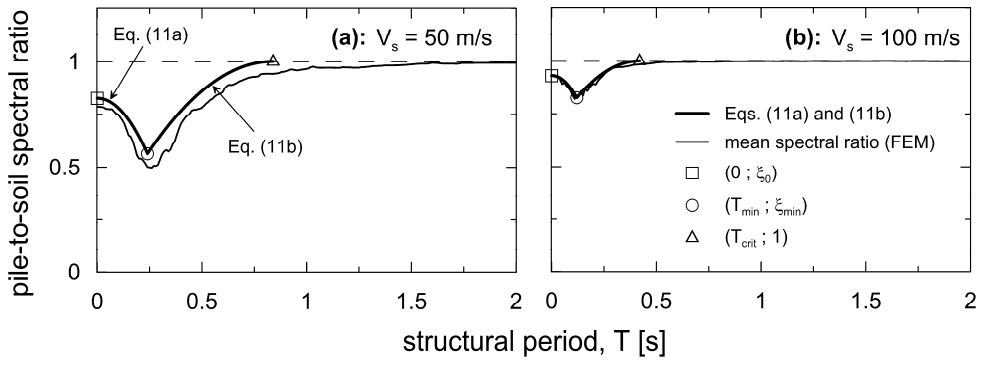


Figure 7. Mean spectral ratios for homogeneous soil conditions and corresponding proposed spectral reduction.

5 INERTIAL INTERACTION ANALYSIS

The study discussed in section 4 has been focused on linear elastic soil behavior and an ideal subsoil consisting of a two layer deposit underlain by a rigid layer. It is therefore believed that further investigations are needed, particularly for subsoil conditions other than those considered in this work, to confirm the general validity of the equations for design spectrum reduction. Before anything else, however, the potential coming from the piles in reducing the seismic demand has to be verified against real structures, i.e. Multi Degree Of Freedom (MDOF) systems, that can behave quite differently from the Single Degree Of Freedom (SDOF) systems. To address this point, the study has been focused on the response of

linear frame buildings excited by either the filtered input motion or the free-field input motion, to quantify the beneficial effect coming from the piles on the seismic performance of non-dissipative structures.

Five planar reinforced concrete (RC) frames have been considered for such analyses (Fig. 7), each of these assumed to be representative of a 3D structure having identical 2D frames 4 meters spanned one each other. Concrete having characteristic compressive cylinder strength f_{ck} equal to 25 MPa and steel reinforcement with characteristic yield strength f_{yk} equal to 450 MPa have been considered.

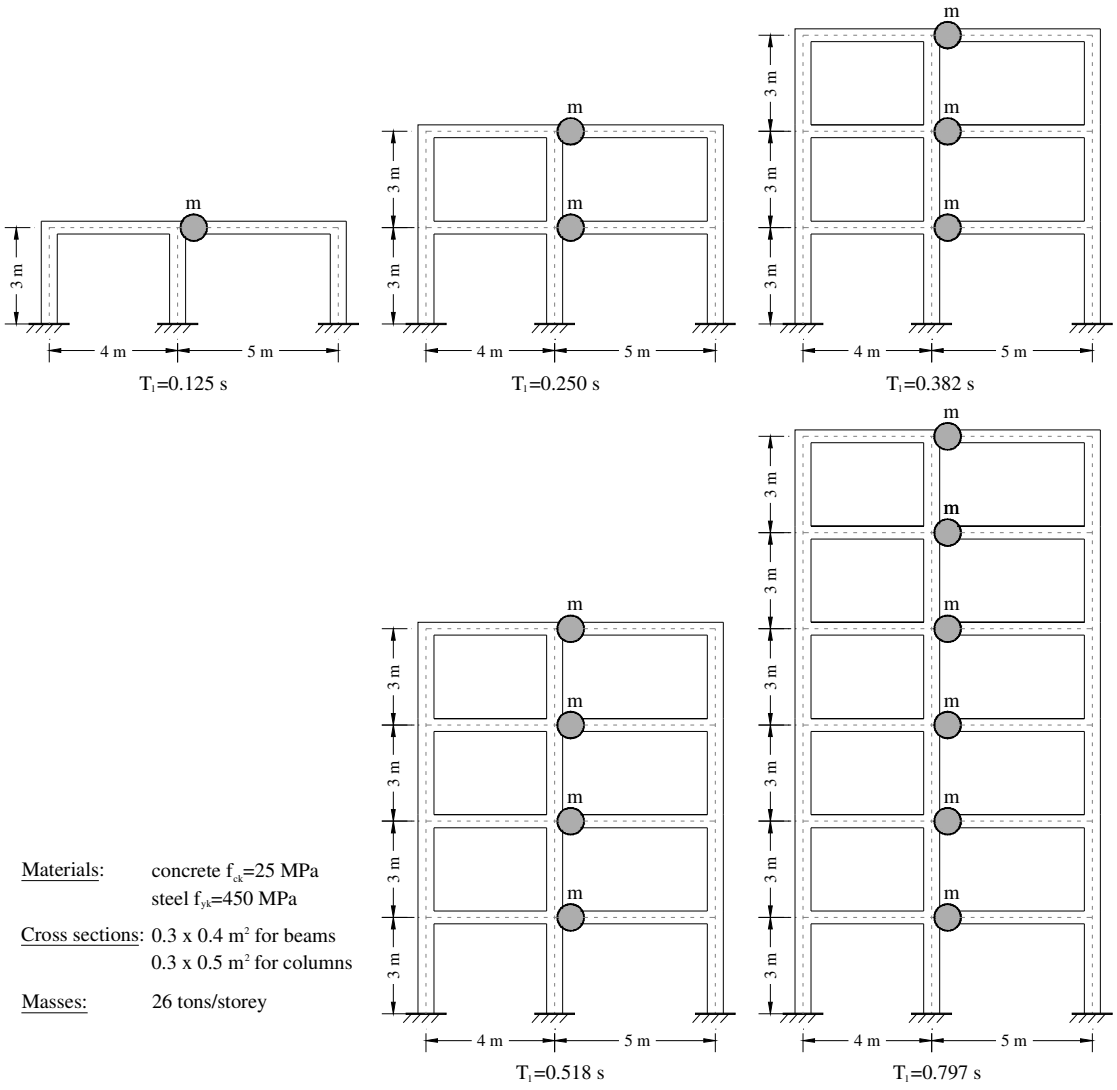


Figure 8. The five RC frame structures considered as case-studies for the dynamic analyses.

The structural design has been performed according to Eurocodes 2 and 8 [26, 27], using the lateral force method of analysis and assuming the following input data: (i) residential use of the buildings; (ii) structures located in L'Aquila (central Italy); (iii) ductility class DCM (medium); (iv) 50 years of lifetime; (v) ground type C; (vi) one way RC slabs subjected to characteristic permanent structural, permanent non-structural and variable actions equal to 1.8 kN/m^2, 2.0 kN/m^2 and 2.0 kN/m^2 respectively; (vii) storey masses (related to both self-weight of elements and above additional loads) of 26 tons.

Frames differ in terms of number of storeys (1, 2, 3, 4 and 6), whereas they have the same interstorey height (3 m) and cross sections' dimensions (0.3x0.4 m^2 and 0.3x0.5 m^2 for beams

and columns, respectively). A lumped mass model has been built for each frame. Masses are ideally concentrated in the corresponding center of masses of each storey. The fundamental periods of vibration are indicated in Fig. 8, falling in the range [0.13, 0.80 s].

Linear time-history analyses have been performed with SAP2000 [28] for each of the above frame structures under the action of the 9 natural earthquakes previously discussed. For any particular earthquake event, the structure has been excited by considering the free-field input motion and then by using the filtered signal. This has been done with reference to 3 subsoil configurations (i.e. respectively h_1/d=5, V_{s1}=50 m/s, V_{s2}/V_{s1}=4; h_1/d=10, V_{s1}=50 m/s, V_{s2}/V_{s1}=4 and h_1/d=10, V_{s1}=100 m/s, V_{s2}/V_{s1}=2) for a total of 9x2x3=54 analyses. Roof displacement and base shear time-histories have been recorded for each analysis as output results. Then the structural demand reduction due to the pile filtering effect has been evaluated assessing: (i) the absolute value of the ratio between maximum roof displacements corresponding to pile filtered and free-field conditions respectively; (ii) the similar ratio expressed in terms of base shear.

It is worth noting that these indexes are such that the smaller value corresponds to a higher reduction of the seismic demand on the superstructure due to the beneficial presence of the piles. All the values resulted from the analyses have been graphically synthesized in Fig. 9 as a function of the previously cited dimensionless parameter $\omega_s d/V_{s1}$, ω_s being an average circular frequency defined as:

$$\omega_s = \frac{2\pi f_m + 2\pi f_p}{2} \tag{12}$$

where f_m is the mean frequency as defined by Rathje et al. [29] and f_p the predominant frequency (corresponding to the maximum spectral acceleration).

Different indicators (circle, rhombus, square) refer the data to the three different subsoil conditions. The following comments can be drawn:

a. the values of response reduction in terms of base shear and top displacement are very close to each other; actually they derive from linear time-history analyses of regular, first-mode dominated structures, therefore such similarity was expected;
b. all the ratios resulted to be less than or equal to 1, demonstrating that the way in which piles alter the seismic demand imposed to the superstructure is never harmful for the latter, indeed is beneficial in most cases;
c. the general trend is that the demand reduction remains almost constant or increases with the dimensionless frequency $\omega_s d/V_{s1}$, consistently with Fig. 2(a);
d. the first subsoil condition (see circles) generally resulted in the largest response reduction, physically due to the lower value of the soil stiffness and the shallower position of the layer interface;
e. the second (rhombuses) subsoil type also corresponds to a significant reduction of structural demand for all the cases analyzed;
f. for both first (circles) and second (rhombuses) subsoil conditions, the highest reduction occurs for the two-storey frame (T_1=0.250 s), as expected from Fig. 7(a);
g. the third subsoil condition (h_1/d=10, V_{s1}=100 m/s, V_{s2}/V_{s1} = 2; see squares) resulted in a significant reduction of displacements and forces demand only for the one-storey building (T_1 = 0.125 s). This is consistent with Fig. 7(b) where, with reference to a homogeneous subsoil having V_s = 100 m/s, it is shown that appreciable reduction of the spectral demand occurs for vibration periods around 0.125 s, quickly going to be negligible when the period gets longer.

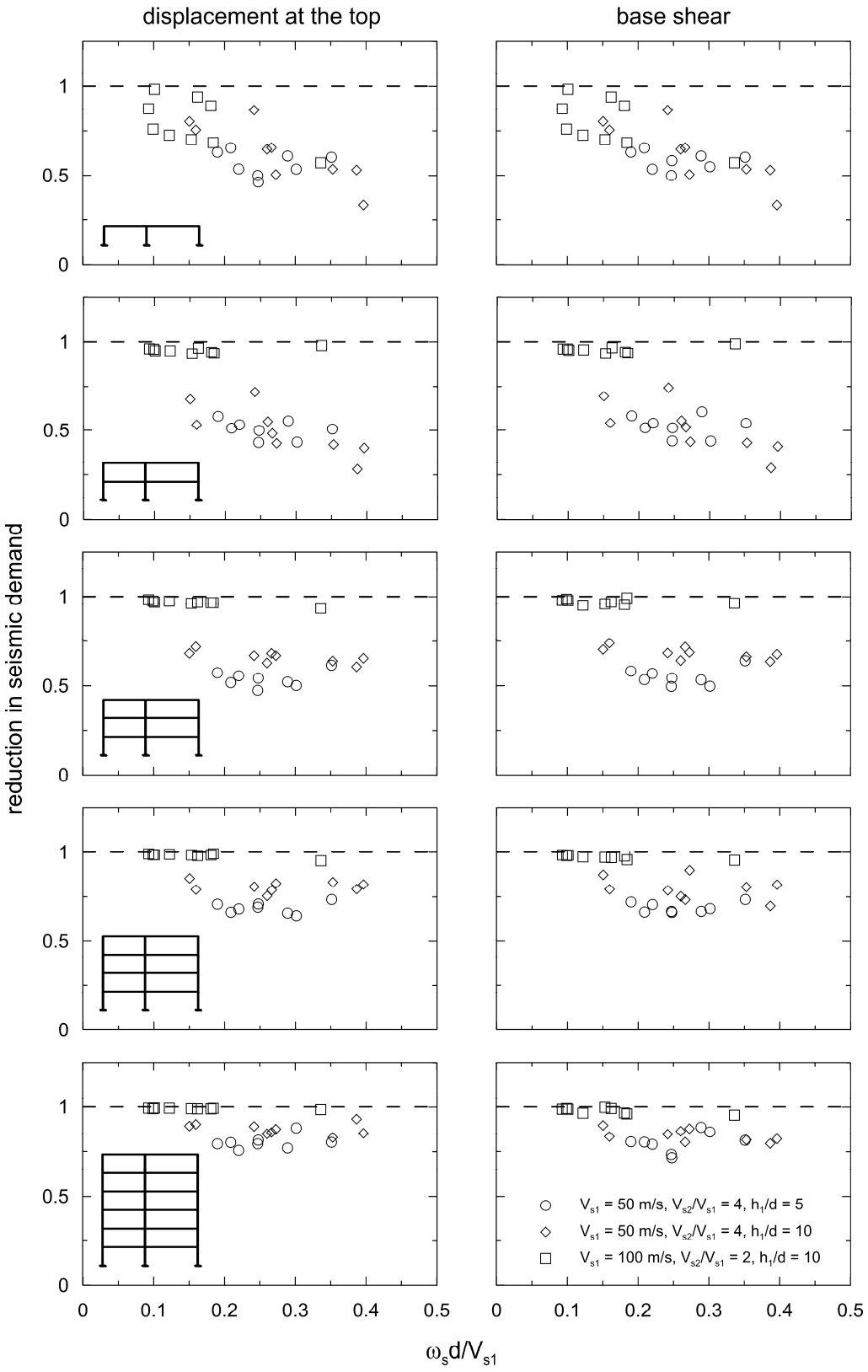


Figure 9. Reduction in top displacement and base shear demand for the five case-study structures.

Such results can be further discussed from a different perspective, i.e. observing the trend of the reduction in seismic demand as a function of the fundamental structural period, taking the average of the values corresponding to each earthquake. This representation (Fig. 10) allows to include, for comparison, the mean spectral ratios for the examined subsoil (thinner line) and the proposed spectral reduction for homogeneous soil conditions (thicker line), described in the previous section. Fig. 10 refers separately to the three subsoil cases (see parts (a), (b) and (c) respectively). Circles correspond to mean ratios of maximum base shear whereas rhombuses to mean ratios of maximum top displacements. It can be observed that: (i) the values of ratios in terms of base shear and top displacement are very close to each other as already observed with reference to the disaggregated data in Fig. 9; (ii) all the response reduction indicators result to be almost aligned on the thin lines representing mean spectral ratios; this indicates that the filtering effect due to the presence of the piles measured on SDOF does not change dramatically when referred to MDOF systems.

Nonlinear behavior of materials [30] and stiffness/strength irregularities of structures in plan [31] and in elevation could affect these results. Further analyses in such direction have been planned by authors, being the subject of a future paper. With reference to the same above case-study buildings, authors are also working on the comparison, via decision making procedures already applied to civil engineering problems [32], of the two alternative design strategies addressed to the adoption of shallow and deep foundations respectively. Finally the effect of pile filtering on the seismic response of a benchmark bridge [33, 34] is currently under investigation, to evaluate the results with reference to a MDOF very different from buildings for dynamic characteristics.

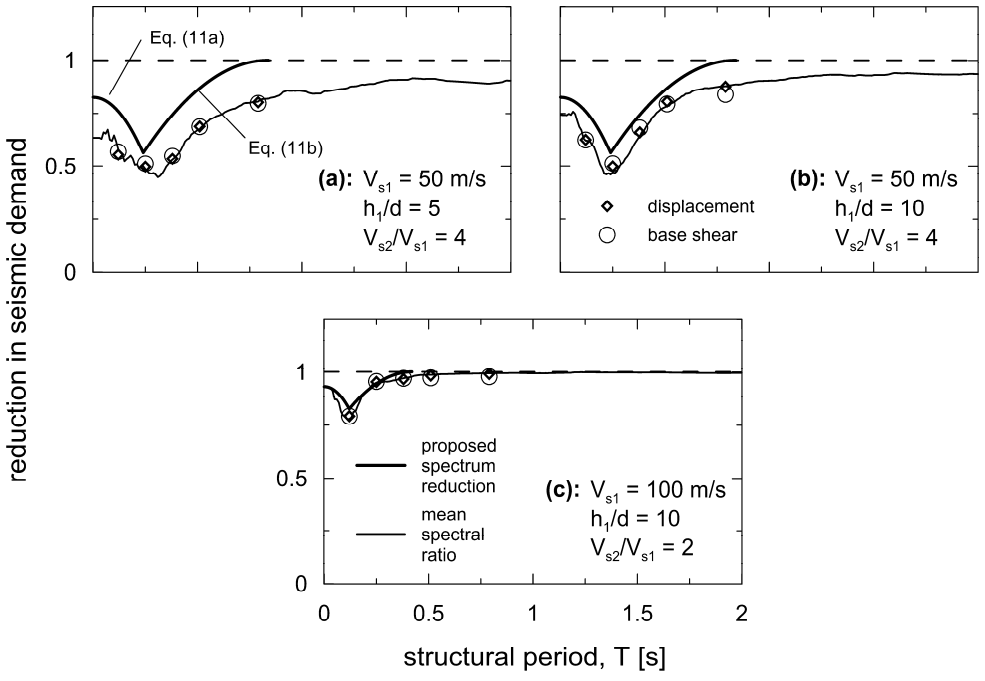


Figura 10. Mean response reduction in terms of top displacement and base shear. Mean spectral ratios. Proposed spectral reduction for homogeneous soil conditions.

6 CONCLUSIONS

The inertial interaction analysis of the superstructure is usually performed by assuming that the foundation input motion is merely that of the free field, thus neglecting the filtering action exerted by the piles. In this work, the concept of piles as seismic demand reducers has been introduced and discussed.

First, emphasis has been placed on the mechanism of the filtering effect. From results undertaken by FE analyses carried out in the frequency domain the following conclusion can be drawn: (i) the phenomenon of the filtering action is governed by soil stiffness, pile diameter and excitation frequency; (ii) the amount of the filtering action is lowered by the spectral ratio function pertaining to the homogenous soil deposit; (iii) the ratio of the spectral accelerations between the filtered motion over that of the free field has a somewhat 'root' shape, characterized by a critical structural period, after which the filtering effect becomes negligible.

Based on the above results, a coefficient for the reduction of design spectra has been suggested. This can be conveniently adopted within strategies for seismic risk reduction to assess the seismic vulnerability of existing structures founded on piles. It can be also employed within the framework of the substructure method to evaluate the convenience to carry out the computational cost associated to the analysis of pile-soil kinematic interaction.

Moreover, the potential coming from the piles in reducing the seismic demand has been verified against real structures, i.e. MDOF systems. The performance of structures with gradually increasing vibration period has been analyzed performing linear time-history analyses to quantify the beneficial effect coming from the piles for earthquake that are likely to occur during the life span of the structure. Five reinforced concrete frame structures have been designed according to Eurocode 8 so as to make their fundamental vibration periods range in the interval [0.13, 0.80 s]. Measures of response reduction due to the piles expressed in terms of base shear and top displacement resulted to be very close to each other, as expected from linear analysis of first-mode dominated structures. On average, the percentage reduction in seismic demand (in some cases even equal to about 50%) resulted to be similar to that measured in terms of spectral ratios, so confirming also for MDOF the beneficial effect that a pile foundation may lead to, acting as a mechanical filter between soil and superstructure.

Nonlinear behavior of materials and stiffness/strength irregularities of structures along the height could affect these results. Further analyses addressed to investigate in such direction have been planned by authors and will be the object of a future paper.

REFERENCES

[1] L. de Sanctis, G. Russo, Analysis and performance of piled rafts designed using innovative criteria. *Journal of Geotechnical and Geoenvironmental Engineering*, **134**(8), 1118-1128, 2008.

[2] G. Russo, C. Viggiani, L. de Sanctis. *Piles as settlement reducers: a case history. Proc. of the Skempton Conference 'Advances in Geotechnical Engineering: The Skempton conference. Proc. of a three day conference on advances in Geotechnical Engineering, organized by the Institution of Civil Engineers.* London, Thomas Telford, 1143-1154, 2012.

[3] R. Flores-Berrones, R.V. Whitman, Seismic response of end bearing piles. *Journal of the Geotechnical Engineering Division,* **108**(4), 554-569, 1982.

[4] G. Gazetas, Seismic response of end-bearing single piles. *International Journal of Soil Dynamics and Earthquake Engineering*, **3**(2), 82-93, 1984.

[5] K. Fan, G. Gazetas, A. Kaynia, E. Kausel, S. Ahmad, Kinematic seismic response analysis of single piles and pile groups. *Journal of the Geotechnical Engineering Division*, **117**(12), 1860-1879, 1991.

[6] G. Anoyatis, R. Di Laora, A. Mandolini, G. Mylonakis, Kinematic response of single piles for different boundary conditions: analytical solutions and normalization schemes. *Soil Dynamics and Earthquake Engineering*, **44**, 183-195, 2013.

[7] A.S. Nikolaou, G. Mylonakis, G. Gazetas, T. Tazoh, Kinematic pile bending during earthquakes analysis and field measurements. *Géotechnique*, **51**(5), 425-440, 2001.

[8] R.M.S. Maiorano, L. de Sanctis, S. Aversa, A. Mandolini, Kinematic response analysis of piled foundations under seismic excitations. *Canadian Geotechnical Journal*, **46**(5), 571-584, 2009.

[9] L. de Sanctis, R.M.S. Maiorano, S. Aversa, A method for assessing kinematic bending moments at the pile head. *Earthquake Engineering and Structural Dynamics*, **39**(10), 1133-1154, 2010.

[10] S. Sica, G. Mylonakis, A.L. Simonelli, Transient kinematic pile bending in two-layer soil. *Soil Dynamics and Earthquake Engineering*, **31**(7), 891-905, 2011.

[11] R. Di Laora, G. Mylonakis, A. Mandolini, Pile-head kinematic bending in layered soil. *Earthquake Engineering and Structural Dynamics,* **42***,* 319-337, 2013.

[12] S.M. Mamoon, P.K. Banerjee, Response of piles and pile groups to travelling SH waves. *Earthquake Engineering & Structural Dynamics*, **19**(4), 597-610, 1990.

[13] A. Kaynia, E. Kausel. Dynamics of piles and pile groups in layered soil media. *Soil Dynamics and Earthquake Engineering*, **10**(8), 386-401, 1991.

[14] K. Fan, G. Gazetas, A. Kaynia, E. Kausel, S. Ahmad, Kinematic seismic response analysis of single piles and pile groups. *Journal of the Geotechnical Engineering Division,* **117**(12), 1860-1879, 1991.

[15] S. Kawamura, H. Umemura, Y. Osawa, Earthquake motion measurement of a pile-supported building on reclaimed ground. *Proc. 6th WCEE*, India, 1977.

[16] H. Tajimi, Seismic effects on piles. *State-of-the-Art-Report. Spec. Session Proc. 9th Int. Conf. Soil Mech*., Tokyo, 1977.

[17] T. Ohta, S. Uchiyama, M. Niwa, K. Ueno, Earthquake response characteristics of structure with pile foundation on soft subsoil layer and its simulation analysis. *7th World conf. on earthquake engineering*. Vol. 3. Istanbul, Turkey, 1980.

[18] J.M. Roesset. The use of simple models in soil-structure interaction. *ASCE specialty conference*, Knoxville, TN, Civil Engineering and Nuclear Power, vol. 2, 1980.

[19] N. Makris, G. Gazetas, Dynamic pile-soil-pile interaction. Part II: Lateral and seismic response. *Earthquake Engineering & Structural Dynamics* , **21**(2), 145-162, 1992.

[20] E.L. Wilson, Structural analysis of axisymmetric solids. *American Institute of Aeronautics and Astronautics Journal AIAA*, **3**, 2269-2274, 1965.

[21] O.C. Zienckiewicz, N. Bicanic, F.Q. Shen, Earthquake input definition and the transmitting boundary conditions. *Conf. Advances in computational non-linear mechanics*, 109-130. Editor St. Doltnis I, 1988

[22] R. Di Laora, A. Mandolini, G. Mylonakis, Insight on kinematic bending of flexible piles in layered soil. *Soil Dynamics and Earthquake Engineering,* **43**, 309-322, 2012.

[23] G. Scasserra, G. Lanzo, J.P. Stewart, B. D' Elia. SISMA (Site of Italian Strong Motion Accelerograms): a web-database of ground motion recordings for engineering applications. *Seismic Engineering Conference commemorating the 1908 Messina and Reggio Calabria Earthquake*, Reggio Calabria, Italy, Vol. 2, 1649-1656, 2008.

[24] N. Ambraseys, P. Smit, R. Sigbjornsson, P. Suhadolc, B. Margaris. Internet-Site for European Strong-Motion Data. European Commission; Research-Directorate General, Environment and Climate Programme, 2002.

[25] R. Di Laora, L. de Sanctis, Piles-induced filtering effect on the Foundation Input Motion. Soil Dynamics and Earthquake Engineering, **46**, 52-63, 2013.

[26] Eurocode 2, Design of concrete structures - Part 1-1: General rules and rules for buildings, 2004.

[27] Eurocode 8, Design for Structures for Earthquake Resistance – Part 1: General Rules, Seismic Actions and Rules for Buildings, 2003.

[28] SAP2000, Static and Dynamic Finite Element Analysis of Structures, release 15.0, Computers and Structures Inc., Berkeley, CA, 2011.

[29] M. Rathje, N.A. Abrahamson, J.D. Bray. Simplified frequency content estimates of earthquake ground motions. *Journal of Geotechnical and Geoenvironmental Engineering,* **124**(2), 150-159, 1998.

[30] G. Maddaloni, G. Magliulo, E. Cosenza. *Effect of the seismic input on non-linear response of R/C building structures*. Advances in Structural Engineering, **15**(10), 1861-1877, 2012.

[31] G. Magliulo, G. Maddaloni, E. Cosenza. Extension of N2 method to plan irregular buildings considering accidental eccentricity. *Soil Dynamics and Earthquake Engineering*. **43**, 69-84, 2012.

[32] N. Caterino, I. Iervolino, G. Manfredi, E. Cosenza, Multi-Criteria Decision Making for Seismic Retrofitting of RC Structure, *Journal of Earthquake Engineering*, **12**, 1-29, 2008.

[33] G. Maddaloni, N. Caterino, A. Occhiuzzi, Semi-active control of the benchmark highway bridge based on seismic early warning systems. *Bulletin of Earthquake Engineering,* **9**(5), 1703-1715, 2011.

[34] G. Maddaloni, N. Caterino, G. Nestovito, A. Occhiuzzi, Use of seismic early warning information to calibrate variable dampers for structural control of a highway bridge: evaluation of the system robustness. *Bulletin of Earthquake Engineering* (in press).

COMPDYN 2013
4th ECCOMAS Thematic Conference on
Computational Methods in Structural Dynamics and Earthquake Engineering
M. Papadrakakis, V. Papadopoulos, V. Plevris (eds.)
Kos Island, Greece, 12–14 June 2013

EXPERIMENTAL INVESTIGATION OF DYNAMIC BEHAVIOUR OF CANTILEVER RETAINING WALLS

Panos Kloukinas[1], Anna Scotto di Santolo[2], Augusto Penna[3], Subhamoy Bhattacharya[4], Matthew Dietz[4], Luiza Dihoru[4], Aldo Evangelista[2], Armando L. Simonelli[5], Colin A. Taylor[4], George Mylonakis[1,4]

[1] University of Patras
Dep. of Civil Engineering, GR-26500 Patras, GREECE
e-mail: {pkloukin, mylo}@upatras.gr

[2] University of Naples Federico II
Dep. of Hydraulics, Geotech. & Environmental Engrg, Via Claudio, 21, 82125, Naples, ITALY
e-mail: {anscotto, evangeli}@unina.it

[3] CIMA-AMRA
Via Petrile, 83054, Avellino, ITALY
e-mail: aupenna@unina.it

[4] University of Bristol
Dep. of Civil Engineering, 1-90 Queen's Building, University Walk, BS8 1TR Bristol, UK
e-mail: {s.bhattacharya, m.dietz, luiza.dihoru, colin.taylor, g.mylonakis}@bristol.ac.uk

[5] University of Sannio
Dep. of Engineering, Palazzo ex-INPS Piazza Roma, 27-1, 82100 Benevento, ITALY
e-mail: alsimone@unisannio.it

Keywords: Cantilever Retaining Walls, Earthquake Design, Dynamic Earth Pressures, Shaking Table Testing.

Abstract. *The dynamic behaviour of cantilever retaining walls under earthquake action is explored by means of 1-g shaking table testing, carried out on scaled models at the Bristol Laboratory for Advanced Dynamics Engineering (BLADE), University of Bristol, UK. The experimental program encompasses different combinations of retaining wall geometries, soil configurations and input ground motions. The response analysis of the systems at hand aimed at shedding light onto the salient features of the problem, such as: (1) the magnitude of the soil thrust and its point of application; (2) the relative sliding as opposed to rocking of the wal land the corresponding failure mode; (3) the importance/interplay between soil stiffness, wall dimensions, and excitation characteristics, as affecting the above. The results of the experimental investigations are in good agreement with the theoretical models used for the analysis and are expected to be useful for the better understanding and the optimization of earthquake design of this type of retaining structure.*

1 INTRODUCTION

Reinforced concrete cantilever retaining walls represent a popular type of retaining system. It is widely considered as advantageous over conventional gravity walls as it combines economy and ease in construction and installation. The concept is deemed particularly rational, as it exploits the stabilizing action of the soil weight over the footing slab against both sliding and overturning, thus allowing construction of walls of considerable height.

The traditional approach for the analysis of cantilever walls is based on the well-known limit equilibrium analysis, in conjunction with a conceptual vertical surface AD (Fig. 1b,c) passing through the innermost point of the wall base (vertical virtual back approach). A contradictory issue in the literature relates to the calculation of active thrust acting on the virtual wall back, under a certain mobilized obliquity ranging naturally from 0 (a perfectly smooth plane) to φ (a perfectly rough plane). Efforts have been made by different investigators to establish the proper roughness for the analysis and design or this type of structures under static loading [1, 2]. Nevertheless, the issue of seismic behaviour remains little explored. Modern Codes including Eurocode [3] and the Italian Building Code [4], do not explicitly refer to cantilever walls. The current Greek Seismic Code [5] addresses the case of cantilever retaining walls by adopting the virtual back approach in the context of a pseudo-static analysis under the assumption of gravitational Rankine conditions [6] and various geometric constraints.

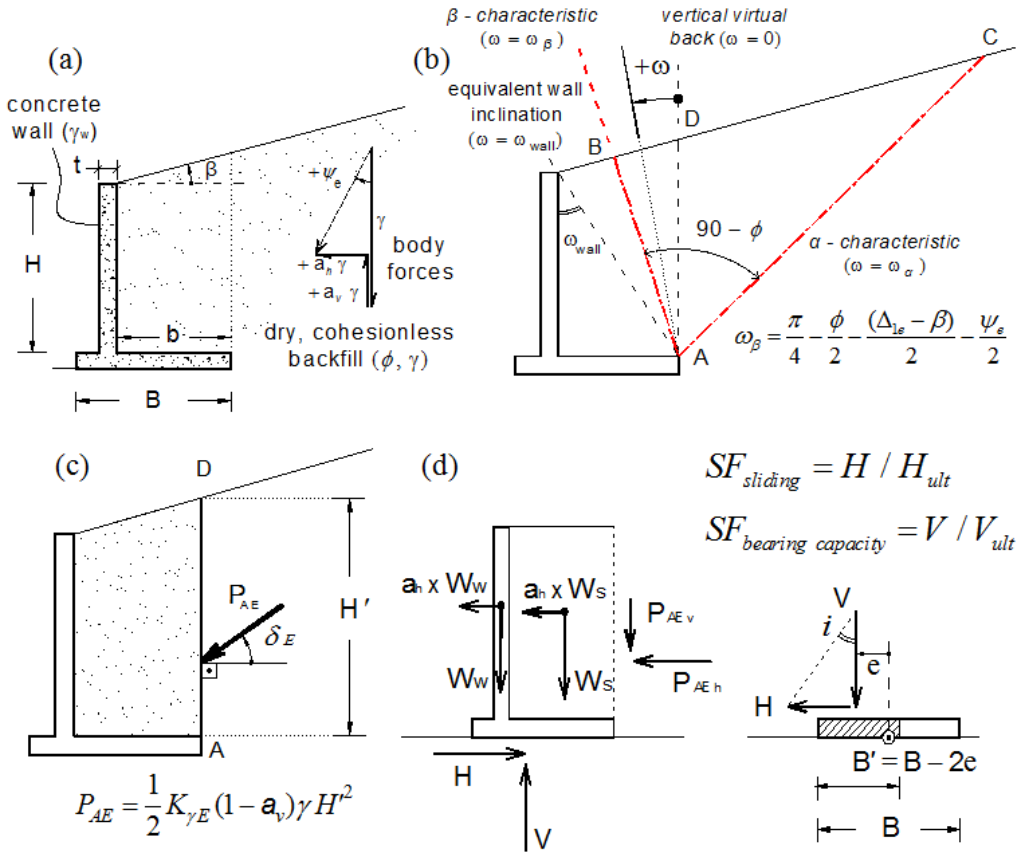


Figure 1: Pseudo-dynamic analysis of cantilever retaining walls for seismic loading: (a) Problem under consideration, (b) seismic Rankine stress field characteristics, (c) Modified virtual back approach by stress limit analysis, (d) Stability analysis of wall foundation according to Meyerhof (EC 7).

Recent theoretical findings obtained by means of stress limit analysis [1, 2, 7] for the seismic problem of Fig. 1a indicate that a uniform Rankine stress field develops in the backfill,

when the wall heel is sufficiently long and the stress characteristics do not intersect the stem of the wall ($\omega_\beta < \omega_{wall}$). Given that the stress characteristics inclination depends on acceleration, Rankine condition is valid for the vast majority of cantilever walls under strong seismic action. This is applicable even to short heel walls, with an error of about 5% [8, 9].

Following the aforementioned stress limit analysis studies, closed-form expressions are available for the pseudo-dynamic earth pressure coefficient K_{AE} and the resultant thrust inclination, δ_E (Fig.1c), given by [2]:

$$\delta_E = \tan^{-1}\left[\frac{\sin\varphi \sin\left(\Delta_{1e} - \beta + \psi_e\right)}{1 - \sin\varphi \cos\left(\Delta_{1e} - \beta + \psi_e\right)}\right] \quad (1)$$

where $\Delta_{1e} = \sin^{-1}[\sin(\beta+\psi_e)/\sin\varphi]$ and $\psi_e = \tan^{-1}[a_h/(1-a_v)]$ are the so-called Caquot angle and the inclination of the overall body force in the backfill. The same result for δ_E has been derived, in a somewhat different form, by Evangelista et al. [1]. In the case of gravitational loading ($\psi_e = 0$), the inclination δ_E equals the slope angle β, coinciding to the classical Rankine analysis. In presence of a horizontal seismic component ($\psi_e > 0$), δ_E is always greater than β, increasing with ψ_e up to the maximum value of φ, improving wall stability. The robustness of the above analysis becomes evident since under a mobilized inclination δ_E, the stress limit analysis and the Mononobe-Okabe formula results coincide. These findings have been confirmed by numerical investigations [1, 7].

A second key issue relates to the stability analysis shown in Figure 1c. Traditionally, stability control of retaining walls is based on safety factors against bearing capacity, sliding and overturning. Of these, only the first two are known to be rationally defined, whereas safety against overturning is known to be misleading, lacking a physical basis [2, 4, 10, 11]. It is important to note that the total gravitational and seismic actions on the retaining wall are resisted upon the external reactions H and V acting on the foundation slab. The combination of these actions together with the resulting eccentricity e, determines the bearing capacity of the wall foundation based on classical limit analysis procedures for a strip footing subjected to an eccentric inclined load (e.g. EC7, EC8). This suggests that the issue of wall stability is actually a footing problem and from this point of view, understanding the role of the soil mass above the foundation slab and the soil-wall interaction is of paramount importance. The above observations provided the initial motivation for the herein-reported work.

2 SHAKING TABLE EXPERIMENTAL INVESTIGATION

The dynamic behaviour of L-shaped cantilever walls was explored by means of 1-g shaking table testing. The aim of the experimental investigation is to provide a better understanding of the soil-wall dynamic interaction problem, the relationship between design parameters, stability safety factors and failure mechanisms, and the validation of the seismic Rankine theoretical model. The test series were conducted to the Bristol Laboratory for Advanced Dynamics Engineering (BLADE), University of Bristol, UK. Details on the experimental hardware, materials, configurations and procedure are provided in the ensuing.

2.1 Experimental hardware

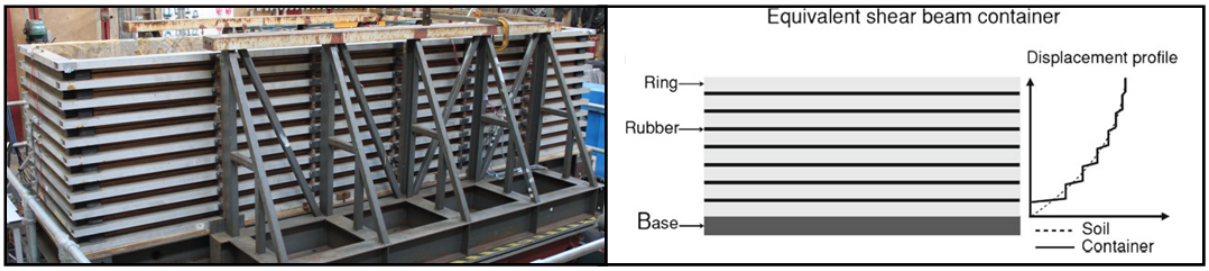
Earthquake Simulator (ES)

The 6DOF ES consists of a 3 m x 3 m cast aluminium platform weighing 3.8 tonnes, with payload capacity of 15 tonnes maximum and operating frequency range of 1-100Hz. The platform sits inside an isolated, reinforced concrete seismic block that has a mass of 300

tonnes and is attached to it by eight 70 kN servo hydraulic actuators of 0.3m stroke length. Hydraulic power for the ES is provided by a set of 6 shared variable volume hydraulic pumps providing up to *900 litres/min* at a working pressure of *205 bar,* with maximum flow capacity of around *1200 litres/min* for up to 16 seconds at times of peak demand with the addition of extra hydraulic accumulators.

Equivalent Shear Beam (ESB) Container

The apparatus, shown in Figure 2a, consists of eleven rectangular aluminium rings, which are stacked alternately with rubber sections to create a flexible box of inner dimensions 4.80m long by 1m wide and 1.15m deep [12]. The rings are constructed from aluminium box section to minimize inertia while providing sufficient constraint for the K_0 condition. The stack is secured to the shaking table by its base and shaken horizontally lengthways (in the x direction). Its floor is roughened by sand-grain adhesion to aid the transmission of shear waves; the internal end walls are similarly treated to enable complementary shear stresses. Internal side walls were lubricated with silicon grease and covered with latex membrane to ensure plane strain conditions.



(a) **(b)**

Figure 2: Equivalent shear beam container ("shear stack")

This type of containers should be ideally designed to match the shear stiffness of the soil contained in it, as depicted in Figure 2b. However, the shear stiffness of the soil varies during shaking depending on the strain level. Therefore, matching of two stiffnesses (end-wall and the soil) is possible only at a particular strain level. The "shear stack" at the University of Bristol is designed considering a level of strain in the soil close to failure (0.01–1%). Therefore, the box is much more flexible than the contained soil and, as a consequence, the soil will always dictate the overall behaviour of the container [13]. Indeed the resonant frequency and damping of the container in the first shear mode in the long direction when empty were measured prior to testing at 5.7Hz and 27% respectively, which is sufficiently different from the soil material properties.

Instrumentation

As seen in Figure 3, 21 1-D accelerometers have been used to monitor the shaking table, the shear stack and the wall-soil system, with the main area of interest laying on the wall itself and the soil mass in its vicinity, as well as the response of the free field. 4 LVDT transducers were employed to measure the dynamic response and permanent displacements of the wall and 32 strain gauges were attached on the stem and the base of the wall, on three cross sections, to monitor the bending of the wall. The signal conditioning was made via appropriate amplifier and filter modules and data acquisitions frequency was set at 1024 Hz. Additionally to the 57 data channels employed overall, a grid of colored sand was used for monitoring the settlement of the backfill surface.

2.2 Shaking table model setup

Model geometry

The dimensions of the model are illustrated in Figure 3, with the type and the positions of the instrumentation used. The model consists of an L-shaped retaining wall supporting a backfill of thickness 0.6m and length 5 times its thickness, resting on a 0.4m thick base soil layer (equal to the wall foundation width, B). The properties of the soil layers and detailed description of the instrumentation and the various wall configurations are provided in below.

The retaining wall was constructed from Aluminium 5083 plates of 32mm thickness. The width of the wall stem is 970mm. A central wall segment of 600mm width was created by two 1mm thick vertical slits penetrating 400mm down into the wall. The location of the slits were 185mm from each side of the wall stem. The base of the wall is subdivided into four 240mm-wide aluminium segments that are each secured to the wall stem using three M12 bolts. Properties of the aluminium alloy are: unit weight γ = 27 kN/m^3, Young's modulus E = 70GPa, Poisson's ratio ν = 0.3.

Soil material properties

The required soil configuration consists of a dense supporting layer and a medium dense backfill. The material proposed for both layers is Leighton Buzzard (LB) sand BS 881-131, Fraction B (D_{50} *=0.82 mm,* G_s*=2.64 Mg/m*^{3}*,* e_{min} *= 0.486,* e_{max} *= 0.78)*. This particular soil has been extensively used in experimental research at Bristol and a wide set of strength and stiffness data is available (detailed references in [13]). The empirical correlation between peak friction angle φ and relative density D_r provided by the experimental work of Cavallaro et al. [14] was used for a preliminary estimation of the soil strength properties.

The packing density for each layer was determined from sand mass and volume measurements during the deposition; corresponding predictions for peak friction angles are summarized in Table 1. The base deposit was formed by pouring sand in layers of *150-200 mm* from a deposition height of 0.6m, and then densifying it by shaking. After densification the height of the layer was reduced to 390mm. The top layer was formed by pouring sand in axisymmetric conditions close to the centre of the desired backfill region, without any further densification. The pouring was carried out by keeping the fall height steady, approximately equal to 200mm, in order to minimize the densification effect of the downward stream of sand.

Model wall configurations

Three different Configurations (#1, #2, #3) for the wall model presented in Fig. 3 were used to provide different response in sliding and rocking of the base. The characteristics of these configurations are shown in Table 2. After testing Configuration 1, the wall model was modified for Configuration 2. The wall heel was shortened by 50mm and the toe was totally removed. In Configuration 3, the geometry of Configuration 2 was retained, after increasing the frictional resistance of the base interface from 23.5^o to 28^o (approximately equal to the critical state angle), by pasting rough sandpaper. The interface friction angles were measured in-situ by means of static pull tests on the wall. The differences between these three Configurations in terms of a pseudo-dynamic stability analysis according to EC7 are summarised in Table 2, ranging from a purely sliding-sensitive wall (Configuration 1), to a purely rotationally sensitive one (Configuration 3).

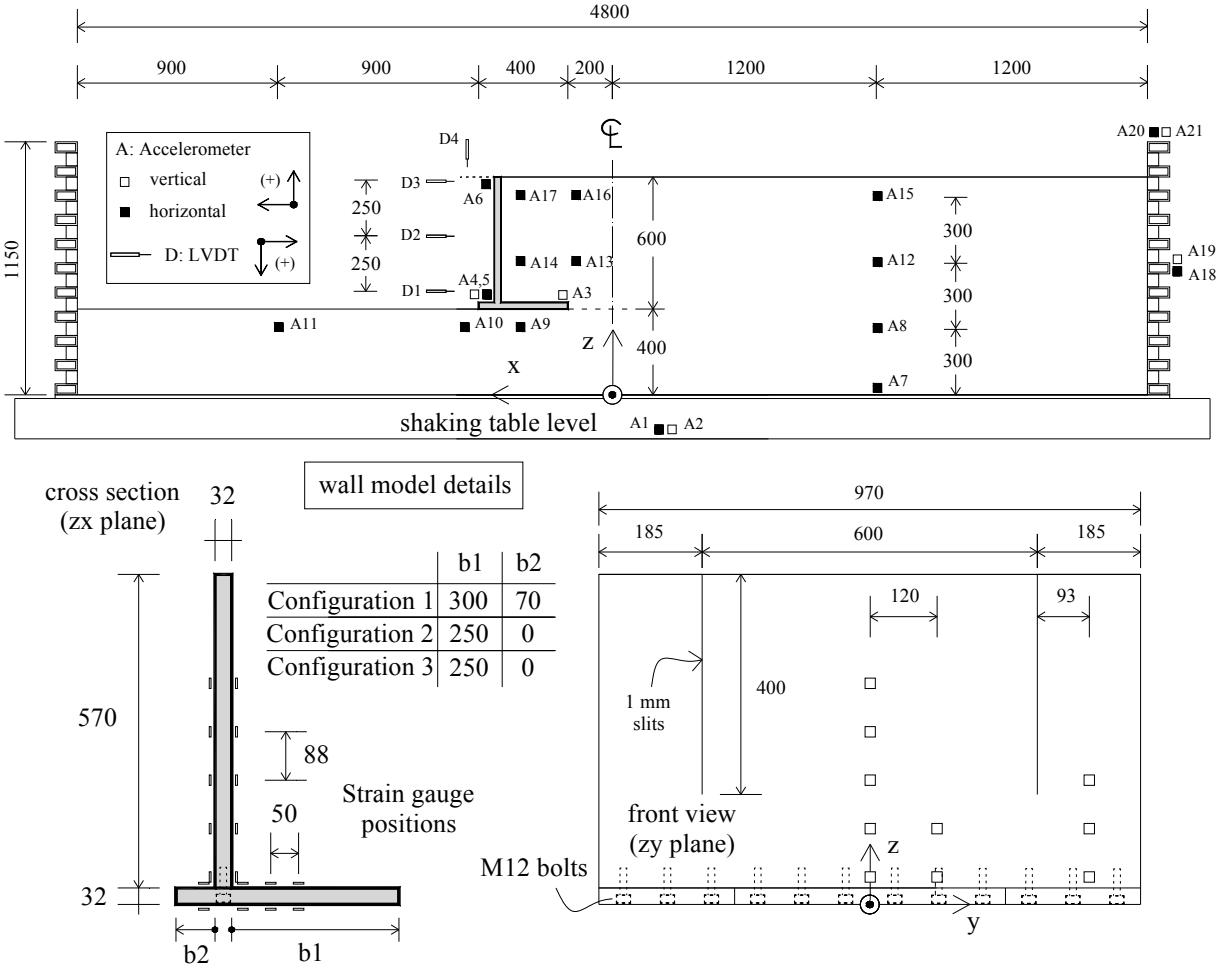


Figure 3: Illustration of geometry and instrumentation of the shaking table model (dimensions in mm)

Soil layers	Thickness (mm)	Voids ratio, e	Relative density, D_r (%)	Unit weight (kN/m^3)	Friction angle, φ(°) Cavallaro et al. (2001)
Foundation	390	0.61	60	16.14	42
Backfill	600	0.72	22	15.07	34

Table 1: Soil properties

Test configuration	Critical acceleration for $SF_{sliding} = 1$	$SF_{Bearing\ capacity}$ at critical sliding acceleration	Critical acceleration for $SF_{Bearing\ capacity} = 1$	$SF_{sliding}$ at critical bearing capacity acceleration
Configuration 1	0.18g	7.45	0.35g	0.68
Configuration 2	0.14g	1.46	0.17g	0.93
Configuration 3	0.23g	0.44	0.17g	1.14

Table 2: Pseudostatic critical accelerations and associated safety factors (SF)

2.3 Experimental procedure

Each model Configuration was tested under the same dynamic excitation, described in detail in the following paragraphs. Two different input motions, harmonic and earthquake, were used in the form of sequential, increasing amplitude time histories. The dynamic properties of the soil layers and the soil-wall interactive system were investigated by means of the white noise exploratory procedure described below. This kind of testing was repeated after every severe yielding of the system to track for significant chances in the dynamic properties.

White noise excitation

During white noise exploratory testing, a random noise signal of bandwidth *1-100 Hz* and *RMS* acceleration = 0.005g was employed. During each exploratory series test, and simultaneous data acquisition, system transmissibility was monitored using a two-channel spectrum analyser. The analyser computes the frequency response function (FRF) between the input and the output signals of interest. Natural frequency and damping values for any resonances up to 40Hz (i.e. within the seismic frequency range) were determined for well-defined resonances using the output of the analyser's curve fitting algorithm by means of a least-squares error technique. Additionally, transfer functions can be determined between any pair of data channels to get a clear view of the system dynamics.

Harmonic excitation

This type of input acceleration was imposed by sinusoidal excitation consisting of 15 steady cycles. To smoothen out the transition between transient and steady-state response, the excitation comprises of a 5-cycle ramp up to full test level at the beginning of the excitation, and a 5-cycle ramp down to zero at the end. With reference to frequency and acceleration level, a set of 5 frequencies (4, 7, 13, 25 and 43 Hz) was used at low acceleration amplitude of 0.05g, to study the dynamic response of the system. The excitation frequency of 7Hz was then selected for a series of harmonic excitations with increasing amplitude, until failure. The conditions of the excitation are considered to be essentially pseudostatic, as the above frequency is much smaller than the resonant frequencies of the system, with respect to both the free field and the soil-wall system.

Earthquake excitation

Three earthquake records from the Italian and American database were selected for the earthquake testing. Specifically, the Tolmezzo record from the Friuli, 1976 earthquake, the Sturno record from Irpinia, 1980 and the Northridge record from Los Angeles, 1994. The authentic signals were scaled by a frequency scale factor of 5, derived from the scaling law $n^{0.75}$, which is valid for 1-g modelling [15], assuming a geometrical scale factor n = 9, corresponding to a prototype of 5.4m high. The frequency-scaled signals were applied at low acceleration amplitude of 0.05g to measure the dynamic response of the model and then the Sturno record was selected for carrying out increasing amplitude dynamic testing, until failure in sliding or rocking of the retaining wall.

3 EXPERIMENTAL RESULTS AND DISCUSSION

Some characteristic experimental measurements are presented in Figures 4 to 8, relative to failure mechanisms, accelerations, dynamic and permanent displacements and bending moments, organized in sets of graphs suitable for direct comparisons. Most of the results presented herein mainly relate to Configurations 1 and 3, for they exhibit yielding near similar acceleration conditions but in different modes. Limited results are presented for Configuration 2, which is significantly weaker compared to the others, failing almost simultaneously in

foundation sliding and rotation (i.e., bearing capacity) mode, thus is less important for comparison reasons.

In Figure 4, measured settlement profiles at the state of failure are plotted together with the assumed failure mechanisms for Configurations 2 and 3. The following are worthy of note: *First,* these failure mechanisms were observed only for transient earthquake loading, whereas in the case of harmonic excitation, the settlement profile could not clearly reveal the emergence of the main failure planes, as it had more-or-less a smooth parabolic shape. This can be explained in view of a non-uniform settlement and deformation mechanism and stronger dynamic effects imposed by earthquake loading. Although there is actually not a "rigid block" response in the retained soil mass, the experimental findings show that the earthquake excitation induces a more uniform acceleration distribution within the retained soil material, which corresponds to a more uniform stress field, as assumed in the pseudo-static analyses. *Second,* the assumed failure mechanisms confirm the estimations based on the material properties, the stability analysis and the yield accelerations presented in Tables 1 and 2 respectively.

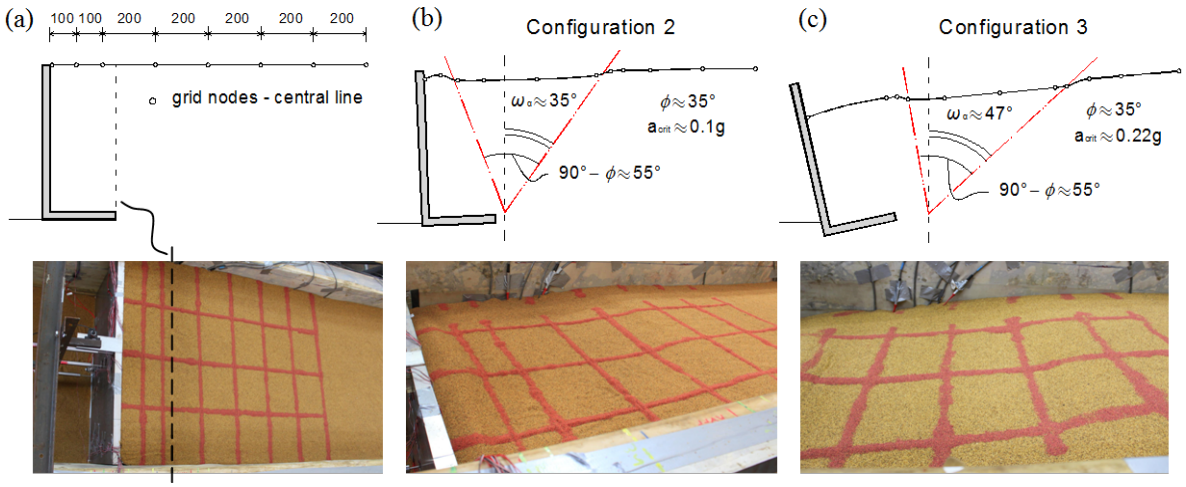


Figure 4: Backfill surface settlement distribution at failure: (a) initial grid geometry - dimensions in mm, (b),(c) settlement distributions for Configurations 2 and 3, respectively.

The measurements of system displacement for all tested configurations are summarized in Figure 5. The total, cumulative settlement and rotation of the wall, for each series of sequential input motions are presented in Figures 5a and 5b, and the incremental displacements for each input motion are presented in Figures 5c-5e, indicating different behaviour of the wall models under the same input. The measurements confirm the predictions for the expected failure modes and the levels of critical acceleration. The sliding failure is clearly visible in Configuration 1, as is the bearing capacity failure in Configuration 3. Configuration 2 although designed to be weaker in sliding, also exhibits significant rotational deformations caused by the high eccentricities induced by the seismic thrust. Rotational deformations are also observed in Configuration 1 for high acceleration levels, revealing that walls resting on a compliant base exhibits local bearing capacity failure near the toe, due to high compressive stress concentration. This observation elucidates the importance of properly designing retaining structures to avoid development of significant rotational response.

Results from Configurations 1 and 3 under harmonic excitation are plotted together in Figure 6. The following can be observed: *First* the response of each Configuration is as

expected. A translational response mode is evident in Configuration 1 and a rocking one in Configuration 3, respectively. Sliding discontinuities are obvious on the acceleration time histories of Configuration 1 (Fig 6a), at a critical acceleration slightly higher than that of Table 2. Note that the translational yield acceleration is not steady, but always increases after every successive yielding, as even a small rotation causes penetration of the wall toe into the foundation soil thus increasing passive resistance. On the other hand, Configuration 3 starts rotating at initiation of yielding, without any evidence of sliding discontinuities on the recorded accelerogram. *Second*, in both cases the wall stem appears to have an amplified response, mainly because of foundation rocking and secondarily of pure bending of the stem. Naturally, this is more evident in Configuration 3. *Third*, both models exhibit a consistent, repeatable, behaviour with respect to yielding.

The same results for earthquake loading on Configurations 1 and 3 are presented in Figure 7. In this case, the input motion contains higher effective peak accelerations, but the number of important strong cycles (half cycle pulses) is only three. A sliding failure pattern is, again, clearly visible in Configuration 1. Likewise, a bearing capacity failure in Configuration 3 is apparent, due to high eccentricities induced by seismic thrust. An important notice about the failure modes arising from the combination of the two comparisons is that the bearing capacity failure is more affected by the input acceleration level, whereas the behaviour of pure sliding mechanisms is mainly controlled by the time interval of the strong motion, as established from sliding block theory. Accordingly, rotational mechanisms appear to be more critical under strong earthquakes, even though they are strong enough against sliding (Fig 6d and Fig 7d). Moreover, some rotational deformation is also observed in Configuration 1 for high acceleration level, revealing that any wall resting on a compliant base exhibits local bearing capacity failure near the toe, due to concentration of high compressive stresses. This observation elucidates the importance of properly designing retaining structures to avoid development of significant rotational response.

From the acceleration distributions of Figs 6c and 7c, it is evident that the earthquake loading results to conditions which are closer to the assumptions of pseudostatic analysis, as a soil mass moving together with the wall is evident, especially for the rotational mode of Configuration 3. Contrary to earthquake excitation, under harmonic loading wall and soil appear to respond in a quite different way.

Peak seismic increments of bending moments are compared in Figs 6e and 7e. A noteworthy observation is that the earth pressure on the wall increases when the system moves towards the backfill, that is for an acceleration not critical for overall stability. On the other hand, at yielding acceleration of the system, earth pressure on the stem is minimum. This is in agreement with the findings of other recent experimental and numerical studies [16, 17]. Comparing Configurations 1 and 3, it can be clearly identified that rotational modes induce lower earth pressure on the wall, but different distribution leading to a higher point of application of the thrust.

Finally, the response of Configuration 2 to harmonic and earthquake excitation with PGA = 0.17g presented in Fig. 8, exhibits a similar behaviour to both Configurations 1 and 3, resulting to simultaneous sliding and rotational failure. As seen from both the acceleration time histories (Fig. 8a) and the failure mechanisms (Fig. 8b) the sliding failure mode prevails, which is consistent to the critical accelerations estimated in Table 2.

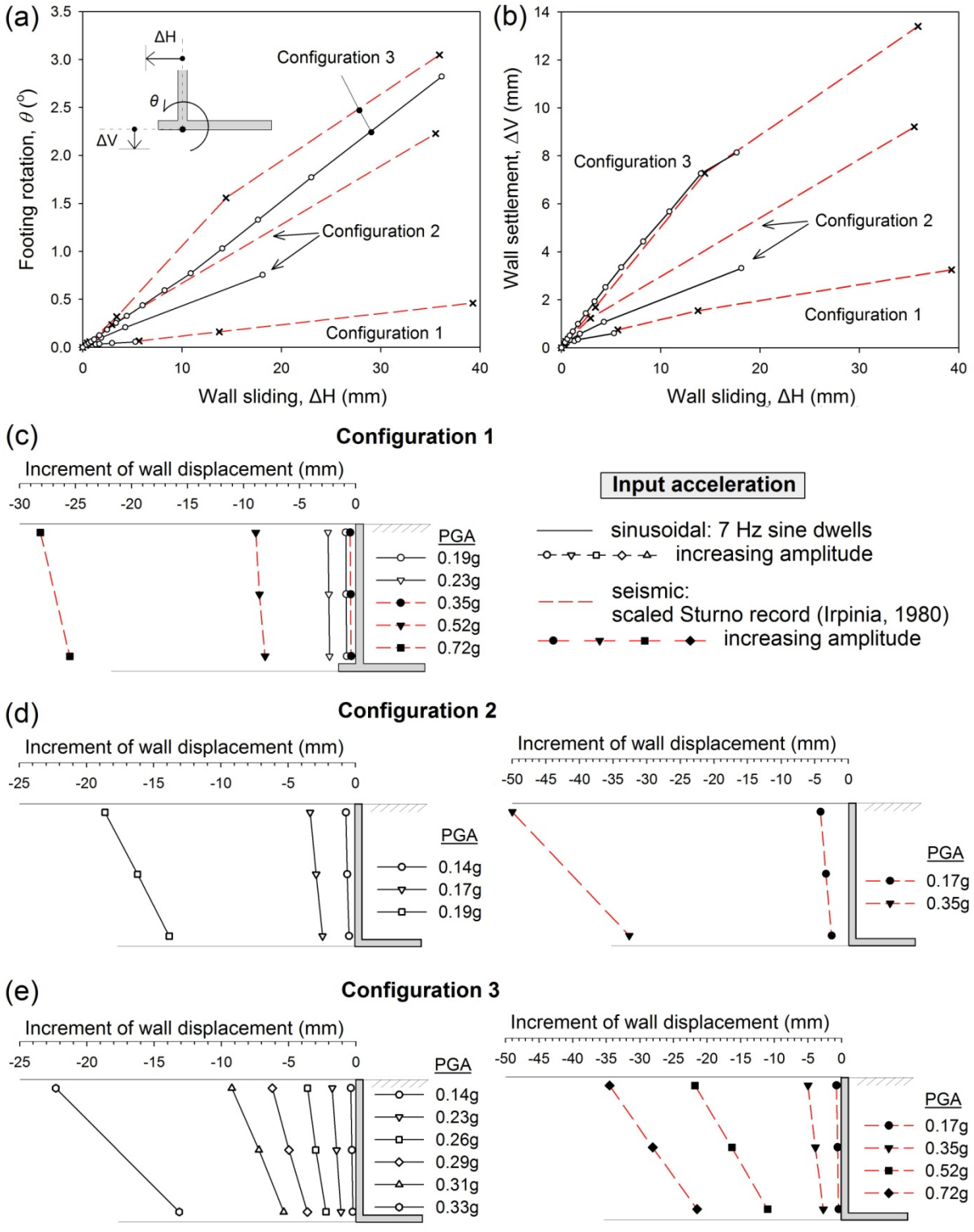


Figure 5: Measurements of wall displacement and rotation for all configurations and various base excitations. (a) Cumulative footing rotation versus sliding (LVDT-D1), (b) Cumulative footing settlement (LVDT-D4) versus sliding, (c), (d) and (e) Incremental wall displacement (LVDTs D1-D2-D3) for configurations 1, 2 and 3, respectively

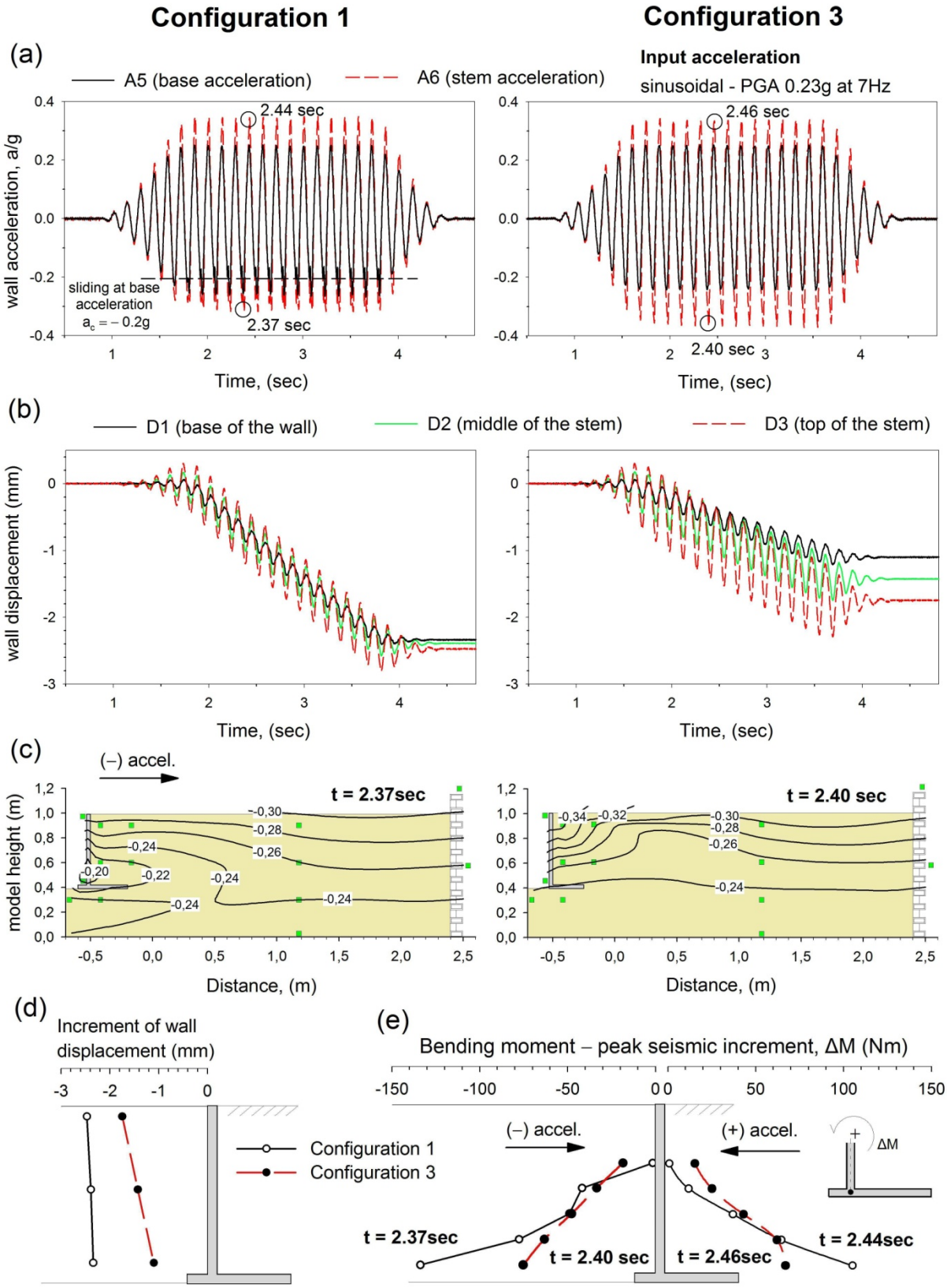


Figure 6: Comparison of typical experimental results for Configurations 1 and 3 under harmonic-sinusoidal excitation: (a) measured wall accelerations, (b) corresponding wall displacements, (c) negative acceleration distribution (maximum inertial forces towards the wall), (d) increment of wall displacement (LVDTs D1-D2-D3) and (e) peak seismic increment of bending moment for positive and negative acceleration.

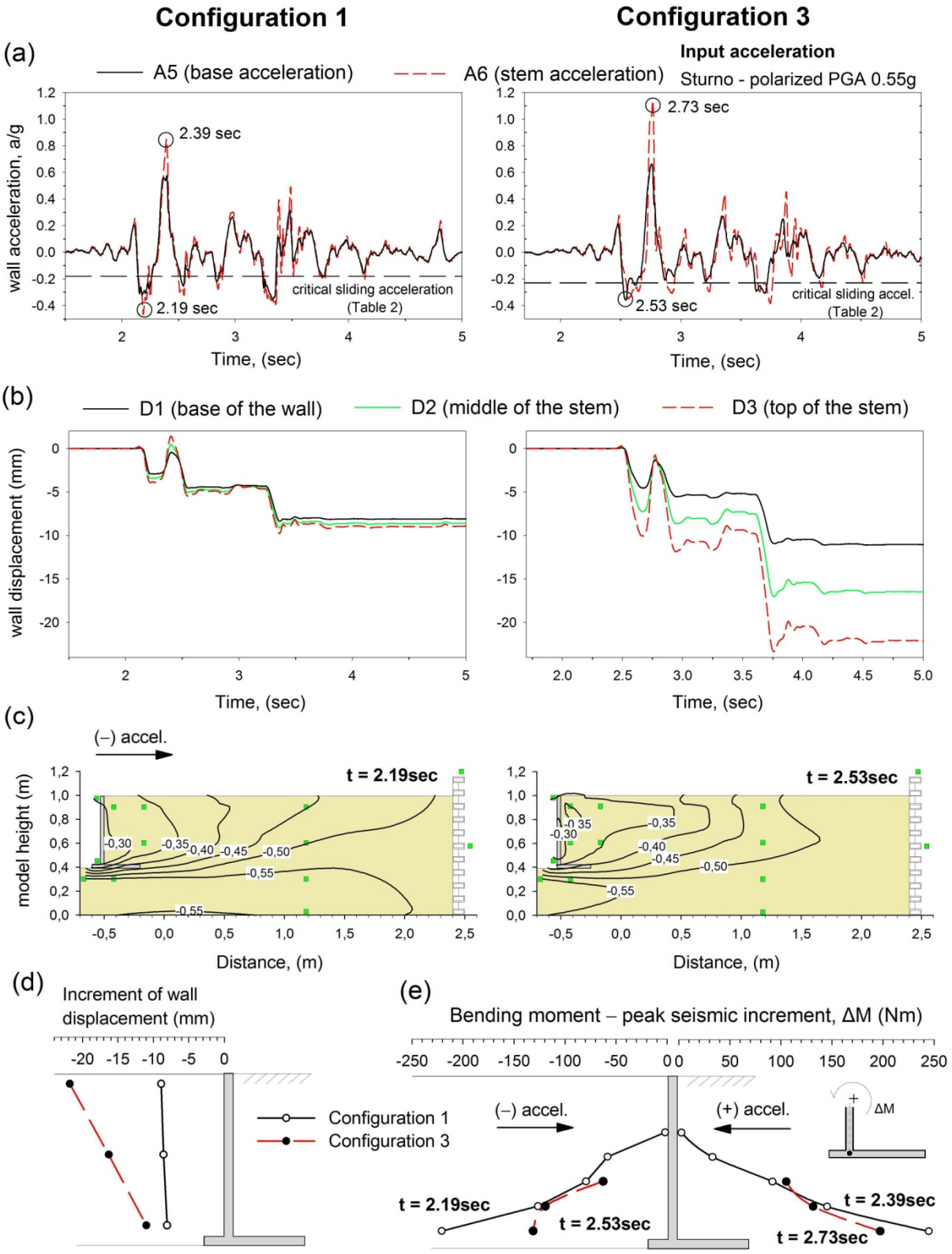


Figure 7: Comparison of typical experimental results for Configurations 1 and 3 under seismic excitation: (a) measured wall accelerations, (b) corresponding wall displacements, (c) negative acceleration distribution (maximum inertial forces towards the wall), (d) increment of wall displacement (LVDTs D1-D2-D3) and (e) peak seismic increment of bending moment for positive and negative acceleration.

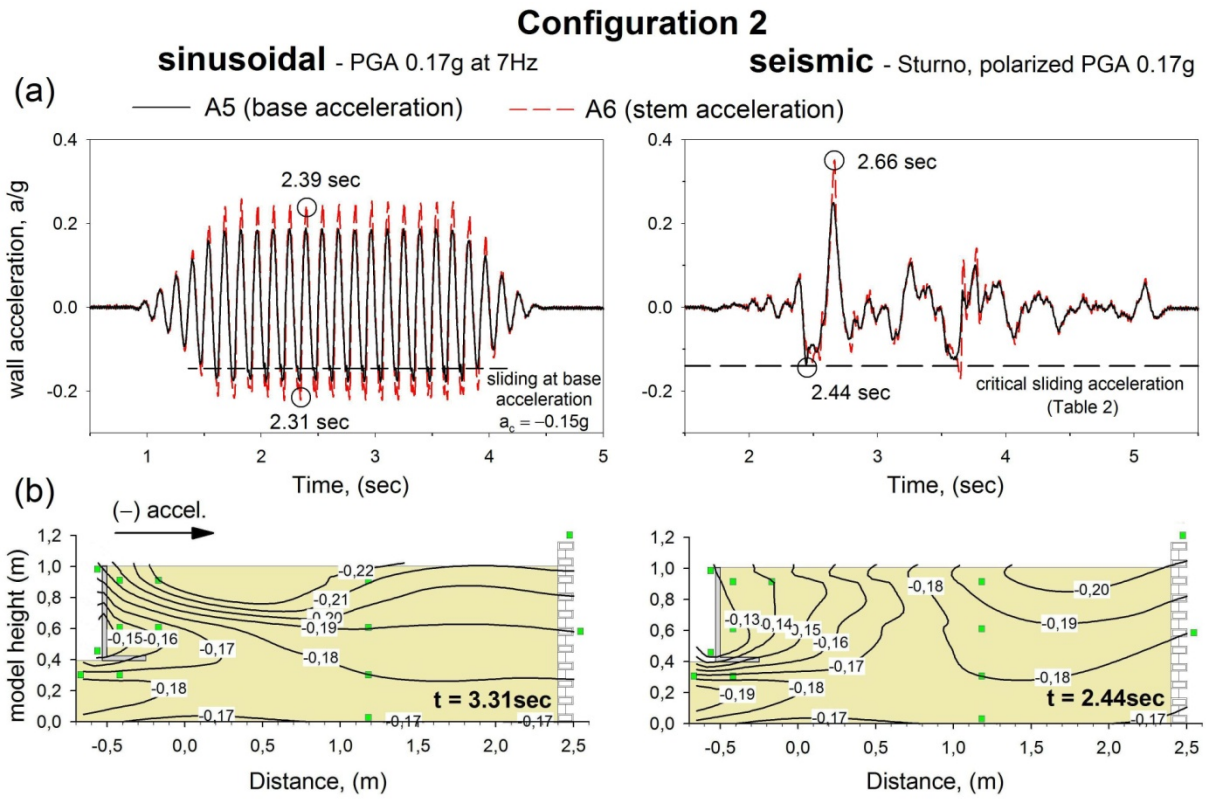


Figure 8: Typical experimental results for Configuration 2: (a) measured wall accelerations for harmonic sinusoidal and seismic excitation, (b) negative acceleration distribution (maximum inertial forces towards the wall)

4 CONCLUSIONS

A series of shaking table tests on scaled models of cantilever retaining walls were conducted in BLADE laboratory at University of Bristol. The initial motivation of this experimental study was the validation of recent stress limit analysis solutions for the seismic design of this type of retaining structures [1, 2] in conjunction with the absence of any specific, relative regulations in established seismic codes, including the EC-8. Special issues related to stability design and response of walls founded on a compliant base were also addressed. Preliminary interpretation of the experimental findings confirms the predictions of the theoretical analysis with reference to the failure mechanisms and the critical yield accelerations of the system. Pseudo-static stability analysis proves to behave adequately for both harmonic and seismic excitation, although important dynamic effects are evident in the first case, dealing with the response of the backfill and the wall stem. On the other hand, earthquake loading results to conditions which are closer to the assumptions of the pseudo-static analysis, namely the uniform distribution of the acceleration and the "rigid block" response of the backfill. Finally, the responses of the various wall configurations confirm the "equivalent footing" interpretation of wall stability and highlight the importance of a proper design of walls founded on compliant base against sliding and rocking.

ACKNOWLEDGEMENT

The research leading to these results has received funding from the European Union Seventh Framework Programme (FP7/2007-2013) under grant agreement n° 227887, SERIES.

REFERENCES

[1] Evangelista A., Scotto di Santolo A., Simonelli A.L., Evaluation of pseudostatic active earth pressure coefficient of cantilever retaining walls. *Soil Dynamics & Earthquake Engineering*, **30:11**, 1119-1128, 2010

[2] Kloukinas, P. and Mylonakis, G., Rankine Solution for seismic earth pressures on L-shaped retaining walls. *5 ICEGE*, Santiago, Chile, January 10-13, 2011

[3] Eurocode 8, *Design provisions for earthquake resistance of structures, Part 5*. CEN E.C. for Standardization, Bruxelles, 2003

[4] NTC, *Italian Building Code*. DM 14 Jan., G.U. n. 29, 4 Feb., n. 30, 2008

[5] EAK 2000, *Greek Seismic Code*. Earthquake Planning and Protection Organization, Athens, 2003

[6] Rankine, W.J.M, On the stability of loose earth. *Phil. Trans. of the Royal Soc. of London*, **147,** 9 – 27, 1857

[7] Evangelista A., Scotto di Santolo A., Dynamic active earth pressure on cantilever retaining walls. *Computers and Geotechnics*, **38:8**, 1041-1051, 2011

[8] Huntington W, *Earth pressures and retaining walls*. New York: John Wiley, 1957

[9] Greco VR., Active earth thrust on cantilever walls with short heel. *Canadian Geotechnical Journal*, **38:2**, 401–409, 2001

[10] Greco, V.R., Stability of Retaining Walls Against Overturning. *Journal of Geotechnical & Geoenviromental Engineering*, ASCE, **123:8**, 778 – 780, 1997

[11] Eurocode 7, *Geotechnical Design.* CEN, E.C. for Standardization, Bruxelles, 2003

[12] Crewe AJ, Lings ML, Taylor CA, Yeung AK, Andrighetto R, *Development of a large flexible shear stack for testing dry sand and simple direct foundations on a shaking table*. In: Elnashai (ed) European seismic design practice, Balkema, Rotterdam, 1995

[13] Bhattacharya S., Lombardi D., Dihoru L., Dietz M. S., Crewe A.J., and Taylor. C.A, *Chapter 8: Model Container Design for Soil-Structure Interaction Studies*", in M.N. Fardis and Z.T. Rakicevic (eds.) Role of Seismic Testing Facilities in Performance-Based Earthquake Engineering SERIES Workshop, Geotechnical, Geological and Earthquake Engineering 22, Springer Science+Business Media B.V, 2012

[14] Cavallaro A, Maugeri M, Mazzarella R., Static and dynamic properties of Leighton Buzzard sand from laboratory tests. *Proc. of 4th int. conf. on recent adv. in geotech. earthquake engrg. and soil dyn. and symposium in honour of Prof. WD Liam Finn*, San Diego, California, March 26–31, 2001

[15] Muir Wood D., Crewe A. & Taylor C.A., Shaking Table Testing of Geotechnical Models. *International Journal of Physical Modelling in Geotechnics*, **2**, 01-13, 2002

[16] Green R.A and Olgun CG., Response and Modeling of Cantilever Retaining Walls Subjected to Seismic Motions. *Computer-Aided Civil and Infrastructure Engineering* **23:4**, 309–322, 2008

[17] Al Atik L., Sitar N., Seismic Earth Pressures on Cantilever Retaining Structures, *Journal of Geotechnical and Geoenvironmental Engineering*, ASCE, **136:10**, 1324-1333, 2010

COMPDYN 2013
4th ECCOMAS Thematic Conference on
Computational Methods in Structural Dynamics and Earthquake Engineering
M. Papadrakakis, V. Papadopoulos, V. Plevris (eds.)
Kos Island, Greece, 12–14 June 2013

SEISMIC PILE-SOIL INTERACTION: EXPERIMENTAL RESULTS VS. NUMERICAL SIMULATIONS

Maria Giovanna Durante [1], Luigi Di Sarno [1], Stefania Sica [1], George Mylonakis [2], Colin A. Taylor [3], Armando L. Simonelli [1]

[1] University of Sannio
Dept. of Engineering, Palazzo ex-INPS Piazza Roma, 27-1, 82100 Benevento, ITALY
e-mail: {mgdurante, ldisarno, stefsica, alsimone}@unisannio.it

[2] University of Patras
Dept. of Civil Engineering, GR-26500 Patras, GREECE
e-mail: mylo@upatras.gr

[3] University of Bristol
Dept. of Civil Engineering, 1-90 Queen's Building, University Walk, BS8 1TR Bristol, UK
e-mail: colin.taylor@bristol.ac.uk

Keywords: Pile-soil interactions, piles, seismic response, period elongation.

Abstract. *The present analytical work discusses the outcomes of a series of 1-g shaking table experimental tests that were carried out to validate numerical models formulated for kinematic and inertial interaction effects on pile-supported systems. Towards this aim, pile models in layered sand deposits were built in the laboratory; such models were subjected to several cyclic tests and an ensemble of earthquake loading. The piles were densely instrumented with accelerometers and strain gauges; therefore, earthquake response, including bending strains along their length, could be measured directly. Different configurations were considered for the shake-table tests; the latter configurations include free-head piles and single-degree-of-freedom (SDOF) systems with short and long caps at foundation level. The experimental data have been assessed accurately to estimate the period elongation of the SDOF structures, if any. Additionally, comparisons between the soil free-field response derived experimentally and advanced numerical simulations are also included. The results of the analyses show that the period elongations of the SDOF structure caused by pile-soil-interactions may be significant, thus affecting the evaluation of structural response under earthquake loading. Implications on the assessment of existing structures and the design of new ones are discussed.*

1 INTRODUCTION

Assessing the seismic behaviour of piled foundations is not an easy task, especially in presence of a superstructure. Soil-structure interaction (SSI) for piled foundations may cause: (i) a variation between the free-field ground motion and the corresponding motion at the base of the superstructure, (ii) kinematic bending, axial and shear stresses along the piles even in the absence of a superstructure. The kinematic bending moments may be particularly significant for piles embedded in soft soils closed to the pile head in presence of a rigid cap or in the vicinity of interfaces between layers having high stiffness contrasts.

The present work is aimed at shedding light into different aspects of soil-pile-structure interaction. To this end, it discusses and simulates the results of a series of high-quality shaking table tests on model piles. The experimental test program was performed at the Bristol Laboratory for Advanced Dynamics Engineering (BLADE), within the framework of the Seismic Engineering Research Infrastructures for European Synergies (SERIES). Tests were carried out on different pile group configurations, with and without pile caps and superstructures, subjected to both lateral and vertical earthquake shaking. Single-degree-of-freedom (SDOF) systems were considered to simulate the response of either buildings or bridge piers on piled foundations. The loading conditions include different input motions such as white noise, sine dwells and recorded earthquakes. The tests aimed at investigating various aspects of seismic Soil-Pile-Structure-Interaction (SPSI), including the natural frequency (in both horizontal and vertical direction) of the system, the natural frequency and damping of embedded piles, the horizontal and vertical soil-pile kinematic interaction and foundation-structure interaction. The experimental data have been analyzed accurately to estimate the period elongation of the superstructure, if any. Additionally, comparisons between measured and simulated free-field soil response are included. It is found that the period elongations caused by pile-soil-interactions may be significant thus affecting the evaluation of the structural response of SDOF under earthquake excitation.

The earthquake response of pile groups was investigated through 1-g shaking table tests. Such laboratory tests were aimed at assessing the effects of both kinematic and inertial effects on the piles. The test campaign consisted of two series of tests: preliminary tests, carried out in November 2010, and a more comprehensive series of tests, including earthquake loading, carried out in June 2011. The 6-degree-of-freedom earthquake simulator of BLADE and the equivalent shear beam (ESB) laminar container were utilized to this end [1 - 2]. The ESB consists of 8 rectangular aluminium rings, which are stacked alternately with rubber sections to create a hollow yet flexible box of inner dimensions 1.190 m long by 0.550 m wide and 0.814 m deep [3].

The sample test model consists of five piles embedded in a bi-layer soil (Figure 1a). The piles consist of an alloy aluminium tube (commercial model 6063-T6) and the superstructure is modeled using different masses and two types of columns (aluminum, steel); the principal characteristics of these elements are listed in Table 1.

Accelerometers were used to monitor the accelerations of the shaking table, the shear stack, the soil along a vertical array, the pile heads and the superstructure. The LVDT transducers were employed to monitor the displacements of the pile in the horizontal and vertical direction. To evaluate the bending response along the piles, 8 strain gauge pairs have been attached on the shafts of piles 4 and 5; additionally, 4 strain gauges are placed on the shaft of pile 1 close to the layer interface. 63 data channels were used in total.

A two-layer soil profile was deposited by pluviation. The top layer is made of Leighton Buzzard sand (LB) fraction E, the bottom layer is a mix of LB fractions B and E (85% and 15%, respectively) The LB sand adopted in the tests has been extensively used in the experi-

mental research activity carried out in BLADE. Material data can be found in previous experimental studies [4 -8].

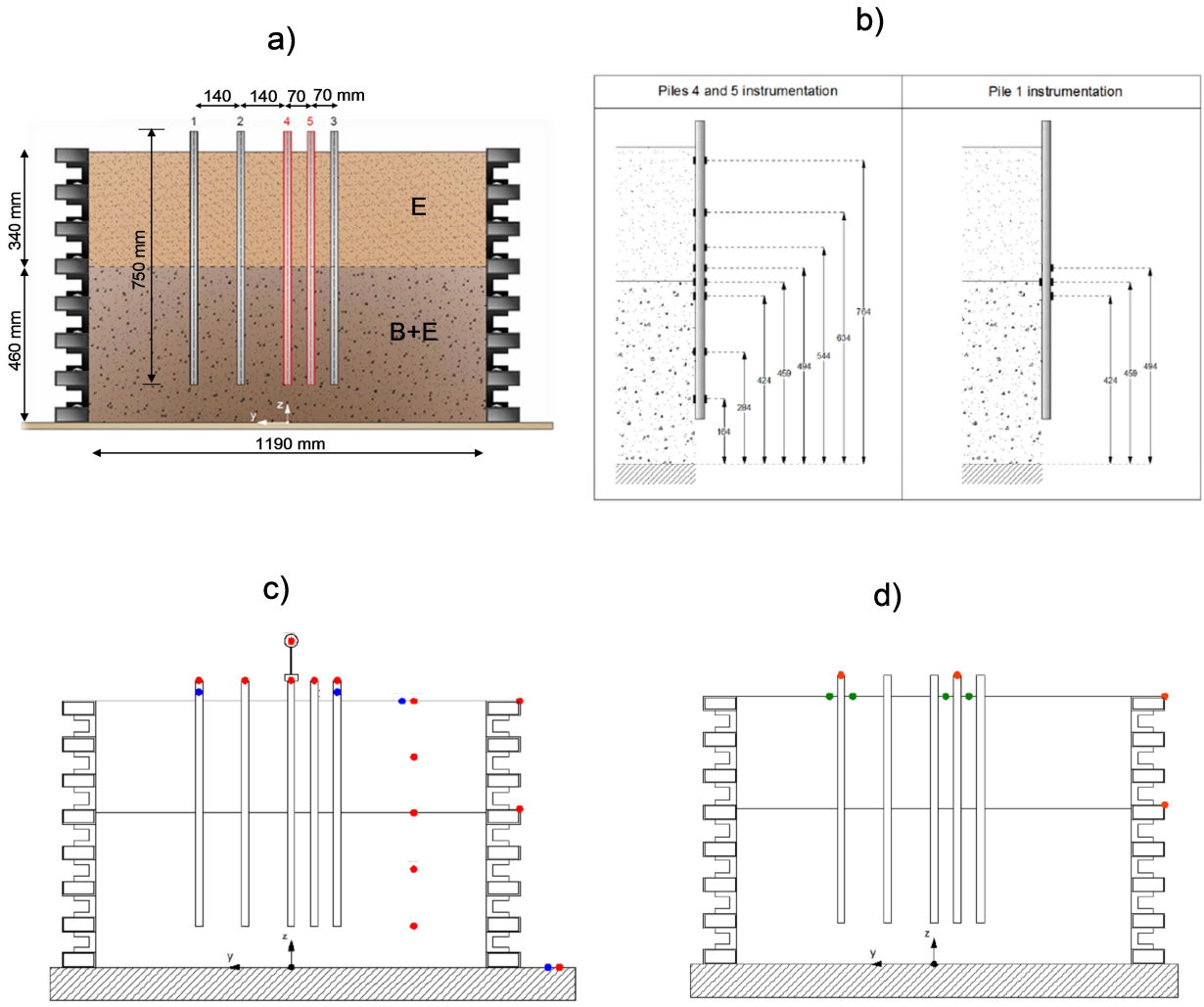


Figure 1. Model setup: (a) subsoil configuration, (b) strain gauge, (c) accelerometer and (d) LVDT location

Element [type]	Geometrical details [mm]	*Unit weight* [kN/m^3]	*Length [mm]*	Young's modulus E [GPa]
Pile	D_e = 22.23 t = 0.71	27	750	70
Aluminum column	Cross section 3x12	27	130 (phase I) 50 -100 (phase II)	70
Steel column	Cross section 3x12	80	100 (phase II)	21

Table 1. Characteristics of piles and columns

Table 2 outlines the sand index properties obtained from different previous studies, while Table 3 presents physical and mechanical properties of the two soil layers as evaluated from the present sample tests.

Materials	Type	G_s [Mg/m^3]	e_{min}	e_{max}	D_{10}	D_{50}	References
LB - fraction E	Sand BS 881-131	2.647	0.613	1.014	0.095	0.14	Tan (1990)
LB - fraction B	Sand BS 881-132	2.647	0.486	0.78		0.82	Ling & Dietz (2004)
LB - fraction E+B		2.647	0.289	0.614			Moccia (2009)

Table 2. LB sand index properties

The shear wave velocity, V_s, was derived from white noise tests carried out before corresponding sine dwell and earthquake tests for each stage of the experimental activity. As can be observed from Table 3, the shear wave velocity contrasts between the bottom and top layer are similar for the two stages of tests; the contrast is about 1.6.

Soil layers	Thickness H (mm)	Void ratio e	Relative density Dr (%)		Dry unit weight γ_d (kN/m^3)		Shear wave velocity Vs (m/s)		Vs_2/Vs_1	
			Nov 2010	June 2011	Nov 2010	June 2011	Nov 2010	June 2011	Nov 2010	June 2011
Top LB(E)	340	0.9	28	10	13.63	13.13	51	54	1.59	1.57
Bottom LB(E+B)	460	0.48	41	50	17.46	17.92	81	85		

Table 3. Soil layer properties

The testing procedure utilized during the experimental campaign includes both cyclic motions and earthquake records; the input motions are summarized as follows:

- White noise excitation: random noise signal of bandwidth 1-100 Hz and peak ground acceleration varying between 0.01 g and 0.10 g.
- Harmonic excitation: sine dwell acceleration time-histories with amplitudes varying between 0.01g÷0.18g and frequencies varying from 5 to 45 Hz.
- Earthquake excitation: three earthquake records from the Italian database: Tolmezzo (Friuli 1976), Sturno (Irpinia 1980) and Norcia (Umbria-Marche 1997). The earthquake motions were modified by a frequency scaling factor of 5 or 12; acceleration amplitude was varied between 0.043g to 0.577g.

The characteristics of all configurations tested and the number of the tests in the two phases of the experimental tests are summarized in Tables 4 and 5, which refer to Phase I and Phase II, respectively. More than 600 tests were carried out during the two phases; these include 366 tests in Phase I and 248 tests in Phase II. White and sinedwell inputs were considered for the first set of preliminary tests, as also shown in Table 4.

	Free Head Pile (FHP)	Short Cap (SC)	Short Cap + Single Degree of Freedom on pile 5 (SC+SDOF pile 5)	Free Head Pile + Single Degree of Freedom on pile 5 (FHP+SDOF pile 5)	Free Head Pile + Single Degree of Freedom on pile 4 (FHP+SDOF pile 4)
White Noise	4	3	15	12	11
Sinedwell	21	15	75	90	90

Table 4. Details tests Phase I (total tests: 366)

A comprehensive set of input motions, including vertical white noise, vertical sinedwell, earthquake records, snapback and pullover tests were considered for the Phase II (see Table 5).

	Free Head Pile (FHP)	Short Cap (SC)	Short Cap + Single Degree of Freedom on pile 5 (SC+SDOF pile 5)	Free Head Pile + Single Degree of Freedom on pile 5 (FHP+SDOF pile 5)	Free Head Pile + Single Degree of Freedom on pile 4 (FHP+SDOF pile 4)	Free Head Pile + Single Degree of Freedom on pile 1 (FHP+SDOF pile 1)	Long Cap (LC)
White Noise	8	1	9	2	3	3	2
Sinedwell	45	1	58	6	26	6	24
Vertical White Noise	2	-	-	-	-	-	-
Vertical Sinedwell	26	-	-	-	-	-	-
Earthquake	5	-	9	5	-	-	-
Snapback	1	-	-	5	-	-	-
Pullover	1	-	-	-	-	-	-

Table 5. Details tests Phase II (total tests: 248)

2 TEST RESULTS

The outcomes of typical tests of the comprehensive laboratory experimental program carried out on the BLADE shaking table are discussed hereafter, with the specific aim of investigating some particular aspects of seismic SPSI.

2.1 Effect of PGA on free-field response

The results reported herein refer to test configuration FHP. Results for sinedwell input motion with frequency of 30 Hz and increasing levels of peak ground acceleration (PGA) applied on the shaking table are reported: 5 tests from PGA=0.008g to 0.069g for the first stage of tests; 6 tests from PGA= 0.016g to 0.105g for the second stage of tests.

In Figure 2 the peak acceleration profiles in the soil (quoted as a_{max}) for the two phases are plotted: as expected, free-field response increases with acceleration level. The overall comparison in Figure 2 shows that the profiles of a_{max} exhibit quite similar shapes for both phases of tests. As regards the amount of amplification, it is believed that the effect of loading history on soil properties plays a key role and should be accounted for in a realistic manner in nonlinear numerical simulations.

Figures 3 and 4 compare experimental data with results of numerical simulations, the latter obtained by linear EERA analyses. Such analyses were carried out by assuming the values of mechanical parameters at low strain level. It is observed that for low values of accelerations (Figures 3a and 4a) there is a close match between the numerical and experimental test results. However, as nonlinearity increases (Figures 3b and 4b) test results tend to diverge from the outcomes of numerical simulations.

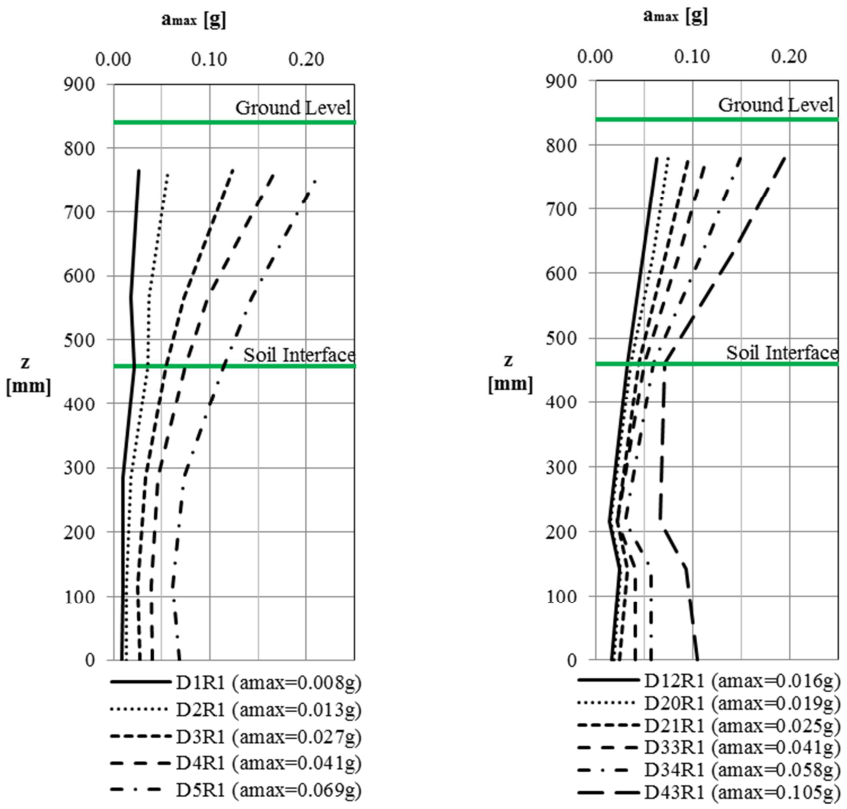


Figure 2. Peak acceleration vs. depth (z) for different amplitudes of input acceleration for Phase I (left) and Phase II (right)

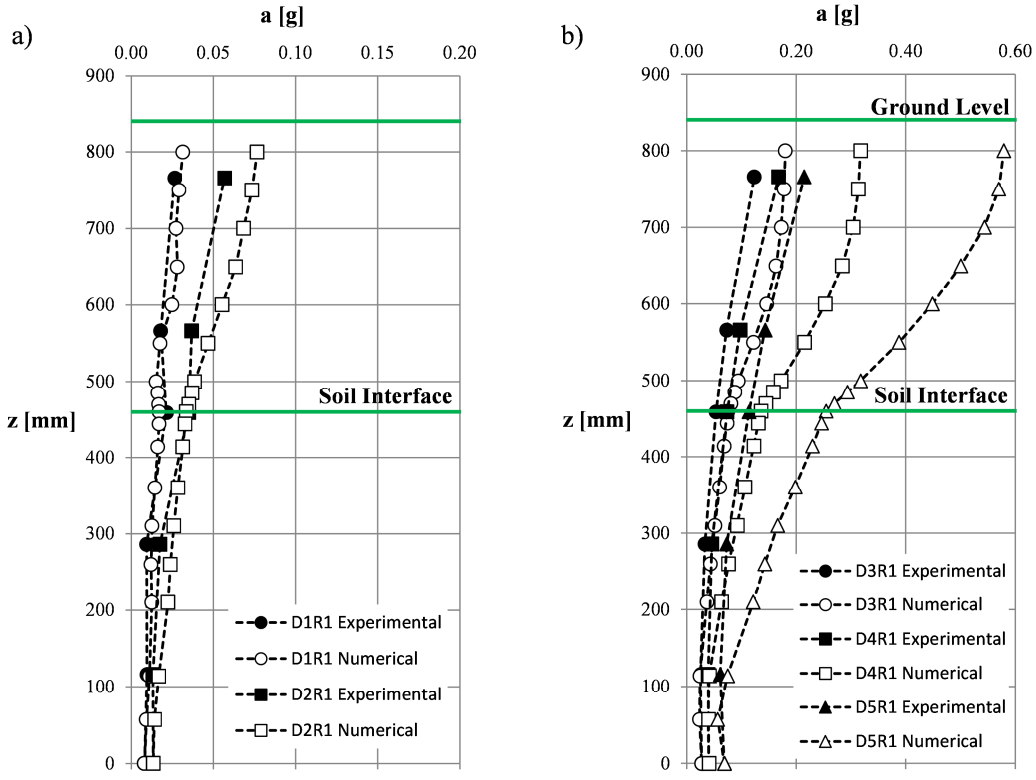


Figure 3. Comparison between experimental and numerical results for Phase I

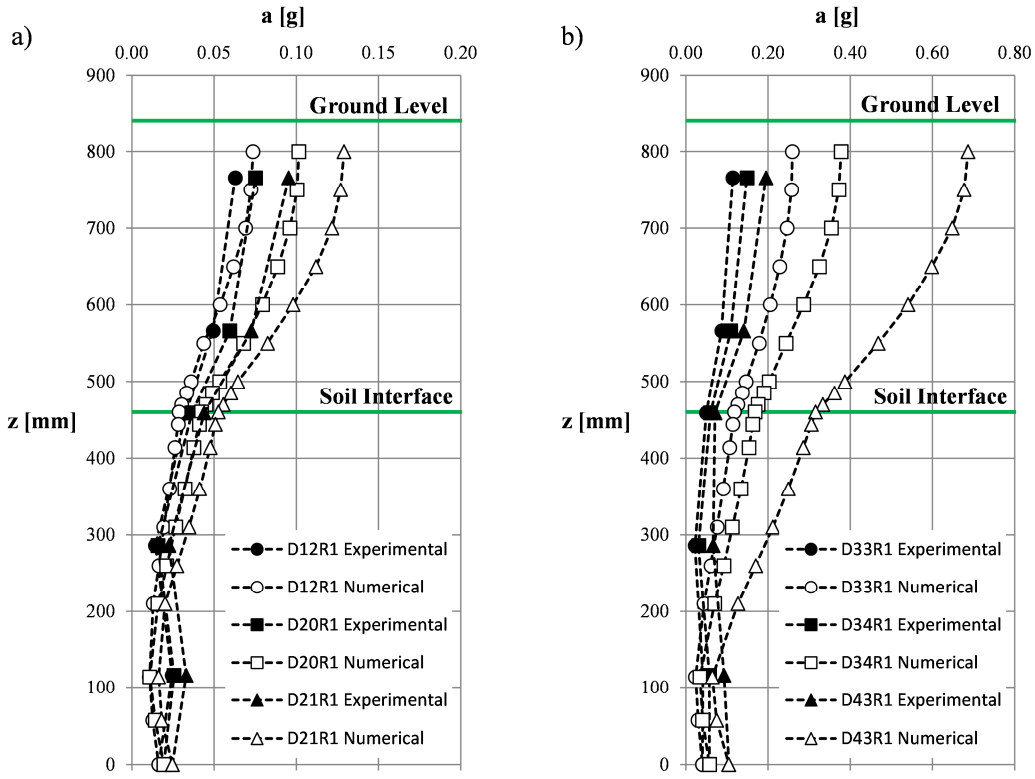


Figure 4. Comparison between experimental and numerical results for Phase II

2.2 Soil-structure interaction effects

In order to investigate the effects of soil-structure interaction on the natural period of vibration of the sample SDOF oscillators, fifteen tests were carried out on different system configurations. Such tests were aimed at assessing the effects on the global system response of following factors:

- amplitude of input excitation;
- stiffness and mass of the attached SDOF oscillators.

The superstructure considered consists of an aluminium column of 3mmx12mm rectangular cross section, 130mm long and 15gr mass. Different natural periods were specified by adding masses on the column top (always placed in a symmetrical way with respect to the column). Preliminary white noise tests were conducted in order to determine the “fixed base” frequency of the oscillator, by fixing it directly on the shaking table. The test results for the different oscillators are outlined in Table 6.

The response of the oscillator placed on the short-cap configuration (SC+SDOF) is examined hereafter. The aim is the evaluation of the period shifting of the whole system (soil, pile and superstructure). Additionally, white noise excitations were utilised for evaluating the influence of input motion amplitude on system response. The amplitude of such excitations varied between 0.02g and 0.09g, as listed in Table 7.

Firstly, transfer functions (TFs) between the oscillator and its base (or the top of the pile 5) and between the oscillator and the shaking table were computed. These TFs allow estimating the fundamental frequencies of the whole system and its sub-assemblage. Figure 5 displays the plots of such TFs for the input motion with PGA≈ 0.02g, computed with reference to the SDOF base (Figure 5a) and the shaking table (Figure 5b). The natural frequencies are close to the “fixed base” ones, as expected. The experimental outcomes confirm that the frequency

decreases as the mass increases. The amplitude of the TFs relative to the shaking table is significantly higher (Figure 5b).

Total added mass [g]	Added mass constituent parts	Fixed base frequency [Hz]
75	Mass-fixing arrangement and accelerometer	38.0
125	Mass-fixing arrangement and accelerometer + 50g	30.5
175	Mass-fixing arrangement and accelerometer + 2 x 50g	26.5
275	Mass-fixing arrangement and accelerometer + 4 x 50g	20.5
475	Mass-fixing arrangement and accelerometer + 8 x 50g	15.0
975	Mass-fixing arrangement and accelerometer + 2 x 50g + 4 x·200g	10.0

Table 6. Results of tests carried out for identifying the fixed-base frequency of the different oscillators

Application order	SIGNAL TYPE	CODE	FREQUENCY [Hz]	AMPLITUDE [g]
1	White noise	X1R1	0.1-100	~ 0.02
2	White noise	X2R1	0.1-100	~ 0.04
3	White noise	X3R1	0.1-100	0.07÷0.09

Table 7. Input motion selected for the tests on the SDOF system

In order to investigate the effects of SSPSI on SDOF response, the shifting of the SDOF fundamental frequencies (and periods) with respect to the SDOF fixed-base configuration has been evaluated. The values for three white noise excitations and different masses are summarized in Table 8.

mass	**Transfer**	**a ~ 0.02g**				**a ~ 0.04g**				**a = (0.07÷0.09)g**			
[grams]	**function**	**f [Hz]**	**T_{SSI} [s]**	**ΔT [s]**	**ΔT [%]**	**f [Hz]**	**T_{SSI} [s]**	**ΔT [s]**	**ΔT [%]**	**f [Hz]**	**T_{SSI} [s]**	**ΔT [s]**	**ΔT [%]**
125	SDOF-S.T.	29.2	0.034	0.001	4.539	28.996	0.034	0.002	5.187	29.002	0.034	0.002	5.167
	SDOF-P.H.	29.8	0.034	0.001	2.488	29.799	0.034	0.001	2.353	29.776	0.034	0.001	2.430
175	SDOF-S.T.	25.2	0.040	0.002	5.014	24.724	0.040	0.003	7.184	24.511	0.041	0.003	8.117
	SDOF-P.H.	25.0	0.040	0.002	6.195	25.117	0.040	0.002	5.507	25.167	0.040	0.002	5.295
275	SDOF-S.T.	20.4	0.049	0.000	0.540	20.379	0.049	0.000	0.596	20.238	0.049	0.001	1.294
	SDOF-P.H.	19.9	0.050	0.001	3.037	19.817	0.050	0.002	3.445	19.812	0.050	0.002	3.475
475	SDOF-S.T.	14.7	0.068	0.001	1.749	14.883	0.067	0.001	0.784	14.888	0.067	0.001	0.746
	SDOF-P.H.	14.5	0.069	0.002	3.323	14.557	0.069	0.002	3.024	14.473	0.069	0.002	3.619
975	SDOF-S.T.	10.0	0.100	0.000	0.000	10.060	0.099	0.000	0.000	10.043	0.100	0.000	0.000
	SDOF-P.H.	9.9	0.101	0.001	1.641	9.897	0.101	0.001	1.545	9.841	0.102	0.002	2.404

Table 8. Input Period shifting for the sample systems. Keys: S.T. shaking table; P.H. Pile head; $\Delta T=T_{SSI}-T_{fix}$; $\Delta T[\%]=(\Delta T/T_{fix})\times 100$

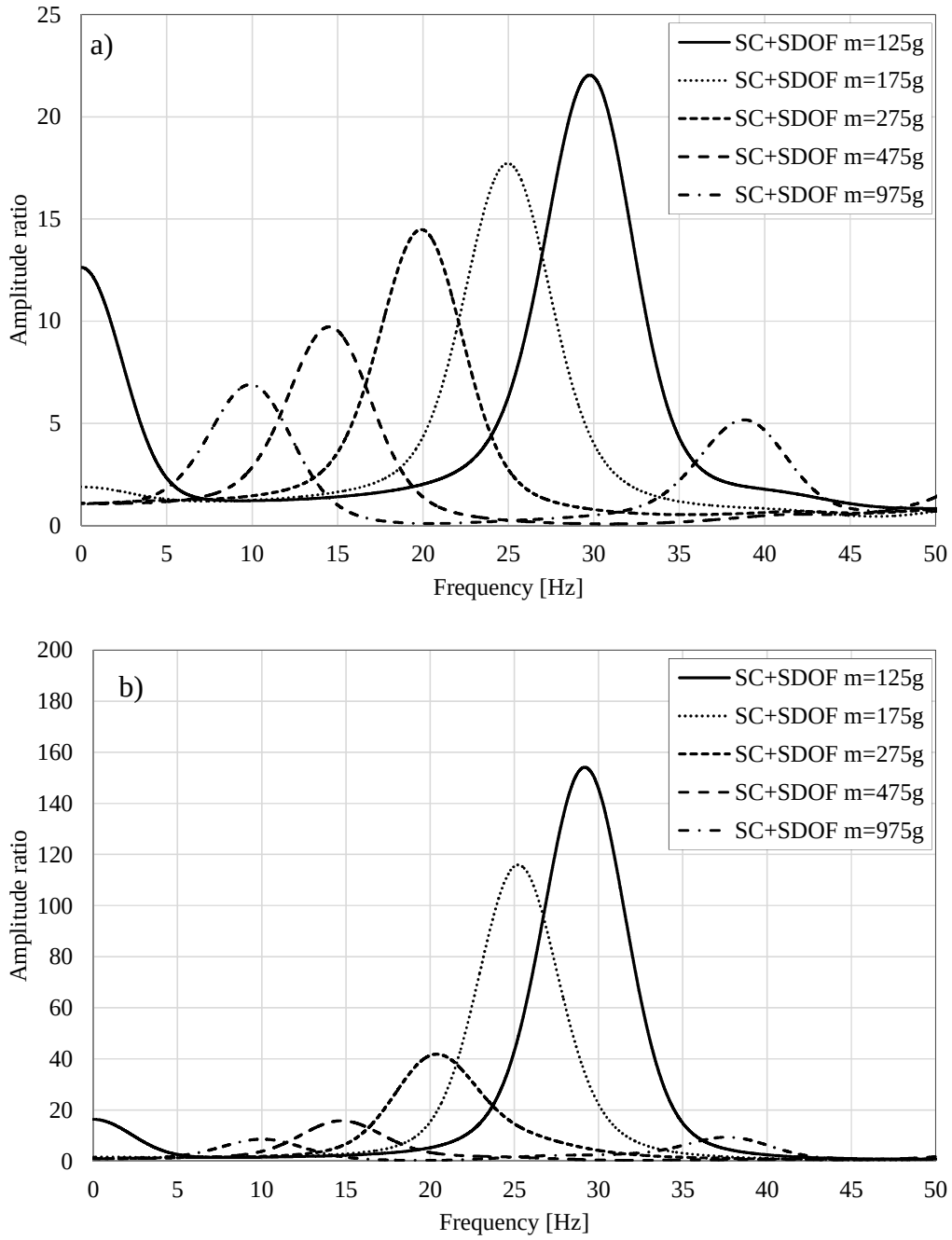


Figure 5. Transfer function between the oscillator and its base (a) and the oscillator and the shaking table (b) (white noise motion with PGA≈ 0.02g)

According to the fundamentals of the SSI theory, the ratio T_{SSI}/T_{fix} does not vary with structural (SDOF) mass. This statement is corroborated by the experimental results shown in Figure 6, where the ratio T_{SSI}/T_{fix} has been plotted against the mass of the SDOF for different system configurations (SC and FHP with SDOF on pile 4 or 5) and peak acceleration at the shaking table (a=0.021g and 0.046g). The assessment of the slight variability of the experimental data with respect to mass values is still under investigation. The results in Figure 6 also show that, at the model scale, period elongation due to SSI is modest, yet not insignificant.

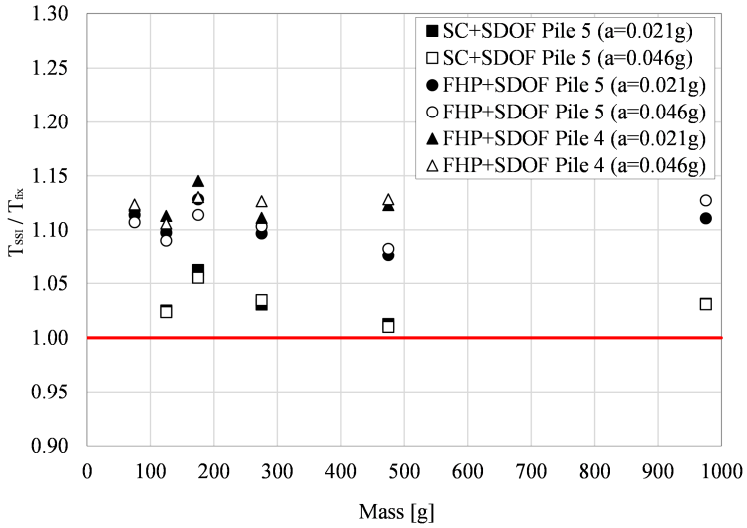


Figure 6. Ratio T_{SSI}/T_{fix} against the mass of the SDOF for different system configuration and peak input acceleration

The period shift ΔT [%], expressed as a percentage of T_{fix}, is represented in Figure 7 against the mass of the SDOF. The plot provided in figure 7 shows a clear dependence on the SDOF mass. The maximum period shift ΔT [%] corresponds to the mass of 175grams, due to a resonance occurring between the fundamental frequencies of the SDOF (f_{SDOF}=26.5 Hz) and of the soil (f_{soil}=22÷28 Hz).

The sample tests show that the period shift ΔT [%] of the SDOFs with SSPSI varies between 1% and 8% at the model scale. Further analyses still on-going are investigating on SSPSI effects on full-scale systems.

3 CONCLUDING REMARKS

The present work has discussed the outcomes of a series of 1-g shaking table tests that were carried out to validate numerical models formulated for kinematic and inertial interaction effects on pile-supported systems. The results of the laboratory tests and numerical simulations conducted on well-calibrated models have indicated that:

- From a purely linear site response analyses, it is observed that for low values of accelerations there is a close match between measured and predicted values; However, as nonlinearity increases the outcomes of numerical simulations tend to diverge from test results, thus highlighting the need for a more suitable modelling of soil behaviour;
- The experimental outcomes indicate that the frequency of the single-degree-of-freedom (SDOF) system in the short cap configuration decreases as the mass increases. The amplitude of TFs relative to the shaking table is significantly higher than TFs relative to the base of the SDOF. This finding contradicts fundamental (linear) SSI theory and can thus be attributed to nonlinear soil effects near the pile head.

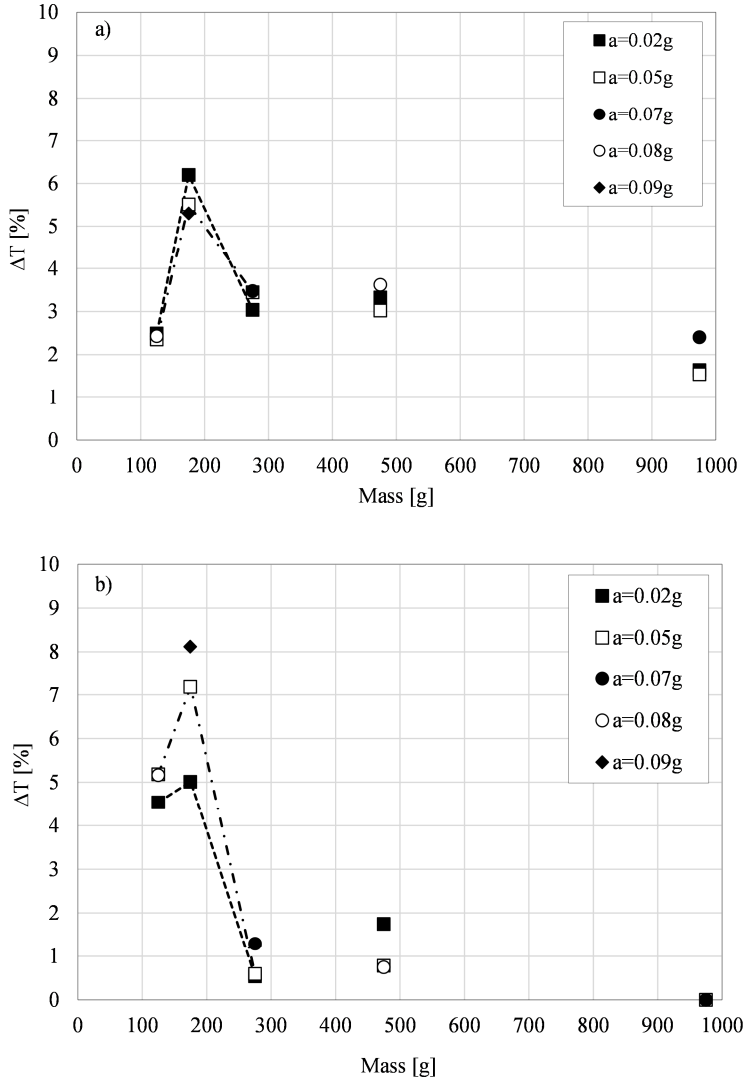


Figure 7. Period shift ΔT [%] vs. the SDOF mass, obtained by TFs between: a) SDOF and Pile Head; b) SDOF and Shaking Table

Further investigations are ongoing to derive the variation, if any, of the equivalent viscous structural damping of the SDOF systems with soilstructure-interaction effects. Design implications will be derived from the assessment of the prototype response of the single piles and group of piles, with or without caps.

Acknowledgments

The research leading to these results has received funding from the European Union Seventh Framework Programme (FP7/2007-2013) for access to the Bristol Laboratory for Advanced Dynamics Engineering (BLADE), University of Bristol, UK under grant agreement n° 227887 [SERIES]. The financial support provided by the project ReLUIS (Task MT2) funded by the Italian Civil Protection is also appreciated.

REFERENCES

[1] Simonelli, A.L., Di Sarno, L., Durante, M.G., Sica, S., Bhattacharya, S., Dietz, M., Dihorou, L., Taylor, C.A., Cairo, R., Chidichimo, A., Dente, G., Anoyatis, G., Mylonakis,

G., Modaressi, A., Todo Bom, L.A. and Kaynia, A.M. (2012). *Performance of soil-pile-structure systems under seismic waves.* II Int. Conf. On Performance-Based Design in Earthquake Geotechnical Engineering, Taormina, I

[2] Simonelli, A.L., Di Sarno, L., Durante, M.G., Sica, S., Bhattacharya, S., Dietz, M., Dihorou, L., Taylor, C.A., Cairo, R., Chidichimo, A., Dente, G., Anoyatis, G., Mylonakis, G., Modaressi, A., Todo Bom, L.A. and Kaynia, A.M. (2012). *Experimental investigation of soil-pile-structure seismic interaction*. 15th World Conference on Earthquake Engineering, Lisbon 2012

[3] Crewe AJ, Lings ML, Taylor CA, Yeung AK and Andrighetto R (1995) *Development of a large flexible shear stack for testing dry sand and simple direct foundations on a shaking table*. In: Elnashai AS (ed) European seismic design practice. Balkema, Rotterdam

[4] Tan, F.S.C. (1990) *Centrifuge and theoretical modelling of conical footings on sand*. PhD Thesis, University of Cambridge, U.K.

[5] Lings ML, Dietz MS (2004) *An improved direct shear apparatus for sand*. Geotechnique **54(4)**:245–256

[6] Moccia F (2009) *Seismic soil pile interaction: experimental evidence*. PhD Dissertation, Università degli Studi di Napoli Federico II, Napoli

[7] Stroud MA (1971) *The behaviour of sand at low stress levels in the simple shear apparatus*. PhD thesis, University of Cambridge, UK

[8] Cavallaro A, Maugeri M, Mazzarella R (2001) *Static and dynamic properties of Leighton Buzzard sand from laboratory tests*. 4th International Conference on Recent Advances in Geotechnical Earthquake Engineering and Soil Dynamics, San Diego, CA, Paper 1.13

COMPDYN 2013
4th ECCOMAS Thematic Conference on
Computational Methods in Structural Dynamics and Earthquake Engineering
M. Papadrakakis, N.D.Lagaros, V. Plevris (eds.)
Kos Island, Greece, 12–14 June 2013

STOCHASTIC RESPONSE DETERMINATION AND RELIABILITY ASSESSMENT OF A NONLINEAR CABLE NET STRUCTURAL SYSTEM

Ioannis A. Kougioumtzoglou[1], Isabella Vassilopoulou[2] and Charis J. Gantes[2]

[1] Institute for Risk & Uncertainty, University of Liverpool
Brodie Tower, Brownlow Street, L69 3GQ, Liverpool, United Kingdom
kougioum@liverpool.ac.uk

[2] Institute of Steel Structures, School of Engineering, National Technical University of Athens
9, Iroon Polytechniou Street, GR-15780 Zografou, Athens, Greece
isabella@central.ntua.gr; chgantes@central.ntua.gr

Keywords: Cable Net, Nonlinear System, Dimension Reduction, Random Vibration, Reliability Assessment, Uncertainty Quantification.

Abstract. *A multi-degree-of-freedom (MDOF) symmetric cable net system with fixed cable ends under Gaussian white noise excitation is considered. First, a dimension reduction approach based on similarity relations is employed to cast the original MDOF system into an equivalent single-degree-of-freedom (SDOF) nonlinear oscillator of the hardening Duffing kind. Next, a numerical path integral (NPI) approach is utilized for determining the reduced system non-stationary response amplitude probability density function (PDF). The main concept of the approach relates to the evolution of the response PDF in short time steps, assuming a Gaussian form for the conditional response PDF. Further, the NPI approach is employed for determining first-passage kind reliability statistics of the Duffing oscillator; these are associated with the probability of cable tensile failure for specific mechanical and geometrical characteristics of the original cable net system. It is noted that the main advantages of the approximate deterministic approach of dimension reduction relate to a) the detection of nonlinear phenomena, such as the occurrence of sub/super-harmonic resonances, jump phenomena, etc, and b) the reduction of the computational effort associated with the nonlinear dynamic analysis of the original MDOF system. The latter advantage becomes significantly more important in the case of stochastic excitation where Monte Carlo simulation (MCS) methodologies can be computationally prohibitive, especially for cases of large scale complex systems. Hopefully, the herein developed approximate stochastic approach can be used as a convenient tool for preliminary reliability based design of the original MDOF structural system.*

1 INTRODUCTION

In 1953, when the first saddle-form cable net was studied and constructed, covering the Raleigh Arena in North Carolina, USA, a new era begun for such tensile structures. Since then, many similar structures have been used as roofs to large span facilities. Their shape is characterized by two opposite curvatures, defined by their sags, realized by two families of prestressed cables, the carrying and the stabilizing ones, which create an orthogonal net. They are called tensile structures because only tension can develop in their elements. Any local slackening of cables may lead to a total failure of the structure, thus their design is focused on ensuring a minimum tension in cables, under any loading combination.

Their behaviour is strongly nonlinear, exhibiting large displacements when they are loaded, leading to a significant change of their stiffness as the deformation evolves. This means that the internal forces do not vary linearly with the applied load. Their static analysis is based on iterative methods calculating the deformed geometry and the stiffness of the system for every load step. Their dynamic response instead, is much more complex due to particular nonlinear dynamic phenomena that may occur [1].

In [2] a preliminary design method was proposed by two of the authors of this paper for estimating the nonlinear dynamic response of a MDOF cable net using the analytical solution of an equivalent SDOF model. Nonlinear dynamic phenomena, such as bending of the response curve, jump phenomena, secondary resonances and dependence of the steady state response on the initial conditions, easily detected by solving analytically the equation of motion of the SDOF model, were verified for the MDOF system with surprising accuracy. This method was the evolution of a work first presented by Gero ([3], [4]) aiming at estimating the static behaviour of a large cable net with fixed cable ends using the response of a smaller similar system. The method was extended by the present authors to elastically supported cable network structures ([5] – [7]), proceeding later to the dynamic response of the net for the case of fixed cable ends [8].

In this paper a further step is achieved towards the design of such systems. In the traces of the previously presented preliminary design method, this investigation focuses on determining the non-stationary stochastic dynamic response and on assessing the reliability of such systems subjected to white noise excitation. In this regard, a numerical path integral (NPI) solution approach, recently proposed by the first author [9], is applied to the reduced SDOF nonlinear system for determining the non-stationary response probability density function (PDF) as well as the reliability function (survival probability). Specifically, based on the concepts of statistical linearization and of stochastic averaging the system response amplitude is modelled as a one-dimensional Markov diffusion process. Further, using a discrete version of the Chapman-Kolmogorov (C-K) equation and the associated first-order stochastic differential equation (SDE), the response amplitude PDF and the corresponding reliability function are derived. The main concept of the approach relates to the evolution of the response PDF in short time steps, assuming a Gaussian form for the conditional response PDF.

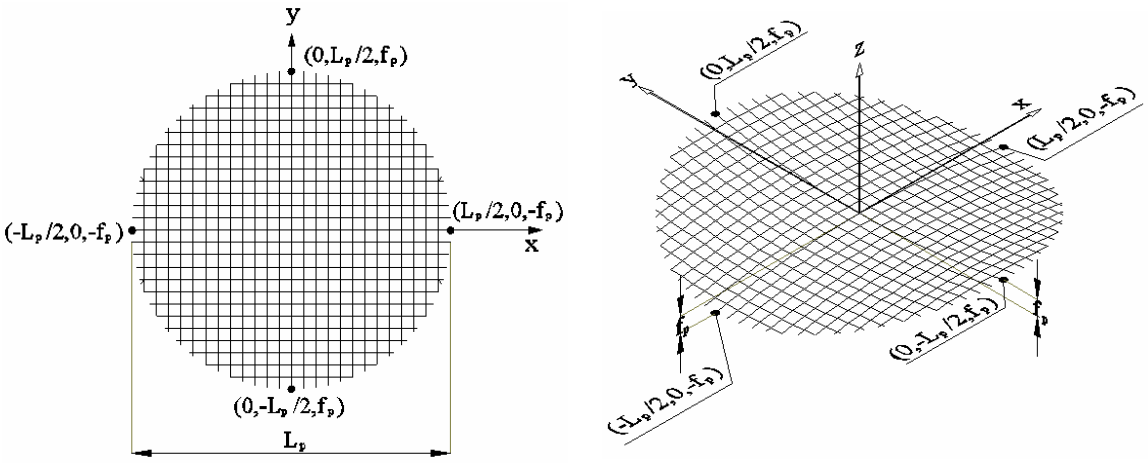
In this manner, the proposed methodology can be utilized for a preliminary reliability based design. In this regard, the mechanical and geometrical characteristics of the structure can be chosen appropriately to avoid large values of the cable tensile failure probability. The accuracy of the proposed method is illustrated by means of an illustrative example.

2 MODELLING ISSUES AND ASSUMPTIONS

Two different models are used in this paper. The first one is a multi-degree-of-freedom (MDOF) symmetric saddle-shaped cable net, called prototype and symbolized as ‘p’, while the second one is a SDOF cable net system, which is referred to as model, and denoted as ‘m’.

2.1 Prototype

The prototype has a circular plan view of diameter L_p and sag f_p, equal in both directions. It consists of N_p cables in each direction, arranged in a quadratic grid (Figure 1). Both groups of cables have a circular cross-section with area A_p, while their material is assumed to be linearly elastic with Young modulus E_p in tension and zero compression branch. The maximum cable stress is assumed equal to the yield stress of the material σ_y, corresponding to a strain $\varepsilon_{max}=\sigma_y/E_p$. The net is uniformly prestressed, considering an initial cable elongation $\varepsilon_p=(N_0)_p/(E_pA_p)$ equal for all cables, where $(N_0)_p$ is the initial pretension. The cable mass density is m_p. A lumped mass matrix is taken into account, thus the distributed mass along the length of the cables is concentrated at the nodes. A Rayleigh damping [10] is also assumed, taking into account a damping ratio ζ_p. All cables are modelled as straight truss elements between two adjacent intersection points. Equal concentrated dynamic loads, defined as $P_p(t)$, are exerted vertically on all nodes of the net, having the same amplitude and time variation. The three translational degrees of freedom are considered as free for all internal nodes of the net, while the cable ends are assumed as pinned. All analyses for the MDOF model are performed with the finite element software ADINA ([11], [12]) considering the geometry and stiffness of the state under pretension; thus, no form-finding analysis is carried out. The error introduced by this assumption is negligible as proved in [1]. The response of the system is represented by the vertical displacement of the central node located at the origins of the axes, where the maximum oscillation amplitude is observed.

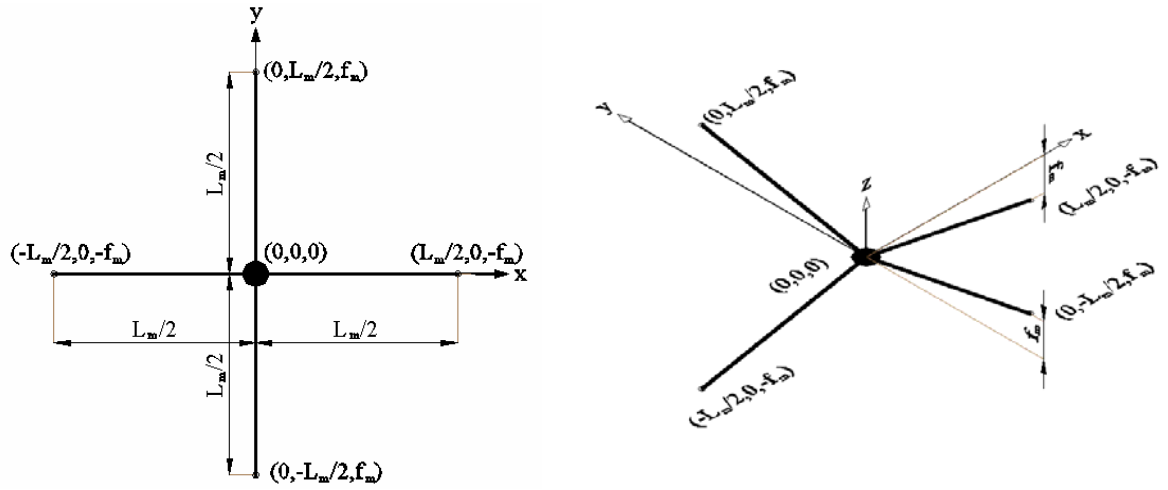


(a) (b)

Figure 1: Geometry of the MDOF cable net (prototype) (a) plan view, (b) perspective view

2.2 Model

The model is the simplest possible cable net system, consisting of two perpendicularly crossing cables, intersecting at their mid-spans. Thus, four straight cable elements are formed between the external nodes and the central one (Figure 2). Both cables have the same initial pretension $(N_0)_m$, material with elastic modulus E_m, cross-sectional area A_m, equal lengths L_m and equal but opposite sags f_m. The damping ratio of the system is ζ_m. The central node is free, while the ends of the cables are fixed. A concentrated mass M_m and a vertical dynamic load $P_m(t)$ are applied on the central node. Due to the symmetry of the structure, the only degree of freedom is the vertical displacement of the central node. As in the case of the prototype, the vertical displacement of the central node represents the response of the model.



(a) (b)

Figure 2: Geometry of the SDOF cable net (model) (a) plan view, (b) perspective view

As demonstrated in [13], the SDOF model can be simulated with great accuracy by a hardening Duffing oscillator [14], given by the following equation of motion:

$$\ddot{x} + 2\zeta\omega_m\dot{x} + \omega_m^2 x + \frac{16E_mA_m}{M_mL_m^3}x^3 = \frac{P_m(t)}{M_m} = w(t) \tag{1}$$

where x represents the vertical displacement of the central node, while its first and second derivatives are the corresponding velocity and acceleration, respectively. The eigenfrequency of the system is expressed as:

$$\omega_m = \sqrt{\frac{4E_mA_m}{M_mL_m}\cdot\left(8\frac{f_m^2}{L_m^2} + 2\frac{(N_0)_m}{E_mA_m} - 4\frac{(N_0)_m}{E_mA_m}\frac{f_m^2}{L_m^2}\right)} \tag{2}$$

3 DIMENSION REDUCTION METHOD

The dimension reduction method is based on the transformation of a large cable net (prototype) into a smaller cable net (model), using similarity relations which include the geometric and mechanical characteristics of both systems.

3.1 Similarity relations

The relations used in this paper are based on the ones provided in [2] and are the following:

$$(P_0)_m = (P_0)_p\left(\frac{E_m}{E_p}\right)\left(\frac{L_m}{L_p}\right)^2\left(\frac{N_p+1}{N_m+1}\right)^2\sqrt{\frac{f_m/L_m}{f_p/L_p}}\text{: load amplitude} \tag{3}$$

$$D_m = D_p\left(\frac{L_m}{L_p}\right)\sqrt{\left(\frac{N_p+1}{N_m+1}\right)\left(\frac{f_p/L_p}{f_m/L_m}\right)}\text{: cable diameter} \tag{4}$$

$$A_m = A_p\left(\frac{L_m}{L_p}\right)^2\left(\frac{N_p+1}{N_m+1}\right)\left(\frac{f_p/L_p}{f_m/L_m}\right)^2 : \text{cable cross-sectional area} \quad (5)$$

$$(EA)_m = (EA)_p\left(\frac{E_m}{E_p}\right)\left(\frac{L_m}{L_p}\right)^2\left(\frac{N_p+1}{N_m+1}\right)\left(\frac{f_p/L_p}{f_m/L_m}\right)^2 : \text{axial stiffness} \quad (6)$$

$$(N_0)_m = (N_0)_p\left(\frac{E_m}{E_p}\right)\left(\frac{L_m}{L_p}\right)^2\left(\frac{N_p+1}{N_m+1}\right): \text{initial pretension} \quad (7)$$

$$M_m = M_p\left(\frac{E_m}{E_p}\right)\left(\frac{L_m}{L_p}\right)\left(\frac{N_p+1}{N_m+1}\right)^2 : \text{nodal mass} \quad (8)$$

$$x_{d,m} = x_{d,p}\left(\frac{L_m}{L_p}\right)\left(\frac{f_m/L_m}{f_p/L_p}\right): \text{nodal dynamic deflection} \quad (9)$$

$$\Omega_m=\Omega_p: \text{loading frequency} \quad (10)$$

where N is the number of cables in each direction, while the subscripts m and p stand for model and prototype, respectively.

Potential discrepancies of the results extracted by this method decrease as the similarities between the two systems increase. In order to minimized the error introduced by the dimension reduction, the cable span, the sag and the elastic modulus of the material are chosen to be equal for both prototype and model, thus, $L_m=L_p$, $f_m=f_p$ and $E_m=E_p$.

3.2 Example

The MDOF cable net is the one described in [2] and also studied in [1]. It has a diameter L_p=100m and a sag-to-span ratio equal to f_p/L_p=1/35 (f_p=2.857m), while the number of cables in each direction is N_p=25. The cable diameter is D_p=50mm with cross-sectional area A_p=0.00196m^2. The Young modulus is E_p=165GPa. The pretension is $(N_0)_p$=600kN, corresponding to approximately 20% of the yield stress, which is considered equal to 1570MPa, considering one of the two most common categories of steel for cables, 1570/1770MPa. Assuming that cable failure occurs when the cable stress becomes equal to the yield stress, the maximum permissible cable tension is:

$$(N_c)_{max,p}=A_p\sigma_y=0.00196\text{m}^2\cdot 157000\text{kN/m}^2=3082\text{kN} \quad (11)$$

corresponding to a strain of cables ε_{max}=0.0095. Thus, the material constitutive law taken into account for all analyses of the prototype is illustrated in Figure 3.

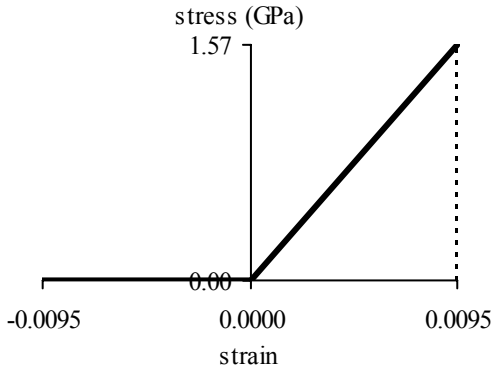


Figure 3: Material constitutive law

The unit weight of the cables is taken equal to ρ_p=100kN/m^3, which corresponds to a concentrated mass on every node equal to:

$$M_p = \frac{2A_p\rho_p L_p}{g\left(N_p+1\right)} = 0.151\text{kN}\sec^2\text{m}^{-1} \tag{12}$$

where g=10m/sec^2. In this work a damping ratio equal to ζ_p=2% is assumed, a common value for such structures, as mentioned in [15]. Performing modal analysis the eigenmodes and eigenfrequencies are calculated. The first six are shown in Figure 4. The first vibration mode is the first symmetric mode having frequency ω_p=9.902sec^{-1}. In this paper this is considered as the main vibration mode.

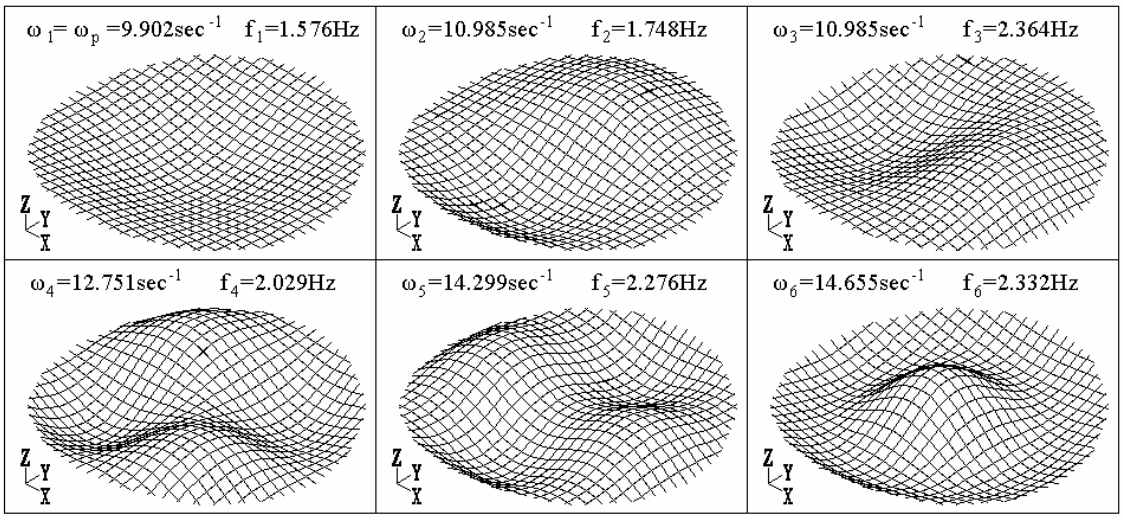


Figure 4: The first six vibration modes of the prototype

Taking into account that for the model N_m=1 cable in each direction, L_m=L_p=100m, f_m/L_m= f_p/L_p=1/35 (f_m=2.857m), and E_m=E_p=165GPa, based on the similarity relations, the equivalent SDOF model has the following characteristics:

$$A_m = A_p\left(\frac{N_p+1}{N_m+1}\right) = 0.00196\cdot\frac{26}{2} = 0.0255\text{m}^2 \tag{13}$$

$$(N_0)_m = (N_0)_p \left(\frac{N_p + 1}{N_m + 1} \right) = 600 \frac{26}{2} = 7800\text{kN} \tag{14}$$

$$M_m = M_p \left(\frac{N_p + 1}{N_m + 1} \right)^2 = 0.151 \cdot \left(\frac{26}{2} \right)^2 = 25.52\text{kN}\,\text{sec}^2\,\text{m}^{-1} \tag{15}$$

In the case of the model the maximum cable tension is:

$$(N_c)_{,max,m} = A_m \sigma_y = 0.0255\text{m}^2 \cdot 157000\text{kN/m}^2 = 40035\text{kN} \tag{16}$$

and the maximum permissible deflection is equal 3.975m, as calculated in [1]. Due to its geometry, the maximum vertical displacement of the central node corresponds to the maximum cable stress.

One of the drawbacks of this method is that the analytical solution of the Duffing oscillator's equation of motion, expressed by Eq. (1), does not take into account an eventual slackening of the cables. This is not an issue in this investigation, as the level of pretension does not allow any cable slackening for any displacement. In Figure 5, where the cable tension is plotted for both cables up to the maximum deflection of the central node, it is noted that both cables remain always under tension.

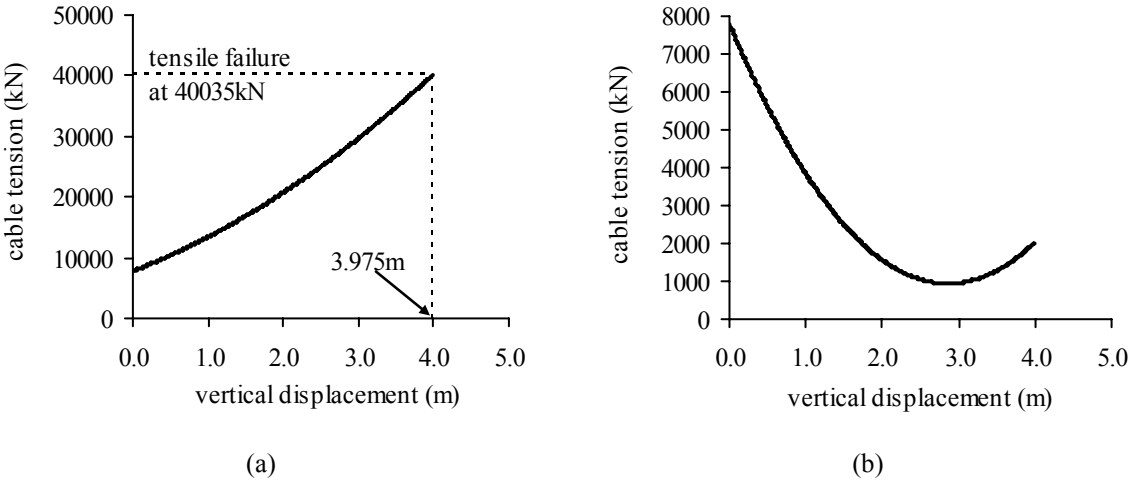


Figure 5: Cable tension diagrams with respect to the vertical displacement of the central node of the model: (a) Carrying cables (b) Stabilizing cables

3.3 Additional and improved similarity relations

For the purposes of the investigation presented in this paper, new transformations are added and some improvements in the similarity relations used in previous works, are introduced. In [2], the interest of the authors was focused on the estimation of the steady-state response of the prototype; thus, the structural response behaviour of the transient phase was neglected. In this investigation it is suggested to scale also time, as it plays an important role in the non-stationary stochastic response determination and reliability assessment of the prototype. In this regard, considering the characteristics of the prototype, given in section 3.2, and using the similarity relations to transform them into the corresponding ones of the model, the response to a harmonic load is calculated and compared for both systems, performing nonlinear time-history analyses with ADINA for the MDOF system and solving the equation

of motion for the SDOF model with MATLAB [16]. In the following, zero damping is chosen for the analyses so that the resonance phenomenon is illustrated more clearly.

The natural frequency of the model is calculated according to Eq. (2) and it is equal to $\omega_m=8.22\text{sec}^{-1}$. The ratio ω_m/ω_p is 0.83 and it is equal to $[(N_m+1)/(N_p+1)]^{0.07}=(2/26)^{0.07}=0.83$. Thus, an improved similarity relation is proposed herein, with respect to the one given in [2], connecting the natural frequencies of the two systems, defined as:

$$\omega_m = \omega_p \left(\frac{N_m + 1}{N_p + 1} \right)^{0.07} \tag{17}$$

A harmonic load acts on every node of the prototype, described as $P_p(t)=(P_0)_p \cos\Omega_p t$, with amplitude $(P_0)_p=1\text{kN}$, which is transformed for the model according to relation (3):

$$(P_0)_m = (P_0)_p \left(\frac{N_p + 1}{N_m + 1} \right)^2 = 1 \cdot \left(\frac{26}{2} \right)^2 = 169\text{kN} \tag{18}$$

Three loading frequencies are chosen for the prototype $\Omega_p=0.33\omega_p$, $\Omega_p=\omega_p$ and $\Omega_p=1.2\omega_p$, while for the model they become $\Omega_m=0.33\omega_m$, $\Omega_m=\omega_m$ and $\Omega_m=1.2\omega_m$. The equation of motion of the undamped SDOF system, expressed by Eq. (1), becomes:

$$\ddot{x} + (8.22\,\text{sec}^{-1})^2 x + (2.64\,\text{sec}^{-2}\,\text{m}^{-2}) x^3 = (6.62\,\text{m/sec}^2) \cos\Omega_m t \tag{19}$$

In case of fundamental resonance without damping each system vibrates with a frequency equal to its eigenfrequency and consequently, the period of the response of each system is related to its natural frequency. Thus, a new similarity relation is generated to scale the time of the model's response in order to match the one of the prototype.

$$t_p = t_m \left(\frac{N_m + 1}{N_p + 1} \right)^{0.07} \tag{20}$$

Figure 6a shows the time history diagrams of the vertical displacement for both systems, as calculated without time transformation. It is concluded that it is necessary to scale time for the SDOF model in order to match the response of the prototype. In Figure 6b the improved diagram of the SDOF system is plotted, where the time of its response is scaled based on relation (20), attaining a better match with the response of the prototype.

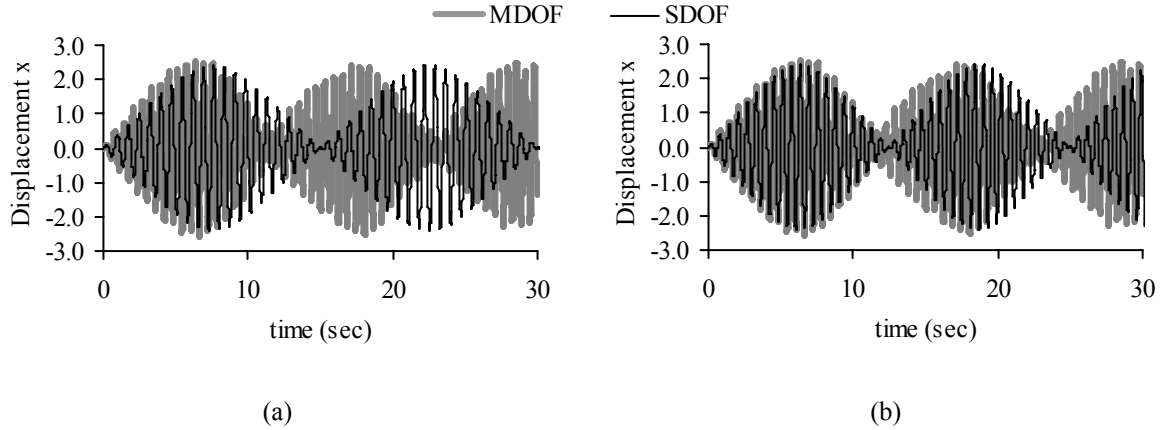
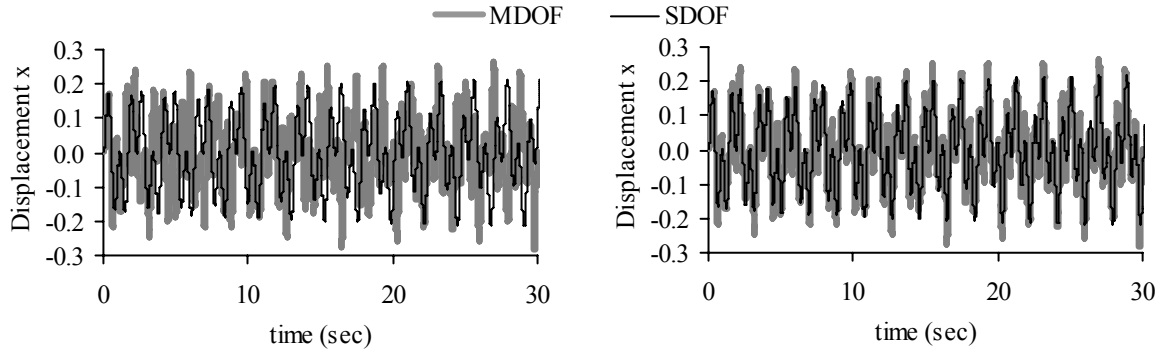


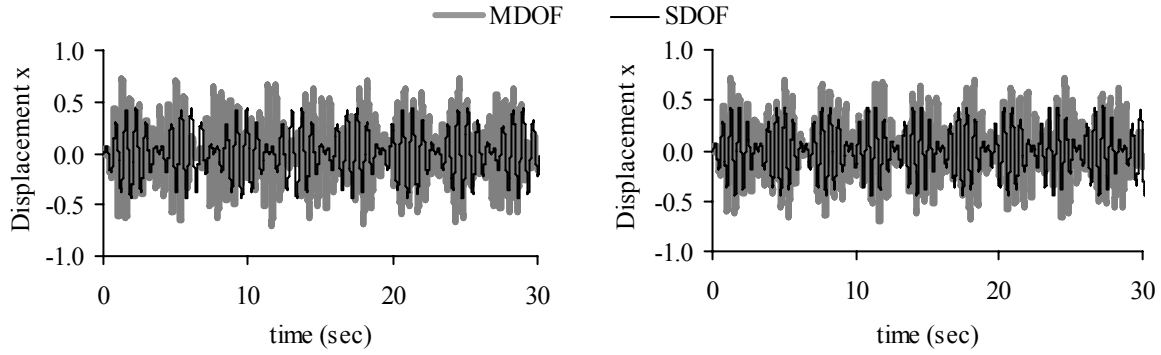
Figure 6: Time-history response diagrams for $P_p(t)=(1\text{kN})\cos(\omega_p t)$ and $P_m(t)=(169\text{kN})\cos(\omega_m t)$
(a) without time scale (b) with time scale for the model

Similar diagrams are plotted in Figure 7 for the case of small loading frequencies and in Figure 8 for loading frequency larger than the eigenfrequency. In all cases, the proposed transformation of time provides improved accuracy regarding the vibration period.



(a) (b)

Figure 7: Time-history response diagrams for $P_p(t)=(1kN)\cos(0.33\cdot\omega_p t)$ and $P_m(t)=(169kN)\cos(0.33\cdot\omega_m t)$ (a) without time scale (b) with time scale for the model



(a) (b)

Figure 8: Time-history response diagrams for $P_p(t)=(1kN)\cos(1.2\cdot\omega_p t)$ and $P_m(t)=(169kN)\cos(1.2\cdot\omega_m t)$ (a) without time scale (b) with time scale for the model

Further, it is noted that structural damping influences the dynamic response of the associated system, affecting significantly the amplitude of the oscillations. In this regard, based on the simulations performed in the current research effort, an improved similarity relation of the damping ratio between the prototype and the model is suggested. This introduction provides with enhanced accuracy regarding the model and the prototype reliability statistics. The new similarity relation proposed herein is given as:

$$\zeta_m = \zeta_p \sqrt[4]{\frac{N_m + 1}{N_p + 1}} \tag{21}$$

In [2] the response curves for both systems at steady state were compared in fundamental and superharmonic resonant conditions, considering $\zeta_p=\zeta_m=2\%$, and achieving a good accuracy. According to similarity relation (21), the damping ratio equal to $\zeta_p=2\%$ assumed for the prototype corresponds to $\zeta_m=1\%$ for the model, thus, Eq. (1) becomes:

$$\ddot{x} + (0.164\,\mathrm{sec}^{-1})\dot{x} + (8.22\,\mathrm{sec}^{-1})^2 x + (2.64\,\mathrm{sec}^{-2}\,\mathrm{m}^{-2})x^3 = (6.62\,\mathrm{m/sec}^2)\cos\Omega_m t \qquad (22)$$

In what follows, the response diagrams presented in [2] are re-plotted based on the new damping ratio for the model, in an attempt to quantify the influence of the new similarity relation with respect to previously published work of the authors. In this regard, in Figure 9 the response diagram under fundamental resonance presented in [2] is compared with the equivalent one which takes into account ζ_m=1%. It is shown that adopting the new damping ratio the steady-state response of the SDOF model does not alter significantly.

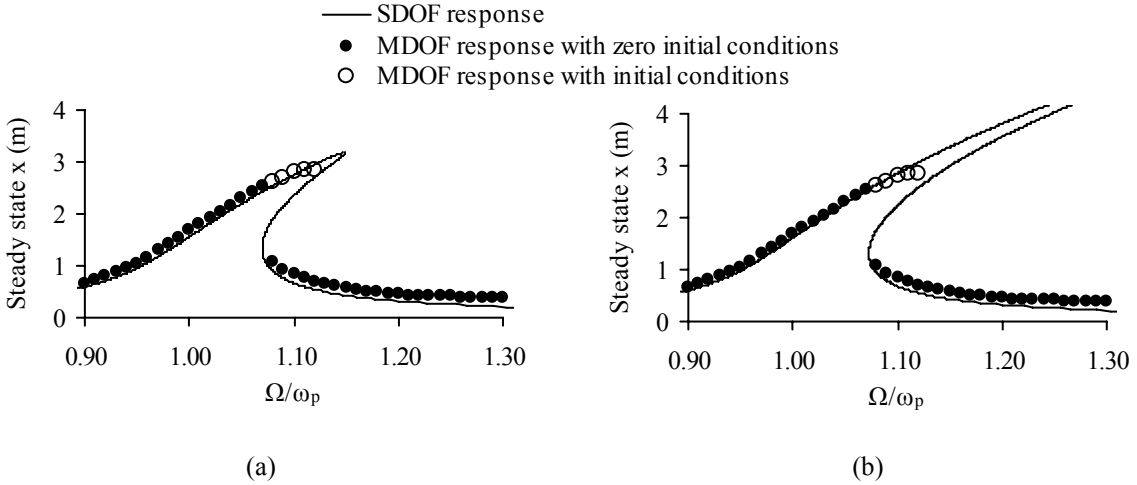


Figure 9: Fundamental resonance: response curve of the MDOF prototype for load amplitude $(P_0)_p$=1.30kN with (a) ζ_m=0.02 (from [2]), (b) ζ_m=0.01

In Figure 10 a time-history diagram of the response under fundamental resonance is plotted, considering both damping ratios for the SDOF cable net. It is observed that changing the damping ratio of the model, the accuracy of the dimension reduction method remains acceptable.

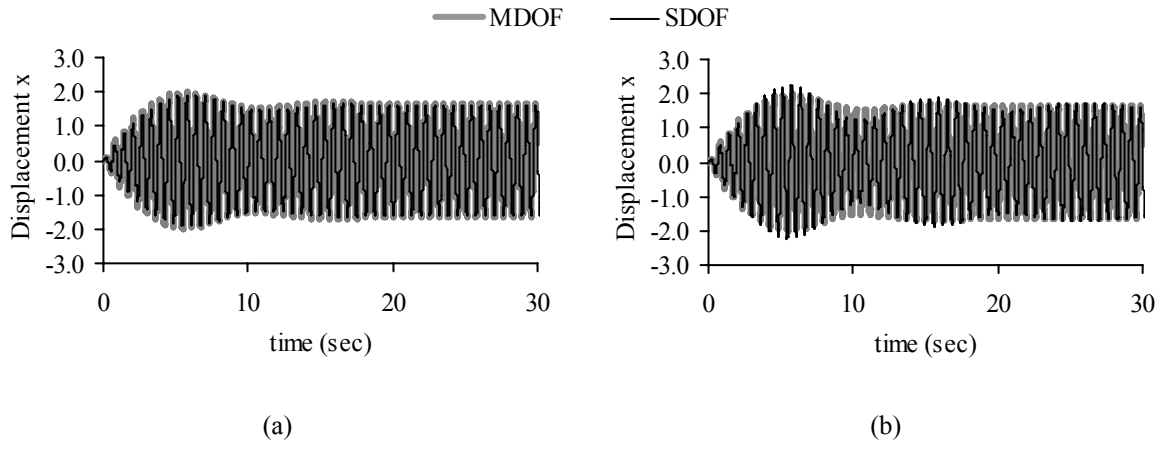


Figure 10: Time-history response diagrams for $P_p(t)=(1.30\text{kN})\cos(\omega_p t)$ and $P_m(t)=(219.7\text{kN})\cos(\omega_m t)$: with (a) ζ_m=0.02, (b) ζ_m=0.01

In Figure 11 the response diagrams at steady state under superharmonic resonance are illustrated, while Figure 12 shows the time-history diagrams for a frequency smaller than the eigenfrequencies of the systems. In those Figures both damping ratios are considered for the

model. It can be readily seen that the different values of the ratio of critical damping do not affect the accuracy of the method significantly.

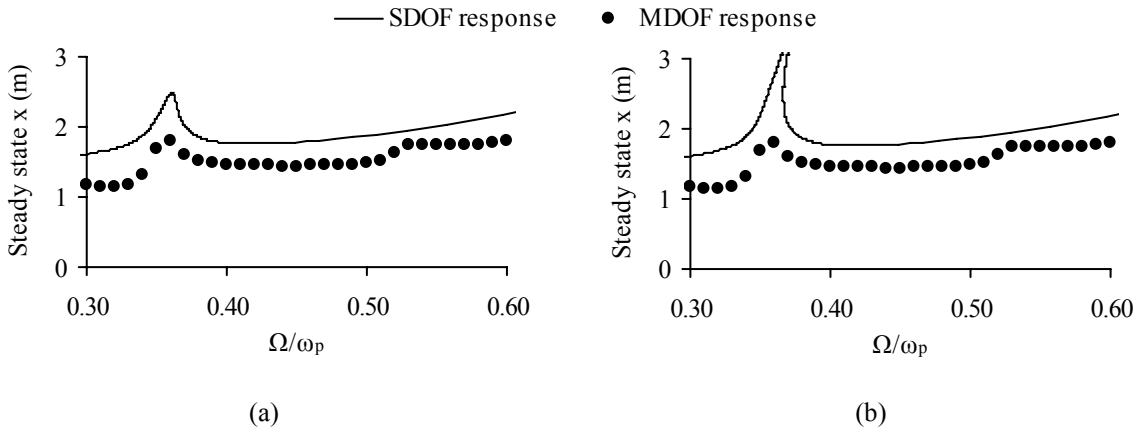


Figure 11: Superharmonic resonance: response curve of the MDOF prototype for load amplitude $(P_0)_p$=14kN with (a) ζ_m=0.02 (from [2]), (b) ζ_m=0.01

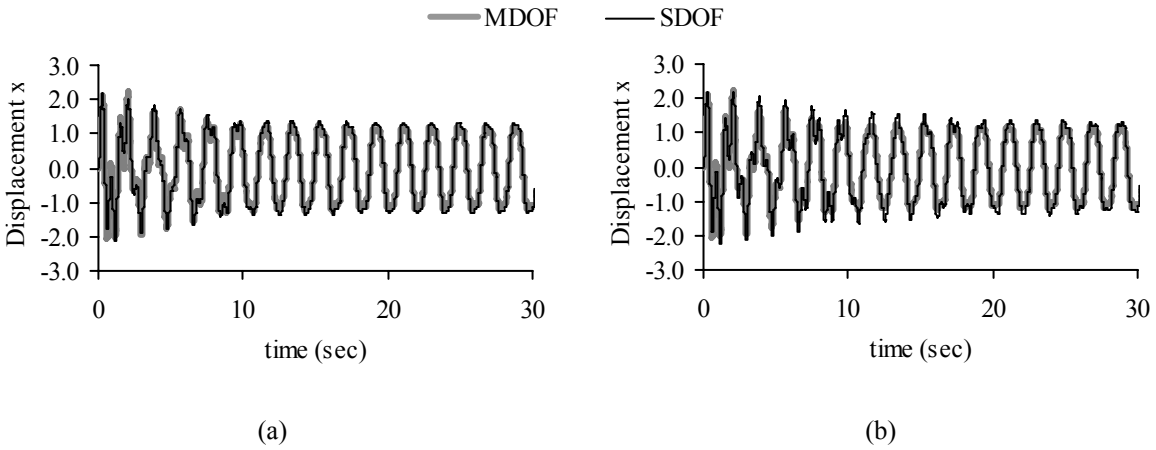


Figure 12: Time-history response diagrams for $P_p(t)=(14kN)\cos(0.33\cdot\omega_p t)$ and $P_m(t)=(2366kN)\sin(0.33\cdot\omega_m t)$ with (a) ζ_m=0.02, (b) ζ_m=0.01

Finally, an additional similarity relation is provided here for the stochastic excitation w(t). Focusing on Eq. (1) each generated realization of the excitation stochastic process w(t) used for exciting the model is transformed into the corresponding one of the prototype, or vice versa, taking into account the similarity relations (3) and (8). Thus,

$$w(t) = \frac{P_m(t)}{M_m} = \frac{P_p(t)}{M_p} \Rightarrow P_p(t) = w(t)M_p \tag{23}$$

4 STOCHASTIC EXCITATION AND THE NUMERICAL PATH INTEGRAL APPROACH

4.1 Introduction

Structural systems are often subject to excitations such as seismic motions, winds, and ocean waves, which can be most realistically described as stochastic processes. Since the pio-

neering work by Caughey and Stumpf [17] several attempts have focused on determining response statistics of linear and nonlinear systems under stochastic excitation (e.g. [18], [19]).

A sustained challenge in the area of stochastic dynamics is the determination of the probability that the system response stays within a prescribed domain within a specified time interval. Such a reliability-based analysis can be beneficial in terms of safety or risk assessment. An alternative equivalent definition of the aforementioned challenge, known as the first-passage problem, is the evaluation of the probability that the response of the system reaches, and possibly crosses, a predetermined level for the first time.

One of the promising frameworks for addressing the stochastic response determination and the first-passage problem challenges is related to the concept of the Wiener Path Integral (WPI). The concept of the functional path integral was introduced by Wiener [20], and was re-invented in a different form by Feynman [21] in the field of theoretical physics. Recently, a Wiener Path Integral based approximate analytical technique was developed by Kougioumtzoglou and Spanos [22] to address certain challenges in the area of engineering dynamics.

Further, numerical versions of the WPI solution have been employed in engineering applications to derive response and reliability statistics of nonlinear systems (e.g. [23] – [25]). Most of the developed numerical path integral approaches constitute, in essence, a discrete version of the well-known Chapman-Kolmogorov (C-K) equation which is associated with Markov processes (e.g. [26]). The basic characteristic of this approach is that the evolution of the response probability density function (PDF) is computed in short time steps, assuming a Gaussian form for the conditional response PDF. It was Wehner and Wolfer [27] who first addressed certain numerical aspects of the approach and established it as a robust numerical tool.

Recently, a generalized numerical path integral approach (NPI) has been developed by one of the authors [9] for determining response and first-passage statistics of nonlinear oscillators subject to evolutionary broad-band stochastic excitation. The NPI approach is utilized in the following to determine the non-stationary response amplitude PDF and the survival probability of the Duffing oscillator of Eq. (1) under Gaussian white noise excitation.

4.2 Mathematical formulation elements

In the following, a brief overview of the NPI approach proposed in [9] is included for completeness. In this regard, consider a nonlinear single-degree-of-freedom system whose motion is governed by the differential equation:

$$\ddot{x} + \beta\dot{x} + z(t, x, \dot{x}) = w(t) \tag{24}$$

where a dot over a variable denotes differentiation with respect to time t; $z(t, x, \dot{x})$ is the restoring force which can be either hysteretic or depend only on the instantaneous values of x and $\dot{x}$; β is a linear damping coefficient; and w(t) represents a Gaussian, zero-mean non-stationary stochastic process possessing an evolutionary broad-band power spectrum, $S(\omega, t)$.

Considering next the case of a lightly damped system, it can be argued that the nonlinear oscillator of Eq. (24) exhibits a pseudo-harmonic behaviour described by the equations:

$$x(t)=A(t)\cos[\omega(A)t+\varphi(t)] \tag{25}$$

and

$$\dot{x}(t) = -\omega(A)A(t)\sin[\omega(A)t + \varphi(t)] \tag{26}$$

where the response amplitude envelope A is a slowly varying function with respect to time and, thus, can be treated as a constant over one cycle of oscillation.

Further, following a statistical linearization approach discussed in [18] and [28], a linearized counterpart of Eq. (24) is:

$$\ddot{x} + \beta(A)\dot{x} + \omega^2(A)x = w(t) \tag{27}$$

For the special case of the Duffing oscillator (see [9] for a more detailed presentation), namely for

$$z(t, x, \dot{x}) = \omega_0^2 x + \varepsilon\omega_0^2 x^3 \tag{28}$$

(ε being a nonlinearity magnitude parameter) the equivalent damping element and the natural frequency are given by the expressions

$$\beta(A)=\beta \tag{29}$$

and

$$\omega^2(A) = \omega_0^2\left(1 + \frac{3}{4}\varepsilon A^2\right) \tag{30}$$

Taking into account Eq. (25) and Eq. (26), the amplitude A can be expressed in the form:

$$A^2(t) = x^2(t)\left(\frac{\dot{x}(t)}{\omega(A)}\right)^2 \tag{31}$$

Relying once more on the assumption of light damping, simplification of Eq. (27) is possible by further application of stochastic averaging (e.g. [18], [29]). This yields the Ito stochastic differential equation [26]:

$$\dot{A} = K_1(A,t) + K_2(A,t)\eta(t) \tag{32}$$

where

$$K_1(A,t) = -\frac{1}{2}\beta(A)A(t) + \frac{\pi S(\omega(A),t)}{2A(t)\omega^2(A)} \tag{33}$$

and

$$K_2(A,t) = \frac{\sqrt{\pi S(\omega(A),t)}}{\omega(A)} \tag{34}$$

which governs approximately the evolution in time of the amplitude A(t). In Eq. (32), $\eta(t)$ is a zero mean and delta correlated Gaussian process of intensity one, i.e., $E(\eta(t))=0$; and $E(\eta(t)\eta(t+\tau))=\delta(\tau)$, with $\delta(\tau)$ being the Dirac delta function. The Fokker-Planck (F-P) equation which corresponds to Eq. (32) takes the form (e.g. [26])

$$\frac{\partial}{\partial t}p(A, t+\Delta t \mid A', t) = -\frac{\partial}{\partial A}[K_1(A,t)p(A, t+\Delta t \mid A', t)] + \frac{1}{2}\frac{\partial^2}{\partial A^2}[K_2^2(A,t)p(A, t+\Delta t \mid A', t)] \tag{35}$$

The significance of Eq. (32) relates to the fact that the amplitude A(t) is decoupled from the phase $\varphi(t)$. Thus, it is feasible to model the amplitude process A(t) as a one-dimensional Markov diffusion process (e.g. [26], [30]). Hence, the C-K equation

$$p(A,t+2\Delta t \mid A'',t)=\int_0^{\infty} p(A,t+2\Delta t \mid A',t+\Delta t)p(A',t+\Delta t \mid A'',t)dA' \tag{36}$$

is satisfied, where $p(A,t+\Delta t \mid A',t)$ represents the conditional PDF of the response amplitude process. Note that the NPI approach proposed in [9] involves the numerical evaluation of one integral only in Eq. (36); this is due to the fact that a stochastic averaging treatment has been utilized to reduce the original second-order SDE Eq. (24) to a first-order SDE of the form of Eq. (32). Although it can be argued that the stochastic averaging treatment introduces additional approximations to the problem, it renders the NPI approach significantly less computationally demanding than alternative NPI approaches applied directly to Eq. (24) (e.g. [23]). In the latter case, Eq. (36) involves a double integral, which increases considerably the computational cost.

Further, the evaluation of the reliability function $R_B(T)$ is possible (e.g. [31]). This is defined as the probability that the system response amplitude stays below the threshold B over the time interval $[t_0,T]$. Specifically, considering the time interval $[t_0,T]$ discretized so that $t_j=t_0+j\Delta t$, $j=0,1,\ldots,n$ and $\Delta t=(T-t_0)/(n)$, and assuming an initial PDF $p(A_0,t_0)$, the reliability function $R_B(t_j)$ becomes

$$R_B(t_j)=\int_0^{B}\int_0^{\infty} p(A_j,t_j \mid A_{j-1},t_{j-1})\ldots\int_0^{B}\int_0^{\infty} p(A_1,t_1 \mid A_0,t_0)dA_1\ldots dA_j \tag{37}$$

It can be readily seen that knowledge of the conditional PDF suffices to evaluate Eq. (37) using Eq. (36). The interesting feature of the F-P Eq. (35) is that the conditional PDF $p(A,t+\Delta t \mid A',t)$, often called short-time propagator, has been shown to follow a Gaussian distribution (e.g. [32]) of the form

$$p(A,t+\Delta t \mid A',t)=\frac{1}{\sqrt{2\pi K_2^2(A',t)\Delta t}}\exp\left(-\frac{(A-A'-K_1(A',t)\Delta t)^2}{2K_2^2(A',t)\Delta t}\right) \tag{38}$$

5 NUMERICAL EXAMPLES

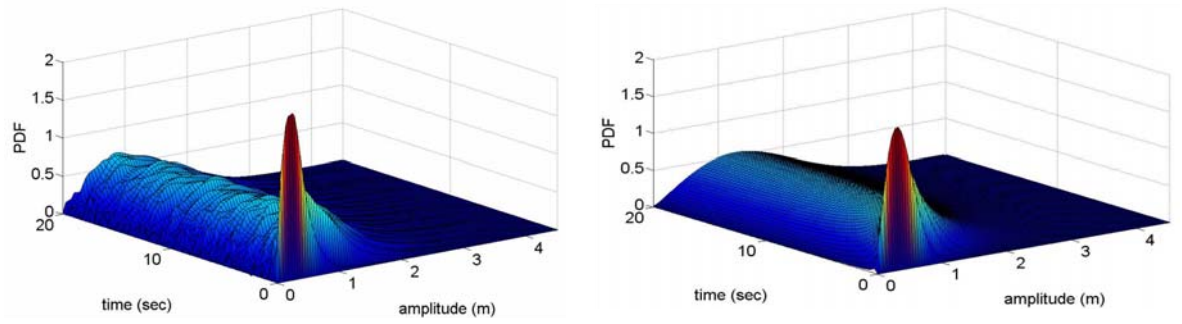
In this section the Duffing oscillator of Eq. (1), or equivalently of Eq. (24) taking into account Eq. (28), is considered with a nonlinearity parameter $\varepsilon=0.039$ subject to Gaussian white noise excitation with a power spectrum $S(\omega,t)=S_0$. The value of parameter ε is computed so that there is an equivalence between Eq. (1) and Eqs. (24) and (28). In the numerical examples, three values of S_0 are chosen, namely $5m^2{\cdot}sec/rad$, $7.5m^2{\cdot}sec/rad$ and $10m^2{\cdot}sec/rad$, corresponding to maximum loading amplitudes $(P_0)_p$ equal to $0.57kN/m^2$, $0.70kN/m^2$ and $0.81kN/m^2$, respectively. These are realistic values of a dynamic load, considering that for an actual project of a similar cable net, the roof of Peace and Friendship Stadium in Greece [33], the wind load of the final design was $1.10kN/m^2$. Further, a total time duration $t_{p,total}=30sec$ is considered for all analyses of the prototype, for which, both systems reach steady-state response. This time duration is transformed for the model according to the inverse relation of (20):

$$t_{m,total}=t_{p,total}\left(\frac{N_p+1}{N_m+1}\right)^{0.07}=35.90\,\text{sec} \tag{39}$$

As far as numerical implementation issues and convergence criteria are concerned for the NPI approach, an extended discussion of conditions to be satisfied for the values of the time increment and the grid size is provided in [27]. Further, the initial distribution chosen for the response amplitude PDF is the Dirac delta function, namely $p(A,t=0)=\delta(A)$, assuming the system is initially at rest. For the Monte Carlo simulations of the prototype MDOF system an ensemble of 500 realizations is used. Although it is recognised that this number is quite small for capturing detailed system response PDF characteristics, it is noted that the main aim of the approach relates to a preliminary (reliability-based) system design. In this regard, the number of realizations is deemed adequate for estimating the general features of the MDOF system non-stationary response PDF.

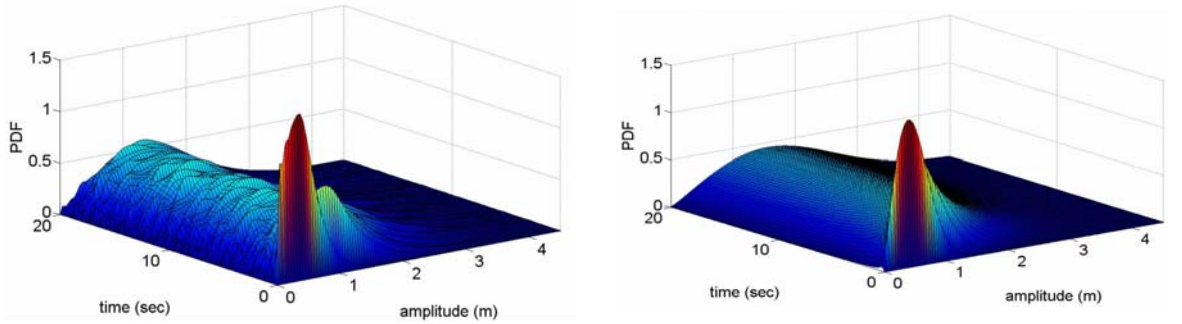
5.1 Non-stationary response amplitude PDF

In Figure 13 the non-stationary response amplitude PDFs for the prototype and the model are shown for $S_0=5m^2$·sec/rad. It is noted that the proposed dimension reduction approach based on the NPI performs satisfactorily in capturing the essential characteristics of the MDOF system non-stationary response PDF. Similarly, in Figures 14 and 15 the non-stationary response amplitude PDFs for the prototype and the model are shown for $S_0=7.5m^2$·sec/rad and for $S_0=10m^2$·sec/rad, respectively.



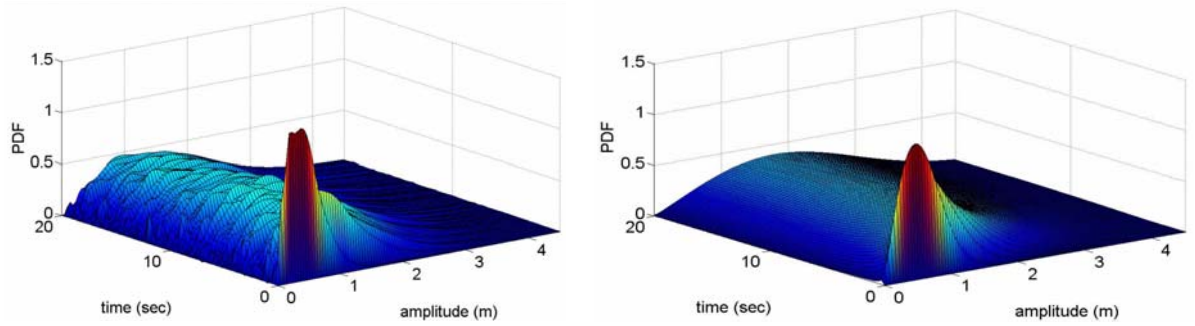
(a) (b)

Figure 13: Non-stationary response amplitude PDF for $S_0=5m^2$·sec/rad: (a) MDOF (MCS) and (b) SDOF (NPI)



(a) (b)

Figure 14: Non-stationary response amplitude PDF for $S_0=7.5m^2$·sec/rad: (a) MDOF (MCS) and (b) SDOF (NPI)



(a) (b)

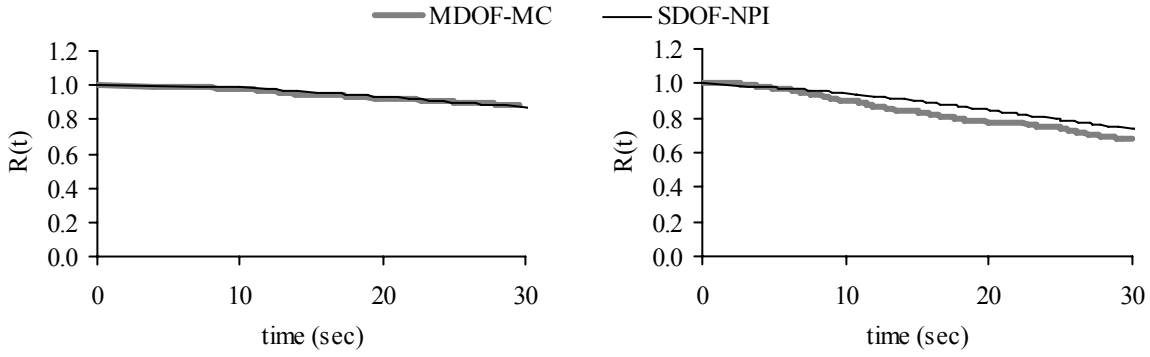
Figure 15: Non-stationary response amplitude PDF for S_0=10m^2·sec/rad: (a) MDOF (MCS) and (b) SDOF (NPI)

The comparison between the diagrams of the SDOF model and the MDOF system shows a satisfactory level of accuracy. Thus, the proposed dimension reduction method based on the NPI approach can be used at a preliminary design stage to estimate the probability for the MDOF cable net to reach a certain value of displacement at a given time, during transient or steady state response, using the equivalent SDOF model.

5.2 Reliability function

The failure barrier level is set to B=3.975m accounting for a maximum permissible cable stress as explained in section 3.2. All analyses performed with ADINA for the prototype have a material law for which the tension branch arrives at the yield stress, as shown in Figure 3. As mentioned in section 5, the total time is 30sec for the prototype and 35.90sec for the model, while the results of the latter are time scaled, according to the inverse relation of Eq. (20), in order to match the time for the prototype.

Figure 16a depicts the reliability function (survival probability) for S_0=7.5m^2 sec/rad. The maximum difference between the MDOF prototype and the SDOF model is found to be approximately 1%. Similarly, in Figure 16b the reliability functions are plotted for S_0=10m^2·sec/rad, which corresponds to a larger excitation magnitude; thus, causing naturally more failure events for both systems. The maximum difference between the prototype and the model, regarding the calculation of R(t) is found to be approximately 16%. In both diagrams, the proposed dimension reduction approach based on the NPI demonstrates a satisfactory level of accuracy.



(a) (b)

Figure 16: Reliability function R(t) vs time for (a) S_0=7.5m^2·sec/rad and (b) S_0=10m^2·sec/rad

Based on those results it can be concluded that the proposed dimension reduction methodology based on a NPI approach is capable of predicting with satisfactory accuracy the reliability of a large cable net, circumventing the computationally prohibitive in many cases MCS based nonlinear dynamic analyses of the original MDOF system.

6 CONCLUSIONS

In this paper, a dimension reduction approach based on a recently proposed NPI technique introduced in [9] has been developed for determining the non-stationary response amplitude PDF and the survival probability of a MDOF symmetric cable net system with fixed cable ends under Gaussian white noise excitation. Specifically, the concept of similarity relationships, as used in [2], has been employed to reduce the original MDOF system to a SDOF nonlinear oscillator of the Duffing kind. Next, a NPI based approach in conjunction with a stochastic averaging treatment has been utilized to determine the non-stationary response amplitude PDF and the survival probability of the Duffing oscillator.

It has been shown that the proposed dimension reduction approach succeeds in capturing the essential characteristics of the original MDOF system response behaviour in an average manner. In this regard, relatively accurate cable tensile failure probability estimates have been derived at a minimum computational cost for a selected illustrative numerical example; thus, rendering the herein proposed dimension reduction approach a strong candidate for preliminary reliability based design of such structures. Specifically, it can be used potentially for the preliminary design of such structural systems by appropriately choosing the geometry of the cable net, the cable diameter and initial pretension so that failure probability values prescribed by relevant code provisions are satisfied. Regarding future work, more sophisticated excitation power spectrum forms modelling wind loads can be used; this is especially important considering the fact that wind loads are the prevalent dynamic loads which threaten the safety of such structures.

REFERENCES

[1] I. Vassilopoulou, *Nonlinear dynamic response and design of cable nets*, Doctoral Thesis. National Technical University of Athens, Greece, 2011.

[2] I. Vassilopoulou and C. J. Gantes, Nonlinear dynamic behaviour of a saddle form cable net modeled by an equivalent SDOF cable net. M. Papadrakakis, M. Fragiadakis, V. Plevris eds. *3rd ECCOMAS Thematic Conference on Computational Methods in Structural Dynamics and Earthquake Engineering – (COMPDYN 2011)*, Corfu, Greece, May 25-28, 2011.

[3] J.S. Gero, The behaviour of cable network structures. *Structures Report SR8*, University of Sydney, Australia, 1975.

[4] J.S. Gero, The preliminary design of cable network structures. *Structures Report SR9*, University of Sydney, Australia, 1975.

[5] I. Vassilopoulou and C.J. Gantes, Behaviour and preliminary analysis of cable net structures with elastic supports. D.E. Beskos, D.L. Karabalis, A.N. Kounadis eds. *4th National Conference on Metal Structures*, Patras, Greece, **2**, 517-525, May 24-25, 2002.

[6] I. Vassilopoulou and C.J. Gantes, Behavior, analysis and design of cable networks anchored to a flexible edge ring. *IASS Symposium on Shell and Spatial Structures from Models to Realization*, Montpellier, France, Extended Abstract, 212-213, 2004.

[7] I. Vassilopoulou and C.J. Gantes, Cable nets with elastically deformable edge ring. *International Journal of Space Structures*, **20**, 15-34, 2005.

[8] I. Vassilopoulou and C.J. Gantes, Similarity relations for nonlinear dynamic oscillations of a cable net. M. Papadrakakis, D.C Charmpis, N.D. Lagaros, Y. Tsompanakis eds. *1st ECCOMAS Thematic Conference on Computational Methods in Structural Dynamics and Earthquake Engineering (COMPDYN 2007)*, Rethymno, Crete, Greece, abstract 373, June 13-16, 2007.

[9] I. A. Kougioumtzoglou and P. D. Spanos, Response and first-passage statistics of nonlinear oscillators via a numerical path integral approach, *ASCE Journal of Engineering Mechanics*, doi:10.1061/(ASCE)EM.1943-7889.0000564, 2012, (In Press).

[10] A. K. Chopra, *Dynamics of structures, theory and applications to earthquake engineering*, Prentice Hall International, Inc., U.S.A., 1995.

[11] ADINA (Automatic Dynamic Incremental Nonlinear Analysis) v8.4, *ADINA User interface command reference manual, Vol. I: ADINA Solids & Structures model definition*. ADINA R & D, Inc., U.S.A., 2006.

[12] ADINA (Automatic Dynamic Incremental Nonlinear Analysis) v8.4, *Theory and modeling guide, Vol. I: ADINA Solids & Structures*. ADINA R & D, Inc., U.S.A., 2006.

[13] I. Vassilopoulou and C.J. Gantes, Nonlinear dynamic phenomena in a SDOF model of cable net. *Archive of Applied Mechanics*, **82**, 1689-1703, 2012.

[14] A. Nayfeh and D.T. Mook, *Nonlinear Oscillations*. John Wiley & Sons, Inc. U.S.A., 1979.

[15] H. A. Buchholdt, *An introduction to cable roof structures*. Thomas Telford, 2nd Edition, Great Britain, 1999.

[16] MATLAB, *The language of technical computing*. v.7.9.0.529 (R2009b), The MathWorks, Inc., U.S.A., 2009.

[17] T. K. Caughey and H. J. Stumpf, Transient response of a dynamic system under random excitation. *Journal of Applied Mechanics*, **27**, 563-566, 1961.

[18] I. A. Kougioumtzoglou and P. D. Spanos, An approximate approach for nonlinear system response determination under evolutionary stochastic excitation. *Current Science, Indian Academy of Sciences*, **97**, 1203-1211, 2009.

[19] P. D. Spanos and I. A. Kougioumtzoglou, Harmonic wavelets based statistical linearization for response evolutionary power spectrum determination. *Probabilistic Engineering Mechanics*, **27**, 57-68, 2012.

[20] N. Wiener, Generalized harmonic analysis. *Acta Mathematica*, **55**, 117-258, 1930.

[21] R. P. Feynman, Space-time approach to non-relativistic quantum mechanics. *Reviews of Modern Physics*, **20**, 367-387, 1948.

[22] I. A. Kougioumtzoglou and P. D. Spanos, An analytical Wiener path integral technique for non-stationary response determination of nonlinear oscillators. *Probabilistic Engineering Mechanics*, **28**, 125-131, 2012.

[23] A. Naess and J. M. Johnsen, Response statistics of nonlinear, compliant offshore structures by the path integral solution method. *Probabilistic Engineering Mechanics*, **8**, 91-106, 1993.

[24] A. Naess, D. Iourtchenko and O. Batsevych, Reliability of systems with randomly varying parameters by the path integration method. *Probabilistic Engineering Mechanics*, **26**, 5-9, 2011.

[25] A. Pirrotta and R. Santoro, Probabilistic response of nonlinear systems under combined normal and Poisson white noise via path integral method. *Probabilistic Engineering Mechanics*, **26**, 26-32, 2011.

[26] C. W. Gardiner, *Handbook for Stochastic Methods for Physics, Chemistry and the Natural Sciences*. Springer-Verlag, Berlin, Heidelberg, New York, 1985.

[27] M. F. Wehner and W. G. Wolfer, Numerical evaluation of path-integral solutions to Fokker-Planck equations. *Physical Review A*, **27**, 2663-2670, 1983.

[28] J. B. Roberts and P. D. Spanos, *Random Vibration and Statistical Linearization*. New York: Dover Publications, 2003.

[29] J. B. Roberts and P. D. Spanos, Stochastic Averaging: an approximate method of solving random vibration problems. *International Journal of Non-Linear Mechanics*, **21**, 111-134, 1986.

[30] T. T. Soong and M. Grigoriu, *Random Vibration of Mechanical and Structural Systems*. Prentice Hall, New Jersey, 1993.

[31] D. Iourtchenko, E. Mo and A. Naess, Reliability of strongly nonlinear single degree of freedom dynamic systems by the path integration method. *Journal of Applied Mechanics*, **75**, 061016-1-061016-8, 2008.

[32] H. Dekker, Time-local Gaussian processes, path integrals and nonequilibrium nonlinear diffusion", *Physica*, **85A**, 363-373, 1976.

[33] R. Alessi, D. Bairaktaris, F. Caridakis, M. Majowiecki and F. Zoulas, The roof structures of the new sports arena in Athens. *World Congress on Shell and Spatial Structures*, Spain, 6.107-6.123, 1979.

COMPDYN 2013
4th International Conference on
Computational Methods in Structural Dynamics and Earthquake Engineering
Kos Island, Greece, 12–14 June 2013

PROBABILISTIC PERFORMANCE-BASED SEISMIC DESIGN OF BRIDGE COLUMNS

Amarjeet S. Saini[1], Ashkan Vosooghi[2], and Mehdi S. Saiidi[3]

[1] Doctoral Student
University of Nevada Reno, Reno, NV 89557, USA
asaini@unr.edu

[2] Bridge Engineer, Ph.D., P.E.
AECOM Transportation, Sacramento, CA 95811, USA
ashkan.vosooghi@aecom.com

[3] Professor, Ph.D., P.E.
University of Nevada Reno, Reno, NV 89557, USA
saiidi@unr.edu

Keywords: bridge columns; damage index; damage states; earthquakes; return periods; reliability index.

Abstract. *Because earthquakes are random events it is reasonable to design structures taking into account the non-deterministic features of response. Performance-based design is intended to provide options to designers and bridge owners to manage the target performance of the structure. Probabilistic damage control approach (PDCA) is a new procedure for seismic design of bridges subjected to earthquakes. As part of a study funded by the California Department of Transportation (Caltrans), this innovative design methodology is developed by incorporating "Damage Index" (DI) and different earthquake return periods to provide flexibility to the designer. The damage level of the bridge is established for each earthquake level as a function of the degree of lateral displacement nonlinearity and is related to six apparent damage states (DS) defined in a previous study at the University of Nevada, Reno. The correlation between DI and DS was determined from a statistical analysis of measured data for 21 bridge column models subjected to seismic loads on shake tables. Extensive analytical modeling of seismic response of two-column bents was conducted. A wide range of variables was included in the study to address the effect of aspect ratio, transverse steel ratio, longitudinal steel ratio, material properties, site class, return period, target DI, and the number of columns in bents. Each column bents was analyzed under fifteen near-field and ten far-field ground motions. A statistical analysis of the demand DIs was performed to develop fragility curves and calculate the reliability index for each DS. The calculated reliability index and fragility curves show that the proposed method can be effectively used in seismic design of new bridges.*

1. INTRODUCTION

Based on the lessons learnt from the previous earthquakes, performance-based seismic design of bridges has become of interest to many researchers and structural engineers. Performance based seismic design [PBSD] is based largely on displacement consideration rather than strength/forces [10]. The fundamental philosophy behind PBSD is that the structure should be designed to achieve a specified performance level under design earthquake. However, most of past research on seismic design of bridge columns is based on deterministic approach and therefore, does not take into account the non-deterministic nature of earthquake events, and scatter in column material and geometric properties. Vosooghi and Saiidi [15] developed fragility curves provide a probabilistic approach to account for uncertainties in the seismic response of bridge columns subjected to earthquakes.

In the present study probabilistic damage control approach (PDCA) is introduced in PBSD of bridge columns subjected to earthquakes. PDCA approach considering the possible uncertainties in earthquake demand and bridge response was developed for probabilistic PBSD of bridge columns. This innovative design methodology is developed by incorporating "Damage Index" (DI) and different earthquake return periods. The concept of PDCA approach by incorporating DI was proposed by Tourzani et al [12], for designing and evaluating bridge column based on predefined or expected performance level. However the uncertainties in earthquake demands and bridge responses were not included in their study.

In this article, PDCA approach was applied to many single column and two columns bents (SCB and TCB). However, in the present study, only TCB's are discussed. TCB's were design for a predefined performance under design earthquake. To quantify the performance of a bridge column, each performance level was correlated to each possible apparent DS and subsequently, each damage state was correlated to their associated DI. DI was defined as the ratio of plastic displacement demand to plastic displacement capacity (Eq. 1). The correlation between DI and damage state (DS) was determined from a statistical analysis of measured data for 21 bridge column models subjected to seismic loads on shake tables [15].

$$\mathrm{DI} = \frac{\mathrm{D_d} - \mathrm{D_Y}}{\mathrm{D_u} - \mathrm{D_Y}} \tag{1}$$

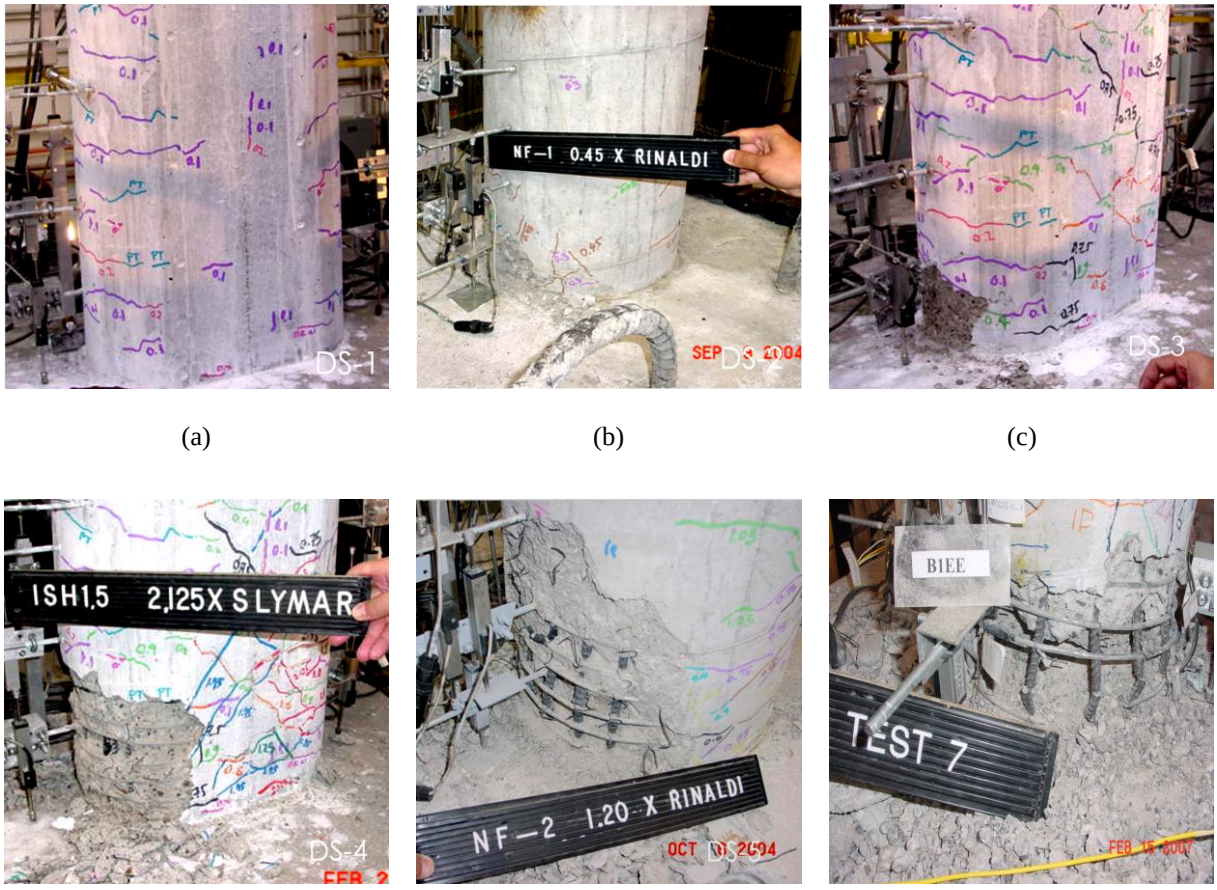
To develop a large database/scatter for damage index demand (DI_d), nearly 400 non-linear dynamic analyses was performed utilizing SAP 2000. To consider uncertainties in DI_d, various column dimensions, support conditions, longitudinal steel ratios, site classes, and distance to active faults were considered in the analyses. A statistical analysis of the demand DI_d was performed to develop fragility curves and calculate the reliability index. Reliability analysis was conducted to calibrate the design DI to obtain a sufficient reliability against failure.

2. DAMAGE STATES AND DAMAGE INDICES

To develop probabilistic performance based design approach various performance levels for different earthquake return periods were defined. Each performance level was quantified in terms of DS. Each DS was correlated to corresponding DI. Damage states defined previously in the study at University of Nevada Reno [14] was utilized. Six possible apparent damage states defined are as follow [15]; DS1 = flexural cracks, DS2 = minor spalling, DS3 = Extensive spalling, DS4 = visible lateral or longitudinal bars, DS5 = imminent core failure, and DS6 = failure/fractured bars. Six apparent damage states are shown in Fig. 1. Figs. 1(a) to 1 (d) represent the DS's from DS1 to DS6, respectively.

The columns were tested under gradually increasing loads in the original studies to cover all possible damage states (DS1 to DS6). The peak displacement was measured at each DS

and subsequently, DI was calculated. DI varies between zero and one corresponds to no damage and failure, respectively. For each DS, large scatter in the calculated DI was observed. To take into account the scatter in DI, fragility analysis for each DS was performed utilizing cumulative lognormal distribution function [15]. Fragility curves were justified utilizing Smirnov-Kolmogorov goodness of fit test [5] with 10% level of significance [6]. Fragility curves for each DS are shown in Fig. 2. DS6 is corresponds to failure with DI equal to one, therefore, even though in some cases where DI was greater than one, it was considered equal to one and consequently, no scatter in the data was considered and no fragility curve was developed for DS6. Also for reliability analysis mean and standard deviation of DS6 for resistance model was considered one and zero, respectively. Fragility curves shown in Fig. 2 are the resistance model for the reliability analysis.



(a) (b) (c)

(d) (e) (f)

Figure 1. Possible apparent damage states of bridge columns

3. PERFORMANCE OBJECTIVES

Apparent damage states were used to define the performance objectives of bridge columns under design earthquake of 1000 year return period. Earthquake of 1000 year return period is corresponds to 7% probability of exceedance in 75 years [1]. Based on the discussion with Caltrans engineers, columns were designed for DS3 under design earthquake. To design columns for DS3, initially tentative target design DI of 0.35 was selected from the fragility curve shown in Fig. 2. Target design DI of 0.35 is corresponds to the 50% probability of exceed-

ance of DS3. To calibrate the target design DI, reliability analysis was performed. The choice of target reliability index for any structure is bit subjective. The AASHTO LRFD recommends target reliability index of 3.5 for gravity loads. In the present study, it was decided to use β of 3 against failure because earthquake loading is non-deterministic and not always present on a structure unlike gravity loads.

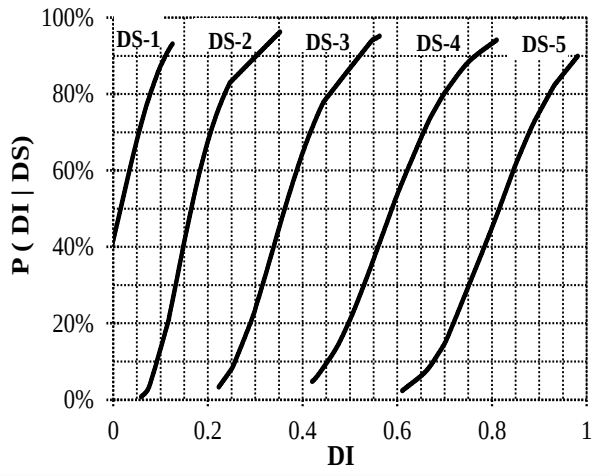


Figure 2. Fragility curves of damage index for various damage states (Vosooghi and Saiidi, 2010)

4 SEISMIC DEMAND ANALYSIS

To determine DI_d non-linear dynamic analysis was performed on various TCB models utilizing SAP 2000. All bents were analyzed under ten far-field and fifteen near-field ground motions selected from PEER strong ground motion data base [9]. Peak displacement of bent for each ground motion was recorded and associated DI_d to peak displacement was calculated. To consider uncertainties in seismic demand, various parameters were considered in the analyses. These parameters are divided mainly into the following categories:

4.1. Bridge site class

Bridge site class was divided into two categories; site B/C and site D. Site B, C, and D is correspond to the rock, soft rock, and stiff soil, respectively [1]. Because site B and C both represents rock, therefore, for sake of simplicity they are lumped together in one site class as B/C. Caltrans ARS online [3] and USGS de-aggregation beta website [13] were utilized to determine design spectrum for site class B/C and D, respectively. For design spectrum shear wave velocity (V_{S30}) of 760 m/s and 270 m/s was used for site B/C and site D, respectively. 760 m/s represents the median of V_{S30} of site class B and C, whereas, 270 m/s represents the average V_{S30} of site class D.

4.2. Ground motion selection

Un-scaled ground motions were selected from PEER strong ground motion database [9]. To consider the uncertainties in the ground motion, various site parameters were considered. The selection criteria of ground motions were based on the V_{S30}, distance to the fault (R_{jb}), and scaling factors (SF). V_{S30} between 500 to 1500 m/s and 200 to 360 m/s were considered to select ground motions for site class B/D and D, respectively. R_{jb} between 0 to 15 km and 15 to 30 km was selected for near-field and far-field ground motions, respectively. Ground motions were selected so that the scale factor calculated based on spectral acceleration associated

with period of one second is not greater than 3. Based on these parameters, fifteen near-field and ten far-field ground motions were selected for each site class.

4.3. Column bent properties

To consider uncertainties in column bent properties, the affect column height to diameter ratio (H/D), longitudinal steel ratio (ρ_l), and column support conditions were considered in the analyses. All bents had circular section with 6 feet diameter. Square cap beam section of seven feet was used in all TCB's. Various TCB models used in the analyses are presented in Table 1. All bents were designed for axial load index of 10%. The expected material properties as specified in SDC Caltrans 2010 were used to design column bents. . The specified concrete strength of 3.6 ksi and steel Gr. 60 were used in the design. The columns were not designed for shear because the intention of this research was to study the scatter on seismic demand of the columns designed for a given DI.

Site class	Config.	H/D	Long. steel ratio	Period	Yield Displacement	Demand Displacement	Ultimate Displacement	Damage Index
			%	secs	in	in	in	in/in
B	Fix-Pin	5	1	1.29	3.80	6.70	12.20	0.34
			2	1.15	4.70	6.10	9.50	0.29
			3	1.05	5.10	5.70	8.60	0.16
D	Fix-Pin	5	1	1.30	4.10	10.70	21.30	0.39
			2	1.16	5.10	9.50	16.20	0.39
			3	1.06	5.70	8.70	14.70	0.34
B	Fix-Fix	5	1	0.69	2.20	3.50	5.60	0.37
D	Fix-Fix	5	1	0.70	2.40	5.10	8.60	0.43
			2	0.64	3.00	4.40	6.70	0.38
			3	0.58	3.20	3.80	5.40	0.27
D	Fix-Pin	10	1	3.62	14.9	26	47.3	0.34
			2	3.13	17.4	23.3	38	0.29
			3	2.81	18.5	21.5	32.8	0.61
D	Fix-Fix	10	1	1.87	8.2	15.3	25.9	0.4
			2	1.63	9.7	13.5	21.2	0.33
			3	1.47	10.2	12	17.7	0.24

Table 1. Two column bent properties and design parameters

5 Analyses results

Non-linear dynamic analysis were conducted using fifteen near-field and ten far-field ground motions scaled at the spectral acceleration associated with the fundamental period of the bent. Nearly 400 analyses were conducted. The peak relative displacement for each analysis was determined and subsequently, DI_d associated to peak displacement was calculated. A large scatter was observed in the calculated DI_d. To take into account the scatter in DI_d, cumulative normal distribution functions were utilized to perform fragility analysis. Fragility analysis was justified utilizing Smirnov-Kolmogorov goodness of fit test [5] with 10% level of significance [6]. The fragility of DI_d is shown in Fig. 3. This DI_d fragility curve represent the load model in the reliability analysis.

Fig. 3 show that 18% of the calculated DI_d data is falling outside the limit curves. It was observed that fragility curve for TCB's using normal distribution function is very sensitive to number of failures (DI = 1) occurred in the analyses. In TCB's six failures were occurred

which cause this data to fall outside the limit curves. Excluding these six data points, only 5% of the total data falls outside the limit curves. Moreover non-cumulative normal frequency distribution of DI_d shows that, calculated DI_d data follow the normal distribution, as shown in Fig. 4. Due to these reasons normal distribution function for TCB's was considered reasonable.

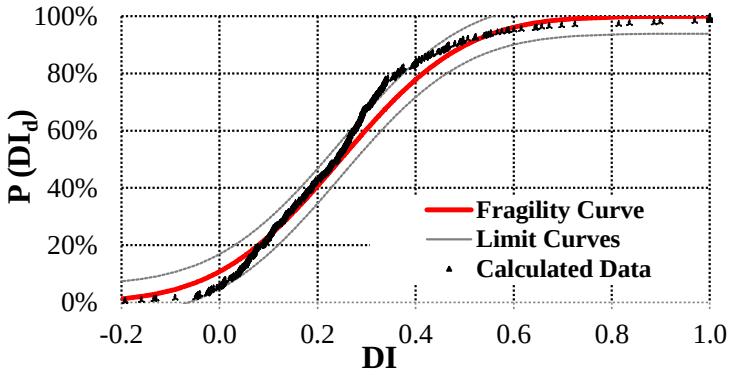


Figure 3. Fragility curve for damage index at different damage state

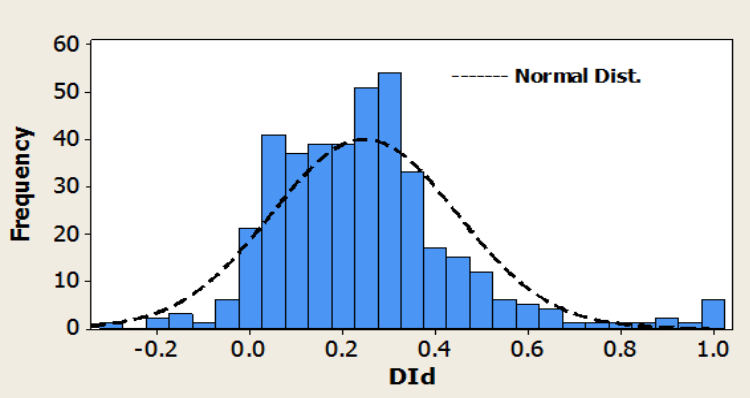


Figure 4. Normal frequency distribution of damage indices

6 RELIABILITY ANALYSIS

The reliability of a structure commonly expressed in terms of reliability index (β) [7]. The reliability analysis presented in this paper is based on large experimental test data and comprehensive analysis of column resistances and load models, respectively. Because the scatter in data was normally distributed, therefore, β corresponds to normal distribution was calculated by utilizing equation Eq. 2 [2, 7]. μ_R and σ_R is the mean and standard deviation of DI corresponds to DS3 in resistance/capacity curve (Fig. 2). μ_Q and σ_Q is the mean and standard deviation of DI corresponds to DS3 in load/demand curve (Fig. 3). The probability of bent failure corresponds to given β can be calculated by using Eq. 3. The β calculated using Eq. 2 does not include probability of earthquake exceednace during the life time of a structure.

$$\beta = \frac{\mu_R - \mu_L}{\sqrt{\sigma_R^2 + \sigma_L^2}} \tag{2}$$

$$\beta = -\Phi^{-1}(P_f) \tag{3}$$

Where, P_f and Φ represent the probability of failure and normal standard distribution function, respectively.

Probability of bent failure is related to the return period or exceedance probability of the design earthquake. In the present paper all bents were designed for an earthquake of 1000 year return period. Therefore, it is important to determine the probability of bent failure combined with the probability of earthquake exceedance during the life time of a structure. Considering annual earthquake events are independent, the probability of earthquake exceedance during lifetime of a structure can be calculated using Eq. 4 [16]:

$$P_{EQ} = 1 - \left(1 - \frac{1}{T}\right)^t \tag{4}$$

Where, P_{EQ}, t and T are the probability of earthquake exceedance during the life time of a structure, life time of a structure and return period, respectively. The P_{EQ} calculated utilizing Equation 4 was equal to 0.072. The probability of bent failure (P_{BF}) and at the same time to have earthquake occurrence can be calculated using conditional probability as:

$$P_{BF} \cap P_{EQ} = \left(P_{BF} \mid P_{EQ}\right) \times \left(P_{EQ}\right) \tag{5}$$

$$P_{BF} \mid P_{EQ} = 1 - \Phi(\beta) \tag{6}$$

$P_{BF} \mid P_{EQ}$ is the probability of bent failure given the design earthquake has occurred. Using β calculated from Eq. 2, $P_{BF} \mid P_{EQ}$, was calculated utilizing Eq. 6.

Having P_{EQ} and $P_{BF} \mid P_{EQ}$, the probability of bent failure (P_{BF}) combined with probability of earthquake exceedance during the life time of a structure was calculated using Eq. 5. Having the combined probability of failure, β was back calculated from Eq. 3. The level of reliability at DS3, DS4, and DS5 was also investigated. Fig. 5 shows the cumulative β combining the DI_d data of all TCB models. The reliability indices presented in Fig. 5 are based on target design DI of 0.35 and earthquake of 1000 year return period.

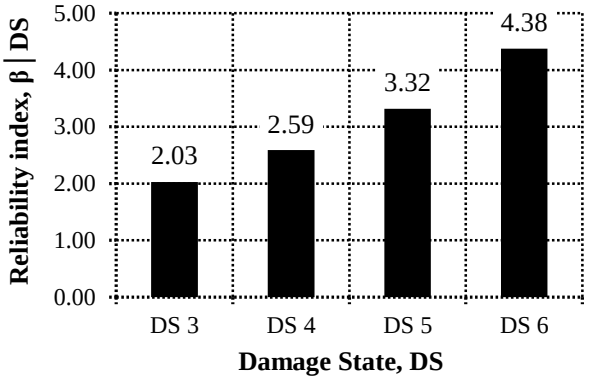


Figure 5. cumulative reliability index at each damage state

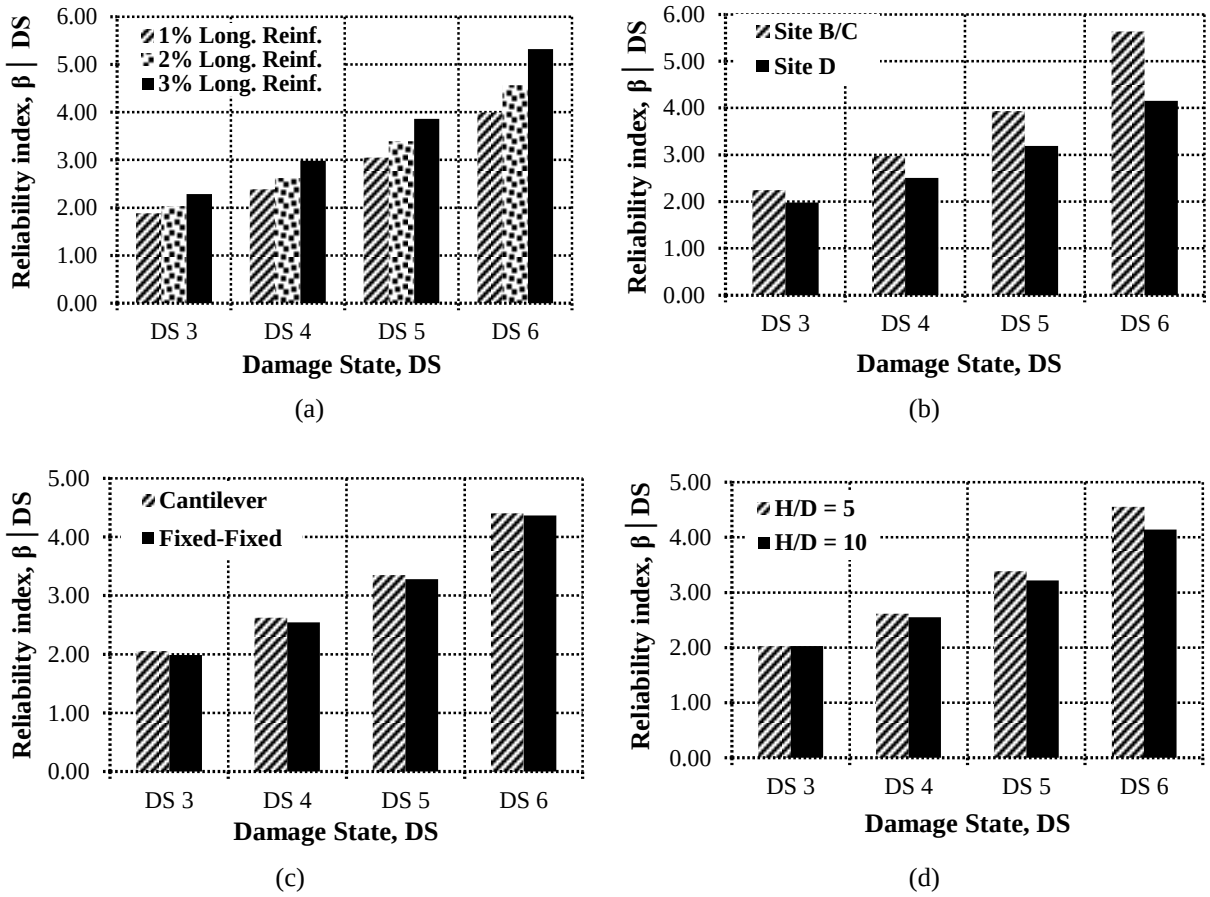


Figure 6. The effect of different parameters on reliability indices at different damage states

Figs. 6 (a) to 6 (d) represent the β for TCB's under various longitudinal steel ratio, site class, support conditions, and column height to diameter ratio (H/D) ratio, respectively. Figs. 6(a) and 6(c) indicate that the reliability indices increase by increasing longitudinal steel ratio and are independent of support conditions, respectively. Fig. 6(b) indicates that TCB's for site class B are more reliable than TCB's for site class D, and Fig. 6(d) indicates that TCB's with H/D = 5 are more reliable than TCB's with H/D = 10.

7 CONCLUSION

The following conclusions were made based on the study presented in this paper:

- Seismic demand of bridge columns is sensitive to bent properties and site class parameters.
- Seismic response of bridges columns is sensitive to bent material properties and bent configurations.
- Reliability index against failure in two column bents is much higher when two column bents are designed for 50% probability of exceeding DS-3 (damage index of 0.35) under 1000-year earthquake. Therefore, to achieve an optimum reliability index against failure, two column bents can be designed for higher probability of exceeding DS-3 without causing a concern for failure.
- The new approach of PDCA by incorporating reliability index provides much flexibility to the structural designers to design a bridge column to reach a given damage state with a specified reliability under an earthquake with a given return period.

ACKNOWLEDGEMNETS

The research presented herein was sponsored by California Department of Transportation (Caltrans) under Grant No. 65A0419. Mr. Abbas Tourzani, Dr. Mark Mahan, Dr. Amir Malek, and Mr. Sam Ataya, of Caltrans are thanked for their feedback and interest in different aspects of the project. Special thanks due to Mr. Peter Lee, the Caltrans Research Program manager, for his support and advice.

REFERENCES

[1] AASHTO 2010, "AASHTO LRFD Bridge Design Specification," American Association of State Highway and Transportation Officials, 5th Edition, Washington, D. C.

[2] Ayyub, B. and McCuen, R. H. 2003. "Probability, Statistics, and Reliability for Engineers and Scientists," CRC Press LLC, Boca Raton, Florida.

[3] Caltrans 2012, "ARS Online," http://dap3.dot.ca.gov/shake_stable/v2/index.php, California Department of Transportation, Sacramento, CA.

[4] Caltrans 2010. "Seismic Design Criteria (SDC)," version 1.6, California Department of Transportation, Sacramento, CA.

[5] Massey, F.J. 1951. "The Kolmogorov-Smirnov Test for Goodness of Fit," Journal of the American Statistical Association, V. 46, No. 253, March, pp. 68-78.

[6] Naeim, F., Hagie, S., Alimoradi, A., and Miranda, E. (2005). "Automated Post-Earthquake Damage Assessment and Safety Evaluation of Instrumented Buildings," Report No. 2005-10639, John A. Martin Associates, Inc., Los Angeles, CA.

[7] Nowak, A.S. and Collins, K.R. 2000. "Reliability of Structures," McGraw-Hills Companies

[8] Nowak, A.S. and Zhou, J. H., 1985, "Reliability Models for Bridge Analysis," Report No. UMCE85-9, University of Michigan, March.

[9] PEER 2011, "Users Manual for the PEER Ground Motion Database Web Application," Beta Version, November, http://peer.berkeley.edu/peer_ground_motion_database/.

[10] Priestley, M. J. N., Calvi G. M., and Kowalsky M. J. 2007, "Displacement-Based Seismic Design of Structures," IUSS Press, Pavia, Italy.

[11] Saiidi, M., Vosooghi, A., and Nelson, R.B. 2013. "Shake Table Studies of a Four-Span Reinforced Concrete Bridge," Journal of Structural Engineering, ASCE, Special Issue on NEES: Advances in Earthquake Engineering, In press, http://ascelibrary.org/doi/abs/10.1061/%28ASCE%29ST.1943-541X.0000790.

[12] Tourzani, A.M, Malek, A.M, Ataya, S, and Mahan, M 2008, "Probabilistic Damage Control Approach (PDCA) and Performance–Based Design of Bridges," Sixth National Seismic Conference on Bridges and Highways: Seismic Technologies for Extreme Loads, Multidisciplinary Center for Earthquake Engineering Research.

[13] USGS 2008. "NSHMP PSHA Interactive Deaggregation," https://geohazards.usgs.gov/deaggint/2008/index.php, Geologic Hazard Science Center.

[14] Vosooghi, A. and Saiidi, M. 2010. "Seismic Damage States and Response Parameters for Bridge Columns," ACI Special Publications, SP271-02, Structural Concrete in Performance-Based Seismic Design of Bridges, V. 271, May 24, pp. 29-46.

[15] Vosooghi, A. and Saiidi, M. 2012. "Experimental Fragility Curves for Seismic Response of Reinforced Concrete Bridge Columns," ACI Structural Journal, V. 109, No. 6, November-December, pp. 825-834.

[16] Yen, B. C. 1970. ''Risks in Hydrologic Design of Engineering Projects,'' Journal Hydrologic Division, ASCE, 96(4), 959–966.

COMPDYN 2013
4th ECCOMAS Thematic Conference on
Computational Methods in Structural Dynamics and Earthquake Engineering
M. Papadrakakis, V. Papadopoulos, V. Plevris (eds.)
Kos Island, Greece, 12–14 June 2013

SYSTEM RELIABILITY ANALYSIS OF SLENDER NETWORK ARCH BRIDGES

Anders Rønnquist[1] **and Arvid Naess**[2]

[1] Department of Structural Engineering
Norwegian University of Science and Technology
NO-7491 Trondheim, Norway
e-mail: anders.ronnquist@ntnu.no

[2] Centre for Ships and Ocean Structures & Department of Mathematical Sciences
Norwegian University of Science and Technology
NO-7491 Trondheim, Norway
e-mail: arvid.naess@ntnu.no

Keywords: System reliability, Network Arch Bridges, Monte Carlo Simulation

Abstract. *In principle, the reliability of complex structural systems can be accurately predicted through Monte Carlo simulation. This method has several attractive features for structural system reliability, the most important being that the system failure criterion is usually relatively easy to check almost irrespective of the complexity of the system. However, the computational cost involved in the simulation may be prohibitive for highly reliable structural systems. Network arched bridges are in their design slender structures which by their efficient configuration can carry loads several times higher than for more traditional tie arched bridges with vertical hangers. These bridges are seen as an attractive structure due to their slenderness which also might make them vulnerable to global system buckling. The buckling reliability of network arch bridges are therefore investigated with emphasis on geometric uncertainties*

1 INTRODUCTION

In recent years, the structural assessments of new and existing structures have included probabilistic methods to get a broader insight into the structural behavior over time. Reliability tools have been shown to be a valuable contribution in the decision making process. For all structures, either already existing or to be built and perhaps especially for large civil engineering structures, these tools can be used to evaluate different alternative methods and scenarios, see e.g. [3].

The improvement of the structural understanding during the life span of large infrastructures has at the present time become an important problem to be addressed. This is partly due to the situation of an ever increasing number of infrastructures reaching their final stage of design life, and partly due to changing loads and nonfulfillment of maintenance, rendering physical signs of wear and tear. Results from these observations will ultimately lead to some major decisions for the elected politicians to make regarding our existing and future infrastructure. Should it be invested in upgrading to achieve an extended service life or rather replace dilapidated structures with new? Both of these alternatives will demand major investments in the immediate future to uphold today's standard and to include future demands.

The solution of realistic structural system reliability problems is generally exceedingly difficult to obtain through conventional reliability methods such as the FORM/SORM methods. The main reason is the high number of limit state functions and basic random variables that may be required to define the problem. The system failure event in a realistic case may be defined by a complex combination of failure modes, in general as a combination of series and parallel systems. The failure criteria are very often associated with nonlinear structural behavior, requiring computationally demanding numerical approaches such as the nonlinear FE analysis to accurately assess the structural capacity.

At least in principle, the reliability of complex structural systems can be accurately predicted through Monte Carlo simulation. With this method the system failure criterion is relatively easy to evaluate almost irrespective of the complexity of the system and the number of basic random variables. However, the system failure probabilities are typically of rather small magnitude and therefore the computational cost involved in the Monte Carlo simulation may be prohibitive. If numerical approaches are used to assess the structural capacity, the problem may be intractable if efficient techniques such as the response surface method were not used.

A new Monte Carlo based method for system reliability estimation that aims to reduce the computational cost was recently proposed in [12]. It exploits the regularity of tail probabilities to set up an approximation procedure for the prediction of the far tail failure probabilities based on the estimates obtained by Monte Carlo simulations at more moderate levels. The method was first applied in [12] to small structural systems and later in [13] to a complex system involving a high number of limit state functions and basic random variables. It was shown that the method provides good estimates for the system failure probability with low to moderate computational cost. In this study the method is used to estimate the global system buckling of a network arch bridge represented by a FE structural model.

2 EFFICIENT SYSTEM RELIABILITY ESTIMATION

Consider a structural system for which several failure modes may be defined, and assume that each failure mode is represented by a safety margin,

$$M_i = G_i\left(X_1, \cdots, X_n\right) \tag{1}$$

with G_i, i = 1, …, m, the limit state function that defines the safety margin M_i as a function of a vector $X = [X_1, \ldots, X_n]^T$ of n basic random variables. The limit state function G_i can be a ra-

ther complicated function of the random vector X. In many cases a closed-form equation is not known and the evaluation of G_i requires computationally demanding numerical models, e.g., non-linear FE-models. Failure in mode i of the system is assumed to occur when $M_i = G_i(X) \leq 0$. For a basic system of m failure modes in series the system failure probability is defined by,

$$p_f = \mathrm{P}\left[\bigcup_{i=1}^{m}\left(M_i \leq 0\right)\right] \tag{2}$$

while for the parallel case it is,

$$p_f = \mathrm{P}\left[\bigcap_{i=1}^{m}\left(M_i \leq 0\right)\right]. \tag{3}$$

These are the elementary cases considered in structural systems reliability analysis [9], which are here introduced as example.

To overcome the computational cost typically involved in the estimation of the failure probability of a system of failure modes, the method proposed in [12] formulates the system safety margins in the following way:

$$M_i(\lambda) = M_i - \mu_i(1-\lambda) \tag{4}$$

where M_i is a system safety margin, given by Eq. (1), and $\mu_i = E[M_i]$ is the mean value of M_i. The parameter λ assumes values in the interval $0 \leq \lambda \leq 1$ and its effect on the system failure probability may be interpreted as a scale factor. The original system is obtained for $\lambda = 1$, and for $\lambda = 0$ the system is highly prone to failure, as the mean value of the system safety margins is $E[M_i(0)] = 0$. For small to intermediate values of λ the increase in the system failure probability is sufficiently high to get accurate estimates of the failure probability by Monte Carlo simulation with moderate computational cost.

As proposed by [12], it is assumed that the failure probability as a function of λ can be written as,

$$p_f(\lambda) \underset{\lambda \to 1}{\approx} q(\lambda)\exp\left\{-a\left(\lambda - b\right)^c\right\} \tag{5}$$

where $q(\lambda)$ is a slowly varying function compared with the exponential function $\exp\{-a(\lambda - b)^c\}$. For practical applications it can be implemented in the following form [12]:

$$p_f(\lambda) \approx q\exp\left\{-a\left(\lambda - b\right)^c\right\} \quad \text{for} \quad \lambda_0 \leq \lambda \leq 1 \tag{6}$$

for a suitable value of λ_0, with the function $q(\lambda)$ replaced by a constant q. An important part of the method is therefore to identify a suitable λ_0 so that Eq. (6) represents a good approximation of $p_f(\lambda)$ for $\lambda \in [\lambda_0, 1]$.

The functional form assumed in Eq. (5) is strictly speaking based on an underlying assumption that the reliability problem has been transferred to normalized Gaussian space where a FORM or SORM (or similar) type of approximation would work for the transformed limit state functions. However, when the basic random variables have 'exponential' type of distributions, like e.g. Weibull, normal, lognormal, Gumbel, there is no need to make a transformation to normalized Gaussian space. One can then instead work in the original space and adopt Eq. (6) there. This is the procedure adopted in this paper.

The practical importance of the approximation provided by Eq. (6) is that the target failure probability $p_f = p_f(1)$ can be obtained from values of $p_f(\lambda)$ for $\lambda < 1$. This is the main concept

of the estimation method proposed in [12], as it is easier to estimate the failure probabilities $p_f(\lambda)$ for $\lambda < 1$ accurately than the target value, since they are larger and hence require less simulations and therefore less computational cost. Fitting the approximating function for $p_f(\lambda)$ given by Eq. (6) to the estimated values of failure probability obtained by Monte Carlo simulation with $\lambda < 1$, will then allow us to provide an estimate of the target failure probability by extrapolation.

It may be noted that the method described above is, in fact, very different from an importance sampling procedure. While importance sampling is very vulnerable to the dimension of the space of basic random variables, this is not at all the case with the method described here [13].

2.1 Monte Carlo based reliability estimation by optimized fitting

To find the four parameters q, a, b and c in Eq. (6) defining the optimal fit between function and estimated values of failure probability obtained by Monte Carlo simulation, an optimized fitting procedure was suggested in [12].

For a sample of size N of the vector of basic random variables $\boldsymbol{X} = [X_1, \ldots, X_n]^T$, let $N_f(\lambda)$ denote the number of samples for which failure of the system is verified. An empirical estimate of the failure probability is then given by,

$$\hat{p}_f(\lambda) = \frac{N_f(\lambda)}{N}. \tag{7}$$

The coefficient of variation of this estimator is,

$$C_v\left(\hat{p}_f(\lambda)\right) = \sqrt{\frac{1-p_f(\lambda)}{p_f(\lambda)N}}, \tag{8}$$

which for small failure probabilities can be approximated by,

$$C_v\left(\hat{p}_f(\lambda)\right) \approx \frac{1}{\sqrt{p_f(\lambda)N}}. \tag{9}$$

A fair approximation of the 95% confidence interval for the value $p_f(\lambda)$ can be obtained as $\mathrm{CI}_{0.95}(\lambda) = [C^-(\lambda), C^+(\lambda)]$, where,

$$C^{\pm}(\lambda) = \hat{p}_f(\lambda)\left[1 \pm 1.96 C_v\left(\hat{p}_f(\lambda)\right)\right]. \tag{10}$$

Considering now that we have obtained empirical estimates of the failure probability using Eq. (7) for a suitable set of λ values, the problem then becomes one of finding the optimal fit between the proposed approximating function for the failure probability given by Eq. (6) and the empirical estimates obtained. As proposed in [12], this optimal fit can be carried out by minimizing the following mean square error function with respect to the four parameters q, a, b and c in Eq. (6) at the log level:

$$F(q,a,b,c) = \sum_{j=1}^{M} w_j \left[\log \hat{p}_f(\lambda_j) - \log q + a\left(\lambda_j - b\right)^c\right]^2 \tag{11}$$

where $\lambda_0 \le \lambda_1 \le \ldots < \lambda_M < 1$ denotes the set of λ values where the failure probability is empirically estimated and w_j denotes a weight factor that puts more emphasis on the more reliable

data points. The choice of the weight factors is to some extent arbitrary. The following definition was suggested in [12]:

$$w_j = \left[\log C^+\left(\lambda_j\right) - \log C^-\left(\lambda_j\right)\right]^{-\theta} \tag{12}$$

with θ = 1 or 2, combined with a Levenberg - Marquardt least squares optimization method. This has proved to work well provided that a reasonable choice of the initial values for the parameters is made. In this study $\theta = 2$ is adopted for the optimized fitting. Note that the definition adopted for w_j puts some restriction on the use of the data. Usually, there is a level λ_j beyond which w_j is no longer defined. Hence, the summation in the mean square error function given by Eq. (12) has to stop before that happens. Also, the data should be preconditioned by establishing the tail marker λ_0 in a sensible way.

Although the Levenberg-Marquardt least squares method as described above generally works well, it may be simplified by exploiting the structure of the mean square error function F. It is realized by scrutinizing Eq. (11) that if b and c are fixed, the optimization problem reduces to a standard weighted linear regression problem. That is, with both b and c fixed, the optimum values of a and $\log q$ are found using closed-form weighted linear regression formulas in terms of w_j, $y_j = \log \hat{p}_f\left(\lambda_j\right)$ and $x_j = \left(\lambda_j - b\right)^c$.

It is obtained that the optimal values of a and q are given by the relations:

$$a^*\left(b,c\right) = -\frac{\sum_{j=1}^{M} w_j\left(x_j - \overline{x}\right)\left(y_j - \overline{y}\right)}{\sum_{j=1}^{M} w_j\left(x_j - \overline{x}\right)^2} \tag{13}$$

and

$$\log q^*\left(b,c\right) = \overline{y} + a^*\left(b,c\right)\overline{x} \tag{14}$$

where

$$\overline{x} = \sum_{j=1}^{M} w_j x_j \Big/ \sum_{j=1}^{M} w_j \tag{15}$$

and

$$\overline{y} = \sum_{j=1}^{M} w_j y_j \Big/ \sum_{j=1}^{M} w_j \tag{16}$$

The Levenberg-Marquardt method may now be used on the function $\tilde{F}\left(b,c\right) = F\left(q^*\left(b,c\right), a^*\left(b,c\right), b, c\right)$ to find the optimal values b^* and c^*, and then the corresponding a^* and q^* can be calculated from Eqs. (13) and (14).

For estimation of the confidence interval for a predicted value of the failure probability provided by the optimal curve, the empirical confidence band given by Eq. (10) is reanchored to the optimal curve. The range of fitted curves that stay within the reanchored confidence band will determine an optimized confidence interval of the predicted value. As a final point, it was verified that the predicted value is not very sensitive to the choice of λ_0 provided that it is chosen with some care.

3 NETWORK ARCH BRIDGE

The concept of network arch bridges has been developed through many years and has been used for road bridges, see [7], as well as train crossings, see [2]. By optimizing the hanger slope configuration of the network the structure can be designed with a significantly lower

mass by steel reduction; over 50 % compared to other similar tie arch bridges with vertical hanger is reported in [17].

Network arch bridges are tied arch bridges with inclined hangers with multiple intersections where the configuration of the tie will follow the arch but with a much larger radius of curvature. This type of arch bridge design is thoroughly described and investigated in several papers by Dr. P. Tveit, e.g. [18]. The inclined hangers are well suited to distribute bending moments and shear forces to the upper and lower chord similar to a truss compared to those in tied arches with vertical hangers where these are relatively large and decisive. Thus, for network arch bridges bending moments in the transverse direction are more important than in the longitudinal direction. This property is one of the main conditions in designing some of the world's most slender bridges.

3.1 Network arch bridge reliability analysis

In the present investigation an enhanced Monte Carlo simulation method is introduced to assess the system buckling reliability of a slender Network arch bridge due to traffic loads. For all slender structures geometric properties are of special interest and their effects on the global system are investigated. Thus, for the presented case study four global imperfections are introduced as basic random variables, width, length, height and the arch out of plumbness. Furthermore, the arch tube member geometric cross section properties are also introduced as random variables. These are the four main steel arch member outer radii's together with corresponding thicknesses. The four arch members are the wind portal frame columns given as the lower part of the arch, wind portal frame girder, wind bracing and the remaining arch members above the wind portal frame, all shown in the Figure 1. These render the 12 basic random variables of the system buckling reliability analysis.

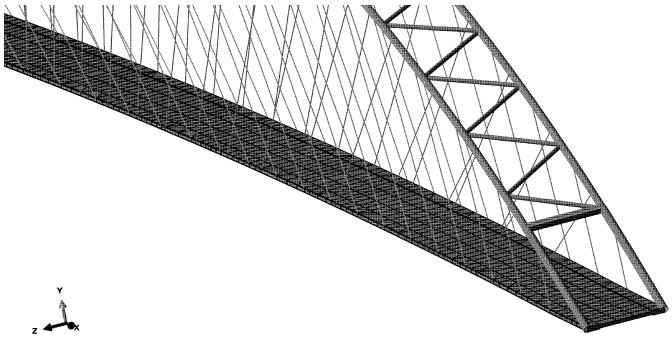


Figure 1. Network arch members with the wind portal frame side columns as part of the arch and top girder as end of the diagonal wind bracing.

All the geometric random variables are assumed uncorrelated normally distributed with the mean values as nominal values (i.e. the dimensions given on drawings). The coefficient of variation (CoV) given in Table 1 are chosen from the guidelines given in [6] with complementation for steel member parameters given in [8].

Random variables	CoV
Tube outer radius, r	2.5 %
Tube thickness, t	2.5 %
Arch length, L	1 / 10.000
Arch height, H	1 / 1000
Arch width, W	1 / 1000
Arch out of plumbness, θ	1.5 $^{o}/_{oo}$

Table 1. Coefficients of variation for basic random variables.

3.2 Model uncertainty

Most civil engineering models are based on an hypothesis of a physical understanding supported by empirical relations between different variables. The engineering models will introduce uncertainties from the inherent physical understanding and the assumed physical model. Incompleteness due to the lack of knowledge and simplifications will give model predictions that differ from real output. This is taken into account in the present analysis by the introduction of a model parameter, *I*, representing the model uncertainties for the load and structural capacity and is treated as a random variable.

A systematic method of choosing and quantify the material and load model uncertainties can be found in the Reliability-Based Classification publication by the Road Directorate, Ministry of Transportation in Denmark [16]. The structural capacity model uncertainty is accounted for by the random variable I_m, introduced by multiplication. This variable is assumed logarithmic normally distributed with a mean value of 1.0 and a coefficient of variation V_{Im}, given by:

$$V_{I_m} = \sqrt{V_{I_1}^{\ 2} + V_{I_2}^{\ 2} + V_{I_3}^{\ 2} + 2\left(\rho_1 V_{I_1} + \rho_2 V_{I_2} + \rho_3 V_{I_3}\right)} \tag{17}$$

Coefficients of variation, V_{Ii}, and correlation coefficients, ρ_i, are determine based on the assumption of three main contributions (i = 1-3). These are the accuracy of the computational mode, uncertainty in determine material parameters and the identity of materials. For the present example selections are made for the structure as a whole. The accuracy of the computational model is assumed normal, uncertainty determining material parameters is set to medium and the identity of materials is assumed normal, rendering $V_i = 0.06$ and $\rho_i = 0.0$ for all three uncertainties.

To quantify the load model uncertainty a similar model can be used [16]. The uncertainty in the computational model for loads are taken into account by introducing a normally distributed stochastic variable, I_f, by addition. The model uncertainty for traffic loading determined from the assumption of medium uncertainty in the loading model can be assumed to have a mean value 0.0 and a coefficient of variation, $V_{If} = 0.15$.

3.3 Traffic load

The Traffic load represents one of the most significant contributions to the total value of the external actions to be considered in the ultimate limit state analysis. In the present reliability analysis is a traffic load model, which represent one of several load cases, sought for a given return period. The traffic loads on bridges will by its nature inherent a great complexity due to the high randomness, thus is difficult to model accurately. This is a natural consequence of the load which varies significantly, also due to its site dependency, especially for long spanning bridges [4].

The uncertainty in the traffic load is dependent on several statistical variables involved describing the problem. Among those which may be considered are the type of vehicle, intervals between vehicles, gross weight of each vehicle, gross weight distribution to axles, spacing

between extreme axles and between any pair of axles, total external length of the vehicle, velocity, daily intensity of vehicles per lane and the density of vehicles over the road, as described in [1]. In most cases there exists no common analytic expression for the total load distribution and correlation coefficients between all these variables.

In [1] it is shown that the traffic load is highly dependent on the type of vehicles as well as their individual load situations. They have identified relations between characteristic load and maximum load effects. It is shown that the axle load distribution, both for loaded as well as unloaded vehicles are skew distributions, assuming that this represents extreme events; they may most likely be assumed to be Gumbel distributed. Furthermore, if a complete description of the different cases is sought then a multimodal distribution must be introduced. Several similar studies are also reported in [4], which show that a detailed description of the traffic load can be modeled by the sum of several assumed independent distributions.

The traffic load extreme values are in the present investigation assumed to be Gumbel distributed where the described load case is assumed representing a uniformly distributed line load. In the design rules given by the Norwegian Public Road Administration (NPRA) it is not clearly stated what the return period of the characteristic traffic load is. However, the Eurocode NS-EN 1991-2 [10] is based on a return period of 1000 years.

The design of the network arch bridge considered in the present investigation is the characteristic design load given by the NPRA used to determine the site specific probabilistic load model for the reliability analysis. By comparison, using the expected distribution of a 250 m queue weight registered in [4], the assumption of Gumbel distribution and a return period equal to 1000 years can an estimate of the mean and standard deviation for the extreme traffic load be fitted. The result from the load distribution estimation gave a mean and standard deviation as m_q= 3.5 N/m and σ_q = 1.1 N/m, respectively. Finally, the Gumbel distribution given by equation 18, where the scale, α, and location, β, parameters relation to the mean, μ, and standard deviation, σ, of the process are given by (as used in [19]):

$$F(x) = \exp\{-\exp[-\beta(x-\alpha)]\} \tag{18}$$

where $\beta = \pi/\sigma\sqrt{6}$ and $\alpha = \mu - 0.57722/\beta$, rendering the scale parameter β = 1.17 and the location parameter α = 3.0.

3.4 Buckling analysis of network arch bridges

Buckling occurs as a small increase in the axial compressive force in the structure causes a sudden outwards displacement as the loading reaches a certain critical level. This may lead to a sudden collapse of the structure without any initial warning. Thus, buckling does not occur as a result of the applied stress reaching a critical level, but rather depends on variations of component dimensions and the overall geometry of the structure.

Shallow arches are more likely to have non-linear pre-buckling behavior with substantial deformation prior to the buckling. This effect needs to be considered and ensured. If classic buckling analysis is used without including these effects might the critical load be incorrectly predict. Thus, it is important to include the pre-loading face with the possibility of any non-linear response, which in the present paper is ensured by the inclusion of bi-linear material strength and geometric stiffness. This will allow for the correct pre-buckling deformation to occur and the correct stiffness to be established. This is to ensure a correct elastic buckling load which is used in the structural reliability analysis. These effects are investigated in [14] and drafted for the in plane buckling but cannot be excluded to be significant also in the out of plane buckling. As stated in [14] may significant pre-buckling deformations, especially for

shallow arches, significantly reduce the buckling resistance and over estimating the buckling load.

For buckling of network arches will the stiffness of the hangers be of special importance and also significantly influence the estimated buckling capacity. Therefore, the hanger configuration will be favorable for network arches compared to tie arches with vertical hangers.

If the network arch tie remains strait the arch will get in-plane buckling modes as can be found from simple columns supported by flexural springs as pointed out by [15]. Simplified solutions may then be found from in-plane arch calculation methods as introduced in both [14] and [15]. However, it can be seen in the present investigation that the out of plane buckling modes can also be expected. In the case of a large network arch bridge with great slenderness may the symmetric as well as the asymmetric modes appear.

In plane buckling modes for network arches was further investigated in [15]. It shows that buckling load for network arches will be dependent on the arch bending stiffness, the number of hangers as well as the arch to hanger angle. However, the bending stiffness and deflection of the tie will have less influence on the global buckling load.

4 THE BRANDANGER NETWORK ARCH BRIDGE, A CASE STUDY

The Brandanger Bridge situated in the western part of Norway is stated to be the world's most slender arch bridge in [18] and [7], see Figure 2.



Figure 2. The Brandanger Bridge opened on the 4th of November 2010.

The design of the bridge was suggested to the Norwegian public road administration in 2004 by dr. P. Tveit and was finally opened on the 4th of November, 2010. In the present case study is an early suggested version of the bridge design used with some further modifications introduced. However, the main description is the same with a length of 220 m, a width of 7.6 m and an arch bow height of 33 m as shown in Figure 3.

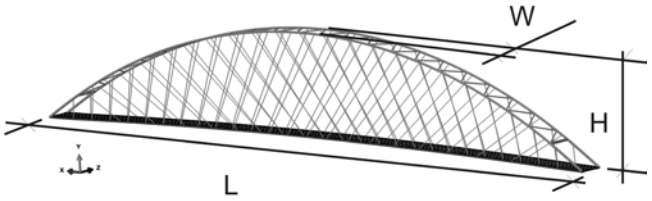


Figure 3. Overall dimensions, width W=7.6m, bow height H=33m and span length L=220m of the network arch bridge.

The bridge consists of a main span with two parallel upper chord steel arches and a lower chord concrete slab tie suspended by 44 hangers on each side. Between the arches is a simple wind portal frame and diagonal wind bracing. The arch as well as the wind bracing consists of steel tube elements, while the inclined hangers are made out of high-strength steel cables. The

bridge deck is constructed by pre-stressed concrete with a total width of just 7.6 meters, creating an extremely light and slender structure. The steel tube profiles of the arch have only some few variations along the arch length. Typically, D·t is 711·40 mm below the wind bracing and 711·35 mm elsewhere. A typical dimension of the concrete slabs is a 250 mm centre thickness, while the first outer 1.1 m on each side has a thickness of 400 mm. below is main material parameters listed.

- Structural steel: density 7850 kg/m3, Young's modulus 210 GPa, yield stress 355 MPa
- Steel hangers: density 7850 kg/m3, Young's modulus 170 GPa, yield stress 1550 MPa
- Concrete bridge deck: density 2200 kg/m3, Young's modulus 28.7 GPa, compressive strength 35 MPa

4.1 Structural response by FE-analysis

The Brandanger Fjord Bridge has in the design stage been subject to extensive numerical analysis such as linear and non-linear static analysis, the prediction of buckling, as well as dynamic time domain analysis. The finite element model for the present analyses is built up of beam elements in the arch with tubular cross sections and the hangers with solid circular cross sections, as well as shell elements for in lower chord bridge deck.

To model the steel network arch in the FE-model are 3-node quadratic Timoshenko beam formulation within Abaqus/Standard used for all arch tube members, wind bracing and wind portal frame girder. For the network hangers is the 2-node linear Timoshenko beam formulation chosen. These beam formulation allows for transverse shear deformation and the beam may be subjected to large axial strains.

The lower chord bridge deck is represented with a simple first order 4-node general purpose conventional shell element with reduced integration formulation within Abaqus/Standard. This element includes thickness changes and transverse shear deformations allowing for large rotations and finite membrane strains.

It is in the FE-analysis procedure distinguishes between general non-linear steps and linear perturbation steps. The general non-linear analysis is defined as sequential events where one state of the model at the end of the step will provide the initial state for the start of the next. The linear perturbation analysis provides the linearized response of the model about the reached state at the end of the last non-linear step. For each step in the analysis can also the procedure account for nonlinear effects from large displacements and deformations. These effects are of special interest in the present buckling investigation, where it is important to account for the pre-buckling deformation.

4.2 Global system buckling reliability estimation

In the present study is a network arch bridge global system buckling limit state function to be evaluated. It includes the derived simplified ultimate traffic load model and the FE linear perturbation eigenvalue solutions of the pre-loaded structure. The system failure is therefore defined as the lowest estimated buckling load exceeding the estimated structural buckling capacity.

Before each evaluation of the system buckling capacity is the system first pre-loaded with the structural self-weight and the nominal traffic load as defined by the Norwegian Public Road Administration design guide Håndbok 185 [5]. This include a uniformly distributed line load of 9 kN/m over a 3 m width and three pairs of point loads, each pair 210 kN, separated by 6 m and 2.5 m. The uniformly distributed traffic load is also introduced as the perturbation load pattern used in the solution. Thus, any pre-load deformation imperfections introduced by

initial loading as well as the geometric stiffness contribution are all established before the buckling analysis.

The reliability of the structure is evaluated by the limit state function defined by the stability failure considered. The bifurcation buckling limit state function can in general terms be stated by:

$$G(\mathbf{X}_R, P_\gamma, I_m, I_f) = P_{cr}(P_B(\mathbf{X}_R), I_m) - P_\gamma\left(P_T(\alpha,\beta), I_f\right) \tag{19}$$

where P_{cr} corresponds to the global system buckling load found by the FE-analysis whereas P_γ is the estimated buckling load estimated from the traffic action. The random variable vector is given by:

$$< \mathbf{X}_R = [t_{arch}, t_{bracing}, t_{port.\,\text{column}}, t_{port.\,girder}, D_{arch}, D_{bracing}, D_{port.\,\text{column}}, D_{por.\,girder}, H, W, L, \theta] \tag{20}$$

The model uncertainty is also introduced by the factors I_m and I_f. The buckling load, P_B, from the FE-analysis is given by the perturbation load and the buckling load factor as:

$$P_B(\mathbf{X}_R) = P_{pert} \cdot \lambda_{cr}(\mathbf{X}_R) \tag{21}$$

whereas the traffic load is estimated from the simplified Gumbel distributed traffic load:

$$P_T = P_T(\alpha,\beta) \tag{22}$$

The remaining structural properties as well as the load distributions are all assumed to be deterministic.

In the present example is the estimated failure probability of the global system buckling event considered. The crude Monte Carlo simulation was used to compute the empirical estimation of failure probability for $\lambda < 1$, as described previously. Each system buckling strength capacity was computed by the bifurcation analysis in Abaqus/Standard with a computational time of approximately 10s on a standard laptop computer, including time to retrieve results and initiate a new analysis. The total number of simulated system buckling analyses was $3.88 \cdot 10^5$ executed in 6 parallel processes, rendering approximately 8 days and nights of computing time. This was deemed as what could be seen as reasonable calculation effort to be invested in the present problem.

Probability of failure for the three first buckling modes are calculated, where the two first are out of plane buckling modes and the third is an in plane buckling mode with significant higher buckling load factor than the first two. Probability of failure is calculated for all three modes using the limit state function in Eq. (19). Typical buckling modes corresponding to the three first modes are shown in Figures 4 – 6.

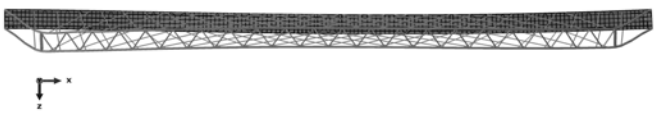


Figure 4. First estimated buckling mode.



Figure 5. Second estimated buckling mode.

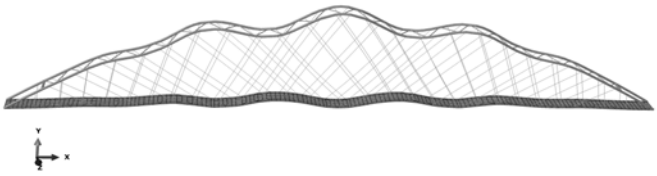


Figure 6. Third estimated buckling mode.

The predicted failure probability and corresponding reliability index at $\lambda = 1$ given by the fitted optimal curves and the re-anchored and optimized 95% confidence interval is given in table 2 and shown in Figures 7-9.

	Pf-	Pf	Pf+	β-	β	β+
M1	4.74·10-7	10.1·10-7	16.9·10-7	4.64	4.75	4.90
M2	1.40·10-7	4.53·10-7	9.66·10-7	4.76	4.91	5.14
M3	0.15·10-9	1.75·10-9	5.01·10-9	5.73	5.91	6.29

Reliability index given by $\beta = -\Phi(P_f)$

Table 2. Network arch bridge probability of failure for global system buckling estimated with the three first buckling modes.

The estimated probabilities of failure comply with expected target probability of failure commonly used in design of civil engineering structures, depending on the consequences of failure and failure modes. In Eurocode NS-EN 1990 [11] are three different target reliabilities in annex B given as 10^{-5}, 10^{-6} and 10^{-7}.

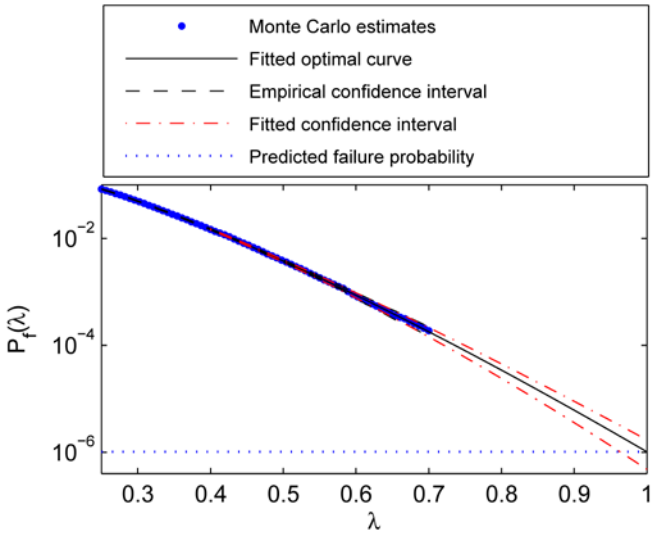


Figure 7. Log plot of failure probability with buckling mode 1. Parameters of the fitted optimal curve: $q = 0.180$, $a = 14.943$, $b = 0.152$ and $c = 1.2825$.

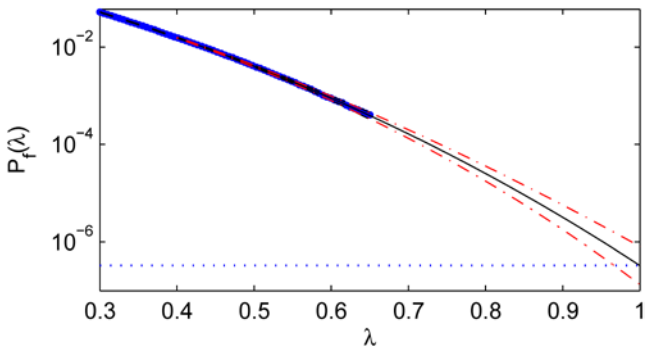


Figure 8. Log plot of failure probability with buckling mode 2. Parameters of the fitted optimal curve: q = 2.452, a = 8.321, b = -0.375 and c = 1.955.

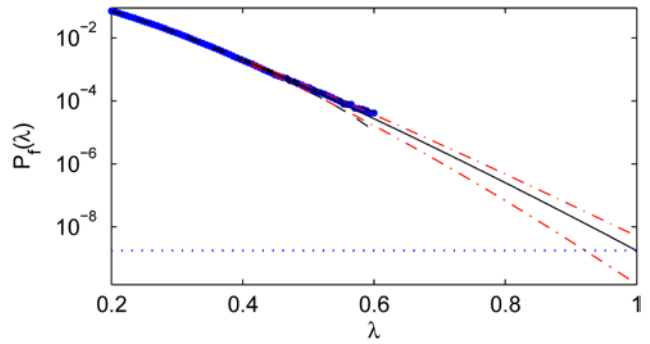


Figure 9. Log plot of failure probability with buckling mode 3. Parameters of the fitted optimal curve: q = 0.087, a = 22.448, b = 0.183 and c = 1.170.

5 CONCLUSIONS

In the present investigation of the global system buckling of a network arch bridge is an efficient enhanced Monte Carlo based method presented to assess the structural reliability. It has been shown that the method provides good estimations of the reliability of the structural global system with a reasonable computational effort. The method is in the study used to estimate the global system buckling failure probability represented by non-linear pre-loaded geometric stiffness and linearized buckling solved by the FE-software Abaqus/Standard. The low values of probability of failure are in agreement with the target values in design codes whit a failure event without warning and with large consequences commonly the set to 10-7. The enhanced Monte Carlo method has shown to be an efficient technique to reduce the necessary number of simulation needed to reach acceptable levels of uncertainty of the estimated reliability index.

6 REFERENCES

REFERENCES

[1] Bez, R. & Bailey, S. 1993. Traffic load models for bridge evaluation: *Second international conference on bridge management*: Surrey, 9 pps

[2] Brunn, B., Schanack, F. & Steinmann, U. 2004, Network arches for railway bridges, *Advvances in Assessment, Structural Design and Construction. CIMNE*, Barcelona

[3] Faber, M.H., 2001. Reliability of Exceptional Structures. World *Congress Safety of Modern Technical Systems*, Cologne Germany,

[4] Getachew, A. 2003. Traffic load effects on bridges, statistical analysis of collected and Monte Carlo simulated vehicle data: *Doctoral thesis at KTH-Stockholm*, 162pps.

[5] Håndbok 185 2009. Bruprosjektering: *Norwegian Public Road Administration*: ISBN 82-7207-591-1, pps. 302

[6] JCSS, 2001. Probabilistic Model Code - Part 1 -3: *Joint Committee on Structural Safety*, ISBN 978-3-909386-79-6

[7] Larsen, R. & Aas-Jakobsen, K. 2006. Brandangersundet Bru – verdens slankeste?: *Nyheter om stål No. 3*. ISSN 1404-9414

[8] Li, K. & Sun, K. 2011. Stochastic parameters analyze for steel highway bridge members: *Geotechnical special publication No. 219GSP, ASCE*: 184-189

[9] Melchers, R.E., 1999, *Structural Reliability Analysis and Prediction*, 2nd Edition, John Wiley & Sons Ltd, Chichester, UK.

[10] NS-EN1991-1-2:2003+NA:2010, Eurocode 1: Actions on Structures - Part 2: Traffic loads on bridges

[11] NS-EN1990:2002+NA:2008, Eurocode : Basis of structural design

[12] Naess, A., Leira, B.J. and Batsevych, O., 2009, System Reliability Analysis by Enhanced Monte Carlo Simulation, *Structural Safety*, Vol. **31**, pp. 349-355.

[13] Naess, A., Leira, B.J. and Batsevych, O., 2010, Efficient Reliability Analysis of Structural Systems with a High Number of Limit States, *Proceedings of the 29th International Conference on Offshore Mechanics and Artic Engineering* (OMAE2010), June 6-11, Shanghai, China.

[14] Pi, Y. L. & Bradford, B. U. 2002. In-plane stability of arches, *International journal of solids and structures*: 105-125

[15] Schanack, F. 2009. Berechnung der Knicklast in Bogenebene von Netzwerkbögen: *Bautechnik* Vol 86, Issue 5 p. 249-255

[16] Scholten, C.v., Enevoldsen, I., Arnbjerg-Nielsen, T., Randrup-Thomsen, S., Sloth, M. & Engelund, S., (2004). *Reliability-Based Classification of the Load Carrying Capacity of Existing Bridges* Road Directorate - Ministry of Transport Denmark, ISBN 87-7923-774-6

[17] Tveit, P. 2006. Optimal network arches for coastal regions: *International conference on bridges*: Dubrovnik pp. 721-728

[18] Tveit, P. 2011. The Network Arch. Bits of Manuscript in February 2011 after Lectures in 50 Countries Internet edition, Grimstad,
way ://home.uia.no/pert/index.php/Home

[19] Xiangyang, W. & Guanghui, Z. 2010. Bridge reliability analysis based on the FEM and Monte Carlo method: *International conference on intelligent computation technology and automation*, Changsha, China: 891-894.

COMPDYN 2013
4th ECCOMAS Thematic Conference on
Computational Methods in Structural Dynamics and Earthquake Engineering
M. Papadrakakis, V. Papadopoulos, V. Plevris (eds.)
Kos Island, Greece, 12–14 June 2013

NUMERICAL INVESTIGATION OF THE PARAMETRIC PENDULUM UNDER FILTERED RANDOM PHASE EXCITATION

Panagiotis Alevras[1], Daniil Yurchenko[1], and Arvid Naess[2]

[1]Department of Mechanical Engineering, Heriot-Watt University
Edinburgh, EH14 4AS, UK
e-mail: {pa132, d.yurchenko}@hw.ac.uk

[2] Department of Mathematical Sciences, NTNU
Trondheim, NO 7491, Norway
e-mail: arvidn@math.ntnu.no

Keywords: Narrow-band Parametric Excitation, Stochastic Modeling, Rotational Motion, Linear SDOF filter.

Abstract. *The parametrically excited pendulum is a highly nonlinear system which has been thoroughly studied regarding the response's stability and the fundamental types of motion that could be established. The rotating potential of a pendulum having its suspension point vertically excited was numerically identified and the appropriate excitation characteristics were presented. In this paper, the excitation is modeled using the random phase modulation and the rotational motion is sought. The resulting stochastic system is analyzed by using a numerical Path Integration (PI) method solving the Chapman-Kolmogorov equation to construct parameter space plots. The Probability Density Function (PDF) is computed and the rotational regions are identified as well as the effect of noise intensity onto them. Previous studies have shown that for small values of noise intensity the stochastic response resembles the deterministic one. However numerical simulations showed that with increasing noise intensity the regions of rotational motion become narrower. In order to improve the system's response a linear single-degree-of-freedom (SDOF) system is intercepted to filter the noisy excitation, forming a base excited SDOF system acting on the pendulum suspension point. The interaction between the moving pendulum mass and the SDOF filter is investigated with the goal being for the former to establish rotational motion.*

1 INTRODUCTION

Parametric excitation is a very well-known phenomenon that could be met in a variety of dynamical mechanical and electrical systems ([1, 2, 3]. These systems are often described as being internally excited since the excitation is inserted to the system through its parameters opposed to externally excited systems. In mechanical systems, such an excitation could be the result of changing stiffness, axial loading of a cantilever or vertical excitation of a pendulum's suspension point. In this paper, the parametric pendulum is considered. By applying Lagrange equations of the second kind in this case, the equation of motion would read:

$$ml^2\ddot{\theta} + \tilde{c}\dot{\theta} + mgl\sin\theta = ml\ddot{f}(t)\sin\theta \tag{1}$$

where θ is the angle of inclination, $\tilde{c}$ is the viscous damping coefficient, $f(t)$ - excitation force, l - the length of the pendulum or the distance from the suspension point to the lumped mass m. If the excitation force is perfectly harmonic - $f(t) = A\cos(\omega t)$ - then the previous equation may be rewritten:

$$\ddot{\theta} + c\dot{\theta} + \left[\frac{g}{l} + \frac{A}{l}\omega^2\cos(\omega t)\right]\sin\theta = 0 \tag{2}$$

The fraction g/l is usually notated as Ω^2, with Ω being the natural frequency of the linearized system. When it comes to linearizing equation (2) by considering a small angles approximation - $\sin\theta \approx \theta$ - the damped widely known Mathieu equation is derived:

$$\ddot{\theta} + c\dot{\theta} + \left[\Omega^2 + \frac{A}{l}\omega^2\cos(\omega t)\right]\theta = 0 \tag{3}$$

Applying the Floquet theory [2], the above equation (3) can be proved to have both bounded and unbounded solutions. Returning to the actual pendulum equation (2) a much colorful response exists. Asymptotically stable, periodic oscillatory, rotational and even chaotic motion can be observed. Numerous studies [4, 5, 6, 7, 8] were devoted to determining the stability-instability boundaries by different methods such as Lyapunov exponents, perturbation analysis, bifurcation analysis and other. Introducing non-dimensionalization of the time domain, $\tau = \Omega t$, transforms the studied equation (2):

$$\begin{gathered}\theta'' + \gamma\theta' + [1 + \lambda\cos(\nu\tau)]\sin\theta = 0, \\ \tau = \Omega t,\ \Omega^2 = \tfrac{g}{l},\ \nu = \tfrac{\omega}{\Omega},\ \lambda = \tfrac{A}{l}\nu^2 = \tfrac{A\omega^2}{g}\end{gathered} \tag{4}$$

where the prime denotes differentiation with respect to τ and γ is the scaled damping coefficient.

In [8], approximate analytical solutions were derived for equation (4) and the boundaries of the stability region were approximated. The resonance zones, with the first resonance region at a frequency ratio $\nu = \omega/\Omega = 2$ being the most important, introduce period doubling bifurcations which result in generation of period-two oscillations. Increasing the amplitude of the excitation makes rotations of period-one and period-two achievable as well as introducing the system into a region of chaos. In [9] and [10] parameter space plots were constructed classifying the response according to not only the stability but the type of the response as well.

In this paper, the scope is concentrated on identifying the rotational regions only. Such an interest is motivated by a recently proposed concept [9, 11] for a Wave Energy Converter that would utilize the wave bobbing motion to provide the vertical excitation to the discussed parametric pendulum. The rotational response is much more preferable for generating electricity from oscillatory or chaotic motion because of the higher energy levels of the motion and the

reliability of the device respectively. Thus, the basic tool here is parameter space plots characterizing the amount of rotations experienced by the pendulum. Up to this point, the dynamical systems considered are deterministic since the excitation $f(t)$ was considered purely periodic. However, this is reductive of the real-world environment, since ocean waves are not purely periodic and should be rather modeled as a narrow-band stochastic process. Throughout this paper, random phase modulation is incorporated into the parametric excitation, as proposed by Wedig [12], describing the real-world phenomena in a more realistic way. So, instead of the purely sinusoidal function, the previous randomness provides the excitation as:

$$f(t) = A\cos q,\ \dot{q} = \omega + \tilde{\sigma}\zeta(t) \tag{5}$$

where $\zeta(t)$ is a Gaussian White Noise of $D = \tilde{\sigma}^2$ intensity for which:

$$E[\zeta(t)] = 0,\ E[\zeta(t)\zeta(t+\rho)] = D\delta(\rho) \tag{6}$$

This formulation leads to the following system:

$$\begin{gathered} \theta'' + \gamma\theta' + (1 + \lambda\cos q)\sin\theta = 0 \\ q' = \nu + \sigma\zeta(\tau) \end{gathered} \tag{7}$$

Equation (7) is strongly nonlinear, for which an analytical approach would be much more difficult to be applied even for the deterministic system. Thus, a numerical approach is adopted dealing with the discrete dynamical system:

$$\begin{gathered} x_1 = x_1' + x_2'\Delta\tau \\ x_2 = x_2' - \gamma x_2'\Delta\tau - [1 + \lambda\sin x_3']\sin x_1'\Delta\tau \\ x_3 = x_3' + \nu\Delta\tau + \sigma\Delta W(\tau) \end{gathered} \tag{8}$$

where x_1 represents the angle, x_2 the angular velocity, x_3 the excitation phase, $\sigma = \tilde{\sigma}/\Omega$, $\Delta\tau$ the scaled discretization time step, the prime stands for the previous time step and $\Delta W(\tau) = W(\tau) - W(\tau - \Delta\tau)$ is a standard Wiener process. Note that formally, the Wiener process is not differentiable. However, it has been observed in particle physics and the Brownian motion of particles that the following approximation is rather representative, $\zeta(t)\Delta t = \Delta W(t)$. In the discretized equation (8) a simple Euler-Maruyama scheme has been applied. In order to increase the accuracy of the solution a 4^{th} order Runge-Kutta-Maruyama scheme is adopted which utilizes the widely known Runge-Kutta techniques instead of the Euler one.

A widely used technique for analyzing equations (8) is the Monte-Carlo (MC) simulations. These include sampling of the stochastic response process and statistical exploitation of the results. These methods require a random number generator and usually a number of realizations is performed. The nowadays high computing capabilities make such techniques rather quick. However, due to their sampling nature they are always reductive. In this paper, a numerical Path Integration (PI) method [13] is implemented based on invoking the total probability law:

$$p(\mathbf{x}, t) = \int_{-\infty}^{\infty}\int_{-\infty}^{\infty}\int_{-\pi}^{\pi} p(\mathbf{x}, t|\mathbf{x}', t')p(\mathbf{x}', t')d\mathbf{x}'. \tag{9}$$

where $\mathbf{x}$ is the variables vector, $p(\mathbf{x}, t)$ is the joint probability density function (PDF) at time t and $p(\mathbf{x}, t|\mathbf{x}', t')$ is the transitional probability density function (TPD). The method applies

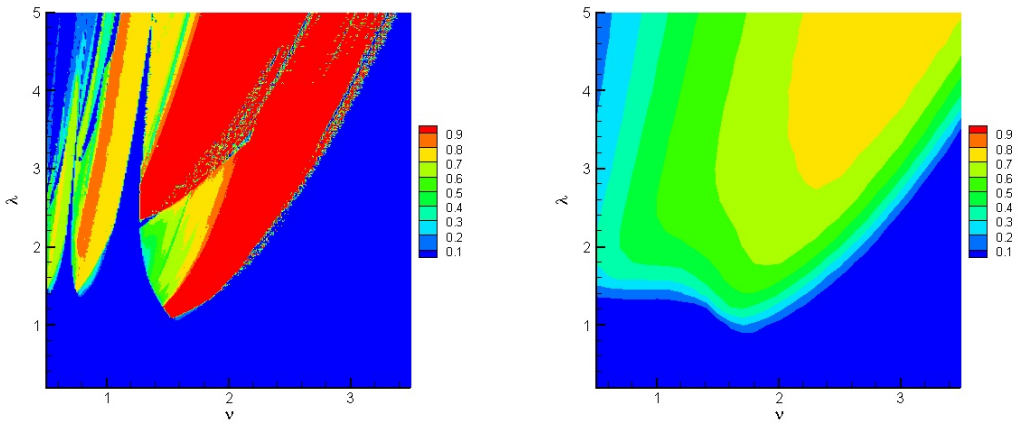
an iterative approach by moving an initial PDF forward in time up until the point where the stationary solution is obtained. The TPD function in the case of equation (8) takes the following form:

$$p(\mathbf{x},t|\mathbf{x}',t') = \delta(x_1 - x_1' - r_1(\mathbf{x}',\Delta t))\delta(x_2 - x_2' - r_2(\mathbf{x}',\Delta t))\tilde{p}(x_3,t|x_3',t') \tag{10}$$

where δ denotes the Dirac function and r_i stands for the Runge-Kutta evolution of the i^{th} variable. Since the stochastic excitation is of Gaussian nature and is inserted to the system only by the last equation, the former equation includes:

$$\tilde{p}(x_3,t|x_3',t') = \frac{1}{\sqrt{2\pi D dt}} \exp\left(-\frac{(x_3 - x_3' - r_3(\mathbf{x}',\Delta t))^2}{2Ddt}\right) \tag{11}$$

The PI method has been used and proved very efficient for constructing the PDFs of different, even strongly nonlinear, systems [14, 15] as well as some reliability problems [16, 17]. In [18], both MC methods and the PI method were used to analyze equation (8). The effect of increasing noise onto the rotational response of the parametric pendulum was investigated. Parameter space plots, figure 1, were constructed characterizing the amount of rotational motion. Particularly, red stands for $> 90\%$ and blue for $< 10\%$, counting different types and directions of rotations as one [18].



(a) (b)

Figure 1: Parameter space plot with ratio of rotational motion for $\gamma = 0.3$ and $y(0) = 0$. (a) $D = 0.0$; (b) $D = 0.3$;

As it can be seen from figures 1(a) and 1(b) increasing the noise intensity causes the rotational motion to drop from purely rotational response to around 75%. Even though such an amount cannot be considered as negligible, different ways to enhance the rotational motion in a random environment are sought. In the following, a linear single-degree-of-freedom spring-mass- damper system is intercepted between the excitation and the pendulum, acting as a noise filter and their coupled dynamics are investigated.

2 LINEAR SDOF FILTER

A linear SDOF system is proposed to filter the vertical stochastic excitation acting on the pendulum's suspension point as depicted in figure 2. The system constitutes of a base-excited

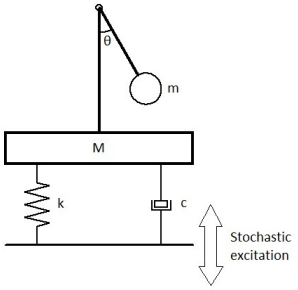


Figure 2: Sketch of the parametrically excited pendulum of mass m through a base-excited linear SDOF system of mass M.

linear SDOF system and the parametircally excited pendulum. The following system of differential equations describe the coupled dynamics:

$$\begin{gathered}\ddot{\theta} + c\dot{\theta} + (\Omega^2 - \ddot{x}/l)\sin\theta = 0 \\ \ddot{x} + 2\alpha\dot{x} + \eta^2 x = \eta^2 A\cos q(t) - 2\alpha\omega A\sin q(t) + g + \tfrac{m}{M+m} l\ddot{\theta}\sin\theta + \tfrac{m}{M+m} l\dot{\theta}^2\cos\theta \\ \dot{q}(t) = \omega + \tilde{\sigma}\zeta(t)\end{gathered} \tag{12}$$

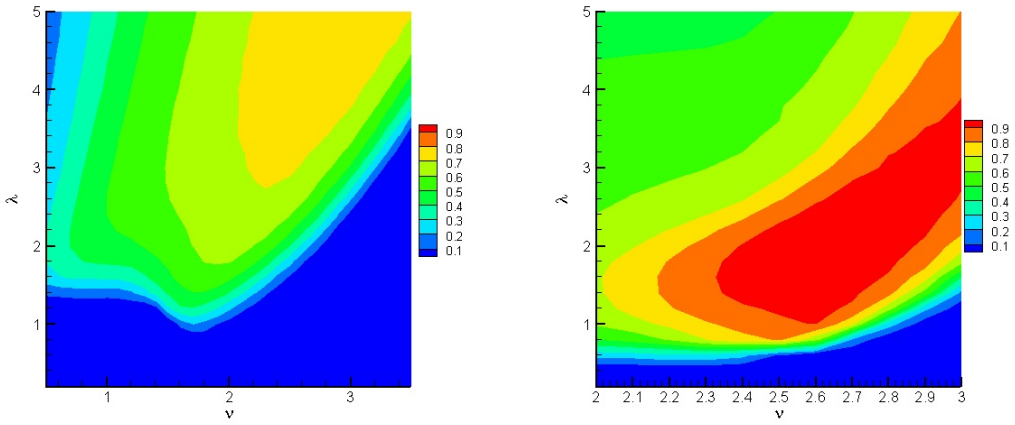
where ω - the mean excitation frequency, A - the excitation amplitude, α - the linear system's damping coefficient, η - its natural frequency and M - the total mass of the secondary SDOF system. Applying the same time non-dimensionalization as before, $\tau = \Omega t$, as well as setting $y = x/l,\ m_r = m/(M+m)$ and using the definitions $\nu = \omega/\Omega,\ \lambda = A\nu^2/l$, the filter's scaled natural frequency $e = \eta/\Omega$ and the scaled damping coefficient $\beta = \alpha/\Omega$, equations (12) become:

$$\begin{gathered}\theta'' + \gamma\theta' + (1 - y'')\sin\theta = 0 \\ y'' + 2\beta y' + e^2 y = \tfrac{e^2\lambda}{\nu^2}\cos q - \tfrac{2\beta\lambda}{\nu}\sin q + 1 + m_r\theta''\sin\theta + m_r\theta'^2\cos\theta \\ q' = \nu + \sigma\zeta(\tau)\end{gathered} \tag{13}$$

In the case of $m \ll M$ then $m_r \approx 0$ and thus the two last terms in the RHS of the system's (12) second equation might be omitted. Then the linear system is a typical base-excited SDOF system having random exciting phase. Furthermore, from basic trigonometry, the remaining sinusoidal terms in the RHS of the same equation could as well be represented by an imperfect harmonic function, say $g(\tau) = A^*\sin(q + \phi)$. Among other, the PI method has also been used to analyze this system, calculating the joint PDF of the response and its derivative.

Moreover, in [19], the coupled system described as in equation (13) has been studied with regard to the rotational motion of the pendulum when the random excitation is filtered, assuming that the mass ratio is negligible. That is, no influence of the pendulum onto the linear SDOF system was taken into account. Figure 3 compares the rotation-wise response of the pendulum alone with the one of the coupled system's. In both figures 3(a) and 3(b), the provided vertical excitation is the same meaning that the parameter pair $(\nu,\ \lambda)$ describes the characteristics of the random phase excitation. In that way, the addition of the linear SDOF system was able to be evaluated. Comparing the level of rotational motion in these two figures, it is obvious that the addition of linear SDOF system is extremely beneficiary for establishing and maintaining the rotational response. In figure 3(a) the corresponding value is only 75% while in figure 3(b) the same value is $> 90\%$ with the shape and position of the maximal rotational region having been changed and brought at a lower amplitude level. Of course, changing the natural

frequency of the linear SDOF filter or the value of its damping coefficient will change the response significantly providing another option for controlling the system as well, but such a discussion exceeds the scope of this paper.



(a) (b)

Figure 3: Parameter space plot with ratio of rotational motion for $D = 0.3$, $\gamma = 0.3$. (a) wihtout filter; (b) with filter and $e = 2.5,\ \beta = 0.3,\ m_r = 0$;

Also, one could notice that the parameter space plot in figure 3(b) is extended to a shorter range at the ν axis. This is because the response of the linear filter will retain the narrow-band property of the excitation only under certain conditions, one of which is low detuning value between the excitation frequency ω and the system's natural one η.

3 INFLUENCE OF PENDULUM'S MASS

In this section, the rotational motion of the pendulum is investigated when the influence of its mass m onto the response of the linear SDOF filter cannot be neglected. The problem now is formulated by the full equations (13) and the parameter m_r becomes a subject of study. Figure 4 shows parameter space plots characterizing the amount of rotational motion in the same way as in figure 3(b). The left column of the plots depicts the numerical results for the value of damping coefficient, $\beta = 0.1$, while the right column for $\beta = 0.5$. A first observation can be made with regard to the influence of the damping coefficient, β. Considering that the natural frequency of the linear SDOF filter is $e = 2$, the filter is a system at or around its resonance. When the β value is small, the amplification of the response leads it to very high amplitude values forcing the pendulum to move closer to the region above the rotational one, thus reducing the rotational amount in comparison with the higher β values. The latter values drive the pendulum inside the rotational parameter region providing a better response for the pendulum to rotate. Obviously, there is a critical damping value, larger ones than which get the filter's response smaller in amplitude up until the point it dies out.

Furthermore, the plots in the same line present results for the same mass ratio, m_r. Figures 4(a) and 4(b) correspond to cases with $m_r = 0$ and have been added for comparison purposes. When the mass ratio gets slightly bigger, and particularly equal to $m_r = 0.1$ shown in figures 4(c) and 4(d), the whole plots resemble the ones without the pendulum's influence (figures 4(a) and 4(b)), with the only difference being a slight increase in the experienced rotational motion.

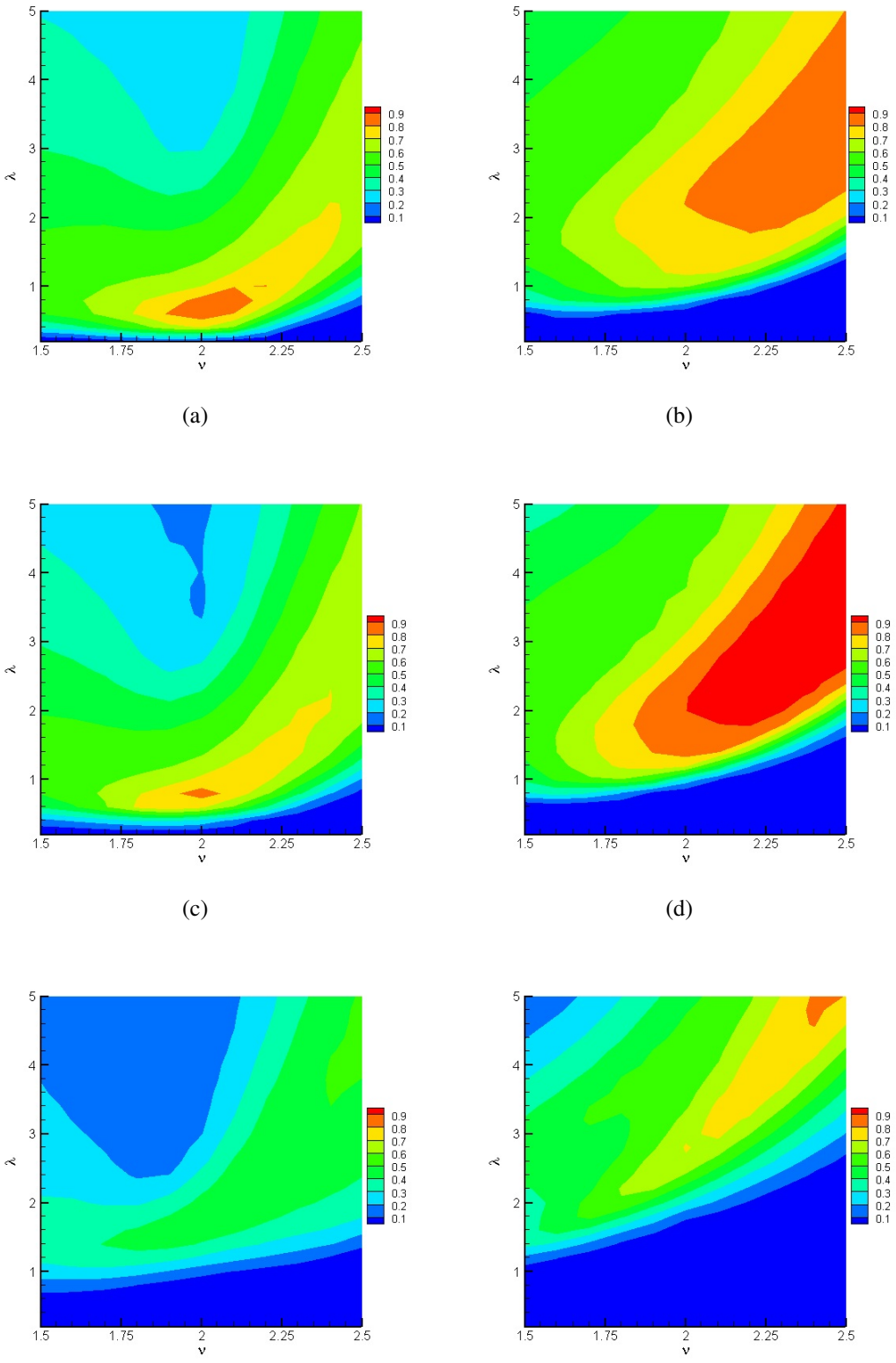


Figure 4: Parameter space plot with ratio of rotational motion for $D = 0.3, \gamma = 0.3, e = 2$. (a) $m_r = 0.0,\ \beta = 0.1$; (b) $m_r = 0.0,\ \beta = 0.5$; (c) $m_r = 0.1,\ \beta = 0.1$; (d) $m_r = 0.1,\ \beta = 0.5$; (e) $m_r = 0.5,\ \beta = 0.1$; (f) $m_r = 0.5,\ \beta = 0.5$;

However, when the value of the mass ratio gets even higher, as in figures 4(e) and 4(f)) for which the pendulum mass equals the filter's, the response of the pendulum contains less rotations than before, keeping nevertheless at the appropriate damping conditions a respectable amount of around 75% in place. Also, it is observed that some lower amplitudes points of the plot get stabilized, turning into blue asymptotically or marginally stable points.

4 CONCLUSIONS

The coupled dynamics of a parametric pendulum vertically excited by a random phase imperfect harmonic function were in question. The characteristics of the excitation were improved by filtering it through a linear SDOF system acting at small detuning values. The effect of the filter on the pendulum's rotational motion has proven beneficiary when the pendulum's mass is very much smaller than the filter's. In this paper, the latter assumption is removed and the influence of the pendulum's mass onto the response of the linear SDOF filter is investigated. As it was seen through the numerical construction of parameter space plots, small values of the ratio of the pendulum's mass over the filter's slightly enhance the rotational motion, while when these masses are equal the desired response decreases. However, the rotational motion is still maintained even at a lower level, around 75%, when the damping coefficient is chosen properly. The latter also gives rise to the option of using the filter for controlling purposes as well.

REFERENCES

[1] Y.K. Lin, G.Q Cai, *Probabilistic Structural Dynamics*, McGraw-Hill, New York, 1995.

[2] A.H. Nayfeh, D.T. Mook, *Nonlinear Oscillations*, Wiley, New York, 1979.

[3] K.L. Turner, S.A. Miller, P.G. Hartwell, N.C. MacDonald, S.H. Strogatz, S.G. Adams, Five parametric resonance in a MEMs, *Nature*, **396**, 149-152, 1998.

[4] M.J. Clifford, S.R. Bishop, Rotating periodic orbits of the parametrically excited pendulum, *Physics Letters A*, **201**, 191-196, 1995.

[5] R.W. Leven, B.P. Koch, Chaotic behavior of a parametrically excited damped pendulum, *Physics Letters A*, **86**, 71-74, 1981.

[6] R.W. Leven, B. Pompe, C. Wilke, B.P. Koch, Experiments on periodic and chaotic motions of a parametrically forced pendulum, *Physica D*, **16**, 371-384, 1985.

[7] W. Szemplinska-Stupnicka, E. Tyrkiel, The Oscillation-rotation attractors in the Forced Pendulum and their Peculiar Properties, *International Journal of Bifurcation and Chaos*, **12**(1), 159-168, 2002.

[8] X. Xu, M. Wiercigroch, Approximate analytical solutions for oscillatory and rotational motion of a parametric pendulum, *Nonlinear Dynamics*, **47**, 311-320. 2007.

[9] X. Xu, M. Wiercigroch, M.P. Cartmell, Rotating orbits of a parametrically-excited pendulum, *Chaos, Solitons & Fractals*, **23**, 1537-1548. 2005.

[10] B.W. Horton, J. Sieber, J.M.T. Thomson and M. Wiercigroch, Dynamics of the nearly parametric pendulum. *International Journal of Non-Linear Mechanics*, **46**(2), 436-442, 2011.

[11] S. Lenci, M. Brocchini, C. Lorenzoni, Experimental rotations of a pendulum on water waves, *Journal of Computational and Nonlinear Dynamics*, **7**, 011007 (9 pages), 2012.

[12] W.V. Wedig, Invariant measures and Lyapunov exponents for generalized parameter fluctuations, *Structural Safety*, **8**, 13-25, 1990.

[13] A. Naess, V. Moe, Efficient path integration methods for nonlinear dynamic systems, *Probabilistic Engineering Mechanics*, **15**, 221-231, 2000.

[14] D.V. Iourtchenko, A. Naess, E. Mo, Response probability density functions of strongly nonlinear systems by the path integration method, *International Journal of Non-linear Mechanics*, **41**, 693-705, 2006.

[15] A. Naess, F.E. Kolnes, E. Mo, Stochastic spur gear dynamics by numerical path integration, *Journal of Sound and Vibrations*, **302**, 936-950, 2007.

[16] D.V. Iourtchenko, E. Mo, A. Naess, Reliability of strongly nonlinear SDOF dynamic systems by the path integration method, *Journal of Applied Mechanics*, **75**, 2008.

[17] A. Naess, D.V. Iourtchenko, O. Batsevych, Reliability of systems with randomly varying parameters by the path integration method, *Probabilistic Engineering Mechanics*, **26**, 5-9, 2011.

[18] D. Yurchenko, A. Naess, P. Alevras, Pendulum's rotational motion governed by a stochastic Mathieu equation, *Probabilistic Engineering Mechanics*, **31**, 12-18, 2013.

[19] D. Yurchenko, P. Alevras, Stochastic Dynamics of a parametrically base excited rotating pendulum, *Procedia IUTAM (2012)*, to be published.

COMPDYN 2013
4th ECCOMAS Thematic Conference on
Computational Methods in Structural Dynamics and Earthquake Engineering
M. Papadrakakis, V. Papadopoulos, V. Plevris (eds.)
Kos Island, Greece, 12–14 June 2013

VISK: A GIS-COMPATIBLE PLATFORM FOR MICRO-SCALE ASSESSMENT OF FLOODING RISK IN URBAN AREAS

R. De Risi[1], F. Jalayer*[1,2], I. Iervolino[1,2], G. Manfredi[1,2], and S. Carozza[1]

[1] Università degli studi di Napoli Federico II, Naples, Italy.

[2] Analisi e Monitoraggio dei Rischi Ambientali s.c.ar.l., Naples, Italy.

*Corresponding author

e-mail: {raffaele.derisi, fatemeh.jalayer, iunio.iervolino, gaetano.manfredi} @unina.it

Keywords: Fragility, vulnerability assessment, portfolio of structures, Bayesian parameter estimation, Graphical user interface.

Abstract. *Evaluation of the vulnerability of buildings in urban areas to flooding is a fundamental step in flooding risk mitigation. In this work, a new GIS-compatible computer platform with Matlab®-based graphical user interface is presented: VISK, "Visual Vulnerability & Risk", flooding module. This platform performs detailed (micro-scale) flood risk assessment for building stock with more-or-less similar characteristics. The GIS compatibility allows for graphical processing of both input and output to the program, providing an efficient visualization of flooding risk. At the core of the platform lies a comprehensive probability-based algorithm for the assessment of the vulnerability of a class of buildings to flooding. This Bayesian algorithm is based on assigning prescribed analytic uni- and bi-modal probability distributions for characterizing the flooding structural fragility functions. This allows for efficient evaluation of structural fragility based on a small number of (around 30-50) Monte Carlo simulations. The fragility calculations are performed on a bi-dimensional finite-element structural model considering the openings (door and windows) constructed using open-source software Opensees. The uncertain structural modeling parameters are characterized through, orthophoto recognition, sample in-situ building survey, laboratory test results for material mechanical properties and literature survey. Finally, the risk map is generated by integrating the flooding hazard and fragility taking into account additional information on the exposure (e.g., repair costs, population density, etc.). The results can be visualized both in a detailed building-to-building scale (of potential interest to single house-holds) or as overall estimates for the entire area (of interest to policy makers).*

1 INTRODUCTION

Delineation of flood prone areas and the evaluation of the vulnerability of buildings in the urban areas to flooding are fundamental steps in taking adaptive measures for flooding risk. This demands cross-cutting scientific and technical support from different disciplines, such as but not limited to, climate modeling, hydraulic engineering, structural engineering, risk modeling and urban policy making. In recent years, increasing attention is focused on flooding risk assessment. In fact, several publications document and discuss the consequences of flooding, such as loss of life [1], economic losses [2-4] and damage to buildings [5-8]. These research efforts have many aspects in common, such as a direct link between the flooding intensity and the incurred damage, and that they are based on real damage observed in the aftermath of a flooding event. On the other hand, many research efforts are starting to galvanize in the direction of proposing analytical models for flood hazard and vulnerability assessment taking into account various sources of uncertainties. For instance, in [9] a stochastic method for assessment of the direct impact of flood actions on buildings is proposed. A general methodological approach to flood risk assessment is embedded in the HAZUS procedures for risk assessment [10, 11]. Moreover, [12] provides a classification of flood risk assessment methods based on their degree of complexity and precision. In this context, development of tools that allow for quantifying flooding risk efficiently and with sufficient accuracy is essential. These methods serve as technical support to the stakeholders and policy makers, for flood risk mitigation, emergency preparedness, response and recovery, both in short- and long-term.

In this work, a new software tool for flood risk assessment for individual buildings is presented. VISK, acronym of Visual Vulnerability and (*Flooding*) Risk, is a GIS-compatible platform that performs micro-scale flood risk assessment for buildings located in homogenous (i.e., characterized as a single *class* of buildings) urban areas. Figure below demonstrates the graphical user interface for VISK.

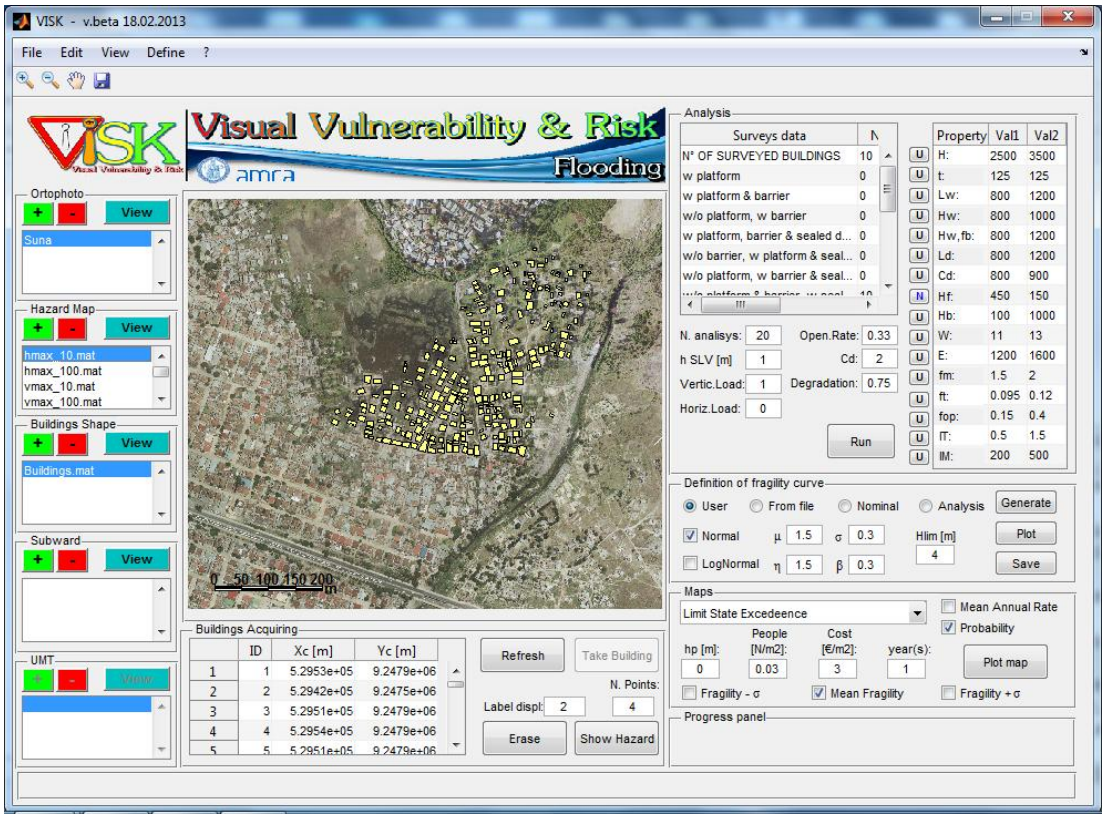


Figure 1: The graphical user interface for VISK.

The main parts of the graphical user interface for VISK are: (1) the central display panel in which the orthophoto of the case study area is demonstrated. The orthophoto can be overlaid on the spatial polygons representing buildings' foot-prints (i.e., a GIS shape file) and the flooding height/velocity profile for a prescribed return period; (2) the orthophoto input panel where an orthophoto of the case-study area can be up-loaded; (3) the flood profile panel where a lattice of nodes containing maximum flood depth and velocity pairs for each node for a given return period can be up-loaded; (4) building shape panel where the GIS shape file of the buildings' spatial boundary can be up-loaded; (5) a panel for miscellaneous information in which data such as spatial delineation of administrative boundaries can be up-loaded; (6) a panel for the acquisition of data regarding buildings' spatial foot-prints, where in lieu of shape files, for each building, the spatial foot-print can be specified manually and processed by the program; (6) a digital survey sheet where the results of building-specific field survey can be specified. This digital panel is matched with a building-specific survey sheet; (7) a structural analysis panel where a specified number of structural model realizations are generated and analyzed based on the data provided by the digital survey sheet; (8) a fragility assessment panel where the fragility curves for a specified limit state are derived based on the results of the simulations performed in the structural analysis panel. This panel also envisions up-loading of user-defined fragility curves; (9) risk map generation panel where risk maps are plotted for various risk metrics such as the frequency of exceeding a given limit state, expected repair/replacement costs, etc; (10) a progress panel which visualizes the progress of the program. In the following, various functionalities of VISK are discussed in detail. In order to render the description more accessible, each section is accompanied by a numerical example.

Background: VISK is created inside the European FP7 project CLUVA**:** Climate change and urban vulnerability in Africa. The original idea was to create a tool for vulnerability assessment of informal settlements in Africa. The problem of vulnerability assessment for a portfolio of "informal" and non-engineered buildings is particularly challenging due to many aspects such as lack of complete information and poor construction details. In fact, the core vulnerability assessment methodology created for VISK is organized in a manner so that various sources of uncertainty can be taken into account, with particular attention to structural detailing and water-tightness. Moreover, due to lack of precise survey data, the software uses sample surveys as a basis and constructs probability distributions for the probability of observing/not observing certain structural details in a given building in a Bayesian framework. Needless to say, VISK as a visual interface and platform for vulnerability and risk assessment is applicable not only to the non-engineered structures in an African context but also to other structural typologies in alternative contexts.

2 INPUT DATA

The input data required by platform VISK are: orthophoto of the case-study area, spatial foot-print of the buildings, flooding height/velocity profiles for prescribed return periods and the uncertainties in structural modeling parameters related to both material mechanical properties, construction details and geometry (in the form of probability distributions). In this section, each input category is described in more detail.

2.1 Othophoto and the footprint of the buildings

The orthophoto of the case-study area needs to have the following characteristics: at least 300 dpi of resolution, aspect ratio of about one, georeferenced in a specific coordinate system (e.g., UTM,WGS 1984) that remains the same for all the other input (i.e. flood hazard maps, buildings shape). As far as it regards the spatial foot-print of the buildings to be analyzed, the

program accepts a dataset containing the information stored for each spatial polygon that defines the building boundary (i.e., a GIS shape file format). In case such a spatial dataset is not available, VISK can extract the plan dimensions by performing orthophoto boundary recognition guided by the user. User's role is to manually define the nodes of the polygon that define building's footprint as illustrated in Figure 2 below. The user-guided boundary recognition operation not only helps in creating a digital database of buildings for which risk assessment is later going to be performed but also helps in characterizing the building-to-building variability in the dimension of the wall which is going to resist the flood action.[1]

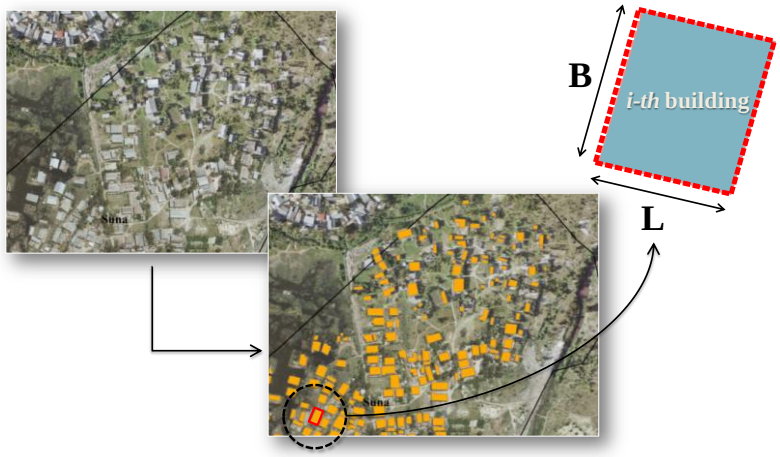


Figure 2: Acquisition of data regarding building footprint.

2.2 Characterization of uncertainties:

VISK can be used for flooding risk assessment for individual buildings located in a homogenous urban area. Therefore, the main function of VISK as software for vulnerability assessment is the definition of fragility curves for a single class of structures. Therefore, the uncertainties considered are primarily related to building-to-building variability in material properties, geometry and construction details. In the following sub-sections, the procedure for characterizing these uncertainties is described in detail. As mentioned in the previous section, orthophoto recognition can be used in order to capture the variation of buildings' footprints in the case-study area. However, building specific field surveys are needed in order to gain better understanding of the geometry and construction details. As far as it regards survey-based input requirements for VISK, information on the uncertain parameters can be specified in two alternative ways: (1) discrete binary uncertain parameters based on a logic-tree approach; (2) continuous uncertain parameters.

2.2.1 Discrete binary uncertain parameters/logic statements:

Presence of raise-foundation / Platform	*PL*
Presence of Barrier	*Ba*
Are the doors sufficiently water-proof	*DS*
Are the windows sufficiently water-proof	*WS*

[1] Neglecting the effect of internal walls or embedded columns in reducing the "free" loading span.

Is There a door in the wall panel	*D*
Are there windows in the wall panel	*W*
Are there signs of material degradation	*DG*

Table 1 - Discrete binary uncertain parameters considered by VISK

Table 1 reports the list of discrete binary uncertain parameters/logic statements considered and the related input accepted by VISK. Examples of the uncertain binary parameters considered are, presence of a raised foundation (platform) *Pl*, presence of a barrier *Ba*, water-tightness of the door *DS*, water-tightness of the windows *WS*, and presence of a visual degradation in the building *DG*. It can be noted that also the presence of openings (doors *D* and windows *W*) in the model wall panel is randomized. This is due to fact that in the current version of VISK, the specific building wall hit first by the flood (and its angle) are assumed to be unknown. The vulnerability assessment module uses the logic-tree approach in order to propagate the uncertainties in discrete binary uncertain parameters listed in Table 1. Organization of the binary parameters in a logic-tree, among other things, enables the user to define the correlation between various uncertain parameters. Figure 3 below illustrates the two logic-trees employed by VISK: (a) the logic tree illustrated in Figure 3a is used in order to evaluate whether the building is sufficiently waterproof or not; (b) the logic-tree illustrated in Figure 3b is used in order to randomize the wall panels in terms of the presence of openings (door and windows). The red arrows indicate the information that should be input to VISK.

n° OF SURVEYED BUILDINGS	100
n° of buildings with visual signs of degradation DG	0
n° of buildings with ***Pl***	30
n° of buildings with ***Ba given Pl***	10
n° of buildings with ***Ba given not Pl***	50
n° of buildings with DS given ***Pl*** and ***Ba***	5
n° of buildings with DS given ***Pl*** and not ***Ba***	15
n° of buildings with DS given not ***Pl*** and ***Ba***	30
n° of buildings with DS given not ***Pl***, not ***Ba***	8
n° of buildings with WS given ***Pl***, ***Ba***, and ***DS***	2
n° of buildings with WS given ***Pl***, not ***Ba***, and ***DS***	5
n° of buildings with WS given not ***Pl***, ***Ba***, and ***DS***	10
n° of buildings with WS given not ***Pl***, not ***Ba***, and ***DS***	3
n° OF SURVEYED WALLS	400
n° of walls with ***D***	100
n° of walls with W given ***D***	80
n° of walls with W given not ***D***	200

Table 2 - Example: Discrete binary uncertain parameters in a sample survey data input to VISK.

Logic-trees: Logic-tree [13] is an efficient and visual method for modeling the joint probability distribution for several discrete uncertain variables represented as logic statements. A logic tree is consisted of *nodes*, *branches* and *paths*. Each node represents a logic statement (e.g., given value of an uncertain parameter). Each branch in a logic-tree represents the degree of belief (conditional probability) for the logic statement in the destination node given all the statements corresponding to the nodes along the path leading to (and including) the node in the origin of the branch. For example, In Figure 3(a),(b), the degrees of belief or the condi-

tional probability values are written in grey characters on the corresponding branch **(**|, reads as *given* or *conditional on***)**. Each path in a logic-tree is consisted of nodes and branches that connect them; where the nodes belong to progressively increasing levels within the tree. The degree of belief in a path (or the joint probability for the specific values of the corresponding uncertain parameters) is equal to the product of the probabilistic corresponding to the branches that construct the path. Finally, for any vertical cut to the tree, the sum of the degrees of belief for all the paths trimmed by the cut should be equal to unity. That is, the paths trimmed by vertical cuts represent mutually exclusive and collectively exhaustive logic statements.

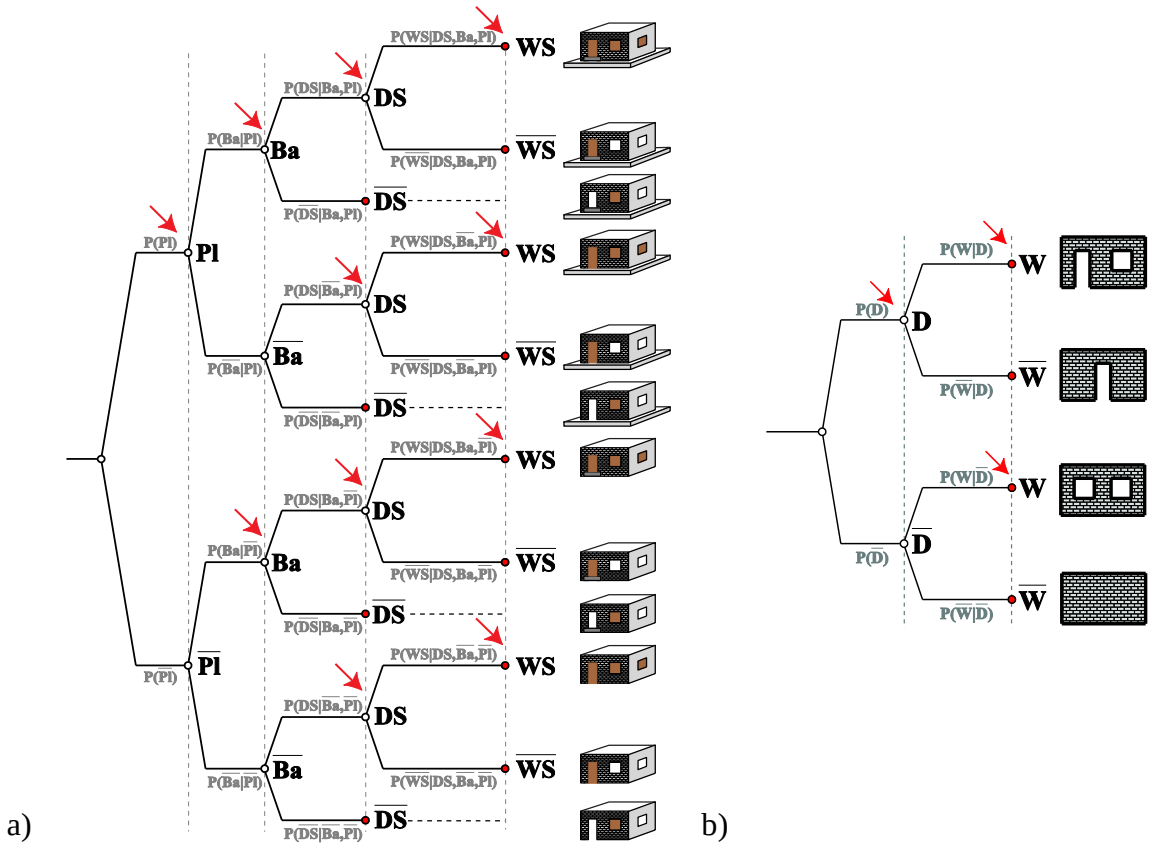


Figure 3: a) logic tree for the waterproofness, b) logic tree for the modeling generation.

Estimating the logic-tree probabilities/degrees of belief: VISK's operative way to assess the conditional probability/degree of belief for each node of the logic tree, consists in cataloging of the survey information, following the conditions imposed by path leading to the node in question. The conditional probabilities corresponding to each branch can be constructed by classifying progressively the building survey results based on the logical value (truth value) of each binary statement. In fact, the visual survey panel in the graphical interface allows the user to progressively input the survey results based on the specific conditions imposed by the path. This provides the possibility to take into account the correlation between uncertain parameters/logic statements. It can be observed from Table 2 that the input data accepted by VISK for a binary uncertain parameter/logic statement denoted as BV is in the form of the number r of surveyed buildings (progressively classified as described above) for which the logic statement is TRUE out of number n of all the buildings surveyed. Therefore, the probability π that BV is true can be calculated as a complete Beta-function [14]:

$$p(\pi \mid r,n) = \frac{(n+1)!}{r!(n-r)!}\pi^{r}(1-\pi)^{n-r} \quad (1)$$

where $p(\pi|r,n)$ denotes the probability distribution for the degree of belief in statement BV given r "success" out of a total of n. After evaluating the above probability distribution, VISK platform provides three possibilities as much as it regards the estimation of π: a) only use the mode of the distribution in Eq. 1: $\pi = r/n$ b) only use the expected value $\pi = (r+1)/(n+2)$, that is the first moment approximation, or c) sample from the entire distribution.

Numerical example: With reference to the survey information reported in Table 2, using the mode of the Beta distribution in Eq. 1, referred to as approach (a) above: $P(Ba|Pl)$ is equal to 10/30=0.33; $P(DS|Ba,Pl)$ is equal to 5/10=0.5; and finally $P(WS|DS,Ba,Pl)$ is equal to 2/5=0.40.

2.2.2 Continuous uncertain parameters:

The VISK input for continuous uncertain parameters consists of the choice of a probability distribution (e.g., Normal or Uniform) and its relevant statistics. In the current version of VISK possible correlations between the continuous uncertain parameters are not considered. However, the future updates will allow for modeling of possible correlations between a chosen subset of the continuous parameters. These user-specified probability distributions will be used later during the simulation process.

Table 3, 4 and 5 list the continuous uncertain parametersparameter considered in VISK. It can be observed that the continuous parameters considered are classified into three categories: (1) parameters related to the building geometry; (2) parameters related to the mechanical material properties; (3) parameter related to structural loading.

Geometrical property	Distribution type	Mean Min	Standard Deviation Max
L (m) - wall length	Normal	11.17	3.39
H (m) - wall height	Uniform	2.50	3.50
t (m) - wall thickness	Deterministic	0.125	0.00
L_w (m) - window length	Uniform	0.80	1.20
H_w (m) - window height	Uniform	0.80	1.00
H_{wfb} (m) - window rise	Uniform	0.80	1.20
L_d (m) - door length	Uniform	0.80	1.20
C_d (m) - corner length	Uniform	0.80	0.90
H_f (m) - foundation rise	Lognormal	0.45	0.15
H_b (m) - barrier height	Uniform	0.10	1.00

Table 3: The continuous uncertain parameters considered by VISK: building geometry.

In the first category, parameters such as structural height, wall thickness, window length and height, window height from the bottom, door length, distance between the corners and the openings, the foundation (platform) height. As far as it regards the second category, parameters such as elastic modulus (E), Poisson ratio (ν), compressive strength (f_m), shear strength(τ_0), flexural strength (f_{fl}) for the wall panels are considered. Moreover, it possible to take into account a parameter that measures the amount of material deterioration due to the elongated contact with water.

Mechanical properties	Distribution type	Mean Min	Standard Deviation Max
f_m (MPa) - compression strength	Uniform	1.50	2.00
τ_0 (MPa) - shear strength	Uniform	0.095	0.12
f_{fl} (MPa) - flexural strength	Uniform	0.14	0.40
E (MPa) - linear elastic modulus	Uniform	1200	1600
G (MPa) - shear elastic modulus	Uniform	500	667
γ (kN/m^3) - self weight	Uniform	11	13

Table 4: The continuous uncertain parameters considered by VISK: material mechanical properties.

Ideally, input statistics related to structural material properties should be obtained based on the results of case-specific laboratory tests. The laboratory tests are aimed to mimic the construction materials and relevant techniques used in the field, in order to evaluate the main mechanical characteristics of the wall material. In lieu of case-specific laboratory tests, existing literature results can be used. Third category is related to uncertain loading parameters. Table 5 report the uncertain parameters *a* and *b* related to the hydro-dynamic flood loading profile. These parameters describe the flooding velocity as a power-law function ($a \cdot h^b$) of flooding height at a given point.

Loading parameter	Distribution type	Median	Standard Deviation
B	Lognormal	1.57	0.54
A	Fully correlated with b[2]		

Table 5: The continuous uncertain parameters considered by VISK: loading parameters

Numerical example: The histogram in Figure 4 illustrates the histogram of platform heights based on the results of sample field survey. A Lognormal distribution is fit to the histogram and its two parameters (median and logarithmic standard deviation) can be provided as input to VISK.

[2] b is sampled from a probability distribution fit to various (a, b) data pairs calculated based on the inundation profile. Therefore, after simulating b from its probability distribution, the closest (a, b) pair is taken.

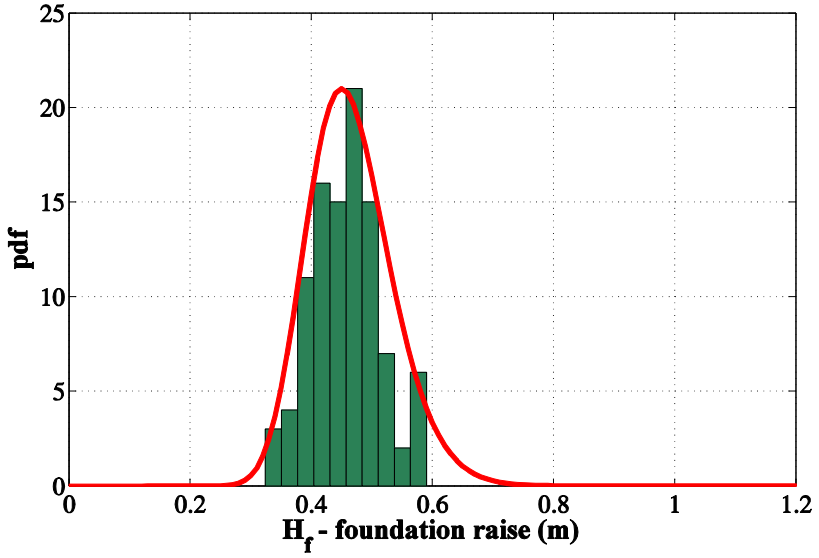


Figure 4: Histogram of platform height [17].

2.3 Hydraulic results and flooding hazard curves

Inundation profiles calculated for various return periods are one of the main input data fed into VISK. The inundation profile is generally expressed in terms of flood depth and velocity, for different return periods of the extreme precipitation event, for each node within a lattice that covers the entire case study area. This information is usually obtained through a general hydrologic/hydraulic routine. VISK acquires inundation profiles for various return periods, in terms of gridded data set in Arc ASCII grid format, typical output file of commercial software that develop mono/bi-dimensional diffusion models [15, 16].

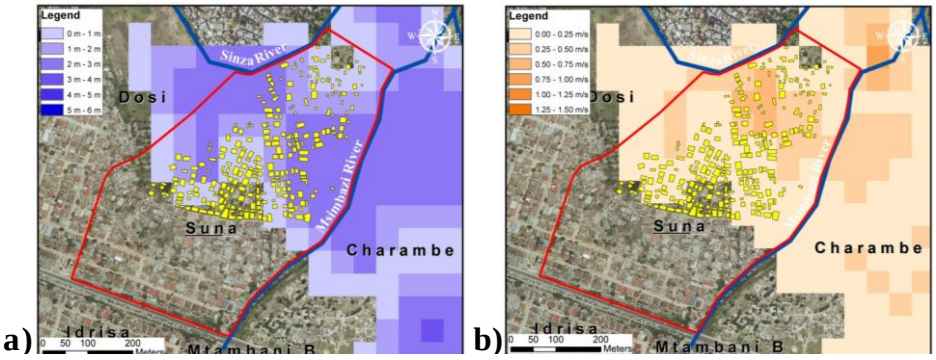


Figure 5: Inundation profiles for a given return period in terms of a) flood depth and b) flood velocity [17].

Once the grid dataset of the inundation profiles has been acquired by VISK, the software creates an overlay of the inundation profile (for various return periods and classified by flooding height and/or velocity) and the uploaded orthophoto of the case-study area.

Extracting flooding hazard curves: VISK has the capability of extracting flooding hazard curves in terms of the mean annual frequency of exceeding (equal to the inverse of return period for a homogenous Poisson process) a given flooding height or velocity for a given point within the case-study area (e.g., centroid of a given building), based on the input grid data set described in the previous paragraph. This is done by a spatial interpolation between the point

(identified as *G* in Figure 6 below) and the flood height/velocity values at the vertex of the lattice grid containing the point in question.

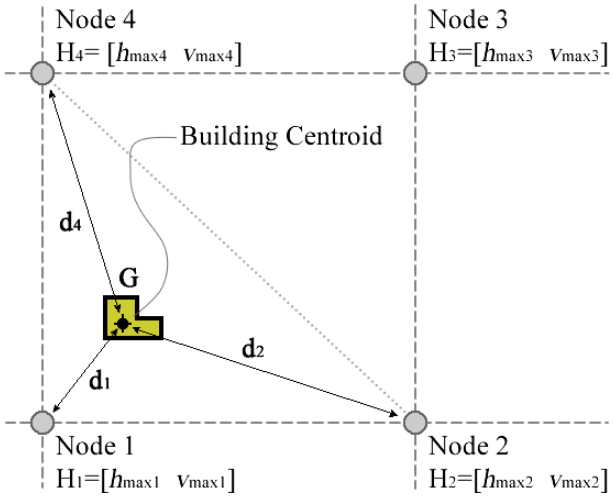


Figure 6: Graphical representation of the spatial interpolation for point G.

The flooding height and velocity vector denoted by $\mathbf{H}=[h_{max}, v_{max}]$ at a given point can be evaluated as follows:

$$H_G = \frac{\frac{H_1}{d_1} + \frac{H_2}{d_2} + \frac{H_4}{d_4}}{\frac{1}{d_1} + \frac{1}{d_2} + \frac{1}{d_4}} \tag{2}$$

where d_i denotes the distance to node i and H_i represents the flooding height and velocity vector for node i. It can be observed in Eq. 2, that the flood height and velocity vector H_G is calculated as the spatial weighted average of H_i; where the weights are equal to the inverse of the distance d_i. It is worth noting that for each building only the three closest nodes are considered.

Velocity/height relationship: For each point/centroid of a building, An analytic power-law relation of the form of $h_{max}=a\ v_{max}^{\ b}$ is fitted by employing a linear regression in logarithmic scale to $\mathbf{H}=[h_{max}, v_{max}]$ pairs for all the return periods considered. Figure 7 below demonstrates 3 different power-law fits for three different points within a case-study area. This power-law fit helps in transforming an otherwise vector-based risk assessment using $\mathbf{H}=[h_{max}, v_{max}]$ as the hazard/fragility interface variable to a scalar risk assessment problem using only h_{max} as the interface variable.

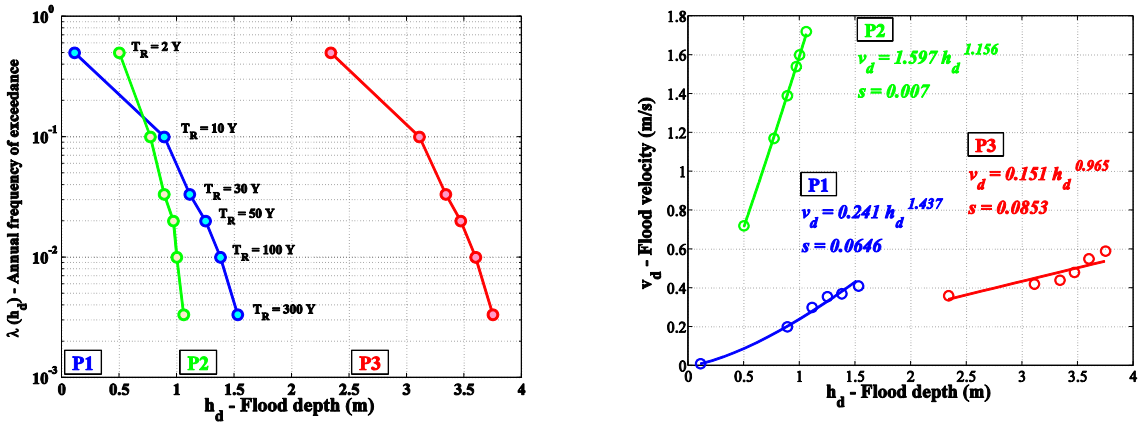


Figure 7: (a) Hazard curves, (b) Flood height versus flood velocity power-law relation [18]

Demonstration: Using the above-mentioned capabilities, VISK can generate hazard curves for centroid points of all the buildings identified within the case-study area as illustrated in Figures 8.

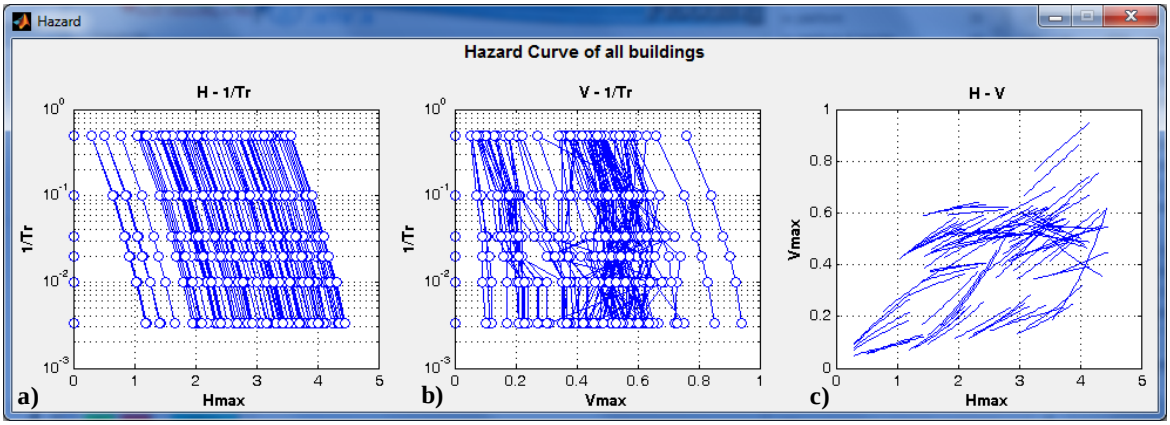


Figure 8: Hazard curves in terms of maximum flood a) height, b) velocity and c) relation between height and velocity, [17].

Figures 8a and 8b illustrate the hazard curves for all the building centroid points within a given case-study area for flooding height and velocity, respectively. For each building centroid, the set of $\mathbf{H}=[h_{max}, v_{max}]$ pairs and the power-law relation fitted to them are plotted in Figure 8c.

3 VISUAL VULNERABILITY ASSESSMENT PLATFORM

Structural vulnerability assessment lies in the core of VISK platform. The vulnerability assessment results are represented as the fragility curves, expressing the probability of exceeding a prescribed limit state. The software envisions various modes for acquiring the necessary input: (a) calculating the fragility curves based on the input provided to VISK; (b) creating Normal/Lognormal fragility curves based on the first two moments (i.e., mean and standard deviation); (c) creating fragility curves based on data uploaded by the user from a file; (d) creating step-function fragilities, referred to in the program as the Nominal fragilities. In this section the methodology used for calculating the fragility curves based on approach (a) listed above is described.

3.1 The limit states

The fragility curves are calculated for three limit states, namely, serviceability (SE), life safety (LS), and structural collapse (CO). In VISK, limit state thresholds are expressed in terms of the critical flooding height. Serviceability is marked by the critical water beyond which the normal activities in the household is going to be interrupted, most probably due to water infiltration. For example, for an insufficiently water-tight buildings built on a raised foundation, the critical serviceability water height is equal to the height of raised foundation above the ground level. For buildings constructed according to flood-resistant criteria, the critical water height for limit state of serviceability is taken asymptotically equal to the critical height needed for exceeding collapse limit state assuming brittle failure modes. Collapse limit state is defined as the critical flooding height in which the most vulnerable section of the most vulnerable wall in the building is going to break. Life safety limit state defines the critical flooding height in which lives of the inhabitants is going to be in danger. This can be caused either due to the infiltration of water inside the building (with the increasing risk of drowning in water), or the structural collapse (defined in the same manner as the critical height for collapse limit state). The critical water height for structural collapse is calculated in VISK by employing structural analysis taking into account the various sources of uncertainties in geometry, material properties and construction details. As far as it regards life safety considerations, VISK allows the consideration of judgment-based or code-based nominal water height.

For all the limit states considered within VISK, a simulation-based routine is employed in order to propagate the various sources of uncertainties described in Section 2.2. VISK employs an efficient simulation-based procedure relying on a small number of simulations (e.g., in the order of 50-100).

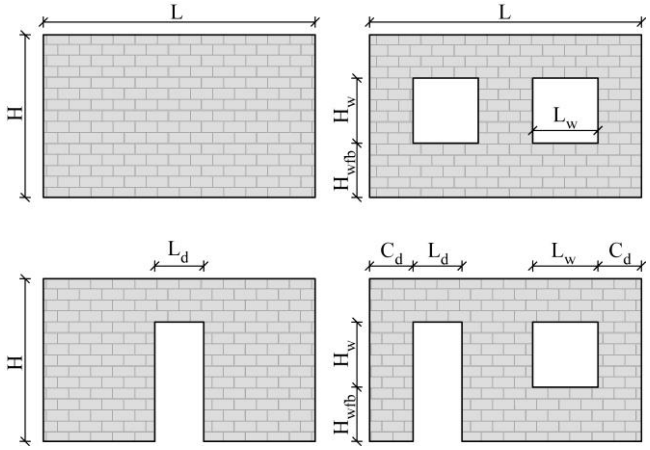
Assuming that vector $\boldsymbol{\theta}$ consists of all the uncertain parameters considered in the problem, simulation *i* corresponds to the i^{th} realization of vector $\boldsymbol{\theta}$. Each $\boldsymbol{\theta}_i$ is sufficient for defining the structural configuration, flood action, and material strength values for i^{th} simulation realization. Having this information, the critical water height can be calculated for each realization of the structural model/action. With reference to the uncertain parameters considered by VISK and described in Section 2.2, vector $\boldsymbol{\theta}$ is partitioned in two sections: $\boldsymbol{\theta}_1$ lists the discrete binary uncertain parameters considered; and $\boldsymbol{\theta}_2$ is related to continuous uncertain parameters. Each simulation realization is generated according to the probability distributions for vector $\boldsymbol{\theta}$ (at present, correlation structure is considered only for the discrete parameters defined using logic trees).

It is important to emphasize that the sampling procedure is going to involve both the structural model (configuration and material properties) and the flooding action. In particular, the load considered in the structural analysis is going to depend on the degree of water-tightness assigned to the structure based on the quality of doors and windows. Moreover, the parameters identifying the hydro-dynamic pressure profile have been simulated based on the variability of velocity profile with respect to the flooding height profile in the zone of interest, as demonstrated in detail in the section relative to the loading.

3.3 The structural analysis

VISK platform relies on the open-source structural finite element analysis software OpenSees [19] for structural analyses. The structural models developed herein are consisted of two-dimensional elastic shell finite element panels with openings (considered as voids). Three types of transversal boundary condition restraints are considered: (a) fixed end; (b) hinged; (c) free. For example, if a good transversal connection between two orthogonal walls is verified, wall panel with fixed-end restraints can be used. Based on the uncertain parame-

ters related to the geometrical configuration of the buildings, four different types of structural models are generated. These models are distinguished based on the type, number and relative positioning of openings (door and windows). Figure 9 below illustrates various configurations generated in the simulation procedure.



L (m) - wall length
H (m) - wall height
t (m) - wall thickness
L_w (m) - window length
H_w (m) - window height
H_{wfb} (m) - window rise
L_d (m) - door length
C_d (m) - corner length
H_f (m) - foundation rise
H_b (m) - barrier height

Figure 9: Four structural configurations considered in the analysis.

The current version of VISK considers three kinds of flood action on the structure: (1) hydrostatic; (2) hydrodynamic pressure; (3) waterborne debris impact; (4) material property deterioration (due to elongated contact with water). Detailed description of the above-mentioned flood actions can be found in [20]. As far as it regards the flooding pressure, the flooding profile across structural height is considered and the resulting forces are discretized to the panel joints. The discretized force on the openings (if they are sealed) is applied to the joints located at the opening boundary (neglected if the opening is not sealed).

3.3.1 Incremental flood loading analysis

The critical flooding height for the structure is established through a procedure referred to as incremental flood loading analysis. In this procedure, for increasing levels of flooding height, the structural model is analyzed considering the above-mentioned combination of actions (assuming that waterborne debris are going to hit the structure at the flooding water level assumed). The critical water-height for a given limits state is considered as the water-height in which the limit state in consideration is exceeded for the first time. For each flooding height level, this consists in controlling whether the section force, or demand, denoted by *D*, exceeds the corresponding section resistance, or capacity, denoted by *C*, for the specified limit state, for zones of stress concentration.

Safety-checking: For all the identified zones of stress concentration (described in detail in the next section) and for each water height level, safety-checking is performed in terms of both shear force and out-of-plane bending moment. It should be noted that safety-checking for bending moment is differentiated with respect to horizontal and vertical sections, due to the presence of axial forces. Denoting the flexural strength of a horizontal section by ($M_{Rd,H}$); the flexural strength of a vertical section by ($M_{Rd,V}$); and the shear strength by (V_{Rd}):

$$V_{Rd} = A_{section} \cdot \tau_0 \tag{3}$$

$$M_{Rd,H} = \frac{N \cdot t}{2} \cdot \left(1 - \frac{N}{0.85 \cdot f_m \cdot A_{section}}\right) \tag{4}$$

$$M_{Rd,V} = \frac{f_{fl} \cdot H_{section} \cdot t^2}{6} \tag{5}$$

where $A_{section}$ is the area of the section/sub-section; $H_{section}$ is the height of the section/sub-section, and N is the axial force acting on the section/sub-section. The formula for shear strength neglects interactions between shear/axial forces. The flexural strength for a horizontal section/sub-section in Eq. 4 is calculated assuming that the out-of-plane bending moment strength reached by exceeding the ultimate compression strength. This is while the flexural strength for a vertical section/sub-section in Eq.5 is calculated by assuming that the bending moment strength is reached by exceeding the ultimate tensile strength.

Calculating the critical demand-to-capacity ratio: VISK provides an iterative procedure for identification of the zones high stress concentration by searching through prescribed critical sections. Figure 10 below illustrates various critical sections (highlighted) identified in relation to structural configuration and geometry.

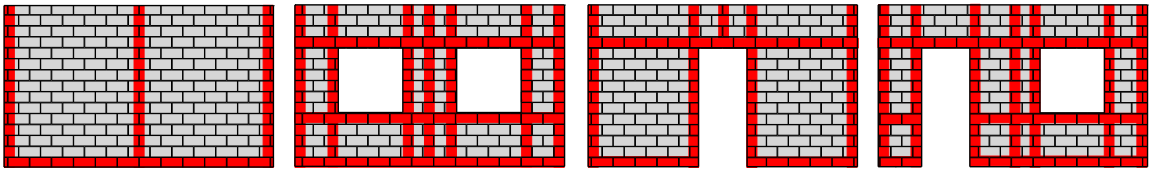


Figure 10: Zones of panel in which is searched the critical section.

Zones of high stress concentration can verify due to, debris impact, asymmetric boundary conditions, and geometrical configurations/presence of openings. Strictly speaking, local stress concentrations do not necessarily translate into global failure mechanisms; however, – in lieu of more accurate information – they can be considered as precursors to failure for a brittle structure. For each critical section *i* considered, the zone(s) of high stress concentration are identified by: (a) discretizing in smaller *sub-sections* (with a discretization step of 25 cm); (b) calculating the demand to capacity ratio (for both flexure and shear), for each sub-section *j* of the critical section considered, denoted by D_{ji}/C_{ji}. This is done in an exhaustive manner considering all the possible sub-sections; (c) defining the zone(s) of high stress concentration as those having the largest demand to capacity ratio $\max_j D_{ji}/C_{ji}$. In this manner, VISK can determine, for each water height level *h*, the critical demand to capacity ratio as the demand to capacity ratio *Y(h)* that takes the structure closer to the onset of specified limit state [21]:

$$Y(h) = \max_i \max_j \frac{Dji}{Cji} \tag{6}$$

VISK platform registers the critical section *i*, the mode of failure (shear/flexure), and the water height h_{cr} that corresponds to $Y(h_{cr})=1$.

For each Monte Carlo realization of the structural model identified by vector θ, a value for the critical water height $h_{cr}(\theta)$ is obtained, for a given limit state, defined as $Y(h_{cr}(\theta))=1$. The dependence of critical water-height on θ is dropped for convenience hereafter.

Numerical Example: Figure 11 below shows the histrogram of critical section/mode of failure corresponding to h_{cr} for a set of $N=200$ simulations performed by VISK. The red column marked as *no collapse* identifies the simulations in which, for all the water height levels considered, the critical height for which $Y(h_{cr})=1$ is not verified.

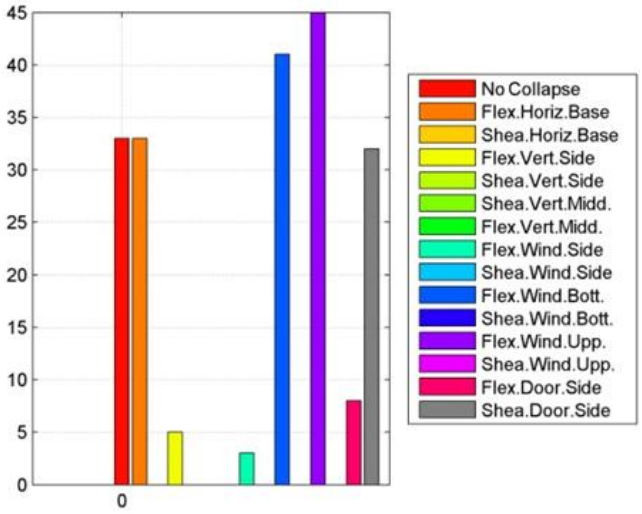


Figure 11. Histogram of critical section/mode of failure corresponding to h_{cr} for a set of $N=200$ simulations.

3.5 The analytical fragility curves

For each limit state considered, the simulation procedure provides a set of critical water height values as described in the previous section. These critical water height values are used then as *data* in order to calculate, using Bayesian parameter estimation [22], the *posterior* probability distribution for the parameters of prescribed analytic fragility functions. Finally, the *robust fragility* [23, 24] is calculated as the expected fragility based on the posterior probability distribution calculated for the parameters of the prescribed analytic fragility functions. Note that this posterior probability distribution can be interpreted as degrees of belief in the various analytic fragility models that are defined based on a specific set of parameters. VISK adopts three analytical fragility models corresponding to each of the three limit states considered:

(SE) $$F\left(h_f \mid \pi_0, \eta_{SE}, \beta_{SE}\right) = P\left(h_{SE} \le h_f\right) = \pi_0 \cdot \Phi\left(\frac{\ln \frac{h_f}{\eta_{SE}}}{\beta_{SE}}\right) + \left(1-\pi_0\right) \cdot I_0\left(h_f\right) \tag{7}$$

(CO) $$F\left(h_f \mid \eta_{CO}, \beta_{CO}\right) = P\left(h_{CO} \le h_f\right) = \Phi\left(\frac{\ln \frac{h_f}{\eta_{CO}}}{\beta_{CO}}\right) \tag{8}$$

(LS) $$F\left(h_f \mid \pi, \eta_{SL}, \beta_{SL}\right) = P\left(h_{SL} \le h_f\right) = \pi \cdot \Phi\left(\frac{\ln \frac{h_f}{\eta_{SL}}}{\beta_{SL}}\right) + \left(1-\pi\right) \cdot I\left(h_f\right) \tag{9}$$

where parameters π, η and β reported after the conditioning sign (|) are the three parameters that define the analytic probability distribution/fragility function for the serviceability (SE) and life safety (SL) limit states. Meanwhile, for the collapse (CO) limit state, only two parameters denoted by η and β are needed. 1-π_0 is the ratio of cases for which the serviceability critical height is equal to zero; *1-*π is the ratio of cases for which the life safety height is equal to a nominal prescribed value; η and β are respectively the median and the logarithmic standard deviation for the critical water height given that the critical water height is greater than zero for (SE) and given that the critical water height is not equal to the nominal value for (LS); Φ(.) denotes the standard Gaussian (Normal) cumulative probability distribution and $I_0(h_f)$ and $I(h_f)$ are index function defined as follows:

(SE)
$$I_0\left(h_f\right)=\begin{cases}0 \ if \ h_f=0\\1 \ if \ h_f>0\end{cases} \tag{10}$$

(LS)
$$I\left(h_f\right)=\begin{cases}0 \ if \ h_f\le h_{nominal}(LS)\\1 \ if \ h_f>h_{nominal}(LS)\end{cases} \tag{11}$$

$I_0(h_f)$ and $I(h_f)$ depict two step functions identified respectively by zero (Figure 12a) and the nominal water height ($h_{nominal}(LS)$) (Figure 12d). Note that the derivative *I* functions is equal to the Dirac delta function at $h=0$ and $h=h_{nominal}(LS)$.

The analytical fragility model proposed in Eq. 7 and Eq. 9 can be interpreted as an application of the total probability theorem [25] on the two mutually exclusive outcomes marked by probabilities π_0 and π. The probability distributions in Eqs. 7 and 9 are also known as the *three-parameter* distributions [25, 26] which are bi-modal probability density function (PDF)/cumulative distribution function (CDF) expressed as a linear combination of a Lognormal PDF/CDF and a Dirac delta function/step function. In particular, the three-parameter cumulative distribution functions expressed in Eq. 7 and illustrated in Figure 12(c) is a linear combination (with weight π_0) of the step function $I_0(h_f)$ depicted in Figure 12(a) and the Lognormal CDF depicted in Figure 12(b). In a similar manner, the three-parameter cumulative distribution functions expressed in Eq. 9 and illustrated in Figure 12(f) is a linear combination (with weight π) of the step function $I(h_f)$ depicted in Figure 12(d) and the Lognormal CDF depicted in Figure 12(e).

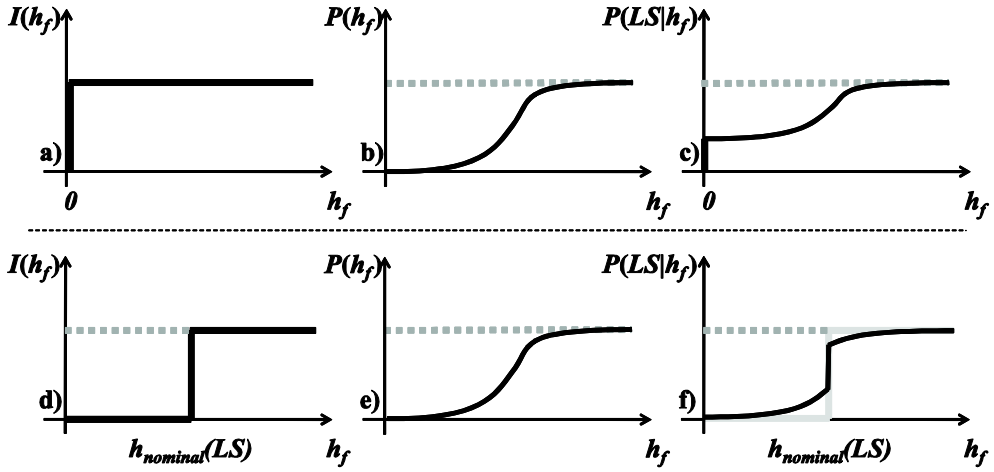


Figure 12: schematic diagrams of: a) step function for SE; b) the Lognormal CDF for SE; c) the three-parameter CDF for SE; d) step function for LS; e) the Lognormal CDF for LS; f) the three-parameter CDF for (LS)

3.6 The robust fragility estimation

Denoting the parameters of the analytic fragility function as χ (e.g., $\chi=[\pi,\eta,\beta]$ for LS), the joint probability distribution for the vector of parameters χ can be expressed as $p(\chi)$. Using Bayesian parameter estimation, the probability distribution for the parameters of the fragility function for a given limit state can be updated using formulas described in [22] based on the set of critical height values obtained from simulation. The updated or posterior probability distribution can be denoted as $p(\chi|\mathbf{H_c(LS)})$ [3] where $\mathbf{H_c(LS)}$ is the vector of simulation-based critical height values for limit state LS. This probability distribution represents the uncertainty in the vector χ due to limited number of simulations.

The robust fragility denoted by $F(h_f|\ \mathbf{H_c})$ is calculated as the expected value of the analytic function $F(h_f|\chi)$ in Eqs. 3, 4 and 5, over the entire domain of vector χ and according to the updated joint probability distribution $p(\chi|\mathbf{H_c})$:

$$F\left(h_f \mid \boldsymbol{H_c}\right) = E\left[F\left(h_f \mid \chi\right)\right] = \int_{\Omega} F\left(h_f \mid \chi\right) \cdot p\left(\chi \mid \boldsymbol{H}_c\right) \cdot d\chi \tag{12}$$

where $E[.]$ is the expected value operator and Ω is the domain of the vector χ. The variance σ^2 in fragility estimation can be calculated as:

$$\sigma^2\left[F\left(h_f \mid \chi\right)\right] = E\left[F\left(h_f \mid \chi\right)^2\right] - E\left[F\left(h_f \mid \chi\right)\right]^2 \tag{13}$$

where $E[F(h_f|\chi)]^2$ can be calculated from Eq. 12 replacing $F(h_f|\chi)$ with $F(h_f|\chi)^2$.

Numerical Example: Figure 13 below illustrates the robust fragility curves and their plus/minus one standard deviation interval, corresponding to the three limit states (SE, LS and CO) taken into account into in VISK, based on N=50 Monte Carlo simulations.

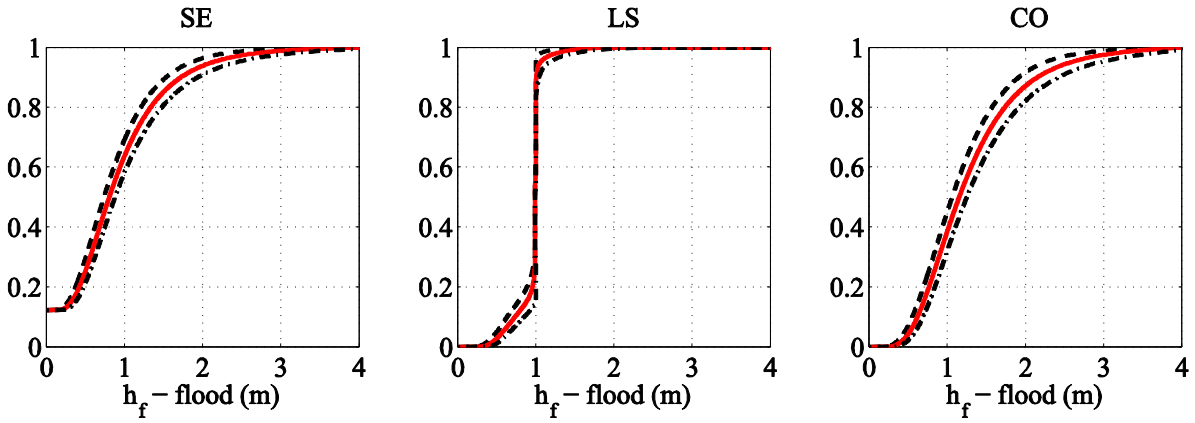


Figure 13: Robust Fragility curves and their plus/minus one standard deviation interval (SE), (LS) and (CO), respectively.

[3] LS is dropped hereafter for brevity.

4 VISUAL RISK ASSESSMENT PLATFORM

4.1 The risk maps

VISK renders point estimates of flooding risk by integrating the robust fragility and its plus/minus one standard deviation intervals ($F \pm \sigma_F$) and the flood hazard at a given point in the zone of study:

$$\lambda_{LS}(\mathbf{H_c}) = \int_x \mathrm{F}\left(x \mid \mathbf{H_c}\right) \cdot \left| d\lambda\left(x\right) \right| \cdot dx \tag{14}$$

In this case, the flooding risk is $\lambda_{LS}(\mathbf{H_c})$ is expressed in terms of the mean annual rate of exceeding[4] a prescribed limit state LS (i.e., exceeding the critical flooding height corresponding to the limit state in question) for a given point. The annual probability of exceeding a limit state *P(LS)*, assuming a homogeneous Poisson process model with rate λ_{LS} is:

$$P\left(LS\right) = 1 - \exp\left(-\lambda_{LS}\right) \tag{15}$$

Numerical Example: Figure 14 illustrates risk maps in terms of mean annual rate λ_{LS} and annual probability *P(LS)* of exceeding the collapse limit state.

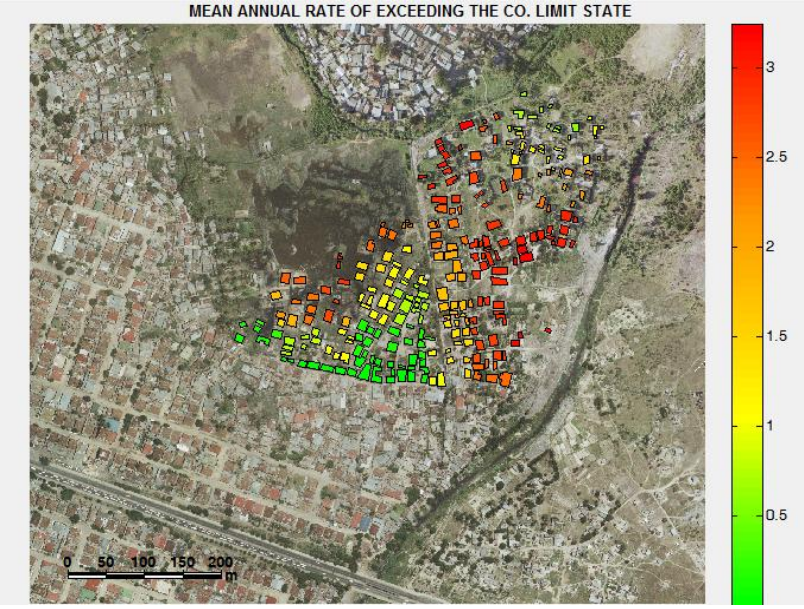


Figure 14 a: Risk maps in terms of mean annual rate of exceeding the collapse limit state [17]

[4] $\mathbf{H_c}$ is dropped hereafter for brevity.

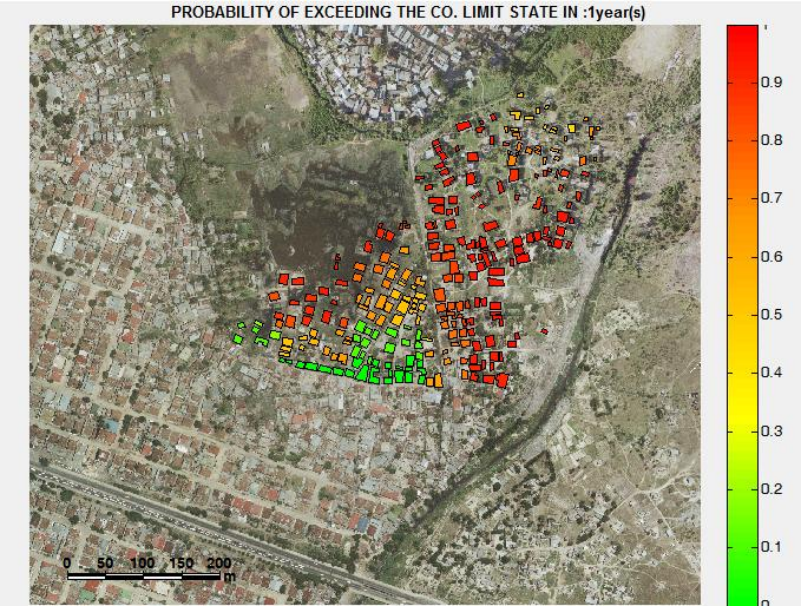


Figure 14 b: Risk maps in terms of the annual probability of exceeding the collapse limit state [17]

Exposure to risk: VISK estimates the exposure to risk by calculating the total expected loss or the expected number of people affected for all the buildings identified (see Section 2.1) in the case-study area. The expected repair cost (per building or per unit residential area), E[R], can be calculated as a function of the limit state probabilities and by defining the damage state *i* as the structural state between limit states *i* and *i*+1:

$$E[R] = \sum_{i=1}^{N_{LS}} \left[P\left(LS_{i+1}\right) - P\left(LS_i\right) \right] \cdot R_i \tag{16}$$

where N_{LS} is the number limit states that are used in the problem in order to discretize the structural damage; R_i is the repair cost corresponding to damage state *i*; and $P\left(LS_{N_{LS}+1}\right) = 0$. The expected number of people affected by flooding can also be estimated as a function of the limit state probabilities from Eq. (16) replacing R_i by the population density (per house or per unit residential area).

Numerical Example: Considering a population density of 0.03 per residential square meter and a rebuilding cost of 3 € per square meter (for a single limit state, CO), the expected replacement cost and the expected number of casualties is calculated from Eq. 16 (with $N_{LS}=1$). Figure 15 and 16 illustrate the expected number of casualties and expected replacement cost for the buildings considered in the case-study area.

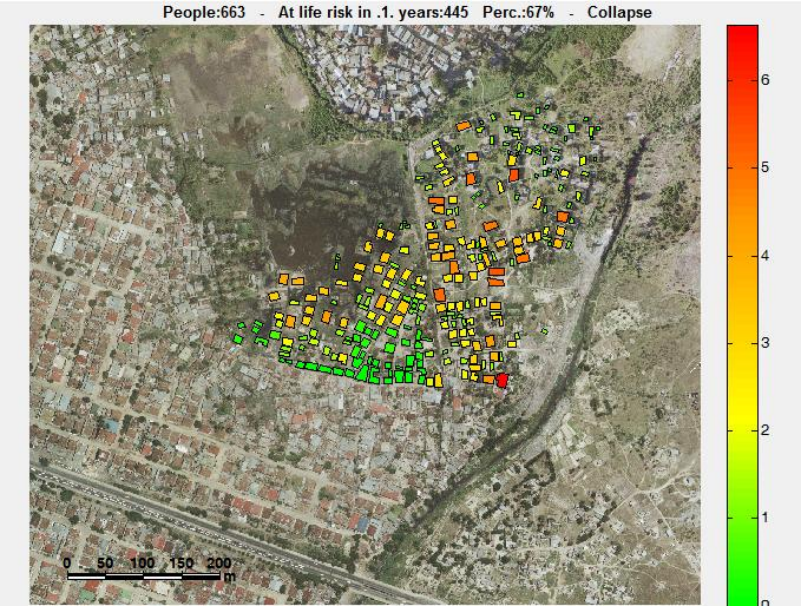


Figure 15: The expected number of casualties [17]

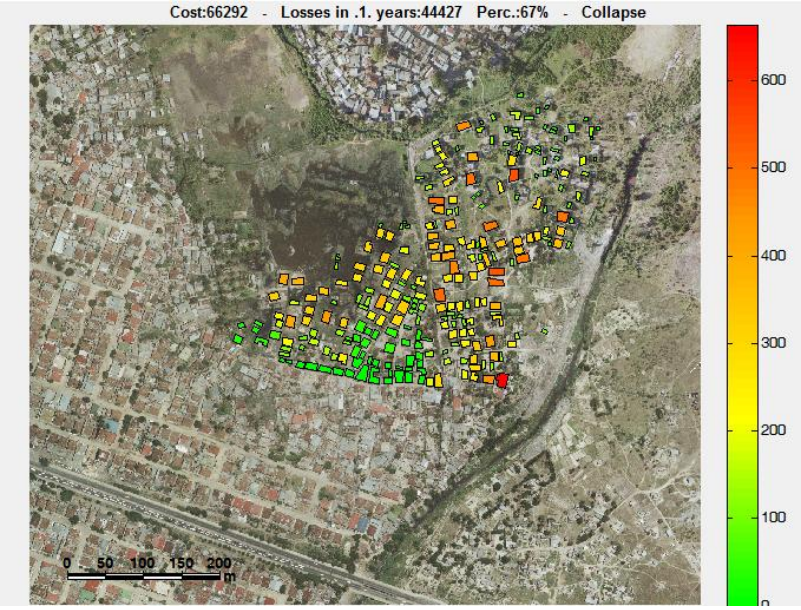


Figure 16: The expected replacement cost [17]

2 CONCLUSION

VISK is a new software platform with a graphical user interface for micro-scale flood risk assessment for a single class of buildings. This software, which has been developed in the context of the European FP7 project CLUVA for flood vulnerability assessment of informal settlements ("non-engineered" buildings), is particularly suitable for risk assessment based on incomplete information. This paper has discussed the novel features of VISK. These novel features include: using manual orthophoto boundary recognition in order to capture the footprint of the buildings considered; propagation of several sources of uncertainties (e.g., building-to-building variability, incomplete knowledge, limited number of surveys, limited number of simulations) in the calculation of structural fragility for a class of buildings; considering the correlation between discrete binary parameters; using Bayesian parameter estimation based on sample field survey results in order to characterize uncertainties; calculating the structural

fragility using an efficient Bayesian small-sample simulation method; an exhaustive iterative procedure for localizing the structural damage in the model structure; considering the openings in the model structure; taking into account flood actions such as the hydro-static and hydro-dynamic pressure, the debris impact and material deterioration due to elongated contact with water, taking into account the effect of water-seepage in structural analysis. The fragility curves for the class of buildings are calculated for three limit states of serviceability (SE), structural collapse (CO), and life safety (LS). Various point-wise risk metrics are adopted in VISK for evaluating the flooding risk, the mean annual rate and annual probability of exceeding a prescribed limit state, the expected loss, and the expected number of people affected by flooding.

It should be noted that, although VISK is developed for micro-scale flood risk assessment of informal settlements, it could be applied to other building types in general.

ACKNOWLEDGEMENTS AND DATA SOURCES

This work was supported in part by the European Commission's seventh framework program Climate Change and Urban Vulnerability in Africa (CLUVA), FP7-ENV-2010, Grant No. 265137. This support is gratefully acknowledged. The authors gratefully acknowledge Prof. F. De Paola, Prof. M. Giugni and M. E. Topa for providing the inundation profiles; E. Mbuya and A. Kyessi for the field survey results for informal settlements in Suna Sub-ward of Dar es Salaam City.

REFERENCES

[1] Jonkman S.N., Vrijling J.K., and Vrouwenvelder A.C.W.M., *Methods for the estimation of loss of life due to floods: a literature review and a proposal for a new method.* Natural Hazards, 2008. **46**: p. 353-389.

[2] Pistrika A.K. and Jonkman S.N., *Damage to residential buildings due to flooding of New Orleans after hurricane Katrina.* Natural Hazards, 2009. **54**: p. 413-434.

[3] Pistrika A. and Tsakiris G., *Flood risk assessment: A methodological framework*, in *Water Resources Management: New Approaches and Technologies. European Water Resources Association, Chania, Crete-Greece*. 2007.

[4] Pistrika A., *Flood Damage Estimation based on Flood Simulation Scenarios and a GIS Platform*, in *EWRA 7th International Conference "Water Resources Conservancy and Risk Reduction Under Climatic Instability"*. 2009: Limassol, Cyprus. p. 419-427.

[5] Smith D., *Flood damage estimation- A review of urban stage-damage curves and loss functions.* Water S. A., 1994. **20**(3): p. 231-238.

[6] Kang J., Su M., and Chang L., *Loss functions and framework for regional flood damage estimation in residential area.* Journal of Marine Science and Technology, 2005. **13**(3): p. 193-199.

[7] Schwarz J. and Maiwald H., *Empirical vulnerability assessment and damage for description natural hazards following the principles of modern macroseismic scales*, in *14th WCEE - World Conference of Earthquake Engineering*. 2012: Lisboa, Portugal.

[8] Schwarz J. and Maiwald H., *Damage and loss prediction model based on the vulnerability of building types*, in *4th International symposium of Flood Defence*. 2008: Toronto, Canada.

[9] Nadal N.C., Zapata R.E., Pagán I., López R., and Agudelo J., *Building damage due to riverine and coastal floods.* Journal of Water Resources Planning and Management, 2009. **136**(3): p. 327-336.

[10] Scawthorn C., Flores P., Blais N., Seligson H., Tate E., Chang S., Mifflin E., Thomas W., Murphy J., and Jones C., *HAZUS-MH flood loss estimation methodology. II. Damage and loss assessment.* Natural Hazards Review, 2006. **7**(2): p. 72-81.

[11] Scawthorn C., Blais N., Seligson H., Tate E., Mifflin E., Thomas W., Murphy J., and Jones C., *HAZUS-MH flood loss estimation methodology. I: Overview and flood hazard characterization.* Natural Hazards Review, 2006. **7**(2): p. 60-71.

[12] Apel H., Aronica G.T., Kreibich H., and Thieken A.H., *Flood risk analyses—how detailed do we need to be?* Natural Hazards, 2008. **49**: p. 79-98.

[13] Faber M.H., *Statistics and Probability Theory: In Pursuit of Engineering Decision Support*. Vol. 18. 2012: Springer.

[14] Jaynes E.T., *Probability theory: The logic of science*. 2003: Cambridge university press.

[15] O'Brien J., Julien P., and Fullerton W., *Two-dimensional water flood and mudflow simulation.* Journal of hydraulic engineering, 1993. **119**(2): p. 244-261.

[16] FLO-2D S.I., *FLO-2D® User's Manual*. 2004: Nutrioso, Arizona.

[17] DeRisi R., Jalayer F., DePaola F., Iervolino I., Giugni M., Topa M.E., Mbuya E., Kyessi A., Manfredi G., and Gasparini P., *Flood Risk Assessment for Informal Settlements, Under Review.* Natural Hazards, 2013.

[18] DeRisi R., Jalayer F., Iervolino I., Kyessi A., Mbuya E., Yeshitela K., and Yonas N., *Guidelines for vulnerability assessment and reinforcement measures of adobe houses*, deliverable in CLUVA project - Climate Change and Urban Vulnerability in Africa. 2012. Available from: http://www.cluva.eu/deliverables/CLUVA_D2.4.pdf. Data last access: 01/01/2013.

[19] McKenna F., Fenves G., and Scott M., *OpenSees: Open system for earthquake engineering simulation.* Pacific Earthquake Engineering Center, University of California, Berkeley, CA., http://opensees. berkeley. edu, 2006.

[20] Kelman I. and Spence R., *An overview of flood actions on buildings.* Engineering Geology, 2004. **73**(3): p. 297-309.

[21] Jalayer F., Franchin P., and Pinto P., *A scalar damage measure for seismic reliability analysis of RC frames.* Earthquake Engineering & Structural Dynamics, 2007. **36**(13): p. 2059-2079.

[22] Box G.E.P. and Tiao G.C., *Bayesian Inference in Statistical Analysis*, ed. W. Interscience. 1992: John Wiley & Sons, Inc.

[23] Jalayer F., Elefante L., Iervolino I., and Manfredi G., *Knowledge-based performance assessment of existing RC buildings.* Journal of Earthquake Engineering, 2011. **15**(3): p. 362-389.

[24] Papadimitriou C., Beck J.L., and Katafygiotis L.S., *Updating robust reliability using structural test data.* Probabilistic Engineering Mechanics, 2001. **16**(2): p. 103-113.

[25] Benjamin J.R. and Cornell C.A., *Probability, Statistics, and Decision for Civil Engineers*. 1970: McGraw-Hill, New York.

[26] Shome N., *Probabilistic seismic demand analysis of nonlinear structures*. RMS Program. 1999, Stanford University.

COMPDYN 2013
4th ECCOMAS Thematic Conference on
Computational Methods in Structural Dynamics and Earthquake Engineering
M. Papadrakakis, V. Papadopoulos, V. Plevris (eds.)
Kos Island, Greece, 12–14 June 2013

A SIMPLIFIED METHODOLOGY TO OBTAIN RELIABILITY INDEXES FOR CALIBRATION OF DESIGN CODE FOR BUILDINGS

L.E Pérez-Rocha[1], **M.A. Fernández,**[1] **L.E. Manjarrez,**[1] **J. D. Maldonado,**[1] **L. Esteva**[2]

[1] Instituto de Investigaciones Eléctricas
62490 Cuernavaca, Morelos, México
e-mail: {lepr, marco.fernandez, lorena.manjarrez, david.maldonado}@iie.org.mx

[2] Instituto de Ingeniería, UNAM
México, D.F.,
{LEstevaM}@iingen.unam.mx

Keywords: Reliability index, code calibration, load combinations, safety load factor, FOSM.

Abstract. *The aim of this work is to give support in the update of the Complementary Technical Standards for Actions for Structural Design of the buildings of the Federal District of Mexico. A methodology based on probability concepts was developed to obtain reliability indexes for some typical structural elements (columns, beams and walls). Structural element designs were performed using Mexican requirements. An interval of load factors values was analyzed including current values. Gravitational and gravitational plus accidental actions load combinations formats were analyzed in which variations of reliability index as a function of load factors were presented and discussed.*

1 INTRODUCTION

Provisions are set out in building codes in order to furnish a protection from the view point of society, so that by complying with them there is assurance that the design will not drift excessively from what is optimum for society and at the same time it will exist an appropriate level of security against unwanted states. This in particular, requires proof that the structure meets those requirements, being capable of withstanding all load assumed to occur during the envisaged lifetime. The requirements are mainly comprised of design criteria such as design actions, factors and load combinations, limit states, resistance factors, as well as, general analysis and design procedures for a number of structural elements and materials.

Actually, a challenge faced by group of code writers it to keep regulations up to date. This process requires the constant development of basic research and incorporation of the new advanced techniques, technological progress and practical experience. Rational methodologies and judgment to assess safety levels are of paramount significant.

Quantifying the safety level can be carried out applying reliability theory. Early works like those performed by [1 and 2] have given us a guideline on reliability code formats and reliability indexes. Recently, groups from different countries have been conducting code calibrations using reliability techniques. Amongst the ones it could be highlighted are the following: the reference [3] for the American National Standard A58 standard in force at that year; [4, 5 and 6], for ASCE regulations; [7 and 8] for ACI regulations; [9] for Danish codes; and [10 and 11] for the Eurocodes [12 and 13].

Recognizing the need for evaluation safety levels in code building regulations, this paper aims to obtain measures of reliability indexes that can be achieve in keeping with the requirements of the Complementary Technical Standards for Criteria and Actions for the Structural Building Design at the Distrito Federal in México [14]. The developed methodology is applied to conventional structural elements. Quantitative measures of reliability for columns, beams and walls are obtained. Finally, a discussion of the findings of this study is presented.

1.1 Trend of load combinations formats and load factors

Building regulations have been improving and overcoming several past limitations that hindered the establishment of common criteria for an adequate level of safety of the structures, the assurance of consistency in similar structures, and in many cases, the experience extrapolation for materials to other building systems. This has been overcome mainly by recognizing the random nature of the variables involved (loads and resistance) and by providing procedures for dealing with uncertainty in the various stages of the design process in a rational and simple way.

Table 1 shows a summary of the factored load combinations and load factors on international codes. As it can be appreciated, all cases of load combination comprising dead load only, with no other action accompanying, a factor of 1.4 is applied. When using load combinations which include wind or earthquake loads, the load factor for dead load decreases from 1.4 to values between 0.9 and 1.25 because of the transient nature of wind and earthquake loads; that is based on the assumption that simultaneous occurrence of maximum value of each one it is not possible (this assumption is based on the fact that there is a very low probability of occurrence), and if they act at the same time, then it is possible that some load components may counteract other components.

Code/Standard	Dead Load (D)	Wind Load Factor	Seismic Load Factor
[15] ASCE/SEI 7-05	1.4	[1] 1.6	[1] 1.0
[16] UBC, Uniform Building Code	1.4	[1] 1.3	[1] 1.0
[17] IBC, International Building Code	1.4	[1] 1.6	[1] 1.0
[14] Normas Técnicas Complementarias	1.4	[2] 1.1	[2] 1.1
[18] NSR – 10	1.4	[1] 1.6	[1] 1.0
[19] SEAOC	1.4	[1] 1.3	[1] 1.0
[20] National Building Code of Canada	1.4	[3] 1.4	[4] 1.0
[21] ACI 318-08	1.4	[5] 1.6	[5] 1.0

[1] 1.2D + [2] 1.1D + [3] (1.25D o 0.9D) + [4] 1.0D+ [5] (1.2D o 0.9D) +

Table 1: Summary of load factors and factored load combinations

1.2 Theoretical framework - Structural Reliability

Despite of the effort made to understand, quantify and reduce uncertainties, there is always a finite probability of failure.

Failure is often understood as the condition in which the loading effect (S) exceeds the resistance (R), it means that $S > R$. In other words, there is a chance that a limit state will be reached or exceed – this conditions means that the behavior is no longer acceptable. Ultimate limit state and Serviceability limit state are the most well-known. The first limit state is used to restrict system or structural element total capacity of load-bearing, i.e., creep, brittle fracture, fatigue, instability, buckling and overturning. The serviceability limit state allows deformations with certain tolerances that do not exceed the overall system load-bearing capacity. Examples include cracking, corrosion, permanent deformation and vibration.

In structural design, component or system reliability is evaluated according to one or more failure modes. By means of a set of random variables grouped into a vector **X,** the strength, stiffness, geometry and loading of the component is modeled. Variables are considered as stochastic in the sense that, according to its variability and other possible uncertainties, they can take random degrees of outcomes agreeing to a distribution function. For the failure mode been studied, the possible outcome of $\mathbf{X}$ can be separated into two groups: 1) the set of events in which the structural component is said to be safe (safe set) and 2) the set where it fails (failure set). The area of basic variables between the set of failure and safe assembly space is denoted as limit-state surface. Then reliability problem can conveniently be described through the limit state function g(X), defined as:

$$\mathrm{g}(\mathbf{X}) \begin{cases} > 0 & \text{for X in the safe set} \\ = 0 & \text{for X on failure surface} \\ < 0 & \text{for X in the failure set} \end{cases} \tag{1}$$

The limit state function should be based on mathematical models that more closely reflect true mechanical behavior. The probability of failure can be defined as:

$$P_f = P\left[g(\mathbf{X}) \le 0\right] = \int_{g(\mathbf{X}) \le 0} f(\mathbf{x}) d\mathbf{x} \tag{2}$$

Where $f(\mathbf{x})$ is the joint probability density function of $\mathbf{X}$ and represents the uncertainty of variables $\mathbf{X}$.

The probability that a component or structural system does not fail, or more precisely, that it does not exceed a limit state is called reliability of the structure. The probability of failure P_f is one of the means to measure the reliability of a structure.

For example, a case in which $\mathbf{X}$ consists only of two variables, load, S, and resistance, R, the limit state function can be specified as $g(\mathrm{X}) = \mathrm{R} - \mathrm{S}$. Assuming both variables are statistically independent, probability of failure becomes a convolution integral.

$$\begin{aligned} P_f &= P[\mathrm{R} - \mathrm{S} < 0] = \int_{R-S\le 0} f_{\mathrm{R}}(r) f_{\mathrm{S}}(s) dr ds \\ &= \int_{-\infty}^{\infty}\int_{-\infty}^{\infty} f_{\mathrm{R}}(r) f_{\mathrm{S}}(s) dr ds \\ &= \int_{-\infty}^{\infty} F_{\mathrm{R}}(s) f_{\mathrm{S}}(s) ds \end{aligned} \tag{3}$$

Where f_{R} and f_{S} are the probability density functions of R and S, respectively, and $f_{\mathrm{R}}(r) = dF_{\mathrm{R}}(r)/dr$, where F_{R} is the cumulative distribution function R.

An alternative measure of reliability of a structure is obtained through the reliability index β, which can be related to the probability of failure by:

$$\beta = -\Phi^{-1}(P_f) \tag{4}$$

Where $\Phi(\cdot)$ is the cumulative distribution function of the standard normal distribution. Reliability index also represents standard deviations times that the critical value of the variable is far away from the expectation.

The reliability index β can be obtained through a structural reliability analysis either by numerical integration methods, first and second order analytical methods (FORM, SORM, and FOSM) or simulation methods. Some of them can lead to obtain approximate results of the reliability index. On one hand, the numerical integration is only recommended when $\mathbf{X}$ consists of few stochastic variables. Solution with the methods of first and second order is often accurate enough and has advantage over simulation methods when failure probabilities are small. A complete discussion of these methods can be found in the following literature [22, 23, 24, and 25].

A rough estimate of the probability of failure corresponding to a value of β is given by the expression proposed by [2]:

$$P_f = 460e^{-4.3\beta} \tag{5}$$

2 METHODOLOGY

The methodology proposed for this study is based on an approximation of first order and second moments. Random parameters influencing the design appear only through its expectation and covariance. It is assumed that probability density functions of the random variables can be described by a normal distribution function, because only the first moment are required to recover statistical moments. Subsequently, the variables are transformed into standardized normal distribution with zero expectation and unit variance. This transformation and approximation of random variables to the standard normal distribution integration simplifies the procedure for determining the probability of failure taking advantages of the normal distribution function properties. Although it is true that limit state function can be nonlinear, it can be linearized in order to carry out major simplifications. This technique is known as the method of

first order. These techniques of limit state approximation of first order and second moments of the random variables are known as First Order Second Moment (FOSM) reliability method and it is used in the present work.

To apply the first order approximation to the general design process, it should consider that variables may consist of one or more random variables, in the form:

$$y = \mathrm{g}\left(X_1, X_2, ..., X_n\right) \tag{6}$$

Then, statistical moments of independent variables can be obtained through a development in Taylor series approach around the expectation of each variable, and then taking into account only terms of its first derivatives. If it is assumed a condition of independency between random variables, the expectation of the dependent variable will be obtained by applying the function to the expectation of each one of the independent variables. This is formulated as follows:

$$m_y = \mathrm{g}\left(m_{X_1}, m_{X_2}, ..., m_{X_n}\right) \tag{7}$$

The variance is obtained as the sum of variances of the independent variables weighted by a factor whose value depends on its own influence on the variability of the dependent variable. This weighted factor is equal to the partial derivative of the limit state function with respect to each independent variable which, in turn, will be calculated by replacing the value of its expectation:

$$\sigma_y^2 = \sum_{l=1}^{n} \left(\frac{\partial \mathrm{g}}{\partial X_l} \right)_{m_{x_l}}^2 \cdot \sigma_{X_l}^2 \tag{8}$$

With this methodology, main contribution is to determine the implicit reliability of structural elements in various design situations according to the regulations currently in force for the Federal District of Mexico [14].

First, it is necessary to obtain, from the design values, the mean value and the coefficient of variation of load actions and resistance. All these variables will also be a function of special considerations concerning accuracy.

Secondly, with above data, variation on the structural element reliability under certain loading conditions and design can be obtained, using the method described in the previous section. For this study the following structural elements were analyzed because they can be found among the most widely used elements type for building structures, usually built in the Federal District:

- Reinforced concrete beam
- Structural steel beam
- Reinforced concrete column
- Structural steel column
- Masonry wall

The methodology to determine reliability indexes is summarized in Table 2 and it will be described in the following paragraphs.

I.	**Specification: member geometry and boundary conditions**
II.	**Evaluation: load combinations, design and load effects**
	• *Load combination: only gravitational loads*
	• *Load combination: gravitational loads plus accidental loads*
III.	**Design: member design for each load combination**
IV.	**Determination: expected values of total load effect and resistance**

•	*Load and resistance bias factors*
•	*Coefficients of variations*
V.	**Determination: reliability index**

Table 2: Methodology phases.

2.1 Specification of member geometry and boundary conditions

For each of the selected structural elements their geometry and support conditions as shown below in Figure 1. It is assumed that those structural elements are representative of typical they are at are characteristic of each element are frequently used in many structural designs.

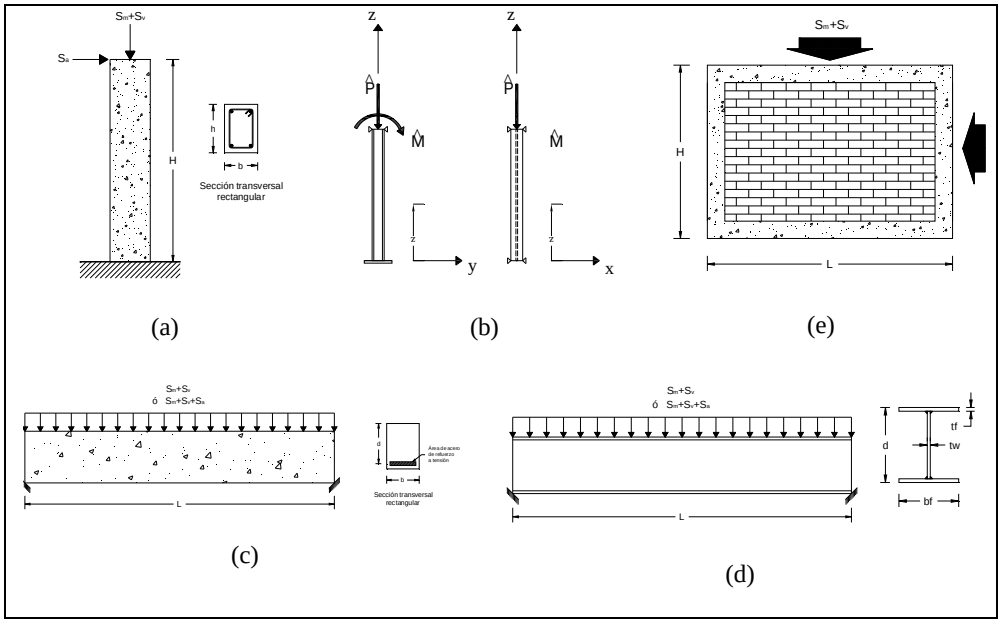


Figure 1: Selected structural elements for analysis: (a) R.C. column, (b) Steel column, (c) R.C. beam, (d) Steel beam, and (e) masonry wall.

2.2 Evaluation of load combinations, design loads and load effects

Load combinations adopted are those stipulated at [14]. Accordingly to the requirements, design actions are defined as:

- Permanent actions
- Variable actions
- Accidental actions

In the present work, structural elements will be designed to comply with the following criteria of load combinations and the associated load factors:

Load Combination	Load Factor
1. Permanent and variable actions	1.4
2. Permanent actions, variable and accidental	1.1

Table 3: NTC load factors.

In addition to the above load factors, structural elements are designed for a wide range of load factors for both prescribed load combinations that of course, cover those values prescribed by the actual code and others. This sketch allows us to study the effects on reliability index as load factors are decreased or increased.

An overview to obtain load effects on members is provided in Table 4. Knowing the nominal load effects and the load factors the mechanical elements, such as axial and shear forces and moments are derived.

Total Design Effect	
$S = (\gamma \text{ ó } \delta) \cdot \hat{S}$	
Total design effect = Load factor * Total nominal effect	
Load Combination	
Gravitational	Gravitational plus accidental
1) $S = \gamma (\hat{S}_m + \hat{S}_v)$	**2)** $S = \delta (\hat{S}_m + \hat{S}_v + \hat{S}_a)$
Total Nominal Effect	
$\hat{S} = (\hat{S}_m + \hat{S}_v)$	$\hat{S} = (\hat{S}_m + \hat{S}_v + \hat{S}_a)$
Range of Load Factors **(14)**	
$\gamma \in [1.2 \text{ a } 1.6]$ @ 0.05 (=1.4, [14])	$\delta \in [0.9 \text{ a } 1.2]$ @ 0.05 (=1.1, [14])
Action Effects in Terms of Mechanical Forces and Moments	
$P_{d1} = \gamma (\hat{P}_1)$	$P_{d2} = \delta (\hat{P}_2)$
$V_{d1} = \gamma (\hat{V}_1)$	$V_{d2} = \delta (\hat{V}_2)$
$M_{d1} = \gamma (\hat{M}_1)$	$M_{d2} = \delta (\hat{M}_2)$

Table 4: Actions effects derived in terms of mechanical forces and moments.

Where: S is the total design effect of the action pattern; γ y δ are load factors for gravitational and gravitational plus accidental load combinations, respectively. $\hat{S}$ represents the total nominal effect of the action, and the subscripts m, v or a indicate what kind of load is causing de action, permanent loads, variables or accidental, respectively. P, V and M represent the total action effects in terms of axial and shear forces and bending moment, respectively. The subscripts 1 and 2 indicate the load combination type. The subscript d is used to denote design condition. Finally, the symbol $\wedge$ on S, P, V and M , denotes the nominal effect of the corresponding action (i.e. denotes a value that has not yet been affected by load factors).

Gravity loads include dead loads such as the weight of the structural element and variable loads (live loads). In order to cover different load intensities and scenarios for both type of loads, representative values were adopted, being equal or proportional to the weight of the structural element.

2.3 Element design for each load combination

In real design situations, the actions effects on structural systems should be evaluated by a structural analysis. Usually, the response is obtained in terms of internal forces and deformations. In this work, for simplicity, instead of a structural system, a series of structural elements were chosen. That strategy omits the need for a structural analysis, so that to define action effects through defining representative ranges of the load intensity. That tries to cover many possible schemes, at which the structural element might be subjected during its lifetime into a structural system configuration.

For this study, only mechanical forces and moments will be taken into account as a result of any action effect on the structural element, coming from specific load combination and load factor. We are aware that certain situation may generate deformations and stresses, but now their incorporation within this methodology is out of scope of the present work.

The structural elements are designed for load combinations 1 and 2 (i.e. gravitational and gravitational loads plus accidental) and with respect to the failure modes listed in Table 6. It is pretended with this parametric work to a range of designs and to calculate the effect of the variation of the load factors on the reliability index values for each load combination.

2.4 Expected values of total load effects and resistance

2.4.1. Load bias factors

Fluctuations in loads constitute a significant proportion of the uncertainties that must be considered in the proposal of nominal load values for design. The estimation of the load intensities are affected by wide margins of uncertainty, lower for permanent actions and higher for accidental.

The current value adopted for a design action must be taken as the load action leading to the worst effects on the system; in general, this involves taking the maximum value that can be presented. However, uncertainties due to load fluctuations are only possible to determine if it is accepted a previously prescribed probability to be exceeded during a given time. The probability of this load must be small enough, but not zero. The assigned value will depend on how much conservatism it is desired to achieve, or it can be based on what is socially accepted for failure. Building Code [14] defines a nominal load value to that with a probability ranging from two to five percent of being exceeded during the lifetime of the structure (percentile 98).

The probability associated of a certain variable value to be exceeded o not achieved, may be formulated as function of the expected (or mean value), $\overline{m}_S$, and the standard deviation, σ_S, or coefficient of variation, V_S. For example, to calculate the nominal value, $\hat{m}_S$, which has 2 percent probability of being exceeded, and if there are knowledge to assume that the random variable has a distribution function similar to normal distribution function, $\hat{m}_S$ can be calculated with the following expression:

$$\hat{m}_S = \overline{m}_S + 2\,\sigma_S = \overline{m}_S\left(1 + 2\,V_S\right) \tag{9}$$

In this study it is assumed that all load variables can be described by a normal distribution, so that, the relations between the nominal values and the mean values (bias factors) of these loads are:

Permanente load $\hat{S}_m = \bar{S}_m \cdot (1 + 2\ V_m)$ (10)

Variable load $\hat{S}_v = \bar{S}_v \cdot [1 + 2\ V_v]$ (11)

Accidental load $\hat{S}_a = \bar{S}_a \cdot (1 + 2 V_a)$ (12)

where:

$\hat{S}_m, \bar{S}_m$ are nominal and expected permanent load value, respectively;

$\hat{S}_v, \bar{S}_v$ are nominal and expected variable load value, respectively;

$\hat{S}_a, \bar{S}_a$ are nominal and expected accidental load value, respectively;

V_m, V_v and V_a are de coefficient of variation for the permanent, variable and accidental loads, with representatives values of 0.08, 0.3 and 0.3, respectively [26].

The adimentional coefficient resulting from the division of expected values between nominal ones will be named, in this work, as bias factor, and it will denoted with the Greek symbol λ.

Bias factor	
$\frac{\text{Expected or mean load effect}}{\text{Nominal load effect}} = \left(\frac{\bar{S}}{\hat{S}}\right) = \lambda_S$	
Load Combination	
Gravitational	Gravitational plus accidental
$\lambda_{S1} = \left(\frac{\bar{S}}{\hat{S}}\right)_{S1} = \frac{\bar{S}_m + \bar{S}_v}{\hat{S}_m + \hat{S}_v}$ 13)	$\lambda_{S2} = \left(\frac{\bar{S}}{\hat{S}}\right)_{S2} = \frac{\bar{S}_m + \bar{S}_v + \bar{S}_a}{\hat{S}_m + \hat{S}_v + \hat{S}_a}$ (14)
Mean total load	
$\bar{S} = \bar{S}_m + \bar{S}_v$	$\bar{S} = \bar{S}_m + \bar{S}_v + \bar{S}_a$

Table 5: Load bias factors derivation for load combinations

The bias factors can also be expressed as functions of coefficients of variation:

$$r = \frac{\bar{S}_m}{\bar{S}_m + \bar{S}_v} \tag{15}$$

And

$$r' = \frac{\bar{S}_a}{\bar{S}_m + \bar{S}_v + \bar{S}_a} \tag{16}$$

Where:

r is a parameter that relates the effect of the permanent load with respect to the total effect (permanent load plus variable load). It can be noticed that r take values between 0 to 1 (when r tends to 0 means that $\bar{S}_m >> \bar{S}_v$, and when r equals 1, $\bar{S}_v = 0$).

$$\lambda_{S1} = 1/[1 + 2rV_m + 2(1-r)V_v] \tag{17}$$

$$\lambda_{S2} = 1/\{1 + (1-r')[2rV_m + 2(1-r)V_v] + 2r'V_a\} \tag{18}$$

Equations (17) and (18) describe bias factors for gravitational and gravitational plus accidental load combinations as a function of the coefficients of variation (permanent load, variable and accidental), and the parameters r and r '. It is noted that if there is no accidental load, the bias factor for the second combination will be the same as those prescribed by equation 17.

2.4.2. Coefficients of variation of total load effect

The coefficients of variation of the total loading effect is obtained by applying a first order approximation, using expressions (7) and (8) for the expected and the variance, respectively. The coefficient of variation is obtained by dividing variance between the square of the mean value.

For gravitational load combination of gravitational load, this coefficient of variation of total load effect is obtained as follows:

$$V_S = \sqrt{V_p^2 + r^2 V_m^2 + (1-r)^2 V_v^2} \tag{19}$$

For gravitational plus accidental load combination, the coefficient of variation of total load effect is:

$$V_S = \sqrt{V_p^2 + (1-r')^2 \left[r^2 V_m^2 + (1-r)^2 V_v^2 \right] + (r')^2 V_a^2} \tag{20}$$

The values of the coefficients of variation for V_p is equal to 0.15. V_p is he coefficient of variation to take into account for the lack of precision in the analysis. The values of the parameters, V_p , V_m and V_v were taken from [26].

2.4.3. Resistance bias factors

The design strength is obtained by multiplying nominal value by a factor which minor than unity, named resistance factor.

Nominal resistance value of a structural element must be a conservative value of its minimum capacity to withstand the actions effects. This value is also set with probabilistic basis. The determination of the resistance of a section or structural element may be analytically or experimentally, following procedures set forth in buildings regulations or codes of practice in association recognized techniques. In general, for nominal resistance values codes set up probabilities values between 0.02 y 0.05 that should be attained, i.e., the fact that a lower strength will be presented.

Analytically, the resistance should be expressed in terms of the internal forces or as the combination (axial forces, shear forces, bending moments and torsion), which are produced by the actions. This evaluation should be considered uncertainties in calculation formulas and variability of the factors involved in such expressions.

When resistance is obtained by testing, it is necessary to determine the nominal value or that with minimum probability from statistical information. If it only allowed to obtain the mean and the coefficient of variation of resistance, the nominal value can be approximated through the expression:

$$\hat{m}_R = \frac{\overline{m}_R}{1+\varsigma V_R} \tag{21}$$

Where:

$\hat{m}_R$ is the nominal strength value; $\overline{m}_R$ is the expected strength; V_R is the strength coefficient of variation; and ς is a factor in Mexican regulations equals 2.5 (corresponding to a probability of 0.02 of being reached).

The values adopted for coefficient of variations were adopted from the references [26, 27, 28, and 29]. A summary is presented in Table 6.

Structural element	Failure mode	Bias Factor (Mean/nominal)	Coefficient of variation
R.C. Beam	Bending*	1.34	12%
	Bending**	1.34	12%
Steel Beam	Bending*	1.11	12%
	Bending**	1.28	14%
R.C. Column	Axial Compression*	1.42	15%
	Bending-axial compression**	1.49	15%
Steel Column	Compression*	1.20	15%
	Bending-axial compression**	1.24	14%
Masonry wall	Axial Compression*	1.37	15%
	Shear**	1.87	35%

* Gravitational load combination

**Gravitational plus accidental load combinación

Table 6: Strength bias factors and coefficients of variation

2.5 Reliability index

In the case of defining as failure criterion the relationship $R - S = 0$, where R and S are the elements (or critical section) strength and action effect of an element, respectively, the reliability index may be formulated as follows:

$$\left(\frac{R}{S}\right) - 1 < 0 \tag{20}$$

$$\text{or } \log R - \log S < 0 \tag{21}$$

Taking as basic variables of R and S, $\log R$ and $\log S$, failure criterion can be rewritten as in the form $\log R - \log S < 0$. The reliability index is calculated as:

$$\beta = \frac{\left(\overline{\log R}\right) - \left(\overline{\log S}\right)}{\sqrt{\sigma^2(\log R) + \sigma^2(\log S)}} \tag{22}$$

Applying a first order approximation to the mean values and variances, we obtain:

$$\overline{R} = \overline{S}\exp\left(\beta_0\sqrt{V_R^2 + V_S^2}\right) \tag{23}$$

V_R and V_S are the coefficients of variation of R and S, respectively, and β is a reliability index.

3 RESULTS

Results show the measure of safety associated with particular design in terms of β. In figures 2 to 9 it is illustrated the variation of the reliability index with respect to the load factor in accordance with a specific load combination. Contour plots are also included for each structural element (R.C. Columns, R.C. Beams, Steels Columns, Steel Beams and masonry walls). Through each contour line it is intended to represent the reliability index for different load factors values in combinations which may include either first load combination (gravitational only) or second load combination (gravitational plus accidental). A contour plot allows us to distinguish and to combine load factors in order to obtain constant reliability index on structural elements analyzed.

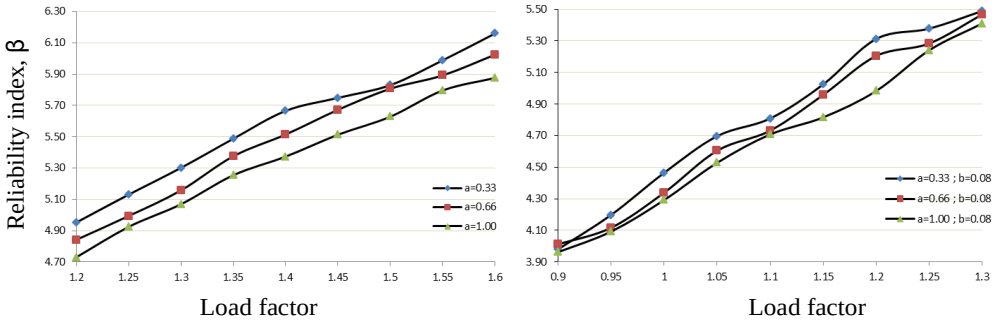


Figure 2: Reliability indexes, R.C. Column, (a) gravitational load combination, failure mode: axial compression; (b) gravitational plus accidental load combination, $c = 0.08$, failure mode bending and axial compression

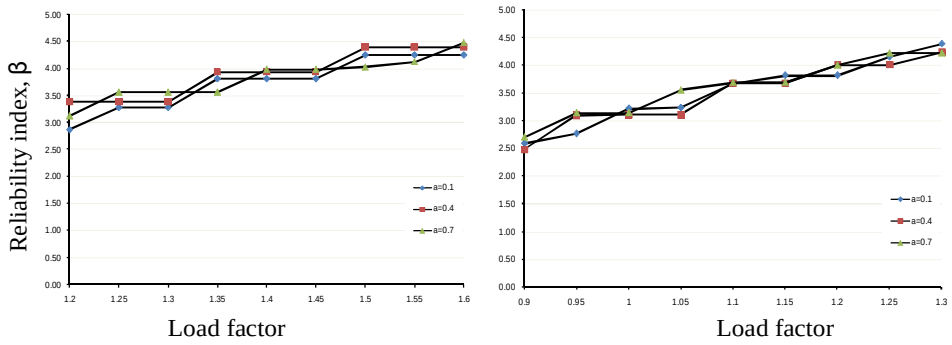


Figure 3: Reliability indexes, Steel Column, (a) gravitational load combination, failure mode: axial compression (according to the maximum KL/r value); (b) gravitational plus accidental load combination, $c = 0.33$, failure mode bending and axial compression

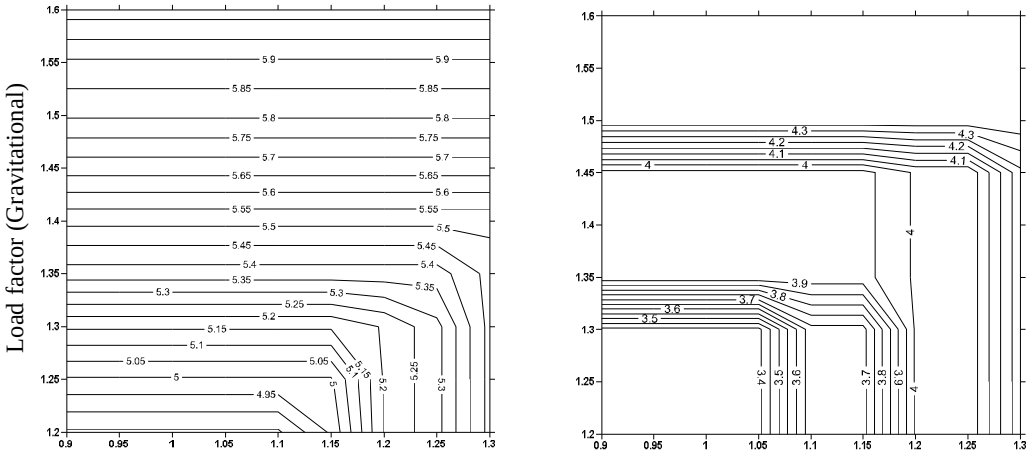


Figure 4: Reliability indexes for various load factors in each load combination, (a) R.C. Column, $a = 0.66$ and $c = 0.08$; (b) Steel Column, $a = 0.4$ and $c = 0.33$.

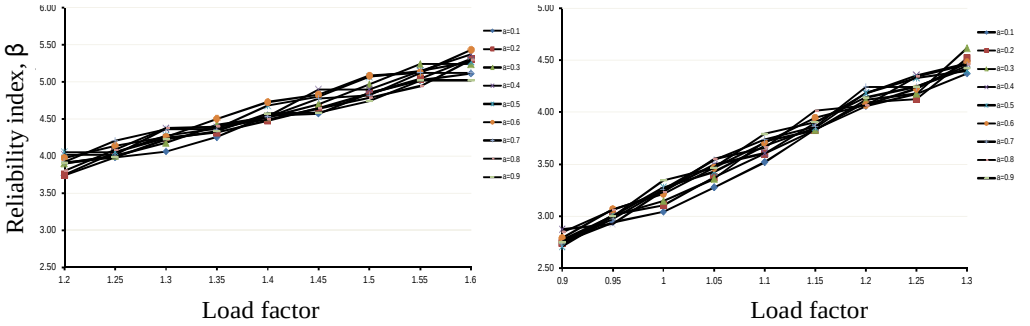


Figure 5: Reliability indexes, R.C. Beams, (a) gravitational load combination, failure mode: bending; (b) gravitational plus accidental load combination, $c = 0.50$, failure mode: bending.

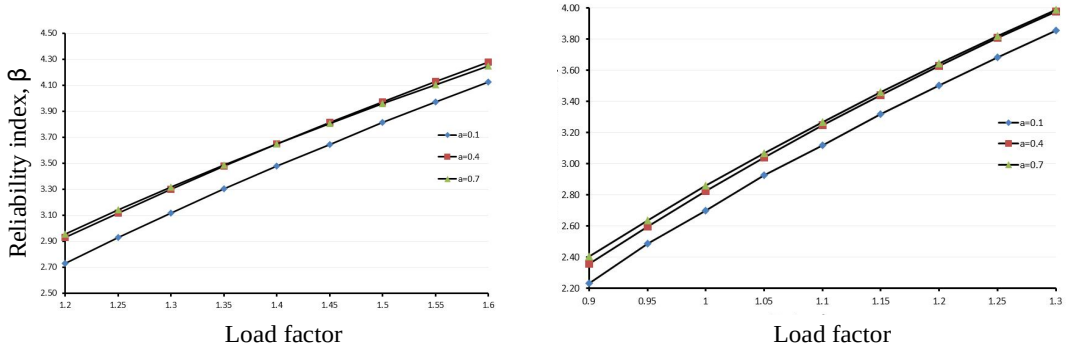


Figure 6: Reliability indexes, Steel Beams, (a) gravitational load combination, failure mode: bending; (b) gravitational plus accidental load combination, $c = 0.5$, failure mode: bending

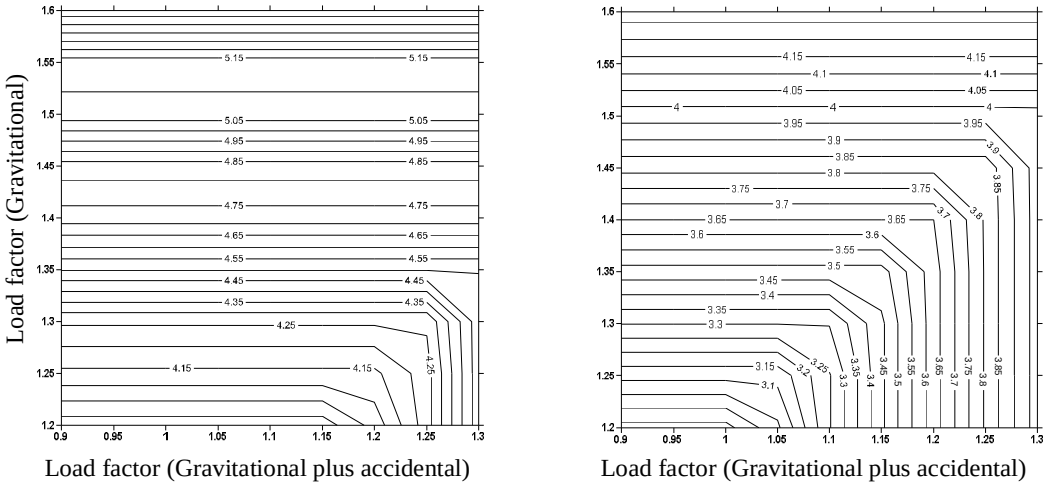


Figure 7: Reliability indexes for various load factors in each load combination, (a) R.C. Beams; (b) Steel Beams, $a = 0.4$ and $c = 0.5$.

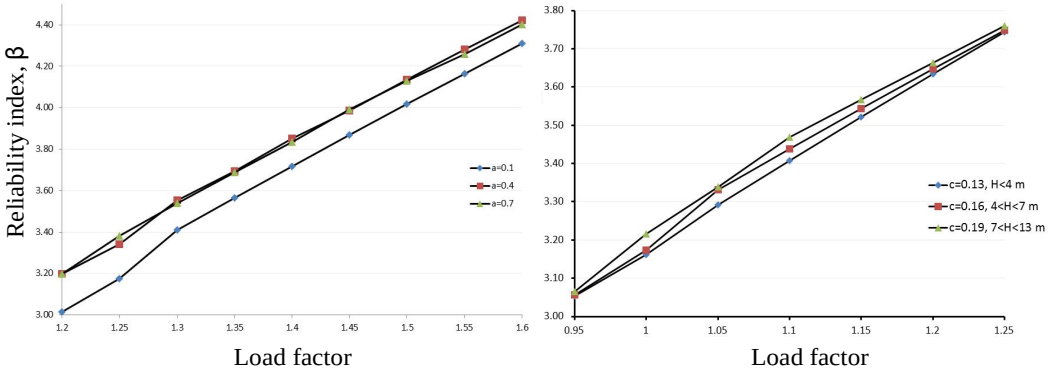


Figure 8: Reliability indexes, Masonry wall, (a) gravitational load combination, failure mode: axial compression; (b) gravitational plus accidental load combination, $a = 0.4$, failure mode: shear

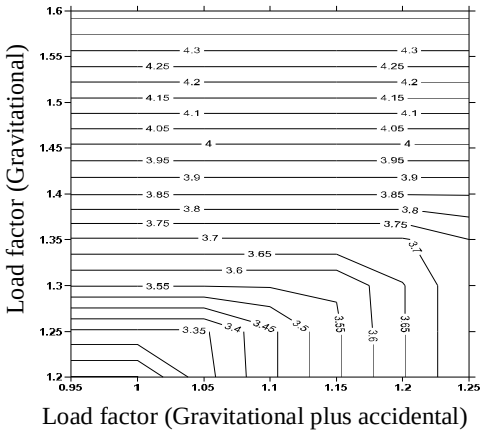


Figure 9: Reliability indexes for various load factors in each load combination, masonry walls, $a = 0.4$ and $c = 0.16$.

A summary of some important β values are show in Table 7 and Table 8. Maximum and minimum values are compared with the current values of the standard. The parameters a and c represent load ratios for variable load / dead load and accidental load/ permanent load, respectively. It is showed in the last column of Table 7 the reliability indices for structural elements considering the load combination for gravity loads established in [14]. From the same Table, it should be noted that reliability indices for reinforced concrete elements are larger compared to those obtained for structural steel elements and masonry.

Structural element / Failure mode	**Reliability index**		
	Minimum (F.C.=1.2)	**Maximum (F.C.=1.6)**	**F.C.=1.4 (Currently)**
R.C. Column/ Axial compression, $a = 0.66$	4.84	6.02	5.51
Steel Column/ Axial compression, $a = 0.4$	3.43	4.43	3.90
R.C. Beam, bending, $a = 0.4$	3.90	5.40	4.56
Steel Beam, bending, $a = 0.4$	2.96	4.25	3.65
Masonry wall, axial compression, $a = 0.4$	3.20	4.42	3.83

Table 7: Reliability indices for structural elements under gravitational load combination.

In Table 8 it is showed the reliability indices for the gravitational plus accidental load combination. In this case, the trend is almost the same as the previous table, but it can be noted an important decrease in reliability indices magnitudes compared to that presented in Table 7 for the gravitational load combination.

Structural element / Failure mode	**Reliability index**		
	Minimum (F.C.=0.9)	**Maximum (F.C.=1.3)**	**F.C.=1.1 (Currently)**
R.C. Column/Bending- axial compression, $a = 0.66$, $c = 0.20$	4.08	5.50	4.84
Steel Column/Bending- axial compression, $a = 0.4$, $c = 0.33$	2.49	4.23	3.65
R.C. Beam, bending, $a = 0.4$, $c = 0.33$	2.70	4.48	3.60
Steel beam, bending, $a = 0.4$, $c = 0.33$	2.34	3.96	3.21
Masonry wall/ shear, $a = 0.4$, $c = 0.16$	3.06 (F.C.=0.95)	3.75 (F.C.=1.25)	3.44

Table 2: Reliability indices for structural elements under the gravitational plus accidental load combination.

4 CONCLUSIONS

- Load factors and combinations of standards established in some national and international norms were reviewed. It was found that almost standards consider a factor of 1.4 in the case of load combination format that include only gravitational loads. For other combination like that including accidental loads, load factors change according to the nature of concerning load (seismic, wind, etc): for wind loads, factors can range from 1.3 to 1.6, for earthquake loads usually factors are unitary, but in both cases, the gravitational loads are affected by 1.1 or 1.2 with particularities. In the standard studied [14], it is considered a factor of 1.1 for the load combination format that includes gravity loads and accidental. It is thought that regarding the international scheme and results obtained, load factor for load combination format for facing accidental actions should be reviewed.
- A methodology to obtain quantitative measure of reliability for some typical structural elements where presented. The format provides a major benefit in permitting the individual contribution to uncertainty in structural performance to be separated, studies individually, and then incorporated in a consistent manner. The central idea is the use of only second order moments and associated approximations to express the influences of uncertainty. Coefficients of variation are introduced to express the dispersion of variation in these best estimates of measurable uncertainty and unmeasurable uncertainty.
- It was observed that there is a strong correlation between load factors and reliability indices, in both load combinations formats, i.e. gravitational loads and gravitational loads plus accidental load, in which of course, the reliability indices increase with increasing load factors.
- Reliability indices were obtained for some ratios of variable load / dead load and accidental load / dead load. From this, it was noted that all the curves follow the same trend, regardless of the ratio values.The largest values of reliability indices were observed in reinforced concrete columns, while the opposite were observed in structural steel beams, for both load combinations.
- The convenience of adopting a factored load combination format in terms of reliability index can for a specific structural element be evaluated through the use of contour plots.

REFERENCES

[1] A.C. Cornell, A probability-based structural code. *Journal of the American Concrete Institute*, **66 -85**, 974-985, 1969.

[2] E. Rosenblueth, L. Esteva, Reliability basis for some Mexican Codes, *In Probabilistic Design of Reinforced Concrete Buildings, ACI,* **SP-31**, 1973.

[3] B. Ellingwood, T.V. Galambos, J.G. MacGregor, C.A. Cornell, Development of a Probability Based Load Criterion for American National Standard A58. Building Code Requirements for Minimum Design Loads in Buildings and Other Structures. *NBS Spec. Publ. 577*, U.S. Department of Commerce, National Bureau of Standards. June ,1980.

[4] M.K. Ravindra, T.V. Galambos, Load and Resistance Factor Design for Steel. *ASCE. Journal of the Structural Division*, **104**, No. ST9, 1337-1353, 1978.

[5] T.V. Galambos, B. Ellingwood, J.G. MacGregor, C.A. Cornell, Probability based load criteria: Assessment of Current Design Practice. *Journal of the Structural Division, ASCE*, **108**, No. ST5, Proc. Paper 17067, 959-977, 1982.

[6] B. Ellingwood, J.G. MacGregor, T.V. Galambos, C.A. Cornell, Probability based load criteria - Load Factors and Load Combination. *Journal of the Structural Division, ASCE*, **108**, No. ST5, Proc. Paper 17068, 978-997, 1982.

[7] M.M. Szerszen, A.S. Nowak, Calibration of design code for buildings (ACI 318): Part 2 - Reliability Analysis and Resistance Factors. *ACI Structural Journal*, **100 (**3), May-June, 383-391, 2003.

[8] A.S. Nowak, M.M. Szerszen, Calibration of design code for buildings (ACI 318): Part 1 - Statistical models for resistance. *ACI Structural Journa*l, **100 (3)**, May-June, 377-382, 2003.

[9] J.D. Sørensen, S.O. Hansen, A. Nielsen, Calibration of partial safety factors for danish structural codes. *Proc. Conf IABSE Safety, Risk and Reliability - Trends in Engineering*, Malta, IABSE, Zurich, 179-184, 2001.

[10] SAKO, SAKO: Probabilistic Calibration of Partial Safety Factors in the Eurocodes, 1999.

[11] H. Gulvanessian, M. Holicky, Eurocodes: using reliability analysis to combine action effects. *Structures and Buildings, the Proceedings of the Institution of Civil Engineers*, Proc. Paper I3680. August I58, Issue SB4, pp. 243-252, 2005.

[12] EN 1990: 2002, Eurocode: Basis of structural design, 2002.

[13] EN 1991-1-1, Eurocode 1 Actions on structures Part 1-1: General actions. Densities, self-weight, imposed loads for buildings,.2003.

[14] GDF (Federal District), Normas Técnicas Complementarias sobre Criterios y Acciones para el Diseño Estructural de la Edificaciones del Reglamento de Construcciones para el Distrito Federal (NTC CADEE). Mexico, 2004.

[15] ASCE (American Society of Civil Engineers), ASCE 7-05 Minimum Design Loads for Buildings and Other Structures.USA, 2010.

[16] ICBO (International Council of Building Officials), UBC - Uniform Building Code, USA, 1997.

[17] ICC (International Code Council), IBC - International Building Code, USA, 2009.

[18] AIS (Colombian Association for Earthquake Engineering), NSR - 10, Rules Colombian Earthquake Resistant Construction, Colombia, 2010.

[19] Recomended lateral force requirements and commentary SEAOC, Structural Engineers Association of California, USA, 1999.

[20] NRCC (National Research Council Canada), National Building Code of Canada, Canada, 2005.

[21] ACI (American Concrete Institute), ACI 318-08 Building Code Requirements for Structural Concrete and Commentary.USA, 2008.

[22] International Organization for Standarddization, *ISO 2394 General principles on reliability for structure, Second Edition*, 1998.

[23] H.O. Madsen, S. Krenk, N.C. Lind, *Methods of Structural Safety*. Prentice Hall, Inc. Englewood Cliffs, NJ, 1986.

[24] AH-S, Ang, W.H. Tang, *Probability Concepts in Engineering, 2nd Edition*, John Wiley & Sons, Inc, 2007.

[25] O. Ditlevsen, H.O. Madsen, *Structural Reliability Methods*. John Wiley & Sons Ltd, Chichester, 1996.

[26] R. Meli, Bases para los criterios de diseño estructural del proyecto del reglamento de construcciones para el Distrito Federal. *Blue Series*, Institute of Engineering, UNAM, Mexico, D.F., **375**, 1976.

[27] C.J. Mendoza, (1984)**,** Propiedades mecánicas de los concretos fabricados en el Distrito Federal. Master Degree Thesis. UNAM, Mexico DF, UNAM, Mexico, D.F., 1984.

[28] M. Rodriguez, J.C. Botero, Aspectos del comportamiento sísmico de estructuras de concreto reforzado considerando las propiedades mecánicas de aceros de refuerzo producidos en México, *Blue Series*, Institute of Engineering, UNAM, Mexico, D.F., **575**,1996.

[29] L. Esteva, Comportamiento de muros de mampostería sujetos a carga vertical. *Blue Series*, Institute of Engineering, UNAM, Mexico, D.F., **No. 46,** 1961.

COMPDYN 2013
4th ECCOMAS Thematic Conference on
Computational Methods in Structural Dynamics and Earthquake Engineering
M. Papadrakakis, V. Papadopoulos, V. Plevris (eds.)
Kos Island, Greece, 12–14 June 2013

A BAYESIAN MODEL UPDATING PROCEDURE FOR DYNAMIC HEALTH MONITORING

Edoardo Patelli[1], **Matteo Broggi**[2], **and Pierre Beaurepaire**[2]

[1]Institute of Risk and Uncertainty, University of Liverpool
Brodie Tower, L69 3GQ Liverpool, UK
e-mail: edoardo.patelli@liverpool.ac.uk

[2] Virtual Engineering Centre, University of Liverpool
STFC Daresbury Laboratory, Daresbury Science and Innovation Campus, WA4 4AD Warrington, UK
e-mail: {matteo.broggi,pierre.beaurepaire}@liverpool.ac.uk

Keywords: Bayesian Model Updating, Transitional Markov Chain Monte Carlo, Fatigue, Crack Detection, Dynamic Excitation, Health Monitoring.

Abstract. *Structures under dynamic excitation can undergo phenomena of crack growth and fracture. For safety reasons, it is of key importance to be able to detect and classify these cracks before the unwarned structural failure. Additionally, the cracks will also change the dynamic behaviour of the structures, impacting their performance.*

Here, a Bayesian model updating procedure has been implemented for the crack detection location and length estimation on a numerical model of a spring suspension arm. A high-fidelity finite element model has been used to simulate experimental data, by inserting cracks of different extent at different locations and obtaining reference frequency response functions. In the following, a low fidelity parametric model has been used in the Bayesian framework to infer the crack location and length by comparing the dynamic responses. It is shown that the proposed methodology can be successfully adopted as a structural health monitoring tool.

1 INTRODUCTION

Fatigue is the most dangerous failure mode for mechanical components subject to alternating loads: one or several cracks can be initiated and propagated through the cross section of the structure. Once a critical crack length is exceeded, the structure can catastrophically fail even for stress level much lower than the design stress [1]. In particular, interactions may occur between the structural responses and cracks in components subject to high frequency dynamic excitations, leading to vibration-induced fatigue. In this case, the stress field in the structure is mainly determined by the high frequency resonance modes, leading to very fast cycles of loading and accelerated fatigue crack growth. Hence the service life of the structure may be considerably reduced.

Several strategies are possible to avoid fracture; for instance, non-destructive inspections may be performed at predetermined time intervals in order to detect the cracks; however failure can happen between inspections [2]. Alternatively, a continuous monitoring of the dynamic response of the structure can allow for real-time crack detection and for a timely intervention with maintenance procedures [3]. Repair actions are taken in case the monitoring procedure successfully identifies a crack which jeopardizes the structure.

In both cases, the procedure may fail in identifying a crack, leading to fatigue failure. Thus, efficient crack detection before fracture occurs is required in order to avoid the loss of the structure, and more importantly to mitigate the consequences that such loss could cause, both from an economical and safety point of view. Once the crack is successfully detected, corrective maintenance or substitution of the damaged component can be performed.

Thanks to the advancements in the field of computational mechanics, new detection techniques could be developed to assist in the monitoring of the health of the structures. These numerical techniques allow for a synthetic analysis of experimental and sensor data. More specifically, these techniques modify some specific parameters in a numerical model to ensure a good agreement with the data, leading to a so-called inverse problem. A computational framework well fitted for the solution of such inverse problems is the model updating [4].

In this paper, an efficient numerical framework, based on a Bayesian model updating procedure [5], is implemented for the identification of cracks within structures under dynamic excitation. The influence of the cracks on the mechanical behaviour is quantified using the Frequency Response Functions (FRF) at a specific locations. A suspension arm, as normally used by automotive industry, has been analysed. Two finite elements models have been used: one high-fidelity model to simulate experimental data of the arm under dynamic excitation (i.e., the reference model). Cracks of random dimension and positions determined by stress intensity are introduced in the simulated experimental suspension arm.

The second low-fidelity model is used in the Bayesian model updating procedure. The updating procedure adjusts the length of cracks inserted at candidate crack locations in the low-fidelity model in order to minimize the difference between the frequency response function of this model and the reference frequency response function. This allows reconstructing efficiently the crack pattern of the reference model.

Particular attention is given to the efficiency of the numerical simulation. As a matter of fact, a high number of model evaluation is required, thus a strategy for the parallelization of the simulations as provided by the general purpose software COSSAN-X [6] is employed.

The paper is structured as follows: Section 2 deals with the modelling of fracture in a Finite Element framework. Section 3 outlines the main concept of Bayesian model updating and the efficient simulation algorithm employed in the particular case of structure with cracks under dy-

namic excitation. A numerical example will be introduced in Section 4, and the crack detection routine will be tested in different configurations. Finally, some conclusions and final remarks will be pointed out in Section 5.

2 MODELLING OF FRACTURE MECHANICS

The mechanical behaviour of structures may be modified by the presence of cracks. The effective cross section of the component is reduced, which causes a reduction of the stiffness. Moreover, the stress field is also modified in the vicinity of a crack.

Specific methods allow modelling efficiently the mechanical behaviour of structures containing cracks. The extended finite elements method (XFEM) [7, 8] has received considerable attention over the past few years. It consists of using a particular element formulation in the vicinity of a crack. Additional degrees of freedom and shape functions are used to describe the displacements within an element affected by a crack and such elements are said to be *enriched*. The displacement field in these elements is then expressed using a combination of the standard and of the shape functions devoted to enrichment.

In case an element is crossed by a crack, the additional shape function consists of a Heaviside function centered on the crack. The discontinuity of this function accounts for discontinuity of the displacements between the two lips of the crack.

In case an element includes the crack tip, the corresponding nodes of the finite element model are enriched with specific shape functions. These functions correspond to the asymptotic displacement field at the vicinity of a crack tip, which can be determined analytically (see [7] for more details about the enrichment of the tip elements). This allows capturing efficiently the displacement and strain fields near the crack tip, without excessive refinement of the mesh.

Details on the implementation of the extended finite element method may be found e.g. in [7, 9, 8, 10].

However, mesh refinement in the vicinity of the crack tip may be necessary when the extended finite elements method is used, in spite of the enrichment of the nodes at the crack tip [11]. Nevertheless, the mesh does not have to be compatible with the crack, which considerably simplifies the re-meshing.

In case the behaviour of a cracked structure under dynamic excitation needs to be determined, the stiffness matrix may be computed using the XFEM, as stated above. The mass matrix is not modified by the presence of cracks, and no special action needs to be taken. The problem is subsequently solved using the standard procedure for linear dynamics: the modes and frequency of vibration are determined by solving the eigen-value problem associated with the mass and stiffness matrices; and the FRFs associated with any pair of DOF of the node of the finite element model are determined.

3 BAYESIAN MODEL UPDATING FOR CRACK DETECTION

3.1 Bayesian updating of structural models

A Bayesian model updating procedure is based on the well known Bayes theorem [12]. This theorem was first introduced by Thomas Bayes in the 18th century, then was rediscovered and largely redeveloped by Laplace in the 19th century, and finally has been widely accepted and applied only in recent times. Its general formulation is

$$P\left(\theta|D,I\right) = \frac{P\left(D|\theta,I\right)P\left(\theta|I\right)}{P\left(D|I\right)} \tag{1}$$

where θ represents any hypothesis to be tested, e.g., the value of the model parameters, D is the available data or observations, and I is the background information. Three main terms can be identified in the Bayes theorem:

- $P(\theta|I)$ is the prior probability density function (PDF) of the parameters
- $P(\theta|D, I)$ is the posterior PDF
- $P(D|\theta, I)$ is the likelihood function of the data D.

Finally, the term $P(D|I)$ at the denominator is a normalization factor ensuring that the posterior PDF integrates to 1.The theorem introduces a way to update some *a priori* knowledge on the parameters θ by using data/observations, conditional to the available information.

Bayes theorem has been successfully applied in the updating of structural models [13, 14]; in particular the Bayesian structural model updating has been successfully used to update large finite element models using experimental modal data [5].

In a structural model updating framework, the initial knowledge about the unknown adjustable parameters is expressed through the prior PDF. A careful choice of this distribution has to be taken, in order to accurately represent the knowledge available, e.g., from prior expertise. As an example, a proper prior distribution can be a uniform distribution in the case when only a lower and upper bound of the parameter is known, or a Gaussian distribution when the mean and a relative error of the parameter is known.

The likelihood function gives a measure of the agreement between the available experimental data and the corresponding numerical model output. Particular care has to be taken in the definition of the likelihood, and the choice of likelihood depends on the type of data available, e.g., whether the data is a scalar or a vector quantity.

Finally, the posterior distribution expresses the revised knowledge about the parameters, providing information on which parameter ranges are more probable based on the initial knowledge and the experimental data.

3.2 Transitional Markov-Chain Monte-Carlo

The Bayesian updating expressed in equation 1 needs the computation of a normalizing factor, that can be very complex to compute and computationally expensive. An efficient stochastic simulation algorithm, called Transitional Markov Chain Monte-Carlo [15], can be used to avoid the computation of this factor. This algorithm allows the generation of samples from the complex shaped unknown posterior distribution through an iterative approach. In this algorithm, m intermediate distributions P_i are introduced,

$$P_i \propto P(D|\theta, I)^{\beta_i} P(\theta|I) \tag{2}$$

where the contribution of the likelihood is scaled down by an exponent β_i, with $0 = \beta_0 < \ldots < \beta_i < \ldots < \beta_m = 1$, thus the first distribution is the prior PDF, and the last is the posterior. These intermediate distributions show a more gradual change in the shape from one step to the next when compared with the shape variation from the prior to the posterior. The value of β_i is automatically set to allow a more slow variation for the first steps, and a faster variation towards the end. The variation of β between two steps is controlled by the value of the coefficient of variation of the intermediate posterior, that is compared to a target CoV value set as an input of the algorithm.

In a first step, samples are generated from the prior PDF using direct Monte-Carlo. Then, sample from the P_{i+1} distribution are generated using Markov chains with the Metropolis-Hasting algorithm [16], starting from selected samples taken from the P_i distribution. This step is repeated until the distribution characterized by β_i is reached. By using the Metropolis-Hasting algorithm, samples are generated from the posterior PDF without the necessity of ever computing the normalization constant.

3.3 Model updating for crack detection

The approach introduced so far has been successfully applied to structural model updating, thus reducing the uncertainties in the numerical model parameters and improving the agreement between the numerical results and experimental data. Within the model updating framework, the cracks' extent and position present in the damaged structure are seen as uncertain model properties.

Knowing that cracks will develop most likely in locations characterized by high concentration of stresses, these candidate positions are inserted in the undamaged model, analysed using XFEM assuming the crack length and shape as random parameters.

In the updating procedure, the prior distribution will use a uniform distribution for the crack parameters, allowing the possibility of crack in any stress concentration point and with any possible physically acceptable length.

Experimental data from the reference structure are available in the form of Frequency Response Functions (FRF). These reference data are compared with the numerical FRF of the numerical model, by computing the root mean squared error (RMSE), in order to include the experimental data information in the likelihood. It is assumed that the prediction error is distributed according to a Gaussian PDF, thus the likelihood can be expressed as

$$P\left(D|\theta, I\right) \propto \exp\left(-\frac{1}{2\delta}\sum_{k=1}^{N_{freq}}\left(h_{exp}\left(\omega_k\right) - h\left(\omega_k;\theta\right)\right)^2\right) \tag{3}$$

where $h_{exp}\left(\omega_k\right)$ is the experimental FRF, $h\left(\omega_k;\theta\right)$ represents the numerical FRF, and δ is the variance of the RMSE. After the updating procedure, the posterior will provide a qualitative indication on both crack length and position, i.e., the length of the crack will go towards zero if the crack is not present in the candidate location, and otherwise, it will concentrate around the unknown length.

4 Numerical Example

4.1 Model description

In this numerical example, the proposed framework is applied to detect cracks in a suspension arm similar to those used in the automotive industry [17]. The structure, shown in Figure 2 can freely rotate along the axis indicated by the dashed line, and the suspension spring and the wheel structure is connected at the location indicated by S. The stress concentration points, and candidate crack locations, are indicated in the figure by the numbers 1 to 6.

In this example, "simulated" experimental data are generated using a high-fidelity FE model, characterized by a very refined mesh near the crack (Figure 2b). The software used to construct the model and in the analysis is Code_ASTER [18]. A crack with fixed length is inserted in one of the candidate position, and the reference FRF is computed at the position indicated by "O". Both the FRF in direction X and Y are considered, while no FRF is obtained in the direction Z

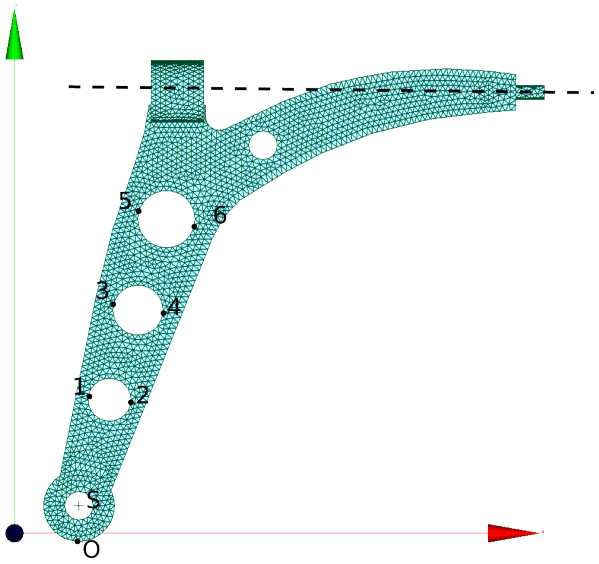


Figure 1: Finite Element model of a suspension arm.

since the structure is not constrained in that direction. Figure 3 shows the inertance FRF in the two directions X and Y when a crack with the length of 5mm is inserted in the possible positions. A clear difference is shown between the inertance FRF, especially at the high frequencies.

4.2 Bayesian model updating

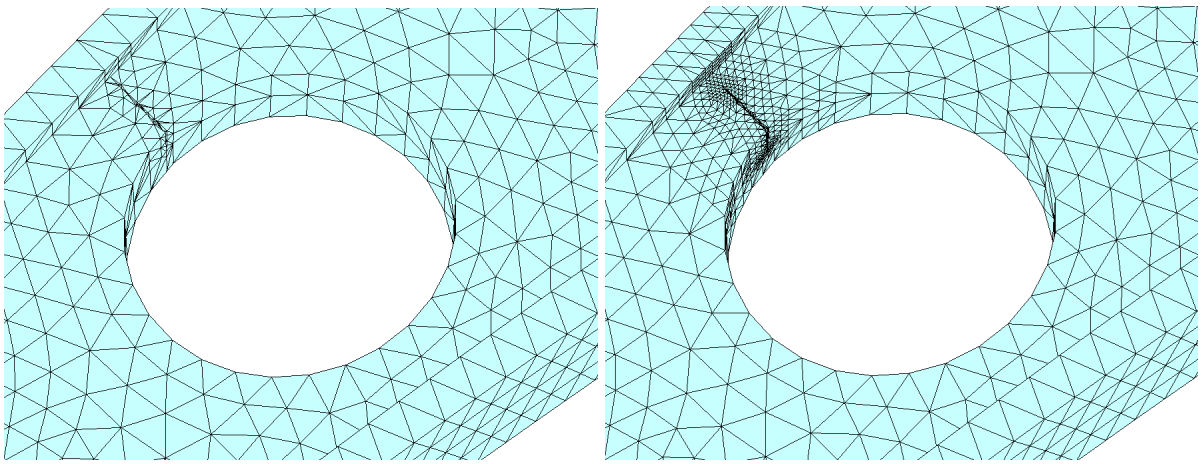
The Bayesian model updating procedure is employed using the low-fidelity FE model, where a more coarse mesh is used. The crack lengths are considered as uncertain parameters, and are modelled using uniformly distributed random variables. Since the crack is physically constrained to not touch the flanges of the arm, a maximum crack length of 5mm is assigned to the cracks in position 1 and 2, while the length is limited to 10mm for the cracks in positions 3 to 6. Thus the prior uncertain parameters and their prior distributions are:

$$\theta = \left\{ \begin{array}{c} l_1 \\ l_2 \\ l_3 \\ l_4 \\ l_5 \\ l_6 \end{array} \right\}, \qquad \theta_0 \sim \left\{ \begin{array}{c} U(0, 5\text{mm}) \\ U(0, 5\text{mm}) \\ U(0, 10\text{mm}) \\ U(0, 10\text{mm}) \\ U(0, 10\text{mm}) \\ U(0, 10\text{mm}) \end{array} \right\} \tag{4}$$

The sampled values of the random variables are inserted into the FE model by using the ASCII file injection routine provided by COSSAN-X [6].

The Bayesian updating procedure has been executed with one crack. A reference FRF has been obtained with the high fidelity model with a 5mm crack located in position 3. Then, 1000 samples from the prior distribution have been generated. The low-fidelity FE model is run in parallel on a computer cluster allowing a reduction of the overall computational time. Figure 4 shows the variation of the inertance FRFs of the low-fidelity model with 1600 random values of crack length sampled from the prior distributions.

The FRFs are compared with the reference FRFs from the high-fidelity model, computing the RMSE. In order to speed up the analyses needed for the bayesian updating, a Multi Layer Perceptron Artificial Neural Network has been constructed. The network is constituted by $N_{inp} = 6$



(a) Low fidelity model (b) High fidelity model

Figure 2: Low fidelity (a) and high fidelity (b) model of the suspension arm. High mesh refinements near the crack tips are included in the high fidelity model.

inputs, that are the length of the cracks at positions 1 to 6, and $N_{out} = 2$ outputs, the RMSE computed between the reference FRF and that of the low-fidelity model in bot the x and y direction. An automated training procedure has been implemented such that various network topologies are tested and the best network, characterized by the highest R^2 value is kept. R^2 is defined as

$$R^2 = 1 - \frac{\sum_{i=1}^{N_{data}} \left(h_i^2 - \hat{h_i}^2 \right)}{\sum_{i=1}^{N_{data}} \left(h_i^2 - \overline{h_i}^2 \right)}, \tag{5}$$

where h_i is the RMSE computed using the real model outputs, $\overline{h_i}$ is the average of h_i, and $\hat{h_i}$ is the RMSE predicted by the neural network. The best network is structured with 2 hidden layers, with 13 nodes in the first hidden layer and 11 nodes in the second. The R^2 is 0.972 for the RMSE of the FRFs in the x direction, and 0.969 for that of the FRFs in the y direction.

4.3 Discussion of the results

The results of the updating procedure are shown in Figure 5, where the prior and posterior distributions of the six random crack lengths is shown, while Figure 6 shows the value of the RMSE of the two FRFs using the prior and posterior distributions of the parameters. The procedure successfully updated the model parameters and identified the position of the crack as being position 3 and length 5mm. The posterior distribution of the crack length clearly remove any possibility of having cracks at positions 1, 5 and 6, since their final PDF is very peaked in the vicinity of zero (see Figures 5a, 5e and 5f).

However, a perfect model updating would have resulted in posterior distributions very peaked around zero for the position 2 and 4 as well, and peaked around 5 for the posterior of the crack length at position 3 as the synthetic numerical simulated data is noise free. This is not the case: instead, some uncertainty is still shown in the posterior distribution for the crack in positions 2, 3 and 4. Nevertheless, it can be reasonably assured that the crack is indeed located in position 3, since the posterior of the crack length at position 3 is the only one having a significant mean value (see Figure 5c). Additionally, the posterior PDF in position 3 is the only PDF not including zero as a possible value of the distribution, as opposed for the distributions relevant to

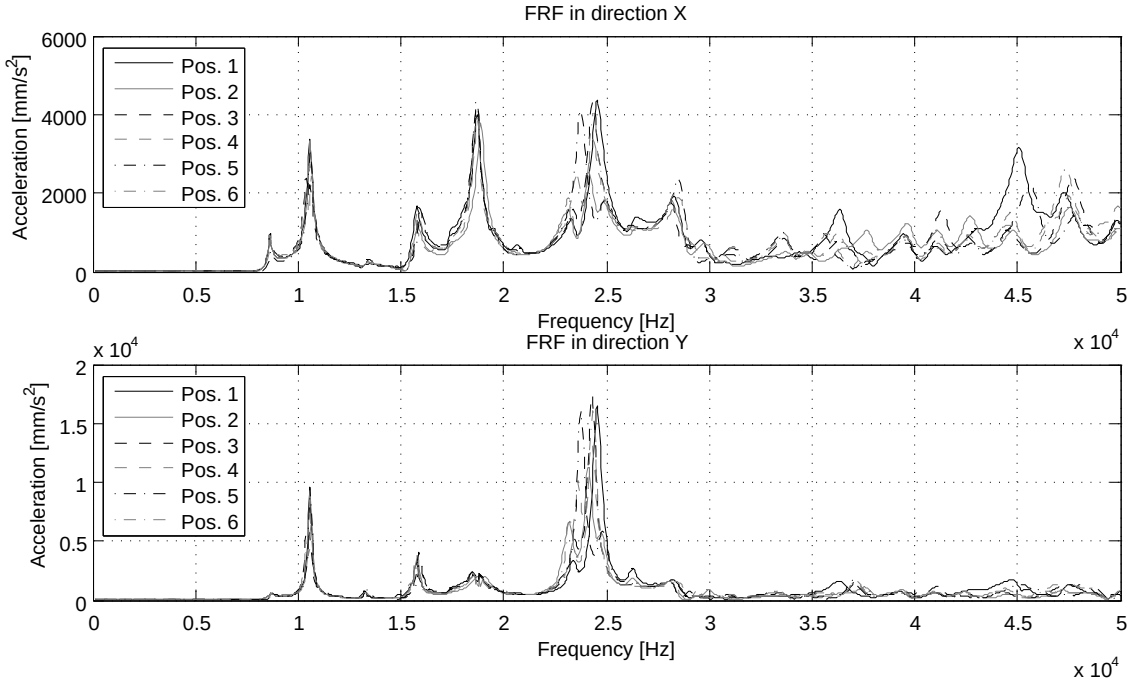


Figure 3: Frequency response functions of the high fidelity FE model. A single crack of 5mm length is inserted in each of the stress concentration points.

the cracks in position 2 and 4 (see Figures 5b and 5d). The reason for the non perfectly peaked posterior is two-fold: first, limited amount of reference data is available, and second, the RMSEs are already very close to zero (thus, within the target of the model updating procedure) for the model responses computed using crack length distributed according to the posterior PDF, as shown in Figure 6.

As a matter of fact, only two reference inertance FRFs are obtained from the high-fidelity FE model at a single location. Additional data, e.g., retrieved from a different point or with different loading condition, can improve the computation of the posterior at the expense of a more complex likelihood. It should be noted anyway that the approach carried out in this numerical example is a "worst case scenario" with regards to the availability of data, although the methodology was capable of giving a very good answer anyways.

5 CONCLUSIONS

A Bayesian updating procedure has been successfully employed as a computational framework to detect crack location and length. Reference dynamic data from vibration analysis has been used as target for the updating procedure.

The proposed framework allowed for successful updating and identification of crack position and length using simulated FE data. These preliminary results clearly show the possibility to apply this methodology to detect crack given data retrieved from sensors. To further validate this procedure, the updating procedure needs to be executed with additional numerical tests, e.g. with varying position and length of the crack. The results will show the performance of the framework, in particular with different crack length and location.

Future development and additional research will be taken by using real experimental data to further validate and expand the proposed approach, and using advanced more efficient Monte-

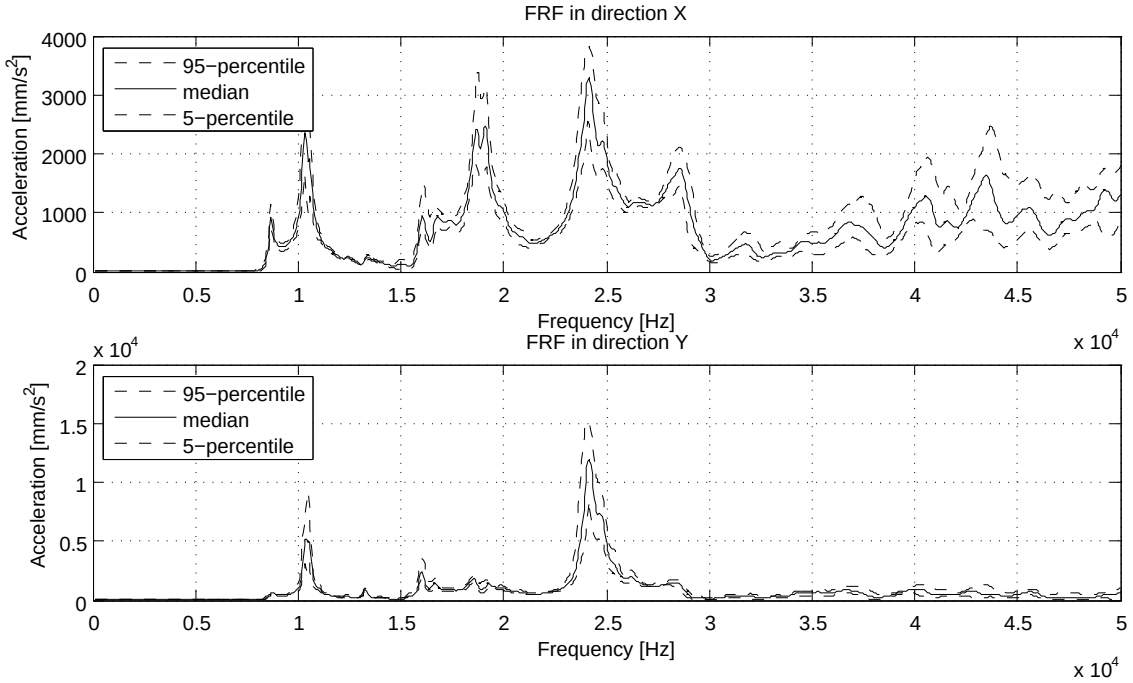


Figure 4: Variation of the FRFs with the crack length sampled from the prior distributions using the low-fidelity model. Random cracks of random length are inserted in all the possible positions.

Carlo procedures, i.e., sequential Monte-Carlo or Particle Filtering methods.

Acknowledgement

This work was undertaken at the Virtual Engineering Centre. The Virtual Engineering Centre is a University of Liverpool project partially funded by the Northwest Regional Development Agency and European Regional Development Fund.

REFERENCES

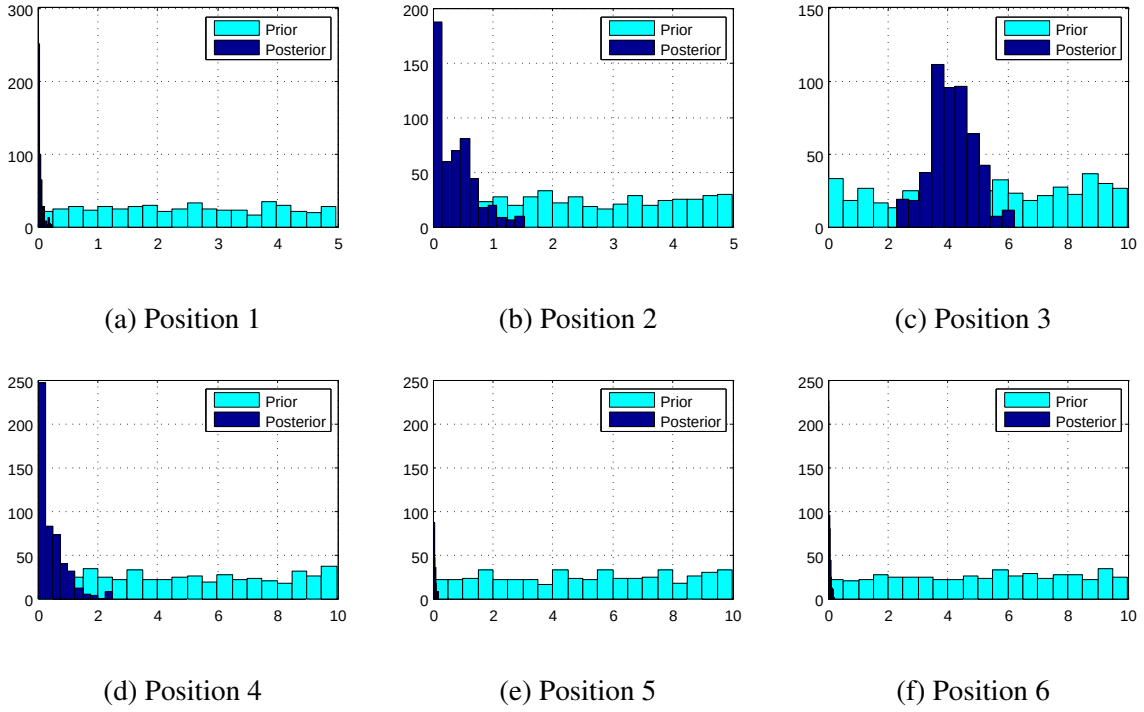
[1] P. Paris, F. Erdogan, A critical analysis of crack propagation laws. *Transactions of the ASME. Series D, Journal of Basic Engineering*, Volume 85, p. 52834, 1963.

[2] Beaurepaire, P., Valdebenito, M., Schuller, G., Jensen, H., 2012. Reliability-based optimization of maintenance scheduling of mechanical components under fatigue. *Computer Methods in Applied Mechanics and Engineering,* Volume 221-222, pp. 24-40.

[3] P. Chang, A. Flatau, S. Liu, Review paper: health monitoring of civil infrastructure. *Structural Health Monitoring*, Volume 2, 2003.

[4] C.-P. Fritzen, D. Jennewein, T. Kiefer, Damage detection based on model updating methods. *Mechanical Systems and Signal Processing*, 12(1), pp. 163-186, 1998.

[5] B. Goller, M. Broggi, A. Calvi, G.I. Schuëller, A stochastic model updating technique for complex aerospace structures. *Finite Elements in Analysis and Design*, 47(7), p. 739752, 2011.



(a) Position 1 (b) Position 2 (c) Position 3

(d) Position 4 (e) Position 5 (f) Position 6

Figure 5: Prior (cyan) and Posterior (blue) distributions of the lengths of the cracks at the 6 candidate positions.

[6] E. Patelli, H.M. Panayirci, M. Broggi, B. Goller, P. Beaurepaire, H.M. Pradlwarter, G.I. Schuëller, General purpose software for efficient uncertainty management of large finite element models, *Finite Elements in Analysis and Design*, Volume 51, pp. 31-48, 2012.

[7] N. Moes, J. Dolbow, T. Belytschko, A finite element method for crack growth without remeshing, *International Journal for Numerical Methods in Engineering*, Volume 46 , pp. 131-150, 1999.

[8] G. Zi, T. Belytschko, New crack-tip elements for XFEM and applications to cohesive cracks, *International Journal for Numerical Methods in Engineering*, Volume 57, pp. 2221-2240, 2003.

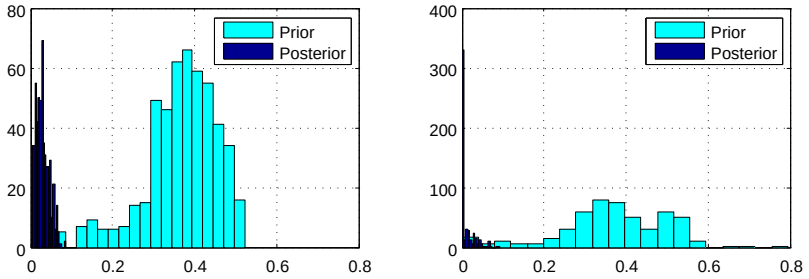
[9] T. Belytschko, T. Black, Elastic crack growth in finite elements with minimal remeshing. *International Journal for Numerical Methods in Engineering*, 45(5), pp. 601-620, 1999

[10] Y. Abdelaziz, A. Hamouine, A survey of the extended finite element. *Computers & Structures,* 86(11-12), pp. 1141-1151, 2008

[11] S. Geniaut, *Code Aster, notice d'utilisation de la methode X-FEM* (in French). Technical Report U2.05.02, 2011.

[12] Bayes, T. An essay towards solving a problem in the doctrine of chances,. *Philosophical Transactions of the Royal Society of London,* Volume 53, pp. 370-418, 1763.

[13] J. L. Beck, L. S. Katafygiotis, Updating models and their uncertainties, I: Bayesian statistical framework. *Journal of Engineering Mechanics*, 124(4), p. 455, 1998.



(a) x direction (b) y direction

Figure 6: RMSE between the FRFs of the reference high-fidelity model with 5mm crack in position 3 and of the low-fidelity model with random crack lengths in (a) x and (b) y directions. The cyan histogram denotes the random crack lengths of the low-fidelity model that have been extracted from the prior distribution, while in the blue histogram the crack lengths are distributed according to the posterior distribution.

[14] L. S. Katafygiotis, J. L. Beck, Updating models and their uncertainties. II: Model identifiability, *Journal of Engineering Mechanics*, 124(4), p. 463, 1998.

[15] J. Ching, Y.-C. Chen, Transitional Markov chain Monte Carlo method for Bayesian updating, model class selection, and model averaging, *Journal of Engineering Mechanics*, Volume 133, pp. 816-832, 2007.

[16] W. Hastings, Monte Carlo sampling methods using Markov chains and their applications. *Biometrika*, 57(1), pp. 97-109, 1970.

[17] M. Mrzyglod, A. Zielinski, Numerical implementation of multi-axial high-cycle fatigue criterion to structural optimization. *Journal of Theoretical and Applied Mechanics*, 44(3), pp. 691-712, 2006.

[18] Code_Aster, 2004. Code d'Analyse des Structures et Thermo-mcanique, pour des Etudes et des Recherches. [Online] Available at: http://www.code-aster.org/ [last access: 01-03-2013].

COMPDYN 2013
4th ECCOMAS Thematic Conference on
Computational Methods in Structural Dynamics and Earthquake Engineering
M. Papadrakakis, V. Papadopoulos, V. Plevris (eds.)
Kos Island, Greece, 12–14 June 2013

THE RATIONAL IMPERATIVE OF PROFESSIONAL RISK MANAGEMENT

Jatin Nathwani[1], **Niels C. Lind**[2]

[1]Waterloo Institute for Sustainable Energy (WISE)
University of Waterloo
Waterloo, ON Canada
e-mail: nathwani@uwaterloo.ca

[2] Department of Civil and Environmental Engineering
University of Waterloo
Waterloo, ON Canada
e-mail: lindniels@gmail.com

Keywords: Quantified risk, Acceptable risk, Welfare economics, Life Quality Index (LQI).

Abstract. The conundrum of *modern post-industrial societies is extraordinary level of overall social well-being punctuated by concerns over multiple risks to which our management responses are ill-adapted. Risks are mostly foreseen but uncertain and often dreadful, but some risks are unforeseen in their likelihood and can have disastrous consequences. The public's trust in the capabilities of professionals to manage the risks is often a matter of contention but, in our view, the primary obligation of risk regulators and professional risk managers is to make paramount the duty to serve the public interest. Risks must therefore be assessed scientifically and quantified: "Numbers, not adjectives" must guide decisions. Relative valuation of what is at risk and what can be sacrificed to reduce the risk is fundamental.*

Societal preferences about longevity vs. prosperity is expressed by a social indicator, the Life Quality Index LQI. The LQI reflects fundamental human life values and allows explicit balancing of risk with life benefits. It is derived from the economics of human welfare to give a clear guide to risk evaluation. We summarize the derivation of the LQI and derive a paradigm for consistent management of risks in all areas of public exposure to risk. The literature gives many examples that have been implemented in structural engineering and disaster management.

It is concluded that the LQI together with the marginal life saving principle provides a reliable and rational approach to quantify, judge and manage public risks with transparency.

1 INTRODUCTION

For millennia structural design has relied solely on judgment based on experience. During the last few centuries we have been judging the extreme actions upon a structure over its projected service life in order to calculate the stresses and deflections. Further, during the last few decades we have become able to calculate the probabilities of extreme structural states (including collapse) and compared them to specified limits – these limits, too, have been based on judgment.

Professional judgment remains fundamental to structural engineering, but history shows how professional practice has been moving towards the ideal of scientific objectivity and accountability. To this end it is imperative not just to guess but to have a *measure* of risk and of safety. During much of the past 100 years we have developed probabilistic structural analysis, but until recently probabilistic standards of acceptable risk have been based on guesswork and calibration to resemble past practice. Accountability to society that the safety levels are optimal has not yet been served. 'Judgment' may be just a nice euphemism for guesswork.

An objective quantification of 'acceptably safe', derived from revealed preferences by the economics of human welfare, is described here to provide an answer. Risk and of safety both require clear definition – "*numbers, not adjectives*." The 'scientific' meaning of *risk* is a set of events over a specified future period, each with a probability of occurring.

How safe is safe enough? This innocent question makes safety into a quantity and is germane in the development of engineering codes and standards, just as it is in the risk regulations in many other areas. The question of appropriate safety concerns the designer of every structure. It is essential in regulation, whether of design codes, consumer products, medical devices or procedures, and so on.

The safety question is universally important, but there is wide room for divergent opinion: Just what do we mean by "safe"? What do we mean by "risk"? The professional engineer, the regulatory authority, the general public and those exposed all see risk very differently. The engineer has a professional obligation to serve the clients' best interest, and so must judge safety objectively and dispassionately. Also, life safety is about surviving a long time in good health, so engineering risk management must harmonize with societal risk management in general. Engineering risk management should be rational and justifiable in the public interest.

In developed society safety concerns every person – is it safe enough to walk alone at night? The popular notion of risk is very different -- fear and dread. This might not normally matter much, but the difference can be extremely important. When the population in L'Aquila, Italy in 2009 suffered a disastrous earthquake that killed some 300 persons, there was anger and disappointment directed at the six scientists and civil protection officials who just a week prior had sensibly recommended against evacuation. In 2012 a local court convicted them of manslaughter and sentenced them to jail and payment of compensation [1]. Such misunderstandings of risk and the limits of our professional capacity to predict future events must be avoided. Communication about risks to non-specialists should and can be improved, e.g., by following a specified standard protocol as has just been proposed [2]. Meanwhile, we serve the public best by dispassionate risk assessment.

The rational imperative of professional risk management is to quantify risk and risk acceptability.

2 ALARA

Widely cited in risk regulation is the so-called *As Low As Reasonably Achievable or Possible/Practicable (ALARA or ALARP) principle.* Risks are classified by estimate or convention

as either negligible, tolerable or non-acceptable. What is "reasonably" possible, practicable or achievable depends on who and when, and may well be decided by the feelings of a few people sitting around a table, as if 'possible' meant the same as 'practicable'. If risks are deemed negligible (sometimes *de minimis*) they need no regulation. Otherwise risks are considered with regards to how efficiently they may be reduced. According to the ALARA principle these risks shall be reduced until the costs associated with further reductions become disproportionate to the risk reductions and the risks are called 'tolerable'.

Moreover, much risk regulation also exhibits *risk aversion*. A risk-averse attitude implies that the loss of many lives in individual accidents is less important that the loss of just as many lives in one single accident. Risk aversion is clearly problematic as it does not provide equity in the societal regulation of risk [3, 4].

The scientific study of risks is well advanced. We can calculate the probability of any set of events that is worth studying, using available measured data. There is a problem: uncertainty – data and hence risks are never certain. However, Bayesian processing of data allows us to assign probabilities in a transparent manner, incorporating uncertainty and supporting decisions while satisfying the demands of objectivity and accountability. Thus, quantifying a particular risk is not the problem.

Rather, the main problem is twofold: (1) assessing the *disutility* (for the want of a better word) of sets of multi-dimensional outcomes (loss of life, health, assets, production . . .) and (2) choosing a standard of what their associated risks are worth, whether tolerable, acceptable or optimal.

Risk is intrinsic to life itself. Any activity that we undertake to secure a benefit has some associated risk that varies with context and can be changed, but this changes the net benefit and leads to a problem of prioritization: (3) How shall limited resources be allocated for life-saving purposes for the collective benefit of society? (4) It is important to ensure transparency of the decision-making process and (5) maintain respect for societal values. The LQI paradigm described below addresses these five issues. It is also compatible with the ALARA convention.

3 FUNDAMENTAL PRINCIPLES OF RATIONAL RISK MANAGEMENT

Nathwani et al. [5] presented four principles for managing risks to the public:

Accountability: Decisions for the public in regards to health and safety must be open, quantified, defensible, consistent and apply across the complete range of hazards to life;

Benefit: Risks shall be managed to maximize the total expected net benefit to society;

Measure: The measure of health and safety benefit is the expectancy of life in good health; and

Kaldor-Hicks Compensation: A policy is to be judged socially beneficial if the gainers receive enough benefits that they can compensate the losers fully and still have some net gain left over [6].

These principles are fundamental and explicitly satisfied in the application of the LQI paradigm.

4 THE LQI RATIONALE

The control of risk takes resources and thus presents a problem in resource allocation, an issue of broad societal importance. How much life safety can we afford from a societal perspective, what is the societal capacity to commit resources to safety? Phrased in this way, the "safe enough?" question becomes one of *sustainable resource allocation*. It is also important for communication between administration, industry and the public on how priorities are set

in sharing common resources for the purpose of risk management. Professional engineering ethics in this context demands that risks and costs be balanced transparently and justifiably.

The governing principle in health economics for supporting decisions on health and life safety management is the *marginal life saving cost (MLS) principle*, see e.g. [4, 7]. The basic idea behind this principle is that investments into activities that affect health and life safety must be pursued until the costs associated with saving one more life year in good health exceeds a certain amount, the *marginal life savings cost limit.* The assessment of this amount has been subject to some scientific debate and various proposals, with significant variability in the amounts and philosophical basis that have been suggested in the literature. We suggest that the LQI provides the best way to satisfy the quality requirements of risk assessment because of its derivation and accurate calibration.

In conjunction with the marginal life saving cost principle the LQI has found application into a wide range of practical contexts in both public and industrial health and life safety management [8, 9, 10]. Presently this framework is being implemented in the new edition of ISO 2394 "General Principles on Reliability of Structures" and will thus form the fundamental rationale on how and how much societies shall invest into structures for what concerns risk reduction with respect to, e.g., natural disasters, safety against terrorist attacks, industrial disasters, and effects of climate change, safety of nuclear power, offshore and marine activities.

5 THE LQI FORMULATION

The gross national product per person (GNP) and the life expectancy at birth are aggregate descriptors of what one may loosely call the total average quality of life per person and use as utility function. The utility of wealth production is a positive monotonic function $h(g)$ of g, the GNP per person while the time to enjoy it can be taken as a positive monotonic function $f(e)$ of the expectancy at birth, e, of life in good health. Each enhances the other, so the appropriate measure is a product of the two. Averaged over society, the utility per person can be written as the life product $f(e)h(g)$.

Lind et al. [11] describe how separation of the variables shows that $f(.)$ and $g(.)$ should be powers of e and g respectively, leading to the life product index format $L = g^b e^c$ where b and c are positive constants. Since the utility is invariant under a monotonic transformation, this expression can be simplified to $L = g^a e$.

Further, it is observed that people produce wealth by assigning some of their life to the task of work. People's choice of how much of their life they give to work thus shows how much life-value they attribute to the GDP per person.

The societal capacity to commit resources to risk reduction is derived from the LQI by setting the first variation of L equal to zero: $dL/L = adg/g + de/e$. Any project or regulation that produces small changes dg and de to g and e respectively, contributes positively (negatively) to the Life Quality Index utility if and only if de/dg is greater (less) than $S = ae/g$. S is a statistical time series that represents the societal capacity to commit resources sustainably. In risk assessment S is a yardstick for assessing life risks, applied just like the "societal value of a statistical life" or the "societal willingness to pay" found in the literature; both have shortcomings. We propose an alternative terminology, based on the fact that S is the limit between interventions that are beneficial and those that consume too many resources for the benefit they deliver. S is called the *limit of benefit* to risk reduction.

R. Rackwitz has given a lucid argument for optimization based on the LQI when there is risk to life, deriving from principles of human rights and equality that are found in all modern, democratic constitutions and the 1948 United Nations' Universal Declaration of Human Rights. Rackwitz also illustrated several applications in the assessment of structural safety, proposing a social benefit rate for public interventions close to the long term growth rate of

the GDP (around 2% for developed countries). Correspondingly, the interest rate used in evaluating projected time sequences of cash flow and risk flow should be slightly smaller. Further, Rackwitz concluded broadly that optimal structures are almost always also acceptable, but that just acceptable structures are almost always suboptimal [12].

The exponent *a* reflects the relative value of duration of life and economic benefit. There have been several calibrations of *a* from observed human preference. Pandey and Nathwani [13] provided a rigorous approach to this calibration, deriving the exponent parameter from the economics of human welfare [6]. Using a Cobb-Douglas formulation of GDP they derived *a* as $a=wb^{-1}(1-w)^{-1}$, where b is the Cobb-Douglas labour exponent [13]. With this formulation, using economic data for each of 27 developed OECD countries over the period 1976-2004, Nathwani et al. [8] found *a* to be practically constant, established the LQI in the form $L=eg^{0.2}$ and the limit of benefit as *5e/g*.

Lind et al. [11] showed that parameter *a* in practice need not be very precise. They considered a wide selection of 26 implemented risk reducing regulations in the USA analyzed by Morrall [14]. The cost to prevent [i.e., postpone] a death ranged from $100,000 to $132 million; the expected number of lives saved ranged from 0.06 to 1850 per year, and the annual cost ranged from 840,000 to $8.9 billion. 14 of the 26 regulations were found to have an expected benefit above the limit, i.e. were cost-effective, with $a = 1/6$; the rest were not. The same result would be obtained with any value of *a* between 0.102 and 0.25, in particular the preferred value $a = 0.2$. This standard value is now widely used; it should be generally applicable for developed countries for a long time in the future.

Thomas and Stupples [15] developed the LQI approach further, introducing the J-value of a risk-mitigation pair, a dimensionless ratio of cost per QALY to *1/S*. A series of more than twenty publications by P. Thomas and his collaborators describe multiple applications to a broad range of life- health- and environmental mitigation, e.g., [16].

6 APPLICATIONS

The applications of the LQI are of two kinds. Conventionally, such social indicators are used to rank countries or other social groupings. More important, the LQI implies a relative valuation of longevity and the production of goods, services and capital. In applications it is generally convenient to normalize *e* and *g* with respect to a country, date or currency, etc.

The dimensionless $L = EG^{0.2}$, may be considered the standard or *canonical form of the LQI*, in which $E = e/e^*$ and $G = g/g^*$ respectively denote values of *e* and *g* normalized with respect to specified constant reference values e^* and g^* respectively.

More than 200 publications apply the LQI or have developed it further. With a few exceptions the applications address practical problems of acceptable risk in various areas of technology or public health.

The MLS-LQI paradigm thus provides the basis for decisions involving all health and life safety investments nationally and even globally [17] if calibrated accordingly. This framework, in contrast to much present practice, accounts for rational societal preferences for investments into health and life safety improvements and thus greatly enhances sustainable societal development.

Safety or health provisions taken at present have economic and life-saving consequences that extend into the future, and so it is in general necessary to take discounting into account. For details see the expositions by Faber et al. [7, 17].

7 CONCLUSIONS

- It is imperative that risks to the public be managed rationally and dispassionately in the exclusive interest of the public. This entails that resources committed to risk mitigation be distributed rationally.
- The overriding goal in risk regulation is to preserve life in good health and resources.
- Engineers and other professionals who manage these risks are subject to professional ethics. This requires the risks to be analyzed scientifically and quantified.
- The measure of value in life risk is the expected duration of life in good health.
- The marginal life saving cost (MLS) principle requires that risk reduction measures be quantified and that the effective measures be preferred to ineffective ones.
- The Life Quality Index (LQI) reflects the compound societal valuation of disposable time and economic activity. Maximizing the contribution of a life risk reduction to the LQI is a reliable objective of regulation to reduce risk.
- The relative reduction of a risk to life in good health by x% is justified if the cost is less than 5x% of the GDP per capita in a developed country.
- Many examples in the literature and summarized in the Bibliography [10] illustrate the practical application of the MLS-LQI paradigm.

REFERENCES

[1] T. van Stiphout, S. Wiemer, W. Marzocchi, Are short term evacuations warranted? Case of the 2009 L'Aquila earthquake. *Geophysical Research Letters,* **37**, L06306, doi:10.1029/2009GL042352. 2010.

[2] M.H. Faber, N. Lind, The need for a protocol on risk communication and accountability. *2nd OECD High Level Risk Forum,* Paris, France.13-14 December 2012.

[3] M. Schubert, M.H. Faber, J.W. Baker, Decision making subject to aversion of low frequency high consequence events, *Special Workshop on Risk Acceptance and Risk Communication*, Stanford, USA, March 26-27, 2007.

[4] M.H. Faber, M. Maes, Sustainable Management of Life Safety Risks. *International Journal of Engineering under Uncertainty, Hazards, Assessment, and Mitigation,* **2**, 9-17, 2010.

[5] J.S. Nathwani, N.C. Lind, M.D. Pandey, Affordable Safety by Choice: The Life Quality Method. Institute for Risk Research, University of Waterloo, Waterloo, Ontario, 1997.

[6] J.R. Hicks, The foundation of welfare economics. *The Econ. Journal* **49(196),**696-712, 1939.

[7] M.H. Faber, E. Virguez-Rodriguez, Supporting decisions on global health and life safety investments, *11th International Conference on Applications of Statistics and Probability in Civil Engineering, ICASP11*. August 1-4, Zurich, 2011.

[8] J.S. Nathwani, M.D. Pandey, N.C. Lind, Engineering Decisions for Life Quality: How Safe is Safe Enough? Springer Verlag Series in Reliability Engineering, London, 189 pp., 2009.

[9] R. Rackwitz, A. Joanni, H. Streicher, Cost-Benefit Optimization and Risk Acceptability for Existing, Aging but Maintained Structures. *Structural Safety*, **30**, Issue 5, 375-393, 2008.

[10] N.C. Lind, J.S. Nathwani, LQI Bibliography and Abstracts. *LQI Symposium, August, Lyngby*, Denmark, 2012. http://www.jcss.byg.dtu.dk

[11] N.C. Lind, J.S. Nathwani, E. Siddall, *Managing Risks in the Public Interest*, Institute for Risk Research, University of Waterloo, Waterloo, Ontario IRR, June 1991, 2nd ed., 1993.

[12] R. Rackwitz, Optimization and Risk Acceptability Based on the Life Quality Index. *Structural Safety* **24**, 297-332, 2002.

[13] M.D. Pandey, and J.S.Nathwani, Foundational Principles of Welfare Economics Underlying the Life Quality Index for Efficient Risk Management. *Int. J. Risk Assessment and Management*, **7**, 6/7, 862-883, 2007.

[14] J.F. Morrall, A review of the record. *Regulation*, November/December 25-34, 1986.

[15] P. Thomas, D. Stupples, J-value: a universal scale for health and safety spending, Special Feature on Systems and Risk, *Measurement & Control*, **39**/9, 273-276, November, 2006. [Awarded the Best Paper Prize, 2006, by the Worshipful Company of Scientific Instrument Markers].

[16] P.J. Thomas, R.D. Jones, Extending the J-value framework for safety analysis to include the environmental costs of a large accident, *Process Safety and Environmental Protection*, **88**, 5, September, 297-317, 2010.

[17] M.H. Faber, N.C. Lind, J.N. Nathwani, P. Thomas, T. Vrouwenvelder, A Common Rationale for Health and Life Safety Management. *2nd OECD High Level Risk Forum*, 13-14 December 2012, Paris, France, 2012.

COMPDYN 2013
4th ECCOMAS Thematic Conference on
Computational Methods in Structural Dynamics and Earthquake Engineering
M. Papadrakakis, V. Papadopoulos, V. Plevris (eds.)
Kos Island, Greece, 12–14 June 2013

DERIVATION OF FRAGILITY CURVES FOR TRADITIONAL TIMBER-FRAMED MASONRY BUILDINGS USING NONLINEAR STATIC ANALYSIS

Leonidas S. Kouris[1] **and Andreas J. Kappos**[2]

[1] Aristotle University of Thessaloniki
Dept. of Civil Engineering, Division of Structural Engineering, GR-54124, Greece
e-mail: lakouris@civil.auth.gr

[2] City University London
Dept. of Civil Engineering, London EC1V 0HB, UK
e-mail: Andreas.Kappos.1@city.ac.uk

Keywords: Timber-Framed Masonry, Fragility Curves, Pushover Curves, Lefkas traditional buildings.

Abstract. *Recent earthquakes and two experimental campaigns on timber-framed masonry walls have shown that timber-framed masonry buildings possess a good displacement capacity and hence can withstand severe earthquakes without collapse. In the present paper, timber-framed masonry panels with diagonal braces are studied. Using a simplified model based on non-linear (NL) lumped plasticity strut elements, NL analyses are carried out of typical traditional buildings in Lefkas (Greece) with diagonally braced timber-framed masonry walls in their lateral load resisting system. Furthermore, an investigation is carried out regarding the foundation of the buildings. The key feature of the Lefkas buildings is their dual structural system. The primary system consists of a stone masonry ground floor and all upper floors are made of timber-framed masonry walls. Timber posts in the ground floor, a few centimetres apart from the stone masonry, constitute the secondary structural system which is connected to the upper floors. This latter system is activated once the ground floor stone masonry piers fail. Two different structural models are developed to simulate each system. Pushover curves are derived from the NL analyses of the buildings and are then converted into capacity curves assuming the fundamental mode dominates. On these curves four damage states (slight damage, moderate damage, heavy damage and collapse) are defined on the basis of criteria related to the actual response of the building. The first three damage states are defined on the capacity curve of the primary system, whilst the ultimate damage state is related to the response of the secondary system. Then, fragility curves in terms of spectral displacement are generated, adopting a log-normal statistical distribution of the probability of damage.*

1 INTRODUCTION

Timber-framed Masonry (TFM) is a traditional structural system that in seismic areas has proved to effectively resist earthquakes. It is well known that un-reinforced masonry (URM) is a system that in general cannot resist strong earthquakes; its high vulnerability, documented during several recent earthquakes (e.g. [1]), originates from its low tensile and shear strength, and the low ductility of its components. On the other hand, the combination of wood braces and masonry can provide adequate lateral load resisting capacity. Buildings made in some form of TFM are found in Ancient Greece from the Bronze Age (16^{th} century B.C.), and since then TFM has a continuous history, as well as widespread occurrence.

A relatively recent development in TFM is the inclusion of diagonal timber members in the frame. A very advanced, from the structural engineering point of view, TFM construction is found in Lefkas Island in the Ionian Sea (western part of Greece). This structural system was produced by local builders in the region at least since the 17^{th} century AD; it is reported that after the destructive earthquake that hit Lefkas in 1825 the local authorities decided to rebuild collapsed buildings of the island using this system [2]. Erecting such a structural system which comprises wood and masonry in harmonious proportions is a challenging task that could be properly carried out only by highly-skilled builders.

The development of this structural system, which is to some extent follows the principles of displacement-based design (a very recent trend in earthquake engineering), has strongly benefitted from the experience gained by frequent, yet moderate intensity, earthquakes in the area, that permitted observations and inspired improvements with the course of time. In its historical context, the system is a pioneer construction, which is the key reason why it has been listed as a monument of world heritage by the United Nations [3]. However, construction of these traditional buildings came to an abrupt end during the last century; hence nowadays most of them date back at least a century ago. TFM buildings have been given a considerable amount of attention by architects and archaeologists. On the other hand very little has been done so far to assess their seismic capacity and vulnerability/fragility.

Empirical fragility curves have been published for TFM buildings using data from the 2003 Lefkas earthquake. After this 2003 earthquake that had an epicentre very close to the NE end of the island, a detailed survey of damage and collapse has been carried out by Karababa [4,5]. Processing this data Karababa & Pomonis generated fragility curves for the TFM buildings of Lefkas [6]. To the authors' best knowledge, no analytically derived fragility curves exist for this type of building; such curves are developed in the remainder of this paper.

2 ANALYSIS OF THE STRUCTURAL SYSTEM

2.1 'Dual' structural system of buildings with more than one storey

The ground floor of TFM buildings in Lefkas when they have more than one storey is constructed in URM, typically stone masonry. Walls in the upper floors are made in TFM. Stones of the URM ground floor, usually calcareous limestone, are extracted from local quarries or those of the neighbouring Epirus coast [3]. The ground floor height is on average 3 m and the thickness of the walls may vary from 0.6 to 1.0 m. The external façade is made of ashlar-work, while the internal one is made of roughly dressed and worked stones or even rubble walls in irregular courses.

TFM of the upper floors consists of timber elements forming a 3D timber-frame, and masonry infills. Timber sections are on average 10×10 (±2) cm^2. The timber frame comprises spans that vary from around 1.0 up to 2.2 m. Diagonal members join opposite corners but sometimes one of them may miss or be halved. An important feature of the TFM is the use of

curved timber elements to stiffen the connection of timber posts to beams. These angles are L-shaped for one-sided connections (Figure 1) or T-shaped for two-sided connections. It is apparent that local builders had comprehended the substantial lateral load capacity of timber elements and tried to exploit it as much as possible.

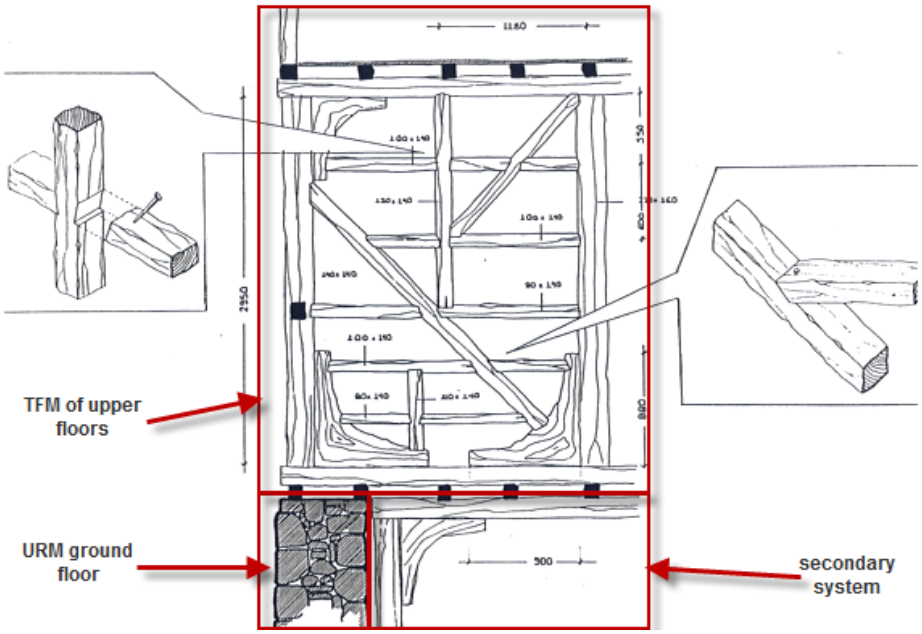


Figure 1. Connection of TFM super-structure with the URM ground floor and the secondary system (after [2]).

Nevertheless, the key structural feature of Lefkas buildings is their dual system. In fact, apart from the URM ground floor there is a secondary structural system on the internal side of the walls comprised of timber posts. Normally to every pier corresponds a single timber post a few centimetres apart the walls (Figure 1). This small distance of the timber posts from the walls results from the plinth foundation of the posts which is usually on a compact massive stone appropriately curved and usually equipped with thin metal plates serving that clamp the base of the column (Figure 2). These timber posts are connected to the beams, as well as the TFM walls, of the upper floor. Hence, the beams of the floors and the TFM walls are supported by both the primary and the secondary system. This sophisticated connection is realised by embedding floor beams into the URM ground floor walls and at the same time joining them to the timber columns of the secondary system.

Timber columns are not acted by gravity loads under normal service conditions in the building and support to the upper floors gravity loads is provided by the primary system (i.e. the URM ground walls). During an earthquake, if its intensity is so high as to drive the URM ground floor walls to partial or full collapse the secondary system will be activated. Due to the much higher deformability of the timber columns compared to the URM walls, this secondary system has displacement reserves able to accommodate the increased displacement demand of the earthquakes, at the expense of significant damage. Collapse of the URM walls of the ground floor may be classified as ‘severe damage’ state. Consequently, the building will be able to avoid collapse but damage will be high or possibly irreparable due to permanent displacements after seismic shaking; however, adequate life safety is ensured.

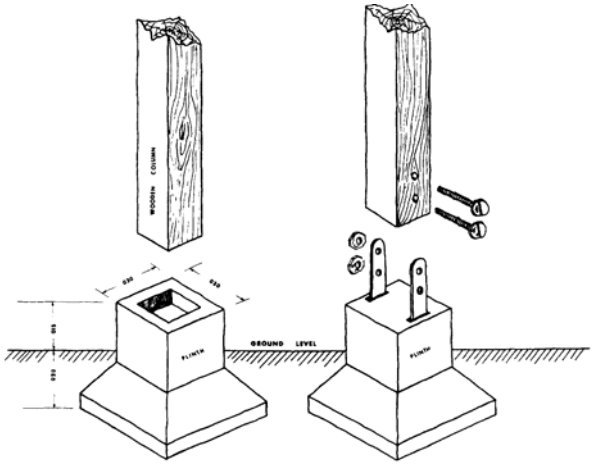
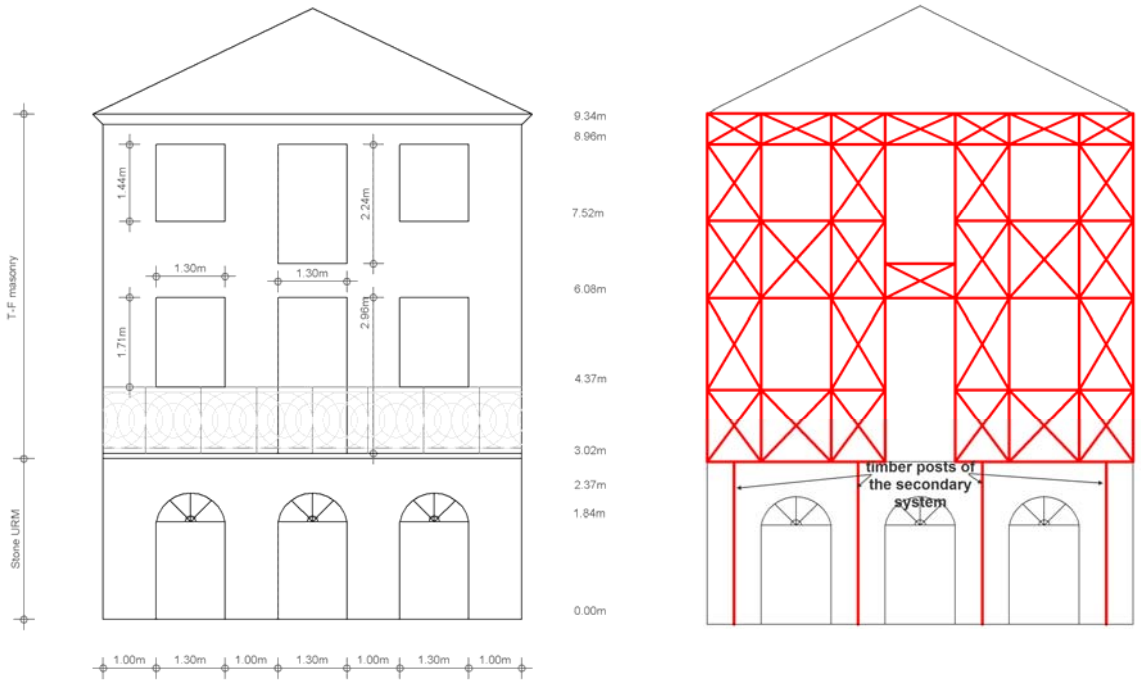


Figure 2. Stone foundations of timber posts of the secondary system of Lefkas' buildings (after [7]).

2.2 Typical building studied

A TFM building with the previously described dual system, situated in the central square of Lefkas city, called the 'Berykiou' building, is selected for further analysis as its geometrical and mechanical characteristics are typical of those found in the island (Figure 3). The ground floor is made of limestone with stonework texture in courses and walls 0.8 m thick. The TFM of the upper storeys is covered with thin galvanized iron sheeting for their protection against weathering. The configuration of the diagonals of the TFM is not exactly known due to the presence of the opaque metal sheathing. It is assumed here that every TFM panel consists of two diagonals as illustrated in Figure 3b, and a previously developed model for TFM with two diagonal braces [8] is utilised.



(a) (b)

Figure 3. Berykiou building in the centre of Lefkas city: (a) façade geometry and (b) timber elements of TFM walls and the ground floor secondary system (shown in red).

The timber frame of the upper storeys is supported by both the ground floor URM and the timber posts of the secondary system shown in Figure 3. A typical section of timber elements of TFM is assumed (10×10 cm) and the thickness of TFM is also assumed as 10 cm. Timber posts of the secondary system have a section 15×15 cm^2. Referring to Figure 2, two bounding cases are considered for column end restraint, i.e. fully clamped or free to rotate.

	Masonry	Wood
Compressive strength $f_{c,x}$ [MPa]	3.50	18.9
Compressive strength $f_{c,y}$ [MPa]	3.50	4.77
Tensile strength $f_{t,x}$ [MPa]	0	18.9
Tensile strength $f_{t,y}$ [MPa]	0	4.77
Modulus of elasticity E_x [MPa]	1750	11000
Modulus of elasticity E_y [MPa]	1750	370
Shear modulus G [MPa]	673	690
Weight [kN/m^3]	20	3.5
Poisson ratio v	0.2	0.3

Table 1. Mechanical properties for the materials used in the model in the longitudinal (x) and transverse (y) direction.

Mechanical properties of wood correspond to timber class C24 and service class II according to EC5 (see Table 1). Experiments in traditional stone masonry specimens made of two outer wythes of ashlar stones and an inner core of rubble have shown that these walls present relatively low strength compared to that of stones [9]. In this regard a conservative value of compressive strength is adopted (Table 1). Masonry is considered isotropic here, as the strength differences in the two axes are not substantial [10]. Finally, a simplified beam model is adopted.

2.3 NL static analysis

A 2D plane model of the façade is set up in SAP2000 [11]. TF walls are modelled by axial force vs. axial deformation (N-ε) lumped plasticity hinges in the diagonals [8]. Modification of the axial stiffness of the diagonals is required to take into account their sliding:

$$k_s = \frac{\left(H^2 + L^2\right)^{3/2} + H^3}{EA} \cdot \frac{1}{L^2} \cdot \frac{V_y}{\delta_y} \tag{1}$$

In Equation (1) E is the Young's modulus of timber, A is the area of the section, δ_y and V_y are the corresponding displacement and shear force at yielding and L, H the panel dimensions.

The URM piers of the ground floor were modelled using moment vs. rotation (M-θ) lumped plasticity hinges according to [12,13].

The primary and secondary systems are modelled separately for two reasons:

(i) the considerable differences in modal characteristics of these two systems result in different shape of the pushover curve, and

(ii) introducing a softening branch in the curve is prone to numerical instabilities that can cause errors and/or early termination of the analysis.

The failure mechanism of the primary system after its NL static analysis is depicted in Figure 6 where plastic hinges are indicated by a different colour associated to their damage state. 'Collapse' of the building is due to the development of a ground floor mechanism. However, upper floor TFM has suffered considerable damage as shown by the widespread

inelastic deformations of the TFM panels. Indeed, development of hinges in the ground floor is preceded by the occurrence of the TFM wall hinges. However, the evolution of plastic deformation in the ground floor is rather quick and finally dominates the failure mechanism.

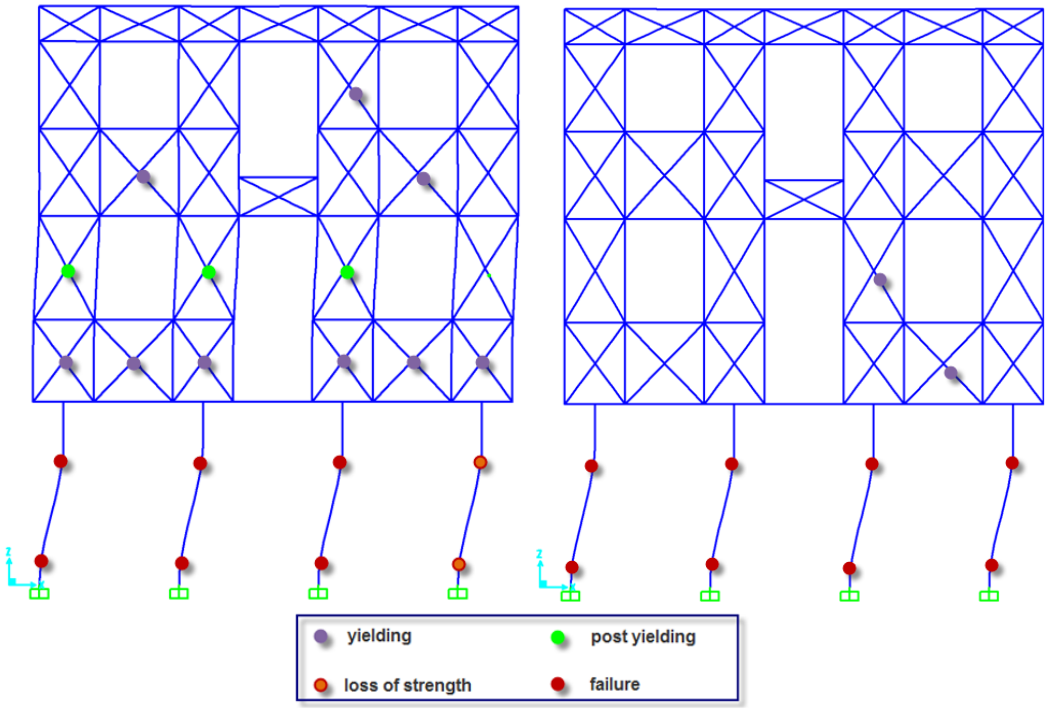
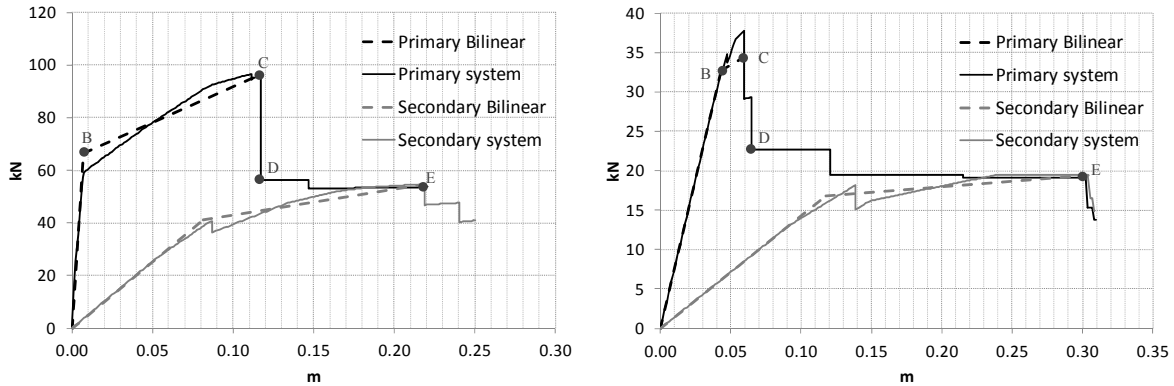


Figure 4. Failure mechanism of the primary (left) and the secondary (right) system of Berykiou TF building.

On the contrary, NL static analysis of the secondary system leads to collapse of the timber posts of the ground floor, with negligible inelastic deformation in the upper floors; the latter remain almost intact and the whole plastic deformation is concentrated in the ground floor.



(a) (b)

Figure 5. Pushover curves of the primary and secondary system of 'Berykiou' TFM building with: (a) full restraints and (b) flexible supports (SSI).

These two mechanisms in the real building coexist and interact; activation of the secondary system occurs after failure of the URM piers, but from then on it follows the deformation of the primary system. Consequently, combination of the pushover curves is in order; failure of

the ground floor piers constitutes the point wherein the two curves should be joined. Then, the resulting curve is idealised by a multi-linear one that allows definition of a yield point.

Previous analyses have been carried out without considering any interaction between the building and the soil as full restraints have been applied at the basis of the piers. However, the city of Lefkas is situated on soft alluvial deposits [14] which give rise to compliance of the URM foundations. These URM foundations are usually strengthened with a substructure made of layers of tree trunks to increase their stiffness [7,15]. Dynamic impedances for this kind of foundation and this type of soil have been estimated as $\boldsymbol{k_{sdv}}$=2400 kN/m^3 for the vertical direction and $\boldsymbol{k_{sdh}}$=1600 kN/m^3 for the horizontal one, to account for soil – structure interaction (SSI).

3 DERIVATION OF FRAGILITY CURVES

Fragility curves are derived based upon the key assumption [16] that the 'Berykiou' building represents a typical TFM building of this typology, displaying ‘average’ response. The seismic behaviour of this building type can then be expressed in terms of an ‘average’ pushover curve. The capacity spectrum method [17] based on inelastic demand spectra [18] is used here to relate pushover curves with seismic demand. So, pushover curves are transformed into capacity curves, i.e. the pushover curve of the corresponding SDOF (single degree of freedom) system. This transformation is implemented using properties of the predominant mode in the considered direction. The validity of this procedure depends on the contribution of the first mode, which in this case is over 90%, which ensures reliable results.

A capacity curve is generally characterized by two points; (i) the yield point B that represents the transition from elastic to inelastic deformations, and (ii) the maximum capacity point C which represents failure of the piers of the primary system. Nevertheless, in Lefkas’ dual system buildings there are two more significant points: (iii) point D related to the yielding of the secondary system and (iv) point E representing collapse of the secondary and eventually of the entire building. This sequence of points specifies the main four representative stages of the seismic performance of TFM buildings with a dual system.

It is well documented in the current literature that fragility curves can be described by (cumulative) normal, lognormal, or beta distributions [19]. The lognormal distribution (eq. 2) is adopted here since it describes adequately the evolution of seismic damage [16].

$$\mathrm{P}\left[ds \geq ds_i \middle| A_g\right] = \Phi\left[\frac{1}{\beta_{ds,i}} \ln\left(\frac{A_g}{\overline{A}_{g,dsi}}\right)\right] \tag{2}$$

In Equation (2) Φ is the cumulative distribution function of the lognormal distribution, $\beta_{ds,i}$ is the standard deviation of the natural logarithm of the damage state i and $\overline{A}_{g,dsi}$ the mean value of the appropriate measure that represents seismic intensity (here spectral displacement) at which the building reaches the threshold of damage state i. $\overline{A}_{g,dsi}$ is computed according to the previous discussion of the damage stages through the following expressions:

$$\overline{S_{d1}} = \delta_y = \delta_B \tag{3a}$$

$$\overline{S_{d2}} = 0.4 \times (1.5\delta_y + \delta_C) \tag{3b}$$

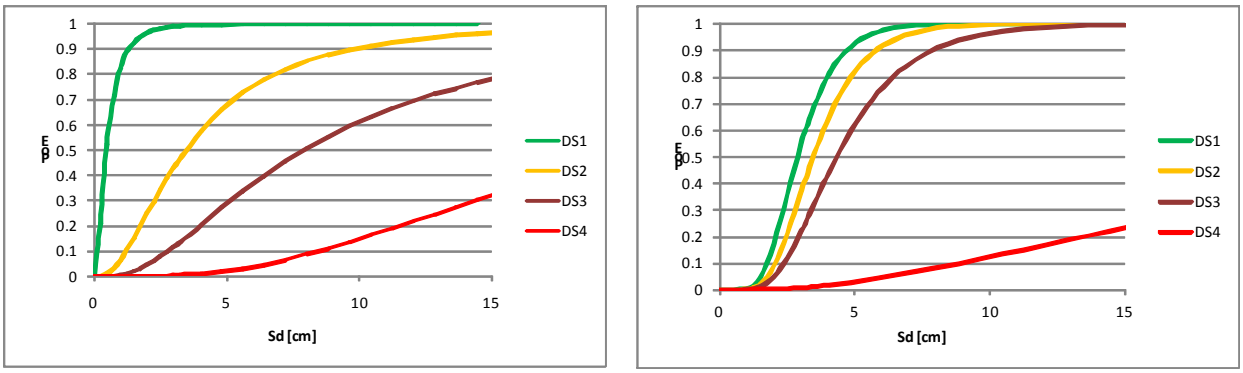
$$\overline{S_{d3}} = \delta_C \tag{3c}$$

$$\overline{S_{d4}} = \delta_u = \delta_E \tag{3d}$$

In the absence of other information, the following assumption is made in order to calculate the standard deviation $\beta_{ds,i}$ [20,21]; first the binomial distribution (eq. 4) is adopted since it depends only on one parameter, i.e. the mean value of the spectral displacement:

$$P_i = \frac{n!}{i!\cdot(n-i)!}\cdot\left(\overline{S_{d,i}}\right)^i\cdot(1-\overline{S_{d,i}})^{n-i}\;|_{i=1-n} \tag{4}$$

Consequently, for the mean spectral displacement of each damage state i defined from (3), the probability of exceedance of all other damage states may be computed using Equation (4).



(a) (b)

Figure 6. Fragility curves for 3storeys TFM buildings in Lefkas island on: (a) fully restrained and (b) flexible foundation (SSI).

Figure 6 shows the fragility curves for three-storey TFM buildings with a dual system. It is seen that DS1 (light damage) will be reached for rather low earthquake intensity. Taking into account the deformability of soil, DS1 shifts to higher displacements, which in general would mean higher intensities (Figure 6b); however, this depends on the type of response spectrum used for estimating demand. A similar trend is noted with respect to DS4, whose probability of exceedance decreases for the same values of spectral displacement. On the contrary, intermediate damage states (DS2 and DS3) shift towards lower intensities which leads to the conclusion that there is lower probability for a building on soft soil to reach DS1 and DS4 compared to a building on rock; the opposite holds for DS2 and DS3. Clearly, these issues have to be verified with additional analyses.

4 CONCLUSIONS

The key findings from this study can be summarised as follows:

- TFM buildings in Lefkas having a dual structural system (described in section 2) can be thought of as an early realisation of displacement based 'design', as they are expected to resist strong earthquakes through their displacement capacity rather than their strength.
- The primary system aims to support gravity loads and, under low to moderate intensity earthquakes, to prevent premature cracking and noticeable deflection of the building.
- The secondary system renders displacement capacity to the building and provides the necessary deformability to survive a severe seismic event.
- The study of the above two systems using a different model for each, is a reasonable analysis procedure since the presence of the secondary system has a negligible effect on the response when the primary system is still intact.

- Pushover curves of TFM buildings are best idealised by four points on a multi-linear curve representing the transition of the building through four discrete response states.
- Damage states were related to the response phases of the building, defined in terms of displacements. So, three (DS1, DS3 and DS4) out of the four damage states are related directly to the response phases, establishing a robust definition.
- The derived fragility curves for TFM buildings show that although these may suffer cracks and damage for low intensity earthquakes, they are expected to avoid collapse due to their high displacement capacity. These findings agree with observed response of TFM buildings in past earthquakes in Greece.

REFERENCES

[1] M. Indirli, L.A.S. Kouris, A. Formisano, R.P. Borg, F.M. Mazzolani, Seismic damage assessment of unreinforced masonry structures after the Abruzzo 2009 earthquake: The case study of the historical centers of L'Aquila and Castelvecchio Subequo, *International Journal of Architectural Heritage,* **7,** 536-578, 2013.

[2] P. Touliatos, D. Gante, "Local traditional earthquake-resistant construction: the paradigm of Lefkas", National Technical University of Athens, 1995 (in Greek).

[3] United Nations, The traditional aseismic techniques and the everlasting principles they reveal, *Newsletter - Stop Disasters. International decade for natural disasters reduction "Seismic Vulnerability Reduction",* 4-5, 1993.

[4] F.S. Karababa, P.M. Guthrie, Vulnerability Reduction through Local Seismic Culture, *Technology and Society Magazine, IEEE,* **26,** 30-41, 2007.

[5] F.S. Karababa, Local seismic construction practices as a means to vulnerability reduction and sustainable development, *A case-study in Lefkada Island,* PhD Thesis, University of Cambridge, 2007.

[6] F.S. Karababa, A. Pomonis, Damage data analysis and vulnerability estimation following the August 14, 2003 Lefkada Island, Greece, Earthquake, *Bulletin of Earthquake Engineering,* **9,** 1015-1046, 2011.

[7] D.T.G. Porphyrios, Traditional Earthquake-Resistant Construction on a Greek Island, *The Journal of the Society of Architectural Historians,* **30,** 31-39, 1971.

[8] L.A.S. Kouris, A.J. Kappos, Detailed and simplified non-linear models for timber-framed masonry structures, *Journal of Cultural Heritage,* **13,** 47-58, 2012.

[9] A.W. Hendry, Structural Masonry, Macmillan Press, 1998.

[10] K. Naraine, S. Sinha, Cyclic Behavior of Brick Masonry Under Biaxial Compression, *Journal of Structural Engineering (ASCE),* **117,** 1336-1355, 1991.

[11] Computers and Structures Inc., *SAP2000: Three dimensional static and dynamic finite element analysis and design of structures*, Berkeley, California, 1999.

[12] A.J. Kappos, G.G. Penelis, C.G. Drakopoulos, Evaluation of simplified models for lateral load analysis of unreinforced masonry buildings, *Journal of Structural Engineering,* **128**, 890-897, 2002.

[13] G.G. Penelis, An efficient approach for pushover analysis of unreinforced masonry (URM) structures, *Journal of Earthquake Engineering,* **10,** 359-379, 2006.

[14] C. Karakostas, V. Lekidis, T. Makarios, T. Salonikios, I. Sous, M. Demosthenous, Seismic response of structures and infrastructure facilities during the Lefkada, Greece earthquake of 14/8/2003, *Engineering Structures,* **27,** 213-227, 2005.

[15] T. Makarios, M. Demosthenous, Seismic response of traditional buildings of Lefkas Island, Greece, *Engineering Structures,***28,** 264-278, 2006.

[16] C.A. Kircher, R.V. Whitman, W.T. Holmes, HAZUS earthquake loss estimation methods, *Natural Hazards Review,* **7,** 45, 2006.

[17] S. Freeman, Development and use of capacity spectrum method, *6th US NCEE Conference on Earthquake Engineering/EERI*, Washington, USA, May 31 - June 4, paper No. 269, 1998.

[18] P. Fajfar, Capacity spectrum method based on inelastic demand spectra, *Earthquake engineering and structural dynamics,* **28,** 979-994, 1999.

[19] R.V. Whitman, Anagnos, T., Kircher, C.A., Lagorio, H.J., Lawson, R.S., Schneider, P. Development of a national earthquake loss estimation methodology, *Earthquake Spectra*, **13**(4), 643–661, 1997.

[20] A.H. Barbat, L.G. Pujades, N. Lantada, Seismic damage evaluation in urban areas using the capacity spectrum method: Application to Barcelona, *Soil Dynamics and Earthquake Engineering,* **28,** 851-865, 2008.

[21] S. Lagomarsino, On the vulnerability assessment of monumental buildings, *Bulletin of Earthquake Engineering,* **4,** 445-463, 2006.

COMPDYN 2013
4th ECCOMAS Thematic Conference on
Computational Methods in Structural Dynamics and Earthquake Engineering
M. Papadrakakis, V. Papadopoulos, V. Plevris (eds.)
Kos Island, Greece, 12–14 June 2013

SEISMIC LOAD ASSESSMENT FOR MASONRY MONUMENTAL BUILDINGS

Thomas N. Salonikios, Konstantinos E. Morfidis, and Vasilios A. Lekidis

Earthquake Planning and Protection Organization (EPPO)
5 Agiou Georgiou Str., Patriarchika Pylaia, 55535 Thessaloniki, Greece
e-mails: salonikios@itsak.gr, morfidis@itsak.gr, lekidis@itsak.gr

Keywords: Masonry, Monument, Seismic Loads, Equivalent Damping, Earthquake Records, Exact Response, Inelastic Analysis, Masonry Frames, National Strong Motion Network.

Abstract. *In present work, selected experimental data of the last 25 years are used together with the inelastic analysis of masonry frames and the postprocessing of the records of strong earthquakes in Northern Greece, for the estimation of rational seismic loads that are appropriate for the seismic evaluation and/or upgrade of existing masonry buildings. The estimated rational seismic loads have significantly lower values than the seismic loads that are suggested by modern seismic codes. It is commonly accepted that modern codes usually suggest very high seismic loads. This happens even in the case that in these codes are foreseen provisions appropriate for masonry structures. These provisions usually refer to modern masonry buildings where is possible to provide high strength. Through the literature review was found that in existing unreinforced masonry buildings is possible to be developed an "equivalent" damping around 20%. Also was found that the eigenfrequency of masonry buildings is reduced at 2/3 - 1/2 of the elastic one and the corresponding reduction of the stiffness is at least 50% of the elastic one. These reductions happen close after the "yielding" point of the "equivalent" bilinear elastoplastic diagram of the structure. The performance points of such structures are located after that "yielding" point. Through the nonlinear analyses of masonry frames, resulted the base shear that these frames is possible to resist and its value is 25% of the total vertical loads of the frames. This value was found for the models with nonlinear frame elements and for the models with discrete brick – mortar joint elements. The models, where bricks and mortar joints were simulated by continuous elements, had higher strength than two aforementioned models. Through the postprocessing of recorded accelerograms of strong earthquakes, resulted spectral accelerations with values around 70%g. The corresponding normalized accelerations resulted 50%g and correspond to damping 5%. By considering "equivalent" damping 20% (as was found above) the normalized spectral accelerations resulted around to 25%g that are close to the value noticed above as the resisted accelerations of the examined frames. These spectral accelerations were found for the records of Achaia – Ilia earthquake. For this earthquake were not observed any collapses of monumental masonry structures at the stricken area with the exception of some local damages and local failures. This way, many of the conclusions - suggestions of the present work are confirmed. It is also concluded that additional experimental and analytical research effort is necessary in the aforementioned fields for the legislation of the conclusion of the present work.*

1 INTRODUCTION

The estimation of the seismic loads that should be used for the seismic evaluation of masonry monumental buildings is the field of extensive research, last decades, in countries with high seismic activity. These loads are strongly affected by parameters such as the "equivalent" damping, the variation of the eigenproperties of the building and the available capacity of the masonry monumental buildings for inelastic deformation. According Beucke and Kelly [1], the total damping of masonry walls is composed by two parts, the viscous and the friction parts. The viscous part of the damping is divided to "constant" and to "kinetic" Coulomb damping. All aforementioned parts give the "equivalent" damping "ξ_{eq}". This consideration is a simplified expression of the damping and according parametric analyses the exact solution is appropriately approached. Calvi, Kingsley and Magenes [2], utilize laboratory tests of masonry specimens, pseudo-dynamic loading as well as seismic table tests on building specimens to examine the type of the response of the specimens (shear or flexural rocking) in relation with the capacity for seismic energy damping. Through specimens' tests was found that the response of the specimens is strongly affected by the aspect ratio. For high aspect ratios the flexural rocking dominates while for low aspect ratios dominates the shear response. In the second case (shear response) the dissipated energy is higher than the energy that is dissipated by flexural rocking response. During rocking the unloading path of the load – response curve is parallel with the loading path with slightly lower values. This way is indicated that an important amount of the seismic energy that is needed for the maximum deformation of the tested walls return to the specimen during the unloading procedure. During diagonal shear response the unloading path is almost a vertical line resulting thus to higher area of the hysteresis loops than in the case of flexural response. In the case of sliding shear response the absorbed and dissipated energy is higher than in the aforementioned two cases. The main disadvantage in this case is the high permanent deformations along the base sliding cracks. In some cases the shear response of masonry walls is ductile. This is observed in masonry piers with low aspect ratio ($\leq$1.0) that are subjected to shear loads. In this case the failure cracks are formed in mortar joints. After this type of cracking, remain significant strength reserves to gravity and live loads. Also through the development of friction resistance at the cracks there is a capacity for resistance to shear loads. According Magenes and Calvi [3], masonry walls respond in flexural, diagonal shear or sliding shear ways and for each case of response are given the corresponding shear forces. Also in this work is extensively studied the damping capacity during each considered way of response. During flexural – rocking response the hysteretic damping is 10% and the viscous damping 5% should be added to this value. During diagonal shear response the "equivalent" damping results 10%. In the case of sliding shear response, resulted "equivalent" damping 64% for high level of deformation. In every test, in this study, was observed a combined response of flexural, diagonal shear and sliding shear response. For this reason the value of 64% is very high and for the definition of reliable damping factors all possible responses should be taken into account. Before 1997 there were not adequate experimental data for the consideration of the contribution of the sliding shear mechanism to the damping during combined shear – flexural response. In this work is suggested that in the case of flexural – rocking response should be considered "equivalent" damping 15% and ultimate drift 1.0%, in the case of diagonal shear response the corresponding values are suggested as 15% and 0.5% while in the case of sliding shear response are suggested "equivalent" damping 20% (considered as conservative) and ultimate drift 1.0%. The definition of the type of the response (flexural, diagonal shear, sliding shear) is achieved by simplified equations that are given by Magenes and Calvi in [3]. The design response spectrums that are given by Eurocode 8 are reduced by 1.8 times when "equivalent" damping is

considered. This reduction is higher, when are used response spectrums that resulted from the records of real earthquakes. It is concluded that the proposed behavior factor, 1.5, is very conservative and higher values should be used when are taken into account the complete model of the masonry building as well as the activation of inelastic mechanisms, the "equivalent" damping and the variation of the eigenperiods of the building. In the study by Tomazevic and Weiss [4], are given results from the test of a 1:5 scale building model at the seismic table. During the tests resulted reduction at the eigenfrequencies of the tested building model about 40% and the resulted behavior factor was found q=2.84. The Eurocode value q=1.5 is conservative but seems reasonable in the case that are not desired any damages at the masonry buildings. In the study by Bothara et al [5], are described the tests at the seismic table of a 1:2 scale masonry building model. The seismic loads were applied in two directions. A part of the study was related with the estimation of the dissipated energy for various levels of deformation and vulnerability. From the postprocessing of the recorded response resulted "equivalent" damping factors up to 36%. This way is shown a significant capacity of the masonry buildings for a steady nonlinear response under high seismic loading. This nonlinear response is attributed to the flexural – rocking response and to the reduction of the eigenfrequencies of the building (softening) due to the development of cracks at the shear mechanisms. Ahmad et al. [6], suggest that the energy that is dissipated by masonry structures that are subjected to seismic loads should be defined in relation with the achieved ductility: $\xi=0.05+c.(\mu-1)/(\pi.\mu)$. The coefficient "c" resulted from experiments on masonry piers and was found c=0.32. In this work the hysteretic damping varied between 9% and 14%. These values vary due to the influence of aspect ratio and the level of axial compression. In the study by Michel et al [7], was found that the main eigenfrequency of the masonry buildings is reduced at 60% when are applied accelerations about 0.20g. Also the drop to the eigenfrequency is about 50% for inter storey drifts 0.5% - 1.0%. These values resulted from pseudo-dynamic tests at two masonry buildings that were constructed in natural scale.

Through the literature review is concluded that there are many reasons for the consideration of an "equivalent" damping that represents the viscous and hysteretic response of the masonry walls that are subjected to seismic loading, with value over 5%. In the case of the seismic evaluation of masonry buildings for a predefined level of damage, is concluded that these buildings have adequate capacity for seismic energy dissipation. This capacity is attributed to the "equivalent" damping that was found during the literature review, about 20%. Another important conclusion from the literature review is that the main eigenfrequency of the masonry buildings is reduced by 40% to 50% for drift values 0.1% - 1.0%. From the aforementioned conclusion, the stiffness of the masonry buildings seems to be reduced by 50% of the initial one (elastic) at the yield point of the bilinearized diagram of the response of the building. This way are developed lower stresses at the masonry structural elements than in the case of consideration of the elastic stiffness.

2 PARAMETRIC ANALYSES

In this section are given results from the inelastic analysis of masonry frames that are subjected to seismic loading that is applied by horizontal step by step increased forces [8]. Two types of frames are considered. One frame is constructed with two piers (1BAY) and the other is constructed with eight piers (7BAY), both frames are two-storey. The frames were selected, by taking into account that masonry buildings are generally short in height while is possible to form two-pier to multi-pier frames. The frames were modeled with inelastic properties and were analyzed by the CAST3M Code (Visual CAST3M, 2000) [8]. The frames were modelled by two dimension finite elements with two different property types. In "Continuous" models, masonry is considered as a two-dimensional homogeneous material under the plane

stress assumption (homogenized media) so that bricks and mortar joints are not represented separately. The numerical model chosen is the model of Mazars existing in the code CAST3M: it is an isotropic scalar damage model suitable for concrete structures under monotonic loadings. The damage variable varies from 0 (virgin material) to 1 (fully destroyed material). The elastic characteristics are Young modulus 1650MPa and Poisson coefficient 0.2 and tension/compression strengths 0.1MPa and 3.0 MPa respectively. The parameters governing the post-peak behaviour of the model have been chosen so as to obtain a brittle softening in tension and a more ductile softening in compression (1BAY, 7BAY frames). In "Discontinuous" models, masonry is considered as a two-dimensional heterogeneous material under the plane stress assumption: the bricks are modeled separately (elastic material) and the mortar joints are represented by elasto-plastic interface elements [8]. The plastic yielding of the interface is governed by a composite yield locus featuring a usual Mohr-Coulomb criterion, a tension cut-off and a compression cut-off. The post-peak regime is controlled by three uniaxial evolutions featuring respectively the behaviors in pure shear, pure tension and pure compression. The elastic characteristics of the brick and mortar joint are usually very different (the former are much stiffer than the latter). The Young moduli of the two materials (2400MPa for brick and 400MPa for mortar) have been chosen so as to give in average (owing to the bond pattern, masonry is orthotropic) a value around 1650MPa. The friction angle of the interface was 30^o and the cohesion 0.15MPa. The tension/compression strengths of the masonry (0.1MPa and 3.0MPa) have been affected to the tension/compression cut-offs of the interface [8]. The post-peak behaviour was again chosen very brittle in tension and more ductile in compression and shear (1BAY, 7BAY frames). The loading is imposed on the structures in a two step sequence. In the first step the vertical uniform distributed loads are applied and in the next step the lateral loads are imposed. The values of the latter are then increased monotonically step by step [8]. The analysis is carried out until a prescribed displacement value at a prescribed (control) node is developed. In the parametric solutions, three different lateral load distribution were used:

- Loadcase ACC: A lateral force is applied at each node, that is proportional to the mass tributary to that node.
- Loadcase MODE: Application of a load pattern in lateral direction that is proportional to the product of a specified mode shape times the mass tributary to that node. For this case the first mode is used.
- Loadcase LOAD: A triangle distribution of lateral loads proportional to the mass and height of each floor.

From the different analysis cases, resulted the load – displacement curves for the examined masonry frames. By the use of these strengths and the existing axial loads are defined the "equivalent" seismic load coefficients that can be withstood by the considered frames (Table 1).

From table 1, is concluded that by modeling the masonry frames by continuous elements results higher strength than in the case that are used discrete elements or frame elements. By the use of seismic loads according "ACC" load case, results increased strength of the frames in comparison with the distribution of seismic loads according " LOAD" or "MODE" load cases. By the use of inelastic analyses and table 1, is concluded that the considered frames, with properties similar to the ones of ordinary masonry buildings, can resist an "equivalent" seismic load coefficient around 0.25g.

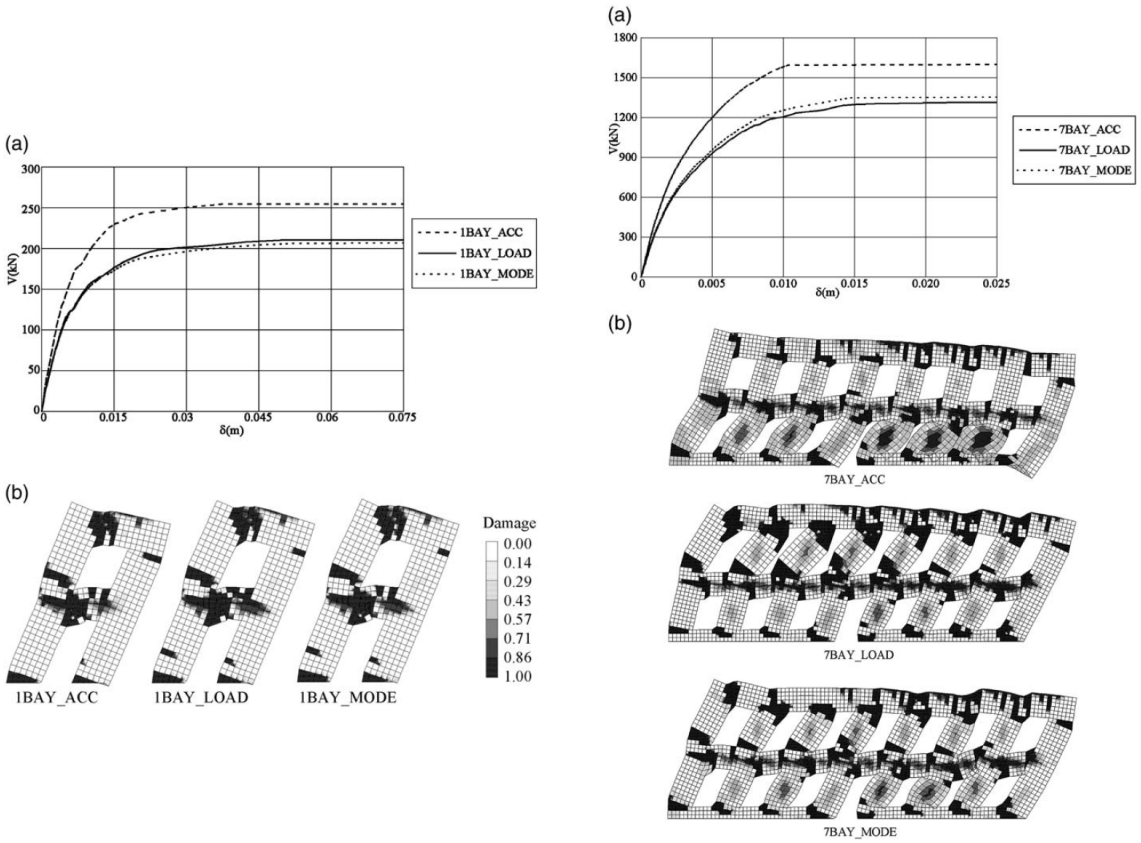


Figure 1: (a) Load – displacement curves (b) Failure types of considered frames. Continuous models.

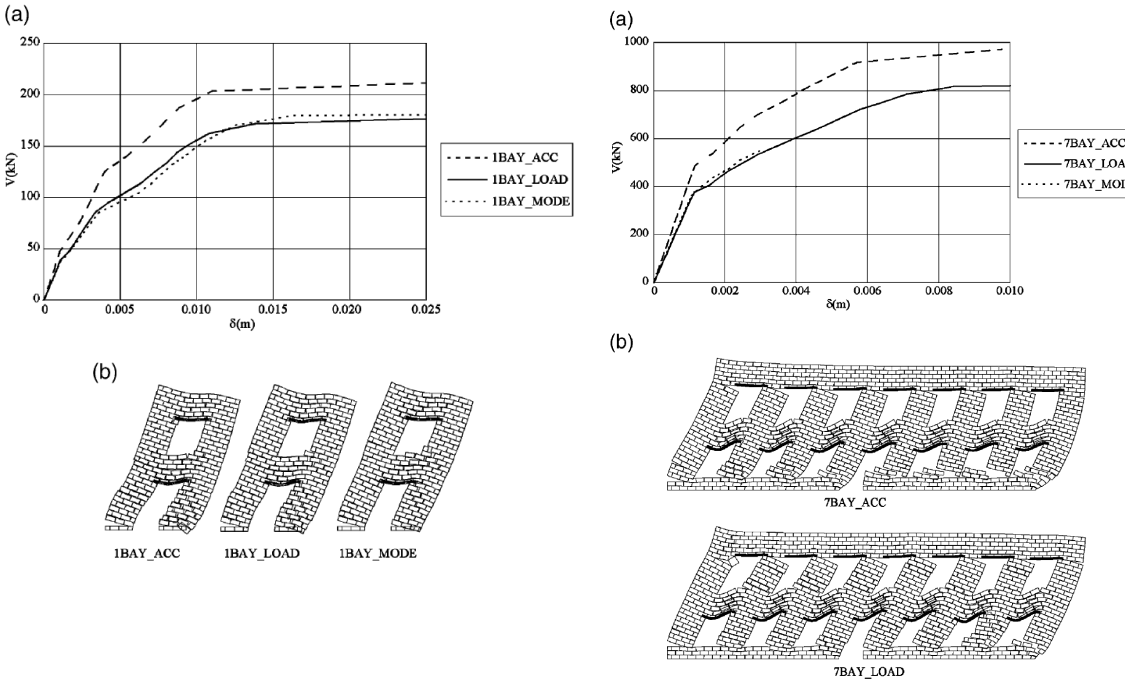


Figure 2: (a) Load – displacement curves (b) Failure types of considered frames. Discrete models.

"Equivalent" seismic load coefficients				
FRAME TYPE	1 BAY		7 BAY	
LOAD TYPE	LOAD, MODE	ACC	LOAD, MODE	ACC
SAP2000 Nonlinear Frame Elements	0.26g		0.24g	
Continuous Model	0.30g	0.36g	0.47g	0.55g
Discrete Model	0.25g	0.31g	0.29g	0.33g

Table 1. "Equivalent" seismic load coefficients for the various model types and various loading schemes.

3 RESULTS FROM THE POSTPROCESSING OF RECENT EARTHQUAKES

In this paragraph are postprocessed the records of four strong earthquakes that happened in Peloponnesus (in southern Greece), during last years, and were recorded by the Strong Motion Network of EPPO. The epicenters of these earthquakes and the records are given in figures 3-8. The response spectrums of these earthquakes are given in figures 9-11. The response spectrum of Achaia – Ilia earthquake has the highest ordinates. The spectral accelerations for these earthquakes are elevated for periods between 0.18sec to 0.30sec. Through simplified considerations the main eigenperiod of this earthquake is close to the main eigenperiod of two storey masonry buildings that are located close to epicentral area. For the rest earthquakes the response spectrum accelerations are lower with Koroni earthquake having the lowest values. In table 2, the maximum observed response spectrum accelerations (column 2) are compared with the corresponding code accelerations (column 4). The highest different result for Achaia – Ilia earthquake. The normalized spectral accelerations that are given at column 5, denote that many monumental masonry buildings should been collapsed especially for Achaia – Ilia earthquake with normalized Sa_{max}=0.57g. From the in-situ inspections resulted that for Koroni earthquake were not observed any damages to monumental masonry buildings (MMB), for Kithira earthquake were observed slight damages while for Achaia – Ilia earthquake were observed extended damages to some MMBs. This is attributed to the development of high "equivalent" damping coefficient by the MMBs in contrast with the norms of many Seismic Codes. It is obvious that the suggested values of damping coefficient, 5% is very low. The same value is suggested by similar codes for the damping of reinforced concrete walls. It is obvious that a masonry wall of 0.60m thick is not possible to have the same damping coefficient as a reinforced concrete wall of the same thickness. In two records of Achaia – Ilia earthquake are calculated the response spectrums for damping 5%, 10% and 20%. These spectrums are normalized at 66% of the maximum ordinate, Figures 12-13.

EQ	Sa_{omax}	Sa_{max}	T	2.5*Ao/ q	(2/3)*Sa_{max}
	(1)	(2)	(3)	(4)=2.5*0.24/1.5	(5)=2/3*(2)
Koroni	0.07g	0.31g	0.28sec	0.6g/1.5=0.40g	0.20g
Kythera	0.15g	0.65g 0.46g	0.55sec 0.32sec	0.6g/1.5=0.40g	0.43g 0.31g
Achaia - Ilia	0.21g	0.87g	0.18sec	0.6g/1.5=0.40g	0.57g

Table 2. Calculation of Spectral Accelerations

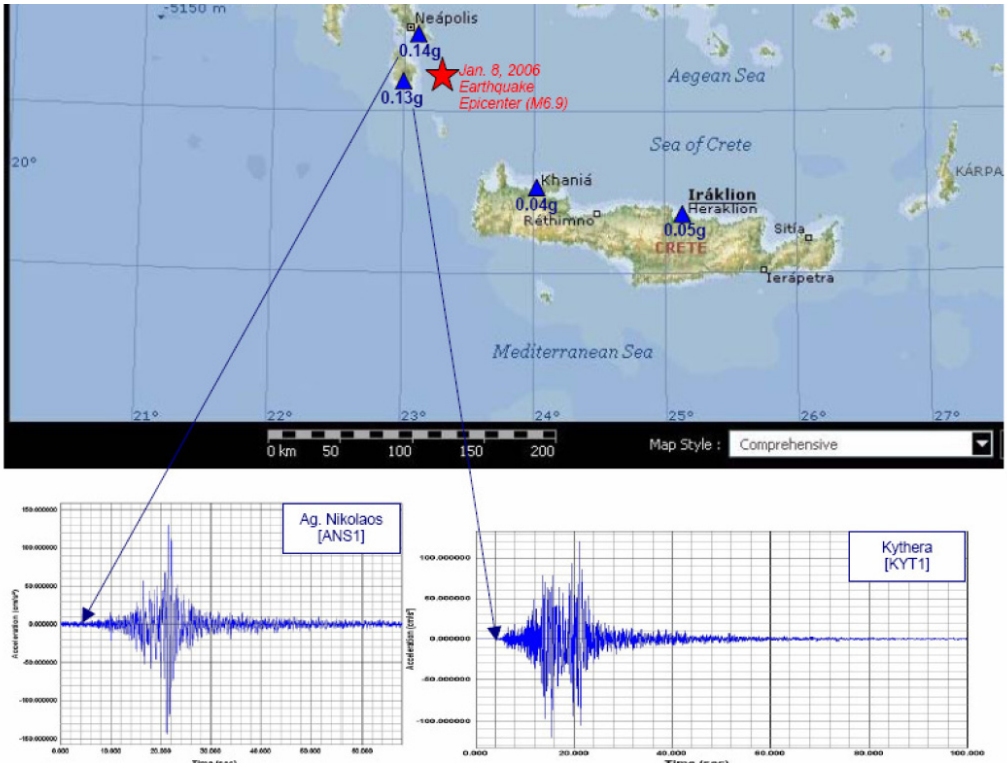


Figure 3. Kithira Earthquake 8/1/2006, (M6.9). Epicenter, Accelerometric Network and records.

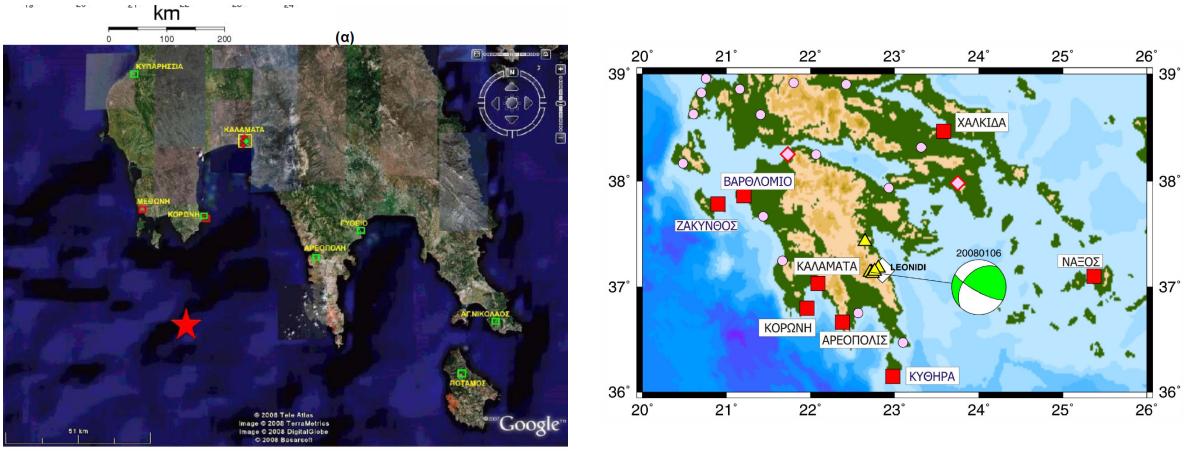


Figure 4. Left: Koroni Earthquake 14/2/2008, (M6.7). Right: Leonidio Earthquake 6/1/2008 (M6.5).

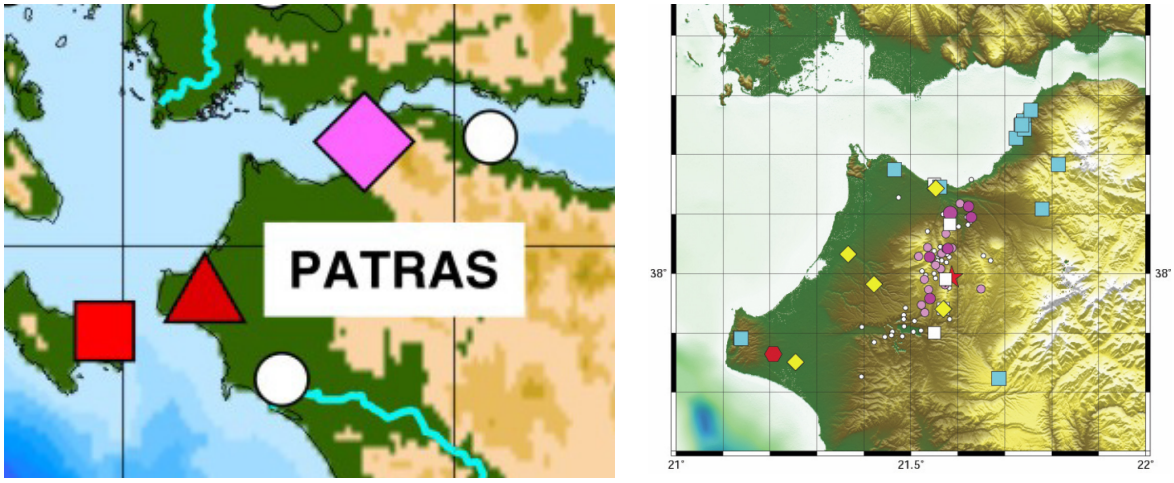


Figure 5. Achaia – Ilia Earthquake 8/6/2008 (M6.5). Left: Accelerometric Network, Right: Epicenters of the seismic activity.

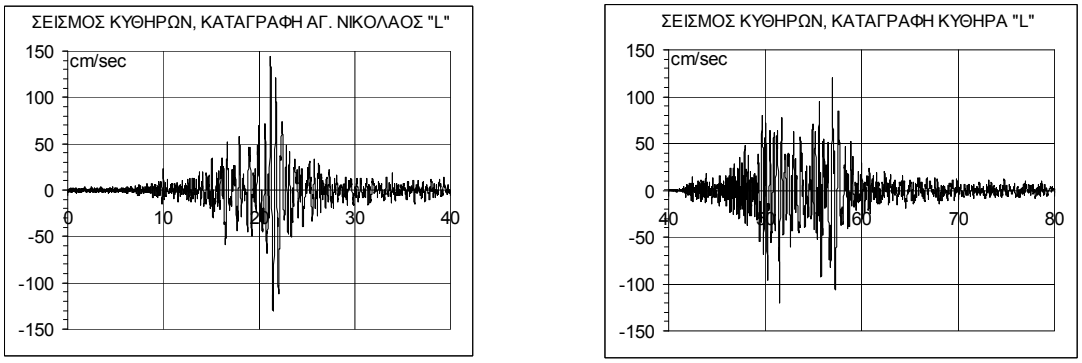


Figure 6. Accelerograms of Kithira earthquake. Left: records at Agios Nikolaos, Lakonia. Right:Records at Kithira.

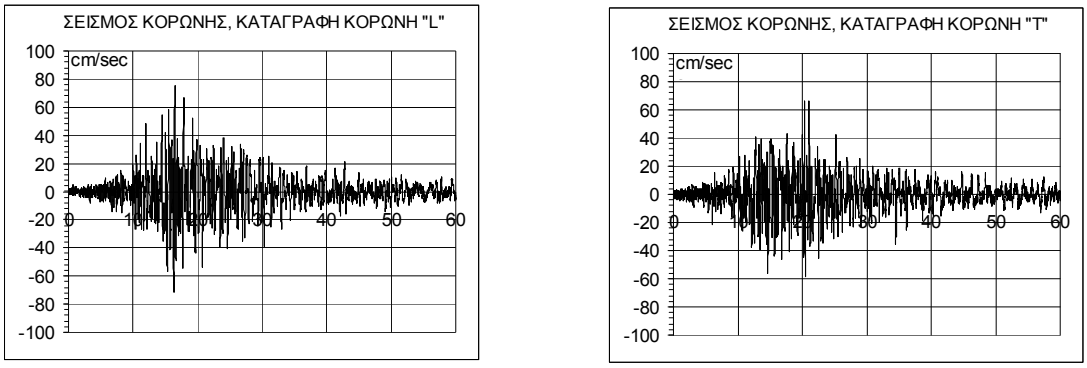


Figure 7. Accelerograms of Koroni earthquake. Left: Longitudinal (L) direction. Right: Transverse (T) direction.

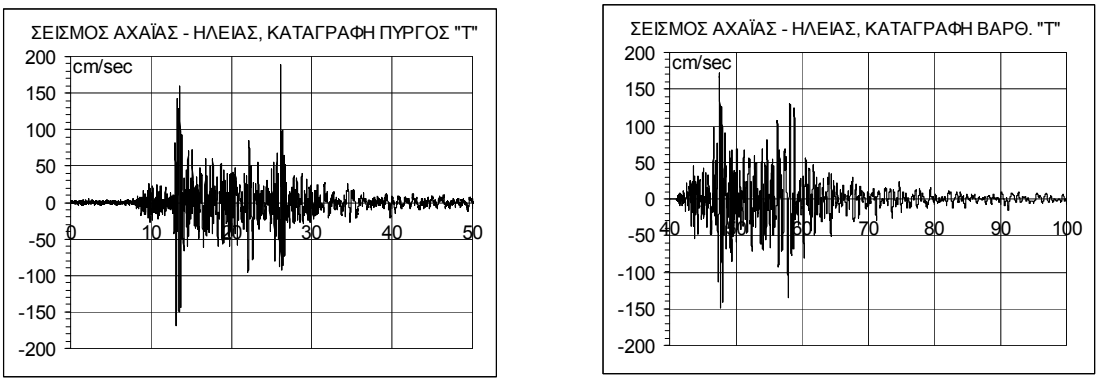


Figure 8. Accelerograms of Achaia – Ilia earthquake. Left: "T" Record at Pyrgos. Right: "T" Record at Vartholomio



Figure 9. Response spectrums for Kithira earthquake. Bold line "L", "T" records at Agios Nikolaos, Lakonia. Smooth line "L", "T" records at Kithira. (ζ=0.05)

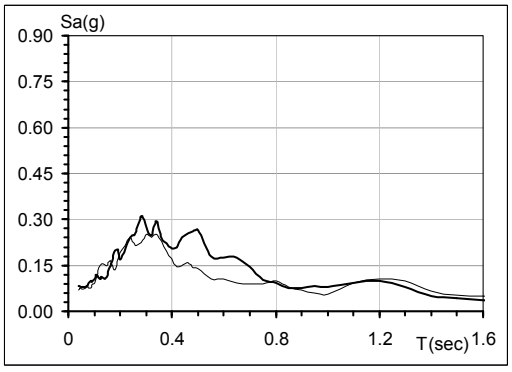


Figure 10. Response spectrums for Koroni earthquake. (ζ=0.05)

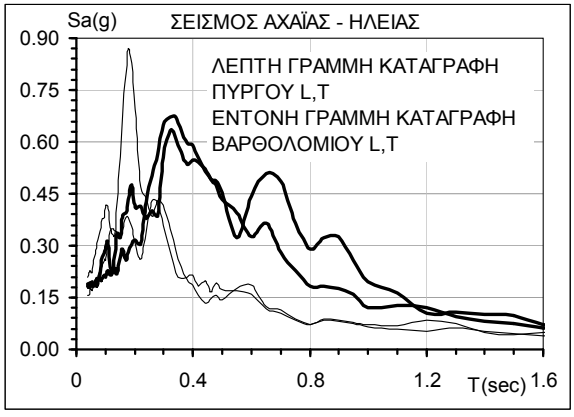


Figure 11. Response spectrums for Achaia - Ilia earthquake. Bold line "L", "T" records at Vartholomio. Smooth line "L", "T" records at Pyrgos. (ζ=0.05)

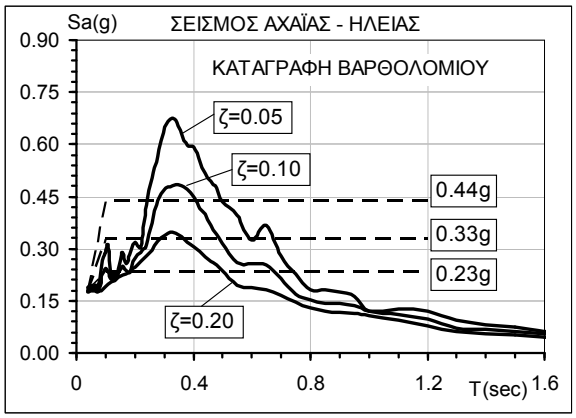


Figure 12. Response spectrums of Achaia – Ilia earthquake from records at Vartholomio (continuous lines) for 5%, 10%, 20% damping. Normalization of response spectrums at 66% of the maximum value (discontinuous lines).

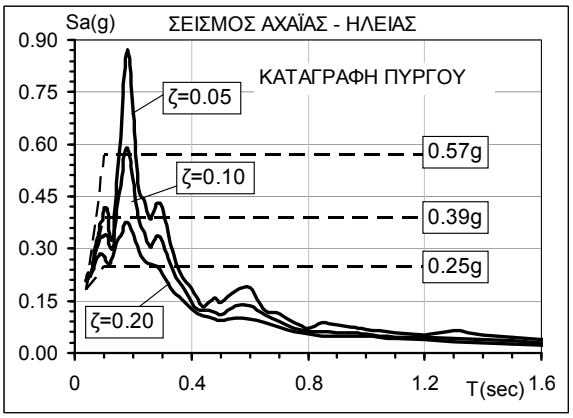


Figure 13. Response spectrums of Achaia – Ilia earthquake from records at Pyrgos (continuous lines) for 5%, 10%, 20% damping. Normalization of response spectrums at 66% of the maximum value (discontinuous lines).

4 CONCLUSIONS

Through present studies, result conclusions about the seismic loads that should be used for the seismic evaluation of monumental masonry buildings. The seismic loads that are suggested by modern seismic codes have usually very high values. This happen even in the cases that in these codes are foreseen provisions for existing masonry buildings (e.g. Eurocode 8, Part 3). The proposed provisions were instituted for new constructed buildings, where can be easily designed to withstand such loads.

- Through the literature review is concluded that existing masonry monumental buildings can develop an "equivalent" damping (both viscous and "hysteretic") about 20%. Also, was found that the actual initial eigenfrequency of these buildings is reduced at 2/3 to 1/2 of calculated analytical one. The resulted reduction of the actual stiffness is at least 50% of the analytically calculated one. These reductions happen close to the bending point of the bilinear elastoplastic diagram that represents the response of the building to horizontal loading and in generally is located before the performance point for the check of the deformations of the piers and spandrels.
- Through the nonlinear analysis of masonry frames, resulted that these frames can resist horizontal loading about the 25%.g of their total mass. This value was verified for the models with frame elements as well as for the models with discrete elements (brick – masonry). For the frames with continuous elements the aforementioned value was higher. Also higher value was found, when the seismic loads were calculated as a percentage of the mass at each node (ACC) in comparison with the other two loadcases (MODE, LOAD).
- From the postpossessing of recorded earthquakes resulted spectral acceleration about 70%g for 5% damping. The normalized value was 50%g. By considering "equivalent" damping 20% (as defined after literature review) the normalized spectral accelerations resulted 25%g that are close to the value of previous conclusion. These values are considered rational and were resulted by the postprocessing of Achaia – Ilia recorded earthquake, where only damages and no collapses of monuments were observed.

REFERENCES

[1] K. Beucke, J. Kelly, Equivalent Linearization for Practical Hysteretic Systems, *Int. Journal of Non-Linear Mechanics*, Vol. 23 (4), pp. 211 – 238, 1985.

[2] M. Calvi, G. Kingsley, G. Magenes, Testing of Unreinforced Masonry Structures for Seismic Assessment", *Earthquake Spectra, Journal of Earthquake Engineering Research Institute*, Vol. 12 (1), 1996.

[3] G. Magenes, M. Calvi, In-Plane Seismic Response of Brick Masonry Walls, *Earthquake Engineering and Structural Dynamics Journal*, Vol. 26 (11), pp. 1091 – 1112, 1997.

[4] M. Tomazevic, P. Weiss, Seismic Behavior of Plain and Reinforced Masonry Buildings, *Journal of Structural Engineering ASCE*, Vol. 120(2), pp. 323 – 338, 1994.

[5] J. Bothara, R. Dhakal, J. Mander, Seismic Performance of an Unreinforced Masonry Building: An Experimental Investigation, Earthquake *Engineering and Structural Dynamics Journal*, Vol. 39(1), pp. 45 – 68, 2010.

[6] N. Ahmad, H. Crowley, R. Pinho, Q. Ali, Simplified Formulae for the Displacement Capacity, Energy Dissipation and Characteristic Vibration Period of Brick Masonry Buildings, *8th Int. Masonry Conference in Dresden*, pp. 1385 – 1394, 2010.

[7] C. Michel, B. Zapico, P. Lestuzzi, F. Molina, F. Weber, Quantification of Fundamental Frequency Drop for Unreinforced Masonry Buildings from Dynamic Tests, *Earthquake Engineering and Structural Dynamics Journal*, Vol. 40(11), pp. 1283 – 1296, 2011.

[8] T. Salonikios, C. Karakostas, V. Lekidis, A. Anthoine, Comparative Inelastic Pushover Analysis of Masonry Frames, *Engineering Structures Journal*, Vol. 25 (12), pp. 1515 – 1523, 2003.

COMPDYN 2013
4th ECCOMAS Thematic Conference on
Computational Methods in Structural Dynamics and Earthquake Engineering
M. Papadrakakis, N.D.Lagaros, V. Plevris (eds.)
Kos Island, Greece, 12–14 June 2013

ANALYTICAL PROCEDURE FOR SEISMIC ASSESSMENT OF MASONRY BUILDINGS WITH HISTORICAL VALUE

Stylianos J. Pardalopoulos[1], Maria Th. Kontari[1], Stavroula J. Pantazopoulou[2,1]

[1] Demokritus University of Thrace
Dept. of Civil Engineering, Xanthi, Greece
spardalo@civil.duth.gr, marikont@civil.duth.gr

[2] University of Cyprus
Dept. of Civil Engineering, Nicosia, Cyprus
pantaz@ucy.ac.cy

Keywords: Masonry buildings, Seismic assessment, Heritage buildings

Abstract. *Today, about 60 years after the proliferation of reinforced concrete in urban construction, structures that are classified as heritage buildings carrying a significant value from the past belong mostly to the class of unreinforced load-bearing masonry construction (URM), dating back to the 19th and early 20th Century. Extending current practices for seismic assessment to these buildings is not straightforward, as, in contrast with conventional frame structures, they are characterised by distributed stiffness and mass and poor diaphragm action. Interventions are often restricted by international treaties for non-invasiveness and reversibility of the intervention - given the practical requirements for the buildings' intended reuse. Poor understanding of the mechanics of masonry and the inherent brittleness of the material further compounds the uncertainties in analytical methods used for assessment and rehabilitation. Simplified procedures that produce dependable results for estimating seismic demand for this class of structures are a primary objective of this paper. In a displacement-based context, requirements are determined from the spectral acceleration and displacement at the end of the constant acceleration range, T_c, in light of the fact that these structures seldom exceed two storeys in height above ground. Displacement demand at the reference point is then distributed through the structure following a simplified estimate of the fundamental mode of vibration; this is calculated in each of the two principal directions of the building in plan, by applying a lateral load distribution analogous to its mass distribution. The intensity of local demand and likelihood of damage are estimated as relative drift ratios, in plan and in height, of the masonry piers of the structure. A case study of two neoclassical buildings damaged in the 1978 earthquake in Thessaloniki are used as a point of reference for illustration of concepts - results are correlated based on their ability to reproduce the patterns of damage observed during post-earthquake reconnaissance evaluations of the building.*

1 INTRODUCTION

Historic and cultural buildings of the 19th and 20th Century are a significant part of the built environment in many cities across Europe. Having a lifetime of more than a hundred years, load-bearing masonry buildings of this class are a living part of the European history and as such, they are protected by international treaties and organizations. Over the several decades of their service life, most of those buildings have suffered from structural damages of different severity level, especially in countries of the Mediterranean basin with high seismicity. Yet, even today they remain in good condition, being operational in many cases (Fig. 1). Due to those buildings' historical importance and their significance as examples of an architectural school of thought, an increasing interest for their rehabilitation has recently emerged, often regulated by international treaties for noninvasiveness and reversibility of the intervention combined with the practical requirements for the buildings' modern day intended reuse.



Figure 1: Heritage buildings of the 20th Century located in the center of Thessaloniki, Greece.

2 PRACTICAL DIFFICULTIES IN COMPUTER MODELLING OF URM STRUCTURES

Eurocode 8-III [1] provides guidance for assessment of existing structures, which rides on analytical estimations of seismic demand that are calculated from a number of analytical alternative representations of the structure. Those representations are ranging from equivalent single degree of freedom systems to detailed three-dimensional modeling of the geometrical details with consideration of the regions of nonlinearity; the seismic hazard may also be represented simply, through an acceleration spectrum or through an acceleration time history which requires step by step integration through time; the spectral representation of the seismic hazard lends itself to modal superposition, provided that the structural model is linearly elastic, or to "performance-point evaluation" if a "static" pushover curve may be independently established for the structural system. These two general options regarding choices of representation of the structural and the loading degrees of complexity, when combined in all possible ways, yield an array of several different possible alternative methods that may be used for demand estimation, all more or less acceptable in practice. This variety rides on the assumptions that (a) where needed, available computer software supports nonlinear modeling of the individual member components and (b) no premature, brittle modes of failure that would macroscopically cause a post-peak softening branch identifiable trough a negative or zero pivot in the stiffness matrix of a structure would occur over the range of calculated seismic response.

The above assessment code builds on established computer modeling technologies for lumped systems, mostly frames, for which most commercial codes enable modeling of lumped or spread nonlinearity and detailed time history calculations. And because it calls on concepts that are general in principle, it is considered applicable and easily extendable to all types of structures, including URM buildings. However, when attempting to practically apply the above ideas to the simplest of these structures, a number of stumbling blocks may be encountered. For one, the state of the art in structural software today does not address the requirement (b) above: URM is brittle and thus, maintaining a positive definite stiffness of pier members after cracking is not possible particularly in tension-controlled modes of failure. Furthermore, most of the available commercial software packages today do not offer the option for 3-D analysis using nonlinear shell elements that are needed to model masonry wall behavior. So, accounting for nonlinearity in this class of structures is restricted to either one-dimensional elements (beams, trusses, springs and gap elements) that can be used to modeling secondary elements (such as timber beams in diaphragms and roof trusses) or points of contact (such as unilateral contact at the point of embedment of a timber beam in a masonry wall using gap elements, contact between foundation masonry with the surrounding soil using springs with asymmetric properties, etc.). Last, most commercial software packages today do not offer complete options for dynamic response estimations, except for combinations of modal response maxima (which, being based on the principle of superposition, precludes the option for even considering secondary sources of nonlinearity). An added difficulty emanates from the distributed character of URM structures. As the number of modes generated is proportional to the total number of degrees of freedom in the structure, there is no clearly prevelant "first" or "fundamental" mode. The mode with the highest period is oftentimes associated with vibration of a single secondary component (such as a diaphragm timber beam), with insignificant ratio of mobilized mass. Previous studies by the authors and co-workers [2, 3] have illustrated that in some cases with flexible diaphragms, several hundreds of modes need to be included in the calculation just so as to mobilize 70% of the total mass in lateral translation. This numerical circumstance in practice nullifies the so called equivalent single degree of freedom representation of the structure, which, combined with the pushover analysis methods, forms the backbone of modern code methods for seismic assessment and design (see EC8-I, Appendix B [4]).

Special – research-oriented software may be used instead to conduct detailed time history analysis of URM structures (e.g. ABAQUS, DIANA, etc.); the effort required is disproportionately higher than the degree of confidence in the actual values of the input parameters concerning both the materials and the description of the seismic hazard, violating a fundamental principle of modern simulation. Therefore an urgent research need is facing the earthquake engineering community, regarding formulation of a simple framework for seismic assessment of URM structures that could also be used to guide seismic retrofit. This objective is the motivating interest in the present paper: a seismic assessment method that produces results of equivalent accuracy to detailed time-history dynamic analysis-based assessment procedures, yet requires significantly shorter computational time, is presented, specifically tailored to the morphology and particularities of older URM structures. Here, the seismic hazard is specified in its spectral format (total acceleration and relative displacement) so as to render the methodology compatible to design code formats. To deal with the uncertainty associated with a dependable estimation of the structural period, all structures up to two storey heights (the most common sample of the URM heritage building population in southern Europe) are evaluated at the end of the constant acceleration range of the spectral plateau. The principles of generalized single degree of freedom representation of complex distributed systems are used to convert the structure to an ESDOF system consistent with the established code procedures – the

fundamental response shape is almost a heuristic approximation of the fundamental translational mode of vibration, used as a tool for a global to local transformation of displacement demands thereby identifying locations of anticipated damage. The behavior factor q is obtained from the peak ratio of demand to supply in terms of out-of-plane moments of the free standing walls of the structure and is subsequently used to modify spectral displacement estimates through pertinent q-μ-T relationships.

Application of the proposed method provides information about the condition assessment of the structure and the anticipated damage localization at the state of the building's maximum seismic response, based on the translational modal characteristics of the building. As illustrated in the presented example analyses of two neoclassical buildings of the late 19th Century the proposed method can lead to equally dependable estimates as the results of complicated and time-consuming dynamic time-history analysis.

3 PROCEDURE FOR SEISMIC ASSESSMENT OF HISTORICAL BUILDINGS BASED ON THEIR FUNDAMENTAL MODE SHAPE

The significance of the fundamental response shape as a diagnostic tool for seismic assessment of existing structures has been illustrated in recent studies in the field of seismic assessment [5 - 7]. The fundamental translational shape is a compound property that conveys information about the tendency for localization of deformation demand in the structure. Therefore, the fundamental shape of a structure can be used to identify likely points of concentration of anticipated damage through the distribution of relative drift, while at the same time identifying lack of stiffness and the relative significance of possible mass or stiffness discontinuities (Fig. 2).

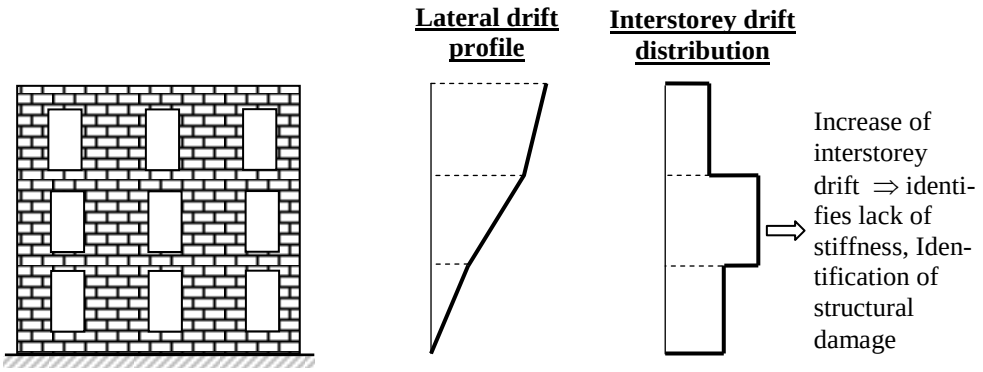


Figure 2: Use of the building's deformed shape in the identification of developed structural damage points.

Furthermore, the fundamental response shape of any structure with established diaphragm action at the floor levels has been proven to correlate very well with the structure's displacement profile at the state of maximum roof displacement [5, 8]. This conclusion was derived from the results of parametric dynamic analyses of several R.C. building models, both simplified and detailed, accounting for different types of geometric configuration that were subjected to ground accelerations of different characteristics. It was shown that the deformed shape of any multi-storey structure in the presence of diaphragms resembles the fundamental mode shape (i.e. the mode shape that mobilizes the greatest percentage of its total mass) at the point of maximum roof displacement, especially when the period of a building's fundamental mode is in the range of the predominant period of the seismic vibration. This conclusion was further extended to nonlinear systems, where the fundamental shape refers to the eigen-mode associated with the secant stiffness matrix at the instant of peak response.

Given the fact that some floor types used in historical or heritage masonry buildings of the 19th and 20th Century provide adequate diaphragmatic response, the fundamental mode shape of those buildings has also been used to identify potential damage locations under earthquake; recent studies (Karantoni et al. [3], Pardalopoulos and Pantazopoulou [2], Kontari [9]) have tested application of the same concept in URM buildings with flexible diaphragms, with good success. To do so, a three-step procedure for seismic assessment of the URM historical buildings is presented, which produces results of equal accuracy as compared to complex time-history dynamic analyses. The three steps of the proposed procedure are:

- *Determination of the fundamental translational mode of the URM building*: The determination of the fundamental translational mode in each of the two principal plan directions of the examined building can be accomplished by subjecting a three-dimensional finite element model of the building to a notional gravitational field in the corresponding direction of lateral translation (i.e. along the longitudinal and transverse directions of the plan geometry). In light of the fact that gravitational forces are proportional to the mass of the structure whereas the restoring forces in free vibration are equilibrating these mass-proportional inertia forces, the deflected shape of the structure obtained from this solution is thought to be the closest approximation to the translational mode of vibration since the associated natural frequency would result from the ratio of the work-equivalent inertia force and restoring force [10]. This procedure is more suitable for the determination of the fundamental translational modes of load-bearing masonry structures that are simulated using three-dimensional finite element models of spread mass area elements rather than the execution of modal analysis, as in most cases modal analyses of this type of finite element models leads to a large number of very similar translational modes with closely spaced periods, each having a small participation factor, leading to the requirement of including several modes in the calculation in order to mobilize the structural mass. On the contrary, the building's fundamental translational modes which are determined with the use of a notional gravitational field in the direction of lateral translation correspond to a mass participation factor in the direction of action, in the range of 90% or more [2]. Taking into consideration the brittle response of URM, which cannot secure a positive definite stiffness of pier members after cracking, the examined building can be simulated as a linear finite element model, with localized points of non-linear response (i.e. at points of contact or in modeling secondary elements).
- *Calculation of the seismic response of the building at the state of its maximum seismic response*: Based on the postulated proportionality between the fundamental translational mode of a structure and the corresponding deformed shape at the state of its maximum seismic response [5, 8], the building's maximum seismic response can be determined using the spectrum seismic demand that is applicable at the site [4]. For this reason, the amplification factor f_i is introduced:

$$f_i = S_{d,i}(T) / U_{Roof,i} \quad (1)$$

where, $S_{d,i}(T)$ is the seismic demand in plan direction i (x, or y) in terms of spectral relative displacement and $U_{Roof,i}$ is the horizontal translation at the roof level of the building in the corresponding direction, i, as calculated in the previous step of the proposed procedure. According to this procedure, maximum seismic response of the examined URM historical structure in terms of developed deformations along its structural system can be determined by multiplying the building's fundamental translational modes with the amplification factor f_i. Furthermore, f_i allows the determination of the developed forces/stresses along the building's structural system at the same time segment of the earthquake excitation; the developed forces/stresses at the state of the building's maximum seismic response are equal to the corresponding value of

the building's fundamental mode, multiplied by f_i. The building's fundamental period, T, by which $S_{d,i}(T)$ can be calculated according to EC8-I [4], as:

$$T = \mathrm{C_t} \cdot H^{3/4} \tag{2.a}$$

In Eq. (2), H is the total building height, in m, measured from the level of foundation or the level of rigid basement and C_t a constant given by the relationship:

$$C_t = 0,075 / \sqrt{A_c} \leq 0,05 \tag{2.b}$$

The upper level in Eq. (2.b) refers to URM buildings with flexible diaphragms (Karantoni and Pantazopoulou [3]). A_c depends on the total area of load-bearing walls in the ground floor of the building (in m^2) and is calculated from:

$$A_c = \Sigma\left[A_i \cdot \left(0,2 + \left(l_{wi} / H\right)\right)^2 \right] \tag{2.c}$$

A_i is the active cross section of the i-th wall in the direction of seismic action considered in m^2, and l_{wi} is the length of the i-th wall in the direction of seismic action, in m.

- *Determination of local seismic demand and application of acceptance criteria*: Bearing capacity in URM historical structures can be best identified by the amount of deformation occurring in the various components of the structures. The use of deformation demand for the purpose of seismic assessment of structures is more meaningful than force demand estimation – based on the equal displacement rule, elastic displacement demands are close to the inelastic ones, whereas forces in the nonlinear analysis are vastly different from the elastic values. Performance criteria are also specified in terms of relative drift ratio – the drift capacity may refer either to URM piers deforming laterally so that drift refers to the relative deviation of the pier ends from vertical, or alternatively, it may refer to URM facades deviating from their horizontal initial orientation. These parameters, are referred to as relative drift ratios in height and in plan of the examined building, θ_{height} and θ_{plan} respectively, defined in case of θ_{height} as the horizontal displacement difference that occurs between the top and the bottom of each of the vertical structural elements (i.e. piers and walls) at each storey of the building, divided by their vertical length, whereas θ_{plan} is defined as the relative lateral displacement of any two points of the plan perimeter divided by their horizontal distance. In this regard, the most meaningful pair of points to be used at the crest of the building (or at the floor levels) is the point of peak outwards deflection in the wall orthogonal to the earthquake action, and the point at the corners where transverse walls are intersected by walls parallel to the earthquake.

Deformation measures calculated above can be used to determine the performance level (characterization of damage level) attained by the structure in response to the design earthquake. Cracking rotations (drift ratios) in masonry elements are in the order of 0.15%, but the available ductility capacity varies depending on the type and reinforcement (e.g. timber lacing) of the URM walls. In well-constructed masonry a drift capacity of 0.5% (drift ductility of 3.5) may be attainable, and timber-laced or adobe masonries even larger values may be well depended upon. But plain unreinforced masonry without timber lacing is unlikely to be able to support rotation or drift ductilities in excess of 2 (a drift ratio of 0.3%).

4 EXAMPLE ANALYSES OF TWO NEOCLASSICAL BUILDINGS OF THE 18TH CENTURY

To investigate the accuracy of the proposed analysis procedure as compared to the corresponding results obtained from detailed time-history dynamic analysis, the proposed analysis method has been performed in three-dimensional finite element models of two neoclassical

building located in the center of the city of Thessaloniki, Greece. The buildings were constructed in the end of the 19th Century, according to the designs of Ernst Ziller, in order to house at that time the Hellenic high school and the Hellenic consulate of Thessaloniki, respectively. Both buildings operated continuously for more than 80 years until June of 1978, when both buildings suffered damages by a strong earthquake of 6.5 M_w that struck the city of Thessaloniki, with its epicenter located about 40 km North-East of Thessaloniki, in the Volvi lake region.

4.1 Description of the examined buildings

The *Hellenic High School* of Thessaloniki is a two-storey building with a basement and a timber-framed roof (Fig. 3(a)), constructed in 1893 according to the designs of Ernst Ziller, as those modified of the architects Kabanakis and Kokkinakis; the project was financed by Andreas Sygros and the Hellenic community of Thessaloniki [11].

The building has a 20.83m x 16.05m plan, symmetrical with respect to a main corridor that is spanning from the northern side of the building to the southern, whereas the external building height, from ground level to the roof top, is 14.20m. The first storey comprises six rooms, symmetrically located on both sides of the storey's corridor (Fig.3(c)). The second storey was originally constructed to have four halls, one big hall on each side of the corridor spanning from the front view of the building (north view) to the south and two smaller ones in the southern part of the plan. Over the years, the two big halls were divided, the eastern one with the addition of a 0.15m thick brick wall and the western one with the addition of a wooden panel (Fig. 3(d)). The basement comprises five rooms that were used as storage rooms and sanitary facilities, after the addition of miscellaneous infill brick walls (Fig. 3(b)). Floors were connected with a wooden stair in the southern part of the main corridor.

The walls of the basement are made of stone, having a thickness equal to 0.75m in the perimeter of the building and 0.65m in the inner plan. Walls of the first and the second storey were built of solid brick. Perimeter walls have 0.50m width, whereas internal walls were 0.40m thick. Floors of the first and the second storey were made of double T iron beams having a 60mm x 180mm cross section, spaced at 0.70m along the small sides of the rooms and the corridors (i.e. having an E-W orientation over the building's corridors and a N-S orientation over the building's halls), whereas brick-arches spanning in the transverse direction between successive iron beams were encased between the upper and lower flanges of the double T beams. The total thickness of building's floors (including the finishing) is 0.33m at the location of the iron beams and 0.25m at the highest point of the arches. The last storey is covered by a roof made of timber trusses spanning in the east to west direction of the building.

The building had operated continuously as a school from its construction until the June of 1978, when it suffered moderate damages mainly in the area of connection of the roof with the 2nd storey walls and operated again as a school in 1985, after the restoration of the damages.

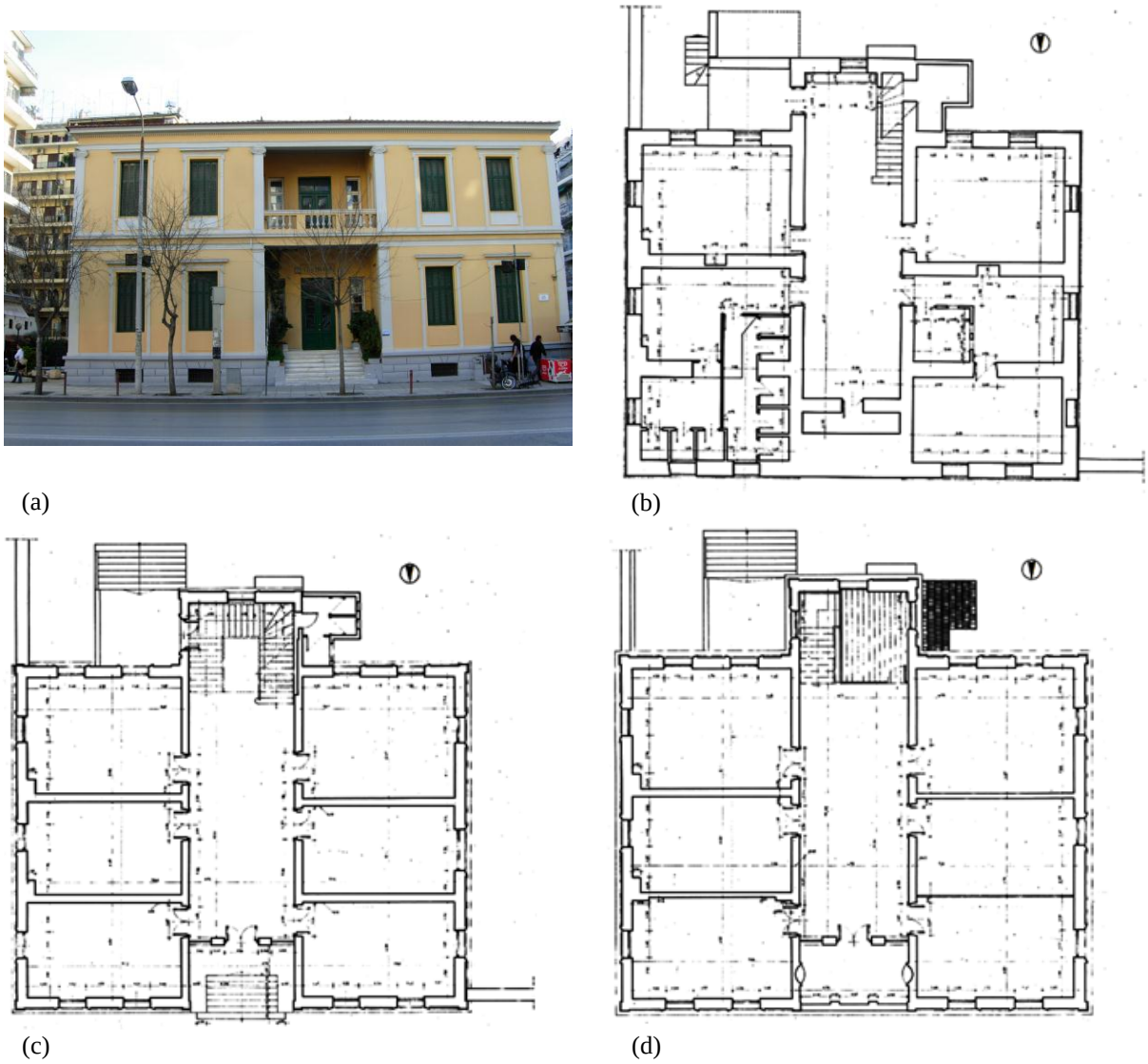


Figure 3: The *Hellenic High School* of Thessaloniki: (a) North view, (b – d) plan views of the building's basement, 1st and 2nd storey, respectively [12].

The *Hellenic Consulate* of Thessaloniki is also a two-storey building with a basement and a roof (Fig. 4(a)), constructed in 1898 in the center of Thessaloniki. The building was also made according with the designs of Ernst Ziller and again, it was financed by Andreas Sygros [12, 13], to house the consulate of Greece during the Ottoman occupation of the city of Thessaloniki, whereas after the liberation of Thessaloniki in 1912 the building had operated as a primary school until 1978, when it suffered heavy damages from the earthquake.

The building has a 15.20m x 19.00m orthogonal plan, whereas the external building height, including the roof, is 14.45m. The first storey (Fig. 4(c)) is of total area of 288.80 m^2 and comprises five rooms, located in both sides of the storey's corridor. Communication between the first storey and the basement is achieved via a stairwell located at the west end of the 1st storey's corridor, whereas a second stairwell located at the north-eastern corner of the building leads to the second storey of the building. The second storey of the building (Fig. 4(d)) has six rooms of various sizes, located on both sides of the storey's corridor. The basement comprises four rooms at the north side of the main corridor that were used as storage rooms and a large room along the building's southern side (Fig. 4b)).

The walls of the basement are made of stone, having a thickness equal to 0.65m in the perimeter of the building and 0.55m in the inner plan. Walls of the first and the second storey were built of solid brick. Perimeter walls are 0.55m thick, whereas internal walls' thickness varies from 0.10m to 0.45m. Floors of the first and the second storey were made of double T iron beams, whereas brick-arches spanning in the transverse direction between successive iron beams were encased between the upper and lower flanges of the double T beams. The last storey is covered by a roof made of timber trusses spanning in the north to south direction of the building.

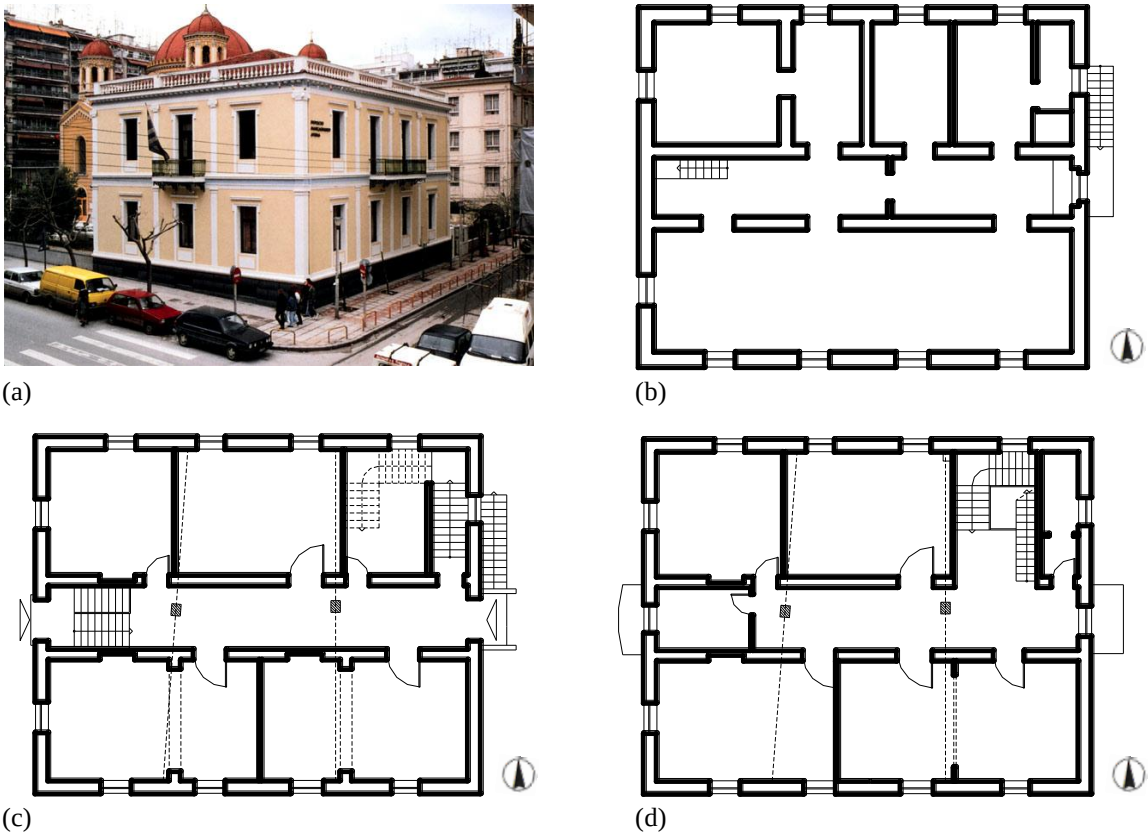


Figure 4: The *Hellenic High School* of Thessaloniki: (a) North-West corner of the building, (b – d) plan views of the building's basement, 1st and 2nd storey, respectively.

4.2 Modeling and analyses of the two examined buildings

In order to investigate the seismic response of the two buildings during the 1978 earthquake, three-dimensional finite models were produced (Fig. 5) using a finite element analysis program [13]. In all building models walls were idealized using four-node shell elements, capable of supporting forces and moments (6 d.o.f. per node), whereas floors were simulated using linear elements for the iron beams and shell elements to represent the brick arches spanning between steel beams. Linear elements were used at the roof level, accounting for the horizontal timber beams of the roof trusses. In all models, the response of the shell and the linear elements was considered elastic. The modulus of elasticity of stone and bricks was considered 1000 times the value of the corresponding compressive strength, f_k; this variable was taken equal to the following: (a) in the case of the *Hellenic High School* for stone f_k = 5.5 MPa, for solid bricks f_k = 4.0 MPa and for voided bricks f_k = 1.5 MPa, whereas in the case (b) of the *Hellenic Consulate*, for stone f_k = 6.3 MPa and for solid bricks f_k = 5.2 MPa. In the case of

frame (iron and timber) elements, the modulus of elasticity was taken equal to 150 GPa for the iron beams, 10 GPa for timber in the longitudinal direction of the beams and 1GPa in the other two sectional directions. In all cases self weight of the building was calculated according to the material density; for stone 28.5 kN/m^3, for solid bricks 18 kN/m^3 and for voided bricks 14kN/m^3. A roof weight equal to 1.5 kN/m^2 was assumed, uniformly distributed along the linear elements of the roof trusses according to their tributary area. Service loads were considered equal to 2.50 kN/m^2 for the roof and 3.50 kN/m^2 for the floors of both buildings.

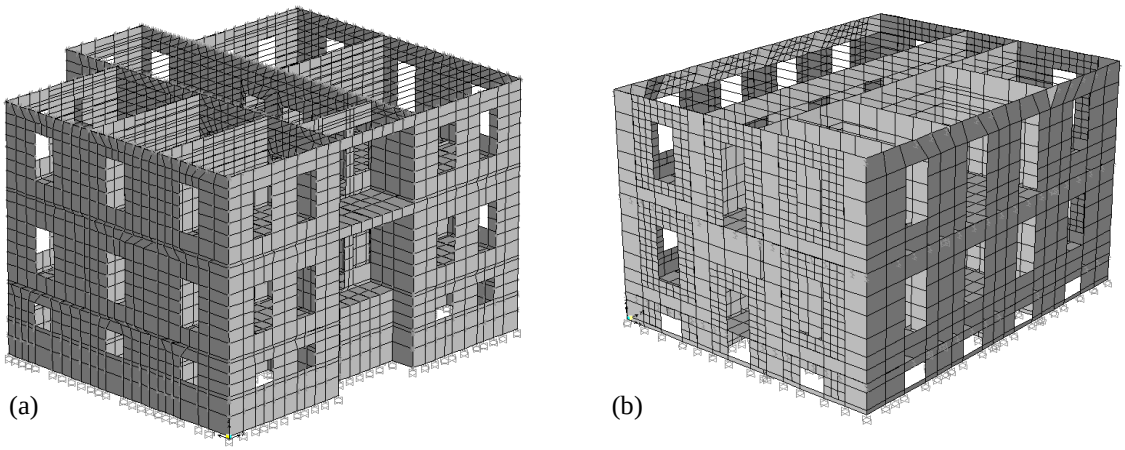


Figure 5: Three-dimensional finite element models of (a) the *Hellenic High School* and (b) the *Hellenic Consulate* of Thessaloniki.

For each building two building models were produced, referred to as *A* and *B*, in order to investigate the influence of modeling assumptions for the various mechanisms that develop in the structural system of the 19th and 20th Century load-bearing URM piers owing to the construction practices and the influence these have on the overall seismic response of the buildings. In both cases parameters of investigation were the developed mechanisms at the floors and the roof. In finite element models *A* the linear elements that were used to simulate the floors' iron beams were considered fixed at their ends to the shell elements accounting for the constraint provided by the infill brick arches. Fixed connections were also considered at the ends of timber beams of the roof trusses to the wall elements. In finite element models *B*, gap elements were added between the nodes of the shell elements that represented the brick arches and the corresponding nodes of the iron beams, replacing the fixity condition for the same contact detail in models *A* (Fig. 6(a)). Thus, gap elements were intended to model the separation between the brick arches and the iron beams when in tension whereas they were considered rigid in compression (perfect contact). Also added in models *B* were springs between the nodes of the wall elements and the timber beams over the wall, which were meant to account for friction between the wall and the timber beams. Spring-response was described by a multilinear force-displacement relationship (Fig. 6(b)) that was calculated according with the development capacity over the beams' contact surfaces when accounting for friction with the building walls.

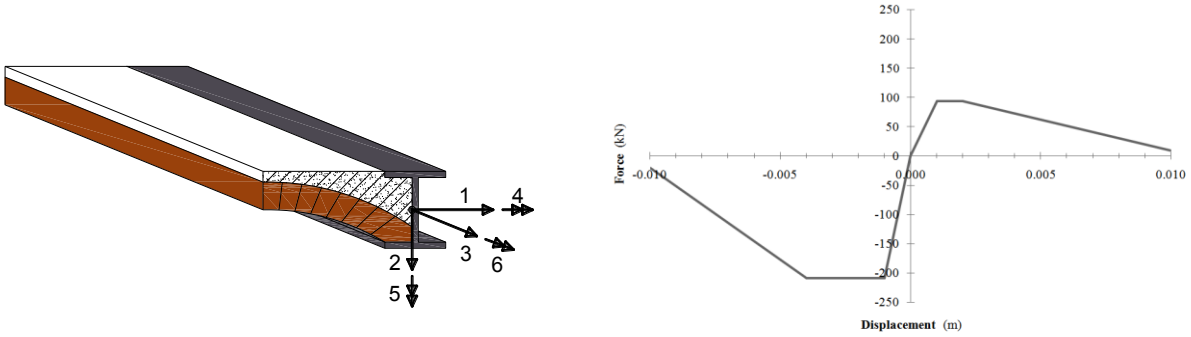


Figure 6: (a) Simulation of the connection of iron beams and infill brick arches at the buildings' floors by the addition of gap elements functioning in degree of freedom 1 (b) Force-displacement relationship used in the friction springs that connect the timber beams with the walls of the second storey.

In order to investigate the accuracy of the simulation for the two buildings, all finite element models were subjected to time-history dynamic analyses based on the 1978 Thessaloniki earthquake ground accelerations that were recorded at locations near the buildings site [14]. Figure 7 illustrates the E-W (blue color) and N-S (red color) components of the recorded ground accelerations, as well as the corresponding elastic response spectra calculated for the case of 5% damping. Masses considered in the time-history analyses were automatically calculated by the program, by multiplying each element (shell or linear) volume by their respective density.

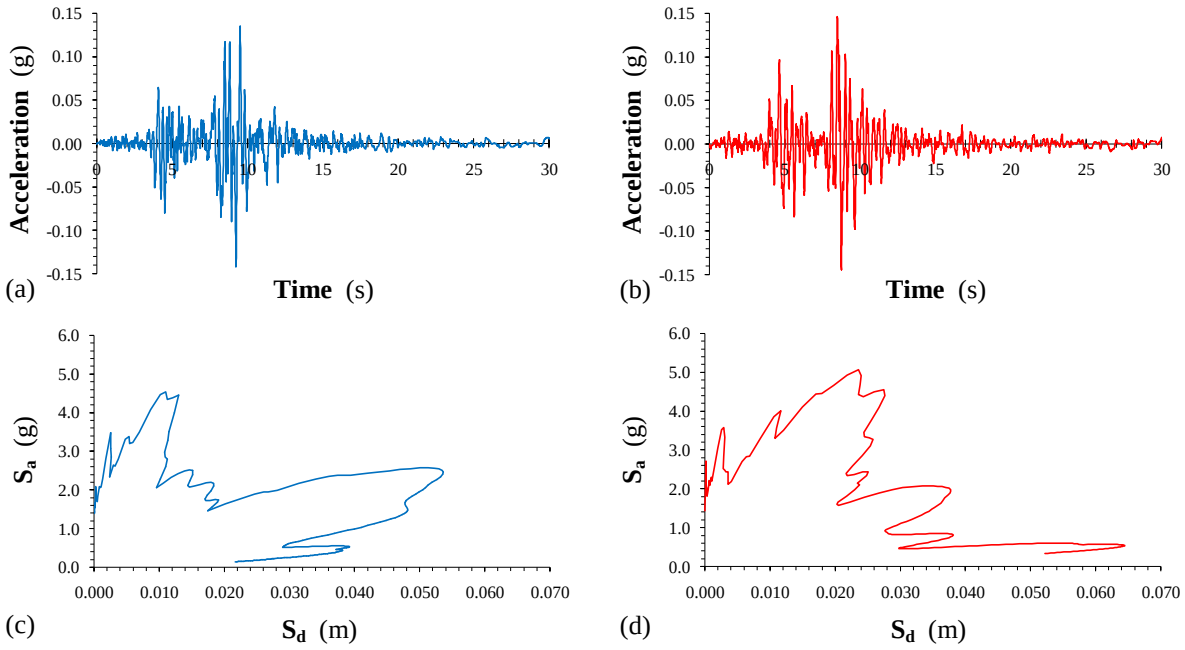


Figure 7: 1978 Thessaloniki earthquake: (a, b) Recorded ground accelerations in E-W (blue color) and N-S (red color) directions at the center of Thessaloniki, Greece, (c, d) Elastic response spectra of the corresponding earthquake components calculated for 5% damping (ADRS format).

From the examination of the dynamic response of models' *A* and *B* of each building interesting conclusions have derived concerning the significance of simulation of the special mechanisms that develop in the 19th and 20th Century load-bearing masonry buildings due to the construction practices followed at that era. From the analyses results it is evident that the simulation of the separation between the brick arches and the iron beams when tension stress-

es develop in the floor diaphragms (with the aid of gap elements), results in significant reduction in the developed stresses and deformations throughout the buildings' structural system. Figure 8 illustrates the shear reactions acting on each one of the two principal plan directions of the *Hellenic High School* (i.e. in the E-W and the N-S directions) during the earthquake excitation. As illustrated in Fig. 8, in the time range of the building's maximum seismic response the base shear in model *B* are reduced by 22% in E-W and by 18% in N-S direction, respectively, as compared to the corresponding values developed in model *A* for the same time range. Also reduced in building model *B* were the developed horizontal displacements along the buildings' height at the time of peak response by an average of 25% and 21% in E-W and N-S directions, as compared with the same measures for model *A* (Fig. 9). Similar reductions in the developed base shear and horizontal displacements at the time of building's response were also seen between models A and B of the *Hellenic Consulate*.

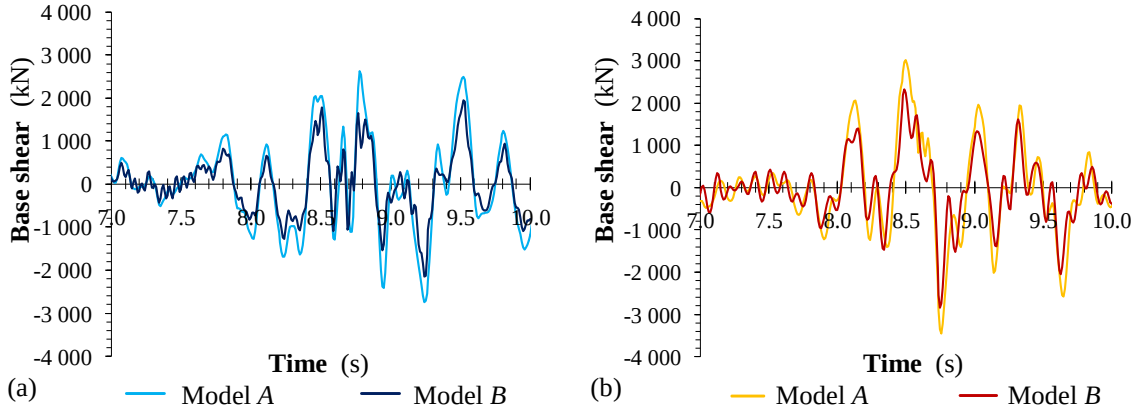


Figure 8: Time-history of base shear of models *A* and *B* of the *Hellenic High School* (a) in E-W and (b) in N-S directions.

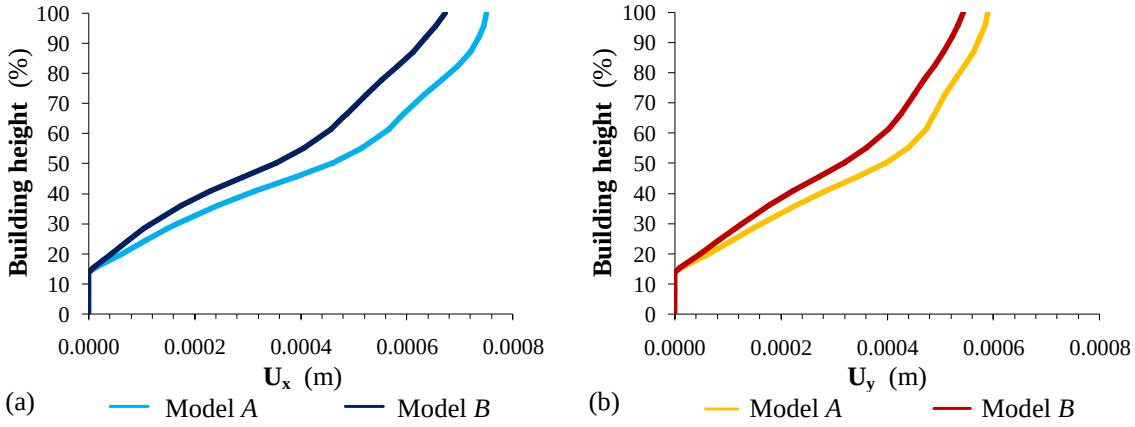


Figure 9: Deformed shape of the North-East corner axis of models *A* and *B* for the *Hellenic High School* at the time of peak dynamic response (a) in E-W and (b) in N-S directions.

Also tested using models *B* of the two neoclassical buildings was the accuracy of the results that derive from the application of the proposed analytical method for seismic assessment of historical buildings, as compared with the corresponding results at the time of peak response obtained from time-history dynamic analysis. Figure 10 plots deformed shapes obtained for both buildings by subjecting each structure to a uniform uniform horizontal acceleration (i.e. a static pushover procedure where inertia forces proportional to the self-weight is applied pointwise throughout the nodes of the F.E. mesh). Also shown, for the sake of com-

parison, are the corresponding shapes at peak building top displacement response, obtained from dynamic time history analyses as shown in Fig. 9. Clearly, correlation of the results between the two procedures is excellent. Also evident is the proportionality of the results that derive from the two procedures in terms of the developed stress patterns along the buildings' structural systems, which is presented in the case of the north view of the *Hellenic Consulate* in Fig. 11.

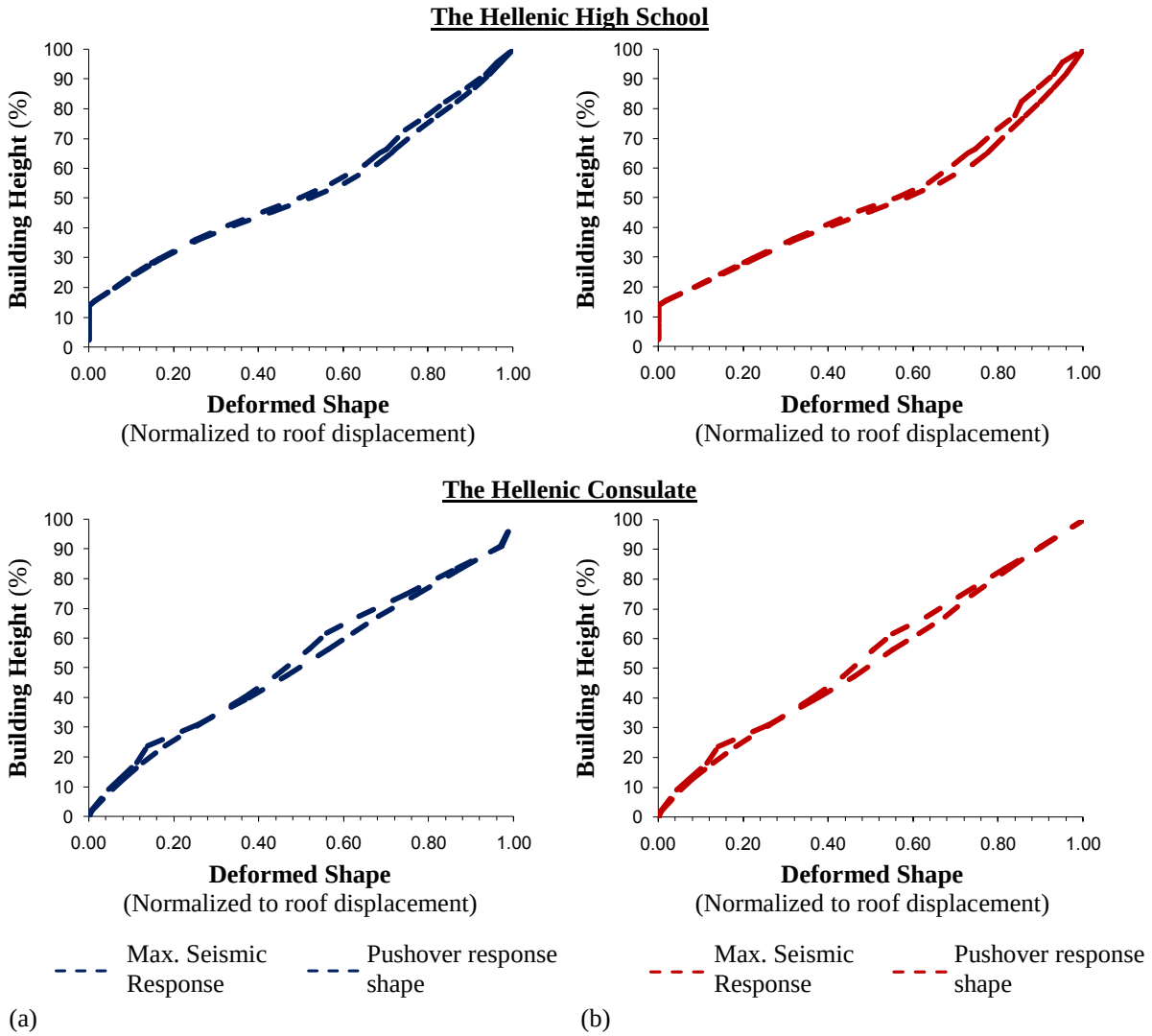


Figure 10: Comparison between the deformed shape of the North-East corner axis of the two buildings at the state of peak seismic response and their estimated translational mode: (a) E-W direction, (b) N-S direction.

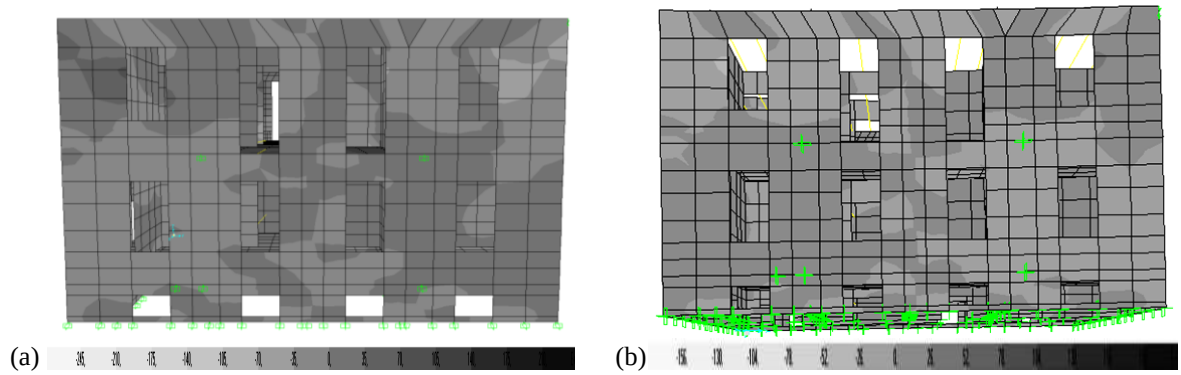


Figure 11: Developed patterns of shear stresses on the north view of the *Hellenic Consulate* (a) at the time of the building's maximum seismic response according to time-history dynamic analysis and (b) according to static analysis of the building with lateral loading proportional to the building's mass distribution.

Seismic assessment of the examined buildings was performed by the examination of the values of θ_{height} and θ_{plan} at each storey of the buildings. Presenting the application of the proposed assessment procedure for the case of the *Hellenic High School*, the building's spectral relative displacements in E-W and N-S plan directions, $S_{d,E\text{-}W}$ and $S_{d,N\text{-}S}$ respectively, were calculated from the elastic response spectra of the corresponding earthquake components (Fig. 7c – 7d) according to the periods of the fundamental translational modes of the building in the corresponding directions ($T_{E\text{-}W}$ = 0.303 sec, $T_{N\text{-}S}$ = 0.262 sec; Eq. 2) as: $S_{d,E\text{-}W}$ = 6.56 mm and $S_{d,N\text{-}S}$ = 5.42 mm. Note that $S_{d,E\text{-}W}$ and $S_{d,N\text{-}S}$, as calculated according to the proposed procedure, correlate very well with the average value of the horizontal roof displacements at the corresponding plan directions at the time of the building's maximum seismic response ($U_{Roof,E\text{-}W}$ = 6.73 mm and $U_{Roof,N\text{-}S}$ = 5.54 mm), as those were calculated from time-history dynamic analysis. Amplification factors in E-W and N-S plan directions, $f_{E\text{-}W}$ and $f_{N\text{-}S}$ respectively, were calculated according to $S_{d,E\text{-}W}$, $S_{d,N\text{-}S}$ and the average values of roof displacement in the corresponding directions derived from static analysis of the building with lateral loading proportional to its mass distribution ($U_{Roof,E\text{-}W}$ = 18.34 mm and $U_{Roof,N\text{-}S}$ = 26.65 mm, Figs. 12 & 13), as: $f_{E\text{-}W}$ = 6.56 / 18.34 $\Rightarrow$ $f_{E\text{-}W}$ = 0.36 and $f_{N\text{-}S}$ = 5.54 / 26.65 $\Rightarrow$ $f_{N\text{-}S}$ = 0.20.

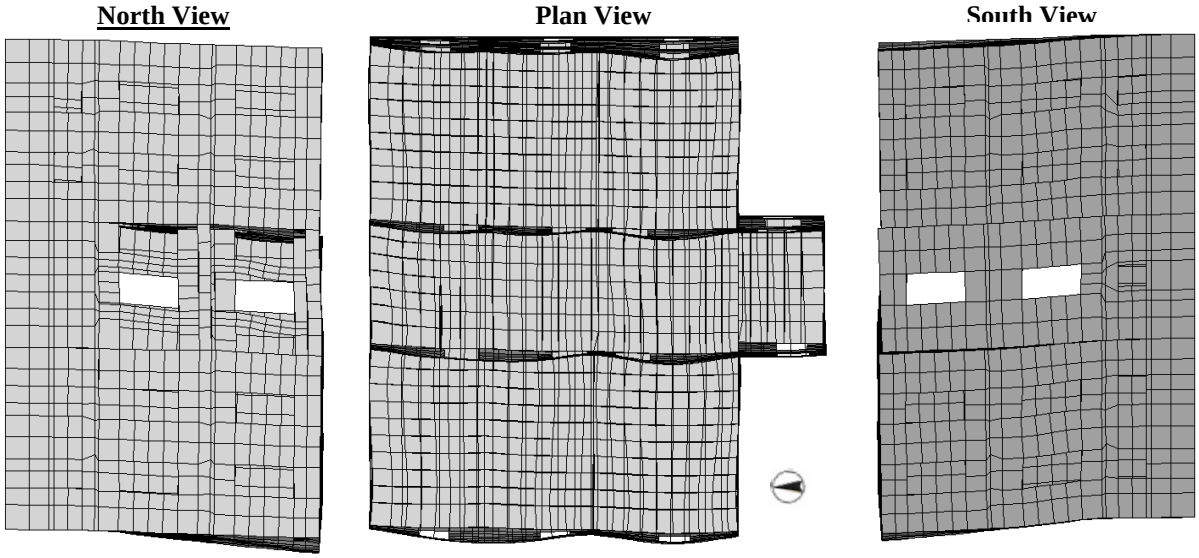


Figure 13: Deformed shape of the *Hellenic High School* calculated from static analysis with lateral loading proportional to the building's mass distribution in E-W direction.

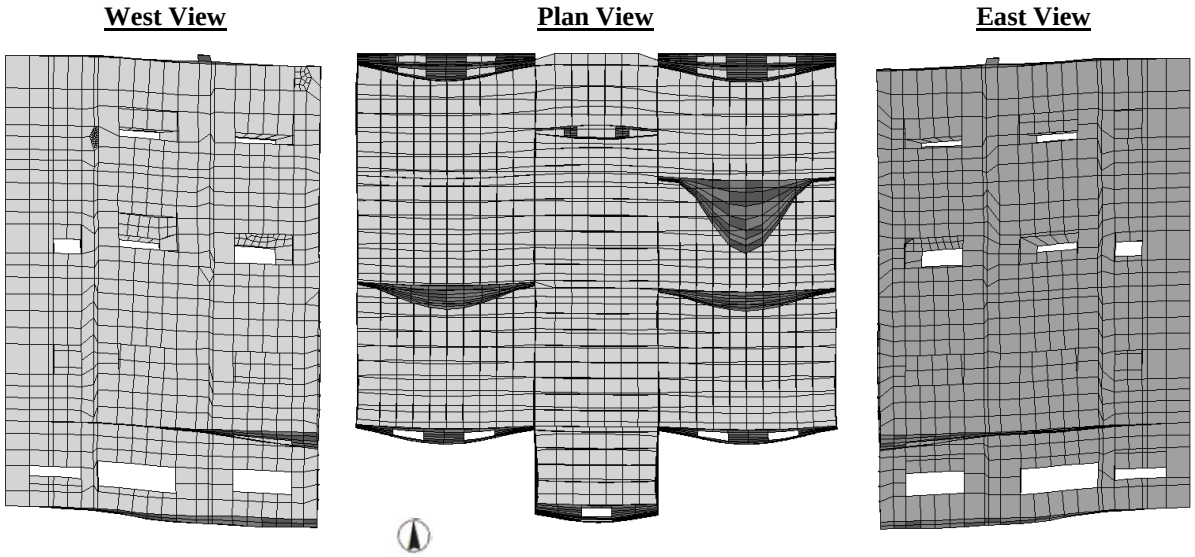
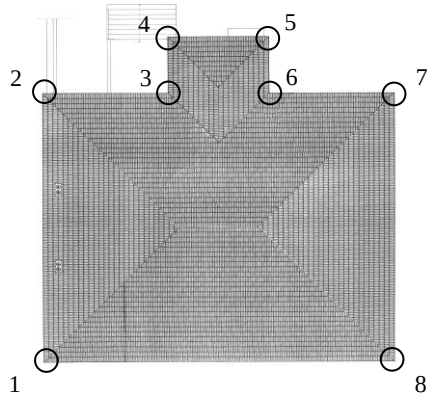


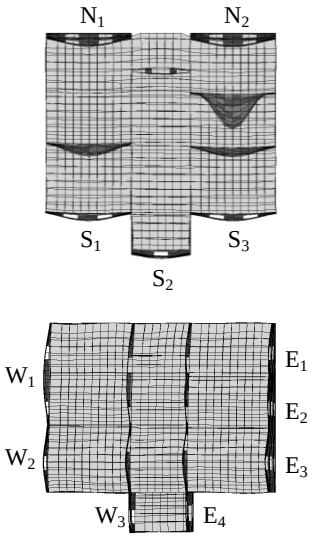
Figure 12: Deformed shape of the *Hellenic High School* calculated from static analysis with lateral loading proportional to the building's mass distribution in N-S direction.

Relative drift ratios in height and in plan, θ_{height} and θ_{plan} respectively, were calculated from the horizontal displacements of the structural system in E-W and N-S directions that derived from static analyses (Figs. 11 & 12) after their multiplication with the corresponding amplification factors. Table 1 presents the values of θ_{height} that were calculated at the edges of the first and the second storey, in both E-W and N-S plan directions. From the values of θ_{height} it is evident that during the 1978 Thessaloniki earthquake the walls of the first storey of the building were subjected to larger deformations than the walls of the second storey. Nevertheless, the developed deformations were not capable to cause severe damages to the building (max. value equals to drift ductility 1.2). Similar conclusions have derived from the evaluation of θ_{plan} in all storeys of the building. The only exception was the case of the infill wall that was added in the second storey some years before the 1978 earthquake in order to divide the big room at the N-E corner of the building (Fig. 12). At the time of the building's maximum seismic response during the earthquake this wall was estimated that had developed θ_{plan} = 0.817%, a value equal to drift ductility 5.45 and as such it was anticipated to develop savvier damage, a conclusion that was confirmed by the examination of the actual seismic response of the building.



	θ_{height} - 1st Storey (%)		θ_{height} – 2nd Storey (%)	
Edge	E-W	N-S	E-W	N-S
1	0.07	0.06	0.06	0.03
2	0.15	0.06	0.08	0.03
3	0.15	0.07	0.07	0.03
4	0.12	0.06	0.08	0.03
5	0.12	0.07	0.08	0.03
6	0.17	0.06	0.08	0.03
7	0.17	0.06	0.09	0.03
8	0.07	0.06	0.06	0.03

Table 1: Values of θ_{height} at the building edges of the first and the second storey, calculated in E-W and N-S directions.



View	Point	θ_{plan} (%)
North	N_1	0.18
	N_2	0.18
South	S_1	0.17
	S_2	0.14
	S_3	0.17
East	E_1	0.23
	E_2	0.09
	E_3	0.10
	E_4	0.10
West	W_1	0.23
	W_2	0.22
	W_3	0.10

Table 2: Values of θ_{plan} of the facades of the second storey of the building at the time of its maximum seismic response.

5 CONCLUSIONS

Seismic assessment of load-bearing buildings of the 19th and 20th Century is an emerging interest for engineering community, as this class of buildings are a living part of the European modern history. Current assessment procedures, often regulated by international treaties for non-invasiveness and reversibility of the intervention combined with the practical requirements for the buildings' modern day intended reuse, are based on a vast variety of analytical methods, ranging from the use of simplified mechanical models to the use of sophisticated finite element analyses programs combined with powerful computational means. Yet, the obtained results are often of limited reliability when these assessment procedures, which are a modification of design procedures used in frame structures with ductile behavior, are applied on URM brittle piers. Therefore, an urgent research need is facing the earthquake engineering community, regarding formulation of a simple framework for seismic assessment of URM structures that could also be used to guide seismic retrofit.

In this paper an analytical method for seismic assessment of URM historical buildings, which produces results of equivalent accuracy to detailed time-history dynamic analysis based assessment procedures, yet requires significantly shorter computational time is presented. According to the proposed method, seismic demand is estimated in terms of displacement demand at the building's roof, based on the principles of generalized single degree of freedom representation of complex distributed systems, consistent with the established code procedures. Then the displacement demand is distributed through the structure following a simplified estimate of the fundamental mode of vibration in each of the two principal directions of the building in plan.

REFERENCES

[1] European Committee for Standardization (CEN), *EN 1998-3 Eurocode 8: Design of Structures for Earthquake Resistance – Part 3: Assessment and Retrofitting of Buildings*, Brussels, 2005.

[2] S. J. Pardalopoulos, S. J. Pantazopoulou, *Seismic Assessment of 19th Century Heritage building Through Simulation*, COMPDYN 2011 – Computational Methods in Structural Dynamics and Earthquake Engineering, M. Papadrakakis, M. Fragiadakis, V. Plevris (eds.), Corfu, 2011.

[3] F. V. Karantoni, M. Papadopoulos and S. Pantazopoulou, *Criteria Guiding Seismic Assessment Strategies of Traditional Masonry Buildings*, Second Conference on Smart Monitoring, Assessment and Rehabilitation of Civil Structures (2SMAR), Istanbul, 2013.

[4] European Committee for Standardization (CEN), *EN 1998-1 Eurocode 8: Design of Structures for Earthquake Resistance – Part 1: General Rules, Seismic Actions and Rules for Buildings*, Brussels, 2004.

[5] S. J. Pardalopoulos, *Seismic Design of Natural Gas Pipeline Networks Attached in Existing and New Constructions*, PhD Thesis, Demokritus University of Thrace, Xanthi, Greece, 2012.

[6] G. E. Thermou, S. J. Pantazopoulou, A. S. Elnashai, *Global Interventions for Seismic Upgrading of Substandard RC Buildings*, ASCE Journal of Structural Engineering, ASCE, 138(3): pp. 387-401, 2012.

[7] G. E. Thermou, S. J. Pantazopoulou, *Assessment Indices for the Seismic Vulnerability of Existing R.C. Buildings*, Earthquake engineering and Structural Dynamics, DOI: 10.1002/eqe.1028, Wiley InterScience, 2010.

[8] S. J. Pardalopoulos, S. J. Pantazopoulou, *Spatial Displacement Patterns of R.C. Buildings Under Seismic Loads*, Computational Methods in Earthquake Engineering, Computational Methods in Applied Sciences 21, M. Papadrakakis et al., Springer, pp. 123-145, 2011.

[9] M. Th. Kontari, *Seismic Assessment of Neoclassical Buildings through Computer Simulation*, MASc thesis, Depart. Of Civil Engineering Demokritus University of Thrace, Xanthi, Greece, 2011 (*in greek*).

[10] R. W. Clough, J. Penzien, *Dynamics of Structures*, Second Edition, MacGraw-Hill Inc., 1993.

[11] M. Papadopoulos, H. Cotta, T. Gounarido, *The history of the school of the "Hellenic high school"of Thessaloniki*, Municipality of Thessaloniki, Thessaloniki, Greece, 2001 (in Greek).

[12] National Service for Management of Earthquake Damages in Northern Greece (Υ.Α.Σ.Β.Ε.), *Restoration of the damages caused to the General Hellenic Consulate due to earthquake,* Ministry of public works, Thessaloniki, Greece, 1979.

[13] SAP2000, Computers and Structures, Inc., University Avenue, Berkeley, California 94704, USA.

[14] ITSAK, *Institute of Technical Seismology and Earthquake Resistant Structures*, Thessaloniki, Greece.

COMPDYN 2013
4th ECCOMAS Thematic Conference on
Computational Methods in Structural Dynamics and Earthquake Engineering
M. Papadrakakis, V. Papadopoulos, V. Plevris (eds.)
Kos Island, Greece, 12–14 June 2013

SEISMIC ASSESSMENT OF A NON – SYMMETRIC STONE MASONRY BUILDING WITH FLEXIBLE FLOORS

F.V. Karantoni[1], I.C.Manalis[2]

[1] University of Patras
University Campus, Patras, Greece
e-mail: karmar@upatras.gr

[2] University of Patras
University Campus, Patras, Greece
e-mail: yiannismanalis@gmail.com

Keywords: masonry buildings, strengthening, seismic assessment, relative drift, flexible floor

Abstract. *For the rehabilitation of a 150 years old water mill, seismic assessment was necessary. According to provisions of Eurocode 8, Part 3, it is not applicable to stone masonry buildings. However, due to the lack of a code in force for this type of structures, it was applied to a structure consisted of two buildings which share the adjacent wall. Three alternatives for the simulation of the cooperation of the common wall is considered and also the two alternative analysis methods compatible with the limited knowledge level which was obtained, the lateral force method and the response spectrum modal method is used. The inconsistencies of the code with relevant structures are pointed out and results for each case and analysis method in terms of demanded relative drifts are compared to capacity of the masonry. The main conclusion is that the large gap of codes in force must be filled otherwise the existing non-monumental stone masonry structures will stay unprotected if their strengthening will become a process which demands explicit calculations and inspection works of high cost.*

1 INTRODUCTION

During the redesign process of an existing building a variety of problems arises which are not encountered during the design process of a new building. In stone masonry buildings uncertainties related to the unknown properties of structural masonry, the bonding of the masonry units at the corners or through the width of the wall, the number of wythes, the way floors and beams are supported by the walls etc, are risen. Non destructive tests (NDT) and high technology devices are available nowadays for both the inspection of the masonry and the determination of its properties and not only the choice of each NDT, but also the extent of application depends on the importance of the structure and the budget of the project, as well. Another subject is the way all the collected data about the construction details of a masonry building should be used when modeling the structure for seismic assessment. It is reasonable that treating with a unique monumental structure, the cost for the analysis is of minor importance. The later is the cost to supply a computer program of high capabilities as well as the cost of person hours to model in detail the structure and to evaluate the huge amount of results. But the cost of analysis for the assessment of a more or less non-monumental structure is critical and engineers are often obligated to simplify the modeling by adopting reasonable assumptions which are accepted or proposed by the codes in force.

Worldwide, industrial buildings from the early industrial era, left functionless for decades, were restored and rehabilitated. Being hundreds, their survival is essential for the preservation of both the architectural heritage and the historical memory; they often stand for milestone of a location. Nevertheless, this is not a strong reason to treat them as unique monuments in which renovation cost and especially computational cost is of minor importance. The permissible simplifications are a matter of code and engineer's experience as well.

Eurocode EN 1998-3:2005 [1] is pertained to existing structures but it is mainly oriented to frame structures and especially to reinforced concrete ones. According to EN 1998-3:2005 the capacity of a structure, in terms of deformation, is calculated in control node and it is compared to the demanded deformation which depends on the performance level adopted. This procedure is simple in structures with rigid floors and roof where the control node is the center of the mass at the top of the building. The following methods may be used for the analysis of new structures, depending on the restrictions for the application of each one: (a) the simple equivalent single degree of freedom representation where demand is obtained directly from the spectrum (see appendix B in EN 1998-1), [2], (b) the linear lateral force analysis procedure (static), (c) the multi modal response spectrum analysis (linear, with CQC or SRSS type modal response combination), (d) the non-linear static (pushover) analysis and (e) the non-linear time history (dynamic) analysis. In EN 1998-3 the same methods are adopted for existed structures but instead of design spectra, the elastic spectra must be used. Additionally in informative Annex C of EN 1998-3, it is mentioned that it is not applicable to stone masonry buildings leaving a gap relating to the vast majority of traditional buildings.

It is well known and it is well documented in [3] that the use of non-linear static analysis in case of structures with deformable floors and roof presents difficulties and codes have not yet taken these issues into consideration. In the absence of diaphragms the choice of the control node cannot be the center of mass because each wall is deformed almost independently and this is a matter of study in this paper. Because of the wide variety of masonry types, the non-linear behavior of each type, especially for the out of plane response is not yet well documented. In order to overcome these time consumer and doubtful for these particular structures methods, in [4] and [5] a simple procedure for the seismic assessment of ordinary traditional masonry structures is proposed. Herein, emphasis is given to aspects related to the control node and the analysis method used. A structure consisted of two buildings which are con-

structed at different time periods, not bonded together is used as benchmark; it is analyzed: a) considering three alternatives for the simulation of the sheared adjacent wall and b) by both a lateral force analysis and a response spectrum analysis considering both the fundamental modes only and mode superposition of the twenty first modes. Displacements of each wall and the maximum relative drift in plane and in elevation is calculated for each one of the analysis methods and of simulation methods.

2 DESCRIPTION OF THE STRUCTURE

The structure is a water mill constructed in two phases from uncoursed stones of local schist in island Andros, Greece, during the years 1876-1900. The older building (Building A in Fig. 1) of dimensions 18,72x12,07m in plan and 19,16m in elevation consists of only external load bearing walls of width ranging from 1,09m to 0.55m as seen in Fig. 2. The newer building B of maxima dimensions in plan 11,34mx8.53m has three external load bearing walls sharing the adjacent wall W2 of building A. The area of ground floor because of the slope of the ground is smaller than of the upper floors (see Fig. 2(d)). As seen in Fig.1 the complex is L-shaped in plan. It is noteworthy to point out that the wall W2 bears loads from both buildings A and B. Another point of interest is that there is not bonding between the masonry units of walls W5 and W7 and the ones of the wall W2 as it is clearly seen in the picture of Fig. 1(c). Although the structure is located in an earthquake prone area, there is no evidence or signs of structural damage except environmental one. This is actualy surprising because of: a) the height of the structure, b) the "open plan" of building B due to lack of connection of one end of the walls W5 and W7, c) the existence of wall W5 which could pound the wall W2 in the middle of its span, and d) the different seismic response of the two buildings.

For the seismic assessment both the properties and the loads of the structure must be known, so for the study of the structure under consideration, in order to calculate the live loads it was proposed a rehabilitation concept fully compatible with the nature of the old water mill and the needs and history of island Andros which exhibits a remarkable cultural life with museum of modern art, libraries, naval museum, municipal theater etc. The proposal does not alter the configuration of load bearing walls and gives the possibility of any use provided the live load does not exceed 2kN/m^2.

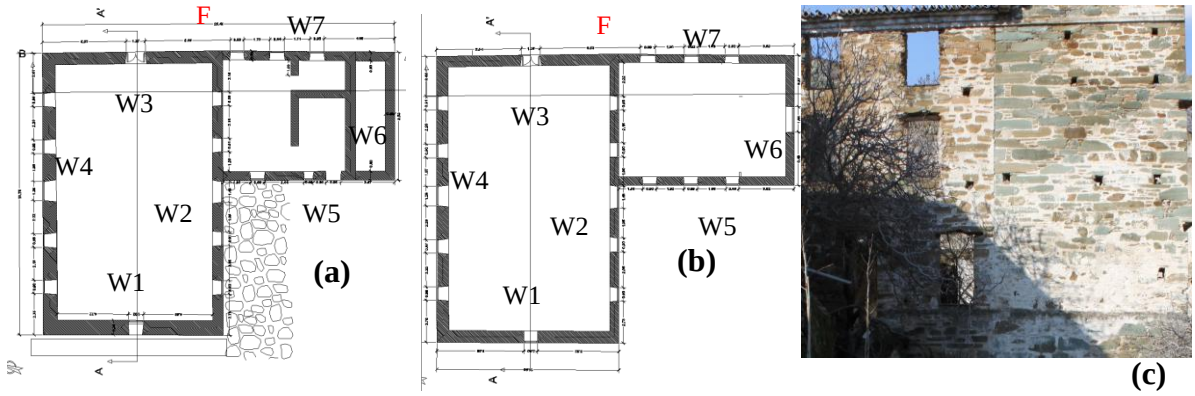


Figure 1: Plans at levels z= 11.22m a), z=13,96m b) and a picture taken from point F which shows the lack of connection among the buildings (c)

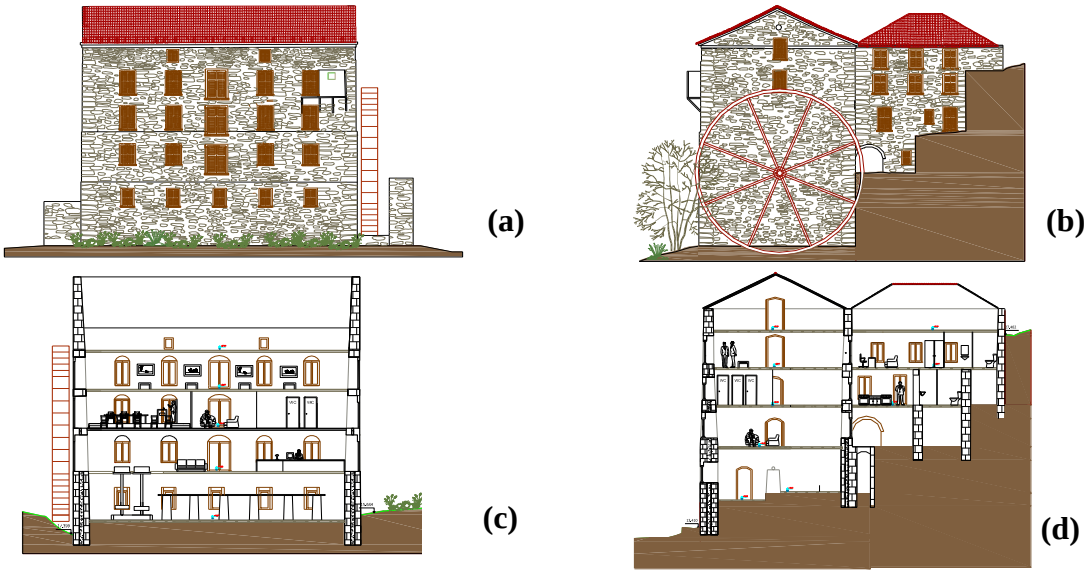


Figure 2: The north, (a) and west facade, (b) and elevations A-A, (c) and B-B, (d)

3 ASSUMPTIONS FOR THE ANALYSIS

3.1 Mechanical properties of masonry

All load bearing walls are of uncoarced stones of local schist. For the determination of compressive strength of stone the Schmidt rebound hammer test was used, (see Fig. 3). The test was performed in twenty seven different locations of lower parts of the walls because due to destroyed floors, there was not access to upper parts the walls. In Table 1 the corrected, according to hammer instructions, values of the compressive strength of masonry units are presented and one can notice the variation of mechanical properties of masonry over the structure. The mean compressive strength of masonry units derived as f_b=36,79 MPa with a standard deviation σ=13,82 MPa. The compressive strength of mortar f_m was estimated equal to 1.0MPa. The compressive strength of masonry f_w =3.03MPa was calculated from equation 1 which was proposed in [6] in which α=1.5 for the uncoursed stones of the structure under consideration.

$$f_w = \frac{2}{3}\sqrt{f_b} - a + 0{,}5 f_m \tag{1}$$

In the analysis the Young modulus E* = *0,5E* was taken so that cracking is considered, where E=1200f_w from [6]. The specific weight of masonry was estimated 22kN/m^3. The equations of En 1996-1-1 [7] are not applicable to uncoursed stone units.

12,0	45,0	45,0	60,0	26,0	12,0	27,0	46,0	42,0	12,0
25,0	37,0	26,0	50,0	30,0	34,0	26,0	34,0	45,0	39,5
39,0	39,0	62,0	34,0	34,0	59,0	54,0			

Table 1: Compressive strength in (MPa) of masonry units after Schmidt rebound hammer test

3.2 Loads

For the calculation of dead loads the weight of masonry, the timber roof and the timber floors as well was taken into consideration. The floors consist of steel beams parallel the

small side of each building which transfer the loads to the longitudinal walls. The roof trusses of building A are supported by the walls W4 and W2, part of the later and the walls W5, W6, W7 transfer the loads of the roof of building B.

Type I spectrum of EN 1998-1:2005 with a_g= 0,16g from the Greek National Annex and S=1.0 because of the rocky soil was used for the seismic analysis. More details about the seismic analysis are presented in a separate following section.



Figure 3: Hammer Schmidt test

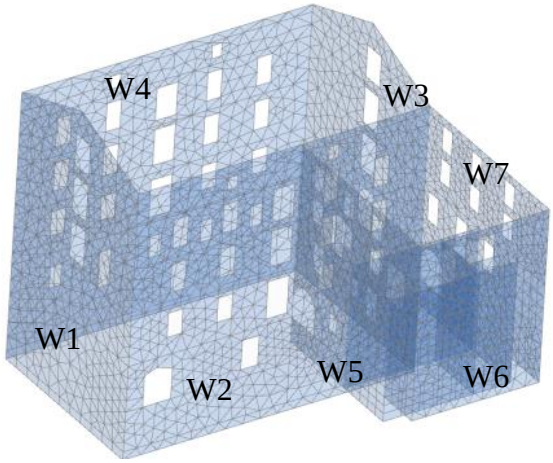


Figure 4: Finite element discritization

4 ALTERNATIVE SIMULATIONS

In Section 2 it is pointed out the lack of bonding of walls W5 and W7 of building B with the adjacent wall W2 of building A, which however bears part of the loads of building B. This fact raises the question for the proper simulation of the entire structure and its response under earthquakes. For a very eligible simulation the use of special contact elements provided by program codes, not so familiar to everyday practice of engineers, is recommended. The scope of this study is to compare the results of the three possible alternative simulations which an engineer may proceed using wide spread program codes. In all three cases, the spatial model of the structures is discritized with shell finite elements which take into account the in-plane and the out -of -plane response of the walls in the absence of rigid diaphragms. The finite elements are of dimensions about 0,5 x 0,5 m in their plane and of width equal the actual one of each wall. In Figure 4 the finite element discritization is shown. The three alternative cases considered in the present study are:

Case I: in this case the two buildings are considered as a unique non-symmetrical in plan structure, namely as if the masonry units of wall W2 are bonded to the ones of walls W5 and W7. In case steel connectors will be placed to tie the walls together, the assumption of the considered full cooperation of the walls is valid.

Case II: in this case there is no connection between the two buildings and each one is more or less symmetrical building independently analyzed, provided a wall transverse the free ends of the walls W5 and W7 and parallel the wall W2 is constructed to outcome a cellular formation of load bearing walls in the plan of building B.

Case III: in this case, the addition of the wall of case II is omitted and the building B is of an open U-shaped plan. For comparison reasons, no redistribution of loads was considered in this case; taking into account the low values of dead and live loads of wooden floors, this assumption does not affect the response of structure.

5 SEISMIC ANALYSIS

According to modern codes for structural performance to near linear behavior, the linear analysis is adequate and economical because behavior will be essentially elastic in regular structures with short periods and linear static procedures are adequate. For regular structures with long periods and all irregular structures, linear dynamic procedures are better and response spectra is accurate enough. In EN 1998-3, Annex C it is clarified that the code is not in force for stone masonry buildings as well as linear analyses may be performed in case of floors and roof stiff enough that service like horizontal diaphragms, conditions which is not fulfilled in the majority of existing masonry structures and hence nonlinear procedures are requested. However also according to EN 1998-3, nonlinear analysis is not applicable in case of limited knowledge level, KLI. Herein, knowledge level higher than KL1 was not possible at a reasonable cost and the two permitted methods of analyses for this level of knowledge are performed for a stone masonry structure with flexible floors despite the fact the conditions for their application are not fulfilled. The linear methods performed are:

- A modal response spectrum analysis using the Type I elastic spectrum of EN 1998-1:2005 with ground acceleration a_g = 0,16g ground of type A with S=1.0 and characteristic periods T_B and T_C 0,15 and 0,40 sec respectively.
  Seismic codes demand a combination of modal maxima in order to estimate “design” values, but contrary to what is seen in lumped systems, where the fundamental mode is usually the translational mode, engaging very large fractions of mass participation (over 75%), several tens to hundreds of modes need to be considered when applying the same procedures in structures with distributed mass before a tolerable amount of mass may be excited (less than 65%), whereas it is very difficult to identify the fundamental translational mode from among the multitude of modes estimated, which can be related to the vibration of a subordinate component (such as a spandrel or an intermediate wall, or even a beam). Herein, results are presented for the superposition of the twenty first eigen modes as well for the first fundamental eigenmode for each direction (herein an eigenmode identified as fundamental when the effective mass is over 10% of the total mass). In Table 2 the effective mass as percentage of total mass participated in each egeinmode (denoted as "mpf") is presented for the first twenty modes for each one of the cases examined as well as the corresponding periods, in sec. In the relevant Figures 5 and 6 the deformation in plan and in perspective for both the fundamental modes and the superposition of the twenty modal shapes, are depicted. In case I, the mass participated in each mode is very low and a small percentage of mass (about 41%) is activated even twenty modes are considered. When 50 eigenmodes are considered, (66% in x and 70,1% in y of the mass is participated) both the time cost and the required free computer space increased disproportionally the accuracy of the results as it will be discussed in the next. Practically, it is difficult to point out the fundamental eigenmode in case I. In case II, where each building is considered separate from the other, the mass contributed after the twenty eigen modes considered, is about 70%; the same states for case III. Difficult, but easier than in case I, one can distinguish first modes for the building A and higher modes for the building B, as fundamental ones.
- A linear later force analysis (LF) procedure (static) loading the structure with an horizontal force F uniformly distributed along the height of the building from Equation 2, along horizontal axes x and y combined with dead and live vertical loads.

$$F = mS(e) \tag{2}$$

  where m is the mass of the structure and $S(e)$=0,40g (m/sec^2) a uniform acceleration from the equation 3.

$$T_B \le T \le T_C : \quad S(e) = a_g \cdot S \cdot \eta \cdot 2{,}5 \tag{3}$$

where for ground of type A, S=1,00, T_B = 0,15sec, T_C=0,40sec, damping ratio ξ=5% (η= $\sqrt{\frac{10}{5+100\xi}}$ =1 for ξ=5%)

mode	Case I			Case II-Building A			Case II-Building B			Case III-Building B		
	T(sec)	mpf x %	mpf y %	T(sec)	mpf x %	mpf y %	T(sec)	mpf x %	mpf y %	T(sec)	mpf x %	mpf y %
1	0,35	**10,8**	0	0,52	0	**27,8**	0,26	0	0	0,51	11,6	0
2	0,32	4,5	0,6	0,35	**15,2**	0	0,25	0	0	0,28	0	0
3	0,29	0,3	**18,4**	0,32	6,5	0,1	0,25	0	0	0,26	0	0
4	0,26	0	0	0,29	0,3	0	0,23	**24,1**	0	0,25	0	0
5	0,25	0	0	0,23	0	0	0,21	0	0	0,25	0	0
6	0,25	0	0	0,23	0	0	0,2	0	**33,9**	0,24	2,2	0
7	0,23	0	0	0,23	0	19,5	0,19	0,1	0	0,2	0	27,6
8	0,23	0	0	0,21	0	0	0,18	0	4,9	0,19	0	0
9	0,22	0	0	0,21	13,1	0,9	0,15	0	0	0,18	**18,7**	0
10	0,22	7,2	0,2	0,21	1	5	0,14	14	0,1	0,18	0,1	0
11	0,22	1,5	6,1	0,2	0	0	0,13	8,5	0,6	0,16	0,8	0,1
12	0,21	0	0	0,2	0	11,9	0,12	0,1	30,5	0,13	0,4	**33,1**
13	0,21	8	0,6	0,19	0	0	0,11	0	0,4	0,13	2,2	1,9
14	0,2	0	0	0,19	0	0	0,1	6,2	0,4	0,12	0	0
15	0,19	0,2	12,9	0,19	15,1	0	0,1	8,3	0,2	0,11	0	0,7
16	0,19	0	0	0,17	0	0	0,1	5	0	0,11	9,3	0,1
17	0,18	1,5	3,4	0,16	0	0	0,09	0	0	0,11	11,8	0,9
18	0,18	7,1	0,4	0,15	0,7	0,6	0,08	2,3	0	0,1	1,2	1,8
19	0,17	0	0	0,14	11	0	0,08	0,2	0	0,1	0,2	0,2
20	0,16	0	0	0,14	0	0	0,08	0,3	0,2	0,09	12,1	0,1
total		***41,0***	***42,6***		***63,0***	***66,0***		***69,0***	***71,3***		***70,5***	***66,7***

Table 2: modal mass participated (mpf) in each case

		Mode supp. x		Mode supp. y		Fundamental Mode x		Fundamental Mode y		LF-x		LF-y	
	wall	u	v	u	v	u	v	u	v	u	v	u	v
Case I	**1**	36,2	2,4	16,5	7,7	12,4	-0,1	-7,1	5,40	25,3	-0,2	1,3	7,6
	2	2,8	6,4	2,8	**25,3**	1,3	0,5	1,2	**23,6**	5,3	-0,4	1,9	17,0
	3	**54,4**	1,1	9,9	1,9	**46,3**	0,5	-0,4	0,1	**26,5**	-0,2	-0,6	2,4
	4	3,4	7,7	3,9	24,9	2,5	-3,2	2,3	23,0	6,1	1,6	-1,3	**17,4**
	5	**16,1**	2,3	6,3	4,6	1,8	-0,3	-1,8	**3,5**	9,7	-0,7	1,1	5,4
	6	1,7	12,4	1,5	**21,7**	-0,1	-0,2	0,80	2,9	2,6	-1,2	0,4	**10,2**
	7	16,1	0,8	5,8	1,7	**-2,5**	0,2	-1,0	-0,3	**10,4**	-0,5	1,20	2,8
Case II	**1**	37,4	1,0	5,3	5,4	12,1	0,2	2,9	2,8	25,4	-0,2	2,0	8,4
	2	4,2	5,2	2,80	54	2,8	3,9	0,40	52,2	5,9	2,1	0,2	54,2
	3	**57,6**	2,8	9,5	6,0	**49,7**	0,1	-4,3	3,6	**28,4**	0,2	-2,4	9,8
	4	4,0	5,0	2,8	**54,5**	2,5	-3,3	-0,3	**53,0**	6,1	2,1	-0,9	**55,7**
	5	**15,7**	1,8	2,5	2,7	**15,2**	-0,9	-1,40	2,5	11,0	-0,9	0,8	3,1
	6	2,2	2,9	0,5	**18,1**	0,4	1,7	0,3	**16,3**	2,5	0,7	0,2	**9,2**
	7	15,6	1,8	2,3	2,6	**15,2**	0,9	1,8	2,2	**11,6**	-0,3	0,8	3,0
Case III	**5**	52,0	1,1	3,0	2,9	**-11,1**	0,6	-1,5	1,80	55,1	-0,4	-0,8	2,9
	6	1,8	1,2	0,9	**16,0**	1,1	0,6	-0,6	**-4,5**	2,8	-1,2	-0,2	**9,1**
	7	**52,2**	1,1	2,8	2,8	-8,3	-0,6	-1,7	1,7	**55,9**	-1,4	0,8	2,8

Table 3: Maximum displacements u, along x and v, along y, in mm, of each wall for each case and analysis method

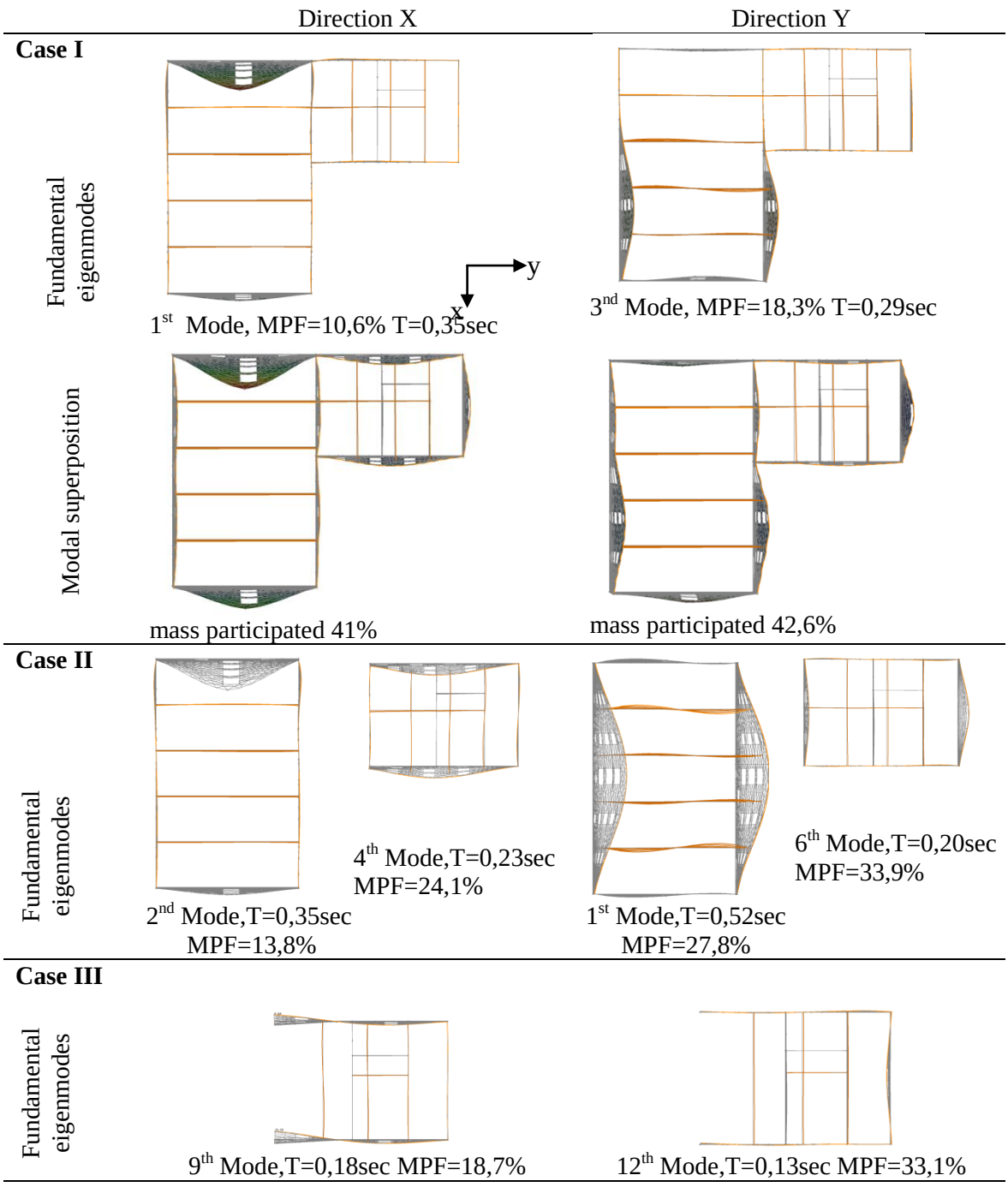


Figure 5: Modal shapes along X (left) and Y (right) axes

For the analyses, the program code Acord-expert [8] was used. The maxima displacements u and v along x and y axis, respectively, of each external load bearing wall of the building, are depicted in Table 4 for the three simulation and the two analysis methods. In bold letters the maximum displacement of the whole structure (case I), for both the buildings A and B (case II) and only the building B in case III is denoted. From the table and the Figures 5 and 6, it is obvious that the out of plane bending is the dominate response of the walls. In case I, the displacements of building A are smaller than in case II when each building considered separate from the other, especially those ones of the wall W4, which is at the opposite of building B. On the contrary, displacements of building B are greater in case I than in case II when

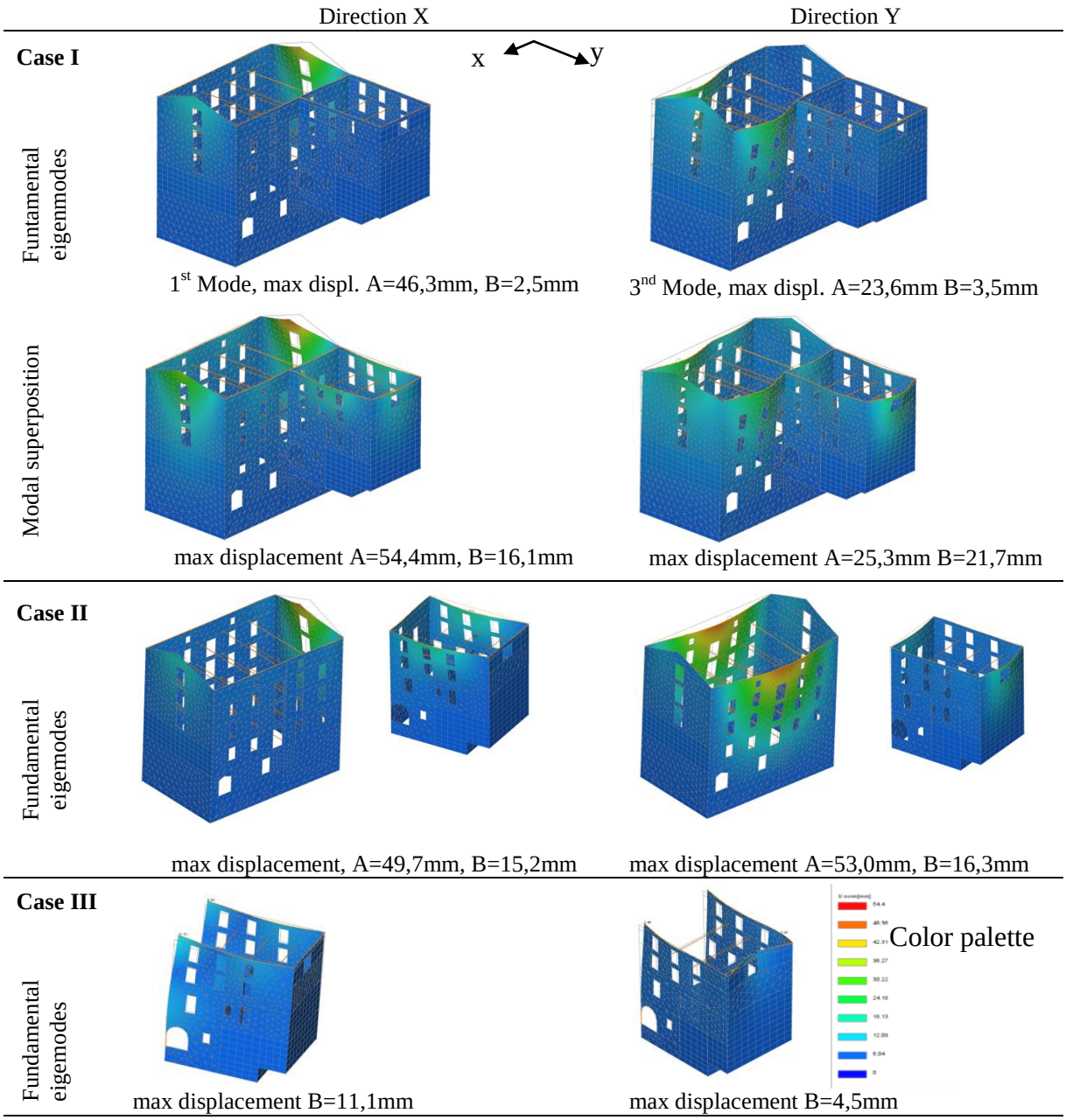


Figure 6: maxima displacements of buildings A and B, for excitation along x (left) and along y (right)

superposition of modes was considered, but times smaller if only the fundamental mode shape is regarded. In case III, as it was expected, when walls W5 and W7 are free at one edge, the deformations of building B along x axis are three to four times larger than in cases I and II. On the other hand, not only the value of maximum displacement but also the associated wall differs according to the analysis method. At this point it must be added that when fifty modes are superimposed, the displacement u of the wall W3 is 55,0 mm instead of 54,4m or 1% greater in case of twenty modes and of the wall W7 16,6mm instead of 16,1mm, or 3% greater. According to EN 1998-3 for the seismic assessment the seismic demand for the performance level considered, e.g. the drift at the top of the structure, is compared with the corresponding capacity of the structure. In case of flexible roof as it is seen in Table 4 the displacement of each external wall is different irrespectively the modeling considered. In [4] and [5] the introduction of two relative drifts with the greater one to be a measure of the seismic

demand, which will be compared to the capacity of the structure, in terms of relative drifts, is discussed in detail.

Relative drift (in height) measures the rotation of the structure at the point of peak lateral response from the vertical axis: θ_v is defined by the ratio of relative displacement occurring between two reference points located at different heights (z_1 and z_2) on the same vertical line, divided by their distance, (z_1-z_2). θ_v is owing primarily to the shear distortion of walls oriented parallel to the ground motion, (θ_{sh}), as well as to the out of plane flexural action of walls oriented in the orthogonal direction (θ_{fl}). Figure 7 clarifies the concept of the relative drifts. For the out of plane response, *relative drift in plan*, θ_{plan}, refers to the relative displacement of the point with peak outwards deflection as compared to the wall corner. In Table 4, where the maximum relative drift for in-plane and out-of-plane deformation is presented for the three alternatives of modeling and the two methods of analysis, the maximum relative drift irrespective of the analysis method is in bold. In Figure 8 the relative drifts are presented in diagrams for better comparison. In all the three cases, the relative drift θ_{sh} is very small compared to θ_{plan}. Relative drift θ_{plan} is almost three times greater than θ_{fl} in cases I and II of "close" plans and almost equal in case III of "open" plan. Shear relative drift is very limited compared to flexural drift. The results obtained from the lateral force method are closer to those from multimodal response spectrum than the ones obtained from modal response only in case III.

			Modal sup.		Fundamental Mode		LF	
	Building		‰	wall	‰	wall	‰	wall
Case I	**A and B**	θ_{plan}	***9,161***	3	7,857	3	3,661	3
		θ_{sh}	0,402	1	**0,647**	1	0,397	1
		θ_{fl}	**2,839**	3	2,416	3	1,383	3
Case II	**A**	θ_{plan}	***9,571***	3	*8,964*	4	5,271	4
		θ_{sh}	**0,282**	1	0,271	3	0,618	3
		θ_{fl}	3,006	3	3,340	4	**3,510**	4
	B	θ_{plan}	**3,919**	6	3,565	6	1,587	7
		θ_{sh}	0,254	5	0,235	5	**0,256**	5
		θ_{fl}	**1,704**	6	1,535	6	0,957	7
Case III	**B**	θ_{plan}	4,394	7	2,585	5	**4,629**	7
		θ_{hs}	**0,248**	5	0,149	5	0,239	5
		θ_{fl}	4,307	7	0,916	5	**4,612**	7

Table 4: Maximum relative drifts

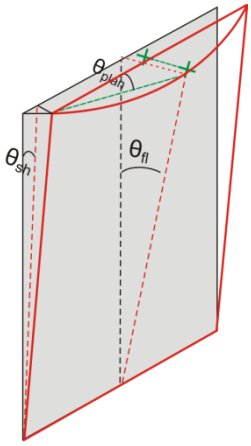


Figure 7: Relative drifts

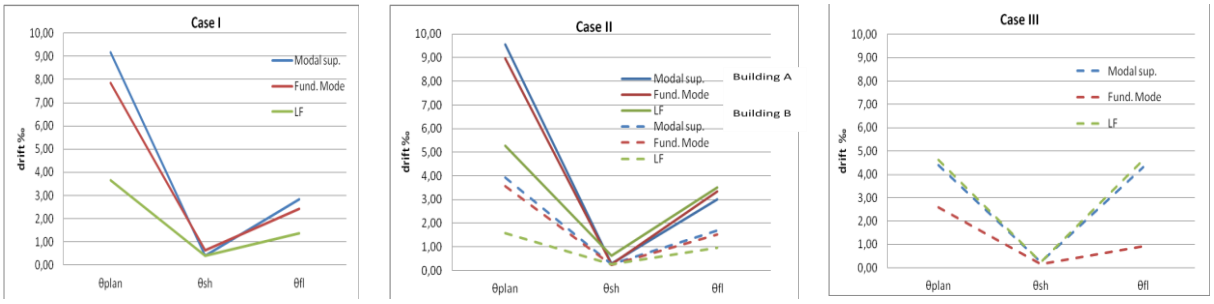


Figure 8: Relative drifts for the three simulation cases and the analysis methods

The relative drifts θ_v and θ_{plan} is the seismic demand and must be compared to the capacity of masonry. In EN1998-3 for the limit state "severe damage" the capacity of a wall of plain masonry (from brick or concrete units) for primary members in terms of drift is 0,004 if governed by shear and 0,008 H_o/D if governed by the in plane bend, where H_o is the distance between the section to be verified and the contraflexure point and D is the depth of the wall. As pointed out the structure of the current study is governed by the out of plane bending so EN 1998-3 does not suggest the capacity of masonry. It is clear that 4‰ is higher than the maximum demanded 0,6‰ and shear failure is not expected under the design earthquake. If we make the assumption that the relation suggested for the in-plane bending is also valid for the out-of-plane capacity, we must accept a rather high capacity of unreinforced stone masonry walls. As an example, for the wall W3 with depth, D=12,07m and H_o =19,16m the capacity in terms of maximum drift for in plane bending equals 10‰ which is greater than the maximum demanded θ_{plan} =9,57‰ (see Table 4). According to this, no strengthening of the structure is required. It is necessary to draw attention that regardless EN 1998-3 is not applicable to stone masonry structures, this conclusion derived from two assumptions which is not allowed to apply in this particular structure, in the lack of any other codified choice : a) nevertheless the absence of horizontal diaphragms linear analyses were performed because the knowledge level achieved did not allow non-linear ones, and b) capacity, in terms of relative drifts, suggested for in plane response is adopted for the out of plane one as well.

6 CONCLUSIONS

Although the existing stone masonry buildings with flexible floors and roof represent a large part of the building stock of Europe, part 3 of Eurocode 8 does not cover them for seismic assessment. As suggested, in order the analysis methods of EN 1998-1 to be performed, detail documentation is available so that a knowledge level higher than limited (KL1) to be obtained; for ordinary traditional masonry buildings this is a matter of cost.

The outcome of the application for both the lateral force method and the modal response spectrum analysis (in the later considered either the fundamental mode or the modes superposition), is different drift ratios without any systematic deviation to the three cases examined.

In case of adjacent buildings, the impact of sharing the adjacent wall may be either positive or negative to the building considered. A trend to conservative results in case the adjacent structures were not considered is coming into view.

The need for accounting the out-of-plane response by the codes is of great importance. The large gap of codes must be filled otherwise the existing non-monumental stone masonry structures will stay unprotected if their strengthening will become a process which demands explicit calculation and inspection works of high cost.

REFERENCES

[1] CEN. EN 1998-3 Eurocode 8: Design of Structures for Earthquake Resistance - Part 3: Assessment and retrofitting of Buildings, *European Committee for Standardization*, Brussels, 2005

[2] CEN. EN 1998-1 Eurocode 8: Design of Structures for Earthquake Resistance-Part 1: General Rules, Seismic Actions and Rules for Buildings, *Europ. Comm. for Standardization*, Brussels, 2004

[3] Galasco, A., Lagomarsino, S., Penna, A., (2006) "On the use of pushover analysis for existing masonry buildings" *Proc. First European Conference on Earthquake Engineering and Seismology*, 2006, Geneva, Switzerland – paper n. 1080, CD-ROM.

[4] Karantoni, F.V, Papadopoulos M, Pantazopoulou S., Criteria Guiding Seismic Assessment Strategies of Traditional Masonry Buildings, *SMAR2013*, Istanbul, 2013

[5] Karantoni, F.V, Pantazopoulou S,. Criteria Guiding Seismic Upgrading of Traditional Masonry Buildings, *12th Canadian Masonry Symposium*, Vancouver, 2013

[6] Tassios, Th. & Cronopoulos, M.P. (1986), "A seismic dimensioning of interventions (repairs/strengthenings) on low-strength masonry buildings", *Proceedings of M.East and Mediterranean Regional Conference, Ankara*

[7] CEN. EN 1996-1-1 Eurocode 6: Design of Masonry Structures - Part 1-1: General Rules for Reinforced and Unreinf. Masonry Structures, *Europ. Comm. for Standardization*, Brussels, 2005

[8] ACORD-CP http://www.itech-soft.com/en/acordCP/acordCP.htm

COMPDYN 2013
4th ECCOMAS Thematic Conference on
Computational Methods in Structural Dynamics and Earthquake Engineering
M. Papadrakakis, V. Papadopoulos, V. Plevris (eds.)
Kos Island, Greece, 12–14 June 2013

REHABILITATION OF A PARTIALLY COLLAPSED MASONRY TRADITIONAL TOBACCO WAREHOUSE OF THE LATE 19TH CENTURY

Constantin E. Chalioris[1], Maria J. Favvata[1], Venetia G. Alexandri[1], and Chris G. Karayannis[1]

[1]Democritus University of Thrace, School of Engineering, Department of Civil Engineering
Xanthi 67100, Greece
e-mail: chaliori@civil.duth.gr

Keywords: Traditional Masonry Building, Partial Collapse, Rehabilitation Plan, Photogrammetry, Temporary Supporting Steel Towers.

Abstract. *This study presents morphology, pathology, recording method, applied rehabilitation procedure and constructional problems of a four-storey masonry building in Alexandroupoli which today is partially collapsed. It was constructed before 1900 and enlarged in 1924 to be used as tobacco warehouse. From 1950s onwards, it has been neglected and because of the total lack of maintenance it has sustained structural and architectural deterioration; intervention works for its re-use as Municipal Library began in 2004. The first approved rehabilitation plan based on false strategy adopted the total removal of the interior structural members including wooden diaphragms, beams and columns and the construction of a new internal reinforced concrete frame structure. It proved to be catastrophic since in 2005 a sudden partial collapse of masonry and the roof was caused. The building has remained partially collapsed and difficult to approach due to the danger of a potential further collapsing. Recording of the present state has been based on photogrammetry. A proper intervention plan is applied. This work is a contribution in the field of structural rehabilitation of partially collapsed historic masonry buildings that constitute an extremely unsafe working environment.*

1 INTRODUCTION - ANAMNESIS

The building is located in the center of the city of Alexandroupolis which is a significant port at the most North-East side of Greece. In the late of the 19th century and the beginning of the next century still under the Turkish occupation an exponential growth of the city occurred as a result of the immigration of many catholic families from west Europe. Most of them were railway technicians and employees, consulate staff and merchants. Before 1900 this well established catholic community constructed the building under examination to be used as a school. It was one of the most well-constructed buildings of the city. It seems though that it was only a part of the structure as it looks today since the community was but 5000 people and a larger school building was really not realistic. In 1904 a major fire during a student exhibition destroyed part of the existing building along with its equipment and facilities. The fire damages in conjuncture with the eventual economical decay of the community had as a result the utter forlornness of the structure.

In the year 1924 under the Greek rule anymore the rapid economical growth of the area due to the intensive cultivation of fine local tobacco allowed the reconstruction and simultaneously the enlargement of the building to its final shape. It became one of the largest and most prestigious and well-constructed buildings of the whole area and its new usage was the base of the renowned "Companie general de Tabac" (General Tobacco Company).

After the reconstruction and enlargement of the building size in the year 1924 the structure has taken its final L-shaped plan, as shown in Figure 1. The length of the building is 26.75 m, while its width is 12.30 m and 10.30 m at the northern and the southern side, respectively. The total height of the structure is 12.45 m. The building consists of four storeys; a basement, a ground floor, an upper floor and an attic under a gabled roof (Figure 2).

In World War II the building was used as prison by the Bulgarian army of occupation. After the war and until early 1950s the building was used as a shelter for the accommodation of the refugees. Henceforth the building remained completely forlorn and derelict. As a result of the long period of neglect and lack of maintenance the building had sustained damages to a considerable extent.

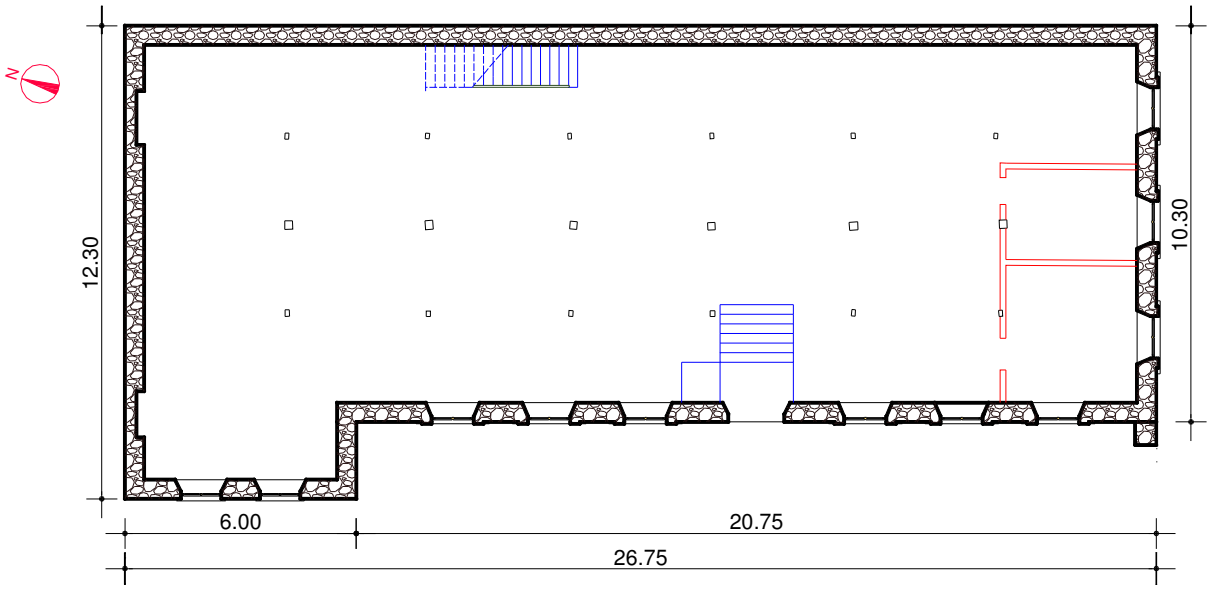


Figure 1: Plan view with the external dimensions of the ground floor of the building.



Figure 2: Outside south-western view and inside views of each floor of the tobacco warehouse (the photos were taken in 2003, before the intervention works of 2004-05).

2 STRUCTURAL CHARACTERISTICS

The building can be considered as a historic load-bearing masonry structure. It is an excellent sample of industrial architecture initially influenced by the urban architecture of the late 19th century. After the reconstruction and enlargement of the building in the year 1924 it was composed by the basement, ground floor, upper floor and an attic. The area of a typical floor is approximately 293 m^2 in a building plot of approximately 846 m^2. The building has a gabled roof composed by wooden trusses and terracotta tiles forming gables on the façades. The roof consists of 13 wooden trusses having a slope of 27°.

The basic building materials that prevail are stone and wood and secondly also used are cement and metal. Metal is used at the window recesses and in some cases as steel beams. Concrete is used for the middle row of columns in the basement only. The roof, the floor diaphragms, the beams and the columns except of the middle ones in the basement are made of wood.

The structural system consists of load-bearing masonry made of ashlars of regional granite connected with mud mortar. The hierarchical way of the construction of the perimetric wall at the floors in a way that the thickness of the masonry is being reduced as we reach the higher levels of the building is something worthy of remark. This reduction of thickness is attributed to the reduction of the loads. Thus the thickness of the masonry at the basement is almost 60 cm, at the ground floor it becomes 50 cm and finally at the floor and the attic it is only 45 cm. The masonry was lime - casted on inside and outside surfaces. The thickness of the foundation masonry is a little bigger than the thickness of the basement walls whereas the depth of the foundation level is approximately 1.50 m. The building as it is today neighbors with a multi-floor Reinforced Concrete (RC) residential structure at the east side.

3 FALSE REHABILITATION STRATEGY - BUILDING'S SITUATION

3.1 Rehabilitation plan

Recently, the building was bought by the municipality with the purpose of its future use as the Municipal Library. At that time despite the large extent of the damages due to the forlornness and the thieveries the building was a stable structure as it can be observed in the photographs of Figure 2. The wooden diaphragms of the basement, the ground floor, the first floor and the attic were intact and in a relatively good condition. These diaphragms and the roof connected the opposite perimetric masonry walls and maintained this way a stable equilibrium for the whole structure.

A reasonable rehabilitation strategy would provide for the repair and the total restoration of the existing structural members and materials and further where it was necessary for the possible reinforcement with materials friendly to the existing old materials if possible. Grout injections, deep repointing, jacketing and partial reconstruction are some well-known and widely-applied strengthening techniques for deficient or damaged masonry walls [1, 2]. A combination of these intervention methods on the same wall could be applied too. Furthermore the excessive use of cement or concrete in restoration works of historic buildings, and especially the construction of a whole new RC multi-storey frame that replaces all the existing old members is usually considered invasive for the preservation of the authenticity of historical heritage. Therefore, official authorities or bodies of experts involved in the conservation of cultural heritage usually prescribe the use of cement or concrete to be limited, whereas in some cases it is strictly prohibited (for example in classical and Byzantine monuments and antiquities). Besides, grout injections, deep repointing and partial reconstruction have proved quite successful restoration techniques for bearing masonry walls [3].

Instead, the approved rehabilitation plan for the re-use of the building under consideration as the Municipal Library included first the removal of the all the parts of the interior of the building and then the construction of a new, interior RC frame structure inside the existing masonry historic building. According to this plan in the first step all wooden diaphragms, the wooden beams and the wooden and concrete columns were to be removed. After that an entirely new interior structure was panned to be built. This interior structure consisted of new foundations, columns, beams and slabs, all made of RC, which were intended to serve the new purpose of the building and its bear increased loads.

Thus, in the year 2004 the intervention works for the rehabilitation of the building and the forthcoming re-use as the Municipal Library began. However, these works during the years 2004-05 proved to be inappropriate and catastrophic for the building because the removal of all the interior old structural members without the proper shoring of the perimetric walls and the roof had as a result the sudden partial collapse of the building; part of the eastern and northern wall along with part of the roof collapsed, as displayed in Figures 3a & b. After that incident the works stopped and the building has remained heavily damaged, partially-collapsed, unsafe and apparently unapproachable to anyone due to the immediate danger of further collapsing.

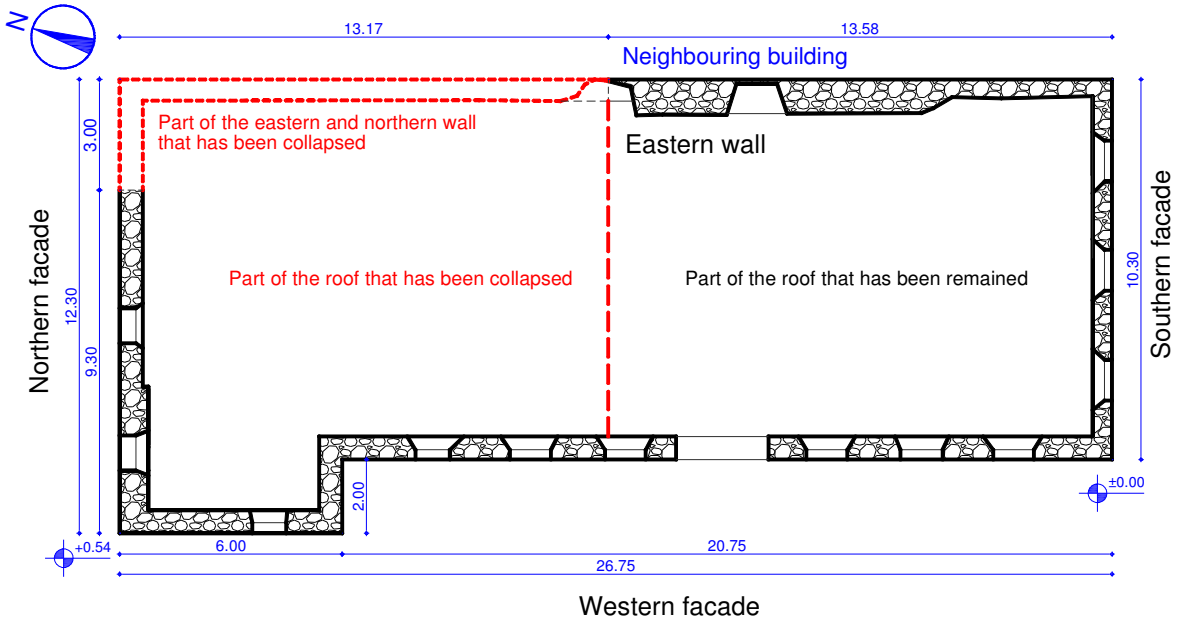




Figure 3: (a) Plan view and (b) external view (western façade) of the building after the partial-collapse of 2005.

3.2 Pathology

The building sustained severe damages due to (a) its age, the many years of non-use, the total lack of maintenance and the utter forlornness (b) the inappropriate and catastrophic rehabilitation plan which included the total removal of all the interior structural members: the wooden diaphragms, wooden beams and wooden and concrete columns; and (c) the partial-collapse of the eastern and northern wall along with part of the roof (in 2005), during the intervention works.

According to the approved restoration plan of 2004-05 almost all the wooden floors and columns of the building were removed (see also Figure 4a) without shoring the walls or any other safety measures, although it is well known that floors of multi-storey bearing masonry buildings are very important structural components since they form horizontal diaphragms that connect and restrain the perimetric masonry walls of the building. After the partial collapsing the few remained columns can hardly bear any loads and even more some remained parts of wooden columns are literally hanging from the roof making the working environment quite risky and dangerous.

After the collapse the building consisted of the perimetric masonry walls (except for parts of the eastern and northern walls that have fallen), two columns per floor and part of the roof. The masonry walls sustained ageing, damages and cracks. The main entrance at the west façade has become a very dangerous point for anyone who wants to enter the building due to its inappropriate widening of the opening during the intervention works (Figure 4b). Further, the eaves of the walls (the ridge was made of concrete) sustained serious damages and cracks, whereas at some parts they have been destroyed by the fallen parts of the roof. Figures 5a & b shows the partially-collapsed masonry walls (northern and eastern walls). The masonry wall that sustained the greater damage is the eastern one. Further there are three vertical and one horizontal deep grooves on the internal side of the eastern wall (Figure 5c).

According to the plan of the recent interventions those grooves were meant to be the positions of the RC columns (vertical grooves) and beam (horizontal groove) of the new internal RC structure. In order to gain space, the new RC columns and beams at the eastern side of the inner structure were designed to be placed inside the existing masonry walls. For this reason the cutting and creation of vertical and horizontal grooves in the masonry of the existing eastern wall was planned. However, this intervention proved to be quite inappropriate, very dangerous and in effect catastrophic for the stability of the existing masonry walls and the old structure as a whole.



Figure 4: (a) Inside and (b) outside views of the building after the partial-collapse of 2005.

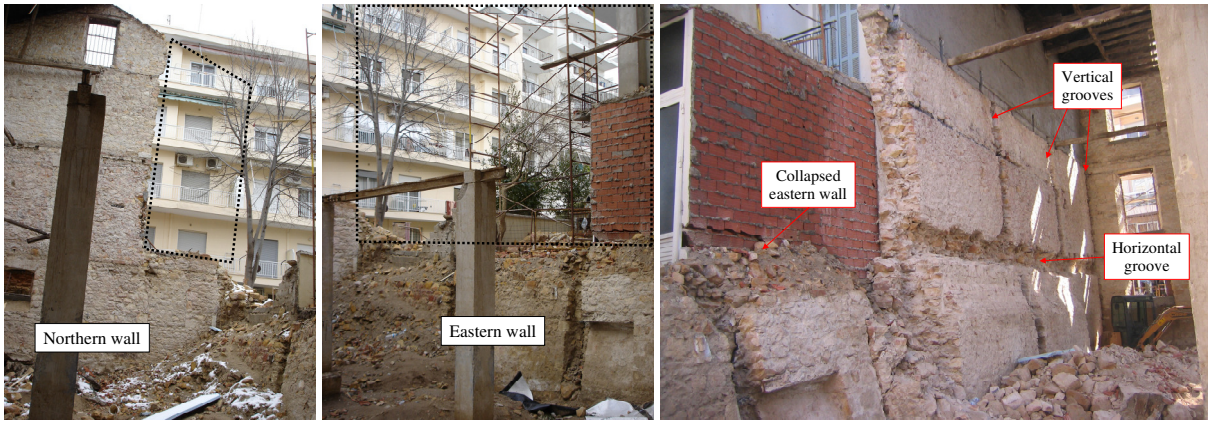


Figure 5: Inner views of the (a) northern and (b) eastern masonry walls of the building after the partial-collapse of 2005. (c) Eastern masonry has three vertical grooves and one horizontal groove on the internal part of the wall.

4 RECORDING USING PHOTOGRAMMETRY

Due to the dangerous conditions of the heavily damaged and partially-collapsed masonry building, the geometrical details of the structure could not be recorded using common procedures and a rather special refined survey was required. For this reason, photogrammetric image processing is used in order to create the orthoimages of the façades, as background information to digitize details of the building in a CAD environment with accuracy 1 cm [4]. Details of the recording procedure along with rectified images - mosaics of the building and a spherical 3D panorama of the inner of the building are given in Refs [5, 6].

5 REHABILITATION PROCEDURE

After the partial collapse of the building a different methodology has been adopted for the rehabilitation and reconstruction of the partially-collapsed historic masonry building in order it to be reused as the Municipal Library. This new approach is based on the cautiousness and the safety of the structure and the working personnel [7] and yet it is also constrained by the initial concept of the approved plan for a new internal RC structure. The presented rehabilitation procedure includes the following steps:

- Temporary support of the façades using external, non-permanent steel towers.
- Strengthening of the severely damaged eastern masonry wall using cast-in-place concrete or shotcrete and steel reinforcement in order to fill the dangerous vertical and horizontal grooves of the masonry and to form a permanent RC beams-columns supporting system.
- Construction of a new, interior RC frame structure inside the existing masonry that will bear the increased design loads of the new usage as the Municipal Library. This frame will also be the permanent support of the north, south and west façades. For this purpose efficient connection between the RC structure and the masonry walls will be applied. The construction of the new RC frame is unavoidable part of the approved initial rehabilitation plan of the building which has not been changed despite the partial collapsing of the old building.
- Restoration of the damaged masonry walls and removal of the temporary supporting system of the steel towers is the last step.

5.1 Temporary support of the remained walls

Supporting and securing the façades of the building is of great importance for the stability of the whole structure and the creation of a safe working environment. For this purpose, special non-permanent structural system has been used. The aim is to prevent potential horizontal displacements that would induce further damages or further collapsing of the entire building.

The geometry of the building, the condition of the damaged masonry walls, the urban character of the project, the free space inside the building plot, the neighboring buildings, the foundation soil and the seismicity of the region were the parameters that have defined the supporting system of the façades. Thus, vertical steel towers placed outside of the building comprise the temporary supporting system of the masonry walls, as shown in Figure 6. These towers will be removed when the rehabilitation procedure will be completed. It is mentioned that before the installation of these supports, it is necessary all the openings (windows and entrance) of the building to be properly stabilized. This can be achieved by mounting wooden frames and beams inside these openings (see also Figures 6 and 7).



Figure 6: Outside view of the external non-permanent steel towers for the temporary support of the façades.



Figure 7: Inside view of the temporary supporting system of the substantially damaged eastern masonry wall.

5.2 Support and strengthening of the eastern masonry

One of the challenges of the rehabilitation design plan is how to face the problem of the supporting and strengthening of the heavily damaged and unsecure eastern masonry, since at this side of the building there is an adjacent multi-storey apartment building and there is no space for the installation of an exterior steel tower. Part of this masonry wall has collapsed and furthermore some very deep and dangerous vertical and horizontal grooves have been formed on this stone wall during the works of 2005. These grooves have been cut for the construction of the RC columns and beam of the new internal frame structure that was the next step of the rehabilitation plan.

However, the depth of the grooves is approximately half of the total width of the wall and the capacity and stability of this stone masonry is considerably decreased. Further, the wall at the upper floor and the attic has been reconstructed during the recent interventions using low capacity cinder blocks. Furthermore the removal of the three horizontal wooden floors of the building has made the 11 m height wall extremely unsafe and totally unpredictable in any new intervention.

The problem can be approached with the use of cast-in-place concrete or shotcrete with dry-mix process that can fill the vertical and horizontal grooves, forming a RC beams-columns supporting system of the masonry [8-12]. These new RC members will also be part of the new internal RC structure. Geometrical outline figures of the RC internal frame of the eastern masonry wall are presented in Figure 8. The RC members can be designed according to the specifications of Eurocode 2 and 8 [13-16].

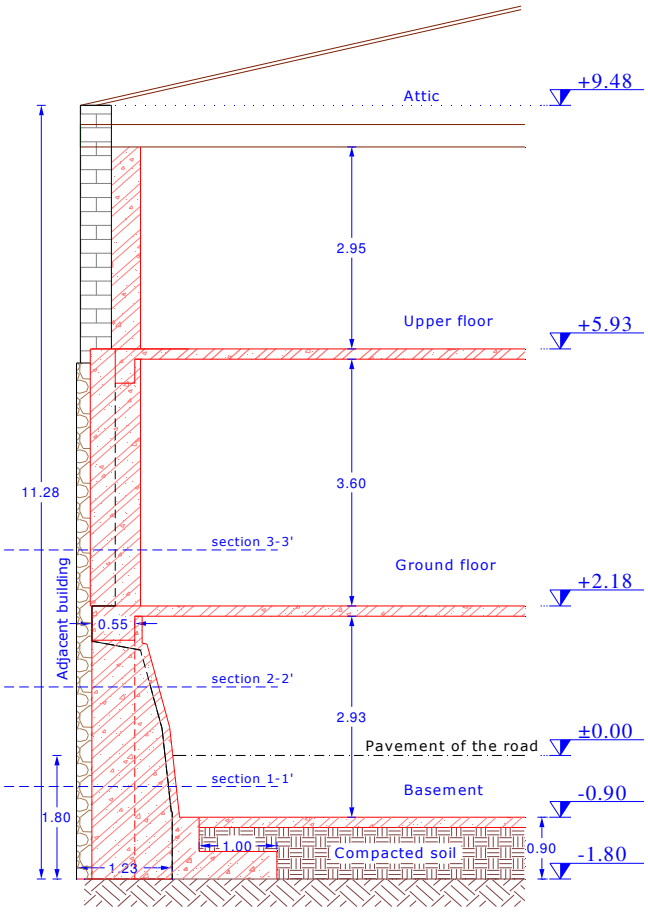


Figure 8: Geometrical outline figure of potential internal reinforced concrete frame inside the grooves of the eastern masonry wall.

5.3 The new internal RC structure - Connection with the masonry walls

According to the approved rehabilitation plan a new interior RC frame structure inside the existing masonry historic building is planned to be constructed. This internal structure will also serve as a permanent support of all the masonries of the façades. Apparently, the temporary steel towers will be removed after the completion of the construction of the internal RC structure and after the full connection between the internal new frame and the old perimetric masonry walls has been achieved. The efficiency of this connection is of vital importance for the safety of the walls and the integrity of the rehabilitated building.

The cast in-situ RC slabs of the new interior structure will have significant importance for the stability and seismic capacity of the restored building, since they will form horizontal diaphragms that connect the perimetric masonry walls and distribute the seismic forces induced by the mass of the walls into the internal structural system [17, 18]. Simultaneously with the construction of the slabs, perimetric bond-beams are planned to cast inside the stone walls. The positions of the perimetric bond-beams are the existent holes inside the masonry walls that have been formed during the recent interventions when the wooden floors of the building were inappropriately removed.

Especially for the eastern masonry wall the proposed RC columns-beams supporting system which is part of the interior RC structure will also permanently support the masonry wall and connect it with the new frame structure.

5.4 Restoration of the damages on the masonry walls

After the construction of the new interior RC frame structure that will permanently support the cracked masonry walls of the building the next step is to repair the damages and the cracks on these masonries. The following restoration methods are planned to be used, depending on the features of the damages.

First, cement grouting [19, 20] is suitable to restore cracking of the basement and ground floor masonry walls with width greater than 45 cm and crack width less than 10 mm. According to this technique, cracks are filled with injected cementitious grout that is composed of cement, natural or artificial pozzolanes and admixtures for the cement dry contraction and to liquefy the grout. The grout is injected into the cracks with a pressure less than 0.1 MPa in order to avoid any additional damages to the wall.

Secondly, deep repointing [3] is suitable for the masonry walls whose old and low-strength mortar needs to be replaced with a stronger one. The joint-gaps between the stones of the masonry walls and the cracks have to be deeply filled using a thin trowel and a mortar with a very particular composition. The mortar contains terra theraic (earth of Thera): hydraulic lime: sand, with proportions 0.417: 1: 3.333. This new mortar is considered quite compatible with the existing mortar, but it has higher strength and improved durability capacities. Moreover, the hydraulic lime conduces to the mortar mixture, as it regards the pasting. Cement-based mortar should be avoided in these cases because it exhibits high compressive strength compared to the traditional-made, existing one.

Further, the deteriorated architectural features of the building also have to be restored according to their original shape and with respect to the historic value of the building. These features include the destroyed main entrance, the damaged frames of the windows and the damaged decorative cornices that rim the perimeter of the building and distinguish the floors of the warehouse from the external. The bricks and the stones that are missing have to be replaced with new ones having the same shape with the original ones. For this purpose mortar with terra theraic as described above is also suitable for this usage in order the building to obtain its original form and shape.

6 CONCLUSIONS

Inappropriate rehabilitation strategy and intervention plan in historic masonry buildings could be catastrophic both for the architectural cultural value of the structure and for the structure safety and integrity. Cautiousness and structural safety are fundamental issues in the field of rehabilitation of historical heritage. The masonry building under examination had suffered indelible damage due to failure of recently-applied interventions. These works caused the partial collapse of the masonry walls and created a quite unsafe working environment. The constructional characteristics the damages and the pathology in general of the historic building under examination have been recorded using photogrammetry and have been detailed in this paper.

The choice of a proper and feasible restoration process for a partially collapsed historic masonry structure that constitutes a dangerous and risky working environment is a difficult task. The presented rehabilitation methodology aims to successfully support, strengthen and restore the existing building, minimizing the risks of further collapse and personal injury. This procedure in general could include (a) a specially developed securing and temporary supporting system for the façades using external steel towers; (b) a permanent RC beam-column internal frame for the strengthening of the heavily damaged eastern masonry wall that will bear the increased design loads and serve as a permanent support for the façades; it is noted that the construction of a new interior RC frame structure inside the existing masonry building is the main concept of the approved rehabilitation plan and (c) the repair of the masonry cracks and the restoration of the architectural features of the building.

REFERENCES

[1] F.V. Karantoni, M.N. Fardis, Effectiveness of seismic strengthening techniques for masonry buildings. *Journal of Structural Engineering New York*, **118**, 1884-1902, 1992.

[2] F.V. Karantoni, Seismic behaviour and strengthening of a vulnerable structure. *WIT Transactions on the Built Environment*, **98**, 333-342, 2008.

[3] M. Corradi, C. Tedeschi, L. Binda, A. Borri, Experimental evaluation of shear and compression strength of masonry wall before and after reinforcement: Deep repointing. *Construction and Building Materials*, **22**, 463-472, 2008.

[4] V.E. Tsioukas, Simple tools for architectural photogrammetry. *XXI CIPA - Cultural Heritage Documentation International Symposium*, Athens, Greece, 2007.

[5] V.E. Tsioukas, V.G. Alexandri, C.G. Karayannis, C.E. Chalioris, Photogrammetry as a tool to record a historic building at risk. *22nd CIPA Symposium on Digital Documentation, Interpretation and Presentation of Cultural Heritage*, Kyoto, Japan, paper number 44, 2009.

[6] C.E. Chalioris, V.E. Tsioukas, M.J. Favvata, C.G. Karayannis, Recording historic masonry buildings using photogrammetry - Two case studies. *4th International Conference on Computational Methods in Structural Dynamics and Earthquake Engineering (COMPDYN 2013)*, Kos Island, Greece, paper number 1597, 2013.

[7] C. Modena, Criteria for cautious repair of historic buildings. L. Binda, C. Modena eds. *Evaluation and strengthening of existing masonry structures*. France, RILEM, 25-42, 1997.

[8] C.G. Karayannis, C.E. Chalioris, K.K. Sideris, Effectiveness of RC beam-column connection repairing using epoxy resin injections. *Journal of Earthquake Engineering*, **2**, 217-240, 1998.

[9] C.G. Karayannis, C.E. Chalioris, G.M. Sirkelis, Local retrofit of exterior RC beam-column joints using thin RC jackets - An experimental study. *Earthquake Engineering and Structural Dynamics*, **37**, 727-746, 2008.

[10] C.E. Chalioris, M.J. Favvata, C.G. Karayannis, Reinforced concrete beam-column joints with crossed inclined bars under cyclic deformations. *Earthquake Engineering and Structural Dynamics*, **37**, 881-897, 2008.

[11] C.E. Chalioris, M.J. Favvata, C.G. Karayannis, A new method for the seismic rehabilitation of old exterior reinforced concrete beam-column joints. *7th European Conference on Structural Dynamics (Eurodyn 2008)*, Southampton, UK, paper number E245, 2008.

[12] A.G. Tsonos, Performance enhancement of R/C building columns and beam-column joints through shotcrete jacketing. *Engineering Structures*, **32**, 726-740, 2010.

[13] M.J. Favvata, B.A. Izzuddin, C.G. Karayannis, Modelling exterior beam–column joints for seismic analysis of RC frame structures. *Earthquake Engineering and Structural Dynamics*, **37**, 1527-1548, 2008.

[14] C.G. Karayannis, B.A. Izzuddin, A.S. Elnashai, Application of adaptive analysis to reinforced concrete frames. *Journal of structural engineering New York*, **120**, 2935-2957, 1994.

[15] Eurocode 2: *Design of concrete structures - Part 1-1: General rules and rules for buildings*. EN 1992-1-1, CEN Tech. Com. 250/SC2, 2004.

[16] Eurocode 8: *Design of structures for earthquake resistance - Part 1: General rules, seismic actions and rules for buildings*. EN 1998-1, CEN Tech. Com. 250/SC8, 2004.

[17] Eurocode 8: *Design of structures for earthquake resistance - Part 3: Assessment and retrofitting of buildings*. EN 1998-3, CEN Tech. Com. 250/SC8, 2005.

[18] P.B. Lourenço, N. Mendes, L.F. Ramos, D.V. Oliveira, Analysis of masonry structures without box behavior. *Journal of Architectural Heritage*, **5**, 369-382, 2011.

[19] E. Vintzileou, T.P. Tassios, Three-leaf stone masonry strengthened by injecting cement grout. *Journal of Structural Engineering ASCE*, **121**, 848-856, 1995.

[20] L. Binda, G. Cardani, D. Penazzi, A. Saisi, Performance of some repair and strengthening techniques applied to historical stone masonries is seismic areas. *ICPCM a New Era of Building*, Cairo, Egypt, **2**, 1195-1204, 2003.

COMPDYN 2013
4th ECCOMAS Thematic Conference on
Computational Methods in Structural Dynamics and Earthquake Engineering
M. Papadrakakis, V. Papadopoulos, V. Plevris (eds.)
Kos Island, Greece, 12–14 June 2013

RECORDING HISTORIC MASONRY BUILDINGS USING PHOTOGRAMMETRY- TWO CASE STUDIES

Constantin E. Chalioris[1], Vassilios E. Tsioukas[2], Maria J. Favvata[1], and Chris G. Karayannis[1]

[1]Democritus University of Thrace, School of Engineering, Department of Civil Engineering
Xanthi 67100, Greece
e-mail: chaliori@civil.duth.gr

[2]Aristotle University of Thessaloniki, School of Rural and Surveying Engineering
Thessaloniki 54124, Greece
e-mail: tsioukas@auth.gr

Keywords: Masonry Building, Partial Collapse, Surveying, Photogrammetry.

Abstract. *The use of conventional and photogrammetric surveys is presented for the recording of two historic masonry buildings in Greece. The first one is a four-storey traditional tobacco warehouse of the late 19th century in Alexandroupoli which has been partially collapsed in 2005 and constituted an extremely dangerous working environment. The second is an old customs house that is located in the old historic town of Nafplio and specifically in front of the central part of the port. It was built around the middle of the 19th century by the well-known Architect Stamatios Kleanthis. The architectural, structural and morphological characteristics along with the pathology of these buildings have been recorded through photogrammetric and conventional topographic surveys. This way, all the necessary information for the structures have been acquired with an appropriate accuracy in order to assist Engineers to choose the proper repairing and strengthening techniques for the renovation and the re-use of these historic buildings. The old tobacco warehouse in Alexandroupoli is planned to be the new Municipal Library, whereas the old customs house in Nafplio will be a museum for cultural exhibitions. The recording procedure used, combines the conventional topographic surveys and the photogrammetric image processing for the formation of all the façades' orthoimages. The orthoimages were used as background information to digitize details of the buildings façades in a CAD environment. The Photomodeler software and the freeware application Hugin has been used to create respectively a detailed 3D model and an interactive panorama file of the buildings.*

1 INTRODUCTION - HISTORICAL REFERENCES AND STRUCTURAL CHARACTERISTICS

1.1 The partially-collapsed building in Alexandroupolis

The building has been first constructed before 1900 in the center of the city of Alexandroupolis by the catholic community to be used as a school. After a major fire that destroyed part of the existing building in 1904, the building has been reconstructed and enlarged to its final shape in 1924 in order to be used as a tobacco warehouse. It was one of the largest, most prestigious and well-constructed buildings of the area and its new usage was the base of the renowned "Companie general de Tabac" (General Tobacco Company), as shown in Figure 1.

The length of the L-shaped plan building is 26.75m, while its width is 12.30m and 10.30m at the northern and the southern side, respectively. The total height of the structure is 12.45 m and it consists of four storeys; a basement, a ground floor, an upper floor and an attic under a gabled roof. The area of a typical floor is approximately 293 m^2 in a building plot of approximately 846 m^2. It has a gabled roof composed by wooden trusses and terracotta tiles forming gables on the façades. The building is a load-bearing masonry structure made of ashlars of regional granite connected with mud mortar. The thickness of the masonry at the basement is almost 60 cm, at the ground floor it becomes 50 cm and finally at the floor and the attic it is only 45 cm. It can be considered as an excellent sample of industrial architecture initially influenced by the urban architecture of the late 19th century. Supplementary features of the examined building are also provided in Ref [1].



Figure 1: Vintage photograph of the building in Alexandoupolis. It was a tobacco warehouse of the corporate named “Compagnie General de Tabac”. At the top of the gable, “1924” is displayed as the year when the building was first used as a tobacco warehouse.

1.2 The customs house in Nafplio

The historic building is situated in Nafplio, a seaport town in the Peloponnese in southern Greece. Nafplio was the first capital of modern Greece, from the start of the Greek War of Independence (also known as the Greek Revolution) in 1821 to 1834. Count Ioannis Kapodistrias, first governor of modern Greece, set foot on the Greek mainland for the first time in Nafplio on 7 January 1828 and made it the official capital of Greece in 1829. Nafplio remained the capital of the state until 1834, when King Otto decided to move the capital to Athens.

The old customs house is located in the old town of Nafplio, and specifically in front of the central part of the port (Figure 2). It was built in 1832 by the architect Stamatios Kleanthis. He is best known for his urban plan of Athens, which he designed in cooperation with Edward Schaubert, and his designs for various public buildings in the same city. It should be mentioned that Kleanthis and Edward Schaubert were students of perhaps the most important German neo-classical architect Karl Friedrich Schinkel [2]. Kleanthis along with the architects Edward Schaubert and G. Luders carried out the plans of many historic buildings of Nafplio at the time that Nafplio was the Seat of State.



Figure 2: Vintage and nowadays views of the western façade of the old customs house taken from Filellinon Square of Nafplio.

The building has been designated by the Minister of Culture as a Historic Monument and as a Work of Art in 1998. From 1999 till today, it is used as a warehouse for the needs of the customs authority.

The main (northern) façade consists of three parts with an arcade supported on pillars (Figure 3). The specific plan recalls the Venetian Arsenal that houses the Nafplio Archeaological Museum in Syntagma (Constitution) Square. Generally the Customs House is simple in design, rectangular, with symmetrical entrances and windows. It creates a sense of balance and harmony, in keeping with the neo-classical movement. The building consists of a ground floor and a small loft (mezzanine) as well as the arcade supported on pillars. The covered surface of the plot is approximately 376 m^2. The area of the ground floor is 322 m^2 (see also the plan view of the building in Figure 4) and the one of the loft 34 m^2.

The future use of the old customs house was decided by the Municipality of Nafplio to be a museum of custom houses as well as a space where cultural exhibitions will take place. For this reason, detailed recording and structural analysis of the building was required.



Figure 3: Northern façade of the old customs house.

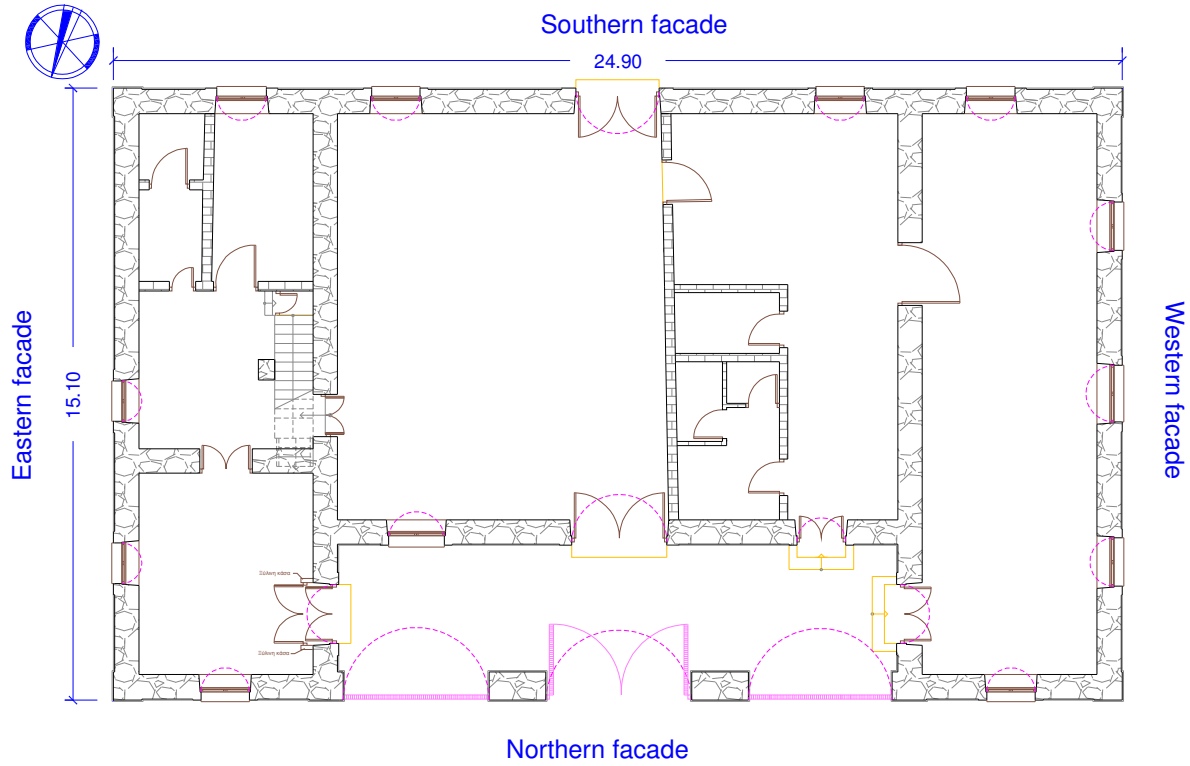


Figure 4: Plan view of the old customs house.

This historic masonry building has a hip roof composed by wooden trusses and byzantine type terracotta tiles. It consists of a ground floor and a small loft (mezzanine) at its north-eastern corner and an arcade supported on pillars at north. The main building materials are stone and wood. Steel only appears in certain architectural elements of the building. In fact it is used at window's metal railings for the protection of the building as well as at arch shaped transom windows recesses. There are two rectangular skylights at the north-eastern corner of the building as well as a circular (bullseye window) at the eastern façade. The main entrance is protected by a metal double-door whereas the two double doors at north and south are wooden. Though the main entry door was supposed to be at the western façade, nowadays there is a window instead of a door. The roof, the floors and the stair that leads to the loft are

wooden. The floor of the western room on the ground floor is paved with plastic tiles; the floors of the two central rooms are paved with mosaic.

The foundation of the building is made of bearing masonry and follows the outside perimetric walls of the basement in approximately 95 cm below the ground level whereas the aquifer is 85 cm below the ground level making the foundation soil's characteristics not safe. Due to that fact, one meter below the ground the foundation is probably composed by wooden piles. It should be mentioned that the building was constructed on an embanked section of the coast line.

The thickness of masonry is 60 cm and the height is 6.60 m. The masonry is unreinforced composed of natural stones. The main ingredient of the mortar is clay and its thickness varies from 1 to 3 mm. The walls are covered on the inside as well as on the outside with a rubber coating. The original color of the outside of the walls was a mix of ochre iron with white. The decorative cornices of the windows are composed of solid bricks coated with cement. The pillars that form the arcade at north are covered with carved limestone. Also the four corners of the building are covered from their base to the top with carved limestone resembling four columns. Under the hip roof, there is a stone moulding, quadrant shaped, that covers all the perimeter of the building.

2 PATHOLOGY AND DAMAGES

2.1 Partially-collapsed building in Alexandroupolis

The building sustained severe damages due to (a) its age, the many years of non-use, the total lack of maintenance and the utter forlornness (b) the inappropriate and catastrophic rehabilitation plan which included the total removal of all the interior structural members such as wooden diaphragms, wooden beams and wooden and concrete columns; and (c) the partial-collapse of the eastern and northern wall along with part of the roof in 2005, during the intervention works. Details can also be found in Ref [1].

After the partial-collapse and in order first to support the existing walls and make the working environment safe and second to repair and reconstruct the building, a detailed recording of the existing situation is required. In particular, a thorough recording of the morphology and the pathology of the partially-collapsed building was necessary. The method of photogrammetry was chosen as one of the most appropriate for this recording due to the unsafe and precarious nature of the building, and to the fact that access inside the building and to the upper parts of the masonry walls is hazardous and practically impossible.

2.2 The customs house in Nafplio

The building suffers from damages and wears due to the aging of the materials, to the high humidity due to its seaside location as well as the neglect and lack of maintenance. The damages that are related to the structural system of the building (masonry) are local wears and cracks at the arches of the lintels as well as at certain masonries. Cracks are also observed at the connections of the inner masonries. The majority of the cracks are transversal with rather small to medium width (under 10 mm). Some slight longitudinal cracks (width < 3 mm) are also detected near the windows (lintels and sills). Finally, some carved limestones, without any coating, that cover the pillars of the arcade sustain wears due to aging. Further, as it was expected, all the construction materials of the masonry, natural stones, clay mortars, carved limestone and bricks contain soluble salts, mostly chloroide, because of their exposure to the marine environment according to the results of their examination at the laboratory. A vertical displacement of 14 cm is also observed at the roof (see also Figure 3). This deformation is

located mainly at the northern and the southern façade. The wooden elements of the roof (trusses, batters, sheeting) are more or less in a good condition given their age. However certain wooden elements should be replaced due to aging and the lack of maintenance.

3 RECORDING USING PHOTOGRAMMETRY

Concerning the partially-collapsed tobacco warehouse, due to the dangerous conditions of the heavily damaged building, the geometrical details of the structure could not be recorded using common procedures and a rather special refined survey was required. For this reason, photogrammetric image processing is used in order to create the orthoimages of the façades, as background information to digitize details of the buildings in a CAD environment with accuracy of 1 cm [3]. The recording data via photogrammetry consists of rectified images and mosaics of the building and a spherical 3D panorama of the inner of the building. Photomodeler software and the freeware application Hugin has been used to create the detailed 3D model and the interactive panorama file of the building, respectively [4, 5].

The same recording procedure has been also used for the case of the old customs house in Nafplio. The detailed and accurate geometrical shape of the digitized façades of both building provides a rich database of their structural features. Further, all the irregularities of their geometry are detected in detail and can be given as input data to the structural analysis models [6, 7]. Obviously, these data have fundamental importance for the stability assessment of the partially-collapsed warehouse. This way, photogrammetry is used as a refined tool that would help to implement a safe and efficient supporting solution and an integrated rehabilitation procedure of this problematic masonry structure. Further, the interactive spherical panorama has placed virtually the engineer inside the partially-collapsed building, helping him to zoom in the details of the structure without exposing him to the danger of a potential collapse.

The recording through the photogrammetric process was providing the required safety just because its remote sensing nature. All the images were corrected from lens and manufacturing distortions and were calibrated since a common digital camera was used to obtain the complete set of images. The camera used was a Canon dSLR EOS 400D of 10 Mpixel imaging sensor equipped with a accompanied low quality 18-50mm lens. The procedure of the recording was accomplished in the three following described steps; measurements, calibration and photogrammetric processing and digitization.

3.1 Measurements

The capturing of the outer space images of the examined buildings was realized and a set of appropriate control points were measured in a unique rectangular coordinate system. A rough 3D model of the building was created through conventional surveying methodology. An accurate topographic network of ground control points was established in accuracy appropriate to realize in the architectural scale (1:50) all the drawings (sections, façades and top-views and bottom views) of the buildings. The topographic measurements did not include cracks and other important details of the masonries. These were digitized from the rectified images created in a next stage.

For the recording of the buildings, Ground Control Points (GCPs) were measured on the façades and these points were also used to obtain the shape of the construction. A triangulation network, covering the buildings from the outside and its inside, was established. The topographic instrument's stations were installed in the yard, the area around the buildings and on the terrace of neighboring buildings. Only one instrument station was installed inside the partially-collapsed tobacco warehouse for security reasons. From the instrument's stations additional GCPs were measured for the 2D rectification of the façades' images.

3.2 Calibration

In order to obtain the best results two calibration procedures have been applied before the main process of the photogrammetric image processing. Photomodeler's calibration module and a homemade application were used for this reason [4]. The camera calibration module of the commercial application Photomodeler was used to obtain a more precise draft model of the buildings while for the correction of the radial distortion of the images to be rectified, a homemade software application has been used.

Photomodeler's calibration module leads to a solution with an accuracy of 0.45 pixel and the camera's focal distance was estimated at 17.66 mm. The homemade software Calib has been developed using the Open Source Computer Vision Library created by Intel (OpenCV) and has provided similar results [3, 5]. The calibration procedure is using a regular grid (grid of circular points or a printed chessboard) that is supposed to be photographed from different camera positions. The algorithms are identifying the targets of the patterns with sub pixel accuracy and then calculate the exterior orientation parameters of the camera during the image capture and its intrinsic calibration parameters.



Figure 5: Rectified mosaic of images (left) and corresponding digitized façade (right) of the western and the southern façades of the partially-collapsed tobacco warehouse in Alexandroupolis

3.3 Photogrammetric processing and digitization

Special image capturing (vertical image capturing) was realized to create rectified images and orthomosaics of the façades of the examined buildings. In every façade a set of Ground Control Points (GCPs) were measured to obtain the 2D rectification of the images. These GCPs were also connected to the generic 3D coordinate system that is describing the draft 3D

model of the building. The connection (transformation and rotation parameters) between the 3D model and the GCPs was used to provide the georeference of every rectified image, mosaic or digitized drawing to the 3D space. The accuracy of the digitization of the images was compatible to the final printout scale (1:50). Additionally, convergent image shooting and the Photomodeler software application were used to obtain a photogrammetric 3D model of the building.

The generated rectified images were created in VeCAD-Photogrammetry [5]. GCPs collected for the 2D rectification of images (radial distortion free) were inserted in the software and simple procedures lead to the desired results. The digitization was accomplished from the rectified images and mosaics after the processing the nearly vertical images of the façades of the buildings (see Figures 5 and 6). Snaps of the interactive spherical panorama are also displayed in Figure 7.

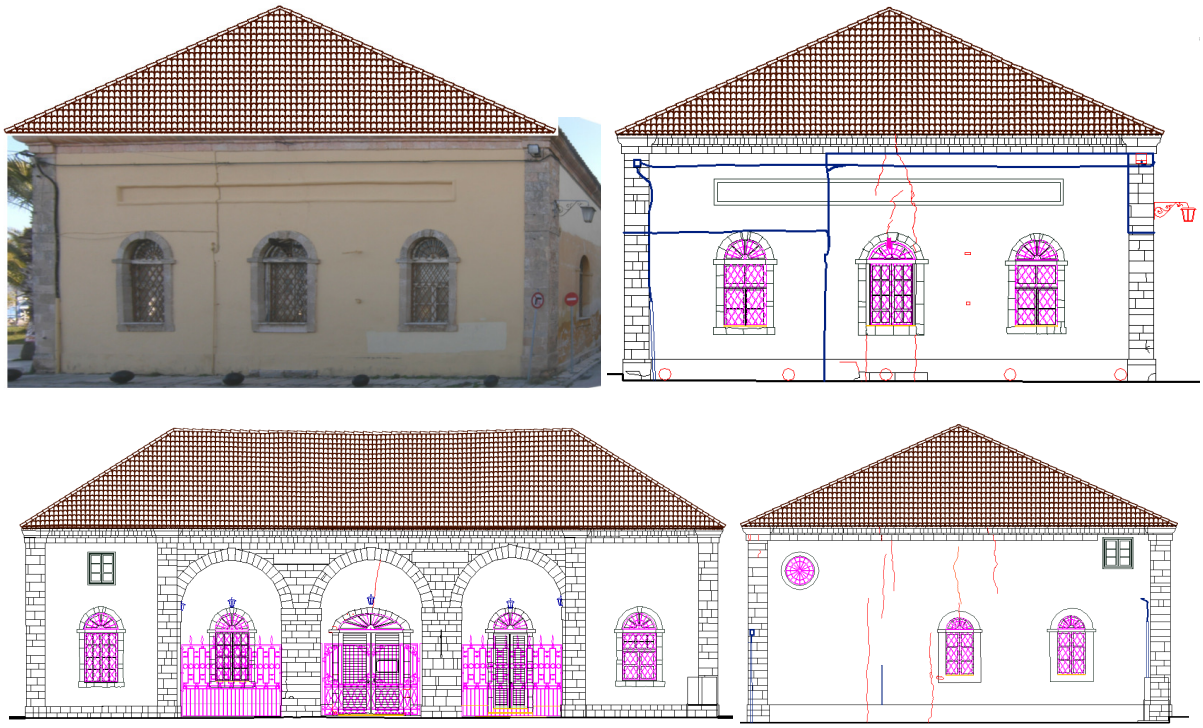


Figure 6: Rectified mosaic of image of the western façade and digitized façades (western, northern and eastern) of the old customs house in Nafplio along with the detected cracking of the masonries.



Figure 7: Snaps of the interactive spherical panorama of the partially-collapsed building in Alexandroupolis.

4 CONCLUSIONS

Application of image rectification to complete 2D drawings of historical buildings has been presented. The conventional 2D drawings have been enriched by the visual information of the geometrically corrected texture images of the masonry structures, thus providing a more comprehensive and understandable representation of the construction, the damages and the materials. The visualization of the examined buildings through the rectified images, mosaics, orthoimages and 2D drawings increased surveying speed and constituted a useful implementation guide.

Additionally, low-cost (Photomodeler), open-source (Hug-in) and home-made software (VeCAD-Photogrammetry [8]) were used to obtain the minimum number of measurements and achieve the desired results and products in the appropriate accuracy (1 cm) for the final (1:50 scale) drawings' reprints. The total budget for the purchase of the specific hardware (camera) and software (Photomodeler), at the time of the project, were under 2,000 €. Taking into account also the reduced time to obtain the measurements on the field and the complete digitization in the office of all the structural details and fractures on the buildings facades, we can conclude that photogrammetry is the most appropriate technique to record in short time with the lowest cost a historic building that is under a renovation process or at risk.

REFERENCES

[1] C.E. Chalioris, M.J. Favvata, V.G. Alexandri, C.G. Karayannis, Rehabilitation of a partially collapsed masonry traditional tobacco warehouse of the late 19th century. *4th International Conference on Computational Methods in Structural Dynamics and Earthquake Engineering (COMPDYN 2013)*, Kos Island, Greece, paper number 1596, 2013.

[2] K. Biris, *Athenian Studies*, Athens, **1**, 10-30, 1938.

[3] V.E. Tsioukas, V.G. Alexandri, C.G. Karayannis, C.E. Chalioris, Photogrammetry as a tool to record a historic building at risk. *22nd CIPA Symposium on Digital Documentation, Interpretation and Presentation of Cultural Heritage*, Kyoto, Japan, paper number 44, 2009.

[4] *Photomodeler Software*, www.photomodeler.com

[5] V.E. Tsioukas, Simple tools for architectural photogrammetry. *XXI CIPA - Cultural Heritage Documentation International Symposium*, Athens, Greece, 2007.

[6] G. Pavlidis, A. Koutsoudis, F. Arnaoutoglou, V. Tsioukas, C. Chamzas, Methods for 3D digitization of cultural heritage. *Journal of Cultural Heritage*, **8**, 93-98, 2007.

[7] E. Andaroodi, Z. Taqipour, Architectural photogrammetry by non-metric cameras: CAD-based 2D drawing of facades from rectified photos. M. Ioannides et al. eds. *Progress in Cultural Heritage Preservation, Lecture Notes in Computer Science*, **7616**, 477-485, 2012.

[8] *VeCAD-Photogrammetry*, Free software download link: http://blogs.auth.gr/tsioukas/2011/08/21/vecad-photogrammetry/

COMPDYN 2013
4th ECCOMAS Thematic Conference on
Computational Methods in Structural Dynamics and Earthquake Engineering
M. Papadrakakis, V. Papadopoulos, V. Plevris (eds.)
Kos Island, Greece, 12–14 June 2013

STRUCTURAL UPGRADING OF A 3-STOREY HERITAGE STRUCTURE OF 1925 IN THESSALONIKI

Chris G. Karayannis[1], **Constantin E. Chalioris**[1], **and Maria J. Favvata**[1]

[1]Democritus University of Thrace, School of Engineering, Department of Civil Engineering
Xanthi 67100, Greece
e-mail: chaliori@civil.duth.gr

Keywords: Reinforced Concrete Structure, Infilled Masonry, Upgrading, Jacketing.

Abstract. *The structural upgrading and rehabilitation procedure of a historic building representative of 1920s construction in Thessaloniki, Greece is presented. The case study building is a listed three-storey reinforced concrete flat-slab frame structure sited in Nikis Avenue in front of the old seaside of the city of Thessaloniki. Reinforced concrete columns and beams frames along with wide infilled masonry walls are the load-bearing elements of the structure. The building was designed in 1925 without Seismic Code requirements and constructed in 1926. The ground floor was used for many years as a cinema, whereas the upper floors are areas where people may congregate since they are used as assembly halls (dining halls, reading and conference rooms). Concrete core tests and in-situ non-destructive tests were first performed to evaluate the compressive strength of the concrete and to detect - determine the existing steel reinforcements of the reinforced concrete members. The concrete strength was low and the steel reinforcement of several columns of the ground floor and slabs of the upper floors was found to be corroded. Analytical evaluations of the original and the strengthened structure were carried out in order to identify the weak members of the structural system and to justify the decisions of the strengthening methods adopted. Comparisons between the capacity of the existing or/and the strengthened members with the design requirements derived from the initial and the strengthened structural system analyses are also presented. Special attention has been given in issues regarding the simulation of actual details encountered in mixed structural system. The upgrading methods used along with the uncovering of latent defects during the strengthening works and how these were managed are also commented in this paper.*

1 STRUCTURAL CHARACTERISTICS OF THE HERITAGE STRUCTURE

The building is sited in Thessaloniki, in Nikis Avenue in front of the old seaside of the city. It is a three-storey Reinforced Concrete (RC) flat-slab frame structure that was designed in 1925 and constructed in 1926. The ground floor was used for many years as a cinema, whereas the upper floors as assembly halls (dining halls, reading and conference rooms). The load-bearing elements of this structure consist of RC columns and beams frames along with wide infilled masonry walls.

This listed heritage structure has remarkable exterior decoration and noticeable architectural features as it can be observed in Figure 1. In this Figure the front façade of the building as it has been designed in a drawing of 1925 and as it is shown today in a recent photograph are presented. It should be mentioned that authorities responsible for potential preservations of heritage buildings do not allow interventions that may alter its front façade.

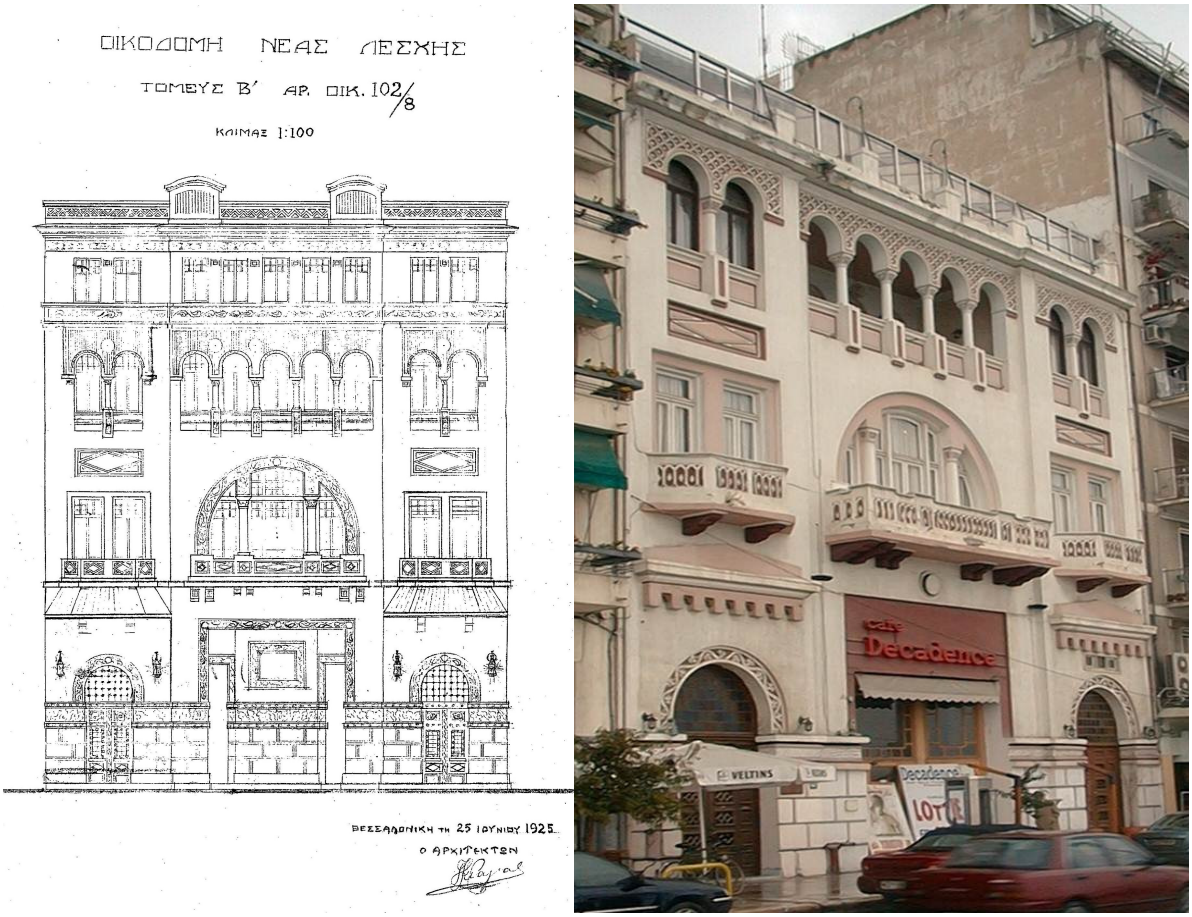
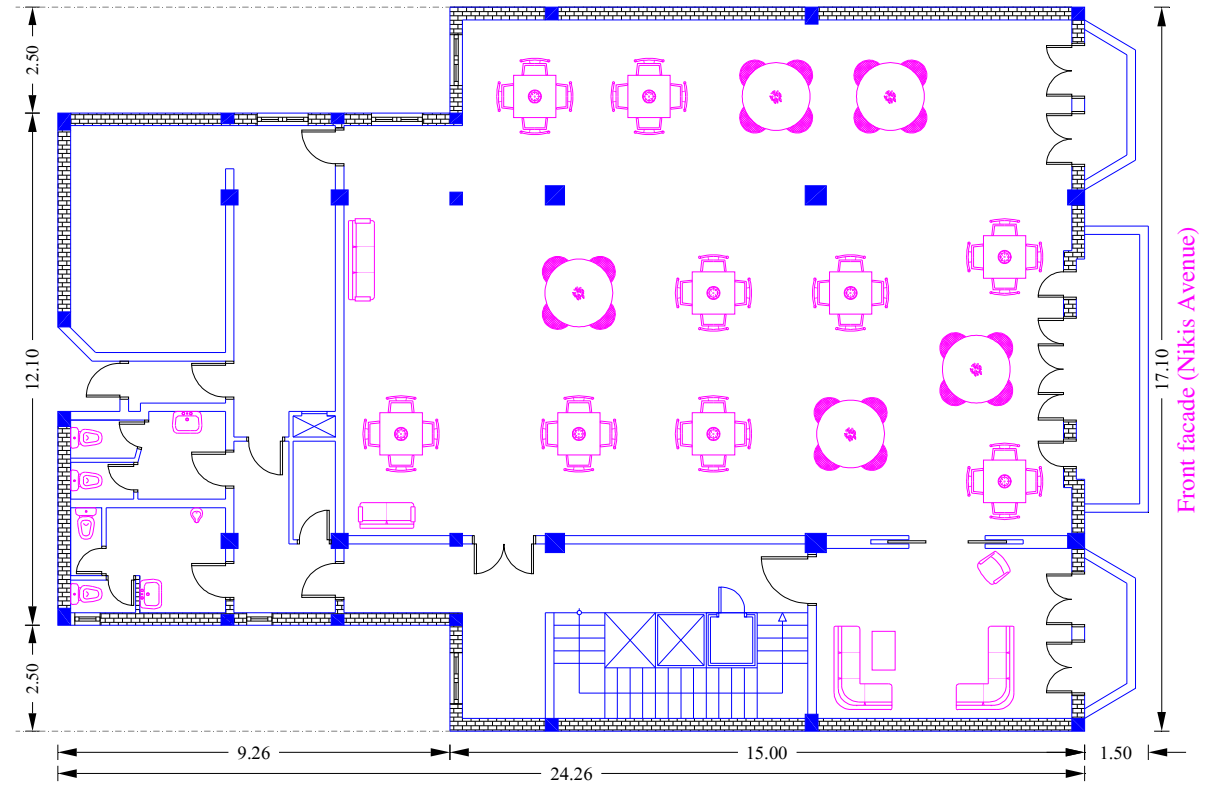
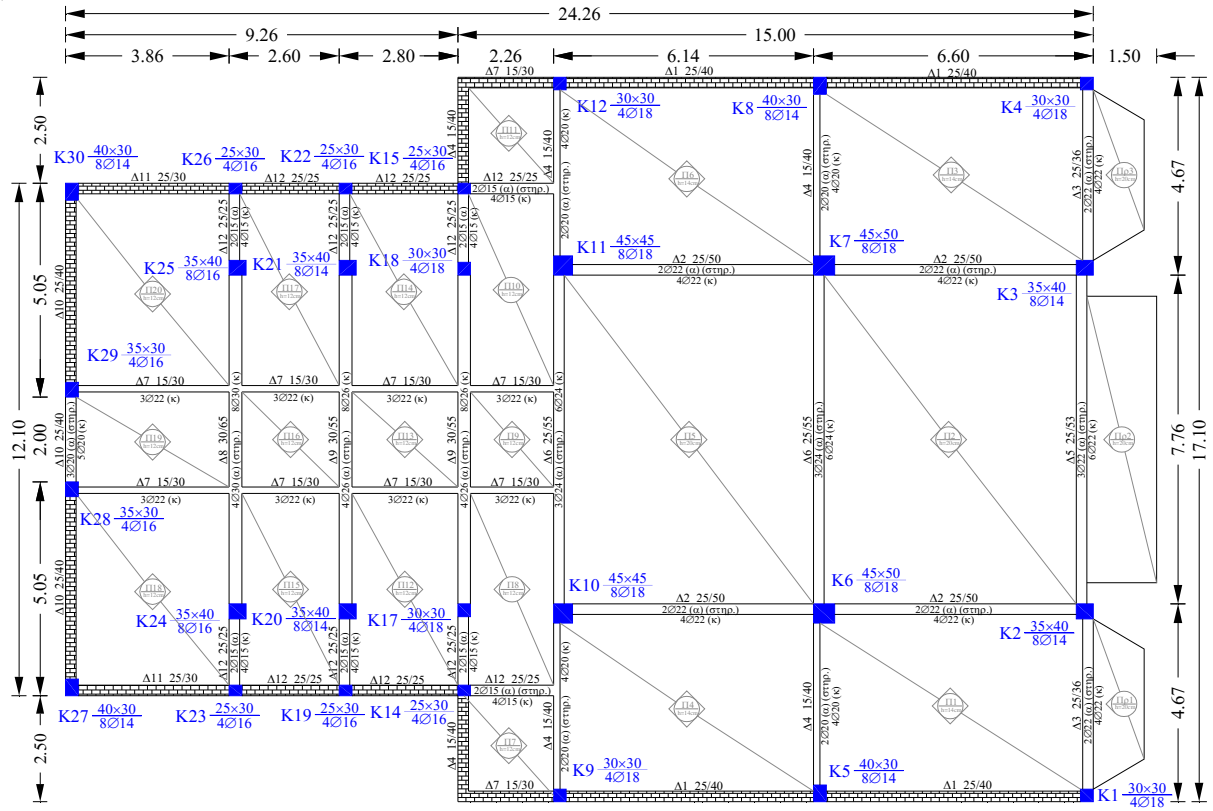


Figure 1: The front façade of the building as it was first designed (drawing of 1925) and as it is today (recent photograph).

The total length of the building is 24.26 m, while the width of its front façade is 17.10 m. This width remains the same for a length equal to 15.00 m and then it is reduced symmetrically to 12.10 m (see also the plan view of Figure 2a). The area of a typical floor is approximately 370 m^2 and the total height of this three-storey structure is 17.40 m. The examined heritage structure stands between two adjacent multi-storey modern apartment buildings, as shown in the photograph of Figure 1.



(a) Plan view



(b) Formworks plan

Figure 2: Drawings of the first floor (typical floor) of the initial status of the building.



Figure 3: Corrosion of the steel reinforcement of the RC columns K17, K21, K24, K28 and K29 (ground floor).



Figure 4: Extensive corrosion of the steel reinforcement of the RC slabs.

There are 30 RC columns in the ground floor and 28 in the upper two floors. These columns and the infilled masonry walls at the perimeter of the structure consist of the vertical load-bearing elements, whereas RC beams and slabs are the horizontal elements, as shown in the formworks plan of Figure 2b.

The building has been constructed very close to the coast line where the soil's characteristics are not safe due to the presence of underground water. For this reason, the foundation of the building consists of a rigid RC raft foundation system with RC ribs that connect the existing RC columns.

The main damages of the building come from the aging of concrete and the extensive corrosion of the reinforcing steel, as shown in the photographs of Figures 3 and 4. Limited and rather expecting cracking has also been observed in the RC beams and slabs of the structure

with rather large spans. The condition of the masonry walls could be characterized as satisfactory since no severe cracks or damages in the bricks or the mortars have been observed.

2 METHODOLOGY

First, extensive in situ non-destructive tests have been performed in order to determine the present status of the building, to estimate the concrete strength and to record the dimensions and the steel reinforcement arrangements (bars and stirrups) of the RC elements, mainly of the columns and the beams. The concrete strength has also been evaluated by core tests of concrete cylindrical core samples that have been taken from five columns and three foundation beams of the building. These tests showed that the mean compressive concrete cylinder strength is today 15.9 MPa with standard deviation 4.6 MPa. Thus, the concrete strength class is very low (C8/10) with characteristic strength 8 MPa.

Plain round mild steel bars and stirrups have been used for the reinforcement of the concrete elements of the building. The characteristic strength of the mild steel used is 220 MPa. Further, in situ observations and half-cell potential measurements highlighted the problem of corrosion in the steel reinforcement of many RC elements (see also Figures 3 and 4).

The vulnerability of the building was mainly originated from the following aspects: (i) The low quality of the building materials (concrete and steel), (ii) the significant corrosion of steel reinforcement, (iii) the lack of seismic design and consequently its inadequate seismic resistance, (iv) the minor cross-sectional dimensions and the low reinforcement ratio of several RC columns and (v) the lack of adequate ductility.

It is known that the strengthening of heritage structures located in seismic areas is a very complex problem due to the wide variety of involved aspects, such as the quality of the materials (concrete, steel and masonry), the building structural assemblages and, apparently, the economical implications. Further, the analysis of the seismic response of such buildings needs a proper knowledge of the traditional constructive techniques, the identification of the damage and collapse mechanisms activated by the earthquake and the check of the effectiveness of the most applied retrofitting techniques [1-3].

Experimental tests of RC beam-column joints and frames with or without infilled masonry sub-assemblages [4-7] have shown that the excessive damage or failure of joints, in particular exterior joints, can lead to the global collapse of a building [8, 9]. The poor joint behavior of older construction can be attributed to the inadequate shear reinforcement in joint region, the poor bond properties of plain round bars reinforcement and the deficient anchorage details into the joint region [10, 11]. Various retrofit or seismic rehabilitation schemes have been previously proposed and implemented for RC beam-column joints and frames [12]. The majority of these methods involve either the strengthening of the joint only or both the joint and column in order to induce plastic hinging in the beams.

Jacketing is one of the most favorable and well-known strengthening method of poor detailed or deficient members and structures. It has long been recognized that RC jackets do provide increased strength, stiffness and overall enhancement of the structural performance. Jackets constructed by conventional cast-in-place concrete [13], premixed, non-shrink, flowable, rapid and high-strength cement-based mortar [14], shotcrete [15], self-compacting concrete [16] and FRP sheets [17, 18] have been examined as rehabilitation methods in existing inadequate or damaged RC members.

The upgrading scheme selected for the examined heritage structure is presented in Figure 5. Most of the existing RC columns have been strengthened using RC jacketing. The checking and design procedure of the existing and the strengthened columns, respectively, is presented and briefly described in Figures 6-10 for four representative columns of the building.

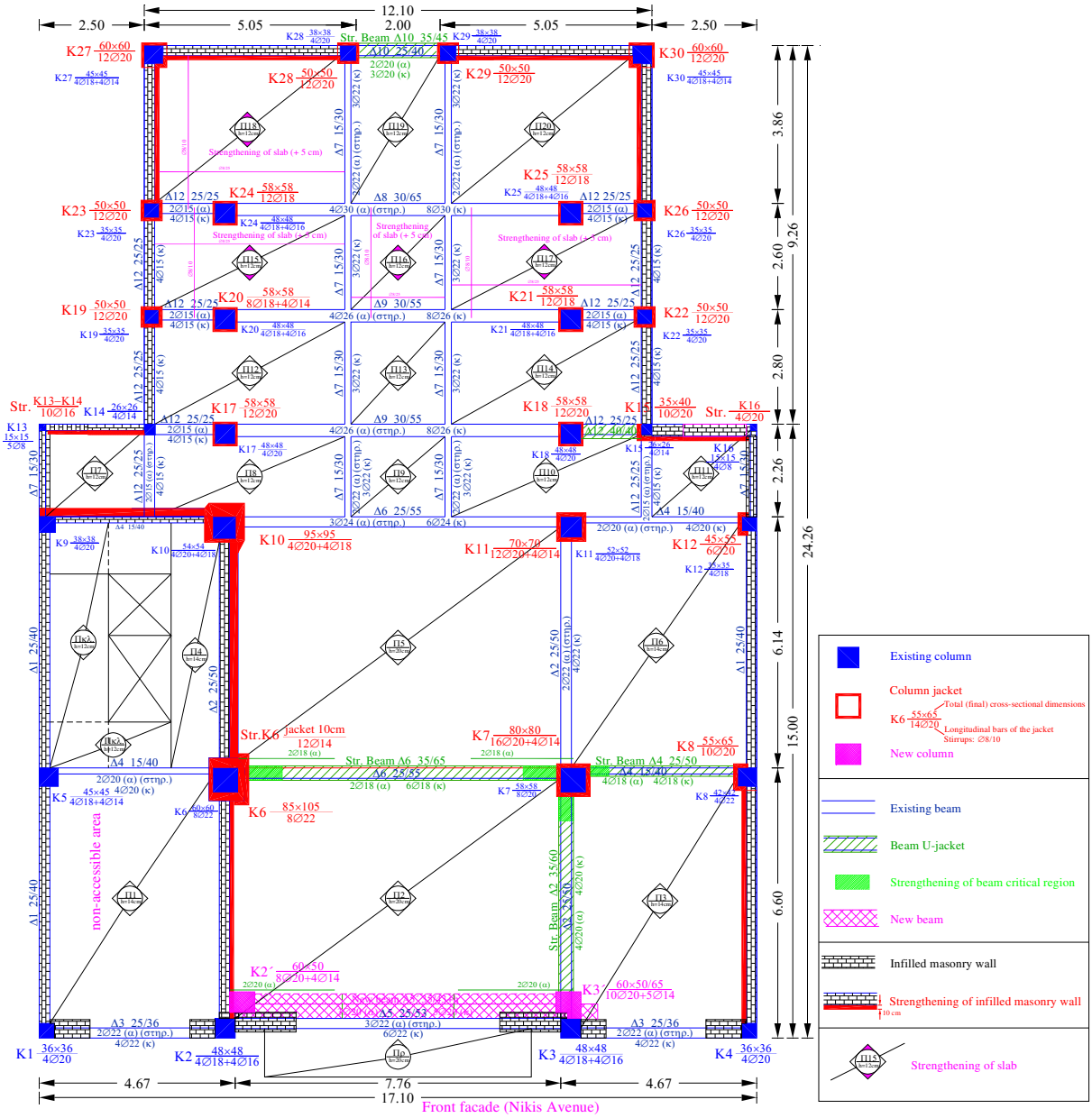
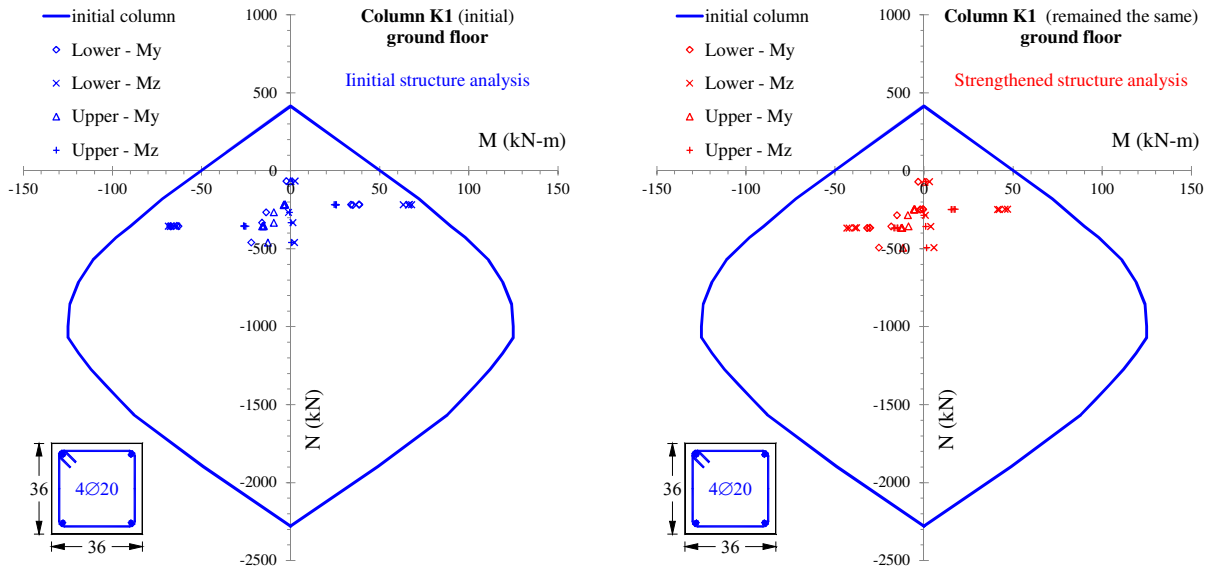


Figure 5: Formworks plan of the ground floor of the strengthened building.

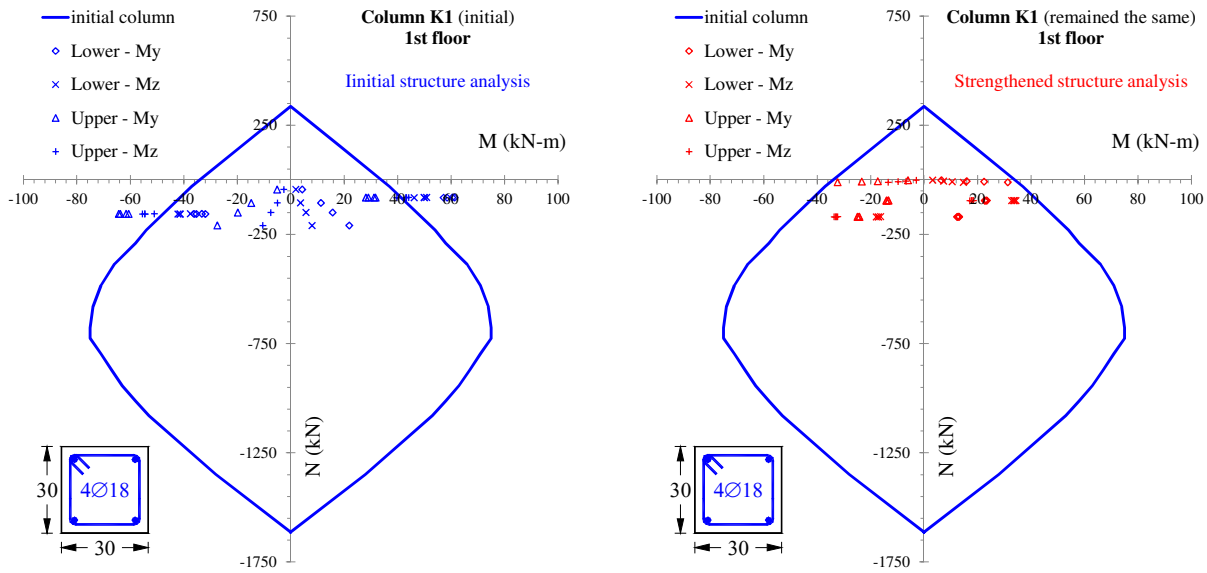
Further, selected infilled masonry walls along with the deficient beams and slabs due to corroded steel reinforcement have also been strengthened using new steel reinforcement and shotcrete, as shown in Figure 5. Moreover, since the front façade of the upgrading heritage building should be remained intact, a new two columns - beam RC frame has been constructed in the interior of the structure. This frame is in contact and connected with the structural RC elements of the front façade.

The new and the strengthened RC elements are designed according to the specifications of the Greek Code for Concrete Structures [19] and the Greek Seismic Code [20] for concrete strength class C20/25, steel reinforcement class S500s, design ground acceleration 0.16g, ground type C, importance factor 1.00, behavior factor 1.5 for the initial structure and 3.5 for the strengthened structure and live loads 5 kN/m^2. Eight seismic combinations were examined: G+0.30Q±E_x±0.3E_y and G+0.30Q±0.3E_x±E_y, where G and Q are the dead and live loads respectively, and E_x and E_y are the seismic loads along the x and y axes, respectively.



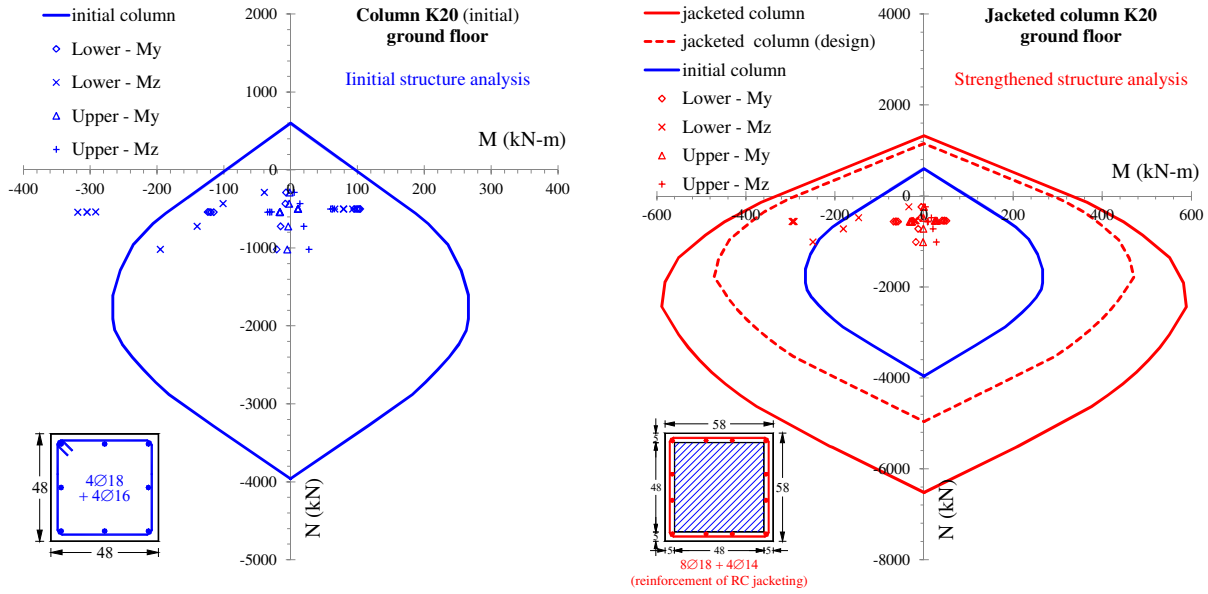
(a) Initial structure (b) Strengthened structure

Figure 6: Bending moment (M) versus axial force (N) interaction curves for the column K1 of the ground floor. The data points (M, N) represent the design values of the applied M and N derived from the seismic analyses of the (a) initial and (b) strengthened structural system. It is concluded that there is no need column K1 of the ground floor to be strengthened since its strength satisfy the design requirements in all cases.



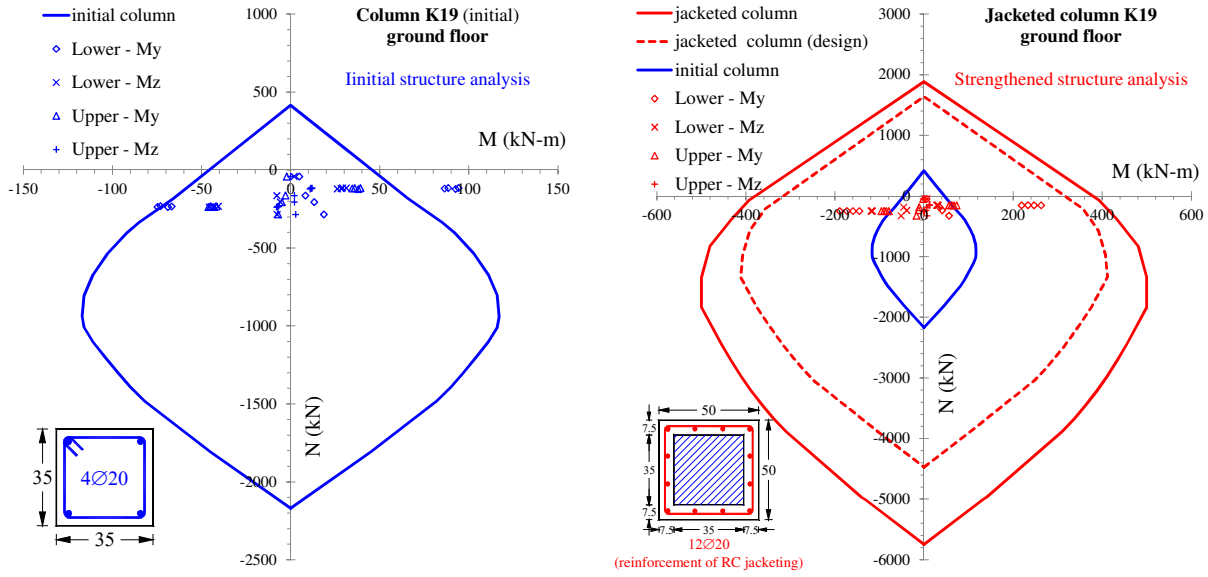
(a) Initial structure (b) Strengthened structure

Figure 7: Bending moment (M) versus axial force (N) interaction curves for the column K1 of the first floor. The data points (M, N) represent the design values of the applied M and N derived from the seismic analyses of the (a) initial and (b) strengthened structural system. It is concluded that although the strength of the existing column does not satisfy the design requirements of the initial structure analysis in all cases, the design requirements of the strengthened structure analysis become lower and henceforth proved to be satisfied. Thus, there is no need column K1 of the first floor to be strengthened.



(a) Initial structure (b) Strengthened structure

Figure 8: Bending moment (M) versus axial force (N) interaction curves for the column K20 of the ground floor. The data points (M, N) represent the design values of the applied M and N derived from the seismic analyses of the (a) initial and (b) strengthened structural system. The strength of the existing column does not satisfy the design requirements of both analyses (initial and strengthened). Thus, column K20 of the ground floor is strengthened by applied RC jacket.



(a) Initial structure (b) Strengthened structure

Figure 9: Bending moment (M) versus axial force (N) interaction curves for the column K19 of the ground floor. The data points (M, N) represent the design values of the applied M and N derived from the seismic analyses of the (a) initial and (b) strengthened structural system. The strength of the existing column does not satisfy the design requirements of both analyses (initial and strengthened). Thus, column K19 of the ground floor is strengthened by applied RC jacket.

3 STRENGTHENING WORKS

Selected strengthening works applied in the examined heritage building are presented in the photographs of Figure10.



(a) Masonry walls and columns of the ground floor



(b) Connection with the infilled masonry wall



(c) Jacketing of the ground floor columns



(d) U-jacketing of a beam with large span



(e) Slab strengthening of the second floor



(f) Shotcrete application

Figure 10: Reinforcement arrangement and shotcrete application of the jacketing - strengthening works in the existing RC elements of the building

4 CONCLUSIONS

This study presents the upgrading procedure of a three-storey historic building with mixed structural system. Reinforced concrete slabs and beam-column frames along with wide infilled masonry walls are the load-bearing elements of the structure. The building was designed in 1925 without seismic design provisions. In situ non-destructive and core tests have been performed in order to evaluate the concrete strength and to record the present status of the building. The compressive concrete cylinder characteristic strength found to be 8 MPa. The steel reinforcement in several columns of the ground floor and in some slabs of the upper floors was found to be substantially corroded. Analyses of the initial and the strengthened structural system were carried out and comparisons between the capacity of the existing or/and the strengthened members with the design requirements are presented and discussed. Most of the existing RC columns have been jacketed, whereas selected infilled masonry walls and deficient beams and slabs have been strengthened using new steel reinforcement and shotcrete. During the strengthening works, covered problems such as extended steel reinforcement corrosion and severe cracking in beams with long spans have been revealed and supplementary interventions were carried out. In this case study, an integrated upgrading procedure is presented as a contribution in the field of structural upgrading of historic buildings with mixed structural system.

REFERENCES

[1] F.V. Karantoni, M.N. Fardis, Effectiveness of seismic strengthening techniques for masonry buildings. *Journal of Structural Engineering New York*, **118**, 1884-1902, 1992.

[2] C. Modena, Criteria for cautious repair of historic buildings. L. Binda, C. Modena (eds). *Evaluation and strengthening of existing masonry structures*. France: RILEM, 25-42, 1997.

[3] T.C. Triantafillou, M.N. Fardis, Strengthening of historic masonry structures with composite materials. *Materials and Structures/Materiaux et Constructions*, **30**, 486-496, 1997.

[4] C.G. Karayannis, M.J. Favvata, D.J. Kakaletsis, Seismic behaviour of infilled and pilotis RC frame structures with beam-column joint degradation effect. *Engineering Structures*, **33** (10), 2821-2831, 2011.

[5] C.E. Chalioris, M.J. Favvata, C.G. Karayannis, Reinforced concrete beam-column joints with crossed inclined bars under cyclic deformations. *Earthquake Engineering and Structural Dynamics*, **37**, 881-897, 2008.

[6] C.G. Karayannis, C.E. Chalioris, Capacity of RC joints subjected to early-age cyclic loading. *Journal of Earthquake Engineering*, **4**, 479-509, 2000.

[7] C.G. Karayannis, C.E. Chalioris, K.K. Sideris, Effectiveness of RC beam-column connection repairing using epoxy resin injections. *Journal of Earthquake Engineering*, **2**, 217-240, 1998.

[8] C.G. Karayannis, B.A. Izzuddin, A.S. Elnashai, Application of adaptive analysis to reinforced concrete frames. *Journal of structural engineering New York*, **120**, 2935-2957, 1994.

[9] M.J. Favvata, B.A. Izzuddin, C.G. Karayannis, Modelling exterior beam-column joints for seismic analysis of RC frame structures. *Earthquake Engineering and Structural Dynamics*, **37**, 1527-1548, 2008.

[10] S. Hakuto, R. Park, H. Tanaka, Seismic load tests on interior and exterior beam-column joints with substandard reinforcing details. *ACI Structural Journal*, **97**, 11-25, 1997.

[11] W.Y. Kam, S. Pampanin, Selective weakening techniques for retrofit of existing reinforced concrete structures, Proceeding of 14th World Conference on Earthquake Engineering, Beijing, China, 2008.

[12] FIB, *Seismic Assessment and Retrofit of Reinforced Concrete Buildings: State-of-the-art report*. International Federation for Structural Concrete, Lausanne, Switzerland, 2003.

[13] S.N. Bousias, D. Biskinis, M.N. Fardis, A.L. Spathis, Strength, stiffness, and cyclic deformation capacity of concrete jacketed members. *ACI Structural Journal*, **104**, 521-531, 2007.

[14] C.G. Karayannis, C.E. Chalioris, G.M. Sirkelis, Local retrofit of exterior RC beam-column joints using thin RC jackets - An experimental study. *Earthquake Engineering and Structural Dynamics*, **37** (5), 727-746, 2008.

[15] A.G. Tsonos, Performance enhancement of R/C building columns and beam-column joints through shotcrete jacketing. *Engineering Structures*, **32**, 726-740, 2010.

[16] C.E. Chalioris, C.N. Pourzitidis, Rehabilitation of shear-damaged reinforced concrete beams using self-compacting concrete jacketing, *ISRN Civil Engineering*, Article ID 816107, 12 pages, 2012.

[17] C.E. Chalioris, Analytical model for the torsional behaviour of reinforced concrete beams retrofitted with FRP materials. *Engineering Structures*, **29**, 3263-3276, 2007.

[18] C.G. Karayannis, G.M. Sirkelis, Strengthening and rehabilitation of RC beam-column joints using carbon-FRP jacketing and epoxy resin injection. *Earthquake Engineering and Structural Dynamics*, **37**, 769-790, 2008.

[19] *Greek Code for Concrete Structures*, Earthquake Planning and Protection Organisation, Athens, 2000.

[20] *Greek Seismic Code*, Earthquake Planning and Protection Organization, Athens, 2003.

COMPDYN 2013
4th ECCOMAS Thematic Conference on
Computational Methods in Structural Dynamics and Earthquake Engineering
M. Papadrakakis, V. Papadopoulos, V. Plevris (eds.)
Kos Island, Greece, 12–14 June 2013

ESTIMATING THERMAL INERTIA AND TEMPERATURE DISTRIBUTION CONSISTENT WITH MONITORED DATA FROM A RAILWAY BRIDGE

Fabio Casciati[1], Sara Casciati[2], Lucia Faravelli[1], Daniele Bortoluzzi[1] and Thomas B. Messervey[3]

[1]Department of Civil Engineering and Architecture, University of Pavia
Via Ferrata 1, 27100 Pavia, Italy
e-mail: fabio@dipmec.unipv.it

[2] Dept. DICA, Dipartimento di Ingegneria Civile e Ambientale, School of Architecture, University of Catania at Siracusa, Piazza Federico di Svevia, 96100 Siracusa, Tel.: (+39) 338 5953658
e-mail: saracasciati@msn.com

[3]R2M Solution srl
Via Monte Sant'Agata 16, 95100 Catania, Italy
thomas.messervey@r2msolution.com

Keywords:, FBG sensors, Monitoring, Railways Bridge, Temperature.

Abstract. *This paper proposes a sequence of analyses allowing the designer to quantify the changes in the structural response due to the temperature variation. This is illustrated for a case study on a railway bridge. The SHM (Structural Health Monitoring) system installed on the bridge consists of Fiber Bragg Grating (FBG) sensors. A numerical model of the bridge was created. The plot of the daily variation of the vertical displacement of a node, when numerically computed for a temperature field interpolating the readings of the temperature sensors, shows a curve similar to the recorded history plot, but the latter one is delayed. This delay is due to both the thermal inertia of the deck, the reinforced concrete of the superstructure, and the actual temperature distribution across and along the deck. Thus, a refined study of the temperature time histories was conducted by a suitable thermo-mechanical model driven by the temperatures measured at the sensor locations. The obtained field of temperature is then used as input for a stress-strain analysis. The resulting displacements are eventually compared with the measured values. Using a first set of data, the numerical model parameters are calibrated, while a second set of data is used for a validation of the whole procedure.*

1 INTRODUCTION

In Structural Monitoring one collects data on the kinematics of the structural response, but these readings are strictly correlated with the temporal and spatial distribution of the temperature. It is a rule of thumb to associate temperature sensors to the units detecting the mechanical performance of the structural system [1-3]. Nevertheless, these temperature sensors are only covering a few points around the structure and this obliges one to find a way to model the spatial variability of the temperature. Furthermore, a virtual laboratory approach, i.e., a tool aiming at simulating numerically the behavior detected by the sensors, requires the availability of initial conditions of temperature even inside the structural elements.

The first aspect is well documented in the literature. Among others, in the book [4], one finds on page 59 a reconstruction of the temperature in the upper side and in the lower side of a bridge deck plotted together with the measured environment temperature.

Another study is reported in [5], where a further plot of recorded data is provided confirming a significant daily peak in the upper side of the deck, a lower peak for the lower side of the deck and valleys of the two plots at the values of the ambient temperature.

In this paper, the authors start from the standard situation of having collected data of both temperature and displacement, adopt a finite-element numerical model of the structural system and investigate the possibility of reconstructing the actual temperature field from the available data, so that the computed displacements match the recorded values.

2 GOVERNING RELATIONS

Following [6], a finite element model is created in *Mentat* [7-8] based on the available information on the bridge design and dimensional/sectional properties.

The boundary conditions are assigned as temperature time histories, moving from initial conditions which should be assigned on the boundary surface of the deck as well as at the internal points.

The following notations are introduced:

- B denotes the deck body;
- ∂B denotes the external surface of the deck body which can be partitioned in:
- ∂B_1 , i.e., the lateral surface of the deck, exposed to the air temperature variations;
- ∂B_2 , i.e., the end surfaces of the deck;
- ∂B_3 , i.e., the deck surface at the support location;
- $\Theta(x,y,z)$ denotes the temperature field;
- $u(x,y,z)$ denotes the displacement field. In any point the displacement should be a vector, but attention is focused here on the vertical component which is supposed to be measured by sensors at M locations.

The thermo-mechanical problem, then, can be formulated as follows: at any instant of time t, find the displacement field u resulting from a temperature variation accounting for the support settlement

$$u(x,y,z|t) = F_A(\Theta(x,y,z|t), \Theta(x,y,z|t=0), u(x,y,z|t=0), u(\partial B_3|t) \quad (1)$$

Such a problem, however, cannot be directly approached since the temperature field at any time t is ignored. One only knows the time evolution of the temperature in a small number of points, say N.

Thus the true problem becomes:

$$\Theta(x,y,z|t) = F_B(u(x_i,y_i,z_i|t)\ i=1,...,M;$$
$$\Theta(x_j,y_j,z_j|t)\ j=1,...,N|\Theta(x,y,z|t=0),\ u(u,y,z|t=0),\ u(\partial B3|t) \quad (2)$$

but the available information does not cover all the degrees of freedom. Heuristic models must be introduced to cover the ignored quantities. In particular one assumes that:

$$\Theta(x,y,z \in B\ |t) = F_C\ (\ \Theta(x,y,z \in \partial B_1, \partial B_2) \text{ constant along } t+\Delta t)) \quad (3)$$

$$\Theta(x,y,z \in \partial B_1, \partial B_2) = F_D\ (\Theta(x_j,y_j,z_j\ |t)\ j=1,...,N) \quad (4)$$

Equation (4) assumes that one can extrapolate from the knowledge of the temperature in a few point the temperature on the whole lateral surface. Equation (3) expresses that from the knowledge of the temperature on the whole lateral surface, the temperature field at regime can be computed and it is independent from the initial conditions for Δt sufficiently long.

3 THE ROLE OF THERMAL INERTIA

One neglects first Eq. (4), which mainly means to work at the time t_w during the day that sees the upper deck and the lower deck to show the same value of temperature.

3.1 Thermal inertia

In Equation (3) the length of the time interval depends on the thermal inertia, which is here introduced as the system property which determines the decay from the initial conditions to the stationary one for the thermo-elastic problem. The first step, discussed in this section, is to check how this phenomenon affects the temperature measurement time-stepping.

With reference to a given rectangular geometry, which will be illustrated when the application is introduced in next section, and for a given day the following analysis is developed. From the uniform temperature of 292.9°K assigned to all nodes of a finite element model (initial condition), the four corner areas, where the temperature sensors are located, should be driven to the temperature read at time t_w, each different from the others. Since the driving temperature has to be assigned over the whole external surface (lateral, lower, upper and ends), the simple partition scheme in Figure 1 was adopted. In this way a sort of an external "thermal coat" is assigned all around the surface of the deck (boundary condition).

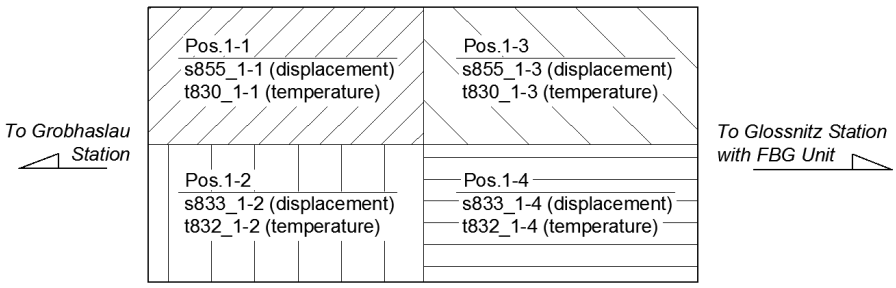


Figure 1. Zones of the deck of equal lateral surface temperature (view from above).

Once the boundary conditions are assigned a dynamic transient analysis was conducted. Two representative transversal sections of the deck were selected: the section in the middle of the support area, and the mid-span section. Figures from 2 to 4 summarize the distribution of the temperature at three different time steps: after 3840 sec (nearly 1 h), after 86400 sec (nearly 1 day) and after 240000 sec (nearly 3 days), respectively.

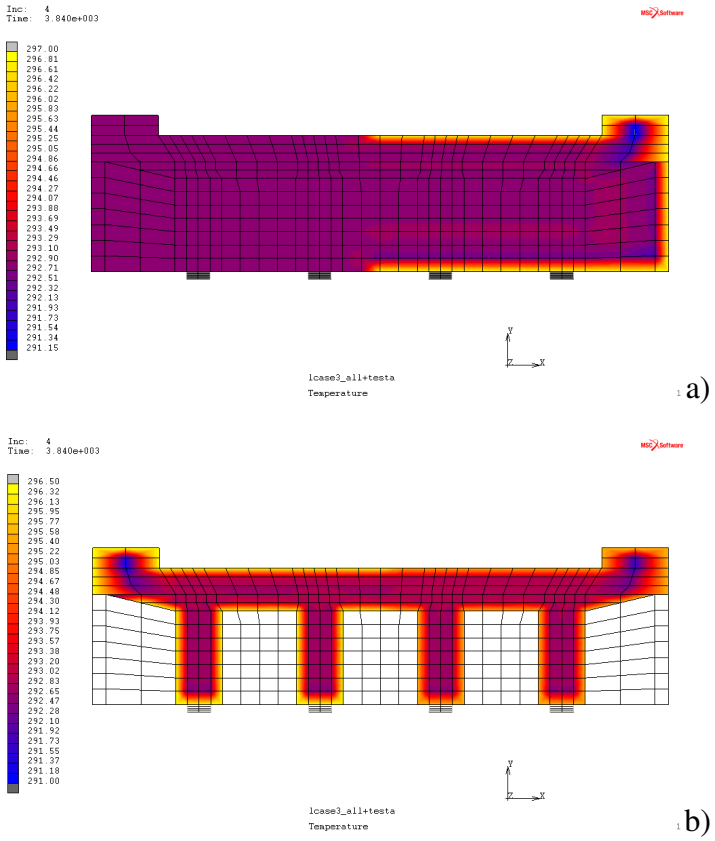


Figure 2. Temperature distribution after 1 h0ur: a) end section; b) mid-span section.

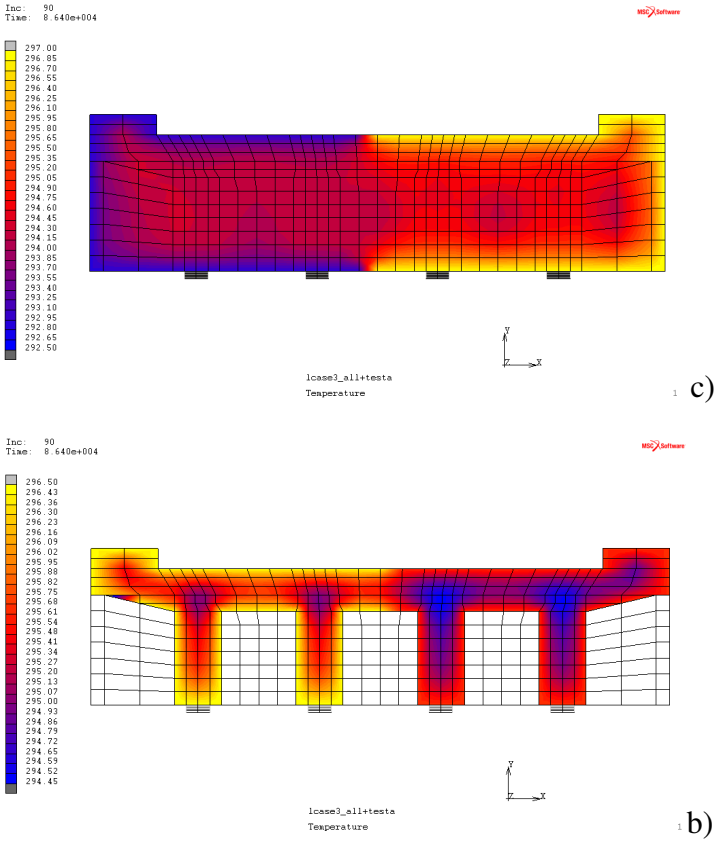


Figure 3. Temperature distribution after 1 day: a) end section; b) mid-span section.

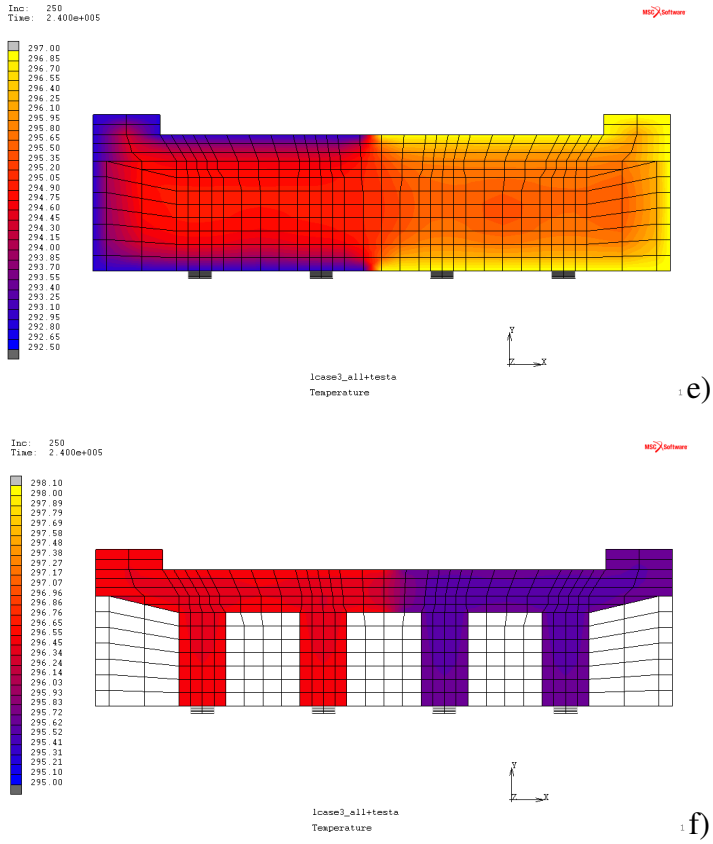


Figure 4. Temperature distribution after 3 days: a) end section; b) mid-span section.

Figure 5 provides the temperature time histories for- two central nodes of the sections considered above, namely node 4552 and 17664, respectively..

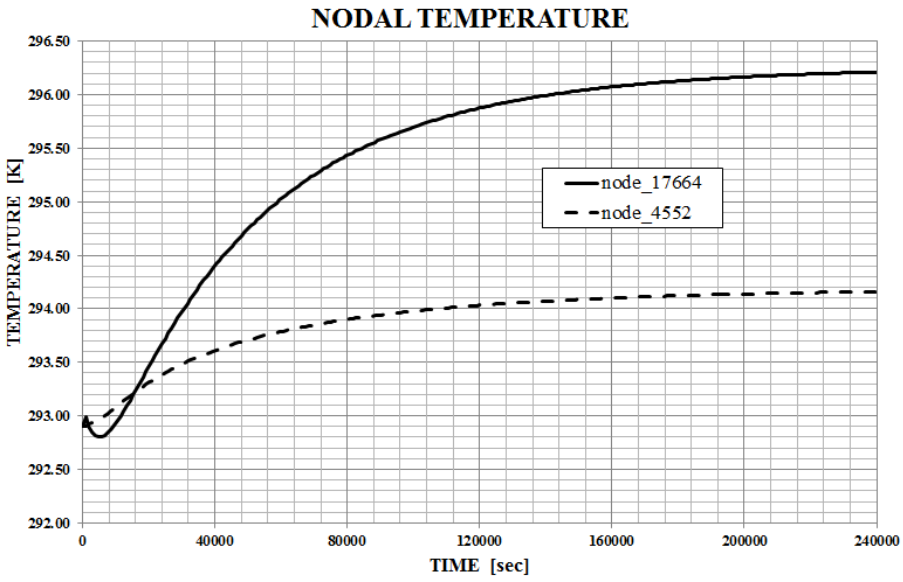


Figure 5. Temperature time histories for node *17664* (belonging to the mid-span cross section) and node *4552* (belonging to terminal cross section).

It is seen from Figure 5 that the stationary solution is reached after 240000 seconds (i.e., nearly 3 days). It follows that the thermal inertia plays a significant role within the problem. It is worth noticing that temperature measures are taken every two hours.

3.2 Temperature distribution on the body surface

The preceding methodology is an operative approach to Eq. (3). But one has also to give a form to Eq. (4), which is an implicit expression of the temperature variability when moving from the top of the deck to its bottom.

Following [4] and [5] three different levels were introduced: upper deck, lateral surface and lower deck. The second level is associated with the temperature recorded by the sensor installed at the deck corner. The different temperature values for the three levels were obtained on the basis of the plot on page 59 of the book [4]:

- starting time: when the three temperature are equal each to the other;
- the lateral surface temperature follows the values read by the sensors;
- the lower deck temperature is increased, within a temporal window, from the read value;
- the upper deck temperature is increased, within a temporal window, from the read value;

In this way a representation of the actual trend is pursued. An example of the distribution of the three levels of temperature according to the partition in Figure 1, is given in Figure 6.

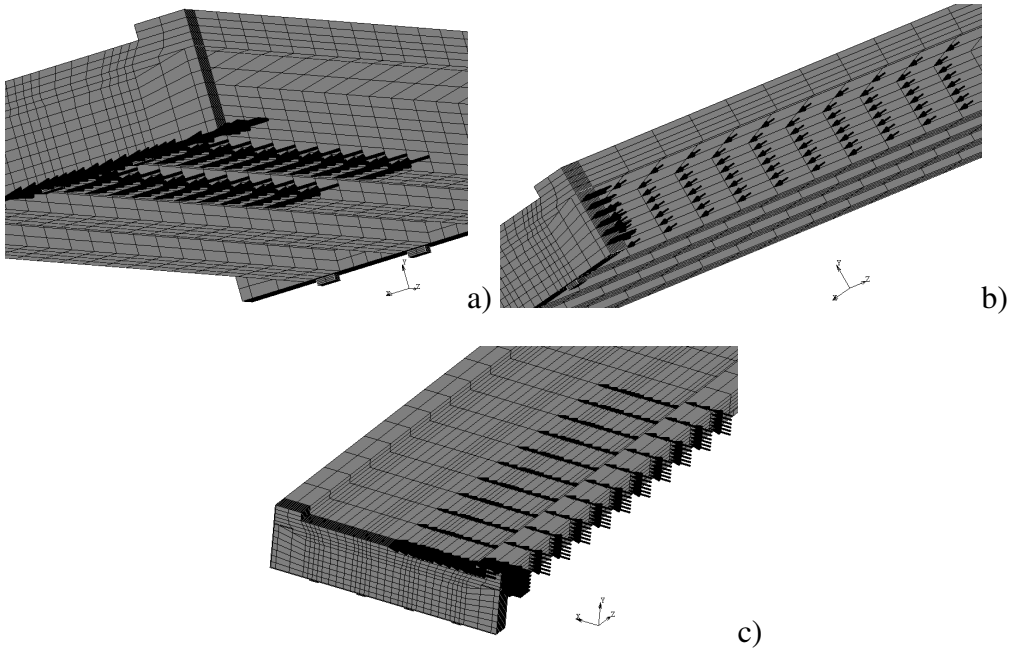


Figure 6. a) Lower deck distribution of temperature; b) Lateral surface distribution of temperature; c) Upper deck distribution of temperature.

4 THE CASE STUDY

The structural system analysed in this paper is the railway bridge called the ÖBB Brucke Großhaslau which is located in the South part of Austria. It belongs to the railway "ÖB Martinsberg – Schwarzenau", and was built in 2009-2010 to cross the road "Zwettler Straße – B36" at a height of 6.70 m. The geometry of the bridge deck is shown in Figure 7. The deck

of the bridge consists of a single span, reinforced concrete T-beam, which supports dual-lane rail traffic. The length is 30.80 m and the width 8.65 m. More details are given in [6]. Elastomeric supports under the deck are mounted and their response to temperature variations must be considered.

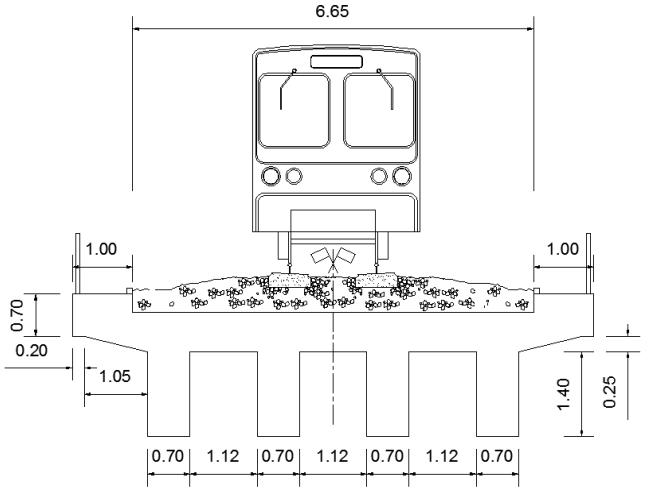


Figure 7. Transversal section of the deck for the bridge case study.

The structural health monitoring (SHM) system installed on the bridge consists of Fibre Bragg Grating (FBG) sensors [9-10]. The implemented monitoring system includes two different kinds of sensors. The first one is able to detect the variation of displacement induced by both environmental actions and train crossing events, while the second set tracks the variation of temperature. The sensors are located close to the supports. In total, ten displacement sensors and four temperature sensors were used (Figure 8). The data are recorded at different time steps (namely, every 10 s for the temperature values, every second for the displacement sensors and every 0.01 second for the displacement during the train crossing event), stored in a data-logger, and then sent to a PC situated in an Operation Centre. Finally, they are uploaded in a Web page were the enabled users can access them by FTP.

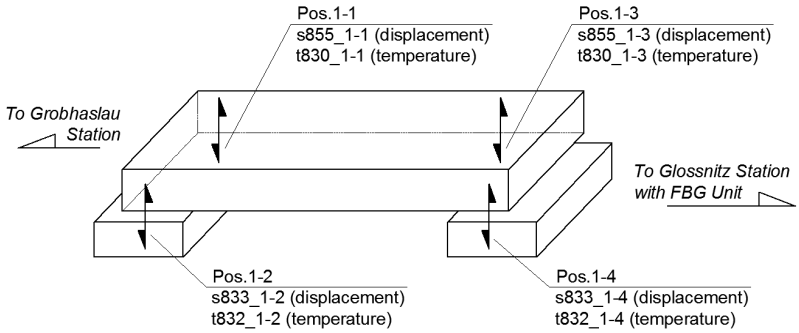


Figure 8. Position of the sensors along the bridge's deck.

Before performing the FEM modelling and analysis, all the data were managed using MatLab and Microsoft Excel. The preliminary task consists of checking the quality of the recorded data to manage gaps, zero readings from malfunctioning sensors, or obvious outliers.. Both displacements and temperature data are separately plotted against time to track their seasonal and monthly trends. As an example, Figure 9 shows the trend of the vertical displacement recorded by sensor s833_1-4 during June, 2011. More details about the data elaboration can be found in [11-12].

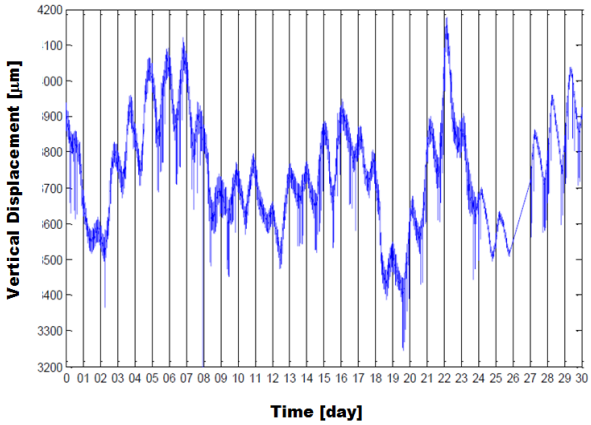


Figure 9. Trend for vertical displacements recorded by sensor s833_s1-4 – June, 2011.

4.1 Calibration of the temperature distribution

The 24 hours period from 12.00 of June 3rd, 2011 to 12.00 of June 4th. 2011 is first considered. The temperature distribution arising from the data in [4] is summarized in Table 1.

Table 1. Temperature values (in bold) recorded by sensor *t832_1-2* from 12:00 a.m. of June 3rd to 12:00 a.m. of June 4th, 2011 assigned to the lateral surface. Additional per cent increments provide a possible temperature distribution for upper and lower deck.

Day	Time [h]	Θ_{lower} [°C]	$\Theta_{lateral}$[°C]	Θ_{upper} [°C]	$(\Theta_{lower} - \Theta_{lateral})/\Theta_{lateral}$ [%]	$(\Theta_{upper} - \Theta_{lateral})/\Theta_{lateral}$ [%]
June 3rd, 2011	12:00	293.4	**292.9**	296.9	0.1707	1.366
	14:00	292.8	**292.3**	297.8	0.1711	1.881
	16:00	297.4	**296.4**	303.4	0.3373	2.361
	18:00	291.9	**290.4**	299.4	0.5165	3.099
	20:00	287.9	**286.7**	293.7	0.4186	2.441
	22:00	289.8	**288.7**	294.7	0.3810	2.078
June 4th, 2011	0:00	290.1	**289.1**	294.6	0.3459	1.902
	2:00	286.2	**285.7**	288.2	0.1750	0.875
	4:00	286.3	**285.8**	287.3	0.1749	0.525
	6:00	295.2	**294.2**	295.2	0.3399	0.3399
	8:00	295.5	**295.5**	295.5	0	0
	10:00	299.95	**299.7**	300.7	0.0834	0.3336
	12:00	296.4	**295.9**	299.9	0.1690	1.352

The numerical analyses carried out made evident the appropriateness of the lower curve while the upper one should be effective, and less sharping, only in the temporal window from 18.00 to 6.00. Figure 10 summarizes the adopted temperature distribution.

A basic role is played by the initial conditions which are achieved by a preliminary evolution, from a uniform temperature distribution, to the sensor readings applied to the boundary of the 4 zones of competence. Such preliminary analysis is run over a period of 8 hours, to include the thermal inertia effect.

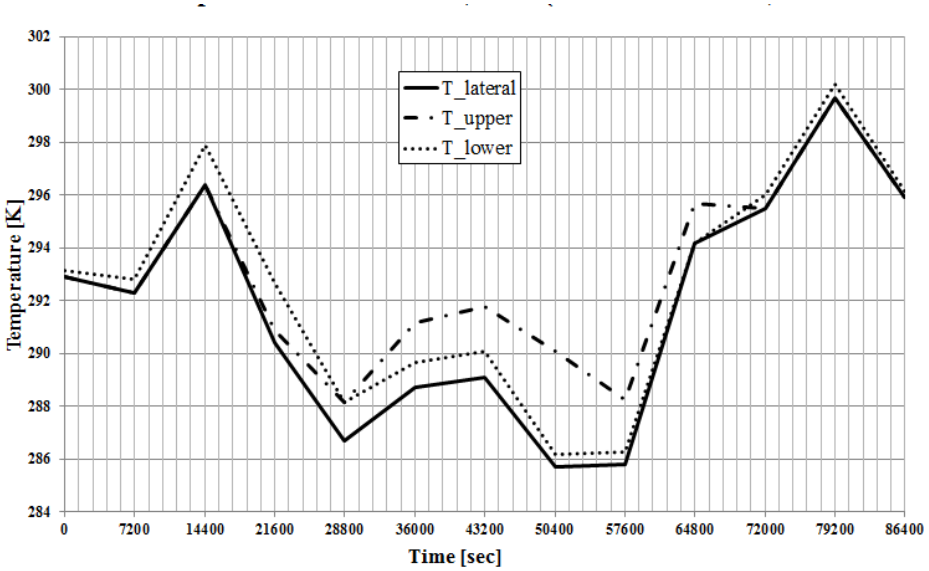


Figure 10 - Temperature recorded by sensor *t830_1-1* from 12:00 a.m. of June 3rd, 2011, to 12:00 a.m. of June 4th together with the upper and lower deck temperature distributions adopted in the analysis

4.2 Calibration of the procedure

The thermo-mechanics properties of the materials are assigned and the period specified in the previous sub-section is adopted to calibrate the procedure. The calibration of the whole proposed procedure pursues the matching of the computed vertical displacements with the values recorded during the data acquisition. The initial conditions are assigned accounting for the thermal inertia and the boundary conditions on the temperature distribution as achieved in the previous subsection. The result in terms of absolute variation of the vertical displacement for sensor s855_s1-3 (node *8682*) is represented (dotted line) in Figure 11, where it is compared with the recorded time history (continuous line).

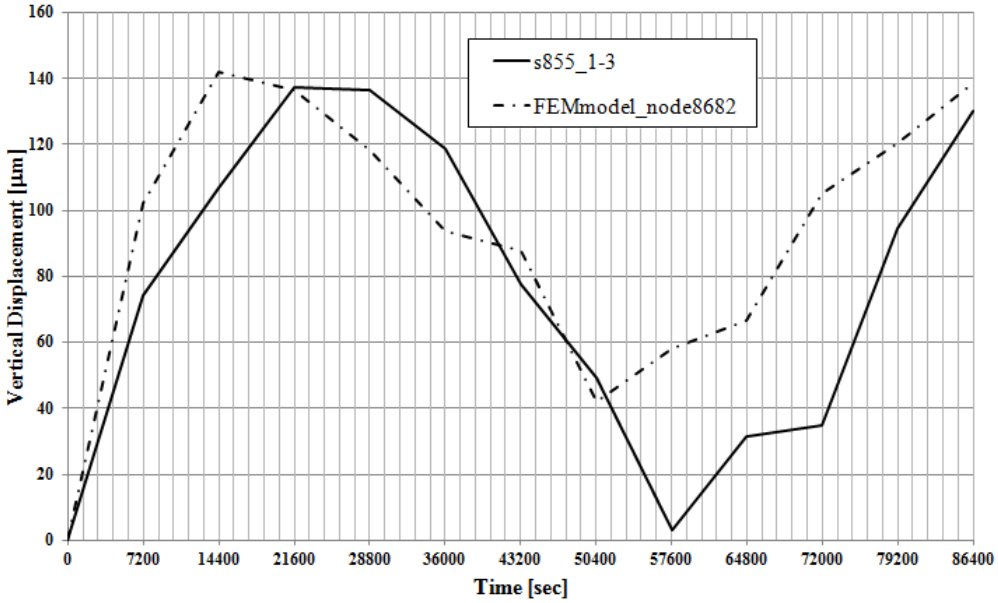


Figure 11. Absolute variation of the vertical displacement for sensor s855_s1-3 from 12:00 a.m. of June 3rd, 2011 to 12:00 a.m. of June 4th.

4.3 Validation of the procedure

The procedure then tested on a different set of data: it covers the same hours of the days 14 and 15 June, 2001. The two days are selected close each to the other to avoid the influence of seasonal variations of some parameters.

The resulting time history of the absolute variation of the vertical displacement for sensor s855_s1-3 from the model (*ID8682*) is plotted in Figure 12 together with the measured values (continuous line).

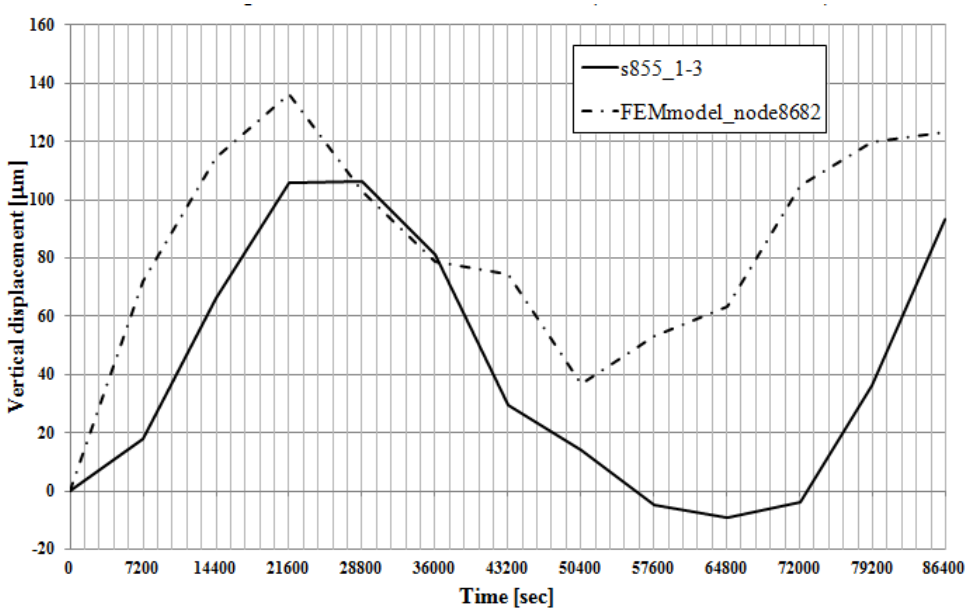


Figure 12. Absolute variation of vertical displacement for sensor s855_s1-3 from 12:00 a.m. of June 14th, 2011 to 12:00 a.m. of June 15th.

5 CONCLUSIONS

The actual temperature distribution across the deck of a bridge plays a dominant role on the estimation of the displacement field [13]. But very often only a reduced number of temperature sensors are deployed. Thus a refined study of the temperature time histories was conducted by a suitable thermo-mechanical model driven by the temperatures measured at the sensor locations. The obtained field of temperature is then used as input for a stress-strain analysis. The resulting displacements are compared with the measured one. Using a first set of data, the numerical model parameters ate calibrated, while a second set of data is used for a validation of the whole procedure.

ACKNOWLEDGMENTS

The authors are grateful to the Czech instrumentation and monitoring company *Safibra* for making the data available.

REFERENCES

[1] B. Peeters, G. De Roeck. One-year monitoring of the Z24-Bridge: environmental effects versus damage events, *Earthquake Engineering & Structural Dynamics*, 30 (2), 149-171, 2001.

[2] J. Kullaa. Eliminating Environmental or Operational Influences in Structural Health Monitoring using the Missing Data Analysis, *Journal Of Intelligent Material Systems And Structures*, 20 (11), 1381-1390, 2009.

[3] J. Kullaa, J. Distinguishing between sensor fault, structural damage, and environmental or operational effects in structural health monitoring, *Mechanical Systems And Signal Processing*, 25 (8), 2976-2989, 2011.

[4] H. Wenzel and D. Pichler, *Ambient Vibration Monitoring*, John Wiley & Sons, 2005.

[5] Y. Cao, J. Yim, Y. Zhao and M.L. Wang, Study of Temperature Induced Displacement for Cable Stayed Bridge Using Health Monitoring System, in F-K. Chang (ed.), *Structural Health Monitoring 2009*, DEStech Publications Inc., Lancaster, PA, Vol. 2, 1987-1994, 2009.

[6] L. Faravelli, D. Bortoluzzi, T. B.Messervey, and L. Sasek. Temperature Effects On The Response Of The Bridge "ÖBB Brucke Großhaslau". In: *Proceedings of the International Conference on Advanced Dynamics and Model Based Control of Structures and Machines. Invited contribution. ABC12*, Saint Petersburg, Russia, July 1-4, 2012.

[7] Marc and Mentat® 2010 – Release Guide, 2010.

[8] http://www.mscsoftware.com.

[9] http://www.safibra.cz.

[10] D. Inaudi, S. Vurpillot, Monitoring of Concrete Bridges with Long-Gage Fiber Optic Sensors, *Journal of Intelligent Materials Systems and Structures*,10, 280-292, 1999.

[11] B. Moro. Sistema Di Monitoraggio Per il Ponte "ÖBB Bruke Großhaslau": effetti della temperatura, Master Degree Thesis, University of Pavia, 2012.

[12] M. Orlandoni. Simulazione Numerica Dell'effetto Della Temperatura Sul Ponte "ÖBB Bruke Großhaslau: effetti della temperatura, Master Degree Thesis, University of Pavia, 2012.

[13] H. Sohn, M. Dzwonczyk, E.G. Straser, A.S. Kiremidjian, K.H. Law and T. Meng, An Experimental Study on Temperature Effect on Modal Parameters of the Alamosa Canyon Bridge, *Earthquake Engineering and Structural Dynamics*, 28, 879-897, 1999.

COMPDYN 2013
4th ECCOMAS Thematic Conference on
Computational Methods in Structural Dynamics and Earthquake Engineering
M. Papadrakakis, N.D. Lagaros, V. Plevris (eds.)
Kos Island, Greece, 12–14 June 2013

FINITE ELEMENT MODEL UPDATING OF A FOOTBRIDGE BASED ON STATIC AND DYNAMIC MEASUREMENTS

Mario Solís[1], Leqia He[2], Geert Lombaert[2] and Guido De Roeck[2]

[1] E.T.S. Ingeniería - Universidad de Sevilla
Camino de los Descubrimientos s/n, 41092 Sevilla (Spain)
e-mail: msolis@us.es

[2] Structural Mechanics Division, KU Leuven
Kasteelpark Arenberg 40, bus 2448, B 3001 Heverlee, Belgium
e-mail: {Leqia.He, Geert.Lombaert, Guido.Deroeck}@bwk.kuleuven.be

Keywords: Footbridge, Model updating, Static response, Operational Modal Analysis, Foundation contribution

Abstract. *The Palmas Altas footbridge is a recently built bridge in Sevilla (Spain) designed by architect Richard Rogers. It is a 78.6m long steel-concrete box girder. The bridge has three spans, with two pairs of intermediate oblique piers. The cross section of the box girder and the piers are variable along the bridge length. The footbridge has a cylindrical roof with a complex structural geometry, made of elliptical crossing bars and a cylindrical shell. Before being taken in use, the structural response of the footbridge was experimentally identified by an operational modal analysis. Mode shapes and frequencies have been clearly identified. In addition, the static response of the structure was obtained from a static load test. A detailed finite element model has been built for analyzing both the static as well as dynamic behavior of the bridge. A model updating process has been performed to improve static and dynamic response predictions. The present analysis is mainly focused on the in plane behavior of the bridge, for which both static and dynamic experimental information is available. Special attention is paid to the role of the bearings and foundations in the structural response. It is shown that the measured static response provides useful information about the response of the bridge and its foundation, which is not available from a dynamic analysis only.*

1 INTRODUCTION

In the last decade, new civil engineering design challenges have emerged from the construction of new footbridges [1, 2]. Due to the small service loads, they are usually light and slender structures that must withstand dynamic loads from pedestrians, wind, and traffic or water flow underneath. Some structural dynamics problems are arising, including human induced vibrations and human-structure interaction. These problems have to be addressed and new design guidelines are required. For this purpose, information about the behavior of footbridges has to be collected and analyzed.

Experimental information about the behavior of a civil engineering structure can be obtained from Operational Modal Analysis (OMA). The experimental modal parameters give information about the actual properties of the structure and can be compared to predicted values from numerical models. By performing a model updating, a more accurate and realistic model can be obtained. The updating process can be used to understand the actual behavior of the structure.

This paper presents the updating process of a recently constructed footbridge in Sevilla (Spain). A detailed finite element model of the structure has been built to obtain a good approximation of the real structural response. The experimental identification includes an OMA and a static load test. The paper includes not only the dynamic response but also the static one in the updating process. Special attention is paid to the influence of the neoprene bearings, foundations and structural contribution of architectural elements. Useful information is obtained about the foundation contribution when combining the satic and dynamic response in the model updating.

The paper is organized as follows. The next section describes the structure and the finite element model. In the third section, the experimental results from the static and dynamic tests are presented. The model updating process and the discussion of the most significant results are presented next. Finally, some remarks and conclusions are drawn from the results.

2 Description of structure and FE model

The footbridge is a three-span steel box girder bridge built in Sevilla (Spain) in 2011. The bridge is 78.65 m long, including the main span of 39.15 m and two equal side spans of 19.25 m. Fig. 1 shows a side and perspective view of the bridge. The bridge is simply supported at both abutments and is also supported by two pairs of intermediate oblique piers. A detailed finite element model of the bridge was built to represent its structural response.



Figure 1: The Palmas Altas footbridge.

Fig. 2 shows the standard cross section of the bridge and a front view of one of the bridge ends. The cross section contains a steel box girder with a concrete slab of 150 mm thickness. The geometry of the girder is changing along the bridge, providing more stiffness towards the joints with the piers. The height of the girder varies from 0.56 m to 1.32 m, the thickness of the upper flange (steel part of the deck) varies from 12 to 20mm, the thickness of the bottom flange varies from 10 to 20mm and the thickness of the webs varies from 10 to 20 mm. Fig. 2(c) shows a schematic drawing of a side view of the bridge, including the foundation of the abutments and the piers. The foundations consist of a pile cap and 4 piles of 850 mm diameter and a length of 20 m (the drawing does not include the whole piles). A concrete beam connects the foundation of piers and abutments at both sides.

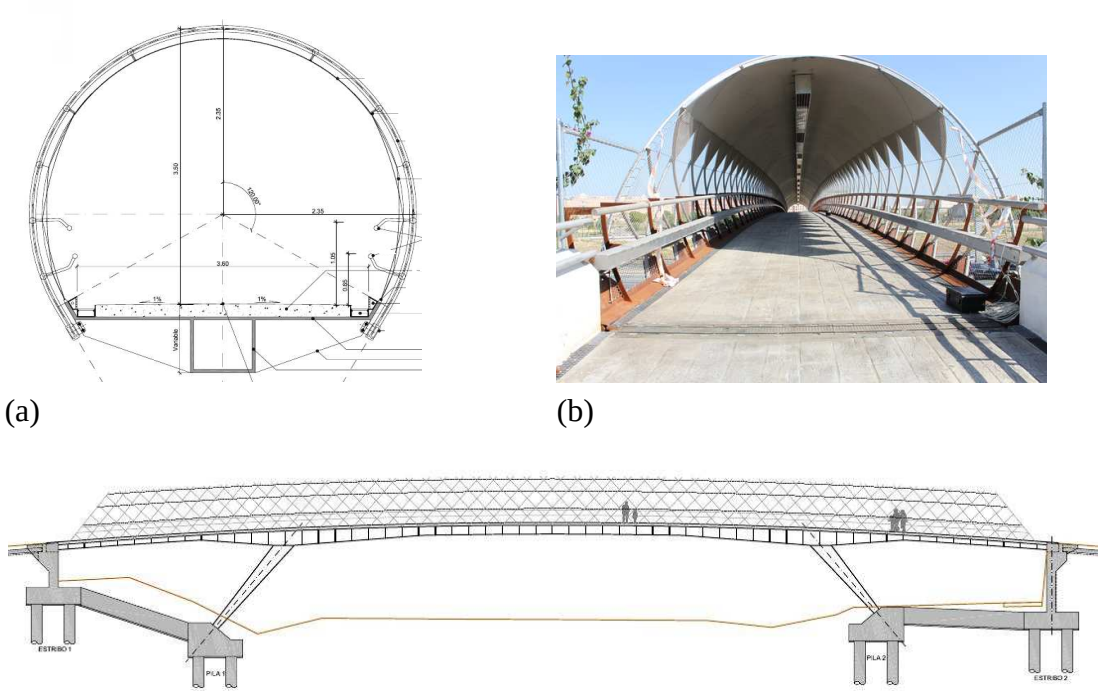


Figure 2: (a) Standard section of the bridge (b) Front view of one end of the bridge (c) Lateral drawing of the bridge including foundation

The triangular stiffeners of the girder (16 mm thickness) are located every 1.30m along the bridge. Inside the concrete slab, there are 5 longitudinal bar stiffeners and also one transversal bar stiffener every 1.30m. There is also one longitudinal stiffener on the bottom flange of the box girder and transversal stiffeners inside the box girder every 1.30m.

The roof consists of a cylindrical cover along the bridge. It is formed by elliptical inclined arched bars, geometrically defined as inclined sections of the cylindrical cover along the bridge. There are arched bars with two different orientations, so that the final assembly looks like a kind of three dimensional arched truss.

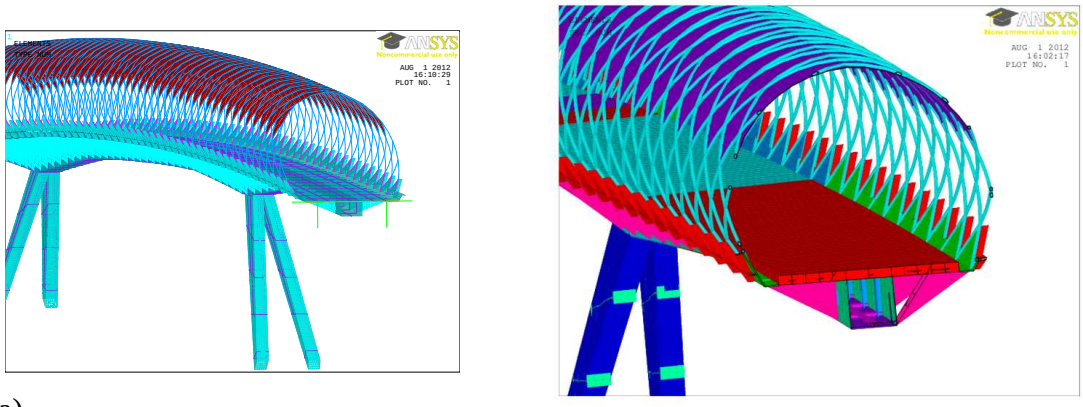
The roof provides a singular aesthetic appearance to the bridge and is an element of a clear major architectural significance. However, its structural contribution was not that clear. It was originally not considered as part of the structure in the design phase of the footbridge. However, its final construction design (robust bars and anchorage to the deck) makes the roof a significant

structural element, as found from the numerical and experimental analysis.

The piers are inclined, tapered and with a hollow cross section. The cross section of the piers varies from 0.5 mx0.5 m at the bottom to 0.4 mx1.62 m on top. The wall thickness is 20 mm. It must be noted that the South pier (5.125 m height) is shorter than the North pier (6.35 m height). Because of that, there is a lack of symmetry in the bridge.There are also 4 longitudinal and 3 transversal bar stiffeners inside the piers.

Fig. 3 shows a three dimensional representation of the finite element model. The whole girder as well as the piers are modeled with shell elements. Their internal bar stiffeners are modeled with beam elements. The concrete slab and the steel counterpart of the girder are modeled as a shell with composite material properties. The composite material is defined by one layer of concrete and one layer of steel. For the roof, curved 3 node bar elements and curved 8 node shell elements were used to represent its complex curved geometry.

The mechanical properties for steel and concrete in the finite element model are, respectively: Young's modulus $E = 210$ GPa and $E = 31.1$ GPa, density $\rho = 7850\ \mathrm{kg/m^3}$ and $\rho = 2400\ \mathrm{kg/m^3}$, Poisson modulus $\nu = 0.3$ and $\nu = 0.15$.



(a) (b)

Figure 3: (a) General view of the finite element model (b) Three dimensional representation of cross section

3 Experimental Analysis

3.1 Static load test

After construction, the bridge was subjected to a static load test. An equivalent load of $250\ \mathrm{kg/m^2}$ was applied by putting cement bags on top of the bridge deck (Fig. 4a). Vertical displacements were measured at eleven points along the bridge with a total station laser theodolite (Fig. 4b). Fig. 4c shows the measured displacements. It can be observed that there were significant vertical displacements on top of the piers. This behavior can only be explained by some displacements occurring at the foundations of the piers. This phenomenon and its implications on the updating process will be further discussed in the following sections.

3.2 Operational Modal Analysis

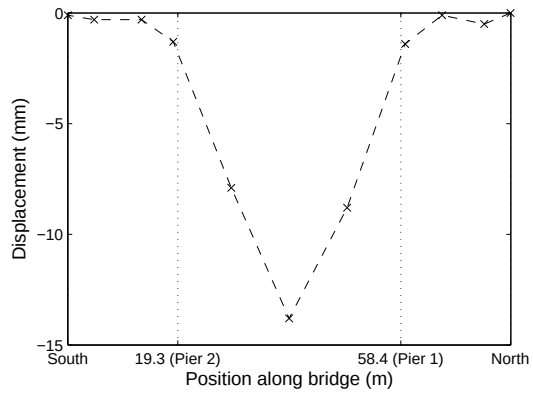
The dynamic properties (natural frequencies and mode shapes) of the bridge were obtained from an Operation Modal Analysis. The experimental test was carried out before the structure



(a)



(b)



(c)

Figure 4: (a) Applied load (b) Static measuring equipment (c) Experimental displacements

was taken in use. It was only subjected to ambient vibration produced mainly by road traffic of the highway underneath the bridge.

In total, the dynamic response at 27 points was measured (Fig. 5c). The measurement nodes were located on top of the bridge deck (Fig. 5b). Accelerations in three directions were collected by triaxial wireless units (Fig. 5a). Three of the measurement points (11, 12 and 16 in fig.5c) were reference nodes that were measured by sensors with fixed locations. The other nodes were measured by nine roving sensors through 3 setups. One longitudinal line of measuring points, in addition to the reference nodes, was considered for each setup. The measurement duration was 15 minutes in each setup.

The measured vibration data were analyzed using MATLAB toolbox MACEC [3]. System identification was performed for each setup using the reference based covariance driven stochastic subspace identification algorithm (SSI-cov) [4].

In the following, modes below 10Hz are considered, as these are of most interest for ambient excitation and human induced vibrations. Table 1 shows the identified frequencies and damping ratios of the mode shapes in that frequency range. The table also includes information about the standard deviation of frequencies and damping ratios, and the Modal Phase Collinearity [5]. These parameters provide information about the stability and quality of the modal results.

The mode shapes are presented in fig. 6. Besides giving a three dimensional view of the deck, the vertical and horizontal movements of the three longitudinal lines of measuring points are shown as well. Torsional, vertical bending or lateral bending components of each mode can be observed.

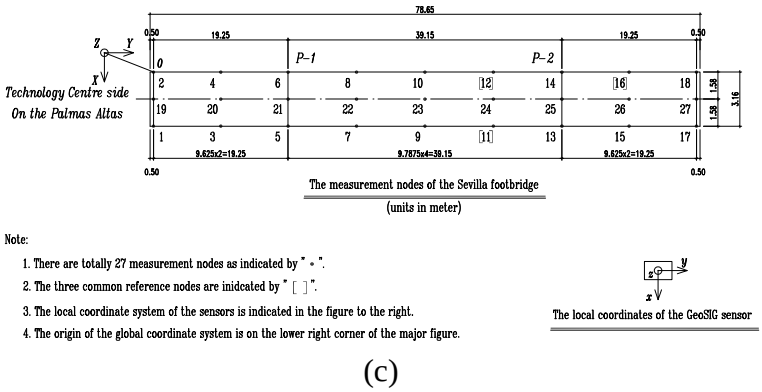
It can be seen that the first mode is at 2.364 Hz and combines lateral and torsional movements of the bridge. The lateral bending component of this first mode is very similar to that of the third mode (3.298 Hz) but the latter does not show any torsional behavior. Additional measuring points on the roof would give complementary information about these modes and allow a clearer distinction between these modes. From the FE model results, it could be observed that the first mode is mainly a lateral mode of the roof, which leads to a lateral and torsional deformation of



(a)



(b)

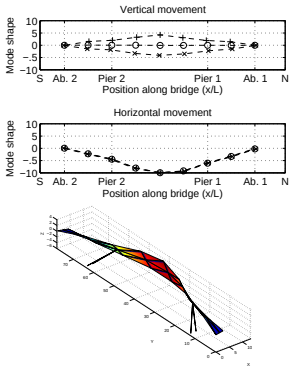


(c)

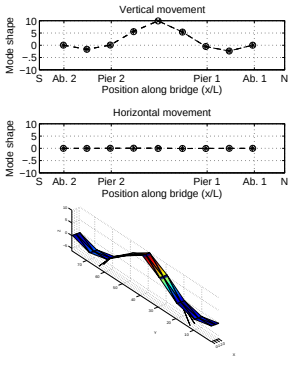
Figure 5: (a) Set of wireless sensor units (b) Sensor units during measuring process (c) Scheme of measuring points distribution

Mode Number	Freq (Hz)	Std. Dev. Freq.(%)	Damping ratio (%)	Std. Dev. damp.	M.Ph. Coll.	Description
1	2.364	0.001	0.23	0.01	1.00	Torsion + lat. bending
2	3.038	0.005	0.58	0.03	1.00	1^{st} bending.
3	3.298	0.006	1.11	0.19	0.99	First lateral bending
4	3.656	0.020	1.60	0.02	0.99	2^{nd} bending.
5	5.461	0.019	1.05	0.22	0.96	Lateral bend + torsion
6	5.727	0.008	0.92	0.07	0.97	Symmetric to 5
7	6.574	0.018	1.18	0.35	0.98	4^{th} bending.
8	6.903	0.031	1.75	0.14	0.95	Lat. bending
9	7.326	0.010	1.36	0.48	0.95	5^{th} bending
10	8.622	0.007	0.42	0.07	0.94	Torsion + lat. bend
11	8.855	0.018	1.05	0.07	0.98	6^{th} bending

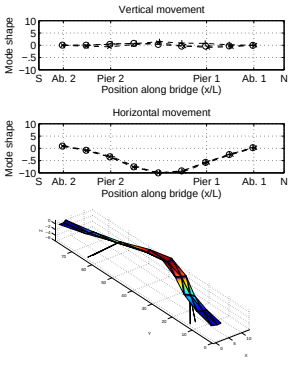
Table 1: Identified modes from Operational Modal Analysis below 10Hz



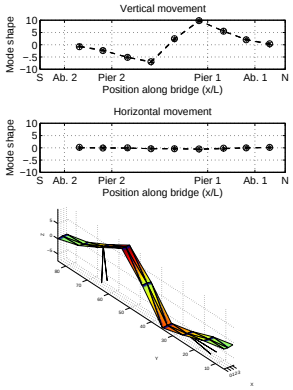
Mode 1 (2.364Hz)



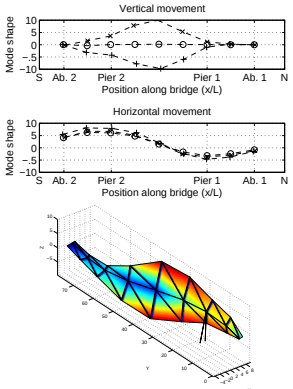
Mode 2 (3.038Hz)



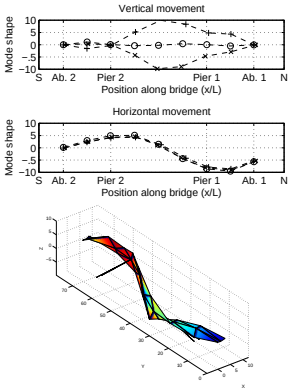
Mode 3 (3.298Hz)



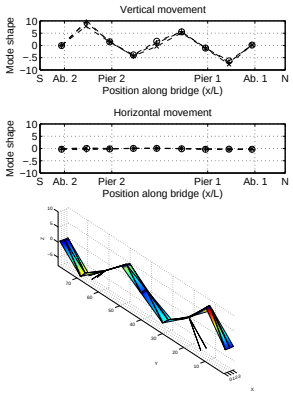
Mode 4 (3.656Hz)



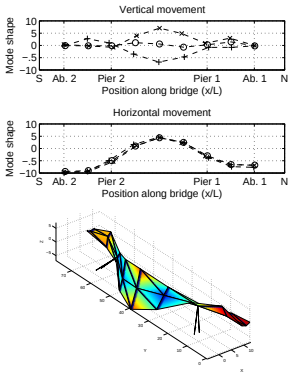
Mode 5 (5.461Hz)



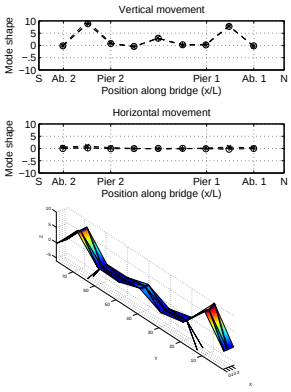
Mode 6 (5.727Hz)



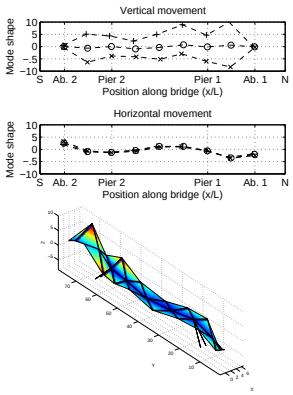
Mode 7 (6.574Hz)



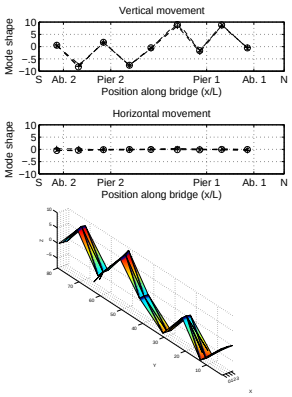
Mode 8 (6.903Hz)



Mode 9 (7.326Hz)



Mode 10 (8.622Hz)



Mode 11 (8.855Hz)

Figure 6: Identified mode shapes from OMA

the deck. The third mode is a lateral mode of the whole bridge. If the roof is not considered in the FE model, only one of these modes is obtained (mainly a lateral bending mode). So it seems that the roof must be considered as part of the structure in order to obtain results in good agreement with the experimental observations. If it is considered as a non-structural element the number of mode shapes would be underestimated and the model would not be realistic [6].

Similar lateral and torsional deformation is also present in modes 5 (5.461 Hz) and 6 (5.727 Hz). They are second type lateral bending modes, with high lateral modal displacements at only one of the abutments. Mode 8 ($6.903Hz$) is a higher order lateral bending mode, including high modal displacements at both abutments. For all these lateral bending modes, the movement of the roof produces also a torsional deformation of the deck. Finally, there a pure torsional mode is found at 8.622 Hz (mode 10).

Regarding the vertical bending modes, the first one is mode 2 (3.038 Hz) and the second ones is mode 4 (3.656 Hz). It is worth to mention that the second bending mode, which is an antisymmetric mode, shows very high longitudinal modal displacements, including a high movement on top of the piles. Maximum longitudinal displacements values are 60% of the maximum vertical displacement. This illustrates how important it can be to take longitudinal movements into account when performing a modal analysis. This component of displacements is often neglected and can provide significant information about the behavior of the bridge, which should be considered for model updating.

Modes 7 (6.574 Hz) and 11 (8.855 Hz) are bending modes of higher order. There is also another bending mode which consists of a bending of both side spans (mode 9 at 7.326 Hz).

To resume, out of the 11 mode shapes identified below 10 Hz, 5 are vertical bending modes, 4 are lateral bending combined with torsional modes, and only 2 are purely torsional and purely lateral bending, respectively. In this paper, the 5 vertical bending modes will be the most relevant for combination with the in plane static bending response during the model updating.

The modal transfer norm [5] obtained for each mode gives information about their relevance in the measured response. According to that parameter, the most important modes in the ambient vibration response are (in order of relevance) the first bending mode (mode 2), the first lateral and torsion mode (mode 1) and the second bending mode (mode 4).

Fig. 6 also includes the MAC matrix for the eleven presented modes. The MAC matrix is almost diagonal, showing that the identified modes are mostly orthogonal. However, a high MAC value is observed between modes 1 and 3. As previously explained, these modes contain a significant roof motion. Because of the lack of measuring points on the roof, it is hard to distinguish between both modes.

4 MODEL UPDATING PROCESS

4.1 Objective function

The model updating process is used to solve an inverse problem so that the finite element model reproduce the experimental static and dynamic response of the structure as close as possible to the real (experimental) one. An optimization problem must be solved for which an objective function and updating parameters have to be properly chosen [7]. The objective function includes the difference between the experimental and numerical results. In this applications the objective function can be written as follows

$$\mathbf{p}^* = \arg\min_{\mathbf{p}} \frac{1}{2} \left[\sum_i \left[w_s r_i^s(\mathbf{p}) \right]^2 + \sum_j \left[w_f r_j^f(\mathbf{p}) \right]^2 + \sum_j \left[w_M r_j^M(\mathbf{p}) \right]^2 \right] \tag{1}$$

where $\mathbf{p}$ is the set of updating parameters, r_i^s is the residuals of the static displacement at measuring point i, r_j^f is the residual of frequency of mode j, and r_j^M is the residual of the MAC value of mode j. w_s, w_f and w_M are the weights applied to the residuals of static displacements, frequencies and mode shapes (MAC), respectively. The values of the weights are chosen in order to have good convergence and a trade-off between the influence of each part on the value of objective function, so none of them becomes dominant in the optimization process.

The residuals of the static displacement at each measuring point are defined as

$$r_i^s(\mathbf{p}) = \frac{u_i^s(\mathbf{p}) - \tilde{u}_i^s}{\tilde{u}_{max}^s} \tag{2}$$

where $u_i^s(\mathbf{p})$ is the displacement computed from the finite element model, $\tilde{u}_i^s$ is the experimental result and $\tilde{u}_{max}^s$ is the maximum experimental displacement.

The frequency residuals can be written as

$$r_j^f(\mathbf{p}) = \frac{f_j(\mathbf{p}) - \tilde{f}_j}{\tilde{f}_j} \tag{3}$$

where $f_j(\mathbf{p})$ is the computed natural frequency and $\tilde{f}_j$ is the corresponding experimental one of mode j.

The residuals in mode shapes computed is computed through the MAC values as follows:

$$r_j^M(\mathbf{p}) = 1 - MAC(\phi_j(\mathbf{p}), \tilde{\phi}_j) \tag{4}$$

where $\phi_j(\mathbf{p})$ is the computed mode vector j and $\tilde{\phi}_j$ is the corresponding experimental one.

The optimization problem is solved using a Newton trust region method, which is a gradient based iterative algorithm. The jacobian of the objective function is computed numerically using a finite difference scheme. One of the key issues in a model updating based on modal results is the matching of the computed and the experimental modes. In this paper, each experimental mode is paired to the computed mode that gives the highest MAC value.

4.2 Updating parameters

A detailed finite element model of the structure is set up to give a good approach of the behavior of the structure. However, the response is highly influenced by the actual boundary conditions, which could deviate form the idealized case. Therefore, the updating process considers equivalent springs simulating the contribution of the foundation. The stiffness values of these springs are considered as updating parameters. This paper focuses on the in plane static and dynamic behavior of the bridge, so that a total of 6 stiffness constants considered in the analysis. Fig. 7 show an schematic representation of the updating parameters. In the definition of the updating parameters, it has been assumed that the abutments and pier foundations at both sides of the bridge have the same stiffness.

The footbridge is supported by neoprene bearings at both ends. Based on the dimensions of the rubber and the steel layers [8, 9], the stiffness of each neoprene bearing in the vertical direction (k_{N-V}), transversal direction (k_{N-L}) and rotation ($k_{N-\theta}$) is estimated to be in the range $[1e8 - 1e9]$ N/m, $[1e6 - 2e6]$N/m and $[5e5 - 1.5e6]$N/m respectively.

Regarding the foundation of piers (4 piles of $850mm$ diameter and 20m long), an estimation of the equivalent horizontal (k_{P-L}), vertical (k_{P-V}) and rotational ($k_{P-\theta}$) stiffness of the piles working together as cantilever beams is 9.2×10^6N/m , 16×10^{10} N/m and 35×10^{10} Nm/rad

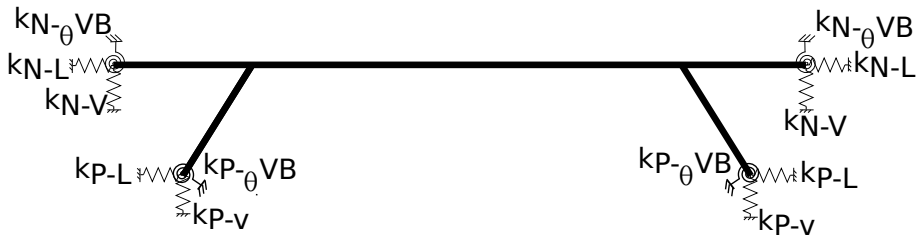


Figure 7: Schematic representation of the springs at foundations of the piers and abutments considered as updating parameters

	Case							
Parameter (N,m)	1	2	3	4	5	6	7	8
k_{N-V}	∞	5e8	5e8	5e8	5e8	5e8	5e8	5e8
k_{N-L}	0	1.5e6	1.5e6	1.5e6	1.5e6	1.5e6	1.5e6	1.5e6
$k_{N-\theta VB}$	0	1e6	1e6	1e6	1e6	1e6	1e6	1e6
k_{P-V}	∞	∞	1e9	1e8	∞	∞	∞	∞
k_{P-L}	∞	∞	∞	∞	∞	∞	1e8	1.5e7
$k_{P-\theta VB}$	∞	∞	∞	∞	∞	1e8	∞	∞

Table 2: Different combinations of values of updating parameters for manual calibration based on the static response

respectively. These values are considered only as estimated references and realistic values for the equivalent springs. The actual values of equivalent stiffness should be higher due to the soil contribution.

5 STATIC RESPONSE ANALYSIS

5.1 Manual calibration

A manual calibration and sensitivity analysis of the selected updating parameters is very useful for interpretation of the results. Table 2 gives different combinations of foundation stiffness parameters and fig. 8 shows the static results obtained for each combination together with the experimental results.

Case 1 is a simulation of the ideal boundary conditions that would be usually considered during the structural design process (simply supported deck and fixed piers). This “theoretical” approach gives results that are far from the experimental values. The provided displacement values as well as the overall deflection shape are different from the experimental results. If the roof is removed from the FE model (case 1 bis) the contribution of the superstructure of the roof is clear. It is worth to remark that if the superstructure was not considered in the structural design process, the predicted results would be definitely wrong. However, the static deflection of case 1bis is also qualitatively different from the experimental one. So the reason for the difference between the numerical values in case 1 and the experimental ones is not only the contribution of the roof.

If some springs (k_{N-V}, k_{N-L}, $k_{N-\theta VB}$ in fig. 7) are introduced to model more realistically the contribution of the neoprene bearings (case 2), the results are almost identical to the ideal boundary conditions (case 1). Therefore, some additional relaxation of the boundary conditions

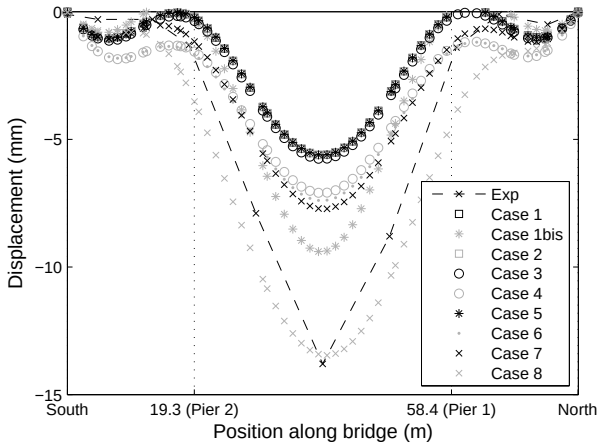


Figure 8: Static displacements for different sets of values of updating parameters according to table 2

is required. As a matter of fact, significant vertical displacements were measured on top of the piers. If the bridge response is analyzed assuming that the structural elements have infinite axial stiffness (which is reasonably close to reality), the only explanation for these vertical displacements is a displacement of the foundation of the piers. Since this foundation is composed of vertical piles and the piers are inclined, horizontal reactions are transmitted to the foundation and the most likely foundation displacement is a horizontal one.

Cases 3 and 4 consider the vertical stiffness of the pier foundations (k_{P-V} in fig. 7) and show that real stiffness values should be in the range $[1e9 - 1e8]$N/m, since the experimental static displacements at the piers are much higher than the computed values of case 3 and much lower than those of case 4. Results with $1e9$N/m could be considered equivalent to an infinite stiffness (ideal boundary condition). In the considered range, the computed static displacements are not in agreement with the experimental ones, the deflection shape still being different from the experimental one. Similar conclusions can be drawn from cases 5 and 6 and the effect of rotational springs in the pier foundations.

Finally, cases 7 and 8 show that the displacement values and the deflection shape are very sensitive to the longitudinal stiffness of the pier foundations(k_{P-L} in fig. 7). The equivalent stiffness is likely to be in the range $[1e8 - 1.5e7]$ N/m.

5.2 Optimization of the static model

By giving null values to the weights of residuals in frequencies and mode shapes in eq. (1), the objective function in the optimization process only includes the residuals in static displacements. Table 3 shows the initial values of the updating parameters and the final values that give the optimum value in the updating process.

Fig. 9 shows that the updated model provides a good approximation to the experimental displacements. The most sensitive and relevant parameter is the longitudinal stiffness of the foundation of the piers (k_{P-L}), as predicted from the manual calibration and sensitivity analysis. The rest of the updated parameters are in agreement with their corresponding theoretical values and can assume a rather broad range of values without affecting the optimum solution. Some of them are not sensitive above a certain threshold value, which is equivalent to an infinite value (table 3), since similar results are obtained as in the case of a fixed boundary condition.

Parameter (N,m)	Initial Values	Final Values	Comment
k_{N-V}	5e8	"∞"	$> 5e8$, not sensitive
k_{N-L}	1.5e6	1e7	Medium influence [0.5e7-1.5e7]
$k_{N-\theta VB}$	1e7	1e6	Not sensitive
k_{P-V}	1e8	"∞"	$> 1e9$, not sensitive
k_{P-L}	1.5e7	**2.398e7**	Extremely sensitive
$k_{P-\theta VB}$	1e8	"∞"	$> 1e9$, not sensitive

Table 3: Results for updating parameters of static response

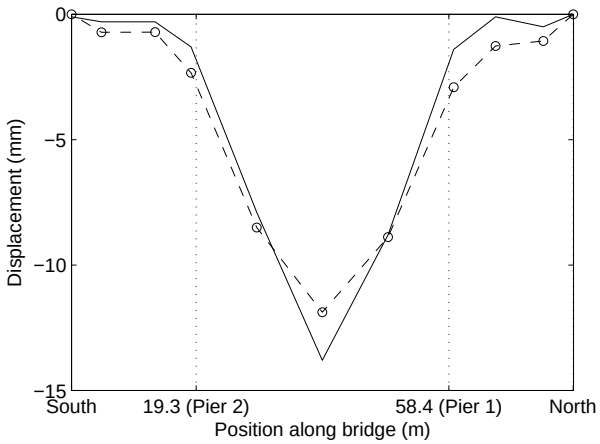


Figure 9: Static displacements of the updated model (o) according to the static experimental displacements (solid line)

Mode Exp.	Mode FEM	Description	MAC	Δf (%)
1	1	Tors. + lat. bend.	0.971	-39.0
2	2	Vert. bend.	0.905	-12.8
3	3	Lat. bend.	0.901	-8.1
4	4	Vert. bend.	0.886	-9.13
5	5	Lat. bend + tors.	0.499	-23.8
6	5	Lat. bend + tors.	0.492	-27.3
7	8	Vert. bend.	0.422	-1.14
8	13	Lat. bend.	0.729	20.0
9	9	Vert. bend.	0.614	-7.6
10	23	Tors. + lat. bend	0.665	71.8
11	6	Vert. bend.	0.395	-30.7

Table 4: Dynamic results with updating parameters from the updating of the static response (table 3)

6 UPDATING DYNAMIC AND STATIC RESPONSE

Whereas the previously considered static response affects only the in-plane behavior, the vertical bending modes as well as the rest of the previously presented modes are considered for model updating. These out of plane modes should be included in order to check that realistic results for the overall response of the bridge are obtained. However, the analysis will be focused on the in plane bending modes. The lateral out of plane stiffness of the foundation is now additionally included in the model updating. Transversal springs in the out-of-plane direction with stiffness k_{N-T} and k_{P-T} are introduced for the neoprene bearings of the abutments and the pier foundations respectively.

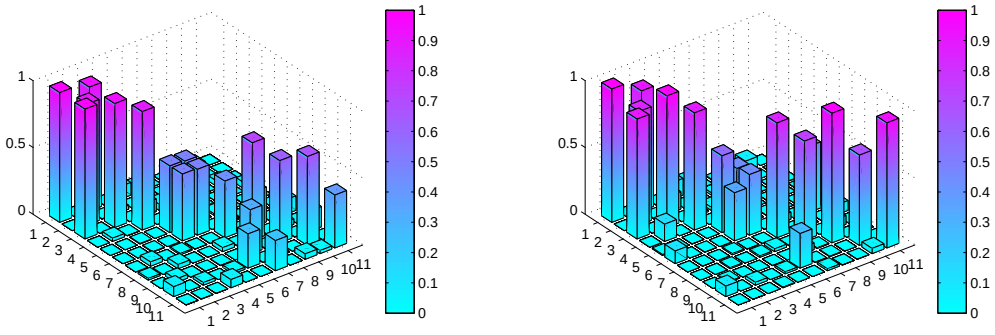
6.1 Manual calibration of dynamic model

Once the static model has been updated, the natural frequencies and mode shapes can be obtained with the updated parameters presented in the previous section. For doing so, it is considered that the transversal stiffness of the neoprene bearings (k_{N-T}) is similar to the one in the longitudinal direction (k_{N-L}). Table 4 summarizes the corresponding dynamic results and fig. 10(a) shows the MAC matrix between the numerical and experimental mode shapes. The difference in frequencies of table 4 is defined in the same way as the corresponding residual of the objective function (eq. 3) but applying percentages. The model updated according to the static results does no not give a good approximation of the modal parameters.. Low MAC values and large differences in frequencies between computed and experimental values are obtained.

After the manual sensitivity analysis of the updating parameters, it was found that good results are obtained if the piers are considered to be fixed. Table 5 summarizes the results in that case. Computed mode shapes and frequencies are now much closer to the experimental values. Fig. 10(b) shows a better MAC matrix than in the previous case. The increase in MAC values is particularly significant for the in plane behavior of the experimental bending modes 7, 9 and 11.

Mode Exp.	Mode FEM	Description	MAC	Δf (%) (%)
1	1	Tors. + lat. bend.	0.997	-0.46
2	3	Vert. bend.	0.849	12.4
3	2	Lat. bend.	0.984	-28.65
4	4	Vert. bend.	0.876	1.54
5	5	Lat. bend + tors.	0.575	1.96
6	6	Lat. bend + tors.	0.452	-2.77
7	7	Vert. bend.	0.858	6.10
8	12	Lat. bend.	0.741	32.0
9	8	Vert. bend.	0.969	2.54
10	22	Tors. + lat. bend	0.676	79.58
11	15	Vert. bend.	0.936	-26.87

Table 5: Dynamic results with values of parameters from static updating (table 3) at abutments and considering the piers as fixed elements



(a) (b)

Figure 10: MAC matrix between experimental modes and computed modes obtained with (a) values of parameters from static updating and (b) the same values but with the piers considered to be fixed

Parameter (N,m)	Initial Values	Final Values	Comment
k_{N-V}	5e9	"∞"	$> 5e8$, not sensitive
k_{N-L}	1.5e7	1.58e7	Sensitive
k_{N-T}	7.5e7	1.51e7	Sensitive
$k_{\theta-VB}$	1e7	2e6	Not sensitive

Table 6: Values of updating parameters at abutments considering the measured static and dynamic response

Mode Exp.	Mode FEM	Description	MAC	Δf (%)
1	1	Tors. + lat. bend.	0.997	-0.50
2	3	Vert. bend.	0.880	13.6
3	2	Lat. bend.	0.983	2.98
4	4	Vert. bend.	0.902	2.19
7	7	Vert. bend.	0.858	-0.08
8	8	Lat. bend.	0.899	-0.43
9	9	Vert. bend.	0.970	-4.79
11	16	Vert. bend.	0.936	8.85

Table 7: Dynamic results with updating parameters at abutments based on the measured dynamic and static response (table 6)

6.2 Optimization of the static and dynamic model

When considering the static and dynamic response, all terms in the objective function in equation (1) are considered. The applied weights were $w_M = 0.5$ for the mode shapes (MAC values), $w_f = 0.2$ for the frequencies and $w_s = 0.2$ for the static displacements. These values provided good convergence and avoided that any term of the objective function dominated the optimization process.

Since the targeted modes are the in plane vertical bending modes, only the most significant lateral and torsional modes are retained in the analysis. Vertical bending modes $(2, 4, 7, 9, 11)$ and lateral and torsion modes $(1, 3, 8)$ were eventually considered.

The updating parameters include only the stiffness of the neoprene bearings at the abutments (k_N). Table 6 includes the corresponding values after updating the FE model. The optimization process gives precise values for the longitudinal (k_{N-L}) and transversal (k_{N-T}) springs, whereas it is not very sensitive to the other two.

Table 7 shows the MAC values and relative frequency differences between the experimental and computed modes in the updated model. The updated finite element model gives high MAC values and low discrepancies in frequencies for the vertical bending modes as well as for the considered lateral and torsional modes. Fig. 11 compares the experimental vertical bending modes and the computed form the updated model.

Despite the fact that good results are obtained for the dynamic behavior, the displacements for the static load case obtained with the updated parameters do not agree well with the experimental results (fig. 12). This figure shows also the results obtained when springs at the bottom

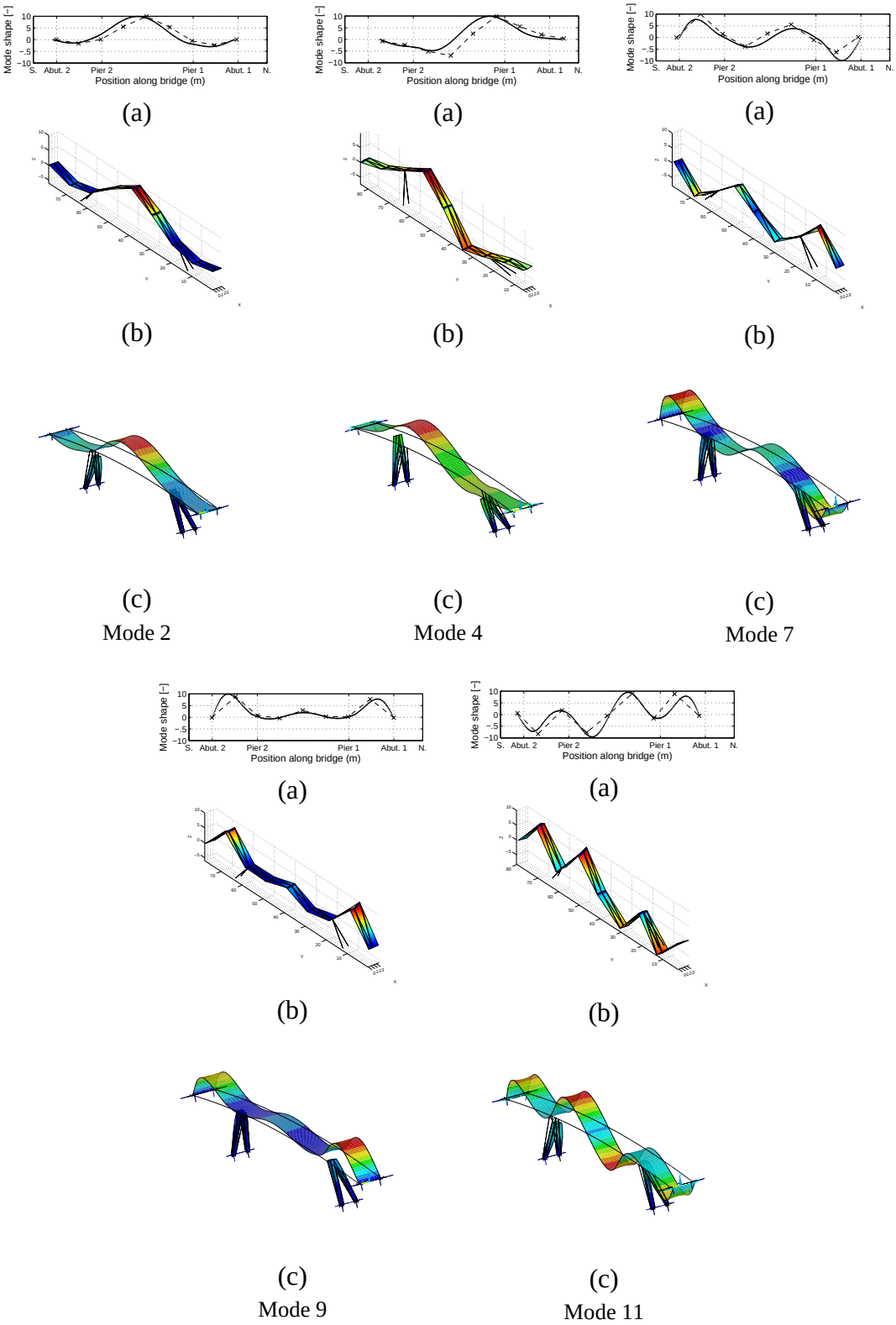


Figure 11: (a)Vertical bending modes from the FE model (solid lines) and experimental ones (discontinuous lines with “x” marks). (b) 3D view of experimental mode shape. (c) 3D view of numerical mode shape (including only deck and piles from the FE model)

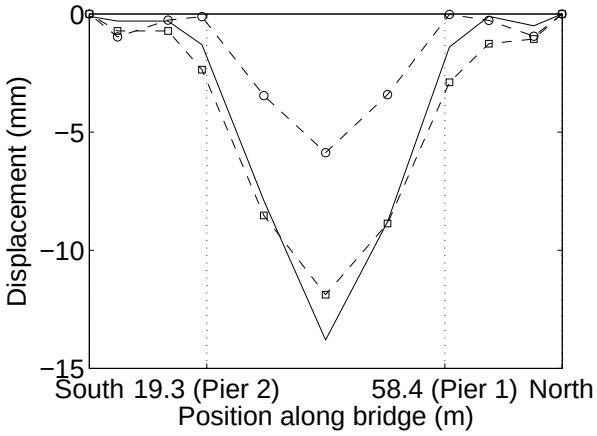


Figure 12: Static displacements from the updated model with fixed piers considering dynamic and static response (o), from the updated model including springs at piers foundation (□) and experimental values (solid line).

of the piers are additionally considered as updating parameters (table 3, fig. 9).

7 DISCUSSION OF RESULTS

The finite element updating process has allowed obtaining a good approximation of either the measured static and dynamic behavior of the bridge. However, compatible bearing stiffness at the abutments have been determined for the static and the dynamic response, whereas non compatibility in the longitudinal stiffness of piers foundation is encountered.

As discussed for the manual calibration of the static model, the measured vertical displacements on top of the piles must be produced by a horizontal displacement of the foundation of the piers. The structural design of the foundation (long vertical piles) and the piers (inclined piers) justifies the low horizontal stiffness at the foundation. Thus, the static model response "needs" a flexible foundation to approach the experimental results.

On the other hand, the dynamic model requires a rigid foundation (infinite stiffness) to simulate the mode shapes and frequencies obtained from the Operational Modal Analysis. The proposed explanation for this is that the mass of the foundation and surrounding soil is sufficiently large to make the foundation behave as a fixed point from a dynamic point of view. In order to address this phenomenon, the FE model should consider an equivalent mass of the foundation and the soil, so mass elements would be introduced as new updating parameters. Thus, static as well as dynamic soil-foundation-structure interaction could be considered and a more accurate updating process could be performed. Ongoing work is focused on the analysis of a new model that accounts for the dynamic soil structure interaction effect.

8 CONCLUSIONS

This paper has successfully combined the static and dynamic experimental response of a footbridge to obtain a finite element model that accurately reproduces the static and dynamic response. The updating process has provided useful information about the actual behavior of the bridge and the interaction with its foundation. The static load test has provided relevant information. The role of the foundation of the piers would probably not have been clear from a dynamic test. In addition, static results are easier and faster to analyze than the dynamic results.

Possible soil-structure interaction effects require further analysis. The finite element model should include a more complex model for the soil and foundation.

9 ACKNOWLEDGEMENTS

This research was funded by the Spanish Ministry of Economy and Competitiveness (*Ministerio de Economía y Competitividad*) through research project BIA2010-14843. Financial support is gratefully acknowledged.

References

[1] P. Dallard, A. J. Fitzpatrick, A. Flint, S. L. Bourva, A. Low, R. M. R. Smith, and M. Willford, "The london millennium footbridge," *Structural Engineer*, vol. 79, no. 22, pp. 17–33, 2001.

[2] S. Zivanovic, A. Pavic, and P. Reynolds, "Vibration serviceability of footbridges under human-induced excitation: a literature review," *Journal of Sound and Vibration*, vol. 279, pp. 1–74, 1/6 2005.

[3] K. L. Structural Mechanics Division, "Macec," *http://bwk.kuleuven.be/bwm/macec*.

[4] B. Peeters and G. D. Roeck, "Reference-based stochastic subspace identification for output-only modal analysis," *Mechanical Systems and Signal Processing*, vol. 13, no. 6, pp. 855–878, 1999.

[5] E. Reynders, J. Houbrechts, and G. D. Roeck, "Fully automated (operational) modal analysis," *Mechanical Systems and Signal Processing*, vol. 29, pp. 228–250, 5 2012.

[6] E. Matta, R. Ceravolo, A. D. Stefano, A. Quattrone, and L. Z. Fragonara, "Structural system identification in the presence of resonant non-structural appendages," in *Proceedings of the Eleventh International Conference on Computational Structures Technology*, 2012.

[7] A. Teughels, *Inverse modelling of civil engineering structures based on operational modal data*. Ph.D. Thesis, Katholieke Universiteit Leuven, 2003.

[8] N. Yazdani, S. Eddy, and C. Cai, "Effect of bearing pads on precast prestressed concrete bridges," *Journal of Bridge Engineering*, vol. 5, no. 3, pp. 224–232, 2000. http://ascelibrary.org/doi/pdf/10.1061/224

[9] AASHTO, *AASHTO LRFD bridge design specifications*. Washington,DC: AASHTO, 1996.

COMPDYN 2013
4th ECCOMAS Thematic Conference on
Computational Methods in Structural Dynamics and Earthquake Engineering
M. Papadrakakis, V. Papadopoulos, V. Plevris (eds.)
Kos Island, Greece, 12–14 June 2013

UKF ESTIMATION OF SP-TAR MODELS FOR THE IDENTIFICATION OF TIME-VARYING STRUCTURES

Minas D. Spiridonakos and Eleni. N. Chatzi

ETH Zurich, Institute of Structural Engineering,
Department of Civil, Environmental and Geomatic Engineering,
Wolfgang-Pauli Str. 15, 8093 Zurich, Switzerland,
e-mail: {spyridonakos,chatzi}@ibk.dbaug.ethz.ch

Keywords: Time-varying structures, Autoregressive, Smoothness Priors, Unscented Kalman Filter.

Abstract. *An important class of methods for the effective identification of time-varying structures based on random vibration response data records is that of stochastic parameter evolution methods. Methods of this class rely on parametric time-varying models with a stochastic structure imposed on the time evolution of their parameters. The latter are considered as random variables allowed to vary in time, with their evolution being subject to stochastic smoothness constraints (smoothness priors constraints). In the present study, Smoothness Priors Time-dependent (SP-TAR) models characterized by stochastic smoothness constraint equations with unknown a-priory coefficients are considered. The SP coefficients of the model along with the time-varying AR coefficients have to be estimated based on the measured response of the structure. This is achieved by expressing the generalized SP-TAR model in a nonlinear state-space form and employing the Unscented Kalman Filter (UKF) algorithm. The introduced method is validated through its application for the identification of a simulated gantry crane system.*

1 INTRODUCTION

The increasing interest among engineers for lightweight configurable mechanisms and structures such as the ones based on the principle of tensegrity, brings forth the need for more efficient identification methods able to handle inherent structural variability. Structures characterized by properties, either physical or geometrical, that vary with time are commonly referred to as time-varying or non-stationary structures, and are encountered in numerous applications such as heavy vehicle-bridges systems, cranes, robotic devices and others.

The available time-varying identification methods may be distinguished into three distinct classes (outlined in order of increasing structural complexity; [1, 2]): (i) unstructured parameter evolution methods , (ii) stochastic parameter evolution methods, and (iii) deterministic parameter evolution methods.

Methods of the first class are based on the assumption that the time-varying characteristics of the system to be identified evolve slowly with time. Thus, they employ stationary (short-time or recursive) methods in windowed versions of the signal, within which the stationarity assumption is approximately valid. These methods impose no-structure on their model parameters which are thus free to vary with time. Typical methods of this class include stationary models applied on short segments of the non-stationary signal, and recursive methods that employ exponential windows in order to estimate their parameters based only on recent values of the non-stationary signal [3, Ch. 11].

On the other hand, deterministic parameter evolution methods rely on functional series time-varying models, that is models with coefficients expanded on a time-dependent functional basis [4]. These types of models have been widely used over the last years and are particularly effective for the identification of systems with properties that evolve in a deterministic way [1, 5].

Stochastic parameter evolution methods stand between the aforementioned extreme cases. They are based on time-varying models with parameters that are considered as random variables, allowed to vary with time, with their evolution being subject to stochastic smoothness constraints [6]. These constraints are often referred to as *smoothness priors constraints* and they may be tuned in order to track a wide range of evolutions: from random walk processes to deterministic evolutions described by low order polynomial functions [7].

Although in the vast majority of engineering applications the time-variability of structural properties is designed to be deterministic, disturbances, control errors and random effects lead to deviation from the predetermined variability thus introducing stochasticity. In this way, stochastic parameter evolution methods may be deemed as appropriate for the identification of time-varying structures.

However, the main limitation of the stochastic parameter evolution methods is that they commonly use pre-determined coefficients for the stochastic equation of their parameters. The aim of the present study is to overcome this drawback by using generalized smoothness priors constraints for the time-varying parameters with initially unknown or rather uncertain coefficients. This is achieved by expressing a general Smoothness Prior Time-dependent AutoRegressive (SP-TAR) model in a nonlinear state-space form and estimating its unknown parameters by means of the Unscented Kalman filter (UKF) method. The introduced method is validated through its application on a numerical case study.

2 SMOOTHNESS PRIORS TIME-DEPENDENT AR MODELS

A Time-dependent AutoRegressive (TAR) model of order n is given by the following equation:

$$y[t] + a_1[t]y[t-1] + a_2[t]y[t-2] + \ldots + a_n[t]y[t-n] = e[t], \qquad e[t] \sim \text{NID}(0, \sigma_e^2[t]) \quad \text{(1a)}$$

where t designates discrete time (with $t = 1, 2, \ldots, N$), $y[t]$ the observed nonstationary signal, $e[t]$ the residual sequence, that is the unmodeled part of the signal, which is assumed to be normally identically distributed with zero mean and time-varying variance $\sigma_e^2[t]$, and $a_i[t]$ the time-varying AR parameters.

In the case of smoothness priors models, stochastic difference equations of the following general form govern each of the AR parameters.

$$a_i[t] + \delta_1 a_i[t-1] + \delta_2 a_i[t-2] + \ldots \delta_p a_i[t-p] = w_i[t], \qquad w_i[t] \sim \text{NID}(0, \sigma_w^2[t]) \quad \text{(1b)}$$

In the equation above p designates the difference equation order, and $w_i[t]$ zero-mean, uncorrelated, mutually uncorrelated and also uncrosscorrelated with $e[t]$, Gaussian sequences with time-dependent variance $\sigma_w^2[t]$. The smoothness of evolution of the AR parameters is controlled by this variance, where a small variance indicates smooth evolution of the corresponding time-varying parameter and vice-versa. This fact may be easily demonstrated by considering the two parts of the solution of Eq. (1b): the solution of the corresponding homogeneous equation $a_i[t] + \delta_1 a_i[t-1] + \ldots \delta_p a_i[t-p] = 0$ and the particular solution for a given driving input noise $w_i[t]$. In the limiting case of $w_i[t] = 0$, the difference equation is deterministic and its solution is an initial values problem, as long as the values $a_i[-p+1], \ldots, a_i[-1], a_i[0]$ are sufficient to solve recursively for any $a_i[t]$ with $t = 1, \ldots, N$. On the other hand, a driving input noise $w_i[t]$ with large variance would manifest the solution of the inhomogeneous stochastic difference equation and the AR parameters would vary almost randomly.

The significant difference of the general SP-TAR model defined in Eq. (1) compared to the conventional approach [6], is that the coefficients of the stochastic difference equations are not predetermined, but assumed unknown. Thus, they have to be estimated from the observed non-stationary signal along with the time-varying AR parameters. In this way, the smoothness priors constraint equation is able to adapt to a specific identification problem under study.

It should be mentioned that for the conventional approach the smoothness priors constraints are typically of the form $\Delta^p a_i[t] = w_i[t]$ where Δ^p is the p order difference operator ($\Delta^p = (1 - \mathcal{B})^p$; where $\mathcal{B}$ the backshift operator $\mathcal{B}^i y[t] = y[t-i]$).

The model parameter estimation problem of the general SP-TAR model of Eq. (1) is considered in the following section.

2.1 Parameter estimation

The parameter estimation problem for the SP-TAR model of Eq. (1) involves estimation of both the parameter vector $\boldsymbol{\delta} = [\delta_1 \ \delta_2 \ \ldots \ \delta_p]^T$ and the time-varying AR parameters $a_1[t]$, $a_2[t]$, $\ldots$, $a_n[t] \ \forall \ t$. This problem may be treated by expressing the SP-TAR model in a non-linear state space form. Toward this end, the model parameters are concatenated into an augmented joint state vector

$$\boldsymbol{z}[t] = \left[\ a_1[t] \ldots a_n[t] \vdots a_1[t-1] \ldots a_n[t-1] \vdots \ \ldots a_1[t{-}p{+}1] \ldots a_n[t{-}p{+}1] \vdots \delta_1 \ldots \delta_p \ \right]^T_{p(n+1)\times 1}$$

and the SP-TAR$(n)_p$ model may be expressed as:

$$\boldsymbol{z}[t] = \boldsymbol{F}(\boldsymbol{z}[t-1]) \cdot \boldsymbol{z}[t-1] + \boldsymbol{G} \cdot \boldsymbol{w}[t] \tag{2a}$$

$$y[t] = \boldsymbol{h}[t]^T \cdot \boldsymbol{z}[t] + e[t] \tag{2b}$$

with:

$$F(z[t-1]) = \left[\begin{array}{ccccc:c} -\delta_1 \cdot \boldsymbol{I}_n & -\delta_2 \cdot \boldsymbol{I}_n & \cdots & -\delta_{p-1} \cdot \boldsymbol{I}_n & -\delta_p \cdot \boldsymbol{I}_n & \boldsymbol{0}_{n\times p} \\ \boldsymbol{I}_n & \boldsymbol{0}_{n\times n} & \cdots & \boldsymbol{0}_{n\times n} & \boldsymbol{0}_{n\times n} & \boldsymbol{0}_{n\times p} \\ \boldsymbol{0}_{n\times n} & \boldsymbol{I}_n & \cdots & \boldsymbol{0}_{n\times n} & \boldsymbol{0}_{n\times n} & \boldsymbol{0}_{n\times p} \\ \vdots & \vdots & \vdots & \ddots & \vdots & \vdots \\ \boldsymbol{0}_{n\times n} & \boldsymbol{0}_{n\times n} & \cdots & \boldsymbol{I}_n & \boldsymbol{0}_{n\times n} & \boldsymbol{0}_{n\times p} \\ \hdashline \boldsymbol{0}_{p\times n} & \boldsymbol{0}_{p\times n} & \boldsymbol{0}_{p\times n} & \cdots & \boldsymbol{0}_{p\times n} & \boldsymbol{I}_p \end{array}\right]_{p(n+1)\times p(n+1)}$$

$$\boldsymbol{G} = \left[\begin{array}{cc} \boldsymbol{I}_n & \boldsymbol{0}_{n\times n(p-1)+p} \end{array}\right]^T_{p(n+1)\times n}$$

$$\boldsymbol{w}[t] = \left[\begin{array}{cccc} w_1[t] & w_2[t] & \ldots & w_n[t] \end{array}\right]^T_{n\times 1}, \quad \boldsymbol{w}[t] \sim \text{NID}\left(\boldsymbol{0}_{n\times 1}, \boldsymbol{Q}[t]\right), \text{ with } \boldsymbol{Q}[t] = \sigma_w^2[t] \cdot \boldsymbol{I}_n$$

$$\boldsymbol{h}[t] = \left[\begin{array}{cccc:ccc} -x[t-1] & -x[t-2] & \ldots & -x[t-n] & 0 & \ldots & 0 \end{array}\right]^T_{p(n+1)\times 1}$$

where $\boldsymbol{I}_{\text{dim}}$ and $\boldsymbol{0}_{\text{dim}}$ designate identity and zero matrices, respectively, of the indicated dimension. This state space model is non-linear since $\boldsymbol{F}$ is a function of the joint state vector $\boldsymbol{z}[t-1]$ and more specifically of the parameter vector $\boldsymbol{\delta}$.

Several techniques have been proposed for nonlinear identification applications in Civil Engineering, including the Least Squares Estimation (LSE) [8], the Extended Kalman Filter (EKF) [9], the sequential Monte Carlo methods (particle filters, PF) [10] and the Unscented Kalman Filter (UKF) [11]. Presently, the UKF algorithm is employed for the recursive estimation of the joint state vector $\boldsymbol{z}[t]$. The UKF algorithm is known to offer a number of advantages compared to the Extended Kalman Filter (EKF) algorithm, which has been the standard approach for nonlinear state and/or parameter estimation problems [12]. This is mainly due to the first-order linearization approach adopted by the EKF algorithm that may introduce large errors in the posterior mean and covariance of the estimated random variables. In addition, the EKF algorithm necessitates the analytic differentiation of the nonlinear functions for the derivation of the Jacobian, in contrast to the UKF algorithm which derives this information implicitly.

The UKF algorithm is based on the propagation of a minimal set of carefully chosen sample points through the true non-linear system. These sample points, refereed to as sigma points, completely capture the true mean and covariance of the Gaussian random variables to be estimated, while they also capture the posterior mean and covariance by propagating these sigma points through the nonlinear system [12]. The versatility of the filter has been demonstrated in joint-state and parameter identification problems relating to nonlinear hysteretic structural systems in [13], [14].

A summary of a normalized version of the estimation method, based on the use of the UKF algorithm, is provided in Table 1. For this version, the time-varying state and measurement noise processes are normalized by $\sigma_e^2[t]$. In this way the problem of introducing arbitrary values for the normally a-priori unknown $\sigma_w^2[t]$ and $\sigma_e^2[t]$ values is overcome.

Finally, the structure of a specific SP-TAR model is completely defined by the AR model order n and the smoothness constraints order p, which may be selected based on a suitable criterion such as the Mean Square Error (MSE) or the Akaike Information Criterion (AIC) [6].

Table 1: Unscented Kalman filter for the estimation of generalized SP-TAR models.

Calculate sigma points:

$$\mathcal{Z}_{t-1} = \left[\hat{\boldsymbol{z}}[t-1|t-1] \quad \hat{\boldsymbol{z}}[t-1|t-1] + \gamma\sqrt{\widetilde{\boldsymbol{P}}[t-1|t-1]} \quad \hat{\boldsymbol{z}}[t-1|t-1] - \gamma\sqrt{\widetilde{\boldsymbol{P}}[t-1|t-1]}\right]$$

Time update (prediction):

$$\mathcal{Z}^*_{t|t-1} = \boldsymbol{F}\left(\mathcal{Z}_{t-1}\right)$$

State prediction
$$\hat{\boldsymbol{z}}[t|t-1] = \sum_{i=0}^{2L} W_i^{(m)} \mathcal{Z}^*_{i,t|t-1}$$

"Covariance" update
$$\widetilde{\boldsymbol{P}}[t|t-1] = \sum_{i=0}^{2L} W_i^{(c)} \left\{\mathcal{Z}^*_{i,t|t-1} - \hat{\boldsymbol{z}}[t|t-1]\right\}\left\{\mathcal{Z}^*_{i,t|t-1} - \hat{\boldsymbol{z}}[t|t-1]\right\}^T + G\widetilde{\boldsymbol{Q}}[t]G^T$$

Redraw sigma points
$$\mathcal{Z}_{t|t-1} = \left[\hat{\boldsymbol{z}}[t|t-1] \quad \hat{\boldsymbol{z}}[t|t-1] + \gamma\sqrt{\widetilde{\boldsymbol{P}}[t|t-1]} \quad \hat{\boldsymbol{z}}[t|t-1] - \gamma\sqrt{\widetilde{\boldsymbol{P}}[t|t-1]}\right]$$

$$\mathcal{Y}_{t|t-1} = \boldsymbol{h}[t]^T \mathcal{Z}_{t|t-1}$$

$$\hat{y}[t|t-1] = \sum_{i=0}^{2L} W_i^{(m)} \mathcal{Y}_{i,t|t-1}$$

Observation update (filtering):

$$\boldsymbol{P}_{\tilde{y}_t\tilde{y}_t} = \sum_{i=0}^{2L} W_i^{(c)} \left\{\mathcal{Y}_{i,t|t-1} - \hat{y}[t|t-1]\right\}\left\{\mathcal{Y}_{i,t|t-1} - \hat{y}[t|t-1]\right\}^T + 1$$

$$\boldsymbol{P}_{z_t y_t} = \sum_{i=0}^{2L} W_i^{(c)} \left\{\mathcal{Z}_{i,t|t-1} - \hat{\boldsymbol{z}}[t|t-1]\right\}\left\{\mathcal{Y}_{i,t|t-1} - \hat{y}[t|t-1]\right\}^T$$

Gain
$$\mathcal{K}_t = \boldsymbol{P}_{z_t y_t}\boldsymbol{P}^{-1}_{\tilde{y}_t\tilde{y}_t}$$

State update
$$\hat{\boldsymbol{z}}[t|t] = \hat{\boldsymbol{z}}[t|t-1] + \mathcal{K}_t(y[t] - \hat{y}[t|t-1])$$

"Covariance" update
$$\widetilde{\boldsymbol{P}}[t|t] = \widetilde{\boldsymbol{P}}[t|t-1] - \mathcal{K}_t\boldsymbol{P}_{\tilde{y}_t\tilde{y}_t}\mathcal{K}_t^T$$

$\gamma = \sqrt{L+\lambda}$, where λ is the composite scaling parameter and $L = p(n+1)$ the dimension of the joint state.

Weights: $W_0^{(m)} = \frac{\lambda}{L+\lambda}, \quad W_0^{(c)} = \frac{\lambda}{L+\lambda} + (1-\alpha^2+\beta), \quad W_i^{(m)} = W_i^{(c)} = \frac{1}{2(L+\lambda)}, \quad i = 1,\ldots,2L.$

Initialization: $\hat{\boldsymbol{z}}[0|0] = \boldsymbol{0}$, $\widetilde{\boldsymbol{P}}[0|0] = \boldsymbol{I}$

Normalization: $\widetilde{\boldsymbol{P}}[t|t] = \frac{\widetilde{\boldsymbol{P}}[t|t]}{\sigma_e^2[t]}, \qquad \widetilde{\boldsymbol{P}}[t|t-1] = \frac{\boldsymbol{P}[t|t-1]}{\sigma_e^2[t]}, \qquad \widetilde{\boldsymbol{Q}}[t] = \frac{\boldsymbol{Q}[t]}{\sigma_e^2[t]} = \frac{\sigma_w^2[t]}{\sigma_e^2[t]}\boldsymbol{I}_n$

Ratio $\nu = \frac{\sigma_w^2[t]}{\sigma_e^2[t]}$ assumed to be constant over time.

3 NUMERICAL CASE STUDY

In order to validate the introduced method, a numerical case study is presently considered. The setup is based on the simplified model of a planar gantry crane system consisting of a trolley moving over a girder (Fig. 1).

The crane lifts a payload of mass m from point A and deposits it at point D following the route A-D as shown in Fig. 1(a). The variability of the system stems from the varying length of the steel wire rope $\ell(t)$ and the corresponding stiffness coefficient $k_2(t) = \frac{EA}{\ell(t)}$ (see Fig. 2). The simulation study is based on the simplified 2-DOF mass-spring-damper system depicted in Fig. 1(b). The analysis focuses on the vertical vibration response of the trolley mass M and more specifically on the acceleration $\ddot{y}_1(t)$. The system is excited by the random unobservable force $F_2(t)$ generated from the disturbances of the payload. Assuming $\theta \approx 0$ the equations of motion

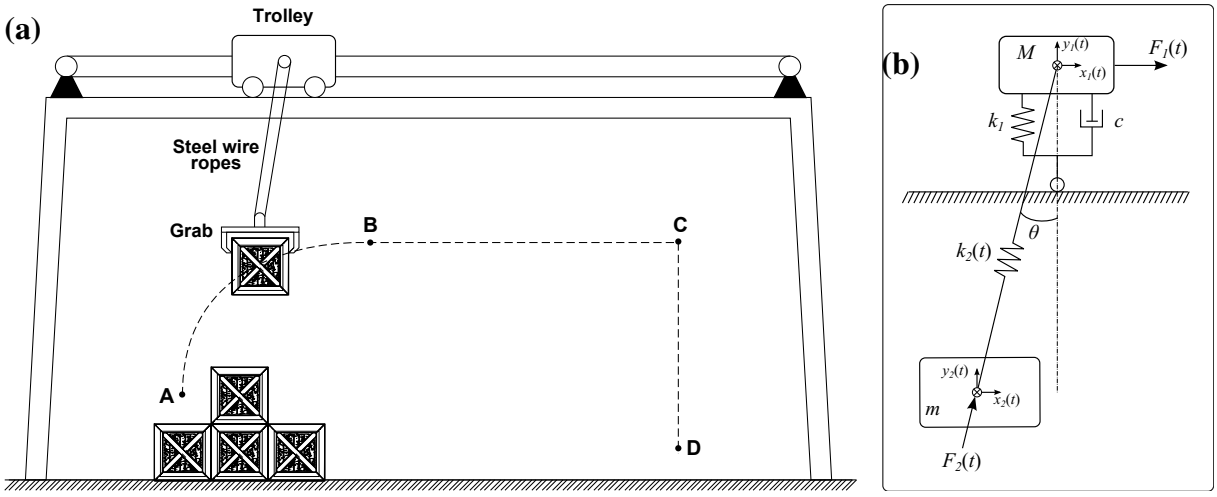


Figure 1: (a) The gantry crane, and (b) the equivalent mass-spring-damper system.

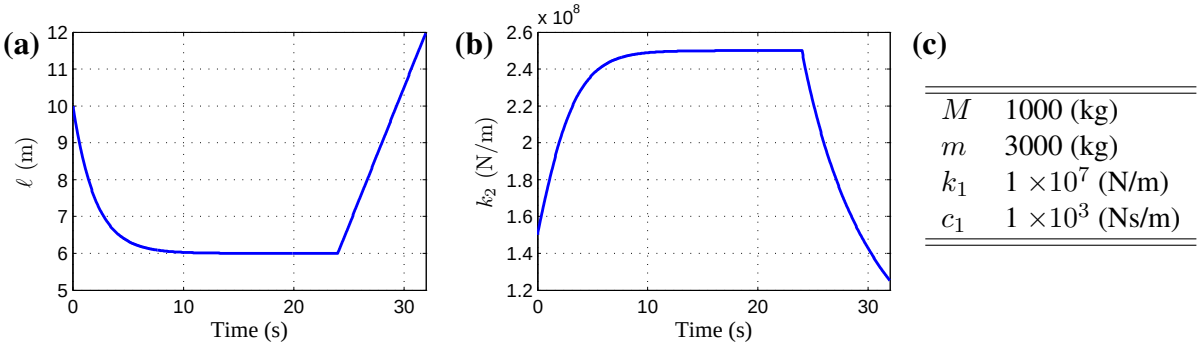


Figure 2: (a) The steel wire rope length, (b) the corresponding stiffness coefficient, and (c) the time-invariant properties of the gantry crane system.

may be written as follows:

$$M\ddot{y}_1(t) + c\dot{y}_1(t) + k_1 y_1(t) + k_2(t)[y_1(t) - y_2(t)] = 0 \quad (3a)$$

$$m\ddot{y}_2(t) + mg + k_2(t)[y_2(t) - y_1(t)] = F_2(t) \quad (3b)$$

Given a realization of the excitation force $F_2(t)$ which is assumed to follow a normal distribution with zero mean value and standard deviation equal to 100 N, the vibration response of the gantry crane model is simulated by solving the equations of motion by utilizing the Runge-Kutta 4/5 method (MATLAB *ode45* function). Simulation time is defined as $t \in [-16s, 32s]$, while a constant integration step equal to $T_s = 0.004$ s is selected. In order to minimize initialization effects, the first 4000 samples (16 s) of the response signal are discarded, resulting in a 8000 samples long response realization. The latter along with its instantaneous power spectral density estimate based on the Short-Time Fourier Transform (STFT) is depicted in Fig. 3.

The identification of the simulated system is based on a SP-TAR model of AR order equal to four estimated through the UKF method described in the previous section (parameter $\alpha = 1, \beta = 2, \kappa = 0$) [15]. The algorithm is applied in three sequential passes over the data – forward, backward and a final forward pass – in order to minimize the effects of arbitrary initial conditions. The Rauch-Rung-Striebel smoother is also applied as a last step [15].

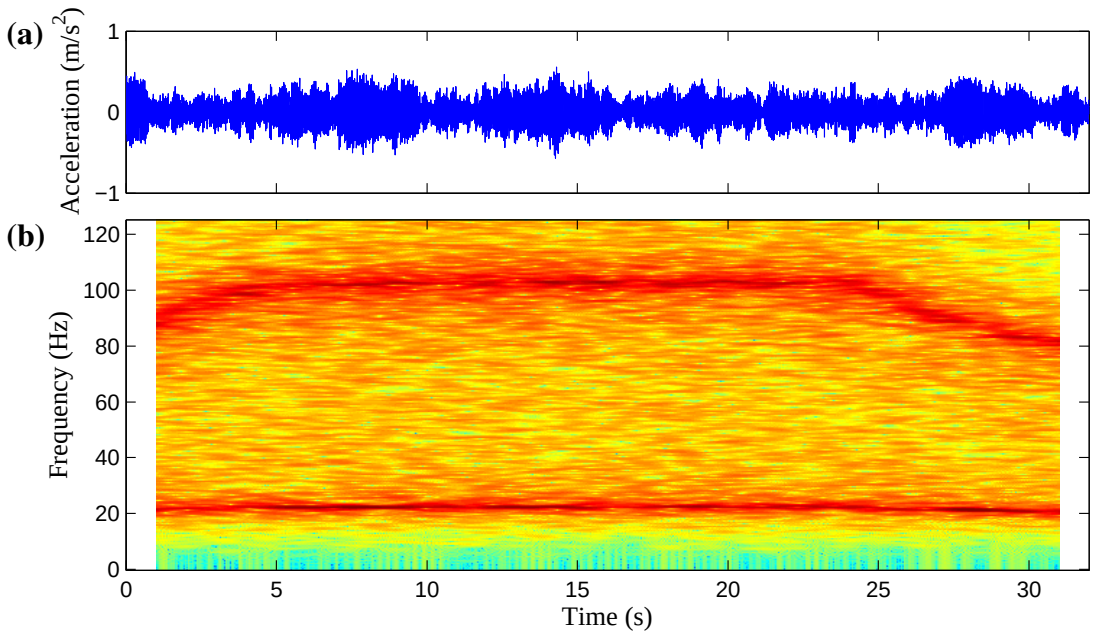


Figure 3: (a) The simulated vibration response signal and (b) the non-parametrically obtained instantaneous power spectral density estimate (STFT method).

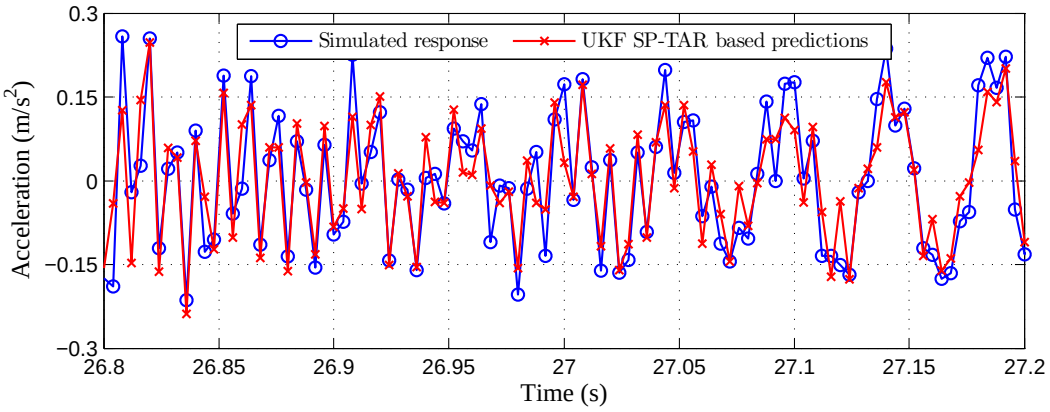


Figure 4: Segment of the simulated response signal and SP-TAR$(4)_6$ based predictions.

The mean squared error (MSE) given by the following expression

$$\text{MSE} = \frac{1}{N}\sum_{t=1}^{N}(y[t] - \hat{y}[t|t-1])^2 \tag{4}$$

is used for selecting the appropriate SP equation order p (search space $[1, 2, \ldots, 6]$) and the variance ratio ν (search space $[10^{-1}, 10^{-2}, \ldots, 10^{-5}]$). Based on the MSE values obtained by the various estimated models an SP-TAR$(4)_6$ model with ratio $\nu = 10^{-2}$ is finally selected as appropriate for the representation of the time-varying structural dynamics. Indicative signal predictions ($\hat{y}[t|t-1]$) obtained by this model are compared to the actual simulated response $y[t]$ in Fig. 4, while the estimated time-varying AR parameters and the coefficients of the SP equation are shown in Fig. 5.

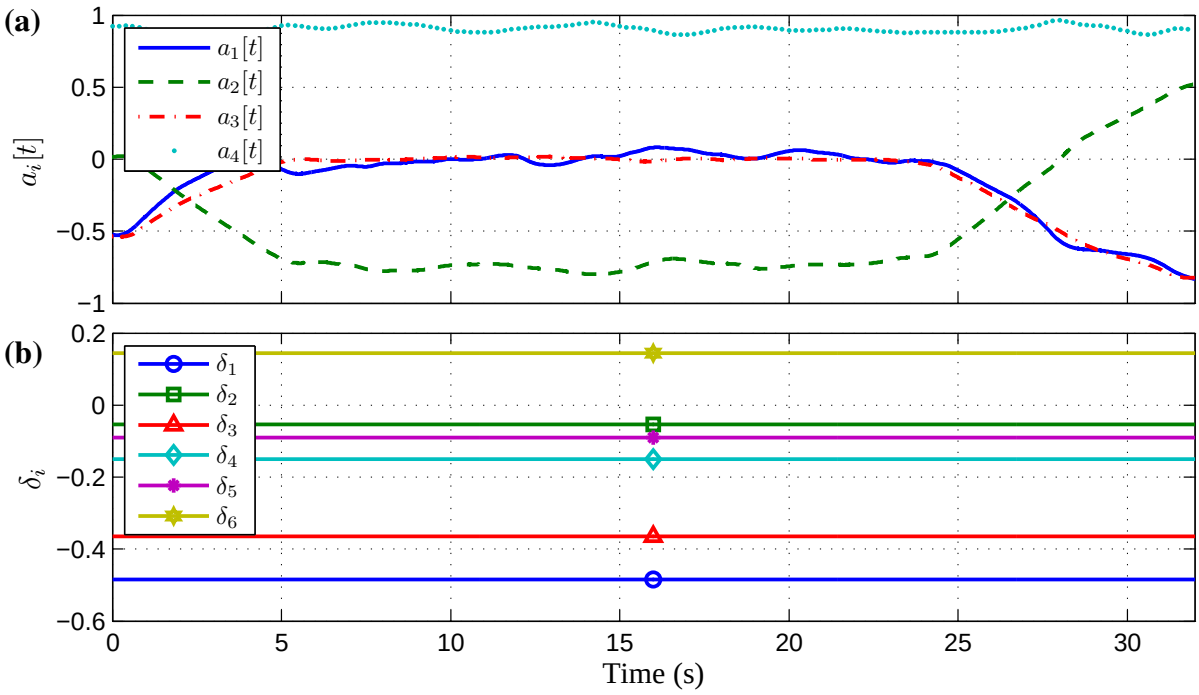


Figure 5: UKF estimated SP-TAR$(4)_6$ parameters: (a) The time-varying AR parameters, and (b) the smoothness priors equation coefficients.

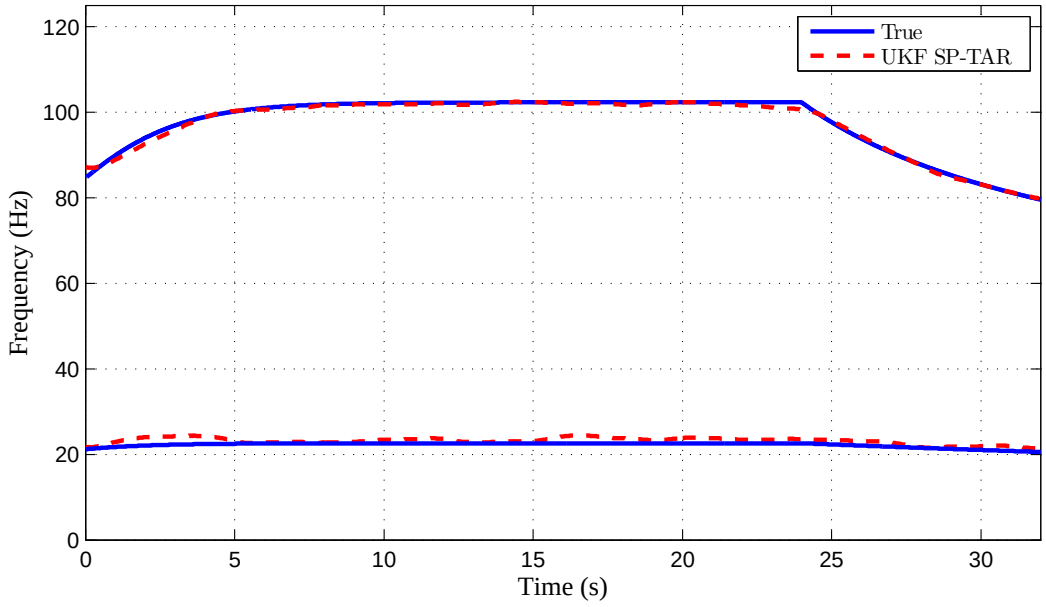


Figure 6: SP-TAR$(4)_6$ based instantaneous natural frequency estimates contrasted to those of the true simulated gantry crane system.

Finally, the SP-TAR$(4)_6$ based instantaneous natural frequency estimates are contrasted to those of the true system in Fig. 6. It should be noted that the tracking errors of the instantaneous natural frequencies achieved by the estimated SP-TAR$(4)_6$ model are below 1.5 $\%$ for both frequencies and all time instants t.

4 CONCLUSIONS

A time-varying identification method based on generalized SP-TAR models and UKF-based parameter estimation was presently proposed. The introduced method uses a smoothness priors constraint equation with unknown a-priori coefficients in contrast to the conventional approach. In this way, the potential of the SP-TAR method for accurate tracking of the time-varying dynamics of a structural system is enhanced. A primary investigation of the method's effectiveness has been carried out via its successful implementation on the identification of a simulated planar gantry crane system.

REFERENCES

[1] A.G. Poulimenos, S.D. Fassois, Parametric time-domain methods for non-stationary random vibration modelling and analysis: A critical survey and comparison. *Mechanical Systems and Signal Processing*, **20**(4), 763–816, 2006.

[2] M. Niedźwiecki, *Identification of time-varying processes*. John Wiley, 2000.

[3] L. Ljung, *System identification – Theory for the user, 2nd Edition*. PTR Prentice Hall, 1999.

[4] M.D. Spiridonakos, S.D. Fassois, Parametric identification of a time-varying structure based on vector vibration response measurements. *Mechanical Systems and Signal Processing*, **23**(6), 2029–2048, 2009.

[5] M.D. Spiridonakos, A.G. Poulimenos, S.D. Fassois, Output-only identification and dynamic analysis of time-varying mechanical structures under random excitation: A comparative assessment of parametric methods. *Journal of Sound and Vibration*, **329**(7), 768–785, 2010.

[6] G. Kitagawa, W. Gersch, *Smoothness priors analysis of time series*. Springer-Verlag, 1996.

[7] H. Clergeot, Filter-order selection in adaptive maximum likelihood estimation. *IEEE Transactions on Information Theory*, **30**(2), 199–210, 1984.

[8] A.W. Smyth, S.F. Masri, E.B. Kosmatopoulos, A.G. Chassiakos, T.K. Caughey, Development of adaptive modeling techniques for non-linear hysteretic systems. *International Journal of Non-Linear Mechanics*, **37**(8), 1435-1451, 2002.

[9] S. Mariani, A. Corigliano, Impact induced composite delamination: state and parameter identification via joint and dual extended Kalman filters. *Computer Methods in Applied Mechanics and Engineering*, **194**(5052), 5242-5272, 2005.

[10] J. Ching, J.L. Beck, K.A. Porter, R. Shaikhutdinov, Bayesian state estimation method for nonlinear systems and its application to recorded seismic response. *Journal of Engineering Mechanics*, **132**(4), 396–410, 2006.

[11] S.J. Julier, J.K. Uhlmann, A new extension of the Kalman filter to nonlinear systems. *Proceedings of AeroSense: The 11th International Symposium on Aerospace/Defense Sensing, Simulation and Controls*, Orlando, 1997.

[12] E.A. Wan, R. van der Merwe, The unscented Kalman filter, *in Kalman filtering and neural networks (ed S. Haykin)*. John Wiley & Sons, 2002.

[13] E.N. Chatzi, A.W. Smyth, The unscented Kalman filter and particle filter methods for nonlinear structural system identification with non-collocated heterogeneous sensing. *Structural Control & Health Monitoring*, **16**(1), 99–123, 2009.

[14] E.N. Chatzi, A.W. Smyth, S.F. Masri, Experimental application of on-line parametric identification for nonlinear hysteretic systems with model uncertainty. *Journal of Structural Safety*, **32**(5), 303–328, 2010.

[15] S. Särkkä, J. Hartikainen, A. Solin, EKF/UKF toolbox for Matlab V1.3. *http://becs.aalto.fi/en/research/bayes/ekfukf/*.

COMPDYN 2013
4th ECCOMAS Thematic Conference on
Computational Methods in Structural Dynamics and Earthquake Engineering
M. Papadrakakis, V. Papadopoulos, V. Plevris (eds.)
Kos Island, Greece, 12–14 June 2013

MODE SHAPE ASSEMBLY FOR AMBIENT MODAL ANALYSIS USING A TWO-STAGE BAYESIAN SPECTRAL DENSITY APPROACH

Wang-Ji YAN[1], and Lambros S. KATAFYGIOTIS[2]

[1] Department of Civil and Environmental Engineering, The Hong Kong University of Science and Technology, Clear Water Bay, Hong Kong, China.
e-mail: wjyan@ust.hk

[2] Department of Civil and Environmental Engineering, The Hong Kong University of Science and Technology, Clear Water Bay, Hong Kong, China.
e-mail: lambros@ust.hk

Keywords: Ambient Modal Analysis, Bayesian Approach, Mode Shape Assembly, Wireless Sensors, Structural Health Monitoring.

Abstract. *A two-stage Bayesian spectral density approach was formulated for ambient modal analysis recently. The interaction between spectrum variables (e.g., frequency, damping ratio as well as the magnitude of modal excitation and prediction error) and spatial variables (e.g., mode shape components) can be decoupled so that they can be identified separately. The proposed method can be implemented in the environment of a wireless sensor network through a distributed computing strategy so that local mode shapes as well as their uncertainties confined to different clusters can be identified. However, the difficulty on how to assemble these local mode shapes estimated from multiple clusters is still a problem required to be resolved properly. In this study, a Bayesian mode shape assembly methodology is proposed so that the weight for different clusters is accounted for properly according to their data quality. The optimal values for the global mode shape components corresponding to all measured dofs can be obtained by a fast iterative scheme, while the associated uncertainties can be derived analytically. There is no need to share the same set of reference dofs for all clusters for scaling purpose when using ambient vibration data. The proposed mode shape assembly method is investigated with a shear building model. Results show that the overall mode shape can be effectively identified by the proposed method.*

1 INTRODUCTION

Ambient modal analysis, which aims to identify structural modal properties by using output-only measured response without the knowledge of the input, has aroused increasing attention in industrial applications due to its efficiency and economic implementation. It has also been one of the most important issues in wireless sensor network (WSN) based structural health monitoring (SHM) systems. Recent interest has arisen to calculate the uncertainties of identified modal parameters by using Bayesian approaches [1]. In the context of ambient modal analysis, a number of Bayesian approaches have been proposed [2, 3, 4]. These methods provide rigorous means for obtaining optimal modal properties as well as their uncertainties. However, computational difficulty has severely hindered the wider application of these approaches in real-life engineering applications.

A breakthrough was made by Au [5, 6, 7] recently to address the computational challenges of conventional Bayesian FFT approach. Motivated by Au's work, a two-stage fast Bayesian spectral density approach has been proposed for ambient modal analysis when there are separated modes and closely spaced modes [8]. The proposed method is able to separate spectrum variables (e.g., frequency, damping ratio as well as the magnitude of modal excitation and prediction error) and spatial variables (e.g., mode shape components) so that these two kinds of variables can be identified independently in two stages. The proposed method can be implemented through a distributed computing strategy in the environment of wireless sensor networks. As a result, a group of local mode shapes identified from different sensor clusters sharing some reference sensors can be obtained. The local mode shapes identified from different clusters may have different senses and scaling factors since they are normalized individually [9]. The assembly of these local modes shapes to form a global mode shape is an important issue in modal analysis. A novel global least square method with an automated procedure for determining the global mode shape by minimizing a measure-of-fit function was proposed recently by Au [9]. However, the global least square approach assigns the same weights for all setups. There is still room for improvement since the quality of originally well-identified clusters may be corrupted by the quality of some more problematic setups [10]. Therefore, it is reasonable to try to incorporate the uncertainty information of different clusters into the mode shape assembly procedure. In particular, local mode shapes not well identified in particular clusters should be assigned less weight due to their relatively unreliable data quality. As a sequel to the global least square method [9], a Bayesian mode shape assembly approach is developed in this study so that the weight for different clusters can be accounted for properly according to the data quality.

2 REVISITING THE TWO-STAGE BAYESIAN APPROACH FOR AMBIENT MODAL ANALYSIS

Bayesian spectral density approach (BSDA) [4] proposed previously is novel since it can consider different kinds of uncertainties and provides a rigorous means for obtaining modal properties as well as their uncertainties which is useful for further risk assessment. However, there are some challenges related to its practical implementation: (1) BSDA requires solving a high-dimensional numerical optimization problem whose computational effort grows with the number of measured dofs and the number of modes to be identified. (2)When calculating the posterior covariance function, BSDA involves computing the inverse of a Hessian matrix, for which the computational effort and required memory space grow with the number of measured dofs and the number of modes. (3) BSDA involves repeated evaluations of the determinant and inverse of a rank deficient (singular) matrix. Therefore, the minimization problem may be ill-conditioned. (4) The dofs of interest will be always measured and processed sepa-

rately in different setups or clusters, resulting in different tour size among different setups. Therefore, BSDA encounters the difficulty on how to combine the parameters and their uncertainties identified from different setups.

To address the problems aforementioned, a two-stage Bayesian spectral density approach has been developed [8]. Following a “divide and conquer” strategy, the frequency band can be divided into multiple sub-bands and one can only focus on a specified sub-band each time. There are two possible cases over each selected frequency band: case of separated modes and case of closely spaced modes. For both cases, the interaction between spectrum variables (e.g., frequency, damping ratio as well as the magnitude of modal excitation and prediction error) and spatial variables (e.g., mode shape components) can be decoupled so that they can be conquered in two consecutive stages. In the first stage, the spectrum variables as well as their uncertainties can be identified through ‘fast Bayesian spectrum trace approach’ (FBSTA) by employing the statistical properties of the trace of the spectral density matrix. The information contained in all measured dofs from different setups can be collected together, thus avoiding the difficulty of posterior data fusion. Once the spectrum variables are extracted, the spatial variables as well as their uncertainties can be identified in a second stage by ‘fast Bayesian spectrum density approach’ (FBSDA) using the statistical information of the spectrum density matrix. In this stage, the matrix determinant lemma and matrix inverse lemma are employed to avoid the ill-conditioning of conventional BSDA. The proposed method can deal with the practical difficulties of conventional Bayesian spectrum density approach even for a large number of measured dofs. The case of separated modes and the case of closely spaced modes are discussed separately in [8].

3 HIERARCHICAL ARCHITECTURE OF WSN

As shown in Figure 1, the proposed two-stage Bayesian spectrum density approach for ambient modal analysis can be implemented through a distributed computing strategy, which is formed as a three-level hierarchical architecture. Wireless sensors can be divided into hierarchical communities, with each community composed of a cluster head node and several leaf nodes. All cluster head nodes can report to the manager node, while the manager node can report to the base station node directly connected to a PC. The ambient modal analysis can be implemented in two stages. In the first stage, the auto-spectrum density of all measured dofs is collected centrally in the manager node so that the spectrum variables and their associated uncertainties can be identified by FBSTA. The identified results will be transmitted to the cluster head nodes from the manager node in the second stage. Then the optimal local mode shapes and their covariance matrix for each community can be identified by FBSDA. Global mode shapes and their uncertainties can then be assembled with the aid of the overlapping nodes public for different clusters, as will be shown in next section.

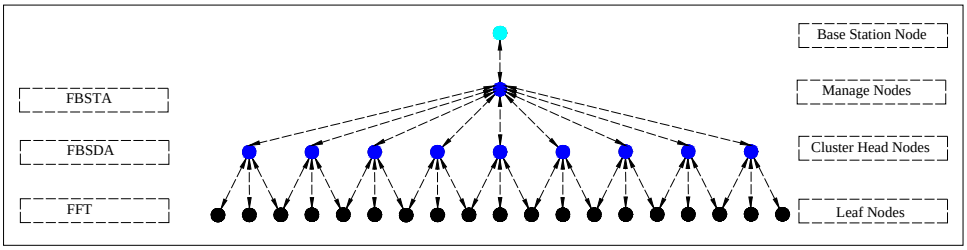


Figure 1: Three-level hierarchical architecture of WSN.

4 ASSEMBLING MODE SHAPE FROM MULTIPLE CLUSTERS

4.1 Negative Logarithm Likelihood Function

For the r-th given mode, let $\hat{\boldsymbol{\psi}}_{r,i} \in \mathbb{R}^{n_i}$ and $\mathbf{C}_{\boldsymbol{\psi}_{r,i}} \in \mathbb{R}^{n_i \times n_i}$ be the optimal values and covariance matrix of the mode shape confined to the measured dofs of the i-th cluster $(i = 1, 2, \cdots, n_t)$; n_i is the number of sensors measured in the i-th cluster and n_t is the total number of clusters included in the ambient vibration test. Assume that n_l is the total number of distinct measured dofs from all clusters, which should satisfy $n_l < \sum_{i=1}^{n_t} n_i$ since some dofs are shared by more than one cluster.

Let $\boldsymbol{\varphi}_r \in \mathbb{R}^{n_l}$ be the r-th given global mode shape covering all measured dofs, and $\boldsymbol{\varphi}_{r,i} \in \mathbb{R}^{n_i}$ be the components of $\boldsymbol{\varphi}_r$ corresponding to the measured dofs in the i-th cluster. The local mode shape $\boldsymbol{\varphi}_{r,i}$ can be mathematically related to the assembled global mode shape $\boldsymbol{\varphi}_r$ as [9]

$$\boldsymbol{\varphi}_{r,i} = \mathbf{L}_i \boldsymbol{\varphi}_r \tag{1}$$

where $\mathbf{L}_i \in \mathbb{R}^{n_i \times n_l}$ is a selection matrix, where $\mathbf{L}_i(j,k) = 1$ if the j-th sensor in the i-th cluster gives the k-th dof of the global mode shape and zero otherwise. The mode shape assembly problem under the Bayesian framework is to determine the global mode shape so that it can best fit the identified counterparts by assigning different weight for various clusters according to their data quality. It is worth noting that $\hat{\boldsymbol{\psi}}_{r,i}$ is normalized to unity when it is identified by FBSDA. Therefore, the measure-of-fit should be implemented based on the discrepancy between $\boldsymbol{\varphi}_{r,i} / \|\boldsymbol{\varphi}_{r,i}\|$ and $\hat{\boldsymbol{\psi}}_{r,i}$ both of unit norms. Since the identified local mode shape can be well-approximated by a Gaussian PDF with mean $\hat{\boldsymbol{\psi}}_{r,i}$ and covariance matrix $\mathbf{C}_{\boldsymbol{\psi}_{r,i}}$, the likelihood function of the i-th local mode shape is given by,

$$p(\hat{\boldsymbol{\psi}}_{r,i}, \mathbf{C}_{\boldsymbol{\psi}_{r,i}} | \boldsymbol{\varphi}_{r,i}) = \exp[-\frac{1}{2}(\boldsymbol{\varphi}_{r,i} / \|\boldsymbol{\varphi}_{r,i}\| - \hat{\boldsymbol{\psi}}_{r,i})^T (\mathbf{C}_{\boldsymbol{\psi}_{r,i}}^{-1})(\boldsymbol{\varphi}_{r,i} / \|\boldsymbol{\varphi}_{r,i}\| - \hat{\boldsymbol{\psi}}_{r,i})] \tag{2}$$

It is assumed that local mode shapes identified from different setups are statistically independent. Therefore, the likelihood function of the local mode shapes measured from all setups is given by,

$$p(\{\hat{\boldsymbol{\psi}}_{r,i}, \mathbf{C}_{\hat{\boldsymbol{\psi}}_{r,i}} : i = 1, \cdots, n_t\} | \boldsymbol{\varphi}_r) = \prod_{i=1}^{n_t} p(\hat{\boldsymbol{\psi}}_{r,i}, \mathbf{C}_{\boldsymbol{\psi}_{r,i}} | \boldsymbol{\varphi}_{r,i}) \tag{3}$$

Under the Bayesian framework, the updated probabilities of the global mode shape given the measured local mode shapes $\wp = \{\hat{\boldsymbol{\psi}}_{r,i}, \mathbf{C}_{\hat{\boldsymbol{\psi}}_{r,i}} : i = 1, \cdots, n_t\}$ should be

$$p(\boldsymbol{\varphi}_r | \wp) = c_0 \, p(\boldsymbol{\varphi}_r) \, p(\wp | \boldsymbol{\varphi}_r) \tag{4}$$

In the case where a non-informative prior is used, the posterior PDF of $\boldsymbol{\varphi}_r$ is proportional to the likelihood function $p(\boldsymbol{\varphi}_r | \wp)$, which can be written in terms of the 'negative logarithm likelihood function' (NLLF), where the index 'as' stands for 'assembly',

$$L_{as} = \frac{1}{2} \sum_{i=1}^{n_t} (\boldsymbol{\varphi}_{r,i} / \|\boldsymbol{\varphi}_{r,i}\| - \hat{\boldsymbol{\psi}}_{r,i})^T \mathbf{C}_{\boldsymbol{\psi}_{r,i}}^{-1} (\boldsymbol{\varphi}_{r,i} / \|\boldsymbol{\varphi}_{r,i}\| - \hat{\boldsymbol{\psi}}_{r,i}) \tag{5}$$

Writing (5) explicitly in terms of the global mode shape $\boldsymbol{\varphi}_r$ gives

$$L_{as} = \frac{1}{2}\sum_{i=1}^{n_t}(\mathbf{L}_i\boldsymbol{\varphi}_r / \|\mathbf{L}_i\boldsymbol{\varphi}_r\| - \hat{\boldsymbol{\psi}}_{r,i})^T(\mathbf{C}_{\boldsymbol{\psi}_{r,i}})^{-1}(\mathbf{L}_i\boldsymbol{\varphi}_r / \|\mathbf{L}_i\boldsymbol{\varphi}_r\| - \hat{\boldsymbol{\psi}}_{r,i}) \tag{6}$$

To enforce the norm constraint of $\boldsymbol{\varphi}_r$, i.e. $\|\boldsymbol{\varphi}_r\|^2 = 1$, (6) can be rearranged by using the Lagrange multipliers [9],

$$L_{as} = \frac{1}{2}\sum_{i=1}^{n_t}(\mathbf{L}_i\boldsymbol{\varphi}_r / \|\mathbf{L}_i\boldsymbol{\varphi}_r\| - \hat{\boldsymbol{\psi}}_{r,i})^T(\mathbf{C}^{-1}_{\boldsymbol{\psi}_{r,i}})(\mathbf{L}_i\boldsymbol{\varphi}_r / \|\mathbf{L}_i\boldsymbol{\varphi}_r\| - \hat{\boldsymbol{\psi}}_{r,i}) + \gamma_r(1-\boldsymbol{\varphi}_r^T\boldsymbol{\varphi}_r) \tag{7}$$

where γ_r is Lagrange multiplier that enforces $\|\boldsymbol{\varphi}_r\|^2 = 1$. As seen, (7) is not a quadratic function of $\boldsymbol{\varphi}_r$, thus the optimal value of $\boldsymbol{\varphi}_r$ cannot be determined analytically. To avoid the above difficulty, the auxiliary variables $\chi_{r,1},\cdots,\chi_{r,n_t}$ similar to [9] are introduced

$$\chi_{r,i}^2 = 1/\|\mathbf{L}_i\boldsymbol{\varphi}_r\|^2 \tag{8}$$

As a result, the objective function can be re-formulated by using the Lagrange multipliers approach:

$$L_{as} = \sum_{i=1}^{n_t}\frac{1}{2}(\chi_{r,i}\mathbf{L}_i\boldsymbol{\varphi}_r - \hat{\boldsymbol{\psi}}_{r,i})^T(\mathbf{C}^{-1}_{\boldsymbol{\psi}_{r,i}})(\chi_{r,i}\mathbf{L}_i\boldsymbol{\varphi}_r - \hat{\boldsymbol{\psi}}_{r,i}) + \gamma_r(1-\boldsymbol{\varphi}_r^T\boldsymbol{\varphi}_r) + \sum_{i=1}^{n_t}\beta_{r,i}(\chi_{r,i}^2\|\mathbf{L}_i\boldsymbol{\varphi}_r\|^2 - 1) \tag{9}$$

where $\beta_{r,i}$ are Lagrange multipliers that enforce equation (8).

4.2 Most Probable Values

The full set of parameters to be identified includes $\boldsymbol{\lambda}_{as} = \{\boldsymbol{\varphi}_r, \gamma_r, \beta_{r,i}, \chi_{r,i} : i = 1,2,\cdots,n_t\}$. Direct solution for the optimal global mode shapes from the objective function (9) is not trivial due to its high-dimensional as well as nonlinear features. In this study, an iterative solution strategy will be employed. The optimal values of $\chi_{r,i}$ and $\beta_{r,i}$ in terms of $\boldsymbol{\varphi}_r$ and γ_r are first derived analytically firstly, following which the optimal value of $\boldsymbol{\varphi}_r$ and γ_r given the remaining parameters are derived. A sequence of iterations comprised of the following linear optimization problems can be implemented:

(1) Optimization for $\beta_{r,i}$ and $\chi_{r,i}$

The gradient of $L_{ass}(\boldsymbol{\varphi}_r)$ with respect to $\chi_{r,i}$ is given by

$$\frac{\partial L_{as}}{\partial \chi_{r,i}} = \chi_{r,i}(\mathbf{L}_i\boldsymbol{\varphi}_r)^T(\mathbf{C}^{-1}_{\boldsymbol{\psi}_{r,i}})(\mathbf{L}_i\boldsymbol{\varphi}_r) - (\hat{\boldsymbol{\psi}}_{r,i})^T(\mathbf{C}^{-1}_{\boldsymbol{\psi}_{r,i}})(\mathbf{L}_i\boldsymbol{\varphi}_r) + 2\beta_{r,i}\chi_{r,i}\|\mathbf{L}_i\boldsymbol{\varphi}_r\|^2 \tag{10}$$

Setting $\frac{\partial L_{as}}{\partial \chi_{r,i}} = 0$ and solving for $\chi_{r,i}$ gives

$$\chi_{r,i} = \frac{(\hat{\boldsymbol{\psi}}_{r,i})^T(\mathbf{C}^{-1}_{\boldsymbol{\psi}_{r,i}})(\mathbf{L}_i\boldsymbol{\varphi}_r)}{(\mathbf{L}_i\boldsymbol{\varphi}_r)^T(\mathbf{C}^{-1}_{\boldsymbol{\psi}_{r,i}})(\mathbf{L}_i\boldsymbol{\varphi}_r) + 2\beta_{r,i}\|\mathbf{L}_i\boldsymbol{\varphi}_r\|^2} \tag{11}$$

Substituting (11) into (8) leads to two roots for $\beta_{r,i}$

$$\beta_{r,i} = -\frac{(\mathbf{L}_i\hat{\boldsymbol{\varphi}}_r)^T(\mathbf{C}^{-1}_{\boldsymbol{\psi}_{r,i}})(\mathbf{L}_i\boldsymbol{\varphi}_r)}{2\|\mathbf{L}_i\boldsymbol{\varphi}_r\|^2} \pm \frac{(\hat{\boldsymbol{\psi}}_{r,i})^T(\mathbf{C}^{-1}_{\boldsymbol{\psi}_{r,i}})(\mathbf{L}_i\boldsymbol{\varphi}_r)}{2\|\mathbf{L}_i\boldsymbol{\varphi}_r\|} \tag{12}$$

It is worth noting that the Hessian of L_{as} with respect to $\chi_{r,i}$ is given by

$$\frac{\partial^2 L_{as}}{\partial \chi_{r,i}^2} = (\mathbf{L}_i \boldsymbol{\varphi}_r)^T (\mathbf{C}_{\boldsymbol{\psi}_{r,i}}^{-1})(\mathbf{L}_i \boldsymbol{\varphi}_r) + 2\beta_{r,i} \left\| \mathbf{L}_i \boldsymbol{\varphi}_r \right\|^2 \tag{13}$$

The minimum of L_{as} occurs only when $\frac{\partial^2 L_{as}}{\partial \chi_{r,i}^2} > 0$, which implies that

$$\beta_{r,i} = -\frac{(\mathbf{L}_i \boldsymbol{\varphi}_r)^T (\mathbf{C}_{\boldsymbol{\psi}_{r,i}}^{-1})(\mathbf{L}_i \boldsymbol{\varphi}_r)}{2\left\| \mathbf{L}_i \boldsymbol{\varphi}_r \right\|^2} + \left| \frac{(\hat{\boldsymbol{\psi}}_{r,i})^T (\mathbf{C}_{\boldsymbol{\psi}_{r,i}}^{-1})(\mathbf{L}_i \boldsymbol{\varphi}_r)}{2\left\| \mathbf{L}_i \boldsymbol{\varphi}_r \right\|} \right| \tag{14}$$

Substituting (14) into (11) leads to,

$$\chi_{r,i} = \frac{\hat{\boldsymbol{\psi}}_{r,i}^T \mathbf{C}_{\boldsymbol{\psi}_{r,i}}^{-1} (\mathbf{L}_i \boldsymbol{\varphi}_r)}{\left| \hat{\boldsymbol{\psi}}_{r,i}^T \mathbf{C}_{\boldsymbol{\psi}_{r,i}}^{-1} \mathbf{L}_i \boldsymbol{\varphi}_r \right| \left\| \mathbf{L}_i \boldsymbol{\varphi}_r \right\|} = \operatorname{sgn}\left(\hat{\boldsymbol{\psi}}_{r,i}^T \mathbf{C}_{\boldsymbol{\psi}_{r,i}}^{-1} \mathbf{L}_i \boldsymbol{\varphi}_r \right) \left\| \mathbf{L}_i \boldsymbol{\varphi}_r \right\|^{-1} \tag{15}$$

Here $\operatorname{sgn}(\cdot)$ denotes the signum function.

(2) Optimization for $\boldsymbol{\varphi}_r$ and γ_r

The gradient of L_{as} with respect to $\boldsymbol{\varphi}_r$ is given by

$$\frac{\partial L_{as}}{\partial \boldsymbol{\varphi}_r} = \sum_{i=1}^{n_t} (\chi_{r,i} \mathbf{L}_i)^T (\mathbf{C}_{\boldsymbol{\psi}_{r,i}}^{-1})(\chi_{r,i} \mathbf{L}_i) \boldsymbol{\varphi}_r - \sum_{i=1}^{n_s} (\chi_{r,i} \mathbf{L}_i)^T (\mathbf{C}_{\boldsymbol{\psi}_{r,i}}^{-1}) \hat{\boldsymbol{\psi}}_{r,i} - 2\gamma_r \boldsymbol{\varphi}_r + \sum_{i=1}^{n_t} 2\beta_{r,i} \chi_{r,i}^2 (\mathbf{L}_i)^T (\mathbf{L}_i) \boldsymbol{\varphi}_r \tag{16}$$

Setting $\frac{\partial L_{as}}{\partial \boldsymbol{\varphi}_r} = 0$ and solving for $\boldsymbol{\varphi}_r$ gives

$$\mathbf{A}_r \boldsymbol{\varphi}_r + \mathbf{b}_r = \gamma_r \boldsymbol{\varphi}_r \tag{17}$$

where $\mathrm{A}_r = \frac{1}{2} \sum_{i=1}^{n_t} (\chi_{r,i} \mathbf{L}_i)^T (\mathbf{C}_{\boldsymbol{\psi}_{r,i}}^{-1})(\chi_{r,i} \mathbf{L}_i) + \sum_{i=1}^{n_t} \beta_{r,i} \chi_{r,i}^2 (\mathbf{L}_i^T)(\mathbf{L}_i)$ and $\mathbf{b}_r = -\frac{1}{2} \sum_{i=1}^{n_t} (\chi_{r,i} \mathbf{L}_i)^T (\mathbf{C}_{\boldsymbol{\psi}_{r,i}}^{-1}) \hat{\boldsymbol{\psi}}_{r,i}$. Equation (17) is subject to the constraint $\left\| \boldsymbol{\varphi}_r \right\|^2 = 1$, which forms a constrained eigenvalue problem different than the conventional eigenvalue problem. It can be solved by constructing an augmented vector that satisfies the standard eigenvalue equation [9]. As a result, all optimal parameters can be obtained in groups given the remaining ones until convergence is achieved instead of optimizing the full set of parameters simultaneously.

4.3 Posterior Uncertainties

The posterior uncertainty of the global mode shape can also be obtained by inversing the Hessian matrix of L_{as} with respect to $\boldsymbol{\lambda}_{as}$. The uncertainty of model parameters well approximated by a Gaussian distribution centered at the most probable parameter values and with covariance matrix equal to the inverse of the Hessian of the function $\boldsymbol{\Gamma}_{as}$ calculated at the optimal parameters $\hat{\boldsymbol{\lambda}}_{as}$. This Hessian matrix is given by

$$\boldsymbol{\Gamma}_{as} = \begin{pmatrix} \mathbf{L}^{(\varphi_r \varphi_r)} & \mathbf{L}^{(\varphi_r \chi_r)} & \mathbf{L}^{(\varphi_r \beta_r)} & \mathbf{L}^{(\varphi_r \gamma_r)} \\ \mathbf{L}^{(\chi_r \varphi_r)} & \mathbf{L}^{(\chi_r \chi_r)} & \mathbf{L}^{(\chi_r \beta_r)} & \mathbf{L}^{(\chi_r \gamma_r)} \\ \mathbf{L}^{(\beta_r \varphi_r)} & \mathbf{L}^{(\beta_r \chi_r)} & \mathbf{L}^{(\beta_r \beta_r)} & \mathbf{L}^{(\beta_r \gamma_r)} \\ \mathbf{L}^{(\gamma_r \varphi_r)} & \mathbf{L}^{(\gamma_r \chi_r)} & \mathbf{L}^{(\gamma_r \beta_r)} & \mathbf{L}^{(\gamma_r \gamma_r)} \end{pmatrix} \tag{18}$$

In (18), $\boldsymbol{\chi}=[\boldsymbol{\chi}_1^T,\cdots,\boldsymbol{\chi}_r^T,\cdots,\boldsymbol{\chi}_{n_m}^T]^T$ with the r-th block $\boldsymbol{\chi}_r^T=[\chi_{r,1},\cdots,\chi_{r,i},\cdots,\chi_{r,n_t}]^T$; $\boldsymbol{\beta}=[\boldsymbol{\beta}_1^T,\cdots,\boldsymbol{\beta}_r^T,\cdots,\boldsymbol{\beta}_{n_m}^T]^T$ with the r-th block $\boldsymbol{\beta}_r^T=[\beta_{r,1},\cdots,\beta_{r,i},\cdots,\beta_{r,n_t}]^T$. $\mathbf{L}^{(\boldsymbol{\varphi}_r\boldsymbol{\varphi}_r)}$ denotes the second order derivatives of L_{as} with respect to $\boldsymbol{\varphi}_r$. Similar explanation can be given to other blocked members in (18). $\boldsymbol{\Gamma}_{as}$ is a symmetrical matrix, and only the blocked members in the upper triangle $\mathbf{L}^{(\boldsymbol{\varphi}_r\boldsymbol{\varphi}_r)}$, $\mathbf{L}^{(\boldsymbol{\varphi}_r\boldsymbol{\chi}_r)}$, $\mathbf{L}^{(\boldsymbol{\varphi}_r\boldsymbol{\beta}_r)}$, $\mathbf{L}^{(\boldsymbol{\varphi}_r\boldsymbol{\gamma}_r)}$, $\mathbf{L}^{(\boldsymbol{\chi}_r\boldsymbol{\chi}_r)}$, $\mathbf{L}^{(\boldsymbol{\chi}_r\boldsymbol{\beta}_r)}$, $\mathbf{L}^{(\boldsymbol{\chi}_r\boldsymbol{\gamma}_r)}$, $\mathbf{L}^{(\boldsymbol{\beta}_r\boldsymbol{\beta}_r)}$, $\mathbf{L}^{(\boldsymbol{\beta}_r\boldsymbol{\gamma}_r)}$ and $\mathbf{L}^{(\boldsymbol{\gamma}_r\boldsymbol{\gamma}_r)}$ need to be computed analytically. Among these blocks, $\mathbf{L}^{(\boldsymbol{\chi}_r\boldsymbol{\gamma}_r)}\in\mathbb{R}^{n_t}$, $\mathbf{L}^{(\boldsymbol{\beta}_r\boldsymbol{\beta}_r)}\in\mathbb{R}^{n_t\times n_t}$, $\mathbf{L}^{(\boldsymbol{\beta}_r\boldsymbol{\gamma}_r)}\in\mathbb{R}^{n_t}$ and $\mathbf{L}^{(\boldsymbol{\gamma}_r\boldsymbol{\gamma}_r)}\in\mathbb{R}^{1}$ are all zero matrixes. The non-zero blocks can be derived analytically as follows:

(1) Derivatives of $\mathbf{L}^{(\boldsymbol{\varphi}_r\boldsymbol{\varphi}_r)}$

$\mathbf{L}^{(\boldsymbol{\varphi}_r\boldsymbol{\varphi}_r)}\in\mathbb{R}^{n_l\times n_l}$ can be obtained by taking the derivative of (9) with respect to $\boldsymbol{\varphi}_r$, which can be formulated as

$$\mathbf{L}^{(\boldsymbol{\varphi}_r\boldsymbol{\varphi}_r)}=\sum_{i=1}^{n_t}(\chi_{r,i}\mathbf{L}_i)^T(\mathbf{C}_{\boldsymbol{\psi}_{r,i}}^{-1})(\chi_{r,i}\mathbf{L}_i)+\sum_{i=1}^{n_t}2\beta_{r,i}\chi_{r,i}^2\mathbf{L}_i^T\mathbf{L}_i-2\gamma_r\mathbf{I}_{n_l} \tag{19}$$

(2) Derivatives of $\mathbf{L}^{(\boldsymbol{\varphi}_r\boldsymbol{\chi}_r)}$

$\mathbf{L}^{(\boldsymbol{\varphi}_r\boldsymbol{\chi}_r)}\in\mathbb{R}^{n_l\times n_t}$ is a matrix formulated as

$$\mathbf{L}^{(\boldsymbol{\varphi}_r\boldsymbol{\chi}_r)}=[\mathbf{L}^{(\boldsymbol{\varphi}_r\chi_{r,1})},\cdots,\mathbf{L}^{(\boldsymbol{\varphi}_r\chi_{r,i})},\cdots,\mathbf{L}^{(\boldsymbol{\varphi}_r\chi_{r,n_t})}]_{n_l\times n_t} \tag{20}$$

where $\mathbf{L}^{(\boldsymbol{\varphi}_r\chi_{r,i})}$ can be expressed as

$$\mathbf{L}^{(\boldsymbol{\varphi}_r\chi_{r,i})}=2\chi_{r,i}(\mathbf{L}_i^T)(\mathbf{C}_{\boldsymbol{\psi}_{r,i}}^{-1})(\mathbf{L}_i)\boldsymbol{\varphi}_r-(\mathbf{L}_i^T)(\mathbf{C}_{\boldsymbol{\psi}_{r,i}}^{-1})\hat{\boldsymbol{\psi}}_{r,i}+4\beta_{r,i}\chi_{r,i}(\mathbf{L}_i^T)(\mathbf{L}_i)\boldsymbol{\varphi}_r \tag{21}$$

(3) Derivatives of $\mathbf{L}^{(\boldsymbol{\varphi}_r\boldsymbol{\beta}_r)}$

$\mathbf{L}^{(\boldsymbol{\varphi}_r\boldsymbol{\beta}_r)}\in\mathbb{R}^{n_l\times n_t}$ is a matrix formulated as

$$\mathbf{L}^{(\boldsymbol{\varphi}_r\boldsymbol{\beta}_r)}=[\mathbf{L}^{(\boldsymbol{\varphi}_r\boldsymbol{\beta}_{r,1})},\cdots,\mathbf{L}^{(\boldsymbol{\varphi}_r\boldsymbol{\beta}_{r,i})},\cdots,\mathbf{L}^{(\boldsymbol{\varphi}_r\boldsymbol{\beta}_{r,n_t})}]_{n_l\times n_t} \tag{22}$$

where the i-th block $\mathbf{L}^{(\boldsymbol{\varphi}_r\boldsymbol{\beta}_{r,i})}\in\mathbb{R}^{n_l}$ can be expressed as:

$$\mathbf{L}^{(\boldsymbol{\varphi}_r\boldsymbol{\beta}_{r,i})}=2\chi_{r,i}^2\mathbf{L}_i^T\mathbf{L}_i\boldsymbol{\varphi}_r \tag{23}$$

(4) Derivatives of $\mathbf{L}^{(\boldsymbol{\varphi}_r\boldsymbol{\gamma}_r)}$

$\mathbf{L}^{(\boldsymbol{\varphi}_r\boldsymbol{\gamma}_r)}\in\mathbb{R}^{n_l}$ is a vector which can be expressed as

$$\mathbf{L}^{(\boldsymbol{\varphi}_r\gamma_{r,i})}=-2\boldsymbol{\varphi}_r \tag{24}$$

(5) Derivatives of $\mathbf{L}^{(\boldsymbol{\chi}_r\boldsymbol{\chi}_r)}$

$\mathbf{L}^{(\boldsymbol{\chi}_r\boldsymbol{\chi}_r)}\in\mathbb{R}^{n_t\times n_t}$ is a diagonal matrix shown as follows

$$\mathbf{L}^{(\boldsymbol{\chi}_r\boldsymbol{\chi}_r)}=diagonal(\mathbf{L}^{(\chi_{r,i}\chi_{r,i})}) \tag{25}$$

whose i-th diagonal entry can be derived analytically as follows,

$$\mathbf{L}^{(\chi_{r,i}\chi_{r,i})}=(\mathbf{L}_i\boldsymbol{\varphi}_r)^T(\mathbf{C}_{\boldsymbol{\psi}_{r,i}}^{-1})(\mathbf{L}_i\boldsymbol{\varphi}_r)+2\beta_{r,i}\left\|\mathbf{L}_i\boldsymbol{\varphi}_r\right\|^2 \tag{26}$$

(6) Derivatives of $\mathbf{L}^{(\boldsymbol{\chi}_r\boldsymbol{\beta}_r)}$

$\mathbf{L}^{(\chi_r,\boldsymbol{\beta}_r)} \in \mathbb{R}^{n_t \times n_t}$ is a diagonal matrix shown as follows

$$\mathbf{L}^{(\chi_r,\boldsymbol{\beta}_r)} = diagonal(\mathbf{L}^{(\chi_{r,i},\boldsymbol{\beta}_{r,i})}) \tag{27}$$

whose i-th diagonal entry can be derived analytically as follows,

$$\mathbf{L}^{(\chi_{r,i},\boldsymbol{\beta}_{r,i})} = 2\chi_{r,i}\left\|\mathbf{L}_i\boldsymbol{\varphi}_r\right\|^2 \tag{28}$$

5 NUMERICIAL STUDY

To illustrate the accuracy of the proposed approach, simulated data of a linear and time-invariant system are processed. The system is a 15-story shear building with a uniformly distributed mass and stiffness at each floor. The stiffness to mass ratio is chosen to be $2500s^{-2}$. Rayleigh damping is assumed here, and the damping ratios for the first two modes are set to be 1%. The structure is assumed to be excited with a ground acceleration $\ddot{x}_g$ which can be adequately modeled as Gaussian white noise with auto spectral intensity $0.25m^2s^{-3}$. The prediction error level is taken to be 10%. It is assumed that the 15 dofs are measured using sensors arranged in 3 clusters as shown in Table 1.

Setup	Measured dofs
1	1, 2, 3, 4, 5,6,7
2	6, 7, 8, 9, 10,11,12
3	11, 12, 13, 14, 15

Table 1: Setup information.

It is assumed that 20 sets of acceleration data of 500-seconds duration are available in each dof. Figure 2 shows the most probable global mode shapes of the first four modes of the structure by using the method introduced in section 4. The solid line denotes the exact mode shapes, whereas the squares represent the identified global mode shape assembled from local ones. These two mode shapes almost coincide. The MAC between the identified global mode shape and the exact one is calculated to be 0.999, 0.999, 0.995 and 0.985 for the first to fourth modes, respectively. The numericial example indicates that the Bayesian mode shape assembly approach yields satisfactory results. Moreover, there is no need to share the same reference dofs for all setups.

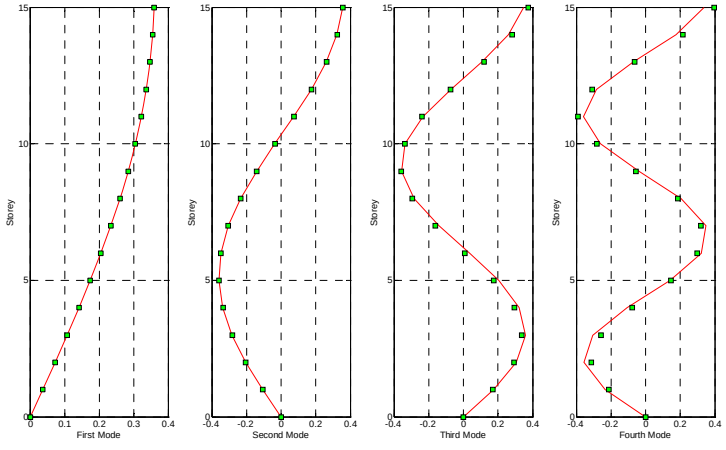


Figure 2: Assembled global mode shape from multiple setups.

6 CONCLUDING REMARKS

A two-stage Bayesian spectrum density approach proposed for ambient modal analysis can be implemented in the environment of wireless sensor networks through a distributed computing strategy. The local mode shapes as well as their uncertainties confined to different clusters can be identified. To assemble the local mode shapes, a Bayesian assembly methodology is proposed in this study so that the weights for different clusters can be accounted for properly according to their data qualities. The optimal values for the global mode shape confined to all measured dofs can be obtained by a fast iterative scheme. The associated uncertainties can also be obtained analytically. A shear building model subject to ground motion is employed to demonstrate and verify the proposed method. Results show that the global mode shapes can be effectively and accurately identified by the proposed method.

ACKNOWLEDGEMENTS

This research has been supported by the Hong Kong Research Grants Council under grants 613511 and 613412. These supports are gratefully acknowledged.

REFERENCES

[1] K.V. Yuen, *Bayesian methods for structural dynamics and civil engineering*. John Wiley & Sons Ltd, 2010.

[2] K. V. Yuen, L.S. Katafygiotis, Bayesian time-domain approach for modal updating using ambient data. *Probabilistic Engineering Mechanics*, 16(3), 219-231, 2001.

[3] K.V. Yuen, L.S. Katafygiotis, Bayesian fast Fourier transform approach for modal updating using ambient data. *Advance in Structural Engineerin*g, 6(2), 81-95, 2003.

[4] L.S. Katafygiotis, K.V. Yuen, Bayesian spectral density approach for modal updating using ambient data. *Earthquake Engineering and Structural Dynamics*, 30(8), 1103-1123, 2001.

[5] S.K. Au, Fast Bayesian FFT method for ambient modal identification with separated modes. *ASCE Journal of Engineering Mechanics*, 137 (3), 214-226, 2011.

[6] S.K. Au, Fast Bayesian ambient modal identification in the frequency domain, Part I: Posterior most probable value. *Mechanical Systems and Signal Processing*, 26, 60-75, 2011.

[7] S.K. Au, Fast Bayesian ambient modal identification in the frequency domain, Part II: Posterior uncertainty. *Mechanical Systems and Signal Processing*, 26, 76-90, 2012.

[8] W.J. Yan, *Wireless Sensor Network (WSN) based Structural Health Monitoring Accommodating Multiple Uncertainties*. PhD thesis draft, Department of Civil and Environmental Engineering, The Hong Kong University of Science and Technology, 2013.

[9] S.K. Au, Assembling mode shapes by least squares. *Mechanical System Signal Processing*, 25(1), 163-179, 2011.

[10] S.K. Au, F.L. Zhang, Fast Bayesian ambient modal identification incorporating multiple setups, *ASCE Journal of Engineering Mechanics*, 138(7), 800-815, 2012.

COMPDYN 2013
4th ECCOMAS Thematic Conference on
Computational Methods in Structural Dynamics and Earthquake Engineering
M. Papadrakakis, V. Papadopoulos, V. Plevris (eds.)
Kos Island, Greece, 12–14 June 2013

DESIGN OF ONE STOREY BUILDING WITH PRECAST CONCRETE SANDWICH PANELS IN EARTHQUAKE REGIONS

Andreas P. Christou[1]

[1] A.P.Christou & Accosiates
9th klm Thessalonikis – Thermis, P.O.Box 8107, GR 57001 Thessaloniki
e-mail: info@apchistou.com

Keywords: Precast building, Seismic design, prefabricated elements connections.

Abstract. *The object of this study is the development of a structural precast system for a supermarket chain in order to have the same quality of product construction all over Greece regardless of its application site and independently of the area seismicity. The dimensions of one typical storey building was approximately 50.0x25.0x0.50 (AxBxH m). The load bearing structure of the building consists of columns restrained in the foundation with special anchors or Koecher – Foundation. Between the columns were placed double-walls (precast Sandwich panels) with insulation and for the earthquake resistance some walls placed in certain positions along the external perimeter. These walls were designed by special connections with the foundations and columns in order to achieve restrain. The panels were connected on the top with beams by hinges (so called Dual Type), define as the combination of structural walls and frames. It is well known that precast concrete structures generally provide poor performance in earthquakes and the existing codes do not provide adequate guidelines for the designing of prefabricated structures so it is very important that the modeling of such structures must be very precise in order to be able to make the design of the connections. The structure was calculated with linear and finite surface elements (3d- modeling) by taking in mind every peculiarity of the building. Slab is acting as diaphragm. The seismic behavior was calculated according to the Dynamic Spectral Method (Norm: EC8). Seismic Behavior Factor q=1.5. Specially calculated and designed connections between the elements (columns- walls, column – beams, column/ wall – foundation, metal structure – concrete elements) is giving the ability to the system for uniform action.*

1 INTRODUCTION

The scope of this paper is the development of an earthquake-resistant [5] prefabriced structural system that may be implemented in all stores of a large food supermarket chain, maintaining the same structural quality regardless of the installation area and its seismic activity.

Due to the particular nature of the structural system, the creation of an accurate calculation model that takes into consideration the method of connecting the different structural elements is a crucial factor in the investigation of an optimum solution. The results of the analysis, in combination with a good knowledge of the features and properties of connecting materials (quality, resistance, etc.) may then make the basis for the proper implementation of the construction.

2 DESCRIPTION OF THE BUILDING AND BEARING STRUCTURE

The aforementioned stores have a typical floor plan measuring 50.00 X 25.00m and have a height of approx. 5.50m; they consist of two main areas: a) the retail area, 18 or 22m wide and b) the storage area with a width of approx. 6.50m. The final dimensions and the configuration of any offsets on the plan are determined based on the architectural requirements and the position of the loading ramp on the site. It is noted that the store entrance is marked with an L-shaped canopy (bottom left of the floor plan in Figure 1).

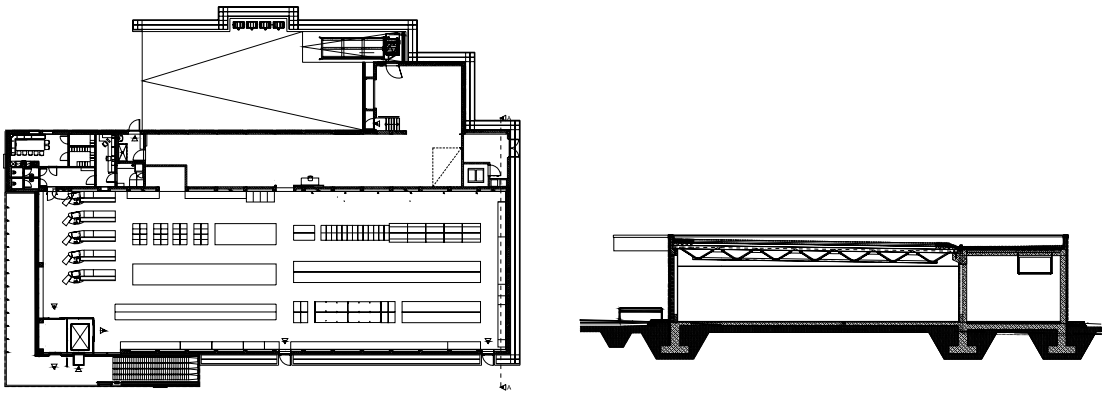


Figure 1: Floor plan (left) and section (right) of a typical store

The load bearing structure of the building consists of prefabricated reinforced concrete columns and beams. Between the columns were placed double-wall (precast Sandwich panels) with insulation and for the earthquake resistance some walls placed in certain positions along the external perimeter. The roof of the retail area is covered by means of large trusses made of structural steel with a span of 18 or 22 m, while the storage area is covered with prefabricated reinforced concrete one-way slabs. The foundation is made of cast strip footings equipped with specially configured sockets where the prefabricated columns are fixed (anchored) or, alternatively, with custom elements where the columns are bolted. The beams are connected to the columns by joints and designed to bear the vertical loads of the steel structure and participate in the transfer of the roof's seismic loads to the columns and walls.

3 SIMULATION MODEL

The simulation of the carrier is performed using a 3D model, where the system's structural elements are simulated as linear and surface finite elements [4] with their exact geometric features. A diaphragm action is simulated on roof level (invariable relative distances of the col-

umns' top points under horizontal and vertical torsion), which is ensured in the area of the steel roof by the use of a special trapezoid metal sheet specifically bonded to the trusses.

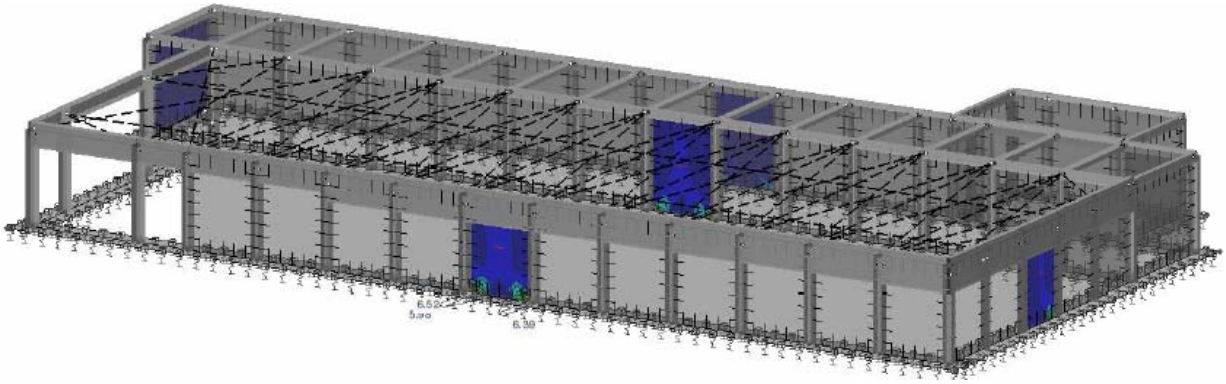


Figure 2: Simulation 3D model

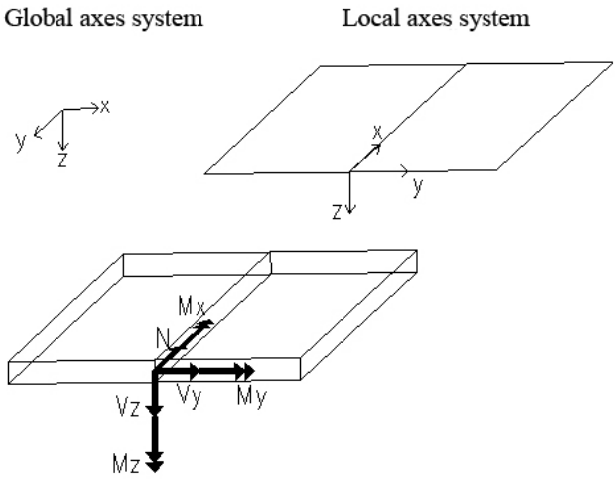


Figure 3: Axes and cross-section loads on the bonding surface of two structural elements

Particularly important are the boundary conditions which are obtained by computer-aided-calculation for the connections of different structural elements. The columns' bases are considered restrained, while the beam-to-column connections are considered joints.

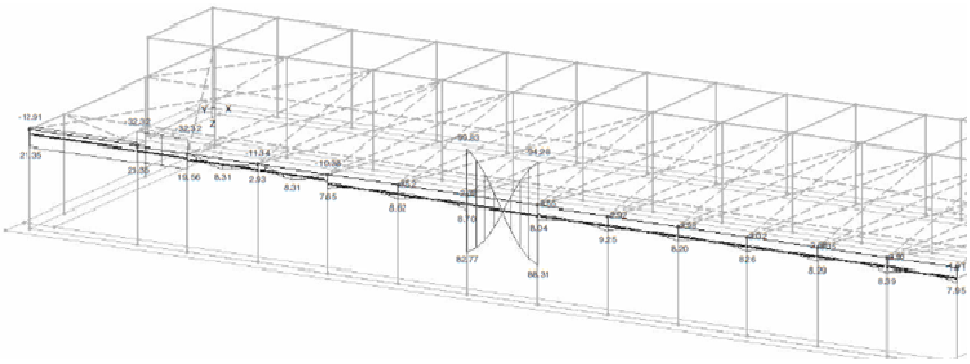


Figure 4: Axial forces of modular beams

The infilled walls are connected to the strip footings, at their bottom, and to the beams, at their top edge, by joints. The simulation of these connections assumes a bound displacement only along the connecting surface of the different structural elements (Vy = Vz = Mx = My = Mz = 0). Moreover, the connection of the wall with the columns is assumed as a joint blocked the displacement only in the direction transversal to the interface of the different elements (N = Vy = Mx = My = Mz = 0). The following diagrams show the envelope results for the cross-sectional loads, where we assume only the loads n-x, D along the connecting surface for the connection of a infilled wall with the foundation, and only the loads n-x transversal to the connecting surface for their connection with the columns.

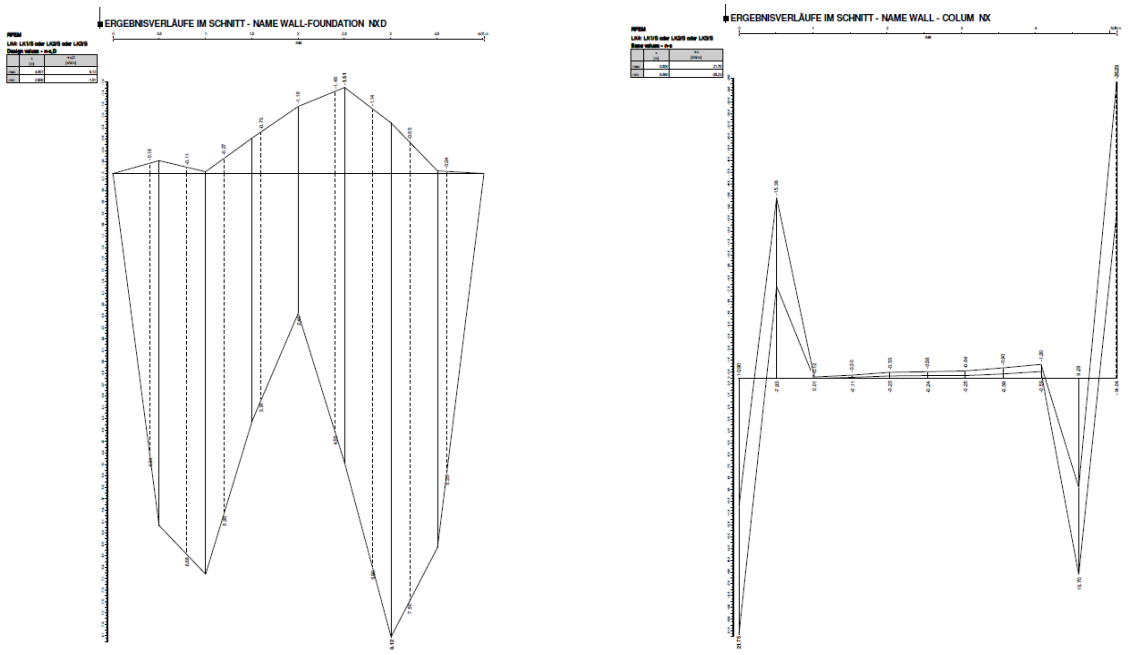


Figure 5: Design envelope for load on the infilled wall-foundation (left) and infilled wall-column (right) connecting surfaces

In relation to the earthquake-resistant (shear) walls (marked blue in Figure 2), the same apply for their connection to the roof beams as in the case of infilled walls, but at their connection to the strip footing, the joint receives only loads in three axes (Mx = My = Mz =0). The joint connections of the earthquake-resistant (shear) walls with the columns vary depending in different site locations, as these depend on the seismic risk zone. For instance, in zone I with a horizontal ground acceleration A=0.16g, the joint must only receive the force that is transversal to the structural elements' interface (N = Vy = Mx = My = Mz = 0), contrary to the other zones where the joint must additionally receive the force parallel to the connecting surface of the different structural elements (Vy = Mx = My = Mz = 0).

The following Figures 6 and 7 show the envelope results of the cross-sectional loads for the connection of the earthquake-resistant (shear) walls with the foundation and the columns, where n-y signifies the loads tending to separate structural elements (i.e. Vy in Figure 3) and n-x signifies the corresponding loads transversal to the connecting surface (i.e. Vz in Figure 3). Figure 8 below shows clearly loads n-y appearing only on the earthquake-resistant wall.

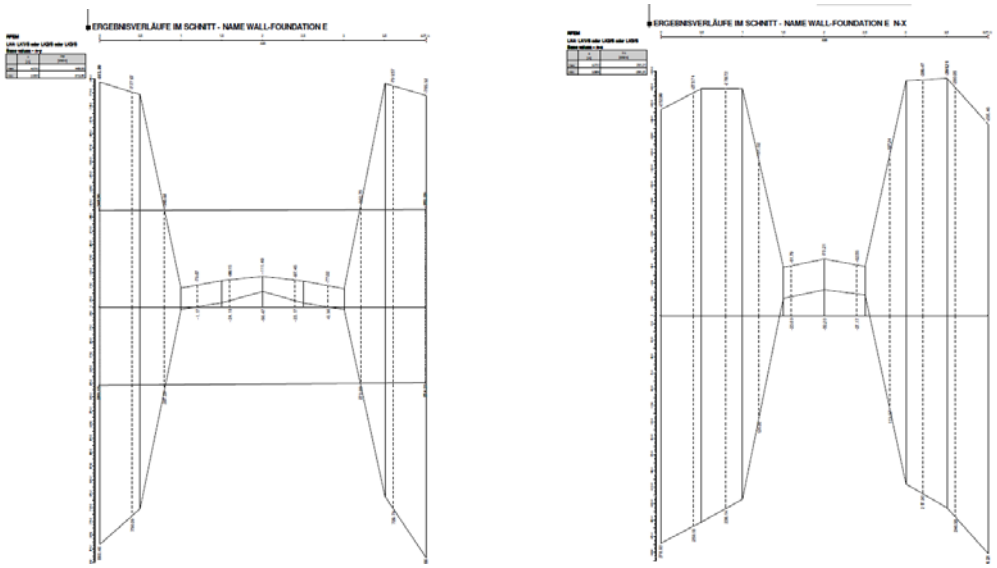


Figure 6: Design envelope for ‘n-y’ load perpendicular to (left), and ‘n-x’ load envelope transversal (right) to the connecting surface between earthquake-resistant (shear) wall - foundation

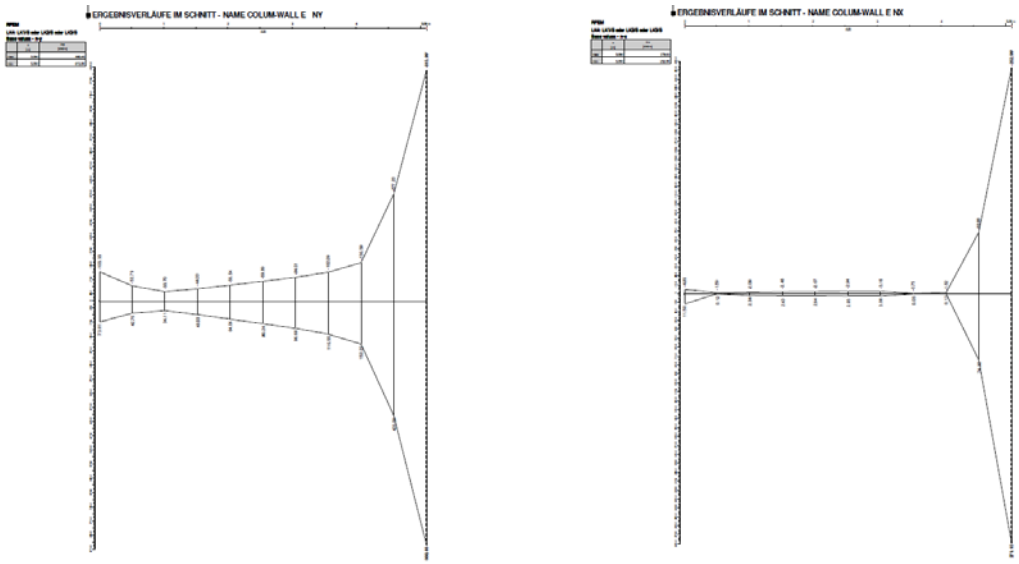


Figure 7: Design envelope for ‘n-y’ load vertically (left) and ‘n-x’ transversely (right) of the connecting surface between the (earthquake-resistant) shear wall –column

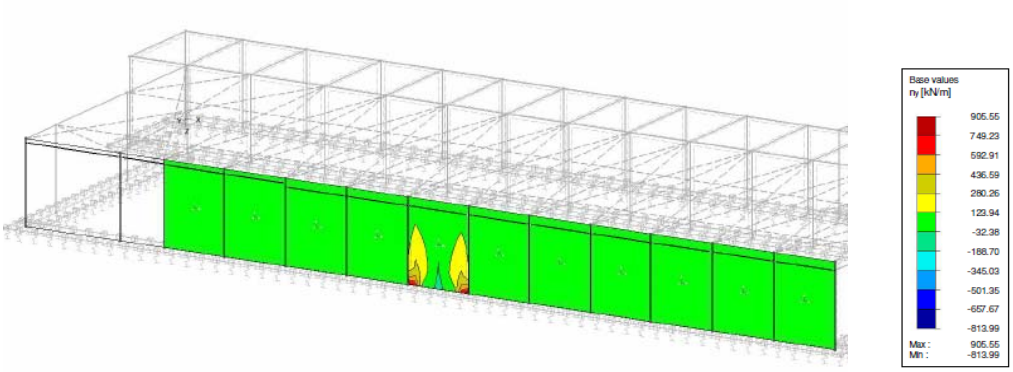


Figure 8: Design envelope for 'n-y' load at the connection between earthquake-resistant (shear) wall - foundation

In essence, all the aforementioned calculation results are evaluated before the realization of the connections with materials and reinforcements [2] that can withstand the loads at the connection, as indicated in Figure 9 for the connection between earthquake-resistant (shear) wall and strip footing (see also 'n-y' loads of Figures 6 and 8).

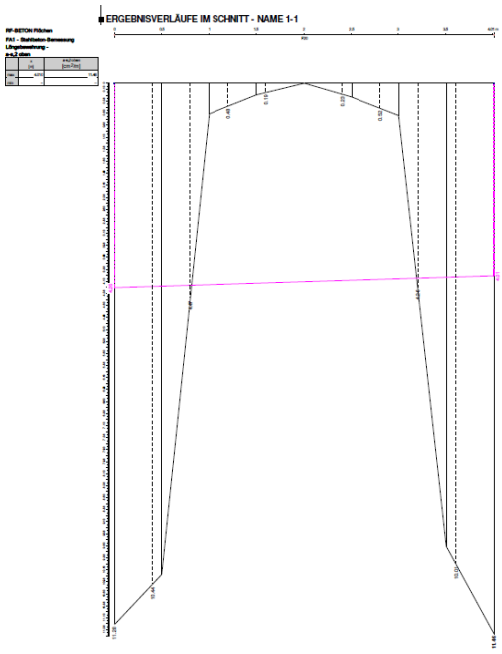


Figure 9: Required reinforcement at the connection between earthquake-resistant (shear) wall and foundation

The last diagram shows the load along the connecting surface between infilled walls and prefabricated beams.

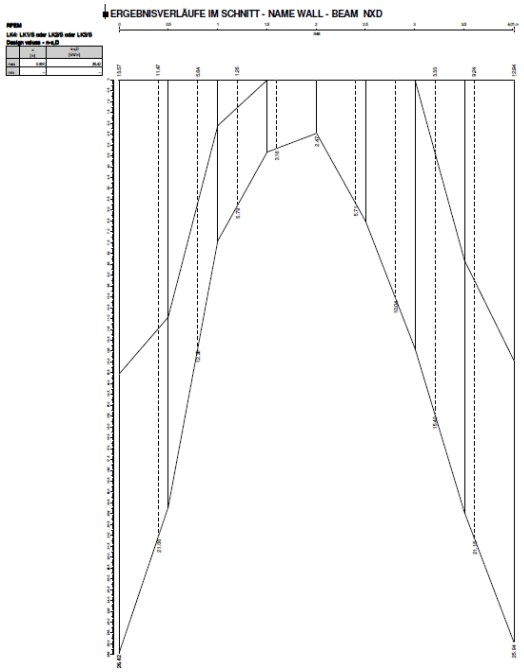


Figure 10: Design envelope for load at the connecting surface between infilled wall and beam

With regard to the loads stressing the structure, vertical dead and live loads are taken as static loads, and the dynamic spectral analysis is applied for seismic loads as per EC8 / National Annex [3]. The dynamic features are determined by modal analysis, and a design spectrum acting in three dimensions (two horizontal and one vertical) is introduced. In the spectrum, the horizontal ground acceleration is A=0.16g or 0.25g or 0.36g, depending on the location of the store; the behavior factor of the structure is taken as q=1.50. The calculation is performed for the modes in which 90% mass participation is achieved in every direction, which requires 23 modes in this particular model, a rather large number resulting from the modular connections of the infilled walls with the columns.

The calculation is performed for load combinations determined in accordance with Eurocodes EC1/EC3, taking into consideration EC8 / National Annex, while the loads cases [1] participating in the combinations are the follows: a) LC1: self weight of the structure, b) LC2: dead load of the slab, c) LC3: additional dead load of the slab (HVAC), d) LC4: dead load of the canopy, e) LC5: dead load of the trusses (point loads on columns), f) LC6: live load of slab, g) LC7: live load of canopy, h) LC8: live load of trusses, i) CA1: seismic load on X-axis, j) CA2: seismic load on Y-axis, and k) CA3: seismic load on Z-axis. The schematics of the three main modes are shown below, as they result from the calculation of the structural model.

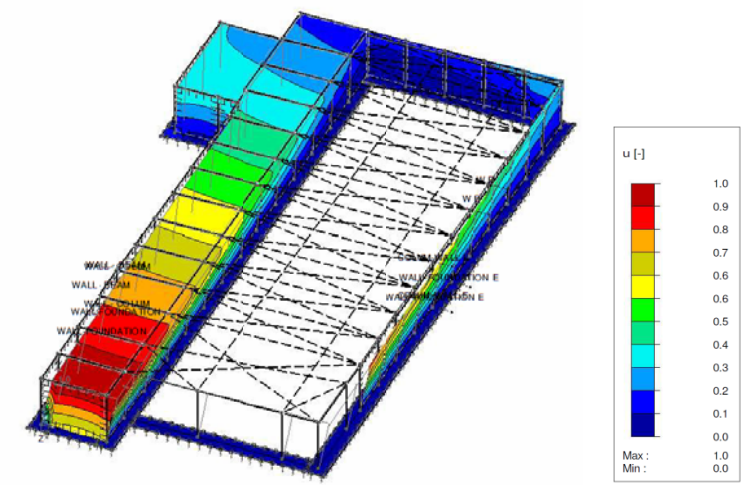


Figure 11: 1st mode (natural frequency 2.76Hz)

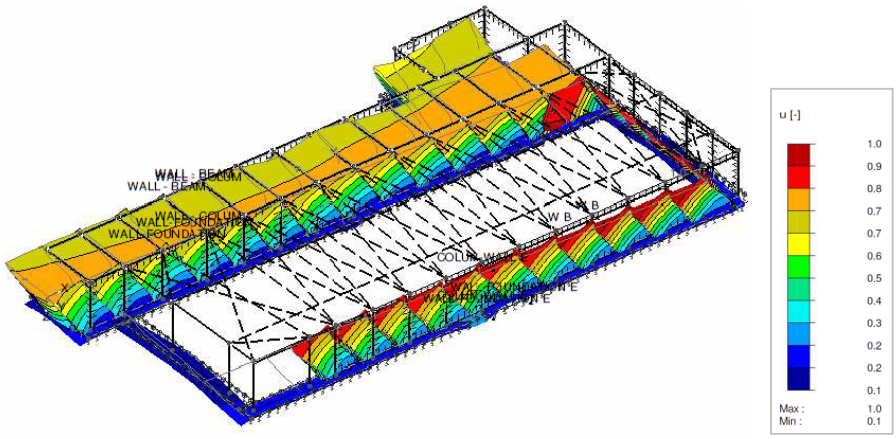


Figure 12: : 2nd mode (natural frequency 4.54Hz)

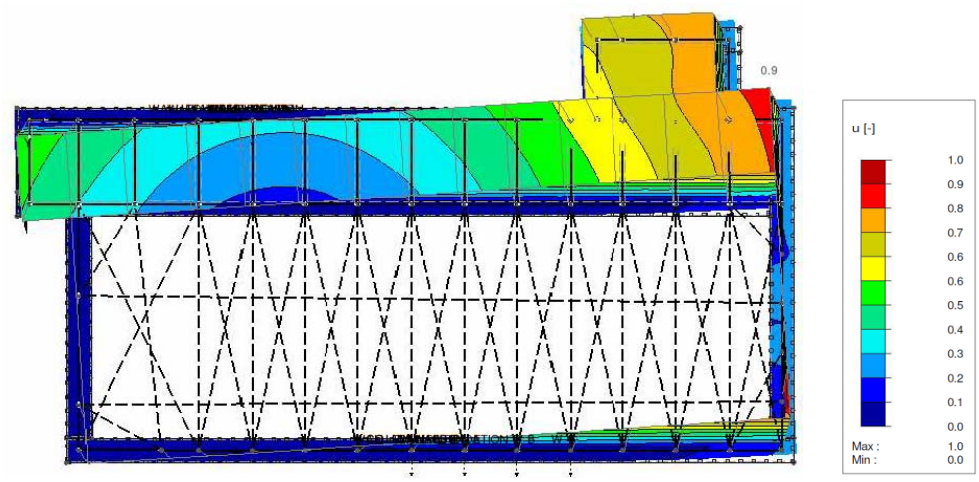


Figure 13: 3rd mode (natural frequency 4.82Hz)

The program RFEM has been used for analysis. The results also have been checked with the program Sap2000.

4 STRUCTURAL DETAILS

The proper implementation of connections [6] is particularly important in prefabrication systems, in order to properly block displacements, according to the calculation model described in detail in chapter 3.

The columns are restrained on the strip footings by use of preconfigured encasement pockets (koecher); wherever this solution is not viable, the columns are restrained using special anchor bolts that are standardized and certified for use to receive specific loads.

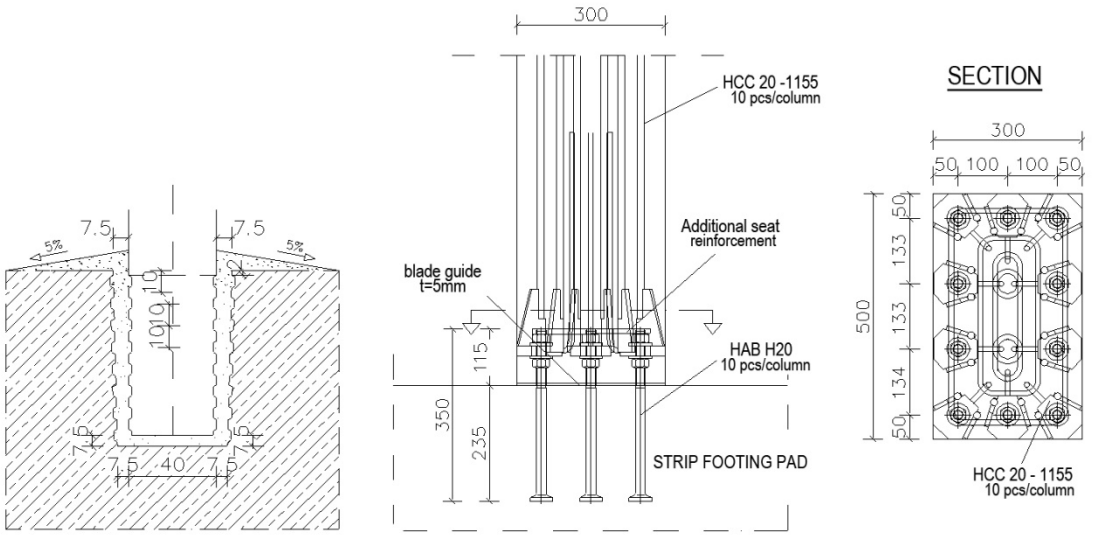


Figure 14: Fixed support of columns by means of pockets (left) and anchor bolts (right)

The sandwich-type walls provide full thermal insulation. They consist of three layers, the outer skin, 7 cm thick with an Ø8/20 steel mesh, the inner skin, 30 cm thick with an Ø12/20 rebar grid, and the 5 cm thick thermal insulation between the two skins. The inner skin is connected with the outer skin by means of special stainless pieces able to transfer their self weight, wind pressure loads and seismic loads to the inner skin.

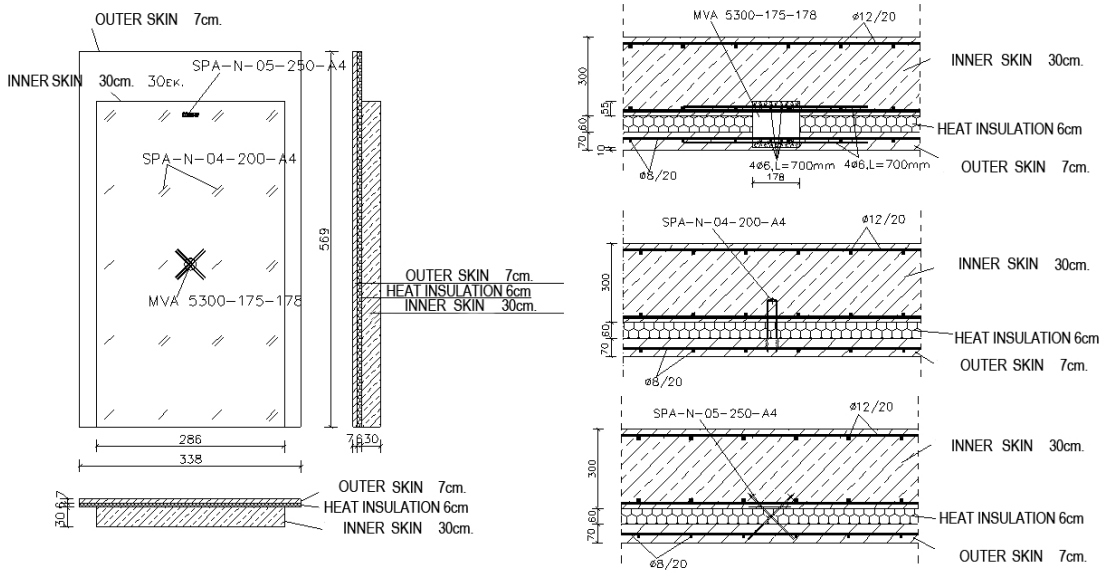


Figure 15: “Sandwich”-type wall: Elevation and typical sections

Depending on their load bearing role, the walls are distinguished as infilled walls and earthquake-resistant (shear) walls; their connections to the remaining structural elements is accordingly arranged. Infilled walls are connected with joints to the strip footings with the use of special reinforced dowel sleeves on the bottom of the walls, which fit in specially configured cavities in the strip footings in order to be able to receive loads point out during the analysis; on the other hand, they are connected with the columns by means of anchoring channels, bolts and L shape steel plates (for the bindings achieved with such connections, see chapter 3).

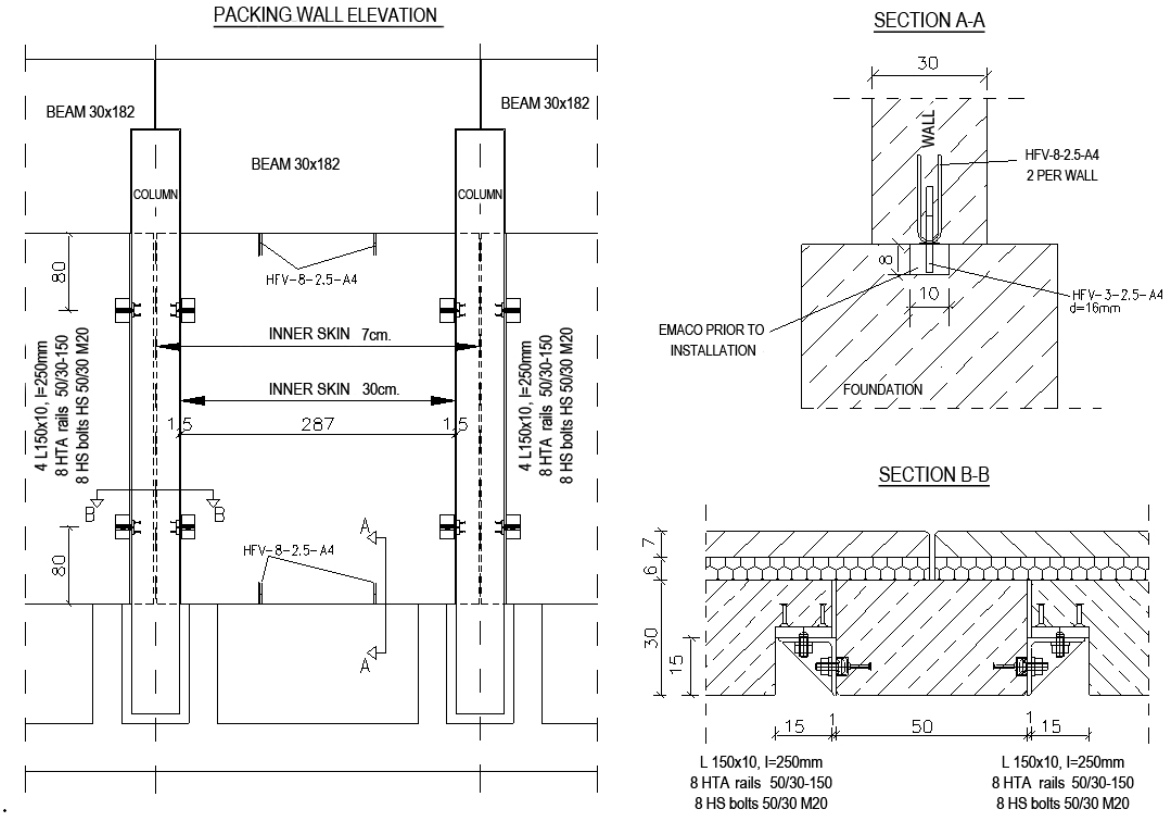


Figure 16: "Sandwich"-type wall: Connections of packing wall with strip footing and column

The connection of earthquake resistant (shear) walls to the foundation is provided by special anchor bolts at 2 points of the walls' bottom, which are placed in the strip footing before the concrete is poured. This type of connection is dimensioned for compression and tensile forces resulting from seismic combinations (Figure 6). The connection of earthquake (shear) walls with columns for seismic risk zone I (A=0.16g), as mentioned in chapter 3, matches the connection implemented on infilled walls. On the contrary, for the other connections, the columns are equipped with special casings with rebend starters, toothing in transverse direction for optimal force transmission and for exposure to longitudinal shear forces parallel to the joint (Figure 19) in order to achieve connection and cooperation between walls and columns in receiving the loads.

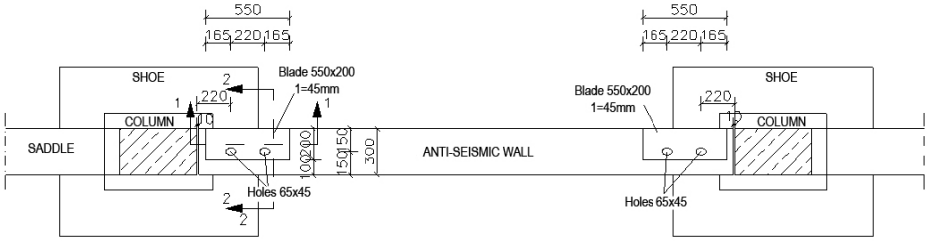


Figure 17: Sandwich"-type wall: Connection between earthquake-resistant (shear) wall and strip footing (floor plan)

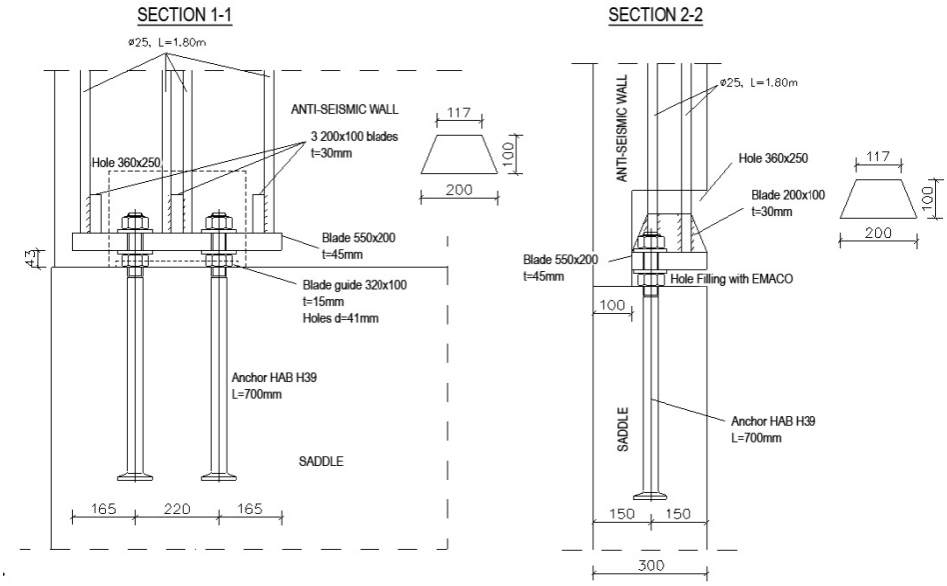


Figure 18: "Sandwich"-type wall: Connection between earthquake –resistant (shear) wall and strip footing (sections, see Figure 17)

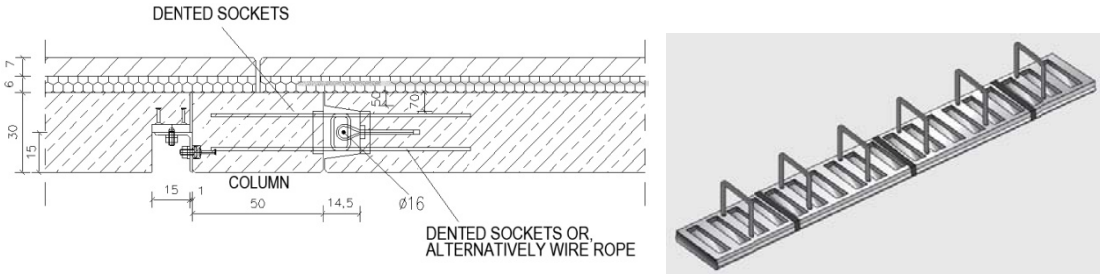


Figure 19: Connection between shear wall and columns using special casing rebend starters (right)

Upon completion of the connections of vertical structural elements, they are connected with the horizontal elements of the structure, i.e. with beams and slabs. At positions of beam-column joints, pins are implemented on the columns to fit in holes inside the beams in order to receive the cross-sectional loads of the joint. Moreover, the bottom side of the beams is connected to the columns by use of special incorporated cast-in channels.

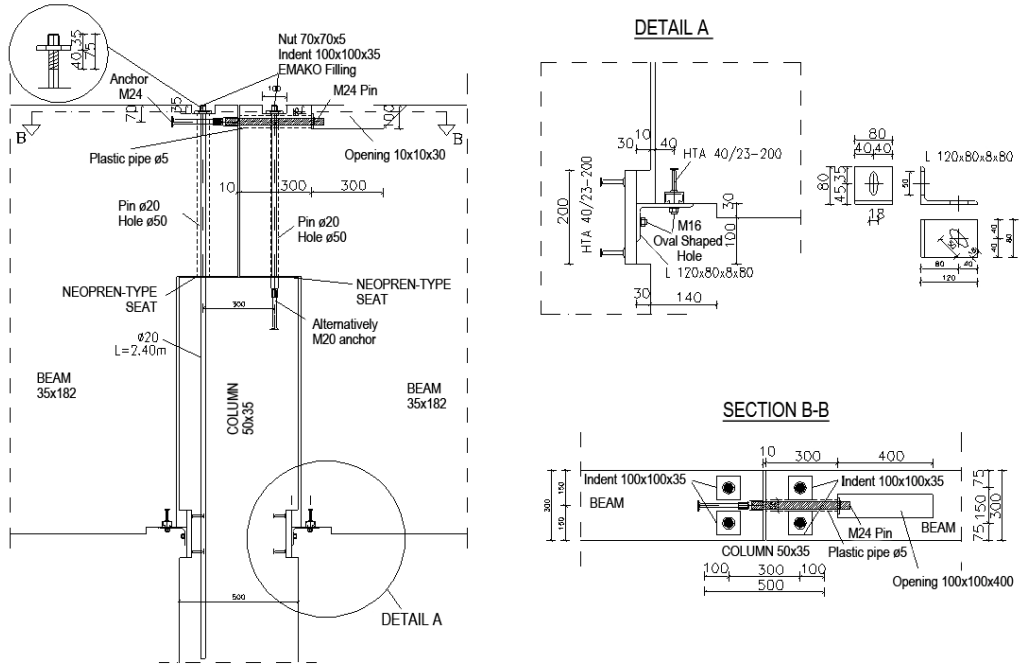


Figure 20: Beam-column joint connection

The storage area roof is laid with 7 cm thick one-way preslabs; during the assembly, these slabs rest on a 4 cm wide support zone on the wall of each side, while their starter bars are anchored through the entire width of the beam. Apart from the rebar mesh, latticed girders as well as connector bars are factory incorporated wherever it is deemed necessary (in order to create hidden beams within the storage roof slab, additional reinforcement areas around slab holes etc.). A top rebar mesh is added on-site and an 18 cm thick layer of concrete is poured to achieve a final slab thickness of 25 cm. The connection between preslab-wall (with hidden beam)-column in the storage area is considered monolithic, due to the on-site concrete pouring procedure. The beam-column connection near the aforementioned slab is implemented using special stud connectors placed at the system points where concrete is poured in order to achieve monolithic connection.

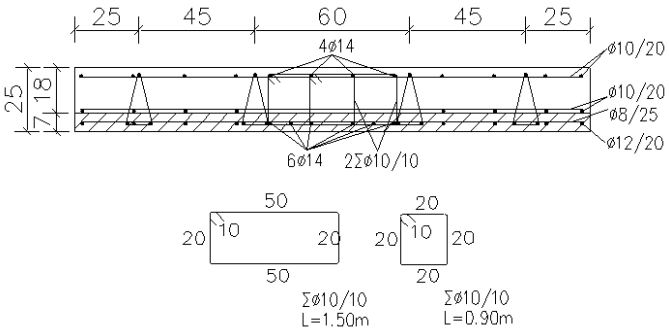


Figure 21: Formation of preslab near the hidden beam

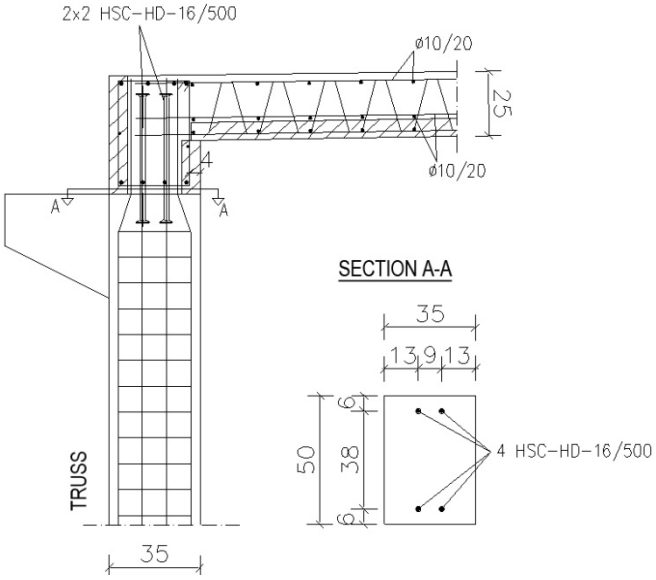


Figure 22: Beam-column monolithic connection near the slab

5 CONCLUSIONS

- Except for linear, surface elements may also be implemented in prefabrication structural systems.
- Modeling the structure model and particularly the connections between structural elements, as well as matching the results to the construction are the determining factors for a complete construction design of prefabrication projects.
- Due to the particularity of the construction, numerous different structural elements and variety of connection types and materials, the creation of a reliable calculation model is a quite strenuous task.
- The prefabrication method may be the ideal solution for mass construction of standard buildings in any location, irrespective of the seismic activity of the area.
- Prefabricated walls can be applicable in strengthening existing buildings.

COMPDYN 2013
4th ECCOMAS Thematic Conference on
Computational Methods in Structural Dynamics and Earthquake Engineering
M. Papadrakakis, V. Papadopoulos, V. Plevris (eds.)
Kos Island, Greece, 12–14 June 2013

SAFECAST PROJECT: EUROPEAN RESEARCH ON SEISMIC BEHAVIOUR OF THE CONNECTIONS OF PRECAST STRUCTURES

Giandomenico M. Toniolo

Politecnico di Milano
p.za Leonardo da Vinci 32, Milan (I)
e-mail: toniolo@stru.polimi.it

Keywords: Precast structures, connections, cyclic & dynamic tests.

Abstract. *SAFECAST Project is the last of a long series of co-normative researches that supported the standardisation of precast structures within Eurocode 8. The paper presents the activity performed by the 16 European partners. The seismic behaviour of four classes of connections is investigated: floor-to-floor, floor-to-beam, beam-to-column and column-to-foundation. The experimental qualification is made in terms of strength, ductility, dissipation, deformation, decay and damage. More than 100 cyclic and dynamic tests have been performed in the laboratories of Lisbon, Milan, Ljubljana, Athens and Istanbul. But the most relevant series of tests have been performed at ELSA Laboratory of the JRC of Ispra, where a full-scale prototype of a three storeys precast structure has been subjected to pseudodynamic and cyclic tests. Other authors are presenting the details of any specific testing activity. This paper presents the design criteria deduced from these activities, as collected in the final document of design rules.*

1 INTRODUCTION

The first testing campaign has been carried out on 1994 when a first draft of Eurocede 8 has been prepared with a section dedicated to precast structures. To make up for the lack of experimental data, a number of cyclic and pseudodynamic tests has been performed on precast columns in pocket foundations at ELSA Laboratory of Ispra (see Figure 1). These tests gave the required demonstration that precast columns behave very well, like the corresponding cast-in-situ ones, but also better because there are no bar splices and no danger of stirrup packaging due to their horizontal casting position [1].

In the typical arrangement of one storey industrial buildings (see Figure 2), the role of the hinged connections had to be investigated in comparison to the monolithic joints proper of cast-in-situ construction. This has been done first with non linear dynamic numerical comparative simulations made on two similar prototypes of one storey structures, one precast and the other cast-in-situ, designed with the same base shear resistance [2].

The experimental verification of the numerical results came from the pseudodynamic tests performed on 2002/2003 again at ELSA Laboratory of Ispra within an European Ecoleader Programme. Two full scale prototypes of one storey structures (see Figures 3a-b) with the same base shear resistance have been submitted to the same accelerogram. The results gave the expected demonstration that the two arrangements have the same seismic capacity: the cast-in-situ structure in its more numerous critical regions dissipates the same amount of energy dissipated by the precast structure in its fewer and larger critical regions dimensioned as they are for higher moments. It is the global volume involved in dissipation and not the number of plastic hinges that gives the measure of the energy dissipation [3].

These results have been taken to the competent CEN Technical committee that, on 2004 in Vienna under the presidency of prof. Fardis, approved the final version of Eurocode 8 with the full equalisation between precast and cast-in-situ frame systems

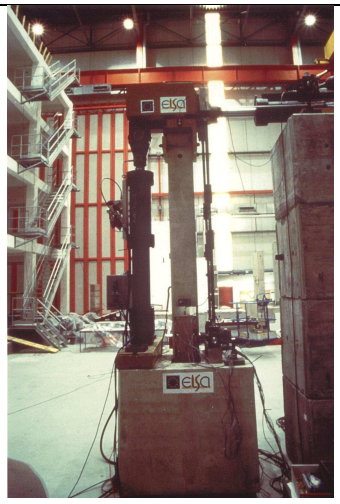


Figure 1: Assobeton tests 2004/06
20 cyclic and 8 PsD tests



Figure 2: precast structure of industrial building
in erection stage .

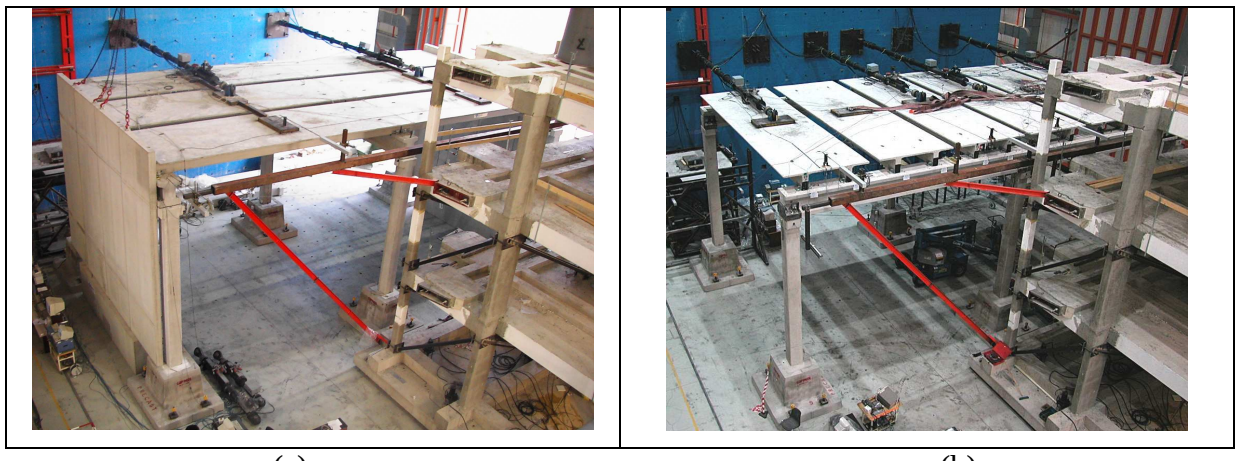


(a) (b)

Figure 3: Ecoleader PsD tests 2002/03 on full scale prototypes: precast (a) and cast-in-situ (b)

In the meantime BIBM, the international association of prefabrication industry, had expressed its interest on the research, so that an other wider testing campaign has been launched within the European Growth programme. “Precast structures EC8” concerned in general the seismic behaviour of precast concrete structures for industrial buildings with respect to Eurocode 8 and was supported by ten partners from Italy, Portugal, Slovenia and Greece. Also the Tongji University of Shanghai participated:

Figures 4a-b show the images of the full scale prototypes tested at ELSA Laboratory of Ispra with the pseudodynamic procedure. But also in Lisbon, Athens and Shanghai important tests have been performed. The role of cladding panels has been investigated together with the effectiveness of the diaphragm action. The quoted PsD tests are reported in [4]. A more exhaustive interpretation of results is presented in [5].



(a) (b)

Figure 4: Precast structures EC8 2003/06 – full scale prototypes ready for PsD tests
(a) with cladding panels (b) turned roof arrangement

2 GENERAL SPECIFICATIONS

Through their very large crop of results, the previous researches pointed out the importance of the connections on the overall behaviour of the structures. This was a problem still pending with a general lack of knowledge. So a new project has been launched within the scope of the European FP7-SME-2007-2 Programme.

Safecast project started on 2009 with the participation of 16 partners coming from Portugal, Spain, Italy, Slovenia, Germany, Greece and Turkey:

Associaions	*Research providers*	*Users (producers)*
1. Assobeton (I – coord.)	6. EC DG JRC – Elsa Lab.	14. DLC (I)
2. Andece (E)	7. Politecnico di Milano	15. Rphorsa (E)
3. Anipb (P)	8. Nat. Techn. Univ. Athens	16. Halfen (D)
4. Sevips (GR)	9. Istanbul Techn. Univ.	
5. Tpca (TR)	10. LNEC of Lisbon	
	11. Univ. of Ljubljana	
	12. Labor (I)	
	13. Lugea (I)	

It has been closed on March 2012. More than 4 million Euro has been the cost, partly supported by the European Commission.



Figure 5: Beam-to-column joint NTUA Lab. – Athens



Figure 6: Beam-to-column joint ITU Lab – Istanbul



Figure 7**:** Column-to-found. joint POLIMI – Milan

A large number of cyclic and dynamic tests have been performed on sub-assemblies of structural elements connected at their joints. Figure 5 shows a beam-to-column connection placed on the shaking table of the Technical University of Athens. Figure 6 shows a different type of beam-to-column connection placed in an overturned position in the laboratory of the Istanbul Technical University. Figure 7 shows the prototype of a column-to-foundation connection installed in the testing plant of the Politecnico di Milano. Figure 8 shows a frame modulus placed in the National laboratory of civil engineering of Lisbon and finally Figure 9

shows the laboratory of the University of Ljubliana where additional tests on beam-to-column connections have been made.



Figure 8: Frame modulus
LNEC Lab. – Lisbon

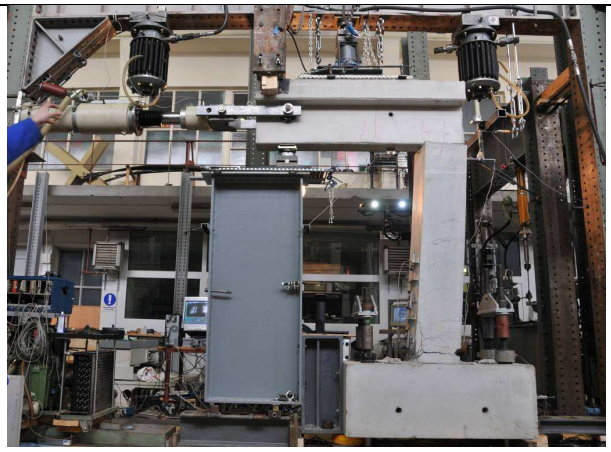


Fig.ure 9: Beam-to-column joint
ULJ Lab – Ljubliana

More than one hundred of such tests have been performed in all in the quoted laboratories providing a large data-base that is now the basis for any possible improvement of the related technology and design. Following the due interpretations a manual containing the Design rules for connections of precast structures has been drafted as presented in Chapter 3.



Figure 10: Three storey prototype in erection
ELSA Lab. – Ispra



Figure 11: Three storey prototype completed
ELSA Lab. – Ispra

But the most important series of tests has been performed between June and August 2011 at ELSA Laboratory of Ispra. Figure 10 shows the full scale prototype of three storeys structure installed against the reaction wall of that laboratory at an advanced stage of erection, while Figure 11 shows the same prototype completed with all its components. The dimensions are about 16 by 16 m in plan and more than 10 m in elevation. It is the biggest prototype ever tested in that laboratory and one of the biggest ever tested in the world. From the experimentation a complete information has been obtained about the seismic behaviour of this type of structures in terms of reliability of the analysis, displacement control and effectiveness of connections system, as reported in [6] and [7].

3 DESIGN RULES FOR CONNECTIONS

The main supply delivered to Safecast purchasers (that is the five national associations of small and medium enterprises) is the manual containing the "Design guidelines for connections of precast structures".

The purpose of this document is to give simple design rules for practical applications, drafted in the format of a manual for designers. The rules of this manual have a theoretical derivation supported by the experimental results of the testing campaign and by the numerical simulations performed within the research. General know-how on production practice and international literature on the matter have been also considered.

The rules refer to the connections in precast frame systems of one-storey and multi-storey buildings. Four orders of connections are considered: floor-to-floor, floor-to-beam, beam-to-column and column to foundation. Different types of connections are treated for any order belonging to the three main systems of typical joints, that is dry joints with mechanical connectors, emulative joints, that is wet joints with rebar splices and cast-in-situ concrete, and mechanical joints, that is joints with bolted flanges as used in steel construction. Simple bearings working by gravity load friction are not considered. Sliding and elastic deformable supporting devices neither, being all these types of connections not suitable for the transmission of seismic actions.

Some fundamental requirements give the basic design criteria to which the document is shaped:

"Any type of connection shall be experimented with an initial type testing in order to quantify its strength and possibly the other properties that affect its seismic behaviour. From this experimentation a design model may be deducted, by means of which a verification by calculation can be applied on the different connections of the same type. For a specific application one can refer to the available results of previous experimentations like those provided in this document or in other reliable documents such as official regulations (Eurocodes, CEN product standards and CEN Technical specifications, …). "

"Non ductile connections can be used provided they are opportunely over-proportioned by capacity design with respect to the resistance of the critical dissipative regions of the structure."

The main parameters that characterize the seismic behaviour of the connections, as measured through monotonic and cyclic tests, refer to the six properties of:

-*strength*, that is the maximum value of the force which can be transferred between the parts;

-*ductility*, that is the ultimate plastic deformation compared to the yielding limit, where the plastic deformation can be replaced by other physical phenomena like friction;

-*dissipation*, that is the specific energy dissipated through the load cycles related to the correspondent perfect elastic-plastic cycle;

-*deformation*, that is the ultimate deformation at failure or functional limit;

-*decay*, that is the strength loss through the load cycles compared to the force level;

-*damage*, that is the residual deformation at unloading compared to the maximum displacement or the details of rupture.

For any single type of connection strength is specified with the definition of:

-the *behaviour models* related to the resisting mechanisms of the connection;

-the *failure modes* of the resistant mechanisms;

-the *calculation formulae* of the ultimate strength for any failure mode.

For what concerns ductility the connections are classified on the basis of the force-displacement diagrams obtained from the experimentation:

-*brittle connections* for which failure is reached without relevant plastic deformations;

-*over-resisting connections* for which, at the functional limit, failure has not been reached:

-*ductile connections* for which a relevant plastic deformation has been measured.

Ductile connections are again classified in:

-*high ductility* with a displacement ductility ratio of at least 4,5;

-*medium ductility* with a displacement ductility ratio of at least 3,0;

-*low ductility* with a displacement ductility ratio of at least 1,5.

This classification of ductility refers to the connection itself. This ductility has not direct reference to the global ductility of the structure. Ductile connections may give or not a relevant contribution to the energy dissipation at the no-collapse limit state of the structure depending on their location within the structural assembly and on their relative stiffness. In general all the connections, ductile or not ductile, shall be over-proportioned by capacity design with respect to the critical regions of the structure.

For what concerns dissipation the connections are classified on the basis of the specific histograms obtained from the experimentation:

-*non dissipative* with specific values of dissipated energy lower than 0,10;

-*low dissipation* with specific values between 0,10 and 0,30;

-*medium dissipation* with specific values between 0,30 and 0,50;

-*high dissipation* with specific values of dissipated energy over 0,50.

Medium dissipation corresponds to well confined reinforced concrete sections under alternate flexure and high dissipation can be achieved with the use of special dissipative devices.

For a direct comparability of the results, the quantification of the properties quoted above has been carried out by means of tests performed following the procedures described in a special Protocol for connection testing. From monotonic (push-over) tests the first information about the yielding limit, the maximum force, the ultimate deformation and the ductility ratio is obtained. From cyclic tests, performed following a standard loading history, information about the strength variation, the force decay and the energy dissipation is obtained.

3.1 Beam-to-column dowel connections

Among the different types of beam-to-column connections the qualification of a traditional wide spread one is presented. Figure 12 shows this type with the details of a beam placed on a supporting column. In the case (a) two dowels protrude from the top of the column and enter into the sleeves inserted in the beam. The sleeves are filled with no-shrinkage mortar of adequate strength to ensure by bond the anchorage of the dowels. The

anchorage can also be ensured providing the dowels with a cap fixed at the top with a screwed nut. In any case the sleeve shall be filled in with mortar to avoid hammering under earthquake conditions. The case (b) refers to the same technology but with only one dowel. In the transverse direction the use of two dowels improve the resistance against overturning moments. Due to the much lower stability against overturning moments the use of one only dowel is not recommended especially with reference to the uneven load conditions during the construction stages. The beam usually is placed over a pad to localise the load out of the peripheral edges of the connected elements. The rules given in the following clauses are based on tests made only on connections with flexible rubber pads and adherent dowels [8].

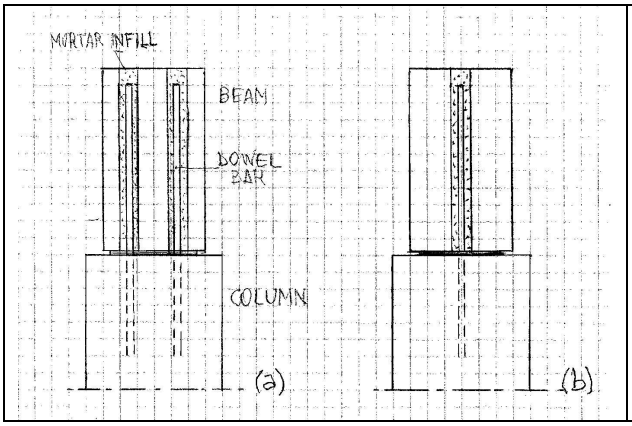


Figure 12: beam-to-column connection with two dowels (a) or one dowel (b)

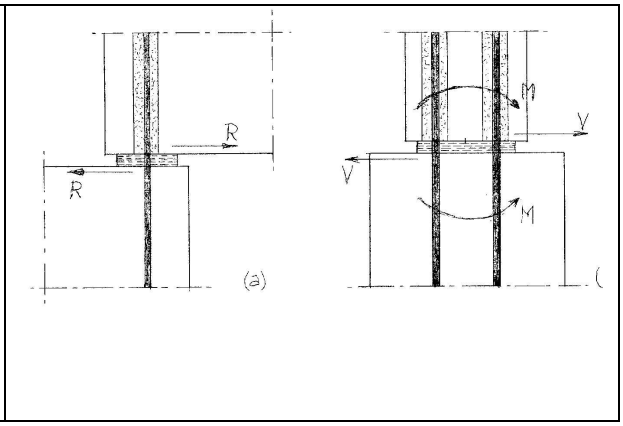


Figure 13: behaviour models for longitudinal (a) and transverse (b) action

The following indications about the mechanical behaviour of this type of connection leaves out of consideration the friction that sets up between the parts due to the weight of the supported element. In fact in seismic conditions, under the contemporary horizontal and vertical shakes, the connection may work instantly also in absence of weight.

This type of connection provides an hinged support in the vertical plane of the beam and a full support in the orthogonal vertical plane. In the longitudinal direction of the beam the horizontal force R is transmitted through the shear resistance of the connection (see Figure 13a), which is given by the shear resistance of the dowels and their local flexure between the elements in correspondence of the bearing pad. In the transverse direction, omitting the vertical gravity loads, the connection transmits a shear force V together with the corresponding moment M (see Figure 13b).

The principal failure modes are listed below together with the corresponding verification formulae. With reference to Figure 13a for the longitudinal action of a given force R evaluated by capacity design, as deduced from tests performed on connection with flexible pads, the following verifications shall be made:

a – breaking of the dowel connection due to combined shear, tension and flexure on steel bar and bearing stresses on concrete;

$$R_{Rd} = 0{,}90\, n\, \phi^2 \sqrt{[\, f_{yd}\, f_{cd}\, (\, 1 - \alpha^2\,)\,]} \geq R$$

with n number of dowels, ϕ diameter of dowels, f_{cd} design strength of concrete, f_{yd} design strength of steel, $\alpha = \sigma / f_{yk}$ with σ normal tensile stress due to other possible contemporary effects on the dowel;

b/c – spalling of the concrete edge of the beam or of the column due to tensile stresses;

$$R_{Rd} = \kappa 1{,}6\ \phi^{\alpha} h^{\beta} \sqrt{(f_{ck,cube}\, c^3)} / \gamma_C \geq R \qquad \alpha = 0{,}1\ (h / c)^{0{,}5} \qquad \beta = 0{,}1\ (\phi / c)^{0{,}2}$$

where $f_{ck,cube}$ is the characteristic cubic strength of concrete, ϕ is the diameter of the dowel, c is the edge distance of the dowel axis, $h=8\phi$ is the effective length of the dowel and $f_{ck,cube}$ is expressed in N/mm^2, R and R_{Rk} in N and d, h, c, ϕ in mm.

With reference to Figure 13b, for the transverse action of a force V and a moment M evaluated by capacity design, the following verifications shall be made:

d – flexural failure of the bearing section due to the action of M:

$$M_{Rd} = A_s\, f_{yd}\, z \geq M$$

with z lever arm of the internal forces and A_s sectional area of the dowels;

e – pull-out of the tensioned dowel under the action due to M:

$$l_b\, u\, f_{bd} \geq \gamma_R\, A_s\, f_{ym}$$

where $f_{bd}=0{,}45f_{cd}$ is the ultimate bond strength, $f_{ym}=1{,}08f_{yk}$ is the mean yielding stress of the steel, l_b is the anchorage length of the dowels, A_s is the sectional area of a dowel and u is its perimeter;

f – sliding shear failure under the action of V:

$$V_{Rd} = 1{,}3\, A_s \sqrt{(f_{cd}\, f_{yd})} + 0{,}25\, b\, x\, f_{cd} \geq V$$

where A_s is the sectional area of the dowels not yielded by flexure and b and x are the width and the depth of the compressed part of the concrete section.

In testing, failure mode *a* of dowel connection displayed a local shear ductility, due to the flexural and tensional deformation of the dowels within the joint gap, evaluated in $\mu=4{,}0$ to $\mu=6{,}0$. For $c/\phi<6$, with a failure mode *b* or *c*, the ductility decreased to $\mu=2{,}5$ to $\mu=3{,}5$**.** Cyclic tests performed in the longitudinal direction of the beam showed a *medium dissipation* capacity due to the alternate deformations of the dowels within the joint gap. In any case, due to their location in the structural assembly and to their high stiffness in comparison to the column flexibility, no contribution of ductility and dissipation are expected from this type of connections to the global ductility of the structure. They shall be over-proportioned by capacity design with respect to the critical sections of the column base.

3.2 Foundations with bolted sockets

Figure 14 shows a new type of connection of a column to the foundation obtained with steel sockets inserted in the column base and bolted to the foundation. The sockets are anchored to the column by means of couples of bars welded to them and spliced to the current longitudinal reinforcement by overlapping. Other transverse links can be welded to the sockets to avoid their lateral detaching. At the lower part of the connections, stud-bolts are protruding from the foundation, one for any socket. They consist of headed fasteners of adequate length previously inserted in the foundation element. A mortar embedding fills the lower joint in.

In expectation, under seismic conditions, of a plastic hinge at the base of the column, the length of this plastic hinge finds some difficulties to be determined because of the uncertain effectiveness of the longitudinal reinforcement in the lap zone of the bars. In any case the formation of the plastic hinge in a raised position over the lap length shall be avoided since for this position the displacement ductility of the column would be reduced. More reliable

results and possibly a higher displacement ductility can be obtained moving upwards the lap zone so to leave a sufficient length of single (non overlapped) reinforcement at the base of the column, provided these lower bars are weaker and connected to the sockets with proper provisions that don't endanger their ductility.

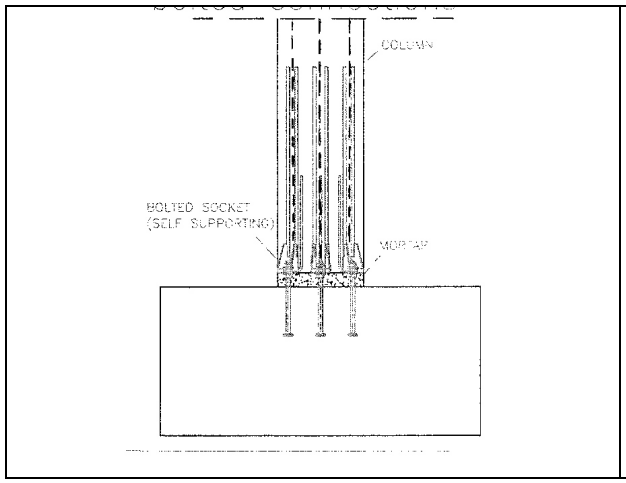


Figure 14: column-to-foundation with bolted sockets

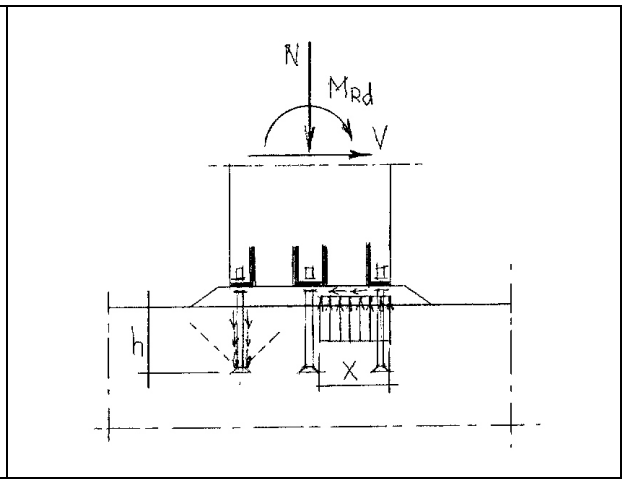


Figure 15: design model of the resisting mechanism

The connection shall be verified for the action of the (plastic) ultimate moment $M_{Rd}=M_{Rd}(N)$ at the base of the column with the correspondent contemporary axial force N and of the shear V. This calculation can be performed in the two main directions independently. The due overstrength factor γ_R shall be added as specified hereunder. The lap length of the lower bars with the upper bars of the column shall be overproportioned applying the same factor γ_R and this calculation is taken for granted in the following points. Due to their expected brittle failure modes, in general terms for a good ductile behaviour the local devices (sockets, bushes, bolts,…) with their coupling provisions (welding, threading, pressing,…) shall be over-dimensioned by γ_R with respect to the connected elements to which a ductile behaviour is required.

Figure 15 shows the detail of the resisting mechanism of the foot section of the column subjected to the combined bending moment $\gamma_R M_{Rd}$ and axial action N and to the shear $\gamma_R V$. Assuming that at this level of action the tensioned lower steel bars are at their maximum ultimate capacity F_u, the anchorage verification shall be referred to a correspondent pull-out force. The failure modes are listed hereunder together with the corresponding verification formulae:

For fasteners well spaced among them and from the foundation edges, with reference to the symbols described in Figure 15 and with γ_R overstrength factor, the following verifications shall be performed.

a – failure of the fastener subjected to the tensile force coming from the upper reinforcement:

$$F_{Rmin} \geq \gamma_R A_s f_{ym}$$

where F_{Rmin} is the minimum steel ultimate capacity of the fastener declared by the producer, A_s is the sectional area of the corresponding upper reinforcement, $f_{ym}=1{,}08f_{yk}$ is the mean yielding stress of the steel bars.

b – pull-out of the head-fastener subjected to the maximum upper force F_u with concrete cone-failure:

$$k \sqrt{(f_{ck,cube} h^3)} / \gamma_C \geq \gamma_R F_u$$

where $F_u=\min\{A_s f_{ym} , F_{Rmax}\}$, $F_{Rmax}=1,2F_{Rmin}$ and for current products k=7,0 may be assumed.

c – sliding shear failure at the foot section in the design situation corresponding to $\gamma_R M_{Rd}$, N and $\gamma_R V$:

$$1,5 A_d \sqrt{(f_{cd} f_{yd})} + 0,25 b x f_{cd} \geq V$$

where V is the shear corresponding to $\gamma_R M_{Rd}$, A_d is the sectional area of the dowel not yielded by the moment, f_{yd} is design strength and b and x are the width and the depth of the compressed part of the concrete section.

Tests have been performed on different prototypes with different arrangements of the connection showing different ductility capacities [9]. Some early failure occurred due to the rupture of defective welding of the socket, pointing out the importance of a correct coupling technology. When a correct coupling is made, the arrangement of weak bars under the lap zone moved in an upper position can save the full “medium” ductility and dissipation capacity of the column.

4 CONCLUSIONS

The work done in Safecast Project allowed to achieve a good knowledge on the behaviour of the connections of precast structures, enabling to have a reliable design under seismic action. All the rules given by the specific manual for the calculation of the resistance are based on the assumption to apply the capacity design criterion for the calculation of the action. In some cases the application of capacity design for the proportioning of the connections is simple and immediate: with reference to the hinged beam-to-column connections of one storey structure, the horizontal force at the top of the columns can be calculated from the resisting moment M_{rd} of the section at the critical region at the base of the columns with $H=\gamma_R M_{rd}/h$, where h is the height of the column and γ_R is the due overstrength factor. For multi-storey structures the equilibrium around the base support gives $H_1z_1+H_2z_2+H_3z_3+\ldots=\gamma_R M_{rd}$ and the problem remains indeterminate, depending on the ratio between the storey forces H_i that are applied at the different levels z_i. Some approximate solutions are proposed in [10] and [11]. Also indeterminate remains the distribution of the diaphragm forces transmitted among the floor elements through their connections. A solution is suggested in [12] with reference to the roofs of one storey structures. But an inadequate approach is still now applied to the design of the fastening systems of cladding panels as pointed out by lesson of recent earthquakes [13]. This is a pending problem on which the new ongoing Safecladding research project is addressed in the present years.

5 ACKNOWLEDGMENTS

The present work has been performed within the scope of the Research Project SAFECAST supported by the contribution of the European Commission in the FP7-SME-2007-2 Programme with Grant agreement n. 218417 of 2009.

REFERENCES

[1] Saisi A. & Toniolo G. (1998). Precast r.c. columns under cyclic loading: an experimental programme oriented to EC8. *Studi e ricerche, Scuola di specializzazione.* Politecnico di Milano.

[2] Biondini F. & Toniolo G. (2002). Probabilistic calibration of behaviour factors of EC8 for cast-in-situ and precast frames. *17th BIBM Congress.* Istanbul 2002

[3] Biondini F. & Toniolo G. (2004). Validation of seismic design criteria for concrete frames based on Monte Carlo simulation and full scale pseudodynamic tests. *ECEE 13th World Conference.* Vancouver 2004.

[4] Biondini F., Toniolo G. & Zaho Bin (2008). Pseudodynamic tests on full scale prototypes of precast structures. *14th WCEE World Conference.* Beijing 2008.

[5] Biondini F. & Toniolo G. (2009). Probabilistic calibration and experimental validation of seismic design criteria for one storey concrete frames. *Journal of Earthquake Engineering, Vol. 13 No 4.* Taylor & Francis.

[6] Negro P., Bournas D.A. & Molina F.J. (2012), Pseudodynamic testing of the Safecast three-storey precast building. *15th WCEE World Conference*, Lisbon 2012

[7] Bournas D.A. & Negro P. (2012), Performance of innovative mechanical connections in the Safecast three-storey precast building, *WCEE World Conference*, Lisbon 2012

[8] Psycharis I.N. & Mouzakis H.P. (2012), Assesment of the seismic design of precast frames with pinned connections from shaking table tests, *Bulletin of earthquake engineering*

[9] Dal Lago B., Lamperti M. & Toniolo G. (2012), Experimental investigation on mechanical column-to-foundation connections for precast structures, *WCEE World Conference*, Lisbon 2012

[10] Biondini F., Tsionis G. & Toniolo G. (2010), Capacity design and seismic performance of multi-storey precast structures, *European Journal of environmental and civil engineering*, Vol. 14 n.1

[11] Fischinger M., Rejek K. & Isakovic T. (2010), Shear magnification factors for rc structural walls, *14th European Conference on Earthquake Engineering,* Ohrid 2010

[12] Ferrara L. & G. Toniolo (2008), Design approach for diaphragm action of roof decks on precast concrete buildings under earthquake, fib Symposium Amsterdam 2008

[13] Colombo A. & Toniolo G. (2012), Precast constructions: the lesson learned from L'Aquila earthquake, *Structural concrete*, 2012

COMPDYN 2013
4th ECCOMAS Thematic Conference on
Computational Methods in Structural Dynamics and Earthquake Engineering
M. Papadrakakis, V. Papadopoulos, V. Plevris (eds.)
Kos Island, Greece, 12–14 June 2013

EARTHQUAKE EXPERIENCE OF TURKISH PRECAST INDUSTRY

S. Ozden[1], G. Barka[2], H. Atakoy[3], B. Hancioglu[4], U. Ozkan[5]

[1] Turkish Precast Concrete Association, TPCA Technical Advisor
Associate Professor, OKAN University, Tuzla Campus, Akfirat-Tuzla Istanbul
sevketozden@yahoo.com

[2] Turkish Precast Concrete Association, TPCA Technical Committee Chairman
Turkiye Prefabrik Birligi, Farabi Sk., 39/10, Ankara, Turkey
gbarka@barkamuh.com

[3] Turkish Precast Concrete Association, TPCA Technical Committee Member
Turkiye Prefabrik Birligi, Farabi Sk., 39/10, Ankara, Turkey
h.atakoy@afaprefabrik.com.tr

[4] Turkish Precast Concrete Association, TPCA Technical Committee Member
Turkiye Prefabrik Birligi, Farabi Sk., 39/10, Ankara, Turkey
bhancioglu@alacali.com.tr

[5] Turkish Precast Concrete Association, TPCA Technical Committee Member
Turkiye Prefabrik Birligi, Farabi Sk., 39/10, Ankara, Turkey
umit.ozkan@adimltd.com.tr

Keywords: Earthquake Performance, Precast Concrete Structure

Abstract. *The high seismic activity of the three fault zones in Turkey developed damaging earthquakes in the last five decades that affected the precast-concrete building structures in the region. Among others, the 1998 Adana, 1999 Kocaeli, 2003 Bingol and 2011 Van earthquakes are considerably important regarding the seismic performance of the precast structures. Earthquake performance of frame structures in the form of industrial-halls, shopping malls, multi-storey residential buildings and gymnasiums along with the wall structures mainly in the form of residential housing, under these seismic actions, revealed valuable information on the effectiveness of the prevailing technology and the design practice. The quality control system, inherently developed within the member companies of the Turkish Precast Concrete Association, TPCA, resulted better performance of the precast structures. The structural system of the multi-storey residential buildings in Bingol, Kocaeli and Van, regardless of the structural system, were in the state of immediate occupancy, while the cast-in-place buildings in the vicinity experienced damage ranging from life safety up to total collapse. Beside the residential buildings, bigger span structures like shopping malls gymnasiums and the industrial structures of TPCA members after the Adana and the devastating Kocaeli earthquakes responded between immediate occupancy and life safety.*

1 INTRODUCTION

Turkey is located in a seismically active region and frequently experiences large earthquakes. The high seismicity of the region is mainly caused by the North and East Anatolian fault zones. The North Anatolian Fault Zone (NAF) is a strike-slip fault in Northern Anatolia which runs between the Eurasian and the Anatolian Plates having an approximate length of 1500 km [1]. On the other hand the East Anatolian Fault (EAF) is another 550 km length strike-slip fault zone in South-Eastern Turkey, forming the boundary between the Anatolian Plate and the northbound moving Arabian Plate (*Fig. 1*).

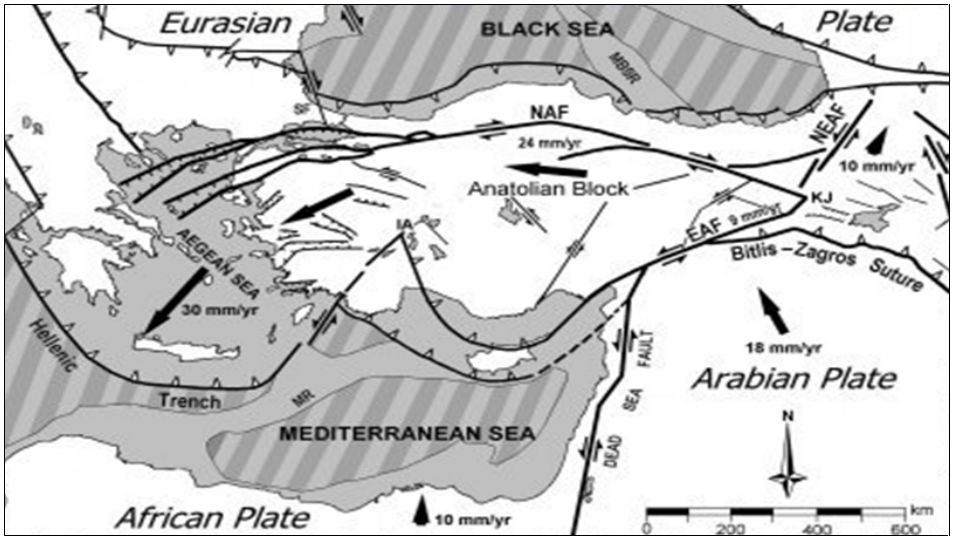


Figure 1 – The Anatolian Fault Zone [2]

Year	Location	Magnitude
1930	Hakkari	7.2 *(M_s)*
1939	Erzincan	7.8 *(M_s)*
1942	Erbaa	7.0
1943	Ladik	7.4
1944	Gerede	7.5
1953	Yenice	7.2 *(M_s)*
1957	Abant	7.1
1964	Manyas	7.0 *(M_s)*
1966	Varto	6.7
1967	Mudurnu	7.2
1971	Bingol	6.9
1976	Muradiye	7.5 *(M_s)*
1983	Erzurum	6.9 *(M_s)*
1992	Erzincan	6.8
1995	Dinar	6.1 *(M_s)*
1998	Adana-Ceyhan	6.2 *(M_s)*
1999	İzmit	7.6
1999	Duzce	7.2
2003	Bingol	6.4 *(M_w)*
2011	Van	7.2 *(M_w)*

Table 1 – Some Earthquakes of the Anatolian Fault Zone

Since the disastrous 1939 Erzincan earthquake (*Table 1*) on the East bound of Turkey, there have been several earthquakes on NAF and EAF zones hitting the residential and commercial areas, causing casualties and economic losses. Approximately 95 percent of the Turkish land, as well as residential and industrial facilities, are under the direct thread of earthquakes. The residential housing in the form of brick and adobe structures form the main percentage of the building stock in small residential centers, while cast-in-place reinforced concrete frame type of structures and precast concrete frame or wall systems are more common in the big residential cities and in the industrialized regions.

Precast concrete in Turkey has a wide range of application ranging from highway bridges to city furniture, and to single- and multi-storey building structures. The precast concrete building structures, as compared to the cast in place counterparts, are mostly preferred for the shopping centers, gymnasiums, multi-storey housing, and for single or multi-storey industrial facilities. The building structures for the industrial facilities among the others cover the highest percentage within the precast concrete production in Turkey.

2 PERFORMANCE OF PRECAST INDUSTRIAL FACILITIES

Precast construction was introduced in Turkey in the 1960s. During the 1990s, approximately 90% of the warehouse and light industrial facilities were constructed using precast members [3]. The most common structural system for these facilities is based on a structural configuration that was developed in Western Europe to carry gravity loads only [4]. However Turkish engineers modified the unique connection details for each producer company so that the precast buildings have the capacity to resist seismic lateral loads. The connection and other details of such structures vary appreciably from producer to producer [5].



Figure 2 – Industrial Building under Construction in Adana in 1998 [6]

Adana (on EAF), Kocaeli and Sakarya (on NAF) are the industrial heartlands of Turkey and hit by two devastating earthquakes in the year 1998 and 1999 respectively. The precast construction in Adana was mainly in the form of single storey industrial buildings, while multi-storey industrial buildings also exist in the Kocaeli region. The structural system of single storey industrial buildings consists of cantilever columns, fixed at the base and pin connected to the roof beams at the top. It is reported that the workmanship and the material quality of the precast concrete elements in Adana were significantly over those of the cast in place residential buildings (Fig.2). It is also reported that the Schmidt hammer measurements of the concrete elements yielded a mean value for the compressive strength of f_c= 60 N/mm^2 while the yield strength of the reinforcement steel is assumed to be f_y = 420 N/mm^2 [6]. The local damage of such buildings were confined to the connections where roof beams were pin con-

nected to the columns. The structures conforming to the Turkish Earthquake Code experienced minimal damage confined to the partition walls and some connections, while the ones not conforming to the code experienced local failures. The column dimensions played an important role on the damage distribution in such buildings.

One year after Adana earthquake, Posada and Wood [5] reported similar results for the industrial buildings. Authors investigated the industrial buildings in Sakarya, Kocaeli, and Gebze. It is reported that the damage level of the industrial buildings are mainly influenced by the drift demand and the drift capacity of the buildings. The damage of precast structures in Sakarya was more pronounced due to the drift demand invoked by the soft soil conditions, as compared to the no damage in Gebze where the soil is basically stiff clay to rock. It is also reported that the buildings with larger column sizes, in other words the buildings conforming the Turkish Earthquake Code (TEC) performed well [5] (Fig.3). The site investigations and elaborations on the structural design calculations revealed that most of the damaged buildings were not conforming to the drift limits of TEC. Besides, the design was made only in the frame direction, and the earthquake loading is not made in the transverse direction. The damage of precast concrete industrial buildings confirming to the TEC drift limits on both orthogonal directions, even in the vicinity of the epicenter, were in the range of immediate occupancy to life safety [7].



Figure 3 – Typical Single- and Multi-Storey Warehouses after Kocaeli Earthquake [5]

In some of the single-storey industrial buildings in Adana earthquake, the damage was confined to the out-of-plane toppling or leaning of the triangular roof beams. TPCA Technical Committee developed a design methodology and enforced the use of double bars to fix the triangular roof beams to the corbel of the columns (Fig.4). The forces Fi resulting from the earthquake excitation is resisted by the moment around a beam corner due to gravity and due to the force couple created by the double bars as shown in Fig.4. [8].

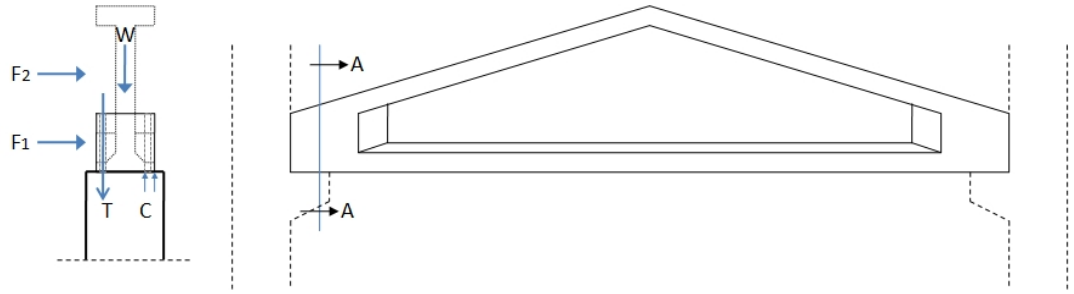


Figure 4 – Forces on the Roof Beams and the Resisting Mechanism

3 PERFORMANCE OF MULTI-STOREY RESIDENTIAL HOUSING

The first multi-storey post-earthquake housing in precast concrete was constructed at Genc-Bingol in 1986 after the damaging earthquake of Bingol in 1971 (Table 1). The housing complex contains 36 blocks with 5 floors including basement; basement having monolithic peripheral walls. The joint system of the precast frame was cast-in-place. Seismic lateral loads were resisted by the precast moment resisting frame system and the cast-in-place reinforced concrete shear walls spanning from the foundation up to the roof level. The plan dimension of the blocks was 8.20x32.90 meters with a story height of 2.70 meters.



Figure 5 – Precast Multi-Storey Building during Construction and After 2003 Bingol Earthquake [9]

Post Earthquake investigation (Bingol-2003) on the Genc-Bingol housing complex revealed that the buildings were in the performance state of immediate occupancy, although the surrounding cast-in-place reinforced concrete structures underwent damages ranging from life safety to collapse.

In 1999, a devastating earthquake hit the city of Kocaeli leaving thousands of casualties and a considerable economic loss both due to the damage in infrastructure and due to the industrial production losses (Table 1). The spread of damage was more pronounced in the sediment basins such as Adapazarı, and in the regions close to the East bound of the Kocaeli Gulf such as Golcuk and Kavaklı. The displacement demand due to the soft sub-layers caused many buildings to collapse, left many beyond the life safety performance limit. The precast wall type of 5 storey residential construction at Golcuk, which was constructed in 1991 experienced no damage (immediate occupancy performance level) while all the surrounding buildings were collapsed. The walls and the slabs of the building complex with 2

blocks were of hollow core slabs. The wall to slab and wall to wall connections were cast-in-place with special reinforcement detail (Fig.7).



Figure 6 – Precast Multi-Storey Wall System Building during Construction and After 1999 Kocaeli EQ. [10]

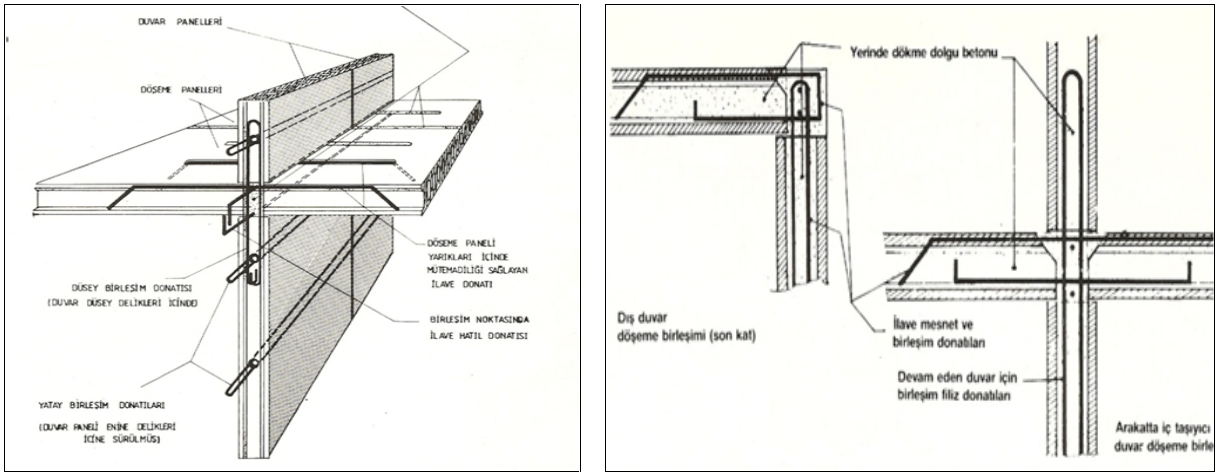


Figure 7 – Slab-to-wall and Wall-to-Wall Connections in Multi-Storey Wall System Building. [10]



Figure 8 – Frame Building with Post Tensioned Connections, and the Performance after 2011 Van EQ. [11]

Starting with the 1990s precast concrete moment resisting frames with post tensioned connections took place in the Turkish Precast Concrete market. Multi-storey industrial and residential buildings with such connections were constructed in Turkey. The recent earthquake in 2011, in the city of Van (Table 1) revealed valuable information on the performance of such connections. The residential multi-storey moment resisting frame building with post tensioned connections in Van had 7 storeys with an approximate foot-print area of 380 m2. Plan geometry was rectangular: two bay by two bay. The bays were Lx=12.30m, Ly=8.00m. Floor system was with hollow core slabs which were supported by the 12.30m spans. The beams spanning in the short direction were 50/70cm, while the ones spanning on the long direction were 60/80cm. The columns of the frame were 75x70cm. The columns of the building were constructed in single pieces with a height of seven storeys (approximately 22m) and transported to the construction site. A cast-in-place socket type of foundations were used and designed as fixed support. Beams with tapered end were seated on square corbels of the columns and post tensioning was used for the connection continuity.

Post-earthquake damage investigation on that specific building revealed no structural damage on neither pre-cast, pre-tensioned members, nor the post-tensioned connections, and post-tensioning ducts. The column to foundation connections were carefully investigated and no flexural or shear cracking was observed. The frame performance during the Van Earthquake of October 2011 was immediate occupancy. However, some the dry partition walls experienced minimal damage.

4 PERFORMANCE OF LARGE SPAN SHOPPING MALLS

The shopping malls, with the economic development of Turkey, became a market field for the precast concrete structures. The spans were relatively long, and the service loads were high in such structures. The shopping center given in Fig.9 was in the epicenter of Kocaeli earthquake (Table 1). The building had a central part with two storeys, while the surrounding



Figure 9 – Performance of a Shopping Mall after 1999 Kocaeli Earthquake [12]

frames were three storey height. The frame connections were cast-in-place. The structural system was in the immediate occupancy performance level. However, the false ceilings and the material racks toppled and service of the mall suspended for a while.

5 CONCLUSIONS

The post earthquake field investigations revealed that the performance level of the precast concrete structures in Turkey is clearly influenced by the building conformity to the Turkish Earthquake Code. None of the buildings designed and constructed by the TPCA members underwent a damage beyond the minimal level.

REFERENCES

[1] Implications for Earthquake Risk Reduction in the United States from the Kocaeli Turkey Earthquake of August 17 1999, *U.S. Geological Survey Circular 1193*, November 22, 1999

[2] 1 Mayıs 2003 Bingöl Depremi Ön Raporu (Reconnaissance Report for Bingol Earthquake, May1 2003), *Boğaziçi Üniversitesi Kandilli Rasathanesi ve Deprem Araştırma Enstitüsü Sismoloji Servisi,* 8 Mayıs 2003, Istanbul

[3] E. Karaesmen, *Prefabrication in Turkey: Facts and Figures*, Department of Civil Engineering, Middle East Technical University, 2001, Ankara, Turkey.

[4] U. Ersoy, T. Tankut, and G. Özceb, *Damages Observed in the Precast Framed Structures in the 1998 Ceyhan Earthquake and their Rehabilitation*, Department of Civil Engineering, Middle East Technical University, 1999, Ankara, Turkey.

[5] M. Posada, S. L. Wood, Seismic Performance of Precast Industrial Buildings in Turkey, *Proceedings, 7th U.S. National Conference on Earthquake Engineering, Earthquake Engineering Research Institute*, Boston, MA, Paper 543, July 2002

[6] The Adana-Ceyhan Earthquake of June 27, 1998, *Report on the Reconnaissance Mission from July 6 - 12, 1998 of the Swiss Society of Earthquake Engineering and Structural Dynamics (SGEB)*

[7] S. Ozden, H. Meydanlı, Seismic Response of Pre-Cast Industrial Buildings During 1999 Kocaeli Earthquake *International Conference in Earthquake Engineering to Mark 40 Years from Catastrophic 1963 Skopje Earthquake and Successful City Reconstruction*, SE 40EEE, Skopje and Ohrid, Republic of Macedonia, August 2003

[8] H. Atakoy, Yapı Guvenligi ve Beton Prefabrikasyonda Tasarım, *İnşaat Mühendisleri Odası İzmir Şubesi, Yapı Güvenliği ve Eğitim Sempozyumu*, October 2001, Izmir

[9] H. Atakoy, 01 Mayıs 2003 Bingol Depremi ve Prefabrike Betonarme Yapılar, *Beton Prefabrikasyon*, N.68-69, October 2003 (Precast Journal, Quarterly Published by the Turkish Precast Concrete Association)

[10] G. Barka, *Seminars on Precast Concrete Building Performance*, Turkish Precast Association.

[11] S. Ozden, E. Akpinar, H.M. Atalay, Reconnaissance Report - Van Earthquake of October 2011, *Structures Laboratory, Department of Civil Engineering, Kocaeli University*, pp.28

[12] H. Atakoy, Prefabrike Betonarme Yapılar ve Deprem, *Beton Prefabrikasyon*, N.57-58, January 2001 (Precast Journal, Quarterly Published by the Turkish Precast Concrete Association)

COMPDYN 2013
4th ECCOMAS Thematic Conference on
Computational Methods in Structural Dynamics and Earthquake Engineering
M. Papadrakakis, V. Papadopoulos, V. Plevris (eds.)
Kos Island, Greece, 12–14 June 2013

ANALYTICAL PREDICTION OF THE SHEAR RESISTANCE OF PRECAST RC PINNED BEAM-TO-COLUMN CONNECTIONS

Georgia D. Kremmyda[1], Yasin M. Fahjan[2], and Ioannis N. Psycharis[1]

[1] National Technical University of Athens, Greece
9 Heroon Polytechneiou str., Zografos 15780, Greece
gkrem@ath.forthnet.gr
ipsych@central.ntua.gr

[2] Gebze Institute of Technology, Turkey
Gebze, 41400 Kocaeli, Turkey
fahjan@gyte.edu.tr

Keywords: Precast; Pinned beam-to-column connections; Shear resistance; Monotonic and cyclic loading; Numerical model; Non linear analysis

Abstract. *In the research presented herein, analytical investigation was undertaken with regard to the behaviour of precast RC pinned beam-to-column connections provided by steel dowels, under static, monotonic and cyclic, loading. In particular, the main scope of this investigation was the development of a numerical model and its calibration against available experimental data, which were used to prove the efficiency of the proposed model to provide an analytical prediction of the shear resistance of precast RC pinned beam-to-column connections. The results of sixteen experiments under monotonic and cyclic loading were used for the calibration of the model. The experiments used for the calibration and validation of the model were performed at the Laboratory for Earthquake Engineering of the National Technical University of Athens, Greece in the framework of the European FP7 project, SAFECAST. The numerical model was developed within the environment of Abaqus/Standard general purpose finite element software by applying the Concrete Smeared Cracking Model for the modelling of the concrete. To substantiate the analytical approach, three-dimensional nonlinear simulation of the precast pinned beam-to-column connection was utilized. All related parameters and properties with regard to the materials, boundary conditions, interaction properties etc, are duly described. The obtained numerical results demonstrate that the proposed model provides reasonably accurate prediction of the shear resistance of precast RC pinned beam-to-column connections under static, cyclic and monotonic, actions and, thus, it can be an effective tool for further investigation of the response of precast structures.*

1 INTRODUCTION

The major difference between the traditional monolithic cast in-situ R.C. structures and the prefabricated ones is that the latter are composed of various bearing members cast in a different place of origin than their final position in the structure; therefore the structure is composed of a set of "elements" and "connections" between them. One of the main issues that arise in precast construction is related to the behaviour of the connections (shear resistance, ductility, etc), especially when the structure is imposed to seismic actions.

Although considerable research on prefabrication has been reported worldwide (e.g. PRESSS project [1-3], COST C1 Action [4]), the main part of this research has been focused merely on the behaviour of specific types of connections used by the pre-cast construction industry and does not apply directly to the behaviour of common pinned beam-to-column connections, especially under seismic loading. In pre-cast technology, it is mostly (but not exclusively) desirable to design structures (which usually comprise of prestressed horizontal members) with beam-to-column connections that allow rotations.

A pinned beam-to-column connection that usually appears in frame systems hinged at the top and fixed to the foundation is shown in Figure 1. The role of the connection is to ensure the transfer of the vertical and lateral forces from the beams to the columns without allowing flexural moments to develop at the connection. This type of connection is usually provided by one or two (recommended) steel dowels (made of ribbed or threaded bars). From the phase of the production of the columns, steel dowels are foreseen to protrude from the top of each column (or from the upper face of column corbels in case of multi-storey buildings) while at each beam end vertical holes of proper diameter are provided at the corresponding positions. The gap between the beam holes and the dowels is filled by non shrinking grout of high strength.

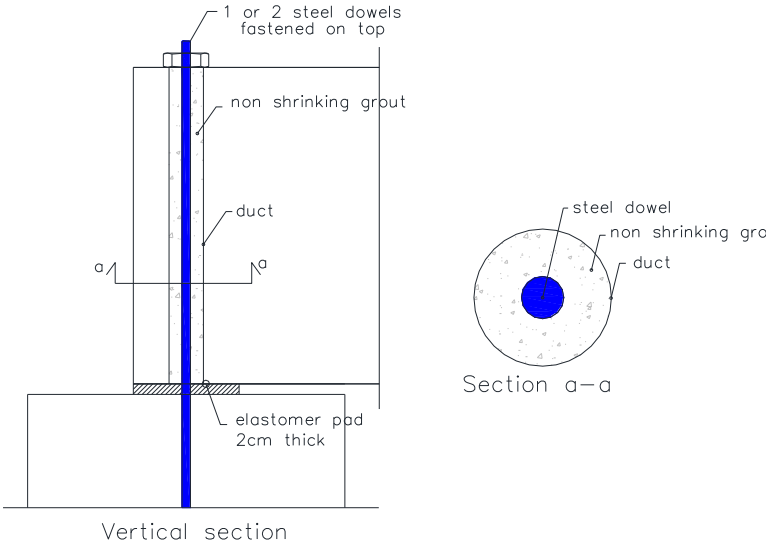


Figure 1: Typical precast pinned beam-to-column connection.

The shear resistance of the connection is controlled by several parameters such as:

- The steel amount and steel grade of the dowels;
- The concrete grade (of the column and/or beam elements);
- The compressive strength of the infill material;
- The thickness of the concrete cover of the dowels;
- The existence or not of confining reinforcement around the dowels.

In the present research, analytical investigation was undertaken with regard to the shear resistance of precast RC pinned beam-to-column connections, provided by steel dowels, under static (monotonic and cyclic) loading. In particular, the main scope of this investigation was the development of a numerical model and its calibration against available experimental data, which were also used to prove the efficiency of the proposed model to provide an analytical prediction of the shear resistance of precast RC pinned beam-to-column connections.

2 EXPERIMENTAL DATA USED

The analytical model described in the following section was calibrated against experimental data that were derived in the framework of the FP7 project "SAFECAST: Performance of innovative mechanical connections in precast building structures under seismic conditions", Research for SME Associations, Grant Agreement number 218417. The tests were conducted at the Laboratory for Earthquake Engineering of the National Technical University of Athens (NTUA), Greece. Description of the performed tests and the obtained results are given in Psycharis and Mouzakis [5], while detailed information on the experimental data can be found in the deliverable 2.5 of SAFECAST [6].

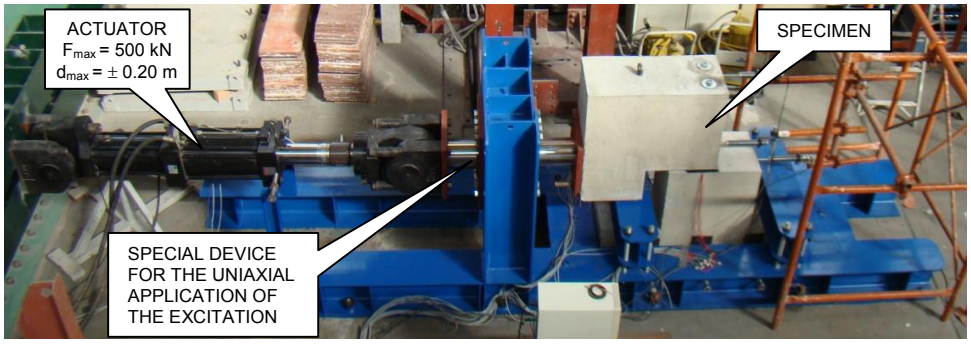


Figure 2: Experimental setup.

The experimental setup is shown in Figure 2. The specimens represented a typical pinned connection of linear precast members and consisted of the end parts of the beam and the column that were connected by steel dowels as shown in Figure 1. The cross section of the column was 0.60 m × 0.40 m and the cross section of the beam was 0.40 m × 0.60 m. For the proper sitting of the beams on the columns, elastomeric (neoprene) pads of 20 mm thickness were used. A mechanism made of two steel plates and four high strength screws was embedded in the rear part of the beam for the fastening with the force application system.

Each specimen was subjected to monotonic or cyclic, displacement-controlled loading, applied at the rear end of the beam, while the column was securely fastened to the strong floor of the Laboratory. The driving force was applied exactly at the level of the joint, while a special device which allowed only uniaxial application of the loading was used, in order to achieve pure shear conditions at the connection.

In total, 22 tests were performed with the experimental investigation being focused on the effect of various parameters including the diameter of the dowels, the number of dowels, the distance of the axis of the dowels from the beam edge in the loading direction and the strength of the grout that is placed in the dowels' ducts. The specimens were tested under monotonic loading in pull and/or push direction and under cyclic excitation up to the failure of the connection, or until the displacement capacity of the hydraulic actuator was reached.

3 NUMERICAL MODEL

3.1 General

Sixteen of the previously described experimental tests were modelled within the environment of ABAQUS software [7], as shown in Figure 3, under the relevant assumptions and properties. Each numerical model was subjected to the same loading history with the corresponding specimen. By comparing the numerical results with the experimental data, the parameters of the numerical model were calibrated and validated.

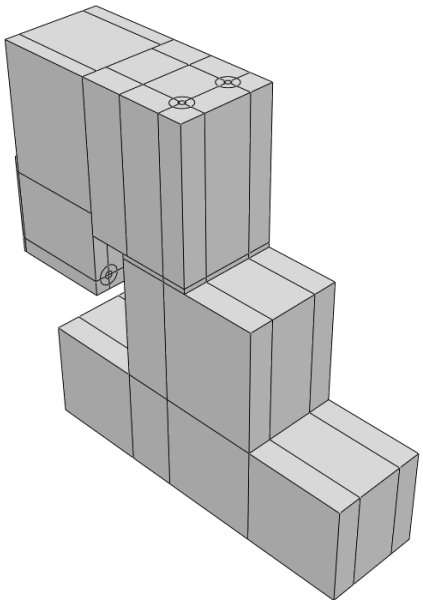


Figure 3: Numerical model of the test specimens.

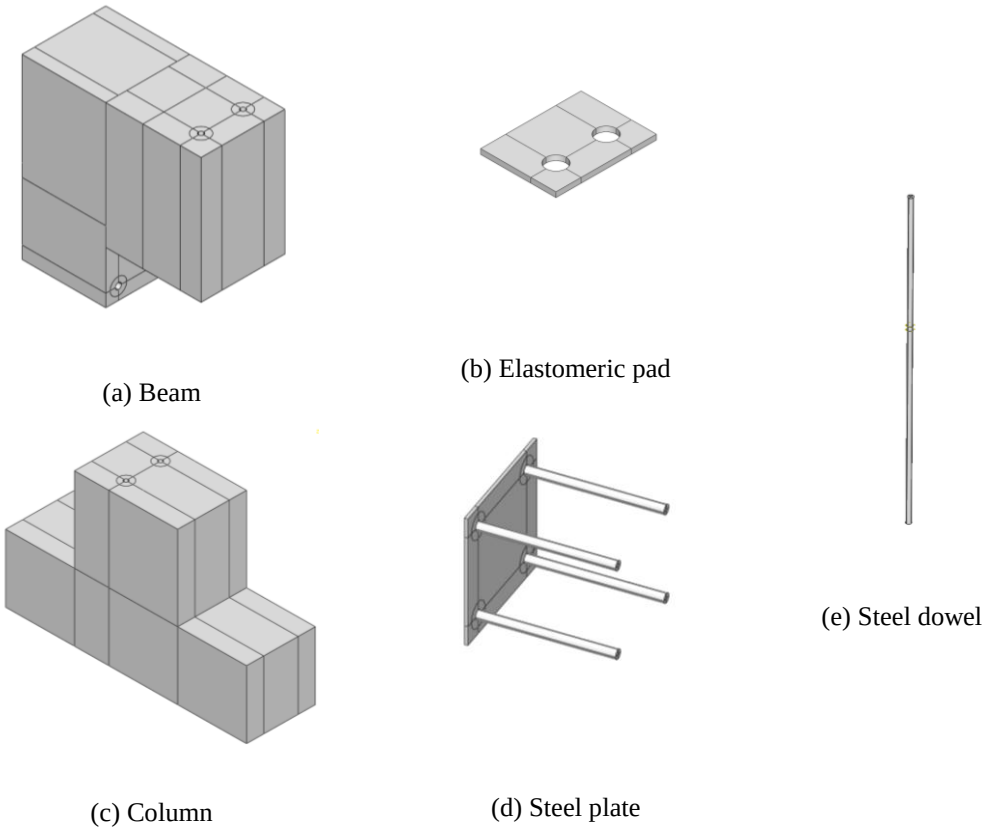
3.2 Model description

All parts of the test specimens were simulated with their exact geometry in the numerical models by 3D solid continuum elements, as shown in Figure 4. Specifically, each model was composed of five parts:

a. the beam;
b. the column;
c. the steel dowels;
d. the elastomeric pad; and
e. the steel plate provided for the application of the imposed loading.

The reinforcements in the concrete parts were not included in the model; however, their effect on the behaviour of the concrete was considered through proper selection of the material properties, as described in the following.

The beam and the column were assumed made of concrete material. The peak unconfined compressive strength was taken equal to 34 MPa according to the attained strengths during the experimental tests. The Poisson modulus was taken equal to 0.20 and the Young's modulus was taken equal to 31 GPa. As mentioned above, the reinforcement bars were not included in the model in order to facilitate the analysis process. However, the contribution of the reinforcement to the behaviour of the concrete was taken into account by considering characteristics of confined concrete. Specifically, the Chang & Mander [8] stress-strain relationship for confined concrete was used.



(a) Beam (b) Elastomeric pad (c) Column (d) Steel plate (e) Steel dowel

Figure 4: Parts considered in each numerical model.

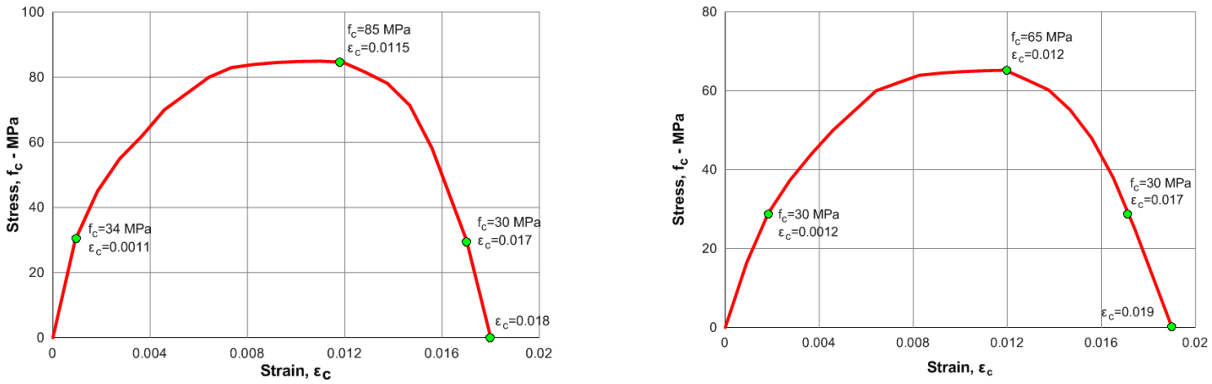
The nonlinear behaviour of the concrete material was modelled using the Concrete Smeared Cracking Model of ABAQUS. The post-cracking behaviour of the concrete was taken into account using the tension stiffening displacement parameter of ABAQUS with a value of u_0 = 0.1 mm.

Different material was used for the infill grout that was placed around the dowels on the beam side, to fill the gap with the ducts. The peak unconfined compressive strength of the grout was taken equal to 23 MPa, according to the attained strengths during the experimental tests. Its behaviour was also based on the Chang & Mander model for confined concrete. The Poisson modulus was taken equal to 0.20 and the Young's modulus was taken equal to 26 GPa. For the grout, the nonlinear behaviour was also approached using the Concrete Smeared Cracking Model of ABAQUS and the post-cracking behaviour was taken into account by the tension stiffening displacement parameter with u_0 = 0.1 mm.

In Figure 5, the stress-strain relationships that were considered for the concrete and the in-fill grout are shown.

The Plastic Model of ABAQUS was used for the steel dowels of the connection, with the same stress-strain relationship with the experimental data. The yield strength was about 580 MPa and the ultimate strength was 700 MPa. The Poisson modulus was taken equal to 0.15 and the Young's modulus was set equal to 200 GPa.

The elastomeric pad was considered to behave elastically. The Elastic model of ABAQUS for isotropic materials was used with Poisson ratio equal to 0.20 and Young's modulus equal to 1.7 MPa.



(a) (b)

Figure 5: Stres-strain relationship of: (a) concrete material; (b) grout material.

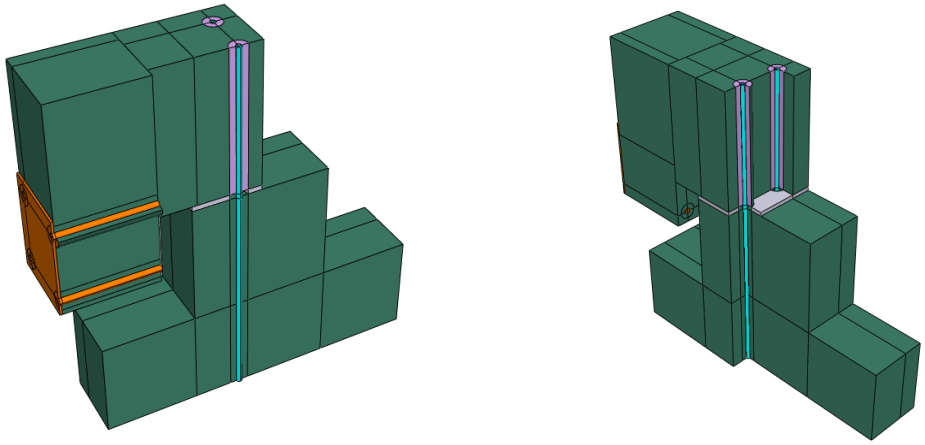


Figure 6: Overview of the model with indication of the various materials applied.

Elastic behaviour was also assigned to the steel plate that was provided at the back end of the beam, which was used for the application of the loading. In this case, the Poisson ratio was considered equal to 0.15 and the Young's modulus equal to 200 GPa.

In Figure 6, an overview of the model is given, with each material shown with different colour.

3.3 Dowel – concrete interaction

At the interface between the dowels and the surrounding infill grout at the beam side and at the interface between the dowels and the surrounding concrete at the column side, the following interaction properties were assigned in the tangential and the normal (to the longitudinal axis of the dowel) directions: in the normal direction, hard contact with allowed separation was assigned, while in the tangential direction a friction coefficient of 0.60 was considered. In Figure 7, the interaction between dowels and grout is given schematically.

3.4 Boundary conditions

The model was considered fully fixed at the bottom of the column. The vertical motion at the back end of the beam was restrained, since this motion was not allowed in the experiments. In Figure 8, the applied boundary conditions are presented schematically.

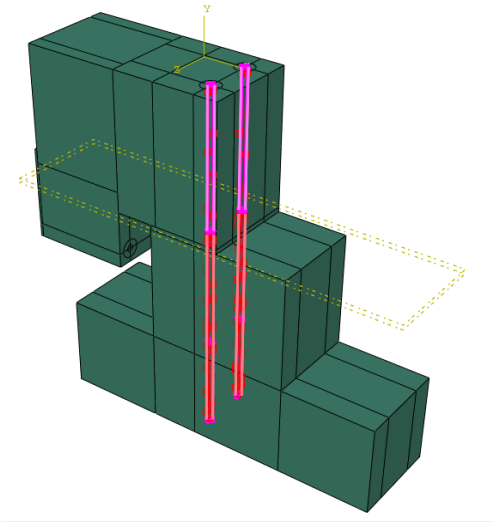


Figure 7: Interaction between dowels, grout infill and concrete.

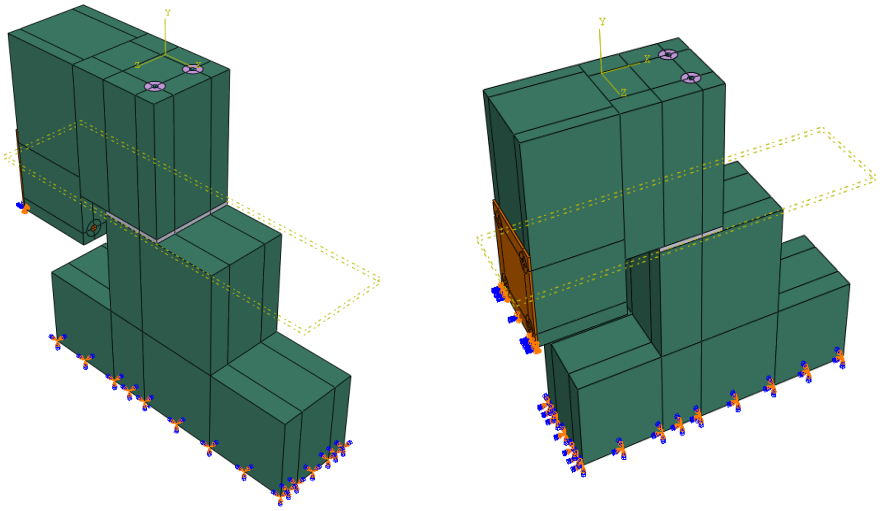


Figure 8: Boundary conditions of the numerical model.

3.5 Loading protocol

For each experimental test, a model was developed for the corresponding characteristics of the connection (number and diameter of the dowels, concrete cover etc). Then monotonic or cyclic loading was applied, similarly to the corresponding experiment. The loading was applied to the steel plate at the back end of the beam as shown in Figure 9.

For cyclic loading, the protocol that was followed during the experiments was also applied to the numerical models (Figure 10). Specifically, three cycles were performed at each displacement level, which was increasing in steps of d_y, with d_y being the yield displacement. In some tests, a smaller step, equal to $0.5 \cdot d_y$, was used during the first stages of the loading procedure. The yield displacement was determined from the point of bend of the force-displacement curve for monotonic pull or monotonic push loading. In cases in which the value of d_y was different in the pull and in the push direction, the minimum value was considered.

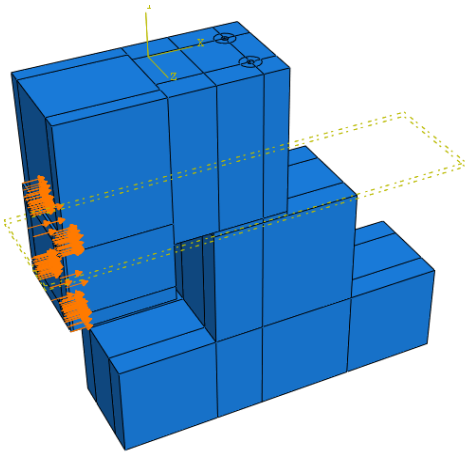


Figure 9: Application of loading to the numerical model.

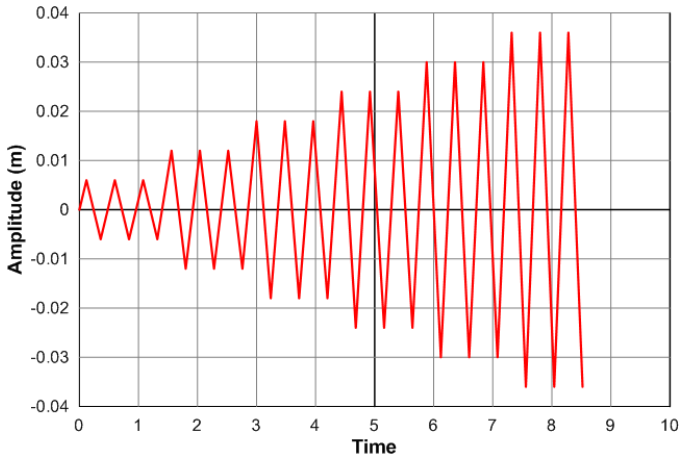


Figure 10: Protocol used for cyclic loading.

3.6 Finite element mesh

The model was meshed using the structured and the free meshing technique of ABAQUS. The structured technique was applied for the meshing of the dowels and the infill grout, where extra numerical accuracy was needed during the analysis. The free meshing technique was used for all other parts of the model. The dowels and the infill grout were modelled by C3D8R elements (8-node linear bricks with reduced integration) while all other parts were modelled by C3D4 elements (4-node linear tetrahedrons).

In total the model was composed of 3.815 nodes, 11.345 elements and 10.629 degrees of freedom. In Figure 11 the generated mesh of the model is shown.

4 NUMERICAL RESULTS - COMPARISONS WITH EXPERIMENTAL DATA

Sixteen of the connections that were tested experimentally at the laboratory were modelled numerically for the corresponding geometry. The numerically reproduced experiments concerned connections with one or two dowels, with dowels of different cross section (∅16, ∅25 or ∅32 mm) and with varying concrete cover (10, 15 or 20 mm). Different types of loading were also applied: monotonic push, monotonic pull or cyclic. Indicative snapshots of the deformed shape of the numerical models are shown in Figure 12.

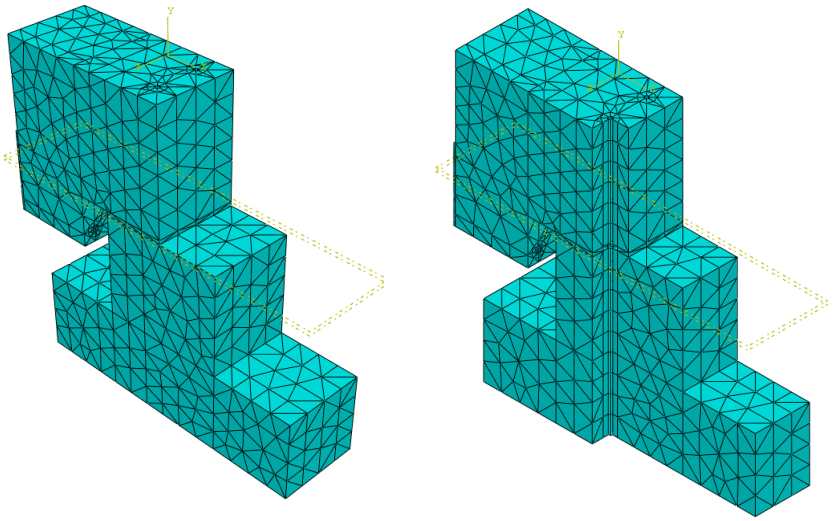
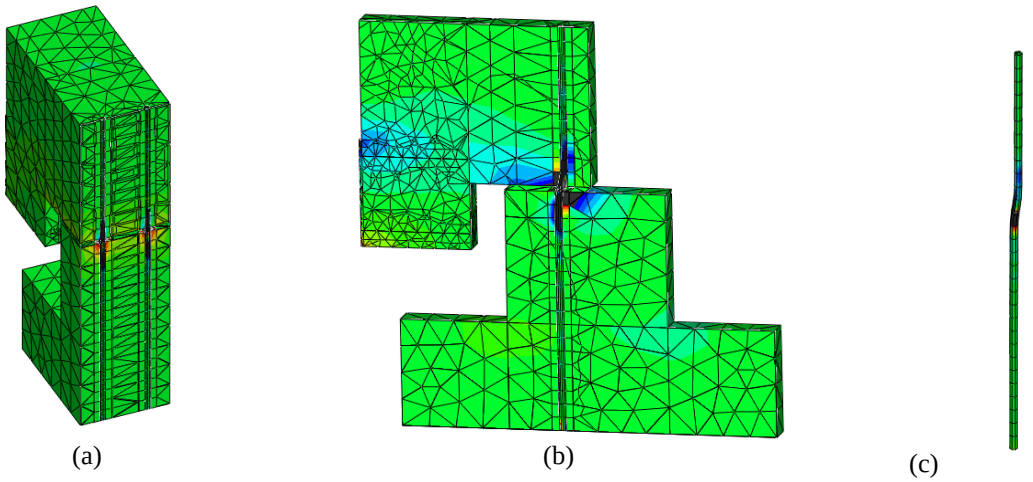


Figure 11: Generated mesh of the model.



(a) (b) (c)

Figure 12: Snapshots of the deformed shape of the model: (a) transverse section; (b) longitudinal section; (c) steel dowel.

For each model and for each loading pattern, the force-displacement relation was calculated and compared with the recorded force-displacement diagram during the corresponding experiment. The results are presented in figures 13 and 14 for monotonic and cyclic loading, respectively. It is seen that the numerical models can predict very well the real response, except of the cases involving large displacements in the pull direction. This discrepancy is due to the severe damage that occurred to the cover concrete of the dowels in such cases, which cannot be captured by the numerical model. In all other cases, however, the numerical analysis predicted quite accurately the response: the yield points were accurately calculated, the slope of the curves was right and the hysteretic loops were estimated with satisfactory accuracy.

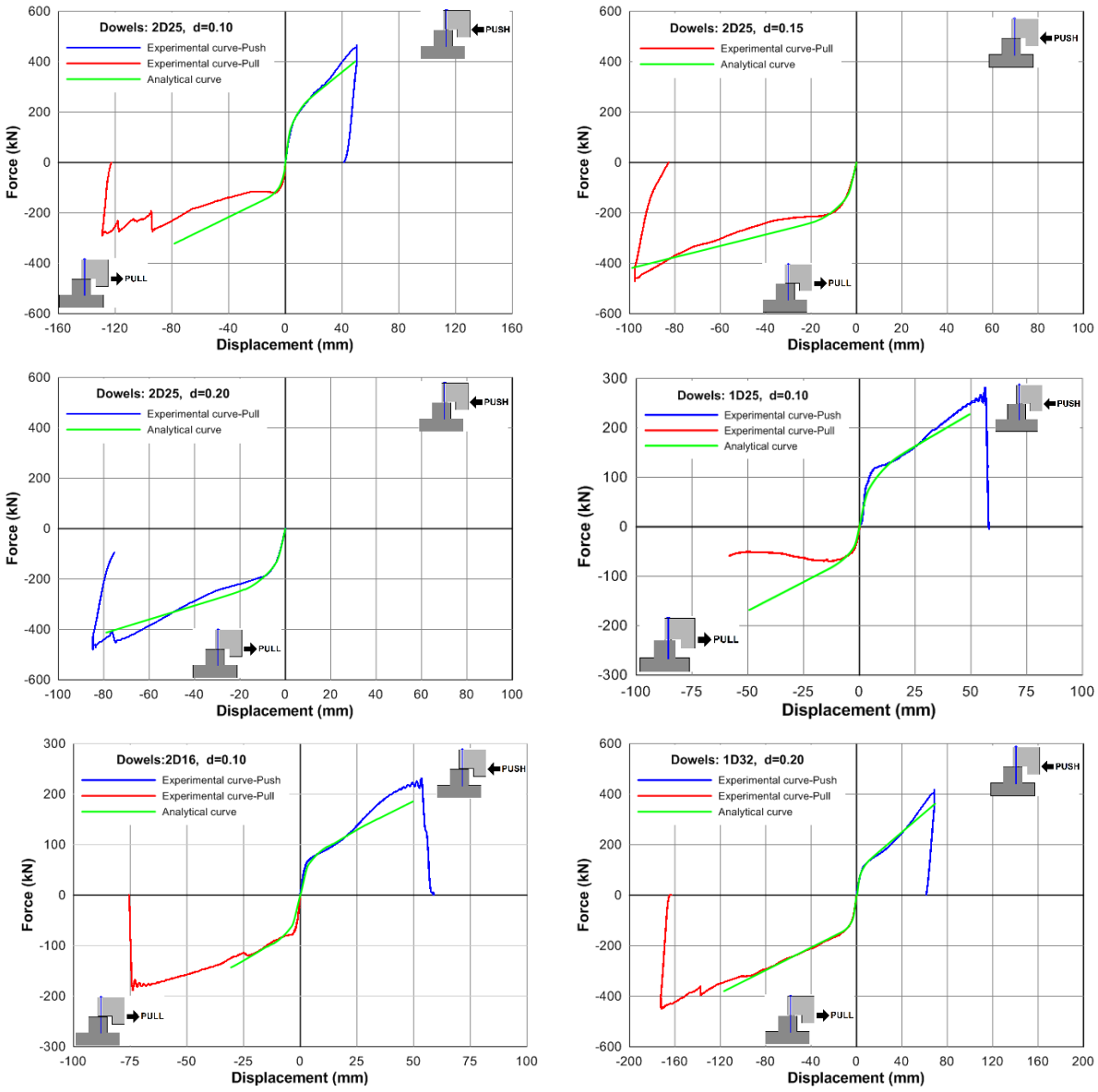


Figure 13: Comparison of analytical force-displacement diagrams with experimental data for monotonic loading.

The validation of the numerical analysis allows its use for the calculation of other quantities that were not measured during the experiments. For example, in Figure 15 characteristic stress diagrams along the infill grout are shown for two instances: when yielding of the connection occurs and at the maximum displacement at the end of the analysis. In these diagrams, "grout back" and "grout front" refer to the position of the considered side of the grout in relation to the direction of the loading. Similarly, in Figure 16, the stress distribution along the steel dowel is presented at yielding and at the end of the analysis.

It should be noted that the end of the analysis does not necessarily coincide with the failure of the connection. In some cases, especially for cyclic loading, the analysis stopped before the failure of the connection due to convergence problems that arose.

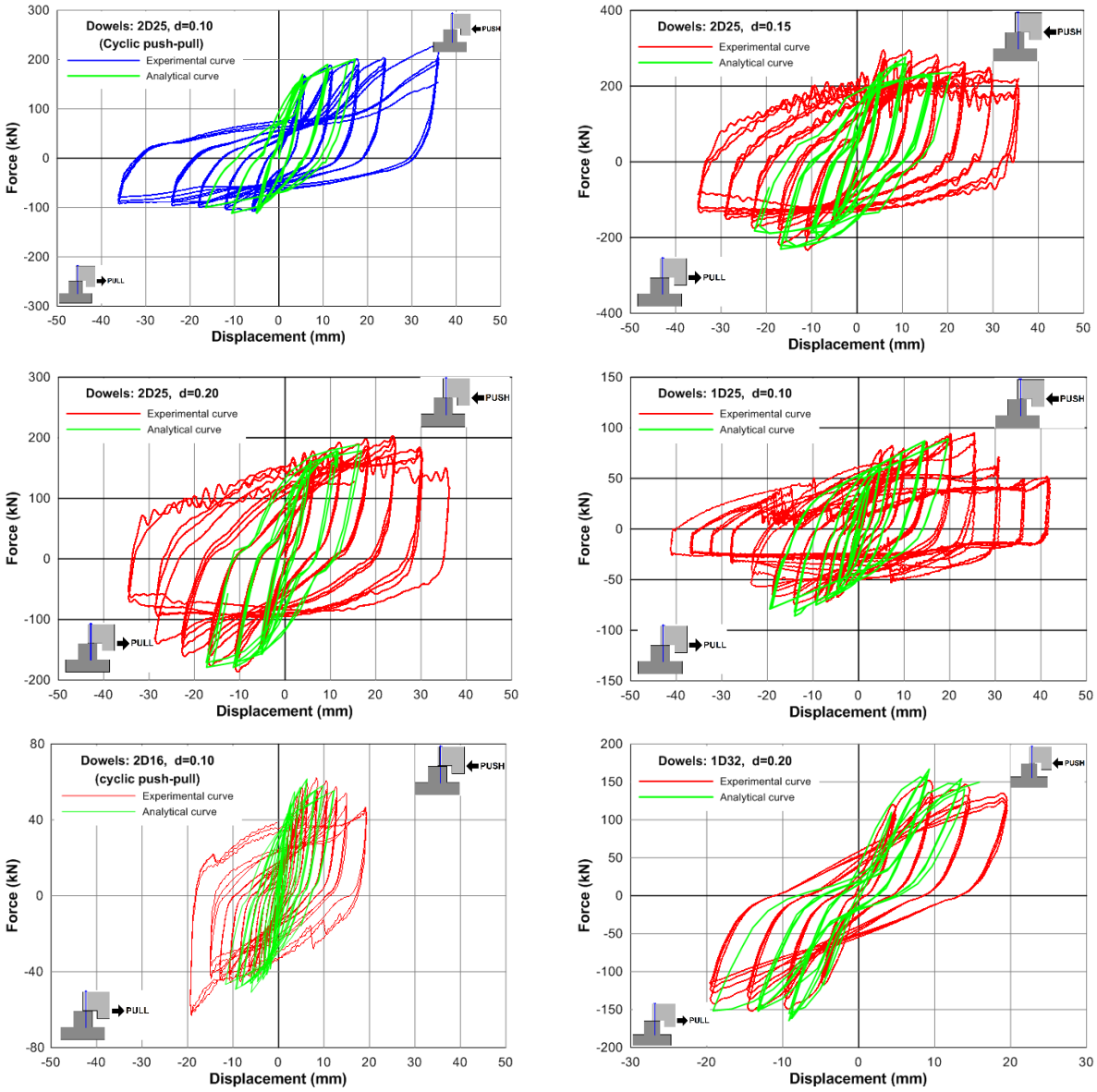
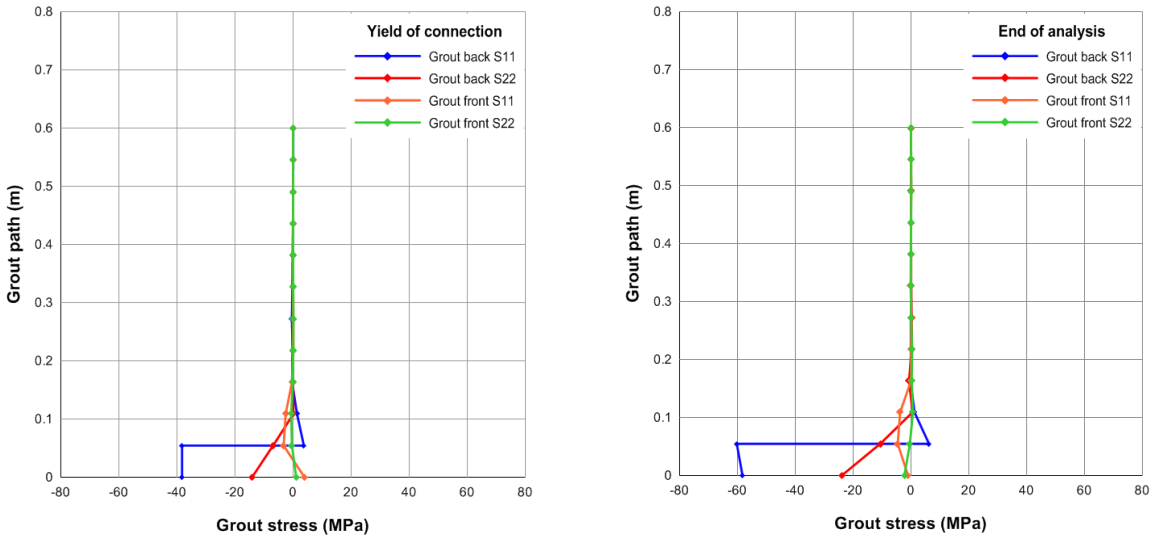


Figure 14: Comparison of analytical force-displacement diagrams with experimental data for cyclic loading.

5 CONCLUSIONS

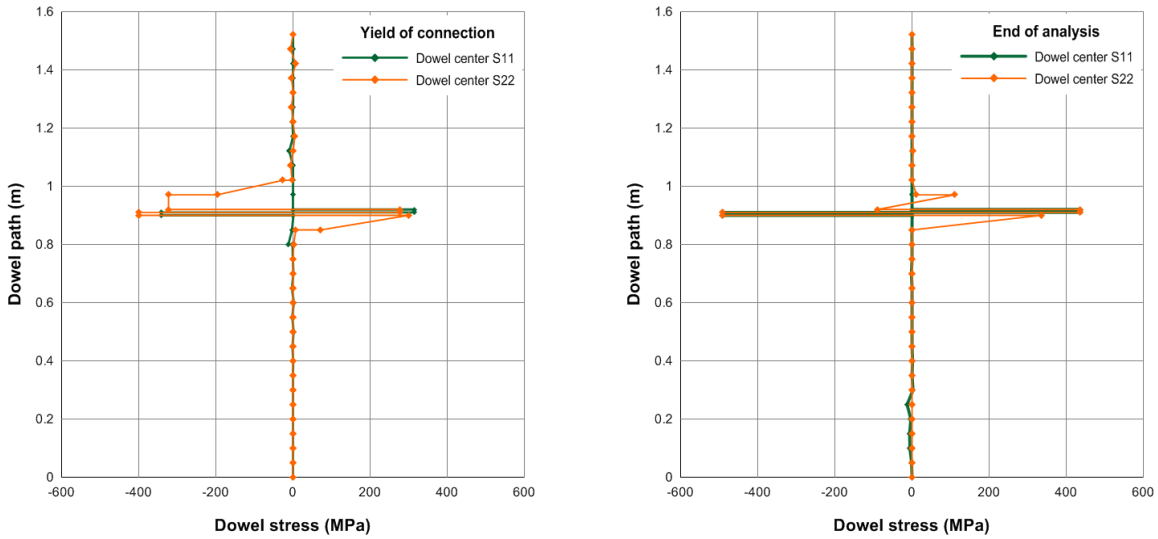
The three-dimensional numerical models that were developed using ABAQUS for the nonlinear analysis of the shear behaviour of precast RC pinned beam-to-column connections provide reasonably accurate results compared with experimental data for static loading (cyclic and monotonic). Therefore, such models can be used for the in-depth analytical investigation of the response of precast structures, beyond the experimental investigation.

Nevertheless, in some cases and especially for cyclic loading, the analysis stopped prior to the failure of the connection. This is attributed to the fact that the reinforcement bars were not modelled explicitly and thus, the deformability of the connection was limited. Although the contribution of the reinforcements was taken into account by applying characteristics of confined concrete to the beam and the column, convergence issues arose that interrupted the completion of the analysis before the failure of the connection.



(a) (b)

Figure 15: Characteristic stress diagrams along the infill grout: (a) at the yielding of the connection; (b) at the end of the analysis.



(a) (b)

Figure 16: Characteristic stress diagrams along the dowel: (a) at the yielding of the connection; (b) at the end of the analysis.

During the calibration of the numerical models it was found that the accuracy of the analysis is significantly affected by:

- The proper modelling of the behaviour of the concrete and the grout material. The Concrete Smeared Cracking Model of ABAQUS was found to be very effective.
- The correct modelling of the interaction properties between the dowel and the surrounding concrete or grout.

The conclusions that can be drawn from the numerical analyses are:

- The critical stresses that define the shear resistance of the connection develop in the dowels and the infill grout that surrounds them.

- The critical section of the dowel, where a plastic hinge develops, is located close to the joint in depth of about 10 cm.
- In the infill grout, large stresses develop up to depth of about 20 cm from the connection joint under monotonic loading, and up to about 30 cm under cyclic loading. In both cases, the lower 5 cm of the grout are imposed to very large stresses.
- By increasing the concrete cover of the dowels, the developed stresses evolve in smaller depth at the concrete and infill grout.
- Confinement reinforcement is recommended to be placed at the lower part of the beam and at the higher part of the column, as close as possible to the joint and close to the location where the plastic hinge of the dowel develops.

REFERENCES

[1] M. J. N. Priestley, The PRESSS program – Current status and proposed plans for phase III. *PCI Journal*, **41** (2): 22-40, 1996.

[2] H. F. Stanton, The PRESSS program in the USA and Japan – Seismic testing of precast concrete structures. *Proceedings of the COST C1 International Conference on Control of the Semi-rigid Behaviour of Civil Engineering Structural Connections*, Liege, 13-24, 1998.

[3] H. Shiohara, F. Watanabe, The Japan PRESS precast concrete connection design. *Proceedings f the 12th WCEE*, Aukland, 2000.

[4] COST C1, Control of the semi-rigid behaviour of civil engineering structural connections. *Final Report European Commission EUR 19244*, November 1999.

[5] I. N. Psycharis and H. P. Mouzakis, Shear resistance of pinned connections of precast members to monotonic and cyclic loading. *Engineering Structures*, Vol. 41, pp. 413–427, 2012.

[6] SAFECAST, Card files of the different types of connections with the performance data for seismic design – *Deliverable 2.5. FP7 Project No. 218417*; 2012.

[7] ABAQUS Inc., *Abaqus/Standard Users' Manual*, U.S.A., 2004

[8] G. A. Chang, J. B. Mander, Seismic energy based fatigue damage analysis of bridge columns: Part I — evaluation of seismic capacity. *NCEER Technical Report No. NCEER–94–0006*, State University of New York, Buffalo, New York, 1994.

COMPDYN 2013
4th ECCOMAS Thematic Conference on
Computational Methods in Structural Dynamics and Earthquake Engineering
M. Papadrakakis, V. Papadopoulos, V. Plevris (eds.)
Kos Island, Greece, 12–14 June 2013

SEISMIC BEHAVIOUR OF THE BEAM-TO-COLUMN DOWEL CONNECTIONS: FEM ANALYSIS

Blaz Zoubek[1], Matej Fischinger[2], Tatjana Isakovic[3]

[1]University of Ljubljana, Faculty of Civil and Geodetic Engineering
Jamova 2, 1000 Ljubljana, Slovenia
e-mail: blaz.zoubek@fgg.uni-lj.si

[2,3] University of Ljubljana, Faculty of Civil and Geodetic Engineering
Jamova 2, 1000 Ljubljana, Slovenia
{matej.fischinger, tatjana.isakovic}@ fgg.uni-lj.si

Keywords: Seismic behavior, precast industrial buildings, dowel connection, FE model

Abstract. *To analyze the failure mechanism of the typical precast beam-to-column dowel connection, the numerical model in the FEA software ABAQUS [8] was defined and calibrated using the results of the experimental investigations. Cyclic as well as monotonic response was analyzed. The most important observations are: 1) standard theory assuming that the failure mechanism is initiated by flexural yielding of the dowel and crushing of the surrounding concrete has been confirmed [5-7]; 2) the strength of the connection considerably depends on the depth of the plastic hinge in the dowel, 3) in the case of the cyclic loading the strength is reduced due to the smaller depth of the plastic hinge, 4) neoprene bearing pad can considerably increase the strength of the connection, particularly when large relative displacements between the beam and the column are developed. The proposed FEM based tool supports additional parametric studies and the analysis of the buildings damaged in the recent European earthquakes.*

1 INTRODUCTION

Although the dowel type of the connection is the most common in Europe, the knowledge about its seismic behavior was incomplete and poorly understood. The connections were investigated only on simplified models where many important structural components were neglected. The lack of knowledge reflected in the seismic codes and in particular in the design practice. When the capacity design had become mandatory it became obvious that the existing knowledge about the behavior of realistic dowel connections was insufficient. The recent experimental research [1, 2, 3] on realistic connections provided more empirical data, however the mechanisms of failure have still not been adequately explained. For this reason a FEA model and a macro model supported by the FEA model were developed. In this article, the FEA model is presented while the macro model is described in companion article - Seismic Behavior of the Beam-to-Column Dowel Connections: Macro Modeling [4].

2 PREVIOUS STUDIES OF THE DOWEL FAILURE MECHANISM

Behavior of the precast beam-to-column connections analyzed in this paper is mainly characterized by the dowel action mechanism for which simplified numerical models assuming idealized conditions have already been developed in some previous studies [5-7].

If the dowel is located relatively far from the edges of the connected beam and column (the distance from the edge is more than six diameters of the dowel), it can be assumed that the strength of the dowel is reached at simultaneous yielding of the dowel and crushing of the surrounding concrete (see Fig. 1).

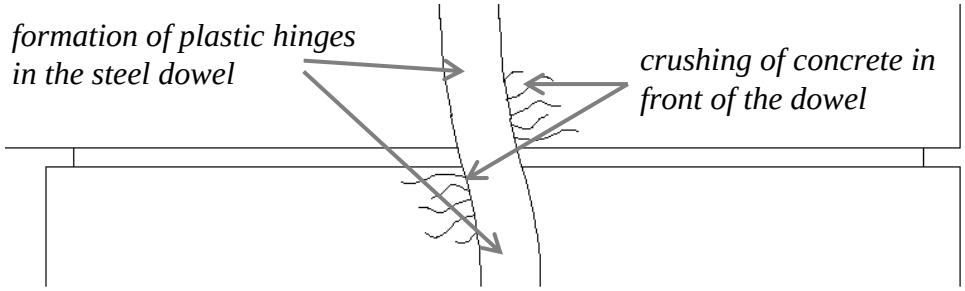


Figure 1: Failure mode of the dowel mechanism

If the concrete compressive strength, the steel yield strength and the diameter of the dowel are known, the following expression, according to [6, 7], can be used to analytically evaluate the ultimate resistance of the dowel connection at monotonic loading:

$$R_{u,m} = F_{u,m} = 1.3 \cdot {d_b}^2 \cdot \sqrt{f_{cc} \cdot f_y} = Fu, \quad (1)$$

$f_{cc}\ [MPa]$ … *uniaxial compressive strength of concrete*

$f_y\ [MPa]$ … *yield strength of steel*

Expression (1) is appropriate only for monotonic loading. In the case of cyclic loading, the capacity of the connection is notably lower due to the cyclic degradation of concrete and steel. In [6] the following formula is proposed to account for the decrease of the dowel ultimate resistance in the case of cyclic loading:

$$R_{u,c} = 0.5 \cdot R_{u,m} = 0.65 \cdot {d_b}^2 \cdot \sqrt{f_{cc} \cdot f_y}, \quad (2)$$

Based on the results of the experiments performed in the frame of the SAFECAST project (see [1, 2] and Section 3), a modified formulas have been proposed, which account for cyclic behavior of the realistic beam-to-column dowel connections:

$$R_{u,sr} = 1.1 \cdot {d_b}^2 \cdot \sqrt{f_{cc} \cdot f_y}, \tag{3}$$

$$R_{u,lr} = 0.9 \cdot {d_b}^2 \cdot \sqrt{f_{cc} \cdot f_y}, \tag{4}$$

$R_{u,sr}$ *... ultimate resistance of the connection if small rotations between beam and column are expected*
$R_{u,lr}$ *... ultimate resistance of the connection if large rotations between beam and column are expected*

It should be noted that the expressions (3) and (4) predict substantially higher resistance than formula (2). However, expressions (3) and (4) are predominantly empirical and no detailed analysis of the failure mechanism leading to this result was done within the SAFECAST project. Therefore the understanding of the behavior was incomplete and consequently the generalization of the formula to the cases not tested within the project was complex.

3 EXPERIMENTS

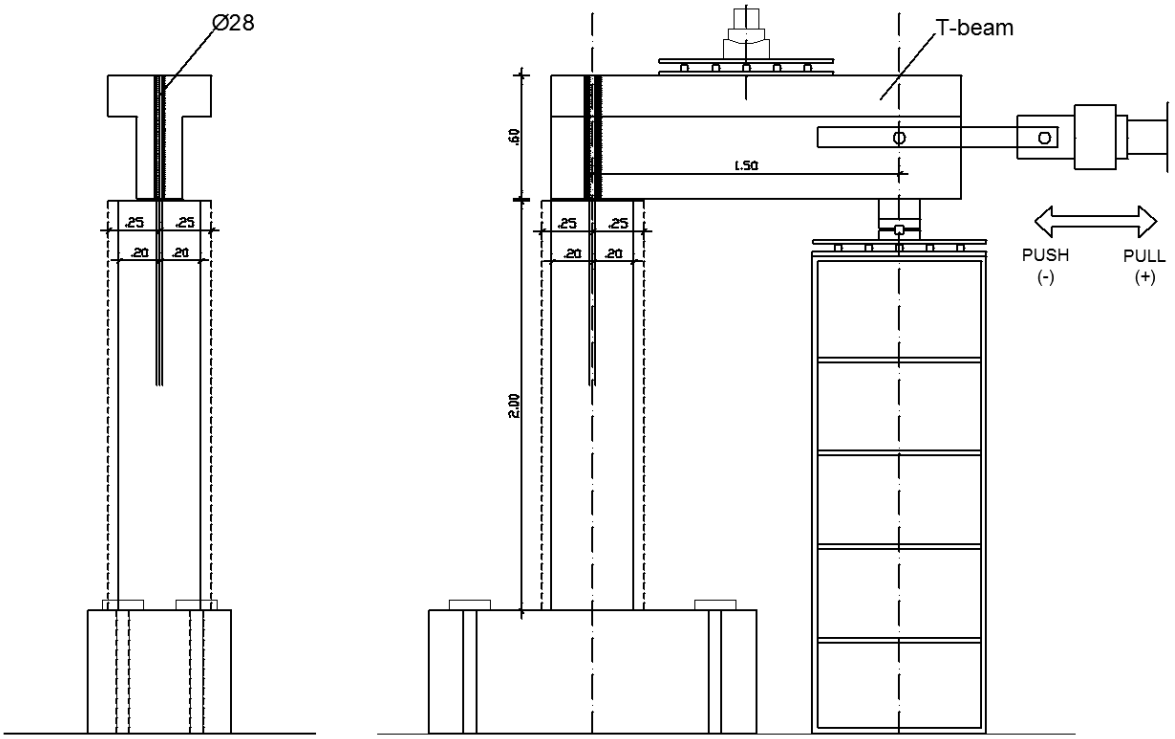


Figure 2: Scheme of the experimental set up.

The test set-up is shown in Fig. 2. The column was fixed to the ground through a special foundation, which was anchored to the laboratory floor. On the opposite side the beam was supported by a roller bearing, which allowed its horizontal movement. A vertical load was applied at the mid-span of the beam by means of a vertical hydraulic jack. The magnitude of the vertical load was 100 kN in all cases. The horizontal force was applied in the direction of the beam by means of another hydraulic actuator, attached to the reaction steel frame.

Vertical steel dowel of diameter Φ = 28 mm was located at the centre of the column cross-section. The dowel was anchored deep into the body of the column (90 cm) and protruded into

the steel socket within the beam. The empty space between the dowel and the socket was filled with a fine non-shrinking grout (f_{ck} =15 - 20MPa). The neoprene pad (the thickness was 10 mm) was placed between the column and the beam in order to enable the relative rotations between the elements.

The T-shape beams were 60 cm high and 22/50 cm wide. At the location of the connection they were provided with a steel tube (80/50/2 mm) which was surrounded by a number of horizontal U-shape stirrups (Φ10/10 cm). The purpose of these stirrups was to partly confine the dowel and first of all to provide resistance against the splitting of the beam. For this reason, two additional stirrups of larger diameter (Φ14) were applied at the bottom of the beam. Similarly, the hoops in the beam (perpendicular to these stirrups) were closely spaced (Φ8/5 cm) within the location of the connection at a distance of 50 cm from the edge of a beam.

The columns had a square section (50x50cm). They were 2 meters high and therefore very stiff (small displacements of the column were expected). The confinement at the top of the column was substantial (Φ10/4 cm).

4 NUMERICAL MODEL

The specimen presented in Figures 3 and 4 was modeled using Abaqus FEA software [8]. The following structural components were included into the model: dowel, beam, column, infill, steel tube and neoprene bearing pad (Fig. 3). Modeling of each component is described in section 4.2.

To adequately simulate the experimentally observed response it was particularly important to properly model the connections between structural components listed above. Three different contacts were identified: dowel-to-concrete contact, dowel-to-grout contact and neoprene-to-concrete contact (Fig. 3). Modeling of the contacts is explained in detail in section 4.1.

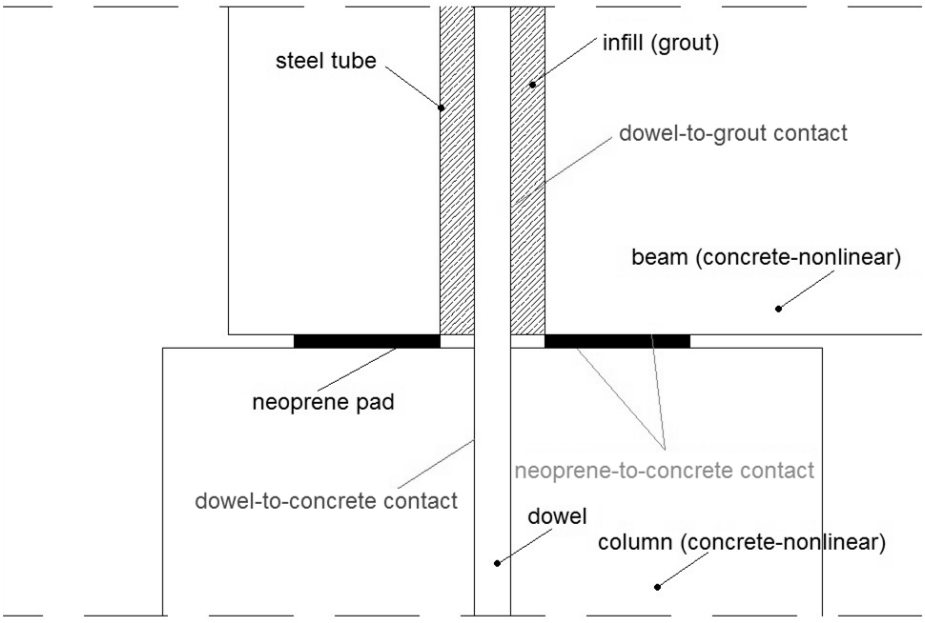


Figure 3: Close-up of the connection: presentation of the contact and material assignments

4.1 INTERACTION BETWEEN THE COMPONENTS OF THE CONNECTION

The contact properties were defined in two orthogonal directions. Hard contact with allowed separation was chosen normal to the surface of the dowel and the concrete. As it was

observed during the experiment, the concrete around the dowel at the top of the column crushed and a crater-like void was formed around the dowel. This loss of the contact between the dowel and the concrete was properly modeled allowing their separation.

The tests described in section 3 showed no pull-out of the dowel. Nevertheless, tangential behavior was described with friction coefficient of 0.8 to simulate bond between the dowel and the concrete.

As long as the rubber pad is exposed to the normal pressure, there is a friction between the concrete and the pad activated, and the neoprene pad contributes to the shear resistance of the whole connection between the beam and the column. The interaction between the neoprene and the concrete surface was defined as a hard contact in normal direction and with a friction coefficient of 0.5 [9] in the tangential direction.

By assuming a totally rigid connection between the reinforcement and the surrounding concrete the slip of the reinforcement is neglected. For reinforcement, embedded elements were used to model total fixity to the surrounding concrete.

4.2 MATERIALS AND TYPES OF ELEMENTS

Material “concrete” as defined in Abaqus [8] was assigned to the beam and column. Material grout was assigned to the infill between the dowel and the steel tube. For the stress-strain relationship of concrete and grout Park & Kent model was used [10]. Nonlinearity of concrete was modeled by approaches based on the concepts of plasticity and damage by using Concrete Plasticity Damage Model (CPDM) included in ABAQUS [8]. All three parts (the beam, the column and the infill) were modeled with standard solid continuum elements with reduced integration C3D8R (an 8-node linear brick).

For modeling steel classical metal plasticity model (included in ABAQUS) with combined isotropic hardening, which uses Misses yield surfaces, was used. Stress and strain values were obtained from uniaxial tension test. The dowel was modeled with standard solid continuum elements with reduced integration C3D8R. For the reinforcement, 2-node linear 3D truss elements were used.

Because no tests have been performed to obtain the stress-strain diagram of the steel tube, bilinear response with maximum strength of 250 MPa and maximum deformation of 10% has been considered.

Neoprene bearing pad was modeled as an ideally elastic material with elastic modulus E=3MPa and Possion's ratio ν=0.49. Standard solid continuum elements with reduced integration C3D8R were used.

5 COMPARISON OF THE EXPERIMENTAL AND NUMERICAL RESULTS

In this section the efficiency of the proposed numerical model is demonstrated. The numerical results obtained by ABAQUS are compared with the test data. Good match with the experimental results was achieved on the global level as well as in all significant details. The comparison of the numerical and experimental relation between the horizontal force F_h in the actuator and the relative displacement between the beam and the column u_r is presented in Fig. 4.

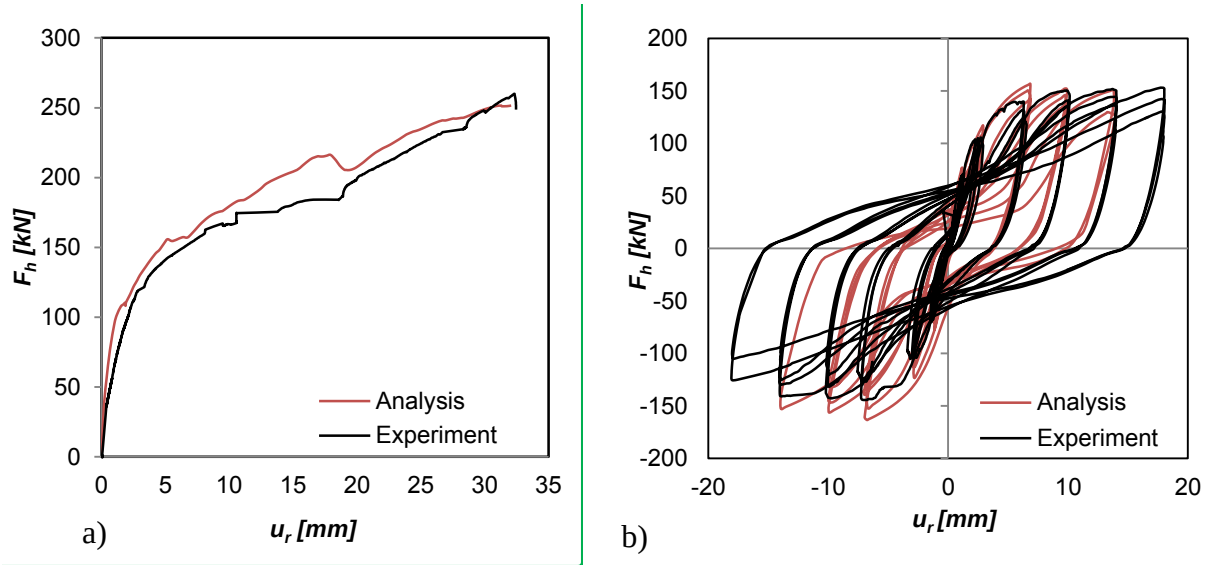


Fig. 4: (a) Global response (horizontal force –relative displacement): Comparison of the experiment and the analysis (a) for monotonic loading and (b) for cyclic loading.

The analysis successfully reproduced the mechanism observed during the test (Fig. 5(a)). First, the yielding of the dowel was observed, corresponding to the displacement of approximately 3 mm. Simultaneously the concrete around the dowel crushed allowing the dowel to develop large plastic deformation. The numerical model also captured well the experimentally observed cyclic strength deterioration (Fig. 5(b)).

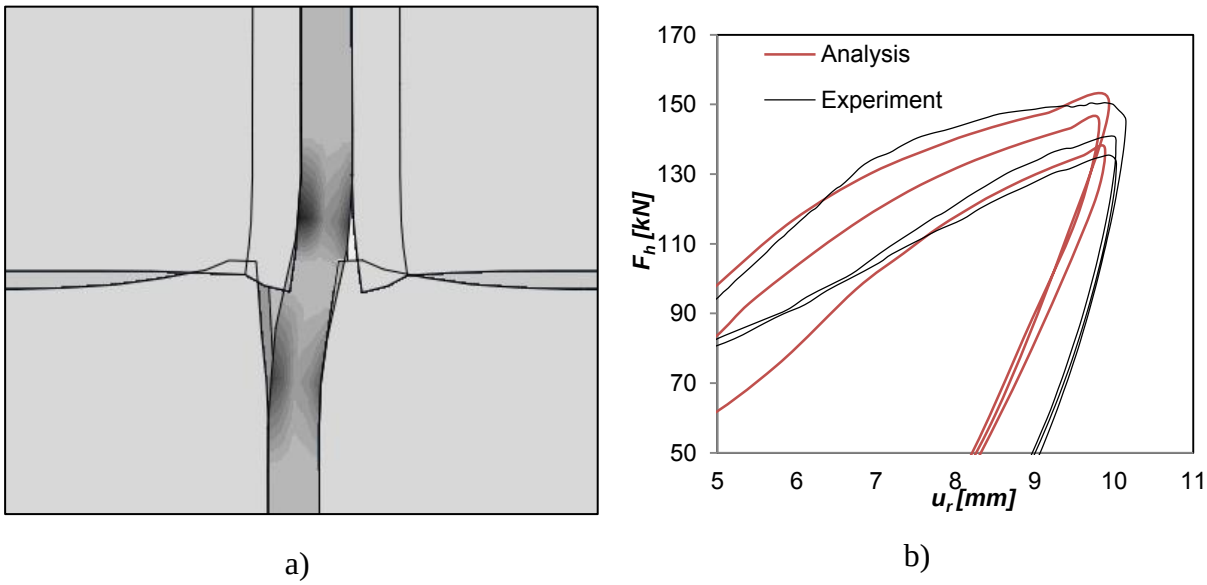


Fig. 5: (a) Failure of the dowel as predicted by the numerical analysis. (b) Experimentally observed cyclic deterioration was successfully captured by the model

The strain hardening in the case of monotonic loading (Fig. 4(a)) after the displacement of 20 mm was contributed by the neoprene pad, and the total strength of 250 kN was observed in the experimental as well as in the analytical response.

In the case of the cyclic response no hardening (typical for the monotonic response – Fig. 4(b)) was observed, neither in the analysis nor in the experiment. This was because of the

smaller contributions (10% of the total force) of the elastomer to the total shear strength due to smaller relative displacements between the beam and the column. Additionally, the depth of the plastic hinge was smaller than in the case of monotonic loading, therefore smaller strength was obtained. Consequently the final difference of the monotonic and cyclic resistance was about 40%.

6 CONCLUSION

The research presented in this paper has provided a numerical tool, based on the ABAQUS FEA software, which is able to describe the characteristics of inelastic seismic behavior of dowel connections on the global and component level. Comparisons with experimental results obtained with monotonic and cyclic tests on realistic connections demonstrated the soundness and efficiency of the proposed model. Considering the complexity of the problem the match of the results is very good. The model was able to explain the failure mechanism as well as the most important features of the monotonic and cyclic response on the component level. It therefore helped to develop a less computationally demanding macro model presented in the accompanying paper - Seismic Behavior of the Beam-to-Column Dowel Connections: Macro Modeling [4].

7 ACKNOWLEDGEMENTS

The presented research was supported by the SAFECAST project “Performance of Innovative Mechanical Connections in Precast Building Structures under Seismic Conditions” (Grant agreement no. 218417-2) in the framework of the Seventh Framework Programme (FP7) of the European Commission. Experiments were completed at the Slovenian National Building and Civil Engineering Institute (ZAG). The specimens were constructed at Primorje d.d. company.

REFERENCES

[1] SAFECAST Performance of Innovative Mechanical Connections in Precast Building Structures under Seismic Conditions. http://www.safecastproject.eu/, 2012.

[2] I.N. Psycharis, H.P. Mouzakis, Shear resistance of pinned connections of precast members to monotonic and cyclic loading, Eng. Struct., **41**: 413-427, 2012.

[3] M. Fischinger, B. Zoubek, M. Kramar, T. Isakovic, Cyclic Response of Dowel Connections in Precast Structures. *15th World Conference on Earthquake Engineering*, Portugal, Lisbon, 24-28th September, 2012.

[4] B., Zoubek, M., Fischinger, T., Isakovic, Seismic Behaviour of the Beam-to-Column Dowel Connections: Macro Modeling, International Conference on Computational Dynamics and Earthquake Engineering –COMPDYN 2013

[5] H. Dulascska, Dowel action of reinforcement crossing cracks in concrete, *J. ACI,* **69-70**:754-757, 1972.

[6] E.N. Vintzeleou, T.P. Tassios, Behaviour of Dowels under Cyclic Deformations, *ACI Struct. J.*, **84(1)**: 18-30, 1987.

[7] E.N. Vintzeleou, T.P. Tassios, Mathematical model for dowel action under monotonic and cyclic conditions, *Mag. Concr. Res.*, **38**: 13-22, 1986.

[8] ABAQUS Theory Manual, version 6.11-3, Dassault Systèmes, 2011.

[9] G. Magliulo, V. Capozzi, G. Fabbrocino, G. Manfredi. Neoprene-concrete friction relationships for seismic assessment of existing precast buildings, *Eng. Struct.*, **33**:532-538, 2010.

[10] D.C. Kent, R. Park. Flexural members with confined concrete, *J. Struct. Div.*, **7**:1969-1990. 1997.

COMPDYN 2013
4th ECCOMAS Thematic Conference on
Computational Methods in Structural Dynamics and Earthquake Engineering
M. Papadrakakis, V. Papadopoulos, V. Plevris (eds.)
Kos Island, Greece, 12–14 June 2013

SEISMIC BEHAVIOUR OF THE BEAM-TO-COLUMN DOWEL CONNECTIONS: MACRO MODELLING

Matej Fischinger[1], Blaz Zoubek[2], Tatjana Isakovic[3]

[1]University of Ljubljana, Faculty of Civil and Geodetic Engineering
Jamova 2, 1000 Ljubljana, Slovenia
e-mail: matej.fischinger @fgg.uni-lj.si

[2, 3] University of Ljubljana, Faculty of Civil and Geodetic Engineering
Jamova 2, 1000 Ljubljana, Slovenia
{blaz.zoubek, tatjana.isakovic}@fgg.uni-lj.si

Keywords: Seismic behavior, precast industrial buildings, dowel connection, macro model

Abstract. *Since the knowledge about the response of dowel connections was quite limited, the adequate numerical models were almost not available. Using the results of experiments, performed within the SAFECAST, the numerical models for monotonic as well as cyclic response of dowel connections were defined. Firstly the detailed FEM modeling has been performed in order to identify the important parameters influencing the response. Based on these analyses the results of the experiments were generalized (for more details see the accompanying paper [2]). After that, quite robust hysteretic macro-model [10], which can be used for monotonic as well as dynamic analyses of dowel connections, was defined. First the procedure that can be used to define the input parameters, based on the material data and construction details of the dowel connection, will be proposed. The adequacy of the procedure will then be tested by comparing the analytical and experimental results.*

1 INTRODUCTION

Precast buildings have been frequently used in many European countries. Predominant type of these structures consists of an assemblage of columns tied together with beams. Among many types of different connections between precast elements, the connection using steel dowel is the most common. Nevertheless, the quantified knowledge of their inelastic response to earthquakes has been poor. This is partly due to the fact that the predominant mechanisms of the seismic response of the connections are complex and difficult to model. In practice connections are predominantly designed by engineering feeling and numerical verifications are seldom done. The cyclic behaviour of the dowel connections was systematically experimentally tested on the series of full-scale models in the frame of the European project SAFECAST [1, 2]. The main European associations of the precast manufacturers and different research institutions (including the University of Ljubljana) from the most earthquake prone areas in Europe, joint their efforts to define the design procedures for different types of connections in precast buildings. The supporting experimental campaign has been without comparison in the past. A large number of different connections (traditional, innovative, dissipative, connecting different structural elements) and structural assemblages in large scale have been tested. Monotonic, cyclic, PSD and shake table tests were performed. The results from these experiments and findings of FE analysis performed with ABAQUS [2] helped to define appropriate macro models. These models are much less complex and time consuming than FE models and therefore allow for parametric and probabilistic studies. They are essential for satisfactory modeling of the global response of the precast structures.

2 ANALYTICAL INVESTIGATION OF THE RESPONSE

In the past, some research on the dowel mechanism has been already done [3-5]. However, the knowledge about the whole response envelope under monotonic and cyclic loading remains quite poor. In this section, analytical investigation of the force – displacement relationship is presented (Fig. 1) and the procedure for the input parameters for hysteretic macro-models is proposed. First three characteristic points of the monotonic response will be defined based on the experimental and FEA results [2] (Fig. 1) – 1.) yielding of the dowel and crushing of the concrete; 2.) midpoint; 3.) maximal resistance. After that, cyclic degradation will be evaluated.

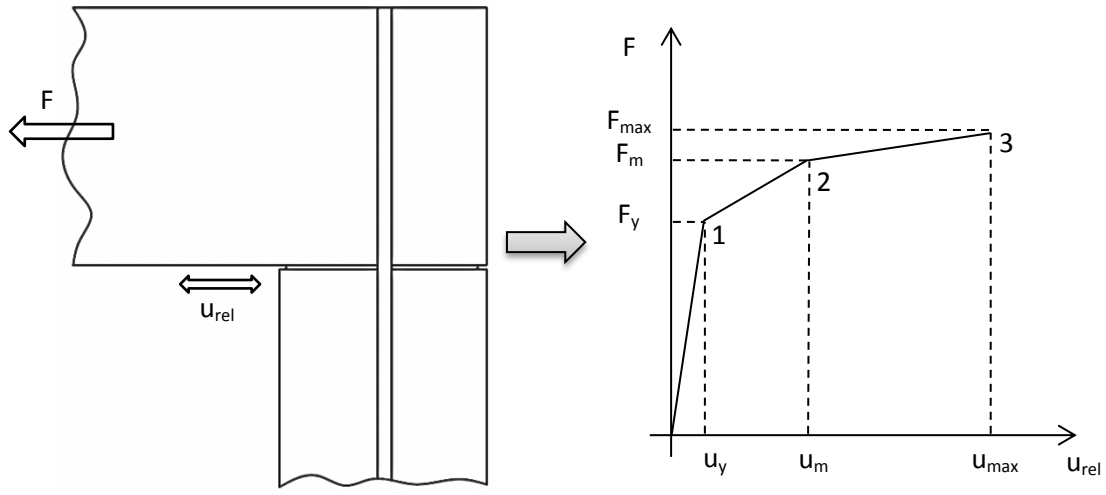


Figure 1: Schematic presentation of the force – displacement response of the dowel connection.

2.1 YIELDING OF STEEL DOWEL AND CRUSHING OF CONCRETE

At certain level of loading a plastic hinge is formed in the dowel at some depth in the column (Fig. 2). The concrete in front of the dowel starts to crush. For that reason larger deformations (rotations) of the dowel are allowed.

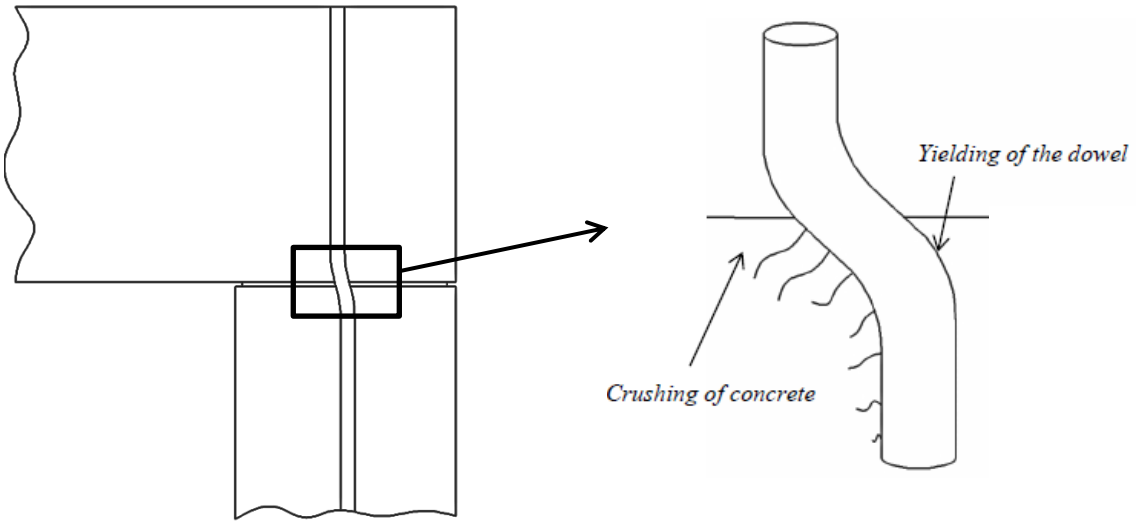


Figure 2: Yielding of the steel dowel and crushing of the surrounding concrete.

At the moment right before the plastification in the dowel starts, the stress state in the concrete in front of the dowel is as presented in Fig. 3. The figure shows the results of finite element analysis and the simplification which will be later used for the calculation of the first characteristic point of the monotonic response envelope. It is assumed that up to this point the behavior of the concrete remains elastic. Therefore the usage of the theory of the beam on the elastic foundation is appropriate. If this is the case, the depth of the intercept can be estimated at L=2.5 d_d, where d_d is the diameter of the dowel [5] (Fig. 3).

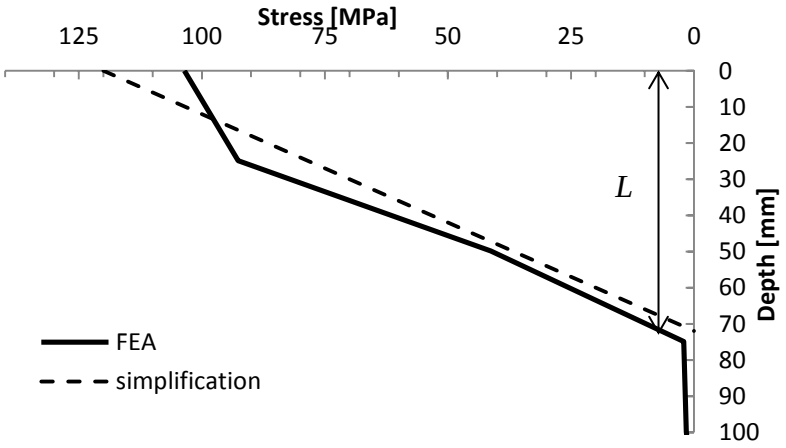


Figure 3: Compressive stresses in front of the dowel obtained from the FE analysis and the simplification of the stress-path at the start of yielding

FEM analysis [2] and previous studies [4, 5] indicate that due to the confining effects the maximal compression stresses reached in the concrete are much higher than its uniaxial compression strength (1).

$$f_{cc}{}^{*} = k_{conf}\, f_{cc} \quad (1),$$

In the equation (1), f_{cc} is the uniaxial compressive strength of concrete, $f_{cc}{}^{*}$ the maximal compressive strength of concrete under confining effects and k_{conf} the factor of confinement. Vintzeleou and Tassios [5] suggest value of 5 for k_{conf}. The results of the FE analysis presented in the accompanying paper [2] reveal much lower values – $k_{conf} \approx 2$. In Fig. 4 principal stresses in front of the dowel obtained from the analysis are shown. It can be seen that the second and the third principal stresses are approximately 1/3 of the first principal stresses (the compressive stresses in the direction of loading). In this case, according to different studies [6], the maximal compressive strength of concrete ranges from 2 to 3 the uniaxial compressive strength which confirms the findings of the FE analysis.

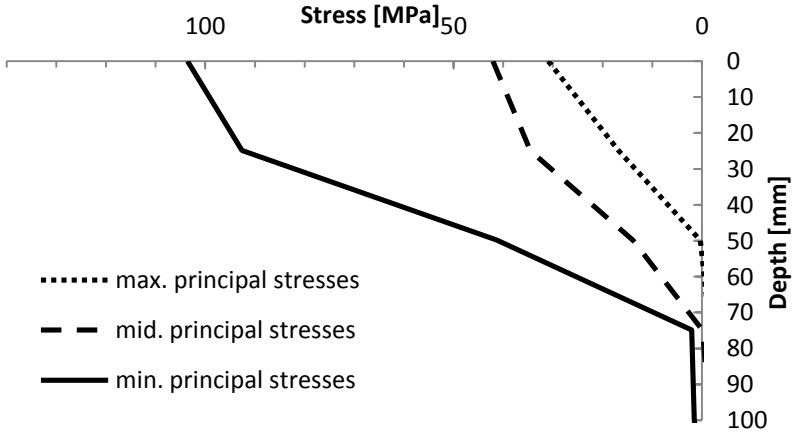


Figure 4: Principal stresses in the concrete in front of the dowel

Now it is possible to calculate the force in the connection at the moment of yielding of the dowel by simply integrating the stresses under the dowel (2).

$$F_y = k_{conf}\ f_{cc}\, d_d\, (\, 8 \cdot 0.314\, d_d\,)/2 \quad (2)$$

The relative displacement is calculated using the theory of the beam on the elastic foundations [7, 8]:

$$u_{y,rel} = 2\, F_y\, (1 - \beta e)/(2\beta^3 E_s I) \quad (3)$$

Where:

$\beta = (Kd/4EI)^{1/4}$ [8] and

$K = 269 f_{cc}{}'^{0.5}/d_d{}^{2/3}$ [9]

e…eccentricity (half of the thickness of the neoprene bearing pad)

$I = \frac{\pi\, d_d{}^4}{64}$…moment of inertia of the dowel section

E_s…elastic modulus of the steel used for the dowel

2.2 MAXIMAL RESISTANCE

When the connection fails, the maximum flexural resistance of the dowel is reached. The analytical stress-path in the concrete in front of the dowel with the simplification is presented in Fig. 5.

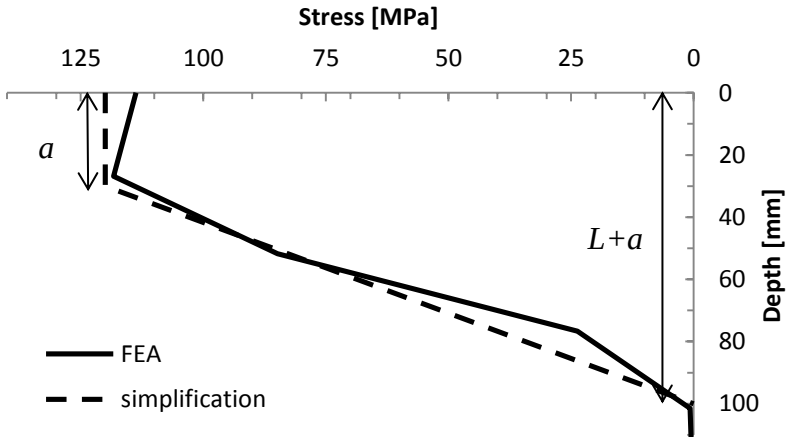


Figure 5: Compressive stresses in front of the dowel obtained from the FE analysis and the simplification of the stress-path when the maximal resistance is reached

Fig. 5 shows that the stresses are approximately constant up to the depth of the plastic hinge *a*. *a* can be easily determined from the equilibrium in Fig. 6 (4).

$$a = \sqrt{2\, M_{pl} / k_{conf}\, f_{cc}\, d_d} \tag{4},$$

M_{pl} (please see equation (4) and Fig. 6) is the flexural strength of the steel dowel which can be calculated with the following expression (5):

$$M_{pl} = k_{h,a}\, W_{pl}\, f_y \tag{5}$$

$k_{h,a}$ is the factor of hardening of steel and reduction in strength due to the axial forces in the dowel (6). W_{pl} is the plastic section modulus of the dowel section.

$$k_{h,a} = f_u / f_y\, (1 - \alpha^2) \tag{6}$$
$$\alpha = \sigma_{s,N} / f_y$$
$$\sigma_{s,N} = N / A_d,$$

where *N* is the axial force in the dowel, A_d is the area of the dowel section, f_y is the yield strength and f_u is the maximal strength of the steel used for the dowel.

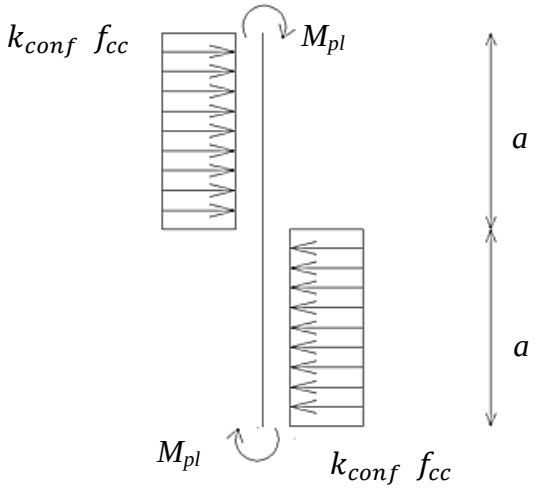


Figure 6: The equilibrium from which the depth of the plastic hinge can be determined.

Under the plastic hinge, the compressive stresses linearly decrease up to the depth of the intercept, which can be estimated at $L+a$ (Fig. 5). In short, from the top surface to the depth of the plastic hinge a nonlinear behavior of concrete is assumed. Under the plastic hinge, the concrete remains elastic, therefore the dowel behaves as a beam on the elastic foundations.

The strength of the connection can now be simply calculated by integrating the compressive stresses in front of the dowel (Fig. 5):

$$F_{max} = k_{conf}\ f_{cc}\ d_d\ (a + (2.5\ d_d - a)/2) \tag{8}$$

Relative displacement at maximal resistance u_{max} is determined from the equation (9). It is assumed that the rotation of the dowel arises mainly from the rotation in the plastic hinge. Based on the result of the FE analysis it is assumed that the length of the plastic hinge is approximately 2 d_d (Fig. 7).

$$u_{u,rel} = 2\ \tan(rot_{max}) \cdot a \tag{9}$$

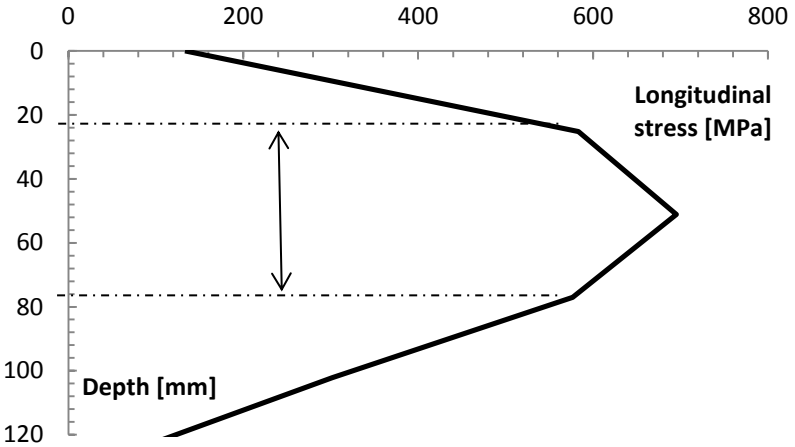


Figure 7: Longitudinal stresses in the dowel – the length of the plastic hinge is approximately 2 d_d

2.3 MIDPOINT

To capture the response more accurately, another characteristic point was defined at the force

$$F_m = (F_y + F_{max})/2 \tag{10}$$

The relative displacement at this force can be determined using a formula suggested by Vintzeleou and Tassios [5]:

$$u_{i,rel} = 1.15\ u_y\ \ u_{max}\ ((F_m/F_{max})^4 - 0.5\ (F_m/F_{max})^3 \tag{11}$$

2.4 CONTRIBUTION OF THE NEOPRENE BEARING PAD

To take into account the additional resistance of the neoprene bearing pad, its stiffness should first be calculated (12).

$$k_e = G_n\ A_{eff}/\ t_n \tag{12}$$

G_n is the shear modulus of the elastomer (neoprene), t_n is the thickness of the neoprene bearing pad and A_{eff} is the compressed area of the pad. The force in the neoprene pad is then

simply calculated with the equation (13). It is assumed that the neoprene bearing pad behaves elastically.

$$F_{neo}(u_{rel}) = k_e\, u_{rel} \tag{13}$$

The total response of the connection is then obtained by adding the contribution of the pad to the forces calculated under 2.1, 2.2, 2.3, 2.4 (Fig. 8).

In the experiment and FE analysis a quite large contribution of the neoprene bearing pad was observed when monotonic loading was applied [2]. In the case of cyclic response, the influence of the pad was much smaller due to smaller relative displacements (and rotations) between the beam and column [2]. For this reason the contribution of the neoprene bearing could be neglected if modeling cyclic response of the connection.

2.5 CYCLIC DEGRADATION

Due to cyclic degradation of concrete and steel the resistance of the connection in the case of cyclic loading is much lower. Maximal resistance of the connection is therefore reduced by the factor k_{cyc} (14).

$$k_{cyc} = 1 - \frac{1}{7}\sqrt{n-1} \quad [5] \tag{14}$$

In the equation (14) n is the number of cycles at constant amplitude. The maximal force in the connection is then determined with the following expression (14):

$$F_{max,cyc} = k_{cyc}\, F_{max} \tag{15}$$

3 APPLICATION OF THE PROPOSED PROCEDURE

The results of the experiments performed at the University of Ljubljana in the frame of the SAFECAST project [1, 2] were used to test the procedure proposed in the previous chapter. The procedure was used for the determination of the input data for the hysteretic model included in the Opensees software [10].

The material data and the construction details of the investigated dowel connection are given in Table 1. The input data for the hysteretic model are given in Tables 2 and 3.

variable	
f_{cc}	60 MPa
k_{conf}	2
f_y	580 MPa
f_u	700 MPa
E_s	200000 MPa
d_d	28 mm
α	0.09
G_n	1 MPa
A_{eff}	24200 mm^2
t_n	10 mm

Table 1: The data about the materials and construction details

According to the finite element analysis, values of 2 for k_{conf} and 0.09 for α were taken. If there are no FEA results available, the values should be chosen reasonably by the user.

Char. point	*F [kN]*	*u [mm]*
1	121	1.5
2	168	9
3	241	30

Table 2: The input data for the hysteretic model in Opensees [10] – monotonic response

Char. point	*F [kN]*	*u [mm]*
1	118	1.5
2	150	9
3	150	30
Parameter		
pinchX	0.67	
pinchY	0.5	
damage1	0.0	
damage2	0.035	

Table 3: The input data for the hysteretic model in Opensees [10] – cyclic response

The selection of the parameters pinchX, pinchY, damage1 and damage 2 was based on the experimental results (Table 3). The contribution of the neoprene pad was neglected in the case of the macro-model used for cyclic loading.

4 RESULTS

The comparison between the experimental and analytical results is presented in Fig. 8 and 9. The match between the experiment and the analysis is quite good for the monotonic and cyclic loading. Not only the force-displacement relationship, but also the dissipated energy is more or less similar (Fig. 9).

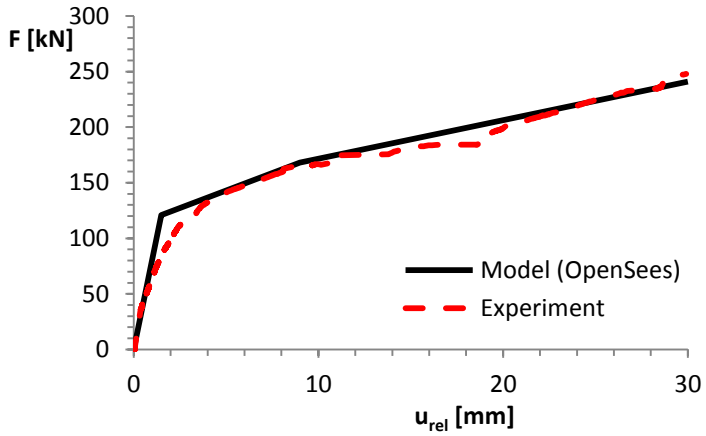


Figure 8: Comparison between the experimental and analytical results – a) force-displacement relationship and (b) dissipated energy.

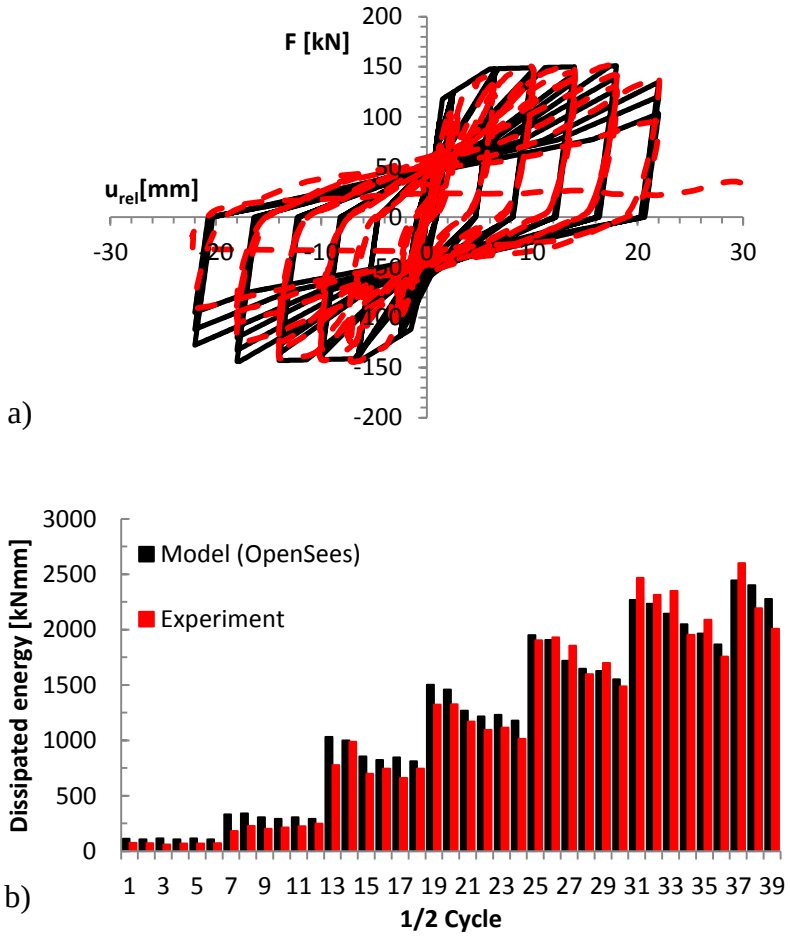


Figure 9: Comparison between the experimental and analytical results – a) force-displacement relationship and (b) dissipated energy.

5 CONCLUSION

The paper represents macro-modeling of the typical beam-to-column dowel connection used in precast industrial buildings. With the support of the experiments and finite element analysis a simple procedure for the determination of the input parameters for the hysteretic macro-model included in the Opensees software [10] was proposed. The model gives promising results for monotonic and cyclic loading. Too sophisticated FE models did not allow for some extended parametric and probabilistic studies of the precast industrial buildings due to their computational inefficiency. However, with the here presented macro-models this is feasible.

6 ACKNOWLEDGEMENTS

The presented research was supported by the SAFECAST project “Performance of Innovative Mechanical Connections in Precast Building Structures under Seismic Conditions” (Grant agreement no. 218417-2) in the framework of the Seventh Framework Programme (FP7) of the European Commission. Experiments were completed at the Slovenian National Building and Civil Engineering Institute (ZAG). The specimens were constructed at Primorje d.d. company.

REFERENCES

[1] SAFECAST Performance of Innovative Mechanical Connections in Precast Building Structures under Seismic Conditions. http://www.safecastproject.eu/, 2012.

[2] B., Zoubek, M., Fischinger, T., Isakovic, Seismic Behaviour of the Beam-to-Column Dowel Connections: FEM Analysis, International Conference on Computational Dynamics and Earthquake Engineering –COMPDYN 2013

[3] H. Dulascka, Dowel Action of reinforcement crossing cracks in concrete. *J. ACI*, **69-70**: 754-757, 1972.

[4] E.N. Vintzeleou, T.P. Tassios, Behaviour of Dowels under Cyclic Deformations, *ACI Struct. J.*, **84(1)**: 18-30, 1987.

[5] E.N. Vintzeleou, T.P. Tassios, Mathematical model for dowel action under monotonic and cyclic conditions, *Mag. Concr. Res.*, **38**: 13-22, 1986.

[6] A.H. Gandomi, S.K. Babanajad, A.H.Alavi, Y. Farnam, Novel Apporach to Strength Modeling of Concrete under Triaxial Compression, *J. Mater. Civ. Eng.*, **24(9)**: 1132-1143, 2012.

[7] B.F. Friberg, Design of dowels in transverse joints of concrete pavements. *American Society of Civil Engineers, Proceedings*, **64(2)**: 1809-1828, 1938.

[8] S. Timoshenko, Strength of materials, Part II, advanced theory and problems. *American Society of Civil Engineers, Proceedings*, Third ed. Princeton, NJ: Van Nostrand; 1956.

[9] S. Dei Poli, S. M. Di Prisco, P.G. Gambarova, Shear Response, Deformations and Subgrade Stiffness of a Dowel Bard Embedded in Concrete, *ACI Struct. J.*, **89(6)**: 665-675, 1992.

[10] S. Mazzoni, F. Mckenna, M.H. Scott, G.L. Fenves, B. Jeremic. Open System for Earthquake Engineering Simulation (OpenSees) - Command Language Manual, UCB, PEER, Berkeley, http://opensees.berkeley.edu/, 2009.

COMPDYN 2013
4th ECCOMAS Thematic Conference on
Computational Methods in Structural Dynamics and Earthquake Engineering
C. Soydan, E. Yüksel, E. İrtem (eds.)
Kos Island, Greece, 12–14 June 2013

NUMERICAL MODELING OF SINGLE-STOREY PRECAST FRAME'S PINNED CONNECTIONS WITH A SPECIAL DAMPER

C. Soydan[1], E. Yüksel[2], and E. İrtem[3]

[1] Namık Kemal University
Namık Kemal University, Department of Civil Engineering, Tekirdağ, Turkey
e-mail: csoydan@nku.edu.tr

[2] İstanbul Technical University
İstanbul Technical University Faculty of Civil Engineering, İstanbul, Turkey
yukselerc@itu.edu.tr

[3] Balıkesir University
Balıkesir University, Department of Civil Engineering, Balıkesir, Turkey
eirtem@balikesir.edu.tr

Keywords: Single Storey Precast Frames, Pinned Beam-Column Connections, Numerical Modeling, Lead Extrusion Damper.

Abstract. *Single-storey precast frames with pinned beam-column connections are widely used in Turkey. This type of precast structures had suffered extensive damages during the recent major earthquakes (Ceyhan (1998), Kocaeli (1999), Duzce (1999)). The damages had been generally concentrated on the pinned connections as failure of dowels or at the column bases as large plastic deformations.*

A special lead extrusion damper (LED) has been developed in an ongoing PhD study in Istanbul Technical University. The damper is going to be installed into the pinned connection regions of the single storey precast frames.

Nearly half scaled specimens representing existing features of precast frames are planned to be tested on the shake table. Prior the experimental work, an extensive blind prediction study has been carried out through the nonlinear dynamic time history analyses of the numerical models which are representing the specimens with and without damper. The numerical models are generated with Seismostruct. The comparison of the structural behaviors between the bare frame and the frame with LED has been discussed. Although the relative drifts of the precast frame has been significantly reduced, the observed base shear demand moderately increased by the installation of the LED.

1 INTRODUCTION

Single storey precast frames are adopted worldwide especially as industrial buildings. In Turkey, simple dry pinned connections are widely used for beam-column joints of industrial buildings. Pinned beam-column connections of single storey precast frames have usually two dowels at the top of the columns. These dowels are installed into the beams where the holes are released at the appropriate places during production process of the beams. These holes are located at the end regions and filled with non-shrinking mortar to actualize the adherence anchorage of the dowels. Generally, the dowels are not bolted if the anchorage length of the dowels through the precast elements is sufficient.

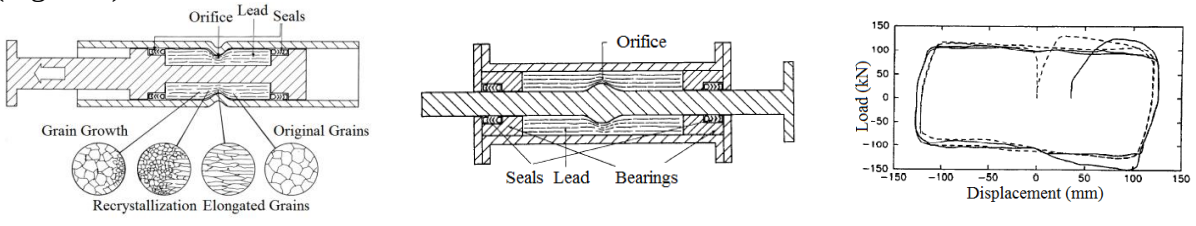
The structures consisting of single storey precast frames had suffered extensive damages during the recent major earthquakes (Ceyhan (1998), Kocaeli (1999), Duzce (1999)) in Turkey. These damages had been generally concentrated on the pinned connections as failure of dowels or at the column bases as large plastic deformations. The seismic design of precast structures with pinned beam-column connections is based on formation of plastic deformations within the critical regions of the columns through column bases. The energy dissipation actualized in the prescribed regions in the columns while the connections remain in the elastic range.

A special lead extrusion damper (LED) has been developed in an ongoing PhD study in Istanbul Technical University. The damper is placed into the pinned connection regions of the single storey precast frames. The main purpose of this application is to reduce the top displacement of the precast frames and the base rotation of the columns so decreasing the relative drifts of precast frames and the effect of geometric nonlinearity on columns.

Nearly half scaled specimens representing one half of a precast frame with a pinned beam-column connection are going to be tested on the shake table. A blind prediction study has been carried out with the numerical models representing the precast specimens. The nonlinear dynamic time history analyses are executed for the bare frame and the frame with LED using Seismostruct which is a computer program for the static and dynamic nonlinear analysis of framed structures. The comparison of the structural behaviors between the bare frame and the frame with LED has been discussed.

2 LEAD EXTRUSION DAMPERS

LED utilizes the hysteretic energy dissipation properties of lead. The process of extrusion consists of forcing a material through a hole or an orifice, thereby altering its shape [1]. The pressure applied to the ram forces the lead to flow through the orifice, producing a microstructure of elongated grains containing many crystal lattice defects. A proportion of the energy required to extrude the lead appears immediately as heat, but some is stored in the deformed lead and is the primary driving force for three interrelated processes (recovery, recrystallization and grain growth) which tend to restore the lead to its original condition [2, 3] (Figure 1).



(a) (b) (c)

Figure 1: LED; (a) Longitudinal section of a constricted tube LED showing the changes in microstructure of the lead [4] (b) Longitudinal section of a bulged shaft LED [5] (c) Hysteresis loops of LED [6].

A special lead extrusion damper (LED) has been developed in an ongoing PhD study in Istanbul Technical University. A bulged shaft LED design is adopted in this study (Figure 2). There is a sphere shaped bulge at the center of the shaft. The space between the elements is filled with lead. The diameter of the shaft and the bulge are 32 mm and 44 mm, respectively. The internal diameter of the tube is 60 mm and the thickness of the tube is 12 mm. The gap between the bulge and the tube is 8 mm. The displacement capacity of the LED is ±33 mm.

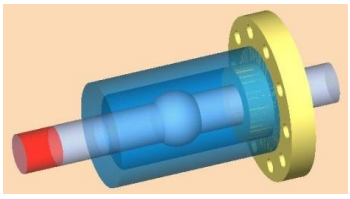


Figure 2: 3D demonstration of LED.

3 LITERATURE REVIEW

The dowel mechanism was investigated and the recommendations for the calculation of dowel strength both under monotonic and cyclic loading conditions were proposed by Vintzeleou and Tassios (1985, 1987) [7, 8]. The shear resistance of the connections between precast elements under monotonic and cyclic loading was investigated by Tsoukantas and Tassios (1989) [9] and design values for the shear resistance of each connection were proposed.

A friction damper was inserted in the region of beam-to-column connections of a precast industrial building to provide additional damping to the structure by Martinelli and Mulas (2009) [10]. A prototype building was designed for a medium-to-high seismic risk. The device efficiency in modifying favorably the structural behavior was analyzed by comparing the seismic response of the bare and redesigned frame to twelve accelerograms having a PGA equal to the design value. A non-critical shear increase in the zones where the device was inserted was found, largely counteracted by the reduction in extreme values for top displacement, bending moment at the column base and amount of energy dissipated in the hysteresis of materials.

The strength and deformation capacity of the pinned beam-to column connection with one dowel located at the center of the column were investigated with monotonic and cyclic tests by Kramar et al. (2010) [11] where rotations were controlled by different flexural strength of columns. It was stated that the strength and deformation capacity of the connections both for the monotonic and cyclic loading were much larger than determined according to the existing analytical expressions.

The monotonic test was carried out up to the failure of the specimen to obtain the load-displacement curve of the dowel connection and an analytical model of the beam-column pin connection for weak mechanism was presented by Capozzi et al. (2012) [12].

The cyclic response of single centrically, single eccentrically and double eccentrically located dowel connections was experimentally investigated and the parameters which control the type of the failure were identified by Fischinger et al. (2012) [13]. A numerical non-linear macro-model which was included in SAP2000 via multilinear plastic nonlinear type uniaxial link element (pivot type) of the investigated connections was identified.

The numerical model for beam-column dowel connection behavior was proposed and the results from the analytical research for different type of beam-column connections under seismic action were presented by Apatolska et al. (2012) [14]. The nonlinear behavior of con-

nection was modeled by using multi-linear pivot hysteretic plastic property in SAP2000. Non-linear time history analyses were conducted with the constructed analytical model.

Precast beam and column elements connected with dowels were tested under monotonic and cyclic pure shear loading by Psycharis and Mouzakis (2012a) [15]. The research was focused on several design aspects as the shear ductility capacity of the connections and the effect of various parameters on their strength. The diameter and the number of the dowels, the distances of the dowels from the edges of the beam in the longitudinal and transverse direction, and the strength of the grouts in the ducts were examined as parameters. The strength of the connection was lower in the pull direction than that in the push direction for both monotonic and cyclic loading due to the early spalling of the concrete for small ratios of "the distance of the dowels from the edge of the beam in the longitudinal direction/the diameter of the dowel". The cyclic response of the connections showed lower resistance, less than half of the monotonic response. Significant values of shear ductility could be achieved by dry pinned joints if the concrete cover of the dowels had sufficient thickness for cyclic loading. A formula was proposed for the calculation of the shear strength of pinned connections.

The behavior of precast frames with pinned connections was investigated with shaking table tests by Psycharis and Mouzakis (2012b) [16]. The frames that had different sections of columns having varying longitudinal reinforcement ratios were adopted in the tests while beam sections remain the same. The frame columns were designed as flexible and weak (under-reinforced) in which large rotations were induced at the joints, flexible and strong (over-reinforced) in which significant rotations and shear forces were induced at the joints and stiff and strong (over-reinforced) in which small rotations and large shear forces induced at the joints within the frame. The base motions were applied in the plane of the frame was piecewise increasing up to the point that significant damage observed. The results were compared with those of connections of the same geometry subjected to pure shear cyclic loading.

4 DESCRIPTION OF THE SPECIMENS

The specimens consist of a beam attached to a column with a doweled connection on the corbel that is located at the top of the column. Nearly one half of the single storey one bay frame was modeled due to the 2.35 m×2.35 m plan dimensions of the shake table, the capacity of the hydraulic jack and the laboratory facilities (Figure 3).

The dimensions of the column cross section are 30 cm×30 cm and the height of the column is 2.28m. The length of the column inside the foundation socket is 60 cm. The areal reinforcement ratio of longitudinal bars for the column is 1% (8Ø12) (Figure 4) which also represents the minimum (lower) limit of longitudinal reinforcement for columns in Turkish Earthquake Code 2007 [17]. The transverse reinforcement for the column is located with 7.5 cm and 15.0 cm spacing inside and outside of the plastic hinge region respectively.

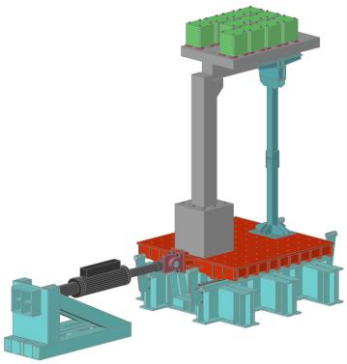


Figure 3: 3D demonstration of experimental setup.

The dimension of the corbel can be seen in Figure 5 and 6. The beam is located on the corbel with a 2.5 cm gap between the beam and the column face.

The beam has a constant T-shape cross section with a 1.25 m slab width (Figure 4). This slab width is needed for the installation of 3.5 tons additional mass on the top of the specimen. The beam is located on the column corbel with a rubber pad of 1cm thickness and 18.5 cm×21 cm plan dimensions between the column and the beam. Two M14 dowels are used through the pinned connection of precast frame. The distance of the axes of the dowels is 10 cm and the distance of the axes of the dowels from the beam edge (perpendicular to the loading direction) is 7.5 cm (5.4Ø). On the other hand, the distance of the axes of the dowels from the beam edge in the loading direction is 11.25 cm (8.0Ø) (Figure 5).

The dowels are inserted in the holes of section 60 mm×40 mm that are released at the end region of the beam. These holes are filled with non-shrinking mortar to actualize the adherence anchorage of the dowels in practice. The dowels are surrounded with six horizontal U-shape hoops at connection region and these hoops continue for a length of 70 cm from the beginning of the beam. The spacing of the transverse reinforcement is 7.5 cm in the same region and 8.0 cm in the rest of the beam. Total length of the beam is 2.05 m.

The height of the specimens is 2.64 m from the top of the foundation socket. The total height of the specimen including the additional mass and the foundation socket is 3.865 m. The foundation sockets are fixed to the shake table (Figure 6).

The class of concrete and the grade of reinforcing steel that is used for the specimens are C30 and S420, respectively.

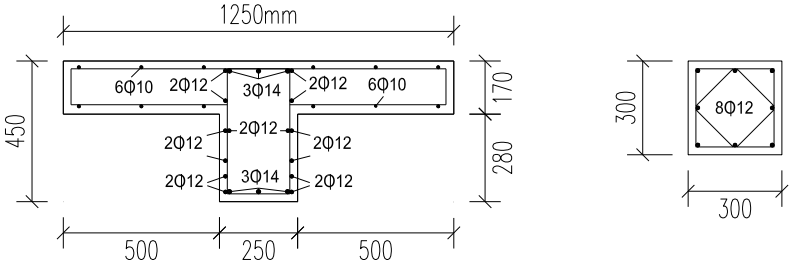


Figure 4: Sections of beam and column.

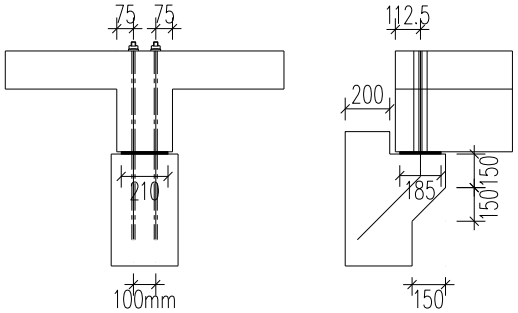


Figure 5: Dimensions of connection region.

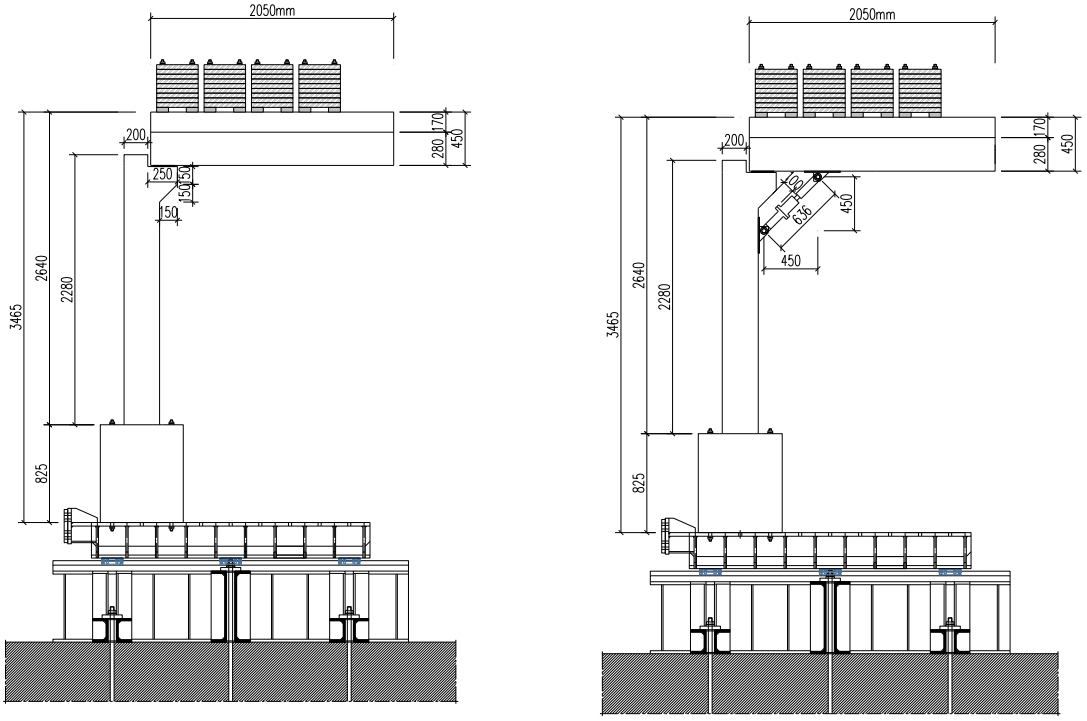


Figure 6: Pinned beam-column connections (bare and with LED)

5 ANALYTICAL MODEL

A plane frame model is created to represent the aforementioned specimen. Seismostruct [18] is adopted in modeling process and also in static and dynamic analysis of the constructed model. Seismostruct is a finite element package capable of predicting the large displacement behavior of space frames under static or dynamic loading, taking into account both geometric nonlinearities and material inelasticity.

The column has a square cross-section with dimensions 30 cm×30 cm and is designed with C30 class of concrete. The beam is designed with T-shape with 45 cm high and 25/125cm wide with the same class of concrete (Figure 4). The grade of transverse and longitudinal reinforcement is S420 that is used for the column and the beam. The column height and the span of the beam are 2.5 m and 1.625 m respectively.

The column is modeled with an inelastic plastic hinge frame element that exists in Seismostruct. This element features a distributed inelasticity forced-based formulation but concentrates such inelasticity within a fixed length of element. The formation of plastic deformations is expected within the critical regions of the columns through column bases. The length of plastic hinge is determined from Equation 1 [19].

$$l_p = 0.08l + 0.022 f_y d_b \tag{1}$$

In Equation 1 l_p, l, f_y and d_b expresses the plastic hinge length, the length of the relevant element, the yield strength of longitudinal reinforcement and the diameter of longitudinal reinforcement respectively.

The core and the cover concrete behavior are modeled via nonlinear concrete model. This is a uniaxial nonlinear constant confinement model, initially programmed by Madas (1993) [20], that follows the constitutive relationship proposed by Mander et al. (1988) [21] and the cylic rules proposed by Martinez-Rueda and Elnashai (1997) [22]. The confinement effects

provided by the lateral transverse reinforcement are incorporated through the rules proposed by Mander et al. [1988] whereby constant confining pressure is assumed throughout the entire stress-strain range [18]. The confinement factor is taken into account due to quality and quantity of longitudinal and transverse reinforcement of the column.

The behavior of the longitudinal reinforcement is modeled by bilinear steel model. This is a uniaxial bilinear stress-strain model with kinematic strain hardening, whereby the elastic range remains constant throughout the various loading stages, and the kinematic hardening rule for the yield surface is assumed as a linear function of the increment of plastic strain [18].

The beam section is overdesigned to realize the expected plastic deformation within the column base or as the failure of dowels. Therefore the beam is modeled with an elastic frame element. The additional masses on the beam slab are modeled with relatively stiff elastic frame elements where distributed mass is assigned. Similarly, the elements which connect the additional masses with beam are modeled with relatively stiff elastic frame elements but no mass is assigned to these elements (Figure 7).

The elements in the corbel region of column and the initial region of beam, which are perpendicular (orthogonal) to the axes of column and beam respectively (Figure 7), are modeled with elastic frame elements that are relatively stiff. All elements, except the additional mass representing and connecting elements, are assigned with their own masses.

The rubber pad is located between the beam and the column and modeled with 11 linear springs which are connected in parallel (Figure 7). These springs are only compression members (the springs in green) except the central one. The central spring is modeled as a tension and compression member (the spring in blue) that has the tension characteristics due to the dowels and the compression characteristics due to the rubber pad. The tension and compression stiffness of the springs are obtained with elongation stiffness of the related members. The central spring also has a lateral link element characteristic (the spring in magenta) to represent the shear resistance and shear ductility capacity of the connection.

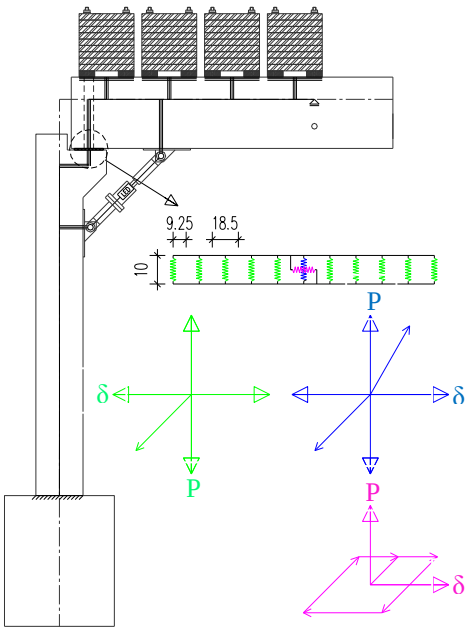


Figure 7: Analytical model of pinned beam-column connections

The stiffness of the uniaxial springs in compression is related to modulus of elasticity (100 MPa), area (185 mm×210 mm) and thickness (10 mm) of the rubber pad. Similarly the stiffness of the uniaxial spring in tension is related to the elasticity modulus (200000 MPa), the area (2M14) and the length of the dowels (10 mm).

The shear resistance of pinned connections to be used in the seismic design of precast structures is obtained by Equation 2 which is proposed by Psycharis and Mouzakis (2012a) [15].

$$R_d = \frac{C_0}{\gamma_R} nD^2 \sqrt{f_{cd} f_{yd}} \quad \text{for } d/D > 6.00 \tag{2}$$

$$R_d = \frac{C_0}{\gamma_R} \left(0.25 \frac{d}{D} - 0.50\right) nD^2 \sqrt{f_{cd} f_{yd}} \quad \text{for } 4.00 \leq d/D \leq 6.00 \tag{3}$$

In Equation 2 and 3 the d and D represents the distance of the axis of the dowels from the beam edge in the loading direction and the diameter of the dowels respectively. C_0 is a coefficient varying from 0.90 and 1.10 depending on the magnitude of expected joint rotations. If large joint rotations may occur (flexible columns) a value of 0.90-0.95 is suggested. The maximum value of C_0 is 1.10 for practically zero joint rotations. γ_R represents a general safety factor for the uncertainties in the experimental procedure and the limited number of experimental data used in the derivation of these equations. It is suggested that $\gamma_R \approx 1.30$. The n, f_{cd} and f_{yd} represent the number of the dowels, the compression design value of concrete and the yield design value of the dowel, respectively [15].

In Psycharis and Mouzakis (2012a) [15] the shear ductility capacity of the connections was calculated from their cyclic response, considering as ultimate displacement the one that corresponds to 20% drop in the strength. If the distance of the dowels from the beam edge was large enough ($d/D \geq 6$) quite satisfactory values of shear ductility capacity were attained, ranging from 4 to 6.

In this study Equation 2 is adopted because d/D is approximately 8 and the shear resistance is calculated as 24 kN for the considered connection. For the same reason the expected shear ductility capacity is between 4 and 6. The displacement value of maximum shear strength of the connections is read as approximately 5mm from the test results that are presented in Psycharis and Mouzakis (2012a) [15]. Because of a nearly half-scaled specimen examined in this study, the displacement that is corresponding to the maximum shear strength of the connection is accepted as 2.5 mm. The ultimate displacement value can be obtained as 10 mm with the consideration of the shear ductility capacity is 4 (the lower limit for shear ductility capacity).

The lateral link element characteristic of the central spring is modeled via bilinear kinematic curve. This is a kinematic-hardening bilinear symmetrical curve frequently employed to model idealized elastic-plastic behavior [18]. Three parameters need to be defined in order to fully characterize this response curve. These are initial stiffness (K_o), yield force (F_y) and post-yield hardening ratio (r) (Figure 8). The initial stiffness and yield force are considered as 9600 kN/m and 24 kN respectively. The post yield hardening ratio is adopted as 0.

The LED is also represented with the aforementioned link element. The initial stiffness, the yield strength and the post-yield hardening ratio is considered as 350000 kN/m, 75 kN and 0.0003 respectively for the LED. The elements which connect the LED to column and beam elements are modeled with relatively stiff elastic frame elements but no mass is assigned to these elements (Figure 8).

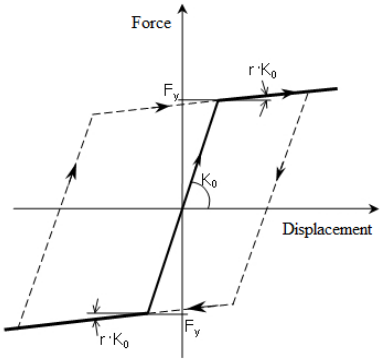


Figure 8: Kinematic-hardening bilinear symmetrical curve [18].

6 GROUND MOTIONS

The nonlinear dynamic time history analyses are executed with the bare frame and the frame with LED using Seismostruct which is a computer program for the static and dynamic nonlinear analysis of framed structures. Seven near fault and seven far fault type ground motions are considered in nonlinear dynamic time history analyses. The accelerograms used in this study are selected from the PEER NGA database [23].

The acceleration response spectra of the original accelerograms and the arithmetic mean of these accelerograms for 5% damping are given in Figure 9. The response spectrum for the 2nd earthquake zone (where effective acceleration coefficient is 0.3) and the ground soil type Z3 (which represents the firm soil with spectrum characteristic periods of 0.15 s and 0.60 s) that is defined in Turkish Earthquake Code [17] is also presented in Figure 9. The ground motions and the related station name which are used in this study are listed in Table 1.

Fault Type	Station Name	Earthquake	Year	Magnitude	Component	PGA (g)	PGV (cm/s)
Near	El Cen. Array #4	Imp. Valley	1979	6.53	140	0.485	37.39
	TCU076	Chi-Chi	1999	7.62	N	0.416	64.20
	El Cen. Array #5	Imp. Valley	1979	6.53	140	0.519	46.87
	Sarat. Aloha Ave	Loma Prieta	1989	6.93	000	0.512	41.15
	S5051	Super. Hills	1987	6.22	315	0.377	43.88
	LA Dam	Northridge	1994	6.69	334	0.349	50.81
	Erzincan	Erzincan	1992	6.69	East-West	0.496	64.28
Far	Saticoy	Northridge	1994	6.69	090	0.368	28.88
	TCU067	Chi-Chi	1999	7.62	N	0.325	66.69
	Delta	Imp. Valley	1979	6.53	352	0.351	33.00
	Sun Vall.-Roscoe	Northridge	1994	6.69	090	0.444	38.21
	Poe Road	Super. Hills-02	1987	6.54	360	0.300	32.78
	Holl. Diff. Array	Loma Prieta	1989	6.93	165	0.269	43.86
	TCU079	Chi-Chi	1999	7.62	N	0.393	48.82

Table 1: Main characteristics of the accelerograms.

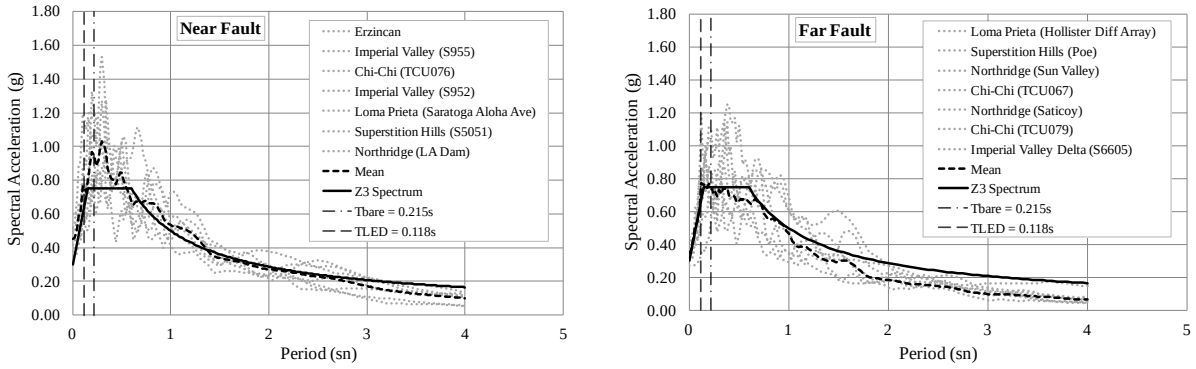


Figure 9: Response spectrum for near and far fault type ground motions

7 NUMERICAL ANALYSIS

The nonlinear dynamic time history analyses are executed with the bare frame and the frame with LED using Seismostruct which is a computer program for the static and dynamic nonlinear analysis of framed structures.

The base shear vs. top displacement relationship of the specimen, the moment vs. rotation relationship of the specimen column base section, the lateral force vs. slip of the dowels and the axial force vs. axial displacement of the LED are monitored through these analyses for near fault and far fault type ground motions.

The Newmark time integration method ($\beta = 0.25$, $\gamma = 0.50$) is adopted for all nonlinear time-history analyses, with a time step equal to the related ground motion acceleration record time step (0.005 s or 0.01 s). A Rayleigh type viscous damping is assumed, with the damping matrix proportional to the mass and initial stiffness matrix. A damping ratio of 5.0% is imposed for the first two modes of the model where T_1 and T_2 are 0.215 s and 0.027 s for the bare specimen and 0.118 s and 0.015 s for the specimen with LED, respectively.

7.1 Base shear vs. top displacement of the specimens

The base shear vs. top displacement relationships for the bare specimen and the specimen with LED that are obtained from dynamic time history analyses are presented in Figure 10 and Figure 11. It can be seen that the lateral stiffness of the specimen is increasing with the installation of the LED. The top displacement and plastic deformations of the specimen are decreasing both for near and far fault type ground motions.

The maximum base shear for the considered near and far fault type ground motions are 28.96 kN (Imperial Valley, El Centro Array #5) and 28.25 kN (Northridge, Sun Valley) respectively for the bare specimen. Similarly, the maximum values of top displacement are 26 mm (Imperial Valley, El Centro Array #4) and 22 mm (Chi-Chi, TCU067) for the near and far fault type ground motions respectively.

The base shear of the specimen with LED is increased 19% (34.57 kN for Imperial Valley, El Centro Array #5) while the top displacement is decreased 54% (12 mm for Imperial Valley, El Centro Array #4) for the near fault type ground motions. The increment in the base shear is obtained as 18% (33.30 kN for Northridge, Sun Valley) and the decrement in the top displacement is obtained as 50% (11 mm for Northridge, Saticoy) for the far fault type ground motions with the comparison of the maximum values. These values are presented bold in Table 2.

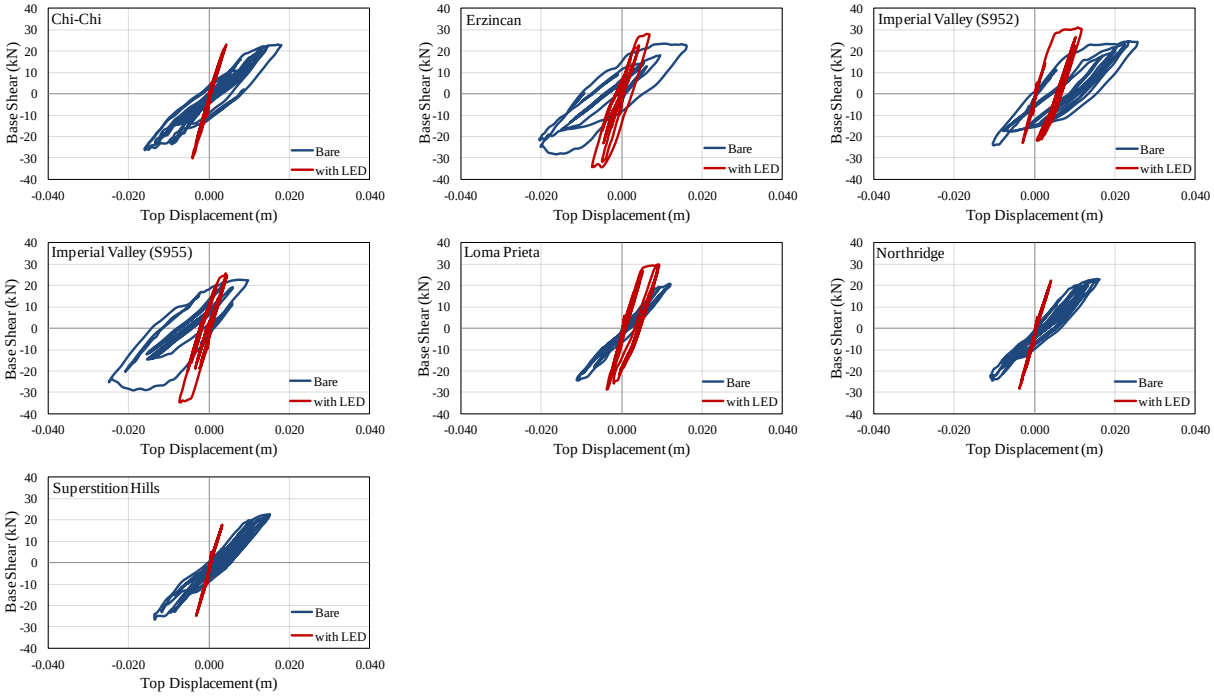


Figure 10: Base shear vs. top displacement relationships of specimen for near fault type ground motions

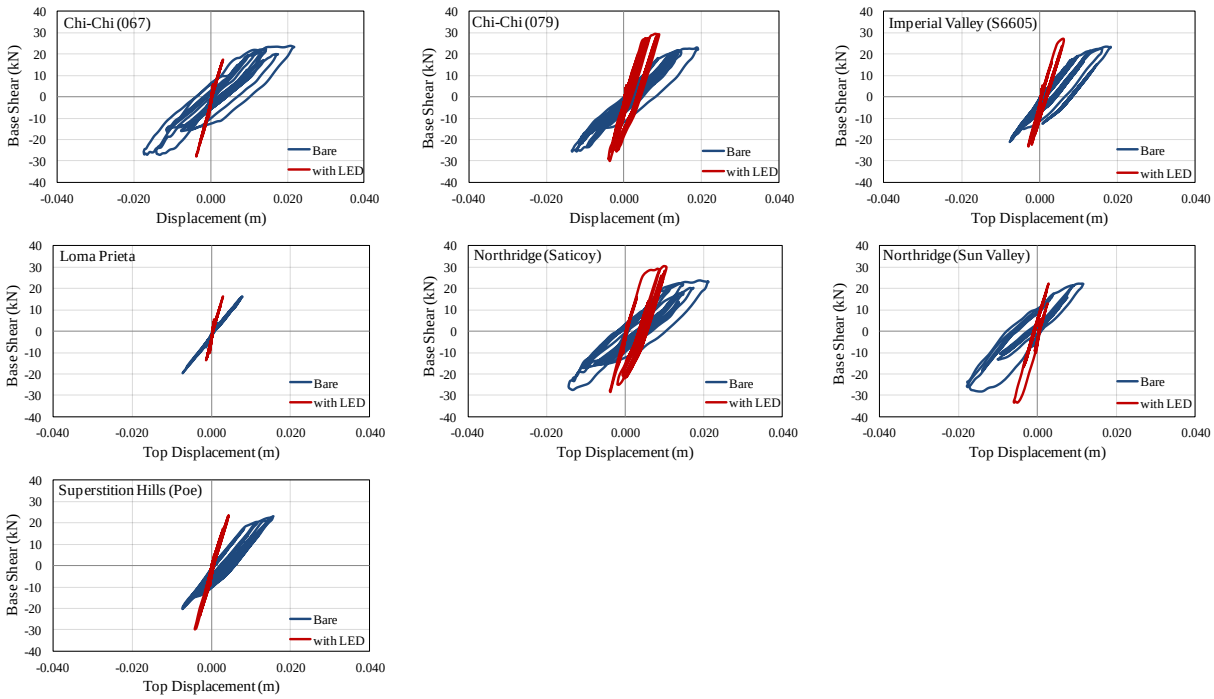


Figure 11: Base shear vs. top displacement relationships of specimen for far fault type ground motions

Fault Type	Station Name	Earthquake	Bare Specimen		Specimen with LED	
			Base Shear (kN)	Top Displacement (mm)	Base Shear (kN)	Top Displacement (mm)
Near	El Cen. Arr. #4	Imp. Valley	24.71	**26**	31.09	**12**
	TCU076	Chi-Chi	26.56	18	31.14	4
	El Cen. Arr. #5	Imp. Valley	**28.96**	25	**34.57**	7
	Saratoga Aloha	Loma Prieta	24.63	12	29.71	9
	S5051	Super. Hills	26.82	15	25.06	3
	LA Dam	Northridge	24.54	16	28.33	4
	Erzincan	Erzincan	28.35	20	34.24	7
Far	Saticoy	Northridge	27.41	21	30.39	**11**
	TCU067	Chi-Chi	27.20	**22**	28.14	4
	Delta	Imp. Valley	23.51	18	27.07	6
	Sun Valley	Northridge	**28.25**	18	**33.30**	6
	Poe Road	Super. Hills	22.82	15	29.95	4
	Holl. Diff.	Loma Prieta	19.73	8	16.32	3
	TCU079	Chi-Chi	25.81	19	30.18	9

Table 2: Top displacement and base shear of specimen.

7.2 Moment vs. rotation of the columns

The moment vs. rotation relationships for the column base section of the bare specimen and the specimen with LED are presented in Figure 12 and Figure 13. The moment and rotation of the column are decreasing both for near and far fault type ground motions. It can also be seen that plastic deformations are reduced for considered ground motions.

The maximum moment for the column base section are 49.55 kNm (Imperial Valley, El Centro Array #5) and 49.05 kNm (Northridge, Sun Valley) for the near and far fault type ground motions respectively for the bare specimen. The maximum values of rotation for the same section are 0.011 rad (Imperial Valley, El Centro Array #4) and 0.010 rad (Chi-Chi, TCU067) for the near and far fault type ground motions respectively.

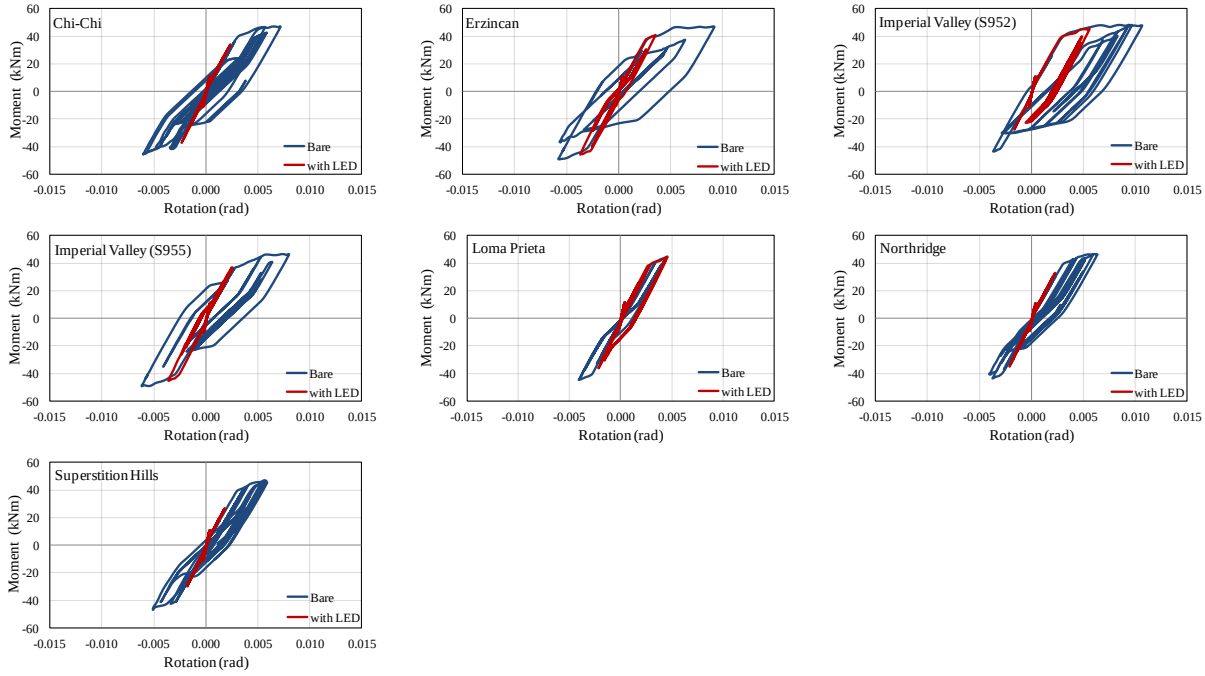


Figure 12: Moment vs. rotation relationships of column base section for near fault type ground motions

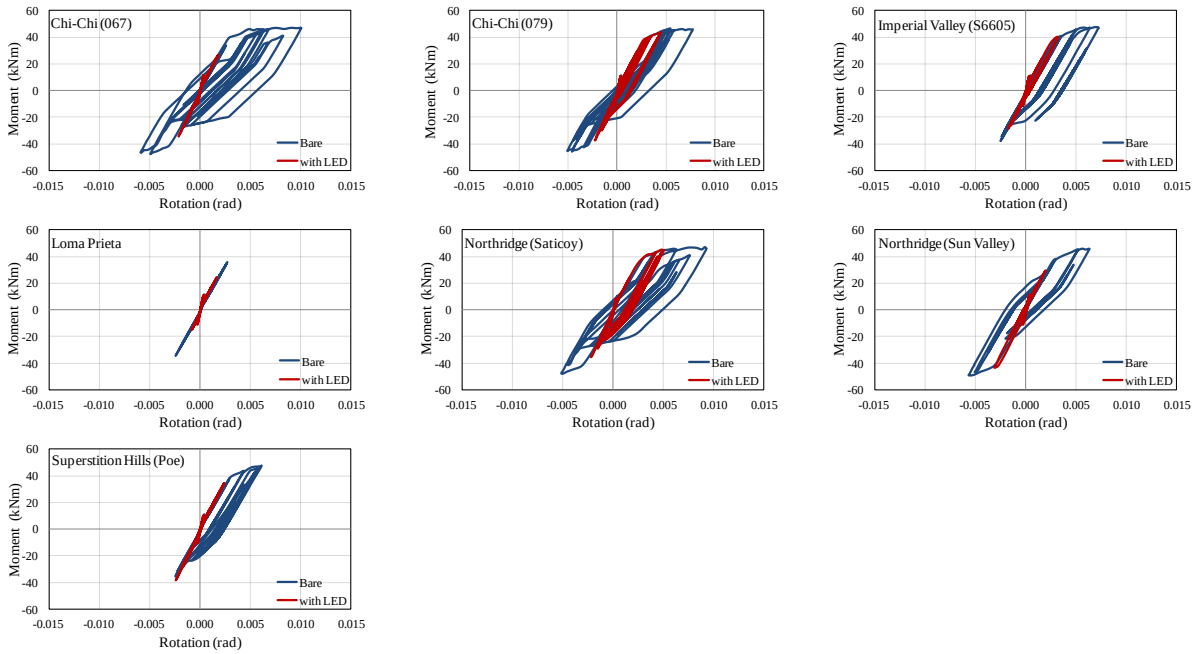


Figure 13: Moment vs. rotation relationships of column base section for far fault type ground motions

The moment of the specimen column base section with LED is decreased 7.4% (45.87 kNm for Erzincan) while the rotation is decreased 45% (0.006 rad for Imperial Valley, El Centro Array #4) for the near fault type ground motions. The decrement in the moment is obtained as 7.8% (45.24 kNm for Northridge, Saticoy) and the decrement in the rotation is obtained as 50% (0.005 rad for Northridge, Saticoy) for the far fault type ground motions with the comparison of the maximum values. The maximum values for the monitored relationships are presented bold in Table 3.

Fault Type	Station Name	Earthquake	Bare Specimen		Specimen with LED	
			Moment (kNm)	Rotation (rad)	Moment (kNm)	Rotation (rad)
Near	El Cen. Arr. #4	Imp. Valley	48.14	**0.011**	45.67	**0.006**
	TCU076	Chi-Chi	47.13	0.007	37.45	0.002
	El Cen. Arr. #5	Imp. Valley	**49.55**	0.008	45.60	0.004
	Saratoga Aloha	Loma Prieta	44.70	0.005	44.23	0.005
	S5051	Super. Hills	47.00	0.006	30.27	0.002
	LA Dam	Northridge	46.68	0.006	34.98	0.002
	Erzincan	Erzincan	49.14	0.009	**45.87**	0.004
Far	Saticoy	Northridge	48.10	0.009	**45.24**	**0.005**
	TCU067	Chi-Chi	47.68	**0.010**	34.59	0.002
	Delta	Imp. Valley	47.72	0.007	39.91	0.003
	Sun Valley	Northridge	**49.05**	0.006	43.59	0.003
	Poe Road	Super. Hills	47.07	0.006	38.24	0.002
	Holl. Diff.	Loma Prieta	35.71	0.003	24.45	0.002
	TCU079	Chi-Chi	46.71	0.008	43.75	0.004

Table 3: Moment and rotation values for the column base section of the specimen.

7.3 The lateral force vs. slip of the dowels

The maximum shear strength is obtained as 24 kN and the displacement that is corresponding to the maximum shear strength of the connection is accepted as 2.5 mm. The ultimate dis-

placement value can be obtained as 10 mm with the consideration of the shear ductility capacity is 4 (the lower limit for shear ductility capacity).

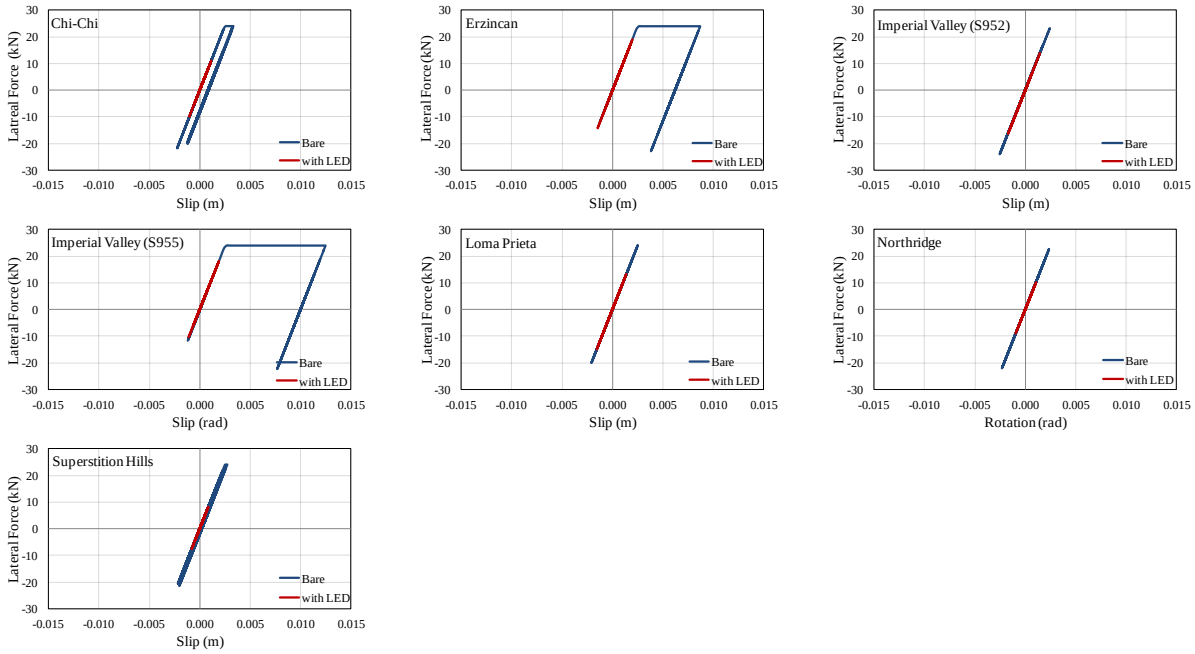


Figure 14: Lateral force vs. slip relationships of dowels for near fault type ground motions

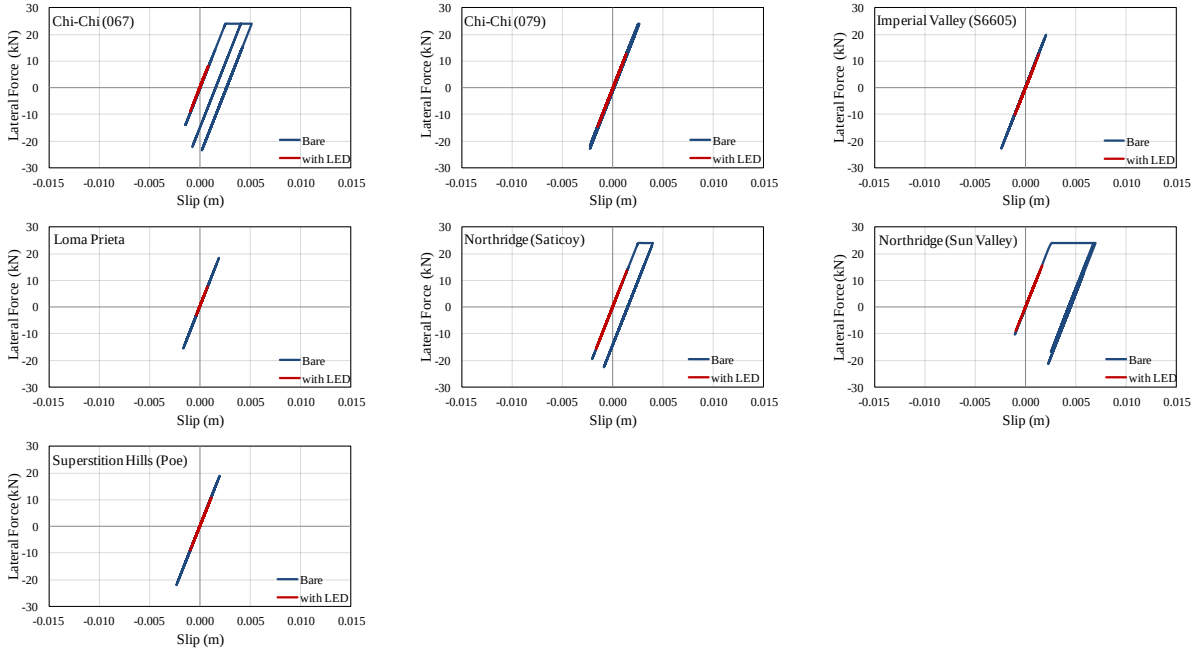


Figure 15: Lateral force vs. slip relationships of dowels for far fault type ground motions

The shear capacity of the dowels is reached and the plastic deformation of dowels is occurred in some of the ground motions that are considered in this study (Figure 14 and Figure 15). On the other hand the dowels are remained in elastic range for some of the considered ground motions. The ultimate displacement of 10 mm is not exceeded in most cases except Imperial Valley (S955) which is a near fault type ground motion for the bare specimen.

After the installation of the LED the lateral force and slip are quite decreased and all of the dowels are remained in the elastic range both for the near and far fault type ground motions.

7.4 The axial force vs. axial displacement of the LED

The axial force-axial displacement hysteresis of the LED can be seen in Figure 16 and Figure 17. The plastic deformations in the LED are occurred in most of the ground motions except two in both the near and far fault type ground motions. These ground motions are Northridge and Superstition Hills for near fault type and Chi-Chi and Loma Prieta for far fault type.

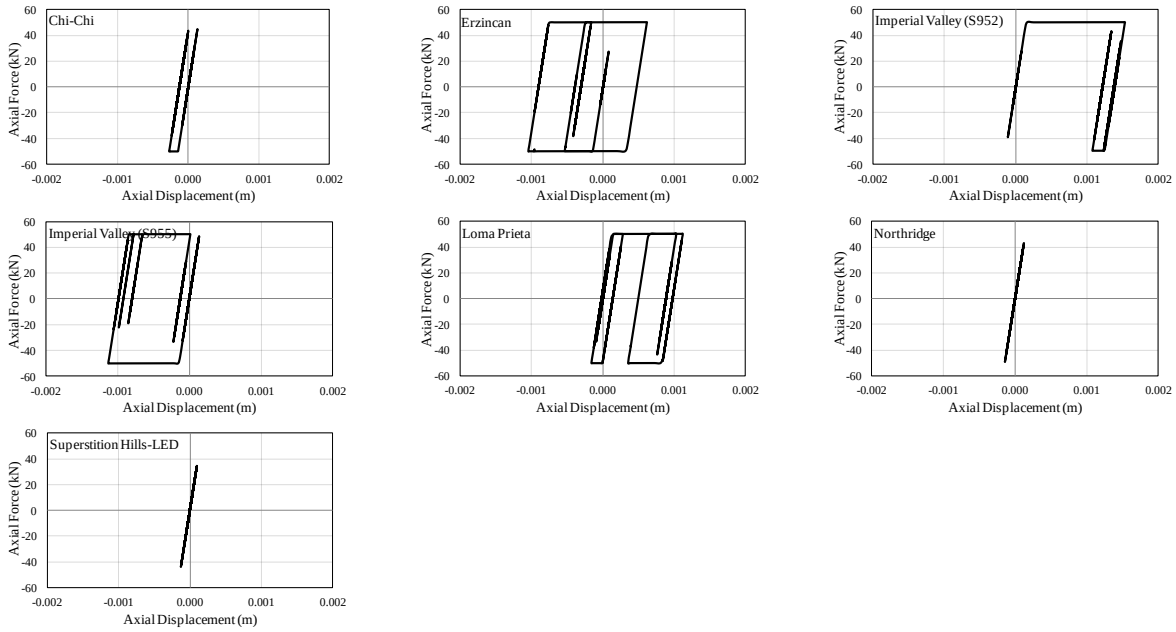


Figure 16: Axial force vs. axial displacement relationships of LED for near fault type ground motions

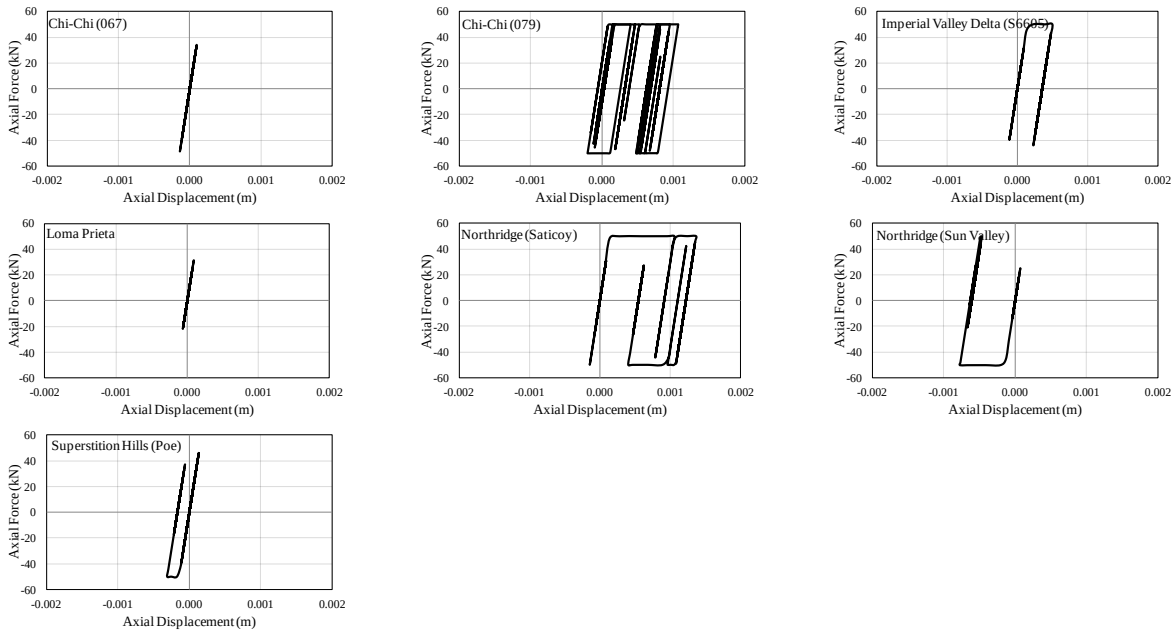


Figure 17: Axial force vs. axial displacement relationships of LED for far fault type ground motions

8 CONCLUSIONS

The results of the analytical study have been evaluated for the bare frame and the frame with the LED in order to express the effectiveness the applied method for seismic retrofitting. The following conclusions could be drawn:

- The lateral stiffness of the specimen is increasing with the installation of the LED.
- The top displacement and plastic deformations of the specimen with the LED are considerably smaller than the bare specimen for near and far fault type ground motions.
- Base shear demand of the specimen with the LED are relatively bigger than the bare frame.
- ·At the column lower end, bending moment and rotation are decreasing both for near and far fault type ground motions with the installation of the LED.
- The dowel's inelastic behavior is exceedingly affected by the existence of the LED.
- LED is operative for near and far fault type earthquakes.
- The applied retrofitting technique is effective to reduce the in-plane seismic risk of single-story precast frames with pinned beam-column connections.

REFERENCES

[1] F. Sadek, B. Mohraz,A.W. Taylor, R.M. Chung, Passive energy dissipating devices for seismic applications. *Report NISTIR 5923*. Building and Fire Research Laboratory, National Institute of Standarts and Technology, Gaithersburg, Maryland, 1996.

[2] J. Wulf, J.F. Taylor, A.J. Shaler, *Metallurgy for engineers*. John Wiley and Sons, New York, 1956.

[3] C.E. Birchenall, *Physical metallurgy*. McGraw-Hill, London, 1959.

[4] W.H. Robinson, L.R. Greenbank, Properties of an extrusion energy absorber. *Bulletin of the New Zealand Society for Earthquake Engineering*, **8(3)**, 187-191, 1975.

[5] W.H. Robinson, L.R. Greenbank, Extrusion energy absorber suitable for the protection of structures during an earthquake. *Earthquake Engineering & Structural Dynamics*, **4(3)**, 251-259, 1976.

[6] W.H. Robinson, W.J. Cousins, Recent developments in lead dampers for base isolation. *Pacific Conference on Earthquake Engineering*, **Vol. 2**. New Zealand, 1987.

[7] E.N. Vintzeleou, T.P. Tassios, Mechanics of load transfer along interfaces in reinforced concrete, prediction of shear force vs. shear displacement curves. *Studie de Reserche, No.7*, Corpo di Perfezionamento per le Construzioni in Cemento Amato, Italcementi Societa per Azioni (S. p:A), Bergamo, pp. 121-161, 1985.

[8] E.N. Vintzeleou, T.P. Tassios, Behavior of dowels under cyclic deformations. *ACI Structural Journal*, **84(1)**, 18-30, 1987.

[9] S.G. Tsoukantas, T.P. Tassios, Shear resistance of connections between reinforced concrete linear precast element. *ACI Structural Journal*, **86(3),** 242-249, 1989.

[10] P. Martinelli, M.G. Mulas, An innovative passive control technique for industrial precast frames. *Engineering Structures*, **32(4)**, 1123-1132, April 2010.

[11] M. Kramar, T. Isakovic, M. Fischinger, Experimental invesitigation of pinned beam-to-column connections in precast industrial buildings. *14th European Conference on Earthquake Engineering*, Ohrid, Republic of Macedonia, 30 August-03 September, 2010.

[12] V. Capozzi, G. Magliulo, G. Manfredi, Nonlinear mechanical model of seismic behaviour of beam-column pin connections. *15th World Conference on Earthquake Engineering*, Lisbon, Portugal, 24-28 September, 2012.

[13] M. Fischinger, B.Zoubek, M. Kramar, T. Isakovic, Cyclic response of dowel connections in precast structures. *15th World Conference on Earthquake Engineering*, Lisbon, Portugal, 24-28 September, 2012.

[14] R. Apostolska, G. Necevska-Cvetanovska, J. Bojadziev, M. Fishinger, T. Isakovic, M. Kramar, Analytical investigations of beam-column connections in precast buildings under seismic loads. *15th World Conference on Earthquake Engineering*, Lisbon, Portugal, 24-28 September, 2012.

[15] .N. Psycharis, H.P. Mouzakis, Shear resistance of pinned connections of precast members to monotonic and cyclic loading. *Engineering Structures*, 41:413-427, 2012a.

[16] I.N. Psycharis, H.P. Mouzakis, Assessment of the seismic design of precast frames with pinned connections from shaking table tests. *Bull Earthquake Engineering*, 10:1795-1817, 2012b.

[17] Turkish Earthquake Code 2007.

[18] SeismoStruct, "Computer program for static and dynamic nonlinear analysis of framed structures". (http://www.seismosoft.com).

[19] T. Paulay, M.J.N. Priestley, *Seismic design of reinforced concrete and masonry buildings*. John Wiley & Sons Inc., New York, 1992.

[20] P. Madas, *Advanced Modeling of Composite Frames Subjected to Earthquake Loading*, PhD Thesis, Imperial College, University of London, London, UK, 1993.

[21] J.B. Mander, M.J.N. Priestley, R. Park, Theoretical stress-strain model for confined concrete. *Journal of Structural Engineering*, Vol. 114, No. 8, pp. 1804-1826, 1988.

[22] J.E. Martinez-Rueda, A.S. Elnashai, Confined concrete model under cyclic load. *Materials and Structures*, Vol. 30, No. 197, pp. 139-147, 1997.

[23] PEER NGA Database. Pacific earthquake engineering research center: NGA database. (http://peer.berkeley.edu/peer_ground_motion_database/)

COMPDYN 2013
4th ECCOMAS Thematic Conference on
Computational Methods in Structural Dynamics and Earthquake Engineering
H.F. Karadogan, S.Z. Yuce, E.Yuksel, I.E. Bal and F.B.Hasel (eds.)
Kos Island, Greece, 12–14 June 2013

SINGLE STORY PRECAST STRUCTURES IN SEISMIC ZONES - I

H.F. Karadogan[1], S. Ziya Yüce[2], E. Yüksel[3], I.E. Bal[4], and F.B.Hasel[2]

[1] Istanbul Technical University, Faculty of Civil Engineering, Istanbul, Turkey
e-mail: karadogan@itu.edu.tr

[2] Istanbul Technical University
Graduate School of Science Engineering and Technology, Istanbul, Turkey
e-mail: yuceser@itu.edu.tr, fbhasel@itu.edu.tr

[3] Istanbul Technical University, Faculty of Civil Engineering, Istanbul, Turkey
e-mail: yukselerc@itu.edu.tr

[4] Istanbul Technical University
Institute of Earthquake Engineering and Disaster Management, Istanbul, Turkey
e-mail: iebal@itu.edu.tr

Keywords: Single story precast frame type structures, Column, Displacement Ductility Ratio, Lateral Load Reduction Factor.

Abstract. *The theoretical and experimental research performed recently in the Structural and Earthquake Engineering Laboratory of Istanbul Technical University on prefabricated square columns will be presented here as a set of complementary research work. The deformability limits, failure modes of columns, the performance of columns exhibited under the different type of cyclic displacement protocols versus monotonic loading, rehabilitation by different type of complete and partial jacketing with and without CFRP sheets using both ordinary or self-leveling-self compact concrete, damping ratios and Earthquake Load Reduction Factors based on experiments, plastified regions observed etc. were taking place in this research program.*

The investigation essentially covers the test results of 1/1 scale 13 specimens with different cross sections and longitudinal reinforcement ratios. Nine of them were tested again after having applied different types rehabilitation referring to the corresponding displacement protocols.

The presented part of the research covers the test results of virgin specimens, displacement ductilities obtained, overstrength factors and hence earthquake load reduction factors. An attempt to find out the most probable displacement demands of precast individual square columns has been presented as well in order to set up a more reliable design philosophy based on dynamic displacement considerations. The purpose is to find ways of overcoming the selection of initial stiffness and displacement ductility. In order to does that, 12 groups of earthquake records cover the cases of far field, near field, firm soil, soft soil possibilities for 2/50, 10/50 and 50/50 earthquakes with minimum scale factors. The selection has been done by using two different approaches which suggest modifying the frequency content of the record or not.

1 INTRODUCTION

Single story precast frame type structures are widely used in the construction of industrial facilities and commercial malls in Turkey. This building type consists of cantilever columns connected by simply supported precast and/or pre-stressed beams. Connection of the non-moment resisting beams to the columns is achieved on site. The lateral strength and stiffness of the structure depend entirely on the cantilevered columns as shown in Figure 1a and 1b, respectively.

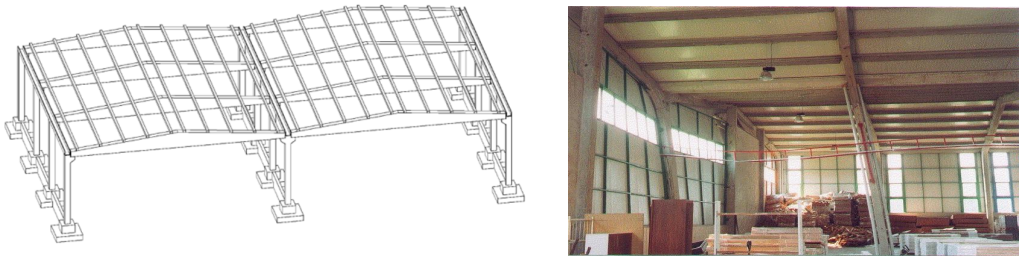


Figure 1: a-Typical view of a precast frame type structure b- Insufficient lateral stiffness.

After August 1999 Kocaeli and November 1999 Düzce Earthquakes, site investigations revealed that structural damage and collapse of one-story precast structures were common Saatcioglu et al. (2001) [1], Ataköy (1999) [2], Sezen et al. (2000) [3], Bruneau (2002) [4], Sezen and Whittaker (2006) [5]. Various types of structural damage were frequently observed in one-story precast structures, such as flexural hinges at the base of the columns, axial movement of the roof girders that led to pounding against the supporting columns or falling of the roof girders, Figure 2, Wood (2003) [6].



a- Flexural hinge at the bottom of column b- Overtopping of beam

Figure 2: Structural damages, [1].

The post-earthquake observations of one-story precast frame type structures indicate also that

- *i- Lateral stiffness may not be high enough to limit the lateral displacement of column tops which may differ from peripheral columns to center columns simply because of the lack of inplane rigidity of roofing system, Figure 1b,*
- *ii- Hence the excessive top rotations of columns and the relative displacement in the plane of roof become perfect reasons to dislocate the long span heavy slender roof beam together with the other two component of earthquake, Figure 2b. They are creating perfect imperfections as well, for out of plane buckling of beams which have very simple insufficient hinge connections to the columns.*
- *iii- Incompatible column displacement ductility achieved in the field and the lateral load reduction factor used in design, Figure 2a.*

In addition to the observations listed above it is also known that, structural alterations done after construction, the effects of nonstructural elements used unconsciously, oversimplified details of connections can be counted among the other important deficiencies of these buildings.

At the design stage of that type of buildings, the seismic weight coming from the tributary area of columns are determined easily for predicting the earthquake loads. However the *Lateral Displacement Ductility Ratio* which is the main parameter of *Lateral Load Reduction Factor* has to be selected at the beginning of design which is not an easy estimation and has its own uncertainties. Another difficulty is to estimate the lateral rigidity of column which is going to be used to calculate the fundamental period of vibration to go to the spectrum curves. Finally the proposed displacement limits based on static considerations are no longer satisfying the requirements of dynamic displacement calculations.

The following three general critics to the design procedures adopted, should be properly satisfied at the end:

i- What should be the initial stiffness of the structure on which the fundamental period will be based?

ii- What should be the displacement ductility factor or lateral load reduction factor on which the design forces will be based?

iii- To what extent is valid the story drifts calculation based on static considerations?

Those are the factors to be discussed experimentally and theoretically in these set of papers, Karadogan [7], Karadogan et al. [8].

2 EXPERIMENTAL STUDY

Full scale 13 virgin reinforced concrete column specimens have been fabricated and tested in the Structural and Earthquake Engineering Laboratory of Istanbul Technical University, Karadogan et al. (2006), [9]. Square columns containing 1~2.4% of longitudinal reinforcement were 30×30 ~ 40×40 cm in cross section. The columns had a height of 4.0 m measured from the top of the precast socket foundation. The typical column elevation and cross section are shown in Figure 3.

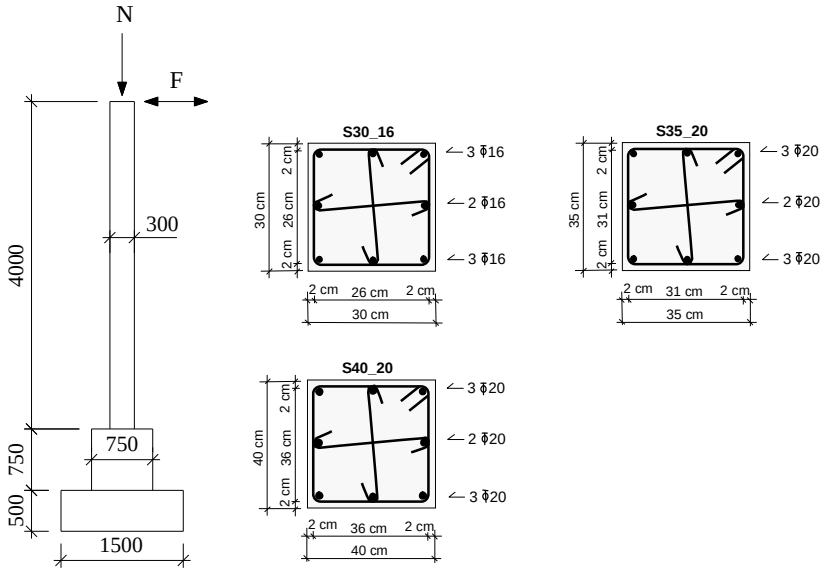


Figure 3: Typical column dimensions, [9].

The column-socket foundation connection surfaces were smooth for ten specimens, whereas the other connections were roughened as shown in Figure 4.

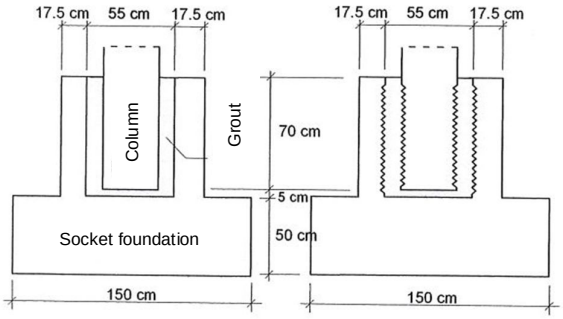


Figure 4: Geometry of the socket foundation.

The typical cross section consists of 8 vertical rebars with one hoop and 2 ties. Transverse reinforcements were selected as ϕ8/10 in the confinement zone which is the lower 1.60 m of the columns, and as ϕ8/15 or ϕ8/20 in the remaining part of the columns. The concrete and the rebar quality were C45 and S420, respectively. Detailed information about each column is presented in Table 1. Specimens S30_14 and S30_14M are identical columns except for the loading pattern used in the tests.

Specimen	Cross Sec cm×cm	Comp. Strength MPa	Long. Rein.	Long. Rein. Ratio %	Surface Type in Socket Foundation
S30_14	30×30	45.9	8 Φ14	0.014	Smooth
S30_14M	30×30	40.9	8 Φ14	0.014	Smooth
S30_16	30×30	47.7	8 Φ16	0.018	Smooth
S30_18	30×30	45.8	8 Φ18	0.023	Smooth
S30_18Z	30×30	44.0	8 Φ18	0.023	Roughened
S35_1416	35×35	45.8	4 Φ14+4 Φ16	0.012	Smooth
S35_18	35×35	45.8	8 Φ18	0.017	Smooth
S35_20	35×35	45.8	8 Φ20	0.021	Smooth
S35_20Z	35×35	45.8	8 Φ20	0.021	Roughened
S40_16	40×40	45.9	8 Φ16	0.010	Smooth
S40_20	40×40	45.9	8 Φ20	0.016	Smooth
S40_2020	40×40	45.9	12 Φ20	0.024	Smooth
S40_2020Z	40×40	45.9	12 Φ20	0.024	Roughened

Table 1: Properties of the columns.

The testing setup utilized during the whole course of this research program is given in Figure 5. It consists of one 250 kN loading capacity displacement controlled electro-hydraulic actuator, a hydraulic jack and load cell connected to a specially developed convex adaptor on top for having more or less conservative constant axial load acting on the specimens. All specimens have been tied down on the testing bed by post-tensioned high strength bolts.

All specimens have been instrumented so that the lateral displacements along the height of columns in addition to the top displacement and the relative vertical displacements shown in,

Figure 5, were measured and recorded to obtain the possible relative rotations between the selected sections around the critical zones. All the necessary additional measurements have been done in order to relay on the readings. It has been observed that the slippage of the specimens and the rotation of foundations were at the negligible order in every stage of the experiments. Strain gauges were mounted on some of the rebars in the critical zones.

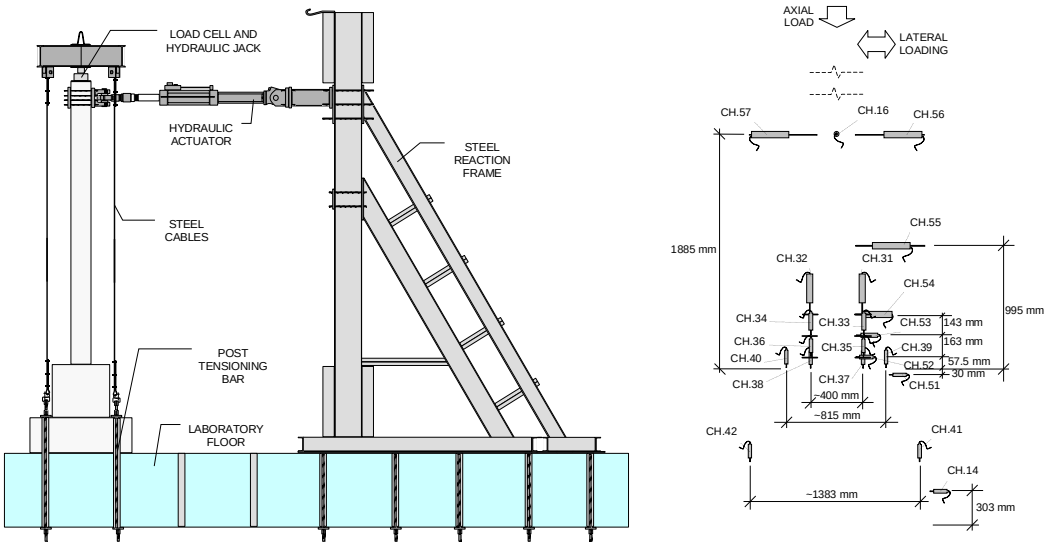
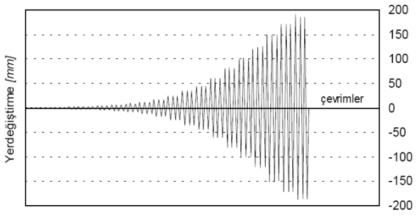


Figure 5: Testing and measuring set-up.

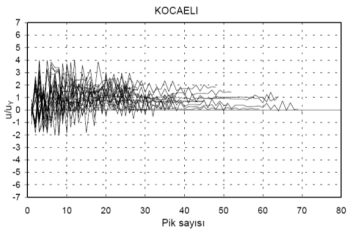
The specimens were subjected to constant vertical load which is equivalent to 5% of the column axial load carrying capacity and cyclic lateral displacement reversals repeated three times for each displacement threshold. The displacement protocol used in general is given in Figure 6a. In addition to that a different displacement protocol developed and used hopefully has better simulations of the earthquake characteristics recorded around Izmit Bay area, Figure 6b. For that purpose the records of Kocaeli 1999 Earthquake obtained from the four different stations normalized to the biggest PGA which was 0.379g and used in the nonlinear time history analyses of 30×30, 35×35, 40×40 cm square columns. The envelope of the response was normalized once again according the expected ductility ratio 4 and then was smoothed. The displacement protocol achieved at the end is presented in Figure 6e and used for two full scale specimens namely S35_20Z and S40_2020Z. It should be noted that the last one is not a symmetric one and at the end of the tests two or three big cycles have been added to see the final behavior of the specimens.



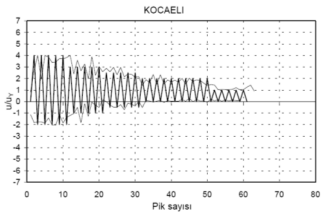
a- Generally used displacement pattern

Station	Component	PGA [g]	PGV [cm/s]	PGD [cm]
Duzce	DZC180	0.312	58.8	44.11
	DZC270	0.358	46.4	17.61
Izmit	IZT180	0.152	22.6	9.81
	IZT090	0.220	29.8	17.12
Sakarya	SKR090	0.376	79.5	70.52
Yarımca	YPT060	0.268	65.7	57.01
	YPT330	0.349	62.1	50.97

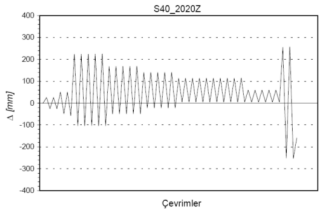
b- The earthquake records considered in nonlinear time history analyses



c- Real nonlinear behaviour



d- Approximate idealized envelop of real nonlinear behaviour



e- Modified idealized envelop of real nonlinear behaviour

Figure 6: Displacement protocols used in several tests.

2.1 Load Displacement Relations

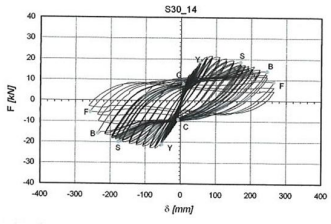
Each column was tested till considerable crushing of concrete and buckling of longitudinal bars were observed at the maximum moment region of the cantilever. No significant damage was observed in the socket foundation and column-socket interface.

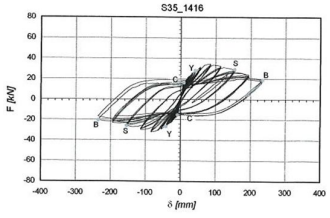
The columns developed flexural cracks at the bottom edge after cycling to 0.2% drift. Yielding of the longitudinal reinforcement was observed around 1.4% drift and the corresponding width of the flexural cracks was about 0.5 mm. Cycling to 2% drift caused widening of these flexural cracks to more than 0.7 mm. Crushing of the concrete of all the columns was observed at 4% drift. Buckling of the longitudinal bars was observed nearby 6.25% drift, Figure 7.

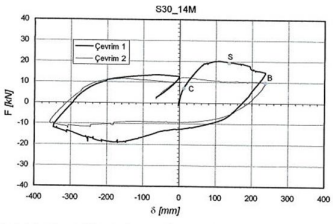


Figure 7: Typical damages observed in the columns.

The performance of each specimen is presented in terms of the lateral load-top displacement curves shown in Figure 8. The columns displayed stable hysteretic behavior for the whole course of the tests. The most distinct difference in the behavior observed is the strength capacity of the columns which arose from variation in the longitudinal reinforcement ratio.







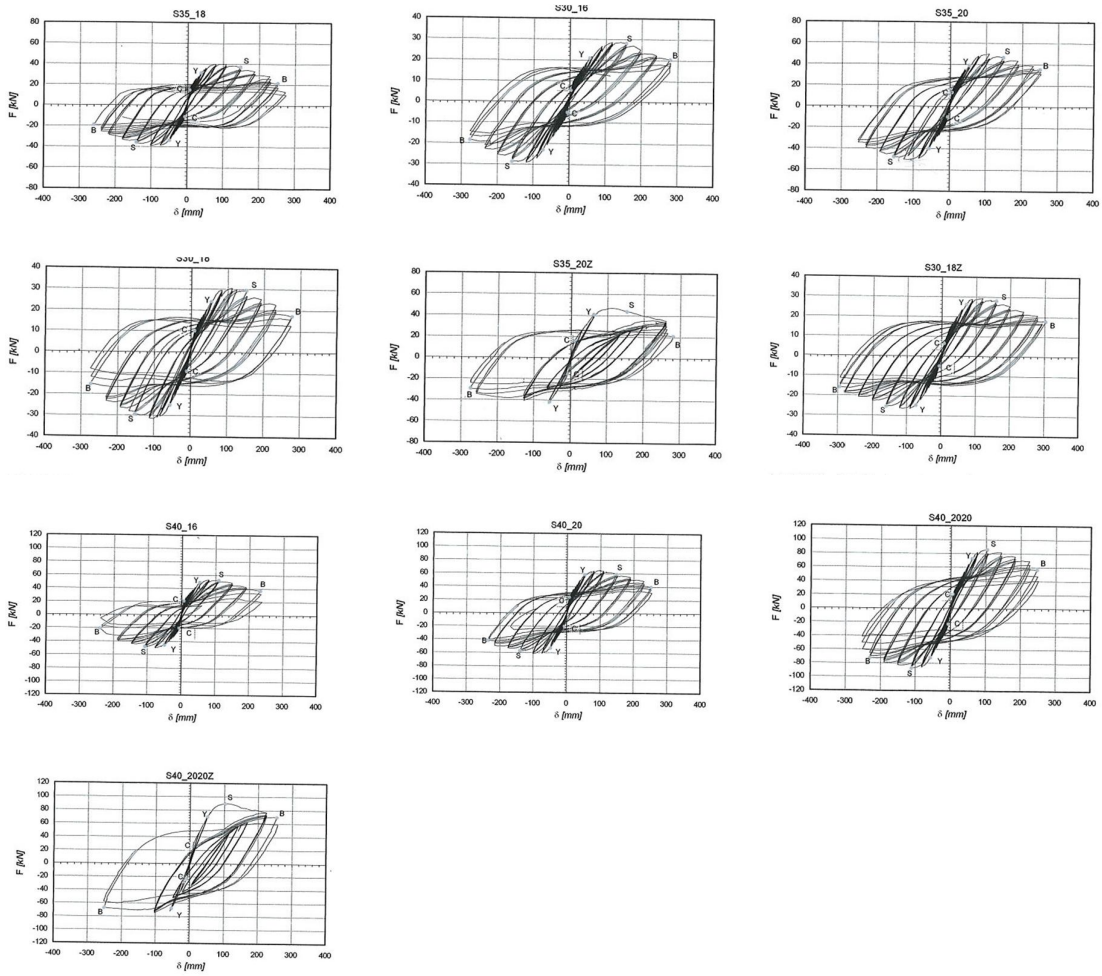
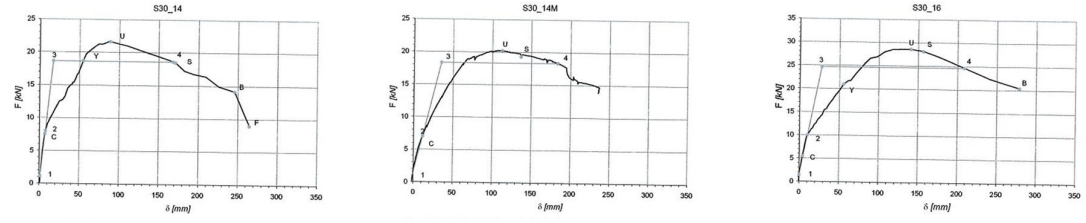


Figure 8: The lateral load vs. top displacement hysteresis of the columns.

2.2 Envelopes of Load Displacement Relations

It is generated the envelopes of the lateral load top displacement hysteresis of the columns. The points corresponding to the cracking, yielding, ultimate strength, and buckling events are exposed on the envelopes, Figure 9. The idealization of the envelopes in the bi-linear form which is established by means of the energy equivalence is accomplished and given away on the same diagrams.



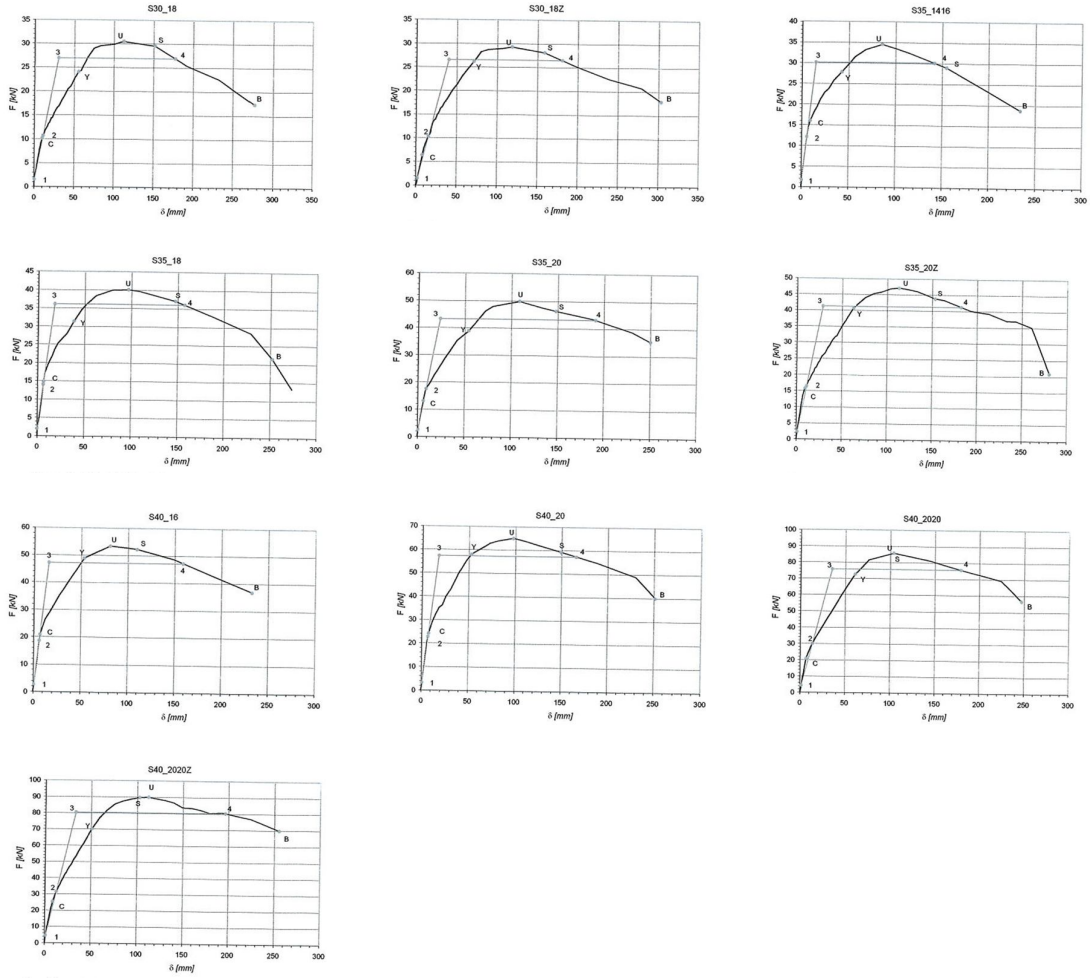


Figure 9: Envelope of load displacement hysteresis and bi-linear idealization.

2.3 Evaluation of the Test Results

The achieved test results are summarized in Table 2. The displacements and forces corresponding to the cracking (C), yielding (Y), ultimate strength (U), 10% strength decaying (S), and longitudinal rebars buckling (B) are offered for each specimen. The ratio of effective flexural stiffness to the gross flexural stiffness is calculated and given as $\alpha=EI_e/EI_g$ in the table. An average value of 0.78 is obtained which is almost double of the code suggested value. The critical points, 1 to 4, of the bi-linear idealized form, four alternative ductility ratios (δ_i/δ_j) and one strength ratio (β) which is the proportion of bi-linearized strength to the ultimate strength are also given in Table 2.

Typical behavior of a structure or structural member having energy dissipating capability, subjected to cyclic loading is schematically illustrated in Figure 10. The energy dissipated in the structure is given by the area E_H enclosed in the hysteresis loop. *Equivalent damping ratio* is defined according to Chopra [10] in terms of dissipated energy (E_H) and strain energy (E_{S0}). The equivalent damping ratio ζ_{eq} is given by Eq.1. Variation of the e*quivalent damping* respect to the top displacement of the columns is illustrated in Figure 11. In the undamaged part of the tests the equivalent damping ratio is smaller than 5%.

Specimen		C	Y	U	S	B	α	1	2	3	4	δ_4/δ_3	δ_4/δ_2	δ_U/δ_3	δ_U/δ_2	β
S30_14	δ [mm]	7.7	54.4	88.8	170.7	245.8	0.98	1.3	7.0	16.8	167.9	10.0	23.9	5.3	12.6	0.862
	F [kN]	8.0	18.7	21.6	18.5	14.2		1.1	7.6	18.7	18.7					
S30_14M *	δ [mm]	11.4		112.4	136.5		0.46	-0.9	11.6	34.8	183.6	5.3	15.8	3.2	9.7	0.906
	F [kN]	7.0		20.3	19.4			1.0	7.1	18.4	18.4					
S30_16	δ [mm]	4.1	55.2	140.6	156.4	278.7	0.79	0.1	10.3	27.6	208.5	7.6	20.3	5.1	13.7	0.863
	F [kN]	5.4	21.2	28.6	28.1	20.5		1.4	10.0	24.7	24.7					
S30_18	δ [mm]	10.0	55.3	112.1	151.5	276.8	0.78	0.6	11.2	30.1	177.3	5.9	15.8	3.7	10.0	0.883
	F [kN]	10.1	24.0	30.5	29.5	17.4		1.5	10.7	26.9	26.9					
S30_18Z	δ [mm]	8.0	71.1	118.5	158.4	303.2	0.58	2.3	15.5	40.0	180.5	4.5	11.6	3.0	7.6	0.906
	F [kN]	6.4	26.2	29.3	28.2	17.9		1.5	10.3	26.5	26.5					
S35_1416	δ [mm]	9.1	42.5	85.5	154.6	233.9	0.96	0.5	5.8	14.8	141.7	9.5	24.6	5.8	14.8	0.872
	F [kN]	16.0	27.8	34.5	29.0	18.7		1.7	12.1	30.1	30.1					
S35_18	δ [mm]	6.6	38.5	96.6	147.4	252.1	0.97	0	6.2	17.7	157.1	8.9	25.2	5.5	15.5	0.900
	F [kN]	14.8	31.4	40.1	37.1	21.5		2.0	14.0	36.1	36.1					
S35_20	δ [mm]	6.1	54.1	108.6	148.0	250.1	0.88	0.7	9.0	23.4	190.7	8.1	21.1	4.6	12.0	0.868
	F [kN]	13.0	38.8	49.9	46.4	35.3		2.5	17.5	43.3	43.3					
S35_20Z	δ [mm]	9.5	62.6	113.2	153.1	280.6	0.68	1.1	11.1	28.7	182.2	6.4	16.4	3.9	10.2	0.876
	F [kN]	15.8	40.7	47.2	43.9	21.0		2.4	16.5	41.3	41.3					
S40_16	δ [mm]	6.9	53.1	80.5	109.4	232.5	0.85	0.7	6.0	15.4	158.8	10.3	26.6	5.2	13.5	0.886
	F [kN]	20.9	48.9	53.4	52.3	36.9		2.7	18.7	47.3	47.3					
S40_20	δ [mm]	7.4	52.6	97.5	149.5	251.4	0.91	0.8	6.8	17.6	165.7	9.4	24.2	5.5	14.3	0.882
	F [kN]	24.2	58.0	65.1	59.3	40.1		3.3	22.8	57.4	57.4					
S40_2020	δ [mm]	6.7	60.7	103.9	103.9	247.0	0.60	1.5	13.5	35.0	179.1	5.1	13.2	3.0	7.7	0.884
	F [kN]	20.8	72.6	85.8	85.8	56.7		4.3	30.0	75.8	75.8					
S40_2020Z	δ [mm]	8.5	50.6	112.2	102.5	255.2	0.67	1.1	12.4	33.1	196.3	5.9	15.8	3.4	9.0	0.894
	F [kN]	25.4	70.1	90.0	89.8	69.9		4.5	31.5	80.4	80.4					

* *The authors keep their hesitation about the reliability of this particular test.*

Table 2: Critical points, stiffness, ductility and strength ratios of the columns.

$$\zeta_{eq} = (1/4\pi)\,(E_H/E_{S0}) \qquad (1)$$

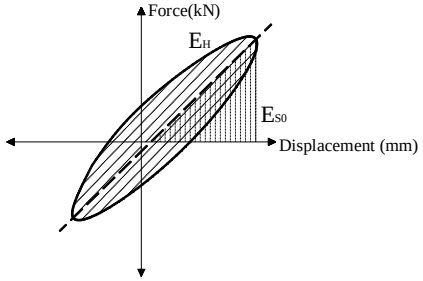


Figure 10: Definition of the dissipated and strain energies, [10]

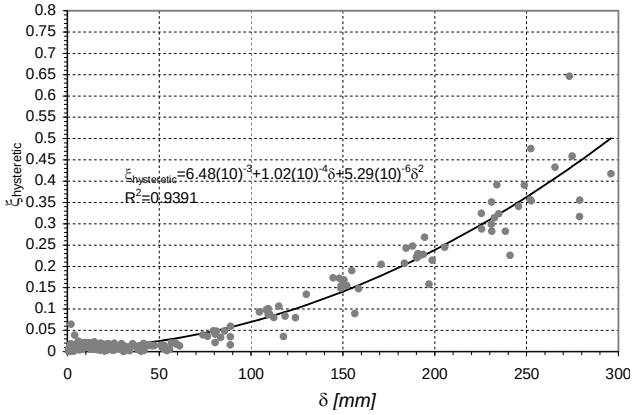


Figure 11: Equivalent damping calculated for the columns.

3 ANALYTICAL STUDY AND OVER-STRENGTH FACTORS

Seismostruct [11] which is a finite element package capable of predicting the large displacement behavior of space frames under static or dynamic loading taking into account both geometric and material nonlinearities, is adopted in modeling process and also in static and dynamic analysis of the columns.

The column is modeled with *an inelastic fiber frame element* that exists in Seismostruct. This element features a distributed inelasticity forced-based formulation but concentrates such inelasticity within a fixed length of element. The formation of plastic deformations is expected within the critical regions of the columns through column bases.

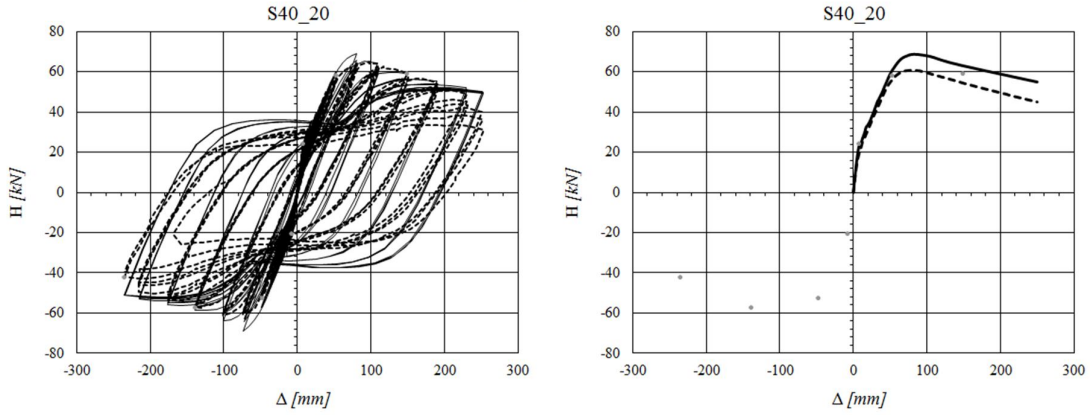
The core and the cover concrete behavior are modeled via *nonlinear concrete model*. This is a uniaxial nonlinear constant confinement model. The behavior of the longitudinal reinforcement is modeled by *Menegotto-Pinto model* which is a uniaxial steel model based on a simple stress-strain relationship coupled with the isotropic hardening rules.

As a specific example; for the column having 400×400 mm cross section with 1.6% longitudinal reinforcement ratio has been studied. Two sorts of analyses have been performed. They are *i.* the nonlinear static analysis in which the reversal test displacement pattern has been used, *ii.* pushover analyses with two diverse material coefficient sets.

The parameters of the material behavior models are as follows: For unconfined concrete, compressive strength is 45.9 MPa, strains at the peak stress and the crushing are 0.002 and 0.004, respectively. For confined concrete, compressive strength is 52.8 MPa, strains at the peak stress and the crushing are 0.0035 and 0.008, respectively. For steel, the yield stress is f_y=540 MPa, the maximum stress is f_u=616 MPa, the hardening and the ultimate strains are ε_{sh}=0.0135 and ε_u=0.25, respectively.

The column height is 4 m and the lower 1.6 m part is defined as confined zone. The axial load top of the column is 373 kN which includes one half of the column's own weight. The geometric-nonlinearity is considered in the analyses.

The result of the nonlinear static analysis for the reversal test displacement pattern is presented together with the experimental result. The broken and solid lines represent experimental and analytical results respectively. It seems good correlation between them, Figure 12a. Two pushover curves are presented in Figure 12b. The solid line is obtained for the material coefficient of γ_c=1.0 and γ_s=1.0 for concrete and steel. The broken line represent the case of γ_c=1.4 and γ_s=1.15 for concrete and steel, respectively.



a- Comparison of experimental and analytical results b- The effect of material coefficient

Figure 12: Analytical evaluation of S40_20 column.

Material coefficients used for concrete and reinforcement for precast members are respectively 1.40 and 1.15 according to the current Turkish codes. It is known that the design based defined these coefficients provide a kind of reserve strength margin over the targeted strength of the columns to be subjected to earthquakes. Since the individual contributions of these two different materials with two different coefficients can not be estimated, same displacement reversals used in the tests summarized above, have been theoretically applied to the columns with material coefficients γ_c=1.4 for concrete and γ_s=1.15 for steel. Deformation characteristics of the materials are kept same for two different set of nonlinear analyses. The ultimate strengths obtained from these analyses are given in the first two rows of Table 3.

The existing over strength due to load coefficients 1.4 and 1.6 of the *G dead* and *Q live loads* respectively, were assumed that they will compensate more or less the additional strength demand for earthquake affects in the load combination of *1.0 G + 1.0 Q + 1.0 E*.

Over-strength factors, OSF, for all the tested columns have been determined as the ratio of $P_{u(\gamma=1)}/P_{u(\gamma\neq1)}$ which correspond to the ultimate loads calculated by material coefficients equal to unity or not, respectively. The OSF is given in Table 3 together with the displacement ductility ratios achieved in the tests and the possible *lateral load reduction factors* calculated. The displacement ductility μ, referred in the fourth line of the table corresponds to (δ_U/δ_3) ratio given in Table 2.

SPECIMEN	1 S30_14	2 S30_14M	3 S30_16	4 S30_18	5 S30_18Z	6 S35_1416	7 S35_18	8 S35_20	9 S35_20Z	10 S40_16	11 S40_20	12 S40_2020	13 S40_2020Z
$P_{u\,(\gamma=1)}$	21.30	21.00	29.10	32.60	30.40	33.50	42.50	50.40	48.00	49.30	68.50	88.30	89.76
$P_{u\,(\gamma\neq1)}$	19.00	19.50	25.20	28.60	26.80	29.70	37.70	44.30	42.20	43.70	60.70	77.73	77.40
OSF	1.12	1.08	1.15	1.14	1.13	1.13	1.13	1.14	1.14	1.13	1.13	1.14	1.16
μ	5.30	3.20	5.10	3.70	3.00	5.80	5.50	4.60	3.90	5.20	5.50	3.00	3.40
OSF × μ	5.94	3.44	5.89	4.22	3.40	6.54	6.20	5.23	4.44	5.87	6.21	3.41	3.94

Table 3: Overstrength factors, displacement ductility datios and possible lateral load reduction factors.

It has to be kept in mind that because of the excessive plastic deformations accumulated around the critical regions of column, the stability load of the column will decrease and the safety margin against buckling load will drop down. This may cause early collapse of column or columns may experience a very large unacceptable lateral displacement which is strongly related to the earthquake records selected to check the design completed according the code defined target spectrums.

4 SELECTION OF EARTHQUAKE RECORDS

Two different techniques have been used to select the proper records for nonlinear time increment analyses. Seismomatch [12] software has been utilized first for having *fully code compatible records* with minimal discrepencies. As a other way of earthquake selection, the records which are naturally get closer to the target spectrum in three levels, have been modified sligtly to stay around the acceleration spectrums in *a selected period region* only. For that purpose the soil for which the shear wave velocity is bigger than 300 m/sec and the soil for which the shear wave velocity is lower than 700 m/sec have been considered as two different group of soils and they have been designated as *firm soil* and *soft soil* respectively. This should not be considered as a limitation to the earthquake selection process. Because more refined classification for soil types are always possible.

4.1 First Approach: Fully Compatible Records

Seven near fault and seven far fault type ground motions are considered in this approach. The accelerograms were selected from the PEER NGA database [13]. The main properties of the ground motions are listed in Table 4.

The acceleration response spectra of the original accelerograms and the arithmetic mean of these accelerograms for 5% damping are given in Figure 13. The response spectrum for the 2nd earthquake zone and the ground soil type Z3 which is defined in Turkish Earthquake Code [14] is also illustrated in Figure 13. Seismomatch [12] software was used to obtain spectrum compatible acceleration records.

Fault Type	Station Name	Earthquake	Year	Magnitude	Component	PGA(g)	PGV(cm/s)
Near	El Centro Array #4	Imperial Valley	1979	6.53	140	0.485	37.39
	TCU076	Chi-Chi	1999	7.62	N	0.416	64.20
	El Centro Array #5	Imperial Valley	1979	6.53	140	0.519	46.87
	Saratoga Aloha Ave	Loma Prieta	1989	6.93	000	0.512	41.15
	S5051	Superstition Hills	1987	6.22	315	0.377	43.88
	LA Dam	Northridge	1994	6.69	334	0.349	50.81
	Erzincan	Erzincan	1992	6.69	East-West	0.496	64.28
Far	Saticoy	Northridge	1994	6.69	090	0.368	28.88
	TCU067	Chi-Chi	1999	7.62	N	0.325	66.69
	Delta	Imperial Valley	1979	6.53	352	0.351	33.00
	Sun Valley-Roscoe	Northridge	1994	6.69	090	0.444	38.21
	Poe Road	Superstition Hills-02	1987	6.54	360	0.300	32.78
	Hollister Diff. Array	Loma Prieta	1989	6.93	165	0.269	43.86
	TCU079	Chi-Chi	1999	7.62	N	0.393	48.82

Table 4: Two set of accelerograms.

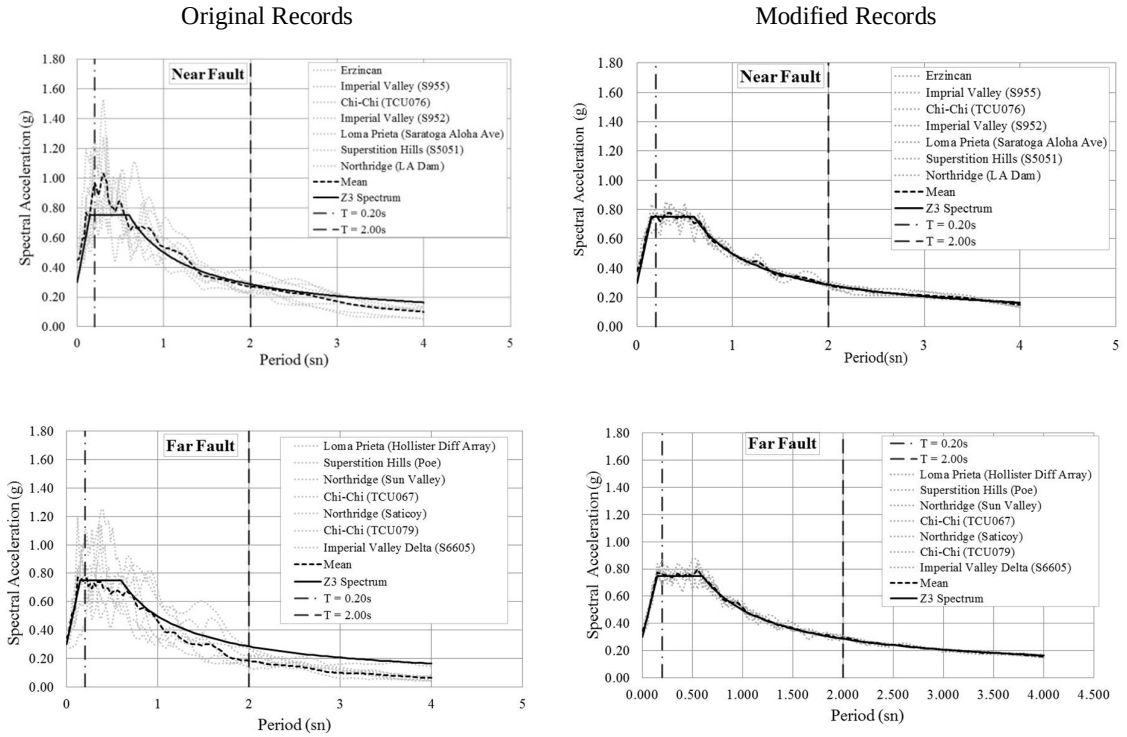


Figure 13: Response spectra for near and far fault type ground motions.

4.2 Second Approach: Partially Compatible Records

A simple engineering approach is being proposed herein to adopt real earthquake records for nonlinear time increment analyses of the columns designed according to a valid code, for design checking process.

The record selection has been done by using the PEER NGA database [13] where 7025 recorded motions were available. An in-house developed software was used to list and download the record automatically and plot the spectra for acceleration at 5% damping, velocity and displacement. The spectra have been saved into a file so that every time a filter is applied, spectra are not re-calculated.

Twelve bins of records, [15], are created where:

1. Earthquake intensity (2/50, 10/50 or 50/50 earthquakes, 3 bins)
2. Far field or near field issue (2 bins)
3. Soil type (firm soil and soft soil, 2 bins)

parameters are checked. Each of these 12 bins have 20 records,

The selected region of the acceleration spectrum curves is a structure oriented decission which is based on the expected displacement ductility proposed at the very beginning of the design. Free standing peripheral columns of a single story precast building may or may not be connected to each other by rigid connection of beams or claddings. Any one of these connections make the structure relatively rigid in comparision to the free standing column. Because of the plastic deformations of the columns and/or connections, on the other hand, structure becomes more flexible with longer fundamental period. It may not be so difficult to define two extreme periods wherein between compatibility will be enforced to the records by scaling them. For this research program the realistic two boundaries have been specified as 0.2 and 2.0 seconds.The upper one corresponds more or less to displacement ductility 4. The lower one is sligthly above the frames rigitly connected to cladding panels. Most of the buildings which are dealt with are generally simple structures with structural behavior essentially similar to first vibration mode of predominat period.

In terms of the selection algorithm, first the acceleration spectrum of the original record is compared to that of the target, in the period window of 0.2 to 2.0sec. The scale factor needed to equate the area below the spectrum of the original record to the area below the target spectrum. The scale factor is applied to the ordinates, so only to the acceleration of the original record. Then the near field vs. far field comparison is made where the distances above 15km are assumed as far field. Finally a comparison is made in terms of the soil type where the records taken on soil with Vs30 higher than 300m/sec are assumed to be recorded on firm soil while records taken on soils with Vs30 lower than 700m/sec are assumed to be recorded on soft soil. There is certainly an overlap in the soil criteria; this is nevertheless unavoidable if one checks the firm and soft soil borders in the guidelines and codes.

The criteria applied have resulted the number of available records, but it should be mentioned that some each bin does not return the same number of available records. For instance, records which are recorded on soft soil and farm field consist of more than 60% of the record pool, thus the rest is shared between three different groups which are far field – firm soil, near field – soft soil, and near field – firm soil. Thus fitting the criteria in far field – soft soil is much easier as compared to setting criteria in the other bins.

The scale factors are set such that average of 20 records does not go below the target spectrum in certain percentages and most of the cases the average spectrum is not allowed to go below the target spectrum at all. Similarly, the average spectrum is not allowed to go above 30% of the target spectrum in any point within the period window. In order to control the difference of the positive and negative peaks, where positive peaks refer to the peaks

above the target spectrum and vice versa, another criterion is also applied to check the indi-individual records. According to this, the individual record is not allowed to go below the target spectrum less than 50%, or above more than 200-300% in any of the peaks. This criterion dictates to select rather smooth records with less peaks, however it is a very harsh criterion to be satisfied. The scale factors in overall are not allowed to be below 0.5 and above 2 in any of the selected records so that the energy content can be controlled.

Two more criteria have been applied to control the energy content, one is the PGV and the other is the Arias Intensity. The purpose of the inclusion of these two criteria is to decrease the scatter, i.e. record-to-record variability of the selected records. In order to do so, a record that fits the target spectrum with the least error has been assigned as the best record, and the selected records are not allowed to have PGV or Arias Intensity values above or below certain ratios as compared to those obtained from the best record. The limits for these criteria had be set so high in some of the bins that they were practically not much effective because the number of available records was already low even without these criteria. Generally, the selected records are not allowed to have PGV and Arias ıntensity values, after scale factors are applied, above 1/0.6 – 1/0.7 and below 0.6-0.7 of that of the best record.

An alternative record selection approach has also been applied in order to see if the application of linear scale factors could be justified. In this approach, all spectra of the relevant bin, i.e. 10/50 earthquake – soft soil – near field etc., have been plotted over the target spectrum and no scale factor is used. In this approach, a cloud analysis is done to find the best matching 20 records.

As an example, acceleration spectrums of 2/50, 10/50 and 50/50 earthquakes for far field firm soil conditions are demonstrated in Figure 14.

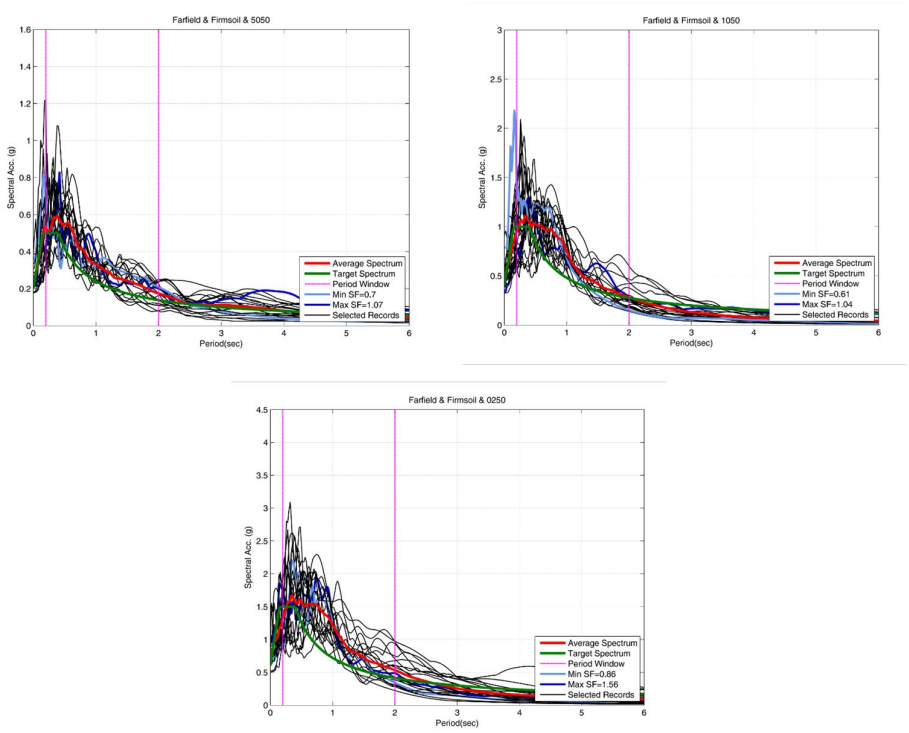


Figure 14: Acceleration spectrums of 2/50, 10/50 and 50/50 earthquakes, [15].

5 NUMERICAL ANALYSES

Two columns namely S30_16 and S40_20 are studied here to define the top displacement demands. Properties of S40_20 column are accessible in Chapter 3. The column of S30_16 has a cross section of 300×300 mm with 1.8% longitudinal reinforcement ratio. The parameters of the material behavior models are as follows: For unconfined concrete compressive strength is 47.7 MPa, strains at the peak stress and the crushing are 0.002 and 0.004, respectively. Confined concrete compressive strength is 55.8 MPa, strains at the peak stress and the crushing are 0.0038 and 0.008, respectively. For steel, the yield stress is f_y=506 MPa, the maximum stress is f_u=616 MPa, the hardening and the ultimate strains are ε_{sh}=0.0126 and ε_u=0.27, respectively.

Lumped mass used on top of the columns are 19.0 and 37.3 kNsec^2/m for S30_16 and S40_20 columns, respectively. The first vibration mode periods of S30_16 and S40_20 columns are 0.80 and 0.65 sec, respectively. A constant damping of 5% is assigned during the dynamic time history analyses. Newmark integration method is used with the parameters of Beta=0.25 and Gamma=0.50.

The attained ultimate top displacements for numerous acceleration records are presented in Figures 15 and 16.

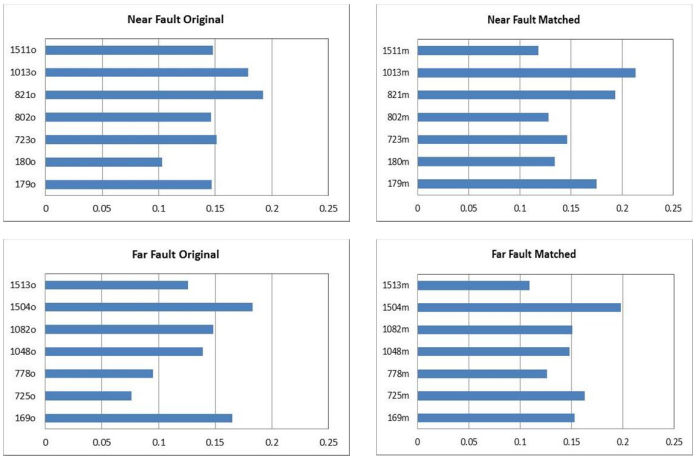
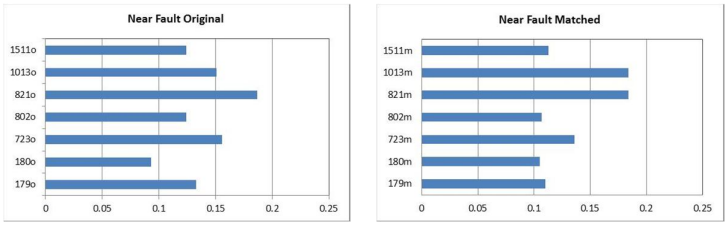


Figure 15: Top displacement demands of S30_16 column.



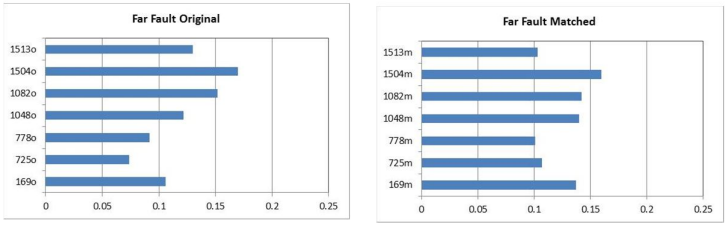


Figure 16: Top displacement demands of S40_20 column.

For S30_16 column, minimum and maximum mean values obtained for different cases are 13.3 cm and 15.8 cm, respectively, Table 5.

	Far Fault Earthquakes		Near Fault Earthquakes	
	Modified	Original	Modified	Original
Mean	15.0 cm	13.3 cm	15.8 cm	15.2 cm
St. Dev.	2.8 cm	3.8 cm	3.6 cm	2.8 cm
CoV	19%	28%	23%	19%

Table 5: Top displacement demands of S30_16 column.

For S40_20 column, minimum and maximum mean values obtained for different cases are 12.1 cm and 13.8 cm, respectively, Table 6.

	Far Fault Earthquakes		Near Fault Earthquakes	
	Modified	Original	Modified	Original
Mean	12.7 cm	12.1 cm	13.4 cm	13.8 cm
St. Dev.	2.3 cm	3.3 cm	3.5 cm	3.0 cm
CoV	18%	28%	26%	22%

Table 6: Top displacement demands of S40_20 column.

The third column is an outer column of the benchmark structure, 2×2 bay, used in the *Safecladding Project*. The column has a cross section of 600×600 mm with 12 longitudinal reinforcement of 25mm diameter. The concrete is C30 and the steel is S420. The free height of the column is 7.2m and it carries a lumped weight of 285kN on top. The analyses have been conducted in OpenSees v2.4 [16] in an in-house developed software that control the OpenSees batch analyses also performs the post-processing. A constant damping of 5% is assigned during the dynamic time history analysis. The achieved ultimate top displacements for numerous acceleration records are presented in Figure 17.

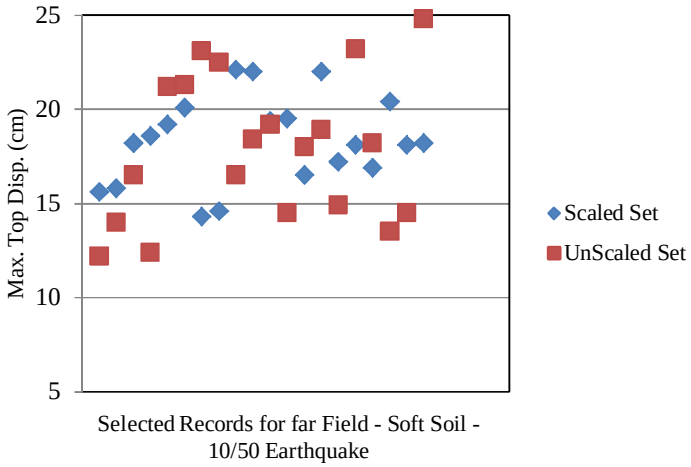


Figure 17: Top displacement demands of the column having a cross section of 600×600 mm.

For this column, mean values of the top displacement demand for the original and scaled accelerograms are 17.89 cm and 18.34 cm, respectively, Table 7.

	Max. Top Disp. (cm)	
	Scaled	Original
Mean	18.34	17.89
St. Dev.	2.33	3.86
CoV	13%	22%

Table 7: Top displacement demands of 600×600 mm column.

The selection has been made once again by using the cloud approach where a scale factor of 1.0 is used for all records, also considering the 12 bins explained above, and the best-matching 20 records are selected without considering any other filter. The results suggest that the coefficient-of-variation, a parameter that represents the scatter of the results, is 13% in the scaled records and 22% when the cloud analysis is used for the selection of the records. This justifies the efforts made for selecting the records by using the criteria mentioned above and using scale factors to multiply the ordinates of the records.

6 CONCLUSIONS

A study is presented in an effort on the response of columns in single story precast structures in seismic areas. Based on the partial results of the experimental and analytical works, the following conclusions can be drawn for the time being:

- The assessment of the test results indicated that the application of smooth or roughened column-socket foundation connection detail doesn’t have negative effects on the overall behavior.
- The displacement protocol proposed to represent the near-fault effects of earthquakes have been applied to two of the tests .The observed behavior, especially the back bone curves, were almost similar irrespective to the shape of the cycles applied.

- Almost all the envelopes of the lateral load-displacement hysteresis obtained from tests were close to the capacity curves or backbone curves determined through not only by *pushover* but by *nonlinear static analysis* for constant axial load as well.
- After having bilinearized the backbone P-δ curves of tested specimens realistic displacement ductilities and initial stiffnesses have been achieved. It is interesting to note that the lateral load reduction factors obtained are generally above the corresponding values specified by present Turkish Earthquake Code. On the other hand the top displacements estimated through nonlinear time history analyses based on nearly code compatible real earthquake records are generally bigger than the same code limits. Therefore static considerations to limit the top displacements are not coinciding with displacement demands obtained through nonlinear time history analyses. Additional provisions are needed. The design proposed by existing code should be revised accordingly. During this process, it would be important to notice that attained equivalent damping ratio for undamaged condition is smaller than 5%. In addition to this it can be concluded that the cracked to virgin flexural stiffness ratio is observed as almost double of the code suggested value.
- The second approach about acceleration selection namely p*artially compatible records case* are efficient on the selection of most proper real earthquakes among the reliable and available data, being on the safe side for nonlinear time history analyses. It should be noted that the scale factors are only *0.80* and *1.87* which means that their influence on the energy content is almost negligible.
- It was employed a large database of recorded and processed motions, the PEER NGA database, where more than 7000 records are available. The software developed in-house for the *Safecladding Project* is used to select, filter and scale the records in 12 different bins depending on the earthquake intensity, soil type and the near- or far-field conditions. The results suggest that the selection can be made by constraining the scale factors between 0.8 and 2.0 for all cases, something that is required if one does not wish to alter the energy and cycle content of the natural record during the linear scaling process.

REFERENCES

[1] Saatcioglu M, Mitchell D, Tinawi R, Gardner NJ, Gillies AG, Ghobarah A, et al. The August 17, 1999, Kocaeli (Turkey) Earthquake – Damage to Structures. *Can J Civ Eng* 28: 715-37, 2001.

[2] Ataköy H, 17 August Marmara Earthquake and the Precast Structures Built by TPCA Members. *Turkish Precast Concrete Association*, Ankara, Turkey, 1999.

[3] Sezen H, Elwood KJ, Whitaker AS, Mosalam KM, Wallace JW, Stanton JF, *Structural Engineering Reconnaissance of the August 17, 1999*, Kocaeli (Izmit), Turkey. Earthquake Rep No 2000/09. Pacific Engineering Research Center. University of California, Berkeley, CA, 2000.

[4] Bruneau M, Building Damage from the Marmara, Turkey Earthquake of August 17, 1999. *J Seismo* 6(3): 357-77, 2002.

[5] Sezen H, Whittaker AS, Seismic Performance of Industrial Facilities Affected by the 1999 Turkey Earthquake. *J Per Const Fac* ASCE 20(1): 28-36, 2006.

[6] Wood SL, Seismic Rehabilitation of Low-Rise Precast Industrial buildings in Turkey In: Wasti T, Ozcebe G (eds) *Advances in Earthquake Engineering for Urban Risk Reduction*. NATO Science Series. IV. Earth and Environmental Sciences: Kluwer Academic Publishers 66: 167-77, 2003.

[7] Karadogan F., 'Prefabricated Industrial Type Structures of Adapazarı', *Irregular Structures*, European Association of Earthquake Engineering, Task Group 8, Asymmetric and Irregular Structures, Istanbul, Vol. 2, October 1999.

[8] Karadogan F., Yuksel E., Ilki A., 'Deformability Limits and Ductility of Reinforced Concrete Bare Frames', *First Japan – Turkey Workshop On Earthquake Engineering*, Istanbul,Vol.1, March 1997.

[9] Karadogan F, Yuksel E, Yuce S, Taskın K, Saruhan H, Experimental Study on the Original and Retrofitted Precast Columns. *Technical Report (in Turkish)*, Istanbul Technical University, 2006.

[10] Chopra AK. *Dynamics of Structures Theory and Applications to Earthquake Engineering*, Prentice Hall: Englewood, 2001.

[11] SeismoStruct, "Computer program for static and dynamic nonlinear analysis of framed structures". (http://www.seismosoft.com).

[12] Seismomatch Software, (http://www.seismosoft.com/en/HomePage.aspx).

[13] PEER NGA Database. Pacific earthquake engineering research center: NGA database. (http://peer.berkeley.edu/peer_ground_motion_database/)

[14] Turkish Earthquake Code, 2007.

[15] http://web.itu.edu.tr/~iebal/Dr_Ihsan_Engin_BAL/SafeCladding_EU_Project.html

[16] Opensees Software, (http://opensees.berkeley.edu/).

COMPDYN 2013
4th ECCOMAS Thematic Conference on
Computational Methods in Structural Dynamics and Earthquake Engineering
M. Papadrakakis, V. Papadopoulos, V. Plevris (eds.)
Kos Island, Greece, 12–14 June 2013

SHAKE TABLE TESTING OF A FULL-SCALE FIVE-STORY BUILDING: SEISMIC PERFORMANCE OF PRECAST CONCRETE CLADDING PANELS

Elide Pantoli[1*], Michelle Chen[1], Tara Hutchinson[1], Glen A. Underwood[2], and Mark Hildebrand[3]

[1] University of California, San Diego, 9500 Gilman Drive, La Jolla, CA 92093-0085
elide.pantoli@yahoo.it; mchen.ucb@gmail.com; tara@ucsd.edu

[2] Clark Pacific, 1980 South River Road, West Sacramento, CA 95691
gunderwood@clarkpacific.com

[3] Willis Construction Co., Inc., 2261 San Juan Hwy, San Juan Bautista, CA 95045
mhildebrand@pre-cast.org

Keywords: Façades, Precast concrete cladding, shake table tests.

Abstract. *Precast concrete cladding (PCC) is used in many regions of the world as an architectural façade for buildings. Use of PCC is appealing in that panels can be constructed off-site and quickly installed on a finished structural skeleton to complete the building envelope. Detailing of the PCC panel joints and connections to the building must carefully consider the movement that the building will undergo during its service life – including the potentially intense effects of an earthquake. Although code prescribed seismic design requirements provide nominal guidance regarding the desirable features of the PCC and its connections, much is still unknown regarding their actual behavior during an earthquake. Moreover, to date, only a handful of full-scale tests have been conducted to investigate the behavior of the PCC under earthquake loading, and even fewer have been conducted with the PCC attached to a full-scale building.*

To address the need for system-level experimental data, a full-scale five-story building was tested on the Network for Earthquake Engineering Simulation (NEES) Large Outdoor High-Performance Shake Table at the University of California, San Diego. This structure was seismically tested in two phases, namely, while isolated and fixed at its base. Two different types of façades were installed on the building, namely a lightweight metal stud system overlaid with stucco and a punchout window-style PCC system. Push-pull, sliding, flexing, and a new yielding connection were investigated within the PCC system. In addition variation in the panel corner details were implemented. This paper describes the performance and the measured experimental response of the precast concrete cladding panels installed at the upper levels of the test building.

1 INTRODUCTION

Recent earthquakes have demonstrated that damage to nonstructural components and systems (NCSs) in buildings pose life safety hazards to the building occupants and lead to significant economic losses and repair downtime [1]. A particularly important and sensitive NCS is that which provides the exterior enclosure. Not only does this subsystem represent a significant portion of the cost of the building, varying between 9% and 18% of the total cost for different types of buildings [2], but exterior enclosures have also realized extensive damage in past earthquakes [3]. A prevalent type of façade commonly used worldwide is the precast concrete cladding (PCC) panelized system. In this type of façade, concrete panels are fabricated at a precast facility and brought to the site just prior to installation. They are attached to the building with steel connections that must provide a load path to the structure transferring not only their own weight, but also any lateral forces (wind/seismic) imposed on the panels. The connection system, however, must allow relative motion of the panel and structure due to the horizontal building displacements – both in-plane and out-of-plane – during seismic motions. Connections that hold the panels to the structure for out-of-plane forces while accommodating these *interstory drift* displacements are designated as *push-pull* or *tie-back* connections. In practice, two types of push-pull connections are used, namely, sliding connections and flexing rod connections. In both cases the out-of-plane force is resisted by the axial action of the rod. In a sliding connection, the panel is allowed to move in the in-plane direction via sliding of the connection rod in a slot. In contrast, a flexing rod connection allows movement through the bending of the connection rod. In either case, the sliding or bending capacity must be enough to allow the maximum interstory drift. The performance of the connections can vary considerably by changing the length (L) to diameter (Φ) ratio of the rods. For sliding rod connections, a longer rod may facilitate the installation of the panels, however, if the rod is too long it might not be stiff enough and may begin to yield under bending during a large earthquake. For the flexing rod connections, a shorter rod might not be able to provide enough ductility but a longer rod might occupy too much space. Another detail of critical importance for the performance of the PCC panels is the size of the panel-to-panel joints: the joints have to be big enough to avoid collision of the panels during earthquake motion. However, for aesthetic reasons, large joints are undesireable.

Historically, this construction method has performed well in past earthquakes – including the 1994 Northridge event, which resulted in large story drifts in buildings with limited damage to precast cladding systems [4]. Nonetheless, instances of damage to these panel systems have been reported in several earthquakes. Recently for example, during the Christchurch earthquake in 2011 in New Zealand several panels failed due to inadequate detailing. Moreover, extensive cracking, corner crushing, residual displacement of the panels and rupture of the seal at panel interfaces were reported [3]. During the Chile earthquake in 2010, several PCC panels collapsed in the out-of-plane direction. In one case, the cause of collapse was local bending failure of the flanges of an embedded anchor channel, which allowed pullout of the sliding bolt [5]. Several pullout failures of tie-back connections were also observed following the L'Aquila earthquake in Italy in 2006 [6]. Large scale testing of these PCCP, particularly if integrated within a building system would help understand their behavior. However, such testing is highly complex and costly, therefore to-date only a few full-scale experiments on these panels have been conducted [7,8].

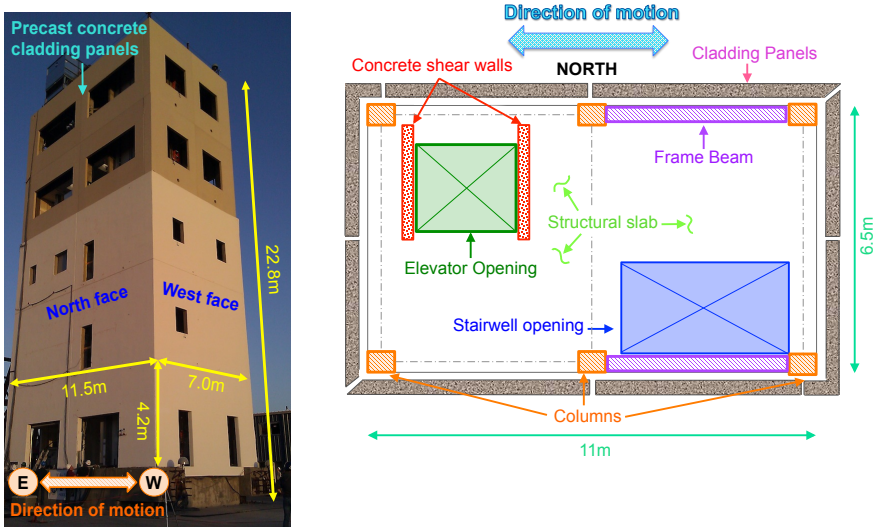
1.1 Scope of this Paper

In April and May 2012, a landmark test of a five-story building constructed at full-scale and completely furnished with nonstructural components and systems (NCSs) was conducted

at the University of California, San Diego (UCSD) Network for Earthquake Engineering Simulation (NEES@UCSD, 2013) facility. The project, coined *Building Nonstructural Components and Systems (BNCS)* was realized by a unique collaboration between Academe, Industry and Government and hundreds of individuals with expertise in structural and nonstructural design, earthquake engineering, and construction and management practices (BNCS, 2013). The full-scale building-NCS system was seismically tested in a base isolated and fixed based configuration on the Large High-Performance Outdoor Shake Table (LPOSHT) at the UCSD-NEES facility. Wrapping the exterior of this building were two types of façades, namely; light weight metal stud balloon-framing overlaid with a synthetic stucco finish (first three floors) and precast concrete cladding panels (PCC panels) (two upper floors). This paper will describe the test parameters considered in the design of the PCC panels installed at the upper floors of the building, their instrumentation, the overall test protocol, and select physical and analog measured results specific to the PCC panels.

2 DESCRIPTION OF THE EXPERIMENT

The poured in place reinforced concrete five story building was fully equipped with a wide range of NCSs, including a fully functional passenger elevator, stairs, mechanical and electrical services, ceiling and piping subsystems, as well as roof mounted equipment. Different occupancy types were specified for each floor level within the building. The fourth and the fifth floor were equipped as medical floors (resembling an intensive care unit and a surgical suite, respectively). The overall height of the specimen, including its foundation, was 22.8m, its length was 11.5m and its width 7m. The bare structure had an estimated weight of 3010 kN, excluding the foundation which weighed 1870 kN. Including the NCSs, the building weighed approximately 4420 kN. The floor plan was characterized by the presence of two large openings (one for the stairs and one for the elevator) and two walls encasing the elevator shaft (Figure 1). It is important to underline that the LHPOST at NEES@UCSD allows movement only in the East-West direction (longitudinal direction of the building). Two bays in the longitudinal (shaking) direction and one bay in the transverse direction provided the load bearing system. Lateral seismic resistance was provided by a pair of identical one-bay special moment resisting frames in the Northeast and Southeast bays.



(a) (b)

Figure 1: General views of the test building: (a) photograph of the North and West sides of the building and (b) plan view of a typical floor

The building was initially tested while isolated from the shake table with four high damping rubber bearings installed between at each of the four corners of the structure. Following the base isolation (BI) test phase, the foundation was fixed to the table and the building was then tested with a fixed base configuration (FB). The building was subjected to a suite of earthquake motions of increasing intensity: seven motions were used while in the BI configuration and six motions while in the FB configuration. In addition, white noise and pulse base excitation were input before and after earthquake motion input. Initial motions were selected and scaled to an intensity associated with a serviceability event. Motions from the Maule, Chile (2010) and the Pisco, Peru' (2007) earthquakes were chosen due to their inherently long duration of strong shaking. The latter record was also input into the model multiple times at increasing amplitudes. Two final motions were spectrally matched and scaled records obtained during the Denali earthquake in Alaska (2002). The goal of these motions was to reach and surpass the design level earthquake. The sequence of motions applied in the first portion of the BI test phase was repeated for a portion of the FB test phase. In some cases the actual motion (AM) was used as the target, while in other cases the original motion was spectrally matched (SM) to the ASCE 7-05 design spectrum assuming a high seismic zone in Southern California (site class D). The LAC motion was run twice in the BI configuration. The full test protocol is shown in Table 1.

Base	Station-scale (Earthquake)	Name	Type	Notes
Isolated (BI)	Canoga Park-100% (1994 Northridge earthquake)	BI-1: CNP100	SM	Serviceability level
	LA City Terrace-100% (1994 Northridge earthquake)	BI-2:LAC100	SM	Serviceability level
	LA City Terrace-100% (1994 Northridge earthquake)	BI-3:LAC100	SM	Serviceability level
	San Pedro-100% (2010 Maule-Chile earthquake)	BI-4:SP100	AM	Long duration
	ICA-50% (2007 Pisco-Peru earthquake)	BI-5:ICA50	AM	Long duration, multiple runs
	ICA-100% (2007 Pisco-Peru earthquake)	BI-6:ICA100	AM	Long duration, multiple runs
	ICA-140% (2007 Pisco-Peru earthquake)	BI-7:ICA140	AM	Long duration, multiple runs
Fixed (FB)	Canoga Park-100% (1994 Northridge earthquake)	FB-1:CNP100	SM	Serviceability level
	LA City Terrace-100% (1994 Northridge earthquake)	FB-2:LAC100	SM	Serviceability level
	ICA-50% (2007 Pisco-Peru earthquake)	FB-3:ICA50	AM	Long duration, multiple runs
	ICA-100% (2007 Pisco-Peru earthquake)	FB-4:ICA100	AM	Long duration, multiple runs
	Pump Station #9-67% (2002 Denali eq.)	FB-5:DEN67	SM	~Design Earthquake
	Pump Station #9-100% (2002 Denali eq.)	FB-6:DEN100	SM	~>50% larger than Design Earthquake

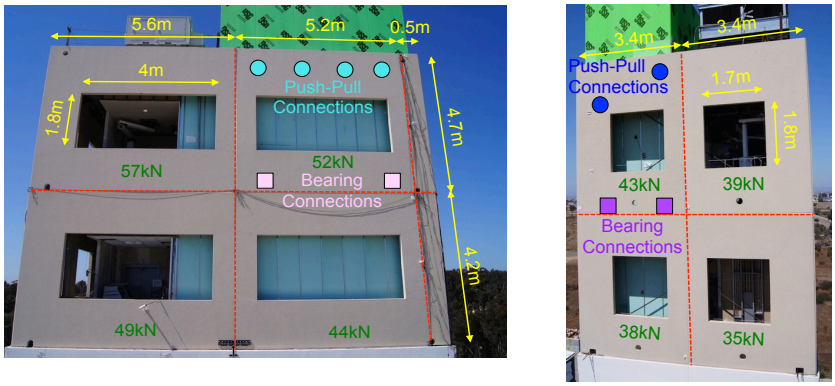
Table 1: Seismic test protocol (AM = actual motion as target; SM = spectrally matched motion as target).

3 DESCRIPTION OF THE PRECAST CONCRETE CLADDING PANELS

Through support of the Charles Pankow Foundation and an industry advisory board within the Precast Concrete Institute (PCI), a team of researchers and precast concrete producers worked closely on the design, construction, installation, and instrumentation of the precast concrete panels tested within the BNCS building specimen.

3.1 Overview

Panels selected for this test program were punched window wall units, meaning they spanned from floor to floor with openings provided only for windows. Two panels per side of the building were installed at each floor, resulting in a total of 16 panels mounted on the test building. Eight panels translate predominantly in the in-plane direction (denoted as *IP* panels) and eight panels tilt predominantly in the out-of-plane direction (denoted *OP* panels). Connection of the panels to the building skeleton were facilitated by steel embeds installed in the slab, beams and columns. Each panel was supported by two bearing connections at the bottom welded to embeds in the floor slab, and push-pull connections at the top (four in the IP panels and two in the OP panels). The IP panels had an average dimension of 5.4m x 4.4m and an average weight of 50 kN, while the OP panels were smaller, with an average dimension (not considering the return corner) of 3.4m x 4.4m and an average weight of 39 kN. All panels were 125 mm in thickness and generally reinforced with #4 bars at 305mm o/c spacing in both directions. Details of the panel geometry can be found in Figure 2. Nomenclature adopted in this paper to describe the various panels and connections is shown in Figure 3. Two different types of corner joints were tested, namely, miter joints and butt joints (Figure 4). Miter joints were installed in the South-West and North-East corners, while butt joints were installed on the North-West and South



(a) (b)

Figure 2: View of the panels showing the geometry and the typical location of the connections: (a) IP panels on the South side and (b) OP panels on the East side

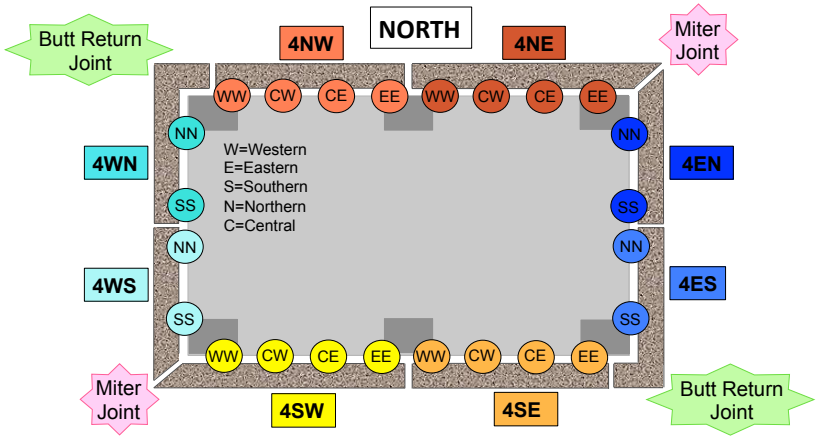
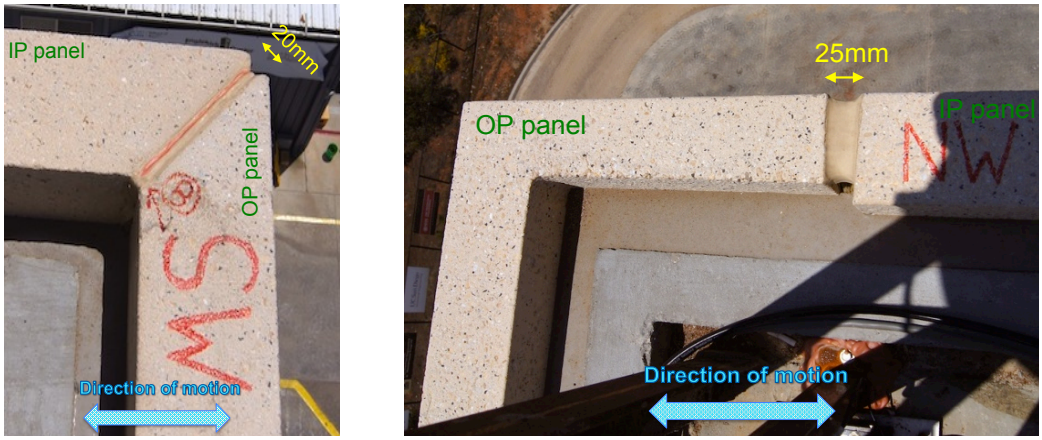


Figure 3: Nomenclature used to identify the panels and connections on the fourth floor. Nomenclature for the fifth floor panels are similar, with the exception that the first digit becomes "5".



(a) (b)

Figure 4: Corner joints: (a) miter joint in the SW corner and (b) butt return joint in the NW corner

3.2 Parameters of specific interest in the test program

The behavior of PCCP connections and panel joints was of paramount interest in this experiment because panel collisions and connection failures greatly affect whether panels become separated from a structure in a seismic event. Incidental damage and resulting affects on serviceability of the PCCP are also affected by panel joints and connectivity. For the IP panels, the main purpose of the connections is to absorb the relative drift from floor to floor, or interstory drift, while maintaining the ability to support the panel in the out-of-plane direction. This is commonly facilitated in practice via sliding or flexing rod connections (Figure 5), and is codified in United States practice within ASCE 7, Section 13.5.3 as follows [9]:

> ***13.5.3 Exterior Nonstructural Wall Elements and Connections***. *Exterior nonstructural wall panels or elements that are attached to or enclose the structure shall be designed to accommodate the seismic relative displacements defined in Section 13.3.2 and movements due to temperature changes. Such elements shall be supported by means of positive and direct structural supports or by mechanical fasteners in accordance with the following requirements:*

> *a. Connections and panel joints shall allow for the story drift caused by relative seismic displacements (D_p) determined in Section 13.3.2, or 0.5 in. (13mm), whichever is greatest.*
> *b. Connections to permit movement in the plane of the panel for story drift shall be sliding connections using slotted or oversize holes, connections that permit movement by bending of steel, or other connections that provide equivalent sliding or ductile capacity.*
> *c. The connecting member itself shall have sufficient ductility and rotation capacity to preclude fracture of the concrete or brittle failures at or near welds.*

These code provisions provide a good basis for design of cladding joints and connections, but still leave designers to their own devices when it comes to defining the meaning of qualitative terms like *"sufficient ductility and rotation capacity"*, especially considering the allowance of yielding in a connection to accommodate story drift displacements.

In the tested connections, the key variables for these mechanisms to work properly are the ratio of rod length to rod diameter (L/Φ), and the ratio of relative seismic displacements, D_p to rod length, L (D_p/L). It should also be noted that flexing rod connections need to be constructed of mild steel such as ASTM A36 or a ductile SAE range of ASTM A108 material to preclude a premature brittle fracture during cyclic bending. Sliding connections are often facilitated by a sliding rod and oversized hole in the support clip angle, with long plate washers either side to maintain contact (Figure 5a-b). Sliding connections can also be constructed with an embedded channel that allows the bolt to slide inside the channel on the panel side of the connection. This configuration was not tested. In general, a sliding connection works best when the surface with the slot is close to the surface that is sliding, i.e. when the rod is short. If the sliding rod is too long, bending and rotation of the rod will cause the connection to bind, leading to a shear failure of the rod. On the other hand, flexing rod connections benefit from longer rod lengths. The longer rod length helps reduce inelastic strains in the rod for a given displacement (Figure 5c-d). However, it should be noted that from a practical point of view, long rods may require too much space, infringing on interior finishes rather than being concealed in the perimeter framing spaces.

In these tests, several rod lengths were tested for each of the sliding and flexing rod connections, as summarized in Table 2. The diameter of the rods was 20mm for all IP panel connections. Pictures of a sliding connection with a long rod (SRL) and flexing rod connection with long rod (FRL) are provided in Figure 6. The IP panels on the West side of the building were installed with sliding rod connections, while those on the Eastern side were installed with flexing rod connections. The exact distribution of the upper connections in the panels is shown in Figure 7.

Type of connection	Short rod length (mm)	Short rod L/Φ	Medium rod length (mm)	Medium rod L/Φ	Long rod length (mm)	Long rod L/Φ
Sliding	snug	-	90	4.6	180	9.3
Flexing rod	300	16	405	21.3	510	26.6

Table 2: Summary of rod lengths tested

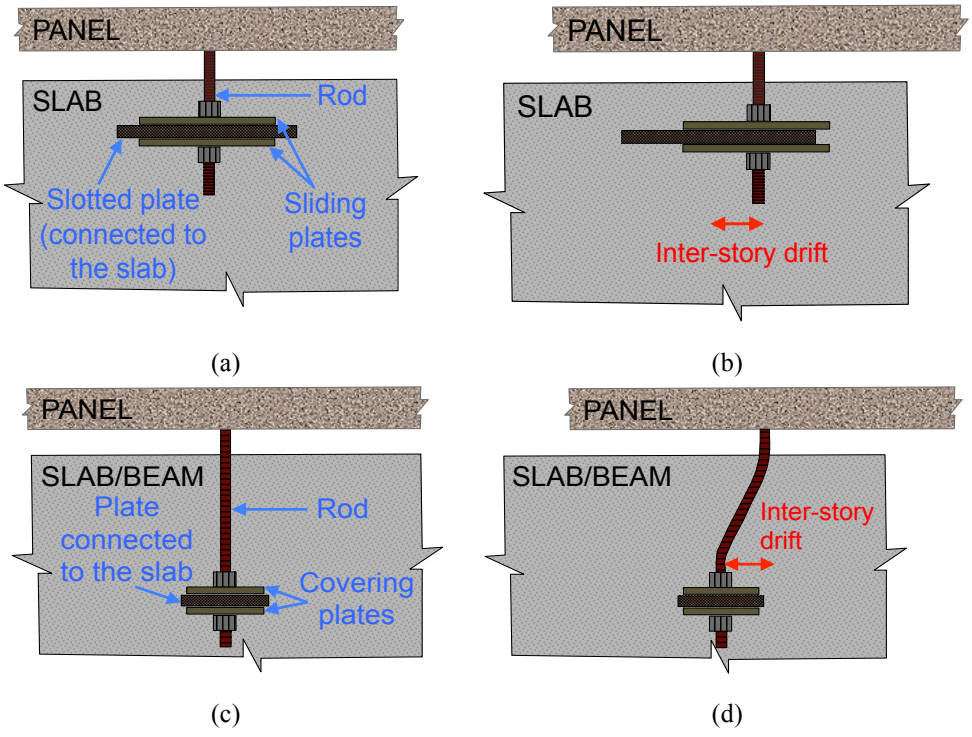


Figure 5: PCCP connections between structural skeleton and panel (schematic on left, desired behavior on right): (a), (b) sliding rod connection, and (c), (d) flexing rod connection.

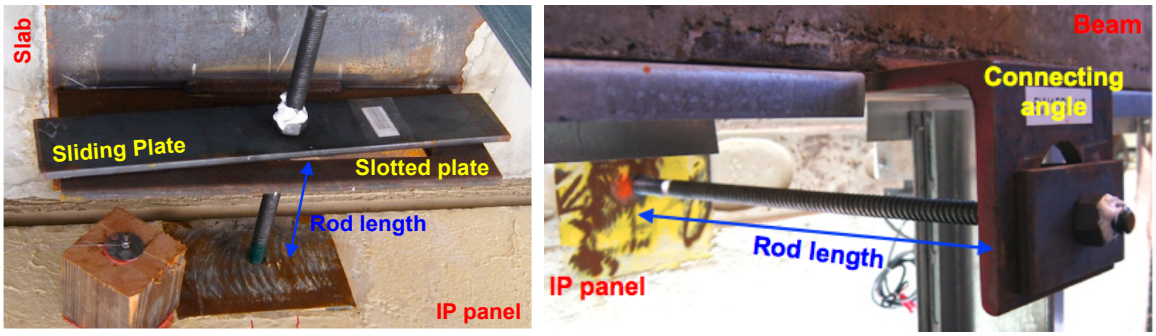


Figure 6: Photographs of the connection details for the IP panels: (a), sliding rod connection with long rod and (b) flexing rod connection with long rod.

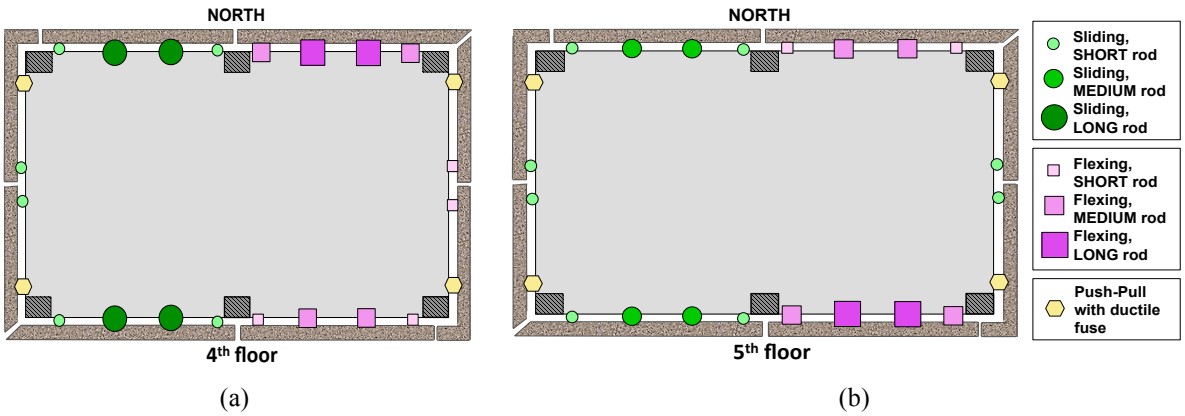


Figure 7: Location of the different types of connections: (a) fourth floor and (b) fifth floor.

In addition to the traditional sliding and flexing connections, which are designed with the intent of allowing movement of the panels relative to the building, a new connection detail was explored. This detail would allow for smaller vertical joints between panels at the corners of the building, which is an architecturally appealing performance feature. This strategy was implemented within the OP panel connections at corner columns. Here, the width of vertical corner joints was intentionally undersized to 25mm (butt joint) and 19mm (miter joint). These joint sizes are intended to be sufficient to accommodate the elastic interstory drift of the structure without closing, but would not accommodate inelastic displacements that can be expected in the design basis earthquake (DBE). For this case, panel tilt (and joint closures) ranged on the order of 100mm for the most severe motions tested. Upon panel collision at the joint, the panel connection would activate a ductile fuse in the form of a cantilevered bending plate designed to yield as the structural column drifts along the shaking direction, while the panel motion is restrained by the contracted joint during contact (Figure 8). The ductility is provided by ensuring the expected plastic flexural capacity of the plate is less than the capacity of the welds, the rod in tension, and the concrete anchorages of the embeds in the column and the panel itself. For these connections, the rod was 700mm long, and the diameter was 25mm. Each of the OP panels had two push pull connections at the top of the panel, namely a corner push pull connection with ductile fuse (PPDF) as shown in Figure 8, and either a sliding rod connection with snug rod (SRS) or a flexing rod connection with short rod (FRS) connection (for the exact location see Figure 7).

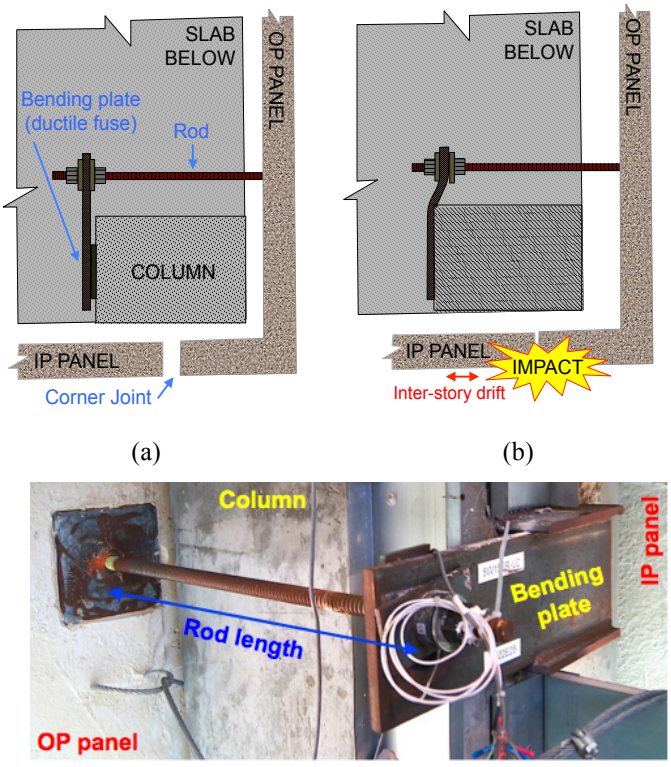


Figure 8: Push-pull connection with ductile fuse on the OP panels: (a), (b) drawings showing their desired behavior and (c) photograph.

3.3 Design, material properties and installation

Panel design, construction, and installation were performed by a U.S. West-Coast precaster with expertise in precast concrete cladding systems. Structural design criteria and detailing conformed to requirements of ASCE 7-05, ACI 318-08, PCI MNL 120-04 and ANSI/AISC 360-05 [9,10,11,12] for regions of high seismicity. Nonlinear time history analyses of the building were conducted and used to predict interstory drift ratios (IDRs) anticipated during design and maximum credible earthquake events [13] and thereby size the joints and design the slotted and flexing rod connections. Design forces were estimated using the building target S_{DS} and the linear force distribution estimate of ASCE 7 (equations 13.3-1). Panels were 127mm thick and reinforced with #4 bars A615 Grade 60 rebar spaced at 300mm on center. Additional #5 bars were added around window openings, and #3 horizontal bars at 150mm o/c were used in piers adjacent to windows. The specified compressive strength of concrete at 28 days was 34MPa with a unit weight of 2400 kg/m^3. Coil rods and bolts were ASTM A108 steel with yield and ultimate strengths of f_y = 410MPa and f_u = 550MPa, respectively.

Panels were cast off-site at a precast plant and shipped to the NEES@UCSD facility on the day of installation. In total, installation of the 16 panels on the building was performed during approximately five days, with the following activities:

- Day one: All connections were prepared, including welding of connection angles to the structural embeds cast in the building and placement of the rods;
- Day two and three: Eight panels per day were installed on the building; and
- Day four and five: Welding of all bearing connections at the base of the panels to the embeds in the structural slab and frame was complete.

Finally, several days were needed to place caulking between panel-to-panel joints and between the balloon framing-to-panel joints.

3.4 Instrumentation

A total of 65 analog sensors monitored the behavior of the cladding panels. The main goals were to monitor:

- The displacement at the top of the panel relative to the structural skeleton. In particular the in-plane movement of the IP panels and the out-of-plane movement of the OP panels were closely monitored;
- The acceleration in both IP and OP panels in order to understand a possible magnification of the acceleration in the panels. Vertical and East-West accelerometers were deployed to reach this goal; and
- Force in the connection rods, especially for the PPDF connections.

Due to the large number of panels and connections compared to the number of sensors available, measurement locations were concentrated in the South-East corner of the building, as this was considered the most flexible. In addition to the analog sensors, four video cameras were installed to monitor the behavior of the panels during the FB testing: these recorded the behavior of the two types of corner joints, namely a PPDF connection and a flexing rod connection.

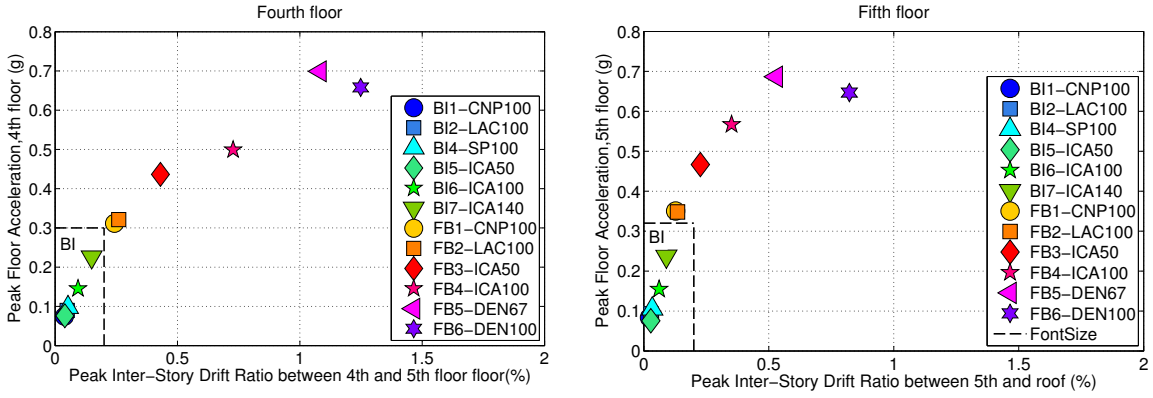
3.5 Physical inspections

Interior inspection of the cladding panels and connections was performed after each test (except for the first BI motions). In addition, exterior inspections, as time allowed, were per-

formed to evaluate the state of crack patterns on the panels as well as condition of the sealant between the panels. Upon observation of permanent displacement of a rod, selected connection rods were replaced between earthquake events. In addition, a complete replacement of the rods in the IP panels was performed prior to FB-4: ICA100, as the impending motion FB-5: DEN67 was intended to serve as the design earthquake event.

4 GLOBAL BUILDING RESPONSE

Figure 9 shows the peak floor accelerations (PFA) and peak interstory drift ratios (PIDR) of the building at its fifth and fourth floor. It is noted that accelerations were measured at every corner of each floor of the building, and displacements were obtained by double integration of these accelerations. The peaks in Figure 9 are the average of the maximum values of each of the four corners. As can be seen from Figure 9, the values of the PIDR and PFA were quite small for all BI tests, with the PIDR no greater than 0.15% at the 4-5th floor and the peak acceleration no greater than 0.23g on the fifth floor, during motion BI-7: ICA140. The first two FB motions, which were scaled to achieve serviceability demands within the building, reported peak accelerations and interstory drift ratios only slightly larger then those obtained in the final BI motion. The maximum value of PFA was obtained during motion FB-5: DEN67, when the structure observes considerable plastic deformation. The PFA at fifth floor was 0.68g, while 0.99g was measured at the roof slab. The largest PIDRs obtained on levels 4-5 and 5-roof were observed during the final motion FB-6: DEN100, with 1.2% and 0.8% attained on levels 4-5 and 5-roof, respectively. These values were lower anticipated, as soft story mechanism developed in the lower levels of the building, with very large PIDRs approaching 6% for the first two floors [14].



(a) (b)

Figure 9: Peak interstory drift ratio versus peak floor acceleration: (a) fourth floor, (b) fifth floor

5 DEVELOPMENT OF DAMAGE IN THE IP PANEL CONNECTIONS

Physical observations determined that, where it occurred, the damage to connections between the IP panels and building both for sliding rod and flexing rod connections, manifested primarily as a permanent bending of the rods. Even so, none of the rods actually fractured. This is likely due to a combination of ductile steel rod materials, bending mechanisms in the welded angle support clips, and the drifts imposed which were less than 1.5% (Figure 9). In what follows, the damage level will be indicated with the estimated lateral plastic distortion and angle of permanent bending of the rods.

5.1 Sliding rod connections

The sliding connections with snug rod (SRS) behaved well, as rod bending is virtually eliminated when the rod is snug to its connecting plate. Short rods within a sliding connection manifested no visible damage. These observations were confirmed during removal of the panels. In contrast, medium rod length sliding connections (SRM) developed plastic yielding during progressively increasing interstory drift demands, potentially due to abutting of the rod against the slotted plate or binding of the connection. Table 3 summarizes the physical observations, including noting when the rods were replaced during the motion sequence for the SRM at the 5th floor. The first notable damage to these connections was observed following motion FB-1. The plastic bend of the connection was barely visible and it was measured after the rod was removed. Subsequently, no additional visible damage to the SRM connections was noted until motion FB4-ICA100, during which one of the rods was severely permanently bent (25mm of residual drift in the connection, forming a 27° angle with the straight direction) as can be seen in Figure 10. The PIDR during this motion was only 0.35%. Interestingly, the residual deformation of the rod of 25mm was greater than the PID of 15mm, suggesting that the connection accumulated drift deformations through a ratcheting mechanism as the connection cycled back and forth, binding in one direction, while sliding in the other. This connection was replaced and was not damaged further, despite the much larger PIDR in subsequent motions.

Test	PID(PIDR) 5th floor-roof	Panel 5SW		Panel 5NW	
		Connection CW [Residual Deformation]	Connection CE [Residual Deformation]	Connection CW [Residual Deformation]	Connection CE [Residual Deformation]
BI	4mm(0.09%)	OK	OK	OK	OK
FB1	5mm(0.13%)	2mm *Replaced*	OK	OK	OK
FB2	6mm(0.14%)	OK	OK	OK	OK
FB3	10mm(0.23%)	OK *Replaced*	OK *Replaced*	OK *Replaced*	OK *Replaced*
FB4	15mm(0.35%)	25mm/27° *Replaced*	OK	OK	OK
FB5	23mm(0.53%)	OK	OK	OK	OK
FB6	35mm(0.82%)	OK	OK	OK	OK

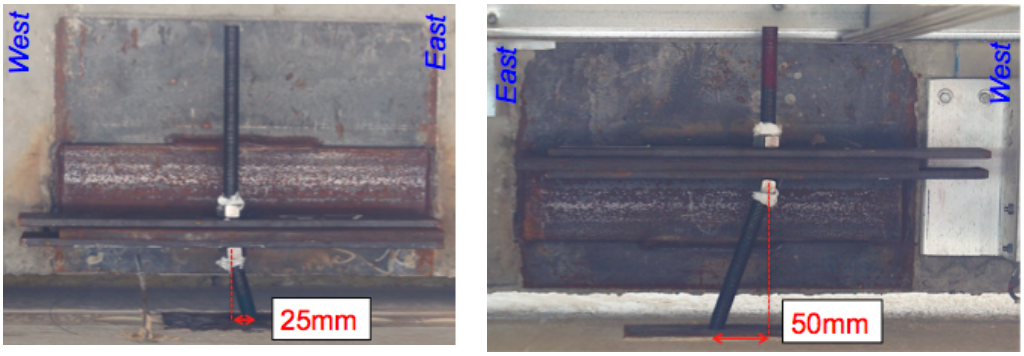
Table 3: Progression of damage to SRM connections

Table 4 presents the progression of damage for the sliding connection with long rods (SRL) and their associated times of replacement. Similarly, these connections were not damaged during the BI tests, however, significant permanent deformation was observed during the FB motion sequence. In particular during FB-2:LAC100, when a PIDR of only 0.2% was reached, three of four connections were observed with permanent bends during post-event inspection. As it was clear that this configuration was not optimal, during replacement of these rods, the outside nut was not reinstalled to allow the rod to only carry tension, and to alleviate binding from clamping of the plate washers during rotation. This new configuration performed reasonably well during motion FB-4: ICA100 (with only one connection slightly damaged). During motions FB-5 and FB-6 (PIDR=1.2%), however, these connections were severely

plastically bent again, demonstrating the difficulty of utilizing a very long rod for this type of connection. Examples of the physical damage to the SRL connections are shown in Figure 10.

Test	PID(PIDR) 4th-5th floor	Damage to panel 4SW		Damage to panel 4NW	
		Connection CW [Residual Deformation]	Connection CE [Residual Deformation]	Connection CW [Residual Deformation]	Connection CE [Residual Deformation]
BI	6mm(0.15%)	OK	OK	OK	OK
FB1	10mm(0.24%)	25mm (14°) *Replaced*	OK	OK	OK
FB2	11mm(0.26%)	25mm (14°)	25mm (14°)	OK	30mm (17°)
FB3	18mm(0.43%)	55mm (30°) *Replaced (no nut)*	50mm (27°) *Replaced (no nut)*	OK *Replaced (no nut)*	60mm (32°) *Replaced (no nut)*
FB4	31mm(0.72%)	OK	OK	10mm (<1°)	OK
FB5	47mm(1.11%)	OK	25mm (14°)	0mm	OK
FB6	53mm(1.24%)	OK	60mm (32°)	5mm (<1°)	25mm (14°)

Table 4: Progression of damage to SRL connections



(a) (b)

Figure 10: Example of damage to sliding rod connections. (a) SRM type, connection CW/panel SW after FB4-ICA100 and (b) SRL type, connection CE/Panel 4SW after FB3-ICA50.

5.2 Flexing rod connections

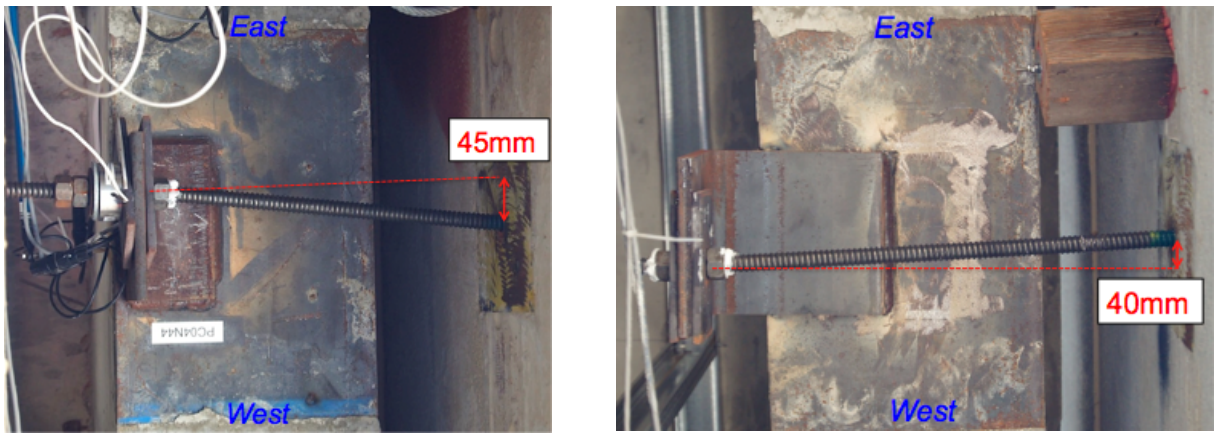
Similarly, a synthesis of visible damage to the flexing rod connection is presented in Tables 5 and 6, with example photographs shown in Figure 11. Damage was manifested via plastic hinging of the rod at the nut location (Figure 11). Residual damage to the flexing rod connections with short rods was not detected. It should be noted that inspection of these connections was possible only on the fifth floor, noting that this level attained smaller PIDRs. The flexing rod connections with a medium length rod (FRM) on the fourth floor were permanently bent during motions FB5 and FB6 at the fourth floor while only during FB6 did they plastically yield at the fifth floor (Table 5). Flexing rod connections with long rods (FRL) exhibited residual damage only after motion FB6, and only at the panel on the fourth floor (Table 6).

Test	PID(PIDR) 4-5th floor	Damage to panel 4NE Connection WW [Residual Defor-mation]	Connection EE [Residual Defor-mation]	PID(PIDR) 5th floor-roof	Damage to panel 5NE Connection WW [Residual Defor-mation]	Connection EE [Residual Defor-mation]
BI	6mm(0.15%)	OK	OK	4mm(0.09%)	OK	OK
FB1	10mm(0.24%)	OK	OK	5mm(0.13%)	OK	OK
FB2	11mm(0.26%)	OK	OK	6mm(0.14%)	OK	OK
FB3	18mm(0.43%)	OK *Replaced*	OK *Replaced*	10m(0.23%)	OK *Replaced*	OK *Replaced*
FB4	31mm(0.72%)	OK	OK	15mm(0.35%)	OK	OK
FB5	47mm(1.11%)	30mm (4°)	45mm (6°)	23mm(0.53%)	OK	OK
FB6	53mm(1.24%)	20mm (3°)	40mm (6°)	35mm(0.82%)	OK	25mm (3°)

Table 5: Progression of damage to the connection FRM

Test	PID/PIDR 4th-5th floor	Damage to panel 4NE Connection CW [Amount of bent]	Connection CE [Amount of bent]
BI	6mm(0.15%)	OK	OK
FB1	10mm(0.24%)	OK	OK
FB2	11mm(0.26%)	OK	OK
FB3	18mm(0.43%)	OK *Replaced*	OK *Replaced*
FB4	31mm(0.72%)	OK	OK
FB5	47mm(1.11%)	OK	OK
FB6	53mm(1.24%)	40mm (4°)	OK

Table 6: Progression of damage to the connection FRL



(a) (b)

Figure 11: Damage to flexing rod connections: (a) FRM type, connection EE in panel 4NE after FB5-DEN67, (b) FRL type, connection CW in panel 5NE after FB6-DEN100

6 IN-PLANE DISPLACEMENT OF THE IP PANELS

In each of the eight IP panels, the in-plane displacement absorbed by the push pull connections at the top of the panels (Δ_c^{panel}) was measured. Moreover, it was possible to find the theoretical ID at the centerline of the panels assuming a weighted average of the ID measured at the corners of the building (ID^{panel}). From these measurements, it is clear that the behavior of panels with sliding rod connections and flexing rod connections was quite different. Figure 12 shows a view of the time history of Δ_c^{panel} and ID^{panel} for the panels on the South Side for the fourth floor of the building (4SW, utilizing sliding rod connections, and 4SE, utilizing flexing rod connections) for three different motions. During the final BI motion (BI-7:ICA140, Figure 12a and 12b) Δ_c^{panel} was smaller than ID^{panel} for both panels. However, while at the panel with sliding connections Δ_c^{panel} was quite similar to ID^{panel}, in the panel with flexing rod connections Δ_c^{panel} was half of the total ID^{panel} ,meaning that in this panel half of the drift was absorbed by a deformation of the panel itself.

The behavior changed during FB phase of testing. Figure 12c and 12d show that, even for the small FB-1:CNP100 record, Δ_c^{panel} was slightly larger than ID^{panel} for the panel with sliding connections, while it still was smaller that the ID^{panel} for the panel with flexing rod connections. The behavior of the sliding connection can be understood considering the force-displacement behavior of a frictional system: once the value of the force reaches the force necessary to activate the motion (F_M), the sliding is activated and the displacement can increase without increment in force until the force goes back to be less that F_M and the mechanism locks. The behavior is of course different when the movement is controlled by bending of the steel such as occurs in the flexing rod connections. In this case, resistance of the steel can limit the displacement, especially if the steel is elastic or only slightly plastic. It should be noted that, since the panels were installed at the upper floors, acceleration (and consequently forces), reached considerable values. This behavior observed in FB-1:CNP100 continued up to FB-4:ICA100 with the difference between Δ_c^{panel} and ID^{panel} increasing for the panel with sliding rod connections and decreasing for panel with flexing rod connections. During the last two motions, the amplitude of Δ_c^{panel} for the panel with flexing rod connections approaches the ID^{panel}. Figure 12e and 12f show an asymmetric behavior of the panel with flexing rod connections, namely, Δ_c^{panel} was larger than ID^{panel} for the movement in the positive direction (Eastward), while it was still smaller than the ID^{panel} for movements in the negative direction (Westward). The asymmetry in the behavior might be due to some permanent deformation of the flexing rod (as observed in the inspection phases), which initiated exactly during the design motion FB-5:DEN67.

Scatter plots summarizing the peaks of the ID^{panel} versus the peak Δ_c^{panel} for each motion are presented in Figure 13. Results for the panels at the fourth floor (respectively moving in the Eastward/positive direction and in the Westward/negative direction) are presented in Figure 13a and Figure 13b. As already observed from the time histories, the displacement Δ_c^{panel} was always smaller than ID^{panel} during the BI motions. In addition, the panels with sliding rod connections had a Δ_c^{panel} greater than the ID^{panel} for all of the FB motions. It can be seen also that the increment of Δ_c^{panel} with respect to the ID^{panel} followed a specific trend, and that this trend is more pronounced in the Eastward direction than in the Westward direction. The displacement of the panels with flexing rod connections is asymmetric, namely, in the Eastward direction it follows a trend incrementally similar to that of the sliding rod connections, while in the Westward direction the displacement is mostly smaller than the ID^{panel}, though it approaches a 1:1 line during the last motion. The behavior of the panels on the fifth floor can be seen in Figure 13c (Eastward movement) and Figure 13d (Westward movement). The behavior of the panels with sliding rod connections in the Eastward direction is similar to that ob-

served on the fourth floor. For the Westward movement Δ_c^{panel} is initially smaller than ID^{panel} and then it keeps really similar to it. In this case, the panels with flexing rod connections show a Δ_c^{panel} smaller the ID^{panel} for all the cases.

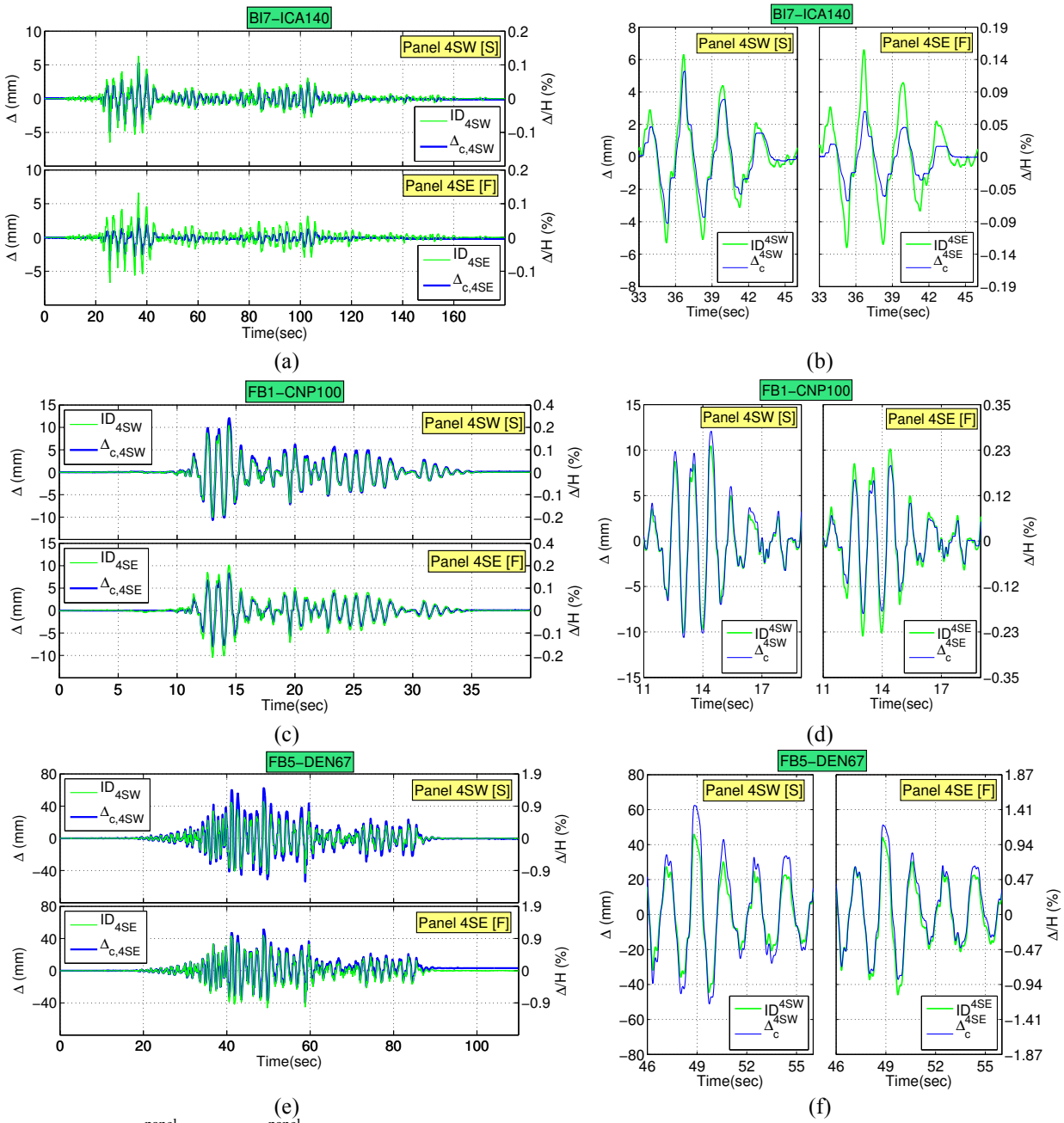


Figure 12: ID^{panel} versus Δ_c^{panel} for panel 4SW(sliding connections) and 4SE(flexing rod connections). (a) BI7-ICA140, (b) FB1-CNP100, (c) FB4-ICA100, (d) FB5-DEN67.

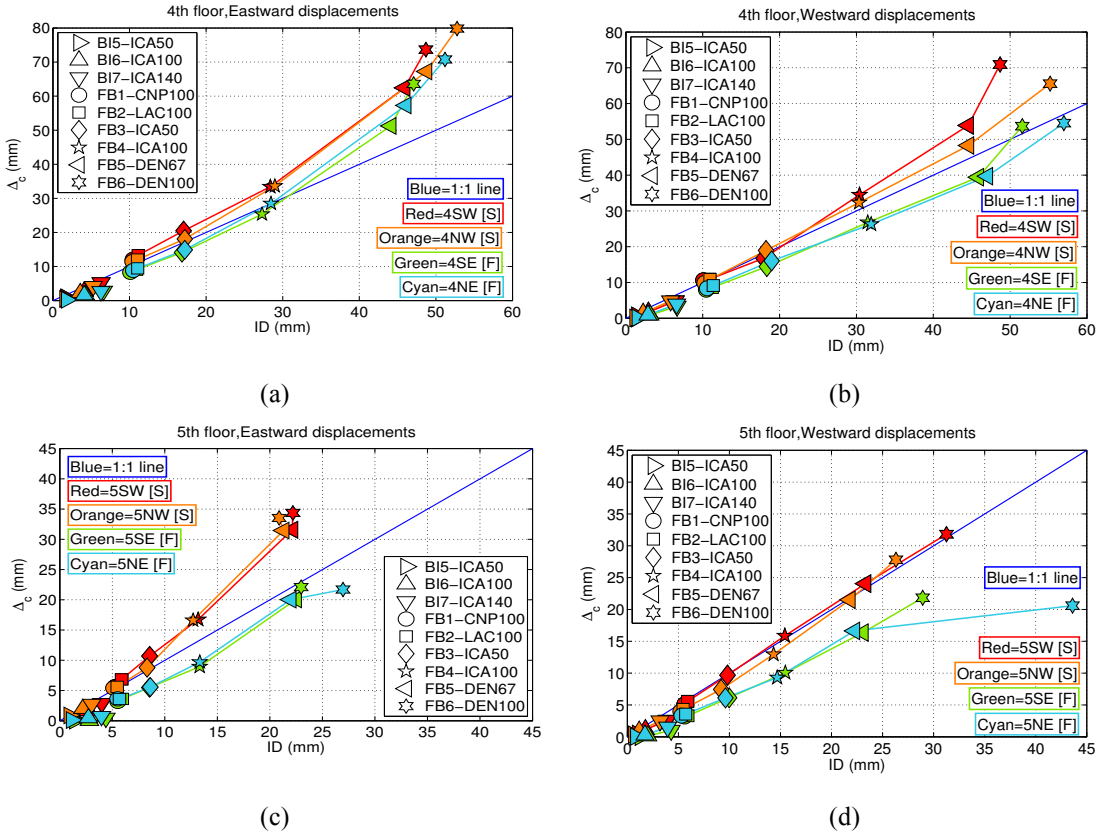


Figure 13: Peak ID versus peak Δ_c : (a) Panels on the fourth floor-Eastward displacement, (b) Panels on the fourth floor-Westward displacement, (c)Panels on the fifth floor-Eastward displacement, (d) Panels on the fifth floor-Westward displacement.

7 CONCLUSIONS

Sixteen precast concrete cladding panels were installed on the upper two floors of a five-story building and subjected to a series of earthquake motions, first with the building in a base-isolated configuration, and then in a fixed-base configuration (BI and FB test phases, respectively). Two types of push-pull connections were tested and their ability to accommodate in-plane story drifts assessed. Namely, flexing rod and sliding rod connections of varying rod lengths were installed and tested in an effort to understand the relationship between rod length and connection performance. Inspection of residual damage after each test motion revealed that the connections did not undergo any substantial damage during the BI motions. During the FB tests however, plastic yielding of both the flexing rod and sliding rod connections were observed, with the exception of the sliding short rod connections, which showed no signs of damage under any test. Sliding rods of a medium length showed minor plastic yielding in most of the tests. Flexing rod connections behaved better, with no residual damage observed in the flexing rod connections with short rods, and plastic yielding observed during the design and maximum credible scaled earthquake motions FB5 and FB6 (PIDR as low as 0.8%), while the one with the long rod was damaged only during FB6 (PIDR 0f 1.2%).

Displacement absorbed by the connection (Δ_c) was compared with the interstory drift (ID) for all of the IP panels. It was found that panels with sliding rod and flexing rod connection behaved in vastly different ways, especially while the building was fixed at its base. During these tests, for the panels with sliding rod connections, the connection displacement Δ_c was greater than the ID because of the frictional behavior of the connections, while for the panels with flexing rod connections Δ_c was smaller than the ID up to FB-4.

A new concept connection was also tested – where the building corner joints were intentionally undersized – forcing a collision of out-of-plane tilting panels with in-plane translating panels around the corner. The push-pull connection accommodated the panel collision through the development of a plastic ductile fuse that limited the force on the connection fasteners and anchorages.

Data from these experiments will lay the foundation for contributing to design guidelines specific to precast concrete cladding, with a focus on defining acceptable behavior of connections and panel joints. The current practice in the U.S. is governed by the requirements of ASCE 7, Section 13.5.3, which provides qualitative performance guidelines for panel joints and connection ductility. The design guidelines supported by this testing will provide a quantitative approach to the existing state of the practice.

ACKNOWLEDGEMENTS

This project is a collaboration between four academic institutions (University of California, San Diego, San Diego State University, Howard University, and Worcester Polytechnic Institute), four government or other granting agencies (the National Science Foundation, the Englekirk Advisory Board, the Charles Pankow Foundation, and the California Seismic Safety Commission), over 40 industry partners, and two oversight committees. A listing of industry project sponsors may be found on the project website: http://bncs.ucsd.edu/index.html. Through the NSF-NEESR program, partial funding is provided by grant number CMMI-0936505, where Dr. Joy Pauschke is the program manager. The above continuous support is gratefully acknowledged. Many individuals contributed to the overall effort of this project. However, we specifically thank core team members Profs. Jose Restrepo and Joel Conte, doctoral students Rodrigo Astroza, Hamed Ebrahimian, Steven Mintz, and Xiang Wang, the NEES@UCSD and NEES@UCLA staff, Mr. Robert Bachman, Dr. Robert Englekirk, Mr. Mahmoud Faghihi, Dr. Matthew Hoehler of Hilti Corp., Prof. Ken Walsh of SDSU, and SDSU students Consuelo Aranda and Elias Espino. Specific to the PCC effort described in this paper, the authors thank the PCI and its R&D Council members, the Charles Pankow Foundation, Clark-Pacific, and Willis Construction, and Regal Industries and specifically Roger Becker and Prof Kurt McMullin for their collaboration and continued support. Opinions, findings, and conclusions expressed are those of the authors, and do not necessarily reflect those of the sponsoring organization.

8 REFERENCES

[1] E. Miranda, G. Mosqueda, R. Retamales, G. Pekcan, Performance of Nonstructural Components during the 27 February 2010 Chile Earthquake. *Earthquake Spectra*, 28(S1), S453–S471, June 2012.

[2] S. Taghavi, E. Miranda, Response Assessment of Nonstructural Building Elements, *Technical Report PEER 2003/05*, Pacific Earthquake Engineering Research Center, University of California, Berkeley.

[3] A. Baird, A. Palermo and S. Pampanin, Façade damage assessment of multi-storey buildings in the 2011 Christchurch earthquake, Bullettin of the New Zealand Society for Earthquake Engineering, **44/4**, 368-376, December 2011.

[4] Iverson, J.K., Hawkins, N.M., "Performance of Precast/Prestressed Concrete Building Structures During Northridge Earthquake" PCI Journal March/April 1994

[5] S. K. Ghosh, N. M. Cleland, Performance of Precast Concrete Building Structures. Earthquake Spectra, **28S1**, S349–S384, June 2012.

[6] Miyamoto International, L'Aquila, Italy, Earthquake Field Investigation Report, West Sacramento, CA, 2009.

[7] K.M. McMullin, M. Ortiz, L. Patel, S. Yarra, T. Kishimoto, C. Stewart and B. Steed, Response of Exterior Precast Concrete Cladding Panels in NEES-TIPS/NEES-GC/E-Defense Tests on a Full Scale 5-story Building. *Structures Congress 2012* (ASCE 2012), Chicago, Illinois, March 29-31 2012.

[8] A. Barid, A. Palermo, S. Pampanin, Experimental and numerical validation of seismic interaction between cladding systems and moment resisting frames. 15th World Conference on Earthquake Engineering (15 WCEE 2012), Lisbon, Portugal, September 24-28, 2012.

[9] American Society of Civil Engineers, ASCE 7-10 Minimum Design Loads for Buildings and Other Structures, ASCE.

[10] American Concrete Institute Committee 318, 318-08: Building Code Requirements for Structural Concrete and Commentary, ACI 2008.

[11] Precast/Prestressed Concrete Institute, PCI MNL-120-0, PCI Design Handbook-Precast and Prestressed Concrete, 6th Edition, 2004.

[12] American Institute of Steel Construction, Specification for Structural Steel Buildings ANSI/AISC 360-05, AISC,2005.

[13] Wang, X., Ebrahimian, H., Astroza, R., Conte, J., Restrepo, J. and Hutchinson, T. (2013). "Shake table testing of a full-scale five-story building: pre-test simulation of the test building and development of a nonstructural components and systems design criteria," Proceedings, *ASCE Structures Congress*, ASCE, Pittsburgh, PA, May 2013.

[14] T. Hutchinson, J. Restrepo, J. Conte, B. Meacham, Overview of the Building Nonstructural Components and Systems (BNCS) project. *Proceedings, ASCE Structures Congress*, ASCE, Pittsburgh, PA, May 2013.

COMPDYN 2013
4th ECCOMAS Thematic Conference on
Computational Methods in Structural Dynamics and Earthquake Engineering
M. Papadrakakis, V. Papadopoulos, V. Plevris (eds.)
Kos Island, Greece, 12–14 June 2013

SEISMIC PERFORMANCE EVALUATION OF A POST-TENSIONED FRAME BUILDING

B.Hancıoğlu[1*], M.S.Kırçıl[2], S.İ.Ulusoy[1]

[1]Alacalı Cons.Ind.Trd.Inc.
Mahmut Bey Mah. K.Halkalı Cad. No:26
34550 Bağcılar-İstanbul, Turkey
bhancioglu@alacali.com.tr
siulusoy@alacali.com.tr

[2]Yıldız Technical University
Department of Civil Engineering,
Davutpaşa Campus, 34544 Istanbul, Turkey
kircil@yildiz.edu.tr

Keywords: post-tensioned frame, performance evaluation, mild-press-joint.

Abstract. *The precast construction technology is used not only for industrial buildings today, but also used for other building types such as residences, schools etc. On the other hand, the requirement of the seismic safety must be satisfied for such buildings constructed in earthquake regions. Thus, seismic safety evaluation of this type of buildings to estimate the potential damage is a critical issue and must be made as realistic as possible. Realistic damage estimation requires considering the nonlinear behavior of structure. In this study, performance evaluation of a seven story post-tensioned frame building which was in the state of immediate occupancy after the Van Earthquakes (October 23rd and November 9th, 2011), is carried out on the basis of Turkish Seismic Design Codes provisions.*

The maximum displacement demand of the design earthquake is estimated by using the push-over curves of the structure. The construction stages of the structure have been taken into account as the initial condition of pushover analysis. Finally, damage of all the structural elements has been determined, based on their plastic deformation demands, under the effect of the design earthquake by using the section damage classification of Turkish Seismic Design Code.

1 INTRODUCTION

The precast construction technology is used not only for industrial buildings today, but also used for other building types such as residences, schools etc. On the other hand, the requirement of the seismic safety must be satisfied for such buildings constructed in earthquake regions. Thus, seismic safety evaluation of this type of buildings to estimate the potential damage is a critical issue and must be made as realistic as possible. In this study, performance evaluation of a seven story post-tensioned frame building which was in the state of immediate occupancy after the Van Earthquake (October 23rd, 2011), is carried out on the basis of Turkish Seismic Design Code provisions [1].

The maximum displacement demand of the design earthquake is estimated by using the push-over curves of the structure. The construction stages of the structure have been taken into account as the initial condition of pushover analysis. Finally, damage of all the structural elements has been determined, based on their plastic deformation demands, under the effect of the design earthquake by using the section damage classification of Turkish Seismic Design Code [1].

2 DESCRIPTION OF THE BUILDING

The investigated structural system is formed of 7 story frames in both two directions. Columns are precast and continuous along the building height. The story height is 3.13m. Post-tensioned tendons are used at column-beam joints so that structural integration can be provided. Prefabricated slabs and topping (7 cm) are used at all story levels to construct the slab system of the building. Topping also helps to provide diaphragm behavior. The typical floor plan is shown in Figure 1.

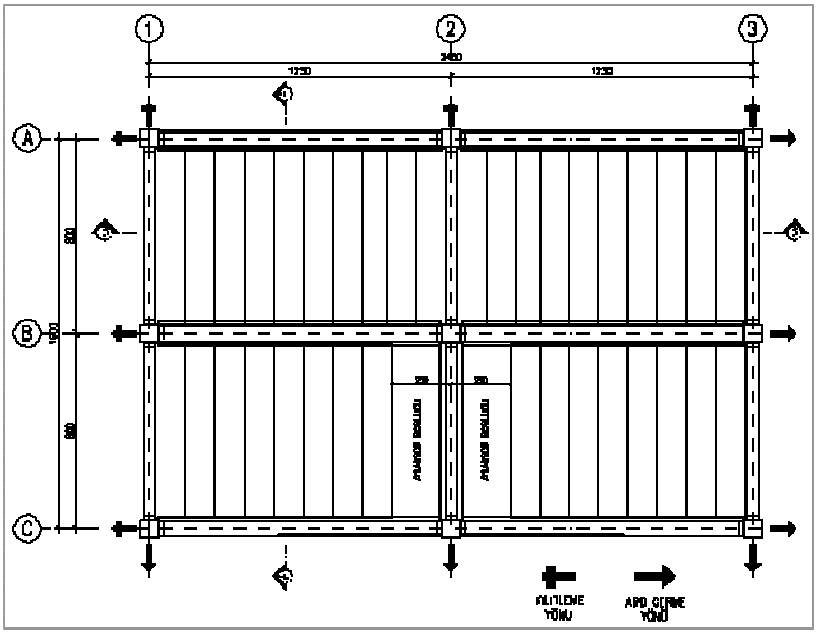


Figure 1: Typical floor plan of the building.

The characteristic concrete strength is 50 MPa and 40 MPa for frames and sabs, respectively. The reinforcement steel's characteristic yield strength is 420 MPa. Low-relaxation prestressing strand with the yield strength of 1700 MPa is used for post-tension tendons. Figure 2 shows a typical column-beam connection.

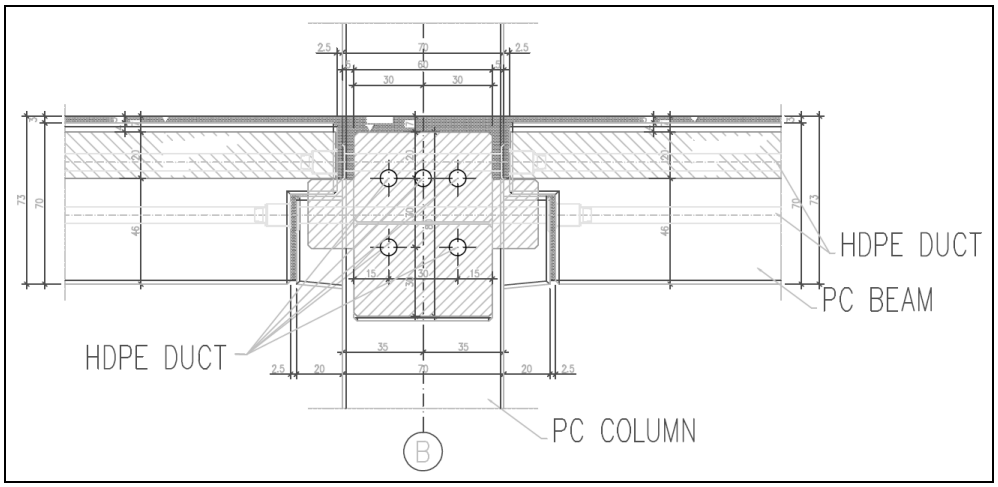


Figure 2: Typical column-beam connection.

3 PUSHOVER ANALYSES OF THE BUILDING

3.1 Material properties

Pushover analyses are carried out -in both two directions- to determine the performance of structural elements under the effect of the design earthquake. Kent&Park model [2] is used for both unconfined and confined concrete. The Figure 3 shows the stress-strain relation of considered model.

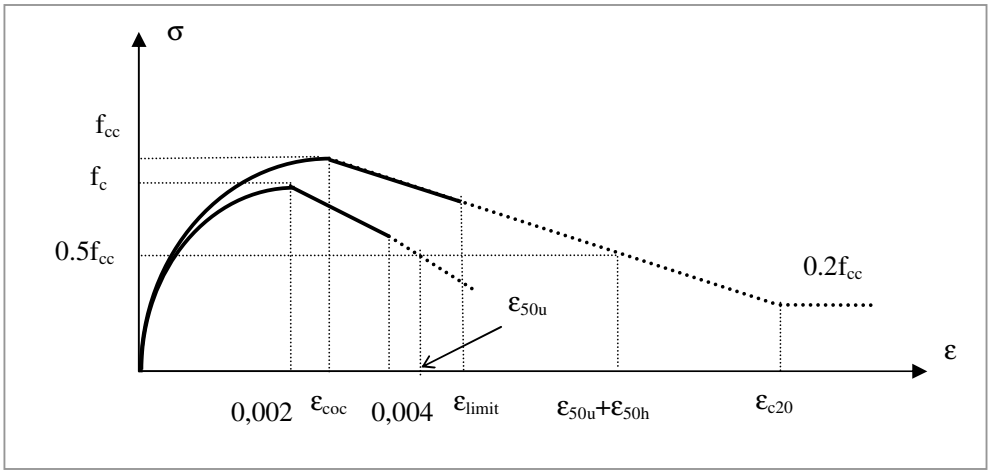


Figure 3: Kent&Park model.

The stress-strain curves of reinforcement steel and post-tension steel are given in Figure 4 and 5, respectively.

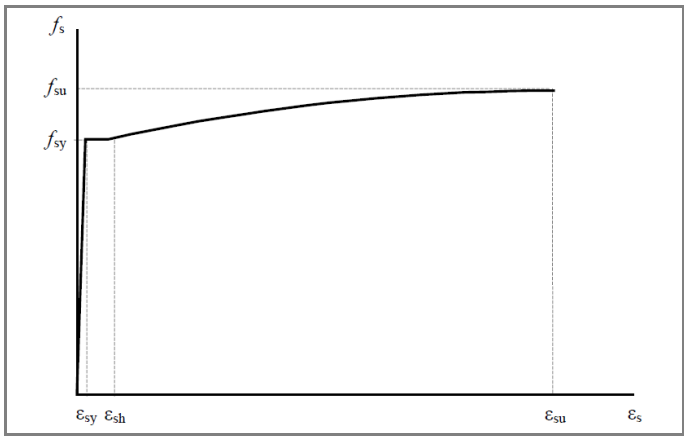


Figure 4: Stress-strain curve of reinforcement steel model.

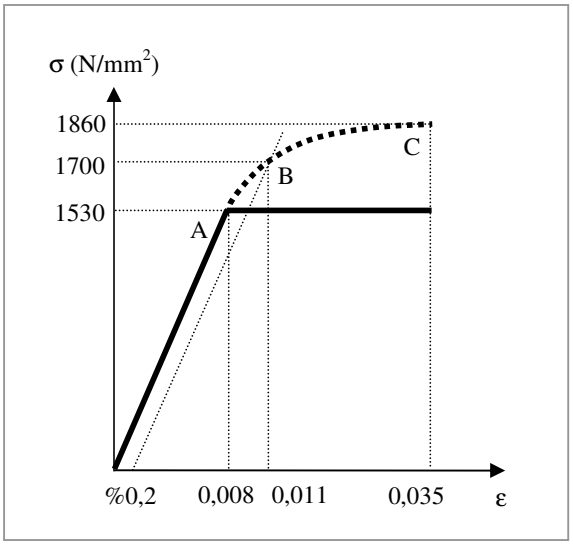


Figure 5: Stress-strain curve of post-tension cable.

3.2 Load-deformation relation for structural system elements

Moment-rotation diagrams and yield surfaces are determined for beam and column end sections where the possible plastic hinges can be occurred. For the beam end sections tri-linear moment-rotation diagram is assigned as shown in Figure 6.

The first reduction in stiffness of the section is observed with cracking (Point I). The second one is observed at Point II with bond slip. Beyond the yield point (Point II) there is no strain-hardening and stiffness is zero. Bond slip is assumed to be occurred when the strain of post-tension cable reaches 0.008. The mean bond stress is assumed to be 1.42MPa for the computation of section rotation [3, 4, 5]. The moment-rotation is assumed to be elastoplastic for columns. A typical yield-surface is given in Figure 7.

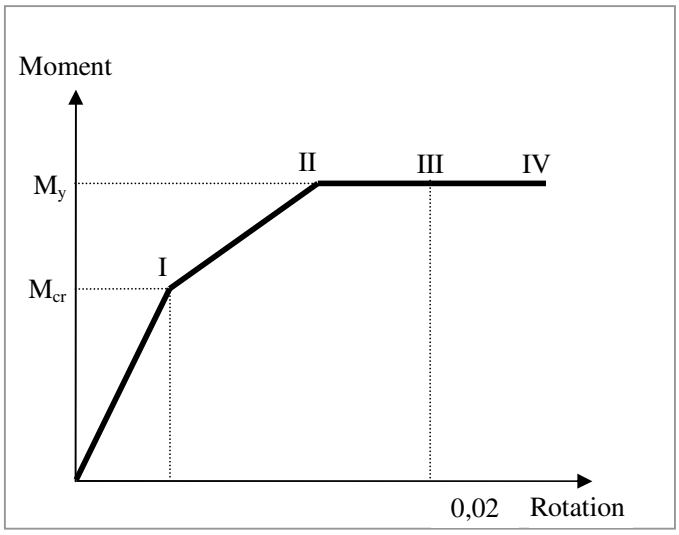


Figure 6: Typical moment-rotation diagram.

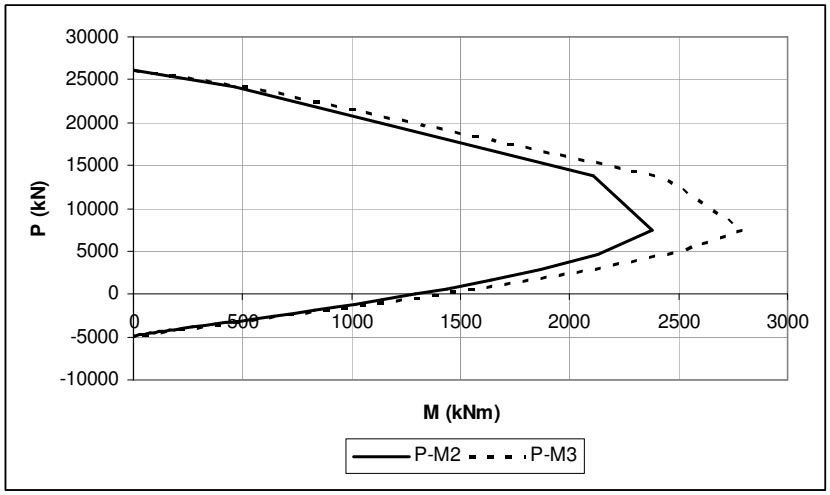


Figure 7: Typical yield-surface for column sections.

3.3 Construction Stages

Construction stages are considered as the initial conditions of pushover analysis. The followings are the sequence of loadings;

a. Installation of columns,
b. Installation of first story beams,
c. Installation of first story slabs,
d. Installation of beams and slabs for other story levels,
e. Post-tensioning of each story level,
f. Topping concrete for each story level,
g. Live and other dead loads.

Figure 8 shows the considered construction stages.

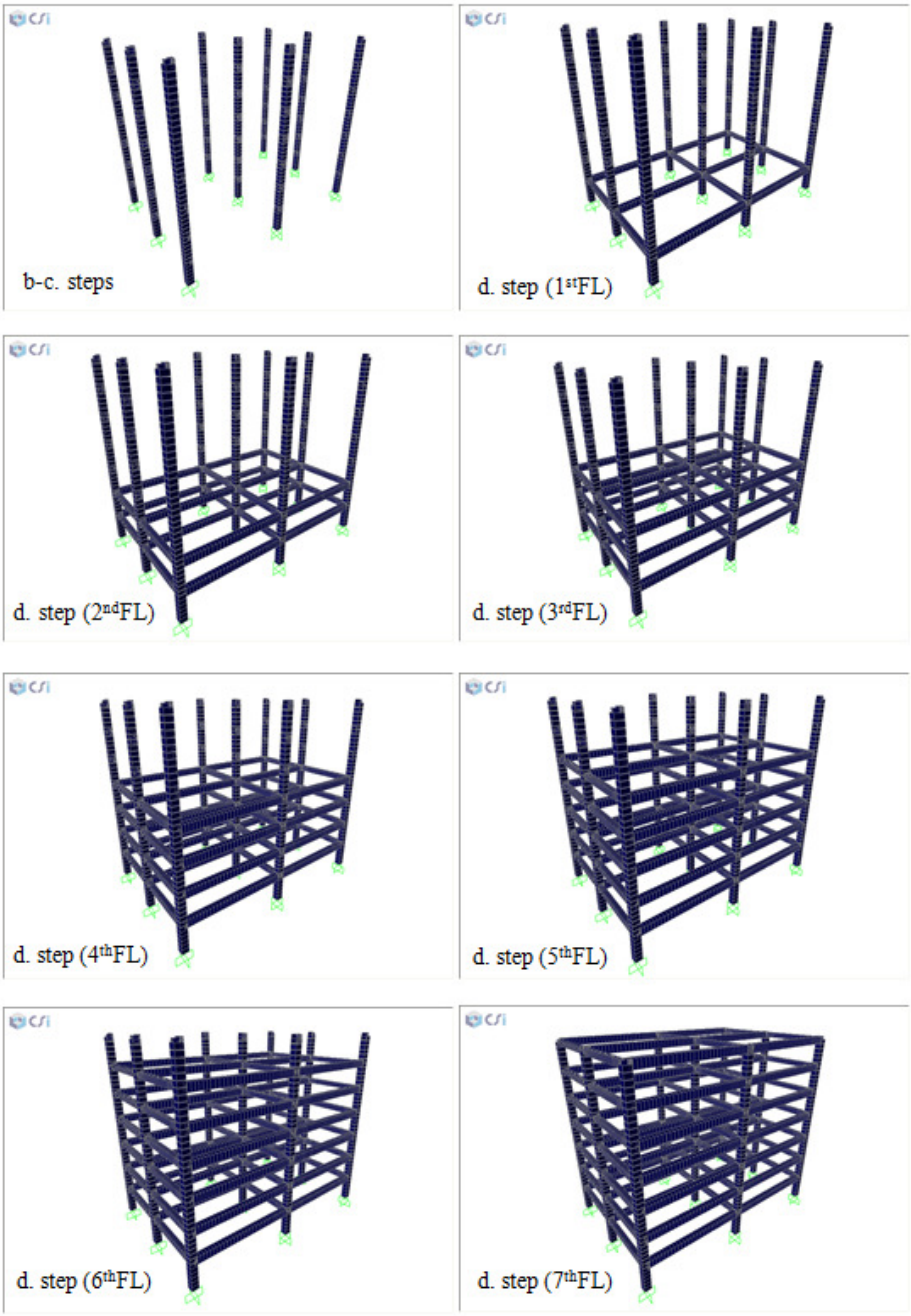


Figure 8: Construction stages

3.4 Pushover Curves

The pushover curves of both two direction are given Figure 9.

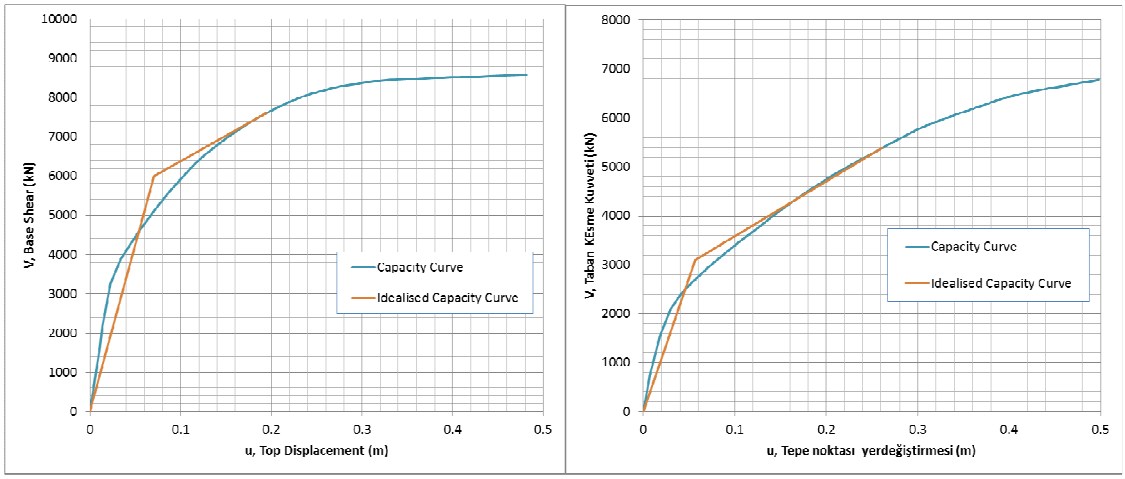


Figure 9: Pushover curves in X and Y direction.

The inelastic displacement demands are determined by using the method given by Turkish Seismic Design Code [1]. Figure 10 shows the design spectrum of Earthquake Zone 2 given by Turkish Seismic Design Code [1].

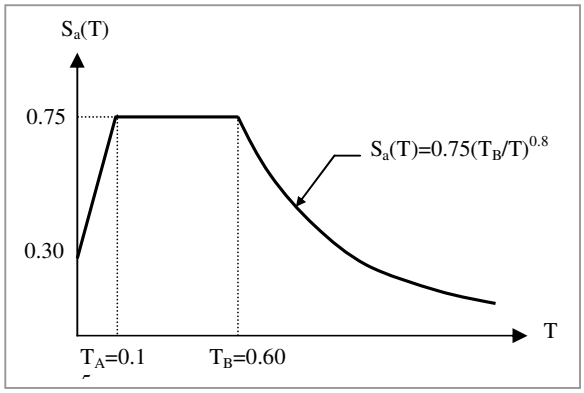


Figure 10: Design spectrum.

Figure 11 shows capacity spectra and inelastic displacement demands of each direction determined by using the method given by Turkish Seismic Design Code [1]. Sakata et. al. [3, 4] showed that origin-oriented hysteresis model can represent the sectional behavior of partially post-tensioned frames. Furthermore, considering the results of the study Ruiz-Garcia and Miranda [6] the inelastic displacement demand of elastoplastic model given by Turkish Seismic Design Code [1] has been increased %20.

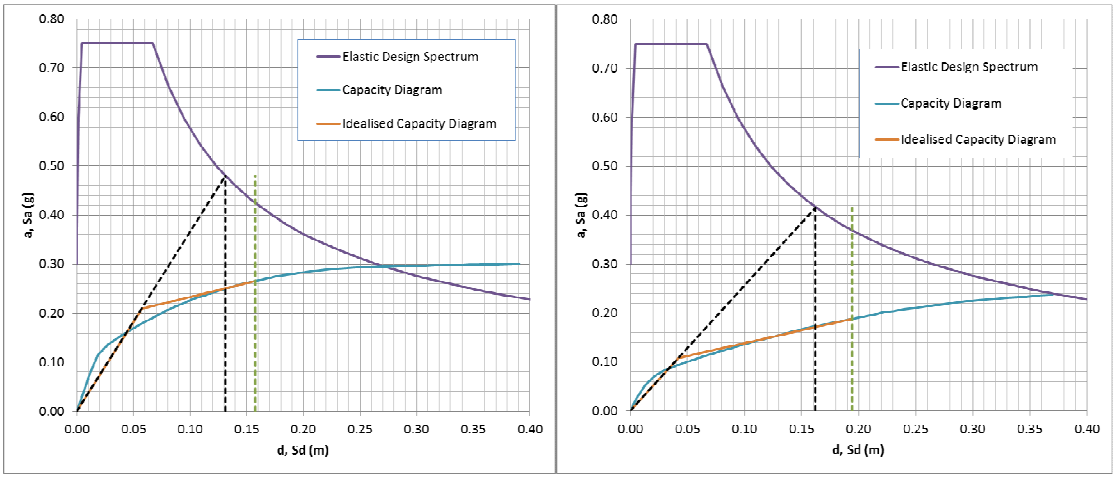


Figure 11: Inelastic displacement demand.

4 PERFORMANCE EVALUATION

The nonlinear deformations of the structural system elements were assessed considering the deformations limits given by Turkish Seismic Design Code [1]. Figure 12 shows the section damage limits.

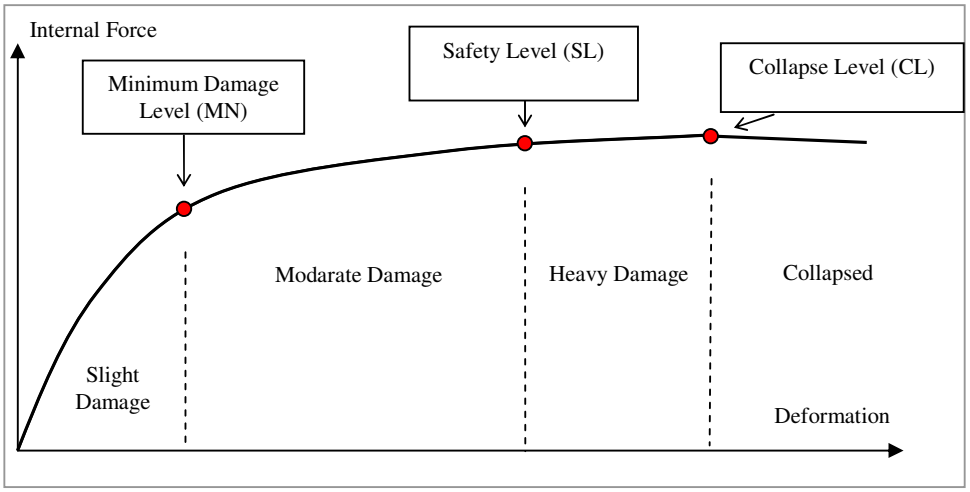


Figure 12: Section damage limits.

The plastic rotation demands of the beam sections are given in Figure 13 and 14 for both directions.

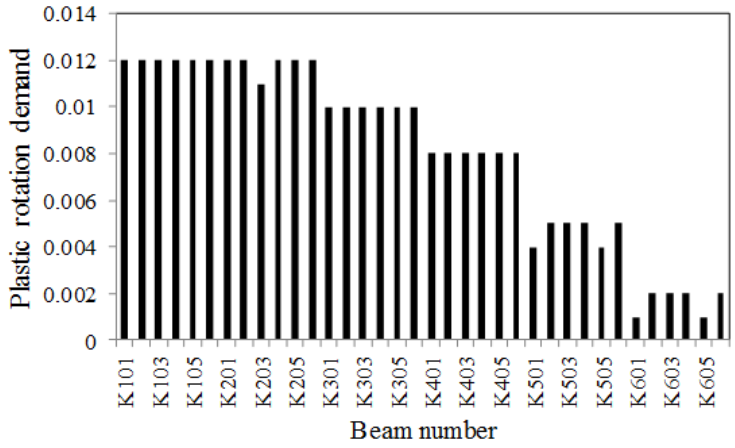


Figure 13: Plastic rotation demands of beams in X direction.

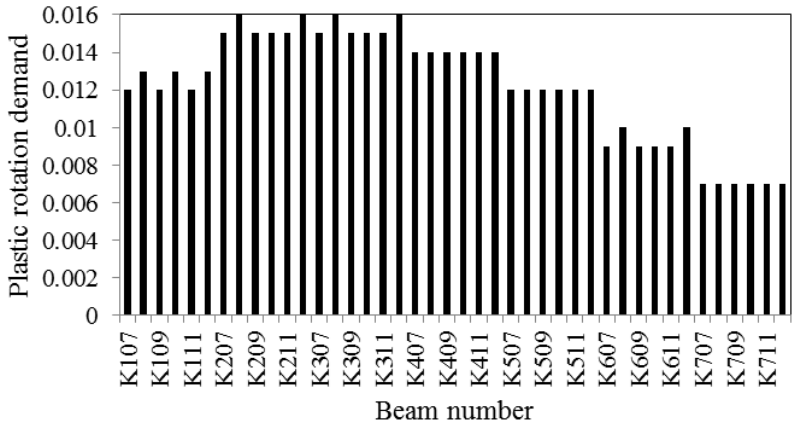


Figure 14: Plastic rotation demands of beams in Y direction.

All the plastic rotation demands of columns can not be given here because of space limitations. However plastic rotation demands and section damage limits for each direction of the mid-column are given in Fig. 15 and 16.

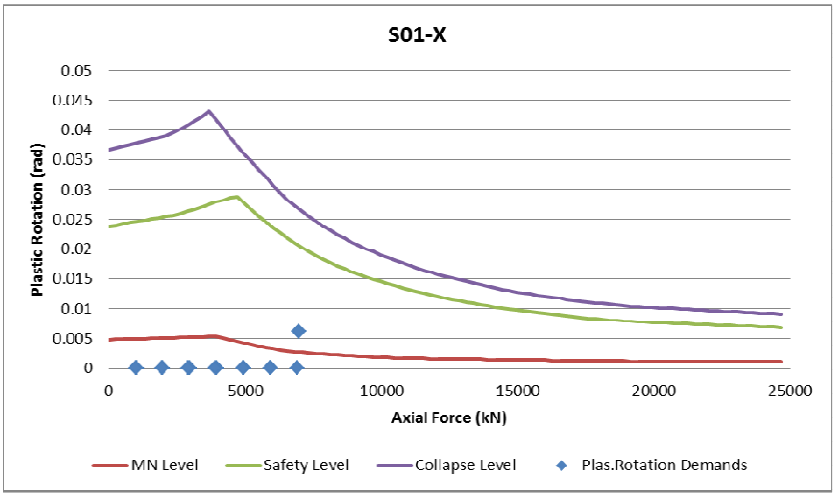


Figure 15: Plastic rotation demands of S101 in X direction.

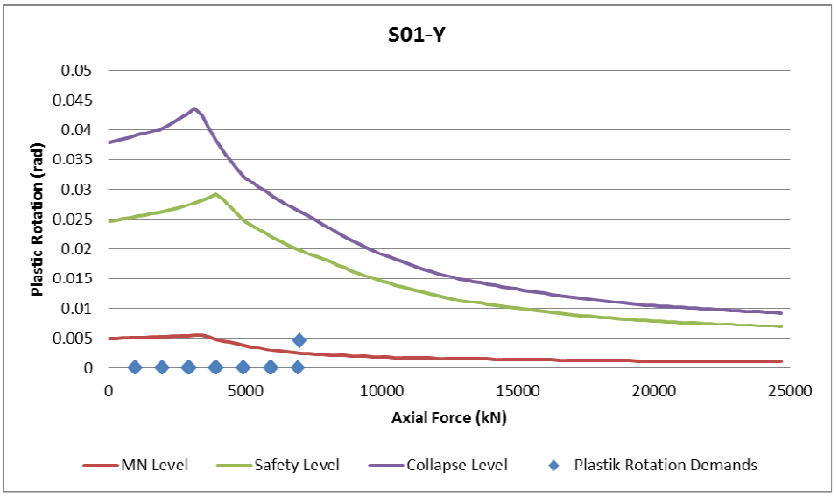


Figure 16: Plastic rotation demands of S101 in Y direction.

Plastic hinge distribution of 2-2 and B-B axis are given in Figure 17 and 18.

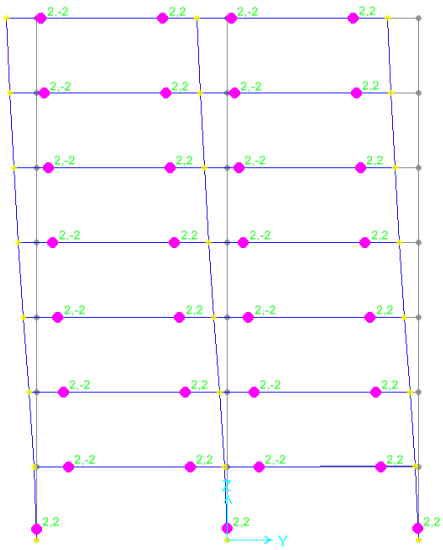


Figure 17: Plastic hinge distribution demands of 2-2 axis.

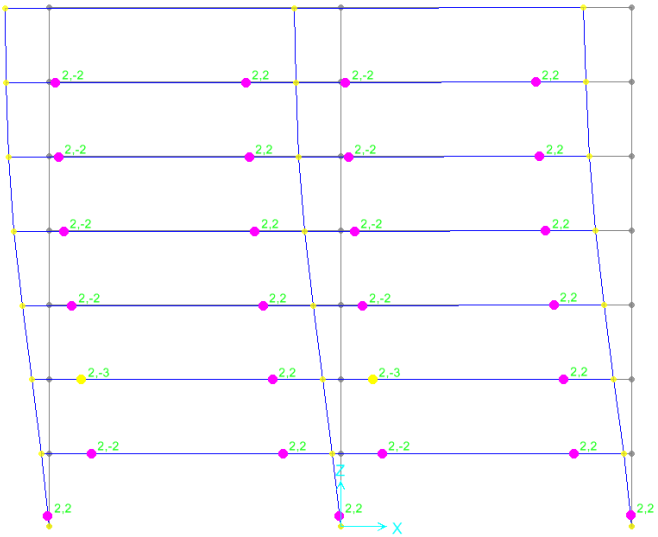


Figure 18: Plastic hinge distribution demands of B-B axis.

5 CONCLUSIONS

- All the plastic hinge rotations of beams are less than 0.02 for the design earthquake (%10 probability of being exceeded in 50 years). The only plastic hinge formation in columns is observed at ground level sections of columns. The plastic hinge mechanism is beam mechanism and damage is under the level of minimum damage for almost all section.

- The maximum interstory drift is %1.28 and %1.43 in X and Y directions, respectively.

- The building performance is Life Safety in both two directions for the design earthquake according to the regulations of Turkish Seismic Design Code.

- The building experienced two major earthquakes in 2011 with the moment magnitudes of 7.2 and 5.6 (October 23rd and November 9th, Van). The distance between the location of the building and the epicenter of the Earthquakes is about 30 km and 16 km, respectively. It should be noted that any structural damage was observed and the building was in the state of immediate occupancy after those Earthquakes.

ACKNOWLEDGEMENT

The authors thank Prof.Dr.H.F. Karadoğan for his valuable contributions.

REFERENCES

[1] Specification for Buildings to be Built in Seismic Zones, Ministry of Public Works and Settlement Government of Republic of Turkey, 2007.

[2] Kent, D.C., and Park, R. Flexural members with confined concrete. *Journal of the Structural Division*, *Proc. of the American Society of Civil Engineers*, 97(ST7), 1969-1990, 1971.

[3] Sakata, H., Wada, A., Nakano K., Matsuzaki, Y., Tanebe, K., Machida, S., Study on damaged controlled precast-prestressed concrete structure with P/C mild press joint/ Part 1- Overview of PC Mild-Press-Joint Building Construction and Practical Applications, *FIB Proceedings of the Second International Congress*, June 5-8, Naples-Italy, 2006.

[4] Sakata, H., Wada, A., Nakano K., Matsuzaki, Y., Tanebe, K., Machida, S., Study on damaged controlled precast-prestressed concrete structure with P/C mild press joint/ Part 2- Experimental Study on Mechanical Behaviour of Frame with PC Mild-Press-Joint, *FIB Proceedings of the Second International Congress*, June 5-8, Naples-Italy, 2006.

[5] Sakata, H., Wada, A., Nakano K., Matsuzaki, Y., Tanebe, K., Machida, S., Study on damaged controlled precast-prestressed concrete structure with P/C mild press joint/ Part 3- Experimental Study on Bond Behaviour of EC Strands, *FIB Proceedings of the Second International Congress*, June 5-8, Naples-Italy, 2006.

[6] Ruiz-Garcia, J., Miranda, E., Performance Based Assessment of Existing Structures Accounting for Residual Displacement, *The John A. Blume Earthquake Engineering Center*, Report No:153, 2005.

[7] MATLAB Release 13, The Mathworks Inc., 2002.

[8] SAP2000 User's Manual, Structural Analysis Program Nonlinear Version 15.1.0, Computers and Structures Inc., 2011.

COMPDYN 2013
4th ECCOMAS Thematic Conference on
Computational Methods in Structural Dynamics and Earthquake Engineering
M. Papadrakakis, V. Papadopoulos, V. Plevris (eds.)
Kos Island, Greece, 12–14 June 2013

THE EMILIA EARTHQUAKES: REPORT AND ANALYSIS ON THE BEHAVIOR OF PRECAST INDUSTRIAL BUILDINGS FROM A FIELD MISSION

Dionysios A. Bournas[1], Paolo Negro[2], and Fabio Taucer[2]

[1] University of Nottingham
Nottingham, NG7 2RD-UK
e-mail: dionysios.bournas@nottingham.ac.uk

[2] Joint Research Centre, European Commission
T.P. 480, I-21020 Ispra (VA), Italy
e-mail: paolo.negro@jrc.ec.europa.eu; fabio.taucer@jrc.ec.europa.eu

Keywords: Industrial buildings, precast structures, connections, cladding elements, simply supported beams, steel storage racks.

Abstract. *A series of earthquakes, the highest of magnitude M_w 5.9, hit a portion of the Po Valley in Northern Italy, which was only recently classified as seismic. The paper reports the findings and the lessons learnt from a preliminary field survey which was conducted immediately after the second event. As a result of the economic attitude of the affected area, and possibly of the characteristics of the event, an unprecedented number of industrial precast buildings were affected, resulting into most of the casualties as well as in large economic losses. Whereas most of the damaged and collapsed buildings were designed for gravity loads only, evidence of poor behavior of some precast buildings designed according to seismic provisions were discovered. The paper provides a description of the performance of precast buildings, highlighting the deficiencies that led to their poor behavior as well as some preliminary recommendations.*

1 INTRODUCTION

There are many evidences about the behavior of precast structures during past earthquakes such as the 1976 Friuli (Italy) Earthquake [1], the 1977 Vrancea Earthquake [2], the 1979 Montenegro Earthquake [3]. More recently, experience has been gained in more modern structures after the Northridge Earthquake [4] and the Kocaeli Earthquake [5,6].

The main causes associated to the damage of the precast structures in these earthquakes were failure of connections, insufficient ductility of the columns, insufficient stiffness of the roof or slab system, being failure of the connections the main factor leading to most of the collapses. However, existing knowledge is rather incomplete and controversial. In fact, in most past earthquake events there is evidence of excellent behavior of precast structures as well as reports of catastrophic collapses, which does not come as a surprise, since performance depends upon the specific structural system, the type of connections, the adequacy of the design and the quality of construction.

Restricting the focus to precast frames, the typology which is most commonly used in Europe, evidences of very good structural behavior go hand in hand with reports of collapses, as in the already mentioned cases of Friuli and Kocaeli Earthquakes. For this kind of structures, recent evidence after the 2009 L'Aquila Earthquake [7] seems to demonstrate that the behavior of such structures is satisfactory, whereas some problems exist with the non-structural components connections, in particular with the heavy cladding elements as was reported by [8].

The present paper follows a technical mission to the area affected by the Emilia earthquakes. The economic activities of the area, in which a large number of small-size industrial facilities were concentrated, and possibly the specific characteristics of the earthquakes, resulted into an unprecedented number of precast buildings being affected by the earthquakes, with a large percentage of them being damaged or destroyed. The lessons which can be learnt from this experience are of much importance because of the coexistence of modern seismically designed buildings and of, still recent, non-seismically designed ones. The consequences are profound both for the risk which is represented by some non-seismically designed precast structures and for the importance of carefully designing the connections in modern buildings.

2 SEISMIC EVENT

The On 20 May 2012, at 02 h 09 min (UTC) – 04h 09min (local time), a 5.9 M_w magnitude (as estimated by the National Institute of Vulcanology and Geophysics of Italy, INGV) earthquake occurred at Finale Emilia, Province of Modena in Northern Italy, at a depth of 6.3 km. The main shock was followed by two very strong aftershocks, the strongest of which (M_L= 5.8) occurred on May 29 at 07h 00 min (UTC) – 09h 00min (local time) at Medolla (Province of Modena). The authors conducted their survey in the affected region immediately after the first aftershock. A last strong aftershock of 5.1 M_w magnitude took place on June 3 at 19h 20 min (UTC) - 17h 20 min (local time) at Novi di Modena. The whole area affected by the earthquakes, including all epicentres, is approximately 60 km (East-West) x 30 km (North-South). The areas mostly affected by the earthquakes comprise the municipalities of San Felice sul Panaro, Sant'Agostino, San Carlo, Finale Emilia, Mirandola, Medolla, Cavezzo, Concordia sulla Secchia and Novi di Modena , with a toll of 23 casualties, 400 injured and a total of approximately 20,000 homeless. The USGS PAGER System estimated that the economic losses were in the range of 1% of the national GDP. According to results provided by the Italian Civil Protection, for a total of 6,700 structures inspected 37% were habitable, 17% temporary uninhabitable but habitable following emergency measures, 6% partially uninhabitable,

2% temporary uninhabitable and to be reviewed in more detail, 33% uninhabitable and 5% uninhabitable due to external factors (such as near-to-collapse neighboring buildings).

A series of accelerometer stations of the RAIS (Strong Motion Network of Northern Italy) and RAN (National Strong Motion Network) networks were installed in the affected area, some already existing, and others installed following the first event. Figure 1 presents the time histories of the E–W, N–S and vertical components of the acceleration recorded at the Mirandola (MRN) station. The maximum recorded peak ground acceleration (PGA) is in the order of 0.30g (Fig. 1).

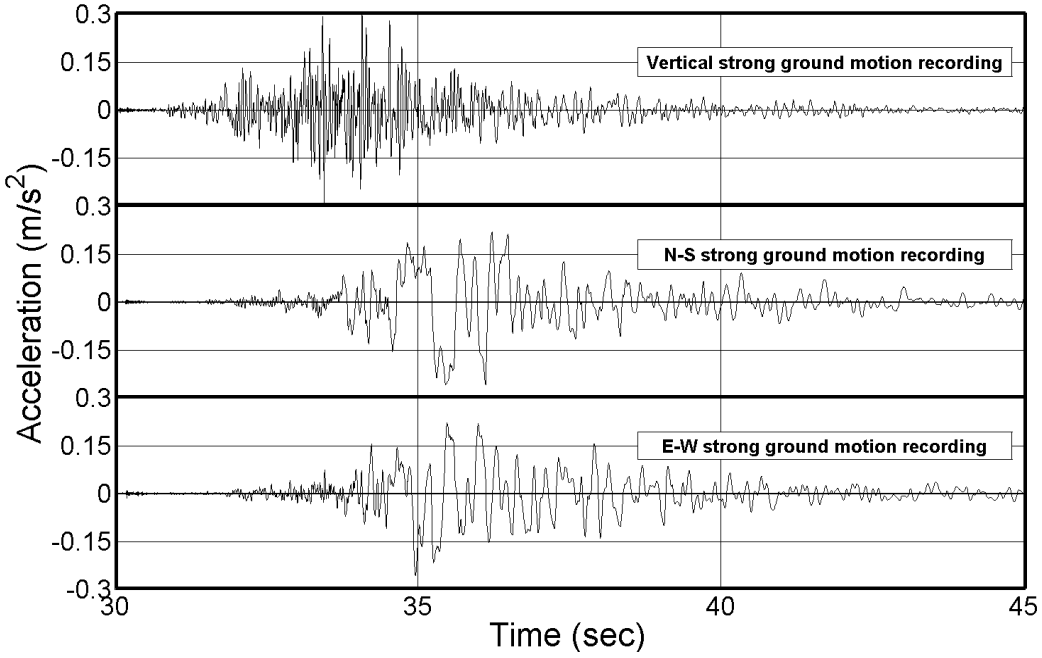


Figure 1: Vertical, N-S and E-W strong ground motion recordings at Mirandola station, 20 May 2012, 04:09 (UTC) ML= 5.9. (Source: Italian Civil Protection).

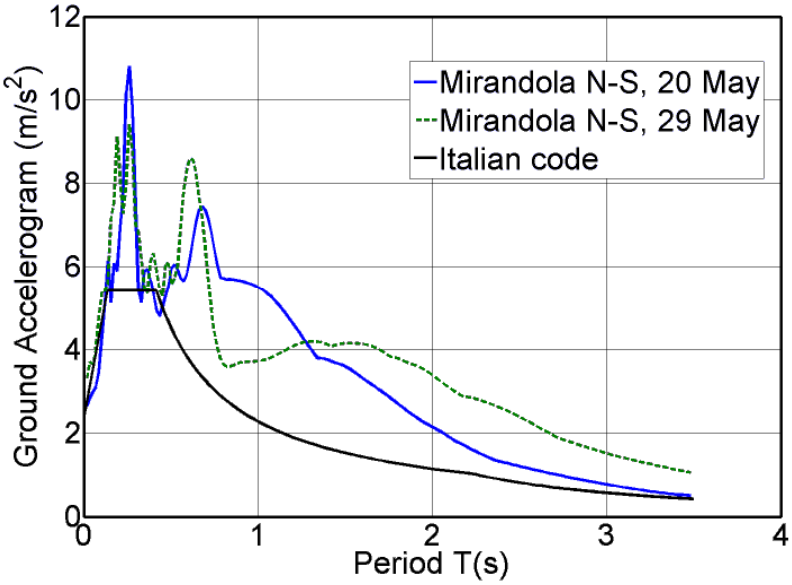


Figure 2: Spectra of the N-S component of the two strongest records compared to the Italian code spectrum.

Figure 2 plots the spectra of the N-S component of the two strongest records at the Mirandola station as compared with the current Italian code, both for ground type B and 5% viscous damping. It can be observed that the spectra from the recorded ground motions are consistently larger than the 475 years spectrum currently specified by the Italian norms. As it can also be observed, beyond the peak value of acceleration, this occurred for low periods; only the N–S component of the response spectra in both earthquakes shows high accelerations for higher periods. In particular, for periods in the range of 0.7-1.8 sec, the spectral acceleration of the N-S component of the 29 May earthquake is approximately equal to half of its peak spectral value. This low frequency content of the N-S component may have added to the high levels of damage experienced by structures with high periods of vibration, such as the relatively flexible precast industrial buildings. It should be noted here that the fundamental period of a typical single-storey industrial precast concrete building, calculated following a benchmark design study among Italy, Greece, Slovenia and Turkey, ranges between 0.8-1.4 s [9]. Finally, it should be also pointed out that the second event was more damaging because of its higher energy content in low periods of vibration.

3 NORMATIVE PROVISIONS FOR THE AFFECTED AREA

A new seismic zoning of Italy was issued in 2003, which practically established a fourth seismic zone for all regions that before 2003 were considered as non-seismic. Figure 3 presents the Italian seismic zoning map for design before and after 2003, and shows that the area affected by the earthquakes was not classified as seismic before 2003. It should be considered that the seismic zoning issued in 2003 was waived during a grace period of 18 months, and in Italy the norms applied in construction are those in force at the time in which the permission is filed at the local authorities and the permission might have been extended for years. As a result, it is very difficult to assess whether seismic provisions were taken into account with the sole estimation of the period of construction.

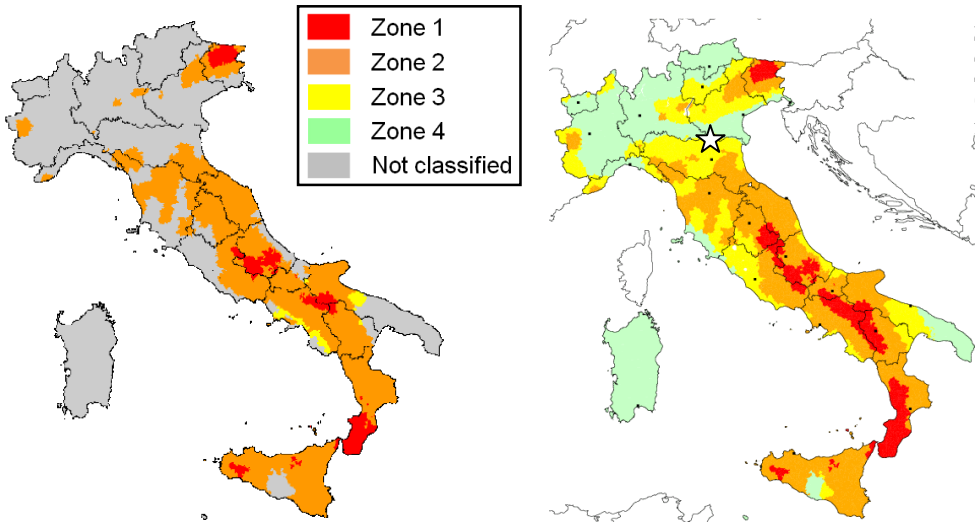


Figure 3: Italian seismic zoning map for design: (a) Before 2003. (b) After 2003.

The current seismic design code of Italy, based on Eurocode 8 and approved in 2008 with its application waived for 18 months, divides the entire country into four regions, assigning peak ground accelerations of 0.05, 0.15, 0.25 and 0.35 g for regions 4, 3, 2 and 1, respectively (Fig. 3b). The area most affected by the earthquakes is presently classified as Zone 3 (Fig. 3b), corresponding to 0.15g PGA for a return period of 475 years. The maximum acceleration rec-

orded at Mirandola (0.30 g) corresponds to twice of the design acceleration given by the current codes (0.15g). These earthquakes revealed that the most vulnerable structures in the area were mainly the precast concrete industrial buildings, particularly those constructed without seismic provisions, and some historical unreinforced masonry buildings (i.e. churches, towers). Slight damage to motor-way bridge structures, to a new *pilotis* building and effects of liquefaction in the town of San Carlo were also observed. The focus of the paper on the performance of precast industrial buildings recognizes the important effect that the Pianura Padana-Emiliana earthquakes had on this type of structures, with no precedent in other earthquakes in Italy and Europe.

4 DAMAGE REVIEW

4.1 General

Most of the precast industrial buildings in the affected area were designed for gravity loads only and were characterized by lack of beam-column joints capable of transferring the seismic forces down to the foundation, insufficient seating and isolated column foundations. A small number of buildings were designed and constructed during the last 5-7 years, presumably conforming to the updated seismic zoning of the area. The findings of the field mission indicate that approximately three quarters of the precast concrete industrial buildings designed with non-seismic provisions in the affected area presented damage and detachment of the exterior cladding elements, with one quarter of the total presenting partial or total collapse of the roof, mainly due to the loss of seating of the main girder. Apart from one building that presented partial collapse, all precast industrial buildings designed with seismic provisions – based on the architecture of the buildings and discussions of the reconnaissance team with the owners and inhabitants of the affected area – presented no damage to the structural elements. The damage on non-structural elements, which typically comprised the detachment of cladding panels from the main structure due to insufficient capacity of the connections, were not significantly reduced in the buildings designed with seismic provisions.

4.2 Structural damage

The weak link in the vast majority of the industrial buildings visited was the absence of mechanical connections between roof-girders and columns. The most common typology corresponded to double-slope beams, simply supported over special openings (forks) at the top of columns as shown in Fig. 4. This typology was used in Italy during the 60s and 70s for agricultural buildings, now being replaced by the more common flat-roof systems. In this connection typology, the capacity of transferring lateral loads depends entirely on the static coefficient of friction between the supporting surfaces of beam and column and on the length of the beam seating when the friction forces are exceeded by the earthquake force demands.

The collapse of most of the precast buildings was due to unseating of the transverse girders from the columns' forks. The seating loss was in the majority of the cases observed in the central column, where the seating length of the girders was rather limited and the relative displacement between the column and girder exceeded the available width, as shown in Fig. 5. In some cases, the collapse of the girders took place in the out-of-plane direction of the girder, after failure at the base of the forks. Figure 6a illustrates the out-of-plane collapse of a double-slope precast beam after unseating, following failure of the lateral restraints of the fork at the seat pocket (the original location of the beam is shown in red dashed lines). Figure 6b presents a detail of the failure of the lateral restraint, showing with red dashed lines the original undamaged geometry of the restrain at the fork.



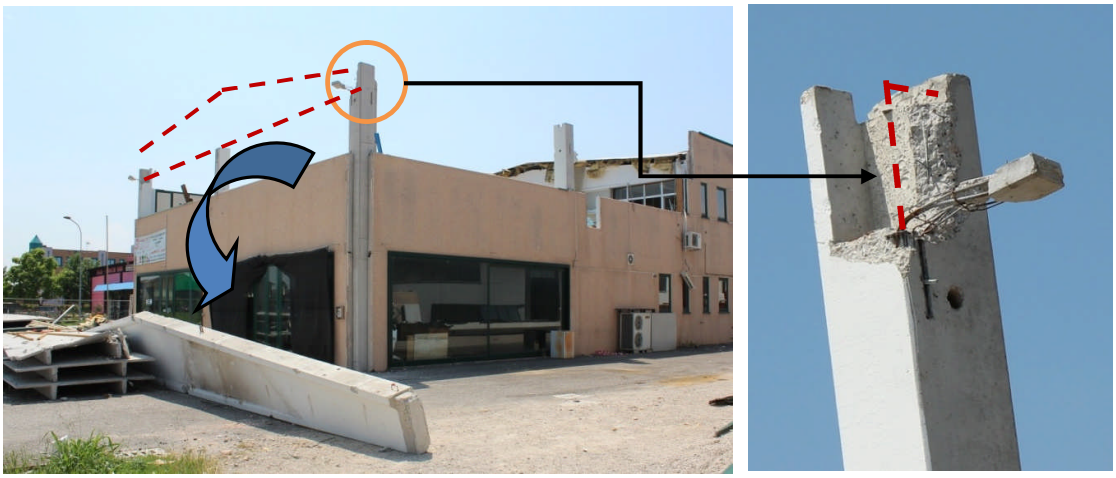
(a) (b)

Figure 4: (a) Seating of double slope precast beams showing the fork at the top of the column: seating at an end column. (b) Seating at an intermediate column of a "T" section beam (with dashed lines indicating the section of the beam at the seat pocket).



(a) (b)

Figure 5: (a) Loss of beam seating from the central column and associated collapse of a double slope precast beam (the blue curved arrow shows direction of collapse and the orange arrow shows the intermediate beam); (b) Longer seating of the end beam at the external column (blue arrow).

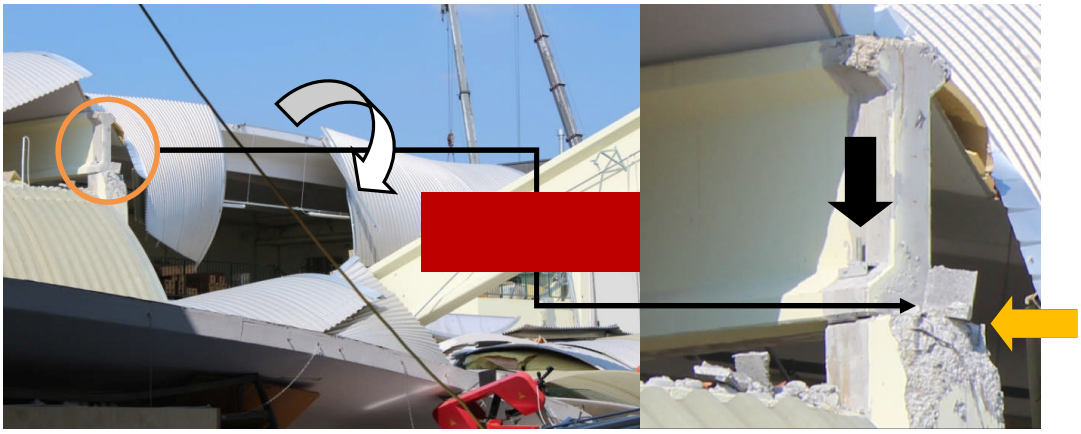


(a) (b)

Figure 6: (a) Out-of-plane collapse of a double slope precast beam after unseating following failure of the lateral restrain of the fork at the seat pocket; (b) Detail of the shear failure of the fork.

The main feature of precast industrial buildings constructed with seismic provisions lies in the type of beam-column connections. When horizontal forces are taken into consideration in design, the most common connection system for the construction of single-storey industrial buildings in Europe comprises hinged beam-column connections by means of dowel bars (shear connectors). This type of connection is able to transfer shear and axial forces resulting from the seismic actions. Practically, the horizontal beam-column connection is established by means of vertical steel dowels (typically one or two) which are protruding from the column into special beam sleeves. This pinned beam-column connections are constructed by seating the beams on the column capitals and by holding the beam ends in place by the use of these vertical steel dowels. In general, recently constructed precast concrete buildings, including a high-rise precast parking structure, which most probably incorporated steel dowels in the beam-column joints, exhibited apparent good performance. It should be noted that, due to safety measures in force immediately after the main shocks, no inspection near or inside these buildings was possible.

It is worth mentioning that a building completed in 2010 showed partial collapse, in spite of having been designed (according to information provided by the owner) with pinned beam-column connections following the new Italian construction standards. Visual inspection revealed failure at the top of one of the central column beam-column connections. This failure was followed by loss of the girder seating and its subsequent collapse (Fig. 7a). The rather limited distance of the dowels from the edge of the column and the limited amount of transverse reinforcement might have resulted into the formation of a shear crack across the concrete cover (Fig.7b), followed by the loss of the dowels anchorage and consequently the loss of the girder seating. This failure reveals the absence of specific provisions for detailing the beam-to-column connections in the current Italian construction standards and the as well as in the Eurocodes [10].



(a) (b)

Figure 7: Loss of girder seating in a recently constructed industrial building after failure of the pinned beam-column connection: (a) General overview of the collapsed beam (red dashed lines); (b) Detail showing failure of the column support at the beam-column pinned connection. Orange arrow shows damaged area at the top of the column, while red arrow shows an undamaged pinned connection.

4.3 Non-structural damage

Most of the inspected buildings – designed with or without seismic provisions – presented failure of the connections of the cladding elements due to their insufficient displacement capacity that led to overturning of the cladding elements. The panel connections were designed to transfer the vertical (self weight) load of the panel, as well as any out-of-plane loading, to

the main elements of the precast structure (beams and columns). For small drifts of the structure, the connections do not provide any in-plane stiffness interaction with the panels. However, during the earthquake the precast buildings might have been subjected to excessive interstorey drifts, as well as high out-of-plane inertial lateral forces, for which these connections were not designed for.

Current design practice for precast industrial buildings is based on a bare frame model, where the peripheral cladding panels enter only as masses, without any stiffness contribution. In addition, some designers introduce only the inertial mass contribution of the walls orthogonal to the plane of the walls. The panels are then connected to the structure with fastenings devices which are dimensioned by means of a local calculation, with anchorage forces orthogonal to the plane of the panels computed based on their mass and design spectral acceleration. The connecting devices are expected to allow for all other relative deformations. However, when the free relative deformation capacity of the connection is exceeded, the panels become an integral part of the resisting system, conditioning its seismic response. The high stiffness of this resisting system leads to much higher forces than those calculated from the frame model. These forces are related to the global mass of the floors and are primarily resisted in the plane of the walls. Furthermore, the seismic force reduction considered in precast structures relies on the energy dissipation resulting from the formation of plastic hinges at the columns bases. Due to the large flexibility of precast structures, very large drifts of the columns are typically needed to activate the energy dissipation mechanism assumed in design. However, the capacity of the connections between the cladding elements and the structure is typically exhausted well before such large drifts can develop.

Figure 8a illustrates the in-plane detachment of an exterior cladding element after failure of the connections (Fig. 8b) with the main structure. The design of the claddings connections proved to be insufficient also in the orthogonal direction. The out-of-plane inertial effects of the panel led to the development of high out-of-plane lateral forces that induced failure in the panel-to-frame and panel-to-panel connections.



(a) (b)

Figure 8: (a) Cladding panel collapse after failure of the connections with the main structure (orange arrows showing the location of connections of the collapsed exterior cladding); (b) Detail showing failure of the mechanical connection.

5 STRENGTHENING MEASURES

5.1 Overall damage and lesson learnt

The high damage and collapse of the precast industrial buildings – designed for gravity loads only –was due mainly to the absence of mechanical connections between beams and columns. Simply supported beam-column connections resulted into a large number of collapses induced by unseating of the transverse girders and longitudinal beams. The loss of seating mainly occurred in the central columns, where the seating length of the girders was shorter. In other cases the collapse of girders took place in the out of plane direction – of the girder –, after failure at the base of the forks. Recently constructed industrial buildings, which most probably incorporated steel dowels in the beam-column joints, exhibited a better seismic performance. However, the partial collapse of a building completed in 2010, in spite of having been designed with pinned beam-column connections following current Italian construction standards, brought in light the lack of specific provisions for the detailing of beam-to-column connections (including the Eurocodes).

The detachment of the cladding panels from the main structure due to the insufficient capacity of the connections was practically not improved in the newly constructed buildings. The panel connections were designed to transfer the vertical load of the panel, as well as any out-of-plane loading, to the precast structure, allowing for free deformations along the other directions. There were two types of loading situations for which the panel was not designed for: i) excessive drifts that exhausted the fastenings sliding capacity and led to the development of high forces and fracture of the fastenings; and ii) high out-of-plane inertial forces that led to the fastenings failure.

After the second main shock it was decided by the local and national authorities that the tagging of precast industrial buildings for usability would have been made by civil engineers being called upon by building owners. For most of the precast buildings existing in the affected area (i.e., designed for gravity loads only) a tagging procedure solely based on damage proved in general to be inadequate, as a number of industrial buildings that survived with no damage the first main shock did collapse during the second one. However, simple procedures for vulnerability assessment do not exist for this class of structures. Even if undamaged, precast buildings designed with no seismic provisions are highly vulnerable and may experience high levels of damage in the event of future aftershocks similar to the main event. Moreover, there is a high potential of indirect economical losses due to the interruption of the economic activities associated to the prefabricated industrial buildings. There is a risk of relocation of activities to areas not affected by the earthquake, which would badly impact on the economy of the affected area.

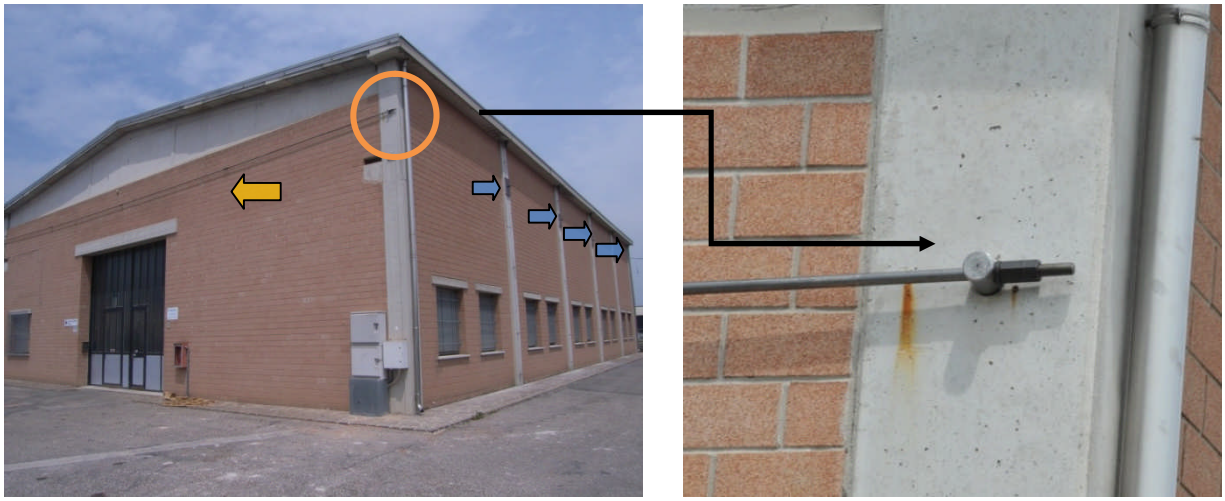
On the basis of the current situation, a series of provisional recommendations concerning the structural performance and safety of new precast buildings and the retrofit of existing ones in seismic regions are presented, regarding: (i) development of guidelines for retrofitting precast buildings designed with non-seismic provisions; (ii) development of guidelines for the rational design of connections of precast buildings in seismic regions; and (iii) improvement of the design of the connections of panels.

5.2 Retrofitting proposal for simply supported precast beams

In response to the risk associated with the seismic response of industrial precast buildings an ordinance comprising general guidelines for vulnerability assessment and intervention was issued by the national authorities [11]. This draft document calls for the need of adopting interventions to reduce the relative displacements between column heads and supporting beams

by means of mechanically connecting the beams with the columns. At present there are not experimentally validated strengthening techniques for the seismic connection of beams simply supported to the column forks, although various retrofitting proposals for this typology of industrial buildings have been proposed.

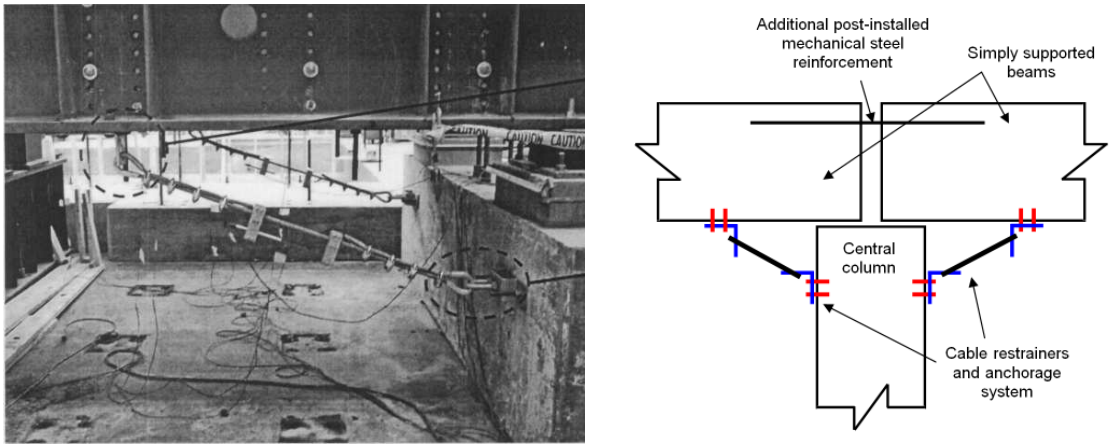
During the field visit the team inspected a precast industrial building that had been retrofitted following the first event (after information gathered from the building owner). The building corresponded to the typology with simply supported beams on columns designed for gravity loads only. The retrofit consisted in a series of steel ties in line and below the main girders, as shown in Fig. 9. The steel ties were anchored at the top of the columns in the transverse direction and might have prevented opening of the columns and loss of seating of the girder during the 29 May event.



(a) (b)

Figure 9: (a) Steel ties anchorage system installed after the main event to stabilize the structure: orange arrow showing the external tie, blue arrows showing the internal ties. (b) Detail of the anchorage at the external tie.

A proposal for the strengthening of existing industrial building consists in adopting a scheme which is used for the seismic retrofit of simply supported bridges: to reduce the likelihood of collapse due to unseating, cable restrainers are used between the girders and the piers/abutments of the bridge. Cable restrainers were first used in the United States after the collapse of several multi-frame bridges that collapsed due to unseating during the 1971 San Fernando earthquake in California [12]. The performance of bridges in the 1989 Loma Prieta and 1994 Northridge earthquakes showed that cable restrainers were effective in limiting damage [13-15]. DesRoches et al. 2003 [16] evaluated the force-displacement behavior of a cable restrainer assembly, used for the seismic retrofit of simply supported bridges. The cable restrainers were connected to the bridge pier using steel bent plates, angles, and undercut anchors embedded in the concrete as specified by typical bridge retrofit plans. The test results demonstrated that this strengthening configuration was effective in cases where seat widths were very small and relative displacements needed to be limited. The results of this study might form a good basis for future research on the use of cable restrainers for the retrofit of industrial buildings with beams simply supported at the top of columns (Fig. 10). The restrainers in such a system would be anchored at the column and beam ends, where the bending moment is minimum, with the advantage that their installation would not significantly disturb the functioning of the building.



(a) (b)

Figure 10: (a) Side view of a full-scale bridge model with seismic cable restrainers (DesRoches et al. 2003); (b) General concept of a retrofit solution for industrial buildings with beams simply supported on the column top comprising seismic cable restrainers and possibly additional steel reinforcement.

5.3 Seismic design of pinned beam-column connections

The partial collapse of the industrial building with pinned beam-column connections completed in 2010 and described in Section 4.2 brought in light the lack of specific provisions for the detailing of beam-to-column connections by the Italian construction standards and the Eurocodes. To address such issues related to the seismic design of precast concrete structures a large amount of pre-normative research [17, 18] for the development and maintenance of the Eurocodes was carried out at the European Laboratory for Structural Assessment (ELSA) of the Joint Research Centre (JRC) of the European Commission at Ispra (Italy). To this end the research project SAFECAST (Performance of innovative mechanical connections in precast buildings structures under seismic conditions, Grant agreement n° 218417-2), financed by the Seventh Framework Programme of the European Commission, was recently undertaken to fill the gap in the knowledge of the seismic behavior of the mechanical connections used in precast concrete structures. A set of guidelines for the design of connections of precast structures in seismic areas was finally delivered in the framework of SAFECAST [19].

The structural capacity of pinned beam-column connections, which represent the most common connection system in construction practice in Europe was investigated by the National Technical University of Athens [20] and the University of Ljubljana [21].

Based on the work of Psycharis and Mouzakis 2012 [20], a rational procedure for the seismic design and proper detailing of pinned beam-to column connections was proposed. Following the concept of Eurocode 8, the connections are overdesigned with respect to the strength of beam and column. The prevailing energy dissipation mechanism of the structure relies on the formation of plastic hinges within the critical regions of the columns, with the connections remaining elastic. The design of the columns is based on a prescribed force reduction factor q, whereas the design of the connections follows the capacity design rule: the design shear force E_d for the connection is obtained assuming that the ultimate flexural resistance is developed at the base of the column, calculated by multiplying its flexural resistance M_{Rd} by the overstrength factor γ_{Rd}. Verification for the shear resistance of the connection R_d is made, namely by satisfying the inequality $E_d \leq R_d$. On the basis of the experimental results obtained by Psycharis and Mouzakis 2012 the following formula for the shear resistance of the connection was proposed:

$$R_d = \frac{C_0}{\gamma_{Rd}} \cdot n \cdot D^2 \cdot \sqrt{f_{cd} \cdot f_{yd}} \cdot \quad \text{for } d/D > 6 \tag{1a}$$

$$R_d = \frac{C_0}{\gamma_{Rd}} \cdot (0.25d/D - 0.50) \cdot n \cdot D^2 \cdot \sqrt{f_{cd} \cdot f_{yd}} \quad \text{for } 4 \le d/D \le 6 \tag{1b}$$

where $C_0 \approx 0.90 \div 1.10$ is a coefficient that depends on the expected joint rotations. For large joint rotations (flexible columns) a value of around 0.90–0.95 is suggested, while for small joint rotations (stiff columns and walls) it may be increased up to the maximum value of 1.10, for practically zero joint rotations. f_{ck} and f_{sy} are the characteristic strengths of concrete and steel (units in MPa), with their design values $f_{cd} = f_{ck}/\gamma_c$ and $f_{yd} = f_{sy}/\gamma_s$, where γ_c and γ_s are the partial safety factors for concrete and steel. The recommended values for these coefficients in Eurocodes 2 and 8 are: $\gamma_c = 1.50$ and $\gamma_s = 1.15$. D is a diameter of the dowel, d the distance from the centre of the dowel to the face of the column (units in mm), and n is the number of dowels. The suggested general safety factor γ_{Rd} is equal to 1.30 as proposed by fib 2008 [22].

In addition, a series of specific provisions for the detailing of hinged beam-column joints were proposed by Psycharis and Mouzakis 2012:

- It was suggested to use a sufficient cover of the dowels (d/D ≥ 6), otherwise spalling might occur, which much decrease their resistance.
- The presence of horizontal hooks in front of the dowels was found to be very important for the hinged joint's seismic response.
- The use of high strength grout inside the sleeves increases the resistance of the connection and improves its cyclic response by decreasing pinching and increasing ductility.
- For flexible columns, large rotations can occur at the joints, which reduces shear strength and increase damage to the connection, which increases with repeated cycles.

Besides the tests on individual beam-column joints, within the SAFECAST project a series of pseudodynamic tests on a full-scale three-storey precast concrete building, comprising pinned beam-column connections, were carried out at the ELSA Laboratory. On the basis of these tests it was shown that in the case of multi-storey buildings with hinged beam-to-column connections, due to the participation of the higher modes, there is no reduction of the inter- storey forces when the structure enters into the nonlinear regime, as one would expect as a consequence of ductility. This resulted into large (i.e., much larger than when taking into account the q factor) forces in the beam-column connections. Therefore, the large magnification of storey forces should be considered in determining the capacity of the pinned connections. A possible conservative simplification could be to multiply the design storey forces in all stories by q [21, 23-24] (Fischinger et al. 2012, Negro et al. 2012, Bournas et al. 2012), even though less conservative approaches have also been developed [21].

5.4 Cladding panels design

The detachment of cladding panels from the main structure due to insufficient capacity of their connections with the main structure demonstrated their high vulnerability. Classifying precast claddings as non-structural elements because they are not expected to contribute to the strength of the building is indeed misleading, since they may provide a stiffness contribution at large drift, inducing failure of their connections resulting in the fall of panels up to 10 tons of weight. In order to ensure the standard design approach in which the claddings do not con-

tribute to seismic response, stringent design criteria for the design of the connections should be enforced: connections devices should be able to provide the required strength in the vertical and out-of-plane directions while accommodating large relative deformations in all other directions (Figure 11a). A viable option would be to prescribe adequate fail-safe restraints, so that the panels would not fall even in case the relative displacement capacity of the connection is exceeded (Figure 11b). Another possibility would be to design the claddings and their connections as being an integral part of the structure, by adequately taking into account their strength and stiffness in the design model. These are the objectives of the recently activated EU-funded project SAFECLADDING (Grant Agreement no. 314122).



(a) (b)

Figure 11: (a) Panel connection device that provides resistance in the vertical and out-of-plane directions and accommodates large relative deformations in the lateral direction. (b) Fail-safe restraints to prevent panel falling.

6 CONCLUSIONS

The present paper follows a technical mission to the area affected by the earthquake focusing mainly on the performance of precast industrial buildings. From the findings of the field reconnaissance mission, the following set of conclusions and recommendations may be drawn:

- Most of the damage experienced by precast industrial buildings in the affected area was observed in buildings designed according to the seismic zoning in force until 2003, which classified the area as non-seismic, corresponding to a design for gravity loads only, with beam-to-column joints not capable of transferring horizontal loads and isolated column foundations.
- Approximately 75% of the precast industrial buildings designed with no seismic provisions presented damage and detachment of the exterior cladding, with 25% presenting partial or total collapse of the roof and girders.
- The weak link in the majority of industrial buildings designed with no seismic provisions only was the absence of a mechanical connection between beams and columns. This resulted in a large number of collapses induced by unseating of the main beams. The loss of seating occurred mainly in the central columns, where the seating length of the girders was rather limited. In other cases the collapse of girders took place in the out of plane direction – of the girder – following failure of the lateral restrains at the top of the column.
- Industrial buildings designed under the seismic zoning in force at the time of the earthquake and corresponding to 0.15g PGA (475 year return period) exhibited better seismic

performance. However, the partial collapse of a building with pinned beam-column connections completed in 2010 and designed following the Italian construction standards brought in light the lack of specific provisions for the detailing of beam-to-column connections.

- The detachment of cladding panels from the main structure was practically not improved in the newly constructed buildings, due to insufficient capacity of the connections between the panels and the structure to accommodate in-plane displacements and resist the out-of-plane inertial forces of the panels.
- It is recommended to develop guidelines for the seismic retrofit of precast buildings designed with non-seismic provisions, in particular for the beam-to-column connections and for the connections of the cladding panels with the structure. Such guidelines will be of very much use in similar areas in Europe that are upgrading their seismic zoning, classifying as seismic areas that have been historically considered as non-seismic.

REFERENCES

[1] EERI (1979), Stratta J, Loring W, Friuli, Italy Earthquakes of 1976, Earthquake Engineering Research Institute.

[2] Tzenov LL, Sotirov, Boncheva P, (1978), Study of some damaged industrial buildings due to Vrancea earthquake. Proc. of 6th ECEE. Dubrovnik, 6: 59-65.

[3] Fajfar P, Duhovnik J, Reflak J, Fishinger M, Breska Z, (1981) The behaviour of Buildings and Other Structures during the Earthquake of 1979 in Montenegro, University of Ljubljana, IKPIR Publication no. 19A.

[4] Bonacina G, Indirli M, Negro P, (1994) The January 17, 1994 Northridge Earthquake - Report to the Sponsor: Earthquake Engineering Field Investigation Team, *Special Publication No.I.94.14,* 1994, Ispra (VA), Italy.

[5] Saatcioglu M, Mitchell D, Tinawi R, Gardner NJ, Gillies AG, Ghobarah A, Anderson DL, Lau D. (2001), The August 17, 1999 Kocaeli (Turkey) earthquake-damage to structures". Can. J. Civil Eng., 28(8): 715-773.

[6] EERI (2000), Kocaeli, Turkey, Earthquake of August 17, 1999, Earthquake Spectra Supplement.

[7] Monitoring and Information Centre (MIC), Community Civil Protection Mechanism, Technical Report Italy Earthquake 2009, http://ec.europa.eu/echo/files/aid/countries/italy_report1.pdf

[8] Toniolo G, Colombo A (2012) Precast concrete structures: the lessons learned from the L'Aquila earthquake. Structural Concrete 13: 73-83.

[9] Olgiati M, Negro P, Bournas D, (2011) Literature survey and identification of needs-Part two: General survey and design procedures. Contribution of the Joint Research Centre. SAFECAST-Deliverable 1.2. Grant agreement no.218417-2: 190p.

[10] CEN (2004) European Standard EN 1998-1: Eurocode 8: Design of Structures for Earthquake Resistance - Part 1: General rules, seismic actions and rules for buildings, European Committee for Standardization, Brussels, 2004.

[11] Consiglio Superiore dei Lavori Pubblici (2012), Valutazione della vulnerabilità e onterventi per le costruzioni ad uso produttivo in zona sismica, http://www.mit.gov.it/mit/mop_all.php?p_id=12505

[12] Jennings PC (1971) Engineering features of the San Fernando earthquake of February 9, 1971. Rep. No. EERL-76/18, Earthquake Engineering. Research Laboratory, California Institute of Technology, Pasadena, Calif.

[13] Saiidi M, et al. (1993) Response of bridge hinge restrainers during earthquakes: Field performance, analysis, and design. Rep. No. CCEER93-6, Center for Civil Engineering Earthquake Research, Univ. of Nevada, Reno, Nev.

[14] Priestley MJN, Seible F, Uang CM (1994) The Northridge earthquake of January 17, 1994: Damage analysis of selected freeway bridges. Rep. No. SSRP-94/06, Department of Applied Mechanics and Engineering Sciences, Univ. of California, San Diego.

[15] Moehle JP (1995) Northridge earthquake of January 17, 1994: Reconnaissance report. Volume 1: Highway bridges and traffic management. Earthquake Spectra, 11 (Suppl.): 287–372.

[16] DesRoches R, Thomas P, Leon RT, Lam T (2003) Full-Scale Tests of Seismic Cable Restrainer Retrofits for Simply Supported Bridges restrainer design methods for simply supported bridges. ASCE J. Bridge Eng. 6 (5): 307–315.

[17] Ferrara L, Colombo A, Negro P, Toniolo G, (2004) Precast vs. cast-in-situ reinforced concrete industrial buildings under earthquake loading: an assessment via pseudodynamic tests. Proceedings of the 13th WCEE.

[18] Ferrara L, Mola E, Negro P, (2006) Pseudodynamic and cyclic testing of full scale prototypes of precast R/C one storey buildings, Proceedings of the *1st European Conference on Earthquake Engineering and Seismology*, Geneva, September 3-8.

[19] Negro P, Toniolo G, (2012) Design Guidelines for Connections of Precast Structures under Seismic Actions, Report EUR 25377 EN, European Commission. http://bookshop.europa.eu/en/design-guidelines-for-connections-of-precast-structures-under-seismic-actions-pbLBNA25377.

[20] Psycharis I and Mouzakis H (2012) Shear resistance of pinned connections of precast members to monotonic and cyclic loading. Elsevier Eng Struct 41: 413-427.

[21] Fischinger M, Isaković T, Kramar M (2012) Experimental behaviour of existing connections-Part two: Contribution of the University of Ljubljana. SAFECAST-Deliverable 2.1. Grant agreement no.218417-2: 68p.

[22] Federation International du Beton (fib), (2008) Structural connections for precast concrete buildings. Bulletin 43.

[23] Negro P, Bournas D, Molina FJ, (2012) Pseudodynamic Tests on a Full-Scale 3-Storey Precast Concrete Building: Global Response. Elsevier Eng Struct J. 2012, submitted.

[24] Bournas D, Negro P, Molina FJ, (2012) Pseudodynamic Tests on a Full-Scale 3-Storey Precast Concrete Building: Behavior of the Mechanical Connections and Floor Diaphragms. Elsevier Eng Struct J. 2012, submitted.

COMPDYN 2013
4th ECCOMAS Thematic Conference on
Computational Methods in Structural Dynamics and Earthquake Engineering
M. Papadrakakis, V. Papadopoulos, V. Plevris (eds.)
Kos Island, Greece, 12–14 June 2013

THE EFFECT OF MULTIPLE EARTHQUAKE EXCITATIONS IN SEQUENCE ON ANCIENT MULTI-DRUM STRUCTURES

Loizos Papaloizou[1], Petros Komodromos[2]

[1,2] Department of Civil and Environmental Engineering, University of Cyprus
P.O. Box 20537, 1678 Nicosia, Cyprus
[1] loizosp@ucy.ac.cy, [2] komodromos@ucy.ac.cy

Affiliation: This project with protocol number "ΑΝΘΡΩ/0609(BE)/23" is co-funded by the European Regional Development Fund and the Republic of Cyprus through the Research Promotion Foundation.

Keywords: Ancient Columns, Earthquake, DEM.

Abstract. *Strong earthquakes are common causes of destruction of ancient monuments, such as classical columns and colonnades. Ancient classical columns of great archaeological significance can be abundantly found in high seismicity areas in the Eastern Mediterranean. Multi-drum columns are constructed of stone blocks that are placed on top of each other, often without connecting material between the individual blocks. The seismic behaviour of these structures exhibits complicated rocking and sliding phenomena between the individual blocks of the structure that very rarely appear in modern structures.*

The investigation of the dynamic response of such monumental structures, combined with the research fields of paleoseismology and archaeoseismology, may reveal certain information from past strong earthquakes that have struck the respective regions. Studying multi-drum structures under different earthquake excitations can provide some insights in defining the frequency content and magnitude of past destructive earthquakes. Furthermore, the understanding of the seismic behaviour of these structures can contribute to the rational assessment for their structural rehabilitation. Multi-drum classical columns have been exposed to large numbers of strong seismic events throughout the many centuries of their life spans. Those that survived have successfully withstood a natural seismic testing that lasted for several centuries.

This research work investigates how multiple earthquake excitations in sequence affect the overall seismic behaviour of multi-drum columns. Specifically, various strong motion excitations are selected from a specific region where these monuments are built, and used in series for the computation of the collective final deformation of multi-drum columns. In order to calculate this cumulative deformation for the series of motions, the individual deformation of the column for each excitation is computed and then used as initial conditions for the next earthquake. For this procedure, the Discrete Element Method (DEM) is utilized by simulating the individual rock blocks as distinct bodies. A specialized software application is developed, using a modern object-oriented programming language, in order to enable the effective and efficient simulation of multi-drum columns under these conditions.

1 INTRODUCTION

Strong earthquakes are common causes of destruction of ancient monuments, such as classical columns and colonnades. Ancient classical columns of great archaeological significance can be abundantly found in high seismicity areas in the Eastern Mediterranean (Figure 1). Multi-drum columns are constructed of stone blocks that are placed on top of each other, often without any connecting material between the individual blocks. The seismic behaviour of these structures exhibits complicated rocking and sliding phenomena between the individual blocks of the structure that are very rare in modern structures.

Today, the remains of most of these temples are often limited to series of columns with an entablature or only an architrave, and in some cases only standalone columns or parts of columns. The investigation of the seismic behaviour of such monuments is scientifically interesting, as it involves complicated rocking and sliding responses of the individual rock blocks. The understanding of the seismic behaviour of these structures contributes to the rational assessment of efforts for their structural rehabilitation and may also reveal some information about the characteristics of past earthquakes that had struck the respective regions.



Figure 1: Multi-drum columns, Jerash, Jordan.

Ancient monuments, compared to modern structures, have been exposed to great numbers of severe seismic events throughout the many centuries of their life spans. Those that survived have successfully withstood a natural seismic testing that lasted for thousands of years. Thus, it is important to understand the mechanisms that allowed them to avoid structural collapse and destruction during very strong earthquakes. Since analytical study of such multi-block structures under strong earthquake excitations is practically difficult, if not impossible for large numbers of blocks, while laboratory tests are very difficult and costly, numerical methods can be used to simulate their seismic response.

A very extensive review of the literature on the usage of numerical methods for the analysis of monuments until 1993 was published by Beskos [1]. The dynamic behaviour of infinitely rigid bodies during horizontal excitations was studied by Housner [2], while, later on, other researchers [3-7] investigated further, both analytically and experimentally, the required

conditions to overturn rigid bodies. Such structures can be simulated utilizing the Discrete Element Methods (DEM), which have been specifically developed for systems with distinct bodies that can move freely in space and interact with each other with contact forces through an automatic and efficient recognition of contacts.

Research efforts to use the DEM in the simulation of ancient structures have already exhibited promising results, motivating further exploitation of this method. Recent research work based on commercial general-purpose DEM software applications [3,8], demonstrated that the DEM can be reliably used for the analysis of such structures, although a sensitivity of the response to small perturbations of the characteristics of the structure or the excitation has been reported. However, similar sensitivity has also been observed in experiments with classical columns [9]. Hence, it is important to perform large numbers of simulations with varying earthquake characteristics and design parameters to properly assess and interpret the simulation results. Yim, Chopra and Penzien [10], through analytical study of rigid blocks under horizontal and vertical ground motion, suggested that the vertical acceleration affects rocking motion significantly but not systematically.

Latest research studies in the fields of paleoseismology and archaeoseismology [11,12] investigate the damage in ancient monument structures and propose various quantitative models to test the seismogenic hypothesis of observed damage. Papaloizou and Komodromos [13] used the Discrete Element Method (DEM) as well as a modern object-oriented design and programming approach, in order to examine the simulation of multi-drum columns and colonnades under harmonic and earthquake excitations.

Stefanou et al. [14,15] showed, by using stability analysis, that rocking is unconditionally unstable and that wobbling is the dominant motion for frustums. Furthermore, the authors suggested that the two dimensional analyses should fail to capture wobbling as the out-of-plane motion is ignored. Dimitri et al. [16], studied the dynamic behaviour of masonry columns and arches on buttresses with the discrete element method. Ambraseys and Psycharis [17] studied the stability of columns and statues under earthquakes, by investigating various parameters that affect their response. Efraimiadou et al. [18] examined the effect of multiple earthquakes on the collision between adjacent reinforced concrete buildings.

In this research project, a custom-made DEM software has been specifically designed [13] and implemented to enable efficient and effective performance of large numbers of numerical simulations with varying parameters, modelling these structures with independent distinct bodies, as they are actually constructed in practice. Such numerical simulations allow the assessment of the influence of different earthquake characteristics as well as the various mechanical and geometrical parameters of these structures on their seismic responses.

2 METHODOLOGY

For the analyses performed, a specialized software application (Papaloizou and Komodromos, [13]) is appropriately extended to take into account the vertical component of the excitation. For the extension of the software application modern object-oriented design and programming is used, in combination with the Discrete Element Method (DEM), in order to include the vertical earthquake component.

Specifically, the interactions between two bodies in contact are created in DEM whenever a contact is detected, kept as long as the bodies remain in contact and removed as soon as the bodies are detached from each other. No tension force can be transmitted between the contact surfaces. In order to be able to consider potential sliding according to the Coulomb friction law, normal and tangential directions are considered during contact. The normal and tangential directions are based on a contact plane, which is defined at each simulation step. The bod-

ies slide along the contact plane relatively to each other, whenever the tangential force exceeds the maximum allowable force in that direction.

The simulations take into account the individual rock blocks as distinct rigid bodies. At any simulation step, when two bodies come in contact, equivalent springs and dashpots are automatically generated, in the normal and tangential directions, to estimate the contact forces that should be applied to the bodies in contact. The interactions between bodies may involve new contacts, renewed contacts, slippages and complete detachments from other bodies with which they were, until that time, in contact. The contact forces, which are applied at contact points during impact, are then taken into account, together with the gravity forces, in the formulation of the equations of motion, which are numerically integrated using the Central Difference Method (CDM) in order to compute the displacements at the next time step.

3 NUMERICAL ANALYSES

Two different types of single standing multi-drum columns are analyzed with the same overall dimensions but with different numbers of drums. Each set of columns analyzed (Figure 2) has a total width of *1 m* and a total height of *6 m*, divided into two and four drums, respectively. The coefficient of friction that is used for the analyses is set to $\mu = 0.485$. A contact stiffness of the order of 10^8 N/m^2 and a damping coefficient of 10^3 $N\,s/m$ are used in the simulations. The time step Δt is selected to be of the order of 10^{-6}.

The columns are examined with horizontal earthquake ground motions selected from regions, where these monuments are often built, such as the Greek region (Table 1). The earthquakes selected have a similar Peak Ground Acceleration (PGA) but significantly different frequency content. Furthermore, the earthquakes have been selected so that they do not overturn the columns analyzed. The response spectra of the horizontal earthquake ground motions are presented in Figure 3, whereas the motion characteristics are shown in Figure 4.

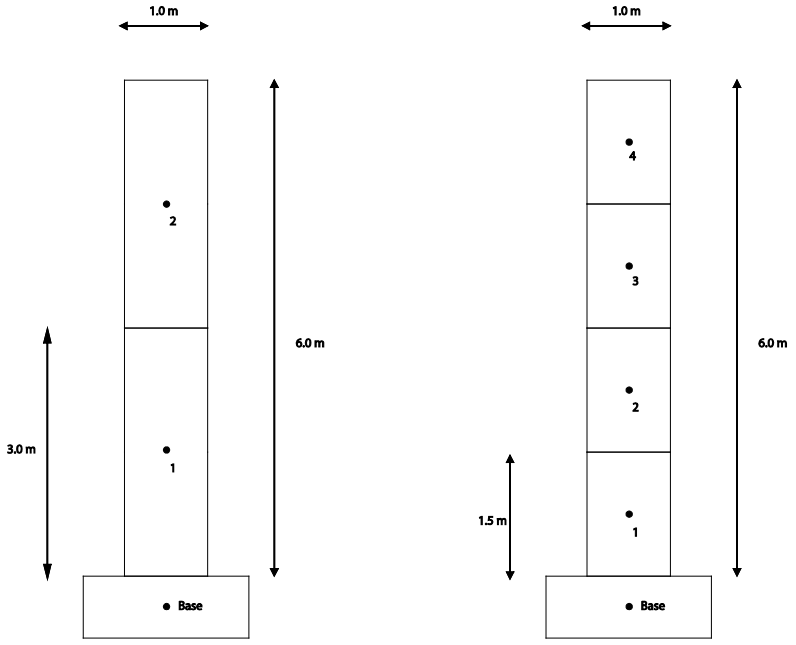


Figure 2: Dimensions of the analyzed columns.

No.	Place	Date and Time	Earthquake Component	PGA *(m/sec^2)*
1	Athens, Greece	11:56:50, SEPTEMBER 7, 1999	KALLITHEA DISTRICT N46	2.602
2	Kalamata, Greece	17:24:31, SEPTEMBER 13, 1986	KALAMATA OTE-BUILDING N10W	2.671

Table 1: List of earthquake records that are used in the analyses.

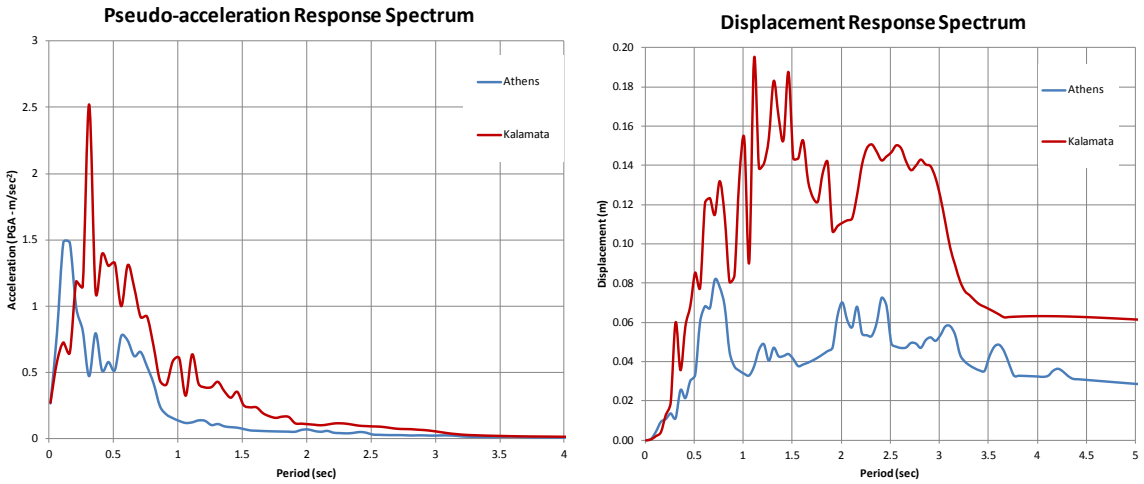
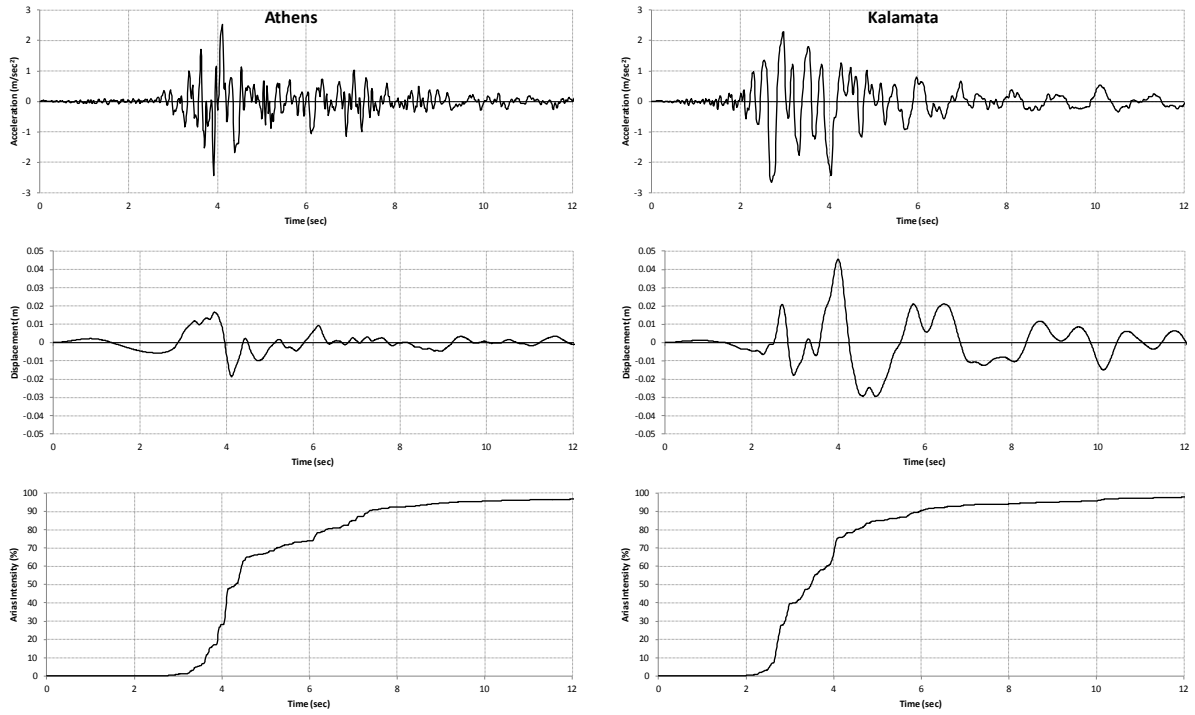


Figure 3: Response Spectra for horizontal components.



(a) (b)

Figure 4: Acceleration, Displacement and Arias Intensity for the Athens (a) and Kalamata (b) earthquake.

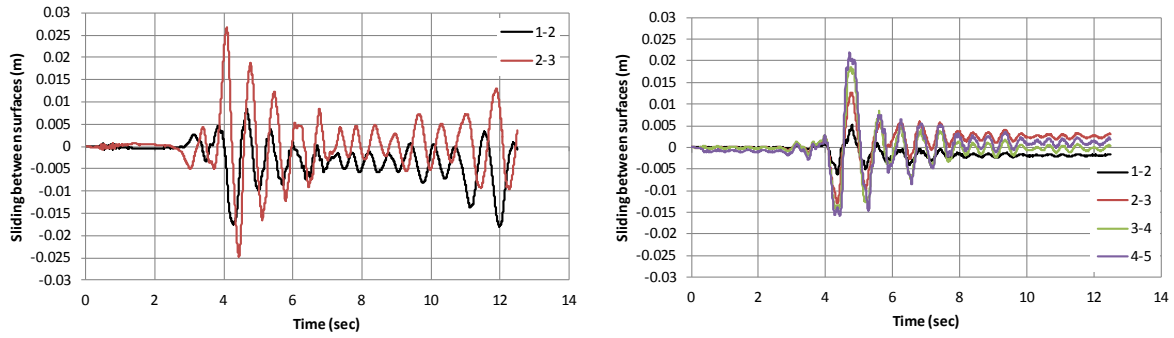
4 ANALYSES RESULTS

A number of parametric studies is performed in order to investigate the collective response of multi-drum columns under a series of strong motion excitations. The two columns previously described (Figure 2) are initially analyzed under the aforementioned Athens and Kalamata earthquake excitations.

The strong motion excitations are then applied repeatedly in series, for the computation of the collective final deformation of the columns. In order to calculate this cumulative deformation for the series of motions, the individual deformation of the column for each excitation is computed and then used as initial conditions for the simulation under the following earthquake excitation.

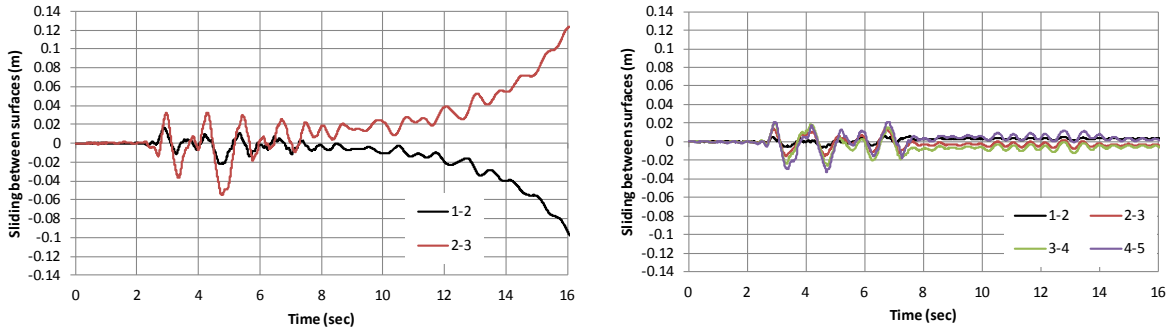
4.1 Single earthquake analyses

Figure 5 and Figure 6 show the horizontal sliding between surfaces for a two-drum column and a four-drum column under the Athens and Kalamata earthquakes, respectively. The results demonstrate that for both excitations a four-drum column seems to be more stable than a two-drum column. Furthermore, the horizontal sliding between the surfaces of the drums is larger for the Kalamata earthquake than for the Athens earthquake.



(a) (b)

Figure 5: Horizontal sliding between surfaces for a two-drum column (a) and a four-drum column (b) under the Athens earthquake.



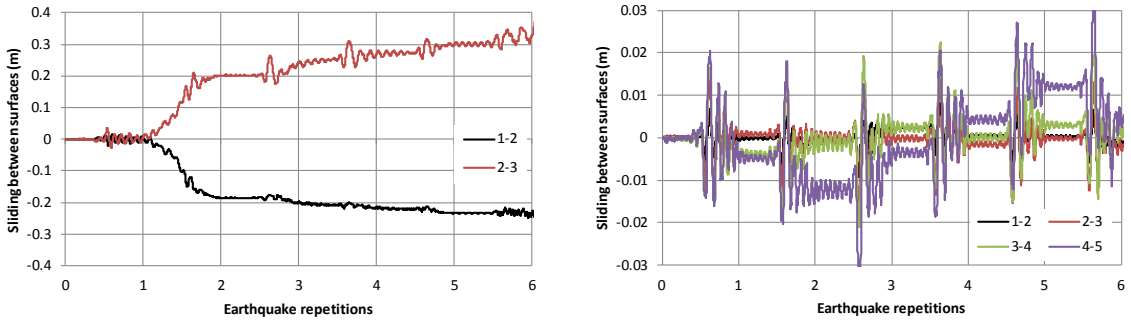
(a) (b)

Figure 6: Horizontal sliding between surfaces for a two-drum column (a) and a four-drum column (b) under the Kalamata earthquake.

4.2 Analyses under earthquakes in series

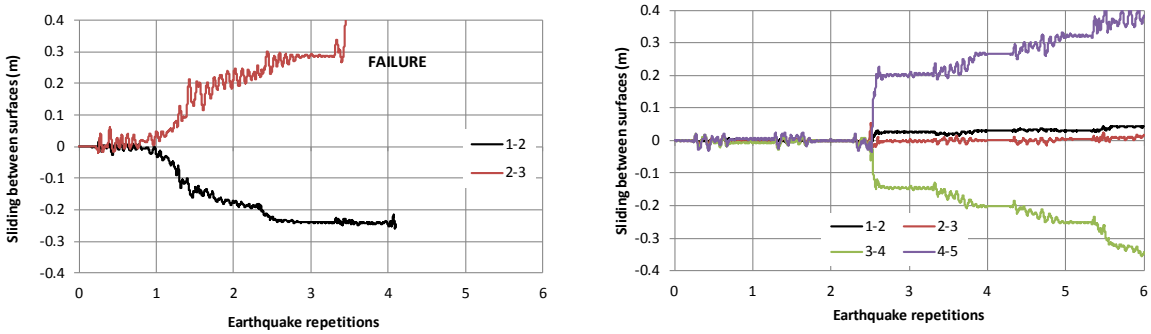
Figure 7 and Figure 8 show the horizontal sliding between surfaces for a two-drum column and a four-drum column under a series of repetitions of the Athens and Kalamata earthquake, respectively. The results show that for both series of excitations a four-drum column seems to be more stable than a two-drum column. In addition, the horizontal sliding between the surfaces of the drums is larger for the Kalamata earthquake, which has almost the same PGA with the Athens earthquake but different frequency content.

The analyses indicate that the cumulative deformation of the columns increases with each recurrence of the earthquake, with a failure occurring for the two-drum column under the Kalamata earthquake series (Figure 8a). Figure 9 shows snapshots of the deformations of a two-drum column under a repeated series of the Kalamata earthquake as well as the horizontal sliding between the drum surfaces. These snapshots show that the cumulative sliding increases on every recurrence of the earthquake, causing the top drum of the column to overturn before the 4th repetition.



(a) (b)

Figure 7: Horizontal sliding between surfaces for a two-drum column (a) and a four-drum column (b) under a series of repetitions of the Athens earthquake.



(a) (b)

Figure 8: Horizontal sliding between surfaces for a two-drum column (a) and a four-drum column (b) under a series of repetitions of the Kalamata earthquake.

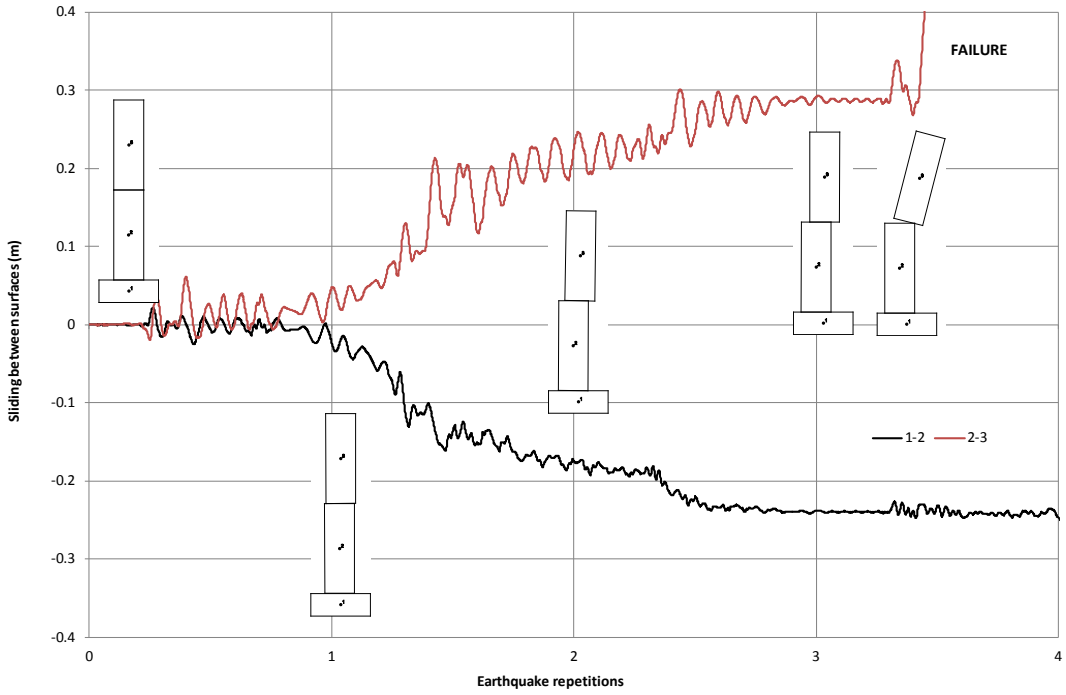


Figure 9: Horizontal sliding between surfaces and snapshots of the deformation for the two-drum column under a series of repetitions of the Kalamata earthquake.

5 CONCLUSIONS

The analysis results indicate that the frequency of seismic excitation, significantly affects the seismic response of multi-drum columns. Specifically, the horizontal sliding between the drums is larger for the Kalamata earthquake, which has lower frequency content than the Athens earthquake. Furthermore, under both excitations the four-drum columns seem to be more stable than the two-drum columns with the same overall dimensions.

By examining the stability of multi-drum columns for earthquakes that have been selected from the Greek region, where these monuments are often built, the simulations show that these multi-drum structures have the capacity to successfully withstand a single strong earthquake motion. However, the simulations results concerning a number of the same excitations applied in series indicate that the cumulative sliding increases on every recurrence of the earthquake, causing in some cases, instability to the multi-drum columns.

REFERENCES

[1] Beskos D. (1993), “Use of finite and boundary elements in the analysis of monuments and special structures”, Association of Civil Engineers of Greece, 217.

[2] Housner G.W (1963), ‘The behavior of inverted pendulum structures during earthquakes”. Bulletin of seismological Society of America, 53, 403-417.

[3] Psycharis I., Lemos J., Papastamatiou D., Zambas C. and Papantonopoulos C. (2003), “Numerical study of the seismic behaviour of a part of the Parthenon Pronaos”, Earthquake Engineering & Structural Dynamics 32, 2063-2084.

[4] Pompei A., Scalia A. and Sumbatyan M.A. (1998), "Dynamics of Rigid Block due to Horizontal Ground Motion", Engineering Mechanics 124, 713-717.

[5] Makris N. and Zhang J., (2001) "Rocking response of anchored blocks under pulse-type motions", Engineering Mechanics 127, 484-493.

[6] Manos G.C., Demosthenous M., Kourtides V., Hatzigeorgiou A., (2001) "Dynamic and earthquake behavior of models of ancient columns and colonnades with or without energy absorbtions systems", Proceedings of Second Greek National Conference on Earthquake Engineering and Seismology, 1, 257-276.

[7] Komodromos P., Papaloizou L., Polycarpou P., (2008) "Simulation of the response of ancient columns under harmonic and earthquake excitations", Engineering Structures 30(8), 2154-2164.

[8] Papantonopoulos C., Psycharis I., Papastamatiou D., Lemos J. and Mouzakis H., (2002), "Numerical prediction of the earthquake response of classical columns using the distinct element method", Earthquake Engineering and Structural Dynamics 31, 1699-1717.

[9] Mouzakis H., Psycharis I., Papastamatiou D., Carydis P., Papantonopoulos C., and Zambas C., (2002). "Experimental investigation of the earthquake response of a model of a marble classical column", Earthquake Engineering and Structural Dynamics 31, 1681-1698.

[10] Yim C., Chopra A., Penzien J., (1980), Rocking response of rigid blocks to earthquakes, Earthquake engineering and structural dynamics, 8, 565-587.

[11] Hinzen, K.-G., Fleischer, C., Reamer, S.K., Schreiber, S., Schütte, S., Yerli, B., (2010), "Quantitative methods in archaeoseismology" Quaternary International, 242, 31-41

[12] Caputo, R., Hinzen, K.-G., Liberatore, D., Schreiber, S., Helly, B., Tziafalias, A., (2011), "Quantitative archaeoseismological investigation of the Great Theatre of Larissa, Greece "Bulletin of Earthquake Engineering. 9 (2), 347-366.

[13] Papaloizou, L., Komodromos, P., (2012) "Investigating the seismic response of ancient multi-drum colonnades with two rows of columns using an object-oriented designed software", Advances in Engineering Software, 44 (1), 136-149.

[14] Stefanou I., Vardoulakis I. and Mavraganis A. (2011), Dynamic motion of a conical frustum over a rough horizontal plane, InternationalJournalofNon-LinearMechanics, 46, 114–124.

[15] Stefanou I, Psycharis I., Georgopoulos I., (2011) Dynamic response of reinforced masonry columns in classical monuments, Construction and Building Materials, 25, 4325-4337.

[16] Dimitri R., De Lorenzis L., Zavarise G., (2011) Numerical study on the dynamic behavior of masonry columns and arches on buttresses with the discrete element method, Engineering Structures, 33, 3172–3188

[17] Ambraseys N. and Psycharis I.N, (2012) Earthquake Stability of Columns and Statues, Journal of Earthquake Engineering, 15:5, 685-710

[18] Efraimiadou S., Hatzigeorgiou G.D and Beskos D.E, (2013), Structural pounding between adjacent buildings subjected to strongground motions. Part II: the effect of multiple earthquakes, Earthquake Engineering & Structural Dynamics, DOI: 10.1002/eqe.2284.

COMPDYN 2013
4th ECCOMAS Thematic Conference on
Computational Methods in Structural Dynamics and Earthquake Engineering
M. Papadrakakis, V. Papadopoulos, V. Plevris (eds.)
Kos Island, Greece, 12–14 June 2013

SEISMIC PERFORMANCE OF ANCIENT MASONRY BUILDINGS: A SENSITIVITY ANALYSIS

Nuno Mendes[1], **Paulo B. Lourenço**[1]

[1] ISISE, Department of Civil Engineering, University of Minho
Azurém Campus, 4800-058, Guimarães, Portugal
{nunomendes,pbl}@civil.uminho.pt

Keywords: Masonry, Ancient Buildings, Earthquake, Seismic Performance.

Abstract. *Ancient masonry structures are usually associated to a high seismic vulnerability, mainly due to the properties of the materials (low tensile and moderate shear strengths), weak connections between floors and load-bearing walls, high mass of the masonry walls and flexibility of the floors. For these reasons, the seismic performance of traditional masonry structures has received much attention in the last decades.*

This paper presents the sensitivity analysis taking into account the deviations on features of the "gaioleiro" buildings - Portuguese building typology. The main objective of the sensitivity analysis is to compare the seismic performance of the structure as a function of the variations of its properties with respect to the response of a reference model. The sensitivity analysis was carried out for two types of structural analysis, namely for the non-linear dynamic analysis with time integration and for the pushover analysis proportional to the mass of the structure. The Young's modulus of the masonry walls, Young's modulus of the timber floors, the compressive and tensile non-linear properties (strength and fracture energy) were the properties considered in both type of analysis. Additionally, in the dynamic analysis, the influences of the viscous damping and of the vertical component of the earthquake were evaluated. Finally, a pushover analysis proportional to the modal displacement of the first mode in each direction was also carried out.

The results shows that the Young's modulus of the masonry walls, the Young's modulus of the timber floors and the compressive non-linear properties are the parameters that most influence the seismic performance of the structure for both sensitivity analyses. Furthermore, it is concluded that that the stiffness of the floors influences significantly the strength capacity and the collapse mechanism of the numerical model, and the strengthening of the timber floors improved significantly the seismic performance of the ancient masonry buildings with flexible floors.

1 INTRODUCTION

The seismic behavior of ancient masonry buildings is particularly difficult to characterize and depends on several factors, namely the material properties, the geometry of the structure, the foundations, the connections between walls and floors, the connections between walls and roof, the stiffness of the horizontal diaphragms and the building condition. Furthermore, the strength of "non-structural" elements (partition walls) and their connection to the load-bearing walls also contribute for the performance of ancient masonry buildings.

Masonry is a composite material that consists of units and mortar, which has been used for construction of housing and some of the most important monuments around the world. Units are such as bricks, blocks, ashlars, irregular stones and others. Mortar can be clay, bitumen, chalk, lime/cement based mortar, glue or other. The huge number of possible combinations generated by the geometry, nature and arrangement of units as well as the characteristics of the joints raises doubts about the accuracy of the term masonry.

The strength of masonry depends on the unit and mortar properties as well as on the construction technique. The compressive strength of the units may range from 5 MPa (limestone units of low quality) to over 130 MPa (limestone units of good quality). The strength of the mortar also presents high deviations and depends on the proportion of its components (cement, lime, sand and water) used in the mix [1]. The compressive strength of the mortar of ancient masonry buildings ranges from 1.5 MPa to 3.5 MPa [2, 3]. Furthermore, the strength and failure modes of the masonry are also dependent on the loading direction and combination of the loads [4]. Nevertheless, the mechanical behavior of different types of masonry has some common features: high specific mass, low tensile strength, low to moderate shear strength and low ductility (quasi-brittle behavior). The specific mass of stone masonry ranges between 1700 kg/m^3 to 2200 kg/m^3 [5].

The features of masonry allow it to be a material mainly for structural elements under compressive stresses caused by vertical static loads (e.g. walls, arches, vaults and columns subject to the self-weight). Masonry properties have direct influence on the seismic performance of unreinforced masonry buildings, therefore, this material has been considered unsuitable for the construction of buildings in seismic zones. The inertial forces induce tensile and shear stresses which may lead to the failure of masonry elements and, consequently, to local or global collapse of the building. More information about the mechanical behavior of the masonry is given in [1, 4, 6].

The in-plane and in-elevation regularity as well as simplicity (geometry, mass and stiffness distribution) are aspects that improve the seismic performance of masonry structures, preventing local damage and decreasing the torsional effects. These criteria as well as a set of material properties requirements, design and detailing rules are present in modern codes [7, 8, 9], which aim at a good seismic performance of masonry buildings in terms of strength capacity and adequate collapse mechanisms. However, ancient masonry buildings were not built according to any particular code and a great number of unreinforced masonry buildings subjected to earthquakes presented serious damage or even total collapse.

Existing masonry buildings present several types of geometry and material properties, which may lead to different damage and collapse mechanisms. However, the types of damage generally occurring in unreinforced masonry buildings due to the seismic action are [6]:

- Cracks between walls and floors;
- Cracks at the corners and at wall intersections;
- Out-of-plane collapse of the perimetral walls;
- Cracks in spandrels beams and/or parapets;
- Diagonal cracks in structural walls;

- Partial disintegration or collapse of structural walls;
- Partial or complete collapse of the buildings.

For more information about the damage occurring in unreinforced masonry buildings see e.g. [10, 11].

Although the seismic performance of unreinforced masonry buildings depends on several aspects, only the seismic behaviour of the masonry walls and of the floors are discussed next.

The in-plane behaviour of masonry walls depends on the geometry of piers, spandrels and openings. In what concerns the seismic behaviour of piers, the typical in-plane collapse mechanisms (Figure 1) are [12, 13]:

- Rocking: the high bending causes horizontal cracks at the top and at the bottom of the pier. The failure of the pier occurs by overturning of the wall;
- Sliding: when the horizontal forces at the piers are larger than the shear strength of the bed joints (low vertical load and low friction coefficient), where horizontal cracks develop and the pier presents sliding movement along the bed joints;
- Diagonal tension: the principal tensile stress caused by the seismic action exceeds the tensile strength of masonry and the pier presents diagonal cracks. The cracks can propagate along the mortar bed joints and head joints or go through the units, depending on the strength of the mortar, mortar-unit interface and unit;
- Toe crushing: the toes of the piers are usually zones of high compressive stresses and when the principal compressive stress caused by the seismic action exceeds the compressive strength of the masonry a compressive failure (crushing) can occur.

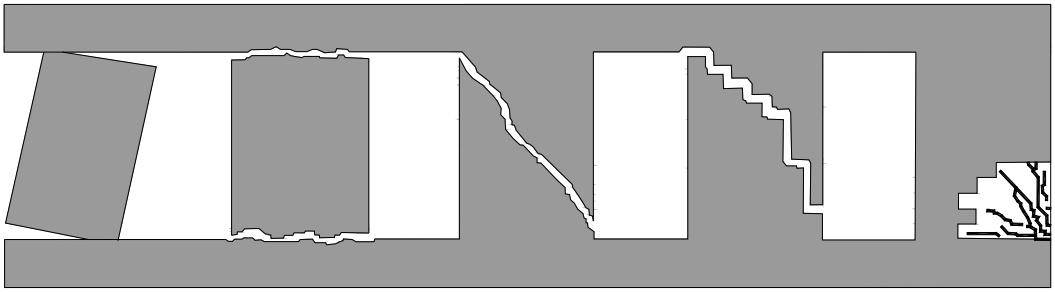
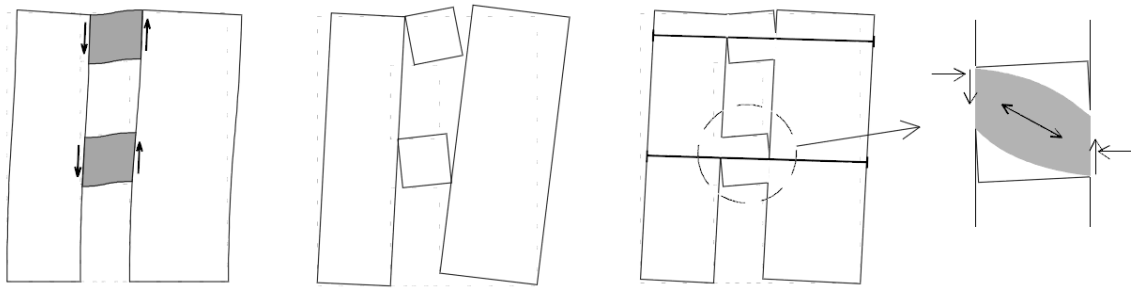


Figure 1: In-plane collapse mechanisms of the piers (adapted from [13]).

The behaviour of spandrels is similar to the behaviour of piers. However, two aspects have to be taking into account: (a) the axis of the spandrel is horizontal and not vertical as in the piers; (b) the normal stress existing in the spandrels, caused by vertical loads, is significant lower than the one in the piers. The first aspect is important for regular masonry, due to orthotropic behaviour, while irregular masonry presents, in general, isotropic behaviour, independent from the load direction. The second aspect has consequences in both types of masonry, as the normal stress influences the seismic behaviour of spandrels. Figure 2a presents the in-plane behaviour of the spandrels subjected to a seismic action, in which shear stresses initially occur and can lead to them to collapse (Figure 2b). In masonry buildings with reinforced elements that prevent such collapse mechanisms (Figure 2c), diagonal compression occurs and this increases the bending strength of the spandrel. In these conditions, the spandrels present two possible collapse mechanisms [14]:

- Collapse due to high compression of diagonal strut (similar to the collapse for combined axial and bending forces of a pier);
- Collapse due to diagonal tension (shear failure).



(a) (b) (c)

Figure 2: In-plane behaviour of the spandrels [14].

The out-of-plane behavior of unreinforced walls is complex and depends on the connection between walls and floors, the connection between walls and roof, and the in-plane stiffness of the floors. When the floors are rigid and have sufficient strength, masonry walls have local effects. On the other hand, when the floors are flexible or the connection between the walls and the floors is weak, the walls present a global behavior (independent of the floor levels) with collapses involving one or more floors and, consequently, present lower stiffness and strength [15].

Diaphragms distribute the inertial forces to the building's vertical resisting elements. The distribution capacity of lateral loads through the diaphragms is dependent on the in-plane stiffness of the diaphragms and on the connection between walls and diaphragms. In contrast to a rigid diaphragm, in which the in-plane stiffness is so large that the distribution among the vertical elements is affected only by the location and lateral stiffness of these structural elements, a flexible diaphragm (timber floors) usually exhibits significant bending and shear deformations under horizontal loads, influencing the distribution of the load among the elements of the structure. The importance of the flexibility of the floor diaphragms and of the connections between these and the masonry walls plays an important role in the global and local response of masonry buildings under seismic load.

This works presents the sensitivity analysis taking into account the deviations on features of the ancient masonry buildings. The main objective of the sensitivity analysis is to compare the response of the structure as a function of the variations of its properties with respect to the response of a reference numerical model. The sensitivity analysis was carried out for two types of structural analysis, namely for the non-linear dynamic analysis with time integration and for the pushover analysis.

2 REFERENCE NUMERICAL MODEL

2.1 Preparation of the reference numerical model

The definition of a reference numerical model was the first step of the sensitivity analysis. The numerical model is representative of a Portuguese masonry building typology – *gaioleiro* buildings [16] and is based on mock-up tested in the 3D shaking table of the National Laboratory for Civil Engineering (LNEC) in Lisbon [17]. The mock-up has four floors, two facades with openings, two gable walls without openings, and timber floors. In the construction of the timber floors, medium-density fibreboard (MDF) panels, with thickness

equal to 0.012 m, connected to a set of timber joists spanning in the direction of the shortest span, were used. The reference numerical model (Figure 3a) was prepared using the Finite Element Method (FEM) and the non-linear analysis software DIANA [18], in which quadratic shell elements with eight nodes (CQ40S) were used for simulating the masonry walls and beam elements with three nodes (CL18B) were used for simulating the MDF panels and the timber joists [18]. All the finite elements are based on the theory of Mindlin-Reissner, in which the shear deformation is taken into account. In the modelling of the floors, shell elements were used aiming at simulating the in-plane deformability (Figure 3b). The thickness of the masonry walls and of the MDF panels is equal to 0.510 m and 0.036 m, respectively, and the dimensions of the cross section of the timber joists are equal to 0.300x0.225 m^2 (width and height), with spacing of 1.05 m. In plan, the numerical model has 9.45x12.45 m^2 and the interstory height is equal to 3.60 m. The translation and rotation degrees of freedom at the base were restrained. In what concerns the connections, tyings providing equal translation of degrees of freedom between walls and floors were assumed. The numerical model involves 5,816 elements (1,080 beam elements and 4,736 shell elements) with 15,176 nodes, resulting in 75,880 degrees of freedom.

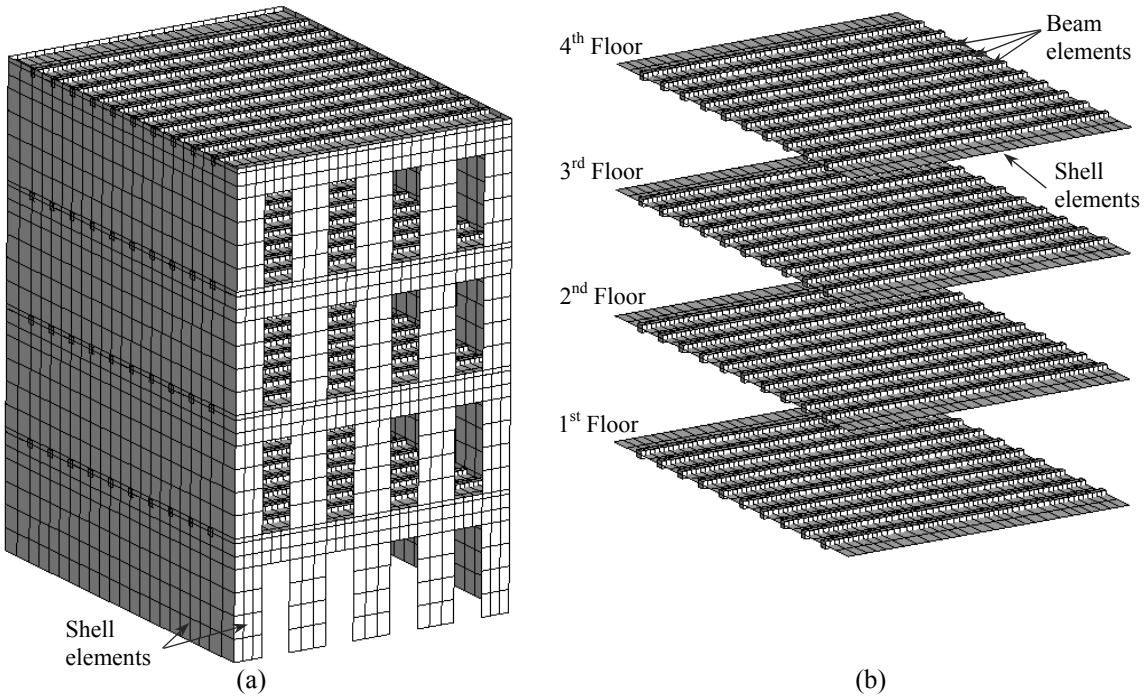


Figure 3: Numerical model: (a) general view; (b) detail of the floors.

The selection of the masonry constitutive model was based on a compromise between accuracy of the results and computation time. The Total Strain Fixed Crack Model [18], which corresponds to a model of distributed and fixed cracks based on total strains, was selected due to its robustness and simplicity. In this model, the cracks are fixed according the principal directions of the strains and remain invariant during the loading of the structure. Several stress-strains relationships were used. Here, and taking into account that only the non-linear behaviour of the masonry was considered, exponential tension-softening for the tensile behaviour and parabolic hardening and softening for the compressive behaviour were adopted. The shear behaviour was simulated by a linear relationship between stress and strains, in which the shear stiffness is reduced after cracking according to the following equation:

$$G^{cr} = \beta G \tag{1}$$

where G^{cr} is the shear modulus after cracking, G is shear modulus without damage and β is the shear retention factor (ranging from zero to one).

The crack bandwidth h for the shell elements was estimated as function of the area of the element A, making the analysis results independent of the size of the finite element mesh:

$$h = \sqrt{A} \tag{2}$$

Table 1 and Table 2 present the linear and non-linear material properties of the reference numerical model, respectively.

	Young's modulus [GPa]	Specific mass [kg/m^3]	Poisson ratio
Masonry walls	1.00	2162	0.2
MDF panels	0.16	760	0.3
Timber joists	12.00	580	0.3

Table 1: Linear material properties of the reference model.

	Compressive strength f_c [MPa]	Compressive fracture energy G_c [N/mm]	Tensile strength f_t [MPa]	Mode I- tensile fracture energy G_t [N/mm]
Masonry walls	1.00	1.60	0.10	0.05

Table 2: Non-linear material properties of the masonry walls of the reference model.

In what concerns damping for the non-linear dynamic analysis, the $\underline{C}$ viscous damping (proportional to the velocity) of Rayleigh was adopted, which is a linear combination between the mass and stiffness matrix in the form [19]:

$$\underline{C}=\alpha\underline{M}+\beta\underline{K} \tag{3}$$

where α and β are the coefficients that weigh the contribution of the mass $\underline{M}$ and $\underline{K}$ matrices, respectively. The α (1.48218) and β (0.00052) were determined through the damping ratios identified in the dynamic identification tests carried out at LNEC.

2.2 Seismic performance of the reference numerical model

Non-linear dynamic analysis with time integration and pushover analyses proportional to the mass were carried out. In the dynamic analysis, two artificial accelerograms were applied in two uncorrelated orthogonal directions (Earthquake 100%). The accelerograms were generated based on stochastic methods and techniques of finite fault modelling, with parameters adequate for Portugal [20] and duration equal to 30 s (intense phase). The response spectrum of the accelerograms is compatible with the type 1 design response spectrum defined by Eurocode 8 [7] and Portuguese National Annex for Lisbon (PGA = 1.5 m/s^2), with a damping ratio equal to 5% and a type A soil (rock, S=1). The pushover analysis is a non-linear static analysis that aims at simulating the structural response during an earthquake, through application of incremental horizontal forces (forced based) or displacements (displacement based) until collapse. The response of the structure is given by the so-called capacity curve, which represents the value of the base shear or seismic coefficient (Equation 4) versus the displacement at a control point (usually at the top of the structure).

$$\alpha_b = \frac{\sum Horizontal\ \ forces\ at\ the\ base}{Self-weight\ of\ \ the\ structure} \tag{4}$$

In the non-linear dynamic analysis with Earthquake 100%, the maximum seismic coefficient at the base is equal to 0.10 and 0.25 in the transversal and longitudinal direction, respectively (Figure 4). According to the pushover analyses, the force based capacity reaches its limit in the transversal direction (α_b=0.10). However, in the longitudinal direction the seismic coefficient obtained from the non-linear dynamic analysis (α_b=0.25) is significantly lower than the force based capacity obtained from the pushover analysis (α_b=0.46). Furthermore, in the non-linear dynamic analysis the displacement is significantly lower than the value obtained from the pushover analysis. As an example, in the transversal direction the maximum displacement at the top obtained from the non-linear dynamic analysis (Earthquake 100%) and from the pushover analysis is about 4.4 cm and 20.0 cm, respectively, which corresponds a difference of about 355%. Thus, the seismic action was increased and a non-linear dynamic analysis with Earthquake 300% was carried out, aiming at exploring the deformation capacity of the structure and obtaining serious damage that allows identifying clearly the collapse mechanism. In the non-linear dynamic analysis of the Earthquake 300% (Figure 4), the force based capacity approaches the one obtained from the pushover analyses. In terms of deformation, in the transversal direction the non-linear dynamic analysis of the Earthquake 300% presents similar maximum displacement at the top. However, in the longitudinal direction the analyses present significant differences.

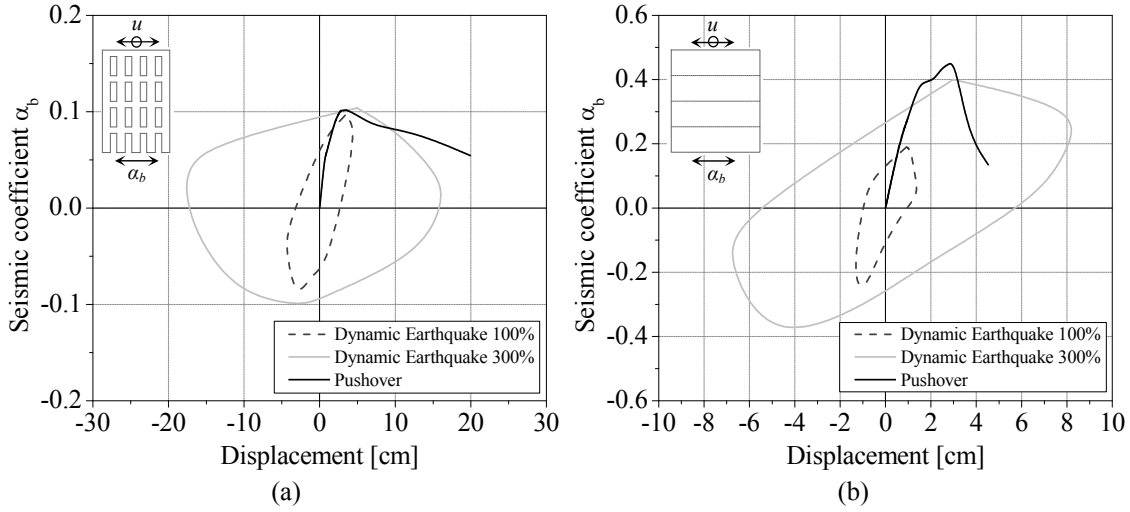


Figure 4: Envelope of the response obtained from the non-linear dynamic analysis with time integration and capacity curve obtained from the pushover analysis of the reference model in the: (a) transversal direction; (b) longitudinal direction.

Figure 5a presents the distribution of the maximum principal tensile strains, which is an indicator of the cracking, for the non-linear dynamic analysis of the Earthquake 100%. It is observed that damage concentrates at the spandrels, due to the diagonal cracking, and at the piers of the top floor, due to in-plane rocking and out-of-plane bending. The gable walls do not present significant damage. In the Earthquake 300% (Figure 5b) the structure presents serious damage, with several spandrels totally damaged and piers at the top floor presenting significant cracks due to in-plane rocking and out-of-plane bending. Furthermore, the piers of the first floor also present severe damage. This damage is related to the damage of the

spandrels, which present significant deformations and do not adequately restrict the relative displacements of the piers, causing damage mainly due to in-plane forces. The gables walls also present damage, with shear cracks, which have origin at the floor levels and progress to the middle of the walls, and vertical cracks at the top of the walls. Furthermore, local damage at the base and at the connections between the gable walls and the joists of the first floor is observed.

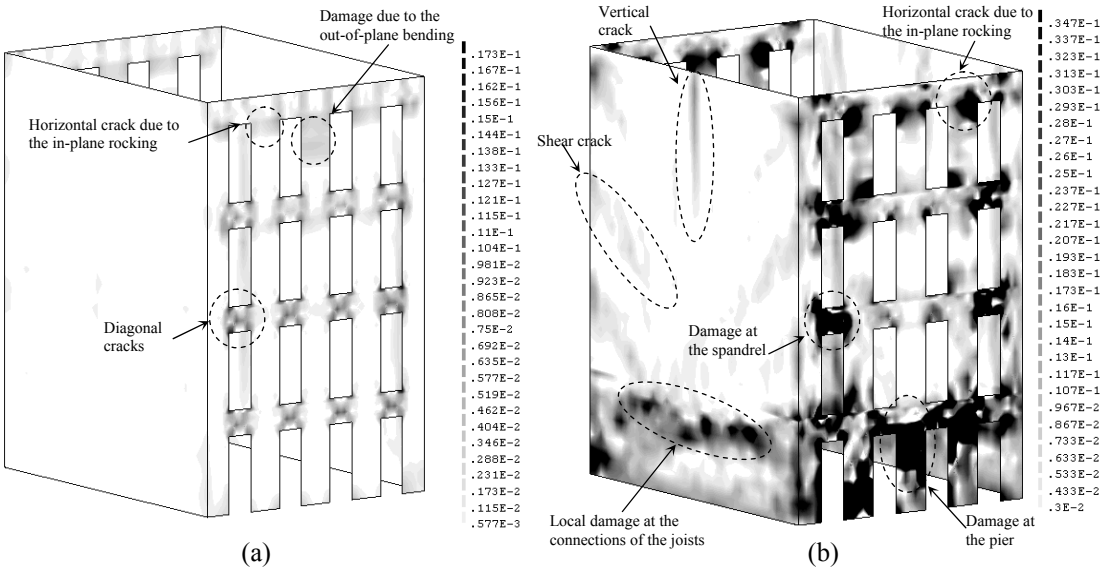


Figure 5: Maximum tensile principal strains at the external surface of the non-linear dynamic analyses of the reference model: (a) Earthquake 100%; (b) Earthquake 300%.

Figure 6 presents the maximum principal strains obtained in the pushover analysis in the transversal and longitudinal direction. The transverse damage (Figure 6a) is according to the one observed in the non-linear dynamic analysis caused by the in-plane forces (Figure 5b), mainly with damage concentration at the piers and horizontal cracks at the piers of the top floor. The piers of the first floor and the base also present damage, but less severe in comparison to the damage observed in the non-linear dynamic analysis. In the pushover analysis in the longitudinal direction (Figure 6b) the piers of the top floor do not presents significant damage caused by the out-of-plane bending as observed in the non-linear dynamic analyses (Figure 5). The damage concentrates mainly in the gable walls, with two vertical shear cracks that have origin at the floor levels and progress to the middle of the base, and one vertical crack. According to this analysis, the numerical model presents a typical collapse mechanism, in which the facades collapse with the vertical cracks occurring at the top floors of the gable walls (near to first joist of the timber floors) and at the corner of the first floor. The MDF panels are rather flexible and are not able to transfer the inertial forces of the facades to the gables, resulting in out-of-plane collapse of the facades. This collapse mechanism is not observed in the non-linear dynamic analysis, because the model reaches its strength capacity firstly in the transversal direction.

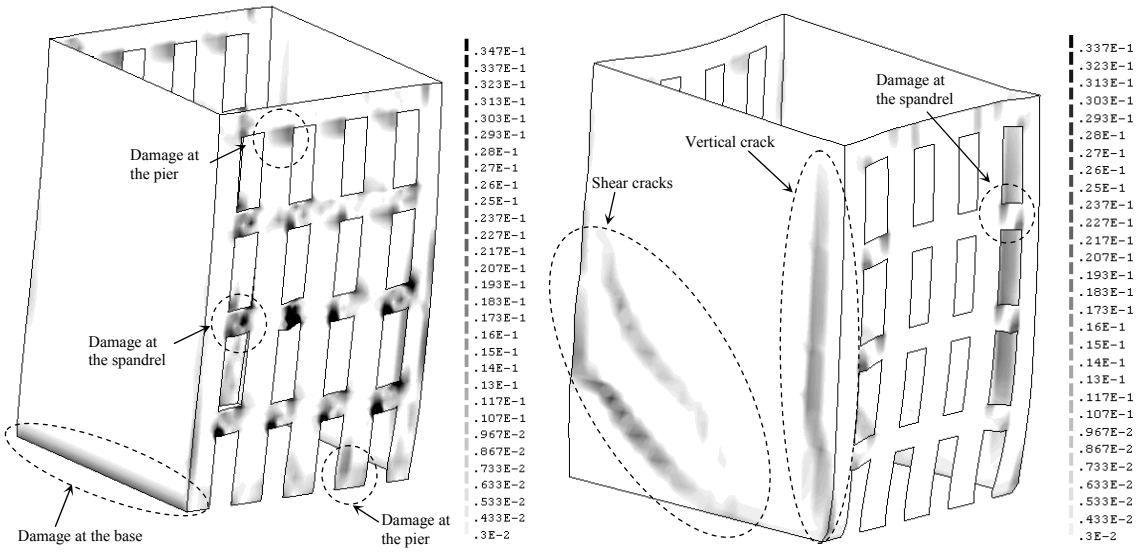


Figure 6: Maximum tensile principal strains at the external surface of the pushover analysis of the reference model in the: (a) transversal direction; (b) longitudinal direction.

3 NON-LINEAR DYNAMIC SENSITIVITY ANALYSIS

The non-linear dynamic analysis with time integration involves several parameters that influence the response in a different way and, consequently, the conclusions about the seismic performance of the structures. Thus, a sensitivity analysis taking into account the main parameters that can influence the seismic behavior of the "gaioleiro" buildings was carried out. Here, the objective is to evaluate the variation of response of the structure, with respect to the reference model, varying the value of each parameter, taking into account the dispersion in the features of the "gaioleiro" building typology. The considered parameters (Table 3) aim at evaluating the response of the numerical models with respect to the variation on stiffness of the masonry walls, on stiffness of the floors, on non-linear properties of the masonry in compression and tension, and on damping ratio. Furthermore, the influence in the response of the vertical component of the earthquake was also studied. Next, the main results of the non-linear dynamic sensitivity analysis (Earthquake 300%) are briefly presented.

	Lower value	Reference value	Upper value
Young's modulus of the walls	0.5x$E_{walls,ref}$	$E_{walls,ref}$ = 1.00 GPa	2.0x$E_{walls,ref}$
Young's modulus of the floors	0.1x$E_{floors,ref}$	$E_{floors,ref}$ = 0.16 GPa	10x$E_{floors,ref}$
Compressive strength	0.5x$f_{c,ref}$	$f_{c,ref}$ = 1.00 MPa	2.0x$f_{c,ref}$
Compressive fracture energy	0.5x$G_{c,ref}$	$G_{c,ref}$ = 1.00 N/mm	2.0x$G_{c,ref}$
Tensile strength	0.5x$f_{t,ref}$	$f_{t,ref}$ = 0.10 MPa	2.0x$f_{t,ref}$
Tensile fracture energy	0.5x$G_{t,ref}$	$G_{t,ref}$ = 0.05 N/mm	2.0x$G_{t,ref}$
Damping ratio	ζ_{Lower}=2.0%	ζ_{ref} =3.3%	ζ_{Upper}=5.0%
Vertical earthquake	vertical component of the earthquake		

Table 3: Parameters considered in the non-linear dynamic sensitivity analysis.

The sensitivity analysis carried out through non-linear dynamic analysis with time integration shows that the Young's modulus of the masonry walls, the Young's modulus of the timber floors and the compressive non-linear properties are the parameters that most influence the seismic performance of the structure. The range of variation of the maximum seismic coefficient assuming 0.50 GPa as lower limit (very poor ancient masonry) and

2.00 GPa as upper limit for the Young's modulus of the masonry walls is about 54% of the reference value. The stiffness of the floors has also an important role on the seismic performance of the structure. The numerical model with very flexible floor presents the typical out-of-plane collapse of the facades with portion of the gable walls and damage at the corners. On the other hand, when increasing the stiffness of the floors the damage concentrates at the facades and the gable walls do not present serious damage. Furthermore, the damage is mainly associated to the in-plane forces (Figure 7).

It is expected that the variation of compressive non-linear properties has limited influence in the response of masonry structures, but here a relevant influence in the strength capacity of the structure has been found. This aspect is related to the low reference value of the compressive strength (1.00 MPa - ancient masonry), the range of the adopted values (0.50 MPa to 2.00 MPa) and the type of failure mode obtained. It is noted that the maximum compressive stress due to the self-weight is about 20% of the compressive strength, which would seem reasonable for the stability against vertical loading.

The response presented low variations when the tensile properties were changed, which is associated to the low range of the adopted values (0.05 MPa $\leq f_t \leq$ 0.20 MPa; 0.025 N/mm $\leq G_t \leq$ 0.100 N/mm). However, these limits correspond to a common feature of masonry – low tensile strength, meaning that the non-linear tensile properties seem not to affect significantly the response under high seismic amplitude.

The response of the structure in the transversal direction does not change significantly decreasing the ratio damping of about 1% (ζ_{Lower}=2.0%). The maximum variation of the response in the longitudinal direction with ζ_{Lower}=2.0% is equal to -8% (displacement at the top). In the transversal direction of the numerical model with ζ_{Upper} =5.0% the maximum seismic coefficient increases about 10% and the maximum displacement at the top decreases about 17%. In the longitudinal direction the response (ζ_{Upper} =5.0%) presents a variation of about 20% for both parameters. The numerical model with ζ_{Lower}=2.0% presents serious damage at the spandrels, piers at the top floor and at the base, and at the first floor of the gable walls. On the other hand, when increasing the damping (ζ_{Upper} =5.0%) the numerical model presents, as expected, a damage reduction.

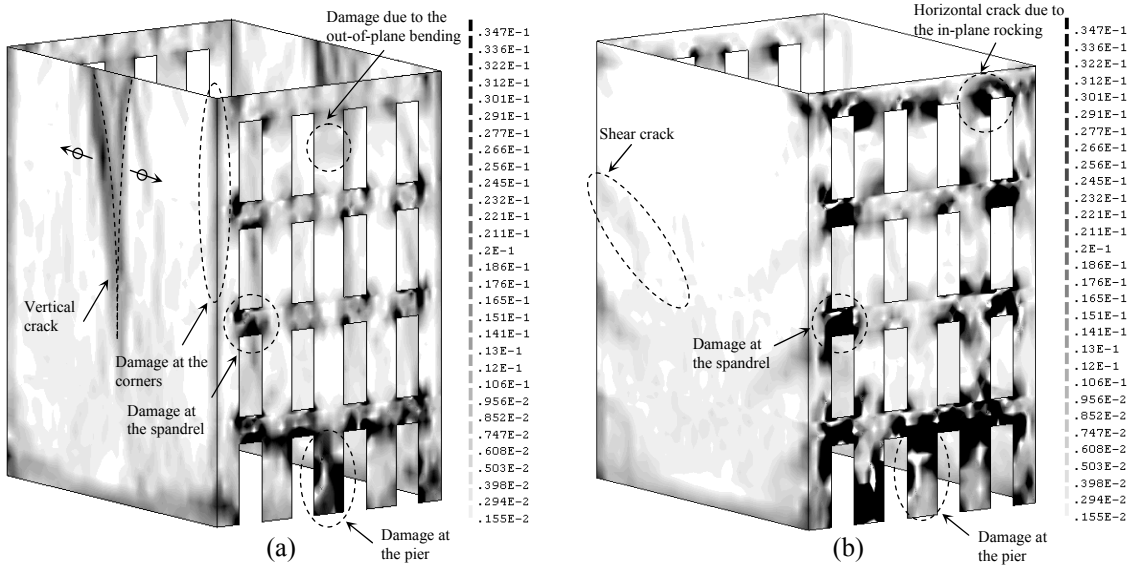


Figure 7: Maximum tensile principal strains at the external surface, obtained from the dynamic analysis, varying the Young's modulus of the floors: (a) 0.1x$E_{floors,ref}$; (b) 10x$E_{floors,ref}$.

The vertical component of the earthquake does not have influence on the response, which is due to the dimensions of the structure and high compressive stresses present, minimizing the effect of the vertical acceleration. Furthermore, the structure is very stiff in the vertical direction and, consequently, presented very small deformation in this direction. Table 4 and Table 5 present the variation of the maximum seismic coefficient and displacement at the top of the structure obtained from the non-linear dynamic parametric analysis for the transversal direction (direction with the lowest strength capacity).

	0.5x$E_{walls,ref}$	0.1x$E_{floors,ref}$	0.5x$f_{c,ref}$	0.5x$G_{c,ref}$	0.5x$f_{t,ref}$	0.5x$G_{t,ref}$	ζ=2%
Seismic coefficient	-10%	10%	-20%	0%	-2%	10%	0%
Displacement	-7%	24%	-16%	-11%	4%	-1%	0%

Table 4: Variation of the response in the transversal direction obtained from the non-linear dynamic parametric analysis for the lower limits of the parameters.

	2.0x$E_{walls,ref}$	10x$E_{floors,ref}$	2.0x$f_{c,ref}$	2.0x$G_{c,ref}$	2.0x$f_{t,ref}$	2.0x$G_{t,ref}$	ζ=5%	Vertical earthquake
Seismic coefficient	39%	20%	70%	20%	20%	10%	10%	10%
Displacement	-17%	-6%	3%	3%	0%	-4%	-17%	-3%

Table 5: Variation of the response in the transversal direction obtained from the non-linear dynamic parametric analysis for the upper limits of the parameters and earthquake vertical component.

4 PUSHOVER SENSITIVITY ANALYSIS

As previously done in the non-linear dynamic sensitivity analysis, in the pushover sensitivity analysis presented next the values of the Young´ modulus of the masonry walls, the Young´ modulus of the timber floors and the compressive and tensile non-linear properties of the masonry were changed and the variations on the response were analyzed. Furthermore, the type of load pattern applied horizontally to the structure was also discussed and a pushover analysis proportional to the modal displacements of the first mode in the applied direction was carried out besides a standard uniform load distribution (Table 6). Here, the objective is to evaluate the variation of the response of the structure under a seismic action based on displacement (first mode proportional) with respect to a loading based in force (proportional to the mass). Next, the most relevant variations of the response are presented.

	Lower value	Reference value	Upper value
Young's modulus of the walls	0.5x$E_{walls,ref}$	$E_{walls,ref}$ = 1.00 GPa	2.0x$E_{walls,ref}$
Young's modulus of the floors	0.1x$E_{floors,ref}$	$E_{floors,ref}$ = 0.16 GPa	10x$E_{floors,ref}$
Compressive strength	0.5x$f_{c,ref}$	$f_{c,ref}$ = 1.00 MPa	2.0x$f_{c,ref}$
Compressive fracture energy	0.5x$G_{c,ref}$	$G_{c,ref}$ = 1.00 N/mm	2.0x$G_{c,ref}$
Tensile strength	0.5x$f_{t,ref}$	$f_{t,ref}$ = 0.10 MPa	2.0x$f_{t,ref}$
Tensile fracture energy	0.5x$G_{t,ref}$	$G_{t,ref}$ = 0.05 N/mm	2.0x$G_{t,ref}$
Load pattern	displacement proportional to the first mode		

Table 6: Parameters considered in pushover sensitivity analysis.

The sensitivity analysis based on the pushover proportional to the mass shows that the Young's modulus of the masonry walls, the stiffness of the timber floors and the compressive strength are the properties that present the highest influence on the strength capacity of the structure. Furthermore, the decrease of the tensile strength causes a significant decrease of the strength capacity in the longitudinal direction (-20%). In the pushover analysis in the transversal direction (direction with the lowest strength capacity) the damage is caused by in-

plane forces and is similar to the one obtained from the non-linear dynamic analysis, in which severe damage at the spandrels and piers is found.

In the pushover analysis when varying the Young's modulus of the timber floors, the maximum seismic coefficient presents on average variations of about 11% and 13% in the transversal and longitudinal direction, respectively (Figure 8). The major differences occur in the pushover analysis in the longitudinal direction, which is more dependent of the stiffness of the timber floors. The numerical model with 10x$E_{floors,ref}$ presents a response stiffer than the reference model and with a high reduction of the lateral forces after post-peak for low deformation (more brittle behaviour). On the other hand, the response of the numerical model with 0.1x$E_{floors,ref}$ presents several losses of stiffness until the maximum seismic coefficient and high deformation (Figure 8b). In the end of the pushover analyses in the longitudinal direction the numerical models with 0.1x$E_{floors,ref}$ and 10x$E_{floors,ref}$ present similar seismic coefficient and significant different displacements. This is related to the serious damage present in the numerical model with 0.1x$E_{floors,ref}$, mainly due to the vertical crack near the corners that cause the out-of-plane collapse of the facades (Figure 9a). In the numerical model with 10x$E_{floors,ref}$ the collapse occurs due to shear failure of the gable walls (Figure 9b).

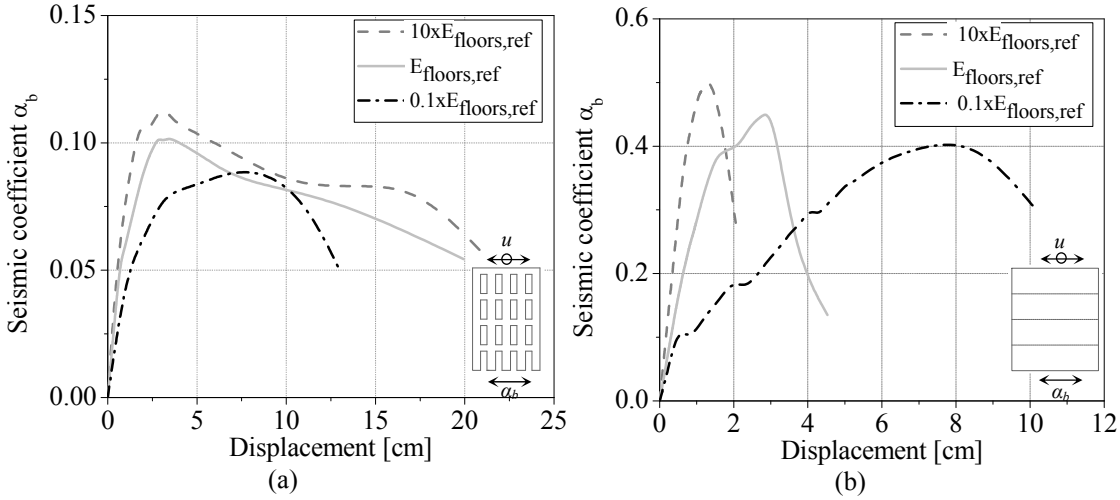


Figure 8: Capacity curves varying the Young's modulus of the timber floors in the: (a) transversal direction; (b) longitudinal direction.

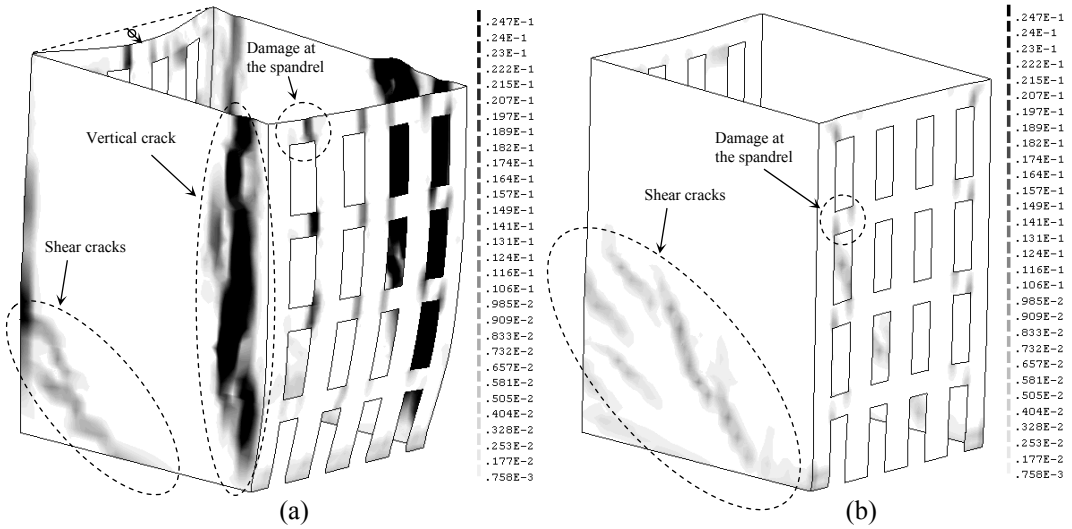


Figure 9: Maximum tensile principal strains at the external surface, obtained from the pushover analysis in the longitudinal direction, varying the Young's modulus of the floors: (a) 0.1x$E_{floors,ref}$; (b) 10x$E_{floors,ref}$.

Finally, the pushover analysis proportional to the modal displacements of the first mode presents lower strength capacity with respect to the pushover analysis proportional to mass and does not provide any improvement in the simulation of the local damage at the piers of the top floor caused by the out-of-plane bending. Table 7 and Table 8 present the variations of the maximum seismic coefficient obtained from the pushover parametric analysis for the transversal and longitudinal directions.

Direction	0.5x$E_{walls,ref}$	0.1x$E_{floors,ref}$	0.5x$f_{c,ref}$	0.5x$G_{c,ref}$	0.5x$f_{t,ref}$	0.5x$G_{t,ref}$
Transversal	-2%	-10%	-32%	-3%	-2%	-6%
Longitudinal	-9%	-14%	-37%	-7%	-20%	-6%

Table 7: Variation of the maximum seismic coefficient obtained from the pushover parametric analysis for the lower limits of the parameters.

Direction	2.0x$E_{walls,ref}$	10x$E_{floors,ref}$	2.0x$f_{c,ref}$	2.0x$G_{c,ref}$	2.0x$f_{t,ref}$	2.0x$G_{t,ref}$	1st Mode
Transversal	25%	11%	34%	13%	11%	8%	-12%
Longitudinal	11%	12%	8%	1%	8%	11%	-27%

Table 8: Variation of the maximum seismic coefficient obtained from the pushover parametric analysis for the upper limits of the parameters and pushover analysis proportional to the first mode.

5 CONCLUSIONS

A sensitivity analysis using different techniques of structural modelling was carried out, namely: (a) non-linear dynamic analysis with time integration; (b) pushover analysis proportional to the mass. The objective was to evaluate the variation of the response taking into account the deviations in the main features of an ancient masonry building typology of the housing stock of Portugal – *gaioleiro* buildings.

The Young's modulus of the masonry walls, Young's modulus of the timber floors, the compressive and tensile non-linear properties (strength and fracture energy) were the parameters considered in both type of parametric analysis. Furthermore, in the non-linear dynamic analysis the influence of the variation of the viscous damping and of the vertical component of the earthquake was also evaluated. Finally, a pushover analysis proportional to the modal displacement of the first mode in each direction was carried out. The results of the sensitivity analysis shows that the Young's modulus of the masonry walls, the Young's modulus of the timber floors and the compressive non-linear properties are the parameters that most influence the seismic performance of the structure for both sensitivity analyses. The vertical component of the earthquake does not have influence on the response of the numerical model, which is related to the dimensions of the structure, high compressive stresses caused by self-weight and high stiffness in the vertical direction. The pushover analysis proportional to the modal displacements of the first mode presents lower strength capacity with respect to the pushover analysis proportional to the mass and does not provide any improvement in terms of failure mode.

Finally, it is concluded that the stiffness of the floors influences significantly the strength capacity and the collapse mechanism of the numerical model. Strengthening timber floors such that they can be considered as rigid diaphragms, with good connection between floors and masonry walls, is a solution to reduce the seismic vulnerability of *gaioleiro* buildings, namely preventing the global collapse of the facades. Here, the strengthening of the floors using timber or steel elements are preferable when compared for example to a solution with concrete slabs, as it allows an increase of the in-plane stiffness of floors without increasing significantly the inertial forces at floor levels.

ACKNOWLEDGMENT

The first author sincerely acknowledges the financial support from the Portuguese Foundation for Science and Technology (FCT) through grant SFRH/BD/32190/2006.

REFERENCES

[1] T. Paulay, M. Priestley, *Seismic design of reinforced concrete and masonry buildings*. John Wiley & Sons Inc, 1992.

[2] E. Toumbakari, *Lime–pozzolan-cement grouts and their structural effects on composite masonry walls*. PhD Thesis, Katholieke Universiteit Leuven, Belgium, 2002.

[3] M. Valluzi, F. Porto, C. Modena, Behaviour and modelling of strengthened three-leaf stone masonry walls. *Materials and Structures,* **37**, No. 3, 184-192, 2004. (doi:10.1007/BF02481618)

[4] P.B. Lourenço, *Computational strategies for masonry structures*. PhD Thesis, Delft University of Technology, Netherlands, 1996. (Available from: http://www.civil.uminho.pt/masonry)

[5] F. Pinho, *Walls from ancient Portuguese buildings*. "Edifícios", Nº8, National Laboratory for Civil Engineering, Lisbon, Portugal, 2000. (In Portuguese)

[6] M. Tomaževič, *Earthquake-resistance design of masonry buildings*. *Series on Innovation in Structures and Construction, Vol. 1*. Imperial College Press, 1999.

[7] EN 1998-1, *Eurocode 8: Design of structures for earthquake resistance – General rules, seismic actions and rules for building*. European Committee for Standardization, 2004.

[8] FEMA 440, *Improvement of nonlinear static seismic analysis procedures*. Applied Technology Council (ATC-55 Project), Department of Homeland Security, Federal Emergency Management Agency, Washington D.C, 2005.

[9] OPCM 3274, *First elements on general criteria for seismic classification of the national territory and technical standards for construction in seismic areas*. Ordinance of the President of the Council of Ministers, 2003. (In Italian)

[10] D. D'Ayala, E. Speranza, An integrated procedure for the assessment of seismic vulnerability of historic buildings. *12th European Conference on Earthquake Engineering*, London, United Kingdom, paper 561, 2002.

[11] C. Carocci, Guidelines for the safety and preservation of historical centres in seismic areas. *Historical Constructions: Possibilities of numerical and experimental techniques*, Guimarães, Portugal, 145-166, 2001.

[12] G. Magenes, G. Calvi, In-plane seismic response of brick masonry walls. *Earthquake Engineering and Structural Dynamics*, **26**, Issue 11, 1091-1112, 1997. (doi:10.1002/(SICI)1096-9845(199711)26:11<1091::AIDEQE693>3.0.CO;2-6).

[13] T. Yi, *Experimental investigations and numerical simulation of an unreinforced Masonry structure with flexible diaphragms*. PhD Thesis, Georgia Institute of Technology, 2004.

[14] G. Magenes, D. Bolognini, C. Braggio, *Simplified methods for non-linear seismic of masonry buildings*. National Group for Earthquakes Protection (GNDT), 2000. (In Italian)

[15] P. Candeias, *Seismic vulnerability assessment of ancient buildings*. PhD Thesis, University of Minho, Portugal, 2008. (Available from: http://hdl.handle.net/1822/9057) (In Portuguese)

[16] J. Appleton, *Rehabilitation of "gaioleiros" buildings – a block in Lisbon. Orion edition*, 2005. (ISBN: 9728620055) (In Portuguese).

[17] N. Mendes, P.B. Lourenço, A. Campos-Costa, Seismic vulnerability assessment of ancient masonry building an experimental method. Advanced Materials Research, **134-134**, 635-640, 2010. (doi: 10.4028/www.scientific.net/AMR.133-134.635)

[18] TNO, *DIsplacement method ANAlyser*. User's Manual, Release 9.4, Netherlands, 2009.

[19] A. Chopra, *Dynamics of Structures: Theory and applications to earthquake engineering, 3rd Edition*. Prentice Hall, 2001.

[20] A. Carvalho, *Stochastic modelling of the seismic action in Mainland Portugal*. PhD Thesis, Technical University of Lisbon, Portugal, 2007. (In Portuguese).

COMPDYN 2013
4th ECCOMAS Thematic Conference on
Computational Methods in Structural Dynamics and Earthquake Engineering
M. Papadrakakis, N.D.Lagaros, V. Plevris (eds.)
Kos Island, Greece, 12–14 June 2013

POST-EARTHQUAKE ASSESSMENT OF A MASONRY TOWER BY ON-SITE INSPECTION AND OPERATIONAL MODAL TESTING

Antonella Saisi[1], **Carmelo Gentile**[2], **and Lorenzo Cantini**[2]

[1] Politecnico di Milano
P.za Leonardo da Vinci, 32 – 20133 Milan, Italy
e-mail: antonella.saisi@polimi.it

[2] Politecnico di Milano
P.za Leonardo da Vinci, 32 – 20133 Milan, Italy
e-mail: carmelo.gentile@polimi.it, lorenzo.cantini@polimi.it

Keywords: Earthquake, Masonry Towers, On-site Survey, Operational Modal Testing

Abstract. *The paper describes the methodology applied to assess the state of preservation of the tallest historic tower in Mantua, the "Gabbia" tower, after the earthquakes of May 2012. An extensive investigation programme – including visual inspection, sonic and flat jack tests, operational modal testing and structural modelling – has been planned to support the future preservation actions of the tower. The paper focuses especially on the information collected during on-site survey and dynamic tests and describes how these results can be employed and cross-correlated to assess the structural condition and seismic vulnerability of the tower.*

1 INTRODUCTION

On May 29th, 2012 a strong earthquake occurred in Emilia-Romagna region but it was significantly felt also in Lombardia region and damages were reported on several historic buildings placed in the town of Mantua, where Politecnico di Milano has a large campus. Consequently, the VIBLAB (Laboratory of Vibration and Dynamic Monitoring of Structures) of Politecnico di Milano was committed to assess the structural condition and to evaluate the seismic performances of the taller historic tower of the city, the *Gabbia* tower [1]. The tower (Fig. 1), about 54.0 m high and surrounded by an important historic building, is a symbol of the cultural heritage in Mantua so that the fall of small masonry pieces from its upper part, reported during the earthquake, provided strong motivations for deeply investigating the seismic vulnerability of the building.

The multi-disciplinary approach planned to assess the structural safety and the seismic vulnerability of the *Gabbia* tower involves both experimental and analytical analysis, including several tasks [2-4]: (a) historic and documentary research; (b) geometric survey and field survey of the crack pattern; (c) non-destructive and slightly destructive tests of materials on site (i.e. sonic pulse velocity tests and flat-jack tests); (d) dynamic tests in operational conditions; (e) F.E. modelling and vibration-based validation of the model; (f) use of the validated model to asses the structural safety and predict the seismic performance, according to the provisions of the current Italian guidelines for the seismic risk mitigation of cultural heritage [5].

After a brief description of the *Gabbia* tower, the paper summarizes the information and the results provided by the execution of visual inspection and dynamic tests, performed between July 30th and August 3rd, 2012 with the support of a mobile platform (Fig. 1).



Figure 1: Views of the *Gabbia* tower in Mantua, Italy.

2 DESCRIPTION OF THE TOWER AND HISTORIC BACKGROUND

The *Gabbia* tower, about 54.0 m high, is the tallest tower in Mantua, overlooking the historic centre listed within the UNESCO Heritage (Figs. 1-3). The Tower, dating back to XIII century [1], is built in solid masonry bricks. An important palace surrounds the tower (Figs. 1-3); even if the building dates back nearly the same age of the tower, the load bearing walls of the palace are not effectively linked but just drawn.

The tower has an almost squared plan and the load bearing walls are about 2.4 m thick until the upper levels (Fig. 3). Precious frescoes, dating back to XIV and XVI centuries, decorate

the tower's fronts embedded in the palace, whereas in 1811 the interior walls were painted with refined decorations [1]. The top part of the building has a two level lodge, which hosted in XIX century the observation and telegraph post reachable by a wooden staircase, no more practicable since several years.

In the XVI century, the *Gabbia* tower was used as open-air jail, hosting a hanged dock on the S-W front (Figs. 1 and 3). Few information is available on the building evolution but the observation of the masonry texture reveals passing-through discontinuities at the top. Traces of past structures are visible on all fronts (Fig. 4) and the presence of merlon-shaped discontinuities (Figs. 4 and 5) suggests modifications and further adding at the top of the tower. Moreover, at about 8.0 m from the top, a clear change of the brick surface workmanship (the bricks of the lower part are superficially scratched) could reveal a first addition (Fig. 6); in the same region concentrated changes of the masonry texture reveal local repair.

The inner access to the tower was re-established recently (October 2012) through provisional scaffoldings; it should be noticed that the entrance is at 17.7 m from the ground level (Fig. 3) and the access to the lower portion and the base of the building is not possible.

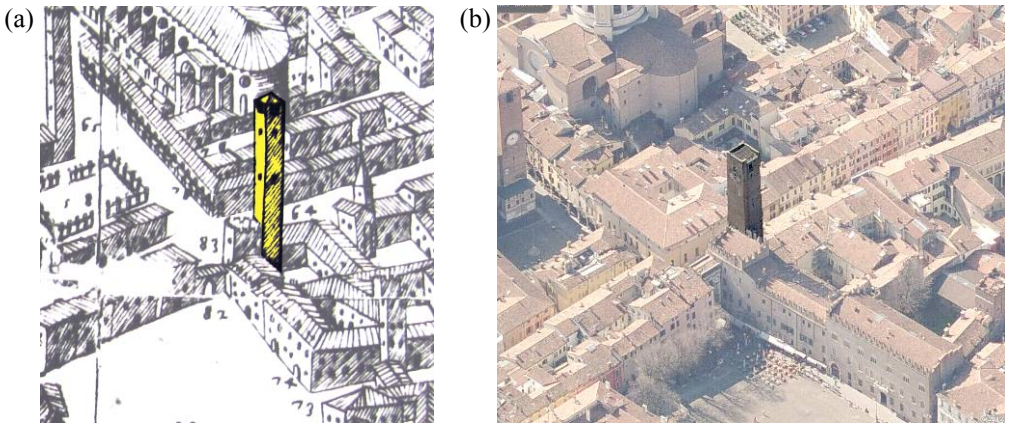


Figure 2: The *Gabbia* tower and the surroundings: (a) view of the XVII century [6]; (b) recent view.

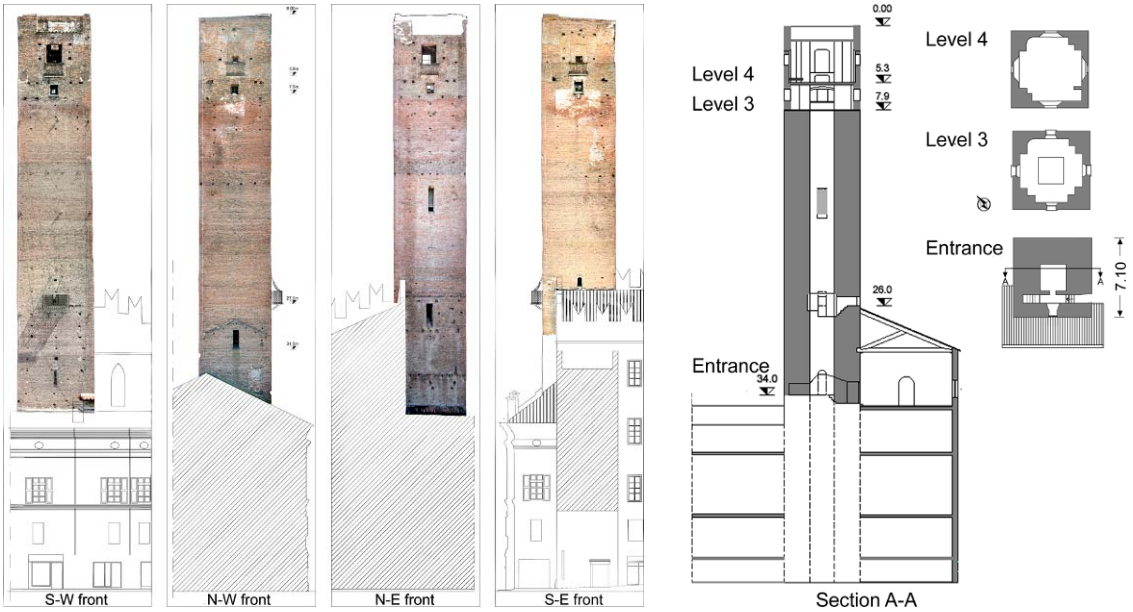


Figure 3: Fronts and section of the tower.

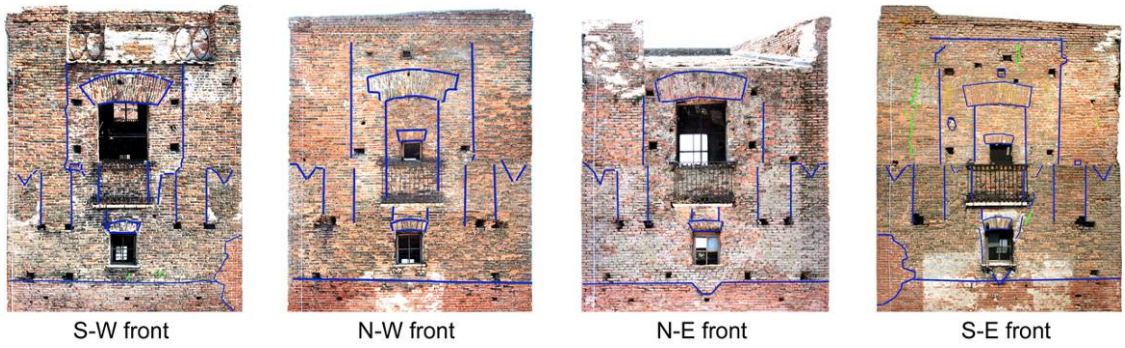


Figure 4: Map of the discontinuities on top of the tower.



Figure 5: Probable merlons embedded in the masonry texture.

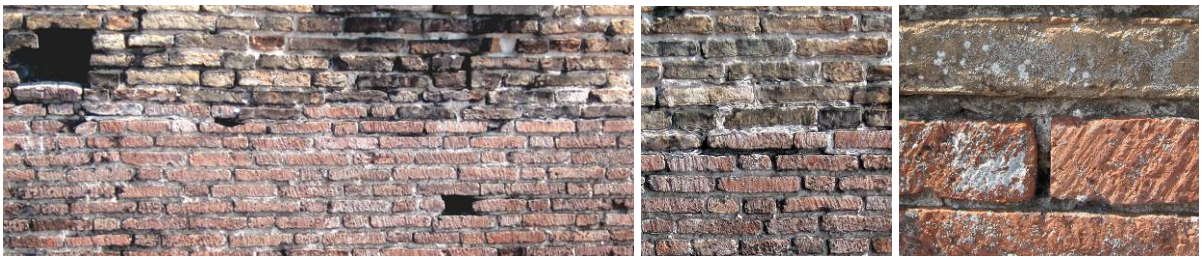


Figure 6: Change of the surface workmanship at about 8.0 m from the top (the bricks of the lower portion are superficially scratched).

3 VISUAL INSPECTION AND ON SITE TESTS

As previously pointed out, an accurate on-site survey of all fronts of the tower was firstly performed using a mobile platform (Fig. 1). This preliminary survey is aimed at providing details on the geometry of the structure and identifying critical areas and irregularities, where more refined inspections are needed. In the meantime, the historical evolution of the structure should be known to explain the signs of damage detected on the building.

Excepting the upper part of the tower, visual inspection did not reveal evident structural damage but only superficial decay of the materials (mainly of the mortars, due to the natural ageing and the lack of maintenance). In the lower part of the tower, the corners exhibit rare thin cracks and the masonry section appears of solid bricks and lime mortars. Subsequent pulse sonic tests and double flat jacks confirm the soundness and the compactness of the masonry of such building portion. Results from pulse sonic tests suggest solid brick section, with high velocity values, ranging between 1100 m/s to 1600 m/s. Double flat jack test carried out on the N-E side at about 32.8 m from the ground level (Fig. 7) revealed that the Young's modulus is larger than 3.00 GPa. Similar information result from the laboratory tests on sampled bricks and mortars.

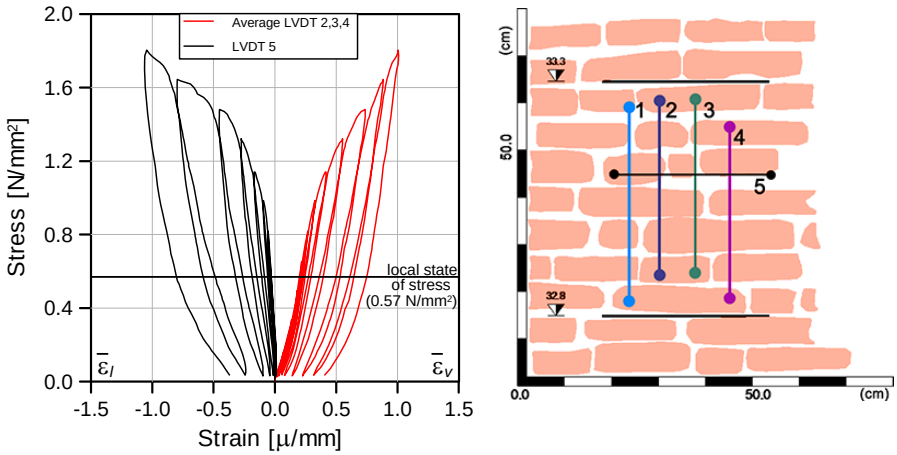


Figure 7: Results of the double flat jack test and superficial texture of the investigated area.



Figure 8: Typical discontinuities on top of the tower and lack of horizontality of the masonry courses.

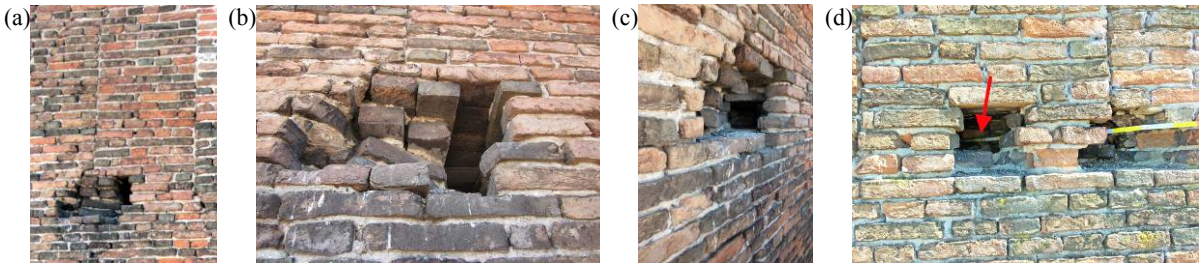


Figure 9: Details of the infillings between the supposed merlons on the N-W front: (a), (b), (c) left side infilling; (d) right side infilling.

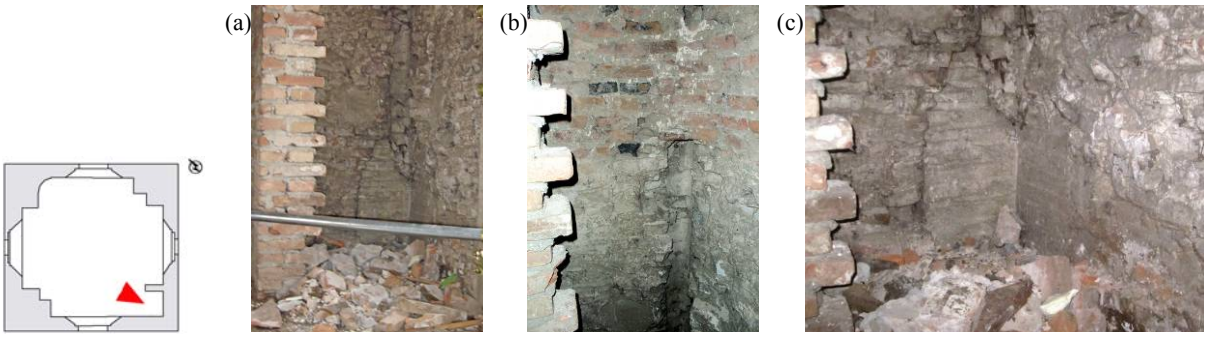


Figure 10: Details of the South corner at level 4: (a) the corner is partially dismantled, (b) with an embedded pipe at the edge and (c) a probable merlon.

On the contrary, the top of the tower (i.e. the upper portion about 8.0 m high, Fig. 3) shows damage related to the detachment of the several construction phases, worsened by the natural decay (Fig. 4). In fact, settlement of the interventions and of the opening infillings coupled

with the highly disordered masonry and mortar erosion causes lack of horizontality of the joints of the crowing and the development of cracks as well (Fig. 8).

Critical areas are the infillings between merlons (Figs. 4 and 9), supported only by few courses of thin masonry due to the unusual layout of the scaffolding holes. The extension of the scaffolding holes beside the base of the infillings weakens the local and overall stability (Fig. 9) so that the prevention of local instability of such masonry portions should be one of the intervention priority on the tower.

It is important to remark the change of the masonry sections and of the plan layout in the upper part (Levels 3 and 4 in Fig. 3), where the nearly squared plan turns into corner masonry piers and un-toothed infillings. The decrease of resisting section is especially significant for the piers on North and South corners at level 4. As shown in Fig. 10, the corner pier at South is partially dismantled, showing an embedded pipe at the edge and the merlon shape. The lack of any mortar encrustation in the merlon surface suggests a weak connection in the other piers at the same level, as well.

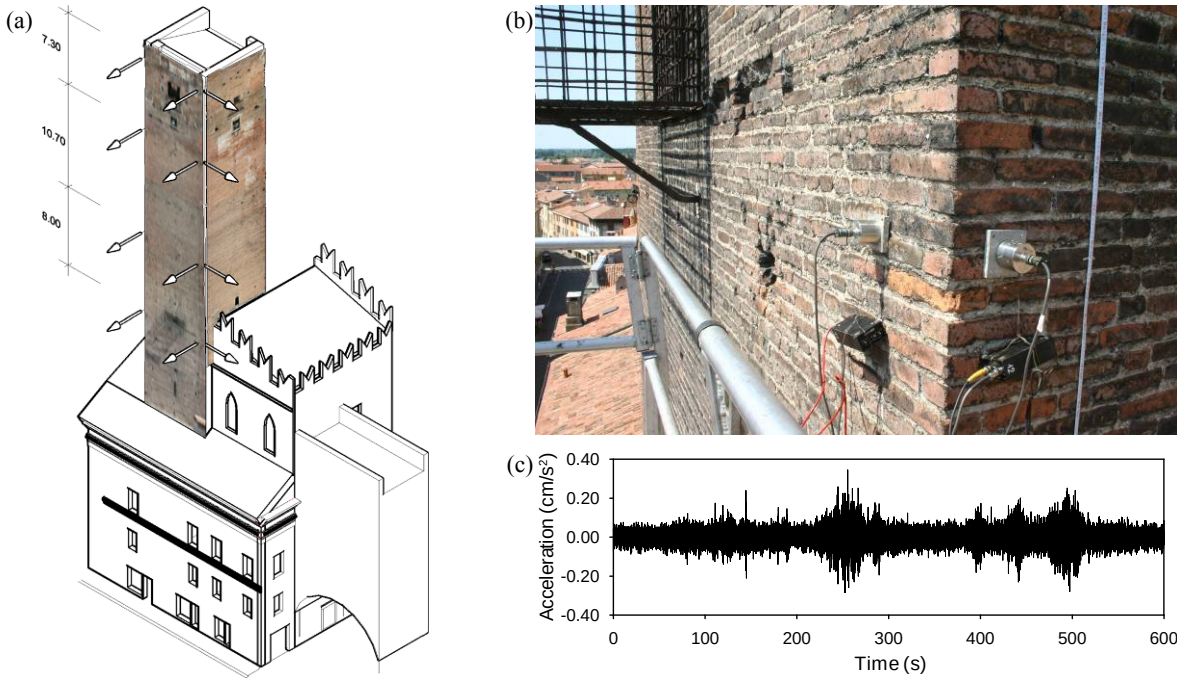


Figure 11: (a) Sensor layout adopted in ambient vibration testing of the *Gabbia* tower (dimensions in m); (b) typical mounting of accelerometers; (c) sample of acceleration recorded at the top of the tower

4 AMBIENT VIBRATION TESTS AND MODAL IDENTIFICATION

4.1 Testing procedures and modal identification

Ambient vibration tests (AVTs) were conducted between July 31st and August 2nd 2012 using a 24-channel data acquisition system (24-bit resolution, 102 dB dynamic range and anti-aliasing filters) and piezoelectric accelerometers (WR model 731A, 10 V/g sensitivity and ±0.50 g peak). A short cable (1 m) connected each sensor to a power unit/amplifier (WR model P31), providing the constant current needed to power the accelerometer's internal amplifier, signal amplification and selective filtering.

The response of the tower was measured in 12 selected points, belonging to 4 different cross-sections along the height of the building, according to the sensor layout shown in Fig. 11a. Figure 11b shows two accelerometers mounted on the corner of the lower instrumented cross-section, corresponding to the level of the hanging dock on the S-W front (about 28.0 m

from the top). It should be noticed that the positioning of the accelerometers at the upper levels was aimed at checking if the change of masonry texture detected in visual inspection (and the thickness decrease of load bearing walls, Fig. 3) affects the dynamic characteristics of the tower. Hence, the upper instrumented sections (Fig. 11a) were at the crowning (about 2.0 m from the top) and just below the change of masonry texture (about 9.3 m from the top).

The excitation was only provided by wind and micro-tremors and acceleration data were acquired for 28 hours: from 16:00 to 23:00 of July 31st 2012 and between 9:00 of August 1st to 6:00 of August 2nd 2013. Figure 11c shows a sample of the acceleration recorded the upper instrumented level: it should be noticed that very low level of ambient excitation was present during the tests, with the maximum recorded acceleration being always lower than 0.4 cm/s^2.

The modal identification was performed using time windows of 3600 s. The sampling frequency was 200 Hz, which is much higher than that required for the investigated structure, as the significant frequency content of signals is below 12 Hz. Hence, low pass filtering and decimation were applied to the data before the use of the identification tools, reducing the sampling frequency from 200 Hz to 40 Hz; after decimation, the number of samples in each 1-hour record was of 144000, with a sampling interval of 0.025 s.

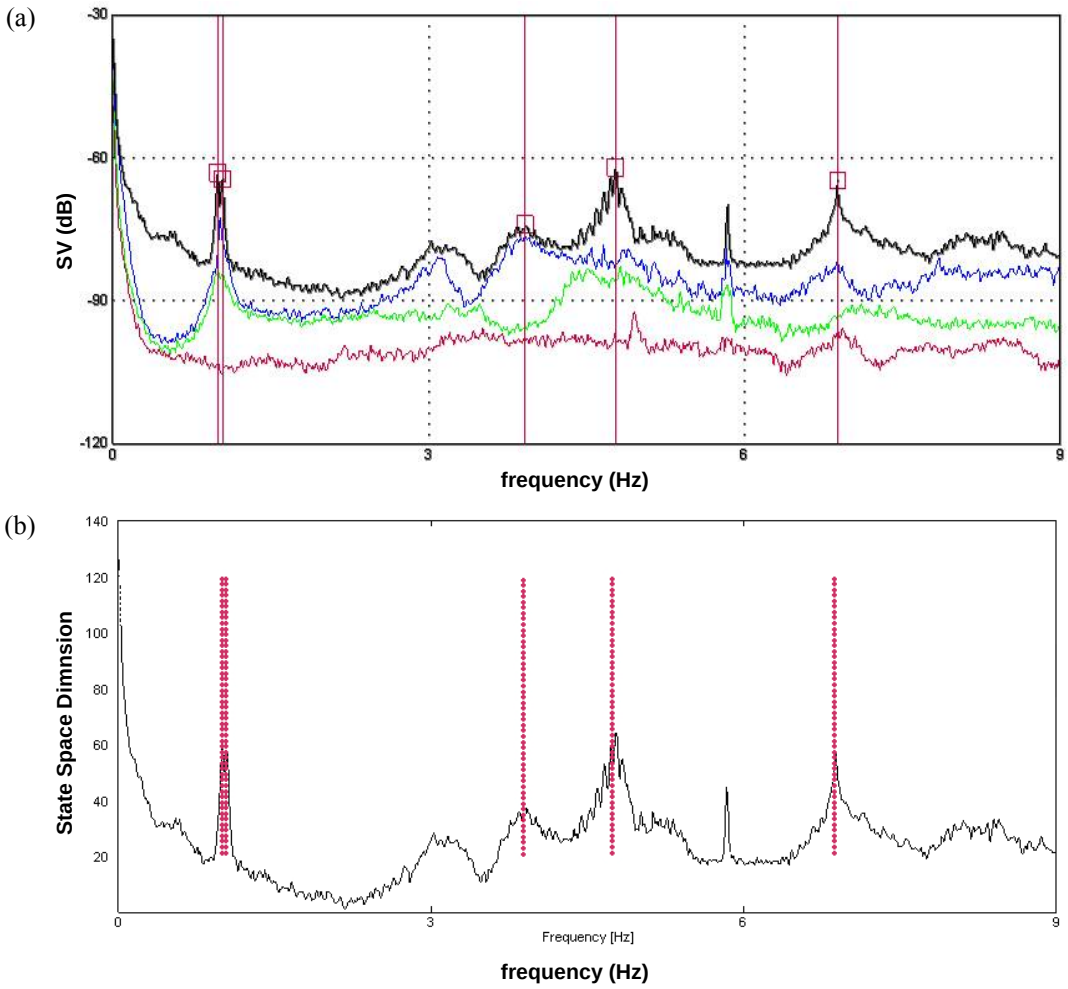
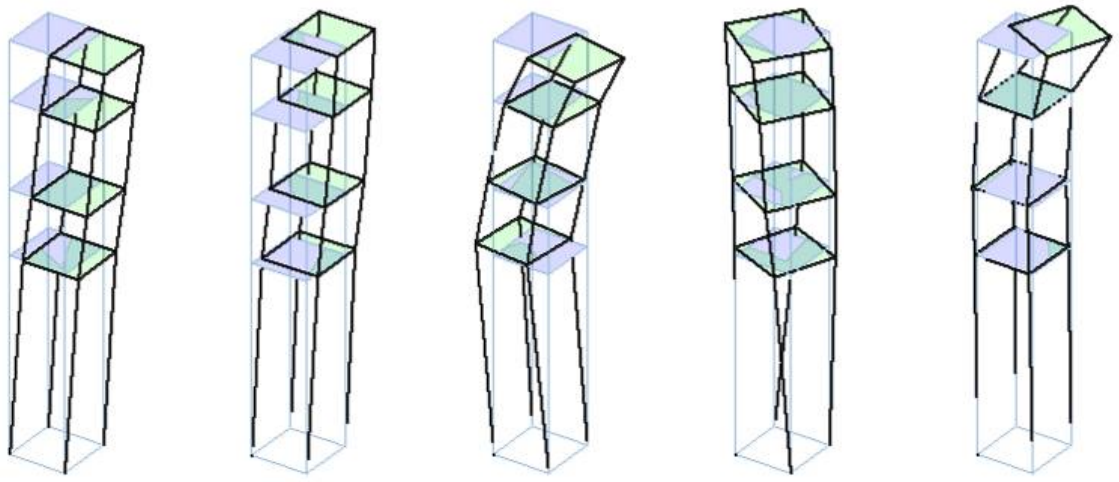


Figure 12: Dataset recorded on July 31st 2013, 16:00-17:00: (a) Singular value (SV) lines and identification of natural frequencies (FDD); (b) stabilization diagram (SSI).

The extraction of modal parameters from ambient vibration data was carried out by using the Frequency Domain Decomposition (FDD) technique [7] in the frequency domain and the

data driven Stochastic Subspace Identification (SSI) method [8-9], in the time domain; these techniques are available in the commercial software ARTeMIS [10]. More specifically, the FDD was mainly applied on site in order to quickly estimate the dynamic characteristics of the structure, whereas back in the office those estimates were refined using the SSI.

During the dynamic tests, a second acquisition system was used to measure the temperature in three different points of the tower: on the S-W front both indoor and outdoor temperature were measured, whereas only the outdoor temperature was measured on the S-E front. It is worth mentioning that the changes of outdoor temperature were very significant and ranged between 25°C and 55°C, whereas slight variations were measured by the indoor sensor (29°C-30°C) due to the high thermal inertia of the load bearing walls.



B1) f_{SSI} = 0.993 Hz B2) f_{SSI} = 1.034 Hz B3) f_{SSI} = 3.916 Hz T1) f_{SSI} = 4.770 Hz L1) f_{SSI} = 6.873 Hz

Figure 13: Vibration modes generally identified from ambient vibration measurements (SSI, July 31st 2013, 16:00-17:00).

4.2 Dynamic characteristics of the Tower

Notwithstanding the very low level of ambient excitation (Fig. 11c) that existed during the tests, the application of both FDD and SSI techniques to all collected data sets generally allowed to identify 5 vibration modes in the frequency range of 0-7 Hz.

Typical results in terms of natural frequencies and mode shapes are shown in Figs. 12 and 13, respectively. The plots in Figs. 12 and 13 refer to the acceleration data recorded in the time window 16:00-17:00 of July 31st 2013. The first Singular Values (SV) of the spectral matrix resulting from the application of the FDD technique is shown in Fig. 11a, whereas Fig. 11b shows the stabilization diagram obtained by using the SSI method; the corresponding mode shapes, identified via SSI, are shown in Fig. 13.

The inspection of Figs. 12 and 13 allows the following comments on the dynamic characteristics of the *Gabbia* tower:

(a) two closely spaced modes were identified around 1.0 Hz. These modes are dominant bending (B) and involve flexure in the two main planes of the tower, respectively: the mode B1 (Fig. 13B1) is dominant bending in the N-E/S-W plane whereas the modal deflections of B2 (Fig. 13B2) belong to the orthogonal N-W/S-E plane;
(b) the third mode B3 (Fig. 13B3) involves bending in the N-E/S-W plane, with slight (but not negligible) components in the orthogonal plane;
(c) just one torsion mode (T) was identified (Fig. 13T1) and the corresponding natural frequency was 4.77 Hz (in the examined time window);
(d) the last identified mode is local (L) and only involves deflections of the upper portion of

the tower (Fig. 13L1). The mode shapes seems dominant bending, with significant components along the two main planes of the tower. The presence (and generalized detection) of a local vibration mode provides further evidence of the structural effect of the change in the masonry quality and morphology (including un-toothed opening infillings and discontinuities) observed on top of the tower during the preliminary visual inspection. On the other hand, both visual inspection and OMA confirm the concerns about the seismic vulnerability of the buildings and explains the fall of small masonry pieces from the upper part of the tower, reported during the earthquake of May 29th 2013.

4.3 Frequency variation and correlation with outdoor temperature

Statistics of the natural frequencies that were identified between 31/07/2012 and 02/08/2012 are summarized in Table 1 through the mean value, the standard deviation, the extreme values and the coefficient of variation of each modal frequency. It should be noticed that the natural frequencies of all modes exhibit slight but clear variation, with the standard deviation ranging between 0.011 Hz (mode B2) and 0.037 Hz (mode L1).

Mode	f_{ave} (Hz)	σ_f (Hz)	f_{min} (Hz)	f_{max} (Hz)	CV (%)
1 (B1)	0.981	0.018	0.957	1.014	1.826
2 (B2)	1.026	0.011	1.006	1.052	1.093
3 (B3)	3.891	0.025	3.857	3.936	0.654
4 (T1)	4.763	0.022	4.714	4.802	0.462
5 (L1)	6.925	0.037	6.849	6.987	0.528

B = bending mode; T = torsion mode; L = local mode

Table 1 Statistics of the natural frequencies identified during 28 hours of dynamic testing

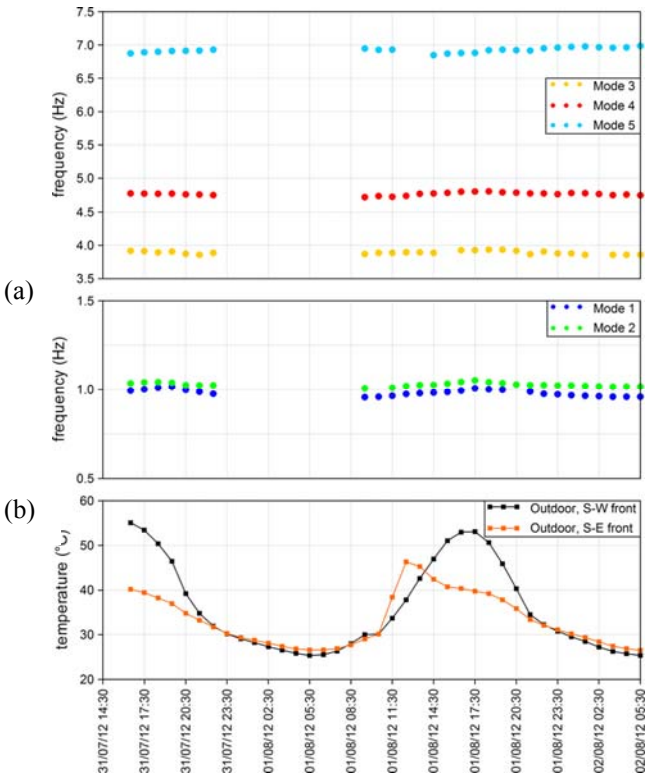


Figure 14: Variation in time of: (a) the natural frequency of identified vibration modes (SSI); (b) the temperature measured outdoor on the fronts S-W and S-E.

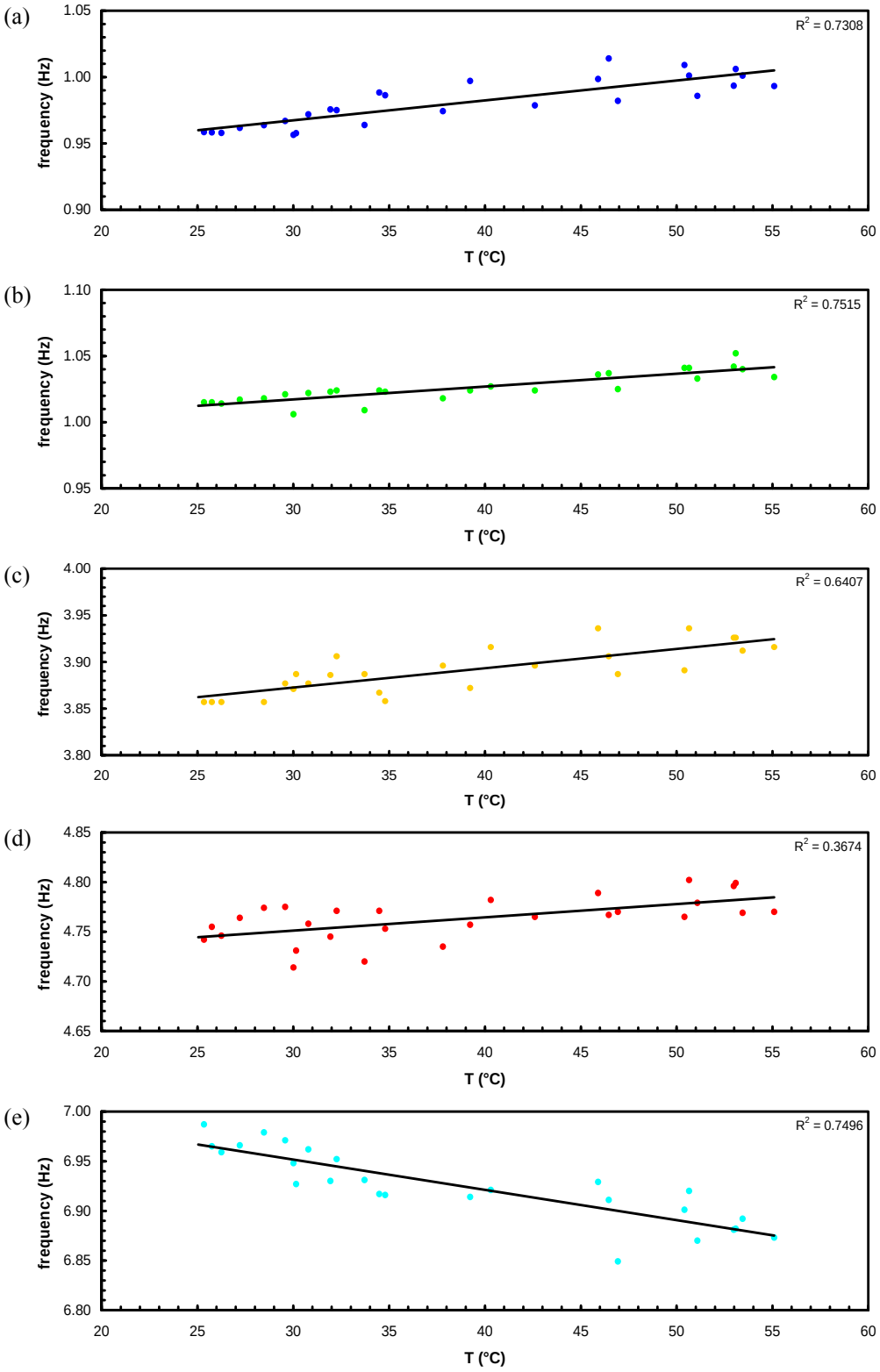


Figure 15: Frequency (SSI) variation versus measured outdoor temperature (S-W front): (a) mode B1; (b) mode B2; (c) mode B3; (d) mode T1; (e) mode L1.

Due to the very low amplitude of ambient excitation that existed during the 28 hours of acquisition, the variation of natural frequencies is conceivably related to the environmental (i.e. temperature) effects. In order to investigate the possible relationships between natural frequencies and temperature, Fig. 14 shows the evolution of natural frequencies, identified via

SSI, and the hourly averaged temperature, measured outdoor on the fronts S-W and S-E. The inspection of Fig. 14 suggests that:

1. the natural frequencies of the lower modes (global modes B1-B3 and T1) seem to increase with increased temperature. This behaviour, observed also in past experiences [4], [11] on masonry structures, can be explained through the closure of superficial cracks, masonry discontinuities or mortar gaps induced by the thermal expansion of materials. Hence, the temporary "compacting" of the materials induces a temporary increase of stiffness and modal frequencies, as well;
2. for the higher mode identified (that is a local mode of vibration), the variation in time of the natural frequency seems quite different.
3. the oscillation in time of natural frequencies of lower modes seems almost perfectly in-phase with the outdoor temperature on the S-W front.

In order to better explore the frequency-temperature correlation, the SSI estimates of all modal frequencies are plotted versus the outdoor S-W temperature in Figs. 15a-e. Each graph also shows the regression line and the coefficient of determination R^2.

R^2 is a dimensionless parameter and measures the variation percentage of Y (i.e. the k-th modal frequency) caused by the X variation (i.e. the temperature). The coefficient of determination ranges from 0 to 1; a value of 1 implies that the statistical model fits perfectly the experimental data whereas R^2 is equal to 0 in absence of correlation between the model and the experimental data.

Figures 15a-c confirm that the natural frequencies of bending modes B1-B3 increase as temperature increases and exhibit an almost linear correlation with the temperature, with R^2 ranging between 0.64 (mode B3, Fig. 15c) and 0.75 (mode B2, Fig. 15b).

The frequency-temperature correlation seems less strong for the torsion mode T1 (Fig. 15d) since R^2 is quite low (0.37) in comparison with the values of the other modes.

Nevertheless, it can be observed that the natural frequencies of all global modes clearly tend to increase with increased temperature.

Unlike the global modes, the natural frequency of the local mode L1 (Figure 15e) decreases as the temperature increases and the coefficient of determination assumes a high value ($R^2 \cong 0.75$). This result suggests that the thermal expansion of materials in a very inhomogeneous area of the structure causes a general worsening of the connection between the masonry portions; hence, further evidence seems to be provided, again in agreement with the main observation of the visual inspection, of the poor state of preservation of the upper part of the tower.

5 CONCLUSIONS

The paper demonstrates the importance of a multi-disciplinary approach in the assessment of historic buildings and especially in prompt post-earthquake investigation. The available information from visual inspection and on-site survey, suggesting the possible building evolution and indicating the masonry changes, provides a preliminary knowledge of utmost importance for planning the sensor layout in dynamic tests as well as for the execution of further tests.

Visual inspection of all main bearing walls clearly indicated that the upper part of the *Gabbia* tower is characterized by the presence of several discontinuities due to the historic evolution of the building, local lack of connection and extensive masonry decay.

The poor state of preservation of the same region was confirmed by the observed dynamic characteristics. In particular, the higher mode identified (having average frequency of 6.93 Hz) turned out to be local and involves only the top portion of the tower; the corresponding mode

shapes is dominant bending, with significant components along the two main planes of the tower. It is further noticed that the local mode was clearly identified by applying different output-only techniques to the ambient response data collected for more than 24 hours on the historic structure.

The presence of a such local mode highlights the relevant structural effects of the change in the masonry quality and morphology observed on top of the tower in the preliminary visual inspection. Furthermore, the natural frequency of the local mode clearly decreases as temperature increases, suggesting that the thermal expansion of materials in a very inhomogeneous area of the structure, causes a general decrease of the connection between the masonry portions.

ACKNOWLEDGEMENTS

The investigation was supported by the Mantua Municipality. M. Antico, M. Cucchi (VIBLAB, Laboratory of Vibrations and Dynamic Monitoring of Structures, Politecnico di Milano) and Eng.. Marco Guidobaldi are gratefully acknowledged for the assistance during the field tests.

REFERENCES

[1] N. Zuccoli, *Historic Research on the Gabbia Tower* (in Italian). Internal Report, Municipality of Mantua, 1988.

[2] L. Binda, A. Saisi, C. Tiraboschi, Investigation procedures for the diagnosis of historic masonries. *Construction and Building Materials*, **14**(4), 199-233, 2000.

[3] C. Gentile, A. Saisi, Ambient vibration testing of historic masonry towers for structural identification and damage assessment. *Construction and Building Materials*, **21**(6), 1311-1321, 2007.

[4] C. Gentile, A. Saisi, A. Cabboi, (2012) Dynamic monitoring of a masonry tower. In: *Proc. 8th Int. Conf. on Structural Analysis of Historical Constructions*. Wroclaw, Poland, 2012.

[5] DPCM (2011). *Valutazione e riduzione del rischio sismico del patrimonio culturale con riferimento alle NTC 14 gennaio 2008*. G.U.R.I. February 26th 2011, Rome, Italy.

[6] G. Bertazzolo, *Urbis Mantuae Descriptio*. 1628.

[7] R. Brincker, L.M. Zhang, P. Andersen, Modal identification from ambient responses using Frequency Domain Decomposition. In: *Proc. 18th Int. Modal Analysis Conference* (IMAC-XVIII). San Antonio, Texas, U.S.A., 2000.

[8] P. van Overschee, B. De Moor, *Subspace identification for linear systems: Theory, implementation, applications*. Kluwer Academic Publishers, 1996.

[9] B. Peeters, G. De Roeck, Reference-based stochastic subspace identification for output-only modal analysis. *Mechanical Systems and Signal Processing*, **13**(6), 855-878, 1999.

[10] SVS. ARTeMIS Extractor 2010 release 5.3, http://www.svibs.com, 2012.

[11] L.F. Ramos, L. Marques, P.B. Lourenço, G. De Roeck, A. Campos-Costa, J. Roque, Monitoring historical masonry structures with operational modal analysis: two case studies. *Mechanical Systems and Signal Processing*, **24**, 1291-1305, 2010.

COMPDYN 2013
4th ECCOMAS Thematic Conference on
Computational Methods in Structural Dynamics and Earthquake Engineering
M. Papadrakakis, V. Papadopoulos, V. Plevris (eds.)
Kos Island, Greece, 12–14 June 2013

SEISMIC RELIABILITY ASSESSMENT OF CLASSICAL COLUMNS SUBJECTED TO NEAR SOURCE GROUND MOTIONS

Ioannis Psycharis[1*], Michalis Fragiadakis[2], Ioannis Stefanou[3]

[1]School of Civil Engineering, National Technical University of Athens, Greece
ipsych@central.ntua.gr,

[2]Department of Civil and Environmental Engineering, University of Cyprus
mfrag@ucy.ac.cy,

[3]Université Paris-Est, Laboratoire Navier (UMR 8205), CNRS, ENPC, IFSTTAR,
F-77455 Marne-la-Vallée
ioannis.stefanou@enpc.fr

Keywords: Classical monuments, multidrum masonry columns, risk assessment, 3D Distinct Element Method (DEM), performance-based design.

Abstract. *A methodology for the performance-based seismic risk assessment of classical columns is presented. Classical columns are articulated structures, made of several discrete bulgy stone blocks (drums) put one on top of the other without mortar. Despite its apparent instability, this structural system is, in general, earthquake resistant, as proven from the fact that many classical monuments have survived many strong earthquakes over the centuries. Nevertheless, due to the fundamental non-linear character and the sensitivity of their response, the quantitative assessment of their reliability and the understanding of their dynamic behaviour are not easy. Consequently, the derivation of general remarks regarding their seismic risk is not trivial. In order to understand the dynamic behaviour and estimate the capacity of multidrum columns, a seismic risk assessment methodology is performed using Monte Carlo simulation with synthetic ground motions. The ground motions adopted contain a high and a low frequency component, combining the stochastic method and a simple analytical pulse model in order to simulate the directivity pulse contained in near source ground motions. Fragility curves are produced first conditional on magnitude and fault distance and then using a scalar intensity measure. The deterministic model for the numerical analysis of the system is three dimensional and is based on the Discrete Element Method (3D DEM). Fragility analysis demonstrates some of the salient features of these spinal systems and provides useful results regarding their reliability and decision-making during restoration process.*

1 INTRODUCTION

Several investigators have examined the seismic response of classical monuments and also that of stacks and of rigid bodies. These studies were analytical, numerical or experimental, mostly using two-dimensional models (e.g. [1] – [6] among others) and lesser using three-dimensional ones (e.g. [7] – [12]). It was shown that the response is non-linear and sensitive even to small changes of the parameters. These characteristics are evident even to the simplest case of a rocking rigid block (Housner [13]).

Previous analyses of the seismic response of classical columns have shown that these structures, despite their apparent instability to horizontal loads, are, in general, earthquake resistant (Psycharis *et al*. [5]), which is also proven from the fact that many classical monuments built in seismic prone areas have survived for almost 2500 years. However, many others have collapsed.

In general, the vulnerability of ancient monuments to earthquakes depends on two main parameters (Psycharis, *et al*. [5]): the size of the structure and the predominant period of the ground motion. Concerning the size, larger columns are more stable than smaller ones with the same aspect ratio of dimensions. Concerning the period of the excitation, it affects significantly the response and the possibility of collapse, with low-frequency earthquakes being much more dangerous than high-frequency ones. In this sense, near field ground motions, which contain long-period directivity pulses, might bring these structures to collapse.

The assessment of the seismic reliability of a monument is a prerequisite for the correct decision making during a restoration process. The seismic vulnerability of the column, not only in what concerns the collapse risk, but also the magnitude of the expected maximum and residual displacements of the drums, is vital information that can help the authorities decide the necessary interventions. This assessment is not straightforward, not only because fully accurate analyses for the near-collapse state are practically impossible due to the sensitivity of the response to small changes in the geometry and the difficulty in modelling accurately the existing imperfections, but also because the results depend highly on the ground motions characteristics.

In this paper, a risk assessment is performed for the case study of a column of the Parthenon Pronaos in Athens, Greece. To this end, we present a vulnerability assessment approach that accounts for the record-to-record variability. Advanced modelling and numerical analysis tools are combined with performance-based earthquake engineering concepts. The performance-based concept is expanded to classical monuments adopting appropriate performance levels and demand parameters to develop a decision-support system that will take into consideration engineering parameters helping the authorities on deciding upon the interventions required.

2 NUMERICAL MODELLING OF MULTIDRUM COLUMNS

The underlying mathematical problem is strongly non-linear and consequently the modelling of the dynamic behaviour of multidrum columns is quite complex. Even in the case of systems with a single-degree-of-freedom in the two dimensional space, i.e. a monolithic rocking block, the analytical and the numerical analysis is not trivial (Housner [13]) and differs from the approaches followed in modern structural analysis. The dynamic response becomes even more complex in three dimensions, where realistic models have to account for several non-linearities related to the three dimensional motion of each drum and the energy dissipation at the joints. For a more extensive discussion on the dynamic behaviour of such spinal systems we refer to Psycharis [3], Mouzakis *et al.* [8], Dasiou *et al.* [10], Stefanou *et al*. [14] among others.

Herein, we used the Discrete (or Distinct) Element Method (DEM) for the numerical modelling of the seismic response of multidrum systems. DEM may not be the only choice for the discrete system at hand, but it forms an efficient and validated manner for the study of the dynamic behaviour of masonry columns in classical monuments. The Molecular Dynamics (smooth-contact) approach was followed here [15] and the three dimensional DEM code 3DEC [16] was used. This software code provides the means to apply the conceptual model of a masonry structure as a system of blocks which may be considered either rigid, or deformable. In the present study only rigid blocks were used, as this was found to be a sufficient approximation and capable to reduce substantially the computing time. The system deformation is concentrated at the joints (soft-contacts), where frictional sliding and/or complete separation may take place (dislocations and/or disclinations between blocks). As discussed in more detail by Papantonopoulos *et al.* [7], the discrete element method employs an explicit algorithm for the solution of the equations of motion, taking into account large displacements and rotations. The efficiency of the method and particularly of 3DEC to capture the seismic response of classical structures has been already examined by juxtaposing the numerical results with experimental data (Papantonopoulos, *et al*. [7]; Dasiou, *et al*. [11]).

The geometry of the column considered in the present study was inspired by the columns of the Parthenon Pronaos on the Acropolis Hill in Athens. The column has a total height of 10.08 m, being composed of a shaft of 9.38 m and a capital. The real column has 20 flutes; however, the shaft in the numerical model was represented in an approximate manner by a pyramidal segment made of blocks of polygonal 10-sided cross section with diameters ranging from 1.65 m at the base to 1.28 m at the top. The shaft was divided into 12 drums of different height according to actual measurements of the columns of the Pronaos (Figure 1).

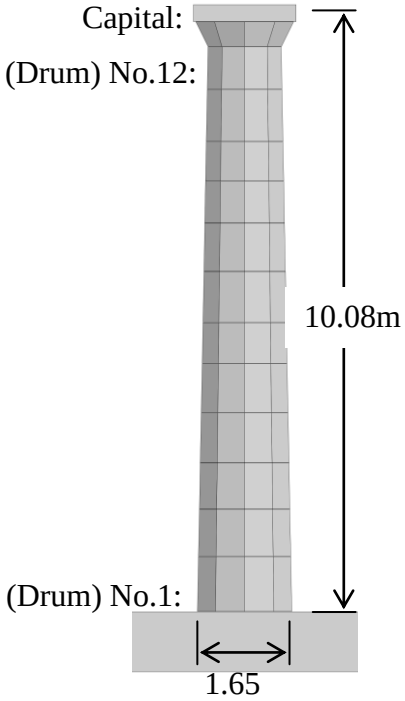


Figure 1. The multidrum column considered in the analyses.

A quite important factor for the numerical analysis is the selection of the appropriate constitutive laws that govern the mechanical behaviour of the joints. In the present paper we made use of a Coulomb-type failure criterion. Moreover, the friction angle was considered equal to 37^o, the cohesion and the ultimate tensile strength were considered equal to zero and

the normal and the shear stiffness of the joints were both considered equal to 1 GPa/m. Note that the stiffness choice might affect considerably the results of the analysis. Furthermore, no connections were considered between the drums, as the only connectors present in the original structure are wooden dowels, the so-called 'empolia', which were used to centre the drums during the erection of the column and not to provide a shear resistant mechanism. The shear strength of the wooden dowels is small and has only marginal effect to the response of the column (Konstantinidis and Makris [6]); for this reason, the wooden dowels were not considered in the numerical model.

3 FRAGILITY ASSESSMENT

Fragility (or vulnerability) curves are a valuable tool for the seismic risk assessment of a system. The seismic fragility F_R is defined as the limit-state probability conditioned on seismic intensity. The seismic intensity can be expressed in terms of magnitude M_w and distance R, resulting to a surface $F_R(M_w,R)$. Therefore, the fragility of a system is the probability that an engineering demand parameter (*EDP*) exceeds a threshold value *edp* and is defined as:

$$F_R(M_w,R)=P(EDP\geq edp\,|M_w,R) \tag{1}$$

Eq. (1) provides a single-point of a limit-state fragility surface, while engineering demand parameters (*EDP*s) are quantities that characterize the system response, e.g., permanent or maximum deformation, drum dislocation. To calculate F_R we performed Monte Carlo Simulation (MCS) using Latin Hypercube Sampling (LHS) for a range of magnitude and distance (M_w, R) scenarios. For this purpose, a large number of nonlinear response history analyses for every M_w–R pair is needed, especially when small probabilities are sought. Therefore, suites of records that correspond to the same M_w and R value must be compiled. Since it is very difficult to come up with such suites of natural ground motion records, we produced synthetic ground motions following the procedure discussed in the following section.

Assuming that seismic data are lognormally distributed, $F_R(M_w,R)$ can be calculated analytically once the mean and the standard deviation of the logs of the *EDP* are calculated, which are denoted as $\mu_{\ln EDP}$ and $\beta_{\ln EDP}$, respectively. Once they are known they can be used to calculate F_R using the normal distribution:

$$F_R=P(EDP\geq edp\,|M_w,R)=1-\Phi\left(\frac{\ln(edp)-\mu_{\ln EDP}}{\beta_{\ln EDP}}\right) \tag{2}$$

where *edp* is the *EDP*'s threshold value that denotes that the limit-state examined is violated and Φ denotes the standard normal distribution.

As the ground motion intensity increases, some records may result in collapse of the structure. When collapsed simulations exist, Eq. (2) is not accurate, since the *EDP* takes an infinite or a very large value that cannot be used to calculate $\mu_{\ln EDP}$ and $\beta_{\ln EDP}$. To handle such cases, Eq. (2) is modified by separating the data to collapsed and non-collapsed ones. The conditional probability of collapse is calculated as:

$$P(C|M_w,R)=\frac{\text{number of simulations collapsed}}{\text{total number of simulations}} \tag{3}$$

If $\mu_{\ln EDP}$ and $\beta_{\ln EDP}$ are the mean and the dispersion of the non-collapsed data respectively, Eq. (2) is modified as follows:

$$P\left(EDP \geq edp \left| M_{\mathrm{w}}, R\right.\right) = P\left(C \left| M_{\mathrm{w}}, R\right.\right) + \left(1 - P\left(C \left| M_{\mathrm{w}}, R\right.\right)\right) \cdot \left(1 - \Phi\left(\frac{\ln(edp) - \mu_{\ln EDP}}{\beta_{\ln EDP}}\right)\right) \quad (4)$$

4 GENERATION OF SYNTHETIC, HAZARD–CONSISTENT GROUND MOTIONS

The assessment of the seismic reliability of the column of Parthenon that is presented herein is based on synthetic ground motions, representative of near-field sites. The synthetic records were generated using the process that has been proposed by Mavroeidis and Papageorgiou [17], which allows for the combination of independent models that describe the low-frequency (long period) component of the directivity pulse, with models that describe the high-frequency component of an acceleration time history. In the present paper, the generation of the high-frequency component was based on the stochastic (or engineering) approach discussed in detail in Boore [18]. Based on a given magnitude-distance scenario (M_{w}–R) and depending on a number of site characteristics, the stochastic approach produces synthetic ground motions.

It must be noted that, due to the high nonlinear nature of the rocking/wobbling response and the existence of a minimum value of the peak ground acceleration that is required for the initiation of rocking, the high frequency part of the records is necessary for the correct simulation of surrogate ground motions. Long-period directivity pulses alone, although they generally produce devastating effects to classical monuments (Psycharis, *et al*. [5]), might not be capable to produce intense shaking and collapse, as the maximum acceleration of pulses of long period is usually small and not strong enough to even initiate rocking.

Classical monuments were usually constructed on the Acropolis of ancient cities, i.e. on top of cliffs; thus, most of them are founded on stiff soil or rock, and only few of them on soft soil. For this reason, the effect of the soil on the characteristics of the exciting ground motion was not considered in the present analysis. It is noted, though, that, although the directivity pulse contained in near-fault records is not generally affected by the soil conditions, soft soil can significantly alter the frequency content of the ground motion and, consequently, affect the response of classical columns. This effect, however, is beyond the scope of this paper.

4.1 Low frequency pulse

For the long-period component of the synthetic ground motions we applied the pulse model of Mavroeidis and Papageorgiou [17]. This wavelet has been calibrated using actual near-field ground motions from all-over the world. The velocity pulse is given by the expression:

$$V(t) = 0.5A_{\mathrm{p}}\left[1 + \cos\left(\frac{2\pi f_{\mathrm{p}}}{\gamma_{\mathrm{p}}}(t - t_0)\right)\right]\cos\left[2\pi f_{\mathrm{p}}(t - t_0) + \nu_{\mathrm{p}}\right],\ t \in \left[t_0 - \frac{\gamma_{\mathrm{p}}}{2f_{\mathrm{p}}}, t_0 + \frac{\gamma_{\mathrm{p}}}{2f_{\mathrm{p}}}\right] \quad (5)$$

where A_{p}, f_{p}, ν_{p}, γ_{p} and t_0 describe the amplitude of the envelope of the pulse, the prevailing frequency, the phase angle, the oscillatory character (i.e., number of half cycles) and the time shift to specify the epoch of the envelope's peak, respectively. All parameters of Eq. (5) have a clear and unambiguous meaning. For every magnitude – distance scenario (M_{w}–R), the velocity amplitude of the directivity pulse (V_{p}) and the frequency f_{p} were obtained using the expressions produced by Rupakhety *et al.* [19]. Specifically, the mean value of V_{p} was obtained by:

$$\log(V_p) = -5.17 + 1.98 \cdot M_w - 0.14 \cdot M_w^2 - 0.10 \cdot \log\left(R^2 + 0.562\right) \quad (6)$$

where M_w cannot exceed M_{sat}, which is considered equal to 7.0. Thus, for magnitude values above M_{sat}, we set $M_w = M_{sat}$ to obtain V_p using Eq. (6). Similarly, the mean pulse frequency f_p is:

$$\log(1/f_p) = -2.87 + 0.47 \cdot M_w \quad (7)$$

Note that equations (6) and (7) use base 10 logarithms. Also, V_p is not in general equal to the envelope amplitude A_p, but one can be calculated from the other if the phase angle ν_p is known.

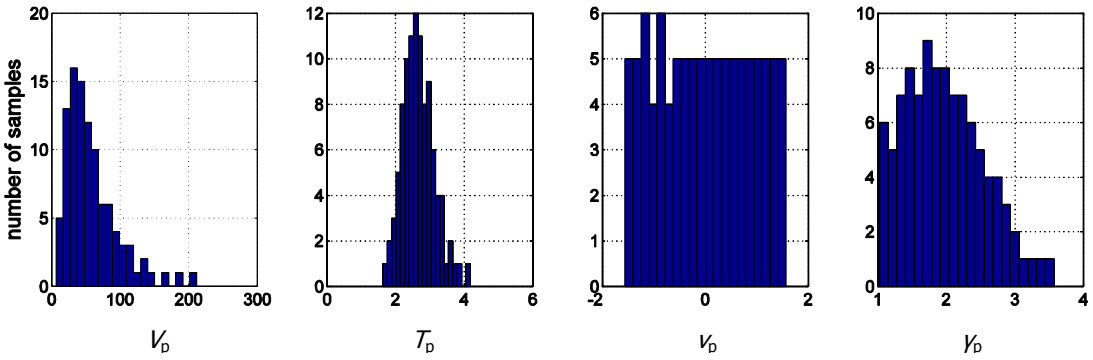


Figure 2. Histogram of the random parameters that describe the low-frequency plot (M_w = 7 and R = 5 km).

We randomly constructed low-frequency pulse-like ground motions using Eq.(5) and giving random values to V_p, f_p, ν_p and γ_p. Sets of pulse-like ground motions were obtained for every M_w–R combination using Latin Hypercube Sampling. We assumed that the logarithms of V_p and f_p follow the normal distribution with standard deviation equal to 0.16 and 0.18, respectively (Rupakhety, *et al*. [19]). The phase angle ν_p was randomly chosen in the [–π/2, π/2] range. Moreover, being consistent with the data of Mavroeidis & Papageorgiou [17], the number of half cycles γ_p was assumed to follow a normal distribution with mean and standard deviation equal to 1.8 and 0.4, respectively. The distribution of γ_p was left-truncated to one, while V_p and f_p were also left-truncated to zero, ensuring that no negative values were sampled. Figure 2 shows the histogram of the four random parameters used for creating pulses for the M_w = 7 and R = 5 km case.

4.2 High frequency component and combined synthetic strong ground motions

The stochastic approach was selected for modelling the high-frequency component of the ground motions. The stochastic method is discussed in detail in Boore [18] and is based on the ground motion radiation spectrum $Y(M_w,R,f)$, which is the product of quantities that consider the effect of source, path, site and instrument (or type) of motion. By separating the spectrum to its contributing components, the models based on the stochastic method can be easily modified to account for different problem characteristics. The shape and the duration of the ground motions depend on an envelope function $w(M_w,R,t)$. All simulations have been performed using the SMSIM program, freely available from http://www.daveboore.com.

The procedure we used to combine the low and high frequency components is discussed in Mavroeidis and Papageorgiou [17]. Using this approach synthetic ground motion records were constructed for magnitudes M_w in the range 5.5 to 7.5 with a step of 0.5 (five values of

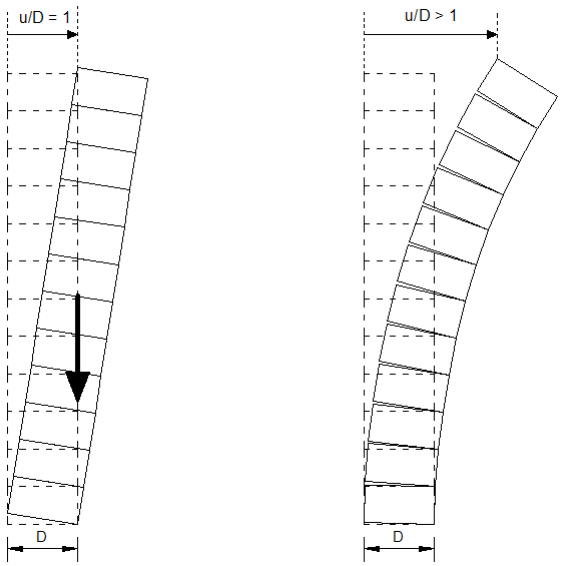
M_w) and distances from the fault R in the range 5 to 20 km with a step of 2.5 km (seven values of R). In total, 35 pairs of M_w–R were considered. For each M_w–R scenario, 100 Monte Carlo Simulations (MCS) were performed for a random sample of V_p, f_p, ν_p, γ_p using Latin Hypercube Sampling to produce the low-frequency pulse, while the high-frequency component was produced using the stochastic method, producing thus 100 random ground motions compatible with the M_w–R scenario considered.

5 PERFORMANCE-BASED RELIABILITY ASSESSMENT OF CLASSICAL MONUMENTS

In order to assess the risk of a monument, the performance levels of interest and the corresponding levels of capacity of the monument need first to be decided. Demand and capacity should be measured with appropriate parameters (e.g. stresses, strains, displacements) at critical locations, in accordance with the different damage (or failure) modes of the structure. Subsequently, this information has to be translated into one or a combination of engineering demand parameters (*EDP*s), e.g., permanent or maximum column deformation, drum dislocation, foundation rotation or maximum axial and shear stresses. For the *EDP*s chosen, appropriate threshold values that define the various performance objectives e.g. light damage, collapse prevention, etc. need to be established.

In the investigation presented here, two engineering demand parameters (*EDP*s) are introduced for the assessment of the vulnerability of classical columns: (a) the maximum displacement at the capital normalized by the base diameter (lower diameter of drum No. 1, see Fig. 2); and (b) the relative residual dislocation of adjacent drums normalized by the diameter of the corresponding drums at their interface. The first *EDP* is the maximum of the normalized displacement of the capital (top displacement) over the whole time history and is denoted as u_{top}, i.e. $u_{top} = \max[u(\text{top})]/D_{base}$. This is a parameter that provides a measure of how much a column has been deformed during the ground shaking and also shows how close to collapse the column was brought during the earthquake. Note that the top displacement usually corresponds to the maximum displacement among all drums. The second *EDP* is the residual relative drum dislocations at the end of the seismic motion normalized by the drum diameter at the corresponding joints and is denoted as u_d, i.e. $u_d = \max(\text{res}u_i)/D_i$. This parameter provides a measure of how much the geometry of the column has been altered after the earthquake increasing thus the vulnerability of the column to future events.

The *EDP*s proposed have a clear physical meaning and allow to easily identify various damage states and setting empirical performance objectives. For example a u_{top} value equal to 0.3 indicates that the maximum displacement was 1/3 of the bottom drum diameter and thus there was no danger of collapse, while values of u_{top} larger than unity imply intense shaking and large deformations of the column, which, however, do not necessarily lead to collapse. It is not easy to assign a specific value of u_{top} that corresponds to collapse, as collapse depends on the 'mode' of deformation, which in turn depends on the ground motion characteristics. For example, for a cylindrical column that responds as a monolithic block with a pivot point at the corner of its base (Figure 3a), collapse is probable to occur for $u_{top} > 1$, as the weight of the column turns to an overturning force from a restoring one when u_{top} becomes larger than unity. But, if the same column responds as a multidrum one with rocking at all joints (Figure 3b), a larger value of u_{top} can be attained without threatening the overall stability. In fact, the top displacement can be larger than the base diameter without collapse, as long as the weight of each part of the column above an opening joint gives a restoring moment about the pole of rotation of the specific part (cf. also video No.1). In the numerical analyses presented here, the maximum value of u_{top} that was attained without collapse was about 1.15.



(a) (b)

Figure 3. Top displacement for two extreme modes of rocking: (a) as a monolithic block; (b) with opening of all joints (displacements are shown exaggerated).

u_{top}	Performance level	Description
0.15	Damage limitation	No danger for the column. No permanent drum dislocations expected.
0.35	Significant damage	Large opening of the joints with probable damage due to impacts and considerable residual dislocation of the drums. No serious danger of collapse.
1.00	Near collapse	Very large opening of the joints, close to partial or total collapse.

Table 1. Proposed performance criteria concerning the risk of collapse.

u_d	Performance level	Description
0.005	Limited deformation	Insignificant residual drum dislocations without serious effect to future earthquakes.
0.01	Light deformation	Small drum dislocations with probable unfavourable effect to future earthquakes.
0.02	Significant deformation	Large residual drum dislocations that increase significantly the danger of collapse during future earthquakes.

Table 2. Proposed performance criteria concerning permanent deformation (residual drum dislocations).

Based on the above defined *EDP*s, the performance criteria of Tables 1 and 2 have been adopted. For u_{top}, three performance levels were selected (Table 1), similarly to the ones that are typically assigned to modern structures. The first level (*damage limitation*) corresponds to weak shaking of the column with very small or no rocking. At this level of shaking, no damage nor severe residual deformations are expected. The second level (*significant damage*)

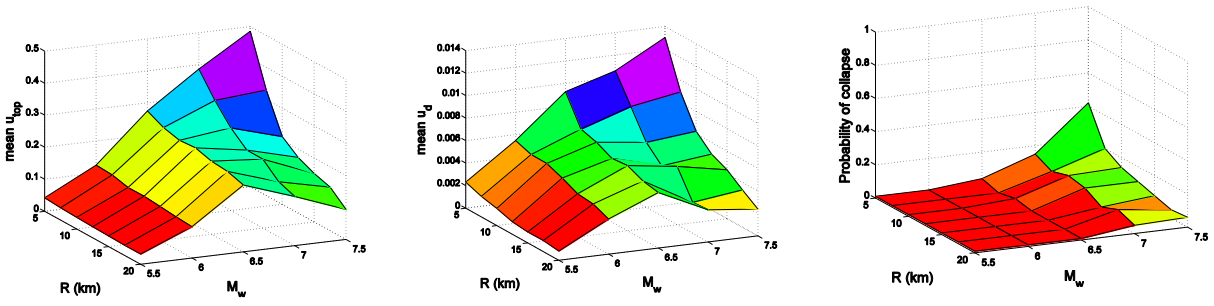
corresponds to intense shaking with significant rocking and evident residual deformation of the column after the earthquake; however, the column is not brought close to collapse. The third performance level (*near collapse*) corresponds to very intense shaking with significant rocking and probably sliding of the drums. The column does not collapse at this level, as $u_{top} < 1$, but it is brought close to collapse. In most cases, collapse occurred when this performance level was exceeded. The values of u_{top} that are assigned at every performance level are based on the average assumed risk of collapse.

Three performance levels were also assigned to the normalised residual drum dislocation, u_d (Table 2). This *EDP* is not directly related to how close to collapse the column was brought during the earthquake, since residual displacements are caused by wobbling and sliding and are not, practically, affected by the amplitude of the rocking. However, their importance to the response of the column to future earthquakes is significant, as previous damage/dislocation has generally an unfavourable effect to the seismic response to future events [20]. The values proposed are based on engineering judgment taking into consideration the size of drum dislocations that have been observed in monuments and also the experience of the authors from previous numerical analyses and experimental tests.

6 FRAGILITY CURVES

The proposed fragility assessment methodology was applied to the classical column of Figure 1. The response of the column was calculated for 35 M_w–R scenarios. For every M_w–R scenario 100 Monte Carlo Simulations (MCS) were performed, thus resulting to 3500 simulations in total.

Figure 4a shows the mean u_{top} displacements of the column and Figure 4b the corresponding u_d displacements. The surface plots of Figure 4a and 4b refer to non-collapsed simulations, while the collapse probabilities as function of magnitude and distance are shown in Figure 4c. Collapse is considered independently of whether it is local (collapse of a few top drums) or total (collapse of the whole column). As expected, the number of collapses is larger for smaller fault distances and larger magnitudes. For example, for $M_w = 7.5$ and $R = 5$ km 40% of the simulations caused collapse, while practically zero collapses occurred for magnitudes less than 6.5.

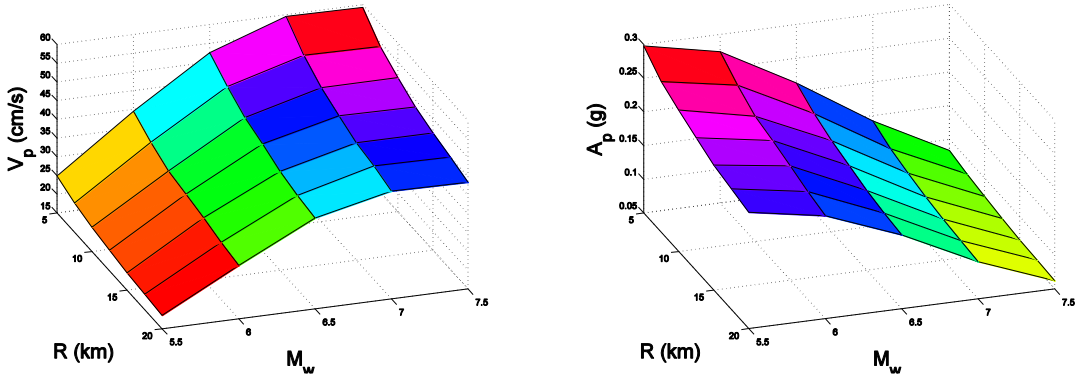


(a) (b) (c)

Figure 4. Mean values of the adopted *EDP*s for the classical column considered: (a) maximum normalised top displacements, u_{top}; (b) normalised residual deformations, u_d; and (c) Collapse probabilities for the multidrum column considered.

An unexpected behaviour is depicted in Figure 4. Concerning the mean top displacement during the seismic motion, Figure 4a shows that for small distances from the fault, up to approximately 7.5 km, the mean value of u_{top} increases monotonically with the magnitude as expected. However, for larger fault distances, the maximum u_{top} occurs for magnitude M_w =

6.5, while for larger magnitudes the top displacement decreases. For example, for R = 20 km, the mean value of u_{top} is approximately 0.4 for M_w = 6.5, while the corresponding value for M_w = 7.5 is about 0.2, i.e. it is reduced to one half. This counter-intuitive response is attributed to the saturation of the *PGV* for earthquakes with magnitude larger than M_{sat} = 7.0 (Rupakhety *et al.* [18], see Eq. (6)) while the period of the pulse is increasing exponentially with the magnitude. As a result, the directivity pulse has small acceleration amplitude for large magnitudes, which is not capable to produce intense rocking (Fig 5).



(a) (b)

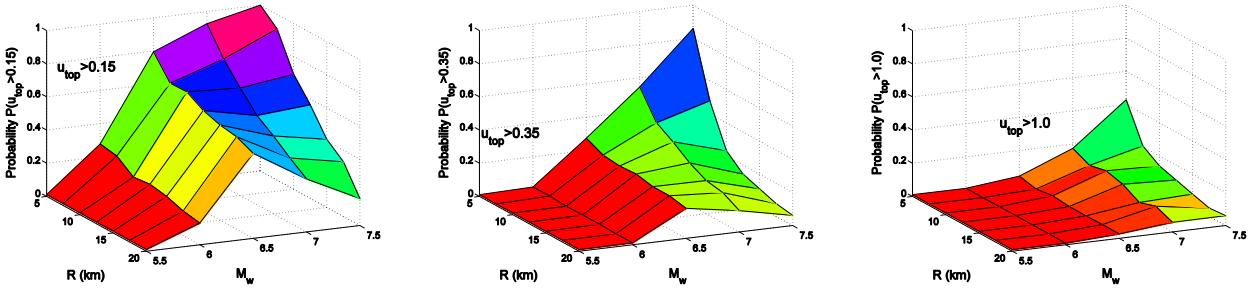
Figure 5. Variation of the mean value of: (a) the velocity amplitude, and (b) the acceleration amplitude of the directivity pulse, according to Eqs (6) and (7), with the magnitude, M_w, and the distance, R, respectively.

Similar, and probably more pronounced, is the behaviour concerning the permanent drum dislocations u_d shown in Figure 4b. Again, u_d increases monotonically with the magnitude for small values of R only, less than 10 km. For larger distances, u_d increases with M_w up to magnitudes equal to 6.5, when it attains its maximum value. For larger magnitudes smaller permanent deformation of the column occurs.

This 'strange' observation was verified for for both horizontal components of 30 real ground motions from the NGA PEER database [21], recorded in distances ranging from 17 to 23 km: the maximum u_{top} demand occurred for M_w = 6.5, while for higher magnitudes the demand gradually decreased as in the case of the synthetic records. It is interesting to note that most values of u_{top} for natural earthquakes lie below the corresponding line of the synthetic ground motions (Fig. 4a). This was expected, since the synthetic records were constructed considering the directivity pulse with its maximum amplitude, i.e. typically that of the fault-normal direction; however natural ground motions were, in general, recorded in various directions with respect to the fault, and thus contain directivity pulses of reduced amplitude.

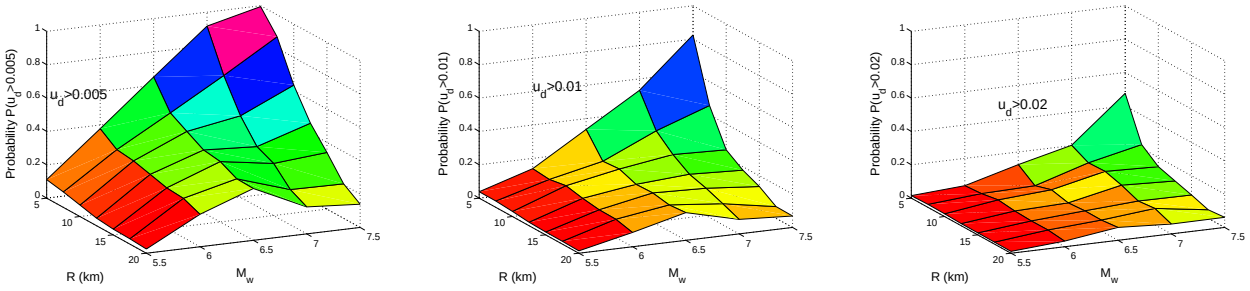
Figure 6 shows the fragility surfaces of the classical column for the three performance levels of Table 1 ranging from damage limitation (u_{top} > 0.15) to significant damage (u_{top} > 1). It is reminded that u_{top} > 0.15 means that the maximum top displacement during the ground shaking is larger than 15% of the base diameter and u_{top} > 1 corresponds to intense rocking, close to collapse or actual collapse. When damage limitation is examined, the exceedance probability is of the order of 0.2 for M_w = 6 and increases rapidly for ground shakings of larger magnitude. For the worst scenario among those examined (M_w = 7.5, R = 5 km), the probability that the top displacement is larger than 15% of D_{base} is equal to unity, while in the range M_w = 6.5–7.5 and R > 15 km a decrease in the exceedance probability is observed as discussed above. Similar observations hold for the exceedance of the significant damage limit state (u_{top} > 0.35), but the probability values are smaller. For the near collapse limit state

(u_{top} > 1.0), the probability of exceedance reduces significantly for large distances, even for large magnitudes. It is interesting to note that the u_{top} > 1.0 surface practically coincides with the probability of collapse of Figure 4c, which shows that, if the top displacement reaches a value equal to the base diameter, there is a big possibility that the column will collapse a little later.



(a) (b) (c)

Figure 6. Fragility surfaces with respect to the maximum capital displacement u_{top} for the performance levels of Table 1: (a) u_{top} > 0.15; (b) u_{top} > 0.35; (c) u_{top} > 1.0.



(a) (b) (c)

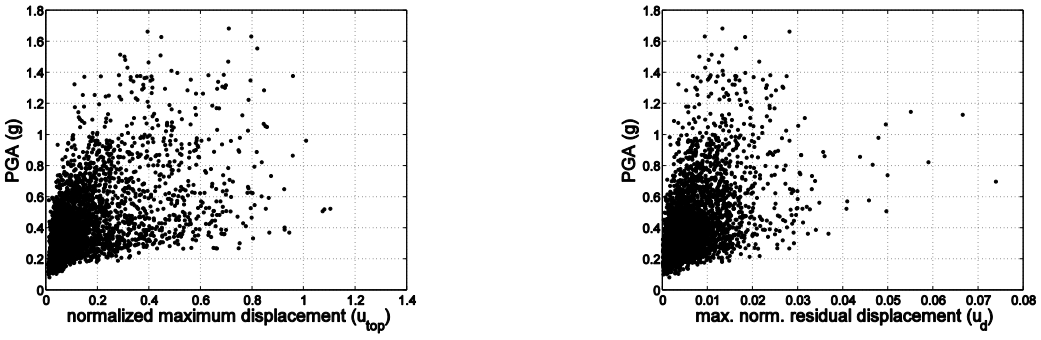
Figure 7. Fragility surfaces with respect to the permanent drum dislocations, u_d for the performance levels of Table 2: (a) u_d > 0.005; (b) u_d > 0.01; (c) u_d > 0.02.

Figure 7 shows the fragility surfaces when the *EDP* is the normalized permanent drum dislocation, u_d, and considering the performance levels of Table 2. For the limited deformation limit state (u_d > 0.005), probabilities around 0.3 are observed for magnitudes close to 6. Note that, for the column of the Parthenon with an average drum diameter about 1600 mm (Figure 1), u_d > 0.005 refers to residual displacements at the joints exceeding 8 mm. The probability of exceedance of the light deformation performance criterion (u_d > 0.01), which corresponds to residual drum dislocations larger than 16 mm, is less than 0.2 for all earthquake magnitudes examined and for distances from the fault larger than 10 km. The significant deformation limit state (u_d > 0.02) was exceeded only in a few cases.

In Figs 8 and 9 the *PGA* and *PGV* are plotted versus the *EDP*s considered, u_{top} and u_d. The scatter in the results is significant in both cases, slightly smaller for *PGV*. However, clear trends can be identified in the response, especially from Figure 9, showing, in average, a generally linear relation between the deformation (maximum and residual) with *PGV*.

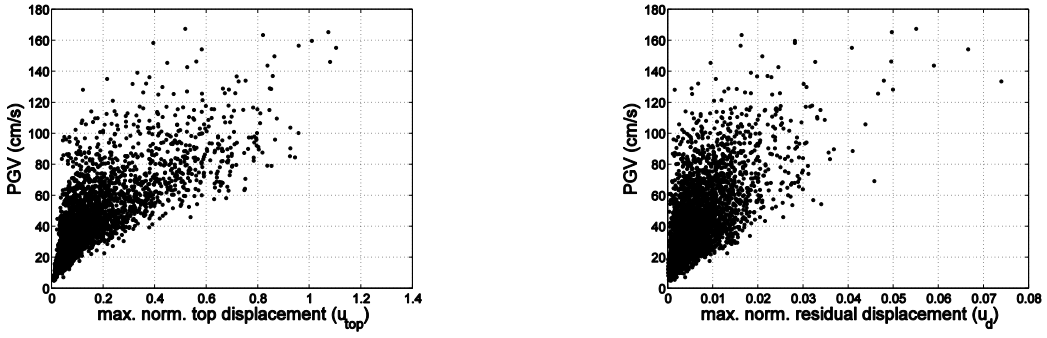
Another conclusion is that very strong earthquakes, with *PGV* that exceeds 150 cm/sec, are required for bringing the column of the Parthenon close to collapse (u_{top} > 1). However, significant dislocations of the drums (u_d > 0.02) can occur for weaker earthquakes with

PGV > 40 cm/sec. These observations are in accordance with findings of previous studies (Psycharis *et al*. [9]).



(a) (b)

Figure 8. Scatter plots of *PGA* versus: (a) maximum normalized displacement u_{top}; (b) maximum normalized displacement u_d.



(a) (b)

Figure 9. Scatter plots of *PGV* versus: (a) maximum normalized displacement u_{top}; (b) maximum normalized displacement u_d.

7 CONCLUSIONS

A seismic risk assessment of a column of the Parthenon Pronaos is performed using Monte Carlo simulation with synthetic ground motions which contain a high- and a low- frequency component. The ground motions considered combine the stochastic method and a simple analytical pulse model to simulate the directivity pulse contained in near source records. The fragility analysis demonstrated some of the salient features of these spinal systems under near-fault earthquake excitations which were not realized up to now.

8 ACKNOWLEDGEMENTS

Partial financial support for this study has been provided by the EU research project "DARE" ("Soil-Foundation-Structure Systems Beyond Conventional Seismic Failure Thresholds: Application to New or Existing Structures and Monuments"), which is funded through the 7th Framework Programme "Ideas", Support for Frontier Research – Advanced Grant, under contract number ERC-2—9-AdG 228254-DARE to professor G. Gazetas.

REFERENCES

[1] Allen RH, Oppenheim IJ, Parker AP, Bielak J. On the dynamic response of rigid body assemblies. *Earthquake Engineering and Structural Dynamics*, **14**, 861–876, 1986.

[2] Sinopoli A. Dynamic analysis of a stone column excited by a sine wave ground motion. *Applied Mechanics Reviews* Part 2, **44**, 246–255, 1989.

[3] Psycharis IN. Dynamic behaviour of rocking two-block assemblies. *Earthquake Engineering and Structural Dynamics*, **19**, 555–575, 1990.

[4] Winkler T, Meguro K, Yamazaki F. Response of rigid body assemblies to dynamic excitation. *Earthquake Engineering and Structural Dynamics*, **24**, 1389–1408, 1995.

[5] Psycharis IN, Papastamatiou DY, Alexandris AP. Parametric investigation of the stability of classical columns under harmonic and earthquake excitations. *Earthquake Engineering and Structural Dynamics*, **29**, 1093–1109, 2000.

[6] Konstantinidis D, Makris N. Seismic response analysis of multidrum classical columns, *Earthquake Engineering and Structural Dynamics*, **34**, 1243–1270, 2005.

[7] Papantonopoulos C, Psycharis IN, Papastamatiou DY, Lemos JV, Mouzakis H. Numerical prediction of the earthquake response of classical columns using the distinct element method, *Earthquake Engineering and Structures Dynamics*, **31**, 1699–1717, 2002

[8] Mouzakis H, Psycharis IN, Papastamatiou DY, Carydis PG, Papantonopoulos C, Zambas C. Experimental investigation of the earthquake response of a model of a marble classical column, *Earthquake Engineering and Structures Dynamics*, **31**, 1681–1698, 2002.

[9] Psycharis IN, Lemos JV, Papastamatiou DY, Zambas C, Papantonopoulos C. Numerical study of the seismic behaviour of a part of the Parthenon Pronaos, *Earthquake Engineering and Structural Dynamics*, **32**, 2063–2084, 2003.

[10] Dasiou M-E, Mouzakis HP, Psycharis IN, Papantonopoulos C, Vayas I. Experimental investigation of the seismic response of parts of ancient temples. *Prohitech Conference 2009 Rome*, 21-24 June, 2009.

[11] Dasiou M-E, Psycharis IN, Vayias I. Verification of numerical models used for the analysis of ancient temples. *Prohitech Conference 2009 Rome*, 21-24 June, 2009.

[12] Stefanou I, Psycharis IN, Georgopoulos I-O. Dynamic response of reinforced masonry columns in classical monuments, *Construction and Building Materials*, **25**, 4325–4337, 2011.

[13] Housner GW. The behavior of inverted pendulum structures during earthquakes, *Bulletin of Seismological Society of America*, **53**, 403–417, 1963.

[14] Stefanou I, Vardoulakis I, Mavraganis A. Dynamic motion of a conical frustum over a rough horizontal plane. *International Journal of Non-Linear Mechanics*, **46**, 114-124, 2011.

[15] Cundall PA, Strack OD. A discrete numerical model for granular assemblies, *Geotechnique*, **29**, 47–65, 1979.

[16] Itasca Cosulting Group, Inc., 3-dimensional Distinct Element Code (3DEC), *Theory and Background*, Minneapolis, Minnesota, 1998

[17] Mavroeidis GP, Papageorgiou AS. A mathematical representation of near-fault ground motions. Bulletin of Seismological Society of America, **93**, 1099–1131, 2003.

[18] Boore DM. Simulation of Ground Motion Using the Stochastic Method. *Pure and Applied Geophysics*, **160**, 653–676, 2003

[19] Rupakhety E, Sigurdsson SU, Papageorgiou AS, Sigbjörnsson R. Quantification of ground-motion parameters and response spectra in the near-fault region, *Bulletin of Earthquake Engineering*, **9**, 893–930, 2011.

[20] Psycharis I. A Probe into the Seismic History of Athens, Greece from the Current State of a Classical Monument, *Earthquake Spectra*, **23**, 393–415, 2007.

[21] Pacific Earthquake Engineering Research Center: NGA Database. http://peer.berkeley.edu/nga

COMPDYN 2013
4th ECCOMAS Thematic Conference on
Computational Methods in Structural Dynamics and Earthquake Engineering
M. Papadrakakis, V. Papadopoulos, V. Plevris (eds.)
Kos Island, Greece, 12–14 June 2013

EFFECT OF DAMAGE ON THE DYNAMIC CHARACTERISTICS OF ST. NICHOLAS CATHEDRAL IN CYPRUS

Renos A. Votsis[1], Nicholas Kyriakides[1], Elia A. Tantele[1], and Christis Z. Chrysostomou[1]
[1] Cyprus University of Technology
P.O.Box 50329, 3603 Limassol, Cyprus
renos.votsis@cut.ac.cy
nicholas.kyriakides@cut.ac.cy
elia.tantele@cut.ac.cy
c.chrysostomou@cut.ac.cy

Keywords: masonry monument, finite element modelling, damage assessment, dynamic characteristics.

Abstract. *The protection of monuments from aging and natural hazards, such as earthquakes, is very important since such structures are part of the cultural heritage of many countries around the world. In order to protect them from earthquakes, their structural system has to be identified and their capacity to withstand dynamic loads has to be clearly understood. Due to the large size of such structures and the limitations imposed by antiquities departments on the methods that can be used to obtain the properties of the materials of these structures and their dynamic characteristics, the ambient vibration survey method seems to be the most appropriate one to be used.*

Once the dynamic characteristics are identified, they will form a bench mark and any deviation in these parameters will be used for the identification and localization of damage caused to the structure, either due to environmental factors and aging, or due to an earthquake. In this work the dynamic characteristics of St. Nicholas Cathedral obtained through ambient vibration survey and the subsequent calibrated FE model are presented. Then a numerical sensitivity analysis is performed, in which damage in inflicted at vulnerable sections of the structure and the effects of this damage on the dynamic characteristics of the structure are recorded. Finally, conclusions are drawn on the type of sensors and locations they should be placed, as well as on the effectiveness of a monitoring system in identifying and localizing damage on the structure.

1 INTRODUCTION

In Cyprus there are plenty of historic monuments, all emerging from the various conquerors of the island who left an indelible mark on the structural heritage. These structures are invaluable, both in cultural and architectural terms. Nowadays there is an ever increasing sensitivity to preserve these monuments through rehabilitation and maintenance. For these historic structures, most of which are constructed of masonry, the assessment of their structural performance is based mostly on modal testing.

However, there are concerns in the application of modal testing (which is based on linear elastic behaviour of structures) to historic masonry monuments due to the complexities of these systems; such complexities include for example the assembly of mortar and masonry units via mortar joints. Field tests and checks on similar structures showed that the linearity assumption is a valid approximation and the analyses prompted accurate results [1].

Due to the sensitive nature of historic monuments, the use of excitators such as impact hammers or shakers is often restricted or prohibited and the tests are normally performed by using the Ambient Vibration Survey (AVS) technique. The results are often used to calibrate a Finite Element (FE) model that can be used for further analyses and for damage identification procedures [2].

Another issue of concern for masonry structures is their vulnerability to earthquakes. The historical investigation on the understudy monument carried-out in section 2 of this study, provides information that the St Nicholas Cathedral has been damaged by earthquakes. Monitoring and field tests can help assess their condition after earthquakes and investigate the effectiveness of any protecting countermeasures [3].

The current study carries-out a numerical damage assessment on the St Nicholas Cathedral in Famagusta, Cyprus. The dynamic characteristics of the monument as obtained from AVS testing, contributed in the calibration of the developed FE models and in the planning of the monitoring strategy that is already implemented at St Nicholas Cathedral. The initial FE models were calibrated basically through modification of the Young's modulus in order to minimise the differences in the frequencies and the mode shapes between the FE models and the measurements. The calibrated models were used to estimate changes in the frequencies after damage has been induced at several locations on the structure, which were identified through a numerical seismic analysis performed on the monument [4].

2 DESCRIPTION OF ST NICHOLAS CATHEDRAL

The earliest documents that mention the cathedral of St. Nicholas at Famagusta go back to 1300 AD. Although the chronicles of Amadi and Florio Bustron state that the construction began in 1308, it is certain that the work was under way from the 3rd August 1300, as reported in the Genoese records of Famagusta published by Cavaliere Desimoni [5]. It was the Bishop of Famagusta at that time (Bishop Guy) who initiated and financed the construction of the St. Nicholas Cathedral. After Bishop Guy's death, his successor Baldwin Lambert continued and completed the construction of the Cathedral. St. Nicholas Cathedral was the appointed place for the coronation of the Lusignan kings as Kings of Jerusalem, after they had been crowned as Kings of Cyprus at the capital of the island, Nicosia. This is probably why the Gothic style of the structure closely resembles that of Rheims Cathedral in Paris, France. The cathedral was damaged by earthquakes in 1546, 1568, and 1735. After the Ottoman conquest of 1571, the cathedral was converted into a mosque with the addition of a mihrab and a minaret and complete removal of internal decorations. Since then it is being used as a mosque. The style of the structure indicates that the architects and the sculptors of the cathedral were brought in from the Champagne region, France. The St. Nicholas cathedral consists of a nave

of seven bays ending in a polygonal apse flanked by aisles ending in apsidal chapels of similar shape (Figure 1). It is a 50m long, 24m wide limestone structure with a height of about 29m. The thickness of the walls is in general 1m while that of the vaults is 0.75m [5].



Figure 1: St Nicholas Cathedral

3 FINITE ELEMENT MODELLING

The field testing was carried out in association with the Kibris Turk Mimar ve Muhendis Odaları Birligi (KTMMOB) under the EuropeAid funded project "Earthquake vulnerability of historical monuments in Cyprus". The FE modelling in this work was implemented by the KTMMOB partner and the purpose of this section is to provide the main steps of that FE modelling process. The details of the latter can be found in [4] and [6].

For the St Nicholas Cathedral three different in details and complexity, 3D FE models have been developed with the level of complexity progressively increasing with each model [6]. The first and second models use only 2D shell elements for all structural members, but in the second model the minarets and the tower staircase were included. For the third model, the 2D shell elements were replaced with 3D solid elements for the peripheral abutments, internal columns and the western façade peripheral wall, to provide a more accurate representation of members with thick cross sections. All other details (material properties, boundary conditions) were the same for the three models.

Their allocated thickness was based on detailed on-site measurements. Prior to the FE modelling, several non-destructive testing (NDT) have been carried out using equipment such as the rock hammer, the ultrasonic pulse velocity, the ground penetrating radar etc, in order to estimate the mechanical properties of the building material and assess the construction details (i.e. foundation type) and the structural condition of the monuments (surface-cracks depth etc). With this information, the material properties such as compressive strength and the Young's modulus of elasticity were set for the FE models. To take into consideration the weathering of the stone, three different masonries were assigned to different sections depending on their exposure.

The numerical results presented in this study are obtained from the linear elastic modal analysis (using the updated FE model after the Young's modulus was adjusted to match the experimental values) after the work in [4] and [6].

4 VIBRATION TESTING

4.1 Testing procedure

A variety of techniques exist for field modal testing, depending on the availability of equipment, the type of structure and the operational conditions. When the input force is not measured, the analysis is undertaken using response data, and is better known as output-only analysis [8]. The modal parameters are subsequently extracted from the measured responses using a wide variety of methods which are nowadays implemented in powerful software such as ARTeMIS [9].

The output-only analysis is associated almost exclusively with the ambient vibration survey (AVS) method [10], although in some cases human activities can be used to excite the structure especially for tests on footbridges and floors. Ambient vibrations are the vibrations caused by excitation experienced by a structure under its normal operating conditions, therefore allowing the structure to remain open. Based on equipment's availability described in [11] and information from previous tests on similar structures, described in [1], it was decided to adopt the AVS approach.

The field testing on the St Nicholas cathedral is described in detail in [11].

5 DATA ANALYSIS

The acquired data obtained from the measurements were analyzed using DASYLab 9.0 [12] and ARTeMIS Extractor Pro 5.2 [9]. The first software was primarily used to obtain the frequencies of vibration contained in the signals using Fast Fourier Transform. The second software which is used exclusively for output-only analysis was utilised to confirm the frequencies obtained from DASYLab but at the same time revealing the mode shapes of the structure that correspond to the identified frequencies. The analysis in ARTeMIS is implemented using the Frequency Domain Decomposition (FDD) and the Stochastic Subspace Identification (SSI) methods [13]. A Hanning window with 67% overlapping and a frequency resolution of 0.015Hz were used. For the correlation of mode shapes, the Modal Assurance Criterion (MAC) has been used [14].

5.1 Dynamic characteristics of the St Nicholas Cathedral

The details of the modal parameter identification of St Nicholas cathedral can be found in [11]. In this study only the results are presented in a tabulated form: the frequencies and mass participation factors from the numerical analysis performed in SAP2000 are listed in Table 1.

In addition, in Table 1 only measured frequencies associated with identified mode shapes are listed and the correlation of the identified mode shapes with their numerical counterpart is expressed using the MAC values. The mode shape correlation has been performed by the FEMtools software which is using the measured data to perform FE model correlation and calibration [15].

Mode	Calculated Freq. Hz	Measured Freq. Hz	MAC	Mode Type	UX	UY
1	0.98	0.98	0.82	Longitudinal	0.6400	0.0126
2	0.99	1.04	0.85	Lateral	0.0107	0.6500
3	1.33	---		Torsional	0.0002	0.0182
4	1.54	1.40	0.89	Lateral	0.0012	0.0005
5	1.64	---		Torsional	0.0000	0.0559
6	1.82	---		Torsional	0.0001	0.0170

Mode	Calculated Freq. Hz	Measured Freq. Hz	MAC	Mode Type	UX	UY
7	1.94	---		Torsional	0.0263	0.0003
8	2.17	---		Torsional	0.0119	0.0000
9	2.30	---		Torsional	0.0051	0.0037
10	2.40	---		Torsional	0.0149	0.0000
11	2.48	---		Torsional	0.0491	0.0085
12	2.55	---		Torsional	0.0554	0.0033

Table 1: Measured and numerical modal parameters for St. Nicholas Cathedral

The mode shapes of the first three translational modes from the updated FE model are shown in Figure 2.

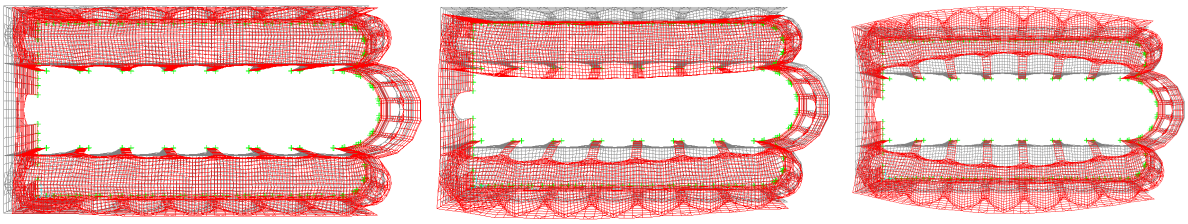


Figure 2: a) 1st longitudinal mode at 0.98Hz b)1st lateral mode, and c) 2nd lateral mode

6 FE MODEL UPDATING

Normally prior to FE model updating (manual or automated), sensitivity analysis is carried out to indicate the important parameters. In this study, a first attempt was made using only modulus of elasticity, E, in order to give an insight for the modes captured but not identified via their mode shapes due to lack of measured points. Other uncertain parameters that are often used in the updating procedure for masonry structures can include the connectivity between structural members (mortar joint), stone's density, etc [16].

The main parameter affecting the dynamic characteristics of masonry monuments is the E value of the stone. This value varies not only between different monuments but even comparing members of the same structure. In this study it was initially assumed that all structural members of the structure have the same value, i.e. a homogeneous distribution in all members. Although other researchers [17] divide the structure using different E for each divided section, the updating process with this assumption provided good correlation between the numerical and measured data, thus a single value for E was considered.

In the current study a simple model (shell elements and considering only one type of masonry) has been employed in the updating procedure. For this FE model the modulus of elasticity of the stone of which the monument is made of was initially set to 603 MPa, based on some compressive tests that were performed on the stone. With that modulus of elasticity the fundamental frequency was 0.834 Hz. In order to match the first recorded frequency shown in Table 1, the modulus of elasticity of all the elements was changed to 702 MPa.

7 RESPONSE SPECTRUM ANALYSIS

The seismic performance of the St Nicholas Cathedral was investigated numerically by Cagnan [4]. She used the three models described in section 3, to study the behaviour of the monument under earthquake loading of 475 years return period and for 5% damping. The results of the earthquake response spectrum analysis indicated different structural behaviour

among the models, where the induced tensile stresses exceeded the calculated structural capacities. The models developed only with shell elements indicated the critical members to be the internal columns, and depending on the condition of the weathered masonry, the crown points of the vaults, the flying buttresses, and the peripheral abutments (Figure 3a-d). The model with the incorporated solid elements restricted definite damage only to the flying buttresses and under conditions to the crown points of the vaults (similar locations as depicted in Figure 3a). The obtained results from Cagnan [4] are shown below.

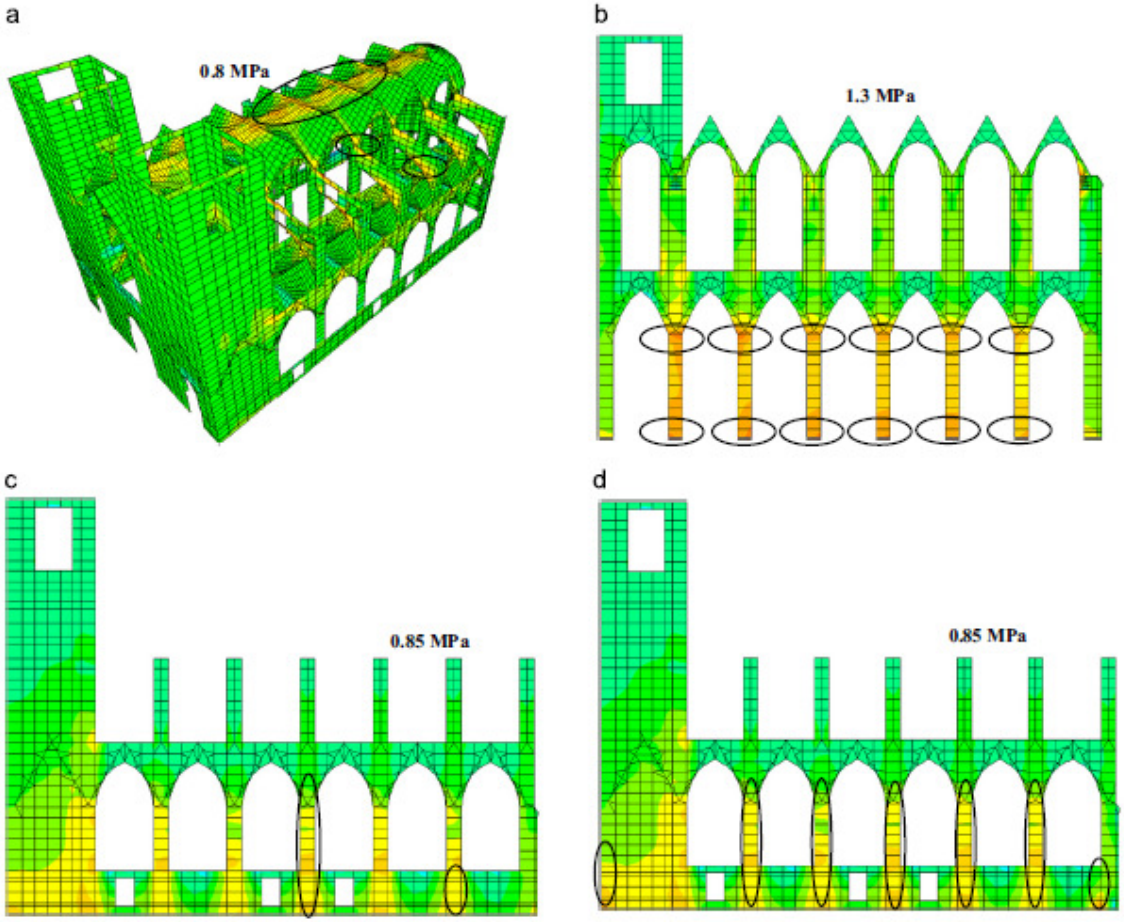


Figure 3: Stress distributions (a) flying buttresses and vaults (b) internal column capitals and bases ;(c) peripheral abutment(d) peripheral abutments (after Cagnan[4]).

Considering the performance of the three models, Cagnan concluded that as the results of model 3 are consistent with damage sustained by the structure reported in historical documents, this model can be considered to represent better the actual structural behaviour of the monument. She concluded that the more simple shell element models are adequate to provide an insight of the dynamic characteristics of complex structures but they may have limitations when coming to stress distribution analyses.

8 SIMULATED DAMAGE SCENARIOS

Considering the findings of the previous section after the work in [4], a damage assessment has been carried-out examining various damage scenarios. The objective was to check if induced damage on the structure at different locations can be identified solely by changes in the frequencies. Generally, in literature a limit of 5% change in frequencies is considered as significant; smaller changes can be attributed to ambient conditions variations such as tempera-

ture, wind etc [18, 19]. This limit has been adopted in this study to indicate the presence of damage in the monument.

Having in mind that a monitoring system is installed on the monument this sensitivity analysis will provide a useful insight of its capabilities.

For every damage scenario, three damage cases are considered, with progressive reduction of masonry's Young modulus, E , from the initial value of 702MPa:

1. 25% damage=25% reduction = 527MPa
2. 50% reduction = 351 MPa
3. 75% reduction = 176MPa.

The chosen damage locations are as shown in Figure 3. Although the results of the more detailed FE model are considered as more accurate, also the findings of the simpler FE models have been considered in the investigation. The damage scenarios and their adverse effect against the 5% frequencies change limit are discussed below.

8.1 Damage scenario 1

This scenario is focused on the behaviour of the flying buttresses. Two damaged locations have been considered as in figure 3a (circled yellow areas): 1) flying buttress-vault connection and 2) underside of flying buttress. Initially only a single flying buttress has been examined under the three damaged cases (progressive, 25%; 50%; 75%, E reduction). The results showed almost no changes in frequencies; the highest change calculated was 0.3%.

8.2 Damage scenario 2

Following the examination of a single flying buttress, the next step was to assume that all the members on one side have been damaged in the same way as in scenario 1. The effect of this damage scenario on frequencies was insignificant with the highest value calculated at 0.9%.

8.3 Damage scenario 3

For this scenario it was considered that all twelve flying-buttresses on both sides are damaged. The changes on frequencies were well below the 5% limit; a variation of 1.8% was calculated for the fourth mode (second lateral).

8.4 Damage scenario 4

In addition to the damage on the flying-buttresses it is considered that all the internal columns have sustained some form of damage. As the damage source has enough intensity to affect all the internal columns, it is safe to assume that the weakest part of the monument (that is the flying-buttresses), are all damaged too. Therefore, the damage described in scenario 3 is extended herein on the twelve internal columns. The damage is simulated with reduction in E on the top and bottom 2 elements (Figure 3b). The results showed that only for the worst case (75% reduction of E) the changes in the frequencies of the two lateral modes exceeded the limit of 5% (6.5% and 5.6% respectively); all other modes had smaller changes. However, the most important observation is the modal re-ordering of the two first modes: the lateral mode is now representing the first mode of the structure whereas the longitudinal mode appears as the second mode.

8.5 Damage scenario 5

For the last scenario, it is assumed that the 5 external columns on one side only, as in Figure 3d, are damaged, in addition to the damaged structural members of scenario 4. The damage is induced on the 12 elements below each column's capital. The same amount of damage is induced simultaneously on external and internal columns; the reduction on the flying-buttresses elements is kept constant at 75%. The analysis showed that for 25% reduction in columns' Young's modulus the frequency changes are not considered as alarming. At 50%, both lateral modes exhibit reduction in their frequencies of over 6%. For 75% reduction this difference is increased to 10%. All other modes are approaching the 5% limit. The modal re-ordering of the first two modes is again observed in this scenario.

8.6 Summary of results

The damage assessment results described above are summarised in Table 2. For the assessment the first ten vibration modes have been considered. It is shown that for the first three scenarios no significant changes in frequencies were observed, even for 75% induced damage on the selected members. For scenarios 4 and 5, the damage is affecting more modes 1 and 4 (lateral modes) and modal re-ordering is also observed.

Mode No & Type	**DS1** 75% Damage	**DS2** 75% Damage	**DS3** 75% Damage	**DS4** 75% Damage	**DS5** 50% Damage	**DS5** 75% Damage
1- longid.	-0.02	0.08	0.22	$6.56^{lateral}$	$6.21^{lateral}$	$10.84^{lateral}$
2- lateral	-0.30	0.19	0.73	$2.45^{longid.}$	$2.55^{longid.}$	$4.92^{longid.}$
3- torsional	0.06	0.76	1.38	3.86	3.42	5.19
4- lateral	0.15	0.93	1.80	5.62	6.09	9.51
5- torsional	0.23	0.31	0.40	2.05	1.90	3.36
6- torsional	0.27	0.88	1.43	3.14	2.92	4.29
7- torsional	-0.06	0.18	0.42	1.95	1.67	2.76
8- torsional	-0.01	0.51	1.04	2.23	2.23	3.22
9- torsional	0.19	0.49	1.15	3.98	3.03	4.69
10-torsional	0.01	0.13	0.28	1.41	1.06	1.76

Table 2: Summarised results of % frequencies changes for damage scenarios (DS).

9 CONCLUSIONS

In this paper the results of a numerical damage assessment for the St Nicholas Cathedral in Famagusta, Cyprus, were presented. For the assessment, calibrated FE models from field testing were used. The objective was to check if induced damage at different locations can be identified by solely changes in the frequencies.

The critical locations which are vulnerable after an earthquake have been identified from the numerical seismic assessment carried out in [4]. The study indicated that the flying buttresses are the most critical structural parts of the monument, which lies in agreement with previous damage sustained by the monument during an earthquake. In addition, other locations such as the internal and external columns and abutments have been considered in the damage assessment.

The damage has been introduced in the selected members as reduction of the masonry's Young's modulus. Three steps of 25% progressive reduction have been applied.

The results showed that severe damage at some parts of the flying buttresses cannot be detected by frequency changes. Additional severe damage to the internal columns can cause concerns over the condition of the structure, even though the damage affects only the lateral modes. Basically, only the extension of 75% damage to the external columns can clearly indicate the presence of damage. This shows that depending solely on frequencies in a damage assessment it is not very effective. High levels of damage are required to cause alarming variations in frequencies. It is well known, that this approach is the first and simplest step in a damage assessment; subsequent studies will include in the assessment the mode shapes (obtained from the sensors of the installed monitoring scheme) and damage identification techniques to investigate whether better evidence for damage detection can be provided. It is clear that monitoring of the individual behaviour of selected structural members is required, when only the frequencies are considered.

REFERENCES

[1] S. Atamturktur, A. Pavic, P. Reynolds, T. Boothy, Full-scale modal testing of vaulted gothic churches: lessons learned, *Journal of Experimental Techniques*, **33/4**, 65-74, 2009.

[2] L.F. Ramos, G. De Roeck, P.B. Lourenco, A. Campos-Costa, Vibration based damage identification of masonry structures, *5th International Conference on Structural Analysis of Histoical Construction*, New Delhi, India, November 6-8, 2006.

[3] C.Z. Chrysostomou, A. Stassis , T. Demetriou, K. Hamdaoui, Application of shape memory alloy prestressing devices on an ancient aqueduct, *Smart Structures and Systems,* **4/2**, 261-278, 2008.

[4] Z. Cagnan, Numerical Models for the Seismic Assessment of St. Nicholas Cathedral, Cyprus, *Journal of Soil Dynamics and Earthquake Engineering*, **39** ,50-60,2012.

[5] C. Enlart, *Gothic Art and the Renaissance in Cyprus, First ed.*, Trigraph, London, 1987.

[6] Z. Cagnan, Computer modelling and seismic performance assessment of a Byzantine basilica, *3rd International Conference on Computational Methods in Structural Dynamics and Earthquake Engineering*, Corfu, Greece, May 26-28, 2011.

[7] SAP2000, *Computers and Structures, v. 14.2.3 user's manual*, 2010.

[8] C.R. Farrar, T.A Duffey, P.J Cornwell, S.W. Doebling, Excitation methods for bridge structures, *17th International Modal Analysis Conference*, Kissimmee, USA, February 8-11, 1999.

[9] ARTeMIS Extractor Pro v. 5.2, Structural *Vibration Solutions A/S*, Aalborg, Denmark, 2011.

[10] I.R. Stubbs, V.R. McLamore, The ambient Vibration survey, *5th World Conference on Earthquake Engineering*, Rome, Italy, June 25-29, 1973.

[11] R.A. Votsis, N. Kyriakides, C.Z. Chrysostomou, E.A Tantele and T. Demetriou, Ambient vibration testing of two masonry monuments in Cyprus, *Soil dynamics and earthquake engineering,***43**,58-68, 2012.

[12] DASYLab v.9, National Instrument Corporation ,2005.

[13] P.V. Overschee, B.D. Moor, *Subspace Identification for Linear Systems: Theory- Implementation-Applications*, Kluwer Academic Publishers, Boston, USA, 1996.

[14] D.J. Ewins, *Modal Testing: Theory, practice and applications, Second edition*, Res. Studies Press, Baldock, 2000.

[15] FEMtools 3.4.0.2, Dynamic Design Solutions N.V., 2009.

[16] S. Atamturktur, J.A. Laman, Finite element model correlation and calibration of historic masonry monuments: review, *The Structural Design of Tall and Special buildings*, 2010.

[17] G. Gentile, A. Saisi, Ambient vibration testing of historic masonry towers for structural identification and damage assessment, *Construction and Building Materials*, **21**,1311–1321,2007

[18] G. Feltrin, Temperature and damage effects on modal parameters of a reinforced concrete bridge, *4th International Conference on Structural Dynamics, Eurodyn 2002*, Munich, Germany, September 2-5, 2002.

[19] C.R. Farrar, S.W Doebling, P.J. Cornwell, E.G. Straser, Variability of modal parameters measured on the Alamosa Canyon bridge, *15th International Modal Analysis Conference*, Orlando, USA, February 3-6, 1997.

SEISMIC PROTECTION OF MONUMENTS AND HISTORICAL BUILDINGS BY A SUSTAINABLE REDUCTION SYSTEM OF THE SEISMIC INPUT MOTION (COMPDYN 2013)

Panayotis G. Carydis[1], Vasileios S. Giannopoulos[2], Egkolfios E. Athanasiou[3], Nikolaos Th. Lebesis[4]

[1]Academician, Professor Emeritus N.T.U.A., Civil Engineer
Panagouli 5A, Kifissia, 14562 Greece
pkary@tee.gr

[2]Civil Engineer
Alonnisou 12, Egaleo, 12241 Greece
bgiannop@tee.gr

[3]Civil Engineer, MSc
Thoukididou 11, Levadia, 32100, Greece
eg_athanasiou@yahoo.gr

[4]Civil Engineer
Epidamnou 4, Athens, 11253, Greece
niklempesis@teemail.gr

Keywords: Seismic isolation, foundations, strengthening, monuments, existing buildings.

Abstract. *The basic idea of the described research work, lies on the exploitation of the incoherency and the out of phase physical phenomenon among the in-coming seismic waves that excite the structures through their foundation. This beneficial function is valid only if the foundation is quite large, stiff and strong along all directions. The ground motion mitigation system consists of a grillage of reinforced concrete beams that are constructed in direct structural contact with its foundation body. The dimensions of the plan of the orthogonal grillage should be longer that the half seismic surface wave's length in order to achieve a substantial reduction. A parametric analysis was carried out considering the foundation as a two dimensional elastic beam and the velocity of the propagation of the ground motion as basic parameters. Two strong ground motions have been used, each one with quite different characteristics compared to the other one. Finally, a combination of 32 cases was examined, and the resulted motions at the center of gravity of the beams as well as the corresponding response spectra were calculated. The ratios of the resulted response spectra over the free field spectral values at various natural periods and for 5% critical damping are calculated, and it was proved that the reduction may reach the 50% of the free field values. The application of the methodology is presented in various case studies of monumental structures such as churches and residential buildings. These results are checked following the FEMA 440 methodology. It was proved that the difference between the two approaches is within engineering acceptable limits given the large amount of parameters involved in the problem.*

1 SCOPE OF THE WORK

With the present work it is aimed to document a design methodology in order to reduce the size of the seismic input motion to monuments and historic building structures. This is achieved by creating a new larger, stiffer and stronger foundation which comes in full structural connection with the existing one. In this methodology are not used any devices. The whole reduction is achieved with structural members that provide sustainability to the whole intervention. This methodology might be proved quite useful for monumental structures where there strengthening unless impossible it is at least difficult and expensive. This difficulty is increasing with the increase of the value of the monument under preservation. On the other hand the intervention in the foundation body starting from a certain depth into the ground does not come to any conflict with the Venice Charter, or other international relevant treaties.

Any strengthening methodology is based on the following well known relation well known inequality:

$$S \leq R \tag{1}$$

where:
S is the loading of a structure, and
R is its resistance.

In the case of the earthquake loading, one could better say that S should be the resulting loading from the earthquake response of the structure. In the present communication we are dealing with monumental structures that we are designing into the elastic – linear domain and ductilities or other nonlinearities are not primarily taken under consideration. Therefore, the loading S is rather proportional to the input motion.

Therefore, the problems from Eq.(1) start when this equation is not satisfied, which means that S>R. Instead of increasing the structural resistance R, one could decrease S by a proportional percentage, without touching the structure. Of course, this procedure involves a limitation, since it is not always possible to decrease S as much as is necessary in order to respect Eq.(1). In that case we must increase the resistance R only for the remaining unsatisfied part of Eq.(1). For example, if it is necessary to increase the resistance R by a percentage 50% to meet Eq.(1), and we can reduce the loading S by 40% only, we have to increase the resistance R of the structure roughly by 10% only.

2 HISTORICAL RETROSPECT

Since about 50 years ago, the influence of the size of the foundation to the earthquake response of structures has attracted the interest of various researchers, a quite eminent of which was the late professor G. Housner with his work [1]. He observed the reduction of about 50% of the free field earthquake ground motion along the longer and stiffer E-W direction of a building structure, see Fig.1, during the Arvin Tohachapi, 1952 earthquake.Along the more flexible and slender N-S direction of the structure almost not any change was noticed compared to the free field motion. The respective response spectra obtained are presented in Fig. 2.

It is self understood that the seismic response of the building structure ay its basement automatically constitutes its seismic design excitation along the two main directions of the building.

The monolithic reinforced concrete box of the Hollywood Storage building possesses the following fundamental periods: Along the longitudinal E-W direction, T=0.49 sec while along the transverse N-S direction, T=1.20 sec. The distance between the building and parking lot (P.L.) is about 37 m, where the accelerograph is functioning into a light metallic shelter 2 m x

3 m in plan. The record of the latter instrument may be considered as the free field earthquake motion. As it is shown in Fig. 2a, along the longer and stiffer side of the building the reduction of the free field motion reaches 50%. From the same figure one may see that the greater reduction of the response spectra values is achieved for shorter than 1.20 sec periods, compared to those of higher natural periods.

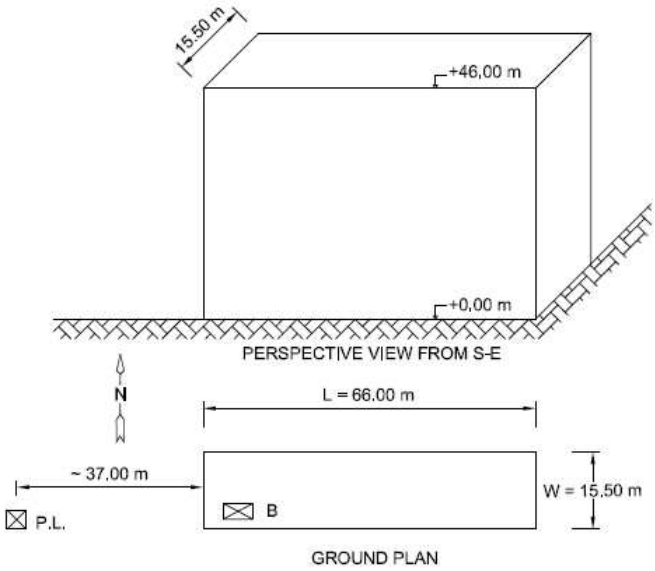


Figure 1: A stiff, large and strong structure of the Hollywood Storage building is instrumented at its basement (B) with a 3-D accelerograph. An other one is recording the free field motion at the parking lot (P.L.), after [1].

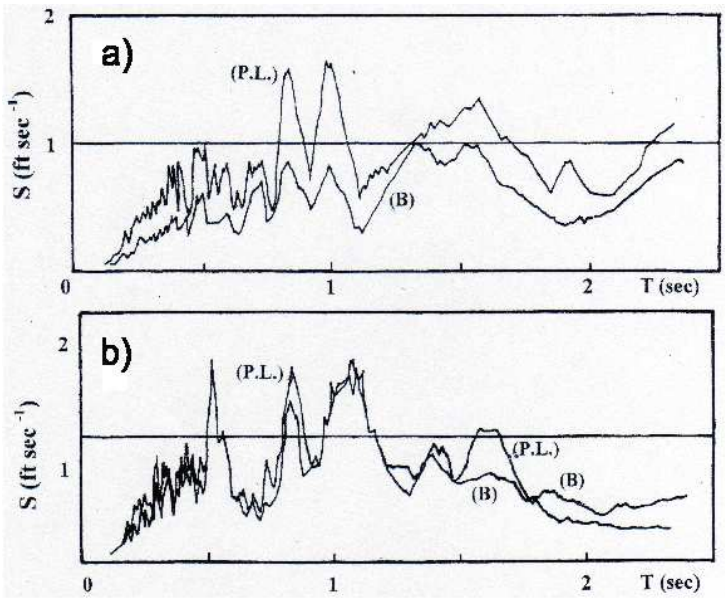


Figure 2: Velocity response spectra for ζ=0% damping in order to compare the ground motion records between the free field (P.L.) and the building response at its basement (B), for (a): along E-W stiff and longer direction and (b): along the N-S shorter and more flexible direction, after [1].

In [1] it is concluded that the reduction of the free field motion along the E-W direction is due to the length of the foundation compared to the half wave length of the seismic waves and, also, due to its high stiffness. Obviously the observed lack of damage is due to the high strength of the structure.

On the other hand, according to the regulations for earthquake resistant structures issued by the Ministry of Construction of U.S.S.R. up to the present [2], [3] long size foundation structures were considered as seismically vulnerable. For this reason limitations for the maximum allowable lengths of the structures and foundations were introduced. In those limitations the seismicity, the structural type and the quality of the material were introduced as parameters. For example, for non seismic regions the maximum length is 150 m independently from the structural type and quality of material. For the lowest seismic zone is 80 m for reinforced concrete frames and for the highest seismic zone the maximum allowable length is reduced to 40 m for simpler structural systems and of lower quality construction materials.

As it is explained, the building length limitations are set in order to avoid misleading or complicated calculations in order to evaluate high tensile and shear stresses in the foundation and to avoid horizontal tensional forces around the vertical axis of the structure. Those observations are documented after strong earthquakes, in which the longer the structure the larger was the damage.

According to [4] it was fully demonstrated by [5] the increase of stresses in a type of a large panel building which reached 1.35 MPa for the tensile stress and 0.74 MPa for the shear stress. In the same publication it was clearly shown that the increase of the length of a building usually will adversely affect its earthquake response. In the same publication it was not explicitly stated but it could be concluded that this is due to the phasing phenomenon of the seismic waves that propagate along the longitudinal direction of the building foundation. A further and more rigorous investigation of this phenomenon can be found in [6], in which it was proved, by using a two dimensional analysis, that important torsional vibrations were created in long buildings excited by seismic waves.

According to the above mentioned, a contradiction seems to exist between the recorded seismic observations at the Hollywood Storage building [1], and the equally well documented analytical calculations and field observations, on which the U.S.S.R. seismic codes since 1957 are based. Actually, there is not any contradiction, since the Hollywood Storage building is constructed out of solid reinforced concrete walls with very limited openings in the façade. At those years the type of structural systems as well as the material used in U.S.S.R., in general, should not be of the type and quality of the Hollywood building. It must be noticed that if the materials of that building were of lower quality, severe seismic damage would unavoidably occur. Therefore, based on the observations of both sides one may conclude that the longer is the foundation structure, the higher are the seismic stresses developed, while smaller becomes the resulting response – input motion to the structure.

In addition to the above mentioned, according to [7], a considerable decrease of the total seismic loads may be expected for building founded on strip foundations of continuous footings. This is compared to the case of the free field motion and the assumption that the ground particles during the earthquake vibrate “synchronously throughout the foundation”. For the first time the averaging concept was introduced by [8] according to the formula shown in Eq. (2):

$$\ddot{a}_b(t) = \frac{1}{L}\int_0^L \ddot{a}(x,t)\,dx \tag{2}$$

where,

$\ddot{a}_b(t)$ is the mean seismic acceleration in the body of the foundation as a function of time (t)

$\ddot{a}(x,t)$ is the point seismic acceleration at the free field along the foundation as a function of position (x) and time (t)

L is the total length of the foundation.

According to Eq. (2) the acceleration $\ddot{a}_b(t)$ will be the design acceleration for the whole structure, and its maximum value is certainly smaller that the maximum value of the free field one.

It is easily understandable that, due to the phasing phenomenon and / or the incoherency of the incident motion at the various points of the foundation body considerable dynamic strains (axial, bending, rotational and shear) may be developed in the body of the foundation. These strains and deformations are increased by a mutual increase of the length of the foundation, up to a certain magnitude. Therefore, it is logical to expect damage in inadequately designed and dimensioned foundations as this is mentioned in [9]. The calculation of those strains and the resulting forces is a rather difficult and time consuming procedure, some times based on various engineering approximation. In case that the various design parameters is difficult to be safely estimated it is better to set limitations related to the allowable maximum length of the foundation as a function of various parameters (seismicity, level of reinforcement and quality of the construction, geometry and mass of the above the foundation structure, stiffness of the foundation, soil conditions, expected motions from far or near field seismic sources).

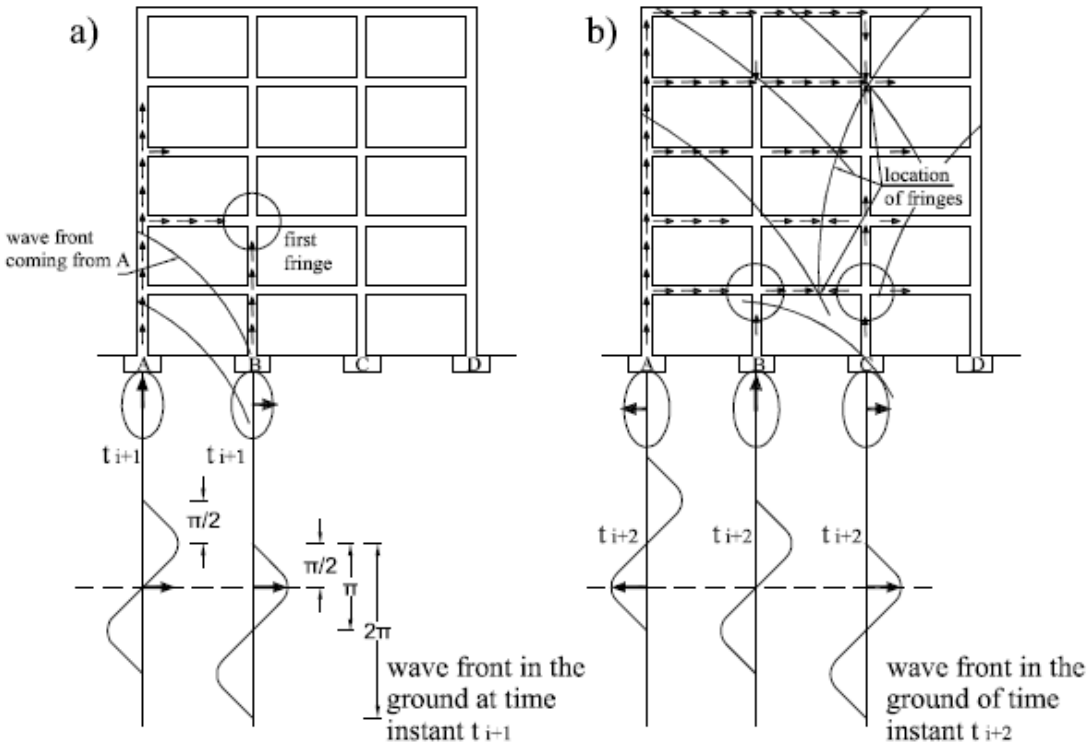


Figure 3: The input motion is inserted at discrete points of the foundation body (A), (B), (C) and (D): a) the earthquake motion, coming from the left of the figure, strikes the left hand parts of the structure first, while the other parts of the structure does not move until; b) the earthquake motion propagates through the foundations (C and D). The various input particle ground motions show a phase lag among themselves.

In the sketch of Fig. 3 the phasing phenomenon is attempted to be presented. The practical meaning of Fig. 3, may be illustrated with the following example. For a length of a building foundation of 45 m and an apparent wave velocity of 150 m/sec, the time required for the seismic motion to cross the foundation from point A to point D, is 45/150 = 0.30 sec. This means that for an oscillation period of the ground particles of the order of 0.60 sec the phase

lag between points A and D can reach 180º. In this case, the maximum amplitude of the resulting input motion will be roughly the 0.75 of the free filed one, according to Eq.(2).

A very important contribution to this subject was given by FEMA 440 [10], in chapter 8 where the base-slab averaging and embedment effects are presented and illustrated in its Fig.8.1. The placement of a rather rigid body between structure and ground absorbs all differences of the spatially variable ground motion and produces an averaging effect. The produced motion at the center of gravity of the slab is more uniform, it is filtered and it is less than the free filed motion in which localized maxima are usually observed and recorded, [10].

The relevant design methodology suggested by FEMA 440, [10], is followed in the arithmetic applications given in the relevant case studies presented in section 6 of the present communication.

Following the above mentioned, it is logical to propose that the engineering design of the foundation must be carried out according to the following approach: in its top side is the interactive building, while in its bottom side, the various incident waves with phase lag should be taken under consideration. These additional considerations must be done in order to maintain the current building design process as it is specified by the codes.

Also, it must be mentioned here, that in epicentral regions of mainly shallow focus earthquakes, it is not fully justifiable to use the term "surface wave velocity", since the surface waves are greatly distorted due to multiple incident wave motions with various reflections and refractions. Thus, "surface waves" although created by the body waves emerging from the source, can not be normally propagated. Instead, the term "apparent surface wave velocity" should rather be used. The well known function $c = \lambda/\tau$ (c=wave velocity, λ=wave length and τ=period) has actually not a pure physical sense, in epicentral regions of shallow focus earthquakes, since no one of these three parameters may belong to one and the same wave. According to various field observations in epicentral regions the apparent wave lengths are rather short compared to the far field ones, where the conditions are more normal and harmonic.

The particles of the ground in Rayleigh waves perform elliptical motions. The longer axis of the ellipse is along the vertical direction and the shorter one is along the horizontal one. The closer to the epicentre, the greater is the ratio between the vertical over the horizontal diameter of the ellipse.

In this way, the seismic motion that excites the foundation of a structure is a motion that results from the convolution of basic motions, plus the initial tectonic motion in the hypocentral region, which are projected on the three perpendiculars to each other axes, horizontal and vertical. This is exactly what accelerographs are recording. Of course, it is useless to say that these instruments record the 3-D true seismic motion of the base on which they are fixed, as for example the two quite different records obtained in [1] and shown in Fig. 2.

3 EARTHQUAKE RESPONSE OF BUILDINGS PROVING THE NECESSITY FOR LARGE, STIFF AND STRONG FOUNDATIONS

It is proved by abundant field observations and [11] the great variation of the ground motion and the resulting response of similar structures built on almost identical ground conditions and in a rather close distance among themselves. This means that the spatial distribution of the ground motion presents maxima and minima even along rather close distances, as already mentioned. Also, supporting the point of view of the U.S.S.R. code there are some cases in which the damage refers to structures of rather long dimensions.

According to [12] and as presented in Fig. 4, a "rhythmic" destruction occurred in a case of six similar multistoried buildings, built along a straight line, at equal distances one from the other. These six apartment buildings were identical to each other because they had been constructed with the same design drawings and the same materials, by the same constructor, with

the same workmanship and at the same time. In addition to that and although there is no reason to assume any alternation of the soil conditions from one plot to its adjacent one, the damage and collapse occurred selectively at every second building. The difference of the earthquake response between one building and its neighboring is striking, i.e. from a total collapse to partial damage only.

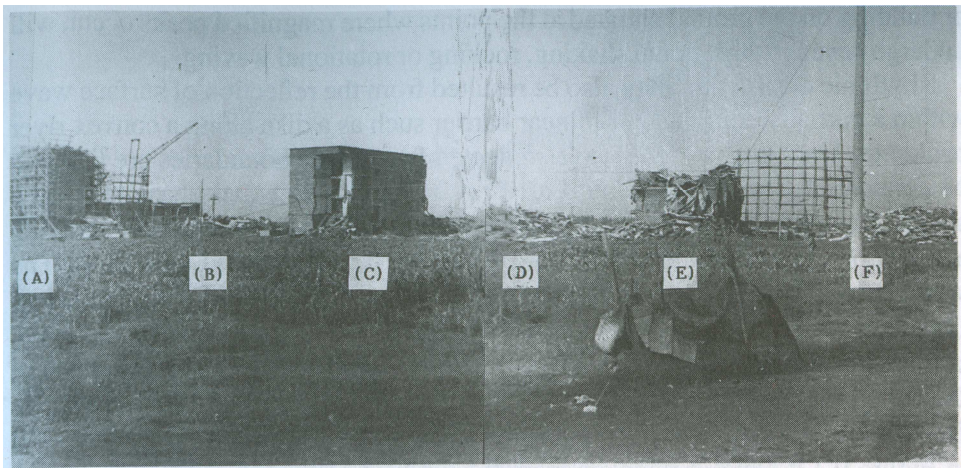


Figure 4: Taken from [12]: Six quite similar buildings responded quite differently from total collapse (B), (D), (F), or partial collapse (E), up to minor damage (A) and (C).

The above mentioned authors reported for the same earthquake, a similar to the above mentioned phenomenon in another location. In that case, six one – storied quite similar houses, located also along a straight line at equal distances suffered, as in the previous case, quite different damage. The first and fourth were safe, while all the rest totally collapsed.

In Fig. 5 are shown three buildings. At the left hand side the first building is located that suffered small damage. The second one suffered some heavier damage, while the third one totally collapsed. All three buildings were identical, constructed at the same time by the same constructor and with the same materials. According to a site inspection carried out by the first author, the soil conditions were all the same, for the three buildings, [13].

Quite interesting is, also, the case shown in Fig. 6, after the Dinar, Turkey, 1995 earthquake, [14]. The two out of five similar four storied apartment buildings totally collapsed, while the other three remained safe. The first author investigated the whole site and concluded that there was not any alternative difference in the underlying soil conditions. The total distance between the left hand side of the first and the right hand side of the fifth building is estimated to be about 120 m. Since all this takes place inside the epicentral region, the apparent surface wave length, is much smaller than the usual, as already mentioned. Therefore, it might be estimated that the apparent surface wave's length is of the order of 50 m. Also, it might be concluded that it was a one pulse damaging shock, that can only be explained with the convolution of the P waves.

In Fig. 7, another similar to the above mentioned rhythmic destruction phenomenon is presented after the Erzincan, Turkey, 1992 earthquake, in which, quite similar buildings within a small distance, with almost the same soil conditions along a street (Fig. 7a) presented a great variation of the observed damage: from almost no damage (Fig. 7b), up to total collapse (Fig. 7c), alternatively, [15].

Considering the above presented five representative cases of rhythmic destruction, it seems logical to support the hypothesis, from a pure engineering point of view, that if the foundations of each one of those building series were connected together rigidly and adequately

strongly, collapse would certainly have been avoided. This is because the destructions occurred not due to the increased seismic vulnerability of the specific buildings that were destroyed, but due to the increased destructiveness of the input motion at the specific plots, see also, Eq. (2). Even more, the distance between the various plots is relatively small.

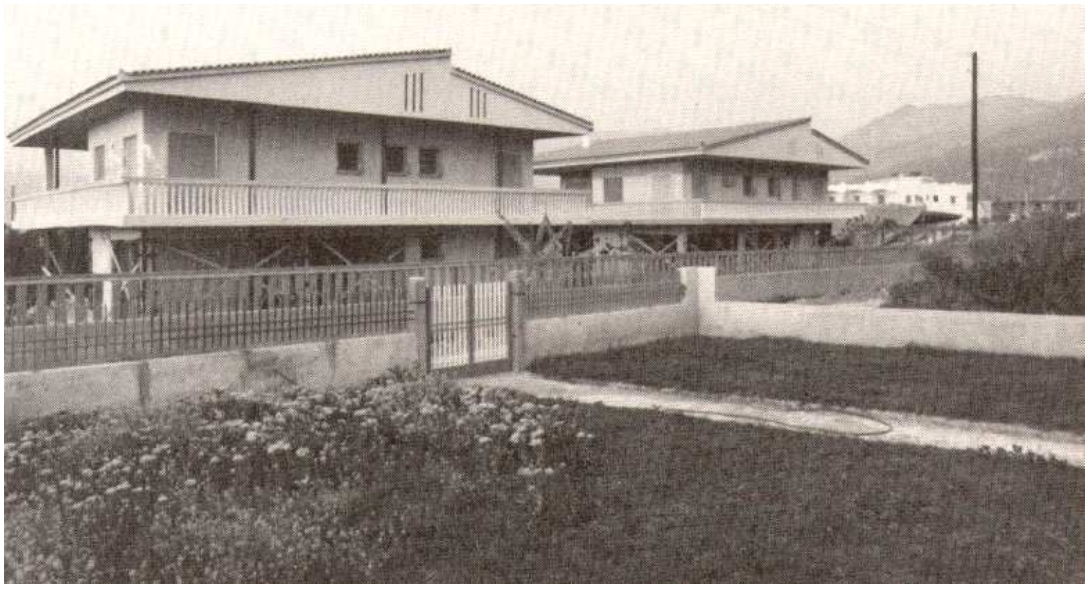


Figure 5: Rhythmic destruction. Three quite similar buildings in close distance to each other, on the same soil conditions, present a different response after the Corinthos, Central Greece earthquakes of 1981. The damage increases from the left hand side of the picture to the right hand side. The third building totally collapsed, [13].

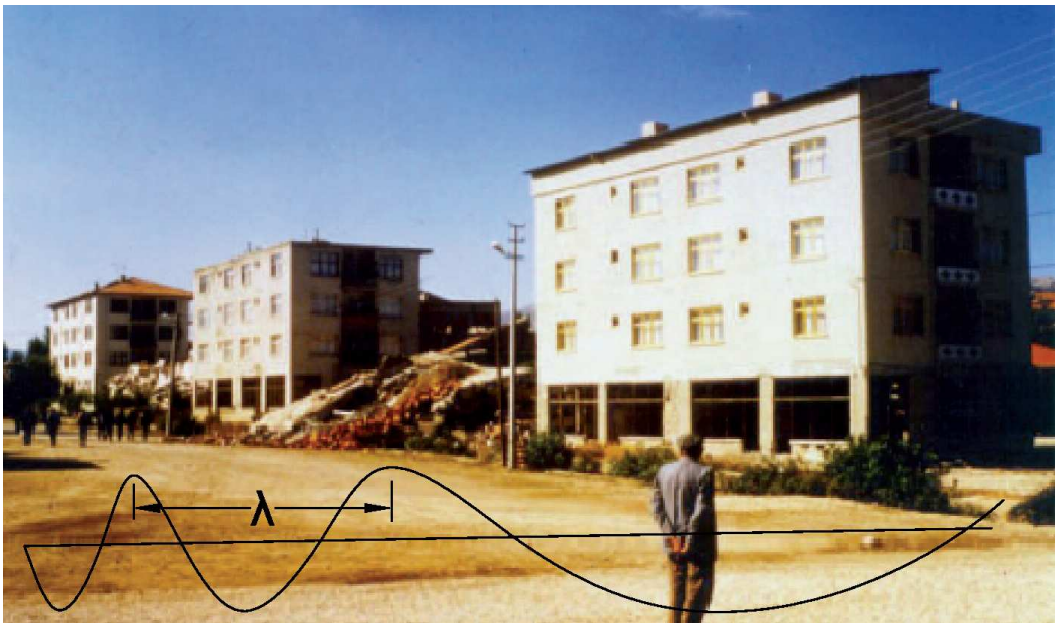


Figure 6: Rhythmic destruction. Two out of five quite similar structures founded on the same soil conditions and constructed by the same constructor totally collapsed after the Dinar, Turkey earthquake of 1995, [14].

The flexibility and strength of the foundation and, further, of the whole building on the vertical plane against the ground deformation due to surface seismic wave propagation, can be checked, during the design, with a simple calculation, as it is schematically shown in Fig. 8. If the stiffness of the foundation is not enough to withstand the subsidence (d) of the ground, the stiffness of the whole building along the vertical plane could be included. As a result, of these

calculations the additional member forces and deformations will probably lead to a new dimensioning of the structural members.

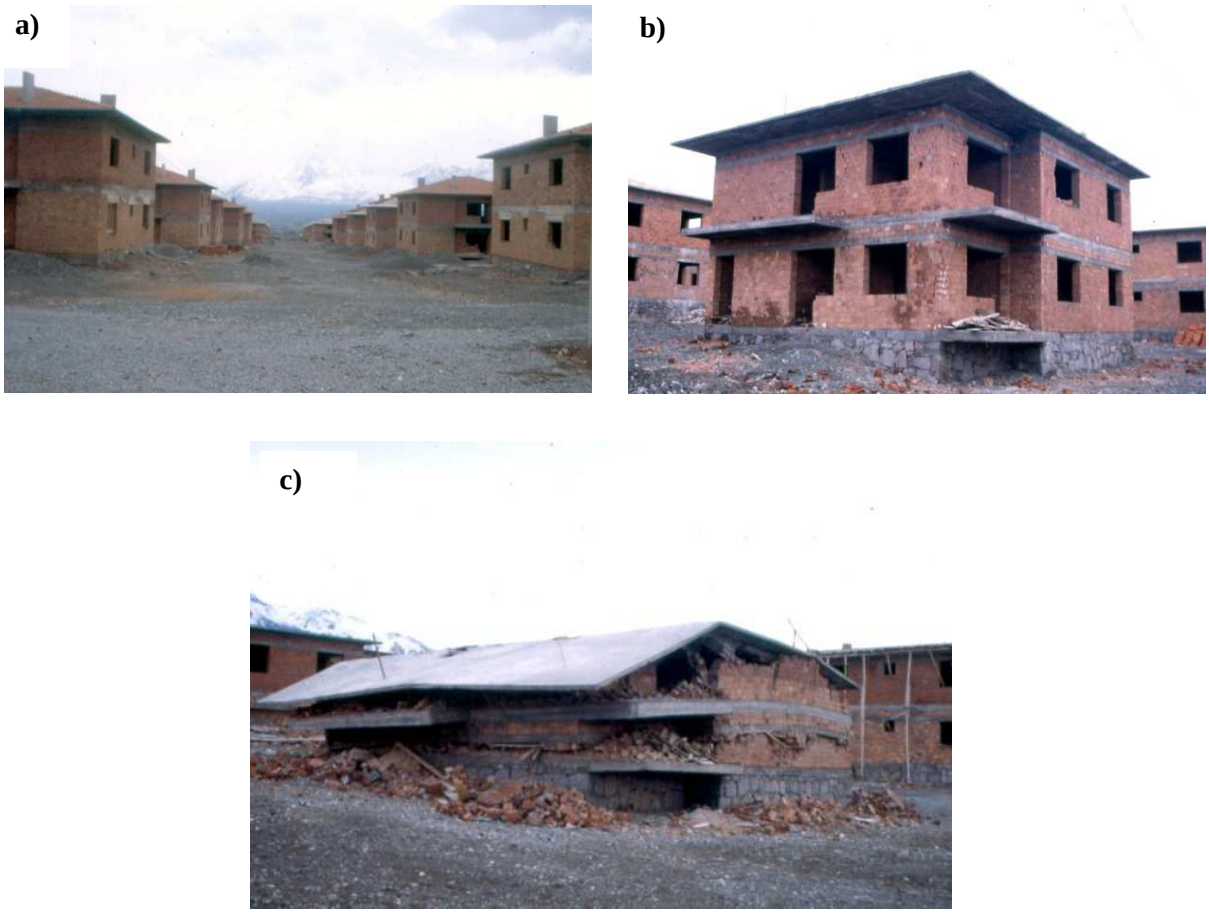


Figure 7: Rhythmic destruction. A series of similar buildings along one and the same street within a rather small distance one to the other (a), suffered damage of quite different intensity alternately. From almost no damage (b), up to total collapse (c). Erzincan, 1992 earthquake, by courtesy of A. Pomonis, [15].

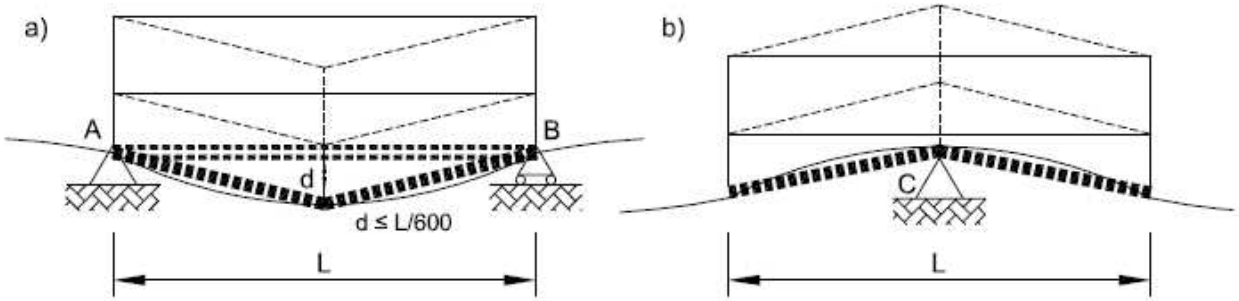


Figure 8: Simple deformational scenario on the vertical plane, may help the design against ground deformation due to the propagation of surface seismic waves. In order to avoid damage also to non bearing elements, the stiffness must be quite high, so that the flexure under its own weight is $d \leq 0.50\ell/300$; (a) a simply supported at A and B massive or Vierendeel beam; (b) a cantilever dual beam supported at C.

In Fig. 9 a partial collapse of an hotel after Egion, Greece, 1995 earthquake, [16] is shown. The building consists out of three parts statically separated by two separation joints of a negligible width. The damage of the remaining two blocks and the remaining part of the third block (Fig. 9b) is rather limited. The ground under the collapsed part did not present any per-

manent deformation (vertically or horizontally). The combination of the vertical components of the "surface waves" and of the body waves at the site of the collapse, with the flexible and weak foundation along the vertical plane could be an explanation of that type of partial collapse. The fact of the almost total lack of damage of the remaining parts supports this approach. During the same earthquake, many other similar partial collapse, while the rest of the building remained intact, were reported, [16]. The characteristics of the focal mechanism through the body P waves being propagated upwards might have a contribution to this result.

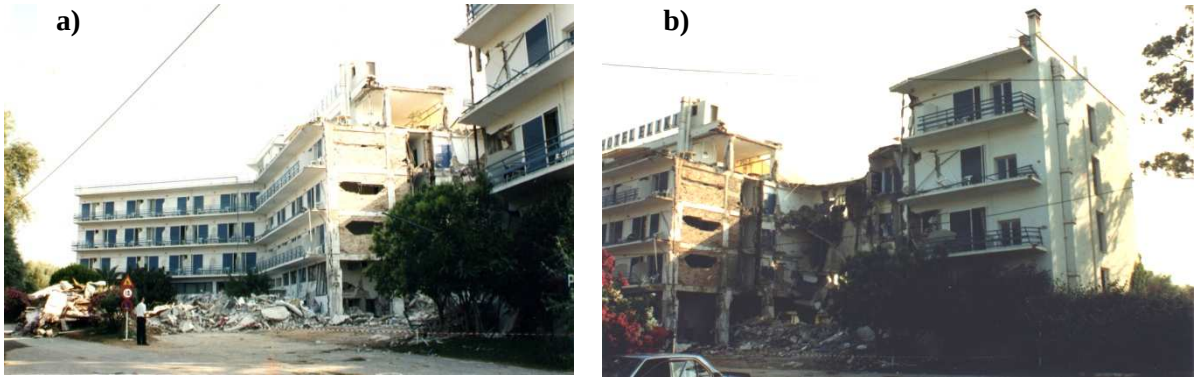


Figure 9: Typical example of partial collapse of buildings after the Egion 1995, M=6.7 earthquake. The rest of the building suffered limited damage, [16], [17].

An other collapse is shown in Fig. 10 after the Tokachi-Oki, 1968 earthquake. This phenomenon might be classified as a rhythmic destruction too, with the same conclusions as mentioned above: if the foundation structure were stiffer and stronger, the collapse would have been avoided.

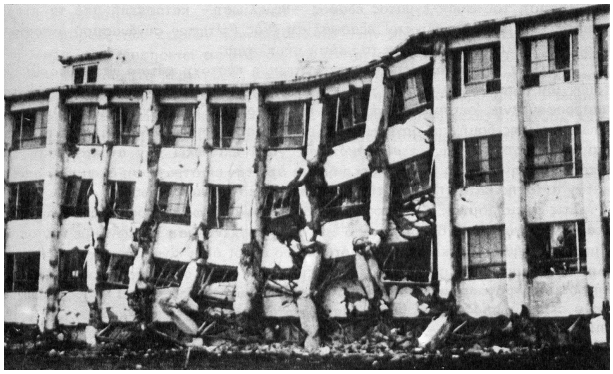


Figure 10: The elongated and without separation joints building suffered partial collapse after the Tokachi-Oki earthquake of 1968, [9].

As a partial practical conclusion of the present chapter is the fact that once the forces and deformations in the foundation body of large dimensions are successfully confronted, the seismic response of the whole structure, or of a group of structures that are bound together through a foundation body, will be less, compared to the case with a foundation of smaller dimensions. According to [18] existing structures separated by construction joints could increase their earthquake resistance just by elastically connecting the above the foundation parts of the structure.

4 SEISMIC ARRAYS AND COHERENCY. A BRIEF REVIEW

The subject under consideration is obviously based on the variation of the input motion along the foundation body. This variation is due to the amplitude, the phase difference and the shape of the seismic waves that travel along the foundation of a structure. A good measure of this variation is the coherency between two motions at points i and j. This coherency according to [19] is expressed in the frequency domain by:

$$\gamma_{ij}(\omega) = \frac{S_{ij}(\omega)}{\sqrt{S_{ii}(\omega) S_{jj}(\omega)}} \tag{3}$$

where:
S_{ij} is the cross spectral function and
S_{ii} or S_{jj} are the auto spectral functions.

The coherency is a normalized complex function, [19]. The coherence is identified as the square of the modulus of the coherency i.e. the quantity $|\gamma_{ij}(\omega)|^2$, which as a real number, may vary from zero (non coherency) up to one (complete coherency).

A great help to the subject under consideration was given by the analysis of the strong motion array records obtained from the various strong motion arrays as it is presented by [7], [19], [20], [21], [22], [23] and many other researchers. Besides this, the practical interest lays on the establishing of time histories of strong motion for the seismic analysis of structures with multiple supports, long structures e.tc..

The recorded motions by the SMART 1 array, [19], are dominated by "incoherent energy" at frequencies above 2 Hz when they are averaged over a large distance.

On the other hand as it is concluded by [21] the peak cross correlation values (P) of the accelerogramms, of the El Centro Differential Array may be approximated by the expression:

$$P = e^{-\frac{0.00035 \times L \times c}{\lambda}} = e^{-0.00035 \times L \times f} \tag{4}$$

where:
L is the distance in (m) between the two stations or the foundation length,
λ is the apparent wave length in (m),
c is the apparent velocity of the wave propagation in (m/sec) along the ground on an adequate depth below the foundation, and
$f=c/\lambda$ is the apparent frequency in (Hz) of the particle ground motion ($T_g=1/f=\lambda/c$).

Based on Eq. (4) it is concluded by [21], that the frequency (f) and the length of the foundation (L), as far as the reduction of the input seismic motions is concerned, are interchangeable quantities. This means that we can get the same values of cross correlation either by long lengths of foundations or by high predominant frequencies of the seismic ground motion.

Eq. (4) is graphically presented in Fig. 11 for a variety of values of parameters L and f.

A considerable contribution must be attributed to the research work by [24] to a better understanding of the earthquake response of rigid foundations to spatially varying ground motion excitations by analytical approach, producing closed mathematical forms including all basic parameters. In that research work the authors used a massless rigid foundation bonded to a viscoelastic half space, excited by a wave passage and they found reduction of the translational component of the motion of the beam at higher frequencies (>1Hz). Also, they found that torsional and rocking components of the motion were created. They noted that these effects highly depend on the degree of spatial incoherence of the free field motion along the foundation.

It is worth mentioning in this chapter that the in depth study of the effects on structures of the spatially variation of the seismic motion, has very much advanced with the help of adequate analytical evaluation of mainly digital recordings obtained from strong motion arrays on the surface of the ground and in bore holes as well. These well known devices are installed and functioning all around the globe since many years. Eminent research efforts are carried out in addition to the ones mentioned above, as for example: by [22] in which the "differential motion $\Delta_{jk}(t)$", also other physical parameters are introduced and studied as well; by [23] using the strong motion data recorded by dense arrays described the spatial variability of the ground motions and stochastic models were produced using the coherency quantity; by [25] in which the effects of the spatially variation of the seismic input motions on a two – span indeterminate beam are parametrically investigated.

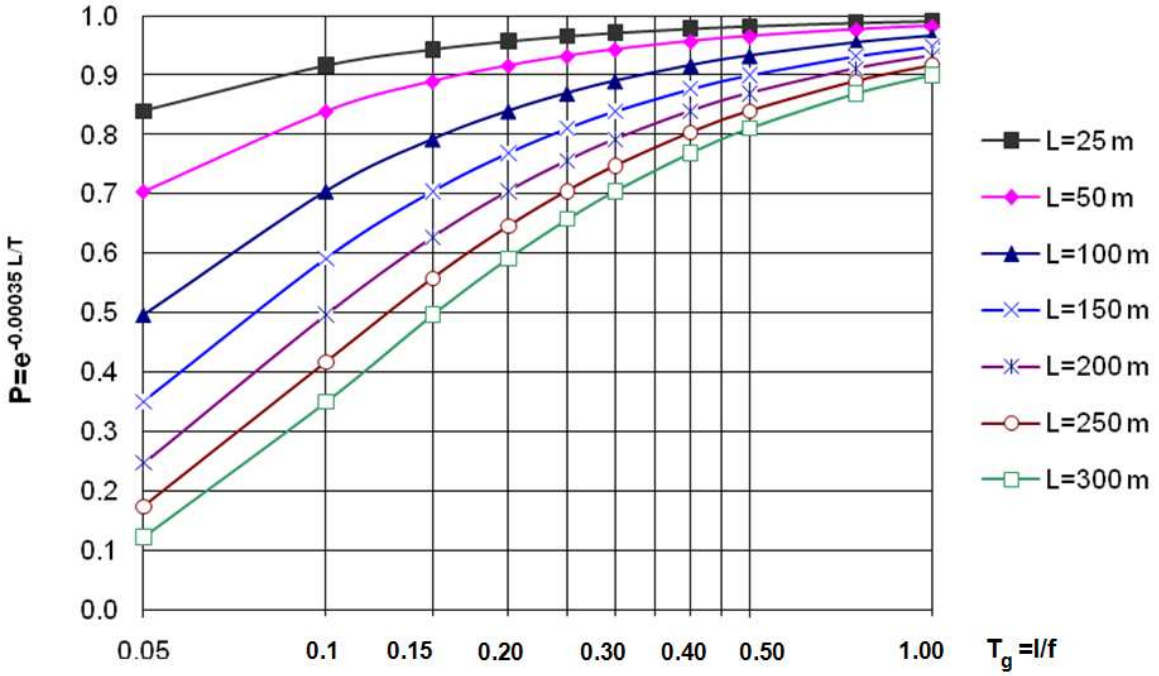


Figure 11: A graph of the function $P=e^{-0.00035\ L/Tg}$, using a variety of values of parameters L and f, (see Eq. 4).

On the other hand, it must be mentioned here, that all these observations might be much more pronounced in epicentral regions of shallow normal or reverse focal mechanisms. This could be attributed more to the fact of the low coherence of the emerging seismic motions, due to multiple reflections and refractions, rather than to the phase lag of the travelling “surface waves”.

In all the above mentioned references it is clearly stated that there is a phase lag among the incident seismic motions along a sizable building foundation as well as other phenomena that lead to reducing the seismic excitation of the structure. On the contrary, [26] the analysis of the earthquake records in 57 building foundations of various sizes, did not verify the decrease of the motion as a function of the size of the foundation body rather than its rigidity. An in depth discussion of the findings of this work should be very interesting, but it is beyond the scope of the present communication.

5 A PARAMETRIC EVALUATION OF THE RESPONSE OF A MASSLESS RIGID FOUNDATIONS BEAM

The parameters studied are a combination of the length of the beam, a variety of the traveling velocity of the acceleration time history and a variety of two types of time histories, [17].

With the advancement of computers and computer codes in Earthquake Engineering it became feasible to carry out quickly and reliably series of parametric analyses under various assumptions in order to examine complex phenomena as the one under consideration.

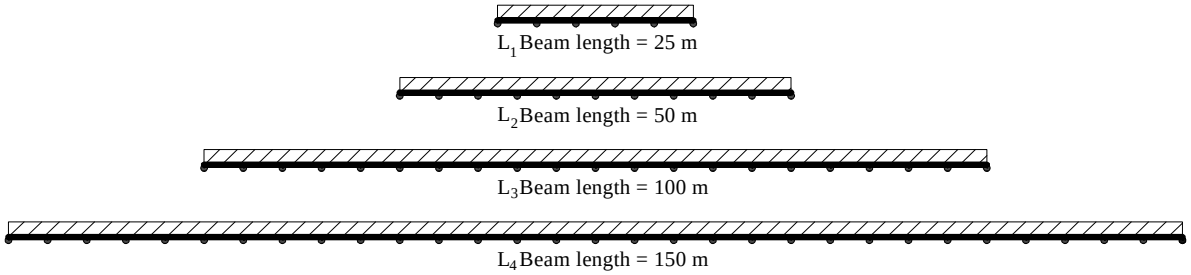


Figure 12: The various beams and points with spring supports – input motions used in the parametric analyses, [17].

As it is shown in Fig. 12 for the parametric study a massless beam out of reinforced concrete with various lengths of L_1=25 m, L_2=50 m, L_3=100 m and L_4=150 m as it is shown in Fig. 14, has been used. The rigidity of the beams is a function of their cross section 0.50 m width x 2.00 m height. The beams rest on elastic springs with a stiffness of:

$$K_h = 4.0\ MN/m \text{ and } K_v = 5.0\ MN/m \tag{5}$$

where

K_h is the horizontal stiffness of the springs

K_v is the vertical stiffness of the springs

their modulus of elasticity is E = 2.90×10^7 kPa and the poison ratio ν = 0.20.

The transient dynamic analysis of the computer code ABACUS has been used throughout the present study, as well as other programs of every day use for minor calculations (response spectra, reinforcement).

The input motion is defined as follows. The time history of an accelerogramm has been selected. The whole accelerogramm is propagated with a certain velocity along the beam and the excitation is applied through the above mentioned supports. The velocity of the propagation of the accelerogramm is selected for the various parametric calculations as follows:

$$c_1 = 100\ m/sec, c_2 = 200\ m/sec, c_3 = 400\ m/sec \text{ and } c_4 = 600\ m/sec \tag{6}$$

For example, for the case of the beam L_3=100m and the velocity c_3=400m/sec its last support starts to be excited at a time lag equal to Δt=0.25 sec after the excitation of the first support of the beam. The coherency of the two input motions in the case under consideration depends also on the predominant period of the motion, as already mentioned. And according to Fig. 11, the higher is the predominant period the higher is the coherency.

For the needs of the present investigation, the following two input time histories have been selected: The first one is an artificial accelerogramm, the response spectrum of which fits to EC-8 Type 1, ground class A, corresponding to a design acceleration value of a_g=0.24g, of a total duration of 2.4 sec, as it is shown in Fig. 13. The second one is the Edessa N – S component due to Griva northern Greece, 21 Dec. 1990, M=5.9 earthquake with max ä=0.10g, re-

corded by the Greek National Institute of Engineering Seismology and Earthquake Engineering, ITSAK. The epicentral distance is 31 km and the depth of the hypocenter is H< 15km. The record is on rather soft soil conditions.

Therefore it is logical to measure predominant periods between 0.5 sec and 0.7 sec. The component used, is shown in Fig. 14.

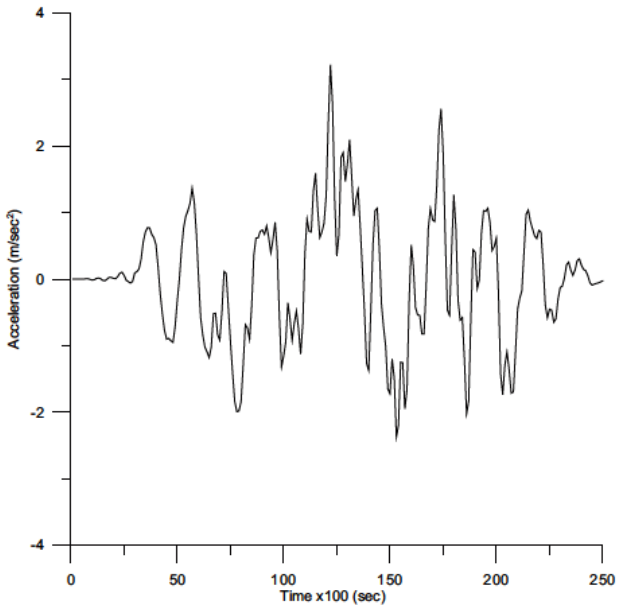


Figure 13: Artificial accelogramm fitting to EC-8 Type 1 response spectrum, ground class A, design acceleration 0.24g.

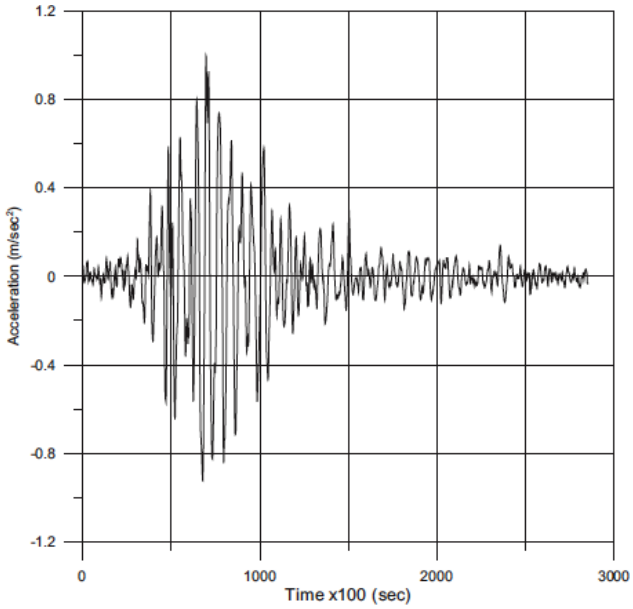


Figure 14: The N – S component of the Edessa, 21 Dec. 1990, M=5.9, northen Greece, Griva earthquake recorded by ITSAK.

In total 34 responses spectra have been calculated (4 seismic wave velocities x 4 beam lengths x 2 types of ground motions = 32 cases + 2 for the free field motions). The obtained horizontal motion at the center of gravity of each beam was used in order to calculate its response spectra for 5% damping ratio. Here, for the sake of brevity, the most representative

response spectra are presented. It was proved, as already shown in [6], that the determining parameter among the various response spectra is the ratio τ=L/c sec. Therefore, in Fig. 15 these response spectra, for τ_1=0 sec (is the corresponding to the free field motion), τ_2=25/200=0.125 sec, τ_3=25/100=0.25 sec, τ_4=100/100=1.0 sec and τ_5=150/100=1.5 sec, are depicted for the artificial ground motion.

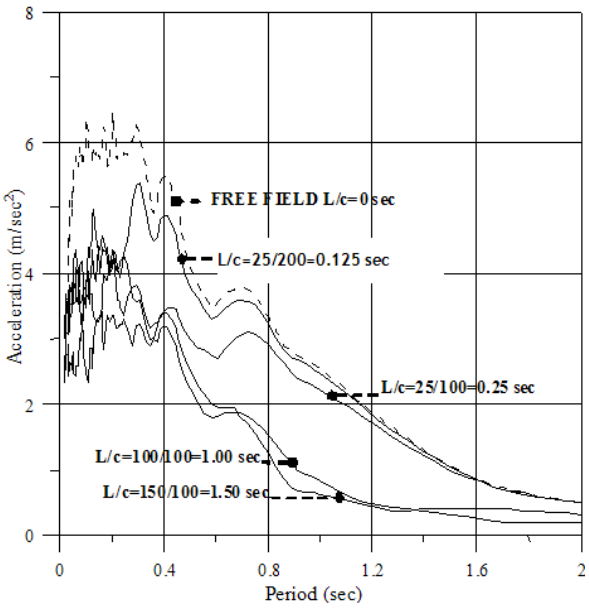


Figure 15: Response spectra at the center of gravity of the beams for the artificial ground motion fitting to EC-8 Type 1, for various τ(sec)=L/c=beam length/wave propagation velocity, and 5% damping ratio.

In Fig. 16 the response spectra, for τ_1=0 sec, τ_2=25/100=0.25 sec, τ_3=150/400=0.375 sec, τ_4=100/100=1.0 sec and τ_5=150/100=1.5 sec, are depicted for the Edessa ground motion.

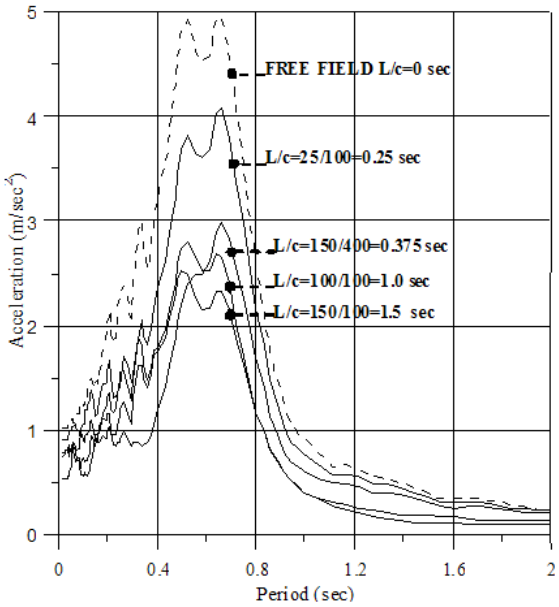


Figure 16: Response spectra at the center of gravity of the beams for the Edessa earthquake, for various τ(sec)=L/c=beam length/wave propagation velocity, and 5% damping ratio.

Although the earthquake excitation records are quite different in shape, duration, and frequency content from the engineering point of view and the resulted response spectra are quite different in shape and magnitude, their resulted reduction is in both cases obvious.

For the discrete set of natural periods of the one DOF oscillator: 0.1, 0.2, 0.4, 0.6, 0.8, 1.0, 1.2, 1.4 and 1.6sec, the ratios of the various response spectra shown in Figs 15 and 16 over the respective values for the free field ground motion are depicted in Fig. 17, always for 5% damping ratio.

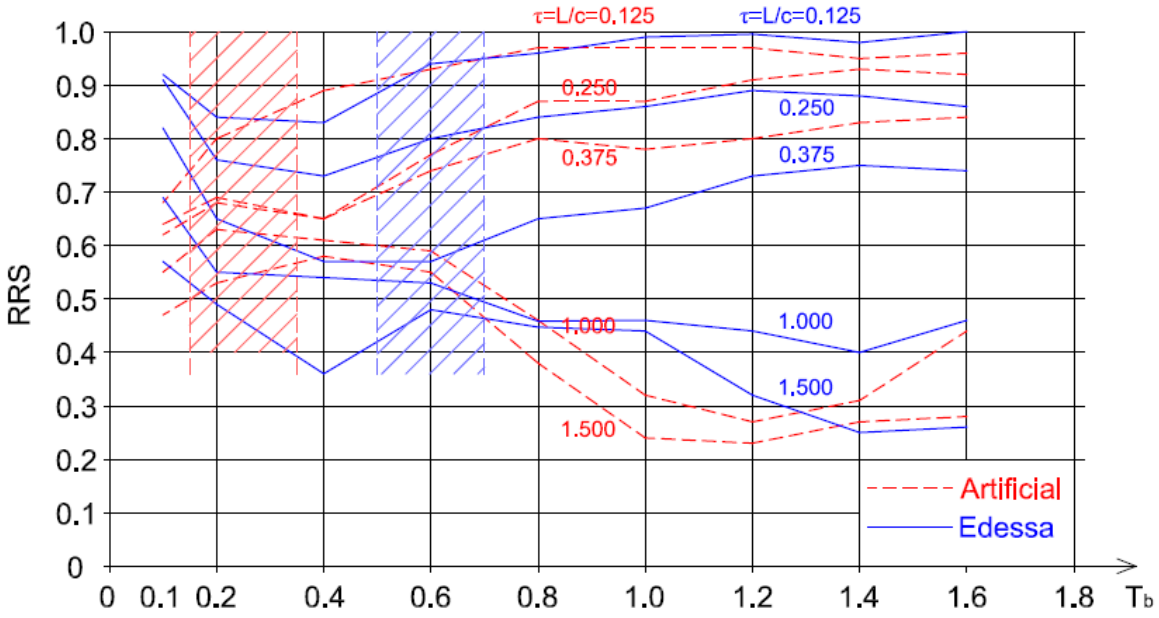


Figure 17: Ratios of Response Spectra (R.R.S.) obtained at the center of mass of the beams over the respective free field ones, all for 5% ratio. The hatched areas indicate zones where the maximum values of the spectra occur.

A lot of results and comments may be drawn based on the findings of Fig. 17. For example the spectral values reduction is extremely high for values of $\tau=L/c \geq 1.0$ sec, for both types of earthquakes, as it is expected.

In Table 1 the ratios of the maximum values of the various response spectra obtained at the beam's center of gravity over the maximum values of the free field motion are shown.

τ =L / c (sec)	0.000	0.125	0.250	0.375	1.000	1.500
Artificial	1.000	0.840	0.760	0.680	0.630	0.580
Edessa	1.000	0.940	0.840	0.600	0.570	0.510

Table 1: Ratios of Response Spectra (RRS) of the obtained at the center of gravity of the beams maximum response to the free field ones.

It must be mentioned that the max S_a values shown in Table 1, do not occur at the same periods of the one DOF oscillator. This means that the interference of the stiff foundation grillage does not only result to the reduction of the amplitude of the free-field motion but also to the modification of its frequency content. The latter is more pronounced in the case of the artificial ground motion which is characterized with a higher frequency content that the Edessa one.

The calculated stresses are quite high at the beams of Fig. 12 The longer the beam the higher the stresses, but to a certain limit. For example, the stresses for L_4=150 m are almost

the same with those yielding for L_3=100 m. The latter ones are a little bit higher than those for L_2=50 m. More specifically, for the L_3=100 m beam length, the maximum calculated stresses are the following: Homogeneous axial stress, about 1.0 MPa (tensional or compressional). Axial stress due to the bending only (without the axial stress) 1.5 MPa and shear stress about 0.6 MPa. These stresses calculated after intergration, over the respective cross section area of the beam (part or whole) give the corresponding forces which finally lead to the appropriate dimensioning and reinforcement of the beams. For example, the main reinforcement that will be put equally distributed all around the cross section of the beam 50/200 is 36Ø22 of which 6Ø22 at the top and 6Ø22 at the bottom side of the beam. Stirrups 2xØ12/15. The geometrical percentage of the main reinforcement is about 14‰.

6 CASE STUDIES OF SOME MONUMENTAL STRUCTURES

It is obvious that the presented methodology may be applied to existing structures by creating long, rigid and strong beams in close contact with the existing foundation. These beams may function as a two – dimensional close orthogonal grillage in order not only to reduce the input seismic motions but also to comply with the plan dimensions of the building. Besides that, the mentioned beam grillage of large dimensions increases, also, the necessary resistance against torsional phenomena that may be created by the non uniform motion of the ground and by the torsional response of the structure itself during strong earthquakes. Also, the sail grillage, in conjunction with the above standing structure, will withstand the ground deformations of the traveling "surface waves" if adequately designed. The so designed and constructed new foundation body will possess a minor kinetic state compared to the underlying ground. It must also be taken under consideration that the new foundation body possesses a higher mass density than the underlying ground. According to well known principles of physics, the travelling seismic waves from a less dense (ground) will be easier reflected on the denser grillage out of R/C beams. Therefore, a transition – interface zone is naturally formed between the moving ground and the less moving and/or out of phase moving foundation grillage. The height (h) of this transition zone is determined in combination with its quality. A useful parameter is the developed shear deformation $\gamma=\Delta d/h$, that must not create excessive permanent – plastic differential deformations (**Δd)**. The latter one is the maximum difference between the two maximum displacements: do (the original of the ground) and d (the resulting in the center of gravity of the grillage). The thickness of this transition – interface zone, might be of the order of 30 to 60 cm. This is in agreement with the proposed method presented in [27]. This transition – interface zone is a path along which an amount of input seismic energy is going to be absorbed. For this reason, it is indicatively shown the respective sketches of the case studies a gradual improvement of the underlying ground from the base of the zone to the base of the grillage, in the case of soft ground. If the ground is harder, the transition – interface zone might be of smaller thickness and could be constructed out of well compacted, by vibration, angular rubbles of almost equale dimensions (about 5 to 7 cm), as it is also shown in some sketches of case studies.

Some basic parameters for the design, besides the above mentioned, are the seismicity and the characteristics of the anticipated earthquake ground motions, the soil conditions, the relief of the ground surface, the characteristics of the structure to be protected, its dimensions e.tc. It is of basic importance to know, if a basement is needed, what is the available area of the plot of the structure and its geometry. It is self – evident that all the life–line connections of the building with the public utility networks must be constructed resiliently in order to continue functioning even after strong earthquakes during which, considerable deformations between the building and the surrounding may occur.

As it is shown in the sketches of the various study cases that are following, there are three types of the new foundation elements that are provided in each intervention. To the first type belong the main load bearing beams that are forming the grillage. To the second type belong the secondary beams that are provided in order both beams to confine the masonry members of the structure. The two types of beams are connected together, usually with cross beams 40/40 cm at horizontal distances of about 1.50 m one to the other, [28]. The confinement of the masonry elements with these beams is indispensable in order to ensure a uniform response of the whole structure given that under the foundation body of the existing structure there is not any transition – interface zone. On the other hand we want to increase, us much as possible, the areas of those zones. An acceptable lower threshold of the total area of the transition – interface zones is to be at least 2.5 times that of the total cross sections of the load bearing masonry walls of the structures. As far as the calculation of the total area of the transition - interface zone is concerned it will be taken under account only those zones that are in close vicinity to the walls as mentioned above. For this reason, the third type of elements constituting the grillage is provided, which consists of a rather thick (25 cm) R/C slab. Those slabs are functioning as retaining – continuous interconnecting structural elements between beams at their bottom. Clarifications are provided in the details of the sketches. If a non structural element is founded on the ground needs to be fixed to the load bearing walls by an adequate horizontal diaphragm.

In this way we are absolutely sure that all bearing and non bearing parts of the existing structure will follow the response of the grillage in case of an earthquake.

For a preliminary design of the case studies presented below two methodologies are followed. The one is based on the procedure already exposed in the present communication and the other follows the FEMA 440, chapter 8 methodology [10]. In general, we prefer to have a rectangular shape of the foot print of the grillage. Nevertheless, if the dimensions of the grillage are large enough, i.e. several times the length of the anticipated seismic waves, as this was realized at Ano Liossia city for the reconstruction of 1,500 houses after the destructive earthquake of 1999 and as it is presented in [29], the said requirement for a rectangular shape of the foot print of the new foundation, is not necessary.

6.1 Case study No 1

In Euboea, Greece, the Prophet Elias church was “strengthened” by applying the already exposed methodology. The plan of the church with the proposed new bean’s grillage with dimensions 75m x 70m is shown in Fig. 18a, while a construction detail is shown in Fig. 18b.

The mean plan dimension of the realized grillage is $L = \sqrt{L_x \times L_y} = 72.50\text{m}$.

The ground quality is medium, of a predominant natural period $T_g = (T_{1g} + T_{2g})/2 = (0.15 + 0.60)/2 = 0.375\,\text{sec}$ (according to EAK-2000 code), and the shear wave velocity is c=300 msc^{-1}. The quantity $\tau = L/c = 72.5/300 = 0.24\,\text{sec}$.

These ground conditions are more consistent to the artificial earthquake fitting to EC-8 Type 1, ground class A. Using Table 1 and after interpolation, one may find RRS=0.77 for the maximum spectral values. The natural period of the building fixed on rigid base is T_b=0.25 sec. By using the respective curves shown in Fig. 17, and after double interpolation for τ=0.24 sec and T_b=0.25 sec one may find RRS_b=0.69.

The thickness of the transition – interface zone can be calculated with the use of adequate computer codes. But for a preliminary design one could estimate it as follows: The achieved reduction of the motion between free field and R/C grillage is of the order of 30%. In engineering terms of the design input acceleration, this means 0.30x0.24g=71.0 $cmsec^{-2}$.

With a mean predominant period T_g=0.375 sec, the differential displacement is $\Delta d=71.0/(2\pi/0.375)^2=0.25$ cm. The normalized shear deformation that can be developed within the transition zone without creating accumulative shear deformations for the specific material quality and compaction, is $\gamma=5.10^{-3}$, [30]. Therefore, $h=\Delta d/\gamma=50$ cm.

On the other hand, following FEMA 440, chapter 8 procedure for the present case study, we find for the foot print of the foundation dimensions 70x75 m^2=230x249 ft^2.

Effective foundation size $L = \sqrt{230 \times 249} = 239\text{ft}$.

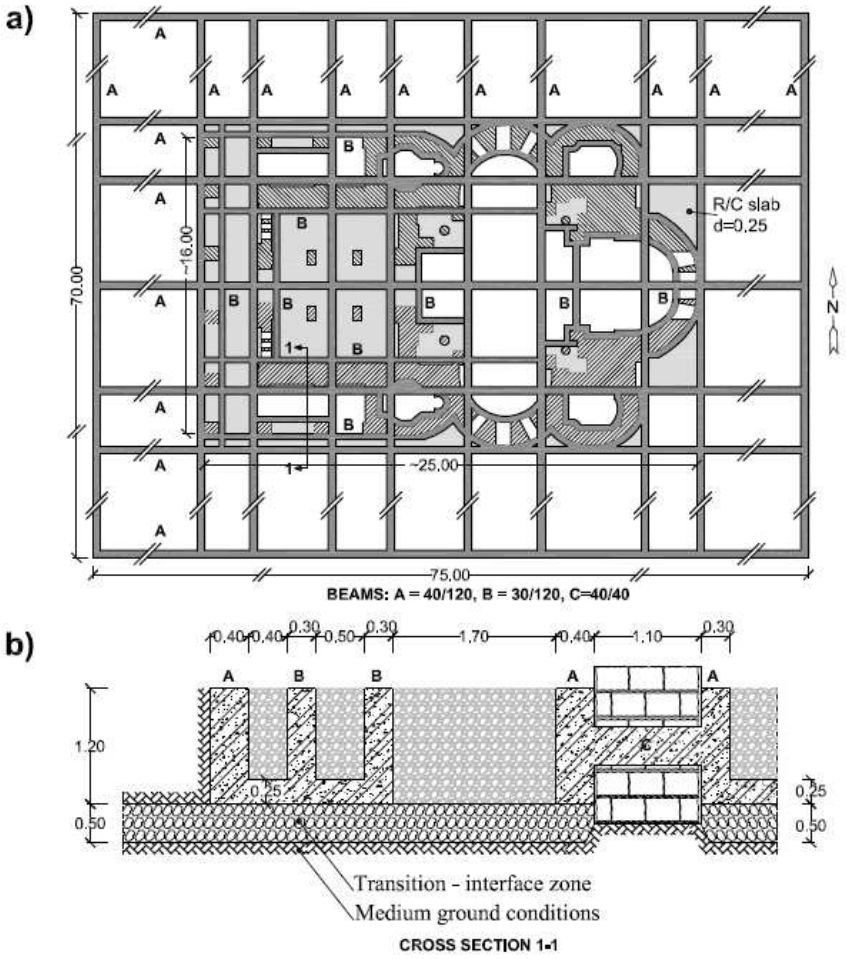


Figure 18: The Prophet Elias, a church at Euboea "strengthened" by applying the methodology exposed in the present communication, (a) general plan; (b) detail at cross section 1-1.

The Ratio of the Response Spectrum (RRS) due to base-slab averaging, according to FEMA 440, chapter 8, formula (8-1), for T_b=0.25 sec:

$$RRS_{bsa}=1-(L/T_b/14{,}100)^{1.2}=1-[(239/0.25/14{,}100)^{1.2}=1-0.27=0.73 \quad (7)$$

An other parameter being considered by FEMA 440, closely related to the subject under consideration is the effect of the foundation embedment, treated under the relationship:

$$RRS_e = cos[\frac{2\pi e}{T_b nc}] \quad (8)$$

where:

e is foundation embedment (ft)

c is the shear wave velocity at a depth L under the foundation (ftsec^{-1})
n is the shear wave velocity reduction factor for the design ground acceleration, according to FEMA 440, Table 8-1.

The total foundation's grillage thickness from its base up to the surface of the ground is about e=9 ft. The shear wave velocity reduction factor for the expected PGA=0.24g (according to the 2000 Greek code for design and construction of earthquake resistant structures - medium seismic zone) is n=0.68.

Therefore applying Eq. (8), and for e=9 ft, T_b=0.25 sec, n=0.68 and c=300 msec^{-1}=984 ftsec^{-1}, one may find $RRS_e = \cos[\frac{2\times\pi\times 9}{0.25\times 0.68\times 984}] = \cos(0.34) = 0.94$.

The total RRS value is:

$$RRS = RRS_{bsa} \text{ x } RRS_e = 0.73 \text{ x } 0.94 = 0.69 \quad (9)$$

Comparing the obtained two values: a) Using the present methodology: RRS_b=0.69, and b) Using the FEMA 440: RRS=0.69, one may conclude that the coincidence of the resupts between the two approaches is quite incidental taken under consideration the abundance of parameters involved in a so complicated phenomenon; we could just accept a good agreement between the results of the two approaches. Nevertheless, the achieved reduction of the earthquake design motion is of the order of 30%.

6.2 Case study No2

Near the city of Alexandroupolis the church of St. Panteleimon was "strengthened", by applying the already exposed methodology. The problem in the case under consideration is that the available area of the plot of the church is rather limited along N-S direction. The finally applied dimensions of the grillage are 65.0 m x 45.0 m, as shown in Fig. 19a. In Fig. 19b a detail of cross section 1-1 is shown. The ground is soft with a predominant period T_g=(0.20+1.20)/2=0.70 sec, (according to EAK 200 code). The shear wave velocity is c=150 msec^{-1}. The mean length of the foot print of the grillage is $L = \sqrt{65\times 45} = 54.0\text{m}$. The quantity τ=L/c=54/150=0.36 sec.

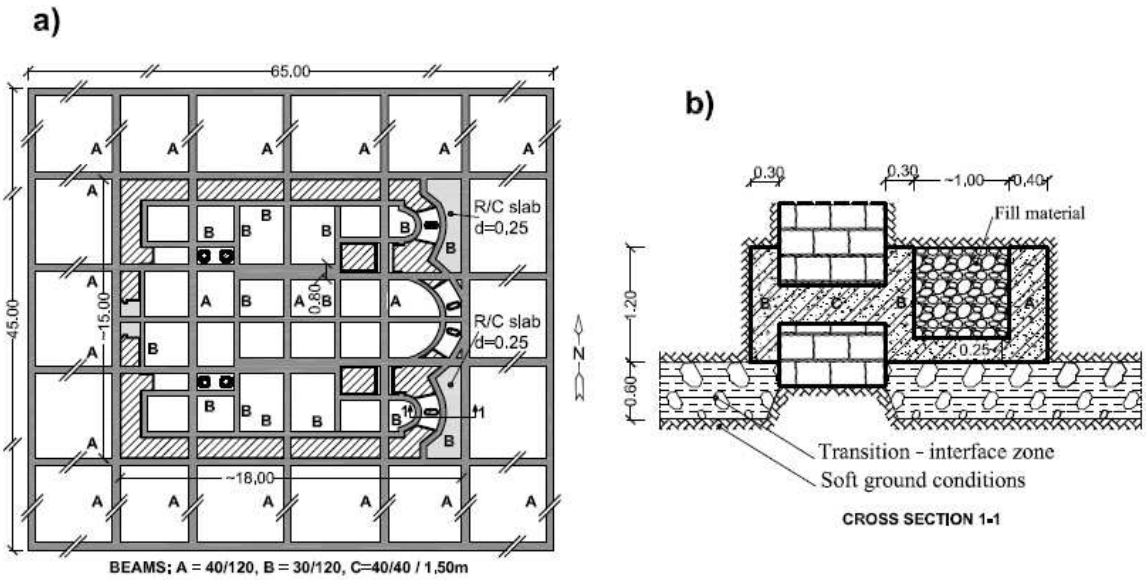


Figure 19: The St. Panteleimon church close to Alexandroupolis, "strengthened", by applying the methodology exposed in the present communication; (a) general plan; (b) detail at cross section 1-1.

The anticipated type of motion is more consistent with the Edessa earthquake time history. The natural period of the fixed on the base structure is T_b=0.23 sec. By using the respective data in Fig. 17 we may obtain RRS_b=0.62.

On the other hand, using the FEMA 440 procedure we may find, with an embedment e=7 ft $RRS=RRS_{bsa}xRRS_e=0.79x0.84=0.66$.

The achieved reduction of the input motion is of the order of 35% as a mean value.

6.3 Case study No3

The plan of the private monumental building in Epirus is shown in Fig. 20, with the beam grillage as designed, based on the present communication. The dimensions of the R/C grillage is 45.0 m x 45.0 m.

The ground conditions are soft to medium, $T_g=(0.2+0.8)/2=0.5$ sec (according to EAK 2000 code). The shear wave velocity is c=200 $msec^{-1}$. The parameter $\tau=L/c=45/200=0.225$ sec. The anticipated type of motion must be something between the Edessa and the artificial ground motions. The fundamental period of the building fixed on its base is T_b=0.30 sec. The building possesses a cellar. The whole embedment height is e=12 ft.

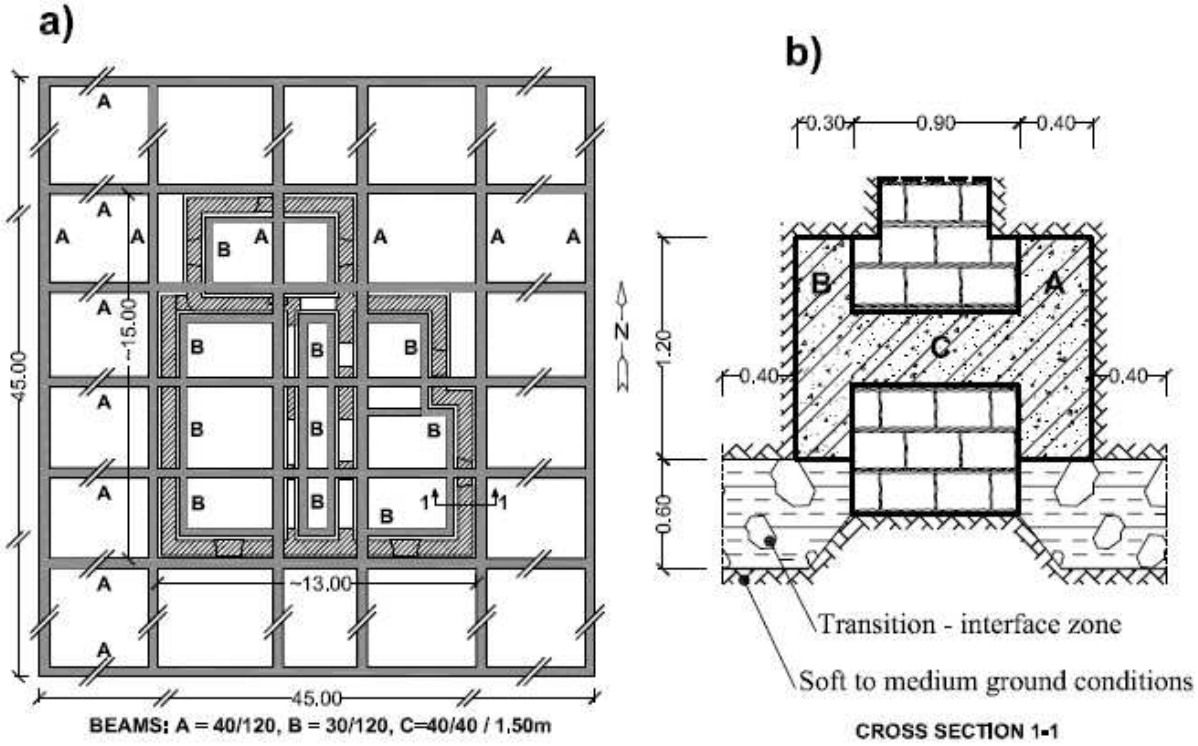


Figure 20: A monumental private building in Epirus, "strengthened" by applying the methodology exposed in the present communication; (a) general plan; (b) detail at cross section 1-1.

The RRS for the Edessa earthquake is RRS_{bED}=0.76.

The RRS for the artificial earthquake is RRS_{bART}=0.71.

Then by an engineering judgment, considering the mean value we obtain: RRS_b=0.74.

By using the FEMA 440 procedure, we may find:

$RRS=RRS_{bsa}xRRS_e=0.88x0.85=0.75$. The reduction of the anticipated input seismic motion is of the order of 25%.

Other study cases related to monumental and new structures are presented in [17].

7 CONCLUSIONS

- A sustainable seismic input reduction system is presented, in which there are not employed any kind of seismic isolation or seismic input energy absorbing devices. The methodology is based on simple principles of engineering mechanics that can be adjusted to any site condition.
- The system may be applied to monumental structures, such as churches, houses and existing buildings in general, in which an intervention to the superstructure might be difficult or even impossible, due to Venice Charter or other international or national relevant treaties. On the other hand interventions in the foundation body could be carried out in a more effective and conventional way.
- The resulted seismic input motion reductions after the application of the system to several case studies were checked following the FEMA 440, chapter 8 procedure. The obtained differences between the two approaches were either null or negligible.
- The reduction of the input motion following the presented methodology may reach 50% of the free filed motion. Therefore, this finding could be used by various means, one of which is as the following example: if the existing earthquake resistance of a monument is keeping behind the nominal by 50%, it might be possible to make it earthquake safe by a structural seismic resistance upgrading of 10% only, and by applying the present methodology that will result to a 40% reduction of the seismic input motion. It is self understood that the required dimensions for the foundation grillage will be available in the plot of the structure.
- The proposed system should be also applied to structures that may possess the adequate earthquake resistance, but they must be secured against future much stronger earthquakes.
- The main parts of the system are: a) an orthogonal grillage of R/C beams that must be longer than the half of the anticipated seismic wave length. These beams are stiff and strong enough in order to withstand the resulting member strains and stresses. The beams must be in structural contact with the existing foundation of the structure; b) a transition – interface zone. In this zone the differential motion between the grillage and the ground must be compensated without creation of permanent and uncontrollable deformations. Using simple engineering mechanics the thickness and the quality of this zone may be defined. As a general guideline a thickness of the order of 30 to 60 cm might be enough for an appropriate material of the zone and adequate dynamic compaction of it.
- In the most of the cases various problems in the foundation body of monumental structures are quite often reported. In those cases the proposed system might be proved extremely effective for curing the said problems of the existing foundation.
- The longer are the dimensions of the grillage, the higher the developed strains and stresses are in the beams. For the examined four beam lengths ℓ_1=25.0 m, ℓ_2=50.0 m, ℓ_3=100.0 m and ℓ_4=150,0 m the largest member strains and stresses were developed in the ℓ_3=100.0 m. This loading level was a little bit higher than that developed in the ℓ_2=50.0 m beam.

REFERENCES

[1] G.W. Housner, Interaction of building and ground during an earthquake, *Bull. Seismol. Soc. Am.*, **47**, 179-186, 1957.

[2] Ministry of Construction of U.S.S.R., Earthquake Resistant Regulations, A World List, *IAEE, 225 – 306* [in Russian], 1957, 1963.

[3] Ministry of Construction of Russia, Earthquake Resistant Regulations, A World List, *IAEE, 43-1 ÷ 43-27* [in Russian], 1995, 2004.

[4] S.V. Polyakov, Earthquake resistant construction, *Translated from Russian, Izdatel' stvo 'VYSSHAIA SHKOLA', 1969*, pp 282, Moscow, 1973.

[5] Y.S. Medvedeva, The Relation of the Seismic Rigidities of a Building and the Ground, *Nos 3,4 Publishing House of the Academy of Sciences of the Tadjik Soviet Socialist Republic*, 1966.

[6] S.V. Polyakov, Design of earthquake resistant structures, *Mir. Publ., Moscow*, 1985.

[7] M. Petronijevic, M. Nefovska, S. Brcic, Multiple – support seismic analysis of bridges including soil – structure interaction, *12th European Conf. Earthquake Engng, Elsevier Science Ltd., London*, paper ref. 180, 2002.

[8] I. Psycharis, D. Papastamatiou, I. Taflambas, P.G. Carydis, The Athens, Greece Earthquake of September 7, 1999, *EERI Special Earthquake Report, November*, pp 8, 1999.

[9] K. Anastassiadis, Earthquake resistant structures, *Ziti publishers*, **1**, pp 400, Thessaloniki [in Greek], 1989.

[10] FEMA 440, Improvement of Nonlinear Static Seismic Analysis Procedures, *Chapter 8, and Appendix E*, 2005.

[11] K. Goda, H.P. Hong, Spatial Correlation of Peak Ground Motions and Response, *Bull. Seismol. Soc. Am.*, **98**, 354-365, 2008.

[12] J.G.Z.O. Wang, K.T. Law, Sitting in Earthquake zones, *A. A. Balkema publishers*, pp 120, 1991.

[13] P.G. Carydis, N.R. Tilford, G.E. Brandow, J.O. Jirsa, The central Greece earthquakes of February-March 1981, A Reconnaissance and Engineering Report, *National Academy Press, Washington DC*, pp 162, 1982.

[14] P.G. Carydis, E. Lekkas, U. Ersoy, S.M. Uzumeri, G. Ozcebe, U. Polat, T. Tankut, M. Erdik, The Dinar, Turkey, Earthquake of October 1, 1995, *EERI special earthquake report*, November, pp 8, 1995.

[15] M.S. Williams (editor), A. Pomonis, E.D. Booth, G. Vaciago, S. Ring, The Erzincan, Turkey earthquake of 13 March 1992, *A field Report by EEFIT*, pp 105, 1993.

[16] P.G. Carydis, K. Holevas, E. Lekkas, T. Papadopoulos, The Egion, Greece, Earthquake of June 15, *EERI special earthquake report, July*, pp 4., 1995.

[17] P.C. Carydis, A Sustainable seismic input reduction system for monuments, for existing and new structures by creating large, stiff and strong foundations – practical applications, *Engegneria Sismica, XXVIII*, **2**, 7-24, 2011.

[18] P.G. Carydis, B.S. Giannopoulos, G.A. Karydis, E.E. Athanasiou, Increase of the seismic resistance of adjacent buildings through resilient connections among themselves, *14th Hellenic Concrete Conf., October 15-17*, p.8, [in Greek], 2003.

[19] B.A. Bolt, Development of the phased strong motion time- histories for the structures with multiple supports, *6th Canadian Conf. Earthquake Engng.*, Toronto, 1991.

[20] N. A. Abrahamson, B. A. Bolt, The spatial variation of the phasing of seismic strong ground motion, *Bull. Seismol. Soc. Am.*, **75**, *1247-1264*, 1985.

[21] M. Niazi, Inferred displacements, velocities and rotations of a long rigid foundation located at El Centro differential array site during the 1979 Imperial Valley California earthquake, *Earthquake Engng Struct. Dyn.*, **14**, pp 531-542, 1986.

[22] A. Zerva, Spatial variability of seismic motions recorded over extended ground surface areas, *in Wave Motion in Earthquake Engng, editors Kausel E., and Manolis, G., WIT press*, 97-139, 2000.

[23] A. Zerva, V. Zervas, Spatial variation of seismic ground motions: An overview, *Appl. Mech. Rev., ASME,* **55**, *No 3*, 271-297, 2002.

[24] J.E. Luco, H.L. Wong, Response of a rigid foundation to a spatially random ground motion, *Earthquake Engng. Struct. Dyn.*, **14**, 891-908, 1986.

[25] R.S. Harichandran, W. Wang, Response of indeterminate two-span beam to spatially varying seismic excitation, *Earthquake Engng Struct. Dyn.*, **19**, 173-187, 1990.

[26] V.W. Lee, M.D. Trifunac, C.C. Feng, Effects of foundation size on Fourier spectrum amplitudes of earthquake accelerations recorded in building, *Soil Dyn. Earthquake Engng*, **1**, No. 2, 52-58, 1982.

[27] D. Benedetti, P. Carydis, M.P. Limongelli, Evaluation of the seismic response of masonry buildings based on energy functions, *Earthquake Engng Struct. Dyn.*, **30**, 1061-1081, 2001.

[28] D. Benedetti, P.G. Carydis, S. Croce, A. Lucchini, P. Pezzoli, Ready-to-use manual for the practical implementation of repairs and strengthenings to reduce the seismic vulnerability of masonry buildings, *ISMES*, pp 136, 1996.

[29] P.G. Carydis, A system for earthquake proofing of structures through a special foundation. Application to the new earthquake resistant city of A. Liossia in Attica, *Society of Civil Engineers of Cyprus*, Nicosia, June, pp 10, 2001.

[30] N.M. Newmark, E. Rosenblueth, Fundamentals of earthquake engineering, *Civil Engineering and Engineering Mechanisms Series, Prentice-Hall, Inc., Englewood Cliffs, N.J.*, pp 640, 1971.

COMPDYN 2013
4th ECCOMAS Thematic Conference on
Computational Methods in Structural Dynamics and Earthquake Engineering
M. Papadrakakis, V. Papadopoulos, V. Plevris (eds.)
Kos Island, Greece, 12–14 June 2013

PERFORMANCE-BASED ASSESSMENT OF THE ARSENAL DE MILLY OF THE MEDIAVEL CITY OF RHODES

S. Cattari [1], A. Karatzetzou [2], S. Degli Abbati[1], K. Gkoktsi [2], D. Pitilakis [2], C. Negulescu [3]

[1] Department of Civil, Chemical and Environmental Engineering, University of Genoa, Italy
Via Montallegro 1, 16145, Genoa, Italy
serena.cattari@unige.it, stefania.degliabbati@unige.it

[2] Department of Civil Engineering, University of Thessaloniki
P.O.B. 424, 54124, Thessaloniki, GREECE
akaratze@civil.auth.gr, kgkoktsi@civil.auth.gr, DPitilak@civil.auth.gr

[3]BRGM, Service DRP
Avenue Claude Guillemin, 45060, Orleans, France
C.Negulescu@brgm.fr

Keywords: nonlinear analyses, structural dynamic identification, FEM model, equivalent frame model, macro-block model, monument

Abstract. *The paper focuses on the performance-based assessment (PBA) of the monument named «Arsenal De Milly» which is located in the Medieval City of Rhodes in Greece. It is an unreinforced masonry structure characterized by an important mass value and is founded on a soil profile that consists of soft and stiff soil layers. As known, usually PBA refers to the use of nonlinear static procedures. In particular, in the paper it has been performed by applying the procedure proposed in the framework of PERPETUATE project (www.perpetuate.eu) for the performance-based earthquake preservation of cultural heritage assets. The seismic response of the structure has been analysed by comparing the results obtained from different modelling strategies, in particular: (i) the finite element approach (through a 3D model using brick finite elements); (ii) the structural element modelling approach (through a 3D model based on the equivalent frame approach); (iii) the macro-block modelling one. Both linear and non linear analyses have been performed. Moreover, the results from some microtremor measurements addressed to the structural identification of the building have been used to calibrate the mechanical parameters to be adopted in the models in the elastic range.*

1 INTRODUCTION

This paper focuses on the performance-based assessment of "Arsenal de Milly", an unreinforced masonry monument located in the Medieval City of Rhodes in Greece. In particular, the procedure proposed in PERPETUATE project for the performance-based earthquake preservation of cultural heritage assets has been applied [1] (funded by the FP7-Theme ENV.2009.3.2.1.1, www.perpetuate.eu).

PERPETUATE methodology adopts a displacement-based approach. A full methodological path for the assessment of cultural heritage assets has been proposed, which is based on three main steps ([1], [2]). The first one includes: 1) classification of the architectonic asset and contained artistic assets; 2) definition of performance limit states (specific for the cultural heritage assets); 3) evaluation of seismic hazard and soil-foundation interaction; 4) as built information (non-destructive testing, material parameters, structural identification). The second step is related to: 5) the definition of structural models for the seismic analysis of the masonry building and the contained artistic assets; 6) verification procedures. Finally, in the third step, rehabilitation decisions are taken and, if necessary, the second step is repeated for the design of strengthening interventions.

In the paper, the application of such procedure is presented focusing the attention on substeps 4), 5) and 6) and briefly summarizing the results on the other ones. In particular, seismic response of the structure has been analysed by comparing the results obtained from different modelling strategies, and in particular: (i) from the finite element approach (through a 3D model using brick finite elements); (ii) from the structural element modelling approach (through a 3D model based on the equivalent frame approach); (iii) from the macro-block modelling.

Moreover, results from some microtremor measurements addressed to the structural identification of the building have been used to calibrate the mechanical parameters to be adopted in the models in the elastic range.

2 ASSET CLASSIFICATION AND PERFOMANCE LEVELS CONSIDERED

Arsenal de Milly is located at the northeast corner of the medieval fortifications of Rhodes and it was built in the middle of the 15th century. It is a one storey rectangular building covered by pointed vaulted ceiling, and characterized by the presence of a very thick and massive fortified wall which supported one of its sides (Figure 1a). This monument was interested by many interventions in the past. Nowadays, it has been restored and the south wall is laterally supported by five buttresses (Figure 1b-c).

In the PERPETUATE project a proper asset classification of the cultural heritage has been proposed ([3],[4]). This classification is based on the prevailing seismic damage modes of assets and on the assumption that their occurrence is closely related to building morphology (architectural form, proportions) and technology (type of masonry, nature of horizontal diaphragms, and effectiveness of wall-to-wall and floor-to-walls connections). It is functional to the proper choice of the models to be adopted for the seismic assessment ([5], [6]). According to this classification, by taking into account the configuration of the building (which is quite simple and not characterized by a significant number of intermediate floors) and the information acquired through the in-depth as built information, it may be mainly classified according to Class B - *Assets subjected to prevailing out-of-plane damage*. This is consistent with the damage pattern, before the restoration too (Figure 2).

In PERPETUATE project specific targets and performance levels have been defined in order to consider the conservation and safety of people in an integrated approach ([3], [6]), and

in particular they are related to: Use and human life (U), Building conservation (B); Artistic asset conservation (A). For each PLs the related earthquake hazard levels, expressed in terms of return period ($T_{RD,PLi}$, with i=1..4) have been indicated; these values maybe eventually modified through a proper coefficient in order to take into account the relevance of the asset ([3]). In the case of Arsenal de Milly (since the building is not used for public functions and not relevant artistic assets are present) the seismic assessment needs to be checked only with regard to the *Collapse Prevention* (Architectonic Asset Target, $T_{RD,PL3}$ =475).

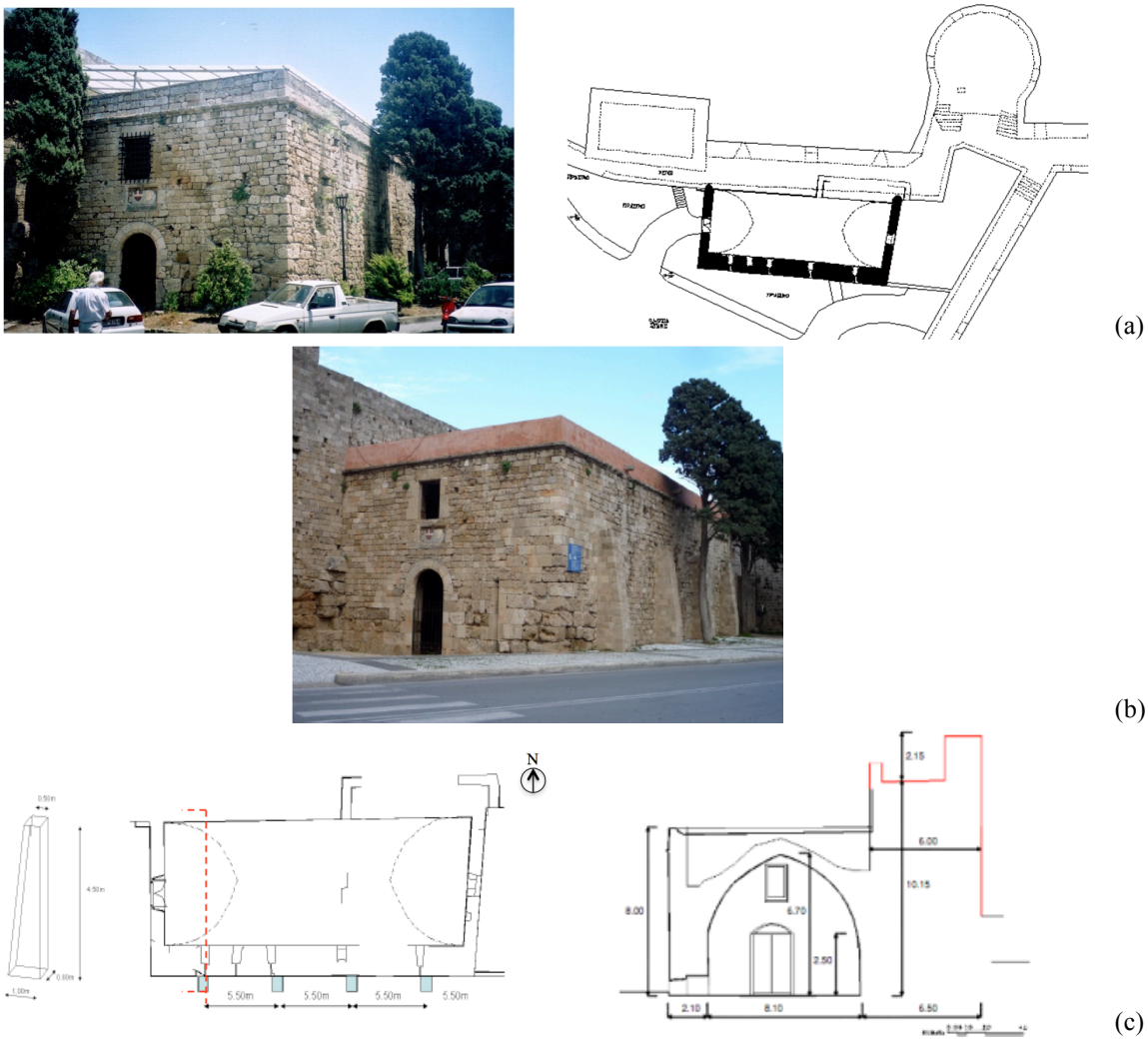


Figure 1: The Arsenal de Milly before (a) and after (b) the restoration ([7], [8]); ground plan (on the left) and cross-section (on the right) after the restoration (c), with the buttresses marked in light blue.

3 AS BUILT INFORMATION

In this sub-step, geometrical, technological and mechanical features of the asset have been analysed in depth. Several data have been acquired related to: geometry of the building; foundations; mechanical parameters; historical data on transformation and damage; state of maintenance; dynamical behaviour ([9]).

From geometrical point of view, it is a building of rectangular plan and average dimensions 10.20m × 23.88m (Figure 1). It is covered by a vaulted ceiling. The vault has not the usual semi-cylindrical shape, but it is pointed at an average height of 6.70m. It consists of the original (bearing) arch at a height of 2.50m at its genesis and thickness 0.25m and has an

overlying layer of mortar (kourasani) and an additional (non-bearing) thin "skin" of masonry (t=0.25m), while in the past it had been filled with a layer of clay material. The support for the vault is achieved monolithically at the south (outer) side with the 2.10m thick outer wall and at the northern tip (internal) is jointed and supported by a large volume of residue Wall of the Medieval Fortifications (thickness 6.00m).

The level of the foundation is at -1.90m with no widening. Arsenal De Milly has accepted many interventions in the past. Its damage pattern, before the restoration, proves the out-of-plane response. Cracks of width up to 8cm at the vertical walls and declinations at the top up to 10cm led to partial detachment of both vault and south wall (Figure 2). As aforementioned, nowadays, it has been restored and the south wall is laterally supported by five buttresses (Figure 1).



Figure 2: Pre-restoration damage pattern: detachment of the south wall (on the left) and longitudinal cracking on the vault (on the right).

In following paragraphs, some additional information related to the investigation plan aimed to the definition of masonry mechanical parameters and structural dynamic identification is illustrated.

3.1 Laboratory tests for the definition of mechanical properties of masonry

In situ and laboratory tests took place in order to determine (i) the constitution of mortars and stones (via chemists and mineralogical analyses) and (ii) the compressive strength of these materials (via core borings). The results show that the mortars are pozzolanic-lime mortars and the stones are sand-limes. The compressive strength of both materials of masonry is low.

More specifically, the pozzolanic-lime mortars have high content of fine aggregate (smooth surface, varying composition, natural origin) and its compressive strength varies from 3.14MPa to 4.56MPa. The stones used are local sandstones (lime stones) with compressive strength varying from 5.81MPa to 9.08MPa and tensile strength at around 0.75MPa.

3.2 Microtremor measurements for the structural dynamic identification

Figure 3 presents the location of the sensors for two different configurations: Figure 3a, the sensors 107, 109, 103 and 104 were placed on the top of the structure while the sensor 102 was placed in the ground surface close to Arsenal De Milly and Figure 3b, the sensors 107, 109, 108 and 104 are placed in the four corners of the structure while the sensor 105 was placed in an excavation inside the structure.

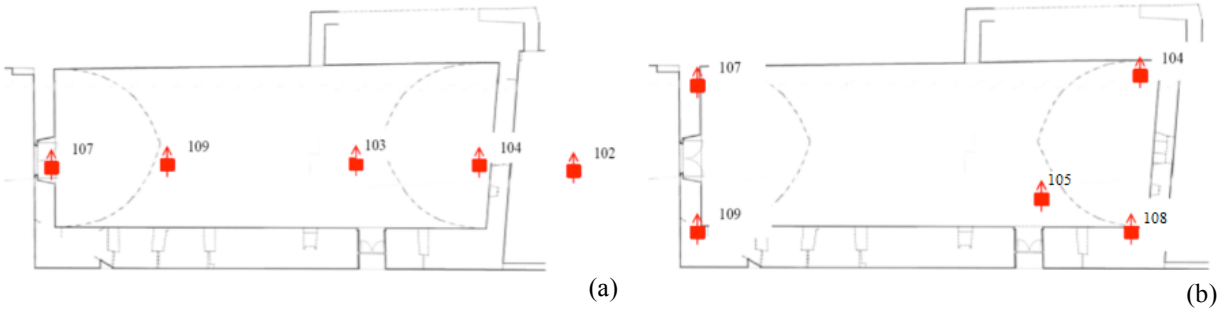


Figure 3: Sensors on the (a) longitudinal and (b) transversal direction

Figure 4a and Figure 4b show the results of the ambient vibration measurements that were performed considering the longitudinal direction ([10]). Figure 4a shows the Fourier spectral ratio given from the sensors situated on the corner near the defensive wall (107 and 104). On this Fourier spectral ratio the first peak appears at the frequency of 8Hz (0.125s) while the second amplification appears at 11.6Hz (0.086s). Figure 4b shows the Fourier spectral ratio given from the sensors placed at the centre of the vault (109 and 103). On this Fourier spectral ratio there is only one peak at the frequency of 8Hz (0.125s). These results verify that the structure is very rigid in the longitudinal direction where no torsional effects appear.

For the transversal direction, Figure 4c shows the Fourier spectral ratio for the sensors placed in the four corners of the structure (107, 109, 108 and 104). The sensor 109 placed in the south-east corner of the structure, present more clear peaks and the higher amplification compared to the other sensors (107, 108, 104). The first peak is at 5.1Hz (0.196 s) that is, in the same time, the predominant peak of the sensor 107 situated in the north-west corner of the structure. The second peak is around 8Hz (0.125s) and the forth peak is around 12Hz (0.083s). The last two peaks (8 Hz and 12 Hz) are also observed for the sensor 108 placed in the south-east corner of the structure. The third peak is at around 10Hz but it is not representative for the behaviour of the structure. The several peaks that appear in the Fourier spectra and confirmed in the Spectral ratio of the sensor 109, situated in the corner of the structure, suggest an important torsional effect. This effect, which is less amplified in the corner with the sensors 108, is due to the different rigidity between the structure and the adjacent defensive wall and due to the openings in the two transversal walls. The fact that there is almost no amplification for the sensors that are placed near the defensive wall (104 and 107) indicates that the structure does not work as a block and that the connections do not play an important role.

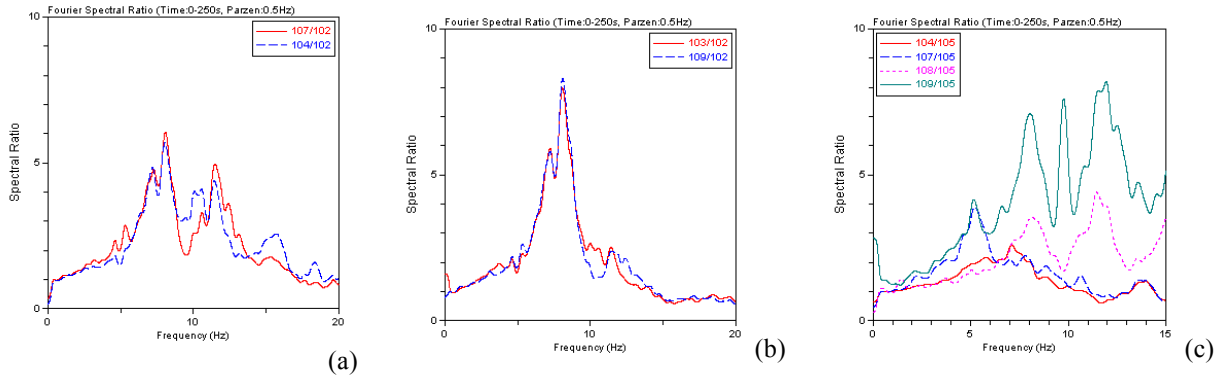


Figure 4: Fourier Spectral Ratio for the longitudinal direction – (a) sensors near the wall, (b) sensors near the centre of the structure and Fourier Spectral Ratio for the transversal direction (c)

3.3 Material properties

Based on the results obtained from laboratory tests and microtremor measurements, the structural identification of the building has been achieved.

Table 1 shows the mechanical properties and the masonry's strength parameters to be adopted in the models in the elastic range. These values have been also adopted in a technical report conducted in the Aristotle University in Thessaloniki [8]. Concerning the masonry's cracked pattern, an effective elastic modulus (E_{eff}) is assumed. To this end, the elastic modulus adopted herein is the one proposed in the abovementioned technical report (E=1800MPa) after a reduction equal to 50% (E_{eff}=900MPa).

Compression strength f_{wd}	Shear limit strength f_{vklim}	Tension Strength f_{wt}	Modulus Elastic E_{eff}	Poisson ratio v	Self weight γ
1.8 MPa	0.2 MPa	0.18 MPa	900 MPa	0.25	22 kN/m^3

Table 1: Masonry's properties

4 MODELING

According to the identified damage modes and asset types proposed in PERPETUATE ([3]), models are classified following two criteria ([5]): scale of discretization (whether material or structural element one) and constitutive modelling of masonry (whether continuous or discrete). Four types of models are identified: 1) Continuum Constitutive Laws Models, 2) Structural Element Models, 3) Interface Models, 4) Macro-Blocks Models. Depending on the different classes of heritage buildings (churches, palaces, towers, defensive walls) the choice of the mode proper model for the seismic assessment can change.

Usually, the MBM models can be mainly useful to perform the seismic assessment of those structures characterized by a prevalent out-of-plane response, as Arsenal de Milly. However, in the examined case, the seismic response is also strongly influenced by the interaction with the defensive wall, as the results of the structural dynamic identification have revealed. For this reason, the global response and the effects of this interaction have been also examined, by using different types of models, in particular CCLM and SEM models.

Following, the models used for the seismic assessment are illustrated in detail, referring to the above mentioned categories (CCLM, SEM and MBM).

4.1 CCLM approach

This model was developed with continuum constitutive laws for material properties. We assumed homogeneous material properties. The Continuum Constitutive Laws Model (CCLM) is simulated using the finite element method and its geometrical and material properties stem from the data obtained during the phase of knowledge. Old studies, field measurements and laboratory surveys were very helpful for the development of the final CCLM that was used herein.

Eight-node brick elements with 3 degrees of freedom at each node were used. The non-linear response is distributed to the whole structure by using Drucker-Prager plasticity law [11]. The Drucker-Prager yield criterion is defined in OpenSees code [12] by the following parameters: the bulk modulus k and the shear modulus G which are functions of the elastic modulus considered, the yield stress σ_Y and the frictional strength parameter ρ. In order to calculate the values of the first two parameters (k and G), the masonry's elastic modulus E is

taken equal to 900MPa as previously mentioned. The Drucker-Prager strength parameters, frictional strength parameter ρ and yield stress σ_Y could be related to the Mohr-Coulomb friction angle φ and cohesive intercept c by evaluating the yield surfaces in a deviatoric plane as described by Chen and Saleeb, 1994 [13]. This relation is based on the shear strength criterion as it is expressed in Equation (1), where the shear strength with no compression is $f_{vk0}=c=0.2$MPa, the frictional coefficient is $\mu=\tan\varphi=0.4$ and σ_n is the compressive stress. The values of these parameters were also adopted in a technical report concerning the Arsenal De Milly [8]. The values used for the Drucker-Prager strength parameters are shown in Table 2. The mass density is equal to 22.4kN/m^3 and the model is considered fixed at its base.

$$f_{vk} = f_{vk0} + \mu \cdot \sigma_n \tag{1}$$

Bulk modulus k	Shear modulus G	Yield stress σ_y	Frictional strength parameter ρ
500 MPa	300 MPa	0.12 MPa	0.272

Table 2: Parameters for Drucker-Prager plasticity law

As a first step we developed an accurate model which is very close to the real structure, which in the following paragraphs will be named as '*global model*' (Figure 5). At this model we assume that the defensive wall is monolithically connected to the rest structure. The CCLM was simulated with OpenSees code.

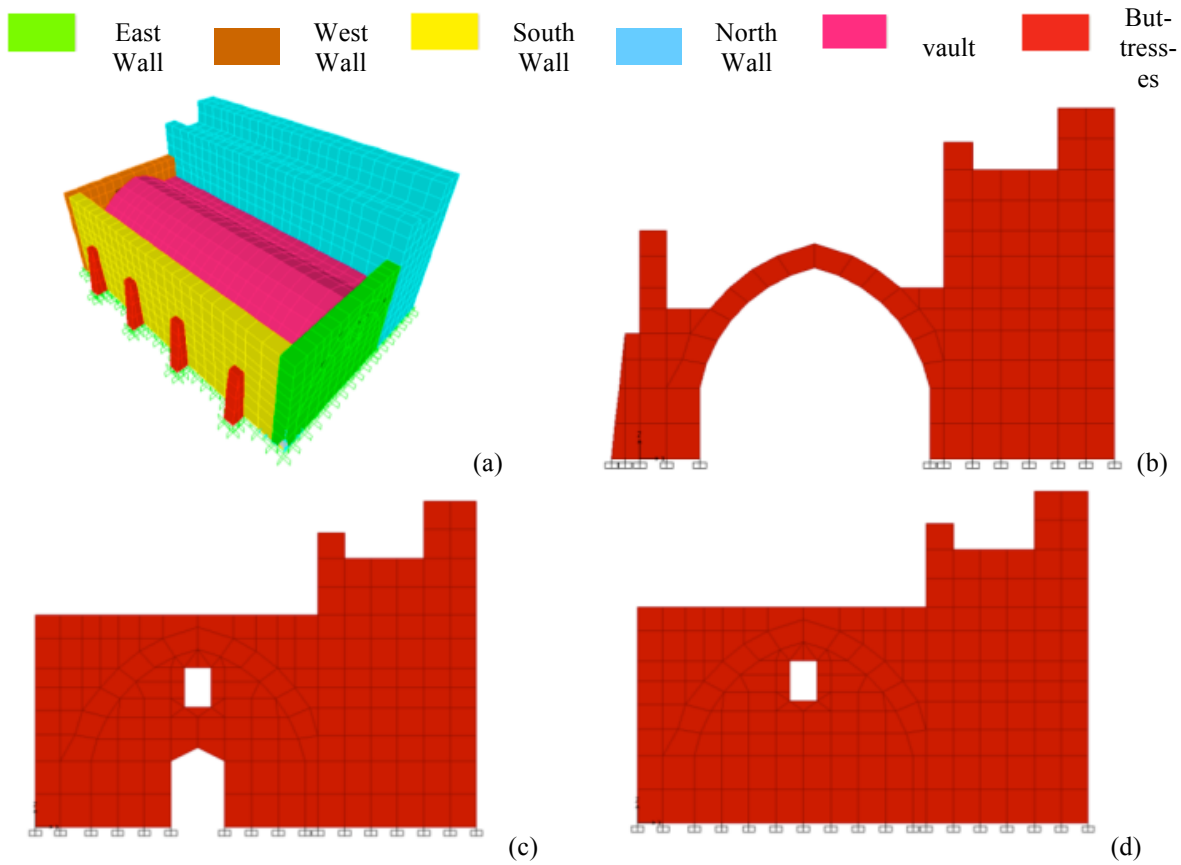


Figure 5: (a) 3D view of the spatial model with the 8 node brick elements (OpenSees), (b) 2D view of a typical cross section, (c) 2D view of the West Wall, (d) 2D view of the East Wall

Then, in order to compare results provided by the CCLM model with those of the Structural Element Model (SEM) developed in TREMURI [14,15] (illustrated in 4.2), in which the defensive wall has not explicitly modelled, the reactions of the defensive wall have been extracted from the base shear in both the directions (thus, by considering only the contribution of walls of Arsenal de Milly). Results related to this second case are called in the following as '*assumed model*'.

4.2 SEM and MBM approaches

In this case, the seismic analyses of the Arsenal de Milly has been performed by using in an integrated way two different types of model: a Structural Element Model (SEM), based on the Equivalent Frame approach (by using the Tremuri software, [14,15]) and a Macro-Block Models (MBM), adopted for the analysis of cross response of system vault-masonry walls (by using the MB-Perpetuate software, developed in the PERPETUATE Project [16]).

In particular, the analysis by the MBM model has been used in order to integrate the assessment of the cross response by including also their out-of-plane contribution, which is ignored in the global analysis (since one of the main hypothesis of the adopted SEM model is to consider only the in-plane response of walls) and which is considered very important in the examined case, due to its specific features (e.g. due to the presence of the buttresses and the high thickness of walls).

According to the SEM model adopted, each wall is discretized by a set of masonry panels (piers and spandrels), in which the non-linear response is concentrated, connected by a rigid area (nodes). Only the in-plane response of masonry walls is considered. Thus starting from the 2D modelling of walls, the complete 3D model is obtained by introducing also floor elements: in particular, they are modelled as orthotropic membrane finite elements [14]. For further detail see also [17,18]. Figure 6 illustrates: the structural model and the definition of the geometry of the structural elements (spandrels and piers) which form each wall in the Equivalent Frame Model; the Equivalent Frame Model of the two most relevant walls of the building.

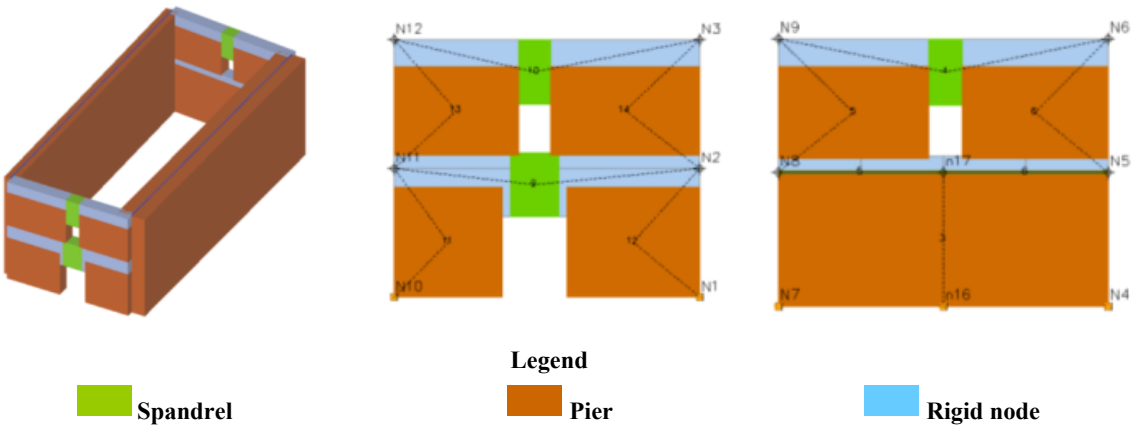


Figure 6: 3D view of the structural model (the visualization of the vault has been switch off) and Equivalent Frame Model of two walls of the building.

The analyses have been performed both in the X and in the Y directions. In the X direction, the effect due to the interaction with the defensive walls has been modelled by considering the hypotheses of the constrained horizontal displacement (Figure 7). In the Y direction, no constraints are considered: in this direction, in fact, it has been assumed that the Arsenal de Milly

is probably added in a second historic phase, so that there is no adequate interconnection with the defensive walls; the analysis has been performed only in negative way by considering the constrain offered by the defensive wall in the other direction (Figure 7).

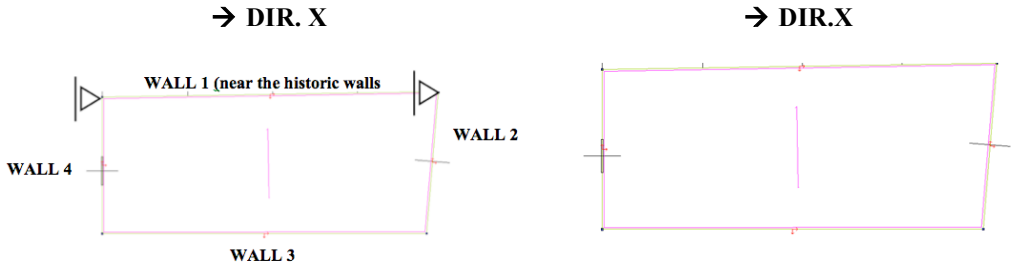


Figure 7: Constrains assumed in X direction.

The analyses have been developed by assuming a multi-linear constitutive laws for piers and spandrels elements by defining adequate drift and strength decay limits, differentiated as a function of the different failure modes that may occur (e.g. Rocking, Diagonal Cracking, Bed Joint Sliding or mixed modes as well) and progressing damage levels reached (like those shown in Figure 8). These laws have been recently implemented in the Tremuri software ([6], [19]). Moreover, the ultimate strength is computed according to some simplified criteria which are consistent with the most common ones proposed in the literature and codes (e.g. in Eurocode 8 [20] and in the Italian Code for Structural Design 2008 [21]) for the prediction of the masonry panels strength as a function of different failure modes which may occur.

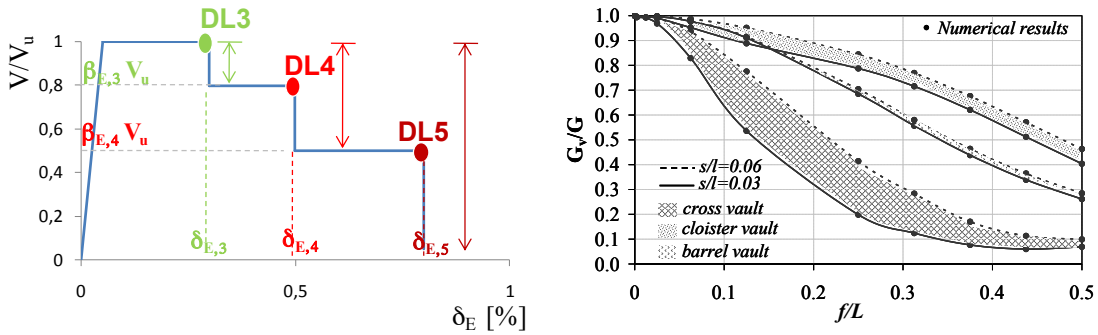


Figure 8: Multi-linear constitutive laws for piers elements (left, [6]); ratio Gv/G by varying the different types of structural vaults (right, [23]).

Table 3 illustrates the values of the mechanical parameters used in the analyses. The strength criterion used for piers and spandrels is a Mann & Muller one ([20]) expressed by eq. (2), with reference to the mortar failure domain:

$$\tau_u = \frac{c}{1+\mu\varphi_b} + \frac{\mu}{1+\mu\varphi_b}\sigma_y = \bar{c} + \bar{\mu}\sigma_y \tag{2}$$

where c and μ are the local cohesion and the friction respectively (assumed equal to 0.2 and 0.6) and ϕ_b is an interlocking parameter (assumed equal to 1).

Floor elements – in this case the vault - are modelled as orthotropic membrane finite elements, in particular: normal stiffness provides a link between piers of a wall, influencing the axial force on spandrels (E_{1v}); shear stiffness influences the horizontal force transferred among the walls (G_v), both in linear and non-linear phases. Regarding the modelling of the

vault, it is important to underline that the definition of the equivalent stiffness properties assigned has been performed referring to the correlation laws proposed in [23] and illustrated in Figure 8, by considering the mechanical properties of masonry, adequately corrected through the use of specific coefficients obtained as a function of the geometrical features of the examined vault (which is similar to a barrel vault). In particular, a value of the rise-to-span ratio equal to 0.3 has been assumed by leading to a ratio of E_{2v}/E and G_v/G equal to 0.3 and 0.55, respectively; moreover, the ratio E_{1v}/E has been assumed equal to 1.6.

Mechanical Properties	
Masonry Panels	*Diaphrams*
$E_{crac.} = 900$ MPa	$E_{1v} = 270$ MPa
$G_{crac.} = 300$ MPa	$E_{2v} = 1440$ MPa
$\bar{c} = 0.125$	$G_v = 165$
$\phi = 0.375$	t = 0.85 m

Table 3: Mechanical parameters associated to masonry panels (piers and spandrels) and to the vault.

The analysis of the cross response has been performed by using the MB-Perpetuate software [16], developed in the PERPETUATE Project. Figure 9 illustrates the analysed model (the initial configuration and the deformed one), where the plastic hinges are represented with an orange circle. In particular, the hinge n.1 at the base of the pillar on the left has been moved inside the section in order to take into account the buttresses' contribution. The position of the hinges has been defined on the basis of the expected response, evaluated from the observation of the recurrent seismic damage of vaulted structures and by taking into account the specific condition of constrains which characterized the examined case.

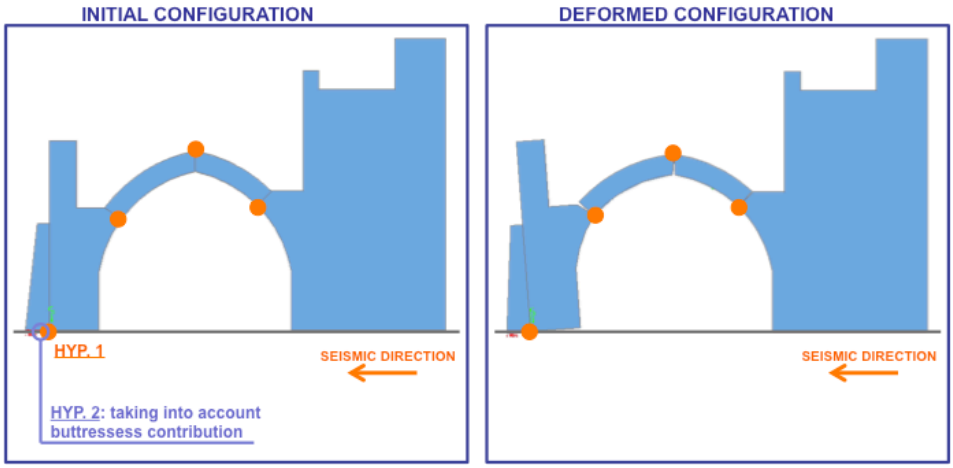


Figure 9: Identification of the collapse mechanism in case of MBM model.

5 SEISMIC ASSESSMENT

5.1 Seismic hazard

In this paragraph the appropriate seismic hazard for Arsenal de Milly will be presented. According to the results of past geophysical surveys and field measurements that conduced in the Medieval city of Rhodes, the studied monument could be classified to soil class C according to EC8 soil classification scheme. Moreover, the appropriate for the studied monument peak ground acceleration values stem from the results of Deliverable 24 [24] of the

PERPETUATE project, where a vector-valued probabilistic seismic hazard assessment (VPSHA) methodology was used for the estimation of a uniform hazard spectrum for Arsenal de Milly of Rhodes for three return periods (T_m=95years, T_m=475years and T_m=2475years).

More specifically, for Arsenal de Milly the seismic hazard is described in the following figures. Figure 10a and Figure 10b show the elastic acceleration response spectra and the elastic demand spectra respectively, for the PGA values proposed in D24 [24] and the three return periods. The assumed importance factor is equal to γ=1. The hazard curve, presented in Figure 11, shows the annual frequency of exceedance (λ_R) as a function of the peak ground acceleration PGA (a_g).

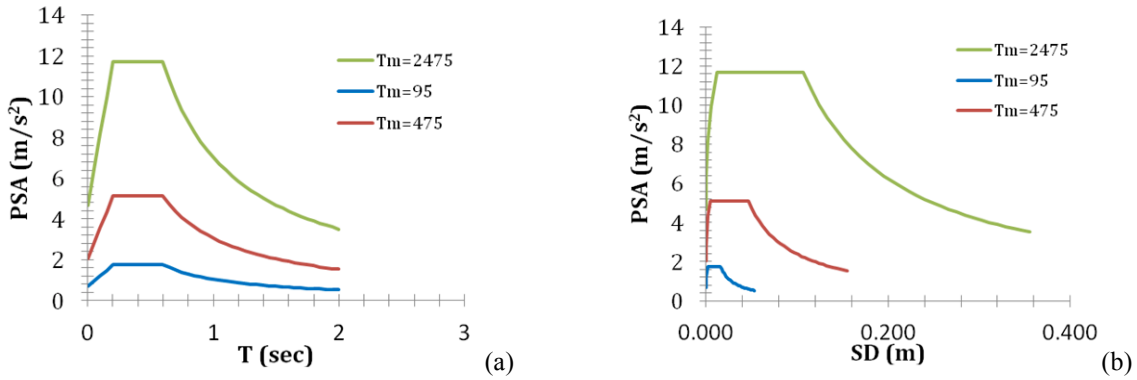


Figure 10: (a) Elastic acceleration response spectra for the PGA values according to D24, for three return periods (95, 475 and 2475 years) for soil class C according to EC8 for importance factor γ=1, (b) Elastic demand spectra for the PGA values according to D24, for three return periods (95, 475 and 2475 years) for soil class C according to EC8 for importance factor γ=1

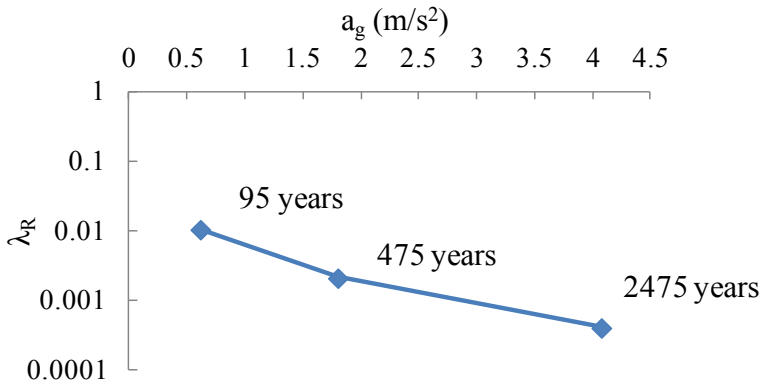


Figure 11: Hazard curve.

5.2 Results of modal analysis

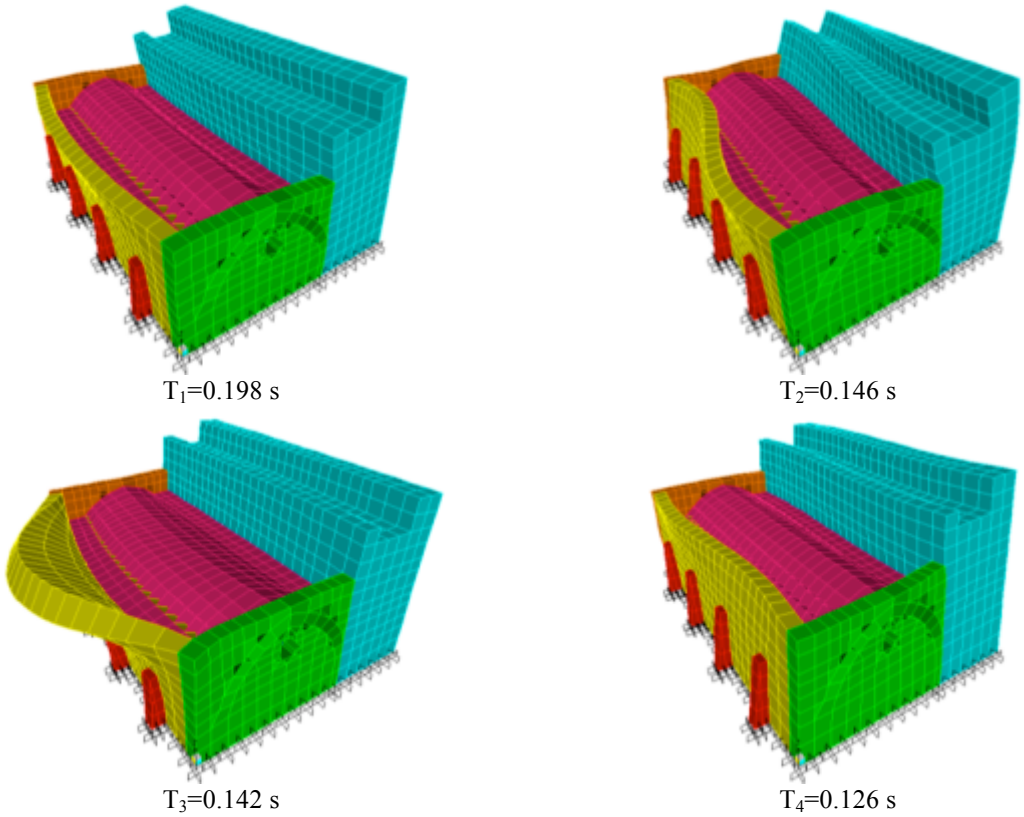
In order to calibrate the elastic behaviour of the model in OpenSees, the modal analysis results in terms of period are compared with the values obtained by microtremor results. As it is indicated in Table 4, the microtremor results are verified for the fixed base model with a modulus elastic equal to 900 MPa.

The first and the forth modes of the model (in OpenSees) are the most significant as a high mass percentage is activated. In the first mode the predominant displacements are in the transversal direction (Table 5). The fundamental period is T_1=0.198s which coincides with the

microtremor results Figure 4c). The second and the third modes activate a negligible mass percentage Table 5). In the forth mode the predominant displacements are in the longitudinal direction (Table 5). The fourth period is T_4=0.126 s which is in agreement with the microtremor results (Figure 4a and b). The modes shapes for the global model in OpenSees are illustrated in Figure 12 and their mass participation factor is indicated in Table 5. Moreover, concerning the rotational modes of vibration, it results that they are important and activate a high percentage of total mass at modes 1st, 2nd and 4th.

	Global model (OpenSees)	microtremor
$T_{transversal}$ (s)	0.198	0.196
$T_{longitudinal}$ (s)	0.126	0.125

Table 4: Comparison of the fundamental periods in the two directions between the model in OpenSees and the microtremor results.



T_1=0.198 s T_2=0.146 s T_3=0.142 s T_4=0.126 s

Figure 12: Modes shapes and the period values obtained by OpenSees for Arsenal de Milly in the 3D model.

MODE	U_X	U_Y	U_Z	R_X	R_Y	R_Z
1	**60.70%**	0.00%	0.04%	0.02%	**23.65%**	**26.97%**
2	0.01%	0.03%	0.00%	0.00%	0.02%	**11.74%**
3	1.06%	0.00%	0.13%	0.08%	0.09%	0.34%
4	0.00%	**68.49%**	0.00%	**22.99%**	0.00%	**30.89%**

Table 5: Modal Participating Mass Ratios for the all the degrees of freedom, translational (Ux, Uy, Uz) and rotational (R_x, R_y, R_z).

5.3 Results of non linear static analyses and definition of performance levels

Figure 13 compares the results in terms of pushover curves as obtained by using the different modelling strategies already discussed (CCLM – *assumed model*, SEM and MBM). These curves have been obtained by performing non linear static analyses in both the seismic directions (in the case of CCLM and SEM models), while for the MBM model, a non linear kinematic analysis has been performed; in this latter case, the curve describes the progressive development of the collapse multiplier α (that induces loss of equilibrium of the system) for increasing finite values of the generalized displacement d, up to the value for which α (d)=0. Pushover curves of SEM and CCLM models are comparable. In general the base shear resulting from the CCLM model is higher than that obtained by the SEM one. Regarding the analyses in OpenSees, it is important noting that it has been possible to reach the convergence just until the part of the curve drawn with a continuous line, and then a suitable trend has been traced (illustrated with the dashed line in Figure 13). Furthermore, it has to be noticed that, referring to the transversal direction, the initial stiffness obtained with the CCLM model is higher; this effect could be associated to interaction between the structure and the defensive walls.

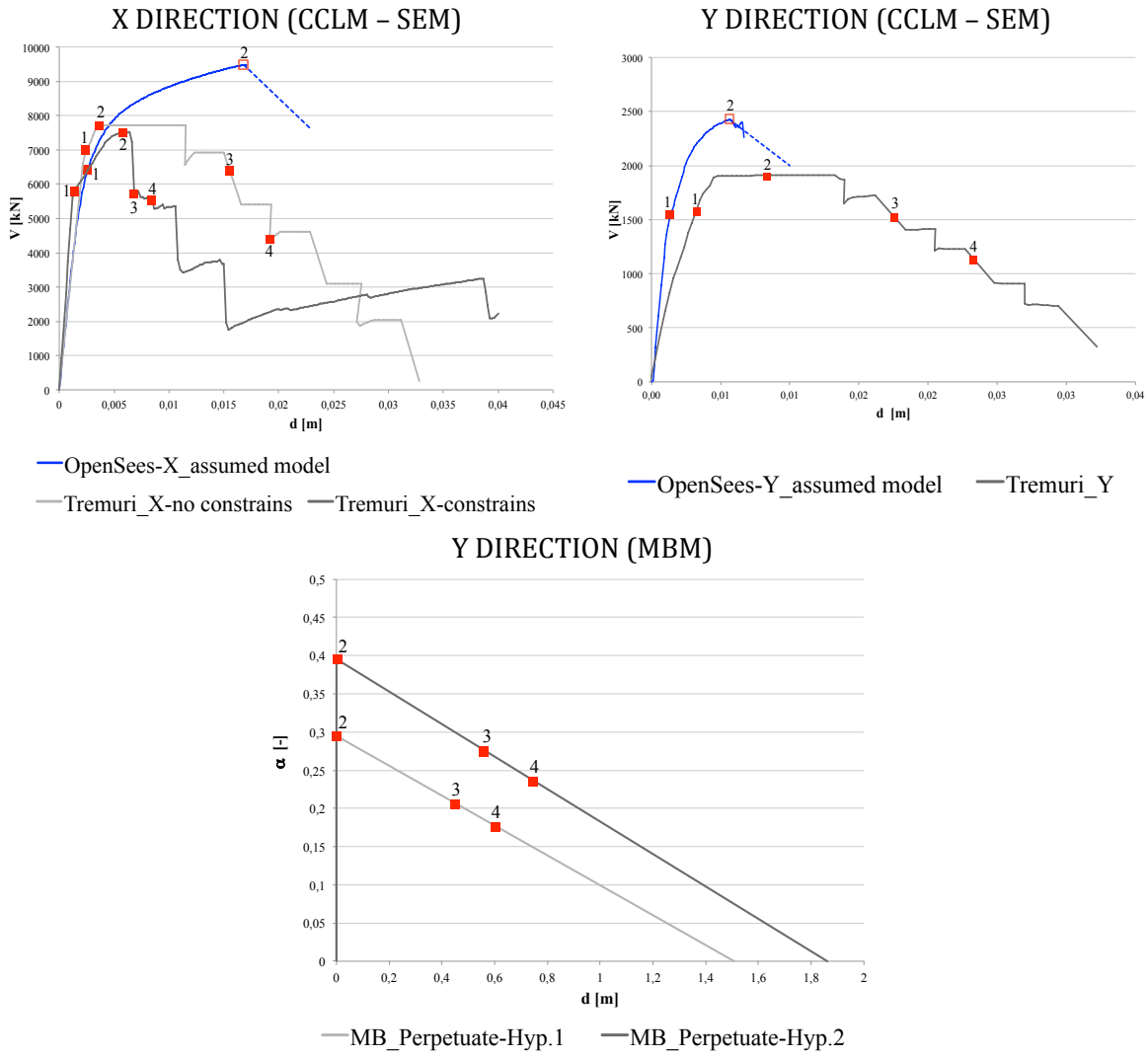


Figure 13: Comparison between the results obtained by using different models.

On each curve, the Damage Level (DL) – assumed coincident with the corresponding PL- are marked in red; they have been obtained by applying the multicriteria approach proposed in ([6], [25]). According to the multicriteria approach, the displacement on the overall pushover curve corresponding to the reaching of the *i-th* Damage Level (*DLi*, with i=1..4) is computed as:

$$d_{DLi} = \min\left(d_{DLi,E}; d_{DLi,M}; d_{DLi,G}\right) \quad i = 1,4 \tag{3}$$

where $d_{DLi,E}$, $d_{DLi,M}$ and $d_{DLi,G}$ are the displacements on the pushover curve corresponding to the attainment of the checks performed at element, macroelement and global scale, respectively.

Table 6 illustrates the limit thresholds assumed to define the damage levels at these different scales (e.g. in terms of drift δ_E, interstory drift δ_{is} or percentage of strength reduction β_E).

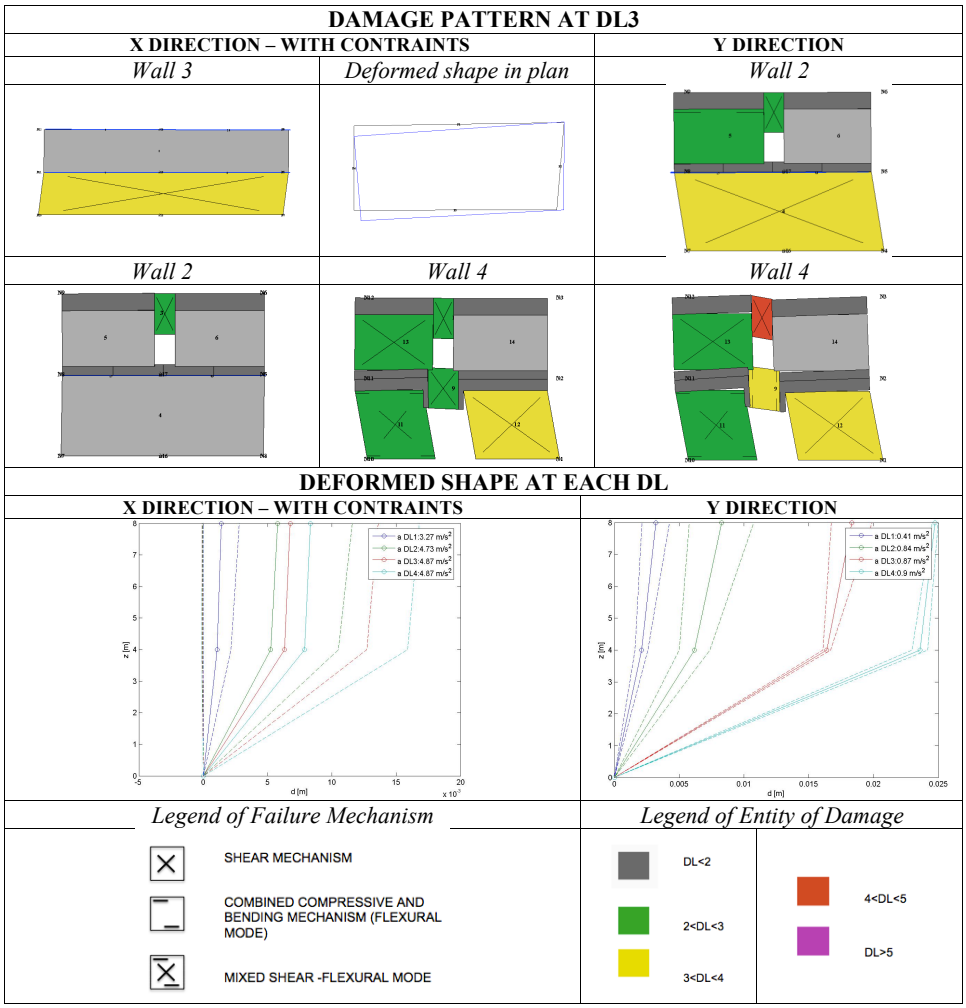


Figure 14: Damage pattern at DL3 of the most significant walls and deformed shape at each DL.

Figure 14 illustrates: the damage pattern at DL3 of the most significant walls (defined in Figure 7), as obtained by the analyses performed in Tremuri; the deformed shape at each DL. As it is possible to deduce by the damage pattern, in X direction the presence of the constrains determines a torsional effect, so that the orthogonal walls (walls 2 and 4) are mainly involved, while in the longitudinal walls only wall 3 is subjected to the seismic action: in fact, the hori-

zontal loads toward this direction in the wall 1 are applied directly to the constrains. Obviously, in Y direction, unlike the walls 1 and 3, the walls 2 and 4 are interested by a quite relevant damage pattern, due to the fact that they are directed toward the seismic action.

DLi	Structural element scale		Macroelement scale	Global scale
	Piers	Spandrels		
	-	-	$\delta_{is,1}$=0.1	-
	Reaching of maximum strength	-	Maximum base shear (V_M) $\delta_{is,2}$=0.3	-
	$\beta_{se,3}$ = 30 $\delta_{se,3}$ =0.3 (shear) – 0.6 (flexural)	$\beta_{se,3}$=50 $\delta_{se,3}$=0.3	$\beta_{M,3}$=30	$\beta_{G,3}$=20
	$\beta_{se,4}$= 60 $\delta_{se,4}$=0.5 (shear) – 1 (flexural)	$\beta_{se,4}$=50 $\delta_{se,4}$=0.6	$\beta_{M,4}$=60	$\beta_{G,4}$=40
	$\delta_{se,5}$= 0.7 (shear) – 1.5 (flexural)	$\delta_{se,5}$=2	-	-

Table 6: Definition of variables x at the different scales and limit thresholds (all limits are in %).

5.4 Safety verification

Figure 15 shows the comparison of results from all the models used (OpenSees – assumed model, OpenSees – global model, TREMURI- SEM model with constrains and MBM models) in terms of maximum acceleration ($a_{g,PLi}$) and return period ($T_{R,PLi}$) compatible with the fulfilment of PL_i (for both X and Y directions). The value of the seismic demand (in terms of PGA and return period) at PL3 is marked in Figure 16 with a red line. The values of $a_{g,PLi}$ have been computed according to the procedure proposed in PERPETUTATE [2], mainly based on the Capacity Spectrum Method [26] and the use of overdamped spectra.

The conversion of the pushover curve into Equivalent Degree of Freedom has been performed by using the Γ and m* factors (related to the assumed modal shape and the participation mass) as proposed by Fajfar in [27] and assumed also in Eurocode 8 [20]. The overdamped spectra have been computed by assuming the reduction factor proposed in Eurocode 8 [20], by computing the equivalent damping of the structure (ξ_{equ}) from the following expression [28]:

$$\xi_{equ}=\xi_{el}+\alpha\left(1-\frac{1}{\mu^{\beta}}\right) \tag{4}$$

where: ξ_{el} is the elastic damping assumed equal to 5%; α and β have been assumed equal to 20 and 1, respectively; and μ is the ductility value.

In the case of the results obtained in OpenSees, the values of a_{gmax} corresponding to PL2, PL3 and PL4 refer to the ultimate value obtained from the nonlinear analyses (marked by the white square in Figure 13).

As it is possible to deduce by Figure 15, the results obtained by the analyses performed in OpensSees ("assumed model") and Tremuri ("with constrains") are quite similar. Regarding the analyses in Y direction (where the prevalent structure seismic response is the out-of-plane one), the more reliable model is the MBM; these results are on the safe side with respect to those of "global model" by OpenSees; in this case, the seismic assessment obtained by using a SEM model is completely conventional (since the out-of-plane contribution is neglected). In

X direction, where the in-plane response is predominant, the SEM model seems adequately describe the seismic behaviour of the structure in comparison with the more refined CCLM model. In general, all the analyses determine results more precautionary than the values obtained in OpenSees with reference to the global model.

Finally, the seismic verification at PL3 is satisfied referring to the MBM model for the Y direction and referring to the other models for the X direction.

Figure 16 shows the safety factors referring to all the considered models in terms of maximum acceleration and return period, obtained by dividing the maximum compatible values of the structure by the design ones.

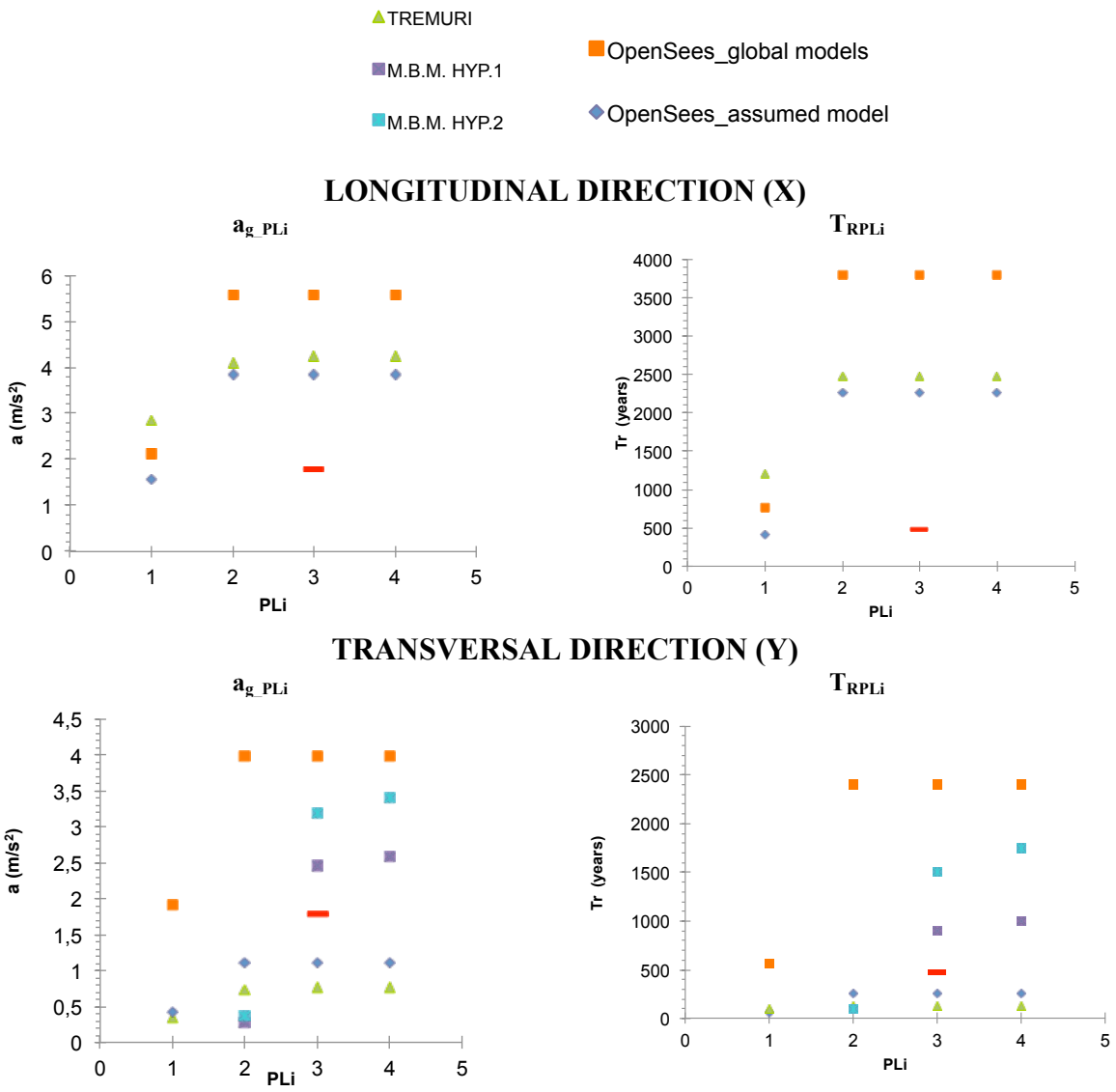


Figure 15: Comparison between maximum acceleration and return period at the four Performance Levels in the models used.

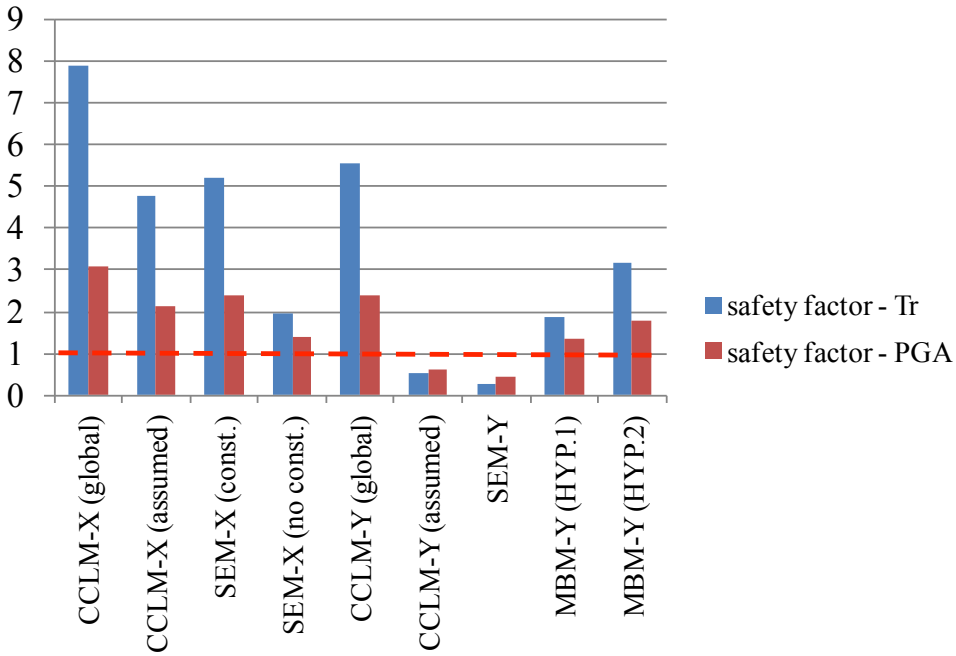


Figure 16: Safety Factors in terms of return period and PGA.

6 CONCLUSIONS

The paper presents the seismic assessment of the Arsenal de Milly according to the procedure proposed in PERPETUATE project, focusing the attention on results provided by different modelling strategies. Although the structure is quite simple from a geometrical point of view, its seismic response is quite interesting due to the interaction effects with the massive adjacent defensive wall. Calibration of models was supported by the results of ambient vibration tests that are very useful in such case in order to highlight torsional modes related to the aforementioned interaction effects. Seismic assessment results proved that the structure is able to fulfil a seismic demand associated to a return period of 475 years. In particular, the MBM (for the transversal direction) and CCLM and SEM models (for the longitudinal direction) seem the more adequate modelling strategies for a reliable assessment. Although the CCLM model is more refined than the SEM one, in non linear range it highlighted some numerical problems: thus, the combined use of the SEM model is useful to corroborate the results achieved. Finally, as future development, the soil structure foundation interaction has to be considered due to the specific feature of this structure (quite massive and founded on a soft soil).

ACKNOWLEDGEMENT

The results proposed in the paper have been achieved in PERPETUATE project (www.perpetuate.eu), funded by the European Commission in the Seventh Framework Programme (FP7/2007-2013, Theme ENV.2009.3.2.1.1), under grant agreement n° 244229.

REFERENCES

[1] S. Lagomarsino, H. Modaressi, K. Pitilakis, V. Bosjlikov, C. Calderini, D. D'Ayala, D. Benouar, S. Cattari, PERPETUATE Project: the proposal of a performance-based approach to earthquake protection of cultural heritage, *Advanced Materials Research Vols. 133-134 (2010) pp 1119-1124, © (2010) Trans Tech Publications, Switzerland.*

[2] S.Lagomarsino, S. Cattari, C. Calderini, *Deliverable D41- European Guidelines for the seismic preservation of cultural heritage assets*, December 2012 (www.perpetuate.eu).

[3] N. Abbas, C. Calderini, S. Cattari, S. Lagomarsino, M. Rossi, R. Ginanni Corradini, G. Marghella, V. Piovanello, G. De Canio, M. Mongelli, P.Giaquinto, D.Rinaldis, A. Karatzetzou, D.Pitilakis, K.Pitilakis, K. Stylianidis, V. Bosiljkov, D.D'Ayala, V.Novelli,D.Benouar, A.Foufa, *Deliverable D4- Classification of the cultural heritage assets, description of the target performances and identification of damage measures*, June 2010 (www.perpetuate.eu).

[4] S. Lagomarsino, N. Abbas, C. Calderini, S. Cattari, M. Rossi, R. Ginanni Corradini, G. Marghella, V. Piovanello, Classification of cultural heritage assets and seismic damage variables for the identification of performance levels, *Proc. of Structural Repairs and Maintenance of Heritage Architecture XII (STREMAH)*, WIT – Transactions on The Built Environment, Vol. 118, pag. 697-708, 2011, WIT press, ISSN 1743-3509 (on-line).

[5] C. Calderini, S. Cattari, S. Lagomarsino, M. Rossi, *Deliverable D7 – Review of existing models for global response and local mechanisms,* September 2010 (www.perpetuate.eu).

[6] S. Cattari and S. Lagomarsino, Performance-based approach to earthquake protection of masonry cultural heritage, *Structural Analysis of Historical Constructions* – Jerzy Jasieńko (ed) © DWE, Wrocław, Poland, ISSN 0860-2395, ISBN 978-83-7125-216-7, pp.2914-2922, 2012.

[7] Mamaloukos et al., *Survey of the Arsenal De Milly at the NE corner of the Fortification Wall of Rhodes*, 1997.

[8] K. Pitilakis, J. Galazoula, A. Sextos, *Stability issues of the foundation of the Fortification of the Medieval City of Rhodes – Arsenal De Milly: Pathology, Static and Earthquake Resistance study of rehabilitation and restoration,* Technical report (in Greek), Laboratory of Soil Mechanics, Foundation & Geotechnical Earthquake Engineering, Civil Engineering Department, Aristotle University of Thessaloniki, 2002.

[9] *Deliverable D40- Final report on the application of the proposed methodology to the case studies selected*, December 2012 (www.perpetuate.eu).

[10] C. Negulescu, B. François, A. Roullé, S. Seyedi, *Deliverable D16 - Report on microtremor measurements for structural Identification*, June 2011 (www.perpetuate.eu).

[11] D. C. Drucker, and W. Prager, Quarterly of Applied Mathematics , Soil mechanics and plastic analysis for limit design., vol. 10, no. 2, pp. 157–165, 1952.

[12] F. McKenna, GL. Fenves, B. Jeremic, MH. Scott, *Open system for earthquake engineering simulation*, http://opensees.berkeley.edu/; 2007.

[13] W.F. Chen and A.F. Saleeb, *Constitutive equations for engineering materials, Vol. I, Elasticity and Modelling*, Elsevier, New York, 1994.

[14] S. Lagomarsino, A. Penna, A. Galasco and S. Cattari, *TREMURI program: Seismic Analyses of 3D Masonry Buildings*, University of Genoa (mailto:tremuri@gmail.com), 2012.

[15] STADATA, 3Muri Program, Release 4.0.5 (*http://www.3muri.com/*), 2012.

[16] S. Lagomarsino, D. Ottonelli, *Deliverable D29 – MB Perpetuate, A Macro-Block program for the seismic assessment (Freeware software for the safety verification of seismic local mechanisms)*, December 2012 (www.perpetuate.eu).

[17] A. Galasco, S.Lagomarsino, A.Penna, S.Resemini, Non-linear Seismic Analysis of Masonry Structures, *In: Proc. 13th World Conference on Earthquake Engineering*, Vancouver, Canada; paper n. 843;2004.

[18] S. Cattari, S. Lagomarsino, Seismic assessment of mixed masonry-reinforced concrete buildings by non-linear static analyses. *Earthquake and Structures*; 4(3);2013.

[19] C. Calderini, S. Cattari, S. Degli Abbati, S. Lagomarsino, S. Ottonelli, M. Rossi, *Deliverable D26 – Modelling strategies for global response and local mechanisms*, October 2012 (www.perpetuate.eu).

[20] Eurocode 8 EN 1998-1. Eurocode 8. Design provisions for earthquake resistance of structures. Part 1-1: General rules – Seismic actions and general requirements for structures. CEN, Brussels, Belgium; 2004.

[21] NTC 2008. Decreto Ministeriale 14/1/2008. Norme tecniche per le costruzioni. Ministry of Infrastructures and Transportations. G.U. S.O. n.30 on 4/2/2008; 2008 (in Italian).

[22] W. Mann, H. Müller, Failure of shear-stressed masonry – An enlarged theory, tests and application to shear-walls. *In: Proc. Int. Symposium on Load-bearing Brickwork*, London, UK: 1980; 1-13.

[23] S. Cattari, S. Resemini, S. Lagomarsino, Modelling of vaults as equivalent diaphragms in 3D seismic analysis of masonry buildings. *In: Proc. 6th Int. Conference on Structural Analysis of Historical Construction*, Bath, UK: 2008.

[24] F. Gherboudj, N. Laouami, D. Benouar, *Deliverable D24 - Report on vector-valued characterization of seismic hazard with respect to strong-motion parameters*, December 2011 (www.perpetuate.eu).

[25] S.Cattari, S.Lagomarsino, D.D'Ayala, V.Novelli, V.Bosiljkov, *Deliverable D17- Correlation of performance levels and damage states for types of buildings*, December 2011 (www.perpetuate.eu).

[26] SA. Freeman, The capacity spectrum method as a tool for seismic design, *In: Proc. 11th European Conference of Earthquake Engineering*, Paris, France; 1998.

[27] P. Fajfar, A non linear analysis method for performance-based seismic design, *Earthquake Spectra*, 16,3: pp.573-591, 2000.

[28] C.A. Blandon, M.J.N. Priestley, Equivalent viscous damping equations for direct displacement based design, *Journal of Earthquake Engineering*, Vol. 9, Special Issue 2, pp. 257-278, 2005.

COMPDYN 2013
4th ECCOMAS Thematic Conference on
Computational Methods in Structural Dynamics and Earthquake Engineering
M. Papadrakakis, V. Papadopoulos, V. Plevris (eds.)
Kos Island, Greece, 12–14 June 2013

EARTHQUAKE BEHAVIOR OF HISTORICAL MINARETS IN ISTANBUL

Eser Çaktı[1], Carlos S. Oliveira[2], Jose V. Lemos[3], Özden Saygılı[4], Serkan Görk[5] and Esra Zengin[6]

[1,4,5,6]Boğaziçi University
Kandilli Observatory and Earthquake Research Institute, Department of Earthquake Engineering,
Çengelköy, Istanbul, Turkey
[1]eser.cakti@boun.edu.tr, [4]ozdenatess@gmail.com, [5]serkangork@hotmail.com.tr,
[6]esrazengin@gmail.com

[2]Instituto Superior Tecnico
Lisbon, Portugal
csoliv@civil.ist.utl.pt

[3]Laboratório Nacional de Engenharia Civil
Lisbon, Portugal
vlemos@lnec.pt

Keywords: Minarets, Dynamic Analysis, Non-linear Modeling, Istanbul, Earthquake Response

Abstract. *Minarets are slender structures. Old ones are mostly made of cut-stone-block masonry and occasionally of brick masonry, while the new ones are generally of reinforced concrete. They have suffered significant damage during past earthquakes, the most recent event being the 23 October 2011 Van, Turkey earthquake. Istanbul is home to many historical and contemporary minarets. Evaluation of their dynamic behavior is significant due to the expectation of a large event in the near future. In a recent study [1] we performed an extensive dynamic characterization campaign in 11 historical minarets in Istanbul, which allowed for the determination of frequencies, modes of vibration and damping. Finite element modeling and analysis of seven of these minarets were performed. Linear dynamic structural analyses were conducted to access their earthquake risk level. This paper summarizes our on-going studies on the same subject, which are: (1) The minaret damage that took place during the 2011 Van earthquake; (2) The new minaret campaign in Istanbul carried out in 30 historical and modern day minarets; (4) Earthquake damage assessment of the minaret of 16th century Mihrimah Sultan mosque based on discrete element modeling, and simulated and real earthquakes; (5) Permanent strong motion instrumentation of the Hagia Sophia Museum and Maltepe Mosque minarets.*

1 INTRODUCTION

Classical Ottoman minarets are essentially composed of a masonry wall tube and an inner core surrounded by a helicoidal stairway going up counter-clock wise, made of single steps spanning from the inner core to the wall. In some cases there are two parallel stairs as it happens in one of Hagia Sophia minarets. The basic elements of the minaret are: footing, boot/pulpit (*kaide*), transition segment (*küp*), cylindrical or polygonal bodyshaft, stairs, balcony (*şerefe*), upper part of the minaret body (*petek*), spire/cap (*külah*) and end ornament (*alem*) (Figure 1). They may be built in cut stone, brick or a mixture of both. The contemporary minarets are reinforced concrete. The top is usually a 3-D timber structure covered by 5-mm-thick lead sheets. In some cases the top can be of stone masonry as is the case with the Nur-u Osmaniye Mosque. Iron clamps hold wall blocks together. Above the upper balcony, the helicoidal stairway stops as well as the stone core. A wooden cylindrical column with slightly smaller diameter gives vertical continuity to the inner core until the base of the spire, serving also as support to a rudimentary vertical wooden stair [2].

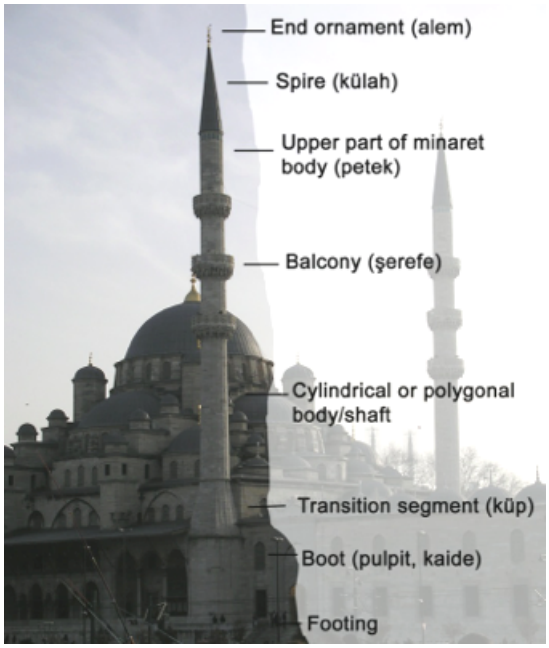


Figure 1: Main elements of a classical Ottoman minaret [1].

Minarets in Istanbul suffered from ground shaking in the past. Most notably in the 1509 earthquake, the Hagia Sophia minarets collapsed [3]. In the 1766 and 1894 earthquakes the minaret of the Mihrimah Sultan Mosque fell [4].

The most recent earthquake, in which minaret damage took place, is the 23 October 2011 Van earthquake. There was widespread damage to the mosques and their minarets. Both masonry and reinforced concrete minarets collapsed in the Van earthquake. Of 194 mosques surveyed in the Van province, 17% received heavy damage, 31% had medium damage and 30% light damage. The majority of them are not historical. Of 76 minarets, affected by the earthquake, 50 had to be demolished as they had either collapsed or had received damage beyond repair. 26 minarets were repaired. The location of the failure in the minarets that received heavy damage during the Van earthquake was mostly found to be at the region near the bottom of the cylinder, where a transition was made from a circular to a square section or where the minaret connects to the adjacent building or is part of it at the lower section. 360° planar cracks at this region were common. The majority of collapses occurred due to failure around

the balcony. Circular cracks along the body and cracks in the pulpit were also common. In Figure 2 images of damaged minarets are shown.



Figure 2: Minaret damage during the 23 October 2011 Van, Turkey earthquake

Istanbul is home to a great number of historical and contemporary minarets. As studies revealed high odds for a strong earthquake event to occur in the next 30 years [5]. It is important to better understand how these structures behave during strong shaking before proposing some retrofitting policy.

2 MINARET CAMPAIGN

Oliveira et al [1] carried out an ambient vibration survey that encompassed 11 minarets located in the historical peninsula of Istanbul. Over the summer and autumn months of 2012 we have extended the survey to 41 minarets by adding 30 further minarets to the inventory. 23 of the minarets are historical. They are of stone-masonry. We have also surveyed 7 minarets that are constructed within the last 50 years. All contemporary minarets are of reinforced concrete. Figure 3 shows the locations of historical and contemporary minarets surveyed in the new campaign and of the historical minarets covered in the survey of Oliveira et al [1], marking them by different colours. In the ambient vibration measurements we have used two three-component Guralp 6TD type seismometers. The first instrument was at the ground level. The second instrument was located at the balcony level. The measurement duration varied between 10min and 15min. The sampling frequency was 200 Hz. In each minaret, in addition to recording its ambient vibrations, we have also measured the step height, number of steps, wall thickness and body diameter.

To find drawings of historical monuments is often difficult. They are either non-existent or non-accessible or when the data are available they generally do not possess the required information or detail. Therefore, we have taken our own measurements and estimated the body height from the number and height of the steps. The body diameter is estimated from the wall thickness, core thickness and the step width. We were able to compare our height estimates for the 14 minarets with their exact heights provided by Kuşüzümü [6] and Sav [7]. We find that our estimations of the body height based on on-site measurements are always within 8% of their exact values. The majority of the minarets are located on C or D type soils.

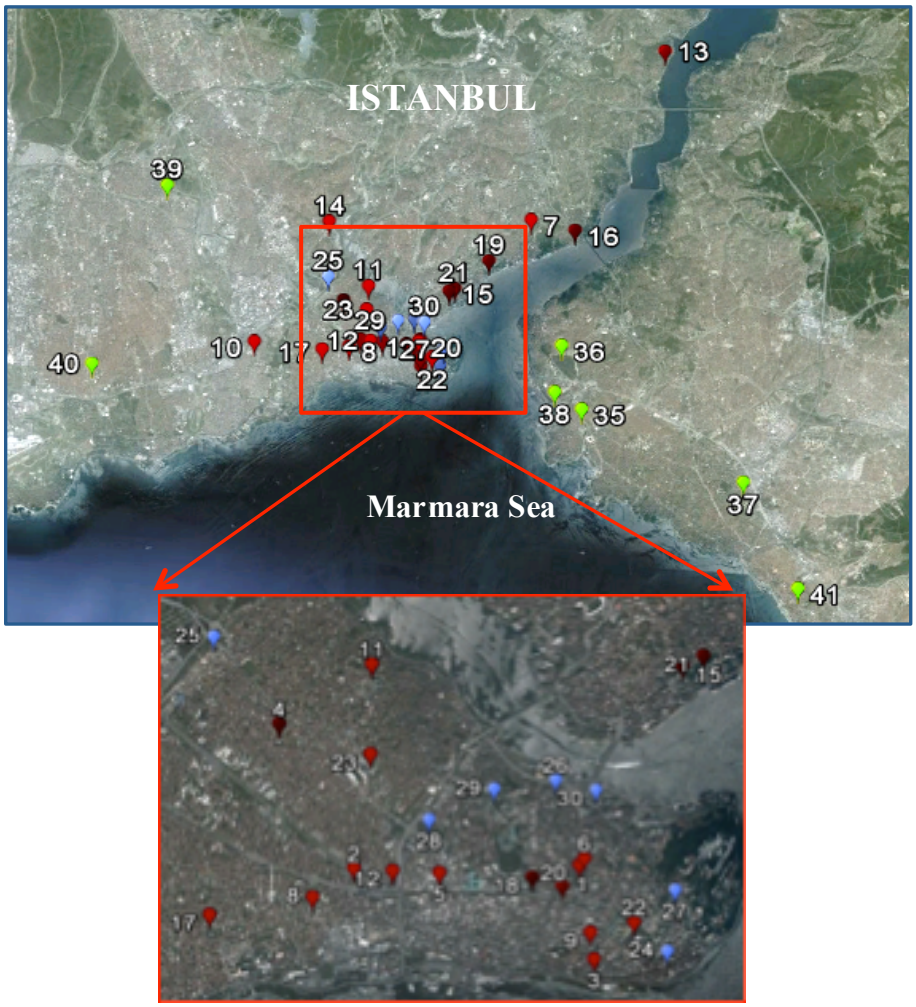


Figure 3: Locations of the mosques, the minarets of which are the subject of this study. The historical minarets covered in the recent survey are shown in red; contemporary minarets are shown in green; minarets surveyed during the previous campaign are in blue..

In each minaret we had three-component recordings from the ground level and the balcony level. Preparation and processing of ambient vibration data involved instrument correction, visual checking, baseline correction and band-pass filtering between 0.1Hz and 10Hz. Dominant frequencies of vibration in north-south and east-west directions were assessed from smoothed Fourier amplitude spectra and transfer functions. The frequencies in two orthogonal directions are very close to each other, as would be expected in symmetrical structures such as minarets. The average ratio of the larger frequency to the smaller one is 1.03.

Derivation of a simple relationship between a geometrical property of a minaret, such as one or more its dimensions, or its stiffness, and its natural vibrational frequencies is desirable. It may provide a simple means for the calculation of the natural frequency of a minaret, when only its basic geometry is known. It is also useful to understand the correlation between its frequency and several of its geometry and stiffness related parameters.

In Figure 4 we plot measured frequencies against body height and slenderness ratio defined as the ratio of the body height to the body diameter. In order to understand the difference between historical and contemporary minarets we create two groups for them.

According to Clough and Penzien [8] the first frequency of vibration for a cantilever is given by eq.1

$$f = \frac{1}{2\pi}(1.875)^2\sqrt{\frac{EI}{\bar{m}L^4}} \tag{1}$$

where E is the modulus of elasticity, I the second moment of area, $\bar{m}$ the mass per unit of length and L the total height of the cantilever.

I of a minaret can be defined can be given by Eq. 2

$$I = \frac{\pi}{4}\left[\left(\frac{\emptyset_{ext3}}{2}\right)^4 - \left(\frac{\emptyset_{ext3}}{2} - wallth_{3.1}\right)^4\right] \tag{2}$$

where $\emptyset_{ext3}$ is the external diameter of the cylindrical body of the minaret and $wallth_{3.1}$ is the wall thickness at the base of the cylindrical body [1]. Assuming that E and $\bar{m}$ are more or less the same for minarets of similar construction material, we define the stiffness parameter S as

$$S = \sqrt{\frac{I}{L^4}} \tag{3}$$

to assess the dependency between experimental frequencies and stiffness parameter. The comparison is shown in Figure 4.

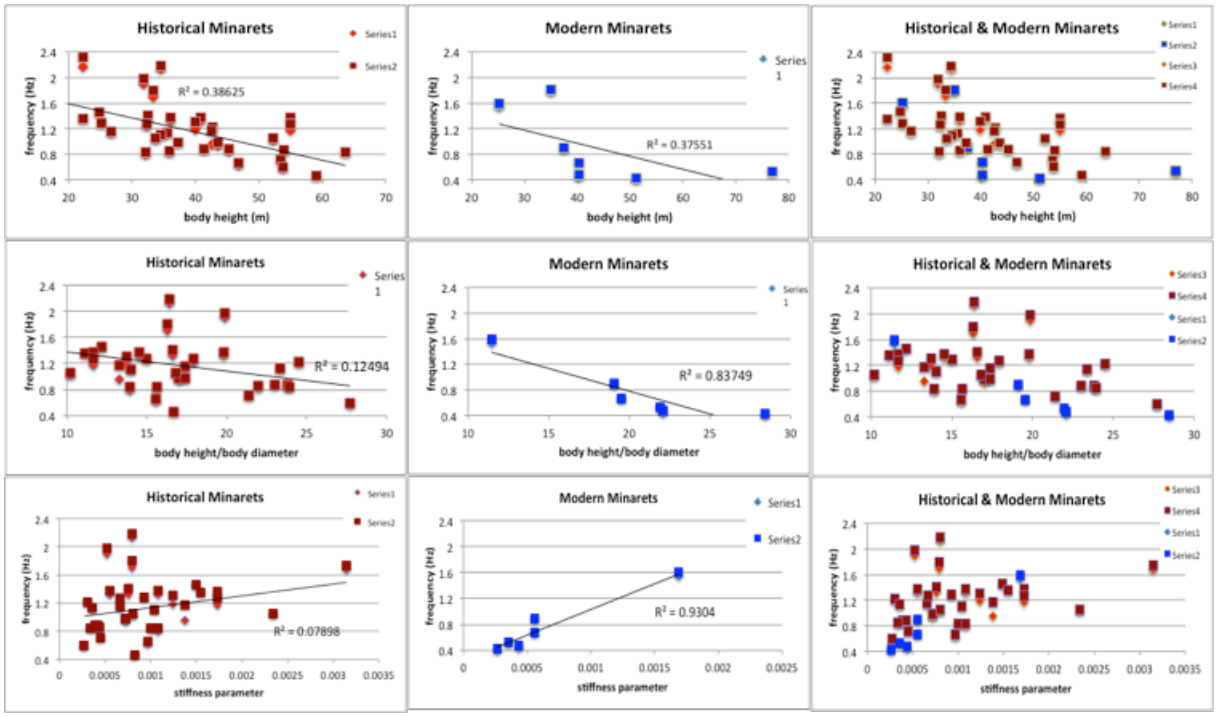


Figure 4: The change of fundamental vibration frequencies with respect to body diameter (upper row), slenderness ratio (middle row) and stiffness parameter (lower row) for the historical minarets (left column), contemporary minarets (center column) and their combination (right column).

There are several interesting features worth discussion in Figure 4. With the introduction of reinforced concrete into minaret practice, it was possible to design and build more slender minarets with lower fundamental frequencies of vibration in comparison to masonry minarets. This is evident in Figure 4 (right column) from their frequency versus body height/slenderness ratio/ stiffness parameter behaviour. The body height is not a good predic-

tive parameter for the contemporary minarets as compared to the slenderness ratio and the stiffness parameter (Figure 4, center column). For the historical minarets, however, it seems that the body height is a better estimator, as it yielded the highest R^2 as 0.39. Although we have limited data representing contemporary minarets, it seems that their behaviour is more stable. This is probably related to the fact that they are of reinforced concrete. The behaviour of masonry minarets is more difficult to predict, yet it can be said that they have their trends.

Oliveira et al. 2012 with data from 11 minarets has presented another fitting equation

$$f = \alpha . A^{c} . I^{\beta} . H^{\delta} \tag{4}$$

where A is the area of the cylindrical cross-section and I is the inertia. The constants were defined as α=38, β=0.7 and δ= -1.1. These values were determined through an iterative process that minimizes the difference between the experimental results and the empirical equation. When we consider the minarets of campaigns 2009 and 2013, Eq. (4) would lead to the values in Table 1.

Campaign	Set	No. minarets	α	c	β	δ
Oliveira et al, 2012	Historical	11	38	-0.5(fix)	0.7	-1.1
2009 data	Historical	11	48.28	-0.631	0.586	-0.968
	Historical	11	42.78	-0.5(fix)	0.51	-0.96
2013 data	All	37	35.95	-0.5(fix)	0.148	-0.879
	Historical	31	18.06	-0.5(fix)	0.374	-0.67
	Modern PC	6	328.6	-0.5(fix)	0.58	-1.572

Table 1: Fitting values of eq. (4) for the different campaigns.

3 MIHRIMAH SULTAN MOSQUE AND MINARET

Mihrimah was the daughter of Suleiman the Magnificent and Hürrem Sultan. She was born in 1522 in Istanbul and died in 1578 in the same city. She was a politically influential and wealthy person. There are two mosque complexes in Istanbul founded by Mihrimah Sultan. The subject of this section is the Mihrimah Sultan Mosque in Edirnekapı located near the land walls of the old city (Figure 5). Architect Sinan built the complex between 1556-1560 according to Müller-Wiener [4] and between 1562-1565 according to its foundation documents [9]. Earthquakes repeatedly caused harm to the mosque, its minaret and adjacent units. The earthquakes of 1719, 1766 and 1894 led to partial collapses [4]. Most recent damage occurred during the 1999, M=7.4 Kocaeli earthquake. The mosque had to be closed to public and had to undergo a comprehensive restoration scheme [9].

The 39.86m tall minaret of the Mihrimah Sultan Mosque is of cut-stone masonry. It received damage during the 1719 earthquake. Its upper 18-step section had to be repaired. It collapsed as a result of earthquakes of 1766 and 1894. An image of the minaret taken after the 1894 earthquake and before its repair in 1907 can be seen in Figure 6. During the recent restoration works, the section of the minaret above the transition segment (küp) was completely disassembled and was rebuilt following the original geometry with new stones [9].

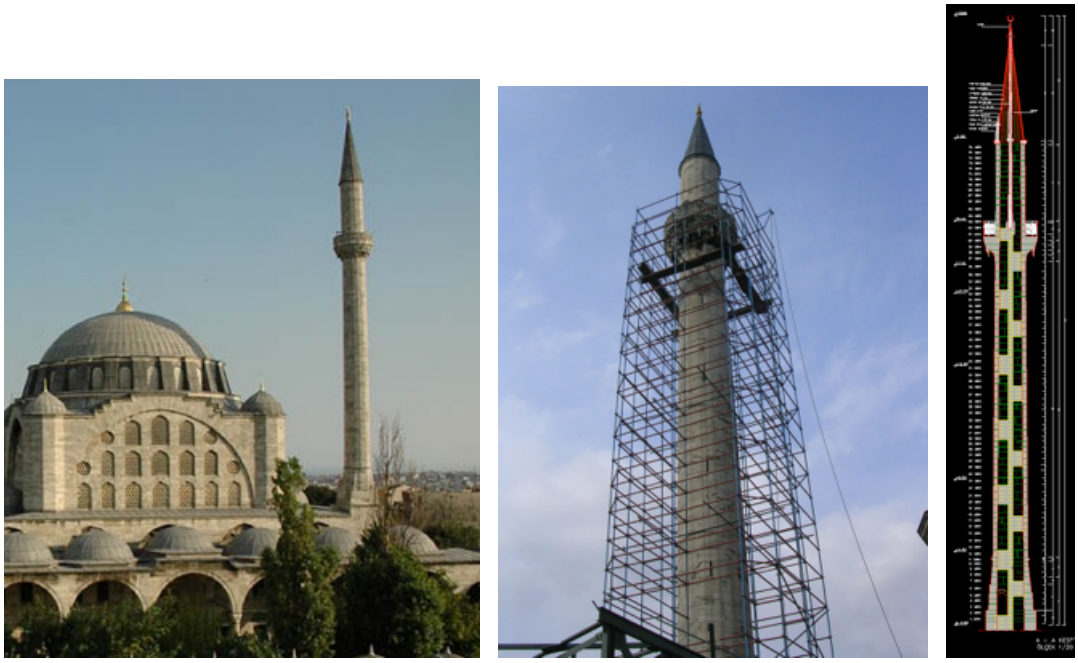


Figure 5: Mihrimah Sultan Mosque (left), its minaret before its dissassemblage (center), cross-section of the minaret (right).



Figure 6: Image of Mihrimah Sultan Mosque with the minaret that collapsed in the 1894 earthquake, from the period between 1894 and 1907 [10].

3.1 Ultrasonic Testing in the Mihrimah Minaret

We have carried out ultrasonic tests in the Mihrimah minaret in January 2013. The timing is significant in the sense that our results are representative of the minaret in its current state, i.e. the footing, the pulpit and the transition segment are original, and the part above the transition segment is new. We have utilized Pundit Lab+ Ultrasonic testing instrument with 54kHz UPV and 250kHz shear wave transducers. The tests are carried out in three different sections of the minaret: in the pulpit, in the transition segment and in the body. 37 direct ultrasonic pulse velocity (UPV) measurements are taken in the pulpit, 20 in the transition segment and 58 in the body. The numbers of readings were 97, 32 and 113 for regions 1, 2 and 3 respectively

The results suggest that the properties of stone used in the pulpit, in the transition segment and in the body are different from each other. The variation in our readings with respect to different regions is justified, as the Vp measurements carried out by two different sensor types

(54kHz and 250kH) confirm each other. It should be noted that the pulpit and the transition segment are original, while the body is newly built. We should point out that there is no evidence that the pulpit and the transition segment date from the same period. We can only say, that the stone used in the transition segment is probably similar to the stones used in the construction of the body. On the other hand, the properties of stone used in the pulpit and the body are clearly different from each other.

4 DISCRETE ELEMENT MODELLING OF THE MIHRIMAH MINARET

4.1 Discrete Element Modeling

It is a complex topic in modeling of masonry structures the choice of a suitable model representing the structure. The method employed in analytical modeling depends on the scale of the problem, the availability of the mechanical properties and the intended calculations. The macro models are used for plastic analysis and they represent the mechanical properties of masonry as a homogeneous material. Discrete models consider the discretization of block or brick masonry walls in terms of rigid or deformable bodies and planar interface or contact elements representing the mortar joints between the blocks. Nonlinear structural behavior of masonry structures depends mostly on the joints where the failure processes are more likely to occur. While deformable discrete models require intensive computation because of the description of each block by means of several finite elements, they are quite capable of treating the complex behavior of masonry walls, considering its elasticity and the progressive damage phenomena that take place after the initiation of cracking.

4.2 Modeling of the Mihrimah Minaret

The numerical models for simulation of the mechanical behavior of Mihrimah minaret were created with the 3DEC software [11]. 3DEC is a three-dimensional numerical modeling program based on the discrete element method for analysis of dis-continuum systems.

Rigid blocks were employed in the numerical model because they significantly reduce computation time in explicit time stepping algorithms. In this study, Mohr–Coulomb type failure criteria were used to represent the mortar interfaces, where the nonlinear behavior is assumed to be concentrated. The deformability of the system is characterized by the joint normal and shear stiffness parameters, which were based on experimental data, and then calibrated in order to match the measured natural frequencies. The nonlinear behavior is characterized by the tensile strength, cohesion and friction parameters.

For static analysis, 3DEC employs a dynamic relaxation algorithm. For dynamic analysis, an explicit time integration algorithm is used with mass proportional Rayleigh damping. The seismic input was applied by prescribing the velocity records in the 3 directions to the centroids of rigid blocks of foundation. The values of a set of variables such as velocity, displacement, normal stress, shear stress, normal displacement, shear displacement, were stored during a model run. Besides providing histories at given locations, it is also possible to find the distribution of peak values of joint displacements and stresses throughout the structure in order to analyze the damage processes.

The model of the Mihrimah minaret is first created in SAP2000 and calibrated for experimental periods and modes of vibration [1]. We have adopted it to 3DEC. The model parameters used in the 3DEC model is given in Table 2. The model can be seen in Figure 7a. Damping ratio was assumed as 0.04. Density is taken as 2 ton/m^3. The iron bars connecting the stone blocks were also represented in the numerical model.

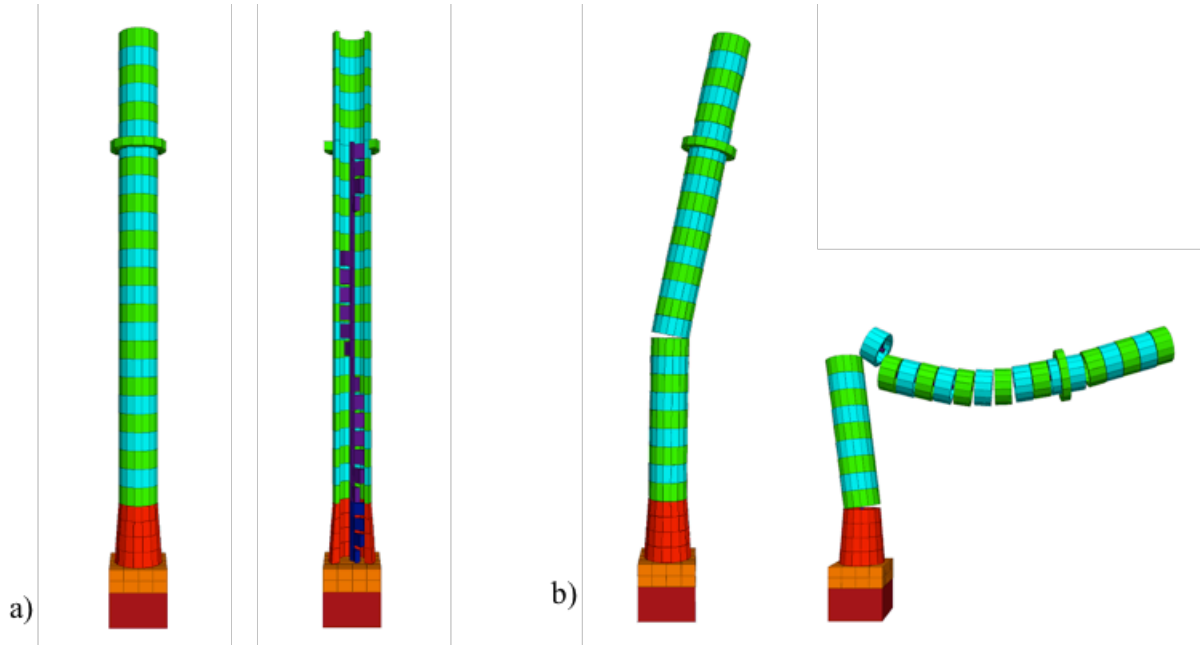


Figure 7: a) 3DEC model of the Mihrimah minaret, general view and cross-section. b) Collapse under simulated earthquake, at 24 s left, at 28 s right.

Location		K_N (MPa/m)	K_S (MPa/m)	Cohesion (MPa)	Tension (MPa)	Friction angle (°)
Wall (body)	**Horizontal joints**	8100	3200	1.0	0.5	35
	Vertical joints	10800	4300	1.0	0.5	35
Wall (trans. segment)	**Horizontal joints**	9900	3900	1.0	0.5	35
	Vertical joints	10200	4100	1.0	0.5	35
Core (trans. segment)	**Horizontal joints**	9900	3900	1.0	0.5	35
Core (body)	**Horizontal joints**	8100	3200	1.0	0.5	35
Core - stair (trans. segment)	**Vertical joints**	14800	5900	1.00E+20	1.00E+20	35
Core - stair (body)	**Vertical joints**	14800	5900	1.00E+20	1.00E+20	35

Table 2: Modeling parameters at the joints

5 CHARACTERISATION AND SELECTION OF INPUT GROUND MOTION

We have used 10 different ground motion time histories as input in the non-linear dynamic analyses. They are all consistent with the earthquake hazard levels and conditions that would be expected at or near the site of the Mihrimah Sultan Mosque in the occurrence of a large earthquake near Istanbul. Two time-history analyses were made with ground motions from the 1999 Kocaeli earthquake: the Yarımca record with a PGA of 0.322 g; and the Fatih record, with a PGA of 0.189 g. Additionally five simulated ground motion time histories were used as

input. They are broadband hybrid simulations due to five rupture scenarios to take place on the central Marmara and northern boundary segments of the North Anatolian Fault in the Marmara Sea. The largest simulated PGA is 0.39 g. Finally we have simulated three ground motion time histories using the stochastic approach by code EXSIM to represent three ruptures on the central Marmara segment. The response spectra of all records used in the analysis are shown in Figure 8.

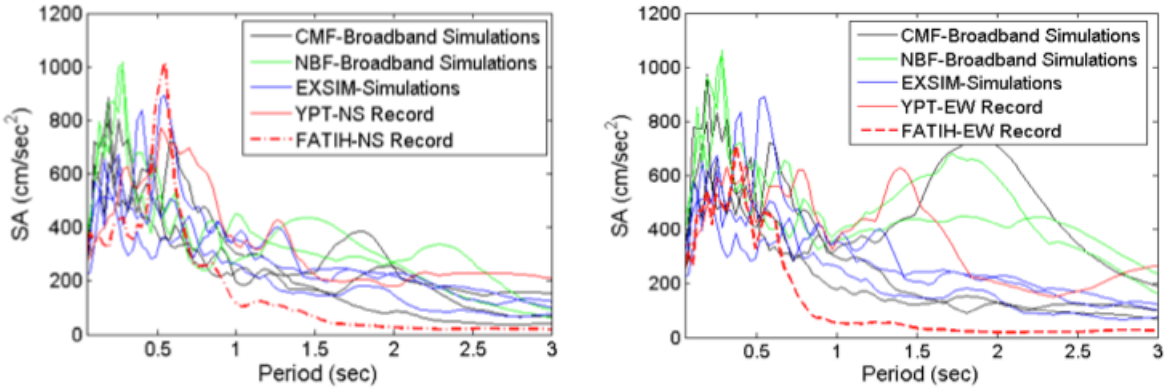


Figure 8: Response spectra of simulated and recorded ground motions used in non-linear dynamic analyses (left: NS components, right: EW components). Note that EXSIM simulates the random component. Therefore three stochastic simulations are shown in both plots.

6 NON-LINEAR DYNAMIC ANALYSIS

We have run the model under 10 earthquakes and assessed its response in terms of peak displacement amplitudes, peak stress amplitudes, their locations and collapse mechanisms. Our preliminary observations are as in the following. There are three zones along the minaret where we observe excess deformations and stresses: at the transition between the body and the so-called transition segment; balcony and its vicinity (just below or above); and at about mid-height of the body. The collapse may occur at any of them depending on ground motion characteristics. This is something we will be concentrating on in the near future. An example for collapse can be seen in Figure 7b. The agreement between the image of the minaret after its collapse in the 1894 earthquake (Figure 6) and the image of the numerical model during collapse (Figure 7b) is remarkable. There is significant rotation in the body, as evidenced by the displacement vectors shown in Figure 9. Among the cases studied, Yarımca record led to largest displacements and stresses. Peak normal joint displacements reached 6.5 cm at about 13 m from the ground level. Shear displacements of 3.2 cm took place above the balcony (Figure 10). The results suggest that failure takes place due to excessive normal deformations and rocking at the base of the minaret body and due to shear deformations at upper levels. Tensile failure on the horizontal joints was widespread, as indicated by the joint normal displacements (separation) observed. Compressive stresses in the horizontal joints attained peaks of about 5 MPa (Figure 10). The disintegration of blocks and as a result their differential displacements are evident from displacement magnitudes and joint shear displacements. Employment of real earthquakes or broadband simulations in the assessment of tall and slender structures is important. The model behaved almost elastically under stochastically simulated earthquakes, while under real and simulated records joint failures developed commonly.

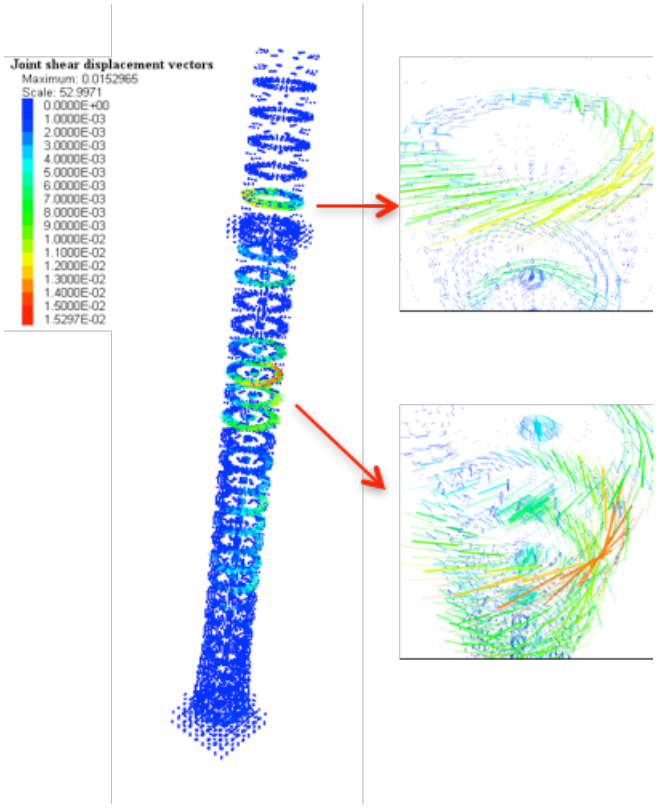


Figure 9: Joint shear displacement vectors, under a simulated earthquake on the northern boundary segment.

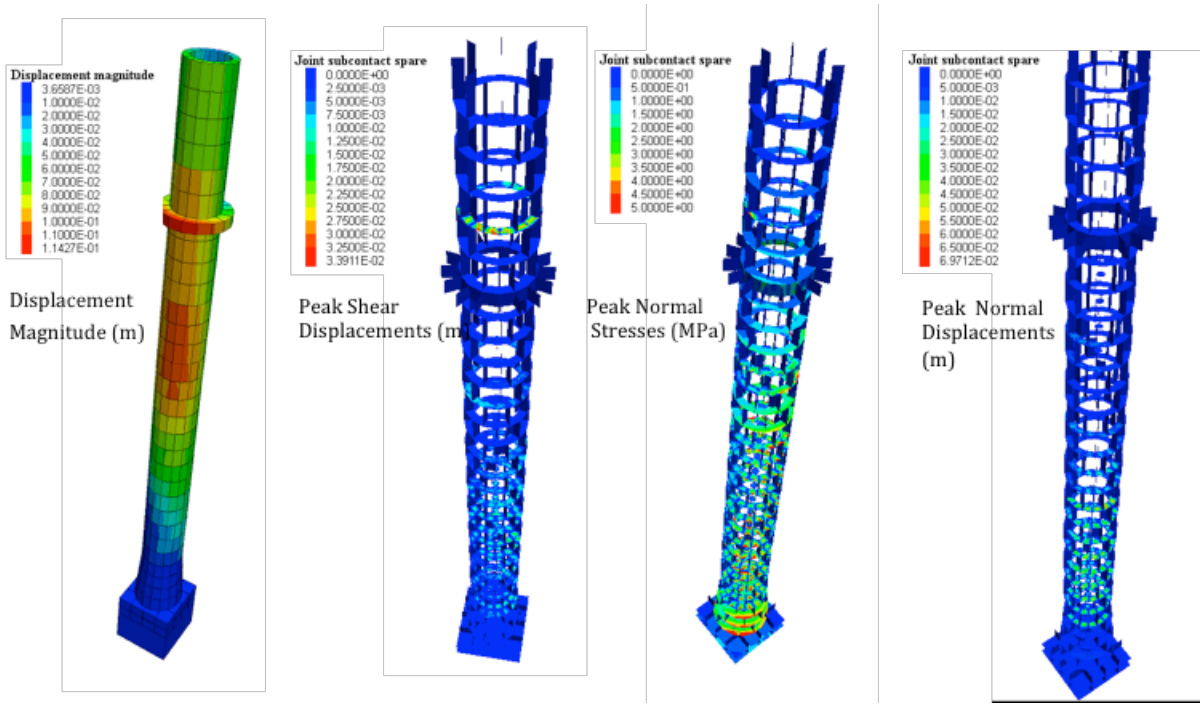


Figure 10: Model response under Yarımca record from the Kocaeli earthquake, Block displacements, maximum joint shear displacements, maximum joint normal stresses and maximum joint normal displacements.

7 CONCLUSIONS

In this paper, we have focused on the modeling and earthquake behavior of the minaret of the Mihrimah Sultan Mosque. We continue to work on understanding the effect of input ground motion on the minaret response, and on the dependence of damage pattern on the minaret geometry.

Very slender, reinforced concrete minarets have been or are being constructed in Istanbul and in other cities of Turkey that are prone to significant earthquake hazard. There is often little and no-control on their design and construction as there are no codes or guidelines concerning them. More research is definitely needed to assess their earthquake performance. Development of codes and guidelines for the maintenance and assessment of old minarets, and design and construction of new ones is also necessary, having witnessed the damage that past earthquake caused to them, and the construction of many new slender minarets.

We will install permanent structural earthquake monitoring networks in two minarets. One system will be installed in one of the Sinan minarets of the Hagia Sophia Museum. The other will be in one of the four minarets of the Maltepe Mosque. Maltepe Mosque has the tallest and most slender minarets among the ones that we have studied. Figure 11 illustrates foreseen systems.



Figure 11: Strong motion instrumentation for the minarets of the Hagia Sophia Museum (top) and of the Maltepe Mosque (bottom).

ACKNOWLEDGEMENTS

We would like to acknowledge following institutions and individuals:

- Istanbul Regional Directorate of Foundations and Istanbul Directorate of Religious Affairs for providing access to the minarets for ambient vibration surveys.
- ITASCA for providing access to 3DEC®.
- Murat Sav of Istanbul Regional Directorate of Foundations for enabling the UPV measurements and his comments and discussions on the minaret of the Mihrimah Sultan Mosque.
- Ahmet Korkmaz, Nafiz Kafadar and Emre Özdemir for their assistance during the ambient vibration tests in the minarets.
- Oktay Çırağ, Emrah Zorbacı and Mehmet Vefa Bektaş for their assistance with the ultrasonic tests in the minaret of the Mihrimah Sultan Mosque.
- State Planning Organization for providing support for instrumentation used in the field tests.
- Boğaziçi University, Instituto Superior Tecnico and Laboratório Nacional de Engenharia Civil for supporting our mutual study visits.

REFERENCES

[1] C.S. Oliveira, E. Çaktı, D. Stengel, M. Branco, Minaret Behaviour under Earthquake Loading: the Case of Historical Istanbul. *Earthquake Engineering and Structural Dynamics*. **41**, 19-39, 2012.

[2] F. Uluengin, B. Uluengin, M B, Uluengin, Classical structural details in Ottoman monument architecture [in Turkish]. Istanbul, Turkey: Yem Publication, 2001.

[3] N. Ambraseys, C. Finkel, The Marmara Sea Earthquake of 1509. Terra Nova, 2i 1989.

[4] W. Müller-Wiener, Bildlexikon Zur Topographie Istanbuls, Deutsches Archaologisches Institute, Verlag Ernst Wasmuth Tübingen, 1977.

[5] T. Parsons, Recalculated probability of M⩾7 earthquakes beneath the Sea of Marmara, Turkey. Journal of Geophysical Research, Vol. **109**, B05304, doi:10.1029/2003JB002667., 2004.

[6] K.H. Kuşüzümü, Yapım Teknikleri Açısından Istanbul Minareleri. *Vakıf Restorasyon Yıllığı*. **1**, 56-64, 2010.

[7] M. Sav, Personal Communication, 2013.

[8] R. Clough, J. Penzien, Dynamics of Structures. McGraw-Hill: U.S.A., 1975.

[9] M. Sav, K.H. Kuşüzümü, Restorasyon Çalışmaları Çerçevesinde Mihrimah Sultan Camii. Vakıf Restorasyon Yıllığı. **1**, 45-55, 2010.

[10] C. Gurlitt, İstanbul'un Mimari Sanatı, Translation: R. Kızıltan, Ankara, 1999.

[11] 3DEC Version 4.10: User's guide. Itasca Consulting Group; 2007.

COMPDYN 2013
4th ECCOMAS Thematic Conference on
Computational Methods in Structural Dynamics and Earthquake Engineering
M. Papadrakakis, V. Papadopoulos, V. Plevris (eds.)
Kos Island, Greece, 12–14 June 2013

EARTHQUAKE PROTECTION OF HISTORICAL BUILDINGS ACCORDING TO PROHITECH

F.M. Mazzolani

Department of Structures for Engineering and Architecture
University of Naples "Federico II", Naples, Italy
fmm@unina.it

Keywords: Seismic protection, Reversible Mixed Technologies, Shaking table tests, Large scale models, Monumental buildings, Numerical models

Abstract.*The FP6 EC PROHITECH research project "Earthquake PROtection of HIstorical Buildings by Reversible Mixed TECHnologies" (2004-2009) developed a wide experimental and numerical activity on structures, sub-structures, elements and devices, involving 16 academic institutions of 12 Countries, mostly belonging to the South European and Mediterranean area (AL, B, EG, GR, I, P, RO, SL, TR, ISR, M, MK). The final results were presented at the International PROHITECH Conference held in Rome on 21-24 June 2009.*

The main objective of this project was to develop sustainable methodologies for the use of reversible mixed technologies in the seismic protection of existing constructions, with particular emphasis to buildings of historical interest. Reversible mixed technologies exploit the peculiarities of innovative materials and special devices, allowing ease of removal if necessary. At the same time, the combined use of different materials and techniques yields an optimisation of the global behaviour under seismic actions.

A challenging activity within the project was devoted to large scale models of monumental buildings, which were tested on shaking table for producing damage and then for evaluating the effectiveness of the proposed consolidation systems. In particular, the following monumental models were tested: the Mustafa Pasha Mosque in Skopje, the Gothic Cathedral in Fossanova, the St. Nikola Byzantine Church in Psacha and the Parthenon temple in Athens. Beside the experimental activity, appropriate numerical models were developed in order to both predict and interpret the testing results.

1 INTRODUCTION

The seismic protection of historical and monumental buildings, namely dating back from the ancient age up to the 20th Century, is faced with greater and greater interest, above all in the Euro-Mediterranean area, its cultural heritage being strongly susceptible to undergo severe damage or even collapse due to earthquake. The cultural importance of historical and monumental constructions limits, in many cases, the possibility to upgrade them from the seismic point of view, due to the potential risk of using intervention techniques, which could have detrimental effects on their cultural value. Consequently, a great interest is growing in the development of sustainable methodologies for the use of Reversible Mixed Technologies (RMTs) in the seismic protection of the existing constructions. RMTs, in fact, are conceived for exploiting the peculiarities of innovative materials and special devices, and they allow ease of removal when necessary.

This paper deals with experimental studies, framed within the FP6 EC PROHITECH research project "Earthquake PROtection of HIstorical Buildings by Reversible Mixed TECHnologies" (Mazzolani, 2009a), on the application of RMTs to the historical and monumental constructions mainly belonging to the cultural heritage of the Euro-Mediterranean area (Mazzolani, 2009b). Within the range of the experimental research activities, shaking table tests were carried out on four large scale models of the following monumental constructions: the Mustafa Pasha Mosque in Skopje, the Gothic Cathedral in Fossanova, the St. Nikola Byzantine Church in Psacha and the Parthenon temple in Athens .

The large scale models of the Mustafa Pasha Mosque (scale 1:6), of the Fossanova Gothic Cathedral (scale 1:5.5) and of the St. Nikola Byzantine Church (scale 1:3.5) were tested on the shaking table at the IZIIS Laboratory in Skopje, Macedonia.

The seismic shaking table tests on the first two models were performed through three main phases with different loading intensities: 1) Testing under low intensity level earthquakes, causing minor damage in the model; 2) Testing under intensive earthquakes, producing a near collapse limit state to the structure; 3) Testing of the strengthened model until reaching heavy damage.

In the case of the third model, the particular consolidation system was able to fully protect the model under the maximum capacity of the shaking table and, therefore it was necessary to remove it for producing damage.

The tests on the large scale model of a part of the Parthenon temple (scale 1:3) was done on the shaking table of the Earthquake Engineering Laboratory of the National Technical University of Athens (NTUA). Three different configurations have been considered: namely three freestanding columns in a row with and without architraves and three columns in corner configuration. In all cases, the influence of metal connectors have been examined.

The carried out experimental activity (Mazzolani, 2011a), together with a systematically related numerical activity (Mazzolani, 2011b), has provided an important contribution to understand the seismic behaviour of monumental constructions, as well as to validate the consolidation interventions based on RMT systems.

2 TESTING EQUIPMENTS

The shaking table of the Laboratory of the Institute for Earthquake Engineering and Engineering Seismology in Skopje (IIZIS) was used for the Prohitech experimental activity (Krstveska et al., 2009). It consists of a 5.0×5.0 m pre-stressed reinforced concrete plate, which is able to both sustain a maximum mass of 40 tons and simulate different types of dynamic/seismic load in horizontal and vertical direction, separately or simultaneously. The table is supported by four vertical hydraulic actuators located at four corners, at a distance of 3.5 m in both orthogonal directions. The table is controlled in horizontal direction by two hydraulic actuators at a distance of 3.5 m with a total force capacity of 850 kN. The four vertical actuators have a total force capacity of 888 kN.

The data acquisition and sequence generation system (DAC) for the shaking table is a computer based system, which allows simultaneous control of eight and data acquisition of 72 channels, storage of the acquired data to a computer recording device (HDD) as well as signal analysis and graphical presentation of the acquired data.

The shaking table of the Earthquake Engineering Laboratory of the National Technical University of Athens consists of a rigid platform and of a system controlling the input motion and the response of the specimen tested on the platform (Mazzolani, 2011a).

The material of the shacking table is steel and the dimensions are 4,0x4,0x0,6 m. The table can move in all six degrees of freedom (three translations and three rotations) independently or simultaneously. The maximum weight of the specimen can be up to 10 tons, if the centre of its mass is 2 m above the simulator platform. The maximum displacement, which can be achieved, is ±0,10 m in each direction and the maximum acceleration is 2,0g in each horizontal direction and 4,0g in the vertical one. The operating frequencies in each degree of freedom range from 0.1 to 50 Hz.

3 THE MUSTAFA PASHA MOSQUE MODEL

3.1 Design phase

The model of the mosque was built at the IZIIS Laboratory, in order to be tested on the biaxial seismic shaking table (Krstveska et al., 2009). Considering the base dimensions of the prototype structure (20x20 m) and its height (22.0 m), the model was built into a scale 1/6. So, the model dimensions were 3.3x3.3 m in plan and 3.6 m in elevation, whereas the minaret was 6.3 m high (Fig. 1).

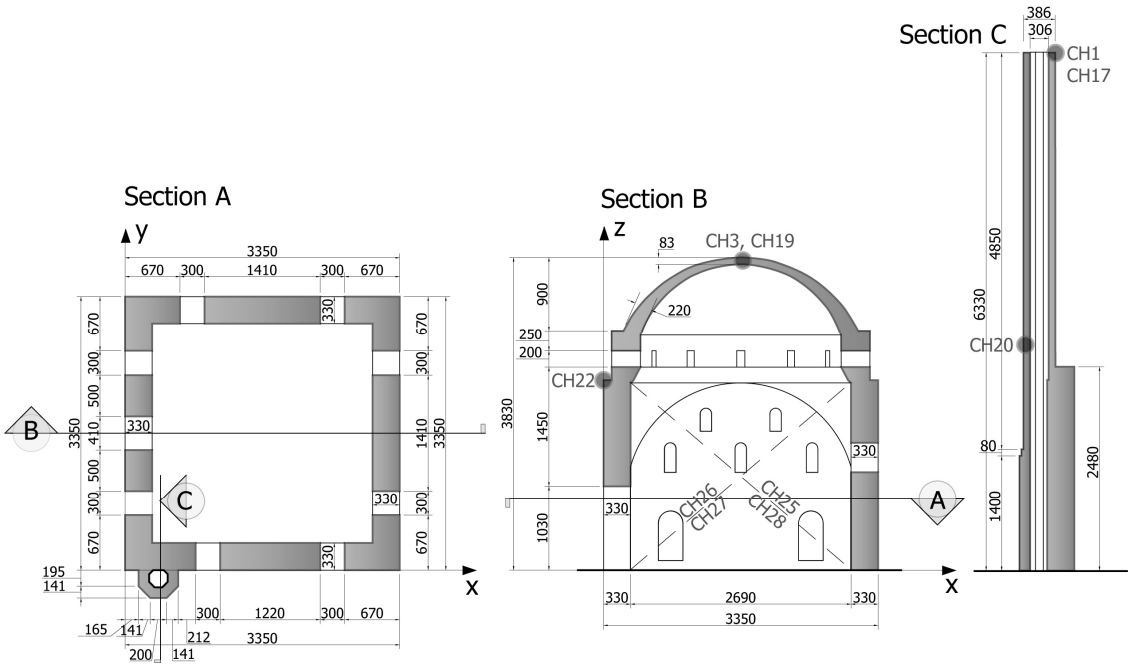


Figure 1: Dimensions of Mustafa Pasha Mosque large scale model.

The model was designed according to "*gravity forces neglected*" modeling principle, using the same materials as in the prototype structure, namely stone (travertine), bricks and lime mortar. The main mechanical properties of this masonry were achieved by experimental tests. The model was constructed on a RC foundation with strong hooks at the corners necessary to transport and lift the model on the shaking table.

The walls of the model were conceived in accordance with the typical Byzantine design: two faces of stone and brick separated by an infill of stone and brick rubble set in lime mortar. Details related to both materials and constructive techniques were provided by the experts of the Institute for Protection of Cultural Heritage in Skopje. Wooden ties – two beams connected in transverse direction –were placed in horizontal mortar joints at each second layer. The construction of the model of the mosque and the completed model fixed to the shake table and ready for testing are shown in Fig. 2.

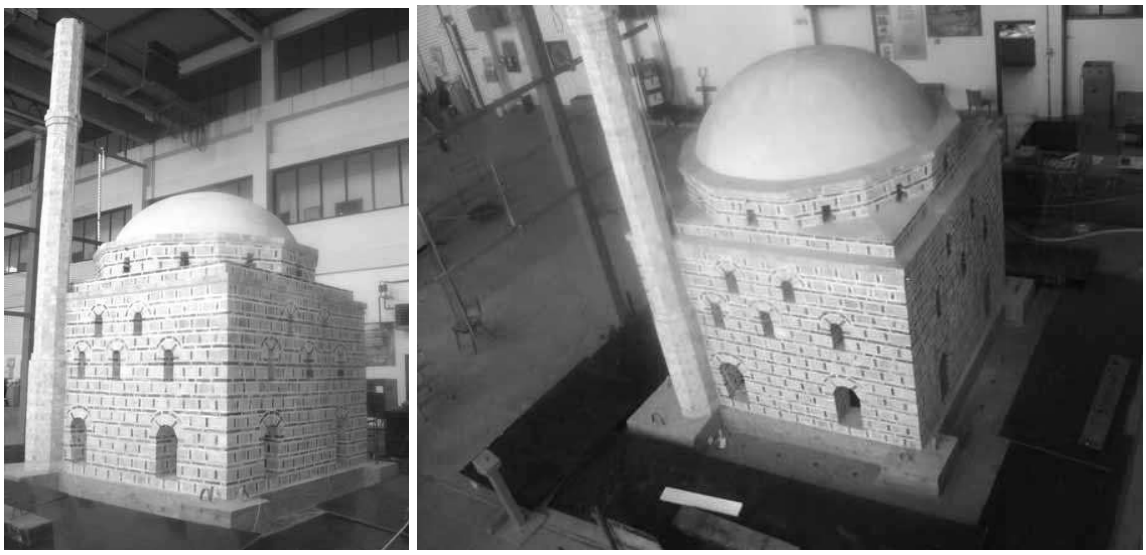


Figure 2: The prototype of the mosque ready for testing.

3.2 Testing set-up

In order to follow the dynamic response during the seismic shaking table testing, the model was instrumented at characteristic points with accelerometers and displacement transducers for measuring the absolute displacements as well as the relative diagonal deformation of the walls in the direction of the excitation (in-plane walls). 13 accelerometers (2 on the minaret, 9 on the mosque and 2 recording the input acceleration) were used. The number of displacement transducers – linear potentiometers and LVDTs – was 11 in total: 3 on the minaret and 8 on the mosque.

The main objective of the testing was to experimentally investigate the effectiveness of the reversible strengthening technology proposed for increasing the seismic resistance of such type of building. With this purpose, the seismic shaking table testing was planned in three main phases:

1) Testing of the original model under low intensity level, with the aim to produce damage to the minaret only;
2) Testing of the model with strengthened minaret under intensive earthquakes, with the aim to produce collapse of the minaret and damage to the mosque;
3) Testing of the strengthened mosque model until reaching heavy damage.

The testing procedure applied to the model consisted of several steps, consisting on the identification of the model dynamic characteristics and on seismic testing on selected earthquake records, whose period, according to the similitude requirements, was reduced 6 times. The excitation was applied in the horizontal direction only.

3.3 Testing phases

Phase 1-Testing of the original model

After the model was located on the shaking table, its dynamic characteristics were defined by means of ambient vibration method as well as by low intensity random excitation in range 0.1–50 Hz.

In this phase the shaking table tests were performed by simulation of the Montenegro-Petrovac earthquake – N-S component, as well as of the El Centro earthquake, N-S component. During this testing phase, nine tests were performed with intensity of 0.01 to 0.10 g, in order to provoke damage only in the minaret. Under input intensity of 2% g, the first horizontal crack appeared at the base of the minaret. In the next tests with intensities up to 10%g, damage in the mosque was observed as well. The reason for this damage was the frequency content of the applied excitation, which was close to the self frequencies of both the minaret and the mosque.

The damaged model is shown in Figure 3. During the last test with input intensity of 10% g, the crack in the minaret was completely developed in the horizontal mortar joint and the minaret continued to vibrate completely freely, reaching the max absolute displacement of 9 mm, while the max displacement at the top of the mosque was 2.6 mm.

Phase 2-Testing of the model with strengthened minaret

After the tests in phase 1, the model of the mosque was repaired by injection in cracks and the minaret was strengthened by application of C-FRP upon a layer of epoxy glue. The vertical strips with a width of 15 cm were placed on four sides along the length of the minaret up to the location of the balcony. They were confined by horizontal wraps, with a width of 10 cm, which were placed at four levels along the height of the minaret, while a strip of 20 cm was placed at its base. Such a strengthening enabled stiffening of the minaret and increasing of its bending resistance (Fig.4a).



Figure 3: The damaged model of the mosque after the first test.

According to the preliminary analysis of the results obtained during the testing of the original model, it was decided to continue with seismic testing applying only the accelerogram of the Montenegro-Petrovac earthquake, N-S component.

Before the seismic tests, the dominant frequencies of the model were checked by random excitation. For the minaret, the dominant frequency was 4.7 Hz, while for the mosque, two frequencies were dominating: f=7.4 Hz and f=9.6 Hz.

During this phase of seismic testing, 11 tests were performed with an input acceleration of 0.2 g to 1.5 g. The accelerogram of the Petrovac earthquake, N-S component was scaled by 6 as in the phase 1 testing.

The first cracks on the minaret were observed under an input intensity of 0.34 g, while on the mosque, the initial cracks appeared at 0.42 g input intensity. During the next tests, cracks developed and, at 0.49 g input acceleration, the upper part of the minaret totally collapsed (Fig. 4b).

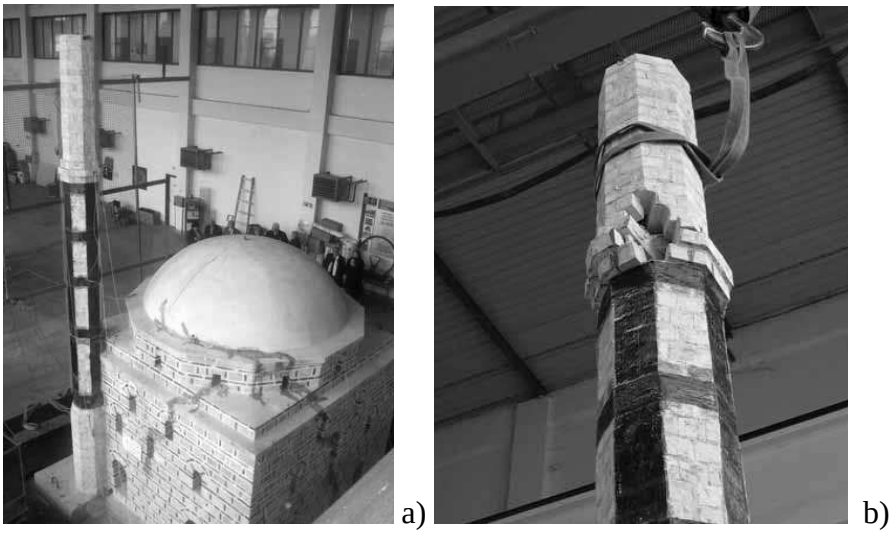


Figure 4: The strengthened model of the mosque (a) and the collapse of the minaret (b).

During the subsequent tests, the cracks on the mosque developed and, after the test with an input acceleration of 1.5 g, the mosque model was heavily damaged and the testing was stopped. The cracking mechanism developed through diagonal cracks in the walls starting from the openings at the upper part of the model and continuing also in the dome. Permanent diagonal deformations were observed and measured due to developed cracks in the walls in the direction of the excitation (in-plane walls). The damaged model is presented in Figure 5. It is interesting to observe that one of the most damaged parts of the mosque was the one where the minaret is inter-connected to the wall of the mosque. This damage was obviously influenced by the bending moment produced by intensive vibrations of the strengthened part of the minaret which remained practically undamaged after the shaking table testing in this phase. This was a good indication of the effectiveness of the applied technique for strengthening of the minaret with C-FRP.

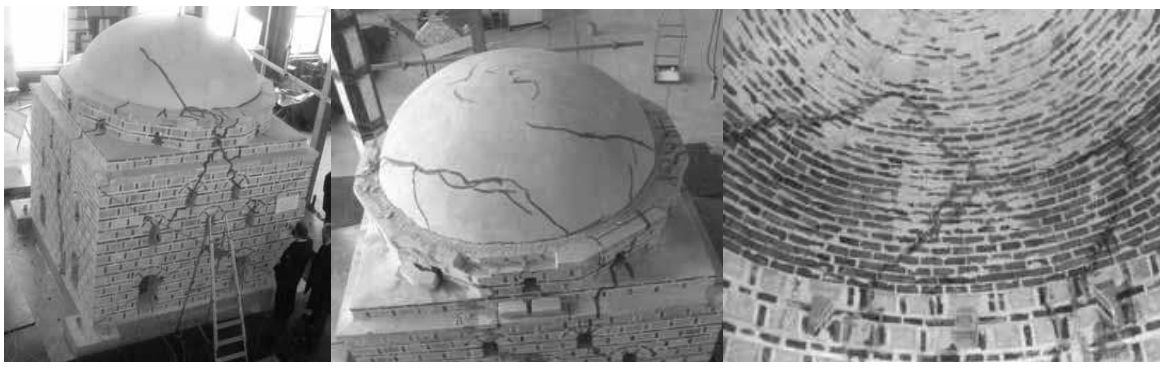


Figure 5: The final model configuration after the second test.

Strengthening of the model

After the end of seismic tests in phase 2, the dominant frequencies of the model were checked by ambient vibration measurements, the minaret was removed and the mosque model was repaired in that part. Then, the model was strengthened according to the proposed technique. The main adopted principle in strengthening the model was that the methodology to be applied be reversible and invisible. Hence, the cracks in the damaged model were not repaired by injection.

The strengthening consisted of incorporation of horizontal belt courses for the purpose of increasing the integrity of the structure at some given levels. The main operations were the following:
– Incorporation of carbon rods in two longitudinal mortar joints around the four walls at two levels: the level above the openings and at the top of the bearing walls, immediately below the tambour. With the incorporation of these carbon rods, two horizontal belt courses were formed and, as a consequence, the tensile resistance of the wall was improved and a synchronous behaviour of the bearing walls was achieved.
– Formation of a horizontal belt course around the tambour by applying a C-FRP wrap with a width of 10 cm.
– Formation of a horizontal belt course at the base of the dome by using C-FRP wraps, with a width of 50 cm.
The strengthened model ready for phase 3 seismic testing is given in Figure 6.

Phase 3-Testing of strengthened mosque model

Before the seismic tests, the dominant frequencies of the model were checked. The frequency of 9.2 Hz obtained by ambient vibrations was compared to the frequency of 8.6 Hz measured after testing in phase 2, i.e. before strengthening. The difference in the frequencies
indicated that, with the strengthening, the resonant frequency of the model was increased for about 8%, which means that the stiffness of the model was not completely recovered compared to the state before testing phase 2, f=9.6 Hz.

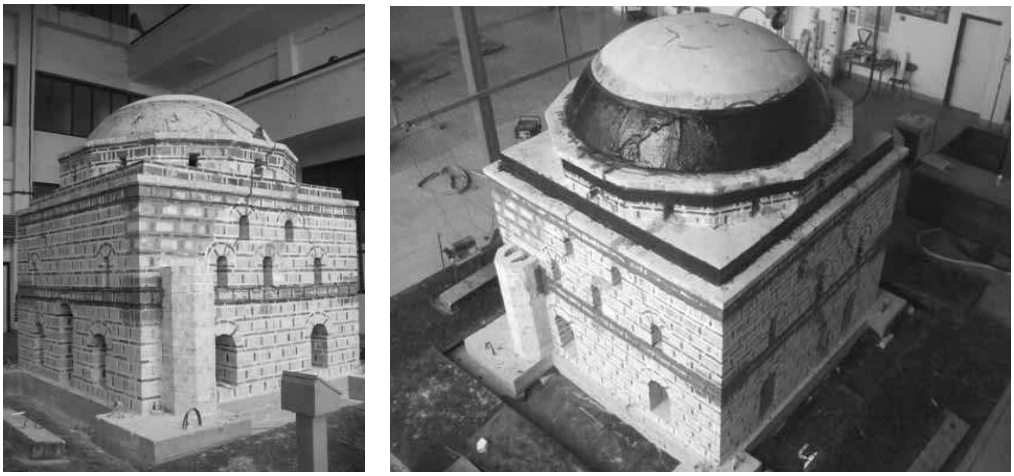
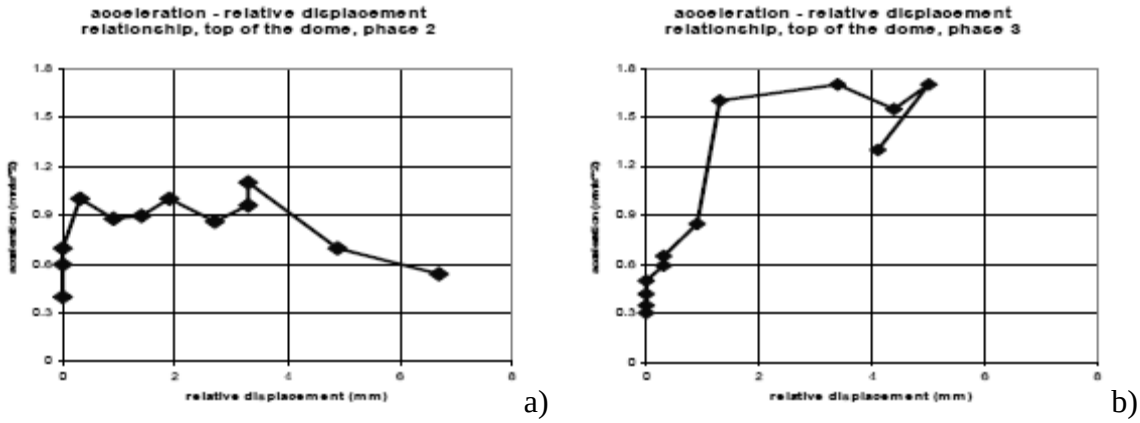


Figure 6. The strengthened model of the mosque ready for the 3rd testing phase

The tests were performed with an input acceleration ranging between 0.15 g and 1.5 g. The accelerogram of the Petrovac earthquake was scaled by 6 in the first 15 tests. During the tests with input intensities of 0.15 g to 0.40 g, the model behaviour was stable, without occurrence of large cracks. In the next 6 tests with an input acceleration of 0.60 to 0.80 g, sliding of the dome took place with a visible horizontal crack at its base. The increasing of the input intensities during the tests with a scaling factor of 6 induced intensive vibrations and sliding along the horizontal crack at the base of the dome as well as dislocation of the stones due to failure of the mortar in the joints. An

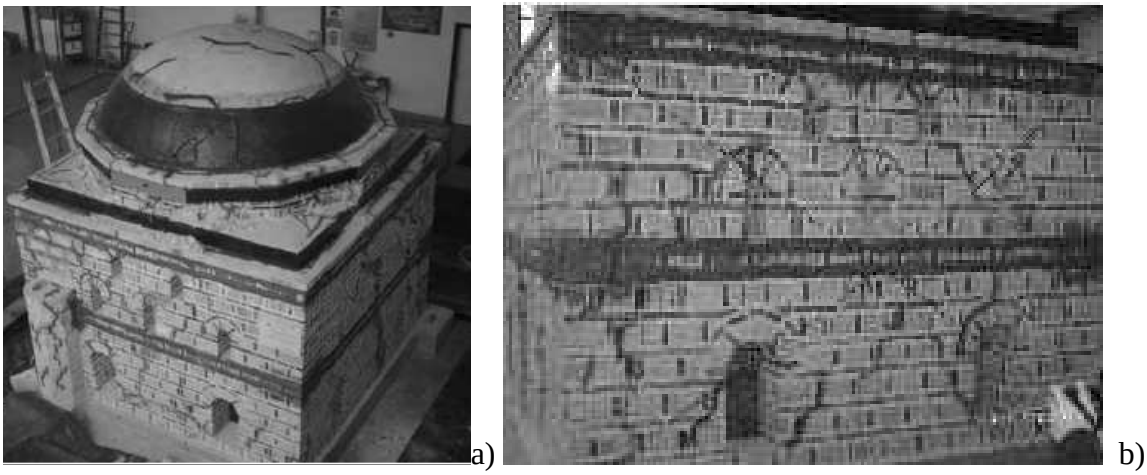
interesting information was obtained comparing the response of the model at the top of the dome and at the top of the walls, by means of the 'push-over' curves obtained for the model during testings in phase 2 and in phase 3 (Fig. 7). As it can be seen from these figures, in the case of the original model (phase 2), the dome lost its integrity by sliding along the base of the dome, while the walls still kept their load-bearing capacity.



a) b)

Figure 7. Pushover curves of the structure in the phases 2 (a) and 3 (b)

Considering phase 3, the curve shows that the effect of recovering and increasing of the dome strength is much bigger than the effect in the case of the walls. To provoke a more intensive response of the model, a time scaling factor of 3 and an input acceleration of 0.46 to1.5 g was used in the next tests. In this series of tests, many new cracks appeared in the walls as well as in the dome, decreasing the dominant frequency of the model to f=4.4 Hz. This frequency value was more than twice lower compared to the initially measured frequency of 9.2 Hz, thus indicating a pre-collapse state of the model. During the test with an intensity of 1.2 g, an initial crack in the epoxy resin of the second belt layer occurred. The next two intensive tests were performed by a scaling factor of 2, with an input acceleration of 0.75 to 1.0 g. Progressive cracks appeared, but still without collapse. The dome was 'moving' intensively, while sliding along the horizontal crack at its base and relative displacement at its top reached 8 cm.



a) b)

Figure 8. Damage into the whole structure (a) and one wall (b) of the mosque after the third testing phase

Diagonal deformation of the walls parallel to the direction of excitation reached 20mm due to the wall crack opening during vibrations.

The final test was performed by a scaling factor of 1 (real earthquake), with an input acceleration of 0.35 g. Heavy damage to many parts of the model was observed. Due to the intensive shaking, one corner of the model was inclined giving rise to damage to the C-FRP belt in that part. The damaged model is presented in Figure 8a, while the damage pattern in one of the walls is given in Figure 8b.

3.4 Numerical analysis

After experimental activity, a numerical model of the mosque based on two different schematization of the material law was implemented aiming at investigating its behaviour in the linear dynamic and non linear static fields (Fig. 9) (Mazzolani, 2011b).

The results of FE model were compared with experimental results. The distribution of first principal plastic strains predicted by the numerical model fits well the crack patterns observed on the large scale model of the Mosque during shaking table tests. As shown by the experimental investigation, in the case of the original Mosque cracks formed on the spandrels between the openings up to the tambour, while in the reinforced model cracks on the bearing walls were observed at the base of the structure, according to the predicted damage pattern. To this regard, it should be noted, however, that sliding of the dome at tambour opening level raised before the collapse of the shear walls.

The sliding mechanism was not predicted by numerical results. This is due to several factors, including the type of performed analysis and the different quality of masonry at the base of the dome, respect to other parts of the Mosque.

The comparison between experimental and numerical responses in terms of PGA and relative displacement at the structure top is shown in Figure 9b. Also in this case, the numerical and experimental results are in good agreement, even if the experimental response is higher than the numerical one, due to the cyclic loading induced by seismic excitations.

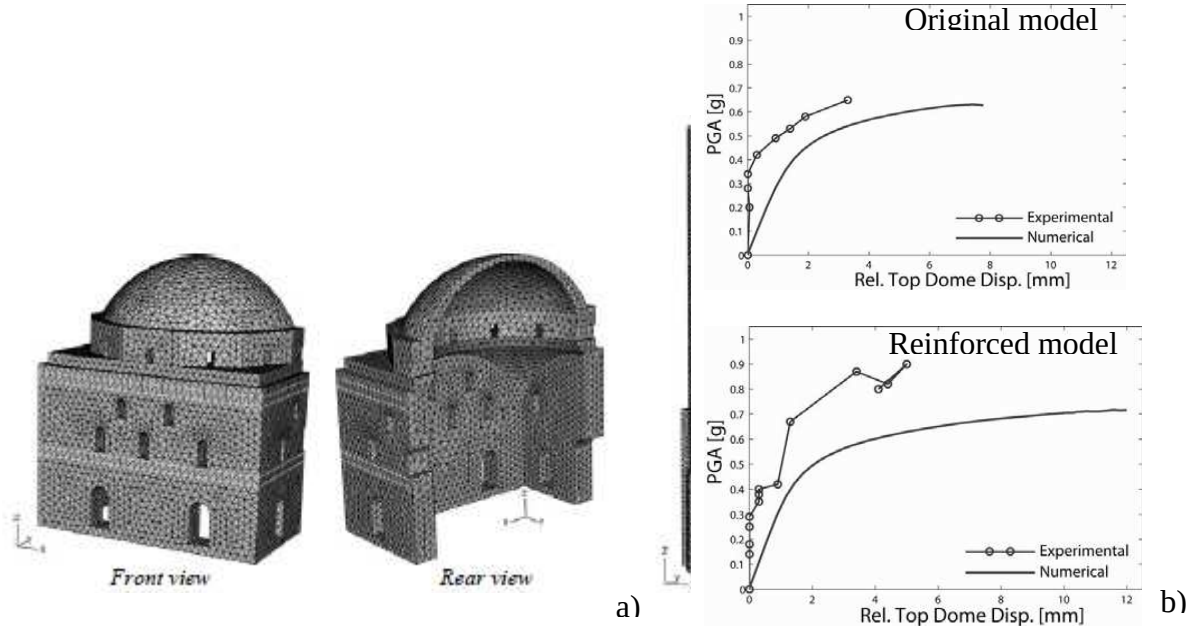


Figure 9. The FEM large scale model of the Mosque (a) and the experimental-numerical comparison in terms of PGA vs. Relative Displacement curves (b)

4 THE GOTHIC CATHEDRAL MODEL

4.1 Design phase

The model of the church was designed in a length scale of 1:5.5, according to the "*true replica*" modelling principles (Tashkov et al., 2009a), in order to investigate the dynamic behaviour of the church in the direction transversal to the main navy. For this reason a structural unit was selected and isolated from the rest of the church. This structural unit presents actual dimension of 20.71 m in the longitudinal direction and 24.00 m in the transversal direction in plane. The maximum height, at the top of the roof structure is of 23.35 m. After construction at the IZIIS Laboratory, the model was transported to the shaking table (Fig. 10).

The main objective of this test was to experimentally investigate the effectiveness of the proposed reversible technology for strengthening and increasing the seismic resistance of this type of structure.

Accordingly, the seismic shaking table testing was performed in two main phases:

– Phase 1: Testing of the original model (as-built model) until occurrence of severe damage.

– Phase 2: Testing of the strengthened model until reaching of heavy damage.

The testing procedure applied to the model consisted of several steps:

– Tests for the evaluation of the dynamic characteristics of the model (before and after the seis mic tests in each phase), in order to check the stiffness degradation of the model produced by micro- or macro-cracks developed during the tests;

– Seismic testing under selected earthquake records.

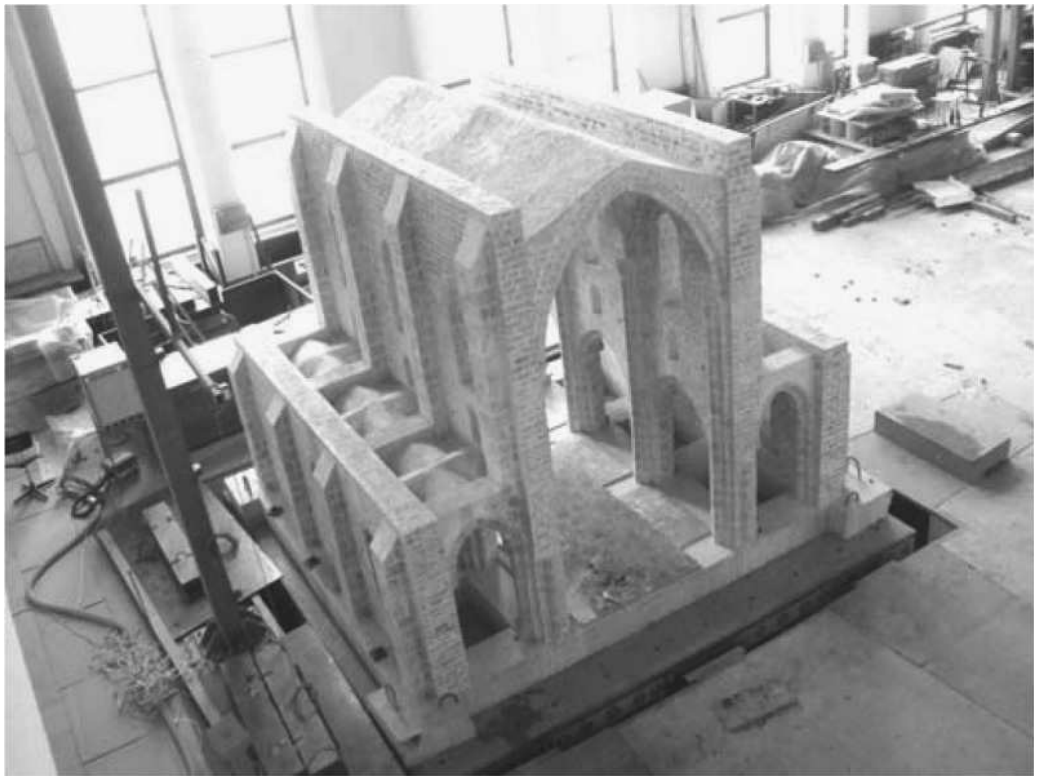


Figure 10. The model of the Fossanova church in scale 1/5.5

4.2 Testing set-up

The dynamic characteristics were evaluated by means of three methods: ambient vibration, sine-sweep and random excitation. The seismic investigation on the model was performed by simulating the Calitri Earthquake (time history – North-South component) selected as the representative one,

being characteristic for the site of the monument. According to the similitude requirements for true-replica models, the original earthquake record was scaled by √5.5 in time domain (compressed).The excitation was applied in horizontal direction only. The acceleration time history and the displacement time history of the scaled earthquake are presented in Figures 11a and 11b, respectively.

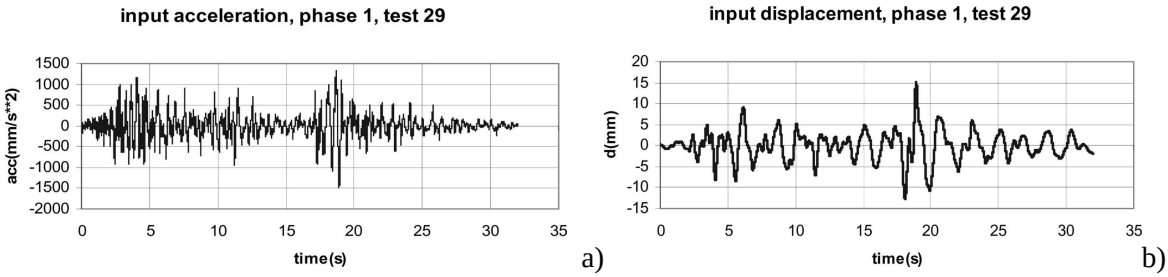


Figure 11. Compressed time history of acceleration (a) and displacement (b) of the Calitri earthquake, N-S component

To follow the dynamic response during the seismic shake-table testing, the original model was instrumented at characteristic points with accelerometers and displacement transducers, for measuring the absolute displacements (LPs) as well as relative deformations between the columns in the direction of the excitation (LVDTs).

4.3 Testing phases

Phase 1-testing of the original model

Initial dynamic characteristics of the model

The dynamic characteristics of the model were defined by means of the ambient vibration method. The mode shapes are shown in Figure 12. The model frequencies compared to the frequencies obtained by in-situ ambient vibration measurements on the Fossanova Church are given in Table 1. The achieved scaling factor model-prototype was very good, which means that the materials for the model construction (stone and mortar) fulfilled the similitude requirements for the material and its mechanical characteristics.

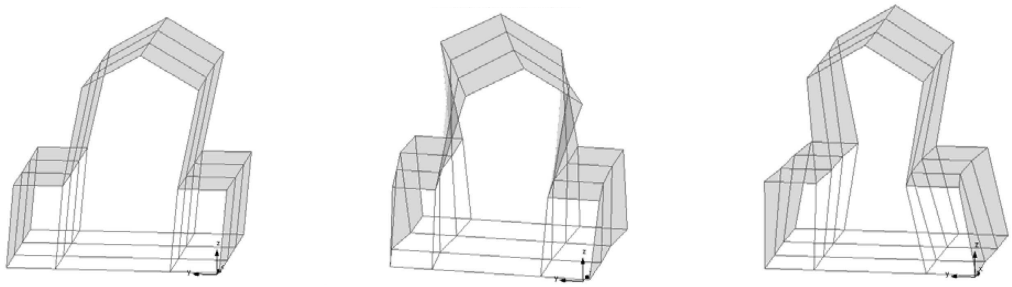


Figure 12: Mode shapes of vibration of the original model

Mode	Prototype/model Hz	Scaling factor required	achieved
Transveral	3.8/8.3	2.35	2.18
Torsional	6.8/15.7	2.35	2.31
Vertical	7.6/19	2.35	2.50

Table 1: Resonant frequencies model/prototype.

Performed seismic tests

The shaking table tests in this phase were performed by using the Calitri earthquake, N-S component, scaled in time by √5.5. During this testing phase, 22 tests were performed with an intensity of 0.004 to 0.14 g. To check the frequency decrease, random and sine-sweep tests were performed after the seismic test with intensity of 10% g. Until the final test, some micro-cracks were observed on vaults and arches at the level of the buttresses. During the final test with 14% g, a severe damage to the model was produced, with development of two main cracks along the central arches of the model and many cracks in the arches and vaults of the buttresses. The reason for this damage was the frequency content of the applied excitation, which was close to the self frequencies of the model. The photos of Figure 13 show details of damage after testing in phase 1. It is interesting to make some comments on the frequency decrease of the model during the seismic testing. It can be observed that the frequency is decreased for more than twice (from 5.8 to 2.5 Hz) after the final test, which leads to the conclusion that the model is near collapse. The push-over curve obtained during the testing of the original model at the levels of the buttresses, and of the central arches is presented in Figures 14a and 14b, respectively. It can be noted that both curves have bi-linear shapes. The cracks at the buttresses appeared at a response acceleration of 0.12 g and relative displacement of 2 mm, when stiffness degradation occurred as well as progressive deformation up to 12 mm, announcing heavy damage state. The cracks in the arches appeared at response acceleration of 0.25 g and relative displacement of about 5 mm, achieving progressive deformation of 35 mm for a small increasing of the acceleration, announcing a near collapse state.



Figure 13: Damage of the model after the first test

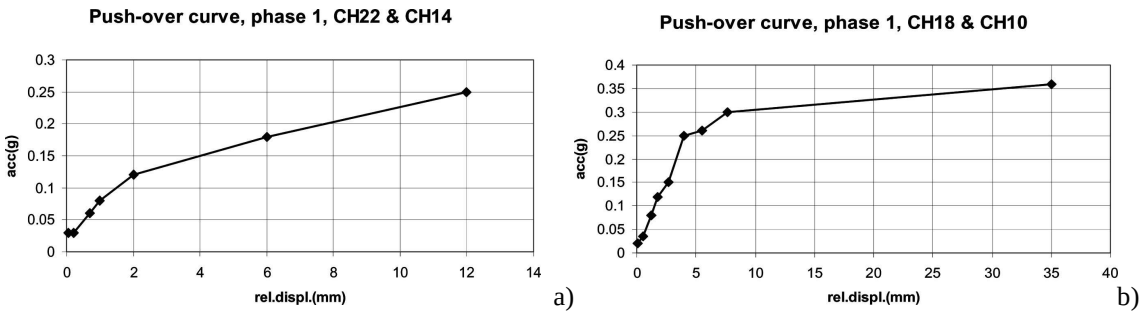


Figure 14: Pushover curve at the level of buttresses (a) and arch (b)

Phase 2- Testing of the strengthened model

Repairing of the model

After the testing of the original model and the development of the failure mechanism, the cracks were repaired by an expansive aluminium-cement mortar. The intention was to recover the contact between the masonry parts without altering significantly the original material properties.
After this reparation, ambient vibration measurements were performed to check the natural frequencies of the model. The obtained value in translational direction was f=9.7 Hz, which is higher than the frequency obtained for the original model f=8.3 Hz, showing that the strength of the model was completely recovered.

Strengthening of the model

The proposed methodology for strengthening consisted in the introduction of pre-stressed vertical and horizontal carbon fiber ties at given position in the model (De Matteis et al., 2009). In the first session of phase 2 (phase 2A), only the upper horizontal ties at the external side (the main central arch and the arches of the buttresses) were introduced; while in phase 2B, horizontal ties at the internal side were added, as shown in Figure 15. In both sub-phases A and B, vertical ties in the columns were always present. The pre-stressing forces in the ties were checked several times during the shaking table testing.

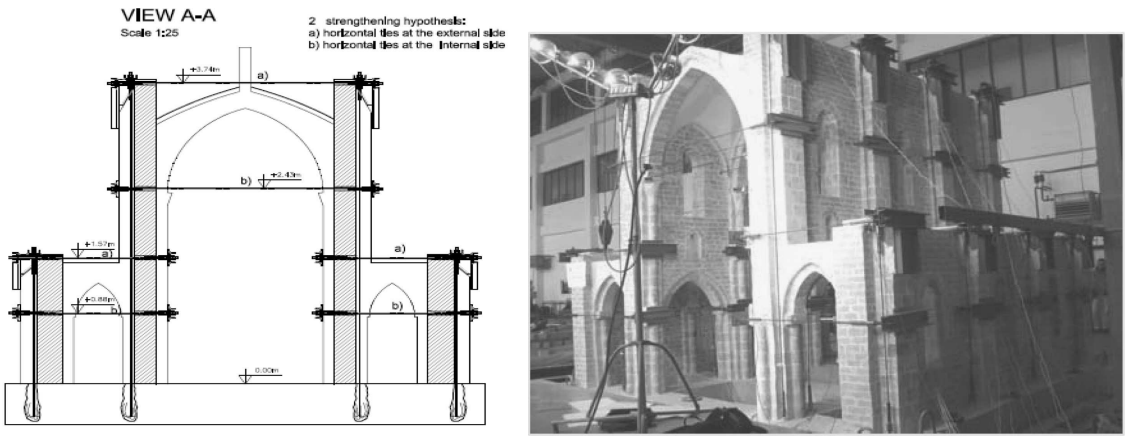


Figure 15. Strengthening of the model with pre-stressed vertical and horizontal external and internal carbon-fiber ties

Seismic tests

During testing phase 2A, 11 seismic tests were performed, with input acceleration between 0.03 g to 0.28 g, by applying the scaled time history of the Calitri Earthquake, as in phase 1. Testing in phase 2A was performed until the development of severe cracks at the level of the main arches and the vaults. In testing phase 2B, when internal ties were also applied to the model together with the external ties, 6 seismic tests were performed with input intensity 0.14 g to 0.40 g.
Actually, the same characteristic horizontal cracks as in phase 1 occurred (Fig. 16a). During the final test of phase 2B, with intensity of 0.4 g, the cracking mechanism developed completely. Severe damage in the model was observed and some of the stones of the central arch fell down. Figure 16b shows details of damage after the accomplishment of the tests.

The push-over curves at the top of the central arch and the top of the buttresses in phases 2A and 2B, respectively, are given in Figures 17 and 18.

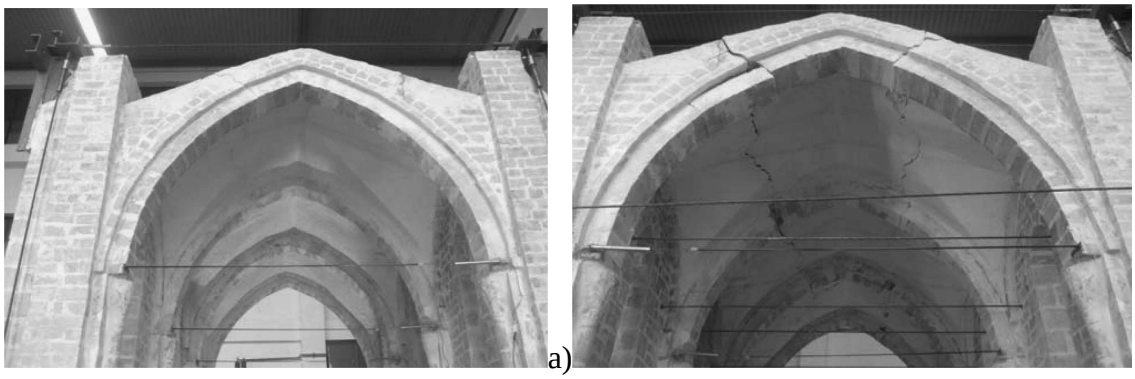


Figure 16. Damage in the model after the phase 2A (a) and 2B (b)

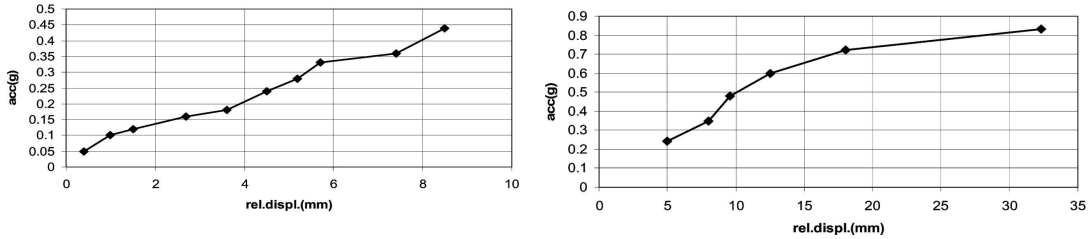


Figure 17. Push-over curves at the top of the central arch obtained in testing phases A and B

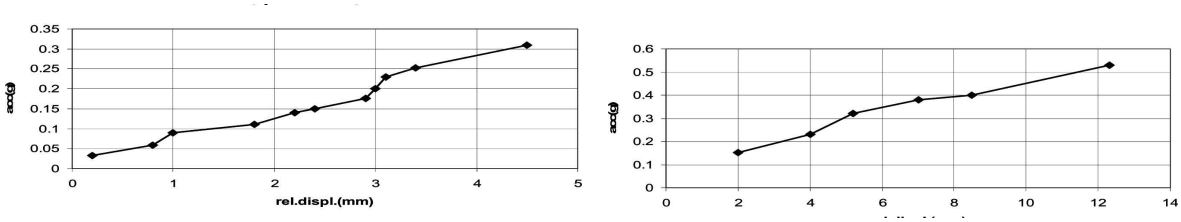


Figure 18. Push-over curves at the top of the buttresses obtained in testing phases A and B

4.4 Numerical analysis

The results achieved in the experimental tests have been numerically reproduced under numerical way (De Matteis et al., 2009). A global 3D view of the church is given in Figure 19a. The material properties were determined on the basis of experimental tests. The first three vibrational modes obtained for the numerical model are shown in Figure 19b and the corresponding eigenvalues compared with the experimental frequency values achieved from ambient vibration tests are reported in Table 2, where it is apparent that a very good agreement among results was reached.

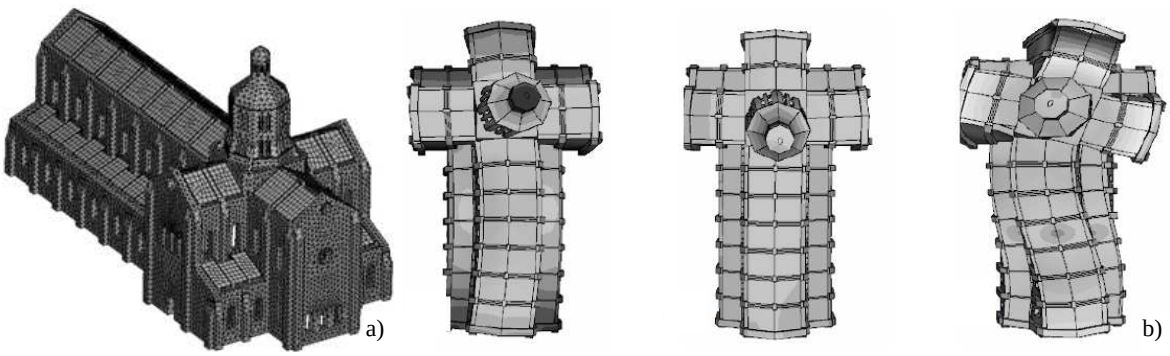


Figure 19. The FEM model (a) and the main modal vibration shapes (b) of the Fossanova church

Direction	Detected natural frequency value [Hz]		
	Ambient Vibration	FEM (1)*	FEM (2)**
Transversal	3.8	3.77	3.65
Longitudinal	4.6	4.63	4.30
Torsional	6.8	6.45	6.15

** with roofing wooden elements*
***without roofing wooden elements*

Table 2: Experimental-numerical comparison in terms of frequencies

As final step of the numerical activity, a non linear analysis was also performed by assuming a macro-modelling-smeared cracking approach (ABAQUS) for masonry. The modal analyses revealed that the more important structural part of the actual complex had to be recognized in the three-central bays of the main nave, as shown in Figure 20a.

This model was considered for the numerical analysis and a symmetry condition about the mid vertical transversal plane was adopted in order to reduce the computational effort. The model was fixed at the base and solid C3D4 (four nodes linear tetrahedron) elements were used with a refined mesh having an average length of 100 mm (Fig. 20b). A proportional load distribution was introduced as an external acceleration applied at the masses.

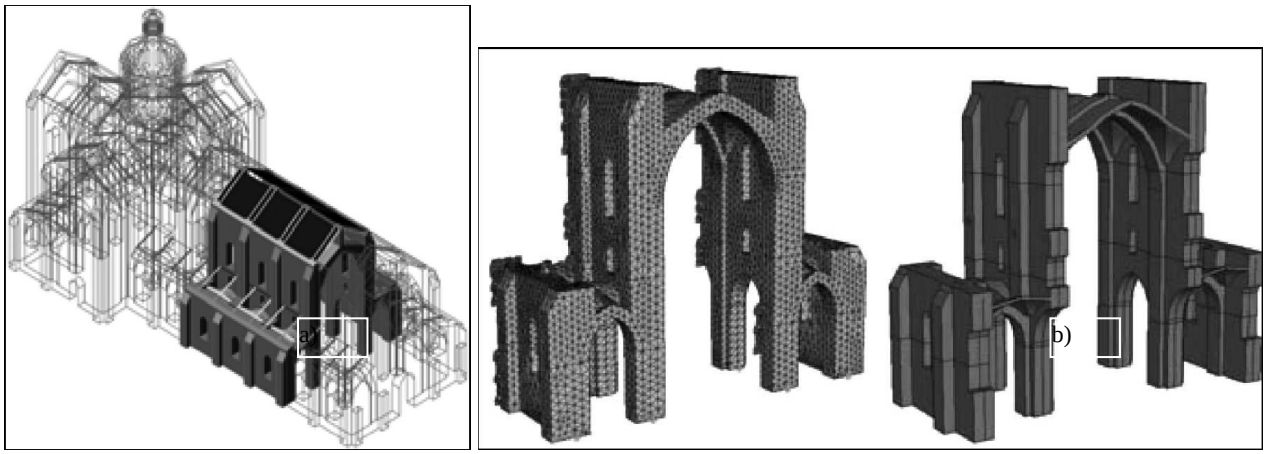


Figure 20. Selected seismic resistant unit in transversal direction (a) and the FEM model for push-over analyses (b)

The analyses on the FEM model showed that the same sequence of damage phases detected in the experimental activity were achieved also in numerical way. Finally, it was noted that when the ultimate experimental control point displacement was applied (d =34 mm), a large deformation appeared at the base of the central piers, whose sections achieved the assumed limit compressive stress.

The global response of the non linear model is synthesized in Figure 21a, whereas in Figure 21b the shear capacity curve of the model, expressed in terms of base-shear/gravity factor versus control point displacement, is plotted. It is apparent that a very good agreement between the non-linear numerical analysis and the experimental tests was achieved in terms of evaluation of the structural capacity of the system.

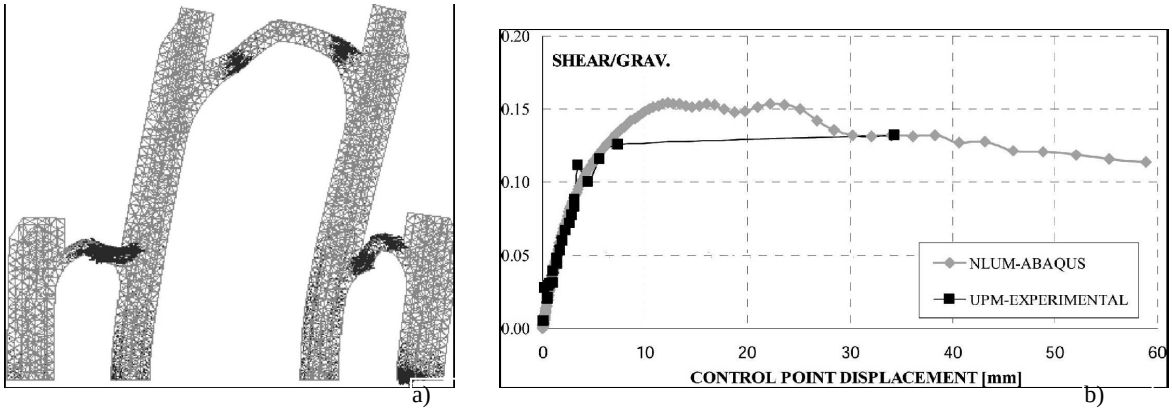


Figure 21. Crack distribution at collapse (a) and experimental-numerical comparison in terms of capacity curves (b)

5 THE GREEK TEMPLE MODEL

5.1 Design phase

Experimental shaking table tests were also carried out at the Earthquake Engineering Laboratory of the National Technical University of Athens on temple sub-assemblages with two different configurations: freestanding columns (Fig. 22a) and columns in a row (Fig. 22b) or in a corner connected by architraves (Fig. 22c) (Dasiou et al., 2009a).



Figure 22: Freestanding (a) and with architraves (in a row (b) and in a corner (c)) columns (C1, C2 and C3 from left to right)

Each column consists of a base, twelve drums and a capital. In order to evaluate the effect of various parameters, the columns were made similar, but not identical. One difference concerns the material used for each column. The capital and the drums of column C1 are made of Dionisos marble, while the base is made of white marble from Kavala. All the blocks of Column C2 and Column C3 are made of Pentelikon marble and Kavala marble respectively. Another important difference is that Column 1 has entasis. In architecture, entasis is the application of a convex curve to a surface for aesthetic purposes and, in particular for classical columns, a small bulge that appears almost at the middle of its height. In accordance with the ancient cuttings, two types of clamps were constructed (Clamp B and Clamp C).

The positioning of the connections in the architraves can be seen in Figure 23. The material of the T-shape clamps used in the experiments is different from the one used in real interventions. In the restoration process, the use of titanium is necessary to avoid corrosion, but since there was not such

need in the experiments, the clamps were made of steel. To secure the connection, leafs of lead were placed between the clamps and the marble. Cement mortar, which is used in practice instead of lead, could not be used in the experiments, due to the scaling restriction (the grain size should be to small).

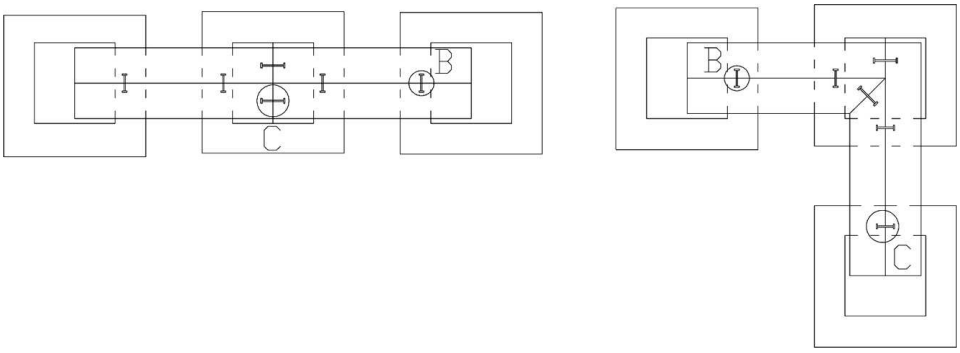


Figure 23: Plan view of the two configurations of the columns and the positioning of the clamps B and C

After these experiments were performed, a new series of tests on these systems upgraded with double T-clamps able to connect architraves was carried out (Mouzakis et al., 2002). The connections are secured in position with cement mortar. The basic criterion for the design of clamps is that, in case of a seismic event, the clamps should absorb the seismic energy and fail before the arble suffers any damage. However, the influence of these connections has not been studied experimentally.

5.2 Testing ser-up

For testing, the following two seismic events, with different characteristics, were chosen from destructive earthquakes in Greece:

- The Kalamata Earthquake (13 September 1986). The magnitude of this earthquake was M=6.2. The accelerogram was recorded on hard soil in a distance of about 9 km from the epicentre. The duration of the strong motion is about 6 sec and the maximum horizontal acceleration is 0.27 g.
- The Lefkada Earthquake (14 August 2003). The magnitude of the earthquake was M=6.4 and the maximum recorded accelerations were 0.42 g and 0.34 g in the two horizontal directions.

Nine displacement transducers, connected, in sets of three, to the midpoints of one side of each capital and to fixed point on the shaking table at the other end, were used in order to record the displacements at the top of the columns. With this setup, the instruments were recording the displacements along their inclined axis and, in order to calculate the displacements of the capitals in the three global axes, proper computations were needed. For each reference point, this was achieved by calculating the intersection of three spheres, centered with the fixed ends of the three transducers connected to it. In addition to the displacement transducers, accelerometers were also used, placed in various positions on the capitals or the architraves.

5.3 Experimental results

Two tests were carried out with the three columns standing free (unconnected). In the first experiment, the columns were subjected to the two horizontal components of the Lefkada record downscaled to 40% of its amplitude. Figure 24a shows the time histories of the absolute displacements of the capitals of the three columns in the longitudinal direction. During the test, each column exhibited different behaviour. The middle column (C2) practically did not move, while the other

two, C1 and C3, experienced large displacements. In the case of column C1, no sliding was observed between the drums and the column was rocking like a monolithic one.

In the second experiment, the Kalamata Earthquake, scaled down to 40%, was used as the base excitation. The columns exhibited different behaviour compared to the first experiment. Column C1 experienced small displacements, while the rotations and displacements of columns C2 and C3 were quite large and similar to each other. In Figure 24b, a comparison of the time histories of the absolute displacement (in the lateral direction) of the capital of column C2 for experiments 1 and 2 is presented.

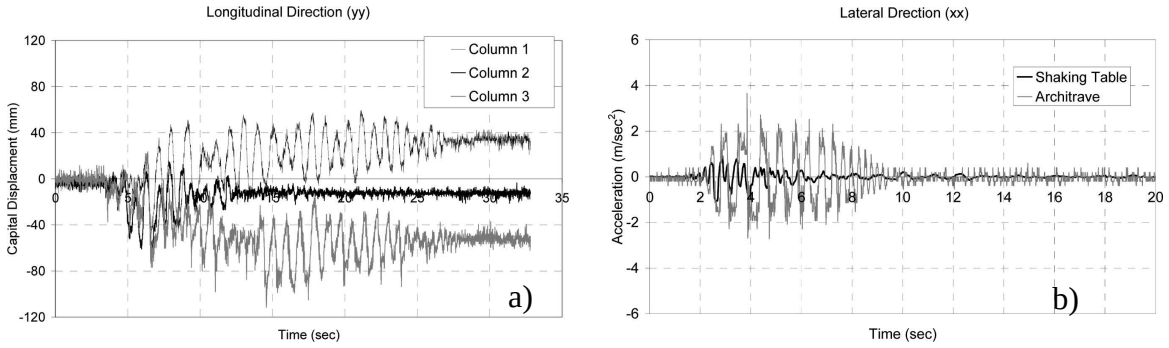


Figure 24: Time histories of the absolute displacements of the capitals of the three columns for Test No.1 (a) and comparison of the time histories of the displacement of the capital of column C2 for tests 1 and 2 (b).

40% of the Kalamata Earthquake. The columns exhibited very small displacements. Columns C1 and C2 and the architraves connecting them moved in phase. All the rocking was occurring at the in the case of temple sub-assemblages without architrave connections, the columns in a row were examined. The test was divided in two phases: in the first phase, the columns were subjected to first drum of the two columns. Column C3 behaved differently: there were many openings and closings of the joints at the middle and the upper part only. Small residual displacements were observed only at column C3 and the architraves.

Since the permanent displacements were not significant, it was decided to submit the specimen to 50% of the Kalamata motion without repositioning the blocks to their initial configuration (Phase 2). This situation corresponds to monuments with structural elements displaced from their intact position, due to previous earthquakes. Figure 25a shows the time histories of the absolute displacements of the capitals of the three columns in the lateral direction. It is noted that the displacements of all columns during the second phase of the experiment were almost twice the ones recorded in the first phase (Fig. 25b). This should not be attributed only to the amplification of the base excitation, but a significant part of the displacement increase might be owed to the initial residual displacements of the drums and the architraves after the first phase.

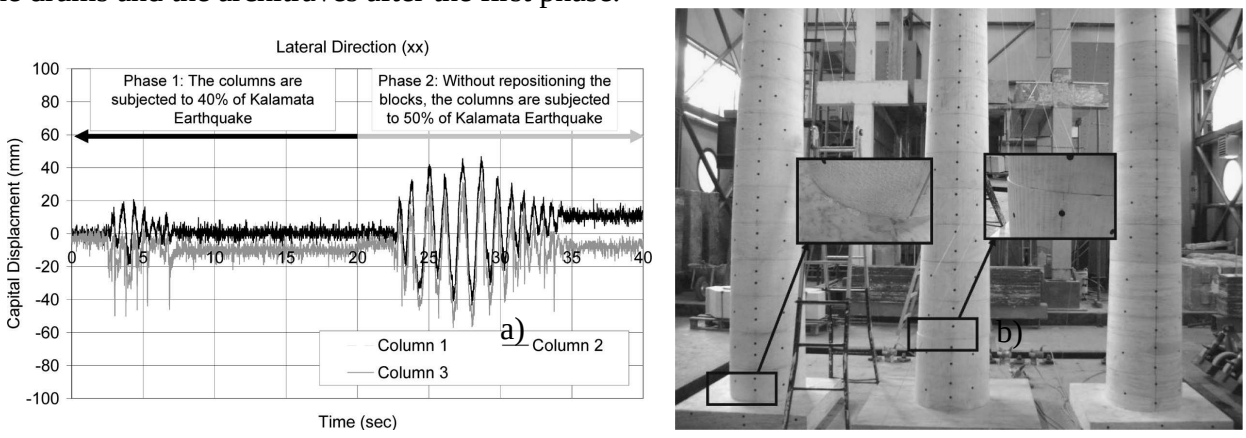


Figure 25. Time histories of the displacement of the capitals of the three columns in test No. 3 (a) and final position of the three columns after test No. 3 (b)

As verified by the experiments, the architraves are the most vulnerable part of the structure and the first to collapse. The purpose of the connections is to prevent this collapse during a seismic event. Although this intervention is used often, the influence of the clamps on the seismic response of the structure has not been studied extensively, neither experimentally nor numerically.

In a further experiment (No. 8), the specimen in a corner configuration with architrave connections was subjected to the Kalamata earthquake scaled down to 40%.

Figure 26a shows the time history of the response of the capital of column C1. On the same diagram, the corresponding displacement for the similar experiment No.7 without connections is also shown for comparison. It was observed that during the first 6 seconds, the column response is not affected by the architrave connections. However, after the strong part of the excitation, the displacement of the column is larger if the architrave beams are clamped. The residual displacement is also larger. Contrary, it was observed that the displacements of the architraves are significantly reduced if they are connected with clamps (not shown in the figure).

Comparison of these experiments with experiments No. 6 and 7 (Fig. 26b), in which the architraves were not connected and the danger of falling was obvious, leads to the conclusion that the use of clamps is in favour of the overall stability of the structure, in spite of the small increase in the response of the columns.

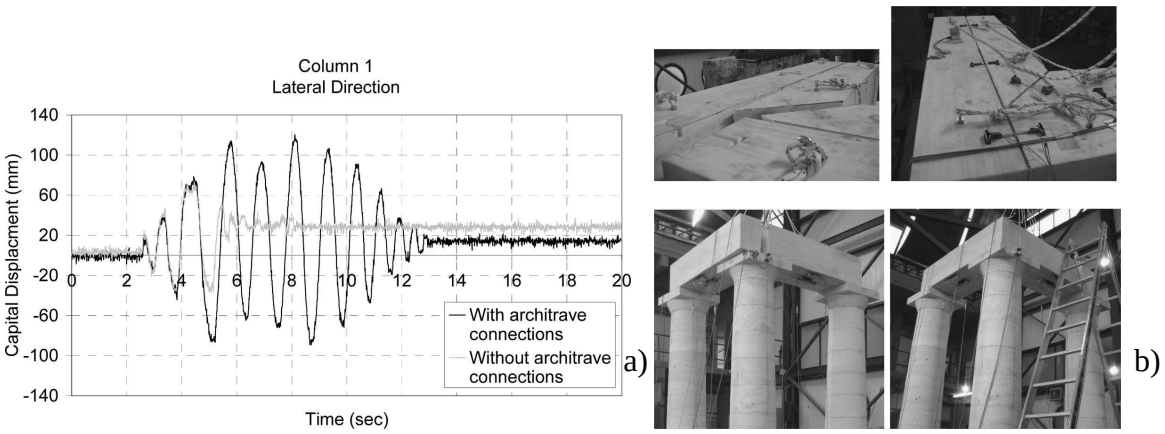


Figure 26. Comparison of the time histories of the displacement of the capital of column C1 for tests No. 7 and 8 (a) and final dislocation of architrave beams after tests No. 7 (left) without connections, and 8 (right) with connections (b).

5.4 Numerical analysis

Three numerical models were created in order to evaluate their efficiency in predicting the seismic response of the considered ancient temples (Dasiou et al., 2009b). For two of them the Finite Element program ABAQUS was used. The geometry of both models was an exact representation of the test specimens. In model 1, the structural elements were assumed to behave as three-dimensional rigid blocks; the contact between the blocks was modelled by means of elastic spring connectors, including a damping coefficient. In model 2, the drums were modelled as three-dimensional elastic deformable bodies (Fig. 27 a). The contact between adjacent blocks was defined by means of mechanical contact-surface interaction elements with friction coefficient equal to 0.70. When surfaces are in contact, these elements transmit shear and normal forces across the interface. In the normal direction, a hard contact approach is considered and interpenetrating is regarded as non-physical and prevented (ABAQUS). The code allows the opening of joints, even complete detachments of the blocks and automatically detects new contacts as the calculation proceeds. Model 3 was created using the code 3DEC of Itasca consulting Group (3DEC), which is based on the distinct (or discrete) element method (Fig. 27 b). The Code was initially designed for the analysis of the behaviour of rock masses, which are modelled as assemblies of discrete rigid bodies and discontinuities are considered as boundary conditions.

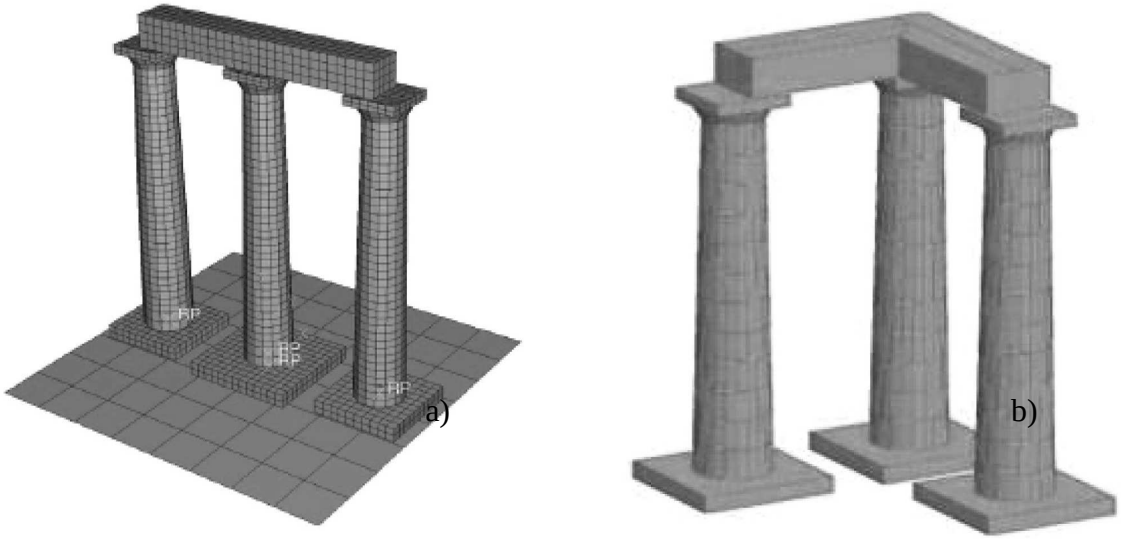


Figure 27. FEM model 2 implemented with ABAQUS (a) and FEM model 3 implemented with 3DEC (b).

Figure 28 presents the comparison of the numerical results for models 2 and 3 with the experimental data for the freestanding columns C1 and C3 obtained in 2007. The accuracy of the numerical analyses is again quite satisfactory.

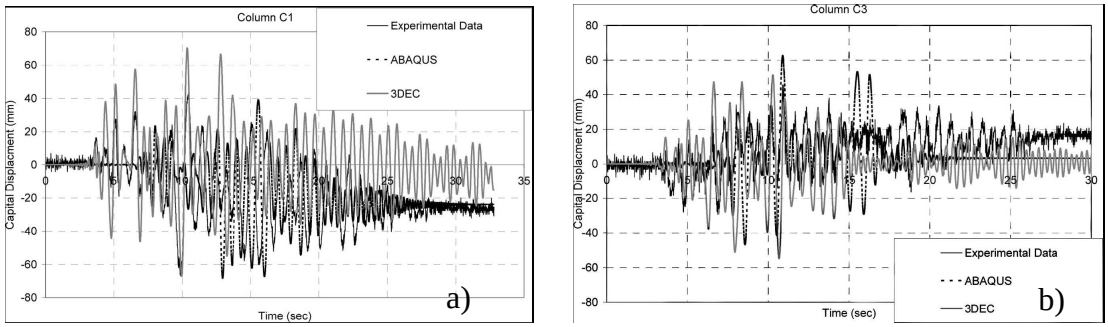


Figure 28. Time histories of the displacement of the capital of freestanding column C1 (a) and C3 (b)

The data from three experiments with specimens in a row or in a corner were reproduced numerically using model 3. It was evident that the numerical model can predict the experimental data very accurately in all cases, better than the response of freestanding columns. Even the out-of-plane slippage could be predicted. This should be attributed to the fact that, as the experiments showed, configurations of columns connected with architraves are less sensitive than freestanding columns.

Finally, it was concluded that:

- Model 1 presented the less accurate results. The results obtained with models 2 and 3 are similar and quite satisfactory.
- More accurate results were obtained for the columns connected with architraves, because the response is less sensitive in this case.
- Model 2 is significantly more time consuming compared to model 3 that makes it practically prohibitive for structure with many elements. However, the stresses induced at the blocks can be obtained. Thus, the selection of the appropriate model depends on the size of the structure and the results needed.

6 THE BYZANTINE St. NiCHOLAS CHURCH MODEL

6.1 Design phase

The shake-table test of the Byzantine church model was performed in Skopje in the period July 15–16, 2008 (Tashkov et al., 2009b). The model of the church was designed to the length scale of 1:3.5 according to the "gravity force neglected" modelling principles (Fig. 29).

The structural system of the church consists of façade walls constructed of hewn stone and brick bound with mortar. In the interior, there are two symmetrically placed rows of columns interconnected by vaults. The wall elements were constructed in the typical Byzantine style of building with two faces of brick and stone masonry and the intervening space filled with a care of rubbish set in a great quantity of mortar. The columns were constructed of the same materials. The vaults and the arches were constructed of hewn tuff, while the tambour and the domes were constructed of bricks in lime mortar. The walls were set on massive masonry foundations. The church in its full size is proportioned 12.7×8.2mat plan and is surmounted by a dome with a height of 10.6 m.

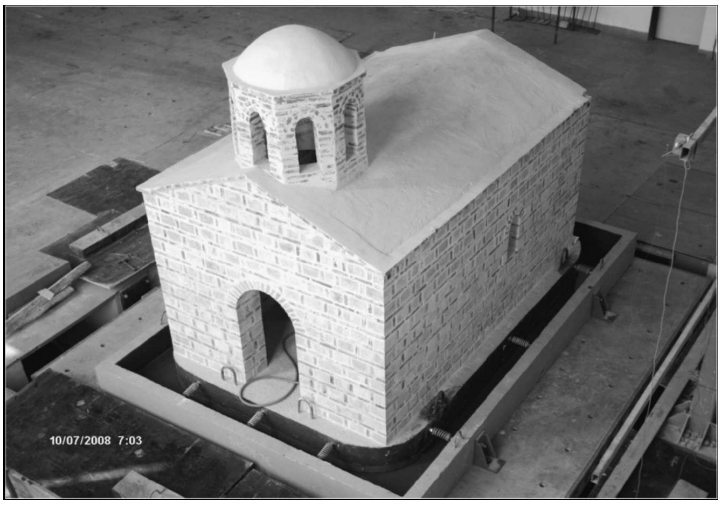


Figure 29. Byzantine St. Nicholas church

The structural system of the church consists of façade walls made of hewn stone and brick bound with mortar. In the interior, there are two symmetrically placed rows of columns interconnected by vaults. The wall elements were constructed in the typical Byzantine style of building with two faces of brick and stone masonry and the intervening space filled with a care of rubbish set in a great quantity of mortar. The columns were made of the same materials. The vaults and the arches were made of hewn tuff, while the tambour and the domes were of bricks in lime mortar. The walls were set on massive masonry foundations. The real church has the full size in plane of 12.7×8.2 m and it is surmounted by a dome with a height of 10.6 m.

6.2 Testing set-up

The model of the church was built at the IZIIS Laboratory in scale 1:3.5 and tested on the biaxial seismic shaking table. The main objective of the testing was to experimentally investigate the effectiveness of the proposed system for increasing the seismic resistance of this type of historical building, which consists on a special type of base isolation, so called ALSC floating-sliding system (Tashkov et al, 2009b).

The seismic shake-table testing was performed in two main phases:

- phase 1 : testing of the base-isolated model with the ALSC floating-sliding system:
- phase 2 : testing of the original fixed-base model.

The model with the sliding base was tested first, because it was expected that no damage will occur. That was confirmed even under the maximum capacity of the shaking table (1.5 g). The second phase was done with the fixed base model, which simulates the original structure on the site.

The automatic system for activation of the working pressure under the sliding plate and keeping it constant as long as needed plays an important role in the effectiveness of the ALSC base-isolation system. Basically, the automatic pressure control system consists of a steel reservoir filled with liquid under pressure, kept constant by means of a compressor and a servo-valve. The servo-valve is closed until the pressure of the liquid under the sliding plate is decreased for more than 10%. After that, the valve opens and the liquid from the steel reservoir comes to the sliding plate increasing the pressure up to the required level. Having this system, the structure does not need to be subjected to a permanent pressure for a long time waiting for the earthquake. It will be activated just a few seconds before the shear seismic waves attack the structure. In the case of the shake table test, the system for pressure control was activated a few seconds before the shake-table started to move and remained active during the testing time (few hours). The testing procedure applied to the model consisted of several steps:

- Preliminary tests (ambient vibration and random excitation) for definition of the dynamic characteristics of the model, in order to check the stiffness degradation of the model produced by micro- or macro-cracks developed during the tests;
- Seismic testing under selected earthquake records (Montenegro Petrovac 1979 earthquake).

To follow the dynamic response during the seismic shake-table testing, the original model was instrumented at characteristic points with accelerometers and displacement transducers, for measuring the absolute displacements (LPs) as well as the relative displacement between the fixed basin and the sliding foundation plate in the direction of the excitation (LVDTs).

6.3 Experimental results

Testing phase 1: Base-isolated model by ALSC system

The test specification is given in Table 3, together with some response parameters for the selected tests.

		Acceleration(g)			Relative displ.(mm)	
Test	Excitation	basin	plate	top	tambour	basin-plate
1	Harm 7 Hz	0.80	0.15	0.12	0.20	7.00
2	Harm 5 Hz	0.60	0.15	0.16	0.22	3.00
3	Petrovac	0.20	0.20	0.18	0.15	3.50
4	Petrovac	0.45	0.25	0.18	0.20	6.00
5	Petrovac	0.80	0.25	0.25	0.30	15.00
6	Petrovac	1.20	0.32	0.35	0.38	20.00
7	Petrovac	1.45	0.25	0.22	0.28	35.00

Table 3: Performed tests in phase 1 – base isolated model

The first two tests were performed with harmonic excitation of 7 and 5 Hz. Other tests were performed with the Petrovac, 1979 earthquake. The earthquake was scaled with a scaling factor of 3.5 according to the modeling principles of "*gravity force neglected*" model. It was compressed 3.5 times of the time scale and 3.5 times of the acceleration scale (0.43 g×3.5=1.5 g). The model was tested with 5 different levels of input acceleration: 0.45 g, 0.8 g, 1.2 g and 1.45 g. Uniform sliding of all parts of the structure was recorded (sliding plate, walls and tambour). The maximum response acceleration of the sliding plate in all cases was about 0.2–0.3 g. This was actually a limitation of the transmissibility of the forces from the basin to the sliding plate. This level of acceleration did not produce any cracks in the model, except an increased relative sliding displacement between the basin and the sliding plate. Under maximum input acceleration of 1.5 g, the relative displacement was about 3.5 cm.

Testing phase 2: Fixed base model

Before testing, the model was fixed by steel bolts and wooden beams. The pressure of the liquid was set to 0. Then, the model was transformed into a classical fixed base structure. The input acceleration was changed in several tests from 0.1 g to 0.7 g. The amplification of the response was: 1.5–2.0 for the top of the wall and 3–4 for the top of the dome. The test results are given in Table 4. The damage pattern is shown in Figure 30. The push-over curve (acceleration response versus relative displacement at the top of the wall) is presented in Figure 31.

		Acceleration (g)			Rel.displ (mm)	
Test	Excitation	basin	plate	top	tambour	basin-plate
1	Petrovac	0.10	0.18	0.25	0.20	0.50
2	Petrovac	0.15	0.25	0.38	0.25	0.70
3	Petrovac	0.20	0.30	0.45	0.40	1.00
4	Petrovac	0.27	0.42	0.60	0.70	1.50
5	Petrovac	0.32	0.50	0.70	0.80	2.00
6	Petrovac	0.38	0.55	1.00	1.00	3.00
7	Petrovac	0.40	0.60	1.50	1.10	13.00*
8	Petrovac	0.45	0.65	/	2.00	/
9	Petrovac	0.50	0.70	/	2.50	/
10	Petrovac	0.60	1.00	/	3.00	/
11	Petrovac	0.70	1.20	/	7.00	/**

*collapse of the tambour.
**heavy damage to the openings and cracks in the walls.

Table 4: Performed tests in phase 2 – fixed base model

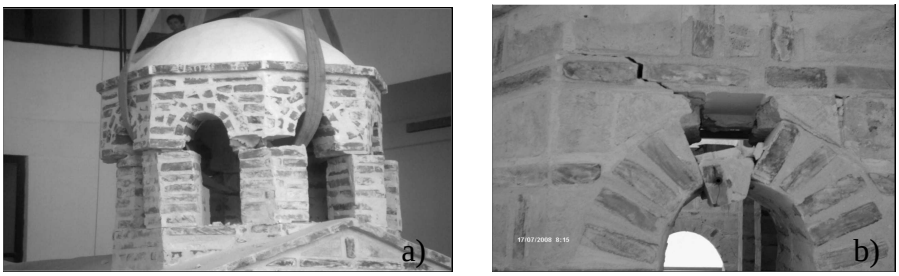


Figure 30. Collapse of the tambour (0.45g) (a) and damages to wall and openings (0.70 g) (b)

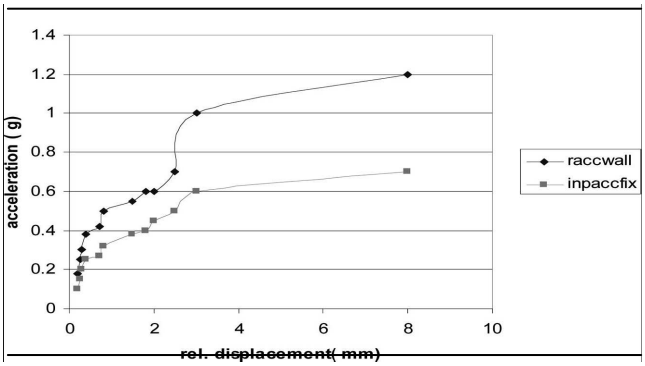


Figure 31. Pushover curve of the church

6.4 Numerical analyses

Two 3D numerical models of the scaled church were set up (Fig. 32) (Kokalanov et al., 2009). The experimental investigations were used for the verification of the mathematical model. The elastic parameters are referred to initial values which were calibrated on the basis of first random vibration tests performed on the original undamaged structure. The non-linear properties were determined on the basis of both compression and shear experimental tests carried out on masonry wall specimens (Gramatikov et al., 2005).

Linear static and dynamic analyses of the models were performed. The results obtained by modal analysis of the model were compared to the experimental results obtained by ambient vibration tests on the actual structure (Table 5).

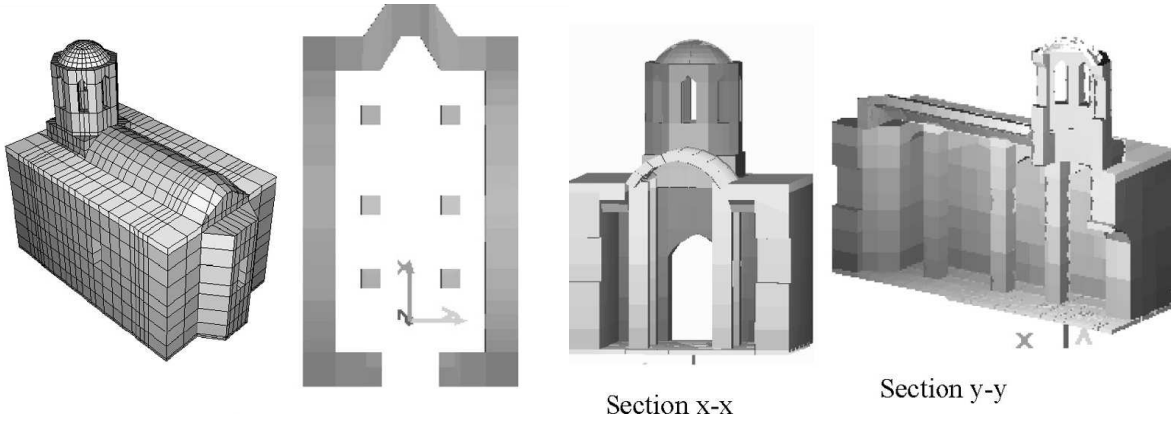


Figure 32. FEM model of the St. Nicholas church

	Module of elasticity MPa	Frequency [Hz]	
		x-x	y-y
Ambient vibration tests		2.8	2.8
Numerical model	290	2.85	2.86

Table 5. Comparison among experimental and numerical frequencies

A linear dynamic analysis was performed by using an actual earthquake record – time history analysis. The record of Petrovac (Montenegro) earthquake was used for simulation. The results from the dynamic analysis confirmed that the most vulnerable part of the church is the lower part of the tambour.

The seismic capacity of the church was obtained by a nonlinear analysis. It is common to use two different loading schemes: a constant acceleration along the total height and the loading defined using the first eigenform in the load direction. In the implemented pushover analyses, a uniform acceleration along the horizontal direction was applied. The numerical results showed that, when collapse of the tambour happened, the rest of the structure was still in good condition. A new model of the church without the tambour was created. This model was used to determinate the seismic capacity of the main structure.

The collapse load on the investigated prototype is 0.68 g, which is very closed to the experimentally determinate collapse of the structure, which happened at seismically exaltation of 0.7 g.
In general, it should be noted that the crack patterns obtained from numerical analyses have always to be ascribed to the attainment of tensile or shear strength, while the compressive resistance is never exceeded. According to the numerical model, the first diagonal tension cracks occur in the shear walls, just over the door opening.

After the analysis on the original church, a new FEM model of the retrofitted church by ALSC system was created (Figure 33).

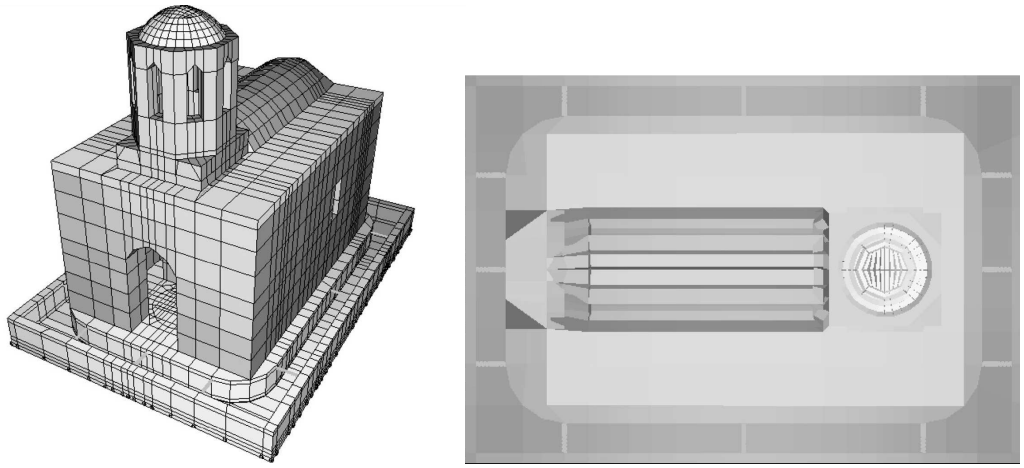


Figure 33. FEM model of the St. Nicholas church retrofitted by ALSC system

The comparison between the original church and the upgraded one by the ALSC system shows frequency shifting from 4.0 Hz (original church) to 1.0 Hz (upgraded church). The ALSC system consequently provides a reduction of relative displacement between top level and the base, from 74 mm to 1 mm, which means that the church translate horizontally over the smooth base in the range of +/−100mm, under an uplifting working pressure of 0.65 bars.

Therefore, the comparison among results shows successful upgrading of the structure by ALSC system, since the acceleration and shear force are reduced about 4.5 times comparing to original structure.

7 CONCLUSIONS

Some experimental and numerical activities, framed within the FP6 EC PROHITECH research project “Earthquake PROtection of HIstorical Buildings by Reversible Mixed TECHnologies”, on the application of RMTs to the historical and monumental constructions of the Euro-Mediterranean area, are presented and discussed in this paper. Within this range, shaking table tests have been car-

ried out on four large scale models of the following monumental constructions: the Mustafa Pasha Mosque in Skopje, the Gothic Cathedral in Fossanova, the Parthenon temple in Athens and the St. Nikola Byzantine Church in Psacha.

Experimental testing on the Mustafa Pasha large scale model was performed to investigate the seismic capacity of the monument after applying a reversible strengthening methodology, for both the minaret and the mosque. Shaking table testing was performed for the original model and for model strengthened by C-FRP. The strengthening of the minaret by application of a C-FRP strips and wraps enabled stiffening and increasing of its bending resistance. The mosque model behaviour, after strengthening by incorporation of carbon rods in longitudinal mortar joints and horizontal belt courses at the base of the tambour as well as at the base of the dome by using C-FRP wraps, was evidently different in respect to that of the original model. Under tests of moderate intensity, the existing cracks were activated, but during the subsequent more intensive tests, the failure mechanism was transferred to the lower zone of the bearing walls, in the direction of the excitation, where typical diagonal cracks occurred due to shear stress. Considering the obtained experimental results for the original model and for the strengthened one, it can be concluded that the applied strengthening technique has significantly improved the seismic resistance of the monument. The results of this experimental investigation were the starting point for the Cultural Heritage authorities of Macedonia to adopt the same consolidation system for the real mosque (Mazzolani et al, 2009).

The experimental study performed on the Fossanova church demonstrated that the seismic performance of the model was significantly improved by the applied strengthening methodology, which represent a modern interpretation of a traditional technology based on the use of ties, which are able to confine the structure. In particular, the ties are mainly effective in preventing and controlling the relative displacements of the columns. This was manifested by controlled “opening” along the two main cracks developed at the level of the main arch during the intensive seismic shaking. In order to make an effective comparison between the original model and the strengthened one, it is important to compare the input intensity which provoked serious damage to both models. For the original model the critical input intensity was 0.14 g, while it was 0.28 g for the strengthened model in phase 2A, and 0.40 g in phase 2B. These values clearly show the effectiveness of the applied strengthening technique.

From the performed experimental activity on the Greek temples the following conclusions were drawn:

- Columns of ancient temples are more stable and their behaviour is less sensitive to small changes of the geometry or the excitation, when connected with architraves than when they are standing free.
- The response is larger for corner configurations than for columns in a row. Especially the architraves of corner columns are the most vulnerable parts of the structure with high danger of collapse during strong earthquakes.
- The nonlinearity of the response was verified during the experiments. Thus, an increase in the base motion does not necessarily result in an increase of the response. In some cases, the residual displacements were reduced by amplifying the excitation.
- The connection of the architrave beams by clamps leads, in general, to a significant decrease of the beams sliding on the capitals and reduces the danger of their collapse. However, the response of the columns might increase. Due to the ambiguous influence of the clamps, numerical investigation is recommended, before they are implemented in the restoration process.

Finally, the comparative test between the base-isolated model by ALSC system and the classical fixed base model of the byzantine church clearly shows the superior behaviour of the ALSC floating-sliding base-isolation system. The excitation of 1.5 g (maximum capacity of the shaking table and maximum peak acceleration of the Montenegro earthquake-scaled by a factor of 3.5) was not enough to produce any damage to the dome and to the walls. The tests show that the system can protect the structure in any frequency and/or amplitude range as well as against the strongest earth-

quake. Contrary, the fixed base model is very vulnerable. The amplification factor ranges from 1.5 for the walls to 3.0 for the dome. The consequence is an early damage to the dome (0.45 g) and severe damage to the walls (0.7 g) in the case of the model, whereas 0.12 g for the dome and 0.2 g for the walls in the case of the real structure.

8 ACKNOWLEDGEMENTS

The author, in his quality of chairman of the Prohitech project, is very pleased to express is sincere thanks to Kiril Gramatikov, leaders of WP7 "Experimental activity" and to Raffaele Landolfo, leader of WP8 "Numerical activity" for their effective work, which this paper is referred to and some parts of which are directly taken from the original papers. The details of the whole Prohitech activity are shown in 6 volumes, now in press, which contain the results of the research work of 150 experts from 16 international institutions involved in this project.

9 REFERENCES

De Matteis, G., Eboli, A., Campitiello, F. & Mazzolani, F.M. 2009. Seismic analysis of the Fossanova gothic church by numerical models and comparison with experimental tests. *Proc. of the Int. Conference "Protection of Historical Buildings" (PROHITECH 09)*, Rome, 21-24 June, Volume 1, CRC Press/Balkema, Leiden, The Netherlands, ISBN: 978-0-415-55804-4, 131-136.

Dasiou, M.E., Mouzakis, H. I., Psycharis, N., Papantonopoulos, C. & Vayas, I. 2009a. Experimental investigation of the seismic response of parts of ancient temples. *Proc. of the Int. Conference "Protection of Historical Buildings" (PROHITECH 09)*, Rome, 21-24 June, Volume 2, CRC Press/Balkema, Leiden, The Netherlands, ISBN: 978-0-415-55805-1, 1617-1622.

Dasiou, M.E., Psycharis, N. & Vayas, I. 2009b. Verification of numerical models used for the analysis of ancient temples. *Proc. of the Int. Conference "Protection of Historical Buildings" (PROHITECH 09)*, Rome, 21-24 June, Volume 2, CRC Press/Balkema, Leiden, The Netherlands, ISBN: 978-0-415-55805-1, 1269-1274.

Gramatikov, K., Tashkov, Lj. & Krstevska, L. 2005. Experimental Analysis, Preliminary study for design of models for shaking table testing. *Report prepared within the WP7 of the PROHITECH Project "Earthquake Protection of Historical Buildings by Reversible Mixed Technologies"*.

Kokalanov, G., Tashkov, Lj., Krstveska, L. & Aleksovska, M. 2009. Analytical and experimental investigations of Byzantine church. *Proc. of the Int. Conference "Protection of Historical Buildings" (PROHITECH 09)*, Rome, 21-24 June, Volume 2, CRC Press/Balkema, Leiden, The Netherlands, ISBN: 978-0-415-55804-4, 149-154.

Krstveska, L., Tashkov, Lj., Gramatikov, K., Mazzolani, F.M. & Landolfo, R. 2009. Seismic Shaking table test of Mustafa Pasha Mosque model in reduced scale. *Proc. of the Int. Conference "Protection of Historical Buildings" (PROHITECH 09)*, Rome, 21-24 June, Volume 2, CRC Press/Balkema, Leiden, The Netherlands, ISBN: 978-0-415-55805-1, 1633-1639.

Mazzolani, F.M. (Editor). 2009a. *Protection of Historical Buildings - PROHITECH 09*. Volumes 1 and 2, CRC Press/Balkema, Leiden, The Netherlands, ISBN: 978-0-415-55804-4 (Vol.1) and 978-0-415-55805-1 (Vol. 2).

Mazzolani, F.M. 2009b. The output of the PROHITECH research project. *Proc. of the Int. Conference "Protection of Historical Buildings" (PROHITECH 09)*, Rome, 21-24 June, Volume 1, CRC Press/Balkema, Leiden, The Netherlands, ISBN: 978-0-415-55804-4, 63-74.

Mazzolani, F.M. (Chairman). 2011a. *Seismic Protection of historical buildings: experimental activity*. FP6 PROHITECH Project "Earthquake Protection of Historical Buildings by Reversible Mixed Technologies", Volume 3, Polimetrica International Scientific Publisher, Monza, Italy, ISBN: 978-88-7699-169-1 (in press).

Mazzolani, F.M. (Chairman). 2011b. *Seismic Protection of historical buildings: numerical activity*. FP6 PROHITECH Project "Earthquake Protection of Historical Buildings by Reversible Mixed Technologies", Volume 4, Polimetrica International Scientific Publisher, Monza, Italy, ISBN: 978-88-7699-169-1 (in press).

Mazzolani, F.M., Sendova V.I. & Gavrilovic P. 2009. Design by testing of seismic restoration of Mustafa Pasha Mosque in Skopje. *Proc. of the Int. Conference "Protection of Historical Buildings" (PROHITECH 09)*, Rome, 21-24 June, Volume 1, CRC Press/Balkema, Leiden, The Netherlands, ISBN: 978-0-415-55805-1, 169-174.

Mouzakis, H. P., Psycharis, I. N., PapastamatiouX, D. Y., Carydis, P. G., Papantonopoulos C. & Zambas, C. 2002. Experimental investigation of the earthquake response of a model of a marble classical column. *Earthquake Engineering and Structural Dynamics* 31:1681–1698.

Tashkov, Lj., Krstveska, L., De Matteis, G., Gramatikov, K. & Mazzolani, F.M. 2009a. Shake-table test of a model of Fossanova church in reduced scale. *Proc. of the Int. Conference "Protection of Historical Buildings" (PROHITECH 09)*, Rome, 21-24 June, Volume 2, CRC Press/Balkema, Leiden, The Netherlands, ISBN: 978-0-415-55805-1, 1683-1689.

Tashkov, Lj., Krstveska, L., Gramatikov, K. & Mazzolani, F.M. 2009b. Shake-table test of the model of St. Nicholas church in reduced scale 1/3.5. *Proc. of the Int. Conference "Protection of Historical Buildings" (PROHITECH 09)*, Rome, 21-24 June, Volume 2, CRC Press/Balkema, Leiden, The Netherlands, ISBN: 978-0-415-55805-1, 1691-1697.

COMPDYN 2013
4th ECCOMAS Thematic Conference on
Computational Methods in Structural Dynamics and Earthquake Engineering
M. Papadrakakis, V. Papadopoulos, V. Plevris (eds.)
Kos Island, Greece, 12–14 June 2013

DETAILED COMPONENT MODELLING OF A SELF-CENTERING ENERGY DISSIPATIVE BRACE SYSTEM

Jeffrey Erochko[1], Constantin Christopoulos[2], and Robert Tremblay[3]

[1] Carleton University
1125 Colonel By Drive, Ottawa, ON Canada
e-mail: jeffrey.erochko@carleton.ca

[2] University of Toronto
35 St. George Street, Toronto, Ontario, Canada
c.christopoulos@utoronto.ca

[3] Ecole Polytechnique Montreal
2900, boul. Édouard-Montpetit, Montreal, Quebec, Canada
robert.tremblay@polymtl.ca

Keywords: Self-Centering Systems, High Performance Structures, Component Modelling, Construction Tolerances, Effective Stiffness

Abstract. *The self-centering energy-dissipative (SCED) brace is a new steel bracing member that provides damping to a structure and a re-centering capability, reducing or eliminating residual building deformations after major seismic events. Recently, the SCED concept has been extended through the design and construction of a new enhanced-elongation telescoping SCED (or T-SCED) brace that allows for self-centering behaviour over a range that is two times as large as the range that could be achieved by the original SCED bracing system. Previous prototype tests of SCED and T-SCED braces have shown that the simplified estimates of the initial brace stiffness that were previously used do not predict the results from the prototype tests well. To accurately model the mechanics of these new systems, a new software tool has been developed that is able to represent the detailed behaviour of SCED braces to determine realistic brace stiffness and the effect of construction tolerances on the brace behaviour. In this paper, the inner workings of the software tool are described and its analysis results are compared to the test results from the two previous experimental studies to demonstrate the software's ability to model SCED and T-SCED behaviour accurately.*

1 INTRODUCTION

The self-centering energy dissipative (SCED) brace is an innovative bracing system for structures that has recently been designed in Canada [1]**.** The mechanics of the SCED brace system are shown in Figure 1. The inner and outer members in the figure are connected to opposite ends of the brace. Two free end plates, one at either end of the two members, abut the ends of both. Post-tensioned tendons connect the two end plates. These tendons elongate both when the brace is in tension and when it is in compression. This provides a restoring force to the system which causes it to be self-centering. An energy dissipation element is also present. This dissipator may consist of a friction, yielding, viscous or shape memory alloy device and it acts on the basis of the relative movement of the inner and outer sections. The effect of the self-centering behavior combines with the energy dissipation to create the flag-shaped hysteretic response shown in Figure 2.

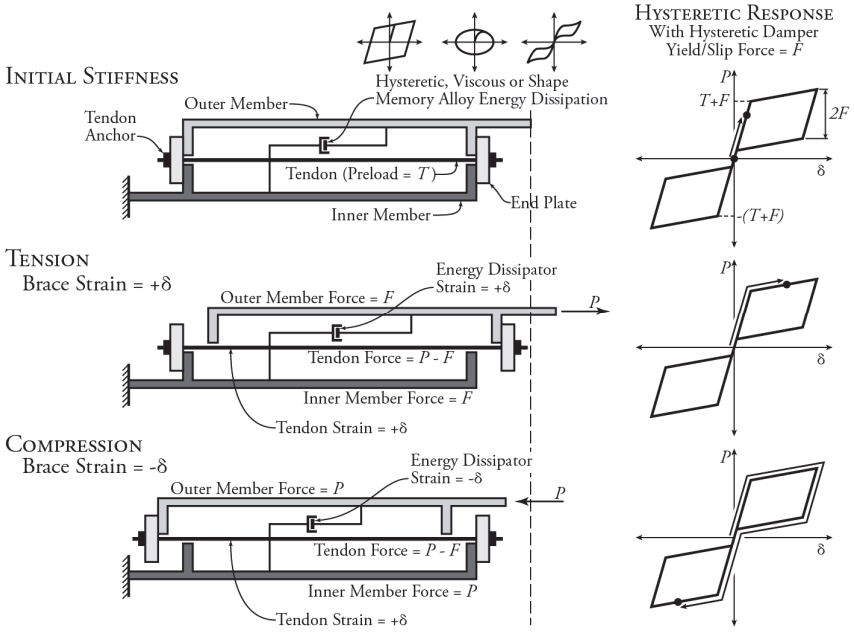


Figure 1: SCED Brace Mechanics (adapted from [1])

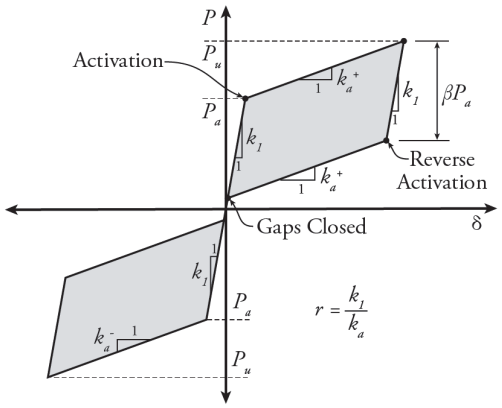


Figure 2: SCED Brace Simplified Hysteresis

The SCED brace concept has recently been extended to achieve double the elongation capacity of the brace for a given type and length of tendons. This concept utilizes one or more intermediate members in between the inner and outer members to allow the use of one or more extra sets of tendons [2]. The extra sets of tendons are effectively in series with the original set, meaning that each set of tendons will share the total deformation of the brace. This new type of SCED brace is called the telescoping SCED or T-SCED and the mechanics of the system are shown in Figure 3.

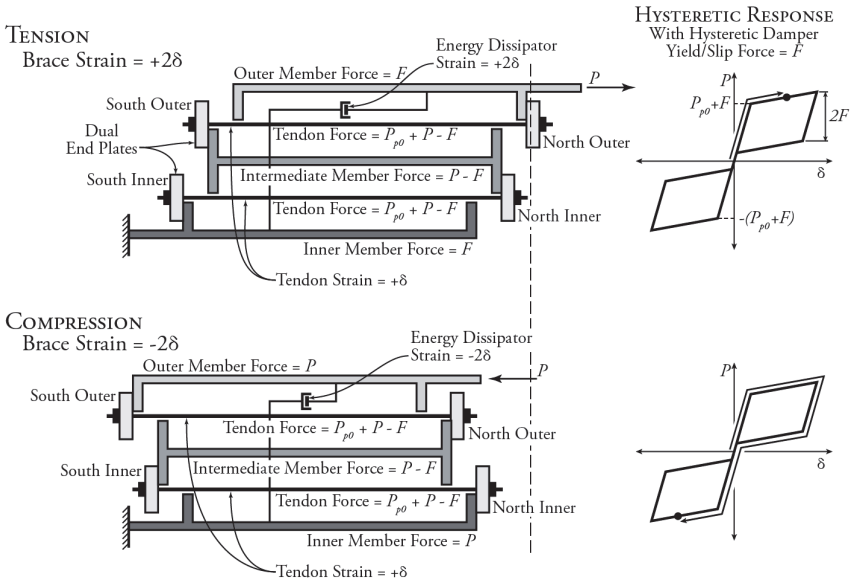


Figure 3: T-SCED Brace Mechanics [2]

Previous tests of SCED and T-SCED braces [1-3] have determined that the initial stiffness of SCED braces as calculated using the simplified method discussed in [1] do not provide a good estimate of the true initial stiffness found during physical testing. It was suspected that this discrepancy may have been caused by imperfect construction tolerances that were applied to the total length of the inner, intermediate and outer members. Since the effect of member length differences on the hysteretic behavior of SCED and T-SCED braces could not practically be developed using a closed-form mechanics solution, a mechanics simulation program was written which uses a nonlinear stiffness method analysis to calculate a more realistic hysteretic behavior. This program is called the SCED Mechanics Simulator and it can simulate the hysteretic effect of any combination of member stiffnesses, arbitrary internal friction damper slip forces at either end of the brace, and member length construction tolerances. It also includes the ability to add viscous damping in parallel with the brace and to simulate the effect of that damping at a specific sinusoidal frequency.

This paper will present the algorithmic implementation of the SCED Mechanics Simulator and the user interface. The Mechanics Simulator will then be used to investigate the effect of construction tolerances on the hysteretic behavior of the brace and the initial stiffness. Then, two previous SCED and T-SCED brace prototype tests will be modeled to show that the simulator provides a good prediction of real brace hysteretic response.

2 THE SCED MECHANICS SIMULATOR MODEL

The SCED Mechanics Simulator requires a web browser in order to run. The program may be found online at "www.erochkoengineering.com/SCED". It was programmed using HTML5 and JavaScript so that it is cross-platform compatible and may be served to users over the web. As such, any computer system with a modern web browser can use the software whether the system is Windows, Mac, or Linux-based. All of the programs inputs, outputs and interactive elements are contained within a single dynamic webpage. The open-source JavaScipt package Sylvester was used to provide linear algebra capabilities for the mechanics calculations [4]. A number of other open-source JavaScript packages were used to facilitate other various user interface capabilities. The package JQuery was used to add dynamic functionality to the HTML page [5]. JQueryUI was used to provide the visual user interface elements for the input forms, buttons and sliders [6]. The JQuery extension Flot was used to provide dynamic data plotting and charts [7]. The dynamic schematic of the SCED brace was drawn using the HTML5 canvas element, but backwards-compatibility support for the canvas element in older browsers was provided using the package ExplorerCanvas [8]. Input box validation to restrict users to appropriate input values and ranges was provided using the LiveValidation javascipt package [9].

2.1 Algorithmic Implementation

The SCED Mechanics Simulator models SCED brace hysteretic behaviour using a nonlinear incremental stiffness method analysis. The stiffness matrix for the analysis contains elements that are connected and arranged as shown in Figure 4. The model itself is effectively one-dimensional; however, for clarity, the figure shows the model elements spaced out in two dimensions. As the figure shows, two different stiffness matrices are possible depending on whether the brace being modelled is an original SCED or a T-SCED. The elements that represent the inner, intermediate and outer members (k_i, k_m, k_o), and the tendons (k_p, k_{p1} and k_{p2}) have a permanent linear stiffness which is dictated by the input parameters. The connection stiffness element (k_{conn}) also has a permanent stiffness dictated by an effective series connection stiffness provided in the inputs. The end plate contact elements ($k_{g[\,]}$) represent the contact between the end surfaces of each of the axial members and the end plates. The stiffness of these contact elements is set at each analysis step to be equal to either the bearing stiffness provided in the inputs (during contact), or a small non-zero stiffness (when not in contact). The internal friction damper elements (k_{f1} and k_{f2}) represent the conditional stiffness of the friction dampers. Similar to the contact elements, at each analysis step the stiffness of each friction damper element is set to the friction interface stiffness provided in the inputs when the damper has not slipped and a small non-zero stiffness when the damper is slipping. For the T-SCED model, the end plate friction elements (k_{ep1} and k_{ep2}) work similarly, changing stiffness based on the friction slip between the inner and outer end plates. These elements simulate the effect of friction between the T-SCED's inner and outer end plates. For each analysis step, the simulator calculates the locations, lengths, axial force, and elongation for every element in the model. The stiffness method analysis was performed using the Payne and Irons method [10].

The first stage of the analysis is to apply the pretensioning to the tendon elements to determine the initial state of the brace prior to external loading. During this stage, it is assumed that the internal friction dampers are not active and, therefore, do not provide any stiffness. The pretensioning force is applied in small force steps. The step increment for this pretensioning force is defined in the software input. The left end of the brace (node 0 in Figure 4) is considered to be restrained. The force increment for each step is applied as a fixed-end force to the tendon elements. For each step in the pretensioning analysis, a new stiffness matrix and

fixed end force matrix are created. The resulting forces and displacements in each element after each step are then calculated and recorded. The pretensioning analysis is complete once the total force in the tendons reached the target pretension force.

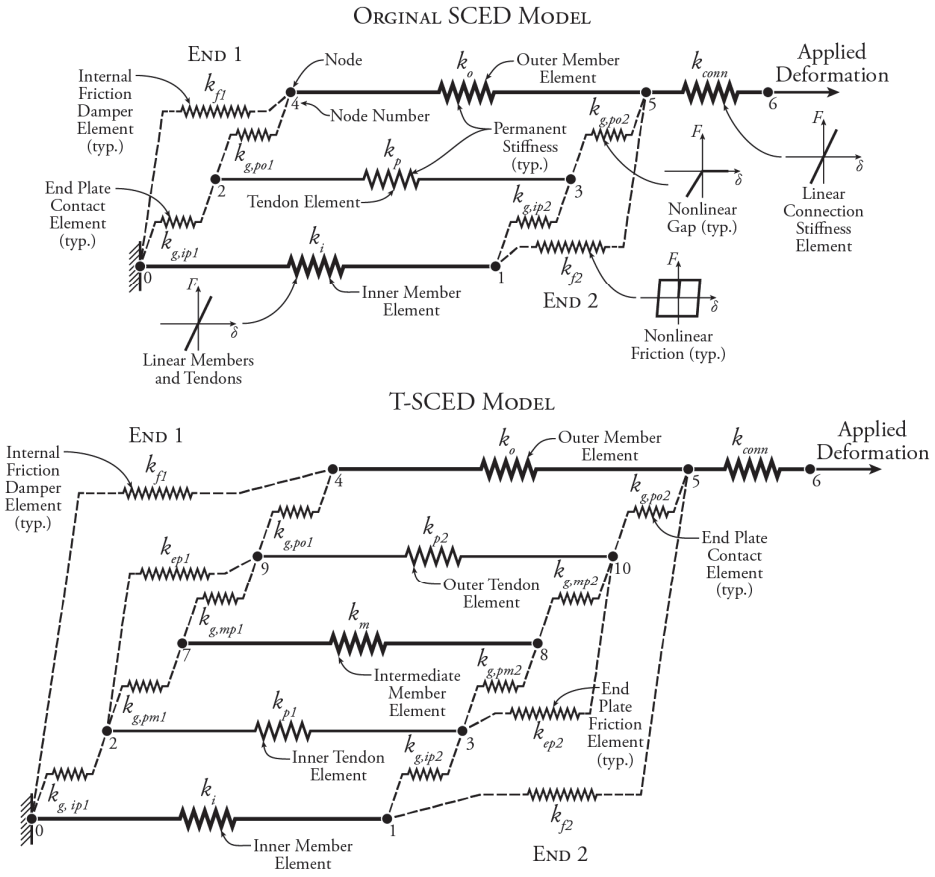


Figure 4: SCED Mechanics Simulator Model.
Note: Both models are one-dimensional, but are shown here separated into two dimensions for clarity

Once the pretension is fully applied, the full brace is deformed in the directions and magnitudes specified in the program input. During this single cycle analysis, node 0 is restrained and the axial deformation of the brace is controlled by applying incremental displacements to the free end of the brace (node 6 in Figure 4). The deformation step increment is defined in the software input. For each step in the hysteretic analysis, a new stiffness matrix and fixed and force matrix are constructed that take into account the locations of the end plates at either end of the brace and the conditional stiffness of the friction damper elements. An end plate contact element is located between the ends of the tendons and the end of each axial member. These end plate contact elements are given a very large or very small stiffness depending on whether the location of the axial member coincides with the end of the tendon or not. If the force in a friction damper exceeds the friction damper slip force, then the stiffness of that element is set to zero, otherwise the friction damper element is given the damper stiffness provided in the input. If viscous damping is specified in the input, the total viscous force for the current step is calculated using the sinusoidal deformation frequency and maximum SCED brace deformation amplitude defined in the input. The hysteretic analysis is complete once the

brace has deformed in both directions up to the maximum specified deformation amplitude and then has returned to zero deformation.

The analysis does not cap the forces in any of the elements, including the friction damper and contact elements. Therefore, it is prone to overshoot force and deformation values if the deformation step increment is too large. A small deformation step increment value is necessary to attain high-quality hysteretic behavior simulation results. This step size will typically be on the order of 0.001 mm to 0.05 mm.

2.2 User Interface

The input form for the SCED Mechanics Simulator begins with inputs for the Young's modulus for the steel sections and the pretensioned tendons. This is followed by inputs for the geometry of each steel member. Input parameters describing the geometry of the inner and outer members are always required, and the 'Middle' member which represents the T-SCED intermediate member is optional. By inputting different initial section lengths for each member, the Mechanics Simulator can simulate the effect of member length tolerances on the behaviour of the brace. The friction inputs specify the slip force for the internal friction dampers at each end of the brace. These may be different from each other and may be set to zero to eliminate internal friction damping. Tendon inputs are provided for the cross-sectional area of the tendons and the tension pretension during brace assembly. Viscous damping inputs are optional. The viscous damping that is specified by the input damping constant adds a force to the model at each step that depends on the specified cycle frequency and the analysis deformation limits. A last set of model inputs allows the user to model a connections in series with the brace.

The user also provides inputs which determine how the analysis is conducted. The first analysis input allows the user to specify the bearing stiffness and friction interface stiffness. The default stiffness values (100000 kN/mm for both) tend to provide the most stable analytical results for most practical design cases. The next inputs specify the force step that is used for applying the tendon pretension as described in the previous section. The deformation step input determines the size of the deformation steps for the hysteretic analysis that follows the pretension analysis. The last two analysis inputs determine the maximum deformations that are applied to the brace model in each direction.

After the 'Calculate SCED' button is pressed, the pretensioning and hysteretic behaviour calculations are performed and the results of the analyses are presented as shown in Figure 5. The top two plots depict the pretension load in each of the members. The left plot shows the axial force in each member as a function of the load step, which shows when each member begins to take tendon pretension force. The right plot shows the axial force in each member as a function of each member's axial deformation. This plot represents the hysteretic behaviour of each member during tendon pretensioning.

Below the pretensioning analysis plots, there is a dynamic schematic showing the forces and deformations of each element of the SCED brace. This schematic is similar in form to the brace schematics shown previously in Figures 1 and 3. The horizontal slider that is below the schematic allows the user to select an analysis step. The state of the brace for the selected step is then shown in the schematic. Text input boxes above and below the slider allow the user to select a step by the step number and to change the horizontal scale of the dynamic schematic so that deformations may be exaggerated. The coloured rectangles immediately below the schematic represent the force present in the internal friction dampers. Both pretension analysis steps and hysteretic behaviour analysis steps may be shown by the dynamic brace schematic.

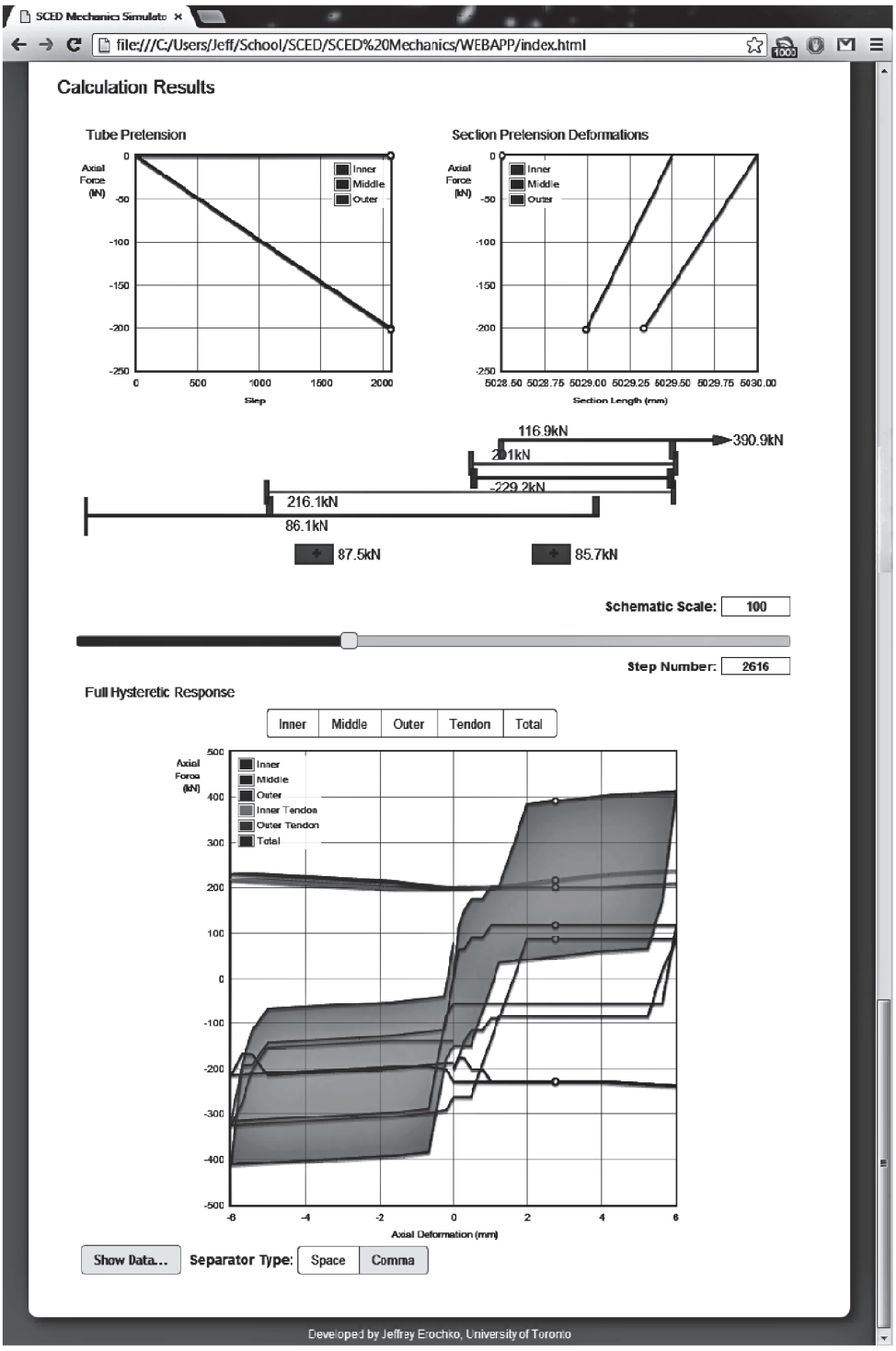


Figure 5: SCED Mechanics Simulator Results

The large bottom plot in the results output shows the total hysteretic behaviour of the SCED brace as well as the hysteretic behaviour of the individual brace elements (the axial members and the tendons). For the individual elements, the hysteretic behaviour is plotted as

the force in that element versus the total deformation of the brace. For each hysteresis shown in that plot, a circular marker identifies the point on the hysteresis that is represented by the step selected by the slider above and the state shown by the dynamic schematic above that.

After the calculation is complete, the full result data set may be output in a text format for further post-processing.

3 VALIDATION OF THE SCED MECHANICS SIMULATOR

For some relatively simple SCED brace design scenarios, closed form solutions have been previously derived for the hysteretic behavior [11]. To validate the SCED Mechanics Simulator, one of these example scenarios was simulated using this tool. A comparison of these two analyses is shown in Figure 6. As the figure shows, both the full step-wise calculations and the simulated response produce identical hystereses. Since there are no practical closed-form solutions for the T-SCED detailed mechanics or for the effect of member length tolerance, there is no way to perform a theoretical comparison for those scenarios; however, real experimental test results will be used to validate the predictions from the SCED Mechanics Simulator to assess its performance when used to model those types of scenarios.

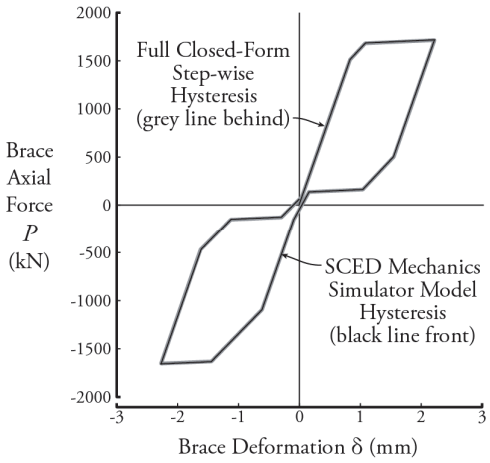


Figure 6: Detailed Mechanics Results vs. Mechanics Simulator Model for a Sample SCED Brace

4 THE EFFECT OF FABRICATION LENGTH TOLERANCES

As mentioned previously, in a real SCED brace, the length of the inner, intermediate and outer members of the brace will not be exactly identical. The axial members will have a construction tolerance that applies to their length. In practice, the manufacturer of the brace may be asked to use any length tolerance to within a fraction of a millimeter; however, tighter tolerances are associated with higher costs, especially for elements that are the size and length of typical SCED brace elements. Since the SCED Mechanics Simulator can effectively simulate the effect of different construction tolerances, it is possible to attain a better understanding of the effect of construction length tolerances on the behaviour of SCED and T-SCED braces. This will help a designer of SCED braces to determine what tolerance is appropriate.

The same sample SCED brace that was used in Figure 6 is used to study the effect of differing axial element lengths as shown in Figure 7. The figure shows a comparison of the low amplitude hysteretic response of the brace under different member length scenarios. These

hystereses are only shown for a deformation amplitude of +/- 2.25mm so that the different transitional stiffnesses are clearly visible.

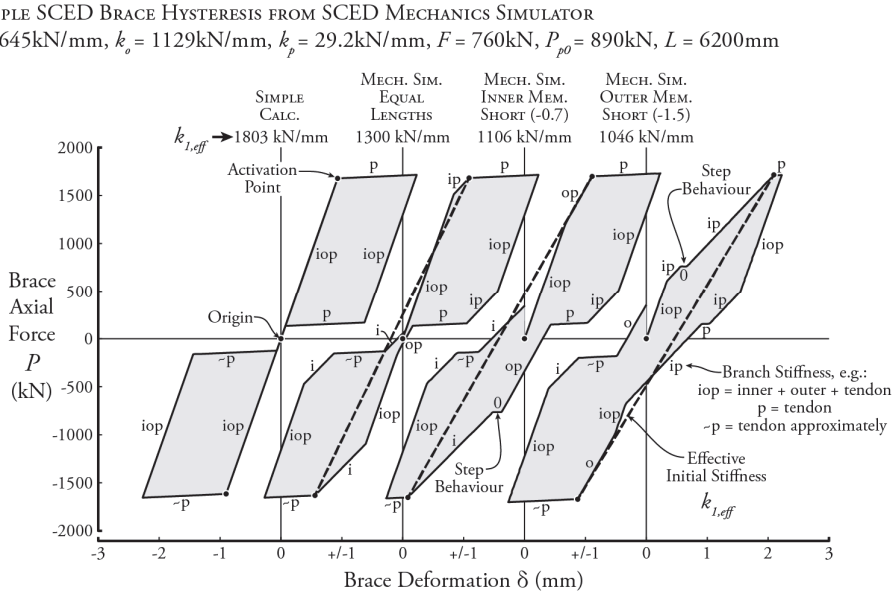


Figure 7: Sample SCED Brace Hystereses - Effect of Length Tolerance

The left hysteresis in the plot represents the idealized simplified behaviour of the brace with a simple initial stiffness equal to the sum of all three axial elements and a post-activation stiffness equal to the stiffness of the tendon. This is the brace behaviour that would be predicted by the simplified design equations [1]. To the right of that simplified hysteresis is the realistic hysteresis of a SCED brace in which the inner and outer members have different stiffnesses but identical lengths. As this plot shows, the initial stiffness before activation for a perfectly constructed brace is multilinear.

The two hystereses on the right of the plot show the effect of different inner and outer member lengths due to construction tolerances. The third hysteresis from the left shows the behaviour of the brace if the inner member is 0.7mm shorter than the outer member and the fourth hysteresis shows the behaviour if the outer member is 1.5mm shorter than the inner member. These values were chosen such that both members still take some load during pre-tensioning, but most of the load is taken by the longer member.

These two hystereses show that the behaviour of the brace becomes significantly more complicated when the lengths are not equal. The initial stiffness branches of these hystereses do not show a consistent pattern with respect to the different element stiffnesses. In addition, there are some portions of the hysteresis that have zero stiffness, causing 'steps' in the response. This step behaviour becomes much more pronounced as the difference between the member lengths becomes greater.

The most significant effect caused by the member length differences is the impact on the effective initial stiffness of the brace. This effective stiffness may be defined as the slope between the positive and negative activation points. The effective stiffnesses of the different brace scenarios are shown above each plot in Figure 7. As the stiffness values show, the effect is significant: even for the SCED with identical length members, the realistic effective initial stiffness of the brace is almost 30% lower than the value that would have been predicted by

the simplified equations. With the modest construction tolerances provided in the two rightmost hysteresis in Figure 7, the initial stiffness may drop by another 10% to 15%. For T-SCED braces, the effect is even greater since they have three axial elements; the effective initial stiffness can be as low as 20% of the assumed simplified value. It is clear that, especially for force-based designs, it is critical that designers use the more realistic values for the effective initial stiffness.

5 COMPARISON OF SIMULATOR MODEL RESULTS WITH TEST DATA

To demonstrate the hysteretic response predictions that may be attained using the SCED Mechanics Simulator, two examples will be presented below. The first is a small-scale conventional SCED brace with construction tolerance issues and the second is a full scale T-SCED brace prototype.

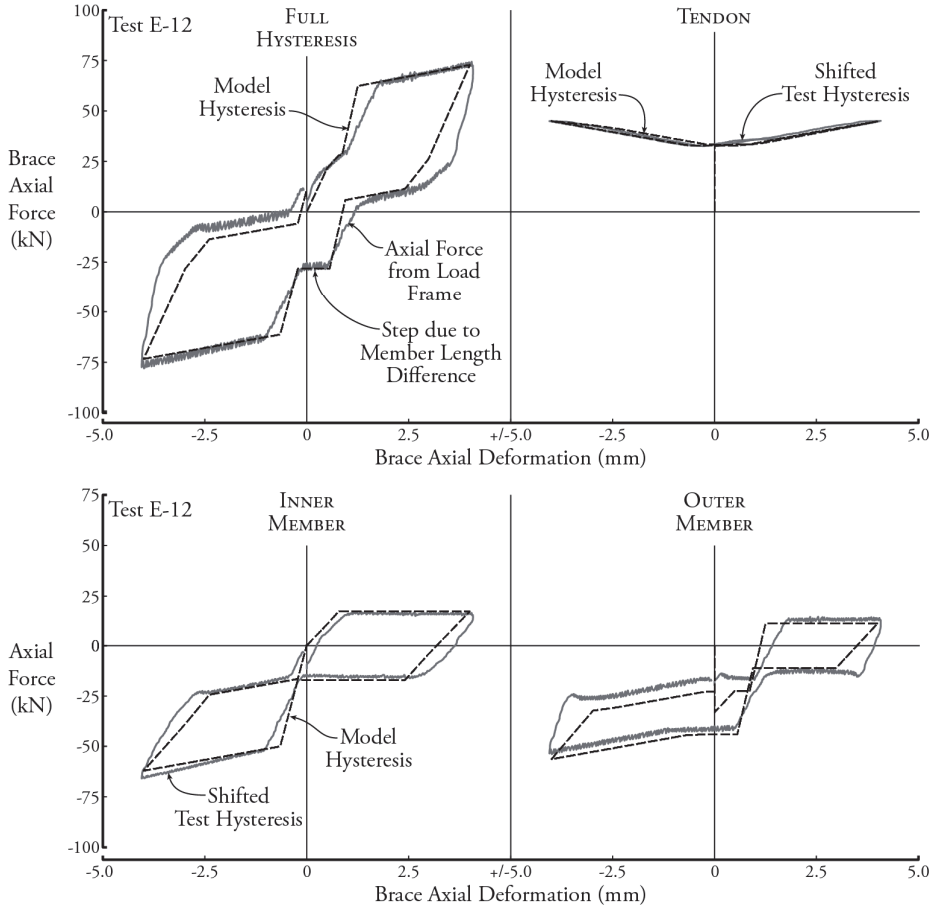


Figure 8: Small-Scale SCED Brace Hysteretic Response Modelled using the SCED Mechanics Simulator

5.1 Small-Scale SCED Brace

The shake table tests of a SCED-braced frame that were previously conducted used small-scale SCED braces [3]. One of these braces had a construction length tolerance problem when it arrived whereby the inner and outer member lengths differed by up to 1mm [11]. This represents a challenging modelling scenario for the SCED Mechanics Simulator because this

brace exhibited the step behaviour caused by unequal member lengths as previously identified in Figure 7. This brace also had unequal internal damper friction slip force at each end. A comparison between the model response and a small amplitude test hysteresis is shown in Figure 8. In the figure, the measured test hystereses were vertically shifted to account for the fact that the measured values do not include the effect of the initial tendon pretension.

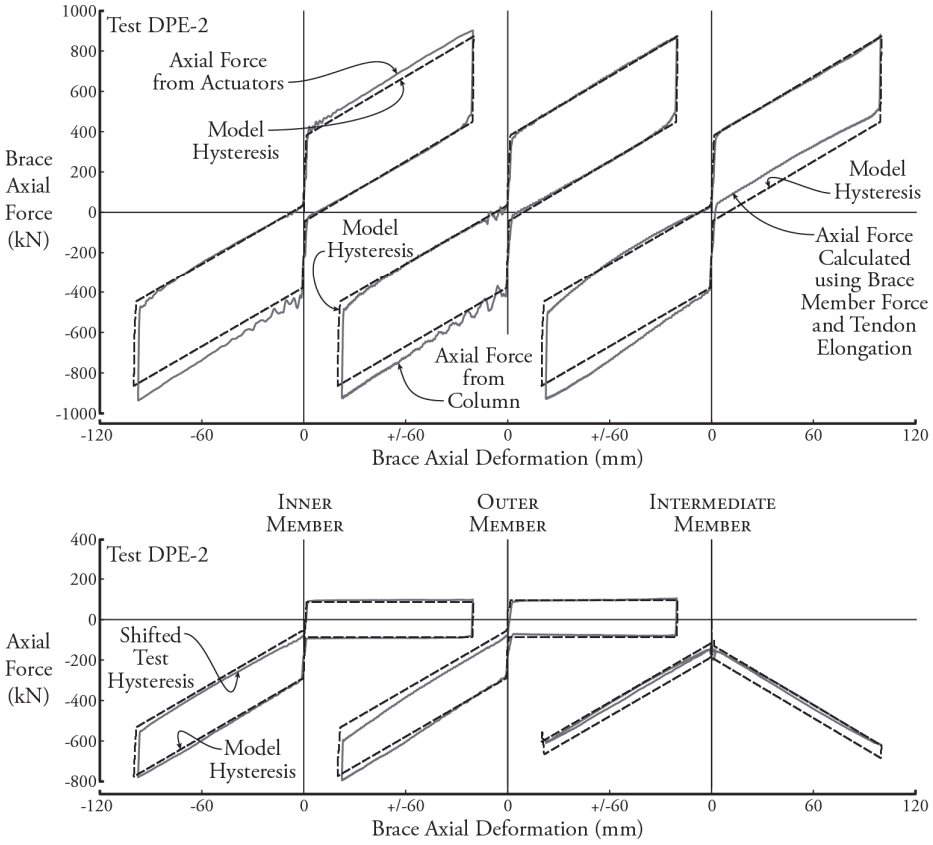


Figure 9: T-SCED Brace Hysteretic Response Modelled using the SCED Mechanics Simulator

This model included a flexible friction interface with a stiffness of 30kN/mm. The tendon pretension force and the damper friction were calculated based on the hysteretic response of the test brace. The division of the internal friction damper force between the two ends was determined based on the relative widths of the inner and outer member hystereses. The member lengths were selected such that they provided a good fit for the test hysteresis data. As the figure shows, using these parameters the SCED Mechanics Simulator model provided a good approximation of the response of the real system, including the step behaviour and the hysteretic response of the individual brace elements.

5.2 Full-Scale T-SCED Brace

A full-scale prototype T-SCED brace has previously been constructed and tested [2]. Figure 9 compares the detailed large-cycle response of the real T-SCED brace to the simulated response of the brace using the SCED Brace Mechanics Simulator. This T-SCED brace was tested within a full scale steel portal frame [2]. The material properties, element areas, and connection geometry were determined using known brace properties. The tendon pretension

and friction forces were calibrated through comparison to the measured element and brace hystereses.

The top axis in Figure 9 shows the overall hysteretic response of the brace. The left hysteresis compares the brace axial load calculated using the actuator force to the simulated response. It shows that this calculation overestimates the response due to the inclusion of friction in the frame and between the frame and the lateral supports. The middle hysteresis uses the brace axial load that was calculated using the projected axial load from the south column of the portal frame. This data shows a vibration in the force response due to the slip and impact of the test portal frame beam connection to the column. Despite these local effects, this response gives the best overall characterization of the envelope of the hysteretic response of the brace. It also compares well to the predicted hysteresis determined using the Mechanics Simulator model. The right hysteresis uses the axial force as calculated from the brace instruments (LVDTs measuring the end plate movements and strain gauges on the inner, intermediate and outer members). This hysteresis does not agree well with the model hysteresis; it under-predicts the width of the flag hysteresis on the tension side and over-predicts the width on the compression side. This effect was caused by friction induced by the rubbing together of the inner and outer end plates at each end. This changes the values of the parameters for the axial force calculation; however, as the hysteresis derived from the axial force in the column shows, this calculation error does not affect the true hysteretic behaviour of the brace. The effect of this end plate friction was included in the Mechanics Simulator model to accurately predict the hystereses of the inner, intermediate and outer members.

The measured effective initial stiffness of the brace that was calculated by finding the secant stiffness between the tension and compression activation points and was approximately equal to 285 kN/mm. The Mechanics Simulator model predicted a value of 340 kN/mm with a member length difference of 0.7mm between the inner and intermediate members and 0.3mm between the intermediate and outer members; this value is reasonably close to the measured effective initial stiffness. These effective initial stiffnesses are much lower than the theoretical initial stiffness for this brace which is 1476 kN/mm. Since this T-SCED brace was fabricated carefully to ensure that the members were the same length, it is unlikely that better fabrication practices could be followed during mass production. Therefore, it is clearly important that a designer considers a realistic effective initial stiffness estimate for the determination of earthquake loads and for drift calculations.

6 CONCLUSIONS

- A newly created software tool called the SCED Mechanics Simulator has been created to model the detailed hysteretic behavior of SCED and T-SCED braces. This software tool is able to consider the effect of axial member length tolerances which significantly affect the effective elastic stiffness properties of SCED and T-SCED braces.
- Use of the software has shown that the initial stiffness of SCED and T-SCED braces is not adequately represented by the simplified design equations. Realistic effective initial stiffness may be as low as 60% of the simplified values for SCED braces and as low as 20% of the simplified values for T-SCED braces.
- Therefore, it is critical that designers use a tool such as the SCED Mechanics Simulator to determine realistic effective initial stiffness values of SCED and T-SCED braces during the design process.
- The SCED Mechanics Simulator provides good predictions of the hysteretic behavior of real SCED and T-SCED brace prototypes.

REFERENCES

[1] C. Christopoulos, R. Tremblay, H.-J. Kim, M. Lacerte, Self-Centering Energy Dissipative Bracing System for the Seismic Resistance of Structure: Development and Validation. *Journal of Structural Engineering*, **134**, 96-107, 2008.

[2] J. Erochko, C. Christopoulos, R. Tremblay, Design and Testing of an Enhanced Elongation Telescoping Self-Centering Energy-Dissipative (T-SCED) Brace. *15th World Conference on Earthquake Engineering*, Lisbon, Portugal. 2012.

[3] J. Erochko, C. Christopoulos, R. Tremblay, Shake Table Testing of a Three-Story Self-Centering Energy Dissipative (SCED) Braced Frame, *Earthquake Engineering and Structural Dynamics* [In press]. 2013.

[4] J. Coglan, Sylvester: *Vector and Matrix math for Javascript (Version 0.1.3)* [Computer Software]. London, UK. Available from http://sylvester.jcoglan.com/ 2012.

[5] JQuery Foundation, *jQuery (Version 1.7.1)* [Computer Software]. Hingham, MA. Available from: http://jquery.com/ 2012.

[6] JQuery Foundation, *jQuery UI (Version 1.8.18)* [Computer Software]. Hingham, MA. Available from: http://jqueryui.com/ 2012.

[7] O. Laursen, O. *Flot: Attractive JavaScript plotting for JQuery (Version 0.7)* [Computer Software] Aalborg, Denmark. Available from: http://www.flotcharts.org/ 2012.

[8] Google Inc. *ExplorerCanvas* [Computer Software]. Mountain View, CA. Available from: http://excanvas.sourceforge.net/ 2006.

[9] A. Hill, *LiveValidation (Version 1.3)* [Computer Software]. London, UK. Available from: http://livevalidation.com/ 2008.

[10] O.C. Zienkiewicz, R.L. Taylor, *The Finite Element Method - Volume 1: The Basis.* Woburn, MA: Butterworth-Heinemann. 2000.

[11] J. Erochko, *Improvements to the Design and Use of Post-Tensioned Self-Centering Energy-Dissipative (SCED) Braces*. Doctoral Thesis, University of Toronto, Toronto, Ontario. 2013.

COMPDYN 2013
4th ECCOMAS Thematic Conference on
Computational Methods in Structural Dynamics and Earthquake Engineering
M. Papadrakakis, V. Papadopoulos, V. Plevris (eds.)
Kos Island, Greece, 12–14 June 2013

R_y-μ-T_n RELATIONS FOR SEISMICALLY ISOLATED STRUCTURES

Anastasios Tsiavos[1], Michalis F. Vassiliou [2], Kevin R. Mackie[2] and Bozidar Stojadinovic[2]

[1] Doctoral Student, Institute of Structural Engineering, Swiss Federal Institute of Technology (ETH) Zürich, HIL E 12.1, Wolfgang-Pauli-Str. 15, 8093 Zürich, Switzerland
tsiavos@ibk.baug.ethz.ch

[2] Post-doctoral Researcher, Institute of Structural Engineering, Swiss Federal Institute of Technology (ETH) Zürich HIL E 13.2, Wolfgang-Pauli-Str. 15, 8093 Zürich, Switzerland
vassiliou@ibk.baug.ethz.ch

[2] Associate Professor, Civil Environmental and Construction Engineering Department, University of Central Florida, Engr II 402, 4000 Central Florida Blvd., Building 91, Suite 211, Orlando, Florida 32816-2450
kmackie@mail.ucf.edu

[2] Professor, Institute of Structural Engineering, Swiss Federal Institute of Technology (ETH) Zürich HIL E 14.1, Wolfgang-Pauli-Str. 15, 8093 Zurich, Switzerland
stojadinovic@ibk.baug.ethz.ch

Keywords: Inelastic isolated structures, Seismic isolation, R_y-μ-T_n relations, Resilience, Extreme hazards

Abstract. *The relations between the strength reduction factor R_y, the displacement ductility μ and the vibration period of the structure T_n have been extensively studied for fixed-base structures by numerous researchers in the past. This project aims at identifying similar relations for base-isolated structures. The investigation is conducted using a two-degree-of-freedom model of a base-isolated structure. The hysteretic behavior of the base isolation devices and the isolated superstructure is simulated in Matlab and OpenSees using a Bouc-Wen model. The results of the observed response are verified through the excitation of the isolated structure by a large number of recorded ground motions. These motions cover a wide range of ground motion types, magnitudes and distances. The effects of base isolation and superstructure design parameters, such as stiffness and strength, are quantified through parametric studies. The resulting R_y-μ-T_n relationship for inelastic seismically isolated structures is based on the statistical processing of the inelastic response data of the isolated superstructure.*

1 INTRODUCTION

The current codes for seismic design of structures focus on preventing their collapse. However, this design approach does not address the short and long-term effects due to the loss or the disruption of the function of the built infrastructure after an earthquake event.

Seismic response modification technologies are used to modify the dynamic response of structures to mitigate their damage and guarantee their post-earthquake functionality. Seismic isolation of structures is a response modification technology which has been widely used in the past for the design of new structures or the seismic retrofit of existing structures [6-9].

Seismic isolation is defined as a system of flexible or sliding structural elements that decouple a structure from the horizontal components of ground excitation. The orthogonality of the structure vibration mode to the seismic isolation vibration mode results in low transmission of energy from the ground motion to the structure [1]. This lower transmission of energy results in the reduction of the earthquake-induced damage to the structure. Furthermore, the fundamental vibration period of the isolated structure is lengthened comparing to a conventional fixed-based structure. This lengthening of the vibration period leads to a significant decrease of the seismic base shear acting on the structure.

However, as the design codes worldwide prohibit extensive yielding of the isolated superstructure, the initial construction cost of an isolated structure is significant. This cost could be reduced if the design base shear for the isolated structure is reduced, thus allowing it to develop ductility demands similar to those permitted for fixed-base structures. The reduction of cost due to a lighter superstructure could then offset the high bearing installation cost. From this point of view, a further insight into the behavior ranges of the inelastic seismically isolated structures is needed for two reasons:

First, to identify the possibility of yielding for a more economical design of new seismically isolated structures. Constantinou and Quarshie [2], Ordonez et al. [3], Kikuchi et al. [4], Thiravechyan et al. [5] have investigated the response of yielding seismically isolated structures and agreed that allowing seismically isolated structures to yield needs careful consideration.

Second, to account for the case in which the applied forces exceed the design forces due to an extreme earthquake event or reduced structural strength in existing seismically isolated structures. This analysis could lead to the identification of the existing base-isolated structures whose strength is not sufficient to keep their response in the elastic range.

This study focuses on the determination of the relations between the force reduction factor R_y, the displacement ductility demand μ and the vibration period of the superstructure T_n, for base-isolated structures. Numerous previous studies have investigated relationships between R_y, μ and T_n for fixed-base structures. Newmark and Hall [10], Lai and Biggs [11] and Riddel and Newmark [12] have proposed piece-wise linear R_y-μ-T_n relations for fixed-base structures. Riddel, Hidalgo and Cruz [13] and Vidic, Fajfar and Fischinger [14] have presented bilinear approximations for R_y-μ-T_n relations. Elgadamsi and Mohraz [15], Arias and Hidalgo [16], Nassar and Krawinkler [17], Miranda [18], and Miranda and Bertero [19] have suggested the use of nonlinear curves for R_y-μ-T_n relations. According to these studies, the seismic response of structures is categorized in three regions: 1) an "Elastic" or "Acceleration sensitive region", which governs the behavior of very stiff structures; 2) a "Hysteretic energy conservation region"; and 3) a "Displacement conservation region", which is observed for very soft structures. The goal of this study is to identify the vibration period delineated behavior ranges for base-isolated structures analogous to those for fixed-base structures.

1.1 Dynamic modeling

The dynamics of a seismically isolated structure, according to the work of Naeim and Kelly [1] can be investigated by using a two-degree-of-freedom system, as presented in Figure 1.1. Masses m_s *and* m_b represent the mass of the superstructure and the mass of the base above the isolation system, respectively. The stiffness and damping are expressed as k_s, c_s, when referring to the superstructure and k_b, c_b when referring to the base. The deformation u_s is the deformation of the superstructure with respect to the base mat, and u_b is the deformation of the bearings with respect to the ground.

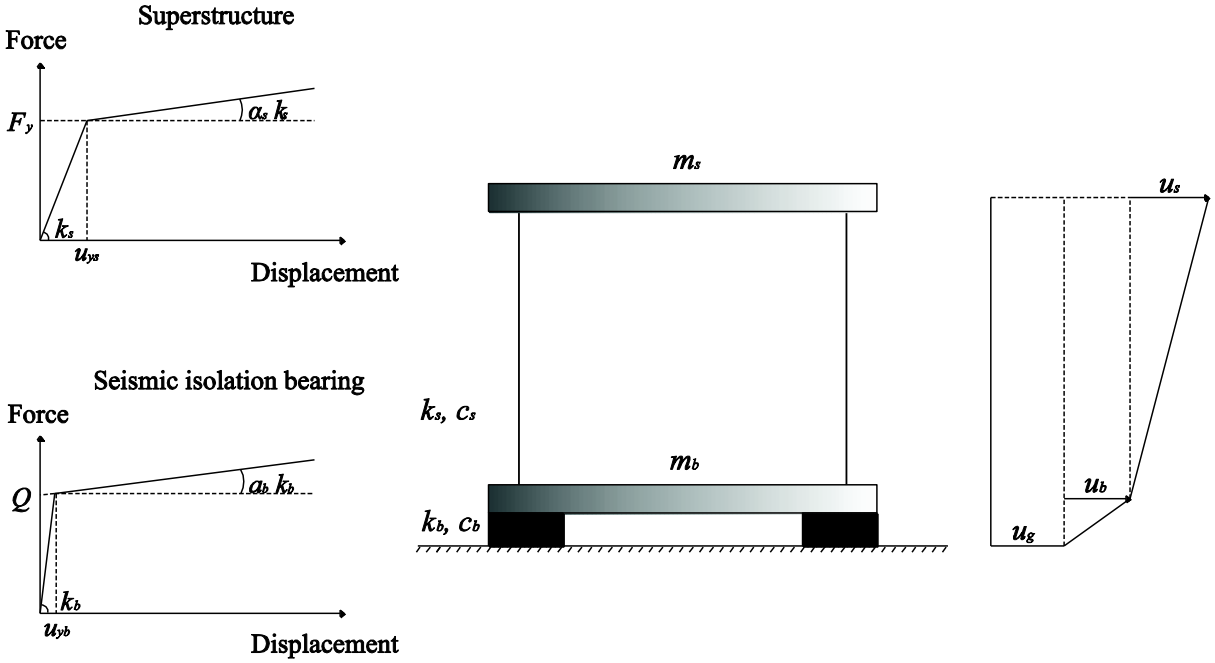


Figure 1.1: Parameters of the 2-DOF model of a base isolated structure.

The following quantities are defined:
1. Fixed-base period and cyclic frequency:

$$T_s = 2\pi\sqrt{\frac{m_s}{k_s}}\,,\ \omega_s = \sqrt{\frac{k_s}{m_s}} \tag{1}$$

2. Isolation period and cyclic frequency:

$$T_b = 2\pi\sqrt{\frac{m_s + m_b}{\alpha_b k_b}}\,,\ \omega_b = \sqrt{\frac{\alpha_b k_b}{m_s + m_b}} \tag{2}$$

3. Non-hysteretic structural and isolation damping ratio:

$$\xi_s = \frac{c_s}{2m_s\omega_s}, \qquad \xi_b = \frac{c_b}{2\left(m_s + m_b\right)\omega_b} \tag{3}$$

4. Mass ratio:

$$\gamma_m = \frac{m_s}{m_s + m_b} \tag{4}$$

A Bouc-Wen [20, 21] model is used to simulate the bilinear hysteretic behavior of the isolation system. The restoring force of the isolation system is modeled as:

$$F_b(t) = -\alpha_b k_b u_b(t) - Q \cdot z_b(t) - c_b \dot{u}_b(t) \tag{5}$$

where α_b is the hardening ratio of post-yield to pre-yield stiffness of the isolation system (Figure 1.1), Q is the strength of the system (force at zero displacement), and $z_b(t)$ is a dimensionless parameter of the Bouc-Wen model.

The strength of the isolation system is determined for friction pendulum bearings using the following equation:

$$Q = (m_s + m_b)\mu_f g \tag{6}$$

where μ_f is the bearing coefficient of friction.

A Bouc-Wen model in parallel with a viscous damper is used to model the bilinear hysteretic behavior of the isolated structure. The restoring force of the isolated structure is given by:

$$F(t) = -\alpha_s k_s u_s(t) - (1-\alpha_s) k_s u_{y_s} z_s(t) - c_s \dot{u}_s(t) \tag{7}$$

where α_s is the hardening ratio of post-yield to pre-yield stiffness of the isolated structure (Figure 1.1), u_{ys} is the yield displacement of the isolated structure and $z_s(t)$ is a dimensionless parameter of the Bouc-Wen model.

The yield strength of the isolated structure is:

$$F_y = k_s u_{ys} \tag{8}$$

Dynamic equilibrium of the isolated structure and the base isolation system gives:

$$(m_s + m_b)\ddot{u}_b + m_s \ddot{u}_s + \alpha_b k_b u_b + Q z_b(t) + c_b \dot{u}_b(t) = -(m_s + m_b)\ddot{u}_g \tag{9}$$

Dynamic equilibrium of the isolated structure gives:

$$m_s \ddot{u}_s + m_s \ddot{u}_b + \alpha_s k_s u_s + (1-a_s) k_s u_{y_s} z_s + c_s \dot{u}_s = -m_s \ddot{u}_g \tag{10}$$

Consequently, equations (9) and (10) become equations of motion of the combined structure-isolation system. When dividing equations (9) and (10) by (m_s+m_b), equations (11) and (12) are derived: The results presented in this study were obtained by solving the derived equations (11) and (12) using Matlab and Opensees:

$$\ddot{u}_b + \gamma_m \ddot{u}_s + \omega_b^2 u_b + \frac{Q}{m_s + m_b} z_b + 2\xi_b \omega_b \dot{u}_b = -\ddot{u}_g \tag{11}$$

$$\ddot{u}_s + \ddot{u}_b + \alpha_s \omega_s^2 u_s + (1-\alpha_s)\omega_s^2 u_{y_s} z_s + 2\xi_s \omega_s \dot{u}_s = -\ddot{u}_g \tag{12}$$

2 ANALYSIS

2.1 Ground motion data

The 160 motions used in this study cover a wide range of ground motion types, magnitudes (5.5 to 7.7) and distances (10 to 60 km). They were taken from the Pacific Earthquake Engineering Research (PEER) Center next generation attenuation (NGA) strong motion database [22, 23].

2.2 Methodology

The analysis method used in this study involves the determination of strength reduction factors R_y for a certain predetermined displacement ductility ratio μ. The structural model shown in Figure 1.1 was subjected to the ground motion ensemble presented in 2.1. The vibration period of the isolation bearings T_b was selected first. The strength of the isolation system was determined by the choice of the bearing friction coefficient μ_f=0.05. Then, for each ground motion record, an elastic analysis is conducted for the calculation of the maximum elastic force and displacement demands of the isolated structure with vibration period $T_n \in \{0.1, 0.5, 1.0, 1.5, 2.0, 3.0, 4.0, 5.0\}$. After the determination of these values, an iterative procedure is performed to compute the maximum strength needed to keep the displacement ductility demand to the predefined level μ within a range of 1%. The strength reduction factors that result in this displacement ductility value can then be easily determined.

2.3 Statistical fit

Based on the analysis presented above, the results obtained for T_b=2 and μ=2 are shown in Figure 1.2. These results (labeled "actual") represent the mean value and the standard deviation of the response of the model subjected to the applied ground motion ensemble. Bilinear curve fitting is carried out to the mean of the data to establish a first approximation of R_y-μ-T_n relation. The proposed bilinear curve representing the statistical fit is also presented in Figure 1.2.

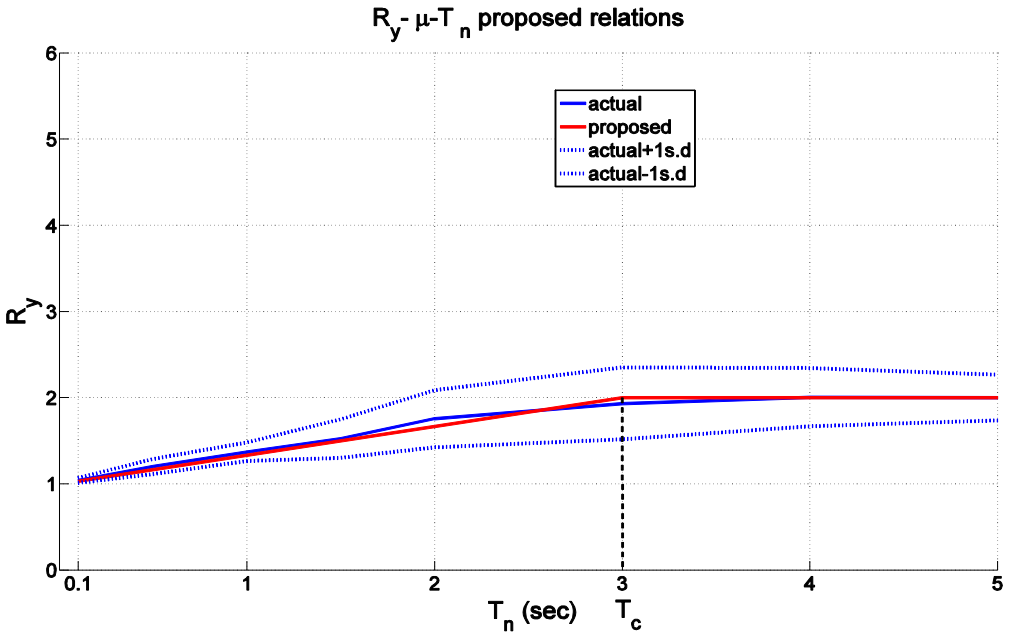


Figure 1.2: R_y-μ-T_n relation for T_b=2 and μ=2 (actual and proposed)

Similar simulations have been performed for a wide variety of values of the isolation period T_b and the ductility demand μ. As the deviation of the results varies with respect to the vibration period of the structure T_n, the maximum standard deviation $\sigma_{max}(T)$ was computed to quantify the dispersion of the results (Table 1.1).

$T_b \backslash \mu$	2	3	4
2 seconds	0.42	0.86	0.98
3 seconds	0.31	0.75	0.97
4 seconds	0.28	0.80	0.86

Table 1.1: Standard deviation $\sigma_{max}(T)$ for alternate values of T_b and μ

3 PARAMETRIC STUDY

As the relation between R_y and μ is non-linear, the period range for which the equal displacement rule applies ($R_y=\mu$) cannot be easily identified. From this point of view, the use of a bilinear curve is more appropriate, it can lead to the determination of the vibration period T_c as an intersection of 2 lines (Figure 1.1). Among other issues, this study attempts to quantify the range of this displacement-sensitive region by taking into account the most crucial parameters that influence this relation:

a) The isolation period T_b.
b) The displacement ductility ratio μ
c) The hardening ratio α_s of post-yield to pre-yield stiffness of the isolated structure

3.1 Proposed R_y-μ-T_n relations for isolated structures

The form of the proposed R_y-μ-T_n relation for isolated structures was adapted from T. Vidic, P. Fajfar and M. Fischinger [14].

$$R_y = 1,\ T < T_a \tag{12}$$

$$R_y = c_\alpha \left(\mu - 1\right)^{c_\mu} \frac{T}{T_b + 1} + 1,\ T < T_c \tag{13}$$

$$R_y = \mu,\ T > T_c \tag{14}$$

The coefficients c_a and c_μ were chosen to quantify the influence of the hardening ratio α_s and the displacement ductility ratio μ on the strength reduction factor R_y. Their values, determined by statistical fitting vary as shown in the following Table 1.2:

α_s	c_a		μ	c_μ
0%	1.00		2	0.85
5%	1.10		3	0.90
10%	1.15		4	0.95

Table 1.2: Coefficients c_a and c_μ for alternate values of α_s and μ

Then, the vibration period, after which the equal displacement rule applies can be determined as an intersection ($R_y=\mu$) between two lines:

$$T_c = \frac{1}{c_\alpha}\left(\mu - 1\right)^{1-c_\mu}\left(T_b + 1\right) \tag{15}$$

3.2 Influence of essential parameters

The essential parameters that influence the proposed R_y-μ-T_n relation are: The isolation period T_b, the displacement ductility ratio μ of the isolated structure and the hardening ratio α_s of post-yield to pre-yield stiffness of the isolated structure. As presented in Figures 1.3 and 1.4, the use of softer isolators giving longer isolation period values T_b significantly increases T_c (moves it to the right), thus reducing the range of the displacement conservation region. Similar, but less pronounced, is the influence of isolated structure post-yield hardening (Figures 1.5 and 1.6): The displacement conservation region decreases for structures with less hardening. Finally, the effect of the displacement ductility ratio μ of the isolated structure on the location of the displacement conservation range is rather negligible and becomes less important for larger displacement ductility values (Figures 1.7 and 1.8).

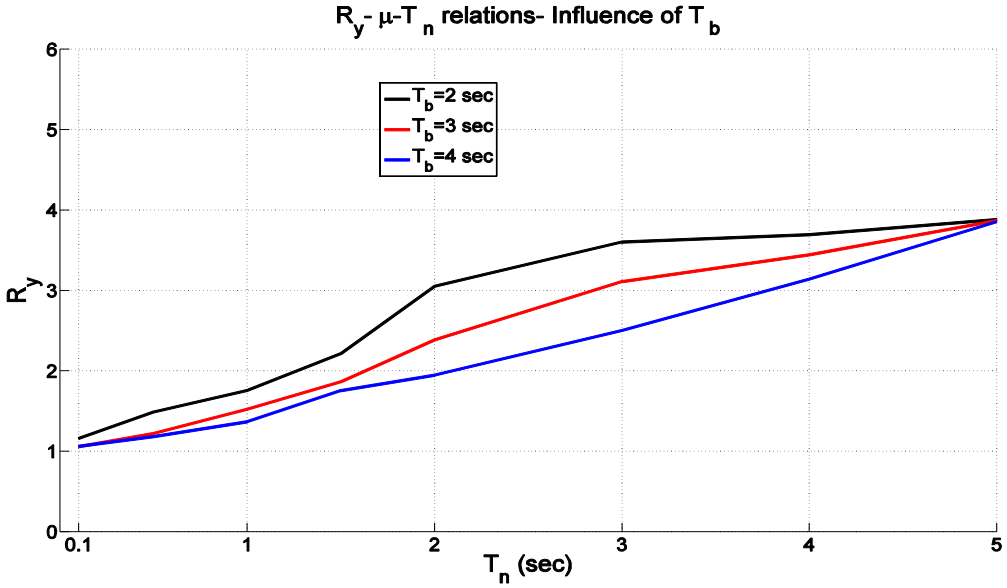


Figure 1.3: R_y-μ-T_n relation for T_b=2,3,4 sec and μ=4 (actual mean values)

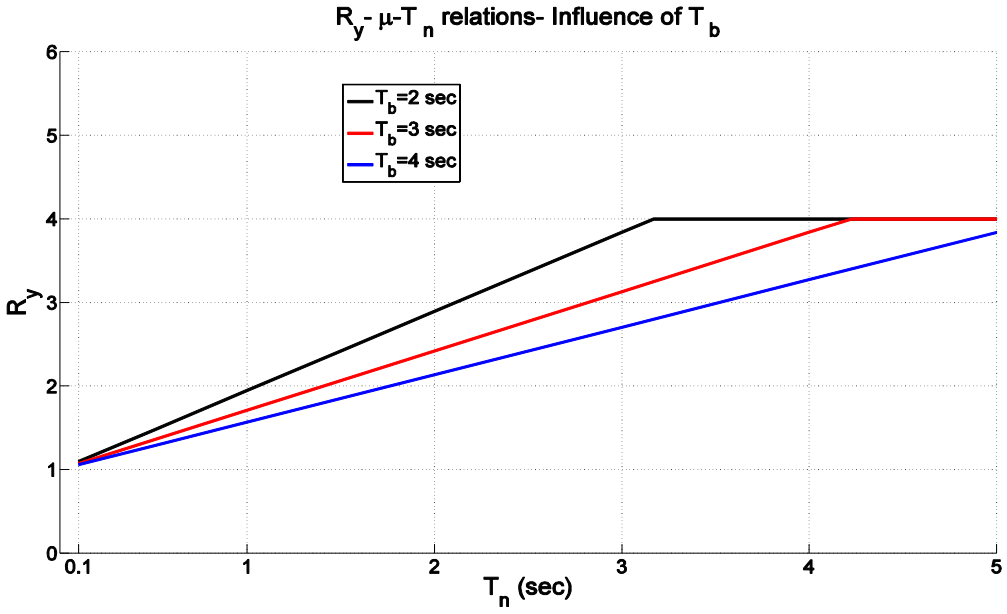


Figure 1.4 R_y-μ-T_n relation for T_b=*2,3,4 sec* and μ=*4* (proposed values)

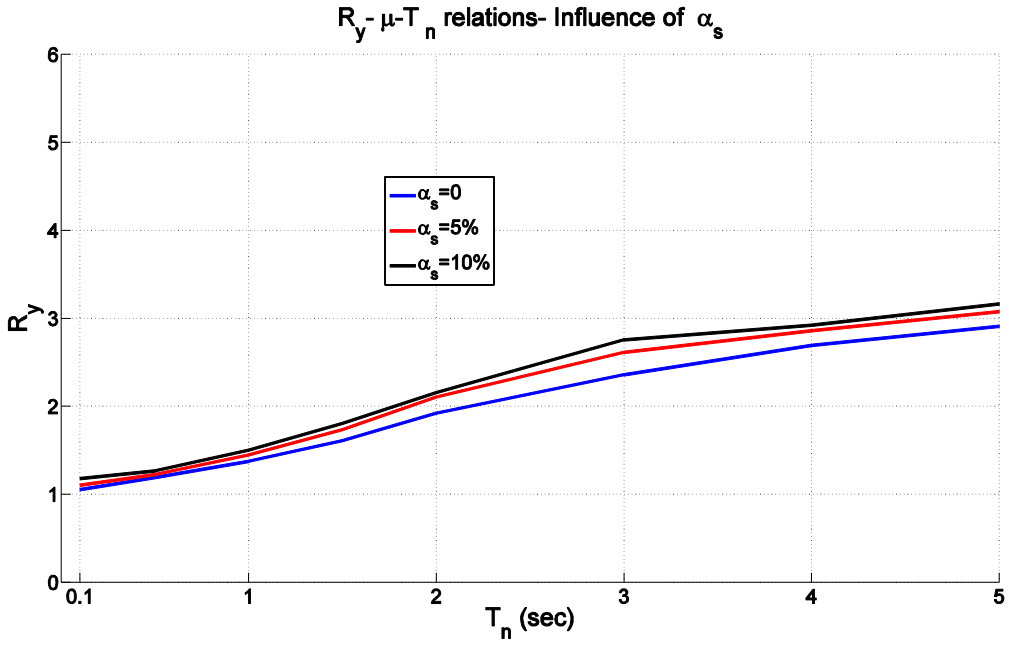


Figure 1.5: R_y-μ-T_n relation for a_s=0, 5%, 10%, μ=3 and T_b=3 sec (actual mean values)

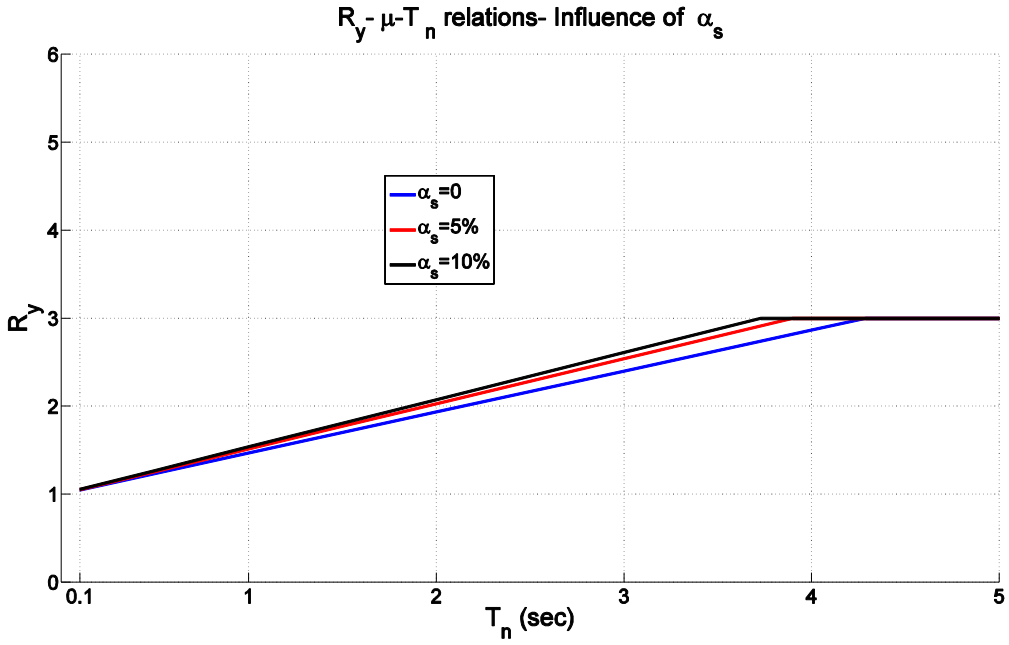


Figure 1.6: R_y-μ-T_n relation for a_s=0, 5%, 10%, μ=3 and T_b=3 sec (proposed values)

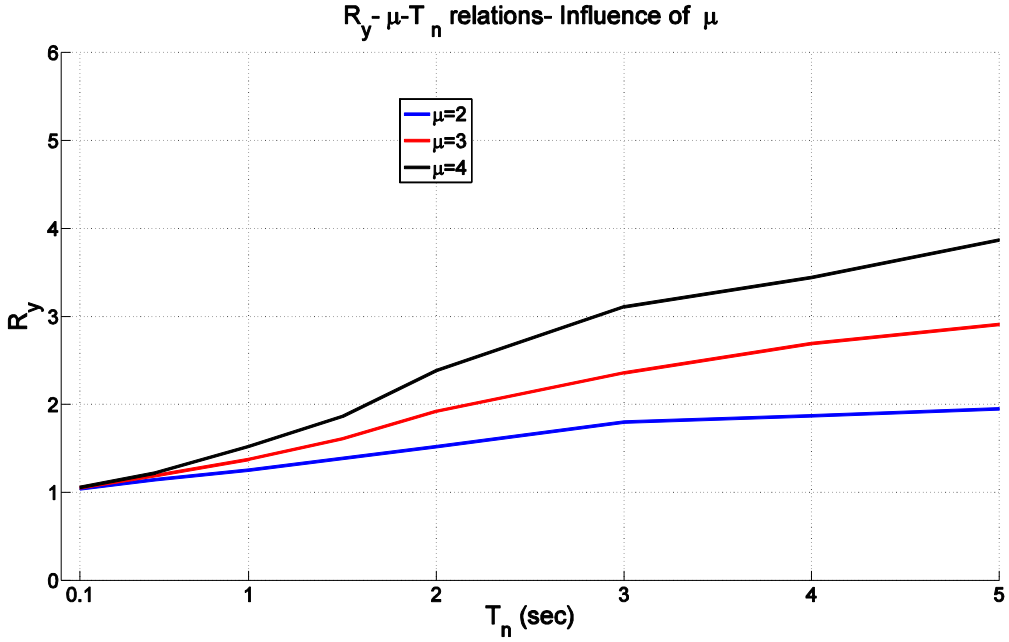


Figure 1.7: R_y-μ-T_n relation for μ=2,3,4 and T_b=3 sec (actual mean values)

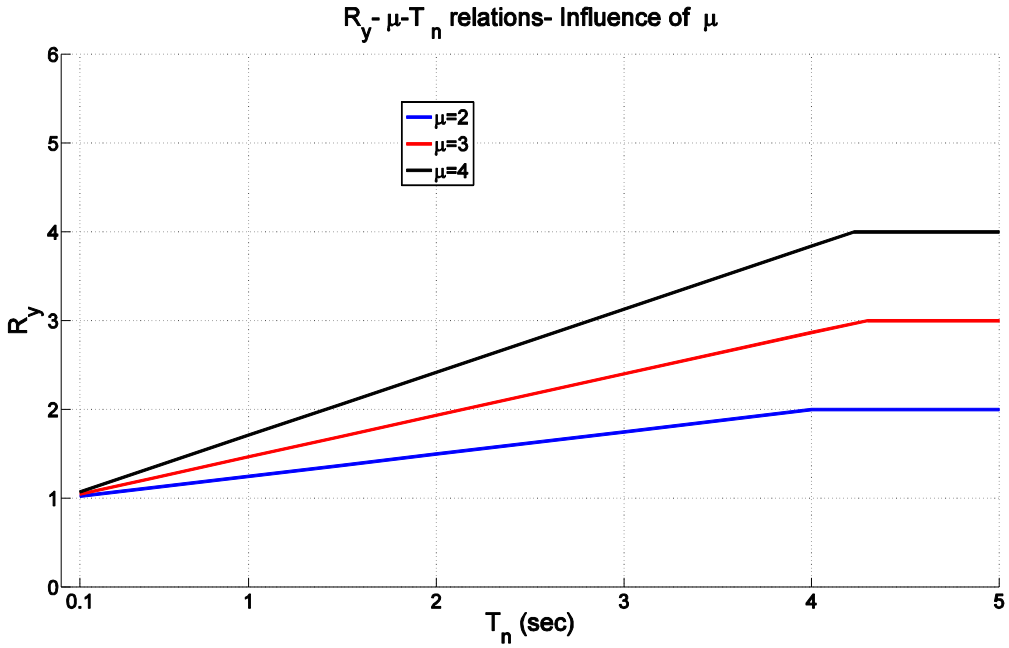


Figure 1.8: R_y-μ-T_n relation for μ=*2,3,4* and T_b=*3 sec* (proposed values)

4 CONCLUSIONS

The results obtained in the parametric analysis conducted in this study indicate the nature of the relation between the force reduction factor R_y, the displacement ductility demand μ and the vibration period of the superstructure T_n, for base-isolated structures. These relations are non-linear and show significant similarity to the ones proposed for fixed-base structures [10-19]. Compared to fixed-base structures, the acceleration sensitive region of the response of inelastic base-isolated structures extends towards longer periods. Moreover, the hysteretic energy and the displacement conservation regions shrink and translate along the period axis.

However, the determination of the exact vibration period T_c, after which the equal displacement rule applies ($R_y=\mu$) is difficult without using linear approximations of the obtained R_y-μ-T_n relations. Therefore, simple bilinear expressions are proposed in this study to quantify the sensitivity of the relations to the selected parameters (3.1).

The isolation period T_b has the largest effect on the proposed R_y-μ-T_n relation for isolated structures. Increasing the isolation period (by using softer isolation bearings) moves the equal displacement range for the isolated structures towards longer period values (T_c moves to the right). The effects of post-yield hardening and displacement ductility of the isolated structure on the proposed R_y-μ-T_n relation are not significant.

The ultimate goal of the R_y-μ-T_n relations proposed in this study is the quantification of the inelastic performance of base-isolated structures for a wide range of earthquake records. The proposed R_y-μ-T_n relation indicates that if the strength of typical seismically isolated structures is selected such that they are allowed to enter their inelastic response range, the structures will develop displacement ductility demands significantly larger than those predicted by the equal displacement rule. The accuracy of the proposed R_y-μ-T_n relation can be improved by using a larger sample of more diverse ground motion records and by widening and denser sampling of the design parameter space.

REFERENCES

1. Kelly JM. *Earthquake Resistant Design with Rubber*. Springer, London, 1997

2. Constantinou MC, Quarshie JK. Response modification factors for seismically isolated bridges. *Report No. MCEER-98-0014, Multidisciplinary Center for Earthquake Engineering Research*, Buffalo, NY, 1998

3. Ordonez D, Foti D, Bozzo L. Comparative study of the inelastic response of base isolated buildings. *Earthquake Engineering and Structural Dynamics*, **32**, 151–164, 2003

4. Kikuchi M, Black CJ, Aiken ID. On the response of yielding seismically isolated structures. *Earthquake Engineering and Structural Dynamics* , **37(5)**, 659–679, 2008

5. Thiravechyan P., Kasai K. Morgan TA, The effects of superstructural yielding on the seismic response of base isolated structures., *Joint Conference proceedings, 9th International Conference on Urban Earthquake Engineering / 4th Asia Conference on Earthquake Engineering*, Tokyo, Japan, 2012

6. Kelly JM. Seismic isolation of civil buildings in the USA. *Progress in Structural Engineering and Materials*, **1**, 279–285, 1998

7. Asher JW, Hoskere S, Ewing R, Van Volkinburg DR, Mayes R, Button M. Seismic performance of the base isolated USC university hospital in the 1994 Northridge earthquake. *Proc., ASME Pressure Vessels and Piping Conf., New York, 1995*

8. De Luca A, Mele E, Molina J, Verzeletti G, Pinto AV. Base isolation for retrofitting historic buildings: Evaluation of seismic performance through experimental investigation. *Earthquake Engineering and Structural Dynamics*, **30**, 1125–1145, 2001
9. Mokha AS, Amin N, Constantinou MC, Zayas V. Seismic Isolation Retrofit of Large Historic Building. *Journal of Structural Engineering*, **122(3)**, 298–309, 1996
10. N. M. Newmark and W. J. Hall, Seismic design criteria for nuclear reactor facilities, Report 46, *Building Practices for Disaster Mitigation, National Bureau of Standards*, pp. 209–236, 1973
11. S.-S. P. Lai and J. M. Biggs, Inelastic response spectra for aseismic building design, *J. struct. diu. ASCE 106*, 1980
12. R. Riddell and N. M. Newmark, Statistical analysis of the response of nonlinear systems subjected to earthquakes. *Structural Research Series No. 468, Civil Engineering Studies, University of Illinois, Urbana-Champaign*, IL, 1979
13. Riddell R, Hidalgo PA, Cruz EF. Response modification factors for earthquake resistant design of short period buildings. *Earthquake Spectra*, **5(3)**, 571–590, 1989
14. T. Vidic, P. Fajfar and M. Fischinger, Consistent inelastic design spectra: strength and displacement, *Earthquake Engng. Struct. Dyn.* **23**, 502–521, 1994
15. Elghadamsi, F. E. and Mohraz, B., Inelastic earthquake spectra. *Earthquake Engng. Struct. Dyn*., **15**, 91–104, 1987
16. P. A. Hidalgo and A. Arias, New Chilean Code for earthquake-resistant design of buildings, *Proc. 4th U.S. earthquake eng., Palm Springs, EERI*, **2**, 927-936, 1990
17. Nassar AA, Krawinkler H. Seismic demands for SDOF and MDOF systems. *Report No. 95, The John A.Blume Earthquake Engineering Center*, Stanford University, Stanford, 1991.
18. Miranda E. Evaluation of site-dependent inelastic seismic design spectra. *Journal of Structural Engineering* (ASCE), **119**(5), 1319–1338, 1993
19. E. Miranda and V. V. Bertero, Evaluation of strength reduction factors for earthquake resistant design, *Earthquake Spectra*, **10**, 357–379, 1994
20. Wen, Y.K. Approximate method for nonlinear random vibration, *J. Eng. Mech. Div.*, **101(4)**, 389–401, 1975
21. Wen, Y.K. Method for random vibration of hysteretic systems, *J. Eng. Mech. Div.*, **102(2)**, 249–263, 1976
22. PEER NGA strong motion database, *Pacific Earthquake Engineering Research Center*, Berkeley, California, 2010
23. Mackie, K.R., and Stojadinovic, B. Fragility basis for California highway overpass bridge seismic decision making. *PEER Report No. 2005/02*, Pacific Earthquake Engineering Research Center, University of California, Berkeley, 2005

COMPDYN 2013
4th ECCOMAS Thematic Conference on
Computational Methods in Structural Dynamics and Earthquake Engineering
M. Papadrakakis, V. Papadopoulos, V. Plevris (eds.)
Kos Island, Greece, 12–14 June 2013

MINIMAL-DAMAGE STEEL FRAMES USING POST-TENSIONED CONNECTIONS WITH WEB HOURGLASS SHAPE PINS: DESIGN AND ASSESSMENT

Athanasios I. Dimopoulos[1], Theodore L. Karavasilis[1], George Vasdravellis[2] and Brian Uy[2]

[1] School of Engineering, University of Warwick
CV4 7AL, Coventry, United Kingdom
e-mail: {A.Dimopoulos,T.Karavasilis}@warwick.ac.uk

[2] Institute for Infrastructure Engineering, University of Western Sydney
Penrith NSW 2751, Sydney, Australia
{G.Vasdravellis,B.Uy}@uws.edu.au

Keywords: Self-centering, Post-tensioned, Seismic Design, Steel connection, Steel MRFs.

Abstract. *A new self-centering steel post-tensioned connection using web hourglass shape steel pins (WHPs) has been recently developed and experimentally validated. The connection isolates inelastic deformations in WHPs, avoids damage in other connection parts as well as in beams and columns, and eliminates residual drifts. WHPs do not interfere with the composite slab and can be very easily replaced without bolting or welding, and so, the connection enables non-disruptive repair and rapid return to building occupancy in the aftermath of a strong earthquake. This paper presents a simplified nonlinear model for the connection and the associated beams and columns that consists of nonlinear beam-column elements, and hysteretic and contact zero-length spring elements appropriately placed in the beam-column interface. The model was calibrated against experimental results and found to accurately simulate the connection behaviour. A prototype building was selected and designed as a conventional steel moment-resisting frame (MRF) according to Eurocode 8 or as a self-centering steel MRF (SC-MRF) using the connection with WHPs. Seismic analyses results show that the conventional MRF and the SC-MRF have comparable peak storey drifts, and highlight the inherent potential of the SC-MRF to eliminate damage in beams and residual drifts. The paper also shows that repair of damage in the conventional MRF will be costly and disruptive after the design basis earthquake, and, not financially viable after the maximum considered earthquake due to large residual drifts.*

1 INTRODUCTION

Conventional ductile steel moment-resisting frames (MRFs) are currently designed to form a global plastic mechanism under strong earthquakes by developing plastic hinges at the ends of the beams and at the base of the columns [7]. This design approach results in softening force-drift behaviour, and so, has many advantages including reduced member forces and low base shear force. However, plastic hinges in structural members involve cyclic inelastic deformations and local buckling which result in difficult to inspect and repair damage as well as residual drifts. The socio-economic losses related to damage and residual drifts are repair costs, loss of building occupation and business interruption, and possibly building demolition due to the complications associated with repairing large residual drifts [19].

A challenge of modern earthquake engineering is the development, standardization and practical implementation of resilient minimal-damage structures having the inherent potential to overcome the socio-economic losses related to earthquake damage by minimizing or avoiding inelastic deformations and residual drifts. Examples of minimal damage steel structures include frames equipped with rate-dependent passive dampers [12, 13, 27], frames with steel energy dissipation devices [14], and, self-centering moment-resisting frames (SC-MRFs) with post-tensioned (PT) connections.

SC-MRFs exhibit softening force-drift behaviour while eliminating inelastic deformations and residual drifts under strong earthquakes as the result of gap openings developed in beam-to-column interfaces and self-centering capability due to elastic pre-tensioning elements (e.g., high strength steel bars) which clamp beams to the columns. PT connections use carefully designed energy dissipation devices which are activated when gaps open and can be classified into yielding devices which dissipate energy through inelastic deformations and devices which dissipate energy through friction. Yielding devices were proposed as angles bolted on the top and bottom flanges of the beam and on the column flanges, dissipating energy through inelastic bending [20, 21, 10]; buckling-restrained steel bars placed between the beam flanges and welded on the beam and column, dissipating energy through axial deformations [6]; reduced flange plates welded around a square-hollow-section column and bolted on the beam flanges [3]; and reduced-section or cross-shaped steel plates placed below the bottom flange of the beam [4]. Friction-based devices were proposed as friction bolted surfaces placed on the top and bottom flanges of the beam [22, 15], on the web of the beam [24] or on the bottom flange of the beam [28, 16].

A new steel PT connection using web hourglass shape steel pins (WHPs) has been recently developed, modeled in ABAQUS and experimentally validated [25, 26]. The connection isolates inelastic deformations in WHPs, avoids damage in other connection parts as well as in beams and columns, and, eliminates residual drifts. WHPs do not interfere with the composite slab and are very easy-to-replace without bolting or welding, and so, the connection enables non-disruptive repair and rapid return to building occupancy in the aftermath of a strong earthquake.

This paper presents a simplified nonlinear model for the PT connection with WHPs and the associated beams and columns that consists of nonlinear beam-column elements, and hysteretic and contact zero-length spring elements appropriately placed in the beam-column interface. The model was calibrated against experimental results and found to accurately simulate the connection behaviour. A prototype building was selected and designed as a conventional steel MRF according to [8] or as a steel SC-MRF using PT connections with WHPs. The design process resulted in the same beam and column cross sections for the conventional MRF and the SC-MRF, while WHPs and the required beam flange reinforcing plates of the SC-MRF have practical sizes. Nonlinear models for the conventional MRF and the SC-MRF were de-

veloped in OpenSees [18] and used to conduct seismic analyses that show that the conventional MRF and the SC-MRF have comparable peak storey drifts. The SC-MRF eliminates damage in beams and residual drifts, and so, avoids disruptive repair after the design basis earthquake (DBE) and the maximum considered earthquake (MCE). On the other hand, repair of damage in the conventional MRF will be costly and disruptive after the DBE, and, not financially viable after the MCE due to large residual drifts.

2 STEEL POST-TENSIONED CONNECTION WITH WHPS

2.1 Structural details

Fig. 1 shows a schematic representation of a SC-MRF incorporating PT connections with WHPs and the details of an exterior PT connection. Two high strength steel bars located at the mid-depth of the beam, one at each side of the web, pass through holes drilled on the column flanges. The bars are post-tensioned and anchored to the exterior column flange, and so, clamp the beam to the column. Four WHPs are inserted in aligned holes drilled on the web of the beam and on strong supporting plates. The supporting plates are welded on the column flanges and have large thickness to provide fixed support boundary conditions to WHPs. Energy dissipation is provided by inelastic bending of the WHPs which are symmetrically placed (close to the top and bottom beam flange) to provide increased lever arm, and so, increased internal moment resistance. WHPs are designed to have an hourglass shape to provide enhanced energy dissipation and fracture capacity [17] as shown in Fig. 2. Both sides of the beam web are reinforced with steel plates to increase the contact surface of the WHPs with the web. In that way, possible ovalization of the holes drilled on the web and the reinforcing plates under the WHP bearing forces will be negligible and pronounced pinching behavior under cyclic deformations can be avoided. The connection includes beam flange reinforcing plates to avoid excessive early yielding in the beam flanges under the high PT bars forces. In addition, the panel zone is strengthened with doubler and continuity plates.

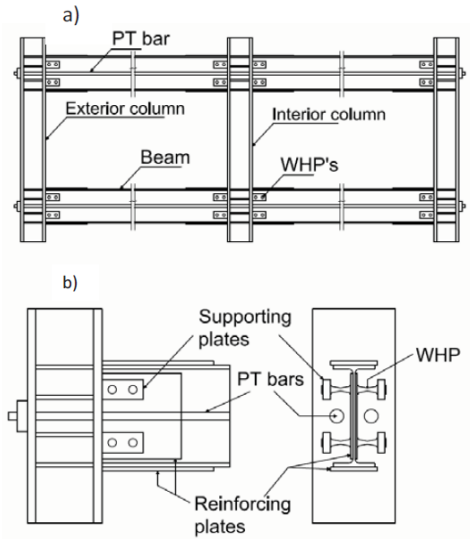


Figure 1: (a) SC-MRF incorporating PT connections with WHPs; (b) exterior PT connection details.

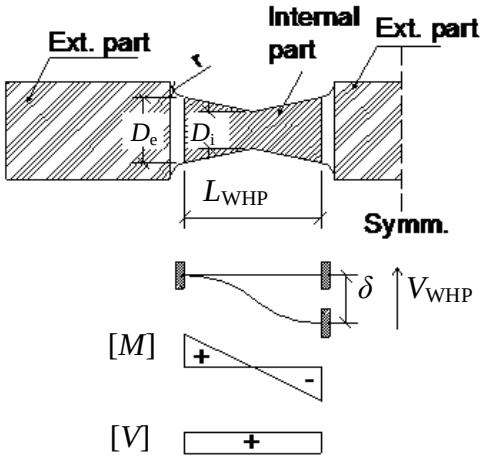


Figure 2: Geometry of half a WHP, assumed static system, and internal forces diagrams.

2.2 Theoretical analysis of cyclic behaviour

The connection behavior is characterized by gap opening and closing in the beam-column interface as a result of the re-centering force in the PT bars. Fig. 3 shows the gap opening mechanism in the connection where d_{1u} and d_{1l} are the distances of the upper and lower WHPs from the center of rotation (COR), respectively; d_2 is the distance of the PT bars from the COR; F_{PT} is the total force in both PT bars; $F_{WHP,u}$ and $F_{WHP,l}$ are the forces in the upper and lower WHPs, respectively; and CF is the compressive force on the beam-column bearing surface. It is assumed that the COR is located at the inner edge of the beam flange reinforcing plate. This assumption has been verified by the large-scale experiments previously conducted by [25].

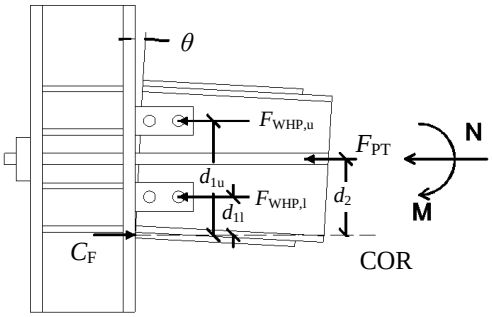


Figure 3: Gap opening mechanism in a PT connection with WHPs

Fig. 4 shows the assumed bilinear elastoplastic force-displacement ($F_{WHP,i}$-δ) behavior of one of the four (i=1 to 4) WHPs, while Fig. 5 shows the assumed cyclic moment-rotation (M-θ) behavior of the connection. M is the sum of the moment contributions from the PT bars, M_{PT}, and the WHPs, M_{WHP}. Fig. 5(b) shows the nonlinear elastic moment contribution of both PT bars. In Fig. 5(b), M_d is the decompression moment, i.e., equal to $F_{PT,i} \cdot d_2$, where $F_{PT,i}$ is the total initial post-tensioning force in both PT bars. Fig. 5(c) shows the moment contribution of the four WHPs. The M_{WHP}-θ curve changes slope two times since the upper WHPs yield at a rotation θ_2 and the lower WHPs yield afterwards at rotation θ_3. Point 1 in Fig. 5(a) corresponds to the decompression moment, M_d, of the connection. After decompression, gap opens and the connection behavior becomes nonlinear elastic. The stiffness K_1 between points 1 and

2 is equal to the sum of the rotational stiffness contribution of the PT bars, K_{PT}, and the rotational stiffness contribution of the WHPs, K_e:

$$K_1 = K_{pT} + K_e = \frac{K_{PT,a}K_b}{K_{PT,a}+K_b} d_2^2 + 2K_{fe}(d_{1l}^2 + d_{1u}^2) \quad (1)$$

where K_{fe} is the elastic stiffness of the force-displacement relationship of one WHP shown in Fig. 4, $K_{pt,a}$ is the total axial elastic stiffness of both PT bars, and K_b is the axial elastic stiffness of the beam. At point 2, the upper WHPs yield and M continues to increase with slope K_2:

$$K_2 = K_{pT} + K_{p1} = \frac{K_{PT,a}K_b}{K_{PT,a}+K_b} d_2^2 + 2(K_{fe}d_{1l}^2 + K_{fp}d_{1u}^2) \quad (2)$$

where K_{fp} is the post-elastic stiffness of the force-displacement relationship of one WHP shown in Fig. 4. At point 3, the lower WHPs yield and M continues to increase with slope K_3:

$$K_3 = K_{pT} + K_{p2} = \frac{K_{PT,a}K_b}{K_{PT,a}+K_b} d_2^2 + 2K_{fp}(d_{1l}^2 + d_{1u}^2) \quad (3)$$

When loading is reversed, the connection begins to unload, from point 4 to point 5, with the same elastic stiffness, K_1. After point 5, the connection unloads with stiffness equal to K_2 between points 5 and 6 and with stiffness K_3 between points 6 and 7 until the gap closes. The behavior of the connection is symmetric, since the WHPs are placed symmetrically to the beam centerline. The moment in the connection, M, is calculated as

$$M = M_{pT} + M_{WHP} \quad (4)$$

where M_{PT} is obtained as

$$M_{pT} = M_d + \frac{K_{PT,a}K_b}{K_{PT,a}+K_b} d_2^2\theta \quad (5)$$

and M_{WHP} is obtained as (see Fig. 3):

$$M_{WHP} = F_{WHP,u}d_{1u} + F_{WHP,l}d_{1l} \quad (6)$$

The assumed static system for half a WHP is shown in Fig. 2. The yield strength, V_{WHP}, of half a WHP is controlled either by the plastic moment of resistance, M_{pl}, or the plastic shear resistance, V_{pl} [8]:

$$M_{pl} = \frac{D_e^3}{6} f_y \quad (7)$$

$$V_{pl} = 0.9\frac{\pi D_i^2}{4} f_y/\sqrt{3} \quad (8)$$

where f_y is the yield strength of the WHP material, D_e is the equivalent external diameter (to be defined later), and D_i is the diameter at the mid-length of half a WHP, as indicated in Fig. 2. The factor 0.9 in Eq. 8 accounts for the relation between the average shear stress and the maximum shear stress in a circular section. The internal WHP part is connected to the external WHP part using a radius of 5 mm to avoid stress concentration and early fracture. It is assumed that D_e, which controls the WHP bending resistance, is equal to the diameter at the start of the round-shaped part with radius r. Plastic analysis assumes that the plastic moment of resistance should be reached at the ends before the plastic shear resistance is reached at the mid-length of half a WHP. By equilibrium, the aforementioned condition can be written as:

$$V_{\mathrm{WHP}} = \frac{2M_{\mathrm{Pl}}}{L_{\mathrm{WHP}}} < V_{\mathrm{pl}} \tag{9}$$

where L_{WHP} is the clear length of the bending parts of half a WHP. The yield force of a WHP, $F_{\mathrm{y,WHP}}$, is then calculated as:

$$F_{\mathrm{y,WHP}} = 2V_{\mathrm{WHP}} \tag{10}$$

Based on the virtual work method along with analytical integration, the elastic stiffness K_{fe} of a WHP is calculated as:

$$K_{\mathrm{fe}} = 2\frac{9\pi D_{\mathrm{e}}^{3} D_{\mathrm{i}} EG}{(40E D_{\mathrm{e}}^{2} L_{\mathrm{WHP}} + 48G L_{\mathrm{WHP}}^{3})} \tag{11}$$

where E is the modulus of elasticity and G the shear modulus of the WHPs material.

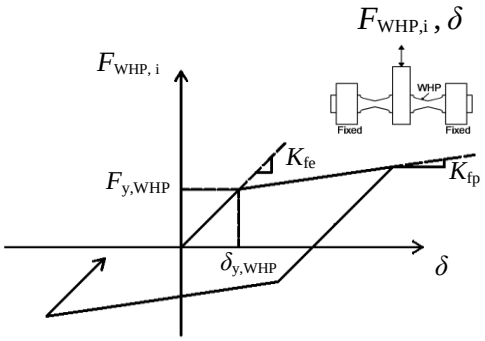


Figure 4: Assumed cyclic behaviour of one WHP

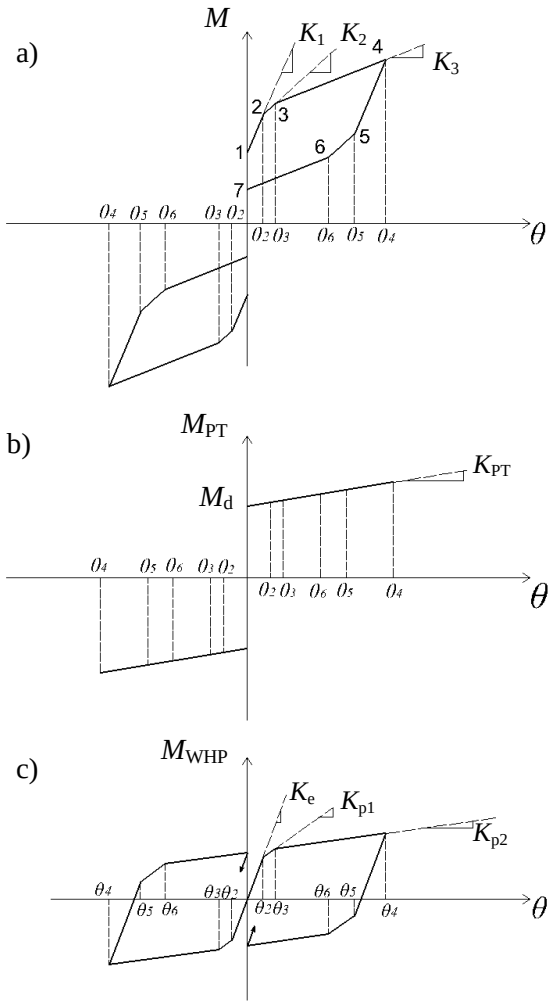


Figure 5: Assumed cyclic behaviour of a PT connection with WHPs

3 MODELING OF PT CONNECTION WITH WHPS FOR NONLINEAR ANALYSIS

3.1 Model development in OpenSees

A model for the PT connection with WHPs and the associated beams and columns was developed in OpenSees as shown in Fig. 6. The beams and columns were modeled using the nonlinear force-based beam-column fiber element which can strictly satisfy equilibrium and accurately capture the distribution of inelasticity along the depth of the section and along the length of the physical member. For the beam, two fiber elements with cross-sections having different flange thickness were used to account for the beam flange reinforcing plates. Each fiber was associated with uniaxial bilinear elastoplastic stress-strain behaviour (Steel01 in OpenSees) with a post-yield stiffness ratio equal to 0.01.

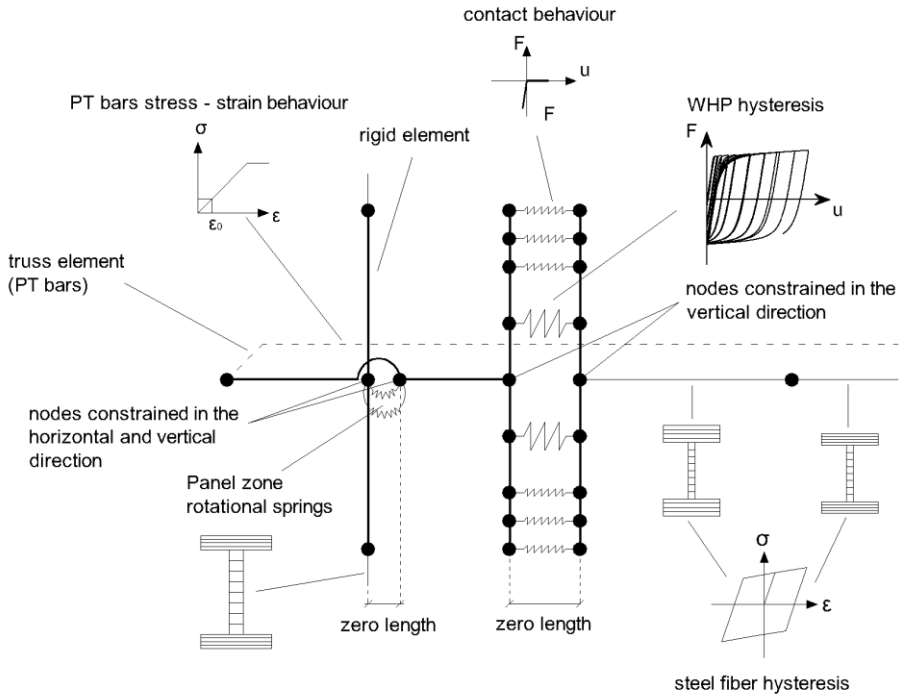


Figure 6: Model for an exterior PT connection with WHPs and associated columns and beam

Rigid elastic beam-column elements were used to model the beam-column interface where gap opening and closing takes place. To accurately capture the gap opening mechanism in the beam-column interface, three zero-length contact spring elements were placed at equal spaces along the beam flange thickness. These contact springs were associated with an elastic compression - no tension force-displacement behaviour (ENT material in Openness). A value of the compression stiffness equal to 20 times the axial stiffness of the beam K_b was assigned to these contact springs. Larger values for this stiffness were found to produce practically the same results but with higher computational cost, i.e., more iterations to achieve convergence and equilibrium in nonlinear analysis. To capture the hysteretic energy dissipation capacity of the connection, two zero-length hysteretic springs were placed at the exact locations of WHPs along the depth of the beam web. These springs were associated with a smooth hysteretic Giuffre-Menegotto-Pinto model with isotropic hardening (Steel 02 material in OpenSees).

To account for panel zone shear deformations and possible yielding, the panel zone was modeled using the Scissors model which introduces four additional rigid elastic beam-column elements and two nodes in the center of the panel zone connected with two zero-length rotational springs. Theses springs are associated with bilinear elastoplastic hysteretic rules (Steel01 material in OpenSees) with properties calculated to reflect the contribution of the column web (including doupler plates) and the column flanges in the shear force - shear deformation panel zone behaviour. This simple panel zone model has been found to produce identical results to those of the more computationally expensive Krawinkler panel zone model [2].

PT bars were modeled using a truss element running parallel to beam center-line axis and connected to the exterior nodes of the panel zones of the exterior columns of the SC-MRF. The truss element has a cross-section area A_{PT} equal to that of both PT bars. To account for post-tensioning, an initial strain equal to $F_{PT,i}/(A_{PT} \cdot E_{PT})$ was first assigned to the truss element where EP_T is the modulus of elasticity of the PT bar material. However, post-tensioning results in shortening of the beams which in turn decreases the post-tensioning force. To account

for this decrease, the initial strain in the truss element was increased to ensure that the post-tensioning force in the PT bars will be equal to $F_{PT,i}$ after the beam shortening.

3.2 Model calibration and assessment

The Steel02 OpenSees hysteretic model used for the WHP force-displacement behaviour was calibrated against experimental results from WHPs component tests previously conducted by Vasdravellis et al. (2012). Fig. 7.a shows the experimental setup for a pair of WHPs with the following properties: D_e=20 mm, D_i=14 mm, L_{WHP}=40 mm, f_y=560 MPa and E=200 GPa. Fig. 7.b compares and confirms a good agreement between the experimental hysteresis and the Steel02 hysteretic model. The Steel02 model has a yield strength equal to $2 \cdot F_{y,WHP}$; initial elastic stiffness equal to $0.6 \cdot (2 \cdot K_{fe})$; strain hardening ratio equal to 0.01; parameters controlling the transition from the elastic to inelastic regions of the hysteresis R_o=30, CR_1=0.925 and CR_2=0.15; and isotropic hardening parameters a_1=0.025, a_2=2.5, a_3=0.0 and a_4=1.0. The factor '2' for the calculation of the yield strength and stiffness reflects that a zero-length spring represents a pair of WHPs.

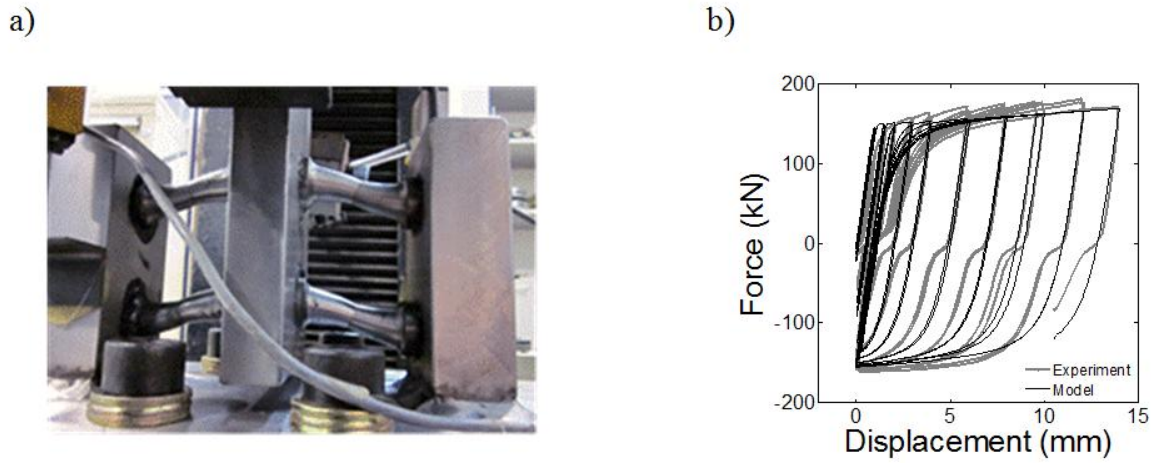


Figure 7: (a) Setup for WHP component tests; (b) comparison of experimental hysteresis and hysteretic model

The accuracy of the model for the PT connection with WHPs and the associated beams and columns (discussed in Section 3.1) was assessed using results from large-scale experimental tests previously conducted by Vasdravellis et al. (2012). Fig. 8.a shows the experimental test setup. A strong 310UC158 column was used along with two additional steel members welded to the column to form a truss system which increases the horizontal stiffness of the test setup. The whole system was bolted on the strong floor. The beam had a 250UB37 cross-section. The length of the beam flange reinforcing plates was 0.7 m. The total post-tensioning force was 504 kN. The displacement history was applied vertically by a hydraulic actuator positioned at a distance of 1800mm from the inner face of the column. The beam sections, column sections and beam flange reinforcing plates were made of steel with yield strength equal to 300 MPa. The WHPs were made of steel with yield strength equal to 560 MPa. The material of the PT bars had nominal yield strength equal to 930 MPa, tensile stress 1050 MPa and elongation capacity 6%, according to the specifications of the supplier. The loading protocol of [1] was used. This protocol consisted of three initial sets of six cycles at 6.75 mm, 9 mm, and 13.5 mm displacements, four subsequent cycles at 18 mm, and six sets of two cycles at 27,

36, and 54 mm. These displacements correspond to drifts equal to 0.00375, 0.005, 0.0075, 0.01, 0.015, 0.02, and 0.03. Fig. 8.b shows the experimental and analytical hysteresis for the PT connection and confirms a good agreement between the proposed model and the test results

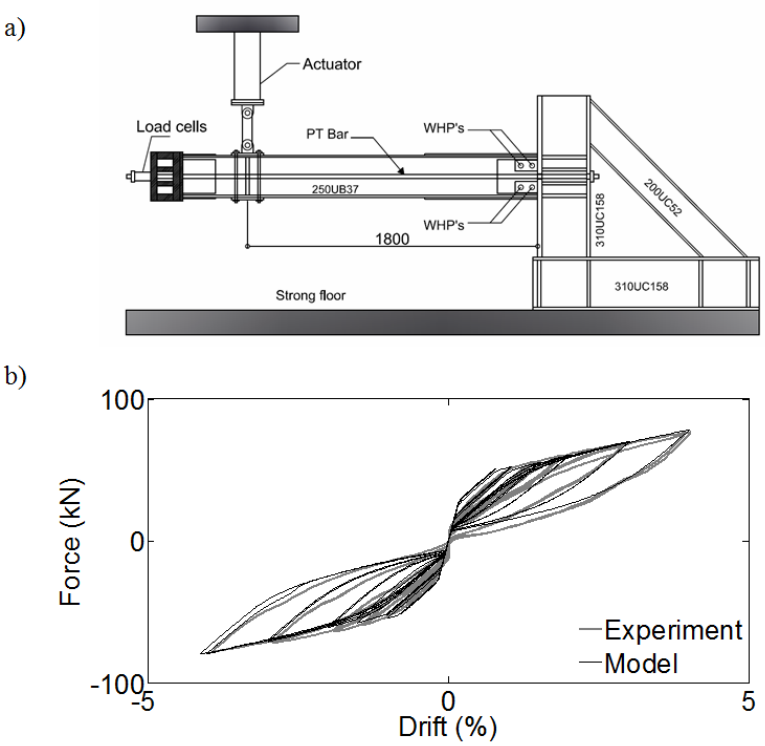


Figure 8: (a) Setup for WHP component tests; (b) comparison of experimental hysteresis and model in OpenSees

4 PROTOTYPE BUILDING

Fig. 9.a shows the plan view of the 5-storey, 4-bay by 3-bay prototype office building used for the study. The building has four identical MRFs to resist lateral loads in the longitudinal plan direction. The design study focused on one of the interior MRFs shown in Fig. 9.b. This MRF was designed either as a conventional steel MRF according to [7] or as a steel SC-MRF using PT connections with WHPs to compare their seismic performance. The dead and live gravity loads considered in the design are selected from [9]. The design seismic action, referred to herein as DBE, has a return period of 475 years and is expressed by the Type 1 elastic response spectrum of [7] with peak ground acceleration equal to 0.30g and ground type B (average shear wave velocity between 360 and 800 m/s.). The MRF was designed according to [8] and [7]. The steel yield strength for columns is assumed equal to 350 MPa and for beams equal to 300 MPa.

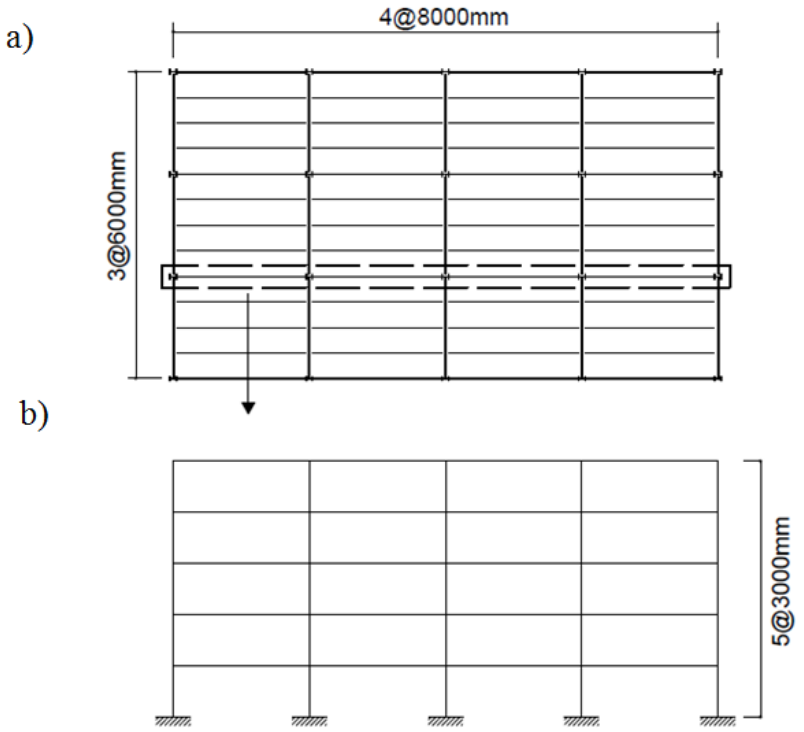


Figure 9: (a) Plan view of prototype building; (b) elevation of interior MRF

5 DESIGN OF THE CONVENTIONAL STEEL MRF

The model used to design the conventional steel MRF was based on the centerline dimensions of the MRF without accounting for the finite panel zone dimensions. The column base and beam-to-column connections were assumed to be fully rigid. A diaphragm constrain was imposed on the nodes of each floor to simulate the effect of the composite slab. The MRF was designed using the modal response spectrum analysis procedure of [7]. The MRF satisfied Ductility Class High [7] by using compact Class 1 cross-sections [8], and so, the behaviour (or 'strength reduction' for the USA) factor was set equal to $5 \cdot a_u/a_1=6.5$, where a_u/a_1 is the overstrength factor with a recommended value of 1.3 for multi-bay multi-storey steel MRFs. The displacement behavior (or 'displacement amplification' for the USA) factor is equal to q, i.e., [7] uses the equal displacement rule to estimate peak drifts associated with inelastic response. These drifts are then used to check second order (P-Δ) effects. Additionally, [7] uses a serviceability limit on the peak storey drift, $\theta_{s\text{-}max}$, under the frequently occurring earthquake (FOE) with a return period equal to 95 years. The FOE has intensity 40% (reduction factor v=0.4 in [7] the intensity of the DBE and the associated limit on $\theta_{s\text{-}max}$ was set equal to 0.75%, assuming ductile non-structural components. The MRF was designed to satisfy the strong column - weak beam capacity design rule of [7], the beam-to-column connections were designed to be fully rigid and the panel zones were strengthened with doubler and continuity plates to avoid yielding. A strength-based design with q=6.5 under the DBE was first performed. Beams and columns cross-sections from strength-based DBE design had to be increased to satisfy the serviceability 0.75% limit on $\theta_{s\text{-}max}$ under the FOE. The final sections were found iteratively by decreasing the value of q, designing the MRF for increased strength under the DBE and then checking storey drifts under the FOE. Table 1 lists the column cross-

sections and the beam cross-sections of the conventional MRF. The fundamental period of vibration is 1.08 s. and the estimated $\theta_{s\text{-}max}$ is 0.64% under the FOE, 1.6% under DBE and 2.4% under the MCE.

Storey	Cross sections MRF & SC-MRF		PT bars		WHPs			Reinf. plates	
	Beams	Columns	$F_{PT,I}$ (kN)	d_{PT} (mm)	D_e (mm)	D_i (mm)	L_{WHP} (mm)	L_{RP} (mm)	t_{RP} (mm)
1	IPE450	HEB400	933	36	36	26	65	1080	15
2	IPE450	HEB400	933	36	36	26	65	1080	15
3	IPE400	HEB400	806	36	33	23	65	1180	15
4	IPE400	HEB360	806	36	33	23	65	1180	15
5	IPE360	HEB360	700	36	32	22	65	1190	15

Table 1: Design details of the conventional steel MRF and the steel SC-MRF using PT connections with WHPs

6 DESIGN OF THE STEEL SC-MRF USING PT CONNECTIONS WITH WHPS

The sections of the conventional MRF were used for designing the SC-MRF so that both frames would have almost the same initial stiffness and fundamental period of vibration. The SC-MRF and the conventional MRF are expected to have similar drifts as it has been shown that self-centering and conventional bilinear elastoplastic systems of the same strength and period of vibration have similar drifts when the self-centering system is designed with adequate energy dissipation capacity and post-yield stiffness [12].

The PT connections with WHPs were designed using the methodology presented in [11] that adopts two performance objectives and associated structural limit states, namely: (1) Immediate Occupancy under the DBE by avoiding damage in beams and columns while permitting gap opening; and (2) Collapse Prevention under the MCE by avoiding PT bar yielding and beam local buckling while permitting minor yielding in beams. To initiate the design procedure, the moment corresponding to point 2 in Fig. 5.a, referred to herein as M_{IGO}, was set equal to 66% of the nominal plastic moment of resistance of the beam section. In addition, M_d was set equal to 69% of M_{IGO}. These M_{IGO} and M_d values provide an energy dissipation factor equal to 0.31 [11]. The post-tensioning force and the length of the reinforcing plates were then designed. PT bars were designed to avoid yielding for $\theta_{s\text{-}max} \leqslant 0.06$ rad. There was no need to increase the beam cross-sections to design the PT connections with WHPs. The design of the PT connections was based on $\theta_{s\text{-}max}$ values equal to 0.64% under the FOE, 1.6% under the DBE and 2.4% under the MCE, i.e., equal to those predicted for the conventional steel MRF. These drifts are significantly lower than those used in previous works which are based on the IBC 2% drift limit under the DBE [22, 11]. Table 1 lists the column cross-sections, beam cross-sections, $F_{PT,i}$, PT bar diameter d_{PT}, D_e, D_i, L_{WHP}, and length LRP and thickness t_{RP} of the beam flange reinforcing plates. The beam flange reinforcing plates are made of steel with yield strength equal to 300 MPa. The WHPs are made of steel with yield strength equal to 235 MPa. The material of the PT bars has nominal yield strength equal to 930 MPa and elongation capacity 6%. The fundamental period of vibration of the SC-MRF is 1.01 sec., i.e., slightly lower than that of the conventional MRF (1.08 sec) because the beam flange reinforcing plates increase the stiffness of the beams of the SC-MRF.

7 NONLINEAR MONOTONIC AND CYCLIC STATIC ANALYSIS

Fig. 10 shows the base shear coefficient (V/W) - roof drift (θ_r) behaviour of the conventional MRF and the SC-MRF from nonlinear monotonic (pushover) static analysis using nonlinear models described in Section 8.2. V is the base shear and W is the seismic weight. An inverted triangular force distribution along with roof displacement control was used in these analyses. The MRF and the SC-MRF have comparable base shear strengths and comparable initial stiffness. The pushover curves are plotted along with points associated with structural limit states and vertical lines corresponding to roof drifts expected under the FOE, DBE and MCE. The structural limit states for the conventional MRF are beam yielding and base column yielding and occur at θ_r equal to 0.82% and 0.92% respectively. The conventional MRF avoids damage under the FOE but experiences significant damage under the DBE. The structural limit states for the SC-MRF are decompression in a PT connection (i.e. point 1 in Fig. 5.a), WHP yielding (i.e. point 2 in Fig. 5.a), base column yielding and beam yielding. Fig. 10 shows that the beams of the SC-MRF are damage-free for θ_r equal or lower than 3%, i.e., drifts higher than the MCE. Damage in the SC-MRF is experienced at the column bases that yield at θ_r equal to 0.97%. No PT bar yielding is observed. The first decompression occurs at θ_r equal to 0.4% while WHPs yield at θ_r equal to 0.62% which is almost equal to the FOE drift. Decompression does not involve damage while yielding of the WHPs is acceptable under low drifts since WHPs can be easily replaced without bolting or welding. The conventional MRF experiences softening at θ_r equal to 1.25% while the SC-MRF shows a more gradual softening behaviour. In particular, the SC-MRF shows softening due to decompression in the PT connections at low drifts and further softening due to plastic deformations at the column bases and yielding of a large number of WHPs at θ_r equal to 1%. Fig. 11 shows the V/W - θ_r behaviour of the MRF and the SC-MRF from nonlinear cyclic (push-pull) static analysis. The first cycle of the analysis is performed up to the DBE drift while the next cycle up to the MCE drift. The SC-MRF shows full re-centering capability under the DBE, adequate energy dissipation and a small residual drift under the MCE due to plastic deformations at the column bases. The conventional MRF shows large energy dissipation capacity due to plastic deformations at the beam ends and at the column bases, and the possibility of experiencing large residual drifts under the DBE and MCE.

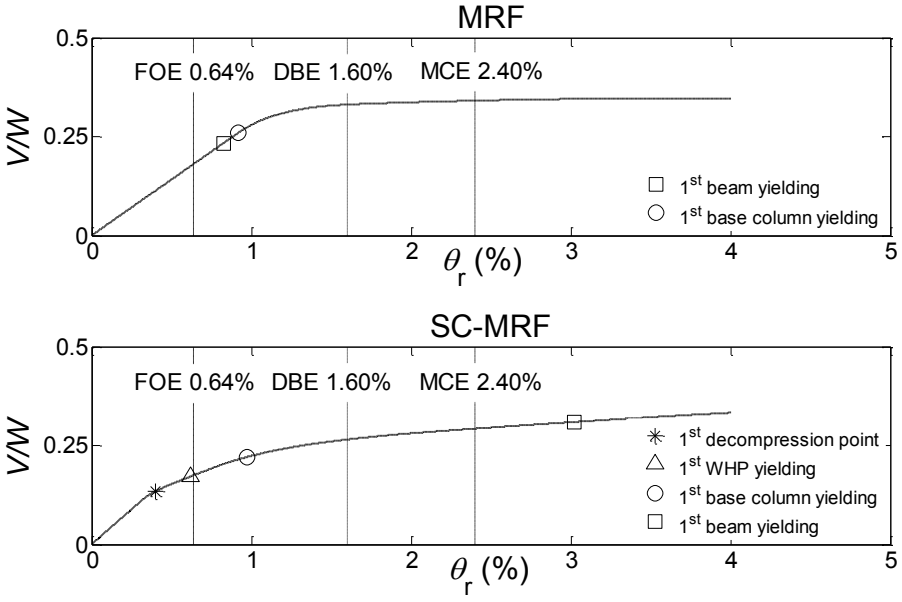


Figure 10: Base shear coefficient - roof drift behaviour from nonlinear monotonic (pushover) static analysis

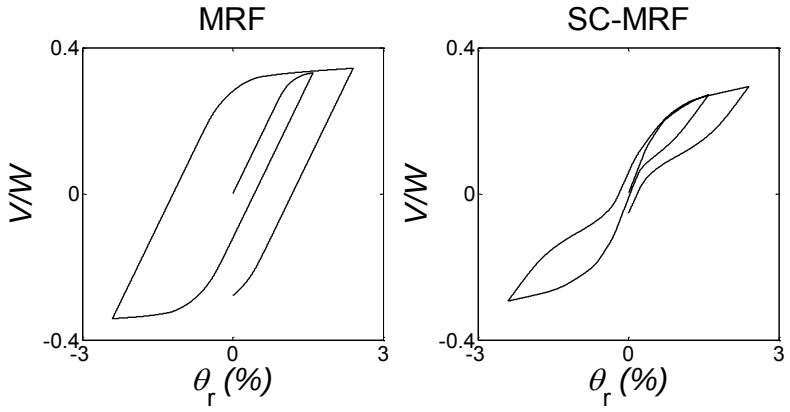


Figure 11: Base shear coefficient - roof drift behaviour from nonlinear cyclic (push-pull) static analysis

8 NONLINEAR DYNAMIC TIME HISTORY ANALYSES

8.1 Ground motions

A set of 20 earthquake ground motions recorded on ground type B were used in 2D nonlinear dynamic time history analyses to evaluate the performance of the SC-MRF and the performance of the conventional MRF. None of the ground motions exhibit near-fault forward directivity effects. The ground motions were scaled to the DBE level using the scaling procedure of [23]. Table 2 provides the scale factors and information on the 20 earthquake ground motions. Fig. 12 compares the DBE elastic response spectrum of [7] with the mean (μ) and mean plus/minus one standard deviation (μ±σ) spectra of the DBE ground motions. The amplitudes of the DBE ground motions were further scaled by 0.4 and 1.5 to represent FOE and MCE ground motions.

Earthquake	Station	Component	Magnitude (M_w)	Distance (km)	Scale factor		
					FOE	DBE	MCE
Imperial Valley 1979	Cerro Prieto	H-CPE237	6.53	15.19	0.82	2.05	3.08
Loma Prieta 1989	Hollister - S & P	HSP000	6.93	27.67	0.29	0.72	1.08
Loma Prieta 1989	Woodside	WDS000	6.93	33.87	1.40	3.49	5.24
Loma Prieta 1989	WAHO	WAH090	6.93	17.47	0.48	1.20	1.80
Manjil 1990	Abbar	ABBAR--T	7.37	12.56	0.28	0.70	1.05
Cape Mendocino 1992	Fortuna - Fortuna Blvd	FOR000	7.01	15.97	0.99	2.47	3.71
Cape Mendocino 1992	Rio Del Overpass - FF	RIO360	7.01	14.33	0.50	1.25	1.88
Landers 1992	Desert – Hot Springs	LD-DSP000	7.30	21.78	0.95	2.37	3.56
Northridge 1994	LA - W 15th St	W15090	6.69	25.60	1.14	2.86	4.29
Northridge 1994	Moorpark - Fire Sta	MRP180	6.69	16.92	0.78	1.94	2.91
Northridge 1994	N Hollywood - Cw	CWC270	6.69	7.89	0.53	1.33	2.00
Northridge 1994	Santa Susana Ground	5108-360	6.69	1.69	0.78	1.95	2.93
Northridge 1994	LA - Brentwood VA	0638-285	6.69	12.92	0.85	2.12	3.18
Northridge 1994	LA - Wadsworth VA	5082-235	6.69	14.55	0.62	1.54	2.31
Kobe 1995	Nishi-Akashi	NIS090	6.90	7.08	0.48	1.19	1.79
Kobe 1995	Abeno	ABN090	6.90	24.85	1.00	2.49	3.74
ChiChi 1999	TCU105	TCU105-E	7.62	17.18	0.96	2.39	3.59
ChiChi 1999	CHY029	CHY029-N	7.62	10.97	0.53	1.32	1.98
ChiChi 1999	CHY029	CHY041-N	7.62	19.83	0.56	1.40	2.10
Hector 1999	Hector	HEC090	7.13	10.35	0.42	1.04	1.56

Table 2: Properties of the ground motions used for nonlinear dynamic analyses

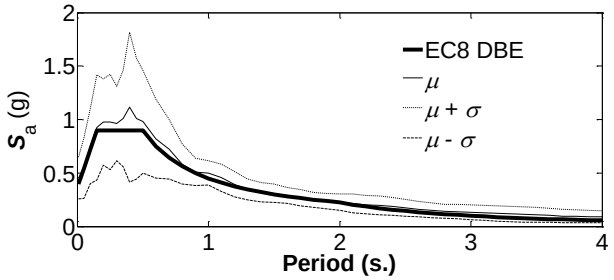


Figure 12: Comparison of the design EC8 spectrum with spectra of the ground motions used for nonlinear analyses

8.2 Modeling for nonlinear dynamic analysis

2D nonlinear analytical models of the conventional MRF and the SC-MRF were developed for nonlinear dynamic analyses in OpenSees. Nonlinear beam-column fiber elements were used for the beams and columns and the Scissors model [2] for the panel zones of the conventional MRF and the SC-MRF. A diaphragm constraint is imposed on each floor level of the conventional MRF. Stiff truss elements were used to connect the internal nodes of each bay of the SC-MRF to allow beam shortening due to post-tensioning, gap opening in PT connections, and to consider the use of a discontinuous slab proposed by [5]. The model of Fig. 6 was used to model the PT connections and the associated beams and columns of the SC-MRF.

The Newmark method with constant acceleration was used to integrate the equations of motion. The integration time step was selected to be 10 times smaller than the input time step of the earthquake ground motions. The Newton method with tangent stiffness was used to minimize the unbalanced forces within each integration time step of the nonlinear dynamic analysis. A Rayleigh damping matrix was used to model the inherent 3% critical damping at the first two modes of vibration. A nonlinear load controlled static analysis under the gravity loads was first performed, and then, the nonlinear dynamic time history analysis for each earthquake ground motion was executed. Each dynamic analysis was extended well beyond the actual earthquake time (the ground motions were padded with zeros) to allow for damped free vibration decay and accurate residual drifts calculation.

8.3 Seismic response results

Fig. 13 compares the roof drift time histories of the conventional MRF and the SC-MRF under the 5082-235 ground motion scaled to the DBE and MCE. Near the end of the time histories the SC-MRF oscillates around the origin, indicating negligible residual drift, while the conventional MRF experiences residual drifts. The peak roof displacements of the MRF and the SC-MRF are similar. Fig. 14 shows the stress-strain hysteresis at points A and B (extreme column base flange fibers), and, C and D (extreme beam flange fibers) of the first storey of the conventional MRF under the 5082-235 ground motion scaled to the DBE and MCE. Fig. 15 presents similar information for the SC-MRF. The stress-strain hysteresis immediately after the end of the beam flange reinforcing plate (points E and F) of the SC-MRF is also shown. The SC-MRF eliminates beam plastic deformations under both the DBE and MCE, while the conventional MRF experiences appreciable beam damage. Figs. 14 and 15 show that the column bases of the SC-MRF experience larger plastic deformations than those of the column bases of the conventional MRF.

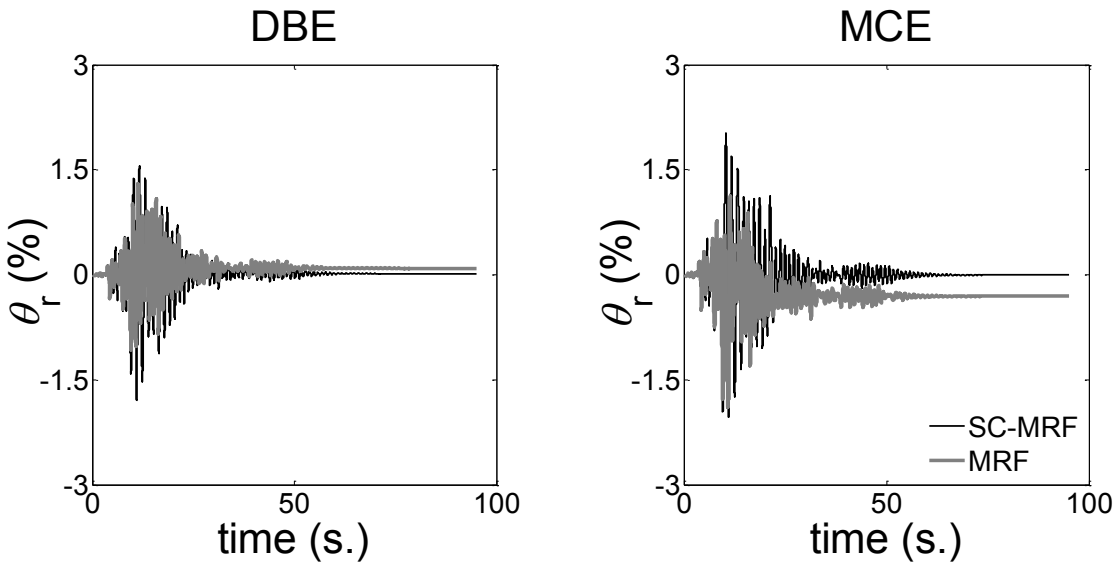


Figure 13: Comparison of the roof drift time histories under the 5082-235 ground motion scaled to the DBE and MCE

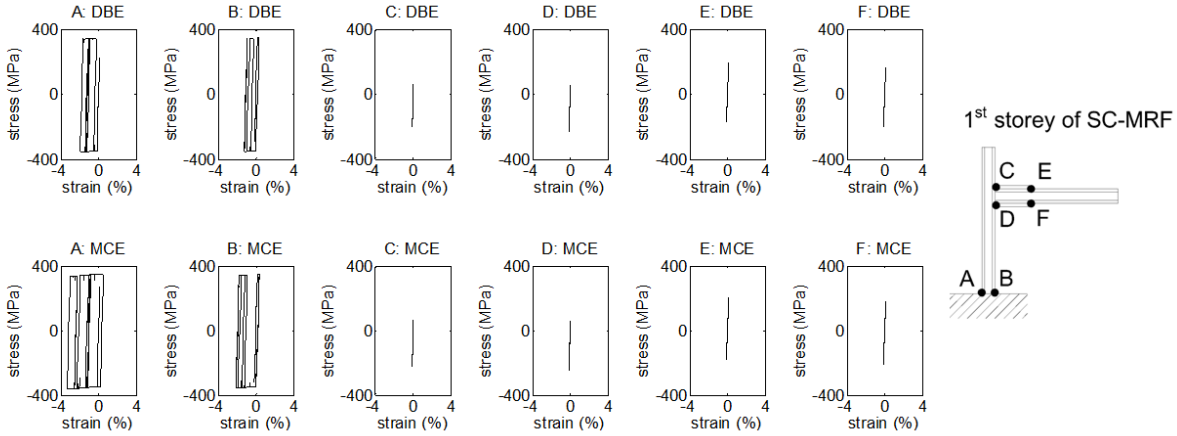


Figure 14: Stress-strain hysteresis at points A, B, C and D of the conventional MRF under the 5083-235 ground motion scaled at the DBE and MCE

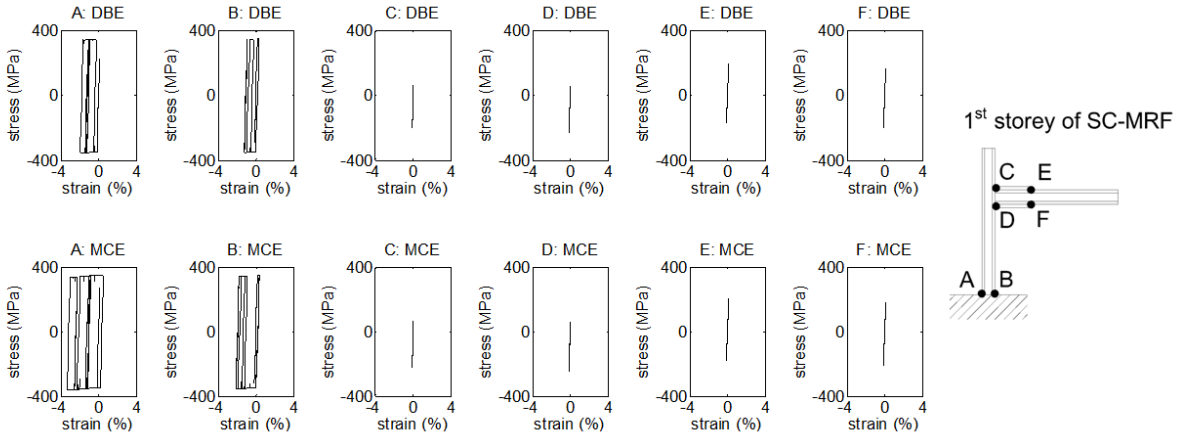


Figure 15: Stress-strain hysteresis at points A, B, C, D, E and F of the SC- MRF under the 5083-235 ground motion scaled at the DBE and MCE

Fig. 16 shows μ, μ + σ and median $\theta_{s\text{-}max}$ values under the earthquake ground motions of Table 2 scaled to the FOE, DBE and MCE. The μ, μ + σ and median height-wise $\theta_{s\text{-}max}$ distributions show identical shapes. The MRF has the largest $\theta_{s\text{-}max}$ in the fourth storey with μ values equal to 0.75% under the FOE, 1.65% under the DBE and 2.2% under the MCE, i.e., close to the design values of 0.64% under the FOE and 1.6% under the DBE, and, smaller than the design value of 2.4% under the MCE. The SC-MRF has the largest $\theta_{s\text{-}max}$ in the fourth storey with mean values equal to 0.75% under the FOE, 1.8% under the DBE and 2.5% under the MCE, i.e., slightly larger than the DBE and MCE design ones. Fig. 17 shows μ, μ + σ and median values of the residual storey drifts, $\theta_{s\text{-}res}$. $\theta_{s\text{-}res}$ show a uniform height-wise distribution for the conventional MRF and large dispersion compared to that of $\theta_{s\text{-}max}$. The largest $\theta_{s\text{-}res}$ of the conventional MRF occurs in the first storey with mean values equal to 0.1% under the DBE and 0.3% under the MCE. The associated μ + σ $\theta_{s\text{-}res}$ values are equal to 0.25% under the DBE and 0.6% under the MCE. The latter $\theta_{s\text{-}res}$ values indicate that repair of damage in the conventional MRF would be costly and disruptive after the DBE and not financially viable after the MCE (Mc Cormick et al. 2008). These results highlight the need for Eurocode 8 to include residual deformations as an additional seismic performance parameter. The SC-MRF practically eliminates residual storey drifts apart from the first storey that has μ and μ + σ $\theta_{s\text{-}res}$ values equal to 0.1% and 0.15% under both the DBE and MCE. The latter $\theta_{s\text{-}res}$ values are lower than the global sway imperfections defined in [8] and so it can be assumed that there will be no need for these residual drifts to be straightened out. Fig. 17 shows small μ + σ $\theta_{s\text{-}res}$ values in the third storey of the SC-MRF due to modest yielding in the beam ends.

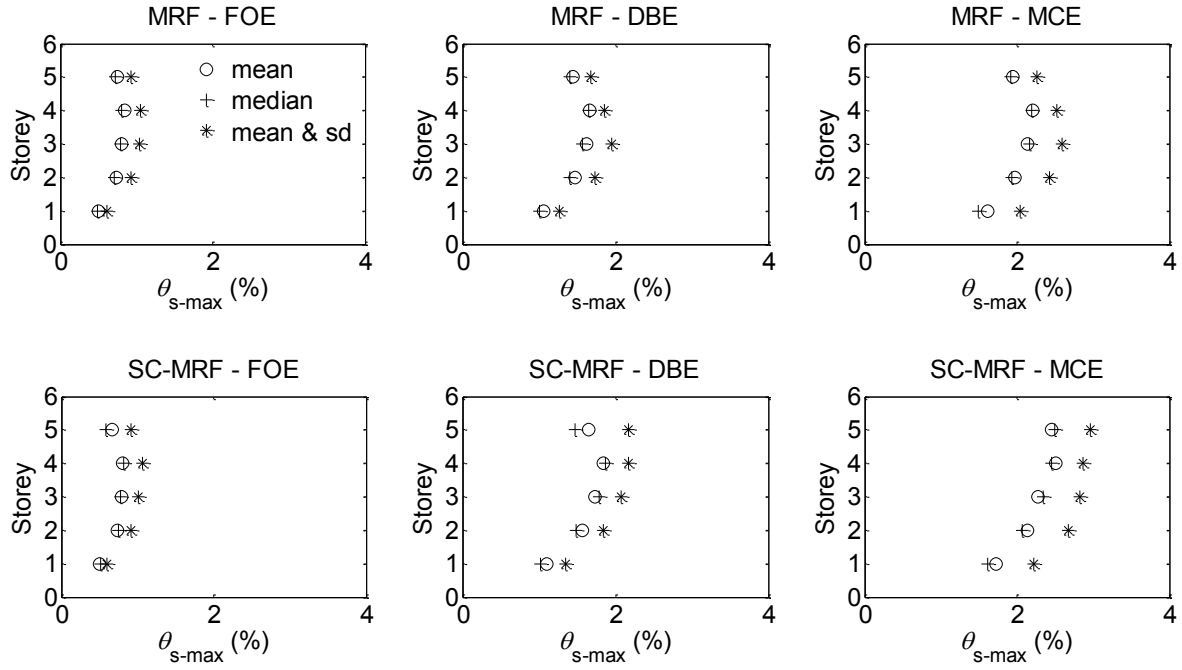


Figure 16: Statistics of peak storey drifts of the conventional MRF and the SC-MRF under 20 earthquake ground motions scaled to the FOE, DBE and MCE

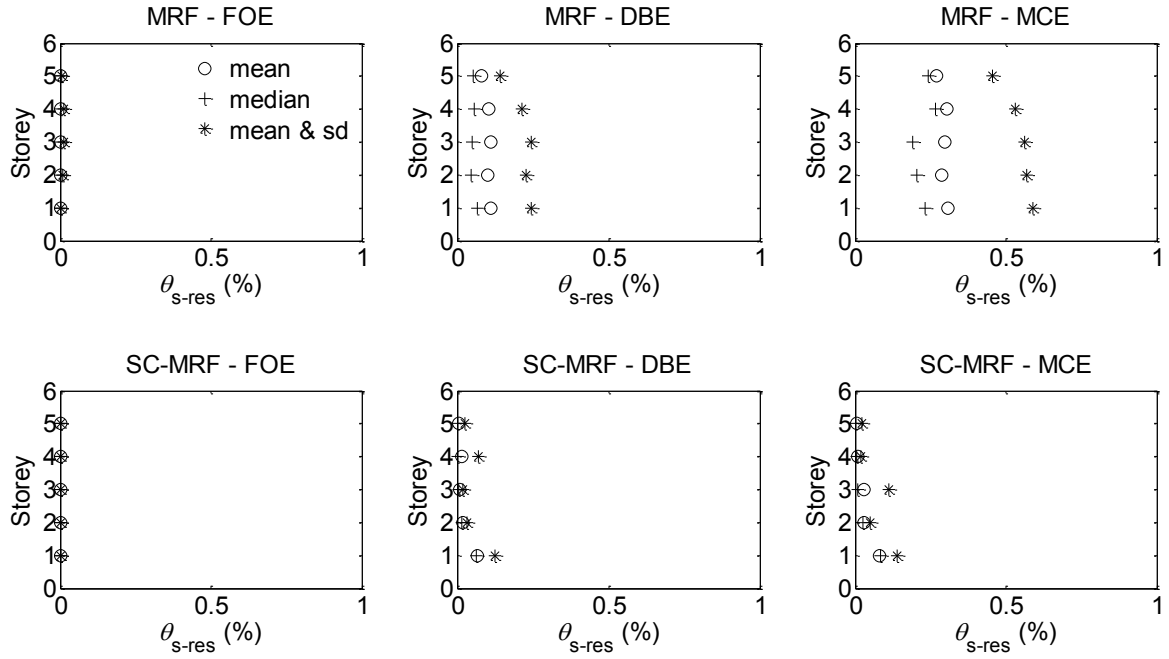


Figure 17: Statistics of residual storey drifts of the conventional MRF and the SC-MRF under 20 earthquake ground motions scaled to the FOE, DBE and MCE

9 SUMMARY AND CONCLUSIONS

This paper presented research on design, modelling and assessment of self-centering steel moment-resisting frames (SC-MRFs) using a recently developed post-tensioned (PT) connection with web hourglass shape steel pins (WHPs). The connection isolates inelastic deformations in WHPs, avoids damage in other connection parts as well as in beams and columns, and eliminates residual drifts. WHPs do not interfere with the composite slab and can be easily repaired without bolting or welding. A simplified nonlinear model has been developed for the PT connection with WHPs and the associated beams and columns. The model consists of nonlinear beam-column elements, and hysteretic and contact zero-length spring elements appropriately placed in the beam-column interface. A prototype building was designed as a conventional steel MRF according to Eurocode 8 or as a steel SC-MRF using PT connections with WHPs. Nonlinear models were developed in OpenSees for the two frames and used to conduct static monotonic (pushover), static cyclic (push-pull) and dynamic (seismic) analyses. Seismic analyses were conducted under a set of ground motions scaled to the frequently occurred, design basis and maximum considered earthquake intensities (FOE, DBE and MCE). Based on the results presented in this paper, the following conclusions are drawn:

- The proposed model for the PT connection with WHPs and the associated beams and columns has been calibrated against experimental results and found to accurately simulate the hysteretic behaviour of the PT connection. Papers should be written following the format of the Latex or Word macros for submission that can be found at the conference website.
- The design process for the prototype building resulted in the same beam and column cross sections for the conventional MRF and the SC-MRF. In addition, the WHPs and the required beam flange reinforcing plates of the SC-MRF have practical sizes. Deadline for the submission of papers posted in the website must be respected.
- Nonlinear static monotonic (pushover) analysis shows that the conventional MRF and the SC-MRF have comparable base shear strength and initial stiffness. The conventional

MRF experiences significant damage in beams at the DBE drift. On the other hand, the SC-MRF has damage-free beams for drifts even higher than the MCE drift.

- Nonlinear static cyclic (push-pull) analysis shows that the SC-MRF has full re-centering capability and adequate energy dissipation capacity under the DBE.
- Seismic analyses show that the conventional MRF and the SC-MRF have comparable peak storey drifts. In particular, the conventional MRF has slightly lower peak storey drifts than the SC-MRF. For both frames though the mean peak storey drifts are close to the design values.
- Seismic analyses show that the SC-MRF practically eliminates residual storey drifts apart from the first storey which sustains small residual drifts due to plastic deformations at the column bases. The mean plus one standard deviation value of the first storey residual drift of the SC-MRF is equal to 0.15% under both the DBE and MCE which is considered small and does not need to be straightened out.
- Seismic analyses show that the mean plus one standard deviation value of the maximum residual storey drift of the conventional MRF is 0.25% under the DBE and 0.6% under the MCE. These values indicate that repair of damage in the conventional MRF would be costly and disruptive after the DBE and not financially viable after the MCE.
- Seismic analyses show that the beams of the SC-MRF do not exhibit any yielding even under the MCE, while significant inelastic deformations are developed in the beams of the MRF under both the DBE and MCE. On the other hand, the column bases of the SC-MRF experience larger inelastic deformations than those of the conventional MRF.

REFERENCES

[1] AISC, Seismic provisions for structural steel buildings, Chicago, Illinois, 2005.

[2] F.A. Charney, W.M. Downs, Connections in steel structures, *V. ESSC/AISC Workshop*, Amsterdam, June 3-4, 2004.

[3] C.C Chou, J.H Chen, Y.C Chen and K.C Tsai, Evaluating performance of post-tensioned steel connections with strands and reduced flange plates, *Earthquake Engineering and Structural Dynamics* **35(9):** 1167-1185, 2006.

[4] C.C. Chou, Y.J. Lai, Post-tensioned self-centering moment connections with beam bottomflange energy dissipators, *Journal of Constructional Steel Research* **65**(10-11): 1931-1941, 2009.

[5] C.C Chou, K.C. Tsai, W.C Yang, Self-centering steel connections with steel bars and a discontinuous composite slab, *Earthquake Engineering and Structural Dynamics* **38**:403-422, 2009.

[6] C. Christopoulos, A. Filiatrault, C.M. Uang, B. Folz, Posttensioned energy dissipating connections for moment-resisting steel frames, *Journal of Structural Engineering* **128(9)**: 1111-1120, 2002b

[7] Eurocode 8, Design of structures for earthquake resistance - part1: General rules, seismic actions and rules for buildings, 2009

[8] Eurocode 3: Design of steel structures - part 1-1: General rules and rules for buildings, 2010

[9] Eurocode 1: Actions on structures - part 1-1: General actions densities, self weight and imposed loads, 2009

[10] M. Garlock, J.M. Ricles, R. Sause R, Experimental studies of full-scale posttensioned steel connections, *Journal of Structural Engineering* **131(3)**: 438-448, 2005

[11] M. Garlock, R. Sause, J.M. Ricles, Behavior and design of posttensioned steel frame systems, *Journal of Structural Engineering* **133(3)**: 389-399, 2009.

[12] T.L. Karavasilis, C.Y. Seo, Seismic structural and non-structural performance evaluation of highly-damped self-centering and conventional systems, *Engineering Structures* **33(8)**: 2248-2258, 2011.

[13] T.L. Karavasilis, J.M. Ricles, R. Sause, C. Chen, Experimental evaluation of the seismic performance of steel MRFs with compressed elastomer dampers using large-scale real-time hybrid simulation, *Engineering Structures* **33(6)**:1859-1869, 2011

[14] T.L. Karavasilis, S. Kerawala, E. Hale, Model for hysteretic behaviour of steel energy dissipation devices and evaluation of a minimal-damage seismic design approach for steel frames, *Journal of Constructional Steel Research* **70**:358-367, 2012.

[15] H.J. Kim, C. Christopoulos, Friction damped posttensioned self-centering steel moment-resisting frames, *Journal of Structural Engineering* **134(11)**: 1768-1779, 2008a.

[16] H.J. Kim, C. Christopoulos, Seismic design procedure and seismic response of post-tensioned self-centering steel frames, *Earthquake Engineering and Structural Dynamics* **38(3)**: 355-376, 2008b

[17] T. Kobori, Y. Miura, E. Fukuzawa, T. Yamada, T. Arita, Y. Takenaka, N. Miyagawa, N. Tanaka N, T. Fukumoto, Development and application of hysteresis steel dampers, *Earthquake Engineering, Tenth World Conference*, Rotterdam: Balkema, 1992.

[18] S. Mazzoni, F. McKenna, M. Scott, G. Fenves, Open system for earthquake engineering simulation (OpenSees). User Command Language Manual, Pacific Earthquake Engineering Research Center, University of California, Berkeley, 2006.

[19] J. Mc Cormick, H. Aburano, M. Ikenaga, M. Nakashima, Permissible residual deformation levels for building structures considering both safety and human elements, *14th WCEE, Beijing, China*, 2008.

[20] J. Ricles, R. Sause, M. Garlock, C. Zhao, Posttensioned seismic-resistant connections for steel frames, *Journal of Structural Engineering* **127(2)**: 113-121, 2001

[21] J. Ricles, R. Sause, S.W. Peng, L.W. Lu, Experimental evaluation of earthquake resistant posttensioned steel connections, *Journal of Structural Engineering* **128(7)**: 850-859, 2002.

[22] P. Rojas, J.M. Ricles, R. Sause R, Seismic performance of post-tensioned steel moment resisting frames with friction devices, *Journal of Structural Engineering* **131(4)**: 529-540, 2004.

[23] P. Somerville, Development of ground motion time histories for phase 2 of the FEMA/SAC steel project, Report No. SAC/DB-97/04, Sacramento, CA, 1997.

[24] K.C. Tsai, C.C. Chou, C.L. Lin, P.C. Chen, S.J. Jhang SJ, Seismic self-centering steel beam-to-column moment connections using bolted friction devices, *Earthquake Engineering and Structural Dynamics* **37**: 627-645, 2008.

[25] G. Vasdravellis, T.L Karavasilis, B. Uy, Large-scale experimental validation of steel post-tensioned connections with web hourglass pins, *Journal of Structural Engineering*, in press, 2012.

[26] G. Vasdravellis, T.L. Karavasilis, B. Uy, Finite element models and cyclic behaviour of self-centering steel post-tensioned connections with web hourglass pins, *Engineering Structures*, in press, 2013.

[27] J. Whittle, M.S. Williams, T.L. Karavasilis, T. Blakeborough, A comparison of viscous damper placement methods for improving seismic building design, *Journal of Earthquake Engineering* **16**:540-560, 2012.

[28] M. Wolski, J.M. Ricles, R. Sause, Experimental study of a self-centering beam-column connection with bottom flange friction device, *Journal of Structural Engineering* **135(5)**: 479-488, 2009.

COMPDYN 2013
4th ECCOMAS Thematic Conference on
Computational Methods in Structural Dynamics and Earthquake Engineering
M. Papadrakakis, V. Papadopoulos, V. Plevris (eds.)
Kos Island, Greece, 12–14 June 2013

MONTE CARLO ANALYSIS FOR THE BLAST RESISTANCE DESIGN AND ASSESSMENT OF A REINFORCED CONCRETE WALL

Pierluigi Olmati

School of Civil and Industrial Engineering, Sapienza University of Rome
Via Eudossiana 18 - 00184 Rome (ITALY)
e-mail: pierluigi.olmati@uniroma1.it

Keywords: Blast Design, Precast Concrete Wall, Fragility Curves, SDOF Method, Non-Linear Analysis.

Abstract. *This paper presents a probabilistic approach for the design and assessment of structural elements under blast loads. The procedure is based on the broadly adopted fragility analysis method, widely implemented in Performance-Based Design procedures for structures subjected to natural hazards such as earthquake and wind. A discussion on the uncertainties related to blast engineering problems and on their implementation in a Performance-Based Design approach is presented, followed by an application aiming at the blast protective performance assessment of panels. The non-linear dynamic analyses are carried out by the equivalent non-linear single degree of freedom (SDOF) method. Consequently, the probability failure is computed using both Monte Carlo simulations and fragility curves.*

1 INTRODUCTION

Extreme loads can produce severe consequences on civil structures since these are not designed to have adequate strength to withstand extreme events. Sensible buildings and critical infrastructures are particularly prone to external man-made bomb attacks. The community is nowadays interested in these issues, especially after the escalation of dramatic events in the 1990's, concluding with the September 11 attacks.

The design for hardened structures to withstand blast loads is a common practice for many federal and commercial buildings. Generally in the design practice, a set of attack scenarios is selected and the structural members are verified using non-linear dynamic analyses with the equivalent single degree of freedom (SDOF) method. In such a way (that is adopting a deterministic approach) the failure probability is not evaluated, principally because there is a lack of knowledge of the hazard probability density function. This is common also for LPHC (Low Probability – High Consequence) events [1].

In the design practice adopting a deterministic approach for structural components subjected to blast loads the mechanical properties of the materials are taken equal to appropriate fractile values, and the demand is not probabilistically characterized. In [2] it is suggested to use a multiplicative coefficient of 20% on the appropriate amount of explosive for the design scenario, but this is limited to a scenario concerning explosive storage facilities. In an antiterrorism design, the amount of explosives used in an attack is generally characterized by an elevated amount of uncertainty.

In recent years, several probabilistic approaches in blast engineering problems have been proposed. In [3] Monte Carlo simulations are performed in order to estimate the failure probability for windows subjected to a blast load from a vehicle bomb. In [4] the fragility curves are presented for two kinds of glazing systems. In this study a similar effort is made focusing on a precast concrete cladding panel.

A cladding system in precast concrete walls has some advantages with respect to traditional masonry claddings (without structural function). In [5] studies are performed for the improvement of traditional masonry cladding. The first advantage of precast concrete panels with respect to the traditional masonry cladding, concerning the blast load considered in this paper, is the greater resistance to this kind of actions. The advantage of using precast concrete walls for protecting steel stud constructions is investigated in [6].

In general, the precast concrete wall façade should be able to protect the inside of the building from different threats such as vehicle impacts and ballistic attacks. Moreover, the concrete cladding panels can be integrated with other materials. The building life-cycle is also enhanced as a consequence of the precast concrete panel resistance to environmental attacks like acid rain and chlorine ion. In [7] the behavior of precast concrete panels with an insulation layer that improves the thermic qualities of the panel is investigated, focusing on the shear ties connecting the two concrete layers confining the insulation layer.

The panel and its surface are durable over time, and do not require expensive maintenance. In fact, this kind of cladding system is economically and ecologically sustainable, having all the advantages of precast structures.

Considering the above, this study focuses on the probabilistic approach for blast resistance assessment, and investigates the failure probability of a precast concrete wall subjected to blast loads (in particular far-field surface-blast loads). The wall under investigation is a non-bearing precast concrete panel used as exterior cladding wall for buildings. Typically the length and the width of these walls are subject to specific architecture requirements while their thickness is approximately 15 cm. The steel reinforcements are generally placed in the

middle of the cross section. From the blast design perspective, these walls should protect people and equipment from external bomb attacks.

The non-linear dynamic analyses are carried out by the well-established method of the equivalent non-linear single degree of freedom (SDOF) system, so the precast concrete wall is made equivalent to a non-linear SDOF. Both the fragility curves and the failure probability of the cladding wall are computed using Monte Carlo simulations.

Since the aim of this paper is to apply a probabilistic approach to the blast design, the fragility curves for a precast concrete cladding panel are computed for each component damage level defined in a Performance-Based Design prospective. Then the fragility curves are used to estimate the failure probability of the cladding panel subjected to a blast load scenario (vehicle bomb). Moreover the failure probability of the cladding panel subjected to the same scenario is estimated by a Monte Carlo simulation without using the fragilities curves.

The rest of this paper is organized as follows: Sections 2 and 3 provide respectively the details of the blast load and of the cladding model. Section 4 focuses on response parameters of the cladding under blast. Section 5 provides some insight on the implementation of fragility curves. Section 6 reports the results. Finally, some brief conclusions and suggestions for further developments are reported in Section 7.

2 BLAST LOAD MODEL

Blast engineering design is characterized by the presence of many uncertainties, which can be divided into three groups:

- load uncertainties: explosive weight, stand-off distance;
- structure uncertainties: stiffness, damping, material characteristic, etc.;
- interaction mechanism uncertainties: typically the reflected pressure, pressure duration, etc.

This classification of the uncertainties in three groups (load, structure, interaction mechanisms) is generally valid for many engineering fields. In [8] and [9] a framework for handling uncertainties implementing Monte Carlo simulation is presented and applied.

The side-on blast pressure P_{s0} [MPa] can be estimated by the formula of Mills [10] (Eq. 1), while the side-on specific impulse i_0 [Pa sec] is estimated by the formula of Held [11] (Eq. 2).

$$P_{s0} = 1.772\left(\frac{W}{R^3}\right) - 0.114\left(\frac{W^{\frac{2}{3}}}{R^2}\right) + 0.108\left(\frac{W^{\frac{1}{3}}}{R}\right) \tag{1}$$

$$i_0 = 300\left(\frac{W^{\frac{2}{3}}}{R}\right) \tag{2}$$

Where W is the explosive (charge) weight (usually in kg_f TNT) and R is the stand-off distance [m].

Both Eq. 1 and Eq. 2 are valid for free-air explosions. In this study detonations occurring on a surface (surface explosions) are considered, therefore the energy of the detonation is confined by the ground surface. This phenomenon is taken into account by using the same equations for the free-air explosions but assuming that a given explosive charge weight (W) on a deformable ground produces the same load as a free-air explosion of a charge weight equal to 1.8 W.

The reflected pressure P_r [MPa] for a normal angle of incidence is computed using Eq. 3. [10]:

$$P_r = 2P_{s0}\left(\frac{7P_{atm} + 4P_{s0}}{7P_{atm} + P_{s0}}\right) \tag{3}$$

Where P_{atm} is the atmospheric pressure (0.1 MPa).

Without loss of generality the negative pressure phase is neglected from the blast load time history [2], while the duration of the positive phase of the blast load is computed by assuming a triangular shape of the load function, given by:

$$t_d = \frac{2i_{s0}}{P_{s0}} \tag{4}$$

The atmospheric pressure is obtained starting from the reflected pressure by means of the Friedlander pulse shape as shown in Eq. 5.

$$P(t) = P_r\left(1 - \frac{t}{t_d}\right)e^{\frac{-\beta t}{t_d}} \qquad t_a \le t \le t_d \tag{5}$$

Where t_a is the arrival time of the blast load, here considered equal to zero, and β is the decay coefficient. In this study a value of 1.8 for β is assumed.

The cleaning effect is neglected in this study since the cladding wall is part of a building façade and no conditions are satisfied for the cleaning of the reflected shock wave [3].

In Figure 1 the blast load time histories computed with the described procedure for different values of the explosive weight W (in kg_f) and the stand-off distance R (in m) are shown. A good agreement can be observed between the obtained curves and the curves obtained by SBEDS [12].

The blast load is considered uniformly distributed on the cladding wall, consistent with a scaled distance higher than approximately 1.2 to 2.0 $m/kg_f^{1/3}$.

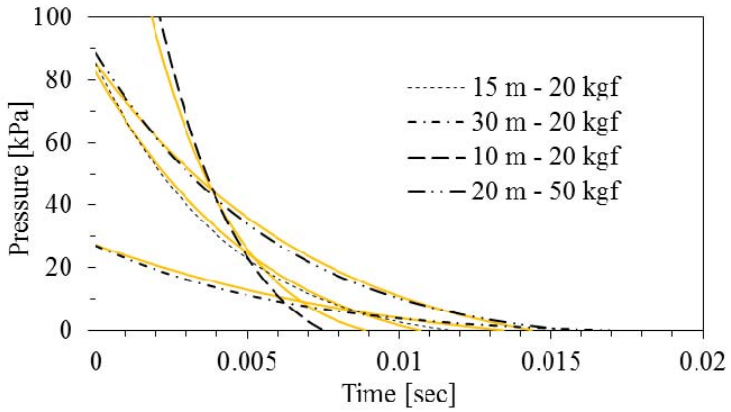


Figure 1: Blast loads (surface explosions) by the adopted model (dotted lines) and the SBEDS model (continuous line).

3 CLADDING PANEL MODEL

The cladding panel examined as case study is part of a frame structure building. A 3500 mm long and 1500 mm wide panel is used, having a cross section thickness of 150 mm. The supports of the panel are placed on the external frame beams of the building. Length, width and cross section thickness are assumed as stochastic variables. Both the assumed mean values and Coefficients of Variations (COVs) are shown in Table 1. The longitudinal reinforce-

ments consist in 10 rebar with a diameter of 10 mm, and they are placed in the middle of the cross section. The strength mean value and coefficient of variation are shown in Table 1 as well. The panel under investigation does not have shear reinforcements and transversal reinforcements are not significant for the purpose of this study.

3.1 Concrete model

The concrete compressive strength f_c is assumed as stochastic variable, while the Young's modulus of the concrete E_c and the concrete density ρ are expressed as functions of f_c.

The mean value of f_c is 28 MPa (4060 psi), with a COV of 0.18 as adopted in [13] for a lognormal probability density function (see Table 1).

The concrete Young's modulus is computed by Eq. 6 [14] and the concrete density is computed by Eq. 7 [15]. Both E_c and f_c are expressed in MPa while ρ is expressed in kg/m^3.

$$\mathrm{Ec} = 22000\left(\frac{\mathrm{f_c}}{10}\right)^{0.3} \tag{6}$$

$$\rho = \left(\frac{\mathrm{E_c}}{0.043\left(\mathrm{f_c}^{0.5}\right)}\right)^{\frac{1}{1.5}} \tag{7}$$

The compressive strength enhancement of the concrete due to the strain velocity is considered in this study. This strength enhancement is taken into account by means of the Dynamic Increasing Factor (DIF), a multiplicative coefficient of the concrete compressive resistance. Furthermore, since for ductile flexural response the compressive strength enhancement of the concrete varies slightly on the range of the strain velocity developed in the ductile flexural response, the DIF can be assumed constant and equal to 1.19 times the static compressive strength. This hypothesis is in accordance with the compressive strength enhancement proposed in [12], and is also convenient for avoiding cyclic iterations in the algorithm of the SDOF equation solver. However, cyclic iterations are necessary for computing the strength enhancement on the reinforcements, which is more crucial for ductile flexural response than the compressive strength enhancement on the concrete.

3.2 Reinforcing steel model

Concerning the reinforcing steel, the characteristic yielding strength is 450 MPa (65250 psi). For estimating the mean value of the yielding strength, an average strength factor equal to 1.1 is adopted as indicated in [12]. However experimental tests should be performed to validate this indication. The COV is of 0.12 as proposed in [13] for a lognormal probability density function (see Table 1). The Young's modulus is assumed as deterministic and equal to 210 GPA (30450 ksi).

The steel strength enhancement due to the strain velocity is taken into account by the Cowper and Symonds model. Thus, the DIF is provided by Eq. 8:

$$\mathrm{DIF} = 1 + \left(\frac{\mathrm{d}\epsilon/\mathrm{dt}}{\mathrm{C}}\right)^{\frac{1}{\mathrm{p}}} \tag{8}$$

Where dε/dt is the strain velocity on the reinforcements, C is taken equal to 500 sec^{-1} and p is taken equal to 6.

Both C and p are estimated by fitting the strength enhancement versus the strain velocity in [15]. Eq. 8 is graphically reproduced in Figure 2. By solving the SDOF equation of motion, the DIF is iteratively updated until a convergence threshold is reached.

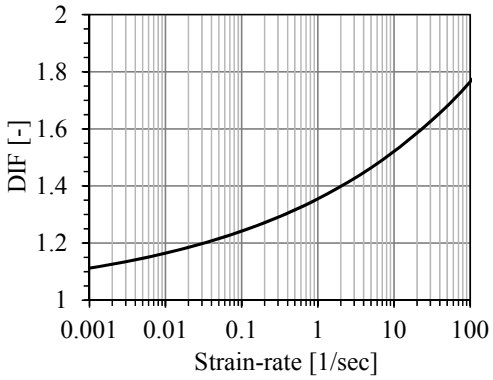


Figure 2: Reinforcing steel strength enhancement for different strain velocities.

The strain velocity of the steel reinforcements (dε/dt) in Eq. 8 is calculated approximately by Eq. 9.

$$\frac{d\varepsilon}{dt} = \frac{dR}{dt}\frac{L}{8}\left(\frac{d}{2E_c I_c}\right) \tag{9}$$

Where L is the length of the cladding panel, E_c is the Young's modulus of the concrete, I_c is the moment of inertia of the cracked cross section, d is the distance from the compressed external fiber of the cross-section to the centroid of the tension reinforcements, and dR/dt is the rate of the resistance force developed by the panel (R) when subjected to the demand load. Eq. 9 is valid for simply-simply supported elements, when the response is governed by the flexural behavior without shear failure.

Symbol	Description	Mean	COV	Distribution
f_c	Concrete strength	28 MPa	0.18	Lognormal
f_y	Steel strength	495 MPa	0.12	Lognormal
L	Panel length	3500 mm	0.001	Lognormal
H	Panel height	150 mm	0.001	Lognormal
b	Panel width	1500 mm	0.001	Lognormal
c	Panel cover	75 mm	0.01	Lognormal
W	Explosive weight	227 kg	0.3	Lognormal
R	Stand-off distance	15 m 20 m 25 m	0.05	Lognormal

Table 1: Input data.

4 COMPONENT DAMAGE LEVELS

For structural components subjected to blast loads, generally two response parameters are of interest: the support rotation angle (θ) and the ductility ratio (μ). These parameters are defined in Eq. 10 and Eq. 11:

$$\theta = \text{arctg}\left(\frac{2\delta_{max}}{L}\right) \tag{10}$$

$$\mu = \frac{\delta_{max}}{\delta_e} \tag{11}$$

Where δ_{max} is the maximum deflection, L is the panel length, and δ_e is the equivalent yield deflection of the resistance function.

A structural component subjected to a blast load is generally expected to yield, and it is impractical to design a member to remain in elastic range. While other significant response

parameters can be defined, this study focuses on the response parameters usually adopted for antiterrorism design [12].

In a performance-based blast design prospective, five Component Damage Levels (CDLs) are usually considered: Blowout (BO), Hazardous Failure (HF), Heavy Damage (HV), Moderate Damage (MD), and Superficial Damage (SD). Following [12] the above mentioned levels are defined as follows:

- Blowout (BO): the component is overwhelmed by the blast load causing debris with significant velocities.
- Hazardous Failure (HF): the component has failed, and debris velocities range from insignificant to very significant.
- Heavy Damage (HD): the component has not failed, but it has significant permanent deflections causing it to be un-repairable.
- Moderate Damage (MD): the component has some permanent deflection. It is generally repairable, if necessary, although replacement may be more economical and aesthetic.
- Superficial Damage (SD): the component has no visible permanent damage.

The thresholds corresponding to these CDLs are defined in terms of the response parameters θ and μ. For a concrete cladding wall without shear reinforcing and by neglecting tension membrane effects, the CDL thresholds are reported in Table 2. In the following the Fragility Curves (FCs) are computed for each component damage level.

Component damage levels	θ [degree]	μ [-]
Blowout	$>10°$	none
Hazardous Failure	$\leq 10°$	none
Heavy Damage	$\leq 5°$	none
Moderate Damage	$\leq 2°$	none
Superficial Damage	none	1

Table 2: Component damage levels, and the associated thresholds in terms of response parameters.

5 FRAGILITY CURVES

The blast load on the panel depends on both the peak pressure and the impulse. The pressure depends directly on the scaled distance (defined as the stand-off distance divided by the cube root of the explosive weight). Nevertheless, the impulse density depends on both the scaled distance and the explosive weight (Eq. 1 and Eq. 2). Consequently, two detonations with the same scaled distance can have different impulse densities, depending on the amount of explosive. Thus, the two explosions have the same peak pressure but different duration.

Summarizing, the blast load depends on the scaled distance and the explosive weight. Therefore the choice of the intensity measure for computing the failure probability using fragility curves (FCs) is a crucial issue. In this study, the scaled distance is taken as intensity measure.

The FCs are consequently plotted in function of the scaled distance and the stand-off distance. This is for taking into account the dependence of the blast demand, and consequently the structural response by both the scaled distance and the amount of explosive.

FCs are developed for each of the CDL (see Figure 3). With reference to the same figure, "i" indicates the i-th point of the FC, "j" is the j-th CDL, and "k" is the k-th FC of the CDL related to the stand-off distance for which the k-th FC is computed. "N" is the maximum val-

ue for "i" and therefore the total number of point forming the FC. "M" is the maximum value for "j" and therefore the total number of the CDLs. Finally "L" is the maximum value of "k" therefore the total number of the stand-off distances for which the j-th FC is computed.

The j-th FC for the k-th stand-off distance (FC CDL (j, k)) is built selecting the j-th CDL and the k-th stand-off distance and varying the explosive weight. The i-th point of the FC (FC CDL (i, j, k)) is therefore computed by considering the blast load at the k-th stand-off distance and by considering a value of the explosive weight. The minimum and maximum amount of explosive weight should be enough for making the value of the FC CDL (j, k) from 1 to 0.

The complete (cyclic) procedure of Figure 3 is hereby described. First a k-th stand-off distance is selected, then the "j" CDL is selected, and consequently the i-th point of the FC CDL (j, k) is computed until tracking the complete FC CDL (j, k). The FC CDL (i, j, k) is obtained by a Monte Carlo simulation. After that a new j-th CDL is considered with the same value of "k". When j=M a different stand-off distance is selected and the previous two described cycles are repeated until k=L.

As said, the failure probability of each CDL is estimated, but the Coefficient of Variance of such Failure Probability (P_f) increases with the decrease of P_f, so the COV is not constant with the P_f values. In order to obtain an acceptable COV it is necessary to increment the number of samples in the Monte Carlo analysis. In this work these samples decrease exponentially with decreasing Z, since for higher values of Z the cladding wall has an inferior structural response than for lower Z values. Thus, it is expected that the P_f is lower for higher values of Z.

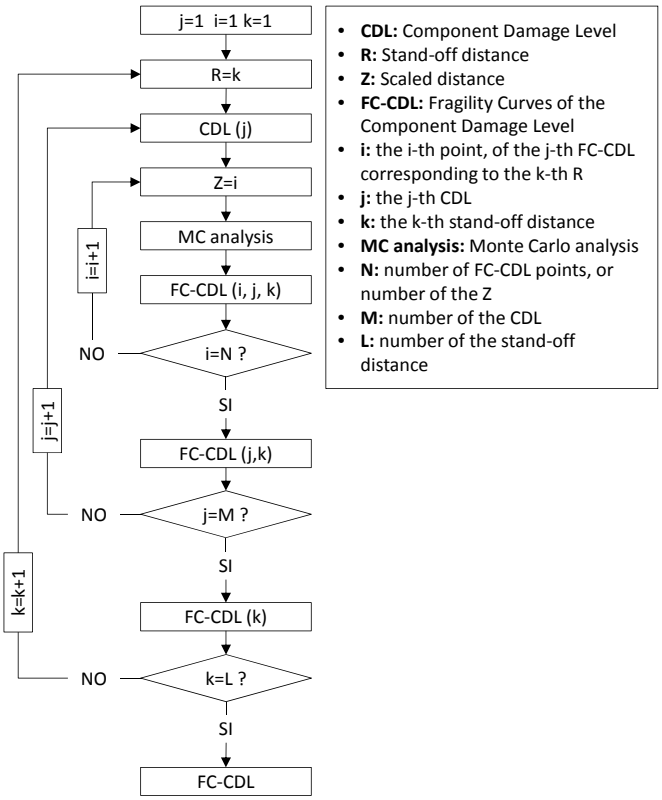


Figure 3: Fragility curve computation flowchart.

6 NUMERICAL RESULTS

This section focuses on the presentation of results on i) the fragility curves of the cladding panel case study, and, ii) the failure probability of such cladding panel estimated by both the fragility curves and the Monte Carlo simulation.

In Figure 4 the computed fragility curves are plotted as a function of the scaled distance. For the specific panel case study, the fragility curves of the SD component damage level appear with a different slope rate compared to the other three component damage levels (HF, HD, and MD). It should be noted that the SD component damage level is based on the ductility (μ) of the component while HF, HD, and MD component damage levels are based on the support rotation (θ). The SD component damage level for a concrete cladding panel prescribes the elastic response of the component, and for the case study panel it appears to be more sensitive to the considered uncertainties compared to the HF, HD, and MD damage levels. By varying the number of samples the maximum obtained COV for the lower failure probability (close to zero), is about 9%. This value is considered acceptable for the specific case, and it is consistent with other studies on blast applications (see [4]). These fragility curves are the probabilistic representation of the mechanical properties of the concrete cladding panel and are useful for computing the failure probability of a set of blast scenarios for the different CDLs. If the stochastic characterization of the blast scenario is neglected, assuming for example the conventional performance demand, the fragility curves of Figure 4 can be used as a design tool. Selecting a blast scenario characterized by both the amount of explosive and the stand-off distance it is possible to establish the failure probability of the panel and check if this failure probability is lower than an acceptable failure probability. Different cladding panels can be certified using these fragility curves, something that facilitates the design process of the specific panel against blast loads. Thus, the fragility curves (Figure 4) can be considered as a design chart when the load is conventionally defined.

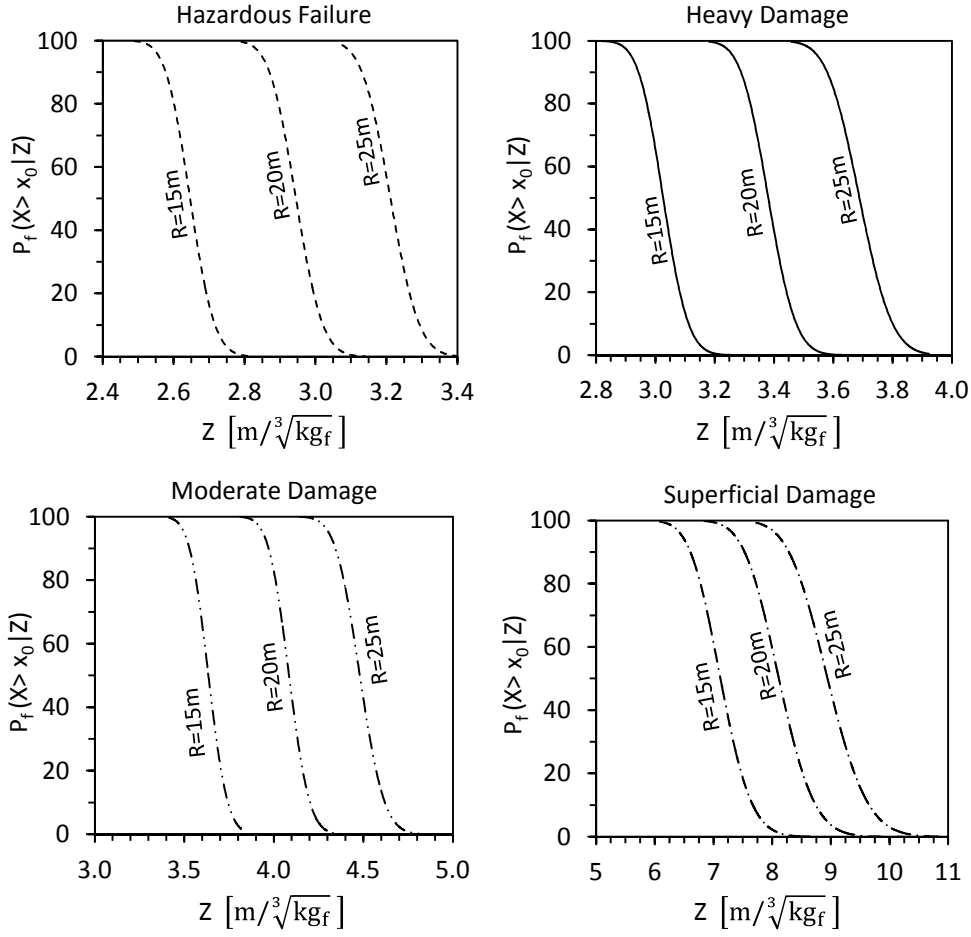


Figure 4: From top left clockwise, fragility curves for the HF, HD, SD, MD component damage levels.

For computing the P_f from the fragility curves it is necessary to characterize stochastically the blast scenario and integrate Eq. 12. In this study a vehicle bomb is considered. The amount of explosive in the vehicle depends among else on the security measures in place, and for each line of security a different mean value of the amount of explosive is expected. The mean value of the amount of explosive decrease with decreasing stand-off distance from the target, since the lines of security system reduce progressively the severity of the possible attacks. In the specific case a vehicle bomb (with about 27 to 454 kg_f of TNT or equivalent) is considered. The mean amount of TNT or equivalent in the vehicle is 227 kg_f with a coefficient of variation equal to 0.3 (see Table 1). This estimation is in line with the data provided in [16]. The stand-off distance is placed at 20 m and its coefficient of variation is 0.05, considering that the vehicle could impact and overpass the fence barrier but without being able to move further. Eq. 12 computes the conditional failure probability of the CDL with respect to the event realization ($P(X>x_0)$). X is the union of the two response parameters characterizing the component damage level (see Table 2). The probability density of the scaled distance (p(Z)) is computed by extracting both the explosive weight and the stand-off distance with a lognormal distribution. The fragility curve ($P(X>x_0|Z)$) for Eq. 12 is the one corresponding to the mean value of the stand-off distance proper of the blast scenario (Table 1).

$$P(X > x_0) = \int_{-\infty}^{+\infty} P(X > x_0|Z)p(Z)dz \cong \sum_{i=0}^{\infty} P(X > x_0|Z)_i \, p(Z)_i \Delta Z_i \tag{12}$$

$P(X>x_0)$ is estimated for three scenarios. The amount of explosive is the same but the mean value of the stand-off distance varies (respectively 15, 20 and 25 meters). As a consequence, the considered fragility curve for each scenario is different. As previously mentioned the fragility curve adopted for solving Eq. 12 is the one for a stand-off distance equal to mean value of the stand-off distance of the blast scenario. In Table 3 the obtained results are shown. The first column reports the CDLs, while the second and third report the conditional failure probability (to the event realize) for each blast scenario obtained respectively by Eq. 12 and by the Monte Carlo analysis.

CDL	Mean W=227 kg_f COV=0.3 lognormal distribution R, COV=0.05 lognormal distribution		
	FC analysis	**MC analysis**	**difference Δ%**
	Mean R = 20 m		
SD	100.0 %	100.0 %	0.0 %
MD	96.6 %	97.5 %	0.9 %
HD	55.7 %	55.5 %	0.3 %
HF	13.6 %	12.1 %	11.0 %
	Mean R = 25 m		
SD	100.0 %	100.0 %	0.0 %
MD	74.6 %	77.3 %	3.5 %
HD	14.2 %	12.6 %	11.2 %
HF	1.02 %	1.02 %	0.0 %
	Mean R = 15 m		
SD	100.0 %	100.0 %	0.0 %
MD	97.9 %	99.9 %	2.0 %
HD	93.6 %	96.9 %	3.4 %
HF	67.8 %	72.6 %	6.6 %

Table 3: Overview of the P_f.

The first consideration is that the amount of explosives in the vehicle has a dominant role on the failure probability. The standard deviation of the explosive weight is 0.3 times the mean value and this level of dispersion is predominant on computing the failure probability for a CDL. If both the explosive weight mean value and the stand-off distance result in a scaled distance on the range of the FC, this leads to a P_f close to 50% since the explosive weight has a higher standard deviation than the other parameters.

From these results the maximum percentage difference between the failure probability computed by the fragility curves and the Monte Carlo simulation is 11%. Further studies are necessary to confirm whether this difference is acceptable or not. However it is also necessary to consider that the amount of explosives in the vehicle has an elevated dispersion, something that amplifies this difference due to the dependence of the impulse density by both the scaled distance and the explosive weight. Thus, being the impulse density proportional to both the explosive weight and the scaled distance, the difference between the failure probability computed by the fragility analysis method and by the MC simulation method increases with the increase of the difference between the stand-off distance with which the fragility curve is computed and the stand-off distance of the blast scenario estimated by $Z\sqrt[3]{W}$. In general such difference can be estimated considering the scaled distance and the explosive weight as the mean values of the blast scenario or by the single Z and W values at each "i" in Eq. 12. A future study could focus on the quantification of this difference and on developing a corrective method that leads to using a fragility curve independently from its stand-off which it is computed.

7 CONCLUSIONS AND FURTHER DEVELOPMENTS

In this paper a probabilistic approach for designing and assessing a cladding panel subjected to a blast load has been proposed. The blast load model has been adopted on the basis of empirical laws, and the geometry and mechanical properties of the panel are assumed as stochastic. A mechanical model equivalent to a SDOF has been adopted for describing the motion of the panel under an impulsive load. The fragility curves for each component damage levels are hence computed for a cladding panel subjected to blast loads, and these fragility curves are used for computing the failure probability, for each component damage level, of the panel subjected to three different blast scenarios. Furthermore, the failure probabilities are estimated using Monte Carlo simulations.

This study highlights the feasibility and effectiveness of a probabilistic approach for the design and assessment of protective structures, having as a principal limitation that the computed failure probability of the component damage level is conditional to the event realization. Computing the unconditional failure probability of the component damage level is tricky since the probability density function of the event in time is unknown. Even if the failure probability was known, it would be difficult to implement in the design phase, since a terroristic vehicle bomb attack is a low probability event. The solution presented in this paper is posed as a basis for the decision making based on the conditional failure probability of the event. However the failure probability of the component damage level has to be fixed on the basis of some criteria.

Future studies could take into account the deterioration of the materials of the different components in the fragility curves, during the entire life cycle - see for example [17]. Moreover, soft-computing methods could be implemented for the more efficient treatment of the uncertainties [18].

ACKNOWLEDGEMENTS

The author gratefully acknowledges the scientific contribution of Dr. Francesco Petrini, Dr. Konstantinos Gkoumas and Prof. Franco Bontempi of the Sapienza University of Rome.

REFERENCES

[1] L. Giuliani, Structural safety in case of extreme actions. *International Journal Lifecycle Performance Engineering*, **1**(1), 22-40, 2012.

[2] UFC 3-340-02, Structures to resist the effects of accidental explosions. United States of America: Department of Defense, 2008.

[3] D.B. Chang, C.S. Young, Probabilistic estimates of vulnerability to explosive overpressures and impulses. *Journal of Physical Security*, **4**(2), 10-29, 2010.

[4] M.G. Stewart, M.D. Netherton, Security risks and probabilistic risk assessment of glazing subject to explosive blast loading. *Reliability Engineering and System Safety*, **93**(4), 627-638, 2008

[5] J.S. Davidson, J.W. Fisher, M.I. Hammons, J.R. Porter, J. Dinan, Failure mechanisms of polymer-reinforced concrete masonry walls subjected to blast. *Structural Engineering*, **131**(8), 1194-1205, 2005.

[6] C.J. Naito, R. Dinan, B. Bewick, Use of precast concrete walls for blast protection of steel stud construction. *Journal of Performance of Constructed Facilities*, **25**(5), 454-463, 2011.

[7] C.J. Naito, J. Hoemann, M. Beacraft, B. Bewick, Performance and characterization of shear ties for use in insulated precast concrete sandwich wall panels. *Journal of Structural Engineering*, **138**(1), 1-11, 2012.

[8] F. Petrini, H. Li, F. Bontempi, Basis of design and numerical modeling of offshore wind turbines. *Structural Engineering and Mechanics*, **36**(5), 599-624, 2010.

[9] F. Petrini, F. Bontempi, Estimation of fatigue life for long span suspension bridge hangers under wind action and train transit. *Structure and Infrastructure Engineering*, **7**(7-8), 491-507, 2011.

[10] C.A. Mills, The design of concrete structures to resist explosions and weapon effects. *1st International Conference for Hazard Protection*, Edinburgh, September 27-30, 1987.

[11] M. Held, Blast waves in free air. *Propellants, Explosives, Pyrotechnics*, **8**(1), 1-7, 1983.

[12] TR-06-01 - US Army Corps of Engineers. Methodology Manual for the Single-Degree-of-Freedom Blast Effects Design Spreadsheets (SBEDS). 2008.

[13] M.P. Enright, D.M. Frangopol, Probabilistic analysis of resistance degradation of reinforced concrete bridge beams under corrosion. *Engineering Structures*, **20**(11), 960-971, 1998.

[14] UNI EN 1992 - Eurocode 2 - Design of concrete structures - Part 1-1: General rules and rules for buildings. European Committee for Standardization, 2005.

[15] ACI 318, *Building Code Requirements for Reinforced Concrete*. American Concrete Institute, 1995.

[16] FEMA 452 The Federal Emergency Management Agency (FEMA). Risk assessment: A How-To Guide to Mitigate Potential Terrorist Attacks Against Buildings, Providing protection to people and buildings, 2005.

[17] L. Sgambi, P.G. Malerba, G. Gotti, D. Ielmini, The influence of degradation phenomena on collapse modes in prestressed concrete beams. *International Journal of Lifecycle Performance Engineering*, **1**(1), 41-63, 2012.

[18] L. Sgambi, K. Gkoumas, F. Bontempi, Genetic algorithms for the dependability assurance in the design of a long-span suspension bridge, *Computer-Aided Civil and Infrastructure Engineering*, **27**(9), 655-675, 2012.

COMPDYN 2013
4th ECCOMAS Thematic Conference on
Computational Methods in Structural Dynamics and Earthquake Engineering
M. Papadrakakis, V. Papadopoulos, V. Plevris (eds.)
Kos Island, Greece, 12–14 June 2013

INVERSE ANALYSIS FOR DETERMINING THE REINFORCED CONCRETE FLEXURAL STIFFNESS OF A STRUCTURE UNDER STRONG COMPRESSION

Alexandre de M. Wahrhaftig [1], **Reyolando M. L. R. F. Brasil** [2]

[1] Federal University of Bahia (UFBa)
Polytechnic School, Department of Construction and Structures
Aristides Novís Street, 02, 5th floor, Federação, Salvador – BA, Brazil, CEP: 40210-910
alixa@ufba.br

[2] University of São Paulo (USP)
Polytechnic School, Department of Structural and Geotechnical Engineering
Prof. Almeida Prado Av., tv. 2, nº 83, University Campus, São Paulo – SP, Brazil, CEP: 05508-900
reyolando.brasil@poli.usp.br

Keywords: Flexural Stiffness, Reinforced Concrete, Structural Dynamics, Inverse Analysis, Strong Compression.

Abstract. *In general, the determination of internal forces along the transverse sections of a piece is made assuming the structure is in its undeformed position. This represents a 1st order theory where the deformations undergone by the piece are neglected. However, when the deformations are considered, the internal forces are no longer proportional to the external forces and the problem then requires a 2nd order theory. The problem worsens when the material is non-linear. Concrete reinforcement structures subjected to high normal effort show both, geometric and physical nonlinearities. The stiffness of bars with a geometric effect is resolved analytically and numerically. There is a need to establish therefore the flexural stiffness to be used. In this work, this is obtained by inverse analysis from the frequency of a real structure in conjunction with a numerical model.*

1 INTRODUCTION

In general, the calculation of the internal forces and moments along the transverse sections of a piece is made assuming the structure is in its undeformed position. Thus, there is proportionality between actions and internal efforts induced. This represents a 1st order theory, because the deformation undergone by the piece is implicitly neglected. However, when the deformations are considered, the internal forces and moments are no longer proportional to the external actions and the problem becomes a 2nd order theory.

Strictly speaking, one should always consider the deformed position of a structure to calculate internal forces, thus 2nd order theory represents a higher degree of approximation. However, from a practical standpoint, for many engineering structures a 1st order theory is a satisfactory approximation, while for others, it is a too inexact to determine the internal stresses. For such structures the efforts and displacements induced must be calculated taking into account the deformations undergone by the system.

The problem worsens when the material is non-linear. Non-linearity is an intrinsic property of material and results in non-proportionality between cause and effect (stress and strain), even in 1st order theory. Concrete reinforcement structures subjected to high normal effort show both, geometric and physical nonlinearities. More information about the characteristics of concrete can be found in Fusco [1] and Metha [2].

A satisfactory solution to most engineering problems can arise from two considerations which are easily implemented in analytical formulations and numerical computing: geometric nonlinearity can be solved through the concept of geometric stiffness, and material nonlinearity through flexural stiffness.

The stiffness of bars with geometric effect is resolved analytically and numerically. There is a need to establish therefore the flexural stiffness to be used. In this work, this is obtained by inverse analysis from the frequency of a real structure in conjunction with a numerical model by using the finite element method to adjust the experimental frequency found.

2 THE STRUCTURE INVESTIGATED

Our case involves an elevated reservoir designed to supply drinking water to a housing development. It is 21.654 meters tall and has a circular hollow section former suit with a diameter of 100 cm and 12 cm uniform thickness along the height. The foundation is superficial, a Pad Footings type. The reservoir is made in *fiberglass* shell and has a capacity of 20,000 liters. The concrete section contains 24 bars 12.5 mm diameter steel reinforcement and has a 2.5 cm cover.

Although there is lateral wind action, the structure behaves more akin to a column than to a beam, in view of the predominance of normal force measured by the ratio between the bending moment and the axial force in section further solicited that is 13 cm. Therefore, the normal force is situated at the section central nucleus of inertia.

The modulus of elasticity of *fiberglass* and density are 4.142857 GPa and 1450 kg/m^3, respectively. The structure has an access ladder to the top, which starts 2 m from the floor, inducing an additional distributed mass of 25 kg/m to structure. There are two working platforms, one located at 10 m and another at 15.60 m from the floor, with masses estimated at 350 kg and 250 kg, respectively. There are also feed and discharge PVC pipes of 25 mm diameter with a wall thickness of 1.7 mm and 20 mm in diameter with a wall thickness of 1.2 mm, which run the entire length of the structure, except underground. In order to model numerically better, the set structure/reservoir was divided into foundation, column (hollow section), head of the column (full section), slab reservoir supporting, reservoir and cap. The height between the lower foundation face and the ground surface is 2.15 m.

The characteristics and dimensions of the assembly are shown in Table 1, corresponding to the discretization of the model, in which ϕ_{ext} is the external diameter, diameter of full section or side of square section, as is the case; and t is the thickness of the section if it exists.

Height (m)	ϕ_{ext} (cm)	t (cm)	Height (m)	ϕ_{ext} (cm)	t (cm)	Height (m)	ϕ_{ext} (cm)	t (cm)
21.654	325.00	0.00	13.66	100.00	12.00	6.28	100.00	12.00
21.650	325.00	0.00	13.29	100.00	12.00	5.75	100.00	12.00
19.700	255.00	0.40	12.91	100.00	12.00	5.22	100.00	12.00
17.750	315.00	0.00	12.53	100.00	12.00	4.68	100.00	12.00
17.650	315.00	0.00	12.15	100.00	12.00	4.15	100.00	12.00
17.450	100.00	0.00	11.62	100.00	12.00	3.82	100.00	12.00
17.071	100.00	12.00	11.08	100.00	12.00	3.48	100.00	12.00
16.693	100.00	12.00	10.55	100.00	12.00	3.15	100.00	12.00
16.314	100.00	12.00	10.02	100.00	12.00	2.82	100.00	12.00
15.936	100.00	12.00	9.48	100.00	12.00	2.48	100.00	12.00
15.557	100.00	12.00	8.95	100.00	12.00	2.15	100.00	12.00
15.179	100.00	12.00	8.42	100.00	12.00	1.40	100.00	12.00
14.800	100.00	12.00	7.88	100.00	12.00	0.65	120.00	0.00
14.421	100.00	12.00	7.35	100.00	12.00	0.20	350.00	0.00
14.043	100.00	12.00	6.82	100.00	12.00	0.00	350.00	0.00

Table 1: The characteristics of the structure.

It is interesting to mention that some of the data were provided by the design engineer and executors of the structure, others were collected in the field and some obtained from the manufacturer of the water tank. The slenderness of the structure is 106. Figure 1 shows a photograph of the structure and Fig 2 details the geometry of the structure.

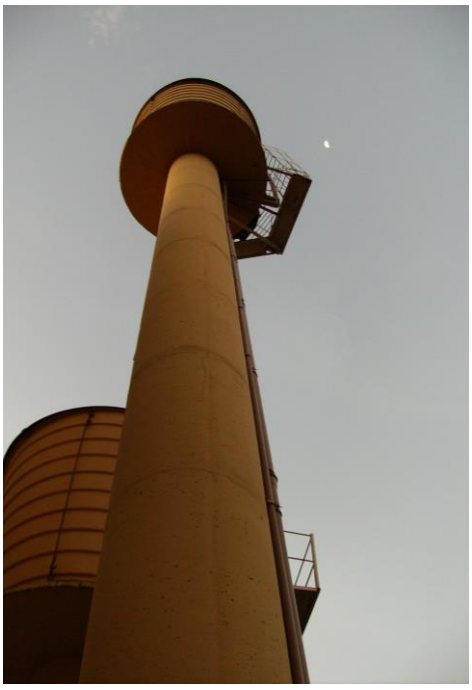


Figure 1: Photograph of the structure.

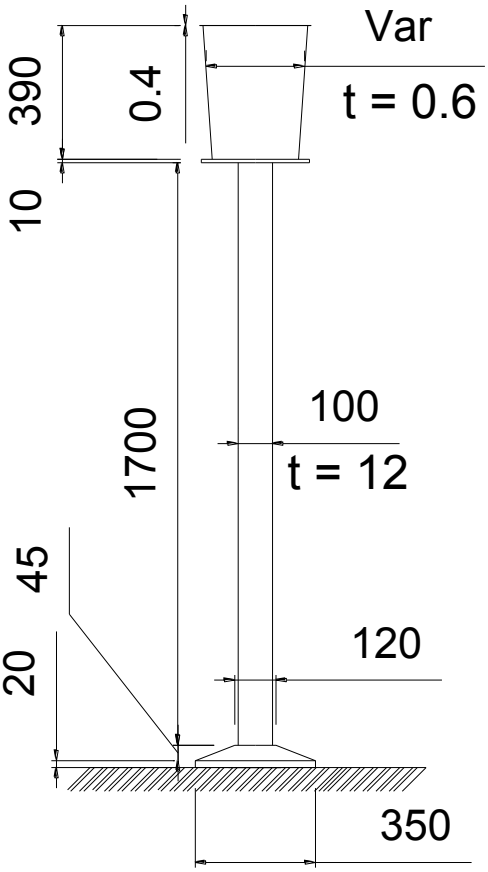


Figure 2: The Geometry of the structure – Measured in centimeters.

The homogenization of the concrete section was necessary due the existence of reinforcement bars in the transverse sections of the column, which was done as follows:

There is a circular ring cross-section with an outside diameter D. A reinforcement bar b_i occupies a position i in the section defined by R_{bi} and θ_i, as shown in Fig.3. R_{bi} determines the center position of each bar in relation to the section center. As all bars have the same radius, for simplicity of notation, $R_{bi} = R_b$, thus:

$$R_b = \frac{D}{2} - \text{cov} - \frac{d_{bi}}{2} \tag{1}$$

where *cov* is the concrete cover of the reinforcement and d_{bi} is the diameter for the i bar.

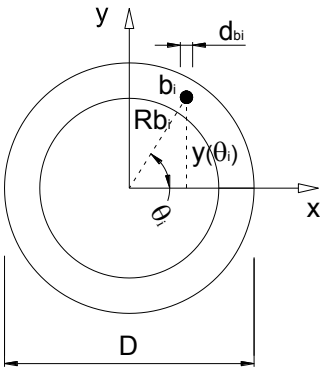


Figure 3: Transversal section homogenizing of the structure analyzed

As θ is the independent variable, the distance between the center of each bar relative to the axis center of inertia of the section is

$$y(\theta_i) = sen(\theta_i) R_b \tag{2}$$

The spacing between the center of each bar section was obtained using $esp = \frac{2\pi R_b}{nb}$, where *nb* is the number of longitudinal bars of reinforcement steel, and for angular phase shift between them for $\Delta\theta = \frac{esp}{R_b}$. Considering θ varying from *0* to 2π at intervals defined by $\Delta\theta$, the total inertia of the steel bars in relation to the section of the structure could be obtained by the theorem of parallel axes with the expression (3).

$$I_s = \sum_{\theta}^{2\pi} \left(\frac{\pi d_{bi}^{\ 4}}{64} + y(\theta_i)^2 \frac{\pi d_{bi}^{\ 2}}{4} \right) \tag{3}$$

The homogenized moment of inertia of the steel bars is therefore:

$$I_{shom} = \sum_{\theta}^{2\pi} I(\theta_i) \left(\frac{E_s}{E_{csec}} - 1 \right) \tag{4}$$

The parcel of concrete inertia is $I_{conc} = I - I_s$, with *I* being the inertia of the circular section. The total homogenized inertia of the section is obtained by $I_{tot} = I_{conc} + I_{shom}$.

Therefore, in order to find a factor *F* which multiplies the nominal inertia of the section in terms of total steel inertia homogenized section we use

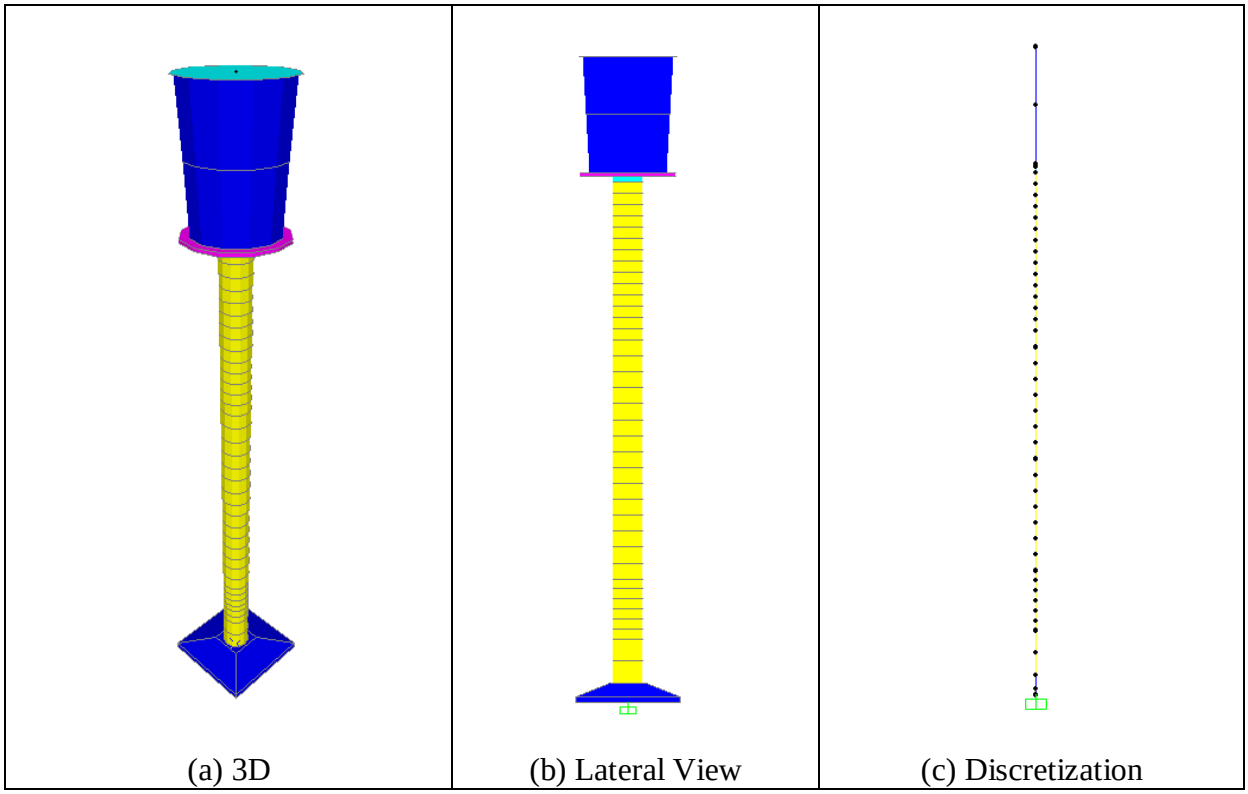
$$F = 1 + \frac{I_{shom}}{I_{tot}} \tag{5}$$

The total homogenized factor of 1.0937 was found to the transversal section of the pillar

3 NUMERICAL MODELLING

The numerical computational modeling of the structure was performed using the Finite Element Method and followed linear and nonlinear criteria from a geometric and material point of view. For the geometric nonlinear criteria we used the portion of the geometric stiffness matrix processing, which allows us to take into account the effect of normal force on the structural frequency of system. It is useful to recall that the 1st portion of the full stiffness matrix is a function of the flexural stiffness *EI*, parameter manipulated in the mathematical model to obtain the same result experimental. It is disregarded the damping system.

In Figure 4 the Finite Element Model can be seen, it is presented in a three-dimensional and lateral view, and with the discretization of the structure, containing 40 bar elements. The vibration modes and frequencies obtained by Finite Element Method are listed in Figure 5, in which GNL stands for Geometric Non-Linearity and MNL Material Non-Linearity. More details about Finite Element Method are presented by Clough [3], Bucalem [4] and Cook [5].



(a) 3D (b) Lateral View (c) Discretization

Figure 4: Finite Element Model.

Natural modes of vibration	1st Mode	2nd Mode	3rd Mode	4th Mode	5th Mode
Linear	0.621513 Hz	4.536457 Hz	9.321836 Hz	9.918722 Hz	11.639488 Hz
GNL	0.606852 Hz	4.511043 Hz	9.298632 Hz	9.918722 Hz	11.610126 Hz
GNL + MNL	0.472836 Hz	3.972319 Hz	8.448274 Hz	9.485529 Hz	10.850828 Hz

GNL is Geometric Non-Linearity and MNL Material Non-Linearity.

Figure 5: Finite Element Processing.

4 EXPERIMENTAL INVESTIGATIONS

The investigation of the natural frequency of the structure under ambient excitement was carried out using a gas-damped DC response accelerometer, manufactured by Bruel & Kjaer, with sensitivity of 1021 mV/g, with an integrated cable, suitable for measuring accelerations between ± 2g (Bruel & Kjaer Product Data, [6]). This device was fixed to the superior extremity of the structure, on the lateral surface of the support slab, as seen in Fig. 6(a). The acquisition of data was carried out by the system ADS2000, AqDados [7], by a Lynx Computer that was connected to a portable computer for the recording of the signals. The equipment was taken to the column top and placed on the superior surface of the support slab, as seen in Fig 6(b). It was registered that the structure was under sufficient excitement of wind, that was able to movement it. Signal acquisition was carried out at the rate of 50 Hz and the elapsed time was 1 h 33 min 22 s.



(a) Accelerometer (b) Data Acquisition System

Figure 6: Signal in frequency domain.

The fundamental frequency of the structure was obtained from the time series of the signals acquisition by Fourier Transform (FFT) in the program AqDAnalysis 7.02 [8]. The obtained result was 0.47 Hz. In Fig. 7 the analysis of the signal in the frequency domain can be seen and the acceleration time series in Fig. 8.

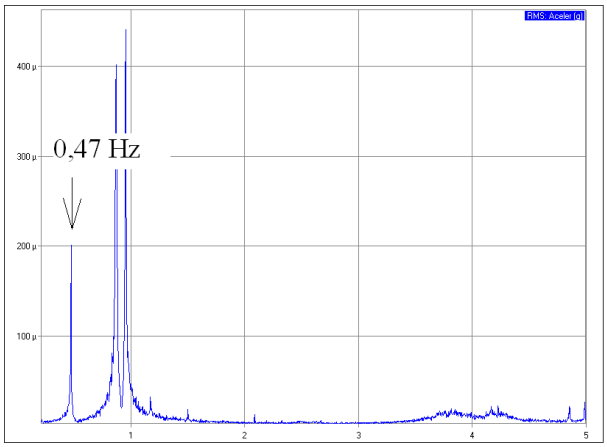


Figure 7: Signal in frequency domain.

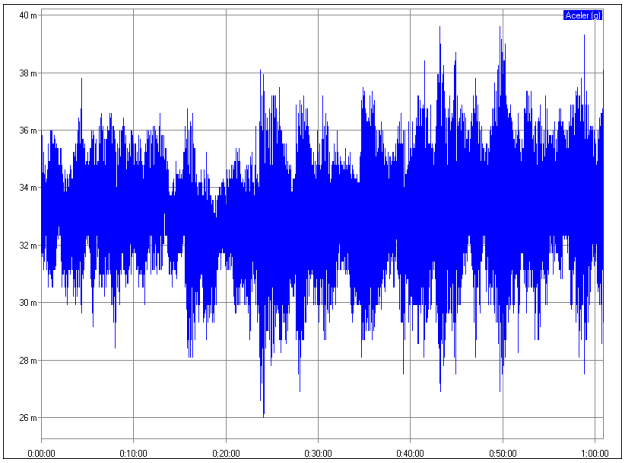


Figure 6: Temporal series.

5 CONCLUSIONS

- The Modulus of Elasticity of concrete was numerically adjusted to obtain the same value as the first vibration frequency mode which obtained experimentally.
- This was possible due to the dependence that the structure stiffness matrix has with the flexural stiffness *EI*, where *E* is the modulus of elasticity of material and *I* is the concrete section inertia homogenized area.
- The mitigation factor of the concrete flexural stiffness used in structures allows us to take into account the non-linear elastic behavior of the material, simplifying structural analysis.
- Similarly, the use of the geometrical stiffness matrix allows us to deal with a geometrically nonlinear problem, linearizing the second-order effects.
- Therefore, the use of the full stiffness matrix structure together with the adjustment factor appropriate for concrete flexural stiffness enables geometric and material nonlinearities solutions, solving the problem without iterative calculations.
- Through inverse analysis, the operator which adjusts the concrete modulus of elasticity, and so to speak the flexural stiffness, in nonlinear analysis, geometric and material, to experimental value, corresponds to 0.62 from linear elastic value, for the specific case studied.
- The first frequency mode of vibration of 0.473 Hz, calculated by the Finite Element Method, with both nonlinear aspects, lies 24% below the purely linear frequency and 2.36% of the frequency with geometric nonlinearity consideration only.
- The structural damping was considered negligible, therefore the adjusted numerical frequency relates to the natural frequency of the system. Uncertainties which may arise from the experimental investigation were discarded as well as the elastic characteristics and soil influence portion situated laterally from structure and above the foundation.

REFERENCES

[1] P.B. Fusco, *Structures of concrete*: *Normal Efforts*. Rio de Janeiro, Guanabara Dois, 1981.

[2] P.K. Metha, P.J.M. Monteiro, *Concrete: structure, properties, and materials*, 2nd Ed., Englewood Cliffs, N.J. Prentice Hall, 1993.

[3] R.W, Clough, J. Penzien, *Dynamic of Structures*, McGraw Hill International Editions, Second Edition, Taiwan, 1993.

[4] M. L. Bucalem, K. J. Bathe, *The Mechanics of Solids and Structures – Hierarchical Modeling and the Finite Element Solution*, Springer, German, 2011.

[5] R. D Cook, *Concepts and Applications of Finite Element Analysis*. John Wiley and Sons, Inc., NJ, USA, 1974.

[6] Bruel & Kjaer, *Product Data*, Nærum – Denmark. 2007.

[7] AqDados 7.02, *Acquisition Program Signals: User Manua*l, ver. 7, Lynx Electronic Technology Ltd., São Paulo, 2003.

[8] AqDAnalysis 7, *Analysis Program Signal: User Manual*, ver 6., Lynx Electronic Technology Ltd., São Paulo, 2004.

COMPDYN 2013
4th ECCOMAS Thematic Conference on
Computational Methods in Structural Dynamics and Earthquake Engineering
M. Papadrakakis, V. Papadopoulos, V. Plevris (eds.)
Kos Island, Greece, 12–14 June 2013

SEISMIC SOIL-PILE INTERACTION — INFLUENCE OF SOIL INELASTICITY

Andreas E. Kampitsis[1], Evangelos J. Sapountzakis[2], Spyros K. Giannakos[3] and Nikos A. Gerolymos[4]

[1] School of Civil Engineering, National Technical University of Athens
Zografou Campus, GR-157 80, Athens, Greece

e-mail: cvakamb@gmail.com [2] e-mail: cvsapoun@central.ntua.gr
[3] e-mail: spigian@hotmail.com [4] e-mail: gerolymos@gmail.com

Keywords: Soil–Pile–Structure Interaction, Nonlinear Winkler, Nonlinear Dynamics, Large Deflections, BEM– FEM.

Abstract. *The main purpose of this study is to investigate the influence of soil p-y nonlinearity in soil–pile–structure kinematic and inertia interaction. Within this context, a beam on nonlinear Winkler foundation model is adopted based on the Boundary Element Method (BEM), accounting for the effects induced by geometrical nonlinearity, rotary inertia and shear deformation, employing the concept of shear deformation coefficients. The soil nonlinearity is taken into consideration by means of a hybrid spring configuration consisting of a nonlinear (*p-y*) spring connected in series to an elastic spring–damper model. The nonlinear spring captures the near–field plastification of the soil while the spring–damper system represents the far–field viscoelastic character of the soil. An extensive case study is carried out on a pile–column–deck system of a bridge, founded in two cohesive layers of sharply different stiffness and subjected in various earthquake excitations.*

1 INTRODUCTION

The seismic response of column-pile systems under transient earthquake excitation is an area of extensive active research, since pile foundation is widely used to support superstructures such as bridges, wind-turbines and offshore platforms. As the seismic shear wave propagates through the soil deposit, the embedded foundation tends to modify the transmitted excitation due to the soil–foundation stiffness contrast, the boundary constrains of the head and tip of the pile as well as the dynamic response of the system (frequency correlation). This interaction develops even in the absence of a superstructure and is referred to as the *kinematic interaction*. At the same time, the dynamic response of the superstructure itself induces additional deformations to the pile and the near–field soil. This effect is known as *inertial interaction. Kinematic and inertial interaction* constitute a complex and unique phenomenon referred to as *Soil–Pile–Structure Interaction* (SPSI) which includes a number of parameters, such as the soil stratigraphy and properties, the non–linear stress–strain behavior of the soil and pile (material nonlinearity) and the geometrical nonlinearities (p–δ effects, separation and slippage).

The main purpose of this study is to investigate the influence of soil p-y nonlinearity in soil–pile–structure kinematic and inertia interaction. Within this context, a beam on nonlinear Winkler foundation model is adopted based on the Boundary Element Method (BEM), accounting for the effects induced by geometrical nonlinearity, rotary inertia and shear deformation, employing the concept of shear deformation coefficients. The soil nonlinearity is taken into consideration by means of a hybrid spring configuration consisting of a nonlinear (p-y) spring connected in series to an elastic spring–damper model. The nonlinear spring captures the near–field plastification of the soil while the spring–damper system (Kelvin–Voigt element) represents the far–field viscoelastic character of the soil. An extensive case study is carried out on a pile–column–deck system of a bridge, founded in two cohesive layers of sharply different stiffness and subjected in various earthquake excitations, providing insight to several phenomena. The results of the proposed model are compared with those obtained from the Beam–FE model employing OpenSees code [1] as well as from a rigorous fully three-dimensional (3–D) continuum FE scheme materialized in the ABAQUS code [2]. The essential features and novel aspects of the present contribution compared with previous ones are summarized as follows.

i. Soil nonlinearity is taken under consideration by means of a hybrid spring configuration consisting of a nonlinear (p-y) spring for the near–field plastification, connected in series to a Kelvin–Voigt element representing the far–field viscoelastic character of the soil.
ii. A calibration methodology of the "spring" and "dashpot" coefficients of the examined hybrid spring configuration is proposed.
iii. Verification of the computational efficiency of the proposed model through the remarkable agreement between its results and those from the sophisticated 3–D model. Moreover, the increased accuracy of the proposed procedure compared with other FEM solutions employing also beam elements is demonstrated.
iv. The proposed method is capable of taking into account both kinematic and inertia interaction to the geometrical nonlinear dynamic response of a column-pile in a layered soil profile.
v. The site seismic response is obtained through one dimensional shear wave propagation analysis.
vi. The pile head and tip are supported by the most general nonlinear boundary conditions. Although a circular pile cross section is investigated, the formulation is capable of analyzing an arbitrary doubly symmetric one.

vii. Shear deformation effect and rotary inertia are taken into account on seismic pile–soil–structure interaction.

2 PROPOSED BEAM FORMULATION

Let us consider a cylindrical column-pile of length l (pile length L, pier length H), diameter d, mass density ρ_p, modulus of elasticity E_p, shear modulus G_p and Poisson's ratio v_p, as this is presented in Fig.1. The pile is embedded in a layered soil profile of Winkler type, materialized by a hybrid spring configuration. As proposed by Wang et al. [3], the soil is separated into two zones, namely a near–field zone implemented by Kelvin–Voigt element (k_{el}, c_{el}) and a far–field one represented by hysteretic element (k_{nl}). More specifically, the adopted hybrid model consists of a nonlinear spring connected in series to a dashpot–elastic spring parallel configuration. The free extremities of the configuration are excited by the free–field (w_{ff}, $\dot{w}_{ff}$) displacement and velocities time histories obtained at each depth from the free–field seismic response analysis (Fig.1).

The column-pile is subjected to the combined action of arbitrarily distributed or concentrated time dependent transverse loading $p_z = p_z(x,t)$ as well as to axial loading $p_x = p_x(x,t)$. Under these actions, the displacement field taking into account shear deformation effect is given as [4]

$$\overline{u}(x,z,t) = u(x,t) + z\theta_y(x,t) \tag{1a}$$

$$\overline{w}(x,t) = w(x,t) \tag{1b}$$

where $\overline{u}$, $\overline{w}$ are the axial and transverse displacement components with respect to the Cyz centroidal coordinate system of axes (Fig.1); $u(x,t)$, $w(x,t)$ are the corresponding components of the centroid C and $\theta_y(x,t)$ is the angle of rotation due to bending of the cross-section with respect to its centroid. It is worth here noting that since the additional angle of rotation of the cross-section due to shear deformation is taken into account, the one due to bending is not equal to the derivative of the deflection (i.e. $\theta_y \neq w'$).

Adopting the strain-displacement relations of the three-dimensional elasticity for moderate displacements and small strains, employing the second Piola–Kirchhoff stress tensor, the governing differential equations and the boundary conditions of the examined problem are obtained based on Hamilton's principle [4]. Following this procedure, the governing equations for the problem at hand are written as

$$\rho_p \mathrm{A}\ddot{u} - E_p A\left(u'' + w'w''\right) = p_x \tag{2a}$$

$$\rho_p \mathrm{A}\ddot{w} - \left(Nw'\right)' - G_p A_z\left(w'' + \theta_y'\right) + k_{nl}\left(w - w_{mnode}\right) = p_z \tag{2b}$$

$$E_p I_y \theta_y'' - G_p A_z\left(w' + \theta_y\right) = \rho_p I_y \ddot{\theta}_y \tag{2c}$$

while the equilibrium of forces at the mid-node of the spring configuration results in an additional equation

$$k_{el}\left(w_{mnode} - w_{ff}\right) + c_{el}\left(\dot{w}_{mnode} - \dot{w}_{ff}\right) = k_{nl}\left(w - w_{mnode}\right) \tag{3}$$

where, $w_{ff} = w_{ff}(z,t)$, $\dot{w}_{ff} = \dot{w}_{ff}(z,t)$ and w_{mnode}, $\dot{w}_{mnode}$ correspond to the free-field and mid-node displacement and velocity, respectively. Moreover, the corresponding time dependent boundary conditions of the problem at hand are given as

$$a_1 u(x,t) + \alpha_2 N(x,t) = \alpha_3 \tag{4}$$

$$\beta_1 w(x,t) + \beta_2 V_z(x,t) = \beta_3 \qquad \gamma_1 \theta_y(x,t) + \gamma_2 \mathrm{M}_y(x,t) = \gamma_3 \tag{5,6}$$

at the column-pile ends $x = 0, l$, together with the initial conditions

$$u(x,0) = \overline{u}_0(x) \qquad \dot{u}(x,0) = \dot{\overline{u}}_0(x) \tag{7a,b}$$

$$w(x,0) = \overline{w}_0(x) \qquad \dot{w}(x,0) = \dot{\overline{w}}_0(x) \tag{8a,b}$$

$$\theta_y(x,0) = \overline{\theta}_{y0}(x) \qquad \dot{\theta}_y(x,0) = \dot{\overline{\theta}}_{y0}(x) \tag{9a,b}$$

In eqns. (2), A is the cross section area, I_y is the moment of inertia with respect to z-axis and GA_z is its shear rigidity of the Timoshenko's beam theory where $A_z = \kappa_z A = (1/a_z) A$ is the shear area, κ_z the shear correction factor and a_z the shear deformation coefficient. This coefficient is evaluated using an energy approach [5]. Moreover, in eqns. (7)–(9), $\overline{u}_0(x)$, $\overline{w}_0(x)$, $\dot{\overline{u}}_0(x)$, $\dot{\overline{w}}_0(x)$, $\overline{\theta}_{y0}$ and $\dot{\overline{\theta}}_{y0}$ are prescribed functions, while in eqns. (4)–(6), N is the axial force, V_z is the transversal force and M_y is the bending moment at the ends of the column-pile accounting for the inertia forces induced from the mass of the superstructure. Finally, α_k, β_k, γ_k ($k = 1, 2, 3$) are functions specified at the column-pile ends $x = 0, l$. Eqns. (4)-(6) describe the most general nonlinear boundary conditions associated with the problem at hand and can include elastic support or restraint. It is apparent that all types of the conventional boundary conditions (clamped, simply supported, free or guided edge) can be derived from these equations by specifying appropriately these functions (e.g. for a free edge it is $\alpha_2 = \beta_2 = \gamma_2 = 1$, $\alpha_1 = \alpha_3 = \beta_1 = \beta_3 = \gamma_1 = \gamma_3 = 0$).

Moreover, a calibration methodology of the "spring" and "dashpot" coefficients of the examined hybrid spring configuration is proposed. The lateral soil reaction against a deflecting pile is expressed as the sum of a hysteretic elastic–perfectly plastic and a visco–plastic component, according to the lumped parameter model, as depicted in Fig. 1. In this way, the frequency–dependent characteristics of the subgrade reaction are realistically captured through a series–parallel assembly of frequency–independent springs and dashpots. In the elastic regime and assuming a sufficiently under-damped response, the small–amplitude frequency–dependent "spring" and "dashpot" coefficients for the lateral soil reaction are approximated by:

$$k_x \approx \frac{k_{el}}{1 + \dfrac{k_{el}}{k_{nl}} + \dfrac{\omega c_{el}}{k_{nl}}} \quad \text{and} \quad c_x \approx \frac{c_{el}}{1 + \dfrac{k_{el}}{k_{nl}} + \dfrac{\omega c_{el}}{k_{nl}}} \tag{10,11}$$

in which ω is the circular frequency. The parameters k_{el}, c_{el} and k_{nl} are appropriately calibrated through an optimization procedure to match the stiffness and dashpot coefficients (Fig. 2) proposed by Makris and Gazetas [6]:

$$k_x = 1.2E_s \quad \text{and} \quad c_x = 6a_0^{-1/4}\rho_s V_s d \tag{12,13}$$

in which E_s, V_s and ρ_s are the Young's modulus, shear wave velocity and mass density of the supporting soil, and α_0 is a dimensionless frequency parameter defined as:

$$\alpha_0 = \frac{\omega d}{V_s} \tag{14}$$

Having calibrated the stiffness k_x and dashpot coefficient c_x according to Eqns. (12) and (13), plastic behavior is then introduced by imposing a threshold value for the reaction force of spring k_{nl} equal to the ultimate soil resistance per unit length of the pile (p_{ult}) as determined by Matlock [7] and Reese et al [8] at near surface (top layer) and at greater depths (bottom layer), respectively. Obviously, when p_{ult} is reached the arranged in-parallel spring and dashpot unit is deactivated and the radiation damping vanishes.

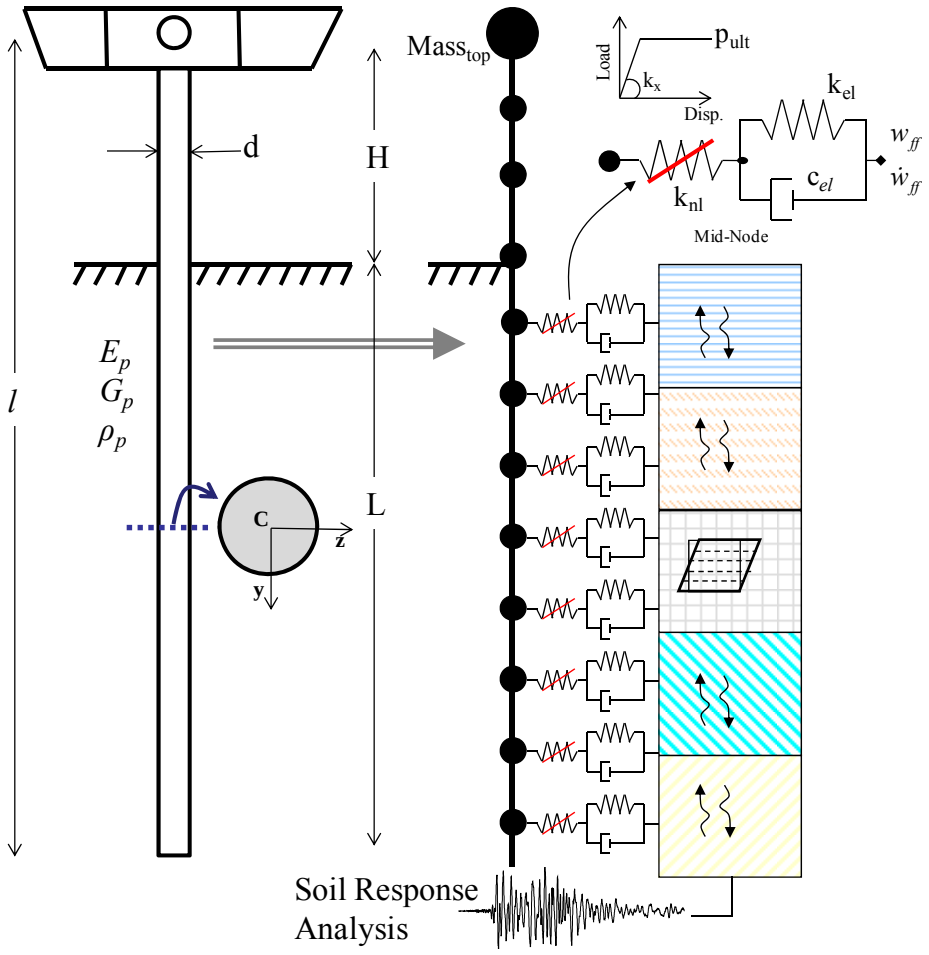
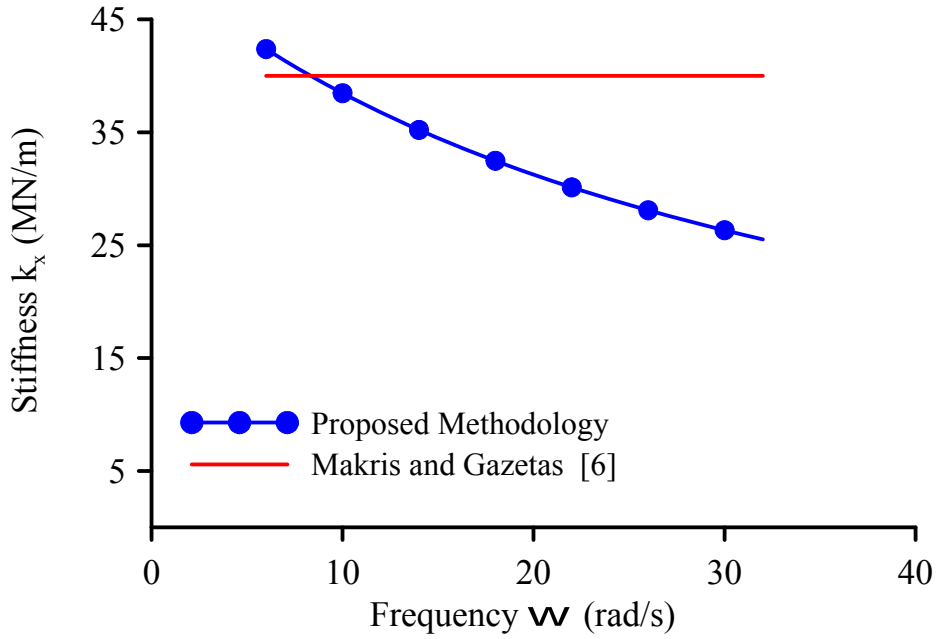
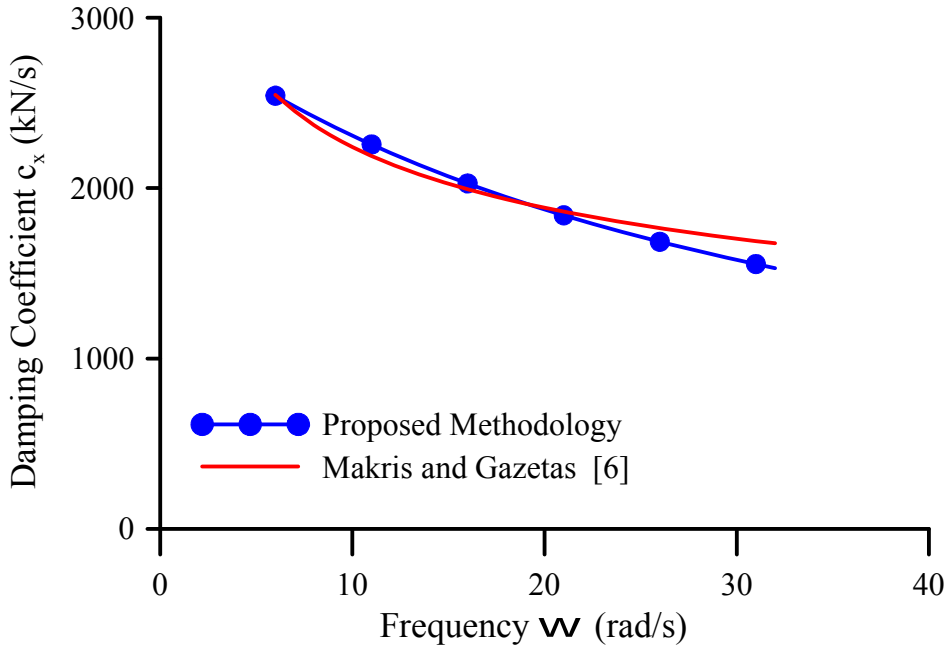


Figure 1: Soil–pile–structure system and adopted model



(a)



(b)

Figure 2: Calibration of stiffness k_x (a) and damping coefficient c_x (b) for the examined configuration.

3 NUMERICAL SOLUTION

According to the precedent analysis, the geometrically nonlinear soil-pile-structure kinematic and inertia seismic interaction of Timoshenko column-pile embedded in a layered nonlinear Winkler-type soil profile, undergoing moderate large deflections reduces in establishing the displacement components $u(x,t)$, $w(x,t)$ and $\theta_y(x,t)$ having continuous derivatives up to the second order with respect to both space x and time t variables. These displacement components must satisfy the coupled governing differential equations (2), (3) inside the column-pile, the boundary conditions (4)-(6) at the pile ends $x = 0,\ l$ and the initial conditions (7)-(9). Application of the boundary element technique yields a system of nonlinear coupled differential-algebraic equations (DAE) of motion, which can be solved iteratively using any efficient direct time integration scheme. In this study, the Petzold-Gear method is used [9] after introducing new variables to reduce the order of the system [10] and obtain an equivalent system with a value of system index $\text{ind} = 1$ [10].

4 MODEL VERIFICATION AND INTERPRETATION OF RESULTS

4.1 Case study

A column-pile monolithically connected to the bridge deck is embedded in two layers of cohesive soil and excited by seismic motion. The concentrated mass at the centre of the deck is $M_{top} = 60tons$, the height of the pier is $H = 10m$, the embedment length of the pile is $L = 30m$, and the diameter of the column-pile equals to $d = 1.5m$. The column-pile is assumed to be linear elastic, while the idealized soil profile from the Agios Stefanos bay was used for the ground response analyses. A soft to medium normally consolidated clay sets on top of a stiff clay. The bedrock is assumed at $50m$ depth. The soft clay has a thickness of $18m$ and a plasticity index $\text{PI}(\%) = 35$. The second layer is 32m thick and has constant undrained shear strength of 100kPa. The maximum shear modulus was calculated by the empirical equations of Seed and Idriss [11].

The influence of shaking on the seismic response is investigated by selecting three well known acceleration records as seismic excitations:

i) the record from Aegion earthquake (1995)
ii) the record from Lefkada earthquake (2003)
iii) the JMA record from Kobe earthquake (1995)

The first two records were chosen as two strong motions of the seismic environment of Greece, with one and many cycles, respectively. JMA record is used to investigate the dynamic response of the soil-pile-structure system to a quite unfavorable incident. All the records were first scaled to a Peak Grand Acceleration (PGA) of 0.5g and 0.8g at the ground surface. Then, through deconvolution analyses conducted with SHAKE91 [12], the bedrock motion as well as the motion at various depths along the pile were estimated.

Both elastic and inelastic soil response are investigated. For the elastic soil response, the proposed beam model is verified against a Beam–FE solution and a refined 3–D continuum FE approach. For the inelastic soil response, the proposed model is verified only against the Beam–FE solution due to the fact that soil response in the 3–D continuum FEM strongly depends on the adopted soil constitutive model

4.2 Additional numerical models

The response of the soil–pile–structure system is investigated further with two different methods; namely a simplified Beam–FE model employing the OpenSees code [1], and a rigorous fully 3–D continuum FE scheme materialized in the ABAQUS [2] code.

In the first model a beam supported in discrete springs is used to model the lateral static and dynamic response of a pile. For seismic loadings, free–field soil response is calculated separately from site response analysis [12] and the obtained displacement time histories are applied to the ends of the soil springs.

In the fully 3–D model the calculations of the site response and the soil–pile–structure interaction are performed in a fully coupled manner with the Finite Element Code ABAQUS [2]. The pile–column and the soil behavior are assumed to be elastic, while P-δ effects (linearized 2nd order analysis) are also taken into account. The soil is modeled with 8-node brick elements. The free-field boundaries were investigated by two different types of boundaries; namely 3 dashpots on each node on the boundaries and alternatively appropriate kinematic constraints i.e. Multi-Point Constrains (MPC) boundaries. The comparison of the acceleration, displacement and rotation time histories at the deck level of the 3–D FE model with the both the boundary types provide identical results. Hence, the MPC boundaries were selected for all of the analyses conducted.

4.3 Results and comparison

The numerical results have been obtained using a set of 6 excitation motions. More specifically, in Figs 3–5 the acceleration time histories at the bridge deck level $\ddot{w}(H,t)$ corresponding to the Lefkada, JMA and Aegion excitation motions scaled to $a_g = 0.8g$, are presented, respectively. In these figures the geometrically linear and nonlinear analysis of the proposed model, taking into account both rotary inertia and shear deformation effect are compared with the Beam-FE and the fully 3–D FE models. From the obtained results it is observed that the proposed nonlinear formulation can capture accurately the response of the 3–D FE model accounting for P–δ effect, while the linear case predicts identical acceleration time histories with the Beam–FE model. From the conducted investigation, it is deduced that instead of executing time–expensive 3–D analyses for the soil–pile–bridge system, the proposed beam model can be employed providing minimum calculation effort while retaining high precision in the obtained results.

Moreover, Figs 6–9 illustrate the displacement time histories at the deck level $w(H,t)$ corresponding to the Lefkada, JMA and Aegion excitation motions, respectively taking into account or ignoring *p-y* soil nonlinearity. Finally, in Tables 1, 2 and 3 the extreme values of the bending moment along with their location are presented for different cases of analysis for all the excitation motions. Both the results from the elastic and the inelastic soil response are illustrated. From these figures and tables it is concluded that the proposed geometrically nonlinear formulation captures accurately the calculated response according to the other methods of analysis used, while all the models predict similar shapes of the moment distribution and the increase of the bending moment at the interface of the two soil layers. The models also predict the same depth of the maximum bending moment as well as the shift of the maximum bending moment at a higher depth as the peak ground acceleration increases for the case of the inelastic soil response.

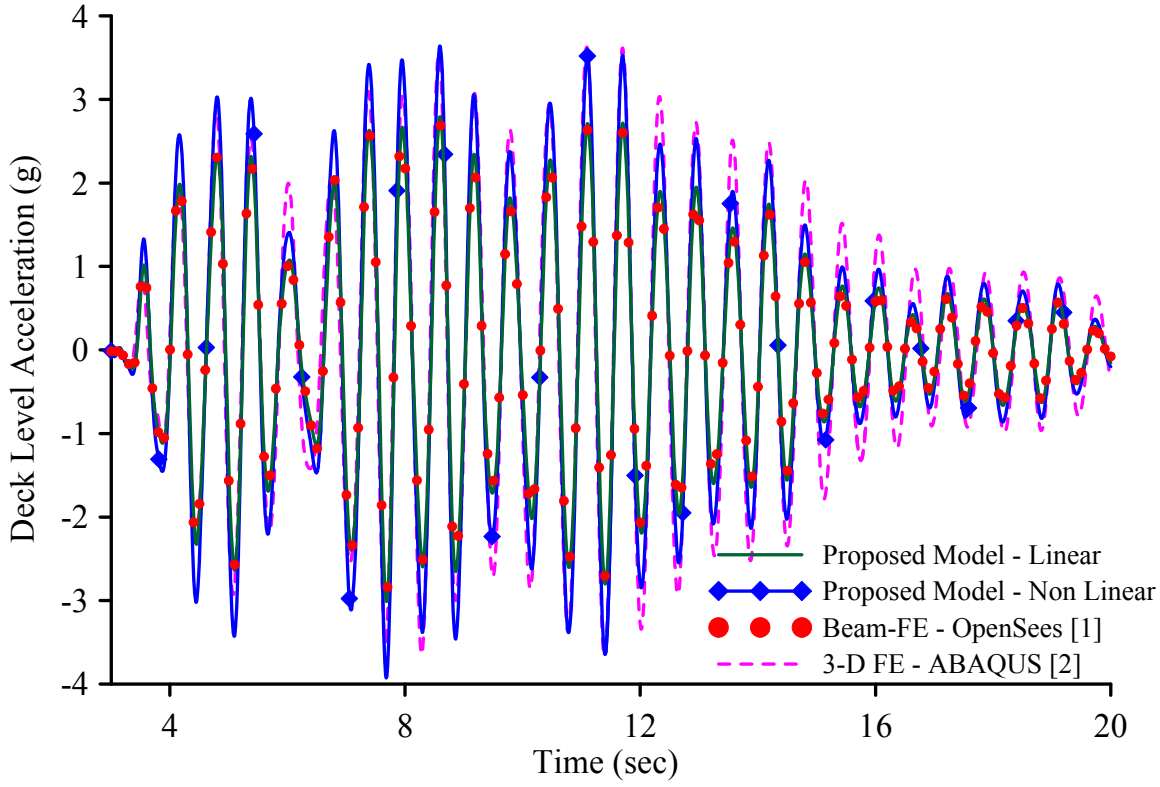


Figure 3: Acceleration time history of the deck level for Lefkada excitation ($a_g = 0.8$g).

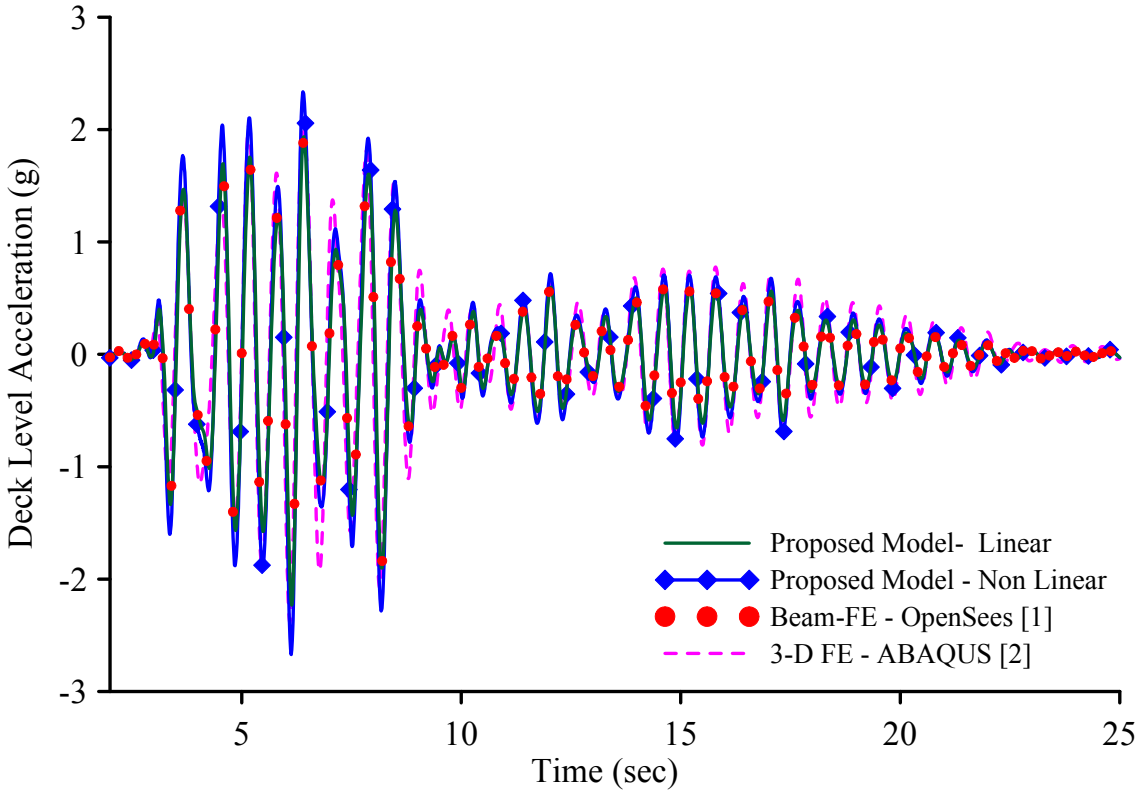


Figure 4: Acceleration time history of the deck level for JMA excitation ($a_g = 0.8g$).

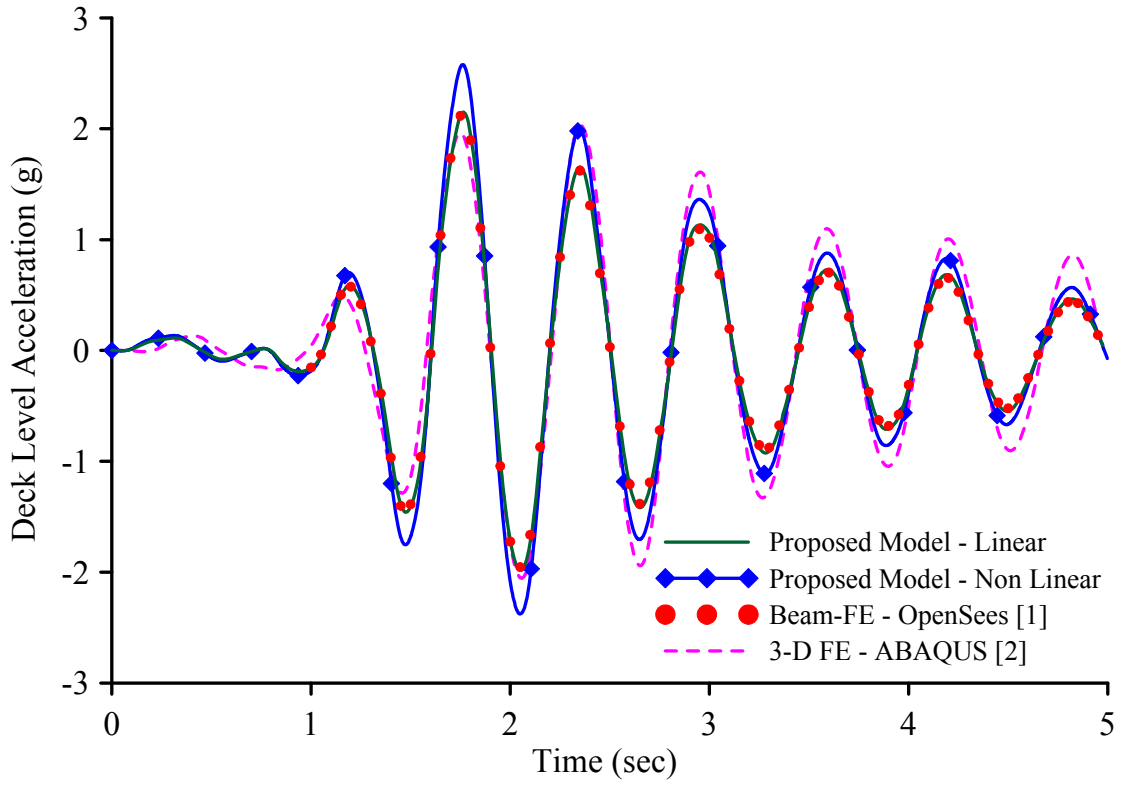


Figure 5: Acceleration time history of the deck level for Aegion excitation ($a_g = 0.8g$).

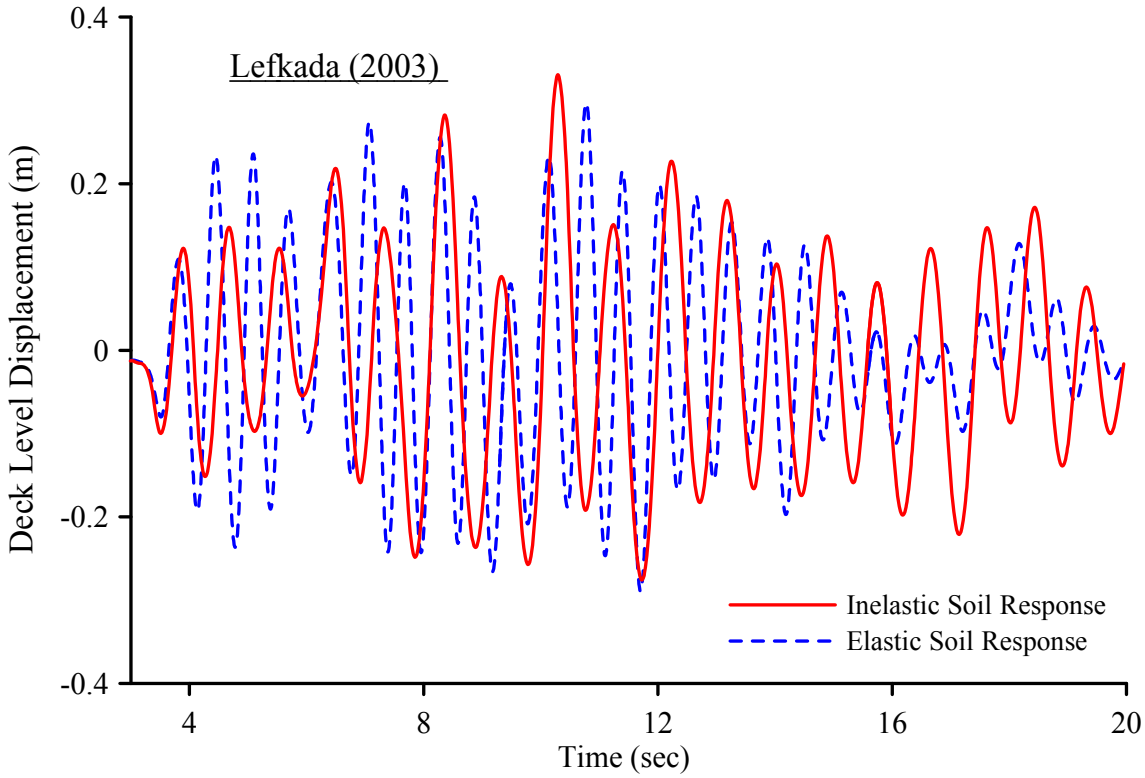


Figure 6: Displacement time history of the deck level for Lefkada excitation ($a_g = 0.8g$).

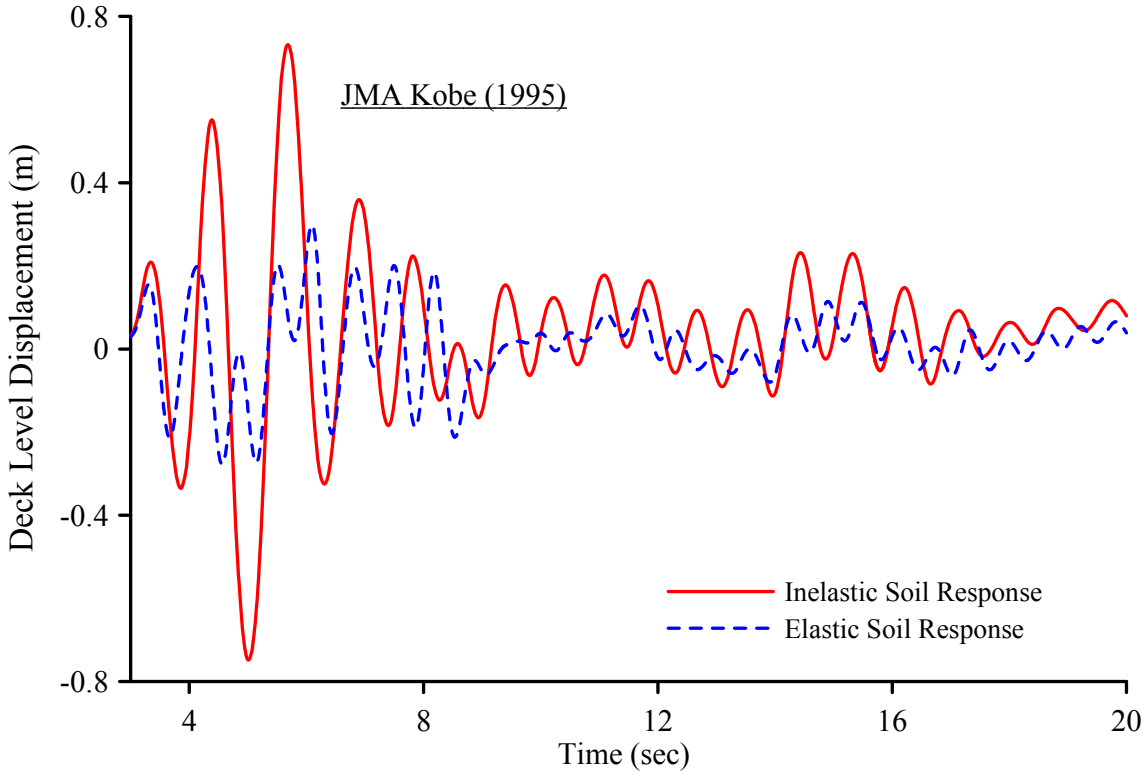


Figure 7: Displacement time history of the deck level for JMA excitation ($a_g = 0.8g$).

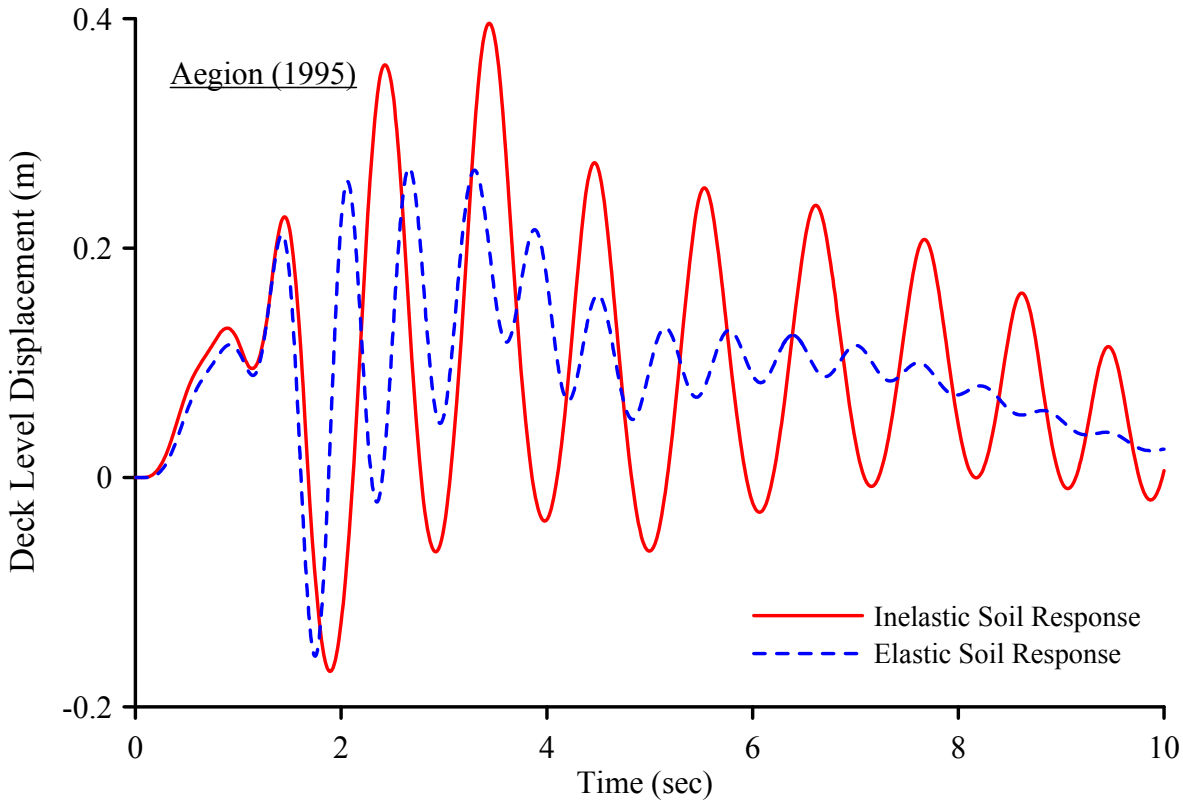


Figure 8: Displacement time history of the deck level for Aegion excitation ($a_g = 0.8g$).

Excitation	Analysis/Model	Elastic Soil		Inelastic Soil	
		M_{el}	Location	M_{pl}	Location
Lefkada (2003) $a_g = 0.5g$	Proposed–Linear	13.68	-1.0	7.19	-4.5
	Proposed–NonLinear	17.01	-1.0	7.16	-4.5
	Beam FE–OpenSees [1]	13.58	-1.0	7.18	-4.5
	3–D FE Abaqus [2]	17.80	-0.5	–	–
Lefkada (2003) $a_g = 0.8g$	Proposed–Linear	21.87	-1.0	12.75	-5.5
	Proposed–NonLinear	27.66	-1.0	12.52	-5.5
	Beam FE–OpenSees [1]	21.72	-1.0	12.60	-5.5
	3–D FE Abaqus [2]	28.48	-0.5	–	–

Table 1: Maximum values of the bending moment for elastic soil M_{el} and inelastic soil M_{pl} in MPa and their location (m) from the ground level, for the Lefkada (2003) excitation motion.

Excitation	Analysis/Model	Elastic Soil		Inelastic Soil	
		M_{el}	Location	M_{pl}	Location
JMA (1995) $a_g = 0.5g$	Proposed–Linear	10.27	-1.0	12.58	-6.5
	Proposed–NonLinear	11.02	-1.0	12.70	-6.5
	Beam FE–OpenSees [1]	10.13	-1.0	12.55	-6.5
	3–D FE Abaqus [2]	11.67	-0.5	.–	–
JMA (1995) $a_g = 0.8g$	Proposed–Linear	16.31	-1.0	19.18	-7.5
	Proposed–NonLinear	17.14	-1.0	19.20	-7.5
	Beam FE–OpenSees [1]	16.21	-1.0	19.16	-7.5
	3–D FE Abaqus [2]	18.67	-0.5	–	–

Table 2: Maximum values of the bending moment for elastic soil M_{el} and inelastic soil M_{pl} in MPa and their location (m) from the ground level, for the Kobe JMA (1995) excitation motion.

5 CONCLUSIONS

In this study, the accuracy of an advanced beam model for the soil–pile–structure kinematic and inertia interaction is investigated and the influence of soil *p-y* nonlinearity is verified. The main conclusions that can be drawn from this investigation are:

- The proposed model takes into account both kinematic and inertia interaction to the geometrical nonlinear dynamic response of a column-pile embedded in a layered soil profile.
- The soil *p-y* nonlinearity strongly influences the system response.
- The proposed formulation captures accurately the response of the 3–D solid model accounting for P-δ effects.
- The proposed model obtains accurate results with minimum computational time required, providing a simple and efficient tool in comparison to fully three dimensional analysis.
- A calibration methodology of the "spring" and "dashpot" coefficients of the examined hybrid spring configuration is proposed.
- The discrepancy between the results of the geometrically linear and the nonlinear analyses is significant especially in the case of an elastic soil behavior.

Excitation	Analysis/Model	Elastic Soil		Inelastic Soil	
		M_{el}	Location	M_{pl}	Location
Aegion (1995) $a_g = 0.5g$	Proposed–Linear	9.94	-1.0	6.75	-4.5
	Proposed–NonLinear	10.00	-1.0	6.72	-4.5
	Beam FE–OpenSees [1]	9.93	-1.0	6.74	-4.5
	3–D FE Abaqus [2]	10.11	-0.5	–	–
Aegion (1995) $a_g = 0.8g$	Proposed–Linear	14.40	-1.0	10.26	-5.5
	Proposed–NonLinear	15.86	-1.0	10.36	-6.5
	Beam FE–OpenSees [1]	15.89	-1.0	10.30	-5.5
	3–D FE Abaqus [2]	16.18	-0.5	–	–

Table 3. Maximum values of the bending moment for elastic soil M_{el} and inelastic soil M_{pl} in MPa and their location (m) from the ground level, for the Aegion (1995) excitation motion.

ACKNOWLEDGMENTS

The authors would like to acknowledge financial support from the EU 7th Framework research project funded through the European Research Council's Programme "Ideas", Support for Frontier Research – Advanced Grant, under Contract number ERC-2008-AdG 228254-DARE, and the Coordinator of the research project Professor George Gazetas.

REFERENCES

[1] S. Mazzoni, F. McKenna, G.L. Fenves, *OpenSees command language manual*, The Regents of the University of California, 2005.

[2] Dassault Systèmes Simulia Corp, *ABAQUS User's Manual, Providence*, RI, USA, 2009.

[3] S. Wang, B.L. Kutter, J.M. Chacko, D.W. Wilson, R.W. Boulanger, A. Abghari, Nonlinear seismic soil-pile-superstructure interaction, *Earthquake Spectra*, **14,** 377-396, 1998.

[4] E.J. Sapountzakis, A.E. Kampitsis, Nonlinear dynamic analysis of Timoshenko beam-columns partially supported on tensionless Winkler foundation, *Computers and Structures,* **88**, 1206–1219, 2010.

[5] E.J. Sapountzakis, V.G. Mokos, A BEM solution to transverse shear loading of beams, *Computational Mechanics*, **36**, 384-397, 2005.

[6] N. Makris, G. Gazetas, Dynamic pile-soil-pile interaction. Part II: Lateral and seismic response, *Earthquake Engineering and Structural Dynamics*, **21**, 145-162, 1992.

[7] H. Matlock, Correlations for design of laterally loaded piles in soft clay, *II Annual Offshore Technology Conference*, Houston, Texas, 1970.

[8] L.C. Reese, W.R. Cox, F.D. Koop, Field testing and analysis of laterally loaded piles in stiff clay, *VII Annual Offshore Technology Conference*, Houston, Texas, 1975.

[9] K.E. Brenan, S.L. Campbell, L.R. Petzold, N*umerical solution of initial-value problems in differential-algebraic equations*, North-Holland, Amsterdam, 1989.

[10] Z.P. Bazant, L. Cedolin, *Stability of structures: elastic, inelastic, fracture and damage theories*, Oxford University Press, New York, 1991.

[11] H.B. Seed, I.M. Idriss, *Soil moduli and damping factors for dynamic response analysis*, Report No. EERC 70-10, University of California, Berkeley, 1970.

[12] I.M. Idriss, J.I. Sun, SHAKE91: *A computer program for conducting equivalent linear seismic response analyses of horizontally layered soil deposits*, Center for Geotechnical Modeling Report, Department of Civil and Environmental Engineering, University of California, Davis, 1991.

COMPDYN 2013
4th ECCOMAS Thematic Conference on
Computational Methods in Structural Dynamics and Earthquake Engineering
M. Papadrakakis, V. Papadopoulos, V. Plevris (eds.)
Kos Island, Greece, 12–14 June 2013

MULTI-SCALE ENERGY PUMPING BETWEEN A MAIN OSCILLATOR INCLUDING SAINT-VENANT TERM AND A NONLINEAR ENERGY SINK

M. Weiss[1], A. Ture Savadkoohi[2], and C.-H. Lamarque[2]

[1] Université de Lyon, École Nationale des Travaux Publics de l'État
LGCB
rue Maurice Audin, F-69518, Vaulx-en-Velin Cedex, France
e-mail: mathieu.weiss@entpe.fr

[2] Université de Lyon, École Nationale des Travaux Publics de l'État
LGCB and LTDS UMR CNRS 5513
rue Maurice Audin, F-69518, Vaulx-en-Velin Cedex, France
e-mail: {alireza.turesavadkoohi,lamarque}@entpe.fr

Keywords: Energy exchange, Saint-Venant, cubic, NES, nonlinear.

Abstract. *Vibratory energy exchange between oscillators can be used for localization, passive control and/or energy harvesting. It has been demonstrated, theoretically and experimentally, that by coupling an essential nonlinear and light oscillator to main oscillators, it will be possible to passively control the main system against externally induced forces. The phenomenon is called energy pumping and the nonlinear oscillator is named as nonlinear energy sink (NES). Some research works have been carried out in order to detect the energy pumping between linear and non-polynomial/nonsmooth NES systems or between a nonsmooth main oscillator and a coupled cubic NES. In this work, multi-scale vibratory energy exchange between a main oscillator including Saint-Venant term and a cubic nonlinear energy sink is studied. Analytically obtained invariant manifold of the system at fast time scale and detected fixed points and/or fold singularities at first slow time scale let us predict and explain different regimes that the system may face during the energy exchange process. The work will be accompanied by two numerical examples confirming our analytical developments.*

1 INTRODUCTION

It has been proved that by endowing nonlinear innate of some special light attachments, namely NES, it is possible to localize the energy of important oscillators which are mainely linear [1, 2, 3, 4, 5]. This localization can be for the aim of passive control and/or energy harvesting. The phenomenon is called energy pumping. The efficiency of NES systems in controlling main systems (e.g. in the field of acoustics, civil and mechanical engineering) has been proved experimentally as well [6, 7, 8, 9, 10, 11, 12]. Some works have been carried out in order to consider other types of nonlinearities for the NES: Nucera et al. [13], Lee et al. [14] and Gendelman [15] studied energy pumping in systems with vibro-impact NES. The energy pumping in a 2 dof system consisting of a linear dof and a nonlinear energy sink with non-polynomial and piece-wise potential investigated by Gendelman [16]. Lamarque et al. [17] pinpointed the targeted energy transfer phenomenon from a linear master dof system to a non-smooth NES under different forcing conditions while the same system in the presence of the gravity pinpointed by Ture Savadkoohi et al. [18]. Some researchers took into account the vibratory energy exchange between a non-smooth main oscillator and a coupled non-smooth/cubic NES: Schmidt and Lamarque [19] by endowing techniques of [20, 21] studied energy transfer from initial single dof system including non-smooth terms of friction type to a cubic NES. The behavior of two coupled non-smooth systems by detecting their invariant manifolds at different scales of time and finally their fixed point are enlightened in [22]. In this paper we would like to analytically investigate on the multi- scale energy exchange between two oscillators, namely a main one including Saint-Venant terms and a coupled cubic NES. Our analytical developments will be accompanied by two numerical examples. Organization of the paper is as it follows:
Academic model of the system, its re-scaling and averaging processes are given in Section 2. Time multi scale behavior of the system by detecting its invariant manifold and fixed points/fold singularities are described in Section 3. Comparison of analytical developments with obtained numerical results are illustrated in Section 4. Finally, conclusions are given in Section 5.

2 Mathematical presentation of the system

We consider a two dof system that is represented in Fig. 1. The main oscillator (M, k, $\tilde{\lambda}$) with a Saint-Venant type behavior ($\tilde{k}_p$, α) is coupled to a NES (m, $\tilde{C}_1$, $\tilde{\lambda}_1$) with cubic potential. The mass ratio between two oscillators is very small i.e., $0 < \epsilon = \dfrac{m}{M} \ll 1$

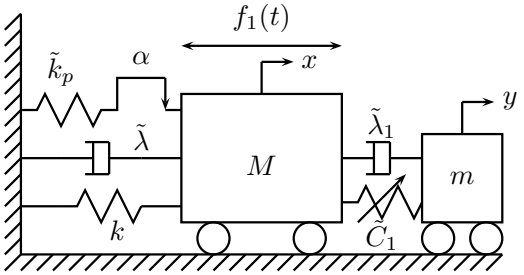


Figure 1: Academic model of the system

Governing equations of the described system in the Fig. 1 is summarized as:

$$\begin{cases} M\frac{d^2x}{dt^2} + \tilde{\lambda}\frac{dx}{dt} + \tilde{\lambda}_1(\frac{dx}{dt} - \frac{dy}{dt}) + kx + \tilde{k}_p u + \tilde{C}_1 F(x-y) = f_1(t) \\ m\frac{d^2y}{dt^2} + \tilde{\lambda}_1(\frac{dy}{dt} - \frac{dx}{dt}) + \tilde{C}_1 F(y-x) = 0 \\ \left(\frac{du}{dt} + \beta(\frac{\tilde{k}_p u}{\alpha})\right) \ni \frac{dx}{dt} \end{cases} \tag{1}$$

with $F : x \mapsto x^3$ and graph of β which is illustrated in Fig.2, is defined as:

$$\beta(x) = \begin{cases} \emptyset & \text{if} \quad x \in]-\infty, -1[\cup]1, +\infty[\\ 0 & \text{if} \quad x \in]-1, 1[\\ \mathbb{R}_- & \text{if} \quad x = -1 \\ \mathbb{R}_+ & \text{if} \quad x = 1 \end{cases} \tag{2}$$

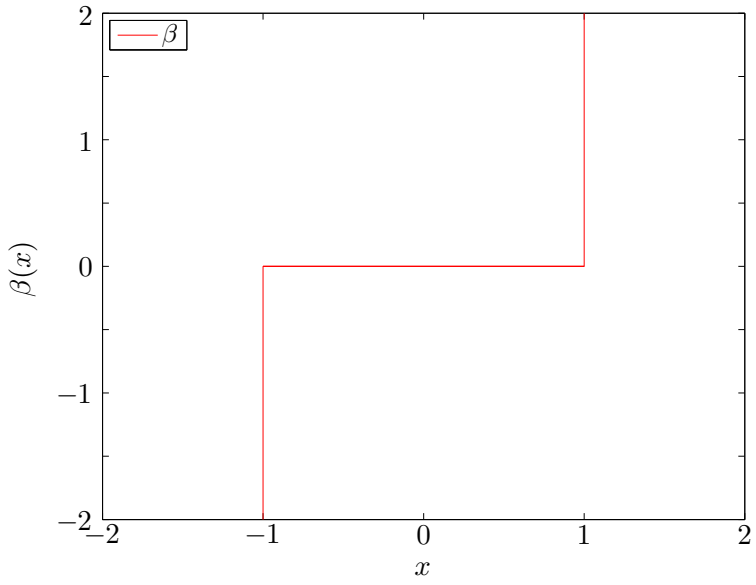


Figure 2: Graph of β

Let us suppose that $\tau = t\sqrt{\frac{k}{M}} = w_1 t$. We introduce following variables: $\frac{\tilde{\lambda} w_1}{M w_1^2} = \epsilon\lambda_0$, $\frac{\tilde{k}_p}{M w_1^2} = \epsilon k_p$, $\frac{\tilde{C}_1}{M w_1^2} = \epsilon C_{10}$, $\frac{\tilde{\lambda}_1}{M w_1^2} = \epsilon\lambda_{10}$, $\frac{f_1(\frac{\tau}{\omega_1})}{M w_1^2} = \epsilon f_{10}\sin(\Omega\tau)$, $\eta = \frac{\alpha}{\tilde{k}_p}$. The system (1) reads (for any arbitrary function V, $\frac{dV}{d\tau}$ is denoted by V'):

$$\begin{cases} x'' + \epsilon\lambda_0 x' + \epsilon\lambda_{10}(x' - y') + x + \epsilon k_p u + \epsilon C_{10} F(x-y) = \epsilon f_{10}\sin(\Omega\tau) \\ \epsilon y'' + \epsilon\lambda_{10}(y' - x') + \epsilon C_{10} F(y-x) = 0 \\ \left(u' + \beta(\frac{u}{\eta})\right) \ni x' \end{cases} \tag{3}$$

Coordinates of the center of mass and relative displacement of two masses are introduced as:

$$\left\{\begin{array}{lcl} v &=& x+\epsilon y \\ w &=& x-y \end{array}\right. \Leftrightarrow \left\{\begin{array}{lcl} x &=& \frac{v+\epsilon w}{1+\epsilon} \\ y &=& \frac{v-w}{1-\epsilon} \end{array}\right. \tag{4}$$

System (3) in new coordinates is defined as:

$$\left\{\begin{array}{l} v''+\epsilon\lambda_0\frac{v'+\epsilon w'}{1+\epsilon}+\frac{v+\epsilon w}{1+\epsilon}+\epsilon k_p u=\epsilon f_{10}\sin(\Omega\tau) \\ w''+\epsilon\lambda_0\frac{v'+\epsilon w'}{1+\epsilon}+\frac{v+\epsilon w}{1+\epsilon}+\epsilon k_p u+(1+\epsilon)(\lambda_{10}w'+C_{10}F(w))=\epsilon f_{10}\sin(\Omega\tau) \\ \left(u'+\beta(\frac{u}{\eta})\right)\ni\frac{v'+\epsilon w'}{1+\epsilon} \end{array}\right. \tag{5}$$

We assume that $\tilde{\tau}=\Omega\tau$ and then following complex variables of Manevitch [23] are introduced to the system (5)(for any arbitrary function V, $\frac{dV}{d\tilde{\tau}}$ is denoted by $\dot{V}$):

$$\left\{\begin{array}{lcl} \phi_1 e^{i\tilde{\tau}} &=& \Omega(\dot{v}+iv) \\ \phi_2 e^{i\tilde{\tau}} &=& \Omega(\dot{w}+iw) \\ \phi_3 e^{i\tilde{\tau}} &=& \Omega(\dot{u}+iu) \end{array}\right. \tag{6}$$

We endow the Galerkin method using truncated Fourier series. In this paper we consider only first harmonic, i.e. $e^{i\tilde{\tau}}$, for each equation. Based on the general periodic behavior of system variables we obtain (see for example [18]):

$$\left\{\begin{array}{l} \Omega\dot{\phi_1}-\frac{\Omega}{2i}\phi_1+\frac{\epsilon\lambda_0(\phi_1+\epsilon\phi_2)}{2(1+\epsilon)}+\frac{\phi_1+\epsilon\phi_2}{2i\Omega(1+\epsilon)}+\frac{\epsilon k_p}{2\Omega i}\phi_3=\epsilon\frac{f_{10}}{2i} \\ \Omega\dot{\phi_2}-\frac{\Omega}{2i}\phi_2+\frac{\epsilon\lambda_0(\phi_1+\epsilon\phi_2)}{2(1+\epsilon)}+\frac{\phi_1+\epsilon\phi_2}{2i\Omega(1+\epsilon)}+\frac{\epsilon k_p}{2\Omega i}\phi_3 \\ +(1+\epsilon)(C_{10}\mathcal{F}+\frac{\lambda_{10}}{2}\phi_2)=\epsilon\frac{f_{10}}{2i} \\ \phi_3=\frac{\phi_1+\epsilon\phi_2}{(1+\epsilon)\pi}\xi\left(\frac{|\phi_1+\epsilon\phi_2|}{(1+\epsilon)\Omega}\right) \end{array}\right. \tag{7}$$

where

$$\forall z\in\mathbb{R}_+,\xi(z)=\left\{\begin{array}{ll} \pi & if\ \ z\leqslant\eta \\ \bar{\tau}_1+e^{-i\bar{\tau}_1}\sin(\bar{\tau}_1)-4e^{-i\frac{\bar{\tau}_1}{2}}\sin(\frac{\bar{\tau}_1}{2})-\frac{4\eta}{z}e^{-i(\bar{\tau}_1+\frac{\pi}{2})} & if\ \ z>\eta \end{array}\right. \tag{8}$$

and

$$\bar{\tau}_1=\arccos(1-\frac{2\eta}{z}) \tag{9}$$

The averaging process (i.e. truncated Fourier series and keeping first harmonic) of the third equation of the system (5) is described in appendix A. We will analyze system behavior around $1:1$ resonance, i.e. $\Omega=1+\epsilon\sigma$.

3 Multi-scale analysis of the system

An asymptotic approach [24] is used by introducing fast time $\tilde{\tau}_0$ and slow times $\tilde{\tau}_1$, $\tilde{\tau}_2$...

$$\tilde{\tau} = \tilde{\tau}_0, \tilde{\tau}_1 = \epsilon\tilde{\tau}_0, ... \tag{10}$$

so

$$\frac{d}{d\tilde{\tau}} = \frac{\partial}{\partial\tilde{\tau}_0} + \epsilon\frac{\partial}{\partial\tilde{\tau}_1} + ... \tag{11}$$

We study the system at different orders of ϵ.

3.1 ϵ^0 order

At the ϵ^0 order, following equations can be derived from the system (7):

$$\frac{\partial\phi_1}{\partial\tilde{\tau}_0} = 0 \Rightarrow \phi_1 = \phi_1(\tilde{\tau}_1) \tag{12}$$

$$\frac{\partial\phi_2}{\partial\tilde{\tau}_0} - \frac{\phi_2}{2i} + \frac{\phi_1}{2i} + C_{10}\mathcal{F} + \frac{\lambda_{10}}{2}\phi_2 = 0 \tag{13}$$

$$\phi_3 = \frac{\phi_1}{\pi}\xi(|\phi_1|) \tag{14}$$

Since we are dealing with cubic nonlinearity of the NES, i.e. $F : x \mapsto x^3$, then it is possible to obtain its average, $\mathcal{F}$, as a function of ϕ_2:

$$\mathcal{F} = \frac{1}{2i}G(|\phi_2|^2)\phi_2 \;\; with \;\; G : x \mapsto \frac{3x}{4} \tag{15}$$

Fixed points, which corresponding to the behavior of ϕ_2 for $\tilde{\tau}_0 \to +\infty$, can be obtained from equation (13):

$$\phi_1 = \phi_2 - C_{10}G(|\phi_2|^2)\phi_2 - i\lambda_{10}\phi_2 \tag{16}$$

If we suppose that $\phi_1 = N_1e^{i\delta_1}$ and $\phi_2 = N_2e^{i\delta_2}$ ($N_1 \in \mathbb{R}_+$,$N_2 \in \mathbb{R}_+$, $\delta_1 \in \mathbb{R}$ and $\delta_2 \in \mathbb{R}$), then equation (16) reads:

$$N_1 = N_2\sqrt{(1 - C_{10}G(N_2^2))^2 + \lambda_{10}^2} \tag{17}$$

$$\begin{cases} \Delta\delta = \delta_2 - \delta_1 = \arctan\left(\frac{\lambda_{10}}{1-C_{10}G(N_2^2)}\right) & \text{if} \quad 1 - C_{10}G(N_2^2) > 0 \\ \Delta\delta = \delta_2 - \delta_1 = \arctan\left(\frac{\lambda_{10}}{1-C_{10}G(N_2^2)}\right) + \pi & \text{if} \quad 1 - C_{10}G(N_2^2) < 0 \end{cases} \tag{18}$$

Equation (17) gives the invariant manifold of the system at fast time scale. Figure 3 represents this invariant for some given system parameters. Now, we would like to seek for local extrema of the Eq. (17). We have:

$$\frac{\partial N_1^2}{\partial N_2^2} = ((1 - C_{10}G(N_2^2))^2 + \lambda_{10}^2) - 2C_{10}N_2^2G'(N_2^2) + 2N_2^2G'(N_2^2)G(N_2^2) = 0 \tag{19}$$

so according to (15)

$$\frac{\partial N_1^2}{\partial N_2^2} = \frac{27}{16}C_{10}^2N_2^4 - 3C_{10}N_2^2 + \lambda_{10}^2 + 1 = 0 \tag{20}$$

$$\Delta = 9 - 4\frac{27}{16}(1+\lambda_{10}^2) \tag{21}$$

and

$$\Delta \geqslant 0 \Leftrightarrow \lambda_{10} \leqslant \frac{1}{\sqrt{3}} \tag{22}$$

Coordinates of local extrema (N_{2+}, N_{1+}) and (N_{2-}, N_{1-}), are summarized as:

$$N_{2+} = \sqrt{\frac{24+8\sqrt{\Delta}}{27C_{10}}} \quad so \quad N_{1+} = N_{2+}\sqrt{(1-C_{10}G(N_{2+}^2))^2+\lambda_{10}^2} \tag{23}$$

$$N_{2-} = \sqrt{\frac{24-8\sqrt{\Delta}}{27C_{10}}} \quad so \quad N_{1-} = N_{2-}\sqrt{(1-C_{10}G(N_{2-}^2))^2+\lambda_{10}^2} \tag{24}$$

These coordinates are shown in Fig. 3. Stability borders of the invariant manifold which are

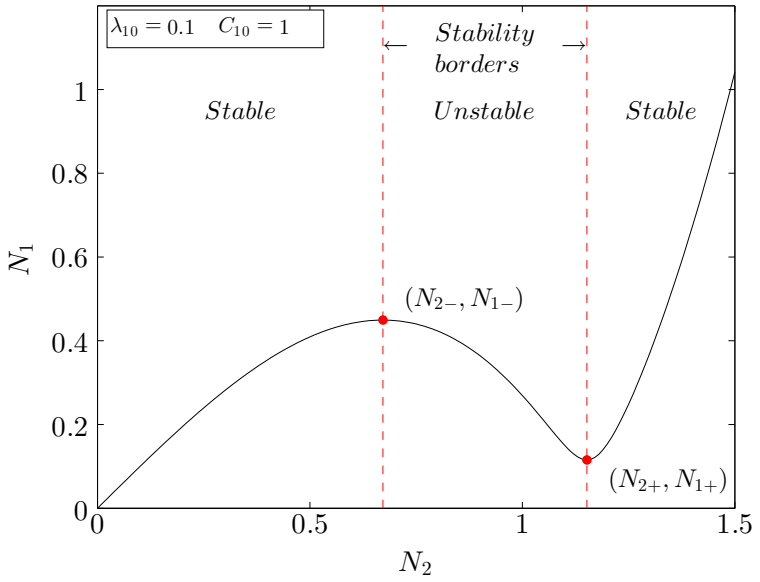


Figure 3: Invariant manifold of the system and its stability borders.

represented in Figure 3 can be detected by perturbing N_2 and δ_2 in system (13) as $N_2 + \Delta N_2$ and $\delta_2 + \Delta\delta_2$ [17, 18].

3.2 ϵ^1 order

The ϵ^1 order of first equation of system (7) gives:

$$\frac{\partial\phi_1}{\partial\tilde{\tau_1}} + \frac{\lambda_0}{2}\phi_1 + \frac{\phi_2}{2i} - \frac{2\sigma+1}{2i}\phi_1 + \frac{k_p}{2i}\phi_3 = \frac{f_{10}}{2i} \tag{25}$$

From this moment on for respecting ϵ^1 order of system of equations, evolution of ϕ_3 at ϵ^0 order which is defined in (14) should be considered in Eq. (25) and all relevant forthcoming analytical developments. If $N_1 > \eta$, ϕ_3 reads:

$$\begin{aligned} \phi_3 &= \tfrac{\phi_1}{\pi}[\bar{\tau_1} + e^{-i\bar{\tau_1}}\sin(\bar{\tau_1}) - 4e^{-i\frac{\bar{\tau_1}}{2}}\sin(\tfrac{\bar{\tau_1}}{2}) - \tfrac{4\eta}{|\phi_1|}e^{-i(\bar{\tau_1}+\frac{\pi}{2})}] \\ &= [\tilde{\mathcal{F}}_{re}(N_1) + i\tilde{\mathcal{F}}_{im}(N_1)]e^{i\delta_1} \end{aligned} \tag{26}$$

where

$$\begin{aligned}\tilde{\mathcal{F}}_{re}(N_1) &= \frac{N_1}{\pi}[\bar{\tau_1} + \sin(\bar{\tau_1})\cos(\bar{\tau_1}) - 4\cos(\frac{\bar{\tau_1}}{2})\sin(\frac{\bar{\tau_1}}{2}) + \frac{4\eta}{N_1}\sin(\bar{\tau_1})] \\ \tilde{\mathcal{F}}_{im}(N_1) &= \frac{N_1}{\pi}[-\sin^2(\bar{\tau_1}) + 4\sin^2(\frac{\bar{\tau_1}}{2}) + \frac{4\eta}{N_1}\cos(\bar{\tau_1})]\end{aligned} \tag{27}$$

If $N_1 \leqslant \eta$, we have the same notations with $\tilde{\mathcal{F}}_{re}(N_1) = N_1$ and $\tilde{\mathcal{F}}_{im}(N_1) = 0$. Considering equation (17), ϕ_3 can be obtained as a function of N_2 and δ_1 with new definitions $\mathcal{F}_{re}$ and $\mathcal{F}_{im}$ which are derived from $\tilde{\mathcal{F}}_{re}$ and $\tilde{\mathcal{F}}_{im}$:

$$\phi_3 = [\mathcal{F}_{re}(N_2) + i\mathcal{F}_{im}(N_2)]e^{i\delta_1} \tag{28}$$

From equation (16) we have:

$$\begin{aligned}\frac{\partial\phi_1}{\partial\tilde{\tau_1}} &= -2\frac{\partial N_2}{\partial\tilde{\tau_1}}N_2C_{10}G'(N_2^2)e^{i\delta_2} + (1 - C_{10}G(N_2^2) - i\lambda_{10})(\frac{\partial N_2}{\partial\tilde{\tau_1}}e^{i\delta_2} + iN_2\frac{\partial\delta_2}{\partial\tilde{\tau_1}}e^{i\delta_2}) \\ &= \frac{f_0}{2i} - \frac{\lambda_0}{2}(1 - C_{10}G(N_2^2) - i\lambda_{10})N_2e^{i\delta_2} - \frac{1}{2i}N_2e^{i\delta_2} \\ &\quad + \frac{2\sigma+1}{2i}(1 - C_{10}G(N_2^2) - i\lambda_{10})N_2e^{i\delta_2} \\ &\quad - \frac{k_p}{2i}(\mathcal{F}_{re}(N_2) + i\mathcal{F}_{im}(N_2))e^{\delta_1}\end{aligned} \tag{29}$$

After separating real and imaginary parts

$$\begin{cases} -2C_{10}N_2^2G'(N_2^2)\frac{\partial N_2}{\partial\tilde{\tau_1}} + \lambda_{10}N_2\frac{\partial\delta_2}{\partial\tilde{\tau_1}} + (1 - C_{10}G(N_2^2))\frac{\partial N_2}{\partial\tilde{\tau_1}} &= \Xi(N_2,\delta_2) \\ (1 - C_{10}G(N_2^2))N_2\frac{\partial\delta_2}{\partial\tilde{\tau_1}} - \lambda_{10}\frac{\partial N_2}{\partial\tilde{\tau_1}} &= \Sigma(N_2,\delta_2) \end{cases} \tag{30}$$

with

$$\begin{aligned}\Xi(N_2,\delta_2) &= -\frac{f_0}{2}\sin(\delta_2) - \frac{(2\sigma+1)\lambda_{10}}{2}N_2 - \frac{\lambda_0}{2}(1 - C_{10}G(N_2^2))N_2 \\ &\quad - \frac{k_p}{2}(\mathcal{F}_{im}(N_2)\cos(\Delta\delta) - \mathcal{F}_{re}(N_2)\sin(\Delta\delta)) \\ \Sigma(N_2,\delta_2) &= -\frac{f_0}{2}\cos(\delta_2) - \frac{2\sigma+1}{2}(1 - C_{10}G(N_2^2))N_2 + \frac{\lambda_0\lambda_{10}}{2}N_2 + \frac{N_2}{2} \\ &\quad + \frac{k_p}{2}(\mathcal{F}_{im}(N_2)\sin(\Delta\delta) + \mathcal{F}_{re}(N_2)\cos(\Delta\delta))\end{aligned} \tag{31}$$

The function C is introduced as:

$$C(N_2) = \lambda_{10}^2 - 2C_{10}N_2^2G'(N_2^2)(1 - C_{10}G(N_2^2)) + (1 - C_{10}G(N_2^2))^2 \tag{32}$$

Then system (30) reads:

$$\begin{cases} C(N_2)\frac{\partial N_2}{\partial\tilde{\tau_1}} &= (1 - C_{10}G(N_2^2))\Xi(N_2,\delta_2) - \lambda_{10}\Sigma(N_2,\delta_2) \\ C(N_2)N_2\frac{\partial\delta_2}{\partial\tilde{\tau_1}} &= \lambda_{10}\Xi(N_2,\delta_2) + (1 - C_{10}G(N_2^2) - 2C_{10}N_2^2G'(N_2^2))\Sigma(N_2,\delta_2) \end{cases} \tag{33}$$

This can be re-written in a compact form as:

$$\begin{cases} \frac{\partial N_2}{\partial\tilde{\tau_1}} &= \frac{f(N_2,\delta_2)}{C(N_2)} \\ \frac{\partial\delta_2}{\partial\tilde{\tau_1}} &= \frac{g(N_2,\delta_2)}{N_2C(N_2)} \end{cases} \tag{34}$$

Functions f and g are given in appendix B. By studying zeros of functions f, g and C in the reduced system (34), one can detect fixed points ($f = g = 0$ and $C \neq 0$) which correspond to periodic regimes and fold singularities ($f = g = C = 0$) which are signs of strongly modulated responses of the system.

4 Numerical examples

The exact behavior of the system will be compared with analytical predictions. The exact response of the system is obtained by numerically integration of the system (3) and then by using explained change of variables in (4) and (6). Analytical predictions will be obtained by using equations (17) as analytical invariant manifold and the system (34) for obtaining fixed points and fold singularities. System (3) is integrated during 100000 unit of time τ with time steps equal to $\Delta\tau = 10^{-5}$ by using an Euler numerical scheme explained in [19]. This scheme is convergent with order 1. Parameters are $C_{10} = 1$, $\lambda_{10} = 0.1$ (as in Figure 3) $\lambda_0 = 0.1$, $\eta = 0.3$, $k_p = 1$ and $\epsilon = 0.001$. Assumed initial conditions are $x(0) = 0.5$, $u(0) = 0.3$, and zero for other coordinates. These initial conditions are illustrated with $\times$ symbol in all relevant figures.

4.1 Example 1: $f_{10} = 0.3$

All possible areas where functions $f(N_2, \delta_2)$, $g(N_2, \delta_2)$ and $C(N_2)$ in Eq. (34) become zero are presented in Figure 4. It can be seen that the system possesses one fixed points and two fold singularities on the lower fold line. Phase portraits of the system around its fixed point is depicted in Figure 5 showing that this fixed point which corresponds to a periodic regime is stable. Analytical invariant manifold of the system which is obtained by Eq. (17) and corresponding numerical ones are illustrated in Figure 6. This shows that the averaged behavior of the system follows its invariant manifold and when it reaches to the stability border, it experiences a bifurcation by a jump to other stable branch. Finally the system is attracted by its fixed point (Point A in Figure 6) which corresponds to a periodic regime. This behavior can be seen more clearly in the time domain by looking histories of system amplitudes that are illustrated in Figures 7 and 8. These histories show that the system after experiencing a bifurcation, which corresponds to sudden energy loss of the NES and almost constat energy level for the main system, finally is attracted to a periodic regime which corresponds to the fixed point A.

4.2 Example 2: $f_{10} = 1$

All possible dynamics of the system are collected in Figure 9. Here, the system possesses one fixed point, A $(5.97, 1.05)$, and two fold singularities, α $(3.66, 0.67)$ and β $(6.06, 0.67)$. Overall view of the phase portrait of the system which is given in Figure 10 shows that α and β are in the form of node and saddle fold singularities. Existence of these fold singularities which are detected by developed analytical techniques give us a hint of possible existence of strongly modulated response (SMR) [17, 25]. Analytical invariant manifold of the system and corresponding numerical results are illustrated in Figure 11 showing that real behavior of the system follows its invariant manifold. This figure highlights the persistent SMR of the system by hysterically jumps between its fold lines (are obtained by setting $C(N_2) = 0$). Variations of system amplitudes which are depicted in Figure 12 and Figure 13 shows that two oscillators present beating response during the SMR. This kind of behavior is very interesting for passive control and/or energy harvesting by proper design of the NES in such a way that the difference

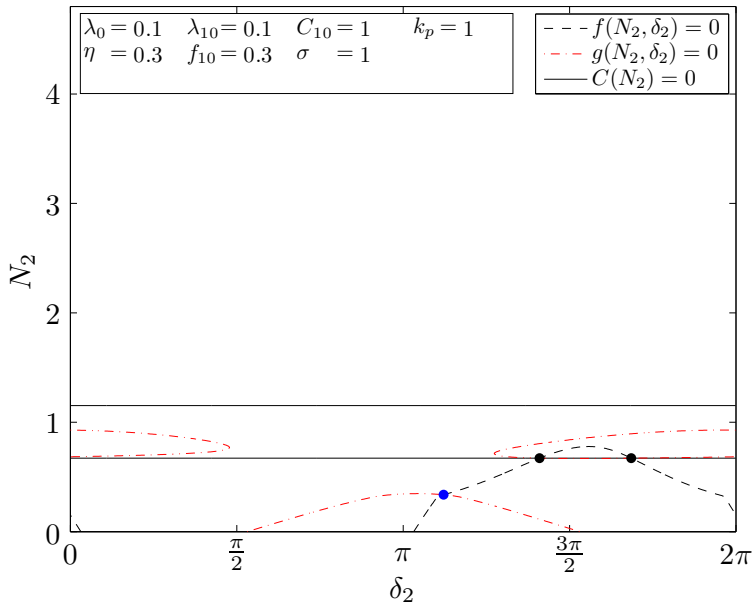


Figure 4: Dynamics of the system under forcing term $f_{10} = 0.3$: positions of fixed point and fold singularities.

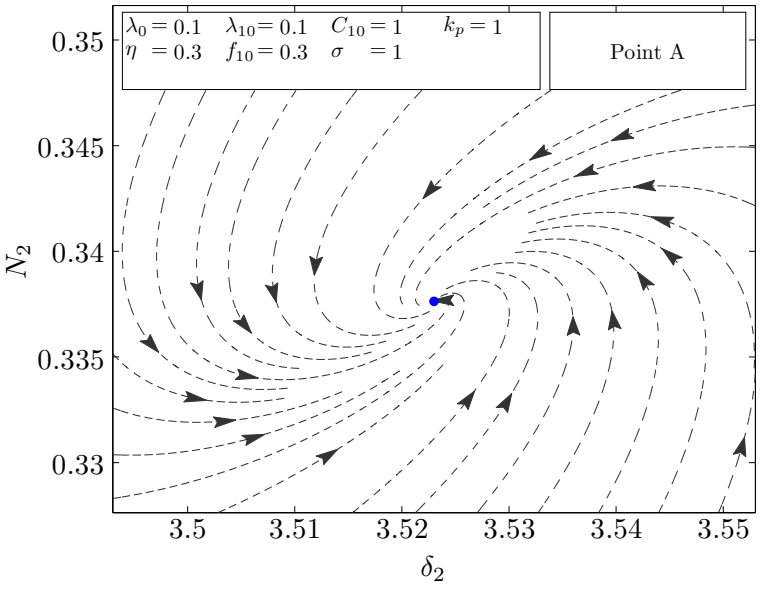


Figure 5: Phase portrait of the system under external forcing term $f_{10} = 0.3$ around its fixed point.

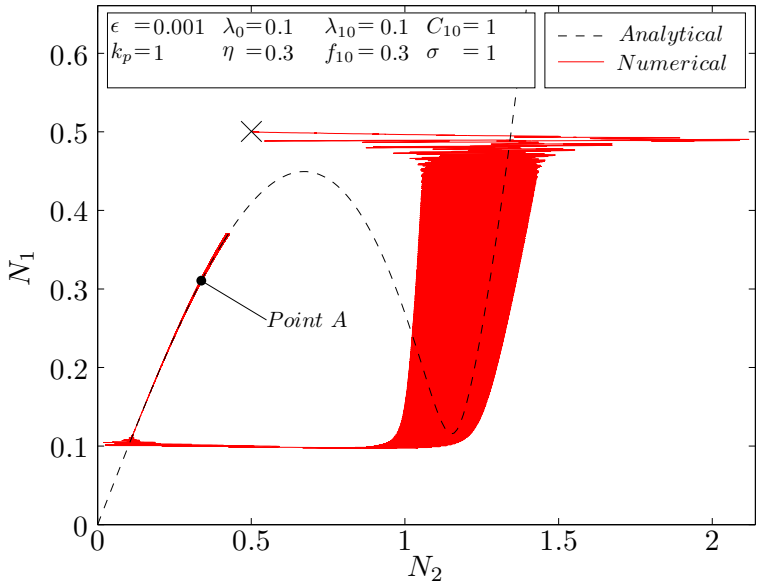


Figure 6: Invariant manifold of the system and corresponding numerical results under forcing term $f_{10} = 0.3$: initial conditions are shown by $\times$ symbol.

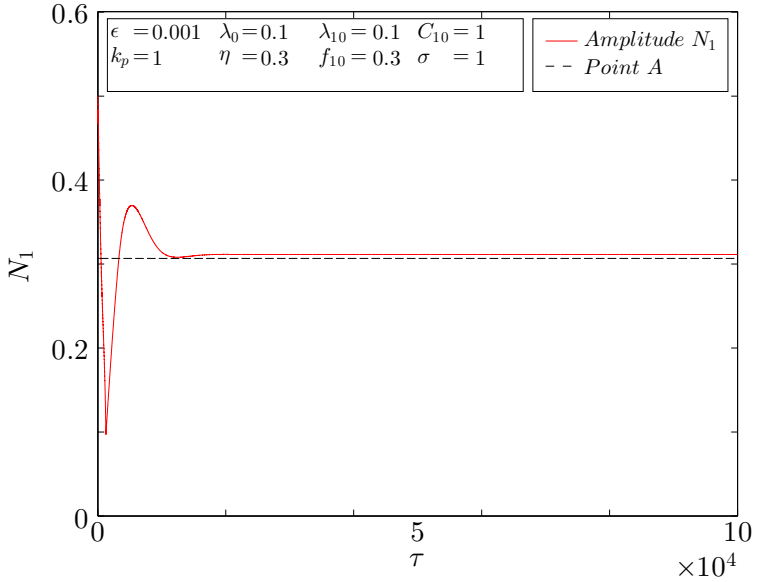


Figure 7: History the N_1 versus time τ for the system under forcing term $f_{10} = 0.3$.

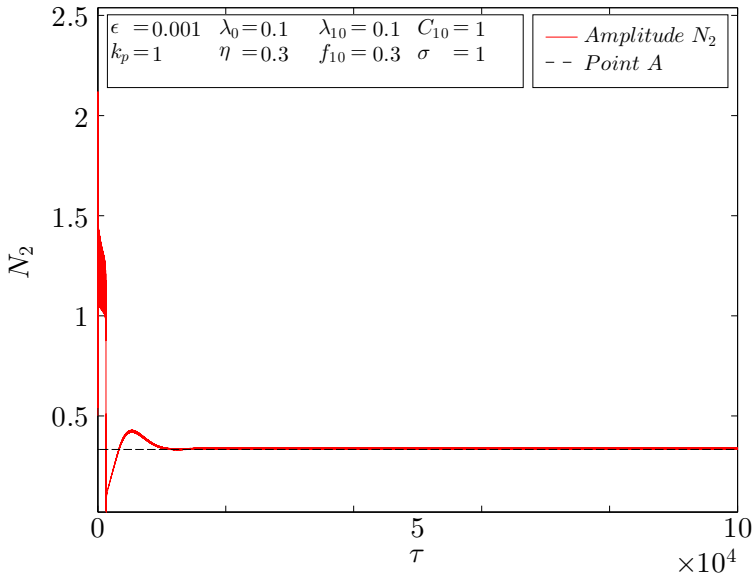


Figure 8: History the N_2 versus time τ for the system under forcing term $f_{10} = 0.3$.

between local maximum and minimum of the invariant, namely N_{1-} and N_{1+}, be small while the same difference in the N_2 direction, i.e. between N_{2-} and N_{2+}, can be large. In this case a high amounts of energy are trapped in a cycle which can be used for harvesting as well.

It is worthwhile to mention that obtained numerical results automatically contain all harmonics of the system while the analytical invariant manifold is based on keeping just first harmonics and truncating higher ones. This is the reason of oscillations of numerical results around the analytical invariant manifold which also causes the start of the bifurcation not to be exactly from the local minimum of the theoretical invariant manifold.

5 Conclusion

We presented the behavior of a two dof nonlinear system. In detail: the main dof includes Saint-Venant terms and the other coupled dof is a nonlinear energy sink with cubic potential. Analytically detected invariant manifold at the fast time scale let us predict the flow of system amplitudes while traced system behavior at first slow time scale let us collect its fixed points and fold singularities. According to external forcing terms (for given initial conditions) the system may face periodic and/or strongly modulated responses. These regimes can represent low or hight energy levels and/or persistently energy exchange between two oscillators by hysteresis bifurcations. Developed techniques in this paper can be used for designing nonlinear energy sink devices for the aim of localization which can be passive control, energy harvesting or both of them.

Acknowledgment

Authors would like to thank the "Ministère de l'Écologie, du Développement Durable et de l'Énergie" for supporting this research.

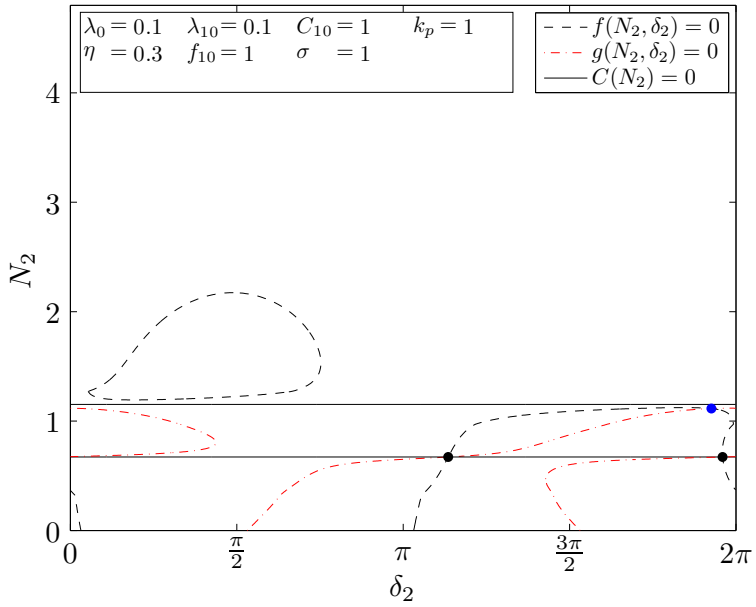


Figure 9: Dynamics of the system under forcing term $f_{10} = 1$: positions of fixed point and fold singularities.

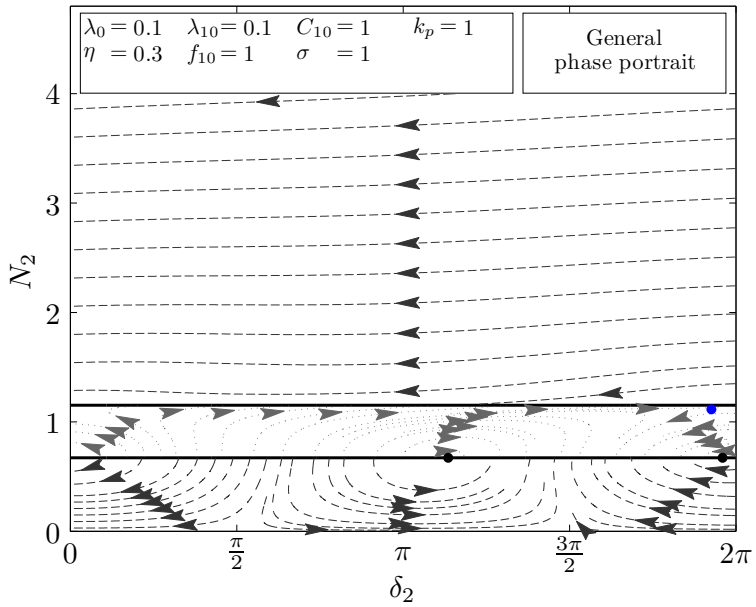


Figure 10: Dynamics of the system under forcing term $f_{10} = 1$: overall view of the phase portrait.

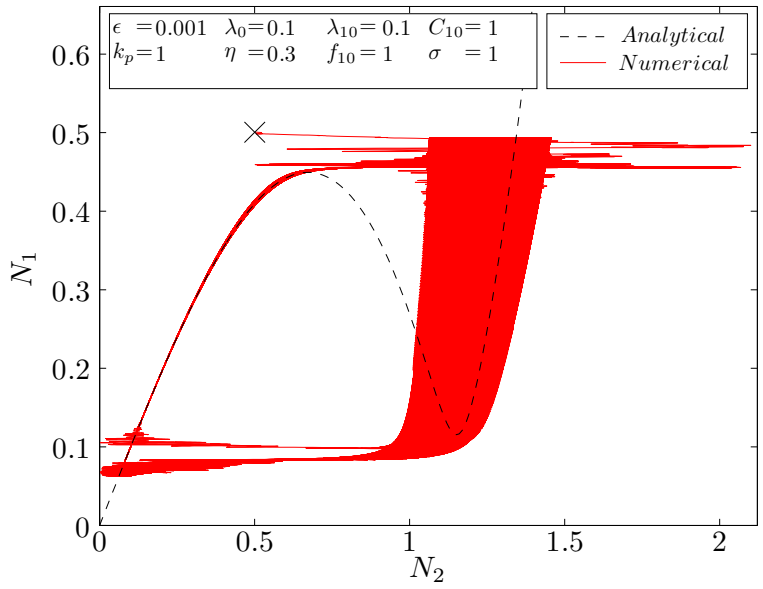


Figure 11: Invariant manifold of the system and corresponding numerical results under forcing term $f_{10} = 1$: initial conditions are shown by $\times$ symbol.

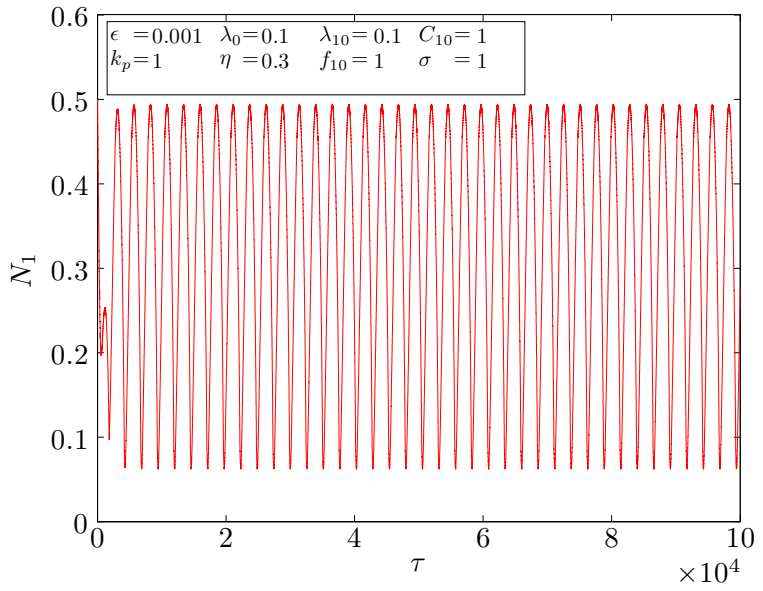


Figure 12: History the N_1 versus time τ for the system under forcing term $f_{10} = 1$.

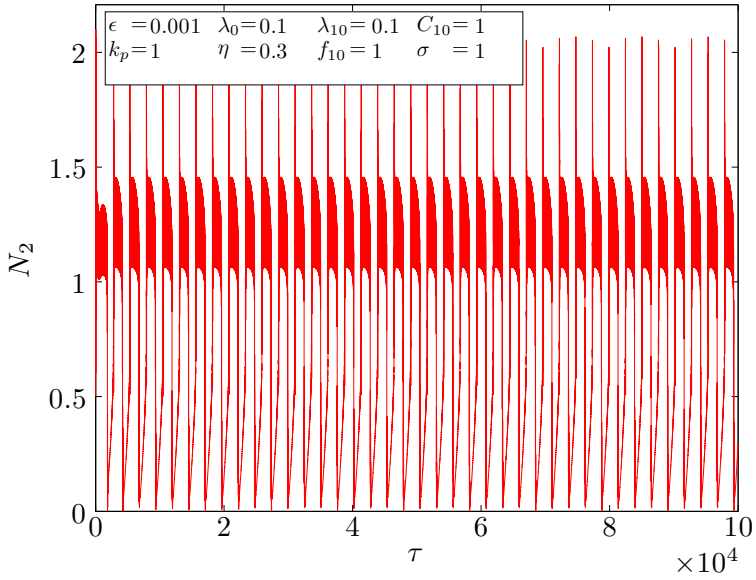


Figure 13: History the N_2 versus time τ for the system under forcing term $f_{10} = 1$.

Appendix

A Averaging ϕ_3

Here, we implement the Galerkin method by using a truncated Fourier series and keeping first harmonic, i.e. $e^{i\tilde{\tau}}$.

ϕ_3 is in relation with the u. u depends on the displacement x, which can be written as (35):

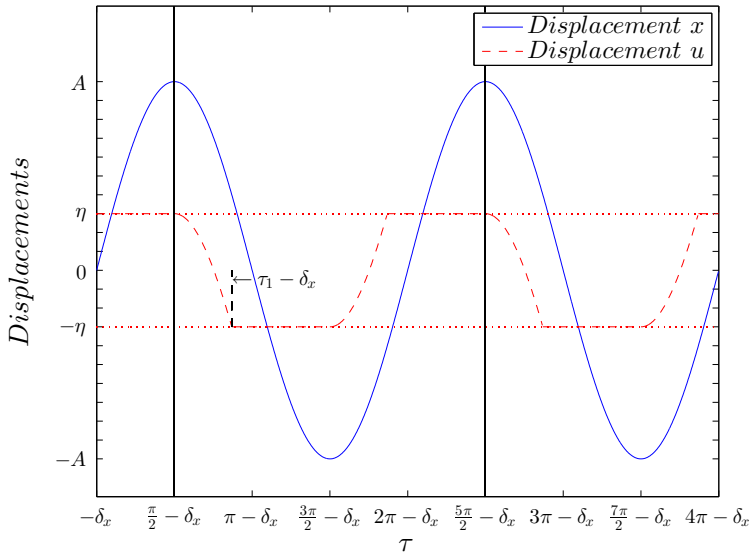


Figure 14: Displacements x and u

$$x(\tilde{\tau}) = A_x \sin(\tilde{\tau} + \delta_x) \tag{35}$$

where:

$$\Omega A_x = \frac{|\phi_1 + \epsilon\phi_2|}{1+\epsilon} \ \ and \ \ \delta_x = Arg\Big(\frac{\phi_1 + \epsilon\phi_2}{1+\epsilon}\Big) \tag{36}$$

If A_x is smaller than η, Saint-Venant element is only a stiffness, $x = u$, so:

$$\phi_3 = \frac{\phi_1 + \epsilon\phi_2}{1+\epsilon} \tag{37}$$

If $A_x > \eta$, the general qualitative behavior of u is presented in Fig. 14. On the interval of $[\frac{\pi}{2} - \delta_x; \frac{5\pi}{2} - \delta_x]$ we have:

$$A_x \cos(\tau_1 - \frac{\pi}{2}) = A_x - 2\eta \ \ so \ \ \tau_1 = \arccos(1 - \frac{2\eta}{A_x}) + \frac{\pi}{2} \tag{38}$$

then,

$$\begin{aligned}
\tfrac{\phi_3}{2i\Omega} &= \tfrac{1}{2\pi}\textstyle\int_{\frac{\pi}{2}-\delta_x}^{\frac{5\pi}{2}-\delta_x} e^{-i\tilde{\tau}}u(\tilde{\tau})d\tilde{\tau} = \tfrac{e^{i\delta_x}}{2\pi}\textstyle\int_{\frac{\pi}{2}}^{\frac{5\pi}{2}} e^{-i\tilde{\tau}}u(\tilde{\tau}-\delta_x)d\tilde{\tau} \\
&= \tfrac{e^{i\delta_x}}{2\pi}\Big[\textstyle\int_{\frac{\pi}{2}}^{\tau_1} e^{-i\tilde{\tau}}[x(\tilde{\tau}-\delta_x) - (A_x-\eta)]d\tilde{\tau} + \int_{\tau_1}^{\frac{3\pi}{2}} e^{-i\tilde{\tau}}(-\eta)d\tilde{\tau} \\
&\quad + \textstyle\int_{\frac{3\pi}{2}}^{\tau_1+\pi} e^{-i\tilde{\tau}}[x(\tilde{\tau}-\delta_x) + (A_x-\eta)]d\tilde{\tau} + \int_{\tau_1+\pi}^{\frac{5\pi}{2}} e^{-i\tilde{\tau}}\eta d\tilde{\tau}\Big] \\
&= \tfrac{e^{i\delta_x}}{\pi}\Big[\textstyle\int_{\frac{\pi}{2}}^{\tau_1} e^{-i\tilde{\tau}}x(\tilde{\tau}-\delta_x)d\tilde{\tau} - \int_{\frac{\pi}{2}}^{\tau_1} e^{-i\tilde{\tau}}(A_x-\eta)d\tilde{\tau} - \int_{\tau_1}^{\frac{3\pi}{2}} e^{-i\tilde{\tau}}\eta d\tilde{\tau}\Big] \\
&= \tfrac{e^{i\delta_x}}{\pi}\Big[\textstyle\int_{\frac{\pi}{2}}^{\tau_1} e^{-i\tilde{\tau}}x(\tilde{\tau}-\delta_x)d\tilde{\tau} - i(A_x-\eta)(e^{-i\tau_1}+i) - i\eta(i-e^{-i\tau_1})\Big] \\
&= \tfrac{e^{i\delta_x}}{\pi}\Big[\textstyle\int_{\frac{\pi}{2}}^{\tau_1} e^{-i\tilde{\tau}}x(\tilde{\tau}-\delta_x)d\tilde{\tau} - iA_x(e^{-i\tau_1}+i) + 2i\eta e^{-i\tau_1}\Big] \\
&= \tfrac{e^{i\delta_x}}{\pi}\Big[\tfrac{A_x}{2i}[(\tau_1 - \tfrac{\pi}{2}) - \tfrac{i}{2}(e^{-2i\tau_1}+1)] - iA_x(e^{-i\tau_1}+i) + 2i\eta e^{-i\tau_1}\Big] \\
&= \tfrac{A_x e^{i\delta_x}}{2\pi i}\Big[(\tau_1 - \tfrac{\pi}{2}) + e^{-i(\tau_1+\frac{\pi}{2})}\cos(\tau_1) + 4e^{\frac{i}{2}(\frac{\pi}{2}-\tau_1)}\cos(\tfrac{\tau_1}{2}+\tfrac{\pi}{4}) - \tfrac{4\eta}{A_x}e^{-i\tau_1}\Big]
\end{aligned} \tag{39}$$

with $\bar{\tau_1} = \tau_1 - \frac{\pi}{2}$, we have:

$$\phi_3 = \frac{\phi_1 + \epsilon\phi_2}{(1+\epsilon)\pi}\Big[\bar{\tau_1} + e^{-i\bar{\tau_1}}\sin(\bar{\tau_1}) - 4e^{-i\frac{\bar{\tau_1}}{2}}\sin(\frac{\bar{\tau_1}}{2}) - \frac{4\eta\Omega(1+\epsilon)}{|\phi_1+\epsilon\phi_2|}e^{-i(\bar{\tau_1}+\frac{\pi}{2})}\Big] \tag{40}$$

so with function ξ as notation with $\bar{\tau_1} = \arccos(1 - \frac{2\eta}{A_x})$:

$$\xi(A_x) = \begin{cases} \pi & if \ \ A_x \leqslant \eta \\ \bar{\tau_1} + e^{-i\bar{\tau_1}}\sin(\bar{\tau_1}) - 4e^{-i\frac{\bar{\tau_1}}{2}}\sin(\frac{\bar{\tau_1}}{2}) - \frac{4\eta}{A_x}e^{-i(\bar{\tau_1}+\frac{\pi}{2})} & if \ \ A_x > \eta \end{cases} \tag{41}$$

Final written of ϕ_3 for all values is:

$$\phi_3 = \frac{\phi_1 + \epsilon\phi_2}{(1+\epsilon)\pi}\xi(\frac{|\phi_1+\epsilon\phi_2|}{(1+\epsilon)\Omega}) \tag{42}$$

B Functions f and g

$$
\begin{aligned}
f(N_2,\delta_2) &= (1-C_{10}G(N_2^2))(-\tfrac{f_0}{2}\sin(\delta_2)-\tfrac{(2\sigma+1)\lambda_{10}}{2}N_2-\tfrac{\lambda_0}{2}(1-C_{10}G(N_2^2))N_2 \\
&\quad -\tfrac{k_p}{2}(\mathcal{F}_{im}(N_2)\cos(\Delta\delta)-\mathcal{F}_{re}(N_2)\sin(\Delta\delta))) \\
&\quad -\lambda_{10}(-\tfrac{f_0}{2}\cos(\delta_2)-\tfrac{2\sigma+1}{2}(1-C_{10}G(N_2^2))N_2+\tfrac{\lambda_0\lambda_{10}}{2}N_2+\tfrac{N_2}{2} \\
&\quad +\tfrac{k_p}{2}(\mathcal{F}_{im}(N_2)\sin(\Delta\delta)+\mathcal{F}_{re}(N_2)\cos(\Delta\delta))) \\
g(N_2,\delta_2) &= \lambda_{10}(-\tfrac{f_0}{2}\sin(\delta_2)-\tfrac{(2\sigma+1)\lambda_{10}}{2}N_2-\tfrac{\lambda_0}{2}(1-C_{10}G(N_2^2))N_2 \\
&\quad -\tfrac{k_p}{2}(\mathcal{F}_{im}(N_2)\cos(\Delta\delta)-\mathcal{F}_{re}(N_2)\sin(\Delta\delta))) \\
&\quad (1-C_{10}G(N_2^2)-2C_{10}N_2^2G'(N_2^2))(-\tfrac{f_0}{2}\cos(\delta_2)-\tfrac{2\sigma+1}{2}(1-C_{10}G(N_2^2))N_2 \\
&\quad +\tfrac{\lambda_0\lambda_{10}}{2}N_2+\tfrac{N_2}{2}+\tfrac{k_p}{2}(\mathcal{F}_{im}(N_2)\sin(\Delta\delta)+\mathcal{F}_{re}(N_2)\cos(\Delta\delta)))
\end{aligned}
$$

REFERENCES

[1] A. F. Vakakis, Inducing passive nonlinear energy sinks in vibrating systems, *ASME Journal of Vibration and Acoustics*, **123**, 324–332, 2001.

[2] O. V. Gendelman, L. I. Manevitch, A. F. Vakakis, R. M'Closkey, Energy pumping in nonlinear mechanical oscillators I: dynamics of the underlying hamiltonian systems, *ASME Journal of Applied Mechanics*, **68**, 34–41, 2001.

[3] A. F. Vakakis, O. V. Gendelman, energy pumping in nonlinear mechanical oscillators II: resonance capture. *ASME Journal of Applied Mechanics*, **68**, 42–48, 2001.

[4] A. F. Vakakis, O. V. Gendelman, L. A. Bergman, D. M. McFarland, G. Kerschen, Y. S. Lee, *Nonlinear Trageted Energy Transfer in Mechanical and Structural Systems I*, Springer, 2009.

[5] A. F. Vakakis, O. V. Gendelman, L. A. Bergman, D. M. McFarland, G. Kerschen, Y. S. Lee, *Nonlinear Trageted Energy Transfer in Mechanical and Structural Systems II*, Springer, 2009.

[6] D. M. McFarland, G. Kerschen, J. J. Kowtko, Y. S. Lee, L. A. Bergman, A. F. Vakakis, Experimental investigation of targeted energy transfers in strongly and nonlinearly coupled oscillators, *The Journal of the Acoustical Society of America*, **118**, 791–799, 2005.

[7] G. Kerschen, J. J. Kowtko, D. M. McFarland, L. A. Bergman, A. F. Vakakis, Theoretical and experimental study of multimodal targeted energy transfer in a system of coupled oscillators. *Nonlinear Dynamics*, **47**, 285–309, 2007.

[8] G. Kerschen, J. J. Kowtko, D. M. McFarland, Y. S. Lee, L. A. Bergman, A. F. Vakakis, Experimental demonstration of transient resonance capture in a system of two coupled oscillators with essential stiffness nonlinearity. *Journal of Sound and Vibration*, **299**, 822–838, 2007.

[9] E. Gourdon, N. A. Alexander, C. A. Taylor, C.-H. Lamarque, S. Pernot, Nonlinear energy pumping under transient forcing with strongly nonlinear coupling: theoretical and experimental results. *Journal of Sound and Vibration*, **300**, 522–551, 2007.

[10] Y. S. Lee, G. Kerschen, D. M. McFarland, W. J. Hill, C. Nichkawde, T. W. Strganac, L. A. Bergman, A. F. Vakakis, Suppressing aeroelastic instability using broadband passive targeted energy transfers, part 2: experiments. *AIAA Journal*, **45**, 2391–2400, 2007.

[11] A. Ture Savadkoohi, B. Vaurigaud, C.-H. Lamarque, S. Pernot S., Targeted energy transfer with parallel nonlinear energy sinks, part II: theory and experiments, *Nonlinear dynamics*, **67** , 37–46, 2012.

[12] R. Bellet, B. Cochelin, R. Côte, P.-O. Mattei, Enhancing the dynamic range of targeted energy transfer in acoustics using several nonlinear membrane absorbers. *Journal of Sound and Vibration*, **331** , 5657–5668, 2012.

[13] F. Nucera, A. F. Vakakis, D. M. McFarland, L. A. Bergman, G. Kerschen, Targeted energy transfers in vibro-impact oscillators for seismic mitigation. *Nonlinear Dynamics*, **50**, 651–677, 2007.

[14] Y. S. Lee, F. Nucera, A. F. Vakakis, D. M. McFarland, L. A. Bergman, Periodic orbits, damped transitions and targeted energy transfers in oscillators with vibro-impact attachments. *Physica D*, **238**, 1868–1896, 2009.

[15] O. V. Gendelman, Analytic treatment of a system with a vibro-impact nonlinear energy sink *Journal of Sound and Vibration*, **331**, 4599–4608, 2012.

[16] O.V. Gendelman, Targeted energy transfer in systems with non-polynomial nonlinearity. *Journal of Sound and Vibration*, **315**, 732–745, 2008.

[17] C.-H. Lamarque, O.V. Gendelman, A. Ture Savadkoohi, E. Etcheverria, Targeted energy transfer in mechanical systems by means of non-smooth nonlinear energy sink. *Acta Mechanica*, **221**, 175–200, 2011.

[18] A. Ture Savadkoohi, C.-H. Lamarque, Z. Dimitrijevic, Vibratory energy exchange between a linear and a non-smooth system in the presence of the gravity, *Nonlinear Dynamics*, **70**, 1473–1483, 2012.

[19] F. Schmidt, C.-H. Lamarque, Energy Pumping for Mechanical Systems involving Non-Smooth Saint-Venant terms. *International Journal of Non-Linear Mechanics*, **45**, 866–875, 2010.

[20] J. Bastien, M. Schatzman, C.-H. Lamarque, Study of some rheological models with a finite number of degrees of freedom. *European Journal of Mechanics A/Solids*, **19**, 277–307, 2000.

[21] C.-H. Lamarque, F. Bernardin, J. Bastien, Study of a rheological model with a friction term and a cubic term: deterministic and stochastic cases, *European Journal of Mechanics, A/Solids*, **24**, 572–592, 2005.

[22] C.-H. Lamarque, A. Ture Savadkoohi, E. Etcheverria, Z. Dimitrijevic, Multi-scales dynamics of two coupled non-smooth systems. *International Journal of Bifurcation and Chaos*, **22**, 125029 1–18, 2012.

[23] L. I. Manevitch, The description of localized normal modes in a chain of nonlinear coupled oscillators using complex variables. *Nonlinear Dynamics*, **25**, 95–109, 2001.

[24] A. H. Nayfeh , D. T. Mook, *Nonlinear oscillations*, John Wiley and Sons, 1979.

[25] Y. Starosvetsky , O. V. Gendelman, Strongly modulated response in forced 2DOF oscillatory system with essential mass and potential asymmetry. *Physica D*, **237**: 1719–1733, 2008.

COMPDYN 2013
4th ECCOMAS Thematic Conference on
Computational Methods in Structural Dynamics and Earthquake Engineering
M. Papadrakakis, V. Papadopoulos, V. Plevris (eds.)
Kos Island, Greece, 12–14 June 2013

LIQUID FREE VIBRATION ANALYSIS IN A CIRCULAR CYLINDRICAL RIGID CAVITY USING THE h-p FINITE ELEMENT METHOD

Mohammed Nabil Ouissi[1], **and Sidi Mohammed Hamza Cherif**[2]

[1]University of Tlemcen
Chetoune – Tlemcen - Algeria
n_ouissi@mail.univ-tlemcen.dz

[2]University of Tlemcen
Chetoune – Tlemcen - Algeria
Sm_hamzacherif@mail.univ-tlemcen.dz

Keywords: Hierarchical finite element method, fluid, cylindrical rigid cavity, free vibration, double hierarchical increment.

Abstract. *A new hierarchical finite element is developed to analyze the free vibration of a fluid in a rigid cylindrical cavity. It is a bi-hierarchical four nodes quadrilateral element with three degrees of freedom (three displacements) by node. The specificity of this element is a double increase of the hierarchical mode number independently according to both axial and radial directions. The first advantage is that the solution is accurate for high ratio dimensions cavities. The second advantage is the possibility of using only one element to idealize the fluid. The third advantage is that the pressure and the velocity potential are not considered as unknowns, only the displacements describe the fluid behavior. Through the comparison results, this element gives good results accuracy with simple idealization for a fluid in a rigid cylindrical cavity.*

1 INTRODUCTION

For coupled systems, obtaining analytical solutions is difficult or impossible however, numerical methods based specifically on the finite element method can easily approach the solution. In general, fluid-structure interaction can be divided into five categories; each category requires a language and unknowns that may not suit others. As shown in Figure 1, the category two is characterized by the non existence of the free surface that reduces the phenomenon only to the fluid vibration. The fluid is the only field that can vibrate and therefore deform.

In the added mass approach, a part of the mass of the fluid is added to the structural model along the interface between the two fields. This approach neglects the compressibility of the fluid. In the Eulerian approach ([1], [2]), the velocity potential, the pressure or velocity describe the behaviour of the fluid, while displacements represent the movements of the structure. The solution of the coupled system can then be obtained by solving the two systems separately but by considering the effects of the interaction in an iterative way ([3]).

In the Lagrangian approach, the fluid behaviour is in general described by a field of displacements ([4], [5]). The motion of the fluid and the structure being both described by only one field of displacement, this approach has the advantage of very easily satisfying the compatibility and the equilibrium conditions along the interface. So a fluid structure system in interaction with a complex geometry can effectively be analyzed with this method.

The liquid in this analysis is regarded as nonviscous, irrotational and incompressible. Such simplification allows displacements, pressures or the velocity potentials to be the variables in the liquid field. But for this study, only displacements will be regarded as variables. This allows a compatibility allowing a facility to incorporate the liquid elements in finished programs of element for the structural analysis.

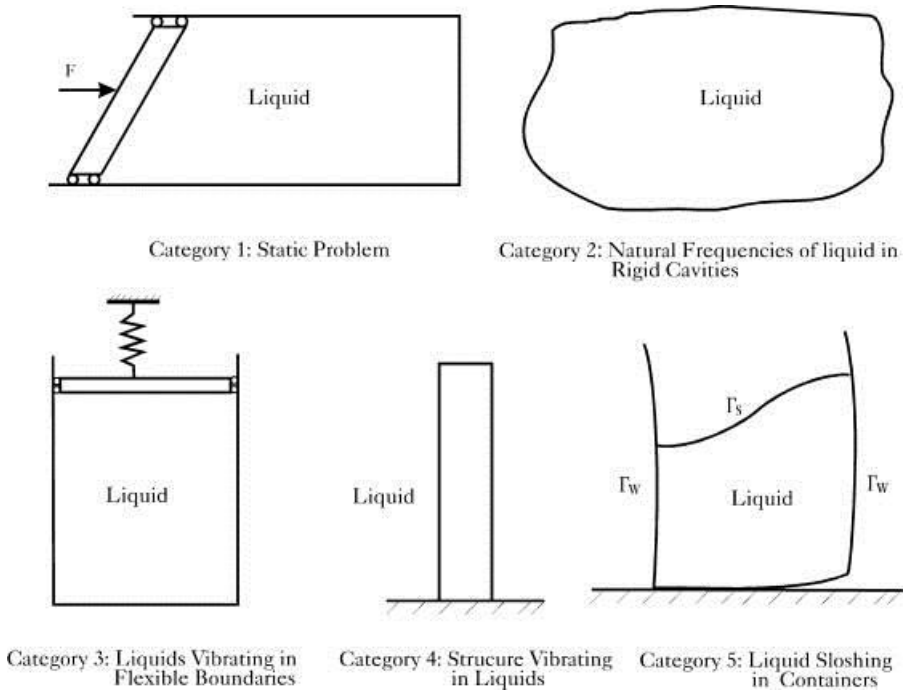


Figure 1: Fluid structure categories

The propose of this work is to present a new displacement based bi-hierarchical finite element to idealize the vibration of a nonviscous, irrotational and incompressible fluid in a cylindrical rigid cavity. This element combined to structural hierarchical finite elements of the same geometrical feathers ([6]) can easily idealize fluid structure interaction. Because of its hierarchical feature, only one element can idealize all the fluid.

2 GOVERNING EQUATION

The fluid motion is governed by the Euler equation:

$$\nabla p = -\rho_f . \dot{v} \tag{1}$$

Where p is the pressure, ∇ is a gradient operator ρ_f is the fluid density and v is the velocity vector of the fluid motion.

In this formulation, velocity and pressure field describe the motion of the fluid. Using the relationship between pressure and volume, one can write:

$$p = -k_f . \nabla^T u \tag{2}$$

Where u is the displacement vector and k_f is the bulk modulus.

Introducing the small amplitude motion assumption expressed by:

$$v = \dot{u} \tag{3}$$

The Euler equation is reduced to an acoustic wave equation:

$$\nabla^2 p = \frac{1}{c^2} . \ddot{p} \tag{4}$$

Where c is the acoustic speed in the fluid given by

$$c = \sqrt{\frac{k_f}{\rho_f}} \tag{5}$$

In the equation (4), only the pressure field describes the fluid motion

The same wave equation can be derived from the following Navier equation for an isotropic, homogeneous and elastic medium:

$$G . \nabla^2 u + \left(k_f + G\right) \nabla \nabla^T u = \rho_f . \ddot{u} \tag{6}$$

Where, G is the shear modulus. For the case of inviscid fluid, the shear modulus equals zero. Equation (6) becomes:

$$k_f . \nabla \nabla^T u = \rho_f . \ddot{u} \tag{7}$$

3 HIERARCHICAL FINITE ELEMENT FORMULATION

The hierarchical finite element method known under the name of the p-version of the finite element method is more precise and its convergence is faster than that of the h-method. Indeed, when the exact solution is analytical everywhere the rate of convergence is exponential, whereas that of the h-method is only algebraic. The quality of the solutions is not very sensitive to the distortions of the elements, which allows the use of flattened elements or great ratio on sides without penalizing the precision too much. The hp version of the finite element method has as a characteristic to increase the precision by increasing both the degree of the polynomial of interpolation and the number of finite elements as for the standard finite element method ([7]).

The equation of motion of the fluid admit the representation of the Radial, circumferential and axial displacement components u, v, and w following respectively R, Z and θ in the following form

$$\begin{cases} u(r,z,\theta) = \bar{u}(r,z).\cos n\theta \\ v(r,z,\theta) = \bar{v}(r,z).\cos n\theta \\ w(r,z,\theta) = \bar{w}(r,z).\sin n\theta \end{cases} \tag{8}$$

Dependence on time is removed by assuming that the displacement varies sinusoidal in phase and at the same frequency. The displacement functions, $\bar{u}(r,z), \bar{v}(r,z)$ and $\bar{w}(r,z)$ are expressed in terms of nodal displacements of the finite element by appropriate interpolation functions.

3.1 Shape functions selection

The hierarchical shape functions are generally selected in the Serendipity space. In this paper, the shape functions are built from the shifted Legendre orthogonal polynomials introduced by ([8]). These polynomials are defined in the interval [0,1]. They can be classified in three categories, nodal shape functions, side shape functions and internal shape functions. Their recurring form is:

$$\begin{cases} f_i(x) = 1 - x \\ f_i(x) = x \\ f_{i+2}(x) = \int_0^x P_i(\alpha).d\alpha \end{cases} \tag{9}$$

Where $P_i(\alpha)$ are the shifted Legendre polynomials defined by :

$$\begin{cases} P_0(\alpha) = 1 \\ P_1(\alpha) = 2.\alpha - 1 \\ P_{i+1}(\alpha) = \dfrac{1}{i+1} \cdot \left[(-2i - 1 + (4i+2)\alpha) \cdot P_i(\alpha) - i \cdot P_{i-1}(\alpha) \right] \qquad \text{i} = 1,2,3,\ldots \end{cases} \tag{10}$$

The shape functions are given on the basis of one-dimensional hierarchical finite element. The origin of the non-dimensional coordinates is at the left end of the element.

Having the shape functions, the displacement functions $\bar{u}(r,z)$, $\bar{v}(r,z)$ and $\bar{w}(r,z)$ can be expressed:

$$\begin{cases} \bar{u}(r,z) = \sum_{1}^{n} N_i(r,z).u_i \\ \bar{v}(r,z) = \sum_{1}^{n} N_i(r,z).v_i \\ \bar{w}(r,z) = \sum_{1}^{n} N_i(r,z).w_i \end{cases} \tag{11}$$

Where $$N_i(r,z) = f_k(r).g_l(z) \tag{12}$$

With: k = 1,..,p+1 et l = 1,..,q+1. p and q being the hierarchical modes number according respectively to ξ and η, and f and g are the shape functions.

A weak form of the expression (7) for a fluid region Ω subject to natural boundary conditions and critical respectively on the boundaries Γ_p and Γ_f can be expressed:

$$\int_{\Omega} \left\{ \rho_f .\tilde{u}^T .\ddot{u} + k_f .\left(\nabla^T \tilde{u}\right)^T .\left(\nabla^T u\right) \right\} d\Omega + \rho_f .g \int_{\Gamma_f} \left(\tilde{u}^T .n\right).\left(n_g^T .u\right) d\Gamma = -\int_{\Gamma_p} \left(\tilde{u}^T .n\right).\bar{p}\, d\Gamma \tag{13}$$

Where $\bar{p}$ is the prescribed pression on Γ_p, n_g the gravity direction vector, n the direction vector normal to corresponding boundary, g the gravitational acceleration, Γ_f the free surface, and $\tilde{u}$ is a virtual displacement field.

The second term of the equation left part, result from the free surface boundary condition relatively to the sloshing movement.

Using the same shape functions matrix for the displacement fields u et $\tilde{u}$, one can write :

$$\{u\} = [N].\{q\} \tag{14}$$

$$\{\tilde{u}\} = [N].\{\tilde{q}\} \tag{15}$$

Where $\{q\}$ is the nodal displacement vector, and $\{\tilde{q}\}$ is an arbitrary constant vector.

Basing on the variationnel form of the expression (13) and replacing u and $\tilde{u}$ by their expressions respectively (14) and (15), one can obtain the following matrix equation:

$$[M_f].\{\ddot{q}\} + \left([K_f] + [S]\right).\{q\} = \{f\} \tag{16}$$

Analogically to (13), this equation gives the mass matrix, the stiffness matrix associated to the volumetric deformation, the sloshing stiffness matrix and the charge vector. the mass and stiffness matrices expressions are respectively:

$$[M_f] = \int_{\Omega} \rho_f .[N]^T .[N] .d\Omega \tag{17}$$

$$\left[K_f\right] = \int_{\Omega} k_f . \left[B_f\right]^T . \left[B_f\right] d\Omega \tag{18}$$

3.2 Idealization of the fluid

The fluid is divided into four nodes hierarchical axisymmetric quadrilateral isoparametric finite elements (Fig.2) with only the volumetric deformation stifeness [K_f]. The element size is arbitrary. They may all be of the same size or may all be different. The fluid can also be idealized by only one element if the geometry is varying linearly or if it is constant.

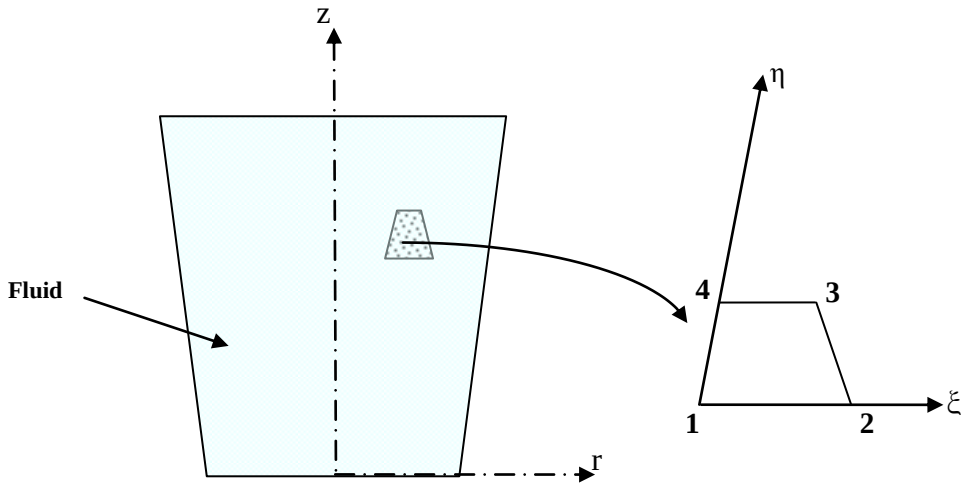


Figure 2: Hierarchical internal axisymmetric fluid finite element

3.2.1 Fluid stiffness matrix

The fluid deformation is given by:

$$\{\nabla\}.\{\delta\} = \frac{\partial u}{\partial r} + \frac{\partial v}{\partial z} + \frac{u}{r} + \frac{1}{r}.\frac{\partial w}{\partial \theta} \tag{19}$$

Where $\{\nabla\}$ is a differential operator. According to generalized displacements, the deformation is written:

$$\{\varepsilon_f\} = \{d_f\}.\{\bar{\delta}\} \tag{20}$$

Where $\{d_f\}$ is a differential operator defined by:

$$\{d_f\} = \left[\left(\frac{\partial}{\partial r} + \frac{1}{r}\right).\cos n\theta \quad \frac{\partial}{\partial z}.\cos n\theta \quad \frac{n}{r}.\cos n\theta\right] \tag{21}$$

The stiffness matrix of the fluid element is given by the expression (18):

$$\left[K_f\right] = \int_{\Omega} k_f .\left[B_f\right]^T .\left[B_f\right] d\Omega$$

Where: k_f is the fluid bulk modulus, Ω is the volume containing the fluid and $\left[B_f\right]$ is a matrix defined by:

$$\left[B_{f\,i}\right] = \left\{d_f\right\}.\left[N_i\right] \tag{22}$$

The element stiffness matrix can be written, as

$$\left[K_{f\,e}\right] = k_f .k.\pi \int_0^1 \int_0^1 \sum_{i=1}^{p+1} \sum_{j=1}^{q+1} \left[B_{f\,i}\right]^T .\left[B_{f\,j}\right] r.\left|J\right| d\xi .d\eta \tag{23}$$

Where k = 2 for n = 0 and k = 1 for n = 1,2,… (n: circumferential wave number)

3.2.2 Fluid mass matrix

The fluid element mass matrix is given by (17):

$$\left[M_f\right] = \int_{\Omega} \rho_f .\left[N\right]^T .\left[N\right] d\Omega$$

Where: ρ_f is the fluid density, and Ω is the volume containing the fluid.

By replacing the matrix $\left[N\right]$ by its submatrices, the fluid element mass matrix can be written:

$$\left[M_{f\,e}\right] = k\pi .\int_0^1 \int_0^1 \rho .\sum_{i=1}^{p+1} \sum_{j=1}^{q+1} \left[N_i\right]^T .\left[N_j\right] \left|J\right| .r.d\xi .d\eta \tag{24}$$

3.4 Numerical integration

The double integral appearing in the forms of the mass and stiffness matrices results in a numerical integration. For his implementation, one uses the Gauss quadrature expressed by:

$$\int_0^1 f(x) d(x) = \sum_{i=1}^{Np} W_i .f(x_i) \tag{25}$$

Where, Np is the integration points number. In order to optimize calculations, the integration points number increase automatically with the of interpolation polynomial degree.

4 RESULTS AND DISCUSSIONS

The convergence and comparison studies must be carried out to ensure the reliability of the results. The results are given by the frequency parameter Ω wich is expressed in terms of the vibration frequency ω by:

$$\Omega = \frac{\omega}{2.\pi} \tag{26}$$

The effectiveness of the proposed fluid element was examined for the vibration of a fluid in a rigid circular cylindrical cavity. It is assumed that the cavity has a radius equal to 1 and a height equal to 1 as shown in Figure (3). The bulk modulus and the density are equal to 1. To validate the results, an ANSYS program has been elaborated, where axisymmetric fluid elements with four nodes were used. Because spurious modes can not be eliminated, the real patterns will be recognized by plotting each mode.

Table 1 shows the convergence of the first six modes in terms of both of hierarchical mode numbers p and q following respectively the radial and axial directions for one and two elements. Considering the square shape of the cavity, the two hierarchical mode numbers will be equal.

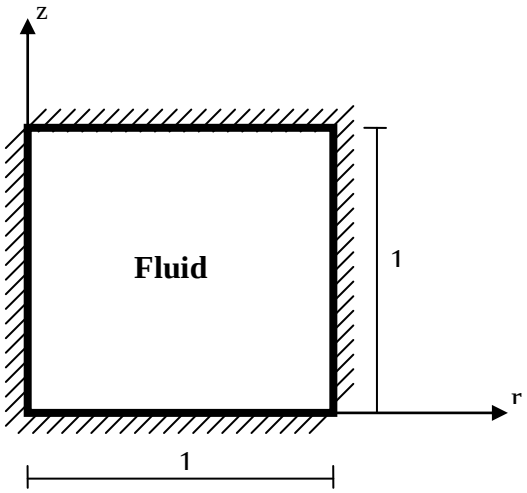


Figure 3: Fluid in a cylindrical rigid cavity

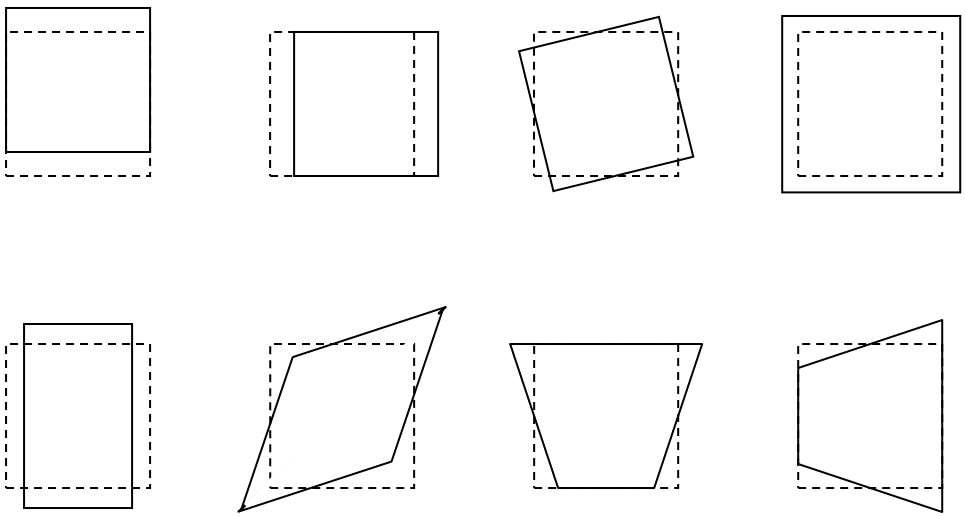


Figure 4: Eight independent displacement modes of a four node fluid element

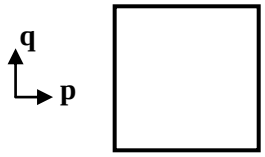
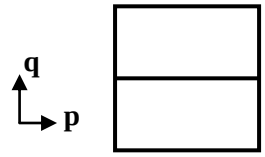
Element number	q	p	Modes							
			1	2	3	4	5	6	7	8
1 	2	2	0.501	0.609	0.789	0.991	1.106	1.152	1.221	1.864
	4	4	0.498	0.605	0.773	0.983	1.091	1.092	1.186	1.483
	6	6	0.496	0.603	0.766	0.970	1.049	1.084	1.157	1.366
	8	8	0.496	0.603	0.766	0.969	1.071	1.079	1.132	1.306
	ANSYS		0.496	0.602	0.757	0.965	1.068	1.077	1.130	1.287
2 	2	2	0.499	0.608	0.785	0.984	1.101	1.136	1.216	1.787
	4	4	0.497	0.604	0.770	0.979	1.082	1.087	1.183	1.411
	6	6	0.496	0.603	0.766	0.969	1.073	1.082	1.145	1.364
	8	8	0.496	0.603	0.766	0.969	1.071	1.079	1.132	1.296
	ANSYS		0.496	0.602	0.757	0.965	1.068	1.077	1.130	1.287

Table 1: Convergence and frequency parameter comparison of a fluid in a circular cylindrical cavity (R =1, H=1).

Table (1) show that for the two idealization one and two elements, an accuracy of two digits after the comma is reached for the first two modes for p=2 and q=2.

For modes 3, 4, 5; the convergence is reached for p=6 and q=6 for a one element model, and for p=4 and q=4 for a two elements model. The sixth mode reaches the convergence for p=8 and q=8 for one element, and p=6 and q=6 for two elements.

It is apparent that by increasing the number of elements, the hierarchical mode numbers p and q necessary to reach convergence are smaller. But the degrees of freedom number becomes more important. The matrices size is smaller if one increases p and q rather than the elements number.

The figure (4) shows the eight independant modes of a four node fluid element. The first six modes are constant-strain modes and the other two are bending modes. One can found these two kind of modes for the bi-hierarchical fluid element in figure (5). The first five modes are constant-strain modes and the other three are bending modes. These modes show the shift of a liquid relative to the walls while being in contact, which reflects the modeling of the interaction that is imposing the same normal displacement to the sides. In this case, the normal displacement is equal to zero because the liquid is in a rigid cavity.

5 CONCLUSION

The bi-hierarchical fluid finite elements presented in this study are able to give accurate frequencies for fluids in axisymmetric cylindrical cavities. The results show clearly that these elements can be easily used for the analysis of the free vibration of a fluid in a closed cavity. With this element one is not constrained any more to have the same number of hierarchical modes in the two main directions (radial and axial) to idealize a fluid in a cavity wich can be slender or lowered. Also, only one element can idealize a fluid in a rigid cavity. Finally these bi-hierarchical finite elements allows triple increase in the accuracy, finite elements number, and radial and axial hierarchical modes numbers.

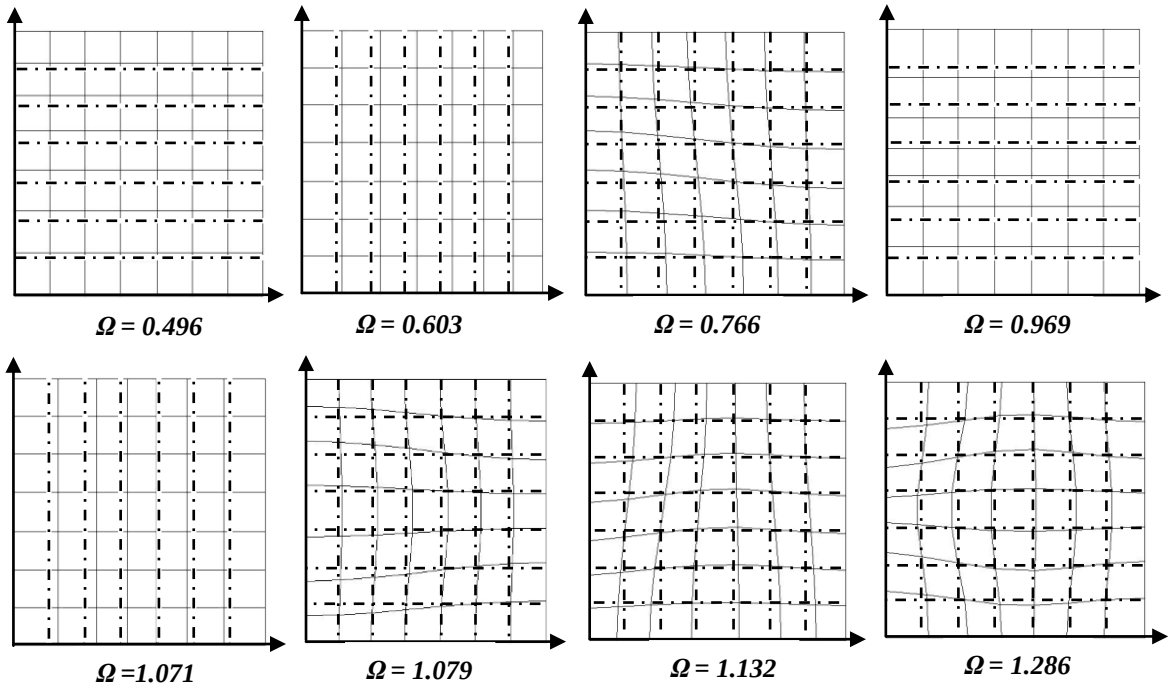


Figure 4: First height acoustic modes of a liquid in a cylindrical rigid cavity

REFERENCES

[1] Haroun, M. A., 1983. Vibration Studies and Tests of Liquid Storage Tanks. J. of Earth. Engng and Struc. Dyn., 11, 179-206.

[2] Veletsos, A.S., Tang, Y. & Tang, H., 1990. Soil-Structure Interaction Effects for Liquid Containing Storage Tanks. Proceedings of the Fourth U.S. National Conference on Earthquake Engineering, California.

[3] Nomura, T. and Hughes, T. J. R., 1992. An arbitrary Lagrangian Eulerian finite element method for interaction of fluid and a rigid body, Comp. Meth . Appl. Mech. Engng., 95, 115-138.

[4] Wilson, E., & Khalvati, M., 1983. Finite Elements For the Dynamic Analysis of Fluid-Solid Systems. International Journal of Numerical Methods in Engineering, 19, 1657-1668.

[5] Chen HC, Taylor RL. 1990. Vibration analysis of fluid-solid systems using a finite element displacement formulation. Int J Numer Methods Eng. 29:683-698.

[6] Ouissi, M.N.,& Houmat, *A. 2009,* Non axisymmetric free vibration analysis of linearly varying thickness shells of revolution by a bi-hierarchical finite element. *Latin American Journal of Solids and Structures,* Vol 6, No 2. 105-129.

[7] Szabo B.A. & Babuska I., Finite element analysis. John Wiley & Sons, 1991.

[8] Houmat A., 2004. Three dimensional hierarchical finite element free vibration analysis of annular sector plates. Journal of Sound and Vibrations. 276, 181-193.

COMPDYN 2013
4th ECCOMAS Thematic Conference on
Computational Methods in Structural Dynamics and Earthquake Engineering
M. Papadrakakis, V. Papadopoulos, V. Plevris (eds.)
Kos Island, Greece, 12–14 June 2013

NONLINEAR DYNAMIC ANALYSIS OF PLATES STIFFENED BY PARALLEL BEAMS WITH DEFORMABLE CONNECTION

J. A. Dourakopoulos[1] and E. J. Sapountzakis[2]

[1] School of Civil Engineering, National Technical University
Zografou Campus, GR-157 80 Athens, Greece
e-mail: jdour@mail.ntua.gr

[2]e-mail: cvsapoun@central.ntua.gr

Keywords: Elastic stiffened plate, plate reinforced with beams, nonlinear dynamic analysis, slab-and-beam structure, deformable connection.

Abstract. *In this paper a general solution to the geometrically nonlinear dynamic analysis of plates stiffened by arbitrarily placed parallel beams of arbitrary doubly symmetric cross section, subjected to arbitrary dynamic loading is presented. The plate-beam structure is assumed to undergo moderate large deflections and the nonlinear analysis is carried out by retaining nonlinear terms in the kinematical relations. According to the proposed model, the arbitrarily placed parallel stiffening beams are isolated from the plate by sections in the lower outer surface of the plate, making the hypothesis that the plate and the beams can slip in all directions of the connection without separation (i.e. uplift neglected) and taking into account the arising tractions in all directions at the fictitious interfaces. These tractions are integrated with respect to each half of the interface width resulting in two interface lines, along which the loading of the beams as well as the additional loading of the plate is defined. Their unknown distribution is established by applying continuity conditions in all directions at the interfaces taking into account their relation with the interface slip through the shear connector stiffness. The utilization of two interface lines for each beam enables the nonuniform distribution of the interface transverse shear forces and the nonuniform torsional response of the beams to be taken into account describing better in this way the actual response of the plate–beams system. Six boundary value problems are formulated and solved using the Analog Equation Method (AEM), a BEM-based method. Application of the boundary element technique leads to a nonlinear coupled system of equations of motion, which is solved employing a distributed mass model. Both free and forced transverse vibrations are considered and numerical examples with great practical interest are presented demonstrating the effectiveness, wherever possible the accuracy and the range of applications of the proposed method. The adopted model permits the evaluation of the shear forces at the interfaces in both directions, the knowledge of which is very important in the design of prefabricated ribbed plates.*

1 INTRODUCTION

Stiffened plate panels are structural elements of practical importance in applications such as ship superstructures, bridge decks and aircraft structures. Stiffening of the plate provides the benefit of added load-carrying capability with a relatively small additional weight penalty, while buckling is prevented especially in case of in-plane loading. The unique peculiarities of the aforementioned structures are obtained due to the behavior of the bond between the plate and the beams; however this bond is the usual reason why these structures are prone to failure. Moreover, since these stiffened plates are frequently subjected to dynamic loading such as air blasts or underwater explosions, a clear understanding of the dynamic response requires development of an efficient dynamic analysis capability.

When the deflections of the structure are small, a wide range of linear analysis tools, such as modal analysis, can be used and some analytical results are possible. As the deflections become larger, the induced geometric nonlinearities result in effects that are not observed in linear systems, making therefore the determination of an analytical solution extremely difficult and in most cases impossible. Moreover, having in mind the importance of weight saving in engineering structures, the study of nonlinear effects in the analysis (large deflection analysis) of stiffened plates becomes essential. These nonlinearities result from retaining the squares of the slopes in the strain–displacement relations (intermediate nonlinear theory), avoiding in this way the inaccuracies arising from a linear or a linearized second-order analysis.

The behavior of composite slab-and-beam structure is affected significantly by the deformability of the shear connection between plate and beams. Therefore, much research effort has been done concerning the linear dynamic analysis of composite beams with deformable connections. On the other hand, less research effort has been made on the free or forced dynamic analysis, taking also account the geometric nonlinearities.

In this paper, a general solution to the geometrically nonlinear dynamic analysis of plates stiffened by arbitrarily placed parallel beams of arbitrary doubly symmetric cross section with deformable connections subjected to arbitrary dynamic loading is presented. The solution is based on the structural model proposed by Sapountzakis and Mokos in [1], according to which the stiffening beams are isolated from the plate by sections in the lower outer surface of the plate, making the hypothesis that the plate and the beams can slip in all directions of the connection without separation (i.e. uplift is neglected) and taking into account the arising tractions in all directions at the fictitious interfaces. These tractions are integrated with respect to each half of the interface width resulting in two interface lines, along which the loading of the beams as well as the additional loading of the plate is defined. The unknown distribution of the aforementioned integrated tractions is established by applying continuity conditions in all directions at the two interface lines taking into account their relationship with the interface slip through the shear connector stiffness. Any distribution of connectors in each direction of the interfaces can be handled. The utilization of two interface lines for each beam enables the nonuniform torsional response of the beams to be taken into account as the angle of twist is indirectly equated with the corresponding plate slope. Six boundary value problems are formulated and solved using the Analog Equation Method (AEM) [2], a BEM based method.

The essential features and novel aspects of the present formulation are summarized as follows.

- The adopted model permits the evaluation of the longitudinal and transverse in-plane shear forces at the interfaces between the plate and the beams in the geometrically nonlinear dynamic analysis of the stiffened plate, taking into account the influence of interface slip, the knowledge of which is very important in the design of shear connectors in plate-beam structures.

- Utilization of two interface lines permits the nonuniform distribution of the in-plane forces along the interface width to be taken into account.
- Both free and forced transverse vibrations are considered taking into account geometric nonlinearities.
- The stiffened plate is of arbitrary shape and is subjected to arbitrary dynamic loading, while both the number and the placement of the parallel beams are also arbitrary (eccentric beams are included).
- The cross section of the stiffening beams is an arbitrary doubly symmetric thin or thick-walled one. The formulation does not stand on the assumption of a thin-walled structure and therefore the cross section's torsional and warping rigidities are evaluated "exactly" in a numerical sense employing the BEM (requiring only boundary discretization for the cross sectional analysis).
- The plate and the beams are supported by the most general boundary conditions including elastic support or restraint.
- The nonuniform torsion in which the stiffening beams are subjected is taken into account by solving the corresponding problem and by comprehending the arising twisting and warping in the corresponding displacement continuity conditions. The distributed warping moment arising from the nonuniform distribution of longitudinal in-plane forces is also taken into account.
- Contrary to previous research efforts where the numerical analysis is based on BEM using a lumped mass assumption model after evaluating the flexibility matrix at the mass nodal points, in this work a distributed mass model is employed.

Based on the numerical solution developed, several examples with great practical interest are presented, demonstrating the effectiveness, wherever possible the accuracy and the range of applications of the proposed method.

2 STATEMENT OF THE PROBLEM

Let us consider a thin plate of homogeneous, isotropic and linearly elastic material with modulus of elasticity E_p, volume mass density ρ_p, shear modulus G_p and Poisson's ratio ν_p, having constant thickness h_p and occupying the two-dimensional multiply connected region Ω of the xy plane bounded by the piecewise Γ_j ($j=0,1,2,...,K$) boundary curves. The plate is stiffened by a set of $i=1,2,...,I$ arbitrarily placed parallel beams of arbitrary doubly symmetric cross section of area A_b^i and length l^i. The material of the beams is considered to be homogeneous, isotropic and linearly elastic with modulus of elasticity E_b^i, mass density ρ_b^i, shear modulus G_b^i and Poisson's ratio ν_b^i. For the sake of convenience the x axis is taken parallel to the beams of length l^i which may have either internal or boundary point supports. The stiffened plate is subjected to the arbitrary lateral dynamic load, $g=g(\mathbf{x},t)$, $\mathbf{x}:\{x,y\}, t\geq 0$. Owing to this loading, the plate and the beams can slip in all directions of the connection without separation (i.e. uplift is neglected). For the analysis of the aforementioned problem a global coordinate system Oxy for the analysis of the plate and local coordinate ones $C^i x^i y^i$ corresponding to the centroid axes of each beam are employed (Figure 1).

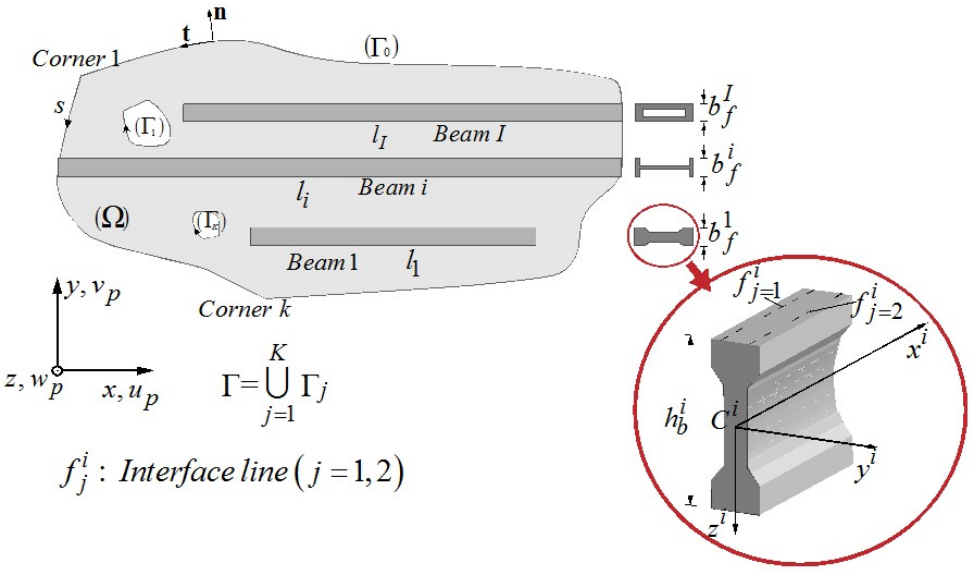


Figure 1: Two dimensional region Ω occupied by the plate.

The solution of the problem at hand is approached employing the improved model proposed by Sapountzakis and Mokos in [1]. According to this model, the stiffening beams are isolated from the plate by sections in its lower outer surface, taking into account the arising tractions at the fictitious interfaces (Figure 2). Integration of these tractions along each half of the width of the i-th beam results in line forces per unit length in all directions in two interface lines, which are denoted by q_{xj}^i, q_{yj}^i and q_{zj}^i $(j=1,2)$ encountering in this way the nonuniform distribution of the interface transverse shear forces q_y^i, which in previous models [3] was ignored. The aforementioned integrated tractions result in the loading of the i-th beam as well as the additional loading of the plate. Their distribution is unknown and can be established by imposing displacement continuity conditions in all directions along the two interface lines, enabling in this way the nonuniform torsional response of the beams to be taken into account. The arising additional loading at the middle surface of the plate and the loading along the centroid of each beam (Figure 3) can be summarized as follows:

a. In the plate (at the traces of the two interface lines j=1,2 of the i-th plate-beam interface)

(i) An in-plane line body force q_{xj}^i at the middle surface of the plate.

(ii) An in-plane line body force q_{yj}^i at the middle surface of the plate.

(iii) A lateral line load q_{zj}^i.

(iv) A lateral line load $\partial m_{pyj}^i / \partial x$ due to the eccentricity of the component q_{xj}^i from the middle surface of the plate. $m_{pyj}^i = q_{xj}^i h_p / 2$ is the bending moment.

(v) A lateral line load $\partial m_{pxj}^i / \partial y$ due to the eccentricity of the component q_{yj}^i from the middle surface of the plate. $m_{pxj}^i = q_{yj}^i h_p / 2$ is the bending moment.

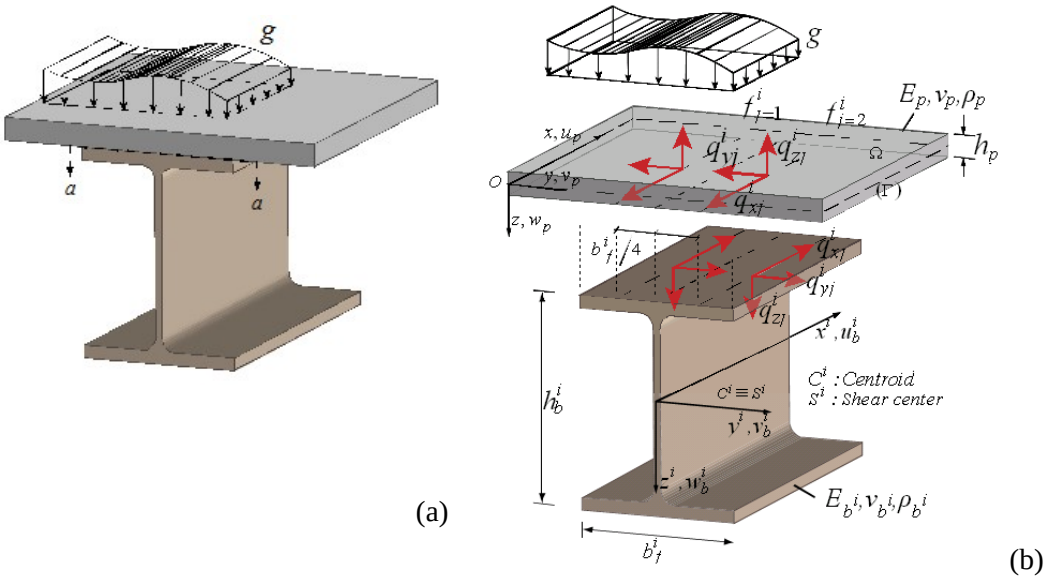


Figure 2: Thin elastic plate stiffened by beams (a) and isolation of the beams from the plate (b).

b. In each (i-th) beam ($C^i x^i y^i z^i$ system of axes)

(i) An axially distributed line load q_{xj}^i along the beam centroid axis $C^i x^i$.

(ii) A transversely distributed line load q_{yj}^i along the beam centroid axis $C^i x^i$.

(iii) A perpendicularly distributed line load q_{zj}^i along the beam centroid axis $C^i x^i$.

(iv) A distributed bending moment $m_{byj}^i = q_{xj}^i e_{zj}^i$ along $C^i y^i$ local beam centroid axis due to the eccentricities e_{zj}^i of the components q_{xj}^i from the beam centroid axis. $e_{z1}^i = e_{z2}^i = -h_b^i/2$ are the eccentricities.

(v) A distributed bending moment $m_{bzj}^i = -q_{xj}^i e_{yj}^i$ along $C^i z^i$ local beam centroid axis due to the eccentricities e_{yj}^i of the components q_{xj}^i from the beam centroid axis. $e_{y1}^i = -b_f^i/4$, $e_{y2}^i = b_f^i/4$ are the eccentricities.

(vi) A distributed twisting moment $m_{bxj}^i = q_{zj}^i e_{yj}^i - q_{yj}^i e_{zj}^i$ along $C^i x^i$ local beam shear center axis due to the eccentricities e_{zj}^i , e_{yj}^i of the components q_{yj}^i , q_{zj}^i from the beam shear center axis, respectively. $e_{z1}^i = e_{z2}^i = -h_b^i/2$ and $e_{y1}^i = -b_f^i/4$, $e_{y2}^i = b_f^i/4$ are the eccentricities.

(vii) A distributed warping moment $m_{bwj}^i = -q_{xj}^i \left(\varphi_S^{Pi}\right)_{fj}$ along $C^i x^i$ local beam shear center axis, which in previous models [1, 3] was ignored. $\left(\varphi_S^{Pi}\right)_{fj}$ is the value of the

primary warping function φ_S^{Pi} with respect to the shear center of the beam cross section (coinciding with its centroid) at the point of the j-th interface line of the i-th plate – beam interface.

On the base of the above considerations the response of the plate and the beams may be described by the following boundary value problems.

a. For the plate

The analysis of the plate is based on the Von Kármán plate theory, according to which the deflection of the plate cannot be regarded as small as compared to the plate thickness, while it remains small in comparison with the rest dimensions of the plate. Due to this assumption, geometrical nonlinearities should be taken into account and the displacement field of an arbitrary point of the plate, as implied by the Kirchhoff hypothesis, is given as

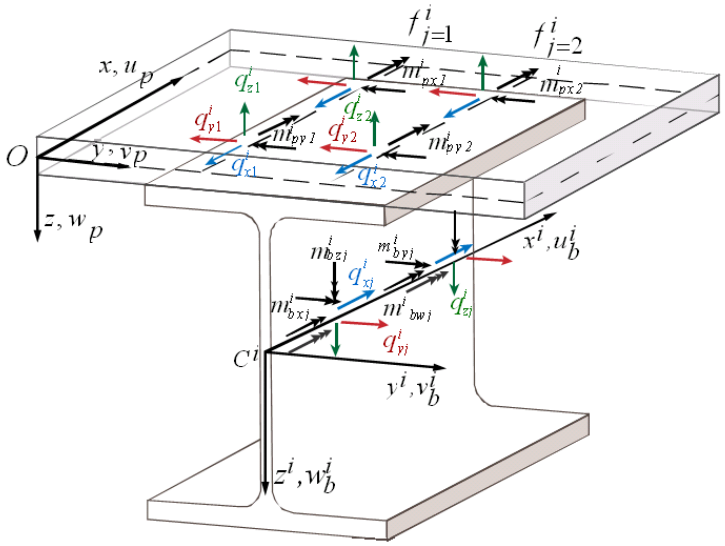


Figure 3: Structural model and directions of the additional loading of the plate and the i-th beam.

$$\bar{u}_p(x,y,z,t) = u_p(x,y,t) - z\frac{\partial w_p(x,y,t)}{\partial x} \tag{1a}$$

$$\bar{v}_p(x,y,z,t) = v_p(x,y,t) - z\frac{\partial w_p(x,y,t)}{\partial y} \tag{1b}$$

$$\bar{w}_p(x,y,z,t) = w_p(x,y,t) \tag{1c}$$

where $\bar{u}_p$, $\bar{v}_p$, $\bar{w}_p$, $t \geq 0$ are the time dependent in-plane and transverse displacement components of an arbitrary point of the plate and $u_p = u_p(\mathbf{x},t)$, $v_p = v_p(\mathbf{x},t)$ and $w_p = w_p(\mathbf{x},t)$ $\mathbf{x}:\{x,y\}, t \geq 0$ are the corresponding components of a point at its middle surface. Employing the strain-displacement relations of the three-dimensional elasticity for moderate large displacements and the stress-strain relations defined by the Hooke's law, the non-vanishing components of the second Piola – Kirchhoff stress tensor are obtained as

$$S_{xx}=\frac{E_p}{\left(1-\nu_p^2\right)}\left\{\left[\frac{\partial u_p}{\partial x}-z\frac{\partial^2 w_p}{\partial x^2}+\frac{1}{2}\left(\frac{\partial w_p}{\partial x}\right)^2\right]+\nu_p\left[\frac{\partial v_p}{\partial y}-z\frac{\partial^2 w_p}{\partial y^2}+\frac{1}{2}\left(\frac{\partial w_p}{\partial y}\right)^2\right]\right\} \tag{2a}$$

$$S_{yy}=\frac{E_p}{\left(1-\nu_p^2\right)}\left\{\nu_p\left[\frac{\partial u_p}{\partial x}-z\frac{\partial^2 w_p}{\partial x^2}+\frac{1}{2}\left(\frac{\partial w_p}{\partial x}\right)^2\right]+\left[\frac{\partial v_p}{\partial y}-z\frac{\partial^2 w_p}{\partial y^2}+\frac{1}{2}\left(\frac{\partial w_p}{\partial y}\right)^2\right]\right\} \tag{2b}$$

$$S_{xy}=\frac{E_p}{2\left(1+\nu_p\right)}\left(\frac{\partial u_p}{\partial y}+\frac{\partial v_p}{\partial x}-2z\frac{\partial^2 w_p}{\partial x\partial y}+\frac{\partial w_p}{\partial x}\frac{\partial w_p}{\partial y}\right) \tag{2c}$$

Subsequently, integrating the stress components over the plate thickness, the stress resultants acting on the plate are written as

$$N_{px}=C\left[\frac{\partial u_p}{\partial x}+\nu_p\frac{\partial v_p}{\partial x}+\frac{1}{2}\left(\frac{\partial w_p}{\partial x}\right)^2+\frac{1}{2}\nu_p\left(\frac{\partial w_p}{\partial y}\right)^2\right] \tag{3a}$$

$$N_{py}=C\left[\frac{\partial v_p}{\partial x}+\nu_p\frac{\partial u_p}{\partial x}+\frac{1}{2}\left(\frac{\partial w_p}{\partial y}\right)^2+\frac{1}{2}\nu_p\left(\frac{\partial w_p}{\partial x}\right)^2\right] \tag{3b}$$

$$N_{pxy}=C\frac{1-\nu_p}{2}\left(\frac{\partial u_p}{\partial y}+\frac{\partial v_p}{\partial x}+\frac{\partial w_p}{\partial y}\frac{\partial w_p}{\partial x}\right) \tag{3c}$$

$$M_{px}=-D\left(\frac{\partial^2 w_p}{\partial x^2}+\nu_p\frac{\partial^2 w_p}{\partial y^2}\right) \tag{3d}$$

$$M_{py}=-D\left(\frac{\partial^2 w_p}{\partial y^2}+\nu_p\frac{\partial^2 w_p}{\partial x^2}\right) \tag{3e}$$

$$M_{pxy}=-D\left(1-\nu_p\right)\frac{\partial^2 w_p}{\partial x\partial y} \tag{3f}$$

where $C=E_p h_p\Big/\left(1-\nu_p^2\right)$, $D=E_p h_p^3\Big/12\left(1-\nu_p^2\right)$ are the membrane and bending rigidities of the plate, respectively.

On the basis of Hamilton's principle, the system of differential equations of motion of the plate can be expressed in terms of the displacement components as

$$G_p h_p\left[\nabla^2 u_p+\frac{1+\nu_p}{1-\nu_p}\frac{\partial}{\partial x}\left(\frac{\partial u_p}{\partial x}+\frac{\partial v_p}{\partial y}\right)+\left(\frac{2}{1-\nu_p}\frac{\partial^2 w_p}{\partial x^2}+\frac{\partial^2 w_p}{\partial y^2}\right)\frac{\partial w_p}{\partial x}+\frac{1+\nu_p}{1-\nu_p}\frac{\partial^2 w_p}{\partial x\partial y}\frac{\partial w_p}{\partial y}\right]-$$

$$-\rho_p h_p\ddot{u}_p=\sum_{i=1}^{I}\left(\sum_{j=1}^{2}q_{xj}^{i}\delta\left(y-y_j\right)\right) \tag{4a}$$

$$G_p h_p \left[\nabla^2 v_p + \frac{1+\nu_p}{1-\nu_p} \frac{\partial}{\partial y} \left(\frac{\partial u_p}{\partial x} + \frac{\partial v_p}{\partial y} \right) + \left(\frac{2}{1-\nu_p} \frac{\partial^2 w_p}{\partial y^2} + \frac{\partial^2 w_p}{\partial x^2} \right) \frac{\partial w_p}{\partial y} + \frac{1+\nu_p}{1-\nu_p} \frac{\partial^2 w_p}{\partial x \partial y} \frac{\partial w_p}{\partial x} \right] -$$

$$-\rho_p h_p \ddot{v}_p = \sum_{i=1}^{I} \left(\sum_{j=1}^{2} q_{yj}^i \delta\left(y - y_j\right) \right) \tag{4b}$$

$$D\nabla^4 w_p - C \left\{ \left[\left(\frac{\partial u_p}{\partial x} + \frac{1}{2} \left(\frac{\partial w_p}{\partial x} \right)^2 \right) + \nu_p \left(\frac{\partial v_p}{\partial y} + \frac{1}{2} \left(\frac{\partial w_p}{\partial y} \right)^2 \right) \right] \frac{\partial^2 w_p}{\partial x^2} + \left(1-\nu_p\right) \cdot \right.$$

$$\cdot \left(\frac{\partial u_p}{\partial y} + \frac{\partial v_p}{\partial x} + \frac{\partial w_p}{\partial x} \frac{\partial w_p}{\partial y} \right) \frac{\partial^2 w_p}{\partial x \partial y} + \left[\left(\frac{\partial v_p}{\partial y} + \frac{1}{2} \left(\frac{\partial w_p}{\partial y} \right)^2 \right) + \nu_p \left(\frac{\partial u_p}{\partial x} + \frac{1}{2} \left(\frac{\partial w_p}{\partial x} \right)^2 \right) \right] \cdot$$

$$\left. \cdot \frac{\partial^2 w_p}{\partial y^2} \right\} + \rho_p h_p \ddot{w}_p - \rho_p h_p \ddot{u}_p \frac{\partial w_p}{\partial x} - \rho_p h_p \ddot{v}_p \frac{\partial w_p}{\partial y} - \frac{\rho_p {h_p}^3}{12} \frac{\partial^2 \ddot{w}_p}{\partial x^2} - \frac{\rho_p {h_p}^3}{12} \frac{\partial^2 \ddot{w}_p}{\partial y^2} =$$

$$= g - \sum_{i=1}^{I} \left[\sum_{j=1}^{2} \left(q_{zj}^i + \frac{\partial m_{pxj}^i}{\partial y} + \frac{\partial m_{pyj}^i}{\partial x} - q_{xj}^i \frac{\partial w_{pj}^i}{\partial x} - q_{yj}^i \frac{\partial w_{pj}^i}{\partial y} \right) \delta\left(y - y_j\right) \right] \tag{4c}$$

where $\delta\left(y - y_i\right)$ is the Dirac's delta function in the y direction.

The governing differential equations (4a)-(4c) are also subjected to the pertinent boundary conditions of the problem at hand

$$a_{p1} u_{pn} + a_{p2} N_{pn} = a_{p3} \tag{5a}$$

$$\beta_{p1} u_{pt} + \beta_{p2} N_{pt} = \beta_{p3} \tag{5b}$$

$$\gamma_{p1} w_p + \gamma_{p2} R_{pn} = \gamma_{p3} \tag{5c}$$

$$\delta_{p1} \frac{\partial w_p}{\partial n} + \delta_{p2} M_{pn} = \delta_{p3} \tag{5d}$$

$$\varepsilon_{1k} w_p + \varepsilon_{2k} \left\| T w_p \right\|_k = \varepsilon_{3k}, \quad \varepsilon_{2k} \neq 0 \tag{5e}$$

and to the initial conditions

$$w_p\left(\mathbf{x}, 0\right) = w_{p0}\left(\mathbf{x}\right) \tag{6a}$$

$$\dot{w}_p\left(\mathbf{x}, 0\right) = \overline{w}_{p0}\left(\mathbf{x}\right) \tag{6b}$$

where a_{pl}, β_{pl}, γ_{pl}, δ_{pl} $(l = 1,2,3)$ are functions specified at the boundary Γ; ε_{lk} $(l = 1,2,3)$ are functions specified at the k corners of the plate; $w_{p0}\left(\mathbf{x}\right), \overline{w}_{p0}\left(\mathbf{x}\right)$, $\mathbf{x}:\{x, y\}$ are the initial deflection and velocity of the points of the middle surface of the plate; u_{pn}, u_{pt} and N_{pn}, N_{pt} are the boundary membrane displacements and forces in the normal and tangential directions to the boundary, respectively; R_{pn} and M_{pn} are the effective reaction along the boundary and the bending moment normal to it, respectively, which employing intrinsic

coordinates (i.e. the distance along the outward normal n to the boundary and the arc length s) are written as

$$R_{pn} = -D\left[\frac{\partial}{\partial n}\nabla^2 w_p - \left(\nu_p - 1\right)\frac{\partial}{\partial s}\left(\frac{\partial^2 w_p}{\partial s \partial n} - \kappa\frac{\partial w_p}{\partial s}\right)\right] + N_{pn}\frac{\partial w_p}{\partial n} + N_{pt}\frac{\partial w_p}{\partial s} \tag{7a}$$

$$M_{pn} = -D\left[\nabla^2 w_p + \left(\nu_p - 1\right)\left(\frac{\partial^2 w_p}{\partial s^2} + \kappa\frac{\partial w_p}{\partial n}\right)\right] \tag{7b}$$

in which $\kappa(s)$ is the curvature of the boundary. Finally, $\left\|Tw_p\right\|_k$ is the discontinuity jump of the twisting moment Tw_p at the corner k of the plate, while Tw_p along the boundary is given by the following relation

$$Tw_p = D\left(\nu_p - 1\right)\left(\frac{\partial^2 w_p}{\partial s \partial n} - \kappa\frac{\partial w_p}{\partial s}\right) \tag{8}$$

The boundary conditions (5a)-(5d) are the most general boundary conditions for the plate problem including also elastic support, while the corner condition (5e) holds for free or transversely elastically restrained corners *k*. It is apparent that all types of the conventional boundary conditions can be derived from these equations by specifying appropriately the functions a_{pl}, β_{pl}, γ_{pl} and δ_{pl} ($l = 1,2,3$) (e.g. for a clamped edge it is $a_{p1} = \beta_{p1} = \gamma_{p1} = \delta_{p1} = 1$, $a_{p2} = a_{p3} = \beta_{p2} = \beta_{p3} = \ = \gamma_{p2} = \gamma_{p3} = \delta_{p2} = \delta_{p3} = 0$).

b. For each (i-th) beam.

Each beam undergoes transverse deflection with respect to z^i and y^i axes, as well as axial deformation and nonuniform angle of twist along x^i axis. Based on the Bernoulli theory, the displacement field of an arbitrary point of a cross section (taking into account moderate large displacements and considering the angle of rotation of twist to have relatively small values) can be derived with respect to those of its centroid as

$$\bar{u}_b^i\left(x^i, y^i, z^i, t\right) = u_b^i\left(x^i, t\right) - y^i\theta_{bz}^i\left(x^i, t\right) + z^i\theta_{by}^i\left(x^i, t\right) + \frac{\partial\theta_{bx}^i}{\partial x^i}\varphi_S^{Pi}\left(y^i, z^i, t\right) \tag{9a}$$

$$\bar{v}_b^i\left(x^i, y^i, z^i, t\right) = v_b^i\left(x^i, t\right) - z^i\theta_{bx}^i\left(x^i, t\right) \tag{9b}$$

$$\bar{w}_b^i\left(x^i, y^i, z^i, t\right) = w_b^i\left(x^i, t\right) + y^i\theta_{bx}^i\left(x^i, t\right) \tag{9c}$$

$$\theta_{by}^i\left(x^i, t\right) = -\frac{\partial w_b^i\left(x^i, t\right)}{\partial x^i} \qquad \theta_{bz}^i\left(x^i, t\right) = \frac{\partial v_b^i\left(x^i, t\right)}{\partial x^i} \tag{9d,e}$$

where $\bar{u}_b^i$, $\bar{v}_b^i$, $\bar{w}_b^i$ are the axial and transverse displacement components with respect to the $C^i x^i y^i z^i$ system of axes; $u_b^i = u_b^i\left(x^i\right)$, $v_b^i = v_b^i\left(x^i\right)$ and $w_b^i = w_b^i\left(x^i\right)$ are the corresponding components of the centroid C^i; $\theta_{by}^i = \theta_{by}^i\left(x^i\right)$, $\theta_{bz}^i = \theta_{bz}^i\left(x^i\right)$ are the angles of rotation of the

cross section due to bending, with respect to its centroid; $\partial\theta_{bx}^{i}/dx^{i}$ denotes the rate of change of the angle of twist $\theta_{bx}^{i}\left(x^{i}\right)$ regarded as the torsional curvature and φ_{S}^{Pi} is the primary warping function with respect to the cross section's shear center (coinciding with its centroid). Employing again the strain-displacement relations of the three-dimensional elasticity for moderate displacements [4], the Hooke's stress-strain law and integrating the arising stress components over the beam's cross section after ignoring the nonlinear terms with respect to the angle of twist and its derivatives, the stress resultants of the beam are derived as

$$N_{b}^{i}=E_{b}^{i}A_{b}^{i}\left[\frac{\partial u_{b}^{i}}{\partial x^{i}}+\frac{1}{2}\left(\left(\frac{\partial v_{b}^{i}}{\partial x^{i}}\right)^{2}+\left(\frac{\partial w_{b}^{i}}{\partial x^{i}}\right)^{2}\right)\right] \tag{10a}$$

$$M_{by}^{i}=-E_{b}^{i}I_{y}^{i}\frac{\partial^{2}w_{b}^{i}}{\partial x^{i2}} \tag{10b}$$

$$M_{bz}^{i}=E_{b}^{i}I_{z}^{i}\frac{\partial^{2}v_{b}^{i}}{\partial x^{i2}} \tag{10c}$$

$$M_{bt}^{Pi}=G_{b}^{i}I_{t}^{i}\frac{\partial\theta_{bx}^{i}}{\partial x^{i}} \tag{10d}$$

$$M_{bw}^{i}=-E_{b}^{i}C_{S}^{i}\frac{\partial^{2}\theta_{bx}^{i}}{\partial x^{i2}} \tag{10e}$$

where M_{bt}^{Pi} is the primary twisting moment [5] resulting from the primary shear stress distribution; M_{bw}^{i} is the warping moment due to torsional curvature. Furthermore I_{y}^{i}, I_{z}^{i} are the principal moments of inertia; I_{S}^{i} is the polar moment of inertia, while I_{t}^{i} and C_{S}^{i} are the torsion and warping constants of the i-th beam with respect to the cross section's shear center (coinciding with its centroid), respectively, given as [6]

$$I_{t}^{i}=\int_{\Omega}\left(y^{i2}+z^{i2}+y^{i}\frac{\partial\varphi_{S}^{Pi}}{\partial z^{i}}-z^{i}\frac{\partial\varphi_{S}^{Pi}}{\partial y^{i}}\right)d\Omega \tag{11a}$$

$$C_{S}^{i}=\int_{\Omega}\left(\varphi_{S}^{Pi}\right)^{2}d\Omega \tag{11b}$$

On the basis of Hamilton's principle, the differential equations of motion are obtained as

$$-E_{b}^{i}A_{b}^{i}\left(\frac{\partial^{2}u_{b}^{i}}{\partial x^{i2}}+\frac{\partial w_{b}^{i}}{\partial x^{i}}\frac{\partial^{2}w_{b}^{i}}{\partial x^{i2}}+\frac{\partial v_{b}^{i}}{\partial x^{i}}\frac{\partial^{2}v_{b}^{i}}{\partial x^{i2}}\right)+\rho_{b}^{i}\mathrm{A}_{b}^{i}\ddot{u}_{b}^{i}=\sum_{j=1}^{2}q_{xj}^{i} \tag{12a}$$

$$E_{b}^{i}I_{z}^{i}\frac{\partial^{4}v_{b}^{i}}{\partial x^{i4}}-N_{b}^{i}\frac{\partial^{2}v_{b}^{i}}{\partial x^{i2}}-\rho_{b}^{i}I_{z}^{i}\frac{\partial^{2}\ddot{v}_{b}}{\partial x^{2}}+\rho_{b}^{i}\mathrm{A}_{b}^{i}\ddot{v}_{b}-\rho_{b}^{i}\mathrm{A}_{b}^{i}\ddot{u}_{b}^{i}\frac{\partial v_{b}^{i}}{\partial x^{i}}=\sum_{j=1}^{2}\left(q_{yj}^{i}-q_{xj}^{i}\frac{\partial v_{b}^{i}}{\partial x^{i}}-\frac{\partial m_{bzj}^{i}}{\partial x^{i}}\right) \tag{12b}$$

$$E_{b}^{i}I_{y}^{i}\frac{\partial^{4}w_{b}^{i}}{\partial x^{i4}}-N_{b}^{i}\frac{\partial^{2}w_{b}^{i}}{\partial x^{i2}}-\rho_{b}^{i}I_{y}^{i}\frac{\partial^{2}\ddot{w}_{b}}{\partial x^{2}}+\rho_{b}^{i}\mathrm{A}_{b}^{i}\ddot{w}_{b}-\rho_{b}^{i}\mathrm{A}_{b}^{i}\ddot{u}_{b}^{i}\frac{\partial w_{b}^{i}}{\partial x^{i}}=\sum_{j=1}^{2}\left(q_{zj}^{i}-q_{xj}^{i}\frac{\partial w_{b}^{i}}{\partial x^{i}}+\frac{\partial m_{byj}^{i}}{\partial x^{i}}\right) \tag{12c}$$

$$E_b^i C_S^i \frac{\partial^4 \theta_{bx}^i}{\partial x^{i4}} - G_b^i I_t^i \frac{\partial^2 \theta_{bx}^i}{\partial x^{i2}} + \rho_b^i I_S^i \ddot{\theta}_{bx}^i - \rho_b^i C_S^i \frac{\partial^2 \ddot{\theta}_{bx}^i}{\partial x^2} = \sum_{j=1}^{2} \left[m_{bxj}^i + \frac{\partial m_{bwj}^i}{\partial x^i} \right] \tag{12d}$$

Moreover, the corresponding boundary conditions of the i-th beam at its ends $x^i = 0, l^i$ are given as

$$a_{b1}^i u_b^i + \alpha_{b2}^i N_b^i = \alpha_{b3}^i \tag{13}$$

$$\beta_{b1}^i v_b^i + \beta_{b2}^i R_{by}^i = \beta_{b3}^i \qquad \bar{\beta}_{b1}^i \theta_{bz}^i + \bar{\beta}_{b2}^i M_{bz}^i = \bar{\beta}_{b3}^i \tag{14a,b}$$

$$\gamma_{b1}^i w_b^i + \gamma_{b2}^i R_{bz}^i = \gamma_{b3}^i \qquad \bar{\gamma}_{b1}^i \theta_{by}^i + \bar{\gamma}_{b2}^i M_{by}^i = \bar{\gamma}_{b3}^i \tag{15a,b}$$

$$\delta_{b1}^i \theta_{bx}^i + \delta_{b2}^i M_{bt}^i = \delta_{b3}^i \qquad \bar{\delta}_{b1}^i \frac{d\theta_{bx}^i}{dx^i} + \bar{\delta}_{b2}^i M_{bw}^i = \bar{\delta}_{b3}^i \tag{16a,b}$$

and the initial conditions as

$$w_b^i \left(x^i, 0 \right) = w_{b0}^i \left(x^i \right) \tag{17a}$$

$$\dot{w}_b^i \left(x^i, 0 \right) = \bar{w}_{b0}^i \left(x^i \right) \tag{17b}$$

where the angles of rotation of the cross section due to bending θ_{by}^i, θ_{bz}^i are given from eqns. (9d,e), R_{by}^i, R_{bz}^i and M_{bz}^i, M_{by}^i are the reactions and bending moments with respect to y^i, z^i axes, respectively, which after applying the aforementioned simplifications are given as

$$R_{by}^i = N_b^i \frac{\partial v_b^i}{\partial x^i} - E_b^i I_z^i \frac{\partial^3 v_b^i}{\partial x^{i3}} \tag{18a}$$

$$R_{bz}^i = N_b^i \frac{\partial w_b^i}{\partial x^i} - E_b^i I_y^i \frac{\partial^3 w_b^i}{\partial x^{i3}} \tag{18b}$$

$$M_{bz}^i = E_b^i I_z^i \frac{\partial^2 v_b^i}{\partial x^{i2}} \tag{19a}$$

$$M_{by}^i = -E_b^i I_y^i \frac{\partial^2 w_b^i}{\partial x^{i2}} \tag{19b}$$

and M_{bt}^i, M_{bw}^i are the torsional and warping moments at the boundaries of the beam, respectively, given as

$$M_{bt}^i = G_b^i I_t^i \frac{\partial \theta_{bx}^i}{\partial x^i} - E_b^i C_S^i \frac{\partial^3 \theta_{bx}^i}{\partial x^{i3}} \tag{20a}$$

$$M_{bw}^i = -E_b^i C_S^i \frac{\partial^2 \theta_{bx}^i}{\partial x^{i2}} \tag{20b}$$

Finally, α_{bk}^i, β_{bk}^i, $\bar{\beta}_{bk}^i$, γ_{bk}^i, $\bar{\gamma}_{bk}^i$, δ_{bk}^i, $\bar{\delta}_{bk}^i$ ($k = 1,2,3$) are functions specified at the i-th beam ends ($x^i = 0, l^i$). The boundary conditions (13)-(16a,b) are the most general boundary conditions for the beam problem including also the elastic support. It is apparent that all types

of the conventional boundary conditions (clamped, simply supported, free or guided edge) can be derived from these equations by specifying appropriately the aforementioned coefficients.

Eqns. (4), (12) constitute a set of seven coupled and nonlinear partial differential equations including thirteen unknowns, namely $u_p, v_p, w_p, u_b^i, v_b^i, w_b^i, \theta_{bx}^i, q_{x1}^i, q_{y1}^i, q_{z1}^i, q_{x2}^i, q_{y2}^i, q_{z2}^i$. Six additional equations are required, which result from the displacement continuity conditions in the directions of x^i, y^i and z^i local axes along the two interface lines of each (i-th) plate – beam interface. Taking into account the displacement fields expressed by eqns. (1a)-(1c) and (9a)-(9d,e) the displacement continuity conditions [7] can be expressed as

In the direction of x^i local axis:

$$u_{p1}^i - u_b^i = \frac{h_p}{2}\frac{\partial w_{p1}^i}{\partial x} + \frac{h_b^i}{2}\frac{\partial w_b^i}{\partial x^i} + \frac{b_f^i}{4}\frac{\partial v_b^i}{\partial x^i} + \frac{\partial \theta_{bx}^i}{\partial x^i}\left(\varphi_S^{Pi}\right)_{f1} + \frac{q_{x1}^i}{k_{x1}^i}\left[1 - \frac{1}{2}\left(\frac{\partial w_b^i}{\partial x^i}\right)^2\right]$$

along interface line 1 ($f_{j=1}^i$) (21a)

$$u_{p2}^i - u_b^i = \frac{h_p}{2}\frac{\partial w_{p2}^i}{\partial x} + \frac{h_b^i}{2}\frac{\partial w_b^i}{\partial x^i} - \frac{b_f^i}{4}\frac{\partial v_b^i}{\partial x^i} + \frac{\partial \theta_{bx}^i}{\partial x^i}\left(\varphi_S^{Pi}\right)_{f2} + \frac{q_{x2}^i}{k_{x2}^i}\left[1 - \frac{1}{2}\left(\frac{\partial w_b^i}{\partial x^i}\right)^2\right]$$

along interface line 2 ($f_{j=2}^i$) (21b)

In the direction of y^i local axis:

$$v_{p1}^i - v_b^i = \frac{h_p}{2}\frac{\partial w_{p1}^i}{\partial y} + \frac{h_b^i}{2}\theta_{bx}^i + \frac{q_{y1}^i}{k_{y1}^i}\left[1 - \frac{1}{2}\left(\theta_{bx}^i\right)^2\right]$$ along interface line 1 ($f_{j=1}^i$) (22a)

$$v_{p2}^i - v_b^i = \frac{h_p}{2}\frac{\partial w_{p2}^i}{\partial y} + \frac{h_b^i}{2}\theta_{bx}^i + \frac{q_{y2}^i}{k_{y2}^i}\left[1 - \frac{1}{2}\left(\theta_{bx}^i\right)^2\right]$$ along interface line 2 ($f_{j=2}^i$) (22b)

In the direction of z^i local axis:

$$w_{p1}^i - w_b^i = -\frac{b_f^i}{4}\theta_{bx}^i$$ along interface line 1 ($f_{j=1}^i$) (23a)

$$w_{p2}^i - w_b^i = \frac{b_f^i}{4}\theta_{bx}^i$$ along interface line 2 ($f_{j=2}^i$) (23b)

where $\left(\varphi_S^{Pi}\right)_{fj}$ is the value of the primary warping function with respect to the shear center of the beam cross section (coinciding with its centroid) at the point of the j-th interface line of the i-th plate – beam interface f_j^i and k_{xj}^i, k_{yj}^i are the stiffness of the arbitrarily distributed shear connectors along the x^i and y^i directions, respectively. It is noted that $k_{xj}^i = k_{xj}^i\left(s_{xj}^i\right)$ and $k_{yj}^i = k_{yj}^i\left(s_{yj}^i\right)$ can represent any linear or nonlinear relationship between the in-plane in-

terface forces and the interface slip s_j^i in the corresponding direction. In all of the aforementioned equations the values of the primary warping function $\varphi_S^{Pi}\left(y^i, z^i\right)$ should be set having the appropriate algebraic sign corresponding to the local beam axes.

3 INTEGRAL REPRESENTATIONS - NUMERICAL SOLUTION

The solution of the presented dynamic problem requires the integration of the set of Eqs. (4a)-(4c), (12a)-(12d) subjected to the prescribed boundary and initial conditions. Moreover, the displacement continuity conditions should also be fulfilled. Due to the nonlinear and coupling character of the equations of motion, an analytical solution is out of question. Therefore, a numerical solution is derived employing the Analog Equation Method [2], a BEM based method. Contrary to previous research efforts where the numerical analysis is based on BEM using a lumped mass assumption model after evaluating the flexibility matrix at the mass nodal points [5], in this work a distributed mass model is employed.

4 NUMERICAL EXAMPLES

On the basis of the analytical and numerical procedures presented in the previous sections, a FORTRAN program has been written and representative examples have been studied to demonstrate the effectiveness, wherever possible the accuracy and the range of applications of the proposed method. It is noted that the term "linear analysis" appearing in all the following sections, refers to the solution of the previously obtained system of equations neglecting all of the nonlinear terms.

Example 1

A rectangular plate ($h_p = 0.2cm$, $E_p = E_b = 3\times10^7\, kN/m^2$, $\rho_p = \rho_b = 2.5tn/m^3$, $\nu_p = \nu_b = 0.2$) with dimensions $L_x \times L_y = 18cm \times 9cm$ subjected to a suddenly applied uniform load $g = 40kN/m^2$ and stiffened by a rectangular beam of $0.5cm$ height and $1.0cm$ width, eccentrically placed with respect to the plate centre line, has been studied. The plate is clamped along its small edges, while the rest of the edges are free according to the transverse and in-plane boundary conditions. The connection between the slab and the beam was accomplished using a linear distribution of shear connectors along each interface (Figure 4). The adopted relationship for the shear connectors' stiffness is given as

$$k_{xj}^i = k_{yj}^i = 250K\left|x^i - \frac{l_{bx}^i}{2}\right| kN/m^2 \qquad (j = 1,2) \quad (24)$$

where K is dimensionless magnification factor. In Table 1 the obtained maximum deflections w_p of the first cycle of motion of the stiffened plate, at the middle of the free edge A are shown for various values of K. In Figure 5, the time histories of the deflection $w_p(t)$ at the same point A for the cases of linear and nonlinear dynamic analysis, for various values of K, are presented. Moreover, in Figure 6 the contour lines of the displacement w_p of the stiffened plate for full and partial connection between plate and beam, at the time of maximum transverse displacement are shown, ignoring (Figure 6a,c) or taking into account (Figure 6b,d) geometric nonlinearities.

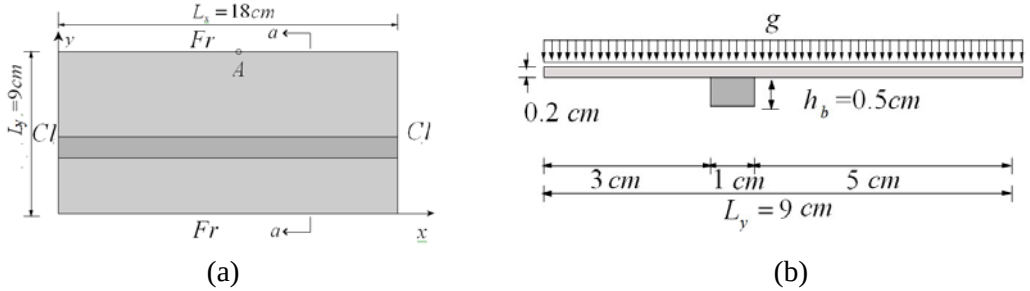


Figure 4: Plan view (a) and section a-a (b) of the stiffened plate of example 1.

K	Linear Analysis	Nonlinear Analysis
Full Connection	0.431	0.402
100.0	0.433	0.403
10.0	0.437	0.406
1.0	0.453	0.420
0.1	0.489	0.452
0.01	0.565	0.520
0.005	0.585	0.530

Table 1: Maximum deflection w_p (m) at the middle point A of the first circle of motion of the stiffened plate for various values of K of example 1.

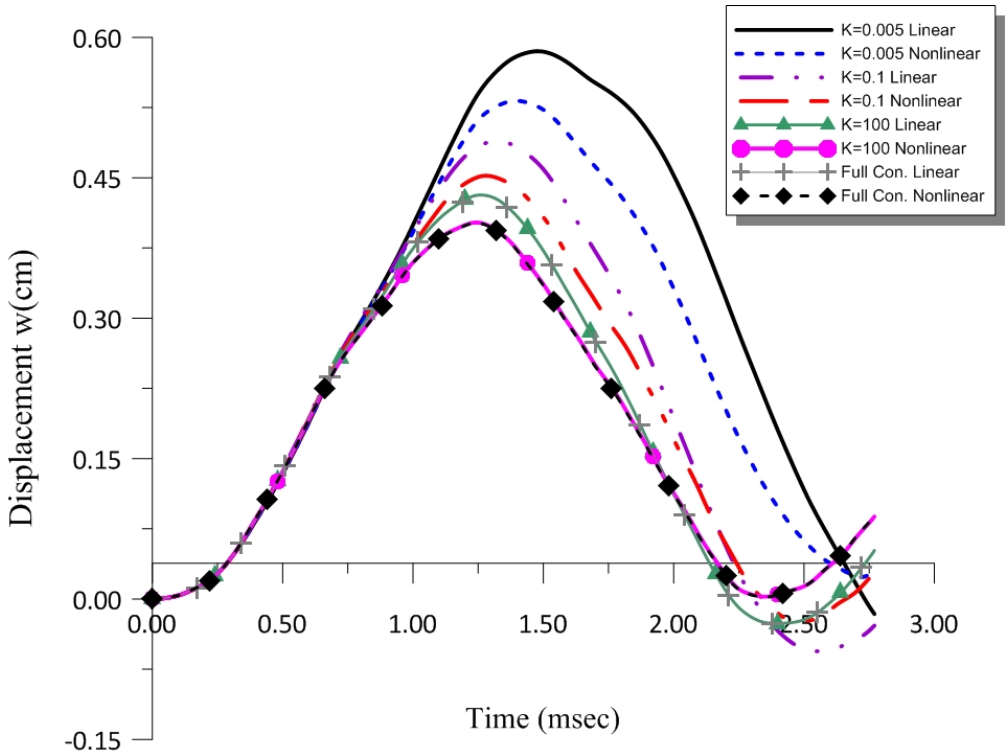
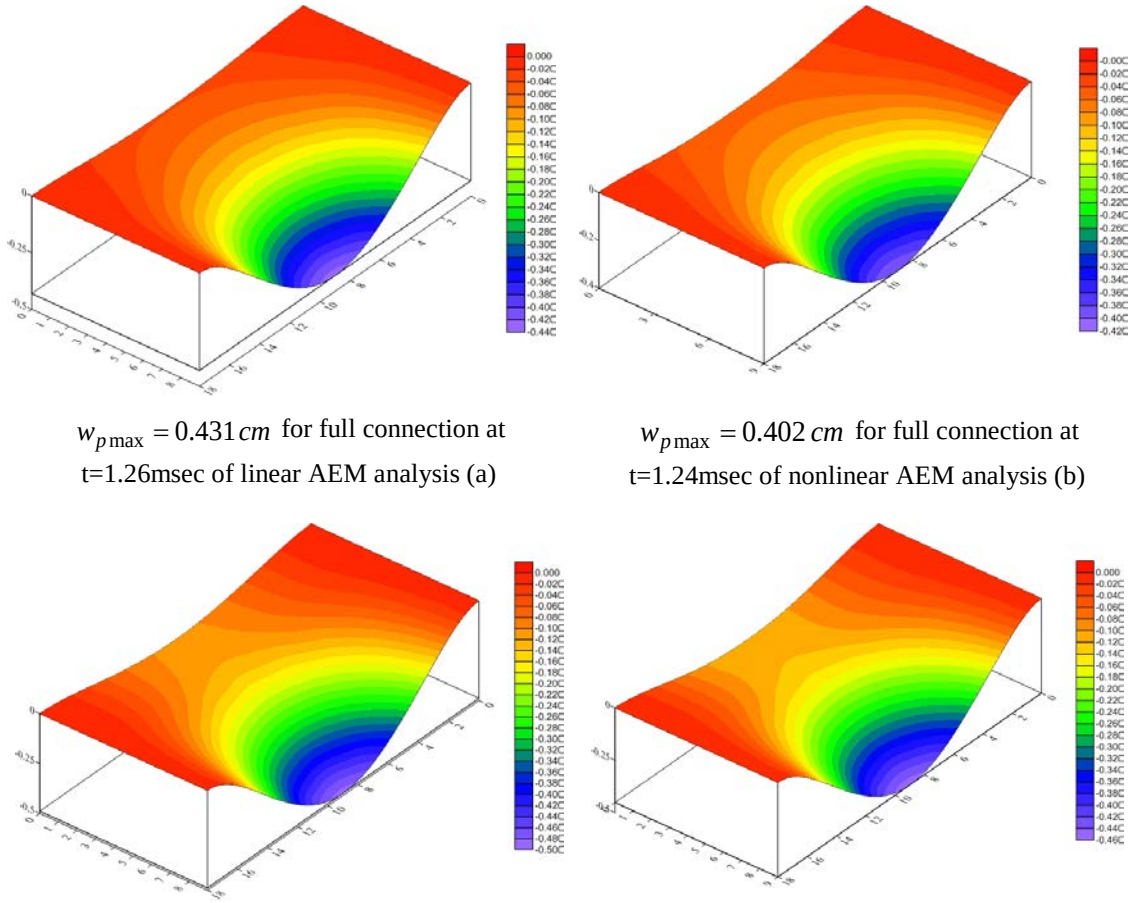


Figure 5: Time history of displacement w(cm) at the middle A of the free edge of the plate of example 1.



$w_{p\max} = 0.431\,cm$ for full connection at t=1.26msec of linear AEM analysis (a)

$w_{p\max} = 0.402\,cm$ for full connection at t=1.24msec of nonlinear AEM analysis (b)

$w_{p\max} = 0.489\,cm$ for K=0.1 at t=1.32msec of linear AEM analysis (c)

$w_{p\max} = 0.452\,cm$ for K=0.1 at t=1.28msec of nonlinear AEM analysis (d)

Figure 6: Contour lines of w_p of the stiffened plate of example 1, for full and partial connection between plate and beam, at the time of maximum transverse displacement ignoring (a,c) or taking into account (b,d) geometric nonlinearities.

5 CONCLUDING REMARKS

A general solution for the geometrically nonlinear dynamic analysis of plates stiffened by arbitrarily placed parallel beams of arbitrary doubly symmetric cross section with deformable connections, subjected to arbitrary loading is presented. The proposed model takes into account the nonuniform distribution of the interface shear forces and the nonuniform torsional response of the beams. The main conclusions that can be drawn from this investigation are

- The proposed model permits the study of the dynamic response of stiffened plates subjected to arbitrary loading, while both the number and the placement of the parallel beams are also arbitrary (eccentric beams are included). The plate and the beams are supported by the most general boundary conditions including elastic support or restraint.
- The adopted model permits the evaluation of the longitudinal and transverse in-plane shear forces at the interfaces between the plate and the beams in the geometrically non-

linear dynamic analysis of the stiffened plate taking into account interface slip in both the x and y directions.

- The nonuniform torsion in which the stiffening beams are subjected is taken into account by solving the corresponding problem and by comprehending the arising twisting and warping in the corresponding displacement continuity conditions. The distributed warping moment arising from the nonuniform distribution of longitudinal in-plane forces is also taken into account.
- The influence of geometrical nonlinearity on the deformation of the examined stiffened plates is remarkable.
- The developed procedure retains most of the advantages of a BEM solution over a FEM approach, although it requires domain discretization.
- The increment of the deflection with the decrement of the connectors' stiffness is easily verified, while this decrement results in a more pronounced influence of the geometrical nonlinearity on the response of the stiffened plate.

Acknowledgments
This work has been funded by the State Scholarships Foundation of Greece as a part of post-doctoral research project.

REFERENCES

[1] E.J. Sapountzakis, V.G Mokos, An Improved Model for the Analysis of Plates Stiffened by Parallel Beams with Deformable Connection, *Computers and Structures*, **86**, 2166-2181, 2008.

[2] J.T. Katsikadelis, The Analog Equation Method. A Boundary – only Integral Equation Method for Nonlinear Static and Dynamic Problems in General Bodies, *Theoretical and Applied Mechanics*, **27**, 13-38, 2002.

[3] E.J. Sapountzakis, V.G. Mokos, Analysis of Plates Stiffened by Parallel Beams, *International Journal for Numerical Methods in Engineering*, **70**, 1209-1240, 2007.

[4] E. Ramm, T.J. Hofmann, *Stabtragwerke*, Der Ingenieurbau, Ed.G. Mehlhorn, Band Baustatik/Baudynamik, Ernst & Sohn, Berlin, 1995.

[5] E.J. Sapountzakis, V.G. Mokos, An Improved Model for the Dynamic Analysis of Plates Stiffened by Parallel Beams, *Engineering Structures*, **30**, 1720-1733, 2008.

[6] E.J. Sapountzakis, V.G. Mokos, Warping Shear Stresses in Nonuniform Torsion by BEM, *Computational Mechanics*, **30**, 131-142, 2003.

[7] E.J. Sapountzakis, I.C. Dikaros, Large Deflection Analysis of Plates Stiffened by Parallel Beams with Deformable Connection, *Journal of Engineering Mechanics*, ASCE, **138**, (8), 1021-1041, 2012.

COMPDYN 2013
4th ECCOMAS Thematic Conference on
Computational Methods in Structural Dynamics and Earthquake Engineering
M. Papadrakakis, V. Papadopoulos, V. Plevris (eds.)
Kos Island, Greece, 12–14 June 2013

NONLINEAR VIBRATIONS OF ROTATING 3D TAPERED BEAMS WITH ARBITRARY CROSS SECTIONS

S. Stoykov[1], **S. Margenov**[1]

[1] Institute of Information and Communication Technologies, Bulgarian Academy of Sciences
Acad. G. Bonchev str., bl. 25A, 1113 Sofia, Bulgaria
{stoykov, margenov}@parallel.bas.bg

Keywords: *p*-version finite element method, warping function, acceleration of Coriolis, setting angle, bending-bending coupling.

Abstract. *The geometrically nonlinear vibrations of 3D beams that rotate about a fixed axis are investigated by the p-version finite element method. The beams are considered to be tapered, i.e. with variable thickness along its length, and with arbitrary cross sections. The beam model is based on Timoshenko's theory for bending and Saint-Venant's theory for torsion, i.e. it is assumed that the cross section rotates about the longitudinal axis as a rigid body but may deform in longitudinal direction due to warping and the torsion is not considered to be uniform. The warping function is obtained preliminarily by the finite element method. For the case of tapered beams, the warping and torsional constants, the cross sectional area, the second moment of inertia and all cross sectional properties are expressed as functions of the longitudinal local coordinate. Geometrical nonlinearity is taken into account and derived from Green's strain tensor. Linear elastic and isotropic materials are considered and generalized Hooke's law is used. The rotation is included in the model through the inertia terms, two coordinate systems are considered: one fixed and one rotating about the fixed one. The equation of motion is derived by the principle of virtual work in the rotating coordinate system but the influence of the rotation of the coordinate system on the displacements of the beam is included in the equation of motion. A setting angle and hub radios are considered, and their influence, as well the influence of the speed of rotation, on the natural frequencies is examined. Forced vibrations in time domain are presented for various setting angles.*

1 INTRODUCTION

Rotating beams are used to model and investigate the dynamics of helicopter blades, jet engine turbine blades, robot arms, wind turbine blades, etc. Many studies have been performed for modeling rotating beams about a fixed axis. The linear natural frequencies of beams that rotate with constant speed were investigated by many researchers, for example in [1-5]. Works that consider geometrically nonlinear models of rotating beams may be found, for example [6-8]. In what concerns modern wind turbine blades, most of them are constructed with load carrying box girder inside the blade and shells on the surface of the blade [9]. The purpose of the box girder is to make the blade stronger and stiffer while the shells around the box girder form the aerodynamic shape. Thus, the dynamic behavior of the wind turbine blade might be determined mainly from the load carrying box, even though the shells contribute small bending strength.

In the current work, a model of beams rotating about a fixed axis with constant speed of rotation is presented. A setting angle and a rigid hub are included in the model. The equation of motion is derived in the rotating coordinate system, and the rotation is taken into account by the inertia forces [10]. The beam may vibrate in space, i.e. it may perform longitudinal, torsional and bending deformations, the model is based on Timoshenko's theory for bending and assumes that under torsion, the cross section deforms only in longitudinal direction due to warping [11]. Geometrical type of nonlinearity is considered and the equation of motion is derived by the principle of virtual work.

Thin-walled box beams with linearly varying thickness and width are investigated. First, the derived model is validated by generating a fine mesh of three-dimensional finite elements. Then, the influence of the setting angle and the speed of rotation on the natural frequencies is examined. Forced vibrations of rotating beams due to harmonic forces are presented.

2 MATHEMATICAL MODEL

Tapered beams with linearly varying thickness and arbitrary cross section, in elastic, homogeneous and isotropic materials, that rotate about a fixed axis with constant angular speed are considered. The beam equation of motion is derived in a rotating coordinate system and the rotation of the coordinate system is taken into account into the equation of motion. Two coordinate systems are used for that purpose: the first one (*XYZ*) is fixed in space, it will be denoted with S_0, the second coordinate system (*xyz*) rotates around the *Z* axis of the fixed coordinate system, it will be called "transport coordinate system" and denoted with S_1. A setting angle φ is considered in the model, i.e. angle which inclines the cross section to the plane of rotation, thus the *z* axis of the transport coordinate system is inclined on angle φ with respect to *Z* axis of the fixed coordinate system, and the *x* axis of the transport coordinate system, which presents the longitudinal direction the beam remains in the plane of rotations, i.e. *XY* (Figure 1). The beam is assumed to be rigidly mounted on hub with radios *R*. The centers of both coordinate systems coincide. The transport coordinate system rotates with a constant speed, $\vartheta(t)$ rad denotes its rotation at time *t*, then $\dot{\vartheta}(t)$ is the speed of rotation (rad/s), or angular velocity. The beam equation of motion is derived with one *p* element and improving the accuracy of the results is achieved by increasing the number of the shape functions.

2.1 Beam equation of motion in transport coordinate system

The displacements of the beam are expressed in the transport coordinate system S_1, assuming Timoshenko's theory for bending [12] and Saint-Venant's theory for torsion [13], including deformation in longitudinal direction due to warping:

$$u(x,y,z,t) = u_0(x,t) - y\,\phi_z(x,t) + z\,\phi_y(x,t) + \psi(y,z)\,\frac{\partial\theta_x}{\partial x}(x,t)$$
$$v(x,y,z,t) = v_0(x,t) + y\cos\big(\theta_x(x,t)\big) - y - z\sin\big(\theta_x(x,t)\big) \quad (1)$$
$$w(x,y,z,t) = w_0(x,t) + y\sin\big(\theta_x(x,t)\big) + z\cos\big(\theta_x(x,t)\big) - z$$

where u presents the longitudinal displacement, v and w present the transverse displacements in y and z directions, the subscript 0 denotes the displacements on the reference line, θ_x is the rotation of the cross section about the longitudinal axis x, ϕ_y and ϕ_z denote rotations of the cross section about axes y and z, respectively and $\psi(y,z)$ is the warping function.

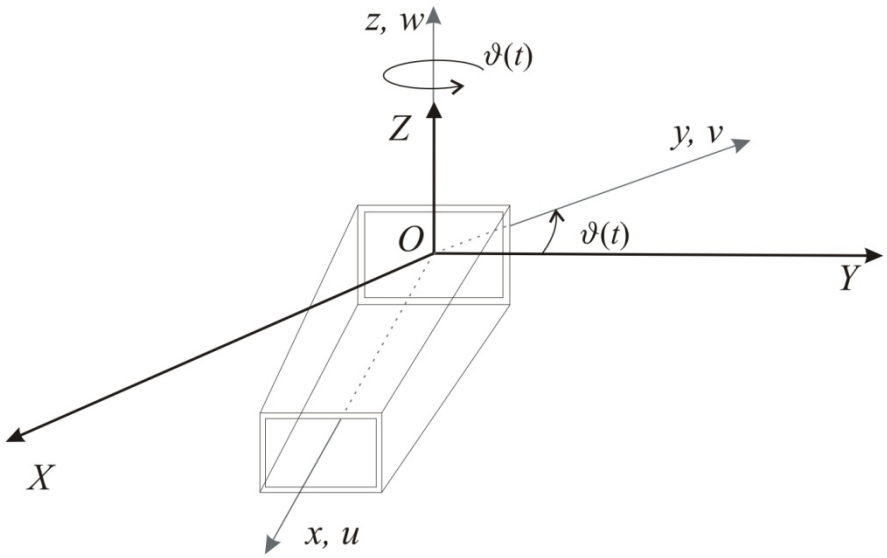


Figure 1. Axes and displacements of rotating beam model.

The equation of motion is derived by the principle of virtual work and the rotation of the beam is considered in the inertia forces by using the absolute acceleration, i.e. the acceleration with respect to the fixed coordinate system [14]. The equation of motion is derived in the rotating coordinate systems, thus the absolute acceleration of an arbitrary point P(x,y,z) from the beam is written at that coordinate system:

$$\boldsymbol{a}_{P_{S_0}} = \boldsymbol{a}_{P_{S_1}} + \boldsymbol{\alpha}_{10} \times \boldsymbol{r} + \boldsymbol{\omega}_{10} \times (\boldsymbol{\omega}_{10} \times \boldsymbol{r}) + 2\,\boldsymbol{\omega}_{10} \times \boldsymbol{v}_{P_{S_1}} \quad (2)$$

where $\boldsymbol{a}_{P_{S_0}}$ is the absolute acceleration of point P, i.e. the acceleration of point P with respect to S_0, $\boldsymbol{a}_{P_{S_1}}$ is the relative acceleration of point P, i.e. the acceleration of point P with respect to S_1, given in (3), $\boldsymbol{v}_{P_{S_1}}$ is the relative velocity of point P, i.e. the velocity of point P with respect to S_1, given in (4), $\boldsymbol{\omega}_{10}$ is the angular velocity of the transport coordinate system (5), $\boldsymbol{\alpha}_{10}$ is the angular acceleration vector of the transport coordinate system which is assumed to be zero, since beams rotating with constant speed are analyzed, and $\boldsymbol{r}$ is the position vector of point P with respect to the origin of S_1 (6). Furthermore, $\boldsymbol{\omega}_{10} \times (\boldsymbol{\omega}_{10} \times \boldsymbol{r})$ is the transport acceleration, and $2\,\boldsymbol{\omega}_{10} \times \boldsymbol{v}_{P_{S_1}}$ is the acceleration of Coriolis.

$$\boldsymbol{a}_{P_{S_1}} = \begin{Bmatrix} \ddot{u}_0 - y\,\ddot{\phi}_z + z\,\ddot{\phi}_y + \psi\frac{\partial\ddot{\theta}_x}{\partial x} \\ \ddot{v}_0 - y\cos(\theta_x)(\dot{\theta}_x)^2 - y\sin(\theta_x)\,\ddot{\theta}_x + z\sin(\theta_x)\big(\dot{\theta}_x\big)^2 - z\cos(\theta_x)\ddot{\theta}_x \\ \ddot{w}_0 - y\sin(\theta_x)(\dot{\theta}_x)^2 + y\cos(\theta_x)\,\ddot{\theta}_x - z\cos(\theta_x)\big(\dot{\theta}_x\big)^2 - z\sin(\theta_x)\ddot{\theta}_x \end{Bmatrix} \quad (3)$$

$$\boldsymbol{v}_{\boldsymbol{P}_{\boldsymbol{S}_1}} = \begin{Bmatrix} \dot{u}_0 - y\,\dot{\phi}_z + z\,\dot{\phi}_y + \psi\dfrac{\partial\dot{\theta}_x}{\partial x} \\ \dot{v}_0 - y\sin(\theta_x)\,\dot{\theta}_x - z\cos(\theta_x)\,\dot{\theta}_x \\ \dot{w}_0 + y\cos(\theta_x)\,\dot{\theta}_x - z\sin(\theta_x)\,\dot{\theta}_x \end{Bmatrix} \tag{4}$$

$$\boldsymbol{\omega}_{\mathbf{10}} = \begin{Bmatrix} 0 \\ \dot{\vartheta}\sin\varphi \\ \dot{\vartheta}\cos\varphi \end{Bmatrix} \tag{5}$$

$$\boldsymbol{r} = \begin{Bmatrix} R + x + u_0 - y\,\phi_z + z\,\phi_y + \psi\dfrac{\partial\theta_x}{\partial x} \\ y + v_0 + y\cos(\theta_x) - y - z\sin(\theta_x) \\ z + w_0 + y\sin(\theta_x) + z\cos(\theta_x) - z \end{Bmatrix} \tag{6}$$

where R is the hub radios.

The absolute acceleration can be written as

$$\ddot{\mathbf{d}} = \begin{Bmatrix} \ddot{u} \\ \ddot{v} \\ \ddot{w} \end{Bmatrix} = \begin{Bmatrix} \ddot{u}_R + \ddot{u}_T + \ddot{u}_C \\ \ddot{v}_R + \ddot{v}_T + \ddot{v}_C \\ \ddot{w}_R + \ddot{w}_T + \ddot{w}_C \end{Bmatrix} \tag{7}$$

where the subscripts $_R$, $_T$ and $_C$ denote relative, transport and acceleration of Coriolis, respectively, given by:

$$\begin{aligned} \ddot{u}_R &= \ddot{u}_0 - y\;\ddot{\phi}_z + z\,\ddot{\phi}_y + \psi\frac{\partial\ddot{\theta}_x}{\partial x} \\ \ddot{v}_R &= \ddot{v}_0 - y\;\cos(\theta_x)(\dot{\theta}_x)^2 - y\;\sin(\theta_x)\,\ddot{\theta}_x + z\sin(\theta_x)\left(\dot{\theta}_x\right)^2 - z\cos(\theta_x)\ddot{\theta}_x \\ \ddot{w}_R &= \ddot{w}_0 - y\;\sin(\theta_x)\left(\dot{\theta}_x\right)^2 + y\;\cos(\theta_x)\,\ddot{\theta}_x - z\cos(\theta_x)\left(\dot{\theta}_x\right)^2 - z\sin(\theta_x)\ddot{\theta}_x \end{aligned} \tag{8}$$

$$\begin{aligned} \ddot{u}_C &= 2\dot{\vartheta}\sin\varphi\left(\dot{w}_0 + y\cos(\theta_x)\,\dot{\theta}_x - z\sin(\theta_x)\,\dot{\theta}_x\right) - \\ &\quad -2\dot{\vartheta}\cos\varphi\left(\dot{v}_0 - y\sin(\theta_x)\,\dot{\theta}_x - z\cos(\theta_x)\,\dot{\theta}_x\right) \\ \ddot{v}_C &= 2\dot{\vartheta}\cos\varphi\left(\dot{u}_0 - y\,\dot{\phi}_z + z\,\dot{\phi}_y + \psi\frac{\partial\dot{\theta}_x}{\partial x}\right) \\ \ddot{w}_C &= -2\dot{\vartheta}\sin\varphi\left(\dot{u}_0 - y\,\dot{\phi}_z + z\,\dot{\phi}_y + \psi\frac{\partial\dot{\theta}_x}{\partial x}\right) \end{aligned} \tag{9}$$

$$\begin{aligned} \ddot{u}_T &= -\dot{\vartheta}^2\left(R + x + u_0 - y\,\phi_z + z\,\phi_y + \psi\frac{\partial\theta_x}{\partial x}\right) \\ \ddot{v}_T &= \dot{\vartheta}^2\sin\varphi\cos\varphi\left(w_0 + y\sin(\theta_x) + z\cos(\theta_x)\right) - \\ &\quad -\dot{\vartheta}^2\cos\varphi^2\left(v_0 + y\;\cos(\theta_x) - z\sin(\theta_x)\right) \\ \ddot{w}_T &= -\dot{\vartheta}(t)^2\sin\varphi^2\left(w_0 + y\sin(\theta_x) + z\cos(\theta_x)\right) + \\ &\quad +\dot{\vartheta}(t)^2\sin\varphi\cos\varphi\left(v_0 + y\;\cos(\theta_x) - z\sin(\theta_x)\right) \end{aligned} \tag{10}$$

The expression of the virtual work of internal forces remains equal to the one derived for non-rotating beams, i.e. the strains are expressed by Green's strain tensor, neglecting the longitudinal displacements of second order, and the stresses are related to the strains by the Hooke's law. The stresses, the strains and the absolute acceleration are functions of the displacement components u, v and w and their derivatives, which are expressed by the displace-

ments on the reference line and the rotations of the cross sections about the reference line. The displacements on the reference line and the rotations of the cross sections are expressed by shape functions and generalized coordinates:

$$\begin{Bmatrix} u_0(\xi,t) \\ v_0(\xi,t) \\ w_0(\xi,t) \\ \theta_x(\xi,t) \\ \phi_y(\xi,t) \\ \phi_z(\xi,t) \end{Bmatrix} = \begin{bmatrix} \mathbf{N^u}(\xi)^{\mathrm{T}} & \mathbf{0} & \mathbf{0} & \mathbf{0} & \mathbf{0} & \mathbf{0} \\ \mathbf{0} & \mathbf{N^v}(\xi)^{\mathrm{T}} & \mathbf{0} & \mathbf{0} & \mathbf{0} & \mathbf{0} \\ \mathbf{0} & \mathbf{0} & \mathbf{N^w}(\xi)^{\mathrm{T}} & \mathbf{0} & \mathbf{0} & \mathbf{0} \\ \mathbf{0} & \mathbf{0} & \mathbf{0} & \mathbf{N^{\theta_x}}(\xi)^{\mathrm{T}} & \mathbf{0} & \mathbf{0} \\ \mathbf{0} & \mathbf{0} & \mathbf{0} & \mathbf{0} & \mathbf{N^{\phi_y}}(\xi)^{\mathrm{T}} & \mathbf{0} \\ \mathbf{0} & \mathbf{0} & \mathbf{0} & \mathbf{0} & \mathbf{0} & \mathbf{N^{\phi_z}}(\xi)^{\mathrm{T}} \end{bmatrix} \begin{Bmatrix} \mathbf{q_u}(t) \\ \mathbf{q_v}(t) \\ \mathbf{q_w}(t) \\ \mathbf{q_{\theta_x}}(t) \\ \mathbf{q_{\phi_y}}(t) \\ \mathbf{q_{\phi_z}}(t) \end{Bmatrix} \tag{11}$$

where $\xi \in$ [-1..1] is the local coordinate.

The shape functions used in the previous works [10, 11] are used here. The equation of motion is derived by the principle of virtual work, it is obtained in the following form:

$$\mathbf{M}\,\ddot{\mathbf{q}} + \beta\,\mathbf{KL}\,\dot{\mathbf{q}} + \mathbf{CR}\left(\mathbf{q},\dot{\vartheta}\right)\dot{\mathbf{q}} + \mathbf{KL}\,\mathbf{q} + \mathbf{KNL}(\mathbf{q})\,\mathbf{q} + \mathbf{T}\left(\mathbf{q},\dot{\vartheta}\right)\mathbf{q} = \mathbf{F} - \mathbf{R}\left(\dot{\vartheta}\right) \tag{12}$$

where $\mathbf{M}$ is the mass matrix due to relative acceleration; matrix $\mathbf{CR}\left(\mathbf{q},\dot{\vartheta}\right)$ is a consequence of Coriolis acceleration, it depends on the vector of generalized displacements, hence introduces a nonlinearity in the system, and linearly on the speed of rotation; $\mathbf{T}\left(\mathbf{q},\dot{\vartheta}\right)$ is a matrix due to the transport acceleration, it depends linearly on the relative displacement $\mathbf{q}$ (also adding non-linear terms) and quadratically on the angular speed; $\mathbf{R}$ is a vector that is a consequence of the transport acceleration, it depends quadratically on the angular speed, and it is related with the centrifugal forces that act on the beam due to the rotation. Two matrices represent the effect of elastic forces: $\mathbf{KL}$ is a stiffness matrix with constant terms and $\mathbf{KNL}$ is a stiffness matrix that depends linearly and quadratically on the vector of generalized displacements. $\mathbf{F}$ is the vector of generalized external forces. Harmonic external excitations, with the excitation frequency represented by ω are considered. Stiffness proportional damping is added to the equation of motion which depends on the damping factor β. The mass and the stiffness matrices were presented in [10], the matrices related with the rotation of the beam were presented in [11], for the cases of beams without considering setting angle and hub radios. For the current model, the setting angle appears in the matrices $\mathbf{T}\left(\mathbf{q},\dot{\vartheta}\right)$ and $\mathbf{CR}\left(\mathbf{q},\dot{\vartheta}\right)$ and the hub radios in the vector $\mathbf{R}\left(\dot{\vartheta}\right)$, they are given in the Appendix.

2.2 Cross sectional modeling

The cross section is assumed to be arbitrary with linearly varying thickness along the longitudinal axis. The cross sectional properties, such as the warping constant, the cross sectional area, the second moment of inertia are constant, for the cases of beams with constant thickness and/or width and can be calculated independently of the derivation of the equation of motion. For beams with variable thickness and/or width, the cross sectional properties are not constants, they depend on the longitudinal axis, thus they are expressed as functions of the longitudinal axis. The equation of motion is derived by integrating over the length of the beam, but including the cross sectional properties in the integration.

The warping function is obtained numerically by solving the Laplace equation with Neumann boundary conditions [15]:

$$\begin{aligned} \nabla^2\psi &= 0 \quad \text{in } \Omega \\ \frac{\partial\psi}{\partial n} &= z\,n_y - y\,n_z \quad \text{on } \Gamma \end{aligned} \tag{13}$$

where Ω denotes the cross section and Γ is the contour of the cross section. Equation (13) is solved by finite element method, as a result the warping and the torsional constants are obtained using Gauss integration points.

The linearly varying thickness of the beam is taken into account by expressing all cross sectional properties as functions of the local coordinate ξ. Let $f(\xi)$ be a linear function which defines the thickness of the beam as a function of the local longitudinal coordinate ξ. The cross sectional properties are express by their values on the left side of the beam, i.e. at ξ = -1, and the function $f(\xi)$. For example, the area of the beam $A(\xi)$, which has dimension m^2 and the warping constant $C_w(\xi)$, which has dimension m^6 are expressed as:

$$A(\xi) = A\left(\frac{f(\xi)}{f(-1)}\right)^2$$
$$C_w(\xi) = C_w\left(\frac{f(\xi)}{f(-1)}\right)^6 \tag{14}$$

where A and C_w are the cross sectional area and the warping constant at the left side of the beam, ξ = -1. The expressions $A(\xi)$, $C_w(\xi)$ plus the additional cross sectional properties are used for the derivation of the equation of motion. As an example, the bending matrix $\mathbf{K1}_{33}$, defined in [10] for constant cross sections, is obtained here on the following way:

$$\mathbf{K1_{33}} = \lambda G \int_V \frac{d\boldsymbol{N^w}}{dx}\frac{d\boldsymbol{N^{wT}}}{dx} dV = \lambda G \frac{2}{l}\int_{-1}^{1} A(\xi)\frac{d\boldsymbol{N^w}}{d\xi}\frac{d\boldsymbol{N^{wT}}}{d\xi} d\xi \tag{15}$$

where λ is the shear correction factor, l is the length of the beam and G is the shear modulus. The rest of the matrices are obtained on similar way.

3 VALIDATION

The proposed model for tapered beams with arbitrary cross sections is first validated by generating a fine mesh of three-dimensional elements. The natural frequencies and the static deformations are compared. A thin-walled beam with rectangular cross section is used. The length of the beam is chosen to be 0.58 m, the left side is with dimensions 0.02 x 0.015 m and thickness 0.001 m and the right side is with dimensions 0.01 x 0.0075 m and thickness 0.0005 m. The material properties are (aluminium): $E = 7.0^{10}\ N/m^2$, $\rho = 2778\ kg/m^3$, $\nu = 0.34$. The beam is with clamped-free boundary conditions. The beam model presented at the previous section, is derived using 10 shape functions for each displacement, i.e. 60 DOF.

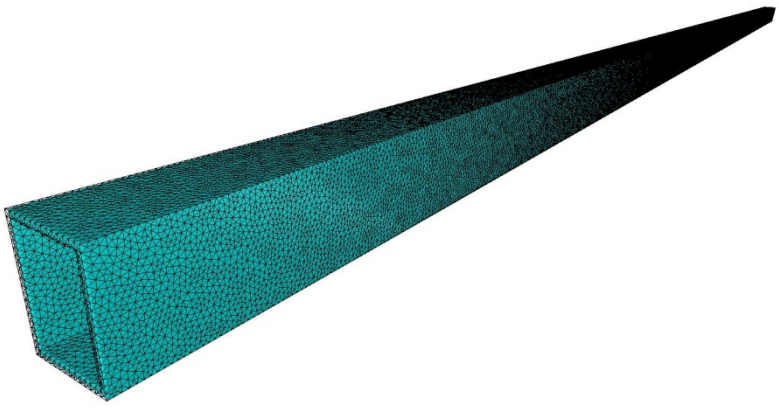


Figure 2. Three-dimensional beam structure used for validation of the proposed model.

The FEM software Elmer [16], which is suitable for large deformation problems, is used to validate the thin-walled beam. A fine mesh of quadratic tetrahedrons is generated using Gmsh

[17]. The mesh has 235914 elements which results into 462725 nodes, each node has three DOF, i.e. the resulting system has more than 1 million DOF. It is solved by parallel computing, using the library Mumps (MUltifrontal Massively Parallel Solver) [18] which is a parallel direct sparse solver. The generated three-dimensional beam is shown on Figure 2. It was verified, by reducing the edges of the tetrahedrons by two, that the results obtained by the large-scale model are converged.

In Table 1 are presented the natural frequencies from the derived beam model and from the three-dimensional software Elmer. Even though the beam is tapered, the cross section remains symmetric with respect to the transverse axes, thus the bending and the torsional modes remain uncoupled.

For further validation of the model, static deformation due to static forces are compared of both models, considering geometrical type of nonlinearity. Uniformly distributed forces are applied along the beam sides in both transverse and longitudinal directions. The results are summarized in Table 2.

The results from both tables confirm that the implemented model for thin-walled tapered beams gives very close results to the same beam structure modeled with three-dimensional finite elements. This beam model, including the rotational terms will be used in the next section. One should note that the beam model is not suitable for large rotations of the cross section, thus the numerical experiments will be limited within the displacements presented and validated in Table 2.

Mode	Beam model	Elmer	Mode shape	Difference %
1	409.65	409.78	Bending xz	0.032
2	514.74	514.97	Bending xy	0.045
3	1725.87	1720.67	Bending xz	0.302
4	2164.70	2160.70	Bending xy	0.185
5	4266.60	4229.38	Bending xz	0.880
6	5335.58	5304.70	Bending xy	0.582
7	8004.81	7869.62	Bending xz	1.718
8	9969.86	9857.35	Bending xy	1.141
9	11449.33	11447.27	Torsion	0.018
10	12913.34	12549.35	Bending xz	2.900

Table 1: First 10 natural frequencies (rad/s) of thin-walled tapered cantilever beam, comparison of the beam model with Elmer.

Total force [N]	Beam model		Elmer model		Difference %	
(F_u, F_v, F_w)	v	w	v	w	v	w
(0, 0, 500)	0.0	0.104911	0.0	0.102897	-	1.92
(0, 500, 500)	0.066618	0.105105	0.065180	0.102138	2.16	2.82
(100, 0, 500)	0.0	0.089321	0.0	0.088223	-	1.23
(100, 500, 500)	0.059885	0.089431	0.058982	0.087738	1.51	1.89
(200, 0, 500)	0.0	0.078108	0.0	0.077448	-	0.84
(200, 500, 500)	0.054517	0.078176	0.053776	0.077114	1.36	1.36

Table 2: Comparison of static deformation (meters) on the free end of the cantilever beam, the applied force is uniformly distributed along the beam's sides, v – transverse displacement in y direction, w – transverse displacement in z direction.

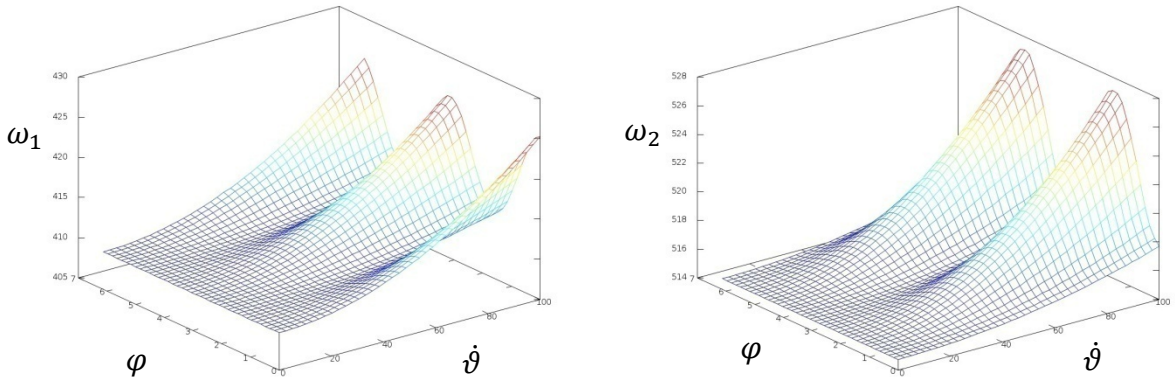
4 NUMERICAL RESULTS

In this section the numerical results of the thin-walled tapered beam rotating at constant speed are presented. First, the influence of the setting angle and the speed of rotation of the natural frequencies and mode shapes is discussed and then the nonlinear forced vibrations at time domain are presented.

4.1 Free vibrations of rotating beams

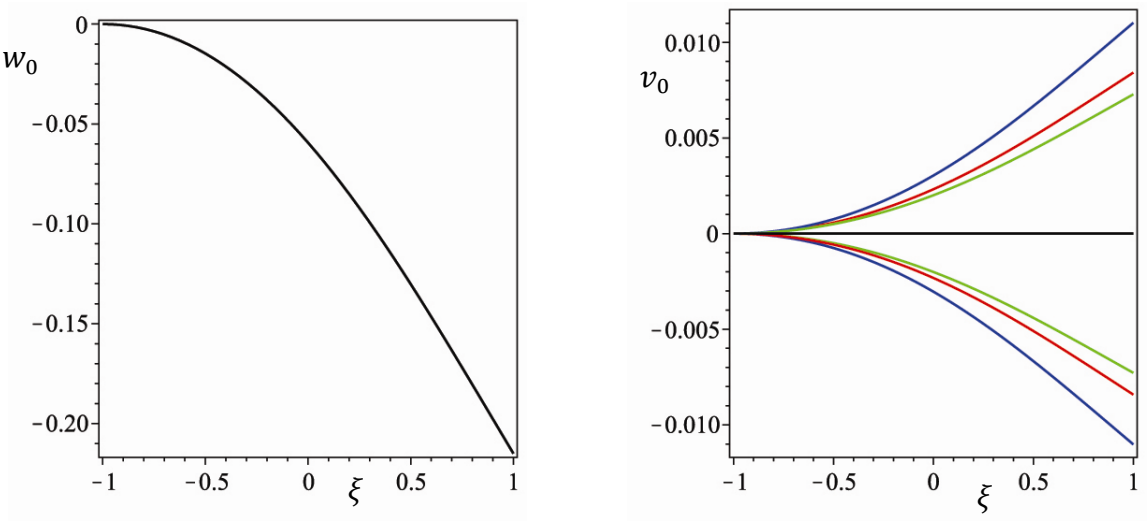
It is well known that the speed of rotation makes the beam stiffer and increases the natural frequencies [1-3], as well that the hub radios increases the natural frequencies of rotating beams. In this subsection, special attention is given to the influence of the setting angle on the natural frequencies. On Figure 3 is presented the variation of the first and second natural frequencies with the speed of rotation and the setting angle.

It should be pointed out that the transverse displacements v_0 and w_0 couple in the linear modes of rotating beams when the setting angle is different from zero or $k\pi/2\,, k \in \mathbb{Z}$ (even though the cross section is symmetric). The coupling comes from the transport acceleration, i.e. from sub-matrices $\mathbf{T}_{23}$ and $\mathbf{T}_{32}$, which are non-zero if the setting angle is different from $k\pi/2\,, k \in \mathbb{Z}$. On Figure 4 are presented the transverse components of the first linear mode of rotating beam with angular velocity $\dot{\vartheta} = 100$ rad/s, for different setting angles. For value of the setting angle $\varphi = 0$ rad or $\varphi = 2\pi$ rad, only the component of w_0 is excited and the vibration is perpendicular to the plane of rotations. i.e. the mode is flapwise. For setting angel $\varphi = \pi$ rad, also only the component of w_0 is excited, but now it vibrates in the plane parallel to the plane of rotation i.e. it is lagwise mode. For all other values of the setting angel φ, both components of the transverse displacements v_0 and w_0 are excited and the vibration is not fixed in a plane parallel or perpendicular to the plane of rotation.



(a) (b)

Figure 3. Variation of the (a) first and (b) second natural frequency with the speed of rotation and setting angle.

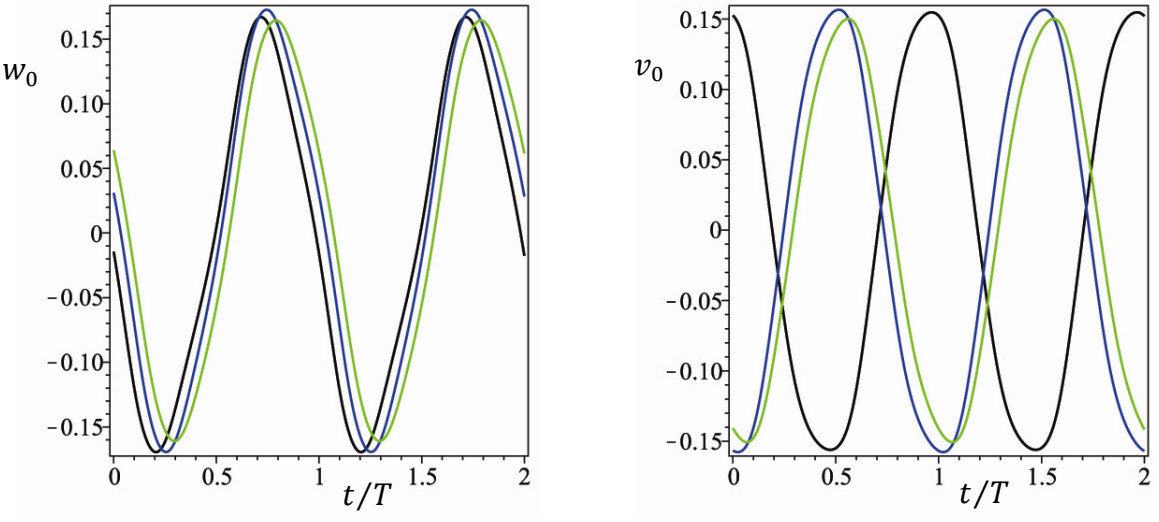


(a) (b)

Figure 4. Linear mode shapes of the beam rotating at angular speed 100 rad/s for various setting angles, (a) component of transverse displacement w_0, (b) component of transverse displacement v_0, — $\varphi = 0, \pi/2, \pi$; — $\varphi = \pm\pi/8$, — $\varphi = \pm\pi/4$, — $\varphi = \pm 3\pi/8$, negative setting angle results into component of transverse displacement v_0 with negative amplitude.

4.2 Forced vibrations of rotating beams

Forced vibrations in time domain due to harmonic excitations are presented and investigated in this section for beams rotating with constant speed $\dot{\vartheta} = 100$ rad/s. An external force with amplitude 50 000 N and excitation frequency 425.25 rad/s is applied in Z direction of the fixed coordinate system, i.e. the force is perpendicular to the plane of rotation. A damping proportional to the linear stiffness matrix with $\beta = 0.0001$ is considered. The steady-state responses of the transverse displacements of the beam are presented for different setting angles.



(a) (b)

Figure 5. Steady-state forced responses of the transverse displacements of the beam on the free end due to external force $F_Z = 50000\cos(425.25\,t)$, — $\varphi = 0$, — $\varphi = \pi/8$, — $\varphi = \pi/4$, $\dot{\vartheta} = 100$ rad/s, t – time, T – period of vibration.

On Figure 5, are shown the forced responses of the beam for three different setting angles: 0, $\pi/8$ and $\pi/4$. It is noted that with changes of the setting angle, the force remains in the

same direction (perpendicular to the plane of rotation), and changes of the setting angle spread the external force in y and z directions in the transport coordinate system. It can be seen that for the three different setting angles, the amplitudes of vibration change slightly. Also, in the case of zero setting angle, $\varphi = 0$, i.e. when the transverse force is applied only in z direction of the beam, the transverse displacement v_0 is excited with amplitude similar to the transverse displacement w_0. One could expect that for that case, $\varphi = 0$, the transverse displacement v_0 will be excited due to acceleration of Coriolis and it will vibrate with smaller amplitude in comparison to w_0. Nevertheless, Figure 5 shows that the response amplitude of v_0 is similar to the amplitude of w_0.

Further, to investigate the influence of the acceleration of Coriolis, the responses at time domain of the same example, $\varphi = 0$, but without Coriolis forces, were obtained and shown in Figure 6. The difference between the responses of the models with and without Coriolis forces is significant (Figure 6 (a)), it is also verified that the transverse displacement v_0 is not excited, in the absence of Coriolis forces. It is concluded that the big amplitudes of the transverse displacement v_0, on Figure 5 (b) are related with loose of stability of the beam, due to interaction of both transverse modes. Even though when the external force is applied only in z direction (in the case $\varphi = 0$), the transverse displacement v_0 is excited, if there is small disturbance (Figure 6 (b)). This phenomenon is due to symmetry-breaking bifurcation point, similar bifurcation point, but for clamped-clamped beams was presented in [19]. In Figure 5, the small excitation of v_0 comes from the Coriolis forces. Thus, the solution obtained when the acceleration of Coriolis is neglected on Figure 6 (a), corresponds to the unstable solution, which presents vibration in one plane (v_0 is not excited). An unstable solution is obtained with time integration method, such as Newmark, because v_0 is not excited and there is no coupling between both transverse displacements, and the problem to solve is two dimensional, where the symmetry-breaking bifurcation point does not exists. It was also verified that, for the current case, the Coriolis forces slightly change the response –Figure 6 (b). The significant difference of the phase of the transverse displacement v_0 for $\varphi = 0$, in comparison with the rest cases of the setting angle (Figure 5 (b)), is explained by the two stable branches which arise from the symmetry-breaking bifurcation point.

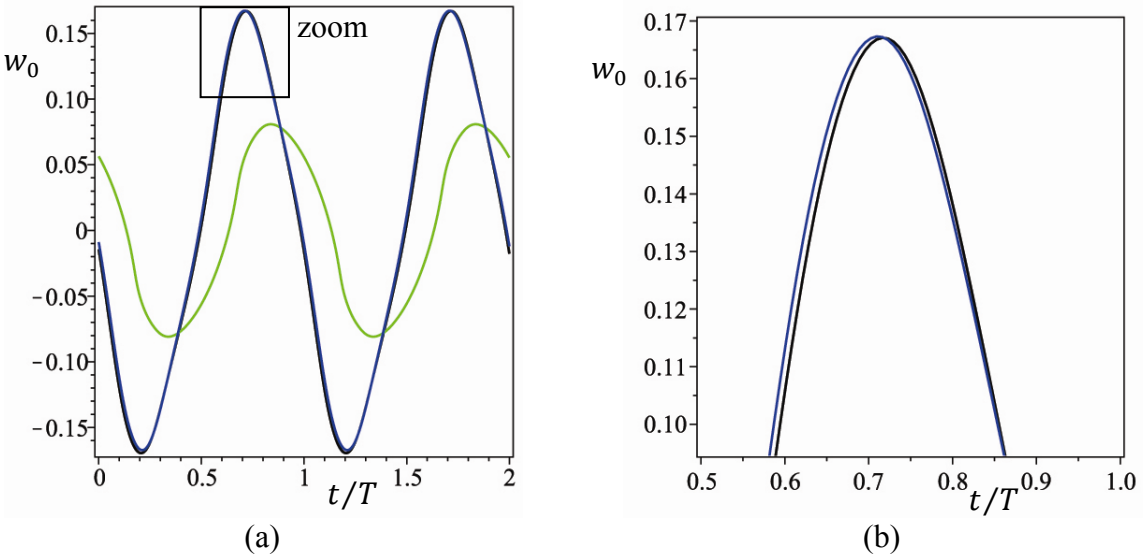
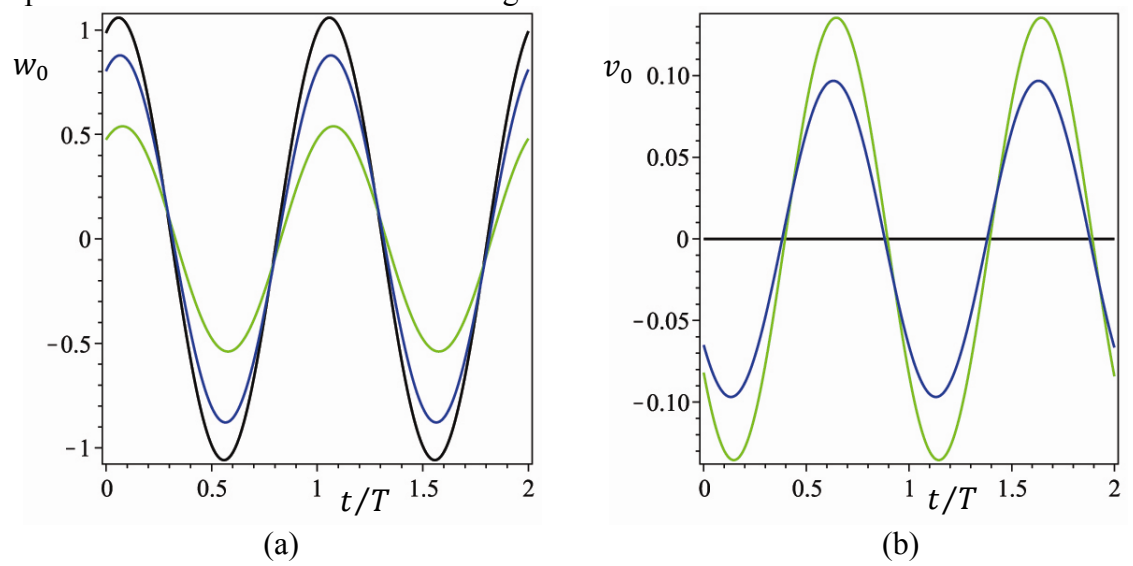


Figure 6. (a) Steady-state forced responses of the transverse displacement w_0 of the beam on the free end due to external force $F_Z = 50000\cos(425.25\,t)$, $\varphi = 0$, $\dot{\vartheta} = 100$ rad/s, ━ with Coriolis forces, ━ without Coriolis forces, ━ without Coriolis forces, but with initial disturbance of v_0, (b) zoom of (a), t – time, T – period of vibration.

Finally, a discussion about the equality of the amplitudes of vibration for the different setting angles is presented. One could expect that increasing the setting angle will decrease the amplitude of w_0 and will increase the amplitude of v_0, because the external force is decreased in z direction and it is increased in y direction (for $0 \leq \varphi \leq \pi/2$). However, the amplitudes remain similar. It is because of the nonlinear terms and the fact the excitation frequency remains the same, i.e. in nonlinear vibrations the amplitude depends on the frequency of vibration [20]. This is not true for linear vibrations and the influence of the setting angle on the amplitude of vibration can be seen on Figure 7.



(a) (b)

Figure 7. (a) Steady-state forced responses of the transverse displacements w_0 and v_0 of the linear beam model on the free end due to external force $F_Z = 50000\cos(425.25\,t)$, $\dot{\vartheta} = 100$ rad/s, ━ $\varphi = 0$, ━ $\varphi = \pi/8$, ━ $\varphi = \pi/4$, t – time, T – period of vibration.

5 CONCLUSION

Nonlinear vibrations of rotating beams due to harmonic excitations were investigated. First a model of 3D beams rotating at constant speed about a fixed axis was presented, a setting angle and hub radios ware included in the model. The equation of motion was derived in the rotating coordinate system, and the rotation was taken into account by the inertia forces. Then, it was shown how the cross section was modeled and the tapered ratio considered in the equation of motion.

The beam model was validated by generating an equivalent beam structure with three-dimensional finite elements. The natural frequencies and the static deformations, of non-rotating beam, were compared and it was demonstrated that the reduced model gives results in agreement with the large-scale model. It should be outlined, that the reduced model is suitable for problems where the cross section does not change in its own plane and the rotations of the cross section about the transverse axes are moderate.

Thin-walled box beams with linearly varying thickness and width were investigated. The influence of the speed of rotation and the setting angle on the natural frequencies was presented. It was shown that in linear free vibrations, both transverse displacements are coupled, for values of the setting angle different from zero, due to the inertia forces, which result from the rotation.

Nonlinear forced steady-state responses were examined for different setting angles. The amplitude of vibration changes slightly with the setting angle, due to the geometrical nonlinear terms, while in linear models this change is significant. Steady-state responses which

correspond to the stable branches which arise from symmetry-breaking bifurcation point were obtained and presented.

ACKNOWLEDGEMENT

The research work carried out in the paper is supported by the project AComIn "Advanced Computing for Innovation", grant 316087, funded by the FP7 Capacity Programme (Research Potential of Convergence Regions) and Bulgarian NSF Grant DCVP 02/1.

APPENDIX

In this appendix the matrices and vectors that result from the transport acceleration and acceleration of Coriolis are presented. The transport acceleration results in the following matrix and vector:

$$\mathbf{T}(\mathbf{q},\dot{\vartheta}) = \begin{bmatrix} \mathbf{T_{11}} & \mathbf{0} & \mathbf{0} & \mathbf{0} & \mathbf{0} & \mathbf{0} \\ \mathbf{0} & \mathbf{T_{22}} & \mathbf{T_{23}} & \mathbf{0} & \mathbf{0} & \mathbf{0} \\ \mathbf{0} & \mathbf{T_{32}} & \mathbf{T_{33}} & \mathbf{0} & \mathbf{0} & \mathbf{0} \\ \mathbf{0} & \mathbf{0} & \mathbf{0} & \mathbf{T_{44}} & \mathbf{0} & \mathbf{0} \\ \mathbf{0} & \mathbf{0} & \mathbf{0} & \mathbf{0} & \mathbf{T_{55}} & \mathbf{0} \\ \mathbf{0} & \mathbf{0} & \mathbf{0} & \mathbf{0} & \mathbf{0} & \mathbf{T_{66}} \end{bmatrix}$$

$$\mathbf{R}(\dot{\vartheta}) = \begin{Bmatrix} \mathbf{R_1} \\ \mathbf{0} \\ \mathbf{0} \\ \mathbf{R_4} \\ \mathbf{0} \\ \mathbf{0} \end{Bmatrix}$$

where

$$\mathbf{T_{11}} = -\dot{\vartheta}(t)^2\,\rho \int_V \mathbf{N^{u}}^{\mathrm{T}}\,\mathbf{N^{u}}\,dV$$

$$\mathbf{T_{22}} = -\dot{\vartheta}(t)^2\,\rho\,\cos\varphi^2 \int_V \mathbf{N^{v}}^{\mathrm{T}}\,\mathbf{N^{v}}\,dV$$

$$\mathbf{T_{23}} = \dot{\vartheta}(t)^2\,\rho\,\cos\varphi\sin\varphi \int_V \mathbf{N^{v}}^{\mathrm{T}}\,\mathbf{N^{w}}\,dV$$

$$\mathbf{T_{32}} = \dot{\vartheta}(t)^2\,\rho\,\cos\varphi\sin\varphi \int_V \mathbf{N^{w}}^{\mathrm{T}}\,\mathbf{N^{v}}\,dV$$

$$\mathbf{T_{33}} = -\dot{\vartheta}(t)^2\,\rho\,\sin\varphi^2 \int_V \mathbf{N^{w}}^{\mathrm{T}}\,\mathbf{N^{w}}\,dV$$

$$\mathbf{T_{44}} = \dot{\vartheta}(t)^2\,\rho\,(\cos\varphi^2 - \sin\varphi^2) \int_V (y^2 - z^2)\,\mathbf{N^{\theta_x}}^{\mathrm{T}}\,\mathbf{N^{\theta_x}}dV +$$

$$+\dot{\vartheta}(t)^2\,\rho\,\cos\varphi\sin\varphi \int_V (z^2 - y^2)\,\mathbf{N^{\theta_x}}^{\mathrm{T}}\,\mathbf{N^{\theta_x}}\,\theta_x\,dV - \dot{\vartheta}(t)^2\,\rho \int_V \psi^2 \frac{\mathrm{d}\mathbf{N^{\theta_x}}^{\mathrm{T}}}{\mathrm{d}x}\frac{\mathrm{d}\mathbf{N^{\theta_x}}}{\mathrm{d}x}dV$$

$$\mathbf{T_{55}} = -\dot{\vartheta}(t)^2\,\rho \int\limits_V z^2\,\mathbf{N^{\phi_y}}^{\mathrm{T}}\mathbf{N^{\phi_y}}\,dV$$

$$\mathbf{T_{66}} = -\dot{\vartheta}(t)^2\,\rho \int\limits_V y^2\,\mathbf{N^{\phi_z}}^{\mathrm{T}}\mathbf{N^{\phi_z}}\,dV$$

$$\mathbf{R_1} = \dot{\vartheta}(t)^2\,\rho \int\limits_V (R+x)\,\mathbf{N^{u}}^{\mathrm{T}}\,dV$$

$$\mathbf{R_4} = \dot{\vartheta}(t)^2\,\rho\,\cos\varphi\sin\varphi \int\limits_V (-y^2+z^2)\,\mathbf{N^{\theta_x}}^{\mathrm{T}}\,dV$$

The acceleration of Coriolis results in the following matrix:

$$\mathbf{CR}(\mathbf{q},\dot{\vartheta}) = \begin{bmatrix} \mathbf{0} & \mathbf{CR_{12}} & \mathbf{CR_{13}} & \mathbf{0} & \mathbf{0} & \mathbf{0} \\ \mathbf{CR_{21}} & \mathbf{0} & \mathbf{0} & \mathbf{0} & \mathbf{0} & \mathbf{0} \\ \mathbf{CR_{31}} & \mathbf{0} & \mathbf{0} & \mathbf{0} & \mathbf{0} & \mathbf{0} \\ \mathbf{0} & \mathbf{0} & \mathbf{0} & \mathbf{0} & \mathbf{CR_{45}} & \mathbf{CR_{46}} \\ \mathbf{0} & \mathbf{0} & \mathbf{0} & \mathbf{CR_{54}} & \mathbf{0} & \mathbf{0} \\ \mathbf{0} & \mathbf{0} & \mathbf{0} & \mathbf{CR_{64}} & \mathbf{0} & \mathbf{0} \end{bmatrix}$$

where

$$\mathbf{CR_{12}} = -2\,\dot{\vartheta}(t)\,\rho\cos\varphi \int\limits_V \mathbf{N^{u}}^{\mathrm{T}}\,\mathbf{N^{v}}\,dV$$

$$\mathbf{CR_{13}} = 2\,\dot{\vartheta}(t)\,\rho\sin\varphi \int\limits_V \mathbf{N^{u}}^{\mathrm{T}}\,\mathbf{N^{w}}\,dV$$

$$\mathbf{CR_{21}} = 2\,\dot{\vartheta}(t)\,\rho\cos\varphi \int\limits_V \mathbf{N^{v}}^{\mathrm{T}}\,\mathbf{N^{u}}\,dV$$

$$\mathbf{CR_{31}} = -2\,\dot{\vartheta}(t)\,\rho\sin\varphi \int\limits_V \mathbf{N^{w}}^{\mathrm{T}}\,\mathbf{N^{u}}\,dV$$

$$\mathbf{CR_{45}} = -2\,\dot{\vartheta}(t)\,\rho\cos\varphi \int\limits_V z^2\;\mathbf{N^{\theta_x}}^{\mathrm{T}}\,\mathbf{N^{\phi_y}}\,dV + 2\,\dot{\vartheta}(t)\,\rho\sin\varphi \int\limits_V z^2\;\mathbf{N^{\theta_x}}^{\mathrm{T}}\,\mathbf{N^{\phi_y}}\,\theta_x\,dV$$

$$\mathbf{CR_{46}} = 2\,\dot{\vartheta}(t)\,\rho\sin\varphi \int\limits_V y^2\;\mathbf{N^{\theta_x}}^{\mathrm{T}}\,\mathbf{N^{\phi_z}}\,dV + 2\,\dot{\vartheta}(t)\,\rho\cos\varphi \int\limits_V y^2\;\mathbf{N^{\theta_x}}^{\mathrm{T}}\,\mathbf{N^{\phi_z}}\,\theta_x\,dV$$

$$\mathbf{CR_{54}} = 2\,\dot{\vartheta}(t)\,\rho\cos\varphi \int\limits_V z^2\,\mathbf{N^{\phi_y}}^{\mathrm{T}}\,\mathbf{N^{\theta_x}}\,dV - 2\,\dot{\vartheta}(t)\,\rho\sin\varphi \int\limits_V z^2\,\mathbf{N^{\phi_y}}^{\mathrm{T}}\,\mathbf{N^{\theta_x}}\,\theta_x\,dV$$

$$\mathbf{CR_{64}} = -2\,\dot{\vartheta}(t)\,\rho\sin\varphi \int\limits_V y^2\,\mathbf{N^{\phi_z}}^{\mathrm{T}}\,\mathbf{N^{\theta_x}}\,dV - 2\,\dot{\vartheta}(t)\,\rho\cos\varphi \int\limits_V y^2\,\mathbf{N^{\phi_z}}^{\mathrm{T}}\;\mathbf{N^{\theta_x}}\,\theta_x\,dV$$

REFERENCES

[1] D. Hodges, M. Rutkowski, Free vibration analysis of rotating beams by a variable-order finite-element method. *AIAA Journal*, 19, 1459-1466, 1981.

[2] T. Yokoyama, Free vibration characteristics of rotating Timoshenko beams. *International Journal of Mechanical Sciences*, 30, 743-755, 1988.

[3] A. Bazoune, Y. Khulief, N. Stephen, Further results for modal characteristics of rotating tapered Timoshenko beams. Journal *of Sound and Vibration*, 219, 157-174, 1999.

[4] S. Lin, K. Hsiao, Vibration analysis of a rotating Timoshenko beam. *Journal of Sound and Vibration*, 240, 303-322, 2001.

[5] H. Yoo, S. Shin, Vibration analysis or rotating cantilever beams. *Journal of Sound and Vibration*, 212, 807-828, 1998.

[6] E. Pesheck, C. Pierre, S. Shaw, Modal reduction of a nonlinear rotating beam through nonlinear normal modes. *Journal of Vibration and Acoustics*, 124, 229-236, 2002.

[7] Ö. Turhan, G. Bulut, On nonlinear vibrations of a rotating beam. *Journal of Sound and Vibration*, 322, 314-335, 2009.

[8] D. Younesian, E. Esmailzadeh, Non-linear vibration of variable speed rotating viscoelastic beams. *Nonlinear Dynamics*, 60, 193-205, 2010.

[9] F.M. Jensen, P.H. Nielsen, A. Roczek-Sieradzan, T. Sieradzan, K. Branner, R. Bitsche, On innovative concepts of wind turbine blade design. *European Wind Energy Conference and Exhibition 2011, EWCE 2011*, 275-279, 2011.

[10] S. Stoykov, P. Ribeiro, Vibration analysis of rotating 3D beams by the p-version finite element method. *Finite Elements in Analysis and Design*, 65, 76-88, 2013.

[11] S. Stoykov, P. Ribeiro, Nonlinear forced vibrations and static deformations of 3D beams with rectangular cross section: The influence of warping, shear deformation and longitudinal displacements. *International Journal of Mechanical Sciences*, 52, 1505-1521, 2010.

[12] C. Wang, J. Reddy, K. Lee, *Shear deformable beams and plates*, Elsevier, Oxford, 2000.

[13] G. Wempner, D. Talaslidis, *Mechanics of solids and shells. Theory and Application*, CRC Press, Boca Raton, Florida, 2003.

[14] A.A. Shabana, *Dynamics of multibody systems*, Cambridge University Press, 2005.

[15] I. Sokolnikoff, *Mathematical theory of elasticity*, McGraw-Hill, 1956.

[16] Elmer web site: www.csc.fi/elmer (last time visited 15/02/2013).

[17] C. Geuzaine and J.-F. Remacle, Gmsh: a three-dimensional finite element mesh generator with built-in pre- and post-processing facilities. *International Journal for Numerical Methods in Engineering*, 79, 1309-1331, 2009.

[18] P. R. Amestoy, A. Guermouche, J. Y. L'Excellent, S. Pralet, Hybrid scheduling for the parallel solution of linear systems. *Parallel Computing*, 32, 136-156, 2006.

[19] S. Stoykov, P. Ribeiro, Stability of nonlinear periodic vibrations of 3D beams. *Nonlinear Dynamics*, 66, 335-353, 2011.

[20] G. Kerschen, M. Peeters, J. C. Golinval, A. Vakakis, Nonlinear normal modes, Part I: A useful framework for the structural dynamicist. *Mechanical Systems and Signal Processing*, 23, 170-194, 2009.

COMPDYN 2013
4th ECCOMAS Thematic Conference on
Computational Methods in Structural Dynamics and Earthquake Engineering
M. Papadrakakis, V. Papadopoulos, V. Plevris (eds.)
Kos Island, Greece, 12–14 June 2013

COUPLING OF FINITE ELEMENTS AND HIERARCHICAL BOUNDARY ELEMENTS FOR DYNAMIC SOIL–STRUCTURE INTERACTION PROBLEMS

Pieter Coulier, Stijn François, Geert Lombaert, and Geert Degrande

KU Leuven, Department of Civil Engineering
Kasteelpark Arenberg 40, 3001 Leuven, Belgium
e-mail: {pieter.coulier,stijn.francois,geert.lombaert,geert.degrande}@bwk.kuleuven.be

Keywords: FE–BE coupling, iterative methods, interface relaxation, $\mathscr{H}$–matrices, dynamic soil–structure interaction.

Abstract. *This paper discusses the coupling of finite element and fast boundary element methods based on hierarchical matrices to solve problems of visco–elastodynamic wave propagation involving dynamic soil–structure interaction in the frequency domain. Three coupling methodologies are presented and their computational performance is assessed through numerical examples. It is demonstrated that a direct coupling approach, in which the boundary element domain is condensed into an equivalent dynamic stiffness matrix, is the least efficient. Iterative procedures provide a valuable alternative; the efficiency of these algorithms strongly depends on the kind of boundary conditions applied to each subdomain, however. The fastest convergence is observed if Neumann boundary conditions are imposed on the most stiff subdomain. Aitken's Δ^2–method is employed in these schemes for the calculation of an optimized interface relaxation parameter in order to ensure and speed up the convergence. A monolithic coupling approach is presented as well, providing a simultaneous solution of the governing equations while avoiding the assembly of a dynamic soil stiffness matrix.*

1 INTRODUCTION

The numerical prediction of three–dimensional (3D) visco–elastodynamic wave propagation in a stratified halfspace arises in a variety of problems, such as the simulation of seismic site effects [1], the modelling of railway induced vibrations [2] and other applications involving dynamic soil–structure interaction (SSI) [3]. A domain decomposition approach is often introduced in computational models, where distinct numerical methods are used for different subdomains. A well–known methodology is the coupled finite element – boundary element (FE–BE) approach, which combines the flexibility offered by the FE method to model complex geometries with the possibility to take the radiation of waves towards infinity into account by means of the BE method. The complementarity of both methods can either be exploited in the time [4] or in the frequency domain [5].

In the past decades, the development of efficient algorithms for the coupling of FE and BE methods has been the subject of numerous investigations [6, 7, 8]. Direct and iterative coupling methodologies exist; the former requires the assembly of a global set of coupled equations, while the governing equations are solved separately in the latter approach. Conforming or non–conforming interface discretizations can be distinguished, imposing the coupling conditions in a strong or weak sense, respectively. The latter allows for an independent mesh size adaptation for each subdomain. FE–BE coupling algorithms for elastostatics are discussed, among others, by Elleithy et al. [9] and Margonari et al. [10], while Rüberg et al. [11] present an algorithm for time–domain elastodynamics using non-conforming interfaces where the coupling conditions are incorporated in a weak sense by means of Lagrange multipliers.

The applicability of classical BE formulations to large scale problems is hindered, however, due to stringent memory and CPU requirement resulting from the dense, fully populated unsymmetric matrices arising in the formulation. This has led to the development of fast BE methods to improve the computational efficiency, including the fast multipole method (FMM) [12] and methods based on hierarchical matrices ($\mathscr{H}$–matrices) [13]. Recently, a $\mathscr{H}$-BE method for visco–elastodynamics in the frequency domain incorporatings Green's functions for a horizontally layered halfspace has been presented [14]. These Green's functions are computed by means of the direct stiffness method [15], as no closed form analytical expressions are available; their application avoids meshing of the free surface and the layer interfaces in the modelling of wave propagation in a stratified medium.

This paper focuses on the coupling of FE and $\mathscr{H}$-BE methods for the solution of dynamic SSI problems. Various FE–$\mathscr{H}$-BE coupling procedures are presented and their computational performance is assessed. Throughout this paper, non–overlapping domains with conforming interface meshes are considered, and all methods are formulated in the frequency domain. The text is organized as follows. Section 2 briefly summarizes the governing equations of the FE and $\mathscr{H}$-BE method. Three different FE–$\mathscr{H}$-BE coupling procedures are subsequently introduced in section 3. First, a classical direct coupling strategy is discussed, which requires the assembly of a dynamic soil stiffness matrix. Next, iterative algorithms are presented; special attention is paid to optimized interface relaxation techniques in order to ensure and/or speed up the convergence. Finally, a monolithic coupling approach is proposed. Numerical examples are investigated in section 4 to validate the coupling strategies and to provide additional insight in the effectiveness of the algorithms. This allows for the formulation of guidelines concerning the choice of an appropriate coupling strategy for a specific dynamic SSI problem.

2 FINITE ELEMENT AND BOUNDARY ELEMENT METHODS

The governing equations of the FE and $\mathscr{H}$-BE method are summarized in this section. It is assumed in the following that finite elements are used to model a structural domain Ω, while boundary elements are employed to model wave propagation in the surrounding soil domain Ω_{s}. The domain Ω should be understood as a generalized structure, which could comprise the actual structure and part of the soil domain. The soil–structure interface is denoted as Σ.

2.1 Finite element formulation

Finite element equilibrium equations of a domain Ω can be obtained by introducing a FE discretization in the weak variational formulation of the equilibrium of Ω, and subsequently applying a Galerkin procedure. This provides the following set of equations [3]:

$$\left[\mathbf{K} + i\omega\widehat{\mathbf{C}}(\omega) - \omega^2\mathbf{M}\right]\hat{\underline{\mathbf{u}}}(\omega) = \hat{\underline{\mathbf{f}}}(\omega) \tag{1}$$

where a hat above a variable denotes its representation in the frequency domain. $\hat{\underline{\mathbf{u}}}(\omega)$ collects the nodal degrees of freedom, while $\mathbf{K}$ and $\mathbf{M}$ are the frequency independent stiffness and mass matrices; the damping matrix $\widehat{\mathbf{C}}(\omega)$ might be frequency dependent. The bracketed term on the left hand side of equation (1) is identified as the dynamic stiffness matrix $\widehat{\mathbf{K}}(\omega)$ of the structure. The vector $\hat{\underline{\mathbf{f}}}(\omega)$ represents the force excitation to which the structure is subjected. Adequate solvers which account for the sparsity and symmetry of the system can be employed to solve equation (1).

2.2 Hierarchical boundary element formulation

The BE method is based on the discretization of the boundary Σ of a domain Ω_{s} with an appropriate number of boundary elements in order to numerically solve a (regularized) boundary integral equation. The method leads to a reduction of the spatial problem dimension (i.e. surface instead of volume discretization), but the storage of the resulting BE collocation matrices requires a quadratic amount of memory with respect to the number of degrees of freedom N_{DOF}, while a cubic amount of numerical operations is needed to solve the corresponding set of BE equations by means of direct numerical solvers. The use of $\mathscr{H}$–matrices provides an elegant way to treat fully populated matrices with almost linear complexity [16], as they approximate the original matrices (with an arbitrary prescribed accuracy) by means of data–sparse, memory–efficient representations. The construction of $\mathscr{H}$–matrices is based on the identification of admissible and inadmissible hierarchical cluster pairs in the BE mesh; the partially pivoted adaptive cross approximation (ACA) algorithm [17, 18] is employed to compute low rank approximations of matrix blocks corresponding to admissible cluster pairs. A major advantage of ACA is its purely algebraic character, avoiding the need for (semi–)analytical expressions of the Green's functions employed in the BE formulation (e.g. allowing for the incorporation of Green's functions for a horizontally layered halfspace [14]). The reader is referred to the literature [13, 16, 19] for a detailed description of the methodology regarding $\mathscr{H}$–matrices. All BE methods discussed in the remainder of this paper involve to application of $\mathscr{H}$–matrices.

For an unbounded domain Ω_{s}, the displacements $\hat{\underline{\mathbf{u}}}(\omega)$ and tractions $\hat{\underline{\mathbf{t}}}(\omega)$ at the collocation points of the boundary Σ are related as follows in the $\mathscr{H}$-BE method:

$$\left[\widehat{\mathbf{T}}_{\mathscr{H}}(\omega) + \mathbf{I}\right]\hat{\underline{\mathbf{u}}}(\omega) = \widehat{\mathbf{U}}_{\mathscr{H}}(\omega)\hat{\underline{\mathbf{t}}}(\omega) \tag{2}$$

where $\widehat{\mathbf{T}}_{\mathscr{H}}(\omega)$ and $\widehat{\mathbf{U}}_{\mathscr{H}}(\omega)$ are hierarchical representations of the BE collocation matrices $\widehat{\mathbf{T}}(\omega)$ and $\widehat{\mathbf{U}}(\omega)$, respectively, while $\mathbf{I}$ represents a unit matrix. The computation of $\widehat{\mathbf{T}}_{\mathscr{H}}(\omega)$ and $\widehat{\mathbf{U}}_{\mathscr{H}}(\omega)$ requires integration of the Green's tractions and displacements over the boundary Σ. Equation (2) can be rewritten as:

$$\widehat{\mathbf{A}}_{\mathscr{H}}(\omega)\hat{\underline{\mathbf{x}}}(\omega) = \hat{\underline{\mathbf{b}}}(\omega) \tag{3}$$

where the vector of unknowns $\hat{\underline{\mathbf{x}}}(\omega)$ contains displacements, tractions or both, depending on whether a Neumann, Dirichlet or mixed Neumann–Dirichlet problem is considered, respectively. In order to solve equation (3), iterative Krylov subspace methods such as the generalized minimal residual method (GMRES) [20] are well suited. The matrix–vector multiplication forms the core of iterative solvers, and the complexity of this operation is only $\mathcal{O}(N_{\mathrm{DOF}} \log N_{\mathrm{DOF}})$ for $\mathscr{H}$–matrices [19]. A tolerance of 10^{-6} is specified in the iterative solver for the relative residual norm $||\hat{\underline{\mathbf{b}}}(\omega) - \widehat{\mathbf{A}}_{\mathscr{H}}(\omega)\hat{\underline{\mathbf{x}}}(\omega)||_2/||\hat{\underline{\mathbf{b}}}(\omega)||_2$ in all numerical examples presented in this paper.

As will be clarified in section 3, equation (3) has to be solved multiple times with a varying right hand side $\hat{\underline{\mathbf{b}}}(\omega)$ in FE–$\mathscr{H}$-BE coupling algorithms, and the implementation of a suitable preconditioner is therefore desirable to reduce the computation time. A right preconditioner $\widehat{\mathbf{M}}(\omega)$ is used throughout this paper in order to lower the condition number of the coefficient matrix $\widehat{\mathbf{A}}_{\mathscr{H}}(\omega)$:

$$\widehat{\mathbf{A}}_{\mathscr{H}}(\omega)\widehat{\mathbf{M}}^{-1}(\omega)\hat{\underline{\mathbf{y}}}(\omega) = \hat{\underline{\mathbf{b}}}(\omega) \tag{4}$$

with $\widehat{\mathbf{M}}(\omega)\hat{\underline{\mathbf{x}}}(\omega) = \hat{\underline{\mathbf{y}}}(\omega)$. An example of an efficient preconditioner is the approximate $\mathscr{H}$–LU decomposition proposed in [21]; its computation requires, however, additional arithmetic operations. A much simpler strategy is applied in this paper, following the approach recently adopted by Chaillat et al. for the acceleration of FMM calculations for elastodynamics [23]. A block diagonal preconditioner $\widehat{\mathbf{M}}(\omega) = \mathrm{blkdiag}\left(\widehat{\mathbf{A}}_{\mathscr{H}}(\omega)\right)$ is employed, where the size of the diagonal blocks is determined by the lowest hierarchical cluster level. An inner GMRES solver with a moderate tolerance of 10^{-2} is applied to solve the preconditioning linear systems, resulting in a nested inner–outer iteration scheme. Furthermore, the flexible GMRES (FGMRES) algorithm [22] is employed for the outer iteration in order to avoid the explicit application of $\widehat{\mathbf{M}}^{-1}(\omega)$ to the Krylov vectors. As $\widehat{\mathbf{M}}(\omega)$ is already computed and stored, the proposed approach is very cheap in terms of computational resources.

3 FE–$\mathscr{H}$-BE COUPLING PROCEDURES

Three procedures for the coupling of FE and $\mathscr{H}$-BE models are outlined in this section. The numerical validation and the assessment of the computational efficiency of the proposed methods are subsequently addressed in section 4.

3.1 Direct FE–$\mathscr{H}$-BE coupling

In a classical direct coupling strategy [24], the governing equations of the FE and BE subdomain are straightforwardly combined, accounting for continuity of displacements and equilibrium of tractions at the soil–structure interface Σ. This results in a global coupled system of equations:

$$\left(\begin{bmatrix} \widehat{\mathbf{K}}_{11}(\omega) & \widehat{\mathbf{K}}_{12}(\omega) \\ \widehat{\mathbf{K}}_{21}(\omega) & \widehat{\mathbf{K}}_{22}(\omega) \end{bmatrix} + \begin{bmatrix} \mathbf{0} & \mathbf{0} \\ \mathbf{0} & \widehat{\mathbf{K}}^{\mathrm{s}}_{22}(\omega) \end{bmatrix}\right) \begin{Bmatrix} \hat{\underline{\mathbf{u}}}_1(\omega) \\ \hat{\underline{\mathbf{u}}}_2(\omega) \end{Bmatrix} = \begin{Bmatrix} \hat{\underline{\mathbf{f}}}_1(\omega) \\ \hat{\underline{\mathbf{f}}}_2(\omega) \end{Bmatrix} \tag{5}$$

where a subdivision into block matrices according to degrees of freedom $\underline{\hat{\mathbf{u}}}_2(\omega)$ on the soil–structure interface Σ and degrees of freedom $\underline{\hat{\mathbf{u}}}_1(\omega)$ internally in the structural domain Ω is introduced. $\widehat{\mathbf{K}}^{\mathrm{s}}_{22}(\omega)$ represents the dynamic soil stiffness matrix and is defined as:

$$\widehat{\mathbf{K}}^{\mathrm{s}}_{22}(\omega) = \int_{\Sigma} \mathbf{N}_2^{\mathrm{T}}(\mathbf{x})\mathbf{N}_2(\mathbf{x})\underline{\hat{\mathbf{t}}}(\mathbf{N}_2(\mathbf{x}))(\omega)\,\mathrm{d}S = \mathbf{T}_{\mathrm{q}}\,\underline{\hat{\mathbf{t}}}(\mathbf{N}_2(\mathbf{x}))(\omega) \tag{6}$$

where $\mathbf{N}_2(\mathbf{x})$ indicates the FE shape functions on the soil–structure interface Σ, corresponding to the BE interpolation functions (as conforming FE and BE meshes are considered). The frequency independent matrix $\mathbf{T}_{\mathrm{q}} = \int_{\Sigma} \mathbf{N}_2^{\mathrm{T}}(\mathbf{x})\mathbf{N}_2(\mathbf{x})\,\mathrm{d}S$ links the FE and BE discretizations.

Although equation (5) provides a straightforward solution to the dynamic SSI problem, it suffers from some major drawbacks. Equation (6) requires the evaluation of tractions $\underline{\hat{\mathbf{t}}}(\mathbf{N}_2(\mathbf{x}))(\omega)$ by means of the $\mathscr{H}$-BE method, which implies that equation (4) has to be solved for multiple right hand sides (i.e. for all shape functions $\mathbf{N}_2(\mathbf{x})$ on Σ); the implemented FGMRES algorithm is only able to handle one right hand side at a time. Furthermore, addition of the dense unsymmetric dynamic soil stiffness matrix $\widehat{\mathbf{K}}^{\mathrm{s}}_{22}(\omega)$ to $\widehat{\mathbf{K}}(\omega)$ strongly affects the sparsity of the system, reducing the efficiency of sparse finite element solvers applied to equation (5). The numerical examples in section 4 will demonstrate that this conventional approach, in which the dynamic soil stiffness matrix $\widehat{\mathbf{K}}^{\mathrm{s}}_{22}(\omega)$ is explicitly evaluated, does not provide an efficient solution procedure, especially in case large scale problems are considered.

3.2 Iterative FE–$\mathscr{H}$-BE coupling

Iterative coupling procedures provide a valuable alternative to the conventional direct strategy outlined in the previous subsection, as the evaluation of the dynamic soil stiffness matrix $\widehat{\mathbf{K}}^{\mathrm{s}}_{22}(\omega)$ is avoided. The governing equations are solved separately for each subdomain in such an approach, while the boundary conditions at the soil–structure interface are updated until convergence is achieved. This methodology avoids the assembly and solution of a global system of coupled equations; it hence allows for the coupling of black box FE and $\mathscr{H}$-BE solvers. Iterative schemes are often used for dynamic SSI problems in the time domain to allow for the use of different time discretization schemes [4, 25, 26]. Their application in the frequency domain remains rather limited, however, especially due to convergence difficulties [27]. Frequency domain iterative algorithms described in the literature mainly involve acoustic–acoustic [28] and acoustic–elastodynamic [27] coupling, although Grasso [29] discusses the iterative coupling of FE and fast multipole BE models for visco–elastodynamics in the frequency domain.

Four different iterative algorithms for the coupling of FE and $\mathscr{H}$-BE model are outlined in the following subsections. These methodologies are denoted as sequential Neumann–Dirichlet or Dirichlet–Neumann algorithms, and parallel Neumann–Neumann or Dirichlet–Dirichlet algorithms, respectively, indicating which kind of boundary conditions are imposed on the FE and BE subdomain.

3.2.1 Sequential Neumann–Dirichlet algorithm

At iteration step k of the sequential Neumann–Dirichlet procedure, the finite element subdomain is analyzed with Neumann boundary conditions $\underline{\hat{\mathbf{q}}}^{(k)}(\omega)$ at the soil–structure interface Σ:

$$\begin{bmatrix} \widehat{\mathbf{K}}_{11}(\omega) & \widehat{\mathbf{K}}_{12}(\omega) \\ \widehat{\mathbf{K}}_{21}(\omega) & \widehat{\mathbf{K}}_{22}(\omega) \end{bmatrix} \begin{Bmatrix} \underline{\hat{\mathbf{u}}}_1^{(k)}(\omega) \\ \underline{\hat{\mathbf{u}}}_2^{(k)}(\omega) \end{Bmatrix} = \begin{Bmatrix} \underline{\hat{\mathbf{f}}}_1(\omega) \\ \underline{\hat{\mathbf{f}}}_2(\omega) \end{Bmatrix} + \begin{Bmatrix} \underline{\mathbf{0}} \\ \underline{\hat{\mathbf{q}}}^{(k)}(\omega) \end{Bmatrix} \tag{7}$$

where $\underline{\hat{\mathbf{q}}}^{(k)}(\omega)$ denotes the soil–structure interaction forces. Solving equation (7) by means of a standard finite element solver provides the internal and interface displacements $\underline{\hat{\mathbf{u}}}_1^{(k)}(\omega)$ and $\underline{\hat{\mathbf{u}}}_2^{(k)}(\omega)$. The latter are subsequently imposed as Dirichlet boundary conditions on the boundary element subdomain, allowing to solve the preconditioned system of equations (4) for the interface tractions $\underline{\hat{\mathbf{t}}}^{(k)}(\omega)$ using the FGMRES solver. These tractions are used to calculate equivalent nodal forces $\underline{\hat{\mathbf{q}}}^{(k+\lambda)}(\omega)$:

$$\underline{\hat{\mathbf{q}}}^{(k+\lambda)}(\omega) = -\int_{\Sigma} \mathbf{N}_2^{\mathrm{T}}(\mathbf{x})\mathbf{N}_2(\mathbf{x})\underline{\hat{\mathbf{t}}}^{(k)}(\omega)\,\mathrm{d}S = -\mathbf{T}_{\mathrm{q}}\,\underline{\hat{\mathbf{t}}}^{(k)}(\omega) \tag{8}$$

The interaction forces are finally relaxed using an iteration dependent relaxation parameter $\lambda^{(k)}$:

$$\underline{\hat{\mathbf{q}}}^{(k+1)}(\omega) = \lambda^{(k)}\underline{\hat{\mathbf{q}}}^{(k+\lambda)}(\omega) + (1-\lambda^{(k)})\underline{\hat{\mathbf{q}}}^{(k)}(\omega) \tag{9}$$

Once the relaxed interaction forces $\underline{\hat{\mathbf{q}}}^{(k+1)}(\omega)$ are computed, a subsequent step in the iterative procedure is performed until convergence is obtained; an accuracy of 10^{-4} is prescribed for the relative residual norm $||\underline{\hat{\mathbf{u}}}_2^{(k+1)}(\omega) - \underline{\hat{\mathbf{u}}}_2^{(k)}(\omega)||_2 / ||\underline{\hat{\mathbf{u}}}_2^{(k+1)}(\omega)||_2$ of the interface displacements and $||\underline{\hat{\mathbf{q}}}^{(k+1)}(\omega) - \underline{\hat{\mathbf{q}}}^{(k)}(\omega)||_2 / ||\underline{\hat{\mathbf{q}}}^{(k+1)}(\omega)||_2$ of the interaction forces.

The choice of a suitable relaxation parameter $\lambda^{(k)}$ in equation (9) is of great importance in order to ensure and/or speed up the convergence of the iterative algorithm. Constant relaxation parameters are considered, among others, by Elleithy et al. [9, 30] for linear elastostatics, von Estorff et al. [4] for transient elastodynamics, Hagen [31] for fluid–soil–structure interaction, and Grasso [29] for visco–elastodynamics in the frequency domain. Convergence conditions have been established [9, 30] and parametric studies have been performed to identify the optimal choice of a constant relaxation parameter [4, 31]. Soares et al. [27] present an iterative procedure for the solution of fluid–solid interaction problems in the frequency domain, in which an optimized relaxation parameter is calculated in each iterative step by minimizing the square error functional of the interface fluxes.

In this paper, Aitken's Δ^2–method [32] is employed for the determination of an iteration dependent relaxation parameter $\lambda^{(k)}$. This method provides a simple but efficient procedure to determine $\lambda^{(k)}$, based on the results of two subsequent iterations. It is often applied in the iterative solution of fluid–structure interaction problems [33, 34] and has already been adopted for transient elastodynamic problems [26]. Figure 1a shows a graphical illustration of the main idea behind this method, for a general iteration process in terms of a scalar x and a function $f(x)$, with solution $\overline{x} = f(\overline{x})$. An estimation $x^{(k+\lambda)} = f(x^{(k)})$ is computed in step k of the iterative procedure; if no relaxation is applied (i.e. $\lambda^{(k)} \equiv 1$), the new approximation of $\overline{x}$ yields $x^{(k+1)} = x^{(k+\lambda)}$. In Aitken's Δ^2–method, however, the estimation $x^{(k+\lambda)} = f(x^{(k)})$ is combined with the result of the previous iteration step $k-1$, which allows for the determination of $x^{(k+1)}$ as the intersection of the linearized function $\tilde{f}^{(k)}(x)$ through the points $\left\{x^{(k-1)}, x^{(k-1+\lambda)}\right\}^{\mathrm{T}}$ and $\left\{x^{(k)}, x^{(k+\lambda)}\right\}^{\mathrm{T}}$, and the function $y = x$, respectively. This clearly corresponds to a single step of the secant method [34]. The relaxation parameter $\lambda^{(k)}$ can hence be written in function of $x^{(k-1)}$, $x^{(k-1+\lambda)}$, $x^{(k)}$ and $x^{(k+\lambda)}$:

$$\lambda^{(k)} = \frac{x^{(k)} - x^{(k-1)}}{x^{(k)} - x^{(k+\lambda)} - x^{(k-1)} + x^{(k-1+\lambda)}} \tag{10}$$

Introducing the relation $x^{(k)} - x^{(k-1)} = \lambda^{(k-1)}\left(x^{(k-1+\lambda)} - x^{(k-1)}\right)$ provides a recursive relation

for the relaxation parameter $\lambda^{(k)}$:

$$\lambda^{(k)} = \lambda^{(k-1)} \frac{x^{(k-1+\lambda)} - x^{(k-1)}}{x^{(k)} - x^{(k+\lambda)} - x^{(k-1)} + x^{(k-1+\lambda)}} \tag{11}$$

$$= -\lambda^{(k-1)} \frac{r^{(k-1)}}{r^{(k)} - r^{(k-1)}} \tag{12}$$

with the residual $r^{(k)}$ defined as $r^{(k)} = x^{(k)} - x^{(k+\lambda)}$.

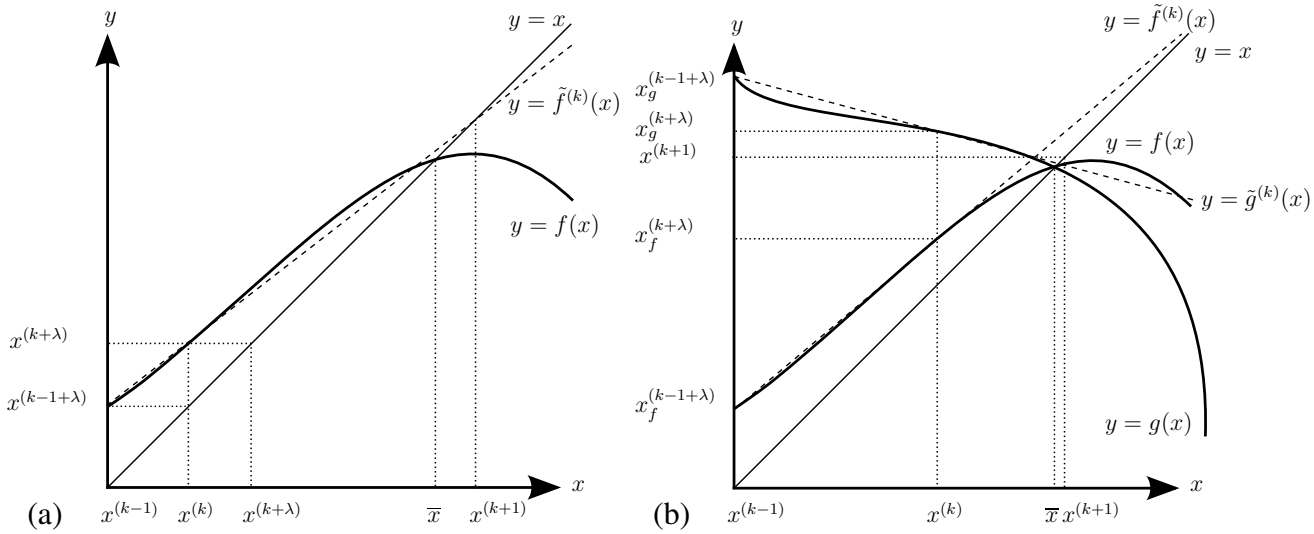


Figure 1: Graphical illustration of Aitken's Δ^2–method employed in (a) sequential and (b) parallel iterative algorithms.

For the vectorized interaction forces $\hat{\underline{\mathbf{q}}}(\omega)$ considered in this subsection, however, the division in equation (12) is impossible. Following the approach presented by Irons and Tuck [35], the vectors are projected in the direction $\hat{\underline{\mathbf{r}}}^{(k)}(\omega) - \hat{\underline{\mathbf{r}}}^{(k-1)}(\omega) = \hat{\underline{\mathbf{q}}}^{(k)}(\omega) - \hat{\underline{\mathbf{q}}}^{(k+\lambda)}(\omega) - \hat{\underline{\mathbf{q}}}^{(k-1)}(\omega) + \hat{\underline{\mathbf{q}}}^{(k-1+\lambda)}(\omega)$:

$$\lambda^{(k)} = -\lambda^{(k-1)} \frac{\left(\hat{\underline{\mathbf{r}}}^{(k)}(\omega) - \hat{\underline{\mathbf{r}}}^{(k-1)}(\omega)\right)^{\mathrm{T}} \hat{\underline{\mathbf{r}}}^{(k-1)}(\omega)}{||\hat{\underline{\mathbf{r}}}^{(k)}(\omega) - \hat{\underline{\mathbf{r}}}^{(k-1)}(\omega)||^2} \tag{13}$$

with $\lambda^{(0)} = 1$. Equation (13) can be evaluated at low computational cost, providing a simple and robust way to calculate an iteration dependent relaxation parameter, hence avoiding the need for an empirical trial–and–error process [4]. As all calculations are performed in the frequency domain, the relaxation parameter $\lambda^{(k)}$ is a complex number. Although the amplitude of this number could be limited (e.g. $||\lambda^{(k)}|| \leq 1$), it is chosen not to do so in this paper, as Soares et al. [27] have observed that faster convergence could be achieved with a non–restricted relaxation parameter (in case of acoustic–elastodynamic FE–BE coupling in the frequency domain).

The convergence of the algorithm can be further accelerated by using the relaxed tractions $-\mathbf{T}_{\mathrm{q}}^{-1}\, \hat{\underline{\mathbf{q}}}^{(k)}(\omega)$ obtained in iteration $k-1$ as an initial guess in the iterative FGMRES algorithm employed to solve equation (4) for $\hat{\underline{\mathbf{t}}}^{(k)}(\omega)$ in iteration k. Furthermore, if a loop with a sufficiently fine frequency sampling is considered, the converged solution at a particular frequency can be used as an initial guess for the first iteration at the subsequent frequency.

A major disadvantage of the proposed algorithm lies in the fact that it does not allow to determine the static solution, as application of Neumann boundary conditions to the unconstrained structural domain Ω results in a singularity of the FE equations. The convergence behaviour at low frequencies is hence expected to be poor, and the frequency sweep is therefore performed from high to low frequencies. Singularity of the FE equations is also encountered if the structure is excited at one of its (undamped) natural frequencies; incorporation of structural damping remediates this issue.

3.2.2 Sequential Dirichlet–Neumann algorithm

The second iterative algorithm considered in this paper consist of a sequential Dirichlet–Neumann scheme; the type of boundary conditions applied to each subdomain is reversed compared to the procedure outlined in subsection 3.2.1. At iteration step k, Dirichlet boundary conditions $\underline{\hat{\mathbf{u}}}_2^{(k)}(\omega)$ are imposed on the interface Σ of the FE subdomain, providing the interaction forces $\underline{\hat{\mathbf{q}}}^{(k)}(\omega)$ through the solution of equation (7) (and condensation of the internal degrees of freedom $\underline{\hat{\mathbf{u}}}_1^{(k)}(\omega)$). The corresponding interface tractions $\underline{\hat{\mathbf{t}}}^{(k)}(\omega) = -\mathbf{T}_{\mathrm{q}}^{-1}\,\underline{\hat{\mathbf{q}}}^{(k)}(\omega)$ are applied to the BE subdomain, and unrelaxed interface displacements $\underline{\hat{\mathbf{u}}}_2^{(k+\lambda)}(\omega)$ are obtained by solving the preconditioned system of equations (4) using the FGMRES solver. Aitken's Δ^2–method is finally employed for the determination of an optimized relaxation parameter $\lambda^{(k)}$ (with equation (13) in that case based on interface displacements instead of interaction forces), allowing for the computation of relaxed interface displacements $\underline{\hat{\mathbf{u}}}_2^{(k+1)}(\omega)$. This iterative procedure is repeated until convergence is achieved.

As displacements are imposed on the boundary of the FE subdomain, the iterative scheme also succeeds in solving the coupled problem for static excitation or excitation near a natural frequency (in case of an undamped structure), in contrast to the Neumann–Dirichlet algorithm presented in subsection 3.2.1.

3.2.3 Parallel Neumann–Neumann algorithm

A parallel Neumann–Neumann iterative scheme is obtained if the interaction forces $\underline{\hat{\mathbf{q}}}^{(k)}(\omega)$ and corresponding interface tractions $\underline{\hat{\mathbf{t}}}^{(k)}(\omega) = -\mathbf{T}_{\mathrm{q}}^{-1}\,\underline{\hat{\mathbf{q}}}^{(k)}(\omega)$ are simultaneously imposed as Neumann boundary conditions on the interface Σ of the FE and BE subdomain, respectively. Solving equations (7) and (4) provides (incompatible) interface displacements $\underline{\hat{\mathbf{u}}}_{2,\mathrm{FE}}^{(k)}(\omega)$ and $\underline{\hat{\mathbf{u}}}_{2,\mathrm{BE}}^{(k)}(\omega)$, respectively. The discrepancy of interface displacements $\Delta\underline{\hat{\mathbf{u}}}_2^{(k)}(\omega) = \underline{\hat{\mathbf{u}}}_{2,\mathrm{BE}}^{(k)}(\omega) - \underline{\hat{\mathbf{u}}}_{2,\mathrm{FE}}^{(k)}(\omega)$ is subsequently employed to calculate an increment of interaction forces $\Delta\underline{\hat{\mathbf{q}}}^{(k)}(\omega)$. The displacement discrepancy $\Delta\underline{\hat{\mathbf{u}}}_2^{(k)}(\omega)$ can either be imposed on the FE or the BE subdomain to compute this increment; this either yields unrelaxed interaction forces $\underline{\hat{\mathbf{q}}}_{\mathrm{FE}}^{(k+\lambda)}(\omega) = \underline{\hat{\mathbf{q}}}^{(k)}(\omega) + \Delta\underline{\hat{\mathbf{q}}}_{\mathrm{FE}}^{(k)}(\omega)$ or $\underline{\hat{\mathbf{q}}}_{\mathrm{BE}}^{(k+\lambda)}(\omega) = \underline{\hat{\mathbf{q}}}^{(k)}(\omega) + \Delta\underline{\hat{\mathbf{q}}}_{\mathrm{BE}}^{(k)}(\omega)$. Application of Aitken relaxation finally provides relaxed interaction forces $\underline{\hat{\mathbf{q}}}_{\mathrm{FE}}^{(k+1)}(\omega)$ or $\underline{\hat{\mathbf{q}}}_{\mathrm{BE}}^{(k+1)}(\omega)$, which are used in a subsequent step of the iterative scheme.

One can expect that the fastest convergence will be achieved if the force increment $\Delta\underline{\hat{\mathbf{q}}}^{(k)}(\omega)$ is calculated by imposing the displacement discrepancy $\Delta\underline{\hat{\mathbf{u}}}_2^{(k)}(\omega)$ on the most flexible subdomain. It is difficult, however, to estimate the flexibility of each subdomain a priori, especially as the latter is frequency dependent. Choosing either the FE or the BE subdomain for the calculation of $\Delta\underline{\hat{\mathbf{q}}}^{(k)}(\omega)$ hence requires a profound understanding of the dynamic behaviour of

each subdomain; a wrong choice can significantly deteriorate the convergence of the iterative procedure.

A more robust variant of the algorithm is therefore presented in this paper, where $\underline{\hat{\mathbf{q}}}_{\mathrm{FE}}^{(k+\lambda)}(\omega)$ and $\underline{\hat{\mathbf{q}}}_{\mathrm{BE}}^{(k+\lambda)}(\omega)$ are simultaneously accounted for in the determination of the relaxed interaction forces $\underline{\hat{\mathbf{q}}}^{(k+1)}(\omega)$. The concept is illustrated in figure 1b for a general iteration process in terms of a scalar x and two functions $f(x)$ and $g(x)$, with solution $\overline{x} = f(\overline{x}) = g(\overline{x})$. The basic idea is to apply Aitken relaxation to both $f(x)$ and $g(x)$. At iteration step k, two estimations $x_f^{(k+\lambda)} = f(x^{(k)})$ and $x_g^{(k+\lambda)} = g(x^{(k)})$ are calculated. These estimations are combined with the data points $\{x^{(k-1)}, x_f^{(k-1+\lambda)}\}^{\mathrm{T}}$ and $\{x^{(k-1)}, x_g^{(k-1+\lambda)}\}^{\mathrm{T}}$ obtained in the previous iteration step $k-1$ to define linear approximations $\tilde{f}^{(k)}(x)$ and $\tilde{g}^{(k)}(x)$ of the functions $f(x)$ and $g(x)$, respectively. The ordinate of the intersection of these linearized functions $\tilde{f}^{(k)}(x)$ and $\tilde{g}^{(k)}(x)$ provides a new approximation $x^{(k+1)}$ of the solution $\overline{x}$:

$$x^{(k+1)} = \frac{r_g^{(k)}}{r_g^{(k)} - r_f^{(k)}}\, x_f^{(k+\lambda)} - \frac{r_f^{(k)}}{r_g^{(k)} - r_f^{(k)}}\, x_g^{(k+\lambda)} \tag{14}$$

with $r_f^{(k)} = x_f^{(k+\lambda)} - x_f^{(k-1+\lambda)}$ and $r_g^{(k)} = x_g^{(k+\lambda)} - x_g^{(k-1+\lambda)}$. These residual vectors are defined differently compared to equation (12).

For the vectorized interaction forces $\underline{\hat{\mathbf{q}}}(\omega)$, however, a projection in the direction $\underline{\hat{\mathbf{r}}}_{\mathrm{BE}}^{(k)}(\omega) - \underline{\hat{\mathbf{r}}}_{\mathrm{FE}}^{(k)}(\omega) = \underline{\hat{\mathbf{q}}}_{\mathrm{BE}}^{(k+\lambda)}(\omega) - \underline{\hat{\mathbf{q}}}_{\mathrm{BE}}^{(k-1+\lambda)}(\omega) - \underline{\hat{\mathbf{q}}}_{\mathrm{FE}}^{(k+\lambda)}(\omega) + \underline{\hat{\mathbf{q}}}_{\mathrm{FE}}^{(k-1+\lambda)}(\omega)$ is introduced in equation (14):

$$\begin{aligned}\underline{\hat{\mathbf{q}}}^{(k+1)}(\omega) = {} & \frac{\left(\underline{\hat{\mathbf{r}}}_{\mathrm{BE}}^{(k)}(\omega) - \underline{\hat{\mathbf{r}}}_{\mathrm{FE}}^{(k)}(\omega)\right)^{\mathrm{T}} \underline{\hat{\mathbf{r}}}_{\mathrm{BE}}^{(k)}(\omega)}{||\underline{\hat{\mathbf{r}}}_{\mathrm{BE}}^{(k)}(\omega) - \underline{\hat{\mathbf{r}}}_{\mathrm{FE}}^{(k)}(\omega)||^2}\, \underline{\hat{\mathbf{q}}}_{\mathrm{FE}}^{(k+\lambda)}(\omega) \\ & - \frac{\left(\underline{\hat{\mathbf{r}}}_{\mathrm{BE}}^{(k)}(\omega) - \underline{\hat{\mathbf{r}}}_{\mathrm{FE}}^{(k)}(\omega)\right)^{\mathrm{T}} \underline{\hat{\mathbf{r}}}_{\mathrm{FE}}^{(k)}(\omega)}{||\underline{\hat{\mathbf{r}}}_{\mathrm{BE}}^{(k)}(\omega) - \underline{\hat{\mathbf{r}}}_{\mathrm{FE}}^{(k)}(\omega)||^2}\, \underline{\hat{\mathbf{q}}}_{\mathrm{BE}}^{(k+\lambda)}(\omega)\end{aligned} \tag{15}$$

Equation (15) clearly indicates that $\underline{\hat{\mathbf{q}}}_{\mathrm{FE}}^{(k+\lambda)}(\omega)$ and $\underline{\hat{\mathbf{q}}}_{\mathrm{BE}}^{(k+\lambda)}(\omega)$ are simultaneously accounted for in the determination of a new estimate $\underline{\hat{\mathbf{q}}}^{(k+1)}(\omega)$, with iteration dependent weighting factors based on data of two subsequent iterations; these weighting factors can be calculated at low computational cost. This approach hence avoids the need for a priori information concerning the flexibility of the FE and BE subdomain.

3.2.4 Parallel Dirichlet–Dirichlet algorithm

The final iterative algorithm discussed in this paper is a parallel Dirichlet–Dirichlet strategy, which is very similar to the procedure outlined in subsection 3.2.3. Imposing Dirichlet boundary conditions $\underline{\hat{\mathbf{u}}}_2^{(k)}(\omega)$ on Σ allows for the computation of interaction forces $\underline{\hat{\mathbf{q}}}_{\mathrm{FE}}^{(k)}(\omega)$ and $\underline{\hat{\mathbf{q}}}_{\mathrm{BE}}^{(k)}(\omega)$ through equations (7) and (4), respectively. The resulting force discrepancy $\Delta\underline{\hat{\mathbf{q}}}^{(k)}(\omega) = \underline{\hat{\mathbf{q}}}_{\mathrm{BE}}^{(k)}(\omega) - \underline{\hat{\mathbf{q}}}_{\mathrm{FE}}^{(k)}(\omega)$ is employed to calculate interface displacement increments $\Delta\underline{\hat{\mathbf{u}}}_{2,\mathrm{FE}}^{(k)}(\omega)$ and $\Delta\underline{\hat{\mathbf{u}}}_{2,\mathrm{BE}}^{(k)}(\omega)$, and unrelaxed displacements $\underline{\hat{\mathbf{u}}}_{2,\mathrm{FE}}^{(k+\lambda)}(\omega) = \underline{\hat{\mathbf{u}}}_{2,\mathrm{FE}}^{(k)}(\omega) + \Delta\underline{\hat{\mathbf{u}}}_{2,\mathrm{FE}}^{(k)}(\omega)$ and $\underline{\hat{\mathbf{u}}}_{2,\mathrm{BE}}^{(k+\lambda)}(\omega) = \underline{\hat{\mathbf{u}}}_{2,\mathrm{BE}}^{(k)}(\omega) + \Delta\underline{\hat{\mathbf{u}}}_{2,\mathrm{BE}}^{(k)}(\omega)$ can subsequently be obtained. The relaxed interface displacements $\underline{\hat{\mathbf{u}}}_2^{(k+1)}(\omega)$ are finally computed by means of the relaxation procedure introduced in subsection 3.2.3; equation (15) is in that case based on interface displacements instead of interaction forces. The procedure is repeated until convergence is achieved.

3.3 Monolithic FE–$\mathscr{H}$-BE coupling

A third FE–$\mathscr{H}$-BE coupling approach consists of a monolithic coupling, in which the governing equations of both subdomains are solved simultaneously, while the assembly of a dynamic soil stiffness matrix is avoided. This approach fundamentally differs from the conventional direct coupling approach outlined in subsection 3.1. Combining equations (1) and (2) and accounting for continuity of displacements and equilibrium of tractions at the soil–structure interface Σ yields:

$$\begin{bmatrix} \widehat{\mathbf{K}}_{11}(\omega) & \widehat{\mathbf{K}}_{12}(\omega) & \mathbf{0} \\ \widehat{\mathbf{K}}_{21}(\omega) & \widehat{\mathbf{K}}_{22}(\omega) & \mathbf{T}_{\mathrm{q}} \\ \mathbf{0} & \widehat{\mathbf{T}}_{\mathscr{H}}(\omega) + \mathbf{I} & -\widehat{\mathbf{U}}_{\mathscr{H}}(\omega) \end{bmatrix} \begin{Bmatrix} \underline{\hat{\mathbf{u}}}_1(\omega) \\ \underline{\hat{\mathbf{u}}}_2(\omega) \\ \underline{\hat{\mathbf{t}}}(\omega) \end{Bmatrix} = \begin{Bmatrix} \underline{\hat{\mathbf{f}}}_1(\omega) \\ \underline{\hat{\mathbf{f}}}_2(\omega) \\ \underline{\mathbf{0}} \end{Bmatrix} \tag{16}$$

where the coupling matrix $\mathbf{T}_{\mathrm{q}}$ is defined as in equation (6). The system size in this monolithic approach is significantly larger than in the classical direct coupling strategy of subsection 3.1. The coefficient matrix is never assembled explicitly, however, as equation (16) is solved by means of an iterative GMRES solver. This requires an efficient evaluation of the matrix–vector product, indicating that the monolithic formulation (16) is only advantageous if a fast BE method (i.e. a formulation based on $\mathscr{H}$–matrices) is employed. Although Margonari et al. [10] have used a monolithic approach for the coupling of FE and fast multipole BE models for elastostatics, it is rarely used in elastodynamics [29]. This strategy is often applied for solving strongly coupled fluid–structure interaction problems [36, 37], however, as the discretization methods commonly used for the fluid and the structure lead to sparse matrices.

The coefficient matrix in equation (16) is likely to be ill–conditioned, as the matrix entries arising from the FE and BE discretizations differ by several orders of magnitude. Convergence of the iterative solver will therefore be slow, and the incorporation of a suitable preconditioner is indispensable. Following simple right preconditioner $\widehat{\mathbf{M}}(\omega)$ is employed:

$$\widehat{\mathbf{M}}(\omega) = \begin{bmatrix} \mathrm{diag}\left(\widehat{\mathbf{K}}_{11}(\omega)\right) & \mathbf{0} & \mathbf{0} \\ \mathbf{0} & \mathrm{diag}\left(\widehat{\mathbf{K}}_{22}(\omega)\right) & \mathbf{T}_{\mathrm{q}} \\ \mathbf{0} & \mathrm{blkdiag}\left(\widehat{\mathbf{T}}_{\mathscr{H}}(\omega)\right) + \mathbf{I} & \mathrm{blkdiag}\left(-\widehat{\mathbf{U}}_{\mathscr{H}}(\omega)\right) \end{bmatrix} \tag{17}$$

where the size of the diagonal blocks of $\widehat{\mathbf{T}}_{\mathscr{H}}(\omega)$ and $\widehat{\mathbf{U}}_{\mathscr{H}}(\omega)$ is determined by the lowest hierarchical BE cluster level. The nested FGMRES solution procedure discussed in subsection 2.2 is employed here as well, avoiding the explicit assembly of $\widehat{\mathbf{M}}^{-1}(\omega)$.

4 NUMERICAL EXAMPLES

In the following subsections, two examples are considered to validate the numerical implementation of the proposed FE–$\mathscr{H}$-BE coupling algorithms and to assess their computational performance. While the first example is related to a full space geometry, the second example involves Green's functions for a layered halfspace. All calculations have been performed on Intel® Xeon® E5520 (2.26 GHz) CPUs.

4.1 3D spherical cavity surrounded by a spherical layer and a full space subjected to an internal pressure

Consider a 3D spherical cavity with inner radius $r_{\mathrm{i}} = 1\,\mathrm{m}$ surrounded by a spherical layer with outer radius $r_{\mathrm{o}} = 2\,\mathrm{m}$ and embedded in a homogeneous full space, which is loaded by

an internal pressure $\hat{p}(\omega) = 1\,\mathrm{Pa/Hz}$ (figure 2a). The full space is characterized by a shear wave velocity $C_\mathrm{s} = 150\,\mathrm{m/s}$, a dilatational wave velocity $C_\mathrm{p} = 300\,\mathrm{m/s}$ and a density $\rho = 1800\,\mathrm{kg/m^3}$. Material damping ratios $\beta_\mathrm{s} = \beta_\mathrm{p} = 0.025$ in both deviatoric and volumetric deformation are specified. The wave velocities in the spherical layer are defined as $\alpha C_{\mathrm{s,full}}$ and $\alpha C_{\mathrm{p,full}}$ (with $C_{\mathrm{s,full}}$ and $C_{\mathrm{p,full}}$ the wave velocities in the full space), respectively, where following values are considered for the ratio α: (i) $\alpha = 1/2$, (ii) $\alpha = 1$ and (iii) $\alpha = 2$. The same material damping ratios and density as in the full space are used.

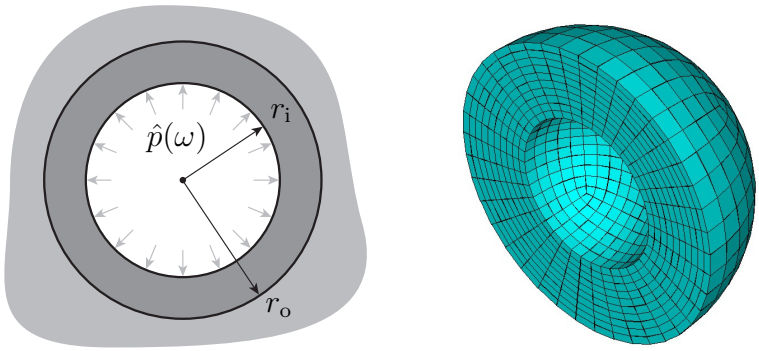


Figure 2: (a) 3D spherical cavity surrounded by a spherical layer with inner radius r_i and outer radius r_o and a homogeneous full space, subjected to an internal pressure $\hat{p}(\omega)$, and (b) half of the FE discretization of the spherical layer.

The spherical layer is discretized by means of 6000 eight–node solid finite elements, which are coupled to a conforming BE mesh consisting of 600 four–node quadrilateral elements for the surrounding full space (figure 2b). A nodal collocation scheme is used for the latter to facilitate the FE–BE coupling, resulting in 19866 FE and 1806 BE degrees of freedom. Up to 6.67 elements per dilatational wavelength $\lambda_\mathrm{p} = C_\mathrm{p}/f$ are provided at a frequency of $100\,\mathrm{Hz}$ in case (i). Analytical full space fundamental solutions [38] are employed in the $\mathscr{H}$-BE formulation.

Each of the FE–$\mathscr{H}$-BE coupling strategies outlined in the section 3 is employed to calculate the response in a frequency range between $0\,\mathrm{Hz}$ and $100\,\mathrm{Hz}$, with a frequency step of $1\,\mathrm{Hz}$. A maximum of 200 global iterations is prescribed for the iterative algorithms. Figure 3 shows the real and imaginary part of the radial displacement at $r = r_\mathrm{o}$, for the three values of the wave velocity ratio α introduced above. All methods yield accurate results in very good agreement with the analytical solution [39] for all values of the ratio α, with exception of the sequential Neumann–Dirichlet algorithm, which is unable to retrieve the correct solution at every frequency for a wave velocity ratio $\alpha = 1/2$ within the prescribed number of iterations.

The integral representation theorem subsequently allows for the computation of the radiated wavefield in the soil from the displacements and tractions on the FE–$\mathscr{H}$-BE interface. Figure 4 shows the real and imaginary part of the radial displacement at $r = 10\,\mathrm{m}$. The solutions of the various coupling procedures are clearly in good correspondence with each other and agree with the analytical solution, except for the aforementioned Neumann–Dirichlet algorithm.

Figures 3 and 4 validate the numerical implementation of the FE–$\mathscr{H}$-BE coupling strategies presented in this paper. The computational performance of each method strongly differs from one another, however. Figure 5 shows the CPU time required in each algorithm in function of the frequency, for the three wave velocity ratios considered. It is observed that the computation time in the direct coupling approach significantly exceeds the computational effort of the alternative procedures due to the drawbacks summarized in subsection 3.1, rendering the conventional method the least efficient. The computation time remains quasi independent of

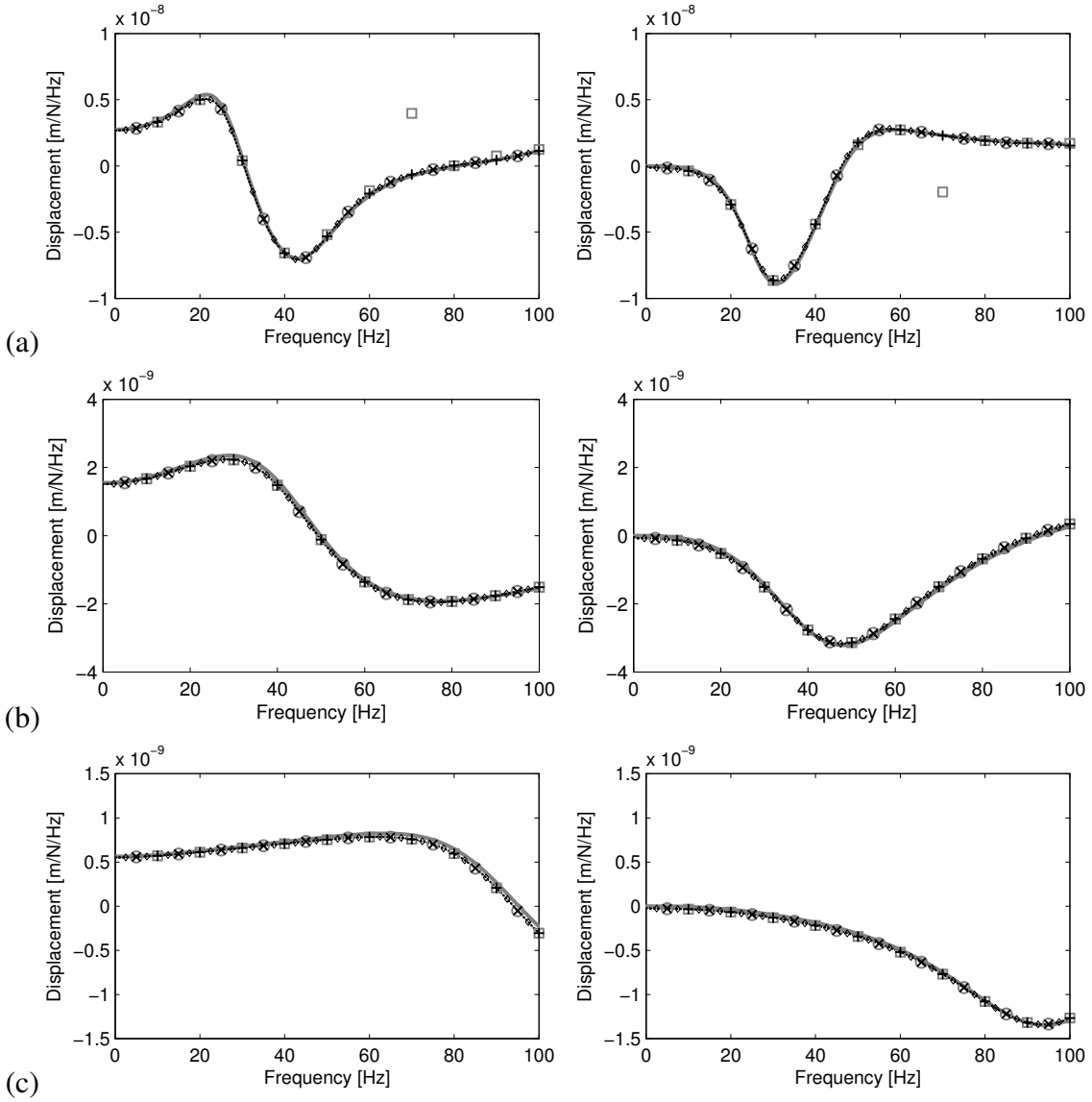


Figure 3: Real (left) and imaginary (right) part of the radial displacement at $r = r_\mathrm{o}$ due to a unit harmonic pressure applied to a spherical cavity surrounded by a spherical layer and a homogeneous full space, for (a) $\alpha = 1/2$, (b) $\alpha = 1$ and (c) $\alpha = 2$. The solutions of the classical direct coupling approach (dashed black line), the iterative Neumann–Dirichlet (grey squares), Dirichlet–Neumann (black plus signs), Neumann–Neumann (grey circles) and Dirichlet–Dirichlet (black crosses) algorithms, and the monolithic coupling procedure (black rhombuses) are compared to the analytical solution (solid grey line) [39].

the wave velocity ratio, but exhibits an increase with frequency. This is related to the fact that the time required to assemble and solve the set of $\mathscr{H}$-BE equations increases at higher frequencies [14], and such a trend is also observed for the other coupling methodologies. The computational efficiency of the iterative coupling schemes, however, is much stronger affected by the wave velocity ratio α. This is in particular the case for the sequential variants: the CPU time in the Neumann–Dirichlet algorithm strongly decreases for increasing values of α, while the reverse is observed for the Dirichlet–Neumann approach. This confirms the idea that Neumann boundary conditions should be applied to the most stiff subdomain in order to achieve the fastest convergence. The efficiency of the parallel iterative algorithms depends less

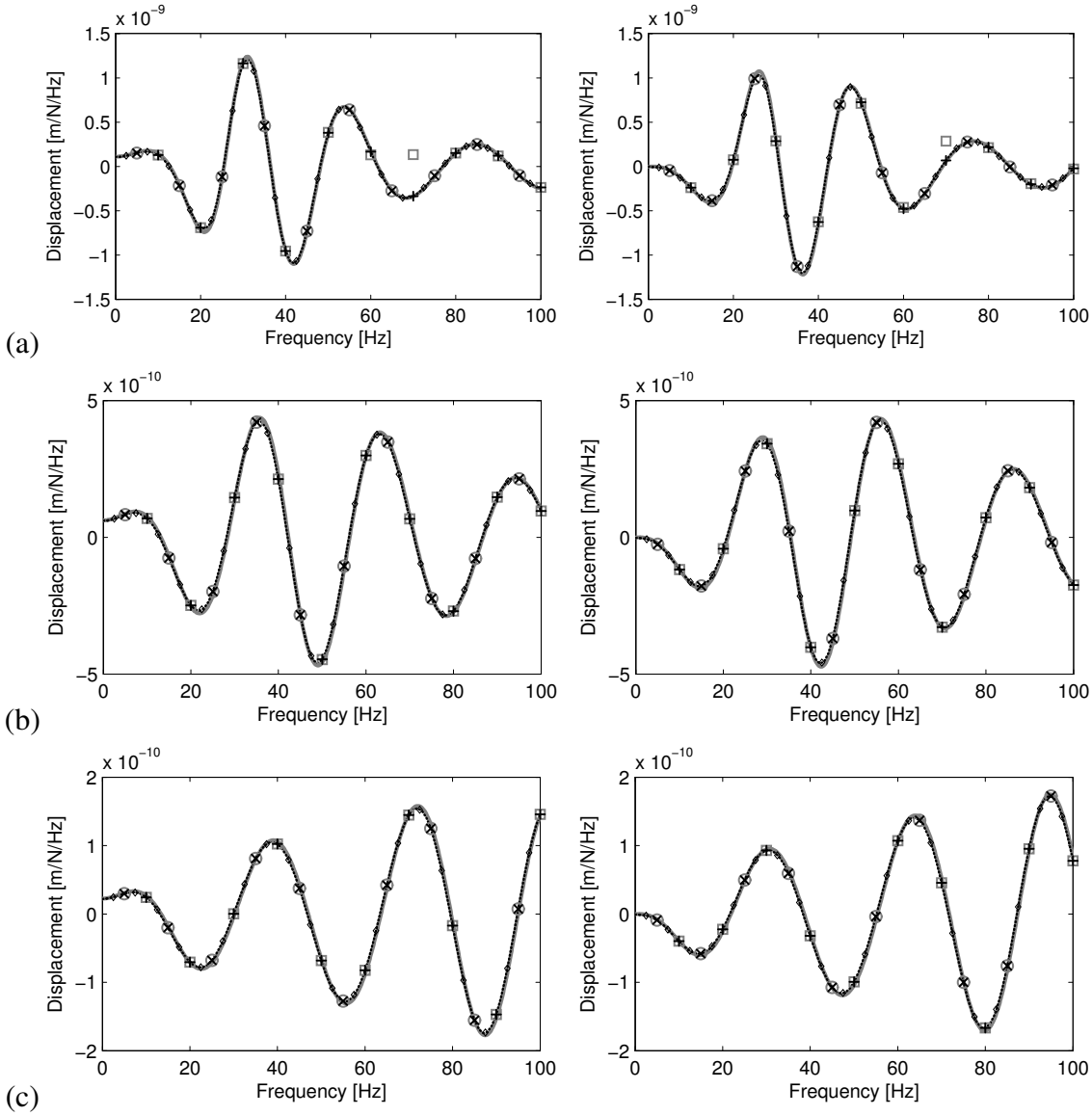


Figure 4: Real (left) and imaginary (right) part of the radial displacement at $r = 10\,\mathrm{m}$ due to a unit harmonic pressure applied to a spherical cavity surrounded by a spherical layer and a homogeneous full space, for (a) $\alpha = 1/2$, (b) $\alpha = 1$ and (c) $\alpha = 2$. The solutions of the classical direct coupling approach (dashed black line), the iterative Neumann–Dirichlet (grey squares), Dirichlet–Neumann (black plus signs), Neumann–Neumann (grey circles) and Dirichlet–Dirichlet (black crosses) algorithms, and the monolithic coupling procedure (black rhombuses) are compared to the analytical solution (solid grey line) [39].

strongly on α due to the relaxation procedure introduced in subsection 3.2.3, as the contribution of each subdomain to the relaxed interaction forces or displacements is balanced in every step of the iterative procedure. Finally, figure 5 illustrates that the monolithic coupling scheme is also relatively insensitive to the value of α, but the overall computational performance of this methodology remains relatively poor compared to the iterative algorithms. The implementation of a more rigorous preconditioner than the one applied in this paper might result in an improved convergence behaviour. Algebraic multigrid preconditioning strategies adapted for hierarchical matrices [40] or approaches based on the sparse approximate inverse (SPAI) of the BE matrices [10] are worthwhile to be considered in future research.

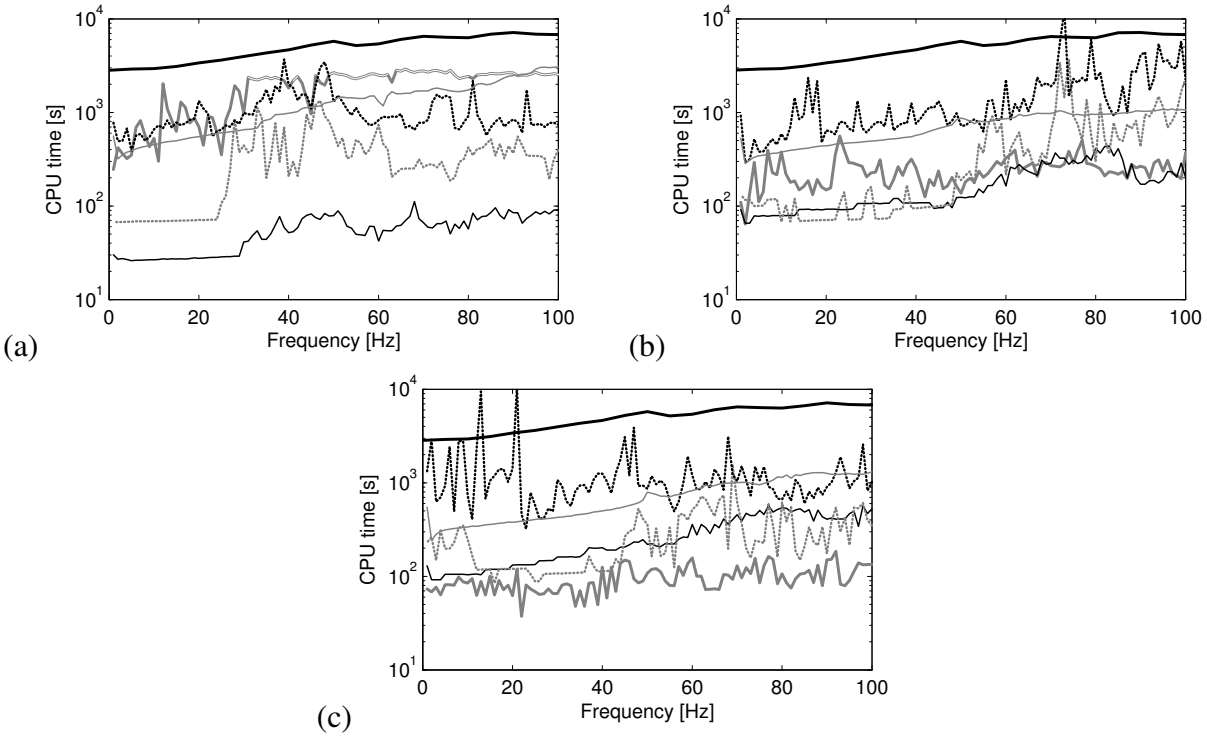


Figure 5: CPU time required in the classical direct coupling approach (thick black line), the iterative Neumann–Dirichlet (thick grey line), Dirichlet–Neumann (thin black line), Neumann–Neumann (dotted grey line) and Dirichlet–Dirichlet (dotted black line) algorithms, and the monolithic coupling procedure (thin grey line), for (a) $\alpha = 1/2$, (b) $\alpha = 1$ and (c) $\alpha = 2$. The lines are only drawn if the correct numerical solution is obtained.

Some important conclusions can be drawn from the results presented in figure 5. It is clear that the classical direct approach is not well suited to provide an efficient coupling of FE and $\mathscr{H}$-BE models; application of the alternative procedures is more appropriate. In particular, if there exists a strong stiffness contrast between the subdomains, a sequential iterative algorithm is preferred. It is recommended to impose Neumann boundary conditions on the most stiff subdomain; the reverse choice can significantly deteriorate the convergence behaviour. If such a contrast is not apparent, however, the parallel iterative algorithms as well as the monolithic approach provide a reliable and robust coupling of FE and $\mathscr{H}$-BE models.

The efficiency of the sequential iterative procedures is now investigated in more detail. In each global iterative step k, an iterative FGMRES solver is used to solve equation (4) for tractions $\hat{\underline{\mathbf{t}}}^{(k)}(\omega)$ or interface displacements $\hat{\underline{\mathbf{u}}}_2^{(k+\lambda)}(\omega)$ in the Neumann–Dirichlet or Dirichlet–Neumann algorithm, respectively. Figures 6 and 7 show the number of FGMRES–iterations in these algorithms in function of the frequency and the iteration step k. The number of FGMRES–iterations generally decreases in subsequent iteration steps, as the relaxed solution obtained in iteration $k-1$ is used as an initial guess in the FGMRES solver in iteration k. The number of global iterations strongly decreases for increasing values of α in figure 6, while the reverse is observed in figure 7.

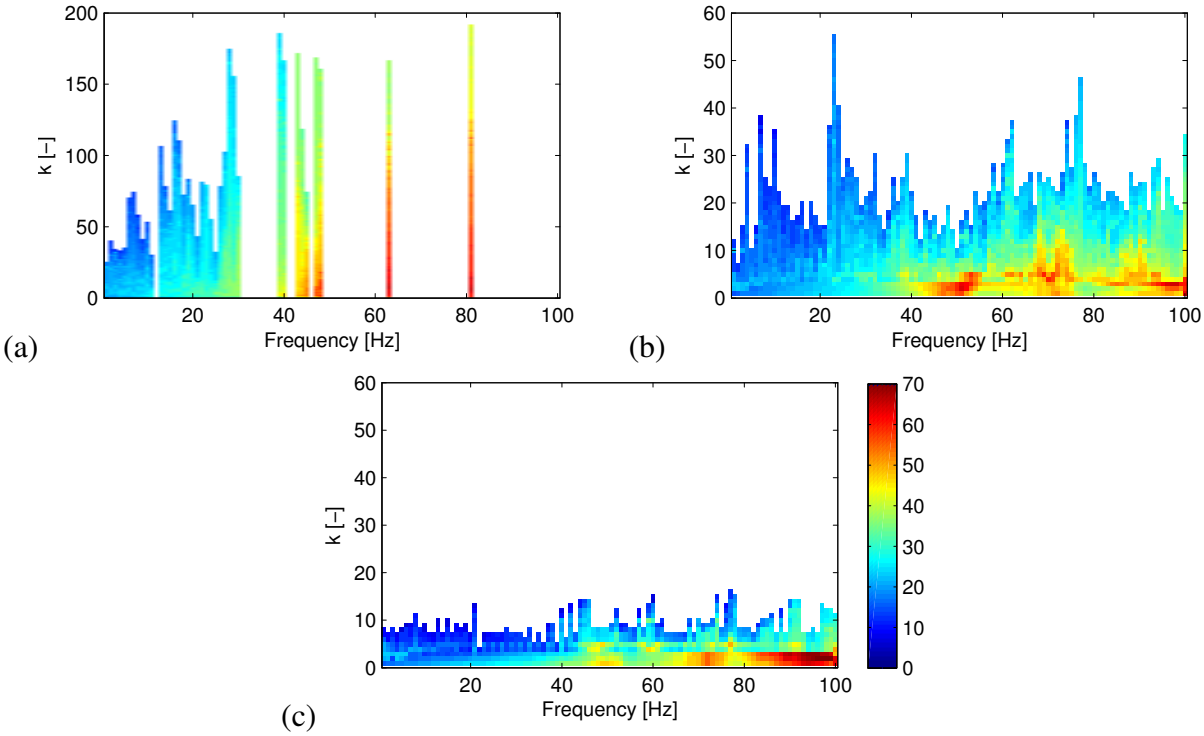


Figure 6: Number of FGMRES–iterations to solve the $\mathscr{H}$-BE equation (4) for tractions in the iterative Neumann–Dirichlet algorithm in function of the frequency and the iteration step k, for (a) $\alpha = 1/2$, (b) $\alpha = 1$ and (c) $\alpha = 2$. The bars are only drawn if the correct numerical solution is obtained.

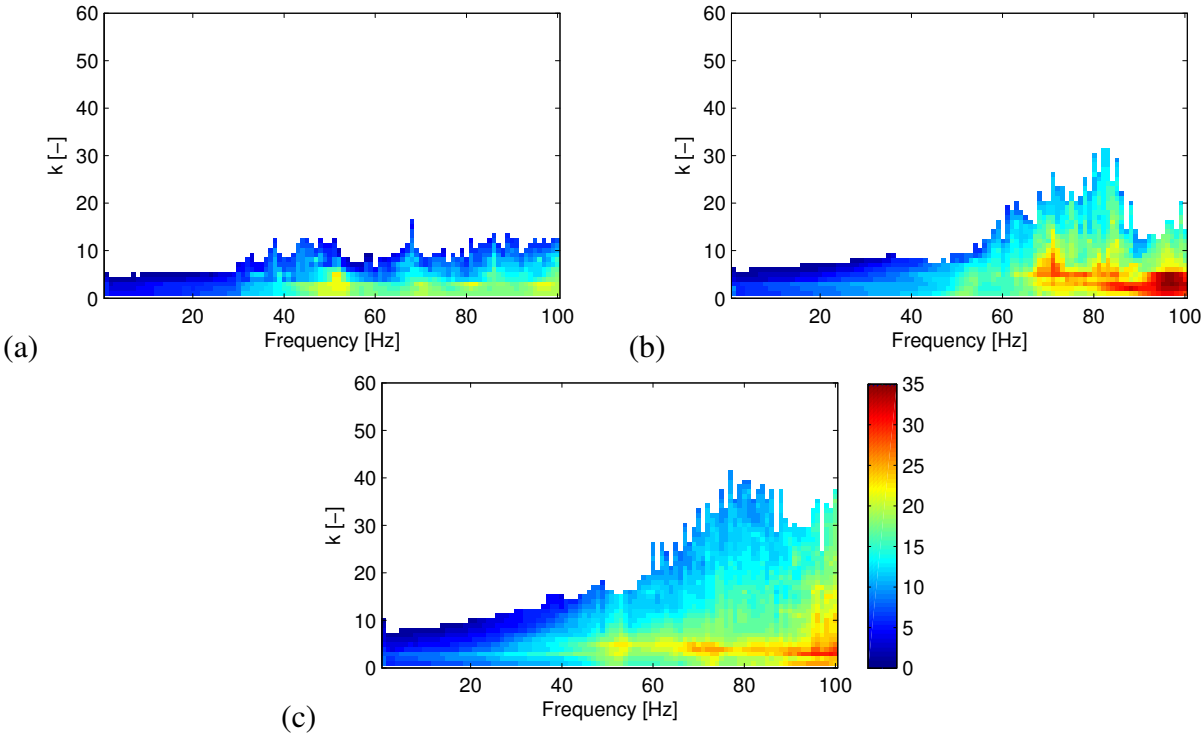


Figure 7: Number of FGMRES–iterations to solve the $\mathscr{H}$-BE equation (4) for interface displacements in the iterative Dirichlet–Neumann algorithm in function of the frequency and the iteration step k, for (a) $\alpha = 1/2$, (b) $\alpha = 1$ and (c) $\alpha = 2$.

Numerical simulations have furthermore demonstrated that application of Aitken's Δ^2–method for the interface relaxation is crucial in order to ensure convergence in the sequential iterative algorithms. No convergence could be obtained with these algorithms in any of the examples under concern in case a fixed value was attributed to the relaxation parameter $\lambda^{(k)}$ (where several constant values between 0 and 1 have been considered), in the entire frequency range of interest. Figure 8 shows the variation of $\lambda^{(k)}$ in the sequential Neumann–Dirichlet algorithm at a frequency of $100\,\mathrm{Hz}$ for $\alpha = 1$, clearly illustrating the dependency of the relaxation parameter on the iteration step.

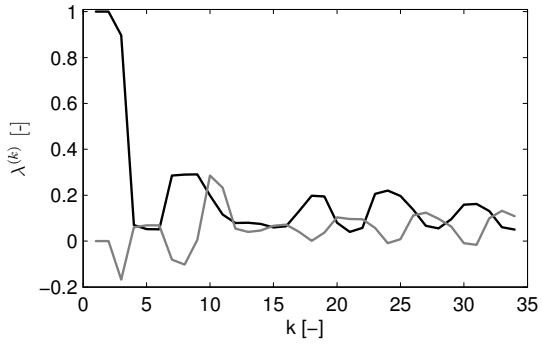


Figure 8: Real (black line) and imaginary (grey line) part of the Aitken relaxation parameter $\lambda^{(k)}$ at $100\,\mathrm{Hz}$ in the sequential Neumann–Dirichlet iterative algorithm, for $\alpha = 1$.

Finally, the effectiveness of the relaxation procedure for the parallel iterative algorithms introduced in subsection 3.2.3 is demonstrated. Figure 9 compares the CPU time in the iterative Neumann–Neumann algorithm using equation (15) for the determination of relaxed interaction forces $\hat{\underline{\mathbf{q}}}^{(k+1)}(\omega)$ to the cases where either $\hat{\underline{\mathbf{q}}}^{(k+1)}_{\mathrm{FE}}(\omega)$ or $\hat{\underline{\mathbf{q}}}^{(k+1)}_{\mathrm{BE}}(\omega)$ is employed, respectively. As indicated in subsection 3.2.3, the fastest convergence is achieved if the displacement discrepancy $\Delta\hat{\underline{\mathbf{u}}}^{(k)}_2(\omega)$ is imposed on the most flexible subdomain, i.e. on the FE subdomain for $\alpha = 1/2$ and on the BE subdomain for $\alpha = 2$. The reverse choice strongly affects the convergence behaviour, however, and the algorithm does even not convergence at some frequencies if $\hat{\underline{\mathbf{q}}}^{(k+1)}_{\mathrm{BE}}(\omega)$ is employed for $\alpha = 1/2$. The relaxation procedure corresponding to equation (15) proves to be a reliable alternative, as the associated CPU times only moderately depend on α and are often bounded by the computation times of the two other approaches.

4.2 Flexible surface foundation on a horizontally layered halfspace

A flexible square surface foundation resting on a horizontally layered halfspace is considered in this subsection. The foundation has dimensions $5\,\mathrm{m} \times 5\,\mathrm{m} \times 0.25\,\mathrm{m}$ and consists of concrete with a Young's modulus $E = 33\,\mathrm{GPa}$, a Poisson's ratio $\nu = 0.20$, and a density $\rho = 2500\,\mathrm{kg/m^3}$. Rayleigh damping is assumed, allowing to write the frequency independent proportional damping matrix as $\mathbf{C} = a_0\mathbf{M} + a_1\mathbf{K}$. The Rayleigh damping coefficients a_0 and a_1 are determined by attributing a modal damping ratio $\xi = 0.03$ to the first two non rigid body modes. As indicated in subsection 3.2.1, structural damping is included to avoid singularity of the FE equations if a sequential Neumann–Dirichlet algorithm is employed. A unit harmonic vertical point excitation is applied to the center of the foundation, within a frequency range between $0\,\mathrm{Hz}$ and $100\,\mathrm{Hz}$.

The soil consists of two layers on a halfspace, each with a thickness of $2\,\mathrm{m}$. The shear wave

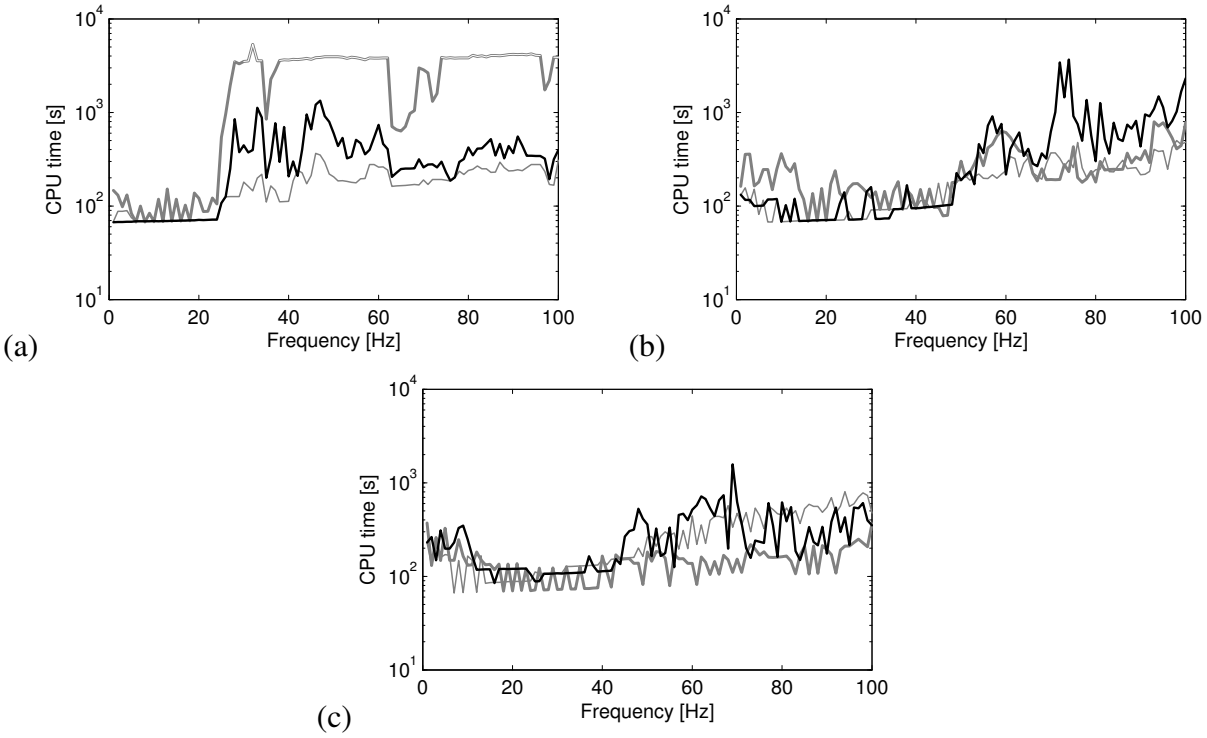


Figure 9: CPU time required in the parallel Neumann–Neumann algorithm in case the displacement discrepancy is imposed on the BE subdomain (thick grey line), on the FE subdomain (thin grey line), and in case the relaxation procedure corresponding to equation (15) is employed (black line), for (a) $\alpha = 1/2$, (b) $\alpha = 1$ and (c) $\alpha = 2$. The lines are only drawn if the correct numerical solution is obtained.

velocity C_s is equal to $150\,\mathrm{m/s}$ in the top layer, $250\,\mathrm{m/s}$ in the second layer, and $300\,\mathrm{m/s}$ in the underlying halfspace. The Poisson's ratio ν is $1/3$ everywhere, resulting in dilatational wave velocities C_p of $300\,\mathrm{m/s}$, $500\,\mathrm{m/s}$, and $600\,\mathrm{m/s}$, respectively. Material damping ratios $\beta_\mathrm{s} = \beta_\mathrm{p} = 0.025$ in both deviatoric and volumetric deformation are attributed to the layers and the halfspace, while a uniform density $\rho = 1800\,\mathrm{kg/m^3}$ is considered throughout the medium.

The foundation is discretized by means of 30×30 equally sized shell elements based on Kirchhoff plate theory, which are coupled to a conforming BE mesh using a nodal collocation scheme for the soil. Up to nine elements per shear wavelength $\lambda_\mathrm{s} = C_\mathrm{s}/f$ are provided at the maximum frequency of $100\,\mathrm{Hz}$ (determined by the shear wave velocity of the top layer). Green's functions for a layered halfspace are incorporated in the $\mathscr{H}$-BE formulation [14, 15, 41], avoiding the necessity to discretize the free surface and the layer interfaces. It is expected that the foundation will behave much stiffer than the soil in the frequency range of interest. In accordance with the findings of subsection 4.1, an iterative Neumann–Dirichlet coupling scheme is therefore employed. The monolithic coupling approach is considered as well.

Figure 10 shows the real and imaginary part of the vertical displacement $\hat{u}_z(\mathbf{x}, \omega)$ at the center of the foundation, calculated with both coupling procedures; a perfect agreement between the results is observed. The iterative Neumann–Dirichlet is unable, however, to determine the static solution, and the frequency sweep is therefore performed from high to low frequencies. The vertical displacement of the foundation and the surrounding soil is shown in figures 11a and 11b at $25\,\mathrm{Hz}$ and $100\,\mathrm{Hz}$, respectively. While the wave fronts at the surface of the soil remain almost perfectly cylindrical at $25\,\mathrm{Hz}$, this is no longer the case at $100\,\mathrm{Hz}$ due to the dynamic interaction between the foundation and the soil.

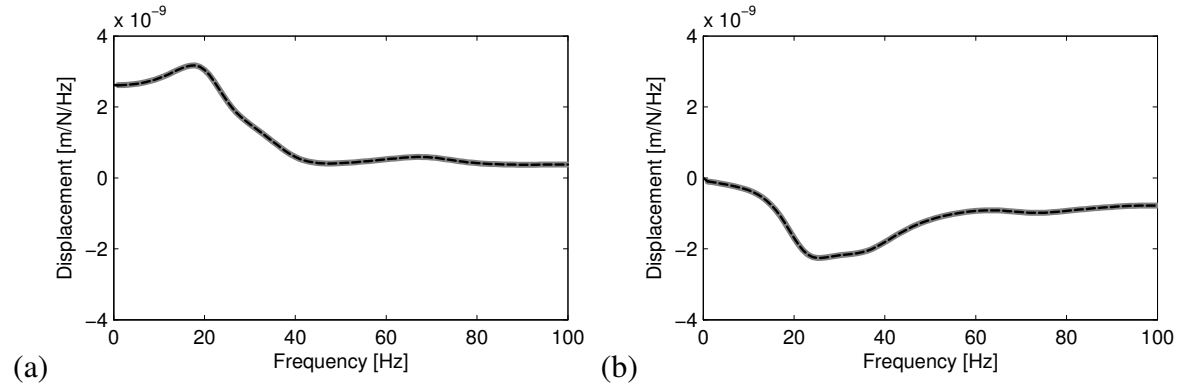


Figure 10: (a) Real and (b) imaginary part of the vertical displacement $\hat{u}_z(\mathbf{x}, \omega)$ at the center of a flexible surface foundation on a layered halfspace excited by a unit harmonic vertical point load. The solution of the iterative Neumann–Dirichlet algorithm (grey solid line) is compared to the solution of the monolithic coupling procedure (black dashed line).

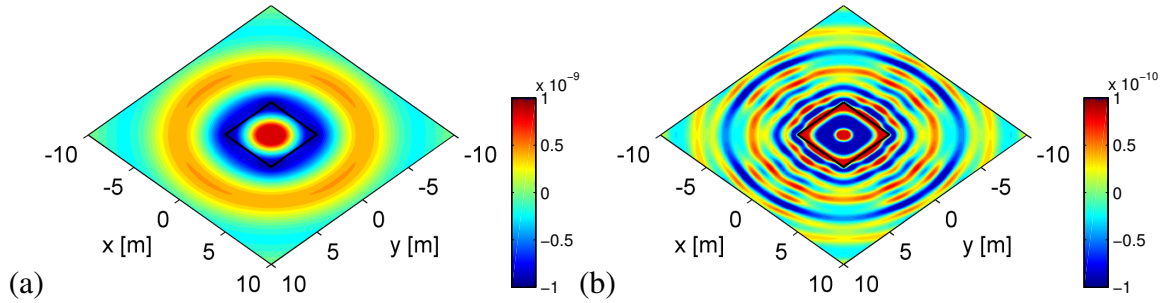


Figure 11: Real part of the vertical displacement $\hat{u}_z(\mathbf{x}, \omega)$ of the foundation and the soil for a flexible surface foundation on a layered halfspace excited at its center by a unit harmonic vertical point load at (a) $25\,\mathrm{Hz}$ and (b) $100\,\mathrm{Hz}$.

Figure 12a shows the number of FGMRES–iterations in function of the frequency and the iteration step k for the sequential Neumann–Dirichlet algorithm. Imposing the relaxed interaction forces obtained in step $k-1$ as initial guess in the FGMRES–solver of step k is clearly beneficial, as the number of FGMRES–iterations in subsequent steps is strongly reduced. This number remains almost constant, however, if no initial guess is used (figure 12b). Furthermore, employing the converged solution at a particular frequency as initial guess in the first iteration at the next frequency is also advantageous, resulting in a lower number of iteration steps in the iterative algorithm. Peaks at $40\,\mathrm{Hz}$ and $62\,\mathrm{Hz}$ correspond to natural frequencies of the foundation.

5 CONCLUSIONS

In this paper, the coupling of FE and $\mathscr{H}$-BE methods has been discussed, illustrating that a subdomain approach is well suited to efficiently solve dynamic SSI problems in the frequency domain. The application of $\mathscr{H}$–matrices enables the fast evaluation of large BE models, and the incorporation of Green's functions for a layered halfspace avoids the need to discretize the free surface and the layer interfaces in the modelling of visco–elastodynamic wave propagation in a stratified medium.

Direct, iterative and monolithic coupling strategies have been considered throughout this

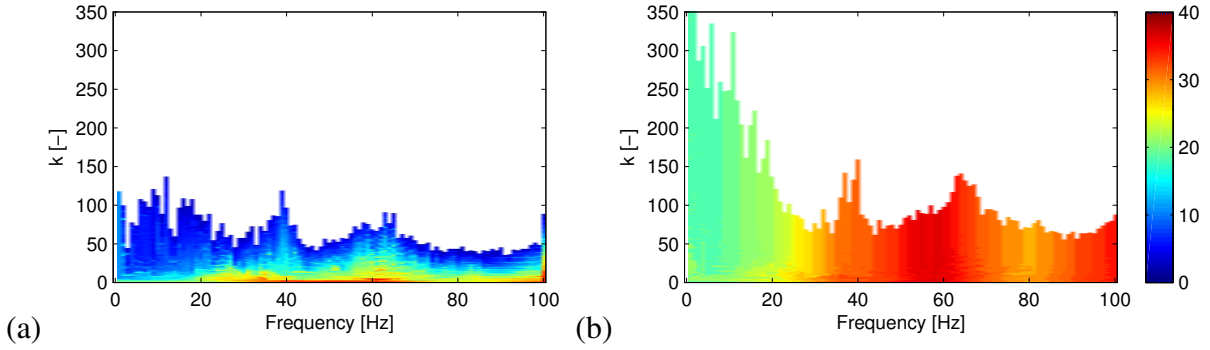


Figure 12: Number of FGMRES–iterations to solve the $\mathscr{H}$-BE equation (4) for tractions in the iterative Neumann–Dirichlet algorithm in function of the frequency and the iteration step k, for a flexible surface foundation on a layered halfspace. The numbers are shown (a) in case the relaxed tractions in iteration $k-1$ are used as an initial guess in iteration k, while the converged solution at a particular frequency is used as an initial guess for the first iteration at the subsequent frequency, or (b) in case no initial guess is provided in the FGMRES solver.

paper, and the numerical validation of each algorithm is presented. An assessment of the computational performance reveals that the direct coupling approach is the least efficient, as the assembly of a dynamic soil stiffness matrix requires the solution of a large amount of $\mathscr{H}$–BE equations. Iterative coupling procedures are more efficient, provided that suitable boundary conditions are applied to each subdomain. It is demonstrated that sequential iterative algorithms should be preferred if there exists a strong stiffness contrast between the FE and $\mathscr{H}$-BE subdomain, with Neumann boundary conditions to be imposed on the most stiff subdomain. The application of Aitken's Δ^2–method for the determination of a proper interface relaxation parameter ensures and speeds up the convergence of these sequential algorithms. Parallel iterative algorithms provide a valuable alternative for cases where an a priori estimation of the flexibility of each subdomain is not obvious, and an appropriate relaxation procedure has been proposed for these algorithms. An efficient combination of FE and $\mathscr{H}$–BE models can also be achieved by means of a monolithic coupling scheme, although the convergence in the examples considered turns out to be relatively slow. This might be improved by the incorporation of an enhanced preconditioner; this is the subject of further research.

ACKNOWLEDGEMENTS

The first author is a doctoral fellow and the second author is a postdoctoral fellow of the Research Foundation Flanders (FWO). The financial support is gratefully acknowledged.

REFERENCES

[1] J.-F. Semblat, A.M. Duval, and P. Dangla. Seismic site effects in a deep alluvial basin: numerical analysis by the boundary element method. *Computers and Geotechnics*, 29(7):573–585, 2002.

[2] G. Lombaert, G. Degrande, and D. Clouteau. Numerical modelling of free field traffic induced vibrations. *Soil Dynamics and Earthquake Engineering*, 19(7):473–488, 2000.

[3] D.E. Beskos, T. Krauthammer, and I. Vardoulakis, editors. *Dynamic soil-structure interaction*. A.A. Balkema, 1984.

[4] O. Von Estorff and C. Hagen. Iterative coupling of FEM and BEM in 3D transient elastodynamics. *Engineering Analysis with Boundary Elements*, 29:775–787, 2005.

[5] D. Clouteau, M.L. Elhabre, and D. Aubry. Periodic BEM and FEM-BEM coupling: application to seismic behaviour of very long structures. *Computational Mechanics*, 25:567–577, 2000.

[6] O.C. Zienkiewicz, D.W. Kelly, and P. Bettes. The coupling of the finite element method and boundary solution procedures. *International Journal for Numerical Methods in Engineering*, 11:355–375, 1977.

[7] G.C. Hsiao. The coupling of boundary element and finite element methods. *Zeitschrift für Angewandte Mathematik und Mechanik*, 70:493–503, 1990.

[8] M. Costabel and E.P. Stephan. Coupling of finite and boundary element methods for an elastoplastic interface problem. *SIAM Journal on Numerical Analysis*, 27(5):1212–1226, 1990.

[9] W.M. Elleithy, H. J. Al-Gahtani, and M. El-Gebeily. Iterative coupling of BE and FE methods in elastostatics. *Engineering Analysis with Boundary Elements*, 25:685–695, 2001.

[10] M. Margonari and M. Bonnet. Fast multipole method applied to elastostatic BEM-FEM coupling. *Computers and Structures*, 83(10–11):700–717, 2004.

[11] T. Rüberg and M. Schanz. Coupling finite and boundary element methods for static and dynamic elastic problems with non-conforming interfaces. *Computer Methods in Applied Mechanics and Engineering*, 198(3–4):449–458, 2008.

[12] S. Chaillat, M. Bonnet, and J.-F. Semblat. A multi-level fast multipole BEM for 3-D elastodynamics in the frequency domain. *Computer Methods in Applied Mechanics and Engineering*, 197(49–50):4233–4249, 2008.

[13] W. Hackbusch. A sparse matrix arithmetic based on $\mathscr{H}$-matrices. Part I: Introduction to $\mathscr{H}$-matrices. *Computing*, 62(2):89–108, 1999.

[14] P. Coulier, S. François, G. Lombaert, G. Degrande, A hierarchical boundary element method for elastodynamics based on Green's functions for a horizontally layered halfspace, Engineering Analysis with Boundary Elements, Submitted for publication.

[15] E. Kausel and J.M. Roësset. Stiffness matrices for layered soils. *Bulletin of the Seismological Society of America*, 71(6):1743–1761, 1981.

[16] L. Grasedyck and W. Hackbusch. Construction and arithmetics of $\mathscr{H}$-matrices. *Computing*, 70:295–334, 2003.

[17] S. Rjasanow and O. Steinbach. *The Fast Solution of Boundary Integral Equations (Mathematical and Analytical Techniques with Applications to Engineering)*. Springer-Verlag New York, 2007.

[18] M. Bebendorf and S. Rjasanow. Adaptive low–rank approximation of collocation matrices. *Computing*, 70:1–24, 2003.

[19] M. Bebendorf. *Hierarchical Matrices: A Means to Efficiently Solve Elliptic Boundary Value Problems*. Springer Publishing Company, 1st edition, 2008.

[20] Y. Saad and M.H. Schultz. GMRES: a generalized minimal residual algorithm for solving nonsymmetric linear systems. *SIAM Journal on Scientific and Statistical Computing*, 7(3):856–869, 1986.

[21] M. Bebendorf. Hierarchical LU decomposition based preconditioners for BEM. *Computing*, 74:225–247, 2005.

[22] Y. Saad. A flexible inner-outer preconditioned GMRES algorithm. *SIAM Journal on Scientific and Statistical Computing*, 14(2):461–469, 1993.

[23] S. Chaillat, J.-F. Semblat, and M. Bonnet. A preconditioned 3-D multi-region fast multipole solver for seismic wave propagation in complex geometries. *Communications in Computational Physics*, 11(2):594–609, 2012.

[24] O. Von Estorff and E. Kausel. Coupling of boundary and finite elements for soil-structure interaction. *Earthquake Engineering and Structural Dynamics*, 18:1065–1075, 1989.

[25] O. Von Estorff and M. Firuziaan. Coupled BEM/FEM approach for nonlinear soil/structure interaction. *Engineering Analysis with Boundary Elements*, 24:605–621, 2000.

[26] S. François, H.R. Masoumi, and G. Degrande. An iterative coupled boundary-finite element method for the dynamic response of structures. In P. Sas and M. De Munck, editors, *Proceedings of ISMA2006 International Conference on Noise and Vibration Engineering*, pages 1701–1716, Leuven, Belgium, September 2006.

[27] D. Soares Jr. and L. Godinho. An optimized BEM–FEM iterative coupling algorithm for acoustic–elastodynamic interaction analyses in the frequency domain. *Computers and Structures*, 106–107:68–80, 2012.

[28] D. Soares Jr., L. Godinho, A. Pereira, and C. Dors. Frequency domain analysis of acoustic wave propagation in heterogeneous media considering iterative coupling procedures between the method of fundamental solutions and Kansa's method. *International Journal for Numerical Methods in Engineering*, 89(7):914–938, 2012.

[29] E. Grasso. *Modelling visco-elastic seismic wave propagation: a fast-multipole boundary element method and its coupling with finite elements*. PhD thesis, Université Paris-Est, 2012.

[30] W.M. Elleithy and M. Tanaka. Interface relaxation algorithms for BEM-BEM coupling and FEM-BEM coupling. *Computer Methods in Applied Mechanics and Engineering*, 192:2977–2992, 2003.

[31] C. Hagen. *Wechselwirkungen zwischen Bauwerk, Boden und Fluid unter transienter Belastung*. PhD thesis, Technischen Universität Hamburg-Harburg, 2005.

[32] A.C. Aitken. Studies in practical mathematics II: The evaluation of the latent roots and latent vectors of a matrix. *Proceedings of the Royal Society of Edinburgh*, 57:269–304, 1937.

[33] D.P. Mok, W.A. Wall, and E. Ramm. Accelerated iterative substructuring schemes for instationary fluid-structure interaction. In K.J. Bathe, editor, *Computational Fluid and Solid Mechanics*, pages 1325–1328. Elsevier, 2001.

[34] U. Küttler and W.A. Wall. Fixed-point fluid-structure interaction solvers with dynamic relaxation. *Computational Mechanics*, 43(1):61–72, 2008.

[35] B.M. Irons and R.C. Tuck. A version of the Aitken accelerator for computer iteration. *International Journal for Numerical Methods in Engineering*, 1(3):275–277, 1969.

[36] B. Hübner, E. Walhorn, and D. Dinkler. A monolithic approach to fluid-structure interaction using space-time finite elements. *Computer Methods in Applied Mechanics and Engineering*, 193(23–26):2087–2104, 2004.

[37] C. Michler, S.J. Hulshoff, E.H. van Brummelen, and R. de Borst. A monolithic approach to fluid-structure interaction. *Computers and Fluids*, 33:839–848, 2004.

[38] E. Kausel. *Fundamental solutions in elastodynamics: a compendium*. Cambridge University Press, New York, 2006.

[39] S. Chaillat, M. Bonnet, and J.-F. Semblat. A new fast multi-domain BEM to model seismic wave propagation and amplification in 3D geological structures. *Geophysical Journal International*, 177:509–531, 2009.

[40] U. Langer and D. Pusch. Data-sparse algebraic multigrid methods for large scale boundary element equations. *Applied Numerical Mathematics*, 54(3–4):406–424, 2005.

[41] M. Schevenels, S. François, and G. Degrande. EDT: An ElastoDynamics Toolbox for MATLAB. *Computers & Geosciences*, 35(8):1752–1754, 2009.

COMPDYN 2013
4th ECCOMAS Thematic Conference on
Computational Methods in Structural Dynamics and Earthquake Engineering
M. Papadrakakis, V. Papadopoulos, V. Plevris (eds.)
Kos Island, Greece, 12–14 June 2013

BRIDGE-WIZARD: EXPERT SYSTEM FOR FINITE ELEMENT MODELING AND POST PROCESSING OF BRIDGE STRUCTURES

Anastasios G. Sextos[1], Nikolaos D. Lesgidis[2],

[1]Aristotle University of Thessaloniki, Department of Civil Engineering, Thessaloniki, Greece, Assistant Professor

[2]Aristotle University of Thessaloniki, Department of Civil Engineering, Thessaloniki, Greece, Civil Engineer

Keywords: Finite Element Analysis, Bridge Engineering, Software, Expert System

Abstract. *Notwithstanding the abrupt increase in computational power and the subsequent advances in finite element analysis, many pre- and post-processing tasks still require a high level of engineering judgment while others remain significantly time consuming. Furthermore, commercial software, being inevitably of general purpose, does not always provide specific elements or constitutive laws tailored to the assessment of seismic response of structures. Powerful software for earthquake engineering has also been developed but, in most cases, it is equally lacking of a user-friendly interactive environment. Along these lines, the scope of this paper is to present the architecture and features of Bridge Wizard, an interactive front-end software for the seismic analysis and assessment of bridge structures, that takes advantage of a sophisticated, Open-Source software for Earthquake Engineering Simulation (OpenSees) to provide through its graphical user's interface: (a) conceptual assistance during the finite element analysis pre- and post-processing (b) finite element model development automations and (c) expert advice for modeling various bridge-specific issues that are key for the reliable prediction of structural response (such as boundary conditions, pier-deck connections, soil-structure interaction etc). It is deemed that the development of Bridge Wizard improves the efficiency and credibility of the finite element modeling developed, particularly for the case of complex bridge structures and gives the designer more control in critical modeling decisions affecting the overall system response.*

1. INTRODUCTION

Similarly to every other scientific area, the technological advancements of the last two decades have greatly affected structural engineering as well. The use of advanced finite element software and analysis methods has become a vital part of the structural engineer's every

day work and it is even prescribed in modern seismic codes and design guidelines. Nonetheless, this major breakthrough has also triggered a number of second order sources of epistemic (modeling) uncertainty that tend to undermine to some extent the credibility of the structural design and assessment process as a whole. More precisely:

(a) General-purpose commercial finite element software is not tailored to the assessment of seismic response of structures. The inherent formulations are analytically articulate but inevitably generic, hence, requiring careful adaptation before simulating the salient features of structural response under earthquake loading. On the other hand, rigorous software has been developed during the last decades specifically for earthquake engineering purposes but still, in most cases, equally lacks of an illustrative and user-friendly interactive environment.

(b) Particularly for the case of long structures, such as bridges subject to seismic hazard, this problem is even more profound because, in contrast to ordinary buildings, the soil-structure system is significantly more extensive and coupled. Few software packages exist that could possibly combine, at equal rigor, all the features required for the advanced simulation of both the (non-linear) dynamic pier-foundation-subsoil [1], [2] and deck-abutment-embankment interaction [3–10], the shear deformation and flexural failure of reinforced concrete members (i.e. piers and piles) as well of any potential geometric non-linearity that commonly arises under large seismic forces (i.e. closure of gaps or joints at the deck level). The same applies to the selection of a realistic earthquake scenario and an appropriate set of representative ground motions [11–13] to be used for dynamic analysis, particularly considering that bridges are subject to multiple support excitation due to the spatially variable nature of seismic waves [14], [15].

(c) Modern seismic codes, acknowledge the progress made in numerical analysis and the present state-of-knowledge regarding the complex phenomena affecting the seismic response of bridges, but they only provide limited practical guidance on how to define the necessary level of modeling refinement, estimate the parameters involved and handling the corresponding uncertainty.

The side effect of the above three conditions is that the designer has a set of powerful numerical tools in hand and the necessary hardware to conduct extremely complex commutations in a limited amount of time, but at the same time, the epistemic uncertainty associated with his/her finite element modeling decisions remains disproportionally high. An additional issue is that, this uncertainty is also not easily quantified, an issue that is of paramount importance in the framework of Performance-Based Earthquake Engineering whose fundamental objective is to design structures to meet specific performance goals for specific probability levels.

To address the above limitations and link more efficiently state-of-the-art research with engineering practice, specialized software has been recently developed [16–18]. Along the same lines, a front-end software has also been developed and is presented herein that utilizes the widely used finite element program OpenSees (Open System for Earthquake Engineering Simulation; http://opensees.berkeley.edu) [19] as the core computational algorithm of a generalized expert system for the seismic analysis of bridges. The main features of the software are presented in the following sections.

2. SOFTWARE CONCEPT

Bridge Wizard is a windows-based application developed in Microsoft® Visual Studio as a stand-alone platform for facilitating the performance of static, modal and (linear/nonlinear) response history analysis of bridges. The main program is written in Visual Basic 2010 and is essentially translating in real time the user decisions into a Tool Command Language (tcl/tk) script. It also processes analysis results for visual illustration purposes. The software concept is based in five main principles, namely:

(a) A *wizard-like* process flow, restricting the user from navigating freely through the software. The user is requested to answer a uni-directional sequence of logical, qualitative and quantitative questions in order to describe the structural configuration of the bridge. Depending on the user response and decisions, the set of questions is modified accordingly.

(b) *Background automations* that minimize the time required for pre-processing by calling internal element generators and completing missing data without the aid of the user (described in detail in Section 4).

(c) *Expert suggestions* at every step of the simulation process for selecting the most appropriate modeling approach for each bridge sub-component (pier, abutment, deck, foundation) and accurately defining the material or analysis parameters involved.

(d) *State-of-the-art add-ons* that call and execute external Matlab scripts in the background.

(e) *An ad-hoc developed 3D visualization engine* for reviewing the structural system while generating the FE model or assessing the analysis results.

3. MODELING STRATEGY ADOPTED BY THE EXPERT SYSTEM

3.1. Pier and deck topology and constitutive behavior

The front-to-end analysis stages involve ten distinct steps, each one retrieving and storing into a large number of matrices, the information necessary to build the finite element model. The first three steps request information related to the general geometry of the Bridge, primarily the number and length of spans (Figure 2), the bridge curvature and elevation. In the following step, the user defines the (uniform or non-uniform along the length) deck properties by picking pre-defined, parameterized sections or drawing, point-by-point a more complex, hollow deck section. For cases that deck dimensions are varying with length, the user has the option to draw a finite number of separate sections at specific locations and the software will interpolate in between to define the section properties at all intermediate points (Figure 3). The coordinates of the deck center of gravity and subsequently of the 3D beam elements used are also computed based on the deck section and the bridge curvature and elevation. The deck is by default considered linear elastic under earthquake loading unless otherwise defined by the user. Regarding element discretization, the deck is initially divided into 20 elements within each span and a post-analysis check verifies that further mesh refinement by a factor of 2 does not modify the dominant natural frequencies (i.e., the ones that overall activate more than 80% of the modal mass) by more than 2%. In case that the prescribed accuracy threshold values are not satisfied, meshing refinement and successive analyses are repeated in the background until convergence is met.

Pier section properties are defined through a similar process. In the case that nonlinear response is sought, the user is navigated to define concrete and steel material properties. Both

Eurocode 8 compliant materials and user-defined constitutive laws are provided (Figure 4). Piers are then modeled with fiber finite elements and non-linear constitutive laws (Kent & Park model for unconfined concrete, Park et al. for confined concrete, bilinear stress-strain relationship for reinforcing steel).

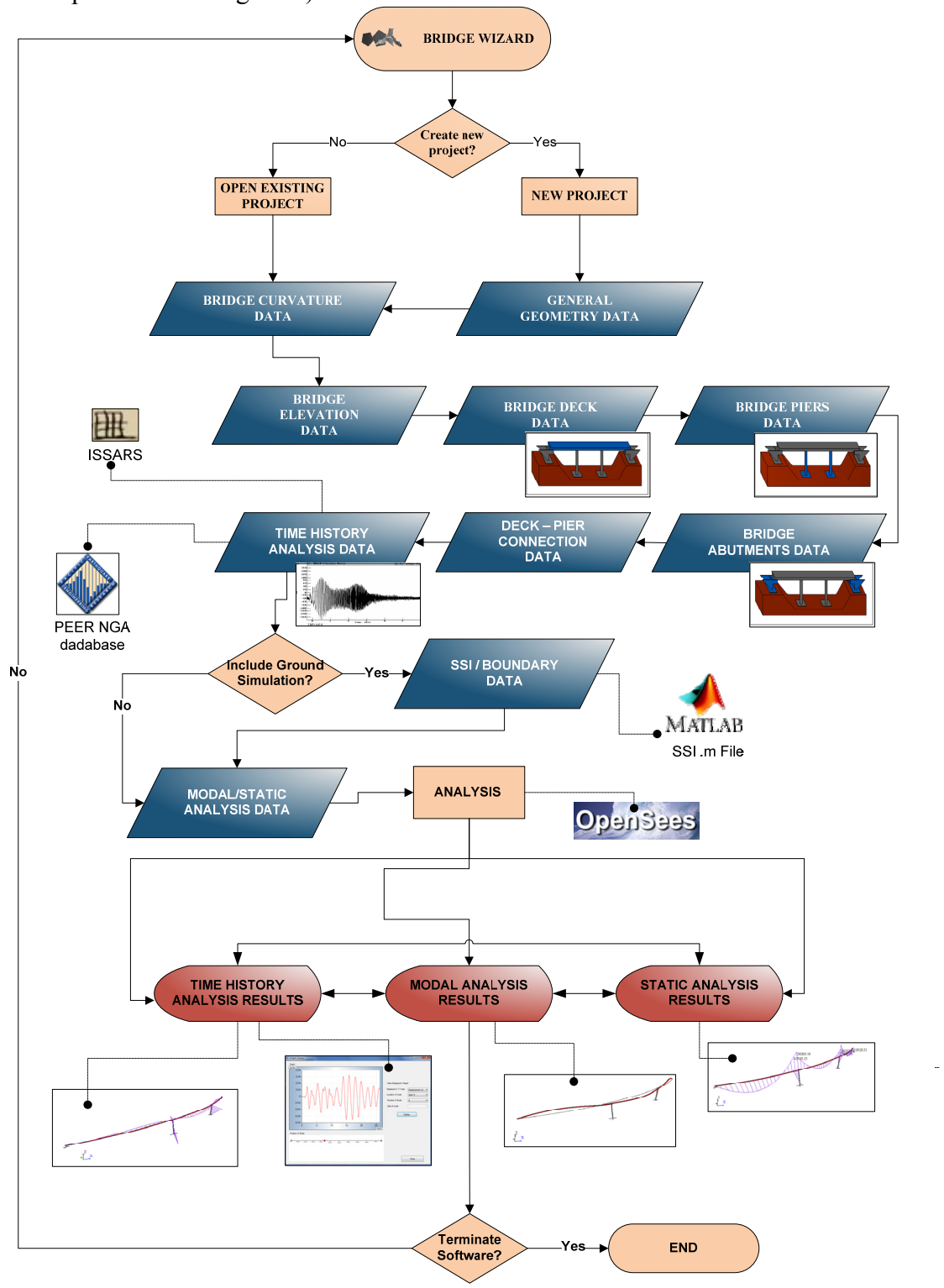


Figure 1: Program flow

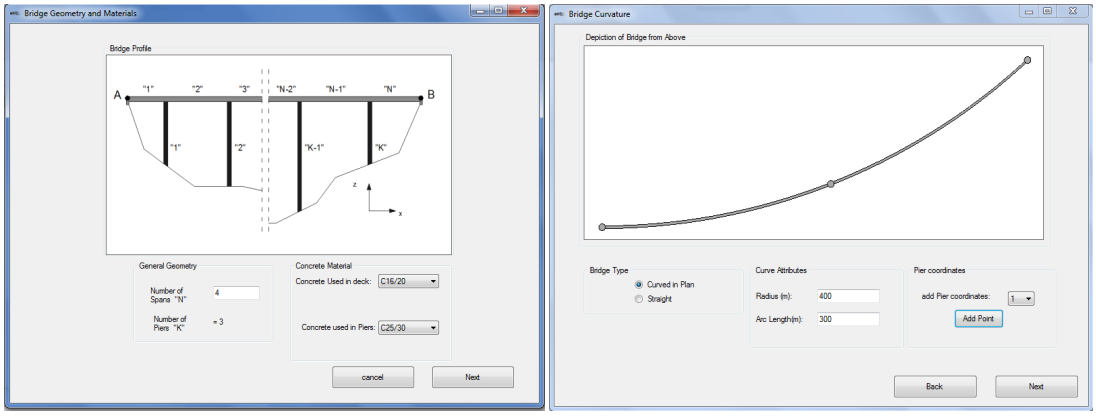


Figure 2. Bridge geometry input

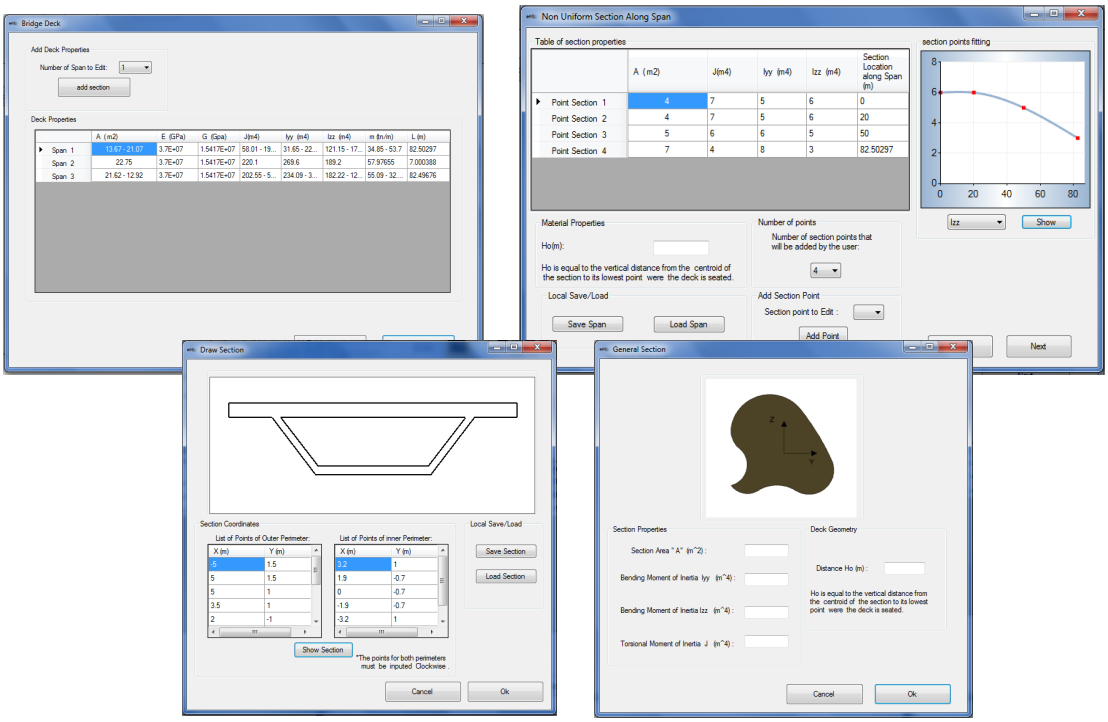


Figure 3. Definition and interpolation of deck section properties along the bridge length.

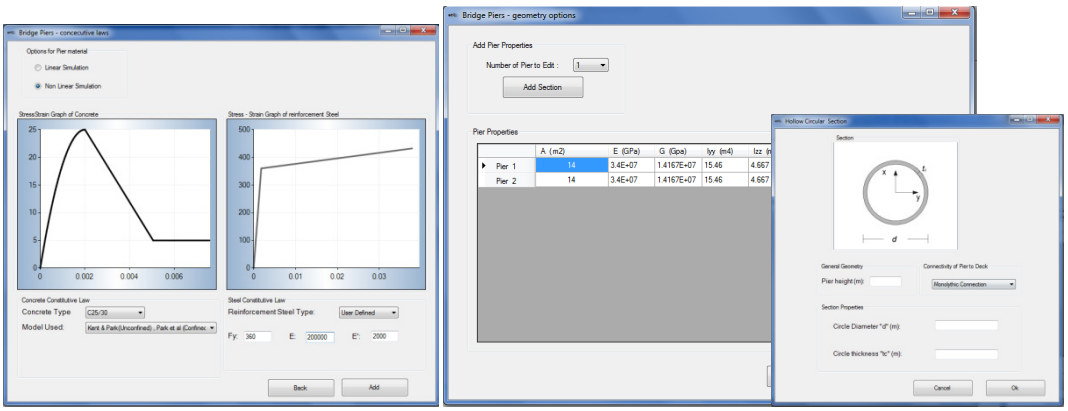


Figure 4. Definition of material properties

3.2 Pier-deck and abutment-deck connection

The deck can be supported on the piers either monolithically or through bearings utilizing the "elastomeric bearing element" of OpenSees and following a linear, bi-linear or tri-linear force-displacement relationship. The number of bearings, input by the user, defines the properties of the single, equivalent bearing element introduced in the finite element model by geometrically coupling the translational and rotational bearing stiffness along each degree of freedom. For the abutments in particular, the option is also given to release certain degrees of freedom or prescribe gaps along the two principal horizontal directions (Figure 5).

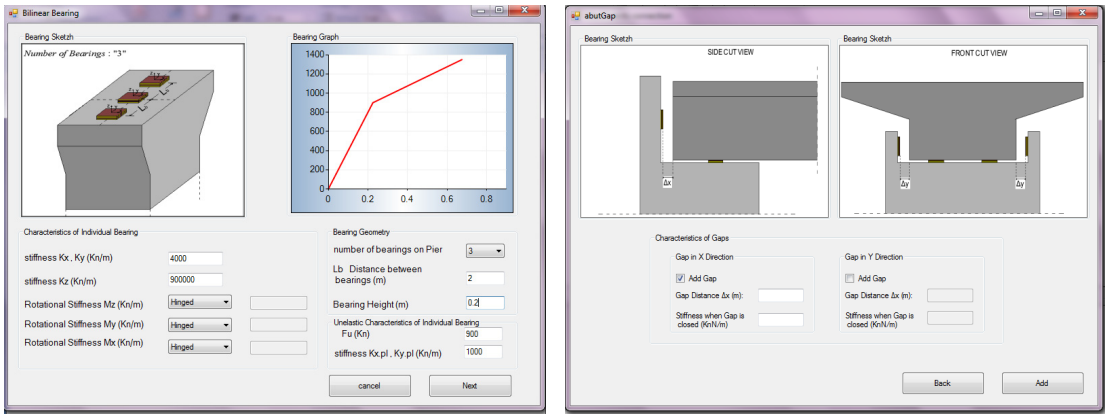


Figure 5: Bilinear force-displacement rule for elastomeric bearings (left) and consideration of deck-abutment gaps along the two principal directions.

3.3 Boundary conditions and soil-structure interaction

Unless the user specifies point fixity, the 6-DOF pier foundation dynamic impedance matrix is computed by calling an external Matlab script. Soil properties and geometry of foundation is required both for the case of shallow footings and *nxm* pile groups according to the literature [20–23]. In particular, the complex dynamic interaction factors α_{ij}^{dyn} are calculated for all modes of vibration (α_z for vertical, α_{uH} for horizontal and $\alpha_{\theta M}$, $\alpha_{\theta H}$ for rocking interaction). By assuming that interaction factors involving rocking vibration ($a_{\theta H}$, $a_{\theta M}$) are taken equal to zero, the static stiffness matrix of the pile group is expressed in the following form:

$$\begin{bmatrix} K_{HH}^{st} & K_{HM}^{st} \\ K_{MH}^{st} & K_{MM}^{st} \end{bmatrix}_{group} = \frac{1}{(f_{uH}^{st} \cdot f_{\theta M}^{st} - f_{MH}^{st\,2})} \begin{bmatrix} f_{\theta M}^{st} & -f_{uM}^{st} \\ -f_{\theta H}^{st} & f_{uH}^{st} \cdot \sum_{i=1}^{n}\sum_{j=1}^{m} a_{uH_{ij}} \end{bmatrix} \quad (2)$$

and the dynamic stiffness matrix of the pile group is then written similarly by introducing the damping coefficients ζ_{HH}, ζ_{MH}, ζ_{MM}:

$$\begin{bmatrix} K_{HH}^{dyn} & K_{HM}^{dyn} \\ K_{MH}^{dyn} & K_{MM}^{dyn} \end{bmatrix}_{group} = \begin{bmatrix} f_{\theta M}^{st} \cdot (nxm) \cdot (1 + 2\zeta_{HH}(\omega)i) / \Delta & -f_{uM}^{st} \cdot (nxm) \cdot (1 + 2\zeta_{MH}(\omega)i) / \Delta \\ -f_{\theta H}^{st} \cdot (nxm) \cdot (1 + 2\zeta_{HM}(\omega)i) / \Delta & f_{MM}^{st} \cdot (nxm) \cdot (1 + 2\zeta_{MM}(\omega)i) / \Delta \end{bmatrix} \quad (3)$$

where $\Delta = (f_{uH}^{st} \cdot \sum_{i=1}^{n}\sum_{j=1}^{m} a_{uH_{ij}} \cdot f_{\theta M}^{st} - f_{uM}^{st\,2})$. The predominant frequency of the motion, required for the computations is defined implicitly by computing the mean period (T_m), a weighting the amplitudes over a specified range of the Fourier Amplitude Spectrum [24]:

$$T_m = \frac{1}{f_m} = \frac{\sum c_i^2 \cdot \frac{1}{f_i}}{\sum c_i^2} \qquad for\ 0.25\ Hz \le f_i \le 20\ Hz\ with\ \Delta f \le 0.05\ Hz \tag{4}$$

where c_i and f_i are the Fourier amplitudes and frequencies, respectively.

Abutment-embankment interaction can be optionally taken into consideration by introducing linear springs according to Caltrans [25], the most widely used expression currently provided in modern seismic codes. In particular, for fill materials that comply with the Caltrans Standard Specifications requirements, the initial longitudinal stiffness of the embankment can be taken equal to 28.7 kN/mm per meter of the width of the wall. In case of other fill materials, the value of 14.35kN/mm/m is to be used. The ultimate abutment load is then limited by a maximum passive resistance of 239kPa. Given the limitations that arise from the use of the particular expression, the user has also the option to utilize more refined force-displacement (P-y) relationships that consider the contribution of the abutment foundation prior to the backwall failure [26].

3.4 Analysis control and post-processing

Having described the structural configuration in maximum possible detail, the parameters for static, modal and (linear/ non-linear) response history analysis are then defined. Ground motions can be imported in the PEER-NGA [27] format for all three components. The software is also capable of importing records selected by an external Matlab-based software ISSARS [28] according to specific seismological, geotechnical and structural criteria. Having accomplished the problem description, a tcl/tk file is automatically generated to be used in OpenSees. The particular *.tcl input file consists of four distinct parts controlling the finite element model topology, the mechanical properties, the analysis method and the desirable post processing output data. OpenSees is automatically called and executed in the software background before the software switches to the post-processing visualization engine (Figure 6). Deformed shapes and eigenmodes are illustrated graphically while the user may easily generate plots of the variation of all the critical engineering demand parameters with time. Projects can also be saved for future reference and modification. Validation with alternative finite element software SAP2000 [29] for the case of real bridge structures [30] has shown satisfactory agreement in the predicted natural frequencies and time-variant action effects that did not exceed 5% (the average deviation found was of the order of 2%).

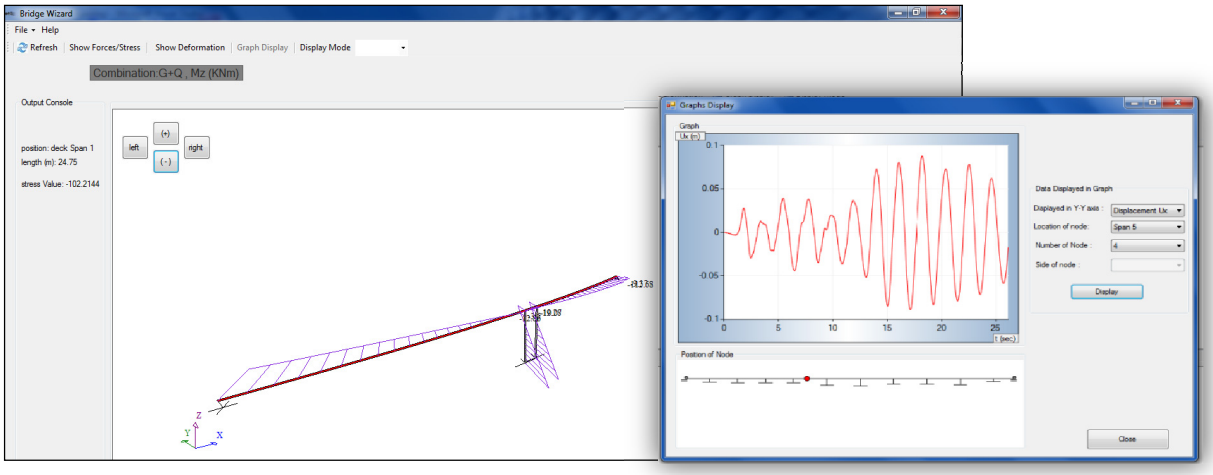


Figure 6: 3D visualization engine for post-processing the analysis results

4. CONCLUSIONS

This paper presents the development of an expert system aiming to (a) eliminate the time required for the numerical analysis of bridges using Opensees (b) improve the credibility of the FEM pre-processing by automatically generating critical model parts and (c) introduce, in an efficient and user-friendly manner, state-of-the art knowledge regarding the seismic response of bridges that the designers are often reluctant to consider during numerical analysis. The software is currently freely available at www.asextos.net/software and is currently under further development.

5. REFERENCES

[1] G. E. Mylonakis, S. Nikolaou, and G. Gazetas, "Footings under seismic loading: analysis and design issues with emphasis on bridge foundations," *Soil Dynamics and Earthquake Engineering*, vol. 26, no. 9, pp. 824–853, May 2006.

[2] G. E. Mylonakis and G. Gazetas, "Seismic soil-structure interaction: beneficial or detrimental?," *Journal of Earthquake Engineering*, vol. 4, no. 3, pp. 277–301, 2000.

[3] N. Makris and G. Kampas, "The eigenvalues of isolated bridges with transverse restraints at the end abutments," *Earthquake Engineering & Structural Dynamics*, vol. 39, no. 8, pp. 869–886, 2010.

[4] M. Dicleli and S. Erhan, "Effect of soil–bridge interaction on the magnitude of internal forces in integral abutment bridge components due to live load effects," *Engineering Structures*, vol. 32, no. 1, pp. 129–145, 2010.

[5] P. Tasiopoulou, E. Smyrou, and G. Gazetas, "Bridge pile − abutment − deck interaction in laterally spreading ground : Lessons from Christchurch vement : from Kobe to Christchurch," in *15th World Conference on Earthquake Engineering*, Lisbon. Portugal, 2012.

[6] A. Shamsabadi, M. Ashour, and G. Norris, "Bridge Abutment Nonlinear Force-Displacement-Capacity Prediction for Seismic Design," *Journal of Geotechnical and Geoenvironmental Engineering*, vol. 131, no. 2, pp. 151–161, 2005.

[7] A. Kotsoglou and S. Pantazopoulou, "Assessment and modeling of embankment participation in the seismic response of integral abutment bridges," *Bulletin of Earthquake Engineering*, vol. 7, no. 2, pp. 343–361, 2009.

[8] A. G. Sextos and O. N. Taskari, "Comparative assessment of advanced computational tools for embankment-abutment-bridge superstructure interaction," in *14th World Conference on Earthquake Engineering*, Beijing, China, 2008.

[9] A. G. Sextos, K. R. Mackie, B. Stojadinović, and O. N. Taskari, "Simplified P-y relationships fro modeling embankment-abutment systems of typical California bridges," in *14th World Conference on Earthquake Engineering*, Beijing, China, 2008.

[10] S. D. Tegou, S. A. Mitoulis, and I. A. Tegos, "An unconventional earthquake resistant abutment with transversely directed R/C walls," *Engineering Structures*, vol. 32, no. 11, pp. 3801–3816, 2010.

[11] E. I. Katsanos, A. G. Sextos, and T. Notopoulos, "ISSARS : An integrated systems for structural analysis and record selections," in *3rd ECCOMAS Thematic Conference on Computational Methods in Structural Dynamics and Earthquake Engineering (COMPDYN), Corfu, Greece*, 2011.

[12] N. Buratti, P. J. Stafford, and J. J. Bommer, "Earthquake accelerogram selection and scaling procedures for estimating the distribution of drift response," *Journal of Structural Engineering*, vol. 137, no. 3, pp. 345–357, 2011.

[13] N. Jayaram, T. Lin, and J. W. Baker, "A computationally efficient ground-motion selection algorithm for matching a target response spectrum mean and variance," *Earthquake Spectra*, vol. 27, no. 3, pp. 797–815, 2011.

[14] A. G. Sextos, A. J. Kappos, and K. D. Pitilakis, "Inelastic dynamic analysis of RC bridges accounting for spatial variability of ground motion, site effects and soil-structure interaction phenomena. Part 2: Parametric study," *Earthquake Engineering & Structural Dynamics*, vol. 32, no. 4, pp. 629–652, 2003.

[15] A. Zerva, *Spatial Variation of Seismic Ground Motions: Modeling and Engineering Applications (Advances in Engineering Series)*. CRC Press, Taylor & Francis Group, FL, 2009.

[16] K. R. Mackie, J. Lu, and A. Elgamal, "Performance-based earthquake assessment of bridge systems including ground-foundation interaction," *Soil Dynamics and Earthquake Engineering*, vol. 42, pp. 184–196, 2012.

[17] M. H. Scott, "Extensions of OpenSees for Bridge Management Applications Overview of OpenSees," in *18th Analysis and Computational Specialty Conference, ASCE*, Vancouver, British Columbia, 2008.

[18] B. Aygün, L. Dueñas-Osorio, J. E. Padgett, and R. Desroches, "Seismic Vulnerability of Bridges Susceptible to Spatially Distributed Soil Liquefaction Hazards," in *6th National Seismic Conference on Bridges and Highways*, Charleston, U.S., 2008.

[19] S. Mazzoni, F. McKenna, M. H. Scott, and G. Fenves, "Open System for Earthquake Engineering Simulation, User Language Manual, Version 1.7.3. University California Berkeley, CA.," 2008.

[20] S. Nikolaou, G. E. Mylonakis, G. Gazetas, and T. Tazoh, "Kinematic pile bending during earthquakes: analysis and field measurements," *Geotechnique*, vol. 51, no. 5, pp. 425–440, 2001.

[21] G. E. Mylonakis, S. Nikolaou, G. Gazetas, and A. Nikolaou, "Soil-pile-bridge seismic interaction: kinematic and inertial effects. part I: soft soil," *Earthquake Engineering and Structural Dynamics*, vol. 26, pp. 337–359, 1997.

[22] G. E. Mylonakis, G. Gazetas, S. Nikolaou, and A. Chauncey, "Development of Analysis and Design Procedures for Spread Footings. Technical Report MCEER-02-0003," 2002.

[23] A. G. Sextos, K. D. Pitilakis, and A. J. Kappos, "Inelastic dynamic analysis of RC bridges accounting for spatial variability of ground motion, site effects and soil-structure interaction phenomena. Part 2: Parametric study," *Earthquake Engineering & Structural Dynamics*, vol. 32, no. 4, pp. 629–652, 2003.

[24] E. M. Rathje, F. Faraj, S. Russell, and J. D. Bray, "Empirical relationships for frequency ground motions," *Earthquake Spectra*, vol. 20, no. 1, pp. 119–144, 2004.

[25] Caltrans, "Seismic Design Criteria Version 1.6," *California Department of Transportation: Sacramento, CA, U.S.*, 2010.

[26] O. N. Taskari and A. G. Sextos, "Stiffness and Ultimate Capacity of Typical Abutment- Embankment Systems," in *15th World Conference on Earthquake Engineering*, 2012, Lisbon, Portugal.

[27] M. Power, B. Chiou, N. A. Abrahamson, Y. Bozorgnia, T. J. Shantz, and C. Roblee, "An Overview of the NGA Project," *Earthquake Spectra*, vol. 24, no. 1, pp. 3–21, 2008.

[28] E. I. Katsanos and A. G. Sextos, "ISSARS: An integrated software environment for structure-specific earthquake ground motion selection," *Advances in Engineering Software*, vol. 58, pp. 70–85, 2013.

[29] C&S, "SAP2000, Integrated Finite Elements Analysis and Design of Structures, Computers and Structures," Berkeley, CA, US, 2008.

[30] S. P. Papadopoulos and A. G. Sextos, "On the excitation of higher modes of long bridges due to spatial variability of earthquake ground motion," in *Innovations on Bridges and Soil-Bridge Interaction (IBSBI), Athens, October 13-15.*, 2011.

COMPDYN 2013
4th ECCOMAS Thematic Conference on
Computational Methods in Structural Dynamics and Earthquake Engineering
M. Papadrakakis, V. Papadopoulos, V. Plevris (eds.)
Kos Island, Greece, 12–14 June 2013

ROBUSTNESS, REPEATABILITY AND RESILIENCE OF INTERCONTINENTAL DISTRIBUTED COMPUTING FOR THE PURPOSES OF SEISMIC ASSESSMENT OF BRIDGES

Olympia N. Taskari[1], **Anastasios G. Sextos**[2]

[1] Aristotle University of Thessaloniki, Greece, Ph.D. Student
e-mail: taskari@civil.auth.gr

[2] Aristotle University of Thessaloniki, Greece, Assistant Professor
asextos@civil.auth.gr

Keywords: Multi-platform simulation, geographical distributed simulation, SimCor

Abstract. *Hybrid simulation is a promising tool that permits the integration of different laboratories in real time to undertake a set of joint experiments on individual components assembling a structural system. The components studied either analytically or experimentally can be physically distributed and thus potentially located anywhere. The same concept has also been applied for the numerical coordination of distributed sub-structures in the framework of multi-platform simulation. The advantage of the latter approach is that it permits the use of different numerical analysis packages, enabling the concurrent use of the most sophisticated constitutive laws, element types and features that each specialized software provides for each individual part of the system. Notwithstanding the major advancements made so far in hybrid experimentation, it is notable that the vast majority of such trans-laboratory campaigns has taken place within the U.S. The scope of this paper therefore, is to present the recent findings and technical challenges encountered in an attempt to run similar (hybrid and multi-platform) experiments both within Europe and between E.U. and the U.S. for the study of seismic soil-structure interaction effects in bridge structures. The paper also discusses the parameters that were found to affect the efficiency and repeatability of distributed analysis while it investigates the resilience of the procedure in cases of abrupt network failure. It also foresees the conditions under which the implementation of a geographically distributed hybrid simulation is indeed feasible, robust and repetitive between transatlantic partners. For this scope, the seismic response of a 110m long, four span, reinforced concrete bridge is preliminary assessed, through its numerical sub-structuring into five structural components (modules) that are analyzed in computers located in the cities of Thessaloniki (Greece), Patras (Greece), Naples (Italy), Urbana-Champaign (U.S.), and Toronto (Canada). The analyses results as well as the implications of the parameters involved in the feasibility of an intercontinental hybrid experiment are also critically discussed.*

1 INTRODUCTION

Experimental methods or analytical models can be used for the seismic evaluation of structures. Despite the increasing capabilities of the laboratories, parameters related with space or equipment capacity limit the full-scale testing of the entire structures. On the other hand, analytical methods cannot fully capture the real complex seismic behavior of the modeled structures inducing an uncertainty level which in many cases cannot be neglected. The combination of the experimental and analytical methods is a very promising tool introduced as hybrid simulation.

Specifically, a number of laboratories could combine their capabilities to undertake a set of integrated component tests of structures. In fact, this multi-site, Real Time Hybrid Simulation (RTHS) approach has already been developed in the United States for the assessment of complex interacting systems. It is supported by NSF through the Network for Earthquake Engineering Simulation (NEES, www.nees.org) scheme [1–4] and it aims to raise the limitations related to the laboratory capacities. In this framework, there is no need for using a single experimental facility neither there is need for physical proximity of the multiple subcomponents tested. Moreover, since communication is solely web-based, using the same protocols, some components of the system can be analyzed numerically while others can be physically tested. The dynamic response of full scale specimens that are discretized into sub-structures is properly controlled with the use of purpose-specific coordination software. Two such specialized software platforms exist to date, i.e. the OpenFresco [5-6] and SimCor [7]. The components (analytical, experimental or a combination of both) are treated on different networked computers and, can thus be located anywhere in the world. Another major advantage of hybrid simulation is that it removes a large source of uncertainty compared to pure numerical simulations, by replacing structural elements with complex non-linear behavior with physical specimens tested on the laboratory floor. Apparently, drawbacks also exist and are related to the necessity for in-depth knowledge of specialized experimental and analytical tools as well as for considerable programming effort and computational cost.

The same concept has also been successfully applied [8] for the coordination of purely numerical analysis modules (where no physical testing is performed, in contrast to the hybrid simulation application). This, so called, “multi-platform simulation” is another promising alternative to the aforementioned hybrid simulation approach primarily because it permits the sub-structured analysis of a complex system using purely analytical tools, similarly physically distributed as was the previous case. The advantage of this approach is that the appropriate selection and combination of different analysis packages, enables the concurrent use of the most sophisticated constitutive laws, element types and features of each package for each corresponding part of the system. In other words, different software can be used for different system components (i.e. abutments, superstructure and supporting pile groups for instance in the case of a long bridge), depending on the foreseen inelastic material behavior, level and nature of the seismic forces and the geometry of the particular problem. It is believed that this approach leads to combined capabilities that no finite element program currently provides, nor is it probable to provide in the near future. On the contrary, it has the minimum assumptions possible and permits the best available option to simulate each component using the most appropriate analytical model, while integrating the various contributions into a fully interacting system. As for the case of Hybrid Simulation though, the computational cost and level of expertise is relatively high compared to a conventional all-inclusive simulation package.

The EU Framework 7 project, EXCHANGE-SSI, enables a number of earthquake engineering centers in Europe and the U.S to collaborate on the application of distributed,

hybrid or multi-platform experimentation for the study of seismic soil-structure interaction effects in bridge structures. In this framework, a four span seismically isolated reinforced concrete bridge of a total length of 110.40m was selected to be assessed by implementing the geographically distributed simulation concept. Although this approach has been used by several research groups, in most cases, the experimentally tested component was a reinforced concrete or a steel structural member. However, in the case of the EXCHANGE-SSI project, it is a rate-dependent member (i.e., bearing) that is to be experimentally tested. In this case, the required time for the communication among the modules is the most critical parameter for the successful conduct of the hybrid experiment.

The scope of this study is therefore, to optimize the parameters that delay the distributed analysis as well as to investigate the conditions under which the implementation of a geographically distributed hybrid simulation concept becomes robust, repetitive and resilient in the case of an intercontinental experiment. For this purpose, it was deemed necessary, before proceeding with hybrid experimentation, to implement a first multi-platform analysis simulation for the system studied. Along these lines, the bridge was divided into four structural components (modules), each one being analyzed using specific software in a different computer station located in Aristotle University of Thessaloniki (AUTH), University of Patras (UPATRAS), University of Illinois at Urbana Champaign (UIUC), University of Naples (UNAPLES) and University of Toronto (UTR). In the subsequent stage, the bearing will be physically tested at the University of Patras, thus replacing the computational node with an experimental component. In both cases, the SimCor [10] communication platform was used as the analysis coordinator (Figure 1). Clearly such a five-partner, intercontinental hybrid experiment is a challenging task which has only limited applications so far, the only successful known to the authors being the specimen test between two UC Berkeley and University of Kassel in Germany [9].A full description of the analytical sub-structured modules, the parametric scheme followed for the optimization of the distributed simulation in terms of computational cost, the analyses results as well as the limitations and future developments are discussed in the following.



Figure 1: Geographical distributions of the numerical and experimental sub-structures involved in the multi-platform and hybrid experiments (www.exchange-ssi.net).

2 OVERVIEW OF THE CASE STUDIED

The seismic evaluation of a four span reinforced concrete bridge of a total length of 110.40m was selected for the particular study. The bridge is located in the region of northeastern Greece and is part of the perpendicular EGNATIA highway axis connecting Greece and Bulgaria. The two outer spans have a 24.20m length each, while the two inner spans have a 31.00m length. A prestressed hollow deck is supported on two piers which consist of circular reinforced concrete sections of a diameter equal to 2.0m. Two series of 65Ø25 longitudinal bars spaced equally around the perimeter were used for the piers. For the transverse reinforcement, a double Ø14 spiral at 8.5cm was used throughout the entire pier length (5.85m). A bearing type pier-to-deck connection was adopted permitting movement along the two principal, longitudinal and transverse direction. For each pier-to-deck connection, two 900x900x328 ALGABLOC NB4 bearings were used computed according to the Greek seismic code for bridges, E39/99 [11] and the relevant DIN4141 specifications. The deck is supported on seat type abutments with a backwall height equal to 1.5m. At the abutments, the deck is connected through two pot bearings that permit sliding along the two principal bridge axes, while a sliding joint of 22cm length separates the deck from the backwall. Seismic forces are also resisted by the activation of stoppers (activated in the transverse direction) located at the seating of the abutments. A general overview of the bridge configuration and the deck section at various locations are illustrated in Figures 2-3.

The foundation is deep due to the soft soil formations existing in the overall area. The presence of loose cohesionless saturated soil deposits, the low N_{30} values measured in the loose silty sand layers and the high water table level are evidence of liquefaction susceptibility. For this purpose, a group of gravel piles of a diameter equal to 0.80m was constructed in the area, at a depth that was determined from the SPT and CPT results. Consequently, the piers and the abutments are supported on 1.2m diameter group of piles (3x2) with a total length equal to 32.00m that cross the liquefaction susceptible layers until the healthy sand formations are reached.

The Greek Seismic Code [12] that was put into force at the time of design, prior to the introduction of Eurocodes, prescribed a peak ground acceleration of 0,24g and soil class “C” which are identical to the ones defined in Eurocode 8 – Part 2, for bridge design [13]. The importance factor was set equal to 1.0, while the behavior (or force reduction) factor was also selected equal to unity, since the bridge under study is seismically isolated, thus, no ductile behavior at the reinforced concrete pier members is anticipated for the design earthquake.

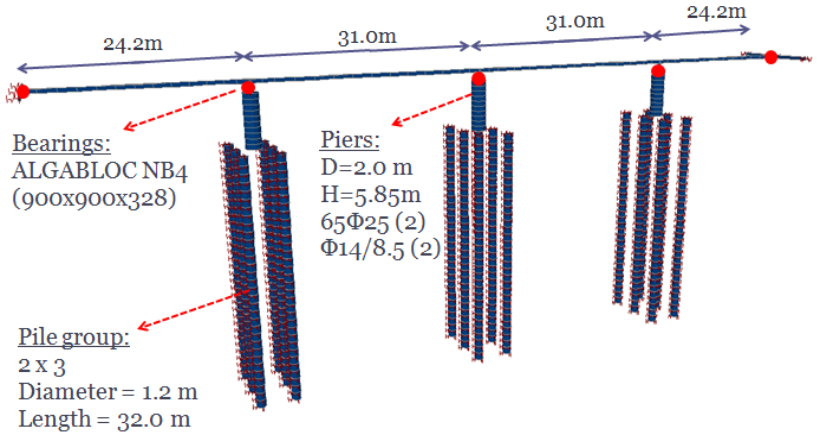


Figure 2: Layout of the bridge configuration.

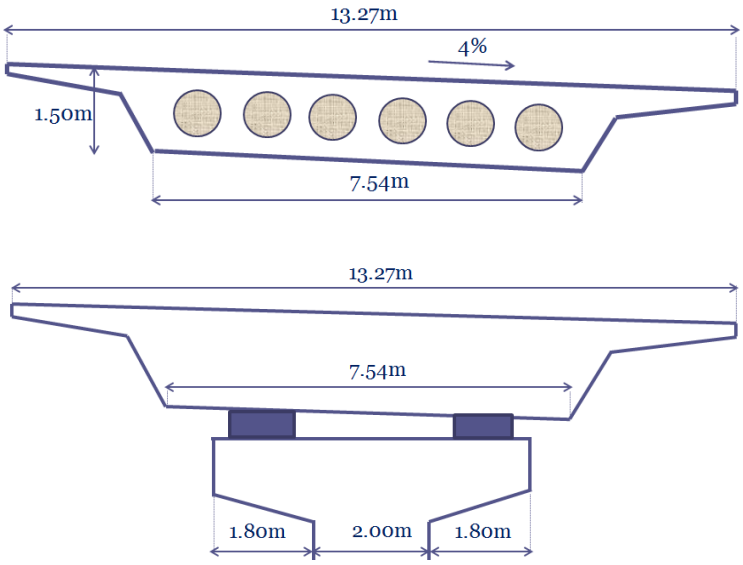


Figure 3: Deck section at the middle of the span (top) and at the location of the piers (bottom).

3 MULTI-PLATFORM ANALYSIS

The specialized software platform SimCor [7] developed by the research group of the University of Illinois was used for coordinating the preliminary multi-platform analysis used to optimize the envisaged hybrid experiment. SimCor concerns an enhanced Matlab-based script which coordinates software or hardware components supporting the NEESgrid Teleoperation Control Protocol (NTCP), as well as TCP-IP connections outside of the NEES system. The basic concept of SimCor is that analytical models of some parts of the structure or experimental specimens representing specific parts of the same structure, are all considered as super-elements with many DOFs. Specially developed interface programs permit the interaction with different analysis software such as Zeus-NL [14], OpenSees [15], FedeasLab [16], and ABAQUS [17]. After the initialization step where the connection between the modules is achieved, the stiffness matrix of the whole structure is evaluated using predefined deformation values. The gravity forces are considered during the static loading stage where displacements due to gravity forces are imposed. Finally, SimCor performs Newmark numerical integration as it steps through the seismic record by utilizing the OS method with a modified α- parameter (a-OS method) which applies numerical damping to the undesired oscillations.For the purpose of the EXCHANGE-SSI program, the bridge under study is sub-structured into an number of modules which are analyzed in different computer stations located at different institutes (AUTH, UPATRAS, UNAPLES, UIUC, UTR). An overview of the distinct modules is provided below.

3.1 Description of the multi-platform simulation modules

The four-span reinforced concrete bridge was divided into four different components (modules) each one analyzed in a different computer station after appropriate definition of the control points at the joint DOFs of interest. At each analysis step, a predefined displacement was imposed by the analysis coordinator and forces were measured to each specific module to establish the initial stiffness matrix of the sub-structured system. The established matrix is then used in the static and dynamic loading stage to determine the desirable target displacements. A brief description of the four modules is illustrated in Figure 4 and is presented in the following.

- Module 1 @UTR: Consists of the 110.40m bridge deck along with the middle and the right pier and the corresponding two bearings, all modeled and analyzed using the OpenSees software. The superstructure is expected to remain linear and is thus modeled using linear elastic beam-column elements, while fiber sections with distributed plasticity are used for the piers. Each fiber of the cross-section is modeled with an appropriate stress–strain relationship depending on whether it represents confined concrete, unconfined concrete or a longitudinal reinforcing bar. The median design strength of concrete and the yielding strength of reinforcing steel are taken equal to 38 and 550MPa, respectively. The bearings are modeled using the elastomeric bearing element where the initial stiffness is calculated using the geometry of the pad [18]. In this study, the right abutment-embankment system (described in the following) initially modeled using solid elements, is represented as a set of 6-DOF linear springs and is considered as part of the same module.
- Module 2 @UPAT: The bearings connecting the left pier to the deck is considered as an individual module and is modeled as an elastomeric bearing element whose initial stiffness is calculated by the geometry of the pad [18]. The same module will be used to link the actual bearing, to be experimentally tested at the University of Patras during hybrid simulation.
- Module 3 @UIUC: The abutment-embankment system is simulated using the OpenSees software, through solid elements but again considered herein as non-linear translational springs. The stiffness of the springs is a function of the passive resistance of the soil as well as the stiffness of the abutment foundation piles. In fact, the backwall is intended to break off and mobilize the longitudinal resistance of the approach fill [13-14] in order to protect the foundation from excessive deformations and distress. Therefore, the backwall-backfill interaction, as well as the passive earth resistance behind the abutments, that is, by design, the main mechanisms activated during a strong seismic event are considered according to the recent literature [21].
- Module 4 @UNAP: The left pier, below the critical bearing is also deemed as an individual module numerically analyzed with OpenSees using fiber sections as previously.
- Analysis Coordinator @AUTH: As previously mentioned, the integration of the analytical modules is conducted in SimCor.

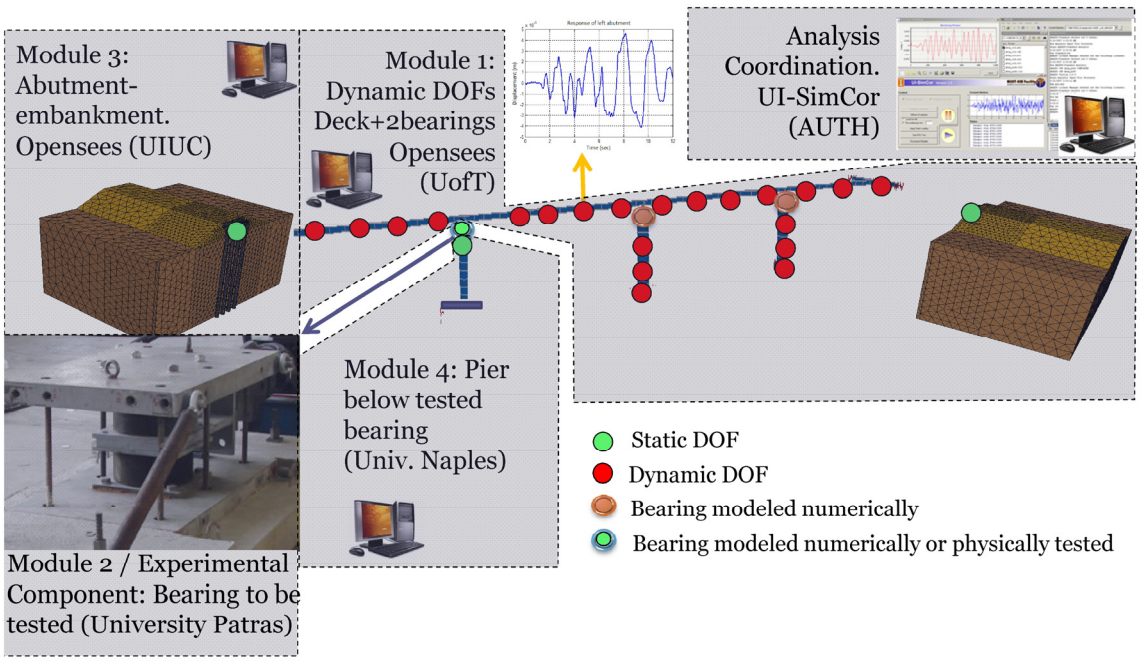


Figure 4: Layout of the bridge substructuring.

3.2 Robustness of the multi-platform model

For comparison purposes, the bridge was also modeled as a whole in OpenSees in order to ensure that the multi-platform analysis yields similar results to that of the full model. The two models were subjected to the same artificial input motion that matched the target Eurocode 8 design spectrum. The force-displacement loops of the middle bearing for the sub-structured and the entire model are presented in Figure 5. It is observed that, despite the system sub-structuring to modules widespread all over the world, there is an excellent match between the two models and therefore the multi-platform scheme is deemed an acceptably robust method for analysis and assessment.

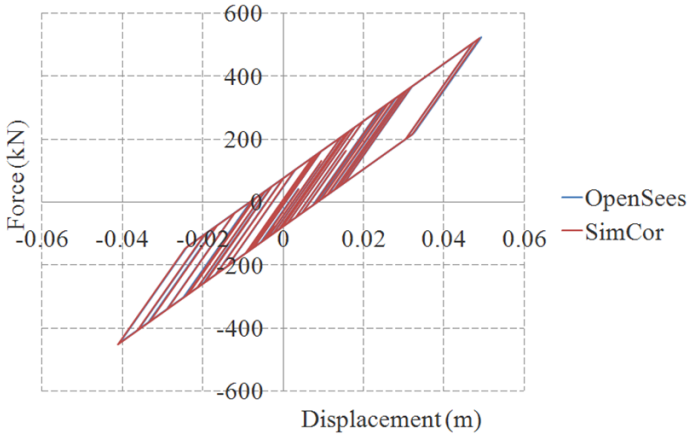


Figure 5: Comparison of the force-displacement loops between the full and the sub-structured model.

4 CONDITIONS FOR AN INTERCONTINENTAL MULTI-PLATFORM AND HYBRID EXPERIMENT

Having established a level of confidence regarding the ability of the multi-platform analysis to represent the non-linear behavior of the bridge structure, a parametric analysis scheme was implemented in order to investigate the conditions under which an intercontinental geographically distributed hybrid simulation becomes robust and repetitive. More specifically, an effort was made to decide whether the analysis time depends on the geographically distributed scheme adopted among the five partners. For this scope, different modules were assigned to each partner at all possible combinations, while retaining the analysis coordination role at AUTH. The distributed parametric scheme and the required analysis time for each run are summarized in Table 1. It is seen that the total analysis time, indeed varies between 45 and 65 minutes for the entire seismic excitation time window, despite the fact that the sub-structured modules are in all cases identical.

In a similar parametric manner, the importance of the time zone was also investigated. Figure 6 presents the average analysis time as a function of the Greek time zone in which the multi-platform analysis tool place. It can be noticed that due to network traffic, different execution times lead to different analysis time, inducing a coefficient of variation of approximately 15% to the analysis time. It is also notable that the most favorable time for conducting the intercontinental multi-platform simulation is between 2:00am-4:00am and 12:00 and 14:00pm Greek time, essentially corresponding to off-peak networking times for the American partners.

AUTH	UIUC	U of T	UPATRAS	UNAPLES	Time (min)
SimCor	Module 1	Module 2	Module 3	Module 4	*47*
SimCor	Module 1	Module 3	Module 4	Module 1	*47*
SimCor	Module 1	Module 4	Module 1	Module 2	*45*
SimCor	Module 2	Module 1	Module 3	Module 4	*65*
SimCor	Module 2	Module 3	Module 4	Module 1	*57*
SimCor	Module 2	Module 4	Module 1	Module 3	*54*
SimCor	Module 3	Module 1	Module 2	Module 4	*54*
SimCor	Module 3	Module 2	Module 4	Module 1	*65*
SimCor	Module 3	Module 4	Module 1	Module 2	*48*
SimCor	Module 4	Module 1	Module 2	Module 3	*54*
SimCor	Module 4	Module 2	Module 3	Module 1	*65*
SimCor	Module 4	Module 3	Module 4	Module 2	*56*

Table 1: Parametric analysis of partners' roles and overall analysis time during the geographically distributed seismic analysis of the bridge studied. .

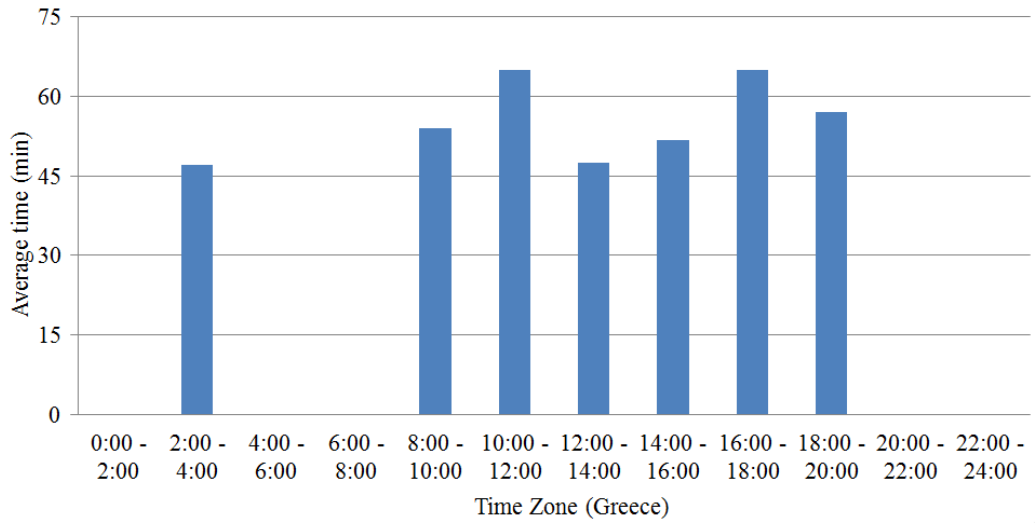


Figure 6: Effect of the analysis time window on the overall time analysis daytime during the geographically distributed analysis.

After deciding the optimum distributed simulation scheme and the most efficient time window of analysis, an effort was made to determine the relative contribution of all the parameters affecting the computational cost, i.e. (i) finite element analysis – related time (Opensees) (ii) module coordination (SimCor) and (iii) clear networking time. Figure 7 presents the breakdown of the total analysis time to the individual sources of delay. It can be seen that networking time is the dominant delay factor as it corresponds to the 70% of the overall analysis, while it is only 10% of time related to module coordination and handling and even less dedicated to finite element analysis. Though the latter is clearly a function of the active degrees of freedom, the intensity level and the corresponding material and geometrical non-linearity which would eventually increase finite element-related computational cost especially in the case of a non-seismically isolated bridge, the network communication is still deemed as the most critical factor.

It is also interesting to notice that the total analysis time increases significantly when the modules run in the U.S. and Canada are introduced (Figure 10). This is further verified by the latency rates between the Greek partners (Aristotle University and University Patras), the University of Naples in Italy and the University of Toronto (Canada) and Illinois at Ubrana-Champaign (U.S.). It is seen that for a 100 megabit network more than 50% of the latency can

be attributed to crossing the Atlantic. In fact, it takes 7-10 hops and approximately 60ms to link to the last European hop (i.e., Paris or Frankfurt) while more than 70ms are spent before connecting to the first transatlantic hop in Toronto. It has to be noted however, that for the particular hybrid test envisioned, it is the time step that is of interest and not the overall experiment time, hence the challenge is to retain the networking time as low as possible and compensate the actual bearing force accordingly.

A final comment that needs to be made is that, at least during the preparatory stage of intercontinental multi-platform analysis, the need for manual action in case of abrupt network or analysis failure is still evident, thus yielding the analysis as not fully resilient. Overall though, it is deemed that extensive calibration of the multi-platform distributed computation has established a level of confidence prior to conducting the final intercontinental hybrid experiment.

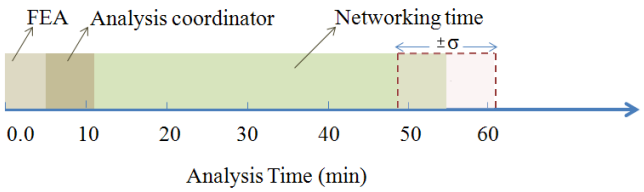
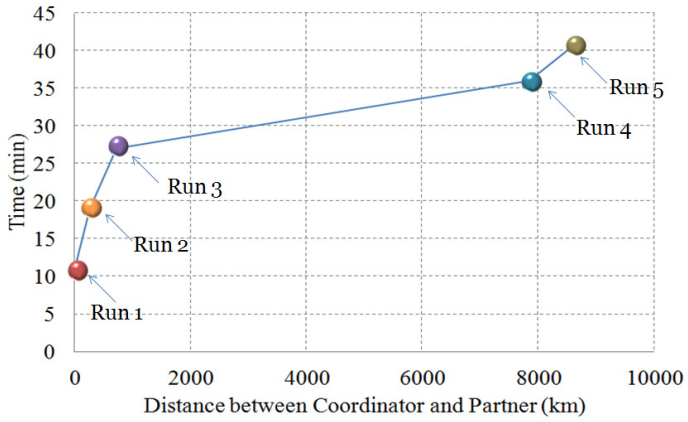


Figure 7: Contribution of various analysis stages to the overall analysis time.



	Coordinator	Module 1	Module 2	Module 3	Module 4
Run 1	AUTH	AUTH	AUTH	AUTH	AUTH
Run 2	AUTH	AUTH	AUTH	AUTH	UPATRAS
Run 3	AUTH	AUTH	AUTH	AUTH	UNAPLES
Run4	AUTH	AUTH	AUTH	AUTH	U of T
Run 5	AUTH	AUTH	AUTH	AUTH	UIUC

Figure 8: Total analysis time as the distance between the coordinator and the partner increases (communications executed over a 100 megabit network, and latency between AUThessaloniki and University Toronto at 132-172ms after 10-15 intermediate hops, respectively).

5 CONCLUSIONS

This study describes the procedure followed to investigate the conditions under which the implementation of a geographically distributed hybrid simulation concept becomes robust, repetitive and resilient, in the case of an intercontinental experiment among five partners (three in Europe, one in Canada and one in the U.S.). A four span, seismically isolated, reinforced concrete bridge of a total length of 110.40m was assessed under earthquake loading, implementing, at a preliminary stage, the geographically distributed multi-platform simulation concept. Through an extensive parametric analysis scheme, it was seen that among the various sources of analysis delay, i.e., the geographical distribution of modules, the partners' role in the sub-structured analysis, the daytime the simulation took place, as well as

pure network connection time, the latter clearly is the most dominating factor. As a result and given the rate-dependency of the bearing that is to be physically tested at the University of Patras during the next stage of hybrid experimentation, careful tuning of the above parameters is of paramount importance. Based on the experience gained, it is also seen that, overall, the concept of multi-platform simulation for earthquake engineering applications between intercontinental partners is fully robust, fully repetitive but only partially resilient, while the foreseen intercontinental hybrid experiment is also expected to be fully repetitive and robust provided that the time step delay is efficiently compensated. Further investigation is currently under progress.

6 ACKNOWLEDMENTS

This work carried out was funded by the 7th Framework Programme of the European Commission, under the PIRSES-GA-2009-247567-EXCHANGE-SSI grant (Experimental & Computational Hybrid Assessment Network for Ground-Motion Excited Soil-Structure Interaction Systems, www.exchange-ssi.net). The authors would like to thank Prof. Luigi di Sarno at the University Sannio, Prof. Alain Pecker at Geodynamique et Structures and particularly Prof. Stathis Boussias at University Patras, Prof. Oh-Sung Kwon at University of Toronto and Prof. Amr Elnashai at University of Illinois at Urbana-Champaign for their precious contribution to the distributed analysis sequence and the preparation of the hybrid experinment.

REFERENCES

[1] O.-S. Kwon, N. Nakata, A. S. Elnashai, and B. F. Spencer, “A framework for multi-site distributed simulation and application to complex structural systems,” *Journal of Earthquake Engineering*, vol. 9, no. 5, pp. 741–753, 2005.

[2] P. Pan, M. Tada, and M. Nakashima, “Online hybrid test by internet linkage of distributed test-analysis domains,” *Earthquake Engineering & Structural Dynamics*, vol. 34, no. 11, pp. 1407–1425, Sep. 2005.

[3] Y. Takahashi and G. Fenves, “Software framework for distributed experimental–computational simulation of structural systems,” *Earthquake Engineering & Structural Dynamics*, vol. 35, no. 3, pp. 267–291, Mar. 2006.

[4] V. Saouma, D.-H. Kang, and G. Haussmann, “A computational finite-element program for hybrid simulation,” *Earthquake Engineering & Structural Dynamics*, vol. 41, pp. 375–389, 2012.

[5] Q. Wang, J.-T. Wang, F. Jin, F.-D. Chi, and C.-H. Zhang, “Real-time dynamic hybrid testing for soil–structure interaction analysis,” *Soil Dynamics and Earthquake Engineering*, vol. 31, no. 12, pp. 1690–1702, Dec. 2011.

[6] G. Haussmann, “Evaluation of OpenFresco and SIMCOR for Fast Hybrid Single Site Simulation, CU-NEES-07-02, University of Colorado,” 2007.

[7] B. F. Spencer, A. S. Elnashai, K. Park, and O.-S. Kwon, “Hybrid Test Using UISimCor, Three-Site Experiment,” 2006.

[8] O.-S. Kwon and A. S. Elnashai, “Seismic analysis of meloland road overcrossing using multiplatform simulation software including SSI,” *Journal of Structural Engineering*, vol. 134, no. 4, pp. 651–660, 2008.

[9] S. Gunnay and A. Schellenberg, “Continous Intercontinental Hybrid Testing.” pp. 1–7, 2012.

[10] O.-S. Kwon, A. S. Elnashai, B. F. Spencer, and K. Park, "UI-SIMCOR : A global platform for hybrid distributed simulation," in *9th Canadian Conference on Earthquake Engineering*, 2007, no. June, pp. 139–149.
[11] Ministry of Public Works (1999) *"Circular E39/99, Guidelines for the seismic analysis of bridges" (in Greek).*
[12] Ministry of Public Works of Greece, *Greek Seismic Code—EAK 2000, Athens, 2000 (amended June 2003) (in Greek).*
[13] CEN (Comité Européen de Normalisation) *"Eurocode 8: Design of structures for earthquake resistance. Part 2: Bridges"*. EN 1998-2, Brussels., 2004.
[14] A. S. Elnashai, V. Papanikolaou, and D. Lee, "Zeus NL – A System for Inelastic Analysis of Structures," Univ. of Illinois at Urbana-Champaign, 2002.
[15] F. McKenna, G. Fenves, and M. Scott, "Open system for earthquake engineering simulation," University of California, Berkeley, 2002.
[16] F. Filippou and M. Constantinides, "FEDEASLab Getting Started Guide and Simulation Examples," 2004.
[17] K. Hibbit and N. Sorenson, "ABAQUS ver. 6.6, User's Manual," Pawtucket, USA, 2006.
[18] F. Naeim and J. M. Kelly, *Design of Seismic Isolated Structures*. N.Y.: Wiley & Sons, Inc., 1999.
[19] Caltrans, "Seismic Design Criteria Version 1.6," *California Department of Transportation: Sacramento, CA, U.S.*, 2010.
[20] ATC, "Improved seismic design criteria for California bridges," *Redwood City, California, Report No. ATC-32, 1996.*, 1996.
[21] O. N. Taskari and A. G. Sextos, "Stiffness and Ultimate Capacity of Typical Abutment- Embankment Systems," in *15th World Conference on Earthquake Engineering*, 2012, no. 1987.

COMPDYN 2013
4th ECCOMAS Thematic Conference on
Computational Methods in Structural Dynamics and Earthquake Engineering
M. Papadrakakis, V. Papadopoulos, V. Plevris (eds.)
Kos Island, Greece, 12–14 June 2013

CABLE-STAYED BRIDGES SUBJECTED TO NEAR-FAULT VERTICAL MOTION

M. Kuleli[1] **and A. S. Elnashai**[1]

[1] Department of Civil and Environmental Engineering, University of Illinois at Urbana-Champaign, USA
e-mail: {kuleli2, aelnash}@illinois.edu

Keywords: Vertical Ground Motion, Near-Fault Effects, Cable-Stayed Bridge.

Abstract. *The existence of a horizontal large velocity pulse that contains a substantial proportion of the seismic energy, often referred to as a 'fling', tends to increase seismic demand on medium-to-long period structures. Vertical ground motion is most intense and damaging in near-fault region, which openings the possibility that vertical motion may also include strong velocity pulses. An investigation of possible 'fling' features in vertical ground motion and their effects on cable-stayed bridge structures is presented in this paper. It is endeavored to identify and explain the reasons for strong velocity pulses in vertical ground motion. A set of earthquake records from recent large thrust events, which provided abundant near-fault vertical ground motion records, was selected and analyzed to identify large velocity pulses. Comparison is made with a set of normal acceleration records. Detailed numerical models of a class of cable-stayed bridges were developed, based on an existing bridge structure. The strong-motion ensemble is used for dynamic geometrically-nonlinear response history analysis of the cable-stayed bridges. Global and local response parameters were monitored and compared. The results indicate that pulse-like vertical ground motion increases moment and rotation demands along the bridge deck and should therefore be considered in seismic design and assessment.*

1 INTRODUCTION

The vertical component of earthquake ground motion has only recently received considerable investigative attention. In contrast, both near- and far-fault horizontal seismic excitations have been extensively studied and considered in the design process. One of the most important features of near-fault ground motions is the presence of strong velocity pulses. Strong velocity pulses cause most of the seismic energy from the rupture zone to arrive during a short period of time. Investigations on pulse-like horizontal ground motion in the last few decades have highlighted their distinct seismic response amplification characteristics. It was shown that pulse-like ground motion tends to amplify the seismic demand in the long period range of the acceleration response spectrum [1]. Furthermore, many studies investigated the seismic response characteristics of building structures subjected to pulse-like horizontal ground motion. It was indicated that strong velocity pulses tend to result in higher inelastic demands on buildings that have long fundamental periods [2, 3] and the structures in the intermediate-to-long period range are more susceptible to directivity pulses in horizontal ground motion [4, 5]. Moreover, it was suggested that the pulse-like ground motion forces the structure to dissipate the seismic energy input in a short period of time with a few inelastic cycles and hence increase the ductility demand [6, 7]. Moreover, recent studies of the engineering seismology community on the dynamics of faults have revealed that vertical ground motion may also contain strong velocity pulses. However, the effects of pulse-like vertical ground motion have not been studied by the structural engineering community before.

Recently a limited number of studies suggested that the vertical ground motion may increase not only the axial force demand on columns and piers but also the bending moment demand on bridge girders. The effects of vertical ground motion on precast segmental bridge girders were investigated with 2D models which were based on the Otay River Bridge and the San Francisco-Oakland Bay Bridge [8]. A suite of ten near-fault earthquake records were employed to perform non-linear time history analyses. It was concluded that segment joint rotations increased at least 400% and 90% for negative and positive bending moment, respectively as a result of the vertical ground motion. Furthermore, a parametric study on two short span reinforced concrete bridges considering various span lengths and pier heights was conducted to investigate the effects of vertical ground motion [9]. Although the focus of the study was on the pier response, it was consistently observed that the bending moment demand on the girders at the face of the bent cap was amplified. It was concluded that the contribution of the vertical ground motion to the moment demand was up to 155% and scaled with the V/H ratio. Six different configurations of ordinary standard highway bridges and overcrossings were utilized to investigate the effects of vertical ground motion on the response of bridge decks [10]. A data set of 56 records was formed based on horizontal peak accelerations (> 0.5g). The results of the nonlinear time history analysis were presented relative to the dead load demands to provide a comparison with the Seismic Design Criteria 2006 (SDC) guidelines. It was concluded that the negative bending moment demands at the mid-span (center of the main span) and positive bending moment demands at the face of the bent cap were significantly increased when the vertical ground motion was included in the analysis.

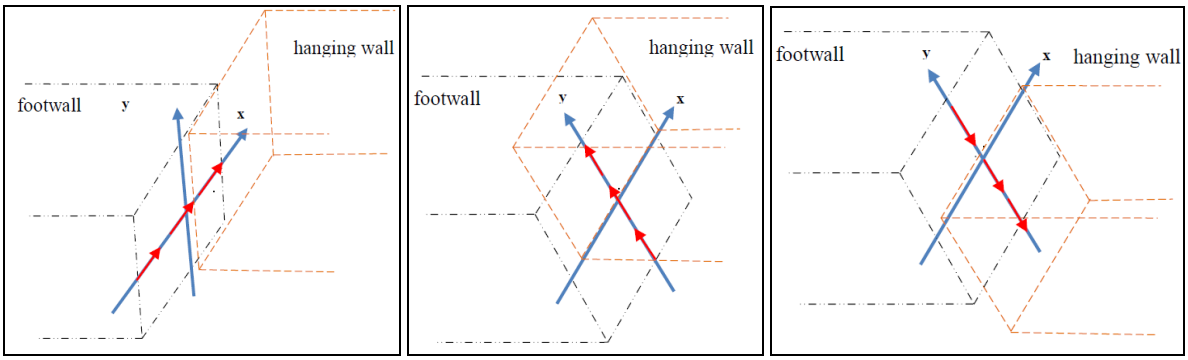
In this study, it is endeavored to identify and explain the reasons for strong velocity pulses in vertical ground motion. Previous studies on dynamics of faults are summarized. A ground motion selection procedure is described. Furthermore, the effects of pulse-like vertical ground motion on a class of cable-stayed bridges were investigated through detailed numerical models.

2 NEAR-FAULT EFFECTS IN VERTICAL GROUND MOTION

Directivity, fling step and existence of asperities are the reasons for strong velocity pulses in ground motion. Near-fault horizontal ground motion have been extensively studied and considered in the design process. Especially, directivity effects of fault-normal component resulting from strike-slip events have been investigated extensively in the last two decades. However, recent studies on fault dynamics, supported with increasing numbers of near-fault records (especially after the 1999 earthquakes), suggest that near-fault effects in vertical ground motion may have been underestimated.

2.1 Strong velocity pulse

Forward directivity is caused by constructive interference of shear waves when rupture propagates toward a site at a velocity close to the shear-wave velocity. Furthermore, fling step is the tectonic deformation associated with the permanent static offset of the ground due to surface rupture. In strike-slip events (Figure 1a), directivity and fling step effects are polarized on two components; strike-normal and strike-parallel, respectively. Therefore, directivity and fling step effects are usually considered uncoupled. Forward directivity and fling step effects can also occur on dip-slip faults [11]. For example, Figure 1b and 2 illustrate the orientation of the slip vector and rupture propagation in a thrust fault mechanism, respectively. The plane perpendicular to fault plane represents the neutral directivity orientation. The slip vector and rupture propagation both directed toward up dip. Shear waves travelling toward the site constructively interfere with each other in both vertical (Figure 2) and horizontal (strike-normal) directions. Therefore, the site located above the neutral plane is forward directivity site. Furthermore, fling step effects are also directed up-dip aligned with the slip vector. Thus, strong velocity pulses due to directivity and fling step effects are coupled on the vertical component and the horizontal component (strike-normal) of ground motions [12].



(a) Strike-slip fault (b) Thrust fault (c) Normal fault

Figure 1: Rupture and slip directions of symmetric and asymmetric faults

The third contributor to strong velocity pulses in vertical ground motion is the hanging wall effect [13]. As the rupture propagates towards up-dip a gap is formed between the hanging wall and footwall of the fault. The seismic energy is trapped between two opaque surfaces; the gap on the fault plane and the free field. Greater particle motion was observed on the hanging wall of thrust faults due to continuous reflection of seismic waves between the two surfaces during the rupture propagation [13]. This physical phenomenon has been also supported by many analytical [14, 15, 16] and experimental studies [17, 18, 19, 20] conducted to understand the ground motion characteristics resulted from asymmetric fault events.

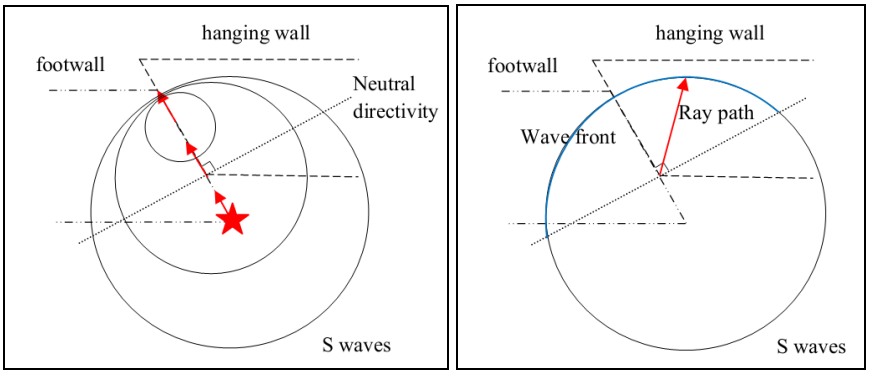


Figure 2: Directivity and fling step orientation in thrust fault mechanism

Furthermore, the directivity model which has been used so far is a one dimensional model which assumes a unidirectional rupture [11]. In strike-slip fault events, the rupture is assumed to be oriented only in the strike direction and the heterogeneities in depth are ignored. Similarly, in the case of dip-slip faults the rupture is assumed to propagate only in the dip direction hence is independent of heterogeneities along the strike direction. The assumption of unidirectional rupture led to two results. First, the widely accepted velocity pulse definition considers only the largest velocity cycle. Second, the directivity effects in dip-slip events are assumed to be concentrated only on the region located directly above the hypocenter.

However, rupture heterogeneity may arise from many reasons such as; existence of asperities or irregularities in the geometry of the fault (i.e. asymmetric faults). Large magnitude earthquakes are especially likely to be far from homogeneous [21]. When rupture heterogeneity is considered, multiple velocity cycles should be taken into account. Recently, a strong relationship between directivity pulses and slip heterogeneity was observed and a new ground motion selection procedure, which considers multiple velocity cycles, was suggested [22]. This selection procedure is further discussed in the following section.

Moreover, vertical ground motion is often assumed to be more of a manifestation of P-waves. However, it has been proven that when the crustal heterogeneity and source finiteness in vertical extent is considered, SV waves also significantly contribute to vertical ground motion in near-fault sites due to the refraction on certain horizontal boundaries [23]. The distance where SV waves are dominant may be extended to 10~20km [24]. Thus, strong velocity pulses in vertical ground motion can be observed not only in the region concentrated up dip from the hypocenter but also in the near-fault region where SV wave contribution is not negligible.

Near-fault effects on vertical component may also be observed in oblique, normal and even in strike-slip fault events depending on the rupture propagation and slip directions. However, strong velocity pulses in vertical ground motion are most prominent in thrust fault mechanism due to coupling of directivity, fling and hanging wall effects as explained above. Thus, in this study only recent thrust events which provided abundant near-fault ground motion records are considered.

2.2 Characteristics of pulse-like vertical ground motion

91 records from four recent large thrust events are selected to investigate the characteristics of pulse-like vertical ground motion. These events are as follows: 1994 Northridge (US), 1999 Chi-Chi (Taiwan), 2010 Darfield (New Zealand) and 2011 Christchurch (New Zealand). The selection of the records is based on the following criteria: 1) peak vertical acceleration (PVA) $\geq$ 0.1g, 2) peak vertical velocity (PVV) $\geq$ 10 cm/s, 3) Mw $\geq$ 6.0, epicentral distance < 25 km or closest distance < 20 km (when available).

Two procedures were proposed to identify pulse-like horizontal ground motion. The first procedure is described as follows [25]: The largest velocity pulse which starts and ends at zero crossing times or where the velocity is equal to 10% of the peak ground velocity [26] is extracted from the original record by using a wavelet-based signal processing analysis. The remaining record is designated as the residual record. The classification of the signals is defined by two parameters. The first parameter is the peak ground velocity (PGV) ratio which is defined as the PGV of the residual record divided by the PGV of the original record. The second parameter is the energy ratio which is the ratio of the energy of the residual record to the energy of the original record. Moreover, pulse period (single cycle) is determined using the period corresponding to the maximum Fourier amplitude of a wavelet. Recently, a new ground motion selection procedure, which considers multiple velocity cycles, was suggested [22]. This procedure uses a velocity pulse definition based on a specific level of threshold energy. By inspection of the selected 308 horizontal ground motion records, this threshold energy is designated as 35% of the total energy of the original record which is carried by certain number of cycles. The maximum number of cycles is specified as three. Furthermore, a new pulse period definition called, Tp^{eff}, effective pulse period was also proposed. Tp^{eff} is designated as the time width of the total velocity cycles which corresponds to the specified threshold energy. It is also concluded that the effective pulse period is more related to the magnitude of the event than the period of a single cycle.

In this study, the ground motion selection procedure proposed by [22] is modified to fit natural trend of the selected vertical ground motion records. First, velocity time histories of each record are inspected manually and the data set is grouped in two categories. The first group of ground motions is those which contain "coherent" pulses (Figure 3a) and the second are those which contain "incoherent" pulses (Figure 3b). Here a coherent pulse refers to a wave signal that consistently keeps the increasing or decreasing trend in local and global levels. On the other hand, an incoherent pulse refers to a signal that is less coherent at the local level (sometimes including several zero crossings) yet keeps its increasing/decreasing global trend through the velocity time history. For example, the spikes in signal at the local level can be seen in Figure 3b. On the other hand, the global increasing/decreasing trends of the signal at the global level are also shown by the black arrows in Figure 3b. Although the energy concentration is continuous in the case of incoherent pulses, it results in response amplification in a shorter period range when it is compared to their coherent counterparts. Because the shorter the predominant period of the ground motion, the smaller is the period range at which the response amplification occurs.

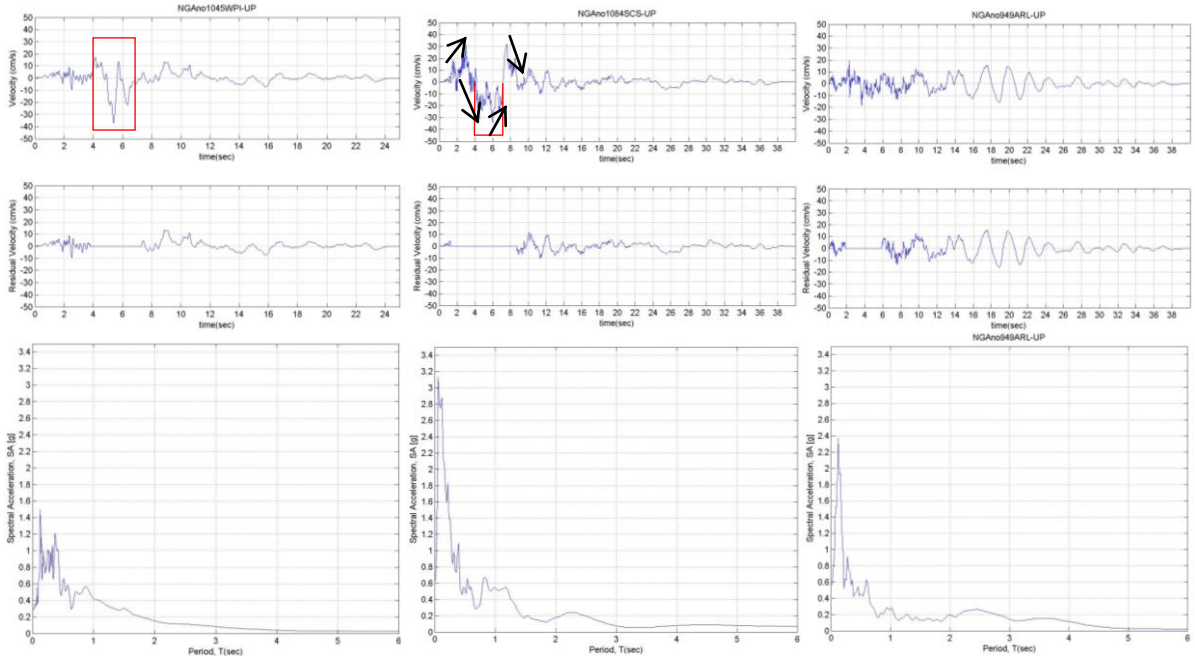
It has been consistently observed that the ground motions which have up to four successive full velocity cycles tend to exhibit pulse-like characteristics. For each record the cycle with highest amplitude (PGV) is obtained using zero crossing time definition. Then, the successive (or preceding) velocity pulse which has minimum amplitude of about 50% of the amplitude of the preceding/following half cycle is determined. The minimum considered amplitude of a half cycle is 10 cm/s which are of engineering interest. For each record, the wave trains which contain up to four full cycles are extracted from the original record. It is important to note that, for records which have $10 < PGV < 20$ cm/s, the half cycles with 10cm/s or less amplitude are also included in the wave train to be in accordance with the selection criteria of half cycle which has a minimum amplitude of about 50% of the amplitude of the preceding/following half cycle. After extraction of the wave train, the ratio of the energy of the residual record to the energy of the original record is calculated. The energy of each record is calculated as the integration of the squared velocity time history. It has been consistently observed that records which contain strong velocity cycles (up to four cycles) and have an "energy ratio" smaller than a certain threshold level tend to exhibit "pulse-like" characteristics which result in ampli-

fication of response in the medium-to-long period range. The limits of the energy ratio are presented in Table 1. Here it is important to note that the energy ratio limits for classification of the incoherent records are smaller than their coherent counterparts due to their different response amplification. For instance, when two wave trains of the same PGV, number of cycles and their amplitudes and same total period are considered, the coherent record provides higher seismic energy than the incoherent record and hence results in higher response amplification. As incoherency increases, ground motions tend to exhibit ordinary characteristics where response amplification is most effective in very short period range (< 0.5sec).

	Energy Ratio		
	min	max	Class
Coherent	0.0	0.4	Pulse
	0.4	0.6	Ambiguous
	0.6	1.0	Ordinary
Incoherent	0.0	0.2	Pulse
	0.2	0.4	Ambiguous
	0.4	1.0	Ordinary

Table 1: Energy ratio intervals for ground motions

Figure 3 represents original and residual velocity time history records of a coherent pulse-like, an incoherent pulse-like and an ordinary vertical ground motion, and their acceleration response spectra. From Figure 3 it is evident that ordinary vertical ground motions are most effective in the small period range where the pulse-like ones tend amplify the response in medium-to-long period range of response.



(a) (b) (c)

Figure 3: Original and residual velocity record of (a) Newhall – W Pico Canyon Road (coherent pulse) (b) Sylmar – Converter (incoherent pulse) (c) Arleta-Nordoff Fire Stations (ordinary) from Northridge, 1994

Furthermore, Figure 4 compares the frequency content of representatives of a pulse-like and an ordinary vertical ground motion. It can be seen that ground motion records classified as "pulse-like" tend to have smaller frequency contents when compared to ordinary counterparts. Thus, it can be concluded that the presence of strong velocity pulses in vertical ground motion tend to amplify the response not only in the short period range but also in the medium-to-long period range of vertically vibrating structures.

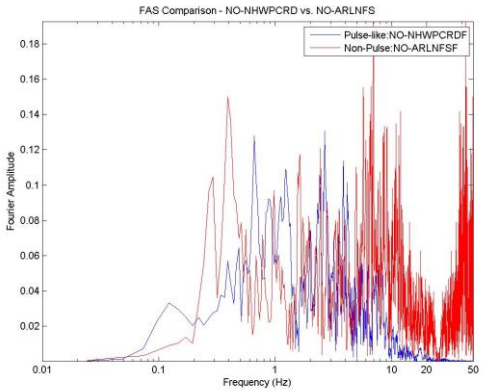


Figure 4: Frequency content comparison for Newhall – W Pico Canyon Road (coherent pulse) Arleta-Nordoff Fire Stations (ordinary) from Northridge, 1994 Earthquake

In summary, 44 of the 91 ground motions in the data set were classified as pulse-like, 29 of them were classified as ambiguous and 18 of them were classified as ordinary vertical ground motions. Here it is important to note that an ambiguous class may contain both pulse-like and ordinary ground motions. Further study is needed for more elaborate classification of this class.

3 ANALYTICAL INVESTIGATION

This study focuses on the investigation of the effects of the pulse-like vertical ground motions on a class of medium-to-long-span bridge girders. Cable-stayed bridges are sensitive to three dimensional earthquake excitations due to the strong coupling between their modes of vibration in the three orthogonal directions unlike such as suspension bridges where modes of vibration can be categorized as bending, torsional and sway [27]. Thus, a class of cable-stayed bridge configurations was chosen to represent medium-to-long span length which allows seismic response assessment over a large range of periods.

3.1 Structural modeling and dynamic characteristics of the selected bridges

The general and tower configurations of a class of cable-stayed bridges are depicted in Figures 5 and 6 [27]. The main span lengths are 1120 and 2200 ft. for Bridge I and Bridge II, respectively.

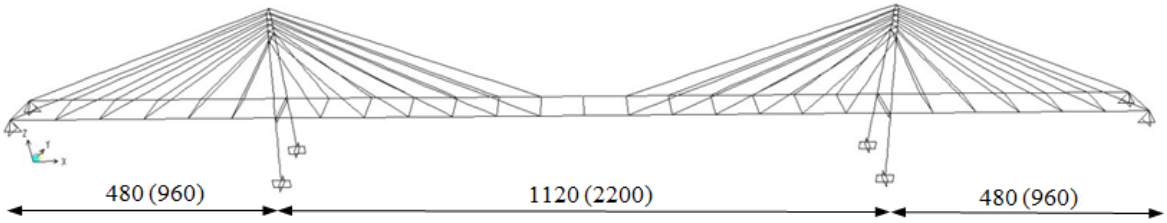


Figure 5: Cable and deck configuration of Bridge I (Bridge II), units: ft.

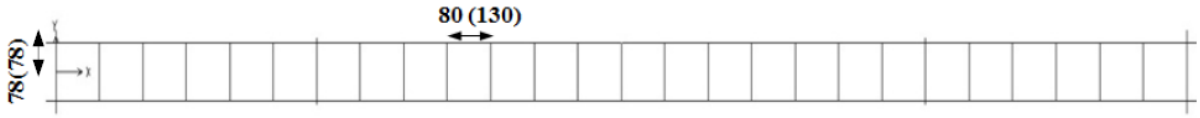


Figure 5 (cont'd): Cable and deck configuration of Bridge I (Bridge II), units: ft.

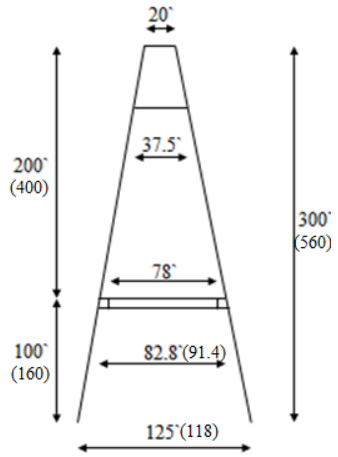


Figure 6: Tower configuration of Bridge I (Bridge II), units: ft.

Cable-stayed bridges are sensitive to three dimensional excitations due to the strong coupling between modes of vibrations. Thus, detailed three dimensional models are developed to account for torsional effects and torsional modes of vibration. The structural properties of the elements in these two bridges were based on several existing bridges in the eastern region of the United States and further details of the section and material properties can be found in [27]. Each cable is represented by a single bar element with equivalent tangent (or instantaneous) modulus approach. Reinforced concrete pylons, pylon struts and steel girders and cross beams are modeled with elastic beam elements. The decks are simply supported at both ends of the girder and connected to the pylons and pylon struts with the elastic links as depicted in Figures 5 and 6.

Static nonlinear analyses which include P-Delta effects are conducted for dead loads to obtain the tangent stiffness matrix of the structures. The dead load tangent stiffness is employed as the initial stiffness for all other analysis cases, namely live load, modal analysis and nonlinear time history analysis. Eigen value analyses are performed to obtain dynamic behavior characteristics with utilization of the tangent stiffness matrix of the dead load deformed state. 200 modes are employed to obtain 95% or higher mass participation in longitudinal, transverse and vertical directions. The first modes of cable-stayed bridges are usually deck modes, followed by coupled cable and deck modes and coupled tower and deck modes [28]. Thus, deck modes are coupled with all other modes through almost all 200 modes of vibrations and cover a period range from 3.25s to 0.027s for Bridge I and from 5.13s to 0.05s for Bridge II. Accumulated mass participation ratios in the vertical direction over the periods of vibration modes for both Bridges I and II are depicted in Figure 8. Hence deck modes of Bridge I and II cover a large period range in vertical direction, the effects of pulse-like and ordinary vertical ground motions can be investigated.

3.2 Selection of strong ground motion

4 raw ground motion records from "coherent pulse-like", 3 records from "incoherent pulse-like" and 4 records from "ordinary" classes were selected as shown in the Table 2. The peak

acceleration ratios of the vertical to horizontal component (V/H), identified pulse period of wave trains (Tp^{wt}) and the energy ratios of the residual record to the original record are also listed in Table 2. Time lag effects between the vertical and horizontal ground motion peaks were not taken into account.

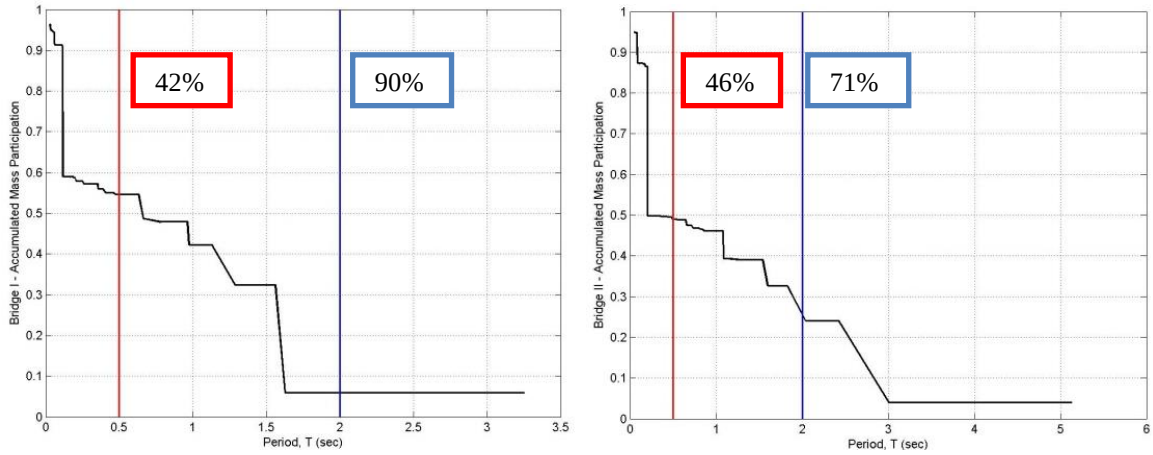


Figure 8: Accumulated mass participation ratio (vertical) vs. Period, T (sec)

The selected ground motions were scaled by utilizing the PGA scaling procedure. The peak vertical ground acceleration among all 11 records is 0.834g. All vertical ground motion records, whether pulse-like or ordinary, were scaled to this peak ground acceleration. For each record, only the horizontal component with the largest PGA was applied in the longitudinal direction of the bridge. Each horizontal ground motion component was scaled with the same scaling factor of its vertical counterpart to keep the V/H ratios constant.

Set	Event	Station	Vertical	Horizontal		Site	Dist.	V/H	scale factor	Tp^{wt}	Energy Ratio	Reference Name
			PGA [g]	PGA [g]	PGA [g]		km			[sec]		
Coherent Pulse	Northridge [1994] Mw = 6.69	Newhall - W Pico Canyon Rd.	0.290	0.455	0.325	D	5.50	0.64	2.88	3.50	0.276	NO-NHWPCRD
		Canyon Country - W Lost Cany	0.318	0.482	0.410	D	12.40	0.66	2.62	4.55	0.277	NO-CCWLC
	Chi Chi [1999] Mw = 7.62	TCU120	0.162	0.225	0.193	C	7.40	0.72	5.15	13.05	0.481	CHI-TCU120
		CHY028	0.337	0.821	0.653	C	3.10	0.41	2.47	5.97	0.296	CHI-CHY028
Incoherent Pulse	Northridge [1994] Mw = 6.69	Sylmar - Con. Sta.	0.586	0.897	0.612	C	5.40	0.65	1.42	7.45	0.138	NO-SCS
	Chi Chi [1999] Mw = 7.62	TCU088	0.222	0.522	0.508	C	18.20	0.43	3.76	13.95	0.111	CHI-TCU088
		CHY080	0.724	0.968	0.902	C	2.70	0.75	1.15	7.21	0.161	CHI-CHY080
Ordinary	Northridge [1994] Mw = 6.69	Arleta - Nordhoff Fire Sta	0.552	0.344	0.308	D	8.70	1.60	1.51		0.950	NO-ARLNFS
		Beverly Hills - 14145 Mulhol	0.327	0.516	0.416	D	17.20	0.63	2.55		0.433	NO-BH14145
		Rinaldi Receiving Sta	0.834	0.825	0.487	D	6.50	1.01	1.00		0.686	NO-RRS
	Chi Chi [1999] Mw = 7.62	TCU079	0.388	0.743	0.393	C	11.00	0.52	2.15		0.446	CHI-TCU079

Table 2: Selected records for analytical investigation

3.3 Live load analysis and response measures

Moving load analyses were carried out by utilizing the tangent stiffness obtained by non-linear analysis of dead loads. The goal of the live load analysis was to obtain possible maxi-

mum demands along the bridge girders for comparison with seismic demands. The load factors used for permanent and live loads [29] are listed in Table 3. Strength II combination considers permit live loading [30]. Furthermore, the live load factor, γ_{EQ}, in Extreme I load combination [29], which represents the possibility of partial live loads during earthquakes events was assumed to be zero in order to obtain only the seismic demands. This way, a conservative comparison between maximum live load and seismic demands is allowed. In total, 4 load combinations are considered to obtain the maximum dead/live load bending moment and rotation demand on girders, one for Strength I and three for Strength II combination considering the restricted permit loads.

Limit State	Permanent Load	LL_{HL93}	LL_{Permit}	EQ
STRENGTH I	1.25	1.75	-	-
STRENGTH II	1.25	-	1.35	-
EXTREME I	1	γ_{EQ}	-	1
SERVICE II	1	1.3	-	-

Table 3: Load combinations and load factors

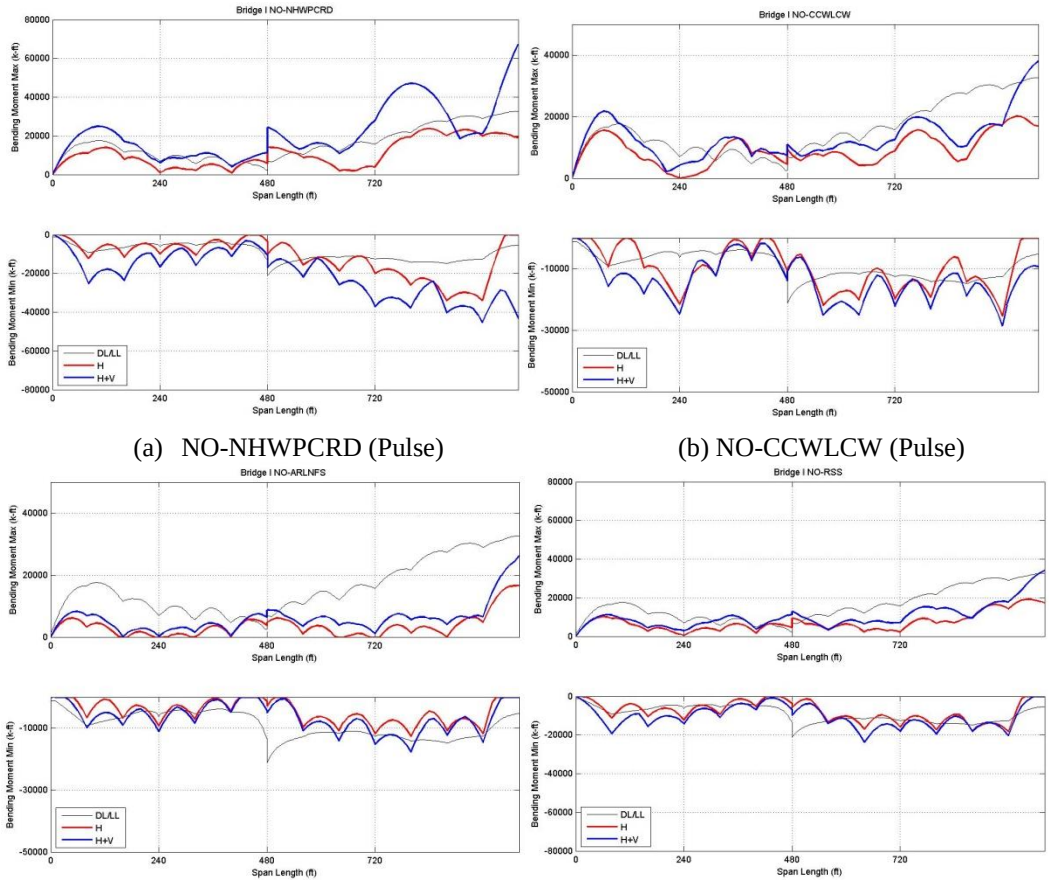
The deflection criterion was checked according to the Service II limit state. The maximum vertical deflections at mid-span (center of main span) are 0.70ft and 1.30ft for Bridges I and II, respectively. For most long-span cable-stayed bridges, acceptable deflection values are in between 1/400 and 1/500 of the central span length, which equals to 2.24ft and 4.40ft (1/500) for Bridge I and Bridge II, respectively.

3.4 Dynamic analysis results

Geometrically-nonlinear time history analyses were conducted by utilizing the dead load deformed state initial stiffness conditions to obtain seismic response characteristics of the bridges when subjected to the selected ground motions. Newmark implicit integration scheme was employed with $\delta = 0.5$and $\alpha = 0.25$ values. A time step, $\Delta t = 0.02$ which allows high frequency modes to participate in response, was adopted. Here, it is important to note that usually a sensitivity analysis should be carried out to determine the time step. However, for simplicity the commonly accepted and suggested time step value was used in this study.

Two bridges were analyzed with the selected 29 ground motions which are listed in Table 2. The envelope maximum responses obtained from dead load and live load combinations are compared with the seismic demands resulting from only horizontal, H, and horizontal and vertical, H+V, ground motions. Global and local earthquake response parameters were monitored and compared.

Figures 9 and 10 compare the bending moment and rotation demands along the girder of the Bridge I with and without vertical excitation for selected representatives of pulse-like and ordinary ground motion records from the Northridge, 1994 earthquake. All representative records are from the same distances (due to scaling) and site conditions (refer Table 2). Results are presented only from end support to the center of the main span (mid-span) since multi-support excitation was not considered in analyses. As shown in legends, the responses obtained from dynamic analyses are compared with the maximum demand values obtained from the dead and live loads.



(a) NO-NHWPCRD (Pulse) (b) NO-CCWLCW (Pulse)

(c) NO-ARLNFS (Ordinary) (d) NO-RRS (Ordinary)

Figure 9: Moment demand comparison along girder (Bridge I)

From Figures 9 and 10 it can be concluded that both positive and negative moment were amplified along the bridge deck when the pulse-type vertical ground motion was included in the analysis. The moment amplification ratio at the mid-span changes from 16% to 158% for the positive bending moment and from 63% to 1137% for the negative bending moment (Figure 9 and Table 4). The reason for those exceptionally high amplification ratios, especially in negative bending moment, is that the negative bending moment under dead/live loads and horizontal ground motion is very small (Table 4).

In some cases although the record consists of strong velocity pulses, high amplification of moment demand was not observed. For example, although NO-CCWLCW (Figure 9b and 11b) record classified as "pulse-like" and has almost the same energy ratio with NO-NHWPCRD (Table 2), its response amplification is accumulated in a short period range at round 2 seconds (Figure 10) where the response amplification for NO-NHWPCRD record is on a larger period range (Figure 9a and 11a). This may result from the different response amplification characteristics due to carried total seismic energy by wave train as discussed earlier (Figure 10). Furthermore, Bridge I has a mass participation ratio of only about 10% around the 2 second period as shown in Figure 8. Thus, NO-CCWLCW ground motion record excites a smaller portion of mass when compared to NO-NHWPCRD record. Furthermore, a relationship between the pulse properties and amplification of response over the medium-to-long period range should be quantitatively defined. In addition, it is important to remember that PGA scaling was used in this study and medium-to-long period range of structures is sensitive to velocity rather than acceleration. Thus, developing a scaling procedure that takes into account

the sensitivity of different period ranges could increase the consistency between the seismic demands and allow a better comparison. Such a scaling procedure may be possible with an energy based approach. However, both developing an identification procedure of pulse characteristics, i.e. pulse period, and such an elaborate scaling procedure for ground motions are beyond the scope of this study.

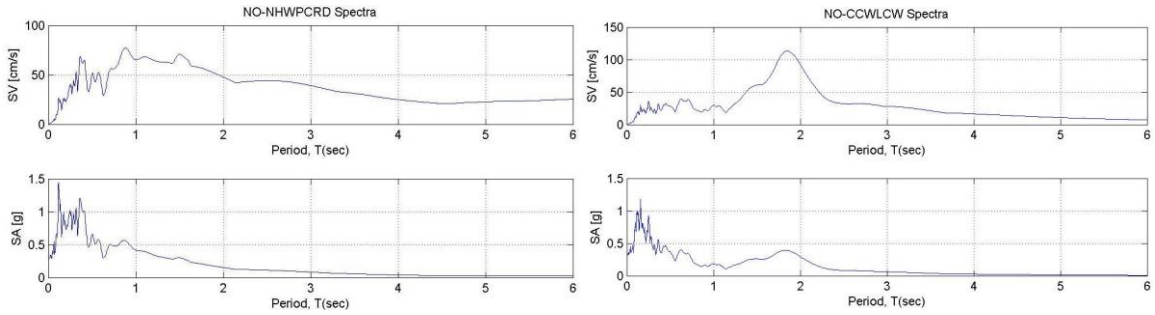


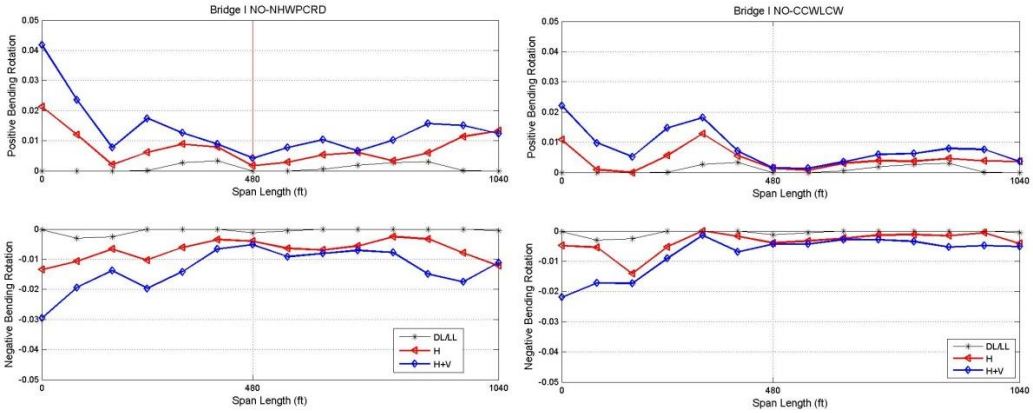
Figure 10: Response amplification comparison for NO-NHWPCRD and NO-CCWLCW

Furthermore, Figures 9 (c) and (d) show the moment demand along the bridge deck from representative ordinary vertical ground motion. It is important to note that these two records are commonly utilized ground motion records in the investigation of vertical ground motion effects. As depicted in the figures, the inclusion of the vertical component in the analysis leads to a very small amplification of moment demand when it is compared to the case of pulse presence, and usually maximum moment demands do not exceed the demand values provided by vehicular load. The moment demand comparison between all selected records for Bridge I are given in Table 4 with amplification ratios with respect to DL/LL maximum and positive and negative bending moment demand values for both H and H+V cases at mid-span.

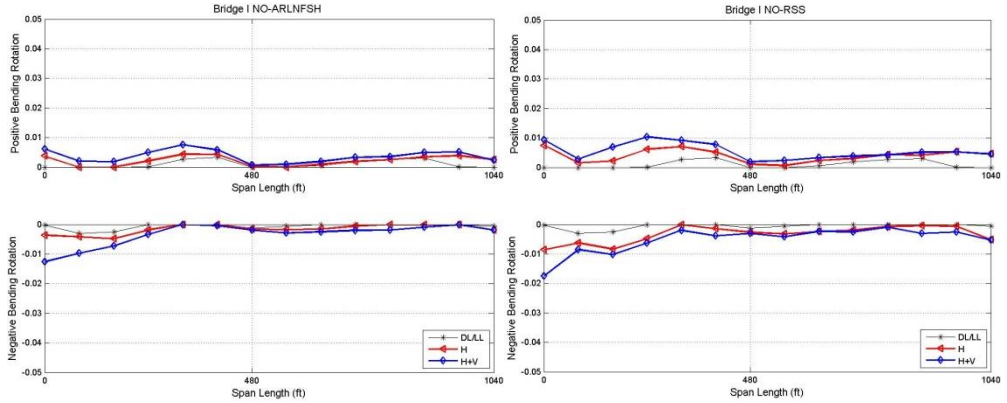
Set	Reference Name	Maximum Positive Moment (k-ft)			Amplification Ratio (%) w.r.t DL/LL	Contribution of VGM to maximum negative moment (%)	Maximum Negative Moment (k-ft)			Amplification Ratio (%) w.r.t DL/LL
		DL/LL	HGM	H+VGM	H+VGM		DL/LL	HGM	H+VGM	H+VGM
Coherent Pulse	NO-NHWPCRD	32613.8	19275	67358	106.5	249.5	-5252	0	-43346	725.3
	NO-CCWLC		16945	38062	16.7	124.6		0	-9302	77.1
	CHI-TCU120		19423	84093	157.8	333.0		0	-64963	1136.9
	CHI-CHY028		30069	53911	65.3	79.3		-6758	-37992	623.4
Incoherent Pulse	NO-SCS		18905	42964	31.7	127.3		0	-8549	62.8
	CHI-TCU088		16177	41991	28.8	159.6		0	-11581	120.5
	CHI-CHY080		18015	37940	16.3	110.6		0	-13259	152.4
Ordinary	NO-ARLNFS	32613.8	16655	26219	-19.6	57.4	-5252	0	0	-
	NO-BH14145		18286	34179	4.8	86.9		0	-11340	115.9
	NO-RRS		17371	34037	4.4	95.9		0	0	-
	CHI-TCU079		16305	16433	-49.6	0.8		0	0	-

Table 4: Bridge I - Summary of analysis results

From Figure 11(c) and (d), it can be concluded that the amplification of rotation demands along the deck due to ordinary vertical ground motions are relatively smaller when compared to the pulse-like counterparts. Similarly, increase in both positive and negative bending moment rotations are also observed along the Bridge II deck. However, the assessment of the increase in rotation demands needs special attention and requires a more detailed modeling approach, i.e. support conditions. Thus, this study focuses only on the moment demand amplification in detail.



(a) NO-NHWPCRD (Pulse) (b)NO-CCWLCW (Pulse)



(c) NO-ARLNFS (Ordinary) (d) NO-RRS (Ordinary)

Figure 11: Rotation demand comparison along girder (Bridge I)

Table 5 provides comparison between the moment amplification ratios at mid-span obtained from all selected records with respect to DL/LL maximum for Bridge II. The table shows that the contribution to negative and positive bending moment, especially at the mid-span of the bridge deck, by coherent type pulse-like vertical ground motion is significantly more than ordinary vertical ground motion. The moment amplification ratio at the mid-span changes from 20% to 355% for the positive bending moment and from 0% to 2133% for the negative bending moment. The reason for those exceptionally high amplification ratios, especially in negative bending moment, is that the negative bending moment under dead/live loads and horizontal ground motion is very small.

Set	Reference Name	Maximum Positive Moment (k-ft)			Amplification Ratio (%) w.r.t DL/LL	Contribution of VGM to maximum negative moment (%)	Maximum Negative Moment (k-ft)			Amplification Ratio (%) w.r.t DL/LL
		DL/LL	HGM	H+VGM	H+VGM		DL/LL	HGM	H+VGM	H+VGM
Coherent Pulse	NO-NHWPCRD	74561.9	76724.95	168631.75	126.2	119.8	-15973.5	-8823.831	-45177.85	182.8
	NO-CCWLC		47596.122	143967.89	93.1	202.5		0	-80095.88	401.4
	CHI-TCU120		83225.718	339355.81	355.1	307.8		-21516.91	-356648.5	2132.8
	CHI-CHY028		65165.693	143150.08	92.0	119.7		-2859.393	-94046.65	488.8
Incoherent Pulse	NO-SCS		73467.654	89610.582	20.2	22.0		0	-42893.12	168.5
	CHI-TCU088		43724.151	89606.636	20.2	104.9		0	-5824.326	-
	CHI-CHY080		58385.957	96427.725	29.3	65.2		0	-29571.29	85.1
Ordinary	NO-ARLNFS		44188.922	111381	49.4	152.1		0	-30814	92.9
	NO-BH14145		66248.228	87633.841	17.5	32.3		-1117.707	0	-
	NO-RRS		53536.973	84410.399	13.2	57.7		0	-1565.612	-
	CHI-TCU079		56747.378	77758.79	4.3	37.0		0	-3486.802	-

Table 5: Bridge II - Summary of analysis results

When Table 4 and 5 are compared, the contributions to seismic moment demands at the mid-span vary in some cases of ground motion records for Bridge I and II as expected. For example, when NO-CCWLCW record is considered the negative bending moment amplification ratios are 77.1% and 401.4% for Bridge I and Bridge II, respectively. However, when NO-NHWPCRD record is considered, the moment amplification ratios are 725.3% and 182.8% for Bridge I and Bridge II, respectively. Thus, NO-CCWLCW record results in higher amplification ratio for Bridge I than NO-NHWPCRD record. On the contrary, NO-CCWLCW record results in a smaller amplification ratio for Bridge II than NO-NHWPCRD record. Here it is important to note that both records are classified as "pulse-like" and have almost the same energy ratio (Table 2). The change in response amplification trends of the two ground motions is due to different dynamic behavior characteristics of the two bridges as pointed out earlier. The mass distribution over the periods, the characteristics of the ground motion, and response amplification characteristics of the pulse are the parameters that cause different seismic response characteristics. The largest amplification factors are obtained from the Chi-Chi earthquake records for both bridges. This is mainly due to the large magnitude of this event. The larger the magnitude, the more coherent the pulse is. Furthermore, the input of seismic energy carried by the pulse is also increasing as the magnitude of the event increases. Thus, the response amplification is more coherent in a larger period range for large magnitude earthquake events when compared to the records from smaller magnitude earthquakes.

4 CONCLUSIONS

In this paper, strong velocity pulse features in vertical ground motion records and their effects on a class of cable-stayed bridge structures are investigated. The most important findings are summarized below.

The existence of a vertical strong velocity pulse tends to reduce the high frequency content of the record and hence increase the seismic demand on medium-to-long period structures. For the structures considered and the earthquake record set used, the bending moment and rotation demands along the bridge deck are substantially increased with respect to maximum dead and live load demands due to pulse-like vertical ground motion records. Since the assessment of rotation demands requires a more detailed modeling approach, i.e. support conditions, the results of this study focuses on the assessment of bending moment demands. The high increase in moment was observed at the center of the main span (mid-span) for both bridges. The increase in positive moment at the mid-span is between 16% and 158% for Bridge I and between 20% and 355% for Bridge II. The corresponding negative bending moment increase is between 63% and 1137% for Bridge I and between 0% and 2133% for Bridge II. The reason for such exceptionally high amplification ratios, especially in negative bending moment, is that the negative bending moment under dead and live loads and horizontal ground motion is very small. It was also observed that the response amplification characteristics of the pulse-like vertical ground motion records related to the pulse characteristics such as the coherency of the pulse signal and the pulse period. The characteristics of the velocity pulse are closely related to the source parameters, i.e. geometry and dimension of the fault, slip duration, correlation between directivity and fling step, and size of asperities. For instance, the most distinct observation is that the coherency of the pulse signals increases as the magnitude of the event increases which often results in longer pulse periods. Further investigation of the pulse characteristics and their correlations with the above-mentioned parameters is required to gain better understanding of the response amplification features of the pulse-like vertical ground motions.

The results also suggest that observations from only the acceleration or velocity spectrum may be misleading in assessing the damage potential of pulse-like vertical ground motion rec-

ords and hence they need to be examined concurrently. In a similar manner, utilizing only one ground motion parameter, e.g., peak ground acceleration, to scale the ground motions could result in unreliable assessment of seismic demand when pulse-like vertical ground motion is considered. Especially in the case of structures which have complex and coupled modes of vibration, i.e. cable-stayed bridges, a scaling procedure that is sensitive to all vibration periods would provide more realistic seismic demand assessment. Such a scaling procedure may be based on an energy criterion and provide better insight into the differences of the response amplification characteristics between normal and pulse-like vertical ground motions.

Taking into account the above observations, medium-to-long period bridge decks subjected to pulse-like vertical components of earthquake strong-motion could be more vulnerable than those subjected to the horizontal ground motion only or combined horizontal and ordinary vertical ground motions. Therefore, incorporating a vertical pulse model for the development of near-fault ground motions and including pulse-like vertical ground motion in the analysis is recommended for reliable seismic assessment and design of medium-to-long period structures in the vicinity of active faults.

REFERENCES

[1] Golesorkhi, R., and Gouchon, J. (2002). "Near-source effects and correlation to recent recorded data", Proceedings, 6th U.S. National Conference on Earthquake Engineering, Seattle, Wash.

[2] Hall, J. F., Heaton, T. H., Halling, M. W., and Wald, D. J. (1995). "Near source ground motion and its effects on flexible buildings", Earthquake Spectra, Vol. 11(4), 569–605.

[3] Heaton, T.H., Hall, J.F., Wald, D.J. and Halling, M.W (1995). "Response of High Rise and Base-Isolated Buildings to a hypothetical Mw 7.0 Blind Thrust Earthquake", Science, Vol. 267, 206-211.

[4] Anderson, J. C., and V. V. Bertero (1987). "Uncertainties in establishing design earthquakes", J. Struct. Eng. 113, no. 8, 1709–1724.

[5] Alavi, B., and Krawinkler H. (2001). "Effects of near-fault ground motions on frame structures", Blume Center Report 138, Stanford, California.

[6] Manfredi, G., Polese, M., and Cozenza, E. (2000). "Cyclic demand in the near-fault area", Proceedings, 6th U.S. National Conference on Earthquake Engineering, Seattle, Wash.

[7] Kalkan E. and Kunnath S.K. (2006). "Effects of Fling-Step and Forward Directivity on the Seismic Response of Buildings", Earthquake Spectra. 22, No. 2, 367-390.

[8] Veletzos, M. J., Restrepo, J. I., Seible, F., 2006 : Response of precast segmental bridge superstructures, Report submitted to Caltrans - SSRP-06/18, University of California, San Diego, California.

[9] Kim, S. J. and Elnashai, A. S. (2008). "Seismic Assessment of RC Structures Considering Vertical Ground Motion", Report No. MAE 08-03, University of Illinois at Urbana-Champaign, Urbana, Illinois.

[10] Kunnath, S. K., et al. (2008). "Development of guidelines for incorporation of vertical ground motion effects in seismic design of highway bridges", Report No. CA/UCD-SESM-08-01, University of California, San Diego, California

[11] Somerville, P.G., et al. (1997). "Modification of empirical strong ground motion attenuation relations to include the amplitude and duration effects of rupture directivity", Seismological Research Letters, Vol. 68(1), 199-222.

[12] Somerville, P.G. (2002). "Characterizing near fault ground motion for the design and evaluation of bridges" Proceedings of the Third National Seismic Conference and Workshop on Bridges and Highways. *This paper is posted on the test bed website.*

[13] Allen, C. R., Brune, J. N., Cluff, L. S., and Barrows, A. G. Jr. (1998). "Evidence for Unusually Strong Near-fault Ground Motion on the Hanging Wall of the San Fernando Fault During the 1971 Earthquake", Seismological Research Letters, Vol. 69(6), 524-531.

[14] Brune, J. N. (1996). "Particle Motions in a Physical Model of Shallow Angle Thrust Faulting", Earth and Planetary Sciences, Proceedings of the Indian Academy of Sciences, Vol. 105 (2), L197-L206.

[15] Shi, B., Anooshehpoor, A., Brune, J. N., and Zeng, Y. (1998). "Dynamics of Thrust Faulting: 2D Lattice Model, Bulletin of the Seismological Society of America, Vol. 88, 1484–1494.

[16] Shi, B., Brune, J. N. (2005). "Characteristics of Near-Fault Ground Motions by Dynamic Thrust Faulting: Two-Dimensional Lattice Particle Approaches", Bulletin of the Seismological Society of America, Vol. 95, 2525–2533.

[17] Oglesby, D. D., and Day, S. M. (2001). "Fault Geometry and the Dynamics of the 1999 Chi-Chi (Taiwan) Earthquake", Bulletin of the Seismological Society of America, Vol. 91(5), 1099-1111.

[18] Oglesby, D. D., and Day, S. M. (2001). "The effect of the Fault Geometry on the 1999 Chi-Chi (Taiwan) Earthquake", Geophysical Research Letters, Vol. 28, 1831-1834.

[19] Oglesby, D. D., Archuleta, R. J. and Nielsen, S. B. (1998). "Earthquakes on Dipping Faults: The Effect of Broken Symmetry", Science, Vol. 280, 1055-1059.

[20] Oglesby, D. D., Archuleta, R. J. and Nielsen, S. B. (2000). "The Three-Dimensional Dynamics of Dipping Faults", Bulletin of the Seismological Society of America, Vol. 90(3), 616-628.

[21] Rowshandel, B. (2006). "Incorporating Source Rupture Characteristics into Ground-Motion Hazard Analysis Models", Seismological Research Letters, Vol. 77(6), 708-722.

[22] Mena, B., Mai, P. M. (2010). "Selection and Quantification of Near-Fault Velocity Pulses Due to Source Directivity", ETH Zurich – Report

[23] Kawase, H. and Aki, K. (1990). "Topography effect at the critical SV-wave incidence: Possible explanation of damage pattern by the Whittier Narrows, California, earthquake of 1 October 1987", Bulletin of the Seismological Society of America, Vol. 80, 1-30.

[24] Silva, W. (1997). "Characteristics of vertical strong ground motions for applications to engineering design," FHWA/NCEER Workshop on the National Representation of Seismic Ground Motion for New and Existing Highway Facilities; Burlingame; CA;

Proceedings, Technical Report NCEER-97-0010, National Center for Earthquake Engineering Research, Buffalo, New York.

[25] Baker, J. W. (2007). "Quantitative Classification of Near-Fault Ground Motions Using Wavelet Analysis", Vol. 97(5), 1486-1501.

[26] Bray, J. D., and Rodriguez-Marek, A. (2004). "Characterization of forward-directivity ground motions in the near-fault region." Soil Dynamics and Earthquake Engineering, 24, 815-828.

[27] Nazmy, A. S., and Abdel-Ghaffar, A. M. (1987). "Seismic Response Analysis of Cable-Stayed Bridges Subjected to Uniform and Multi-Support Excitations." Report No. 87-SM-1, Department of Civil Engineering, Princeton University, Princeton, N.J.

[28] Abdel-Ghaffar, A. M. and Nazmy, A. S. (1991). "3-D nonlinear seismic behavior of cable-stayed bridges." Journal of Structural Engineering, ASCE, 117 (11), pp. 3456-3476.

[29] AASHTO (2011). LRFD Bridge Design Specifications - 4th edition. American Association of State Highway and Transportation Officials, Washington, D. C.

[30] Caltrans (2011). "California Amendments to the AASHTO LRFD Bridge Design Specifications –Fourth Edition".

COMPDYN 2013
4th ECCOMAS Thematic Conference on
Computational Methods in Structural Dynamics and Earthquake Engineering
M. Papadrakakis, V. Papadopoulos, V. Plevris (eds.)
Kos Island, Greece, 12–14 June 2013

VALIDATION OF NUMERICAL MODELS FOR RC COLUMNS SUBJECTED TO CYCLIC LOAD

C. Del Vecchio[1*], L. Di Sarno[2], O. Kwon[3], A. Prota[4]

[1]University of Napoli "Federico II"
Department of Structural Engineering, via Claudio 21, 80125 Napoli, Italy
ciro.delvecchio@unina.it

[2]University of Sannio
Department of Engineering, Piazza Roma, 21, 82100 Benevento, Italy
ldisarno@unisannio.it

[3]University of Toronto
Department of Civil Engineering, 35 St. George St., M5S 1A4, Toronto, ON, Canada
os.kwon@utoronto.ca

[4]University of Napoli "Federico II"
Department of Structural Engineering, via Claudio 21, 80125 Napoli, Italy
aprota@unina.it

Keywords: Reinforced Concrete, Numerical Model, Shear, Columns, Validation.

Abstract. *The paper presents results from numerical analyses of reinforced concrete (RC) elements subjected to cyclic load. Many nonlinear numerical models have been proposed in literature to capture the cyclic behaviour of reinforced concrete (RC) elements. Depending on the expected level of accuracy and computational efficiency, numerical models employ different assumptions. These assumptions ultimately affect the stiffness, strength, energy dissipation capacities and hysteretic behaviours such as strength/stiffness degradation and pinching. All of these sensitively affect the dynamic response of a structure subjected to seismic load. The objective of this work is to investigate the effects of adopted numerical models on predicted seismic performances of RC structures. Three numerical elements that are widely used in research and practice are employed; fiber element in OpenSees, frame element in VecTor5, and continuum element in VecTor2. In an element level, the behaviour responses of the different numerical models are closely compared. A few representative experimental results from PEER Column Test Database are used to investigate the accuracy of each numerical model depending on the shear demand/capacity ratio of the columns. The paper concludes with a suggestion for the applicability of different numerical models for the seismic performance assessment.*

1 INTRODUCTION

Since the philosophy of performance based seismic design (PBSD) was first introduced in mid-1990s, there has been significant efforts to implement the philosophy in structural design practice. The most salient feature in PBSD is that structures are designed to meet certain level of performance criteria at different levels of seismic hazards. For example, a structure should satisfy fully operational, damage controllable, or collapse prevention limit states depending on the level of seismic intensity. In the second and third limit states, designers allow a structure to sustain damage as long as the damage is either controllable or the structure does not collapse. To follow this design philosophy, it is essential to evaluate the seismic performance of a structure in the inelastic range, which is still quite challenging task to most practicing designers. In current state of practice, design is carried out primarily based on elastic analysis. With the development of advanced and refined numerical models, large capacity storage, and fast processing speed, however, practicing engineers tend to employ inelastic analysis. By running inelastic analyses, engineers and researchers try to model 'real' behavior of structural elements when subjected to earthquake load. The global structural response is influenced by the inelastic hysteretic behaviour of elements. Hence, it is essential to employ accurate yet computationally efficient numerical models for structural elements. With this purpose, numerous elements have been developed and proposed by researchers. For example, there exist a wide range of numerical elements for reinforced concrete (RC) elements ranging from lumped springs, fiber-based section elements, sophisticated continuum model with smeared reinforcement bars, and detailed finite element (FE) model in which concrete and reinforcement bars are modeled as FE element. Simplified models frequently employ several assumptions and they may yet require thorough and cumbersome parameter calibrations. On the other hand, sophisticated models tend to be more accurate and may often require less number of assumptions. The hysteretic behaviour used to simulate the structural response may also vary significantly with the analysis model. Thus, it is vital to shed light in the limitations and applicability of numerical models to perform seismic response analyses. The present study is aimed at understanding the limitations and/or applicability of different numerical models for RC elements. The study emphasizes the difficulties and limitations of using numerical models to predict the inelastic response of RC members and structures, especially those that are controlled by shear failure. The outcomes of the present analytical work prove that the matching between experimental and numerical simulations is acceptable for flexural-controlled failure modes. However, brittle failure modes caused by shear requires sophisticated and refined finite element models. Furthermore, existing technical guidelines and code provisions are yet far for being exhaustive for shear-dominated response of RC structures.

2 SEISMIC BEHAVIOUR OF RC STRUCTURES

Reinforced concrete structures enter into the inelastic region when subjected to moderate to high-magnitude earthquakes. Several surveys carried out in the aftermath of major earthquakes have reported widespread brittle failure to structural members and joints (i.e. Figure 1a,b), especially in existing buildings designed primarily for gravity loads. Earthquake resistant structures are nowadays designed using strength reduction, nonlinear response is generally expected for ordinary buildings which are compliant with modern seismic building codes. Such buildings are intended to experience significant structural damage before collapse; hence dissipative zones, e.g. plastic hinges, are required to dissipate and absorb seismic energy. A reliable estimate of the actual seismic capacity of RC structural systems can be obtained through accurate nonlinear analyses [3,4]. Due to the complex nonlinear behavior of structural system a in-depth knowledge at element level is required.



(a) (b)

Figure 1: Field surveys after major devastating earthquake: (a) Shear failure of a squat column during L'Aquila earthquake 2009 [1]; (b) Soft storey mechanism with plastic hinges on columns during Emilia earthquake 2012 [2].

Numerous studies carried out in recent years have demonstrated that the cyclic behaviour of RC elements is affected by various parameters [e.g. 5,6, among many others]. The reliable assessment of the earthquake response of RC members, especially when subjected to a combination of biaxial bending moment and axial load, is still a challenging problem [7]. Based on large and comprehensive datasets of experimental tests, novel formulations which may reproduce closely the seismic behaviour of RC elements, have been developed. Many researchers [8,9] have focused on confined concrete behaviour which led to development of complex yet accurate theories. The most commonly approach to assess the cyclic behaviour of RC members is the lumped plasticity model; it consists of locating or "lumping" the system nonlinearities in ad hoc points of the members, such as the member ends. The plastic hinge length is often not an easy task to accomplish [e.g. 10]. Whenever the use of lumped models is inadequate, fiber models may be employed to account for the spreading of nonlinearities along the members (e.g. [11], among others). The classical Finite Element Method (FEM) tends to be accurate to simulate the large displacement of highly non linear systems. Nevertheless, FEM is often cumbersome for earthquake response analyses of large structures. Advanced theories have been formulated for the applications of FEM to RC structures [e.g. 12-14, among others]. The availability of high computational power has recently promoted the development of advanced and efficient algorithms and computer programs (e.g. OpenSees [15], VecTor programs [16] among others) that may simulate reliably the cyclic behaviour of RC elements or complex structural systems using refined numerical models. New cutting edges simulation capabilities have been achieved especially in interdisciplinary fields, as for instance in the assessment of soil-structure interaction [17]. The integration of such interactions with structural models is often not straightforward.

Brittle failure mechanisms of typical RC members are illustrated in Figure 2b. Brittle failure modes lead to a displacement capacity remarkably lower than the deformations experienced in ductile failure mechanisms. High ductility lateral resisting systems are required by modern earthquake-resistant design to prevent brittle failure in high seismic risk areas. However, numerous existing buildings do not conform to such design rules. Conversely, they tend to exhibit brittle shear failure of critical members, thus impairing the seismic capacity of the structural system as a whole (i.e. Figure 3). Vertical ground motion effects may also endanger the shear capacity of RC members, especially for non-conforming columns in existing framed buildings [20]. Additionally, the accurate assessment of shear critical structures is of para-

mount importance to calibrate appropriate strengthening solutions [21]. As a result, the accurate investigation of the shear response is a key point in the assessment procedure of structures. Shear response, especially when large inelastic deformations are experienced by either the members or the structure, is difficult to predict. In shear critical elements, the cracks may rapidly propagate.

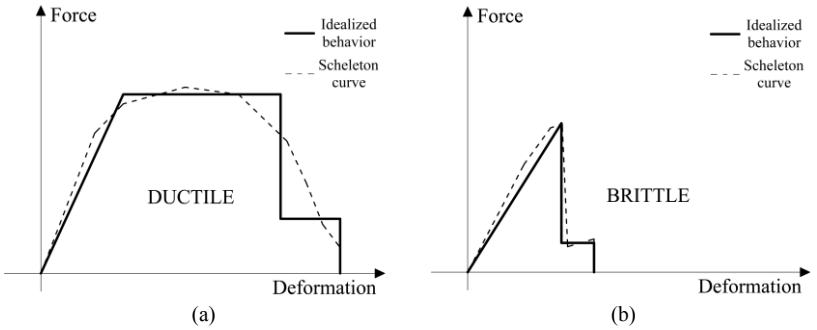


Figure 2: Typical failure modes of R.C. elements: (a) Ductile failure; (b) Brittle failure.

The most common approach to assess the shear strength of RC members uses the truss model. The shear behaviour is thus investigated by assuming that in the cracked element the resisting mechanism includes the compressive field, above the neutral axes, the diagonal concrete struts and the longitudinal. The transverse reinforcement may also be accounted for. The assumption of inclined compression diagonals, with a 45° angle [22], was removed by Mörsch [23]. The truss-based theories were largely adopted in the past and they have inspired several building codes worldwide; however, new developments have been achieved in the recent years. Extensive experimental and field investigations have shown that complex phenomena affect the shear behaviour of RC elements. From the experimental standpoints, it is worth mentioning that innovative theories have been developed; such theories are aimed at characterizing the stiffness, strength and deformability of shear critical elements (e.g. MCFT [12] and DSFM [13]). The validation of the above formulation has been achieved with the implementation of the shear response in a number of dedicated computer programs (VecTor suite [16] and tools [24]).

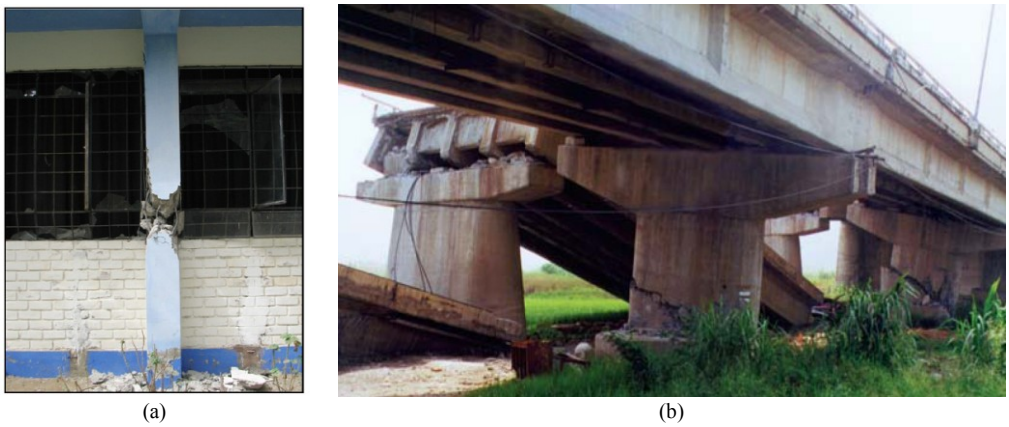


Figure 3: (a) Column shear failure during the 2007 Pisco-Chincha earthquake [18]; (b) Bridge collapse due to pier shear failure during Chi-Chi, Taiwan earthquake 1999 [19].

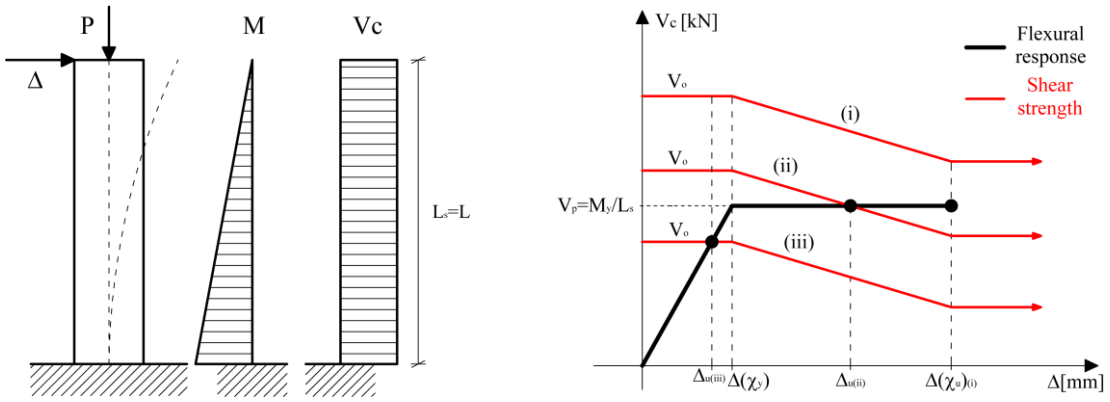
1 RESEARCH OBJECTIVES

Numerical models are powerful tools to simulate the nonlinear behaviour of structural elements subjected to multi-axial (shear, axial, and moment) cyclic loading. However, numerous effects that affect the seismic behaviour of RC structures are often neglected in numerical models or they not accounted for by non-expert users. This is the case, for example, of the accurate description of shear behaviour, bar buckling and reinforcement slipping. The objective of the present study is to investigate the effects of the numerical models on the seismic performance of RC members, such as beams, columns and frames. Thus, three different numerical models have been adopted: fiber element in OpenSees [15], frame element in VecTor5 [16], and continuum element in VecTor2[16]. Realistic physical and mechanical parameters are utilized to set up a sound and general purpose methodology. The first step of the proposed procedure is the validation of the numerical model with respect to basic components. Then, sophisticated models with high level of accuracy are also considered. At an element level, the global hysteretic behaviour is closely assessed. A few representative experimental results from available literatures are used to investigate the accuracy of each modelling approach.

2 VALIDATION OF NUMERICAL MODELS

2.1 Specimen Selection

Reference experimental tests for structural elements and structural systems are selected such that typical failure modes in RC structures can be evaluated. The shear strength may degrade with increasing ductility demand (e.g. [20]) and shear failure after the flexural yielding may thus be attained. According to Setzler [25], five failure modes may typically occur in RC structures. Shear, flexural and mixed flexural-shear failure modes are considered the basic failure mechanisms; two additional cases are also considered when failure mode is not well detected due to the simultaneous occurrence of the two failure modes. The latter approach is also implemented in ACI 369-R11 [26].



	ACI 318/318M conforming seismic details with 135-degree hooks	Closed hoops with 90-degree hooks	Other (including lap-spliced transverse reinforcement)
$V_p/V_o \leq 0.6$	i*	ii	ii
$1.0 \geq V_p/V_o > 0.6$	ii	ii	iii
$V_p/V_o > 1.0$	iii	iii	iii

Figure 4: Failure modes: “i” Flexural; “ii” Flexural-Shear; “iii” Shear according to ACI369R-11 [26].

The ACI code is based on a large number of experimental observations; it classifies the failure mode as a function of the ratio between the shear at the flexural yielding, quoted as V_p, and the shear strength for an imposed ductility level of 1, named V_0. As reported in Figure 4, the failure mode depends also on the transverse reinforcement details. In the present study the ACI 369-R11 [26] approach is adopted to select sample specimens corresponding to three different failure modes. Experimental results from PEER Column Test Database [27] are used to investigate the accuracy of selected numerical models. At the element level, three columns are selected to represent the three failure modes.
The selected specimens are summarized in Table 1 which includes details such as cross section shape, i.e. rectangular (R) or circular (C); concrete cylindrical compressive strength (f_c); span-to-depth ratio (Ls/D); axial load ratio (ν); transverse reinforcement ratio (ρ_s) and predicted and experimental failure mode.

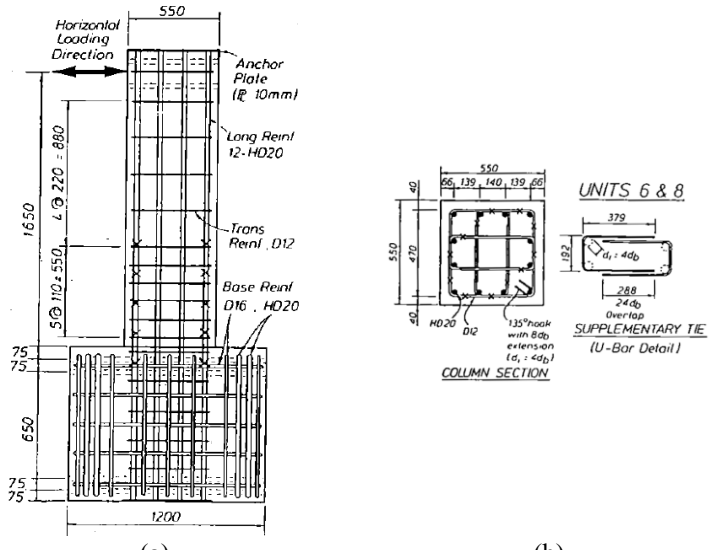
Reference	Spec.	Section	f_c [MPa]	Ls/D	ν	ρ_s [%]	Failure Mode		Numerical Model		
							ACI 369 [26]	Exp.	Open Sees	VecTor 5	VecTor 2
Tanaka [28]	6	R	32	3	0.10	0.8	i	i	●	●	●
Lynn [29]	3CMD12	R	27.6	3.22	0.26	0.2	ii	ii	●	●	●
Umehara [30]	CUS	R	34.9	1.11	0.16	0.3	iii	iii	●	●	●

Table 1: Summary of specimen properties and numerical models adopted for the validation.

Additional details on specimen geometry, reinforcements, test setup and main experimental results can be found in the PEER Database [27] and in the related references.

2.2 Adopted numerical models

The sample numerical models were validated by investigating the cyclic behaviour of four RC columns. The experimental behaviour of a simple cantilever column with a flexural failure mode, Tanaka et al. [28] (Figure 5), is used to validate the proposed numerical models.

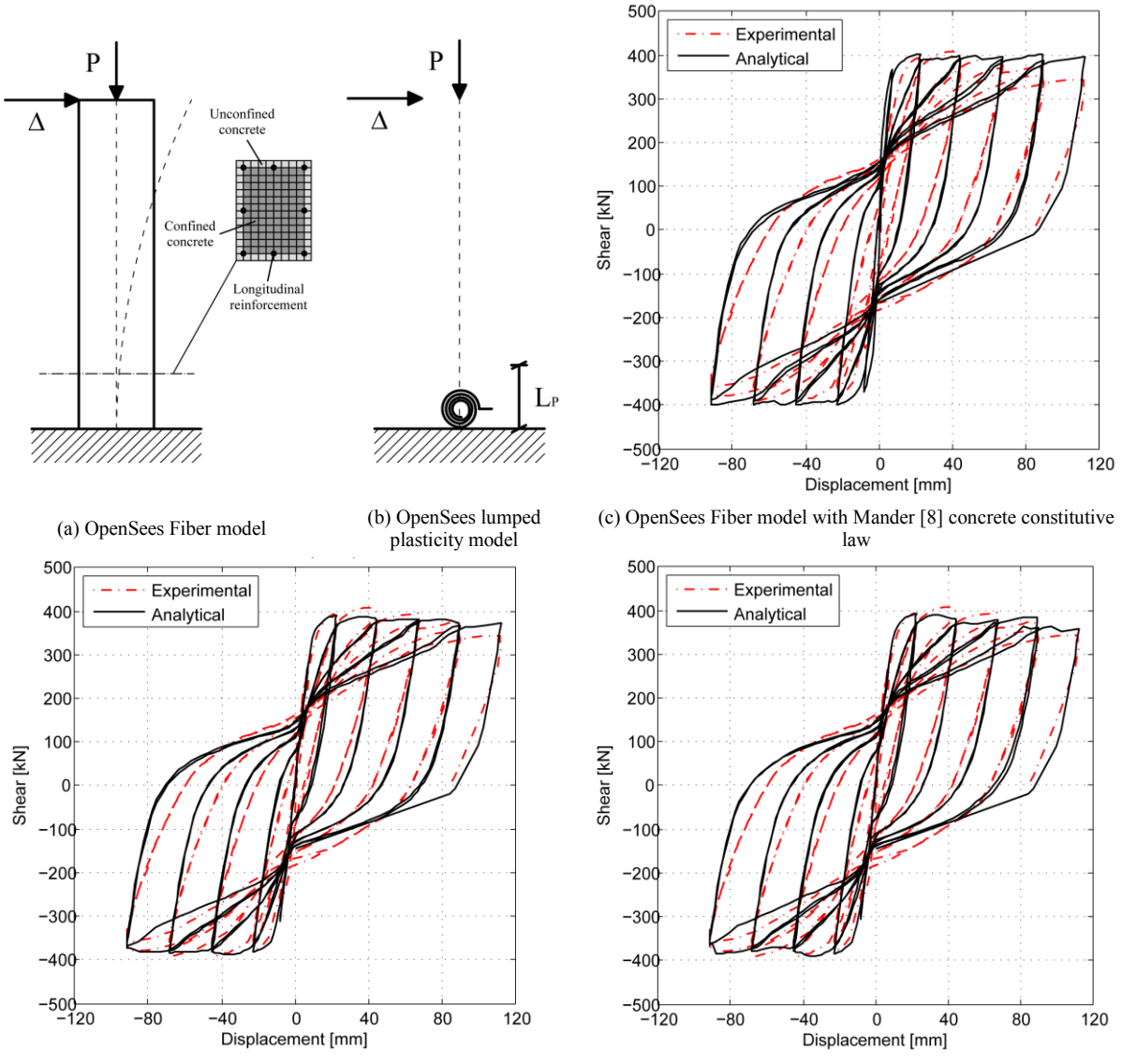


(a) (b)

Figure 5: Tanaka [28] specimen 6 details (unit *cm*).

- *OpenSees models*

Both OpenSees [15] fiber (Figure 6a) and lumped plasticity models (Figure 6b) are adopted herein. In the fiber model, three different materials are used to represent the cyclic behaviour of column cross sections: the confined and unconfined concrete is simulated with the nonlinear *Concrete02* material; the longitudinal reinforcement is modelled with the *Steel02* uniaxial material with isotropic strain hardening. The confining effects of transverse reinforcement on the mechanical properties of the concrete core are calculated according to Mander et al. [8]. The novel *ConfinedConcrete01* (CC01) material is also adopted to account for the confining effects of the stirrups; it is computed by defining transverse reinforcement geometry and mechanical properties. The ultimate compressive strain of confined concrete is calculated according to Biskinis et al. [31] as suggested by Fardis [6].



(a) OpenSees Fiber model

(b) OpenSees lumped plasticity model

(c) OpenSees Fiber model with Mander [8] concrete constitutive law

(d) OpenSees lumped plasticity model with Mander [8] concrete constitutive law

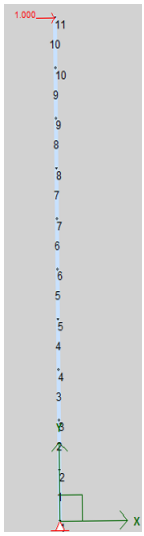
(e) OpenSees lumped plasticity model with CC01 [9] constitutive law

Figure 6: OpenSees model validation with Tanaka [28] spec. 6 experimental result.

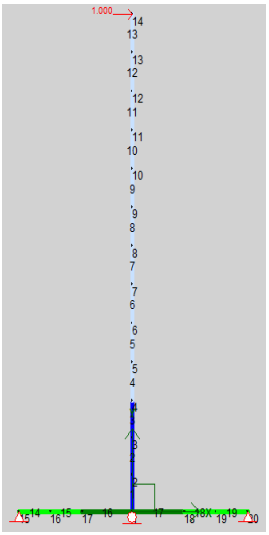
Five integration points along the finite elements have been adopted, thus allowing the spreading of inelasticity to be accurately described. The cross section is uniformly divided into sixteen elements to represent closely small stress-strain variations. For the lumped plasticity model, the 2D *Beam with hinges* command line is set to concentrate all system nonlinearities at the base of the column [10]. The plastic hinge length is set according to Bae et al. [32] and hinges properties are calculated assigning a fiber section. Plastic hinge stiffness is defined according to the experimental-based formulation of Elwood et al. [33]. Applied axial load (P) and cyclic displacement (Δ) are determined in accordance to the actions registered during the experimental test taking into account of P-Δ effects by means of the geometric transformation tool *PDelta Transformation*. The Newton-Raphson solution algorithm is adopted to solve model nonlinear equations. Comparisons between numerical and experimental results for the three OpenSees models in term of shear vs. imposed displacement are provided in Figure 6. Figure 6c shows the close match of experimental hysteresis loop with the OpenSees fiber model numerical results. The match is acceptable with respect to strength, deformability, and pinching. The analytical model provides an initial stiffness higher than the experimental one. This response may be related to model which do not account for the effects of bar slipping, column base cracking, support concrete block confining effects. Both the OpenSees lumped plasticity models (Figures 6d,e) provides accurate predictions of the experimental results also in terms of initial stiffness. This is due to the adoption of a realistic stiffness from a large number of experimental tests on column specimen with negligible shear deformation [33].

- *VecTor5 models*

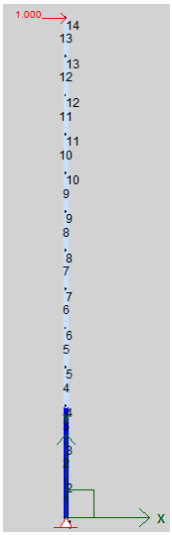
VecTor5 is a nonlinear sectional analysis program, with a distributed nonlinearity fiber model approach, for two dimensional frame-related structures consisting of beams, columns and shear walls, subjected to static and dynamic loading. VecTor5 is based on MCFT [12] and DSFM [13] theories and is capable of considering geometric and material nonlinearities. In the model development, attention should be paid to define geometric and mechanical properties. Starting from element cross-section properties, as suggested in the manual [34] and in related literature studies [35], different thickness and mechanical properties should be assigned to each fiber. The effect of transverse and out-of-plane reinforcements is considered by assigning a specific percentage to each fiber element. Geometric and mechanical material properties of concrete, longitudinal and transverse reinforcements are defined based on experimental specimen. All analyses were performed with the use of *basic* default material behaviour models and analysis options. The Popovic [36] and Mander [8] constitutive law is adopted to reproduce concrete compressive behaviour. The nonlinear sectional analysis is performed using the Parabolic Shear Strain Distribution (Single-Layer Analysis) as shear analysis option. Optimum segment lengths, 50% of the cross section depth [35], is adopted in column modelling. Comparative analyses are carried out in order to assess the influence of the footing block. The cyclic behaviour of three different analytical models are compared in the following: a simple cantilever scheme with the length measured by column-foundation intersection (Figure 7a), an accurate model of footing schematized with beam elements according to [35] (Figure 7b), and a simplified model of the footing, modeling only the portion that goes to column base to foundation block centerline (Figure 7c). Figure 7 shows the close match with experimental results for the VecTor5 proposed models. In details the proposed VecTor5 numerical models give a good fit of experimental results in terms of peak strength, energy dissipation, pinching without neglect strength degradation effects related to large inelastic deformations. The comparisons also pointed out the importance of an appropriate modeling of the footing in order to achieve a more accurate match of element cyclic behavior.



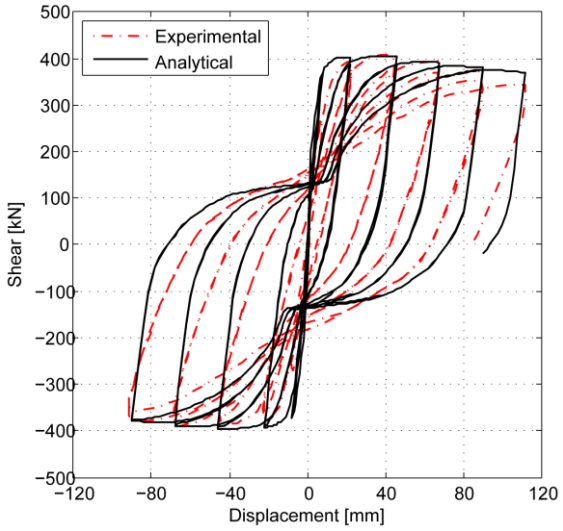
(a) Vector5 cantilever model



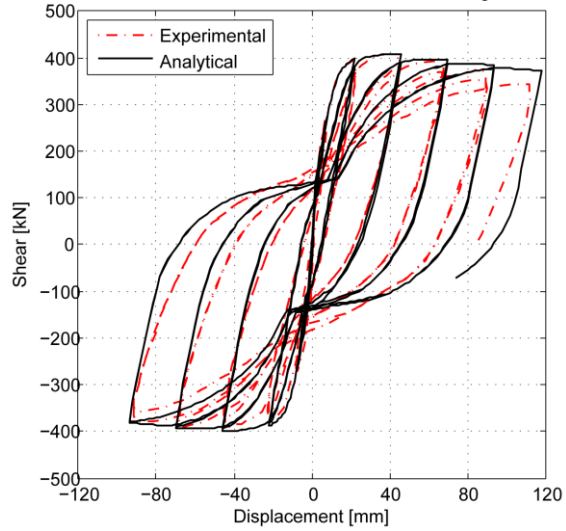
(b) Vector5 model including foundation block



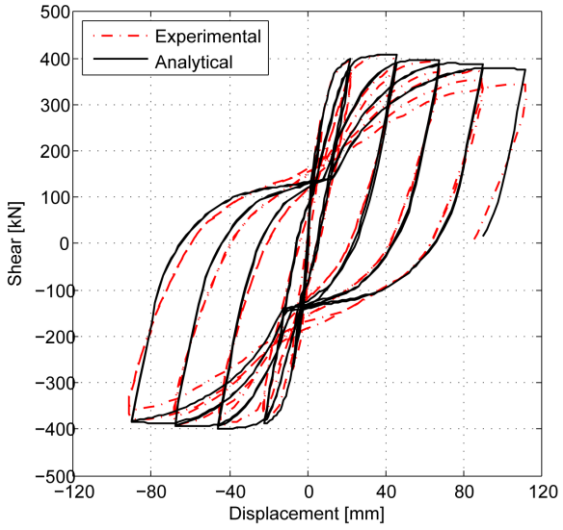
(c) Vector5 simplified model



(d) VecTor5 cantilever model (fig. 7a) with Popovic [36] and Mander [8] concrete constitutive law.



(e) VecTor5 model with Popovic [36] and Mander [8] concrete constitutive law, including foundation block (fig.7b).



(f) VecTor5 model with Popovic [36] and Mander [8] concrete constitutive law, including simplified model of foundation (fig.7c).

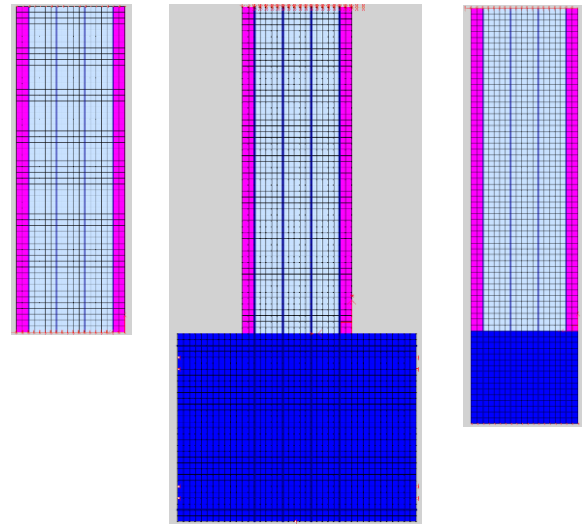
Figure 7: VecTor5 model validation with Tanaka [28] spec. 6 experimental result.

The numerical modeling of the foundation block led to more realistic estimations of the initial stiffness (Figure 7e,f). The use of a simplified scheme of the footing, i.e. adding the column portion from column base to block centerline, leads to results close to the accurate model (Figure 7f).

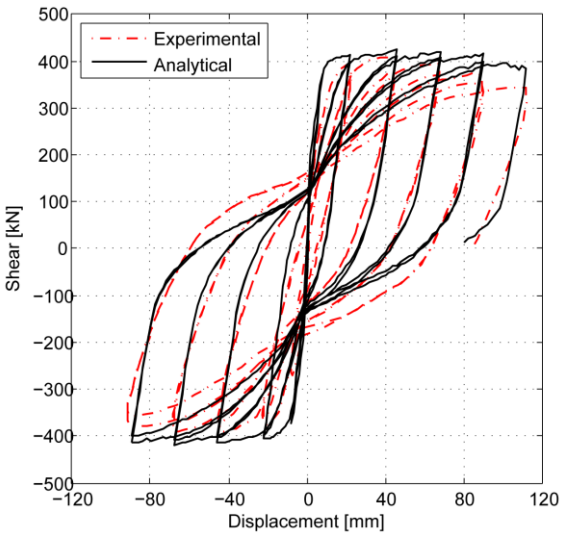
- *VecTor2 models*

VecTor2 is a program based on the MCFT/DSFM for nonlinear finite element (FEM) analysis of reinforced concrete membrane 2D structures that permits accurate assessments of structural performance (strength, post-peak behaviour, failure mode, deflections and cracking). The Vector2 bundle [24] includes: FormWorks, a graphics-based preprocessor program that simplifies the model building; Augustus, a complete VecTor2 post-processor that may provide all the global and local results in useful numeric or graphic formats. It is also able to display the specimen crack pattern at each stage of imposed displacement and this represents a very useful tool to detect numerical model failure mode. The FEM elements require a differ-

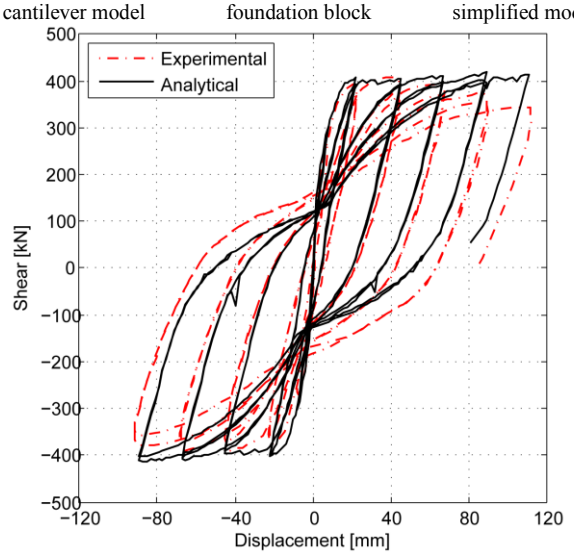
ent and more complex modelling approach. As showed in Figure 8a column model is composed by two different materials, confined and unconfined concrete. Confinement effects are taken into account by means of the geometric percentage of in-plane and out-of-plane reinforcements [37]. Longitudinal reinforcements are modelled with truss elements assuming perfect bond with the surrounding concrete.



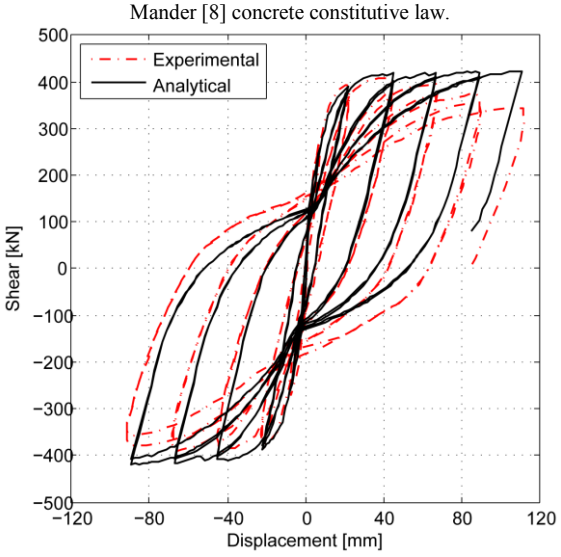
(a) VecTor2 cantilever model (b) VecTor2 model including foundation block (c) VecTor2 simplified model



(d) VecTor2 cantilever model (fig. 8a) with Popovic [36] and Mander [8] concrete constitutive law.



(e) VecTor2 model with Popovic [36] and Mander [8] concrete constitutive law, including foundation block (fig. 8b).

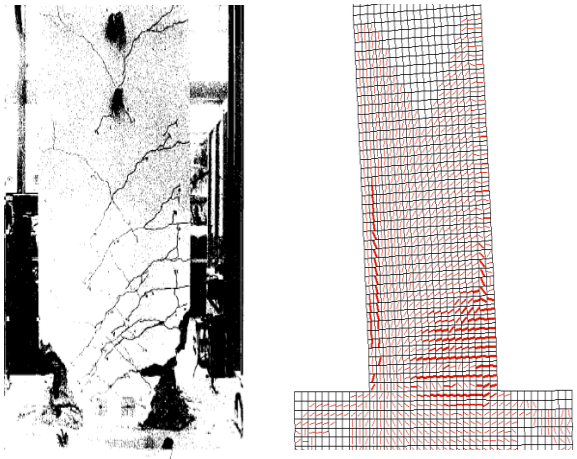


(f) VecTor2 model with Popovic[36] and Mander [8] concrete constitutive law, including simplified model of foundation (fig.8c).

Figure 8: VecTor2 model validation with Tanaka [28] spec. 6 experimental result.

The FormWorks automatic mesh generator is used to create a model with appropriate mesh size (variable in the optimal range 30-35 mm [38]). As in the experimental test, column models are subjected to cyclic displacement and axial load is applied at the top column as a distributed load. Restrain conditions are imposed at column basement. As in the previous modeling approach, three different schemes are proposed to simulate basement effects: a simple cantilever scheme preventing the translation of column base joints (Figure 8a); foundation block accurate modeling with realistic material and reinforcement properties (Figure 8b); a simplified model of foundation block (Figure 8c). Default *basic* options are selected for material constitutive laws and analysis mode [38], except for concrete compressive behaviour

schematized with Popovic [36] and Mander [8] relations. Comparative analysis between experimental and analytical test results are depicted in Figure 8.
Also for the proposed FEM models a good match with experimental results is obtained. It is also confirmed that the foundation modelling appears to be important to correctly estimate the initial stiffness (Figure 8e); however, it can be easily simplified as in Figure 8f with a substantial reduction in computation time.



(a) (b)

Figure 9: Tanaka [28] spec. 6 crack pattern: (a) experimental; (b) VecTor2 analytical model (Augustus view[24]).

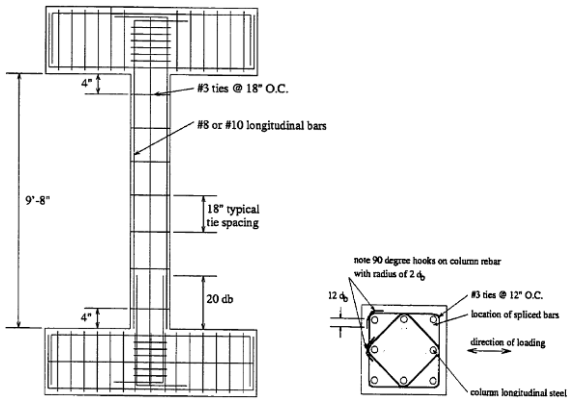
A close match between experimental and analytical crack pattern (Figure 9) with flexural cracks concentrations at column base ar the top part of the footing was also found.

2.3 Validation procedure

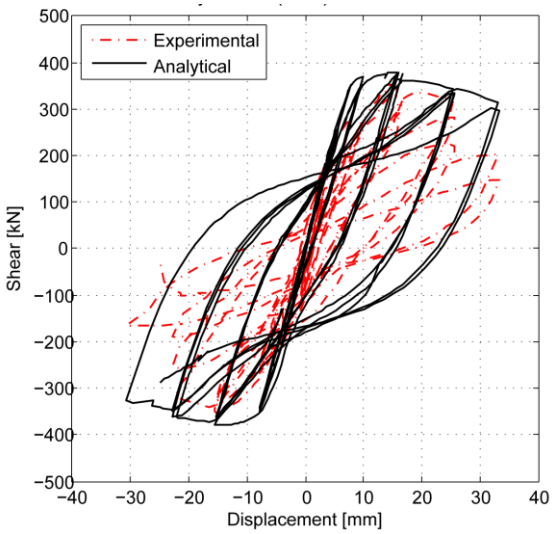
The validation of the numerical models presented earlier is generalized hereafter to specimens with different failure modes (see Table 1). The aim is to provide a unified modelling procedure that may lead to reasonable matches with experimental results regardless of the failure mode. Thus, in the following analyses, the models employed in the previous sections are adopted without changes or numerical calibrations. The adopted numerical models include: OpenSees lumped plasticity model with Mander [8] concrete constitutive law; VecTor5 model with Popovic [36] and Mander [8] concrete constitutive law, including simplified model of foundation; VecTor2 model with Popovic [36] and Mander [8] concrete constitutive law, including simplified model of foundation.

- *Lynn spec. 3CMD12 [29]*

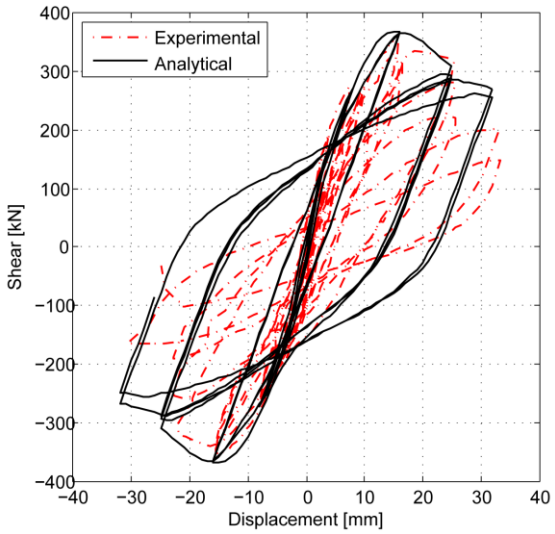
A column with a combined flexural-shear failure mode [26] with non-negligible inelastic shear deformation is used to validate the numerical models. Specimen details are illustrated in Figure 10a. For this specimen a double curvature scheme is adopted in the numerical models.
The comparisons between analytical and experimental results show that the OpenSees model (Figure 10b) led to significant overestimations of the lateral stiffness. The elastic shear deformation, neglected in the numerical model, may affect significantly the initial stiffness. Although the numerical model gives rise to a reasonable prediction of the peak strength (flexural dominated), it is not able to accurately describe the strength degradation related to shear strength degradation after column yielding. This led to significant overestimations of the dissipated energy, especially for the last cycles.



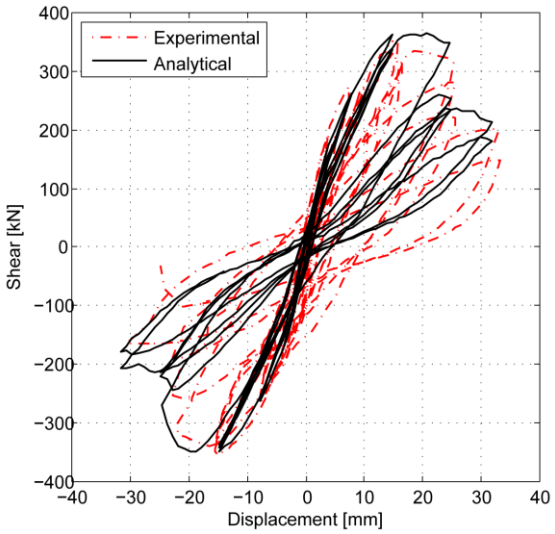
(a) Specimen details



(b) OpenSees lumped plasticity model with Mander [8] concrete constitutive law



(c) VecTor5 model with Popovic [36] and Mander [8] concrete constitutive law



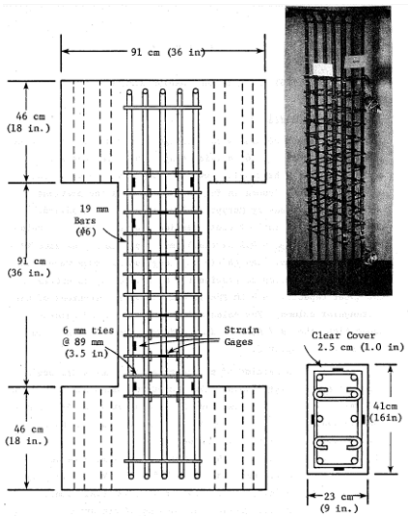
(d) VecTor2 model with Popovic [36] and Mander [8] concrete constitutive law.

Figure 10: Validation of proposed numerical models with Lynn [29] spec. 3CMD12 experimental result.

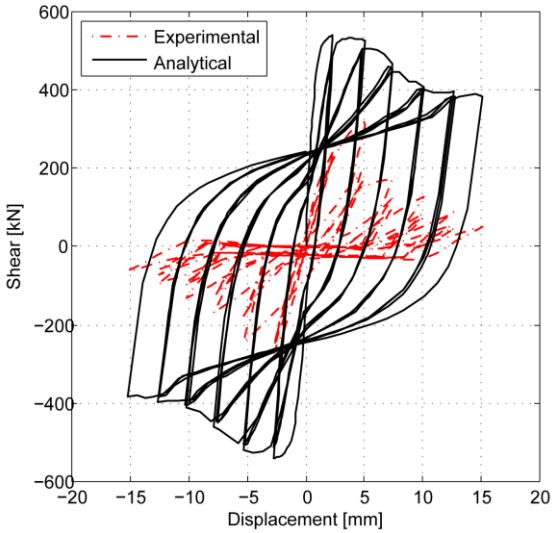
The VecTor5 model (Figure 10c) provides a matching of the strength at the peak stage and in the degradation phase. It also describes closely the column stiffness especially at the initial stages. In the last cycle, when the effects of the shear failure became dominant, a sensitive overestimation of the dissipated energy is shown. For this kind of failure the best fit of experimental results is achieved with the VecTor2 FEM model (Figure 10d), that is able to predict with reasonable accuracy experimental test behaviour at all the stages.

- *Umehara et al. spec. CUS [30]*

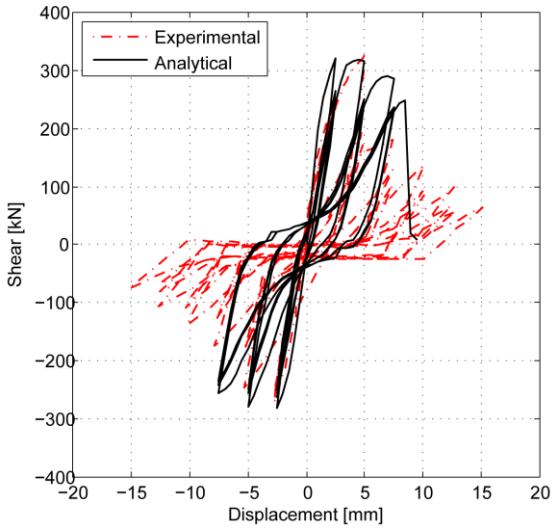
The following step of the validation procedure is to compare the analytical results of the proposed numerical models with an experimental test characterized by shear failure. Geometries and reinforcement details of the selected squat column are presented in Figure 11a.



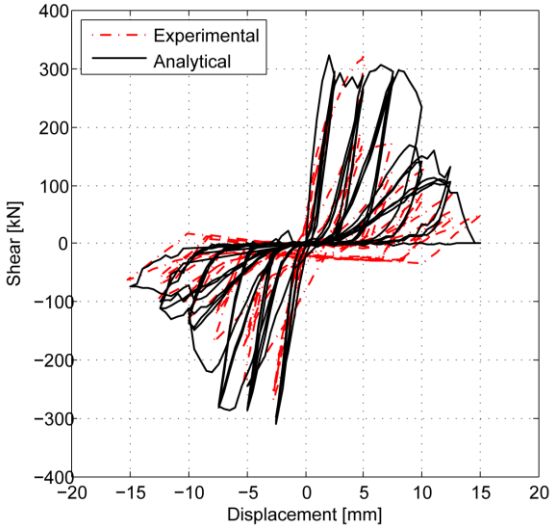
(a) Specimen details



(b) OpenSees lumped plasticity model with Mander [8] concrete constitutive law



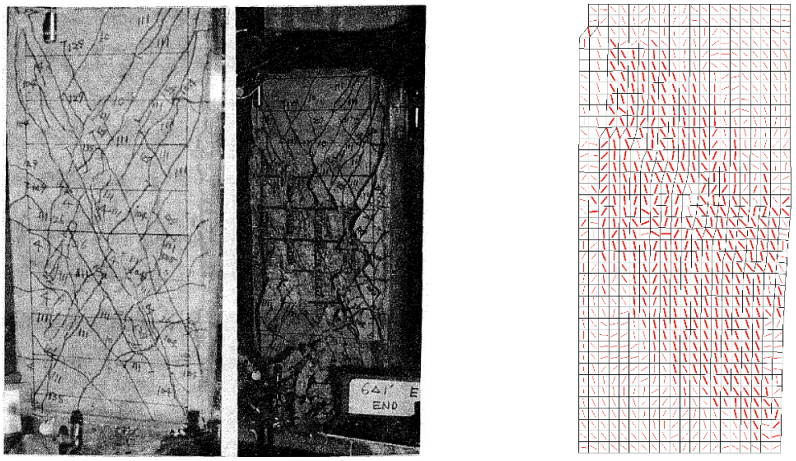
(c) VecTor5 model with Popovic [36] and Mander [8] concrete constitutive law



(d) VecTor2 model with Popovic [36] and Mander [8] concrete constitutive law

Figure 11: Validation of proposed numerical models with Umehara [30] spec. CUS experimental result.

According to the experimental test setup, a double cantilever scheme is adopted. For the VecTor5 model the single change is the segment length in the range of 10% of the cross section depth as suggested for shear walls [35]. Graphic comparisons depicted in Figure 11b show as the analytical models that do not account for shear effects in terms of strength and deformability may led to capacity estimation sensitively different from experimental results. Both the VecTor (Figure 11c,d) models match very well with experimental results, in terms of initial stiffness, peak strength and in the degradation branch for small displacement imposed. VecTor5 capacity curve (Figure 11c) drops to zero when shear crack check detects values not compatible with specimen stability [34]. On the other hand Vector2 is able to achieve a reasonable accordance with experimental results also for high imposed displacement and important strength reductions.



(a) (b)

Figure 12: Umehara [30] spec. CUS crack pattern: (a) experimental; (b) VecTor2 analytical model.

Comparisons between analytical and experimental crack pattern (Figure 12) confirm the ability of Vector2 to predict crack evolution during the cyclic test.

5. DISCUSSION AND CONCLUSIONS

The structural response of RC shear critical elements may lead to simplified models based on the regression approach on experimental data. Such models are limited to an estimation of the strength capacity and are not useful to conduct advanced nonlinear analysis aimed to reproduce both the strength and deformation behaviour of shear critical elements. To achieve accurate estimation of RC buildings seismic capacity, the structural response of structural subassembly or simple elements should be more accurate. Thus, the estimation of the plastic behaviour requires a thorough assessment when the effects of strength and stiffness degradation can be significant. Especially for redundant structures, as RC frames, the failure of one or more structural elements usually does not result in a structural collapse.

In the present paper different advanced numerical model are presented and their capacity to predict the cyclic behaviour of different RC elements is closely investigated. Columns exhibiting flexural failure mode were initially selected to get the best fit between experimental and numerical results. Thus, a validation procedure was proposed to validate the three presented numerical models: OpenSees lumped plasticity model with sectional behaviour; VecTor5 nonlinear fiber model; VecTor2 FEM model. The numerical comparisons showed the accuracy of proposed models in predicting the cyclic behaviour of a flexural critical column. Relevance should be given in the modeling of the footing used to simulate the realistic boundary conditions in the experimental test. This work also pointed out the importance of an accurate modeling of shear effect in the case of shear critical elements. Neglecting elastic and inelastic effects related to shear action (as in the proposed OpenSees models) may give rise to unrealistic estimations of member capacity in terms of strength and deformability. The VecTor software may be an accurate tool to reproduce the behaviour of shear critical elements. The VecTor2 FEM models provide accurate estimations of the element capacity regardless of the failure mode. The selected software also accurately predicts the crack pattern.

Finally, it can be argued that having accurate and complete information of the cyclic behaviour of RC components might be very useful to create a reliable numerical model that will be able to take into account the full nonlinear behaviour including strength and stiffness degradation. The use of the presented models could lead to realistic estimations of the seismic

capacity of the structural system without limitations imposed by traditional capacity models and with appropriate estimation of shear deformability effects.

6. ACKNOWLEDGMENTS

This work carried out was funded by the 7th Framework Programme of the European Commission, under the PIRSES-GA-2009-247567-EXCHANGE-SSI (**Ex**perimental & **C**omputational **H**ybrid **A**ssessment **N**etwork for **G**round-Motion **E**xcited **S**oil-**S**tructure **I**nteraction Systems), grant (www.exchange-ssi.net). The authors would like to thank Prof. F.J. Vecchio at University of Toronto for providing VecTor softwares used for numerical modeling.

REFERENCES

[1] G.M. Verderame, I. Iervolino, P. Ricci, Report on the damages on buildings following the seismic event of 6th of april 2009, V1.20. Laboratories University Network of seismic engineering (ReLUIS), http://www.reluis.it, 2009.

[2] M. Ercolino, C. Petrone, O. Coppola, G. Magliulo, Report sui danni registrati a San Felice sul Panaro (MO) in seguito agli eventi sismici del 20 e 29 maggio 2012 – v. 1.0 (in Italian). Laboratories University Network of seismic engineering (ReLUIS), http://www.reluis.it, 2012.

[3] Department of Homeland Security, Federal Emergency Management Agency, FEMA 440: Improvement of Nonlinear Static Seismic Analysis Procedures; June 2005; Washington, D.C.

[4] G. Maddaloni, G. Magliulo, E. Cosenza, Effect of the seismic input on non-linear Response of R/C building structures. *Advances in Structural Engineering* Vol. 15, No. 10, 2012, pp. 1861-1877.

[5] T. Paulay, M.J.N. Priestley, *Seismic Design of Reinforced Concrete and Masonry Buildings*. John Wiley and Sons, Inc, 1992.

[6] M.N. Fardis, *Seismic Design, Assessment and Retrofitting of Concrete Buildings*. Springer, Vol. 8, Series: Geotechnical, Geological, and Earthquake Engineering, 2009.

[7] M. Di Ludovico, G.M. Verderame, A. Prota, G. Manfredi, E Cosenza. Experimental behavior of non-conforming rc columns with plain bars under constant axial load and biaxial bending. *ASCE-Journal of Structural Engineering*, ISSN: 0733-9445, DOI: 10.1061/(ASCE)ST.1943-541X.0000703, (in printing).

[8] J.B. Mander, M.J.N. Priestley, R. Park, Theoretical Stress-Strain Model For Confined Concrete. *Journal of Structural Engineering*, Vol. 114, No. 8, August, 1988; Paper No. 22686.

[9] F. Braga, R. Gigliotti, M. Laterza, Analytical Stress–Strain Relationship for Concrete Confined by Steel Stirrups and/or FRP Jackets. *Journal of Structural Engineering*, September, 2006; pp. 1402-1416.

[10] M.P. Berry, D.E. Lehman, L.N. Lowes, Lumped-Plasticity Models for Performance Simulation of Bridge Columns. *ACI Structural Journal*, V. 105, No. 3, May-June 2008; pp. 270-279.

[11] L. Di Sarno, G. Manfredi, Seismic retrofitting with buckling restrained braces: application to an existing non-ductile RC framed building. *Soil Dynamics and Earthquake Engineering*, 30(11), 2010, pp. 1279-1297.

[12] F.J. Vecchio, M.P. Collins, The modified compression-field theory for reinforced concrete elements subjected to shear. *ACI Journal*, March-April 1986; pp. 219-231.

[13] F.J. Vecchio, Disturbed stress field model for reinforced concrete: formulation. *Journal of Structural Engineering*, vol.126, n°9, September 2000; paper n° 21621, pp. 1070-1077.

[14] F.J. Vecchio, Disturbed stress field model for reinforced concrete: implementation. *Journal of Structural Engineering*, vol.127, n°1, January 2001; paper n° 22148, pp. 12-20.

[15] The Regents of the University of California, OpenSees: Open system for earthquake engineering simulation. Pacific Earthquake Engineering Research Center. 1999-2000. http://opensees.berkeley.edu.

[16] F.J. Vecchio, VecTor softwares and tools. VecTor Analysis Group C/O F.J. Vecchio Department of Civil Engineering University of Toronto. http://www.civ.utoronto.ca/vector/.

[17] A. Mwafy, O. Kwon, A. Elnashai, Seismic assessment of an existing non-seismically designed major bridge-abutment-foundation system. *Engineering Structures*, 32 (2010) 2192-2209.

[18] O. Kwon, E. Kim, Case study: Analytical investigation on the failure of a two-story RC building damaged during the 2007 Pisco-Chincha earthquake. *Engineering Structures* 32 (2010) 1876_1887.

[19] Risk Management Solutions, Inc., Event Report: Chi-Chi Taiwan Earthquake; Sept 1999; California, USA; www.riskinc.com.

[20] L. Di Sarno, A.S. Elnashai, G. Manfredi, Assessment of RC columns subjected to horizontal and vertical ground motions recorded during the 2009 L'Aquila (Italy) earthquake. *Engineering Structures*, 33(5), 2011, 1514-1535.

[21] R. Frascadore, M. Di Ludovico, A. Prota, G.M. Verderame, G. Manfredi, M. Dolce, E. Cosenza, Local strengthening of RC structures as a strategy for seismic risk mitigation at regional scale. *Earthquake Spectra*, (submitted).

[22] W. Ritter, Die bauweise hennebique. *Schweizerische Bauzeitung*, 1899, 33 (7), pp. 59-61.

[23] E. Mörsch, *Concrete-Steel Construction*. McGraw-Hill, New York, 1909 (English translation by E. P. Goodrich of the original manuscript of the 1902).

[24] F.J. Vecchio, E.C. Bentz, M.P. Collins, Tools for forensic analysis of concrete structures. *Computer and Concrete*, vol. 1, n°1 (2004) 1-14.

[25] E.J. Setzler, H., Model for the lateral behavior of reinforced concrete columns including shear deformations. *Earthquake Spectra***,** vol. 24, issue 2, May 2008, pp. 493-511.

[26] AMERICAN CONCRETE INSTITUTE, COMMITTEE 369**,** ACI 369R-11: Guide for seismic rehabilitation of existing concrete frame buildings and commentary. Feb. 2011; U.S.A.

[27] PEER. Pacific Earthquake Engineering Research Center: Structural Performance Database, *University of California*, Berkeley, *http://nisee.berkeley.edu/spd/*.

[28] H. Tanaka, R. Park, Ph.D. Thesis: Effect of lateral confining reinforcement on the ductile behaviour of reinforced concrete columns. Rep. No. 90-2, 1990; Dept. of Civil Engineering, Univ. of Canterbury, U.K.

[29] A. Lynn, Ph.D. Thesis: Seismic evaluation of existing reinforced concrete building columns. University of California at Berkeley, Berkley, California, 1999, 284 pages.

[30] H. Umehara, J.O. Jirsa, Shear strength and deterioration of short reinforced concrete columns under cyclic deformations. *PMFSEL Report* No. 82-3, Department of Civil Engineering, University of Texas at Austin, Austin Texas, July 1982, 256 pages.

[31] D.E. Biskinis, Resistance and deformation capacity of concrete members with or without retrofitting. Ph.D Thesis, Civil Engineering Department, University of Patras, Greece.

[32] S. Bae, O. Bayrak, Plastic hinge length of reinforced concrete columns. *ACI Structural Journal*, 105 (3) , May-June 2008, pp. 290-300.

[33] K.J. Elwood, M.O. Eberhard, Effective Stiffness of Reinforced Concrete Columns. *A publication of the Pacific Earthquake Engineering Research Center*, Research Digest No. 2006-1.

[34] S. Güner, F.J. Vecchio, User's manual of VecTor5. 2008. VecTor Analysis Group C/O F.J. Vecchio Department of Civil Engineering University of Toronto. *http://www.civ.utoronto.ca/vector/.*

[35] S. Güner, Performance assessment of shear-critical reinforced concrete plane frames. Ph.D Thesis, Department of Civil Engineering University of Toronto, 2008.

[36] S. Popovics, A numerical approach to the complete stress-strain curve of concrete. *Cement and Concrete Research*, Vol. 3, No.5, 1973, pp. 583-599.

[37] P.S. Wong, F.J. Vecchio, VecTor2 & Formworks user's manual. 2002. VecTor Analysis Group C/O F.J. Vecchio Department of Civil Engineering University of Toronto. *http://www.civ.utoronto.ca/vector/.*

[38] F.J. Vecchio, W. Shim, Experimental and analytical reexamination of classic concrete beam tests. *Journal of Structural Engineering*, vol.130, n°3, March 2004, pp. 460-469.

COMPDYN 2013
4th ECCOMAS Thematic Conference on
Computational Methods in Structural Dynamics and Earthquake Engineering
M. Papadrakakis, V. Papadopoulos, V. Plevris (eds.)
Kos Island, Greece, 12–14 June 2013

RIGID BODY DYNAMICS USING A NOVEL APPROACH BASED ON LIE GROUP THEORY

Elias Paraskevopoulos[1] **and Sotirios Natsiavas**[1]

[1] Department of Mechanical Engineering
Aristotle University
54 124 Thessaloniki, Greece
e-mail: natsiava@auth.gr

Keywords: Lie Groups; Left, Right and Parallel Translation; Canonical Connection; Canonical Coordinates; Rigid Body Kinematics and Dynamics.

Abstract. A systematic theoretical approach is presented, in an effort to provide a complete and illuminating study on motion of a rigid body rotating about a fixed point. Since the configuration space of this motion is a differentiable manifold possessing group properties, this approach is based on some fundamental concepts of differential geometry. A key idea is the introduction of a canonical connection, matching the manifold and group properties of the configuration space. This is sufficient for performing the kinematics. Next, following the selection of an appropriate metric, the dynamics is also carried over. The present approach is theoretically more demanding than the traditional treatments but brings substantial benefits. In particular, an elegant interpretation is provided for all the quantities with fundamental importance in rigid body motion. It also leads to a correction of some misconceptions and geometrical inconsistencies in the field. Finally, it provides powerful insight and a strong basis for the development of efficient numerical techniques in problems involving large rotations.

1 INTRODUCTION

The study of rigid body motion has been in the epicenter of many previous investigations due to both the great theoretical importance and the large practical significance of the subject. The main objective of this work is to present a new look into the old but practically significant and still challenging mechanics problem of finite rotations, based on sound geometrical concepts. These concepts are known in the mathematics and physics literature for a long time. However, with a few exceptions (e.g., [1,2]), they are still not fully explored by the engineering community, despite their large value and usefulness. Here, an effort is made to use these concepts in order to create a clear and complete geometrical picture of large rigid body rotation. In this way, more light is thrown into the meaning of some of the most commonly employed quantities in describing rigid body motion. This, in turn, provides an alternative view and better interpretation of the related formulas employed frequently in the classical engineering literature. At the same time, this helps to identify and correct some common misconceptions in the field and achieve another objective of the present work. The latter refers to providing the means for building a reliable theoretical basis for developing better and more effective numerical integration methodologies for studying and investigating dynamics of single or multiple rigid bodies (e.g., [3-5]).

The geometrical route chosen in the present study deviates significantly from that taken in previous studies of mechanics problems. In those studies the underlying manifold is assumed to possess a Riemannian structure from the outset. A typical path is to introduce a set of coordinates and employ a natural coordinate basis in order to define a metric and then produce a metric compatible connection, having as components the classical Christofell symbols [6]. Usually, the same route is also chosen even for dynamics problems [7]. However, a more primitive and natural path is more beneficial and followed in this work. Namely, after creating the manifold corresponding to the configuration space of the motion, a connection operator is first established in an appropriate manner. This proves to be sufficient for performing a complete study of the kinematics. A canonical connection is selected [8], so that one can fully exploit the benefits associated to matching the special curves related to the manifold and the group properties of the configuration space. Then, a study of the dynamics requires the introduction of a metric. In this work, a suitable metric is chosen, which is not compatible with the connection, but allows for a complete, simple and concise treatment of the dynamics.

The classical treatment of spherical motion is briefly summarized in the following section. Then, some useful concepts of differential geometry are presented in Sect. 3. In the fourth section, rigid body kinematics is examined, based on the geometry of an appropriate three dimensional manifold. The basic properties of this manifold are extracted by the special orthogonal group $SO(3)$. Then, a suitable metric is introduced in Sect. 5, providing a useful tool for examining the dynamics of a rigid body. Finally, the most important conclusions are summarized in the last section.

2 A SUMMARY OF THE CLASSICAL APPROACH

Study of the spherical motion about a point O is typically performed in the ordinary Euclidean space $\mathbb{R}^3$ [9]. A basis $\mathfrak{B}$ is introduced, consisting of three fixed orthonormal vectors $\vec{E}_i$ (with $i=1,2,3$), having point O as origin. These vectors form a right-handed Cartesian inertial frame of reference. This basis will also be denoted $\{\vec{E}_i\}$. On the other hand, another basis, $\mathfrak{B}'$ or $\{\vec{e}_i(t)\}$, is formed by considering a new set of three orthonormal vectors $\vec{e}_i(t)$, having O as origin, but rigidly attached to and following the motion of the rigid body. These vectors form the so-called body frame of reference [10].

The two bases $\mathfrak{B}$ and $\mathfrak{B}'$ coincide originally. During the subsequent motion, they are related through a linear mapping

$$\vec{e}_i(t) = \Re(t)\,\vec{E}_i, \quad i = 1,2,3 \tag{1}$$

Then, the position vector of an arbitrary point of the body is

$$\vec{x}(t) = \sum_{i=1}^{3} x_i(t)\,\vec{E}_i = \sum_{i=1}^{3} X_i\,\vec{e}_i(t),$$

where x_i and X_i represent the components in the spatial and body frame, respectively. Adopting the notational convention of dropping the sum operator for products involving repeated indices [11], the last relations can be rewritten as

$$\vec{x}(t) = x_i(t)\,\vec{E}_i = X_i\,\vec{e}_i(t). \tag{2}$$

Next, if the components of the transformation $\Re$ in the basis $\mathfrak{B}$ are expressed by matrix R, that is $M_{\mathfrak{B}}^{\mathfrak{B}}(\Re) = R = [r_{ij}]$, then, Eq. (1) can be rewritten in the form

$$\vec{e}_i(t) = r_{ji}(t)\vec{E}_j.$$

Therefore, from Eqs. (1) and (2) one gets

$$x_i(t) = r_{ij}(t)X_j \quad \text{or} \quad \underline{x}(t) = R(t)\underline{X}, \tag{3}$$

with

$$\underline{x} = (x_1 \quad x_2 \quad x_3)^T \quad \text{and} \quad \underline{X} = (X_1 \quad X_2 \quad X_3)^T.$$

Then, employing the rigidity assumption of the body leads to

$$R^T R = I, \tag{4}$$

where I is the 3×3 identity matrix. This implies that $R(t)$ is orthogonal. Moreover, it easily turns out that the matrix

$$\tilde{\Omega}(t) \equiv R^T(t)\dot{R}(t) \tag{5}$$

is skew-symmetric (as indicated by $\sim$), with general form

$$\tilde{\Omega} = spin(\underline{\Omega}) \equiv \begin{bmatrix} 0 & -\Omega_3 & \Omega_2 \\ \Omega_3 & 0 & -\Omega_1 \\ -\Omega_2 & \Omega_1 & 0 \end{bmatrix}. \tag{6}$$

The corresponding axial vector associated with $\tilde{\Omega}$ is

$$\underline{\Omega} = vect(\tilde{\Omega}) \equiv (\Omega_1 \quad \Omega_2 \quad \Omega_3)^T.$$

In a similar manner one can show that $R\,R^T = I$ and by differentiation obtain the new skew-symmetric matrix

$$\tilde{\omega}(t) \equiv \dot{R}(t)\,R^T(t). \tag{7}$$

Therefore, combination of Eqs. (4), (5) and (7) yields

$$\dot{R} = \tilde{\omega}R = R\tilde{\Omega}. \tag{8}$$

Next, direct differentiation of Eq. (3) with a simultaneous application of Eqs. (7) and (8) yields

$$\underline{v} = \dot{\underline{x}} = \dot{R}\underline{X} = \dot{R}R^T\underline{x} = \tilde{\omega}\underline{x}. \tag{9}$$

Finally, Eqs. (7), (8) and (4) lead to

$$\tilde{\omega} = R\tilde{\Omega}R^T \quad \Rightarrow \quad \underline{\omega} = R\underline{\Omega}\,. \tag{10}$$

After establishing the kinematics, one can evaluate all the quantities needed in dynamics. First, the (convective) angular momentum of the body relative to the origin O is obtained by

$$\underline{H}_O(t) = J_O\underline{\Omega}(t)\,, \tag{11}$$

where

$$J_O = \int_m \tilde{X}^T\tilde{X}\,dm = \int_m [(\underline{X}\cdot\underline{X})I - \underline{X}\,\underline{X}^T]dm \tag{12}$$

is the mass moment of inertia matrix of the body with respect to the origin O [9]. Then, the dynamics of the rigid body is expressed by Euler's law in the form

$$J_O\dot{\underline{\Omega}} + \underline{\Omega}\times\underline{H}_O = \underline{M}_O\,, \tag{13}$$

where $\underline{M}_O$ are the body components of the resultant external moment about O [9]. Finally, by performing straightforward operations the kinetic energy of the motion is found in the form

$$T = \tfrac{1}{2}\underline{\Omega}^T J_O\,\underline{\Omega} = \tfrac{1}{2}\underline{H}_O\cdot\underline{\Omega}\,. \tag{14}$$

3 SOME ELEMENTS OF DIFFERENTIAL GEOMETRY

The set of orthogonal matrices $R(t)$ introduced in Sect. 2 forms a Lie group. Specifically, each matrix $R(t)$ represents a point in the space of 3×3 matrices, coinciding with the Euclidean space $\mathbb{R}^9$. Considering the orthogonality condition (4), this point lies on a three dimensional subset of $\mathbb{R}^9$ [12]. Since these conditions are nonlinear, this subset is not a vector subspace of $\mathbb{R}^9$ but it forms a three dimensional manifold, instead, which can be viewed as a surface in $\mathbb{R}^9$. In addition, since composite rotations are represented by products of orthogonal matrices [13], which are also orthogonal matrices, this subset is a Lie group, having as product the matrix multiplication and as identity element the 3×3 identity matrix I. Moreover, since $R(0) = I$, its determinant at t=0 is equal to +1 and because there can occur no jump to the value -1 during the subsequent motion, this matrix belongs to the special orthogonal group of order three, denoted by $SO(3)$.

Lie groups present some extra mathematical structure. For instance, if g and h are elements of a Lie group G, then one can define the left translation by g through the mapping

$$L_g(h) = gh\,. \tag{15}$$

Likewise, the right translation by g is defined as a mapping

$$R_g(h) = hg\,. \tag{16}$$

These operations are smooth mappings and give rise to useful gradients. Specifically, let $h(t)$ be a curve on G, with $h(0) = h$ and tangent vector $\dot{h}(0)$ at $t = 0$. This vector is denoted by $\underline{X}_h$ and belongs to the tangent space to G at h, denoted by T_hG. Then, according to Eq. (15), the set of points $p(t) = L_g(h(t))$ represents the image curve of $h(t)$ on G, obtained with a left translation by g. The velocity vector of $p(t)$ at point $L_g(h)$ is given by

$$\dot{p} = \tfrac{d}{dt}\{L_g(h(t))\}\big|_{t=0} = L_{g*}\dot{h}(0)\,, \tag{17}$$

where L_{g*} defines a linear transformation from T_hG to T_pG, known as the differential of L_g at h [12]. In this way, one can take a basis $\{\underline{e}_i(e)\}$ of T_eG at the identity element e of the group and left translate it to a basis $\{\underline{e}_i(p)\}$ of T_pG, with

$$\underline{e}_i(p) = L_{p*}\underline{e}_i(e), \tag{18}$$

on all of G. Then, any vector of the vector space T_pG, of dimension n, can be expressed in the form

$$\underline{v}(p) = \sum_{i=1}^{n} v^i(p)\underline{e}_i(p) = v^i(p)\underline{e}_i(p). \tag{19}$$

Moreover, if $\underline{v}$ is a left invariant vector field on G, then

$$\underline{v}(p) = L_{p*}\underline{v}(e) = L_{p*}[v^i(e)\underline{e}_i(e)] = v^i(e)L_{p*}\underline{e}_i(e) = v^i(e)\underline{e}_i(p).$$

Direct comparison of the last result with (19) yields

$$v^i(p) = v^i(e). \tag{20}$$

Left or right translation on a Lie group is important in the study of its one parameter subgroups. These are specific curves, satisfying the group homomorphism

$$g(t+s) = g(t)g(s) = g(s)g(t). \tag{21}$$

It can be shown that the most general monoparametric subgroup of G must pass from the identity element e and is determined by the exponential map, with

$$g(t) = \exp[tg'(0)]. \tag{22}$$

It can also be shown by using Eq. (21) that

$$g'(t) = L_{g(t)*}g'(0) = R_{g(t)*}g'(0), \tag{23}$$

which reveals that the one parameter subgroup of G, with tangent vector $g'(0)$ at the identity, coincides with the integral curve through the identity of the vector field, which results by a left translation of $g'(0)$ over all of G.

Given a Lie group G, one can construct its Lie algebra. This consists of the vector space T_eG, equipped with a special operator, known as Lie bracket [10]. For Lie groups, this bracket can be defined by employing the idea of left (or right) invariant vector fields. For instance, consider two vectors $\underline{X}_e$ and $\underline{Y}_e$ of T_eG and extend them by left translation to the vector fields $\underline{X}^L$ and $\underline{Y}^L$ on all of G. Then, their Lie bracket is

$$[\underline{X}_e, \underline{Y}_e] \equiv [\underline{X}^L, \underline{Y}^L]_e. \tag{24}$$

In fact, it has been proved that there exist three such canonical connections [8]. The first two of them, known as left and right invariant canonical connection, are defined by

$$\nabla^R_{\underline{X}}\underline{Y} = [\underline{X}^L, \underline{Y}] \quad \text{and} \quad \nabla^L_{\underline{X}}\underline{Y} = [\underline{X}^R, \underline{Y}], \tag{25}$$

where $\underline{X}^L$ and $\underline{X}^R$ is a left and a right invariant vector field, respectively, extending an element $\underline{X}$ of the tangent space at a point of a Lie group G to all of G, while $\underline{Y}$ is a vector field on G. Finally, a symmetric canonical connection is defined by

$$\nabla^S_{\underline{X}}\underline{Y} = \tfrac{1}{2}[\underline{X}^L + \underline{X}^R, \underline{Y}]. \tag{26}$$

All these connections are described completely by the Lie bracket and left/right translation. Some of their important properties are summarized in the sequel.

First, let $\{\underline{e}_i^L(p)\}$ (or simply $\{\underline{e}_i(p)\}$) be a basis created at point p by left translating a basis $\{\underline{e}_i(e)\}$ at the identity, using Eq. (18). Since $\underline{e}_i(p)$ is L_g-related to $\underline{e}_i(e)$ [12]

$$L_{g*}[\underline{e}_i(e),\underline{e}_j(e)] = [L_{g*}\underline{e}_i(e), L_{g*}\underline{e}_j(e)] = [\underline{e}_i(p),\underline{e}_i(p)].$$

By using the definition of the structure constants c_{ij}^k of a basis $[\underline{e}_i,\underline{e}_j] = c_{ij}^k\underline{e}_k$, this implies that

$$c_{ij}^k(p) = c_{ij}^k(e). \tag{27}$$

Also, the Lie bracket of the vector fields $\underline{X}$ and $\underline{Y}$ is given by

$$[\underline{X},\underline{Y}] = (X^j\partial_j Y^i - Y^j\partial_j X^i + c_{jk}^i X^j Y^k)\underline{e}_i. \tag{28}$$

Then, if both $\underline{X}$ and $\underline{Y}$ are left invariant vector fields on G

$$[\underline{X},\underline{Y}] = (c_{jk}^i X^j Y^k)\underline{e}_i \equiv Z^i\underline{e}_i.$$

Therefore, since the quantity $Z^i = c_{jk}^i X^j Y^k$ remains constant everywhere on the manifold, this shows that the Lie bracket of two left invariant vector fields is a new left invariant vector field. In a similar manner, if $\underline{X}$ is a left invariant vector field while $\underline{Y}$ is a right invariant vector field on G, it can be shown that their Lie bracket vanishes identically [12], that is

$$[\underline{X}^L,\underline{Y}^R] = \underline{0}. \tag{29}$$

Then, it becomes apparent from Eq. (29) that

$$\nabla_{\underline{X}}^R\underline{Y}^R = \underline{0}, \tag{30}$$

for any right invariant vector field $\underline{Y}$ on G. This means that the parallel translation of a vector on a manifold equipped with a left invariant canonical connection is equivalent to a right translation of it.

Next, by employing the definition of the left invariant canonical connection one arrives at

$$\nabla_{\underline{X}}\underline{Y} = (\partial_j Y^i + c_{jk}^i Y^k)X^j\underline{e}_i, \tag{31}$$

since then $\underline{X} = \underline{X}^L$ and $\partial_j X^i = 0$. On the other hand, the covariant differential of $\underline{Y}$ along $\underline{X}$ is evaluated in the form

$$\nabla_{\underline{X}}\underline{Y} = (\partial_j Y^i + \Lambda_{jk}^i Y^k)X^j\underline{e}_i,$$

where the affinities Λ_{jk}^i of the connection ∇ in the basis $\{\underline{e}_i\}$ are introduced by the following definition

$$\nabla_{\underline{e}_j}\underline{e}_k = \Lambda_{jk}^i\underline{e}_i. \tag{32}$$

It can be shown [14] that the affinities and the structure constants provide the components of the torsion tensor through

$$\tau_{jk}^i = \Lambda_{jk}^i - \Lambda_{kj}^i - c_{jk}^i. \tag{33}$$

Therefore, direct comparison of (32) with Eq. (31) reveals that

$$c_{jk}^i = \Lambda_{jk}^i. \tag{34}$$

Consequently, by substitution in (33) it follows that $\tau^i_{jk} = -\Lambda^i_{kj}$. This indicates that the left invariant canonical connection possesses torsion when $\Lambda^i_{jk} \neq 0$. On the other hand, direct evaluation shows that in such a case, all the components of the curvature tensor vanish ($R^i_{jkl} = 0$), which means that the curvature tensor of this connection is zero [8].

Similar results are also available for the right invariant canonical connection $\nabla^L_{\underline{X}} \underline{Y}$. However, the picture obtained for $\nabla^S_{\underline{X}} \underline{Y}$ is different. First, if $\{\underline{e}^R_i(p)\}$ is a basis created at p by a right translation of the basis $\{\underline{e}_i(e)\}$, then

$$c^i_{jk} = 2\Lambda^i_{jk}. \tag{35}$$

Therefore, by direct substitution in Eq. (33) it follows that

$$\tau^i_{jk} = -\Lambda^i_{jk} - \Lambda^i_{kj}.$$

Also, based on (39), the affinities of the connection are found to be anti-symmetric in their lower indices, i.e.,

$$\Lambda^i_{jk} = -\Lambda^i_{kj}. \tag{36}$$

This implies eventually that $\tau^i_{jk} = 0$. On the other hand, direct evaluation shows that the curvature tensor is non-zero.

For a Lie group, the choice of a canonical connection is a natural way to match the special integral curves associated with its properties as a manifold and as a group. Specifically, by definition the structure constants are anti-symmetric [12]. Consequently, Eqs. (34) and (35) reveal that the canonical connections considered lead to anti-symmetric affinities, satisfying Eq. (40). Then, it can be shown that the tangent vector at each point of an autoparallel curve has constant components on a local frame produced by a left translation. Therefore, each canonical connection relates the affinities Λ^i_{jk} (which express a manifold property) to the structure constants c^i_{jk} of the basis, so that the one parameter Lie subgroups and the curves resulting by their left translation (which are related to the group properties only) coincide with autoparallel curves (which are related to the manifold properties only). These results have remarkable implications in rigid body kinematics and dynamics, examined in the following two sections.

4 RIGID BODY KINEMATICS USING LIE GROUPS

In this section, spherical motion is reconsidered, by employing concepts of differential geometry. A new manifold is introduced, drawing its basic properties through a group representation on the classical $SO(3)$ group.

4.1 Introduction of a new manifold *M(3)*

A new manifold is introduced for the description of rigid body rotation. This manifold belongs to the same abstract group as $SO(3)$, but possesses different geometrical properties. For this reason, this manifold is named $M(3)$. Next, the emphasis is placed in identifying its critical geometrical properties.

First, the orientation of a rigid body can be represented by a point, say p, on $M(3)$. After choosing an appropriate local coordinate system, each point on $M(3)$ is described by three coordinates (or rotation parameters). Then, the spherical motion of a rigid body can be viewed

as a motion of a point on a single parameter curve, say $\gamma(t):\mathbb{R}\to M(3)$. Moreover, the angular velocity of the body is expressed by the tangent vector to $\gamma(t)$

$$\underline{w}(t)=\sum_{i=1}^{3} w^i(t)\underline{e}_i(t)=w^i(t)\underline{e}_i(t), \tag{37}$$

where $w^i(t)$ are the components of $\underline{w}(t)$ in a local basis $\{\underline{e}_i(t)\}$ (with $i=1,2,3$) of $T_pM(3)$ at the current position.

A useful concept in detecting changes of a vector field $\underline{v}(t)$ on $M(3)$ is the covariant differential of this field along the direction of vector $\underline{w}$ [12]. This quantity is determined by

$$\nabla_{\underline{w}}\underline{v}(t)=(\dot{v}^i+\Lambda^i_{jk}w^jv^k)\underline{e}_i.$$

In particular, a parallel translation of vector $\underline{v}$ along the curve $\gamma(t)$, with tangent vector $\underline{w}$, is defined by

$$\nabla_{\underline{w}}\underline{v}=\underline{0} \quad\Rightarrow\quad \dot{v}^i+\Lambda^i_{jk}w^jv^k=0. \tag{38}$$

This represents a set of three coupled linear ordinary differential equations in $v^i(t)$, possessing a unique solution for a given set of initial conditions $v^i(0)$. However, in the general case, the affinities Λ^i_{jk} depend on position. Nevertheless, there exists a special occasion where one can select the affinities so that the solution $\underline{v}(t)$ can be obtained in a convenient closed form, in terms of an exponential matrix, as explained next.

First, in the particular case with $\underline{v}=\underline{w}\equiv\underline{n}$, satisfaction of the condition of parallel translation leads to special curves on the manifold, known as autoparallel curves [15]. If, in addition, the affinities of the connection are anti-symmetric, as in Eq. (36), it can be shown that the components of the tangent vector $\underline{n}(t)$ to the autoparallel curve in the local frame remain constant on the whole curve. That is

$$n^i(t)=n^i(0)\equiv n^i. \tag{39}$$

Therefore, if the affinities Λ^i_{jk} are also constant everywhere on the manifold and such that

$$[\Lambda^i_{jk}n^j]=[\tilde{n}^i_k]=\tilde{n}=spin(\underline{n}), \tag{40}$$

the parallel translation of any vector $\underline{u}(t)$ of $T_pM(3)$ along the autoparallel curve of $M(3)$ connecting point $p(t)$ to any other point of $M(3)$ is described by the following system

$$\begin{pmatrix}\dot{u}^1\\ \dot{u}^2\\ \dot{u}^3\end{pmatrix}=-\begin{bmatrix}0 & -n^3 & n^2\\ n^3 & 0 & -n^1\\ -n^2 & n^1 & 0\end{bmatrix}\begin{pmatrix}u^1\\ u^2\\ u^3\end{pmatrix} \quad\text{or}\quad \dot{\underline{u}}=-\tilde{n}\underline{u}. \tag{41}$$

Simple inspection verifies that Eq. (40), together with condition (36), can be fulfilled simultaneously, indeed, provided that the non-zero affinities take the following constant values

$$\Lambda^1_{23}=-\Lambda^1_{32}=\Lambda^2_{31}=-\Lambda^2_{13}=\Lambda^3_{12}=-\Lambda^3_{21}=1, \tag{42}$$

on all of $M(3)$. Therefore, there appears the need for the selection of an appropriate non-natural basis. Since $M(3)$ forms a Lie group, this basis can conveniently be obtained by extending a basis $\{\underline{e}_i(e)\}$, defined in $m(3)\equiv T_eM(3)$, on all of $M(3)$ through a right or left translation. Taking into account Eq. (1), the latter choice is preferred, leading to

$$\underline{e}_i(p(t))=L_{p(t)*}\underline{e}_i(e), \quad i=1,2,3, \tag{43}$$

so that each basis vector $\underline{e}_i(p(t))$ is part of a left invariant vector field on $M(3)$. In essence, this is identical to Eq. (18), since for a given point p these vectors are fixed and their dependence on t is only implicit. To stress this, the basis vector $\underline{e}_i(p(t))$ will next be denoted simply by $\underline{e}_i(p)$. An immediate consequence of this basis choice is that if $\underline{v}(t)$ is any left invariant vector field on $M(3)$, then its representative vector at point p can be expressed in the form

$$\underline{v}_p(t) = v_p^i(t)\underline{e}_i(p) .$$

Moreover, application of Eq. (20) yields

$$v_p^i(t) = v_e^i(t) \equiv v^i(t) . \tag{44}$$

Then, Eq. (39) can be rewritten in the form $n_p^i(t) = n_e^i(t) \equiv n^i(t)$, illustrating that the tangent vector to an autoparallel curve of $M(3)$ is part of a left invariant vector field on $M(3)$. Therefore, taking into account Eqs. (36) and (42), it is convenient to choose the left invariant canonical connection, expressed by Eq. (25a), as most appropriate for $M(3)$. An immediate consequence of this, with enormous significance, is that the autoparallels of $M(3)$ will coincide with its one parameter Lie subgroups and their left translations (see end of Section 3.2). In this respect, Eq. (41) can be seen as a means of determining the components of any vector $\underline{u}_p(t)$ of $T_pM(3)$, obtained by parallel translation of a vector $\underline{u}_e(t)$ of $T_eM(3)$ along the autoparallel curve of $M(3)$ connecting point $p(t)$ to the identity e. In fact, since the coefficient matrix $\tilde{n}$ in Eq. (41) is constant, this solution can be expressed in the form

$$\underline{u}_p(t) = B(t)\underline{u}_e(t) \quad \Rightarrow \quad \underline{u}_e(t) = A(t)\underline{u}_p(t) , \tag{45}$$

with

$$A(t) = \exp(t\tilde{n}) \tag{46}$$

and

$$B(t) = A^{-1}(t) = \exp(-t\tilde{n}) . \tag{47}$$

Among the infinity of available choices, the specific selection of the affinities expressed by Eq. (42) leads to a 3×3 matrix $A(t)$, given by Eq. (46). Here, this matrix appears in Eq. (45) as a linear transformation from $T_pM(3)$ to $T_eM(3)$.

The ideas presented above can provide a clear interpretation of rigid body kinematics. For instance, the basis $\{\underline{e}_i(p)\}$ obtained by left translation of a basis $\{\underline{e}_i(e)\}$ of $T_eM(3)$ on all of $M(3)$, as specified by (43), corresponds to a basis which remains fixed on the rigid body during its motion (body frame). In addition, the components of the tangent vector $\underline{w}(t)$ to the path $\gamma(t)$ of the motion, are components of the angular velocity of the body in the local basis $\{\underline{e}_i(p)\}$. That is

$$\underline{w}(t) = w^i(t)\underline{e}_i(p) . \tag{48}$$

This vector belongs to $T_pM(3)$ at point p and can be viewed as the outcome of the left translation of a vector of $T_eM(3)$

$$\underline{\Omega}(t) = \Omega^i(t)\underline{e}_i(e) , \tag{49}$$

known as the convective angular velocity [3]. Based on (44), the following choice is made for its components

$$w^i(t) = \Omega^i(t)\,. \tag{50}$$

Alternatively, vector $\underline{w}(t)$ can also be obtained by a parallel transfer of another vector of $T_eM(3)$, through the autoparallel curve of $M(3)$ joining the identity to the current point p. If

$$\underline{\omega}(t) = \omega^i(t)\underline{e}_i(e)\,, \tag{51}$$

then, according to Eq. (49), its components satisfy

$$w^i(t) = B^i_j(t)\omega^j(t) \quad \text{and} \quad \omega^i(t) = A^i_j(t)w^j(t)\,.$$

Next, the results obtained in this section are illustrated by Fig. 1. The actual motion of the body is described by a path $\gamma(t)$ on $M(3)$, starting from the identity element at $t = 0$. Then, for a fixed time t, points on the autoparallel curve of $M(3)$ connecting the current point $p(t)$ to the origin e, say $\eta_p(s)$, are located by another parameter, say s, related to the length of this path. In this case, in order to distinguish the true path $\gamma(t)$ from the autoparallel $\gamma_p(s)$, it is more appropriate to replace matrix $A(t)$ in Eq. (46) by

$$Q(s, \underline{n}(t)) = \exp(s\tilde{n}(t))\,, \tag{52}$$

for $0 \le s \le t$ and $Q(t, \underline{n}(t)) = A(t) = R(t)$. This means that at any given time t, matrices A and Q coincide with matrix R. This is a manifestation of Euler's theorem, stating that one can move a rigid body, rotating about a fixed point, from an initial to any final position, through a pure rotation about a fixed axis [13]. In addition, the tangent vector $\underline{w}(t)$ to the actual path $\gamma(t)$ represents the angular velocity of the body and creates two images, $\underline{\Omega}(t)$ and $\underline{\omega}(t)$, in $T_eM(3)$ at any time t.

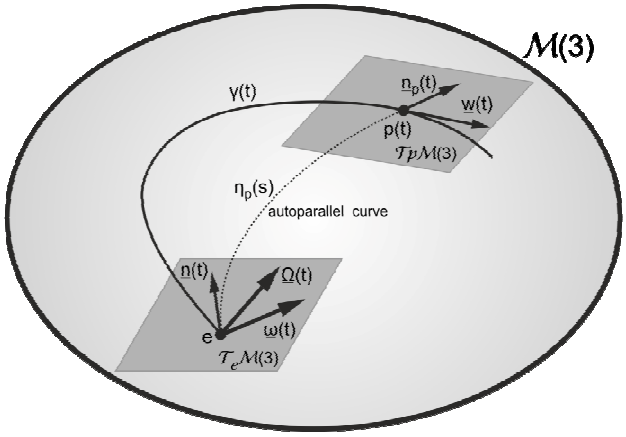


Fig. 1. Geometrical interpretation of spherical motion in $M(3)$

Finally, note that there exist several closed form expressions for matrix $A(t)$ in terms of rotation parameters. Among them, the most commonly known is probably the Rodrigues formula

$$A(t) = \exp[\tilde{\Psi}(t)] = I + \frac{\sin \| \underline{\Psi} \|}{\| \underline{\Psi} \|}\tilde{\Psi} + \frac{1}{2}\frac{\sin^2(\frac{1}{2}\| \underline{\Psi} \|)}{(\frac{1}{2}\| \underline{\Psi} \|)^2}\tilde{\Psi}\tilde{\Psi}\,.$$

Direct comparison with Eq. (50) shows that the quantity $\underline{\Psi}$, known as the Cartesian rotation vector [9], is defined by

$$\underline{\Psi}(t) = t\,\underline{n}(t)\,. \tag{53}$$

4.2 Group representation of *M(3)* on *SO(3)*

The group properties of $M(3)$ can be obtained by a group representation on $SO(3)$, through an appropriate map [16]. This map, say Φ from $M(3)$ to $SO(3)$, is selected to be an isomorphism [14]. In order to derive its explicit form, appropriate coordinates systems on the manifolds and bases on the tangent spaces should first be chosen.

In many occasions, it is beneficial to employ a special set of local coordinates, known as canonical [2]. Specifically, let $\eta(s)$ be the autoparallel curve of a manifold M^n emanating from a point p of the manifold at $s=0$, with a tangent vector $\underline{n}$ on the tangent space T_pM^n. If the coordinates of the origin (or pole) p are selected as

$$p^i = 0\,, \quad i = 1,\ldots,n$$

and the tangent vector $\underline{n}$ is expressed over a basis $\{\underline{e}_i\}$ of T_pM^n in the form $\underline{n} = n^i\underline{e}_i$, then the canonical coordinates of any point q on the curve $\eta(s)$ are uniquely specified to be

$$q^i = s n^i\,. \tag{54}$$

Canonical coordinates specify uniquely any point q of M^n in the vicinity of the pole p. In the special case of a Lie group, it was shown at the end of Sect. 3 that the affinities Λ^i_{jk} can be obtained from the structure constants c^i_{jk}. In the particular case of $M(3)$, it was demonstrated in Sect. 4.1 that the left invariant canonical connection is the most natural choice for it, with affinities given by (42). Then, its autoparallel curves are identified by (39), which leads to (54), with $n=3$. Therefore, (54) defines a canonical coordinate system on $M(3)$ with origin at its identity element e. Moreover, direct comparison of (54) with (53) reveals that the canonical coordinates coincide with the components of the so called Cartesian rotation vector.

Based on the above, a canonical coordinate system is first placed on $M(3)$ with origin at e for locating its points. Next, a basis $\{\underline{e}_i(e)\}$ is selected at $m(3)$, according to conditions that will be stated more explicitly in Sect. 5. This basis is then extended to all points q of $M(3)$ by left translation

$$\underline{e}_i(q) = q\,\underline{e}_i(e)\,, \tag{55}$$

creating a non-natural basis [11].

According to material presented in Sections 3 and 4.1, an autoparallel curve emanating from the identity element e of $M(3)$ coincides with an one parameter Lie subgroup, which corresponds to pure rigid body rotation about an axis determined by the tangent vector to the curve at the identity. Conversely, given any point q on the manifold, one can find a vector on the tangent space at the identity element of $M(3)$, representing an axis of rotation of the body, which is tangent to the unique one parameter subgroup emanating from e and passing from q. Moreover, these special curves are captured by the corresponding exponential map of the group. In fact, the exponential map of a group G is a local diffeomorphism from a neighborhood of zero in T_eG onto a neighborhood of e in G [10]. In addition, this map can be extended over all of G through a left translation. Therefore, guided by Eq. (46), the mapping Φ

from $M(3)$ to $SO(3)$ is selected in the form

$$\Phi(q) = \exp(s\tilde{n}), \tag{56}$$

where $\tilde{n} = spin(\underline{n})$ and $\underline{n}$ is the vector of $m(3)$ which is tangent to the autoparallel curve starting from the identity e and passing from point q of $M(3)$. Based on (54), the components of q depend on the parameters s and $\underline{n}$. Therefore, the quantity

$$Q(s, \underline{n}) = \Phi(q(s, \tilde{n})) \tag{57}$$

represents a 3×3 exponential matrix. Since matrix Q is orthogonal, it is an element of $SO(3)$, indeed. In view of Eq. (54), this matrix represents a map from the canonical coordinates of point q to $\mathbb{R}^9$. Moreover, since the identity element e of $M(3)$ has canonical coordinates $(0,0,0)$, it turns out from Eqs. (56) and (57) that

$$\Phi(e) = Q(0, \underline{n}) = I, \tag{58}$$

which verifies that Φ maps the identity element e of $M(3)$ to the identity element I of $SO(3)$.

This information is enough to determine the tangent mapping of Φ at the identity point e of $M(3)$ by

$$\Phi(e)_*(\cdot) = spin(\cdot). \tag{59}$$

Then, the Lie bracket of the Lie algebra $m(3)$ is defined by

$$[\underline{X}_1(e), \underline{X}_2(e)] = vect([Y_1(I), Y_2(I)]), \tag{60}$$

while the tangent mapping of Φ at an arbitrary point q of $M(3)$ is obtained in the form

$$\Phi(q)_* = \Phi(q)\Phi(e)_* = Q\Phi(e)_*.$$

This completes the geometrical picture of the mapping between $M(3)$ and $SO(3)$, shown in Fig. 2.

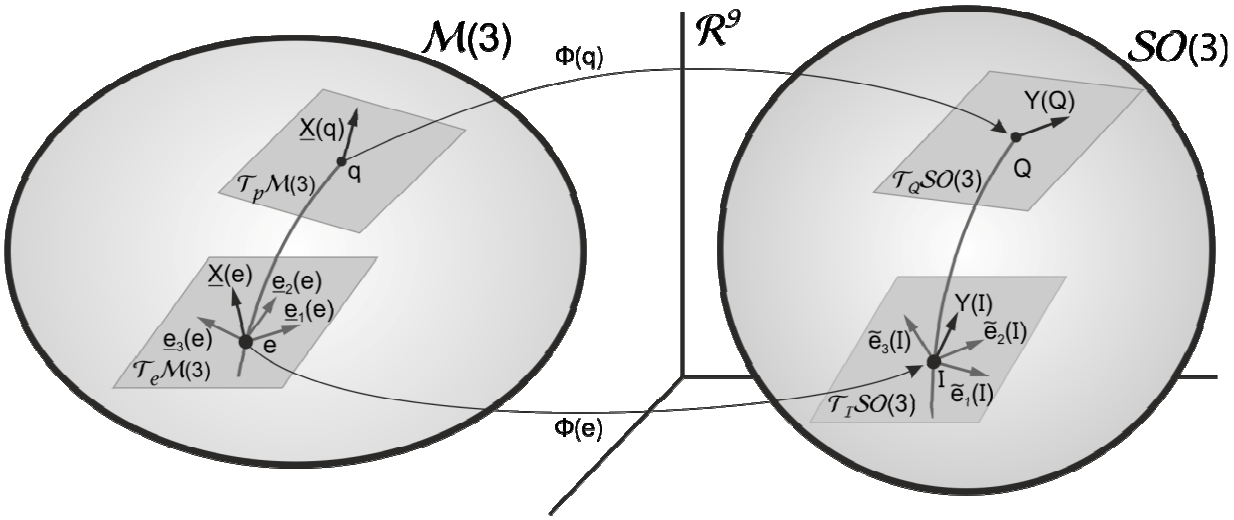


Fig. 2. Definition of mapping Φ for a group representation of $M(3)$ on $SO(3)$.

Finally, direct computation yields

$$c_{ij}^{k} = \tilde{c}_{ij}^{k}, \tag{61}$$

which determines the structure constants c_{ij}^{k} in $m(3)$ and consequently completes the definition of its Lie bracket in terms of the structure constants $\tilde{c}_{ij}^{k}$ of the basis in $so(3)$. At the same time, this result establishes the affinities of the connection on all of $M(3)$, through Eqs. (27), (34) and (42).

5 APPLICATION TO RIGID BODY DYNAMICS

Study of rigid body dynamics necessitates consideration of the dual space $T_pM(3)^*$ to $T_pM(3)$. This space includes elements known as covectors, which are linear functionals on $T_pM(3)$ [12]. More specifically, if $\underset{\sim}{v}$ is a vector of $T_pM(3)$, then there exists a covector $\underset{\sim}{v}^*$ of $T_pM(3)^*$, such that

$$\underset{\sim}{v}^*(\underset{\sim}{u}) \equiv \langle \underset{\sim}{v}, \underset{\sim}{u} \rangle, \quad \forall \underset{\sim}{u} \in T_pM(3), \tag{62}$$

where $\langle \cdot, \cdot \rangle$ denotes the inner product of $T_pM(3)$. In addition, a basis $\{\underset{\sim}{e}^i\}$ (with $i = 1,2,3$) of $T_pM(3)^*$ is called dual basis to the basis $\{\underset{\sim}{e}_i\}$ of $T_pM(3)$, provided that

$$\underset{\sim}{e}^i(\underset{\sim}{e}_j) = \delta_j^i, \tag{63}$$

where δ_j^i is a Kronecker delta symbol. Then,

$$\underset{\sim}{v}^* = v_i \underset{\sim}{e}^i,$$

with components v_i determined by

$$v_i = g_{ij} v^j, \tag{64}$$

where the scalars

$$g_{ij} = \langle \underset{\sim}{e}_i, \underset{\sim}{e}_j \rangle \tag{65}$$

are components of the metric tensor in basis $\{\underset{\sim}{e}_i\}$ of $T_pM(3)$.

The choice of the body frame can now be performed. First, it turns out successively that

$$\underset{\sim}{w}^*(\underset{\sim}{w}) = \langle \underset{\sim}{w}, \underset{\sim}{w} \rangle = w^i w^j g_{ij} = \Omega^i g_{ij} \Omega^j .$$

Therefore, direct comparison of the last result with Eq. (14) shows that the kinetic energy of the body can be expressed by

$$T = \tfrac{1}{2} \langle \underset{\sim}{w}, \underset{\sim}{w} \rangle = \tfrac{1}{2} \Omega^i g_{ij} \Omega^j, \tag{66}$$

provided that

$$g_{ij} = J_{ij}, \tag{67}$$

with $J_O = [J_{ij}]$. Next, a basis $\{\underset{\sim}{e}_i(e)\}$ can be selected for the tangent space $m(3)$ through (65), so that it satisfies

$$\langle \underset{\sim}{e}_i(e), \underset{\sim}{e}_j(e) \rangle = J_{ij}. \tag{68}$$

This basis is then left translated at any point p of $M(3)$, according to (55). Therefore, if the metric tensor is chosen to be left invariant, then

$$\langle \underset{\sim}{e}_i(p), \underset{\sim}{e}_j(p) \rangle = J_{ij}, \qquad \forall p \in M(3). \tag{69}$$

The geometry of manifold $M(3)$ presents some significant differences with the classical rotation group $SO(3)$. The first appears in the connection. Specifically, it was shown in Sect. 4.1 that the most convenient choice for describing spherical motion on $M(3)$ is the left invariant canonical connection, defined by Eq. (25a). This choice leads to a non-Riemannian manifold, with torsion and no curvature, which is in sharp contrast to the geometrical properties of the ordinary $SO(3)$.

Another important deviation between $M(3)$ and $SO(3)$ occurs in the metric tensor. By employing the orthogonality property (4), the components of the metric tensor in $SO(3)$ can be determined in the form

$$\hat{g}_{ij} = 2\delta_{ij}. \tag{70}$$

This metric is symmetric and positive definite and can be shown to be compatible with the connection chosen [11]. This verifies that $SO(3)$ is a Riemannian manifold, since it also possesses curvature and is torsionless. However, the components of the metric tensor of $SO(3)$ are different than those of the inertia tensor in $M(3)$, whose components are defined by (67).

The picture of the dynamics of rigid body spherical motion can now be completed by illuminating the role of $T_pM(3)^*$ and the selection of $\gamma(t)$. Direct comparison of (67) and (13) demonstrates that the covector $\underset{\sim}{w}^*$ corresponding to the angular velocity vector $\underline{w}$, is the angular momentum vector. Namely

$$\underset{\sim}{w}^* = \underset{\sim}{H}_O \quad \Rightarrow \quad H_i = J_{ij}\Omega^j. \tag{71}$$

Also, comparison of Eqs. (62) and (66) shows that the dual product of the angular velocity vector $\underline{w}$ with the angular momentum $\underset{\sim}{H}_O$ yields the kinetic energy of the body. That is,

$$T = \tfrac{1}{2}\underset{\sim}{w}^*(\underline{w}) = \tfrac{1}{2}\underset{\sim}{H}_O(\underline{w}),$$

which is equivalent to Eq. (14). In addition, the selection of the solution curve $\gamma(t)$ on $M(3)$ is performed by Euler's law

$$\dot{\underset{\sim}{H}}_O = \underset{\sim}{M}_O, \tag{72}$$

where $\underset{\sim}{M}_O = M_i \underset{\sim}{e}^i$ is the resultant moment with respect to point O. Therefore, by employing (71) and taking into account that the components J_{ij} are constant, (72) becomes

$$J_{ij}\dot{\Omega}^j + \tilde{\Omega}^j_i J_{jk}\Omega^k = M_i, \tag{73}$$

which matches Eq. (15), with

$$[-\Lambda^j_{ki}\Omega^k] \equiv [\tilde{\Omega}^j_i] = \tilde{\Omega} = spin(\underline{\Omega}). \tag{74}$$

Finally, the affinities selected for $M(3)$ according to (42) match its group and manifold properties but are not compatible with its metric, expressed by (67). This implies that the metric is not preserved under parallel transfer along an arbitrary path. For instance, differentiation of both sides of (66) with respect to time and simultaneous application of the symmetry condition of the inertia tensor $J_{ij} = J_{ji}$, yields eventually

$$\dot{T} = \Omega^i J_{ij} \dot{\Omega}^j . \tag{75}$$

Among all the possible paths, only on the real one it is true that $\dot{\Theta}^m = \Omega^m$. Therefore, for $\underset{\sim}{M}_O = \underset{\sim}{0}$, i.e., for torque free motion

$$J_{ij} \dot{\Omega}^j = -\tilde{\Omega}^j_i J_{jk} \Omega^k = -(-\Lambda^j_{mi} \Omega^m) J_{jk} \Omega^k = \Lambda^j_{mi} \Omega^m H_j ,$$

which after substituting in (75) yields

$$\dot{T} = \Omega^i (\Lambda^j_{mi} \Omega^m H_j) = (\Lambda^j_{mi} \Omega^i \Omega^m) H_j = 0 ,$$

due to the anti-symmetry property of the affinities selected for $M(3)$. This shows that the kinetic energy is conserved along the path corresponding to the actual motion of the body.

6 SYNOPSIS

Finite rigid body rotation has been treated in this study. Borrowing ideas from Lie group theory provided a solid foundation for a thorough and consistent investigation of rigid body kinematics and dynamics. As a result, the following elegant geometrical picture emerged.

First, the orientation of a rigid body was represented by a single point, while the motion over a finite time interval was described by a curve on a three dimensional manifold. Then, it was demonstrated that, contrary to common belief, the well known special orthogonal group $SO(3)$ is not appropriate for describing either the kinematics or the dynamics of large rigid body rotation. In fact, a new manifold was introduced, named $M(3)$, which is diffeomorphic to $SO(3)$. Specifically, a significant contribution of this work was the selection of a canonical connection for $M(3)$, so that its autoparallel curves, representing pure rotation of the body, coincide with its one parameter Lie subgroups, which are located conveniently by the exponential map. This led to a manifold possessing torsion and no curvature, in contrast to the classical rotational group $SO(3)$, which is a Riemannian manifold with curvature and no torsion. Moreover, the exponential map provided the ground for choosing a holonomic coordinate system in determining uniquely the points on $M(3)$. In particular, the components of the classical Cartesian rotation vector were picked up as canonical coordinates. However, an anholonomic coordinate frame was selected for expressing the vectors of the tangent space at the current point. This frame is fixed on the body (body frame) and was obtained mathematically by a left translation of an appropriate basis at the identity. Moreover, all the important geometrical properties of $M(3)$, were also selected by a suitable representation on the rotation group $SO(3)$.

Next, the emphasis was put on dynamics. The components of the metric tensor were chosen to match the components of the mass moment of inertia tensor of the body. This provided the body frame at the identity. Then, the equations of motion were derived by applying Euler's law. Finally, since the connection and metric of $M(3)$ are not compatible, in contrast to the case of $SO(3)$, the inner product in the tangent space (representing kinetic energy) is not preserved along any arbitrary curve. However, it was proved that the kinetic energy is conserved along the true path, during a torque-free motion.

The theoretical results of this study provide valuable tools for developing efficient techniques for their geometrically exact temporal discretization in all areas of mechanics, involving rigid body rotation. This will be demonstrated in future publications.

REFERENCES

[1] J. Argyris, V.F. Poterasu, Large rotations revisited application of Lie algebra, *Computer*

Methods in Applied Mechanics and Engineering, **103**, 11-42, 1993.

[2] R.M. Murray, Z. Li, S.S. Sastry, *A Mathematical Introduction to Robot Manipulation*, CRC Press, Boca Raton, Florida, 1994.

[3] J.C. Simo, L. Vu-Quoc, A geometrically-exact rod model incorporating shear and torsion-warping deformation, *Int. J. Solids Struct*., **27**, 371-393, 1991.

[4] D. Negrut, E.J. Haug, H.C. German, An implicit Runge-Kutta method for the integration of differential-algebraic equations of multibody dynamics, *Multibody System Dyn.*, **9**, 121-142, 2003.

[5] O. Brüls, A. Cardona, M. Arnold, Lie group generalized-α time integration of constrained flexible multibody systems, *Mechanism and Machine Theory*, **48**, 121-137, 2012.

[6] W. Flugge, *Tensor Analysis and Continuum Mechanics*, Springer-Verlag, New York, 1972.

[7] D.H. Sattinger, O.L. Weaver, *Lie Groups and Algebras with Applications to Physics, Geometry and Mechanics*, Springer-Verlag, New York, 1986.

[8] W. Bertram, Differential Geometry, Lie Groups and Symmetric Spaces over General Base Fields and Rings, *Memoirs of the American Mathematical Society*, **192**, 1-202, 2008.

[9] M. Geradin, A. Cardona, *Flexible Multibody Dynamics*, John Wiley & Sons, New York, 2001.

[10] J.E. Marsden, T.S. Ratiu, *Introduction to Mechanics and Symmetry, second ed.*, Springer Science+ Business Media Inc., New York, 1999.

[11] J.G. Papastavridis, *Tensor Calculus and Analytical Dynamics*, CRC Press, Boca Raton, 1999.

[12] T. Frankel, *The Geometry of Physics: An Introduction*, Cambridge University Press, New York, 1997.

[13] A.A. Shabana, *Dynamics of Multibody Systems, third ed.*, Cambridge University Press, New York, 2005.

[14] E. Paraskevopoulos, S. Natsiavas, A new look into the kinematics and dynamics of finite rigid body rotations using Lie group theory, *Int. J. Solids Struct.*, **50**, 57-72, 2013.

[15] S.V. Shabanov, Constrained systems and analytical mechanics in spaces with torsion, *J. Phys. A: Mathematical and General*, **31**, 5177-5190, 1998.

[16] B.C. Hall, *Lie Groups, Lie Algebras and Representations: An Elementary Introduction*, Springer-Verlag, New York., 2003.

COMPDYN 2013
4th ECCOMAS Thematic Conference on
Computational Methods in Structural Dynamics and Earthquake Engineering
M. Papadrakakis, V. Papadopoulos, V. Plevris (eds.)
Kos Island, Greece, 12–14 June 2013

UNCERTAINTY ANALYSIS ON A PUMP ASSEMBLY USING COMPONENT MODE SYNTHESIS

S. Audebert[1*], Fatou Fall-Lo[1]

[1]Electricité de France R&D
Acoustics and Mechanical Analyses
1 avenue du Général de Gaulle
92141 CLAMART Cedex FRANCE
sylvie.audebert@edf.fr

Keywords: Parametrical uncertainty, Model form uncertainty, Component Mode Synthesis, Structural Dynamics, Built-up structure, Modal characterisation.

Abstract. *The combined use of the component mode synthesis and the probabilistic uncertainty analysis is studied on an industrial structure. Component mode synthesis (CMS) methods are useful for the analysis of structures that are built-up of several components. The components are modeled individually and their dynamic models, represented by modal bases, are assembled to produce a much smaller model of the whole structure. In the component mode synthesis framework, uncertainties in properties can be naturally and straightforwardly introduced at the component level; properties concerned can be either component or joint model parameters, such as material characteristics, or component modal characteristics. Variations on component modal characteristics both reflect the model and parametric component uncertainties.*

The structure considered is a free-free two pump component assembly. The whole pump was designed by SULZER Pumps and is used in EDF thermal units. The two frame and bearing support components are assembled using two bolted joints. The variables of interest are the eigenfrequencies of the built-up structure. The uncertain properties are the eigenfrequencies of the two sub-structures: they are modelled in a probabilistic frame as independent random variables defined on intervals determined as a result of 2008-2010 SICODYN international benchmark.

A Monte Carlo approach with 1000 runs is applied in order to estimate eigenfrequency statistics on the built-up structure. The following tendencies can be shown:

- the coefficient of variation of the assembly eigenfrequency values is much lower than the coefficient of variation introduced in the sub-structure eigenfrequency values;

- the first assembly eigenfrequencies depend on the frame eigenfrequencies and not on the bearing support eigenfrequencies, which is a stiffer component.

The present research work has been carried out within the FUI 2012-2015 SICODYN project.

1 INTRODUCTION

A main objective of industrial companies is to quantify the confidence they have in numerical models used either in design purpose or in expertise purpose. The systems of interest include proposed or existing systems that operate at design conditions, at off-design conditions and at failure-mode conditions that apply in accident scenarios. In particular, the dynamical behaviour of engineered systems that equipped power plants must be confidently predicted. The numerical models built to do so in a design purpose must be able to represent the characteristics of the structure itself, its coupling with its environment, the usually unknown excitations and the corresponding error sources and uncertainties; in an expertise purpose, where measurements can be carried out on the existing structure and used to improve the numerical-experimental correlation, the numerical models are generally generic and must be able to reproduce the behaviour of the whole family of nominally-identical structures. The confidence level of a numerical simulation can be quantified by what is called the total numerical uncertainty, which can be divided into parametrical uncertainty and model form uncertainty. Several methodologies such as the probabilistic, interval or possibilistic analyses are commonly used to a priori determine the uncertainty related to output quantities of interest due to input parameter error or uncertainty. Quantifying the model form uncertainty is not so developed and is generally undirectly performed.

The combined use of the component mode synthesis and the probabilistic uncertainty analysis is a possible way to estimate the total numerical uncertainty. Component mode synthesis (CMS) methods are useful for the analysis of structures that are built-up of several components. The components are modeled individually and their dynamic models, represented by modal bases, are assembled to produce a much smaller model of the whole structure. In the component mode synthesis framework, uncertainties in properties can be naturally and straightforwardly introduced at the component level; properties concerned can be either component or joint model parameters, such as material characteristics, or component modal characteristics. Variations on component modal characteristics both reflect the model and parametric component uncertainties. The method has been presented and tested on academic test cases in [1]; it is here applied on an industrial built-up structure.

After the FUI SICODYN 2012-2015 project is presented, the uncertainty analysis in the framework of component mode synthesis is described. Uncertainty quantification and propagation are applied in view of modal characterisation of a built-up two-component pump assembly. Following are quantitative results and concluding remarks.

2 THE 2012-2015 FUI SICODYN PROJECT

The financed FUI (Fonds Unique Interministériel) project, untitled SICODYN (pour des Simulations crédibles via la COrrélation calculs-essais et l'estimation d'incertitudes en DYnamique des structures) is based on an a complex built-up demonstrator in industrial environment ; it gathers 13 French partners, which are industrials, academic, and small and medium size enterprises (cf. Appendix 1).

2.1 Scientific structuration

The idea underlying the project is to give easy tools, based on tested methodologies, to a priori estimate the confidence associated to a dynamical simulation-based prediction [1, 6]. The general organisation of the 6 parts of the project is described in Fig. 1. In Part 1, an inventory of the benchmarks in structure dynamics and a review of methods which estimate the

total uncertainty (model parameter uncertainty plus model form uncertainty) will be made. Two benchmarks (Parts 2 and 3) will permit to observe the total numerical variability, as in the preceeding SICODYN benchmark [7-9], and the experimental variability, related to nominally-identical structures [10], or different operators. Part 4 will be devoted to test-analysis correlation, using notably a collection of numerical results and a collection of experimental measurements [11]. In Part 5, both parametric and non parametric methods will be confronted in order to quantify the uncertainties, either in a deterministic (method of intervals…) or probabilistic context [12-17].

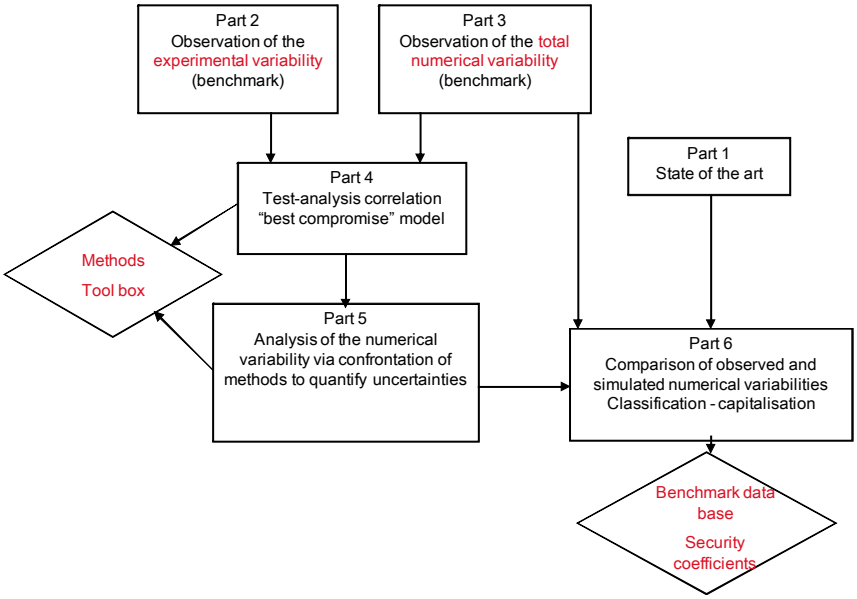


Figure 1: Organisation of the 6 parts of the SICODYN project

In Part 6, the observed (via the benchmark) and simulated (in Part 5) numerical variabilities will be compared. The most appropriate methods, from an industrial point of view, will be retained and possibly derived in simple security coefficients and margins applied in classes of dynamical problems to determine.

2.2 Description of the demonstrator

The chosen equipment is a pump used in EDF thermal units (Fig. 2). It is a one-stage booster pump, composed of a diffuser and a volute, with axial suction and vertical delivery (body with volute called "snail"), mounted on a metallic frame. It was designed forty years ago by Sulzer Pumps.

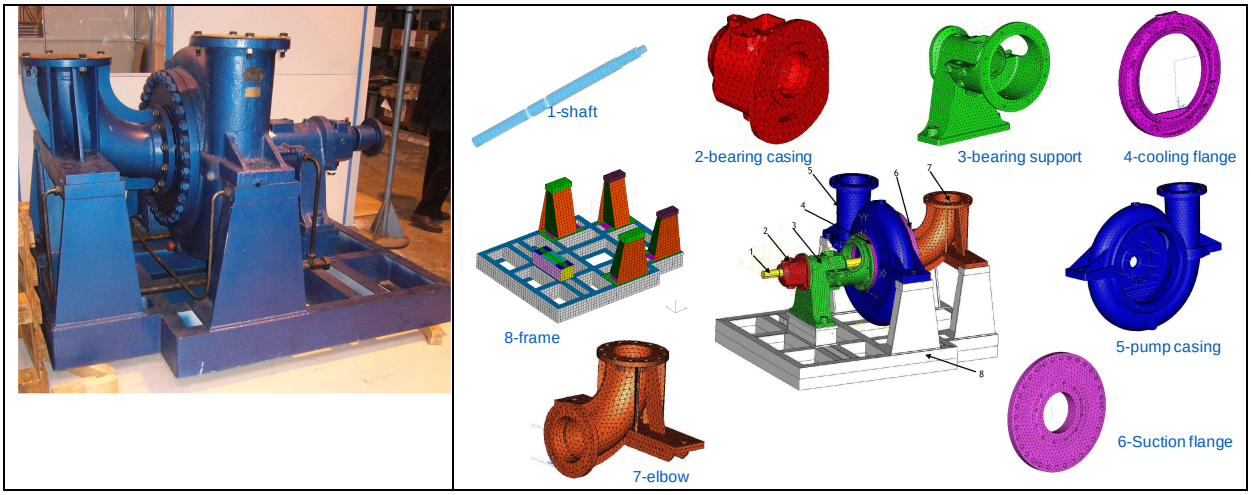


Figure 2: The pump assembly and its main components

3 UNCERTAINTY ANALYSIS AND COMPONENT MODE SYNTHESIS

The component mode synthesis as a framework for uncertainty analysis has been described and applied on academic examples in [1]. The component mode synthesis is a well adapted method to numerically analyse structures that are built-up of several components, as is generally the case in industrial applications. The components are modeled individually and their dynamic models, represented by modal bases, are assembled to produce a much smaller model of the whole structure, and so less time consuming simulations.

A first benefit is, in the context of analysis of structures with uncertain properties, that the computer time related to repeated deterministic problems is drastically reduced, which allows to take into account the statistical independency of the components and the joints. As a consequence, reanalysis, only required for uncertain elements, is less time consuming.

The second benefit is that uncertainties in properties can be naturally and straightforwardly introduced at the component level; properties concerned can be either component or joint model parameters, such as material characteristics, or component modal characteristics. What is making a distinction between well-known methods to estimate parametrical uncertainty estimation and the present methodology is that variations on component modal characteristics both reflect the model and parametric component uncertainties. In that way, it constitutes an original means to take into account the model form uncertainty. Furthermore, one can have a precise idea of the uncertainties related to modal component characteristics, directly issued for instance from variability observed via a numerical benchmark.

Third qualitatively different uncertainty descriptions can be combined, with some components being described probabilistically, some possibilistically. This method has been applied in [1] on an academic test-case.

4 MODAL CHARACTERISATION OF A TWO-COMPONENT PUMP ASSEMBLY USING COMPONENT MODE SYNTHESIS

The dynamical system studied is the assembly of the bearing support and the frame, respectively made of cast iron and steel: their CAD models are shown in the Figure 3. The components are rigidly connected to each other by two bolts; the two-component system is considered in a free-free configuration.

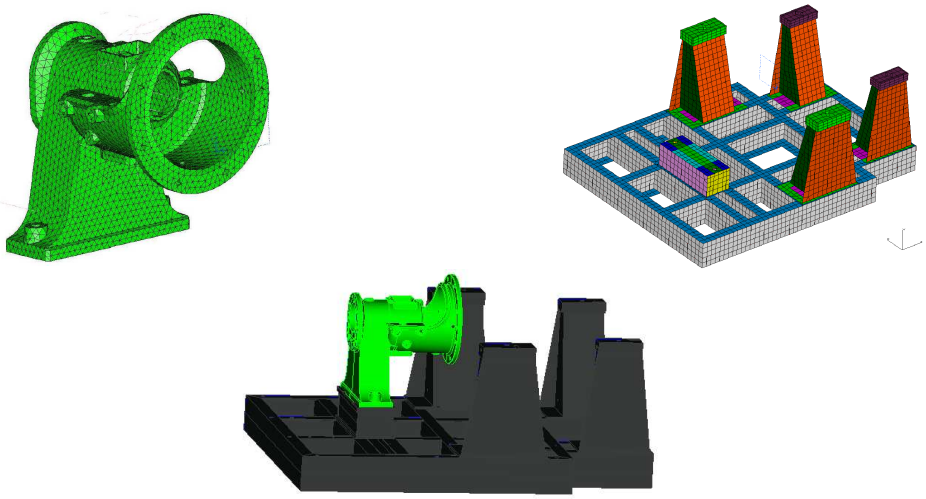


Figure 3: Bearing support and frame CAD models, two-component pump assembly

The modal analysis using component mode synthesis has been carried out with 30 Craig-Bampton interface modes and 20 modes with fixed interfaces for each component. Corresponding modal results are validated by comparison with results issued from direct simulation: the eigenfrequency gap is about 0.1% on the 14 first modes (maximum is 0.2% on the second mode) and the MAC correlation is excellent, as the diagonal MAC values are greater than 0.99 (see Figure 4).

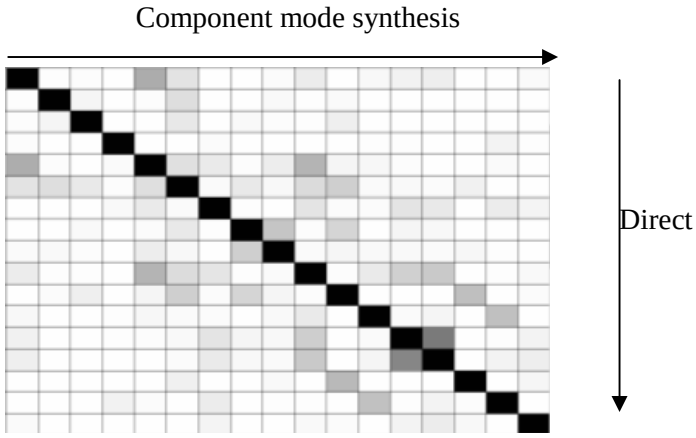


Figure 4: MAC matrix (direct / component mode synthesis)

5 UNCERTAINTY QUANTIFICATION AND PROPAGATION

Uncertainty analysis is performed considering variation in component eigenvalues only, which are supposed to follow a uniform distribution. The variation intervals relative to eigenfrequencies with fixed interfaces have been deduced from variability observed in the numerical benchmark for sub-structures in free-free configuration [7-9].

A Monte Carlo approach with 1000 runs was applied in order to estimate eigenfrequency statistics. Table 1 shows the first eigenfrequency statistics of the two-component assembly function of the eigenfrequency statistics of the components. It can be seen that the coefficient of variation (i.e. ratio of the mean standard deviation to the mean value) of the assembly ei-

genfrequency values is much lower than the variation coefficient introduced in the sub-structure eigenfrequency values.

	Bearing support		Frame		Two-component assembly	
Mode number	Eigenfrequency with fixed interfaces				Free-free eigenfrequency	
	Mean value (Hz)	Coefficient of variation (%)	Mean value (Hz)	Coefficient of variation (%)	Mean value (Hz)	Coefficient of variation (%)
1	91.4	43.2	13.9	103.8	37.6	23.1
2	133.8	46.4	27.6	207.6	48.8	12.8
3	251.1	45.3	35.3	145.3	96.5	6.4
4	262.7	44.3	94.1	69.2	108.7	6.2
5	314.3	43.9	98.9	76.1	116.7	4.6
6	353.1	45.0	103.2	51.9	123.1	3.3
7	523.0	46.7	120.9	44.3	141.7	3.2

Table 1: First eigenfrequency statistics of the two-component assembly function of the eigenfrequency statistics of the components

The sensitivity of the first eigenfrequency of the two-component assembly function of the first two eigenfrequency values of the bearing support and the frame is illustrated in Figure 5. The point cloud shows that there is no dependence of the first eigenfrequency of the assembly function of the bearing support eigenfrequencies; this conclusion is generalized to the other assembly eigenfrequencies.

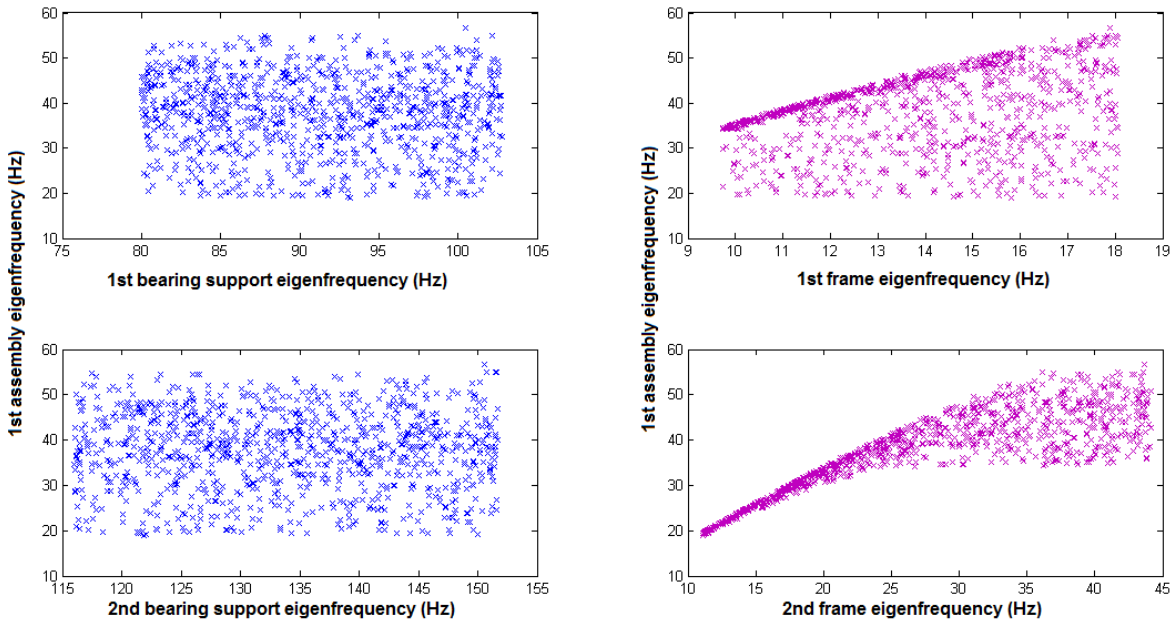


Figure 5: Dependency of the 1st assembly eigenfrequency on the two first component eigenfrequencies

On the other hand, the dependency function of the frame eigenfrequencies is obvious: the first and second assembly eigenfrequencies depend on the two first frame eigenfrequencies (cf.

Fig. 6), the third one depends on the 4th frame eigenfrequency and the fourth one depends on the 3rd frame eigenfrequency. This is related to the fact that the bearing support is much stiffer than the frame, so that the dynamical behaviour of the two-component assembly is essentially directed by the dynamical behaviour of the frame. This indicates that the modal characteristics of the frame must be the more possible precisely determined before studying the modal behaviour of the two-component assembly.

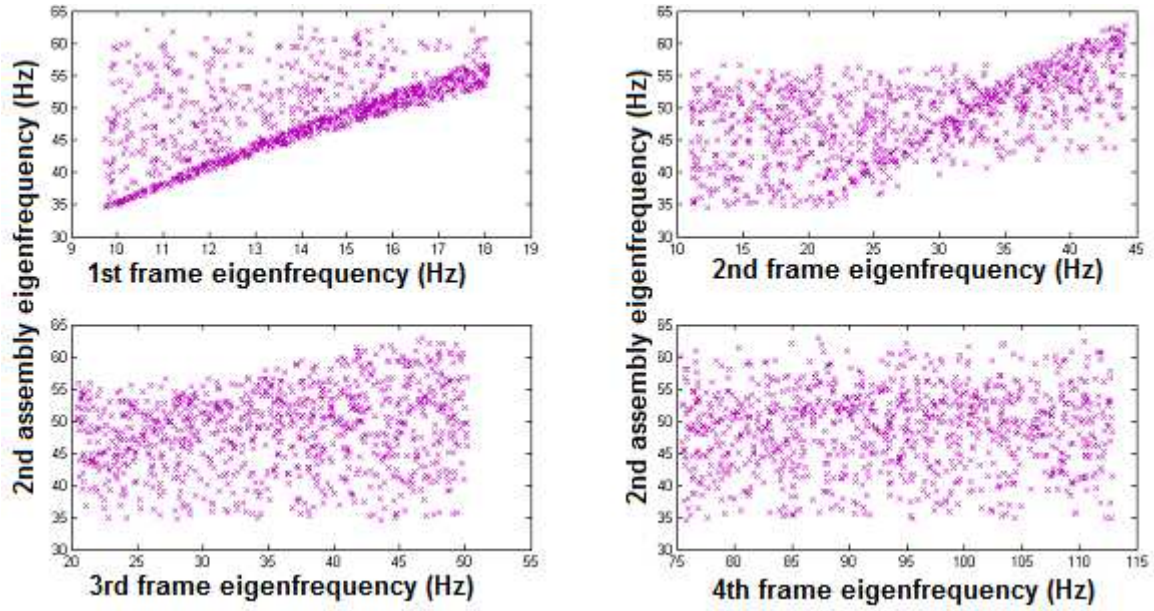


Figure 6: Dependency of the 2nd assembly eigenfrequency on the four first frame eigenfrequencies

6 CONCLUSIONS

The component mode synthesis as a framework for uncertainty analysis, which has been previously described and applied on academic examples in [1], is here tested on an industrial built-up structure. Uncertainty analysis is performed considering variation in component eigenvalues, whose variation intervals have been directly deduced from variability observed in about ten different models built in a previous numerical benchmark. The variability introduced in intermediate result (eigenfrequency) at component level, instead of simply parametrical uncertainty, is a means to represent the total uncertainty, which both reflects the model and parametric component uncertainties.

The application of this framework on a two-component dynamical system permits to show that the dynamical behaviour of the built-up structure is but determined by one sub-structure (frame); furthermore, the dependency of its first eigenfrequency values on the first frame eigenfrequencies can be established. The statistics on the 1000 runs performed give the useful information that the coefficient of variation of the assembly eigenfrequency values is much lower than the coefficient of variation introduced in the frame eigenfrequency values.

Following research will concern the introduction of modeshapes and connection conditions as uncertain properties. When applied to the full pump assembly, comparison with observed variabilities within the benchmark can be performed.

ACKNOWLEDGEMENTS

This research work has been carried out in the context of the FUI 2012-2015 SICODYN Project (pour des Simulations crédibles via la COrrélation calculs-essais et l'estimation d'incertitudes en DYNamique des structures). The support of the FUI (Fonds Unique Interministériel) is gratefully acknowledged.

REFERENCES

[1] L. Hinke, F. Dohnal, B.R. Mace, T.P. Waters, N.S. Ferguson, Component mode synthesis as a framework for uncertainty analysis, *Journal of Sound and Vibration*, 324, 161-178, 2009.

[2] C.J. Roy, W.L. Oberkampf, A comprehensive framework for verification, validation, and uncertainty quantification in scientific computing, *Comput. Methods Appl. Mech. Engrg*. 200 (2011) 2131-2144.

[3] C. Unal, B. Williams F. Hemez, S.H. Atamturktur, P. Mc Clure, Improved best estimate plus uncertainty methodology, including advanced validation concepts, to licence evolving nuclear reactors, *Nuclear Engineering and Design* 241 (2011) 1813-1833.

[4] S. Atamturktur, F. Hemez, B. Williams, C. Tome, C. Unal, A forecasting metric for predictive modelling, Computers and Structures 89 (2011) 2377-2387.

[5] J.R. Langenbrunner, F.M. Hemez, J.M. Booker, T.J. Ross, Model choice considerations and information integration using analytical hierarchy process, Sixth International Conference on Sensitivity Analysis of Model Output, *Procedia Social and Behavioral Sciences* 2 (2010) 7700-7701.

[6] M. Pilch, T.G. Trucano, J.C. Helton, Ideas underlying the quantification of margins and uncertainties, *Reliability Engineering and System Safety* 96 (2011) 965-975.

[7] S. Audebert, SICODYN International Benchmark on dynamic analysis of structure assemblies: variability and numerical-experimental correlation on an industrial pump, *Mécanique et Industries*, 11(6), 439-451, 2010.

[8] S. Audebert, I. Zentner, A. Mikchevitch, Variability and propagation of uncertainties on modal simulations of a built-up structure (SICODYN benchmark), *EURODYN 2011*, Leuwen, Belgium, 4-6 July 2011.

[9] S. Audebert, SICODYN International benchmark on dynamic analysis of structure assemblies: variability and numerical-experimental correlation on an industrial pump (part 2), *XVIIIe Symposium « Vibrations Chocs et Bruit & ASTELAB»*, Clamart, 03-05 July 2012.

[10] A. Batou, C. Soize, M. Corus, Experimental identification of an uncertain computational dynamical model representing a family of structures, *Computers and Structures* 89 (2011) 1440-1448.

[11] Oberkampf W.L., Barone M.F. (2006), Measures of agreement between computation and experiment: validation metrics, *Journal of Computational Physics* 217, 5-36.

[12] B. Van den Nieuwenhof, J.P. Coyette, Modal approaches for the stochastic finite element analysis of structures with material and geometry uncertainties, *Comput. Methods Appl. Mech. Engrg*. 192 (2003) 3705–3729.

[13] D.C. Kammer, S. Nimityonggskul, Propagation of uncertainty in test-analysis correlation of substructured spacecraft, *Journal of Sound and Vibration* 330 (2011) 1211-1224.

[14] M. Guedri, S. Cogan, N. Bouhaddi, Robustness of structural reliability analyses to epistemic uncertainties, *Mechanical Systems and Signal Processing* 28 (2012) 458-469.

[15] A.K. Der Kiureghian, O. Ditlevsen, Aleatory or epistemic? Does it matter?, *Structural Safety* 31 (2009) 105-111.

[16] Hinke L. (2008), Modelling approaches for the low-frequency analysis of built-up structures with non-deterministic properties, *Master Thesis*, University of Southampton, Faculty of Engineering, Science and Mathematics, Institute of Sound and Vibration Research, April 2008.

[17] B.R. Mace, P.J. Shorter (2001), A local modal perturbational method for estimating frequency response statistics of built-up structures with uncertain properties, *Journal of Sound and Vibration* 242(5), 793-811.

Appendix 1

The 13 partners currently involved in 2012-2015 SICODYN project are:

ASTRIUM Space Transportation

CETIM

EDF R&D

LMT ENS Cachan

Institut FEMTO-ST UMR CNRS 6174

LAMCOS UMR CNRS 5259 INSA Lyon

NECS Numerical Engineering and Consulting Service

PHIMECA Engineering

SAMTECH

SOPEMEA

SULZER Pompes France

MSME UMR-CNRS 8208

VIBRATEC

COMPDYN 2013
4th ECCOMAS Thematic Conference on
Computational Methods in Structural Dynamics and Earthquake Engineering
M. Papadrakakis, V. Papadopoulos, V. Plevris (eds.)
Kos Island, Greece, 12–14 June 2013

DYNAMICAL BEHAVIOR OF TRAINS EXCITED BY A NON-GAUSSIAN VECTOR VALUED RANDOM FIELD.

G. Perrin[1,2,3], C. Soize[1], D. Duhamel[2], and C. Funfschilling[3]

[1]Université Paris-Est, Modélisation et Simulation Multi-Échelle (MSME UMR 8208 CNRS).
5 Bd. Descartes, 77454 Marne-la-Vallée, France.
e-mail: guillaume.perrin@enpc.fr, christian.soize@univ-paris-est.fr

[2] Université Paris-Est, Navier (UMR 8205 ENPC-IFSTTAR-CNRS).
Ecole Nationale des Ponts et Chaussées, 6 et 8 Avenue Blaise Pascal, Cité Descartes, Champs sur Marne, 77455 Marne-la-Vallée, Cedex 2, France.
e-mail: denis.duhamel@enpc.fr

[3]SNCF, Innovation and Research Department.
Immeuble Lumière, 40 avenue des Terroirs de France, 75611, Paris, Cedex 12, France.
e-mail: christine.funfschilling@sncf.fr

Keywords: Karhunen-Loève Reduction, Polynomial Chaos Expansion, Random fields, Railway Track Geometry.

Abstract. *Since 2012, European high speed railway networks are meant to have gone to market. Hence, several high speed trains, such as ICE, TGV, ETR 500, Sapsan..., are likely to run on the same tracks, whereas they have been originally designed for specific and different railway networks. Due to different mechanical properties and structures, the dynamic behaviors, the agressiveness of the vehicle on the track and the probabilities of exceeding security and comfort thresholds will be very different from one train to an other. These maintenance, certification and comfort criteria depend on the dynamic interaction between the vehicle and the railway track and in particularly on the contact loads between the wheels and the rail, which are very hard to evaluate experimentally. Therefore, the numerical simulation is bound to play a key role in this context, as it is able to compute these quantities of interest. Nevertheless, the track-vehicle system being strongly non-linear, this dynamic interaction has to be analyzed not only on a few track portions but on the whole realm of possibilities of running conditions that the train is bound to be confronted to during its lifecycle. In reply to this concern, this paper presents a method to analyze the influence of the track geometry variability on the train behavior, which could be very useful to evaluate and compare the agressiveness of different trains. This method is based on a stochastic modeling of the track geometry, for which parameters have been identified with experimental measurements.*

1 INTRODUCTION

If simulation is introduced in certification and conception processes, it has to be very representative of the physical behaviour of the system. The model has thus to be fully validated and the simulations have to be raised on a realistic and representative set of excitations.

Hence, this work presents a three steps method to characterize the influence of the track geometry on the train dynamics. The first step, which is presented in Section 2, corresponds to the classical description of the studied mechanical problem. A particuler attention has to be paid to the definition of the quantities of interest, as this choice will play a major role on the propagation method. Then, Section 3 deals with the characterization of the input variability. At last, Section 3 presents the propagation of the variability through the mechanical system. Two applications of the method will then be analyzed: the influence of an increase of the speed on the train stability and the quantification of the agressiveness of three high speed trains that have different mechanical properties.

2 STEP A: DESCRIPTION OF THE STOCHASTIC MECHANICAL MODELING

This section is devoted to the description of the stochastic modeling of the railway system.

2.1 Description of the railway dynamic problem

As presented in Introduction, a railway dynamic problem can be seen as the excitation of the train by the track geometry through the wheel/rail contact forces, where the wheel/rail contact forces are computed from the wheel profile and the rail profile thanks to the Hertz and Kalker theories. The dynamic $(u_i(t), \dot{u}_i(t))$ of each mass body i of the train at each time step $t \geq 0$, that we describe by the vector of the generalized coordinates,

$$\boldsymbol{U}(t) = (u_1(t), u_2(t), \cdots, \dot{u}_1(t), \dot{u}_2(t), \cdots), \tag{1}$$

can therefore be determined by solving the Euler-Lagrange equation, which reads:

$$\frac{d}{dt}\left(\frac{\partial E_c}{\partial \dot{u}_i}\right) - \frac{\partial E_c}{\partial u_i} = L_i(\boldsymbol{U}, \mathcal{T}), \tag{2}$$

with E_c the total kinetic energy of the train, and $L_i(\boldsymbol{U}, \mathcal{T})$ the general load that is applied to the mass body i, which depends on the track geometry $\mathcal{T}$ and on the generalized coordinates $\boldsymbol{U}$. Eq. (2) can be rewritten in a matricial form as:

$$[A(\boldsymbol{U})]\dot{\boldsymbol{U}} = \boldsymbol{F}(\boldsymbol{U}, \mathcal{T}), \tag{3}$$

with $[A]$ and $\boldsymbol{F}$ two strongly **non-linear** operators. This system is usually solved with an explicit scheme.

The generalized coordinates $\boldsymbol{U}$, for which evolution is computed from Eq. (3), are then post-treated to define the final outputs of the railway simulation. In this work, three criteria are introduced to analyze the vehicule dynamics on a given track geometry of total length S^{tot}:

- a shifting criterion:

$$(Y_\ell + Y_r)_{max} = \max_{\text{wheelset } w} \max_{0 \leq s \leq S^{\text{tot}}} \left\{Y_\ell^w(s) + Y_r^w(s)\right\}, \tag{4}$$

- a derailment criterion:

$$(Y/Q)_{max} = \max_{\text{wheel } q} \max_{0 \leq s \leq S^{\text{tot}}} \{Y_q(s)/Q_q(s)\}, \tag{5}$$

- a wear criterion:

$$(T\gamma) = \sum_{\text{wheel } q} \int_0^{S^{\text{tot}}} T_q(s)\gamma_q(s)ds, \tag{6}$$

where:

- Y_ℓ^k and Y_r^k are the left and right lateral forces of the same wheelset k, such that the higher $(Y_\ell + Y_r)_{max}$ is, the more chance for a shifting of the track there is;
- Y_q and Q_q are the lateral and vertical components of the wheel/rail contact force at wheel q, such that the higher $(Y/Q)_{max}$ is, the more on the flange a wheel of the train can be;
- T_q and γ_q are respectively the creep force and the slip at wheel q, such that the higher $(T\gamma)$ is, the higher the contact wear is likely to be for one run of the complete train.

Finally, the deterministic railway problem, corresponding to the dynamics of a vehicle $\mathcal{V}$ on a track geometry $\mathcal{T}$ can be expressed as:

$$(\mathcal{V}, \mathcal{T}) \mapsto \boldsymbol{c} = \boldsymbol{g}(\mathcal{V}, \mathcal{T}), \quad \boldsymbol{c} = ((Y_\ell + Y_r)_{max}, (Y/Q)_{max}, (T\gamma)), \tag{7}$$

where it is reminded that $\boldsymbol{g}$ is a complex and non-linear operator.

2.2 Stochastic problem

In this work, it is supposed that a normalized model of a train is available, for which mechanical parameters are fixed and have been accurately identified. Moreover, two description scales can be distinguished for the track geometry:

- on the first hand, the track design, which corresponds to the parameters of the mean line position, that is to say the vertical curvature c_V, the horizontal curvature c_H, and the track superelevation c_L, is decided once for all at the building of a new track for economical and political reasons;
- on the second hand, for a fixed track design, the track irregularities are in constant evolution, due to the interactions between the train and the track, to the maintenance operations, and to the wheather conditions. There are four kinds of track irregularities: the horizontal and vertical alignment irregularities, x_1 and x_2, the cant deficiencies x_3, and the alignement irregularities x_4.

It is supposed in this work that the track irregularities characterization can be separated from the track design description. Hence, in the following, a measured track design is chosen and only the track irregularities will be supposed to be variable. In this prospect, let

$\boldsymbol{X} = (X_1, X_2, X_3, X_4)$ be the vector-valued random field corresponding to the four track irregularities, for which statistical characteristics have to be identified from experimental data. As a consequence, vector $\boldsymbol{c}$, which gathers the three criteria of interest, becomes a random vector $\boldsymbol{C}$, and the stochastic problem can be expressed by:

$$\boldsymbol{X} \mapsto \boldsymbol{C} = \boldsymbol{G}(\boldsymbol{X}). \tag{8}$$

The choice of the quantities of interest is crucial as it will rule the choice of the propagation method. In this work, we are interested in the PDF of each criterion, that are denoted by p_{C_i}, $1 \leq i \leq 3$.

3 STEP B: CHARACTERIZATION OF THE INPUT VARIABILITY

We assume in this work that the track irregularities can be seen as a vector-valued random field, $\boldsymbol{X} = (X_1, X_2, X_3, X_4)$, which gathers the four kinds of track irregularities. Characterizing the input variability of the railway stochastic problem amounts thus to identifying the distribution of $\boldsymbol{X}$ from experimental measurements.

To this end, the measurement train IRIS 320 has been running continuously since 2007 over the French railway network, measuring and recording the track geometry of the main national lines. Based on these experimental measurements, this section aims at developing a methodology to parameterize the physical properties as well as the variability of track irregularities random field $\boldsymbol{X}$. This modeling will allow the numerical generation of track geometries that are physically realistic and statistically representative of a whole railway network.

3.1 Local-global approach and available information

In this work, it is supposed that the track irregularities of a whole high speed line of total length S^{tot} has been measured. The track irregularity vector,

$$\left\{\boldsymbol{X}(s) = (X_1(s), X_2(s), X_3(s), X_4(s)),\ s \in [0, S^{\text{tot}}]\right\}, \tag{9}$$

is a random field with values in $\mathbb{R}^4$, for which realizations are continuous functions. It is moreover assumed that $\boldsymbol{X}$ is a centered random field, such that:

$$E[\boldsymbol{X}(s)] = \boldsymbol{0}, \quad s \in [0, S^{\text{tot}}], \tag{10}$$

with $E[\cdot]$ the mathematical expectation.

Due to the specific interaction between the train and the track, this random field is neither Gaussian nor stationary, which motivates a local-global approach for the characterization of the distribution of $\boldsymbol{X}$. This approach is based on the hypothesis that a whole railway track can be considered as the concatenation of a series of independent track portions of same length S, for which physical and statistical properties are the same. Therefore, this asumption should allow us to reduce the complexity of the problem, by restricting the characterization of $\boldsymbol{X}$ to its projection on the interval $\Omega = [0, S]$, with $S \ll S^{\text{tot}}$. Length S plays therefore a key role in the modeling procedure, and its value has to be carefully evaluated. Indeed, S has to be long enough for the statistical and spectral information of $\boldsymbol{X}$ to be accurately taken into account. However, the higher S is, the little number of independent realizations for $\boldsymbol{X}$ can be extracted from the complete measurement of the railway network.

For confidentiality reasons, length S is not given in this work, and it is assumed that it has been carefully chosen as an optimum of the compromise between computational cost and modeling precision. In the same manner, the spatial quantities will be normalized by length S in the following.

Under the local-global hypothesis, it is now supposed that $\nu^{\exp}$ track portions of same length S, that are denoted by $\left\{\boldsymbol{x}^1, \cdots, \boldsymbol{x}^{\nu^{\exp}}\right\}$, can be extracted from the experimental measurements. It is reminded that these measurements are supposed to be $\nu^{\exp}$ independent realizations of random field $\boldsymbol{X}$, which defines the maximum available information for the stochastic modeling of the track geometry.

3.2 Track geometry stochastic modeling

3.2.1 Definition of the local model

The objective of the stochastic modeling is to identify in inverse the statistical properties of $\boldsymbol{X}$ from its $\nu^{\exp}$ independent realizations. This modeling is based on a two steps decomposition. First, a Karhunen-Loève (KL) expansion is performed (see [1, 2, 3, 4, 5, 6, 7, 8, 9, 10, 11, 12, 13, 14, 15, 16, 17, 18, 19] for further details):

$$\boldsymbol{X} = \sum_{k=1}^{+\infty} \sqrt{\lambda_k}\boldsymbol{u}^k \, \eta_k, \tag{11}$$

where couples $(\boldsymbol{u}_k, \lambda_k)$ are solution of the Fredholm eigenvalue problem, such that for all $(s, s') \in \Omega \times \Omega$:

$$E\left[\boldsymbol{X}(s)\boldsymbol{X}(s')^T\right] \approx [R_{\boldsymbol{XX}}(s, s')] = \frac{1}{\nu^{\exp}} \sum_{i=1}^{\nu^{\exp}} \boldsymbol{x}^i(s) \left(\boldsymbol{x}^i(s')\right)^T, \tag{12}$$

$$\int_\Omega [R_{\boldsymbol{XX}}(s, s')]\boldsymbol{u}^k(s)ds = \lambda_k \boldsymbol{u}^k(s'), \tag{13}$$

$$\int_\Omega \boldsymbol{u}^k(s)\boldsymbol{u}^\ell(s)ds = \delta_{k\ell}, \quad \lambda_1 \geq \lambda_2 \geq \ldots \to 0, \tag{14}$$

where $\delta_{k\ell}$ is the Kronecker symbol, equal to one if $k = \ell$ and zero otherwise, and $\{\eta_1, \eta_2, \ldots\}$ are uncorrelated but *a priori* dependent random variables that verify by construction the following equalities:

$$E\left[\eta_k \eta_\ell\right] = \delta_{k\ell}. \tag{15}$$

As an illustration, a particular projection of the empirical estimation of the covariance matrix-valued function of $\boldsymbol{X}$, $[R_{\boldsymbol{XX}}]$, is represented in Figures 1, whereas four particular eigenfunctions, $\boldsymbol{u}^1$, $\boldsymbol{u}^5$, $\boldsymbol{u}^{10}$ and $\boldsymbol{u}^{25}$, are shown in Figure 2. It can be noticed that the vectorial approach allows us to take into account the spatial dependencies between the different track irregularities.

From a practical point of view, this sum is truncated to its N_η most influential terms:

$$\boldsymbol{X} \approx \boldsymbol{X}^{(N_\eta)} = \sum_{k=1}^{N_\eta} \sqrt{\lambda_k}\boldsymbol{u}^k \, \eta_k, \tag{16}$$

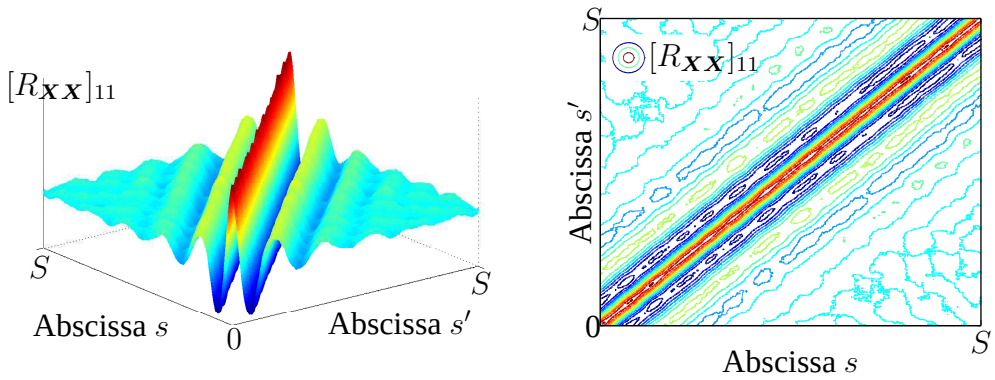


Figure 1: Graphs of $[R_{\boldsymbol{XX}}]_{11}$.

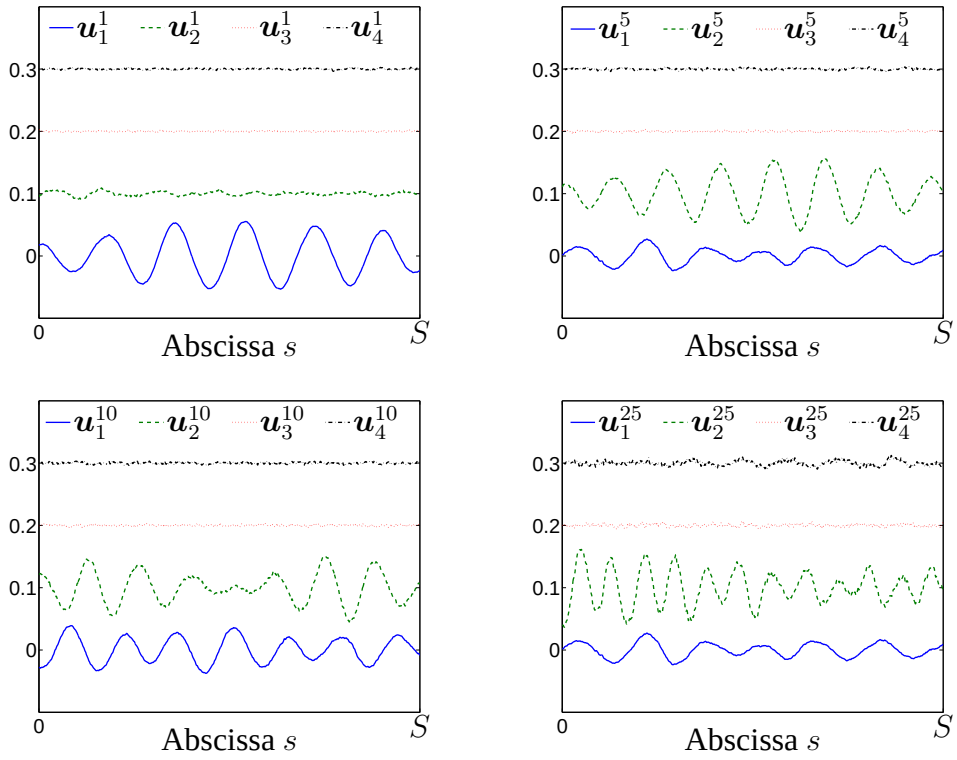


Figure 2: Graphs of four particular eigenvectors $\boldsymbol{u}^1$, $\boldsymbol{u}^5$, $\boldsymbol{u}^{10}$ and $\boldsymbol{u}^{25}$ ($\times 10^{-3} S$).

where the amplitude of the truncation residue, $\boldsymbol{X} - \boldsymbol{X}^{(N_\eta)}$, is evaluated by the normalized L_2 error, $\varepsilon_{KL}^2(N_\eta)$, such that:

$$\varepsilon_{KL}^2(N_\eta) = \frac{\left\| \boldsymbol{X} - \boldsymbol{X}^{(N_\eta)} \right\|_2^2}{\|\boldsymbol{X}\|_2^2} = 1 - \frac{\sum_{k \leq N_\eta} \lambda_k}{\|\boldsymbol{X}\|_2^2}, \tag{17}$$

where for all second order and mean-square continuous vector-valued random field $\boldsymbol{Z}$,

$$\|\boldsymbol{Z}\|_2^2 = E\left[\int_\Omega \int_\Omega \boldsymbol{Z}(s)^T \boldsymbol{Z}(s') ds ds' \right]. \tag{18}$$

The higher N_η, the more precise the characterization of the track geometry, but the more difficult the characterization of the random vector $\boldsymbol{\eta} = \left(\eta_1, \ldots, \eta_{N_\eta}\right)$. As a good compromise, the truncation parameter N_η is fixed to the value 940 in the following, which corresponds to an error threshold of 1% for ε_{KL}^2.

The second step of the modeling of $\boldsymbol{X}$ is the characterization in inverse of the multidimensional probability density function (PDF) of $\boldsymbol{\eta}$, $p_{\boldsymbol{\eta}}$. In this prospect, a polynomial chaos expansion (PCE) method (see [20, 21, 22, 23, 24, 25, 26, 27, 28, 29, 30] for further details about the PCE identification in inverse) is used, which corresponds to a direct projection of $\boldsymbol{\eta}$ on a chosen polynomial hilbertian basis $\mathcal{B}_{\text{orth}} = \{ \psi_j(\boldsymbol{\xi}),\ 1 \leq j \}$ of all the second-order random vectors with values in $\mathbb{R}^{N_\eta}$, such that:

$$\boldsymbol{\eta} = \sum_{j=1}^{+\infty} \boldsymbol{y}^{(j)} \psi_j(\boldsymbol{\xi}). \tag{19}$$

This sum is once again truncated with respect to two truncation parameters, N and N_g, such that:

$$\boldsymbol{\eta} \approx \boldsymbol{\eta}^{\text{chaos}}(N) = \sum_{j=1}^{N} \boldsymbol{y}^{(j)} \psi_j(\xi_1, \ldots, \xi_{N_g}), \tag{20}$$

where projection basis $\left\{\psi_1(\xi_1, \ldots, \xi_{N_g}), \cdots, \psi_N(\xi_1, \ldots, \xi_{N_g})\right\}$ is now defined as the set gathering the N polynomial functions of total degree inferior to p, which are normalized with respect to the PDF $p_{\xi_1,\ldots,\xi_{N_g}}$ of $\left(\xi_1, \ldots, \xi_{N_g}\right)$:

$$\psi_j(\xi_1, \ldots, \xi_{N_g}) = \sum_{q=1}^{N} c_{qj}\ \xi_1^{\alpha_1^{(q)}} \times \cdots \times \xi_{N_g}^{\alpha_{N_g}^{(q)}}, \quad \sum_{\ell=1}^{N_g} \alpha_\ell^{(q)} \leq p, \tag{21}$$

$$\int_{\mathbb{R}^{N_g}} \psi_j(\boldsymbol{x}) \psi_n(\boldsymbol{x}) p_{\xi_1,\ldots,\xi_{N_g}}(\boldsymbol{x}) d\boldsymbol{x} = \delta_{jn}. \tag{22}$$

For given values of N and N_g, identifying the distribution of $\boldsymbol{\eta}^{\text{chaos}}(N)$ amounts therefore to identifying the values of the PCE projection coefficients, $\left\{\boldsymbol{y}^{(j)},\ 1 \leq j \leq N\right\}$, from the available information about $\boldsymbol{\eta}$. According to Eqs. (11), (14) and (15), this available information corresponds to the ν^{exp} independent realizations of $\boldsymbol{\eta}^{\text{chaos}}(N)$, $\{\boldsymbol{\eta}^1, \cdots, \boldsymbol{\eta}^{\nu^{\text{exp}}}\}$, which can be deduced from the ν^{exp} independent realizations of $\boldsymbol{X}$, $\{\boldsymbol{x}^1, \cdots, \boldsymbol{x}^{\nu^{\text{exp}}}\}$, such that:

$$\eta_k^i = \frac{1}{\sqrt{\lambda_k}} \int_\Omega \left(\boldsymbol{x}^i(s)\right)^T \boldsymbol{u}^k(s) ds,\ \ 1 \leq i \leq \nu^{\text{exp}},\ \ 1 \leq k \leq N_\eta. \tag{23}$$

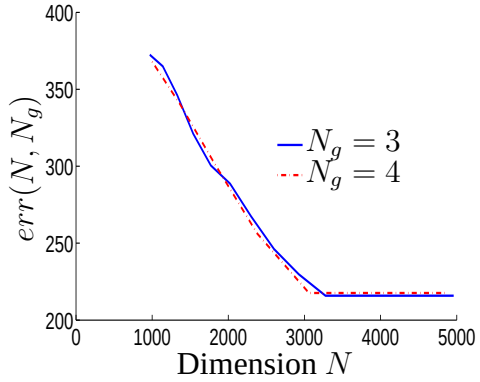


Figure 3: Convergence analysis for the PCE expansion of $\boldsymbol{\eta}$.

In [28, 29], it has been shown that a good approach to identify such coefficients is to search them as the arguments that maximize the likelihood of random vector $\boldsymbol{\eta}^{\text{chaos}}(N)$ at the experimental points $\{\boldsymbol{\eta}^1, \cdots, \boldsymbol{\eta}^{\nu^{\text{exp}}}\}$.

Finally, the last step of the identification of the distribution of $\boldsymbol{\eta}^{\text{chaos}}(N)$ is the justification of the values for the truncation parameters N and N_g. In this prospect, the log-error function $err(N, N_g)$ is introduced to quantify the amplitude of the residue of the PCE truncation, $\boldsymbol{\eta} - \boldsymbol{\eta}^{\text{chaos}}(N)$, such that:

$$err(N, N_g) = \sum_{k=1}^{N_\eta} err_k(N, N_g), \tag{24}$$

$$err_k(N, N_g) = \int_{\text{BI}_k} \left| log_{10}\left(p_{\eta_k}(x_k)\right) - log_{10}\left(p_{\eta_k^{\text{chaos}}}(x_k)\right) \right| dx_k, \tag{25}$$

where BI_k is the domain bounding the experimental values of η_k, p_{η_k} and $p_{\eta_k^{\text{chaos}}}$ are the PDFs of η_k and $\eta_k^{\text{chaos}}(N)$ respectively. Truncation parameters N and N_g can thus be chosen with respect to a given error threshold for $err(N, N_g)$.

For our study, $\boldsymbol{\xi}$ is a N_g-dimension random vector, whose components are independent and uniformly distributed between -1 and 1. According to Figure 3, which represents the convergence of error function $err(N, N_g)$ with respect to N and N_g, truncation parameters N and N_g are chosen equal to $3,276$ and 3 respectively.

To conclude, once truncation parameters N_η, N, N_g have been identified according to convergence analysis, once PCE projection coefficients $\left\{\boldsymbol{y}^{(j)},\ 1 \leq j \leq N\right\}$ have been computed with the advanced algorithms described in [29] and [28], the track irregularity random field is completely characterized and can finally be estimated as:

$$\boldsymbol{X} \approx \sum_{k=1}^{N_\eta} \sqrt{\lambda_k}\boldsymbol{u}^k \sum_{j=1}^{N} y_k^{(j)} \psi_j(\xi_1, \ldots, \xi_{N_g}). \tag{26}$$

For each realization of random vector $(\xi_1, \ldots, \xi_{N_g})$, a representative and realistic track geometry of length S can finally be generated.

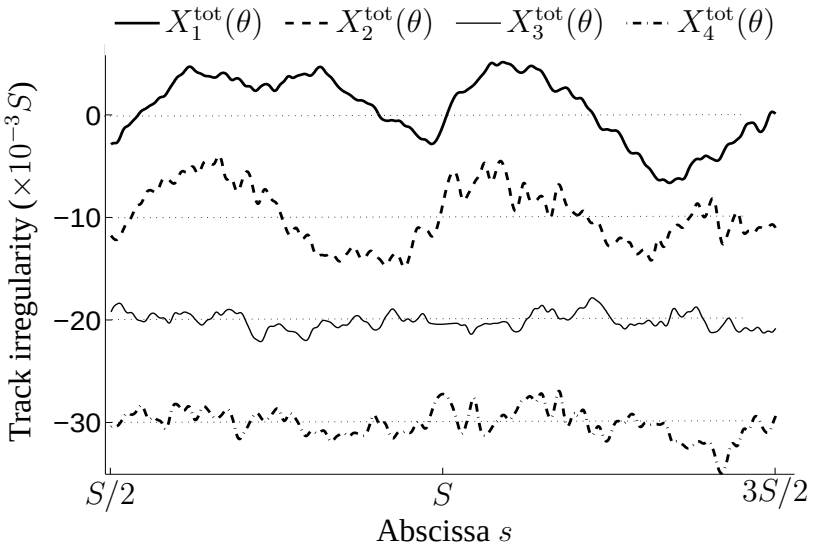


Figure 4: Extract of a simulated track geometry.

3.2.2 Definition of the global model

According to Section 2 and to the local-global hypothesis, a realistic track geometry of length $S^{\mathrm{tot}} = N_{\mathcal{T}} S$ can be generated from the concatenation of $N_{\mathcal{T}}$ track geometries of same length S. However, a particular attention has to be paid to the interface between two different realizations of $\boldsymbol{X}$. Indeed, these junctions have to guarantee the continuity of the track irregularity vector and at least the continuity of its first and second order spatial derivatives in order to avoid an artificial perturbation of the train dynamics. Spline interpolations on a length corresponding to the minimal wavelength of the measured irregularities are then used to fulfill these continuity conditions.

From the local stochastic modeling developed in Section 3.2.1, it is now possible to generate track geometries of length S^{tot}, which are representative of the whole track geometry of the measured high speed line. As an illustration, an extract of length S of a complete generated track geometry $\boldsymbol{X}^{\mathrm{tot}}(\theta)$ is represented in Figure 4. This graph is centered at a junction between the two first realizations that stem from the local stochastic modeling of $\boldsymbol{X}$. The values of the four irregularity fields, for which mean value is zero, have been translated on purpose to allow a better visualization of the results.

4 STEP C: PROPAGATION OF THE TRACK VARIABILITY TO THE TRAIN RESPONSE

Sections 2 and 3 have presented the railway stochastic modeling and the characterization of the input variability. This variability has now to be propagated through the model. After presenting the chosen method for this propagation, this Section describes two applications of the whole method. The first one analyses the influence of an increase of the train speed on the three criteria of interest. The second one underlines in what extent such methods can be used to compare the dynamical response of different high speed trains.

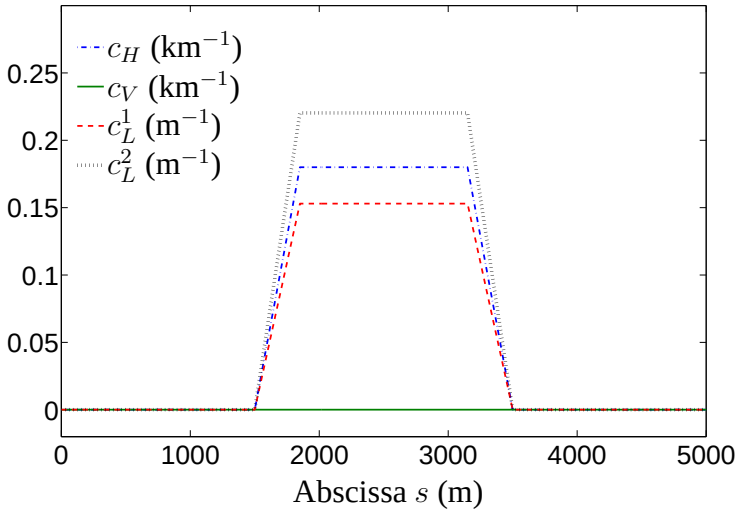


Figure 5: Track Design of the simulated railway track.

4.1 Monte Carlo simulation

From Section 2, three outputs of the railway simulation are studied in this work: a shifting criterion, $C_1 = (Y_\ell + Y_r)_{max}$, a derailment criterion, $C_2 = (Y/Q)_{max}$, and a wear criterion, $C_3 = (T\gamma)$.

As the relation between the three criteria and the track irregularity random field, $\boldsymbol{X}$, is very complex and strongly non-linear, the Monte Carlo method is a good approach to characterize the statitical properties of C_1, C_2 and C_3, as the convergence of these properties is independent of the statistical dimension, N_η, of the KL approximation of $\boldsymbol{X}$ that is very high.

In this prospect, a measured track design of length $5km$ around a high speed line horizontal curve is considered. The track superelevations c_L^1 and c_L^2 have been introduced to compensate the inertial acceleration in curve for a train that runs at speeds $\mathcal{S}$ and $1.2\mathcal{S}$ respectively. For confidentiality reasons, the value of $\mathcal{S}$ is not given in this paper. Then, $\nu = 500$ independent track irregularities, $\left\{\boldsymbol{X}^{\text{tot}}(\theta_1), \ldots, \boldsymbol{X}^{\text{tot}}(\theta_\nu)\right\}$, of total length $5km$ are generated thanks to the local-global approach and to the stochastic modeling of random field $\boldsymbol{X}$ on a length S, such that $\nu = 500$ realistic and representative running conditions around the same curve are available.

Coupled to the model of a train, these geometries can now be used in any rigid-multibodies railway software to characterize its dynamic behavior. For our study, a commercial code, which is called Vampire, has been used.

4.2 Influence of an increase of the speed on the quantities of interest

The first application of the whole method deals with the influence of the speed on the distributions of the three criteria considered for a normalized high speed train. Railway simulations are therefore performed on the same ν realistic and representative track geometries, at the four speeds $\mathcal{S}1 = \mathcal{S}$, $\mathcal{S}2 = 1.1\mathcal{S}$, $\mathcal{S}3 = 1.2\mathcal{S}$ and $\mathcal{S}4 = 1.3\mathcal{S}$. Two other sets of simulations have then been carried out for a different value of the track superelevation at speeds $\mathcal{S}3 = 1.2\mathcal{S}$ and $\mathcal{S}4 = 1.3\mathcal{S}$ in order to quantify the importance of this track design parameter with respect to the three criteria studied.

For each speed, the PDFs of each criterion C_1, C_2 and C_3 are then estimated using kernel smoothing on the $\nu = 500$ independent railway simulations. These PDFs are represented in

Figure 7. In this figure, the non-linearity of the system can be noticed, as the consequences of an increase of the speed of 10% to 30% are much higher than 30% for each criterion considered. In particular, an increase of 30% of the speed of the train can lead to an increase of more than 500% of the contact wear if the track superelevation is not adjusted. In addition, this figure emphasizes the importance of the adjustment of the track superelevation to the speed, in terms of minization of the wear, of the shifting risk and of the risk of derailment.

4.3 Comparison of three high speed trains

In this section, it is supposed that three different models of three concurrential high speed trains, $\mathcal{V}1$, $\mathcal{V}2$ and $\mathcal{V}3$ are available, for which parameters have been carefully identified from experimental measurements. Therefore, the method proposed in this paper allows us to compare the dynamical response of these three trains when they are excited at speed $\mathcal{S}$, by a representative set of the variable track conditions they can be confronted to during their lifecycle. The results of this analysis are shown in Figure 7. In particular, criteria C_1 and C_3 could be interessant indicators to compare the agressiveness of each train, whereas criterion C_2 could be used to quantify the global stability in curve of each train.

5 CONCLUSIONS

A method to propagate the track geometry variability through railway mechanical simulations is nowadays of great interest to face always more challenging railway issues. In this prospect, this paper has presented a general method to completely parametrize the track geometry and its variability. This method is based on a local-global approach, and a double projection, which can be applied to many other mechanical systems. First, a Karhunen-Loeve expansion is used to decompose the projection of the random field as a truncated weighted sum of deterministic spatial functions, for which weights are *a priori* dependent but uncorrelated random variables. The distribution of the high dimension random vector that gathers all these weights is then characterized thanks to a truncated PCE. At last, complete track geometries that are realistic and representative of a whole railway network can be generated. These geometries can finally be used in any railway software to characterize the dynamic behavior of trains. To this end, two applications of the whole method have been described in this paper. The first one analyses the impact of an increase of the speed on the train stability, whereas the second one shows in what extent such an approach could be used to compare competitive high speed trains with respect to their response on a set of representative track conditions.

REFERENCES

[1] C. Allery, A. Hambouni, D. Ryckelynck, and N. Verdon. A priori reduction method for solving the two-dimensional burgers' equations. *Applied Mathematics and Computation*, 217:6671–6679, 2011.

[2] J.A. Atwell and B.B. King. Proper orthogonal decomposition for reduced basis feedback controllers for parabolic equations. *Math. Comput. Modell.*, 33 (1-3):1–19, 2001.

[3] G. Berkooz, P. Holmes, and J.L. Lumley. The proper orthogonal decomposition in the analysis of turbulent flows. *Annu. Rev. Fluid Mech.*, 25:539–575, 1993.

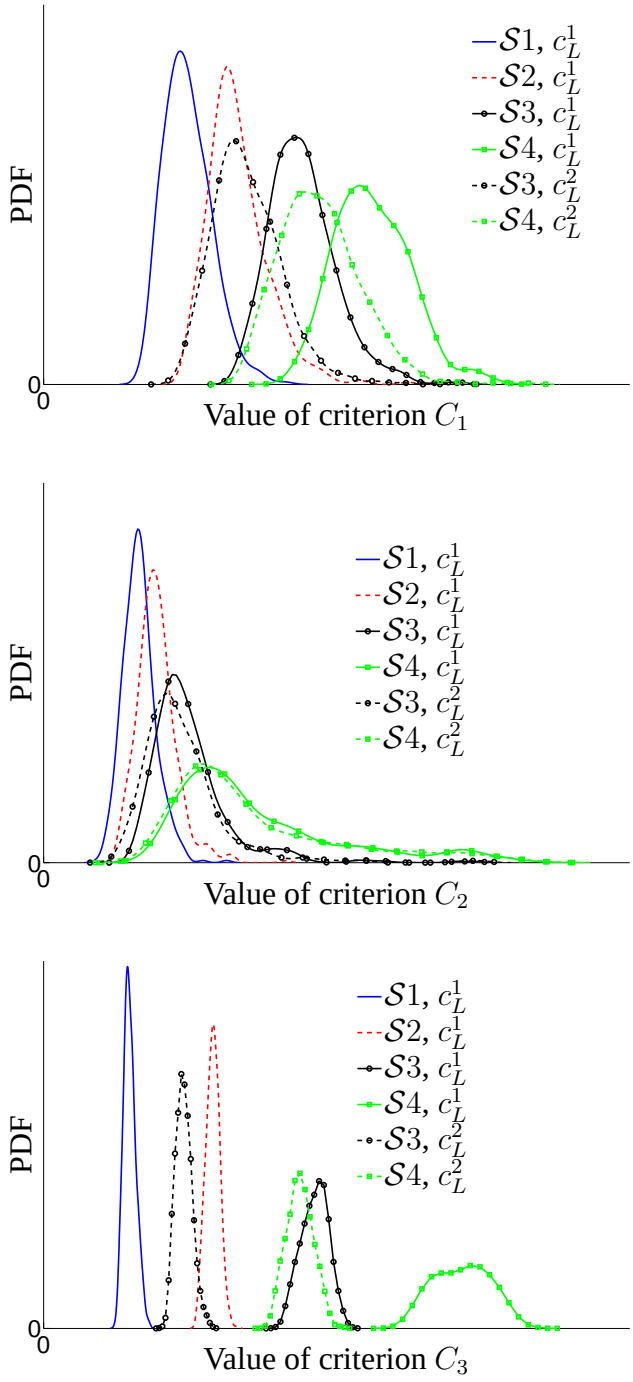


Figure 6: Representation of the evolutions of the PDFs of the three criteria considered with respect to an increase of the train speed.

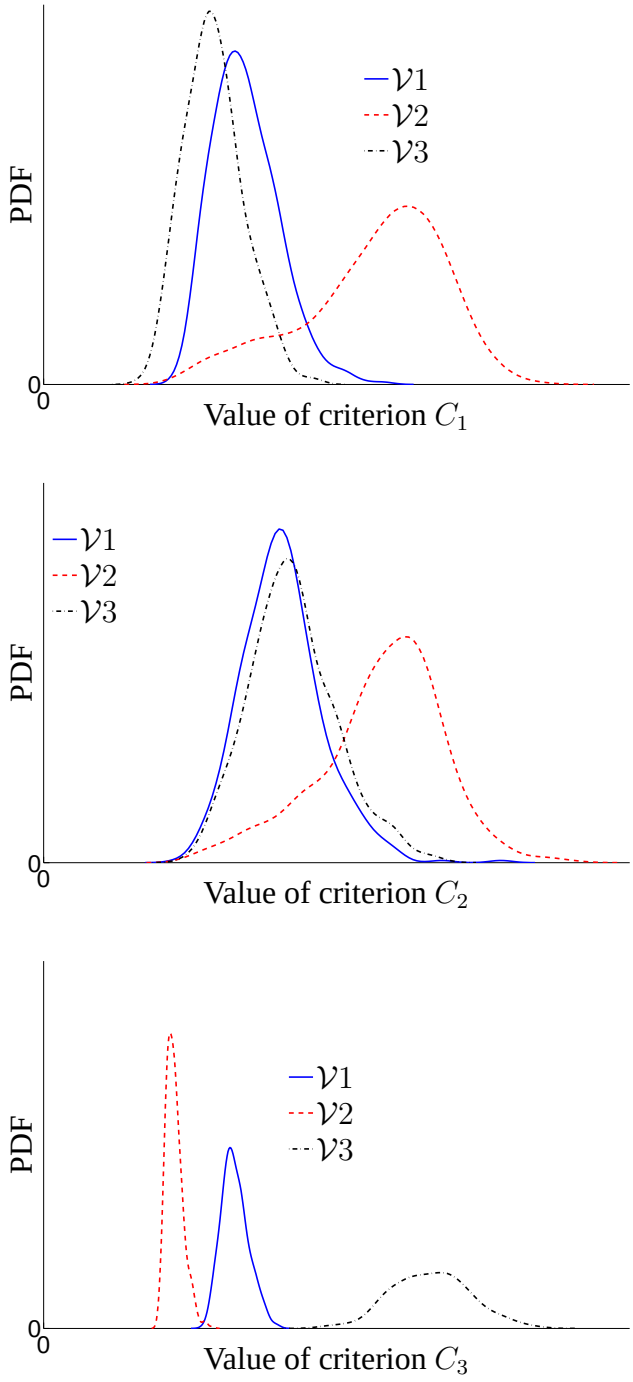


Figure 7: Comparison between the PDFs of the three criteria considered with respect to the train characteristics.

[4] G. P. Brooks and J. M. Powers. A karhunen-loève least-squares technique for optimization of geometry of a blunt body in supersonic flow. *Journal of Computational Physics*, 195:387–412, 2004.

[5] E.A. Christensen, M. Brons, and J.M. Sorensen. Evaluation of proper orthogonal decomposition-based decomposition techniques applied to parameter dependent nonturbulent flows. *SIAM J. Sci. Comput*, 21 (4):1419–1434, 2000.

[6] S.P. Huang, S.T. Quek, and K.K. Phoon. Convergence study of the truncated karhunen-loève expansion for simulation of stochastic processes. *Int J Num Meth Engng*, 52 (9):1029–43, 2001.

[7] K. Kunisch and S. Volkwein. Galerkin proper orthogonal decomposition methods for parabolic problems. *Numer. Math.*, 90 (1):117–148, 2001.

[8] L. Li, K. Phoon, and S. Quek. Comparison between karhunen-loève expansion and translation-based simulation of non-gaussian processes. *Computers and Structures*, 85:264–76, 2007.

[9] X. Ma and N. Zabaras. Kernel principal component analysis for stochastic input model generation. *Comptes rendus de l'Académie des sciences de Paris*, 220, 1945.

[10] Y. M. Marzouk and H. N. Najm. Dimensionality reduction and polynomial chaos acceleration of bayesian inference in inverse problems. *J. Comput. Phys.*, 228:1862–1902, 2009.

[11] A. Nouy and O.P. Le Maître. Generalized spectral decomposition method for stochastic non-linear problems. *J. Comput. Phys.*, 228 (1):202–235, 2009.

[12] K.K. Phoon, S.P. Huang, and S.T. Quek. Implementation of karhunen-loeve expansion for simulation using a wavelet-galerkin scheme. *Probabilistic Engineering Mechanics*, 17:293–303, 2002.

[13] K.K. Phoon, S.P. Huang, and S.T. Quek. Simulation of strongly non-gaussian processes using karhunen-loeve expansion. *Probabilistic Engineering Mechanics*, 20:188–198, 2005.

[14] Christoph Schwab and Radu Alexandru Todor. Karhunen-loeve approximation of random fields by generalized fast multipole methods. *Journal of Computational Physics*, 217:100–122, 2006.

[15] P.D. Spanos and B.A. Zeldin. Galerkin sampling method for stochastic mechanics problems. *Journal of Engineering Mechanics*, 120 (5):1091–1106, 1994.

[16] P.D. Spanos, M. Beer, and J. Red-Horse. Karhunen -loève expansion of stochastic processes with a modified exponential covariance kernel. *Journal of Engineering Mechanics*, 133 (7):773–779, 2007.

[17] B. Wen and N. Zabaras. A multiscale approach for model reduction of random microstructures. *Computational Materials Science*, 63:269–285, 2012.

[18] M.M.R. Williams. The eigenfunctions of the karhunen-loeve integral equation for a spherical system. *Propabilistic Engineering Mechanics*, 26:202–207, 2011.

[19] S. Q. Wu and S. S. Law. Statistical moving load identification including uncertainty. *Probabilistic Engineering Mechanics*, 29:70–78, 2012.

[20] R. Ghanem and P.D. Spanos. Polynomial chaos in stochastic finite elements. *Journal of Applied Mechanics*, Transactions of teh ASME 57:197–202, 1990.

[21] R. Ghanem and P. D. Spanos. *Stochastic Finite Elements: A Spectral Approach, rev. ed.* Dover Publications, New York, 2003.

[22] M. Arnst, R. Ghanem, and C. Soize. Identification of bayesian posteriors for coefficients of chaos expansions. *Journal of Computational Physics*, 229 (9):3134–3154, 2010.

[23] S. Das, R. Ghanem, and S. Finette. Polynomial chaos representation of spatio-temporal random field from experimental measurements. *J. Comput. Phys.*, 228:8726–8751, 2009.

[24] C. Desceliers, R. Ghanem, and C. Soize. Maximum likelihood estimation of stochastic chaos representations from experimental data. *Internat. J. Numer. Methods Engrg.*, 66:978–1001, 2006.

[25] C. Desceliers, C. Soize, and R. Ghanem. Identification of chaos representations of elastic properties of random media using experimental vibration tests. *Comput. Mech.*, 39:831–838, 2007.

[26] R.G. Ghanem and A. Doostan. On the construction and analysis of stochastic models: Characterization and propagation of the errors associated with limited data. *J. Comput. Phys.*, 217:63–81, 2006.

[27] Y. M. Marzouk, H. N. Najm, and L. A. Rahn. spectral methods for efficient bayesian solution of inverse problems. *J. Comput. Phys.*, 224:560–586, 2007.

[28] G. Perrin, C. Soize, D. Duhamel, and C. Funfschilling. Identification of polynomial chaos representations in high dimension from a set of realizations. *SIAM J. Sci. Comput.*, 34(6):2917–2945, 2012.

[29] C. Soize. Identification of high-dimension polynomial chaos expansions with random coefficients for non-gausian tensor-valued random fields using partial and limited experimental data. *Computer Methods in Applied Mechanics and Engineering*, 199:2150–2164, 2010.

[30] C. Soize. Generalized probabilistic approach of uncertainties in computational dynamics using random matrices and polynomial chaos decompositions. *Internat. J. Numer. Methods Engrg.*, 81:939–970, 2010.

COMPDYN 2013
4th ECCOMAS Thematic Conference on
Computational Methods in Structural Dynamics and Earthquake Engineering
M. Papadrakakis, V. Papadopoulos, V. Plevris (eds.)
Kos Island, Greece, 12–14 June 2013

GENERATION OF RESPONSE SPECTRUM COMPATIBLE ACCELEROGRAMS USING THE MAXIMUM ENTROPY PRINCIPLE

A. Batou[1] **and C. Soize**[1]

[1]Université Paris-Est, Laboratoire Modélisation et Simulation Multi Echelle, MSME UMR 8208 CNRS
5 bd Descartes, 77454 Marne-la-Vallee, France
e-mail: anas.batou@univ-paris-est.fr

Keywords: accelerogram, response spectrum, Eurocode, PGA.

Abstract. *The research addressed here concerns the generation of seismic accelerograms compatible with a given response spectrum and other associated properties. The time sampling of the stochastic accelerogram yields a time series represented by a random vector in high dimension. The probability density function (pdf) of this random vector is constructed using the Maximum Entropy (MaxEnt) principle under constraints defined by the available information. In this paper, a new algorithm, adapted to the high stochastic dimension, is proposed to identify the Lagrange multipliers introduced in the MaxEnt principle to take into account the constraints. This novel algorithm is based on (1) the minimization of an appropriate convex functional and (2) the construction of the probability distribution defined as the invariant measure of an Itô Stochastic Differential Equation in order to estimate the integrals in high dimension of the problem.*

1 INTRODUCTION

This research is devoted to the generation of seismic accelerograms which are compatible with some design specifications such as the Velocity Response Spectrum, the Peak Ground Acceleration (PGA), etc. The Maximum Entropy (MaxEnt) principle [3] is a powerful method which allows us to construct a probability distribution of a random vector under some constraints defined by the available information. This method has recently been applied in [5] for the generation of spectrum-compatible accelerograms as trajectories of a non-Gaussian non-stationary centered random process represented by a high-dimension random vector for which the probability density function (pdf) is constructed using the MaxEnt principle under constraints relative to (1) the mean value, (2) the variance of the components and (3) the mean value of the Velocity Response Spectrum (VRS). The objective of this paper is to take into account additional constraints which characterize the natural features of a seismic accelerogram. To achieve this objective, the methodology proposed in [5] is extended to take into account constraints relative to statistics on (1) the end values for the velocity and the displacement, (2) the PGA, (3) the Peak Ground Velocity (PGV), (4) the envelop of the random VRS and (5) the Cumulative Absolute Velocity (CAV). The MaxEnt pdf is constructed and a generator of independent realizations adapted to the high-stochastic dimension of an accelerogram is proposed. Furthermore an adapted method for the identification of the Lagrange multipliers is developed. In Section 2 the MaxEnt principle is used to construct the pdf of the acceleration random vector under constraints defined by the available information. Finally, Section 3 is devoted to an application of the methodology for which the target VRS is constructed following the Eurocode 8.

2 CONSTRUCTION OF THE PROBABILITY DISTRIBUTION

The MaxEnt principle is a powerful method to construct the probability distribution of a random vector associated with a sampled stochastic process under some constraints defined by the available information.

The random acceleration of the soil is modelled by a second-order centered stochastic process $\{A(t), t \in [0,T]\}$. A time sampling of this stochastic process is introduced yielding a time series $\{A_1, \ldots, A_N\}$ for which the $\mathbb{R}^N$-valued random vector $\boldsymbol{A} = (A_1, \ldots, A_N)$ is associated with. We then have $T = N\Delta t$ in which Δt is the sampling time step. Finally, we have to construct the probability distribution of the random vector $\boldsymbol{A}$.

2.1 Maximum entropy principle

The objective of this section is to construct the pdf $\boldsymbol{a} \mapsto p_{\boldsymbol{A}}(\boldsymbol{a})$ of the random vector $\boldsymbol{A}$ using the MaxEnt principle under the constraints defined by the available information relative to random vector $\boldsymbol{A}$. The support of the pdf is assumed to be all the set $\mathbb{R}^N$. Let $E\{.\}$ be the mathematical expectation. We suppose that the available information is written as

$$E\{\boldsymbol{g}(\boldsymbol{A})\} = \boldsymbol{f}\,, \tag{1}$$

in which $\boldsymbol{a} \mapsto \boldsymbol{g}(\boldsymbol{a})$ is a given function from $\mathbb{R}^N$ into $\mathbb{R}^\mu$ and where $\boldsymbol{f}$ is a given (or target) vector in $\mathbb{R}^\mu$. Equation (1) can be rewritten as

$$\int_{\mathbb{R}^N} \boldsymbol{g}(\boldsymbol{a}) p_{\boldsymbol{A}}(\boldsymbol{a}) \mathrm{d}\boldsymbol{a} = \boldsymbol{f}\,. \tag{2}$$

An additional constraint relative to the normalization of the pdf $p_{\boldsymbol{A}}(\boldsymbol{a})$ is introduced such that

$$\int_{\mathbb{R}^N} p_{\boldsymbol{A}}(\boldsymbol{a})\mathrm{d}\boldsymbol{a} = 1\,. \tag{3}$$

The entropy of the pdf $\boldsymbol{a} \mapsto p_{\boldsymbol{A}}(\boldsymbol{a})$ is defined by

$$S(p_{\boldsymbol{A}}) = -\int_{\mathbb{R}^N} p_{\boldsymbol{A}}(\boldsymbol{a}) \log(p_{\boldsymbol{A}}(\boldsymbol{a}))\mathrm{d}\boldsymbol{a}\,, \tag{4}$$

where $\log$ is the Neperian logarithm. Let $\mathcal{C}$ be the set of all the pdf defined on $\mathbb{R}^N$ with values in $\mathbb{R}^+$, verifying the constraints defined by Eqs. (2) and (3). Then the MaxEnt principle consists in constructing the probability density function $\boldsymbol{a} \mapsto p_{\boldsymbol{A}}(\boldsymbol{a})$ as the unique pdf in $\mathcal{C}$ which maximizes the entropy $S(p_{\boldsymbol{A}})$. Then by introducing a Lagrange multiplier $\boldsymbol{\lambda}$ associated with Eq. (2) and belonging to an admissible open subset $\mathcal{L}_\mu$ of $\mathbb{R}^\mu$, it can be shown (see [3]) that the MaxEnt solution, if it exists, is defined by

$$p_{\boldsymbol{A}}(\boldsymbol{a}) = c_0(\boldsymbol{\lambda}^{\mathrm{sol}}) \exp(-\langle \boldsymbol{\lambda}^{\mathrm{sol}}, \boldsymbol{g}(\boldsymbol{a})\rangle)\,, \tag{5}$$

in which $\boldsymbol{\lambda}^{\mathrm{sol}}$ is such that Eq. (2) is satisfied and where $c_0(\boldsymbol{\lambda})$ is the normalization constant defined by

$$c_0(\boldsymbol{\lambda}) = \left\{ \int_{\mathbb{R}^N} \exp(-\langle \boldsymbol{\lambda}, \boldsymbol{g}(\boldsymbol{a})\rangle)\, \mathrm{d}\boldsymbol{a} \right\}^{-1}\,. \tag{6}$$

2.2 Calculation of the Lagrange multipliers

In this section, we propose a general methodology for the calculation of the Lagrange multipliers $\boldsymbol{\lambda}^{\mathrm{sol}}$.

2.2.1 Objective function and methododology

Using Eqs. (7) and (2), vector $\boldsymbol{\lambda}^{\mathrm{sol}}$ is the solution in $\boldsymbol{\lambda}$ of the following set of μ nonlinear algebraic equations

$$\int_{\mathbb{R}^N} \boldsymbol{g}(\boldsymbol{a})\, c_0(\boldsymbol{\lambda}) \exp(-\langle \boldsymbol{\lambda}, \boldsymbol{g}(\boldsymbol{a})\rangle) = \boldsymbol{f}\,. \tag{7}$$

A more convenient way to calculate vector $\boldsymbol{\lambda}^{\mathrm{sol}}$ consists in solving the following optimization problem (see [2]),

$$\boldsymbol{\lambda}^{\mathrm{sol}} = \arg \min_{\boldsymbol{\lambda} \in \mathcal{L}_\mu \subset \mathbb{R}^\mu} \Gamma(\boldsymbol{\lambda})\,, \tag{8}$$

in which the objective function Γ is written as

$$\Gamma(\boldsymbol{\lambda}) = \langle \boldsymbol{\lambda}, \boldsymbol{f}\rangle - \log(c_0(\boldsymbol{\lambda}))\,. \tag{9}$$

Let $\{\boldsymbol{A}_{\boldsymbol{\lambda}}\,,\ \boldsymbol{\lambda} \in \mathcal{L}_\mu\}$ be a family of random variables for which the pdf is defined, for all $\boldsymbol{\lambda}$ in $\mathcal{L}_\mu$, by

$$p_{\boldsymbol{A}_{\boldsymbol{\lambda}}}(\boldsymbol{a}) = c_0(\boldsymbol{\lambda}) \exp(-\langle \boldsymbol{\lambda}, \boldsymbol{g}(\boldsymbol{a})\rangle)\,. \tag{10}$$

Then the gradient vector $\boldsymbol{\nabla}\Gamma(\boldsymbol{\lambda})$ and the Hessian matrix $[H(\boldsymbol{\lambda})]$ of function $\boldsymbol{\lambda} \mapsto \Gamma(\boldsymbol{\lambda})$ are written as

$$\boldsymbol{\nabla}\Gamma(\boldsymbol{\lambda}) = \boldsymbol{f} - E\{\boldsymbol{g}(\boldsymbol{A}_{\boldsymbol{\lambda}})\}\,. \tag{11}$$

$$[H(\boldsymbol{\lambda})] = E\{\boldsymbol{g}(\boldsymbol{A}_{\boldsymbol{\lambda}})\boldsymbol{g}(\boldsymbol{A}_{\boldsymbol{\lambda}})^T\} - E\{\boldsymbol{g}(\boldsymbol{A}_{\boldsymbol{\lambda}})\}\,E\{\boldsymbol{g}(\boldsymbol{A}_{\boldsymbol{\lambda}})\}^T\,, \tag{12}$$

in which $\boldsymbol{u}^T$ is the transpose of $\boldsymbol{u}$. It is assumed that the constraints defined by Eq. (2) are algebraically independent. Consequently, the Hessian matrix is positive definite and therefore, function $\boldsymbol{\lambda} \mapsto \Gamma(\boldsymbol{\lambda})$ is strictly convex and reaches its minimum for $\boldsymbol{\lambda}^{\text{sol}}$ which is such that $\boldsymbol{\nabla}\Gamma(\boldsymbol{\lambda}) = \boldsymbol{0}$ for $\boldsymbol{\lambda} = \boldsymbol{\lambda}^{\text{sol}}$. It can then be deduced that the minimum of function $\boldsymbol{\lambda} \mapsto \Gamma(\boldsymbol{\lambda})$ corresponds to the solution of Eq. (7). The optimization problem defined by Eq. (8) is solved using the Newton iterative method

$$\boldsymbol{\lambda}^{\text{i+1}} = \boldsymbol{\lambda}^{\text{i}} - \alpha\,[H(\boldsymbol{\lambda}^{\text{i}})]^{-1}\,\boldsymbol{\nabla}\Gamma(\boldsymbol{\lambda}^{\text{i}})\,, \tag{13}$$

in which α belongs to $]0\,,\,1]$ is an under-relaxation parameter which ensures the convergence towards the solution $\boldsymbol{\lambda}^{\text{sol}}$. In general, for the non-Gaussian case, the integrals defined by Eqs. (11) and (12) cannot explicitly (such as in the Gaussian Case) be calculated and cannot be discretized in $\mathbb{R}^N$. In this paper, these integrals are estimated using the Monte Carlo simulation method for which independent realizations of the random vector $\boldsymbol{A}_{\boldsymbol{\lambda}}$ are generated using a specific algorithm presented below.

2.2.2 Generator of independent realizations

The objective of this section is to provide a generator of independent realizations of the random variable $\boldsymbol{A}_{\boldsymbol{\lambda}}$ for all $\boldsymbol{\lambda}$ fixed in $\mathcal{L}_\mu$. A generator of independent realizations for MaxEnt distributions has been proposed in [4, 5] in the class of the MCMC algorithms. This methodology consists in constructing the pdf of random vector $\boldsymbol{A}_{\boldsymbol{\lambda}}$ as the density of the invariant measure $p_{\boldsymbol{A}_{\boldsymbol{\lambda}}}(\boldsymbol{a})\mathrm{d}\boldsymbol{a}$, associated with the stationary solution of a second-order nonlinear Itô Stochastic differential equation (ISDE). The advantages of this generator compared to the other MCMC generators such as the Metropolis-Hastings algorithm are: (1) The mathematical results concerning the existence and the uniqueness of an invariant measure can be used, (2) a damping matrix can be introduced in order to rapidly reach the invariant measure and (3) there is no need to introduce a proposal distribution which can induce difficulties in high dimension. Below, we directly introduce the generator of independent realizations using a discretization of the ISDE. Details concerning the construction of this generator can be found in [4, 5].

As proposed in [4, 5], the ISDE is discretized using a semi-implicit integration scheme in order to avoid the resolution of an algebraic nonlinear equation at each step while allowing significantly increase of the time step compared to a purely explicit scheme.

We assume that the function $\boldsymbol{a} \mapsto \boldsymbol{g}(\boldsymbol{a})$ introduced in Eq. (1) and defining the available information is written as $\boldsymbol{g}(\boldsymbol{a}) = (\boldsymbol{g}_{\text{L}}(\boldsymbol{a}), \boldsymbol{g}_{\text{NL}}(\boldsymbol{a}))$ in which $\boldsymbol{a} \mapsto \boldsymbol{g}_{\text{NL}}(\boldsymbol{a})$ is a nonlinear function from $\mathbb{R}^N$ into $\mathbb{R}^{\mu_{\text{NL}}}$ and where $\boldsymbol{a} \mapsto \boldsymbol{g}_{\text{L}}(\boldsymbol{a})$ is a quadratic function from $\mathbb{R}^N$ into $\mathbb{R}^{\mu_{\text{L}}}$ whose components are such that

$$\{\boldsymbol{g}_{\text{L}}(\boldsymbol{a})\}_i = \frac{1}{2}\langle \boldsymbol{u}, [K_i]\boldsymbol{u}\rangle\,, \tag{14}$$

in which $\{[K_i]\}_{i=1,\ldots,\mu_{\rm L}}$ are $\mu_{\rm L}$ symmetric $(N \times N)$ real matrices which are assumed to be algebraically independent. Let $\boldsymbol{u} \mapsto \Phi(\boldsymbol{u}, \boldsymbol{\lambda})$ be a potential function defined by

$$\Phi(\boldsymbol{u}, \boldsymbol{\lambda}) = \langle \boldsymbol{\lambda}, \boldsymbol{g}(\boldsymbol{u}) \rangle \,. \tag{15}$$

Let us introduce the decomposition $\boldsymbol{\lambda} = (\boldsymbol{\lambda}_{\rm L}, \boldsymbol{\lambda}_{\rm NL}) \in \mathcal{L}_\mu$ of the Lagrange multipliers. Then for all $\boldsymbol{\lambda} \in \mathcal{L}_\mu$, the potential function can be written as

$$\Phi(\boldsymbol{u}, \boldsymbol{\lambda}) = \frac{1}{2} \langle \boldsymbol{u}, [\mathcal{K}_{\boldsymbol{\lambda}_{\rm L}}] \boldsymbol{u} \rangle + \Phi_{\rm NL}(\boldsymbol{u}, \boldsymbol{\lambda}_{\rm NL}) \,, \tag{16}$$

in which $[\mathcal{K}_{\boldsymbol{\lambda}_{\rm L}}] = \sum_{j=1}^{\mu_{\rm L}} \{\boldsymbol{\lambda}_{\rm L}\}_j [K_j]$ is assumed to be positive definite for all $\boldsymbol{\lambda}_{\rm L}$ in $\mathcal{L}_\mu$ and where $\Phi_{\rm NL}(\boldsymbol{u}, \boldsymbol{\lambda}_{\rm NL}) = \sum_{j=1}^{\mu_{\rm NL}} \{\boldsymbol{\lambda}_{\rm NL}\}_j \{\boldsymbol{g}_{\rm NL}(\boldsymbol{u})\}_j$. Therefore, the gradient of the potential function with respect to $\boldsymbol{u}$ is written as

$$\boldsymbol{\nabla}_{\boldsymbol{u}} \Phi(\boldsymbol{u}, \boldsymbol{\lambda}) = [\mathcal{K}_{\boldsymbol{\lambda}_{\rm L}}] \boldsymbol{u} + \boldsymbol{\nabla}_{\boldsymbol{u}} \Phi_{\rm NL}(\boldsymbol{u}, \boldsymbol{\lambda}_{\rm NL}) \,, \tag{17}$$

in which $\boldsymbol{\nabla}_{\boldsymbol{u}} \Phi_{\rm NL}(\boldsymbol{u}, \boldsymbol{\lambda}_{\rm NL}) = \sum_{j=1}^{\mu_{\rm NL}} \{\boldsymbol{\lambda}_{\rm NL}\}_j \boldsymbol{\nabla}_{\boldsymbol{u}} \{\boldsymbol{g}_{\rm NL}(\boldsymbol{u})\}_j$. Thus the gradient function $\boldsymbol{\nabla}_{\boldsymbol{u}} \Phi(\boldsymbol{u}, \boldsymbol{\lambda})$ is decomposed into a linear part with respect to $\boldsymbol{u}$ and a nonlinear part.

Let $\Delta r_{\boldsymbol{\lambda}}$ be the integration step size relative to the discretization of the ISDE. Let $\Delta \boldsymbol{W}^1, \ldots, \Delta \boldsymbol{W}^M$ be M mutually independent second-order Gaussian centered random vector with covariance matrix equal to $\Delta r_{\boldsymbol{\lambda}} \, [I_N]$. We then introduce the time series $\{(\boldsymbol{U}^k, \boldsymbol{V}^k), k = 1, \ldots, M\}$ with values in $\mathbb{R}^N \times \mathbb{R}^N$ for all k in $\{1, \ldots, M\}$ and the second-order random vector of the initial condition $(\boldsymbol{U}_0, \boldsymbol{V}_0)$ with values in $\mathbb{R}^N \times \mathbb{R}^N$ and which is independent of the time series $\{(\boldsymbol{U}^k, \boldsymbol{V}^k), k = 1, \ldots, M\}$.

For $\ell = 1, \ldots, n_s$, using n_s independent realizations $\{\Delta \boldsymbol{W}^{k+1,\ell}, k = 1, \ldots, M-1\}$ of the family of random vectors $\{\Delta \boldsymbol{W}^{k+1}, k = 1, \ldots, M-1\}$ and n_s independent realizations $(\boldsymbol{U}_0^\ell, \boldsymbol{V}_0^\ell)$ of the random initial conditions $(\boldsymbol{U}_0, \boldsymbol{V}_0)$ (which are also independent of $\{\Delta \boldsymbol{W}^{k+1}, k = 1, \ldots, M-1\}$), the n_s independent realizations $\boldsymbol{U}^{M,\ell}$ of the vector random $\boldsymbol{U}^M$ are generated by solving n_s times, for $k = 1, \ldots, M-1$, the following equations (which correspond to the discretization of the ISDE, see [4])

$$\begin{aligned}
[\mathcal{E}_{\boldsymbol{\lambda}}] \boldsymbol{V}^{k+1,\ell} &= [\mathcal{B}_{\boldsymbol{\lambda}}] \boldsymbol{V}^{k,\ell} - \Delta r_{\boldsymbol{\lambda}} [\mathcal{K}_{\boldsymbol{\lambda}_{\rm L}}] \boldsymbol{U}^{k,\ell} + \Delta r_{\boldsymbol{\lambda}} \boldsymbol{L}_{\rm NL}^{k,\ell} + [S_{\boldsymbol{\lambda}}] \Delta \boldsymbol{W}^{k+1,\ell} \,, \\
\boldsymbol{U}^{k+1,\ell} &= \boldsymbol{U}^{k,\ell} + \tfrac{1}{2} \, \Delta r_{\boldsymbol{\lambda}} \, (\boldsymbol{V}^{k+1,\ell} + \boldsymbol{V}^{k,\ell}) \,, \\
\boldsymbol{U}^{1,\ell} = \boldsymbol{U}_0^\ell \quad &, \quad \boldsymbol{V}^{1,\ell} = \boldsymbol{V}_0^\ell \,.
\end{aligned} \tag{18}$$

in which $[\mathcal{E}_{\boldsymbol{\lambda}}] = [I_N] + \frac{1}{4} \, \Delta r_{\boldsymbol{\lambda}} \, [D_{\boldsymbol{\lambda}}] + \frac{1}{4} \, \Delta r_{\boldsymbol{\lambda}}^2 \, [\mathcal{K}_{\boldsymbol{\lambda}_{\rm L}}]$ and $[\mathcal{B}_{\boldsymbol{\lambda}}] = [I_N] - \frac{1}{4} \, \Delta r_{\boldsymbol{\lambda}} \, [D_{\boldsymbol{\lambda}}] - \frac{1}{4} \, \Delta r_{\boldsymbol{\lambda}}^2 \, [\mathcal{K}_{\boldsymbol{\lambda}_{\rm L}}]$ where $[I_N]$ is the $(N \times N)$ identity matrix and where $[D_{\boldsymbol{\lambda}}]$ is a symmetric positive-definite damping matrix and the lower triangular matrix $[S_{\boldsymbol{\lambda}}]$ is such that $[D_{\boldsymbol{\lambda}}] = [S_{\boldsymbol{\lambda}}][S_{\boldsymbol{\lambda}}]^T$. The vector $\boldsymbol{L}_{\rm NL}^k$ is defined by $\boldsymbol{L}_{\rm NL}^k = -\{\boldsymbol{\nabla}_{\boldsymbol{u}} \Phi_{\rm NL}(\boldsymbol{u}, \boldsymbol{\lambda}_{\rm NL})\}_{\boldsymbol{u} = \boldsymbol{U}^k}$.

Then, if M is sufficiently large, the n_s independent realizations of the random vector $\boldsymbol{A}_{\boldsymbol{\lambda}}$ are constructed such that $\boldsymbol{A}_{\boldsymbol{\lambda}}^\ell \simeq \boldsymbol{U}^{M,\ell}$ for $\ell = 1, \ldots, n_s$.

Concerning the initial conditions, the more the probability distribution of the initial conditions is close to the invariant measure, the shorter is the transient response.

2.2.3 Estimation of the mathematical expectations

The mean value $E\{\boldsymbol{g}(\boldsymbol{A}_{\boldsymbol{\lambda}})\}$ and the correlation matrix $E\{\boldsymbol{g}(\boldsymbol{A}_{\boldsymbol{\lambda}})\boldsymbol{g}(\boldsymbol{A}_{\boldsymbol{\lambda}})^T\}$ are estimated using the Monte Carlo simulation method by

$$E\{\boldsymbol{g}(\boldsymbol{A}_{\boldsymbol{\lambda}})\} \simeq \frac{1}{n_s}\sum_{\ell=1}^{n_s} \boldsymbol{g}(\boldsymbol{A}_{\boldsymbol{\lambda}}^{\ell})\,, \tag{19}$$

$$E\{\boldsymbol{g}(\boldsymbol{A}_{\boldsymbol{\lambda}})\boldsymbol{g}(\boldsymbol{A}_{\boldsymbol{\lambda}})^T\} \simeq \frac{1}{n_s}\sum_{\ell=1}^{n_s} \boldsymbol{g}(\boldsymbol{A}_{\boldsymbol{\lambda}}^{\ell})\boldsymbol{g}(\boldsymbol{A}_{\boldsymbol{\lambda}}^{\ell})^T\,. \tag{20}$$

3 APPLICATIONS

The acceleration stochastic process is sampled such that the final time $T = 20$ s. The time step is $\Delta t = 0.0125$ s. We then have $N = 1600$ (we assume $A(0) = 0$ ms^{-2} almost surely).

3.1 Available information

The available information relative to random vector $\boldsymbol{A}$ is defined by:

(1) The random vector $\boldsymbol{A}$ is centred.

(2) The standard deviation of the component of $\boldsymbol{A}$ are imposed. The target values are plotted in Fig. 1.

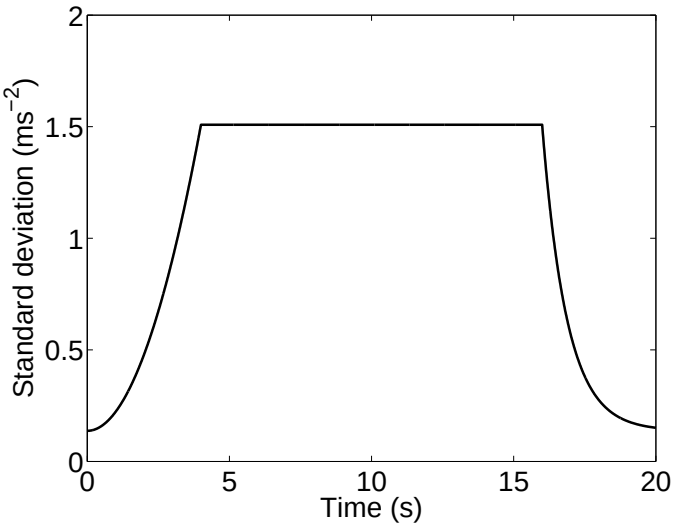


Figure 1: Target standard deviation.

(3) The variance of the end-velocity (resulting from a numerical integration of random vector $\boldsymbol{A}$) is zero.

(4) The variance of the end-displacement (resulting from two successive numerical integrations of random vector $\boldsymbol{A}$) is zero.

(5) The target mean VRS [1] is constructed following the Eurocode 8 for a A-type soil and a PGA equal to 5 ms^{-2}. It is defined for $\xi = 0.05$ of the damping ratio and for 20 frequencies which are (in rad/s) 1.04, 1.34, 1.73, 2.23, 2.86, 3.69, 4.74, 6.11, 7.86, 10.11, 13.01, 16.74,

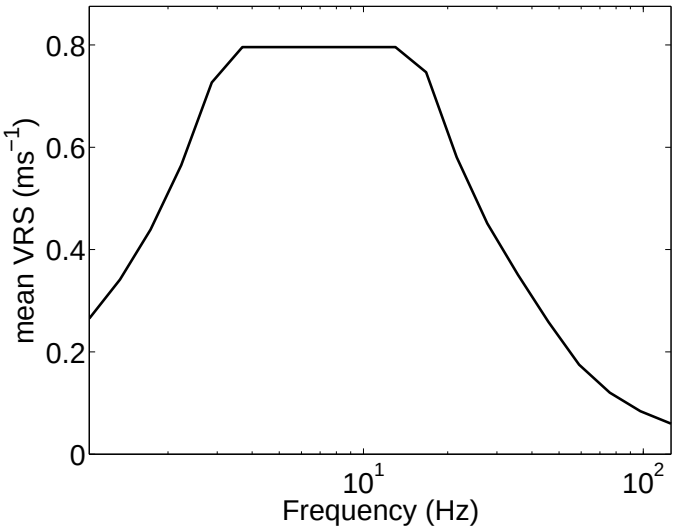


Figure 2: Mean VRS.

21.53, 27.70, 35.64, 45.86, 59.00, 75.91, 97.67 and 125.66. The target mean VRS is plotted in Fig. 2.

(6) Let $\boldsymbol{s}^{\text{low}}$ be the lower envelop defined by $\boldsymbol{s}^{\text{low}} = 0.5 \times \underline{\boldsymbol{s}}$ and $\boldsymbol{s}^{\text{up}}$ be the upper envelop defined by $\boldsymbol{s}^{\text{up}} = 1.5 \times \underline{\boldsymbol{s}}$. The probability for random vector $\boldsymbol{A}$ of being inside the region delimited by the two envelops is 0.99.

(7) The mean PGA is 5 ms^{-2}.

(8) The mean PGV is 0.45 ms^{-1}.

(9) The mean CAV is 20 ms^{-2}.

3.2 Results

The step size for the ISDE is $\Delta r_{\boldsymbol{\lambda}} = 2\,\pi/(\beta\,\sqrt{2\,\lambda_{\max}})$, in which $\lambda_{\max} = \max\{\{\boldsymbol{\lambda}_L\}_i, i = 1, \ldots, N\}$ and $\beta = 80$. At each iteration, the damping matrix $[D_{\boldsymbol{\lambda}}]$ is a diagonal matrix such that $[D_{\boldsymbol{\lambda}}]_{ii} = 2\,\xi_{\text{ito}}\,\sqrt{2\,\{\boldsymbol{\lambda}_L\}_i}$, in which $\xi_{\text{ito}} = 0.7$. For the ISDE, the number of integration steps is $M = 600$. At each iteration, $n_s = 900$ Monte Carlo simulations are carried out. The methodology developed in Section 2.2.1 is applied using 30 iterations. The under-relaxation parameter is $\alpha = 0.3$. Figure 3 shows two independent realizations of the random vector $\boldsymbol{A}_{\boldsymbol{\lambda}_{\text{sol}}}$ which is generated using a classical generator for Gaussian random variable and which are representative of two independent realizations of the random accelerogram. The corresponding trajectories of the velocity times series $\mathbb{V}$ and of the displacement times series $\mathbb{D}$ result from two successive numerical integrations of each realization of the random accelerogram and are plotted in Figs. 4 and 5. As expected, it can be seen that the end velocity and the end displacements are both equal to zero. Figure 6 displays a comparison of the estimated standard deviation of the components with the target values. Figure 7 shows a comparison of the mean VRS with the target mean VRS. The Figure 8 shows 100 trajectories of the random VRS and the envelops $\boldsymbol{s}^{\text{low}}$ and $\boldsymbol{s}^{\text{up}}$. It can be seen in Figs. 6 to 8 a good matching between the estimated values and the target values. Concerning the PGA, the PGV and the CAV, the results are summarized in Table 1. It can be seen a good matching of the estimated means values for the PGA, the PGV and the CAV with the target values.

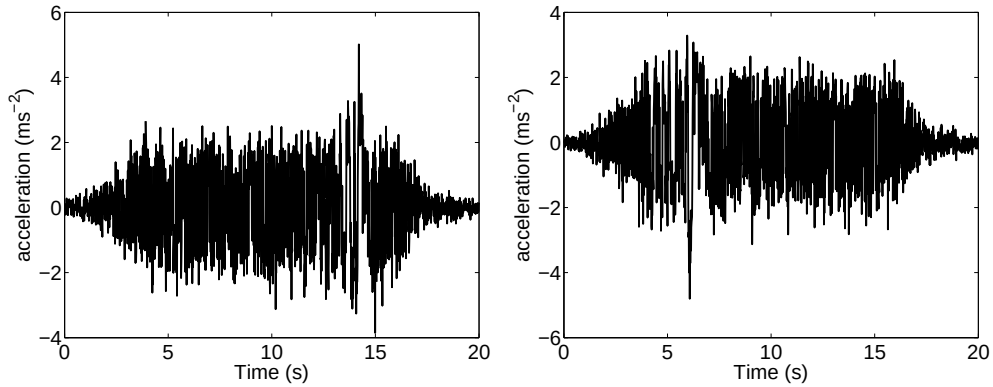


Figure 3: Two independent realizations of the random accelerogram.

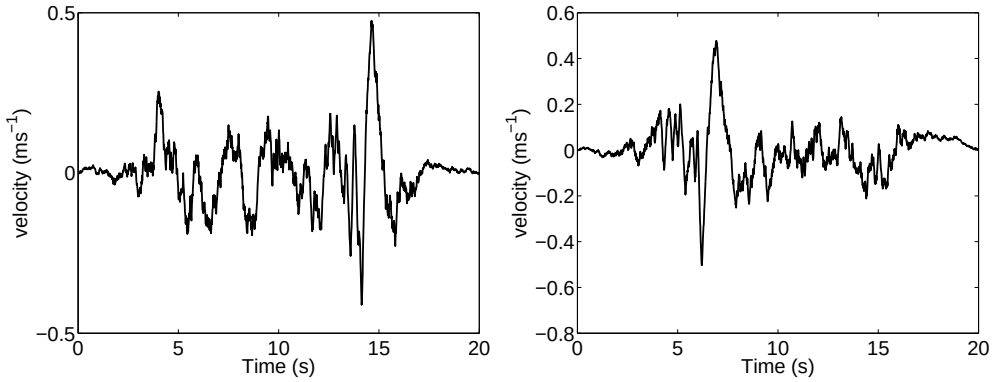


Figure 4: Two independent realizations of the random velocity.

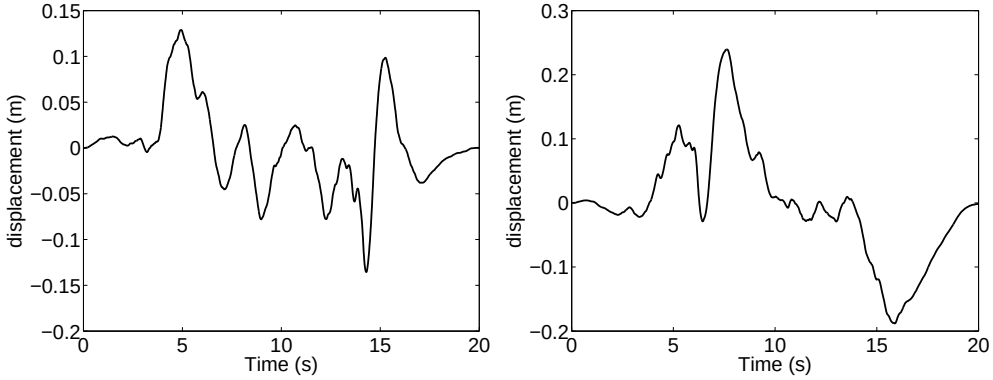


Figure 5: Two independent realizations of the random displacement.

Constraint	Estimation	Target
Mean PGA (ms^{-2})	5.08	5
Mean PGV (ms^{-1})	0.46	0.45
Mean CAV (ms^{-1})	19.99	20

Table 1: For the PGA, the PGV, the CAV: comparision of the estimated mean value with the target value.

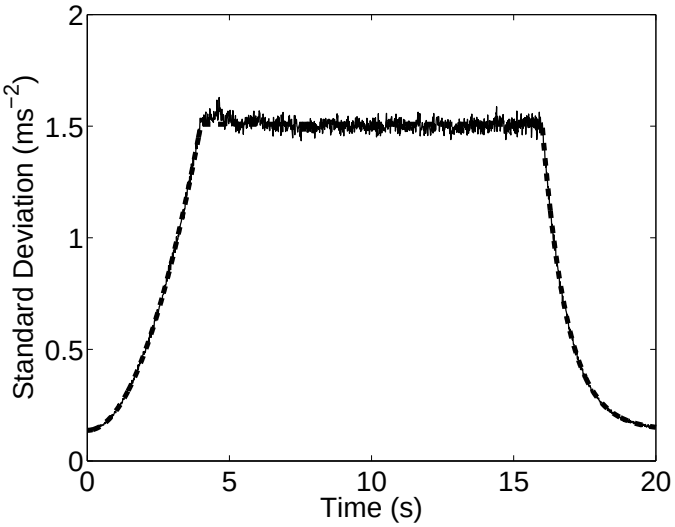


Figure 6: Variance: Target (thick dashed line) and estimation (thin solid line).

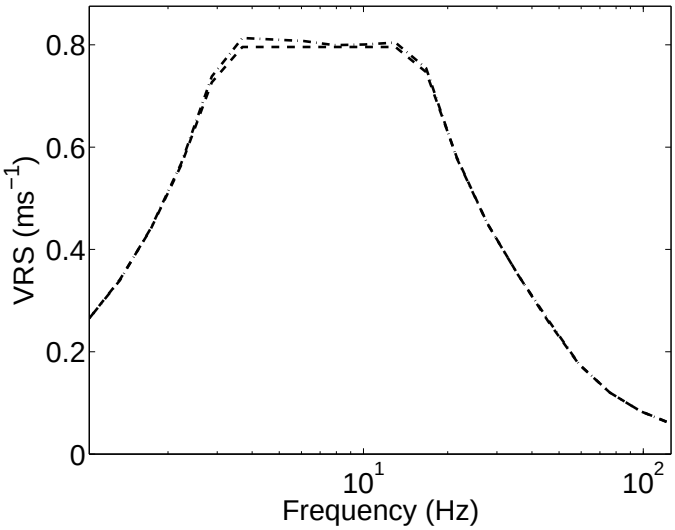


Figure 7: Mean VRS: Target (dashed line), estimation (mixed line).

4 CONCLUSIONS

We have presented a new methodology for the generation of accelerograms compatible with a given VRS and other properties. If necessary, additional constraints can easily be taken into account in addition to those developed in this paper. The application shows a good matching between the estimated values and the target values.

5 ACKNOWLEDGMENT

This research was supported by the ”AgenceNationale de la Recherche”, Contract TYCHE, ANR-2010-BLAN-0904.

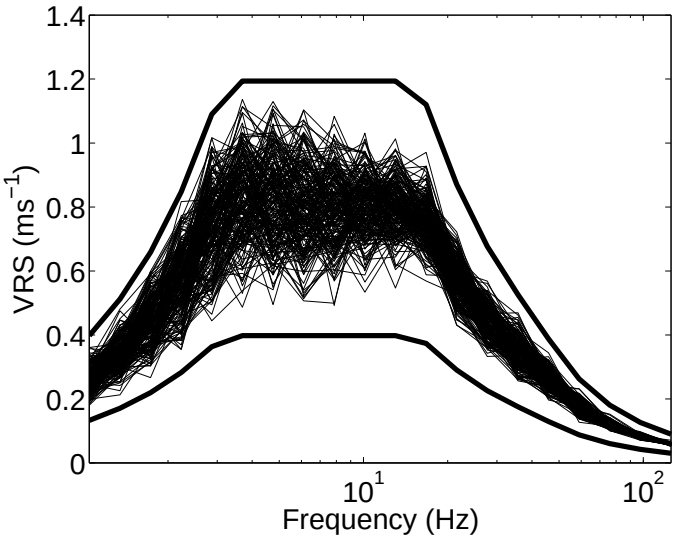


Figure 8: Random VRS: 100 trajectories (thin lines), lower and upper envelop (thick lines)..

REFERENCES

[1] R. W. Clough, J. Penzien, *Dynamics of Structures*, McGraw-Hill, New York, 1975.

[2] A. Golan, G. Judge, D. Miller, *Maximum entropy econometrics: robust estimation with limited data*, Wiley, New York, 1996.

[3] J. N. Kapur, H. K. Kevasan, *Entropy Optimization Principles with Applications*, Academic Press, San Diego, 1992

[4] C. Soize, Construction of probability distributions in high dimension using the maximum entropy principle. Applications to stochastic processes, random fields and random matrices, *International Journal for Numerical Methods in Engineering*, **76**(10), 1583–1611, 2008.

[5] C. Soize, Information theory for generation of accelerograms associated with shock response spectra, *Computer-Aided Civil and Infrastructure Engineering*, **25**, 334–347, 2010.

COMPDYN 2013
4th ECCOMAS Thematic Conference on
Computational Methods in Structural Dynamics and Earthquake Engineering
M. Papadrakakis, V. Papadopoulos, V. Plevris (eds.)
Kos Island, Greece, 12–14 June 2013

UNCERTAINTY QUANTIFICATION OF THE NONLINEAR DYNAMICS OF ELECTROMECHANICAL COUPLED SYSTEMS

Roberta de Queiroz Lima[1,2] **and Rubens Sampaio**[1]

[1]Pontifícia Universidade Católica do Rio de Janeiro
Marquês de São Vicente, 225, Gávea, RJ, CEP: 22453-900, Brazil
e-mail: rsampaio@puc-rio.br

[2] Universit Paris-Est, Laboratoire Modlisation et Simulation Multi Echelle
MSME UMR 8208 CNRS, 5 bd Descartes, 77454 Marne-la-Valle, France
e-mail: roberta.dequeirozlima@univ-paris-est.fr

Keywords: Nonlinear dynamics, coupled systems, friction, stochastic analysis.

Abstract. *This paper analyzes the nonlinear stochastic dynamics of electromechanical systems with friction in the coupling mechanism and in the mechanical parts. Two different electromechanical systems were studied. The first one is composed by a cart whose motion is excited by a DC motor and in the second a new element,a pendulum, is attached to the cart. The suspension point of the pendulum is fixed in cart, so that exists a relative motion between them. The influence of the DC motor in the dynamic behavior of the system is considered. The coupling between the motor and the cart is made by a mechanism called scotch yoke, so that the motor rotational motion is transformed in horizontal cart motion over a rail. In the model of the system, it is considered the existence of friction in the coupling mechanism and in between the cart and the rail. The embarked pendulum is modeled as a mathematical pendulum (bar without mass and particle of mass m_p at the end). The embarked mass introduces a new feature in the system since the motion of the pendulum acts as a reservoir of energy, i.e. energy from the electrical system is pumped to the pendulum and stored in the pendulum motion, changing the characteristics of the mechanical system. Due to the consideration of friction, the dynamic of the problem is described by a system of differential algebraic equations. One of the most important parameters of the problem is the amplitude of the cart motion that is given by the position of the pin used in the coupling mechanism. The behavior of the system is very sensitive to this parameter because it controls the nonlinearities of the problem. In the stochastic analysis, this parameter is considered uncertain and is modeled as a random variable. The Maximum Entropy Principle is used to construct its probability model. Monte Carlo simulations are employed to compute the mean motion and the 90% confidence interval of the displacements of the pendulum, of the cart and of the angular speed of the motor shaft.*

1 INTRODUCTION

The wide occurrence of the electromechanical coupling in manufacturing processes turns the research on this topic an area of interest for engineering practice. By coupling it is meant a mutual influence between the systems. In the two systems studied in this paper the source of energy is the imposed voltage that will be taken as constant. The dynamics of the motor is heavily influenced by the coupled mechanical system. It is believed that the theoretical knowledge on couplings between electric motors and mechanical systems can provide improvements in the design of mechanical systems and can help in the development of control techniques.

Electromechanical coupled systems is not a new subject, in [1] there is a chapter dedicated to the coupled problem and it is remarked that it is a problem different from parametric resonance. In [2] the whole book is dedicated to the problem but the analytical treatment supposes some small parameter, a hypothesis avoided here. Recently, the problem is been intensely studied again, see [3, 4, 5], but the literature is vast. It is important to remark that the nonlinearity of this problem is not prescribed by a function, as is unfortunately found in several papers, but it comes from the coupling and the nonlinearity varies with the coupling conditions. This means that the no linearity varies with the dynamics, one cannot that it a sine, or a cubic nonlinearity, as seen in some papers, for example. Coupled problems have a very rich system dynamics due to presence of nonlinearities arising from the mutual interaction of the coupled systems, see [6, 7, 8, 9, 10].

In this paper, it is analyzed and compared two electromechanical systems. The first one is a very simple system composed by a cart whose motion is driven by a DC motor. The coupling between the motor and the cart is made by a mechanism called *scotch yoke*. In this simple system the coupling is a sort of master-slave condition: the motor drives, the cart is driven, and that is all. The second system has the same two elements of the first and also a pendulum that can move relative to the cart. The pendulum introduces a new feature since the motion of the pendulum acts as a reservoir of energy, i.e. energy from the electrical system is pumped to the pendulum and stored in the pendulum motion, changing the characteristics of the mechanical system. The pendulum is the embarked system and its motion is driven by the motion of the cart or, better said, by the motor. The motor is influenced by the attached mass and the heavier the mass the greater the nonlinearities involved. Normally, problems of this type are modeled saying that the forcing is harmonic with frequency given by the nominal frequency of the motor. It will be shown here that this hypothesis is far from true.

Without simplifying hypothesis about the terms, the behavior of the system variables are analyzed, as the motor current over time, rotational movement of the motor shaft and force and torque exerted by the DC motor in the mass. The influence of the pendulum embarked in the cart is investigated and it is shown the changes it causes in the dynamics of the second system with respect to the first.

To better see the effects of coupling, two different analysis are developed to the coupled systems. In the first one, it is considered that the mechanical system has no dissipation, the only dissipation is in the electrical part. In the second one, it is considered the existence of friction in the mechanical part.

The two most important parameters of the coupled problem are the attached mass and the amplitude of its motion that is given by the position of the pin used in the coupling. With some simplifying hypothesis a lot of analytical results could have been derived as well as results about chaotic behavior, but this is not the object of the paper. The object is to show the dynamics without undue simplifications.

This paper is organized as follows. Section 2 describes the two coupled electromechanical systems analyzed. Section 3 presents the results of the deterministic simulations developed to each one of them in the case of consideration and no consideration of friction. The influence of the attached mass and the amplitude of its motion are discussed. Also in Section 3, it is presented a configuration of the coupled system that leads to the phenomenon of energy pumping and causes revolution, i. e. the inversion of the master-slave relation. The probability model to the parameter that is considered uncertain is construct in Section 4 and the results of the simulations of the stochastic systems are presented in Section 5. Section 6 presents some conclusions.

2 DYNAMICS OF THE COUPLED SYSTEMS

Next, it is presented the elements of the two coupled systems (motor, cart, and pendulum). The coupling between the motor and the mechanical systems are shown and the two coupled problems are described and mathematically formulated as initial-value problems.

2.1 Electrical system: motor DC

The mathematical modeling of DC motors is based on the Kirchhoff's law [11]. It is constituted by the equations

$$l\dot{c}(t) + r\,c(t) + k_e\dot{\alpha}(t) = v\,, \tag{1}$$

$$j_m\ddot{\alpha}(t) + b_m\dot{\alpha}(t) - k_t\,c(t) = -\tau(t)\,, \tag{2}$$

where t is the time, v is the source voltage, c is the electric current, $\dot{\alpha}$ is the angular speed of the motor, l is the electric inductance, j_m is the motor moment of inertia, b_m is the damping ratio in the transmission of the torque generated by the motor to drive the coupled mechanical system, k_t is the torque constant, k_e is the motor electromagnetic force constant and r is the electrical resistance. Figure 1 shows a sketch of a DC motor. The available torque to the coupled mechanical system is represented by τ, that is the component of the torque vector $\vec{\tau}$ in the z direction shown in Fig. 1.

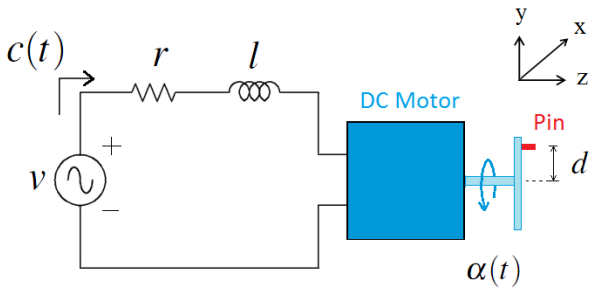


Figure 1: Electrical motor DC.

Assuming that the load applied in the motor and source voltage are constant in time, the motor achieves a steady state. Thus, the electric current and the angular speed become constant

and $\ddot{\alpha}(t) = 0 = \dot{c}(t) = 0$, $\forall t \in \mathbb{R}^{\geq 0}$. By equations (1) and (2), the angular speed of the motor shaft and the current in steady state, respectively $\dot{\alpha}_{steady}$ and c_{steady}, can be calculated by

$$\dot{\alpha}_{steady} = \frac{-\tau\, r + k_t\, v}{b_m\, r + k_e\, k_t} \quad , \quad c_{steady} = \frac{v}{r} - \frac{k_e}{r}\left(\frac{-\tau\, r + k_t\, v}{b_m\, r + k_e\, k_t}\right) . \tag{3}$$

When the hypothesis of constant load is not verified, the angular speed of the motor shaft and the current do not reach a constant value. This kind of situation happens when, for example, a mechanical system is coupled to the motor. In this case, $\dot{\alpha}$ and c variate in time in a way that the dynamics of the motor will be influenced by the coupled mechanical system.

Two more situations are relevant when we analyze electrical motors. The first one is when there is no load applied in the motor (i.e. $\tau(t) = 0$, $\forall t \in \mathbb{R}^{\geq 0}$) and the source voltage is constant in time. Then, the motor achieves its maximum angular speed that is called the *no load speed*. It is calculated by

$$\dot{\alpha}_{no\ load} = \frac{k_t\, v}{b_m\, r + k_e\, k_t} . \tag{4}$$

The second one is when the motor delivers the maximum torque. This torque is achieved when the load applied in the motor is such that the motor does not move at all. This is called the *stall torque*. If the source voltage is constant in time, it is calculated by

$$\tau_{stall} = \frac{k_t\, v}{r} . \tag{5}$$

In the problems discussed here, there is the constraint $\tau(t) < \tau_{stall}$. In Sec. 3 it is taken care do not reach this condition.

2.2 Coupled motor-cart system: a master-slave relation

As described in the introduction, the system analyzed in this paper is composed by a cart whose motion is driven by the DC motor sketched in Fig. 1. The motor is coupled to the cart through a pin that slides into a slot machined on a plexiglas plate that is part to the cart, as shown in Fig. 2. The pin hole is drilled off-center on a disk fixed in the axis of the motor, so that the motor rotational motion is transformed into horizontal cart motion over a rail.

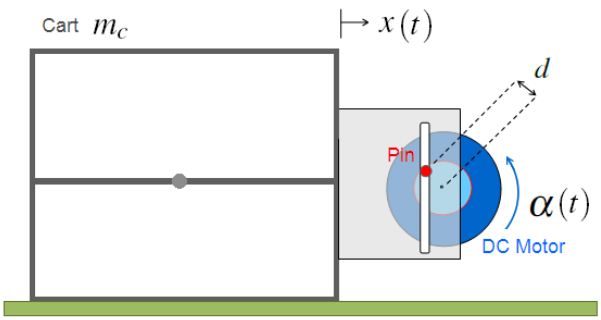


Figure 2: First Mechanical System.

It is noticed that with this configuration, the center of mass of the mechanical system is always located in the center of mass of the cart, so its position does not change.

The mass of the mechanical system, m, is equal the cart mass, m_c, and the horizontal cart displacement is represented by x. Due to constraints, the cart is not allowed to move in the vertical direction. Due to the problem geometry, and noting $||\vec{d}|| = d$, the horizontal motion of the cart and the angular displacement α of the motor are related by the constraint

$$x(t) = d\cos\alpha(t)\ . \tag{6}$$

To model the coupling between the motor and the mechanical system, it is assumed that the motor shaft is rigid. Thus, the available torque to the coupled mechanical system, $\vec{\tau}$, can be written as

$$\vec{\tau}(t) = \vec{d}(t) \times \vec{f}(t)\ , \tag{7}$$

where $\vec{d}$ is the eccentricity of the pin of the motor and $\vec{f}$ is the coupling force between the DC motor and the cart. By the problem geometry, the module of $\vec{d}$ is the nominal eccentricity of the pin. Besides this, the component of $\vec{d}$ that is perpendicular to the plane of the cart movement is always zero and, the others horizontal and vertical components can be calculated from the angular displacement α of the motor.

Assuming that there is no friction between the pin and the slot machined on an acrylic plate, the vector $\vec{f}$ only has a horizontal component, f (the horizontal force that the DC motor exerts in the cart). Thus, $\vec{d}$ and $\vec{f}$ are written as

$$\vec{d}(t) = \begin{bmatrix} d\cos\alpha(t) \\ d\sin\alpha(t) \\ 0 \end{bmatrix} \qquad \vec{f}(t) = \begin{bmatrix} f(t) \\ 0 \\ 0 \end{bmatrix}\ . \tag{8}$$

Substituting Eq. (8) in Eq. (7), the module of $\vec{\tau}(t)$ is

$$\tau(t) = -f(t)d\sin\alpha(t)\ . \tag{9}$$

Since the cart is modeled as a particle, it satisfies the equation

$$m\,\ddot{x} = f(t)\ . \tag{10}$$

Substituting the Eq. (9), (6) and (10) in the equations of the electric motor, we obtain a system of differential equations to the coupled system.

The initial value problem for the motor-cart system is: given the source voltage of the motor, v, find $(\alpha,\ c)$ satisfying

$$\begin{aligned} &l\dot{c}(t) + r\,c(t) + k_e\dot{\alpha}(t) = v\ , \\ &\ddot{\alpha}(t)\ \left[j_m + md^2(\sin\alpha(t))^2\right] + \dot{\alpha}\ \left[b_m + md^2\dot{\alpha}(t)\cos\alpha(t)\ \sin\alpha(t)\right] - k_t\ c(t) = 0\ , \end{aligned} \tag{11}$$

for given initial conditions.

Comparing Eqs. 1, 2, and 11 it is seen that the attached mass influences the motor in a parametric way, [12].

2.3 Coupled motor-cart system with friction

In the model developed to the cart-motor system described in the last subsection, the only mechanism of energy dissipation is associated to the electrical motor. The absence of friction in the mechanical part turns this model unrealistic since the motor can drive the cart for any value of the mass of the mechanical system, m.

Next, it is presented a model to the cart-motor system considering friction between the cart and the rail and in the coupling mechanism, i.e. between the pin and the slot. Therefore, part of the energy provided by the source voltage is dissipated.

As written to the cart-motor system without friction, the available torque to the mechanical system, $\vec{\tau}$, is

$$\vec{\tau}(t) = \vec{d}(t) \times \vec{f}(t) \,, \tag{12}$$

The vector $\vec{f}$ has a horizontal component, f_x, that is the horizontal force that the DC motor exerts in the cart, and has a vertical component, f_y, that is the vertical force that the DC motor exerts in the cart due to friction between the pin and the slot. Thus, $\vec{d}$ and $\vec{f}$ are written as

$$\vec{d}(t) = \begin{bmatrix} d\cos\alpha(t) \\ d\sin\alpha(t) \\ 0 \end{bmatrix} \qquad \vec{f}(t) = \begin{bmatrix} f_x(t) \\ f_y(t) \\ 0 \end{bmatrix} . \tag{13}$$

Substituting Eq. (13) in Eq. (12), the module of $\vec{\tau}(t)$ is

$$\tau(t) = f_y(t)\, d\cos\alpha(t) - f_x(t)\, d\sin\alpha(t) \,. \tag{14}$$

The friction in the couple mechanism makes a vertical friction force, fat_c, in the pin. The adopted model to this force is

$$fat_c(t) = -\,|f_x(t)|\,\mu_1\ \mathrm{sgn}\left(\dot{\alpha}\cos\left(\alpha(t)\right)\right) , \tag{15}$$

where μ_1 is the coefficient friction between the pin and the slot and the term $\mathrm{sgn}\left(\dot{\alpha}\cos\left(\alpha(t)\right)\right)$ indicates the sign of the pin velocity. The vertical force that the DC motor exerts in the cart is

$$f_y(t) = -fat_c(t) \,. \tag{16}$$

The friction force between the cart and the rail is written as

$$fat_r(t) = -\,|n(t)|\,\mu_2\ \mathrm{sgn}\left(\dot{x}(t)\right) , \tag{17}$$

where n is the normal force exerted by the rail in the cart, μ_2 is the coefficient between the cart and the rail. Since the cart is modeled as a particle, its movement in the horizontal direction satisfies the equation

$$m\,\ddot{x} = f_x(t) + fat_r(t) \,, \tag{18}$$

and since the cart is not allowed to move in the vertical direction, the sum of all forces acting on the cart in the vertical direction must be zero, i.e.

$$0 = n(t) - m\,g + f_y(t) \,, \tag{19}$$

where g is the gravitational acceleration.

Substituting the Eq. (14), (15), (16) and (17) in the equations of the electric motor, and considering Eq. (18), (19), we obtain a system of differential algebraic equations to the coupled motor-cart system with friction.

The initial value problem is: given v, find $(\alpha,\ c)$ satisfying

$$
\begin{aligned}
& l\dot{c} + r\,c + k_e\dot{\alpha} = v\ , \\
& j_m\ddot{\alpha} + b_m\dot{\alpha} - k_t c = -\,|f_x|\,\mu_1\ \operatorname{sgn}(\dot{\alpha}\cos\alpha)d\cos\alpha + f_x d\sin\alpha\ , \\
& m(-\ddot{\alpha}d\sin\alpha - (\dot{\alpha})^2 d\cos\alpha) = f_x + |n|\,\mu_2\ \operatorname{sgn}(\dot{\alpha}\sin\alpha)\ , \\
& 0 = n - mg + |f_x|\,\mu_1\ \operatorname{sgn}(\dot{\alpha}\cos\alpha)\ ,
\end{aligned}
\tag{20}
$$

for given initial conditions.

2.4 Coupled motor-cart-pendulum system: introduction of a mechanical energy reservoir

In the second system, a third element, a pendulum, is attached to the cart. It is placed inside the cart, as shown in Fig. 3. The suspension point O is fixed in the cart, hence moves with it. The important point is that it can have a relative motion with respect to the cart. That is the meaning we give to *embarked*.

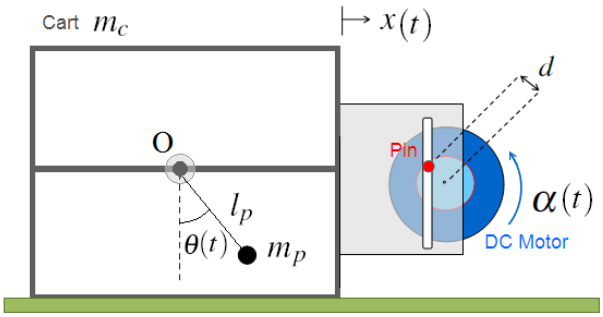


Figure 3: Second Mechanical System.

The embarked pendulum is modeled as a mathematical pendulum (bar without mass and particle of mass m_p at the end). The pendulum length is represented by l_p and the pendulum angular displacement by θ.

Using the Lagrangian equation $\mathcal{L} = \mathcal{T} - \mathcal{V}$, with the angle θ and displacement x of the cart as generalized coordinates, the kinetic and potential energies of the mechanical system, are defined respectively as

$$
\mathcal{T} = \frac{1}{2}m_p[(l_p\dot{\theta}\cos\theta + \dot{x})^2 + (l_p\dot{\theta}\sin\theta)^2] + \frac{1}{2}m_c\dot{x}^2\ , \tag{21}
$$

$$
\mathcal{V} = -m_p g(l_p\cos\theta)\ . \tag{22}
$$

Thus, the equation of the cart-pendulum are

$$
m_p l_p^2\ddot{\theta}(t) + m_p l_p\ddot{x}(t)\cos\theta(t) + m_p g l_p\sin\theta(t) = 0\ , \tag{23}
$$

$$(m_p + m_c)\ddot{x}(t) + m_p l_p \ddot{\theta}(t)\cos\theta(t) - m_p l_p \dot{\theta}^2(t)\sin\theta(t) = f(t)\ , \tag{24}$$

where, again, f represents the horizontal coupling force between the DC motor and the cart, g is the gravity and the horizontal cart displacement is x.

The relative motion of the embarked pendulum causes a variation in the position of the center of mass of the mechanical system. In this case, the mass of the mechanical system, m, is equal the cart mass plus the pendulum mass, $m_c + m_p$.

As in the first coupled system, the cart is not allowed to move in the vertical direction. Due to the problem geometry, the horizontal motion of the cart and the angular displacement α of the motor are related by Eq. (6).

Once again, it is assumed that the motor shaft is rigid and that there is no friction between the pin and the slot machined on the acrylic plate. Thus, the available torque to the coupled mechanical system, $\vec{\tau}$, is written as Eq. (9).

Substituting the Eq. (9), (6) and (24) in the equations of the electric motor and in Eq. (23), we obtain a system of differential equations for the coupled system.

Given the source voltage of the motor, v, the dynamic of the coupled system is written in terms of the variables α, c and θ. Thus, the initial value problem for the motor-cart-pendulum system is: given the source voltage of the motor, v, find $(\alpha,\ c,\ \theta)$ satisfying

$$\begin{aligned}
&l\dot{c}(t) + rc(t) + k_e\dot{\alpha}(t) = v\ ,\\
&\ddot{\alpha}(t)\ \left[j_m + (m_c+m_p)d^2(\sin\alpha(t))^2\right] +\ \dot{\alpha}(t)\ \left[b_m + (m_c+m_p)d^2\dot{\alpha}(t)\cos\alpha(t)\ \sin\alpha(t)\right] +\\
&\qquad +k_t\ c(t)\ -\ \ddot{\theta}(t)\ [m_p l_p\cos\theta(t) d\sin\alpha(t)] + \dot{\theta}(t)\ \left[m_p\ l_p\dot{\theta}(t)\sin\theta(t) d\sin\alpha(t)\right] = 0\ ,\\
&\ddot{\theta}(t)\ \left[m_p\ l_p^2\right] - \ddot{\alpha}(t)\ [m_p\ l_p\ \cos\theta(t) d\sin\alpha(t)] -\ \dot{\alpha}(t)\ [m_p\ l_p\cos\theta(t) d\cos\alpha(t)\dot{\alpha}(t)] +\\
&\qquad\qquad + m_p\ g\ l_p\sin\theta(t)\ =\ 0\ ,
\end{aligned} \tag{25}$$

for given initial conditions.

2.5 Coupled motor-cart-pendulum system with friction

Next, it is presented a model to the motor-cart-pendulum system considering friction between the cart and the rail and in the coupling mechanism, i.e. between the pin and the slot.

As written to the motor-cart-pendulum system without friction, the module of the available torque to the mechanical system, $\vec{\tau}$, is

$$\tau(t) = f_y(t)\ d\cos\alpha(t) - f_x(t)\ d\sin\alpha(t)\ . \tag{26}$$

where f_x is the horizontal component of the force that the DC motor exerts in the cart and f_y is its vertical component. The friction in the couple mechanism makes a vertical friction force, fat_c, in the pin. The adopted model to this force is equal to the model adopted in the motor-cart system with friction, i.e.

$$fat_c(t) = -\left|f_x(t)\right|\mu_1\ \mathrm{sgn}\left(\dot{\alpha}\cos\left(\alpha(t)\right)\right)\ , \tag{27}$$

where again μ_1 is the coefficient friction between the pin and the slot and the term $\text{sgn}(\dot{\alpha}\cos(\alpha(t)))$ indicates the sign of the pin velocity. The vertical force that the DC motor exerts in the cart is

$$f_y(t) = -fat_c(t) \, . \tag{28}$$

The friction force between the cart and the rail is written as

$$fat_r(t) = -|n(t)|\,\mu_2\ \text{sgn}(\dot{x}(t)) \, , \tag{29}$$

where again n is the normal force exerted by the rail in the cart, μ_2 is the friction coefficient between the cart and the rail.

Using the Lagrangian equation, the obtained equation of the cart-pendulum is

$$m_p l_p^2 \ddot{\theta}(t) + m_p l_p \ddot{x}(t)\cos\theta(t) + m_p g l_p \sin\theta(t) = 0 \, , \tag{30}$$

$$(m_p + m_c)\ddot{x}(t) + m_p l_p \ddot{\theta}(t)\cos\theta(t) - m_p l_p \dot{\theta}^2(t)\sin\theta(t) = f_x(t) + fat_r(t) \, , \tag{31}$$

Since the cart is not allowed to move in the vertical direction, the sum of all forces acting on the cart in the vertical direction must be zero. Thus the sum of the normal force exerted by the rail in the cart, the gravitational force, the vertical force f_y and the vertical component of the force exerted by the pendulum in the cart must be zero, i.e.

$$0 = n(t) - (m_c + m_p)\, g + f_y(t) + m_p l_p \ddot{\theta}(t)\sin(\theta(t)) + m_p l_p \dot{\theta}^2(t)\cos(\theta(t)) \, . \tag{32}$$

Substituting the Eq. (26), (27), (28) and (29) in the equations of the electric motor, and considering Eq. (30), (31) and (32), we obtain a system of differential algebraic equations to the coupled motor-cart-pendulum system with friction.

The initial value problem is: given v, find $(\alpha,\, c)$ satisfying

$$\begin{aligned}
&l\dot{c} + r\,c + k_e\dot{\alpha} = v \, ,\\
&j_m\ddot{\alpha} + b_m\dot{\alpha} - k_t c = -|f_x|\,\mu_1\ \text{sgn}(\dot{\alpha}\cos\alpha) d\cos\alpha + f_x d\sin\alpha \, ,\\
&\ddot{\theta}\ \left[m_p\, l_p^2\right] - \ddot{\alpha}\ \left[m_p\, l_p\ \cos\theta d\sin\alpha\right] - \ \dot{\alpha}\ \left[m_p\, l_p \cos\theta d\cos\alpha\dot{\alpha}\right] + \ m_p\, g\, l_p \sin\theta\ =\ 0 \, ,\\
&m(-\ddot{\alpha}d\sin\alpha - (\dot{\alpha})^2 d\cos\alpha) + m_p l_p \ddot{\theta}\cos(\theta) + m_p l_p \dot{\theta}^2\sin(\theta) = f_x + |n|\,\mu_2\ \text{sgn}(\dot{\alpha}\sin\alpha) \, ,\\
&0 = n - (m_c + m_p)g + |f_x|\,\mu_1\ \text{sgn}(\dot{\alpha}\cos\alpha) + + m_p l_p \ddot{\theta}\sin(\theta) + m_p l_p \dot{\theta}^2\cos(\theta) \, ,
\end{aligned} \tag{33}$$

for given initial conditions.

3 NUMERICAL SIMULATIONS OF THE DYNAMICS OF THE COUPLED SYSTEMS

To better comprehend the behavior of the coupled system composed by the DC motor and the mechanical systems, we started analyzing the deterministic models. Simulations of the two systems are compared in order to observe the influence of the pendulum in the rotational motion of the motor shaft.

3.1 Simulations of the motor-cart system

Looking at the initial value problem Eq. (11), it is observed that if the nominal eccentricity of the pin, d, is small, Eq. (11) tends to the linear system equations of the DC motor, Eq. (1) and (2), in case of no load. But as the eccentricity grows, the non-linearities become more pronounced. The nonlinearity also increases with the attached mass, m. To better comprehend the increase of nonlinearity, the system Eq. (11), was integrated in a range of $[0.0,\ 2.0]$ seconds for different values of d and m.

The specifications of the motor parameters used in all simulations were obtained from the specifications of the motor Maxon DC brushless number 411678. The source voltage was assumed to be constant in time and equal to 2.4 [Volt]. This value is just 10% of the nominal voltage of this motor, 24 [Volt], but it ensures the respect to the constraint $\tau(t) < \tau_{stall}$ for the parameters considered for the coupled system. So the simulations reflect realizable situations.

In the integration, the initial conditions assumed for the current in the motor and for the angular position and velocity of the motor shaft were, in all simulations:

$$\alpha(0) = 0.0 \text{ [rad]}\,, \qquad \dot{\alpha}(0) = 0.0 \text{ [Hz]}\,, \qquad c(0) = v/r = 7.81 \text{ [Amp]}\,. \tag{34}$$

Due to the coupling mechanism, coupling torque, τ, variates in time. Thus, the angular speed of the motor shaft and the current are not constant values after the transient. As the motor-cart system does not have any mechanism of storing energy, after the transient the dynamics achieves a periodic state.

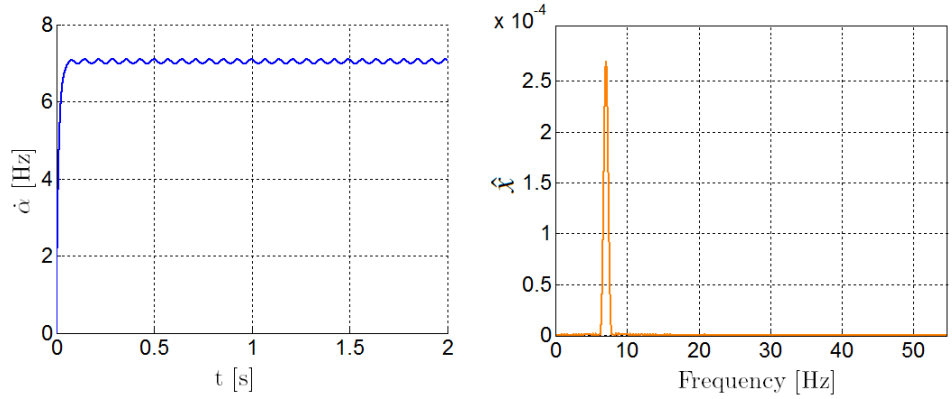
To study the variation of the motor current, the coupling force and torque, the mass was fixed to 5 [Kg] and two values of d were selected: 0.001 [m] and 0.010 [m]. The selection guarantees that the stall torque is not reached in the simulations.

The Fast Fourier Transform of the cart displacement over time, $\hat{x}$, was computed for the two different values of d. Figures 4(b) and 5(b) show the obtained results. It is noted that when d is small, as 0.001 [m], the angular speed of the motor shaft oscillates with a small amplitude around 7 [Hz] and the FFT graph of x presents only one peak at this frequency. In contrast to this, when d is bigger, the amplitude of the oscillations of $\dot{\alpha}$ grows and, due to the non-linearity effects, the FFT graph of x presents more than one peak. The first one of them is at 6.56 [Hz] and, the following are at odd multiples of this value.

As said in the introduction of this paper, normally problems of coupled systems are modeled saying that the force is imposed, so no coupling, and it is harmonic with frequency given by the nominal frequency of the motor. The dynamic of the motor is not considered. The graphs of Fig. 4(a) and 5(a) confirm that this hypothesis does not correspond to reality. Even when d is small, the angular speed of the motor shaft do not reach a constant value. After a transient it achieves a periodic state. It oscillates around a mean value and these oscillations are periodic.

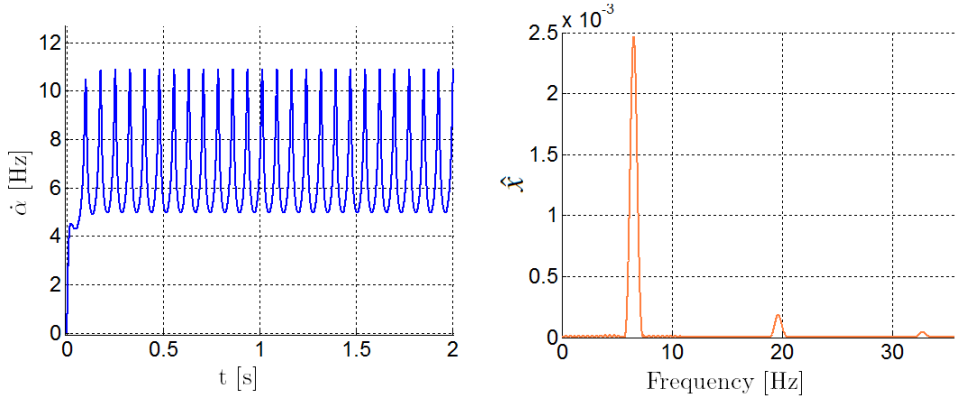
Others graphs to be analyzed are the $f(t)$ and $\tau(t)$ variation during one n-th cart movement cycle. This type of graph will be called *phase portrait*. The Fig. 6(a) and 6(b) shows these graphs for the fourth cycle, i.e., $n = 4$ and $\alpha(t) \in [8\pi, 10\pi]$.

Observing the f graph and remembering the constrain $x(t) = d\cos\alpha(t)$, it is verified that the horizontal force presents its maximum value when $x(t) = -d$ [m] and its minimum value when $x(t) = d$ [m]. Besides this, the cart positions corresponding to the points where f changes sign are $x(t) = -0.00415$ [m] and $x(t) = 0.00415$ [m]. At this values, the angular positions of the motor shaft, in the n-th cart movement cycle, are equals to $\alpha(t) = n2\pi + 1.99$ [rad] and $\alpha(t) = n2\pi + 5,14$ [rad].



(a) (b)

Figure 4: Motor-cart system $d = 0.001$ [m]: (a) angular speed of the motor shaft over time and (b) Fast Fourier Transform of the cart displacement.



(a) (b)

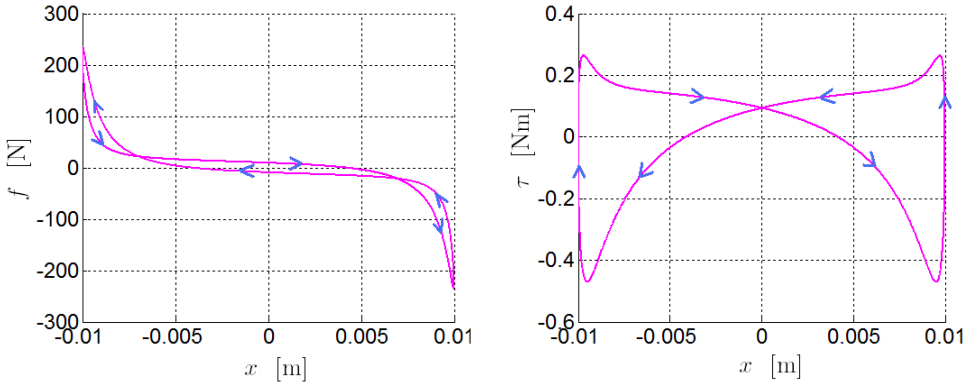
Figure 5: Motor-cart system $d = 0.01$ [m]: (a) angular speed of the motor shaft over time and (b) Fast Fourier Transform of the cart displacement.

Observing the τ graph, it is verified that the torque presents four points of sign changes. Two of them occur when $x(t) = -d$ and $x(t) = d$, corresponding respectively to α multiple of π and α multiple of 2π. This changes were expected from Eq. (9). The others two changes occur exactly in the same cart positions that we have the f sign changing, i.e., when $x(t) = -0.00415$ [m] and $x(t) = 0.00415$ [m]. In each cart movement cycle, the horizontal force f and the torque τ follow once the paths shown in Fig. 6(a) and 6(b).

The Fig. 7(a) and 7(b) show the graphs of the current variation during the fourth cart movement cycle and the torque variation in function of the current. In the left graph, it is noted that the current presents four points of sign changing. They occur when the x value are 0.00891 [m], -0.00728 [m], -0.00891 [m] and 0.00728 [m]. The corresponding angular positions of the motor shaft in the n-th cart movement cycle, α, at these points are $n2\pi + 0.47$ [rad], $n2\pi + 2.38$ [rad], $n2\pi + 3.61$ [rad] and $n2\pi + 5.53$ [rad].

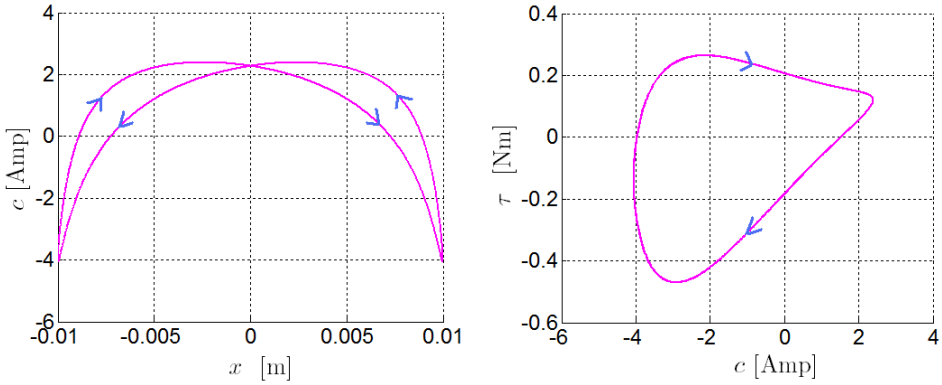
3.2 Simulations of the motor-cart system with friction

Looking at the system of differential algebraic equations to the coupled motor-cart system with friction, Eq. (20), it is possible observe that the two frictions forces considered in the



(a) (b)

Figure 6: Motor-cart system with $d = 0.01$ [m]: (a) horizontal force f and (b) torque τ during one cycle of the cart movement.



(a) (b)

Figure 7: Motor-cart system with $d = 0.01$ [m]: (a) current variation during the fourth cart movement cycle and (b) torque variation in function of the current.

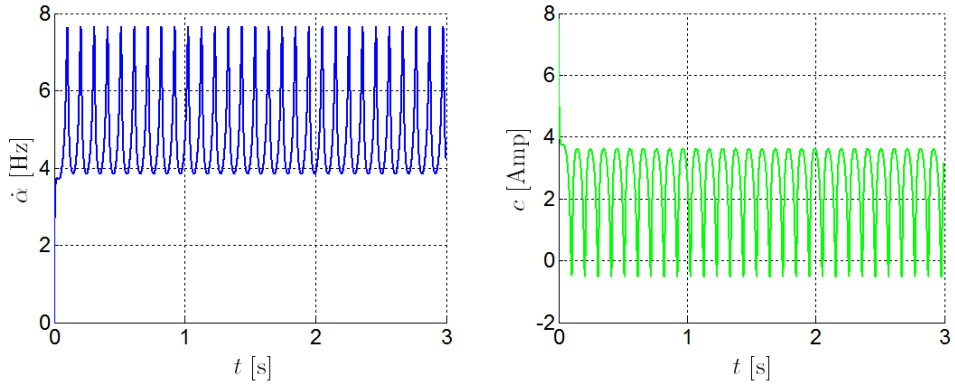
problem are coupled, i.e. there is mutual influence between them.

To better understand the influence of each friction force in the system and the effects of the coupling between them, Eq. (20) was integrated numerically in a range of $[0.0,\ 3.0]$ seconds in tree different situations. In the first one, it was considered the existence of friction only in the coupling mechanism. In the second one, it was considered the existence of friction only between the cart and the rail and, in the third one, the two frictions were considered.

In all simulations, the values used to the initial conditions for the angular position and velocity of the motor shaft were $\alpha(0) = \dot{\alpha}(0) = 0.0$, and for the current in the motor was $c(0) = v/r = 7.81$ [Amp]. The specifications of the motor parameters were equal to the ones used in the previous integrations. The source voltage was assumed to be constant in time and equal to 2.4 [Volt]. The values of the mass and nominal eccentricity of the pin were $m = 5.0$ [Kg] and $d = 0.010$ [m].

The values of the friction coefficients were obtained from [13]. It was assumed that the pin is made of steel and the slot is machined on a plexiglas plate. The used value to the friction coefficient in the coupling mechanism was $\mu_1 = 0.4$. To determine the second friction coefficient, it was assumed that the cart is made of steel and the rail made of cast iron. The used value to μ_2 was 0.1.

Next are shown the results of the integration of Eq. (20) considering the existence of friction only in the coupling mechanism. As in the previous simulations, due to the coupling mechanism, the coupling torque, τ, variates in time. Thus, the angular speed of the motor shaft and the current are not constant values after the transient. Despites the consideration of friction, after a transient period the dynamics achieves a periodic state that can be observed in Fig. 8(a) and 8(b).



(a) (b)

Figure 8: Motor-cart system with friction in the coupling mechanism: (a) angular velocity of the motor shaft and (b) current over time.

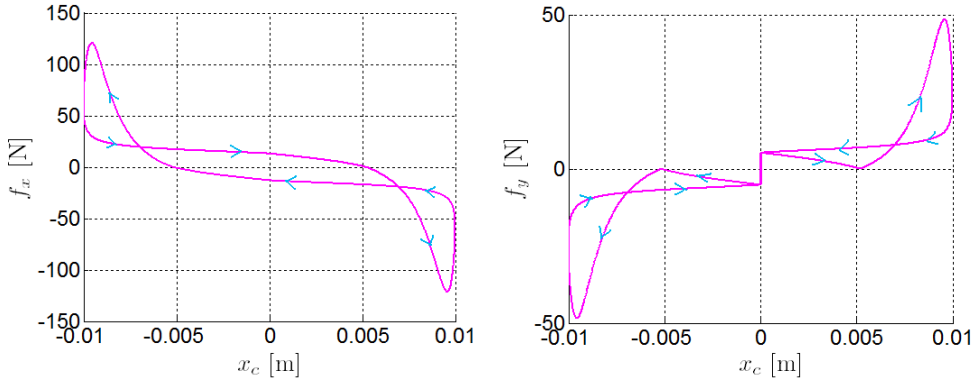
The phase portraits of the horizontal and vertical forces during one cycle of the cart movement are shown in Fig. 9(a) and 9(b). Comparing the graph of f_x with Fig. 6(a) it is possible observe that the horizontal force does not presents anymore its maximum and minimum value at the extremities positions of the cart trajectory. They occur at $x(t) = -0.00957$ [m] and $x(t) = 0.00957$ [m]. Besides this, the cart positions corresponding to the points where f_x changes sign were also modified. They occur at $x(t) = -0.00518$ [m] and $x(t) = 0.00518$ [m].

The graph of f_y presents its minimum value at $x(t) = -0.00957$ [m], its maximum value at $x(t) = 0.00957$ and presents a discontinuity at $x(t) = 0.0$ [m]. This discontinuity occurs because at this position, the friction force in the coupling mechanism changes its sign due to the term $\text{sgn}(\dot{\alpha}\cos(\alpha(t)))$ that appears in Eq. (15) and because $f_y(t) = -fat_c(t)$, see Eq. (16). Another characteristic of this graph is that f_y is zero at the same positions that occurs the sign changing of f_x ($x(t) = 0.00518$ [m] and $x(t) = 0.00518$ [m]). This result is expected since the friction force in the coupling mechanism is proportional to the module of f_x, see Eq. (15).

Figures 10(a) and 10(b) show the normal force and coupling torque during one cycle of the cart movement.

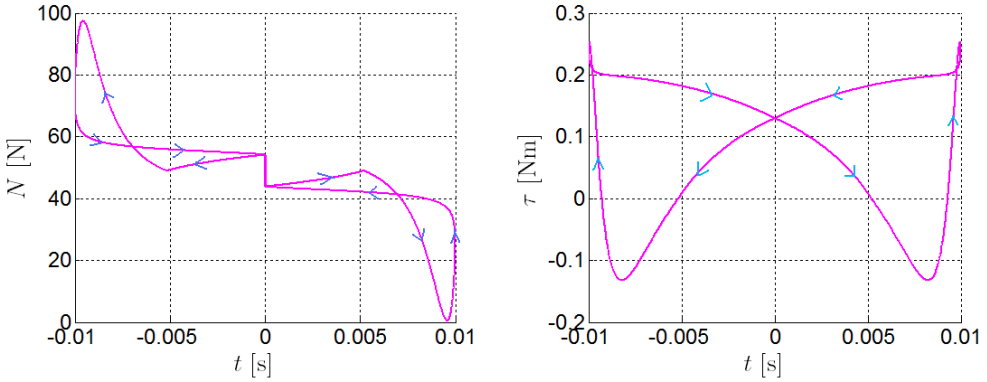
The results of the integration of Eq. (20) considering the existence of friction only between the cart and the rail are presented next. Figures 11(a) and 11(b) show the phase portrait graphs to the horizontal force and torque. Comparing the graph of f_x with Fig. 8(a) it is possible observe that different to the previous case, the horizontal force presents its maximum and minimum value at the extremities positions of the cart trajectory. The cart positions corresponding to the points where f_x changes sign are at $x(t) = -0.00526$ [m] and $x(t) = 0.00526$ [m].

Next are presented the results of the integration of Eq. (20) considering the two friction forces, in the coupling mechanism and between the cart and the rail. Figures 12(a) and 12(b) show the phase portraits of the horizontal and vertical forces. Comparing these graphs with the previous phase portraits of the coupling forces, Fig. 9(a) and 9(b), it is possible observe that



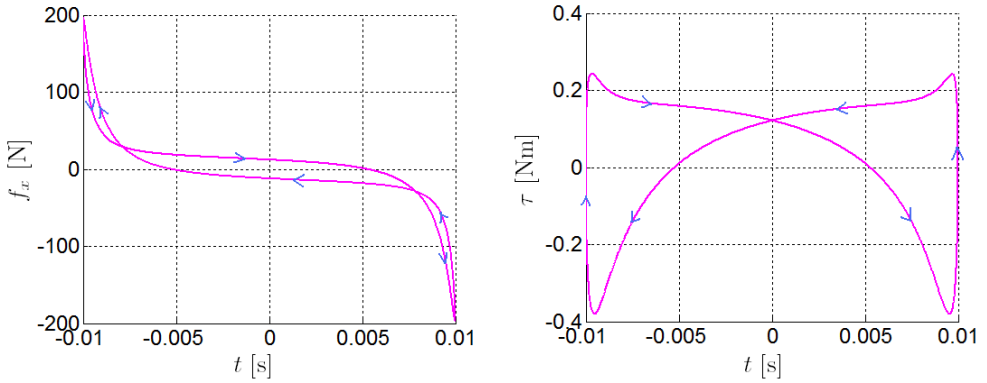
(a) (b)

Figure 9: Motor-cart system with friction in the coupling mechanism: (a) horizontal and (b) vertical forces during one cycle of the cart movement.



(a) (b)

Figure 10: Motor-cart system with friction in the coupling mechanism: (a) normal force and (b) torque during one cycle of the cart movement.

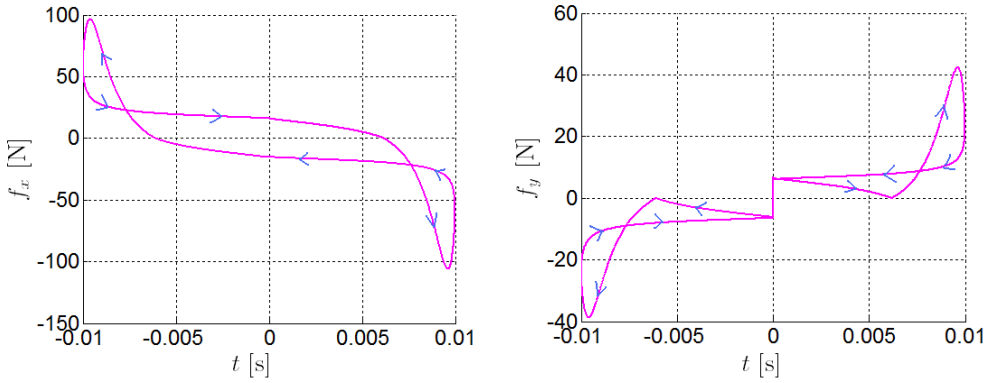


(a) (b)

Figure 11: Motor-cart system with friction between the cart and rail: (a) horizontal force and (b) torque during one cycle of the cart movement.

they present similar shapes to the previous ones but they have lost their symmetry in relation to the maximum and minimum values of the forces. For example, the maximum horizontal force

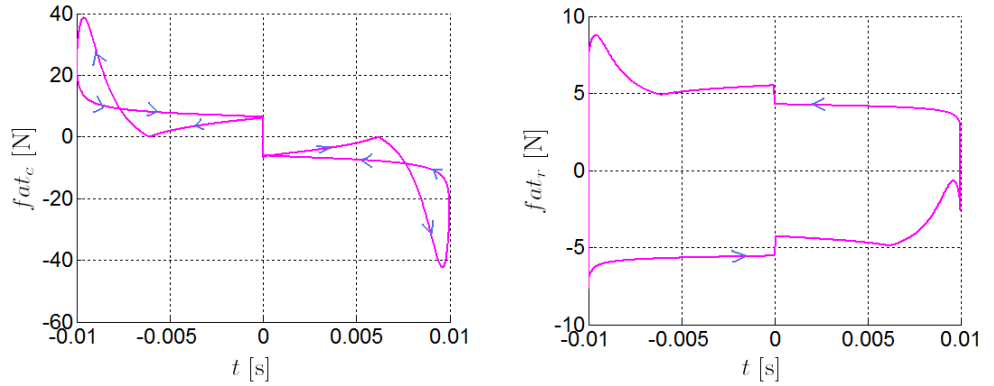
in the new phase portrait is 96.7 [N] and the minimum is −105.9 [N].



(a) (b)

Figure 12: Motor-cart system with friction in the coupling mechanism and between the cart and rail: (a) horizontal and (b) vertical forces during one cycle of the cart movement.

The same phenomenon occurs with the phase portraits of the friction forces, fat_c and fat_r, shown in Fig. 13(a) and 13(b).



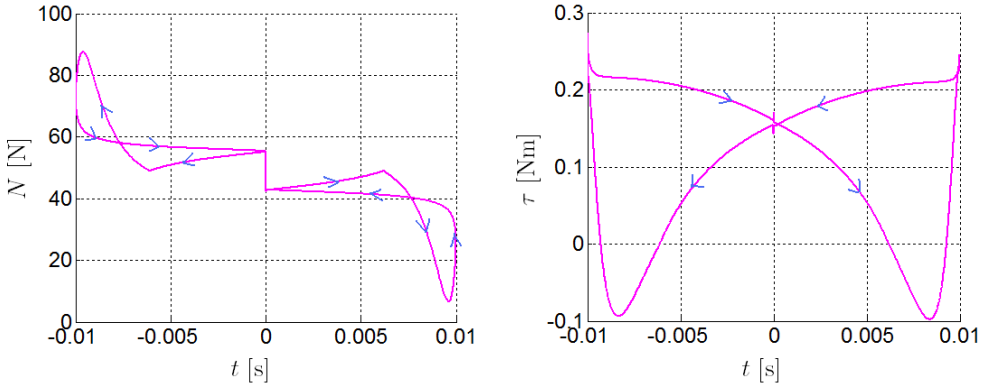
(a) (b)

Figure 13: Motor-cart system with friction in the coupling mechanism and between the cart and rail: friction (a) in the coupling mechanism and (b) between the cart and the rail during one cycle of the cart movement.

Figures 14(a) and 14(b) show the phase portraits of the normal force and the coupling force. In the graph of τ is possible observe that there is a discontinuity at $x(t) = 0.0$ [m] due to discontinuity that exists in phase graph of f_y at this position.

The lost of symmetry in the phase portraits in the case that the two frictions are considered is due to difference of the nature of the forces acting on the cart in horizontal and vertical direction, see Eq. (18) and (19). While in the balance of horizontal forces there are only dynamic forces (f_x and fat_r), in the balance of vertical forces there are two types of forces, dynamics (f_y and n) and constant (the weight $m\,g$).

To verify this, one simple test was donne. In the the integration of Eq. (20), the value of acceleration of gravity was assumed to be equal to zero, making vanish the weight force in Eq. (19). As result, all the phase diagrams became symmetrical.



(a) (b)

Figure 14: Motor-cart system with friction in the coupling mechanism and between the cart and rail: (a) normal force and (b) torque during one cycle of the cart movement.

3.3 Simulations of the motor-cart-pendulum system

A similar analysis to the one made to the motor-cart system was developed for the motor-cart-pendulum system.

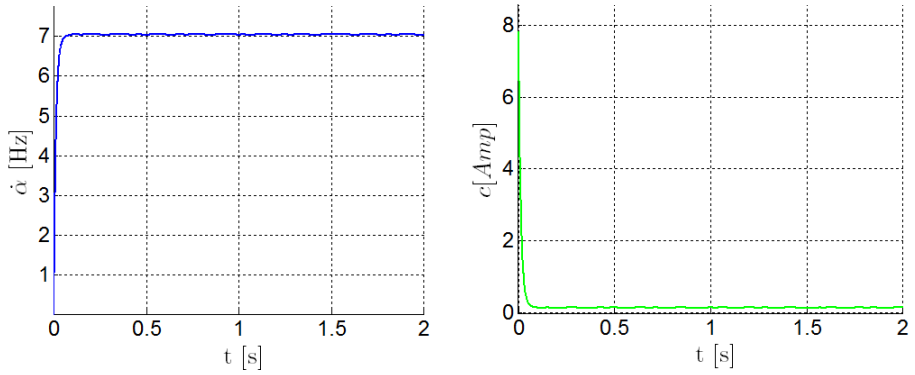
Looking at the initial value problem Eq. (25), it is observed that if the nominal eccentricity of the pin, d, is small and the angle $\theta(t)$ is near zero, Eq. (25) tends to a linear system. But as the eccentricity grows, the nonlinearities become more pronounced. To better comprehend the increase of nonlinearities, the system Eq. (25), was integrated in a range of [0.0, 50.0] seconds for two different values of d: 0.001 [m] and 0.010 [m].

It was considered as initial conditions for the angular position and velocity of the motor shaft, $\alpha(0) = \dot{\alpha}(0) = 0.0$, and for the current in the motor $c(0) = v/r = 7.81$ [Amp] and for the angular position and velocity of the pendulum $\theta(0) = \dot{\theta}(0) = 0.0$. The specifications of the motor parameters used in the simulations are equal to the ones used in the simulations of the motor-cart system. The source voltage was assumed to be constant in time and equal to 2.4 [Volt]. The values of the cart and the pendulum masses were $m_c = 0.0$ [Kg] and $m_p = 5.0$ [Kg], so that the total mass, $m = m_c + m_p = 5.0$ [Kg], is equal to the embarked mass. Although the masses are equal, this configuration contrasts with the one of the motor-cart system used in the previous simulations. In spite of having the same masses, the pendulum has a relative motion with respect to the cart, and this make a huge difference. The pendulum length was assumed to be 0.075 [m].

The results obtained with the integration of Eq. (25), considering $d = 0.001$ [m], are shown in Fig. 15(a) and 15(b). These results reveal that when d is small, the angular speed of the motor shaft oscillates over time with a very small amplitude around 7 [Hz] and the current also oscillates with a small amplitude around 0.13 [Amp].

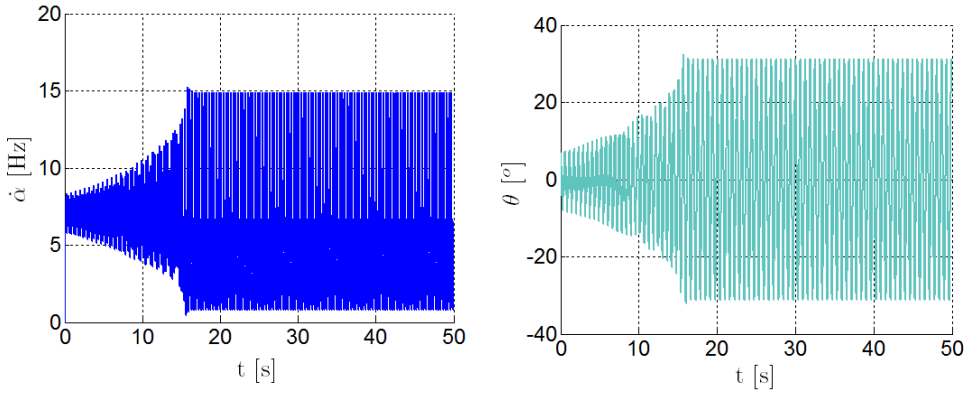
When d is bigger, the amplitude of the oscillations of $\dot{\alpha}$ is bigger when compared with the result obtained with the smaller d. Figures 16(a) and 16(b) show the angular speed of the motor and angular displacement pendulum over time as result to the integration of Eq. 25 with $d = 0.01$ [m].

The presence of the pendulum, that is a mechanism energy reservoir, presents reflects in the graphs of f and τ during one cart movement cycle. Figures 17(a) and 17(b) show these two graphs for the last cycle in the period $[0,\ 50]$ seconds of the integration of Eq. 25. It is possible to observe that the graphs of τ and f have lost their symmetry in relation to a vertical axis drawn



(a) (b)

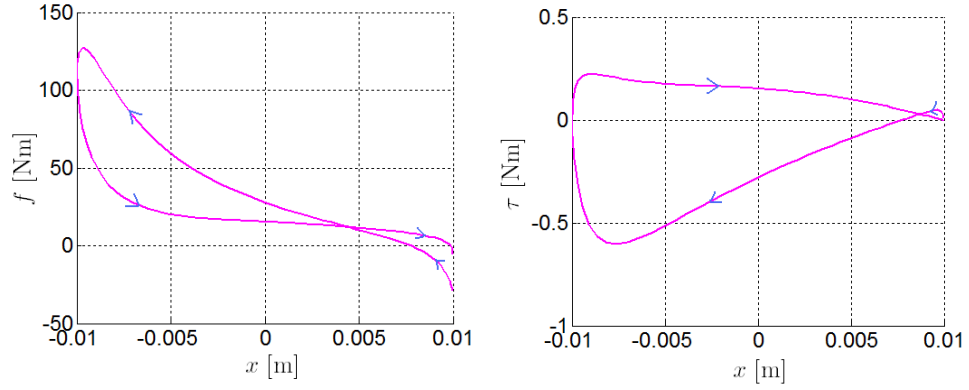
Figure 15: Motor-cart-pendulum system with $d = 0.001$ [m]: (a) angular velocity of the motor shaft and (b) current over time.



(a) (b)

Figure 16: Motor-cart-pendulum system with $d = 0.01$ [m]: (a) angular velocity of the motor shaft and (b) pendulum displacement over time.

at $x = 0$. Thus, the pendulum changes the dynamic behavior of the cart and of the motor. More details could be found in [14] and [15].



(a) (b)

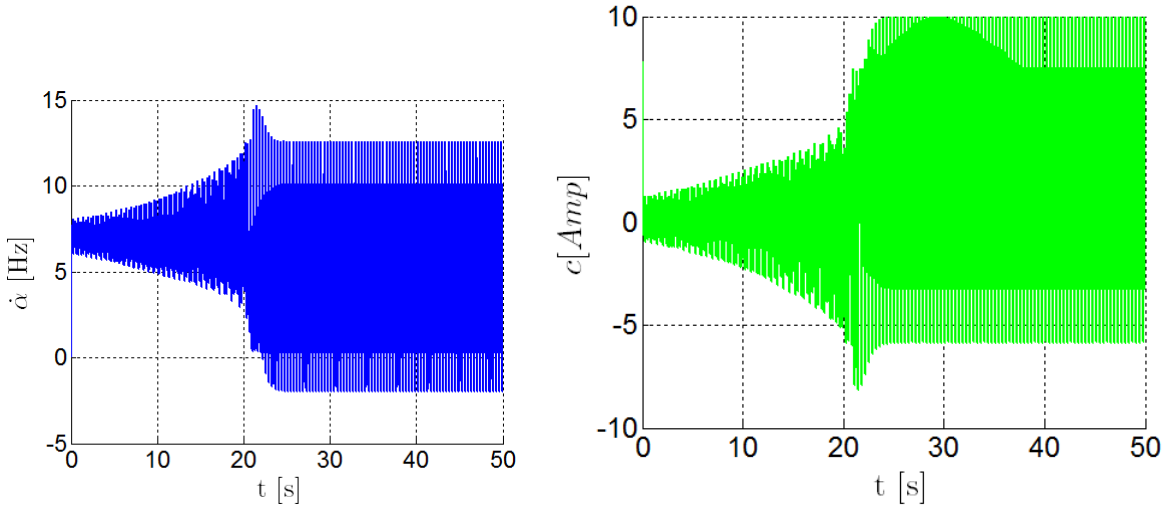
Figure 17: Motor-cart-pendulum system with $d = 0.01$ [m]: (a) horizontal force f and (b) torque τ during the last cycle of the cart movement.

3.4 Simulations of the motor-cart-pendulum system: pumping leads to revolution

In the analysis developed to the the motor-cart-pendulum system, in the previous section of the paper, the cart mass was considered to be zero and the pendulum mass 5.0[Kg]. Next, it is presented an analysis of the behavior of this system with a different mass configuration. The cart mass is kept as 0.0 [Kg] and a smaller value is selected to the pendulum mass, $m_p = 4.0$ [Kg], so that the total mass, $m_c + m_p = 4.0$ [Kg], is still equal to the embarked mass.

To observe the influence of this new configuration in the system behavior, the Eq. 25 was integrated in a range of $[0,\ 50]$ seconds with the null initial conditions to $\alpha(0)$, $\dot{\alpha}(0)$, $\theta(0)$ and $\dot{\theta}(0)$. The initial current was considered equal to $c(0) = v/r = 7.81$ [Amp] and the nominal pin eccentricity 0.01 [m]. The source voltage was assumed to be constant in time and the specifications of the motor parameters were equal to the used in the previous simulations

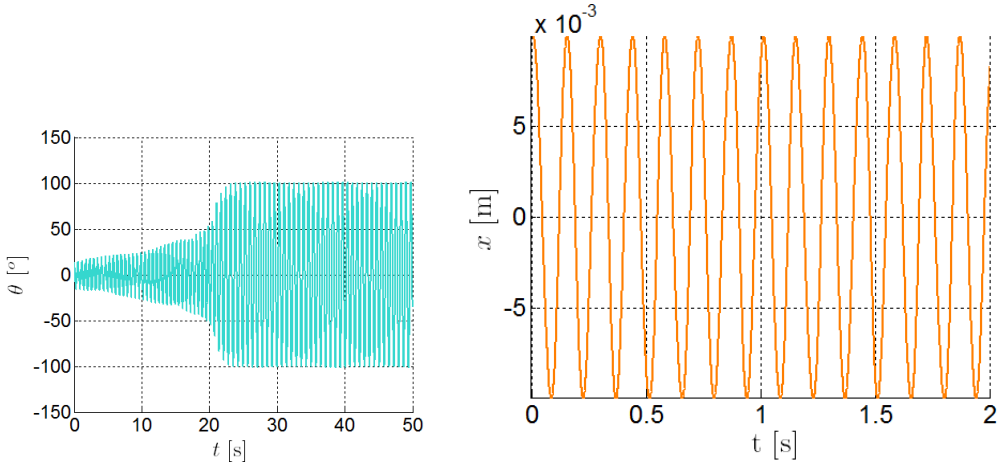
The obtained results for the angular speed of the motor shaft, for the current and cart and pendulum displacements are shown in Fig. 18(a), Fig. 18(b), Fig. 19(a) and Fig. 19(b). The mechanical system pumps energy from the motor and the amplitude of the pendulum grows reaching a point where the mechanical system starts to drive the motion, [16, 17, 18]. This is seen nothing that $\dot{\alpha}$ takes negatives values, meaning that the motor shaft changes its motion direction sometimes. When the angular speed of the motor shaft is positive, it is considered that the motor drives the cart motion, the cart is driven. But in the period when it is negative, the motor looses the control over the cart and drives it no more, it is now driven by the mechanical system. In these situations, it will be said that the relation master-slave is reverted.



(a) (b)

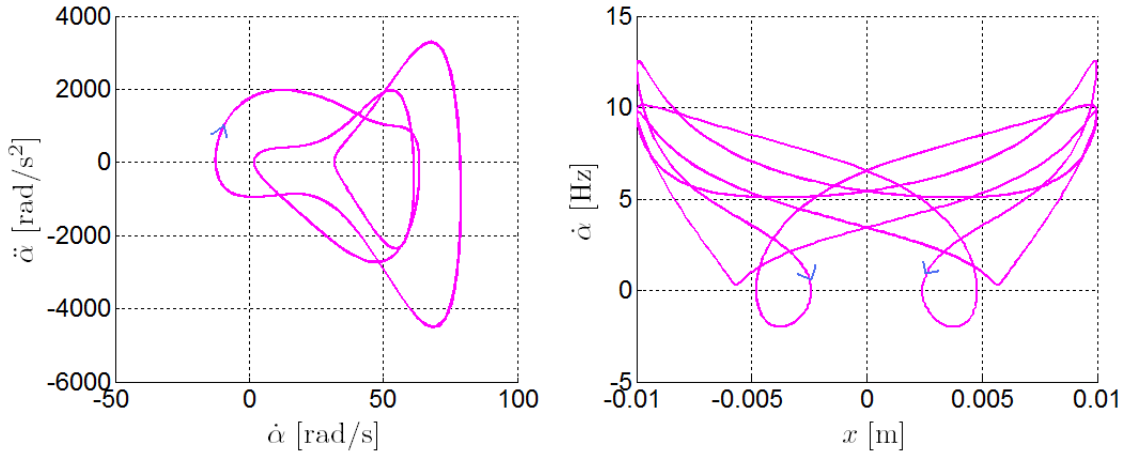
Figure 18: Motor-cart-pendulum system with $d = 0.01$ [m]: (a) angular velocity of the motor shaft and (b) current over time.

To better comprehend the sign changing of the angular speed of the motor shaft, some phase portrait graphs were plotted. Figures 20(a) and 20(b) show the $\ddot{\alpha}$ graph in function of $\dot{\alpha}$ and the $\dot{\alpha}$ graph in function of x during one movement cycle. It is verified that when $\dot{\alpha}(t)$ turns negative, the motor shaft has a negative acceleration. After a short period of time, its acceleration becomes positive and brakes the motor shaft motion. This causes other sign changing in $\dot{\alpha}(t)$ and consequently, it turns positive again. Thus, the motor recovers the control over the cart motion.



(a) (b)

Figure 19: Motor-cart-pendulum system with $d = 0.01$ [m]: (a) pendulum and (b) cart displacement over time.

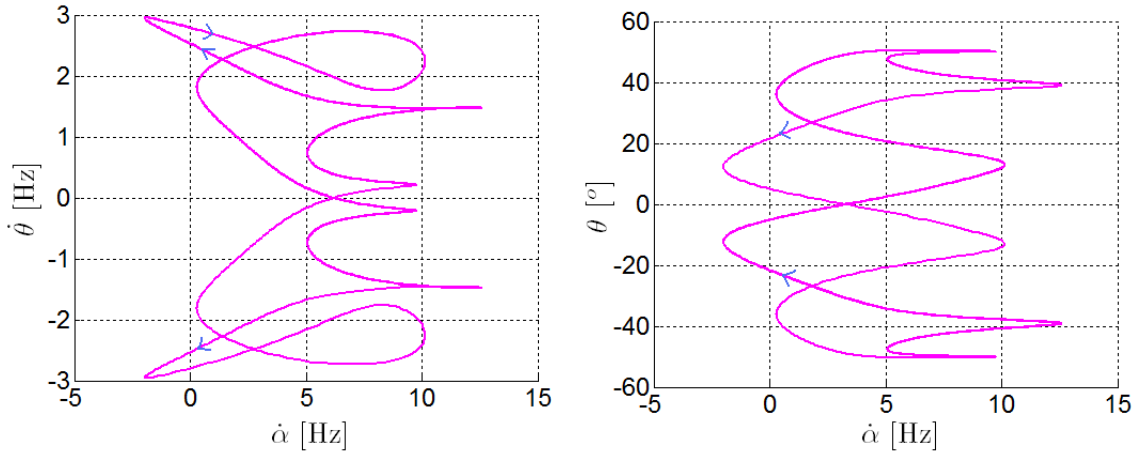


(a) (b)

Figure 20: Motor-cart-pendulum system with $d = 0.01$ [m]: portrait graphs of (a) $\ddot{\alpha}$ graph in function of $\dot{\alpha}$ and (b) $\dot{\alpha}$ graph in function of x.

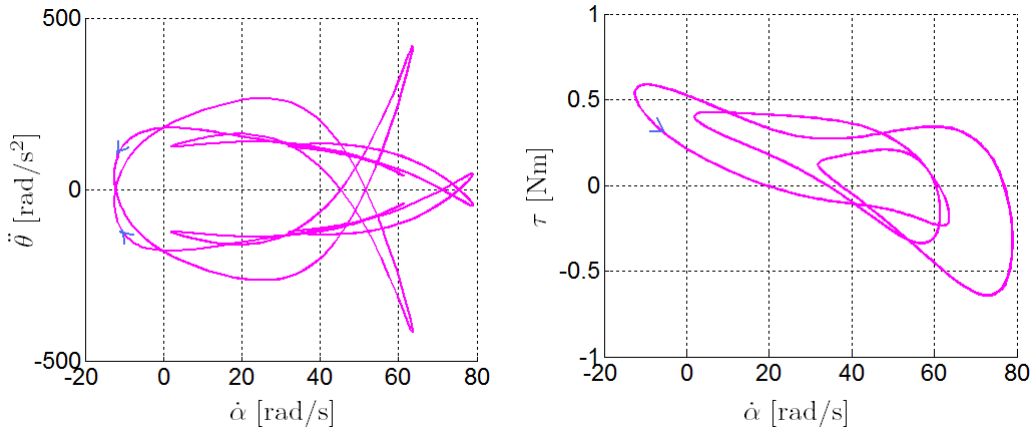
Looking at Fig. 20(b), it is noted that this reversion in the relation master-slave occurs two times in each movement cycle. The position and angular speed of the pendulum, at the moment of the reversion, can be discovered by the graphs of $\dot{\theta}$ in function of $\dot{\alpha}$ and θ in function of $\dot{\alpha}$. They are shown in Fig. 21(a) and 21(b). It is verified that when the the motor looses the control over the cart by the sign changing of $\dot{\alpha}$, the pendulum angle is around 21.6 [^{o}] or around -21.6 [^{o}]. When the motor recovers the control, the pendulum angle is around 6.0 [^{o}] or around -6.0 [^{o}].

It is also noted that, during the period of reversion, the pendulum does not change its direction of motion in spite of its angular speed presents a change of behavior. In the beginning of the reversion the modulus of $\dot{\theta}$ grows, but when it achieves the value 2.95 [Hz], it starts to decrease. This change occurs due to the sign changing in the tangent angular acceleration of the pendulum, as can be observed in Fig. 22(a). The graph of the torque variation in function of the angular speed of the motor shaft shows that the maximum torque is achieved during the period of reversion.



(a) (b)

Figure 21: Motor-cart-pendulum system with $d = 0.01$ [m]: portrait graphs of (a) $\dot{\theta}$ graph in function of $dot\alpha$ and (b) θ in function of $dot\alpha$.



(a) (b)

Figure 22: Motor-cart-pendulum system with $d = 0.01$ [m]: portrait graphs of (a) tangent $\ddot{\theta}$ graph in function of $dot\alpha$ and (b) τ in function of $dot\alpha$.

3.5 Simulations of the motor-cart-pendulum system with friction

The differential algebraic equations to the coupled motor-cart-pendulum system with friction, Eq. (33), was integrated numerically in a range of [0.0, 25.0] seconds.

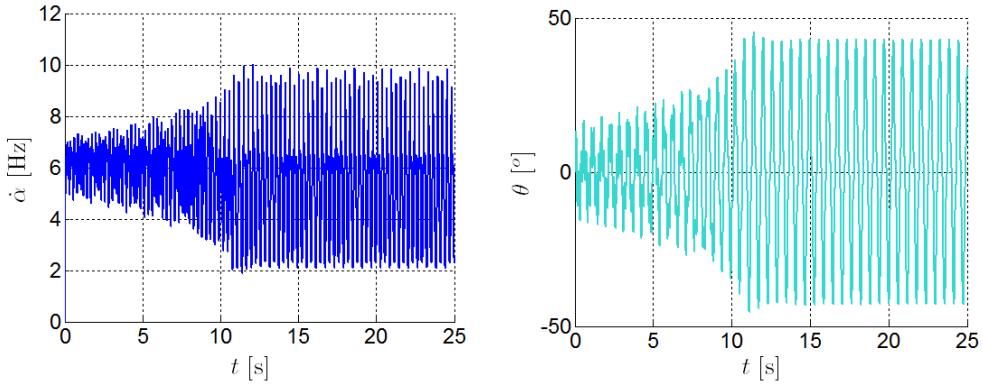
In the integration, the same parameters used in the previous simulations of the motor-cart-pendulum system without friction were adopted. That is, the same initial conditions, specifications of the motor, source voltage, and pendulum length. Also, the values used to the friction coefficients, μ_1 and μ_2, were equal to the values considered in the simulations of the motor-cart system with friction.

The values adopted to m_c, m_p and d were equal to the values used in the simulations of the motor-cart-pendulum system without frictions in the case where occurs the reversion in the relation master-slave. Thus, $m_c = 0.0$ [Kg], $m_p = 4.0$ [Kg] and $d = 0.01$ [m].

The results obtained to the angular speed of the motor and angular displacement pendulum over time are shown in Fig. 23(a) and 23(b). It is possible observe that with the consideration

of the friction, the phenomena of the reversion in the relation master-slave between the cart and the motor does not occur anymore.

Considering the frictions forces, the angular velocity of the motor shaft oscillates between 2.0 [Hz] and 10.0 [Hz] and the angular displacement of the pendulum between -43.0 [^{o}] 43.0 [^{o}]. Should be noted that this maximum angle displacement archived by the pendulum, 43.0 [^{o}], is much lower than the maximum angle in the case of non consideration of the frictions, 100.0 [^{o}] (see Fig. 19(a)). This result verifies the friction reduces the capability of the pendulum to act as a reservoir of energy.



(a) (b)

Figure 23: Motor-cart-pendulum system with friction in the coupling mechanism: (a) angular velocity of the motor shaft and (b) pendulum displacement over time.

4 PROBABILISTIC MODEL

To make a stochastic analysis of the proposed systems, a system parameter is considered uncertain. It is assumed that the value of the nominal eccentricity of the pin, d is a random variable represented by the capital letter D.

The Maximum Entropy Principle (PEM) is used to construct the probability density function of this random variable, "Jaynes (1957)", "Shannon (1948)", "Sampaio and de Queiroz Lima (2012a)" and "Souza de Cursi and Sampaio (2012)", and it is assumed that the only available information is the support of D: $[d_{min}, d_{max}]$. Therefore, the Maximum Entropy Principle using Shannon entropy measure of the probability density function, p, of D, $S(p) = -\int_{d_{min}}^{d_{max}} \ln(p(d))p(d)\,dp$, yields the uniform probability density function, given by

$$p(d) = \mathbb{1}_{[d_{min},d_{max}]}(d)\,\frac{1}{d_{max}-d_{min}}\,. \tag{35}$$

where $\mathbb{1}_{[d_{min},d_{max}]}(d)$ is an indicator function that is equal to 1 for $d \in [d_{min}, d_{max}]$ and 0 otherwise.

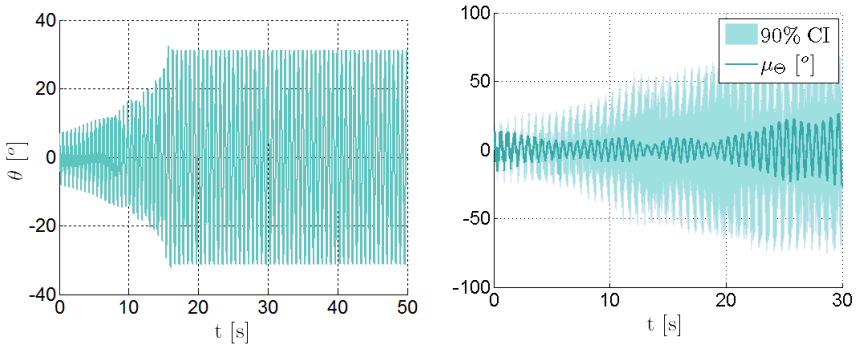
5 NUMERICAL SIMULATIONS OF THE STOCHASTIC MOTOR-CART-PENDULUM SYSTEM WITHOUT FRICTION

As it was assumed that the value of the nominal eccentricity of the pin is a random variable, the output variables of the stochastic coupled systems are random process with parameter t. Therefore, the horizontal cart displacement is represented by the random process $\mathcal{X}$, the pendulum displacement by Θ, the angular displacement of the motor shaft by $\mathcal{A}$, the angular velocity of the motor shaft by $\dot{\mathcal{A}}$, the current by $\mathcal{C}$, the horizontal force by $\mathcal{F}$ and the torque by $\mathcal{T}$.

To make the stochastic analysis of the motor-cart-pendulum system, Monte Carlo simulations were employed to compute the mean and variance of the the random processes listed above. The support of D was assumed to be $[d_{min}, d_{max}] = [0.005,\ 0.015]$ (units in [m]).

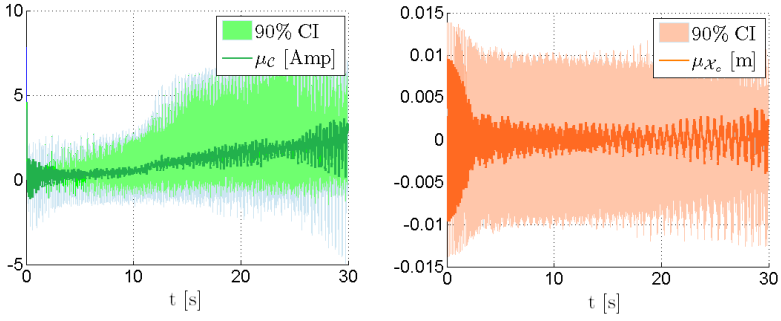
Figure 24(a) shows one realization of Θ and, figures 24(b), 25(a) and 25(b) show the envelope graphs of $\mathcal{C}$, $\mathcal{X}$ and Θ constructed with 10^3 realizations of these random process after a convergence analysis. In each realization, the system Eq. (25), was integrated in a range of $[0.0,\ 30.0]$ seconds. The cart mass was considered to be $m_c = 1.0$ [Kg], the pendulum mass $m_p = 4.0$ [Kg], the pendulum length $l_p = 0.075$ [m], the source voltage 2.4 [Volt] and, the specifications to the motor parameters are from the motor Maxon DC brushless number 411678.

It is possible observe that the variations on the value of the nominal eccentricity of the pin bring significant dispersions to the oscillation frequencies and to the oscillation amplitude of the output variables. As shown in the deterministic analysis of the motor-cart system without friction, the FFT graphs of $\hat{x}$, $\hat{\theta}$ and $\hat{c}$ are very sensitive to variation of the parameter d. A more detailed analysis is presented in "de Queiroz Lima and Sampaio (2012b)".



(a) (b)

Figure 24: Motor-cart-pendulum system with $d = 0.01$ [m]: (a) one realization of Θ and (b) envelope graph of Θ constructed with 10^3 realizations.



(a) (b)

Figure 25: Motor-cart-pendulum system: (a) envelope graph of $\mathcal{C}$ constructed with 10^3 realizations and (b) envelope graph of $\mathcal{X}$ constructed with 10^3 realizations.

6 CONCLUSIONS

The purpose of this paper was to analyze and compare the behavior of two electromechanical systems. The first one is composed by a cart whose motion is driven by a DC motor and in the

second one a embarked mass, a pendulum, was attached to the cart. The motor-cart system has no capacity to pump energy from the motor, it is a master-slave system: the motor drives the cart motion, the cart is driven. The only interesting feature is how the nonlinearity changes with d and m, the mass of the cart. The nonlinearity of the coupled system comes from the coupling. The motor-cart-pendulum system has a new feature, the capacity to store energy in the motion of the pendulum. With this the mechanical system can pump energy from the motor. For the motor-cart-pendulum system, for a fixed mass $m = m_c + m_p$, the relation between m_c and m_p is important. The study of the relation and how it affects the dynamics will be object of a future work. The influence of a embarked mass was demonstrated and it was shown the changes it causes in the solutions of the dynamic equations.

The nominal eccentricity of the pin of the motor, d, was characterized as a parameter that controls the nonlinearities of the equations of motion of both systems, and its influence in the dynamic equations was analyzed by the Fast Fourier Transform.

The consideration of the friction forces in the systems turned their simulations more realistic. In the case of the motor-cart-pendulum system, it was verified that the friction forces can avoid the reversion in the relation master-slave between the cart and the motor.

In the stochastic analysis, d was modeled as a random variable and the Maximum Entropy Principle was used to construct the probability model. Monte Carlo simulations were employed to compute the mean and the 90% confidence interval of the displacements of the random process that characterize the output variables of the stochastic coupled systems. It was observed that the most important effect of the variations on d were the generation of dispersions to the oscillation amplitudes and frequencies of the output variables.

As future work, a study of the distribution of mass between the cart and the pendulum in the motor-cart-pendulum system will be done. In this paper, the total mass of the motor-cart-pendulum system was considered equal to the embarked mass, a extreme case. So would be interesting to study others configurations.

7 ACKNOWLEDGMENTS

This work was supported by the Brazilian Agencies CNPQ, CAPES and Faperj.

REFERENCES

[1] Y. Rocard, *Dynamique Générale des Vibrations*, Masson et Cie., Éditeurs, Paris, France, 1943.

[2] V.O. Kononenko, *Vibrating Systems with a Limited Power Supply*, London Iliffe Books LTD, England, 1969.

[3] D. Belato, *Análise Não Linear de Sistemas Dinâmicos Holônomos Não Ideais, PhD thesis*. Department of Mechanical Engineering, Universidade Estadual de Campinas, 2002.

[4] R.R. Aguiar, *Experimental investigation and numerical analysis of the vibro-impact phenomenon, PhD thesis*. Department of Mechanical Engineering, PUC-Rio, Rio de Janeiro, Brazil, 2010.

[5] J.M. Balthazar, D.T. Mook, H.I. Weber, R.M.L.R.F. Brasil, A. Felini, D. Belato, J.L.P. Felix, An Overview on Non-Ideal Vibrations. *Meccanica*, **38**, 613–621, 2003.

[6] A.H. Nayfeh, D.T. Mook, *Nonlinear Oscillations*, John Wiley and Sons, USA, 1979.

[7] R.M. Evan-Iwanowski, *Resonance oscillations in mechanical systems*, Elsevier Publ. Co., Amsterdam, 1976.

[8] A. Fidlin, *Nonlinear Oscillations in Mechanical Engineering*, Springer, Netherlands, 2006.

[9] P. Hagedorn, *Non-linear Oscillations, 2nd Edition*, Clarendon Press, Oxford, 1988.

[10] H. Troger, A. Steindl, *Nonlinear Stability and Bifurcation Theory: An Introduction for Engineers and Applied Scientists*, Springer-Verlag, Wien, 1991.

[11] D.C. Karnopp, D.L. Margolis, R.C. Rosenberg, *System Dynamics: Modeling and Simulation of Mechatronic Systems, 4th Edition*, John Wiley and Sons, New-York, USA, 2006.

[12] W. Lacarbonara, Stuart Antman, *What is parametric excitation in Structural Dynamics? (ENOC-2008)*, Saint Petersburg, Russia, 2008.

[13] B. J. N. Persson, *Sliding Friction: Phisical Principles and Applications, 2nd Edition*, Springer-Verlag, Germany, 2000.

[14] R. Sampaio, R. de Queiroz Lima, Stochastic Analysis of an Electromechanical Coupled System with Embarked Mass. *Mecânica Computacional*, **XXXI**, 2783–2800, 2012b.

[15] R. Sampaio, R. de Queiroz Lima, Uncertainty quantification of coupled electromechanical systems with an embarked pendulum. *Diname 2013*, 2012c.

[16] E. Gourdon, N.A. Alexander, C.A. Taylor, C.H. Lamarque, S. Pernot, Nonlinear energy pumping under transient forcing with strongly nonlinear coupling: Theoretical and experimental results. *Journal of Sound and Vibration*, **300**, 522–551, 2007.

[17] E. Gourdon, *Contrôle passif de vibrations par pompage énergétique, PhD thesis*. Ecole Centrale de Lyon, France, 2006.

[18] E. Cataldo, S. Bellizzi, R. Sampaio, *Free vibrations of an uncertain energy pumping system*, Tecnical Report, PUC-Rio, 2012.

[19] E. Jaynes, Information theory and statistical mechanics. *The Physical Review*, **106**, No.4, 620-630, 1957.

[20] C.E. Shannon, A mathematical theory of communication. *Bell System Tech. J.*, **27**, 379–423 and 623–659, 1948.

[21] R. Sampaio, R. de Queiroz Lima, *Modelagem Estocástica e Geração de Amostras de Variáveis e Vetores Aleatórios*, Vol. 70, electronic address: http://www.sbmac.org.br/arquivos/notas/livro_70.pdf, Notas de Matemática Aplicada, SBMAC, 2012a.

[22] R. Sampaio, E. Souza de Cursi, *Modelagem Estocástica e Propagação de Incertezas*, Vol. 66, electronic address: http://www.sbmac.org.br/arquivos/notas/livro_66.pdf, Notas de Matemática Aplicada, SBMAC, 2012.

COMPDYN 2013
4th ECCOMAS Thematic Conference on
Computational Methods in Structural Dynamics and Earthquake Engineering
M. Papadrakakis, V. Papadopoulos, V. Plevris (eds.)
Kos Island, Greece, 12–14 June 2013

UNCERTAINTIES IN MULTISTAGE ROTORS MODELED BY THE POLYNOMIAL CHAOS EXPANSION

Bartolomé Seguí, Béatrice Faverjon and Georges Jacquet-Richardet

Université de Lyon, CNRS, INSA-Lyon, LaMCoS UMR5259, F-69621, France
e-mail: {bartolome.segui,beatrice.faverjon,georges.jacquet}@insa-lyon.fr

Keywords: stochastic modal analysis, bladed discs, multistage cyclic symmetry, Polynomial Chaos Expansion.

Abstract. *In this work the effects of uncertainties in turbomachinery rotors is assessed using the Polynomial Chaos Expansion. The multistage cyclic symmetry approach is used to reduce the size of the problem and the uncertainties are modeled as variations in the material properties of the blades. A numerical example consisting in an assembly of two bladed disc is presented. Results obtained by polynomial chaos are validated by comparisons with Monte-Carlo simulations. As a consequence of the included uncertainties changes in nature of modes are observed.*

1 INTRODUCTION

The assessment of variability induced by uncertainties is now recognized as an important part in the design process of any mechanical system. The methodology proposed in this work allows to include uncertainties in the analysis of turbomachinery rotors using the Polynomial Chaos Expansion (PCE) [1]. The rotors considered are composed of several stages of bladed discs for which uncertainties may arise from in-use wear of the blades, temperature changes or manufacturing tolerances. As a first approach, only uncertainties that are the consequence of uniform in-use wear of the set of blades will be included.

Recent designs in turbomachinery tend to have more flexible inter-stage rims and to be more lightly damped, resulting in configurations where modes may not be confined to only one stage. This dynamic coupling between stages is discussed, for example, in [2]. To capture all possible multistage dynamic couplings the computationally costly analysis of the whole structure becomes mandatory. A recently introduced multistage cyclic symmetry approach [3, 4] can be used for reducing the cost of modeling rotors composed of several stages even when the stages have different numbers of sectors. This approach takes advantage of the inherent cyclic symmetry of each stage and uses a specific assumption that results in decoupled subproblems for each spatial Fourier harmonic.

The considered uncertainties are modeled as global variation of the material properties of the set of blades. The multistage cyclic symmetry approach can then be used to reduced the size of the problem because the underlying assumption of identical sectors is respected. In bladed disc systems the modes shapes are considered to be important design parameters and in this work their variability is assessed by solving the stochastic modal analysis using the PCE, as in [5]. The positiveness of the random matrices involved is assured by using gamma-distributed random variables which imply the use of Laguerre's polynomials as basis for the polynomial chaos.

2 MODELING THE DYNAMICS OF MULTISTAGE ROTORS

The rotors considered are composed of several stages of bladed discs. If considered separately, each stage has the property of cyclic symmetry. This allows to carry out the analysis of a stage by modeling only one reference sector. Multistage rotors as a whole are not cyclic symmetric because the number of blades in each stage is generally different.

The equation of motion of the multistage structure at rest is

$$\mathbf{M}\ddot{\mathbf{x}} + \mathbf{C}\dot{\mathbf{x}} + \mathbf{K}\mathbf{x} = \mathbf{F} \tag{1}$$

where $\mathbf{M}$, $\mathbf{C}$ and $\mathbf{K}$ are the mass, damping and stiffness matrix respectively, $\mathbf{x}$ is the displacement vector and $\mathbf{F}$ the vector of external forces. All quantities are expressed in physical coordinates.

Using a recently developed modeling technique called multistage cyclic symmetry [3, 4], the analysis of the whole structure can be carried out by modeling one reference sector of each stage. First, for each stage the displacement in the circumferential direction is decomposed using a discrete Fourier transform as in classical cyclic symmetry. This yields uncoupled subproblems for each Fourier order which are defined on the reference sector. Second, an assumption of compatible Fourier orders of different stages is used to couple this subproblems into fundamental multistage subproblems

$$\tilde{\mathbf{M}}_f\ddot{\tilde{\mathbf{x}}}_f + \tilde{\mathbf{C}}_f\dot{\tilde{\mathbf{x}}}_f + \tilde{\mathbf{K}}_f\tilde{\mathbf{x}}_f = \tilde{\mathbf{F}}_f \tag{2}$$

where f is associated to the fundamental multistage harmonic and the symbol $\tilde{.}$ indicates quantities expressed in cyclic coordinates.

The total number of fundamental multistage subproblems to be solved is given by the stage with the smallest number of sectors. Also, the Fourier orders that are assumed compatible are defined using a rule that is based on the aliasing of the Fourier transform of this stage. Accordingly each fundamental multistage subproblem may group one or more Fourier orders of a particular stage. Displacements $\tilde{\mathbf{x}}_f$ (or other quantities) in cyclic coordinates are easily transformed into physical coordinates of the whole structure.

The normalized modal analysis of the undamped system for the fundamental multistage Fourier order f is governed by

$$\tilde{\mathbf{K}}_f \boldsymbol{\Phi}_l = \omega_l^2 \tilde{\mathbf{M}}_f \boldsymbol{\Phi}_l \quad \text{with} \quad \boldsymbol{\Phi}_l^T \tilde{\mathbf{M}}_f \boldsymbol{\Phi}_l = 1 \tag{3}$$

where ω_l and $\boldsymbol{\Phi}_l$ are the lth natural frequency and mode shape in cyclic coordinates respectively.

3 POLYNOMIAL CHAOS EXPANSION (PCE) REPRESENTATIONS

For simplicity uncertainties are introduced by considering a random Young's modulus $\hat{E}(\tau)$. In order for the Young's modulus $\hat{E}(\tau)$ to remain positive it is modeled as

$$\hat{E}(\tau) = \xi(\tau) \langle \hat{E}(\tau) \rangle \tag{4}$$

where $\xi(\tau)$ is a positive random variable that follows a gamma distribution of shape parameter $\alpha > -1$. Argument τ and the symbol $\hat{\bullet}$ are used to indicate the random character of the variables. The variation coefficient of the random Young's modulus δ_E^2, which is assumed to be known, determines the shape parameter of the distribution as $\alpha = -1 + 1/\delta_E^2$. Random stiffness matrix $\hat{\tilde{\mathbf{K}}}_f(\tau)$ is written using the $\hat{E}(\tau)$ as

$$\hat{\tilde{\mathbf{K}}}_f(\tau) = \xi(\tau) \tilde{\mathbf{K}}_f(\langle \hat{E}(\tau) \rangle) \tag{5}$$

3.1 Modal analysis

The random modal analysis is obtained by using random stiffness matrix $\hat{\tilde{\mathbf{K}}}_f$

$$\hat{\tilde{\mathbf{K}}}_f \hat{\boldsymbol{\Phi}}_l = \hat{\omega}_l^2 \tilde{\mathbf{M}}_f \hat{\boldsymbol{\Phi}}_l \quad \text{with} \quad \hat{\boldsymbol{\Phi}}_l^T \tilde{\mathbf{M}}_f \hat{\boldsymbol{\Phi}}_l = 1 \tag{6}$$

with $\hat{\omega}_l$ and $\hat{\boldsymbol{\Phi}}_l$ being the lth random natural frequency and mode shape. Quantities $\hat{\omega}_l$ and $\hat{\boldsymbol{\Phi}}_l$ are expressed in the Polynomial Chaos representation truncated to $p+1$ terms as

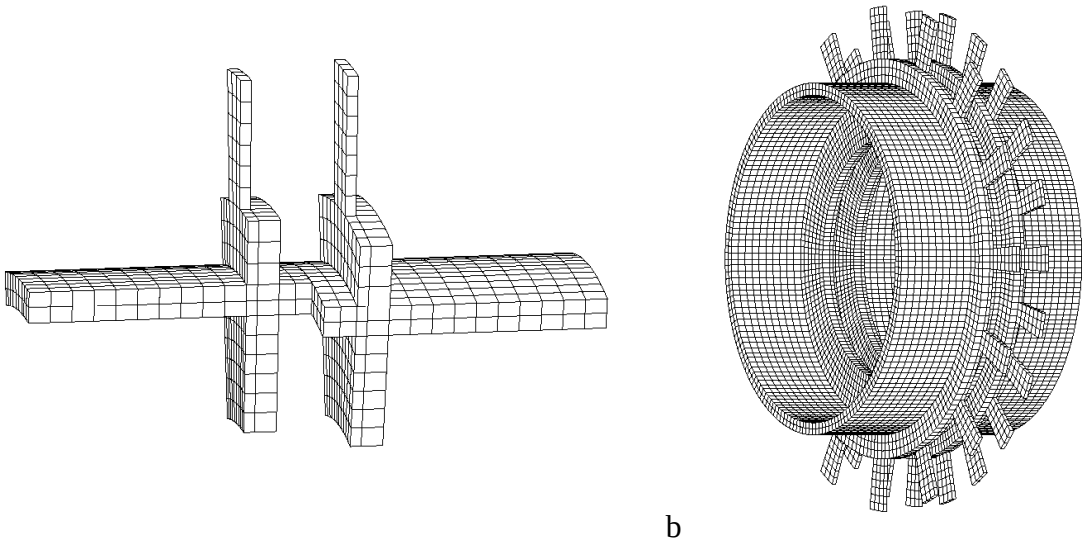
$$\hat{\omega}_l = \sum_{i=0}^{p} \psi_i w_l^{(i)}, \quad \hat{\boldsymbol{\Phi}}_l = \sum_{i=0}^{p} \psi_i \boldsymbol{\Phi}_l^{(i)} \tag{7}$$

where $\psi_i(\xi)$ are the Laguerre's polynomial which are functions of the random variable and form an orthogonal basis with respect to the gamma distribution [6].

Solution of the random modal problem consists in determining coefficients

$$\left\{ w_l^{(0)} \quad , \quad \dots \quad , \quad w_l^{(p)} \quad , \quad \boldsymbol{\Phi}_l^{(0)} \quad , \quad \dots \quad , \boldsymbol{\Phi}_l^{(p)} \right\} \tag{8}$$

which are deterministic quantities that completely describe the stochastic behavior of $\hat{\omega}_l$ and $\hat{\boldsymbol{\Phi}}_l$.



a b

Figure 1: Finite element discretization. a.- one reference sector per stage, b.- complete model.

The solution method consists in substituting the expressions of $\hat{\tilde{\mathbf{K}}}_f$ and $\hat{\omega}_l$ and $\hat{\boldsymbol{\Phi}}_l$ into Eq. 6 and projecting into the basis of Laguerre's polynomials ψ_m for $m = 0, \ldots, p$. This results in a system of $(p+1)(n+1)$ nonlinear equations, n being the size of $\boldsymbol{\Phi}_l$, that is solved by an iterative method such as Newton-Raphson.

In order to study the changes in the modes induced by the uncertainties, the random mode shapes $\hat{\boldsymbol{\Phi}}_l$ are decomposed a posteriori onto the deterministic modal basis [5] as

$$\hat{\boldsymbol{\Phi}}_l = \sum_{i=1}^{n} \hat{e}_i^l \boldsymbol{\Phi}_i \tag{9}$$

where $\hat{e}_i^l$ are random coefficients. The statistics of coefficients $\hat{e}_i^l$ allow to quantify the contributions of the random mode shapes to the deterministic mode shapes.

4 NUMERICAL CASE STUDY

A rotor composed of two bladed discs having 15 and 23 blades is considered. Using the multistage cyclic symmetry assumption only one sector per stage is modeled. Figure 1 shows the finite element discretization of one reference sector per stage and the complete model. The main physical characteristics are, for the discs: thickness 15 mm, inner/outer diameter 150/250 mm; and for the shaft (drum): inner/outer diameter 200/215 mm, total length 220 mm. The length of the blades is 66 mm in stage 1 and 60 mm in stage 2. The material properties used are: density 7820 kg/m^3 and Young's modulus 210 GPa.

The deterministic natural frequencies of the multistage system are plotted as a function of the fundamental Fourier order in Figure 2. The lines drawn help distinguish between families of modes predominantly having blade dominated motion or disc dominated motion. Families of blade dominated modes appear as nearly horizontal lines while the slanted lines correspond to disc dominated modes. Modes corresponding to global deformations of the shaft are not assimilated to any of the families. The stochastic modal analysis for the six modes pointed out in Figure 2, which correspond to Fourier order 3, is shown next.

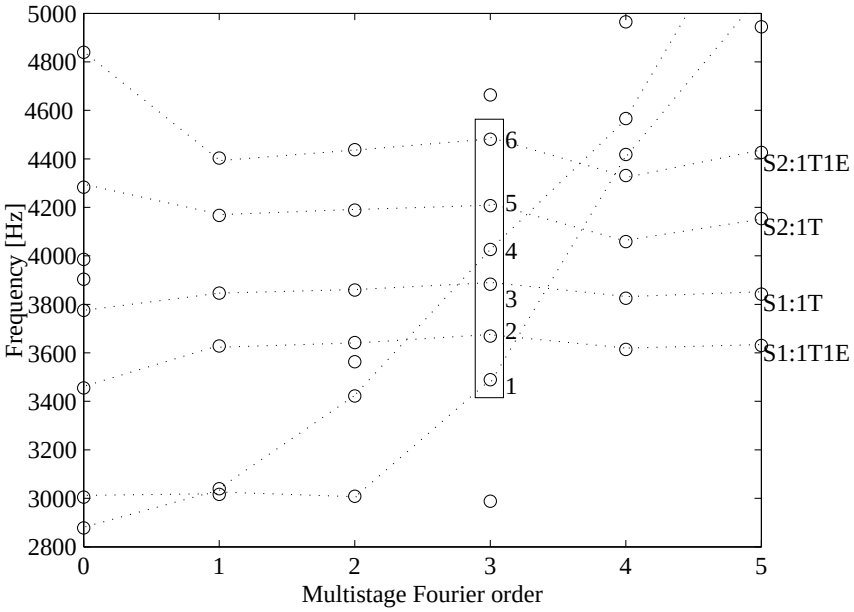


Figure 2: Natural frequencies vs multistage Fourier orders. Families of blade deformations are: S2:1T1E stage 2, torsion–edgewise bending; S2:1T stage 2, 1st blade torsion; S1:1T stage 1, 1st blade torsion; S1:1T1E stage 1, torsion–edgewise bending.

Table 1: Statistical moments of natural frequencies calculated using PCE and Monte-Carlo simulations

	PCE			Monte-Carlo		
Mode	$\langle\hat{\omega}\rangle$ [Hz]	σ_ω [Hz]	δ_ω [%]	$\langle\hat{\omega}\rangle$ [Hz]	σ_ω [Hz]	δ_ω [%]
1	3488.36	5.66	0.16	3488.36	5.63	0.16
2	3669.02	33.61	0.92	3668.99	33.41	0.91
3	3882.75	40.91	1.05	3882.72	40.67	1.05
4	4025.99	4.14	0.10	4025.99	4.10	0.10
5	4206.87	43.26	1.03	4206.83	43.01	1.02
6	4480.33	44.77	1.00	4480.30	44.51	0.99

4.1 Random frequencies and mode shapes

Only uncertainties arising from uniform in-use wear of the set of blades are included. These are modeled by considering a random Young's modulus for the set of blades with a variation coefficient of $\delta_E = 2.5\%$. Hence, only the portion of the stiffness matrix that corresponds to the blades is considered as random.

The Polynomial Chaos expansion of second order ($p = 2$) is used and the obtained results are compared to Monte-Carlo simulations carried out by solving the modal problem for 5000 independent samples of the random variable. Excellent accuracy is found for frequency mean and standard deviation as shown in Table 1. The standard deviations for the modes 1 and 4 are small because they correspond to modes with predominantly disc deformations, however light coupling in frequency between disc and blade dominated modes is evidenced by their non-zero values.

Probability density functions of the frequencies can be obtained using Eq. 7 to calculate the frequencies for a large number of independent samples of the random variable by inexpensive evaluations of polynomials.

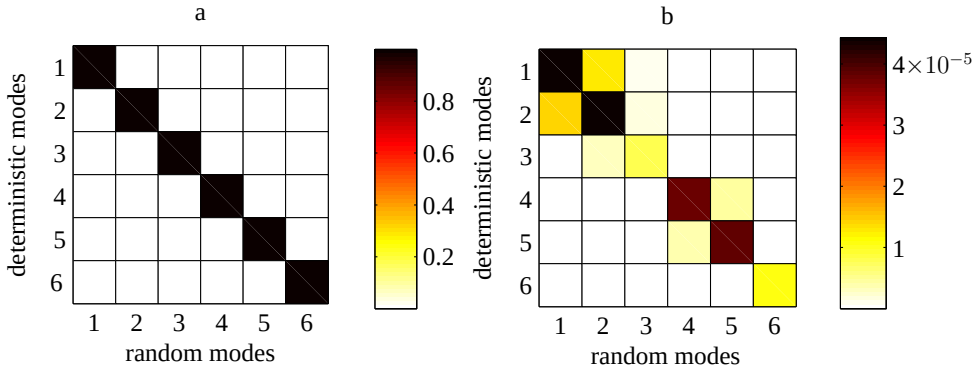


Figure 3: Contributions of the random mode shapes to the deterministic mode shapes. a.- mean $\langle \hat{e}_i^l \rangle$, b.- variance×mean $\sigma^2(\hat{e}_i^l) \times \langle \hat{e}_i^l \rangle$.

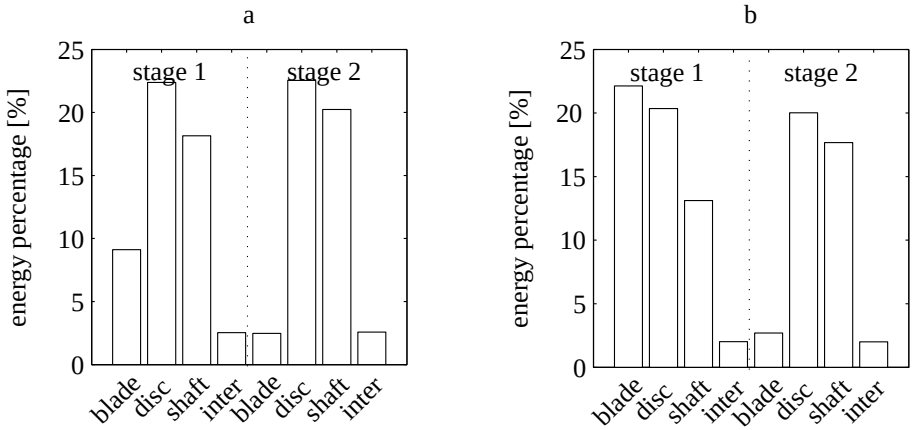


Figure 4: Energy distribution across the components. a.- deformation of mean mode 1, b.- deformation of mode 1 for stochastic realization $\hat{E} = 0.925 \times \langle \hat{E} \rangle$.

The contributions of the random mode shapes to the deterministic mode shapes are illustrated in Figure 3 using the statistics of coefficient $\hat{e}_i^l$ from Eq. 9. The two quantities represented are the mean $\langle \hat{e}_i^l \rangle$ and the variance×mean $\sigma^2(\hat{e}_i^l) \times \langle \hat{e}_i^l \rangle$. Figure 3(a) shows that the mean random modes are very similar to the deterministic modes while Figure 3(b) suggests that changes in the modes induced by the uncertainties are possible. For example, it appears from Figure 3(b) that stochastic mode 1 may have contributions from deterministic modes 1 and 2. Since the later correspond to deformations of the discs and the blades respectively, it is expected that stochastic mode 1 be a combination of both. To further illustrate this, a particular representation for mode 1 of the mean and one stochastic realization is shown in Figure 4. The representation consists on the energy distribution across different components, the components being the blades, disc, shaft and inter-stage region for either stage 1 or 2. The energy distribution for the mean mode 1 suggests a disc dominated mode, however the energy in the blades of stage 1 is significantly increased for the stochastic realization. Furthermore, this change in the nature of the mode is associated to only a very small variation in frequency.

5 CONCLUSIONS

A methodology for solving the stochastic modal analysis using the Polynomial Chaos expansion is briefly presented and illustrated using a numerical example. The size of the underlying problem is reduced using the multistage cyclic symmetry approach and the PCE is applied to the quantities associated to each multistage Fourier order. The uncertainties introduced are

modeled using positive gamma-distributed random variables. Frequency mean and standard deviation results obtained by PCE are compared to Monte-Carlo simulations results showing excellent correspondence. Finally, the analysis shows how small uncertainties in the material properties of the blades may induce significant changes in the nature of the modes which might not be visible if looking at variations in frequency only.

REFERENCES

[1] R Ghanem and P Spanos. *Stochastic finite elements: a spectral approach*. Courier Dover Publications, 2003.

[2] R. Bladh, M. P. Castanier, and C. Pierre. Effects of multistage coupling and disk flexibility on mistuned bladed disk dynamics. *Journal of Engineering for Gas Turbines and Power*, 125(1):121–130, 2003.

[3] D Laxalde, J-P Lombard, and F Thouverez. Dynamics of multistage bladed disks systems. *Journal of Engineering for Gas Turbines and Power*, 129(4):1058–1064, 2007.

[4] D. Laxalde and C. Pierre. Modelling and Analysis of Multi-Stage Systems of Mistuned Bladed Disks. *Computers & Structures*, 89(3-4):316–324, 2010.

[5] R. Ghanem and D. Ghosh. Efficient characterization of the random eigenvalue problem in a polynomial chaos decomposition. *International Journal for Numerical Methods in Engineering*, 72(4):486–504, 2007.

[6] C. Soize and R. Ghanem. Physical systems with random uncertainties: Chaos representations with arbitrary probability measure. *SIAM Journal on Scientific Computing*, 26(2):395–410, 2004.

COMPDYN 2013
4th ECCOMAS Thematic Conference on
Computational Methods in Structural Dynamics and Earthquake Engineering
M. Papadrakakis, V. Papadopoulos, V. Plevris (eds.)
Kos Island, Greece, 12–14 June 2013

STABILITY AND RESPONSE ANALYSIS OF A PIPE WITH INTERNAL FLOW ANALYZED WITH AN UNCERTAIN COMPUTATIONAL MODEL

T.G. Ritto[1], C. Soize[2], F.A. Rochinha[1], and Rubens Sampaio[3]

[1]Federal University of Rio de Janeiro, Dept of Mechanical Engineering
Centro de Tecnologia, Ilha do Fundão, 21945-970, Rio de Janeiro, Brazil
e-mail: tritto@mecanica.ufrj.br, faro@mecanica.ufrj.br

[2] Université Paris-Est, Laboratoire de Modélisation et Simulation Multi-Echelle
MSME UMR 8208 CNRS, 5bd Descartes, 77454 Marne-la-Vallée Cedex 2, France
e-mail: christian.soize@univ-paris-est.fr

[3] PUC-Rio, Dept of Mechanical Engineering
Rua Marquês de São Vicente, 225, 22453-900, Rio de Janeiro, Brazil
e-mail: rsampaio@puc-rio.br

Keywords: stochastic dynamics, fluid-structure model uncertainty, stability analysis, uncertainty quantification

Abstract. *This paper treats the problem of pipes conveying fluid, which has several engineering applications, such as micro-systems and drill-string dynamics. The aim of this work is twofold: (1) propose a stochastic model for the fluid-structure interaction considering modeling errors and (2) analyze the stability of the stochastic system. The Euler-Bernoulli model is used to model the pipe and the plug flow model is used to take into account the presence of the internal flow. The resulting differential equation is discretized by means of the finite element method and a reduced-order model is constructed with the normal modes of the beam model. A variation of the nonparametric probabilistic approach is used to model uncertainties in the fluid-structure interaction, since this approach is able to take into account modeling errors. The numerical results show how the random response of the system changes for different levels of uncertainties. The probability of instability is also computed for different levels of uncertainties.*

1 INTRODUCTION

Slender flexible tubes with internal flow or pipes conveying fluids are present in a number of applications ranging from micro-systems to biological devices, drill-strings or heat exchangers [1, 2, 3]. Typically, the standard configuration is a straight tube mounted over supports carrying a steady flow of constant velocity U [4]. Ambient perturbations might entail low amplitude vibrations of the structure around the standard configuration if the velocity is kept below a certain threshold. Above the critical speed, the coupled system formed by the structure and the flow might undergo large vibrations and complex nonlinear dynamical response. To understand this unstable behavior [5] becomes instrumental for improving the design of the systems and mitigate damage effects. Besides, this large diversity in the vibrations response renders this problem quite attractive for theoretical and numerical studies.

Computer models are nowadays widespreadly used in the design and analysis of standard engineering systems. Many noncritical decisions are taken based on computational simulations. Despite the consolidation of powerful and reliable methods leading to small numerical errors, the extension of this common practice to more critical systems is hindered by the presence of inevitable uncertainties associated to the modeling. Fluctuations around nominal values of parameters, initial and boundary conditions, or production tolerances might entail, after a number of nonlinear calculations, a large variation on the output of the simulations. So, in order to improve the reliability of predictions, those uncertainties must be taken into account. Here, this is carried out within a probabilistic framework in which physical quantities involved in the modeling are represented by random variables or fields. Design criteria are then based on failure probabilities and reliability analysis [6].

On the initial stages of the analysis, low order models considering simplified physics are employed. The use of simple models makes feasible to analyze a significant number of scenarios. Complying with that, the flexible tubes are modeled here as Euler-Bernoulli beams and the internal fluid motion is described through a one-space dimension plug flow model, such that the resulting coupled model consists on a one-dimensional linear partial differential equation parametrized by the flow speed U. The deterministic analysis of the stability of this system has been studied [7], thus we propose an analysis of the stability of the stochastic system. In [8] the stochastic stability analysis is done considering stochastic time varying loads, which differs from the present analysis, in which the system is uncertain.

The coupling is responsible for the existence of unstable modes of the system and, therefore, plays a central role in the present analysis. In order to endow the model with an improved capacity of describing the fluid-structure coupling, a probabilistic model relying upon the nonparametric approach for uncertainties introduced in [9] is proposed. That approach has been applied in many different areas [1, 10, 11] to cope with uncertainties arising from different sources along the modeling process.

This nonparametric probabilistic approach, to be described in more details later, consists in deriving for the reduced-order model of the original problem, random matrices corresponding to a probabilistic density function obtained with the available information through the principle of maximum entropy [12]. Here, two matrices are obtained associated to damping and stiffness engendered by the flow. They replace the ones derived based on simplifications of the coupled system kinematics. Thus, the stability analysis considering randomness relies on solving a stochastic eingenvalue problem. The eingenvalues are now random variables and the stability is dictated by the probability of their sign to be positive. A number of results is presented with emphasis on the statistics characterization of the eingenvalues.

This paper is organized as follows: the deterministic system is depicted in Sections 2, 3, 4 and 5, where the equations, the dimensionless quantities and the stability analysis are presented. The probabilistic model is developed in Section 6. Finally, the numerical results are shown in Section 7 and the concluding remarks are made in Section 8.

2 DETERMINISTIC MODEL

Figure 1 sketches the system considered in the analysis.

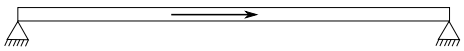


Figure 1: Sketch of the system considered in the analysis (the arrow represents the internal fluid flow).

Using the Euler-Bernoulli beam theory, the partial differential equation governing the dynamics of the structure is written as [13]:

$$m\frac{\partial^2 v(x,t)}{\partial t^2} + EI\frac{\partial^4 v(x,t)}{\partial x^4} = f(x,t) \qquad x \in [0,L]\,,\; t \in [0,T]\,, \tag{1}$$

with appropriate boundary and initial conditions, where v is the transversal displacement, L is the length of the beam, m is the mass per unit length, E is the elasticity modulus, I is the area moment of inertia and f is the external force.

To model the inside flow, the plug flow model [14] is used. Let $\mathbf{r} = x\mathbf{i} + y\mathbf{j}$ be a point measured from the origin, where $(\mathbf{i},\mathbf{j})$ is fixed in a inertial reference, with $\mathbf{j}$ in the transverse direction and $\mathbf{i}$ perpendicular to it, in the axial direction. The velocity of the fluid is given by

$$\mathbf{v}_f \simeq U\mathbf{i} + U\frac{\partial v}{\partial x}\mathbf{j} + \frac{\partial v}{\partial t}\mathbf{j}\,, \tag{2}$$

where U is the speed of the fluid, and it is assumed that $\partial v/\partial x$ is the (small) rotation of the beam cross sectional area. Hence, the fluid acceleration, which is the material derivative of $\mathbf{v}_f$, is given by

$$\mathbf{a}_f = \frac{D\mathbf{v}_f}{Dt} = \frac{\partial \mathbf{v}_f}{\partial t} + (\mathbf{v}_f \cdot \nabla)\mathbf{v}_f \tag{3}$$

If U is constant dU/dt=0, then we arrive to

$$\mathbf{a}_f = \left(\frac{\partial^2 v}{\partial t^2} + 2U\frac{\partial^2 v}{\partial x \partial t} + U^2\frac{\partial^2 v}{\partial x^2}\right)\mathbf{j}\,. \tag{4}$$

The force per unit length is obtained multiplying the acceleration by the fluid mass per unit length M_f

$$\mathbf{f}_f = \left(M_f\frac{\partial^2 v}{\partial t^2} + 2M_f U\frac{\partial^2 v}{\partial x \partial t} + M_f U^2\frac{\partial^2 v}{\partial x^2}\right)\mathbf{j}\,. \tag{5}$$

Including this force in Eq. (1), we arrive in:

$$(m+M_f)\frac{\partial^2 v}{\partial t^2}+2M_fU\frac{\partial^2 v}{\partial x\partial t}+M_fU^2\frac{\partial^2 v}{\partial x^2}+EI\frac{\partial^4 v}{\partial x^4}=f\,. \tag{6}$$

The above equation shows that the fluid contributes linearly to the mass, damping and stiffness of the system. Equation (6) is discretized by means of the finite element method: $v^{(e)}(\xi,t)=\mathbf{N}(\xi)\mathbf{u}^{(e)}(t)$, where the shape functions, $\mathbf{N}$, are Hermitian functions and the element displacement vector $\mathbf{u}^{(e)}=[v_1 \quad \partial v_1/\partial\zeta \quad v_2 \quad \partial v_2/\partial\zeta]$, in which $\xi=x/l_e$ is the local coordinate and l_e is the element length. The element matrices (mass, fluid damping, fluid stiffness, bending stiffness) are the following: $[M]^{(e)}=(m+M_f)\int_0^1\mathbf{N}^T\mathbf{N}l_e d\xi$, $[C_f]^{(e)}=2M_fU\int_0^1\mathbf{N}^T\mathbf{N}'d\xi$, $[K_f]^{(e)}=-M_fU^2\int_0^1\mathbf{N}'^T\mathbf{N}'\frac{1}{l_e}d\xi$, $[K_b]^{(e)}=EI\int_0^1\mathbf{N}_v''^T\mathbf{N}_v''\frac{1}{l_e^3}d\xi$. The resulting global discretized system is given by:

$$[M]\ddot{\mathbf{u}}(t)+[C_f]\dot{\mathbf{u}}(t)+([K_b]+[K_f])\mathbf{u}(t)=\mathbf{f}(t)\,, \tag{7}$$

where $[M]\in\mathbb{R}^{mxm}$ is the positive–definite mass matrix, $[K_b]\in\mathbb{R}^{mxm}$ is the positive–definite bending matrix and $[K_f]\in\mathbb{R}^{mxm}$ is the negative–definite fluid stiffness matrix ($forU>0$). $\mathbf{u}(t)\in\mathbb{R}^m$ is the response vector and $\mathbf{f}(t)\in\mathbb{R}^m$ is the force vector. Matrix $[C_f]\in\mathbb{R}^{mxm}$ in general is not symmetric and can be separated in a symmetric positive-definite part and a skew-symmetric part. Due to the boundary conditions of our application, $[C_f]$ is skew-symmetric, however, we still call it damping matrix, even though it not responsible to dissipate energy. In the frequency domain, Eq. (7) can be written as

$$-\omega^2[M]\hat{\mathbf{u}}(\omega)+i\omega[C_f]\hat{\mathbf{u}}(\omega)+([K_b]+[K_f])\hat{\mathbf{u}}(\omega)=\hat{\mathbf{f}}(\omega)\,, \tag{8}$$

where $\hat{\mathbf{u}}(\omega)\in\mathbb{C}^m$ is the response vector and $\hat{\mathbf{f}}(\omega)\in\mathbb{C}^m$ is the force vector.

3 DIMENSIONLESS QUANTITIES

To be able to do a more general analysis, some dimensionless quantities are introduced:

$$\begin{aligned}
&\zeta=\frac{x}{L}\,, \qquad \eta=\frac{v}{L}\,, \qquad \varpi=\omega L^2\left(\frac{m+M_f}{EI}\right)^{1/2}\,,\\
&\beta=\frac{M_f}{m+M_f}\,, \quad u=UL\left(\frac{M_f}{EI}\right)^{1/2}\,, \quad f=F\frac{L^3}{EI}\,.
\end{aligned} \tag{9}$$

where ζ is the dimensionless length, η is the dimensionless transverse displacement, β is the ratio of fluid mass, u is the dimensionless speed, f is the dimensionless force, and ϖ is the dimensionless frequency.

4 REDUCED-ORDER MODEL

A reduced–order model [15, 16] is going to be construct for the system given by Eq.(8). Lets first write the homogeneous equation associated to Eq.(8):

$$(-\omega^2[M]+i\omega[C_f(U)]+[K_f(U)]+[K_b])\hat{\mathbf{u}}(\omega)=\mathbf{0}\,, \tag{10}$$

The following generalized eigenvalue problem is solved to compute the reduction basis that will be used:

$$(-\omega^2[M] + [K_b])\boldsymbol{\phi} = \mathbf{0}\,, \tag{11}$$

corresponding to U equals to zero. With this choice, (1) we guarantee a good basis ($[M]$ and $[K_b]$ are positive–definite) and (2) it is not necessary to compute a different basis for each value of U. The displacement is written as $\hat{\mathbf{u}}(\omega) = [\Phi]\hat{\mathbf{q}}(\omega)$ and the response in the frequency domain is computed using the reduced-order model:

$$(-\omega^2[M_r] + i\omega[C_r(U)] + [K_r(U)])\hat{\mathbf{q}}(\omega) = \hat{\mathbf{f}}(\omega)\,. \tag{12}$$

The reduced matrices are given by

$$\begin{aligned}
&[M_r] = [\Phi]^T[M][\Phi]\,, && [C_r(U)] = [\Phi]^T[C_f(U)][\Phi]\,,\\
&[K_{fr}(U)] = [\Phi]^T[K_f(U)][\Phi]\,, && [K_{br}] = [\Phi]^T[K_b][\Phi]\,,\\
&[K_r(U)] = [K_{fr}(U)] + [K_{br}]\,,
\end{aligned} \tag{13}$$

where $[\Phi] = [\boldsymbol{\phi}_1\ \boldsymbol{\phi}_2\ ...\ \boldsymbol{\phi}_n]$, with $(n < m)$. It should be noted that $[M_r] = \delta_{ij}$ and $[\Phi]^T[K_b][\Phi] = \delta_{ij}\omega_i^2$, in which δ is the Dirac delta.

5 STABILITY ANALYSIS

To perform the stability analysis we will double the size of the system in the following way:

$$\underbrace{\begin{bmatrix} [0] & [I] \\ -[K_r(U)] & -[C_r(U)] \end{bmatrix}}_{B_r(U)} \underbrace{\begin{pmatrix} \hat{\mathbf{q}} \\ i\omega\hat{\mathbf{q}} \end{pmatrix}}_{\mathbf{y}} = i\omega \underbrace{\begin{bmatrix} [I] & [0] \\ [0] & [M_r] \end{bmatrix}}_{D_r} \begin{pmatrix} \hat{\mathbf{q}} \\ i\omega\hat{\mathbf{q}} \end{pmatrix} \tag{14}$$

Therefore, a generalized eigenvalue problem associated with Eq.(14) is written as:

$$B_r(U)\mathbf{y} = \lambda D_r\mathbf{y}\,. \tag{15}$$

where the eigenvalues $\lambda = Re(\lambda) + iIm(\lambda)$, in which $Re(\cdot)$ and $Im(\cdot)$ refer to real and imaginary parts. If $Re(\lambda) > 0$ the system is unstable. If $Re(\lambda) = 0$ the system is unstable is the corresponding eigenvalues are not simple.

6 PROBABILISTIC MODEL

To model the uncertainty in the fluid-structure interaction we will make an adaptation of the nonparametric probabilistic approach [9, 17] because it is able to cope with model uncertainties. The adaptation consists in using the reduced-order model and the random matrix theory. Since the damping and stiffness matrices come from the same model, they may be statistically correlated and one must find a way to find their joint distribution. In order to achieve this goal, we

propose to gather the information of both damping and stiffness of the fluid in a single operator, in the following way:

$$[A(U)] = i[C_r(U)] + [K_{fr}(U)]\,, \tag{16}$$

such that they will be generated randomly together (explained in the sequence) and later we can extract individually the random matrices $[\mathbf{C}_r(U)]$ and $[\mathbf{K}_{fr}(U)]$ as it will be explained further in this section. The operator needs to pass through some transformations before we can apply the nonparametric probabilistic approach, similar to what was done in [18]. Lets first do the polar decomposition (omitting the dependence on U to simplify the notation):

$$[A] = [Q][P]\,, \tag{17}$$

where $[Q]$ is a unitary matrix ($[Q]^*[Q] = [Q][Q]^* = [I]$), in which * is the conjugate transpose, and $[P]$ is a Hermitian positive-definite matrix. Note that $[A]$ is invertible for all $U > 0$, since $[K_{fr}(U)]$ is symmetric negative-definite and thus invertible for $U > 0$. This decomposition will be computed using the singular value decomposition [19]: $[A] = [U][S][V]^*$, with $[P] = [V][S][V]^*$ and $[Q] = [U][V]^*$. The Cholesky decomposition can be applied to matrix $[P]$:

$$[P] = [L]^*[L]\,. \tag{18}$$

The uncertainty in the fluid-structure interaction model is assumed to be mainly due to the uncertainty on the operator $[P]$, obtained through the polar decomposition. Finally, introducing the random germ $[\mathbf{G}]$:

$$[\mathbf{P}] = [L]^*[\mathbf{G}][L]\,, \tag{19}$$

where $[\mathbf{P}]$ and $[\mathbf{G}]$ are random matrices (note that the boldface is used for a random matrix). Thus, we have the random operator

$$[\mathbf{A}] = [Q][\mathbf{P}] = [Q][L]^*[\mathbf{G}][L]\,. \tag{20}$$

And the random damping and stiffness matrices happen to be:

$$[\mathbf{C}_r] = Im([\mathbf{A}]) \quad \text{and} \quad [\mathbf{K}_{fr}] = Re([\mathbf{A}])\,. \tag{21}$$

Without going into further details, the probability density function of the random matrix $[\mathbf{G}]$ and its random generator can be found in [9].

The level of uncertainty related to the fluid-structure interaction model is controlled by the dispersion parameter δ of matrix $[\mathbf{G}]$ defined as:

$$\delta = \left\{ \frac{1}{n} \mathcal{E}\{ ||[\mathbf{G}] - [I]||_F^2 \} \right\}^{\frac{1}{2}}\,, \tag{22}$$

where n is the dimension of $[\mathbf{G}]$, $[\,I\,]$ is the identity matrix, $\mathcal{E}\{\cdot\}$ denotes the mathematical expectation and $||[A]||_F = (\text{trace}\{[A][A]^T\})^{1/2}$ denotes the Frobenius norm. The random eigenvalue problem related to Eq.(14) is given by:

$$\underbrace{\begin{bmatrix} [0] & [I] \\ -[\mathbf{K}_r(U)] & -[\mathbf{C}_r(U)] \end{bmatrix}}_{\mathbf{B}_r(U)} \mathbf{Y} = i\Omega \underbrace{\begin{bmatrix} [I] & [0] \\ [0] & [M_r] \end{bmatrix}}_{D_r} \mathbf{Y} \tag{23}$$

where $[\mathbf{K}_r(U)] = [\mathbf{K}_{fr}(U)] + [K_{br}]$, and the random generalized eigenvalue problem that has to be solved is the following:

$$\mathbf{B}_r(U)\mathbf{Y} = \Lambda D_r \mathbf{Y}\,. \tag{24}$$

where the eigenvalues are random variables $\Lambda = Re(\Lambda) + iIm(\Lambda)$. Writing $\hat{\mathbf{U}}(\omega) = [\Phi]\hat{\mathbf{Q}}(\omega)$, the stochastic system related to Eq. (12) is given by:

$$(-\omega^2[M_r] + i\omega[\mathbf{C}_r(U)] + [\mathbf{K}_r(U)])\hat{\mathbf{Q}}(\omega) = \hat{\mathbf{f}}(\omega)\,, \tag{25}$$

where $\hat{\mathbf{U}}(\omega)$ is the random response.

7 NUMERICAL RESULTS

The beam is divided in 40 finite elements (after convergence check) and the first four normal modes are considered in the analysis. There are two important dimensionless parameters: β (mass relation) and u (dimensionless flow speed). In this analysis we fix $\beta = 0.24$ and vary the dimensionless speed u.

7.1 Deterministic analysis

Figure 2 shows the stability charts using the real (Fig. 2(a)) and imaginary parts (Fig. 2(b)) of half of the eigenvalues. As u increases, the system gets more unstable. When $u = \pi$ there is the first divergence mode, when $u = 2\pi$ there is the second divergence mode and the coupled-mode flutter, and when $u = 3\pi$ there is the second divergence mode, as indicated in the figure. Figure 2(b) shows that as u increases, the system gets less stiff, that is the four natural frequencies decrease. These results are in accordance with the ones found in [14].

Figure 3 shows the amplitude of the displacement in the frequency domain for $u = \{1.0, 2.5\}$. The curve related to the higher u is moved to the left (system less stiff). The force applied was $f = 1 \times 10^{-4}$ at each degree of freedom of the beam and the response shown is the absolute value of the dimensionless displacement in the middle of the beam.

The next section analyzes how these results change when the stochastic model is taken into account.

7.2 Stochastic analysis

Now we analyze the stochastic response of the system. We have used 1000 Monte Carlo samples in the analysis, since it is sufficient for a reasonable mean square convergence of the random eigenvalues. Figures 4 and 5 show the 95% confidence region for $\delta = \{0.05; 0.1\}$.

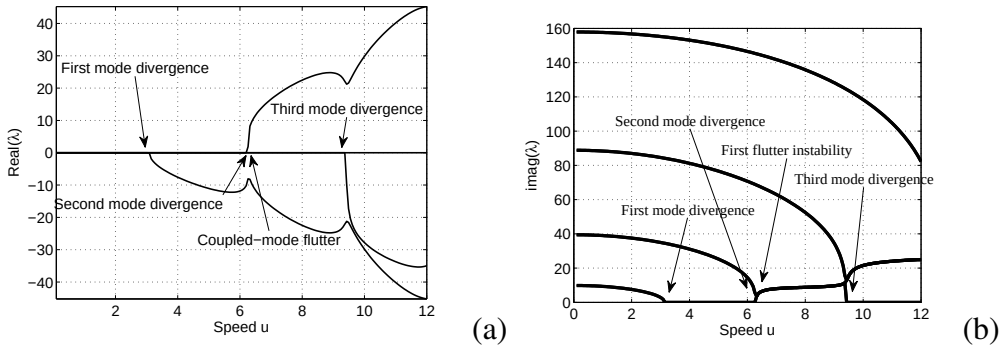


Figure 2: Stability charts. Real (a) and imaginary part (b) of λ.

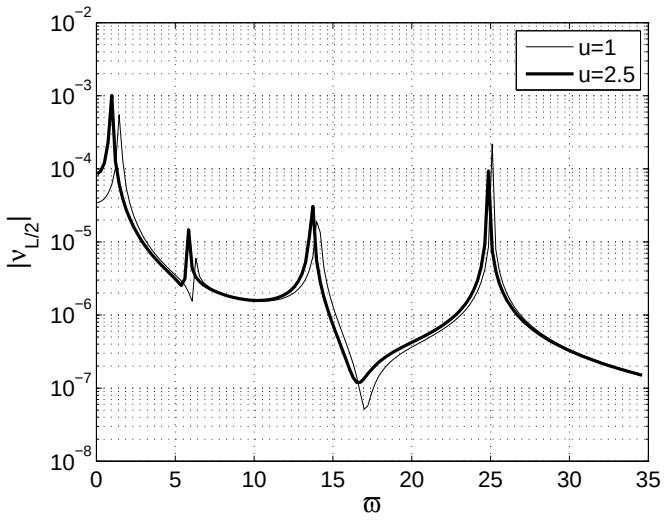


Figure 3: Frequency response amplitude at $\zeta = 0.5$.

When δ increases the confidence region also increases, as expected. It can be seen that when $u = 0$ there is no uncertainty in λ, but the uncertainty then increases. However the robustness of the system varies depending on the speed u, as it is observed for $Re(\lambda)$; between $u = 7$ and 8 the confidence region is thinner and close to $u = 12$ it is wider.

When the lines of the graphics cross each other, it is hard to follow the modes. Instead of analyzing these crossings, lets evaluate the probability of being in a instability region. We define two failure probabilities: (1) one related to the divergence instability and (2) other related to the coupled-mode flutter instability. Figure 6(a) shows that until about $u = 3$ the probability of divergence is close to zero, but for $u > 3.5$ it becomes 100%. The same way, Figure 6(b) shows that until about $u = 5$ the probability of coupled-mode flutter is close to zero, but for $u > 6.5$ it becomes 100%. To get a better feeling of this probability of failure, take a look at Figure 7. It shows the histogram of $Re(\Lambda_2)$ related to the coupled-mode flutter for two different u's. In both cases there is a big probability that $Re(\Lambda_2)= 0$. However, for higher flow speeds, the probability that this random variable is greater than zero increases. An interesting fact to note is that the random variable $Re(\Lambda_2)$ follows a mixed distribution, with a concentrated probability at point zero (stable condition, if only coupled-mode flutter instability is considered) and a continuous distribution above zero (unstable condition relate to flutter).

Now we will detail the analysis of the probability of being in a coupled-mode flutter condi-

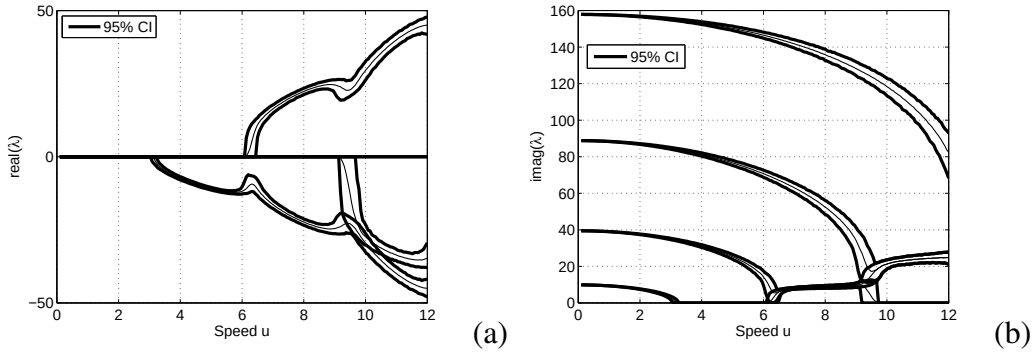


Figure 4: 95% confidence interval for $\delta = 0.05$.

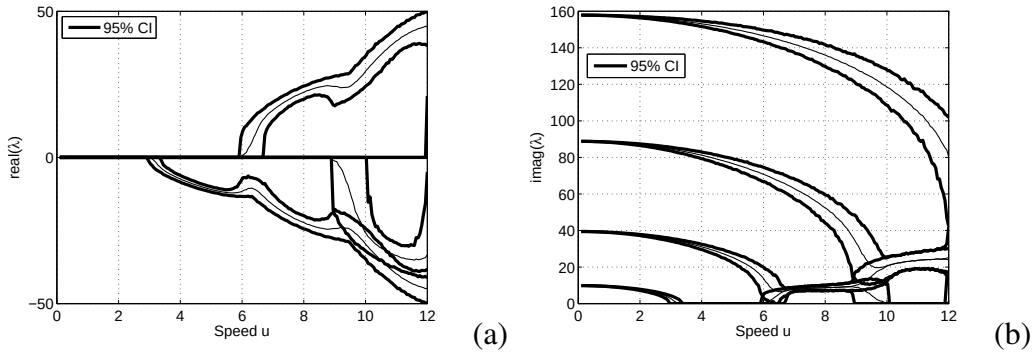


Figure 5: 95% confidence interval for $\delta = 0.1$.

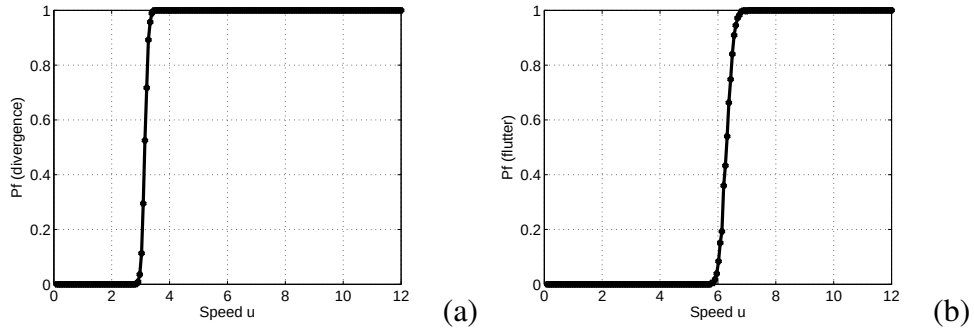


Figure 6: For different values of u and $\delta = 0.1$., (a) probability of being in a divergence region and (b) probability of being in a ccoupled-mode flutter region.

tion for different levels of uncertainties. Figure 8 shows the probability of coupled-mode flutter as a function of the flow speed u for different levels of uncertainty (delta values). The dash-doted arrows show that if the deterministic ($\delta = 0$) limit speed is considered, the probability of failure would be about 50%; which is a bad scenario. This is an important result, and it shows that an uncertainty model should be taken into account.

On the other hand, the solid arrows show that if we define a failure probability, say 20%, depending on the level of uncertainty there will be a limit flow speed for each value of delta: $u = 6.12$ for $\delta = 0.1$, $u = 6.20$ for $\delta = 0.05$, $u = 6.20$ for $\delta = 0.05$ and $u = 6.26$ for $\delta = 0.01$. As expected, if delta increases, the limit u should decrease because the scenario is getting worse. Finally, Figure 9 shows the response in the frequency domain for $u = 3.1$ and

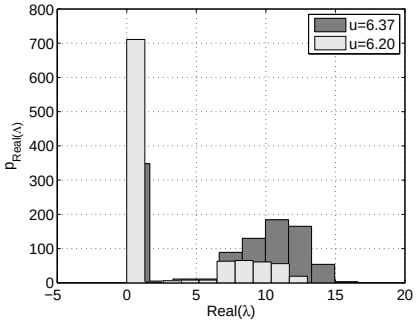


Figure 7: Histogram of $Re(\Lambda_2)$ for two different u's, considering coupled-mode flutter mode instability.

$\delta = 0.1$. It is noted that the uncertain region is bigger when the frequency is close to zero, where the stabilities are put in check.

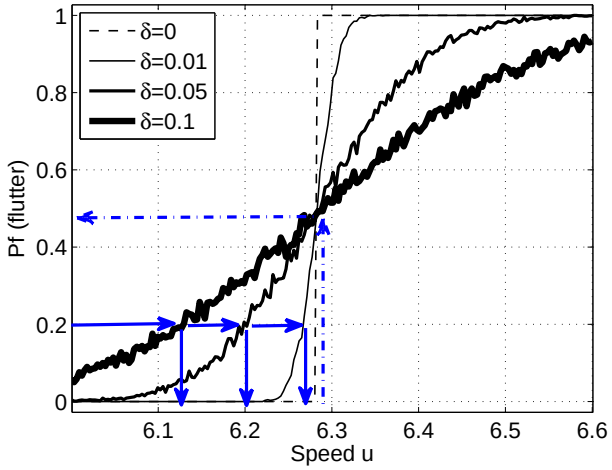


Figure 8: For different values of u and δ, probability of being in a coupled-mode flutter region.

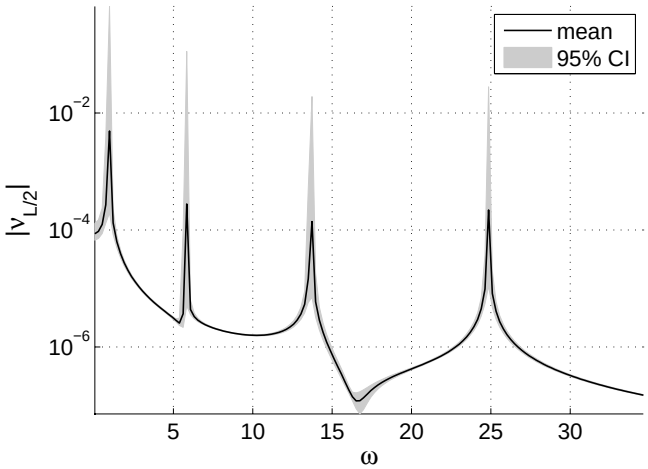


Figure 9: Frequency response amplitude at $\zeta = 0.5$ for $u = 2.5$ and $\delta = 0.1$.

8 CONCLUDING REMARKS

The problem of a tube with internal flow is analyzed in this paper. A probabilistic model based on the nonparametric probabilistic approach was proposed to model uncertainties in the fluid-structure interaction. This probabilistic model is able to take into account modeling errors related to the fluid-structure interaction.

A simple Euler-Bernoulli beam and a plug flow model are considered to model the system, which is discretized by means of the finite element methods and reduced using the normal modes of the beam. The stability analysis is done for different levels of uncertainties showing how confidence limits change for different values of dimensionless flow speed. Also, the probability of instability is computed for different levels of uncertainty of the fluid-structure interaction. An interesting fact is that the random variable related to the real part of the random eigenvalues has a mixed distribution (discrete and continuous). It seems that the proposed probabilistic model is well suited for the problem analyzed, although other analysis should be performed and the previsions compared with experimental data.

Acknowledgements

The authors are grateful to the financial support from the Brazilian agencies: CAPES, CNPq, and FAPERJ. And specifically the project CAPES-COFECUB.

REFERENCES

[1] T. G. Ritto, C. Soize and R. Sampaio, Nonlinear dynamics of a drill-string with uncertain model of the bit-rock interaction. *International Journal of Non-Linear Mechanics*, **44**(8), 865–876, 2009.

[2] S. Rinaldi, S. Prabhakar, S. Vengallatore and M.P Paidoussis, Dynamics of microscale pipes containing internal fluid flow: Damping, frequency shift, and stability. *Journal of Sound and Vibration*, **329**(8), 1081–1088, 2010.

[3] P. Soltani, M.M. Taherian and A. Farshidianfar, Vibration and instability of a viscous-fluid-conveying single-walled carbon nanotube embedded in a visco-elastic medium. *Journal of Physics D: Applied Physics*, **43**(42), art. no. 425401, 2010.

[4] Ritto, T; Sampaio, R.; Rochinha, F.; Model uncertainties of flexible structures vibrations induced by internal flows. *Journal of the Brazilian Society of Mechanical Sciences and Engineering*, **33**, 373-380, 2011.

[5] A. H. Nayefh and B. Balachandran, *Applied Nonlinear Dynamics*, Wiley Series in Nonlinear Science, 1995.

[6] G. I. Schueller, H. J. Pradlwarter and P. S. Koutsourelakis, A critical appraisal of reliability estimation procedures for high dimensions. *Probabilistic Engineering Mechanics*, **19**(4), 463–474, 2004.

[7] M.P. Paidoussis and N. T. Issid, Dynamic stability of pipes conveying fluid . *Journal of Sound and Vibration*, **33**(3), 267–294, 1974.

[8] Y. K. Lin and G. Cai, *Probabilistic Structural Dynamics*, McGraw-Hill, 1995.

[9] C. Soize, A nonparametric model of random uncertainties for reduced matrix models in structural dynamics. *Probabilistic Engineering Mechanics*, **15**, 277–294, 2000.

[10] J. F Durand, C. Soize and L. Gagliardini, Structural-acoustic modeling of automotive vehicles in presence of uncertainties and experimental identification and validation. *J. Accoust. Soc. Am.*, **124**(3), 1513–1525, 2008.

[11] C. Chen, D. Duhamel and C. Soize, Probabilistic approach for model and data uncertainties and its experimental identification in structural dynamics: Case of composite sandwich panels. *Journal of Sound and Vibration*, **194**(1-2), 64–81, 2006.

[12] E. Jaynes, *Probability Theory: The Logic of Science*, Cambridge University Press, 2003.

[13] D. J. Inman, *Engineering Vibration, 4th Edition*, Prentice-Hall, Inc., 2007.

[14] M. P. Paidoussis, *Fluid-Structure Interactions: Slender Structures and Axial Flow, Vol. 1*, Academic Press, 1998.

[15] J. M. Crolet and R. Ohayon, *Computational Methods for Fluid-Structure Interaction*, John Wiley & Sons Inc., 1994.

[16] Z.-Q.S. Qu, *Model Order Reduction Techniques: with Applications in Finite Element Analysis*, Springer, 2010.

[17] C. Soize, Random matrix theory for modeling uncertainties in computational mechanics. *Computer Methods in Applied Mechanics and Engineering*, **194**(12-16), 1333–1366, 2005.

[18] M. Mbaye and C. Soize, J.-P. Ousty and E.Capiez-Lernout, Robust analysis of design in vibration of turbomachines. *ASME Journal of Turbomachinery*, **135**(2), art. no. 021008, 2013.

[19] G. H. Golub and C. F. Van Loan, *Matrix Computations, 3rd Edition*, Johns Hopkins, 1996.

COMPDYN 2013
4th ECCOMAS Thematic Conference on
Computational Methods in Structural Dynamics and Earthquake Engineering
M. Papadrakakis, V. Papadopoulos, V. Plevris (eds.)
Kos Island, Greece, 12–14 June 2013

FORMULATION OF A STOCHASTIC SEMI ANALYTICAL FINITE ELEMENT METHOD FOR UNCERTAIN MEDIA

Faker BOUCHOUCHA[1], Mohamed Najib ICHCHOU[2], and Mohamed HADDAR[1]

[1] Unit of Dynamics of the Mechanical Systems (UDSM)
National School of Engineers of Sfax. BP. W3038 Sfax –Tunisia
e-mail: fakersbouchoucha@yahoo.fr
e-mail: mohamed.haddar@enis.rnu.tn

[2]Laboratory of Tribology and Dynamics of Systems (LTDS)
Ecole Centrale de Lyon. 36 Avenue Guy de Collongues 69130 Ecully. France
Mohamed.Ichchou@ec-lyon.fr

Keywords: Stochastic, semi analytical method, finite element, uncertain media, dispersion.

Abstract. *In the present work, the stochastic semi analytical finite element (S.S.A.F.E) method for uncertain media is formulated. This method leads to the characterisation of the guided wave propagation through the classical linearization of the governing equation of motion. In probabilistic methods, uncertainty in the parameters is considered and is represented by a random variable. The statistics of the propagation constants and the wave modes are offered. The current study extends the S.A.F.E. techniques to stochastic media through the second order perturbation. A parametric approach for uncertainties treatments is considered and combined to the S.A.F.E. technique. The originality of this paper is the study of the second order perturbation. The sensitivity and the precision of the S.S.A.F.E. approach is treated through the second order perturbation introduced in the structural parameters. The question of the statistics of wave characteristics is considered. The second order perturbation of the propagation constants is investigated. The numerical accuracy and the computational efficiency of the method are demonstrated by comparison with analytical results. Comparisons between numerical results and Monte Carlo simulations of the second order stochastic formulation are among the offered originalities of this work.*

1 INTRODUCTION

Guided waves are still a subject of intensive research such as structural forms occur in several engineering areas. This research focuses on the study of guided wave properties and applications. To study wave propagation in structural waveguides, semi-analytical finite element (SAFE) method was investigated by many researchers. Recently, Hayashi and Kawashima [1] derived the SAFE formulation through virtual work principles and proposed a way to calculate the group velocity using the eigensolution at a given frequency. Damljanovic and Weaver [2] developed the linear triangular elements for SAFE method using Lagrange's equations to investigate the elastic waves in waveguides of arbitrary cross-section. Gavric [3] calculated the dispersion relationship in a free rail by using triangular and quadrilateral elements, with those elements obtained from Hamilton's principle. The SAFE method has also be adopted to investigate the wave propagation characteristics for thin-walled structures in [4], where the polynomial interpolation is used in the propagation axis thus leads to the polynomial eigenvalue problems. The method is extended to curved structures in [5], where isoparametric element is used. In the current work, we introduce the semi-analytical numerical method that may be used for wave propagation and dynamic analysis of waveguide structures.

In the literature, however, most of founded numerical issues of wave propagation simulations are mainly limited to deterministic media. In this context the concept of a random field can't be ignored. The nature of variability of the material properties in the structure created a variety of structural problems, in which the uncertainties in different parameters play a major part. Uncertainties can be due to the lack of good knowledge of material properties or due to the change in the load and support condition. The modelling technique is also one of the major sources of uncertainty, in the analysis of waveguides. Hence, when the variations are large, the probabilistic models are advantageous than the deterministic ones. In probabilistic methods, uncertainty in the parameters is considered and is represented by a random variable or field. Among the different probabilistic methods in mechanics, direct Monte Carlo simulation, which involves sampling and estimation, is an example for a frequently used statistical approach [6, 7, 8]. There are also many no statistical methods in probabilistic mechanics. Random perturbation method, orthogonal polynomials expansion methods, Neumann expansion, and numerical integration come under the category of no statistical schemes [9]. Ajith and Gopalakrishnan [10] presented a paper to study the wave propagation responses at high frequencies in composite structures in an uncertain environment using Neumann expansion under the environment of spectral finite element.

The main contribution in the present work is the formulation of the stochastic semi analytical finite element (SSAFE) method through the second order perturbation. We introduce an uncertainty in the structural parameters and using the probabilistic tools, we study the perturbation which affects the wave propagation in the structural waveguide. The numerical accuracy and the computational efficiency of this method are demonstrated by comparison with Monte Carlo simulation and analytical results.

This paper is organised as follows: the next section describes the SAFE method based on the virtual work principle. This method leads to the characterisation of the guided wave propagation through the classical linearization of the governing equation of motion. In the third section, the probabilistic phenomenon is introduced and the SSAFE is formulated using the second order perturbation. Numerical results and discussion are presented in the section 4. The numerical efficiency of this method is demonstrated by comparison with MC simulations and analytical results. A conclusion together with a description of the work in progress is ultimately given.

2 DESCRIPTION OF THE SEMI ANALYTICAL FINITE ELEMENT (SAFE) METHOD

In this section, we introduce the semi-analytical numerical method that may be used for wave propagation and dynamic analysis of waveguide structures. The basic formulations are presented to illustrate the merits and shortcomings of the method. In the following subsection, we briefly introduce the SAFE method based on the virtual work principle.

Consider a structural waveguide with a uniform cross section. The weak form based on the virtual work principle for the dynamic problem may be written as

$$W^e = \int_V \langle \varepsilon^* \rangle \{\sigma\}\, dv + \int_V \langle u^* \rangle \rho \{\ddot{u}\}\, dv = 0 \tag{1}$$

Where W^e is the virtual work of the internal forces, ρ is the density, * denotes virtual quantities, $\varepsilon = \{\varepsilon_{xx} \quad \varepsilon_{yy} \quad \varepsilon_{zz} \quad 2\varepsilon_{xy} \quad 2\varepsilon_{yz} \quad 2\varepsilon_{xz}\}^T$ is the strain vector, $u = \{u_x \quad u_y \quad u_z\}^T$ is the displacement field, $\sigma = \{\sigma_{xx} \quad \sigma_{yy} \quad \sigma_{zz} \quad \sigma_{xy} \quad \sigma_{yz} \quad \sigma_{xz}\}^T$ is the stress vector. The virtual wok principle can be formulated as:

$$W^e(u^*, u) = W_{int} - W_{ext} \tag{2}$$

Where $W_{int} = \int_V \langle \varepsilon^* \rangle \{\sigma\}\, dv$ and $W_{ext} = -\int_V \langle u^* \rangle \rho \{\ddot{u}\}\, dv$ are the internal and external virtual work, respectively.

The harmonic waves in a uniformly cross-sectioned waveguide are described by the orthogonal function $exp(j\omega t - jkx)$. k is the wave number in x direction, ω is the circular frequency. The displacement function can be $u(x,y,z,t) = u(y,z)exp(j\omega t - jkx)$, where $u(y,z)$ describe the amplitudes of the displacements of the waveguide cross-section. Thus the strain-displacement relationship $\{\varepsilon\} = [\mathbf{D}]\{u\}$ becomes

$$\{\varepsilon\} = \begin{bmatrix} \partial/\partial \mathbf{x} & \mathbf{0} & \mathbf{0} \\ \mathbf{0} & \partial/\partial \mathbf{y} & \mathbf{0} \\ \mathbf{0} & \mathbf{0} & \partial/\partial \mathbf{z} \\ \partial/\partial \mathbf{y} & \partial/\partial \mathbf{x} & \mathbf{0} \\ \mathbf{0} & \partial/\partial \mathbf{z} & \partial/\partial \mathbf{y} \\ \partial/\partial \mathbf{z} & \mathbf{0} & \partial/\partial \mathbf{x} \end{bmatrix} \{u\} \tag{3}$$

The strain-displacement relationship can be written in the following form:

$$\{\varepsilon\} = [\mathbf{D_0} + k\mathbf{D_1}]\{u\} \tag{4}$$

Where

$$\mathbf{D_0} = \begin{bmatrix} \mathbf{0} & \mathbf{0} & \mathbf{0} \\ \mathbf{0} & \partial/\partial \mathbf{y} & \mathbf{0} \\ \mathbf{0} & \mathbf{0} & \partial/\partial \mathbf{z} \\ \partial/\partial \mathbf{y} & \mathbf{0} & \mathbf{0} \\ \mathbf{0} & \partial/\partial \mathbf{z} & \partial/\partial \mathbf{y} \\ \partial/\partial \mathbf{z} & \mathbf{0} & \mathbf{0} \end{bmatrix}, \mathbf{D_1} = \begin{bmatrix} -\mathbf{j} & \mathbf{0} & \mathbf{0} \\ \mathbf{0} & \mathbf{0} & \mathbf{0} \\ \mathbf{0} & \mathbf{0} & \mathbf{0} \\ \mathbf{0} & -\mathbf{j} & \mathbf{0} \\ \mathbf{0} & \mathbf{0} & \mathbf{0} \\ \mathbf{0} & \mathbf{0} & -\mathbf{j} \end{bmatrix} \tag{5}$$

The strain-displacement relationship can be written as:

$$\{\varepsilon\} = [\mathbf{D}][\mathbf{N}]\{u_i\} \tag{6}$$

Where $u_i = \{u_{x_i} \quad u_{y_i} \quad u_{z_i}\}^T$ is the displacement vector of the finite element, $[\mathbf{N}]$ is the matrix of the element shape functions.

In the other hand, the relationship between the strain and the stress vectors can be given in the following manner:

$$\{\sigma\} = [\mathbf{C}]\{\varepsilon\} \tag{7}$$

Where $[\mathbf{C}]$ is the material stiffness matrix which can be written as:

$$[\mathbf{C}] = \frac{\mathbf{E}}{(\mathbf{1+\nu})(\mathbf{1-2\nu})} \begin{pmatrix} \mathbf{1-\nu} & \boldsymbol{\nu} & \boldsymbol{\nu} & \mathbf{0} & \mathbf{0} & \mathbf{0} \\ & \mathbf{1-\nu} & \boldsymbol{\nu} & \mathbf{0} & \mathbf{0} & \mathbf{0} \\ & & \mathbf{1-\nu} & \mathbf{0} & \mathbf{0} & \mathbf{0} \\ & & & \mathbf{1-2\nu/2} & \mathbf{0} & \mathbf{0} \\ & & & & \mathbf{1-2\nu/2} & \mathbf{0} \\ \mathbf{sym} & & & & & \mathbf{1-2\nu/2} \end{pmatrix} \tag{8}$$

Where E is the modulus of elasticity and ν is the poisson ration.
The external virtual work can be developed as follows:

$$W_{ext} = \langle u_i^* \rangle [\mathbf{M^e}] \{\ddot{u}_i\} \tag{9}$$

Where $[\mathbf{M^e}]$ is the mass matrix which can be given as:

$$[\mathbf{M^e}] = \int_{\Omega^e} \rho [\mathbf{N}]^{\mathbf{T}} [\mathbf{N}] d\Omega^e \tag{10}$$

Where Ω^e denotes the element domain.
The internal virtual work can be developed as:

$$W_{int} = \langle q_i^* \rangle [\mathbf{K^e}] \{q_i\} \tag{11}$$

Where $[\mathbf{K^e}]$ is the stiffness matrix which can be written as:

$$[\mathbf{K^e}] = \int_{\Omega^e} [\mathbf{N}]^{\mathbf{T}} [\mathbf{D}]^{\mathbf{T}} [\mathbf{C}][\mathbf{D}][\mathbf{N}] d\Omega^e \tag{12}$$

Introducing equation (4) in equation (12) leads to:

$$[\mathbf{K^e}] = \int_{\Omega^e} [\mathbf{N}]^{\mathbf{T}} [\mathbf{D_0} + k\mathbf{D_1}]^{\mathbf{T}} [\mathbf{C}][\mathbf{D_0} + k\mathbf{D_1}][\mathbf{N}] d\Omega^e \tag{13}$$

Then

$$[\mathbf{K^e}] = [\mathbf{K_0^e}] + k[\mathbf{K_1^e}] + k^2[\mathbf{K_2^e}] \tag{14}$$

Where

$$\mathbf{K_0^e} = \int_{\Omega^e} \mathbf{N^T D_0}^{\mathbf{T}} \mathbf{C D_0 N} \, d\Omega^e \tag{15}$$

$$\mathbf{K_1^e} = \int_{\Omega^e} \mathbf{N^T D_1}^{\mathbf{T}} \mathbf{C D_0 N} \, d\Omega^e + \int_{\Omega^e} \mathbf{N^T D_0}^{\mathbf{T}} \mathbf{C D_1 N} \, d\Omega^e \tag{16}$$

$$\mathbf{K_2^e} = \int_{\Omega^e} \mathbf{N^T D_1}^{\mathbf{T}} \mathbf{C D_1 N} \, d\Omega^e \tag{17}$$

Assembly of the element matrices and vectors leads to the governing equation of motion of the waveguide:

$$\left[\mathbf{K_0} - \omega^2\mathbf{M} + k\mathbf{K_1} + k^2\mathbf{K_2}\right]\varphi = \mathbf{0} \tag{18}$$

Where φ denotes the nodal displacement vector.

φ_1 and φ_2 denote the eigenvectors associated to k and $(-k)$, from the equation of motion, we can write:

$$\left[\mathbf{K_0} - \omega^2\mathbf{M} + k\mathbf{K_1} + k^2\mathbf{K_2}\right]\varphi_1 = \mathbf{0} \tag{19}$$

and

$$\left[\mathbf{K_0} - \omega^2\mathbf{M} - k\mathbf{K_1} + k^2\mathbf{K_2}\right]\varphi_2 = \mathbf{0} \tag{20}$$

The linearization of the equation of motion can be given in the following form:

$$\begin{bmatrix} \mathbf{K_1} & \mathbf{K_0} - \omega^2\mathbf{M} \\ \mathbf{K_0} - \omega^2\mathbf{M} & \mathbf{0} \end{bmatrix} \begin{Bmatrix} k\phi_1 \\ \phi_2 \end{Bmatrix} + k^2 \begin{bmatrix} \mathbf{0} & \mathbf{K_2} \\ \mathbf{K_2} & \mathbf{K_1} \end{bmatrix} \begin{Bmatrix} k\phi_1 \\ \phi_2 \end{Bmatrix} = 0 \tag{21}$$

Where $\phi_1 = \varphi_1 + \varphi_2$ and $\phi_2 = \varphi_1 - \varphi_2$

The linearized equation of motion presents the eigenvalue problem of the system.

$$\left(\mathbf{A} - \lambda\mathbf{B}\right)\phi = \mathbf{0} \tag{22}$$

Where $\mathbf{A} = \begin{bmatrix} \mathbf{K_1} & \mathbf{K_0} - \omega^2\mathbf{M} \\ \mathbf{K_0} - \omega^2\mathbf{M} & \mathbf{0} \end{bmatrix}$, $\mathbf{B} = -\begin{bmatrix} \mathbf{0} & \mathbf{K_2} \\ \mathbf{K_2} & \mathbf{K_1} \end{bmatrix}$, $\phi = \begin{Bmatrix} k\phi_1 \\ \phi_2 \end{Bmatrix}$ and $\lambda = k^2$

The resolution of this eigenvalue problem leads to calculate the wave number and provide the dispersion curves.

3 FORMULATION OF THE STOCHASTIC SEMI ANALYTICAL FINITE ELEMENT METHOD

In this section, we formulate the stochastic semi analytical finite element method (SSAFEM). We introduce an uncertainty in the structural parameters and using the probabilistic tools, we study the perturbation which affects the wave propagation in the structure. The stochastic eigenvalue problem is given in the following form:

$$\left(\tilde{\mathbf{A}} - \tilde{\lambda}\tilde{\mathbf{B}}\right)\tilde{\phi} = 0 \tag{23}$$

The random variables are modelled by Gaussian variables through a second order perturbation, mathematically: $\tilde{v} = \overline{v} + v_1\varepsilon + v_2\varepsilon^2$ where $\tilde{v}$ is the random variable, $\overline{v}$ its mean, v_1 is the first order perturbation, v_2 is the second order perturbation and ε is Gaussian variable centred and reduced. The polynomial chaos $(1, \varepsilon, \varepsilon^2)$ is used as a supplementary dimension of the problem. Using the polynomial chaos projection of these variables, we can extract their means (deterministic quantity), their first and second order perturbation. The second order development of stochastic variables is adopted, such that:

$$\tilde{\mathbf{A}} = \overline{\mathbf{A}} + \mathbf{A}_1\varepsilon + \mathbf{A}_2\varepsilon^2, \tilde{\mathbf{B}} = \overline{\mathbf{B}} + \mathbf{B}_1\varepsilon + \mathbf{B}_2\varepsilon^2, \ \tilde{\lambda} = \overline{\lambda} + \lambda_1\varepsilon + \lambda_2\varepsilon^2, \ \tilde{\phi} = \overline{\phi} + \phi_1\varepsilon + \phi_2\varepsilon^2 \tag{24}$$

The eigenvalue equation can be written as a deterministic part and a perturbation part.

The deterministic part is given as:

$$\left(\overline{\mathbf{A}} - \overline{\lambda}\overline{\mathbf{B}}\right)\overline{\phi} = 0 \tag{25}$$

The resolution of the equation (25) leads to calculate the deterministic modes $\overline{\lambda_i}$ and $\overline{\phi_i}$

The perturbation part leads to calculate the first order perturbation of the eigenmode and is given as:

$$\left(\bar{\mathbf{A}} - \bar{\lambda}\bar{\mathbf{B}}\right)\phi_1 + \left(\mathbf{A}_1 - \lambda\mathbf{B}_1 - \lambda_1\mathbf{B}\right)\phi = 0 \tag{26}$$

Multiplying this equation by $\bar{\phi}_i^t$ gives:

$$\bar{\phi}_i^t\left(\bar{\mathbf{A}} - \bar{\lambda}\bar{\mathbf{B}}\right)\phi_1 + \bar{\phi}_i^t\left(\mathbf{A}_1 - \bar{\lambda}\mathbf{B}_1 - \lambda_1\bar{\mathbf{B}}\right)\bar{\phi}_i = 0 \tag{27}$$

The transpose of the deterministic eigenvalue problem gives:

$$\bar{\phi}_i^t\left(\bar{\mathbf{A}}^{\mathbf{t}} - \bar{\lambda}_i\bar{\mathbf{B}}^{\mathbf{t}}\right) = \mathbf{0} \tag{28}$$

Using the symmetry of $\bar{\mathbf{A}}$ and $\bar{\mathbf{B}}$, we have

$$\phi_i^t\left(\bar{\mathbf{A}} - \bar{\lambda}_i\bar{\mathbf{B}}\right) = \mathbf{0} \tag{29}$$

Then, equation (27) can be simplified as follows:

$$\bar{\phi}_i^t\left(\mathbf{A}_1 - \bar{\lambda}\mathbf{B}_1 - \lambda_1\bar{\mathbf{B}}\right)\bar{\phi}_i = 0 \tag{30}$$

The first order perturbation of the eigenvalue can be extracted according to the following equation:

$$\lambda_1 = \frac{\bar{\phi}_i^t\left(\mathbf{A}_1 - \bar{\lambda}\mathbf{B}_1\right)\bar{\phi}}{\bar{\phi}_i^t\bar{\mathbf{B}}\bar{\phi}_i} \tag{31}$$

The orthogonality condition of the eigenmode leads to write:

$$\bar{\phi}_i^t\bar{\mathbf{B}}\,\bar{\phi}_j = \delta_{ij} \tag{32}$$

Therefore

$$\bar{\phi}_i^t\bar{\mathbf{B}}\,\bar{\phi}_i = 1 \tag{33}$$

We can simplify the equation (31) and give the expression of the first order perturbation of the eigenvalue as:

$$\lambda_1 = \bar{\phi}_i^t\left(\mathbf{A}_1 - \bar{\lambda}\mathbf{B}_1\right)\bar{\phi}_i \tag{34}$$

From the definition of first order perturbation of propagation constants, it can be for interest in many applicative engineering cases to consider wave number statistics which can be considered as a random parameter through the second order perturbation:

$$\tilde{k} = \bar{k} + k_1\varepsilon + k_2\varepsilon^2 \tag{35}$$

Indeed, from the knowledge of the mean and the first order perturbation of the eigenvalue and using the relationship $\tilde{\lambda} = \tilde{k}^2$, we can easily express the statistics of $\tilde{k}$ as follows:

$$\bar{k} = \pm\sqrt{\bar{\lambda}} \tag{36}$$

Where $\bar{k}$ is the mean of the wave number.

Developing the first order leads to calculate the first order perturbation of the wave number:

$$k_1 = \frac{\lambda_1}{2\bar{k}} \tag{37}$$

The polynomial chaos projection of the equation (23) leads to give the second order perturbation equation as follows:

$$\left(\mathbf{A}_2 - \bar{\lambda}\mathbf{B}_2 - \lambda_1\mathbf{B}_1 - \lambda_2\bar{\mathbf{B}}\right)\bar{\phi} + \left(\mathbf{A}_1 - \lambda\mathbf{B}_1 - \lambda_1\bar{\mathbf{B}}\right)\phi_1 + \left(\bar{\mathbf{A}} - \bar{\lambda}\bar{\mathbf{B}}\right)\phi_2 = 0 \tag{38}$$

Multiplying this equation by $\bar{\phi}_i^t$ and using the equation (32), we obtain:

$$\bar{\phi}^t\left(\mathbf{A}_2 - \bar{\lambda}\mathbf{B}_2 - \lambda_1\mathbf{B}_1 - \lambda_2\bar{\mathbf{B}}\right)\bar{\phi} + \bar{\phi}^t\left(\mathbf{A}_1 - \lambda\mathbf{B}_1 - \lambda_1\bar{\mathbf{B}}\right)\phi_1 = 0 \tag{39}$$

The second order perturbation is then easily extracted

$$\lambda_2 = \frac{\bar{\phi}^t\left(\mathbf{A}_2 - \bar{\lambda}\mathbf{B}_2 - \lambda_1\mathbf{B}_1\right)\bar{\phi} + \bar{\phi}^t\left(\mathbf{A}_1 - \lambda\mathbf{B}_1 - \lambda_1\bar{\mathbf{B}}\right)\phi_1}{\bar{\phi}^t\bar{\mathbf{B}}\bar{\phi}} \tag{40}$$

Using equation (33), we can write:

$$\lambda_2 = \bar{\phi}^t \left(\mathbf{A}_2 - \bar{\lambda}\mathbf{B}_2 - \lambda_1 \mathbf{B}_1 \right) \bar{\phi} + \bar{\phi}^t \left(\mathbf{A}_1 - \lambda \mathbf{B}_1 - \lambda_1 \bar{\mathbf{B}} \right) \phi_1 \tag{41}$$

The second order perturbation of the wave number is offered as follows:

$$k_2 = \frac{\lambda_2 - k_1^2}{2\bar{k}} \tag{42}$$

4 NUMERICAL RESULTS AND DISCUSSION:

In this section, we present and discuss the numerical results obtained through the SSAFE method. The validation of this method is done using analytical results and MC simulations. We treat many cases of uncertain media in order to prove that the developed technique is general.

The studied structure is illustrated in figure 1. We treat the cylindrical structure which has the following characteristics: radius = 100 mm, thickness = 1 mm, length: d = 20 mm, nodes number = 36 per section and element number= 36. We use a surface element with 4 nodes that include 6 d.o.f. per node.

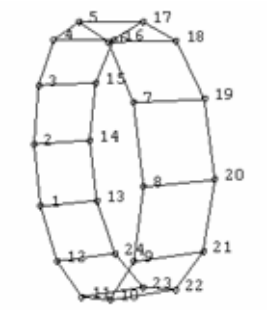


Figure 1: Cylindrical structure.

4.1 Longitudinal wave's case study

Figure 2 shows the deterministic dispersion curves for the longitudinal mode. This illustration is obtained from the equation (36): $\bar{k} = \pm\sqrt{\bar{\lambda}}$ where $\bar{\lambda}$ is extracted by solving the deterministic eigenvalue problem $\left(\bar{\mathbf{A}} - \bar{\lambda}\bar{\mathbf{B}} \right) \bar{\phi} = 0$.

The validation is done using the analytical results and MC simulations. The analytical theory gives the stochastic wave number for the traction compression mode in the following form:

$$\tilde{k}_{TC} = \omega \sqrt{\frac{\rho}{E}} \tag{43}$$

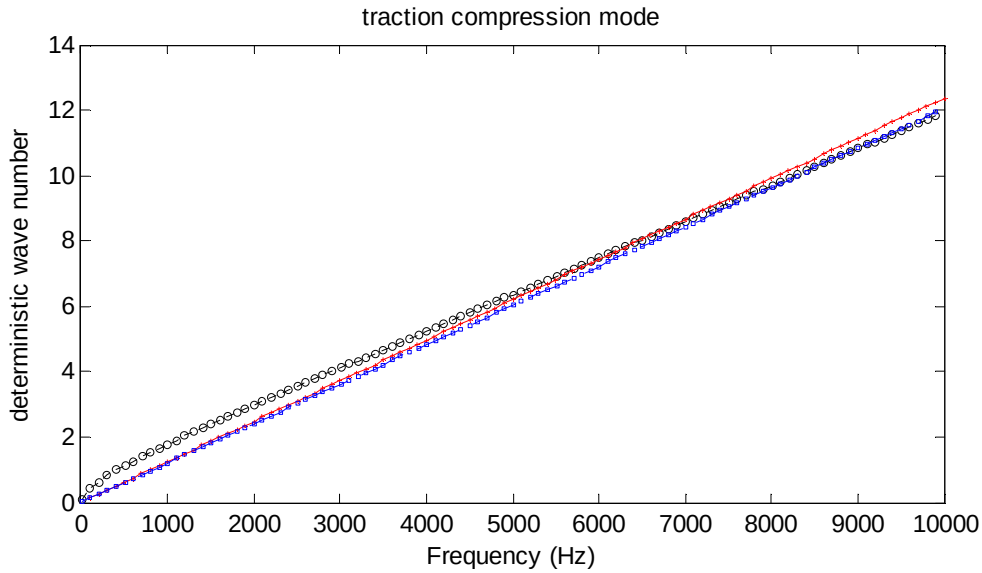


Figure 2: The deterministic wave number for the longitudinal mode

SSAFE Analytical MC

The Young modulus is an important parameter which affects the stiffness matrix. We introduce an uncertainty in this structural parameter through the second order perturbation and it can be written as a Gaussian distribution: $\tilde{E} = \overline{E} + E_1\varepsilon + E_2\varepsilon^2$ where $\overline{E} = 2.1\times 10^5\ MPa$, $E_1 = 0.05\overline{E}$ and $E_1 = 0.05\overline{E}$

Figure 3 presented the first order perturbation of the wave number for the longitudinal mode following an uncertainty introduced in the Young modulus. The first order perturbation of the wave number is given in equation (37).

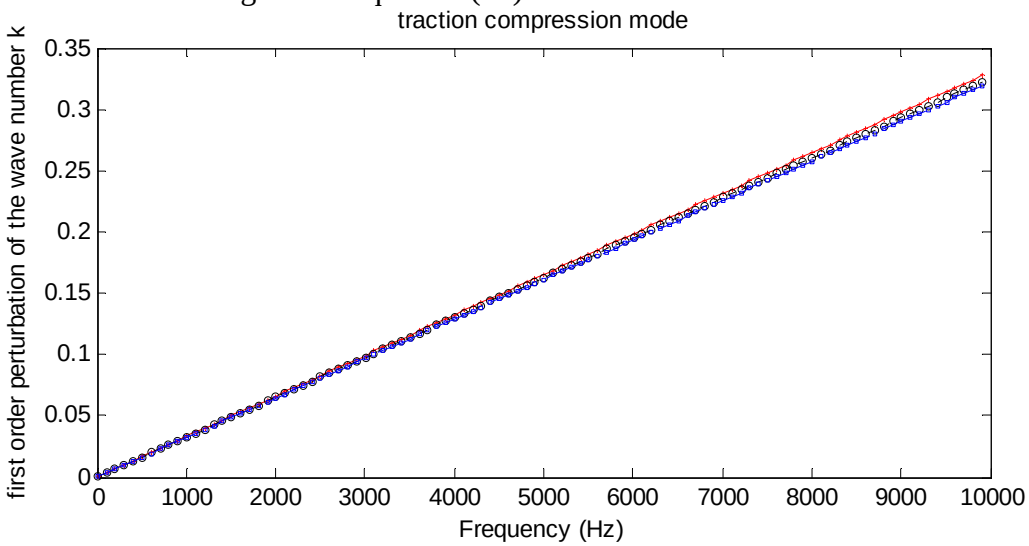


Figure 3: The first order perturbation of the wave number for the longitudinal mode (E stochastic)

SSAFE Analytical MC

Figure 4 shows the second order perturbation of the wave number (equation 42) for the longitudinal mode through the perturbation introduced in the Young modulus.

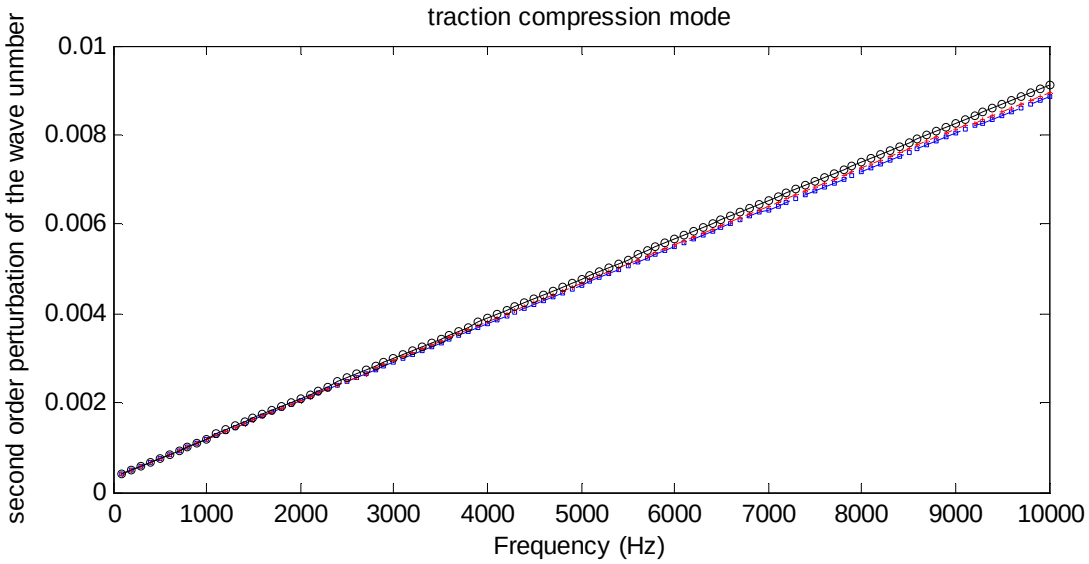


Figure 4: The second order perturbation of the wave number for the longitudinal mode (E stochastic)

SSAFE Analytical MC

4.2 Flexural wave's case study

For the flexural mode, the deterministic, first order and second order perturbation of the wave number are illustrated in figures 5, 6 and 7, respectively. The analytical validation is done using the analytical equation:

$$\tilde{k}_{flexion} = \left(\frac{\rho S \omega^2}{EI} \right)^{1/4} \tag{44}$$

Where EI is the bending stiffness ρ is the mass density, S is the cross section and ω is the pulsation.

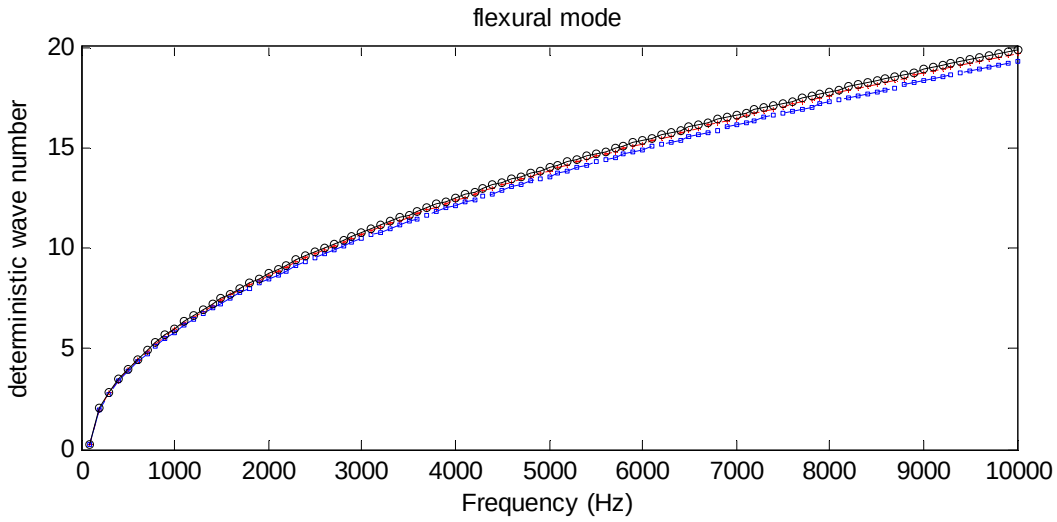


Figure 5: The deterministic wave number for the flexural mode

SSAFE Analytical MC

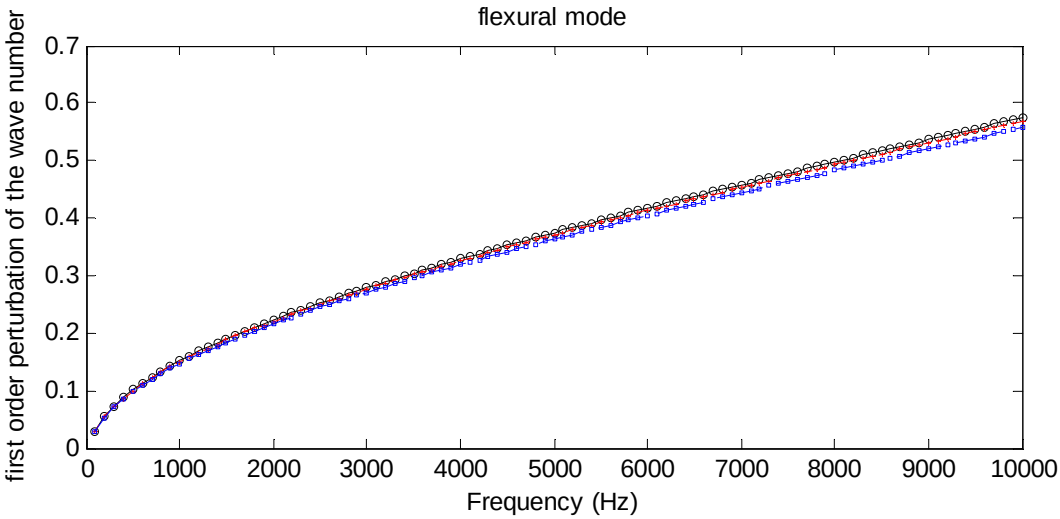


Figure 6: The first order perturbation of the wave number for the flexural mode (E stochastic)

SSAFE Analytical MC

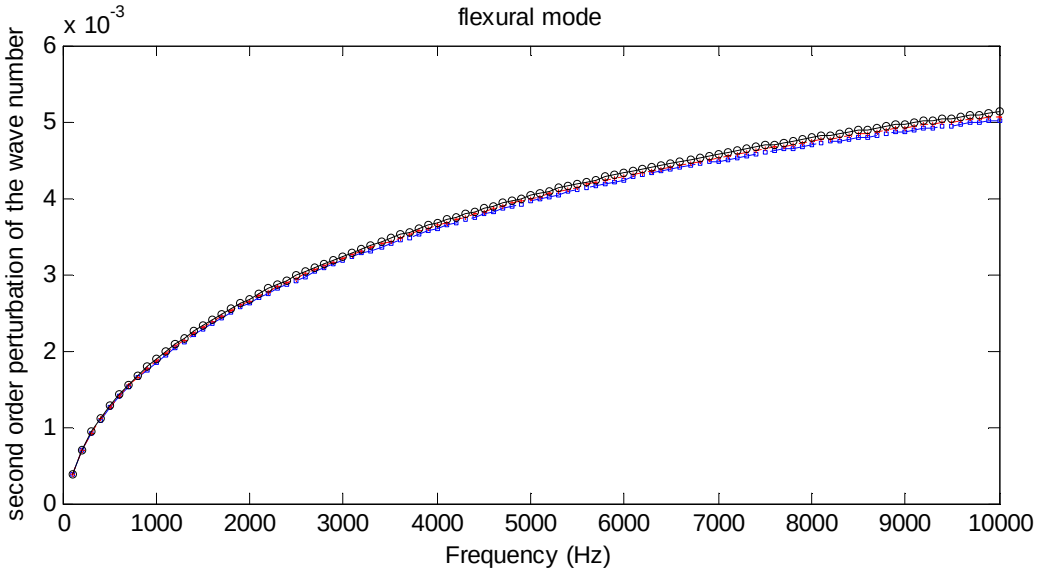


Figure 7: The second order perturbation of the wave number for the flexural mode (E stochastic)

SSAFE Analytical MC

5 CONCLUSION

In this paper, the issue of wave propagation parameters estimations in random waveguide was dealt with. Guided wave properties are an important physical notion for use in many engineering problems, the paper results are expected to be helpful in non-deterministic problems and a formulation named Stochastic Semi Analytical Finite Element was offered. This formulation allows wave characteristics to be defined by means of a stochastic finite element model through a parametric probabilistic approach. The formulation is general and can be applied to various structural shapes. The uncertainty is introduced in the structural parameters through second-order perturbation and using the probabilistic tools, we study the statistics of the wave's dispersion. These statistics are expected to be of use in the sensitivity analysis of guided waves techniques for wave propagation. Ultimately, numerical and analytical comparisons were given. Such analytical developments and numerical experiments showed the

effectiveness of the proposed approach to predict the statistics of guided wave propagation characteristics. The main paper finding can be extracted as follows:
1. The stochastic semi analytical finite element (SSAFE) method is formulated through the second order perturbation. The statistics of the dispersion curves are extracted following an uncertainty introduced in the structural parameters and using the probabilistic tools
2. The numerical accuracy and the computational efficiency of this method are demonstrated by comparison with the MC simulations and the analytical results.
The SSAFE offers some interesting research perspectives. Among future work, the use of SSAFE for energy issues in complex wave guide is an important task. Among the investigations in progress, the mid and high frequencies behaviour is the main target in this case. Further investigations are under progress in order to use such numerical methods in the context of smart materials and structures

REFERENCES

[1] V. Damljanovic , R.L. Weaver, Propagating and evanescent elastic waves in cylindrical waveguides of arbitrary cross section. *Journal of the Acoustical Society of America,* 115, 1572-1581, 2004.

[2] S. Finnveden, Evaluation of modal density and group velocity by a finite element method. *Journal of Sound and Vibration,* 273, 51-75, *2004.*

[3] S. Finnveden, M. Fraggstedt, Waveguide finite elements for curved structures. *Journal of Sound and Vibration,* 312, 644-671, 2008.

[4] L. Gavric, Computation of propagative waves in free rail using a finite element technique. *Journal of Sound and Vibration,* 185, 420-432, 1995.

[5] T. Hayashi, W.J. Song, J.L. Rose. Guided wave dispersion curves for a bar with an arbitrary cross-section, a rod and rail example. *Ultrasonics*, 41, 175-183, 2003.

[6] F. James, Monte Carlo Theory and Practice. *Rep. Prog. Phys,* 43 (9), 1145-1189, 1980.

[7] M.K. Decker, The Monte-Carlo Theory in Science and Engineering: Theory and Application. *Comput. Methods Appl. Mech. Eng,* 89 (1), 463-483, 1991.

[8] G.I. Schueller, Computational Stochastic Mechanics - Recent Advances. *Comput. Struc*, 79 (22-25), 2225-2234, 2001.

[9] J. Li, J.B. Chen, The Probability Density Evolution Method for Dynamic Response Analysis of Non-Linear Stochastic Structures. *Int. J. Numer. Methods Eng,* 65 (6), 882-903, 2006.

[10] V. Ajith, S. Gopalakrishnan. Spectral Element Approach to Wave Propagation in Uncertain Composite Beam Structures. *Journal of Vibration and Acoustics*, 133(5), 2011, DOI: 10.1115/1.4003945.

COMPDYN 2013
4th ECCOMAS Thematic Conference on
Computational Methods in Structural Dynamics and Earthquake Engineering
M. Papadrakakis, V. Papadopoulos, V. Plevris (eds.)
Kos Island, Greece, 12–14 June 2013

CHARACTERIZATION OF THE INFLUENCE OF RAIL WEAR ON TRAIN DYNAMICS

Nicolas Lestoille[1,2], Guillaume Perrin[1,2,3], and Christine Funfschilling[2]

[1]Université Paris Est, Modélisation et Simulation Multi-Echelle (MSME UMR 8208 CNRS)
5 Bd. Descartes, 77454 Marne-la-Vallée, France
e-mail: {nicolas.lestoille,guillaume.perrin}@sncf.fr

[2] SNCF, Innovation and Research Department
Immeuble Lumière, 40 avenue des Terroirs de France, 75611, Paris, Cedex 12, France
e-mail: christine.funfschilling@sncf.fr

[3] Université Paris Est, Navier (UMR 8205 ENPC-IFSTTAR-CNRS)
Ecole Nationale des Ponts et Chaussées, 6 et 8 Avenue Blaise Pascal, Cité Descartes, Champs sur Marne, 77455 Marne-la-Vallée, Cedex 2, France

Keywords: Rail Wear, Railway Dynamics, Wheel-Rail Contact, Statistical Characterization of Contact.

Abstract. *The study presented here aims at characterizing the influence of the rail wear on the train dynamic response. Rail profiles have been measured on a real track and post-processed in order to be used in a mutlibody simulation of the train's response. Wear modes have been extracted from the measures with a Principal Orthogonal Decomposition (POD). The profiles have been projected on these modes, giving a good characterization of the profiles' geometry. In a second step, the train's dynamic response on the measured track is simulated with a multibody software. The result shows that wear reduces the train's stability.*

1 INTRODUCTION

Wheel-rail contact is one of the main sources of excitation of the train. The rail profile is so designed that the wheel is guided by the track and the wheel-rail contact area dissipates as few energy as possible. Then the wheel-rail contact has to guide the vehicles in the curves without any loss of stability. That is why the characterization of the wheel-rail contact is essential for a good understanding of the train dynamics.

The goal of this study is to characterize the influence of rail wear on the train's dynamic response. For this purpose, rail profiles have been measured on a real track, and the train's dynamic behavior is computed with a mutlibody software.

The first section of this proceeding will focus on the analysis of the rail profiles' geometry, projecting the measured profiles on a statistical basis. In the second section, the train's dynamic response on the measured track will be computed and analysed.

2 RAIL PROFILES ANALYSIS

2.1 Post-processing of measures of rail profiles

Rail profiles have been measured experimentally on a real track, using laser cameras fixed under the measuring train, as shown in figure 1. Profiles have been measured each 25 cm during 13 km. The first step of post-processing consists in erasing aberrant points and repositionning the rail profiles to correct the train's roll.

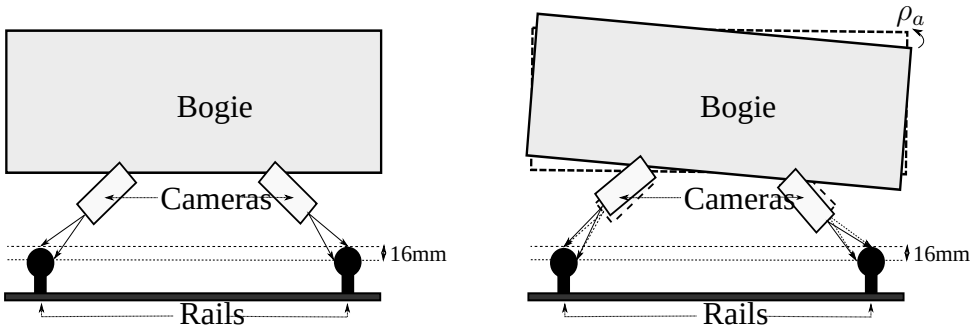


Figure 1: Experimental protocol

Then rail profiles are smoothed to remove the measurement noise. The profiles are written in polar coordinates (r, α). Since coordinates are discrete, $N_\alpha = 250$ equally distributed values of $r(\alpha)$ are taken with α in $[0.5, \pi + 0.1]$ radians (see figure 2). Finally, the profiles are sorted in low and high rails.

2.2 Stochastic characterization of rail profiles geometry

The rail profiles' radius is written as a function of the angle α in polar coordinates (see figure 2), with α in $\Omega = [0.5, \pi + 0.1]$ radians, as in paragraph 2.1. To characterize the rail wear, rail profiles are projected on a statistical basis of dimension M, obtained through a principal orthogonal development (POD) of the profiles' geometry [1] [2].

The space $\mathcal{L}^2(\Omega, \mathbb{R})$ of square integrables functions on Ω, with values in $\mathbb{R}$, is equipped with

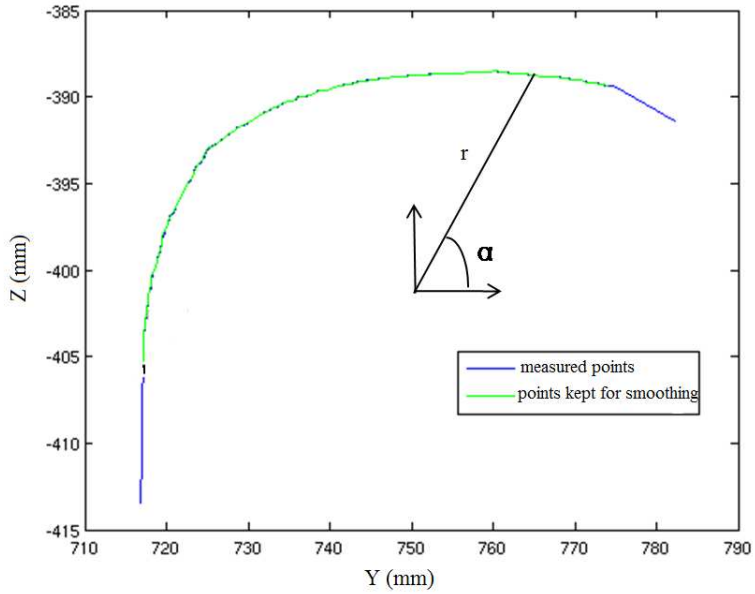


Figure 2: Measured Rail Profile

the inner product $(.,.)$, such that for all u and v in $\mathcal{L}^2(\Omega, \mathbb{R})$,

$$(u, v) = \sum_{i=1}^{N_\alpha} u(\alpha_i)v(\alpha_i). \tag{1}$$

The basis computed through the POD is composed of vectors $\{b_m(\alpha), \alpha \in \Omega\}_{1 \leq m \leq M}$, that can be seen as wear modes. They are orthonormal functions on which the rail radius is projected. The projection is denoted $\hat{r}(\alpha)$ such that, for all $\alpha \in \Omega$,

$$\hat{r}(\alpha) = \sum_{m=1}^{M} b_m(\alpha)C_m, \qquad \sum_{i=1}^{N_\alpha} b_m(\alpha_i)b_p(\alpha_i) = \delta_{mp}, \qquad C_m = \sum_{i=1}^{N_\alpha} r(\alpha_i)b_m(\alpha_i), \tag{2}$$

where δ_{mp} is the kronecker symbol that is equal to 1 if $m = p$ and to zero otherwise. The vector $\mathbf{C} = (C_1, ..., C_M)$ is a M-dimensionnal random vector.

The vector $\mathbf{C}$ is normalized, extracting its determinist norm $\sqrt{\lambda} = (\sqrt{\lambda_1}, ...\sqrt{\lambda_M})$ and computing the normalized random vector $\eta = (\eta_1, ..., \eta_M)$ such that,

$$\eta_m = \frac{(r, b_m)}{\sqrt{\lambda_m}} \qquad \forall m \in [|1, M|] \tag{3}$$

$$E\{\eta_m \eta_p\} = \delta_{mp}, \qquad \forall (m, p) \in [|1, M|]^2 \tag{4}$$

$$\hat{r}(\alpha) = \sum_{m=1}^{M} b_m(\alpha)\eta_m\sqrt{\lambda_m}, \qquad \forall \alpha \in \Omega, \tag{5}$$

where $E\{.\}$ is the mathematical expectation.

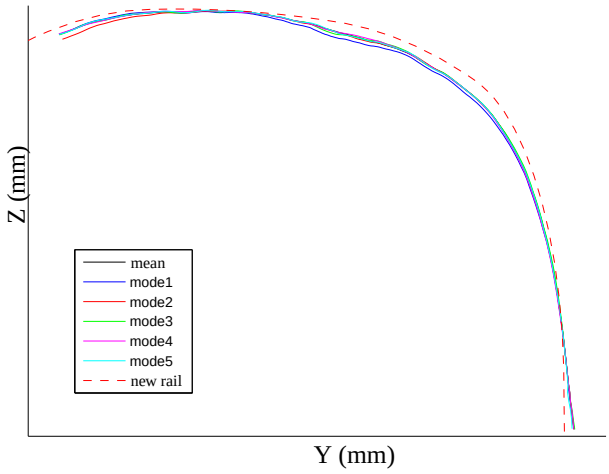


Figure 3: First modes of projection

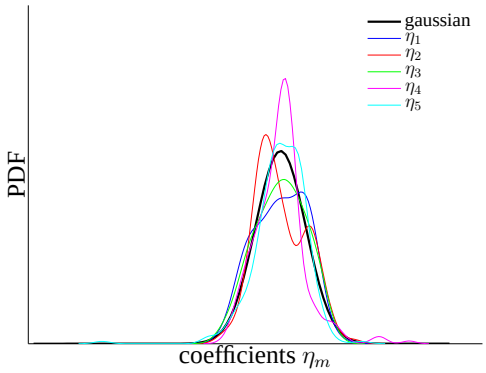


Figure 4: First coefficients η_m for the high rail

One can now observe wear modes and random wear coefficients of the projection basis. The figure 3 confirms that the modes are sorted by descending energy, because higher modes get closer of the mean profile. The first mode appears to be the one which is the most worn.

A look at the first five random coefficients η_m, with $m \in [|1, 5|]$, of the projection basis (see figure 4) gives information about the variability of the rail profiles' geometry. It can be seen that the variability is relatively low, because only high rails are here taken into account.

Nevertheless, one could suppose that wear on both rails (high and low rails) is correlated. This makes take into account rails from both track sides to compute the projection basis, in order to describe the whole track.

2.3 Analysis of the correlation between high and low rails

In order to take into account the correlation between high and low rails in the vectors of the projection basis, both rails have to be described on the same basis. For this reason, no more single rail profiles but pairs of rail profiles are studied, steming from one track section. The geometry of ν pairs of rail profiles has been measured. These experimental data are denoted by

the $\mathbb{R}^2$-vector value $\mathbf{r} = \{(r_1(\alpha), r_2(\alpha)), \alpha \in \Omega\}$ for which each component $\{r_i\}_{1 \leq i \leq 2}$ represents a rail. As in paragraph 2.2, $\mathbf{r}$ is projected on a statistical basis obtained by a POD. The vectors and the coefficients of the projection basis are represented in figure 5 and 6. It can be seen that each vector represents at the same time the high and the low rails, which confirms the assumption that high and low rails should be modeled together.

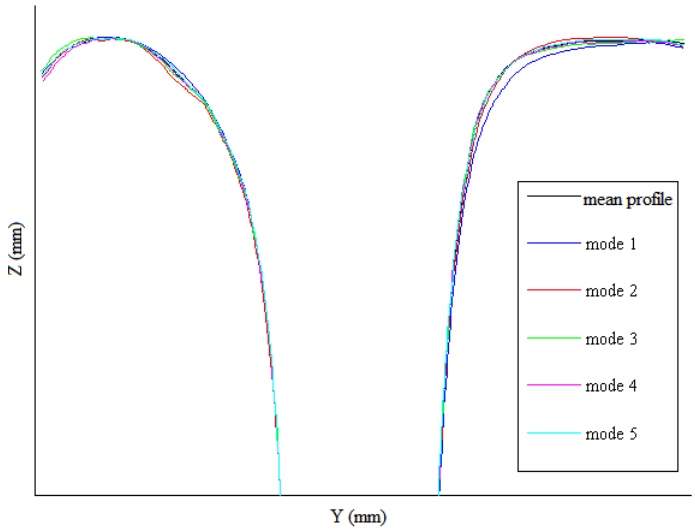


Figure 5: First modes of projection for both rails

Then the norm of each vectors is plotted in figure 7, coloring differently the part due to the high rail and the one due to the low rail. Here again, it can be seen that both high and low rails take part in the projection vectors, so that wear on both rails is highly correlated.

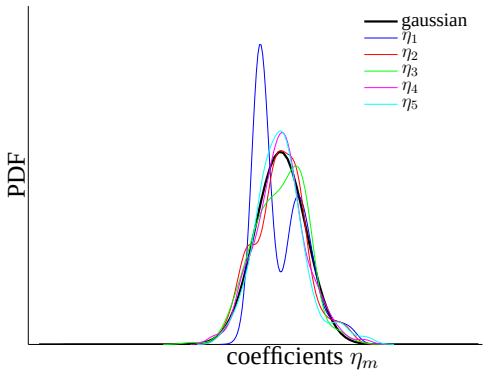


Figure 6: First coefficients η_m for both rails

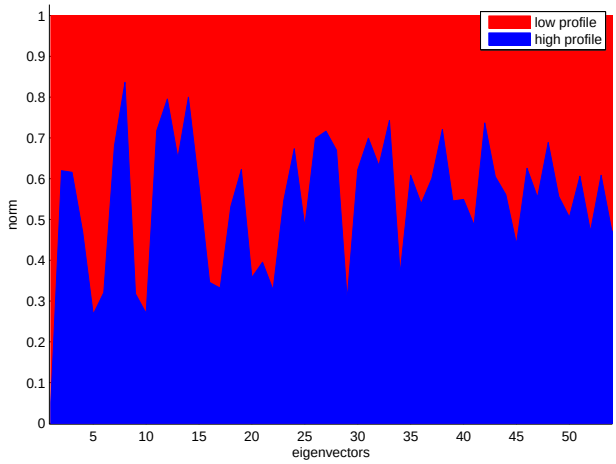


Figure 7: Norms of eigenvectors

3 CHARACTERIZATION OF DYNAMIC FORCES AT WHEEL/RAIL CONTACT

3.1 Model for the wheel-rail contact

The wheel-rail contact is studied in the orthonormal landmark of the track $(Oxyz)$, such as the vertical axle (Oz) points upward and the (Oy) axle points right. Resulting of the contact, an effort is applied to the wheel. This effort can be split into a normal force N and a tangential force T, such as

$$T \leq fN, \tag{6}$$

where f is the friction coefficient [3]. Indeed, the wheel-rail contact includes at the same time sliding and adhesion.

To model the dynamic response of the train, the equations of dynamics are solved considering the wheel-rail coupling. To study the stability and the comfort of the train, only low frequencies ($\leq$20 Hz) are of interest. That is why a multibody software is used to solve the dynamic problem. The software used in this study is Vampire. The contact is modeled with the analytical Hertz model for the normal part of the load and with the semi-analytical Kalker model for the tangential load [4]. Rather than forces N and T, their projections Y and Q in $(Oxyz)$ will be used, as shown in figure 8.

$$Q = N\cos(\delta) + T\sin(\delta) \tag{7}$$

$$Y = N\sin(\delta) - T\cos(\delta), \tag{8}$$

where δ is the angle between the contact surface and the horizontal.

The variations of contact forces trigger instability movements of the train: yaw, roll and pitch movements. While pitch and roll will be neglected in this study, the yaw, which implies an oscillation of the vehicle from right side to left side and could make the train derail, will be studied in detail. Indeed, a transversal displacement of the train triggers a change of the contact point (see figure 9). This change modifies the rolling radius and then the forces in the wheel-rail contact because of the profiled geometry of the wheel and the rail. In alignment, this phenomenon puts the axles centered on the track back. In curves, it allows the inscription of the

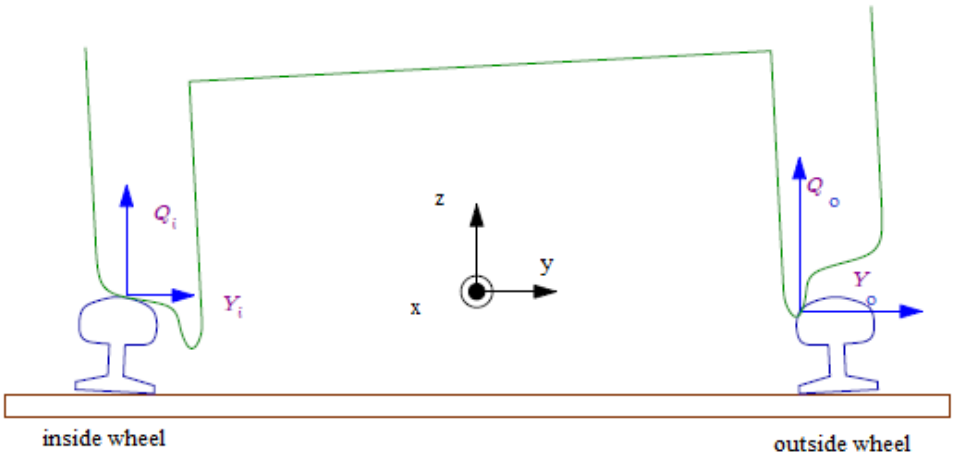


Figure 8: Forces at the wheel-rail contact

axles. That is why the wheel-rail contact can be characterized by the position of the contact and the contact angle. One can notice that the translation of the contact point along the rail profile is not continuous. There can be a gap between two contact points, and there can be two contact points at the same time.

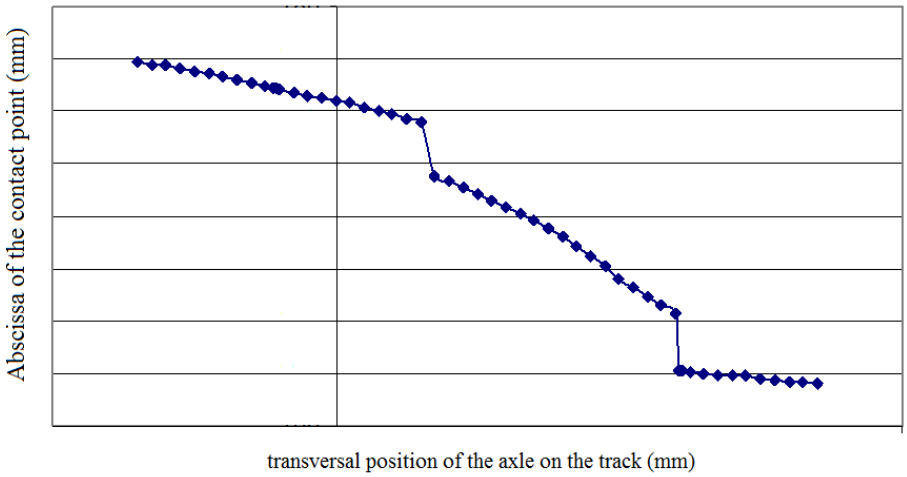


Figure 9: Lateral position of the contact point on the top of the rail

3.2 Dynamical response of the train on a new track

First, the wheel-rail contact is studied in ideal conditions (new rails, new wheels, alignment). The train used is a french Duplex TGV. Contact points are the same on the right and the left sides of the track, as shown in figure 10. There are two gaps in the contact angle and the contact position when the contact skips from the tread to the flange of the wheel. At the equilibrium, the vehicle is centered on the track. Indeed, the curves of contact positions intersect for y=0.

Then, the contact is studied with new rails and new wheels, but in a left curve of zone 4, as defined by UIC [5]. The curve radius is 282 m and the cant equals 120 mm. The goal is

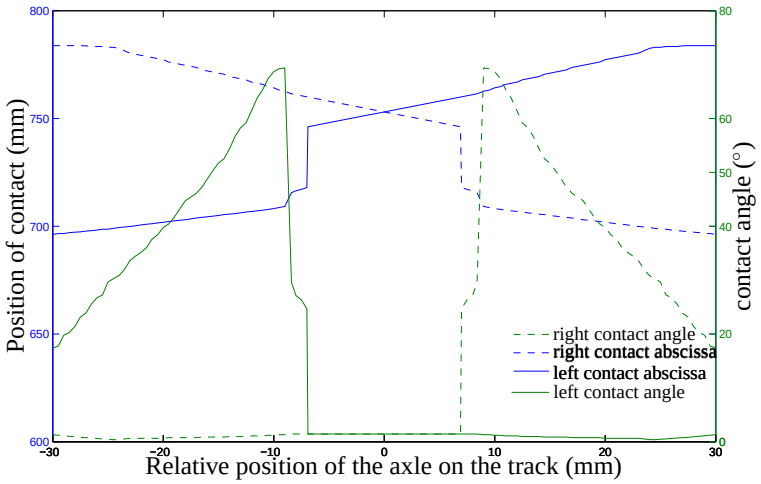


Figure 10: Ideal wheel-rail contact position and angle

to observe the train behavior in the curve (see figure 11). The train goes along the 4 km track at a speed of 70 km/h, and starts turning after 600 m. The cant deficiency in the curve is 85 mm high, and the train should deports on the right side (outside). The lateral displacement of the axles is observed in figure 12. There is a big difference between leading and trailing axles. Whereas the trailing axle moves outward, the trailing axle stays centered because it is steered by the leading axle. In particular, on the leading right wheel (on the high rail), the contact is situated on the flange and not on the tread.

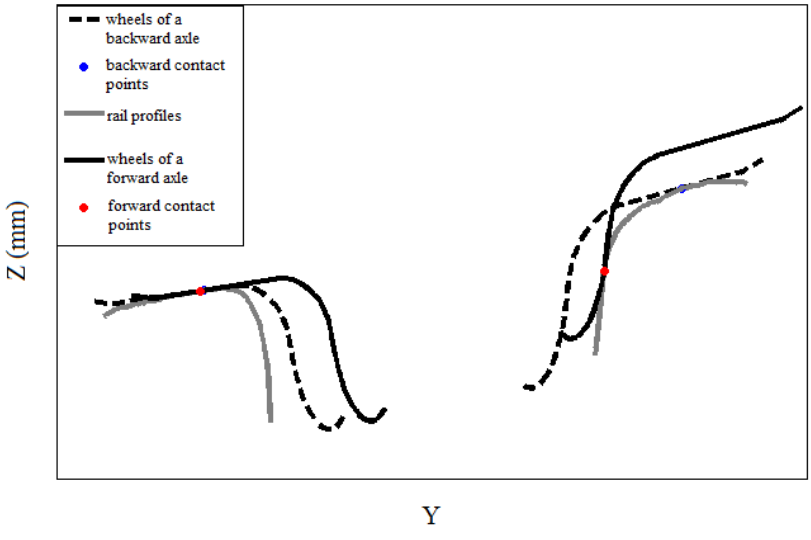


Figure 11: Wheel-rail contact in a zone 4 curve

The lateral forces applied to the axles are drawn in figure 13. For the leading axle, since the axle moves outward, the sum of lateral forces is high and inwardly directed. For the trailing axle, the sum of lateral forces is low because the axle is well centered on the track.

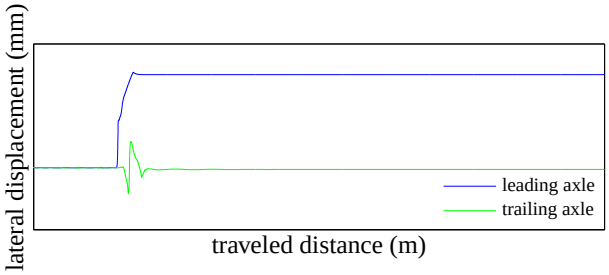


Figure 12: Lateral displacement of the axles in the curve

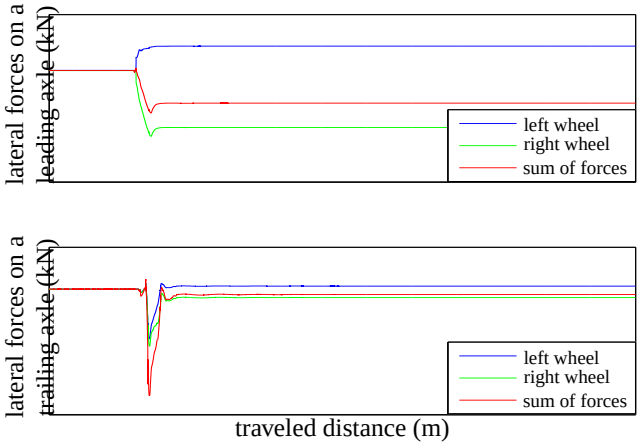


Figure 13: Lateral forces at the wheel-rail contact

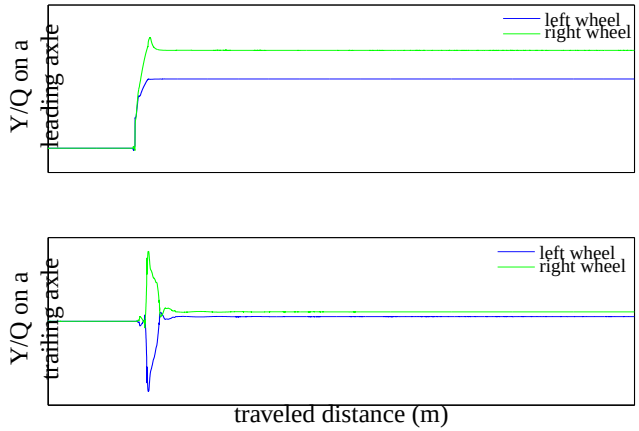


Figure 14: Quotient Y/Q at the wheel-rail contact

As a stability criteria, the quotient of lateral forces on the vertical charge Y/Q is studied in figure 14. For the leading axle, Y/Q rises in the curve, especially for the outer wheel. For the trailing axle, there is a little peak in the curve entrance, but the value stays low.

3.3 Influence of wear on train's dynamic response

Because of the friction between wheels and rails, the rails are worn in curves. Wear modifies the profile's geometry, especially in severe curves. Rail profiles are measured in a curve of zone 4, according to UIC's definition, post-processed as explained in paragraphe 2.1. One can see in figure 15 the difference between worn and new rails. The curve is the one studied in paragraph 3.2. On the high rail (right side), the rail is worn with a side-cutting wear. The low rail is used on the top of the rail. Moreover, wear introduces a gauge irregularity.

Then, the train's behavior on the measured track is computed. The static contact is deeply modified by rails' wear (see figure 16), especially on the high rail. An equilibrium position in the contact position and the contact angle disappears.

A look at the lateral displacement of the axle (see figure 17) shows no big difference betwen worn and new rails for the leading axle. The trailing axle moves inward the curve, increasing the angle between the bogie and the tangent to the track. This phenomenon might be due mostly to the gauge irregularity and not directly to the rail wear.

The lateral forces Y are then observed in figure 18. Since the position of the leading axle is almost the same as with new rails, the lateral forces on this axle have the same shape as with new rails, but around 10% higher. For the trailing axle, the lateral forces rise outward, in order to center the axle back on the track.

Figure 19 shows that the quotient Y/Q is globally the same as with new rails, but the values increase also by around 10 $\%$ in the curve, when one compares with new rails.

As a conclusion, the results show that rail wear implies a loss of stability of the train, without being insecure for the vehicle.

4 CONCLUSION AND PERSPECTIVES

This study allowed to compute the dynamic response of the train on a measured track, taking into account the rail wear. It has been seen that stability of the train decreases because of the

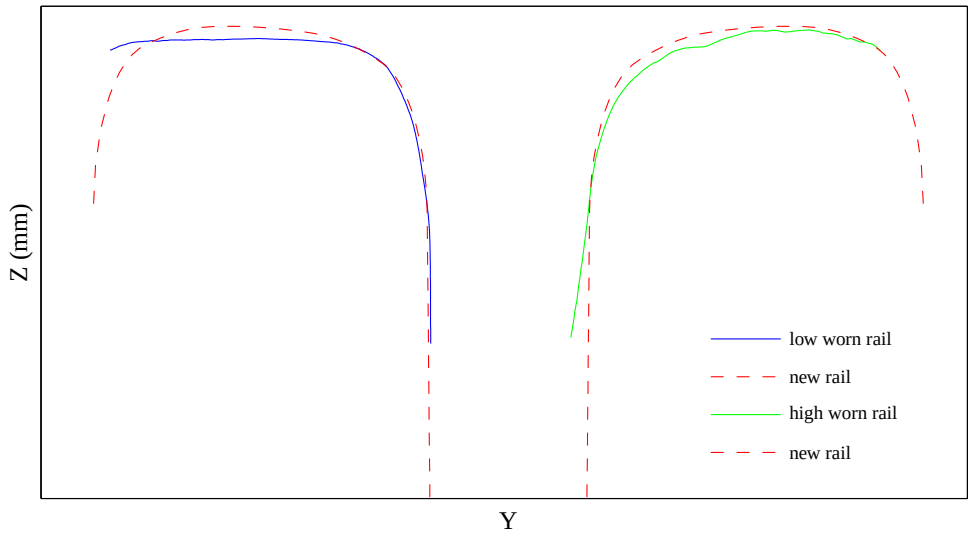


Figure 15: Measured worn rails

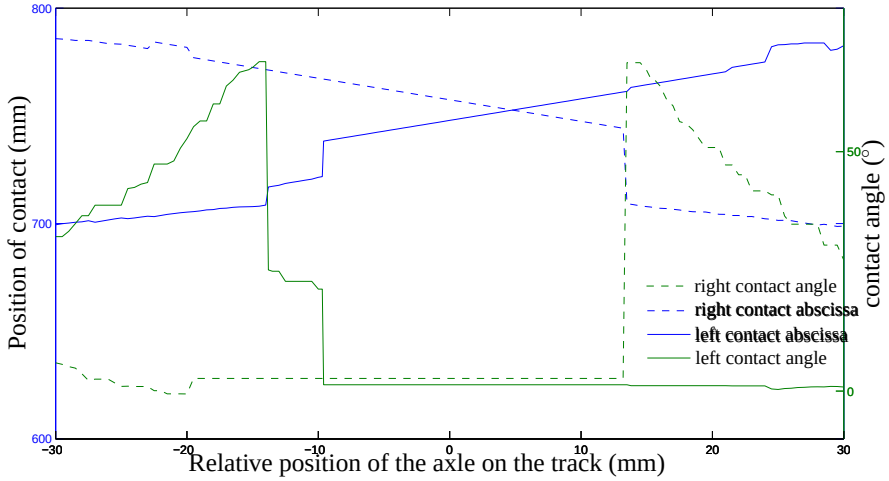


Figure 16: wheel-rail contact position and angle with worn rails

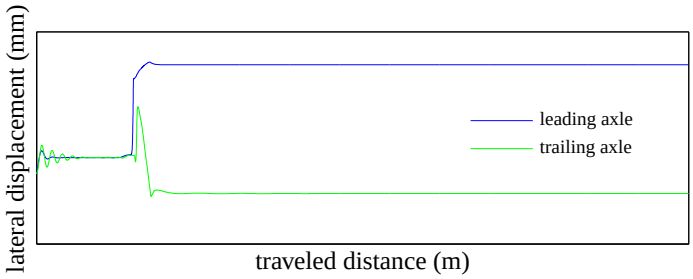


Figure 17: Lateral displacement of the axles in the curve with worn rails

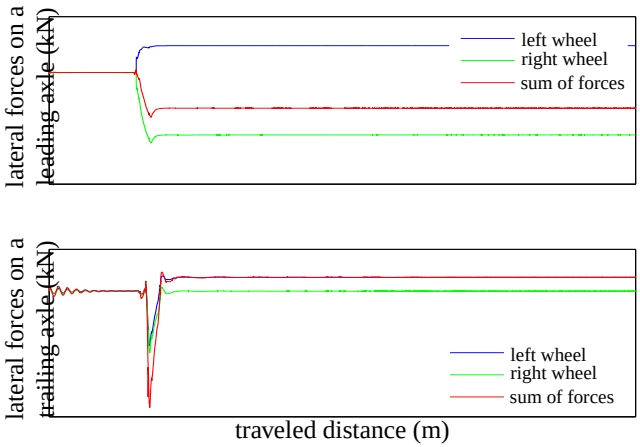


Figure 18: Lateral forces with worn rails

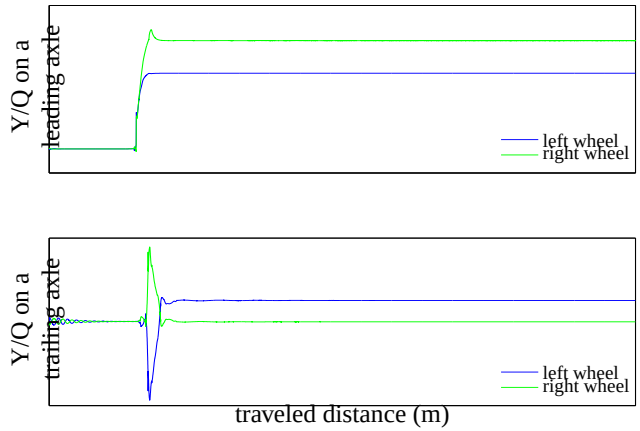


Figure 19: Quotient Y/Q with worn rails

wear, but in a small extent (around 10%). Furthermore, rail profiles have been projected on a statistical basis, in order to characterize rail wear. It has been shown that wear on high and low rails is correlated. Both rails have to be taken into account to have a representative description of the track.

Next step will consist in running a simulation of the train's behavior, using the profiles projected on the statistical basis. The dynamic response will then highlight the link between wear modes and the train stability. A statistical study will be used to characterize this dynamic response.

Acknowledgement. This work was supported by SNCF, Innovation and Research Department.

REFERENCES

[1] O.P. Le Maître, O.M. Knio, *Spectral methods for uncertainty quantification*, Springer, 2010.

[2] G. Perrin, C. Soize, D. Duhamel, C. Funfschilling, Track irregularities stochastic modeling. *Thirteenth International Conference on Civil, Structural and Environmental Engineering Computing*, Chania, Greece, 2011.

[3] B. Soua, *Etude de l'usure et de l'endommagement du roulement ferroviaire avec des modeles d'essieux non rigides*, PhD Thesis, Ecole Nationale des Ponts et Chausses, 1997.

[4] J.J. Kalker, A fast algorithm for the simplified theory of rolling contact, *Vehicle System Dynamics*, **11**, 1–13, 1982.

[5] UIC, *Leaflet 518*, October 2009.

COMPDYN 2013
4th ECCOMAS Thematic Conference on
Computational Methods in Structural Dynamics and Earthquake Engineering
M. Papadrakakis, V. Papadopoulos, V. Plevris (eds.)
Kos Island, Greece, 12–14 June 2013

DISCONTINUOUS GALERKIN METHODS FOR HIGH-DIMENSIONAL FOKKER-PLANCK EQUATIONS IN STOCHASTIC DYNAMICS

Friederike Loerke[1] **and Udo Nackenhorst**[2]

[1]Institute of Mechanics and Computational Mechanics
Appelstr. 9A, 30167 Hannover, Germany
e-mail: friederike.loerke@ibnm.uni-hannover.de

[2] Institute of Mechanics and Computational Mechanics
Appelstr. 9A, 30167 Hannover, Germany
e-mail: nackenhorst@ibnm.uni-hannover.de

Keywords: Fokker-Planck Equation, Discontinuous Galerkin Method

Abstract. *In this contribution, Discontinuous Galerkin methods are investgated as solution techniques for the high-dimensional Fokker-Planck equation (FPE). Time-Discontinuous Galerkin (TDG) methods are identified to provide stable solutions for smooth, as well as non-smooth functions. The TDG method allows for large time steps and are thus very efficient, at least for moderate dimensions. In higher dimensions, they become infeasible due to implicit coupling of the whole domain. For handling high-dimensional problems, spatial Discontinuous Galerkin (DG) methods are suggested, for their allowance of an element-wise split of the domain, and thus parallelization. The implementation of the Discontinuous Galerkin method for arbitrary dimensions is demonstrated.*

1 INTRODUCTION

The Fokker-Planck equation is a very attractive instrument for the analysis of stochastic dynamical systems under white noise excitation. It is of vast interest due to directly providing a probability density function for the system response. This is subject to the acceptance of the Markov process property for the stochastic process under consideration. The Fokker-Planck equation has its origin in the stochastic description of Brownian motion. A thorough discussion on the origin, theory and possible solution techniques is provided by RISKEN in [12]. Beyond this, the solution of the Fokker-Plank equation remains an ambitious task. Analytical solutions can only be provided for very limited special cases. Hence, investigations concentrate on numerical solution techniques. In an early study, [13], a Galerkin type approach, based on polynomial expansions, is used to solve high-dimensional stationary FPEs. A similar approach is presented in [8] for an engineering application. Despite their capability with respect to the treatment of high dimensions, these methods are often restricted regarding the shape of the approximated function. For seeking more general solutions and temporal evolution of the probability density function, Computational Fluid Dynamics solution techniques for advection-diffusion equations are suitable. Just a few contributions within this context are referred to in the following: Finite Element methods are used e.g. by [17], where domain decomposition for higher dimensions is suggested and shown for 2D and 3D. A comparison between Finite Element and Finite Difference methods can be found in [5] using the example of up to 4D non-linear oscillators. To approach the solution of higher dimensional problems, multi-scale Finite Element methods are suggested e.g. in [9], with the presentation of a two-dimensional example, and in [10] with the application to a three dimensional problem.

Within this contribution, alternative numerically stable and efficient solution techniques for the Fokker-Planck equation are investigated. Firstly, a short introduction on the derivation of the FPE is given in section 2. Afterwards, numerical solution techniques are evaluated in section 3: Diverging from traditional semi-discretization techniques, with Finite Element discretization in space and Finite Difference discretization in time, attention is drawn to the Time-Discontinuous Galerkin method. It can be shown, that the TDG method is an efficient technique for the solution of advection-diffusion equations. Nevertheless, in high dimensions the solution becomes impractical. Accordingly, a possibility to overcome this is examined, which is the spatial Discontinuous Galerkin method. Computational tests are presented, as well as the implementation for higher dimensions. Finally, an outlook on further research interests is given.

2 FOKKER-PLANCK REPRESENTATION OF STOCHASTIC DYNAMICAL PROBLEMS

In this section, a brief derivation of the Fokker-Planck equation for an examplary stochastic partial differential equation is outlined. The basis is formed by a stochastic equation of motion of a mass m, with spring constant k and damping constant d,

$$m\ddot{\mathbf{x}}(\theta,t) + d\dot{\mathbf{x}}(\theta,t) + k\mathbf{x}(\theta,t) = \mathbf{f}(\theta,t), \tag{1}$$

subject to random excitation $\mathbf{f}(\theta,t)$. θ denotes a random variable. The system stochastics are restricted by the following assumption: The uncertain excitation is regarded as Gaussian white noise, see [15], which is perfectly characterized by its first and second moments, see[16]. In particular, the ensemble average is $\langle f(t)\rangle = 0$ and the process is delta-correlated for two different instants of time, t and t', meaning that $\langle f(t)f(t')\rangle = \delta(t-t')$, which is further explained in [12]. This implicates that the system response also forms a Markov vector process, meaning

that every state only depends on the known present state, and is fully independent of previous states. With this property, the response statistics of the system can be computed from the transition probability density function. Therefore, they result from the Fokker-Planck equation, which characterizes the temporal evolution of the probability density function. To illustrate this, the probability density of the motion is described as follows

$$p(\mathbf{x},t) = \langle \prod_{i=1}^{n} \delta(x_i - x_i(t)) \rangle, \tag{2}$$

with the $2n$-dimensional vector $\mathbf{x} = [x_1 \ \dot{x}_1 \ \dots \ x_n \ \dot{x}_n]^\mathsf{T}$, consisting of coordinates x_i and velocities $\dot{x}_i$. Equation (2) is transformed into the transport equation

$$\frac{\partial}{\partial t} p(\mathbf{x},t) = -\sum_{i=1}^{n} \frac{\partial}{\partial x_i} \langle \prod_{i=1}^{n} \delta(x_i - x_i(t)) \frac{\partial x_i}{\partial t} \rangle. \tag{3}$$

This reduces to the advection-diffusion-type Fokker-Planck equation:

$$\frac{\partial}{\partial t} p(\mathbf{x},t) = \frac{\partial}{\partial x_i} \left(\mathbf{c}(\mathbf{x},t) p(\mathbf{x},t) \right) + \frac{\partial}{\partial x_i \partial x_j} \left(\mathbf{D}(\mathbf{x},t) p(\mathbf{x},t) \right), \tag{4}$$

wherein the first term is an advection term with the advection velocity vector $\mathbf{c}$ and the second term is the diffusion term with the coefficient $\mathbf{D}$.

3 NUMERICAL SOLUTION

The numerical solution of advection-diffusion equations remains a challenging task, due to the opposed characteristics of advection and diffusion terms. Standard techniques like Finite Difference methods and Finite Volume methods face the difficulty that the advection term is better resolved within explicit time stepping schemes and the diffusion is only efficiently and correctly resolved within implicit time integration, [14]. Otherwise, grave numerical errors due to oscillation would be introduced by the advection term, most notably for non-smooth functions. While explicit treatment of the diffusion term would imply the necessity of very small time steps. Often, the inconvenience of oscillations, induced by the advection term, is coped with the introduction of artificial diffusion, like within the Streamline Upwind/Petrov-Galerkin method (see e.g. [1]). In this work, the introduction of artificial terms is sought to avoid. An efficient solution technique to meet the demands of both advection and diffusion terms turns out to be the Time-Discontinuous Galerkin method, which is discussed in the following subsection. In the subsequent part, attention is drawn to the implementation in higher dimensions. Therefore, the TDG method has to be dropped in favour of a spatial Discontinuous Galerkin method.

3.1 Time-Discontinuous Galerkin Method

Spatial discretization can be either achieved by Finite Volumes or Finite Differences, as well as Finite Elements. Here, the latter is chosen to allow for local high order resolution. Instead of Finite Differences or Runge-Kutta methods, in this work, the time domain is also resolved with Finite Elements, leading to a full Galerkin scheme in space and time. Additionally, element-wise decoupling is allowed in the time domain, to avoid errors induced by oscillations. Those types of schemes are referred to as Discontinuous Galerkin methods. They were proposed amongst others by REED and HILL in [11] with first analyses to be found in [6] and [4]. A

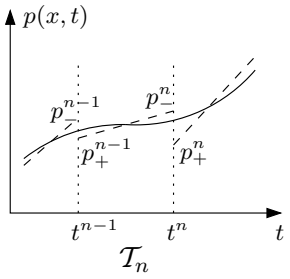


Figure 1: discontinuous shape functions in time

discussion on the TDG method for pure advection is provided in [18].
In particular, the TDG method is conducted as follows: First, the partial differential equation (4) is transformed into a weak form coupled in time and space, by multiplication with a weighting function η and integration over the time and spatial domains $\mathcal{T}_n$ and $\mathcal{B}$:

$$\eta \int_{\mathcal{T}_n} \int_{\mathcal{B}} \frac{\partial p}{\partial t} + \nabla \cdot (\mathbf{c}p - \mathbf{D}\nabla p)\,\mathrm{d}\Omega\,\mathrm{d}t = 0. \tag{5}$$

The dependencies on $\mathbf{x}$ and t are omitted for brevity.
The probability density and the weighting function are approximated by finite element shape functions in space and time, while discontinuities are assumed at the boundaries of each time interval,

$$p_+^n = \lim_{s\to 0}\, p(t^n + s),\; p_-^n = \lim_{s\to 0}\, p(t^n - s) \Rightarrow \text{ jump: } [|p^n|] = p_+^n - p_-^n, \tag{6}$$

as depicted in figure (1). The discrete form of equation (5) for an element Ω_e reads

$$\begin{aligned} &\underbrace{\left[\int_{\mathcal{T}_n} \tilde{N}^T \tilde{N}_{,t}\,\mathrm{d}t + \tilde{N}_+^T(t^{n-1})\tilde{N}_+(t^{n-1})\right]}_{\boldsymbol{\Upsilon}_a} \int_{\Omega_e} \eta_h p_h\,\mathrm{d}\Omega \\ &+ \underbrace{\left[\int_{\mathcal{T}_n} \tilde{N}^T \tilde{N}\,\mathrm{d}t\right]}_{\boldsymbol{\Upsilon}_b} \int_{\Omega_e} \left(-\frac{\partial D_i}{\partial x_i}\eta_h p_h - D_i \eta_h \frac{\partial p_h}{\partial x_i} + D_{ij}\frac{\partial \eta_h}{\partial x_i}\frac{\partial p_h}{\partial x_j} + \frac{\partial \eta_h}{\partial x_i} p_h \frac{\partial D_{ij}}{\partial x_j}\right)\mathrm{d}\Omega \\ &= \underbrace{\left[\tilde{N}_+^T(t^{n-1})\tilde{N}_-(t^{n-1})\right]}_{\boldsymbol{\Upsilon}_c} \int_{\Omega_e} \eta_h p_h^{n-1}\,\mathrm{d}\Omega, \end{aligned} \tag{7}$$

with the temporal shape functions $\tilde{N}$, their time derivatives $\tilde{N}_{,t}$, the discrete test functions η_h and discrete solution p_h, as well as the time matrices $\boldsymbol{\Upsilon}_i$. Inserting continuous shape functions in space $\mathbf{H}$, a non-symmetric linear system of equations is obtained:

$$\underbrace{[\boldsymbol{\Upsilon}_a(t) \otimes \mathbf{M} + \boldsymbol{\Upsilon}_b(t) \otimes \mathbf{Q}]}_{\hat{\mathbf{K}}}[\hat{\mathbf{p}}] = [\boldsymbol{\Upsilon}_c(t) \otimes \mathbf{M}\hat{\mathbf{p}}^{n-1}], \tag{8}$$

with the mass matrix

$$\mathbf{M} = \int_{\Omega_e} \mathbf{H}^T \mathbf{H}\,\mathrm{d}\Omega \tag{9}$$

and the advection and diffusion matrix

$$\mathbf{Q} = \int_{\Omega_e} \Bigg(\underbrace{-\frac{\partial D_i}{\partial x_i}\mathbf{H}^T\mathbf{H} - D_i\mathbf{H}^T\mathbf{H}_{,x_i}}_{\text{advection}} + \underbrace{D_{ij}\mathbf{H}^T_{,x_i}\mathbf{H}_{,x_j} + \mathbf{H}^T_{,x_i}\mathbf{H}\frac{\partial D_{ij}}{\partial x_j}}_{\text{diffusion}} \Bigg) \mathrm{d}\Omega. \tag{10}$$

The TDG scheme enables the use of large time steps and, thus, Courant numbers $Cr = c_i\frac{\Delta t}{\Delta x_i} \gg 1$. Increasing the order of time integration TDG(i) allows for a huge increase in time step size, without negative effects on stability.

To demonstrate the solution of the Fokker-Planck equation, the response of a random white noise excited Van-der-Pol oscillator is computed. The equation of motion for the 1D Van-der-Pol oscillator with system parameters α and β under white noise excitation $\omega(t)$ reads

$$\ddot{x} - (\alpha - \beta x^2)\dot{x} + x = \omega(t). \tag{11}$$

This equation is transformed into the Fokker-Planck equation

$$\frac{\partial p}{\partial t} = -\frac{\partial p}{\partial x} + \frac{\partial}{\partial \dot{x}}\left[\beta x^2\dot{x} - \alpha\dot{x} + x\right] + D\frac{\partial^2 p}{\partial \dot{x}^2} \tag{12}$$

which is solved with the TDG method. In figure (2) the result of the computation is shown, which is a solution on a limit cycle in the phase space, as expected. The Fokker-Planck equation for the one-dimensional oscillator with two degrees of freedom, position and velocity, is a two-dimensional equation, requiring two-dimensional Finite Elements for the solution scheme plus time discretization. Thus, it is easily comprehensible that a system with higher degrees of freedom would lead to a higher *dimensional* Fokker-Planck equation, i.e. a two-mass oscillator with four degrees of freedom, two positions and two velocities, would lead to a four-dimensional Fokker-Planck equation. This is still computable on a desktop computer, but looking on the system matrix growth scheme, the limit of continuous FEM is clearly visible:

matrix size $= (TDG(i)+1)((nel+1)np-nel+1)^n.$

$TDG(i)$: order of TDG
nel: number of elements/dimension
np: order of spatial approx.
n: dimension

Herein, the *curse of dimensionality* comes out very obviously, because the dimension is incorporated in the exponent. To overcome this curse, a split of the spatial domain seems promising, which entails the idea of a Discontinuous Galerkin method in space.

3.2 Spatial Discontinuous Galerkin Method

The spatial Discontinuous Galerkin method for the Fokker-Planck equation is defined according to the representations by COCKBURN and SHU for the classical advection-diffusion equation, see for instance [2]. Initially, the Fokker-Planck equation is rewritten in a compact form,

$$\frac{\partial p(\mathbf{x},t)}{\partial t} + \underbrace{\nabla\cdot(\mathbf{c}p(\mathbf{x},t)}_{\nabla\cdot\mathbf{f}(p(\mathbf{x},t),\mathbf{x},t)} - \mathbf{D}\nabla p(\mathbf{x},t)) = 0, \tag{13}$$

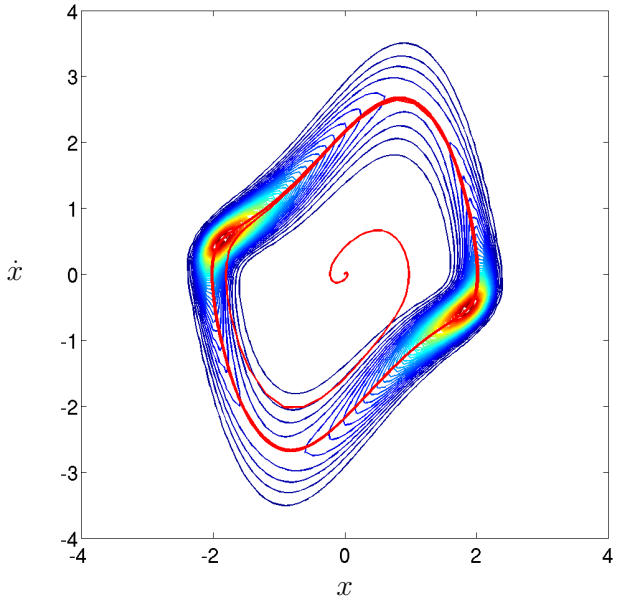


Figure 2: contour plot of the probability density distribution of a white noise excited Van-der-Pol oscillator on the limit cylce (red line)

wherein an advection flux $\mathbf{f}$ and a diffusion flux $\mathbf{D}\nabla p$ can be identified. Again omitting the dependence on $\mathbf{x}$ and t and inserting a variable $\boldsymbol{\sigma} = \bar{\mathbf{D}}\nabla p$, with $\mathbf{D} = \bar{\mathbf{D}}^2$, leads to the system of equations,

$$\frac{\partial p}{\partial t} + \nabla \cdot \mathbf{f}(p) - \nabla \cdot \left(\bar{\mathbf{D}}\boldsymbol{\sigma}\right) = 0 \quad \text{and} \quad \boldsymbol{\sigma} - \bar{\mathbf{D}}\nabla p = 0, \tag{14}$$

analoguous to the formulation in [2]. The coupled weak form after multiplications with the weighting functions η and ζ and integration over the domain reads

$$\begin{aligned} &\frac{\partial}{\partial t}\int_{\mathcal{B}} p\eta \,\mathrm{d}\Omega + \int_{\mathcal{B}} \left[\nabla \cdot \mathbf{f}(p) - \nabla \cdot \left(\bar{\mathbf{D}}\boldsymbol{\sigma}\right)\right] \eta \,\mathrm{d}\Omega \quad = 0 \\ &\text{and} \qquad \int_{\mathcal{B}} \boldsymbol{\sigma}\zeta \,\mathrm{d}\Omega - \int_{\mathcal{B}} \nabla \cdot \mathbf{d}\zeta \,\mathrm{d}\Omega = 0, \end{aligned} \tag{15}$$

with $\mathbf{d} = \bar{\mathbf{D}}p$. Integration by parts of each second term in equations (15) leads to the boundary terms,

$$\int_{\partial\mathcal{B}} \eta \left[\mathbf{f} - \mathbf{D}\boldsymbol{\sigma}\right] \cdot \mathbf{n} \,\mathrm{d}\Gamma \qquad \text{and} \qquad \int_{\partial\mathcal{B}} \zeta \mathbf{d} \cdot \mathbf{n} \,\mathrm{d}\Gamma, \tag{16}$$

including the normal vector $\mathbf{n}$. The boundary terms are non-unique under the precondition of allowing discontinuities at the inter-element boundaries. Consequently, the terms have to be substituted by numerical flux terms, so that the coupled local discretized weak form reads:

$$\begin{aligned} &\int_{\mathcal{B}_e} \mathbf{H}^T\mathbf{H} \,\mathrm{d}\Omega_e \,\hat{\mathbf{p}}_{,t} + \sum_{f\in\partial\mathcal{B}_e} \int_{\mathcal{B}_f} \mathbf{H}_f^T \left(\mathbf{f}^* - (\bar{\mathbf{D}}\boldsymbol{\sigma})^*\right) \,\mathrm{d}\Omega_f - \int_{\mathcal{B}_e} \mathbf{H}_{,x}^T \left[\mathbf{f}(p_h) - \bar{\mathbf{D}}(p_h)\boldsymbol{\sigma}\right] \,\mathrm{d}\Omega_e = 0 \\ &\text{and} \qquad \int_{\mathcal{B}_e} \mathbf{H}^T\mathbf{H} \,\mathrm{d}\Omega_e \hat{\boldsymbol{\sigma}} - \sum_{f\in\partial\mathcal{B}_e} \int_{\mathcal{B}_f} \mathbf{H}_f^T \mathbf{d}^* \,\mathrm{d}\Omega_f + \int_{\mathcal{B}_e} \mathbf{H}_{,x}^T \mathbf{d}(p_h(t,x)) \,\mathrm{d}\Omega_e = 0, \end{aligned} \tag{17}$$

wherein the index e denotes the element domain and f denotes the element face domain. For the numerical flux terms, denoted by an asterisk, any consistent flux can be chosen. COCKBURN and SHU suggest the so-called Local Discontinuous Galerkin (LDG) fluxes in [3]. This is the Lax-Friedrichs flux (see, e.g. [7]) for the advective part,

$$\mathbf{f}^*(p^-, p^+) == \frac{1}{2}\left[\mathbf{f}(p_h^-)\cdot\mathbf{n}_{f,\partial\mathcal{B}_e} + \mathbf{f}(p_h^+)\cdot\mathbf{n}_{f,\partial\mathcal{B}_e} - \alpha_{f,\partial\mathcal{B}_e}(p_h^+ - p_h^-)\right], \tag{18}$$

with the inside element solution value p^- and the outside element solution value p^+, as well as the local maximum flux velocity $\alpha_{f,\partial\mathcal{B}_e}$. The discrete numerical diffusion flux is chosen as

$$\begin{aligned}(\bar{\mathbf{D}}\sigma)^* &= \sum_{i=1}^{dim}\frac{(d_{i,h}^+ - d_{i,h}^-)}{(p_h^+ - p_h^-)}\frac{1}{2}\left[\sigma_{i,h}^-\cdot\mathbf{n}_{f,\partial\mathcal{B}_e} + \sigma_{i,h}^+\cdot\mathbf{n}_{f,\partial\mathcal{B}_e}\right]\\ &\quad + C_{11}(p_h^+ - p_h^-) + \sum_{i=1}^{dim} C_{1i}(\sigma_{i,h}^+ - \sigma_{i,h}^-) \text{ and}\\ \mathbf{d}^* &= \frac{1}{2}\left[d_{i,h}^-\cdot\mathbf{n}_{f,\partial\mathcal{B}_e} + d_{i,h}^+\cdot\mathbf{n}_{f,\partial\mathcal{B}_e}\right] - C_{1i}(p_h^+ - p_h^-).\end{aligned} \tag{19}$$

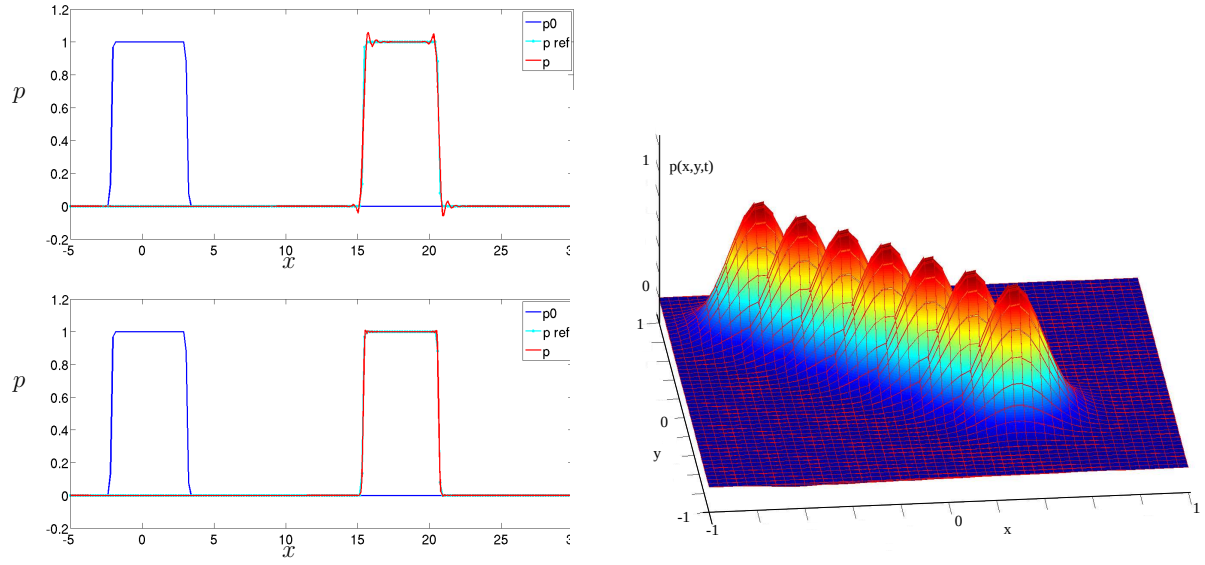
Details on the LDG flux terms can be found in [3].
This brings about a fully local system of equations, so that element-wise decoupling in explicit schemes is applicable without lumping the mass matrices. Here, the significant advantage of the spatial Discontinuous Galerkin method emerges: The problem of working memory deficit can be overcome through element-wise decoupling and even parallel treatment of the possibly high-dimensional system.

Examples

The Discontinuous Galerkin method allows for steep gradients in the approximated function, if the polynomial order of the local shape functions is increased. In figure (3(a)), the decrease of oscillations within the advection of a non-smooth function, computed with DG methods of increasing order is depicted to demonstrate the stability of the method. The quantity $p0$ is the initial condition, p_ref is the analytical reference solution and p the numerically computed solution for the chosen time step.
A second DG-test, shown in figure (3(b)), is the two-dimensional Molenkamp test. This is again a test for pure advection, as the main challenge within the Fokker-Planck equation is the correct resolution of the advection term.

n-Dimensional Discretization

Another challenge is the treatment of high dimensions. Therefore, an arbitrary high-dimensional Finite Element mesher has been implemented for regular meshes. Node coordinates and element incidences can be easily obtained by dimension-dependent permutations, which end up in meshes as depicted in figure (4), for a 4D example. In this example, the domain is discretized with three elements per coordinate direction, meaning that four nodal positions exist per direction. Two exemplary elements (15 and 68) are plotted. Node and element numbering are arranged depending on the dimension, from negative to positive coordinate direction, starting from direction $\mathbf{e}_1$. In this manner, mesh generation is carried out for any number of



(a) 1D DG(3) and DG(7) with steep gradients (b) 2D Molenkamp test

Figure 3: resolution of pure advection with Discontinuous Galerkin methods

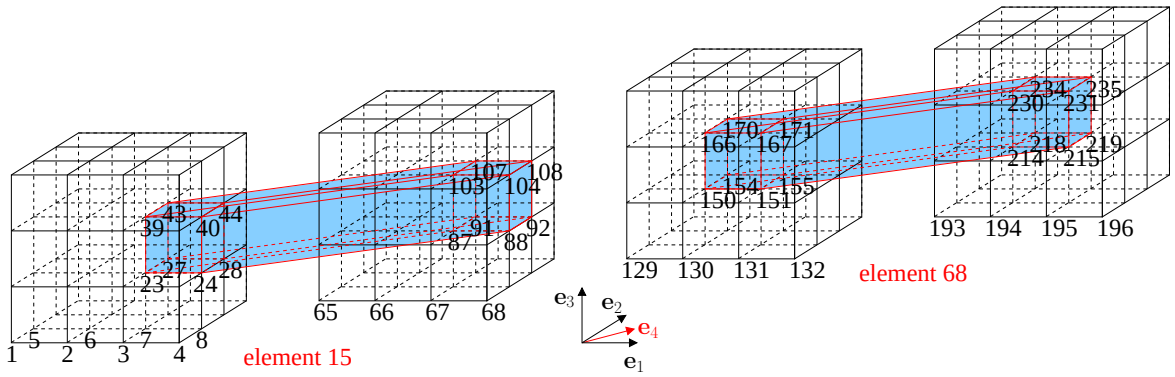
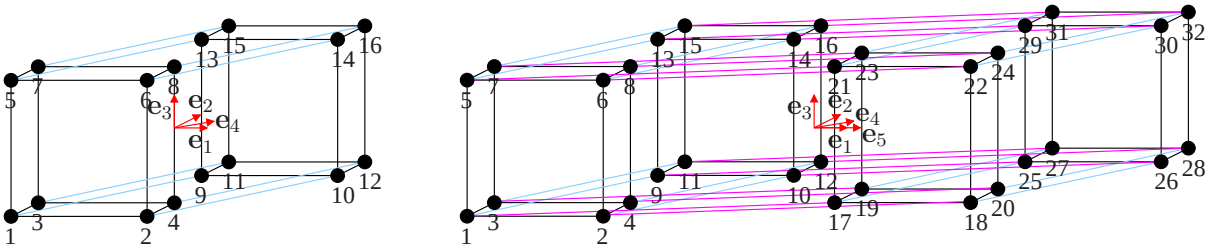


Figure 4: 4-dimensional mesh, 3 elements per dimension, exemplary depiction of element 15 and 68

dimensions n. To support this statement, the generation of n-dimensional unit elements is depicted in figure (5) An n-dimensional element can always be built up through a projection of the $n-1$-dimensional element.

For arbitrary dimensional unit elements, shape functions of polynomial order np can be computed as the n-fold product of the np-order Lagrangian polynomials.

After having defined mesh data and shape functions for n-dimensional problems, it remains to compute the n-dimensional flux vector over all 2^n faces of dimension $n-1$. Therefore, $n-1$-dimensional shape functions are needed, as well as the n-dimensional normal vector in global coordinates. This vector can be computed through orthogonalization of a vector with respect to the row vectors of the surface Jacobian.



(a) 4D element (b) 5D element

Figure 5: unit elements

4 OUTLOOK

The Discontinuous Galerkin method is a promising and applicable technique for the solution of high-dimensional Fokker-Planck equations. It allows for element-wise parallelization, as the system of equations is completely locally decoupled. Adaptive mesh refinement is very suitable for the method, as a result of the allowance of discontinuities at inter-element boundaries. Furthermore, two neighbouring elements can be discretized in completely different scales.
The LDG resolution of the diffusion part with local explicit time integration, is not the perfect choice, due to the time step restriction. In the future, implicit-explicit schemes should be implemented as a replacement.

REFERENCES

[1] Alexander N. Brooks and Thomas J.R. Hughes. Streamline Upwind/Petrov-Galerkin formulations for convection dominated flows with particular emphasis on the incompressible Navier-Stokes equations. *Comput. Meth. Appl. Mech. Eng.*, 32:199–259, 1982.

[2] B. Cockburn and C.W. Shu. Runge-Kutta discontinuous Galerkin methods for convection-dominated Problems. *Journal of Scientific Computing*, 16(3):173–261, 2001.

[3] Bernardo Cockburn and Chi-Wang Shu. The local discontinuous Galerkin method for time-dependent convection-diffusion systems. *SIAM J. Numer. Anal.*, 35:2440–2463, 1998.

[4] C. Johnson and J. Pitkäranta. An analysis of the discontinuous Galerkin method for a scalar hyperbolic equations. *Math. Comput.*, 46(173):1–26, 1986.

[5] Pankaj Kumar and S Narayanan. Solution of Fokker-Planck equation by finite element and finite difference methods for nonlinear systems. *Sadhana-Acad. P. Eng. S.*, 31:445–461, 2006.

[6] P. Lesaint and P.A. Raviart. On a finite element method for solving the neutron transport equation. *Mathematical Aspects of Finite Elements in Partial Differential Equations*, pages 89–122, 1974.

[7] R.J. LeVeque. *Finite Volume Methods for Hyperbolic Problems*. Cambridge Texts in Applied Mathematics. Cambridge University Press, 2002.

[8] Wolfram Martens, Utz von Wagner, and Volker Mehrmann. Calculation of high-dimensional probability density functions of stochastically excited nonlinear mechanical systems. *Nonlinear Dynamics*, 67:2089–2099, 2012.

[9] Arif Masud and Lawrence A. Bergmann. Application of multi-scale finite element methods to the solution of the Fokker-Planck equation. *Computer Methods in Applied Mechanics and Engineering*, 194:1513 – 1526, 2005.

[10] L. Pichler, A. Masud, and L.A. Bergman. Numerical solution of the Fokker-Planck equation by Finite Difference and Finite Element Methods - A comparative study. In Manolis Papadrakakis, George Stefanou, and Vissarion Papadopoulos, editors, *Computational Methods in Stochastic Dynamics*, volume 26 of *Computational Methods in Applied Sciences*, pages 69–85. Springer Netherlands, 2013.

[11] W.H. Reed and T.R. Hill. Triangular mesh methods for the neutron transport equation. *Los Alamos Report LA-UR-73-479*, 1973.

[12] Hannes Risken. *The Fokker-Planck Equation Methods of Solution and Applications*. Springer-Verlag Berlin, 1996.

[13] C. Soize. Steady-state solution of Fokker-Planck equation in higher dimension. *Probabilistic Engineering Mechanics*, 3:196 – 206, 1988.

[14] Gilbert Strang. *Computational science and engineering*. Wellesley-Cambridge Press Wellesley, MA, 2007.

[15] R. L. Stratonovich and Richard A. Silverman. *Topics in the Theory of Random Noise*, volume 1. Gordon and Breach New York, 1963.

[16] N. G. Van Kampen. *Stochastic processes in physics and chemistry*, volume 1. North-Holland, 1981.

[17] W. Yi, B.F. Spencer Jr, and L.A. Bergman. Solution of the Fokker-Planck equation in higher dimensions: application of the concurrent finite element method. In *Shiraishi N, Shinozuka M, Wen YK. 7th International Conference on Structural Safety and Reliability (ICOSSAR97), November*, 1997.

[18] Matthias Ziefle and Udo Nackenhorst. Numerical techniques for rolling rubber wheels: treatment of inelastic material properties and frictional contact. *Comput. Mech.*, 42:337–356, 2008.

COMPDYN 2013
4th ECCOMAS Thematic Conference on
Computational Methods in Structural Dynamics and Earthquake Engineering
M. Papadrakakis, V. Papadopoulos, V. Plevris (eds.)
Kos Island, Greece, 12–14 June 2013

ANALYSIS OF OSCILLATIONS OF ONE-DIMENSIONAL SPATIALLY PERIODIC STRUCTURES. AN UNCONVENTIONAL APPROACH AND SOME NEW EFFECTS

Vladislav S. Sorokin

Institute of Problems in Mechanical Engineering RAS
V.O., Bolshoj pr. 61, St. Petersburg, 199178, Russia
e-mail: slavos87@mail.ru

Keywords: Spatially periodic structures, Long waves, Effective parameters, Averaging, Method of direct separation of motions.

Abstract. *The present study is concerned with the analysis of oscillations of one-dimensional spatially periodic structures. There are many approaches for wave examination in such structures, in particular, methods, based on the utilization of the Floquet theory [1]. However, in the framework of this theory it is problematic to incorporate the (external) boundary conditions. The averaging procedure for processes in periodic systems based on the multiple scales method [2] combined with the averaging method [3] was proposed in the monograph [4].*

In the present paper a new approach for the analysis of oscillations of one-dimensional spatially periodic structures, which is based on the method of direct separation of motions (MDSM) [5,6], is proposed. The approach is introduced in order to detect new effects in such structures' behavior, which may be employed to produce systems with advanced properties.

As an example of the approach application the study of oscillations of a string with variable cross-section is conducted. As the result, analytical expressions for the eigenmodes and the eigenfrequencies of the system are obtained. It is shown that modulation of the string cross-section leads to a change of the eigenfrequencies as compared with their non-modulated values, and to the emergence of a spectrum of additional high eigenfrequencies, which correspond to large wave lengths. A simple physical explanation of the latter effect, which is noted, apparently for the first time, is proposed. It is shown that character of string oscillations may be controlled by modulation of its cross-section, in particular, for given initial conditions the effect of high-frequency components suppression may be achieved.

1 INTRODUCTION

The present study is concerned with the analysis of oscillations of one-dimensional spatially periodic structures. There are many approaches for wave examination in such structures, in particular, methods, based on the utilization of the Floquet theory [1]. The so-called frequency stop bands, i.e. frequencies ranges, in which a wave does not propagate through the considered system, can be determined by their means [7-9]. However, in the framework of this theory it is problematic to incorporate the (external) boundary conditions. The averaging procedure for processes in periodic structures based on the multiple scales method [2] combined with the averaging method [3] was proposed in the monograph [4]. There are several approaches [10, 11] based on this procedure, which are applicable to study other classes of dynamical systems.

In the present paper a new approach for the analysis of oscillations of one-dimensional spatially periodic structures, which is based on the method of direct separation of motions (MDSM) [5, 6], is proposed. The approach is introduced in order to detect new effects in such structures' behavior, which may be employed to produce systems with advanced properties. As an example of the approach application the study of oscillations of a string with variable cross-section is conducted. The aim is to identify the eigenfrequencies and the eigenmodes of this system. Effects revealed for the considered simple model may facilitate solving the practically important problem of design of a periodic structure with tailored characteristics. In particular, a system with advanced performance of sound and vibration suppression may be produced.

It is noted that application of the multiple scales method (MSM) and other classical asymptotic methods for solving the considered equations is rather cumbersome, because an unknown parameter is present in them. The fundamental difference between the MDSM and these methods is specified. In particular, it is shown that the MDSM may be employed for solving equations without small parameter; thereby, the applicability range of this method turns out to be broader than the one of the classical asymptotic methods.

We note that the proposed approach is applicable for solving problems, which are opposite to those studied by the asymptotic method of G. Wentzel, H. Kramers, and L. Brillouin (the WKB method) [12]. Because here long waves in rapidly varying structures are considered that is opposite to short waves in slowly varying structures analyzed by the WKB.

2 OSCILLATIONS OF A STRING WITH VARIABLE CROSS-SECTION. INITIAL EQUATIONS

Consider oscillations of the simplest one-dimensional periodic system – string with variable cross-section, which are described by the equation

$$\rho S \frac{\partial^2 u}{\partial t^2} - \frac{\partial}{\partial x}\left(T \frac{\partial u}{\partial x} \right) = 0 \tag{1}$$

Here ρ is the density of the string material, S is the cross-sectional area, T is the tension force, $u(x,t)$ is the lateral deflection of the string. Spatial modulations of the cross-sectional area are determined by the relation $S = S_0(1+\alpha \sin kx)$, here $0 \le \alpha < 1$, $k >> \frac{\pi}{l}$, where l is the length of the string (Figure 1). The boundary conditions are set to be homogeneous

$$u\big|_{x=0} = u\big|_{x=l} = 0 \tag{2}$$

The classical separation of variables technique is used to solve equation (1)

$$u(x,t) = A(x)B(t) \tag{3}$$

Consequently for the new variable $A(x)$ the following equation is obtained

$$A'' = -\frac{\Omega^2 \rho S_0}{T}(1+\alpha \sin kx)A \tag{4}$$

here Ω is a frequency of string oscillations, which value and order are not given a priori and thence unknown, prime designates the spatial derivative.

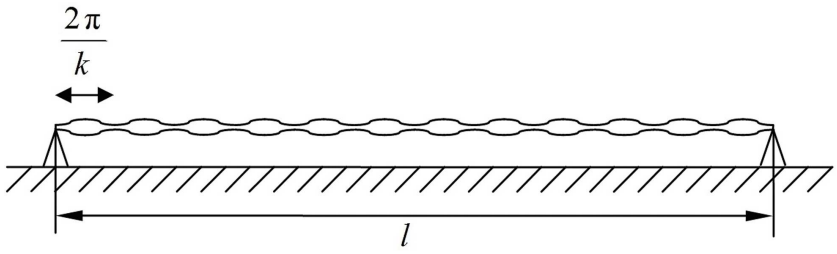


Figure 1: String with variable cross-section.

Generally, application of the averaging method, MSM and other asymptotic methods requires the presence of a small parameter in the equation considered. In addition, orders of all parameters, involved in the equation, must be known to employ these methods. In our case the unknown parameter Ω is present in equation (4). Application of the asymptotic methods for solving such equations is rather cumbersome and may lead to erroneous results. For example Ω may have such value that it will be impossible to assign a small parameter in equation (4).

The condition of the MDSM applicability is the fulfillment of the main assumption of vibrational mechanics, which was formulated in the monograph [5]. In substance, this method also implies the presence of a small parameter. But in contrast to the asymptotic methods, this small parameter must be present in the resulting equation, and not in the initial one. This distinction broadens the applicability range of the MDSM, in particular, enables to apply it for solving the considered equation (4).

So, the applicability range of the MDSM turns out to be broader than the one of the classical asymptotic methods. The validity of this statement is illustrated, particularly, in paper [13], where a classical problem about the stability of a pendulum with vibrating suspension axis is considered at unconventional values of parameters.

3 OSCILLATIONS OF A STRING WITH VARIABLE CROSS-SECTION. SOLUTION BY THE MDSM

The vibrational mechanics approach and the MDSM are employed for solving equation (4). The procedure of the method application remains the same as in conventional cases, but equation with respect to spatial coordinate x, and not to time t, is considered. Solution of equation (4) is sought in the form

$$A = A_1(x) + \psi(x, kx) \tag{5}$$

where A_1 is "slowly varying", and ψ is "rapidly varying", 2π-periodic in dimensionless ("micro") coordinate $x_1 = kx$ variable, with period x_1 average being equal to zero:

$$\langle \psi(x, x_1) \rangle = 0 \tag{6}$$

Here $\langle ... \rangle$ designates averaging in the period 2π on coordinate x_1. The slowly varying component A_1 describes processes taking place at macro scale, which is determined by the characteristic spatial dimension of the problem. In our case this scale is defined by the length of the string l. The rapidly varying component ψ captures processes taking place at micro scale, which is determined by linear dimensions of the inhomogeneity in the considered structure, i.e. by $\frac{2\pi}{k}$. The aim of the method is to compose equations, which describe the spatially averaged processes in periodic system, i.e. equations for the slowly varying variable A_1.

The following equation is obtained for variable A_1 by averaging (4) by x_1

$$\frac{\mathrm{d}^2 A_1}{\mathrm{d}x^2} + \frac{\Omega^2 \rho S_0}{T} A_1 = -\frac{\Omega^2 \rho S_0}{T} \alpha \langle \psi \sin x_1 \rangle \tag{7}$$

Equation for the "rapidly varying" variable ψ may be obtained by subtracting equation (7) from equation (4)

$$\psi'' + \frac{\Omega^2 \rho S_0}{T} \psi = -\frac{\Omega^2 \rho S_0}{T} \alpha \left((A_1 + \psi) \sin x_1 - \langle \psi \sin x_1 \rangle \right) \tag{8}$$

We note that in the absence of modulations these equations will have a natural solution $\psi = 0$ and $A = A_1$.

To achieve more accurate results the MDSM is applied in its modified form [14,15]. We abandon one of the conventional simplifications of the method, which in the considered case has the form: while solving the equation for variable ψ it is possible to consider variable A_1 as constant ("frozen"). Detailed discussion of the reasons for using the modified method is given in section 4.

So, we take into account the dependence of variable A_1 on x while solving equation (8). The solution is sought in the form of series

$$\psi = B_{11} \sin x_1 + B_{12} \cos x_1 + B_{21} \sin 2x_1 + B_{22} \cos 2x_1 + B_{31} \sin 3x_1 + B_{32} \cos 3x_1 + \ldots \tag{9}$$

Taking into account only the first harmonic in the solution, that is sufficient at small α, we obtain the following expression for ψ

$$\psi = \alpha A_1 \frac{\Omega^2 \mu}{1 - \Omega^2 \mu} \sin x_1 + \alpha \frac{2}{k} A_1' \frac{\Omega^2 \mu}{\left(1 - \Omega^2 \mu\right)^2} \cos x_1 \tag{10}$$

here $\mu = \frac{\rho S_0}{T k^2}$. Using this expression, equation (7) for the "slowly varying" variable A_1 is transformed into

$$\frac{\mathrm{d}^2 A_1}{\mathrm{d}x^2} + \frac{\Omega^2 \rho S_0}{T} \left(1 + \frac{\alpha^2}{2} \frac{\Omega^2 \mu}{1 - \Omega^2 \mu} \right) A_1 = 0 \tag{11}$$

Now consider the boundary conditions (2). Taking into account decomposition (5) these conditions may be written in the form

$$A_1(0) + \psi(0,0) = A_1(l) + \psi(l, kl) = 0 \tag{12}$$

Employing expression (10) for ψ, from (12) we obtain
at $x = 0$

$$A_1(0) + \alpha \frac{2}{k} \frac{\Omega^2 \mu}{\left(1 - \Omega^2 \mu\right)^2} A_1'(0) = 0 \tag{13}$$

at $x = l$

$$A_1(l) + \alpha \frac{\Omega^2 \mu}{1 - \Omega^2 \mu} A_1(l) \sin kl + \alpha \frac{2}{k} \frac{\Omega^2 \mu}{\left(1 - \Omega^2 \mu\right)^2} A_1'(l) \cos kl = 0 \tag{14}$$

So, the equation and the boundary conditions for the slowly varying variable A_1 are formulated. As the result, the following equation for the eigenfrequencies Ω is derived

$$\begin{aligned} &\left(\sin \lambda l - \alpha \frac{2}{k} \frac{\Omega^2 \mu}{\left(1 - \Omega^2 \mu\right)^2} \lambda \cos \lambda l \right) \left(1 + \alpha \frac{\Omega^2 \mu}{1 - \Omega^2 \mu} \sin kl \right) + \\ &+ \alpha \frac{2}{k} \frac{\Omega^2 \mu}{\left(1 - \Omega^2 \mu\right)^2} \lambda \left(\cos \lambda l + \alpha \frac{2}{k} \frac{\Omega^2 \mu}{\left(1 - \Omega^2 \mu\right)^2} \lambda \sin \lambda l \right) \cos kl = 0 \end{aligned} \tag{15}$$

Here $\lambda = \sqrt{\frac{\Omega^2 \rho S_0}{T} \left(1 + \frac{\alpha^2}{2} \frac{\Omega^2 \mu}{1 - \Omega^2 \mu} \right)}$ is corresponding wave number. The "macro-scale" eigenmode of the inhomogeneous string is determined by the expression

$$A_1 = \sin \lambda x - \alpha \frac{2}{k} \frac{\Omega^2 \mu}{\left(1 - \Omega^2 \mu\right)^2} \lambda \cos \lambda x \tag{16}$$

4 VERIFICATION OF THE MDSM APPLICABILITY

Verification of the MDSM applicability for solving equation (4) is provided. As it was noted above, in conventional cases criterion of the MDSM applicability is the fulfillment of the main assumption of vibrational mechanics [5]. In the present paper equations with respect to spatial coordinate x and not to time t are considered. However, the procedure of the method application remains the same. So, condition of the MDSM applicability in the considered case is similar to the conventional one. It takes the following form

$$\frac{\psi'}{\psi_0} >> \frac{A_1'}{A_{10}} \tag{17}$$

Here ψ_0 is characteristic amplitude of the rapidly varying variable ψ oscillations, A_{10} is characteristic amplitude of the slowly varying variable A_1 oscillations. Employing expressions (10) and (16) for ψ and A_1, we obtain $\frac{A_1'}{A_{10}} \sim \lambda$, $\frac{\psi'}{\psi_0} \sim k$. So, condition (17) may be reduced to

$$\frac{\lambda}{k} << 1 \tag{18}$$

In substance, this condition may be interpreted as the requirement for variable A_1 to vary "indeed slowly" in comparison with variable ψ. So, only long waves in rapidly varying structures may be studied by means of the MDSM.

As is seen from condition (18), application of the MDSM implies the presence of a small parameter. However, in contrast to the asymptotic methods, this small parameter must be present in the resulting equation, and not in the initial one. In the considered case this parameter is determined by the expression

$$\varepsilon = \frac{\lambda}{k} = \sqrt{\Omega^2 \mu \left(1 + \frac{\alpha^2}{2} \frac{\Omega^2 \mu}{1 - \Omega^2 \mu} \right)} \tag{19}$$

Relation (19) may be considered as an equation for the product $\Omega^2 \mu = \frac{1}{k^2} \frac{\Omega^2 \rho S_0}{T}$, which is present in the initial equation (4). Obtained information about the order of $\Omega^2 \mu$ may facilitate solving equation (4) by means of the asymptotic methods. In our case from relation (19) we obtain $\Omega^2 \mu \sim 1$ and $\Omega^2 \mu \sim \varepsilon^2$. Substituting the first one in (4), equation without small parameter is composed. Such equation can not be properly solved by means of the classical asymptotic methods. If we substitute the second value $\Omega^2 \mu \sim \varepsilon^2$ in (4) and solve this equation by the MSM, then the following equation for the main component A_{1m} will be obtained

$$\frac{\mathrm{d}^2 A_{1m}}{\mathrm{d}x^2} + \frac{\Omega^2 \rho S_0}{T} A_{1m} = 0 \tag{20}$$

As is seen, this equation does not capture the change of the system's effective parameters due to modulation. I.e. application of the MSM in the considered case leads to the erroneous results. Thereby, even the introduction of the small parameter (19), which was determined from the condition of the MDSM applicability, does not allow solving equation (4) by means of the asymptotic methods.

In section 3 the MDSM was applied without one of the conventional simplifications, which in the considered case has the form: while solving the equation for variable ψ it is possible to consider variable A_1 as constant ("frozen"). The abandonment of this simplification complicates the solution of equation (8) for the rapidly varying variable ψ, but in the considered case it turns out to be necessary. To illustrate it we solve equation (8) considering variable A_1 as frozen, or parameter x as constant. Taking into account only the first harmonic in the solution, we obtain

$$\psi = \alpha A_1 \frac{\Omega^2 \mu}{1 - \Omega^2 \mu} \sin x_1 \tag{21}$$

Equation for the slowly varying variable A_1 will, as before, have form (11). But the boundary conditions will change: $A_1(0) = A_1(l) = 0$. As the result, equation for the eigenfrequencies will take the form

$$\lambda = \sqrt{\frac{\Omega^2 \rho S_0}{T}\left(1+\frac{\alpha^2}{2}\frac{\Omega^2\mu}{1-\Omega^2\mu}\right)} = \frac{\mathrm{n}\pi}{l} \tag{22}$$

Solutions of this equation (values of frequencies Ω and wave numbers λ) differ from the correct values Ω and λ, obtained from equation (15).

5 THE EIGENFREQUENCIES AND THE EIGENMODES OF THE INHOMOGENEOUS STRING

To solve equation (15) for the eigenfrequencies the finite-product method [16] is employed. The application of this method implies the representation of $(\sin\lambda l)/\lambda l$ and $\cos\lambda l$ as the following products

$$\frac{\sin\lambda l}{\lambda l} = \prod_{\mathrm{m}'=1}^{\mathrm{m}}\left(1-\left(\frac{\lambda l}{\pi}\right)^2\frac{1}{\mathrm{m}'^2}\right) \tag{23}$$

$$\cos\lambda l = \prod_{\mathrm{m}'=1}^{\mathrm{m}}\left(1-\left(\frac{\lambda l}{\pi}\right)^2\frac{1}{(\mathrm{m}'-\frac{1}{2})^2}\right) \tag{24}$$

Number of retained factors in products (23)-(24) affects the number and the values of the resulting roots of equation (15). We are interested in the frequencies, for which corresponding wave numbers are relatively small $\lambda << k$ (see section 4). To determine such frequencies it is sufficient to retain only a few factors in products (23)-(24). Limiting ourselves to just two factors, we obtain five roots – values of frequency Ω, one of which corresponds to $\lambda = 0$. It should be noted that in the case of a homogeneous string, if we take into account two factors in each product, corresponding equation for the eigenfrequencies $\sin\lambda l = 0$ will have not five, but two roots $\lambda_{1(0)} = \pi/l$ 1/cm, $\lambda_{2(0)} = 2\pi/l$ 1/cm. As an illustration, wave numbers λ and corresponding eigenfrequencies Ω of the inhomogeneous and homogeneous strings are presented in Figure 2 for the following values of the parameters $\rho S_0/T = 1\mathrm{s}^2/\mathrm{cm}^2, l = 5\,\mathrm{cm}, \alpha = 0.5, k = 9\pi/l$ 1/cm.

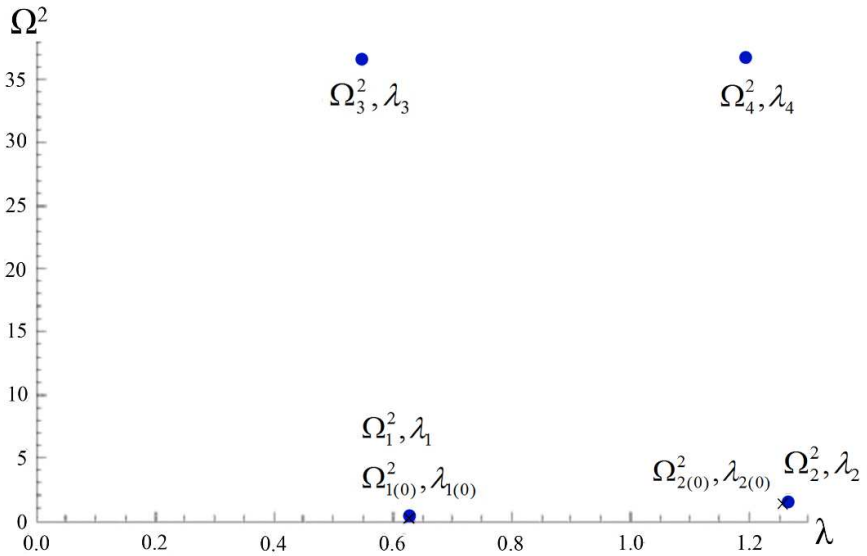


Figure 2: Wave numbers and corresponding eigenfrequencies of the homogeneous (crosses) and inhomogeneous (circles) strings.

As is seen from Figure 2, modulation of the string cross-section leads to a small change of (the basic) eigenfrequencies Ω_1, Ω_2 as compared with their non-modulated values $\Omega_{1(0)}$ and $\Omega_{2(0)}$. Corresponding wave numbers also change due to modulation. Another interesting effect is the emergence of additional eigenfrequencies Ω_3, Ω_4, which values are significantly higher than $\Omega_{1(0)}$ and $\Omega_{2(0)}$. We note that wave numbers, which correspond to these frequencies, are close to $\lambda_{1(0)}$ and $\lambda_{2(0)}$.

The same effects will occur if we retain more factors in products (23)-(24). Thus, if we take into account three factors, equation (15) will have not five, but seven roots, one of which corresponds to $\lambda = 0$. In the case of a homogeneous string we would obtain three roots $\lambda_{1(0)} = \pi/l$ 1/cm, $\lambda_{2(0)} = 2\pi/l$ 1/cm, $\lambda_{3(0)} = 3\pi/l$ 1/cm. Taking into account four factors, we get nine roots of equation (15) etc.

Values of the wave numbers and corresponding eigenfrequencies depend significantly on the character of modulation. To illustrate it wave numbers and corresponding eigenfrequencies are shown in Figure 3 at $\rho S_0/T = 1\text{s}^2/\text{cm}^2, l = 5\text{cm}, \alpha = 0.5$ for different values of parameter k: $k = 8\pi/l$ 1/cm, $k = {}^{17\pi}\!/_{2l}$ 1/cm, $k = 9\pi/l$ 1/cm. As before, we retain two factors in products (23)-(24). It is interesting that at $kl = 2\text{m}\pi$ corresponding wave numbers turn out to be equal to each other $\lambda_1 = \lambda_3$ и $\lambda_2 = \lambda_4$.

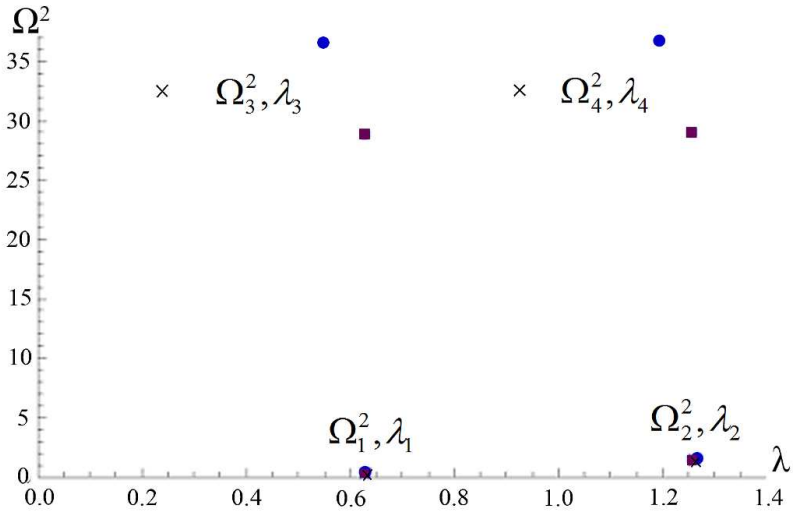


Figure 3: Wave numbers and eigenfrequencies of the inhomogeneous string at different modulations: $k = 8\pi/l$ 1/cm (squares), $k = {}^{17\pi}\!/_{2l}$ 1/cm (crosses), $k = 9\pi/l$ 1/cm (circles).

So, we may conclude that modulation of the string cross-section leads to two effects:1. The emergence of additional high eigenfrequencies, which correspond to small wave numbers or large wave lengths 2. Shift of (the basic) eigenfrequencies Ω_1, Ω_2 etc. as compared with their non-modulated values $\Omega_{1(0)}$, $\Omega_{2(0)}$ etc. This shift may be as in the direction of increasing (e.g. at $k = 9\pi/l$ 1/cm), as in the direction of decreasing (e.g. at $k = 8\pi/l$ 1/cm).

Taking into account relations (10) for ψ and (16) for A_1, the following expression for the eigenmode of the inhomogeneous string, which corresponds to eigenfrequency Ω, is derived

$$A(x)=\left(\sin\lambda x-\alpha\frac{2}{k}\frac{\Omega^2\mu}{\left(1-\Omega^2\mu\right)^2}\lambda\cos\lambda x\right)\left(1+\alpha\frac{\Omega^2\mu}{1-\Omega^2\mu}\sin kx\right)+$$
$$+\alpha\frac{2}{k}\frac{\Omega^2\mu}{\left(1-\Omega^2\mu\right)^2}\lambda\left(\cos\lambda x+\alpha\frac{2}{k}\frac{\Omega^2\mu}{\left(1-\Omega^2\mu\right)^2}\lambda\sin\lambda x\right)\cos kx \tag{25}$$

This expression may be considered as correct at $\alpha<0.5$.

6 ON THE EFFECT OF THE EMERGENCE OF A SPECTRUM OF ADDITIONAL HIGH EIGENFREQUENCIES, WHICH CORRESPOND TO LARGE WAVE LENGTHS

While solving equation (8) for the rapidly varying variable ψ only the first harmonic was taken into account. If we take into account other harmonics, resulting equation for the slowly varying variable A_1 will change. Thus, retaining two harmonics, we will obtain

$$\frac{\mathrm{d}^2A_1}{\mathrm{d}x^2}+\frac{\Omega^2\rho S_0}{T}\left(1+\alpha^2\frac{2\Omega^2\mu(\Omega^2\mu-4)}{(\alpha^2-4)\Omega^4\mu^2+20\Omega^2\mu-16}\right)A_1=0 \tag{26}$$

Corresponding boundary conditions for variable A_1 will also change. As the result, equation for the eigenfrequencies will take the form, which is different from (15). Solving this equation by the finite-product method and retaining two factors in products (23)-(24), we obtain not five, but seven roots - Ω values, one of which corresponds to $\lambda=0$. The first four non-zero roots will differ only slightly from those determined above, for the remaining two the following relations will hold true $\Omega_5^2>>\Omega_3^2$, $\lambda_5\approx\lambda_3$ and $\Omega_6^2>>\Omega_4^2$, $\lambda_6\approx\lambda_4$. Taking into account three harmonics in series (9), we obtain nine eigenfrequencies etc. As an illustration, wave numbers λ and corresponding eigenfrequencies Ω, obtained retaining three harmonics, are shown in Figure 4 for the following values of parameters $\rho S_0/T=1\mathrm{s}^2/\mathrm{cm}^2, l=5\,\mathrm{cm}, \alpha=0.5, k=8\pi/l$ 1/cm.

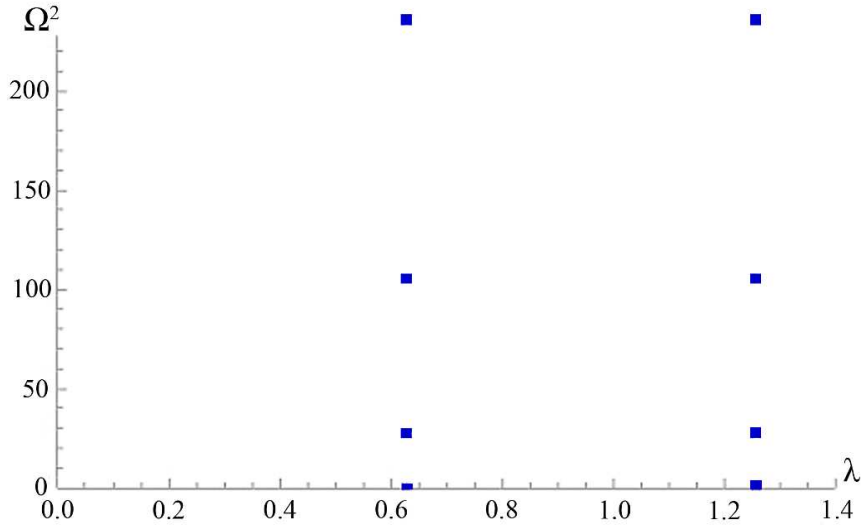


Figure 4: Wave numbers and corresponding eigenfrequencies, obtained retaining three harmonics in series (9), for $k=8\pi/l$ 1/cm.

So, we may conclude that modulation of the string cross-section leads the emergence of a whole spectrum of additional high eigenfrequencies, which correspond to large wave lengths.

A simple physical explanation of this effect is proposed in the paper. Consider oscillations of a homogeneous string fixed at both ends. As is well-known, its first eigenmode is $\sin \lambda_{1(0)} x$ ($\lambda_{1(0)} = \pi / l$ 1/cm), while oscillations on high frequencies occur at micro-level (Figure 5), i.e. large wave lengths correspond to low eigenfrequencies, and small wave lengths to high eigenfrequencies.

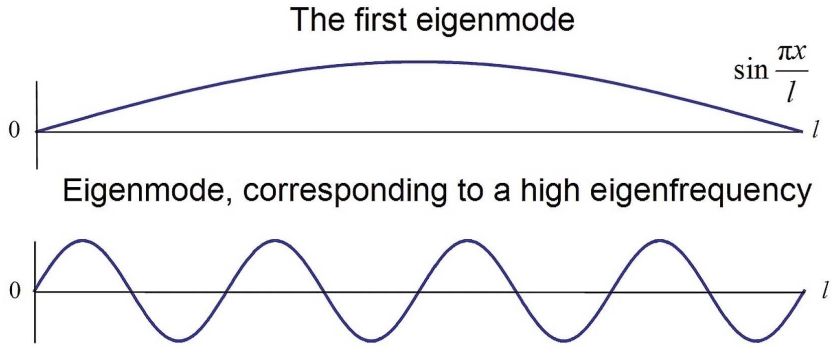


Figure 5: Eigenmodes of a homogeneous string.

Now consider an inhomogeneous string. Due to modulation its eigenmode, corresponding to the first eigenfrequency, is not $\sin \lambda_{1(0)} x$, but is $\sin \lambda_{1(0)} x$ plus imposed additional (small) oscillations on the micro-level. So, this mode is a superposition of the main macro-component $\sin \lambda_{1(0)} x$ and the additional (small) micro-component $(\sin \lambda_{1(0)} x) \sin kx$. As in the case of the low eigenfrequency, oscillations on high eigenfrequencies change due to inhomogeneity of the system and involve both micro and macro (additional) components (Figure 6). The macro-component is small in comparison with the micro-component; low value of the wave number corresponds to it. So, oscillations of the inhomogeneous string on high eigenfrequencies contain long-wave component. And that means spectrum of additional high eigenfrequencies, which correspond to small wave numbers or large wave lengths, is present for the string due to modulation.

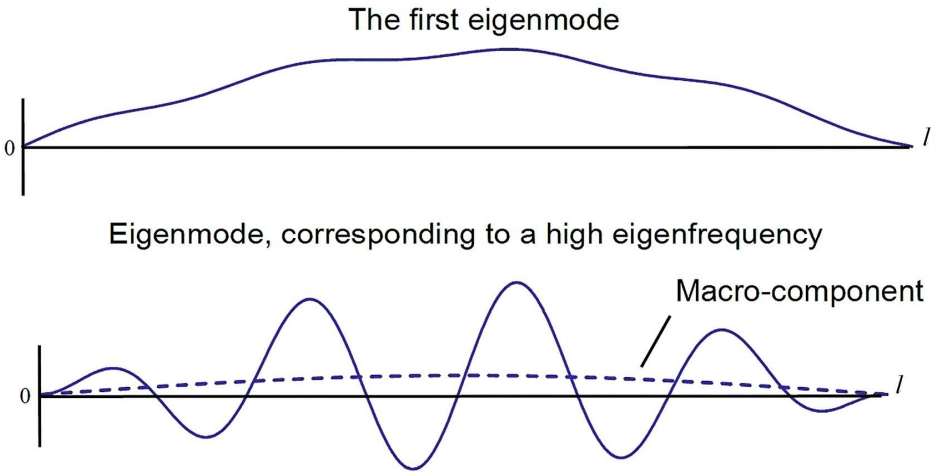
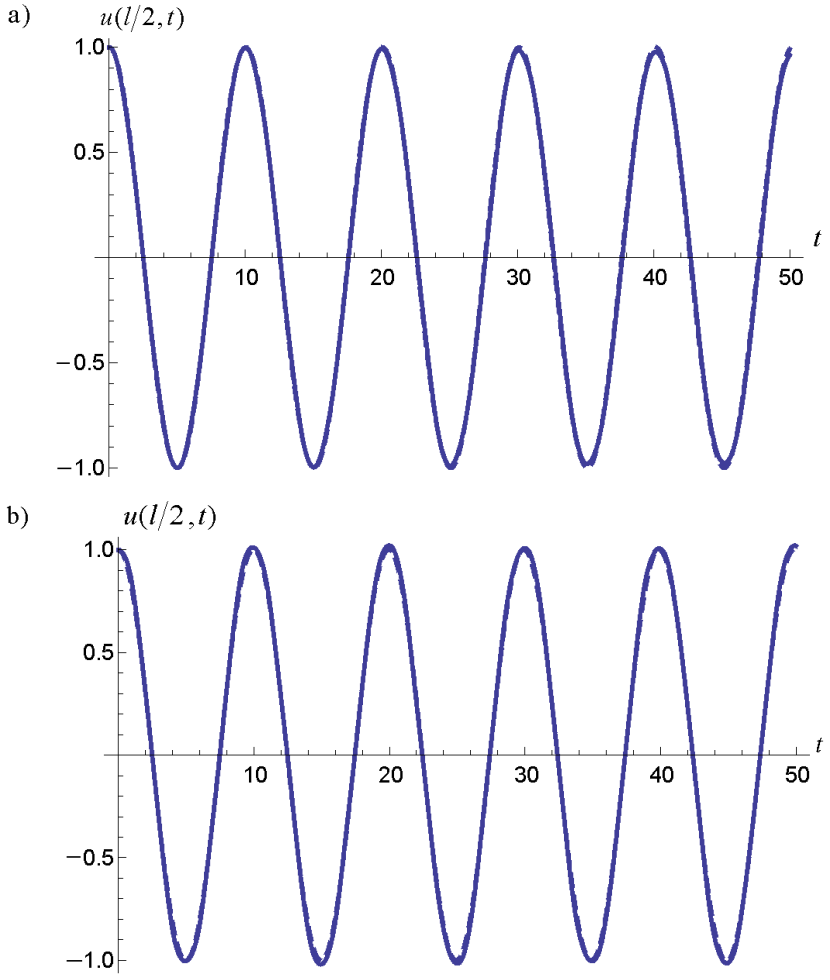


Figure 6: Eigenmodes of an inhomogeneous string.

At $\alpha \to 0$ (the basic) eigenfrequencies Ω_1, Ω_2 etc. tend to their non-modulated values $\Omega_{1(0)}$, $\Omega_{2(0)}$ etc. The long-wave component of string oscillations on high eigenfrequencies vanishes in this limit. This fact is in good agreement with the proposed physical explanation.

7 COMPARISON WITH THE RESULTS OF NUMERICAL EXPERIMENTS

Results obtained in the paper were verified by numerical experiments. Oscillations of an inhomogeneous string at the simplest initial conditions $u\big|_{t=0} = \sin \lambda_{1(0)} x$, $\dot{u}\big|_{t=0} = 0$ were considered. In accordance with our analytical predictions, at such initial conditions the string should oscillate "about the same" as the homogeneous one, because Ω_1 is close to $\Omega_{1(0)}$, and eigenmode (25), which corresponds to this frequency, differs only slightly from $\sin \lambda_{1(0)} x$ since $\lambda_1 \approx \lambda_{1(0)} = \dfrac{\pi}{l}$ 1/cm and $\Omega_1^2 \mu << 1$. The dependences of the deflection of the middle of the string $u(l/2, t)$ on time at $\rho S_0 / T = 1\text{s}^2/\text{cm}^2, l = 5\text{cm}$, $\alpha = 0.5$ are shown in Figure 7 for different values of parameter k: a) $k = 4\pi/l$ 1/cm b) $k = 5\pi/l$ 1/cm; solid line is the numerical solution, dashed line is the analytical solution. To illustrate the effect of modulation on basic eigenfrequencies these dependences, obtained numerically, are presented in Figure 7c) for $k = 4\pi/l$ 1/cm and $k = 5\pi/l$ 1/cm.



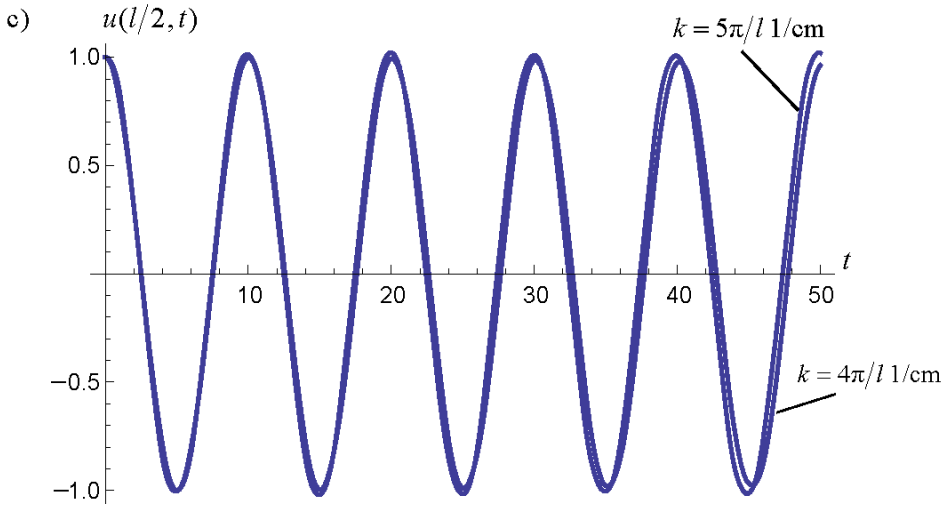


Figure 7: The dependences of the deflection of the middle of the string $u(l/2,t)$ on time t a) $k = 4\pi/l$ 1/cm b) $k = 5\pi/l$ 1/cm c) $k = 4\pi/l$ 1/cm and $k = 5\pi/l$ 1/cm ; solid line is the numerical solution, dashed line is the analytical solution.

As is seen from Figure 7, there is a good agreement between the analytical and numerical results. In particular, value of the eigenfrequency Ω_1 changes due to modulation, as it was predicted.

As follows from the analytical results, at considered initial conditions the additional high-frequency component of the inhomogeneous string oscillations is much smaller than the low-frequency one. In order to check whether this component is present or not, and to verify the value of the corresponding eigenfrequency we study a residual between the numerical solution and the analytically obtained low-frequency component. The dependence of this residual $u(l/2,t) - u_{lf}^{an}(l/2,t)$ on time t is shown in Figure 8 for $\rho S_0/T = 1\text{s}^2/\text{cm}^2, l = 5\,\text{cm}$, $\alpha = 0.3$ and $k = 20\pi/l$ 1/cm.

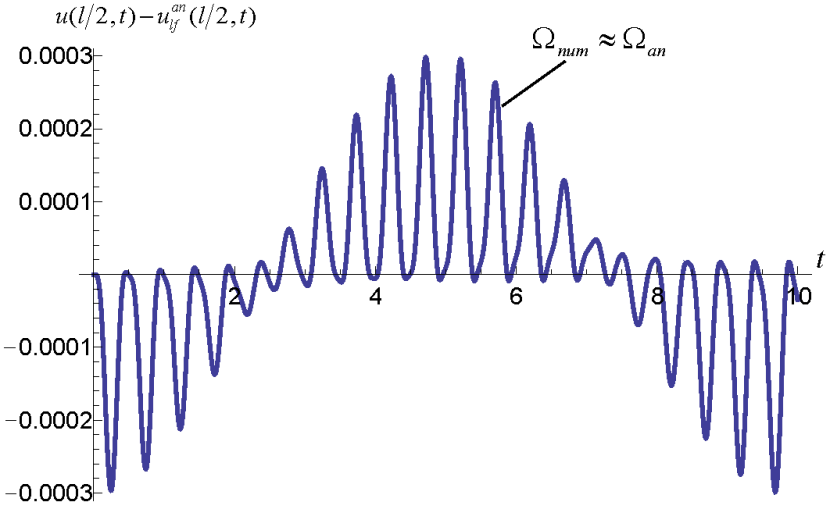


Figure 8: The dependence of the residual between the numerical solution and the analytically obtained low-frequency component of the inhomogeneous string oscillations on time.

As is seen from Figure 8, the conclusion regarding the emergence of a spectrum of additional high eigenfrequencies, which correspond to large wave lengths, is confirmed by the

numerical experiments. It should be noted that values of these frequencies Ω_{an}, predicted analytically, almost coincide with the numerical ones Ω_{num} (for $k > 5\lambda_{1(0)}$). However, numerical experiments have shown that the dependence of the high-frequency component of the string oscillations on time is more complex, than it was predicted. This may be explained by the fact that the equation for variable ψ was solved only approximately, and so the eigenmodes, corresponding to additional high eigenfrequencies, are determined with some degree of error.

It should be noted that structural damping, which is present in every real system, affects the high-frequency motion significantly - it suppresses high-frequency components. However its influence on the low-frequency motion is relatively weak. So, the revealed effect of the emergence of a spectrum of additional high eigenfrequencies, which correspond to large wave lengths, should be less pronounced in real mechanical systems.

8 ON THE EFFECT OF SUPPRESSION OF HIGH-FREQUENCY COMPONENTS OF STRING OSCILLATIONS

If initial deflection of the inhomogeneous string is set as one of its eigenmodes (25), then it will oscillate with corresponding frequency Ω (e.g. with the low frequency Ω_1). However, oscillations of a homogeneous string at such complex initial conditions will involve many high-frequency components. So, we may say that at this initial conditions the inhomogeneous string "behaves better", than the homogeneous one. Thereby, we can control the character of string oscillations by modulation of its cross-section. In particular, for given initial conditions a modulation may be introduced that will compel string to oscillate on certain (e.g. low) frequency. So, the effect of suppression of high-frequency components of string oscillations may be achieved.

To illustrate this effect the dependencies of the accelerations of the inhomogeneous and homogeneous strings on time are presented in Figure 9 for $\rho S_0/T = 1\text{s}^2/\text{cm}^2, l = 5\text{cm}$, $\alpha = 0.8$ and $k = 16.9\dfrac{\pi}{l}1/\text{cm}$. Initial deflection is the eigenmode of the inhomogeneous string (25), which corresponds to the first eigenfrequency Ω_1.

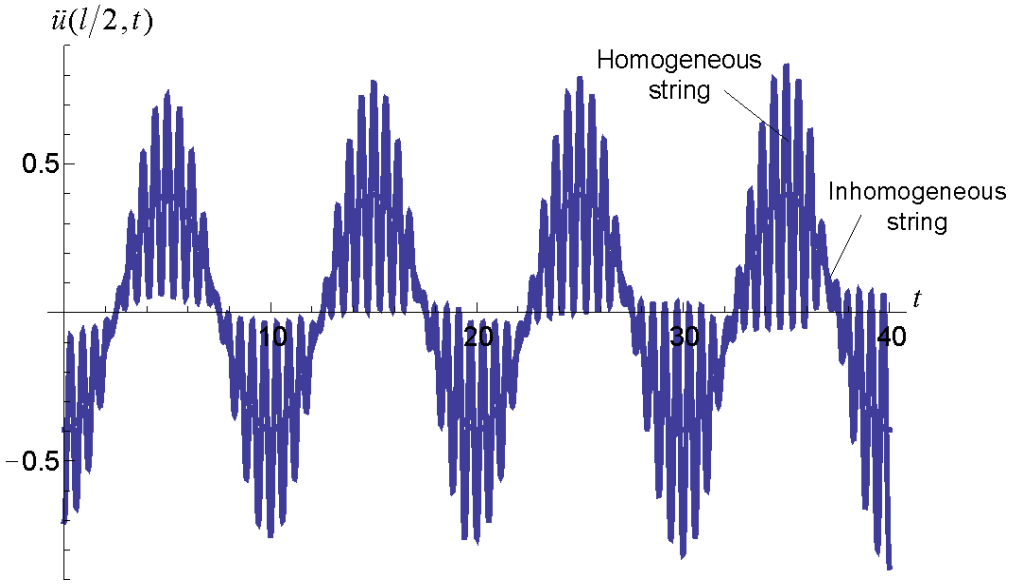


Figure 9: The dependencies of the accelerations of the inhomogeneous and homogeneous strings on time.

As is seen from Figure 9, at considered initial conditions the inhomogeneous string indeed behaves better, than the homogeneous one: there are no high-frequency components, and the amplitude of acceleration is much smaller. Thus, the character of string oscillations may be controlled by modulation of its cross-section, in particular, the effect of high-frequency components suppression may be achieved. This effect, revealed for the considered simple structure, may have various important applications; it may be employed, e.g. to control sound and vibration in spatially periodic systems used in engineering.

9 CONCLUSIONS

In the present paper a new approach for the analysis of oscillations of spatially periodic structures, which is based on the MDSM, is proposed. It is noted that application of the MSM and other classical asymptotic methods for solving the considered equations leads to the erroneous results. The fundamental difference between the MDSM and these methods, which enables to employ the MDSM in the considered case, is revealed. Thereby it is shown that the applicability range of the MDSM is broader than the one of the classical asymptotic methods.

Study of oscillations of a string with variable cross-section is conducted by means of the proposed approach. As the result, analytical expressions for the eigenmodes and the eigenfrequencies of the system are obtained. It is shown that modulation of the string cross-section leads to a change of the eigenfrequencies as compared with their non-modulated values, and to the emergence of a spectrum of additional high eigenfrequencies, which correspond to large wave lengths. A simple physical explanation of the latter effect, which is noted, apparently for the first time, is proposed. It is shown that character of string oscillations may be controlled by modulation of its cross-section, in particular, for given initial conditions the effect of high-frequency components suppression may be achieved.

10 ACKNOWLEDGMENTS

The author is grateful to Professor I.I. Blekhman for specifying the research subject and comments to the paper. Work is carried out with financial support from the Russian Foundation of Fundamental Research (РФФИ), grant 12-08-31136.

REFERENCES

[1] L. Brillouin, *Wave propagation in periodic structures, Second edition*. Dover Publications, 1953.

[2] A.H. Nayfeh, D.T. Mook, *Nonlinear Oscillations*. Wiley-Interscience, 1979.

[3] N.N. Bogoliubov, Y.A. Mitropolski, *Asymptotic Methods in the Theory of Nonlinear Oscillations*. Gordon and Breach, 1961.

[4] N.S. Bakhvalov, G.P. Panasenko, *Homogenization: Averaging Processes in Periodic Media*. Kluwer, 1989.

[5] I.I. Blekhman, *Vibrational Mechanics.* World Scientific, 2000.

[6] I.I. Blekhman, *Selected Topics in Vibrational Mechanics*. World Scientific, 2004.

[7] D.J. Mead, A General Theory of Harmonic Wave Propagation in Linear Periodic Systems with Multiple Coupling. *Journal of Sound and Vibration*, **27**, 235-260, 1973.

[8] D.J. Mead, Wave Propagation in Continuous Periodic Structures: Research Contributions from Southampton. *Journal of Sound and Vibration*, **190** (3), 495-524, 1996.

[9] B.R. Mace, D. Duhamel, M.J. Brennan, L. Hinke, Finite Element Prediction of Wave Motion in Structural Waveguides. *Journal of the Acoustical Society of America*, **117**, 2835–2843, 2005.

[10] G.P. Panasenko, *Multi-Scale Modelling for Structures and Composites*. Springer, 2005.

[11] K.A. Lurie, *Applied Optimal Control Theory of Distributed Systems*. Plenum Press, 1993.

[12] A.D. Pierce, Physical Interpretation of the WKB or Eikonal Approximation for Waves and Vibrations in Inhomogeneous Beams and Plates. *Journal of the Acoustical Society of America*, **48** (1), 275-284, 1970.

[13] V.S. Sorokin, A new approach to the analysis of oscillations of one-dimensional spatially periodic structures. *Journal of Sound and Vibration*, http://dx.doi.org/10.1016/j.jsv.2013.01.037, 2013.

[14] I.I. Blekhman, V.S. Sorokin, On the Separation of Fast and Slow Motions in Mechanical Systems with High-frequency Modulation of the Dissipation Coefficient. *Journal of Sound and Vibration*, **329**, 4936-4949, 2010.

[15] V.S. Sorokin, On Broadening of the Applicability Range of the Method of Direct Separation of Motions. *Proceedings of the 7th European Nonlinear Dynamics Conference (ENOC 2011)*, Rome, Italy, July, 2011.

[16] C.J. Chapman, S.V. Sorokin, The Finite-product Method in the Theory of Waves and Stability. *Proceedings of the Royal Society A: Mathematical, Physical and Engineering Sciences*, **466**, 471-491, 2010.

COMPDYN 2013
4th ECCOMAS Thematic Conference on
Computational Methods in Structural Dynamics and Earthquake Engineering
M. Papadrakakis, V. Papadopoulos, V. Plevris (eds.)
Kos Island, Greece, 12–14 June 2013

ON THE EFFECT OF DAMPING ON DISPERSION CURVES IN PLATES

E. Manconi[1], **S. Sorokin**[2]

[1]Dipartimento di Ingegneria Industriale, Università degli Studi di Parma, Italy
e-mail: elisabetta.manconi@unipr.it

[2] Department of Mechanical and Manufacturing Engineering, University of Aalborg, Denmark
e-mail: svs@m-tech.aau.dk

Keywords: Guided waves, Damping, Viscoelasticity, Dispersion, Finite Element, Rayleigh-Lamb problem.

Abstract. *This paper presents a study on quantitative prediction and understanding of time-harmonic wave characteristics in damped plates. Material dissipation is modelled by using complex-valued velocities of free dilatation and shear waves in an unbounded volume. A Wave Finite Element (WFE) method is used to solve the Rayleigh-Lamb problem for a viscoelastic plate in plain strain, and results are validated using a Finite Product (FP) method. A numerical example concerning a viscoelastic panel is then presented in order to illustrate and discuss the role of dissipation in the cut-off phenomenon and in the phenomenon of veering for dispersion curves. These phenomena are explained in more detail considering a simple model, which allows accurate asymptotic analysis of the perturbation of dispersion curves in the regions of cut-off and veering.*

1 INTRODUCTION

The propagation of waves in plate-like structures has been the subject of a number of studies. Starting from the paper by Lamb in 1917 [1], a lot of effort has been devoted to the analytical, semi-analytical, and numerical prediction of dispersion curves and wave modes up to high frequency. Plates and shells are in fact part, or the main part, of many systems and understanding of guided wave propagation in such structures is fundamental in a number of applications, e.g. shock response, structure-born sound, acoustic emission etc. In particular, theoretical knowledge of dispersive behaviour up to high frequency is of importance in structural health monitoring (SHM) and non-destructive testing (NDT). As an example long-range and short-range ultrasonic guided waves are well established techniques for SHM and material characterisation, e.g. [2, 3]. Understanding of the behaviour of propagating waves modes is thus of direct relevance for better implementation of these techniques. However, many materials and panel constructions (such as metallic panels treated with viscoelastic layers or sandwich panels) show damping which can change the dispersive scenario and attenuate the wave signal, resulting in failure of results prediction and tests if the dissipation is not taken into account in the model.

Only recently the effect of material dissipation on wave propagation characteristics has received attention. The influence of material attenuation on Lamb wave dispersion behavior was investigated analytically in [4]. In this paper it was shown that when the degree of material attenuation is increased, dispersion curves for different modes of the same symmetry can cross instead of veering, which is the typical dispersive behaviour for an elastic plate. Simonetti and Lowe [5] studied shear horizontal wave propagation in elastic plates coated with viscoelastic materials showing the same scenario: compared to non-dissipative structures, real dispersion curve can cross instead of veering if the material attenuation is high enough. In [6] a prediction of energy velocity of attenuative guided waves in plates, together with an experimental validation of some results, was given. In [7] a spectral finite element method (SFEM) was used for modelling wave propagation in viscoleastic plates and evaluating energy velocity and waves attenuation. Comparison between results obtained for an hysteretic and a Kelvin-Voigt viscoelastic model of an orthotropic plate were also presented. In [7] it was also shown that the viscoleastic model has little effect on the phase and energy velocity. In [8] the SFEM was used for studying elastic guided waves in composite viscoelastic plates of different stacking sequences, while in [9, 10] a Wave Finite Element (WFE) method was applied for predicting wave dispersion, wave attenuation, and loss factor in viscoelastic laminated panels.

The aim of this paper is to present a study on quantitative prediction and understanding of wave propagation characteristics in damped plates up to high frequency. In particular Rayleigh-Lamb waves propagating in thick viscoleastic isotropic plate are investigated using an exact method, the Finite Product Method (FPM) [11, 12], and the Wave Finite Element (WFE) method [13, 14, 9]. Compared to other works on the same subject, dispersive behaviour is illustrated and discussed in the complex wavenumber plane and an illustrative example is given to explain and interpret some general features that spatially damped wave modes in plates have, or may have, in common. In the second section of the paper modelling of material losses in terms of complex-valued velocity is discussed. Material properties are obtained from these complex velocities in order to apply the WFE method. In Section 3 the FP method and the WFE method are briefly introduced and reviewed. Section 4 is devoted to numerical results. The propagation of guided waves in a thick viscoleastic plate are interpreted in terms of complex dispersion curves and the main effects of damping are illustrated. It is shown that material losses affect the dispersive behaviour in terms of cut-off frequencies and veering of wavemodes. These are

investigated in section V considering an illustrative model of coupled waveguides, similar to those presented in [15], which allows accurate asymptotic analysis.

2 WAVE PROPAGATION IN DAMPED PLATES.

In damped plates, solving the dispersion relation involves two cases:

a) the real-valued wavenumber and its direction are given and the (complex) frequencies are to be found, that is space-harmonic initial conditions are applied, spatial decay is prevented, and transient vibrations with decaying amplitudes are generated;

b) the real-valued frequency is given and the (complex) wavenumbers are to be found, that is the time-harmonic excitation is considered (time decay is prevented) but spatially attenuating waves are generated.

Thus, according to a) or b) waves are attenuated either in time or in space, respectively. In this work, case b) is considered, that is spatially damped time-harmonic waves are assumed throughout the paper. In particular, for this type of waves, we are concerned with the cut-off and the veering phenomena.

As soon as material losses are accounted for, all wavenumbers become complex-valued. Therefore, the concept of cut-off frequency needs a revision in this context. In a waveguide without damping, the cut-off frequency for a given branch of the dispersion diagram is found from the condition that the imaginary part Im[k] (k is the wavenumber) vanishes, which can occur either when Re[k]$= 0$ or when Re[k]$\neq 0$, where k is the wavenumber. In the 3D space (Ω, Re[k], Im[k]), this corresponds to the sharp turn of the branch onto the Im[k]$= 0$ plane. The presence of damping invalidates this simple definition. In what follows, we identify a cut-off frequency range as the frequency range at which the imaginary part of a wavenumber becomes sufficiently small and, more importantly, its decay rate diminishes and becomes to be "controlled" only by the damping coefficient. For small amounts of damping, the cut-off frequency range is centred at the cut-off frequency for a waveguide without material losses. Veering/mode repulsion is also strongly affected by the presence of material losses. Specifically, in the absence of damping, the veering of propagating waves occurs in the Im[k]$= 0$ plane, whereas in a plate with material losses dispersion curves can avoid intersection in a different manner, as illustrated in this paper.

2.1 Modelling of material losses: complex-valued velocity and material properties.

Modelling material dissipation is a crucial issue and it has been discussed in many studies, e.g. [16]. In modelling the energy dissipation due to viscosity of the material of a waveguide, we adopt the methodology outlined in [17], Vol. II, p. 315, for the linear time-harmonic acoustic waves. We use the complex-valued velocities $c_1 = c_{1r} + \mathrm{i}c_{1i}$ and $c_2 = c_{2r} + \mathrm{i}c_{2i}$ instead of the pure real-valued velocities of dilatation and shear waves. The Young's modulus and Poisson's ratio can thus be obtained as

$$E = \frac{\rho c_2^2\left(3c_1^2 - 4c_2^2\right)}{\left(c_1^2 - c_2^2\right)}; \quad \nu = \frac{\left(c_1^2 - 2c_2^2\right)}{2\left(c_1^2 - c_2^2\right)}. \tag{1}$$

These may be constant or proportional to the frequency and temperature according to the type of damping the analyst is considering.

In what follows the viscoelastic model is used under the assumption that the complex-valued velocities of dilatation and shear waves are frequency independent. Although this is an idealised model, it allows a reasonable and quite general representation of properties of many dissipative materials.

3 The Rayleigh-Lamb problem

In this section the Rayleigh-Lamb problem is solved using a WFE method and FP method. The two methods are briefly described. We consider stationary time-harmonic free waves in an infinitely long straight layer of visco-elastic material with traction-free boundary conditions in plane strain state. The thickness of this layer is h.

3.1 The Wave Finite Element Method

The WFE method is a numerical technique which combines FE analysis and the theory of wave propagation in periodic structures. A detailed description of the method for flat and curved panels can be found in [13, 14] and, for sake of brevity, is not illustrated in details here. The WFE method is a systematic and straightforward approach which combines the theory of wave propagation in periodic structures with conventional FE analysis. As such, it is an application of FE analysis to periodic structures, although in the case considered in this paper the structure is homogeneous in the x and y directions, and hence the periodicity of arbitrary length. Compared to similar methods the WFE approach offers some advantages: (i) typically commercial FE packages can be used to generate the model, (ii) no new elements need to be derived and implemented - as in the the Spectral Finite Element method, (iii) it can be easily applied to 1D and 2D waveguides, and (iv) the computational cost is extremely small. In particular, as also described in [9], using different types of elements and increasing the number of elements meshed through the thickness is a trivial task. This enables the shear distribution to be correctly represented and the energy dissipation to be accurately evaluated, in particular in laminated plates with soft layers or when constrained layer damping treatments are applied. The method has been validated by a number of benchmark cases and it has been seen to provide accurate solutions at small computational cost. In particular viscoelasticity can be straightforwardly included in the WFE formulation in order to predict wave attenuation and the loss factor as shown in [9, 10].

Compared to the 2D formulation in [13], in this paper a 1D formulation (similar to those presented in [18]) is considered. In summary, a section of axial length L is taken from the structure and meshed using a stack of FE elements as indicated in Fig. 1. In this paper, for example, plane elements in plain strain are used, but solid elements or other types of elements can be used. The mass $\mathbf{M}$ and stiffness $\mathbf{K}$ matrices of the FE model are typically found using commercial FE packages. Damping can be included considering viscous matrix $\mathbf{C}$ or structural damping $\mathbf{K} = \mathbf{K}' + \mathrm{i}\mathbf{K}''$ as in this paper, [13, 9]. Therefore FE equation of motion of the section becomes

$$\mathbf{D}\mathbf{q} = \mathbf{f}, \tag{2}$$

where $\mathbf{D} = \mathbf{K} - \omega^2\mathbf{M}$ is the dynamic stiffness matrix of the segment, while $\mathbf{q}$ and $\mathbf{f}$ are the nodal degrees of freedom (DOFs) and nodal forces. The corner's DOFs and nodal forces are then concatenated into sets $\mathbf{q} = [\mathbf{q}_L^{\mathrm{T}}, \mathbf{q}_R^{\mathrm{T}}]^{\mathrm{T}}$ and $\mathbf{f} = [\mathbf{f}_L^{\mathrm{T}}, \mathbf{f}_R^{\mathrm{T}}]^{\mathrm{T}}$ associated with the left L and the right R sides of the segment as shown in Fig. 1, and the FE equations of motion is partitioned into

$$\begin{bmatrix} \mathbf{D}_{LL} & \mathbf{D}_{LR} \\ \mathbf{D}_{RL} & \mathbf{D}_{RR} \end{bmatrix} \begin{bmatrix} \mathbf{q}_L \\ \mathbf{q}_R \end{bmatrix} = \begin{bmatrix} \mathbf{f}_L \\ \mathbf{f}_R \end{bmatrix}. \tag{3}$$

Consider a plane wave propagating in the waveguide according to

$$w(x, y) = We^{\mathrm{i}(-kx+\omega t)}, \tag{4}$$

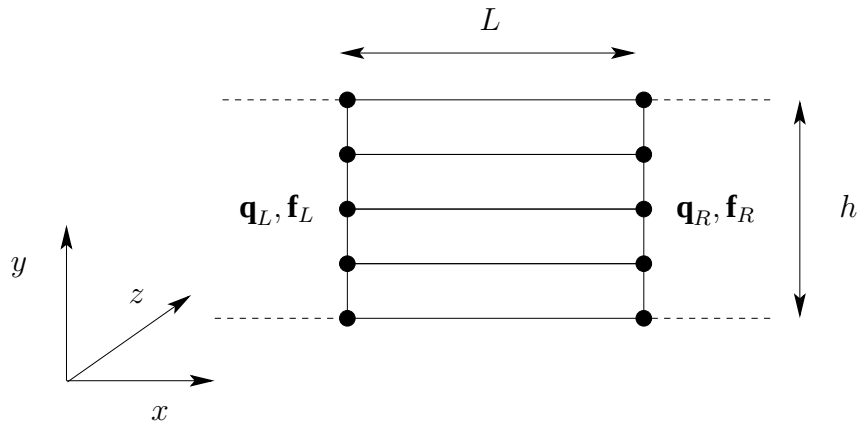


Figure 1: FE model of a section of the waveguide.

where $W(y)$ is the wave mode, ω is the angular frequency and k is the wavenumber. Under the passage of the wave, the nodal DOFs are related by periodicity conditions, [19],

$$\mathbf{q}_R = \lambda \mathbf{q}_L, \tag{5}$$

where $\lambda = e^{-\mathrm{i}kL}$, while equilibrium at the left side of the segment implies

$$[\mathbf{I} \quad \lambda^{-1}\mathbf{I}]\mathbf{f} = \mathbf{0}. \tag{6}$$

The equation of motion of the segment is projected onto the DOFs $\mathbf{q}_L$ using Eqs. (5) and (6), providing a WFE reduced eigenvalue problem whose solutions yield the dispersion curves and the wave mode shapes. For spatially damped waves the real-valued frequency is given and the (complex) wavenumbers are to be found. This involves solving the quadratic polynomial eigenvalue problem in λ

$$[\mathbf{D}_{LR}(\omega)\lambda^2 + (\mathbf{D}_{LL}(\omega) + \mathbf{D}_{RR}(\omega))\lambda + \mathbf{D}_{RL}(\omega)]\mathbf{q}_L = \mathbf{0}, \tag{7}$$

which can be recast as a standard linear eigenvalue problem. Once dispersion curves and wave-modes are obtained, a number of other quantities can be evaluated. For example the forced response can be found straightforwardly, [20, 21].

3.2 Exact Formulation and the Finite Product Method

The standard Lamé decomposition of the displacement field $\mathbf{u} = (u_x, u_y, o)^T$ is employed

$$\mathbf{u} = \nabla \cdot \Phi + \nabla \times \mathbf{i}_z \Psi, \tag{8}$$

where Φ and Ψ are scalar potentials, while $\mathbf{i}_z$ is the unit vector. The potentials Φ and Ψ are governed by the Helmholtz equations (c_1 and c_2 are velocities of dilatation and shear waves, respectively):

$$\nabla^2\Phi + \frac{\omega^2}{c_1^2}\Phi = 0; \quad \nabla^2\Psi + \frac{\omega^2}{c_2^2}\Psi = 0. \tag{9}$$

Due to the symmetry in the boundary conditions at $y = \pm h/2$, the symmetric and skew-symmetric modes are considered independently from each other, and the dispersion equations are:

$$\frac{\tan(q/2)}{\tan(p/2)} = -\frac{4k^2pq}{(q^2-k^2)^2} \tag{10}$$

for symmetric modes, and

$$\frac{\tan(q/2)}{\tan(p/2)} = -\frac{(q^2-k^2)^2}{4k^2pq} \tag{11}$$

for skew-symmetric modes, where $p^2 = \left(\frac{\omega h}{c_1}\right)^2 - k^2$, $q^2 = \left(\frac{\omega h}{c_2}\right)^2 - k^2$. These dispersion equations may be solved by various methods.

In what follows, we apply the FP method. This method was proposed very recently [11, 12], and its fundamental advantage is the absence of spurious roots. The key idea in the FP method for a planar layer is to start with the exact dispersion relations of Rayleigh-Lamb theory, and replace the sine and cosine terms by finite-product polynomials, chosen to have the same roots as the original sines and cosines in a finite region. After this step has been taken, all calculations are performed with polynomials, and the original transcendental dispersion relation is not used again, unless accuracy analysis is required. The dispersion equations are rewritten as follows:

$$L_3^4 S_2 C_1 + K^2 L_1^2 C_2 S_1 = 0 \tag{12}$$

for symmetric modes, and

$$L_3^4 S_1 C_2 + K^2 L_2^2 C_1 S_2 = 0 \tag{13}$$

for skew-symmetric modes. Here $S_i = S(L_i^2/4)$, $C_i = C(L_i^2/4)$, $L_i^2 = \Omega_i^2 - K^2$, $i = 1, 2$ and $L_3^2 = \frac{1}{2}\Omega_2^2 - K^2$, where Ω is the angular frequency. Furthermore, $(K, \Omega_1, \Omega_2) = (kh, \omega h/c_1, \omega h/c_2)$. The functions S and C are defined by $S(s^2) = s^{-1}\sin(s)$ and $C(s^2) = \cos(s)$. The use of S and C, rather than sine and cosine, helps avoid square roots in equations, where the square roots ultimately cancel out in pairs, and so maintains a polynomial form. The finite products are defined as follows:

$$S_{mi} = \prod_{m'=1}^{m}\left(1 - \frac{L_i^2}{4(m'\pi)^2}\right); \quad C_{ni} = \prod_{n'=1}^{n}\left(1 - \frac{L_i^2}{(2n-1)^2\pi)^2}\right); \quad i = 1, 2. \tag{14}$$

If $m = 0$ or $n = 0$, the value of the corresponding finite product is defined as 1. Then the Eqs. (13,12) are approximated by:

$$L_3^4 S_{m2} C_{n1} + K^2 L_1^2 C_{n2} S_{m1} = 0; \quad L_3^4 S_{m1} C_{n2} + K^2 L_2^2 C_{n1} S_{m2} = 0. \tag{15}$$

The dispersion curves presented in the next section (as the reference solution) are obtained by means of the FP method with $m = 13$ and $n = 14$. At this level of approximation, the finite-product results are virtually undistinguishable from the results obtained solving the original transcendental dispersion equations in the considered (k, Ω) windows, while, at the same time, the computational effort to obtain the dispersion diagrams is profoundly less. The polynomial approximations in fact introduce no spurious branches into the dispersion relation, and are ideal for numerical computation. The FP polynomial approximation of dispersion equations is potentially useful for a very wide range of problems in wave theory and stability theory and it is particularly advantageous for calculations of the complex-valued roots.

4 Numerical results and discussion.

In this section numerical results are presented for a $h = 6$ mm thick viscoleastic isotropic plate. The material considered in this numerical example is a high performance polyethylene. Material properties are taken from [6]. In particular it is assumed that complex wave velocity are: $c_1 = 2346.6 - \mathrm{i}99.54$ m s^{-1}, $c_2 = 951 - \mathrm{i}40.31$ m s^{-1}. Material density is $\rho = 953$ kg m^{-3}.

In this example, the WFE model is realized using 150 plane elements (in plane strain) of the type PLANE42 in Ansys. These elements are meshed through the cross sections, see Fig. 1. The length of the element in the x direction is $L = 0.5$ mm. The same value is assumed for the thickness of the element in the y direction. The real valued dispersion curves, which represent propagating waves for the undamped plate and the corresponding real parts of complex wave numbers for the damped plate, are given in Fig. 2(a), while Fig. 2(b) shows the corresponding wave attenuation in the damped plate - notice that the imaginary part of wavenumbers for propagating waves in an undamped plate is zero. Comparison with results obtained using the FP method has shown excellent agreement - dispersion curves obtained using the WFE method and the FP method are indistinguishable. In Fig. 2, for the sake of clarity, only spatially damped waves which propagate in the absence of damping are plotted. Highly attenuated waves with large imaginary parts of wavenumbers are not shown.

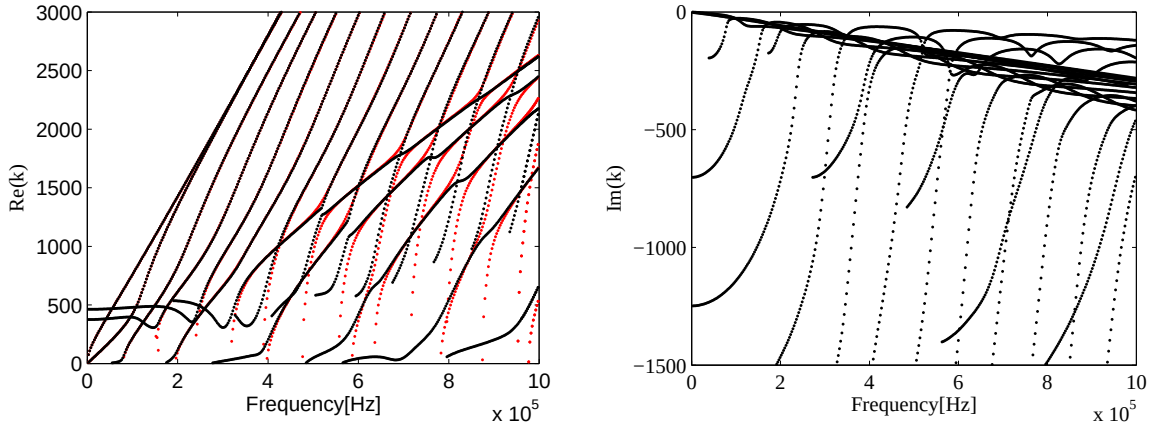


Figure 2: (a) Real valued dispersion curves for the undamped and damped plate; (b) waves attenuation for the damped plate. Black lines: damped case; red lines: undamped case.

Fig. 2 shows that the dispersion curves for the undamped and damped panels differ mainly in terms of cut-off frequencies and veering. The cut-off phenomenon in the complex wavenumber space is illustrated in Fig. 3. Dispersion curves follow two different scenarios for cut-off, which in the absence of damping are: i) dispersion branches cut-off when Re(k)$\neq 0$ but Im(k)$= 0$; ii) dispersion branches cut-off when Re(k)$= 0$ and Im(k)$= 0$. Case i) for the damped plate is shown in Fig. 3(b), (branch 1 and 2). For the sake of clarity only symmetric wave modes are plotted. In the figure negative and positive values of both the real and imaginary part of wavenumbers are plotted in order to highlight some important details of interaction between the branches. Sufficiently far from the "transition zone", branch 1 (plate with damping) is located close to the branch for plate with no damping. In the absence of damping, it can be seen that, as the frequency increases, firstly two complex branches transform into two pure real branches (branches 3 and 4). Then these branches sharply become pure imaginary (branches 5 and 6) and then they transform again into pure real branches (branches 7 and 8). Due to the presence of damping these transitions from pure real to pure imaginary wavenumbers are smoothened, and the damped branches spiral around each other acquiring different imaginary part of the wavenumber (branch 1 and 2). As the frequency grows, branch 1 tends to branch 7. Case ii) is shown in Fig. 3(c). For the sake of clarity only symmetric wave modes are plotted. In the absence of damping, two complex valued branches (branches 10 and 11) become purely imaginary. One of them (branch 12) turns to become two pure real branches (branch

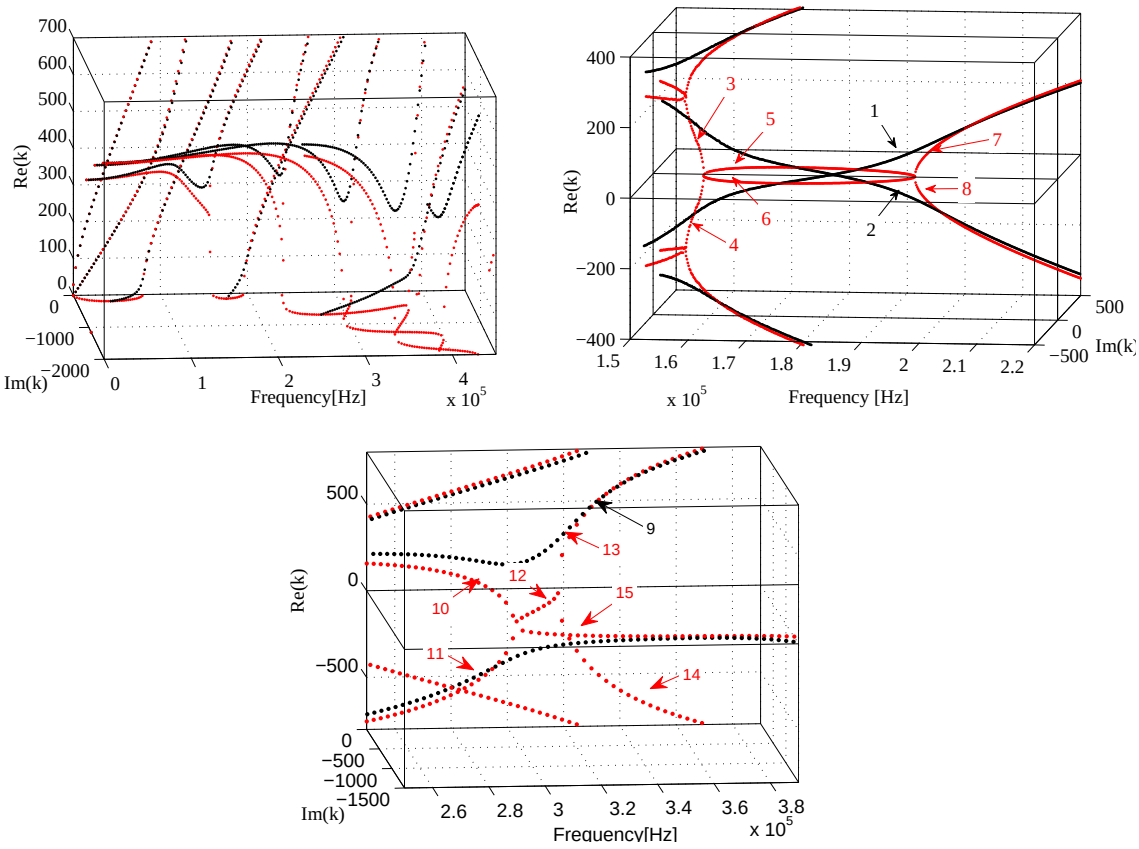


Figure 3: (a) Dispersion curves in the complex wavenumber space; (b) case i) - dispersion curves close to a cut-off frequency; (c) case ii) - dispersion curves (only symmetric waves) close to a cut-off frequency. Black lines: damped case; red lines: undamped case.

13 and branch 14) while the other (branch 15) remains in the imaginary plane until it becomes complex acquiring different signs of the real parts (branches 15 and 16). Again, the presence of damping smoothen the passage between pure real and pure imaginary wavenumbers: as the frequency increases the real and imaginary part of the wavenumber decay up to the real part reaches a minimum in the vicinity of the cut-off frequency of the undamped plate, then the real part grows while the imaginary part stabilises. This phenomenon can readily be captured and quantified in the solution of a simple model problem considered in the next section. In the case of an undamped plate, veering of two branches of the dispersion curves occurs, as seen in Fig. 2(a) and Fig. 4(a). This phenomenon is associated with an exchange of wavemode shapes between these two branches [15]. However, when dissipation is taken into account, curves presenting the frequency dependence of the real parts cross each other instead of veering, as seen in these figures. This behaviour has been noticed by other authors, e.g. [7]. Inspection into spatial location of dispersion curves in the (Ω, Re(k), Im(k)) space reveals that veering still takes place for damped wavemodes, but it occurs in a different manner. This is shown in Fig. 4(b) where dispersion curves are plotted in the complex space in a region close to the frequency around which veering occurs. This phenomenon can readily be captured and quantified in the solution of a simple model problem considered in the next section.

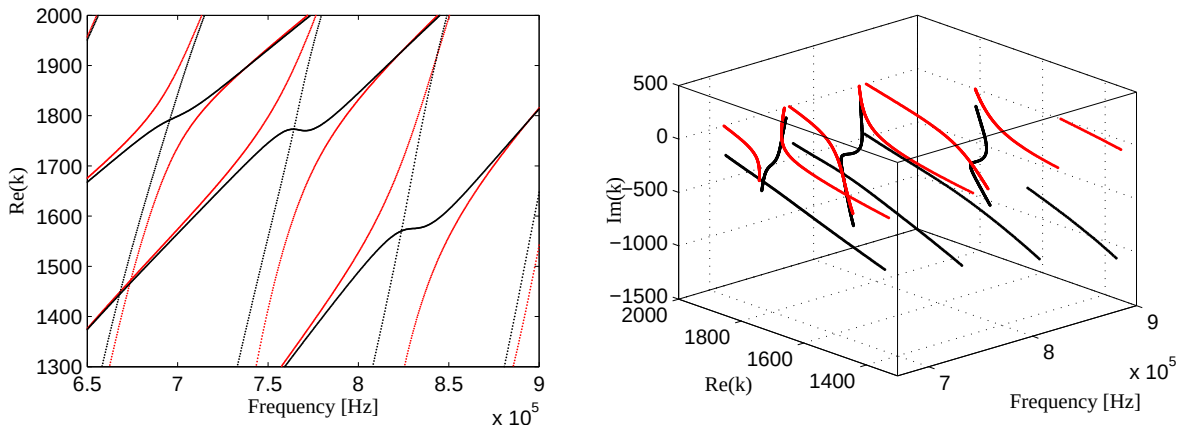


Figure 4: (a) Dispersion curves in a region close to coupling; (b) 3D plot of the complex dispersion curves in a region close to coupling. Black lines: damped case; red lines: undamped case.

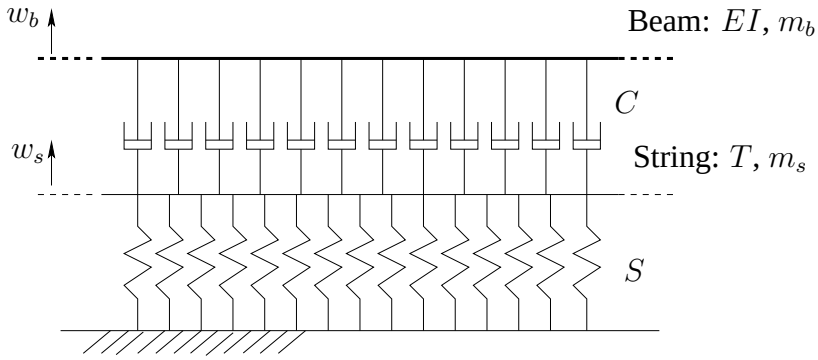


Figure 5: Illustrative example: coupled system.

5 ILLUSTRATIVE EXAMPLE

As it has been shown in the previous section, the material losses change the dispersive scenario. Once the losses are taken into account, the branches of dispersion curves avoid intersection by acquiring different imaginary parts. By these means, the real parts of wave numbers are allowed to be identical, which is impossible for waveguides with no energy dissipation. The presence of damping also features disappearance of cut-off frequencies, since all waves are attenuated at purely real-valued frequencies. These phenomena may be quantified and better understood in the analysis of the wave propagation using the model waveguide similar to the one considered in [15] shown and investigated in the next sections.

5.1 The model waveguide

The model considered in this section consists of a string (membrane) and a beam (plate) coupled as shown in Fig. 5. This is almost the simplest model which allows us to illustrate the veering and cut-off phenomena reported in the previous section. The string is exposed to tension T, it has a mass per unit length m_s and it rests on a Winkler elastic foundation of stiffness S. The beam is characterized by its bending stiffness EI and its mass per unit length m_b. The string is coupled with the beam via locally reacting uniformly distributed dashpot elements with damping coefficient C. The differential equations of motion of this system with respect to

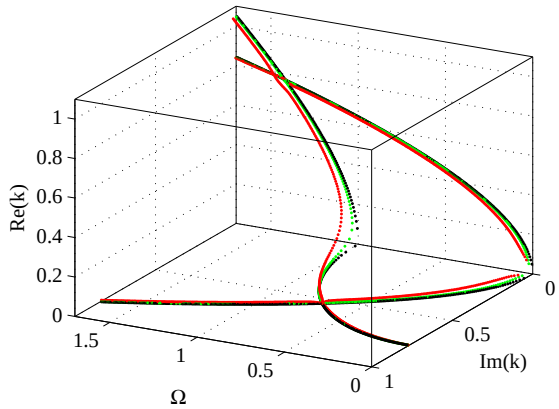


Figure 6: Illustrative example. Dispersion curves. Black lines: $\varepsilon = 0$; green lines: $\varepsilon = 0.01$; red lines: $\varepsilon = 0.05$.

the displacements w_b and w_s are:

$$\begin{gathered} EI\frac{\partial^4 w_b}{\partial x^4} + m_b\frac{\partial^2 w_b}{\partial t^2} + C\left(\frac{\partial w_b}{\partial t} - \frac{\partial w_s}{\partial t}\right) = 0; \\ -T\frac{\partial^2 w_s}{\partial x^2} + Sw_s + m_s\frac{\partial^2 w_s}{\partial t^2} - C\left(\frac{\partial w_b}{\partial t} - \frac{\partial w_s}{\partial t}\right) = 0. \end{gathered} \tag{16}$$

This simple model allows accurate analysis of the perturbations in the location of dispersion curves produced by the purely dissipative coupling elements. Where appropriate, the results of this analysis will be compared with the results obtained for a non-dissipative waveguide, in which spring elements are used instead of dashpots. Solution is sought as $w_b = W_b \exp(\mathrm{i}kx - \mathrm{i}\omega t)$, $w_s = W_s \exp(\mathrm{i}kx - \mathrm{i}\omega t)$. It is convenient to introduce the non-dimensional parameters and write the equations of free propagation of time-harmonic waves as:

$$\begin{gathered} \left(\alpha k^4 - \mathrm{i}\varepsilon\Omega - \delta\Omega^2\right) W_b + \mathrm{i}\varepsilon\Omega W_s = 0; \\ \mathrm{i}\varepsilon\Omega W_s + \left(\beta k^2 + 1 - \mathrm{i}\varepsilon\Omega - \Omega^2\right) W_b = 0. \end{gathered} \tag{17}$$

The notations are: $\Omega^2 = \dfrac{m_s\omega^2}{S}$, $k = k_{dim} r_g$, $\alpha = \dfrac{EI}{Sr_g^2}$, $\beta = \dfrac{T}{Sr_g^2}$, $\delta = \dfrac{m_g}{m_s}$, $\varepsilon = \dfrac{C}{\sqrt{Sm_s}}$, where r_g is the characteristic length scale, say, the gyration radius of the cross-section of a beam. The coupling parameter ε is small, so that classical perturbation methods may be used for the asymptotic analysis. Equating to zero the determinant of the system in Eq. (17) yields the dispersion equation, which is the polynomial of the third order in k^2. It is convenient to introduce the modal coefficient for each wave number, which satisfies the dispersion equation:

$$M = \frac{W_b}{W_s} = -\frac{\alpha k^4 - \mathrm{i}\varepsilon\Omega - \delta\Omega^2}{\mathrm{i}\varepsilon\Omega} = -\frac{\mathrm{i}\varepsilon\Omega}{\beta k^2 + 1 - \mathrm{i}\varepsilon\Omega - \Omega^2}. \tag{18}$$

Since the dispersion equation has the polynomial form, the method of dominant balance as described in [22] is perfectly suitable to find asymptotic formulas for its roots in various regions.

The dispersion diagrams for this waveguide are shown in Fig. 6. The parameters are chosen as $\alpha = 4$, $\beta = 1.4$, $\delta = 0.7$. Black curves are plotted for $\varepsilon = 0$, i.e. in the case of no coupling between a string and a beam. Green curves are plotted for the light damping, $\varepsilon = 0.01$, and red curves are plotted for $\varepsilon = 0.05$. We are interested in the asymptotic analysis of the influence of damping on the location of dispersion curves in the low-frequency $(\Omega \to 0)$ and the cut-off

$(k \to 0)$ limit cases, as well as in the veering zone, not displayed in this diagram. In each case, it is possible to obtain explicit formulas for the wave numbers to the leading order and explore the roles of parameters involved in the problem formulation.

5.2 The cut-off frequencies

The exact dispersion equation for $\varepsilon = 0$ is factorised to yield $k^4 = \frac{\delta\Omega^2}{\alpha}$ (the four branches of dispersion curves for the beam) and $k^2 = \frac{\Omega^2 - 1}{\beta}$ (the two branches of dispersion curves for a string). The asymptotic formulas for the perturbed wave numbers to the leading order are $k^4 = \frac{\delta\Omega^2}{\alpha} + \frac{\mathrm{i}\varepsilon\Omega}{\alpha}$ and $k^2 = \frac{\Omega^2 + \mathrm{i}\varepsilon\Omega - 1}{\beta}$. As seen, the leading order correction to the flexural wave numbers does not contain parameters of the membrane, and, likewise, the leading order correction to the axial wave numbers is independent on the parameters of plate. In the absence of damping, the cut-off frequencies, obviously, are $\Omega^{fl}_{cut-off} = 0$ and $\Omega^{axial}_{cut-off} = 1$. The dispersion diagrams in Fig. 7 are plotted in vicinity of these frequencies for the same three cases as in Fig. 6.

The purely real non-zero cut-off frequencies do not exist for a waveguide with damping, because all wave numbers are complex-valued at any real-valued frequency. In such a waveguide, the wave highly attenuated below cut-off frequency becomes lightly attenuated (only due to the presence of damping) as the frequency exceeds the cut-off value obtained when the damping is set to zero. This aspect was also shown in [5]. In contrast with the model of weak coupling of a string and a beam via distributed spring elements [15], the cut-off frequency for the flexural wave number equals zero. However, its low-frequency (for the fixed damping coefficient) asymptotic behaviour features $k \sim \Omega^{1/4}$, rather than $k \sim \Omega^{1/2}$. This difference is clearly seen in Fig. 7(a). The complex-valued wavenumber for a system with damping departs from the plane Im[k]$= 0$ and it asymptotically tends to this plane as frequency grows. This behaviour differs from the behaviour of dispersion curves for a viscoelastic layer in the vicinity of $\Omega = 0$. When

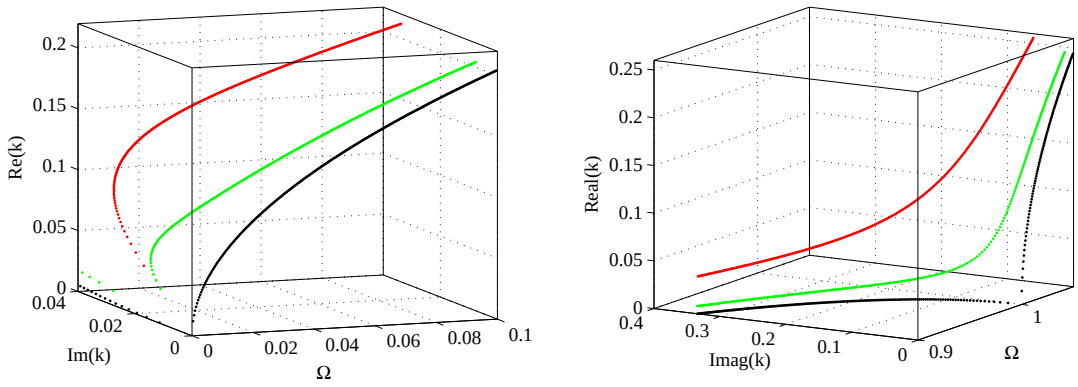


Figure 7: Illustrative example. (a) dispersion diagrams in the vicinity of $\Omega^{fl}_{cut-off} = 0$; (b) dispersion diagrams in the vicinity of $\Omega^{axial}_{cut-off} = 1$. Black lines: $\varepsilon = 0$; green lines: $\varepsilon = 0.01$; red lines: $\varepsilon = 0.05$.

$\varepsilon \neq 0$, it is convenient to determine the wave number of the dominantly axial wave at $\Omega = 1$, i.e. to find how much the dispersion curve is "repelled" from the point $(1, 0, 0)$ in the space of the dispersion diagram. To the leading order, this wave number is given by the formula $k = \sqrt{\frac{\mathrm{i}\varepsilon}{\beta}}$. Comparison of Fig. 3 and Fig. 7(b) shows that the simple model captures the behaviour of

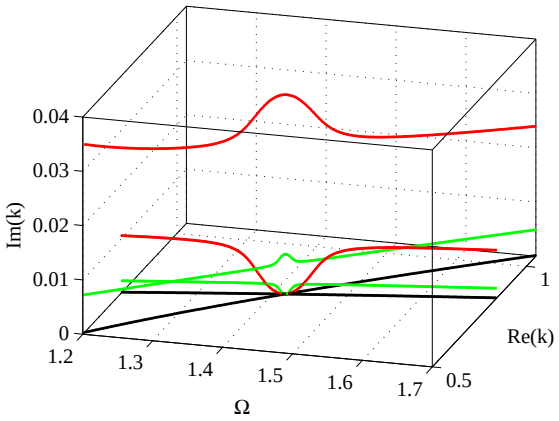


Figure 8: Illustrative example. Dispersion curves. Black lines: $\varepsilon = 0$; green lines: $\varepsilon = 0.01$; red lines: $\varepsilon = 0.05$.

dispersion curve for a viscoelastic layer near the plane Im[k]$= 0$.

5.3 The veering effect

In the case, when $\varepsilon = 0$, dispersion curves cross each other at the "coincidence" frequency $\Omega_c = \sqrt{1 + \frac{\delta\beta^2}{2\alpha} + \frac{\beta\sqrt{4\delta\alpha + \delta^2\beta^2}}{2\alpha}}$. The repeated wave number is $k_c^2 = \frac{\delta\beta}{2\alpha} + \frac{\sqrt{4\delta\alpha + \delta^2\beta^2}}{2\alpha}$. Obviously, the magnitudes of these frequencies and wavenumbers are dependent on all parameters of the waveguide. The dominant balance in the dispersion equation is obtained with the scaling: $\Omega = \Omega_c + \widehat{\Omega}\varepsilon$, $k^2 = k_c^2 + K_2\varepsilon$, $\widehat{\Omega} \sim O(1)$, $K_2 \sim O(1)$. The coefficients $\widehat{\Omega}$ and K_2 have been found in closed analytical form by means of the symbolic manipulator Mathematica 8.0. Dispersion curves shown in Fig. 8 are plotted in the veering zone for the same parameters as in Figs. 6-7. It can be noticed that, compared to the crossing in the (Ω,Re[k]) plane of dispersion curves in the uncoupled waveguide, here the dispersion curves are "repelled" from each other in the direction of Im(k) at the crossing point. This is opposite to the veering in the (Ω,Re[k]) plane which occurs in a waveguide with spring-type coupling elements, see [15].

The dispersion diagram plotted after the asymptotic formulas is compared with the results of direct numerical solution for $\varepsilon = 0.05$. Graphs in Fig. 9 show that these formulas are very accurate in the veering zone. As also seen in Fig. 9, at the "coincidence" frequency, one of the waves becomes purely propagating, whereas its counterpart is more heavily damped, than at other frequencies in the considered range. This effect has a simple physical explanation, which follows from the inspection in the frequency dependence of the modal coefficient shown in Fig. 10. This is the modal coefficient of the wave with the purely real wave number at $\Omega = \Omega_c$. At this frequency, the amplitudes of displacements (and velocities) of both components of the waveguide are the same and they move in phase. It means that the dashpot elements are not activated and the energy is conserved in this wave motion.

5.4 Relevance of the model problem

In a layer of the viscoelastic material considered in the previous section, viscosity influences cut-off frequency and produces veering effect similarly to what seen in the dispersion diagrams in Figs. 3. However, neither magnitude of the imaginary parts of the wave numbers involved in the veering vanishes at $\Omega = \Omega_c$, because each individual mode has its own losses. It is also problematic to identify the sub-waveguides interacting in the visco-elastic layer due to the

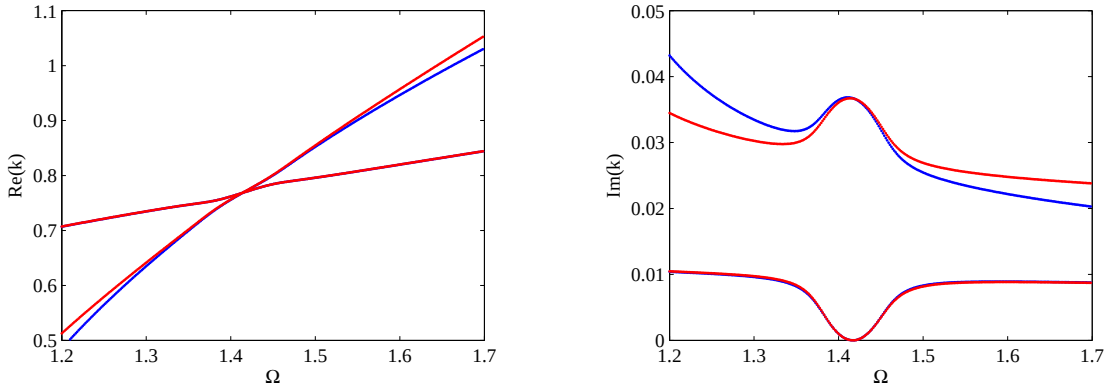


Figure 9: Illustrative example. Dispersion curves in the real and imaginary wavenumber plane, $\varepsilon = 0.05$. Blue lines: numerical solution; red lines: asymptotic solution.

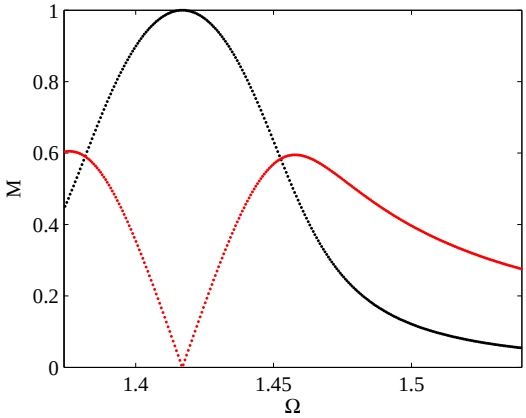


Figure 10: Illustrative example. Modal coefficient. Black lines: Re(M); red lines: Im(M).

energy dissipation as well as the damping coefficient for their coupling. Therefore, the model considered here serves for the qualitative analysis of the damping effects in the waveguides, in particular, in the viscoelastic layer.

6 Conclusion

A study on quantitative prediction and understanding of waveguide properties of viscoelastic plates is presented. A Wave Finite Element (WFE) method is used to solve the Rayleigh-Lamb problem for a viscoelastic plate, and results are validated using a Finite Product (FP) method, with the excellent agreement between these two. It is shown that the material losses affect the location of dispersion curves mainly in the cut-off and veering zones. Two cut-off scenarios in the absence and the presence of damping are identified and compared. In each case, it is shown that the dispersion curves for a plate with damping smoothly follow their counterparts for an undamped plate in 3D space (Ω, Re[k], Im[k]), avoiding sharp turns onto and out of the Im[k]$= 0$ plane. The veering scenarios are also investigated. For damped waves, the curves presenting real parts of complex-valued wavenumbers cross instead of veering (as it occurs for an undamped plate). However, dispersion branches avoid intersection by acquiring different imaginary parts of wavenumbers. An illustrative model of coupled waveguides is also investigated using asymptotic analysis in order to explain and interpret some general characteristics

that spatially damped wave modes have, or may have, in common.

REFERENCES

[1] H. Lamb, On waves in an elastic plate. *Proceedings of the Royal Society of London. Series A*, **93**, 114-128, 1917.

[2] D. E. Chimenti, Guided waves in plates and their use in materials characterization. *Applied Mechanics Reviews*, **50**, 247-284,1997.

[3] P. Wilcox and M. Lowe and P. Cawley, Lamb and SH wave transducer arrays for the inspection of large areas of thick plates. *in D.O Thompson, D.E Chimenti (Eds.), Annual review of progress in quantitative NDE*, **19**, 1049-1056, 2000.

[4] C. W. Chan and P. Cawley, Lamb waves in highly attenuative plastic plates. *Journal of the Acoustical Socitey of America*, **104**, 874-881, 1998.

[5] F. Simonetti and M. Lowe, On the meaning of Lamb mode non-propagating branches. *Journal of the Acoustical Socitey of America*, **118**, 186-192, 2005.

[6] A. Bernard and M. J. S Lowe and M. Deschamps, Guided waves energy velocity in absorbing and non-absorbing plates. *Journal of the Acoustical Socitey of America*, **110**, 186-192, 2001.

[7] I. Bartoli, A. Marzani, F. Lanza di Scalea, E. Viola, Modeling wave propagation in damped waveguides of arbitrary cross-section, *Journal of Sound and Vibration*, **2006**, 685-707, 2006.

[8] L. Taupin, A. Lheémery, G. Inquiété, A detailed study of guided wave propagation in a viscoelastic multilayered anisotropic plate. *Journal of Physics: Conference Series* **269**, 2011.

[9] E. Manconi and B. R. Mace, Estimation of the loss factor of viscoelastic laminated panels from finite element analysis. *Journal of Sound and Vibration*, **329**, 3928-3939, 2010.

[10] E. Manconi, B. R. Mace, R. Garziera, The loss-factor of pre-stressed laminated curved panels and cylinders using a Wave and Finite Element method. *Journal of Sound and Vibration*, **332**, 2013.

[11] C. J. Chapman, S. V. Sorokin, The finite-product method in the theory of waves and stability. *Proceedings of the Royal Society of London. Series A*, **466**, 471-491, 2010.

[12] S. V. Sorokin, C. J. Chapman, 2010. A hierarchy of rational timoshenko dispersion relations. *Journal of Sound and Vibration*, **330**, 5460-5473, 2011.

[13] B. R. Mace, E. Manconi, Modelling wave propagation in two-dimensional structures using finite element analysis. *Journal of Sound and Vibration*, **318**, 884-902, 2008.

[14] E. Manconi, B. R. Mace, Wave characterization of cylindrical and curved panels using a finite element method. *Journal of the Acoustical Socitey of America*, **125**, 154-163, 2009.

[15] B. R. Mace, E. Manconi, Wave motion and dispersion phenomena: veering, locking and strong coupling effects. *Journal of the Acoustical Socitey of America*, **131**, 1015–1028, 2012.

[16] D. J. Jones, Handbook of viscoelastic damping. *John Wiley & Sons, Inc.*, New York, 2001.

[17] L. J. Rayleigh, The Theory of Sound. *Dover*, New York, 1945.

[18] B. Mace, D. Duhamel, M. Brennan, L. Hinke. Finite element prediction of wave motion in structural waveguides. *Journal of the Acoustical Socitey of America*, **117**, 2835-2843, 2005.

[19] L. Brillouin, Wave propagation in periodic structures. *Dover*, New York, 1953.

[20] J. M. Renno, B. R. Mace, Calculating the forced response of two-dimensional homogeneous media using the wave and finite element method. *Journal of Sound and Vibration*. **329**, 5474-5488, 2010.

[21] J. M. Renno, B. R. Mace. Calculating the forced response of two-dimensional homogeneous media using the wave and finite element method. *Journal of Sound and Vibration*. **330**, 5913-5927, 2011.

[22] E. J. Hinch, Perturbation Methods. *Cambridge University Press*, 1991.

COMPDYN 2013
4th ECCOMAS Thematic Conference on
Computational Methods in Structural Dynamics and Earthquake Engineering
M. Papadrakakis, V. Papadopoulos, V. Plevris (eds.)
Kos Island, Greece, 12–14 June 2013

INFINTE PERIODIC STRUCTURE OF LIGHTWEIGHT ELEMENTS: REPRESENTATION OF WAVE PROPAGATION

Parthkumar G. Domadiya[1], Lars V. Andersen[1], and Sergey V. Sorokin[2]

[1] Aalborg University
Department of Civil Engineering, Sohngaardsholmsvej 57
DK-9000 Aalborg, Denmark
e-mail: pdg@civil.aau.dk, la@civil.aau.dk

[2] Aalborg University
Department of Mechanical and Manufacturing Engineering, Pontoppidanstræde 103
DK-9220 Aalborg East, Denmark
e-mail: svs@me.aau.dk

Keywords: Lightweight structure, periodicity, Finite element analysis, bending waves, Timoshenko beam, Euler-Bernoulli beam.

Abstract. *Lightweight wooden structures have become more popular as a sustainable, environmental-friendly and cost-effective alternative to concrete, steel and masonry buildings. However, there are certain drawbacks regarding noise and vibration due to the smaller weight and stiffness of wooden buildings. Furthermore, lightweight building elements are typically periodic structures that behave as filters for sound propagation within certain frequency ranges (stop bands), thus only allowing transmission within the pass bands. Hence, traditional methods based on statistical energy analysis cannot be used for proper dynamic assessment of lightweight buildings. Instead, this paper discusses and compares the use of finite element analysis and a wave approach based on Floquet theory.*

The present analysis has focus on the effect of periodicity on vibration transmission within semi-infinite beam structures. Two models of a semi-infinite Euler-Bernoulli and Timoshenko beam structure with periodic variation of the cross-sectional properties are analyzed. In case of the Euler-Bernoulli beam, vibrational behavior is studied in two dimensions by finite element analysis and Floquet theory. Wave propagation within the two-dimensional periodic Timoshenko beam structure is studied with a finite-element approach and compared with the periodic Euler-Bernoulli beam. The computations are carried out in frequency domain with the load acting as an impact load at the end of a semi-infinite beam. Results of various beam models and analytical approaches are compared and analyzed. A vibration-level distribution and propagation characteristics within the beam are presented for excitation frequencies up to 2 kHz.

1 INTRODUCTION

In recent years, simplifying the design of wooden building structures with adjusting the spacing between ribs and plates, research on formulate them into lightweight has increased. Infinite periodicity has been used as an advantage in process of analyzing the wave transmission phenomena of various panel structures. However, it is a challenge to predict the wave propagation in lightweight building systems due to their design and geometrical complexities.

Wave propagation within periodic structures deals with stop bands where no propagation occurs and pass bands where propagation occurs within certain frequency ranges. Several efforts to study and analyze periodic structures can be found [1, 2, 3, and 4]. Theoretical modelling of the sound transmission loss through double-leaf lightweight partitions stiffened with periodically placed studs was studied by Wang, Lu, Woodhouse, Langley, and Evans [5], who established analytical model for sound transmission through double-leaf partitions to understand the physics involved and allow future work like optimization of partition design for better sound insulation. Mace, Duhamel, Brennan and Hinke [6] also predicted wave transmission in one-dimensional structural waveguides using the finite-element method. The method is seen to yield accurate results for the wavenumbers and group velocities of both propagating and evanescent waves. Finite element analysis of the vibrations of waveguides and periodic structures was done by Duhamel, Mace and Brennan [7] where it was concluded that, point force responses for beams and plates showed the accuracy of the wave finite element approach when the size of the cell is small compared to a wavelength.

Floquet theory has been used by several researchers [8, 9, 10 and 11] to evaluate sound transmission behavior within periodic structures analytically. A periodic structure model using Timoshenko beam theory developed by Heckl could carry compressional waves, torsional waves, horizontal bending waves and vertical bending waves. It was shown that, if a single wave type was present on the beam, its dispersion relation spectrum showed a clear passing/stopping band behavior [12]. Vibrations of Timoshenko beams by variable order finite elements were studied by Houmet and concluded, advantage of this element is that highly accurate frequencies for Timoshenko beams can be obtained with a small number of system degrees of freedom [13].

Wave propagation within a one-dimensional periodic bar and two dimensional beam structures has been studied previously by the authors of the present paper, finding a good correlation between the results obtained by the FEM and Floquet theory [14]. Extensive efforts have been presented to study the problems of wave propagation in periodic structures. Concerning the calculation of wave propagation from one end to another end, three approaches are taken into account: Finite element method (FEM) for Timoshenko and Euler-Bernoulli beam and Floquet theory (Euler-Bernoulli beam).

The paper focuses on flexural wave transmission within a periodic beam structure which is made from Plexiglas and steel. The cross-sectional area is the same along the entire beam structure for the Timoshenko and Euler-Bernoulli beam. Transmitting boundary conditions [15] are introduced to mimic the behavior of a semi-infinite beam structure consisting of material 1, i.e. Plexiglas. The analyses concern the dynamic response of the beam structure to a harmonically varying concentrated force. Pass bands and stop bands that occur due to the periodic nature of the structures are identified in the frequency range 0 to 2 kHz using FEM for both of the beam structure and Floquet theory (Euler-Bernoulli beam). Results from the FE method and Floquet theory are compared and analyzed. Wave propagation behavior using FE method for Euler-Bernoulli and Timoshenko is also examined between 0 to 2 kHz.

2 PROBLEM OVERVIEW

Lightweight building structures are often constructed as panels with plates on beam (stud or joist frames). In the present case, an infinite periodic beam structure has been taken into consideration to study the occurrence of stop bands during various analytical methods like Euler-Bernoulli, Floquet theory, Timoshenko beam theory.

The structure consists of two different materials connected with each other in a periodic manner. The aim of the study is to investigate the wave propagation throughout the beam structure within various ranges of frequencies to predict the effect of periodicity on vibration transmission. Analyses are carried out in frequency domain using finite-element analysis (Euler-Bernoulli, Timoshenko beam theory and Floquet theory). Results from the methods are compared and investigated thoroughly.

2.1 Model geometry and material properties

The two-dimensional beam structure consists of a number of identical cells, each consisting of two materials: Plexiglas and steel. The Plexiglas part and steel part lengths, widths and heights are $0.3 \times 0.03 \times 0.012$ m^3 and $0.05 \times 0.03 \times 0.012$ m^3, respectively. Hence, the two material segments have identical cross-sectional areas throughout the beam structure. The material properties are:

- Material 1 (Plexiglas): Young's modulus, $E_1 = 3.4$ GPa; mass density, $\rho_1 = 1190$ kg/m^3;
- Material 2 (Steel): Young's modulus, $E_2 = 200$ GPa; mass density, $\rho_2 = 7850$ kg/m^3.

3 THEORTICAL FORMULATION

3.1 Euler-Bernoulli finite element formulation

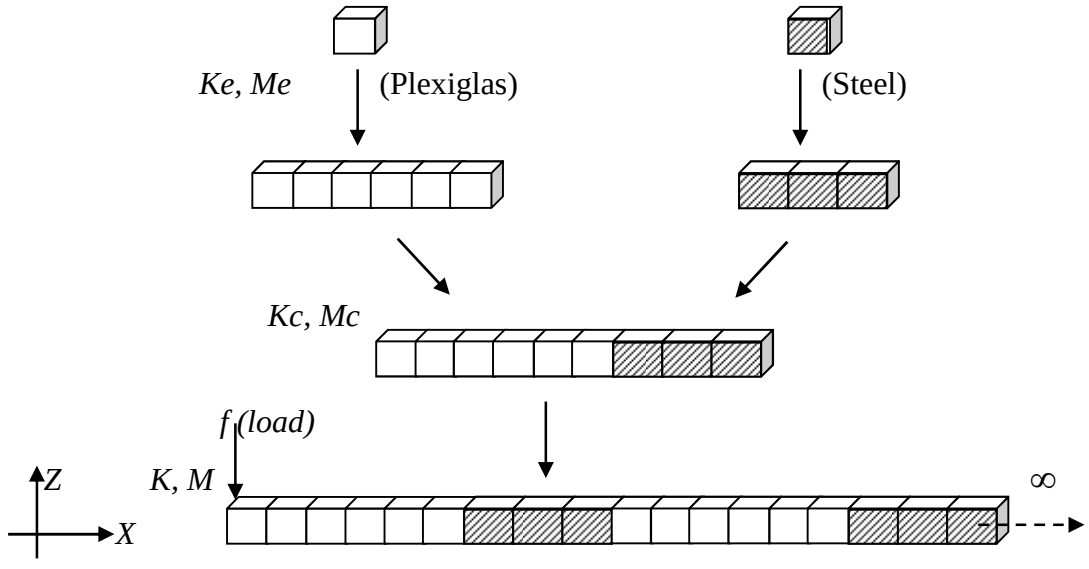


Figure 1: Formation of semi-infinite beam structure using the FEM approach;
Ke, Me = Stiffness and Mass element matrices;
Kc, Mc = Stiffness and Mass cell matrices;
K, M = Stiffness and Mass system matrices.

A semi-infinite beam structure is constructed from Plexiglas$_1$ and Steel$_2$ segments using a finite-element (FE) model. Each of the segments is specified by the following parameters: the segment length l_j, the bending stiffness E_jI_j, the mass density ρ_j, and the cross-sectional area A_j, j = 1, 2. Further, ω is introduced as the circular frequency. An FE code is generated based on the governing equations of motion for linear elastic wave propagation in an Euler-Bernoulli beam undergoing bending vibrations and finite elements with two nodes and two degrees of freedom at each node, i.e. displacement and rotation, and correspondingly two nodal forces, i.e. shear force and bending moment. No forces are applied over the infinite beam structure. The waves form a pair of propagating waves and a pair of evanescent waves at each element. The possible wavenumbers for Plexiglas and steel segments are $\pm k_{b(j)}$, $\pm ik_{b(j)}$, where,

$$k_{b(j)} = \sqrt[4]{\frac{\rho_j A_j \omega^2}{E_j I_j}}, \; j = 1, 2. \tag{1}$$

Figure 1 shows the complete formation of the semi-infinite beam structure. Firstly, the stiffness and mass matrices for the Plexiglas and steel elements are constructed:

$$K_{e(j)} = \frac{2E_jI_j}{l_{e(j)}^3} \begin{bmatrix} 6 & 3l_{e(j)} & -6 & 3l_{e(j)} \\ 3l_{e(j)} & 2l_{e(j)}^2 & -3l_{e(j)} & 2l_{e(j)}^2 \\ -12 & -6l_{e(j)} & 12 & -6l_{e(j)} \\ 6l_{e(j)} & 2l_{e(j)}^2 & -6l_{e(j)} & 4l_{e(j)}^2 \end{bmatrix}, \quad j = 1, 2 \tag{2}$$

$$M_{e(j)} = \frac{\rho_j A_j l_{e(j)}}{420} \begin{bmatrix} 156 & 22l_{e(j)} & 54 & -13l_{e(j)} \\ 22l_{e(j)} & 4l_{e(j)}^2 & 13l_{e(j)} & -3l_{e(j)}^2 \\ 54 & 13l_{e(j)} & 156 & -22l_{e(j)} \\ -13l_{e(j)} & -3l_{e(j)}^2 & -22l_{e(j)} & 4l_{e(j)}^2 \end{bmatrix}, \quad j = 1, 2 \tag{3}$$

Here $l_{e(j)}$ denotes the length of a finite element consisting of material j. The matrices defined by Eqns. (2) and (3) are coupled (i.e. assembled) into one single cell. Secondly, the system matrices are formulated by assembling a number of cell matrices.

3.2 Timoshenko finite element formulation

A semi-infinite Timoshenko beam structure is constructed from Plexiglas1 and steel2 segments using a finite-element (FE) model with the same parameters as the previous Euler-Bernoulli beam. Each of the segments is specified by the following parameters: the segment length $l_{e(j)}$, the bending stiffness E_jI_j, the mass density ρ_j, and the cross-sectional area A_j, shear cross sectional area A_s, phase velocity for longitudinal waves and shear waves c_j^l and c_j^f, frequency ω, shear modulus G_j, radius of gyration r_j, shear coefficient κ; j = 1, 2.

FE code is generated based on the governing equations of motion for linear elastic wave propagation in constant cross sectional beam where shear deformation and rotational inertia effects are taken into account. Each finite element has two nodes and two degrees of freedom at each node, i.e. displacement and rotation, and correspondingly two nodal forces, i.e. shear force and bending moment. The possible wavenumbers for Plexiglas and steel segments are:

$$k_{n(j)} = \pm \sqrt{\frac{1}{2}\left(\frac{\omega^2}{\left(c_j^l\right)^2}+\frac{\omega^2}{\left(c_j^f\right)^2}\right) \pm \frac{1}{2}\left(\frac{\omega^2}{\left(c_j^l\right)^2}-\frac{\omega^2}{\left(c_j^f\right)^2}\right)\sqrt{1+a_j}} \quad , j = 1, 2 \tag{4}$$

Where,

$$a_j = \frac{\left(4\left(c_j^l\right)^2\cdot\left(c_j^f\right)^4\right)}{\left(r_j\right)^2\cdot\omega^2\cdot\left(\left(c_j^l\right)^2-\left(c_j^f\right)^2\right)^2}, \quad c_j^l = \sqrt{\frac{E_j}{\rho_j}}, \quad c_j^f = \sqrt{\frac{A_{s_j} G_j}{\rho_j A_j}}, \quad A_{s_j} = \left(\frac{6}{5}\right)A_j, j = 1, 2. \tag{5}$$

Stiffness matrices $K_{e(j)}$ are obtained by deliberating the exact static solution of an element with forces and moments applied at the two nodes and then consistent mass matrix $M_{e(j)}$ are derived. The stiffness matrix formulation is shown below,

$$K_{e(j)} = \frac{2EI_j}{l_{e(j)}^3\left(1+\phi_j\right)}\begin{bmatrix} 12 & 6l_{e(j)} & -12 & 6l_{e(j)} \\ 6l_{e(j)} & l_{e(j)}^2\left(4+\phi_j\right) & -6l_{e(j)} & l_{e(j)}^2\left(2-\phi_j\right) \\ -12 & -6l_{e(j)} & 12 & -6l_{e(j)} \\ 6l_{e(j)} & l_{e(j)}^2\left(2-\phi_j\right) & -6l_{e(j)} & l_{e(j)}^2\left(4+\phi_j\right) \end{bmatrix}, j = 1, 2 \tag{6}$$

where ϕ is the dimensionless number

$$\phi_{(j)} = \frac{12EI_j}{G_j\kappa_j A_j l_{e(j)}^2} \quad , j = 1, 2 \tag{7}$$

The mass matrix formulation is shown below,

$$M_{e(j)} = \frac{\rho_j A_j l_{e(j)}}{\left(1+\phi_j\right)^2}\begin{bmatrix} m_1 & m_2 & m_3 & m_4 \\ m_2 & m_5 & -m_4 & m_6 \\ m_3 & -m_4 & m_1 & -m_2 \\ m_4 & m_6 & -m_2 & m_5 \end{bmatrix}_j + \frac{\rho_j A_j l_{e(j)}}{\left(1+\phi_j\right)^2}\left(\frac{r_j}{l_{e(j)}}\right)^2\begin{bmatrix} m_7 & m_8 & -m_7 & m_8 \\ m_8 & m_9 & -m_8 & m_{10} \\ -m_7 & -m_8 & m_7 & -m_8 \\ m_8 & m_{10} & -m_8 & m_9 \end{bmatrix}_j, j = 1, 2 \tag{8}$$

$$m_{1(j)} = \frac{13}{35}+\frac{7\phi_j}{10}+\frac{\phi_j^2}{3}, \qquad m_{2(j)} = \left(\frac{11}{210}+\frac{11\phi_j}{120}+\frac{\phi_j^2}{24}\right)l_e \tag{9a}$$

$$m_{3(j)} = \frac{9}{70}+\frac{3\phi_j}{10}+\frac{\phi_j^2}{6}, \qquad m_{4(j)} = -\left(\frac{13}{420}+\frac{3\phi_j}{40}+\frac{\phi_j^2}{24}\right)l_e \tag{9b}$$

$$m_{5(j)} = \left(\frac{1}{105}+\frac{\phi_j}{60}+\frac{\phi_j^2}{120}\right)l_e^2, \qquad m_{6(j)} = \left(\frac{1}{140}+\frac{\phi_j}{60}+\frac{\phi_j^2}{120}\right)l_e^2 \tag{9c}$$

$$m_{7(j)} = \frac{6}{5}, \qquad m_{8(j)} = \left(\frac{1}{10}-\frac{\phi_j}{2}\right)l_e \tag{9d}$$

$$m_{9(j)} = \left(\frac{2}{15}+\frac{\phi_j}{6}+\frac{\phi_j^2}{3}\right)l_e^2, \qquad m_{10(j)} = \left(-\frac{1}{30}-\frac{\phi_j}{6}+\frac{\phi_j^2}{6}\right)l_e^2 \tag{9e}$$

The matrices defined by Eqns. (6) and (8) are coupled (i.e. assembled) into one single cell and the system matrices are formulated by assembling a number of cell matrices.

To study the effects of periodicity in the both of the beam structures (i.e. Euler-Bernoulli beam and Timoshenko beam), 10 cells are coupled in periodic manner as shown in Figure 1. The problem is solved in the frequency domain at the discrete frequencies 0.1, 0.2, …, 2 kHz. At one end of the periodic structure, a nodal force with unit magnitude is applied. At the other end, a transmitting boundary condition is introduced to mimic the behavior of a semi-infinite beam structure consisting of material 1, i.e. Plexiglas.

The element length is adjusted to provide a minimum of ten elements per wavelength at the higher frequency, which provides a very high accuracy given that cubic interpolation of the displacement field is applied. The goal is to predict the characteristics of flanking noise transmission along the beam for flexural motion at each individual frequency. The Euler Bernoulli FE beam results are compared with the propagation characteristics predicted by Floquet theory for an infinite periodic structure. Comparisons between Euler-Bernoulli-beam and Timoshenko-beam FE results are presented.

3.3 Floquet theory for an Euler-Bernoulli beam

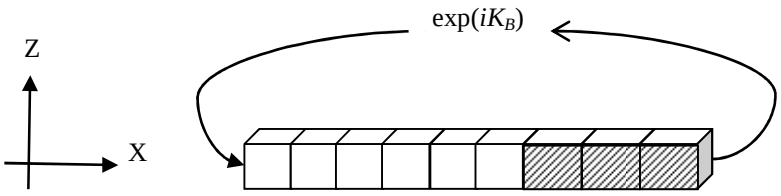


Figure 2: Formation of beam structure using Floquet theory.

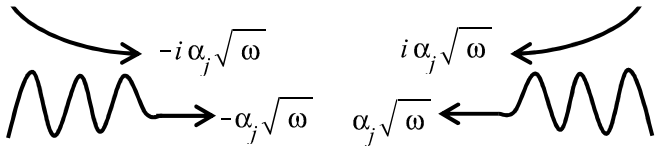


Figure 3: Illustrations of propagating and evanescent waves in a beam structure.

Prediction of wave motion within periodic structures can be done using Floquet theory for the Euler-Bernoulli beam, which eliminates the need to formulate the transfer matrices for the periodic elements. In the present case, the infinite periodic beam is constructed by a periodic repetition of two different segments composed of Plexiglas and Steel, respectively. Each of the segments is specified by the exact same parameters as used in the FEM Euler-Bernoulli model to compare the results from the two different approaches. Thus, the mass per unit length becomes $\mu_j=\rho_j A_j$, and the bending wave velocities are given as

$$c_j = \frac{\omega}{k_j} \Rightarrow c_j = \sqrt{\omega_j}\sqrt[4]{\frac{EI_j}{\rho_j A_j}}, \; j = 1, 2. \tag{10}$$

Floquet theory is applied to the case of bending waves. In frequency domain, the governing equations for flexural waves are fourth order ordinary differential equations for the lateral displacements, $u_1(x)$ and $u_2(x)$, respectively, in the z direction, cf. Figure 2,

$$E_1 \mathrm{I}_1 \left(\frac{\mathrm{d}^4}{\mathrm{d}x^4} u_1(x) \right) - \mu_1 \omega^2 u_1 = 0 , \tag{11a}$$

$$E_2 \mathrm{I}_2 \left(\frac{\mathrm{d}^4}{\mathrm{d}x^4} u_2(x) \right) - \mu_2 \omega^2 u_2 = 0 , \tag{11b}$$

General solutions of these equations are displacements in the form:

$$u_1(\mathrm{x}) = \sum_{n=1}^{4} a_{n,1} \exp\left(ik_{n,1}\mathrm{x}\right) \tag{12a}$$

$$u_2(\mathrm{x}) = \sum_{n=1}^{4} a_{n,2} \exp\left(ik_{n,2}\mathrm{x}\right) \tag{12b}$$

The wavenumbers for propagating waves and evanescent waves are expressed via the frequency parameter. With reference to the illustration of wave directions in Figure 3,

- the term $-\alpha_j\sqrt{\omega}$ is for the waves propagating in the positive direction,
- the term $-i\alpha_j\sqrt{\omega}$ is for the evanescent waves going in the positive direction,
- the term $\alpha_j\sqrt{\omega}$ is for the waves propagating in the negative direction,
- the term $i\alpha_j\sqrt{\omega}$ is for the evanescent waves going in the negative direction.

The wavenumbers are:

$$\begin{aligned} k_{1,1} &= \alpha_1\sqrt{\omega} , & k_{2,1} &= -\alpha_1\sqrt{\omega} , \\ k_{3,1} &= i\,\alpha_1\sqrt{\omega} , & k_{4,1} &= -i\,\alpha_1\sqrt{\omega} , \\ k_{1,2} &= \alpha_2\sqrt{\omega} , & k_{2,2} &= -\alpha_2\sqrt{\omega} , \\ k_{3,2} &= i\,\alpha_2\sqrt{\omega} , & k_{4,2} &= -i\,\alpha_2\sqrt{\omega} , \end{aligned} \tag{13}$$

where,

$$\alpha_j = \sqrt{\frac{\rho_j A_j}{E_j I_j}} , j = 1, 2. \tag{14}$$

Matching conditions at the start of one cell in the periodic beam can be defined as:

$$u_1(0) = u_2(0) , \qquad u_1'(0) = u_2'(0) , \tag{15a}$$

$$E_1 \cdot I_1 \cdot u_1''(0) = E_2 \cdot I_2 \cdot u_2''(0) , \qquad E_1 \cdot I_1 \cdot u_1'''(0) = E_2 \cdot I_2 \cdot u_2'''(0) , \tag{15b}$$

$$u_1(l_2) = u_2(l_2) , \qquad u_1'(l_2) = u_2'(l_2) , \tag{15c}$$

$$E_1 \cdot I_1 \cdot u_1''(l_2) = E_2 \cdot I_2 \cdot u_2''(l_2) , \qquad E_1 \cdot I_1 \cdot u_1'''(l_2) = E_2 \cdot I_2 \cdot u_2'''(l_2) . \tag{15d}$$

Floquet theory is now used to formulate the periodicity conditions (see Fig. 2):

$$u_1(l_2) = \exp\left(i \cdot K_B\right) \cdot u_1(-l_1) , \tag{16a}$$

$$u_1'(l_2) = \exp\left(i \cdot K_B\right) \cdot u_1'(-l_1) , \tag{16b}$$

$$u_1''(l_2) = \exp(i \cdot K_B) \cdot u_1''(-l_1) \ , \tag{16c}$$

$$u_1'''(l_2) = \exp(i \cdot K_B) \cdot u_1'''(-l_1) \ , \tag{16d}$$

These periodicity conditions are substituted into Equation (15), and a system of eight homogeneous equations with respect to eight modal amplitudes grouped in two sets, $A_{n,j}$, n = 1, 2, 3, 4, and j = 1, 2, is derived. This set of equations is solved for each circular frequency, ω, with respect to the Bloch parameter K_B, which is a standard variable in the subject. K_B provides the phase shift in a periodic wave guide at a given frequency. As derived from Floquet theory, if all roots of the characteristic equation are complex numbered, then at a given frequency no propagating waves exist in the periodic beam. Hence, wave propagation in the periodic structure is possible only when the characteristic equation has at least one purely real root K_B for a given frequency, ω. Introducing $\lambda = \exp(-iK_B)$, it means when $|\lambda| \neq 1$ for all roots of the characteristic equation, the frequency falls into a stop band and vibration transmission within the beam is not possible. On the other hand, vibration transmission (i.e. a pass band) is characterized by $|\lambda| = 1$.

4 PREDICTION OF TRANSMISSION LOSS

The transmission loss (TL) for the infinite beam structure is evaluated from the nodal displacements within the frequency range 0 to 2 kHz using the finite-element method using Timoshenko and Euler-Bernoulli beam theory and Floquet theory for the Euler-Bernoulli beam. To get a better, more detailed visualization of the wave propagation properties within the frequency range, three plots are made—one for each 2 kHz frequency range (see Figure 4) where results between FE analyses for the Euler-Bernoulli beam and the Floquet approach are compared. In case of Figure 5, a detailed visualization of wave propagation within low frequency range till 100 Hz obtained by the FE method for Timoshenko and Euler-Bernoulli beams is represented, while results for higher range frequencies are visualized for an FE beam approach for both of the beam theories in Figure 6.

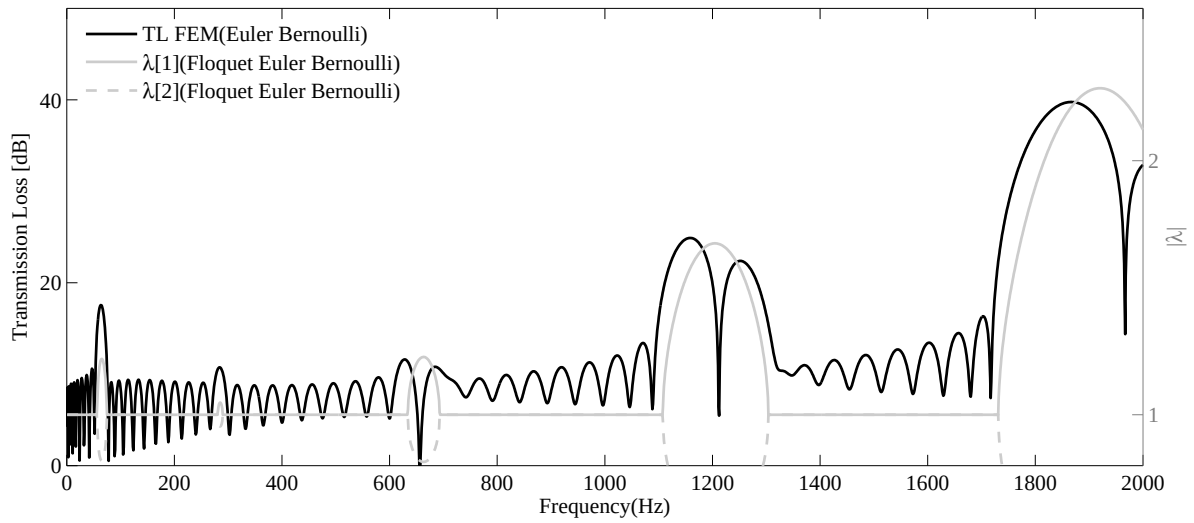


Figure 4: Transmission Loss (TL) in infinite Euler Bernoulli periodic beam structure (FEM) and Bloch parameter ($\lambda = \exp(iK_B)$ – Floquet theory) within the 0 to 2 kHz frequency range.
Note: Different scales on the left and right ordinate axis.

The frequency bands with high transmission loss (TL) broaden with increasing frequency as it is seen in Figure 4. Thus, peaks in the transmission loss are repeated periodically along the frequency axis, and the width of these peaks extends with increasing frequency.

It is furthermore observed that resonance within the pass bands does not lead to infinite (or nearly-infinite) response in the finite-element model. This is a result of the impedance condition introduced in order to mimic the behavior of a semi-infinite beam structure made of Material 1 (Plexiglas). No material damping is introduced in the finite-element model, but the transmitting boundary condition radiates energy into the semi-infinite beam at the end of 10th cell.

Vibration transmission within the infinite beam structure is also calculated using Floquet theory. As a results from this approach, a total of four parameters, $\lambda_n = \exp(-iK_B)$, n =1, 2, 3, 4, (two for bending waves and two for evanescent waves, K_B is the Bloch parameter) are deduced. Values of λ are very high for evanescent waves going in the positive x direction and very low for the corresponding components going in the negative x direction, which shows that the evanescent waves are highly damped. Therefore, these wave components will not provide any transmission of energy along the structure, whether or not it is periodic. Hence, the values of λ for the evanescent waves are not shown in the paper.

Figure 4 shows the results for bending wave propagation in terms of the parameter $\lambda = \exp(-iK_B)$ for the infinite beam in the frequency range from 0 to 2 kHz. Figure 4 shows that pass bands and stop bands can be easily observed in the low-frequency range—even below 100 Hz and the lengths of stop bands increase with increased frequency. It is noted that $|\lambda_1| = 1$ and $|\lambda_2| = 1$ within the pass bands, i.e. waves can propagate in the negative x direction as well as the positive x direction. Propagating waves are suppressed when all $|\lambda_n| \neq 1$, n =1, 2, 3, 4, and by inspection of Figures 4, it can be seen that the stop bands and pass bands equally cover the frequency spectrum from 0 to 2 kHz.

Figure 4 provides a comparison for the evaluation of vibration transmission within the beam structure using the finite-element method (10-cell structure) and the Floquet approach. The two approaches are highly correlated in the sense that stop bands and pass bands appear in the same range of frequencies for both methods. The range of stop band frequencies are 55 Hz to 75 Hz, 280 to 290 Hz, 630 Hz to 690 Hz, 1 kHz to 1.3 kHz and 1.7 kHz till 2 kHz within the prescribed range of frequencies.

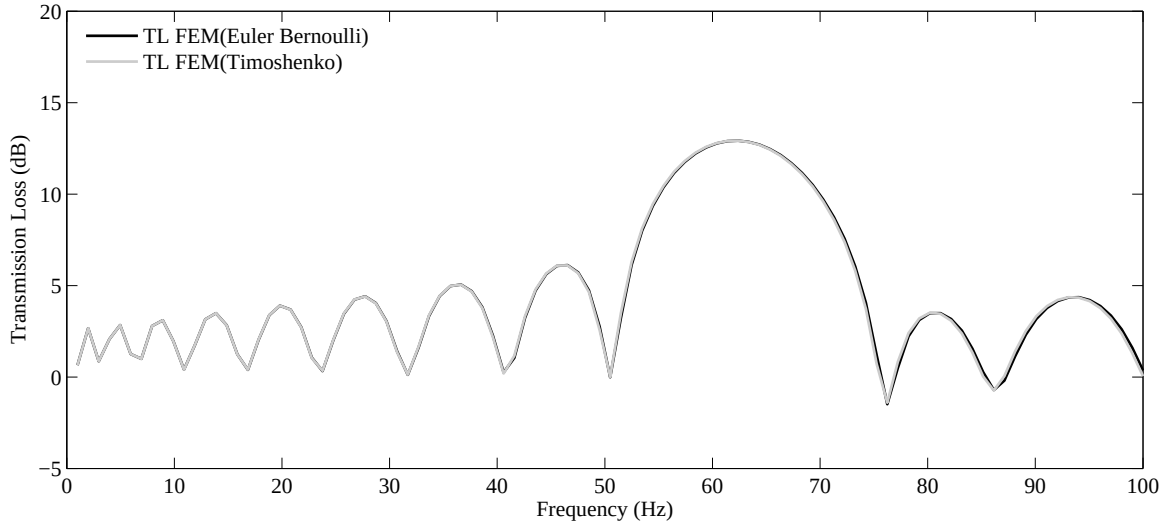


Figure 5: Transmission Loss (TL) in semi-infinite Euler Bernoulli and Timoshenko beam structure within 0 to 100 Hz.

Furthermore, in the case of Figure 5 where results for FE analysis for the various beam theories (Timoshenko and Euler-Bernoulli) are described within the 0 to 100 Hz frequency range. Stop band occurrences within Timoshenko beam show a good correlation with the results obtained by Euler-Bernoulli beam theory in the frequency range till 100 Hz.

Figure 6 provides a complete overview over representation of pass band and stop bands for Euler-Bernoulli and Timoshenko beam till 2 kHz of frequency range. At higher frequencies, a significant change in wave propagation is seen due to the effect of shear deformation and rotational inertia within the Timoshenko beam. Shear deformation effectively lowers the stiffness of the beam, which results into higher deflection and lower the prediction of eigenfrequencies for the semi-infinite beam structure. At higher frequencies within Timoshenko beam, when shear deformation and rotational inertia are present, it lowers the frequency of occurrence of stop bands, while length of the stop bands being close to the length of the stop bands in Euler-Bernoulli beam.

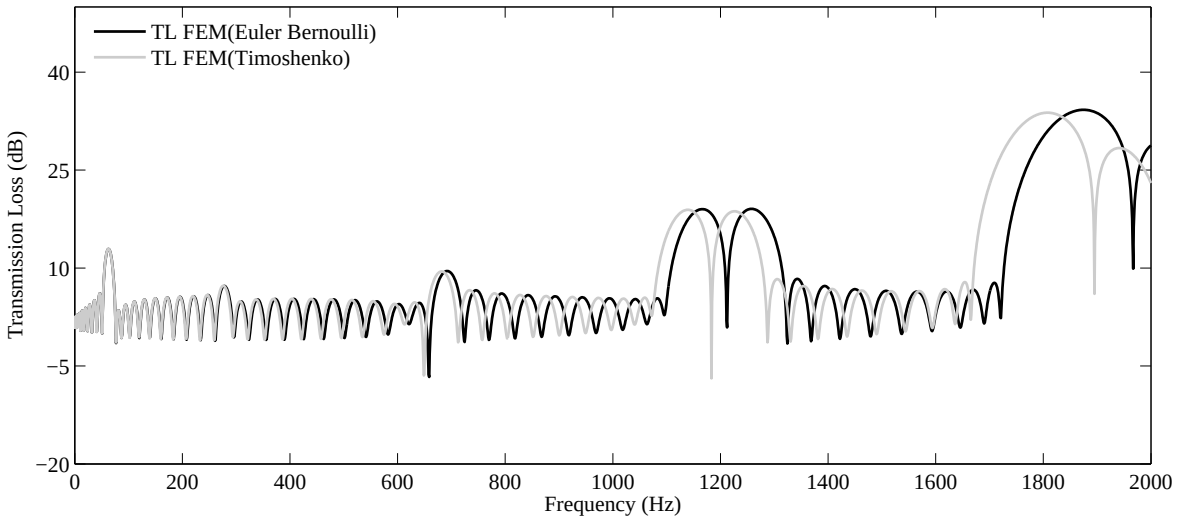


Figure 6: Transmission Loss (TL) in semi-infinite Euler Bernoulli and Timoshenko beam structure within 0 to 2 kHz.

5 CONCLUDING REMARKS

Flanking noise transmission within a periodically connected two-dimensional infinite beam structure made of Plexiglas and steel is analyzed using the finite-element method (FEM) for Timoshenko and Euler-Bernoulli beams and Floquet theory (Euler-Bernoulli beam). In case of the finite-element method, stiffness and mass matrices for Plexiglas and Steel elements were constructed and combined in a periodic manner to generate a beam structure with a finite number of cells, followed by a semi-infinite beam of Plexiglas modeled by means of an impedance condition at the end of the finite-element model.

The transmission loss (TL) is calculated using the FEM for 10 cells in the beam and impedance condition introduced in order to mimic the behavior of an infinite beam structure made of Plexiglas. Stop bands with no wave propagation are visible in certain frequency ranges. Prediction of wave propagation within an infinite two-dimensional beam structure is also evaluated through Floquet theory using Euler-Bernoulli beam, which eliminates the need to generate system matrices as in the FEM. Four parameters, $\lambda_n = \exp(-iK_B)$, n =1, 2, 3, 4, (two for propagating waves and two for evanescent waves) are derived for frequencies in the

range 0 to 2 kHz, where K_B is the Bloch parameter. In case of evanescent waves, the values of $|\lambda|$ are comparatively high in the positive direction and low in the negative direction along the beam, which shows that the structure is highly damped for transmission of evanescent waves. In case of bending wave propagation, pass bands are identified at certain frequency ranges when $|\lambda| = 1$ (bending wave propagation is visible), and stop bands identified by $|\lambda| \neq 1$ (no transmission of vibrations) are obtained in the remaining part of the frequency range.

A comparison between the FEM and the Floquet theory for the Euler-Bernoulli beam approach has been carried out. The methods have shown significant correlation in prediction of vibration transmission within the beam structure. Stop bands with no (or highly damped) wave propagation are surfaced at exactly the same frequency intervals with both approaches.

A comparison between the FEM for Timoshenko and Euler-Bernoulli beam has been carried out as well. It shows quite a significant correlation between results at lower frequencies like below 100 Hz. Results start to vary as the frequency increases, when shear deformation and rotational inertia effect give impact on wave propagation as expected. The FE model for the Timoshenko beam lowers the frequency for occurrence of stop bands in comparison with the Euler-Bernoulli beam, while the lengths of stop bands and pass bands being almost similar within the frequency range 200 Hz till 2 kHz.

Future tasks involve analysis of wave propagation within a thick beam (Timoshenko beam) structure using FEM and Floquet theory as well as an experimental approach, thus identifying the occurrence of stop bands regarding flexural waves within various frequency ranges. Results obtained by numerical and analytical methods will be compared with experimental results. The aim is to get a better understanding of vibration transmission within periodically connected lightweight structures.

ACKNOWLEDGEMENT

The present research is part of the Interreg project “Silent Spaces”, funded by the European Union. The authors highly appreciate the financial support.

REFERENCES

[1] M.A. Heckl, Coupled waves on a periodically supported Timoshenko beam. *Journal of Sound and Vibration*, **252**(5), 849–882, 2002.

[2] J.Y. Yeh, L.W. Chen, Wave propagation of a periodic sandwich beam by FEM and the transfer matrix method, *Composite Structures*, **73**, 53-60, 2006.

[3] B.R. Mace, E. Manconi, Modelling wave propagation in two-dimensional structures using finite element analysis, *Journal of Sound and Vibration*, **318**, 884-902, 2008.

[4] A.S. Knudsen, R. Darula, S. Sorokin, Theoretical and experimental analysis of the stop-band behavior of elastic springs with periodically discontinuous of curvature, *Journal of Acoustical Society of America,* **132** (3), 2012.

[5] J.Wang, T.J. Lu, J.Woodhouse, R.S. Langley, J.Evans, Sound transmission through lightweight double-leaf partitions: theoretical modelling, *Journal of Sound and Vibration*, **286**, 817-847, 2005.

[6] B.R. Mace, D. Duhamel, M.J. Brennan, L. Hinke, Finite element prediction of wave motion in structural waveguides, *Journal of Acoustical Society of America,* **117**(5), 2005.

[7] D. Duhamel, B.R. Mace, M.J. Brennan, Finite element analysis of the vibrations of waveguides and periodic structures, *Journal of Sound and Vibration*, **294**, 205-220, 2006.

[8] A.S. Knudsen, On advantage of derivation of exact dynamical stiffness matrices from boundary integral equations (L), *Journal of Acoustical Society of America*, **128**(2), 2010.

[9] D.J. Mead, Wave propagation in continuous periodic structures: Research contributions from Southampton, 1964-1995, *Journal of Sound and Vibration*, **190**(3), 495-524, 1996.

[10] M. Heckl, Wave propagation on beam-plate systems, *Journal of the Acoustical Society of America*, **33**(5), 640-651, 1961.

[11] D.J. Mead, Free wave propagation in periodically supported, infinite beams, *Journal of Sound and Vibration*, **11**, 181-197, 1970.

[12] M.A. Heckl, Couple waves on a periodically supported Timoshenko beam, *Journal of Sound and Vibration*, **252** (5), 849-882, 2002.

[13] A. Houmat, Vibrations of Timoshenko beams by variable order finite elements, *Journal of Sound and Vibration*, **187** (5), 841-849, 1995.

[14] P.G. Domadiya, L.V. Andersen, S.V. Sorokin, Prediction of vibration transmission within periodic bar structures: analytical Vs numerical approach, *Joint Baltic-Nordic Acoustics Meeting*, June 18th -20th 2012, Denmark.

[15] L. Andersen, S.R.K. Nielsen, P.H. Kirkegaard, Finite element modelling of infinite Euler beams on kelvin foundations exposed to moving loads in convected co-ordinates, *Journal of Sound and Vibration*, **241** (4), 587-604, 2001.

COMPDYN 2013
4th ECCOMAS Thematic Conference on
Computational Methods in Structural Dynamics and Earthquake Engineering
M. Papadrakakis, V. Papadopoulos, V. Plevris (eds.)
Kos Island, Greece, 12–14 June 2013

MULTIMODE CHARACTER OF DYNAMICAL SYSTEMS AS A CAUSE OF THEIR COMPLEX ("CHAOTIC") BEHAVIOR

I. Blekhman

Institute of Problems in Mechanical Engineering RAS
V.O., Bolshoy pr. 61, St.Petersburg, 199178, Russia
e-mail: iliya.i.blekhman@gmail.com

Keywords: dynamical systems, multimode situation, complex behavior, chaos, examples.

Abstract. *This study puts under consideration dynamic systems, whose visible complex ("chaotic") behavior is caused by transition from one motion mode to another. Such motion modes may be represented in particular by some stable in the small periodic motions with different periods. Two types of such systems are singled out. In the first case a number of motion regimes with closely located domains of attraction coexist in the phase space of the system at certain values of parameters. The transition from one stable regime of motion to another is due to the inaccuracy of computer calculations and variation of parameters in the corresponding physical system. In the second case a systematic transition from one regime of motion (which is not necessarily stable) to another occurs due to the internal properties of the system. As an example is the situation, when one of the phase variables may be considered as a relatively slowly varying parameter passing through the existence and steadiness domains of various regimes. The behavior of a particle over a horizontal vibrating plane and emergence of a turbulent surface layer in liquid placed in a vibrating vessel are considered in this paper as illustrative examples. The resemblance of this process to that of the thermoconvection is pointed out. The other example is an analogue of the Lorenz oscillator marked by a phase pattern projection similar to the well-known "butterfly" pattern. Some thoughts corroborating Landau turbulence theory are suggested. It is noted that the complex motion under consideration is characteristic for sufficiently wide scope of dynamic systems such as a pendulum with a vibrating axis, the self-synchronizing oscillating and rotating objects, the systems with period doubling, the parametrically excited distributed systems.*

The author is grateful to A.L. Fradkov for the discussion and comments.

1 INTRODUCTION

A great many papers and monographs dealing with complex ("chaotic") behavior of dynamic systems followed the well-known Lorenz study [1-5]. Most of them ascribed the complex behavior to the instability of trajectories and to closeness to homoclinic structures. Accordingly, a great number of such rather complex "ways to chaos" was listed.

This paper means to discuss a simpler case of complex motions arising in simple systems. The case under study implies multimode behavior i.e. systematic transition of a system from one mode attraction domain to the other. These modes may represent e.g. some stable periodic motions and are not bound to be a totality of instability (diverging) motions.

After a brief general consideration of two such situation types the examples are given when the complexity of the system behavior is taken to be due to said simple circumstances. Among these instances is obtaining "the Lorenz butterfly" from a simple 3D system and emergence of a turbulent gas-saturated layer during water-filled vessel vibration. The attention is drawn to the similarity of the latter process to that of thermo-convection. It is stated that this variety of complexities (chaos) emergence is likely to occur more frequently than it is customary to believe. Above-described considerations are presumably related to L.D.Landau's theory of turbulence.

The term "chaos" is either omitted or accompanied by inverted commas in this paper. The reason is in that there are several definitions of the chaos which are strict and complex enough to be used. So we follow A.N. Kholmogorov's statement that a complex thing is undiscriminated from the accidental one. But definition of the complexity is even more difficult than the definition of the chaos. So when speaking of complexity we mean some speculative subjunctive notion. It was so do the authors of the majority of numerical investigation of dynamical systems.

2 COMPLEX SYSTEM BEHAVIOR DUE TO MULTIMODE PATTERN OF THE "FLAKY PASTRY" TYPE

Let us imagine that in some domain of the parameters space there exist a few or an infinitely great number of motion types such as stable motions in the sense of Lyapunov or motions of different character, e.g. periodic motions with various periods.

Fig. 1 illustrates schematically the polygonal ABCDE representing the existence and stability domain of three different motions 1, 2, 3 for two parameters a and b The space of parameters may have either one or many dimensions, the number of different simultaneously existing motions being other than three.

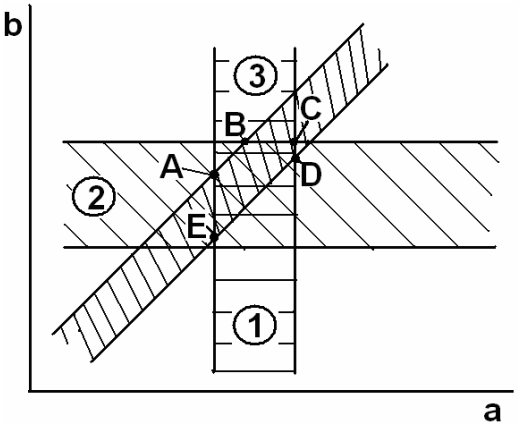


Figure 1: The existence domains of various type motions are superimposed (the case of "flaky pastry").

Let us further assume that in a phase space of the system the modes under study correlate to some attraction domains that are closely spaced or adjacent. Assuming the dimensions of these domains to be similar or less than the domains corresponding to the accuracy of calculations we find that the point reflecting the state of the system is prone to drift in the phase space passing from one attraction domain to the other. As a result of this the trajectories of this point can fill up some space which under numerical investigations may be perceived as a strange attractor.

The examples of such situation are given below.

3 COMPLEX SYSTEM BEHAVIOR DUE TO MULTIMODE PATTERN OF THE "ZEBRA" TYPE

In this case no minuteness of attraction domains or disposition of existence and stability domains in parameter space is presumed. Neither the limited calculation precision is taken into account.

The simplest case of the situation under study is as follows. Suppose there is a system containing some parameter p ,which when changing within a certain range entails the change of the phase pattern, so that the defining point occurs consistent within the attraction domain of various stable motions or even within the domain where all the trajectories either diverge or, if $t \to \infty$, travel to the infinity (see Fig 2).

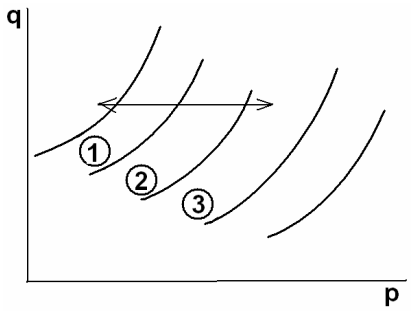


Figure 2: The parameter or the coordinate of a system within the parameter space periodically crosses the existence domains of various motions ("zebra" situation).

Suppose we have designed an additional controlling system where the parameter p is a coordinate varying comparatively slowly within above mentioned range. Then the combined system will eventually pass from one phase pattern to another, staying within for some finite time. It would be natural to expect that after a sufficiently long time interval the system might trace within the phase space a sufficiently complex trajectory, filling up some domain which under numerical investigation may be perceived as a strange attractor. It is safe to suppose that the complexity of this trajectory might increase when the accuracy of calculations, like in the first case, is limited.

The examples of such situation are given below.

Let us describe this situation as "zebra" type multimode behavior.

4 REMARKS

1) The above considerations about the multimode as the cause of the complexity of the movement close to the concepts of amplifiers stochastic in the book [1]

2) One can come across systems combining both of the multimode patterns considered above.

3) Following A.A. Andronov's terminology one can define multimode situation as a rough case of complexity ("chaos").

4) The trajectory of the system in the phase space might appear comparatively simple while its projection on the plane seems to be rather complicated ("chaotic"). By contrast, the trajectory might appear to be chaotic while its projection on some plane would be simple. The same relates to Poincare sections.

5 EXAMPLES

5.1 Lorenz oscillator and its simplest analogue. The "Butterfly effect"

Let us investigate the Lorenz equation system of the following form [1]

$$\ddot{\xi} + (\eta - 1)\xi + \xi^3 + \mu\dot{\xi} = 0, \quad \dot{\eta} = -\frac{\mu}{\sigma + 1}\left[b\eta - (2\sigma - b)\xi^2\right], \tag{1}$$

where μ, σ and b –are positive parameters, parameter μ being a small one. If $\eta = const$, then the first equation of the system (1) represents the Duffing equation. When $\eta - 1 > 0$ it acquires one asymptotic stable equilibrium position $\xi_1 = 0$, while with $\eta - 1 < 0$ –it acquires two such positions $\xi_{2-3} = \pm\sqrt{1-\eta}$.

Now what is to happen to the system when the quantity $\eta - 1$ is slowly and periodically varying as e.g. following the order:

$$\eta - 1 = k^2(\sin\omega t - a), \quad 0 < a < 1, \tag{2}$$

where ω significantly less than k? It is evident that in this case the system with time intervals $t >> 2\pi/\omega$ will intersect bifurcation point $\eta - 1 = 0$ many times, passing from $\eta - 1 > 0$ situation with only one asymptotic stable equilibrium position $\xi_1 = 0$ exist to the situation when $\eta - 1 < 0$ with two such positions $\xi_{2-3} = \pm k\sqrt{1-\eta}$ occurs.

Hence, one may suppose that the motion described by the equation

$$\ddot{\xi} + k^2\xi(\sin\omega t - a) + \xi^3 + \mu\dot{\xi} = 0, \tag{3}$$

with ω significantly less than k? and changing time interval t sufficiently long, is likely to reveal complex behavior.

Fig.3 shows the trajectory corresponding in the equation (3) to the following value of the parameters:

$$k = 10, \quad \omega = 4, \quad \mu = 0.1, \quad a = 0.8$$

with initial conditions: $\xi(0) = 5, \quad \dot{\xi}(0) = 0$

One can see that the motion of this simple system is of a sufficiently complex character, identical to the trajectory of the well-known Lorenz oscillator (1), the projection of the phase trajectory being similar to the well-known "butterfly" pattern.

Similar properties are peculiar to the system where the function $\eta - 1$ is a "control variable" defined by the following autonomous linear equation:

$$\ddot{(\eta - 1)} + \omega^2(\eta - 1) = -k^2 a$$

One can find similar considerations and examples in [7, 8].

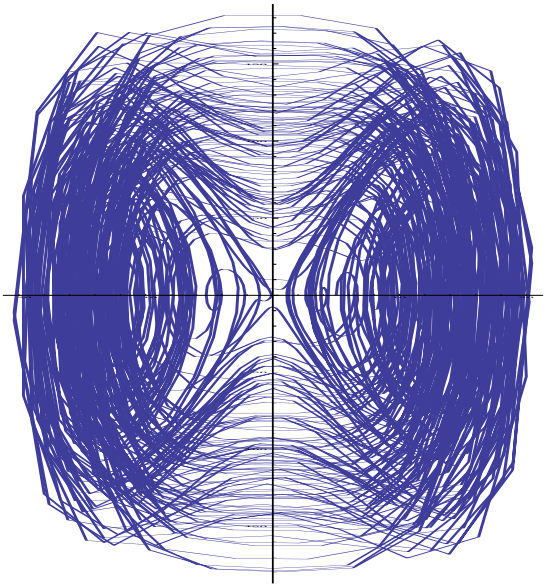


Figure 3: Phase pattern of the system.

5.2 Particle motion over a vertical vibrating plane

Let us consider the motion of a particle bounding over a horizontal plane that is vibrating vertically with amplitude A and frequency ω according to the law (Fig. 4)

$$\eta = A\sin\omega t \tag{4}$$

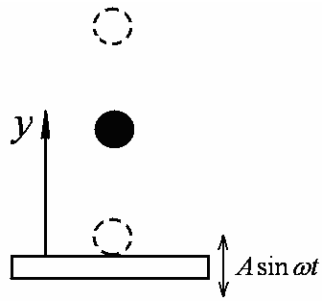


Figure 4: A particle bouncing over a horizontal vibrating plane.

The particle motion character is defined by two non-dimensional parameters, namely the coefficient of overload $w = A\omega^2 / g$ and coefficient of restitution R. It was shown by analytical investigation [9, 10] that on condition

$$\pi p\frac{1-R}{1+R} < w < \frac{\sqrt{\pi p^2(1-R^2)(1+R^2)+4(1+R^2)^2}}{(1+R^2)} \tag{5}$$
$$p = 1, 2, \ldots$$

there exist some stable in small (in Lyapunov's sense) periodic motions (regimes) of a particle when the latter keeps to be positioned over a vibrating plane and is colliding with the same

with a period $T = pT_0 = 2\pi p/\omega$, that is a multiple in relation to the plane vibration period T_0. The domains of existence and stability for such regimes are shown in Fig. 5 (shaded).

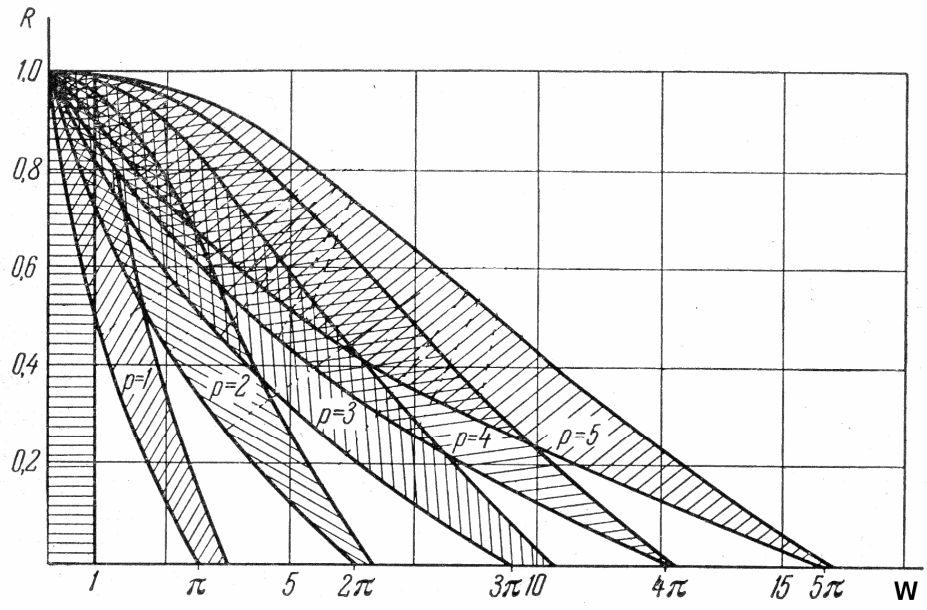


Figure 5: The domains of the existence and stability of periodic motions of a particle over vibrating plane.

As it is seen, with values R relatively close to 1 there exists a great (rather infinitely great) number of regimes to be considered while the domains of their existence and stability in parameter space are superposed. Each of periodic regimes corresponds to a certain sufficiently small domain of attraction within the phase space [9]. So we have the situation of "flaky pastry".

In Fig. 6 phase diagram of a particle behavior on a plane $y, \dot{y}$ corresponding to different values of parameter R are represented

One can see that with $R = 0$ we have periodic motion of the particle, while with $R = 0.95$ – there exists a complex motion, the particle bouncing over the plane by various heights $y_{\max}$. In this case the complexity of the motion increases in accordance with the increase of overload parameter w.

It is to be noted that such multimode behavior and corresponding motion complexity with $R \approx 1$ has been found in other impact - vibration systems including the known Fermi oscillator [11].

The other feature of the system under study is systematic appearance of "fountains", i.e. bouncing of the particle to rather great height (on Fig.6 *b* and 6 *c* conditions – to 1.7 m and 9.5 m accordingly). Similar splashes (fountains) can be observed in behavior of liquid in a vibrating vessel (see item 5.3 below). This is often referred to as intermittence in transition to chaos [1, 2, 5].

Let us emphasize that the above regularities characteristic not only of the mathematical models, but also to the physical systems.

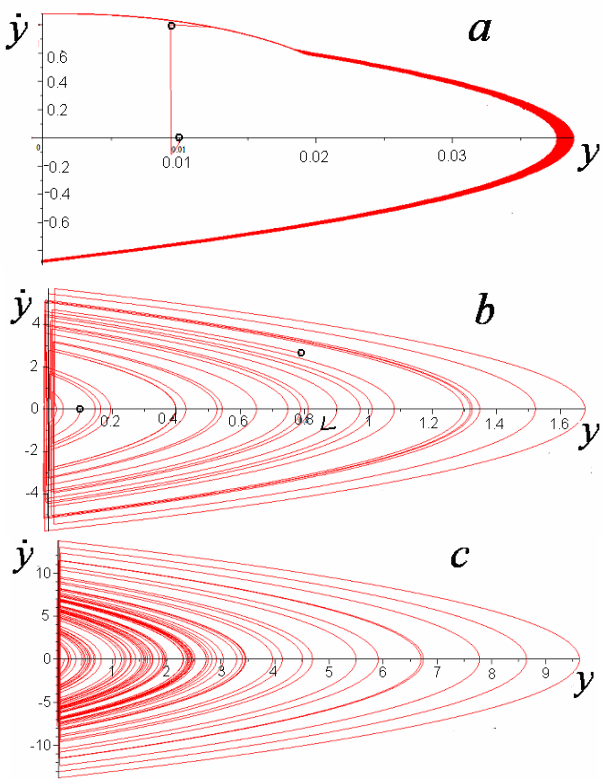


Figure 6: Particle over a vibrating plane. Periodic motion on a phase plane:
$a-\ R=0,\ A=0.025\ m,\ \omega=35\ s^{-1},\ w=\pi;\ \ b-\ R=0.95,\ A=0.016\ m,\ \omega=35\ s^{-1},\ w=2;$
$c-\ R=0.095,\ A=0.024\ m,\ \omega=35\ s^{-1},\ w=3.$

5.3 Liquid in a vibrating vessel. Cellular structures, fountain formation. Generation of turbulent gas-saturated layer. Resemblance to thermoconvection

In our experiments [12] a cylindrical vessel of 60 mm diameter and 450 mm height was filled with water to 20, 50 and 100 mm levels. Vertical vibrations with 1 mm amplitude were imparted to the vessel, the frequencies ω increased from 75 to 240 *rad/s*.

With relatively low vibration frequencies ($\approx$ up to 5 *rad/s*) the liquid surface remained horizontal. The further increase in frequencies resulted in emergence of standing waves ("cellular structures"). Cell dimensions tended to gradually decrease with the increase in ω so that at 146 *rad/s* frequency a gas-saturated turbulent layer of a gradually growing thickness was formed (for more details see [12]). The cells (standing waves) were found by theoretical analysis to correspond by their frequencies to a half of the liquid surface free oscillations in the gravity field λ, thus representing none other than Faraday ripple. As for cell dimensions, they were in correspondence with the dimensions of the free oscillation half waves and only in slight dependence on the volume of water in the vessel.

The other experiments were carried out with a rectangular box of 330 x 245 mm dimensions, shown in Fig.7. One can see clearly visible standing waves forming the cellular structure.



Figure 7: Box with fluid under vibration; cellular structures.

The frequencies $\lambda = \lambda_{n,m}$ of the liquid surface free oscillations in this box may be determined by the formula

$$\lambda_{n,m} = \sqrt{\pi g \sqrt{\left(\frac{n}{a}\right)^2 + \left(\frac{m}{b}\right)^2}\, \tan\left(\pi h_1 \sqrt{\left(\frac{n}{a}\right)^2 + \left(\frac{m}{b}\right)^2}\right)}, \qquad (6)$$

$$n, m = 1, 2, \ldots$$

where *a* and *b* are the box dimensions, h_1 – liquid layer thickness, g - gravity acceleration. Here the number of the cells corresponding to the frequencies $\nu_{n,m} = \frac{1}{2}\lambda_{n,m}$ of the main parametric resonance was $N_{n,m} = \frac{1}{2}(m-1)(n-1)$, while the areas of the cells were equal to $F_{n,m} = 2ab/(m-1)(n-1)$. One can see that the cell dimensions tended to gradually decrease following the increase in the oscillation frequency ν.

The above table shows frequencies λ (*rad/s*) for the test box with water layer height $h_1 = 20$ mm. One can see that with greater n and m values the frequency values get denser. It is to be noted that the parametric resonance frequencies $\omega = 2\lambda_{n,m}$ are in correlation to some close values of *n*, *m*. Thus, for instance, at frequency $\omega = 50$ *rad/s* and $\lambda = \omega/2 = 25$ *rad/s* the difference ± 1 *rad/s* has six frequencies which corresponds to the main parametric resonance.

m	n									
	1	2	3	4	5	6	7	8	9	10
1	4.98	7.13	9.65	12.26	14.86	17.39	19.83	22.16	24.38	26.49
2	8.46	9.84	11.74	13.91	16.18	18.47	20.73	22.91	25.02	27.03
3	12.10	13.05	14.47	16.20	18.10	20.08	22.09	24.08	26.02	27.90
4	15.66	16.35	17.43	18.80	20.37	22.05	23.79	25.56	27.30	29.02
5	19.05	19.58	20.42	21.51	22.79	24.21	25.70	27.24	28.79	30.33
6	22.23	22.65	23.32	24.20	25.25	26.44	27.71	29.04	30.40	31.77
7	25.21	25.54	26.08	26.80	27.67	28.66	29.75	30.90	32.09	33.30
8	27.97	28.24	28.68	29.28	30.00	30.84	31.76	32.75	33.79	34.86
9	30.53	30.75	31.12	31.61	32.22	32.93	33.72	34.58	35.49	36.43
10	32.90	33.09	33.39	33.81	34.33	34.93	35.61	36.36	37.16	37.99

Table: Frequencies (*rad/s*) of liquid free oscillations in the rectangular box

Fig 8. illustrates schematically the domains of parametric instability.

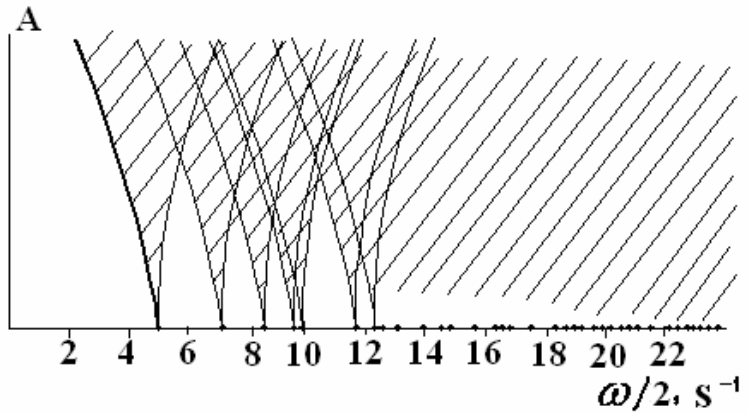


Figure 8: The accumulation and overlap of the instability domains corresponding to the main parametric resonance $\omega/2=\lambda_{n,m}$ (Faraday ripple) in the conditions of Table (shaded).

Each of these domains by presence with some nonlinearity and dissipation is in correlation with a certain steady periodical mode of oscillations, i.e. a certain cellular structure. With relatively great values of ω the domains of parametric resonance get denser and with sufficiently great amplitude *A* they overlap. Thus, the frequency range up to 10 *rad/s* contains 5 frequencies $\lambda_{n,m}$, the range within 10-20 *rad/s* contains 19 frequencies and the range within 20-30 *rad/s* includes 47 frequency values. This causes a complex ("chaotic") motion representing the case of the "flaky pastry".

One may pay attention to the resemblance of the above described picture to the phenomena taking place in thermoconvection when so called Benar's cells are generated. In our case the part of temperature is played by the oscillation intensity. Such resemblance appears to be not casual. As for the theoretical presentation of the thermoconvection by means of Lorenz equations, which suggest quite another way to the chaos ("zebra", see it.5.1), it is to be taken into account that these equations correspond to a double mode approach to the solution of

corresponding partial differential equations. It is to be emphasized that the similarity of oscillatory and thermal influence on the mechanical systems was mentioned in a number of researches (e.g. [13]).

Generation of a gas-saturated turbulent layer during vibration is essential for development of a number of non-linear phenomena, in particular, the submergence of bubbles in a vessel. As far as we know no theoretical explanation of such phenomenon has been given up to now.

Further on it is to be noted that after generation of the turbulent layer some splashes (fountains) appear on its surface. With 23 Hz frequency the height of such splashes was 40-50 mm at about 5 s intervals. Close to the top of the splashes the liquid was broken into separate drops. At 25 Hz frequency the period of splash generation gets shorter – down to about 1 s while the height reached 70 mm. Further increase of oscillation frequency from 28.3 Hz to 38.3 Hz caused simultaneous emergence of a group of splashes reaching maximum height of 110 mm.

As mentioned above the generation of splashes whose height largely exceeds the oscillation amplitude is also characteristic for the behavior of particle over a vibrating plane. It may be of interest that in both cases the splashes are generated at close vibration acceleration amplitudes about $A\omega^2 \approx (3 \div 4)g$.

5.4 Other systems possessing the complex motion due to multimode behavior

Complex motion caused by the multimode situation has been observed to take place in a number of other dynamic systems. Some of these systems are listed below.

5.4.1 A pendulum (or an unbalanced rotor) with a vibrating suspension axis

Under certain conditions the pendulum or an unbalanced rotor reveal a complex ("chaotic") behavior stipulated by multimode situation. The pendulum (rotor) in the process of such motions may transit from vibrations to rotation in various directions [1, 15, 16]. In this case both "zebra" and "flaky pastry" situations are possible.

5.4.2 Synchronization of oscillations and rotations

Multimode situation is characteristic also for systems with self-synchronizing or external synchronized objects, in particular for unbalanced rotors, celestial bodies, pendulum clocks and multi-form oscillators. Such behavior is especially well pronounced in the case of similar objects numbering over three [15, 16].

In this case two kinds of multimode situation are also possible.

5.4.3 Dynamic planes

A flat surface plane formed by two systems of vibrating bars is implied. When vibrating , one system of bars penetrates into another. A particle sufficiently coarse during one part of vibration period will be lying on (over) one system of bars and during the next period part – on the other one. In this case two situations are also likely to occur [17].

5.4.4 Double period system

Systems with bifurcations of period redoubling are often taken into consideration as the models of a large group of dynamic systems marked by transition to chaos. (such as in [1-6]). In such systems any increase in the parameter leads to bifurcations resulting in a stable in the small periodic motion of double period. After a great number of such bifurcations even with

the same parameter value there appears a large number of periodic motions with very small attraction domains, i.e. a “zebra’ type multimode situation takes place.

5.4.5 Arrhythmia of the cardiac systole

A presumption has been made [15, 18] that heart arrhythmia is likely to be explained by the multimode situation.

5.4.6 Parametrical excitation of distributed systems

In elastic bodies like plates and shells the domains of parametric resonance overlap (refer to [20]). Each mode of parametric resonance on condition of possessing non-linearity and dissipation is in correlation to a steady periodic motion. The existence and stability domains of such motions are overlapping (see also item 5.3). In this case “flaky pastry” situation takes place.

5.4.7 Turbulence

Now turning to the formation of turbulent layer in a vibrating water filled vessel (see 5.3) one can suggest that the turbulent motion of liquid should be understood as a simultaneous co-existence of a multitude of stable in the small periodic motions (in this case self-sustained oscillations) Such interpretation is in accordance with the renown Landau turbulence theory which has been put lately to some doubts [1, 2] (supposedly with no reason).

6 CONCLUSION

The present work deals with a relatively simple (“rough”) case study of arising complex motions in dynamic systems. This variety needs no necessity to seek other instability causes because the complex motions can be explained by the presence of several or many stable in the small motions (multimode situation).

Such multimode situation appears to be sufficient for generation of the complex motion in the dynamic system which is likely to be observed as a chaotic one.

Two varieties of such multimode situation referred to as “flaky pastry” and “zebra” have been studied. The formation of turbulent layer in a vibrating water filled vessel has been studied both experimentally and theoretically. The chaotic motion appeared to take place by way of cellular structures (Faraday ripple), the cells diminishing in size with the increase of vibration frequency – this is the “flaky pastry” type situation. It appears to be not accidental that this process is similar to thermoconvection.

It has been shown that the complexity of Lorenz double-mode thermoconvection model may be explained by the multimode situation of “zebra” type. A simple analogue of the Lorenz system has been constructed to prove the emergence of such multimode behavior , the phase pattern obtained resembling the well-known Lorenz butterfly.

The inferences set forth above are in agreement with L.D.Landau turbulence theory.

The instances considered above are thought to illustrate that such variety of complexity in dynamic system behavior (“chaos”) is likely to occur much more frequently than it is thought commonly.

REFERENCES

[1] Yu.I. Neimark, P.S. Landa, *Stochastic and chaotic oscillations, 2nd Edition*. LIBROCOM book house, 2009. (In Russian).

[2] D.I. Trubetskov, *Intruduction into synergetics. Chaos and structures. 4th Edition*. LIBROCOM book house, 2012. (In Russian).

[3] A.L. Fradkov, *Cybernetical physics: principles and practice*. St. Petersburg: Nauka, 2003. (In Russian).

[4] Y. Ueda, *The Road to Chaos – II*. Santa Cruz: Aerial Press, Inc., 2001.

[5] G.A. Leonov, *Strange attractors and classical theory of motion stability*. St. Peterburg: St. Peterburg State University, 2004. (In Russian).

[6] M.V. Zakrczevsky, R.S. Smirnova, I.T. Shchukin, et al, *Non-linear dynamics and chaos.* Riga: Riga Technical University, 2012. (In Russian).

[7] A.Yu. Loskutov, *Non-Feedback Controlling Complex Behavior: An Analytic Approach. Nonlinear Dynamics: New Theoretical and Applied Results*. Berlin: Akademic Verlag GmbH., 126-150, 1995.

[8] I. Kunin, B. Kunin, G. Chernykh. Lorenz – type controlled pendulum. *Inter. Journ. of Engineering Science*, 433-448, 2003.

[9] I.I. Blekhman., G.Yu. Dzhanelidze, *Vibrational Displacement*. Moscow: Nauka Press, 1964. (In Russian).

[10] I.I. Blekhman., K.S. Ivanov, On a vibroimpact system in wich chaos is caused by the rare attractor packing. *Proceedings of the XXXIX International Summer School Conference (APM 2011*), St. Petersburg (Repino), July 1-5, 2011. СПб., 95–100, 2011.

[11] Yu. Guo, A.C.J. Luo, Discontinuity and bifurcation analysis of motions in a Fermi oscillator under dual excitations. *Journ. of Vibroengineering*, **13**, Iss. 1, 66-101, 2011.

[12] I.I. Blekhman, L.I. Blekhman, V.S. Sorokin, V.B. Vasilkov, K.S. Yakimova, Surface and volumetric effects in a fluid subjected to high-frequency vibration. *Journal of Mechanical Engineering Science*, **226(8)**, 2028-2043, 2012.

[13] A.K. Belyaev, V.A. Palmov, Vibration conductance theory. *Dynamics and strength issues*, Riga: : Zinatne, **36**, 93–102, 1980. (In Russian).

[14] V.S. Batalova, G.V. Belyakova, Periodic motion stability diagrams of a pendulum with a vibrating axis. *Applied mathematics and mechanics*, **52**, Iss. 1, 41-48, 1988. (In Russian).

[15] I.I. Blekhman, *Synchronization in Science and Technology*. New York: ASME Press, 1988.

[16] I.I. Blekhman, *Vibrational Mechanics. (Nonlinear Dynamic Effects, General Approach, Applications).* Singapore et al: World Scientific Publishing Co., 2000.

[17] I.I. Blekhman, G.B. Bukaty, The motion of the body which is in contact in turn with two vibrating planes. *Izv. AN SSSR, MTT*, 2, 39–49, 1975. (In Russian).

[18] I.I. Blekhman, Non-linear oscillatory phenomena in functioning of cardiovascular system. *Proceedings of the 6-th ESGCO 2010, April 12-14*, Berlin, Germany, 2010.

[19] E. Surovyatkina, Nonlinear origin of sudden change of heart rhythm. *Proceedings of the 6-th ESGCO 2010, April 12-14,* Berlin, Germany, 2010.

[20] *Vibrations in engineering*. Reference book, **1**, Moscow: Machinostroyeniye, 1978. (In Russian).

[21] L.D. Landau. On Turbulence Problem. *USSR Academy of Sciences Transactions*, **XLIV**, 339-342, 1944. (In Russian).

COMPDYN 2013
4th ECCOMAS Thematic Conference on
Computational Methods in Structural Dynamics and Earthquake Engineering
M. Papadrakakis, V. Papadopoulos, V. Plevris (eds.)
Kos Island, Greece, 12–14 June 2013

INFLUENCE OF STRUCTURAL PERIODICITY ON VIBRATION TRANSMISSION IN A MULTI-STOREY WOODEN BUILDING

Lars V. Andersen

Aalborg University, Department of Civil Engineering
Aalborg, Denmark
e-mail: la@civil.aau.dk

Keywords: Finite element analysis, steady-state response, transient response, periodic structure, substructure.

Abstract. *Noise is a nuisance to people, and buildings should therefore be designed to prevent propagation of sound and vibration in the audible frequency range as well as the range of frequencies relevant to whole-body vibrations of humans. In heavy structures made of concrete and masonry, a source with high energy content is required to mobilise the inertia. However, for lightweight building structures made of wood, less energy is required to produce vibrations since the mass is smaller. This leads to a high risk of sound and vibration propagation in terms of direct as well as flanking transmission.*

However, lightweight structures are typically periodic in the sense that joists and studs are placed with a repetition of the same distance along each panel. Further, in a multi-storey building the geometry of entire rooms may be repeated along the horizontal and vertical directions. Such periodicity is known to result in pass bands and stop bands regarding wave propagation. The paper focuses on analysing and quantifying the effects that a change in the structure, especially regarding the periodicity, has on the overall dynamic performance in the low to mid frequency range up to 250 Hz.

The analysis is performed by means of a finite-element model. Firstly, a rigorous solid finite-element model is made for each wall and floor panel. Secondly, reduced models with significantly fewer degrees of freedom are obtained by component mode synthesis, augmenting Guyan reduction with a number of internal Eigen modes. Using a substructure approach, the panels are then combined to a global model of a multi-storey building. Example Eigen modes of a single floor panel and the global building are presented. Vibration caused by point force excitation is finally analysed in the frequency domain as well as the time domain.

1 INTRODUCTION

Noise and vibration are critical factors regarding human comfort in the built environment. With increasing population density in cities follows a demand of designing buildings with focus not only on structural strength and safety, but also on indoor comfort and sustainability. In this context, timber has number of advantages, but also some shortcomings. With recent advances in structural engineering it has become possible to construct large multi-storey wooden buildings. However, a reliable assessment of sound and vibration transmission in such buildings in the early design phase cannot be carried out by the methods developed for heavy structures made of concrete or masonry. Thus, statistical energy analysis (SEA) [1] and the European standard EN12354-1 [2] have been found to provide inaccurate results for lightweight structures [3]—especially in the low and mid-frequency range.

Regarding the analysis of lightweight wooden building structures, one of the main shortcomings of SEA and related methods lies in the fact that a uniform modal density is assumed. This is contradictory to the dynamic properties of wooden structures. The inherent periodicity of mass and stiffness due to studs and joists in wall and floor panels leads to the existence of pass bands and stop bands for transmission of elastic waves [4]. Whereas this may complicate dynamic analysis, it may, on the other hand, be utilized in the design of a building to avoid transmission of vibration and sound within certain frequency ranges from, for example, foot steps, unbalanced washing machines, air conditioning or elevator motors.

To quantify the effects of periodicity, a finite-element (FE) model is applied in the present paper. FE models have been used for analysis of wooden structures by, among others, Brunskog and Davidsson [5], Løvholt et al. [6], Maluski and Gibbs [7], and Fiala et al. [8]. For large building structures, a solid FE model will contain millions of degrees of freedom if individual joist and studs are to be modelled in detail. Hence, parametric studies become very time consuming. However, Andersen et al. [9] proposed the use of a modular FE model in which the walls and floors are treated as substructures, leading to a significant reduction of the number of degrees of freedom. This approach is employed in the present paper for dynamic analysis of two-storey buildings with different numbers of modules in the length direction and with different distances between the joists and studs. The Eigen modes of the various structures are identified, and analyses of the steady state response to harmonic loading is carried out in the frequency domain within the range 0–250 Hz. Finally, a time-domain analysis is performed to quantify the transient displacement response to a step load on one of the floors.

2 THE COMPUTATIONAL MODEL

2.1 Modular finite-element building model

A finite-element (FE) model of a lightweight wooden building structure has been made, based on a modular approach using substructures for each wall and floor panel. Figure 1 illustrates the overall geometry and principle of the model. The example building shall be named "House 4-3-2" since it is 4 modules long in the x-direction, 3 modules high in the y-direction and 2 modules wide in the z-direction. The module lengths in the x, y and z-directions are denoted L, H and W, respectively. Further, as shown in the figure, rooms and panels are number in accordance with their position within the model. For example, y-Wall 1-2-1 is the first wall in the x and z-directions, and the second wall in the y-direction, with an orientation along the z-axis, cf. Figure 1.

The FE model has been developed with the commercial software code Abaqus 6.12-2 [10] using Python scripting to allow parametric studies in an efficient manner. Firstly, each of the

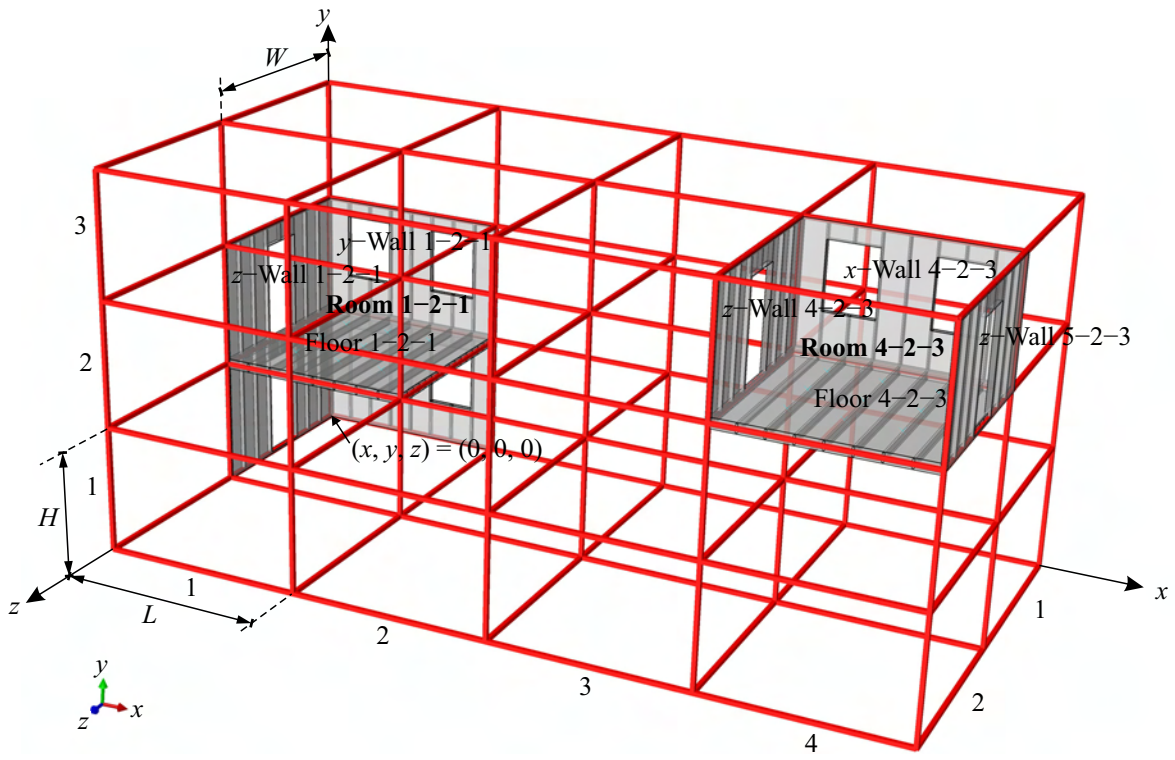


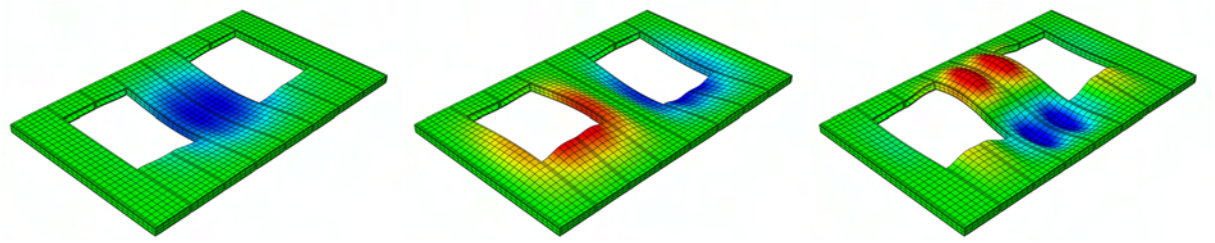
Figure 1: Definition of modular finite-element building model for House 4-3-2.

wall and panels has been modelled in high detail using 20-node solid brick finite elements with full integration and quadratic interpolation of the displacement field. A regular structured hexahedral mesh with a mesh size of maximum 100 mm has been utilized to obtain results of high accuracy in the frequency range below 500 Hz.

The walls are made as double-leaf single-stud panels, assuming all connections to be glued, i.e. fully tied. The plate thickness is 15 mm, whereas the studs are 100 mm thick and 45 mm wide, leading to a total wall thickness of 130 mm. In all considered models within the present analyses, the height of each wall panel is 3.00 m, and the z-wall panels parallel to the (y, z)-plane all have a width of $W = 4.80$ m. The same width applies to the floor panels in all models. Like the walls, the floors are double-leaf single-joist panels. However, the plates are 20 mm thick and the joists have a cross-sectional area of 200×45 mm^2, resulting in a total floor thickness of 240 mm. A 45 mm wide solid frame is placed along the edges of all panels, again assuming glued connections.

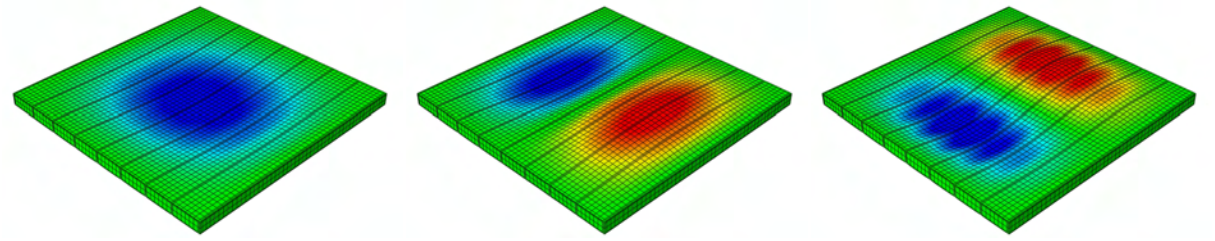
As indicated in Figure 1, 1200×1600 mm^2 (length $\times$ height) window openings are cut into the x-wall panels that form the facade of the building along the x-direction. The first window in every panel is placed 600 mm from the end of the panel along the x-direction and 1000 mm from its base along the y-direction. Depending on the length of the wall module, a number of repetitions are made with a distance of 1200 mm between windows in the x-direction. Likewise, a single door opening is made in the middle of the z-walls with a height of 2445 mm and a width of 1200 mm. The opening is placed 45 mm (the width of the frame) above the base of the wall.

Construction wood and plywood are idealized as an isotropic, linear viscoelastic material with Young's modulus $E = 9.5$ GPa, Poisson's ratio $\nu = 0.3$, mass density $\rho = 455$ kg/m^3. Material dissipation is defined in terms of Rayleigh coefficients providing damping ratios of 2% at 10 Hz and 100 Hz. As a result, a minimum damping ratio of 1.14% occurs at 31.6 Hz.



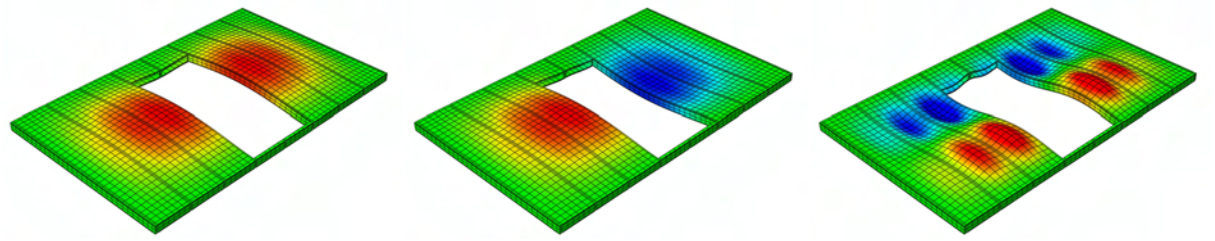
Mode 1 @ 72 Hz Mode 2 @ 98 Hz Mode 7 @ 164 Hz

Figure 2: Example Eigen modes and Eigen frequencies of x-wall panel module with two window openings. The panel dimensions are $(L \times H) = (4.80 \times 3.00)$ m^2, and the joist distance is 600 mm. Red and blue shades indicate positive and negative out-of-plane displacements, respectively.



Mode 1 @ 58 Hz Mode 2 @ 69 Hz Mode 7 @ 138 Hz

Figure 3: Example Eigen modes and Eigen frequencies of y-floor panel module. The panel dimensions are $(L \times W) = (4.80 \times 4.80)$ m^2, and the joist distance is 600 mm. Red and blue shades indicate positive and negative out-of-plane displacements, respectively.



Mode 1 @ 73 Hz Mode 2 @ 73 Hz Mode 7 @ 163 Hz

Figure 4: Example Eigen modes and Eigen frequencies of z-wall panel module with door opening. The panel dimensions are $(W \times H) = (4.80 \times 3.00)$ m^2, and the joist distance is 600 mm. Red and blue shades indicate positive and negative out-of-plane displacements, respectively.

Material dissipation of this magnitude is judged to be realistic for wood. However, for a building including joints and nonstructural elements, e.g. insulation material, it may be unrealistically low. Therefore, in the response predicted by the present FE model may be less damped than the response of a real structure.

Example mode shapes and corresponding Eigen frequencies for an x-wall panel with dimensions $(L \times H \times W) = (4.80 \times 3.00 \times 4.80)$ m^3 and stud distance 600 mm are illustrated in Figure 2. In accordance with the explanation above, two windows are present in this panel. Likewise, Figure 3 shows three modes and the related Eigen frequencies for a floor panel with dimensions $(L \times W) = (4.80 \times 4.80)$ m^2 and joist distance 600 mm, whereas Figure 4 provides an illustration of three modes in a z-wall panel with dimensions $(W \times H) = (4.80 \times 3.00)$ m^2 and stud distance 600 mm. It can be seen in Figures 2 and 4 that the first Eigen mode of each wall occurs at a frequency of about 72–73 Hz, whereas the fundamental mode of the floor occurs at 58 Hz, in all cases assuming that the panels are fully fixed along the edges. These frequencies may be slightly high, but it should be noted that nonstructural mass has been disregarded.

Before assembly of the global building FE model, a system reduction is carried out in order to provide a substructure, i.e. a macro finite element, for each of the wall and floor panels. In the present analyses, nodes are retained along the edges of the panels for every 300 mm. For example, 17 nodes are retained along each side of a floor panel with dimensions $(L \times W) = (4.80 \times 4.80)$ m^2, including two corner nodes. It is noted that only the nodes in the midplane of the panel are retained. However, to allow a coupling of the rotational degrees of freedom from one panel to another, rigid shell elements are introduced in the cross sections of the panel frame at the position of the retained nodes. Hence, six degrees of freedom are retained at each node.

Especially, in the floor panels, additional nodes are retained on the top surface of the floor. These nodes are placed in a grid with the mesh size 1200×1200 mm^2, providing, e.g., an additional $3 \times 3 = 9$ nodes on a 4.80×4.80 m^2 floor panel. The purpose of the nodes placed on the top surface of the floors is to allow application of concentrated forces or discrete nonstructural masses at these positions. Since no external moments or mass moments of inertia are to be applied, only the translational degrees of freedom are retained at the additional nodes.

Taking the approach of Craig and Bambton [11] (see also Ref. [12]), the system matrices achieved by Guyan reduction [13] of the system matrices are enriched by a number of internal modes of a model fixed at the retained degrees of freedom. All modes up to a frequency of 400 Hz are included in the substructures in order to provide an acceptable accuracy of the global model up to 250 Hz. The result of the system reduction is a substructure for each panel with 300 to 600 degrees of freedom. This should be compared to the original 90,000 to 250,000 degrees of freedom present in the rigorous models of the panels. Nonetheless, a very high computational accuracy is maintained.

The individual panels are combined to form a building with a number of rooms in each of the x, y and z-directions. In the present version of the modular FE model, all x-walls are identical, e.g. x-Wall 3-2-1 is identical to x-Wall 2-1-2. The same limitation applies to floor and z-wall panels. Following the idea of Kiel et al. [14], all panels are attached to an artificial skeleton made of beam finite elements as sketched in Figure 1. The skeleton nodes act as a common master, and the retained nodes of the panels act as slaves within the Abaqus "tie" definition. To ensure that the skeleton will not influence the overall behaviour of the building model, the skeleton has a very low stiffness. Further, to avoid spurious modes of resonance in the skeleton within the considered frequency range up to 250 Hz, the beams have a very low mass. In the present case, 3-node Mindlin beam elements with a node distance of 300 mm, a cross-sectional area of 10×10 mm^2, a mass density of 1 kg/m^3, and a Young's modulus of 1 GPa are applied.

Nonstructural mass is included to obtain resonance frequencies of the FE model that more realistically represent the behaviour of a real building. Thus, a discrete mass of 100 kg is applied at each of the retained nodal points on the top surface of the floor panels. As an example of a final model, Figure 5 shows House 3-2-1 with module lengths $(L \times H \times W) = (4.80 \times 3.00 \times 4.80)$ m^3 and a rib distance of 600 mm. This model has a total of 24,940 degrees of freedom. Example Eigen modes are shown in Figure 6.

By inspection of Figure 6 it can be seen that the first modes of resonance related to vibrations in the z-direction (Mode 1), the x-direction (Mode 2), and torsion about the y-axis (Mode 9) lie very close for the present building. This is expected since the x-walls and z-walls have similar stiffnesses regarding bending as well as in-plane shear. Further, it is observed that the first local modes of bending in the floor panels occur between the first three global modes of resonance. Actually, a total of six such local floor modes exist at a frequency of 19 Hz, but only one of the modes is visualized in the figure.

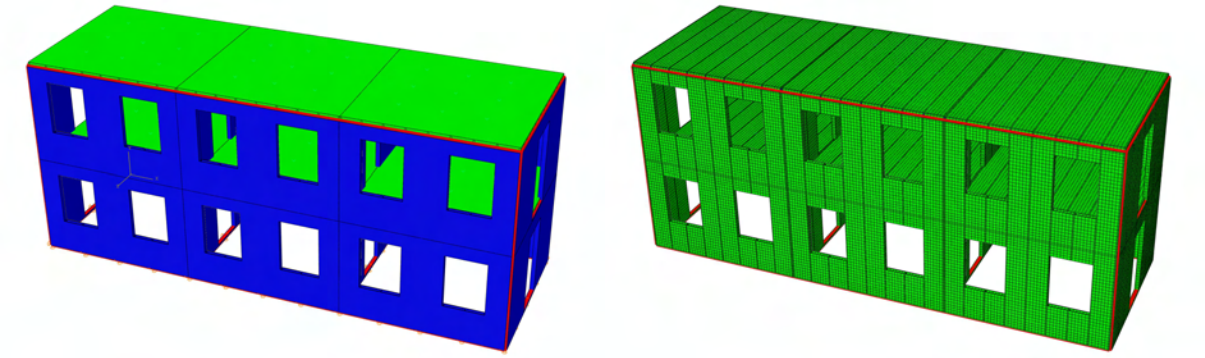
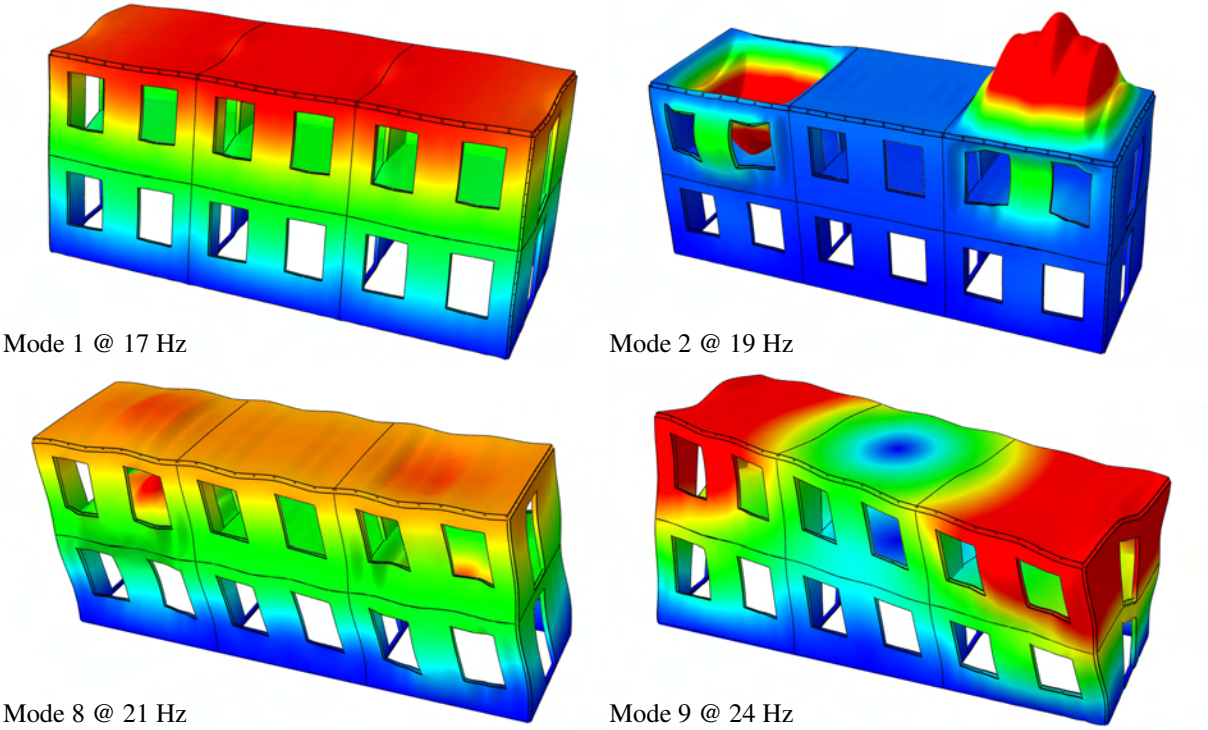


Figure 5: Example of a modular finite-element building model. Left: House 3-2-1 with module lengths $(L \times H \times W) = (4.80 \times 3.00 \times 4.80)$ m^3 and rib distance 600 mm. Wall panels are blue, floor panels are green, and the artificial skeleton is red. Right: Finite-element mesh (mesh size $\leq$ 100 mm).



Mode 1 @ 17 Hz

Mode 2 @ 19 Hz

Mode 8 @ 21 Hz

Mode 9 @ 24 Hz

Figure 6: Example Eigen modes and corresponding Eigen frequencies of House 3-2-1 with the module size $(L \times H \times W) = (4.80 \times 3.00 \times 4.80)$ m^3 and rib distance 600 mm. Red, green and blue shades indicate large, moderate and no displacements, respectively.

2.2 Analyses

Three different comparisons are made in order to analyse the influence of changes in the inherent periodicity due to ribs in the panels or repetitions of rooms along the building:

1. The response of three variants of House 2-2-1 is analysed. The module size is $(L \times H \times W) = (4.80 \times 3.00 \times 4.80)$ m^3 in all three models, but different rib distances of 600, 400 and 300 mm are applied.

2. The response of five buildings with two storeys and one room in the width direction is assessed. The numbers of rooms in the length direction are 2, 3, 4, 5 and 6, respectively. The module size is $(L \times H \times W) = (4.80 \times 3.00 \times 4.80)$ m^3, and the distances between studs and joists are 600 mm.

3. Three buildings with two storeys, one room in the width direction and a total length of 14.40 m are considered. The module height is $H = 3.00$ m and the module width is $W = 4.80$ m in all three models. The module lengths are $L = 7.2$ m, $L = 4.8$ m and $L = 2.4$ m, respectively, leading to 2, 3 or 6 rooms along the building.

In each comparison, three analyses are carried out. Firstly, the undamped Eigen frequencies and the related Eigen modes are identified in the frequency range 0–250 Hz with the purpose of quantifying the modal density related to each building. The Lanczos solver available in Abaqus has been utilized. Secondly, direct steady state analysis is performed in the frequency domain in order to investigate the response of the buildings to vertical harmonic excitation at a point on one of the floors. Again the frequency range 0–250 Hz is considered. Thirdly, the transient response to a step load in the same position as the harmonic force is studied. The load is defined with a smooth amplitude function having the values 0 N at 0 ms, 1 N at 5 ms and 0 N 10 ms. The smoothing implies that the first and second time derivatives of the amplitude function are zero at the instants 0, 5 and 10 ms where the load values are specified [10]. Time integration is performed by the Newmark scheme [15] with a time increment of 0.5 ms.

Results of the transient response obtained in the time domain will be presented in terms of vertical displacements at selected points within the respective buildings. The results in the steady state analyses are evaluated in terms of root-mean-square (RMS) velocities of the retained nodes on the floor in a given room:

$$\langle V \rangle_{\mathrm{RMS}} = \sqrt{\frac{1}{N} \sum_{n=1}^{N} \mathbf{V}_n^H \mathbf{V}_n}, \tag{1}$$

where N is the number of restrained nodes on the floor top surface, whereas $\mathbf{V}_n$ is the complex velocity amplitude vector at node n, and $\mathbf{V}_n^H$ denotes its conjugate transpose. The RMS velocities are evaluated in decibel according to the definition:

$$\langle V \rangle_{\mathrm{RMS}}^{\mathrm{dB}} = 20 \log_{10} \left(\frac{\langle V \rangle_{\mathrm{RMS}}}{V_0} \right), \quad V_0 = 1 \text{ nm/s}. \tag{2}$$

The loss in dB from one room to another can be found, simply, by subtracting the value of $\langle V \rangle_{\mathrm{RMS}}^{\mathrm{dB}}$ in the receiver room from the corresponding value in the source room.

3 Results and discussion

3.1 Eigen frequencies of finite-element building models

Figures 7–9 present a count of the Eigen modes below a given frequency for each of the considered building models. Firstly, mode counts for House 2-2-1 with module size $(L \times H \times W) = (4.80 \times 3.00 \times 4.80)$ m^3 and different distances between studs and joists are provided in Figure 7. As expected, the number of modes present in the building below a certain frequency is generally increasing with an increase of the rib distance. The trend is most pronounced at frequencies above 240 Hz, where the plates may baffle between two adjacent studs in the case with joist and stud distances of 600 mm. However, it may be observed that exceptions to the general trend occur, for example, at frequencies near 220 Hz. Here, more modes are present in the model with a rib distance of 400 mm compared to the model with the higher rib distance of 600 mm. This may be explained by the fact that the additional mass provided by the increased number of ribs reduces the Eigen frequencies related to some modes more than the increase

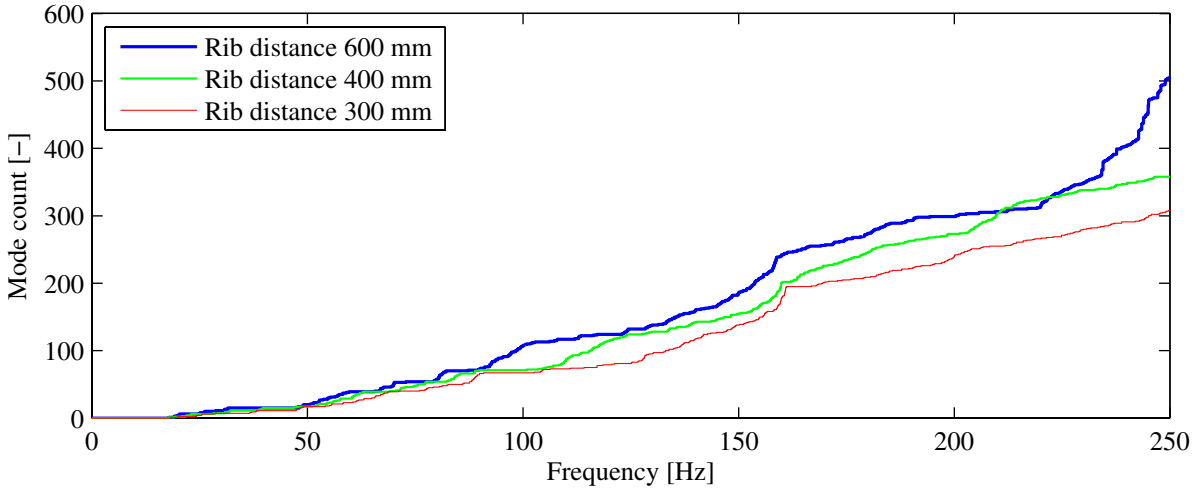


Figure 7: Eigen mode count in House 2-2-1 with module lengths $(L \times H \times W) = (4.80 \times 3.00 \times 4.80)$ m^3 and various rib distances.

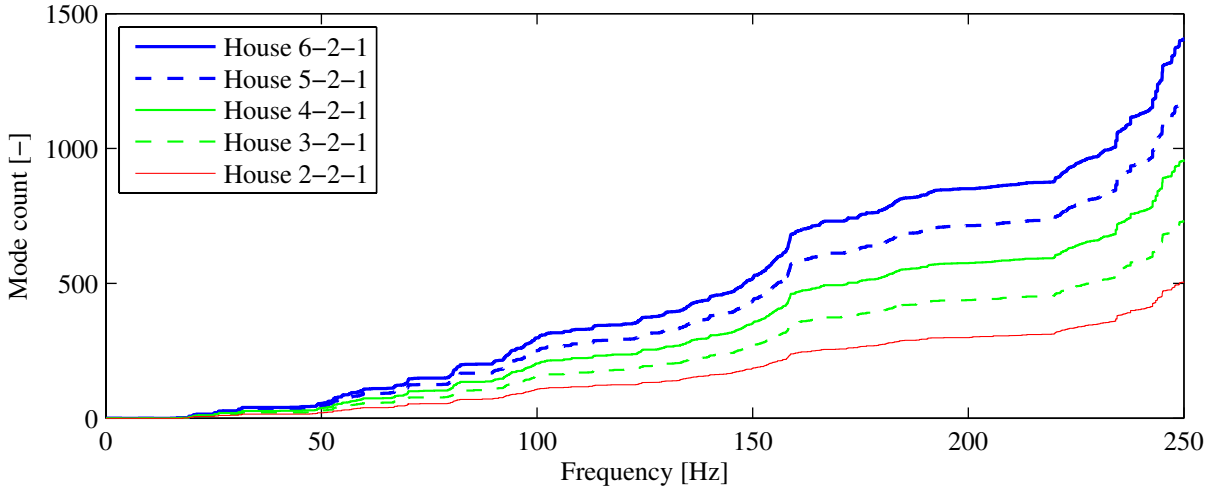


Figure 8: Eigen mode count in buildings with different numbers of modules in the x-direction. The module size is $(L \times H \times W) = (4.80 \times 3.00 \times 4.80)$ m^3, and the rib distance is 600 mm.

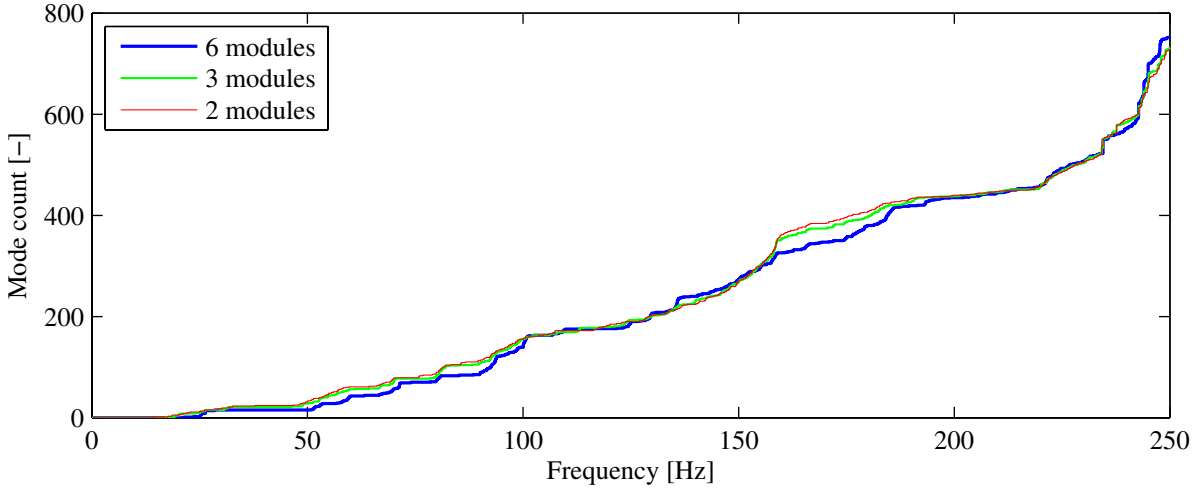


Figure 9: Eigen mode count of House N-2-1, where $N = 6, 3, 2$ is the number of modules in the x-direction. The length of the building is 14.40 m, the module size is $(L \times H \times W) = (14.40/N \times 3.00 \times 4.80)$ m^3, and the rib distance is 600 mm.

provided by the additional stiffness. The opposite effect is clearly seen at frequencies near 100 Hz and, to lesser extent, at frequencies close to 160 Hz.

Figure 8 shows the mode count in five buildings with different numbers of modules in the x-direction. The module size is in all cases $(L \times H \times W) = (4.80 \times 3.00 \times 4.80)$ m^3, and the joist and stud distances are 600 mm. It is noted that the curve for House 2-2-1 in Figure 8 is identical to the curve for a rib distance of 600 mm in Figure 7. Further, it can be observed that the number of modes is almost directly proportional to the number of modules along the building. For example, House 4-2-1 has approximately twice as many modes at all frequencies compared to House 2-2-1. This is due to the fact that only few global modes are present in the considered range of frequencies. Hence, most of the modes are related to local vibrations in the wall and floor panels.

Finally, Figure 9 provides the mode count for three different buildings: House 6-2-1, House 3-2-1 and House 2-2-1. All buildings have a length of 14.40 m, and the module size is $(L \times H \times W) = (14.40/N \times 3.00 \times 4.80)$ m^3, where $N = 6, 3, 2$ is the number of modules along the x-direction. The rib distance is 600 mm. It is observed that the number of modes is nearly the same in all three models, i.e. the number of divisions in the x-direction has marginal influence on the mode count. In the frequency ranges 50–100 Hz and, in particular, 160–190 Hz, the building with few but long modules provides the higher mode count. As opposed to this, more modes are identified in the building with six modules at frequencies near 140 Hz and again at 245 Hz. In this context it may be important to note that the z-walls each have two local modes at 138 Hz and six modes in the frequency range between 242 Hz and 247 Hz. The total number of such modes increases linearly with the number of z-wall panels in the building.

3.2 Steady-state response to harmonic excitation

Figures 10–12 show the steady state RMS velocity response of House 2-2-1 with the module size $(L \times H \times W) = (4.80 \times 3.00 \times 4.80)$ m^3 and three different rib distances. The load is applied as a vertical harmonically varying point force at the retained node placed in the middle of Floor 1-2-1, i.e. the floor of Room 1-2-1 with reference to Figure 1. At frequencies below 20 Hz, no modes exist in any of the buildings. Hence, the response corresponds to quasi-static loading of Floor 1-2-1, and there is a pronounced loss (about 50 dB) from Room 1-2-1 to Room 2-2-1. In Room 1-2-1, the velocities peak at the first few resonance modes of the floor. These modes are also excited in the next room, but with a loss of 10–20 dB.

In the frequency range 70–90 Hz, a relatively high response is observed for the floor to which the load is applied. This peak is a combination of several modes of resonance that are excited by the point force. However, the vibrations in these modes are not all transmitted with equal strength to the neighbouring room. As a result, the peak shifts to a slightly lower frequency in Room 2-2-1. From 120 Hz to 170 Hz, a significant response of Floor 1-2-1 is identified. The pass band is related to global modes that are present in all models. On the other hand, a number of pass bands and stop bands are visible in the frequency range 20-120 Hz, where the loss from Room 1-2-1 to Room 2-2-1 depends significantly on the rib distance. Differences of more than 30 dB occur, and all three models provide the higher loss at some frequencies. Thus, none of the considered rib distances is unconditionally better than the other distances.

Next, Figure 13–18 present the steady state results for five buildings, House N-2-1, with $N = 6, 5, 4, 3$ or 2 modules in the x-direction. The module size $(L \times H \times W) = (4.80 \times 3.00 \times 4.80)$ m^3 and the rib distance 600 mm have been used in all the models, and the harmonically varying vertical point force is applied in the middle of Floor 1-2-1. Firstly, in Figure 13 it is observed that the response of the loaded floor is nearly independent of the number of module repetitions

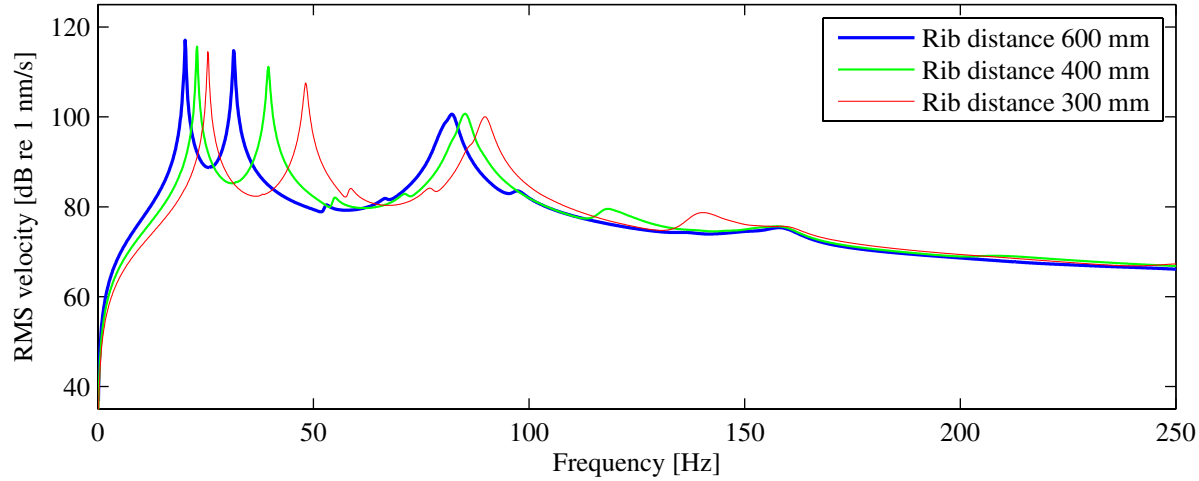


Figure 10: Steady state response in House 2-2-1 (module size $(L \times H \times W) = (4.80 \times 3.00 \times 4.80)$ m^3); RMS velocities of Floor 1-2-1 due to harmonic vertical point force excitation in the middle of Floor 1-2-1.

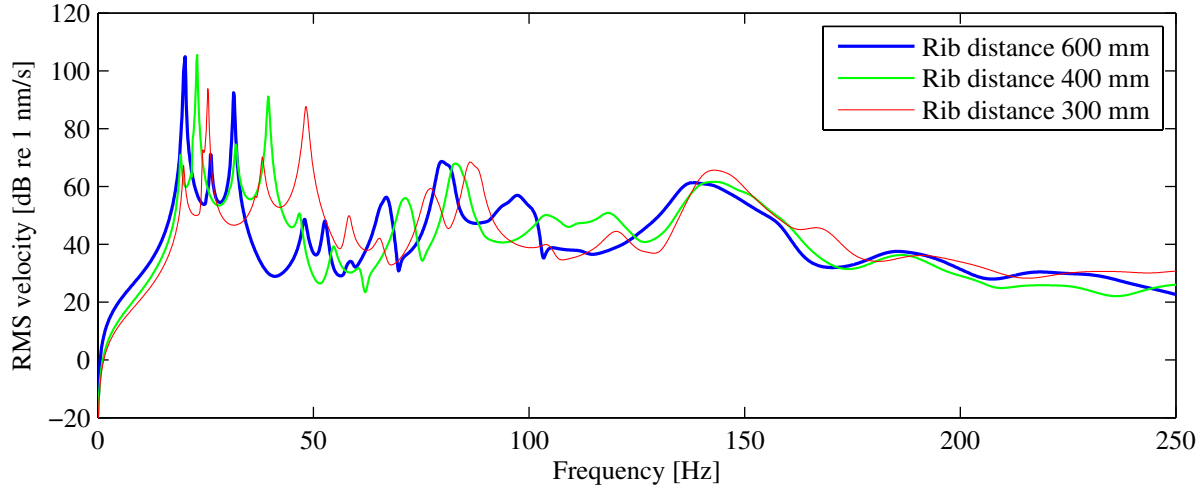


Figure 11: Steady state response in House 2-2-1 (module size $(L \times H \times W) = (4.80 \times 3.00 \times 4.80)$ m^3); RMS velocities of Floor 2-2-1 due to harmonic vertical point force excitation in the middle of Floor 1-2-1.

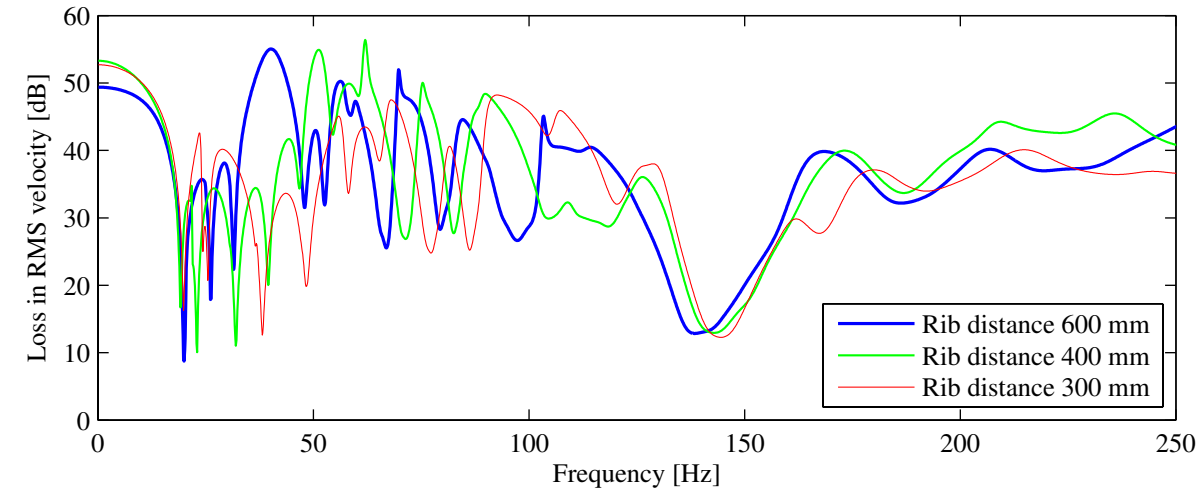


Figure 12: Steady state response in House 2-2-1 (module size $(L \times H \times W) = (4.80 \times 3.00 \times 4.80)$ m^3); loss in RMS velocities from Floor 1-2-1 to Floor 2-2-1 due to harmonic vertical point force excitation in the middle of Floor 1-2-1.

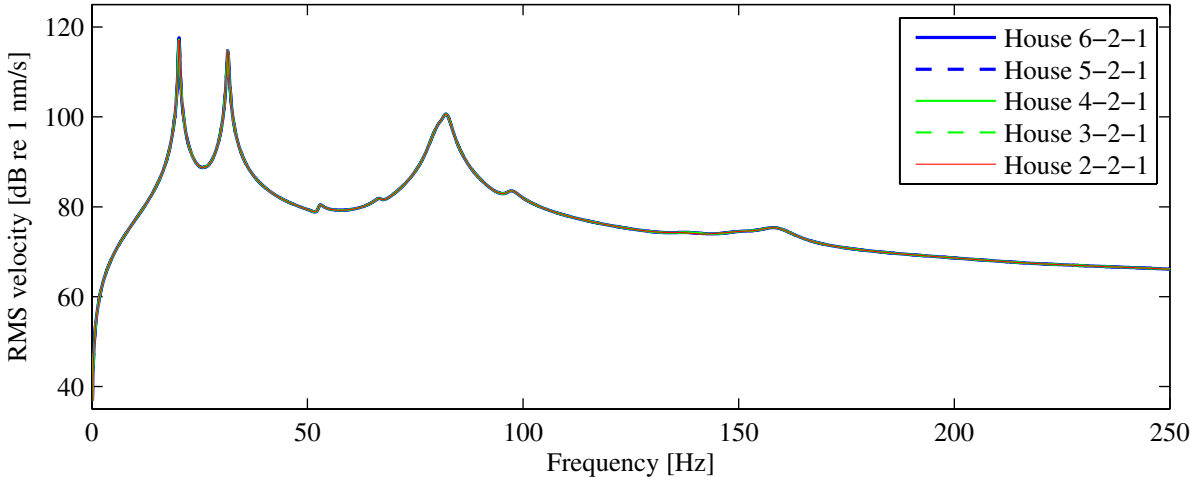


Figure 13: Steady state response in different buildings (module size $(L \times H \times W) = (4.80 \times 3.00 \times 4.80)$ m^3, rib distance 600 mm); RMS velocities of Floor 1-2-1 due to harmonic vertical excitation in the middle of Floor 1-2-1.

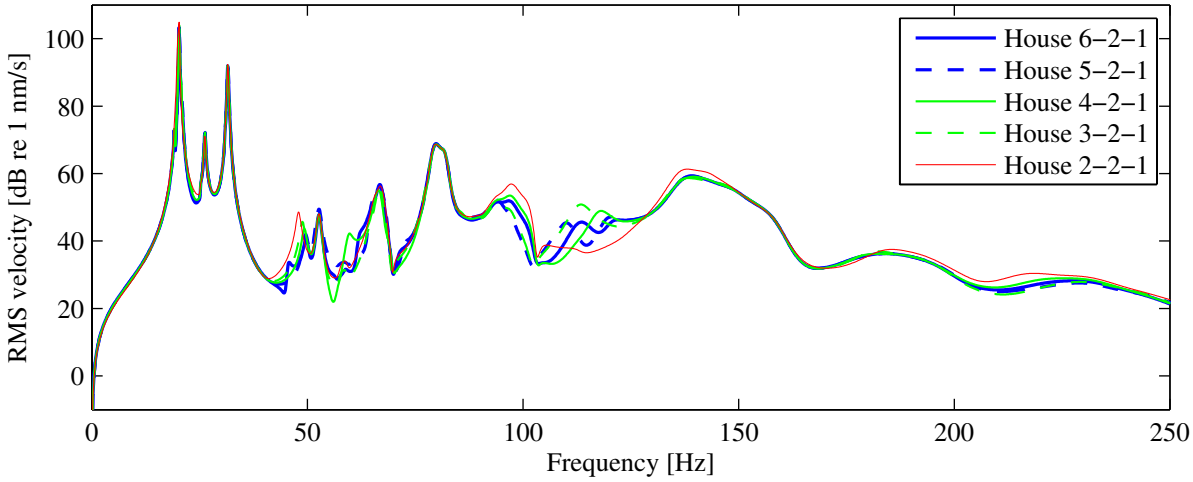


Figure 14: Steady state response in different buildings (module size $(L \times H \times W) = (4.80 \times 3.00 \times 4.80)$ m^3, rib distance 600 mm); RMS velocities of Floor 2-2-1 due to harmonic vertical excitation in the middle of Floor 1-2-1.

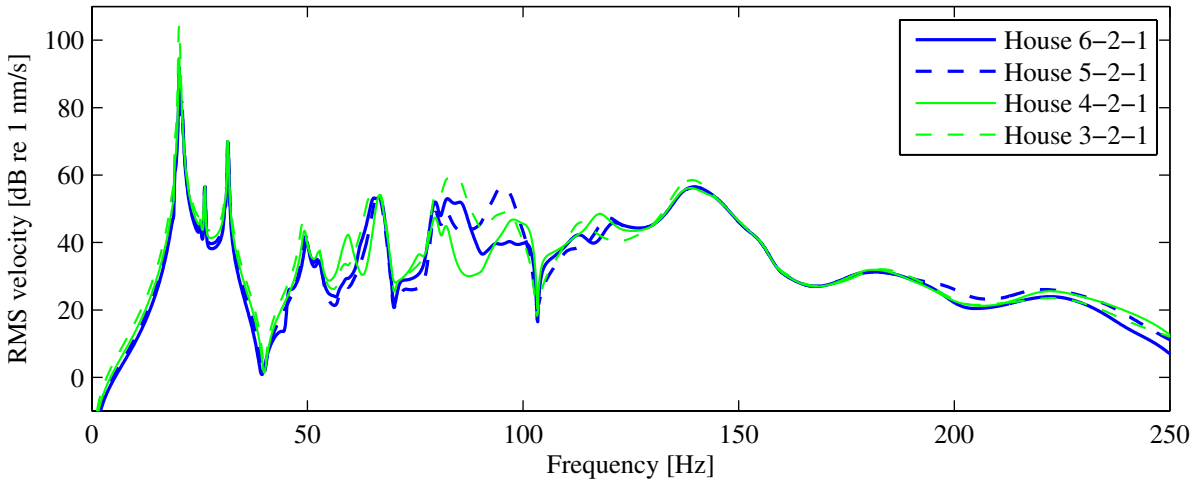


Figure 15: Steady state response in different buildings (module size $(L \times H \times W) = (4.80 \times 3.00 \times 4.80)$ m^3, rib distance 600 mm); RMS velocities of Floor 3-2-1 due to harmonic vertical excitation in the middle of Floor 1-2-1.

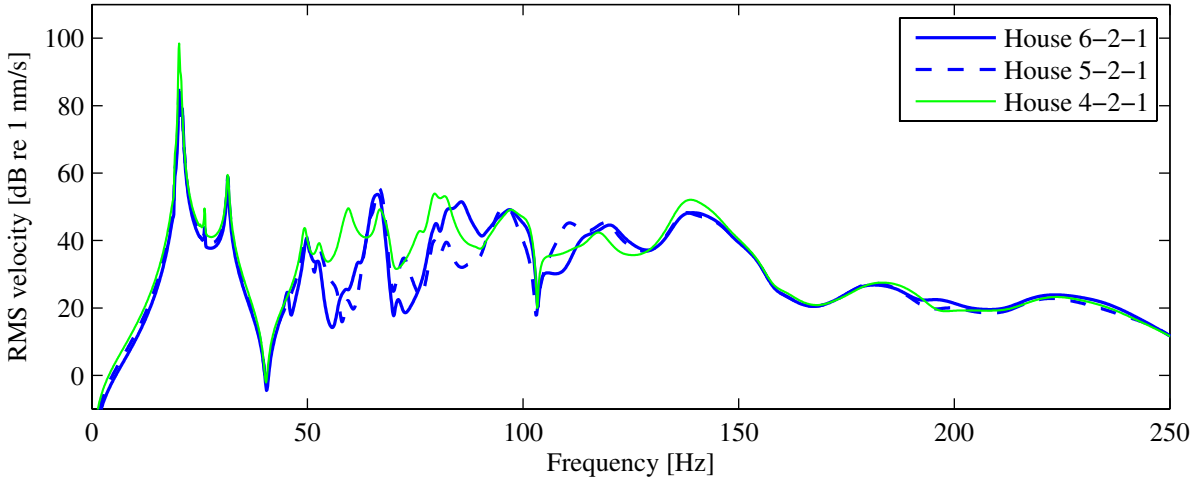


Figure 16: Steady state response in different buildings (module size $(L \times H \times W) = (4.80 \times 3.00 \times 4.80)$ m^3, rib distance 600 mm); RMS velocities of Floor 4-2-1 due to harmonic vertical excitation in the middle of Floor 1-2-1.

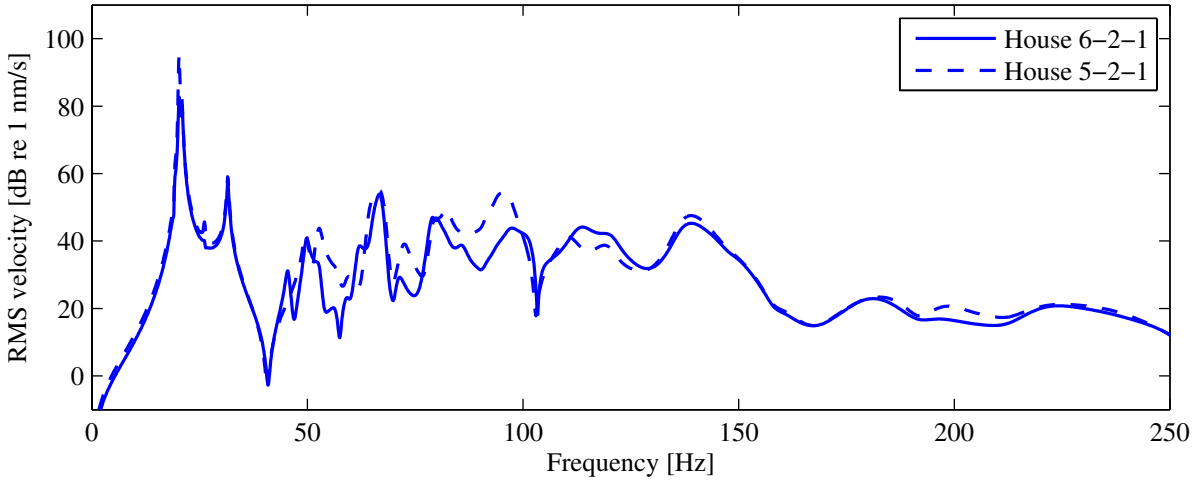


Figure 17: Steady state response in different buildings (module size $(L \times H \times W) = (4.80 \times 3.00 \times 4.80)$ m^3, rib distance 600 mm); RMS velocities of Floor 5-2-1 due to harmonic vertical excitation in the middle of Floor 1-2-1.

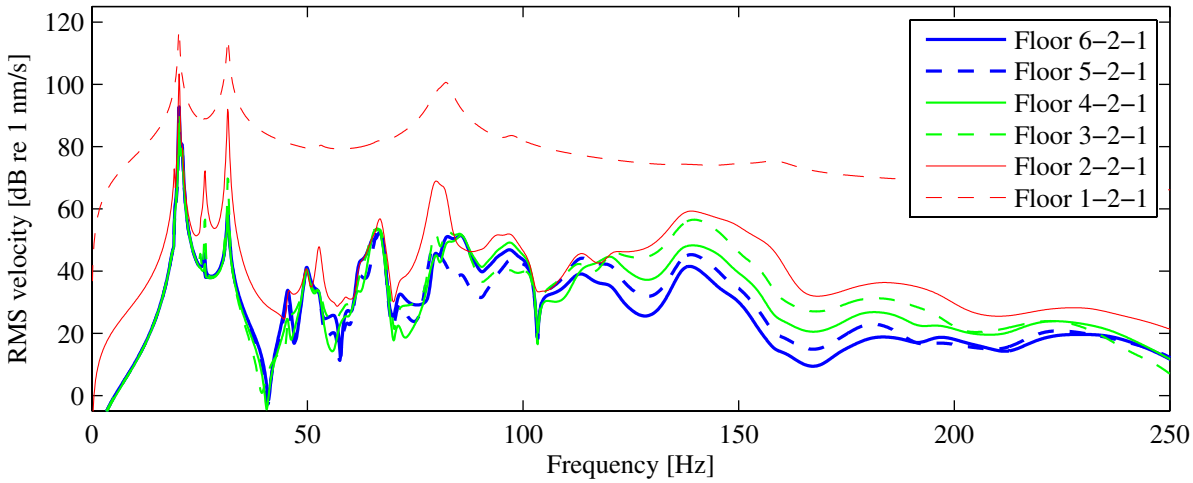


Figure 18: Steady state response in House 6-2-1 (module size $(L \times H \times W) = (4.80 \times 3.00 \times 4.80)$ m^3, rib distance 600 mm); RMS velocities of different floors due to harmonic vertical excitation in the middle of Floor 1-2-1.

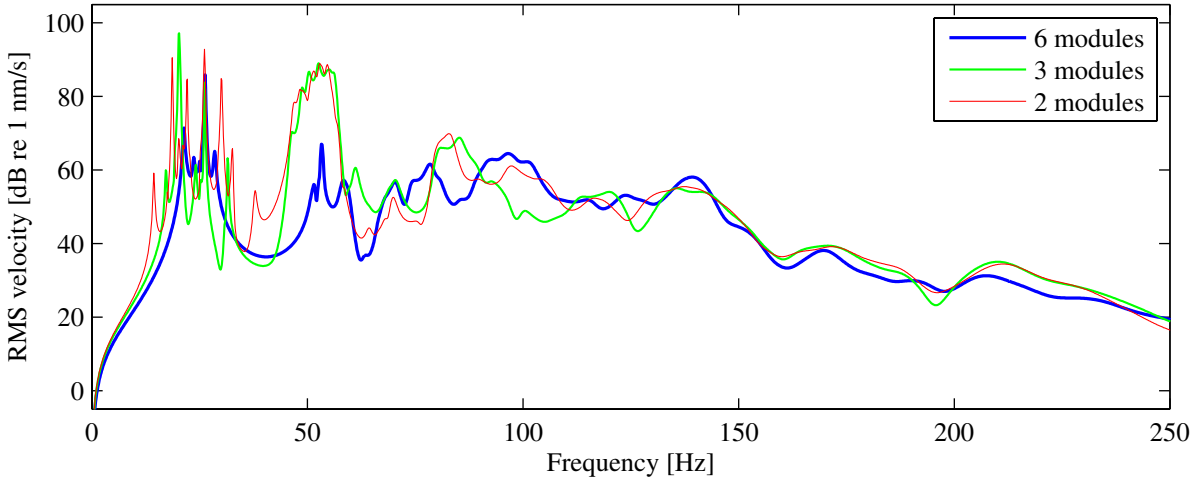


Figure 19: Steady state response in House N-2-1, where $N = 6, 3, 2$ is the number of modules in the x-direction. The length of the building is 14.40 m, the module size is $(L \times H \times W) = (14.40/N \times 3.00 \times 4.80)$ m^3, and the rib distance is 600 mm; RMS velocities of three points in the right end of the building due to harmonic vertical excitation at the point $(x, z) = (1.20, 1.20)$ m^2 on Floor 1-2-1.

along the building. From the subsequent figures it may be concluded that the response in other rooms is also only weakly influenced by the number of modules present in the x-direction. The most significant differences in RMS velocity response occur in the frequency range 40–120 Hz. Here, the response is up to 20 dB higher in some models compared to the response in other models. No clear conclusion can be made whether a building with more modules will provide smaller or larger responses. For example, in some floors and within certain frequency intervals, House 4-2-1 provides a higher RMS velocity level than House 6-2-1, whereas the opposite trend can be seen for other floors or frequencies. On the other hand, in Figure 18 it can be observed that the response in House 6-2-1 is generally decreasing with the distance away from the loaded floor, i.e. the RMS velocities of Floor 6-2-1 are lower than the RMS velocities of Floor 5-2-1, which are again lower than the RMS velocities of Floor 4-2-1 and so on. The trend is particularly clear in the frequency range 120–180 Hz.

Finally, the steady state response in three different buildings of the same length, 14.40 m, are visualized in Figure 19. The response is computed as the RMS value of the velocities in the three retained floor nodes which are as far away from the load as possible. The harmonically varying vertical point force is applied to Floor 1-2-1 at the retained node with coordinates $(x, z) = (1.20, 1.20)$ m^2. The module size is $(L \times H \times W) = (14.40/N \times 3.00 \times 4.80)$ m^3, where $N = 6, 3, 2$ is the number of modules in x-direction, and the rib distance is 600 mm. It should be noted that nonstructural mass has been added only to the retained degrees of freedom on the top surfaces of the floor panels. There are 15 such points on the floor panels with dimensions $(L \times W) = (7.20 \times 4.80)$ m^2 and only three points on the floors with dimensions $(L \times W) = (2.40 \times 4.80)$ m^2. However, the mass of a z-wall panel is about 220 kg which is only slightly less than the 300 kg of nonstructural mass it replaces. As a consequence, the total masses of the three buildings are nearly the same; but the stiffnesses are different.

It may be observed in Figure 19 that a stop band exists in the frequency range around 40 Hz. The width of this stop band increases significantly with the number of divisions in the x-direction. However, at frequencies near 100 Hz the model with six modules provide the higher response. Hence, the results a ambiguous regarding the effect of adding more periodic divisions into the same building.

3.3 Transient response to a step load on a floor

The transient responses obtained by time-domain analyses of the various considered buildings are presented in Figures 20–28. Results of the analyses with different rib distances are provided in Figures 20 and 21, whereas Figures 22–27 show the results of the analyses with different numbers of modules of the same size. Finally, Figure 25 visualizes the response in the three buildings with the same overall length but different numbers of divisions in the x-direction.

In Figure 20 it can be seen that the maximum response of the loaded Floor 1-2-1 occurs immediately after the application of the step load which has a duration of 20 ms. The response of the floor in the model with a rib distance of 300 mm is slightly smaller than the response of the floor in the model with a rib distance of 400 mm and even smaller than the response in the model with a rib distance of 600 mm. The results for the rib distance of 300 mm contain an apparent low-frequency vibration with a frequency of about 3 Hz. However, no mode with such a low frequency has been identified for the building model. Hence, the phenomenon must be caused by modulation due to two (or more) closely spaced modes vibration at higher

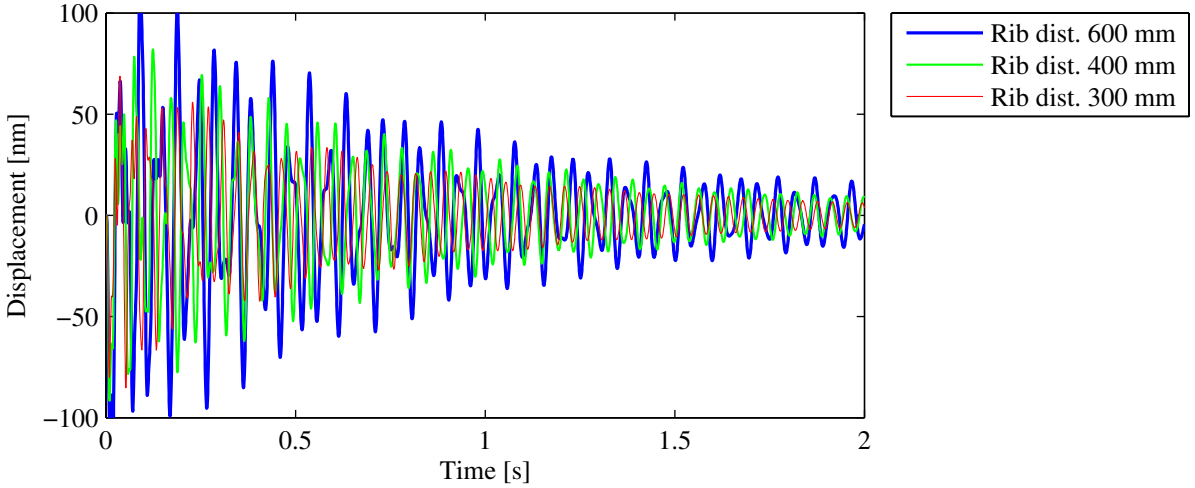


Figure 20: Transient response in House 2-2-1 (module size $(L \times H \times W) = (4.80 \times 3.00 \times 4.80)$ m^3); vertical displacement in the middle of Floor 1-2-1 due to a vertical step load in the middle of Floor 1-2-1.

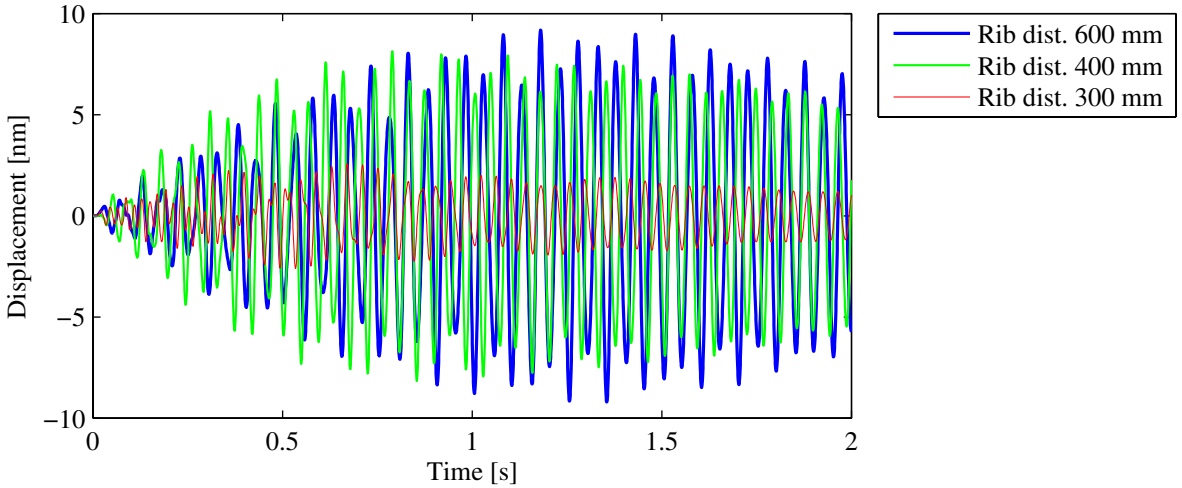


Figure 21: Transient response in House 2-2-1 (module size $(L \times H \times W) = (4.80 \times 3.00 \times 4.80)$ m^3); vertical displacement in the middle of Floor 2-2-1 due to a vertical step load in the middle of Floor 1-2-1.

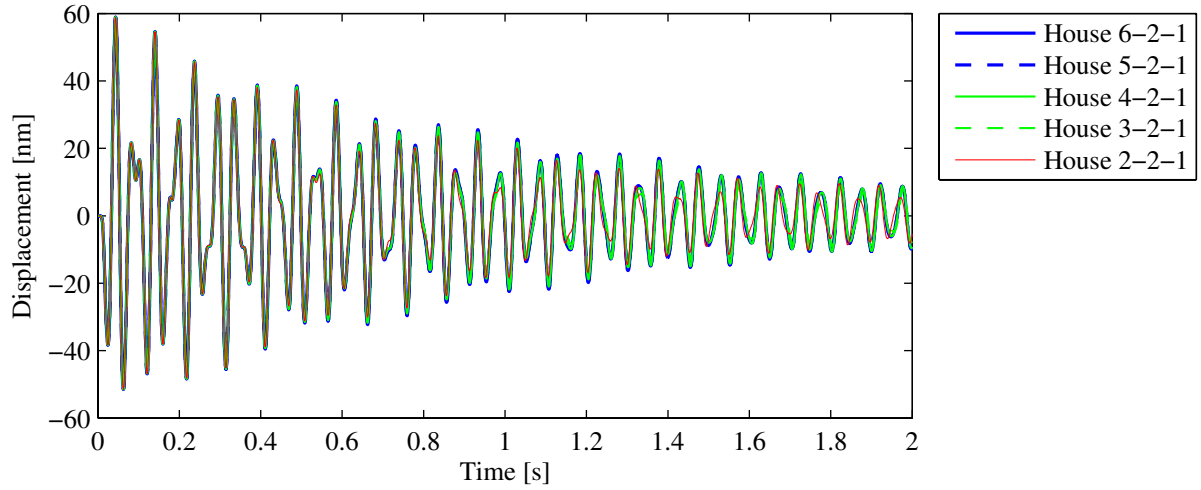


Figure 22: Transient response in different buildings with module size $(L \times H \times W) = (4.80 \times 3.00 \times 4.80)$ m^3 and rib distance 600 mm; vertical displacement in the middle of Floor 1-2-1 due to a vertical step load in the middle of Floor 1-2-1.

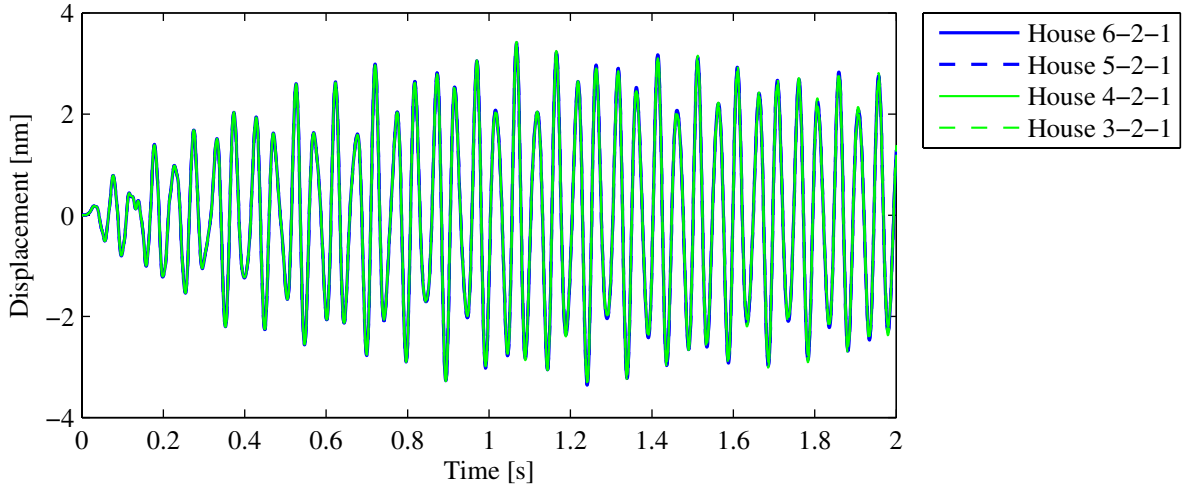


Figure 23: Transient response in different buildings with module size $(L \times H \times W) = (4.80 \times 3.00 \times 4.80)$ m^3 and rib distance 600 mm; vertical displacement in the middle of Floor 2-2-1 due to a vertical step load in the middle of Floor 1-2-1.

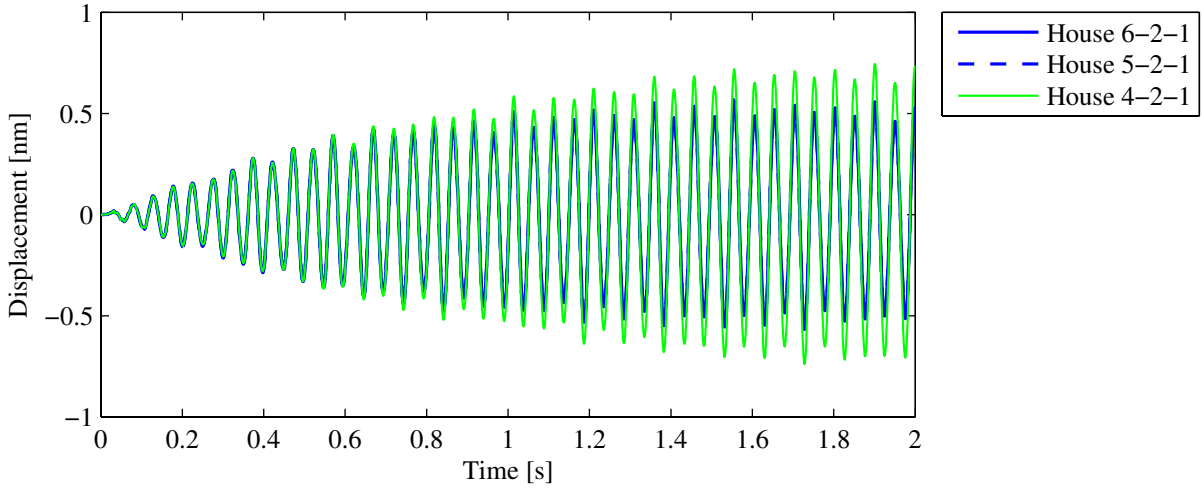


Figure 24: Transient response in different buildings with module size $(L \times H \times W) = (4.80 \times 3.00 \times 4.80)$ m^3 and rib distance 600 mm; vertical displacement in the middle of Floor 3-2-1 due to a vertical step load in the middle of Floor 1-2-1.

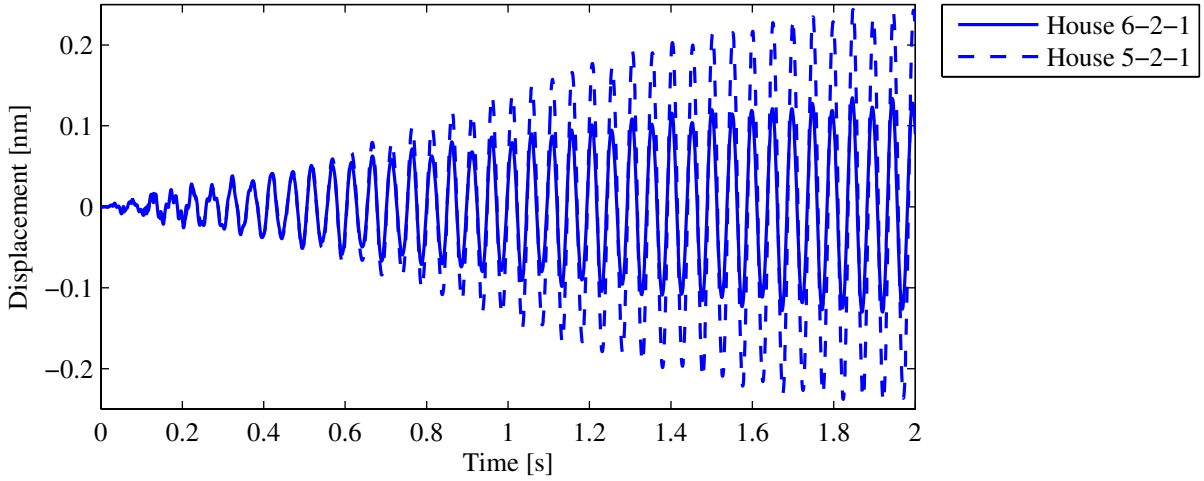


Figure 25: Transient response in different buildings with module size $(L \times H \times W) = (4.80 \times 3.00 \times 4.80)$ m^3 and rib distance 600 mm; vertical displacement in the middle of Floor 4-2-1 due to a vertical step load in the middle of Floor 1-2-1.

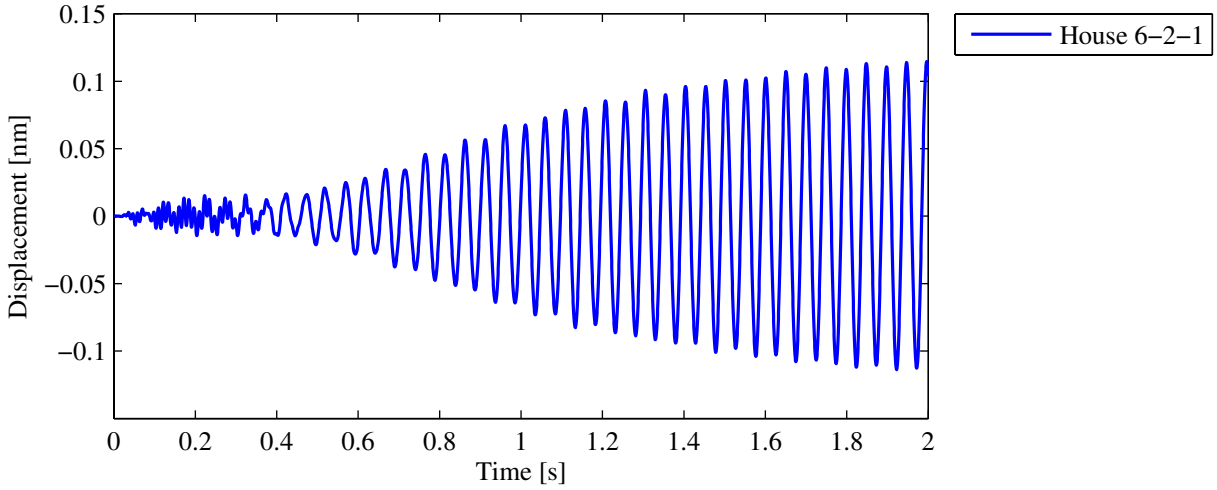


Figure 26: Transient response in House 6-2-1 and module size $(L \times H \times W) = (4.80 \times 3.00 \times 4.80)$ m^3 with rib distance 600 mm; vertical displacement in the middle of Floor 5-2-1 due to a vertical step load in the middle of Floor 1-2-1.

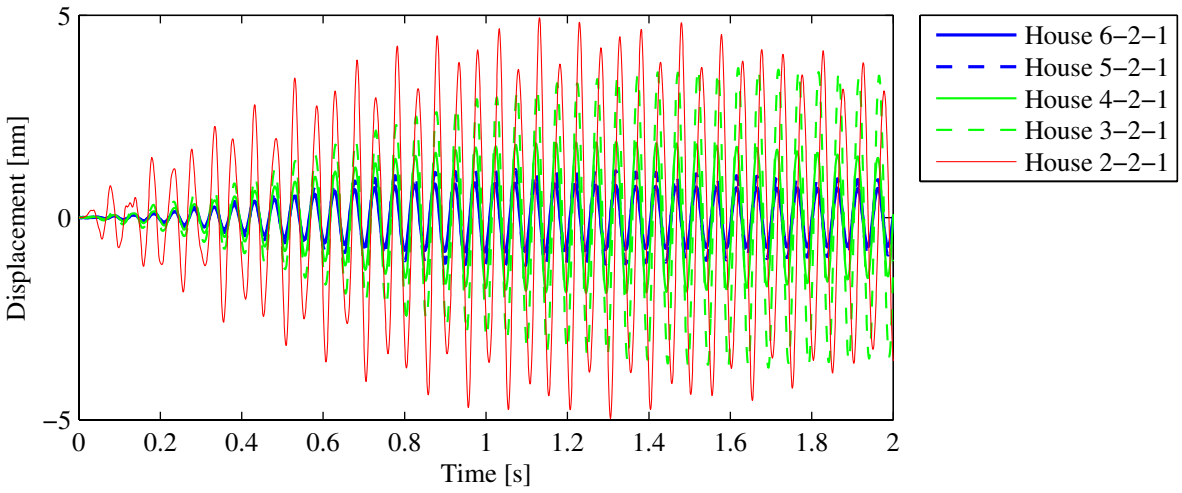


Figure 27: Transient response in House N-2-1, $N = 2, 3, 4, 5, 6$, with module size $(L \times H \times W) = (4.80 \times 3.00 \times 4.80)$ m^3 and rib distance 600 mm; vertical displacement in the middle of Floor N-2-1 due to a vertical step load in the middle of Floor 1-2-1.

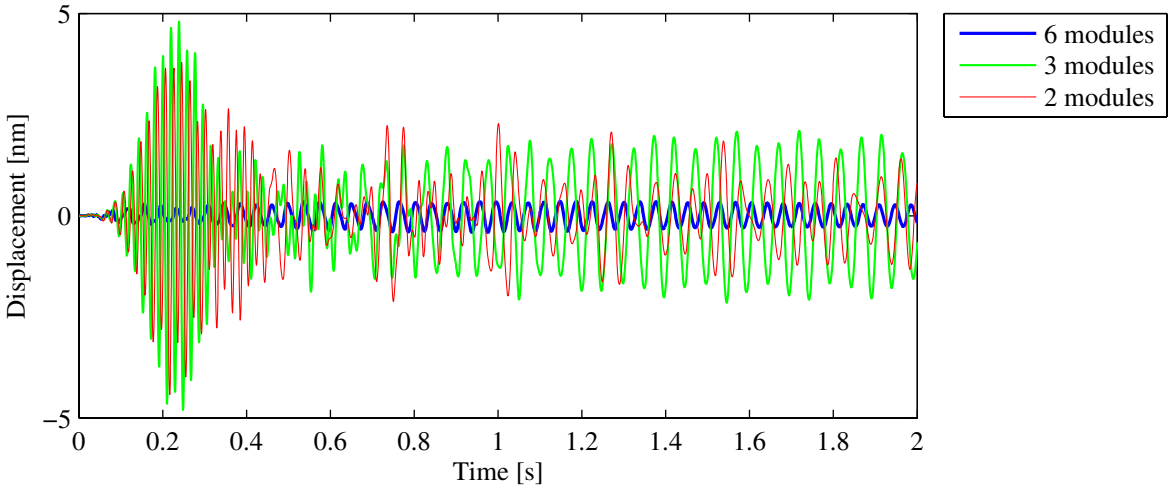


Figure 28: Transient response in House N-2-1, where $N = 6, 3, 2$ is the number of modules in the x-direction. The length of the building is 14.40 m, the module size is $(L \times H \times W) = (14.40/N \times 3.00 \times 4.80)$ m^3, and the rib distance is 600 mm; vertical displacement at the point $(x, z) = (13.20, 3.60)$ m^2 on Floor N-2-1 due to harmonic vertical excitation at the point $(x, z) = (1.20, 1.20)$ m^2 on Floor 1-2-1.

frequencies. Figure 21 reveals that the response of Floor 2-2-1 increases with time. Towards the end of the 2.0 s time interval the response is of the same magnitude in the two floors. Thus, energy is continuously transferred from Floor 1-2-1 to Floor 2-2-1. The tendency is less pronounced for the building with a rib distance of 300 mm, where the response of Floor 2-2-1 is much smaller than the responses recorded in the buildings with rib distances of 400 or 600 mm.

According to Figure 22, the response of Floor 1-2-1 is close to being identical in the five buildings with different number of modules with the same size $(L \times H \times W) = (4.80 \times 3.00 \times 4.80)$ m^3 and rib distance 600 mm. Only in the case of House 2-2-1 is there a small deviation from the other results—especially towards the end of the two-second time interval. From Figures 23–27 it can be seen that the energy introduced by the step load is gradually transferred to the other rooms. An interesting observation regards Figure 25 and especially Figure 26, where a high-frequent vibration signal is observed to appear in the first part of the response. After approximately 0.4 s, these vibrations are damped out and vibrations with a lower frequency take over. A plausible explanation is that the same number of cycles is necessary to transfer energy from one one room to another, independently of the frequency and therefore the high-frequency vibrations are visible in the far end of the building shortly after application of the load. Another essential result is observed in Figure 27 which shows the displacement response at the midpoint of the floor in the room lying in the far end of each building, as far away from the loaded floor as possible but still in the same storey. For example, the response of Floor 2-2-1 is visualized in the case of House 2-2-1, whereas the response of Floor 5-2-1 is provided for House 5-2-1. The response increases with decreasing number of modules in the x-direction. Further, by comparison with Figures 23–27 it can be seen that the response of Floor 3-2-1 of House 3-2-1 is higher than the response of the neighbouring room that lies closer to the load. Similar observations can be made regarding Floor 4-2-1 of House 4-2-1, Floor 5-2-1 of House 5-2-1, and Floor 6-2-1 of Floor 6-2-1. Thus, energy seems to accumulate in the room that lies farthest away from the load.

Finally, Figure 28 compares the vertical displacement at the point $(x, z) = (13.20, 3.60)$ m^2 on Floor N-2-1 due to harmonic vertical excitation at the point $(x, z) = (1.20, 1.20)$ m^2 on Floor 1-2-1, where $N = 6, 3, 2$ refers to the number of modules in the x-direction. In House 2-

2-1 with module size $(L \times H \times W) = (7.20 \times 3.00 \times 4.80)$ m^3 and in House 3-2-1 with module size $(L \times H \times W) = (4.80 \times 3.00 \times 4.80)$ m^3, high-frequency vibrations are transferred to the far corner of the building within the first 0.2 s. This is not the case in House 6-2-1 with module size $(L \times H \times W) = (2.40 \times 3.00 \times 4.80)$ m^3, where the vibrations in the observation point occur with a single frequency for the entire duration of the simulation. Inspection of the displacement response in the remaining floors of House 6-2-1 (not illustrated in the present paper) shows that the high-frequency vibrations are only transmitted to the first couple of rooms away from the source. Thus, a response similar to that of Floor 2-2-1 in House 2-2-1 also occurs in Floor 2-2-1 of House 6-2-1.

4 CONCLUSIONS

A number of comparisons have been made between lightweight wooden building structures with different configurations regarding rib distance, number of modules along the building and size of the module in the length direction of the building. The main findings of the present analyses are:

- A modular finite-element model with substructures generated for each wall and floor panel provides an effective platform for parametric studies of vibration transmission in a large lightweight building structure. The global models contain about 25,000 degrees of freedom, whereas a single panel model has up to 250,000 degrees of freedom before system reduction.

- The distance between studs and joists in wall and floor panels has a significant impact on the modal density in the low and mid-frequency range. Further, the rib distance strongly influences the position and width of stop bands for transmission of vibrations in the steady state. For a transient step load analysed in the time domain, some rib distances may lead to significantly smaller response than others—especially in a room adjacent to the room with excitation of the floor.

- The mode count in a lightweight wooden building structure is proportional to the number of repetitions of an identical module along the building in its length direction, since the majority of modes are related to local vibrations in floor and wall panels. The steady state response to harmonic loading is not very sensitive to the number of modules along the building. For example, the response of the loaded floor is nearly identical for buildings with two and six modules along the building. However, in a building which is several modules long, the response decreases with increasing distance away from the source, in particular in the mid-frequency range. For a step load, the vibrations are gradually transmitted from one room to another along the building. High-frequency vibrations are transmitted faster than low-frequency, but they are also damped out more rapidly.

- Buildings with the same length but divided into different numbers of modules along the building have similar numbers of Eigen modes below a given frequency. When some of the walls, dividing the building in its length direction, are removed, these wall panels will obviously not contribute to the net number of modes. However, this is compensated by an increasing number of modes in the remaining, now longer, wall and floor panels. In any case, inclusion of more walls, resulting in an increase of the number of modules and a reduction of the module size, may have a significant impact on the steady state response to harmonic loads. Hence, stop bands may change width and position. Further, the transient

response in one end of the building due to a step load in the other end of the building depends strongly on the number of modules. For example, high-frequency vibrations may not reach the far end of the building when many walls divide the building in its length direction, whereas strong vibrations occur when only one or two walls intersect the transmission path.

It should finally be mentioned that the analyses have all been based on the assumption of linear viscous material dissipation, implemented in terms of Rayleigh damping. About one to two percent of critical damping has been assumed in the considered frequency range, which may be low for a building structure with frictional joints and nonstructural elements. In future research and further development of the modular building finite-element model, more realistic damping models and damping levels should be identified and implemented.

ACKNOWLEDGEMENT

The present research is part of the Interreg project "Silent Spaces", funded by the European Union. The authors highly appreciate the financial support.

REFERENCES

[1] R. Craik, *Sound Transmission Through Buildings: Using Statistical Energy Analysis*. Gower, Aldershot, 1996.

[2] European Committee for Standardization, *EN 12354-1:2000 Building Acoustics. Estimation of Acoustic Performance in Buildings from the Performance of Elements. Airborne Sound Insulation between Rooms (3rd ed.)*. European Committee for Standardization, 2000.

[3] J. Mahn, *Prediction of flanking noise transmission in lightweight building constructions: A theoretical and experimental evaluation of the application of EN12354-1*. Technical report, University of Canterbury, Acoustics Research Group, 2007.

[4] D.J. Mead, Wave propagation in continuous periodic structures: Research contributions from Southampton, 1964-1995. *Journal of Sound and Vibration*, **190**(3), 495-524, 1996.

[5] J. Brunskog P. Davidsson (2004), Sound transmission of structures. A finite element approach with simplified room description. *Acta Acustica united with Acustica*, **90**, 847–857, 2004.

[6] F. Løvholt, C. Madshus, K. Norén-Cosgriff, Analysis of low frequency sound and sound induced vibration in a Norwegian wooden building. *Noise Control Engineering Journal*, **59**(4), 383–396, 2011.

[7] S. Maluski, B. Gibbs, Application of a finite-element model to low-frequency sound insulation in dwellings. *Journal of the Acoustical Society of America*, **108**(4), 1741–1751, 2000.

[8] P. Fiala, G. Degrande, F. Augusztinovicz, Numerical modelling of ground-borne noise and vibration in buildings due to surface rail traffic. *Journal of Sound and Vibration*, **301**, 718–738, 2007.

[9] L.V. Andersen, P.H. Kirkegaard, K. Persson, B. Niu, A modular finite element model for analysis of vibration transmission in multi-storey lightweight buildings (Paper 189). B. Topping (Ed.), Proceedings of the Eleventh International Conference on Computational Structures Technology, *Civil-Comp Proceedings*, **99**, Civil-Comp Press, Stirlingshire, Scotland, 2012.

[10] Dassault Systèmes Simulia Corp., *Abaqus 6.12 Analysis User's Manual*, Dassault Systèmes Simulia Corp., Providence, RI, USA, 2012.

[11] R. Craig M. Bambton, Coupling of substructures for dynamic analysis. *AIAA Journal*, **6**(7), 1313–1319, 1968.

[12] R. Craig, *Structural dynamics: An introduction to computer methods*. John Wiley & Sons Inc., New York, 1981.

[13] R. Guyan, Reduction of stiffness and mass matrices. *AIAA Journal*, **3**(2), 380, 1965.

[14] N. Kiel, L.V. Andersen, N. Niu, K. Persson, Different modelling approaches to coupling wall and floor panels within a dynamic finite element model of a lightweight building (Paper 190). B. Topping (Ed.), Proceedings of the Eleventh International Conference on Computational Structures Technology, *Civil-Comp Proceedings*, **99**, Civil-Comp Press, Stirlingshire, Scotland, 2012.

[15] N.M. Newmark, A method of computation for structural dynamics. *ASCE Journal of the Engineering Mechanics Division*, **85**(EM3), 67–94, 1959.

COMPDYN 2013
4th ECCOMAS Thematic Conference on
Computational Methods in Structural Dynamics and Earthquake Engineering
M. Papadrakakis, V. Papadopoulos, V. Plevris (eds.)
Kos Island, Greece, 12–14 June 2013

ON OPTIMUM DESIGN AND PERIODICITY OF BAND-GAP STRUCTURES

Niels Olhoff[1], Bin Niu[1], and Gengdong Cheng[2]

[1] Department of Mechanical and Manufacturing Engineering, Aalborg University,
Fibigerstraede 16, DK-9220 Aalborg East, Denmark
e-mail: {no, bni}@m-tech.aau.dk

[2] State Key Laboratory of Structural Analysis for Industrial Equipment,
Dalian University of Technology, 116024 Dalian, China
chenggd@dlut.edu.cn

Keywords: Band-gap Structures, Optimum Eigenfrequency Gap, Periodic Structures.

Abstract. *A band-gap structure usually consists of a periodic distribution of elastic materials or segments, where the propagation of waves is impeded or significantly suppressed for a range of external excitation frequencies. Maximization of the band-gap is therefore an obvious objective for optimum design. This problem is sometimes formulated by optimizing a parameterized design model which assumes periodicity in the design. However, it is shown in the present paper that such an a priori assumption is not necessary since, except for regions adjacent to the structural boundaries, the maximization of the band-gap alone, generally leads to significant design periodicity.*

This paper extends earlier optimum shape design results for transversely vibrating Bernoulli-Euler beams by determining new optimum band-gap beam structures for (i) different combinations of classical boundary conditions, (ii) much larger values of the orders n (n>1) and n-1 of adjacent upper and lower eigenfrequencies of maximized band-gaps, and (iii) different values of a minimum beam cross-sectional area constraint.

In the present paper, instead of maximizing band-gaps between frequencies of propagating waves or forced vibrations excited by external time-harmonic loads, the closely related problem of maximizing the gap between two adjacent eigenfrequencies ω_n and ω_{n-1} of any given consecutive orders n (n>1) and n-1, is considered. This is justified by the fact that external time-harmonic dynamic loads cannot excite resonance with high vibration levels of standing waves, if the eigenfrequencies of the structure are moved outside the range of the external excitation frequencies by the optimization.

Finally, the present study shows that if an infinite beam structure is constructed by repeated translation of an inner beam segment obtained by the aforementioned frequency gap optimization, then a band-gap of traveling waves in this infinite beam is found to correlate almost perfectly with the maximized frequency gap in the finite structure.

1 INTRODUCTION

A band-gap structure can quench vibrations and significantly suppress the propagation of waves for a certain range of frequencies. Such a frequency range is termed a band-gap or stop-band. The phenomenon may occur for elastic, acoustic or electromagnetic waves, see Refs. [1-6]. Except for regions close to the boundaries, a band-gap structure usually consists of a periodic distribution of different elastic materials, or repeated identical segments if a single elastic material is prescribed for the structure. Due to a wealth of potential applications in vibration protection, noise isolation, waveguiding, etc., the study and development of band-gap rod, mass-spring, beam, grillage, disk and plate structures, in most cases by topology optimization, have attracted increasing attention in recent years, see e.g. [5,7-18]. Elastodynamics of finite or infinite periodic 1D rod or beam structures has been studied in [6, 19-21]. Comparisons between Floquet theory ([1]) based unit cell analysis of a band structure and the vibration response analysis of the corresponding finite periodic structure, are presented in [22] for one-dimensional diatomic chains of uncoupled spheres and in [14] for 1D rod structures, respectively.

The problem of design optimization of various types of structures for maximum value of a natural frequency or maximum gap between two adjacent natural frequencies is extensively studied, see, e.g., [23-27] for shape optimization of beam structures, and reference may be given to, e.g., [12,15,16,28,29] for topology optimization of continuum structures, and to [30] for two-scale topology optimization of continuum structures with microstructures. An abundance of other references is available in the exhaustive textbook [31]. The problem of minimization of forced vibration response of structures subjected to external time-harmonic loading has been studied in, e.g., [7,17,29,32-34].

The present paper is based on recent work [35]. Instead of maximizing band-gaps between frequencies of propagating waves or forced vibration excited by external time-harmonic loads, we shall consider the closely related problem of maximizing the gap (also called the separation or difference) between two adjacent natural frequencies (synonym: eigenfrequencies) of free vibration modes (synonym: eigenmodes) of appropriate orders. Note that external time-harmonic dynamic loads cannot excite resonance phenomena with high vibration levels associated with standing waves, if the eigenfrequencies of the structure are moved outside the range of the excitation frequencies of the dynamic loading by the design optimization. We demonstrate that maximization of the frequency gap leads to significant design periodicity. Moreover, the present paper also shows that if an infinite beam structure is constructed by repeated translation of an inner beam segment obtained in the frequency gap optimization above, a band-gap of traveling waves within this infinite periodic beam matches very well with the maximized frequency separation. Thus, the problem of maximizing band-gaps between frequencies of standing or propagating waves can be solved by considering the problem of maximizing the separation between two adjacent eigenfrequencies of free vibration modes of given order.

To the authors' best knowledge, Refs. [24,26,27] were the first publications on problems of optimizing vibrating structures for maximum frequency gap – *albeit* the term difference (or separation) between adjacent natural frequencies (eigenfrequencies) was used rather than the term frequency gap in these papers.

As in the current paper, the structures considered in the papers just cited are thin, elastic, transversely vibrating Bernoulli-Euler beams without damping, and the problems are considered in non-dimensional form. The beams are subjected to shape optimization with the cross-sectional area function as design variable, and no assumption of periodicity is imposed. The cross-sections are assumed to be geometrically similar (e.g. circular), and the total

volume, length and boundary conditions of the beams are assumed to be given.

In fact, Ref. [24] considers the problem of optimizing Bernoulli-Euler beams with any combination of free, simply supported or clamped ends for maximum value of an eigenfrequency ω_n of any prescribed order n, n = 1, 2, 3, …., (see also Section 2), without specifying a minimum constraint for the variable cross-sectional area, thereby allowing vanishing cross-section of the optimized beams. The latter implies that a beam optimized with respect to a higher-order eigenfrequency ω_n (n >1) will turn out to possess n-1 degrees of inner kinematic freedom to perform *rigid-body motions* due to the formation of points of vanishing beam cross-section. At these points, either *inner beam separations* with both zero shear force and bending moment, or *inner hinges* of zero bending moment (but finite shear force) are created in such a way that all the n-1 rigid-body eigenfrequencies $\omega_1, \ldots, \omega_{n-1}$ below the maximized n-th eigenfrequency ω_n reduce to zero.

Thus, without the specification of a minimum cross-sectional area constraint, [24] presents results that simultaneously constitute solutions to the problem of maximizing the n-th eigenfrequency ω_n and the problem of maximizing the gap $\omega_n - \omega_{n-1}$ between the n-th and the (n-1)-th eigenfrequencies of the beams. It should be borne in mind that these solutions must be considered as optimum, *limiting* solutions from the point of view of practical design.

In [24], the governing equations are derived by the calculus of variations and solved numerically by a successive finite difference technique based on a formal integration of the problem for relatively low values of the given order n of the eigenfrequency ω_n. For any higher value of n, the inner beam separations make it possible to solve very easily the maximum ω_n and the maximum $\omega_n - \omega_{n-1}$ problems (including the determination of the corresponding optimum beam designs) with the aid of a very simple quasi-analytical method of "Scaled Optimum Beam Elements" developed in [24]. Thus, it may be stated that for beams with any combination of the classical beam end boundary conditions mentioned above, the optimum solutions corresponding to any given value of n are presented in [24]. These early frequency gap beam results clearly show that already starting at moderate values of n, say n=5, the optimum beam designs exhibit a periodicity that increases significantly with increasing values of n.

In contrast to the paper just discussed, a minimum cross-sectional area constraint (prohibiting creation of inner beam separations and hinges), was taken into account in the follow-up papers [26,27] which present two slightly different mathematical formulations of the problem of directly maximizing the eigenfrequency gap $\omega_n - \omega_{n-1}$ for cantilever beams. The beams are optimized with and without attached non-structural masses, and numerical results are presented for values of n up to 5.

The present paper aims to highlight and extend design results obtained in [24, 26,27] by determining and presenting new optimum frequency gap beam structures in non-dimensional form for (*i*) different combinations of classical boundary conditions, (*ii*) much larger values of the orders n and n-1 of the adjacent upper and lower eigenfrequencies of maximized frequency gaps, and for (*iii*) different values of a positive minimum cross-sectional area constraint. The new results are obtained by finite element and gradient based optimization using analytical sensitivity analysis. The new solutions are compared with corresponding limiting optimum solutions obtained without minimum cross-sectional area constraint by usage of the aforementioned method of "Scaled Optimum Beam Elements" developed in [24].

The remainder of this paper is organized as follows. First, the optimization formulation of maximizing gaps between adjacent eigenfrequencies is presented in Section 2. Section 3

presents sensitivity analysis results and an incremental numerical procedure for solutions of the optimization problems. In Section 4, several numerical examples are presented and discussed. Section 5 contains a discussion of interesting characteristics of the problem when considered in geometrically unconstrained form. In Section 6, a repeated inner segment of the optimized beam is analyzed via Floquet theory and the waveguide finite element (WFE) method to identify the pass-bands and stop-bands of traveling waves. Subsequently, forced vibration of the optimized beam subjected to an external time-harmonic excitation is performed to study the vibration filter effect of the optimized periodic beam. Finally, observations and conclusions are drawn based on the optimization results.

2 FORMULATION FOR MAXIMIZING GAPS BETWEEN ADJACENT EIGENFREQUENCIES FOR BEAM STRUCTURES

Bernoulli-Euler beams of given length L, and volume V are considered for the frequency gap optimization problem, where only free, transverse vibration frequencies (eigenfrequencies) and associated modes (eigenvectors) are included. The beams are made of a linearly elastic material with Young's modulus E and mass density γ, and have variable, but geometrically similar (e.g., circular) cross-sections with the relation $I = cA^2$ between the area moment of inertia I and the cross-sectional area A. The constant c is given by the cross-sectional geometry.

By introducing a dimensionless coordinate $x = X/L$, $0 \le x \le 1$ and cross-sectional area function $\alpha(x) = A(x)L/V$ along the beam, the dimensionless n-th eigenvalue λ_n ($\lambda_n = \omega_n^2$, where ω_n is the dimensionless circular eigenfrequency) associated with free, transverse vibrations takes the form [24]

$$\lambda_n = \omega_n^2 = \frac{\bar{\omega}_n^2 \gamma L^5}{cEV}, \tag{1}$$

where $\bar{\omega}_n$ is the dimensional n-th circular eigenfrequency of the given beam.

In a dimensionless finite element setting where the non-dimensional length and volume of the beam are both assigned unit value, the problem of design optimization with the objective of maximizing the gap between two adjacent frequencies ω_n and ω_{n-1} of given orders n and n-1, can be formulated as follows:

$$\begin{aligned}
&\max_{\alpha_e} \left\{ \Delta(\omega^2) = \omega_n^2 - \omega_{n-1}^2 \right\} && (a)\\
&\text{subject to}\\
&\mathbf{K}\boldsymbol{\phi}_j = \omega_j^2 \mathbf{M}\boldsymbol{\phi}_j,\ j = 1, \ldots, J, && (b)\\
&\boldsymbol{\phi}_j^T \mathbf{M}\boldsymbol{\phi}_k = \delta_{jk},\ j, k = 1, \ldots, J, && (c)\\
&\sum_{e=1}^{N_E} \alpha_e l_e - 1 \le 0, && (d)\\
&0 < \alpha_{\min} \le \alpha_e,\ e = 1, \ldots, N_E. && (e)
\end{aligned} \tag{2}$$

Here, ω_j and $\boldsymbol{\phi}_j$ are the dimensionless j-th eigenfrequency and corresponding eigenvector, respectively, and $\Delta(\omega^2)$ is the difference between the squares of two consecutive eigenfrequencies of given orders n and n-1 (n = 2, 3, …). In Eq. (2b), **K** and **M** are

symmetric positive definite global stiffness and mass matrices (with corresponding element matrices available in [36]) of the generalized structural eigenvalue problem for the vibrating beam structure. Thus, the J candidate eigenfrequencies ($J > n$) considered in the optimization problem will all be real and can be ordered as follows by magnitude:

$$0 < \omega_1 \le \omega_2 \le \ldots \le \omega_J \tag{3}$$

Eq. (2c) imposes the conditions of $\mathbf{M}$ orthonormalization of the corresponding eigenvectors, where δ_{jk} denotes Kronecker's delta.

The dimensionless optimization problem (2) is discretized by subdividing the beam into N_E finite elements of equal lengths $l_e = 1/N_E$ with individual cross-sectional areas $\alpha_e \left(e = 1, \ldots, N_E\right)$, which play the role as design variables of the discretized problem. Hence, Eq. (2d) expresses the non-dimensional (unit) volume constraint for the problem, and in Eq. (2e) a positive minimum cross-sectional area constraint value $\alpha_{\min}$ is prescribed for the design variables $\alpha_e \left(e = 1, \ldots, N_E\right)$. The value of $\alpha_{\min}$ is to be chosen less than the mean (unit) value of the cross-sectional area of the dimensionless beam, and larger than zero to avoid singularity of the stiffness matrix.

Using an extended bound formulation, cf. [37,38,12], the original optimization problem in Eq. (2) can be reformulated as in Eq. (4) where two scalar variables β_1 and β_2 are introduced. These scalar variables denote the upper and lower bound parameters in the constraint equations (4b) and (4c), respectively, and at the same time the difference between them in the objective function will be maximized.

$$\begin{aligned}
&\max_{\beta_1, \beta_2, \alpha_1, \ldots, \alpha_{N_E}} \left\{\beta_2 - \beta_1\right\} && (a)\\
&\text{subject to}\\
&\beta_2 - \omega_j^2 \le 0, \; j = n, n+1, \ldots, J, && (b)\\
&\omega_j^2 - \beta_1 \le 0, \; j = 1, \ldots, n-1, && (c)\\
&\mathbf{K}\boldsymbol{\phi}_j = \omega_j^2 \mathbf{M}\boldsymbol{\phi}_j, \; j = 1, \ldots, J, && (d)\\
&\boldsymbol{\phi}_j^T \mathbf{M}\boldsymbol{\phi}_k = \delta_{jk}, \; j, k = 1, \ldots, J, && (e)\\
&\sum_{e=1}^{N_E} \alpha_e l_e - 1 \le 0, && (f)\\
&0 < \alpha_{\min} \le \alpha_e, \; e = 1, \ldots, N_E. && (g)
\end{aligned} \tag{4}$$

It is emphasized that the two bound variables β_1 and β_2 serve as design variables together with the cross-sectional areas. The bound formulation is convenient for handling of difficulties concerning multiple eigenfrequencies. To accommodate the possibility of existence or creation of multiple eigenfrequencies, sensitivity results for multiple eigenfrequencies are needed (see, e.g., [15,39] for an overview and papers cited therein), and the results will be briefly presented in the next section.

3 INCREMENTAL FORMULATION BASED ON SENSITIVITY RESULTS FOR SIMPLE AND MULTIPLE EIGENFREQUENCIES

The following brief account lends itself to Refs. [15,16].

3.1 Sensitivity results for simple eigenfrequencies

If the *j*-th eigenfrequency is simple (unimodal), the corresponding eigenvector $\boldsymbol{\phi}_j$ is unique (up to a multiplying factor) and the eigenfrequency will be differentiable with respect to the design variables α_e. The derivative of the *j*-th eigenvalue $\lambda_j = \omega_j^2$ with respect to a design variable α_e is given in [40],

$$\frac{\partial \lambda_j}{\partial \alpha_e} = \boldsymbol{\phi}_j{}^T \left(\frac{\partial \mathbf{K}}{\partial \alpha_e} - \lambda_j \frac{\partial \mathbf{M}}{\partial \alpha_e} \right) \boldsymbol{\phi}_j, \; e = 1, \ldots, N_E \,. \tag{5}$$

Here the derivatives of the dimensionless, global matrices **K** and **M** can be calculated explicitly from the element stiffness and mass matrices in [36]. If all the design variables are changed simultaneously, the linear increment $\Delta\lambda_j$ of the simple eigenvalue $\lambda_j = \omega_j^2$ is given by the scalar product

$$\Delta\lambda_j = \nabla\lambda_j^T \, \Delta\boldsymbol{\alpha} \,, \tag{6}$$

where $\Delta\boldsymbol{\alpha} = \left\{ \Delta\alpha_1, \cdots, \Delta\alpha_{N_E} \right\}^T$ is the vector of changes of the design variables $\alpha_e \left(e = 1, \ldots, N_E \right)$ and

$$\nabla\lambda_j = \left\{ \boldsymbol{\phi}_j^T \left(\frac{\partial \mathbf{K}}{\partial \alpha_1} - \lambda_j \frac{\partial \mathbf{M}}{\partial \alpha_1} \right) \boldsymbol{\phi}_j \,, \cdots\cdots, \boldsymbol{\phi}_j^T \left(\frac{\partial \mathbf{K}}{\partial \alpha_{N_E}} - \lambda_j \frac{\partial \mathbf{M}}{\partial \alpha_{N_E}} \right) \boldsymbol{\phi}_j \right\}^T \,, \tag{7}$$

is the vector of sensitivities (or gradients) of the eigenvalue λ_j with respect to the design variables.

3.2 Sensitivity results for multiple eigenfrequencies

If eigenfrequencies are multiple, they are not differentiable with respect to design variables in the usual sense. The difficulty is that any linear combination of the eigenvectors corresponding to a multiple eigenfrequency will satisfy the generalized eigenvalue problem (2b) and (4d), which implies that the eigenvectors are not unique. Hence, Eqs. (5)-(7) are not valid for multiple eigenfrequencies, and the derivation of design sensitivities of such eigenvalues is much more cumbersome, see, e.g. [15,16,39,41].

Our interest in multiple eigenfrequencies in the present context is due to the possibility that, as accounted for by the bound technique in Eqs. (4a-c), the upper eigenfrequency ω_n and lower eigenfrequency ω_{n-1} of the gap $\omega_n - \omega_{n-1}$ may be increased and decreased, respectively, to such an extent that one or both of them become multiple.

Thus, let us assume that the solution to the generalized, *M*-orthonormalized eigenvalue problem, Eqs. (2b,c) and Eqs. (4d,e) included in the optimization problems (2) and (4), yields a *N*-fold multiple eigenfrequency as the *upper* eigenfrequency of the gap to be maximized. The corresponding eigenvalue $\tilde{\lambda}$,

$$\tilde{\lambda} = \lambda_j = \omega_j^2, \quad j = n, \cdots, n+N-1 \tag{8}$$

will then be associated with the N ($N > 1$) eigenfrequencies ω_j with the lowest subscripts j appearing in the bound constraint (4b) in terms of β_2 which will be active for each of the above values of $j = n, \ldots, n+N-1$. In Eqs. (4) and (8) we shall assume $n+N-1 < J$, i.e., that the total number J of eigenfrequencies (counted with multiplicity) considered in problem (4) is chosen such that the J-th eigenfrequency ω_J is larger than the multiple eigenfrequency corresponding to $\tilde{\lambda}$ in Eq. (8).

Analogously, the orthonormalized eigenvalue problem (2b,c) and (4d,e) contained in problems (2) and (4) may yield an R-fold multiple eigenfrequency as the *lower* eigenfrequency of the gap. The corresponding eigenvalue $\hat{\lambda}$,

$$\hat{\lambda} = \lambda_j = \omega_j^2, \; j = n-R, \cdots, n-1, \tag{9}$$

is then associated with the R ($R>1$) eigenfrequencies ω_j with the largest subscripts j included in the bound constraint (4c) in terms of β_1 which will be active for each of the values of $j = n-R, \ldots, n-1$ in Eq. (9). In this case we shall assume that $1 \le n-R$.

Now, following [15,16,39] one finds that both for the upper (possibly N-fold) and lower (possibly R-fold) eigenfrequency of the gap, the increments $\Delta\lambda_j = \Delta(\omega_j^2)$ of the N and R members λ_j of the multiple eigenvalue $\tilde{\lambda}$ in Eq. (8) and $\hat{\lambda}$ in Eq. (9), respectively, are given by the N- respectively R-dimensional algebraic sub-eigenvalue problem

$$\det\left[\mathbf{f}_{sk}^T \Delta\boldsymbol{\alpha} - \delta_{sk}\Delta(\omega^2)\right] = 0, \tag{10}$$

where δ_{sk} is Kronecker's delta, and $\mathbf{f}_{sk}$ denote generalized gradient vectors of the form

$$\mathbf{f}_{sk}^T = \left\{ \boldsymbol{\phi}_s^T \left(\frac{\partial \mathbf{K}}{\partial \alpha_1} - \lambda_j \frac{\partial \mathbf{M}}{\partial \alpha_1} \right) \boldsymbol{\phi}_k, \ldots, \boldsymbol{\phi}_s^T \left(\frac{\partial \mathbf{K}}{\partial \alpha_{N_E}} - \lambda_j \frac{\partial \mathbf{M}}{\partial \alpha_{N_E}} \right) \boldsymbol{\phi}_k \right\}. \tag{11}$$

Note that both in Eqs. (10) and (11), $s,k = n, \ldots, n+N-1$ relate to a N-fold upper eigenfrequency of the gap, cf. Eq. (8), and $s,k = n-R, \ldots, n-1$ pertain to an R-fold lower eigenfrequency of the gap, see Eq. (9).

According to the definition in Eq. (11), each $\mathbf{f}_{sk}$ is a N_E-dimensional vector, and $\mathbf{f}_{sk}^T \Delta\boldsymbol{\alpha}$ in Eq. (10) is a scalar product for each $s,k = n, \ldots, n+N-1$ in the N-dimensional, and each $s,k = n-R, \ldots, n-1$ in the R-dimensional, matrix in Eq. (10). The label 'generalized gradient vector' for $\mathbf{f}_{sk}$ becomes apparent when comparing Eq. (11) with the expression for the gradient vector $\nabla\lambda_j$ of a simple eigenvalue λ_j in Eq. (7). Note also that $\mathbf{f}_{sk} = \mathbf{f}_{ks}$ due to the symmetry of the matrices $\mathbf{K}$ and $\mathbf{M}$, and that the two subscripts s and k refer to the orthonormalized eigenvectors from which $\mathbf{f}_{sk}$ is calculated.

As one may expect, for $N = 1$, i.e., $j = s = k = n$, Eqs. (8) and (10) verify that the upper eigenfrequency of the gap corresponds to the simple (unimodal) eigenvalue $\lambda_n = \omega_n^2$. In this case, Eq. (10) reduces to the simple algebraic equation

$$\mathbf{f}_{nn}^T \Delta\boldsymbol{\alpha} - \Delta\lambda_n = 0, \tag{12}$$

where, according to Eqs. (6), (11) and (7), we have

$$\mathbf{f}_{nn} = \nabla \lambda_n \,, \tag{13}$$

i.e., $\mathbf{f}_{nn}$ is simply the vector of sensitivities of the unimodal eigenvalue $\lambda_n = \omega_n^2$ with respect to the design variables α_e, e = 1, …, N_E, cf. Eqs. (5) and (7).

Analogously, for R=1, i.e., $j = s = k = n - 1$, Eqs. (9) and (10) verify that the lower eigenfrequency of the gap corresponds to the simple eigenvalue $\lambda_{n-1} = \omega_{n-1}^2$.

These observations have the important implication that the computational procedure delineated in the sequential sub-section is applicable independently of whether the upper and/or lower eigenfrequencies that define the gap, are members of a multiple eigenfrequency or are just a simple eigenfrequency.

3.3 Incremental formulation of the optimization problem

Based on the sensitivity analysis results in Sub-sections 3.1 and 3.2, the bound formulation of the optimization problem in Eq. (4) can be written in the following incremental form:

$$\max_{\beta_1, \beta_2, \Delta\alpha_1, \ldots, \Delta\alpha_{N_E}} \{\beta_2 - \beta_1\} \qquad (a)$$

subject to

$$\begin{aligned}
&\beta_2 - \left(\omega_j^2 + \mathbf{f}_{jj}^T \Delta\boldsymbol{\alpha}\right) \le 0,\ j = n + N = J, && (b)\\
&\beta_2 - \left[\omega_j^2 + \Delta\left(\omega_j^2\right)\right] \le 0,\ j = n, \ldots, n + N - 1, && (c)\\
&\left[\omega_j^2 + \Delta\left(\omega_j^2\right)\right] - \beta_1 \le 0,\ j = n - R, \ldots, n - 1,\ (n - R \ge 1), && (d)\\
&\left(\omega_j^2 + \mathbf{f}_{jj}^T \Delta\boldsymbol{\alpha}\right) - \beta_1 \le 0,\ j = n - R - 1,\ (if\ n - R \ge 2), && (e)\\
&\det\left[\mathbf{f}_{sk}^T \Delta\boldsymbol{\alpha} - \delta_{sk} \Delta\left(\omega^2\right)\right] = 0,\ s, k = n, \ldots, n + N - 1, && (f)\\
&\det\left[\mathbf{f}_{sk}^T \Delta\boldsymbol{\alpha} - \delta_{sk} \Delta\left(\omega^2\right)\right] = 0,\ s, k = n - R, \ldots, n - 1, && (g)\\
&\mathbf{K}\boldsymbol{\phi}_j = \omega_j^2 \mathbf{M}\boldsymbol{\phi}_j,\ j = 1, \ldots, J, && (h)\\
&\boldsymbol{\phi}_j^T \mathbf{M}\boldsymbol{\phi}_k = \delta_{jk},\ j, k = 1, \ldots, J, && (i)\\
&\sum_{e=1}^{N_E} \left(\alpha_e + \Delta\alpha_e\right) l_e - 1 \le 0, && (j)\\
&0 < \alpha_{\min} \le \alpha_e + \Delta\alpha_e,\ e = 1, \ldots, N_E. && (k)
\end{aligned} \tag{14}$$

Referring to the algebraic sub-eigenvalue problem in Eq. (10), the solutions of Eqs. (14f,g) correspond to the increments of the upper (possibly N-fold) and lower (possibly R-fold) eigenfrequency of the gap, respectively. These increments $\Delta(\omega_j^2)$ will enter respectively the upper and lower bound constraints Eqs. (14c,d) for the incremented multiple eigenfrequencies. In fact, Eqs. (14f,g) establish a relation between the independent variable increment vector $\Delta\boldsymbol{\alpha}$ and the dependent variables $\Delta(\omega_j^2)$. The incremental formulation in Eq. (14) solves a sub-optimization problem that furnishes optimum values of increments of the design variables. Then, the design variables are updated by iterative addition of the increments obtained until convergence, see [15] with a publisher's erratum [16] for further

details on this two-loop iterative procedure.

With the sensitivity results, the sub-optimization problem in Eq. (14) can be solved by using a mathematical programming method, e.g., MMA (see Ref. [42]). Alternatively, instead of the constraints in Eqs. (14f,g), $N\left(N-1\right)/2$ and $R\left(R-1\right)/2$ constraints $\mathbf{f}_{sk}^{T}\Delta\boldsymbol{\alpha}=0,\ s\neq k$, respectively, may be introduced for the β_2- and β_1-bound constraints, such that it is possible to compute the linear increments of both simple and multiple eigenvalues by the same, simple expression

$$\Delta\left(\omega_j^2\right)=\mathbf{f}_{jj}^{T}\Delta\boldsymbol{\alpha}, \tag{15}$$

where $j=n,\ldots,n+N-1$ for active β_2-bound constraints, and $j=n-R,\ldots,n-1$ for active β_1-bound constraints. In the present paper, the approach of introducing the constraints $\mathbf{f}_{sk}^{T}\Delta\boldsymbol{\alpha}=0,\ s\neq k$ is used for solving the sub-optimization problem. Further details of this approach are available in [43].

As mentioned in the end of the preceding sub-section, the formulation in Eq. (14) is applicable for problems with any mix of multiple and simple eigenfrequencies. Notice that if *N* and *R* are equal to unity, Eqs. (14f,g) reduce to the pertinent single algebraic equation for the increment of a simple eigenfrequency.

4 NUMERICAL EXAMPLES

4.1 Cantilever beams

Here, examples of cantilever beam designs for maximized higher order natural frequency (eigenfrequency) gaps $\Delta\omega_3=\left(\omega_3-\omega_2\right)$, $\Delta\omega_4=\left(\omega_4-\omega_3\right)$, $\Delta\omega_9=\left(\omega_9-\omega_8\right)$, $\Delta\omega_{10}=\left(\omega_{10}-\omega_9\right)$, $\Delta\omega_{19}=\left(\omega_{19}-\omega_{18}\right)$ and $\Delta\omega_{20}=\left(\omega_{20}-\omega_{19}\right)$ will be presented. For reasons of accuracy, an initial finite element study was carried out to ensure that calculated natural frequencies were convergent with respect to the number of elements applied along the length of the beam. Based on this study, 200 elements were adopted for the first two beam designs, and 1000 elements for the last four designs where relatively higher order natural frequencies are considered. The optimized beam designs are shown in Figs. 1, 2, 3(b), 4(d), 6(b) and 7(b). Each of these and subsequent designs in this paper are illustrated to suitable scale by their shape (contour) curves $\pm\sqrt{\alpha\left(x\right)}$, $0\le x\le 1$, after calculation of their linear dimensions $\pm\sqrt{\alpha_e}$ perpendicular to the beam axis. A lower limit $\alpha_{\min}$=0.05 is prescribed for the non-dimensional cross-sectional area in all the examples presented in the present and the two sequential sub-sections.

In order to have a convenient reference for evaluation and discussion of the optimization results, we choose a non-dimensional comparison beam with uniform cross-section and the same material, boundary conditions, (unit) volume, (unit) length, and cross-section parameter *c* as the optimized non-dimensional beams. The gap between the *n*-th and (*n-1*)-th natural frequencies of this uniform beam is denoted as $\Delta\omega_n^u$, and for the frequency gaps to be considered here, we find that $\Delta\omega_3^u$ =39.66, $\Delta\omega_4^u$ =59.20, $\Delta\omega_9^u$ =157.91, $\Delta\omega_{10}^u$ =177.65, $\Delta\omega_{19}^u$ =355.31, and $\Delta\omega_{20}^u$ = 375.04.

The corresponding frequency gaps obtained by optimization are significantly larger. Thus, the optimized cantilever beam designs in Figs. 1, 2, 3(b), 4(d), 6(b) and 7(b) have the

following frequency gaps, $\Delta\omega_3$ =129.72, $\Delta\omega_4$ =195.15, $\Delta\omega_9$ =1144.81, $\Delta\omega_{10}$ =1332.25, $\Delta\omega_{19}$ = 5141.39 and $\Delta\omega_{20}$ = 5542.40.

The designs optimized for maximum frequency gaps $\Delta\omega_3$ and $\Delta\omega_4$ subject to $\alpha_{\min}$ =0.05 in Figs. 1 and 2, respectively, are almost indistinguishable from optimum designs obtained and illustrated in Ref. [24] for the similar problems of maximizing the higher order natural frequencies ω_3 and ω_4 without a minimum constraint for the cross-sectional area of the beams; compare Figs. 1 and 2 in the present paper with Figs. 5 and 6 in [24], where the latter type of problem is treated. The designs in Figs. 1 and 2 are both obtained by using the uniform comparison beam as an unbiased initial design.

As a matter of fact, the number of local optimum designs increases with increasing values of the orders *n* and *n*-1 of the eigenfrequencies that define the frequency gap to be maximized, and with the small lower limit $\alpha_{\min}$ =0.05 prescribed for the cross-sectional area in the current examples, it turned out that for values of $n > 4$, possible optimum designs could no longer be obtained by using the uniform comparison beam as an initial design for the iterative computational procedure. Now, in order to obtain presumed optimum designs maximizing the frequency gap $\Delta\omega_n$, for given values of $n > 4$, we assumed – as was found for the cases of maximizing the frequency gaps $\Delta\omega_3$ and $\Delta\omega_4$ described above – that the design subject to the minimum allowable cross-sectional area $\alpha_{\min}$ =0.05 would be very similar to the design solution to the problem of maximizing the higher order natural frequency ω_n without specification of a minimum cross-sectional area constraint (which, in the current context, corresponds to setting $\alpha_{\min}$ =0). As already indicated in the Introduction, the latter type of problem is quite extensively covered in Ref. [24], and in Section 5 of the present paper it is briefly described how the "Method of Scaled Optimum Beam Elements" developed in [24] may be used to determine the design of a vibrating cantilever beam that maximizes an eigenfrequency of given, higher order when $\alpha_{\min}$ =0.

We shall now present examples of optimizing cantilever beam designs for maximum values of the natural frequency gaps $\Delta\omega_9$, $\Delta\omega_{10}$, $\Delta\omega_{19}$ and $\Delta\omega_{20}$ subject to the minimum cross-sectional area constraint value $\alpha_{\min}$ =0.05, i.e., examples where the possible optimum beam designs could not be obtained by applying the uniform comparison beam as an initial design in the iterative computational procedure presented in this paper.

Thus, in order to obtain the presumed optimum design maximizing the frequency gap $\Delta\omega_9$ subject to $\alpha_{\min}$ =0.05, shown in Fig. 3(b), we applied a *biased* initial design which was very similar to the optimized design obtained by application of the "Method of Scaled Optimum Beam Elements" [24] as described in Section 5 by way of the example of maximizing the 9-th natural frequency of a transversely vibrating cantilever with inner points of zero cross-sectional area and beam separation (due to $\alpha_{\min}$ =0). The design obtained by this approach was only modified by changing the cross-sectional area to be nowhere less than the value of $\alpha_{\min}$, i.e., $\alpha_{\min}$ =0.05, before it was applied as a biased initial design for the maximization of $\Delta\omega_9$ subject to this constraint value.

The resulting optimized design in Fig. 3(b) distinctly exhibits periodicity. The two natural frequencies defining the gap $\Delta\omega_9$ are both unimodal, but very close to neighbouring frequencies. The maximized frequency gap $\Delta\omega_9$ of the design, cf. the caption of Fig. 3(b), is

found to be substantially larger than the corresponding frequency gap obtained when using the uniform comparison beam as an initial design for the optimization. This may indicate that the design in Fig. 3(b) is the "best" optimum solution to the problem considered. Fig. 3(a) shows to suitable scale the free vibration modes $\phi_9(x)$ and $\phi_8(x)$ corresponding to the normalized and mutually orthogonal mode shape vectors $\boldsymbol{\phi}_9$ and $\boldsymbol{\phi}_8$ associated with the eigenfrequencies ω_9 and ω_8 that define the maximized frequency gap $\Delta\omega_9 = (\omega_9 - \omega_8)$ of the presumed optimum design in Fig. 3(b).

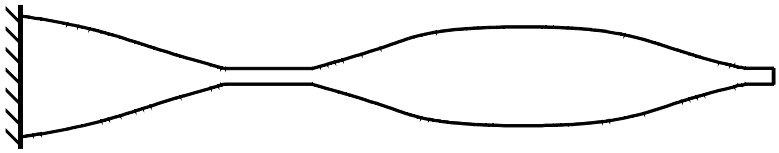


Figure 1: Cantilever with maximized frequency gap $\Delta\omega_3$ = 129.72. $\Delta\omega_3^u$ =39.66 for the comparison design

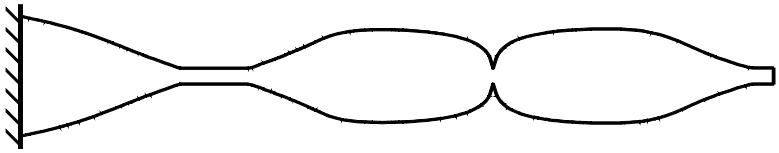


Figure 2: Cantilever with maximized frequency gap $\Delta\omega_4$ =195.15. $\Delta\omega_4^u$ =59.20 for the comparison design

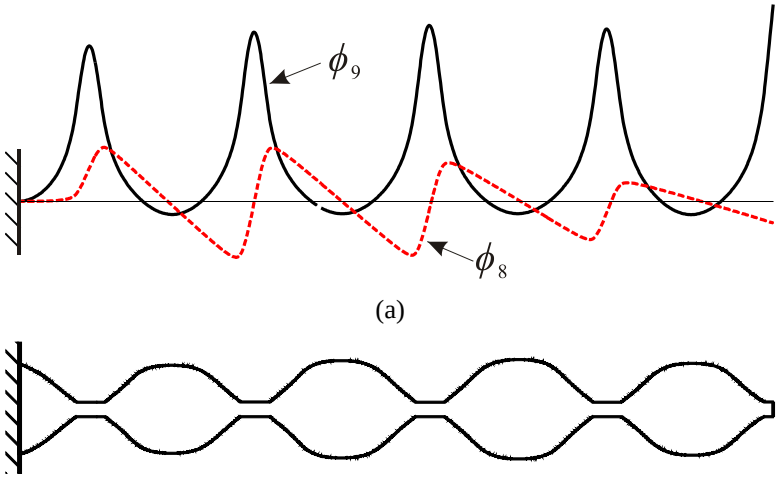


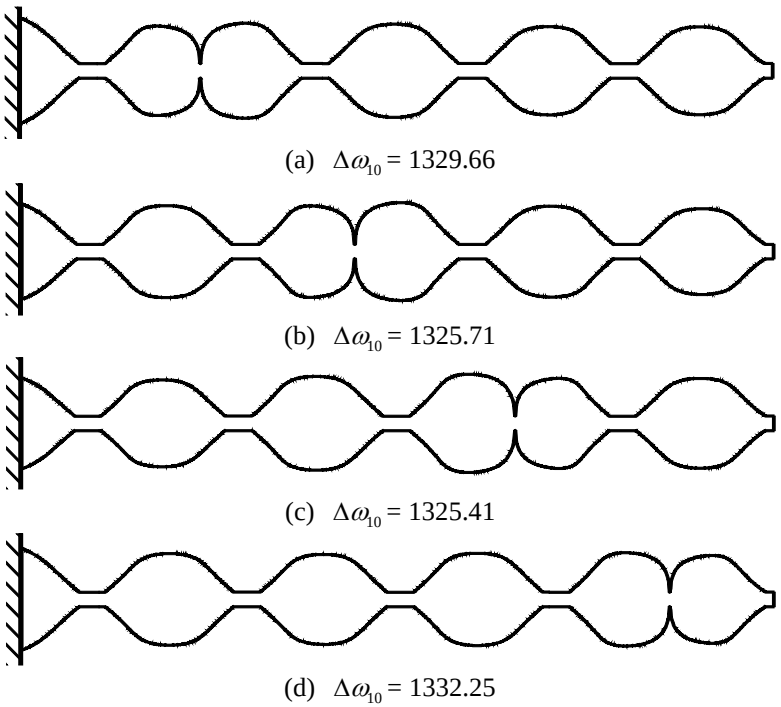
Figure 3: Cantilever with maximized frequency gap $\Delta\omega_9$ =1144.81. $\Delta\omega_9^u$ =157.91 for the comparison design. (a) Mode shapes, (b) Optimized design

With a view to obtain a physical understanding of the frequency gap mechanism, we take a closer look at the variations of the vibration modes $\phi_9(x)$, $\phi_8(x)$ and beam shape $\pm\sqrt{\alpha(x)}$ along the length $0 \le x \le 1$ of the optimized dimensionless beam in Fig. 3. Since $\phi_9(x)$ and $\phi_8(x)$ are normalized eigenfunctions associated with the eigenfrequencies ω_9 and ω_8 for the beam with the cross-sectional area function $\alpha(x)$, then, according to Rayleigh's

principle, the two eigenfrequencies are given by

$$\omega_i^2 = \int_0^1 \alpha^2 \left(\phi_i''\right)^2 dx\,,\ i = 8, 9\,. \tag{16}$$

In this equation, the integral is proportional to the elastic bending energy corresponding to the mode $\phi_i(x)$.



(a) $\Delta\omega_{10}$ = 1329.66

(b) $\Delta\omega_{10}$ = 1325.71

(c) $\Delta\omega_{10}$ = 1325.41

(d) $\Delta\omega_{10}$ = 1332.25

Figure 4: Cantilevers with maximized frequency gaps $\Delta\omega_{10}$. $\Delta\omega_{10}^{u}$ =177.65 for the comparison design. (a), (b) and (c) Local optimum solutions. (d) Presumed global optimum solution



Figure 5: Local optimum cantilever associated with frequency gap $\Delta\omega_{10}$ =901.09

The physical mechanism behind the maximized gap between the natural frequencies ω_9 and ω_8 is as follows. When vibrating with the mode ϕ_9, see Fig. 3(a), a large value of the associated frequency ω_9 is obtained by absorption of large elastic bending energy in the segments with the larger, non-uniform cross-sectional areas, cf. Eq. (16), whereas negligible bending energy is absorbed in the small, uniform segments with high flexibility. When the beam vibrates with the mode ϕ_8, see Fig. 3(a), the associated frequency ω_8 becomes very small (and the frequencies of lower order even smaller) because only the beam segment adjacent to the clamped beam end receives a small amount of bending energy. However, the nota-

ble feature is that each of the other segments of the beam essentially perform rigid body motions in a piecewise linear mode without bending, and therefore support a low value of ω_8. The bending energy from the curvatures of the "kinks" of mode ϕ_8 is negligible in Eq. (16) because the kinks occur in the small, uniform segments with high flexibility.

Figs. 4(a)-(d) depict four design solutions obtained for the problem of maximizing the natural frequency gap $\Delta\omega_{10}$. Although the values of the frequency gaps $\Delta\omega_{10}$ given for the designs in Fig. 4 are very close to each other, the four designs are seen to be distinctly different, and the eigenfrequencies defining the gaps $\Delta\omega_{10}$ are all found to be unimodal. Since the values of the frequency gaps $\Delta\omega_{10}$ are smaller for the designs in Figs. 4(a-c) than the value of the gap $\Delta\omega_{10}$ for the design in Fig. 4(d), the designs in Figs 4(a-c) must be considered to be local optimum designs, and we presume that the design in Fig. 4(d) is the global optimum design for the current problem. We managed to obtain the four different designs by applying a *biased* initial design for each of them that was very similar to one of four alternative, presumed global optimum designs available in [24] for the problem of maximizing the 10-th natural frequency when inner points of vanishing cross-sectional area are allowed.

Fig. 5 shows the design that resulted from applying the uniform comparison beam as an *unbiased* initial design when attempting to maximize the frequency gap $\Delta\omega_{10}$. As is seen from the caption of Fig. 5, the value of the frequency gap $\Delta\omega_{10}$ for this distinctly different design is much lower than that of the design in Fig. 4(d), so the design in Fig. 5 is only a local optimum solution.

Next, we present examples of cantilever beams with maximized gaps between adjacent frequencies of higher orders, i.e., $\Delta\omega_{19} = \left(\omega_{19} - \omega_{18}\right)$ and $\Delta\omega_{20} = \left(\omega_{20} - \omega_{19}\right)$. The optimized designs are shown in Figs. 6(b) and 7(b). Both beam designs are distinct, and the eigenfrequencies defining the maximized frequency gaps of the designs are both found to be unimodal, albeit very close to neighbouring eigenfrequencies.

Figs. 6(b) and 7(b) clearly show the important result that except for beam segments adjacent to the beam ends (whose designs are characteristic for the specific boundary conditions considered), the entire inner part of each of the optimum beam designs exhibit a *significant periodicity in terms of repeated beam segments of the same type*. By comparing the optimized designs in Figs. 6(b) and 3(b) and in Figs. 7(b) and 4(d), respectively, it may be concluded that the degree of this inner periodicity increases with increasing values of the orders *n* and *n-1* of the natural frequencies that define the frequency gap subjected to maximization. The free vibration modes ϕ_{19} and ϕ_{18} are drawn on the basis of the mode shape vectors $\boldsymbol{\phi}_{19}$ and $\boldsymbol{\phi}_{18}$ corresponding to the natural frequencies ω_{19} and ω_{18} that define the frequency gap $\Delta\omega_{19} = \left(\omega_{19} - \omega_{18}\right)$, and are shown in Fig. 6(a). Similarly, the free vibration modes ϕ_{20} and ϕ_{19} corresponding to the natural frequencies ω_{20} and ω_{19} defining the gap $\Delta\omega_{20} = \left(\omega_{20} - \omega_{19}\right)$ are shown in Fig. 7(a). Here, it is interesting to study the influence on the modes of the inner "dip" in the (new) beam segment at the free end of the design in Fig. 7(b). Note finally that it is obvious from Figs. 6 and 7 that the physical frequency gap mechanism described in connection with Fig. 3, also manifests itself in the current examples.

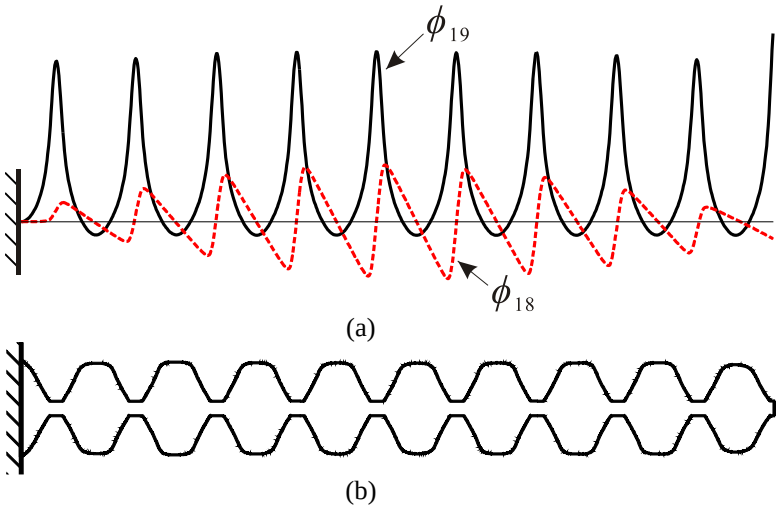


Figure 6: Cantilever with maximized frequency gap $\Delta\omega_{19}$ = 5141.39. $\Delta\omega_{19}^{u}$ =355.31 for the comparison design. (a) Mode shapes, (b) Optimized design

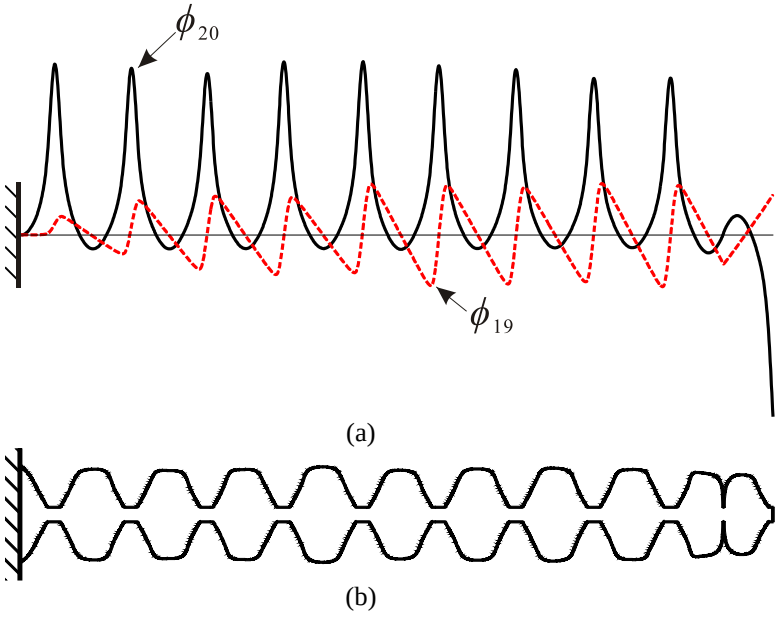


Figure 7: Cantilever with maximized frequency gap $\Delta\omega_{20}$ = 5542.40. $\Delta\omega_{20}^{u}$ =375.04 for the comparison design. (a) Mode shapes, (b) Optimized design

4.2 Clamped-clamped beams

Here, we present a few examples of optimizing clamped-clamped Bernoulli-Euler beams, still assuming a lower limit $\alpha_{\min}$ =0.05 to be prescribed for the non-dimensional cross-sectional area of the beams. The frequency gaps considered are $\Delta\omega_4$, $\Delta\omega_9$ and $\Delta\omega_{10}$, and their maximized values are found to be $\Delta\omega_4$ =309.74, $\Delta\omega_9$ =1411.34 and $\Delta\omega_{10}$ =1617.91,

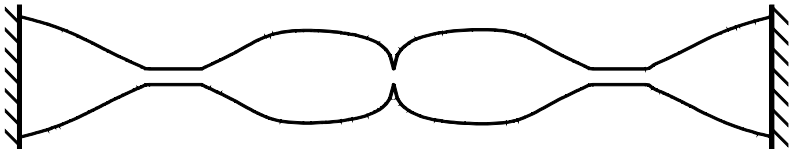


Figure 8: Clamped-clamped beam with maximized frequency gap $\Delta\omega_4$ =309.74. $\Delta\omega_4^u$ =78.96 for the comparison design

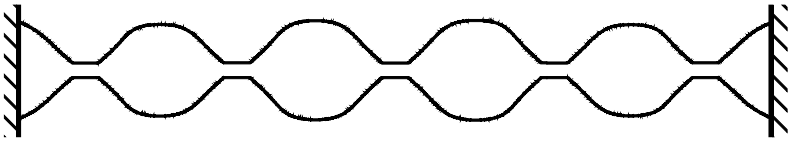


Figure 9: Clamped-clamped beam with maximized frequency gap $\Delta\omega_9$ =1411.34. $\Delta\omega_9^u$ =177.65 for the comparison design

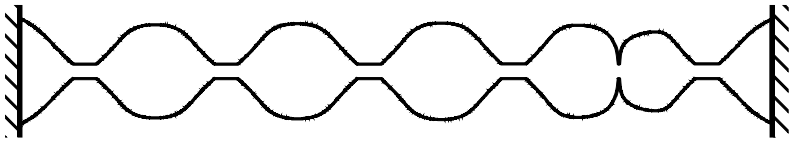


Figure 10: Clamped-clamped beam with maximized frequency gap $\Delta\omega_{10}$ =1617.91. $\Delta\omega_{10}^u$ =197.39 for the comparison design

which are significantly larger than the corresponding values $\Delta\omega_4^u$ =78.96, $\Delta\omega_9^u$ =177.65, and $\Delta\omega_{10}^u$ =197.39 for the uniform, clamped-clamped comparison beam.

The optimized beam designs are shown in Figs. 8, 9 and 10, and it is interesting to compare the design in Fig. 8 in the present paper with that in the bottom of Fig. 13 in Ref. [24]. We note that – as in Figs. 3(b) and 4(d) – it is seen in Figs. 9 and 10 that periodicity, i.e., repetition of segments of the same type, already appears in the inner part of the beam designs with maximized frequency gaps that correspond to relatively low orders of the respective natural frequencies. However, the segments adjacent to the beam ends are generally different due to different characteristics of the specific boundary conditions considered.

4.3 Clamped-simply supported beams

In this section, a few examples of Bernoulli-Euler beams clamped at one end and simply supported at the other end will be optimized. The same lower limit $\alpha_{\min}$ =0.05 as above is prescribed. The frequency gaps considered are $\Delta\omega_4$, $\Delta\omega_9$ and $\Delta\omega_{10}$, and their maximized values are found to be $\Delta\omega_4$ =274.72, $\Delta\omega_9$ =1226.18 and $\Delta\omega_{10}$ =1541.79, i.e., they are significantly larger than the corresponding values $\Delta\omega_4^u$ =74.02, $\Delta\omega_9^u$ =172.72, and $\Delta\omega_{10}^u$ = 192.46 for the uniform, clamped-simply supported comparison beam.

The optimized beam designs are shown in Figs. 11, 12 and 13. Periodicity can be observed in the inner part of the beam designs with maximized band-gaps $\Delta\omega_9$ and $\Delta\omega_{10}$, see Figs. 12 and 13. The segments adjacent to the simply supported end are generally different from those adjacent to the free or clamped end. Two different kinds of segments adjacent to the simple end support are seen in Figs. 12 and 13 that depict the beams maximizing the frequency gaps $\Delta\omega_9$ and $\Delta\omega_{10}$, respectively. This point will be discussed in Section 5.

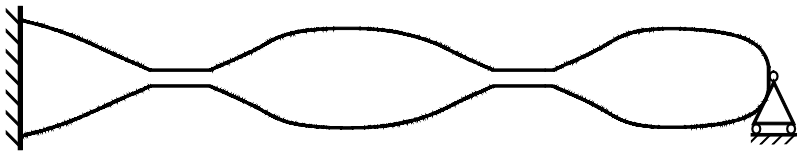


Figure 11: Clamped-simply supported beam with maximized frequency gap $\Delta\omega_4$ =274.72. $\Delta\omega_4^u$ =74.02 for the comparison design

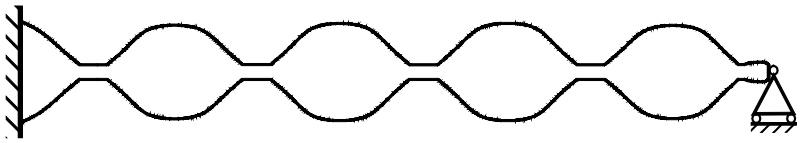


Figure 12: Clamped-simply supported beam with maximized frequency gap $\Delta\omega_9$ =1226.18. $\Delta\omega_9^u$ = 172.72 for the comparison design

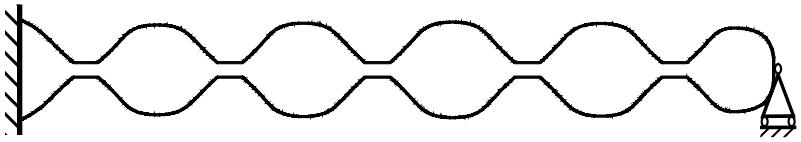


Figure 13: Clamped-simply supported beam with maximized frequency gap $\Delta\omega_{10}$ = 1541.79. $\Delta\omega_{10}^u$ = 192.46 for the comparison design

4.4 Optimum design with larger minimum area constraint value

Figs. 14, 15 and 16 depict the designs obtained by maximizing the frequency gap $\Delta\omega_9$ of a cantilever, a clamped-clamped, and a clamped-simply supported Bernoulli-Euler beam when applying a larger cross-sectional area constraint value, namely $\alpha_{\min}$ =0.5. The values of the frequency gaps $\Delta\omega_9$ for the optimized beams and the gaps $\Delta\omega_9^u$ for the corresponding uniform comparison beams are given in the captions of Figs. 14, 15 and 16.

When comparing the optimized beams in Figs. 14, 15 and 16 with the corresponding ones (same order of frequency gap and same boundary conditions) in Figs. 3(b), 9 and 12, respectively, we make the important observation that pronounced repetitions of similar segments are found in the inner parts of all these beams, and that the same degrees of periodicity in the beams in Figs. 3, 9 and 12 are obtained in the beams in Figs. 14, 15 and 16, although the latter are optimized with the considerably larger value $\alpha_{\min}$ =0.5 of the minimum cross-sectional area constraint.

By the comparison of the above-mentioned figures, we also verify that due to their larger design freedom, the beams optimized with the small value $\alpha_{\min}$ =0.05 of the lower cross-sectional area limit, are associated with significantly larger increases of the maximized frequency gaps.

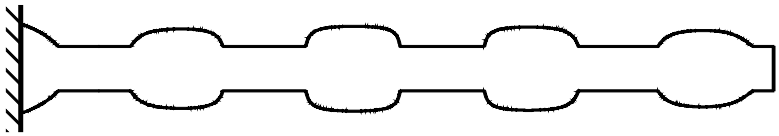


Figure 14: Cantilever with maximized frequency gap $\Delta\omega_9$ =377.91 subject to a minimum cross-sectional area constraint value 0.5. $\Delta\omega_9^u$ =157.91 for the comparison design

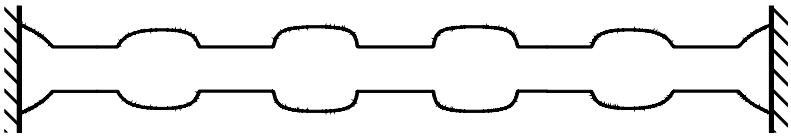


Figure 15: Clamped-clamped beam with maximized frequency gap $\Delta\omega_9$ =460.64 subject to a minimum cross-sectional area constraint value 0.5. $\Delta\omega_9^u$ =177.65 for the comparison design

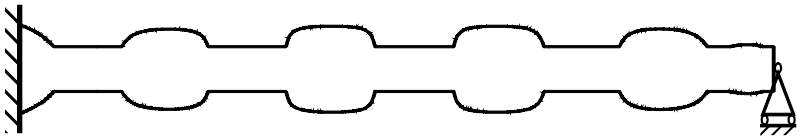


Figure 16: Clamped-simply supported beam with maximized frequency gap $\Delta\omega_9$ = 431.06 subject to a minimum cross-sectional area constraint value 0.5. $\Delta\omega_9^u$ = 172.72 for the comparison design

5 DISCUSSION

Up to now, we have considered optimum design of Bernoulli-Euler beams with the objective of maximizing, for a specified value of *n*, the separation (gap) between the (higher-order) *n*-th and (*n*-1)-th eigenfrequencies, subject to a prescribed positive value of a non-dimensional minimum allowable cross-sectional area $\alpha_{\min}$ which has been chosen as $\alpha_{\min}$ =0.05 in Sub-sections 4.1, 4.2 and 4.3, and $\alpha_{\min}$ =0.5 in Sub-section 4.4.

In this section, we shall briefly discuss the characteristics of this eigenfrequency gap optimization problem in the limiting case where the cross-sectional area function is geometrically unconstrained (except for the given volume). This means that no minimum constraint is specified for the cross-sectional area of the beam, i.e., the cross-sectional area is allowed to attain zero value in discrete points on the beam axis. *In this special case (that corresponds to* $\alpha_{\min}$ = 0 *in the context of this paper), the solutions to our problem of maximizing the gap between the eigenfrequencies* ω_n *and* ω_{n-1} *are the same as the solutions to the problem of maximizing a single, higher order eigenfrequency* ω_n *of given order n for specified volume, length, and boundary conditions of the beam*. The latter problem is treated in Ref. [24], where a large number of optimum designs are available.

The reason why the two different beam optimization problems have identical solutions, may be explained as follows. When a single eigenfrequency ω_n of given higher order *n* is maximized without specification of a minimum constraint on the cross-sectional area, the optimized beam turns out to possess *n*-1 degrees of kinematic freedom to perform rigid motions, since the cross-section vanishes at inner singular points of the beam. At these points, either *inner hinges* of zero bending moment and finite shear force, or, predominantly, *inner separations* with both zero bending moment and zero shear force, are created by the optimization of the *n*-th eigenfrequency. This has the effect that simultaneously with the

maximization of the *n*-th eigenfrequency, the *n*-1 degrees of kinematic freedom of the beam turn all the *n*-1 modes associated with the lower order eigenfrequencies into rigid body motions, and all these frequencies (including that of order *n*-1) are therefore equal to zero.

Thus, besides maximizing the *n*-th eigenfrequency of the beam, the problem formulation in Ref. [24] covers the current problem of maximizing the difference (gap) between the *n*-th and the (*n*-1)-th eigenfrequencies of the beam, if $\alpha_{\min} = 0$.

The optimized beams associated with the small minimum cross-sectional area constraint value $\alpha_{\min}$ =0.05 in Sub-sections 4.1, 4.2, and 4.3 strongly indicate the locations of formation of inner hinges and inner separations in the limiting case of $\alpha_{\min} = 0$. In Fig. 1, for example, the comparatively large inner beam segment with active minimum cross-sectional area constraint will shrink to a single point with the formation of an inner separation between the two parts of the beam in the limiting case of $\alpha_{\min} = 0$. In Fig. 2, the narrow "dip" in the cross-sectional area function indicates a point where an inner hinge with zero bending moment will be created in the case of $\alpha_{\min} = 0$. A large number of similar points with formation of inner beam separations and hinges in the case of $\alpha_{\min} = 0$ are easily identified in the figures. It is worth noting that in each of the optimum designs shown, there is no more than a single inner point with a narrow "dip" in the area function indicating formation of an inner hinge in the case of $\alpha_{\min} = 0$, but an increasing number of points that indicates creation of inner separations, when the given order of the frequency gap is increased. An exception is the design in Fig. 5 which contains several narrow "dips", but this is a *local, and not global optimum solution*.

In the optimum designs with one end clamped and the other end simply supported, see Figs. 12 and 13, we observe two kinds of segments adjacent to the simply supported end. Quite surprisingly, for the design shown in Fig. 12, the beam segment at the simply supported end will shrink to a separation in the limiting case of $\alpha_{\min} = 0$, where both the bending moment and shear force are zero at the end point of the beam. Hence, as is discussed in [24], the beam disconnects from the support, i.e., the separation makes the simple support superfluous. This implies that the optimum solution in the limiting the case of $\alpha_{\min} = 0$ will be the same as that with a free end instead of the original simply supported end. Contrary to this, the beam segment adjacent to the simply supported end in Fig. 13 will not shrink to a separation in the limiting case of $\alpha_{\min} = 0$, but remain connected to the hinge at the end point. Thus, in this case, the optimum solution behaves as expected and takes advantage of the simple support.

In Ref. [24], the dimensionless beam optimization problem is first solved for small values of *n* for various combinations of classical boundary conditions. This is done by successive iterations based on a numerical integration of the governing equations, where singularities in the *n*-th eigenmode and its derivatives are isolated at points of zero beam cross-sectional area for reasons of accuracy and convergence. Hereby a small number of different types of optimally designed, non-dimensional beam elements are produced. By proper scaling, these beam elements can be used as building blocks for optimum beams associated with much larger values of the prescribed order of their *n*-th eigenfrequency.

Since, as mentioned above, at most one inner hinge will appear in a global optimum beam with $\alpha_{\min} = 0$, and an inner hinge can be included in optimized non-dimensional beam elements mentioned above, then all other inner points of vanishing cross-sectional area in an optimum beam associated with a sufficiently large value of *n*, will be inner separations

between optimized beam elements. This is very important because the inner separations provide the means to solve very easily the optimization problem for a sufficiently large value of *n* by an optimum scaling of the optimized non-dimensional beam elements by means of very simple analytical formulas derived in [24].

As an example, let us consider the approach of determining the design of a vibrating cantilever beam that maximizes, say, the 9-th eigenfrequency ω_9 and hence the frequency gap $\Delta\omega_9 = \left(\omega_9 - \omega_8\right)$ of the beam with $\alpha_{\min}$=0. (Note that the optimized beam with $\alpha_{\min}$ = 0.05 is shown in Fig. 3.) The first step of the method consists in applying Table 2 and Eq. (30) in Ref. [24] which easily yields that the optimum cantilever design associated with *n*=9 will have four inner separations and be composed of (or assembled as) five dimensionless, optimized elements (or segments) along the length of the beam: an element "a" consisting of a cantilever optimized for *n*=1 (see Fig. 1 in Ref. [24]), followed by four elements "c" (see Fig. 11 in the reference), each consisting of a free-free beam optimized for *n*=3 (the order of the lowest non-vanishing eigenfrequency for such a beam). The four (identical) "c" elements will endow the resulting optimum beam design with periodicity. The beam elements "a" and "c", together with no more than four other elements, are necessary for the optimization of non-dimensional Bernoulli-Euler beams for any value of *n* and any combination of classical boundary conditions. These elements are all optimized with their designs shown in the first part of Ref. [24], and the elements are listed together with their optimum characteristics in Table 1 of the reference. Finally, very simple explicit algebraic expressions [(30), (57) (63) and (64)] are derived and presented in the reference, for computation of the maximum value of the *n*-th eigenfrequency (in the current example ω_9), of the optimized, assembled beam, and for the proper scaling of the lengths and volumes of the individual, optimized beam elements, such that each of these elements will vibrate at the same frequency as the assembled, optimum beam.

The approach is coined the "Method of Scaled Optimum Beam Elements" [24], and it should be mentioned that for Bernoulli-Euler beams subject to any combination of clamped, simply supported and free end boundary conditions, the geometrically unconstrained optimum solutions to the problem of maximizing the *n*-th eigenfrequency or frequency band-gap corresponding to any value of *n* are available in Ref. [24].

6 FREE WAVE PROPAGATION AND FORCED VIBRATION IN THE OPTIMIZED PERIODIC BEAM STRUCTURE

It is interesting to examine the transverse wave propagation and vibration filter effect in the optimized periodic beam structures obtained in the preceding sections. First, the wave propagation in an infinitely long periodic beam is analyzed, where the infinite beam is constructed by repeated translation of an inner beam segment obtained in the frequency gap optimization above. Subsequently, as an example, a frequency response analysis is conducted for the optimized beam in Fig. 6(b), when the beam is subjected to an external time-harmonic excitation with a view to investigate the attenuation levels in the frequency gap $\Delta\omega_{19} = \omega_{19} - \omega_{18}$.

From the Floquet theory (see [1]) and waveguide finite element (WFE) method [44], the wave propagation through the entire infinite periodic beam mentioned above can be determined by analyzing the wave motion within a single repeated beam segment, which is called a unit cell. The band-gaps can be explored by analyzing the unit cell. The transfer matrix **T** of the unit cell can be defined from the dynamic stiffness matrix of the conventional finite element analysis. Detailed derivation of the transfer matrix is available in [44]. The eigenvalues λ of the transfer matrix **T** are defined by the propagation constant *K* (Bloch

parameter) as [3,45]

$$\lambda = e^{iK} = e^{-K^{\mathrm{Im}}} e^{iK^{\mathrm{Re}}} = e^{-K^{\mathrm{Im}}} \left(\cos\left(K^{\mathrm{Re}}\right) + i \sin\left(K^{\mathrm{Re}}\right) \right), \tag{17}$$

where K^{Re} and K^{Im} represent the real and the imaginary parts of K, respectively. A stop band is found when all eigenvalues λ of $\mathbf{T}$ fulfil the condition $|\lambda| \neq 1$, i.e., $K^{\mathrm{Im}} \neq 0$. In this stop band, free wave propagation is prohibited. Due to two degrees of freedom at each end node of the unit cell, there are four eigenvalues λ_1, λ_2, λ_3, and λ_4 of the transfer matrix.

One of the inner repeated segments in Fig. 3(b) is analyzed as a unit cell in the infinite periodic beam. The magnitude $|\lambda|$ of eigenvalues is plotted as a function of the non-dimensional circular frequency defined in Eq. (1), as shown in Fig. 17, where three stop bands can be identified from the frequency range with $|\lambda| \neq 1$, indicated by three grey domains in Fig. 17. The 8th and 9th non-dimensional circular eigenfrequencies of the uniform, comparison beam and the optimized beam are also shown in Fig. 17. As is well known, no stop band exists in the infinite uniform beam in absence of damping. However, a relatively large stop band for the infinite periodic beam is observed, where bending waves cannot propagate. Similarly, stop bands can be seen in Figs. 18 and 19 for two other examples. These figures demonstrate that there is almost perfect correlation between the band-gap size/location of the emerging band structure and the size/location of the corresponding maximized natural frequency gap in the finite structure.

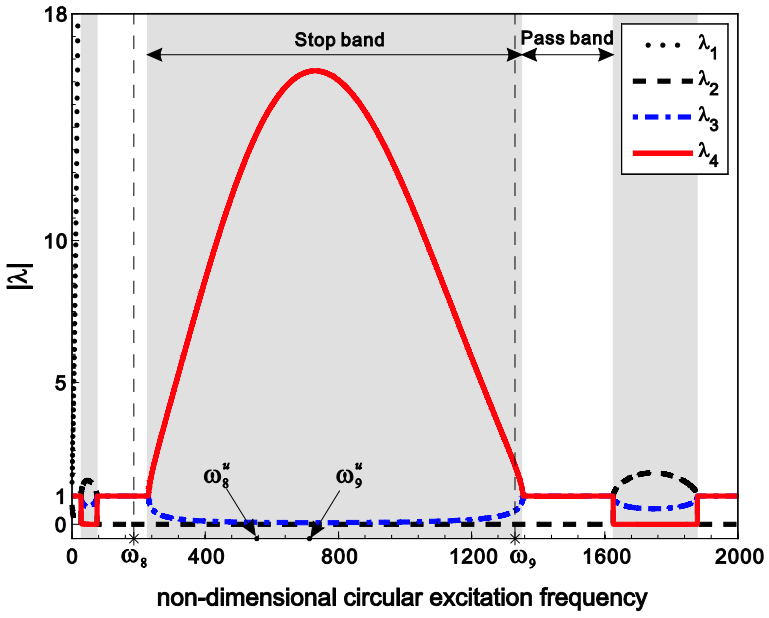


Figure 17: Variation of $|\lambda|$ versus excitation frequency obtained by employing Floquet theory for an inner repeated segment in Fig. 3(b), where the frequency gap $\Delta\omega_9 = \omega_9 - \omega_8$ of the cantilever beam is maximized. The grey domains indicate Floquet-predicted stop bands. The 8th and 9th eigenfrequencies ω_8^u and ω_9^u of the comparison beam with uniform cross-section, and ω_8 and ω_9 of the optimized beam are shown in the figure.

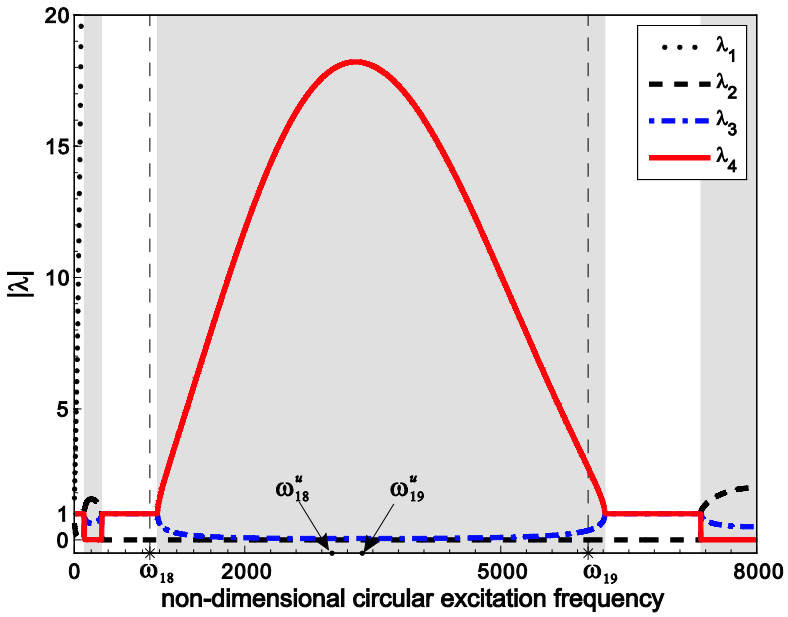


Figure 18: Variation of $|\lambda|$ versus excitation frequency obtained by employing Floquet theory for an inner repeated segment in Fig. 6(b), where the frequency gap $\Delta\omega_{19} = \omega_{19} - \omega_{18}$ of the cantilever beam is maximized. The grey domains indicate Floquet-predicted stop bands. The 18th and 19th eigenfrequencies ω_{18}^{u} and ω_{19}^{u} of the comparison beam with uniform cross-section, and ω_{18} and ω_{19} of the optimized beam are shown in the figure.

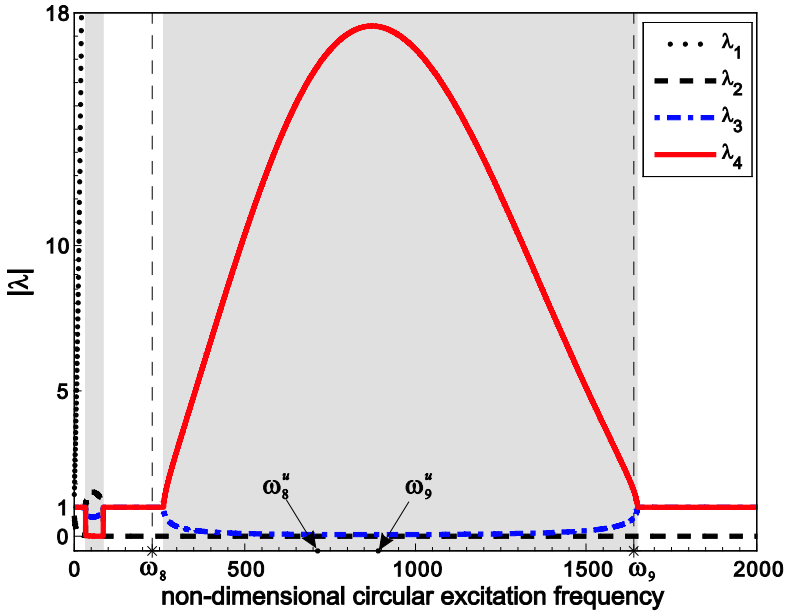


Figure 19: Variation of $|\lambda|$ versus excitation frequency by employing Floquet theory for an inner repeated segment in Fig. 9, where the frequency gap $\Delta\omega_9 = \omega_9 - \omega_8$ of the clamped-clamped beam is maximized. The grey domains indicate Floquet-predicted stop bands. The 8th and 9th eigenfrequencies ω_8^u and ω_9^u of the comparison beam, and ω_8 and ω_9 of the optimized beam are shown in the figure.

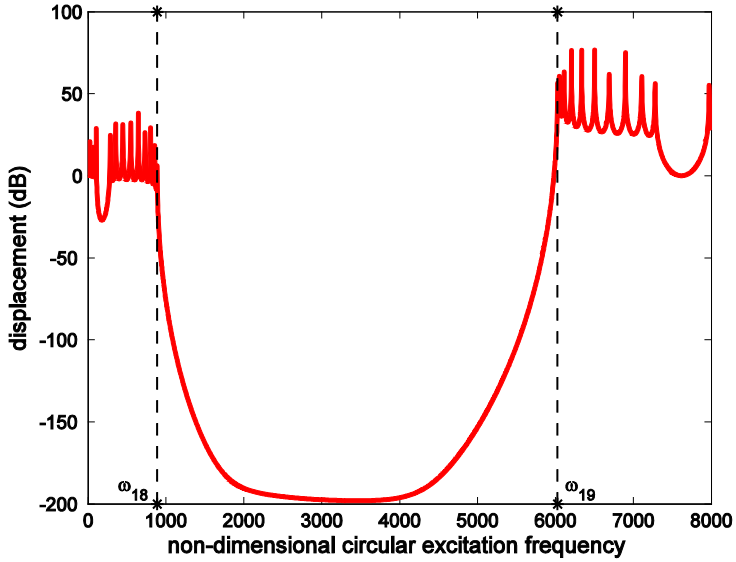


Figure 20: Displacement response at the right hand end from the flexural vibration of the optimized beam in Fig. 6(b) when the beam is subjected to time-harmonic base excitation in the transverse direction at the left hand end. No damping is assumed. The 18th and 19th eigenfrequencies ω_{18} and ω_{19} of the optimized beam are indicated in the figure.

It has been demonstrated in many papers, see e.g. [5,45], that a structure with a finite number of repeated unit cells may significantly suppress propagation of waves with frequencies in the stop band. Fig. 20 shows the displacement response at the right hand end of the optimized beam shown in Fig. 6(b), when the beam is subjected to a time-harmonic base excitation in the transverse direction at the left hand end. The base motion is prescribed with a given displacement amplitude u_0 relative to the fixed reference axis. The transverse displacement u at the right hand end is indicated in Fig. 20 in the form $10\log_{10}\frac{u^2}{u_0^2}$ dB.

It is seen from Fig. 20 that there is a large drop in the response in the stop band frequency range. The stop band calculated from the corresponding unit cell is given in Fig. 18. It demonstrates that the stop band may exist in the optimized beam obtained by maximization of a frequency gap. It is observed from Figs. 18 and 20 that there is a correlation between the value of $|\lambda|$ representing the strength of attenuation in a band gap, and the level of attenuation in the frequency response function for a finite structure composed of the same periodic unit cell. The many resonance peaks observed in Fig. 20 are due to the fact that no damping is included. The resonance peaks can be removed or reduced by including some damping, and we also found that there is no significant change of the band-gap behavior for relatively small damping. The effect of smoothing by including damping is often used in the topology optimization of band-gap structures [7].

7 CONCLUSIONS

Maximizing gaps between two adjacent natural frequencies (eigenfrequencies) of free transverse vibrations of prescribed order is investigated in this paper. The results are obtained by finite element and gradient based optimization using analytical sensitivity analysis. An incremental optimization formulation with consideration of multiple eigenvalues is applied, which can be used for problems with any mix of multiple and simple eigenfrequencies. Non-

dimensional optimum solutions are presented for different classical boundary conditions, different orders of the upper and lower eigenfrequencies of maximized gaps, and values of a minimum cross-sectional area constraint. However, geometrically unconstrained optimum solutions obtained in Ref. [24] are also discussed and utilized in this paper. The results show that, except for beam segments adjacent to the beam ends whose designs are characteristic for the specific boundary conditions considered, all the inner part of the optimum beam designs exhibits a significant periodicity in terms of repeated beam segments, the number of which increases with increasing orders of the upper and lower frequencies of the maximized gaps.

When small values of the minimum cross-sectional area are prescribed, solutions to the current problems are very close to corresponding solutions obtainable by simple non-dimensional analytical expressions for limiting optimum solutions that were derived earlier by a "method of scaled beam elements" [24] in which inner points of vanishing cross-sectional area in the beams were allowed and exploited.

In wave propagation problems, band-gap is found in an infinite beam structure constructed by repeated translation of an inner beam segment obtained by eigenfrequency gap optimization. The band-gap size/location of the emerging band structure is matching very well with the size/location of the corresponding maximized natural frequency gap in the finite structure. For the optimized structures composed of a finite number of repeated segments in the inner part, the motion transmitted from one end will be significantly suppressed by the periodic segments. For the beam structures studied here, it can be concluded that the optimum design maximizing the gap between two adjacent eigenfrequencies of free transverse vibration of given higher order is periodic. It is also demonstrated that the approach tailors a band-gap which is matching very well the maximized frequency gap in the periodic structure characterizing elastic or acoustic wave propagation.

ACKNOWLEDGMENTS

This work was partially supported by the EU InterReg Project "Silent Spaces", Aalborg University, and the National Natural Science Foundation of China (Grant No. 90816025). This support is gratefully acknowledged by the authors.

REFERENCES

[1] L. Brillouin, *Wave Propagation in Periodic Structures, 2nd edition*. Dover Publications. New York, 1953.

[2] M.M. Sigalas, E.N. Economou, Elastic and acoustic-wave band-structure. *Journal of Sound and Vibration*, **158**, 377-382, 1992.

[3] D.J. Mead, Wave propagation in continuous periodic structures: Research contributions from Southampton, 1964-1995. *Journal of Sound and Vibration*, **190**, 495-524, 1996.

[4] J.S. Jensen, O. Sigmund, J.J. Thomsen, M.P. Bendsøe, Design of multi-phase structures with optimized vibrational and wave-transmitting properties. *Proceedings of 15th Nordic Seminar on Computational Mechanics, Aalborg University*. Lund, E., Olhoff, N., Stegmann, J. (Eds). Institute of Mechanical Engineering, Aalborg University, Denmark, p. 63-66, 2002 (ISBN: 87-89206-67-3).

[5] J.S. Jensen, Phononic band gaps and vibrations in one- and two-dimensional mass-spring structures. *Journal of Sound and Vibration*, **266**, 1053-1078, 2003.

[6] M.I. Hussein, G.M. Hulbert, R.A. Scott, Dispersive elastodynamics of 1d banded materials and structures: Analysis. *Journal of Sound and Vibration*, **289**, 779-806, 2006.

[7] O. Sigmund, J.S. Jensen, Systematic design of phononic band-gap materials and structures by topology optimization. *Philosophical Transactions of the Royal Society of London Series A-Mathematical Physical and Engineering Sciences*, **361**, 1001-1019, 2003.

[8] S. Halkjær, O. Sigmund, Optimization of beam properties with respect to maximum band-gap. *Mechanics of the 21st Century, Procedings of 21st International Congress of Theoretical and Applied Mechanics*. Gutkowski, W., Kowalewski, T.A. (Eds.), IUTAM, Warsaw, Poland, 2004 (ISBN: 978-1-4020-3456-5).

[9] A.R. Diaz, A.G. Haddow, L. Ma, Design of band-gap grid structures. *Structural and Multidisciplinary Optimization*, **29**, 418-431, 2005.

[10] M.I. Hussein, K. Hamza, G.M. Hulbert, R.A. Scott, K. Saitou, Multiobjective evolutionary optimization of periodic layered materials for desired wave dispersion characteristics. *Structural and Multidisciplinary Optimization*, **31**, 60-75, 2006.

[11] S. Halkjaer, O. Sigmund, J.S. Jensen, Maximizing band gaps in plate structures, *Structural and Multidisciplinary Optimization*, **32**, 263-275, 2006.

[12] J.S. Jensen, N.L. Pedersen, On maximal eigenfrequency separation in two-material structures: The 1D and 2D scalar cases. *Journal of Sound and Vibration*, **289**, 967-986, 2006.

[13] J.S. Jensen, Topology optimization problems for reflection and dissipation of elastic waves. *Journal of Sound and Vibration*, **301**, 319-340, 2007.

[14] M.I. Hussein, G.M. Hulbert, R.A. Scott, Dispersive elastodynamics of 1D banded materials and structures: Design. *Journal of Sound and Vibration*, **307**, 865-893, 2007.

[15] J.B. Du, N. Olhoff, Topological design of freely vibrating continuum structures for maximum values of simple and multiple eigenfrequencies and frequency gaps. *Structural and Multidisciplinary Optimization*, **34**, 91-110, 2007.

[16] J.B. Du, N. Olhoff, Topological design of freely vibrating continuum structures for maximum values of simple and multiple eigenfrequencies and frequency gaps (vol 34, pg 91, 2007), Editors's Erratum. *Structural and Multidisciplinary Optimization*, **34**, 545-545, 2007.

[17] A.A. Larsen, B. Laksafoss, J.S. Jensen, O. Sigmund, Topological material layout in plates for vibration suppression and wave propagation control. *Structural and Multidisciplinary Optimization*, **37**, 585-594, 2009.

[18] A. Søe-Knudsen, Design of stop-band filter by use of pipe segments and shape optimization. *Structural and Multidisciplinary Optimization*, **44**, 863-874, 2011.

[19] D. Richards, D.J. Pines, Passive reduction of gear mesh vibration using a periodic drive shaft. *Journal of Sound and Vibration*, **264**, 317-342, 2003.

[20] D.L. Yu, Y.Z. Liu, H.G. Zhao, G. Wang, J. Qiu, Flexural vibration band gaps in Euler-Bernoulli beams with locally resonant structures with two degrees of freedom. *Physical Review B*, **73**, 064301, 2006.

[21] L. Liu, M.I. Hussein, Wave motion in periodic flexural beams and characterization of the transition between bragg scattering and local resonance. *Journal of Applied Mechanics*, **79**, 011003-011017, 2012.

[22] A.C. Hladky-Hennion, G. Allan, M. de Billy, Localized modes in a one-dimensional diatomic chain of coupled spheres. *Journal of Applied Physics*, **98**, 054909, 2005.

[23] B.L. Karihaloo, F.I. Niordson, Optimum design of vibrating cantilevers. *Journal of Optimization Theory and Applications*, **11**, 638-654, 1973.

[24] N. Olhoff, Optimization of vibrating beams with respect to higher-order natural frequencies. *Journal of Structural Mechanics*, **4**, 87-122, 1976.

[25] N. Olhoff, Maximizing higher-order eigenfrequencies of beams with constraints on the design geometry. *Journal of Structural Mechanics*, **5**, 107-134, 1977.

[26] N. Olhoff, R. Parbery, Designing vibrating beams and rotating shafts for maximum difference between adjacent natural frequencies. *International Journal of Solids and Structures*, **20**, 63-75, 1984.

[27] M.P. Bendsøe, N. Olhoff, A method of design against vibration resonance of beams and shafts. *Optimal Control Applications & Methods*, **6**, 191-200, 1985.

[28] A.R. Diaz, N. Kikuchi, Solutions to shape and topology eigenvalue optimization problems using a homogenization method. *International Journal for Numerical Methods in Engineering*, **35**, 1487-1502, 1992.

[29] Z.D. Ma, N. Kikuchi, H.C. Cheng, Topological design for vibrating structures. *Computer Methods in Applied Mechanics and Engineering*, **121**, 259-280, 1995.

[30] B. Niu, J. Yan, G. Cheng, Optimum structure with homogeneous optimum cellular material for maximum fundamental frequency. *Structural and Multidisciplinary Optimization*, **39**, 115-132, 2009.

[31] M.P. Bendsøe, O. Sigmund, *Topology optimization: Theory, methods and applications*. Berlin: Springer-Verlag, 2003.

[32] C.S. Jog, Topology design of structures subjected to periodic loading. *Journal of Sound and Vibration*, **253**, 687-709, 2002.

[33] N. Olhoff, J.B. Du, Topological design optimization of vibrating structures. *Proc. The 4th China-Japan-Korea Joint Symposium on Optimization of Structural and Mechanical Systems*, G. Cheng, S. Liu and X. Guo (Eds), Kunming, China, 6-9 November, pp.509-514, 2006.

[34] J.S. Jensen, Topology optimization of dynamics problems with pade approximants. *International Journal for Numerical Methods in Engineering*, **72**, 1605-1630, 2007.

[35] N. Olhoff, B. Niu, G. Cheng, Optimum design of band-gap beam structures. *International Journal of Solids and Structures*, **49**, 3158-3169, 2012.

[36] M. Petyt, *Introduction to finite element vibration analysis, 2nd Ed*. Cambridge University Press, Cambridge, UK, 2010.

[37] M.P. Bendsøe, N. Olhoff, J.E. Taylor, A variational formulation for multicriteria structural optimization. *Journal of Structural Mechanics*, **11**, 523-544, 1983.

[38] N. Olhoff, Multicriterion structural optimization via bound formulation and mathematical programming. *Structural and Multidisciplinary Optimization*, **1**, 11-17, 1989.

[39] A.P. Seyranian, E. Lund, N. Olhoff. Multiple-eigenvalues in structural optimization problems, *Structural Optimization*, **8**, 207-227, 1994.

[40] W.H. Wittrick, Rates of change of eigenvalues, with reference to buckling and vibration problems. *Journal of the Royal Aeronautical Society*, **66**, 590-591, 1962.

[41] W. Zhong, G. Cheng, Second-order sensitivity analysis of multimodal eigenvalues and related optimization techniques. *Journal of Structural Mechanics*, **14**, 421-436, 1986.

[42] K. Svanberg, The method of moving asymptotes - a new method for structural optimization. *International Journal for Numerical Methods in Engineering*, **24**, 359-373, 1987.

[43] E. Lund, *Finite element based design sensitivity analysis and optimization*, Ph.D. Thesis, Special Report No. 23, Dept. of Mechanical Engineering, Aalborg University, Denmark, 1994.

[44] B.R. Mace, D. Duhamel, M.J. Brennan, L. Hinke, Finite element prediction of wave motion in structural waveguides. *Journal of The Acoustical Society of America*, **117**, 2835-2843, 2005.

[45] A. Søe-Knudsen, S.V. Sorokin, Modelling of linear wave propagation in spatial fluid filled pipe systems consisting of elastic curved and straight elements, *Journal of Sound and Vibration*, **329**, 5116-5146, 2010.

COMPDYN 2013
4th ECCOMAS Thematic Conference on
Computational Methods in Structural Dynamics and Earthquake Engineering
M. Papadrakakis, V. Papadopoulos, V. Plevris (eds.)
Kos Island, Greece, 12–14 June 2013

EXCITATION OF PARAMETRIC RESONANCE IN MICRO BEAMS BY JOULE'S HEATING

Timur Sibgatullin, David Schreiber, Slava Krylov*

Microsystems Design and Characterization Laboratory, School of Mechanical Engineering, Faculty of Engineering, Tel Aviv University, Israel
*e-mail: vadis@eng.tau.ac.il

Keywords: MEMS, double clamped micro beam, Joule's heating, parametric resonance, buckling.

Abstract. *In this work we investigate the feasibility of excitation of parametric resonance in micro/nano beams by means of Joule's heating of the beam's material. A time-dependent voltage applied to the beam's ends generates an alternate electric current through the beam, which results in a time-dependent heating of the beam's material and appearance of a time-dependent compressive axial force acting on the beam. By choosing appropriate values of the frequency and magnitude of the voltage, efficient parametric excitation of the beam can be achieved. The main advantage of the suggested approach is its simplicity and compatibility with the existing fabrication processes and common configurations of micro devices. The beam is modeled in the framework of the Euler-Bernoulli theory. The influence of the thermo-elastic effects on the heat generation is neglected and it is assumed that the contribution of the Joule's heating is dominant. The thermo-mechanical coupling is introduced through the thermal expansion of the beam's material due to the heating. The time-harmonic heat-transfer problem is solved analytically. An approximate single degree of freedom (lumped) model of the beam is built by means of Galerkin decomposition. The results provided by the lumped model are verified through comparison with the numerical data obtained by the Finite Differences method. In the framework of the lumped model, the stability properties of the beam are described using the canonical damped Mathieu equation. It was found that within the range of the frequencies below the fundamental frequency of the beam a frequency region always exists such that parametric resonance is possible for the excitation voltages below the critical voltage, corresponding to the Euler buckling of the beam.*

1 INTRODUCTION

Micro- and nanoelectromechanical systems (MEMS and NEMS) find applications in various areas of research and engineering due to their small size, low fabrication cost, unique performance and suitability for integration in complex functional systems [1]. Since the first micromachined electrostatically actuated resonator was introduced by Natanson [2], a large variety of MEMS/NEMS resonators was reported including radio frequency (RF) timing devices and filters [3], inertial sensors [4, 5] as well as mass [6, 7, 8] and stress [9] based sensors for chemical and biological detection. Resonant sensors benefit from the dependence of a device spectral characteristics on device parameters, the latter of which can be extracted with very high accuracy by tracking the changes in the resonant frequency.This principle lies in the foundation of resonant mass sensors [10].

Emerging of new applications and unabated progress in required performance of the devices motivates development of robust architectures for efficient resonant driving. Particularly, efficient parametric excitation, first reported for mechanical microstructures in nineties [11, 12], continues to attract considerable research attention in the realm of MEMS and NEMS as reflected in numerous publications (e.g., see reviews [13, 14] and references therein). Parametric excitation and parametric resonance (PR) are associated with the excitation through time-modulation of the parameters of the system rather than through direct force application to the structure [15]. These systems are distinguished by time-dependent effective stiffness or inertia coefficients of the governing equation and are described by (linear or nonlinear) Mathieu differential equations [15]. Parametrically excited sensors are attractive for a broad range of applications such as mass sensors [16], angular rate sensors [17, 18]) and scanning micro mirrors [19] thanks to their general characteristics of relatively wide bands of operation frequencies, large amplitudes and sharp transition between low-amplitude to high-amplitude response. In MEMS/NEMS devices parametric excitation is typically achieved through controlled modulation of effective stiffness of the mechanical system. In electrostatic devices, the actuation forces are usually nonlinear, time- and configuration-dependent functions, which affect the device effective stiffness [19, 20, 21, 22, 23, 24, 25, 26] and result in parametric excitation of the structures. Recently, parametric excitation has been demonstrated in MEMS/NEMS devices through various rich possibilities, including kinematic excitation of a beam's attachment point [27], direct mechanical stiffness modulation [28], the mass-matrix modulation [29, 30]) and via fringing electrostatic fields [16, 19, 31].

Joule heating of micro structures was considered mainly in the framework of the analysis of electro thermal actuators (e.g., see [32, 33]). Since the characteristic time associated with heating and cooling is typically much longer than the period of free vibrations of these structures, mainly static or low frequency operation of thermal actuators was explored. Some approaches were suggested addressing this intrinsic limitation [34]. Electrothermal heating (by a steady time-independent current) was suggested as an efficient way of tuning the resonant responses of electrostatically actuated devices [35, 36, 37]. Downscaling of the devices's dimensions reduces significantly the thermal response times and allows achieving of resonant thermal excitation of nanoelectromechanical (NEMS) devices using optical heating by means of modulated laser [38, 39, 40, 41]. Parametric excitation and parametric amplification in laser-heated micro beams was reported in [42, 43]. Laser heating was used also for the tuning of the resonant responses of nano beams [44]. Self-excitation of NEMS structures undergoing steady laser irradiation and optomechanical coupling was analyzed as well [38, 45, 46].

In this work we explore a simple but unusual way to excite resonant parametric vibrations of

a slender double clamped beam by means of thermoelectric excitation. Specifically, the modulation of the effective stiffness of the structure is achieved by changing the axial force through the time-periodic heating of the beam's material. An alternating electrical current passing through the beam results in the resistive Joule's heating of the beam's material and in appearance of the time-dependent axial compressive force. Note that combined thermal and magnetic actuation of micro beams was demonstrated theoretically and experimentally in [47]. In the present work we eliminate the magnetic Lorentz force and consider the case of excitation solely by heating. The main goal of the work is to investigate the feasibility of excitation of PR in the beam by means od Joule's heating.

2 FORMULATION

The device under consideration consists of a prismatic double clamped beam with length, width and thickness of L, b and h respectively, Fig. 1. The beam is assumed to be made of a linearly elastic material with the Young's modulus E and mass density ρ. The beam is free to deflect in the $\hat{x}\hat{z}$ (or $\hat{y}\hat{z}$) plane while the ends of the beam are constrained in both lateral $\hat{y},\ \hat{z}$ and axial $\hat{x}$ directions by unmoveable anchors attached to the substrate. The voltage difference V is applied between the anchors of the beam resulting in the current I passing through the beam.

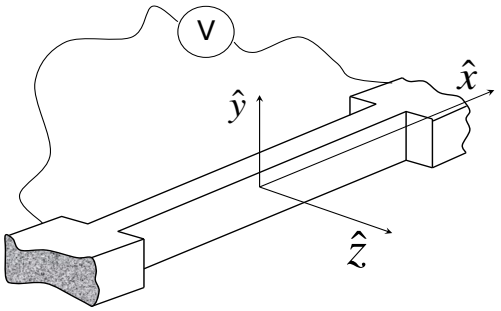


Figure 1: Model of a beam heated by an electric current.

The beam is described in the framework of the Euler-Bernoulli theory and under the assumption that the deflections, while comparable with the thickness of the beam, are small with respect to the beam's length. In addition, we assume that the axial and rotary inertia are negligible compared with the transverse inertia. Under these assumptions, the governing equation of the beam is (e.g., see [48] for the details of the development)

$$\rho A\frac{\partial^2 \hat{w}}{\partial \hat{t}^2} + \hat{c}\frac{\partial \hat{w}}{\partial \hat{t}} + EI_{yy}\frac{\partial^4 \hat{w}}{\partial \hat{x}^4} - \hat{N}\frac{\partial^2 \hat{w}}{\partial \hat{x}^2} = 0 \tag{1}$$

It is completed by homogeneous boundary conditions $\hat{w}(0,\hat{t}) = \hat{w}(L,\hat{t}) = 0,\ \partial\hat{w}(0,\hat{t})/\partial\hat{x} = \partial\hat{w}(L,\hat{t})/\partial\hat{x} = 0$. In Eq. (1) $\hat{x}$ and $\hat{t}$ are dimensional coordinate and time, respectively; A and I_{yy} are the cross-sectional area and the sectional second moment of area; $\hat{w}$ - is the deflection of the beam in the lateral $\hat{z}$ direction; $\hat{c}$ is coefficient of viscous damping. The axial tensile force

$$\hat{N} = \sigma_0 A - \frac{EA}{L}\int_0^L \alpha T\, d\hat{x} + \frac{EA}{2L}\int_0^L \left(\frac{d\hat{w}}{d\hat{x}}\right)^2 d\hat{x} \tag{2}$$

incorporates three terms: the time-independent tensile pre-load $\sigma_0 A$ (e.g., originated in the residual stress arising during the fabrication process), compressive force associated with the thermal stress and the nonlinear, deflection-dependent stretching force. In Eq. (2) $T = T(\hat{x}, \hat{t})$ is the temperature change above a reference temperature and $\alpha = \alpha(T)$ is the (generally speaking temperature-dependent [49]) coefficient of thermal expansion. Note that $T(\hat{x}, \hat{t})$ represents the temperature averaged across the section of the beam [32].

To simplify matters, in this work we adopt an assumption that the coefficient of the thermal expansion α is independent on temperature. In this case Eq. (1) can be written in the form

$$\hat{N} = \sigma_0 A - \frac{EA}{L}\alpha\bar{T} + \frac{EA}{2L}\int_0^L \left(\frac{d\hat{w}}{d\hat{x}}\right)^2 d\hat{x} \tag{3}$$

Here $\bar{T} = \bar{T}(\hat{t})$ is the temperature averaged along the beam. Equation (1) with the axial force given by Eq. (3) shows that changing of the temperature periodically in time will result in a time-dependent axial force. Consequently, Eq. (2) is an homogeneous partial differential equation with a time-dependent coefficient and is of a parametric type. By choosing the frequency and amplitude of the axial force within an appropriate interval, one can anticipate that it could be possible to excite parametric resonance in the beam.

3 Thermal problem

Electric potential difference is applied between the beam's ends. The heat (per unit volume of the beam's material) generated by the electric current is $E_{gen} = J^2\rho_e$ [32]. Here $J = J(x, y, z) = I/A$ is the current density and ρ_e is the electrical resistivity of the beam's material. This Joule's heating is assumed to be the only source of heat generation in the system under consideration while the influence of the thermoelastic coupling arising due to the heat generation associated with the rates of material deformation, is neglected.

For the sake of simplicity, in the analysis of the thermal problem we assume that the material parameters - thermal conductivity, specific heat and resistivity - are independent on temperature. Note that while in reality the temperature dependence of both thermal (conductivity, specific heat) and electrical (resistivity) parameters is significant, this assumption allows to obtain closed-form solutions and is often used in order to simplify development (e.g.,see [50]). In addition, we assume that the current density is distributed uniformly across the section of the beam. Finally, we neglect the term associated with the heat losses to the surrounding fluid and the substrate [51] through the beam's envelope and assume that the cooling of the beam takes place solely through its ends via the conductivity mechanism. Under these assumptions, the heat conduction in the beam can be described by the one-dimensional equation (e.g., see [32] for the reduction of the three-dimensional heat conductance problem to the one-dimensional counterpart)

$$\frac{d}{d\,\hat{t}}(\rho\, C_p\, T) = \frac{\partial}{\partial\,\hat{x}}\left(\kappa\frac{\partial\, T}{\partial\,\hat{x}}\right) + J^2\rho_e \tag{4}$$

Here $T(\hat{x})$ is the temperature (temperature excess above an ambient reference T_∞) averaged across the section of the beam, C_P is the specific heat, κ is the thermal conductivity and ρ is the material density. Note that in Eq. (4) the term $J^2\rho_e$ is the heat generated per unit length of the beam.

The voltage (and consequently the current) applied to the beam's ends contains both steady

V_{dc} and time-periodic V_{ac} components

$$J^2\,\rho_e = \frac{1}{\rho_e\,L^2}\left[V_{dc}^2 + \frac{V_{ac}^2}{2} + 2V_{dc}V_{ac}\cos(\hat{\omega}\,\hat{t}) + \frac{V_{ac}^2}{2}\cos(2\hat{\omega}\hat{t})\right] \tag{5}$$

Here $\hat{\omega}$ is an circular frequency of the driving electrical signal.

First we solve an auxiliary problem of the uniform (in space) harmonic heat source $W\ \cos(\hat{\omega}\hat{t})$. In this case in view of the adopted assumptions, Eq. (4) takes the form

$$\rho\,C_p\,\frac{\partial\,T}{\partial\,\hat{t}} = \kappa\frac{\partial^2\,T}{\partial\,\hat{x}^2} + W\ \cos(\hat{\omega}\,\hat{t}) \tag{6}$$

subject to the boundary conditions $T(\pm\,L/2,\hat{t})\ =\ 0$. For convenience, we introduce non-dimensional quantities

$$x = \frac{\hat{x}}{L},\quad t = \hat{\omega}\hat{t},\quad \theta = \frac{T\kappa}{W\,L^2},\quad \beta = L\sqrt{\frac{\rho\,C_p\hat{\omega}}{2\kappa}} \tag{7}$$

and re-write eq. (6) in the form

$$2\beta^2\,\frac{\partial\theta}{\partial t} = \frac{\partial^2\theta}{\partial x^2} + \cos\,(t) \tag{8}$$

with the boundary conditions $\theta(\pm\,1/2,t)\ =\ 0$. Note that the non-dimensional frequency parameter β represents the ratio between the beam's length to the thermal diffusion length $\mu = \sqrt{2k/(\rho\,C_p\hat{\omega})}$, which can be viewed as a characteristic dimension in the frequency domain, for the case of periodic heating [52].

We are looking for the solution in the following form

$$\theta(t,x) = \theta_s(x)\sin\,(t) + \theta_c(x)\cos\,(t) \tag{9}$$

Substituting of Eq. (9) into Eq. (8) yields the following system of ordinary differential equations for $\theta_s(x)$ and $\theta_c(x)$

$$\left\{\begin{array}{l} 2\beta^2\,\theta_s - \theta_c'' = 1 \\ 2\beta^2\,\theta_c + \theta_s'' = 0 \end{array}\right. \tag{10}$$

completed by the boundary conditions $\theta_s\ =\ \theta_c\ =\ 0$ at $x\ =\ \pm\,1/2$. Hereafter $(\ )'\ =\ d/dx$ or $(\ )'\ =\ \partial/\partial x$. The solution of the system is

$$\theta_s\ =\ \frac{1}{2\beta^2}\left[1-\frac{\cosh(\beta(x-1/2))\cos(\beta(x+1/2))+\cosh(\beta(x+1/2))\,\cos(\beta(x-1/2))}{\cosh(\beta)+\cos(\beta)}\right] \tag{11}$$

$$\theta_c\ =\ -\frac{1}{2\beta^2}\left[\frac{\sinh(\beta(x-1/2))\,\sin(\beta(x+1/2))+\sinh(\beta(x+1/2))\,\sin(\beta(x-1/2))}{\cosh(\beta)+\cos(\beta)}\right] \tag{12}$$

Averaging of $\theta(x,t)$, Eq. (9) over the length of the beam yields

$$\bar{\theta} = \int\limits_{-1/2}^{1/2}\theta(x,t)dx = \bar{\Theta}\cos(t-\phi) \tag{13}$$

where

$$\bar{\Theta}(\beta) = \frac{1}{2\beta^2}\left[\left(1-\frac{\sinh\beta+\sin\beta}{\beta(\cosh\beta+\cos\beta)}\right)^2+\left(\frac{\sinh\beta-\sin\beta}{\beta(\cosh\beta+\cos\beta)}\right)^2\right]^{\frac{1}{2}} \tag{14}$$

$$\phi(\beta) = \arctan\left(\beta\frac{\cosh\beta+\cos\beta}{\sinh\beta-\sin\beta}-\frac{\sinh\beta+\sin\beta}{\sinh\beta-\sin\beta}\right) \tag{15}$$

are the (frequency-dependent) amplitude and the phase, respectively. Note, that in the quasi-static case when $\beta \to 0$ we have

$$\theta_c = \frac{1}{8}-\frac{x^2}{2}, \quad \theta_s = 0, \quad \bar{\Theta} = \frac{1}{12} \text{ and } \phi = 0 \tag{16}$$

where $\bar{\Theta} = \sqrt{\bar{\Theta}_s^2+\bar{\Theta}_c^2}$ is the amplitude, $\phi = \arctan\left(\bar{\Theta}_s/\bar{\Theta}_c\right)$ is the phase and $\bar{\Theta}^s,\ \bar{\Theta}_c$ are the amplitudes $\theta_s,\ \theta_c$ averaged over the length of the beam.

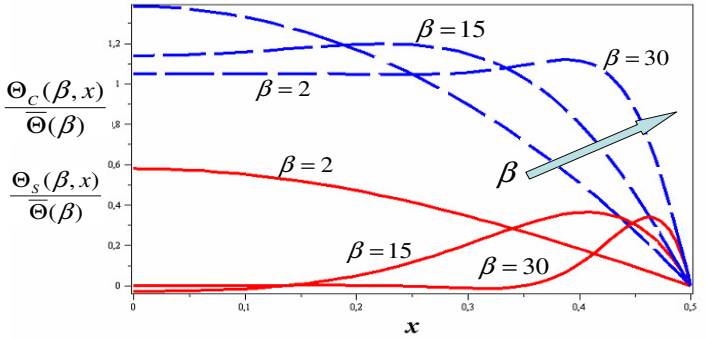


Figure 2: Non-dimensional temperature distribution along the beam: normalized amplitudes $\theta_s(x)$ and $\theta_c(x)$ (solid red and dashed blue lines, respectively) for $\beta = 2, 15$ and 30.

Figure 2 shows the distribution of the sine and cosine components of the temperature for differing values of β (different frequencies). For small β the distribution of the temperature is similar to the quasi-static case. With increase of the frequency, the space dependence of the temperature is less pronounced. The reason for this behavior is that at higher frequencies the diffusion length decreases and heat distribution becomes more local [53], which, combined with uniform heat generation along the beam, results in the temperature distribution close to uniform and justifies the spatial averaging for the case of high frequency excitation. Equation (14) suggests that the amplitude of temperature decreases as $1/2\beta^2$ with the increase of the frequency. Following combination of the solutions for the two limit cases (static and high frequency) allows simple approximation for the $\bar{\Theta}(\beta)$

$$\bar{\Theta}(\beta) \approx \left(\left(\frac{1}{12}\right)^{-1}+\left(\frac{1}{2\beta^2}\right)^{-1}\right)^{-1} = \frac{1}{12}\left(\frac{1}{1+\beta^2/6}\right) \tag{17}$$

The comparison of the approximation (17) with the exact averaged solution $\bar{\Theta}(\beta)$ is illustrated in Fig. 3.

In the case of Joule's heating, the heat propagation in the beam is described by Eq. (4) with the source therm $J^2\rho_e$ given by Eq. (5). Because of linearity of the problem, the temperature

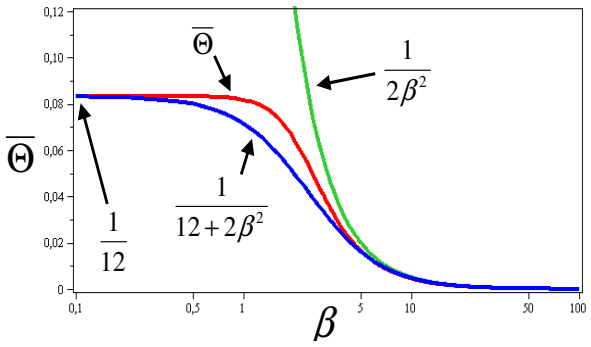


Figure 3: Amplitude $\bar{\Theta}$ of the temperature averaged over the beam's length (red curve) and its approximations for different values of β.

distribution in the beam can be represented as superposition of solutions Eq. (13) obtained for the case of harmonic heating

$$T = \frac{V_{dc}^2 + \frac{1}{2}V_{ac}^2}{8k\rho_e}\left[1 - 4x^2\right] + \frac{2\,V_{dc}\,V_{ac}}{k\rho_e}[\theta_c(x,\beta)\cos t + \theta_s(x,\beta)\sin t] + \\ + \frac{V_{ac}^2}{2k\rho_e}[\theta_c(x,\beta\sqrt{2})\cos 2t + \theta_s(x,\beta\sqrt{2})\sin 2t] \tag{18}$$

where $\theta_s(x,\beta)$ and $\theta_c(x,\beta)$are given by Eqs. (11) and (12). Using Eqs.(13)-(16) we calculate the temperature averaged along the length of the beam

$$\bar{T} = \frac{V_{dc}^2 + V_{ac}^2/2}{12k\rho_e} + \frac{2\,V_{dc}\,V_{ac}}{k\rho_e}\bar{\Theta}(\beta)\cos(t - \phi(\beta)) + \frac{V_{ac}^2}{2k\rho_e}\bar{\Theta}(\beta\sqrt{2})\cos(2t - \phi(\beta\sqrt{2})) \tag{19}$$

Note that Eq. (19) can be simplified for the case of large β (high frequency), when $\phi(\beta) \to \pi/2$, $\bar{\Theta}(\beta) \to 1/2\beta^2$ and $\bar{\Theta}(\beta\sqrt{2}) \to 1/4\beta^2$

$$\bar{T} = \frac{V_{dc}^2 + V_{ac}^2/2}{12k\rho_e} + \frac{V_{dc}\,V_{ac}}{k\rho_e\beta^2}\sin(t) + \frac{V_{ac}^2}{8k\rho_e\beta^2}\sin(2t) \tag{20}$$

In order to estimate the accuracy of the approximate analytical solution the numerical solution of the thermal problem Eq. (4) with the source therm $J^2\rho_e$ given by Eq. (5) was build by means of the finite differences method. The partial differential equation (4) completed by the zero temperature initial conditions and zero boundary conditions is reduced to the system of ordinary differential equations using a spacial finite difference discretization. The integration of the resulting system of linear ordinary differential equations in time is then carried out using fourth-order Runge-Kutta method implemented in Matlab [54]. In all the calculations presented hereafter we used the parameters listed in Table 1 until otherwise is stated. The nodal (discrete) values of the temperature are used for the calculation of the averaged (along the beam) temperature on each time step of the calculation. Figure 4 shows the the analytical steady-periodic and the numerical transient solutions in terms of the average temperatures. Good agreement between the two is observed. One can mention also that in accordance with Eq. (5) the source term $J^2\rho_e$ combines both double and single electrical signal frequencies. Figure 4 illustrates that the increase of the ratio V_{dc}/V_{ac} results in more pronounced response at the (single) frequency of the supplied electrical signal.

Table 1: Parameters of the structure and material properties used in calculations.

Notation	Parameter	Value	Unit
L	Beam's length	2000	μm
b	Beam's width	25	μm
h	Beam's thickness	8	μm
E	Young's modulus	169	GPa
ρ	Density	2330	kg/m^3
α	Thermal linear expansion coefficient	3E-6	$[^\circ C^{-1}$
C_p	Heat capacity	700	$J/kg\,K$
κ	Thermal conductivity	150	$W/\mathrm{m}K$
ρ_e	Electrical resistivity	0.0015	$\Omega\cdot$m

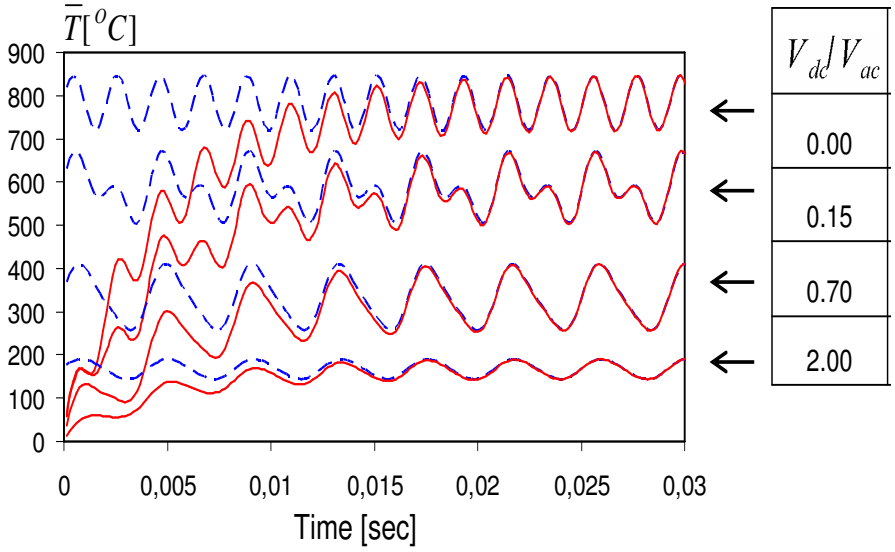


Figure 4: Comparison of the steady-periodic analytical and transient numerical solutions in terms of the average temperature of beam. In the case of dominant V_{ac}, relative to V_{dc}, the double frequency response is dominant. Beam dimensions and material properties correspond to listed in Table 1.

4 Coupled problem and decomposition

The dynamics of the beam heated by a time-dependent current are described by Eq. (1) with the axial force N given by Eq. (3), where the temperature $\bar{T}$, averaged along the length of the beam, is given by Eq. (19). By introducing the non-dimensional quantities

$$x = \frac{\hat{x}}{L}, \quad t = \hat{t}\sqrt{\frac{EI}{\rho A L^4}}, \quad \omega = \hat{\omega}\sqrt{\frac{\rho\, A\, L^4}{EI}} \quad w = \frac{\hat{w}}{r}, \quad c = \hat{c}\sqrt{\frac{EI\rho A}{L^4}} \tag{21}$$

where $r = \sqrt{I/A}$ is the cross-sectional gyration radius, we re-write eq. (1) in the form

$$w^{IV} + c\dot{w} - Nw'' + \ddot{w} = 0 \tag{22}$$

where $\dot{(\,)} = \partial/\partial t$. Note that in accordance with Eq. (21) the frequency was re-scaled. The non-dimensional axial force N is given by the expression

$$N = \gamma_0 + \gamma_1 \cos(\omega\, t - \phi(\beta)) + \gamma_2 \cos(2\omega\, t - \phi(\beta\sqrt{2})) + \frac{1}{2}\int_0^1 (w')^2\, dx \tag{23}$$

where the parameters associated with the driving terms are

$$\gamma_0 = \eta^2 \left[\varepsilon_0 - \frac{\alpha}{k\rho_e}\frac{V_{dc}^2 + V_{ac}^2/2}{12}\right], \quad \gamma_1 = -\frac{2\eta^2\alpha}{k\rho_e} V_{dc} V_{ac} \bar{\Theta}(\beta), \quad \gamma_2 = -\frac{\eta^2\alpha}{2k\rho_e} V_{ac}^2 \bar{\Theta}(\beta\sqrt{2}), \tag{24}$$

Here $\eta = L/r$ is the non-dimensional slenderness ratio of the beam and $\varepsilon_0 = \sigma_0/E$ is an initial tensile strain associated with the residual stress in the beam.

We use Galerkin decomposition in order to construct a single DOF (lumped) model of the beam. By substituting the approximation of the deflection $w = q(t)\psi(x)$ (where $\psi(x)$ is the base function) into eq. (23) we obtain

$$m\,\ddot{q} + c\,m\,\dot{q} + \left[k_B + \gamma_0\, k_S + \gamma(t)\, k_S + \frac{1}{2}\, k_S^2\, q^2\right] q = 0; \tag{25}$$

where

$$m = \int_0^1 \psi^2 dx; \;\; k_S = \int_0^1 (\psi')^2 dx; \;\; k_B = \int_0^1 (\psi'')^2 dx; \tag{26}$$

Equation. (24) suggests that γ_0 decreases with increasing of the electric current. It means that heating reduces the system stiffness, as expected. Note also that γ_0 can be negative and it is limited by the static buckling of the beam. The post buckling behavior is not considered in this work.

5 Static stability

When the axial force engendered by the Joule's heating became higher than the critical Euler's value, the beam becomes unstable and can buckle. The condition of the static instability can be obtained by requiring that the linearized counterpart of the stiffness term in Eq. (25) is zero

$$k_B + k_S\gamma_0 = 0 \tag{27}$$

For convenience, we replace $V_0^2 = V_{dc}^2 + V_{ac}^2/2$ in γ_0, Eq. (25). In analysis of the static buckling we use the buckling mode of the beam $\psi = (1 - \cos 2\pi\, x)/2$ as the base function. Taking into consideration that in this case the integrals m, k_S and k_B, Eq. (26), have the values of $3/8, \pi^2/2$ and $2\pi^4$, respectively we obtain the buckling criterion of the beam

$$\gamma_0 < -4\pi^2 \text{ or } V_0 > \sqrt{\frac{12k\rho_e(4\pi^2 + \eta^2\varepsilon_0)}{\alpha\eta^2}} \tag{28}$$

In the framework of the single DOF nonlinear lumped model, the equilibrium of the beam is described by the equation

$$k_B + k_S\gamma_0 + \frac{1}{2}\, k_S^2\, q^2 = 0 \tag{29}$$

Equation (29) suggests that deflection of the buckled beam is bounded due to the presence of the geometric non-linearity. The non-dimensional and dimensional midpoint deflections of the beam in the post-buckling configuration are as follows (see [55])

$$q^2 = \frac{\alpha\,\eta^2}{3\pi^2\, k\rho_e} V_0^2 - 16 - \frac{4\eta^2}{\pi^2}\varepsilon_0 \text{ and } \hat{q}^2 = \frac{\alpha\, L^2}{3\pi^2\, k\rho_e} V_0^2 - \frac{4t^2}{3} - \frac{4L^2}{\pi^2}\varepsilon_0 \tag{30}$$

where $\hat{q}$ is dimensional midpoint deflection. Note that this result can be obtained by replacing the prescribed axial compressive force by γ_0 in the exact solution for the buckled beam obtained in [55]. Figure 5 illustrates the comparison between the numerical finite differences (blue cycles) and analytical (red line) results for the static bifurcation of the silicon beam with the dimensions listed in Table 1 and without pre-stress (i.e., $\varepsilon_0 = 0$). The critical value of the voltage was found to be $V_{cr} \approx 5.9V$.

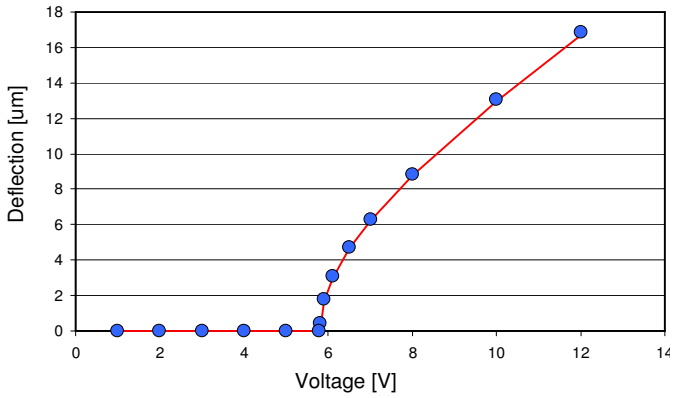


Figure 5: Buckling curves of the beam: comparison between the numerical finite differences (blue cycles) and analytical (red line) solutions describing the static bifurcation of the beam.

6 Parametric excitation

The ordinary differential equation (25) governing the beam's dynamics in the framework of the single DOF model is actually a particular case of a well-known damped Hill's equation (e.g.,see [15]) with an additional nonlinear cubic term. The time-periodic stiffness coefficient contains two time scales-one is proportional to the driving frequency ω (the frequency of the supplied electrical signal) and the second is twice of this frequency, i.e., 2ω. In order to examine the possibility of the PR in the beam under consideration, we reduce Eq. (25) to the form of a canonical Mathieu equation. First, we consider the case of the excitation solely by the ac voltage/current and $V_{dc} = 0$. In this case $\gamma_1(t) = 0$ and the time-dependent coefficient contains only one time scale associated with the excitation at the frequency 2ω. Next, since the parametric instability onset occurs at the straight undeformed configuration of the beam, we neglect the nonlinear cubic term in the equation. In addition, we assume that the beam is initially stress-free, which is typical of the single crystal Si devices considered in this work. By setting the phase lag ϕ (Eq. (19)) to be zero in a homogeneous equation, the single DOF model of the beam takes the form

$$m\ddot{q} + c\,m\dot{q} + [k_B + k_S\gamma_0 + k_S\gamma_2 \cos 2\omega\, t]\, q = 0; \tag{31}$$

where

$$\gamma_0 = -\frac{1}{24}\eta^2 \frac{\alpha}{k\rho_e} V_{ac}^2, \qquad \gamma_2 = -\frac{1}{2}\eta^2 \frac{\alpha}{k\rho_e} V_{ac}^2 \bar{\Theta}. \tag{32}$$

Here the amplitude of the temperature modulation $\bar{\Theta}$ is given by Eq. (14) with β replaced by $\beta\sqrt{2}$ (see Eq. (19)). Note that for convenience, we express the frequency parameter β in terms

of the non-dimensional frequency ω, defined in Eq. (21)

$$\beta = \sqrt{\frac{r\, C_p\, \omega}{2k}\sqrt{\rho\, E}} \tag{33}$$

By re-scaling time $t = \tau/2\omega$ in Eq. (31) we obtain

$$\frac{d^2q}{d\tau^2} + \frac{c}{2\omega}\frac{dq}{d\tau} + \frac{q}{4m\omega^2}\left[k_B - k_S\frac{1}{24}\eta^2\frac{\alpha}{k\rho_e}V_{ac}^2 + k_S\frac{1}{2}\eta^2\frac{\alpha}{k\rho_e}V_{ac}^2\bar{\Theta}\,\cos\tau\right] = 0. \tag{34}$$

This equation is actually the canonical Mathieu equation

$$\frac{d^2u}{d\tau^2} + \tilde{c}\frac{du}{d\tau} + (\delta + \epsilon\,\cos\tau)u = 0 \tag{35}$$

whose two coefficients –δ and ϵ– define the character of the response. The $\delta - \epsilon$ plane is subdivided into two sub-regions corresponding to the "stable" and "unstable" responses. The parametric resonance is possible for the values of δ and ϵ located within the "unstable" region. The location of the boundaries of the unstability region corresponding to the primary parametric resonance is given by the expression [15] (note that this approximation is valid for small ϵ)

$$\epsilon = \sqrt{4\left(\delta - \frac{1}{4}\right)^2 + \tilde{c}^2} \tag{36}$$

In accordance with Eq. (36) the parametric resonance in the damped Mathieu equation is possible for the values of ϵ higher than a certain threshold value (i.e. for $\epsilon > \tilde{c}$ in the case of primary PR [15]).

By comparing Eqs. (34) and (35) it is possible to express the parameters δ and ϵ in terms of the physical parameters of the beam

$$\tilde{c} = \frac{c}{2\omega}, \quad \epsilon = \frac{1}{8m\omega^2}k_S\eta^2\frac{\alpha}{k\rho_e}V_{ac}^2\bar{\Theta}, \quad \delta = \frac{1}{4m\omega^2}\left[k_B - k_S\frac{1}{24}\eta^2\frac{\alpha}{k\rho_e}V_{ac}^2\right] \tag{37}$$

On the other hand, in the beam under consideration, the parameters δ and ϵ are not independent and related through Eq. (37)

$$\epsilon = 12\bar{\Theta}\left(\frac{k_B}{4m\omega^2} - \delta\right) \tag{38}$$

Recall that in Eq. (38) $\bar{\Theta} = \bar{\Theta}(\beta)$, i.e., $\bar{\Theta}$ depends on the excitation frequency, as suggested by Eqs. (14), (33).

Figure 6 shows the location of the stability boundaries given by Eq. (36) on the $\delta - \epsilon$ plane and the lines $\epsilon = \epsilon(\delta)$ given by Eq. (38) each corresponding to a specific prescribed value of the driving frequency ω. Parameters of the beam correspond to listed in Table 1. Note that the frequency dependence of the location of the stability boundaries is due to the dependence of the damping term $\tilde{c}$ in the Mathieu equation on the driving frequency, Eq. (37). One observes that the parametric excitation is possible when the (non-dimensional) driving frequency is lower than a certain threshold value $\omega < \omega_{th} < 5.4$. Note that the natural frequency of the beam with no axial force is $\omega_0 = 4.73^2 = 22.39 >> \omega_{th}$. If the beam is excited at the frequencies above the threshold frequency the excitation of the PR can not be achieved.

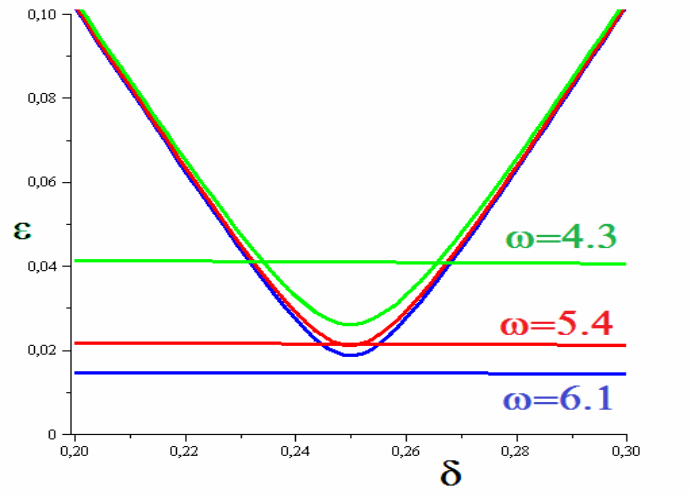


Figure 6: Boundaries Eq. (36) of the stability regions of the damped Mathieu equation. Straight lines $\epsilon = \epsilon(\delta)$, Eq. (38)represent the states of the system corresponding to a constant driving frequency. Parameters of the beam are listed in Table 1, Q-factor is 100.

7 CONCLUSIONS

In this work we investigate the feasibility of the excitation of the parametric resonance by means of time-periodic Joule's heating of double-clamped micro beam. The approach is distinguished by its simplicity and robustness and can be used, for example, in resonant sensors. In thermal micro actuators based on Joule's heating, the characteristic time constants corresponding to heating and cooling are typically much larger than the periods of free or resonant vibrations of micro structures. Our results suggest that in the system under consideration the excitation of PR is possible when the driving frequency (the frequency of the electric potential applied to the ends of the beam) is lower than a certain threshold value. For the parameters of the beam used in calculations and for the case of excitation by the ac voltage, this value was found to be significantly lower than the natural frequency of the beam. This result has a clear physical interpretation. The PR is excited when the frequency of the stiffness modulation, which is in our case the frequency of the temperature fluctuation in the beam, is close to twice the natural frequency. For the given dimensions and material (mechanical and electrical) properties of the structure the achievable "thermal" frequency is limited by the heating/cooling characteristics times and cannot be increased. However, the frequency of the PR cane be pushed down. Joule heating by a time-periodic voltage/current results in appearance of a steady component of the temperature. This steady heating of the beam leads to the appearance of a steady compressive axial force and results in the decrease of the natural frequency of the beam to the required value close to the half of the temperature modulation frequency. Heating allows the decrease of the frequency of the beam to any value below its natural frequency down to zero value, which corresponds to the buckling of the beam. Our results show that a combination of a driving voltage and of the driving frequency can be always found such that the PR frequency is decreased to the value of the driving frequency.

Acknowledgments The research is supported by the consortium PARM-2, FP7-PEOPLE-2011-IAPP, Marie Curie Actions, project no. 284544.

REFERENCES

[1] M. Tanaka, An industrial and applied review of new MEMS devices features. *Microelectronic Eng.,* 84, 1341–1344, 2007

[2] H. C. Nathanson, W. E. Newell, R. A. Wickstrom, and J. R. Davis, The resonant gate transistor. *IEEE Trans. Electron. Devices,* **14** 117-133, 1967.

[3] G. M. Rebeiz, *RF MEMS : Theory Design and Technology.* Hoboken N J : Wiley-Interscience, 2003.

[4] N. Yazdi, F. Ayazi, K. Najafi, Micromachined inertial sensors. *Proceedings of The IEEE* textbf86(8), 1640–1659, 1998.

[5] C. Acar, A. M. Shkel, *MEMS Vibratory Gyroscopes: Structural Approaches to Improve Robustness.* Springer, New York, 2009.

[6] X. M. H. Huang, M. Manolidis, Jun Seong Chan and J. Hone, Nanomechanical hydrogen sensing. *Appl. Phys. Letters*, **86**, 143104, 2005.

[7] B. Ilic, H. G. Craighead, S. Krylov, W. Senaratne, C. Ober, and P. Neuzil Attogram detection using nanoelectromechanical oscillators. *J. Appl. Phys.* **95** 3694-3703, 2004.

[8] B. Ilic, Y. Yang, K. Aubin, R. Reichenbach, S. Krylov, and H. G. Craighead, Enumeration of DNA molecules bound to a nanomechanical oscillator. *Nano Letters,* **5**, 925–929, 2005.

[9] D. J. Joe, Y. Linzon, V. P. Adiga, R. A. Barton, M. Kim, B. R. Ilic, S. Krylov, J. M. Parpia, and H. G. Craighead, Stress-based Resonant Volatile Gas Microsensor Operated near the Critically-buckled State. *Journal of Applied Physics*, **111**(10), pap. 104517 2012.

[10] N. Lobontiu, *Mechanical Design of Microresonators: Modeling and Applications.* McGraw-Hill Nanoscience and Technology, 2005.

[11] D. Rugar and P. Grùtter, *Phys. Rev. Lett.* **67**, 699, 1991.

[12] K. L. Turner, S. A. Miller, P. G. Hartwell, N. C. MacDonald, S. H. Strogatz, and S. G. Adams, Five parametric resonances in a micromechanical syste. *Nature*, **36**, 149–152, 1998.

[13] R. Lifshitz, and M. C. Cross, Nonlinear dynamics of nanomechanical and micromechanical resonators. *Review of Nonlinear Dynamics and Complexity*, Heinz Georg Shuster Ed Wiley-VCH Verlag GmbH & Co KGaA Weinheim, Vol 1 1-52, 2008.

[14] J. Rhoads, S. W. Shaw, K. L. Turner, Nonlinear dynamics and its applications in micro- and nanoresonators. *Proc. DSCC2008 2008 ASME Dynamic Systems and Control Conference October 20-22 Ann Arbor Michigan USA* pap. DSCC2008–2406, 2008.

[15] R. H. Rand, *Lecture Notes on Nonlinear Vibrations, Version 52*, Retrieved from http://audiophile.tam.cornell.edu/randdocs/nlvibe52.pdf, (2005)

[16] W. Zhang, and K. L. Turner, Application of parametric resonance amplification in a single-crystal silicon micro-oscillator based mass sensor. *Sens. Act. A*, **122**, 23-30, 2005.

[17] L. A. Oropeza-Ramos, C. B. Burgner, K. L. Turner, Robust micro-rate sensor actuated by parametric resonance. *Sensors and Actuators A* **152** 80-87, 2009.

[18] Z. Hu, B. J. Gallacher, K. M. Harish, J. S. Burdess, An experimental study of high gain parametric amplification in MEMS. *Sensors and Actuators A* **162** 145-154, 2010.

[19] C. Ataman, O. Kaya, H. Urey, Analysis of parametric resonances in comb-driven microscanners. *Proc. Conf. on MEMS MOEMS and Micromachining Apr. 29-30 2004 Strasbourg France Proc. of The Society Of Photo-Optical Instrumentation Engineers (SPIE)* Vol. 5455, 128–136, 2004.

[20] M. Napoli, R. Baskaran, K. L. Turner, and B. Bamieh, Understanding mechanical domain parametric resonance in microcantilevers. *Proc. IEEE Sixteenth Int. Annual Conference on MEMS (MEMS' 2003)*, 169–172, 2003.

[21] S. Krylov, I. Harari, and Y. Cohen, Stabilisation of electrostatically actuated microstructures using parametric excitation. *J. Micromech. Microeng.,* **15**, 1188–1204, 2005.

[22] J. F. Rhoads, S. W. Shaw, and K. L. Turner, The nonlinear response of resonant microbeam systems with purely-parametric electrostatic actuation. *J. Micromech. Microeng.,* **16**, 890-899, 2006.

[23] J. F. Rhoads, S. W. Shaw, and K. L. Turner, J. Moehlis, B. E. DeMartini, W. Zhang, Generalized parametric resonance in electrostatically actuated microelectromechanical oscillators. *J. Sound Vib.,* **296**, 797-829. 2006.

[24] S. Krylov, Parametric excitation and stabilization of electrostatically actuated microstructures. *Int. J. for Multiscale Comput. Eng.*, **6**(6), 563–584, 2008.

[25] R. M. C. Mestrom, R. H. B. Fey, J. T. M. van Beek, K. L. Phan, and H. Nijmeijer, Modelling the dynamics of a MEMS resonator: Simulations and experiments. *Sens. Act. A*, **142**, 306-315, 2008.

[26] C. van der Avoort, R. van der Hout, J. J. M. Bontemps, P. G. Steeneken, K. Le Phan, R. H. B. Fey, J. Hulshof, J. T. M. van Beek, Amplitude saturation of MEMS resonators explained by autoparametric resonance. *J. Micromech. Microeng.,* **20**, (10), Article-Number 105012, 2010.

[27] A. Vyas, D. Peroulis, A. K. Bajaj, A Microresonator Design Based on Nonlinear 1 : 2 Internal Resonance in Flexural Structural Modes. *Journal of Microelectromechanical Systems*, **18**, No. 3, 744–762, 2009.

[28] S. Krylov, Y. Gerson, T. Nahmias, U. Keren, Excitation of large amplitude parametric resonance by the mechanical stiffness modulation of a microstructure. *J. Micromech. Microeng*., **20**, pap. 015041 2010.

[29] D. Schwartz, D.J. Kim, R.T. MCloskey, Frequency tuning of a disk resonator gyro via mass matrix perturbation. *J. Dyn. Syst. Control* 131 pap. 061004, 2009.

[30] S. Krylov, K. Lurie, A. Ya'akobovitz, Compliant structures with time-varying moment of inertia and non-zero averaged momentum and their application in angular rate microsensors. *Journal of Sound and Vibrations*, **330**, 4875-4895, 2011.

[31] S. Krylov, N. Molinazzi, T. Shmilovich, U.Pomerantz, S. Lulinsky, Parametric excitation of flexural vibrations of micro beams by fringing electrostatic fields. *Proc. ASME Design Engineering Technical Conference IDETC/CIE2010*, v 4, 601–611, 2010.

[32] J. A. Pelesko and D. H. Bernstein *Modeling of MEMS and NEMS.* London-New York-Washington DC: Chapman&Hall A CRC Press Company, 2002.

[33] V. Kaajakari, *Practical MEMS.*, Small Gear Publishing, 2009.

[34] R. Mahameed, D. Elata, Two-dimensional analysis of temperature-gradient actuation of cantilever beam resonators. *J. Micromech. Microeng.*, **15**, 1414–1424, 2005.

[35] T. Remtema, L.Lin, Active frequency tuning for micro resonators by localized thermall stressing effects. *Sensors and Actuators A*, **91**, 326–332, 2001.

[36] Ki Bang Lee, A. P. Pisano, L. Lin, Nonlinear behaviors of a comb drive actuator under electrically induced tensile and compressive stresses. *J. Micromech. Microeng*. **17** 557-566, 2007.

[37] Seong Chan Jun, Hyungbin Son, C.W. Baik, J.M. Kim, S.W. Moon, H. Jin Kim, X.M.H. Huang, J. Hone, Electrothermal noise analysis in frequency tuning of nanoresonators. *Solid-State Electronics*

[38] K. Aubin, M. Zalalutdinov, A. Tuncay, R. B. Reichenbach, R. H. Rand, A. T. Zehnder, J. Parpia, H. G. Craighead, Limit cycle oscillations in CW laser driven NEMS. *J. Microelectromech. Syst.,* **13**, 1018-1026, 2004.

[39] B. Ilic, S. Krylov, K. Aubin, R. Reichenbach, and H. G. Craighead, Optical excitation of nanoelectromechanical oscillators. Appl. Phys. Lett. **86**, 193114, 2005.

[40] B. Ilic, S. Krylov, and H. G. Craighead, Theoretical and Experimental Investigation of Optically Driven Nanoelectromechanical Oscillators," *Journal of Applied Physics*, **107**, 034311, 2010.

[41] M. Pandey, K. Aubin, M. Zalalutdinov, R. B. Reichenbach, A. T. Zehnder, R. H. Rand, H. G. Craighead, Analysis of frequency locking in optically driven MEMS resonators. *J. Microelectromech. Syst.*, **15**, 1564–1554, 2006.

[42] M. Zalalutdinov, A. Olkhovets, A. T. Zehnder, B. Ilic, D. Czaplewski, H. G. Craighead, J. M. Parpia, Optically pumped parametric amplification for micromechanical oscillators. *Appl. Phys. Letters*, **78**, 3142–3144, 2001

[43] T. Sahai, R. B. Bhiladvala, A. T. Zehnder, Thermomechanical transitions in doubly-clamped micro-oscillators. *Int. J. Non-Lin. Mech.*, **42**, 596–607, 2007.

[44] T. Sahai, R. B. Bhiladvala, A. T. Zehnder, Thermomechanical transitions in doubly-clamped micro-oscillators., *International Journal of Non-Linear Mechanics*. **42**, 596 - 607, 2007.

[45] D. Blocher, A. T. Zehnder, R. H. Rand, S. Mukerji, Anchor deformations drive limit cycle oscillations in interferometrically transduced MEMS beams. *Finite Elements in Analysis and Design*, **49**, 52-57, 2012.

[46] S. Zaitsev, O. Gottlieb, E. Buks, Nonlinear dynamics of a microelectromechanical mirror in an optical resonance cavity. *Nonlinear Dynamics*, **69**, 1589-1610, 2012.

[47] D. Schreiber, S. Krylov, Y. Shacham-Diamand, T. Sibgatullin, Electromagnetic microactuators with on-chip resin-bonded permanent magnets. *Proc. of the 9th Biennial ASME Conference on Engineering Systems Design and Analysis ESDA08*, July 7-9, 2008, Haifa, Israel

[48] P. Villagio, *Mathematical Models for Elastic Structures*. Cambridge University Press, Cambridge, 1997.

[49] Y. Okada, and Y. Tokumaru, Precise determination of lattice parameter and thermal expansion coefficient of silicon between 300 and 1500 K. *J. Appl. Phys*. **56**, 314–320, 1984.

[50] R. Hickey, D. Sameoto, T. Hubbard and M. Kujath, Time and frequency response of two-arm micromachined thermal actuators. *J. Micromech. Microeng.* **13,** () 40-46, 2003.

[51] Qing-An Huang and Neville Ka Shek Lee, Analysis and design of polysilicon thermal flexure actuator. *J. Micromech. Microeng*. **9** 64-70, 1999.

[52] E. Marin,Characteristic dimensions for heat transfer.*Lat. Am. J. Phys. Educ.*,**4**,56–60, 2010.

[53] H.S. Carslaw and J.C. Jaeger, *Conduction of heat in Solids*. 2nd ed. Oxford: Clarendon Press, 1986.

[54] L. Shampine, M. Reichelt, The Matlab ODE suite. *SIAM J. Sci. Comput.,* **18**, 1–22, 1997.

[55] A. H. Nayfeh, S. Emam, Exact solution and stability of postbuckling configurations of beams. *Nonlinear Dynamics*,**54**, 395–408, 2008.

COMPDYN 2013
4th ECCOMAS Thematic Conference on
Computational Methods in Structural Dynamics and Earthquake Engineering
M. Papadrakakis, V. Papadopoulos, V. Plevris (eds.)
Kos Island, Greece, 12–14 June 2013

THE LOCATION OF PASS AND STOP BANDS OF AN INFINITE PERIODIC STRUCTURE VERSUS THE EIGENFREQUENCIES OF ITS FINITE SEGMENT CONSISTING OF SEVERAL 'PERIODICITY CELLS'

G. Filippenko

[1] Institute of Problems of Mechanical Engineering of Russian Academy of Sciences
Vasilievsky Ostrov, Bolshoy Prospect 61, St.-Petersburg, 199178, Russia
e-mail: g.filippenko@gmail.com

Keywords: Periodic structures, energy flux, pass and stop bands.

Abstract. *On the classical example of a rod (membrane, string) with periodically located inertial inclusions, it is proved that all eigenfrequencies of a finite periodic structure fall into pass-bands of corresponding infinite system in the symmetrical case. In the unsymmetrical case, some eigenfrequencies may not follow this rule.*

The exact equations for eigenfrequencies and the explicit expressions for power flow are obtained. The asymptotic analysis of power flow in an infinite periodic structure is carried out and the structure of pass- and stop-bands is explored. The modes of free vibrations of a finite periodic structure are analyzed with the special attention to edge effects.

1 INTRODUCTION

Wave phenomena in periodic structures are intensively explored during last years [1-4]. The extensive bibliography is represented in [1] for example. In the process of numerical calculations in [4] was noticed that the eigenfrequencies of a finite periodic structure fall into the pass-bands of corresponding infinite system.

In this work on the classical example of a rod (membrane, string) with periodically located inertial inclusions is analytically proved that all eigenfrequencies of a finite periodic structure fall into pass-bands of corresponding infinite system in the symmetrical case. In the unsymmetrical case, some eigenfrequencies may not follow this rule. The stationary problem is considered.

2 INFINITE PERIODIC STRUCTURE

On the interval $x \in (-\infty, +\infty)$ the following equation is considered

$$u''(x) + k^2 \left(1 + \frac{M}{\mu} \sum_{j=-\infty}^{+\infty} \delta(x - jl) \right) u(x) = 0 \tag{1}$$

It describes propagation of stationary waves in the string (membrane) or longitudinal waves in the rod with periodic point masses (the distance between masses of weight M is equal l). Here $k = \omega / c$, where $c = T / \mu$ - in the case of a string (membrane) or $c = ES / \mu$ - in the case of longitudinal waves in a rod, μ - linear density, T - tension in string, E - Jung modulus, S - cross section of the rod. The dependence on time is $e^{-i\omega t}$ and is omitted. In this model each cell of periodicity consists one mass.

Further we shall use the dimensionless parameters $k := kl$, $m = M / \mu l$, dimensionless variable $x := x / l$ and dimensionless functions $u(x) := u(x) / l$ and $\delta(x) := l\delta(x)$. The equation in terms of dimensionless parameters, variables and functions, having kept former designations is

$$u''(x) + k^2 \left(1 + m \sum_{j=-\infty}^{+\infty} \delta(x - j) \right) u(x) = 0 \tag{2}$$

The Floquet solution of equation (1) is built by the contact method. The following contact conditions are used in the points x_j where the concentrated masses are located:

The continuity of displacements

$$u(x_j + 0) = u(x_j - 0) \equiv u(x_j)$$

The condition of the jump of the forces

$$u'(x_j + 0) - u'(x_j - 0) = -\frac{k^2}{\mu} M u(x_j)$$

Floquet condition

$$u(x+l) = u(x)e^{i\alpha},\ \forall x \in (-\infty, +\infty),$$

where $e^{i\alpha}$ is the Floquet factor between the cells of periodicity and $\alpha = \alpha(k)$ is determined from equality

$$\cos\alpha = \cos k - \frac{m}{2} k \sin k$$

On the interval $x \in [0,1]$ the solution has the view

$$u(x) = A\left(e^{ikx} - f(k)e^{-ik(x-1)}\right) \tag{3}$$

The general solution in arbitrary point $x \in [-\infty, \infty]$ has the form

$$u(x) = Ae^{ik[x]\alpha}\left(e^{ik\{x\}} - f(k)e^{ik}e^{-ik\{x\}}\right) = Ae^{ik[x]\alpha}e^{ik/2}\left(e^{ik(\{x\}-1/2)} - f(k)e^{-ik(\{x\}-1/2)}\right) \tag{4}$$

where $[x]$ is the floor part of x, $\{x\}$ is the fraction part of x, A is the arbitrary constant and

$$f(k) \equiv f(k, \alpha(k)) = \sin\left((\alpha(k)-k)/2\right)/\sin\left((\alpha(k)+k)/2\right) \tag{5}$$

The energy flux (averaged on the period of oscillations) is

$$\Pi(k) = T\frac{\omega}{2}\mathrm{Im}(u'\bar{u}) \quad \text{or} \quad \Pi(k) = ES\frac{\omega}{2}\mathrm{Im}(u'\bar{u})$$

in the case of the string (membrane) or the rod correspondingly. The energy flux of the wave (4) normalized on the energy flux of corresponding wave Ae^{ikx} in the homogeneous system has the view

$$\Pi(k) = 1 - \left|f(k)\right|^2 \tag{6}$$

The elementary analysis of the energy flux shows:

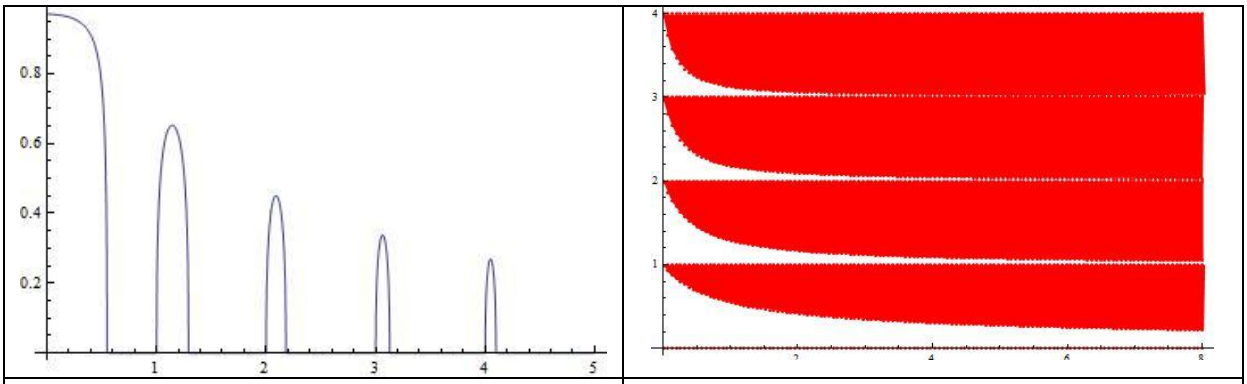
- $\Pi(k) < 1$, if $m \neq 0$.

- Asymptotic: $\Pi(k) = \frac{4}{mk}\left(1+O\left(\frac{1}{k}\right)\right)$, if $k \to \infty$.
- Width of pass bands: $\frac{4}{mk}\left(1+O\left(\frac{1}{k}\right)\right)$, if $k \to \infty$
- $\exists \lim_{k\to 0} \Pi(k,m) \equiv \Pi_0(m) = 1 - \left|\frac{\sqrt{1+m}-1}{\sqrt{1+m}+1}\right|^2$

The typical view of the energy flux dependence on the wave number k (for $m = 1.0$) is shown on the Fig. 1*a* (the numerical results are fulfilled for $k := k/\pi$). The condition of existence of propagating waves in the system will have the form

$$|T(k)| \le 2$$

where $T(k) = mk\sin k - 2\cos k$. The areas on the plain (m,k), where $|T(k)| > 2$ are marked by red color on the Fig. 1*b*. These points are corresponded to nonhomogeneous waves (in the stop bands). The areas outside (where $|T(k)| < 2$) are corresponded homogeneous waves (in the pass bands). The borders between them ($|T(k)| = 2$) are corresponded the special wave regime with zero energy flux.



a) Energy flux, as function of k/π | *b)* k/π as function m (Pass and stop bands)

Figure 1: Infinite periodic structure

3 FINITE PERIODIC STRUCTURE

The finite segment ($x \in [a,b]$), consisting of several (N) cells of periodicity of the infinite periodic system is considered. In the common situation of different masses the equation (2) can be rewritten in the form

$$u''(x) + k^2\left(1+\sum_{j=0}^{N} m_j \delta(x-x_j)\right)u(x) = 0$$

Let us consider the case of one mass for simplicity (the case of greater number of weights is considered similarly)

$$-u''(x)-\lambda\rho(x)u(x)=0 \quad \text{or} \quad Lu(x)=\lambda\rho(x)u(x)$$

where $\rho(x)\equiv 1+m\delta(x)$, $\lambda=k^2$, $L\equiv-\dfrac{d^2}{dx^2}$.

Let's notice that if $\rho(x)$ is continuous positive function then it is a classical case of Sturm-Liouville problem with weight $\rho(x)$. The generalization of this problem on investigated case is based on the following statements.

Operator $L\equiv-\dfrac{d^2}{dx^2}$ is symmetric concerning scalar product in $L_2(a,b)$

$$(Lu,v)=\int_a^b -u''v\,dx=\left(-u'v+uv'\right)\Big|_a^b+(u,Lv) \tag{2a}$$

since extraintegrated members are equal to zero owing to our boundary conditions. For the existence of integral in (2a) it is enough to demand the limitation of energy norm

$$\|u\|^2=\int_a^b\left(|u|^2+|u'|^2\right)dx, \quad \text{i.e.} \quad u\in W_2^1(a,b)\equiv H^1(a,b)$$

By the way in our case expression

$$(\rho(x)u,v)=\int_a^b u(x)\overline{v(x)}dx+mu(0)\overline{v(0)}, \quad m\geq 0$$

sets scalar product with weight $\rho(x)$: $(u,v)_\rho\equiv(\rho(x)u,v)$. By using this scalar product the following facts can be obtained on the traditional way.

The spectrum λ_n, $n=1,2,...$ is discrete and simple. $\lambda_n\geq 0$. Eigenfunctions u_n, v_m are orthogonal via scalar product with weight $\rho(x)$, i.e. $(u_n,v_m)_\rho=0$, if $n\neq m$.

Now the case of odd and even number of point masses will be considered separately.

3.1 The case of odd number of masses N=2n+1

For odd number of point masses the equation (2) on interval $x\in[a,b]$ is transformed to

$$u''(x)+k^2\left(1+m\sum_{j=-n}^{n}\delta(x-j)\right)u(x)=0 \tag{7a}$$

Where $a=-n-1+s$, $b=n+s$, $0<s<1$.

For the particular case of one mass (n=0, N=1) the following equations on eigenfrequencies can be obtained according to the boundary conditions (BC):

If $u(a)=0=u(b)$ (rigid fixing) then $r_1 \equiv r_1(k,s) \equiv mk\sin k(1-s)\sin ks-\sin k=0$ (7b)

If $u'(a)=0=u'(b)$ (free fixing) then $f_1 \equiv f_1(k,s) \equiv mk\cos k(1-s)\cos ks+\sin k=0$ (7c)

If $u(a)=0=u'(b)$ (combined BC) then $g_1 \equiv g_1(k,s) \equiv mk\sin k(1-s)\cos ks-\cos k=0$ (7d)

In the symmetric case ($s=1/2$) these equations are simplified:

$$r_1(k,s)\big|_{s=1/2} \equiv \sin\frac{k}{2}\left(\frac{m}{2}k\sin\frac{k}{2}-\cos\frac{k}{2}\right)=0 \tag{8}$$

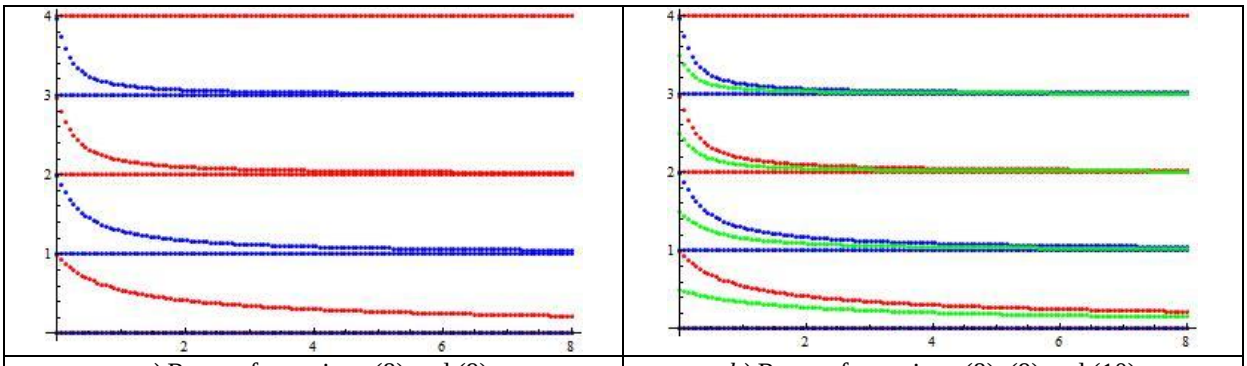
$$f_1(k,s)\big|_{s=1/2} \equiv \cos\frac{k}{2}\left(\frac{m}{2}k\cos\frac{k}{2}+\sin\frac{k}{2}\right)=0 \tag{9}$$

$$g_1(k,s)\big|_{s=1/2} \equiv \cos^2\frac{k}{2}-\sin^2\frac{k}{2}-mk\sin\frac{k}{2}\cos\frac{k}{2}=0 \Leftrightarrow T(k)=0 \tag{10}$$

On the Fig. 2*a,b* is shown the corresponding dependencies of eigenfrequencies on parameter m for fixing (8) and free (9) boundary conditions (red and blue lines accordingly). Green curve on the Fig. 2*b* corresponds combined (10) boundary condition. After multiplication of equations (8) and (9) the following equation can be obtained

$$r_1(k,s)\big|_{s=1/2}\ f_1(k,s)\big|_{s=1/2} \equiv \left(T(k)^2-4\right)/4=0 \Leftrightarrow |T(k)|=2 \tag{11}$$

The curves determined by this equation coincide with the borders of pass and stop bands of consequent infinite periodic system (Fig. 1b).



a) Roots of equations (8) and (9) | *b)* Roots of equations (8), (9) and (10)

Figure 2: Eigenfrequencies as functions m

In the case of $n>1$ the equations on eigenfrequencies have the form

$$r_1(k,s)\prod_{j=1}^{n}\left(T(k)^2-C_j^2\right)=0 \quad \text{or} \quad f_1(k,s)\prod_{j=1}^{n}\left(T(k)^2-C_j^2\right)=0 \tag{12}$$

for rigid and free fixing accordingly.

In the symmetric case ($s=1/2$) the equation for combined fixing has the form

$$T(k)\prod_{j=1}^{n}\left(T(k)^2-B_j^2\right)=0 \tag{13}$$

And multiplication of equations of free and rigid fixing (12) leads to equation

$$\left(T(k)^2-4\right)\prod_{j=1}^{n}\left(T(k)^2-C_j^2\right)^2=0 \tag{14}$$

The multiplication of equations of combined fixing on itself leads to equation

$$T(k)^2\prod_{j=1}^{n}\left(T(k)^2-B_j^2\right)^2=0 \tag{15}$$

Here $C_j, B_j>0$ are the constants depending on N. The first values of them are represented in the tables

	C_1	C_2	C_3
$N=3$	1		
$N=4$	$\sqrt{2}$		
$N=5$	$\left(\sqrt{5}-1\right)/2$	$\left(\sqrt{5}+1\right)/2$	
$N=6$	1	$\sqrt{3}$	
$N=7$	0.445042	1.24698	1.80194
$N=8$	$\sqrt{2-\sqrt{2}}$	$\sqrt{2}$	$\sqrt{2+\sqrt{2}}$

Table 1: The values of constants C_j.

	B_1	B_2	B_3
$N=2$	$\sqrt{2}$		
$N=3$	$\sqrt{3}$		

$N=4$	$\sqrt{2-\sqrt{2}}$	$\sqrt{2+\sqrt{2}}$	
$N=5$	$\sqrt{\left(5-\sqrt{5}\right)/2}$	$\sqrt{\left(5+\sqrt{5}\right)/2}$	
$N=6$	$\sqrt{2}$	$\sqrt{2-\sqrt{3}}$	$\sqrt{2+\sqrt{3}}$

Table 2: The values of constants B_j.

3.2 The case of even number of masses N=2n

For even number of point masses the equation on interval $x\in[a,b]$ is transformed to

$$u''(x)+k^2\left(1+m\sum_{j=-n}^{n-1}\delta\left(x-\frac{2j+1}{2}\right)\right)u(x)=0 \tag{16a}$$

where $a=-\frac{2n+1}{2}+s$, $b=\frac{2n-1}{2}+s$, $0<s<1$.

For the particular case of two masses ($n=1$, $N=2$) the following equations on eigenfrequencies can be obtained according to BC:

If $u(a)=0=u(b)$ (rigid fixing) then $r_2\equiv r_2(k,s)=0$, where

$$r_2\equiv 2\sin 2k+km(2\cos 2k-\cos(2k(s-1))-\cos 2ks+2mk\sin(k(1-s))\sin ks\sin k) \tag{16b}$$

If $u'(a)=0=u'(b)$ (free fixing) then $f_2\equiv f_2(k,s)=0$, where

$$f_2\equiv 2\sin 2k+km\left(2\cos 2k+\cos\left(2k(s-1)\right)+\cos 2ks-mk(\cos k+\cos\left(k(1-2s)\right)\right) \tag{16c}$$

If $u(a)=0=u'(b)$ (combined conditions) then $g_2\equiv g_2(k,s)=0$, where

$$g_2\equiv\left(k^2m^2-4\right)\cos 2k+km\left(km\left(\cos\left(2k(s-1)\right)-\cos 2ks\right)+4\sin 2k+4\cos k\sin\left(k(1-2s)\right)-km\right)$$

In the symmetric case $s=1/2$ these equations on eigenfrequencies are simplified

$$r_2(k,s)\big|_{s=1/2}\equiv\sin\frac{k}{2}\left(\frac{m}{2}k\sin\frac{k}{2}-\cos\frac{k}{2}\right)T(k)=0 \tag{17}$$

$$f_2(k,s)\big|_{s=1/2}\equiv\cos\frac{k}{2}\left(\frac{m}{2}k\cos\frac{k}{2}+\sin\frac{k}{2}\right)T(k)=0 \tag{18}$$

$$g_2(k,s)\big|_{s=1/2} \equiv 2-\left(2\cos k - km\sin k\right)^2 = 2-T^2(k) = 0 \tag{19}$$

The multiplication of equations (17) and (18) gives the equation

$$\left(T(k)^2-4\right)\ T(k)^2 = 0 \tag{20}$$

The multiplication of equation (19) on itself gives the equation

$$g_2(k,s)\big|_{s=1/2}\ g_2(k,s)\big|_{s=1/2} \equiv \left(T^2(k)-2\right)^2 = 0 \tag{21}$$

In the case of $n>1$ the equations on eigenfrequencies have the form

$$r_2(k,s)\prod_{j=1}^{n-1}\left(T(k)^2-C_j^2\right)=0 \quad \text{or} \quad f_2(k,s)\prod_{j=1}^{n-1}\left(T(k)^2-C_j^2\right)=0 \tag{22}$$

for rigid and free fixing accordingly. In the symmetric case ($s=1/2$) the equation for combined fixing has the form

$$\prod_{j=1}^{n}\left(T(k)^2-B_j^2\right)=0 \tag{23}$$

and the multiplication of equations of free and rigid fixing leads to equation

$$\left(T(k)^2-4\right)T(k)^2\prod_{j=1}^{n-1}\left(T(k)^2-C_j^2\right)^2=0 \tag{24}$$

The multiplication of equations of combined fixing on itself leads to equation

$$\prod_{j=1}^{n}\left(T(k)^2-B_j^2\right)^2=0 \tag{25}$$

3.3 The summary for equations on eigenvalues

Further in the table $\Phi_N \equiv \prod_{j=1}^{n-1}\left(T(k)^2-C_j^2\right)$, $\Omega_N \equiv \prod_{j=1}^{n-1}\left(T(k)^2-B_j^2\right)$, $\Psi_N \equiv \prod_{j=1}^{n}\left(T(k)^2-B_j^2\right)$

		$N=2n-1$			$N=2n$		
$n=1$	$s\neq\frac{1}{2}$	$r_1=0$	$f_1=0$	$g_1=0$	$r_2=0$	$f_2=0$	$g_2=0$
	$s=\frac{1}{2}$	$r_1\left(\frac{1}{2}\right)=0$	$f_1\left(\frac{1}{2}\right)=0$	$T=0$	$r_2\left(\frac{1}{2}\right)=0$	$f_2\left(\frac{1}{2}\right)=0$	$T^2-2=0$
		$T^2-4=0$		$T^2=0$	$\left(T^2-4\right)\ T^2=0$		$\left(T^2-2\right)^2=0$
$n\geq 2$	$s\neq\frac{1}{2}$	$r_1\Phi_N=0$	$f_1\Phi_N=0$	$G_N=0$	$r_2\Phi_N=0$	$f_2\Phi_N=0$	$G_N=0$
	$s=\frac{1}{2}$	$r_1\Phi_N=0$	$f_1\Phi_N=0$	$T\Omega_N=0$	$r_2\Phi_N=0$	$f_2\Phi_N=0$	$\Psi_N=0$
		$\left(T^2-4\right)\Phi_N^2=0$		$T^2\Omega_N^2=0$	$\left(T^2-4\right)T^2\Phi_N^2=0$		$\Psi_N^2=0$

Table 3: The view of equations on eigenvalues for different N and s.

4 THE PROOF OF THE STATEMENT

The proof that all eigenfrequencies of a finite periodic structure fall into pass-bands of corresponding infinite system in the symmetrical case ($s=1/2$) is based on two statements:

- The structure of the equations on eigenfrequencies has the above-stated view for any arbitrary finite number of masses.
- All constants C_j, B_j in equations on eigenfrequencies satisfy the inequality $C_j, B_j \leq 2$.

The first statement can be proved by mathematical induction method. In order to prove the second statement let's consider one of the factors $T(k)^2-C^2$ from product $\prod_j$. After selecting $\operatorname{tg} k$ the following expression can be obtained

$$T(k)^2-C^2=\cos^2 k\left(\left(m^2k^2-C^2\right)\operatorname{tg}^2 k-4mk\operatorname{tg} k+4-C^2\right) \tag{26}$$

The multiplier with $\operatorname{tg} k$ can be factorized as a square polynomial

$$R(k,m)\equiv\left(m^2k^2-C^2\right)\operatorname{tg}^2 k-4mk\operatorname{tg} k+4-C^2=\left(m^2k^2-C^2\right)\left(\operatorname{tg} k-A_+(k)\right)\left(\operatorname{tg} k-A_-(k)\right) \tag{27}$$

where

$$A_\pm(k)=\frac{2mk\pm C\sqrt{m^2k^2+4-C^2}}{\left(m^2k^2-C^2\right)} \tag{28}$$

If $4-C^2 \geq 0$ in (28), the simple analyses shows that equation $R(k,m)=0$ has the real roots for every value of m (from geometrical method of solving of the equation at least).
If $4-C^2 < 0$, then the expression $m^2k^2+4-C^2$ under the radical can be made negative by choosing m. The corresponding real root transforms into the complex one and we obtain the violation with Sturm-Liouville problem. So all constants $C_j, B_j \leq 2$ and thereby all eigenfrequencies of a finite periodic structure fall into pass-bands of corresponding infinite system in the symmetrical case ($s=1/2$).

If $s \neq 1/2$ then some eigenfrequencies may not follow this rule. It will be shown in the next item.

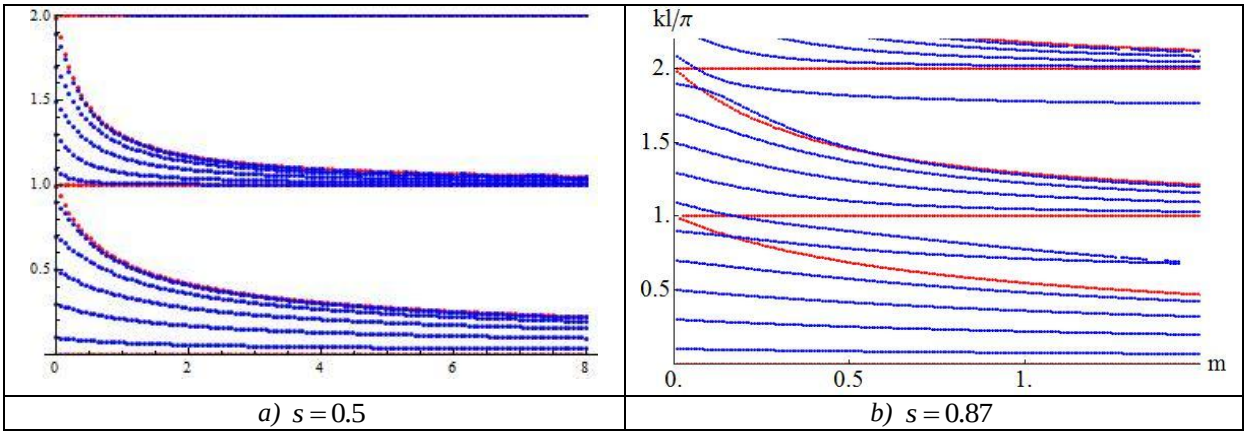
5 THE INFLUENCE OF UNSYMMETRY

In this section the influence of parameter s on the processes is numerically analyzed. The figures are obtained for the case of five point masses and combined BC (the fixed left and free right border). On these figures the curves corresponding dimensionless eigenfrequencies k/π of the finite system as functions of mass m are designated by blue color, and the curves corresponding the boundary of stop bands of the infinite system are designated by red color.

In the case of symmetrical conditions ($s=0.5$, Fig. 3*a*) all the curves corresponding eigenfrequencies do not overstep the bounds of stop bands, according to the proved statement.

In the unsymmetrical case $s=0.27$ as on the Fig. 3b, two curves, in each interval $(n,n+1), n=0,1$ on axes k penetrate into the corresponding stop bands. The modes, corresponding these points of curves when they lie in the stop bands, unlike the corresponding modes for the symmetrical case look like nonhomogeneous waves, i.e. oscillations modulated by decreasing or increasing exponent.

The numerical experiments showed the localization of the mode of finite periodic structure near the boundaries when its eigenfrequency falls into the stop band of corresponding infinite structure. The both direction of decreasing (increasing) are realized for different modes. This "decaying" mode (standing wave) can be interpreted as the combination of non homogeneous waves from the stop band of corresponding infinite periodic structure. This reasoning is analogous to the case of the standing wave as the combination of propagating waves in a finite homogeneous rod.



a) $s=0.5$ | *b)* $s=0.87$

Figure 3: Eigenfrequencies as functions of m for different s. Combined BC

In the case of fixed and free BC the eigenfrequency curves locating in the stop bands are fully determined by the equations (7b), (7c) and (16b), (16c) correspondingly (according to

(12,13) and (22,23)). It can be interpreted as the eigenfrequencies related with the border cells (masses). The calculations show that if the eigenfrequency curve lies in the stop band it lies there wholly in this case.

If combined BC is considered then not only border cells take part in forming of these curves. New opportunities are realized for this situation. For example the curve can cross the border of the stop band several times and interact with another curve in the stop band (as on the Fig. 3b).

6 CONCLUSIONS

These results can be generalised on the case of differential equations of higher order (bending displacements of the ribbed plates, shells e.t.c.). They can be used for design of finite periodical structures with eigenfrequencies located only in the pass bands of corresponding infinite periodical structure. To achieve this goal, the symmetry of cells and special symmetry at the boundaries are requested.

The work was fulfilled in the cooperation with Aalborg University, Department of Mechanical and Manufacturing Engineering, Denmark. The financial support from the Grant Silent Spaces (uk-95-omk-63822-pr-824092) shared between Lund University, Sweden, and AAU and between DMME and Department of Civil Engineering at AAU (Work Package V) is gratefully acknowledged

REFERENCES

[1] D.J. Mead, Wave propogation in continuous periodic structures: research contribution from Southampton, 1964-1995. Journal of Sound and Vibration, **190**(3),495-524, 1996.

[2] E. Glushkov, N. Glushkova, J. Wauer, Wave propagation in an elastically supported string with point-wise defects: gap-band and pass-band effects. *Zeitschrift fur Angewandte Mathematik und Mechanik (ZAMM),* 6 May 2010.

[3] A. Soe-Knudsen, S.V. Sorokin, Modelling of linear wave propogation in spatial fluid filled pipe systems consisting of elastic curved and straight elements. *Journal of Sound and Vibration*, **329**(24), 5116-5146, 2010

[4] N. Olhoff, B. Niu, G. Cheng, Optimum design of band-gap beam structures. *International Journal of Solids and Structures,* **49**, 3158-3169, 2012

COMPDYN 2013
4th ECCOMAS Thematic Conference on
Computational Methods in Structural Dynamics and Earthquake Engineering
M. Papadrakakis, V. Papadopoulos, V. Plevris (eds.)
Kos Island, Greece, 12–14 June 2013

A SIMPLE APPROACH TOWARDS FURTHER ACCURACY IN STRUCTURAL DYNAMIC ANALYSIS

A. Soroushian

[1] International Institute of Earthquake Engineering and Seismology (IIEES)
North Dibajee, West Arghavan, Tehran 19395, Iran
a.soroushin@iiees.ac.ir

Keywords: Time Integration, Accuracy, Computational Cost, Richardson Extrapolation, Proper convergence, Pseudo convergence.

Abstract. *Accuracy and computational cost are of the most important concerns in structural dynamics and especially time integration analyses. In view of the practical need to control the accuracies of time integration, with tolerable computational cost, a simple approach is in this paper proposed for enhancing the accuracies. The mere pre-requisite, which is also essential in conventional practical analyses, is proper convergence. The adequate performance of the approach is tested via a twenty-storey building in linear and nonlinear regimes.*

1 INTRODUCTION

In the complicated world of science and engineering, the considerable distance between our plans/imaginations and the actual analytical capabilities, leads to the essentiality of approximate computational methods. Considering this, and the significant progresses in electronic engineering, entails more advanced methods, for different practical computations and the accuracies evaluation. Together with accuracy, computational cost is of the most important concerns in numerical computations [1-3]. Accuracy is being studied in view of convergence and order of accuracy [1-6], and computational cost is being measured in terms of the computer memory dedicated and the time spent for the analysis [7-9].

Concentrating on semidiscretized equations of motion, i.e.

$$\begin{aligned} &\mathbf{M}\ddot{\mathbf{u}}(t)+\mathbf{f}_{\mathbf{int}}(t)=\mathbf{f}(t) \qquad 0\le t\le t_{end} \\ &\text{Initial conditions}: \left|\begin{array}{l} \mathbf{u}(\mathrm{t}=\mathrm{t}_0)=\mathbf{u}_0 \\ \dot{\mathbf{u}}(\mathrm{t}=\mathrm{t}_0)=\dot{\mathbf{u}}_0 \\ \mathbf{f}_{\mathrm{int}}(\mathrm{t}=\mathrm{t}_0)=\mathbf{f}_{\mathrm{int}_0} \end{array}\right. \\ &\text{Additional constraints}: \mathbf{Q} \end{aligned} \tag{1}$$

(t and t_{end} imply the time and the duration of the dynamic behavior; $\mathbf{M}$ is the mass matrix; $\mathbf{f}_{\mathrm{int}}$ and $\mathbf{f}(t)$ stand for the vectors of internal force and excitation; $\mathbf{u}(\mathrm{t})$, $\dot{\mathbf{u}}(\mathrm{t})$, and $\ddot{\mathbf{u}}(\mathrm{t})$, denote the vectors of displacement, velocity, and acceleration; $\mathbf{u}_0$, $\dot{\mathbf{u}}_0$ and $\mathbf{f}_{\mathrm{int}_0}$ define the initial status of the model [10, 11]; and $\mathbf{Q}$ represents some restricting conditions, e.g. additional constraints in problems involved in impact or elastic–plastic behavior [12, 13]), and their analysis, by time integration, the step by step nature of time integration highlights the importance of accuracy and computational cost in real analyses [1, 3]. Especially, in integration along large numbers of integration steps, the computational costs are considerable, and the accuracies might be affected, by numerical instability [1, 3, 14]. The importance of the concerns increases even further, with attention to the fact that, the main algorithmic parameter, of time integration, i.e. integration step size, affects accuracy and computational cost, in adverse manners [1, 3, 8]. Considering these, a comment for step size selection before any control of the accuracy is [14, 15]

$$\Delta t \cong\le \mathrm{Min}\left(\frac{T}{10}, h\right) \tag{2}$$

(T is the smallest governing period in the response, h is the largest step size preventing numerical stability in linear problems [14-16]). For the sake of the reliability of accuracy, and considering proper convergence [17-19], as an essentiality for practical error evaluation (implied in the inequality in Eq. (2)), it is recommended to repeat the analyses with half steps and compare the responses, while considering the difference of the responses as upper-estimations for the errors (not only in time integration analysis of Eqs. (1), but also, in step-by-step analysis of general ordinary differential equations) [15, 20, 21]. In view of this approach and its enhancement proposed recently [2], and considering time integration, its repetition, and the evaluation of the errors, as a sole computational procedure, the objective in this paper is to increase the efficiency of this practical procedure and arrive at a better approach. A main assumption, in this study, also pre-requisite in practical analyses, is proper convergence, based on which, an approach to implement the recent accuracy-controlling method and materializing less errors with trivial change of computational cost is proposed in this paper. In Section 2,

the theoretical basis is first stated for linear systems and then extended to nonlinear systems. The claims are then examined in Section 3, via analysis of a twenty-storey shear building, in a simple linear case and in a practical nonlinear case subjected to seismic excitations. Later, a complementary discussion is presented in Section 4, and finally, with a brief set of the achievements, the paper is concluded in Section 5.

2 THEORY

2.1 Basis for linear analyses

The method currently recommended for practical time integration analysis consists of a time integration analysis with steps sizes satisfying Eq. (2), and at least once repetition of the analysis with half steps [15], i.e.

$$\Delta t = T_{ord}, \frac{T_{ord}}{2} \tag{3}$$

(Δt_{ord} is the step size obtained from Eq. (2)). This leads to the total computational cost

$$C_{current} = A\frac{30}{T} \tag{4}$$

(A is a constant scalar, depending on the mathematical model in Eqs. (1), and the integration scheme [1, 3]), for cases with $\frac{T}{10}$, as the governing term in Eq. (2). Since, in view of the essentiality of proper convergence, and the Lax-Richtmyer equivalence theorem [4, 22], the study is implicitly limited to numerically stable analyses, unconditional stability and $h \to \infty$ is a comment emphasized in the literature by times, e.g. see [6], and meanwhile, most of the broadly accepted time integration methods are unconditionally stable, e.g. see [23-27], Eq. (4) can be considered valid for general conventional time integration analyses.

Different from ordinary time integration, in time integration analyses with controls of errors based on a recently proposed method [2, 19], at least, two repetitions of the time integration analysis are essential. However because of the additional accuracy obtained from the Richardson extrapolation [28-31], implemented in the recent method [2], the integration step size in the first analysis might be different from that introduced, in Eq. (2). Once again concentrating on unconditionally stable time integration methods and the domination of $\frac{T}{10}$ in Eq. (2), by selecting the step sizes in the first analysis and its two repetitions, as noted below:

$$\Delta t = \frac{10\ T_{ord}}{4}, \frac{10\ T_{ord}}{8}, \frac{10\ T_{ord}}{16} \tag{5}$$

the resulting total computational cost would be

$$C_{proposed} \cong A\frac{28}{T}\frac{1+3n_d}{3n_d} \tag{6}$$

(n_d is the number of the degrees of freedom and the last ratio represents the additional computational effort needed for the Richardson extrapolation). In view of Eq. (4) and (6),

$$C_{proposed} \cong< C_{current} \tag{7}$$

or in other words, when implementing Eq. (5) (as the analyses steps in the recent accuracy controlling method [2]), in stead of implementing Eq. (3), (in two time integration analyses, of the ordinary current approach), the computational costs remain unchanged, and this is while, provided the responses converge properly, the accuracies increases in view of the convergence plot typically depicted in Fig. 1. The convergence trends of the responses computed ordinarily and in the process of the recently accuracy-controlling methods are both as straight lines inclined with integer-valued slopes, in Fig. 1, such that the latter (the line corresponding to Richardson extrapolation and the recent accuracy-controlling method) is steeper. This leads to:

$$E_C < E_B \cong E_A \tag{8}$$

(E implies the error), and since E_A and E_C imply the errors of the most exact obtained in the current analysis approach (implementing Eq. (3)), $E_{current}$, and those obtained in the approach proposed here (implementing Eq. (5) and Richardson extrapolation), $E_{propsed}$, we can conclude:

$$E_{proposed} < E_{current} \tag{9}$$

The validity of Eqs. (8) and (9) (also addressed in Fig. 1) can be proved rigorously in view of [32], Eq. (5), the conventional orders of accuracy, i.e. the range of slopes of the two lines in Fig. 1 [1, 3, 6], and the fifty percent reduction of integration step size in each new analysis (see Eqs. (3) and (5)). Consequently, in view of Eqs. (7) and (9), by considering the integration step sizes stated in Eq. (5), when the responses converge properly, we can increase the accuracy, without additional computational cost. Since, the computational cost and the inaccuracy because of nonlinearities (and specifically the nonlinearity iterations and residuals [16, 18]) are not considered in the discussion, the above claim, regarding arriving at further accuracies with no additional computational cost, is yet limited to linear analyses.

○ Responses under consideration in the ordinary process of analysis and evaluation of accuracy

◎ Responses under consideration in analysis and evaluation of accuracy based on Eq. (5) and a recently proposed accuracy controlling method

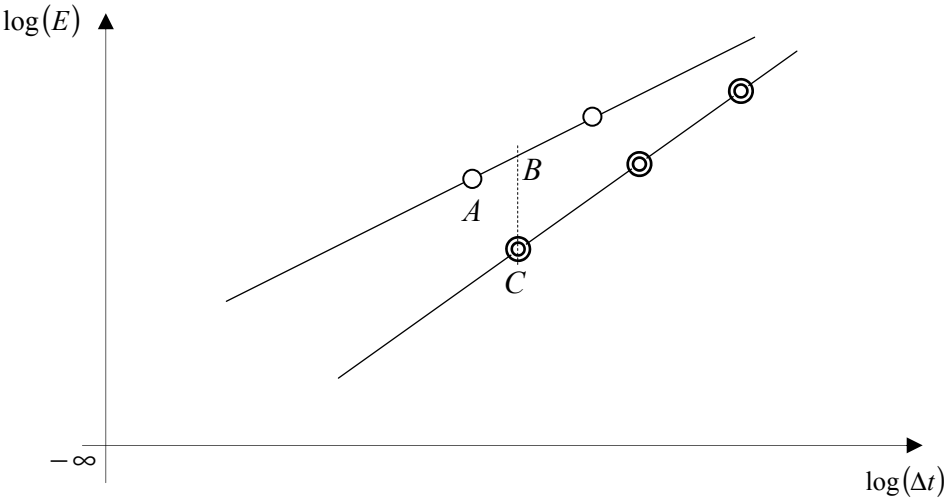


Figure 1: A typical representation of the responses convergence.

2.2 Extension to nonlinear problems

In nonlinear problems, comments regarding integration step size selection, though exist, e.g. see [33] (${}_n\Delta t_{ord} = 0.1\Delta t_{ord}$; ${}_n\Delta t_{ord}$ is the step size recommended for nonlinear problems), are vague; see [18, 34, 35]; special methods are generally essential for maintaining the proper convergence, e.g. see [10, 18, 36, 37]; and proper convergence might not be completely achievable for highly nonlinear problems [18, 38, 39]. Regarding the computational cost, because of the nonlinearity iterations, Eqs. (4) and (6) are not valid, and hence, the validity of Eq. (7) can not guaranteed. Consequently, in presence of nonlinearity, the discussion, presented in Section 2.1, loses its viability. Nevertheless, for low or moderate nonlinear problems (see [38, 39]), where proper convergence is simply achievable [10, 18], and the additional computational cost essential for nonlinearity solutions [40, 41] is small, in view of Eq. (5) and the discussion above, it is reasonable to use the integration step sizes below:

$$\Delta t = \alpha\ {}_n\Delta t_{ord}\ ,\ \frac{\alpha}{2}\ {}_n\Delta t_{ord}\ ,\ \frac{\alpha}{4}\ {}_n\Delta t_{ord} \tag{10}$$

where (see also Eq. (5)),

$$\alpha \cong> 2.5\ \left(=\frac{0.25}{0.1}\right) \tag{11}$$

and expect trivial additional computational cost, and some additional accuracy. Still there would likely exist a limit of nonlinearity severity, after which, the discussion is not valid.

3 NUMRICAL STUDY

The shear frame introduced, in Fig. 2 and Table 1, and subjected to 0.1 meters initial top lateral displacement, is studied, during a fifty seconds time interval. The exact mid-height dis-

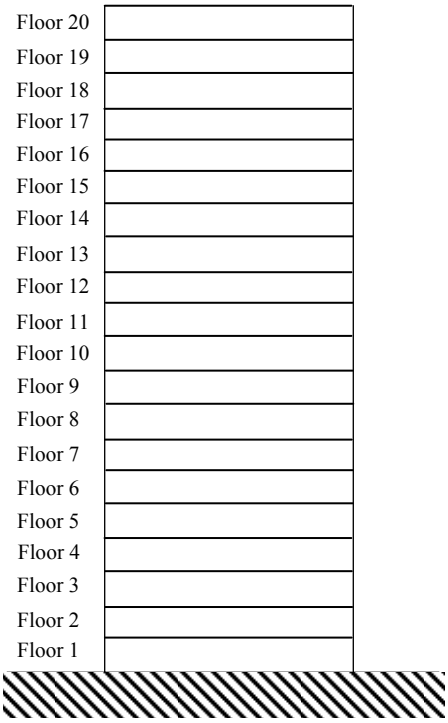


Figure 2: The shear frame under study in the numerical study.

Floor	Mass ($\times 10^{-3}$)	Stiffness ($\times 10^{-3}$)	Damping
1	1060	8600	0
2	1058	8400	
3	1056	8200	
4	1054	7000	
5	1052	6800	
6	1050	6600	
7	1048	6400	
8	1046	6200	
9	1044	6000	
10	1042	5800	
11	1040	5600	
12	1038	5400	
13	1036	5200	
14	1034	5000	
15	1032	4800	
16	1030	4600	
17	1028	4400	
18	1026	4200	
19	1024	4000	
20	1022	3800	

Table 1: Characteristics of the structural system in Fig. 2.

placement is reported in Fig. 3. Considering Fig. 3, and the final displacement therein, an analysis is carried out, with the average acceleration method of Newmark [27] and the integration step size 0.03125, satisfying Eq. (2) and also implying proper convergence; see Fig. 4. Repetition of the analysis with half steps, and then, in the implementation of the new approach, carrying out three analyses with steps satisfying Eq. (5) leads to Table 2. Apparently, Eq. (5), together with conventional time integration, and Richardson extrapolation, has resulted in considerable reduction of errors, i.e. further accuracy, with no additional computational cost (see the third and forth columns of Table 2).

The study is repeated, for a nonlinear seismic case, of the previous problem, by considering linear-elastic/perfect-plastic behaviors, for the columns of the shear frame, in Fig. 2 (the yield limits [42], are all assumed equal to 0.08 meters), and the North-South component of the El Centro strong ground motion, as the excitation [43] (see Fig. 5), the latter affecting Eq. (1) according to the formulation below [15, 43]:

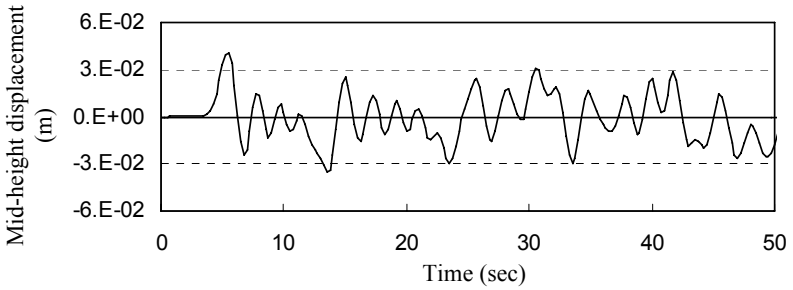


Figure 3: Exact mid-height displacement for the system introduced in Fig. 2 and Table 1 subjected to initial displacement of top floor.

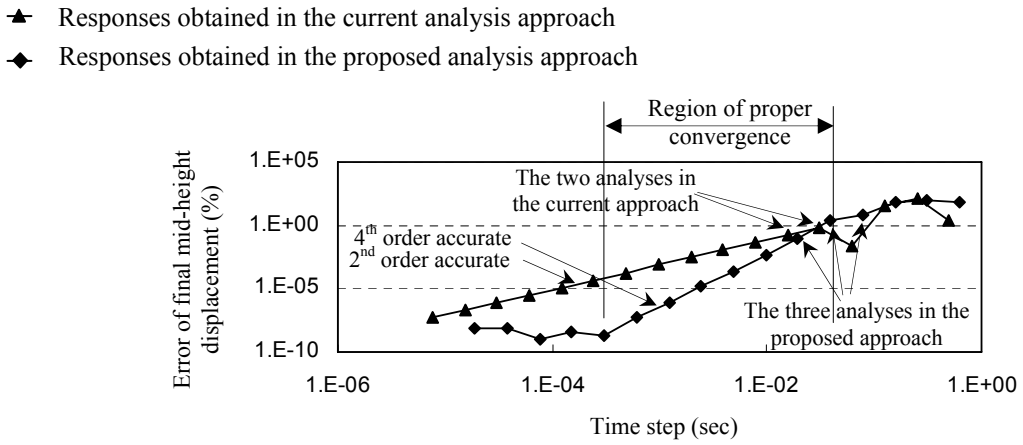


Figure 4: Convergence plots for the final mid-height displacement of the system introduced in Fig. 2 and Table 1 when subjected to initial displacement at top floor and analyzed by the average acceleration.

	Evaluated error (%)	Exact error (%)	Computational cost (Number of steps)
Current approach	0.455	0.1840	4800 (1600+3200)
Proposed approach	0.151	0.0909	4555 (640+1280+2560)*61/60

Table 2: Errors and computational cost for the shear frame introduced in Fig. 2 and Table 1 subjected to top displacement and analyzed by the average acceleration method.

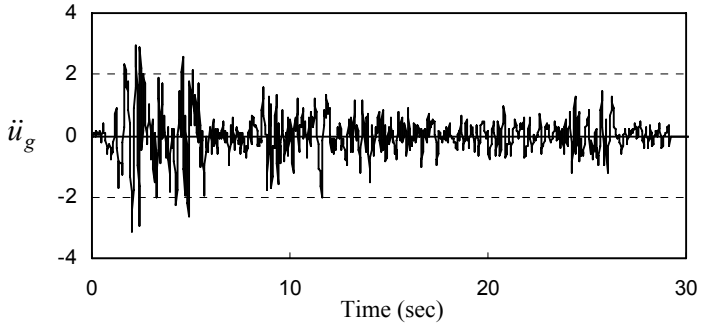


Figure 5: A North-South component of the El Centro strong motion [43].

$$\mathbf{f}(t) = -\mathbf{M}\begin{bmatrix}\alpha_1\\ \alpha_2\\ \vdots\\ \alpha_n\end{bmatrix}\ddot{u}_g \tag{12}$$

where, $\ddot{u}_g$ stands for the ground acceleration, and in general,

$$\alpha_1 = \alpha_2 = \cdots \alpha_n = 1 \tag{13}$$

The almost exact mid-height displacement is as displayed in Fig. 6, with attention to which, the smallest dominant period of the response is very small (at most equal to 0.5 sec), and meanwhile, in view of the smallness of the offset of the static equilibrium position, apparent in Fig. 6, the nonlinearity is not severe (see also [43]). The generalized-α method [44, 45], is selected, for time integration (with $r_\infty = 0.8$, as a conventional value for the parameter of the generalized-α method [44]). The nonlinearity iterations are carried out based on conventional fractional time stepping [46, 47], and the method proposed in [18] is implemented to prevent the improper convergence likely in nonlinear analyses. And, finally, in view of Fig. 6, Eqs. (10) and (11), and the fact that in nonlinear problems the "10" in Eq. (2) is recommended to be replaced with "100" [33] (see also [34, 35]), the integration step size, in the first ordinary (current) and proposed analysis approaches, are considered equal to 0.005 sec and 0.0125 sec, respectively, also satisfying the proper convergence pre-requisite (see Fig. 7). The errors and computational costs of the final mid-height displacement, corresponding to the responses obtained in the current and proposed approaches are addressed in Table 3. Similar to the linear case, the performance of the analysis is enhanced from the point of view of accuracy. This implies the fact that the achievements in this paper are not limited to linear problems. In agreement with the discussion presented in Section 2.2, the above mentioned good performance is diminished in repetition of the study, after increasing the severity of the nonlinear behavior, by multiplying the excitation by numbers greater than and sufficiently large, e.g. 100 (see [38, 39]), not reported here for the sake of brevity.

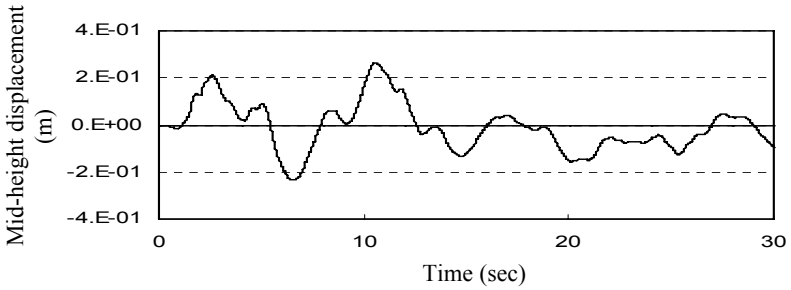


Figure 6: The almost exact response for the nonlinear problem.

Responses obtained in the current analysis approach
Responses obtained in the proposed analysis approach

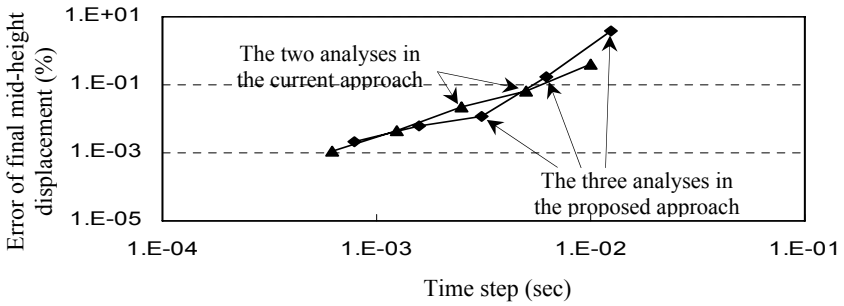


Figure 7: Convergence plots for the final mid-height displacement of the nonlinear problem under consideration when analyzed by the generalized-α ($r_\infty = 0.8$) time integration method.

	Evaluated error (%)	Exact error (%)	Computational cost (Number of steps including the nonlinearity sub-steps)
Current approach	0.0422	0.0224	22879 (8185+14694)
Proposed approach	0.0259	0.0115	24094 (4401+7125+12173)

Table 3: Errors and computational cost for the nonlinear problem under consideration, when analyzed by the generalized-α ($r_\infty = 0.8$) method.

4 DISCUSSION

Based on considering special integration step sizes in the main time integration and repeating the analysis at least twice and extrapolating the computed responses, according to Richardson extrapolation, an analysis approach is proposed for arriving at considerably more accuracy, in price of no or trivial additional computational cost. Proper convergence though is indeed essential even for the current analysis approach (based on at least one repetition of the analysis), it is considered as a key assumption for the approach proposed in this paper. A main question, in this regard, is how can we depict the convergence plot and check the convergence, while, in order to compute the errors,

$$E_{{}_i\mathbf{F}_a} = \left\| {}_i\mathbf{F}_a - \mathbf{F} \right\| \tag{14}$$

($\mathbf{F}$ and ${}_i\mathbf{F}_a$ respectively stand for an approximately computed and the exact values of the arbitrary matrix/vector/scalar under consideration, $E_{{}_i\mathbf{F}_a}$ implies the error and $\| \ \|$ implies an arbitrary norm [48]), the exact response is essential. The answer to this question can be found in the notion of pseudo error and pseudo convergence and their equivalence with error and convergence, from the standpoint of proper convergence [2, 49]. In brief, considering

$$D_i = \left\| {}_i\mathbf{F}_a - {}_{i-1}\mathbf{F}_a \right\| \tag{15}$$

as pseudo error, we can investigate the proper convergence, instead of in the convergence plot, in the log-log plot of pseudo error, D, with respect to integration step size, Δt (being addressed as the pseudo convergence plot), during the analysis repetitions; see also [2].

Another ambiguity in the discussion presented in the previous sections is regarding Eqs. (2), (3), and (5). In fact, in these equations, it is implicitly assumed that the integration step size can be selected continuously from the set of real numbers. This is hardly the case

when the excitation is available as a digitized record, e.g. earthquake records [50]. In these cases, conventionally, Eqs. (2) need to be replaced with

$$\Delta t \cong\leq \text{Min}\left(\frac{T}{10}, h, \Delta t_f\right) \tag{16}$$

(Δt_f is the step size by which the excitation record is available). In view of the typology of the proper convergence region in convergence plot, Eq. (16) affects the proposed approach mainly when instead of the analysis with steps sized Δt_{ord}, in the current analysis approach, we need to carry out an analysis with steps sized $2.5\Delta t_{ord}$, in the proposed approach (see Eqs. (3) and (5)). To explain better, when the integration steps in the current approach equal to Δt_f, how, in the proposed approach, can we consider the integration step size $\Delta t = 2.5\Delta t_f$, while there are not excitation stations at all integration stations. A solution is to replace the excitation with an excitation digitized at steps larger than the steps of the original excitation, such that addressing the steps in the two excitations with ${}_1\Delta t_f$ and ${}_2\Delta t_f$,

$$\frac{{}_1\Delta t_f}{{}_2\Delta t_f} = \frac{z_1}{z_2} \quad , \quad z_1, z_2 \in Z^+ \tag{17}$$

Two formulations are proposed for the replacement; see [8, 51, 52], from which, in view of the convergence based nature of the discussion presented in this paper, the first [8, 51] is already implemented in the analyses of the proposed approach in the second example studied in the previous section.

5 CONCLUSION

Provided the integration step sizes, selected for time integration, correspond to points on the convergence plot, with integer-valued slope (i.e. proper convergence is maintained), the accuracy of time integration analyses can be increased considerably, with trivial change in the total computational costs, including the analyses and their repetitions (for controlling the accuracies). This can be materialized, by replacing Eq. (2) with

$$\Delta t \cong\leq \text{Min}\left(\frac{T}{4}, h\right) \tag{18}$$

for the main analysis, while conventionally assuming unconditional stability in linear problems and $h \to \infty$, considering at least two repetitions of the first (main) analysis (each with half steps compared to the previous analysis), and implementing the Richardson extrapolation. Regarding the performance of the proposed approach (based on the presented theoretical and numerical studies):

- For linear problems, the consequence is guaranteed significant increase of accuracy (not proved in this paper for the sake of brevity), in the price of no additional computational cost.
- For nonlinear problems, when the nonlinearity is not severe, the performance can be similar to linear problems. (In presence of considerably severe nonlinearities, the expectation is to observe better performance, when the nonlinearity solution methods and the methods implemented for maintaining proper convergence are more robust.)
- The performance is independent of the integration scheme.

It is meanwhile worth noting that, though, as implied above, proper convergence is an assumption and pre-requisite for the success of the proposed approach, considering the fact that proper convergence is also essential when implementing the current approach, the assumption on proper convergence is not a weak point for the proposed approach. And, finally, regarding practical implementation of the proposed approach,

- Proper convergence need to be investigated in the pseudo convergence plot instead of the convergence plot (the validity of this replacement is recently demonstrated).
- Some considerations regarding digitized excitations may be essential.

ACKNOWLEDGEMENT

The author sincerely appreciates the kind patience of the organizing committee regarding the late submission of this full paper.

REFERENCES

[1] T. Belytschko, T.J.R. Hughes, *Computational methods for transient analysis*. Elsevier, 1983.

[2] A. Soroushian, P. Wriggers, J. Farjoodi, Asymptotic upper bounds for the errors of Richardson extrapolation with practical application in approximate computations. *International Journal for Numerical Methods in Engineering*, **80**, 565-595, 2009.

[3] W.L. Wood, Practical time stepping schemes. Clarendon, 1990.

[4] P. Henrici, Discrete variable methods in ordinary differential equations. Prentice-Hall, 1962.

[5] J.C. Strikwerda, Finite difference schemes and partial differential equations. Wadsworth & Books/Cole, 1989.

[6] T.J.R. Hughes, The finite element method: linear static and dynamic finite element analysis. Prentice-Hall, 1987.

[7] K.K. Zhou, K.K. Tamma, A new unified theory underlying time dependent first-order systems: a prelude to algorithms by design. *Internatinal Journal for Numerical Methods in Engineering*, **60**, 699-1740, 2004.

[8] A. Soroushian, A technique for time integration with steps larger than the excitation steps. *Communications in Numerical Methods in Engineering,* **24**, 2087-2111, 2008.

[9] D.M. Monro, *Fortran 77*. Edward Arnold, 1982.

[10] A. Soroushian, New methods to maintain responses convergence and control responses errors in the analysis of nonlinear dynamic models of structural systems. *Ph.D. Thesis*, University of Tehran, 2003. (in Persian)

[11] H. Gavin, Structural dynamics, class notes CE 283, Duke University, 2001.

[12] P. Wriggers, Computational contact mechanics. John Wiley & Sons, 2002.

[13] T.J.R. Hughes, K.S. Pister, R.L.Taylor, Implicit–explicit finite elements in nonlinear transient analysis. *Computer Methods in Applied Mechanics and Engineering,* **17/18**, 159–182, 1979.

[14] K.J. Bathe, *Finite element procedures*. Prentice-Hall, 1996.

[15] R.W. Clough, J. Penzien, *Dynamics of structures*. McGraw-Hill, 1993.

[16] A. Soroushian, P. Wriggers, J. Farjoodi, On practical integration of semi-discretized nonlinear equations of motion. Part 1: reasons for probable instability and improper convergence. *Journal of Sound and Vibration*, **284**, 705-731, 2005.

[17] A. Soroushian, Proper convergence a concept new in science and important in engineering. D. Tsahalis ed. *4th International Conference from Scientific Computing to Computational Engineering (4th IC-SCCE)*, Athens, Greece, July 7-10, 2010.

[18] A. Soroushian, P. Wriggers, J. Farjoodi, On practical integration of semidiscretized nonlinear equations of motion: proper convergence for systems with piecewise linear behavior. *Journal of Engineering Mechanics ASCE,* **139**, 114-145, 2013.

[19] A. Soroushian, With nonlinearity iterations towards better control of accuracy in explicit time integration analysis. P.M. Pimenta ed. *10th World Congress on Computational Mechanics (WCCM 2012)*, Sao Paulo, Brazil, July 8-13, 2012.

[20] P. Ruge, A *priori* error estimation with adaptive time-stepping. *Communications in Numerical Methods in Engineering*, **15**, 479-491, 1999.

[21] L. Collatz, The numerical treatment of differential equations. Springer, 1960.

[22] R.D. Richtmyer, K.W. Morton, *Difference methods for initial value problems*. John Wiley & Sons, 1967.

[23] J.C. Houbolt, A recurrence matrix solution for the dynamic response of elastic aircraft. *Journal of the Aeronautical Sciences*, **17**, 540-550, 1950.

[24] R.W. Clough, Numerical integration of equations of motion. *Lectures on Finite Element Methods in Continuum Mechanics*, University of Alabama, pp. 525-533, 1973.

[25] E.L. Wilson, I. Farhoomand, K.J. Bathe, Non-linear dynamic analysis of complex structures. *Earthquake Engineering and Structural Dynamics*, **1**, 241-252, 1973.

[26] K.J. Bathe, E.L. Wilson, Stability and accuracy analysis of direct integration methods. *Earthquake Engineering and Structural Dynamics*. **1**, 283-291, 1973.

[27] N.M. Newmark, A method of computation for structural dynamics. *Journal of Engineering Mechanics, ASCE*, **85**, 67-94, 1959.

[28] L.F. Richardson, J.A. Gaunt, The deferred approach to the limit. *Philosophical Transactions of the Royal Society of London*, **226**, 299–361, 1927.

[29] L.F. Richardson. The approximate arithmetical solution by finite differences of physical problems including differential equations, with an application to the stresses in a masonry dam. *Philosophical Transactions of the Royal Society of London*, **210**, 307–357, 1910.

[30] C. Brezenski, M. Redivo Zagalia, *Extrapolation methods*: *theory and practice*. North-Holland, 1991.

[31] A. Sidi, New convergence results on the generalized Richardson extrapolation process GREP(1) for logarithmic sequences. *Mathematics of* Computation,**71**, 1569–1596, 2002.

[32] A. Soroushian, P. Wriggers, J. Farjoodi, A statement for the convergence of approximate responses and its application in structural dynamics. D. Tsahalis ed. *2nd International Conference from Scientific Computing to Computational Engineering (2nd IC-SCCE)*, Athens, Greece, July 5-8, 2006.

[33] J.F. McNamara, Solution schemes for problems of nonlinear structural dynamics. *Journal of Pressure Vessels*, **96**, 147-155, 1974.

[34] A. Soroushian, On the performance of a conventional accuracy controlling method applied to linear and nonlinear structural dynamics. M.J. Crocker ed. *17th International Conference on Sound and Vibration (ICSV17)*, Cairo, Egypt, July 18-22, 2010.

[35] A. Soroushian, On the adequacy of integration step sizes recommended for nonlinear time integration. D. Tsahalis ed. *5th International Conference from Scientific Computing to Computational Engineering (5th IC-SCCE)*, Athens, Greece, July 4-7, 2012.

[36] J. Farjoodi, A. Soroushian, Robust convergence for the dynamic analysis of MDOF elastoplastic systems. A. Zingoni ed. *1st International Conference on Structural Engineering, Mechanics, and Computation, (SEMC 2001)*, Cape Town, South Africa, April 2-4, 2001.

[37] J. Farjoodi, A. Soroushian, Efficient automatic selection of tolerances in nonlinear dynamic analysis. A. Zingoni ed. *1st International Conference on Structural Engineering, Mechanics, and Computation, (SEMC 2001)*, Cape Town, South Africa, April 2-4, 2001.

[38] A. Soroushian, J. Farjoodi, H. Mehrazin, A new measure for the nonlinear behavior of piecewisely linear structural dynamic models. M.J. Crocker ed. *13th International Congress on Sound and Vibration (ICSV13)*, Vienna, Austria, July 2-6, 2006.

[39] A. Soroushian, J. Farjoodi, H. Mehrazin, A nonlinearity measure for piece-wisely linear structural dynamics. M.J. Crocker ed. *11th International Congress on Sound and Vibration (ICSV11)*, Saint Petersburg, Russia, July 5-8, 2004.

[40] E.L. Allgower, K. Georg, *Numerical continuation methods, an introduction*. Springer, 1980.

[41] A. Soroushian, J. Farjoodi, An improvement in nonlinear analysis. A. Smyth ed. *15th ASCE Engineering Mechanics Conference (EM2002)*, New York, USA, June 2-5, 2002.

[42] J. Lubliner, *Plasticity theory*. McMillan, 1990.

[43] A.K. Chopra, *Dynamics of structures: theory and application to earthquake engineering*. Prentice-Hall, 1995.

[44] J. Chung, G.M. Hulbert, A time integration algorithm for structural dynamics with improved numerical dissipation: the generalized-α method. *Journal of Applied Mechanics, ASME*, **60**, 371-375, 1993.

[45] S. Erlicher, L. Bonaventura, O.S. Bursi, The analysis of the generalized-α method for nonlinear dynamic problems. *Computational Mechanics*, **28**, 83-104, 2002.

[46] J.M. Nau, Computation of inelastic spectra. *Journal of Engineering Mechanics*, *ASCE*, **109**, 279-288, 1983.

[47] S.A. Mahin, J. Lin, Construction of inelastic response spectra for single degree-of-freedom systems. *Report No. UCB/EERC-83/17*, Earthquake Engineering Research Center, University of California, Berkeley, Berkeley, 1983.

[48] B. Noble, J.W. Daniel, *Applied linear algebra,* Prentice-Hall, USA, 1977.

[49] A. Soroushian, J. Farjoodi, Pseudo convergence and its implementation in engineering approximate computations. D. Tsahalis ed. *4th International Conference from Scientific Computing to Computational Engineering (4th IC-SCCE)*, Athens, Greece, July 7-10, 2010.

[50] J. Havskov, G. Alguacil, Instrumentation in earthquake seismology (modern approaches in geophysics). Springer, 2005.

[51] A. Sabzei, A.Y. Reziakolaei, A. Soroushian, More versatility for an integration step size enlargement technique in time integration analysis. M. Papadrakakis, V. Papadopoulos, V. Plevris eds. *4th ECCOMAS Thematic Conference on Computational Methods in Structural Dynamics and Earthquake Engineering (COMPDYN 2013)*, Kos, Greece, June 12-14, 2013.

[52] A. Faroughi, M. Hosseini, Simplification of earthquake accelerograms for quick time history analyses by using modified inverse Fourier transform. S. Kitipornchai ed. *12th East-Pacific Conference on Structural Engineering and Construction (EASEC-12),* Hong Kong SAR, China, January 26-28, 2011.

COMPDYN 2013
4th ECCOMAS Thematic Conference on
Computational Methods in Structural Dynamics and Earthquake Engineering
M. Papadrakakis, V. Papadopoulos, V. Plevris (eds.)
Kos Island, Greece, 12–14 June 2013

ON THE RESPONSE OF THE SMALL BUILDINGS TO VIBRATIONS

L.Munteanu[1], V.Chiroiu[2], and T.Sireteanu[2]

[1] Institute of Solid Mechanics, Romanian Academy
Ctin Mille 15, Bucharest 010141
e-mail: ligia_munteanu@hotmail.com

[2] Institute Solid Mechanics, Romanian Academy
Ctin Mille 15, Bucharest 010141
e-mail: veturiachiroiu@yahoo.com; e-mail: siretimsar@yahoo.com

Keywords: Small building, Electromechanical device, Harmonic excitation, Time-dependent frequency, Random earthquakes.

Abstract. *In this work, the analysis the response to vibrations of a small building equipped with an electromechanical vibration absorber is investigated. In the first part, the case of harmonic excitation with constant or time dependent frequencies is considered, and in the second part, the case of random earthquakes, respectively. The cross correlation functions and the mean square displacements are calculated for the structure when it is equipped with an electromechanical vibration absorber. The stochastic process which characterizes the earth movements is coupled to the cnoidal method which delivers the analytical solutions of the nonlinear problem. The interaction between the structure and the energy source is analyzed via the Sommerfeld effect inside the resonance region. The resonance capture and the vibration reduction are displayed by the time history responses of the displacement and angular velocities above the resonance.*

1 INTRODUCTION

Deterministic evaluation of the response of the buildings subjected to earthquakes is a valuable tool in obtaining information on the behavior of structures under forces which are statistical in nature [1]-[3]. The influence of the time histories of external excitations on the dynamics of structures can be explored both theoretically and experimentally [4], [5].

The theoretical description involves the explicit treatment of both cases, i.e. the harmonic excitation with constant and time dependent frequency. The description asked the temporal characteristics of the seismic data and the response of buildings to transient and seismic excitations.

An attempt to apply the methods of stochastic processes in the analysis of tall buildings to random earthquakes was made by Eringen [6]. This method is based on the cross correlations functions from which the mean square displacements can be evaluated. This model was applied in the electrical circuits [7], in discrete element strings [8] and other problems. The earth movements in the boundary condition can be expressed under the form of expected values.

In this paper, the response of a building to vibrations is analyzed when an electromechanical vibration absorber is attached to the last story of the building.

In the first part of this article the case of harmonic excitation is considered, while the second part will consider the case of random earthquakes.

The reduction of vibrations for a resonant structure was studied by Felix, Balthazar and Brasil [9], [10] and Souza et al. [11] using tuned liquid column. A tuned liquid column connected to the structure works due to the inertial secondary system principle, by which the damper counteracts the forces producing the vibration.

Nagem, Madanshetty and Medhi [12] have experimentally analyzed the reduction of vibrations for a system consisted from a cantilever beam and a motor, by using a linear electromechanical vibration absorber and an ideal eccentrically motor with a sinusoidal force. Bolla et al, [13] have reported approximate analytical solutions to nonlinear vibrating problem, excited by a nonideal motor. A device of nonlinear electromechanical vibration absorber with a nonlinear function of type Rayleigh oscillator was introduced by Yamapi et al. [14].

The case of a nonideal eccentrically motor or a source of limited power supply was investigated by Felix and Balthazar [14] for a nonlinear friction of type cubic-quintic Duffing oscillator. This kind of devices with nonlinear resistor and capacitor were studied by Yamapi et al. [15], Yamapi and Woafo [16], [17] and Mbouna Ngueuteu, Yamapi and Woafo [18].

We are interested in this paper on the case when the vibrating system and the energy source interact with one another. This interaction corresponds to the non-ideal systems or the systems with non-ideal excitation and it is explained by the Sommerfeld effect which says that the steady state frequencies of the DC motor increase with respect to the power, and when the structure resonates with the source, a part of the source energy is used to generate large vibrations. These vibrations can counteract the vibrations of the forced structure, without changing the motor frequency. We must mention that the power is supplied in a step-by-step manner.

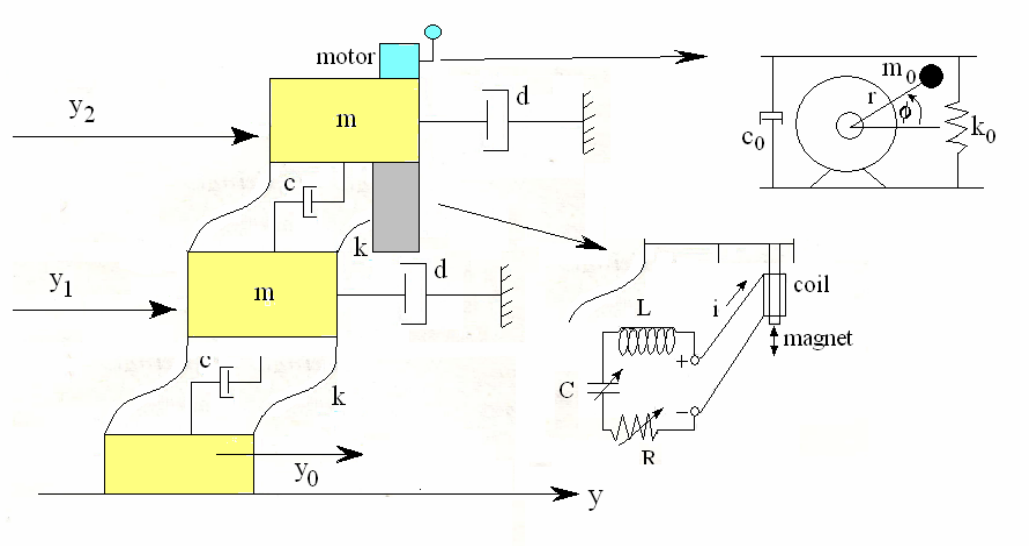


Figure 1. Scheme of the building coupled to a vibration absorber device.

For sufficient motor power, a jump can occur. i.e. the frequency increases and the vibrations decreases, resulting in lower power consumption by the motor [14], [19], [20]. The Sommerfeld effect results from the balance of the energy and it is due to the coupling between the excitation mechanism and the vibrational loads [21].

In this paper we consider a small building with two stories (See Fig, 1). The second floor is equipped with an electromechanical vibration absorber. The structure may be characterized by the stiffness and damping which can be considered to be either the cubic Duffing, cubic-quintic Duffing or Rayleigh, or another such as the Van der Pol with first, second, third, fourth and fifth term.

In the problem considered here, the stiffness is expressed as a sum of a linear and a cubic Duffing term, while the damping is considered to be linear.

Because of the stiffness nonlinearity, the equations cannot be solved by usually applied Fourier-integral type of solutions. The inverse scattering theory generally solves such nonlinear differential equations. Osborne [22] has suggesting that the method is reducible to a generalization of the Fourier series with the cnoidal functions as the fundamental basis function. This is because the cnoidal functions are much richer than the trigonometric or hyperbolic functions, that is, the modulus $\tilde{m}$ of the cnoidal function, $0 \le \tilde{m} \le 1$, can be varied to obtain a sine or cosine function $(\tilde{m} \cong 0)$, a Stokes function $(\tilde{m} \cong 0.5)$ or a solitonic function, sech or tanh $(\tilde{m} \cong 1)$ [23].

The paper is structured as follows: Section 2 presents the model equations for a small building with the electromechanical vibration absorber attached to the last story. The electromechanical device is consisted of a DC motor coupled magnetically by the building. The structure is subjected to external harmonic excitation and also to the excitation of the source with limited power supply. Section 3 presents the solutions written in the terms of the *theta function* representation as a sum of linear and nonlinear superposition of cnoidal vibrations. Some aspects of the dynamics of the building equipped with an electromechanical vibration absorber are discussed in Section 4 for the case of a constant excitation frequency, emphasizing the role of the additional equation which includes the transfer of the source energy to the structure. Next section explores the case of the time-dependent excitation frequency, focusing on the effectiveness of the vibration reduction. The time history responses of the displacement

and angular velocities above the resonance are presented for both cases in order to understand the interaction structure- energy source. Finally, the Section 6 treats the case of random earthquakes modeled as a stochastic or random process. The earthquakes are of short duration and therefore the stationary character of the process is questionable.

2 FORMULATION OF THE PROBLEM

The presence of the vibration absorber device is expressed mathematically by coupling between the motion equations of the building and the equations of the energy source. The resistive torque applied to the motor is neglected. The motion equations are given by

$$m\ddot{y}_1 + c(2\dot{y}_1 - \dot{y}_2 - \dot{y}_0) + d\dot{y}_1 + k_1(2\dot{y}_1 - \dot{y}_2 - \dot{y}_0) + k_2(2\dot{y}_1 - \dot{y}_2 - \dot{y}_0)^3 = 0, \tag{1}$$

$$m_1\ddot{y}_2 + c(\dot{y}_2 - \dot{y}_1) + d\dot{y}_2 + k_1(\dot{y}_2 - \dot{y}_1) + k_2(\dot{y}_2 - \dot{y}_1)^3 = T\dot{q} + m_0 r\ddot{\varphi}\cos\varphi - m_0 r\dot{\varphi}^2\sin\varphi, \tag{2}$$

$$m_0 r\ddot{y}_2\cos\varphi = I\ddot{\varphi} + a\dot{\varphi} - b, \tag{3}$$

$$T(\dot{y}_2 - \dot{y}_1) = -L\ddot{q} + R\left(1 - i_0^{-2}\dot{q}^2\right)\dot{q} - C_0^{-1}q - i_0^2\alpha_3 q^3 - i_0^4\alpha_5 q^5, \tag{4}$$

$$y_0 = f(t). \tag{5}$$

where y_j is the displacement of j^{th} story, $j = 1,2$, m the mass of each story, c the interfloor damping (internal damping), d the external damping constant (velocity damping), k_1 the linear spring constant, k_2 the cubic spring constant, φ the angular displacement of the rotor, r the eccentricity of unbalanced shaft of the electric motor, $m_1 = m + m_0$ with m_0 the mass of unbalanced shaft of the electric motor, I the moment of inertia of the rotor, $T = 2\pi nlB$ the transducer constant, n the number of turns in the coil, l the radius of the coil, B the uniform radial magnetic field strength in the annular gap, L the inductor, C the capacitor, R the resistor, V_{res} the voltage in the resistor, V_{cond} the voltage in the capacitor, i_0 the initial current in the electrical part, C_0 the capacitive characteristic, α_3, α_5 the capacitor coefficients and q the instantaneous electrical charge.

The expression for the driving torque of the motor is $b - a\dot{\varphi}$ (linear in the stationary regime) with b related to the voltage applied across to the armature of the DC motor, and a is a constant depending of the considered motor.

The electric component of the controller is composed by an inductor L, a capacitor C, and a resistor R. The expression of the voltage in resistor and the capacitor are [14]

$$V_{res} = -Ri_0\left(\frac{\dot{q}}{i_0} - \frac{1}{3}\left(\frac{\dot{q}}{i_0}\right)^3\right),\ V_{cond} = \frac{q}{C_0} + \alpha_3 q^3 + \alpha_5 q^5, \tag{6}$$

In (2) the right side term represents the action of the source of energy. Eq. (3) expresses the supplying of the last story with the source energy. Eqs. (4) and (5) represent the boundary conditions for Eqs. (1)-(3).

When loading is deterministic, the function $f(t)$ is known as a function of time. When loading is random, the function $f(t)$ is not known a priori and it is defined statistically. The function $f(t)$ can be viewed as the harmonic excitation

$$f(t) = f_0\sin\Omega t, \quad 0 \le t \le T, \tag{7}$$

with Ω a constant, or the step dependent function $\Omega(t)$

$$\Omega(t)=\omega_1\left[1+\frac{\omega_2-\omega_1}{2\omega_1}\left(1+\frac{1}{2}\tanh(\varepsilon(t-t_s)\right)\right],\ 0\le t\le T, \tag{8}$$

where ω_1 and ω_2 the initial and final frequencies, t_s is the time at which the frequency us changed, and $\varepsilon\to\infty$ is a parameter which describes the step function limit [24].

In the second part of this article, the function $f(t)$ can be viewed as an average of various data y_0 measured from k^{th} earth motions $y_0=f_k(t)$. This is equivalent to obtain $f_k(t)$ from the average curve $E\{f(t)\}$. The earthquakes are of short duration, so the process is not stationary. From this point of view we can not use a purely random stationary Gaussian process.

Eqs. (1)-(5) and (7) are written in a dimensionless version as

$$x_1''+\beta_1 x_1'+A(\alpha+\delta_1 A^2)=0,\quad A=2x_1'-x_2'-x_0', \tag{9}$$

$$x_2''+\beta_1\mu x_2'-\lambda_1 x_4'+B\mu(\alpha+\delta_1 B^2)=(1-\mu)(x_3''\cos x_3-x_3'^2\sin x_3),\ B=x_2'-x_1', \tag{10}$$

$$x_3''-\eta_1 x_2''\cos x_3+ux_3'=v, \tag{11}$$

$$x_4''-\alpha_2 x_4'+\beta_2 x_4'^3+\gamma_2 x_4+\delta_2 x_4^3+\eta_2 x_4^5+\lambda_2 B=0, \tag{12}$$

$$x_0=g(\vartheta), \tag{13}$$

where prime means the differentiation with respect to τ, and

$$\tau=\omega_1 t,\ x_0=\frac{y_0}{r},\ x_1=\frac{y_1}{r},\ x_2=\frac{y_2}{r},\ x_3=\varphi,\ x_4=\frac{q}{q_0},\ \mu=\frac{m}{m+m_0}=\frac{m}{m_1},$$

$$\alpha_1=\frac{c}{m\omega_1},\ \beta_1=\frac{d}{m\omega_1},\ \alpha=\alpha_1+\gamma_1,\ \gamma_1=\frac{k_1}{m\omega_1},\ \delta_1=\frac{k_2 r^2\omega_1}{m}, \tag{14}$$

$$\lambda_1=\frac{Tq_0}{m_1 r\omega_1},\ \eta_1=\frac{rm_0}{I},\ u=\frac{a}{I\omega_1},\ v=\frac{b}{I\omega_1^2},$$

$$\lambda_2=\frac{Tr}{q_0 L\omega_1},\ \alpha_2=\frac{R}{L\omega_1},\ \beta_2=\frac{Rq_0^2\omega_1}{i_0^2 L},\ \gamma_2=\frac{1}{LC_0\omega_1^2},$$

$$\delta_2=\frac{i_0^2\alpha_3 q_0^2}{L\omega_1^2},\ \eta_2=\frac{i_0^4\alpha_5 q_0^4}{L\omega_1^2},\ \vartheta=\frac{\Omega}{\omega_1}.$$

In (14) ω_1 is the first natural frequency of the structure. The unknowns of Eqs.(9)-(13) are the dimensionless displacement of j^{th} story x_j, $j=1,2$, the angular displacement of the rotor x_3, and the dimensionless instantaneous electrical charge x_4. The resonance condition with the building is given by $x_3'=1$. In this case $\dot{\varphi}=\omega_1\varphi'=\omega_1$. The first control parameter is μ which is the ratio between the mass of each story m and $m_1=m+m_0$, with m_0 the mass of unbalanced shaft of the electric motor. The second control parameter is $v=\frac{b}{I\omega_1^2}$ where b is related to voltage applied across to the DC motor, I is the moment of inertia of the rotor and ω_1 is the first natural frequency of the structure.

In the case of (7), the equation (13) becomes

$$x_0 = g_0 \sin(\tau\vartheta), \quad 0 \le \tau \le T_\tau, \quad T_\tau = \omega_1 T, \quad g_0 = \frac{f_0}{r}. \tag{15}$$

In the case of (8), the equation (13) becomes

$$x_0 = g_0 \sin(\tau\vartheta(\tau)), \; 0 \le \tau \le T_\tau, \; T_\tau = \omega_1 T, \quad g_0 = \frac{f_0}{r}, \tag{16}$$

with

$$\vartheta(\tau) = 1 + \frac{\omega_2 - \omega_1}{2\omega_1}\left(1 + \frac{1}{2}\tanh\left(\varepsilon_s(\tau - \tau_s)\right)\right), \tag{17}$$

and

$$\tau_s = \omega_1 t_s, \; \varepsilon_s = \frac{\varepsilon}{\omega_1}. \tag{18}$$

3 SOLUTIONS

The general solution of the system (9)-(13) may be written in the terms of the *theta function* representation

$$\theta(t) = \frac{\mathrm{d}^2}{\mathrm{d}t^2}\log\Theta_n(\eta_1, \eta_2, ..., \eta_n), \tag{19}$$

where Θ is the *theta function* defined as

$$\Theta_n(\eta_1, \eta_2, ..., \eta_n) = \sum_{M \in (-\infty, \infty)} \exp\left(\mathrm{i}\sum_{i=1}^{n} M_i \eta_i + \frac{1}{2}\sum_{i,j=1}^{n} M_i B_{ij} M_j\right), \tag{20}$$

with n the number of degrees of freedom for a particular solutions, and

$$\eta_j = -\tilde{\omega}_j t + \phi_j, \; 1 \le j \le N. \tag{21}$$

In (21), $\tilde{\omega}_j$ are the frequencies and the ϕ_j the phases. Also, we can write

$$M\eta = -\tilde{\Omega}t + \Phi, \; M = [M_1, M_2, ..., M_n], \; \tilde{\Omega} = M\tilde{\omega}, \; \Phi = M\phi.$$

The integer components in M are the integer indices in (16). The matrix B can be decomposed in a diagonal matrix D and an off-diagonal matrix O, that is $B = D + O$.

The solution (19) of Eqs. (9)-(13) can be written as [23]

$$\theta(t) = \frac{2}{\lambda}\frac{\partial^2}{\partial t^2}\log\Theta_n(\eta) = \theta_{lin}(\eta) + \theta_{int}(\eta), \tag{22}$$

where θ_{lin} represents a linear superposition of cnoidal vibrations

$$\theta_{lin}(\eta) = \frac{2}{\lambda}\frac{\partial^2}{\partial t^2}\log G(\eta), \; G(\eta) = \sum_M \exp(\mathrm{i}M\eta + \frac{1}{2}M^T DM), \tag{23}$$

and θ_{int} represents a nonlinear interaction among the cnoidal vibrations

$$\theta_{int}(\eta)=2\frac{\partial^2}{\partial t^2}\log\left(1+\frac{F\ (\eta,C)}{G\ (\eta)}\right),\quad F\ (\eta,C)=\sum_{M^\alpha}C\exp(iM\eta+\frac{1}{2}M^TDM),$$

$$C=\exp(\frac{1}{2}M^TOM)-1. \tag{24}$$

The first term θ_{lin} represents, as above, a linear superposition of cnoidal waves. Indeed, after a little manipulation and algebraic calculus, (19) gives

$$\theta_{lin}=\sum_{l=1}^{n}\alpha_l\left[\frac{2\pi}{\tilde{K}_l\sqrt{m_l}}\sum_{k=0}^{\infty}\left(\frac{q_l^{k+1/2}}{1+q_l^{2k+1}}\cos(2k+1)\frac{\pi\tilde{\omega}_l t}{2\tilde{K}_l}\right)^2\right], \tag{25}$$

with

$$q=\exp(-\pi\frac{K'}{K}),\ \tilde{K}=\tilde{K}(\tilde{m})+\int_0^{\pi/2}\frac{du}{\sqrt{1-\tilde{m}\sin^2 u}},\ \tilde{K}'(\tilde{m}_1)=\tilde{K}(\tilde{m}),\quad \tilde{m}+\tilde{m}_1=1.$$

In (25) we recognize the expression [25]

$$\theta_{lin}=\int_{-\infty}^{\infty}\alpha\,\mathrm{cn}^2[\tilde{\omega}t;\tilde{m}]dt, \tag{26}$$

The second term θ_{int} represents a nonlinear superposition or interaction among cnoidal waves. We write this term as [23]

$$2\frac{\mathrm{d}^2}{\mathrm{d}t^2}\log\left[1+\frac{F(t)}{G(t)}\right]\approx\frac{\beta\,\mathrm{cn}^2(\tilde{\omega}t,\tilde{m})}{1+\gamma\,\mathrm{cn}^2(\tilde{\omega}t,\tilde{m})}. \tag{27}$$

If $\tilde{m}$ take the values 0 or 1, the relation (27) is directly verified. For $0\le\tilde{m}\le 1$, the relation is numerically verified with an error of $|e|\le 5\times10^{-7}$. Consequently, we have in the general case

$$\theta_{int}(t)=\int_{-\infty}^{\infty}\frac{\tilde{\beta}\,\mathrm{cn}^2[\tilde{\omega}t;\tilde{m}]}{1+\tilde{\lambda}\,\mathrm{cn}^2[\tilde{\omega}t;\tilde{m}]}\mathrm{d}t. \tag{28}$$

As a result, the cnoidal method yields to solutions consisting of a linear superposition and a nonlinear superposition of cnoidal vibrations.

In the general case, the solution of the problem (9)-(13) can be written as

$$x_j(t)=\int_{-\infty}^{\infty}K_j(t)g(t-\tau)\mathrm{d}\tau=\int_{-\infty}^{\infty}K_j(t-\tau)g(\tau)\mathrm{d}\tau,\quad j=1,2,...,4 \tag{29}$$

where

$$K_j(t)=\sum_{k=1}^{n}\left[\mathrm{cn}^2[\tilde{\omega}_{jk}t;\tilde{m}_{jk}]+\frac{\tilde{\beta}_{jk}\,\mathrm{cn}^2(\tilde{\omega}_{jk}t,\tilde{m}_{jk})}{1+\tilde{\gamma}_{jk}\,\mathrm{cn}^2(\tilde{\omega}_{jk}t,\tilde{m}_{jk})}\right],\quad j=1,2,..,4. \tag{30}$$

The solution (29) requires the evaluation of unknowns $\tilde{\omega}$, $\tilde{m}$, $\tilde{\beta}$ and $\tilde{\gamma}$. Substitution of (29) into Eqs. (9)-(13) gives a set of identities from which the parameters can be evaluated. The

identities results by equating the coefficients for expression terms containing the functions cn and sn in the same power.

4 CONSTANT EXCITATION FREQUENCY

The solutions (27) and (28) are computed for $n=7$ degrees of freedom for particular solutions and for different values of the parameters of the system and a constant excitation frequency Ω.

Before discussing the results of the numerical calculations, we briefly explain the choice of the control model parameters. Firstly, the range of μ varies from 0.7 to 1. The value $\mu=0.7$ corresponds to the case when the m_0 represents 40% of m, while $\mu=1$ means that the m_0 is negligible compared to m.

The decreasing of the control parameter v with respect to time in the transition interval ($\varphi'=0$) is represented in Fig. 2. The time frames are the following: $0\le\tau\le500$ and $500\le\tau\le800$ above the resonance, $800\le\tau\le1400$ inside resonance, and $1400\le\tau\le1600$, $1600\le\tau\le2000$ below the resonance, respectively. The parameter values were selected as $\mu=0.7$, $\alpha_1=$, $\beta_1=$, $\gamma_1=$, $\delta_1=$, $\lambda_1=$, $\eta_1=$, $u=$, $\lambda_2=$, $\alpha_2=$, $\beta_2=$, $\gamma_2=$, $\delta_2=$, $\eta_2=$ and $\vartheta=1$.

The time variation of the displacement x_1 corresponding to the last story without/with the electromechanical vibration absorber, are plotted in Figures 3 and 4, respectively, during the transition through the resonance region.

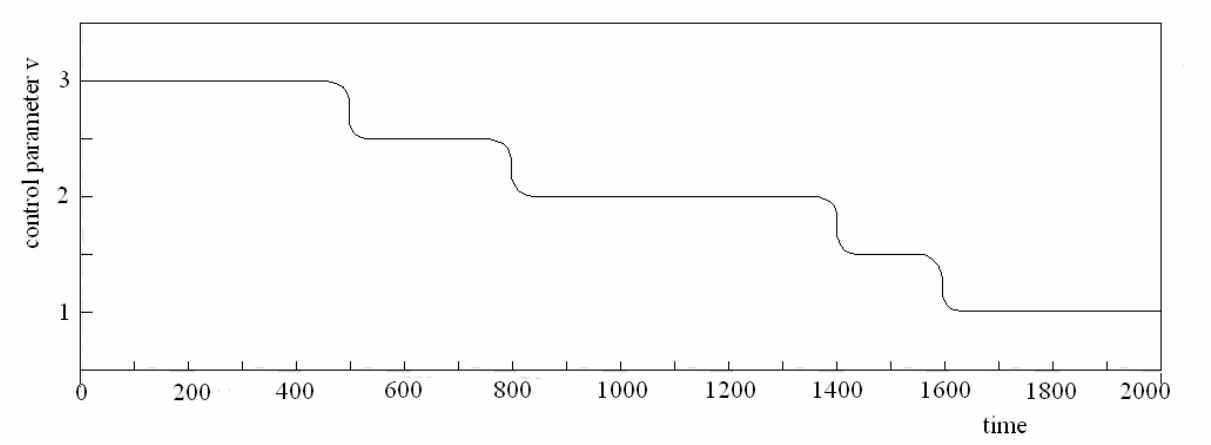


Figure 2.The decreasing of the control parameter v with respect to time in the transition interval.

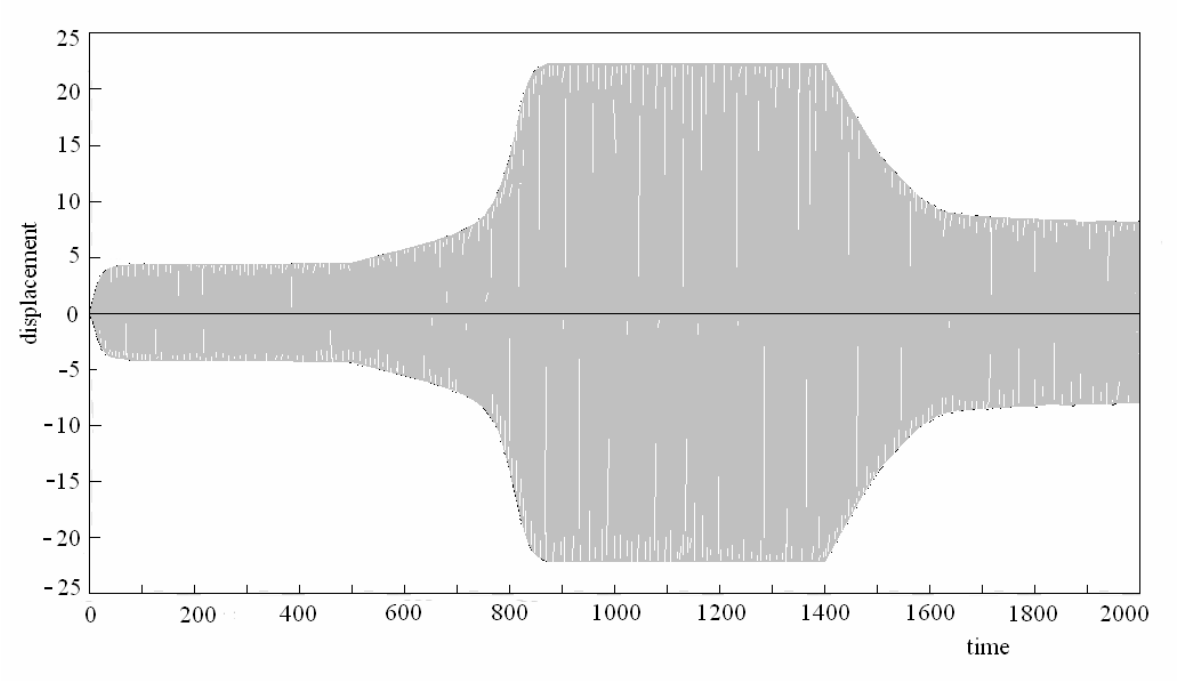


Figure 3. Time history for the last story without the electromechanical vibration absorber.

The time variation of the angular velocity x_3 of the DC motor without/with the electromechanical vibration absorber, are simulated in Figures 3 and 4, respectively, during the transition through the resonance region.

Figure 3 shows that in the case of no coupling between the electromechanical vibration absorber and the structure, the vibration amplitude increase in the time range $800 \le \tau \le 1400$ inside resonance, while Figure 4 shows that in the case of coupling, the vibration amplitude significantly reduce in time ranges $800 \le \tau \le 1400$ inside resonance, and $1400 \le \tau \le 1600$, $1600 \le \tau \le 2000$ below the resonance.

In Figure 5, the capture of the resonance of the angular velocity is put into evidence in the case of no coupling. Fig.6 shows that in the case of coupling, the Sommerfeld effect cancels the resonance of the angular velocity and reduces significantly the vibration amplitudes.

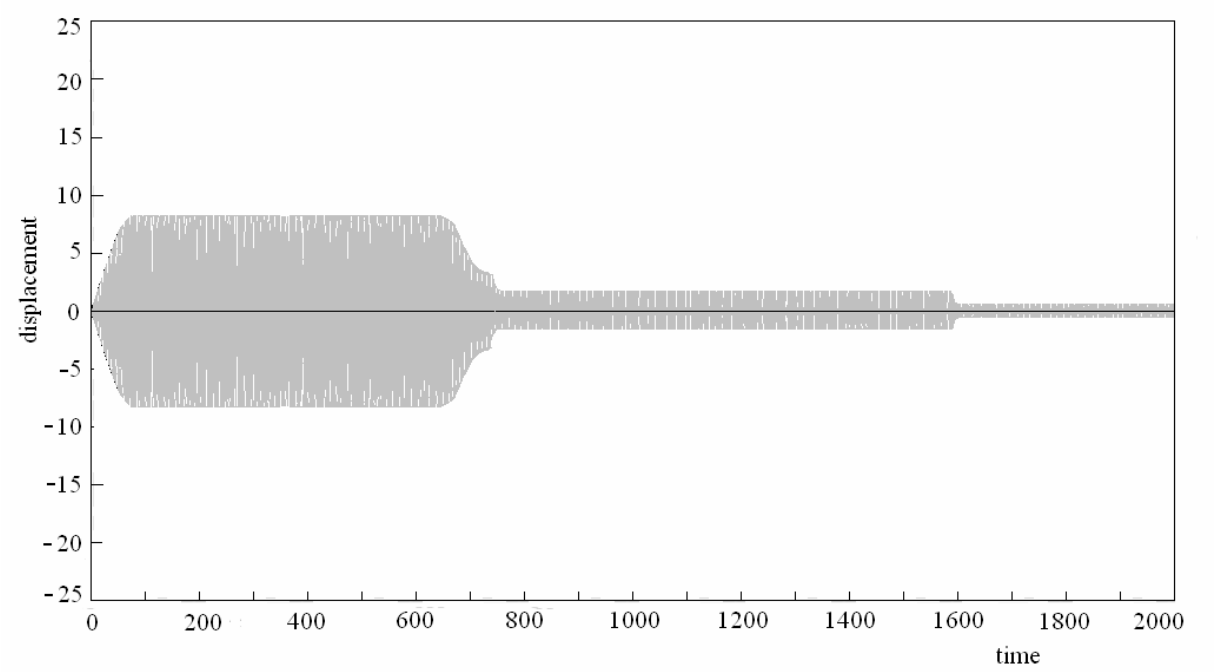


Figure 4. Time history for the last story with the electromechanical vibration absorber.

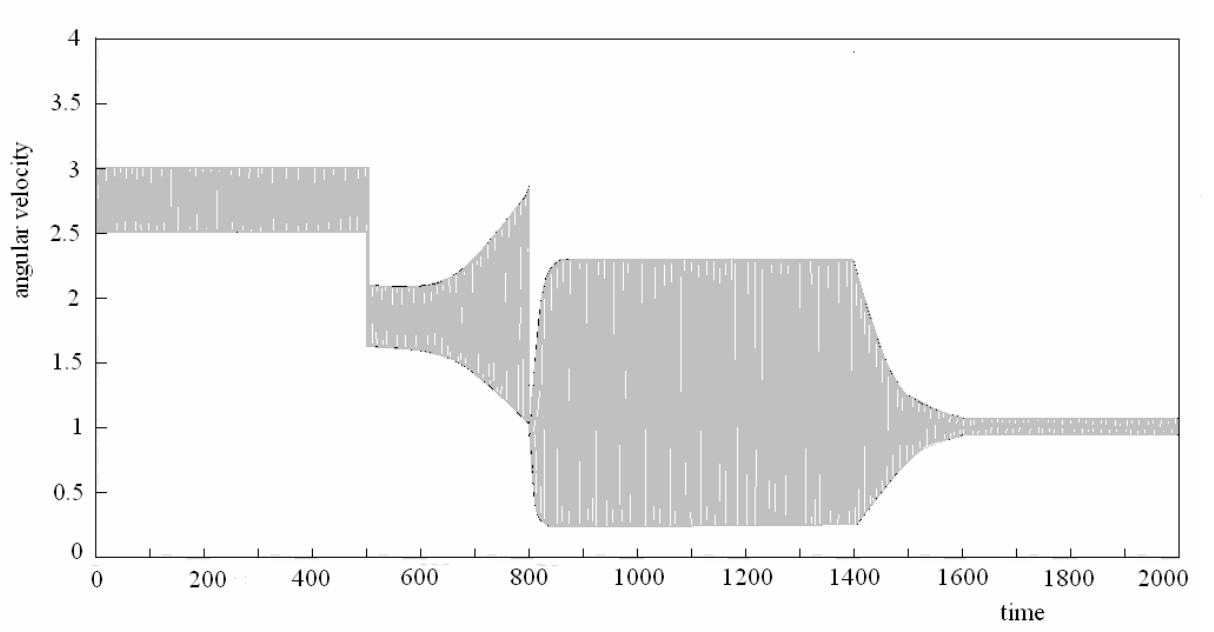


Figure 5. Time history for the angular velocity of the DC motor without the electromechanical vibration absorber.

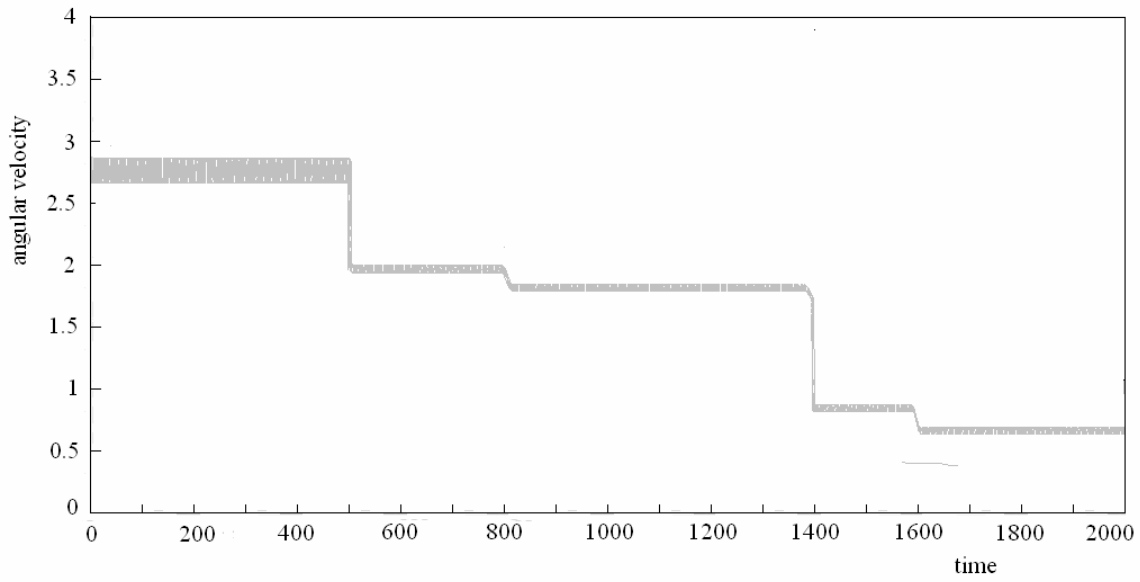


Figure 6. Time history for the angular velocity of the DC motor with the electromechanical vibration absorber.

5 CASE OF THE TIME-DEPENDENT EXCITATION FREQUENCY

The step function (8) is introduces for two cases: (1) $t = 2$ in the interval $0 \le \tau \le 500$ above the resonance and (2) $t = 815$ in the interval $800 \le \tau \le 1400$ inside the resonance. Fig. 7 plots, for example, the step function (9) in the interval $0 \le \tau \le 500$ for $\omega_1 = 1$ and $\omega_2 = 2$ (solid line) and $\omega_2 = 3$ (dash line) and $\varepsilon = 20$, $t_s = 2$. For other intervals, the step function has similar shapes.

In the case (1), the control parameter v knows a sudden variation with respect to time at the beginning of the interval as shown in Figure 8, for both the solid and dash lines, respectively. For $t > 60$, the control parameter is constant and then it jumps to the value 2.5 when $t = 500$.

Upon the matching of two time independent solutions at the time when the step occurs, we obtain the time variation of the displacement x_1 corresponding to the last story without/with the electromechanical vibration absorber, are plotted in Figures. 9 and 10, respectively, during the interval above the resonance, in the case of both solid and dash lines (blue and green contours), respectively. The displacements present squeezing and weaving, and reduction in magnitude for $t > 475$, according to Figure 9. Figure 10 exhibits also squeezing and weaving with increase of the magnitude for $t > 400$. The squeezing and amplitude are enhanced for the dash line (blue and green contours) in both figures. Numerical experiments showed that the squeezing may be enhanced by increasing the frequency difference $\omega_2 - \omega_1$.

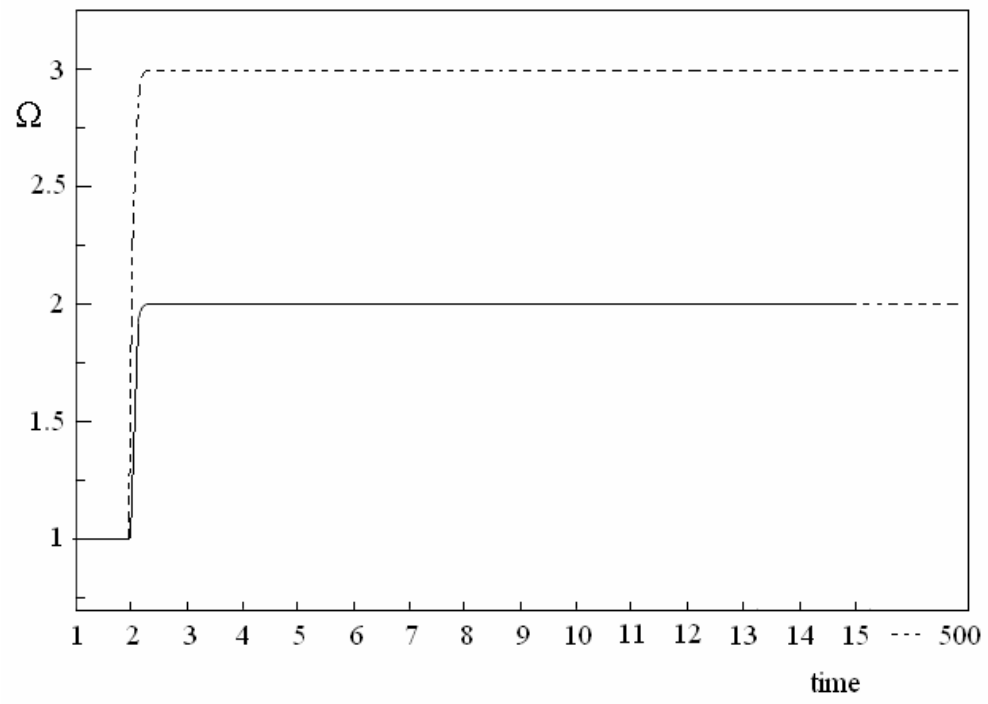


Figure 7. $\Omega(t)$ as a function of t in the interval above the resonance.

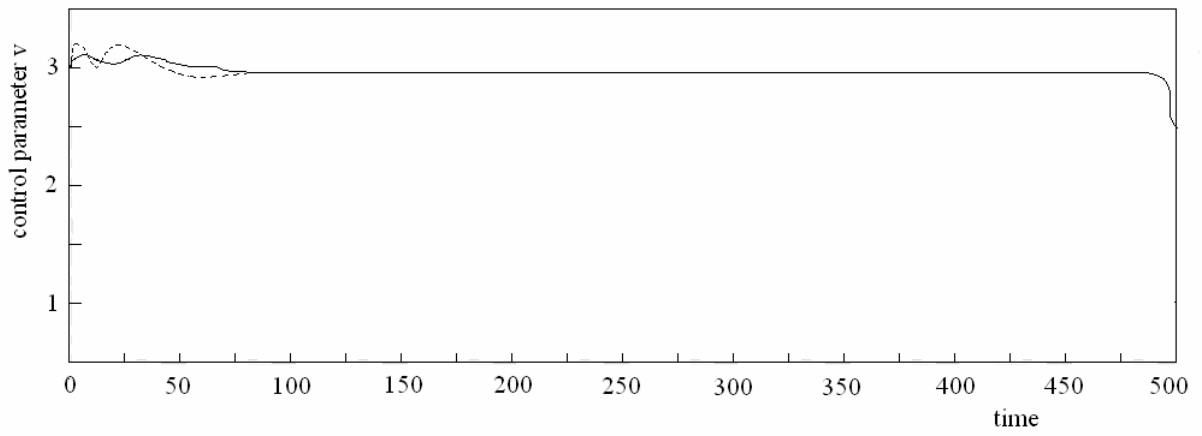


Figure 8. The variation of the control parameter v with respect to time in the interval above the resonance.

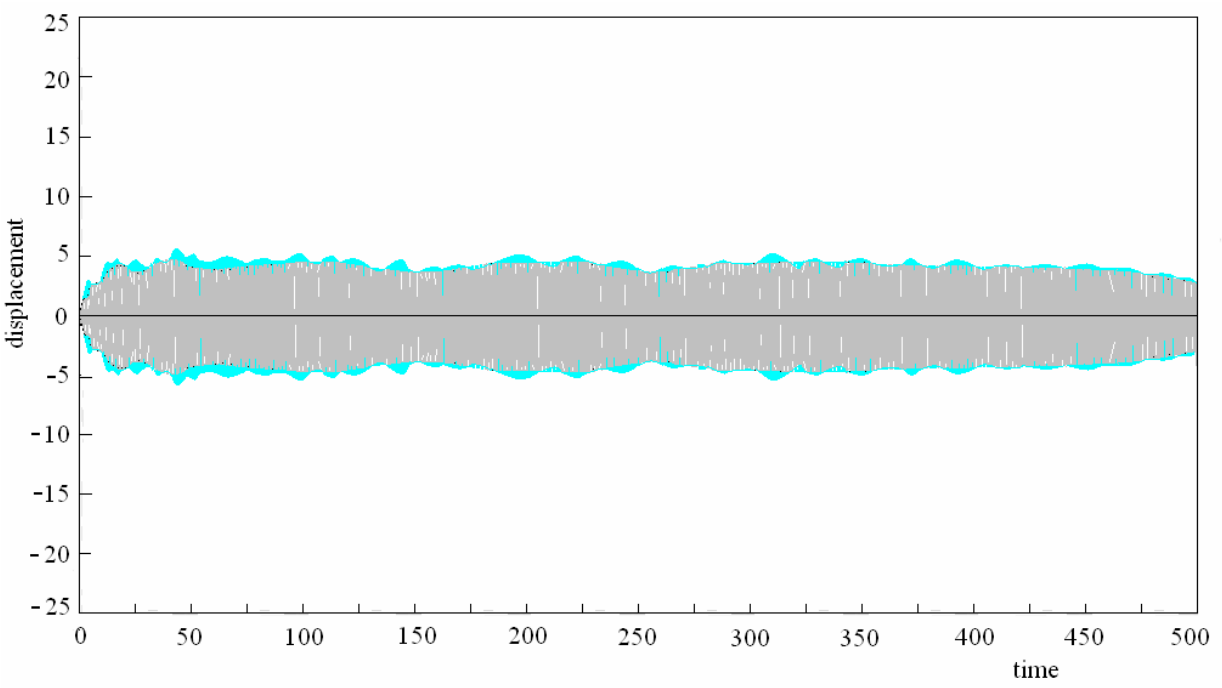


Figure 9. Time history for the last story without the electromechanical vibration absorber, during the interval above the resonance.

In the second case, the variation of the control parameter v is shown in Figure 11. As in the previous case, the control parameter has sudden variations with respect to time at the beginning and at the end of the interval, respectively, for both the solid and dash lines. For $900 < t < 1315$, the control parameter is constant and then it jumps to the value 1.5 when $t = 1400$. The time variation of the displacement x_1 corresponding to the last story without/with the electromechanical vibration absorber, are plotted in Figures 12 and 13, respectively, during the interval inside the resonance, in the case of both solid and dash lines (blue and green contours), respectively. The displacements present squeezing and weaving, and an increasing in magnitude for the last story without the electromechanical vibration absorber, inside the resonance, according to Figure 12.

The squeezing and amplitude are enhanced for the dash line (blue and green contours) in Figure 12. Figure13 exhibits also squeezing and weaving with a substantial decrease of the magnitude for the last story with the electromechanical vibration absorber, inside the resonance.

As a conclusion, by comparing Figure 4 with Figure 13 which presents the history for the last story with the electromechanical vibration absorber for the constant excitation frequency and the time-dependent excitation frequency, respectively, we see that the control system efficiency is higher in the last case.

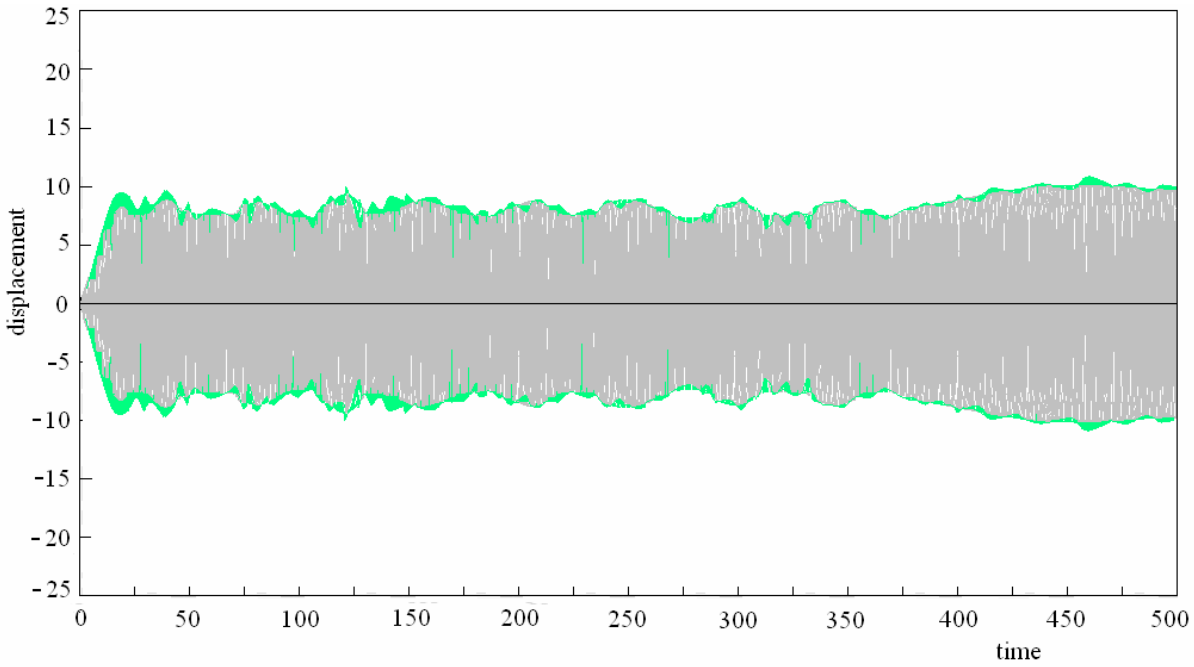


Figure 10. Time history for the last story with the electromechanical vibration absorber, during the interval above the resonance. The green contour corresponds to the dash line.

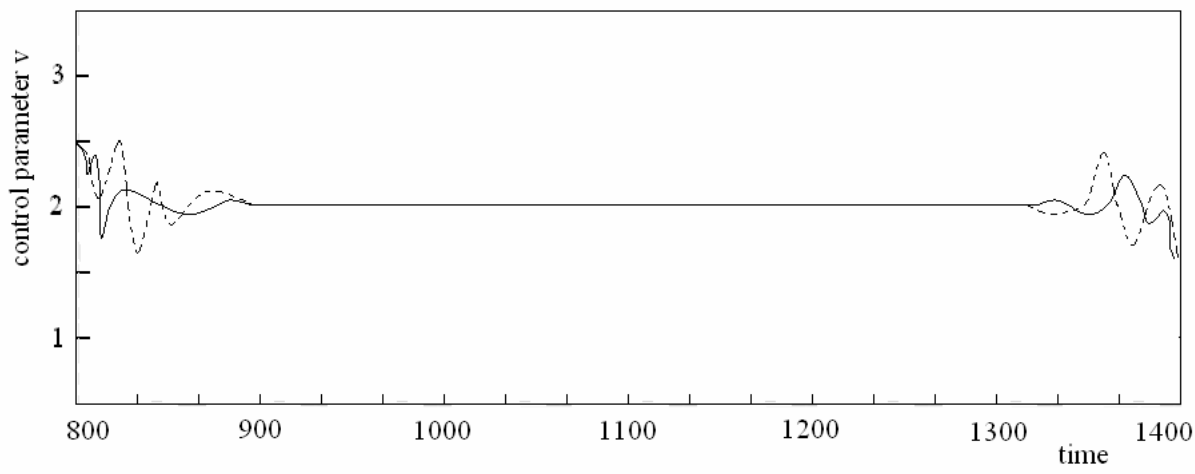


Figure 11. The variation of the control parameter v with respect to time in the interval inside the resonance.

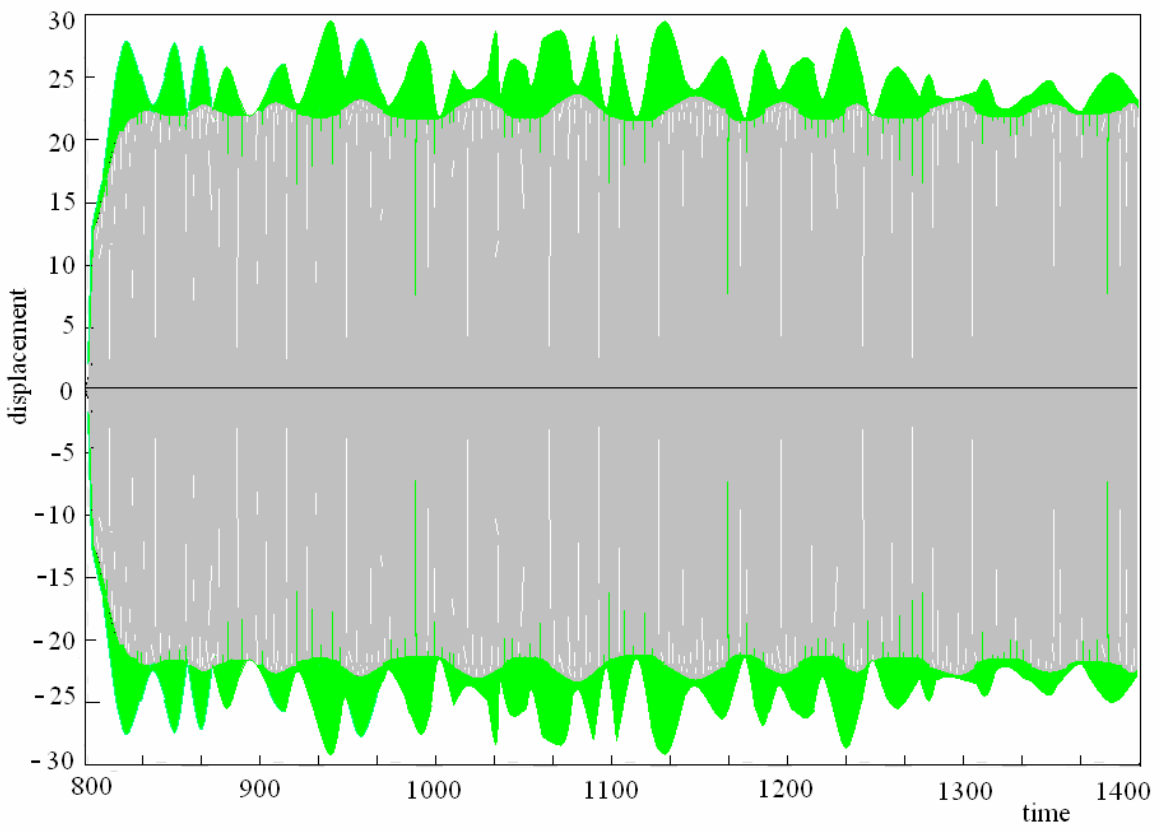


Figure 12. Time history for the last story without the electromechanical vibration absorber, during the interval inside the resonance. The green contour corresponds to the dash line.

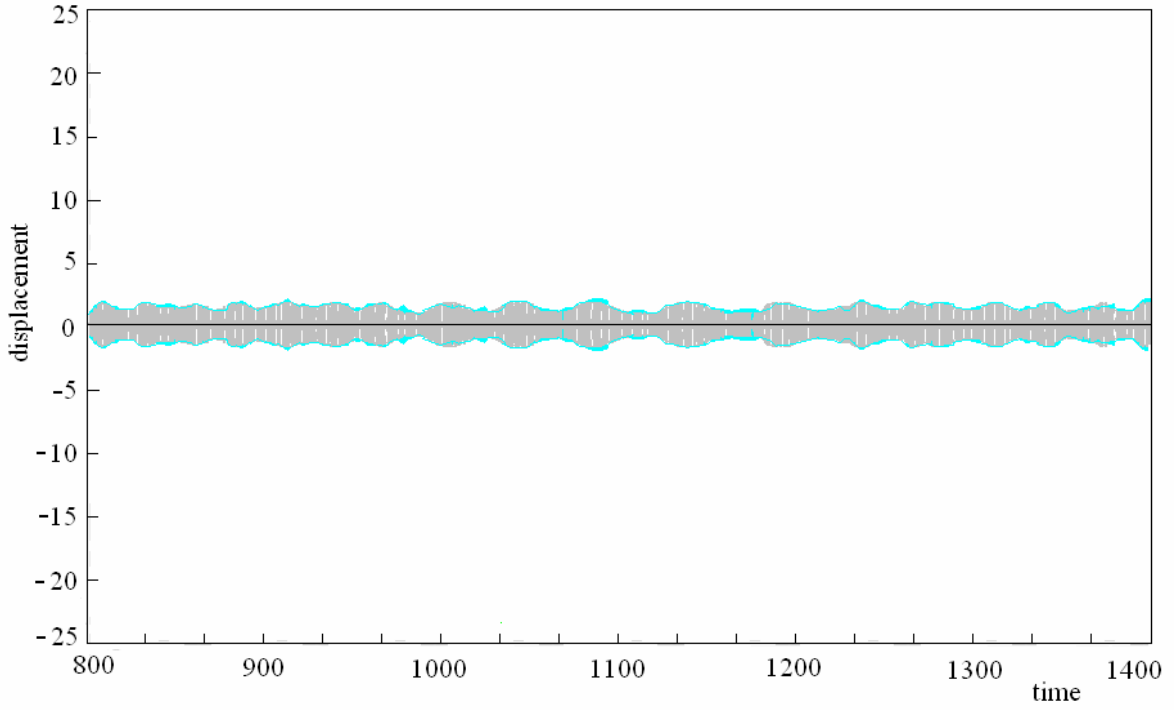


Figure 13. Time history for the last story with the electromechanical vibration absorber, during the interval inside the resonance. The green contour corresponds to the dash line.

6 CASE OF THE RANDOM EARTHQUAKES

In this Section, the function $f(t)$ is viewed as an average of various data y_0 measured from k^{th} earth motions $y_0 = f_k(t)$. This is equivalent to obtain $f_k(t)$ from the average curve $E\{f(t)\}$. The earthquakes are of short duration, so the process is not stationary. From this point of view we can not use a purely random stationary Gaussian process.

We start with 1D expected value $E\{f(t)\}$, and the 2D expected function $E\{f(t_1), f(t_2)\}$ respectively, which are given by [6]

$$E\{f(t)\} = \int_{-\infty}^{\infty} f(t) W_1(f(t)) \mathrm{d}f(t),$$

$$E\{f(t_1) f(t_2)\} = \int_{-\infty}^{\infty} f(t_1) f(t_2) W_2(f(t_1), f(t_2)) \mathrm{d}f(t_1) \mathrm{d}f(t_2), \tag{31}$$

where $W_1(f)$ and $W_2(f(t_1), f(t_2))$ are the 1D probability density function for a given t, and the 2D probability density function, respectively, for given t_1 and t_2. The n^{th} and m^{th} moments ($m, n = 0,1,2,...$) are also calculated

$$E\{f^n(t)\} = \int_{-\infty}^{\infty} f W_1(f) \mathrm{d}f, \quad E\{f^m(t_1) f^n(t_2)\} = \int_{-\infty}^{\infty} f^m(t_1) f^n(t_2) W_2(f^m(t_1), f^n(t_2)) \mathrm{d}f. \tag{32}$$

For $m = n = 1$, the correlation function $R_f(t_1, t_2)$ is obtained

$$R_f(t_1, t_2) = E\{f(t_1) f(t_2)\} = \int_{-\infty}^{\infty} f(t_1) f(t_2) W_2(f(t_1), f(t_2)) \mathrm{d}f(t_1) \mathrm{d}f(t_2). \tag{33}$$

In (7) we can change $f(t)$ with $E\{f(t)\}$ or $R_f(t_1, t_2) = E\{f(t_1), f(t_2)\}$ so that the calculations to remain the same as in the deterministic case. If the correlation function $R_f(t_1, t_2)$ is known, we can calculate the cross correlation functions

$$R_{y_j y_k}(t_1, t_2) = E\{y_j(t_1) y_k(t_2)\} = \int_{-\infty}^{\infty} y_j(t_1) y_k(t_2) W_2(y_j(t_1), y_k(t_2)) \mathrm{d}y_j(t_1) \mathrm{d}y_k(t_2), \tag{34}$$

and the square displacements $E\{y_j^2(t)\}$ for the j^{th}, $j = 1,2$ story

$$E\{y_j^2(t)\} = \int_{-\infty}^{\infty} y_j^2(t) W_2(y_j(t), y_j(t)) \mathrm{d}y(t). \tag{35}$$

The solution (29) allows the calculating of various averages

$$E\{y_j(t)\} = \int_{-\infty}^{t} K_j(t-\tau) E\{f(\tau)\} \mathrm{d}\tau, \tag{36}$$

$$E\{y_j(t_1)y_k(t_2)\}=\int_{-\infty}^{t_1}\int_{-\infty}^{t_2}K_j(t_1-\tau_1)K_k(t_2-\tau_2)E\{f(\tau_1)f(\tau_2)\}\mathrm{d}\tau_1\mathrm{d}\tau_2\,, \tag{37}$$

When $E\{f(\tau)\}=0$, from (36) it results $E\{y_j(t)\}=0$. If the autocorrelation function of $f(t)$ is known, we see from (10) that $R_f(t_1,t_2)$ is also known. So, we obtain from (37)

$$R_{y_jy_k}=\int_{-\infty}^{t_1}\int_{-\infty}^{t_2}K_j(t_1-\tau_1)K_k(t_2-\tau_2)R_f(\tau_1,\tau_2)\}\mathrm{d}\tau_1\mathrm{d}\tau_2\,. \tag{38}$$

Calculation of the mean kinetic energy for each story requires the calculation of the integral

$$R_{\dot y_j\dot y_k}=\int_{-\infty}^{t_1}\int_{-\infty}^{t_2}\dot K_j(t_1-\tau_1)\dot K_k(t_2-\tau_2)\dot R_f(\tau_1,\tau_2)\}\mathrm{d}\tau_1\mathrm{d}\tau_2\,. \tag{39}$$

The shearing force correlation includes the part given by the spring force and the part that is dissipated by the internal damping

$$V_1=c(2\dot y_1-\dot y_2-\dot y_0)+k_1(2\dot y_1-\dot y_2-\dot y_0)+k_2(2\dot y_1-\dot y_2-\dot y_0)^3\,,$$

$$V_2=c(\dot y_2-\dot y_1)+k_1(\dot y_2-\dot y_1)+k_2(\dot y_2-\dot y_1)^3\,.$$

The expression for the shearing force correlation is

$$R_{V_jV_k}(t_1,t_2)=\int_{-\infty}^{t_1}\int_{-\infty}^{t_2}K_j(t_1-\tau_1)K_k(t_2-\tau_2)R_{V_jV_k}(\tau_1,\tau_2)\}\mathrm{d}\tau_1\mathrm{d}\tau_2\,, \tag{40}$$

where $R_{V_jV_k}(t_1,t_2)=R_{j,k}-R_{j,k-1}$.

The 1D and 2D probability density functions are given by [6]

$$W_1(y_j)=\frac{1}{\sigma_j\sqrt{2\pi}}\exp\left(\frac{-y_j^2}{2\sigma_j^2}\right), \tag{41}$$

$$W_2(y_j,y_k)=\frac{1}{\sigma_j\tau_k\sqrt{2\pi(1-\rho_{jk})}}\exp\frac{1}{(1-\sigma_{jk})}\left(-\frac{y_j^2}{2\sigma_j^2}-\frac{y_k^2}{2\tau_j^2}+\frac{2\rho_{jk}y_jy_k}{\sigma_j\tau_k}\right), \tag{42}$$

with

$$\sigma_j^2=E\{y_j^2\}-E^2\{y_j\}=R_{y_j}(t,t)\,,\ \ \sigma_{jk}=\sigma_j\tau_kR_{y_jy_k}(t,t)\,,\ \ \tau_k^2=R_{y_k}(t,t)\,. \tag{43}$$

With (41) or (42), the correlation functions and various moments can be calculated

$$E\{y_j\}=\int_{-\infty}^{\infty}y_jW_1(y_j)\mathrm{d}y_j\,,\ \ E\{y_jy_k\}=\int_{-\infty}^{\infty}\int_{-\infty}^{\infty}y_jy_kW_2(y_j,y_k)\mathrm{d}y_j\mathrm{d}y_k=R_{y_jy_k}\,, \tag{44}$$

$$E\{y_j^n\} = \int_{-\infty}^{\infty} y_j^n W_1(y_j)\mathrm{d}y_j\,, \quad E\{y_j^m y_k^n\} = \int_{-\infty}^{\infty}\int_{-\infty}^{\infty} y_j^n y_k^m W_2(y_j, y_k)\mathrm{d}y_j\mathrm{d}y_k\,. \tag{45}$$

The autocorrelation functions $R_{2,2}$, $R_{1,1}$ and the cross correlation functions $R_{1,2}$ respectively, are divided by $R_0 = \dfrac{4f_0^2}{441\pi^2}$, where f_0^2 is the spectral density (a constant) of R_f which characterizes a Gaussian processes, for which the correlation function $R_f(t_1, t_2)$ given by (10) becomes

$$R_f(t_1, t_2) = E\{f(t_1) f(t_2)\} = f_0^2 \delta(t_1 - t_2)\,, \tag{46}$$

with $\delta(t)$ is the Dirac's delta function.

The autocorrelation functions $R_{2,2}$, $R_{1,1}$ and the cross correlation functions $R_{1,2}$ respectively, are plotted versus the correlation interval in Figs.14-16. The parameters values were selected as $R_0 = \dfrac{4f_0^2}{441\pi^2}$, $\dfrac{k}{m} = 50$, $c = d = 0.2$ [6], [14].

The autocorrelation function $R_{2,2}$ for the second story of the building is plotted versus the correlation interval in Fig.14, with and without the vibration absorber, respectively. The maximum displacement is observed at this story.

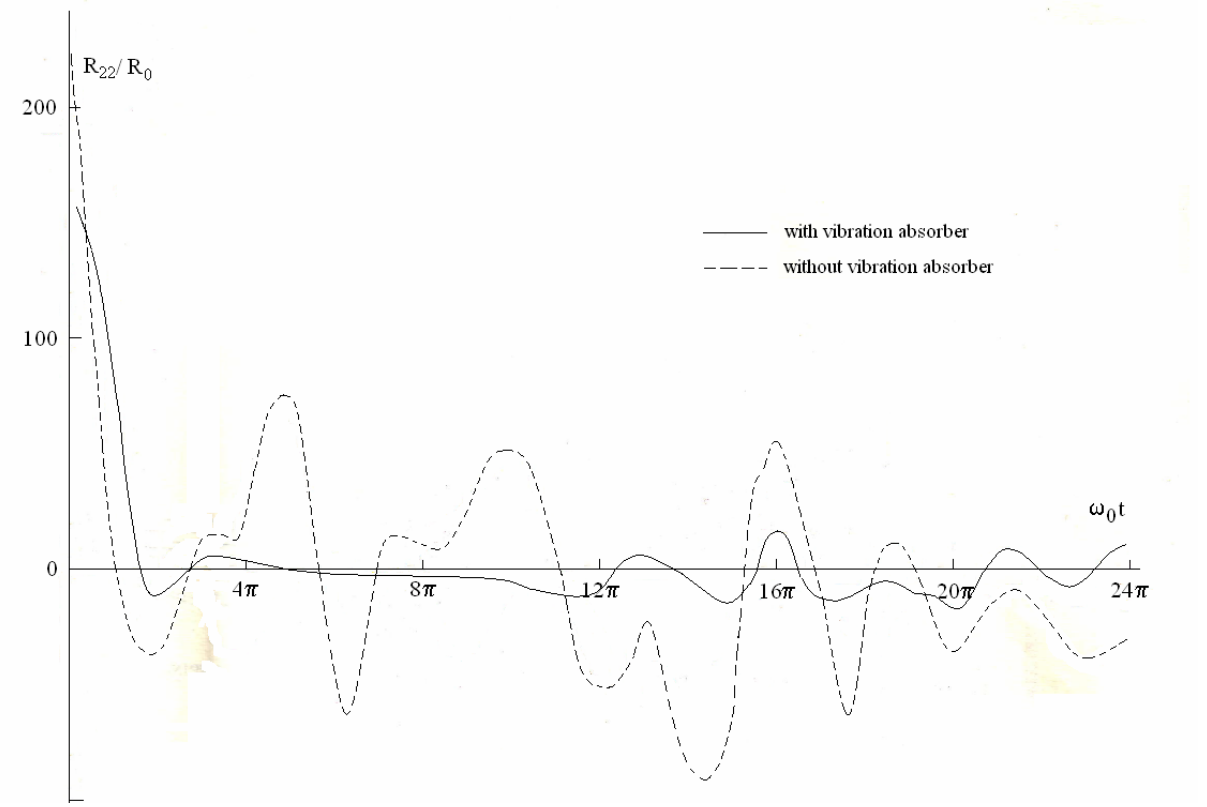


Figure 14. Displacement autocorrelation functions for the second story with and without the vibration absorber.

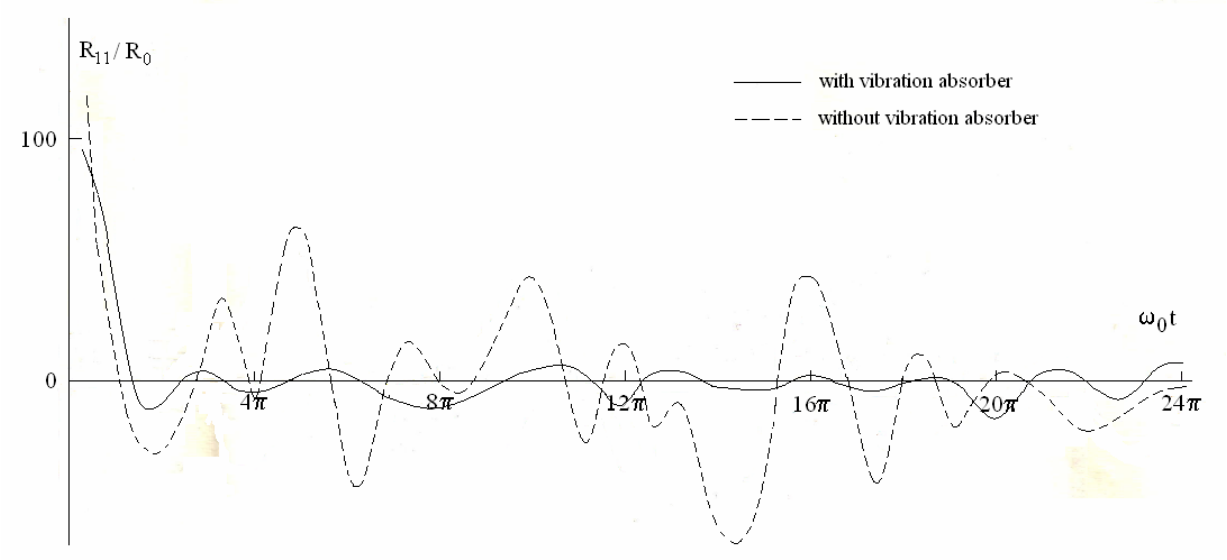


Figure 15. Displacement autocorrelation functions for the first story with and without the vibration absorber.

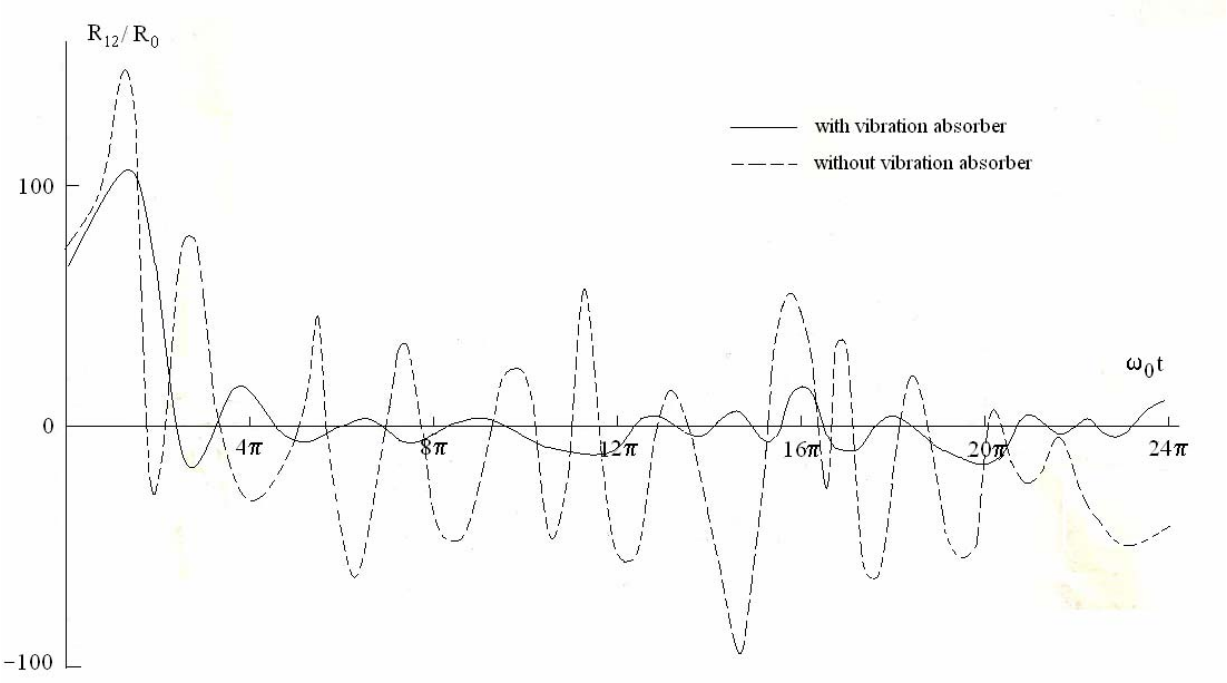


Figure 16. Displacement cross correlation functions with and without the vibration absorber.

7 CONCLUSIONS

This work is dealt with the analysis of the response to vibrations of a small building equipped with an electromechanical vibration absorber. The interaction between the vibrating system and the energy source is investigated for harmonic excitation with constant or step dependent frequencies, and for random earthquakes, respectively. This interaction corresponds to the systems with non-ideal excitation explained by the Sommerfeld effect which results from the balance of the energy and it is due to the coupling between the excitation mechanism and the vibrational loads. The resonance capture and the vibration reduction are displayed by the time history responses of the displacement and angular velocities above the resonance.

Since the earthquakes are of short duration, the stationary character is not available. Therefore, it is shown an attempt for calculation of the mean square displacements and cross correlation functions for this small building equipped with an electromechanical vibration absorber. Because of the stiffness nonlinearity, the equations cannot be solved by usually applied Fourier-integral type of solutions. The stochastic process which characterizes the earth movements is coupled to the cnoidal method which delivers the analytical solutions of the nonlinear problem.

Acknowledgement This research was elaborated through the PN-II-PT-PCCA-2011-3.1-0190 Project of the National Authority for Scientific Research (ANCS, UEFISCSU), contract 149/2012 Romania. The authors acknowledge the similar and equal contributions to this article. The corresponding author is Veturia Chiroiu.

REFERENCES

[1] C.A. Cornell, Engineering Seismic Risk Analysis. *Bulletin of the Seismological Society of America,* **58**, 1583–1606, 1968.

[2] G.H. Powell, R. Allahabadi, Seismic damage prediction by deterministic methods: Concepts and procedures. *Earthquake Engineering Structural Dynamics*, **16**(5), 719–734, 1988.

[3] M. Radulian, G.F. Panza, M. Popa, B. Grecu, Seismic wave attenuation for Vrancea events revisited. *Journal of Earthquake Engineering,* **10**(3), 411–427, 2008.

[4] F. Haas, J. Goedert, Dynamical systems and the Ermakov invariant. *Physics Letters A* **279,** 181, 2001.

[5] S. Bouquet, H.R. Lewis, Extension of Giacomini's results concerning invariants for one-dimensional time dependent potentials. *Journal of Mathematical Physics*, **37**(11) 5496–5509, 1996.

[6] A.C. Eringen, Response of tall buildings to random earthquakes. *Purdue University, Division of Engineering Sciences*, 1957.

[7] M.C. Wang, G.E. Uhlenbeck, On the theory of the Brownian motion II. *Rev. Modern Phys.*, **17** (2), 323–342, 1945.

[8] M.R. Speigel, The random vibrations of a string. *Quarterly of Applied Mathematics* **10**(1), 1952.

[9] J.L.P. Felix, J.M. Balthazar, R.M.L.R.F. Brasil, On saturation control of a nonideal vibrating portal frame foundation type shear-building. *Journal of Vibration and Control*, **11**, 121–136, 2005.

[10] J.L.P. Felix, J.M. Balthazar, R.M.L.R.F. Brasil, On tuned liquid column dampers mounted on a structural frame under a nonideal excitation. *Journal of Sound and Vibration*, 282, 1285–1292, 2005.

[11] S.L.T. Souza, I.L. Caldas, R.L. Viana, J.M. Balthazar, J.M., R.M.L.R.F Brasil, Dynamics of vibrating systems with tuned liquid column dampers and limited power supply. *Journal of Sound and Vibration*, **289,** 987–998, 2006.

[12] R.J. Nagem, S.I. Madanshetty, G. Medhi, An electromechanical vibration absorber. *Journal of Sound and Vibration*, **200**(4), 551–556, 1997.

[13] M. Bolla, J.M. Balthazar, J.L.P. Felix, D.T. Mook, On an approximate analytical solution to a nonlinear vibrating problem, excited by a nonideal motor. *Nonlinear Dynamics*, **50**, 841–847, 2007.

[14] J.L.P. Felix, J.M. Balthazar, Comments on a nonlinear and nonideal electromechanical damping vibration absorber. Sommerfeld effect and energy transfer. *Nonlinear Dynamics,* **55**, 1–11, 2009.

[15] R. Yamapi, J.B. Chabi Orou, P. Woafo, Harmonic oscillations, stability and chaos control in a non-linear electromechanical system. *Journal of Sound and Vibration*, **259**(5), 1253–1264, 2003.

[16] R. Yamapi, P. Woafo, Dynamics and synchronization of coupled self-sustained. *Journal of Sound and Vibratio*n, **285**, 1151–1170, 2005.

[17] R. Yamapi, P. Woafo, Dynamics of an electromechanical damping device with magnetic coupling. *Communications in Nonlinear Science and Numerical Simulation,* **11**, 907–921, 2006.

[18] G.S. Mbouna Ngueuteu, R. Yamapi, P. Woafo, Effects of higher nonlinearity on the dynamics and synchronization of two coupled electromechanical devices. *Communications in Nonlinear Science and Numerical Simulation*, **13**(6), 1121–1130, 2008.

[19] J.M. Balthazar, B.I. Chesankov, D.T. Ruschev, L. Barbanti, H.I. Weber, Remarks on the passage through resonance of a vibrating system with two degrees of freedom, excited by a nonideal energy source. *Journal of Sound and Vibration*, **239**(5), 1075– 1085, 2001.

[20] J.M. Balthazar, D.T. Mook, H.I. Weber, R.M.L.R.F Brasil, A. Fenili, D. Belato, J.L.P. Felix, An overview on nonideal vibrations. *Meccanica*, **38**(6), 613–621, 2003.

[21] K.V. Frolov, T.S. Krasnopolskaya, Sommerfeld effect in systems without internal damping. *International Applied Mechanics*, **23**(12), 1122–1126, 1987.

[22] A.R. Osborne, Soliton physics and the periodic inverse scattering transform. *Physica D*, **86**, 81–89, 1995.

[23] L. Munteanu, St. Donescu, *Introduction to Soliton Theory: Applications to Mechanics.* Book Series Fundamental Theories of Physics, vol.143, Kluwer Academic Publishers, Dordrecht, Boston (Springer Netherlands), 2004.

[24] H. Moya-Cessa, M.F. Duasti,Coherent states for the time dependent harmonic oscillator: the step function. *Physics Letters A*, **311**, 1–5, 2003.

[25] M.J. Ablowitz, H. Segur, *Solitons and the inverse scattering transforms*. SIAM, Philadelphia, 1981.

COMPDYN 2013
4th ECCOMAS Thematic Conference on
Computational Methods in Structural Dynamics and Earthquake Engineering
M. Papadrakakis, V. Papadopoulos, V. Plevris (eds.)
Kos Island, Greece, 12–14 June 2013

More versatility for an integration step size enlargement technique in time integration analysis

A. Sabzei[1], A. Yahyapour Reziakolaei[1], A. Soroushian[1]

[1] International Institute of Earthquake Engineering and Seismology
{a.sabzei,a.yahyapour,a.soroushian}@iiees.ac.ir

Keywords: Structural Dynamics, Time Integration, Computational Cost, Accuracy, Seismic.

Abstract. *A recent technique materializes time integration with steps larger than the steps by which the excitations are digitized. The ratio of integration steps to the digitization steps need to be an integer. By considering linear changes for excitations, between the excitation stations, this paper introduces a generalization, such that the technique becomes applicable when the above ratio can be stated, as a rational number, with a numerator arbitrary greater than the denominator. With a negligble additional computational cost, the proposed generalization entails more efficiency, and, hence, is beneficial in practical time history analysis of structural systems againt strong motions.*

1 INTRODUCTION

Time integration is a versatile tool to analyze semi-discretized equations of motion [1, 2]. In analysis of seismic structural behaviors, the governing equation is as noted below [1, 3-7]:

$$\begin{aligned} &\mathbf{M}\ddot{\mathbf{u}}(t)+\mathbf{f}_{\mathbf{int}}(t)=\mathbf{f}(t) \qquad 0\le t<t_{\text{end}} \\ &\text{Initial Conditions:} \quad \begin{vmatrix} \mathbf{u}(t=t_0)=\mathbf{u}_0 \\ \dot{\mathbf{u}}(t=t_0)=\dot{\mathbf{u}}_0 \\ \mathbf{f}_{\text{int}}(t=t_0)=\mathbf{f}_{\text{int}_0} \end{vmatrix} \\ &\text{Restraining conditions: } \mathbf{Q} \\ &\mathbf{f}(t)=-\mathbf{M}\begin{bmatrix} \alpha_1 \\ \alpha_2 \\ \vdots \\ \alpha_n \end{bmatrix} \ddot{u}_g \end{aligned} \tag{1}$$

where, t and t_{end} imply the time and the duration of the dynamic behavior; $\mathbf{M}$ is the mass matrix; $\mathbf{f}_{\text{int}}$ and $\mathbf{f}(t)$ stand for the vectors of internal force and excitation; $\mathbf{u}(t)$, $\dot{\mathbf{u}}(t)$, and $\ddot{\mathbf{u}}(t)$ denote the vectors of displacement, velocity, and acceleration; $\mathbf{u}_0$, $\dot{\mathbf{u}}_0$ and $\mathbf{f}_{\text{int}_0}$ define the initial status of the model (see [8]); $\mathbf{Q}$ represents some restricting conditions, e.g. additional constraints in problems involved in impact or elastic–plastic behavior [9, 10], and $\ddot{u}_g$ introduces the ground acceleration, available as a digitized record [1, 3, 4, 11], and generally

$$\alpha_1=\alpha_2=\ldots\ldots\alpha_n=1 \tag{2}$$

The size of the digitization, ${}_f\Delta t$, being dependent on the recording facilities [1, 3, 11], may differ from the size of integration steps needed for accuracy. Regarding the latter, the versatility of time integration is provided in the price of some computational error, and considerable computational cost [1, 3, 12]; both the error and the cost mainly depend on the algorithmic parameter [13], i.e. the integration step size, Δt [12]; however, the effects are adverse [1, 3, 12, 14]. This highlights the importance of assigning appropriate values to Δt, leading to:

$$\begin{aligned} \Delta t &= \text{Min}\left(\frac{T}{10},\ {}_s\Delta t\right) \qquad \text{for linear systems} \\ \Delta t &= \text{Min}\left(\frac{T}{100},\ {}_s\Delta t\right) \qquad \text{for nonlinear systems} \end{aligned} \tag{3}$$

as a broadly accepted comment for selecting the integration step size [3, 14, 15]. In seismic time integration analyses, the difference between ${}_f\Delta t$ and the right hand side of Eqs. (3) (addressed above), enforces consideration of ${}_f\Delta t$ as an additional term, after the ${}_s\Delta t$, in Eq. (3). Nevertheless such a selection of integration step size, specifically, when

$$\begin{aligned} {}_f\Delta t &< \text{Min}\left(\frac{T}{10},\ {}_s\Delta t\right) \qquad \text{for linear systems} \\ {}_f\Delta t &< \text{Min}\left(\frac{T}{100},\ {}_s\Delta t\right) \qquad \text{for nonlinear systems} \end{aligned} \tag{4}$$

results in additional computational cost. Recently a technique is proposed to reduce this additional cost, by replacing the excitation with an excitation, with *n* times larger digitization steps, where, *n* is a positive integer, greater than one [16]. The corresponding reduction of computational cost, A_c, is not more than

$$A_c \cong \frac{n-1}{n} \times 100 \quad \% \tag{5}$$

However, since *n* is a positive integer, the computational cost may be still considerably more than the computational cost of the corresponding conventional analysis (that with steps satisfying Eqs. (3), even when leading to integration steps larger than $_f\Delta t$). To say better, in view of the cost reduction values, stated in Table 1 (resulted from Eq. (5)), when, for an integer *n*

$$\begin{aligned} n\ {}_f\Delta t < \text{Min}\left(\frac{T}{10}, {}_s\Delta t\right) < (n+1)\ {}_f\Delta t \qquad & \text{for linear analyses} \\ n\ {}_f\Delta t < \text{Min}\left(\frac{T}{100}, {}_s\Delta t\right) < (n+1)\ {}_f\Delta t \qquad & \text{for linear analyses} \end{aligned} \tag{6}$$

$\frac{\Delta t}{{}_f\Delta t}$	2	3	4	5	6	7	8	9	10	11	12	13	14	15	16	17	18	...
A_c	50	66.6	75	80	83.3	85.7	87.5	89	90	91	92	92	93	93	94	94	94	...

Table1: Reduction of computation cost by considering different values of *n* in implementation of the recent technique (%).

we can analyze with step equal to $n\ {}_f\Delta t$, and save the computational cost according to Eq. (5). However, since *n* is an integer, some considerable additional computational cost cannot be eliminated (specifically $\cong 50\%$ when the right hand side of Eqs. (3) is almost equal but less than twice the digitization step size; see the minimum 50 % in Table 1). In view of the considerable computational cost of real seismic analysis, and hence the practical significance of the computational cost (specifically for smaller values of *n*, for which, according to Table 1, the steps of cost reductions are large), the objective in this paper is to overcome this shortcoming and arrive at more continuous changes of A_c in Table 1.

2 THEORY

Convergence is both the first essentiality in general numerical computation [17-19], and also the key basis in the recently proposed technique [16]. In numerical investigation of convergence and order of accuracy, for problems subjected to digitized excitations, e.g. equations of motion subjected to digitized earthquake records (Eqs. (1)), it is conventional to implement linear interpolation of the digitized records in analyses with smaller steps [12, 19-21]. In view of this idea, we can convert an earthquake record digitized at steps equal to Δt, to a record digitized at smaller steps, by linear interpolation, and expect no loss of accuracy in time integration analysis (compared to the exact responses); though in the price of more computational cost. Considering the new record, as an original record, we can implement the recent technique [16], to arrive at a record with the larger steps to be used in time integration, with reduced computational cost. Since in view of the existing experiences, the recent technique is successful [16, 22-33], the loss of accuracy is trivial. In

other words, by linear interpolation, the original excitation (with digitization steps equal to ${}_f\Delta t$) changes to a new record, digitized at smaller steps equal to $\frac{{}_f\Delta t}{q}$ ($q = 2,3,4,\ldots$), and then, the resulting record can be converted to a record digitized at steps $\frac{{}_f\Delta t}{q}p$ ($p = 2,3,4,\ldots$, $q = 2,3,4,\ldots$), by the recent technique [16]. In consequence, while in implementation of the recent technique, the integration steps can be enlarged by a positive integer greater than one, the integration steps can now be enlarged by a positive rational number (ratio of two positive numbers) greater than one ($p > q$; see also Figure 1), and the reductions of computational cost, i.e.

$$A_c \cong < \frac{p-q}{p} \times 100\% \tag{7}$$

would neither change discontinuously nor would be lower-bounded by 50 % (see Table 1), e.g. consider the case $p = 3$, $q = 2$, leading to $A_c = 33$ %. It is also worth noting that the computational cost of implementing the procedure above is negligible considering the fact that while time integration and specifically implicit time integration analyses are involved in matrix computations depending on the number of degrees of freedom, the computation proposed above is simple and regardless of the number of degrees of freedom. Changing an earthquake record according to the explanation above implies a new technique, or indeed a simple generalization of the recent technique, introduced here, for the first time. Inheriting from the recent technique [16, 22-33], the generalization is independent of the structural system, and integration method, and considers earthquake records digitized at equal steps, as representative of originally smooth phenomena.

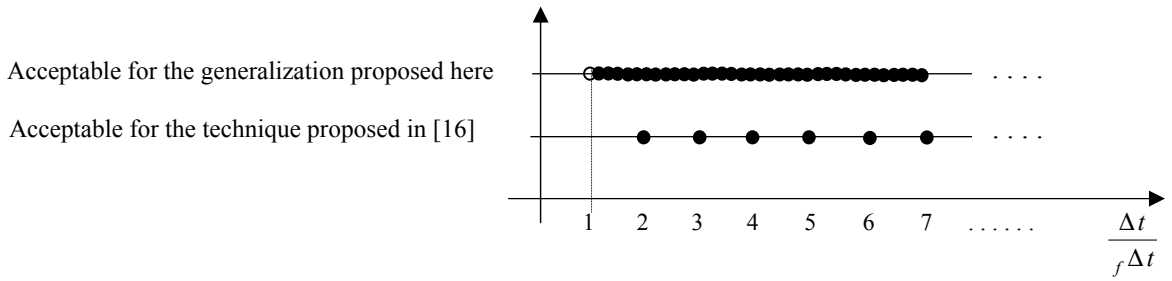


Figure 1: Acceptable values for the ratio of integration step size to the earthquake record digitization step size.

3 NUMERICAL ILLUSTRATION

Consider the single degree of freedom system below:

$$\ddot{u} + 0.2\dot{u} + 25u = -\ddot{u}_g \tag{8}$$

where, $\ddot{u}_g$ is stated in Fig. 2. Implementing the average acceleration method of Newmark [34] for time integration, Figs. 3 and 4, and Table 2, display the performance of the technique discussed in [16, 22-33] and the generalization proposed here for the problem introduced in Eq. (8) and Fig. 2. Clearly the results, and specifically the close resemblance of the responses in Figs. 3(b-d) and Figs. 4(a-d) to that in Fig. 3(a), evidence the adequacy of the provided capability. To explain better, while before the generalization, we could reduce the cost 50% or 67% or 75%, . . as apparent in Table 2 and Figs. 4, the intermediate reductions is now achievable. In this regard, specially, cost reductions less than 50 % is practically notable. A complicated example is studied next.

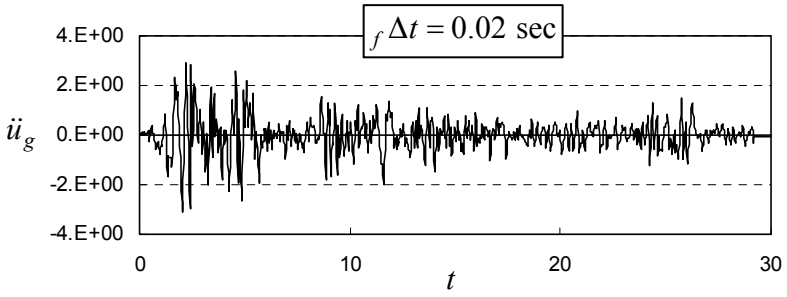


Figure 2: The ground acceleration applied to the structural system in the first example.

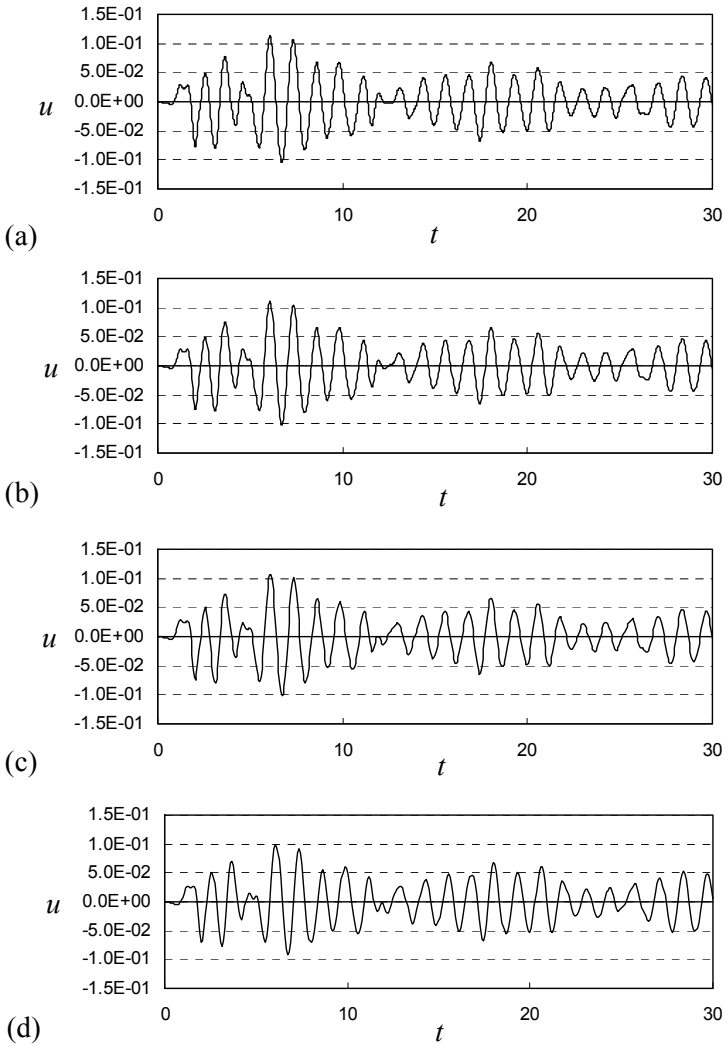


Figure 3: Responses obtained from average acceleration analysis of the problem introduced in Eq. (8) and Fig. 2: (a) ordinary analysis ($n = 1$), (b) implementing the recent technique [16] with $n = 2$, (c) implementing the recent technique [16] with $n = 3$, (d) implementing the recent technique [16] with $n = 4$.

Figure	3(a)	3(b)	3(c)	3(d)	4(a)	4(b)	4(c)	4(d)
Reduction	Basis	50	67	75	33	60	71	78

Table2: Reduction of computation cost (%) in different analyses of the problem introduced in Eq. (8) and Fig. 2, by the average acceleration method.

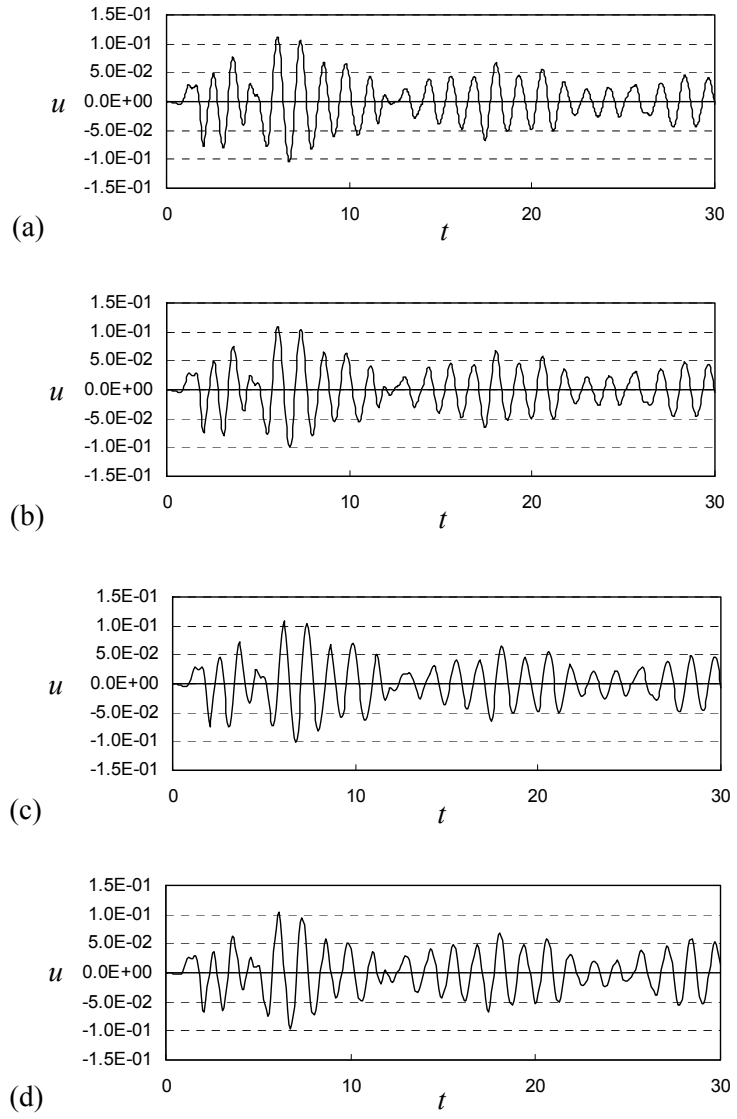


Figure 4: Responses obtained from average acceleration analysis of the problem introduced in Eq. (8) and Fig. 2, after implementing the recent technique [16] with the generalization proposed in this paper: (a) $p = 3$ and $q = 2$, (b) $p = 5$ and $q = 2$, (c) $p = 7$ and $q = 2$, (d) $p = 9$ and $q = 2$.

The second example is introduced in Fig. 5 and Table 3. The objective of the analysis is the mid-height velocity, of the structure, depicted in Fig. 6. The Wilson-θ method [35-37] is implemented

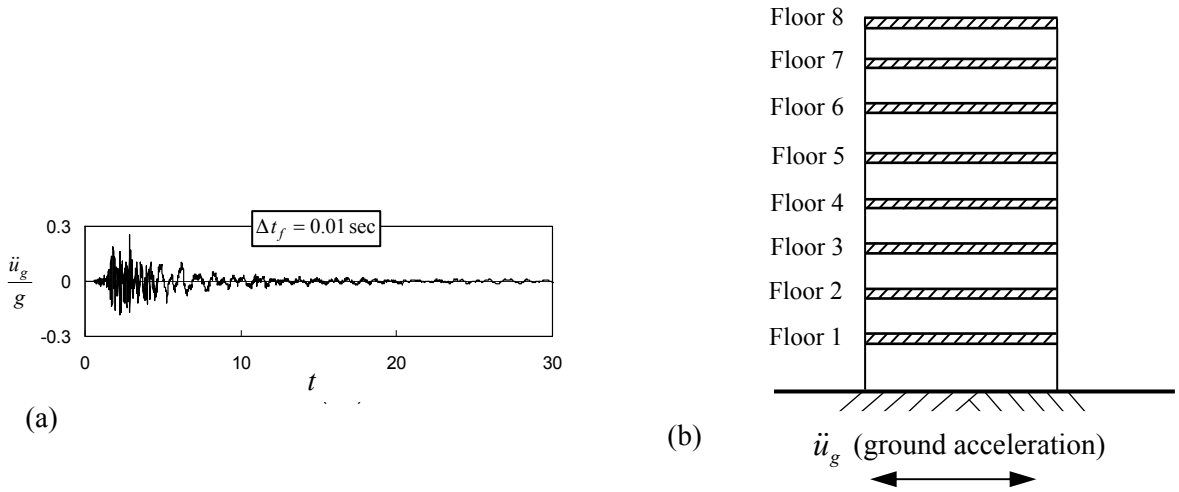


Figure 5: The structural system under consideration in the second example: (a) excitation, (b) shear building.

Floor	1	2	3	4	5	6	7	8
Mass $\times 10^{-3}$ (Kg)	1036	1034	1032	1030	1028	1026	1024	1022
Stiffness$\times 10^{-3}$ (N/m)	8600	8400	8200	7000	6800	6600	6400	6200
Damping (N sec/m)	Negligible (considered zero)							

Table 3: Numerical details of the shear building in Fig. 5(b).

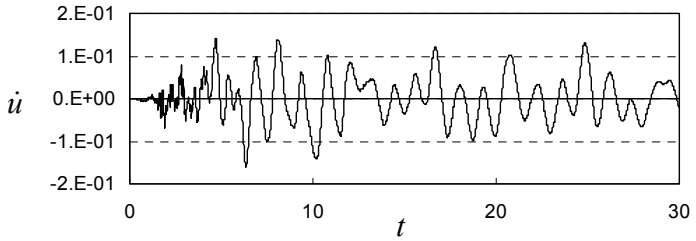


Figure 6: Exact mid-height velocity for the system introduced in Fig. 5 and Table 3.

for the analysis. In view of Fig. 7, when we are interested in high accuracies we would rather use at most $n=2$ in implementation of the recent technique (see the last five seconds in the time histories). This implies 50% reduction of computational cost with a gap of 17% from the case $n=3$, where, the reduction is about 67%. Even if the accuracy demand is between the accuracies provided at cases $n=2$ and $n=3$ (not as much as that corresponding to $n=2$), according to the formulation of the recent technique there is no intermediate response. However, by implementing the generalization proposed in this paper, we can use the sets (9, 4), (10, 4), (11, 4), as (p, q), to materialize accuracies and computational cost reductions between the cases corresponding to $n=2$ and $n=3$ (provided by the recent technique); see Fig. 8 and Table 4. Consequently, this example once again demonstrates the additional versatility provided in this paper for the recently proposed technique, i.e. indeed the capability of reducing more computational cost without sacrificing the accuracy we are interested in.

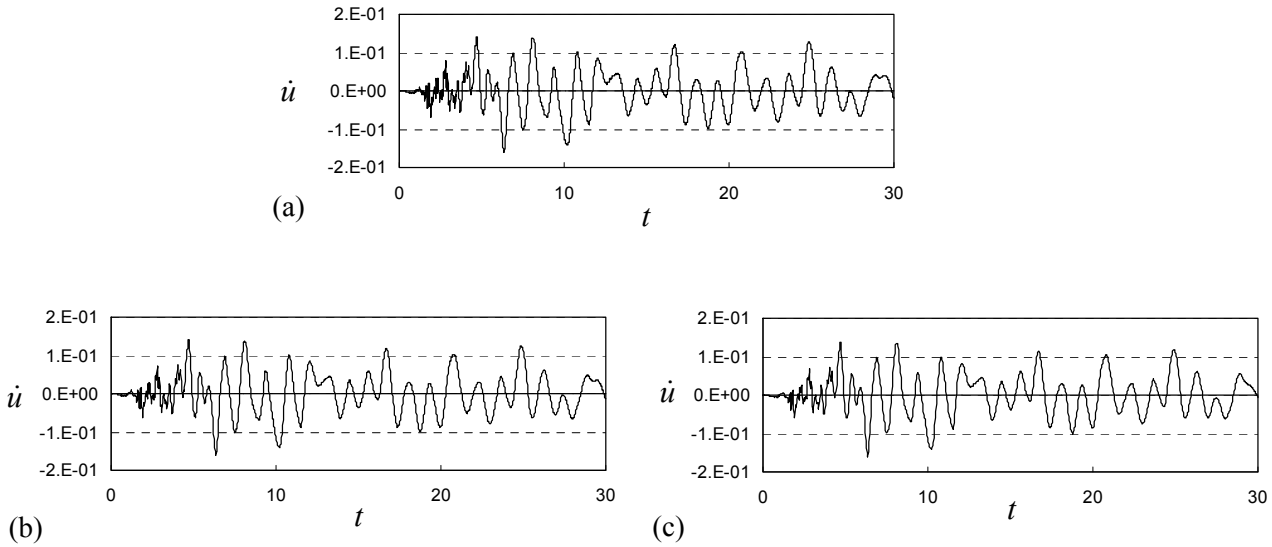


Figure 7: Mid-height velocity for the system in Fig. 5 and Table 3, obtained: (a) from ordinary analysis, (b) when implementing the recent technique [16] with $n = 2$, (c) when implementing the recent technique [16] with $n = 3$.

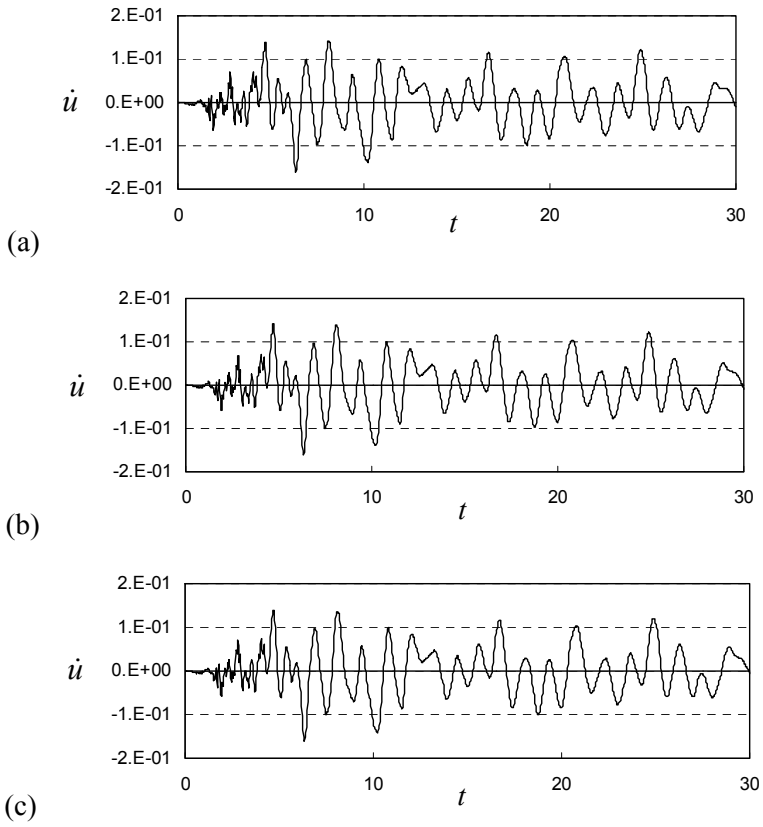


Figure 8: Mid-height velocity for the system in Fig. 5 and Table 3, obtained by implementing the recent technique [16] and the proposed generalization when: (a) $p = 9$ and $q = 4$, (b) $p = 10$ and $q = 4$, (c) $p = 11$ and $q = 4$.

Figure	7(a)	7(b)	8(a)	8(b)	8(c)	7(c)
Reduction	Basis of comparison	50	56	60	64	67

Table 4: Computational cost reduction, corresponding to the analyses reported in the second example (%).

4 CONCLUSION

With the objective of more efficient analysis of structural systems against earthquakes digitized records, attention in this paper is paid to a recent technique [16], proposed for implementing integration steps larger than the excitation steps. A restriction on this technique i.e. a positive integer as the ratio of integration steps to excitation steps, is eliminated, by implementing the practice in numerical analysis of the convergence for time integration analyses with digitized excitations. As the result, the ratio of integration steps to the steps of the earthquake records can now be a rational number, greater than one (with positive integers in the denominator and numerator), and practically the computational cost can be considered as a continuous function of the integration step.

Reference

[1] A.K. Chopra, Dynamics of structures: Theory and application to earthquake engineering. Prentice-Hall, 1995.

[2] J. Chung, G.M. Hulbert, A family of single-step Houbolt time integration algorithms for structural dynamics. *Computer Methods in Applied Mechanics and Engineering*, **118**, 1-11, 1994.

[3] R.W. Clough, J. Penzien, *Dynamics of structures*. McGraw-Hill, 1993.

[4] F. Naeim, S. Zhongzhi. *The seismic design handbook*. 2001.

[5] J. Henrych, *Finite models and methods of dynamics in structures*. Elsevier, 1990.

[6] J. Argyris, J.P. Mlejnek, *Dynamics of structures*. Elsevier, 1991.

[7] T. Belytschko, W.K. Liu, B. Moran, *Non-linear finite elements for continua and structures*. John Wiley & Sons, 2000.

[8] A. Soroushian, New methods to maintain responses convergence and control responses errors in the analysis of nonlinear dynamic models of structural systems. *Ph.D. Thesis*, University of Tehran, 2003. (in Persian)

[9] P. Wriggers, *Computational contact mechanics*. John Wiley & Sons, 2002.

[10] T.J.R. Hughes, K.S. Pister, R.L. Taylor, Implicit–explicit finite elements in nonlinear transient analysis. *Computer Methods in Applied Mechanics and Engineering*, **17**/**18**, 159–182, 1979.

[11] J. Havskov, G. Alguacil, *Instrumentation in earthquake seismology (Modern approaches in geophysics)*. Springer, 2005.

[12] T. Belytschko, T.J.R. Hughes, *Computational methods for transient analysis*. Elsevier, 1983.

[13] C.W. Gear, *Numerical initial value problems in ordinary differential equations*. Prentice-Hall, 1971.

[14] K.J. Bathe, *Finite element procedures*. Prentice-Hall, 1996.

[15] J.F. McNammara, Solution schemes for problems of nonlinear structural dynamics. *Journal of Pressure Vessels, ASME,* **96**, 147–155, 1974.

[16] A. Soroushian, A technique for time integration with steps larger than the excitation steps. *Communications in Numerical Methods in Engineering*, **24**, 2087-2111, 2008.

[17] J.C. Strikwerda, *Finite difference schemes and partial differential equations*. Wadsworth & Books/Cole, 1989.

[18] P. Henrici, *Discrete variable methods in ordinary differential equations*. Prentice-Hall, 1962.

[19] A. Soroushian, P. Wriggers, J. Farjoodi, Asymptotic upper bounds for the errors of Richardson extrapolation with practical application in approximate computations. *International Journal for Numerical Methods in Engineering*, **80**, 565-595, 2009.

[20] A. Soroushian, J. Farjoodi, More reliable responses for time integration analyses. *Structural Engineering and Mechanics,* **16**, 219–240, 2003.

[21] A. Soroushian, Towards a computer program to automate the study of stability and consistency of new time integration methods, Report 7517, Structural Engineering Research Center (SERC), IIEES, Tehran, Iran. (in revision) (in Persian)

[22] A. Soroushian, On the performance of a conventional accuracy controlling method applied to linear and nonlinear structural dynamics. *Proceedings of the 17th International Congress on Sound & Vibration (ICSV 17*), Cairo, Egypt, July 18-22, 2010.

[23] A. Soroushian, A. Aziminejad, A more efficient seismic analysis of tall building by implementing a recently proposed technique. *Proceedings of the 6th International Conference of Seismology and Earthquake Engineering (SEE6),* Tehran, Iran, May 16-18, 2011.

[24] A. Soroushian, A comparison between two methods for disregarding excitation steps in seismic analyses. *Proceedings of the 6th International Conference of Seismology and Earthquake Engineering (SEE6),* Tehran, Iran, May 16-18, 2011.

[25] A. Soroushian, M. Hosseini, A. Vasseghi, On the performance of a technique for more efficient time integration when applied to bridge structures seismic analysis. *Proceeding of the, 3rd ECCOMAS Thematic Conference on Computational Methods in Structural Dynamics and Earthquake Engineering (COMPDYN 2011)*, Corfu, Greece, May 23-28, 2011.

[26] O. Bahar, S. Ramezani, Faster time integration analysis for building structure subjected to 3-component earthquakes. *Proceeding of the, 3rd ECCOMAS Thematic Conference on Computational Methods in Structural Dynamics and Earthquake Engineering (COMPDYN 2011)*, Corfu, Greece, May 23-28, 2011.

[27] F. Nateghi, M. Yakhchalian, Less computational costs for analysis of soils seismic behavior by time integration. *Proceeding of the, 3rd ECCOMAS Thematic Conference on Computational Methods in Structural Dynamics and Earthquake Engineering (COMPDYN 2011)*, Corfu, Greece, May 23-28, 2011.

[28] A. Soroushian, On the performance of a recent technique for more efficient time integration in severe seismic conditions. *Proceedings of the International Conference on Advances in Structural Engineering and Mechanics (ASEM 11)*, Seoul, South Korea, September 18-22, 2011.

[29] A. Soroushian, A. Saaed, M. Arghavani, M. Rajabi, M.M. Sharifpour, Less computational costs in the analysis of seismic behaviors by time integration. *Proceedings of the 10th Biennial Conference on Vibration Problems (ICOVP).* Prague, Czech Republic, September 5-8, 2011.

[30] F. Nateghi, M. Yakhchalian, An investigation into effectiveness of a technique proposed for reducing computational cost of time integration analysis in the analysis of soil seismic behaviors. *Proceedings of the, 11th US National Congress on Computational Mechanics (11th USNCCM)*, Minneapolis, USA, July 25-28, 2011.

[31] A. Soroushian, On the accuracy of accelerations in general implementation of a recently proposed seismic analysis computational cost reduction technique. *Proceedings of the 5th International Conference from Scientific Computing to Computational Engineering (5th IC-SCCE)*, Athens, Greece, July 4-7, 2012.

[32] A. Soroushian, Direct time integration with step larger than the steps by which the excitations are digitized, Report 7510, Structural Engineering Research Center (SERC), IIEES, Tehran, Iran, 2012. (in Persian)

[33] A. Soroushian, A. Sabzei, A.Y. Reziakolai, On the performance of a recent computational cost reduction technique for mid-rise buildings. *In the proceedings of the 2nd National Congress on Civil Engineering*, Zahedan, Iran, May 7-8, 2013.

[34] N.M. Newmark, A method of computation for structural dynamics. *Journal of Engineering Mechanics, ASCE*, **85**, 67-94, 1959.

[35] E.L. Wilson, A computer program for the dynamic stress analysis of underground structures. Report 68-1, University of California, Berkeley, USA, 1968.

[36] K.J. Bathe, E.L. Wilson, Stability and accuracy analysis of direct integration methods. *Earthquake Engineering and Structural Dynamics*, **1**, 283-291, 1973.

[37] E.L. Wilson, I. Farhoomand, K.J. Bathe, Nonlinear dynamic analysis of complex structures. *Earthquake Engineering and Structural Dynamics*, **1**, 241-252, 1973.

COMPDYN 2013
4th ECCOMAS Thematic Conference on
Computational Methods in Structural Dynamics and Earthquake Engineering
M. Papadrakakis, V. Papadopoulos, V. Plevris (eds.)
Kos Island, Greece, 12–14 June 2013

ON THE PERFORMANCE OF A STRUCTURAL ANALYSIS COST REDUCTION TECHNIQUE WHEN APPLIED TO RESIDENTIAL BUILDINGS

A. Y. Reziakolaei[1], A. Sabzei[1], A. Soroushian[1]

[1] International Institute of Earthquake Engineering and Seismology
{a.yahyapour,a.sabzei,a.soroushian}@iiees.ac.ir

Keywords: Seismic Analysis, Time integration, Computational Cost, Accuracy, Step Size.

Abstract. *Time integration is a versatile tool in structural dynamic analysis, suffering from considerable computational cost and inexactness in responses. For the special case of analysis against digitized excitations, recently a technique is proposed for integration with steps larger than the steps of excitation, and is successfully implemented in several practical analyses. In view of the social and financial importance of residential buildings, with five to twenty floors, in this paper, the performance of the recent technique regarding the structural systems of these buildings is examined and specifically it is demonstrated that even with no a priori knowledge about the structure and response, and independent of the analysis method, we can halve the computational cost in the price of trivial loss of accuracy.*

1 INTRODUCTION

Earthquakes are of the most potentially destructive phenomena. Despite the considerable progress, in anti-seismic analysis and design, there exist ambiguities in reliable protection against earthquakes, specially, for the current complicated architectural and structural designs. Considering this, besides the stochastic nature of strong ground motions, a main stage in advanced anti-seismic design is time history analysis against several appropriately selected earthquake records, somehow putting the effects together, and controlling, the adequacy of the resulting structural behavior. Direct time integration is the most versatile tool for time history analysis [1, 2], according to which, after discretization in space [3-5], and arriving at

$$\begin{aligned} &\mathbf{M}\ddot{\mathbf{u}}(t)+\mathbf{f}_{\mathbf{int}}(t)=\mathbf{f}(t) \qquad 0\le t<t_{\text{end}} \\ &\text{Initial Conditions:} \quad \begin{vmatrix} \mathbf{u}(t=t_0)=\mathbf{u}_0 \\ \dot{\mathbf{u}}(t=t_0)=\dot{\mathbf{u}}_0 \\ \mathbf{f}_{\text{int}}(t=t_0)=\mathbf{f}_{\text{int}_0} \end{vmatrix} \\ &\text{Restraining conditions: } \mathbf{Q} \end{aligned} \tag{1}$$

(t and t_{end} imply the time and the duration of the dynamic behavior; $\mathbf{M}$ is the mass matrix; $\mathbf{f}_{\text{int}}$ and $\mathbf{f}(t)$ stand for the vectors of internal force and excitation; $\mathbf{u}$(t), $\dot{\mathbf{u}}$(t), and $\ddot{\mathbf{u}}$(t) denote the vectors of displacement, velocity, and acceleration; $\mathbf{u}_0$, $\dot{\mathbf{u}}_0$ and $\mathbf{f}_{\text{int}_0}$ define the initial status of the model; also see [6]; and, $\mathbf{Q}$ represents some restricting conditions, e.g. additional constraints in problems involved in impact or elastic–plastic behavior [7, 8]), Eqs. (1) need to be analyzed for several strong ground motion (several $\mathbf{f}(t)$) [9-11].

Time integration analyses are not only versatile, but also simple. However, the price is inexactness and computational expensiveness. The most important parameter to control the inexactness and computational cost, also acting as the algorithmic parameter [12], of time integration, is the integration step size, Δt [13]; in seismic analyses, generally constant throughout the integration [1, 14]. Because of this significance and the fact that the effect of Δt on the inexactness and computational cost is adverse, assigning an appropriate value to Δt plays an important role in the efficiency and adequacy of integration and time history analyses. A current comment in this regard is as noted below [14-16]:

$$\begin{aligned} \Delta t &= \text{Min}\left(\frac{T}{10},\ {}_s\Delta t,\ {}_f\Delta t\right) \qquad \text{for linear systems} \\ \Delta t &= \text{Min}\left(\frac{T}{100},\ {}_s\Delta t,\ {}_f\Delta t\right) \qquad \text{for nonlinear systems} \end{aligned} \tag{2}$$

where, T is the smallest dominant period of the response, ${}_s\Delta t$ is the maximum step size, providing numerical stability for linear analyses, and ${}_f\Delta t$ is the step size, by which, the earthquake record is digitized.

Recently, based on the basic essentiality of numerical computations, i.e. convergence [17, 18], a technique is proposed, for reducing the effect of ${}_f\Delta t$, in Eqs. (2), such that the analyses can be carried out with considerably less computational cost, with practically unchanged accuracy [19]; several theoretical studies and numerical investigations are carried out regarding the technique [19-31], successfully. In continuation, in this study, attention is paid to the social and practical importance of low to mid-rise residential buildings, and the performance of the technique in time integration analysis of thirty five- to twenty-story

buildings (with different structural systems and geometries) are studied in detail. In Section 2, the structural systems, the excitations, and the analyses details are set. In Section 3, the outcome of the analyses, once, when implementing the technique, and once, when not implementing the technique, are compared. In Section 4, the observations are discussed, and finally, with a brief set of the achievements, the paper is concluded, in Section 5.

2 The structures of thirty residential buildings

Consider buildings with five, ten, fifteen, and twenty floors, two identical horizontal axes of symmetry, the geometries addressed in Table 1 (only the cases in a vertical column are considered together in a building), and the three structural systems: (a) lateral resistance by moment resisting frames, (b) lateral resistance by bracings, and (c) lateral resistance by moment resisting frame and bracings (cases (a) and (b) are not considered for buildings with twenty floors [11]; for the bracings configuration, see Figure 1 [32]). In view of the selections, stated in Table 2, the structural systems are designed, according to the Iranian codes [11, 33], considering their linear behaviors, when subjected to two two-component strong motions selected in consistence with the design codes (see Figure 2).

Number of bays	4	5	6
Length of bays (m)	4	5	6

Table 1: Variety of geometry of the thirty buildings in horizontal plans, similar for building with different number of floors.

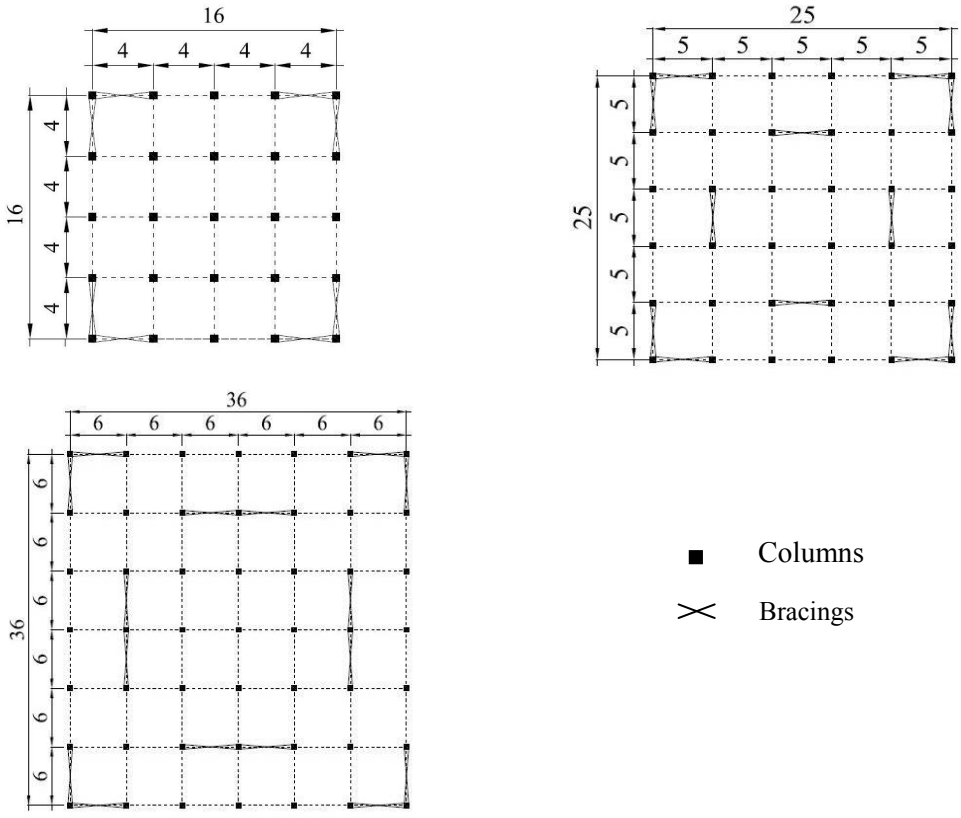


Figure1: Configuration of the bracings: (a) buildings with four bays in each horizontal direction, (b) buildings with five bays in each horizontal direction, (c) buildings with six bays in each horizontal direction [31].

Material	Steel ST-37
Occupancy	Residential
Importance Factor	1
Seismic Zone	0.35
Soil type	II ($375\ \text{m/s} \le Vs \le 750\ \text{m/s}$) [11]
Floor height	3 meters

Table 2: Main details of the structural design.

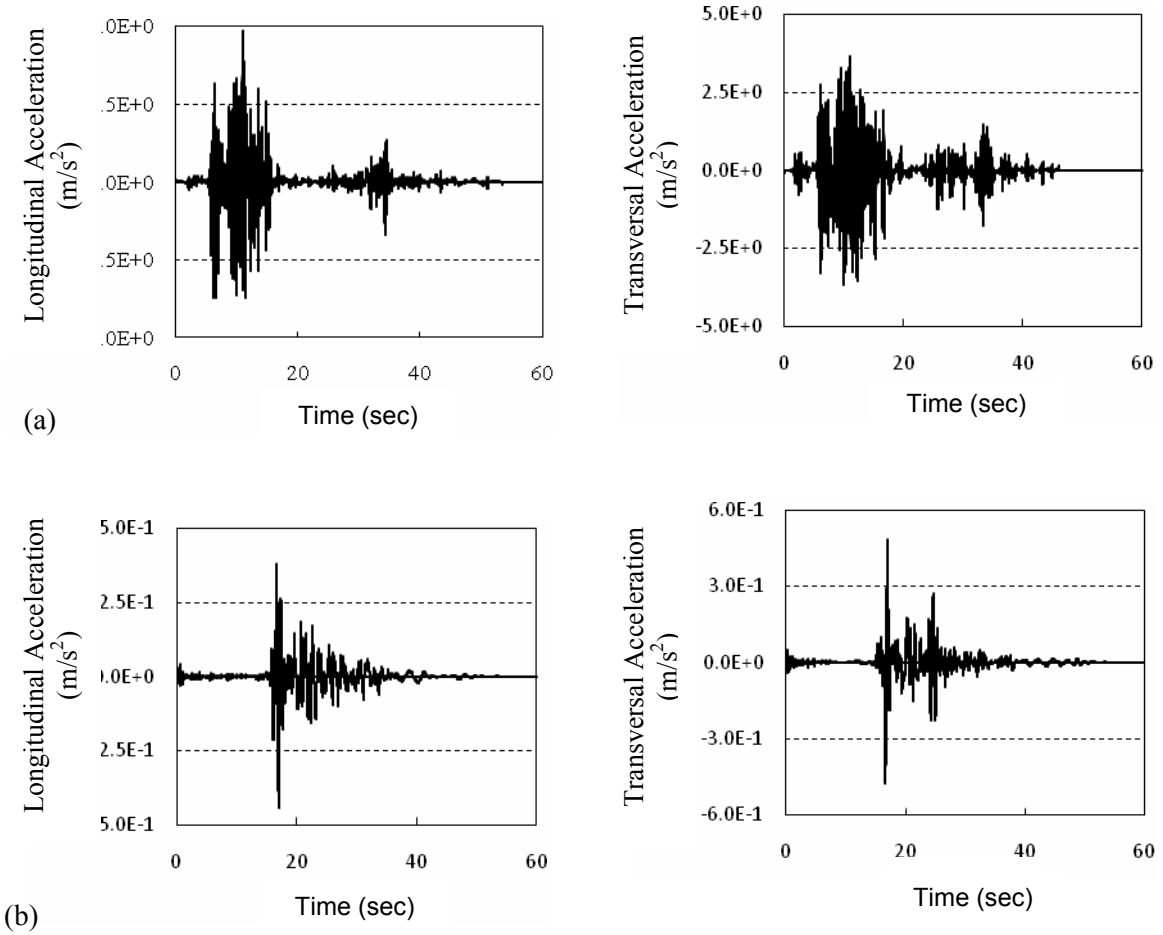


Figure 2: Strong ground motion arbitrarily selected in consistence with the anti-seismic code [11]: (a) record 1 (b) record 2.

Top displacement and base shears are considered as the responses under interest and the average acceleration method of Newmark [1, 14, 34] is set as the integration method. For implementation of the recent technique, the value of T is obtained from the issue 6-3-13 in [11], based on which, and Eq. (2), the parameter of the technique, n, is selected satisfying

$$n_{\ f}\Delta t \le \Delta t \qquad n \in Z^{+} - \{1\} \tag{3}$$

Besides, for the sake of completeness and, in view of Figure 3, the case

$$n = 2 \tag{4}$$

is also numerically studied (see Figure (3).

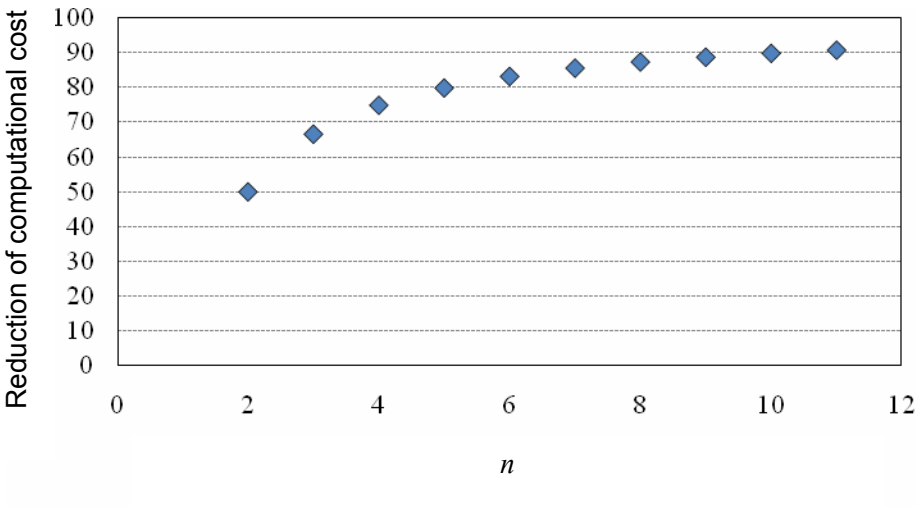


Figure 5: Reduction of computational cost for different values of n.

3 Numerical results

In this section, the results obtained for the ten-story building with dual system (structural system (c) introduced in the previous section) and five five-meter bays in each horizontal direction is pictorially reported, first; see Figures 4 and 5. Then, the detailed results of the thirty buildings are stated in Table 3-6. In view of the fact that the reduction of computational cost corresponding to each row of Tables 3-6 is at least 50% (see Figure 3), and that Tables 3-6 report deviations from conventionally obtained responses, not the corresponding errors, and finally, that the numerical values, in these tables, specifically those in correspondence to $n = 2$, are practically considerably small, the reported observation reveals the good performance of the recent cost reduction technique regarding residential buildings.

4 Discussion

The reported approximations of the results indeed imply a combination of the adequate performance of the recent technique and the good approximation obtained for T from the anti-seismic code [11] (the latter can explain the few larger deviations in Tables 3-6). Regarding the latter, exceptional are the results corresponding to $n = 2$ (see the last columns in Tables 3-6), where, n is not computed based on Eqs. (2) and (3). The results obtained in the case $n = 2$ address 50% reduction of computational cost, with trivial loss of accuracy, as a clear evidence for the adequate practical performance of the recent technique regarding different cases of low to mid-rise buildings structures with different systems and planar geometries. The performance can be explained, in view of [1, 13, 35], according to which

$$_f\Delta t < 0.02 \text{ sec} \tag{5}$$

for many earthquake and the fact that considering the existing engineering experiences, for the responses of mid-rise buildings, the least dominant period, T, satisfies

$$_f\Delta t < 0.02 \text{ sec} \tag{6}$$

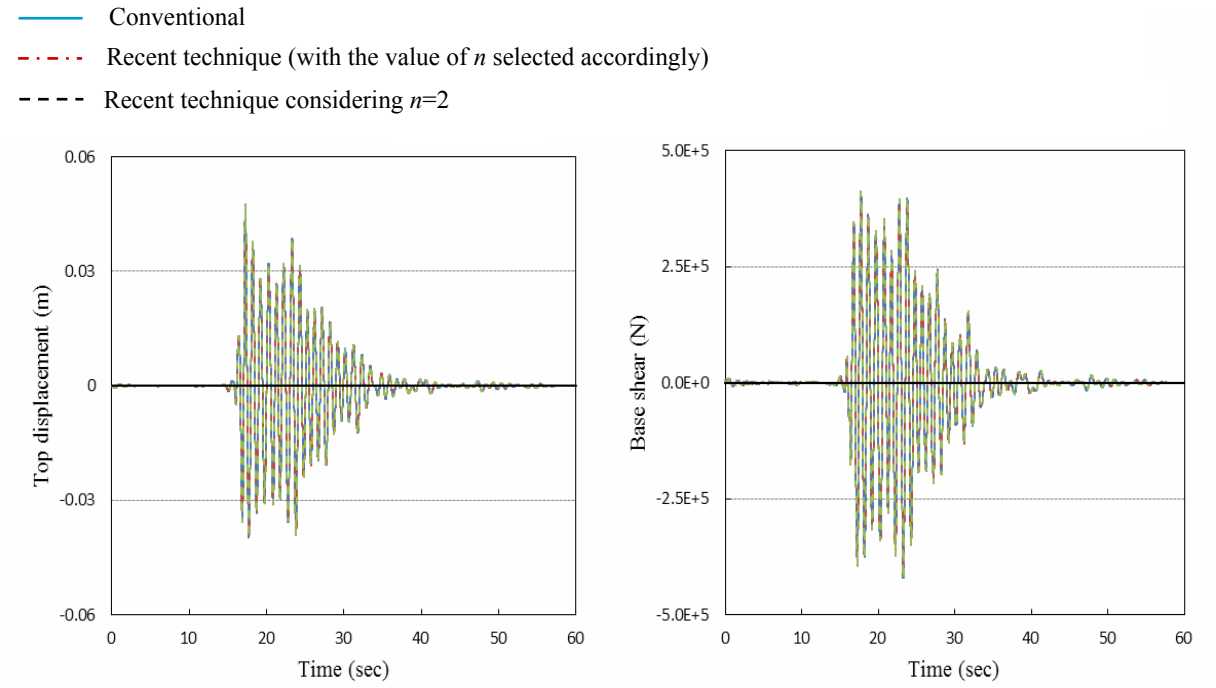


Figure 4: Response history for the ten-story building with dual structural system and five five-meter bays in each horizontal direction when the excitation is as noted in Figure 2(a): (a) top displacement, (b) base shear.

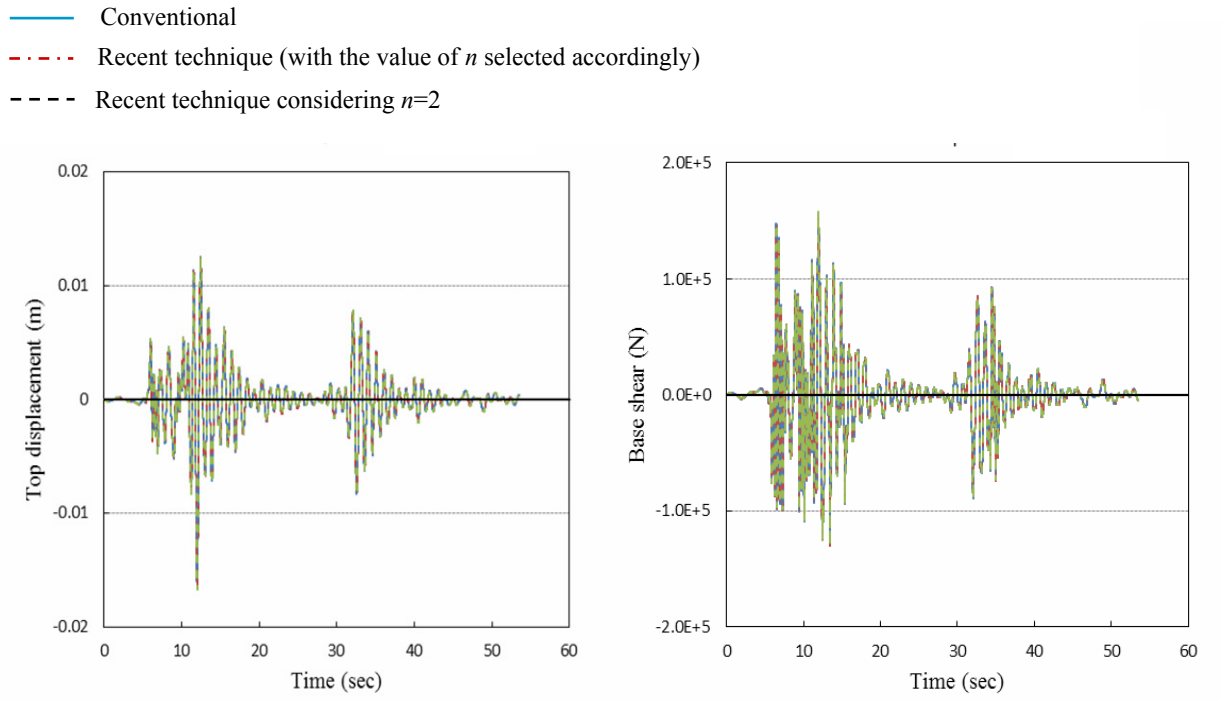


Figure 5: Response history for the ten-story building with dual structural system and five five-meter bays in each horizontal direction when the excitation is as noted in Figure 2(b): (a) top displacement, (b) base shear.

Buildings structural system and geometry in plan	Recent technique with n set according	Recent technique with n=2
Five floors, four four-meters bays, and structural system (a)	26.53	0.181
Ten floors, four four-meters bays, and structural system (a)	17.81	0.132
Fifteen floors, four four-meters bays, and structural system (a)	10.29	0.062
Five floors, four four-meters bays, and structural system (b)	0.569	0.324
Ten floors, four four-meters bays, and structural system (b)	0.622	0.114
Fifteen floors, four four-meters bays, and structural system (b)	2.480	0.111
Five floors, four four-meters bays, and structural system (c)	0.620	0.310
Ten floors, four four-meters bays, and structural system (c)	0.358	0.119
Fifteen floors, four four-meters bays, and structural system (c)	2.660	0.153
Twenty floors, four four-meters bays, and structural system (c)	3.470	0.070
Five floors, five five-meters bays, and structural system (a)	25.93	0.177
Ten floors, five five-meters bays, and structural system (a)	16.75	0.124
Fifteen floors, five five-meters bays, and structural system (a)	9.950	0.062
Five floors, five five-meters bays, and structural system (b)	0.650	0.390
Ten floors, five five-meters bays, and structural system (b)	0.645	0.176
Fifteen floors, five five-meters bays, and structural system (b)	2.750	0.119
Five floors, five five-meters bays, and structural system (c)	0.610	0.305
Ten floors, five five-meters bays, and structural system (c)	0.360	0.120
Fifteen floors, five five-meters bays, and structural system (c)	2.580	0.109
Twenty floors, five five-meters bays, and structural system (c)	4.680	0.090
Five floors, six six-meters bays, and structural system (a)	28.84	0.199
Ten floors, six six-meters bays, and structural system (a)	13.30	0.103
Fifteen floors, six six-meters bays, and structural system (a)	10.62	0.061
Five floors, six six-meters bays, and structural system (b)	0.636	0.380
Ten floors, six six-meters bays, and structural system (b)	0.340	0.154
Fifteen floors, six six-meters bays, and structural system (b)	2.540	0.096
Five floors, six six-meters bays, and structural system (c)	0.608	0.304
Ten floors, six six-meters bays, and structural system (c)	0.351	0.117
Fifteen floors, six six-meters bays, and structural system (c)	0.660	0.120
Twenty floors, six six-meters bays, and structural system (c)	4.680	0.096

Table 3: Deviation from the conventionally computed top displacements in terms of the $\mathbf{L}_\infty$ norm (%), when the excitation is as noted in Figure 2(a).

from which

$$\frac{T}{10_f \Delta t} \cong 2 = n \tag{7}$$

can be obtained in agreement with Eq. (4).

5 Conclusion

The performance of a recent technique for more efficient seismic analyses [18] is studied when implemented in time integration analysis of thirty six residential buildings designed according to seismic codes [11, 33], and the observations are theoretically explained. In conclusion, the parameter of the technique, n, can be set, with attention to the least dominant period approximately obtained from the anti-seismic code [11], leading to appropriate results regardless of the structures. Nevertheless, it is more practical, to upper bound the cost reduction to 50%, and with no *a priori* knowledge about the excitation or structural system, arrive at responses, in trivial deviation from the conventionally computed responses.

Buildings structural system and geometry in plan	Recent technique with n set accordingly	Recent technique with n=2
Five floors, four four-meters bays, and structural system (a)	25.45	0.738
Ten floors, four four-meters bays, and structural system (a)	19.09	0.410
Fifteen floors, four four-meters bays, and structural system (a)	9.400	0.430
Five floors, four four-meters bays, and structural system (b)	1.610	0.939
Ten floors, four four-meters bays, and structural system (b)	1.120	1.610
Fifteen floors, four four-meters bays, and structural system (b)	6.590	1.250
Five floors, four four-meters bays, and structural system (c)	1.820	0.979
Ten floors, four four-meters bays, and structural system (c)	2.070	1.200
Fifteen floors, four four-meters bays, and structural system (c)	7.600	1.260
Twenty floors, four four-meters bays, and structural system (c)	4.760	0.574
Five floors, five five-meters bays, and structural system (a)	25.29	0.695
Ten floors, five five-meters bays, and structural system (a)	21.72	0.938
Fifteen floors, five five-meters bays, and structural system (a)	9.280	0.466
Five floors, five five-meters bays, and structural system (b)	1.390	0.783
Ten floors, five five-meters bays, and structural system (b)	2.360	1.330
Fifteen floors, five five-meters bays, and structural system (b)	2.960	1.110
Five floors, five five-meters bays, and structural system (c)	1.540	0.831
Ten floors, five five-meters bays, and structural system (c)	1.980	1.160
Fifteen floors, five five-meters bays, and structural system (c)	8.290	1.500
Twenty floors, five five-meters bays, and structural system (c)	5.370	0.640
Five floors, six six-meters bays, and structural system (a)	28.55	0.988
Ten floors, six six-meters bays, and structural system (a)	13.35	0.621
Fifteen floors, six six-meters bays, and structural system (a)	9.100	0.618
Five floors, six six-meters bays, and structural system (b)	1.750	0.925
Ten floors, six six-meters bays, and structural system (b)	1.890	0.696
Fifteen floors, six six-meters bays, and structural system (b)	6.050	0.970
Five floors, six six-meters bays, and structural system (c)	1.640	0.914
Ten floors, six six-meters bays, and structural system (c)	1.440	0.875
Fifteen floors, six six-meters bays, and structural system (c)	3.280	1.410
Twenty floors, six six-meters bays, and structural system (c)	5.370	0.640

Table 4: Deviation from the conventionally computed base shears in terms of the $\mathbf{L}_\infty$ norm (%), when the excitation is as noted in Figure 2(a).

Reference

[1] A.K. Chopra, *Dynamics of structures: Theory and application to earthquake engineering*. Prentice-Hall, 1995.

[2] J. Chung, G.M. Hulbert, A time integration algorithm for structural dynamics with improved numerical dissipation: The Generalized-α method. *Journal of Applied Mechanics, ASME*, **60**, 371-375, 1993.

[3] J. Henrych, *Finite models and methods of dynamics in structures*. Elsevier, 1990.

[4] J. Argyris, J.P. Mlejnek, *Dynamics of structures*. Elsevier, 1991.

[5] T. Belytschko, W.K. Liu, B. Moran, *Non-linear finite elements for continua and structures*. John Wiley & Sons, 2000.

[6] A. Soroushian, New methods to maintain responses convergence and control responses errors in the analysis of nonlinear dynamic models of structural systems. *Ph.D. Thesis*, University of Tehran, 2003. (in Persian)

[7] P. Wriggers, *Computational contact mechanics*. John Wiley & Sons, 2002.

Buildings structural system and geometry in plan	Recent technique with n set accordingly	Recent technique with n=2
Five floors, four four-meters bays, and structural system (a)	1.040	0.089
Ten floors, four four-meters bays, and structural system (a)	0.396	0.054
Fifteen floors, four four-meters bays, and structural system (a)	0.515	0.064
Five floors, four four-meters bays, and structural system (b)	0.264	0.132
Ten floors, four four-meters bays, and structural system (b)	0.134	0.095
Fifteen floors, four four-meters bays, and structural system (b)	0.282	0.062
Five floors, four four-meters bays, and structural system (c)	0.303	0.182
Ten floors, four four-meters bays, and structural system (c)	0.144	0.082
Fifteen floors, four four-meters bays, and structural system (c)	0.249	0.049
Twenty floors, four four-meters bays, and structural system (c)	0.360	0.060
Five floors, five five-meters bays, and structural system (a)	1.010	0.089
Ten floors, five five-meters bays, and structural system (a)	0.613	0.042
Fifteen floors, five five-meters bays, and structural system (a)	0.541	0.051
Five floors, five five-meters bays, and structural system (b)	0.240	0.089
Ten floors, five five-meters bays, and structural system (b)	0.135	0.960
Fifteen floors, five five-meters bays, and structural system (b)	0.250	0.044
Five floors, five five-meters bays, and structural system (c)	0.240	0.180
Ten floors, five five-meters bays, and structural system (c)	0.147	0.084
Fifteen floors, five five-meters bays, and structural system (c)	0.281	0.052
Twenty floors, five five-meters bays, and structural system (c)	0.305	0.043
Five floors, six six-meters bays, and structural system (a)	0.971	0.083
Ten floors, six six-meters bays, and structural system (a)	0.501	0.055
Fifteen floors, six six-meters bays, and structural system (a)	0.548	0.069
Five floors, six six-meters bays, and structural system (b)	0.291	0.174
Ten floors, six six-meters bays, and structural system (b)	0.137	0.106
Fifteen floors, six six-meters bays, and structural system (b)	0.351	0.055
Five floors, six six-meters bays, and structural system (c)	0.265	0.199
Ten floors, six six-meters bays, and structural system (c)	0.168	0.105
Fifteen floors, six six-meters bays, and structural system (c)	0.283	0.070
Twenty floors, six six-meters bays, and structural system (c)	0.300	0.043

Table 5: Deviation from the conventionally computed top displacements in terms of the $\mathbf{L}_\infty$ norm (%), when the excitation is as noted in Figure 2(b).

[8] T.J.R. Hughes, K.S. Pister, R.L. Taylor, Implicit–explicit finite elements in nonlinear transient analysis. *Computer Methods in Applied Mechanics and Engineering*, **17/18**, 159–182, 1979.
[9] International Code Council (ICC), *IBC - International building code*. 2003.
[10] F. Naeim, S. Zhongzhi. *The seismic design handbook*. 2001.
[11] Building and Housing Research Center (BHRC). *Iranian code of practice for seismic resistant design, Standard No. 2800 – 05*. 2007.
[12] C.W. Gear, *Numerical initial value problems in ordinary differential equations*. Prentice-Hall, 1971.
[13] T. Belytschko, T.J.R. Hughes, *Computational methods for transient analysis*. Elsevier, 1983.
[14] R.W. Clough, J. Penzien, *Dynamics of structures*. McGraw-Hill, 1993.
[15] K.J. Bathe, *Finite element procedures*. Prentice-Hall, 1996.

Buildings structural system and geometry in plan	Recent technique with n set accordingly	Recent technique with n=2
Five floors, four four-meters bays, and structural system (a)	1.060	0.096
Ten floors, four four-meters bays, and structural system (a)	1.070	0.079
Fifteen floors, four four-meters bays, and structural system (a)	2.550	0.120
Five floors, four four-meters bays, and structural system (b)	0.329	0.176
Ten floors, four four-meters bays, and structural system (b)	0.199	0.109
Fifteen floors, four four-meters bays, and structural system (b)	0.855	0.154
Five floors, four four-meters bays, and structural system (c)	0.328	0.199
Ten floors, four four-meters bays, and structural system (c)	0.197	0.120
Fifteen floors, four four-meters bays, and structural system (c)	0.600	0.112
Twenty floors, four four-meters bays, and structural system (c)	0.920	0.110
Five floors, five five-meters bays, and structural system (a)	1.040	0.095
Ten floors, five five-meters bays, and structural system (a)	0.999	0.100
Fifteen floors, five five-meters bays, and structural system (a)	2.580	0.132
Five floors, five five-meters bays, and structural system (b)	0.320	0.176
Ten floors, five five-meters bays, and structural system (b)	0.170	0.107
Fifteen floors, five five-meters bays, and structural system (b)	0.736	0.127
Five floors, five five-meters bays, and structural system (c)	0.322	0.193
Ten floors, five five-meters bays, and structural system (c)	0.192	0.119
Fifteen floors, five five-meters bays, and structural system (c)	0.760	0.123
Twenty floors, five five-meters bays, and structural system (c)	0.900	0.110
Five floors, six six-meters bays, and structural system (a)	0.991	0.081
Ten floors, six six-meters bays, and structural system (a)	0.949	0.085
Fifteen floors, six six-meters bays, and structural system (a)	2.470	0.139
Five floors, six six-meters bays, and structural system (b)	0.324	0.186
Ten floors, six six-meters bays, and structural system (b)	0.171	0.092
Fifteen floors, six six-meters bays, and structural system (b)	0.564	0.107
Five floors, six six-meters bays, and structural system (c)	0.330	0.197
Ten floors, six six-meters bays, and structural system (c)	0.152	0.098
Fifteen floors, six six-meters bays, and structural system (c)	0.379	0.100
Twenty floors, six six-meters bays, and structural system (c)	0.900	0.110

Table 6: Deviation from the conventionally computed top base shears in terms of the $\mathbf{L}_\infty$ norm (%), when the excitation is as noted in Figure 2(b).

[16] J.F. McNammara, Solution schemes for problems of nonlinear structural dynamics. *Journal of Pressure Vessels, ASME,* **96**, 147–155, 1974.

[17] J.C. Strikwerda, *Finite difference schemes and partial differential equations*. Wadsworth & Books/Cole, 1989.

[18] P. Henrici, *Discrete variable methods in ordinary differential equations*. Prentice-Hall, 1962.

[19] A. Soroushian, A technique for time integration with steps larger than the excitation steps. *Communications in Numerical Methods in Engineering*, **24**, 2087-2111, 2008.

[20] A. Soroushian, On the performance of a conventional accuracy controlling method applied to linear and nonlinear structural dynamics. *Proceedings of the 17th International Congress on Sound & Vibration (ICSV 17*), Cairo, Egypt, July 18-22, 2010.

[21] A. Soroushian, A. Aziminejad, A more efficient seismic analysis of tall building by implementing a recently proposed technique. *Proceedings of the 6th International*

Conference of Seismology and Earthquake Engineering (SEE6), Tehran, Iran, May 16-18, 2011.

[22] A. Soroushian, A comparison between two methods for disregarding excitation steps in seismic analyses. *Proceedings of the 6th International Conference of Seismology and Earthquake Engineering (SEE6),* Tehran, Iran, May 16-18, 2011.

[23] A. Soroushian, M. Hosseini, A. Vasseghi, On the performance of a technique for more efficient time integration when applied to bridge structures seismic analysis. *Proceeding of the, 3rd ECCOMAS Thematic Conference on Computational Methods in Structural Dynamics and Earthquake Engineering (COMPDYN 2011)*, Corfu, Greece, May 23-28, 2011.

[24] O. Bahar, S. Ramezani, Faster time integration analysis for building structure subjected to 3-component earthquakes. *Proceeding of the, 3rd ECCOMAS Thematic Conference on Computational Methods in Structural Dynamics and Earthquake Engineering (COMPDYN 2011)*, Corfu, Greece, May 23-28, 2011.

[25] F. Nateghi, M. Yakhchalian, Less computational costs for analysis of soils seismic behavior by time integration. *Proceeding of the, 3rd ECCOMAS Thematic Conference on Computational Methods in Structural Dynamics and Earthquake Engineering (COMPDYN 2011)*, Corfu, Greece, May 23-28, 2011.

[26] A. Soroushian, On the performance of a recent technique for more efficient time integration in severe seismic conditions. *Proceedings of the International Conference on Advances in Structural Engineering and Mechanics (ASEM 11)*, Seoul, South Korea, September 18-22, 2011.

[27] A. Soroushian, A. Saaed, M. Arghavani, M. Rajabi, M.M. Sharifpour, Less computational costs in the analysis of seismic behaviors by time integration. *Proceedings of the 10th Biennial Conference on Vibration Problems (ICOVP).* Prague, Czech Republic, September 5-8, 2011.

[28] F. Nateghi, M. Yakhchalian, An investigation into effectiveness of a technique proposed for reducing computational cost of time integration analysis in the analysis of soil seismic behaviors. *Proceedings of the, 11th US National Congress on Computational Mechanics (11th USNCCM)*, Minneapolis, USA, July 25-28, 2011.

[29] A. Soroushian, On the accuracy of accelerations in general implementation of a recently proposed seismic analysis computational cost reduction technique. *Proceedings of the 5th International Conference from Scientific Computing to Computational Engineering (5th IC-SCCE)*, Athens, Greece, July 4-7, 2012.

[30] A. Soroushian, Direct time integration with step larger than the steps by which the excitations are digitized, Report 7510, Structural Engineering Research Center (SERC), IIEES, Tehran, Iran, 2012. (in Persian)

[31] A. Soroushian, A. Sabzei, A.Y. Reziakolai, On the performance of a recent computational cost reduction technique for mid-rise buildings. *In the proceedings of the 2nd National Congress on Civil Engineering*, Zahedan, Iran, May 7-8, 2013.

[32] A. Soroushian, Optimization of geometry and structural system of residential complexes. *Ms. Thesis*, Shiraz University, 1995. (in Persian)

[33] Iranian National Building Regulations (INBR), *Iranian National Building Code, Part 10-Steel Structures*. Iran, 1993.

[34] N.M. Newmark, A method of computation for structural dynamics. *Journal of Engineering Mechanics, ASCE* **85**, 67-94, 1959.

[35] J. Havskov, G. Alguacil, *Instrumentation in earthquake seismology (Modern approaches in geophysics)*. Springer, 2005.

COMPDYN 2013
4th ECCOMAS Thematic Conference on
Computational Methods in Structural Dynamics and Earthquake Engineering
M. Papadrakakis, V. Papadopoulos, V. Plevris (eds.)
Kos Island, Greece, 12–14 June 2013

CYCLIC BEHAVIOR MODELING OF RECTANGULAR RC BRIDGE PIERS USING OPENSEES

N. Attarchian[1], A. Kalantari[1], and A.S. Moghaddam[1]

[1] International Institute of Earthquake Engineering and Seismology
No. 21, Arghavan St., North Dibajee, Farmanieh 3913/19395
Tehran Islamic Republic of Iran
{n.attarchian, a.kalantari, moghadam}@iiees.ac.ir

Keywords: Cyclic Behavior, Concrete, Bridge Pier, Fiber Modeling, OpenSees.

Abstract. *Considering various constraints in experimental program tests such as, limitations in budget, time and lab facilities, applying numerical studies in performance evaluation of structures is inevitable. While, conducting numerical analysis without adequate proficiency in modeling and analysis in nonlinear behavior range, could be deceptive. Therefore, in this paper, finite element modeling of reinforced concrete bridge piers has been established in OpenSees and, the experimental results of a couple of cyclic tests has been reproduced and compared. Fiber Modeling methodology has been elaborated and applied in this research and, the paper focuses on numerical assumptions regarding to modeling, analysis and, convergence of numerical computations. In addition the sensitivity of the local and global results to the modeling and analysis assumptions has been discussed. The numerical results obtained in OpenSees have been compared with the experimental and numerical results of previous studies in SeismoStruct program. It can be concluded that via available measures and assumptions, fiber section method has a fair capability of simulating the cyclic behavior of high and medium height piers.*

.

1 INTRODUCTION

The ideal choice for studying the actual seismic behavior of structures is, to apply full scale shaking table tests. However, due to several limitations in the laboratories, experimental tests are generally scaled and simplified to quasi static or dynamic tests. Besides, considering the time constraints and financial costs, the number of the experimental tests which can be done, even in well equipped laboratories is limited. Therefore, numerically investigating the nonlinear behavior of structures via time integration methods is inevitable. Although, this approach can expedite the analysis and, various assumptions and models can be evaluated via numerical methods, the reliability of the obtained results is very significant. Consequently, it is very essential in every numerical study to verify an experimental study which has the most resemblances and similarities with the topic under assessment.

Regarding the essence of numerical analysis in performance evaluation of structures and, the importance of verifying the results obtained from nonlinear numerical analysis, this paper focuses on the various aspects of nonlinear behavior modeling and analysis of a group of reinforced concrete (RC) bridge piers. Considering the available information about the characteristics of the specimens, loading protocols and results, cyclic behavior of piers is modeled in OpenSees [1] and, the results are compared. The studies aim to provide a reliable numerical benchmark model in order to be utilized in seismic performance evaluation of this class of RC piers.

2 SPECIMEN CHARACTERISTICS AND LOADING

The hollow rectangular RC piers under investigation are a part of a four span continuous box girder deck bridge with single column bents. The bridge is representative of typical multi-span bridges and, has been designed according to EC8 [2] provisions. The RC sections were scaled to 1:2.5 and subjected to uniaxial cyclic loading at the Joint Research Center of Ispara [3, 4]. The configuration of the bridge, the cross-sections of the deck and the reinforcement layout of piers, have been shown in Figures 1 and 2 respectively. The height of the scaled piers is 8.4 and, 5.6 m and the deck-pier connection is hinged and the lateral forces are transformed via shear keys (no transmission of moments). The longitudinal steel ratio is equal to 1.15% and the longitudinal rebars consists of $\varphi 8$, $\varphi 12$ and, $\varphi 14$ and the stirrups were $\varphi 6$ (Fig.2). The cylinder compressive strength of concrete (f_{pc}) for tall and medium height piers were 42.9 and 31.5 MPa respectively and all reinforcing bars in the piers are S500 with characteristic yield strength of 500 Mpa. Based on specific weight of concrete (25 kN/m^3), the mass per length of the deck and the column are 2.784 and, 1.664 ton/m respectively. The axial load in the piers is equal to 1700 kN and is applied at the top of the piers by means of actuators [5].

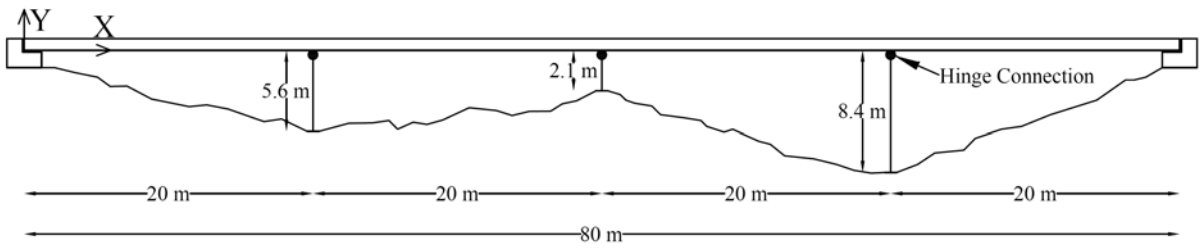


Figure 1: Bridge layout.

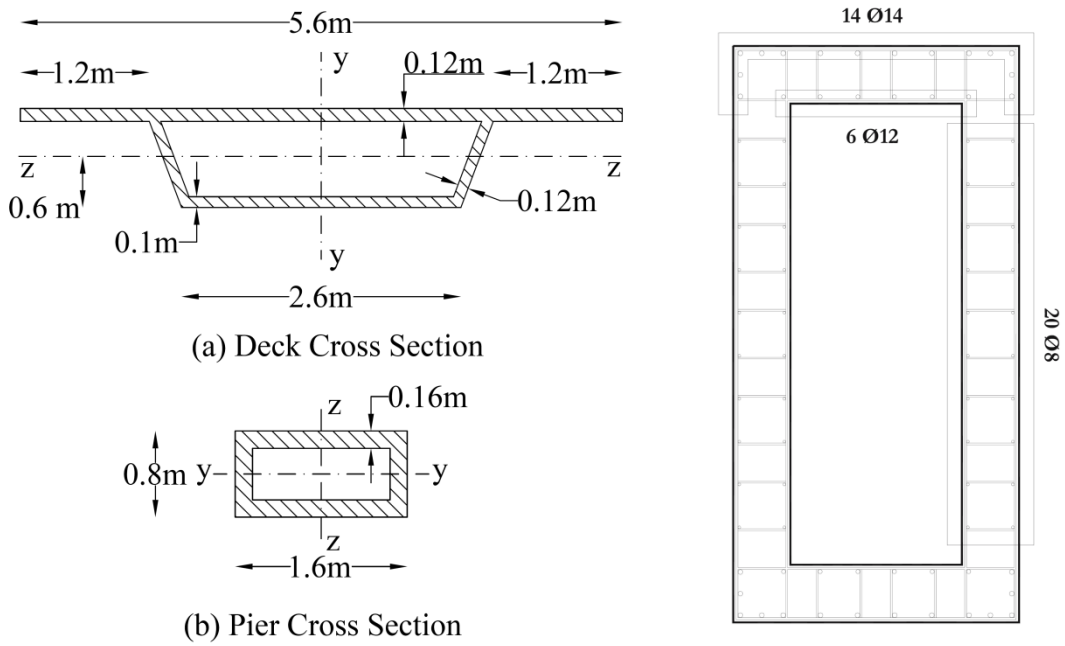


Figure 2: Pier and deck cross sections (left), Reinforcement layout of Pier Section (right).

During the cyclic test, the top of the piers is subjected to the cyclic displacement loading protocol shown in Figure 3. The tall and medium height piers were tested until failure up to 230 and 150 mm, respectively.

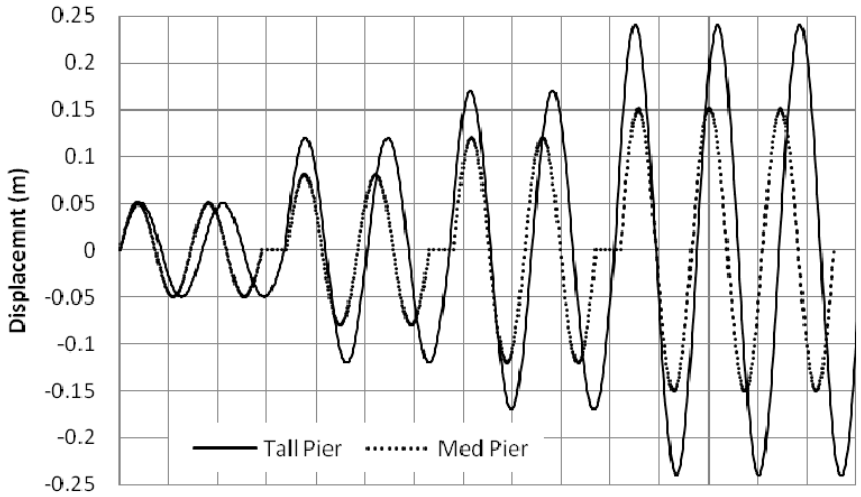


Figure 3: Cyclic test displacement histories.

3 MODELING ASPECTS

Open Source Earthquake Engineering Software (OpenSees) which, can be freely downloaded and used, enables to apply Fiber Modeling (FM) approach. Fiber modeling of frame elements is a widely practiced finite element modeling method and, can inherently account for both geometrical nonlinearities and material inelasticity, without a need for calibration of plastic hinges mechanisms typical in concentrated plasticity models [6].

In this research the piers are modeled using three dimensional beam-column elements. Since the connection of the piers to deck were hinged, piers are modeled like cantilever col-

umns, and the tributary masses are lumped at the nodes in X and Z global direction and 1e-7 mass in assigned in Y direction (Fig. 4). Rotational inertial masses are not included.

In the case of non-rigid connections, the relative rotation of the connection can contribute to the deck drift, proportional to its vertical location. Thus, for better stimulating the deck displacement, the tributary mass of the deck is located at the height of its center of gravity, 0.6 m above the pier top, and connected by a rigid element to the pier. The rigid element was modeled via elastic beam-column element and the stiffness was set 1000 times of the deck element.

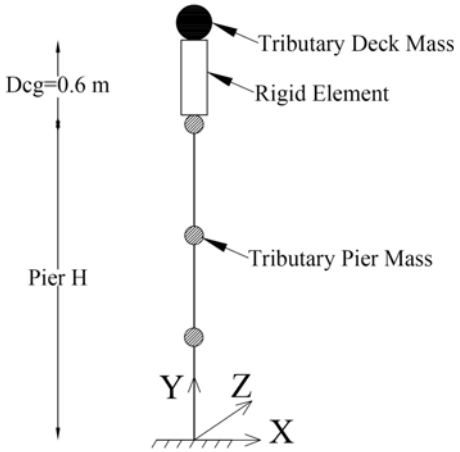


Figure 4: 3D pier modeling in OpenSees.

3.1 Material modeling

'Concrete02' uniaxial material command is used for defining confined and unconfined concrete. This model assumes linear tension softening (Fig. 5). The concrete compressive strength at 28 days is specified for the peak compression strength of unconfined concrete. Given $E_0 = 0.043W^{1.5}\sqrt{f_{pc}}$, the concrete strain at maximum strength (ε_{c0}) can be determined. The ultimate strain of unconfined concrete at crushing strength (ε_u) is specified according to Caltrans [7]. The confined concrete properties are calculated based on Mander's model [8] and the Lambda ratio between unloading slope at second step and initial slope is considered equal to 0.1 in all cases. Concrete material modeling properties for both specimens are presented in Table 1.

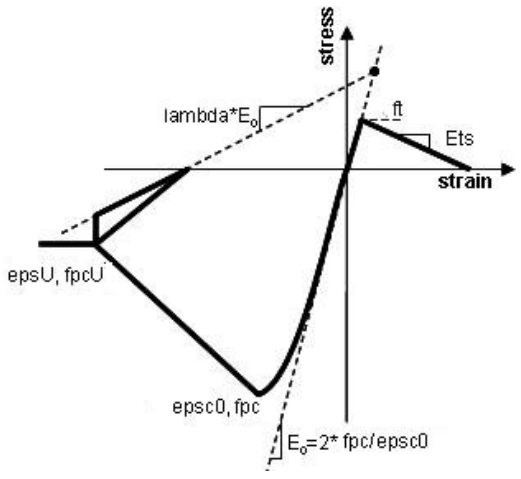


Figure 5: Concrete02 uniaxial material model [5] .

	f_{pc} (MPa)	ε_{c0}	f_{pcu} (MPa)	ε_u	f_t (MPa)	E_{ts} (GPa)
Unconfined Concrete (T)	42.9	0.003	8.6	0.005	3.1	1.05
Confined Concrete (T)	51.5	0.006	30.4	0.02	3.1	0.52
Unconfined Concrete (M)	31.5	0.0025	6.3	0.005	3.1	1.22
Confined Concrete (M)	37.8	0.005	24.2	0.03	3.1	0.6

Table 1: Concrete material modeling properties.

The applied material modeling command for steel material properties were ‘Steel02’ which is in compliance with Menegotto & Pinto constitutive law [9]. The model possesses bi-linear stress strain relationship to account for strain hardening effect (Table 2).

	F_y (MPa)	E_s (GPa)	β	R_0	C_{R1}	C_{R1}
Steel	496	203	0.0036	20	0.925	0.15

Table 2: Steel material modeling properties.

3.2 Elements modeling

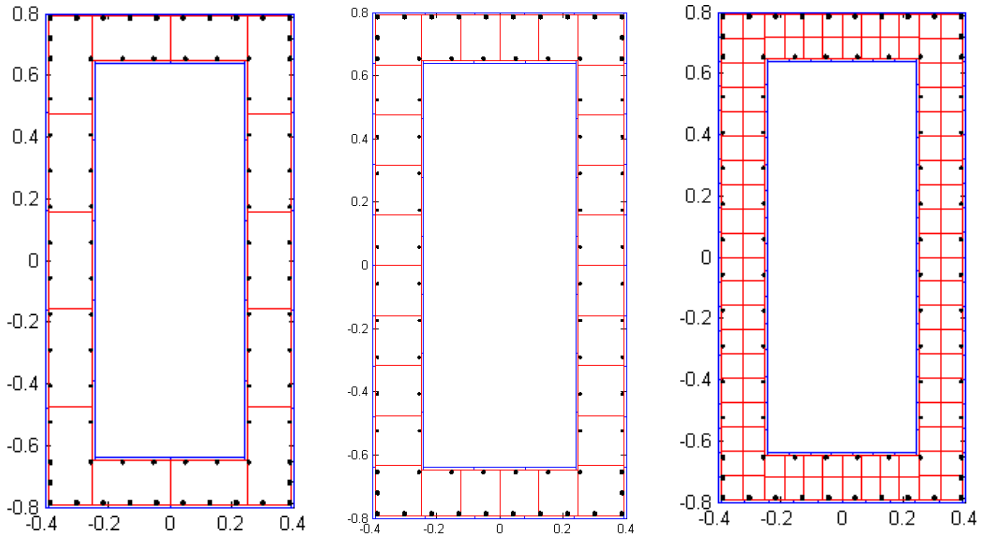
Nonlinear behavior of frame elements can be modeled via concentrated or distributed plasticity models. Although in distributed plasticity models, the interaction of moments and axial force is considered simultaneously and the plasticity is assumed to spread along the entire element length, the computation would not be very time consuming in comparison to lumped plastic hinge models, particularly in bridge systems with concentrated nonlinear behavior in piers. Considering the higher accuracy obtained via distributed plasticity models and, the simplicity of fiber modeling (omitting the need for estimating the plastic hinge length and the appropriate moment curvature relationship in lumped plastic hinges), distributed plasticity model is applied in this research.

OpenSees provides two types of distributed nonlinear beam column elements; ‘forceBeamColumn’ and ‘dispBeamColumn’. The former is based on force formulation (FBE) while the later (DBE) is based on displacement approach and follows standard finite element procedures. Since in DBE the response of the element is approximated by assuming constant axial deformation and linear curvature distribution along the element length, refine meshing of the element is needed to represent higher order distributions of deformations [10]. It should be noted that, for 3D modeling of elements in OpenSees the torsional behavior of the section should be aggregated to the fiber section element. In this regard torsion is modeled via uniaxial elastic material; the torsional rigidity of the section is considered equal to 0.2GJ according to Caltrans [7].

Since inelastic modeling can be computationally demanding, model efficiency is an important consideration. In FM approach the analysis time and the global and local responses are affected by the quantity of elements and number of integration points (NIP) along each element. Previous works [10, 11] indicate that, increasing the quantity of elements and NIPs can enhance the accuracy of global responses but may led to strain concentration and overestimation of local responses. Therefore, determining the appropriate mesh, NIPs and analysis time step which, converge to accurate responses is very significant. In this regard a parametric study is conducted to determine the efficient and accurate element type, element meshing and, NIP. According to the results, FBE provide fastest convergence with less number of elements than DBE. Each pier consists of two equal lengths, ‘forceBeamColumn’ element with 3 integration points. It is to be noted that, increasing the number of elements or NIPs would not led to more accurate results.

3.3 Section modeling

In distributed plasticity models, the cross section is segmented to fine enough fibers with proper material behavior model. In order to increase the efficiency of the model, the minimal number of fibers which could result to accurate responses, has to be specified. In this regard several options for segmenting the fiber section has been studied and the global and local responses are compared with experimental results (Fig. 6). The optimized number of fibers for the cross section is obtained in the second model with 78 fiber segments. The accuracy of the analysis would not be improved by defining more segments.



(a) 42 fiber segments (b) 78 fiber segments (c) 216 fiber segments

Figure 6: Fiber configurations under investigation.

4 ANALYSIS STAGE

Prior to cyclic analysis, gravity analysis should be done on the piers. Each type of analysis in OpenSees consists of a package of commands which will be briefly illustrated in this section. Both cyclic and gravity analysis are in the category of static analysis, and there is a great resemblance between the commands, though to expedite the computation and convergence of results, it is essential to provide compatibility, between the commands of both stages of analysis. The package of commands in each stage of analysis is summarized in Table 3. Details about the function of each of commands and other available options are elaborated further.

	Gravity analysis	Cyclic analysis
constraint	Plain	Penalty
numberer	Plain	Plain
system	BandGeneral	BandGeneral
test	EnergyIncr	EnergyIncr
algorithm	Linear	Newton
integrator	LoadControl	LoadControl
analysis	Static	Static

Table 3: Summary of analysis commands.

4.1 Constraint command

The major difference between the gravity and cyclic analysis is the constraint and algorithm commands. This command is used to construct the ConstraintHandler object. This object determines how the constraint equations are enforced in the analysis. In gravity analysis, 'Plain Constraint' provides homogeneous single point constraints can. In cyclic analysis, the displacement history at the top of the pier is defined via 'sp' command of 'pattern Plain' command and, in order to apply it in the analysis, Penalty constraint handler should be used [6].

4.2 Numberer command

In complex structures with several nonlinear elements, the numbering pattern of nodes and elements can strongly influence the bandwidth and, well planned numbering pattern can minimize the matrix bandwidth. Since in this research the model is very simple, in both stages of analysis 'Plain' numberer is applied in the analysis.

4.3 System command

There are more than six different commands in OpenSees to construct the linear system of equations and linear solver objects to store and solve the system of equations. Based on the bandwidth, population and symmetry of the system of equations, proper system command could be chosen. For efficient analysis, it is very essential to apply compatible system commands in all stages of analysis. In large and complex models, combining proper numberer command and system command could lead to more optimized solutions. Since, the structure under investigation in this research is not a large model, system 'BandGeneral' is applied in both gravity and cyclic analysis.

4.4 Convergence tests

In OpenSees the 'Test' command is used to construct a Convergence Test object over Equation (1). In all types of convergence tests in OpenSees, tolerance and maximum number of iterations have to be specified by the user. If the convergence is not achieved within the tolerance limit, more iteration will be performed. Several test types are available in OpenSees. The convergence equation for some of the options is presented in Table 4. Detailed information is available in OpenSees online manual [6]. The 'EnrgyIncr' test command, with a tolerance of 1.0e-10 and 10 maximum numbers of iterations is used in this study.

$$K\,\Delta U^{i} = R(U^{i}) \tag{1}$$

Test Command	Convergence Equation
NormUnbalance	$\left\|R(U^{i})\right\| < tol$
test NormDispIncr	$\left\|\Delta U^{i}\right\| < tol$
EnergyIncr	$\Delta U^{i} R(U^{i}) < tol$

Table 4: Convergence equations.

4.5 Solution algorithms

Algorithm command determines the sequence of steps taken to solve the equations. Gravity analysis can be done via 'Linear' algorithms, while for non-linear behavior range 'Newton' and 'ModifiedNewton' algorithms are available. The Newton-Raphson method converges rapidly to a solution, if the initial estimate is sufficiently close to the solution, but otherwise

fails to converge. In this method the tangent stiffness is updated at each iteration. In the modified Newton-Raphson method the tangent stiffness is updated only at selected steps, thus avoiding lengthy calculations needed in multi degree of-freedom systems. However, more iteration may be needed to reach a prescribed accuracy [12]. In the cyclic analysis, the nonlinear behavior of single cantilever piers under investigation has been studied via 'Newton' algorithm command. In more complicated cases, combination of both algorithms can be applied to construct the solution algorithm. So, 'ModifiedNewton' would be used as the main solution algorithm and while the convergence is not achieved after the specified maximum number of iteration, with specified tolerance; The 'Newton' algorithm would be specified as the solution algorithm.

4.6 Analysis increment and integration method

The Integrator object is used for determining the predictive step for time t+dt, specifying the tangent stiffness matrix and the residual force vector at any iteration and determining the corrective step based on the displacement increment dU. For performing static analysis, 4 types of integrators are available in OpenSees [12]. The 'LoadControl' command is used to construct a static integrator object for both stages of the analysis. The maximum load increment factor in cyclic analysis should be equal to the input steps which is equal to 0.005. The validity of the results can be verified by repeating the analysis with finer loading factor increments. Also in the cases which convergence cannot be easily obtained, finer loading increments can help to converge to the results. In this research in order to verify the results, the analysis is repeated for 0.0025 loading increment factor too. The average computational time for each of the cyclic analysis, using dual 2.00GHz processor is approximately 5 minutes.

5 ANALYSIS RESULTS

Cyclic analyses are carried out on the introduced piers under displacement loading subjected to the top of the piers. It should be noted that, beside this research, another numerical study has been done by Casarottie and Pinho [5] in SeismoStrut software [13]. For each of the piers, the base shear and displacement at the top of the piers have been derived and plotted.

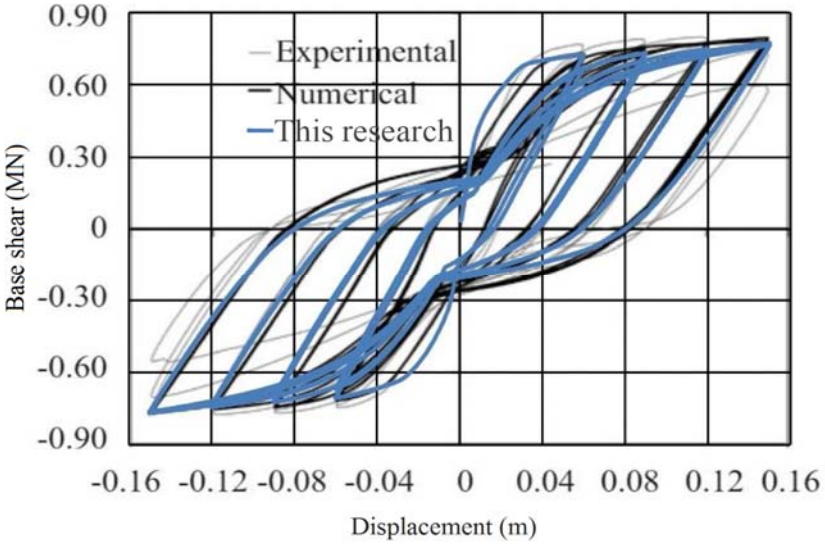


Figure 7: Cyclic experimental and numerical results for Medium Pier.

In Figures 7 and 8, the numerical results of the present study in OpenSees is compared with the previous experimental and numerical investigations, for medium and tall piers, respectively. It can be seen that, there is a very good match between the results of this study and the experimental results. Although, both numerical models cannot simulate the reduction in member strength at the very last cycle, when the failure occurs, due to the characteristic material behavior model of fibers which, would never die, the recent numerical model in OpenSees can satisfactory capture the pinching behavior in the specimens.

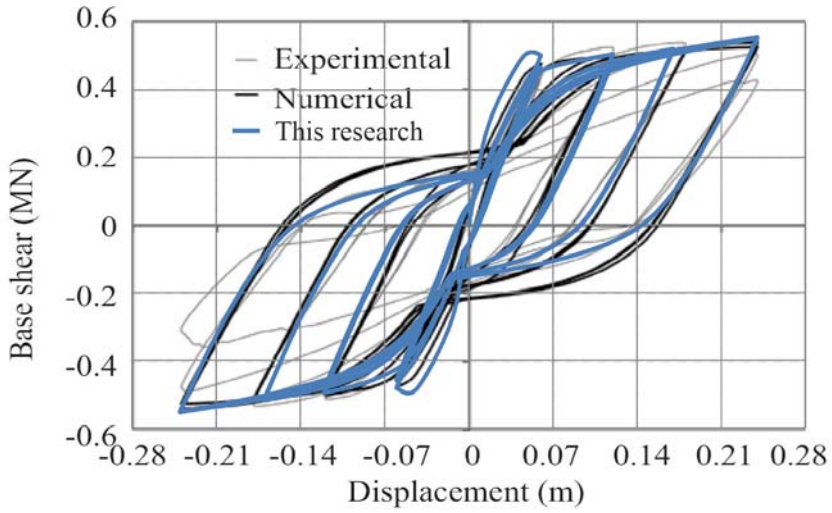


Figure 8: Cyclic experimental and numerical results for Tall Pier.

6 CONCLUSIONS

Considering the significance and necessity of numerical studies in the seismic assessment of the structures, the principals of nonlinear modeling and analysis of hollow rectangular RC bridge piers, has been elaborated in this paper and, two benchmark RC pier models have been established. The piers were modeled via nonlinear fiber section modeling approach and element properties, meshing and number of integration points of each element, also, the material behavior models and properties, have been demonstrated. Furthermore, the nonlinear analysis commands plus available and specified options have been illustrated. Results obtained in the present study indicated that the nonlinear behavior of the piers under investigation have been modeled adequately. It can be recognized that, although, due to the characteristic of material models, numerical simulations cannot capture the reduction in strength in the last cycles of test, the numerical results in the present study can finely can simulate the pinching phenomena in the hysteresis loops.

REFERENCES

[1] OpenSees Development Team, *Open System for Earthquake Engineering Simulations*, Version 2.3.0, [online]. From http://opensees.berkeley.edu, 2012.

[2] European Committee for Normalization, Eurocode 8: Design of Structures for Earthquake Resistance – Part2; Bridges, EN 1998-2: 2005.

[3] A.V. Pinto, G. Verzeletti, P. Pegon, G. Magonetto, P. Negro, J. Guedes, *Pseudo-Dynamic and shaking table tests on RC bridges* ECOEST-PrEC8, Report No.5, Brussels, 1996.

[4] G.M. Calvi, P.E Pinto, *Experimental and numerical investigations on the seismic response of bridges* ECOEST-PrEC8, Report No.4, Brussels, 1996

[5] Ch. Casarotti, R. Pinho, Seismic response of continuous span bridges through fiber-based finite element analysis *Earthquake Engineering and Engineering Vibration* **5**, 119-131, 2006.

[6] OpenSeesWiki, Online Wiki for OpenSees users and developers, Command Manual, from http://opensees.berkeley.edu/wiki/index.php/Main_Page, 2013.

[7] Caltrans Seismic Design Criteria, Version 1.6, November 2010.

[8] J.B. Mander, M.J.N. Priestle, R. Park, Theoretical Stress-strain Model for confined Concrete. *Journal of Structural Engineering, ASCE* **114**, 1804-1826, 1988.

[9] M. Menegotto, P.E. Pinto, Method of Analysis for Cyclically Loaded R.C. Plane Frames Including Changes in Geometry and Non-elastic Behavior of Elements Under Combined Normal Force and Bending. *Symposium on the Resistance and Ultimate Deformability of structures Acted on by Well Defined Repeated Loads*, International Association for Bridge and Structural Engineering, Zurich, Switzerland, September, 15-22, 1973.

[10] Discovering OpenSees, *Force-based Element vs. Displacement-based Element*, Web base semin, from:http://opensees.berkeley.edu/wiki/index.php/Discovering_OpenSees_--_Force-based_Element_vs._Displacement-based_Element, Dec 2011.

[11] M. P. Berry, M.O. Eberhard, *Performance modeling strategies for modern RC bridge columns*. PEER, Report No. 7, 2007.

[12] M. Sadrossadt Zade, M.S. Saiidi, *Pre-test analytical studies for NEESR-SG 4span bridge model using OpenSees*. CCEER, Report No. 7, 2007.

[13] SeismoStrut, SeismoSoft. *A computer program for static and dynamic nonlinear analysis of framed structures*, [online]. From http://www.seismosoft.com , 2005.

COMPDYN 2013
4th ECCOMAS Thematic Conference on
Computational Methods in Structural Dynamics and Earthquake Engineering
M. Papadrakakis, V. Papadopoulos, V. Plevris (eds.)
Kos Island, Greece, 12–14 June 2013

THEORETICAL STUDY ON THE REDUCTION AND RECOVERING METHOD

Mitsuharu Kurata[1], Buntara S. Gan[2] and Eiji Nouchi[3]

[1,2,3] Nihon University, College of Engineering
Department of Architecture

1-Nakagawara, Tokusada, Koriyama City, Fukushima, Japan 963-8642
[1]kurata@arch.ce.nihon-u.ac.jp
[2]buntara@arch.ce.nihon-u.ac.jp
[3]nouchi@arch.ce.nihon-u.ac.jp

Keywords: Dynamic Analysis, Main DOF, Secondary DOF, Reduction, Recovering

Abstract. *A method for reducing Secondary DOF (Degree of Freedom) from a dynamic equilibrium system into was intended to reduce considerably the storage capacity and computation time.*

The most popular Guyan [1] method which is based on superposition of lower modes from the modal analysis is widely adopted as a basis and for further improvements in dynamic reduction procedures. As a result of neglecting the higher modes, after the dynamic responses of structures evaluated by using only the lower modes frequencies, it is not possible to recover back precisely the responses of the other reduced Secondary DOF which are obviously more dominant in higher modes.

In the present works, a new method for reducing and recovering the Secondary DOF in the dynamic equilibrium system which is based on the concept of dynamic sub-structuring method is introduced herein. To improve the computational accuracy after the reduction process, a new so called Differential DOF Replacement method is also introduced.

1 INTRODUCTION

In Japan, the safety and performance of building from damages during the occurrences of earthquake have been given the highest of importance. Therefore, it is necessary to have an understanding of the dynamic response behavior of the buildings.

To achieve the accuracy for design analysis, a designer is often been given an alternative between using a simple design procedure as a design tool combined with seismic design codes and using more complex structural model with ground accelerations applied at the base of the structure. The later tool is often called as the time history analysis with nonlinearities to evaluate the dynamic responses of the building structures. Even though the present rapid development in computing technology and hardware, it seems like for design calculation and practical analysis purposes there is still a need in seeking for a simple and easy yet reliable design procedure.

Most of seismic design codes including charts, tables and graphs are developed based on an equivalent single DOF model for evaluating dynamic responses of building structures against the ground motion excitations. The response spectral of accelerations, velocities and displacements are still a valuable and practical tool for design practice due to its simplicity.

Although in the current state of the art in the dynamic vibration analysis techniques and computing progressions, computers are capable of solving systems with million hundred degrees of freedoms, they still are not adequate for treating directly the mathematical idealizations used in the analysis of complex structures. Moreover, it is seldom of interest to determine more than dozen vibration mode shapes even in the most complex structural system because the mode-superposition method generally is applied to structures in which the loading excites significantly only at the lowest modes. For these reasons, various eigensystem enhancements procedures have been proposed to predict the lower modes precisely for the reduction purposes. Therefore, simplification against the Secondary DOF is made forward-wise and not reversible. Once the responses of reduced structures evaluated by using modes lower frequency modes, it is not possible to get the responses of the reduced higher frequencies of the Secondary DOF precisely.

In present study, a new theory for reduction and recovering degree of freedoms which is based on the Rayleigh-Ritz method and expressed in a series form is formulated. Figure 1 shows a schematic of the proposed reduction and recovering method between the Secondary DOF and Main DOF systems. Present study is a continuation work of several research works [2-4] in an attempt for eliminating the role of modal analysis in the reduction and recovering methods for dynamic analysis problems.

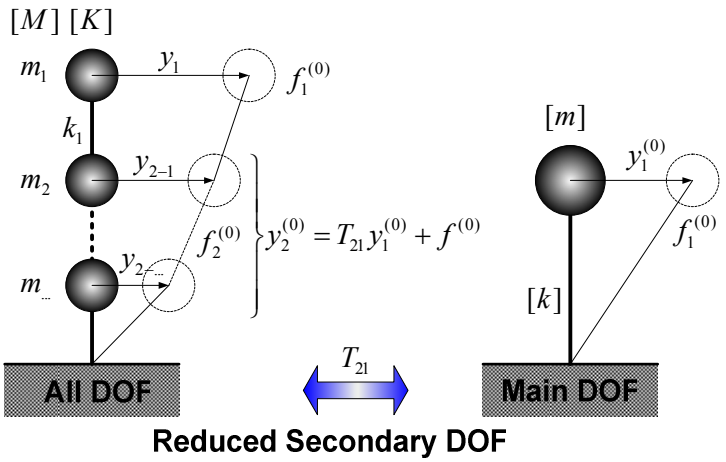


Figure 1: The schematic concept of reduction and recovering methods.

2 RAYLEIGH-RITZ METHOD

The differential equation of motion for an undamped Multi-DOF system can be written in the following

$$[M]\{y_i^{(2)}\}+[K]\{y_i^{(0)}\}-\{f_i^{(0)}\}=\{0\} \tag{1}$$

where, $[M]$, $[K]$, $\{f_i^{(0)}\}$, $\{y_i^{(0)}\}$ and $\{y_i^{(2)}\}$ are the mass matrix, stiffness matrix, external loading vector, displacement vector and acceleration vector, respectively. The time dependent displacement vector and acceleration vector are generally can be expressed in differential form as $y_i^{(n)}=\dfrac{d^n y_i}{dt^n}$; $n=1,2,...,N$ in which t is the time and n is the order of derivative with respect to time. The displacement $\{y_i^{(0)}\}$ and acceleration $\{y_i^{(2)}\}$ vector are then separated into two parts of vectors, a Main DOF vector $\{y_1^{(0)}\}$ and the remaining Secondary DOF vector $\{y_2^{(0)}\}$. The Secondary DOF vector and its characteristic properties, such as mass and stiffness matrices, are going to be reduced into the Main DOF vector and its characteristic properties.

Rewriting the Eq. (1), the following expressions are obtained as

$$\begin{aligned}\{y_i^{(0)}\}&=\begin{Bmatrix}y_1^{(0)}\\y_2^{(0)}\end{Bmatrix}=\begin{bmatrix}I_{11}\\T_{21}\end{bmatrix}\{y_1^{(0)}\}+\begin{Bmatrix}0\\f^{(0)}\end{Bmatrix}=[T]\{y_1^{(0)}\}+\{\overline{F}_i^{(0)}\}\\ \{y_i^{(2)}\}&=\begin{Bmatrix}y_1^{(2)}\\y_2^{(2)}\end{Bmatrix}=\begin{bmatrix}I_{11}\\T_{21}\end{bmatrix}\{y_1^{(2)}\}+\begin{Bmatrix}0\\f^{(2)}\end{Bmatrix}=[T]\{y_1^{(2)}\}+\{\overline{F}_i^{(2)}\}\end{aligned} \tag{2}$$

in which the following relationship can be obtained as

$$y_2^{(0)}=T_{21}y_1^{(0)}+f^{(0)} \tag{3}$$

where $[T]$, I_{11}, T_{21} being the transformation matrix, unit matrix and main to secondary transformation matrix, respectively. By applying the principle of virtual displacement to the Eq. (1) as given below

$$\delta\{y_i^{(0)}\}^T\left([M]\{y_i^{(2)}\}+[K]\{y_i^{(0)}\}-\{f_i^{(0)}\}\right)=0$$

The dynamic equation of motion in Eq. (1) can be rewritten by the following equation

$$[m]\{y_1^{(2)}\}+[k]\{y_1^{(0)}\}-\{f_1^{(0)}\}=\{0\} \tag{4}$$

where the mass matrix, stiffness matrix and external loading vector are given as

$$[m]=[T]^T[M][T]=\begin{bmatrix}I_{11} & T_{21}^T\end{bmatrix}\begin{bmatrix}m_{11} & m_{12}\\ m_{21} & m_{22}\end{bmatrix}\begin{bmatrix}I_{11}\\T_{21}\end{bmatrix}=m_{11}+T_{21}^T m_{21}+m_{12}T_{21}+T_{21}^T m_{22}T_{21}$$

$$[k]=[T]^T[K][T]=\begin{bmatrix}I_{11} & T_{21}^T\end{bmatrix}\begin{bmatrix}k_{11} & k_{12}\\ k_{21} & k_{22}\end{bmatrix}\begin{bmatrix}I_{11}\\T_{21}\end{bmatrix}=k_{11}+T_{21}^T k_{21}+k_{12}T_{21}+T_{21}^T k_{22}T_{21}$$

$$\begin{aligned}\{f_1\} &= [T]^T\left([M]\{\ddot{F}_i^{(2)}\}+[K]\{\ddot{F}_i^{(0)}\}-\{f_i^{(0)}\}\right)\\ &= \begin{bmatrix} I_{11} & T_{21}^T\end{bmatrix}\left(\begin{bmatrix} m_{11} & m_{12}\\ m_{21} & m_{22}\end{bmatrix}\begin{bmatrix} 0\\ f^{(2)}\end{bmatrix}+\begin{bmatrix} k_{11} & k_{12}\\ k_{21} & k_{22}\end{bmatrix}\begin{bmatrix} 0\\ f^{(0)}\end{bmatrix}-\begin{Bmatrix} f_1^{(0)}\\ f_2^{(0)}\end{Bmatrix}\right)\\ &= \left(m_{21}+T_{21}^T m_{22}\right)f^{(2)}+\left(k_{21}+T_{21}^T k_{22}\right)f^{(0)}-\left(f_1^{(0)}+T_{21}^T f_2^{(0)}\right)\end{aligned}$$

3 REDUCTION THEORY

By using matrix notation, the Main and Secondary DOF vectors and matrices of the undamped Multi-DOF dynamic equilibrium equation can be separated into the Main and Secondary DOF equations of rows as given in the following equations,

$$\begin{bmatrix} m_{11} & m_{12}\\ m_{21} & m_{22}\end{bmatrix}\begin{Bmatrix} y_1^{(2)}\\ y_2^{(2)}\end{Bmatrix}+\begin{bmatrix} k_{11} & k_{12}\\ k_{21} & k_{22}\end{bmatrix}\begin{Bmatrix} y_1^{(0)}\\ y_2^{(0)}\end{Bmatrix}-\begin{Bmatrix} f_1^{(0)}\\ f_2^{(0)}\end{Bmatrix}=\begin{Bmatrix} 0\\ 0\end{Bmatrix} \tag{5}$$

$$m_{12}y_2^{(2)}+k_{12}y_2^{(0)}=f_1^{(0)}-m_{11}y_1^{(2)}-k_{11}y_1^{(0)} \tag{5a}$$

$$m_{22}y_2^{(2)}+k_{22}y_2^{(0)}=f_2^{(0)}-m_{21}y_1^{(2)}-k_{21}y_1^{(0)} \tag{5b}$$

with the subscript notations are showing the index of vectors or matrices, and the superscript number in brackets are showing the number of derivative with respect to time.

3.1 Guyan's Reduction

The oldest theory in the dynamic reduction theory was firstly introduced by Guyan [1], where the Eq. (5b) was solved for the Secondary DOF vector $y_2^{(0)}$ as,

$$y_2^{(0)}=-k_{22}^{-1}\left(k_{21}y_1^{(0)}-f_2^{(0)}\right)-k_{22}^{-1}\left(m_{21}y_1^{(2)}+m_{22}y_2^{(2)}\right)$$

and by neglecting the second derivative terms, results in

$$y_2^{(0)}=T_{21}y_1^{(0)}+f^{(0)} \tag{6}$$

where, the transformation matrix which relates the Main DOF and Secondary DOF vectors is given by $T_{21}=-k_{22}^{-1}k_{21}$ and the loading vector is given by $f^{(0)}=k_{22}^{-1}f_2^{(0)}$.

It should be noted that the reduction method introduced by Guyan used this approximation transformation method to recover the Secondary DOF vectors from the Main DOF vectors which is solved by the Eq. (4). Because the reduction method proposed by Guyan is only make use of the Eq. (5b) to obtain the transformation matrix T_{21}, which contains only parts of the stiffness matrix of the dynamic equation, the computed displacement modes are approximated values.

3.2 0^{th}-Order Transformation Matrix

In order to include the influence of Eq. (5a) into the transformation process, the term $y_1^{(2)}$ in the Eq. (5a) is obtained as,

$$y_1^{(2)}=m_{11}^{-1}\left(f_1^{(0)}-k_{11}y_1^{(0)}-m_{12}y_2^{(2)}-k_{12}y_2^{(0)}\right) \tag{7}$$

and substitution into the Eq. (5b) to get the revised $y_2^{(0)}$ term for constructing the new transformation matrix T_{21} can be expressed as,

$$y_2^{(0)} = \bar{k}_{21}^{(0)} y_1^{(0)} + \bar{F}_2^{(0)} + \bar{m}_{22}^{(0)} y_2^{(2)} = \overset{0}{T}_{21}\, y_1^{(0)} + \overset{0}{f}^{(0)} + \overset{0}{m}_{22}\, y_2^{(2)} \tag{8}$$

where,

$\overset{0}{T}_{21} = \bar{k}_{21}^{(0)} = -k_{22}^{(0)-1} k_{21}^{(0)}$, $\overset{0}{f}^{(0)} = \bar{F}_2^{(0)} = k_{22}^{(0)-1} F_2^{(0)}$, $\overset{0}{m}_{22} = \bar{m}_{22}^{(0)} = -k_{22}^{(0)-1} m_{22}^{(0)}$,

$k_{22}^{(0)} = k_{22} - m_{21} m_{11}^{-1} k_{12}$, $k_{21}^{(0)} = k_{21} - m_{21} m_{11}^{-1} k_{11}$

$m_{22}^{(0)} = m_{22} - m_{21} m_{11}^{-1} m_{12}$, $F_2^{(0)} = f_2^{(0)} - m_{21} m_{11}^{-1} f_1^{(0)}$.

The number above the variables, $\overset{*}{(\,)}$, indicates a series of numbering to be summarized the end of the formulations.

By neglecting the second derivative with respect to time of the last third term in the Eq. (8), the equation becomes

$$y_2^{(0)} = \overset{0}{T}_{21}\, y_1^{(0)} + \overset{0}{f}^{(0)} . \tag{9}$$

Because the Eq. (5a) is used in solving the Secondary DOF vector $y_2^{(0)}$ term, the parts of mass matrix from the dynamic system of equation are considered, therefore it will give better approximation and higher accuracy compared to the Guyan's approach. By substituting the Eq. (8) into Eq. (5a), the vector $y_1^{(2)}$ can be obtained as,

$$y_1^{(2)} = \bar{k}_{11}^{(0)} y_1^{(0)} + \bar{F}_1^{(0)} + \bar{m}_{12}^{(0)} y_2^{(2)} \tag{10}$$

where,

$\bar{k}_{11}^{(0)} = -m_{11}^{-1}\left(k_{11} + k_{12}\bar{k}_{21}^{(0)}\right)$, $\bar{m}_{12}^{(0)} = -m_{11}^{-1}\left(m_{12} + k_{12}\bar{m}_{22}^{(0)}\right)$, $\bar{F}_1^{(0)} = m_{11}^{-1}\left(f_1^{(0)} - k_{12}\bar{F}_2^{(0)}\right)$.

3.3 1st-Order Transformation Matrix

In this study, a new concept is introduced by having the dynamic equation of motion in Eqs. (5a) and (5b) are further derived twice with respect to time which results in the following equations,

$$\begin{bmatrix} m_{11} & m_{12} \\ m_{21} & m_{22} \end{bmatrix} \begin{Bmatrix} y_1^{(4)} \\ y_2^{(4)} \end{Bmatrix} + \begin{bmatrix} k_{11} & k_{12} \\ k_{21} & k_{22} \end{bmatrix} \begin{Bmatrix} y_1^{(2)} \\ y_2^{(2)} \end{Bmatrix} - \begin{Bmatrix} f_1^{(2)} \\ f_2^{(2)} \end{Bmatrix} = \begin{Bmatrix} 0 \\ 0 \end{Bmatrix} \tag{11}$$

$$m_{12} y_2^{(4)} + k_{12} y_2^{(2)} = f_1^{(2)} - m_{11} y_1^{(4)} - k_{11} y_1^{(2)} \tag{11a}$$

$$m_{22} y_2^{(4)} + k_{22} y_2^{(2)} = f_2^{(2)} - m_{21} y_1^{(4)} - k_{21} y_1^{(2)} \tag{11b}$$

Under the assumption at $t = 0$, the initial conditions of the Main DOF vector $y_1^{(n)} = 0$, and the Secondary DOF vector $y_2^{(n)} = 0 \ldots (n = 0,1,2,3,4)$ are detained, the solutions for the homogeneous equations in Eq. (5) are exist and hence, all of its derivatives equations can be used to obtain the approximation of the transformation matrix.

By substitution of Eq. (10) into the Eq. (11), the term $y_1^{(4)}$ in the Eq. (11a) can be solved as follow

$$y_1^{(4)} = m_{11}^{-1}\left(-k_{11}\bar{k}_{11}^{(0)} y_1^{(0)} + \left(f_1^{(2)} - k_{11}\bar{F}_1^{(0)}\right) - \left(k_{12} + k_{11}\bar{m}_{12}^{(0)}\right) y_2^{(2)} - m_{12} y_2^{(4)}\right), \tag{12}$$

then, by further substituting the above equation into Eq. (11b), the $y_2^{(2)}$ term can obtained as

$$y_2^{(2)} = \bar{k}_{21}^{(2)} y_1^{(0)} + \bar{F}_2^{(2)} + \bar{m}_{22}^{(2)} y_2^{(4)} \tag{13}$$

where,

$\bar{k}_{21}^{(2)} = -k_{22}^{(2)-1} k_{21}^{(0)} \bar{k}_{11}^{(0)}$, $\bar{m}_{22}^{(2)} = -k_{22}^{(2)-1} m_{22}^{(0)}$, $\bar{F}_2^{(2)} = k_{22}^{(2)-1}\left(F_2^{(2)} - k_{21}^{(0)} \bar{F}_1^{(0)}\right)$.

Substitution of Eq. (13) into the Eq. (8) and rearranging the similar terms, result in

$$y_2^{(0)} = \overset{1}{T}_{21}\, y_1^{(0)} + \overset{1}{f}^{(0)} + m_{22}^1 y_2^{(4)} \tag{14}$$

where,

$\overset{1}{T}_{21} = \bar{k}_{21}^{(0)} + \bar{m}_{22}^{(0)} \bar{k}_{21}^{(2)}$, $\overset{1}{f}^{(0)} = \bar{F}_2^{(0)} + \bar{m}_{22}^{(0)} \bar{F}_2^{(2)}$, $\overset{1}{m}_{22} = \bar{m}_{22}^{(0)} \bar{m}_{22}^{(2)}$.

Neglecting the fourth derivative with respect to time of the last third term in the Eq. (14), results in the following equation,

$$y_2^{(0)} = \overset{1}{T}_{21}\, y_1^{(0)} + \overset{1}{f}^{(0)} . \tag{15}$$

Repeated herein, the number above the variables, $\overset{*}{(\,)}$, indicates a series for summation purpose.

3.4 M[th]-Order Transformation Matrix

By repeating the similar derivation procedures as given in previous sub-sections, for deriving the M[th]-Order transformation matrix can be obtained by further make a $(N-1)$ derivation with respect to time to the dynamic equation which results in,

$$\begin{bmatrix} m_{11} & m_{12} \\ m_{21} & m_{22} \end{bmatrix} \begin{Bmatrix} y_1^{(2n)} \\ y_2^{(2n)} \end{Bmatrix} + \begin{bmatrix} k_{11} & k_{12} \\ k_{21} & k_{22} \end{bmatrix} \begin{Bmatrix} y_1^{(2n-2)} \\ y_2^{(2n-2)} \end{Bmatrix} - \begin{Bmatrix} f_1^{(2n-2)} \\ f_2^{(2n-2)} \end{Bmatrix} = \begin{Bmatrix} 0 \\ 0 \end{Bmatrix} \tag{16}$$

$$m_{12} y_2^{(2n)} + k_{12} y_2^{(2n-2)} = f_1^{(2n-2)} - m_{11} y_1^{(2n)} - k_{11} y_1^{(2n-2)} \tag{16a}$$

$$m_{22} y_2^{(2n)} + k_{22} y_2^{(2n-2)} = f_2^{(2n-2)} - m_{21} y_1^{(2n)} - k_{21} y_1^{(2n-2)} . \tag{16b}$$

Under the same assumption at $t = 0$, the initial conditions of the Main DOF vector $y_1^{(2n-2)} = 0$, and Secondary DOF vector $y_2^{(2n-2)} = 0 \ldots (n = 0,1,2,3,...,N)$ are detained, the solutions for the homogeneous equations in Eq. (5) are exist and hence, all of its derivatives equations can be used to obtain the approximation of the transformation matrix.

If the procedure is repeated following the same procedure as given in the previous section, the $y_2^{(*)}$ terms can be obtained as follow,

$$\begin{aligned} y_2^{(0)} &= \bar{k}_{21}^{(0)} y_1^{(0)} + \bar{F}_2^{(0)} + \bar{m}_{22}^{(0)} y_2^{(2)} \\ y_2^{(2)} &= \bar{k}_{21}^{(2)} y_1^{(0)} + \bar{F}_2^{(2)} + \bar{m}_{22}^{(2)} y_2^{(4)} \\ &\cdots \\ y_2^{(2n)} &= \bar{k}_{21}^{(2n)} y_1^{(0)} + \bar{F}_2^{(2n)} + \bar{m}_{22}^{(2n)} y_2^{(2n+2)} \end{aligned}$$

And in a form of series, all the derivatives of $y_2^{(*)}$ terms can be expressed as

$$y_2^{(0)} = \overset{M}{T}_{21}\, y_1^{(0)} + \overset{M}{f}^{(0)} + \overset{M}{m}_{22}\, y_2^{(2M+2)} \tag{17}$$

with

$$\overset{M}{T}_{21} = \sum_{m=0}^{M} \Pi_{n=0}^{m} \overline{\overline{m}}_{22}^{(2n)} \overline{k}_{21}^{(2m)}$$

$$\overset{M}{f}^{(0)} = \sum_{m=0}^{M} \Pi_{n=0}^{m} \overline{\overline{m}}_{22}^{(2n)} \overline{F}_{2}^{(2m)} \quad .$$

$$\overset{M}{m}_{22} = \Pi_{n=0}^{M+1} \overline{\overline{m}}_{22}^{(2n)} \quad , \quad \overline{\overline{m}}_{22}^{(2n)} = \overline{m}_{22}^{2(n-1)} \quad , \quad \overline{\overline{m}}_{22}^{(0)} = \overline{m}_{22}^{(-2)} = I_{22}$$

4 RECOVERING OF THE SECONDARY DOF

It can be noted that from the Eq. (17), the tolerance of the present reduction theory is due to the negligence of the twice higher order derivatives terms which are considered very small.

$$\left| \overset{M}{T}_{21} y_1^{(0)} + \overset{M}{f}^{(0)} \right| \rangle\rangle \left| \overset{M}{m}_{22} y_2^{(2M+2)} \right|$$

Hence, the Main DOF and Secondary DOF vectors can be written by using the a series form as follow,

$$\begin{Bmatrix} y_1^{(0)} \\ y_2^{(0)} \end{Bmatrix} = \begin{Bmatrix} I_{11} \\ \overset{M}{T}_{21} \end{Bmatrix} y_1^{(0)} + \begin{Bmatrix} 0 \\ \overset{M}{f}^{(0)} \end{Bmatrix} \quad . \tag{18}$$

The second row of the above equation can be used to recover the reduced Secondary DOF vector from the Main DOF vector as a result from solving the reduced dynamic equation in Eq. (4).

5 DIFFERENTIAL DOF REPLACEMENT METHOD

In a complex dynamic system, there are many occasions where the difficulties to determine the Main DOF and Secondary DOF appeared, because different boundary of conditions and loadings will effect the behavior of solutions. If there is a case, still the above formulations can be applied by using relative differences between DOFs instead of each independent DOF. The relative differences between DOFs will make the Secondary DOF vector consists of small values. Components of the Secondary DOF vector $y_2^{(0)}$ are then replaced by $y_{ij}^{(0)}$, where the Secondary DOF components vector now consist of relative difference values to an arbitrarily selected component DOF $y_i^{(0)}$ from the Main DOF which is given as,

$$y_{ij}^{(0)} = y_i^{(0)} - y_j^{(0)} \quad . \tag{19}$$

Rewriting the above equation, each component $y_j^{(0)}$ in the Secondary DOF vector can be expressed by the following relative difference relationship,

$$y_j^{(0)} = y_i^{(0)} - y_{ij}^{(0)} \tag{20}$$

As a result, all the components vector of the Multi-DOF dynamic system consist of only either $y_i^{(0)}$ or $y_{ij}^{(0)}$ terms, where the values of $y_{ij}^{(0)}$ are very small compared to the components $y_i^{(0)}$ in the Main DOF vector.

By successively replacing each other components, the DOF vectors can be reconstructed as $\left\{ y_1^{(0)} \quad y_2^{(0)} \right\}^T$, even with the low order approximation of transformation matrix, high accuracy will be obtained.

6 CONCLUSIONS

- A theory for reduction and recovering methods of large degree-of-freedom in structural dynamic analysis is proposed. The theory is based on the Rayleigh-Ritz method, and then further developed to create a transformation matrix which is finally summarized in a series form; the series form of transformation matrix implies the inclusions of higher order modes inside the formulations. This newly developed theory is expected to give a new kind of reduction theory without using the modal analysis.
- By using the DOF vectors transformation matrix, calculation results from the Main DOF equations can be used to recover back the reduced Secondary DOF while retaining high accuracy results.
- The present proposed method is suitable and recommended for practical design method.

REFERENCES

[1] J. Guyan, Reduction of stiffness and mass matrices. *AIAA*, No.2, 380, 1965.

[2] K. Sugiyama, M. Kurata, B. S. Gan, E. Nouchi, Reduction and Recovering methods of Degree-of-freedom in structural dynamic analysis. *Proceedings of the Eleventh East Asia-Pacific Conference on Structural Engineering & Construction (EASEC-11) "Building a Sustainable Environment"*, Structural Dynamics, No.14, Taipei, Taiwan, November 19-21, 2008.

[3] K. Sugiyama, M. Kurata, B.S. Gan, E. Nouchi, Reduction and recovering method of frame structures into a single degree of freedom system. M. Papadrakakis, N.D. Lagaros, M. Fragiadakis eds. *Proceedings of the ECCOMAS Thematic Conference on Computational Methods in Structural Dynamics and Earthquake Engineering (COMPDYN2009)*, CD447, Rhodes, Greece, June 22-24, 2009.

[4] K. Sugiyama, M. Kurata, B.S. Gan, E. Nouchi, Strain Reduction and Recovering Method. *The Twelfth East Asia-Pacific Conference on Structural Engineering and Construction*, *Procedia Engineering,* 14, 1029–1036, 2011.

COMPDYN 2013
4th ECCOMAS Thematic Conference on
Computational Methods in Structural Dynamics and Earthquake Engineering
M. Papadrakakis, V. Papadopoulos, V. Plevris (eds.)
Kos Island, Greece, 12–14 June 2013

SIMPLIFICATION OF EARTHQUAKE ACCELEROGRAMS FOR RAPID TIME HISTORY ANALYSIS BASED ON THE IMPULSIVE LOAD CONCEPT

Mahmood Hosseini[1] and Iman Mirzaei[2]

[1] Associate Prof., Structural Eng. Research Center, Int'l Inst. of Earthquake Eng. and Seismology (IIEES), Tehran, Iran
Email: hosseini@iiees.ac.ir

[2] Graduate Student, Earthquake Eng. Dept., Science and Research Branch of the Islamic Azad University (IAU), Tehran, Iran
Email: Mirzaei.Iman@gmail.com

Keywords: Digitized accelerograms; Time history analysis; Time step size, Calculation time

Abstract. *Regarding that the time history analysis, as the most realistic seismic response analysis method, is very time consuming, in this paper a method is proposed for simplification of digitized accelerograms by using the concept of impulsive load. In the proposed method, the accelerogram, which is actually a numerical array with the time step size of 0.02, 0.01 or even 0.005 seconds, and usually contains several thousands of time steps with their corresponding acceleration values, is substituted by a limited number (usually less than just a few hundreds) of discrete values, each one equivalent to the area created by the acceleration curve and the time axis between two of its subsequent zero-crossings. These discrete values, which are obviously positive and negative one after the other, multiplied by the mass of the SDOF system, can be considered as a series of impulsive loads, applied consequently to the system, which is subjected to the base acceleration. Using the simple formula of response to impulsive load, response of the SDOF system to base acceleration can be calculated as the summation of its responses to the series of impulsive loads, created by the described method for any given accelerogram. Several numerical examples are presented in the paper to show the efficiency of the proposed simplification technique. Numerical results show that the amount of error of peak response calculation is usually less than 5% for most of earthquake records, while the required time for response calculations is generally only 10% of that of the conventional time history analysis, or even less than that.*

1 INTRODUCTION

Time History Analysis (THA) has been known as the best tool for realistic seismic response analysis of structural systems. However, this type of analysis is very time consuming, mainly due to the very small time step size, used in digitizing the earthquake accelerograms. This is while usually the natural periods of structures are much larger than the digitized accelerogram's time step size. Therefore, if by some way the THA can be done with large time step size, it would be very helpful for quick seismic response analysis any type of structural systems.

A way for achieving this goal is the simplification of accelerograms for seismic response analyses, which goes back to early to mid 70s. Wang (1975) has worked on structural instability during earthquakes and accelerogram simplification [1]. Some simplified dynamic analysis methods have been also presented by researchers in recent years, but each one of them has been focused on some specific type of structures. For example, Kitiyodom and his colleagues (2004) have proposed a simplified dynamic analysis method for piled raft foundation subjected to earthquake load [2], and Ghafari Oskoei and McClure (2009) have presented some simplified dynamic analysis methods for guyed telecommunication masts under seismic excitation [3]. Some simplified THA methods have been also proposed in previous researches based on various means, including the one performed by Domingues Costa and his colleague in 2005 by using theory of plasticity [4].

Recently, Soroushian (2008) has presented a technique for the time integration analysis with steps larger than the excitation steps [5], in which the time step size can be chosen as large as five times of the usual time step size without remarkable error in response calculations. Finally, Faroughi and Hosseini (2011) have proposed a method for quick time history analysis of linear systems by using the modified Inverse Fourier Transform of the accelerogram [6], which makes it possible to perform the analysis by consuming only around 20% of the usual time of the conventional seismic response analysis, with a very little error, mostly less than 5%.

In this paper a method is proposed for increasing the speed of response time history analyses by simplification of the earthquake acceleration digitized record based on using the concept of impulsive load, and the zero-crossing points of the record. By using this method, the required time for response time history analysis is reduced significantly (usually more than 10 times comparing to the conventional analyses), while the amount of error of the response calculations is less than 5% in most cases.

2 THE METHOD

In the proposed simplification method the continuous input accelerogram, which when digitized, is actually a numerical array with the time step size of 0.02, 0.01 or even 0.005 seconds, and usually contains several thousands of time steps with their corresponding acceleration values, is substituted by a limited number (usually less than just a few hundreds) of discrete values, each one equivalent to the area created by the acceleration curve and the time axis between two of its subsequent zero-crossings. These discrete values, which are obviously positive or negative one another, multiplied by the mass of the SDOF system, can be considered as a series of impulsive loads, applied consequently to the system, which is subjected to the base acceleration. Using the simple concept of the impulsive load, which is equivalent to a sudden change of the system's velocity, the response of the SDOF system with the mass of m, un-damped and damped frequencies of, respectively, ω_N and ω_D and damping ratio of ξ to base acceleration, at the instant t_{i+1} can be calculated as:

$$u(t_{i+1}) = e^{-\xi\omega_N \Delta t_{i+1}}\left[\frac{\dot{u}(t_i^+)+\xi\omega_N u(t_i)}{\omega_D}\sin\omega_D\Delta t_{i+1} + u(t_i)\cos\omega_D\Delta t_{i+1}\right] \quad (1)$$

where t_i stands for the instant of applying the i^{th} impulse, $\Delta t_{i+1} = t_{i+1} - t_i$ and $\dot{u}(t_i^+)$ is the suddenly increased velocity of the system at instant t_i just after applying the i^{th} impulse, Imp_i, and is given by:

$$\dot{u}(t_i^+) = \dot{u}(t_i) + Imp_i/m \quad (2)$$

In Equation (2) the velocity of the system at instant t_i just before applying the i^{th} impulse, $\dot{u}(t_i)$, is given by:

$$\dot{u}(t_i) = -\xi\omega_N\Delta t_i e^{-\xi\omega_N\Delta t_i}\left[\frac{\dot{u}(t_{i-1}^+)+\xi\omega_N u(t_{i-1})}{\omega_D}\sin\omega_D\Delta t_i + u(t_{i-1})\cos\omega_D\Delta t_i\right] + e^{-\xi\omega_N\Delta t_i}\{[\dot{u}(t_{i-1}^+) + \xi\omega_N u(t_{i-1})]\cos\omega_D\Delta t_i - \omega_D\sin\omega_D\Delta t_i\} \quad (3)$$

where $\Delta t_i = t_i - t_{i-1}$ (t_0 is assumed to be zero). In Equation (2) the value of the i^{th} impulse, Imp_i, is defined by:

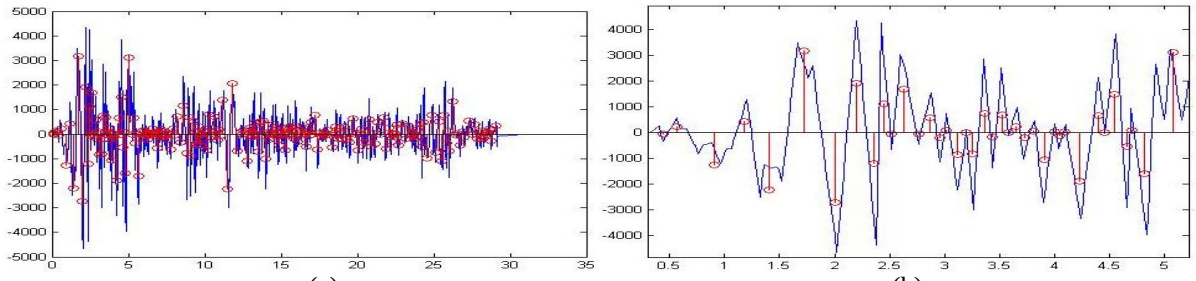
$$Imp_i = -m\int_{t_{zc,i-1}}^{t_{zc,i}} \ddot{u}_g(t).dt \quad (4)$$

In Equation (4) $\ddot{u}_g(t)$ is the earthquake ground acceleration, and $t_{zc,i}$ is the i^{th} zero-crossing of the $\ddot{u}_g(t)$ function. For the first instant (i=1) the condition is expressed as $\dot{u}(t_1) = 0$ and $\dot{u}(t_1^+) = Imp_1/m$. Obviously, at start it is assumed that $\dot{u}(t_0^+) = 0$ and $u(t_0) = 0$. To show the efficiency of the aforementioned formulation for the seismic response time history analysis of structural systems, several numerical examples are presented in the next section of the paper with regard to SDOF systems.

3 NUMERICAL EXAMPLES

To show the efficiency of the proposed method in rapid seismic response calculations the response histories of a set of SDOF systems, which cover a wide range of periods form 0.3 sec to 1.0 sec, have been calculated for a group of accelerograms with various frequency content from low to high, belonging to some well-known earthquakes, including El Centro, Cape Mendocino, Imperial Valley, Humbolt Bay Central California, and Kocaeli. These earthquakes cover a wide range of frequencies. In each case the response calculations have been performed once by using the original accelerogram and the conventional response calculation method, and once by using the simplified accelerogram and the propose formulations, and the two response histories have been compared. To show the capability of the proposed method in the full frequency range the displacement spectra of the used accelerograms have been obtained by using both conventional and the proposed method and have presented for comparison.

Figure 1 shows the accelerogram the main component of El Centro earthquake, as a sample, with its equivalent impulses, calculated by Equation 4, and to see better the details of the equivalent impulses, a small portion of Figure 1-(a) has been magnified as presented in Figure 1-(b).



(a) (b)

Figure 1. Accelerogram of the main component of El Centro earthquake and its equivalent impulses, (a), and a magnified portion of the accelerogram shown in Figure 1 with details of the equivalent impulses, (b)

As the first set of response calculation results the displacement response of a SDOF system with natural period of 0.5 sec and damping ratio of 2% subjected to the main accelerogram of El Centro earthquake, calculated by the conventional response analysis method, and shown in Figure 2, has been calculated once more by the proposed method based on the simplified accelerogram, and the results are shown in Figures 3-a and 3-b, which show the responses obtained by simplifying the accelerogram respectively as single impulses between the subsequent zero-crossings, and double impulses between the subsequent zero-crossings.

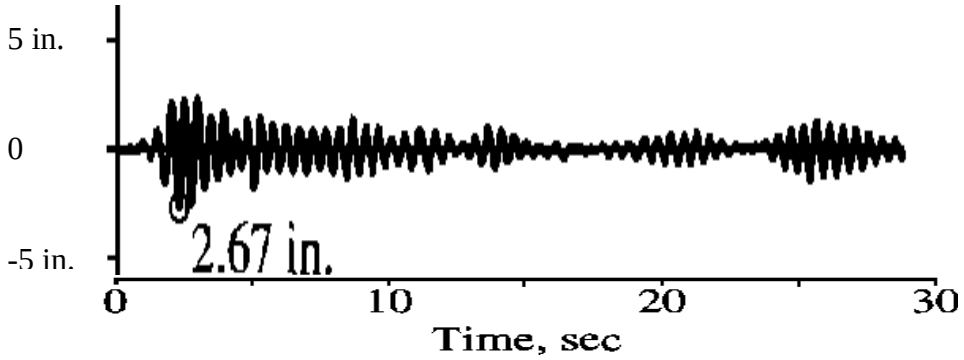
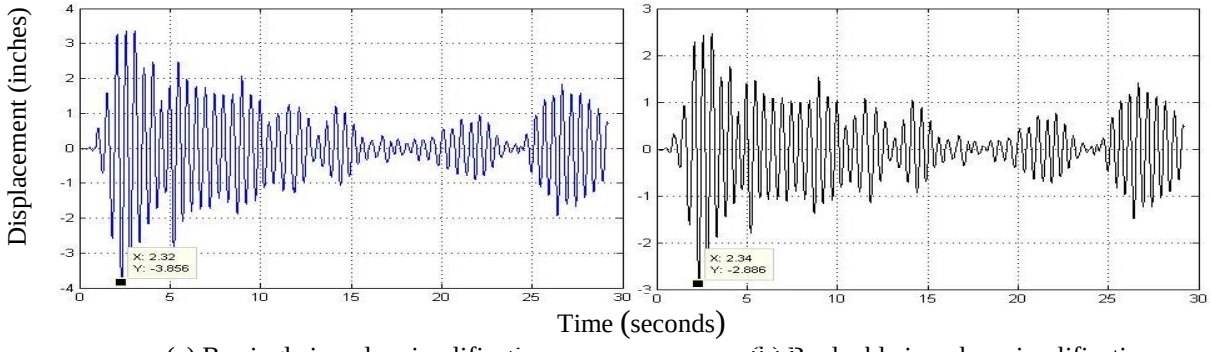


Figure 2. The displacement response history of a SDOF system with natural period of 0.5 sec and damping ratio of 2% subjected to the accelerogram shown in Figure 1, obtained by the conventional analysis method

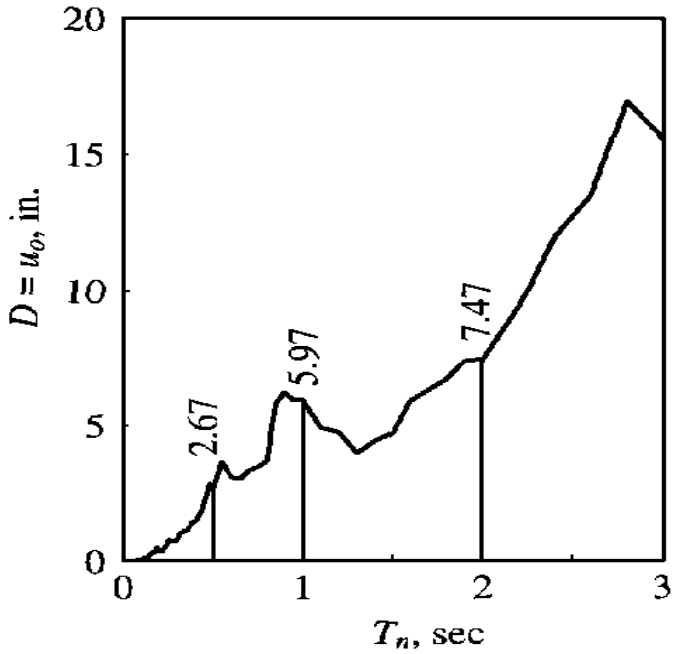


(a) By single impulse simplification (b) By double impulses simplification

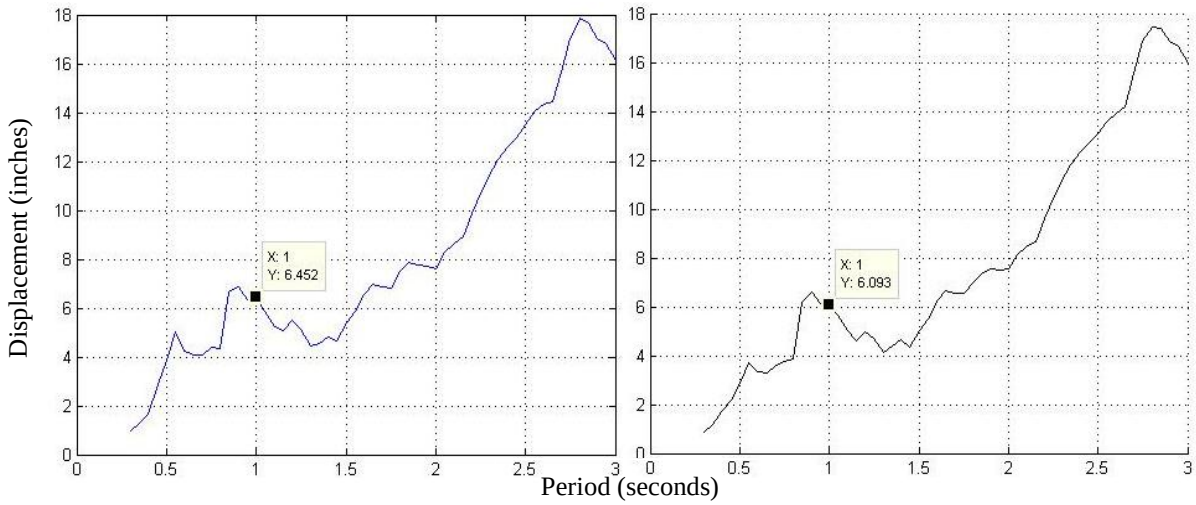
Figure 3. Displacement response histories of the SDOF system with natural period of 0.5 sec and damping ratio of 2% subjected to the accelerogram shown in Figure 1, calculated by the proposed method based on the simplified record as: (a) single impulses between subsequent zero-crossings, and (b) double impulses between subsequent zero-crossings

Comparing the response history shown in Figure 3-a with the one shown in Figure 2 it can be seen that by using the single impulse simplification of accelerogram, although the general trend of the response history is very similar to that of the exact response history, its peak

value has around and 40% error. However, comparison of response history shown in Figure 3-b with the one shown if Figure 3 indicates that by double impulse simplification of the accelerogram the amount of error will decrease to less than 7%. It should be noted that in case of the SDOF system with the natural period of 0.5 sec the relatively high level of error, particularly when single impulse simplification is used, is expected, since the nature of the proposed simplification method results in deletion of high frequencies or low periods of the accelerogram to some extent. On this basis, by increasing the natural period of the SDOF system, the level of error should decrease. This fact can be easily seen in the displacement response spectra of the employed accelerogram, developed by the exact and simplified methods, as shown Figures 4. Comparing the spectrum curves shown in Figures 4-b and 4-c with the one shown in Figure 4-a it can be seen that for a system with the natural period of 1.0 sec the amounts of error for the case of single impulse simplification and double simplification are respectively around 8% and 2%.



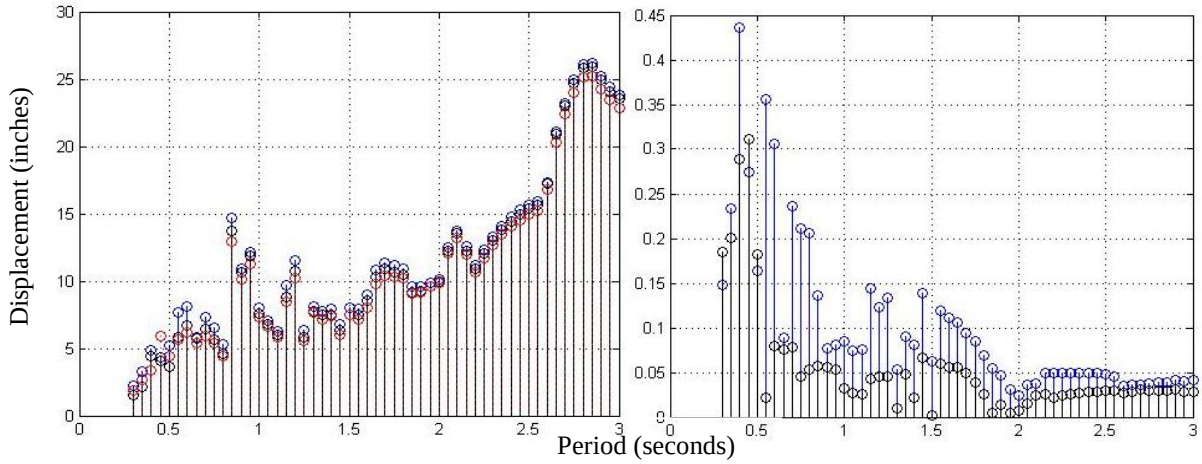
(a) The exact spectrum



(b) By single impulse simplification (c) By double impulses simplification

Figure 4. Displacement response spectra obtained by the original and simplified accelerograms

To see better the difference between the spectrum obtained by the exact method and the one obtained by the simplified method, and also to realize the amounts of error in single impulse and double impulse simplifications all three spectra have been shown in one graph, shown in Figure 5-(a), and the amounts of error are shown in Figure 5-(b).



(a) Displacement response spectrum (b) The amount of error

Figure 5. Displacement response spectra (a) obtained by the original and simplified accelerograms, and the amounts of error (b) in cases of single- and double impulse simplification

In Figure 5-(a) the exact values are shown by red nuts, and the values obtained by single- and double impulse simplification are shown respectively by blue nut and black nuts. It is seen that single impulse simplification leads to higher spectral response comparing to double impulse simplification, and the latter leads to higher values than the exact values. In fact the proposed simplification method always results in overestimated displacement response, and therefore is a conservative simplification.

As other samples of the numerical results the displacement response spectra of some of the employed earthquakes accelerograms, developed by both the exact and the simplified methods, are presented in Figures 6 to 12, in which the result of the exact method is indicated by red curves, and those of the single- and double impulse simplification by, respectively, blue and black curves (more results of this type can not be presented here because of lack of space, and can be found in the main report of the study (Mirzaei 2013), [7]).

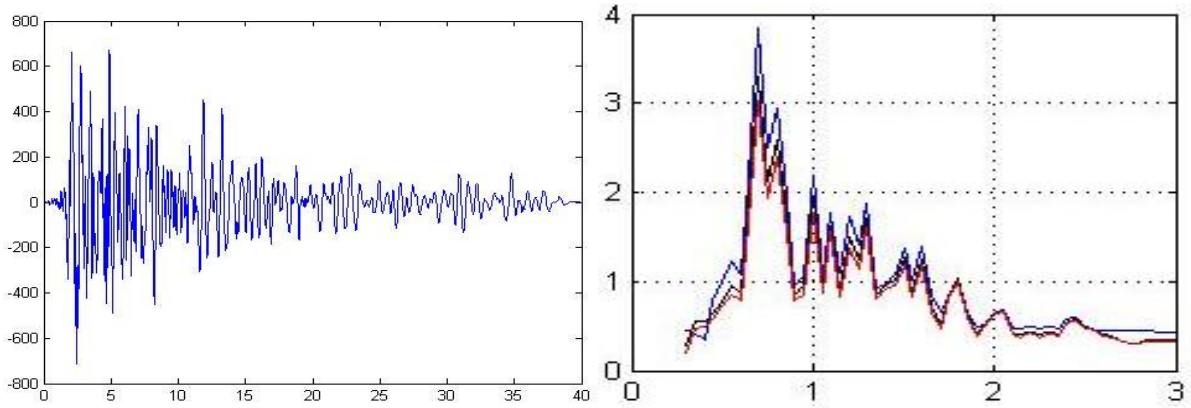


Figure 6. Accelerogram (in Gal units) and displacement spectra (in inches) of the Central Calif earthquake (longitudinal comp.) obtained by exact (in red) and simplified method (in blue and black)

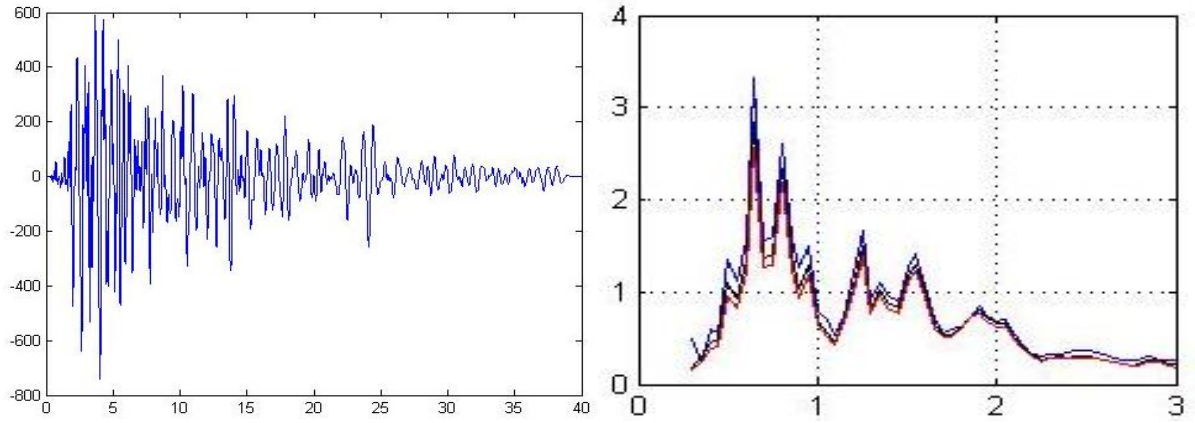


Figure 7. Accelerogram (in Gal units) and displacement spectra (in inches) of the Central Calif earthquake (transverse comp.) obtained by exact (in red) and simplified methods (in blue and black)

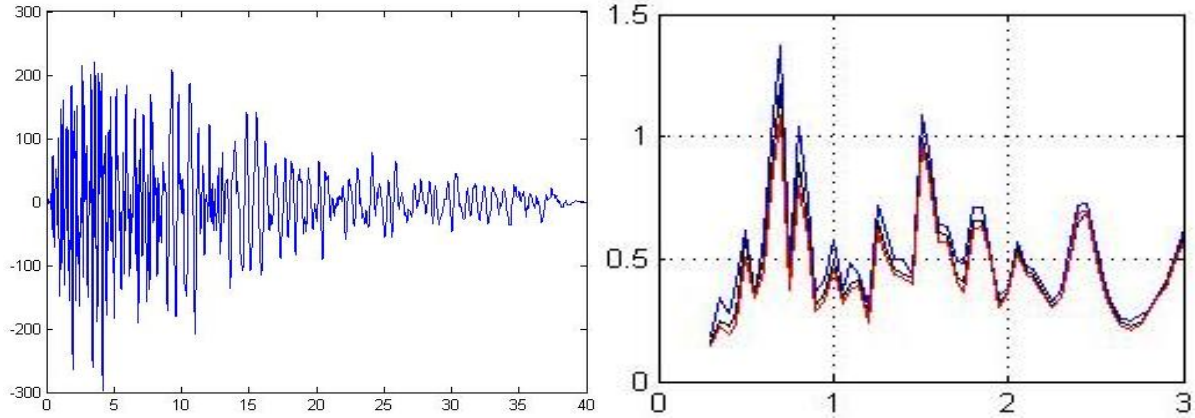


Figure 8. Accelerogram (in Gal units) and displacement spectra (in inches) of the Central Calif earthquake (vertical comp.) obtained by exact (in red) and simplified methods (in blue and black)

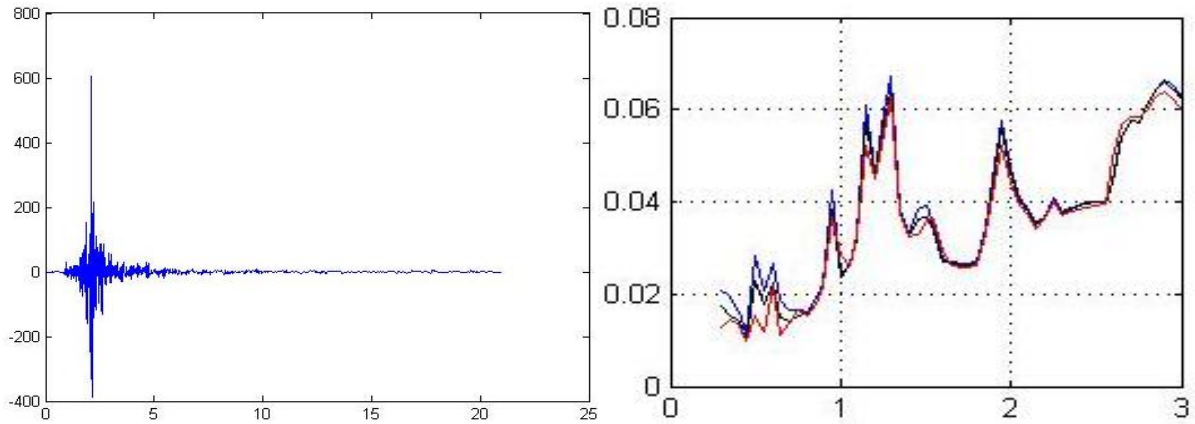


Figure 9. Accelerogram (in Gal units) and displacement spectra (in inches) of the Cape Mendocino earthquake obtained by exact (in red) and simplified methods (in blue and black)

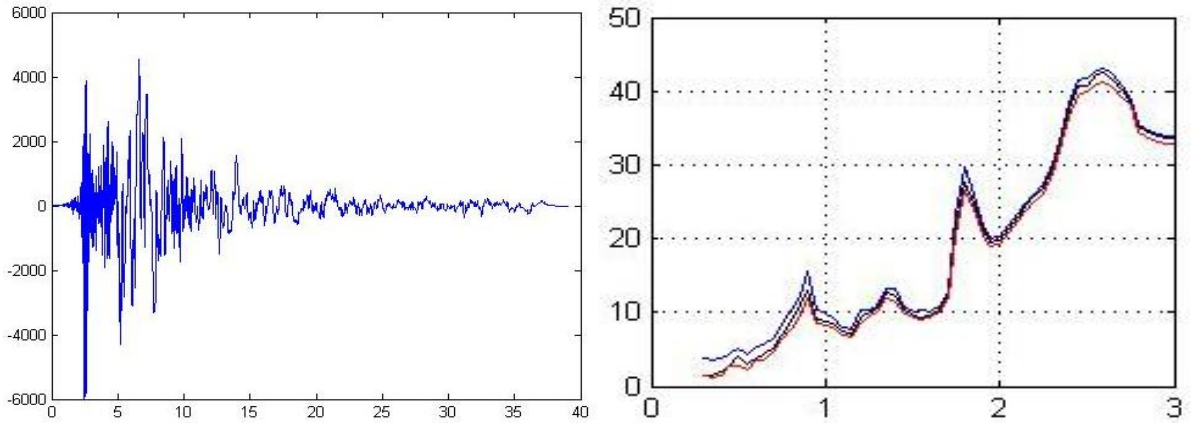


Figure 10. Accelerogram (in Gal units) and displacement spectra (in inches) of the Imperial Valley earthquake obtained by exact (in red) and simplified methods (in blue and black)

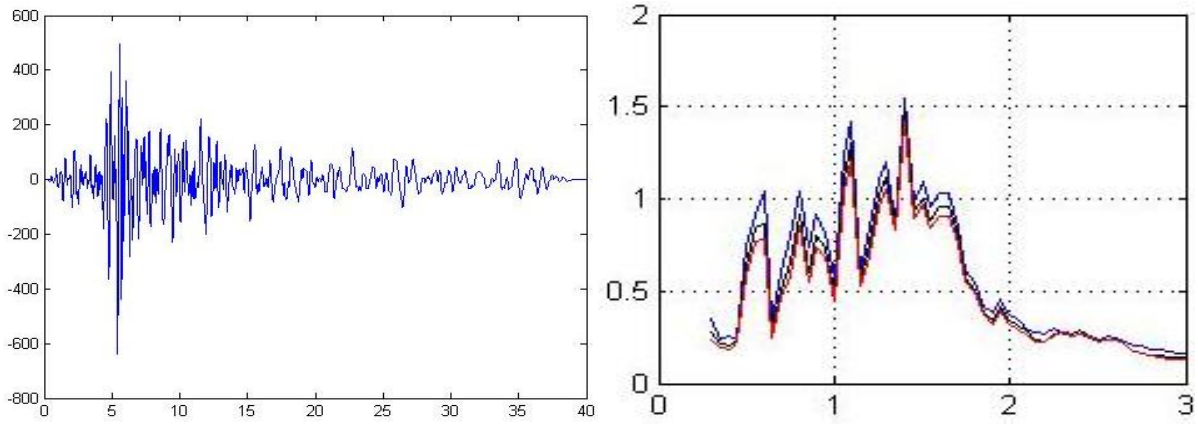


Figure 11. Accelerogram (in Gal units) and displacement spectra (in inches) of the Humbolt Bay earthquake obtained by exact (in red) and simplified methods (in blue and black)

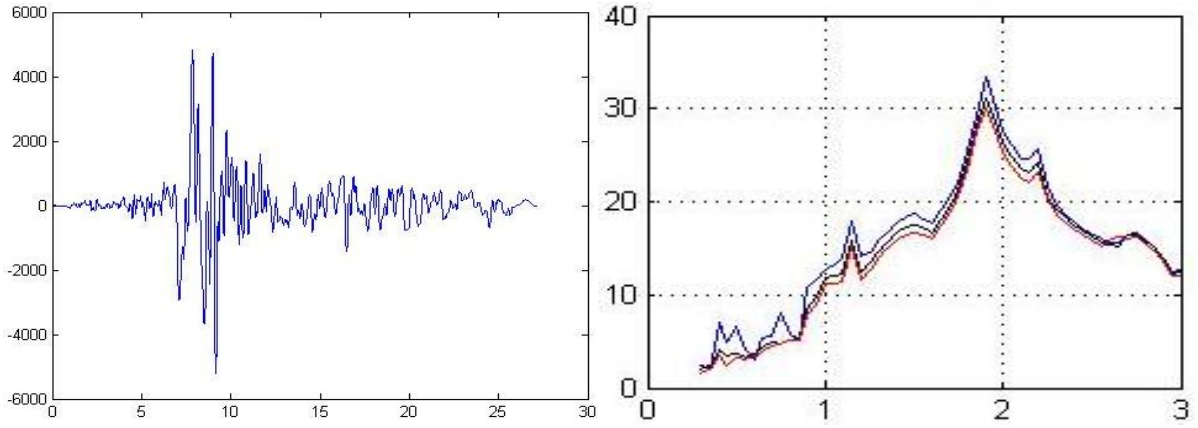


Figure 12. Accelerogram (in Gal units) and displacement spectra (in inches) of the Kocaeli earthquake obtained by exact (in red) and simplified methods (in blue and black)

It can be seen in Figures 6 to 12 that for most of the employed earthquakes the simplified method results in a very good approximation of the displacement response spectrum. As expected the amount of error is relatively high in the range of shorter periods, but in the range of longer periods, results of the exact and simplified method, particularly by double impulse simplification are very close.

4 CONCLUSIONS

Based on the numerical results, obtained by using the accelerograms of several earthquakes, which cover a wide range of frequency content, it can be said that the proposed simplification method leads to very good approximation of the displacement response values, with an average error of less than 10%, particularly when the double impulse simplification (considering two impulses between each pair of the zero-crossing points of the accelerogram) is used. Regarding that the number of equivalent impulses, even in the case of double impulse simplification, is much less than the number of total time steps of the digitized accelerograms, the simplified method results in drastic reduction in the required time for THA.

In some cases, particularly for short period systems subjected to accelerograms, which contain high frequencies, the amount of error in peak responses may be inacceptable. In such cases using three equivalent impulses instead of two for the parts of accelerogram between each pair of its zero-crossings, can improve the precision of the simplification method, while keeps the required time still very little, comparing to the required time for the conventional THA methods.

REFERENCES

[1] W. Y. L. Wang, Structural instability during earthquakes and accelerogram simplification, *Ph.D. Dissertation*, Michigan University, Ann Arbor, USA, 1975.

[2] Pastsakorn Kitiyodom, Ryuuici Sonoda, Tatsunori Matsumoto, Simplified Dynamic Analysis of Piled Raft Foundation Subjected to Earthquake Load, *Proceedings of JIBAN: The 39th Japan National Conference on Geotechnical Engineering*, 2004.

[3] S. Ali Ghafari Oskoei and Ghyslaine McClure, Simplified Dynamic Analysis Methods for Guyed Telecommunication Masts under Seismic Excitation, *Proceedings of the 2009 Structures Congress*, Austin, Texas, April 30-May 2, 2009

[4] J. L. Domingues Costa, R. Bento, V. Levtchitch & M. P. Nielsen, Simplified non-linear time-history analysis based on the Theory of Plasticity, *Proceedings of the 5th Conference on Earthquake Resistant Engineering Structures (ERES 2005)*, Dublin, July 2005.

[5] A. Soroushian, A technique for time integration analysis with steps larger than the excitation steps, *Communications in Numerical Methods in Engineering*, Special Issue, 24 (12), pp. 2087–2111, 2008.

[6] Alireza Faroughi and Mahmood Hosseini, Simplification of Earthquake Accelerograms for Quick Time History Analyses by Using Their Modified Inverse Fourier Transforms, *Proceedings of the Twelfth East Asia-Pacific Conference on Structural Engineering and Construction (EASEC-12)*, Hong Kong Special Administration Region, China, 24-26 January 2011.

[7] Iman Mirzaei, Simplification of Earthquake Accelerograms for Rapid Time History Analysis Based on the Impulsive Load Concept, *M.Sc. Thesis under supervision of Professor Mahmood Hosseini*, Earthquake Engineering Department, Science and Research Branch of the Islamic Azad University (IAU), Tehran, Iran, 2013.

COMPDYN 2013
4th ECCOMAS Thematic Conference on
Computational Methods in Structural Dynamics and Earthquake Engineering
M. Papadrakakis, V. Papadopoulos, V. Plevris (eds.)
Kos Island, Greece, 12–14 June 2013

DESIGN AND IMPLEMENTATION OF A LINEAR CONTROLLER ON A REDUCED MODEL OF A SMART STRUCTURE

Nader Ghareeb[1] **and Ruediger Schmidt**[1]

[1] RWTH Aachen University
Aachen, Germany
e-mail: ghareeb, schmidt@iam.rwth-aachen.de

Keywords: Finite element modeling, Super element, Classical damping, Lyapunov stability theorem.

Abstract. *Active vibration control of smart structures has gained much attention in the last decades. A simple active control system consists of the mechanical structure where vibration occurs, a sensor to perceive the vibration, an actuator to counteract the influence of disturbances and finally, the controller responsible for the generation of the appropriate control signal. The smart structure used in this work comprises a cantilevered beam with a piezoelement glued to it. A finite element model is initially created and then it is reduced to a super element with a finite number of degrees of freedom. Damping properties are also calculated and added to the reduced model, and the model is verified. Finally, a linear control law based on the Lyapunov stability theorem is used to attenuate the vibrations of the smart beam excited with its first eigenmode. The controller is applied directly to the super element model and after that to the extracted state-space model too. Results from both models are then presented and compared.*

1 INTRODUCTION

Optimizing the weight during the design of structures has the advantage of reducing the manufacturing and operational costs by reducing the amount of raw material used. However, reducing material results in lower stiffness and less damping which make the structure prone to vibration. In addition to reducing the performance of the structural system, vibration can also cause fatigue loads that may lead to failure of the structure itself [1]. One way to overcome this vibration problem is to implement active or smart materials that can be controlled in accordance to the disturbances or oscillations sensed by the structure. Structures incorporating such materials are called smart structures. A smart structure comprises a passive structure and distributed active parts working as sensors and/or actuators. Recent innovations in smart materials and developments in control theory have made it possible to control the dynamics of these structures, and has lead to a big amount of research and development activity in this field [2]. The coupled electromechanical properties of smart materials, which are illustrated in this work as piezoelectric ceramics, make them well-suited for being used as distributed sensors and actuators for controling structural response. As for sensors, mechanically induced deformations can be determined by measuring the induced electrical potential (direct piezoelectric effect); whereas in actuator applications, deformation or strains can be controlled through the introduction of an appropriate electric potential (converse piezoelectric effect) [3]. Active vibration control has initially been applied on ships [4], and then on aircraft and spacecraft [5]. Rapid developments in this field have led to the use of point actuators and sensors to control flexible systems based on the knowledge of elastic mode frequencies and mode shapes at their attachment points [6].
The use of piezoelectric materials as actuators and sensors for noise and vibration control has only been demonstrated extensively over the past thirty years [7]. The studies generally emphasized the capabilities and applications of piezoelements as distributed vibration actuators and sensors by simultaneously controling a finite number of modes of the actual system, like in [8, 9, 10].
Consequently, the majority of investigations done in this field were carried out either through experiments on the real model as in [11, 12, 13], or by using 2D or 3D finite element (FE) models of the smart structure as in [14, 15, 16]. However, in the FE work, the damping coefficients were not calculated but rather assumed, which may not reflect the exact performance of the real model.
In the present work, an active linear controller based on Lyapunov stability theorem is designed and implemented to attenuate the vibration of a cantilevered smart beam excited by its first eigenmode. The piezoactuator is modeled, and the relation between voltage and moments at its ends is investigated. A modified FE model of the smart beam based on the first-order shear deformation theory (FOSD) is then created. The damping coefficients are added to the FE model prior to the reduction to a super element (SE) model with a finite number of degree of freedom (DOF). The FE and SE models are validated by performing a modal analysis and comparing the results with the experimental ones. The state-space (SS) model is extracted too. Finally, the Lyapunov controller is integrated into the model to reduce the vibration. The FE package SAMCEF is used for the creation of both the FE and SE models, as well as for the implementation of the controller in the SE model. Consequently, MATLAB/SIMULINK is used for the implementation of the controllers in the SS model.

2 MODELING

In this section, the procedures for modeling a smart structure are examined. The smart structure used in this work is a piezolaminated beam. The same beam model is used later to extract the SE model, derive the SS model, and implement the control strategy. The first step in designing a control system is to build a mathematical model of the structure with all disturbances causing the unwanted vibration. One of the ways to derive the structural analytical model is by using the FE method. The smart beam used consists of a steel beam, a bonding layer and an actuator as seen in Fig. 1.

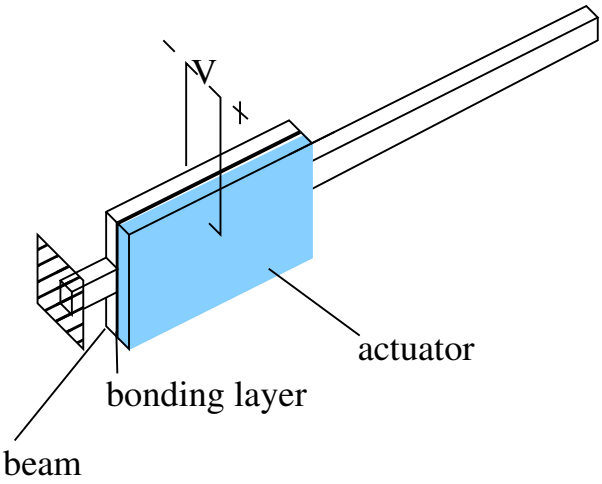


Figure 1: The smart beam.

2.1 Actuator modeling

Using an actuator means implementing an appropriate electric voltage to control the vibration of the smart structure (converse piezoelectric effect). Many FE packages do not offer elements with electrical DOF. Consequently, the voltage applied by the actuator can be represented by two equal moments with opposite directions concentrated at both ends [6]. The relation between actuator moments and actuator voltage can be investigated, so that the moments will then act as the controlling parameters on the smart structure Fig. 2.

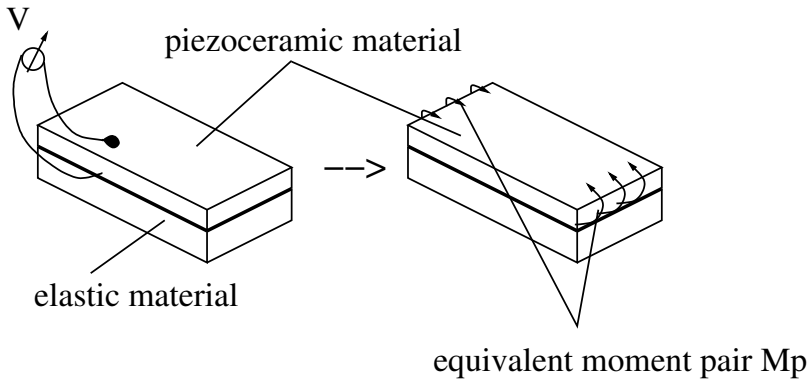


Figure 2: The induced stresses from a piezoceramic actuator.

The procedures to find this relation were already mentioned in [17, 18]. Based on Fig. 3, the relation between actuator moment and actuator voltage is:

$$M_p = \frac{E_p E_a (t_p t_a + t_a^2) + E_p E_b (t_b^2 + t_p t_b + 2 t_a t_b)}{E_p t_p + E_a t_a + E_b t_b} \cdot \frac{d_{31} \cdot b}{2} \cdot V \tag{1}$$

where the indices p, a, and b refer to the piazo-actuator, adhesive layer, and steel beam respectively. t is the thickness and E the Young's modulus of each part. The material properties are shown in Tab. 1.

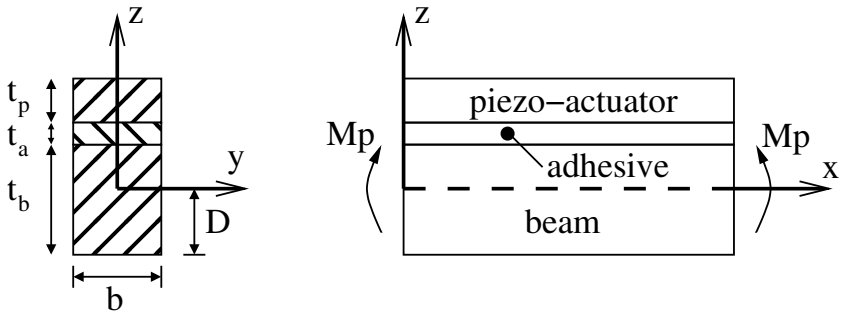


Figure 3: A schematic layout of the composite beam.

Table 1: Parameters of the components of the smart beam.

	Beam	Bonding	Actuator
Material	steel	epoxy resin	$PIC151$
Thickness $[mm]$	0.5	0.036	0.25
Density $[kg/m^3]$	7900	1180	7800
Young's mod. $[MPa]$	210000	3546	66667

2.2 FE modeling

Finding the best FE model that represents the smart beam used in this work means selecting the optimal element type and size. For this reason, a modal analysis of the real beam is experimentally performed and results of the natural frequencies are compared with those from the FE model where different element types. The FE size which yields the best results will be selected. A detailed geometry of the smart beam is shown in Fig. 4.
The smart beam is created as a unique structure but modeled as a composite shell with three layers. This means, all the three components of the model, i.e. beam, bonding layer and actuator are bonded together without any relative slip among the contact surfaces. Consequently, each layer has its own mechanical properties. To validate the choice of the FE type used (a composite shell element with 8 nodes based on the FOSD), a modal analysis of the FE model is done and the first two eigenfrequencies are read and compared to those from the experiment. This is seen in Tab. 2. As a boundary condition, the far left edge of the smart beam is clamped.

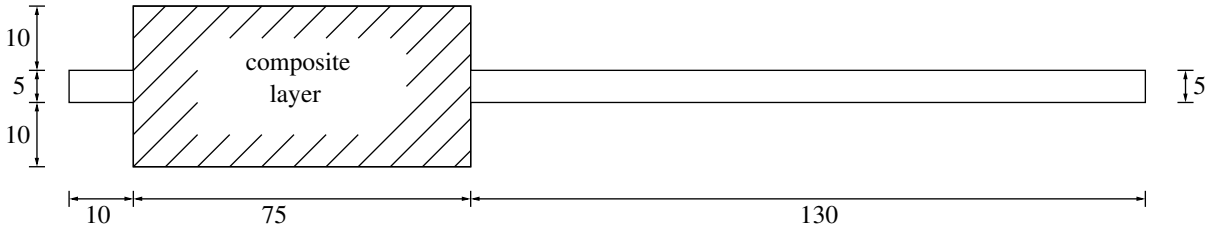


Figure 4: A detailed geometry of the smart beam [dimensions in mm].

Table 2: Validation of element-type based on the modal analysis.

	FE model	Experiment
$1st$ eigenfrequency $[Hz]$	13.81	13.26
$2nd$ eigenfrequency $[Hz]$	42.67	41.14

Concerning the optimal FE size to be used, it's well known that reducing the FE size will improve the solution accuracy. However, especially in the case of large complex structures, the use of excessively fine elements in the FE model may result in unmanageable simulation periods. From Tab. 3, it is seen that using an element size less than $1\ mm$ does not make any significant

Table 3: Effect of element size on the eigenfrequency.

FE size $[mm]$	$1st$ eigenfreq. $[Hz]$	$2nd$ eigenfreq. $[Hz]$
0.25	13.80	42.66
0.5	13.81	42.66
1.0	13.81	42.67
2.5	13.83	42.71
5	13.89	42.81
10	14.09	43.21

change on the values of the $1st$ and $2nd$ eigenfrequencies of the smart beam. This means, it can be regarded as the optimal value for the element size in the FE modeling.

2.3 SE modeling

The main virtue of this technique (also called substructure technique) is the ability to perform the analysis of a complete structure by using the results of prior analysis of different regions comprising the whole structure. When a preliminary analysis of the different parts is performed, the computation time and the size of the whole system are reduced. However, all DOF considered useless for the final solution will be condensed and the rest will be retained. This means, the DOF of the whole system will correspond to the retained nodes plus a number of internal deformation modes (dynamic analysis problems). To construct a SE, or in other words to remove the unwanted nodes and DOF from the substructure, many methods that can be used. The

most popular methods are the ”Guyan reduction technique” [19], and the ”Component-mode method” which is used in this work.

2.3.1 The Component-Mode Method

Also called Craig-Bampton method, it was initially developed by R. Craig and M. Bampton [20]. The idea behind this method is to the basic substructure into a certain number of substructures. The DOF of each substructure are then classified into boundary and internal DOF. The boundary DOF are shared by several substructures, while the internal DOF belong only to the considered substructure.
The behaviour of each substructure is described by the combination of two types of component modes: The constrained modes and the normal vibration modes. The former are determined by assigning a unit displacement to each boundary DOF while all other boundaries DOF are being fixed. The latter correspond to the vibration modes obtained by clamping the structure at its boundary.
It is thus assumed that the behaviour of the substructure in the global system can be represented by superimposing the constrained modes and a small number of normal modes. Hence, by retaining only the low-frequency vibration modes, the substructure's dynamic deformed shape is represented with sufficient accuracy. The method is discussed in details in [21].
Starting from the FE model of the previous subsection, a SE model with a limited number of DOF will be created.
Firstly, the master or retained nodes must be selected. They correspond to the nodes where a boundary condition or a load is applied. The rest of the nodes will be considered as slave or condensed nodes. In the FE model, 5 nodes are considered as retained nodes (Fig. 5).



Figure 5: The retained nodes of the SE.

This means:

- $Node\ 1$ is used to introduce a boundary condition (clamping constraint).
- $Node\ 2$ is used to introduce a load (actuator moment).
- $Node\ 3$ is used to introduce a load (actuator moment).
- $Node\ 4$ is used to measure the displacement (distance sensor).
- $Node\ 5$ is used to measure the tip displacement (distance sensor).

Secondly, 10 modes, which correspond to 97% of the modal effective mass, are selected. The percentage of modal effective mass for each mode is usually found inside the input file created by any FE software.
To check the validity of the SE created, it has to be compared to the FE model which was already validated before. Abstractly said, the reduced model must have the same characteristics as the original model, except that the number of nodes is reduced, as well as the number of DOF. The eigenfrequencies of the first 2 modes resulting from each model are depicted in Tab. 4.

Table 4: Eigenfrequencies of the first two modes.

Mode	SE model $[Hz]$	FE model $[Hz]$	Experiment $[Hz]$
1	14.249	13.811	13.26
2	43.414	42.673	41.14

The physical properties of each model are shown in Tab. 5. It is clear that both models deliver almost the same value of the eigenfrequency for the first two modes. Since the excitation of the beam by its first eigenmode is concerned, furhter readings are not necessary. Compared to the FE model, the SE model has few number of DOF and a very small number of nodes. It consists of a single element and has the advantage that the simulation time becomes short and the controllers are implemented on the SE model itself.

Table 5: Characteristics of the FE and SE models.

	FE model	SE model
Element size $[mm]$	3.07	
Number of elements	2575	1
Number of nodes	8206	5
Number of DOF	16860	40

3 DAMPING CHARACTERISTICS

Damping parameters, which are of significant importance in determining the dynamic response of structures, cannot be deduced deterministically from other structural properties or even predicted by using the FE technique. For this reason, recourse must be made to data from experiments conducted on completed structures of similar characteristics. Such data is scarce in general, but it's very valuable for studying the phenomenon and modeling of damping [22]. For simplicity and convenience, the damping is assumed to be viscous and frequency dependent [23]. This linear approach, which was initially introduced by Rayleigh [24], assumes that the damping matrix is a linear combination of the mass and stiffness matrices. Although this idea was suggested for mathematical convenience only, it allows the damping matrix to be diagonalized simultaneously with the mass and stiffness matrices, preserving the simplicity of uncoupled real normal modes as in the undamped case [25].

The relation is

$$C \;=\; \alpha\, M \;+\; \beta\, K \tag{2}$$

where α and β are real scalars that need to be determined.

The main advantage of this formulation is that the damping matrix will be a diagonal matrix.

This means, the general equation of motion of a damped structure which is given as

$$[M]\,\{\ddot{q}\} \;+\; [C]\,\{\dot{q}\} \;+\; [K]\,\{q\} \;=\; \{F\} \tag{3}$$

can be uncoupled to the form

$$\ddot{u}_r \; + \; 2\,\xi_r\,\omega_r\,\dot{u}_r \; + \; \omega_r^2\,u_r \; = \; \varphi^T\,F \; = \; F_r \tag{4}$$

where q is the vector of nodal displacements, M the inertia (mass) matrix, C the damping matrix, K the stiffness matrix, F the column matrix for equivalent nodal forces.
the subindex r means that (Eq. 4) are uncoupled and they correspond to the rth natural frequency of the rth mode that is considered (ω_r). φ is the vector of mode shapes, $u(t)$ the vector of modal displacements, and ξ_r the damping ratio corresponding to the rth mode.

This form of the equation of motion will be used later on to implement the controller on the analytical model of any structure.

Taking the orthogonality of the mode shapes with respect to the mass and stiffness matrices, the modal form of the damping matrix will become

$$\overline{C} \; = \varphi^T\,C\,\varphi \; = \; \alpha \; + \; \beta\,\omega_r^2 \tag{5}$$

this equation can be written in the form

$$\xi_r \; = \; \frac{\overline{C}}{\overline{C}_c} \; = \; \frac{\overline{C}}{2\,\omega_r} \; = \; \frac{\alpha}{2\,\omega_r} \; + \; \beta\,\frac{\omega_r}{2} \tag{6}$$

with $\overline{C}_c$ as the modal critical damping.

From (6), it can be observed that the damping ratio is proportional to the natural frequencies of the system. Roughly speaking, two values for the eigenfrequency ω_r with the corresponding values of ξ_r are needed to find out the scalars α and β and thus to compute the damping matrix C. Relevant are the first few modes for which there is a significant mass participation, i.e. a mass participation which is not less than 95%. A typical plot of (6) is shown in Fig. 6 [26, 27]. As seen in Fig. 6, the first portion of the curve shows non-linearity (frequency range: $0.1-5$ Hz), in this case the damping is called "mass proportional damping" where α is much greater than β. Beyond this portion, the curve is linear (frequency range: > 5 Hz). The damping is then called "stiffness proportional damping" and β has a big value. To find out α and β , many methods can be applied like the method of Chowdhury and Dasgupta, or the method of damping from normalised spectra (also known as the half-power bandwidth method) [28]. Both methods are used to find the damping characteristics of the smart beam and the results are depicted in Tab. 6. In this work, the average values of both methods are used, and the damping coefficients are

Table 6: Results of α and β using both methods.

Parameter	Chowdhury and Dasgupta	Half-power bandwidth
α	0.02577	0.02955
β	9.918×10^{-6}	9.77×10^{-6}

added to the SE model and to the SS representation.

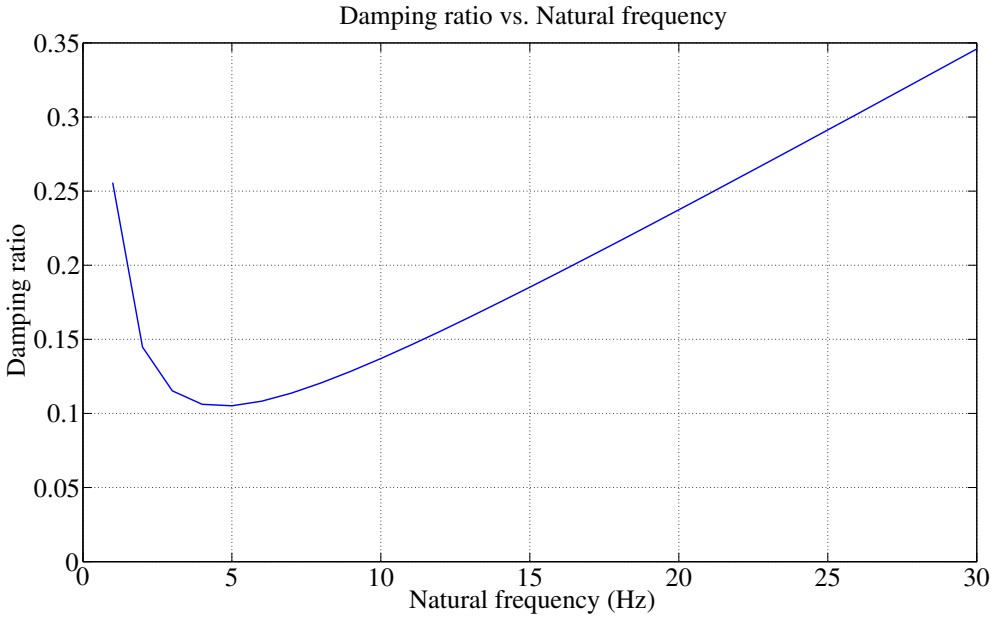


Figure 6: Variation of the damping ratio with natural frequency of a system.

4 STATE-SPACE REPRESENTATION

4.1 Basics of the state-space representation

The SS representation is used as a second approach to implement the controller in order to validate the results of the SE model. The basic idea of the SS repree is to describe a system of equations in terms of n first-order differential equations. However, the increase in the number of state variables, the number of inputs, or the number of outputs does not increase the complexity of these equations [29].
The state equations have the form:

$$\begin{aligned} \dot{x} &= A\,x + B\,u \\ y &= C\,x \end{aligned} \tag{7}$$

and the size of the matrices A, B and C depends on the number of states, inputs and outputs of the system. Upon specifying the type and position of the input and output vectors, a FORTRAN code is used to create the SS model of the smart beam. This model is then integrated in MATLAB/SIMULINK to give the dynamic response of the modelled structure under one or several inputs and outputs.

4.2 Creation and validation of the SS equations for the case of a smart beam

The objective now is to create the SS representation of the smart structure investigated in this work, and to validate it by carrying out a simple simulation, so that the results can be compared to those from the FE model. At the beginning, the inputs and outputs of the system must be specified. Referring to Fig. 5, a sensor is placed at $Node\ 5$ to measure the tip displacement, and the input will be a harmonic force at the same node. Thus, the smart beam will be excited by its first eigenmode. The force F has the form:

$$F = c\,\sin(\omega_1\,t); \qquad \text{with } c \text{ as a constant (amplitude)} \tag{8}$$

Now, there is a single input and a single output. Since $Node\ 1$ is clamped, the number of states is defined as:

$$2p \ = \ 30 \ + \ 10 \ - \ 6 \ = \ 34 \tag{9}$$

There are $30\ DOF$ in the system, in addition to 10 vibration modes. Concerning the dimensions of the matrices $A,\ B,\ C$:

$$\begin{array}{rcl} dim(A) & = & 34 \times 34 \\ dim(B) & = & 34 \times 1 \\ dim(C) & = & 1 \times 34 \end{array} \tag{10}$$

The SS representation of this smart beam is shown in Fig. 7. The simulation is carried out for 40 seconds while the load is kept active for the first 20 seconds. The resulting curve in Fig. 8 shows that both models had the same value of tip displacement throughout the simulation time. This gives more reliance to the results. However, both models will be used in the coming section for the implementation of the controller.

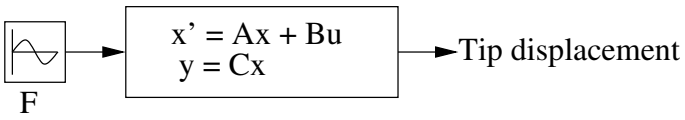


Figure 7: The SS model of the smart beam.

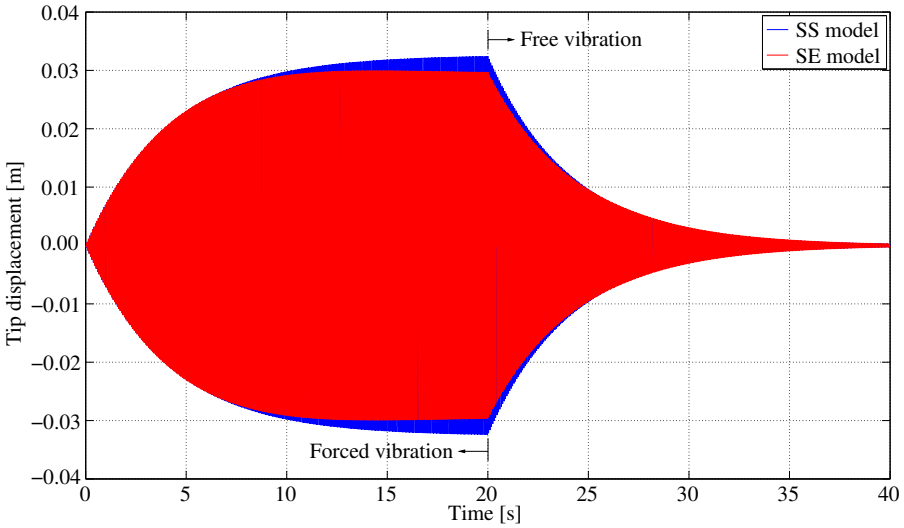


Figure 8: Forced excitation and free vibration of the smart beam.

5 CONTROLLER DESIGN AND IMPLEMENTATION

Although there is no general procedure for constructing a Lyapunov function, yet any function can be considered as a candidate if it meets some requirements, i.e., positive definite, equal to zero at the equilibrium state and with its derivative less or equal to zero [30]. Now, the energy equation of a thin Bernoulli-Euler beam which is modelled as a single FE in a one-dimensional

system with length h and left point coordinate x_i, is considered as a Lyapunov function candidate (Fig. 9).

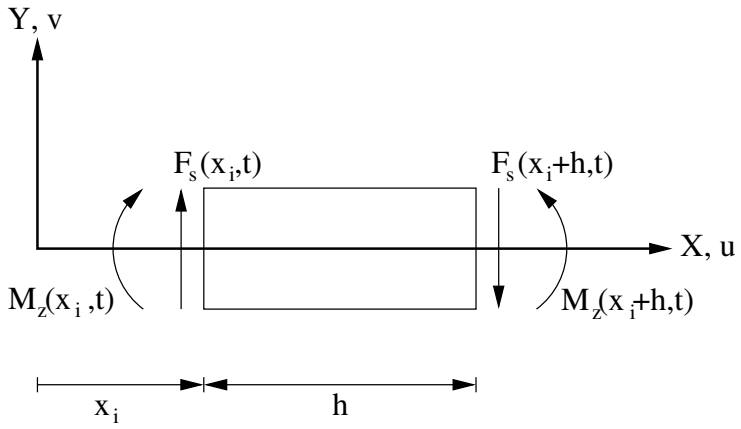


Figure 9: Section of the smart beam where the piezoelement is located.

According to [31], the total energy equation of a beam without any external forces or moments is:

$$U \;=\; \frac{1}{2}\int_{x_i}^{x_{i+h}} \left[\rho A\Big(\frac{\partial v}{\partial t}\Big)^2 \;+\; EI\Big(\frac{\partial^2 v}{\partial x^2}\Big)^2\right] \mathrm{d}x \tag{11}$$

where h is the length of the beam section, u and v are the displacements in longitudinal and transverse directions, E and ρ are the elastic modulus and density of the beam.
According to Fig. 9, M_z is the actuator bending moment, F_s is the shear force on the beam, and I_z is the second moment of inertia of its cross-section about the (bending) z-axis.

The above function is locally positive definite, continuously differentiable and equal to zero at the equilibrium state. Yet, to consider it as a Lyapunov function, the derivative of this function must be smaller or less than zero as well.
Differentiating (11) in time leads to:

$$\dot{U} \;=\; \int_{x_i}^{x_{i+h}} \left[\rho A\frac{\partial v}{\partial t}\frac{\partial^2 v}{\partial t^2} \;+\; EI\frac{\partial^2 v}{\partial x^2}\frac{\partial}{\partial t}\Big(\frac{\partial^2 v}{\partial x^2}\Big)\right] \mathrm{d}x \tag{12}$$

Referring to the relationships for a vibrating beam, which are summarized in any reference about beams like [19], it reveals that:

$$\begin{aligned} \rho A\frac{\partial^2 v}{\partial t^2} \;+\; EI\frac{\partial^4 v}{\partial x^4} \;&=\; 0 \\ M_z \;&=\; EI\frac{\partial^2 v}{\partial x^2} \\ F_s \;&=\; -EI\frac{\partial^3 v}{\partial x^3} \end{aligned} \tag{13}$$

Substituting the derived equations for the bending moment M_z, shear force F_s, and assuming no shear after that, the first derivative yields:

$$\dot{U} \;=\; M_z\Big[\frac{\partial}{\partial t}\left(\frac{\partial v}{\partial x}\right)\Big]_{x_i}^{x_i+h} \;=\; M_z\Big(\dot{v}\prime_{x_i+h} \;-\; \dot{v}\prime_{x_i}\Big) \tag{14}$$

where $\dot{v}\prime_{x_i}$ is a rotational velocity at node x_i.
To ensure that (14) is always smaller or equal to zero, M_z, the actuator moment, can have the value:

$$M_z \;=\; -k\Big(\dot{v}\prime_{x_i+h} \;-\; \dot{v}\prime_{x_i}\Big) \tag{15}$$

with k as a positive constant, sometimes called "the proportionality factor". Varying k has a significant effect on the response. Theoretically, the system is stable for any positive value. Nevertheless, larger values of k tend to "overcontrol the structure" since the moment will have a magnitude larger than that required. Consequently, if k is very small, the added moments will be insufficient and this will reduce the damping ratio. Therefore, a trial-and-error procedure is required to select the best value and customize the control to the application [32].

Substituting (15) in (14) yields:

$$\dot{U} \;=\; -k\Big(\dot{v}\prime_{x_i+h} - \dot{v}\prime_{x_i}\Big)^2 \;\leq 0 \tag{16}$$

and thus, all the requirements to have a Lyapunov function are met. Therefore, (15) can be used as the controller for the smart beam.
To implement this equation on the smart beam, the moments at $node\ 2$ and $node\ 3$, which are equal in magnitude but with opposite directions, are calculated as functions of the rotational velocites at both nodes [33]. They have the form:

$$\begin{array}{rcl} M_{2y} & = & -k\,(\dot{v}_{2y} \;-\dot{v}_{3y}) \\ M_{3y} & = & -k\,(\dot{v}_{3y} \;-\dot{v}_{2y}) \end{array} \tag{17}$$

From the above equations, it is clear that the controller is in fact a connection between the DOF of the nodes composing the SE. To do that in SAMCEF, the nonlinear forces element (FNLI) is used. This element allows the introduction of a list of n general linear or nonlinear internal forces as a function of list of $n\ DOF$ and their derivatives. The control strategy is defined directly inside the input file without the use of any external programming language, and this is one of the merits of the SE technique.
Coming back to the control law of (17), the controller is stable for any positive value of the constant k. Now, the optimal value of the constant k must be found. Since the design of optimal controllers is not the task of this work, the method of trial-and-error is used to find out this optimal value. Best results are got for $k \;=\; 30$, and the corresponding curve of tip displacement vs. time of the smart beam is illustrated in Fig. 10. In the FFT spectrum diagram (Fig. 11), the effect of the controller on the amplitude of the resonance at the natural frequency is shown as well.

As stated before, the SS representation of the smart beam is derived in order to validate the results from the SE model. To do that, the inputs and the outputs are designated in order to find out the matrices $A,\ B$ and C of (7). To implement the controller in the SS model, two steps are performed. In step one, the only input to the system is the forced excitation until the magnitude of vibration does not change anymore, i.e., up to $t \;=\; 20\,s$, and the output consists of the tip displacement, as well as the state vectors exactly at $t \;=\; 20\,s$. The diagram is shown in Fig. 12.

These state vectors are then fed in as initial conditions in the second step. This time, the input comprises both actuator moments at both ends of the actuator, and the output embraces the tip displacement at $node\ 5$, and the velocities at the $node\ 2$ and $node\ 3$.

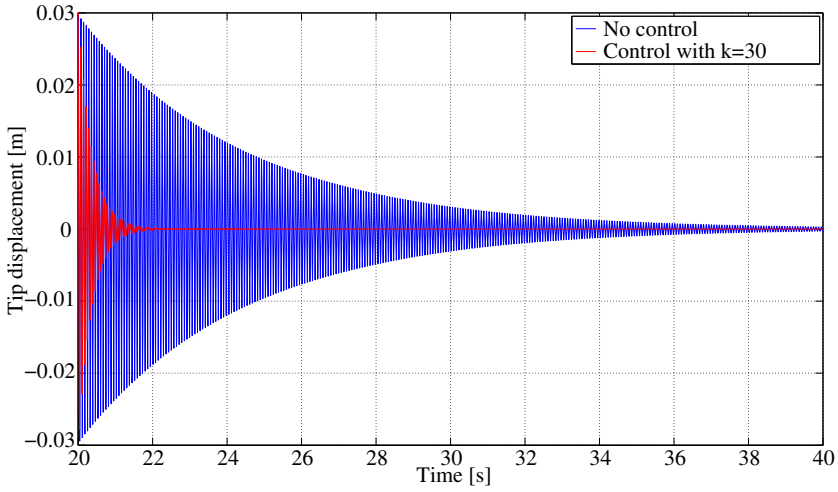


Figure 10: The Lyapunov stability theorem controller for $k = 30$ (SE model).

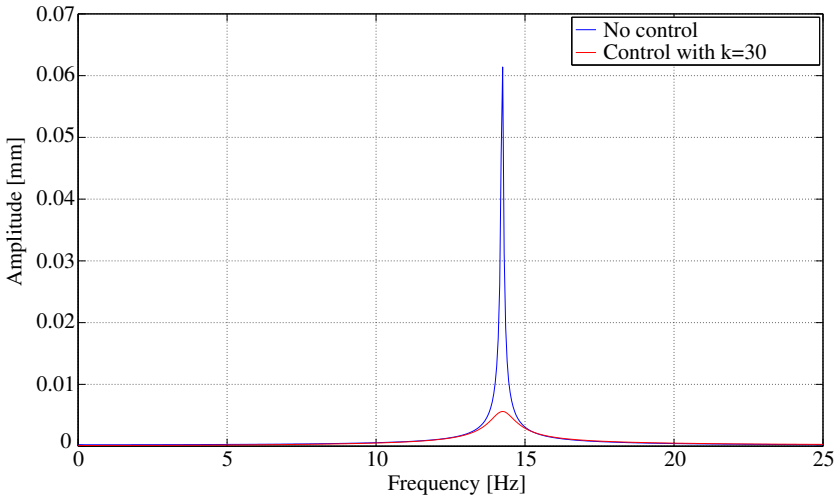


Figure 11: The FFT spectrum of the smart beam using Lyapunov stability controller (SE model).

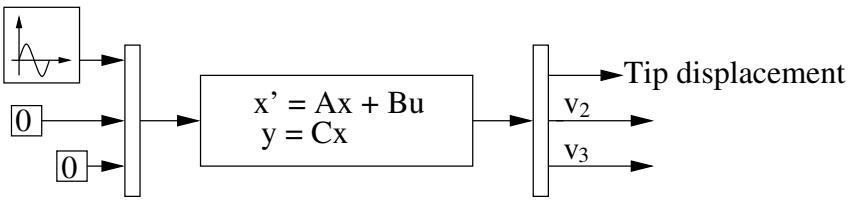


Figure 12: The SS model of the smart beam with controller (step 1).

The steps mentioned above could be also summarized in one step, but in this case a timer must be inserted in the model to deactivate the exciting force when vibrations become stable at $t = 20\,s$. The SS representation of the smart beam in the second step is shown in Fig. 13.
A comparison of the results from the SE model and the SS model is shown in Fig. 14 and Fig. 15 where the time region between 20 and 22 s is magnified. It can be seen that both models yielded the same results. Nevertheless, much more time was needed to carry out the simulation in the

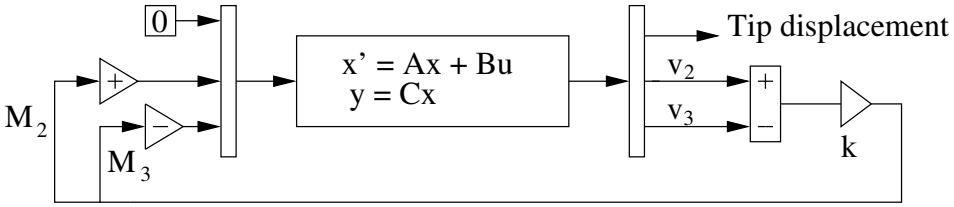


Figure 13: The SS model of the smart beam with controller (step 2).

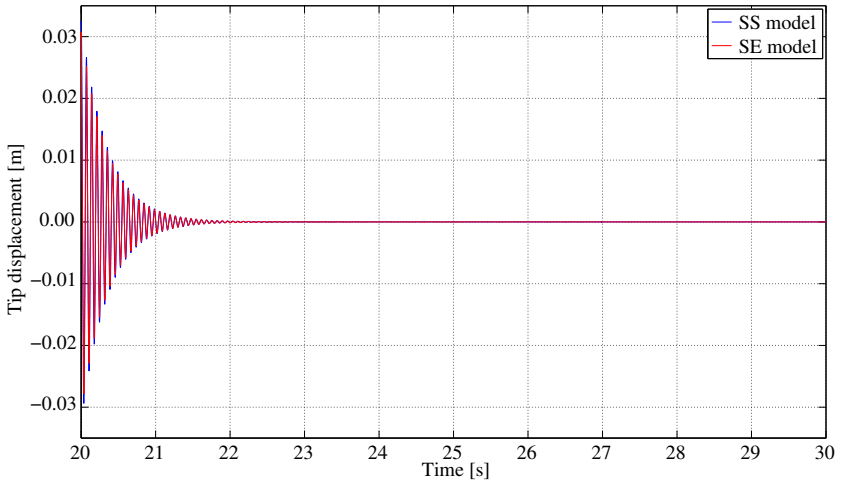


Figure 14: Tip displacement vs. time using SE and SS models.

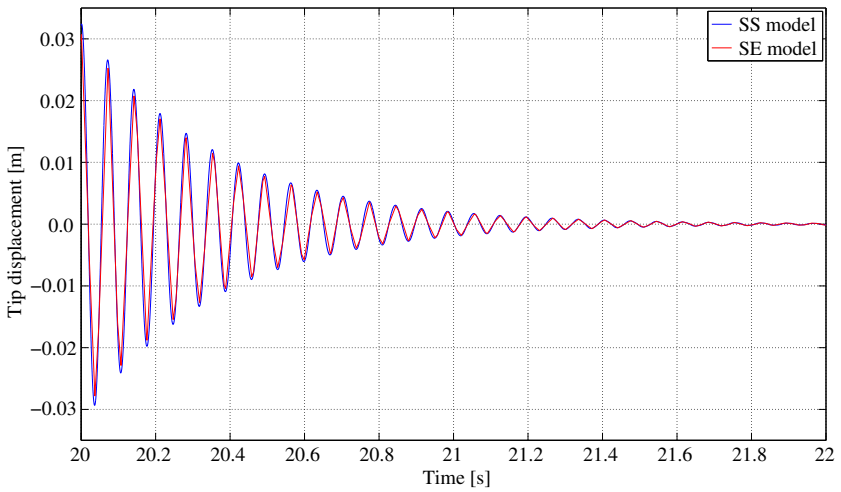


Figure 15: Tip displacement vs. time in a zoomed region of Fig. 14.

SS model (about 35 minutes), while in the SE model, less time (only 3 minutes) was needed. This could be due to the fact that in the SE model a fixed time-step can be assigned (here $0.01\ s$), while in the SS representation the time-step was automatically set. Moreover, the stresses and energy curves, could be requested in addition to the force vectors along the SE model. This is one of the advantages of the SE technique in comparison to the SS representation which is more practical and in which the controller can be easily implemented [33].

6 SUMMARY

In this work, a linear controller based on the Lyapunov stability theorem was designed and implemented on a reduced model of a smart structure. The state-space representation of the same model was extracted as well. The controller was implemented on this model too, and the results from both models were compared.

REFERENCES

[1] N. Ghareeb, Y. Radovcic, Fatigue analysis of wind turbines. *DEWI magasin*, **35**, 12–16, 2009.

[2] R. Vepa, *Dynamics of Smart Structures*. John Wiley & Sons, 2010.

[3] S. Narayanan, V. Balamurugan, Finite Element Modelling of Piezolaminated Smart Structures for Active Vibration Control with Distributed Sensors and Actuators. *Journal of Sound and Vibration*, **262**, 529–562, 2003.

[4] A. Mallock, A Method of Preventing Vibration in Certain Classes of Steamships. *Trans. Inst. Naval Architects*, **47**, 227–230, 1905.

[5] A. Vang, Vibration Dampening. *U.S. Patent US 2,361,071*, Oct. 24, 1944.

[6] M. Balas, Active Control of Flexible Systems. *Journal of Optimization theory and Applications*, **25**, No. 3, 415–436, 1978.

[7] V. Piefort, Finite Element Modelling of Piezoelectric Active Structures. *Universit Libre de Bruxelles, PhD Thesis*, 2001.

[8] J. Fanson, J. Chen, Structural Control by the Use of Piezoelectric Active Members. *Proceedings of NASA/DOD Control-Structures Interaction Conference*, NASA CP-2447, **2**, 809–830, 1986.

[9] A. Preumont, *Vibration Control of Active Structures, An Introduction*. Kluwer Academic Publishers, 2002.

[10] S. Moheimani, A. Fleming, *Piezoelectric Transducers for Vibration Control and Damping*. Springer, 2006.

[11] K.B. Waghulde, B. Sinha, M. Patil, S. Mishra, Vibration Control of Cantilever Smart Beam by Using Piezoelectric Actuators and Sensors. *International Journal of Engineering and Technology*, **2**, No. 4, 259–262, 2010.

[12] A. Gani, A. Salami, R. Khan, Active Vibration Control of a Beam with Piezoelectric Patches: Real-time Implementation with xPC target. *Proceedings of the IEEE Conference on Control Applications, CCA 2003*, **1**, 538–544, 23-25 June 2003.

[13] J. Block, T. Strganan, Applied Active Control for a Nonlinear Aeroelastic Structure. *Journal of Guidance, Control, and Dynamics*, **21**, No. 6, 838–845, 1998.

[14] V.V. Varadan, Y. Lim, V.K. Varadan, Closed loop finite-element modeling of active/passive damping in structural vibration control. *Smart Materials and Structures*, **5**, No. 5, 685–694, 1996.

[15] U. Gabbert, H. Köppe, T. Trajkov, Entwurf intelligenter Strukturen unter Einbeziehung der Regelung (English: Design of intelligent Structures including Regulation). *at - Automatisierungstechnik 50, Oldenbourg Verlag*, **9**, 432–438, 2002.

[16] H. Allik, T. Hughes, Finite Element Method for Piezoelectric Vibration. *International Journal for Numerical Methods in Engineering*, **2**, 151–157, 1970.

[17] N. Ghareeb, R. Schmidt, Modelling and control of a smart beam. *PAMM Proc. Appl. Mech.*, **12**, 703–704, 2012.

[18] N. Ghareeb, Design and Implementation of Linear Controllers for the Active Control of Reduced Models of Thin-Walled Structures. *RWTH Aachen University, PhD Thesis*, 2013.

[19] M. Petyt, *Introduction to Finite Element Vibration Analysis*. Cambridge University Press, 2003.

[20] R. Craig, M. Bampton, Coupling of Substructures for Dynamic Analyses. *AIAA Journal*, **6**, No. 7, 1313–1319, 1968.

[21] C. Rickelt-Rolf, Modellreduktion und Substrukturtechnik zur effizienten Simulation dynamischer, teilgeschädigter Systeme (English: Model Reduction and Substructuring for Efficient Simulation of Dynamic Partially-Damaged Systems). *Technische Universität Carolo-Wilhelmina zu Braunschweig, PhD Thesis*, 2009.

[22] J. Butterworth, J. Lee, B. Davidson, Experimental Determination of Modal Damping From Full Scale Testing. *13th World Conference on Earthquake Engineering*, Vancouver, Canada, August 1-6, 2004.

[23] A. Alipour, F. Zareian, Study Rayleigh Damping in Structures; Uncertainties and Treatments. *The 14th World Conference on Earthquake Engineering*, Beijing, China, October 12-17, 2008.

[24] L. Rayleigh, *Theory of Sound (two volumes)*. Dover Publications, New York, 1877.

[25] S. Adhikari, J. Woodhouse, Identification of Damping: Part 1, Viscous Damping. *Journal of Sound and Vibration*, **243**, No. 1, 43–61, 2001.

[26] I. Chowdhury, S. Dasgupta, Computation of Rayleigh Damping Coefficients for Large Systems. *The Electronic Journal of Geotechnical Engineering*, **8**, Bundle 8C, 2001.

[27] I. Giosan, Dynamic Analysis with Damping for Free-Standing Structures Using Mechanical Event Simulation. *Autodesk Report*, 2010.

[28] D. Ewins, *Modal Testing: Theory and Practice*. John Wiley & Sons Inc., 1984.

[29] K. Ogata, *Modern Control Engineering*. Prentice Hall, 2002.

[30] H. Khalil, *Nonlinear Systems*. Prentice Hall, Madison, 1996.

[31] G. C. Gorain, S. K. Bose, Boundary stabilization of a hybrid Euler-Bernoulli beam. *Proc. Indian Acad. Sci. (Math. Sci.)*, 1999.

[32] S.M. Newman, Active Damping Control of a Flexible Space Structure Using Piezoelectric Sensors And Actuators. *Naval Postgraduate School, Master Thesis*, 1992.

[33] N. Ghareeb, R. Schmidt, Modeling and Active Vibration Control of a Smart Structure. *Proceedings of the 9th international Conference on Informatics in Control, Automation and Robotics (ICINCO 2012)*, **1**, No. 86, 142–147, Rome, Italy, 2012

[34] O.C. Zienkiewicz, R.C. Taylor, *The finite element method, Vol. I, 4th Edition*. McGraw Hill, 1989.

[35] J.T. Oden, T. Belytschko, I. Babuska, T.J.R. Hughes, Research directions in computational mechanics. *Computer Methods in Applied Mechanics and Engineering*, **192**, 913–922, 2003.

[36] J.H. Argyris, M. Papadrakakis, L. Karapitta, Elastoplastic analysis of shells with the triangular element TRIC. M. Papadrakakis, A. Samartin, E. Oñate eds. *4th International Colloquium on Computation of Shell and Spatial Structures (IASS-IACM 2000)*, Chania, Crete, Greece, June 4-7, 2000.

COMPDYN 2013
4th ECCOMAS Thematic Conference on
Computational Methods in Structural Dynamics and Earthquake Engineering
M. Papadrakakis, V. Papadopoulos, V. Plevris (eds.)
Kos Island, Greece, 12–14 June 2013

INFLUENCE OF SOIL-STRUCTURE INTERACTION ON ISOLATED BUILDINGS FOR SF6 GAS-INSULATED SUBSTATIONS

L. E. Pérez Rocha[1], J. Avilés López[2], A. Tena Colunga[3], C. Cordero Macías[4]

[1] Instituto de Investigaciones Eléctricas
Cuernavaca 62490, Morelos, México
e-mail: lepr@iie.org.mx

[2] Instituto Mexicano de Tecnología del Agua
Jiutepec 62550, Morelos, México
e-mail: javiles@tlaloc.imta.mx

[3] Universidad Autónoma Metropolitana
Azcapotzalco 02200, Distrito Federal, México
e-mail: atc@correo.azc.uam.mx

[4] Comisión Federal de Electricidad
Cuauhtémoc 06500, Distrito Federal, México
e-mail: cuauhtemoc.cordero@cfe.gob.mx

Keywords: Soil-structure interaction, seismic isolation, floor spectra.

Abstract. *For earthquake excitation, base isolators have been successfully used in building structures on firm ground. However, the use of these devices in buildings on soft soil for SF6 gas-insulated substations introduces the following concerns: a) the frequency and damping characteristics of the fixed-base structure may change significantly by the combined effects of soil-structure interaction (SSI) and the base isolation device; and b) very large displacements may result because of the translation and rocking of the foundation. In this paper, the effects of SSI on the seismic response of a base-isolated MDOF system are investigated. Both kinematic and inertial effects are considered. The effective input motions (translation and rocking) for an embedded foundation are computed with the averaging Iguchi's method. The soil is replaced by frequency-dependent elastic springs and viscous dampers computed with a finite layer method. The SSI analysis is performed in the frequency domain with the complex frequency method. Numerical results, including floor response spectra of acceleration and displacement, are computed for SSI conditions prevailing in Mexico City, where SF6 gas-insulated substations are being projected. The base isolation device must be capable of accommodating displacements associated with different performance levels.*

1 INTRODUCTION

The dynamic soil-structure interaction (SSI) is a set of kinematic and inertial effects in the structure and the soil as a result of the deformability of the latter before seismic excitation [1]. The SSI modifies relevant dynamic properties that the structure had in the fixed base condition, as well as the ground motion characteristics around the foundation. Elongation of the fundamental period and increment of modal damping are due to inertial interaction. Besides, kinematic interaction reduces translational components (filtering high frequency) but also generates rotational components (rocking and torsion).

In the conventional approach of design free field surface spectra are often used. However, these spectra may not be representative of the motion of foundation. There are two neglected effects: a) the diffraction of incident waves by the foundation (kinematics interaction) and b) the effect on the soil of the inertia forces generated in the structure and foundation (inertial interaction). It is better to determine floor response spectra, computed with the actual motion of foundation that results from a complete SSI analysis. These site spectra with SSI are specific for the soil-structure system and are applied as free-field spectra, assuming fixed base structure.

To evaluate the feasibility of using seismic isolation in buildings for encapsulated substations in the Valley of Mexico, it is necessary to consider the effects of SSI in the model of analysis. To a first approximation, we considered fixed base models and free field excitations. Now we analyze the effects of SSI on the effectiveness of the insulation system, which aims to reduce the seismic forces when the effective flexibility and damping of support are increased.

SSI analysis is based on the principle of superposition in three steps [2], namely:

1. *Kinematic interaction:* Determination of foundation motion supposed rigid and massless under seismic waves propagation.
2. *Impedance Functions:* Computation of dynamic stiffness of the foundation supposed rigid and massless, which are defined by forces and moments required to produce unit harmonic displacements and rotations, respectively.
3. *Inertial interaction:* Determination of structure response supported on springs and dashpots in step 2 and subjected to the effective motion at its base from step 1.

2 FREE FIELD RESPONSE ANALYSIS

The free field response in a soil deposit can be computed with the one-dimensional model of propagation of shear waves [3]. This model allows to consider effects related to soil stratification, flexibility of the base and nonlinearity of materials. The seismic excitation is given in terms of a uniform hazard spectrum (UHS) at rock.

2.1 Design earthquake

The rock UHSs are constructed by the weighted contribution of all possible events, namely subduction earthquakes, normal faulting, and local intraplate. The weighting factor is given mainly by the seismicity of the various sources and their distance to the Valley of Mexico. Rock UHS (5% damping) for return period of 475 years, that is the basis of regulatory design spectra [4] was used in this study. It will be called as design earthquake.

Known the target response spectrum, synthetic accelerograms can be simulated. They are representative of the ground motion to the basement level. From these accelerograms, it is possible to compute the free field response at the surface. Specifically, a simulation method that accomplishes with prescribed spectral amplitudes is used. The principle of the method is to build transient signals whose response spectra iteratively fit the target response spectrum. Figs 1 and 2 show the synthetic accelerograms as well as the achieved compatibility with the objective response spectra. These movements are artificial but conservative, since the calculated spectral ordinates are adjusted in all vibration periods and not only in the characteristic periods of ground motion. These spectra exhibit two peaks in vibration periods near 0.25 and 1 s. The first is associated with near-field earthquakes (local and intraplate normal faulting) and the second far-field earthquakes (subduction).

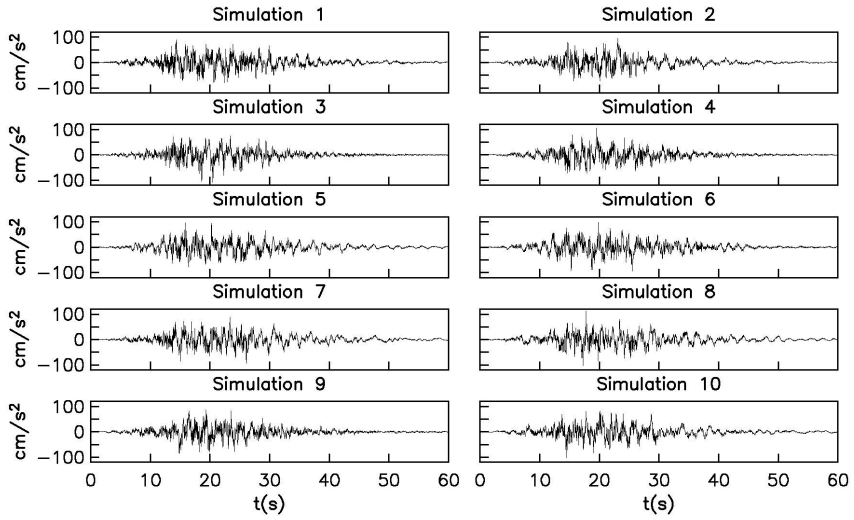


Fig. 1. Synthetic accelerograms on rock (x_g).

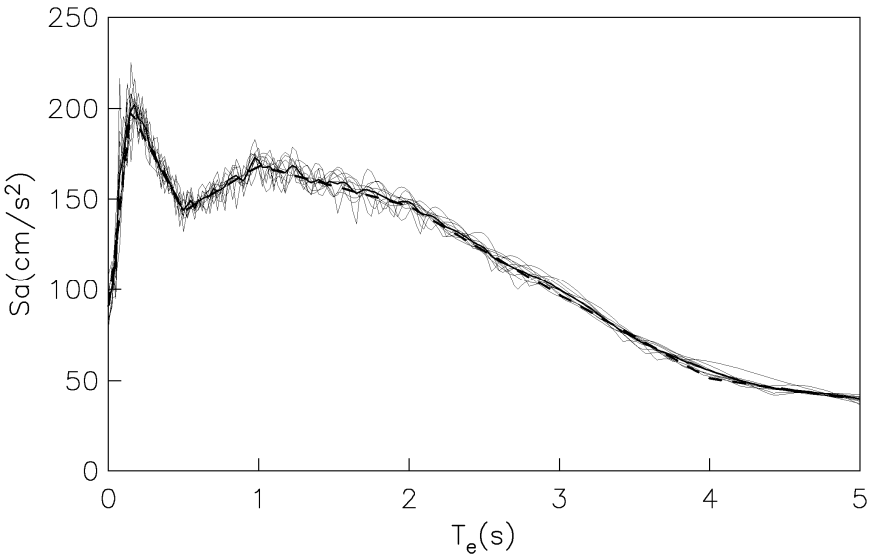


Fig. 2. Response spectra simulations (thin lines), average response spectrum (continuous thick line) and target uniform hazard spectrum (thick dashed line).

2.2 Stratigraphic model

For the specific site, called Narvarte, subsurface data are scarce. To account for the uncertainty in the data, random possible realization of the stratigraphic profile were generated, regarding the dominant period T_s and the depth to the basement H_s specified in regulatory seismic zoning maps [5]. For this site, the period is near 1 s. and the depth of the basement ic near 40 m. The effective velocity of the site is obtained as $V_s = 4H_s/T_s$. Estimated basement shear waves velocity V_r was such that the resonant response of the site, obtained with analytical transfer functions (stratigraphic model), was similar to that obtained with empirical transfer function (spectral ratios). For each simulation of the stratigraphic profile, free field response was calculated assuming vertical propagation of shear waves.

During intense earthquakes, soils may have nonlinear behavior in their dynamic properties. To account for the degradation of stiffness and increment of damping that occurs during great deformations of the soil, the equivalent linear method [6] is applied. This establishes an iterative linear analysis corrected dynamic parameters, which stops until achieve a desired convergence.

2.3 Free field spectra

The shape of the response spectra is strongly influenced by the period of the site. The spectra in free field surface reflect exclusively the amplification effects due to local soil conditions. For 5% damping, Fig. 3 shows the specific site response spectra, corresponding to the design earthquake.

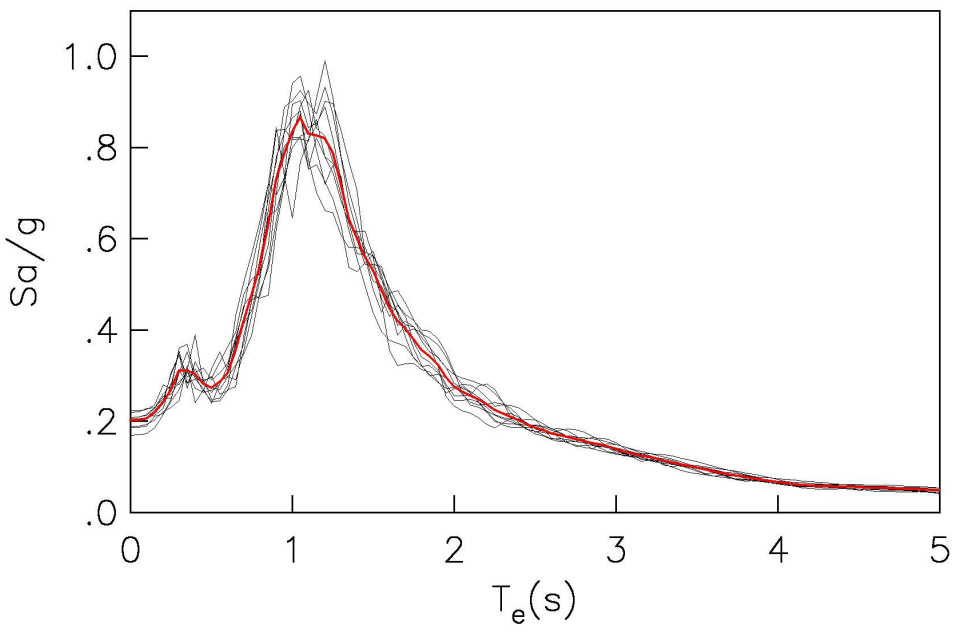


Fig. 3. Response spectra of simulations (thin black lines) and average response spectrum (thick red line), for design earthquake at Narvarte site.

3 EFFECTIVE EXCITATION AT THE BASE

Effective excitation at the base represents the input motion which results from superposing the free field with the field diffracted by the foundation. It is an artificial motion because is obtained by ignoring both the structure and the foundation masses. To calculate it is necessary to solve a complex problem of diffraction waves, hardly to model with commercial computer programs. In practical applications, the effective excitation at the base is calculated with the method of Iguchi [7]. According to this approximation method, the input motion is obtained by a weighted average of displacement and free field stresses around the foundation.

3.1 Normalized input motion

Transfer functions $H_x = \ddot{x}_b / \ddot{x}_g$ and $H_\theta = \ddot{\theta}_b / \ddot{x}_g$ were computed for an embedded foundation in a soil deposit under vertical incidence of shear waves. Damping ratios $\zeta_s = 5\%$ for soil and $\zeta_r = 3\%$ for the basement were used. These functions relate the amplitudes of the input motions (translation and rotation) with the amplitude of the free-field motion. Input motions, as dynamic stiffness are dimensionless function of frequency

$$\eta_m = \frac{\omega r_m}{V_s} \tag{1}$$

where r_m is the radius of a circle equivalent to the supporting surface of foundation with equal area and moment of inertia of that surface, ie:

$$r_x = \left(A/\pi\right)^{1/2} \tag{2}$$

$$r_\theta = \left(4I/\pi\right)^{1/4} \tag{3}$$

where A is the surface area of the foundation and I the corresponding moment of inertia respect to the axial axis of rotation, perpendicular to the direction of analysis.

4 SOIL SPRINGS AND DASHPOTS

Dynamic stiffness of foundation are complex quantities dependent of the frequency excitation. Real part expresses stiffness and inertia of the soil, while the imaginary part expresses material and geometric damping. Physically represent linear springs and viscous dashpots that replace the supporting soil.

4.1 Dynamic stiffness representation

The dynamic stiffness for any mode of vibration of the foundation ($m = h, r, hr$) is often expressed as [8]

$$\tilde{K}_m(\eta_m) = K_m^o[k_m(\eta_m) + i\,\eta_m c_m(\eta_m)](1 + i2\zeta_s) \tag{4}$$

where K_m^o is the static stiffness, k_m and c_m are the impedance coefficients and ζ_s is ground hysteretic damping. If K_m represents a linear spring and C_m a viscous damper, the dynamic stiffness is alternatively defined by expression [8]

$$\tilde{K}_m(\omega) = K_m(\omega) + i\omega C_m(\omega) \tag{5}$$

Therefore, the spring and dashpot are associated with the static stiffness and impedance coefficients by the following expressions:

$$K_m = K_m^o(k_m - 2\zeta_s \eta_m c_m) \tag{6}$$

$$\omega C_m = K_m^o(\eta_m c_m + 2\zeta_s k_m) \tag{7}$$

The spring K_m expresses not only rigidity but also inertia of the soil; dependence on frequency is due to the influence it has on the inertia. Furthermore, the damper C_m expresses material and geometric damping of the soil, the first is due to hysteretic behavior and the second to wave radiation.

Static stiffnesses K_h^o, K_r^o and $K_{hr}^o = K_{rh}^o$, as well as stiffness coefficients k_h, k_r and $k_{hr} = k_{rh}$ and damping coefficients c_h, c_r and $c_{hr} = c_{rh}$ were calculated by using a finite layer method [9] implemented in the computer program SUPELM [10]

5 SOIL-STRUCTURE INTERACTION ANALYSIS

Two approaches are commonly used to evaluate the effects of SSI. The first is to modify the dynamic properties of the original structure and evaluate the response of the modified structure subject to free-field motion. The second is to modify the free-field motion and evaluate the response of the original structure subjected to the motion modified by the foundation. The first approach is useful to consider the effects of SSI only in the fundamental mode of vibration, while the second approach is used to determine floor spectra applicable to all modes of the structure. In this work we adopt the second approach.

5.1 System Modeling

Fig. 4 (left) illustrates the model for the analysis of SSI in buildings with seismic isolation. For each direction of analysis, the structure is modeled as a shear beam with 4 degrees of freedom in horizontal translation and the foundation as a rigid block with two degrees of freedom, one in horizontal translation and the other in rotation. Additionally the deformation of the isolator is considered, which is modeled as a spring and dashpot in the interface between the superstructure and the substructure support. The soil is modeled with spring and dashpots that depend on the excitation frequency, although just the springs are shown, parallely also dashpots exist.

Because the dampings of soil and isolator are significantly higher than the one of the structure and therefore not proportional to its mass and stiffness, the system lacks classical modes of vibration, not allowing to perform a conventional modal superposition analysis.

The free-field motion x_g on the surface becomes an effective excitation in the base, whose translational $\ddot{x}_b$ and rotational $\ddot{\theta}_b$ components depend on the characteristics of the foundation and the soil, as well as on the nature of the seismic excitation. For vertical incidence of shear waves, the torsional component does not exist.

5.2 Equations of Motion

With reference to Fig. 4 (right), the degrees of freedom of the system are the displacements x_1, x_2, x_3, x_4 of the structure relative to its base, the deformation x_o of the isolator and the translation x_c and the rotation θ_c of the foundation relative to the ground. Given a ground motion with translational x_b and rotational θ_b components, the equations of motion can be obtained from the kinetic energy T and the potential energy V of system. Considering first the undamped system (conservative), these energies are given by

$$\begin{aligned} T = {} & \frac{1}{2}M_c(\dot{x}_b+\dot{x}_c)^2+\frac{1}{2}J_c(\dot{\theta}_b+\dot{\theta}_c)^2+\frac{1}{2}M_o(\dot{x}_b+\dot{x}_c+h_o(\dot{\theta}_b+\dot{\theta}_c)+\dot{x}_o)^2 \\ & +\frac{1}{2}M_1(\dot{x}_b+\dot{x}_c+h_1(\dot{\theta}_b+\dot{\theta}_c)+\dot{x}_o+\dot{x}_1)^2+\frac{1}{2}M_2(\dot{x}_b+\dot{x}_c+h_2(\dot{\theta}_b+\dot{\theta}_c)+\dot{x}_o+\dot{x}_2)^2 \\ & +\frac{1}{2}M_3(\dot{x}_b+\dot{x}_c+h_3(\dot{\theta}_b+\dot{\theta}_c)+\dot{x}_o+\dot{x}_3)^2+\frac{1}{2}M_4(\dot{x}_b+\dot{x}_c+h_4(\dot{\theta}_b+\dot{\theta}_c)+\dot{x}_o+\dot{x}_4)^2 \end{aligned} \tag{8}$$

$$\begin{aligned} V = {} & \frac{1}{2}K_h x_c^2+\frac{1}{2}K_{hr}x_c\theta_c+\frac{1}{2}K_r\theta_c^2+\frac{1}{2}K_{rh}\theta_c x_c+\frac{1}{2}K_o x_o^2+\frac{1}{2}K_1 x_1^2+\frac{1}{2}K_2(x_2-x_1)^2 \\ & +\frac{1}{2}K_3(x_3-x_2)^2+\frac{1}{2}K_4(x_4-x_3)^2 \end{aligned} \tag{9}$$

where M_c and J_c are the mass of the foundation and its moment of inertia, respectively, M_o, M_1, M_2, M_3, M_4 are the masses of the floor structure and h_o, h_1, h_2, h_3, h_4 the corresponding heights from the base foundation. Also, $K_h, K_r, K_{hr} = K_{rh}$ are the rigidities of the soil and K_o, K_1, K_2, K_3, K_4 inter-story stifnesses of the structure.

For a system with generalized coordinates $q_i = x_c, \theta_c, x_o, x_1, x_2, x_3, x_4$, the Lagrange equation of motion [11] are given by

$$\frac{d}{dt}\left(\frac{\partial T}{\partial \dot{q}_i}\right)+\frac{\partial V}{\partial q_i}=0 \tag{10}$$

Applying Eq. 10 to Eqs. 8 and 9, equations of motion of the system are obtained. Doing this and adding the damping, the following matrix system of equations are obtained:

$$\boldsymbol{M}_s\ddot{\boldsymbol{U}}_s(t)+\boldsymbol{C}_s\dot{\boldsymbol{U}}_s(t)+\boldsymbol{K}_s\boldsymbol{U}_s(t)=-\boldsymbol{M}_s\left\{\boldsymbol{s}_x\ddot{x}_b(t)+\boldsymbol{s}_\theta\ddot{\theta}_b(t)\right\} \tag{11}$$

where $\mathbf{U}_s=\{\mathbf{X}_e^T, x_o, x_c, \theta_c\}^T$ is the displacement vector of the system, being $\mathbf{X}_e^T=\{x_4, x_3, x_2, x_1\}$, $\mathbf{s}_x=\{\mathbf{0}^T, 1, 0\}^T$ and $\mathbf{s}_\theta=\{\mathbf{0}^T, 0, 1\}^T$. In addition, $\mathbf{M}_s$, $\mathbf{C}_s$ and $\mathbf{K}_s$ are the matrices of mass, damping and stiffness of the system, assembled as follows:

$$\boldsymbol{M}_s = \left[\begin{array}{c|ccc} \boldsymbol{M}_e & \boldsymbol{M}_e\boldsymbol{l}_x & \boldsymbol{M}_e\boldsymbol{l}_x & \boldsymbol{M}_e\boldsymbol{l}_\theta \\ \hline \boldsymbol{l}_x^T\boldsymbol{M}_e & M_o + \boldsymbol{l}_x^T\boldsymbol{M}_e\boldsymbol{l}_x & M_o + \boldsymbol{l}_x^T\boldsymbol{M}_e\boldsymbol{l}_x & M_o h_o + \boldsymbol{l}_x^T\boldsymbol{M}_e\boldsymbol{l}_\theta \\ \boldsymbol{l}_x^T\boldsymbol{M}_e & M_o + \boldsymbol{l}_x^T\boldsymbol{M}_e\boldsymbol{l}_x & M_c + M_o + \boldsymbol{l}_x^T\boldsymbol{M}_e\boldsymbol{l}_x & M_o h_o + \boldsymbol{l}_x^T\boldsymbol{M}_e\boldsymbol{l}_\theta \\ \boldsymbol{l}_\theta^T\boldsymbol{M}_e & M_o h_o + \boldsymbol{l}_\theta^T\boldsymbol{M}_e\boldsymbol{l}_x & M_o h_o + \boldsymbol{l}_\theta^T\boldsymbol{M}_e\boldsymbol{l}_x & J_c + M_o h_o^2 + \boldsymbol{l}_\theta^T\boldsymbol{M}_e\boldsymbol{l}_\theta \end{array}\right] \tag{12}$$

$$\boldsymbol{C}_s = \left[\begin{array}{c|ccc} \boldsymbol{C}_e & \boldsymbol{0} & \boldsymbol{0} & \boldsymbol{0} \\ \hline \boldsymbol{0}^T & C_o & 0 & 0 \\ \boldsymbol{0}^T & 0 & C_h & C_{hr} \\ \boldsymbol{0}^T & 0 & C_{rh} & C_r \end{array}\right] \tag{13}$$

$$K_s = \left[\begin{array}{c|ccc} \boldsymbol{K}_e & \boldsymbol{0} & \boldsymbol{0} & \boldsymbol{0} \\ \hline \boldsymbol{0}^T & K_o & 0 & 0 \\ \boldsymbol{0}^T & 0 & K_h & K_{hr} \\ \boldsymbol{0}^T & 0 & K_{rh} & K_r \end{array}\right] \tag{14}$$

where $\boldsymbol{l}_x = \{1, 1, 1, 1\}^T$ and $\boldsymbol{l}_\theta = \{h_4, h_3, h_2, h_1\}^T$ are vectors of coefficients of influence of the excitation. Also $\boldsymbol{M}_e$ and $\boldsymbol{K}_e$ are the mass and stiffness matrices of the fixed-base structure, given by

$$\boldsymbol{M}_e = \begin{bmatrix} M_4 & 0 & 0 & 0 \\ 0 & M_3 & 0 & 0 \\ 0 & 0 & M_2 & 0 \\ 0 & 0 & 0 & M_1 \end{bmatrix} \tag{15}$$

$$\boldsymbol{K}_e = \begin{bmatrix} K_4 & -K_4 & 0 & 0 \\ -K_4 & K_3 + K_4 & -K_3 & 0 \\ 0 & -K_3 & K_2 + K_3 & -K_2 \\ 0 & 0 & -K_2 & K_1 + K_2 \end{bmatrix} \tag{16}$$

To characterize the isolation system, it is necessary to introduce the following two parameters:

$$T_o = \frac{2\pi}{\omega_o} \quad \text{with} \quad \omega_o = \sqrt{\frac{k_o}{M_o + \sum_{n=1}^{4} M_n}} \tag{17}$$

$$\zeta_o = \frac{C_o}{2\left(M_o + \sum_{n=1}^{4} M_n\right)\omega_o} \tag{18}$$

where T_o is interpreted as the natural period ζ_o as the damping ratio of the isolation system with the structure assumed rigid.

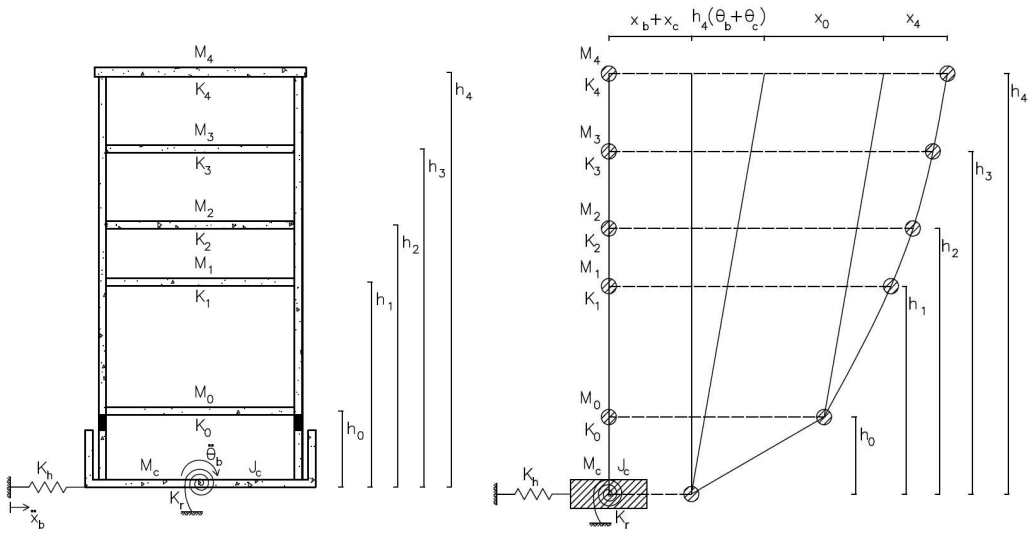


Fig. 4. (Left) Reference model for soil-structure systems with seismic isolation.
(Right) Deformed configuration of the soil-isolator-structure system.

5.3 Consideration of damping

To construct the damping matrix, it is assumed that the fixed-base structure has classical modes of vibration. This idealization is appropriate when the damping is uniformly distributed throughout the structure. So, damping ratios can be assigned to fixed-base natural modes and thus determine the damping matrix.

To construct a classical damping matrix from modal damping ratios, first natural frequencies ω_n and mode shapes matrix $\boldsymbol{\Phi}_e = [\boldsymbol{\Phi}_1, \boldsymbol{\Phi}_2, \boldsymbol{\Phi}_3, \boldsymbol{\Phi}_4]$ must be calculated solving the problem of eigenvalues

$$\left[\boldsymbol{K}_e - \omega_n^2 \boldsymbol{M}_e\right]\boldsymbol{\Phi}_n = \boldsymbol{0} \tag{19}$$

for the undamped structure. If the modes are normalized with respect to the mass such that

$$\boldsymbol{\Phi}_e^T \boldsymbol{M}_e \boldsymbol{\Phi}_e = \boldsymbol{I} = \begin{bmatrix} 1 & 0 & 0 & 0 \\ 0 & 1 & 0 & 0 \\ 0 & 0 & 1 & 0 \\ 0 & 0 & 0 & 1 \end{bmatrix} \tag{20}$$

then, it must be

$$\boldsymbol{\Phi}_e^T \boldsymbol{C}_e \boldsymbol{\Phi}_e = \boldsymbol{\zeta}_e = \begin{bmatrix} 2\zeta_1\omega_1 & 0 & 0 & 0 \\ 0 & 2\zeta_2\omega_2 & 0 & 0 \\ 0 & 0 & 2\zeta_3\omega_3 & 0 \\ 0 & 0 & 0 & 2\zeta_4\omega_4 \end{bmatrix} \tag{21}$$

From here, the damping matrix is deduced as

$$\boldsymbol{C}_e = [\boldsymbol{\Phi}_e^T]^{-1} \boldsymbol{\zeta}_e [\boldsymbol{\Phi}_e]^{-1} \tag{22}$$

The damping ratios ζ_n are reasonably assigned to each mode depending on the characteristics of the structure. Here, 5% damping for all modes is considered. The computation of the damping matrix can be improved by using the orthogonality relation given by Eq. 20. Specifically, it can be seen that

$$[\boldsymbol{\Phi}_e]^{-1} = \boldsymbol{\Phi}_e^T \boldsymbol{M}_e \tag{23}$$

$$[\boldsymbol{\Phi}_e^T]^{-1} = \boldsymbol{M}_e \boldsymbol{\Phi}_e \tag{24}$$

Substituting Eqs. 23 and 24 in Eq. 22, it is has

$$\boldsymbol{C}_e = \boldsymbol{M}_e [\boldsymbol{\Phi}_e \boldsymbol{\zeta}_e \boldsymbol{\Phi}_e^T] \boldsymbol{M}_e \tag{25}$$

In terms of modal superposition, Eq. 25 is expressed as

$$\boldsymbol{C}_e = \boldsymbol{M}_e \left(\sum_{n=1}^{4} 2\zeta_n \omega_n [\boldsymbol{\phi}_n \boldsymbol{\phi}_n^T] \right) \boldsymbol{M}_e \tag{26}$$

Each term of the sum represents the contribution of the n-th modal damping of the damping matrix. The contribution of the higher modes of vibration can be neglected without numerical problems.

5.4 System Response

To determine the response of the system is convenient to use the method of the complex frequency response [11]. Thus, natural frequencies of the system and amplitudes of vibration of the considered degrees of freedom, can be simultaneously computed. Applying the Fourier transform in both sides of Eq. 11, it is has that

$$\left[\boldsymbol{K}_s + i\omega \boldsymbol{C}_s - \omega^2 \boldsymbol{M}_s \right] \boldsymbol{U}_s(\omega) = -\ddot{x}_g(\omega) \boldsymbol{M}_s \left\{ \boldsymbol{s}_x H_x(\omega) + \boldsymbol{s}_\theta H_\theta(\omega) \right\} \tag{27}$$

where $\boldsymbol{U}_s(\omega)$ and $\ddot{x}_g(\omega)$ represent the Fourier transformed of the system response and the excitation on the surface, respectively. Solving Eq. 27 it is obtained the response of the system in the frequency domain, from which the corresponding response can be determined in the time domain through Fourier's synthesis.

Identifying the frequencies of the fixed base structure is possible by the transfer function of the roof

$$H_e(\omega) = \frac{x_b + x_c + h_4(\theta_b + \theta_c) + x_o + x_4}{x_g} \tag{28}$$

For the computation of floor spectra, it is necessary to determine the transfer function of the base

$$H_o(\omega) = \frac{x_b + x_c + h_o(\theta_b + \theta_c) + x_o}{x_g} \tag{29}$$

These complex functions relate the roof or base-structure responses with the excitation on the ground surface.

6 RESULTS FOR THE STUDIED CASE

For the SSI analysis, the structural model SF6 was used (shown in fig 5), properly stiffnessed with perimetral chevron braced to avoid the presence of a soft first floor. This is the model for the building with fixed base, without considering base isolators and supporting soil.

Table 1 contains weights and heights of each floor, as well as inter-story stiffnesses in two orthogonal directions. On the other hand, x direction corresponds to the rigid side, with fundamental period $T_x = 0.5$ s, and y direction corresponds to the flexible one, with fundamental period $T_y = 0.6$ s. The weight of the isolated structure is $W_o = 833.29$ t. The stiffness of the system for a period $T_o = 3.5$ s is $K_o = 4\pi^2 W_o / gT_o^2 = 2.74$ t/cm. The foundation is a rectangular slab of 20.1 m length, 13.80 m width and 3.5 m depth.

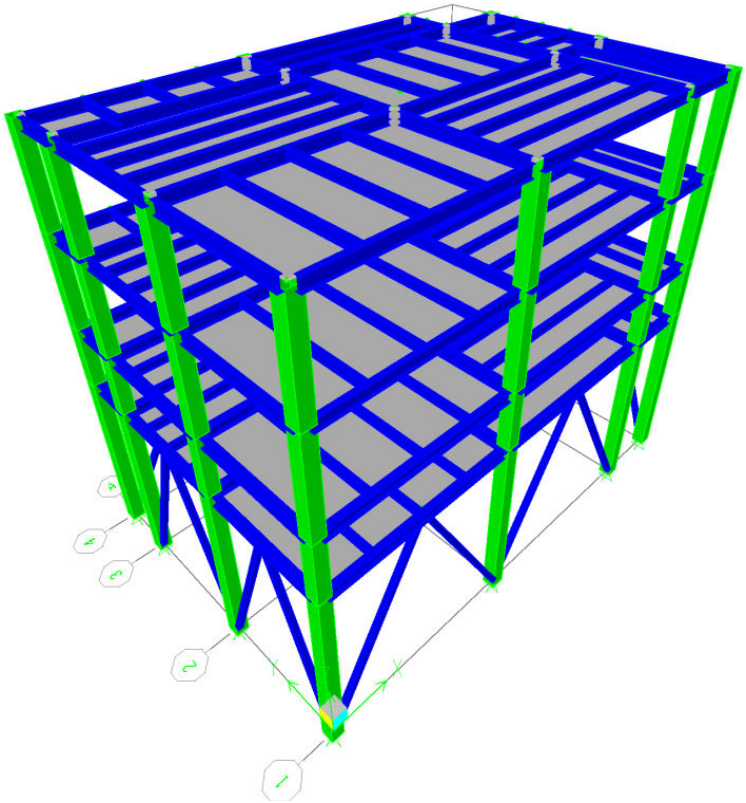


Fig. 5. Model of the SF6 building with fixed base

Level	W (t)	h (m)	Kx (t/cm)	Ky (t/cm)
4	134.79	20.90	79.61	60.41
3	141.66	17.10	119.20	93.84
2	142.75	13.30	298.24	221.61
1	160.25	10.80	219.70	120.52
0	253.84	3.5	2.74	2.74
Base	330.97		Variable	Variable

Table 1. Parameters of the SF6 building isolated at its base

6.1 Transfer functions

Transfer functions allows to simultaneosly identify natural frequencies of the system and amplitudes of vibration of the degrees of freedom. Fig. 6 shows roof transfer functions for the structure with fixed-base ($K_o = \infty$ and $V_s = \infty$) and for the isolated structure without and with SSI effects. Computations were done for the two directions of analysis, considering the damping factors $\zeta_o = 5$ and 15% for the isolation system.

Transfer functions that show major amplifications are the ones corresponding to the fixed-base structure, while functions that show minor amplification are the ones corresponding to the isolated structure without SSI. The SSI effects are little significant in high frecuencies, near to the frequencies of the structure with fixed base. Dynamic decoupling between the isolation period and the fundamental period of the structure grows when SSI is considered, such that the seismic isolation continues to be effective.

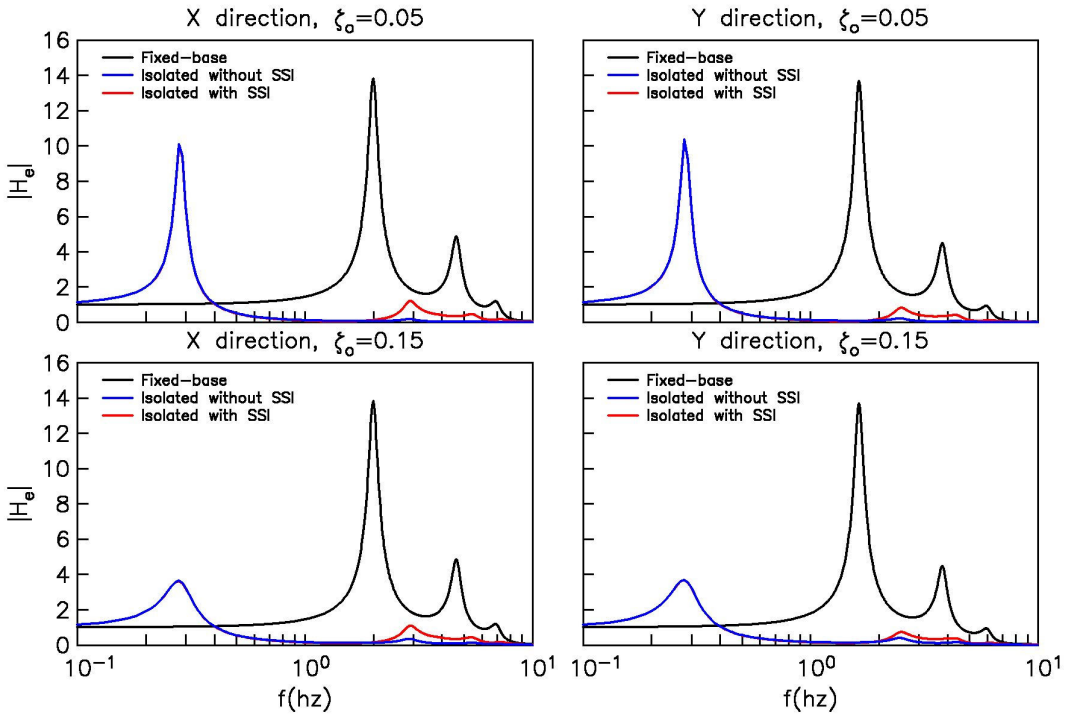


Fig. 6. Roof transfer functions for the fixed-base structure (black) and for the isolated structure without (blue) and with (red) SSI, Narvarte site.

6.2 Displacements and shear forces distribution

To determine the time response under seismic excitation, convolution of the system transfer functions with design simulated earthquakes were done. Average values of peak shear forces and displacements for the fixed-base structure and the isolated structure without and with SSI were computed.

Fig. 7 shows shear force and lateral displacement distributions from the roof to the base foundation, for the fixed-base structure ($K_o = \infty$ and $V_s = \infty$) and for the isolated structure

without and with SSI. Calculations were done for the two directions of analysis, considering damping ratios $\zeta_o = 5$ and 15% for the isolation system.

The SSI effects in the shear force are relatively more important than in the displacement, especially in the superior floors. The effectiveness of the isolation, when SSI is accounted for, is preserved even for low damping ratio. The relative displacements of the structure, behaved as rigid body, become insignificant when compared with the deformations of the isolators, which are less than 30 cm for 5% damping.

It should be noted that the computation of seismic forces and lateral displacements for the design earthquake, was done disregarding the inelastic behavior of the base isolators. Contrarily, the non linear behavior of the supporting soil was accounted for.

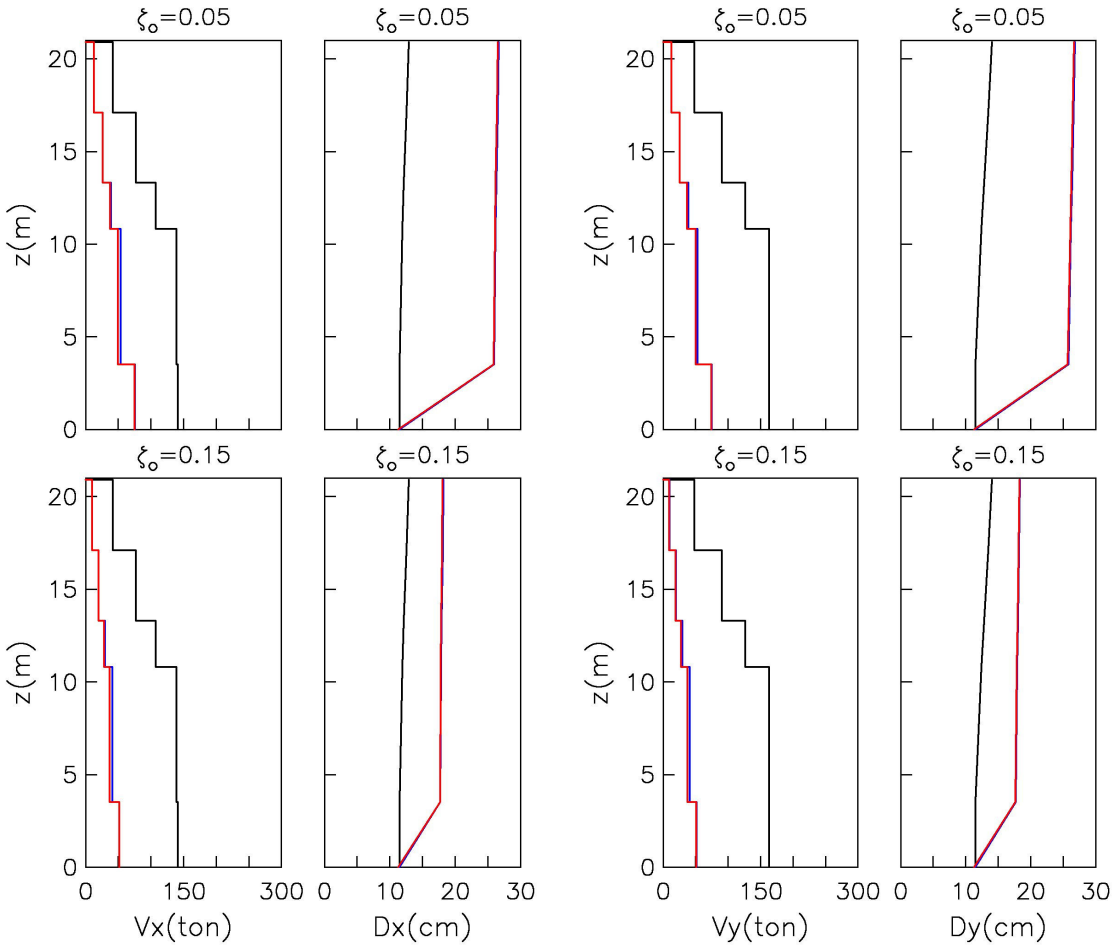


Fig. 7. Variations of shear force and displacement with the heihght for the fixed-base structure (black) and for the isolated structure without (blue) and with (red) SSI. Narvarte site.

6.3 Floor spectra

Floor spectra represent the easiest way to estimate SSI effects in the effectiveness of the isolation. Fig. 8 shows such spectra for the isolated structure without and with SSI effects, compared with the free-field spectrum. Computations were done for both directions of analysis, considering damping ratios $\zeta_o = 5$ and 15% for the isolation system. Changes on response spectra in short periods are due to the SSI effects, being kinematic effects more important than inertial effects. These results show that smaller seismic forces are developed in the structure-isolator system (without SSI) than in the structure-isolator-soil system (with SSI), although SSI effects are relevant only in short periods. Additionally, it is shown that the effectiveness of the isolation is notably increased for 15% damping.

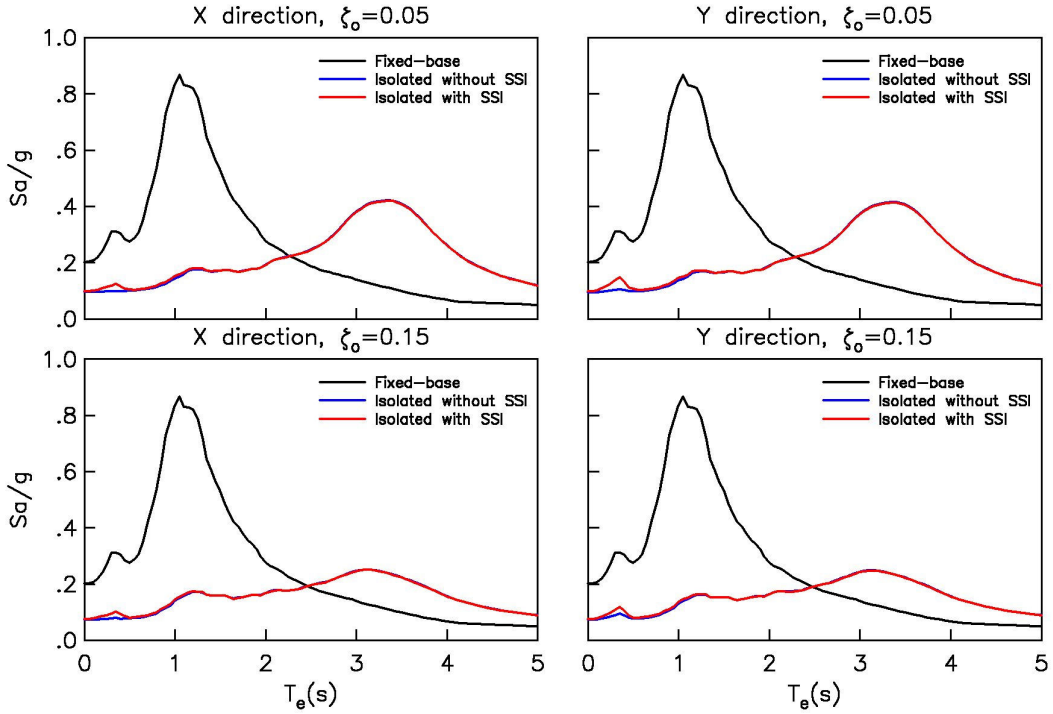


Fig. 8. Response spectra for the fixed-base structure (black) and for the isolated structure without (blue) and with (red) SSI. Narvarte site.

7 CONCLUSIONS

- The aim of this study was to evaluate the feasibility of using seismic isolation in buildings for encapsulated substations in the Valley of Mexico. To do that, it was necessary to consider the effects of SSI (kinematic and inertial) in the model of analysis.
- Seismic excitation was given in terms of a uniform hazard spectrum (UHS) at rock for 475 year return period.
- The studied site, called Narvarte, is near 1 s period, and 40 m depth basement.
- Frequencies identification of the fixed base structure was done by using the transfer function of the roof. For the computation of floor spectra, the transfer function of the base was used.

- Transfer functions that show major amplifications are the ones corresponding to the fixed-base structure, while functions that show minor amplification are the ones corresponding to the isolated structure without SSI. The SSI effects are little significant in high frequencies, near to the frequencies of the structure with fixed base.
- SSI effects in the shear force are relatively more important than in the displacement, especially in the superior floors. The effectiveness of the isolation, when SSI is accounted for, is preserved even for low damping ratio. The relative displacements of the structure, behaved as rigid body, become insignificant when compared with the deformations of the isolators, which are less than 30 cm for 5% damping.
- Results show that smaller seismic forces are developed in the structure-isolator system (without SSI) than in the structure-isolator-soil system (with SSI), although SSI effects are relevant only in short periods. Additionally, it is shown that the effectiveness of the isolation is notably increased for 15% damping.

REFERENCES

[1] A. S. Veletsos, Design concepts for dynamics of soil-structure interaction, Eds. P Gülkan and R W Clough, Kluwer Academic Publishers, 1993.

[2] E. Kausel, R. V. Whitman, J. P. Morray and F. Elsabee, The spring method for embedded foundations, *Nuclear Engineering and Design*, Vol. 48, 1978.

[3] N. A. Haskell, Crustal reflection of plane P and SV waves, *Journal of Geophysical Research*, Vol. 67, 1962.

[4] M. Ordaz, E. Miranda and J. Avilés, Propuesta de espectros de diseño por sismo para la ciudad de México, *Ingeniería de Estructuras*, Vol. 8, 2003.

[5] NTCDS-RCDF (2004), Normas Técnicas Complementarias para Diseño por Sismo, *Reglamento de Construcciones para el Distrito Federal*, Gaceta Oficial del Departamento del Distrito Federal.

[6] H. B. Seed and I. M. Idriss, Influence of soil conditions on ground motions during earthquakes, *Journal of the Soil Mechanics and Foundation Division*, ASCE, Vol. 95, 1969.

[7] M. Iguchi, An approximate analysis of input motions for rigid embedded foundations, *Transactions of Architectural Institute of Japan*, No. 315, 1982.

[8] G. Gazetas, Analysis of machine foundation vibrations: state of the art, *Soil Dynamics and Earthquake Engineering*, Vol. 2, 1983.

[9] J. L. Tassoulas J L and E Kausel, Elements for the numerical analysis of wave motion in layered strata, *Journal of Numerical Methods in Engineering*, Vol. 19, 1983.

[10] E. Kausel, Program SUPELM Ver. 2.0, Foundations Embedded in Layered Media: Dynamic Stiffnesses and Response to Seismic Waves, 1992.

[11] R. W. Clough and J. Penzien, *Dynamics of Structures*, McGraw-Hill, 1975.

COMPDYN 2013
4th ECCOMAS Thematic Conference on
Computational Methods in Structural Dynamics and Earthquake Engineering
M. Papadrakakis, V. Papadopoulos, V. Plevris (eds.)
Kos Island, Greece, 12–14 June 2013

ROT INDEX FOR ASSESSING THE TORSIONAL EFFECT ON THE SEISMIC PERFORMANCE OF RC BUILDINGS

Chrysanthi Stathi[1], Nikolaos P. Bakas[1], Nikos D. Lagaros[1] and Manolis Papadrakakis[1]

[1] Institute of Structural Analysis &Antiseismic Research
School of Civil Engineering
National Technical University of Athens
Zografou Campus
Athens 157 80, Greece
e-mail: {cstathi, nibas, nlagaros, mpapadra}@central.ntua.gr

Keywords: Torsion effect, mass eccentric, center of rigidity, nonlinear dynamic analysis, reinforced concrete, multi-story buildings.

Abstract. *Due to the eccentric setback nature of structures, torsional moments will be induced by a set of lateral loads on buildings. Although the effect on the response of reinforced concrete buildings was the subject of intensive research over the last decades still lacks a criterion valid in both elastic and plastic region. In this study a criterion capable of assessing torsional effect is proposed. In order to evaluate the proposed criterion with code provisions, two test examples are considered. A torsionally stiff, mass eccentric one-storey and a four-storey horizontally irregular building designed according to Eurocode provisions subjected to bidirectional excitation are considered. Nonlinear dynamic analyses are carried out implementing natural record selected for three hazard levels. The performance of the proposed criterion is evaluated and its correlation with other structural response quantities like interstorey drifts, displacements, base torque, shear forces and diaphragm rotation is presented. Through this investigation it was found that the proposed criterion is able to provide a reliable prediction of the magnitude of torsional effects for all test cases considered.*

1 INTRODUCTION

In most current torsional provisions, the effect of torsion is treated implementing accidental and static eccentricity along with imposing restrictions on the design for buildings with irregular layout. Accidental eccentricity is defined as a fraction of the plan dimension of the layout perpendicular to the direction of applied lateral forces. When it comes to static eccentricity interpretation becomes more complicated, since there is no uniformity in definition. Many researchers define as static eccentricity the distance between centre of mass and centre of rigidity, while others the distance between centre of mass and shear centre. For one-story systems, there is a point on the diaphragm owns the following properties: (I) does not rotate when lateral load is applied through it (centre of rigidity), (II) the resultant of shear forces passes through it when no rotation is developed on the diaphragm (shear centre) and (III) remains stationary when the structure is subjected to torque loading (centre of twist). The various centers are coincident and load-independent for one-story systems, but the same does not happen for the multistory ones. Tso [1] clarifies the two approaches aiming to measure the story torsional moments for multistory buildings and concluded that if the proper definitions are used, the result remains the same irrespectively of which one is adopted. Inconsistent conclusions observed have been attributed to the varying model assumptions implemented, while a detailed overview has been presented by Rutenberg [2]. Many researchers also studied the efficiency of torsional codified provisions [3, 4, 5]. Lagaros *et al.* [6] proposed a combined topology and sizing formulation for the optimum design of RC buildings aiming to minimize the cost, the static and strength eccentricities as well as several combinations of them, in order to improve the torsional seismic response of RC buildings in various hazard levels, taking into account both design code and architectural restrictions.

As far as the inelastic state of response is concerned, De la Llera and Chopra [7, 8] proposed the base shear and torque surfaces (BST), which represent all combinations of base shear and torque that would lead to collapse of the structure when applied statically. Furthermore, they suggested a simplified model based on a super-element per building story, capable of representing the elastic and inelastic properties of the story. Paulay [9, 10] presented the centre of resistance and identified the plastic mechanism developed, aiming to estimate the torsional effects on the seismic response of ductile buildings, classified as either torsionally unrestrained or restrained. Myslimaj and Tso [11, 12] proved that the torsional effects can be alleviated for asymmetric wall-type systems by locating the centre of strength and the centre of rigidity on the opposite sides of the centre of mass. Anagnostopoulos *et al.* [13] pointed the inadequacies of the simplified one-story, shear-beam type systems for predicting the inelastic response of real, asymmetric, multistory frame buildings, subjected to torsion due to earthquake motions and consequently for deriving general conclusions about torsional provisions of the codes.

In order to assess the torsional effect on the seismic response of multistory buildings, a new index is proposed. Its performance is evaluated considering a single story and a four-story building. Symmetric counterparts were designed according to Eurocode pre-standards. Intentionally, asymmetry was not considered in the design in order to eliminate any torsional code influence from the results. The Code specified accidental eccentricities $0.05\,L_X$ and $0.05\,L_Y$ are also applied to each building. Two-component seismic excitations are used for the nonlinear dynamic analyses for all states of response. While base torque, diaphragm rotation, interstorey drifts, displacements and shear forces are chosen as response parameters of the buildings examined.

2 TREATMENT OF THE TORSIONAL EFFECT

Some fundamental features of the torsional response for multistory buildings are summarized here. Apart from eccentricity, as mentioned above, centre of rigidity can not be defined also in a strict manner for a story or stories of a multistory building. While Humar [14] interpreted the center of rigidity at a floor as the point through which the resultant lateral forces at that floor can pass without causing rotation at that floor. The other floors may or may not have rotations. Smith and Vezina [15] defined it at a particular level of a multistory building subjected to a particular vertical distribution of horizontal loading as the point in the plane of the floor through which the external horizontal load at that floor must act for it to apply no torque to the structure. There are also more definitions [16, 17] formulated but they are omitted here due to space limitations. Based on the undamped equations of motion for a multistory building, assuming linear behavior, subjected to earthquake ground motion along the x and y directions, the coordinates of the centers of rigidity are given by the equations below:

$$\mathbf{x}_{CR} = \frac{\mathbf{K}_{Y\theta} - \mathbf{K}_{YX}\mathbf{K}_{X}^{-1}\mathbf{K}_{X\theta}}{\mathbf{K}_{Y} - \mathbf{K}_{YX}\mathbf{K}_{X}^{-1}\mathbf{K}_{XY}}$$
$$\mathbf{y}_{CR} = \frac{\mathbf{K}_{X\theta} - \mathbf{K}_{XY}\mathbf{K}_{Y}^{-1}\mathbf{K}_{Y\theta}}{\mathbf{K}_{X} - \mathbf{K}_{XY}\mathbf{K}_{Y}^{-1}\mathbf{K}_{YX}} \tag{1}$$

where $\mathbf{K}_X$, $\mathbf{K}_Y$, $\mathbf{K}_{XY}$, $\mathbf{K}_{X\theta}$ and $\mathbf{K}_{Y\theta}$ are the corresponding submatrices of the building global stiffness matrix. However, the matrices $\mathbf{x}_{CR}$ and $\mathbf{y}_{CR}$ were defined as diagonal matrices and the expressions (1) do not, in general, yield diagonal matrices implying that unique centers of rigidity do not always exist. In such a case, centers of rigidity can still be defined sometimes even if the expressions above does not yield diagonal matrices, but their locations depend on the applied set of static lateral forces (equations (2)).

$$\left\{\mathbf{x}_{CR}\right\} = \left[\mathbf{P}_Y\right]^{-1} \frac{\mathbf{K}_{Y\theta} - \mathbf{K}_{YX}\mathbf{K}_{X}^{-1}\mathbf{K}_{X\theta}}{\mathbf{K}_{Y} - \mathbf{K}_{YX}\mathbf{K}_{X}^{-1}\mathbf{K}_{XY}} \mathbf{P}_Y$$
$$\left\{\mathbf{y}_{CR}\right\} = -\left[\mathbf{P}_X\right]^{-1} \frac{\mathbf{K}_{X\theta} - \mathbf{K}_{XY}\mathbf{K}_{Y}^{-1}\mathbf{K}_{Y\theta}}{\mathbf{K}_{X} - \mathbf{K}_{XY}\mathbf{K}_{Y}^{-1}\mathbf{K}_{YX}} \mathbf{P}_X \tag{2}$$

where $\mathbf{P}_X$ and $\mathbf{P}_Y$ being the vectors of static lateral forces applied. This means that different load distributions would lead to different locations of the centers of rigidity [18]. There is still a special class of building, named buildings with proportional framing, for which the various centers (center of rigidity, shear center and center of twist) exist and are at coincident locations, load independent and lying on a vertical line [18, 19]. The determination of the center of rigidity becomes even more complex in the nonlinear dynamic analysis.

A valid indicator also for the torsional behaviour in the elastic domain is the uncoupled frequency ratio Ω (uncoupled torsional frequency divided by the translational one). For a multi-storey building, whose predominant mode is translational the value of the ratio is greater than unity and is classified as torsionally stiff. A building is classified as torsionally flexible when its predominant mode is torsional. In case of torsionally stiff buildings the displacements on the flexible edge are increased in comparison with its symmetric counterpart. The opposite trend was observed for the stiff edge. Torsionally flexible buildings may exhibit displacement increase at both edges or largest translation at stiff edge. These indices are valid for the elastic range, where the response of all elements remain in the elastic state. When elements start yielding, the characteristics described above are affected. The instantaneous locus

of the centre of rigidity changes, as a consequence the amount of eccentricity is influenced in the elastoplastic range. While for the plastic state of response strength eccentricity considered a more representative indicator, computed as the distance between the center of mass and the center of strength. The center of strength is defined as the point that if resultant of lateral forces act through it and story reaches to mechanism, no rotation happens in that story, when all the degrees of freedom of lower stories are restrained.

3 THE RATIO OF TORSION

Due to the eccentricity of structures, torsional moments will be imposed on the building by the existing lateral loads. These moments are sustained by the system as a pair of shear forces. So the torsion effect on buildings is quantified as torsion-induced displacements via torsion-induced shear forces on certain elements. Applying lateral loading P_i, shear forces V_{ij} are developed at each vertical structural element. Figure 1 shows a generalized floor plan view where shear walls and the corresponding shear forces are depicted.

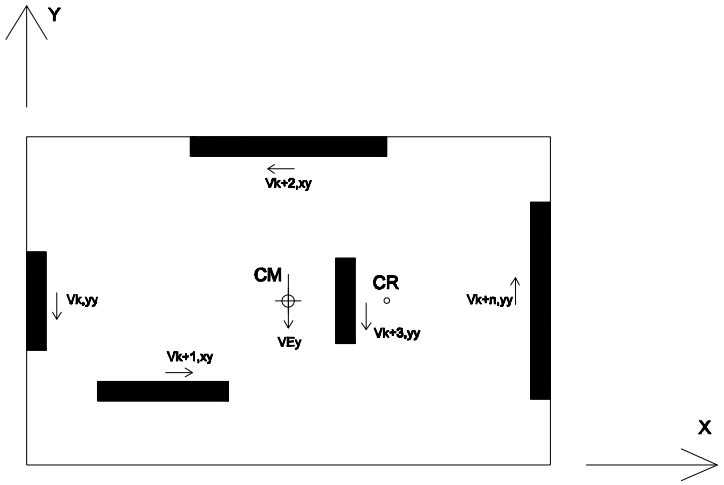


Figure 1: A typical plan view.

Without loss of generality the seismic action is considered along one direction only. While force V_{Ey}, is being developed, with few exceptions, elements along x direction are expected to remain elastic. They will therefore sustain the base torque, as a pair of forces, and restrain the diaphragm rotation. The shear forces acting on the lateral resisting structural elements satisfy the following expression:

$$\sum_{k=1}^{n} \left| V_{kij} \right| \neq \sum_{k=1}^{n} V_{kij} \tag{3}$$

where n is the number of vertical structural elements of the floor diaphragm, while i and j denote the direction of the shear force of the element k and that of earthquake with reference to the structural axes x and y respectively. The sum of the absolute values of resisting elements' shear forces differs from their algebraic. This observation is attributed to torsional components of the shear forces, since torsional moment is sustained by the system as a pair of opposing forces. For the plan view of Figure 1 and seismic action along the y direction only, the following relations are satisfied:

$$\sum_{k=1}^{n}\left|V_{kxy}\right| \neq \sum_{k=1}^{n} V_{kxy} = 0$$
$$\sum_{k=1}^{n}\left|V_{kyy}\right| \neq \sum_{k=1}^{n} V_{kyy} = V_{Ey} \tag{4}$$

The torsion induced in the floor is usually computed from the shear forces of the structural elements, while the elements torsional moments are neglected.

The proposed criterion Ratio Of Torsion (*ROT*) represent a measure to quantify the torsional effect induced by asymmetry in plan layout. The general formulation of *ROT* is defined as:

$$ROT = \frac{\sum_{k=1}^{n}\sum_{i=x,\,j=y}^{y,x}\left|V_{kij}\right| - \left|V_{Ex}\right| - \left|V_{Ey}\right|}{\left|V_{Ex}\right| + \left|V_{Ey}\right|} \tag{5}$$

where V_{Ex} and V_{Ey} the design base shear along x and y directions.

Static equilibrium leads to:

$$\sum_{k=1}^{n}\sum_{j=y}^{x} V_{kxj} = V_{Ex}$$
$$\sum_{k=1}^{n}\sum_{j=y}^{x} V_{kyj} = V_{Ey} \tag{6}$$

ROT formulation take the form:

$$ROT = \frac{\sum_{k=1}^{n}\sum_{i=x,\,j=y}^{y,x}\left|V_{kij}\right| - \left|\sum_{k=1}^{n}\sum_{j=y}^{x} V_{kxj}\right| - \left|\sum_{k=1}^{n}\sum_{j=y}^{x} V_{kyj}\right|}{\left|\sum_{k=1}^{n}\sum_{j=y}^{x} V_{kxj}\right| + \left|\sum_{k=1}^{n}\sum_{j=y}^{x} V_{kyj}\right|} \tag{7}$$

For implementing the proposed index for multi-storey buildings, equation (7) can be computed for every floor of a building. Taking into consideration that the *ROT* value does not follow any particular trend or uniform distribution for the different floors, it is considered more representative for multi-story buildings to be computed equal to the sum of its value of all floors, according to:

$$\sum_{m=1}^{l} ROT \tag{8}$$

where l the number of building's stories. As in the case of one-storey systems, its value is computed for every analysis step and the maximum is compared to maximum values of other response quantities related to torsion as base torque and upper diaphragm's rotation.

4 NUMERICAL MODELING AND SEISMIC LOADS CONSIDERED IN THIS STUDY

Nonlinear static or dynamic analysis needs a proper simulation of the structure in the regions where inelastic deformations are expected to develop. In order to consider the inelastic

behaviour either the plastic-hinge or the fibre approach can be adopted. For some researchers the plastic hinge approach has limitations in terms of accuracy and therefore fibre beam-column elements are preferred [20]. According to the fibre approach, each structural element is discretized into a number of integration sections restrained to the beam kinematics, and each section is divided into a number of fibres with specific material properties (A_{fib}, E_{fib}). Every fibre in the section can be assigned to different material properties, e.g. concrete, structural steel, or reinforcing bar material properties, while the sections are located at the Gaussian integration points of the elements. The main advantage of the fibre approach is that every fibre has a simple uniaxial material model allowing an easy and efficient implementation of the inelastic behaviour. In the numerical test examples section that follows all analyses have been performed using the OpenSEES [21] platform. A bilinear material model with pure kinematic hardening is adopted for the structural steel, while geometric nonlinearity is explicitly taken into consideration. For the simulation of the concrete the modified Kent-Park model, where the monotonic envelope of concrete in compression follows the model of Kent and Park [22] as extended by Scott *et al.* in [23], is employed. This model was chosen because it allows for an accurate prediction of the demand for flexure-dominated RC members despite its relatively simple formulation.

5 NUMERICAL EXAMPLES

The results of time history analyses for the different numerical examples are presented in terms of maximum values of the response parameters over pairs of applied motions. As response parameters interstorey drifts, displacements, shear forces of the columns, base shear and diaphragm rotation were considered and their structural behavior was examined. For this purpose a number of nonlinear time history analyses have been carried out employing three natural ground motion records for each hazard level (2%, 10%, 50%) chosen from the Somerville and Collins [24]. The records of each hazard level are scaled to the same PGA where in order to ensure compatibility between the records, in accordance to the hazard curve taken from the work by Papazachos *et al*. [25]. These records attribute different frequencies and different amount of energy so as to draw more general conclusions.

The design spectrum used correspond to soil type B (characteristic periods T_B = 0.15 sec, T_C = 0.50 sec and T_D = 2.00 sec). Moreover, the importance factor γ_I was taken equal to 1.0, while the damping correction factor η is equal to 1.0, since a damping ratio of 5% has been considered.

The models employed for the verification of the proposed criterion are a single-story torsionally stiff structure and a four-story, torsionally stiff, horizontally irregular building. The models are analysed for bidirectional ground motions. In all test examples the following material properties are considered: Concrete C20/25 with modulus of elasticity equal to 30GPa and characteristic compressive cylinder strength equal to 20MPa, longitudinal and transverse steel reinforcement B500C with modulus of elasticity equal to 210GPa and characteristic yield strength equal to 500MPa. Apart from the symmetric design, three different mass distributions were considered for every system, corresponding to eccentricity 5%, 10%, 20% of the plan dimension. The symmetric counterpart is denoted as *sym*, while the mass eccentric variants characterized by 5%, 10% and 20% eccentricity are denoted as *ecc0.05*, *ecc0.10* and *ecc0.20* respectively. The eccentricity is introduced by assuming non-uniform mass distribution, which results in a shift of the mass centre, while the centre of rigidity coincides to their geometric centre. Each variant differs with reference to the location of CM and the moment of inertia J. Asymmetric brick partition wall and asymmetric live load distribution are some usual causes of mass eccentricity. For the reasons explained above the coordinates of the ri-

gidity center are computed on a floor by floor basis. The first three periods of vibration are listed for the two test examples in Tables 1 and 2. The results presented in the current study apply to maximum values obtained from three time-history analyses for each hazard level.

	T_1	T_2	T_3	$\Omega_x = \frac{T_x}{T_t}$	$\Omega_y = \frac{T_y}{T_t}$
sym	0.3593 ^{x}	0.3484 ^{y}	0.2526 ^{t}	1.4224	1.3793
ecc0.05	0.3620 ^{x}	0.3512 ^{y}	0.2524 ^{t}	1.4342	1.3914
ecc0.10	0.3753 ^{x}	0.3539 ^{y}	0.2519 ^{t}	1.4898	1.4049
ecc0.20	0.4320 ^{x}	0.3549 ^{y}	0.2509 ^{t}	1.7218	1.4145

Table 1: Vibration periods and uncoupled frequency ratios for Test Example 1.

	T_1	T_2	T_3	$\Omega_x = \frac{\omega_t}{\omega_x}$	$\Omega_y = \frac{\omega_t}{\omega_y}$
ecc	1.0074 ^{x}	1.0059 ^{y}	0.6988 ^{t}	1.4416	1.4395
ecc0.05	1.0218 ^{x}	1.0074 ^{y}	0.7006 ^{t}	1.4585	1.4379
ecc0.10	1.0633 ^{x}	1.0074 ^{y}	0.6851 ^{t}	1.5520	1.4704
ecc0.20	1.1933 ^{x}	1.0074 ^{y}	0.6313^{t}	1.8902	1.5958

Table 2: Vibration periods and uncoupled frequency ratios for Test Example 2.

5.1 Test example 1

The first test example is a single-story 3D framed structure. Its symmetric variant is shown in Figure 2, while some properties of the eccentric variants are denoted in grey.

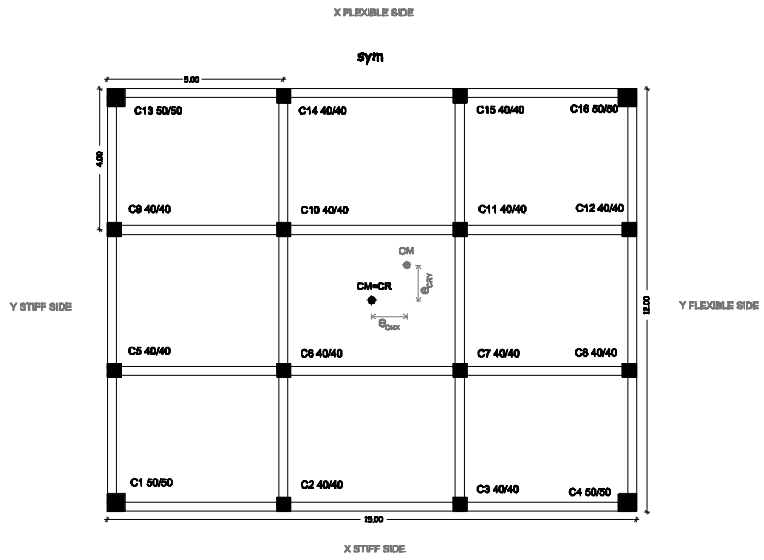


Figure 2: Plan view for Test Example 1.

The basic features of the behaviour of torsionally stiff systems described above is observed for all response quantities. It is noticed that monotonic variation (increase, decrease) of response quantities disappears for eccentricity values greater than 10% percentage. Another

significant remark is that for realistic layouts the established trends are valid for the elastic state of response. Once the system enters the elastoplastic state and elements start yielding, the stiffness is not constant affecting the position of the centre of rigidity. The centre of rigidity in those (elastoplastic, plastic) states is instantaneous preventing us from defining the flexible and stiff side of the system. The above described behaviour was observed for response quantities along both directions but due to space limitations only those of *y* direction will be presented in the current section (see Figures 3a, 3b, 4a, 4b). A decrease is recorded for response quantities for elements at the stiff side (col1, col6), while these quantities for the columns at flexible side (col11, col16) are increasing.

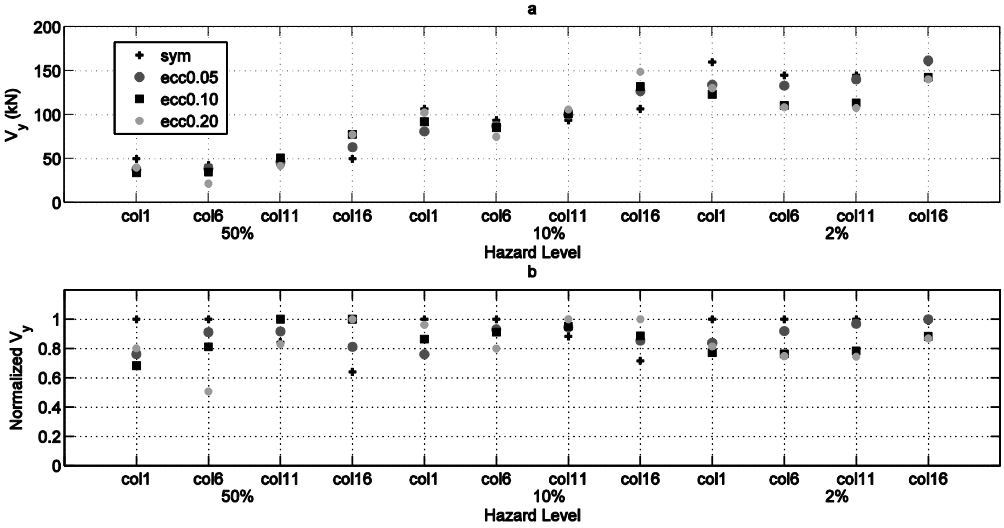


Figure 3: Test example 1 – Column shear forces (a) maximum absolute values and (b) normalized values along *y* direction for each variant and hazard level.

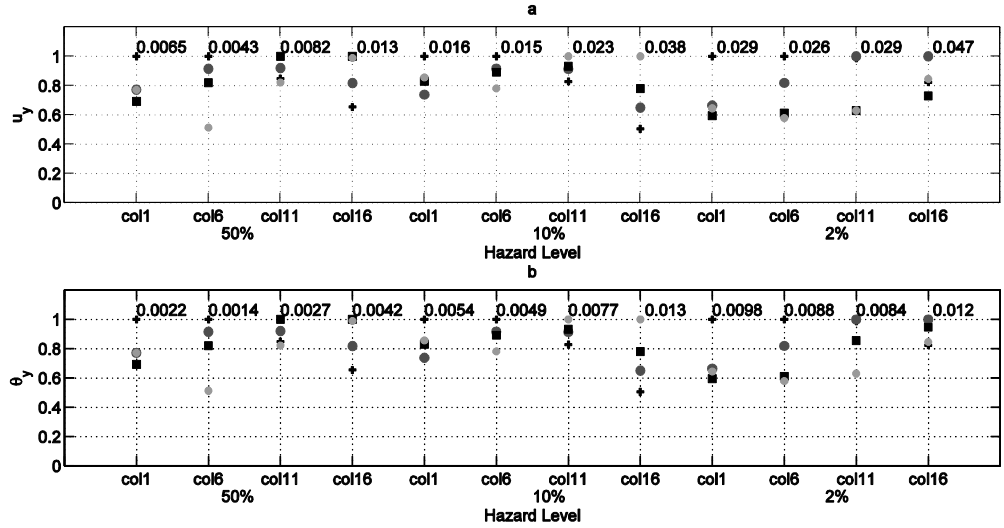


Figure 4: Test example 1 – Column (a) normalized displacement values (in m) and (b) normalized interstorey drift values (%) along *y* direction for each variant and hazard level.

The response values related to torsion (upper diaphragm's rotation, base torque and *ROT*) and their normalized values are shown in Figures 5(a) to 5(f). According to *ROT* , in this case the shear forces imposed were amplified six times for *ecc0.20* in 2/50 hazard level. Another

interesting remark is that maximum base torque values do not always follow the distribution of the maximum diaphragm rotation values. Figures 5b, 5c show that for *ecc0.20* variant a decrease of diaphragm rotation is noticed to its maximum value from 10/50 to 2/50 hazard level, whereas an increase is recorded of maximum base torque values for the corresponding states.

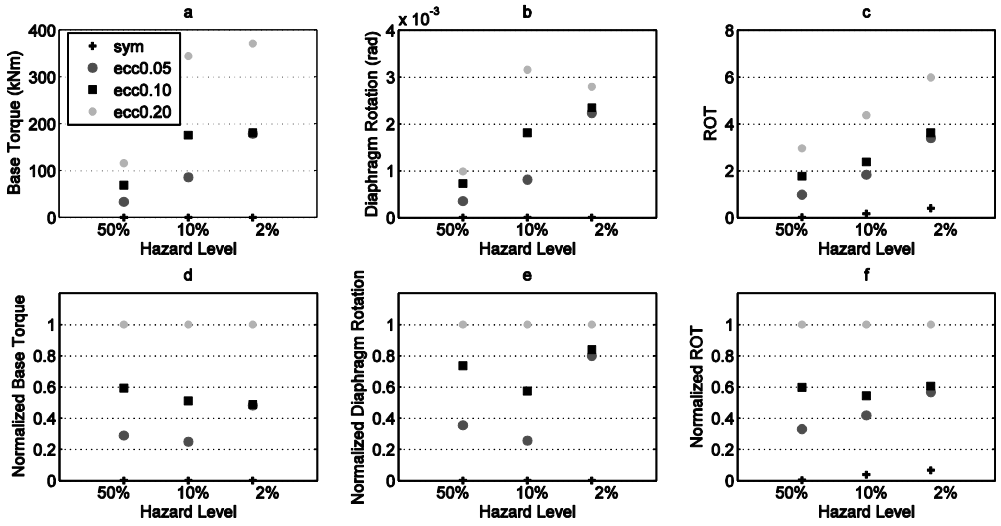


Figure 5: Test example 1 – (a)Base torque, (b) diaphragm rotation, (c) ROT , (d) normalized base torque, (e) normalized diaphragm rotation, (f) normalized ROT for each variant and hazard level.

5.2 Test example 2

For the second test example a horizontally irregular building exhibiting bidirectional eccentricity subjected to two-component ground motion is examined (Figure 6). As expected, it was not possible to design a totally symmetric counterpart that complies with the restrictions imposed by codes [19]. Consequently a small amount of eccentricity 0.9% appears and the reference variant is denoted as *ecc*, instead of *sym* used in the previous cases. The rest variants exhibit the same amounts of eccentricities as in the already examined examples (5%, 10%, 20%).

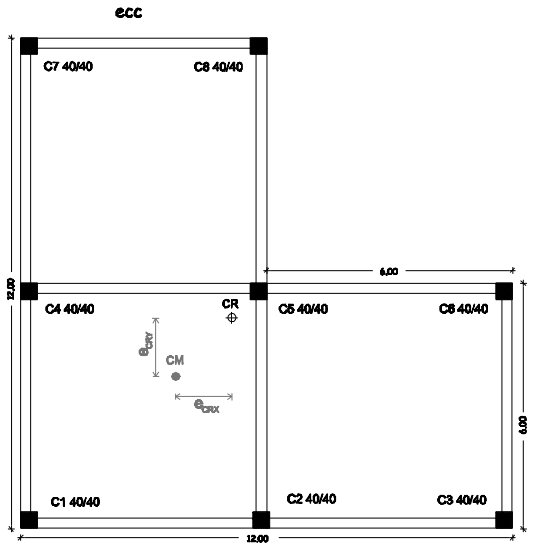


Figure 6: Plan view for Test Example 2.

For all response quantities (shear forces, displacements, interstorey drifts) an already noticed trend has been observed but due to space limitations only those correspond to *y* direction will be presented here. Figures 7 and 8 give consistent increase of response quantities for elements at flexible edge (col1, col7) and the opposite for those at stiff edge (col3, col6) till 10% eccentricity. For *ecc* variant almost zero value was noticed for base torque, diaphragm rotation and *ROT* values for the elastic state of response (50/50). For the other variants, the corresponding values are increased following the eccentricity rule. The same happens for the other two hazard levels. The non-zero *ROT* values for *ecc* variant at 10/50 and 2/50 hazard level may rise due to the fact of asymmetric yielding (the system does not possess two axes of symmetry) which affects the CR position creating eccentricity greater than the initial. The behavioral trend identified previously for horizontally regular systems has been verified also for horizontally irregular systems.

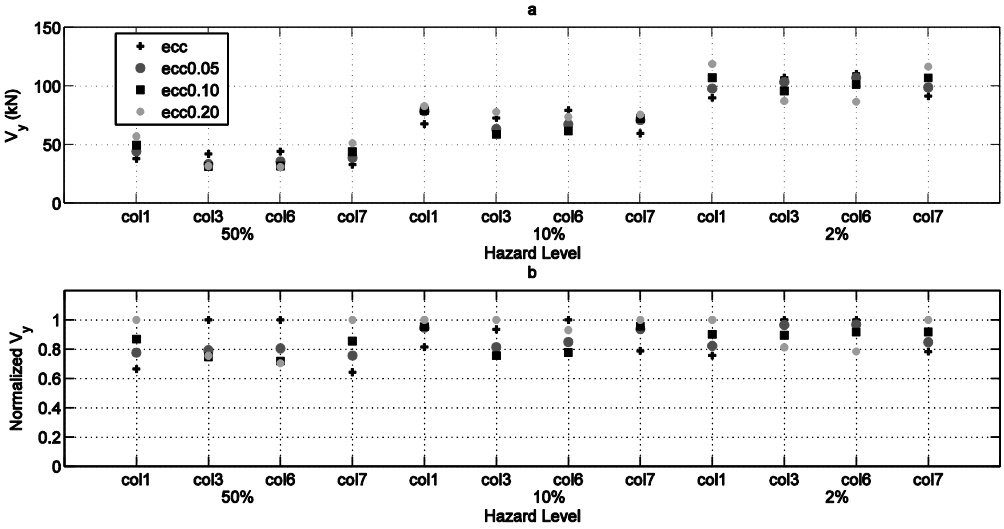


Figure 7: Test example 2 – Column shear forces (a) maximum absolute values and (b) normalized values along *y* direction for each variant and hazard level.

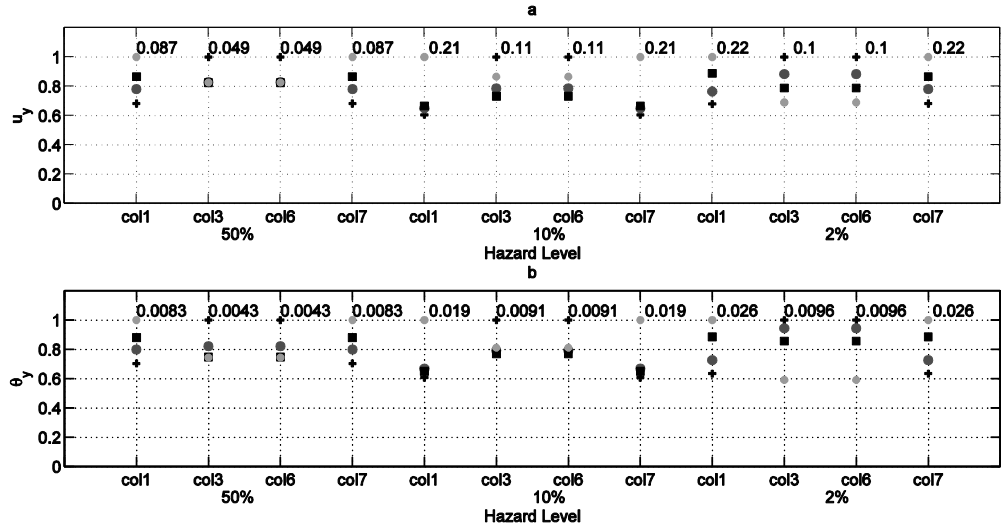


Figure 8: Test example 2 – Column (a) normalized displacement values (in m) and (b) normalized interstorey drift values (%) along *y* direction for each variant and hazard level.

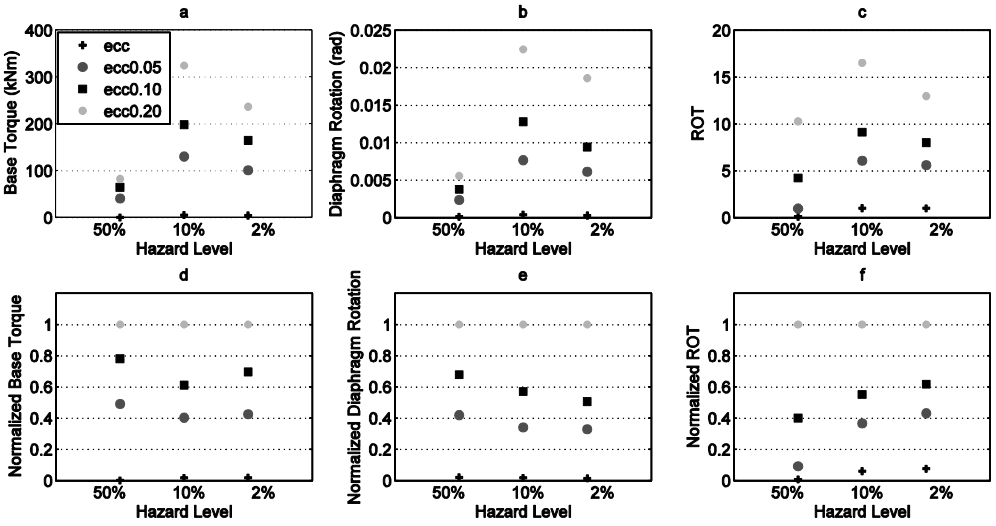


Figure 9: Test example 2 – (a)Base torque, (b) diaphragm rotation, (c) ROT , (d) normalized base torque, (e) normalized diaphragm rotation, (f) normalized ROT for each variant and hazard level.

The response quantities of Figure 7 and 8 are referred to the elements of the fourth floor. Similar variation qualitatively was observed for the other floors. The envelopes of maximum values of shear forces and interstorey drifts for column 7 along the height are shown in Figures 10 and 11 for all variants. Column 7 is located on the stiff side along y direction and on the flexible along x direction. Consistent decrease of the response quantities along x direction for all floors was recorded in the elastic state, while in the elastoplastic and plastic state of response some exceptions appeared due to asymmetric yielding. Along y direction column 7 exhibits monotonic increase till 10% eccentricity for the elastic and elastoplastic range. Some exceptions appeared in 2/50 hazard level.

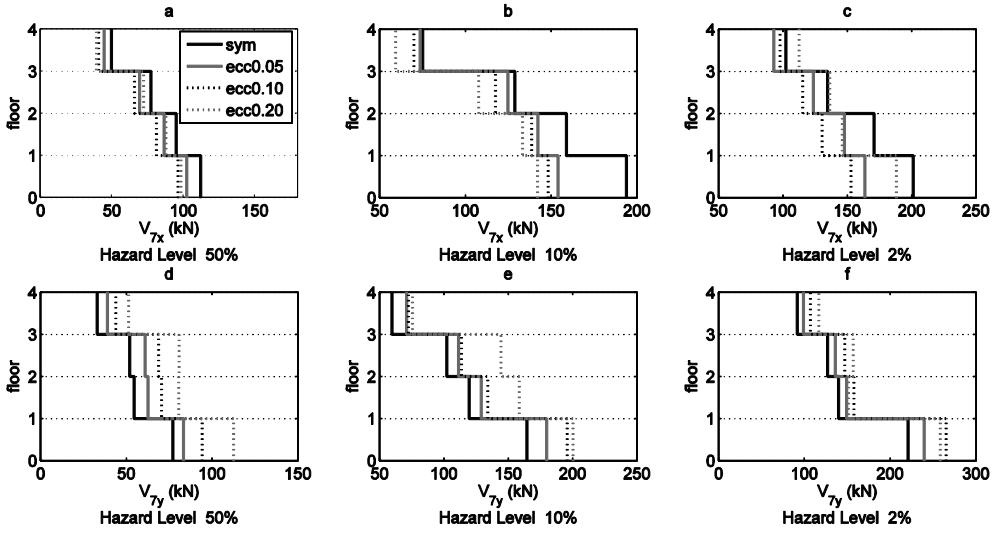


Figure 10: Test example 2 – Column 7 shear forces' maximum absolute values anlong x (a, b, c) and y (d, e, f) direction for all floors and hazard levels.

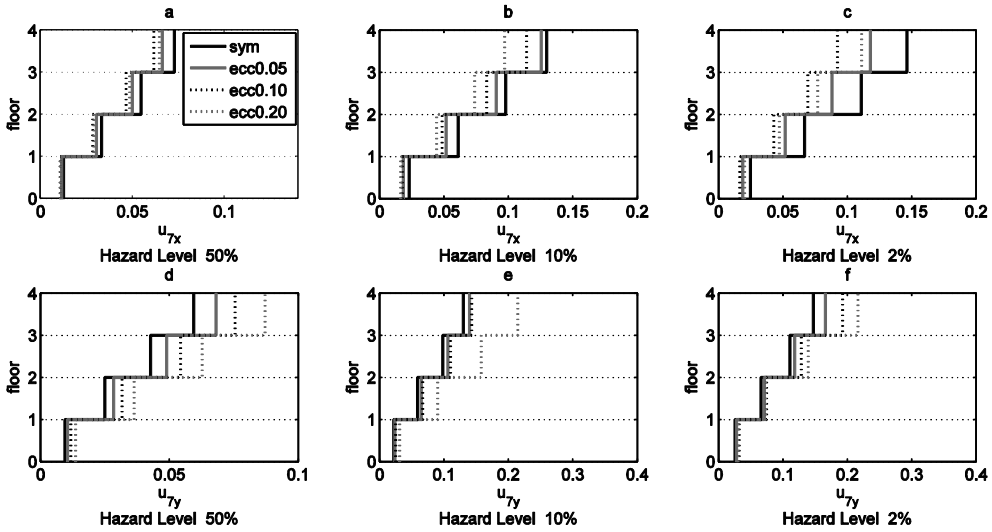


Figure 11: Test example 2 – Column 7 drifts' maximum absolute values anlong *x* (a, b, c) and *y* (d, e, f) direction for all floors and hazard levels.

A remarkable observation, also noticed by other researchers [26, 27], for both test examples considered is that maximum diaphragm rotations do not usually occur at the same time as maximum translations.

6 CONCLUSIONS

In order to investigate the effect of torsion on the seismic response of mass eccentric torsionally-stiff structures, two test examples are considered. In particular, a single-story regular framed structure exhibiting bidirectional eccentricity and a four-story horizontally irregular building are studied. Nonlinear dynamic analyses are conducted using natural accelerograms calibrated for the three hazard levels. The main objective of the current study is to propose a new assessment criterion for the torsional effect on asymmetric plan buildings, defined as the ratio of torsion.

The performance of the suggested index proved to be efficient since it was noticed that its variation follows the one of base torque introduced to a system. According to its formulation, *ROT* quantifies the torsional effect in terms of shear forces calculating the amplification of internal shear forces developed at individual elements due to the introduced torque. It is noteworthy that diaphragm rotation was not in agreement with base torque for all test cases. Specifically, for the first structural model, while values of base torque and *ROT* increase from 10/50 to 2/50 state of response for *ecc0.20* variant, the diaphragm rotation value presents a reduction. Taking into consideration that *ROT* value for the symmetric counterpart of a system is zero, it offers a measure for the torsion-induced shear forces that provides the percentage of their amplification compared to those developed implementing it for the same excitation avoiding analysis procedure of it. Additionally, the fact that *ROT* criterion is based on the internal shear forces, which can be computed by any structural software, it is independent of the arrangement of resisting elements and the geometry of the structure establishing it applicable on any system.

Another important remark is that the already observed trend in most studies from literature for torsionally stiff buildings - increased response quantities at flexible edge and decrease at the stiff one - has been not only noticed in the studied single-story regular system, but also

confirmed for a four-story building exhibiting horizontal irregularity. It was also recorded that maximum diaphragm rotations do not occur for the same time step as maximum translations.

Moreover, during a seismic excitation is difficult to predict the distinct mechanisms mobilized and the number of resisting elements that yield since it depends on various factors such as system properties and the input ground motion. As a consequence, it cannot be predefined if the structure undergoes elastic, elastoplastic or plastic state of response. In the literature many assessment criteria exist exhibiting efficient performance in elastic state and others in plastic state. ROT appeared to be independent of the state of response since its performance was satisfactory for all states of response.

Finally, ROT assessment criterion can be extended to design one through optimization procedure. Since it was observed that the variation of ROT magnitudes follows the variation of magnitude of response parameters correlated to torsion such as base torque. Consequently, minimizing the value of ROT would lead to minimization of the torsion-induced internal shear forces.

Summarizing all the above, a simple criterion is offered to assess structure's performance against lateral-torsional coupling. ROT represents a rational formulation applicable to one-storey as well as multistory buildings for all levels of excitations. The formulation is based on the internal shear forces of the structure, which can be obtained by routine computations, increasing its objectivity and applicability, offering as well a useful tool to engineers. It is encouraging that in a companion study on such multistory buildings similar findings were obtained. Through the optimization procedure ROT can also be extended to a design criterion.

ACKNOWLEDGMENTS

This research has been co-financed by the European Union (European Social Fund – ESF) and Greek national funds through the Operational Program "Education and Lifelong Learning" of the National Strategic Reference Framework (NSRF) - Research Funding Program: Heracleitus II. Investing in knowledge society through the European Social Fund.

REFERENCES

[1] W.K. Tso, Static eccentricity concept for torsional moments estimations, *Journal of Earthquake Engineering*, **116**, 1199-1212, 1990.

[2] A. Rutenberg, Behaviour of irregular and comlex structures-progress since 1998. *Proceedings of the 12th European Conference in Earthquake Engineering*, London, Oxford 2002.

[3] A.M. Chandler, X.N. Duan, Performance of asymmetric code-designed buildings for serviceability and ultimate limit states, *Earthquake Engineering and Structural Dynamics*, **26**, 717-736, 1997.

[4] A.K. Chopra, R.K. Goel, Evaluation of torsional provisions in seismic codes, *Journal of Structural Engineering*, **117**, 3762-3782, 1991.

[5] J. De-la-Colina, Assessment of design recommendations for torsionally unbalanced multistory buildings, *Earthquake Spectra*, **19**, 47-66, 2003.

[6] N.D. Lagaros, M. Papadrakakis, N. Bakas, Automatic minimization of the rigidity eccentricity of 3D reinforced concrete buildings, *Journal of Earthquake Engineering*, **10**, 1-32, 2006.

[7] J.C. De La Llera, A.K. Chopra, Understanding the inelastic seismic behavior of asymmetric plan buildings, *Earthquake Engineering and Structural Dynamics*, **24**, 549-572, 1995.

[8] J.C. De La Llera, A.K. Chopra, A simplified model for analysis and design of asymmetric plan buildings, *Engineering Structures*, **9**, 699-707, 1997.

[9] T. Paulay, Displacement-based design approach to earthquake induced torsion in ductile buildings, *Earthquake Engineering and Structural Dynamics*, **27**, 1101-1121, 1998.

[10] T. Paulay, Torsional mechanisms in ductile building systems, *Earthquake Engineering and Structural Dynamics*, **27**, 1101-1121, 1998.

[11] B. Myslimaj, W.K. Tso, A strength distribution criterion for minimizing torsional response of asymmetric wall-type systems, *Earthquake Engineering and Structural Dynamics,* **31**, 99-120, 2002.

[12] B. Myslimaj, W.K. Tso, A design oriented approach to strength distribution in single-story asymmetric systems with elements having strength-dependent stiffness, *Earthquake Spectra*, **21**, 197-212, 2005.

[13] S.A. Anagnostopoulos, Ch. Alexopoulou, K.G. Stathopoulos, An answer to an important controversy and the need for caution when using simple models to predict inelastic earthquake response of buildings with torsion, *Earthquake Engineering and Structural Dynamics*, **39**, 521-540, 2010.

[14] J.L. Humar, Design for seismic torsional forces, *Canadian Journal of Civil Engineering*, **12**, 150-163, 1984.

[15] S.B Smith, S. Vezina, Evaluation of centers of resistance in multistory building structures, *Proc. Instn. Civ. Engrs., Part 2, Institution of Civil Engineers*, **79**, 623-635, 1985.

[16] R.A. Poole, Analysis for torsion employing provisions of NZRS 4203:1974., *Bulletin of the New Zealand Society for Earthquake Engineering*, **10**, 219-225, 1977.

[17] V., W.-T., Cheung, W.K. Tso, Eccentricity in irregular multistory buildings, Canadian Journal of Civil Engineering, **13**, 46-52, 1986.

[18] H. Reem, A.K. Chopra, *Earthquake Response of Torsionally-Coupled Buildings*. Earthquake Engineering Research Center, College of Engineering, University of California at Berkeley, 1987.

[19] R. Riddel, J. Vasquez, Existence of centres of resistance and torsional uncoupling of earthquake response of buildings, *Proceedings of 8th World Conference on Earthquake Engineering*, 1984.

[20] M. Fragiadakis, M. Papadrakakis, modeling analysis and reliability of seismically excited structures: Computational issues, *International Journal of Computational Methods*, **5**, 483-511, 2008.

[21] F. McKenna, G.L. Fenves, *The OpenSees Command Language Manual* – Version 1.2. Pacific Earthquake Engineering Research Centre, University of California , Berkeley, 2001.

[22] D.C. Kent, R. Park, Flexural members with confined concrete, *Journal of Structural Division*, **97**, 1969-1990, 1971.

[23] B.D, Scott, R. Park, M.J.N. Priestley, Stress – Strain behaviour of concrete confined by overlapping hoops at low and high strain rates, *ACI Journal*, **79**, 13-27, 1982.

[24] P. Somerville, N. Collins, Ground motion time histories for the Humboldt bay bridge, Pasadena, CA, URS Corporation, www.peertestbeds.net/humboldt.htm.

[25] B.C. Papazachos, Ch. A. Papaioannou, N.P. Theodulidis, Regionalization of seismic hazard in Greece based on seismic sources, *Natural Hazards*, **8**, 1-18, 1993.

[26] Peruš I., Fajfar, P., On the inelastic torsional response of single-storey structures under bi-axial excitation, *Earthquake Engineering and Structural Dynamics*, **34**, 931-941, 2005.

[27] Marušić I., Fajfar, P., On the inelastic seismic response of asymmetric buildings under biaxial excitation, *Earthquake Engineering and Structural Dynamics*, **34**, 943-963, 2005.

COMPDYN 2013
4th ECCOMAS Thematic Conference on
Computational Methods in Structural Dynamics and Earthquake Engineering
M. Papadrakakis, V. Papadopoulos, V. Plevris (eds.)
Kos Island, Greece, 12–14 June 2013

SEISMIC BEHAVIOUR OF INNOVATIVE ENERGY DISSIPATION SYSTEMS FUSEIS 1-2

Danai Dimakogianni[1], Georgia Dougka[1] , Ioannis Vayas[1], Phaedon Karydakis[1]

[1] National Technical University of Athens
Zografou Campus, Athens 15780, Greece

e-mail: d_dimakogianni@hotmail.com, yiouli@dougka.gr,
vastahl@central.ntua.gr, karmad44@otenet.gr

Keywords: Innovative, seismic, systems, fuses, pins

Abstract. *Modern seismic codes allow for inelastic deformations in dissipative zones during design earthquakes, accepting damage to a certain extent in the relevant structural parts. As past experience shows, repair works are needed after strong earthquakes, either less or larger than the design one. Structural systems that are easily repairable-replaceable, while maintaining the benefits of high ductility, are therefore beneficial in seismic regions.*

The scope of European Research Program "FUSEIS" was the development and study of two such innovative systems. The first, FUSEIS 1, consists of a pair of strong columns jointed together by fuses forming a shear resistance wall whereas in the second system, FUSEIS 2, the devices are made by introducing a discontinuity on the composite beams of a moment resisting frame. The main advantage of the "FUSEIS" compared to conventional systems is that inelastic deformations are strictly concentrated in controlled zones. The dissipative elements can be positioned in small areas of the building and do not interrupt the architectural plan as braced do. Another advantage of the system is the possibility of easy installation and removal within the structure.

In order to enhance the stiffness, strength and energy dissipation capacity of FUSEIS 1 system, several fuses are provided within each storey. Depending on the geometry of the fuse two cases were examined: FUSEIS 1-1 and FUSEIS 1-2. In FUSEIS 1-1system the dissipative fuses are beams. In FUSEIS 1-2 the fuses consist of beams cut in the middle and connected by short pins. The dissipative zones in this case are formed within the pins while the other parts of the structure remain elastic and protected.

This study focuses on the research carried out to evaluate the behavior of the FUSEIS 1-2 system and includes the results of the full scale tests conducted in NTUA and application examples of the system on real building frames.

1 INTRODUCTION

Opposite to concrete building frames, the lateral stability and seismic resistance of steel buildings may be obtained by a large variety of structural systems. Indeed, due to the monolithic nature of concrete, beam – to – column joints are generally rigid so that concrete buildings constitute 3D - frames with or without shear walls. This is not the case in steel buildings, where the designer has the freedom to form the connections as rigid or flexible and put additional bracing systems or shear walls.

The conventional systems applied worldwide to multi- storey steel buildings, such as moment resisting frames, concentric and eccentric braced frames and frames stabilized by steel or composite shear walls are difficult to repair when damaged after strong earthquakes. Moment resisting frames are ductile but usually flexible. Concentric braced frames are stiffer but less ductile due to buckling of braces. The properties of eccentric braced frames are something between the other two types.

In the frame of the EU supported project FUSEIS two innovative seismic resistant systems, FUSEIS 1 and FUSEIS 2, were developed [1]. In both systems inelastic deformations, and accordingly possible damage after a strong seismic event, concentrate in small easily repairable-replaceable fuses. The system dissipates energy in the fuses maintaining the benefits of high ductility. Easy mounting-dismounting of the fuses within the structure allows for a quick replacement in case of damage. The optimal dissipative fuse consists an economical solution that offers easiness in fabricating and combines the maximum energy dissipation in cyclic behavior with the minimum number of exchangeable part.

This paper presents the second alternative of the FUSEIS 1 system, named FUSEIS 1-2 where the fuses are small pins bolted to the structure. The investigation on FUSEIS1-1 and application examples will be presented in detail in other papers. FUSEIS 2 is presented in [1, 2, 3]. The overall system and a design guide are given in [1, 2].

2 DESCRIPTION OF FUSEIS 1-2

The proposed system is developed to combine the advantages of moment resisting frames in respect to ductility and architectural transparency and those of braced frames in respect to stiffness. Unlike braced frames, the proposed system does not obstruct the bays of the building (Figure 1). In this system, specific seismic elements are inserted in a steel frame that resist the seismic action and provide stiffness, strength and ductility. The seismic resistant system consists of closely spaced strong columns, rigidly connected to multiple beams that run from column to column (FUSEIS 1-1) or alternatively are interrupted and connected by short pins (FUSEIS 1-2). In order to enhance the stiffness, strength and energy dissipation capacity of the system, several beams are provided within each storey.

Under seismic loading the system behaves similarly to a vertical Vierendeel beam. It is important to note, that the fuses do not generally carry vertical loading. Lateral stability of a building may be provided by this system only by appropriate provision of a number of such systems in the relevant directions (Figure 1). The rigidity of the system module varies depending on the selection of element sections, column axial distance and number of intermediate beams (e.g. four to five fuses may be inserted per storey for a typical floor height). Pin sections may vary between floors, following the increase of storey shear from the top to the base of the building, or within the floor, either in respect to their cross-section dimensions or to their length resulting in sequential plasticization. In addition one fuse is provided between columns just above foundation level to minimize the moment transfer to the foundation and enable the realisation of simple pinned bases for FUSEIS columns.

Floor beam to FUSEIS-column connections are simple, while floor beam-to-column connections in the building frame may be formed as simple, semi-rigid or rigid. The formation of semi-rigid or rigid connections provides lateral stiffness of the building frame so that lateral forces are shared between the building frame and the FUSEIS system.

Open or hollow sections may be employed at the FUSEIS columns. In case of hollow sections the connection to the beams is more complex and a T-section can be welded on to ease the connections.

The fuses-to-column joints are formed as rigid to enable the Vierendeel action and are designed to have sufficient overstrength in order to achieve energy absorption only in the fuses. Bolted connections give the possibility of an easy replacement after a very strong seismic event.

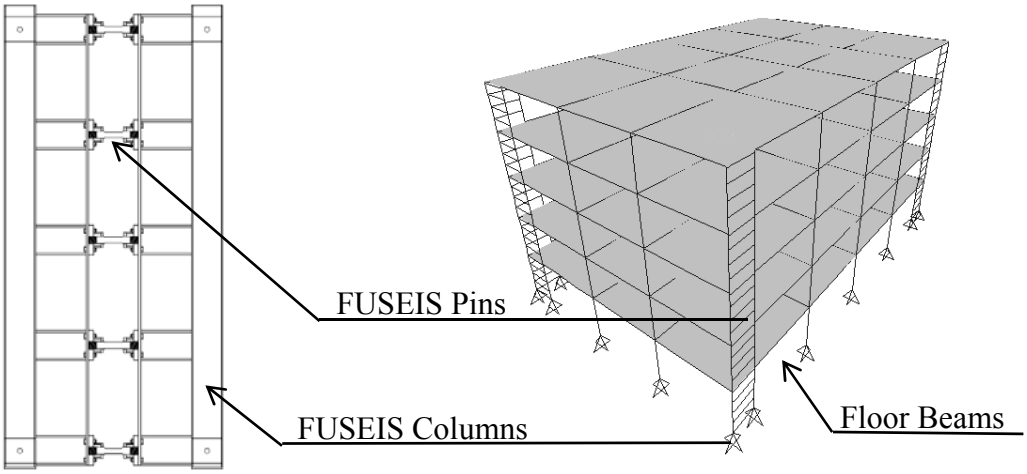


Figure 1: FUSEIS 1-2 system in a building

In FUSEIS1-2, the dissipative zones are the pins that act like fuses. Compared to the other proposed system FUSEIS1-1 their main difference is that the beams are not continuous between two columns. They are cut and connected with the pins (Figure 2). Under strong seismic motion, plastic hinges will develop at the pins that will dissipate a large amount of input energy. The replacement of the fuses is very easy, since it is restricted to the pin. Aiming to lead the plastic hinge formation away from the contact area between the face plate of the receptacles and the pins, the pins diameter is reduced in the middle (similar to the RBS sections). In order to keep the contact area away from the end of the plates, ensuring triaxial stress conditions, pin's diameter decrease starts away from the plate's face and the edges of the plate hole are smoothed (Figure 3). The pins may be circular if the receptacle beams are hollow or rectangular if the receptacle beams are I or H (Figure 2). By appropriate detailing of the pin ends, screwed with inverse directions, their length may be adjusted (Figure 3).



Figure 2: Fuseis 1-2

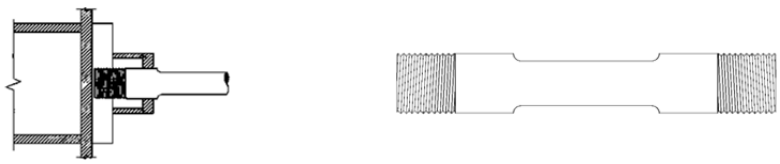


Figure 3: Details of circular pin fuse with weakened middle part and screwed ends

3 FULL SCALE TESTS ON FRAMES WITH FUSEIS 1-2

Numerical and experimental investigations were carried out to study the response of FUSEIS1-2 to cyclic loading. Experimental investigations on individual devices, i.e. on single pins, were performed in the Institute of Steel Construction of Aachen University (RWTH). Based on the understanding gained from these investigations, the necessity to study a real building's performance under a seismic event arose. Two full scale tests on frames with FUSEIS1-2 were conducted in the Steel Structures Laboratory of NTUA.

It is evident that the seismic response of a frame with FUSEIS1-2 depends mainly on the stiffness and strength of the pins. If the same pins are used within a storey all pins are expected to yield at the same time. To achieve a controlled yielding of the pins and a better behaviour of the frame under cyclic loading, the specimens should preferably yield gradually. During the full scale tests, this was realized with the two following ways:

- By using pins with the same cross section but with varying lengths, or
- By using pins with the same length but varying cross sections.

The experimental setup included a resistance space frame – test rig (Figure 4), a computer controlled hydraulic cylinder and the test frame.

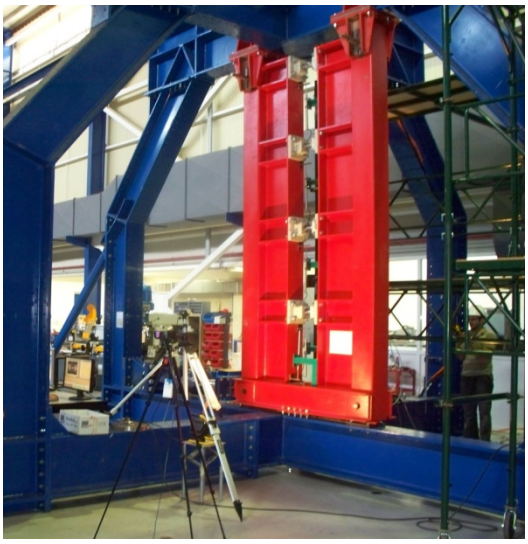


Figure 4: Test Rig

The test frame consisted of two closely spaced strong columns rigidly connected to five fuses as shown in Figure 5. The dimensions of the structural elements corresponded to a real building frame and were defined according to the provisions of EC3 [4] and EC8 [5]. The height of the frame was 3.40 m, the distance (L) between the centrelines of the columns 1,50m, the length (l) of the pins 400mm. The columns of the test frame were pin-jointed at the top and bottom connections and were stiffened by adding stiffening T-sections on their inner side to remain elastic. The fuse consisted of a 400mm pin D60 and two receptacle SHS beams. The pins had a weakened part in the middle aiming to lead the plastic hinge formation within this part. To facilitate mounting and dismounting of the fuse, threads were cut at pin ends in inverse directions to fasten them to the receptacles.

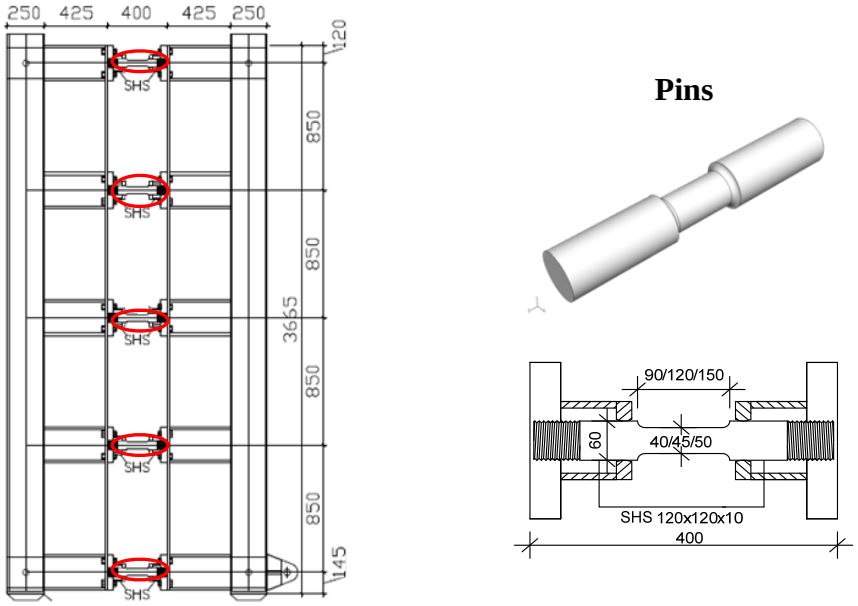


Figure 5: Test Frame & Beam specimens

Based on initial analytical investigations on a variety of reduced sections, three different lengths 90, 120, 150 mm with the same diameter D45 (Test M4) and three different sections with diameters D40, 45, 50 with the same length 120mm of the reduced part (Test M5) were examined. In all cases the diameter's decrease didn't exceed the 30% of the full section based on the provisions of FEMA350 [6] and EC8 [7] for the design of Reduced Beam Sections (RBS).

The actuator was a computer controlled hydraulic cylinder with a maximum displacement capacity of +/-250mm, more than the target displacement of 5% inter-storey drift (=170 mm). It was pin-jointed to the bottom of the column in order to transfer only horizontal forces to the frame and set to the middle course position at the beginning of each test.

In order to determine the material properties of the fuses, material tests were conducted. The range of the determined yielding stresses was usual for steel grade S235.

3.1 Loading Procedures and Experimental measured data

The test procedure was based on the relevant ECCS-recommendation [8]. The cyclic tests were carried out deformation controlled with increasing amplitudes as shown in Figure 6. Starting with an applied displacement of 2.55mm in the axis of the jack the loading was increased up to 170 mm which corresponds to an interstorey drift 5 %.

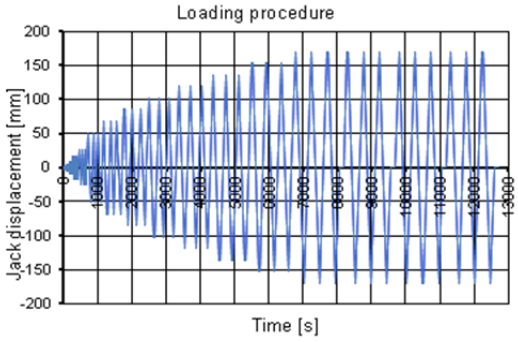


Figure 6: Applied loading protocol

The procedure was continued with amplitudes of 170 mm until total failure. The velocity during the cyclic tests was 1.5 mm/s with a short pause 5sec between the cycles of the same amplitude and 10sec when the amplitude increased.

The data measured during the experimental investigations were: the displacement of the cylinder piston with an electronic displacement transducer, the hydraulic load applied by the cylinder (with the load cell at the end of the piston) and the differential vertical displacement between pin–ends by means of electronic displacement transducers (LVDTs) with a maximum capacity of ±50mm. Special bases were constructed for this purpose. They were bolted to the end plates of the receptacles.

3.2 Test results

All test specimens showed good plastic deformation capacity. It is remarkable that the system's resistance kept increasing after first yield and subsequent plastifications of the pins, due to development of a catenary action in the pins and strain hardening. Plastic deformations took place within the fuse devices, the pins, only while the columns remained elastic and undamaged (Figure 7). The time required for replacing one fuse device was approximately 60 minutes. At the end of the test, the damaged pins were instantly dispatched.

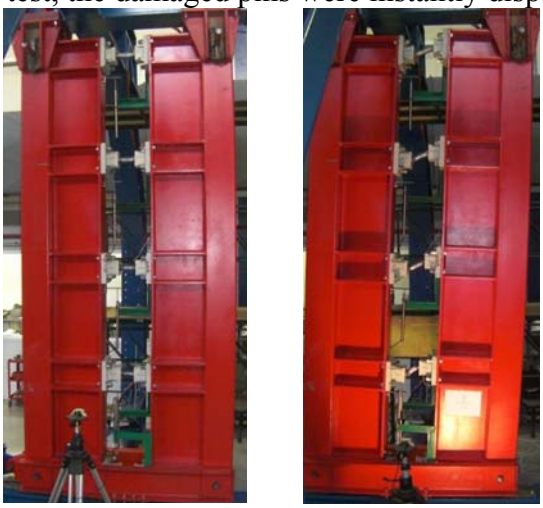
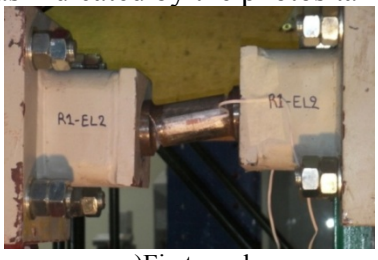
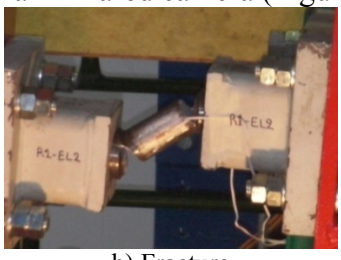


Figure 7: Frame with pin with varying lengths at its initial state and at the end of test

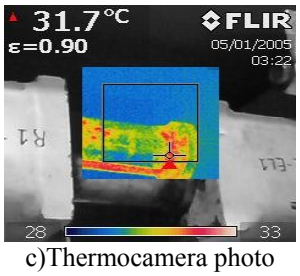
The pin specimen first acted as a beam in flexure, then the resisting mechanism changed to a tension field action and plastic hinges were generated under large deformations. This corresponds to the observed overall behaviors of both tests. At the beginning of the test and during several cycles the measured load was increasing. When the first crack formed at the ends of the weakened part of the pin (Figure 8a) the pins fractured (Figure 8b) and as a result the load dropped. This means that there was local stress concentration at the ends of the weakened pins as indicated by the photos taken by an infrared camera (Figure 8c).



a)First crack



b) Fracture



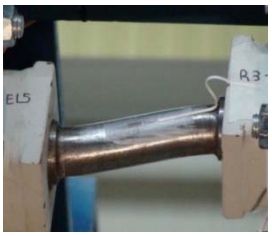
c)Thermocamera photo

Figure 8: Specimen photos during the test

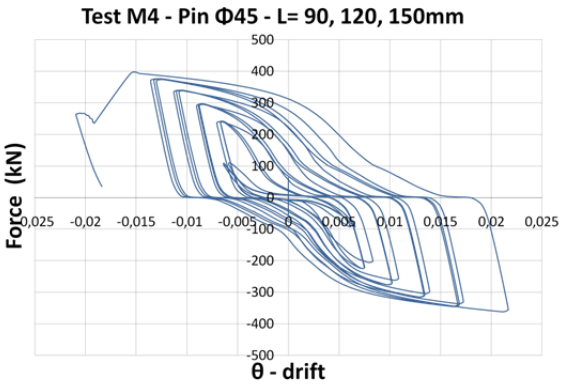
Figure 9 shows the hysteretic diagrams of the tests and photos of the deformed pins during the test. The hysteresis loops have a pinching due to the gap formed between the pin and the plate, as a result of the extensive plastic deformation of the pin and the Poisson effect along the pin circumference. This pinching of the hysteretic curve is accompanied by a substantial drop in the initial stiffness due to the release of the tension field developed in the previous load excursion. Generally, it should be noted that the shorter pins failed at smaller drifts than those of the longer.



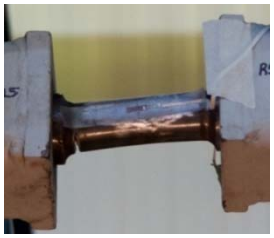
Short pin



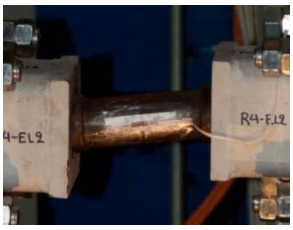
Long Pin



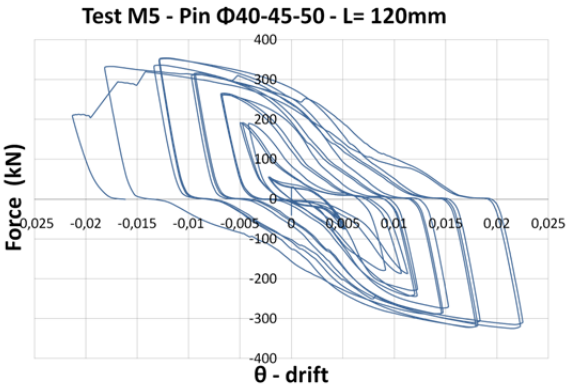
Cyclic Test M4 – Varying lengths



Thin pin



Thick Pin



Cyclic Test M5 – Varying diameters

Figure 9: Force–drift diagrams and photos of the deformed pins

3.3 Low cycle fatigue considerations

Preliminary analyses and experiments on pin fuses, showed that pins can sustain a limited number of cycles in the post-elastic region. The number of cycles to be sustained is dictated by low-cycle fatigue considerations. Low cycle fatigue may be captured by definition of appropriate S-N lines, where S is expressed in terms of deformations rather than in terms of stresses. Such S-N lines may be written as:

$$\log N = -m \log \Delta\varphi \tag{1}$$

where Δφ is the pin rotation, N is the number of rotation cycles and m is the slope constant of the fatigue strength curves.

Using the Palgrem – Miner accumulation law the damage produced by a certain number of constant amplitude cycles is expressed by:

$$D_i = \frac{n_i}{N_{fi}} \tag{2}$$

where: n_i is the number of cycles at specific rotations and N_{fi} is corresponding number of cycles to failure.

For cycles of various amplitudes failure occurs when

$$D = \frac{n_1}{N_{f1}} + \frac{n_2}{N_{f2}} + ... \frac{n_i}{N_{fi}} \geq 1 \quad (3)$$

The S-N lines were derived by evaluation of the cyclic tests on individual devices performed at RWTH and on complete frames performed at NTUA. The test results indicated that the most appropriate value for the slope is m = 3 as proposed in EC3 [10] for high cycle fatigue. The resulting S-N lines are shown in Figure 10. It may be seen that individual devices provide more conservative results. However, the frame results may be considered more realistic due to the combined action of multiple beams. Therefore, following validated relation is proposed to verify low-cycle fatigue:

$$\log \Delta\varphi = -\frac{1}{3} (\log N) - 0{,}30 \quad (4)$$

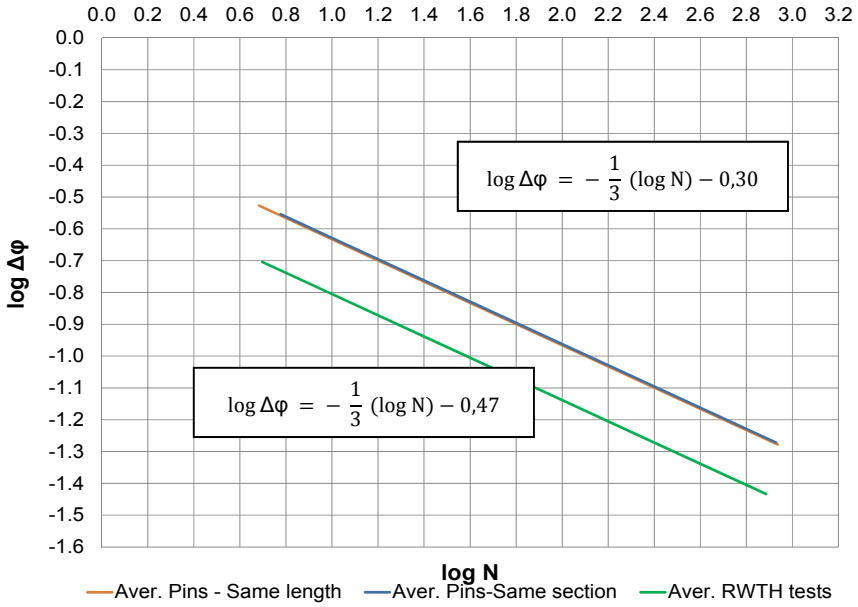


Figure 10: Low cycle fatigue diagrams

3.4 Development and calibration of simple models

The commercial software SAP2000 [11] was used and provided simple engineering models able to simulate the behavior of frames with fuses accurately. The FUSEIS elements were represented by appropriate beam FE-elements. Rigid zones were provided from column centres to column faces to exclude non-existent beam flexibilities. Further on, the net length of the pin fuses was subdivided to 3 zones that represent the full section at the ends and the weakened section in the middle (Figure 11). In this manner, the true system flexibility and strength was accounted for. The columns and the receptacle beams were simulated as usual. Beam-to-column joints were represented as rigid in accordance to the connection detailing of the test.

Two different approaches were followed for the calibration of the tests and the evaluation of the non-linear lateral behaviour of the 2D test frames, a non-linear static (incremental pushover) and a non-linear dynamic (time history) analyses (Figure 12).

Regarding the incremental pushover analysis, the target displacement corresponds to the maximum displacement (170mm) of the experimental tests. Since the ductile elements are the

FUSEIS pins, potential plastic hinges were inserted at the ends of the weakened part of the pin. Initially, the relevant moment rotation curves (hinge property data) were based on the parameters obtained by the RWTH tests on the devices. These parameters were the starting point for the determination of the non-linear hinge properties of the FUSEIS1 devices. Five points labeled A, B, C, D, and E define the moment – rotation behavior of a plastic hinge [12].

In order to fit the analytical results to the experimental, several iterations were made changing the parameters of the hysteresis model. Table 1 summarizes the non-linear hinge parameters that comprised the most suitable approach.

The calibrated models predict with good accuracy the entire behavior of the frames with fuseis indicating that the proposed hinge properties can be applied to study the response of the fuses beyond the elastic state and to estimate expected plastic mechanisms and the distribution of damage.

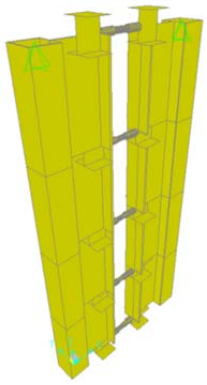


Figure 11: Sap model

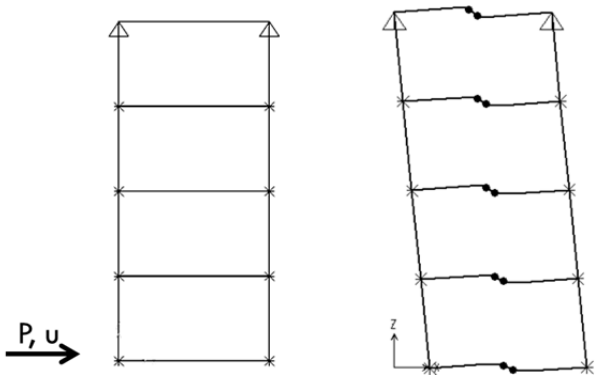
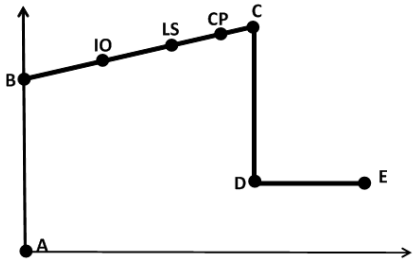


Figure 12: Non-linear static(P) & dynamic(u) loading and hinge formation

HINGE PROPERTIES		
Point	**M/SF**	**Rot./SF**
E-	-0,5	-150
D-	-0,5	-100
C-	-2,5	-100
B-	-2	0
A	0	0
B	2	0
C	2,5	100
D	0,5	100
E	0,5	150
ACCEPTANCE CRITERIA		
IO	30	
LS	45	
CP	60	



M–θ Relation

SF are scale factors corresponding to the moment and rotation yield values

Table 1: Proposed Non-linear hinge parameters

4 LINEAR STATIC ANALYSIS AND DESIGN OF FRAMES WITH FUSEIS 1-2

In the current state of the art, a building frame with Fuseis 1-2 was analyzed with the use of the general purpose software Code SAP 2000. The examined frame was part of a five-

storey composite building with 3,4m storey height and 5 system pins/storey with 2m axial distance of system columns. The geometry and the section properties are given in Figure 13. The systems were placed in the building plan at the outside bays of the frames in a similar manner to shear walls, coupled walls, etc. The beams were composite and the thickness of the slab was 15cm. The system columns were hollow strong columns, jointed together with five horizontal fuses in a tight arrangement. The effective width of the composite beams was calculated based on EC2. The general assumptions for the design of the building frame are given in Table 2.

The models were analyzed and dimensioned according to the provisions of EC3 and 8 and the relevant Design Guide. The Design Guide includes rules to ensure that yielding, takes place in the pins prior to any yielding or failure elsewhere.

The simulation concept for the pins was the same as described in Section 3.4, the reduced pin sections per storey for PGA=0.36g are also presented in Figure 13. The pins were connected to the system columns through receptacle beams SHS 240x240x20 forming a rigid joint to enable the Vierendeel action. The receptacle beams and the system columns were designed to have sufficient overstrength in order to achieve energy absorption only in the fuses.

The remaining structural elements were simulated as usual. The column bases were pinned to limit yielding at the foundation and thereby minimize damage to the columns. Rotational springs were assigned at the composite beams' ends to simulate the connection between the composite beams and the columns (EC 3 part 1.8, §6.3 and EC 4 part 1 - Annex A).

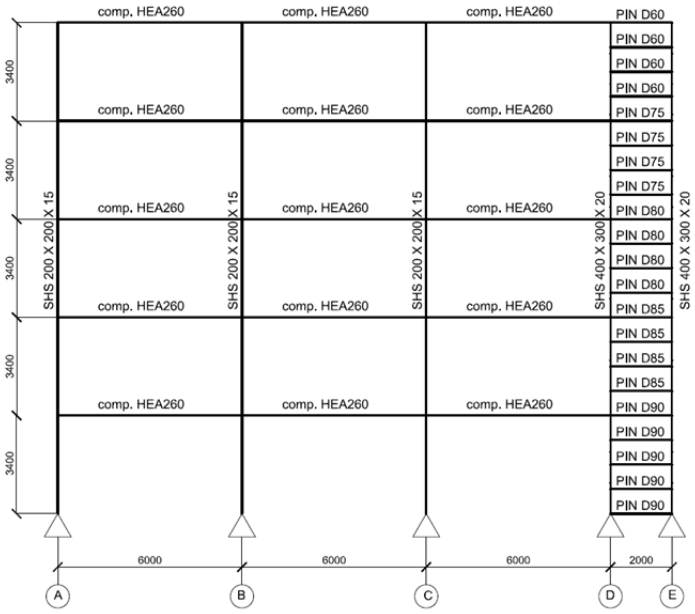


Figure 13: Typical 2D building frame

For the design of the frame the following conditions were fulfilled:

1. Serviceability Limit State: composite beam deflections
2. Ultimate Limit State: composite beam resistance ratio
3. Modal response spectrum analysis: The first mode of vibration activated approximately 75% of the mass
4. Seismic design- EC 8:
   - Limitation of interstorey drift to 0,0075 (buildings with ductile non-structural elements)
   - 2nd order effects via linear buckling analysis, the interstorey drift sensitivity coefficient θ was lower than 0,1

- Design of FUSEIS pins for the most unfavourable seismic combination – Design Guide:
  a. Condition for bending moments
  b. Condition for axial forces
  c. Condition for shear forces
  d. Global dissipative behaviour of the structure: the maximum overstrength of the pins does not differ from the minimum value by more than 25%.
  e. Plastic Rotations Capability θ_p
- Capacity design of Fuseis columns and receptacle beams

Materials	
Concrete	C25/30,γ=25KN/m^3, E=31GPa
Reinforcement	B500C
Structural steel	S 235: Dissipative elements (FUSEIS) S 355: Non dissipative elements (beams - columns)
Vertical loads – calculated for 8m effective width	
Dead loads apart from self-weight –	2.00kN/m^2
Live loads – Q	2.00kN/m^2
Seismic loads	
Elastic response spectra	Type 1
Greek seismic zones	A=0.16g – 0.24g – 0.36g
Importance class	II
Ground type	B
Behaviour factor q (verified in Section 5 through nonlinear analysis)	3
Damping	5%
Factors of operating loads for seismic combinations	φ=1.00 (roof) φ=0.80 (storeys with correlated occupancies)

Table 2: Proposed Non-linear hinge parameters

5 NON- LINEAR STATIC ANALYSIS (PUSHOVER) AND EVALUATION OF THE BEHAVIOUR FACTOR

Non-linear analyses were carried out to estimate the behavior factor of the system, the expected plastic mechanisms and the distribution of damage. The base of the analysis was the target displacement applied at the roof of the frame equal to 0,680m (inter-story drift 4%). The analysis was carried out under conditions of constant gravity loads and monotonically increasing lateral loads taking into account P –Delta effects.

Since the ductile elements are the FUSEIS pins, potential plastic hinges were inserted at the ends of their reduced parts. The nonlinear properties for the pin sections that derived from experimental and analytical investigations are given in Table 1. The rest of the structure - composite beams and columns - remained elastic. Figure 14 demonstrates the formation of plastic hinges within the reduced parts of the pins at the performance point.

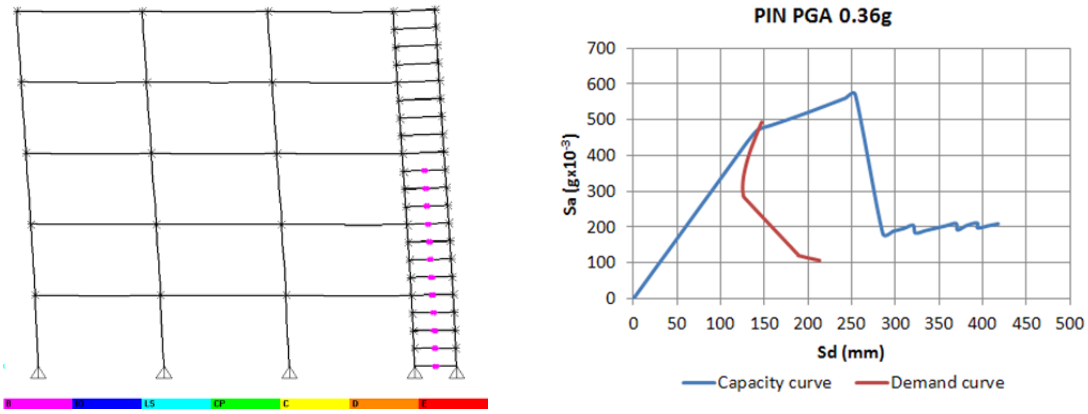


Figure 14: Hinges at the Performance Point and Evaluation of performance point

Besides the assessment of the structural performance of the building frames, pushover analysis also offered the possibility to estimate their behaviour factor. Due to the flexibility of the system $T_1 \geq T_c$ the 'equal displacement rule' was applied. Figure 14: Hinges at the Performance Point and Evaluation of performance pointFigure 15 shows the typical pushover response curve for the evaluation of behaviour factor.

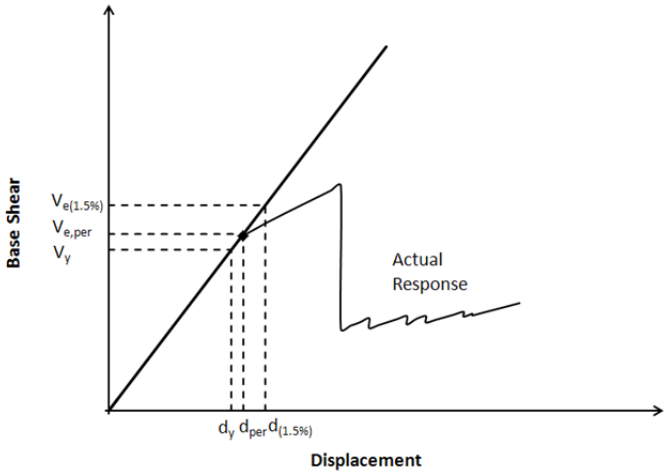


Figure 15: Typical pushover response curve for evaluation of behaviour factors

The behaviour factor, q, accounts for the inherent ductility and overstrength of a structure and may be generally expressed in the following form:

$$q = q_{\mu} \cdot \Omega \tag{5}$$

The structure ductility, q_{μ}, is defined in terms of the Elastic Base Reaction that corresponds to 1,5% drift (V_e) to the Idealised Yield Strength - First hinge (V_y) (Figure 15), as following:

$$q_{\mu} = \frac{V_e}{V_y} \tag{6}$$

The interstorey-drift (ID) adopted, 1,5%, was derived from the experimental results. At approximate this drift the maximum applied force was reached in the tests. This drift corresponds to plastic rotations of the pins of about 20%.

The structural overstrength is defined as the ratio of the Idealised Yield Strength - First hinge V_y to the Design Strength (V_d), as following:

$$\Omega = \frac{V_y}{V_d} \quad (7)$$

The Design Strength (V_d) was based on the fundamental vibration mode which had the largest participation to the vibrating mass and was determined from $V_d = \eta \cdot M \cdot S_d(T)$ where n is the modal participating mass ratio, M is the total mass and $S_d(T)$ is the spectral acceleration that derives from the design spectra for the fundamental mode.

The calculated q factors are given in Table 3 and Figure 16. The system exhibits high over-strength values and relatively low ductility, the q values range between 3 and 6. Conservatively, a maximum value equal to 3 is proposed for the design of buildings with FUSEIS 1-2 system.

0,16g			0,24g			0,36g		
q_μ	Ω	q	q_μ	Ω	q	q_μ	Ω	q
1.74	3.26	5.67	1.38	2.92	4.05	1.28	2.73	3.48

Table 3: Non-linear hinge parameters

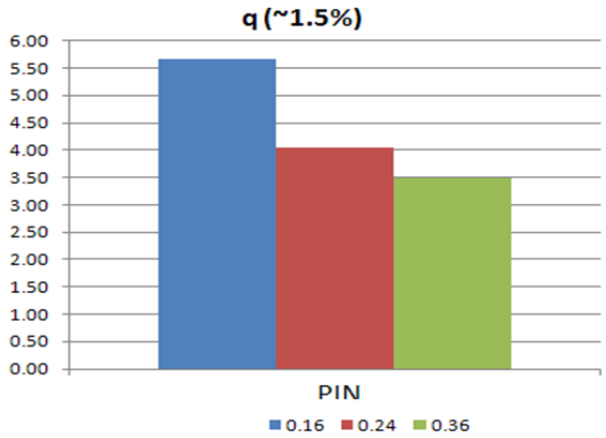


Figure 16: Evaluation of q factors

6 CONCLUSIONS

Innovative fuses systems may be applied to multi-storey steel buildings as an alternative to conventional seismic resistant systems. They combine ductility and architectural transparency with stiffness. Additionally, they offer the possibility of easy mounting and dismounting within the structure. The knowledge obtained is now sufficient to provide all the necessary data for their complete design.

Inelastic deformations are strictly limited to the dissipative elements (pins) preventing the spreading of damage into the rest of the structure. The devices and the frames with the devices have a very good behaviour: strong, stiff, large capacity of energy absorption.

The dissipative elements can be positioned in small areas of the building and do not interrupt the architectural plan as braced systems do. They can also be visible parts of the building indicating its seismic resistant system.

The seismic resistance of a building may be obtained by appropriate provision of a number of FUSEIS systems in the relevant directions. The number of stories and supporting weight strongly affects the required sections and geometry. The system may be designed as more flexible/rigid depending on the section types and their distribution between floor levels. Sequential plastifications may be allowed for by appropriate selection of the sections of the dissipative elements.

The investigations on FUSEIS 1-2 provided a good estimation of the behaviour factor of the system which is approximately 3.

The dissipative elements are easily replaceable if they are damaged after a strong seismic event, since they are small and are not part of the gravity loading resistant system. The assembling and disassembling after test is easy from a practical point of view: the time required for replacing one FUSEIS1 device is approximately 60 minutes.

The damage index of a building with pin fuses may be determined through the low cycle fatigue curve proposed.

The application of FUSEIS devices can provide a more accurate and less expensive design of a building. The steel quality of the dissipative elements can be controlled and thus their resistance can be calibrated avoiding excessive overstrength. The knowledge obtained is now sufficient to provide all the necessary data for their complete design.

ACKNOWLEDGEMENTS

The research presented is made in the framework of the European Research Project RFSR-CT-2008-00032: "Dissipative devices for seismic resistant steel frames (Fuseis)". The financial contribution of the Research Fund for Coal and Steel of the European Community is gratefully acknowledged.

REFERENCES

[1] Vayas, Ph. Karydakis D. Dimakogianni, G. Dougka, C. A. Castiglioni, A. Kanyilmaz et al. Dissipative devices for seismic resistant steel frames - *The FUSEIS Project, Final Report.* Research Programme of the Research Fund for Coal and Steel, 2012.

[2] Vayas, Ph. Karydakis D. Dimakogianni, G. Dougka, C. A. Castiglioni, A. Kanyilmaz et al. Dissipative devices for seismic resistant steel frames - *The FUSEIS Project, Design Guide.* Research Programme of the Research Fund for Coal and Steel, 2012.

[3] Castiglioni, C. A., Calado, L., Kanyilmaz A. Experimental analysis of seismic resistant composite steel frames with dissipative devices. *Journal of Construction Steel Research*, 2012.

[4] EN1993-1-1, Eurocode 3: Design of steel structures - *Part 1-1: General rules and rules for buildings.* Brussels. Comitee Europeen de Normalisation (CEN), 2003.

[5] EN1998-1-1, Eurocode 8: Design of structures for earthquake resistance – *Part 1-1: General rules, seismic actions and rules for buildings.* Brussels: Comitee Europeen de Normalisation (CEN), 2003.

[6] FEMA – 350: *Recommended Seismic Design Criteria for New Steel Moment-Frame Buildings*, 2000.

[7] EN1998-3, Eurocode 8: *Design of structures for earthquake resistance - Part 3: Assessment and retrofitting of buildings*. Brussels: Comitee Europeen de Normalisation (CEN), 2005.

[8] ECCS document: *Recommended testing procedure for assessing the behaviour of structural steel elements under cyclic loads.* Technical committee 1: structural safety and loadings, Technical working group 1.3: seismic design, 1986.

[9] Calado, L., Castiglioni, C. A. *Steel beam-to-column connections under low-cycle fatigue: Experimental and numerical research*. In: Proceedings of XI WCEE; 1996.

[10] EN1993-1-9, Eurocode 3: *Design of steel structures – Part 1-9: General – Fatigue strength*, CEN. 2005

[11] SAP2000, CSI Computers and Structures Inc., www.csiberkeley.com

[12] FEMA – 356: *Prestandard and Commentary for the seismic rehabilitation of Buildings*, 2000.

COMPDYN 2013
4th ECCOMAS Thematic Conference on
Computational Methods in Structural Dynamics and Earthquake Engineering
M. Papadrakakis, V. Papadopoulos, V. Plevris (eds.)
Kos Island, Greece, 12–14 June 2013

SEISMIC BEHAVIOUR OF INNOVATIVE ENERGY DISSIPATION SYSTEMS FUSEIS 1-1

Georgia Dougka[1], Danai Dimakogianni[1], Ioannis Vayas[1], Phaedon Karydakis[1]

[1] National Technical University of Athens
Zografou Campus, Athens 15780, Greece

e-mail: yiouli@dougka.gr, d_dimakogianni@hotmail.com,
vastahl@central.ntua.gr, karmad44@otenet.gr

Keywords: Innovative, seismic, systems, fuses, beams

Abstract. *After strong earthquakes conventional frames used worldwide in multi - storey steel buildings (e.g. Moment resisting, Concentric/Eccentric braced frames) are not well positioned according to reparability. It is therefore advisable to develop structural systems that are simple to repair, i.e. to introduce the reparability as a new property. Two innovative systems for seismic resistant steel frames incorporated with dissipative fuses were developed within the European Research Program "FUSEIS". The FUSEIS systems are able to dissipate energy by means of inelastic deformations in the fuses and combine ductility and architectural transparency with stiffness. In case of strong earthquakes damage concentrates only in the fuses which are exchangeable. Repair work after such an event, if needed, is limited only to replacing the fuses. Experimental and numerical investigations were performed to study the response of the FUSEIS system.*

The first system, FUSEIS1, resembles a shear resistance wall and is composed of two closely spaced strong columns, rigidly connected to multiple beams. The beams run from column to column, FUSEIS 1-1, or alternatively are interrupted and connected by short pins, FUSEIS 1-2. In the second system, FUSEIS2, the devices are made by introducing a discontinuity on the composite beams of a moment resisting frame and connecting the two parts through steel plates.

This study presents the experimental research on overall frames with FUSEIS1-1 and numerical models calibrated on the experimental results. These models provided the design rules and verified the good seismic performance of building frames with FUSEIS1-1.

1 INTRODUCTION

Earthquakes lead frequently to damages to a large extent. Modern seismic codes allow for inelastic deformations in dissipative zones during design earthquakes, accepting damages to a certain extend in the relevant structural parts. As past experience shows, repair works are needed after strong earthquakes, which are usually larger than the design one. Structural systems that are easily repairable-replaceable, while maintaining the benefits of high ductility, are obviously beneficial in seismic regions. Therefore innovation in developing new seismic resistant systems is highly appreciated.

Steel-concrete composite systems (also called mixed or hybrid systems) have seen widespread use in recent decades because of the advantages against conventional construction. The optimal use of two materials and their individual properties result in a very efficient and economical structural solution. Reinforced concrete is inexpensive, massive and stiff, while steel members are strong, ductile, lightweight and easy to assemble. They also give the designer the freedom to form rigid or flexible connections and put additional bracing systems or shear walls.

Conventional systems have advantages and disadvantages. Despite their structural efficiency, conventional frames are not well suited for reparability after a strong earthquake event and this is a new property to introduce. In moment resisting frames the beams are the dissipative elements. They, or their end connections, have been proven to require repair after strong seismic events. However, they are elements resisting gravity loading and difficult to repair. Similar conditions apply to eccentric braced frames where the links, the short parts of the beams between braces, have to be repaired. In concentric braced frames, it is the braces that shall develop inelastic deformations. Damage is therefore expected in the braces, which are long and heavy elements, difficult to handle and repair. The main advantage of FUSEIS 1-1 is that inelastic deformations are strictly concentrated and controlled in zones that constitute easily replaceable fuses. Additionally they offer:

a) easiness in fabricating the fuse
b) maximum energy dissipation in cyclic behaviour
c) minimum number of exchangeable parts
d) reduction of weights, costs and difficulties in replacing the fuse parts.

This study presents the research on FUSEIS1-1, while FUSEIS1-2 is presented in detail in paper “SEISMIC BEHAVIOUR OF INNOVATIVE ENERGY DISSIPATION SYSTEMS FUSEIS 1-2”.

2 DESCRIPTION OF FUSEIS 1-1

This innovative system resembles a shear wall, having the additional advantages of energy dissipation through plastic deformation of the beams and ease of repair and even replacement if necessary. It is composed of two closely spaced strong columns, rigidly connected to multiple beams. The beams run from column to column (FUSEIS 1-1).

The system resists lateral loads as a vertical Vierendeel beam, mainly by combined bending and shear of the beams and axial forces of the columns. The dissipative elements of the system are the FUSEIS beams which are not generally subjected to vertical loads, as they are placed between floor levels.

The seismic resistance of a building may be obtained by appropriate provision of a number of such systems in the relevant directions (Figure 1). When beam-to-column connections of the building are formed as simple, this system provides alone the seismic resistance of the building. When the connections are rigid or semi-rigid, it works in combination with the over-

all moment resisting frame. In any case the connection between the floor beams to the FUSEIS columns shall be formed as simple or semi-rigid.

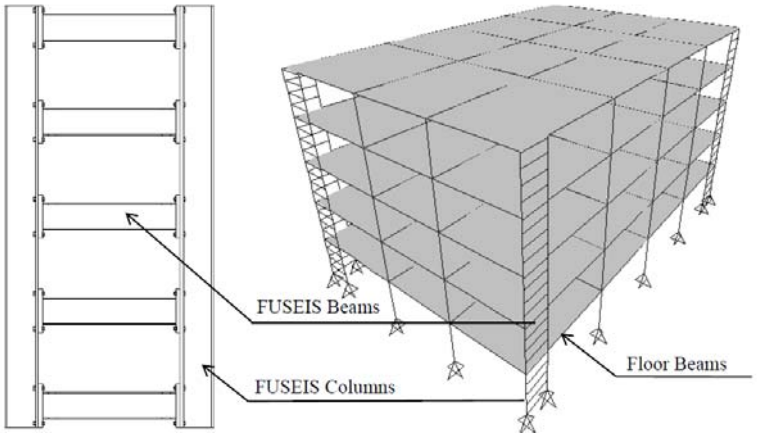


Figure 1: FUSEIS 1-1 system in a building

The fuses-to-column joints are formed as rigid to enable the Vierendeel action and are designed to have sufficient overstrength in order to achieve energy absorption only in the fuses. Bolted end-plate connections which enable an easy replacement of the beams should be used. Considering a typical floor height of 3,4 m, four or five beams may be placed per storey. The beam height depends on the required stiffness with the provision to leave the necessary vertical spacing between them. Additionally, the use of one fuse between columns just above foundation level prevents the moment transfer to the foundation.

FUSEIS columns may be of open or closed section. Open sections are more beneficial, since they offer an easier connection to the beams. When closed sections are used, a T-section can be welded to it to offer the advantage of easier connection.

FUSEIS beams may have hollow sections or open sections (I- or H- sections). To achieve a sequential plasticization of the fuses, beam sections may vary between floors, following the increase of storey shear from the top to the base of the building. In addition, beams may also vary within the floor, either in respect to their cross-sections or to their length.

Aiming to lead the plastic hinge to form away from the connection area and protect the beam to column connections of the system against fracture, beam flanges are reduced near the ends. Constant, tapered or radius cut shapes are possible to reduce the cross sectional area. As an alternative, the connection region could be strengthened by means of additional plates.

3 FULL SCALE TESTS ON FRAMES WITH FUSEIS 1-1

Analytical and experimental investigations on individual FUSEIS 1 -1 devices, i.e. on single beams, were performed in the Institute of Steel Construction of Aachen University (RWTH) which provided an insight of the local behaviour of the system. Full scale tests on a multi-storey building frame were therefore required in order to obtain a more realistic overview of the building's resistance under a seismic event. Six full scale tests on frames with FUSEIS1-1 were conducted in the Steel Structures Laboratory of NTUA. The tests were performed in an experimental rig, available in the Laboratory.

The experimental setup consisted of the test rig (Figure 2), a computer controlled hydraulic cylinder and the test frame. The test frame was designed as a part of a real building frame and consisted of two closely spaced strong columns pin jointed at both ends, rigidly connected to five beams that run from column to column. The dimensions of the structural elements were defined after analysis and seismic design of a complete building frame according to the provi-

sions of EC3 [4] and EC8 [5]. The height of the frame was 3.40 m, the distance (L) between the centrelines of the columns was 1,50m and the length (l) of the fuses varied depending on the stiffness required.

The behaviour of a frame depends on the stiffness and strength of the specimens. Therefore the use of identical beam sections within a storey leads to the simultaneous yielding of all beams. The scope of the tests was to achieve a sequential yielding of the specimens, thus providing a better behaviour under cyclic loading and as a result a better response of the building during a broader spectrum of seismic events. The sequential yielding can be achieved either by using beams with the same cross section but with varying lengths, or by using beams with the same length and varying cross sections. In order to be able to compare and evaluate the behaviour of different types of sections, specimens of similar stiffness and resistance were selected for all tested frames.

Figure 3 shows the FUSEIS 1-1 system tested. The columns were stiffened by adding stiffening T-sections at both sides in order to remain elastic. The connection of the specimens to the column was obtained with the use of receptacle steel plates. The specimens were beams of IPE, SHS and CHS sections. In order to allow a plastic hinge formation away from the beam-column connection, the beam fuses had reduced sections at the ends (RBS). The beams were provided with end plates and were bolted to the columns, to ease the replacement of the fuses after the test.

Based on initial analyses on a variety of RBS sections, the RBS parameters a (distance from face of column) and b (length of RBS) were the same 50mm and 75mm respectively for all fuses beams, while the depth of cut, g was approximately 30% of the beam flange according to FEMA350 [6] and EC8 [7] provisions. The RBS types are also given in Figure 3.



Figure 2: Test rig

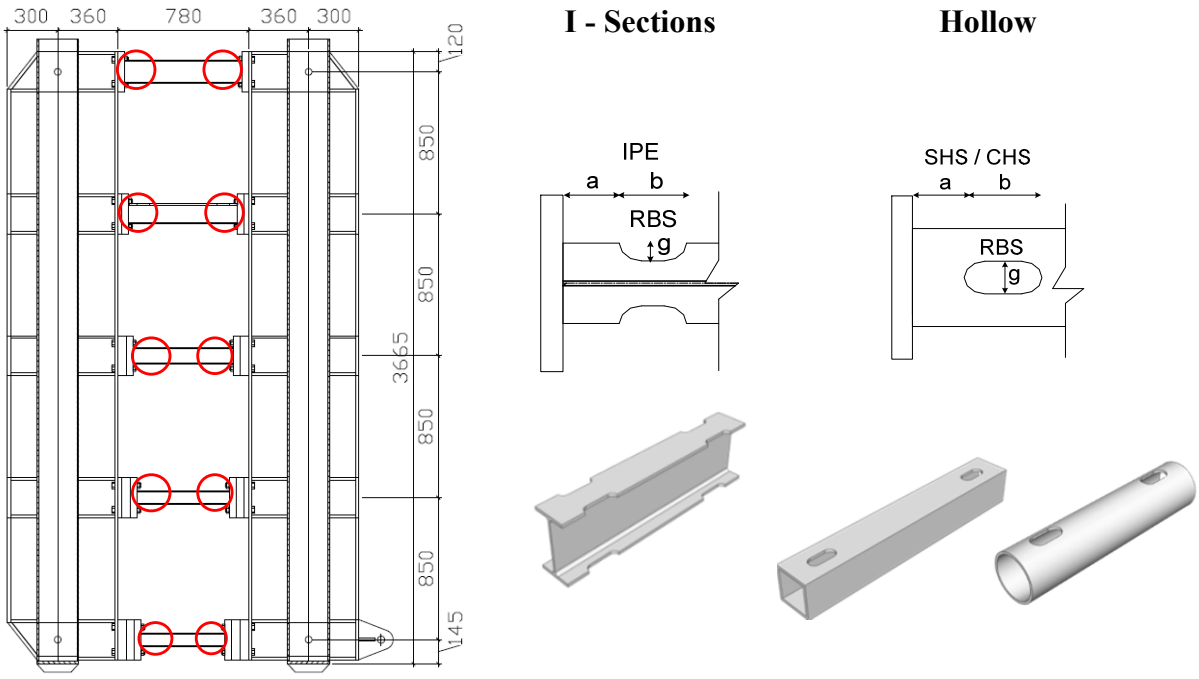


Figure 3: Tested system and beam specimens

The characteristics of the specimens, meaning the specimens sections and lengths, are given in Table 1.

Specimens with variable lengths						
Test	Type	L (mm)	L (mm)	L (mm)	L (mm)	L(mm)
M1	IPE160	700	650	600	550	500
M2	SHS120x8	700	650	600	550	500
M3	CHS 141,3x6	700	650	600	550	500
Specimens with variable sections						
Test	L	Type	Beam	Beam	Beam	Beam
A1	600	IPE	180	160	140	120
A2	600	SHS	140/8	120/8	100/8	80/6
A3	600	CHS	168.3/6	141.3/6	114.3/6	88.9/6

Table 1: Test Matrix

A basic parameter of the design of energy dissipation systems is the steel grade. Low grade steel such as S235 was preferred. Material tests for the test specimen were conducted in order to determine the mechanical characteristics of steel.

The actuator was a computer controlled hydraulic cylinder with a maximum capacity of ±250mm positioned horizontally between the column and a specially designed base via two circular hinges in order to transfer only horizontal forces to the frame. It was calibrated appropriately at the beginning of each test, meaning that it was set to the middle course position.

The above setup (the test rig, a pair of columns and the actuator) and the load application system remained the same for all the tests. The only modification between different tests concerned the replacement of the fuses. The basic problem during the assembly of beam fuses

were the structural imperfections (initial out-of-plane imperfections of the plates, weldings, transportation, residual deformations transferred from one test to the next). Gaps were formed at the contact area between the columns and the receptacle plates, for this reason filler plates were used. Additionally, the surface of the plates in some cases was not plane which was solved by tightening the bolts.

3.1 Loading Procedures and Experimental measured data

Regarding the loading procedures of the experiments, the cyclic loading protocol was defined in terms of the European ECCS – procedures [8]. The yield displacement of the specimens is the reference value that defines the loading protocol. The testing procedure was done in displacement control. The displacement was fed from the computer to the controller, which then displaced the hydraulic actuator to match the demand. The imposed displacement increases linearly, with constant velocity 1,5mm/sec and a short pause 5sec between the cycles of the same amplitude and 10sec when the amplitude increases. The cyclic loading protocol was followed by constant amplitude cycles of 5% until fracture.

Figure 4 shows the cyclic loading protocol, with increasing inter-storey drift, and the correspondent horizontal displacement imposed by the actuator to the frame. The data measured during the experimental investigations were the following:

- Displacement of the cylinder piston with an electronic displacement transducer.
- Hydraulic load applied by the cylinder, with the load cell at the end of the piston.
- Differential displacement of beam ends–shear displacement vertical to the beams with electronic displacement transducers (LVDTs) with a maximum capacity of ±50mm.

No of cycles	Frame Displ. (mm)	Interstorey drift (%)
3	2,55	yield
3	5,10	0,15
3	8,50	0,25
3	17,00	0,50
3	25,50	0.75
3	34,00	1.00
3	51,00	1.50
3	68,00	2.00
3	85,00	2.50
3	102,00	3.00
3	119,00	3.50
3	136,00	4.00
3	153,00	4.50
Until failure	170,00	5.00

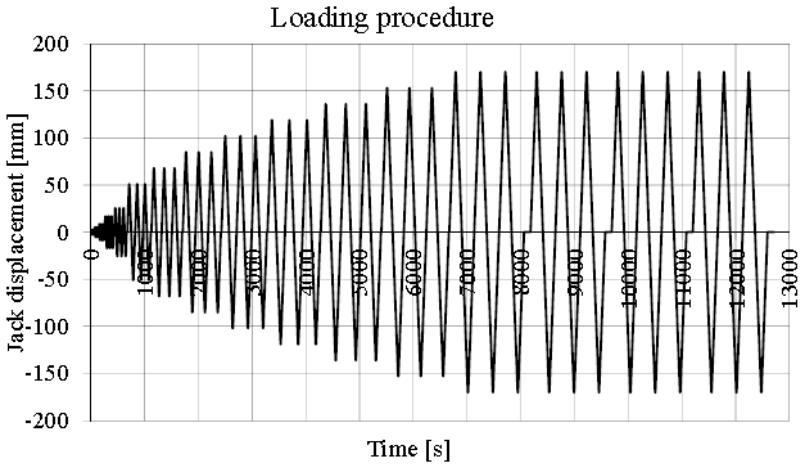


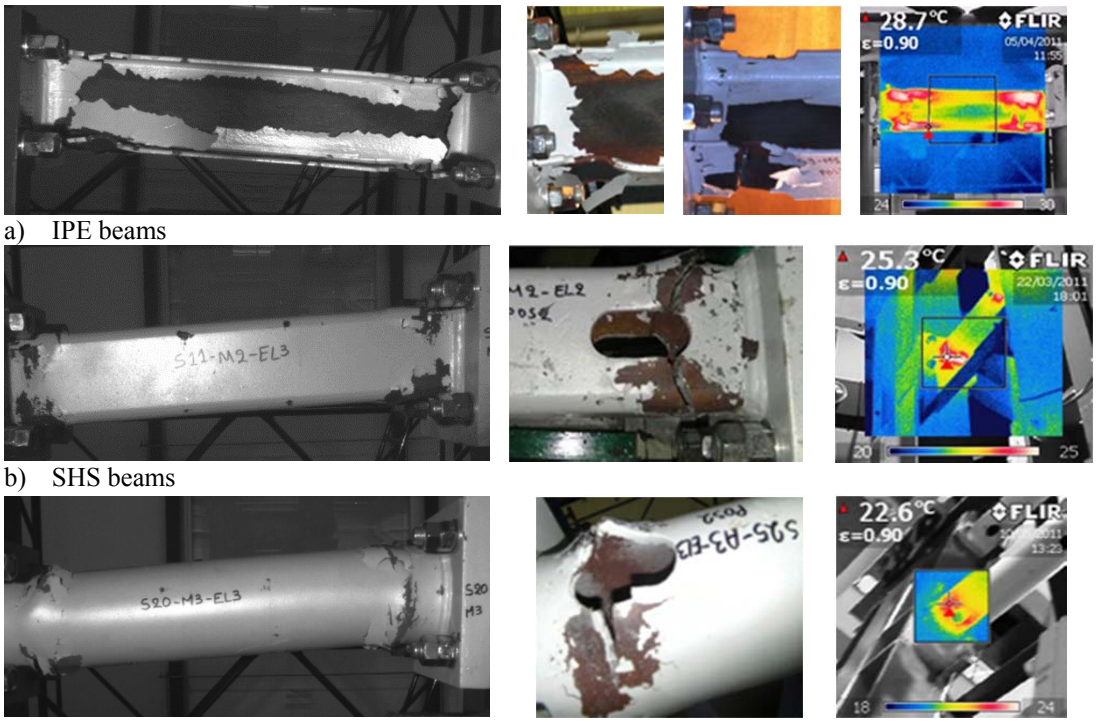
Figure 4: Applied loading protocol

3.2 Test results

All test specimens showed good plastic deformation capacity. It is remarkable that the system's resistance kept increasing after the initial and during the subsequent plastifications, mostly due to hardening, without losing its stability. Plastic deformations took place within the fuse devices only, while the columns remained elastic and undamaged until the completion of the last test. The design and stiffening of the test rig proved to be successful since they

remained almost perfectly rigid. The time required for replacing one fuse device was approximately 60 minutes. At the end of the test, depending on the condition of the fuses, some fuses were cut and removed and others – completely damaged – were instantly dispatched. During the tests, the receptacle and the filler plates did not have any significant damage and were reused.

Yielding of the beam specimens started at the RBS area. Ductile fractures were observed at the curve of the RBS and finally the height of the beam shrank at the same position, as the deformation of the specimens got larger. After attainment of maximum strength, the load degraded gradually with distortion of the RBS. All frames reached an interstorey drift between 2 and 4%. Generally, for the hollow sections it was observed that the load degraded more gradually compared to the IPE sections due to their torsional stiffness and additional resistance provided by the webs. Specifically, the CHS sections behaved even better as the plastification was distributed along the section circumference. The hinge formation during the experiments is clearly shown at the photos taken by an infrared camera, higher temperature values are observed at the RBS. Figure 5 shows photos of the deformed beam fuses.



a) IPE beams

b) SHS beams

c) CHS beams

Figure 5: Photos of the deformed fuseis beams

In some cases, during the first cycles the behaviour of the system was affected significantly by the construction imperfections of the surfaces between the columns and the receptacle plates. This phenomenon diminished at later cycles. The hysteretic diagrams have pinching in the response due to the slippage of the bolts and the construction imperfections.

The force–drift diagrams for all tests are presented in Figure 6.

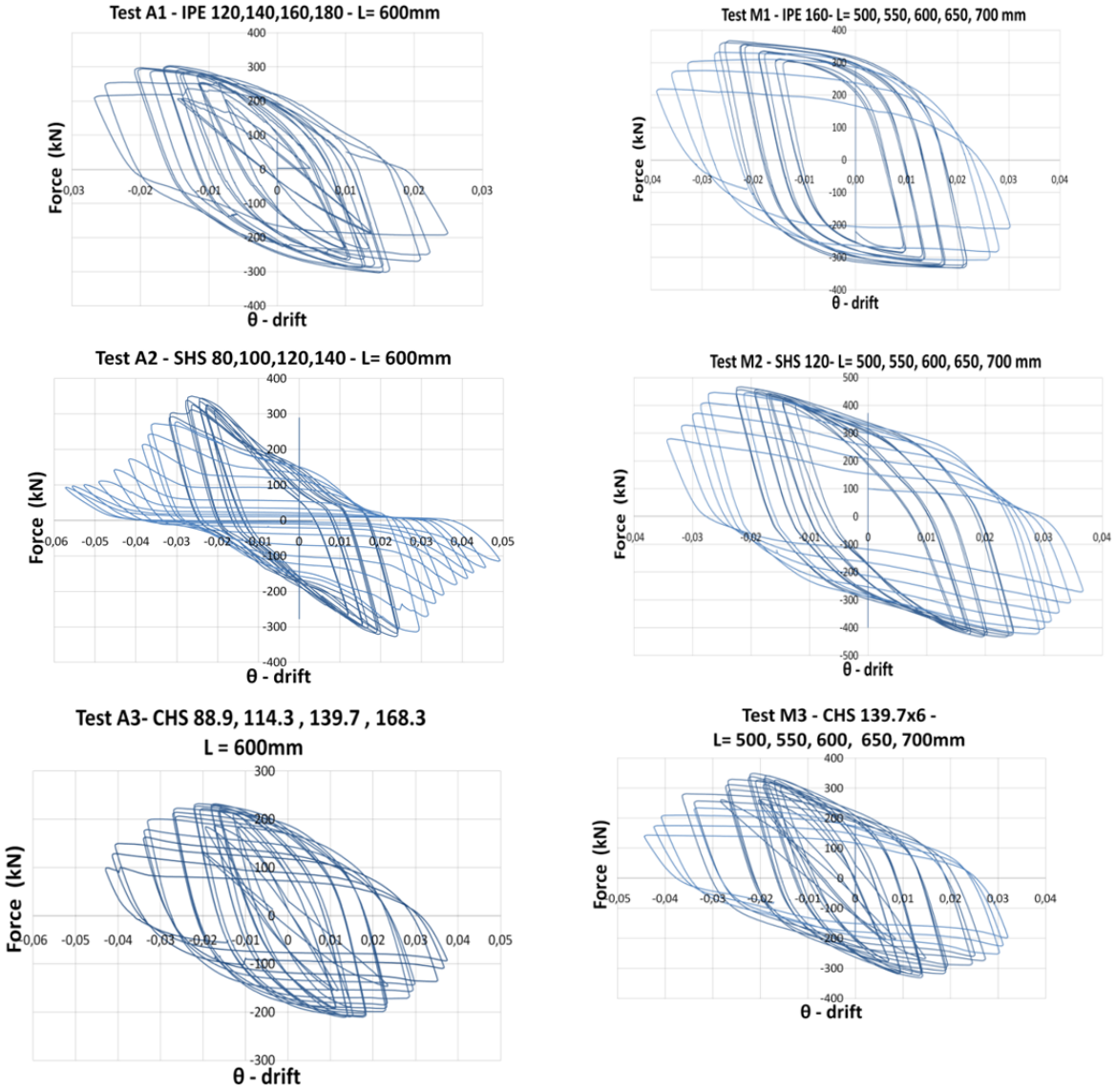


Figure 6: Hysteretic response of tested frames

3.3 Development and calibration of simple models

The commercial software SAP2000 was used and provided simple engineering models able to simulate the behavior of frames with fuses accurately. The FUSEIS elements were represented by appropriate beam FE-elements. Rigid zones were provided from column centres to column faces to exclude non-existent beam flexibilities. Further on, the net length of the beam fuses was subdivided to 5 zones that represent the full sections (ends – middle) and the RBS sections (Figure 7). In this manner, the true system flexibility and strength was accounted for. The remaining structural elements were simulated as usual. Beam-to-column joints were represented as rigid in accordance to the connection detailing of the test.

The non-linear lateral behaviour of the 2D test frames was evaluated by incremental push-over analyses (Figure 7). The target displacement corresponds to the maximum displacement (170mm) of the experimental tests. Since the ductile elements are the FUSEIS beams, potential plastic hinges were inserted at the ends of the beam RBS-sections. Table 2 summarizes the non-linear hinge parameters that comprised the most suitable approach, for each type of fuse section.

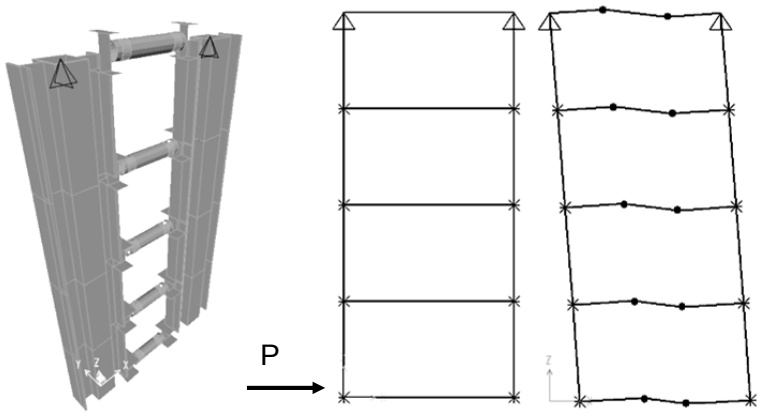
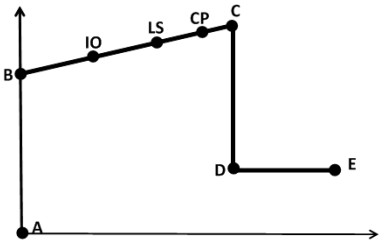


Figure 7: Pushover loading and hinge formation

HINGE PROPERTIES (α_{pl} =shape factor)

	IPE		SHS		CHS	
Point	**M/SF**	**Rot./SF**	**M/SF**	**Rot./SF**	**M/SF**	**Rot./SF**
E-	-0,6	-45	-0,4	-30	-0,2	-30
D-	-0,6	-40	-0,4	-25	-0,2	-25
C-	- α_{pl}	-40	- α_{pl}	-25	- α_{pl}	-25
B-	1	0	-0,6	0	-1	0
A	0	0	0	0	0	0
B	1	0	0,6	0	1	0
C	α_{pl}	40	α_{pl}	25	α_{pl}	25
D	0,6	40	0,4	25	0,2	25
E	0,6	45	0,4	30	0,2	30



M–θ Relation

ACCEPTANCE CRITERIA

	IPE	SHS	CHS
IO	15	5	6
LS	25	12	10
CP	35	18	16

SF are scale factors corresponding to the moment and rotation yield values

Table 2: Non-linear hinge parameters for IPE, SHS, CHS

4 LINEAR STATIC ANALYSIS AND DESIGN OF FRAMES WITH FUSEIS 1-1

Based on the understanding gained from the full scale tests on frames with FUSEIS 1-1 2D building frames with fuses were designed and analyzed using the general purpose software Code SAP 2000. In addition to conventional design, non-linear static analyses were carried out to estimate the behaviour factor of the system. Non-linear analyses based on the response of the devices which have been experimentally investigated.

Several building frames with fuses were designed according to the provisions of EC 3 and EC 8. Additional rules given in the relevant Design Guide were applied to ensure that yielding, takes place in the FUSEIS beams prior to any yielding or failure elsewhere. The FUSEIS beams, able to dissipate energy by the formation of plastic bending mechanisms, were designed to resist the forces of the most unfavourable seismic combination.

Since, this system module is used to ensure lateral stiffness and seismic energy dissipation for building structures, the frames were dimensioned to cover the Seismic zones corresponding to the Greek earthquake intensity conditions 0.16g, 0.24g,0.36g. In order to reflect the

findings obtained during the experimental program the cross sections used were similar to the ones tested (IPE, SHS, CHS) and were reduced near the ends. These models provided an optimal approximation of the behaviour of a steel building.

A typical 2D building frame, part of a five-storey composite building, was used for all the cases examined. The composite building consisted of similar frames at 8m axial distance which was the effective width for both the vertical loads and the lateral mass during earthquake loading. The bays of the main frame were 6.0 m. The beams were composite and the thickness of the slab was 15cm. The effective width of the composite beams was equal to 1.5m in accordance with EC2.

The FUSEIS system consisted of two closely positioned vertical hollow strong columns, jointed together with five horizontal beams in a tight arrangement. The center line distance of the columns was 2m. The simulation concept for the fuses was the same as described in Section 3.3. The column bases were pinned to limit yielding at the foundation level. In order to introduce partial fixity conditions between the composite beams and the columns, rotational springs were assigned at the composite beams' ends according to EC 3 part 1.8, §6.3 and EC 4 part 1 (Annex A).

Vertical loading was equal for all storeys and masses were lumped at the joints. Steel grade of the non-dissipative structural members was S 355 and for the dissipative elements (the fuses) S 235 to eliminate the risk of possible overstrength of the dissipative elements. A preliminary value of the behavior factor q = 5 was employed that is discussed later.

The described layout was followed for all nine frames. All models were designed according to the provisions of EC 3 for ULS and SLS. Limitations on 2nd order effects according to EC8 were also taken into account. In all cases the value of the interstorey drift sensitivity coefficient θ was between 0,1 and 0,2 indicating that a frame with FUSEIS system is flexible. The relevant seismic action effects are then multiplied by a magnification factor 1/(1 - θ). Interstorey drifts were limited to 0,0075 (buildings having ductile non-structural elements) - EC 8. This was the crucial condition for the determination of the controlling structural members (FUSEIS beams and columns).

Design was based on multi modal response spectrum analysis, using a linear-elastic model of the structure and a design spectrum. The analysis showed that the first mode of vibration activated approximately 75% of the mass, while few more modes were needed to reach 90% as required by Codes. Figure 8 presents the building frame with SHS fuses for PGA=0,36g .

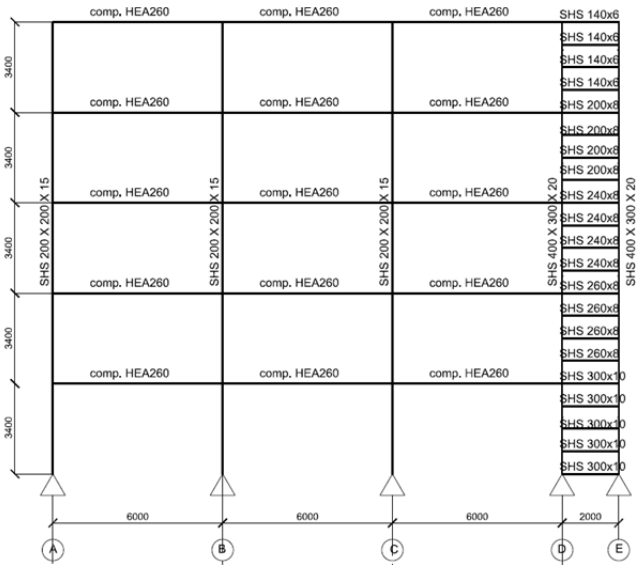


Figure 8: Typical 2D building frame

5 NON- LINEAR STATIC ANALYSIS (PUSHOVER) AND EVALUATION OF THE BEHAVIOUR FACTOR

The structural models used for elastic analysis were extended to include the response of structural elements beyond the elastic state via a non-linear static analysis (Pushover). The principal objective of this investigation was to estimate the behaviour factor q.

The analysis was carried out under conditions of constant gravity loads and monotonically increasing lateral loads. The results of the analysis according to the fundamental mode of vibration, 1st mode, are presented hereafter. The analysis was based on the assumption that the mode shape remains unchanged after the structure yields, P –Delta effects were also taken into account.

In pushover analysis, the behaviour of the structure is characterized by a capacity curve that represents the relationship between base shear force and top displacement and the demand curve for the design earthquake which was based on ATC-40. The performance point is defined as the intersection of the demand curve with the capacity curve (Figure 9).

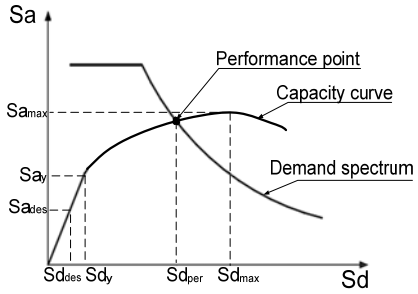


Figure 9: Definition of the performance point

In the implementation of pushover analysis, correct modeling of the hinges is crucial. The model requires the determination of the nonlinear properties of each component in the structure that are quantified by strength and deformation capacities. Non-linear hinge elements were assigned at the ends of the reduced parts and their properties were derived from the calibrated models of the tests (Table 2). At the start of the calculations, potential plastic hinges were also inserted at the ends of the composite beams, the columns and the system columns to check if they also behave inelastic during the seismic event. These analyses showed that at the performance point plastic hinges formed only in the reduced parts of the fuses so in subsequent analyses potential hinges were introduced only in the fuses. The distribution of plastic hinges and the evaluation of the performance point are given in Figure 10.

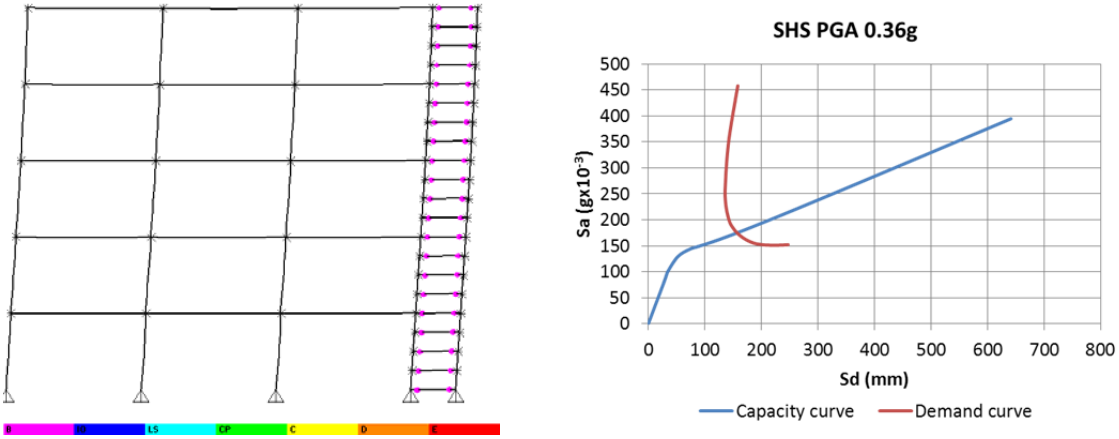


Figure 10: Hinges at the Performance Point and Evaluation of performance point

As expected the weak beam strong column concept was fulfilled for all frames studied.

Besides the assessment of the structural performance of the building frames, pushover analysis also offered the possibility to estimate their behaviour factor. Due to the flexibility of the system $T_1 \geq T_c$ the 'equal displacement rule' was applied. Figure 11 shows the typical pushover response curve for the evaluation of behaviour factor.

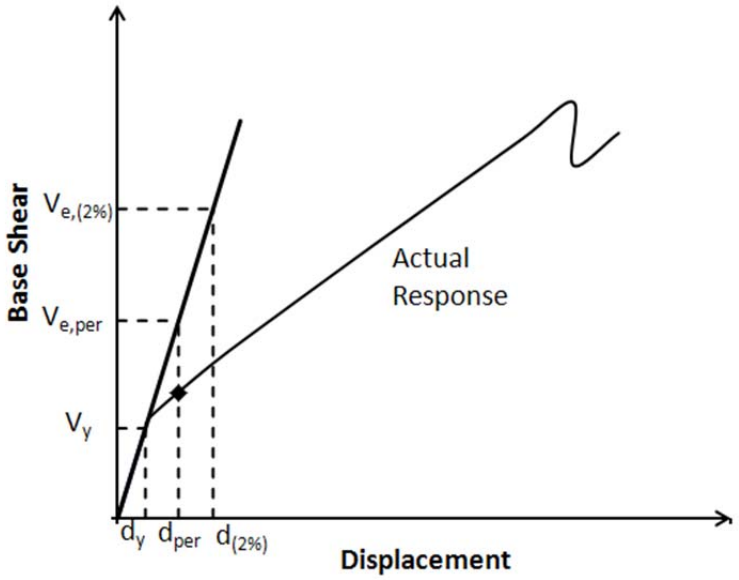


Figure 11: Typical pushover response curve for evaluation of behaviour factors

The behaviour factor, q, accounts for the inherent ductility and overstrength of a structure and may be generally expressed in the following form taking into account the above two components:

$$q = q_\mu \cdot \Omega \tag{1}$$

The structure ductility, q_μ, is defined in terms of the Elastic Base Reaction that corresponds to 2% drift (V_e) to the Idealised Yield Strength - First hinge (V_y) (Figure 11), as following:

$$q_\mu = \frac{V_e}{V_y} \tag{2}$$

The ID equal to 2% was determined experimentally and corresponds to the maximum force reached.

The structural overstrength is defined as the ratio of the Idealised Yield Strength - First hinge V_y to the Design Strength (V_d), as following:

$$\Omega = \frac{V_y}{V_d} \tag{3}$$

The Design Strength (V_d) was based on the fundamental vibration mode which had the largest participation to the vibrating mass and was determined from $V_d = \eta \cdot M \cdot S_d(T)$ where n is the modal participating mass ratio, M is the total mass and $S_d(T)$ is the spectral acceleration that derives from the design spectra for the fundamental mode.

The calculated q factors for each type of cross section are given in Table 3. The system's behaviour is characterised by high values of ductility, its overstrength is dependent on the intensity of the design earthquake. All q values are above 5, the value that was initially considered for the design. However, when high values of q are employed the interstorey drift

sensitivity coefficient θ increases significantly due to 2nd order effects. Therefore, a maximum value of q equal to 5 is proposed for the design of buildings with FUSEIS system.

FUSEIS BEAMS	0,16g			0,24g			0,36g		
	q_μ	Ω	q	q_μ	Ω	q	q_μ	Ω	q
IPE	3.31	2.99	9.91	3.31	1.97	6.51	3.81	1.26	4.79
SHS	3.97	2.26	8.99	3.97	1.51	6.01	5.79	1.09	6.31
CHS	3.18	3.52	11.19	3.18	2.31	7.35	3.82	1.31	5.00

Table 3: Non-linear hinge parameters for IPE, SHS, CHS

The calculated q factors are summarized in Figure 12.

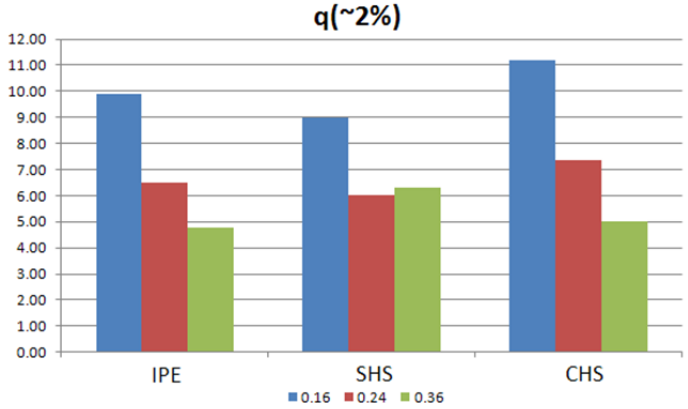


Figure 12: Evaluation of q factors

6 CONCLUSIONS

The above study illustrates the successful application of the innovative FUSEIS system. The following observations are worth noting:

a) The system resists lateral loads as a vertical Vierendeel beam.

b) Inelastic deformations are strictly limited to the dissipative elements preventing the spreading of damage into rest of the structural members (slab, beams, columns). The devices and the frames with the devices have a very good behaviour: strong, stiff, large capacity of energy absorption.

c) It may be designed as more flexible/rigid depending on the section types and their distribution between floor levels. The number of stories and supporting weight strongly affects the required sections and geometry. The seismic resistance of a building may be obtained by appropriate provision of a number of FUSEIS systems in the relevant directions.

d) It consists an architecturally versatile solution for the lateral stability of building structures compared to the braced frames as they can be positioned in small areas of the building and do not interrupt the architectural plan. They can also constitute visible parts of the building indicating its seismic resistant system

e) Sequential plastification may be allowed by appropriate selection of the sections of the dissipative elements.

f) The dissipative elements are easily replaceable if they are damaged after a strong seismic event, since they are small and are not part of the gravity loading resistant system. The assembling and disassembling is easy from a practical point of view.

g) The proposed q-factor for buildings with FUSEIS1-1 is 5.

h) Code relevant design rules for the seismic design of frames with dissipative FUSEIS and practical recommendations on the selection of the appropriate fuses as a function of the most important parameters and member verifications have been formulated and are included in a Design Guide.

ACKNOWLEDGEMENTS

The research presented is made in the framework of the European Research Project RFSR-CT-2008-00032: "Dissipative devices for seismic resistant steel frames (Fuseis)". The financial contribution of the Research Fund for Coal and Steel of the European Community is gratefully acknowledged.

REFERENCES

[1] Vayas, Ph. Karydakis D. Dimakogianni, G. Dougka, C. A. Castiglioni, A. Kanyilmaz et al. Dissipative devices for seismic resistant steel frames - *The FUSEIS Project, Final Report. Research Programme of the Research Fund for Coal and Steel*, 2012.

[2] Vayas, Ph. Karydakis D. Dimakogianni, G. Dougka, C. A. Castiglioni, A. Kanyilmaz et al. Dissipative devices for seismic resistant steel frames - *The FUSEIS Project, Design Guide. Research Programme of the Research Fund for Coal and Steel*, 2012.

[3] Castiglioni, C. A., Calado, L., Kanyilmaz A. Experimental analysis of seismic resistant composite steel frames with dissipative devices. *Journal of Construction Steel Research*, 2012.

[4] EN1993-1-1, Eurocode 3: Design of steel structures - *Part 1-1: General rules and rules for buildings. Brussels.* Comitee Europeen de Normalisation (CEN), 2003.

[5] EN1998-1-1, Eurocode 8: Design of structures for earthquake resistance – *Part 1-1: General rules, seismic actions and rules for buildings.* Brussels: Comitee Europeen de Normalisation (CEN), 2003.

[6] FEMA – 350: *Recommended Seismic Design Criteria for New Steel Moment-Frame Buildings*, 2000.

[7] EN1998-3, Eurocode 8: *Design of structures for earthquake resistance - Part 3: Assessment and retrofitting of buildings*. Brussels: Comitee Europeen de Normalisation (CEN), 2005.

[8] ECCS document: *Recommended testing procedure for assessing the behaviour of structural steel elements under cyclic loads.* Technical committee 1: structural safety and loadings, Technical working group 1.3: seismic design, 1986.

[9] Calado, L., Castiglioni, C. A. *Steel beam-to-column connections under low-cycle fatigue: Experimental and numerical research*. In: Proceedings of XI WCEE; 1996.

[10] SAP2000, CSI Computers and Structures Inc., www.csiberkeley.com

[11] FEMA – 356: Prestandard and Commentary for the seismic rehabilitation of Buildings, 2000.

COMPDYN 2013
4th ECCOMAS Thematic Conference on
Computational Methods in Structural Dynamics and Earthquake Engineering
M. Papadrakakis, V. Papadopoulos, V. Plevris (eds.)
Kos Island, Greece, 12–14 June 2013

Estimation of the behavior factor of steel storage pallet racks

Konstantinos Adamakos[1*], Stella Avgerinou[1], Ioannis Vayas[1]

[1]National Technical University of Athens
Iroon Politexneiou 9, Zografos 15780
kadamakos@hotmail.com, avgerinoustella@gmail.com, vastahl@central.ntua.gr

Keywords : racking, racks, pushover, behaviour factor, pallets, braced, unbraced, storage

Abstract. *European Racking Federation (ERF) is currently developing normative documents for the seismic design of pallet racks due to lack of sufficient design rules and bibliography. The special geometry of these thin-walled members of high slenderness and their non linear behaviour require specific rules for a successful and accurate modeling. The design of these non-traditional steel structures is even more complicated in seismic zones, where they must be able to withstand horizontal and vertical dynamic forces. Furthermore, the analysis must represent the additional limit state of the fall of pallets, which would lead to the subsequent damage to goods, people and to the structure itself. Bracing systems are widely used to enhance the stiffness of the structures under seismic loads. Braced systems exhibit, however, unwanted phenomena, such as torsional dynamic modes. On the other hand, unbraced systems have translational modes and uncoupled behaviour, but they are very flexible.*

In this paper, the earthquake performance of such structures is investigated using pushover analyses. The work presented, is a part of a research project which is carried out within the framework of the European Research Program SEISRACKS 2. Detailed analyses of components using finite elements software are performed in order to clarify their failure and post-failure behaviour. Finally, a comparison of the available q factor and the used value during the design takes place to verify the efficiency of the design procedure

1 INTRODUCTION

The need for a multiple, easier and efficient storage of goods is growing as the logistics are continuously developed. As a consequence a thorough design based on safety and economy is necessary. These special steel structures, otherwise called "storage pallet racks", do not follow the international norms applying for buildings since they are not conventional steel structures. For this reason nowadays multiple attempts are made for the publication of an independent and complete normative document.

Due to the absence of further research and experiments, the seismic performance of racking systems is not yet well known and therefore their members are generally over-calculated. The behaviour factors usually range from 1.5 to 2 although greater values are also allowed [1]. However, these values are not frequently used.

In this report, the results of nine different real case studies are presented, provided by 4 different industrial partners (I.P). Among them there are 6 unbraced and 3 braced racks, which are tested both on down and cross aisle direction.

2 ANALYSIS PROCEDURE

Pushover analysis involves the incremental application of horizontal loads (in a prescribed pattern) on a computer model of the structure. The structure is thus "pushed" until it reaches a limit state or a collapse condition, while the total applied shear force and the respective lateral displacements are plotted at each step.

The horizontal loads coexist with vertical loads, in order to create a real loading situation. The analysis takes into consideration nonlinearities of both geometry and material.

2.1 Geometry

The geometry of the provided racks is shown in figure 1 and 2. The first one refers to a braced system which is actually used for high seismicity zones, while the second one to an unbraced system that can be found in low or medium seismicity zones. Both figures present the longitudinal direction, also called "down aisle" direction.

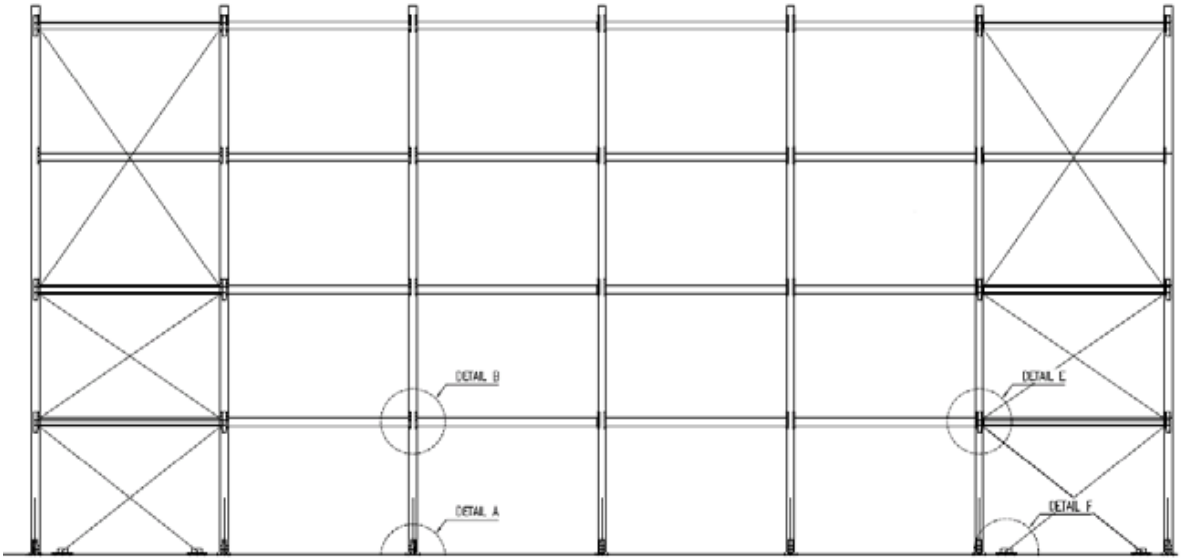


Figure 1- View of braced model at down aisle direction

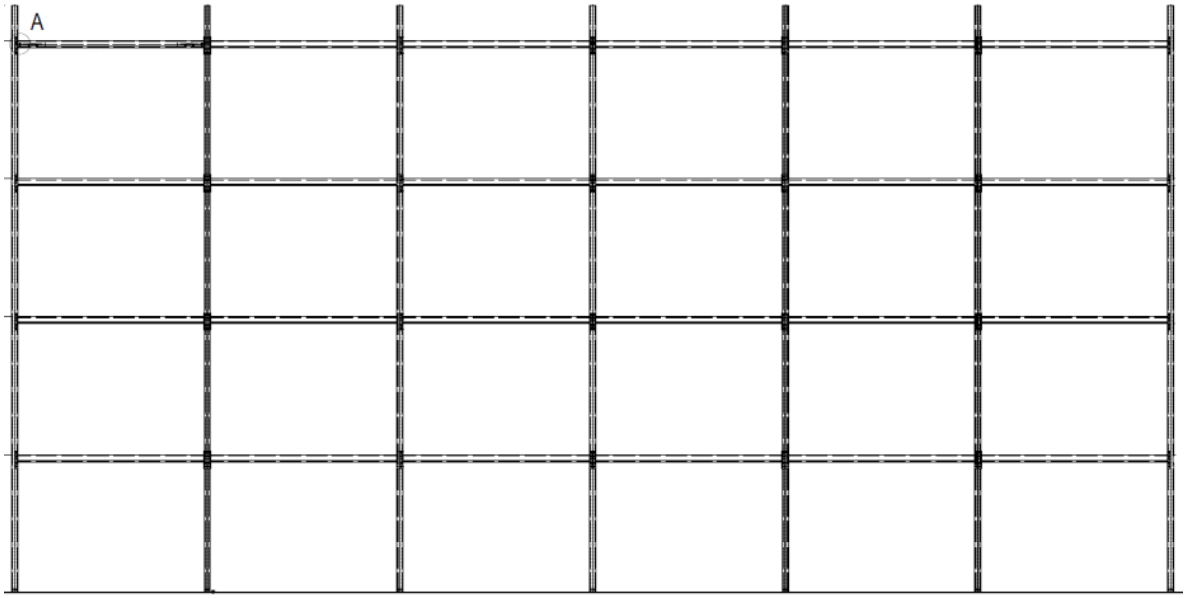


Figure 2- View of unbraced model at down aisle direction

Figure 3 shows the transversal, also called "cross aisle" direction of such a system with two different configurations. The major differences lie on the amount of the used diagonal members and the existence of symmetry or not of the assembly. The first case is used mainly for high seismicity zones. In this picture (on the left) the additional structure of the down aisle bracing system is also evident.

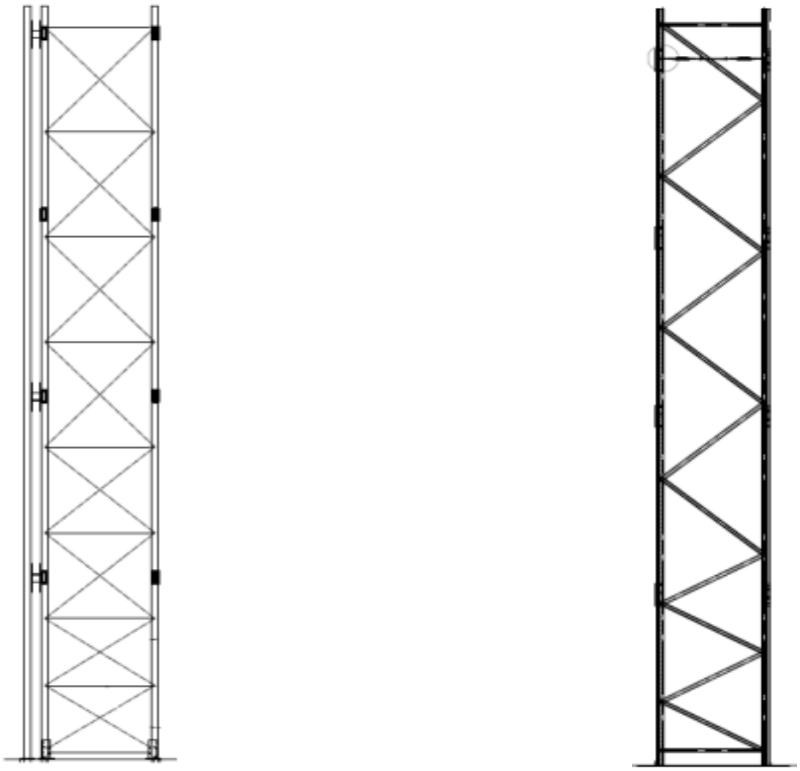


Figure 3- View of cross aisle direction

a) Typical bracing for high seismic zones

b) typical bracing for low seismic zone

2.2 Loads

The applied loads are vertical and horizontal. The vertical loads consist of the dead loads of the structure as well as of the pallets, assuming that the racks are fully loaded. The horizontal load is equivalent to the earthquake load and is applied incrementally. This load is assigned with a uniform distribution along the vertical axis in an attempt to overcome the significant difference between braced and unbraced racks in terms of modal shapes. More specifically, braced racks displayed torsional dynamic modes due to the eccentricity of the spine bracing, thus having lower participating mass ratios and consequently requiring the use of 30 modes in order to reach the required 90% of mass in a multimodal pushover analysis. On the other hand, unbraced racks exhibited a clear translational behaviour. The uniform load was therefore chosen in order to produce comparable results.

It should also be noted that P-delta effects have been taken into account, as the racking systems are generally flexible and the critical buckling factor α_{cr}, where:

$$\alpha_{\mathrm{cr}} = \mathrm{F_{cr}}/\mathrm{F_{Ed}} \qquad (1)$$

was not exceeding the critical value of 10 in most cases. Eurocode 3 suggests neglecting P-Delta phenomena when this factor is greater than 10 for elastic and 15 for plastic analysis [2]. In any case, it is always more accurate even though time consuming.

2.3 Inelastic structural properties

To perform pushover analyses the plastic characteristics of the components have to be defined. In this example, the members are made of thin walled steel sections that belong to class 4 and thus their plastic properties cannot be developed. However, the behaviour of these components is nonlinear and it is simulated as equivalent “plastic”. Therefore what will be referred to as "plastic hinge" and "plastic behaviour" from this point on, actually refers to this aforementioned nonlinear behaviour.

In general, the members/connections where plastic hinges are expected to occur are:

The beam-column connections (beam end connectors), the ground connections (base plates), the uprights and the diagonal members, as past experiments have already indicated [3].

As far as the diagonals are concerned, they can be found in the racking systems in three different versions: those of spine bracing, those of the upright frames and the horizontal ones.

2.4 Beam End Connector

The behaviour of the beam end connectors is crucial for the stability of the whole structure since it provides the frame action (moment resistance) longitudinally. These connectors are hooked, with or without safety pins, and their calculations are only experimental. Each manufacturer is obliged to provide test results in order to specify the rotational stiffness of the connection and its strength. In Figure 4, four different examples of this peculiar connection are displayed, in terms of moment rotation curves. These curves were used in the simulation of the different case studies. More specifically, they were input in the models as nonlinear link elements [4].

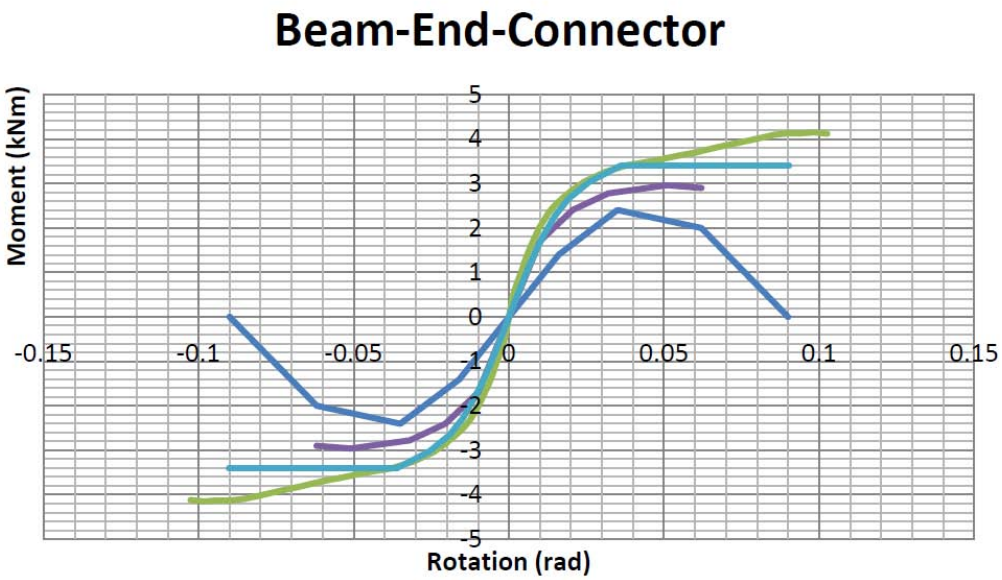


Figure 4- Moment- rotation curve for beam end connectors

2.5 Base- plate

The base-plate connections are also moment resistant connections, the behaviour of which must be defined experimentally. It is important to mention that the total behaviour of the connection is directly influenced by the normal force of the uprights.

Tests for different load levels took place; those with the axial force closest to our case study are presented in Figure 5, in terms of moment-rotation curves, as provided by the experiments of the industrial partners.

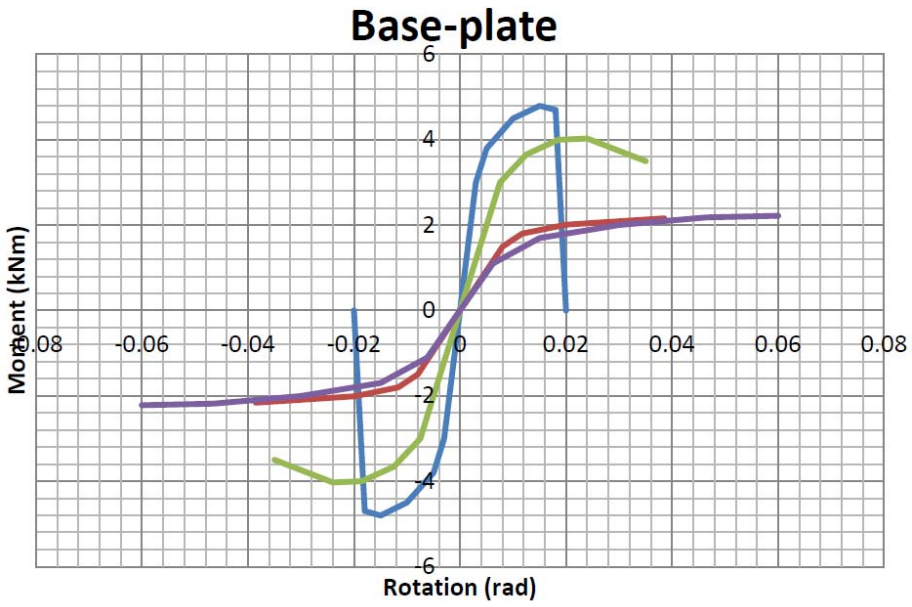


Figure 5- Moment-rotation curve of base plates

2.6 Uprights

The uprights consist of open sections of class 4, so their failure mode is likely to be due to local buckling or lateral- torsional buckling. Using the effective properties in the design stage, the failure is considered to be due to lateral torsional buckling. As is the case with any column, the uprights' behaviour can be described with an interaction curve of biaxial bending moments and axial force. The interaction relation taken into account can be found in Eurocode 3 regarding lateral- torsional buckling.

$$\frac{N_{Ed}}{\chi_{min}A_{eff}f_y/\gamma_M}+\frac{\kappa_y M_{y,Ed}}{\chi_{LT}W_{eff,y}f_y/\gamma_M}+\frac{\kappa_z M_{z,Ed}}{W_{eff,z}f_y/\gamma_M}<1 \qquad (2)$$

Since, the failure occurs before the section enters the plastic region, the interaction relation is linear.

Another point of interest is to define properly the plastic hinges of uprights as well as the post buckling behaviour. Due to lack of experiments, numerical analyses took place in order to determine the moment-rotation curve of such a member. ABAQUS software was used to model a single (upright) member of two meters height, with both ends restrained against torsion and out of plane displacement. The members' base was also restrained in any translation, whereas the top was free to move not only axially but also in the uprights respective down aisle direction.

In the first step an axial force of 48kN was applied, as the one undertaken by an upright of a fully loaded rack, and then a horizontal load pushed the upright to failure.

Regarding the simulation assumptions, shell elements were used, the radius of the real section and the perforations was taken into account, the support was considered as a rolling fixity, and the advantage of symmetry was reckoned. Figure 6 shows the initial modelling and Figure 7 the deformed member at the end of analyses.

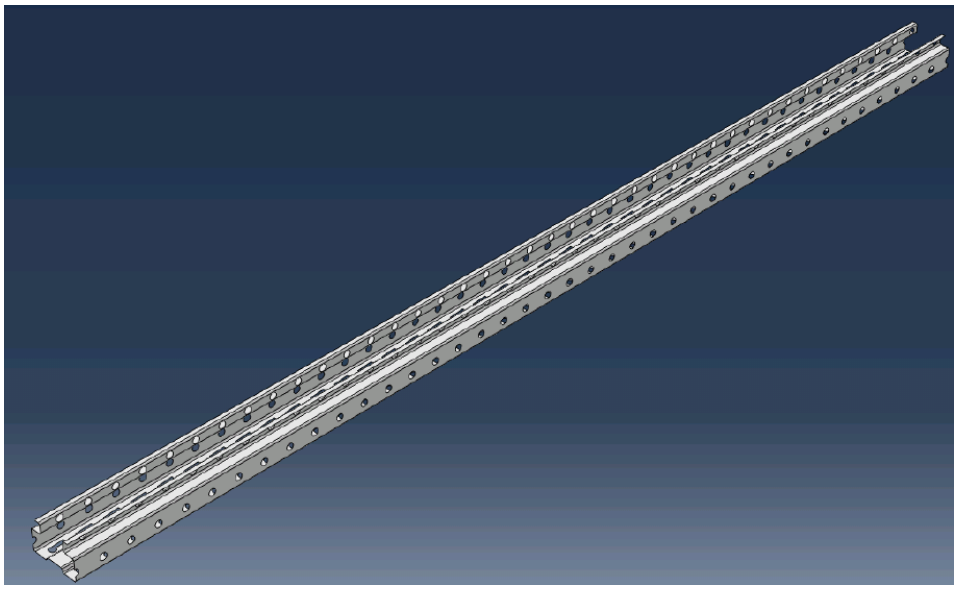


Figure 6- Simulated upright member

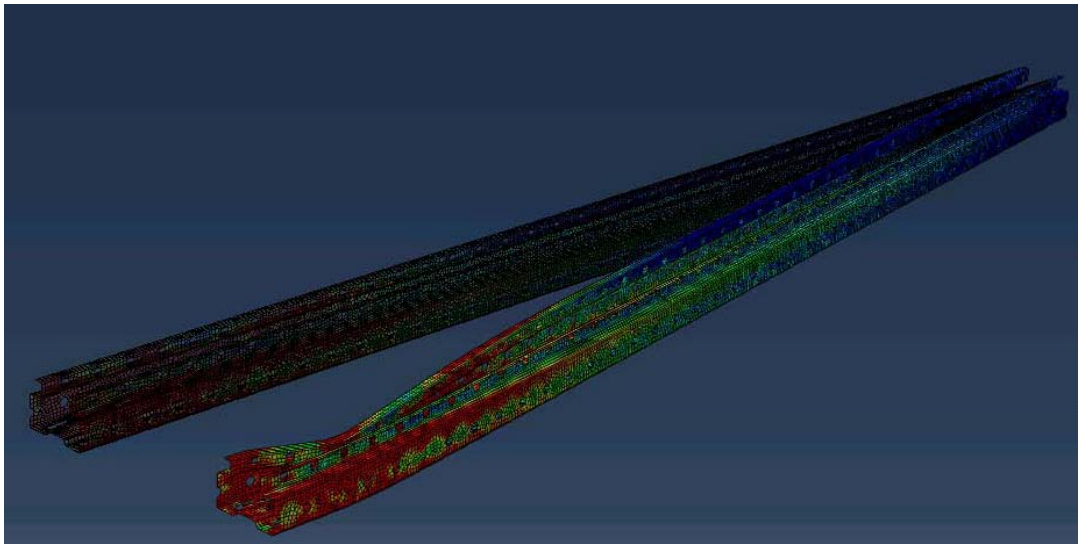


Figure 7- Deformed shape of upright at the end of analysis

The results from the previous analyses are presented to figure 8, as a diagram of moment-rotation.

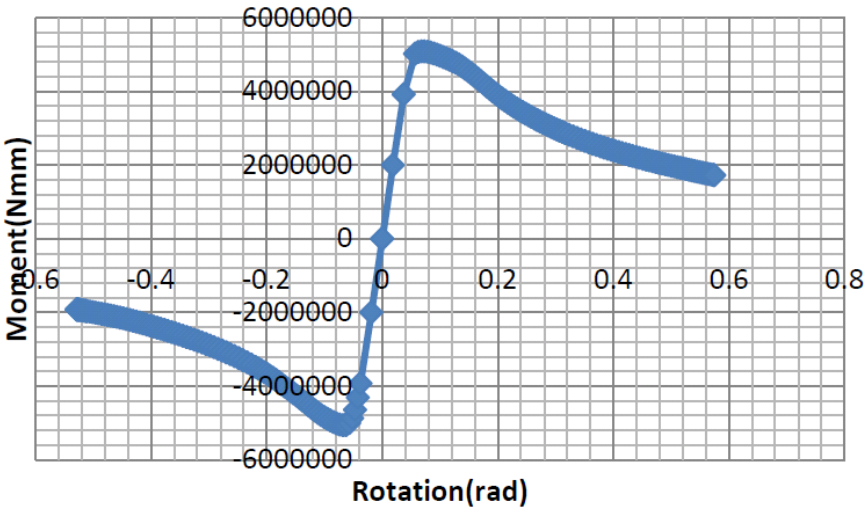


Figure 8- Moment rotation curve of the upright section

2.7 Diagonals

The diagonal members are also significant for the overall behaviour. However, their ultimate capacity is not clear enough, as there is sometimes an interaction between the buckling of the member, the capacity of the section in tension, the shear strength of the bolts and the bearing resistance of the connection. Hence, a further investigation took place numerically, in order to also define the equivalent plastic hinge for each member. The modelling procedure included the use of shell elements and imperfections, to define the theoretical buckling load of the member. Additionally, solid elements were used in a contact model, between holes and bolts, in an attempt to clarify the influence of the bearing resistance in the total behaviour. The results are summarized in Figure 9, and they refer to a channel section, with a single hole in the web.

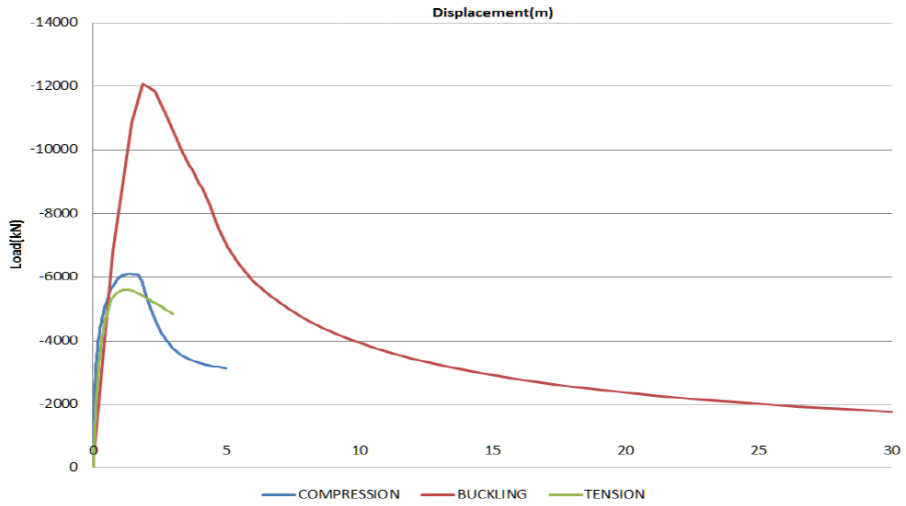


Figure 9- Force displacement curve for different failure modes of diagonals

The critical one is selected to be linearized and simulated as plastic hinge in the software. In this specific case the green and the blue line correspond to the bearing failure of the connection.

3 GLOBAL ANALYSES RESULTS

3.1 General

Nine different case studies of the industrial partners were simulated under equal horizontal loads at all levels as described in previous paragraph. The configurations were considered fully loaded with pallet loads, the inelastic properties of the system are simulated with plastic hinges or nonlinear link elements as described in previous paragraphs. The pushover curves were superimposed in order to compare quantitatively the different configurations. Two main groups of curves were drawn; those referring in down aisle direction and those in cross aisle direction. Figure 26 and 27 present the results for the nine cases on down and cross aisle direction respectively.

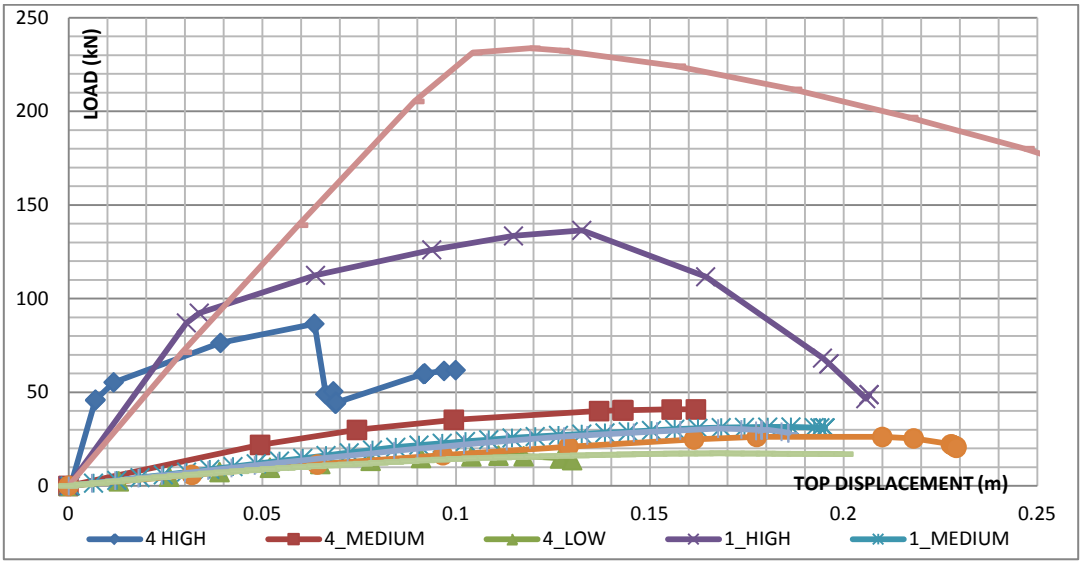


Figure 10- pushover curves for down aisle direction

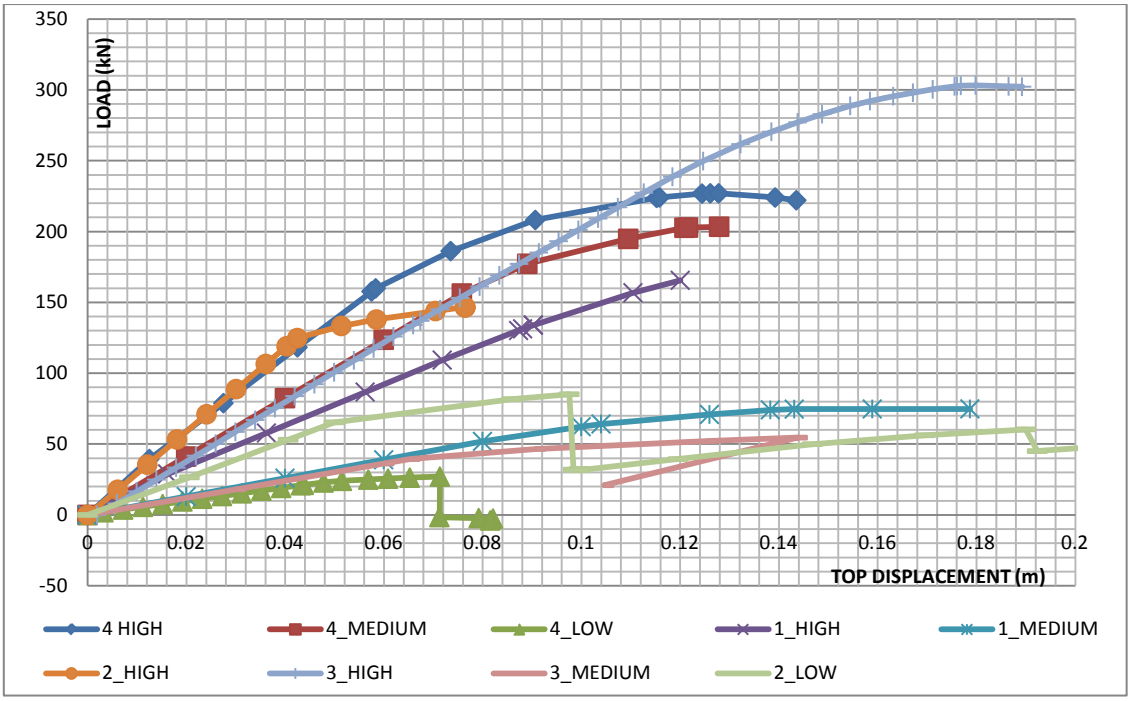


Figure 11- pushover curves for cross aisle direction

One can easily observe that the high seismic zone racks are quite stiffer than those designed for low seismic zones due to the fact that the former possess bracing systems on their back.

3.2 Behaviour factors

In order to estimate the demand imposed by the earthquake the performance points for each structure have to be determined. The relevant calculations are made by SAP2000, based on the procedure described in ATC-40 [5]. The parameters Ca and Cv that define the elastic spectrum are determined as following:

$$C_A = a_g S n \quad (3)$$

$$C_V = 2.5 a_g S n T_c \quad (4)$$

In order to calculate the q- factor the pushover curves have to be linearized. The q- factor is defined as the product of the overstrength Ω and the ductility ratio μ [6], as it is given in eq. (7). The definitions of the overstrength and the ductility are given by equations (5) and (6) respectively. The terms of these equations are defined in figure 12, where the linearization of the pushover curves is presented as well. In absence of other criteria, the "ultimate" state is defined as the state where the base shear reaches its maximum value. The linearized and the original pushover curves, the performance points and the calculated q- factors are illustrated in Figures 13 to 21 for all case studies. The pushover curve is illustrated with blue line, the linearized curve with green line. The performance point is indicated in red, the point of first significant yield in purple. It is interesting to see that in some systems the performance point is below first yielding, indicating that the system is over-dimensioned.

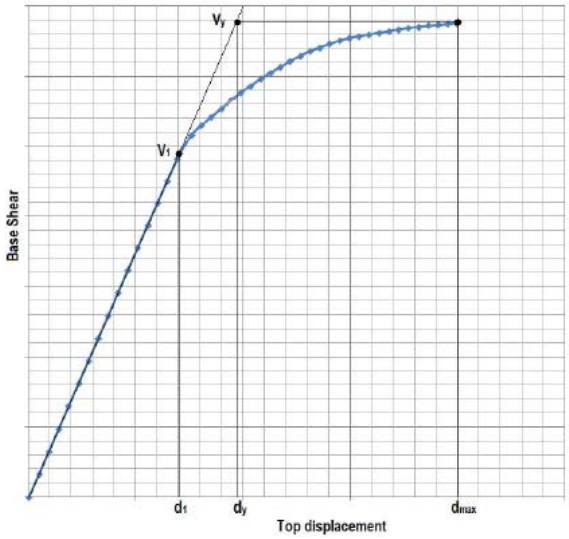
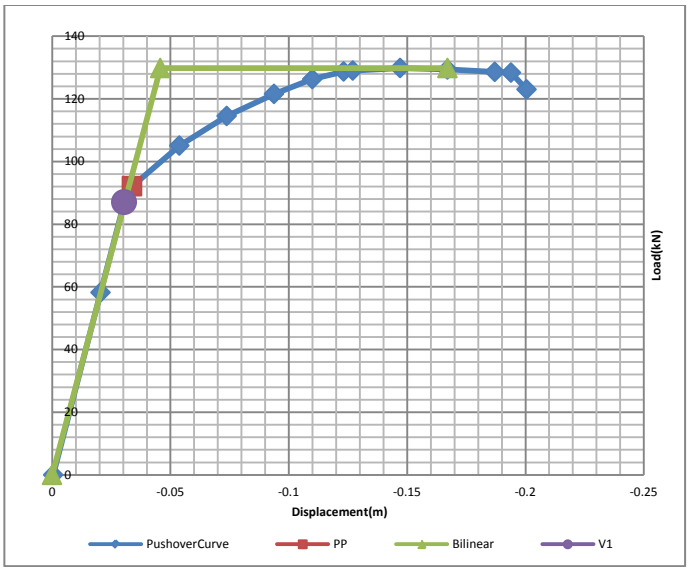


Figure 12- Linearization of a pushover curve

$$\Omega = \frac{V_y}{V_1} = \frac{d_y}{d_1} \quad (5)$$

$$q_0 = \mu = \frac{d_{\max}}{d_y} \quad (6)$$

$$q = q_0 \Omega \quad (7)$$



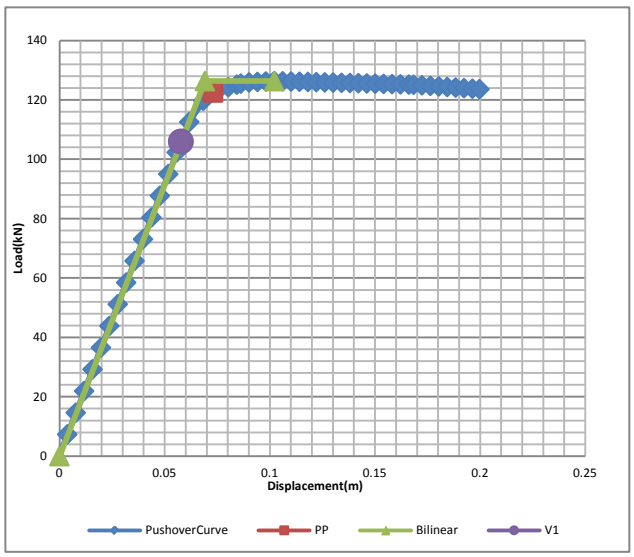


Figure 13 System A, high seismic zone

a) Down aisle b) Cross aisle

Tables 1-9 present the ductility, the overstrength and the q- factor of each system. The system name (A, B, C, or D) indicates the IP.

	μ	Ω	q
Down	3.65	1.50	5.47
Cross	1.47	1.2	1.76

Table 1- Ductility, overstrength and q- factor for system A-high seismic zone

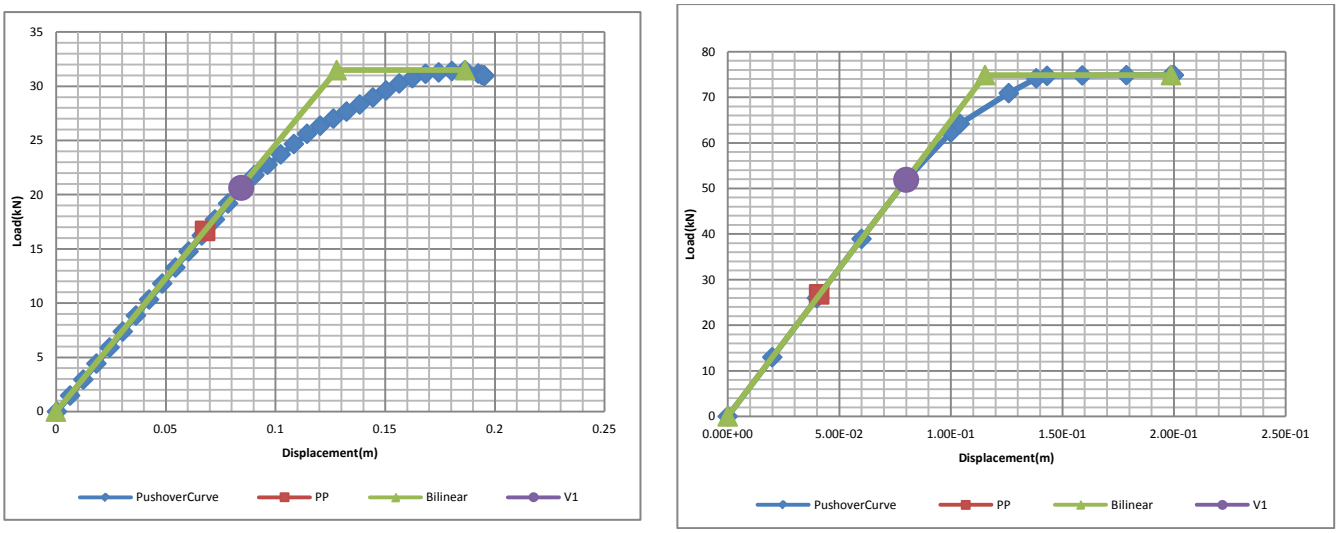


Figure 14- System A, Medium Seismic Zone

a) down aisle b) cross aisle

	μ	Ω	q
Down	1.45	1.52	2.22
Cross	1.72	1.44	2.48

Table 2- Ductility, Overstrength and q- factor for the case study A-Medium seismic zone

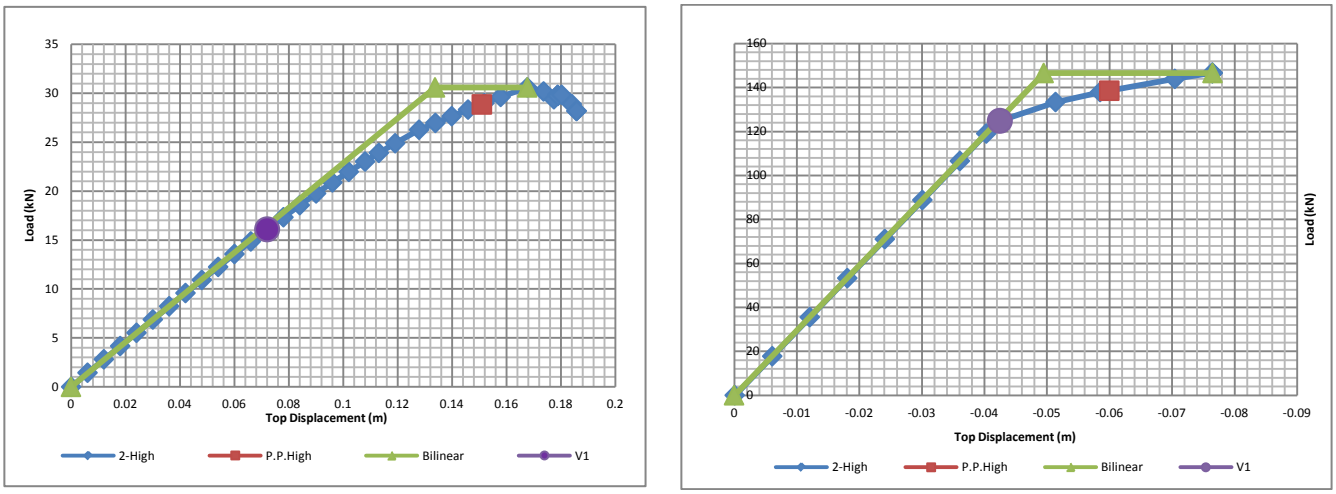
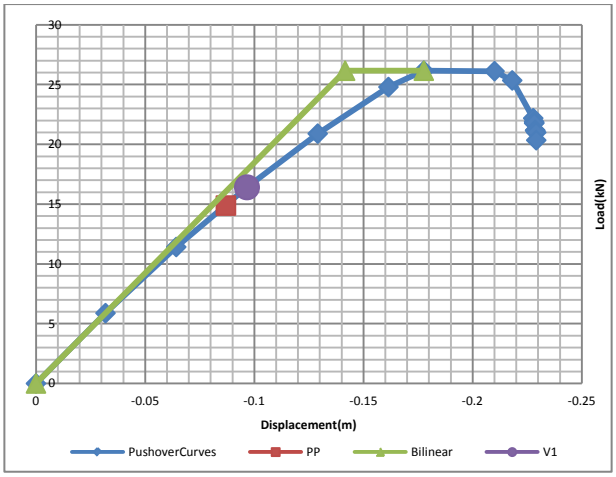


Figure 15- System B, High Seismic Zone

a) down aisle b) cross aisle

	μ	Ω	q
Down	1.25	2.06	2.58
Cross	1.54	1.17	1.81

Table 3- Ductility, Overstrength and q- factor for the case study B-high seismic zone



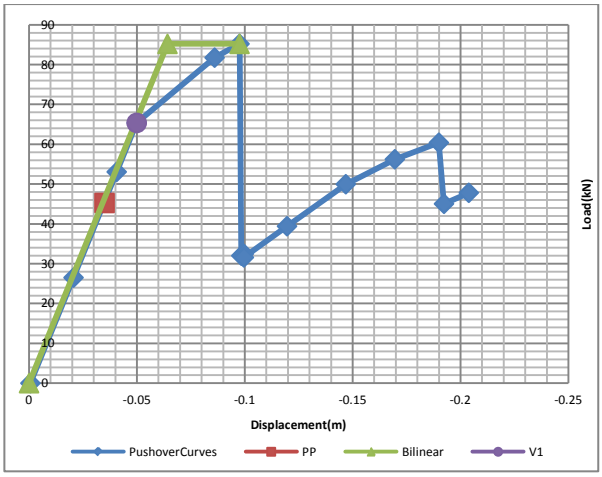
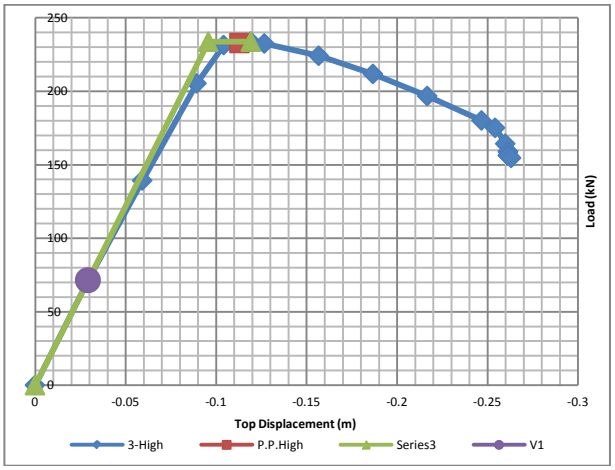


Figure 16- System B, Low seismic zone

a) down aisle b) cross aisle

	μ	Ω	q
Down	1.25	1.59	2.00
Cross	1.52	1.30	1.98

Table 4- Ductility, Overstrength and q- factor for the case study B-Low seismic zone



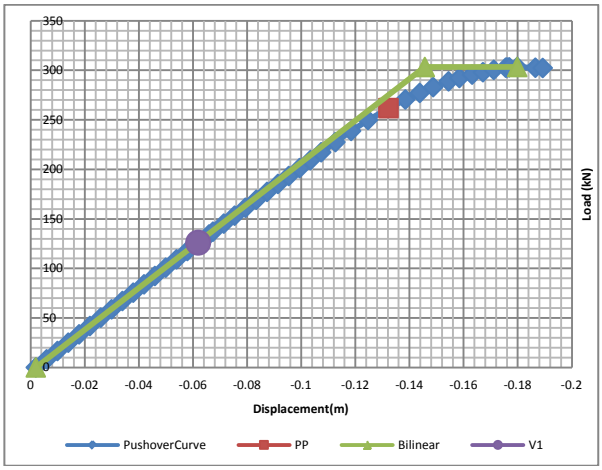
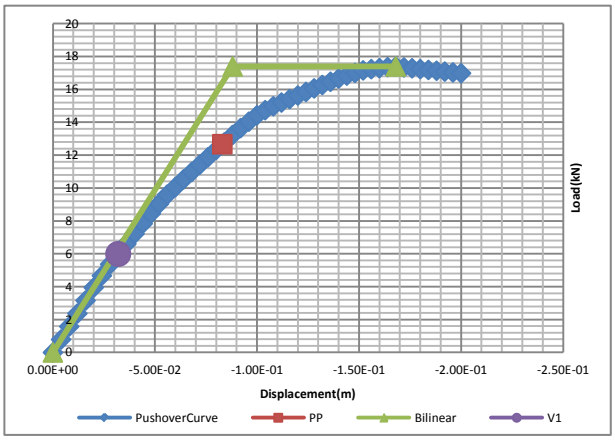


Figure 17- System C, High seismic zone

a) down aisle b) cross aisle

	μ	Ω	q
Down	1.24	3.27	4.07
Cross	1.23	2.4	2.97

Table 5- Ductility, Overstrength and q- factor for the case study C-high seismic zone



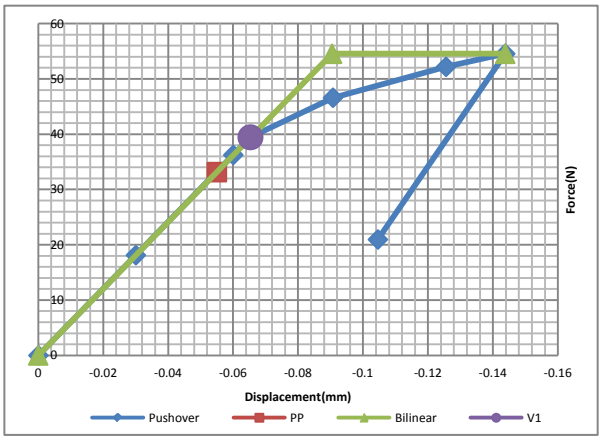
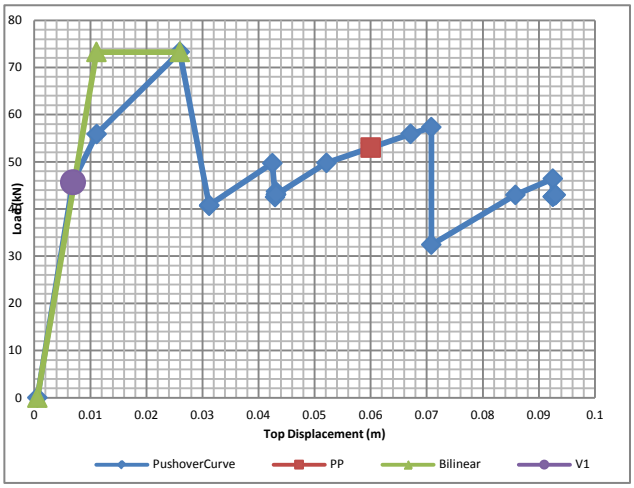


Figure 18- System C, Medium seismic zone

a) down aisle b) cross aisle

	μ	Ω	q
Down	1.90	2.90	5.51
Cross	1.58	1.38	2.2

Table 6- Ductility, Overstrength and q- factor for the case study C- Medium seismic zone



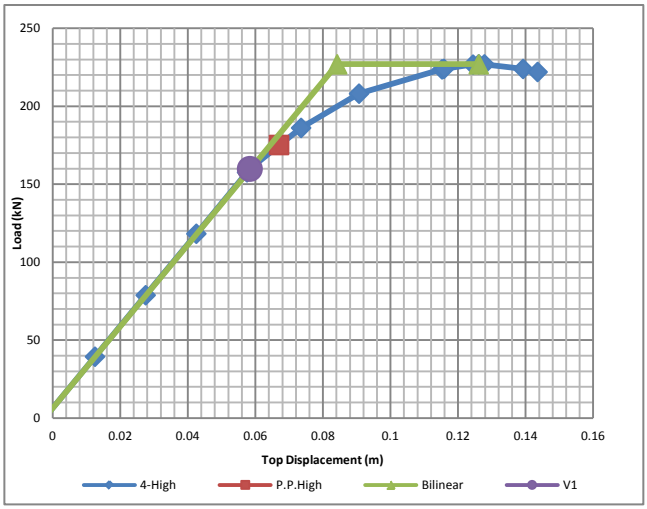


Figure 19- System D, High seismic zone

a) down aisle b) cross aisle

	μ	Ω	q
Down	2.34	1.59	3.72
Cross	1.49	1.42	2.12

Table 7- Ductility, Overstrength and q- factor for the case study D-high seismic zone

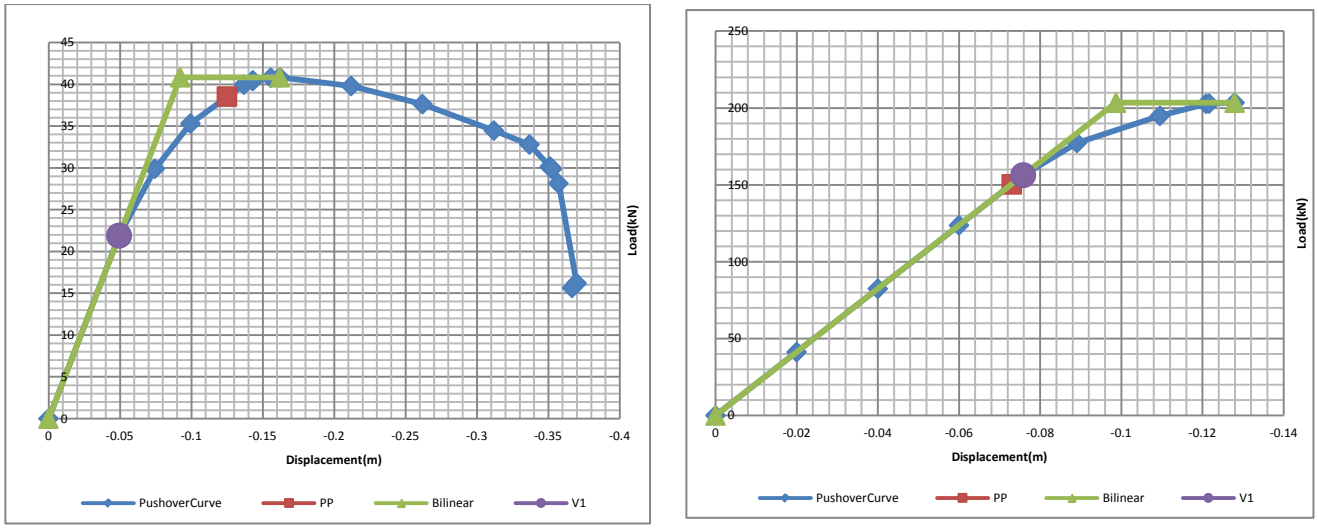


Figure 20- System D, Medium seismic zone

a) down aisle b) cross aisle

	μ	Ω	q
Down	1.75	1.86	3.27
Cross	1.29	1.30	1.68

Table 8- Ductility, Overstrength and q- factor for the case study D- Medium seismic zone

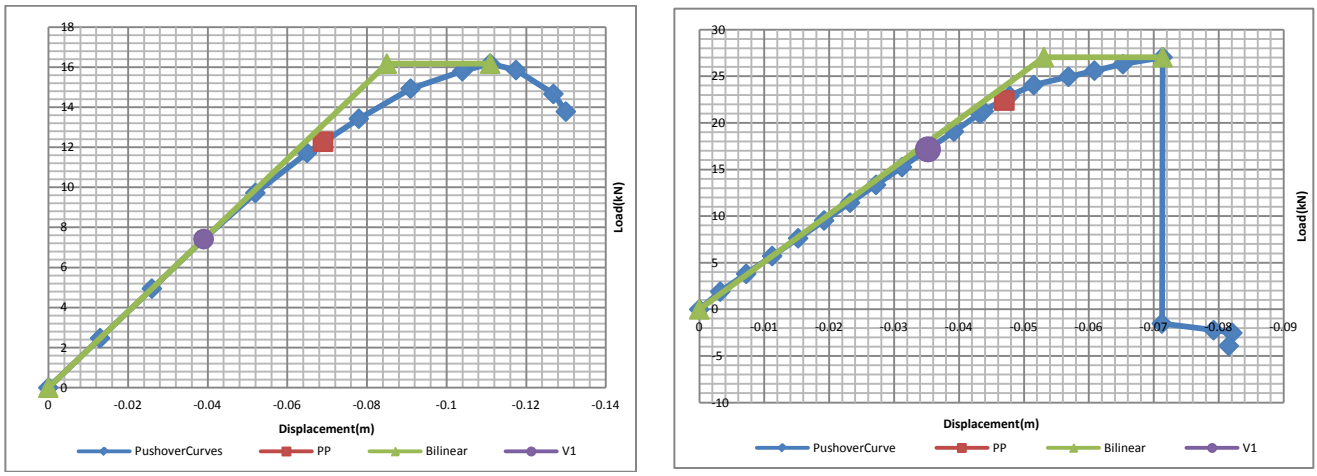


Figure 21- System D, Low seismic zone

a) down aisle b) cross aisle

	μ	Ω	q
Down	1.30	2.18	2.84
Cross	1.34	1.57	2.11

Table 9- Ductility, Overstrength and q- factor for the case study D- Low seismic zone

4 CONCLUSIONS

The previous calculations indicate that q- factor does not follow a specific rule. In general, in down aisle direction there can be calculated has higher values of q- factor than in cross aisle direction. In down aisle direction the braced structures appear to be more ductile compared with the unbraced ones due to the ductility provided by the tension diagonals. The beam end connectors and the base plate connections have a ductile response, although it is relative to the considered yield point. On the other hand, the bracing of the upright frame, which is activated in the cross aisle direction, is not really ductile since buckling; local buckling and bearing failure of thin walled plates appear.

As far as the q factors are concerned, for the analyses in down aisle direction they range from 2 to 5.47, whereas in cross aisle direction they range between 1.68 and 2.97. It should be noted that these values were determined based on the information that was provided by the IPs.

Acknowledgment

The current paper is a part of the research project Seisracks-2 of RFSC (Research Fund for Coal and Steel) and it is funded by European Commission.

REFERENCES

[1]. FEM *Racking and Shelving product group, European Racking Federation, Storage equipment information bulletin no.2: Latest developments in the harmonization of the design and use of storage equipment, ERF Info : FEM 10 / I-02* , July 2010.

[2]. CEN. (1994). *Eurocode 3: Design of Steel Structures – Part 1.1 General Rules and Rules for Buildings*, European Commitee for Standardization

[3]. Castiglioni C.A., *Seismic behaviour of steel storage pallet racking systems*, Structural Engineering Department of Politecnico di Milano, Milano, 2008.

[4]. Computers and Structures Inc., *CSI Analysis Reference Manual for SAP2000®,* ETABS®, and SAFE®, Berkeley, California, USA, 2010.

[5]. ATC 40, *Seismic Evaluation and Retrofit of Concrete Buildings*, Seismic Safety Commission, State of California, November 1996.

[6]. FEMA 356, *Prestandard and commentary for the seismic rehabilitation of buildings*, Federal Emergency Management Agency, November 2000.

COMPDYN 2013
4th ECCOMAS Thematic Conference on
Computational Methods in Structural Dynamics and Earthquake Engineering
M. Papadrakakis, V. Papadopoulos, V. Plevris (eds.)
Kos Island, Greece, 12–14 June 2013

DESIGN AND PERFORMANCE OF STEEL – CONCRETE HYBRID COUPLED SHEAR WALLS IN SEISMIC CONDITIONS

T. Bogdan[1], A. Zona[2], G. Leoni[2], A. Dall'Asta[2], C. Braham[1], H. Degée[1]

[1] University of Liège
Chemin de Chevreuils, 1, 4000, Liège, Belgium
teodora.bogdan@ulg.ac.be / c.braham@ulg.ac.be / h.degee@ulg.ac.be

[2]University of Camerino
Viale della Rimembrenza, 63100 Ascoli Piceno, Italy
alessandro.zona@unicam.it / Graziano.leoni@unicam.it / a.asta@tin.it

Keywords: Hybrid coupled shear walls, dissipative links, innovative steel-concrete hybrid structures, steel frames, and seismic analysis.

Abstract. *In this work innovative hybrid coupled shear walls (HCSW) are considered, their design is discussed, their efficiency and limitations evaluated by means of nonlinear static (pushover) analysis. Different numbers of storeys, wall geometries and design assumptions are studied in order to give an overview of situations of interest in European seismic prone areas. Experimental tests have been designed to study the performance of the connection of a seismic link embedded in a concrete shear wall. This study is part of a larger research project named INNO-HYCO (INNOvative HYbrid and COmposite steel-concrete structural solutions for building in seismic area) funded by the European Commission.*

1 INTRODUCTION

Steel and concrete composite structures are common for buildings in seismic areas, conversely steel and concrete hybrid solutions are less diffused and many open problems and potentially interesting structural solutions require further investigation. In composite structures the deformation demands for the steel and concrete components are in the same range since concrete and steel are part of the same structural member. On the other hand, hybrid structures allow a more efficient design of the reinforced concrete structural elements as well as of the steel structural elements. In fact the deformation demands may be tailored to the capacity of the relevant materials. Thus, it becomes possible to define innovative steel and reinforced concrete hybrid systems for the construction of feasible and easy repairable earthquake-proof buildings through the full exploitation of the properties of both steel and concrete constructions.

Objective of the research project INNO-HYCO (INNOvative HYbrid and COmposite steel-concrete structural solutions for building in seismic area), funded by the European Commission, is the study of steel-concrete hybrid systems obtained by coupling reinforced

concrete elements (e.g., walls and shear panels) with steel elements (e.g., beams and columns). Such systems should permit to exploit both the stiffness of reinforced concrete elements, necessary to limit building damage under low-intensity earthquakes, and the ductility of steel elements, necessary to dissipate energy under medium- and high-intensity earthquakes. Such hybrid systems might represent a cost- and time-effective type of construction since: (i) simple beam-to-column connections could be used for the steel frame constituting the gravity-resisting part, (ii) traditional and well-known building techniques are required for the reinforced concrete and steel components.

Examples of hybrid structural systems are: (i) shear walls with steel coupling beams; (ii) systems made of traditional reinforced concrete shear walls coupled with moment resisting steel frames; (iii) composite walls made of steel frames with infill reinforced concrete panels. Such systems are considered in Eurocode 8 but only limited information is given for their design, e.g., connection between steel components and reinforced concrete components. Hybrid systems may suffer from some drawbacks distinctive of reinforced concrete shear walls and of moment-resisting steel frames. Shear walls are low redundant structures, their post-yielding behaviour is characterised by deformations localized at the base and expensive detailing is required to avoid concrete crushing. Furthermore, the high overturning moments require expensive foundations. In addition, reinforced concrete shear walls are very difficult to restore because the damage could be extended for more than one inter-storey height. On the other hand, moment-resisting steel components have expensive connections and large yielded zones that make repair complicated.

The research project INNO-HYCO aims at developing hybrid systems characterised by innovative conceptions and connection systems between steel and concrete components. Two main typologies are considered: (i) hybrid coupled shear wall (HCSW) systems, and (ii) steel frame with reinforced concrete infill walls (SRCW). In this paper only the HCSW systems are considered and selected results obtained by the research units of the University of Camerino (UNICAM) and of the University of Liège (ULG) are illustrated.

2 COUPLED SHEAR WALLS SYSTEMS

2.1 Conventional systems

Coupled shear wall systems obtained by connecting reinforced concrete shear walls by means of beams placed at the floor levels constitute efficient seismic resistant systems characterised by good lateral stiffness and dissipation capacity. Coupling beams must be proportioned to avoid over coupling, i.e., a system that acts as a single pierced wall, and under coupling, i.e., a system that performs as a number of isolated walls. Extensive past research (e.g. Paulay and Priestley 1992) has led to well established seismic design guidelines for reinforced concrete coupling beams, typically deep beams with diagonal reinforcements, in order to satisfy the stiffness, strength, and energy dissipation demands. The diagonal reinforcement consists of relatively large diameter bars which must be adequately anchored and confined to avoid buckling at advanced limit states. Structural steel coupling beams (Figure 1) or steel-concrete composite coupling beams provide a viable alternative (e.g. El-Tawil et al. 2010), particularly for cases with restrictions on floor height. In contrast to conventionally reinforced concrete members, steel/composite coupling beams can be designed as flexural-yielding or shear-yielding members. The coupling beam-wall connections depend on whether the wall boundary elements include structural steel columns or are exclusively made of reinforced concrete elements. In the former case, the connection is similar to beam-column connections in steel structures. In the latter case the connection is achieved by embedding the coupling beam inside the wall piers and interfacing it with the wall boundary element. In the past dec-

ade, various experimental programs (El-Tawil et al. 2010) were undertaken to address the lack of information on the interaction between steel coupling beams and reinforced concrete shear walls. However, coupled shear wall systems suffer from being difficult to be repaired after strong earthquakes. Design recommendations following the criteria of Performance or Displacement Based Design (PBD and DBD) and Force Based Design (FBD) are still missing or at their early stage of development (ASCE 2009).

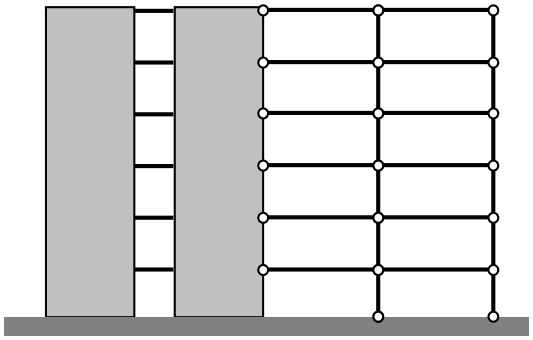


Figure 1. Example of conventional hybrid coupled shear wall system connected to a gravity-resisting steel frame with pinned beam-to-column joints.

2.2 Innovative hybrid systems

An example of innovative hybrid system is the reinforced concrete shear wall with steel links depicted in Figure 2. The reinforced concrete wall carries almost all the horizontal shear force while the overturning moments are partially resisted by an axial compression-tension couple developed by the two side steel columns rather than by the individual flexural action of the wall alone. The reinforced concrete wall should remain in the elastic field (or should undergo limited damages) and the steel links connected to the wall should be the only (or main) dissipative elements. The connections between steel beams (links) and the side steel columns are simple: a pinned connection ensures the transmission of shear force only while the side columns are subject to compression/traction with reduced bending moments. Such a mechanism allows the reduction of the negative effects of the reinforced concrete wall on the foundations.

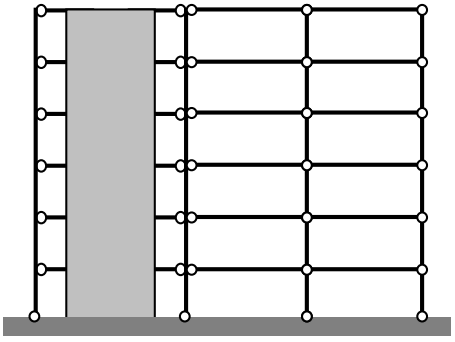


Figure 2. Example of innovative hybrid coupled shear wall system connected to a gravity-resisting steel frame with pinned beam-to-column joints.

The structure is simple to repair if the damage is actually limited to the link steel elements. To this end, it would be important to develop a suitable connection between the steel links and the concrete wall that would ensure the easy replacement of the damaged links and, at

same time, the preservation of the wall. As an alternative, links could include a replaceable fuse (El-Tawil et al. 2010) acting as a weak link where the inelastic deformations are concentrated while the remaining components of the system have to remain elastic. Clearly, the proposed hybrid system is effective as seismic resistant component if the yielding of a large number of links is obtained.

In this paper the problems encountered in a preliminary design of the above described innovative hybrid system based on the recommendations available in the Eurocodes are discussed using selected case studies. The relevant seismic performances of the designed structures are analysed in order to assess both potentiality and limitations encountered during the design for the proposed innovative HCSW systems.

3 DESIGN OF HCSW SYSTEMS

3.1 Case study

Two case studies are considered: 4-storey and 8-storey steel frames with the same floor geometry as shown in Figure 3. For each floor the vertical loads are G_k = 6.5 kN/m^2 and Q_k = 3.0 kN/m^2, while the floor total seismic mass is 1200 tons. Interstorey height is h = 3.40 m. The gravity-resisting frame has continuous columns (Table 1) pinned at the base. Beams (IPE500) are pinned at their ends. Steel S355 is used for columns, beams, and links. Selected materials for the reinforced concrete walls are concrete C25/30 and steel reinforcements S500.

Storey #	4-storey case	8-storey case
8	-	HE 220 B
7	-	HE 220 B
6	-	HE 300 B
5	-	HE 300 B
4	HE 220 B	HE 450 B
3	HE 220 B	HE 450 B
2	HE 300 B	HE 450 M
1	HE 300 B	HE 450 M

Table 1. Wide-flange cross sections of the columns of the vertical-resisting structure.

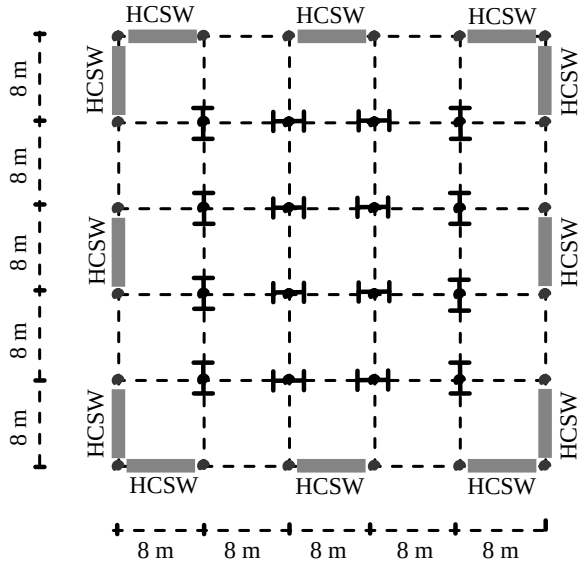


Figure 3. Floor geometry of the benchmark structures with positions of the HCSWs.

The assumed seismic action is represented by the Eurocode 8 type 1 spectrum with a_g = 0.25g and ground type C. Both verifications of the ultimate limit state (ULS) and of the damage limit state (DLS) are required.

3.2 Preliminary design

Preliminary designs based on the conventional force approach were made in order to identify possible optimal geometries. Two conditions were required in the design: (i) strength verification at ULS under the lateral forces derived from the design spectrum following the prescriptions in Eurocode 8, using the behaviour factor q = 3.3 given for composite structural system type 3 according to the definition in 7.3.1.e; (ii) stiffness verification at DLS under the lateral forces assuming ν = 1.0 in formula 4.31 in paragraph 4.4.3.2 of Eurocode 8.

A large number of HCSWs with different dimensions of the reinforced concrete shear walls and link lengths were evaluated in this preliminary design stage by the ULG unit, as detailed in Deliverable 2.1 Part 1 "Description of considered cases, comparison of results and conclusions about the effectiveness in withstanding seismic actions" produced by ULG and included as annex in the INNO-HYCO mid-term report (Dall'Asta et al. 2012). The seismic behaviour of the most promising designs was assessed through nonlinear static (pushover) analysis and multi-record incremental nonlinear dynamic analysis as detailed in Deliverable 2.1 Part 2 "Seismic behaviour assessment by means of incremental dynamic analyses" included in the mid-term report (Dall'Asta et al. 2012). These most promising designs and relevant static and dynamic seismic analyses were presented in Zona et al. (2011, 2012), providing the following indications. In the 4-storey case it is observed that reinforcements in the concrete wall yield together with yielding in bending of the steel links in the first three storeys. Afterwards, further plastic dissipation is fostered by the successive yielding in bending of the links at the last storey. Then the peak strength of the reinforced concrete wall is achieved leading to the maximum sustained base shear before leading the bracing system to failure due to failure of the reinforced concrete wall. A different seismic performance is observed in the 8-storey design, where the steel links at all storeys yield in bending before any damage in the reinforced concrete wall. Afterwards reinforcements yields and shortly afterwards all links yield in shear. The concrete peak strain is attained but the bracing system is still able to exhibit global hardening. Collapse is reached when the link at the fifth storey fails in combined banding and shear. Despite these differences, pushover verifications are satisfied (capacity displacement larger than target displacement) in both case studies. In addition, it is observed that the HCSW systems designed are not prone to soft storey formation, even when the yielding of the steel links is not simultaneous, thanks to the contribution of the reinforced concrete wall.

3.3 Design based on rules inherited from other systems

The results obtained in this first design stage directed the research towards the definition of a design approach that inherits recommendation for capacity design from other structural systems involving similar dissipative mechanisms in the links, i.e. eccentric braces in steel frames, as well as indication to reduce damages in the reinforced concrete wall. The design procedure attempted in this second stage of this research is subdivided in the following steps:

- Step 1: assign dimensions of the reinforced concrete wall by selecting height-to-length ratio and thickness;
- Step 2: design of the steel links based on bending and shear obtained from linear analysis (e.g. spectrum analysis) with assigned uniform over-strength; design of the steel side columns using the summation of the yield shear forces of the links (amplified with $1.1\gamma_{ov}$) as design axial force;

- Step 3: design of the wall longitudinal reinforcements to provide an assigned over-strength compared to the bending moment obtained from linear analysis; design of the transverse reinforcements to avoid shear collapse of the wall considering the maximum shear at the base derived from the limit condition of yielded steel links and yielded wall in bending; reinforcement detailing according to Eurocode 8 DCM rules.

ID step1	Wall aspect ratio H/l_w	Wall length l_w (m)
4F10W25E	10.0	1.36
4F07W25E	7.5	1.81
4F12W25E	12.5	1.09
8F10W25E	10.0	2.72
8F07W25E	7.5	3.63
8F12W25E	12.5	2.18

Table 2. Designed cases: wall geometry.

The application of the above design rules and the necessity to limit the shear force at the base of the wall brought to the adoption of six HCSW systems for each direction (Figure 3) as opposed to the four systems adopted in the preliminary design (Zona et al. 2011, 2012). In order to investigate the main geometric and design parameters, 18 cases were designed, comprising three height-to-length ratios of the wall (Table 2) taken with constant thickness (0.36 m) and relevant links (length 600 mm for the 4-storey case and 660 mm for the 8-storey case) designed with over-strength equal to one (Tables 3 and 4 for the 4-storey and 8-storey cases, respectively, where d = section depth, b = flanges width, t_f = flange thickness, t_w = web thickness), longitudinal reinforcements in order to obtain three values of wall over-strength (1.00 in cases labelled as R10, 1.25 in cases labelled as R12, 1.50 in cases labelled as R15). Reinforcement bars were concentrated in the lateral confined parts of the wall as for Eurocode 8 DCM rules. Significant quantities of longitudinal bars were required, especially for R15, in some cases exceeding Eurocode upper limits. Nevertheless, these design solutions were retained in the following seismic assessment phase in order to gain further insight into the influence of wall over-strength on the nonlinear behaviour up to failure.

ID step1	link #	d (mm)	b (mm)	t_f (mm)	t_w (mm)
4F07W25E	4	330	124	11.5	7.5
	3	400	170	13.5	8.6
	2	450	180	14.6	9.4
	1	500	160	16.0	10.2
4F10W25E	4	330	124	11.5	7.5
	3	400	170	13.5	8.6
	2	450	180	14.6	9.4
	1	500	174	16.0	10.2
4F12W25E	4	330	120	11.5	7.5
	3	400	165	13.5	8.6
	2	450	175	14.6	9.4
	1	500	180	16.0	10.2

Table 3. Designed cases (4-storey): wide-flange links.

Thus, there are a total of nine designs involving 4-storey frames (three wall geometries times three wall over-strengths) and a total of nine designs involving 8-storey frames (again three wall geometries times three wall over-strengths).

ID step1	link #	d (mm)	b (mm)	t_f (mm)	t_w (mm)
8F07W25E	8	400	124	13.5	8.6

	7	400	140	13.5	8.6
	6	550	170	17.2	11.1
	5	550	175	17.2	11.1
	4	600	180	19.0	12.0
	3	600	190	19.0	12.0
	2	600	190	19.0	12.0
	1	550	185	17.2	11.1
8F10W25E	8	400	130	13.5	8.6
	7	400	160	13.5	8.6
	6	550	180	17.2	11.1
	5	550	180	17.2	11.1
	4	600	185	19.0	12.0
	3	600	200	19.0	12.0
	2	600	210	19.0	12.0
	1	600	185	19.0	12.0
8F12W25E	8	400	140	13.5	8.6
	7	400	176	13.5	8.6
	6	550	186	17.2	11.1
	5	550	190	17.2	11.1
	4	600	190	19.0	12.0
	3	600	210	19.0	12.0
	2	600	220	19.0	12.0
	1	600	210	19.0	12.0

Table 4. Designed cases (8-storey): wide-flange links.

4 DESIGN OF THE DOWN SCALED CONNECTION

4.1 General assumptions

The tests aim at characterizing the performance of the connection of a seismic link embedded in a concrete shear wall and the efficiency of the capacity design of such a system, with the objective of developing a plastic hinge in the replaceable part of the link, acting as a fuse, with all other components of the connection remain undamaged. Regarding the materials, design values are used: concrete C 25/30, steel grades S275 for the link, S355 for the embedded part and S500 for reinforcements. The length of the links is defined as being intermediate according to Eurocode 8 chapter 6 classifications. The link stiffeners are determined using a linear interpolation and the link rotation angle value θ_p. Face bearing plates are placed at the face of the concrete wall, in order to keep the integrity of the concrete part and to guarantee the yielding to take place in the profile section or in the rebars. The concrete wall dimensions are consistent with the experimental stand dimensions and the embedment length of the steel profile into the concrete part.

Two topologies are considered for what regards the embedment of the profile in the concrete shear wall and the connection of the replaceable part of the link to the embedded part.

In Configuration No. 1 (Figure 4), the bending moment transferred by the link to the wall is balanced by a couple of horizontal forces and is resisted by shear studs, while the beam splice connection is placed at a distance of 100 mm from the top face of the concrete wall in order to allow an easy bolting of the removable part.

The design assumptions consist in forcing the creation of a plastic hinge in the replaceable part of the link and to capacity-design the part of the fixed part of the link embedded in the shear wall, the link-to-shear-wall connection and the bolted beam splice connection between the fixed and replaceable parts of the link.

The values from the mechanical model presented in Figure 4 are:
M_1 – characteristic maximum bending moment value at the replaceable part of the link;

M_0 – bending moment value at the interface link/concrete;
M_x – the assumed value of the maximum bending moment in the embedded part of the profile.

According to AISC (2010) recommendations, the embedment length values are increased by the concrete cover thickness due to the risk of spalling of the concrete near the wall face. It is assumed that steel link does not behave as having a fixed boundary condition at the face of the wall, and the effective fixed point is taken at one third of the embedment length from the face of the wall.

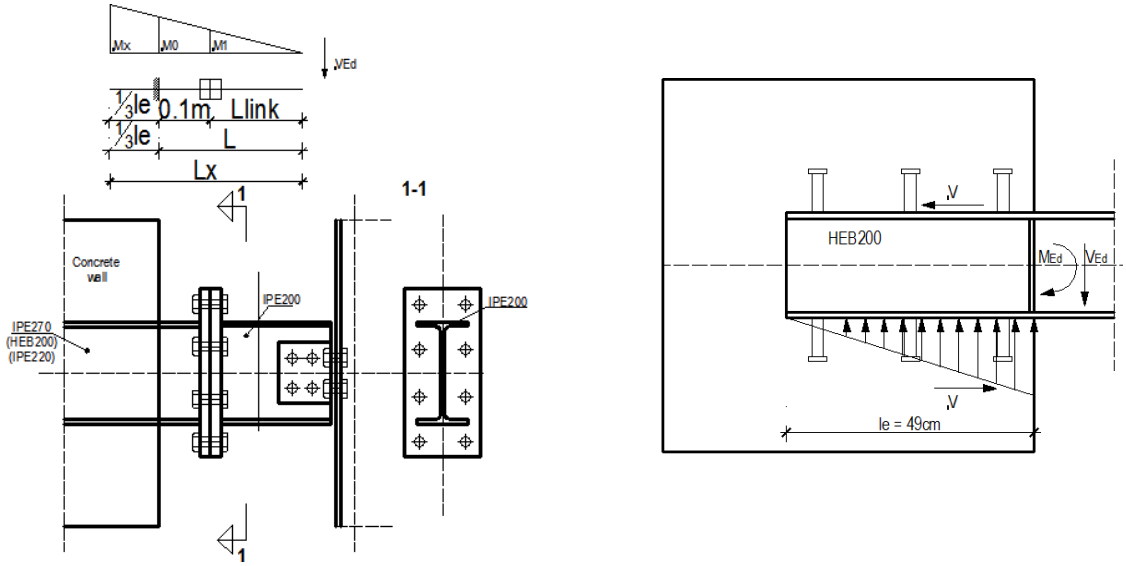


Figure 4. Configuration No. 1- mechanical model.

According to the chosen static scheme and to capacity-design principle, the design is based on the amplified value of the bending moment, with reference to the value at the face.

$$M_{Ed} = 1.1 \cdot \gamma_{ov} \cdot \Omega \cdot M_o \tag{1}$$

$$V_{Ed} = \frac{M_{Ed}}{L_x} \tag{2}$$

The required number of shear studs is governed by the value of the force V, as shown in Figure 4. The embedment length is determined using equilibrium equations of the mechanical model (3) and (4) and shall not be less than 1.5 times the height of the steel profile according to Eurocode 8 recommendations.

$$V_{Ed} = \frac{1}{2} \cdot f_{cd} \cdot l_e \cdot b \tag{3}$$

$$M_{Ed} = V \cdot h - \frac{1}{2} \cdot f_{cd} \cdot l_e \cdot b \cdot \frac{1}{3} \cdot l_e \tag{4}$$

where:
b = 200 mm (HE200B);
h = 200 mm (HE200B);
l_e = 0.49 m – the embedment length of the profile inside the concrete wall.

The number of shear studs is given by (5) and their geometry fulfills the Eurocode 4 Part 1 and 2 specifications.

$$n = \frac{V}{P_{Rd.L}} \tag{5}$$

where:

$P_{Rd.L}$ - the design resistance of a headed stud according to Eurocode 4 Part 2 Annex C;

n – number of shear studs.

For Configuration No. 2 (Figure 5), the bending moment transferred by the link to the wall is balanced by a couple of vertical forces. The connection "link – embedded steel profile" is located right at the face of the wall using threaded bushings.

The design objective is similar to the first configuration but the main differences between the two configurations are:

- The positioning of the beam-splice connection of the fuse with respect to the embedded part of the link. The end-plate is positioned right at the face of the shear wall, acting thus also as face bearing plate. Moreover, the connection is assumed to be realized in practice with threaded bushes instead of regular bolts;
- The assumed load transfer mechanism between the embedded part of the link and the concrete shear wall. In this case, no shear studs are used and a longer embedded part is considered in order to develop a static scheme where the applied bending moment can be resisted by a couple of vertical loads, activating the compression resistance of the contact profile-concrete.

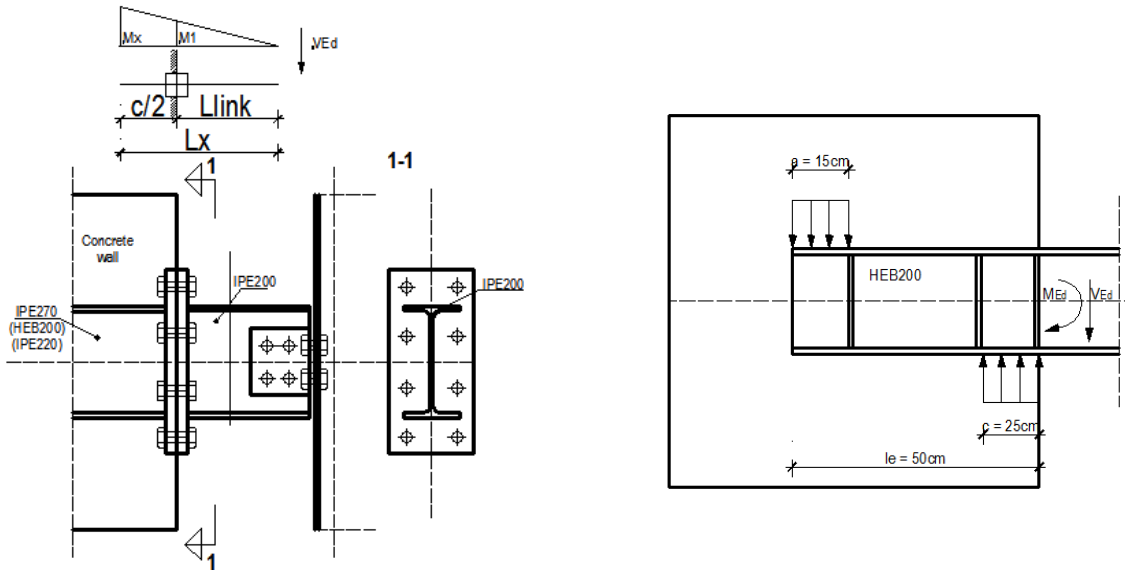


Figure 5. Configuration No.2- mechanical model.

According to the transfer mechanism, the embedded part of the profile is designed assuming conservatively that the bending moment increases linearly until the location of the first reaction force applied by the concrete on the profile. This value is then increased by the overstrength factors similarly to the procedure described in (1) and (2) for Configuration 1. These forces can be largely resisted by an HEB200 profile.

In order to determine the embedded length the following equilibrium equations are used:

$$f_{cd} \cdot a \cdot b + V_{Ed} = f_{cd} \cdot b \cdot c \tag{6}$$

$$M_{Ed} - f_{cd} \cdot a \cdot b \cdot \left(l_e - \frac{a}{2} \right) + f_{cd} \cdot c \cdot b \cdot \frac{c}{2} = 0 \tag{7}$$

where:

b = 200 mm (HEB200);

h = 200 mm (HEB200);
l_e = 0.50 m– the embedment length of the profile inside the concrete wall;
a = 0.15 m;
c = 0.25 m.

The design of the beam-splice connection has been realized with CoP, software developed by Universities of Aachen and Liege, based on the component method. The aimed and governing failure of the connection is the failure of the steel bolts, before yielding of the beam flange of the profile.

4.2 Numerical model

In order to assess the actual behaviour prior to the physical testing to come, the numerical model was developed with the computer program SAFIR used for the analysis of structures under ambient or elevated temperature conditions. The program based on Finite Element Method, was developed at University of Liege and can be used to study the behaviour of one, two or three dimensional structures. The numerical model detailed here for Configuration No.1 presented in Figure 6, along with the test setup of the connection, Figure 7.

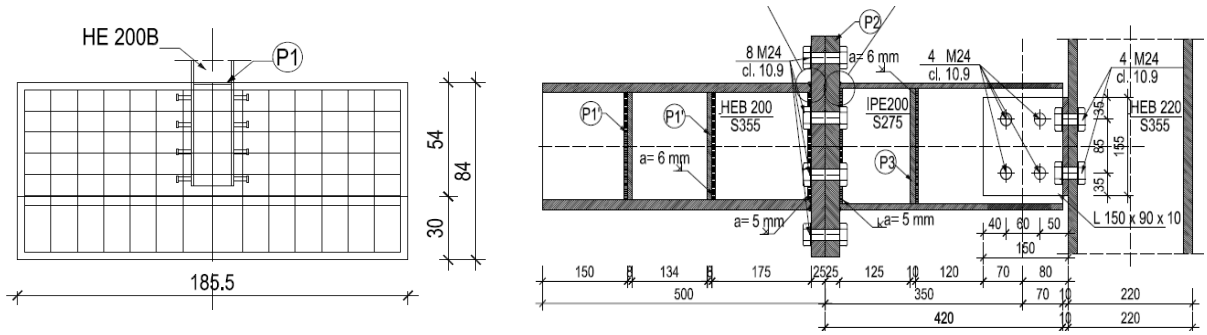


Figure 6. Configuration No.1- design detail drawings.

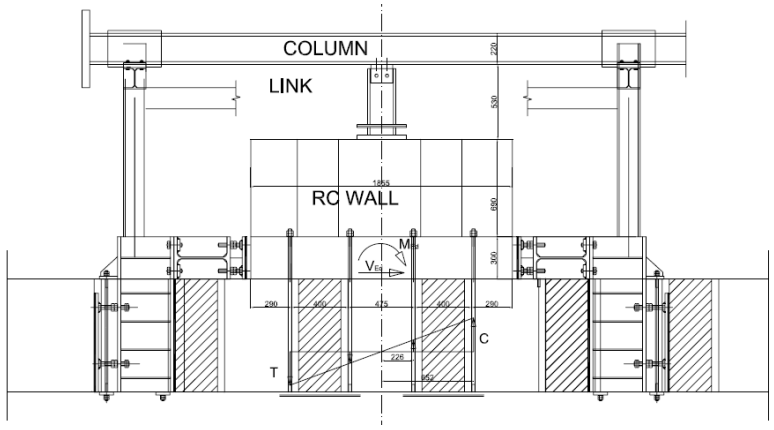


Figure 7. Configuration No.1- test setup.

Concrete wall is defined as a shell element with a constant width all over the wall, reinforcements are defined as truss elements and the steel profile is modelled by means of Bernoulli-type 3D beam elements. Materials properties are the design values defined in Section 4.1. For concrete a parabolic–linear law in compression was used, while the steel part was modeled with a bilinear- elastic-perfectly–plastic law.

Figure 8b) confirms the assumption that the link beam cannot be considered as fixed at the face of the concrete wall and due to that the maximum value of the bending moment occurs inside the concrete wall.

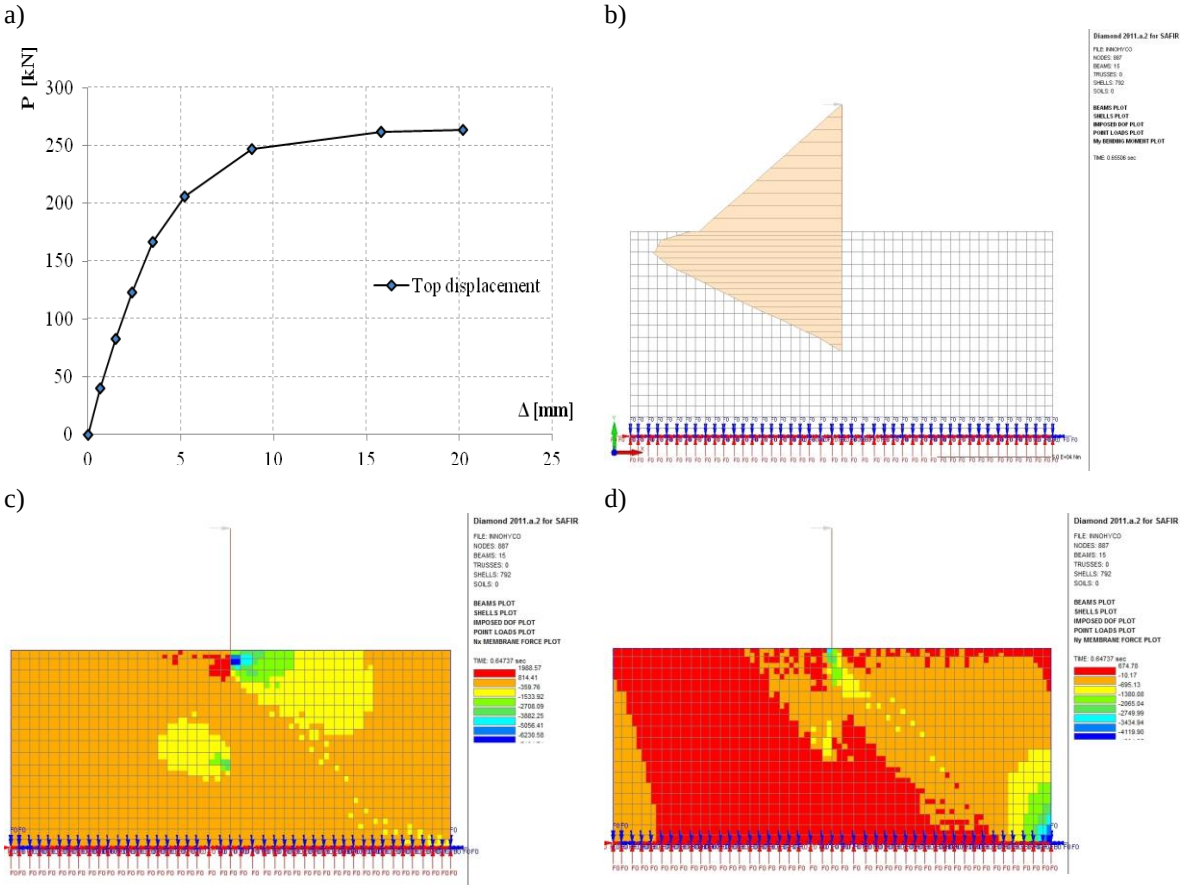


Figure 8. SAFIR-Numerical results: a)Force - top displacement curve; b) M_y – beam link; c) Nx – membrane force plot; d) N_y – membrane force plot.

L_{link}	0.35 m
$M_1 = M_{pl.RdIPE200}$	44.76 kNm
$V_{Ed}=M_1/L_{link}$	127.89 kN
V_{Sdmax} - jack limit	400kN/1.5=266.67 kN
$1.1*\Omega*\gamma_{ov}*V_{Ed}$ - max value	263.76 kN
V_{SAFIR}	258.95kN
$1.1*\Omega*\gamma_{ov}*V_{Ed} / V_{SAFIR}$	98%
$M_x = M_1 \cdot \frac{L_x}{L_{link}}$	60.75 kNm
$1.1*\Omega*\gamma_{ov}*M_x$ -design value	125.30 kNm
M_{SAFIR}	124.6 kNm
$1.1*\Omega*\gamma_{ov}*M_{Ed} / M_{SAFIR}$	100%

Table 5. Comparison between FEM model and design results.

Maximum design values obtained using the simple static scheme shown in Figure 4, are compared with the outcomes of the numerical model and numerical model. It can be observed that the values obtained using SAFIR numerical model are similar to those obtained by hand design. The model will be further calibrated with respect to the last results when available.

5 SEISMIC BEHAVIOUR OF HCSW SYSTEMS

5.1 Modeling assumptions

The seismic behaviour of the designed HCSW systems was assessed through displacement-controlled nonlinear static analysis under applied lateral loads (pushover analysis), using the software FinelG. This software is being developed at the University of Liège for more than 40 years and is used for both academic activities and regular design purposes. It accounts for geometric and material non linear effects. For the sake of simplicity, the evaluation of the seismic performances is based on a plane model of a single HCSW connected to two continuous columns equivalent to the relevant parts of the gravity-resisting steel frame. An illustration of the model is given at Figure 9 for the 4-storey case. Loads and masses are those of the HCSW system as well as loads and masses from the relevant part of the gravity-resisting steel frame

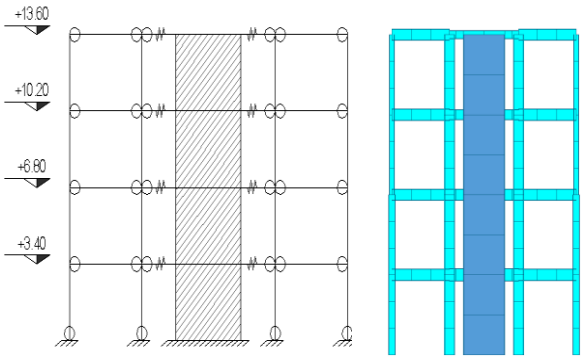


Figure 9. Numerical model.

The reinforced concrete shear wall is represented by beam elements using a fibre description for the behaviour of the concrete in the longitudinal direction, allowing an accurate estimation of the behaviour in bending and thus of the possible plastic hinge at the bottom of the wall. Reinforcement of the shear wall is assumed to be sufficient to avoid a shear failure of the wall. The steel shear links are modelled using non linear frame elements for the bending contribution as well as non linear shear springs introduced at mid span of each steel link to account for the shear deformability of the link and for the possible yielding in shear of the links. This additional shear spring is required for a correct modelling of the system since most links are classified as intermediate according to EC8 definition and are thus more or less equally prone to shear or bending failure. Interaction between flexural and shear plastic deformations is considered in the post-processing of the results.

For all materials, the design values of the resistance are used (f_{cd} = 20 MPa, $f_{y,s}$ = 435 MPa, $f_{y,p}$ = 355 MPa). Steel behaviour is modelled by a bilinear elastic-perfectly-plastic law without strain hardening. Concrete is by a parabola-rectangle in compression and a linear behaviour in tension with tension stiffening. Particular values of the strain are ε_{c2} = 0.002 (end of the parabolic behaviour) and ε_{cu2} = 0.0035 (end of the rectangular behaviour). No confinement is considered for the concrete in compression.

5.2 Selected results for the 4-storey cases

Pushover curves (total base shear versus top displacement) for the 4-storey (15R) cases are shown in Figures 10 to 16. The end of the curves corresponds to reaching the maximum allowed compressive strain in the concrete ($\varepsilon_{cu,2}$= 0.0035).

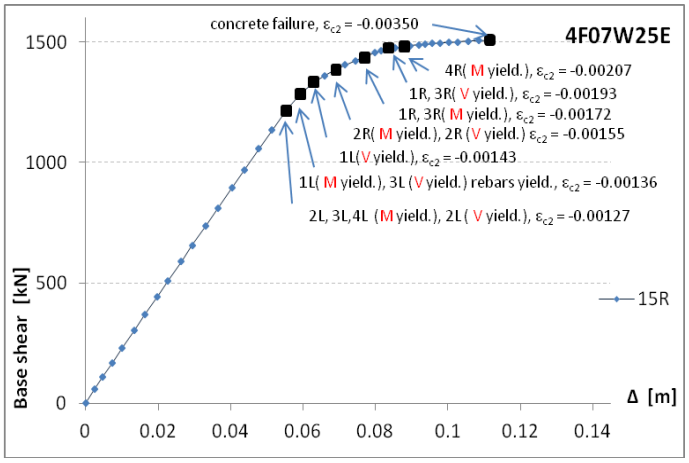


Figure 10. Pushover curve for case 4F07W25E15R and relevant yielding sequence.

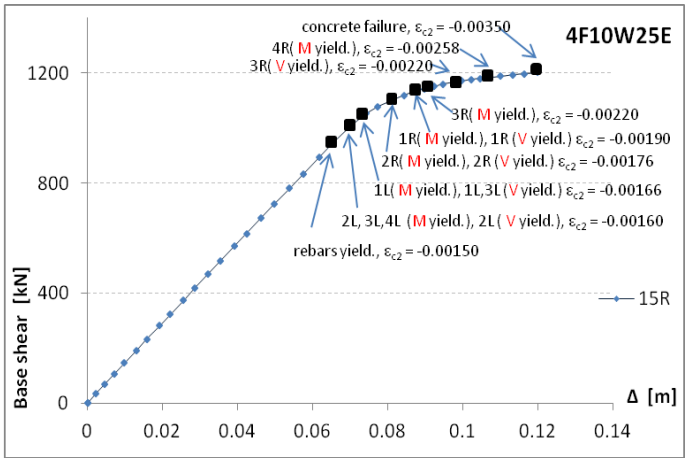


Figure 11. Pushover curve for case 4F10W25E15R and relevant yielding sequence.

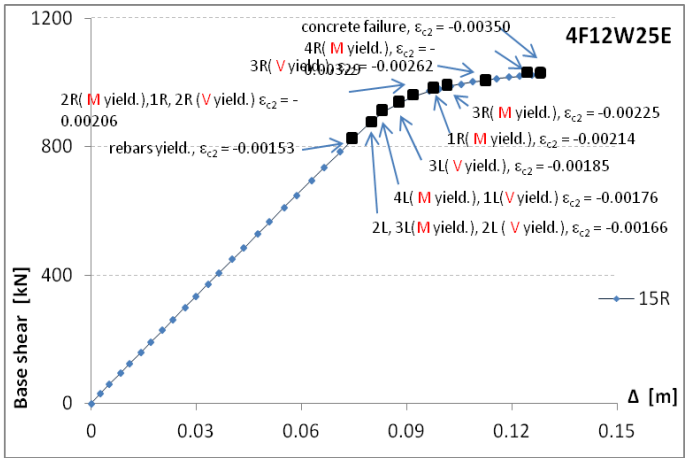


Figure 12. Pushover curve for case 4F12W25E15R and relevant yielding sequence.

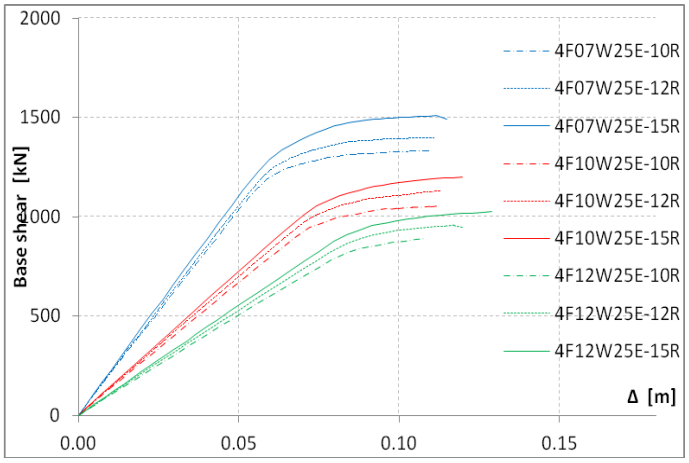


Figure 13. Pushover curve – global comparison

It is observed that increasing the wall over-strength has positive effects as the yielding of reinforcements and failure of the wall (attainment of the ultimate strain in the concrete) are delayed, resulting in an increment of the lateral load capacity as well as in an increment of the global ductility of the HCSW systems. However, these benefits are obtained at the expenses of an often excessive congestion of reinforcements. It is also observed that a reduction of the wall aspect ratio allows a higher lateral load capacity as well as a higher ductility. Given that a reduction of the aspect ratio means smaller steel links and longer walls that allow more space for reinforcements, the design should be based in practice on a limitation of the wall aspect ratio, possibly limited to suggested values $H/l_w \leq 10$.

5.3 Selected results for the 8-storey cases

Pushover curves for the 8-storey (15R) cases are shown in Figures 18 to 29. The observation made for the 4-storey cases can be repeated for these taller structures, where problems for the higher values of the wall aspect ratio H/l_w are even more evident.

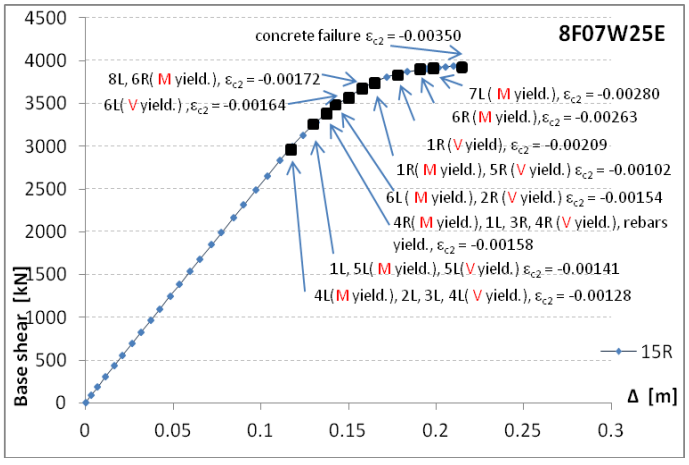


Figure 14. Pushover curve for case 8F07W25E15R and relevant yielding sequence.

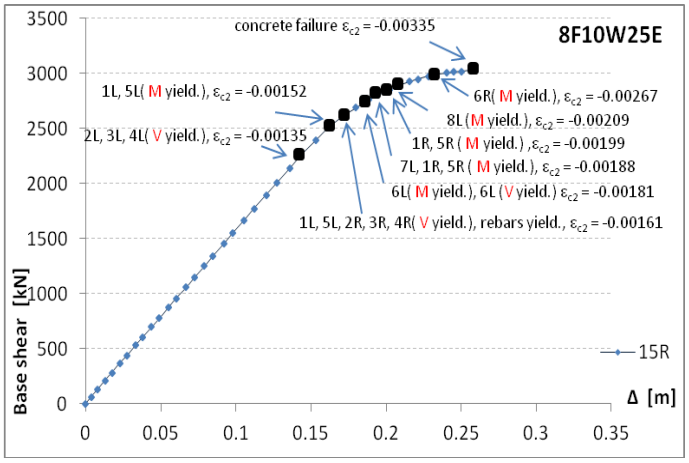


Figure 15 Pushover curve for case 8F10W25E15R and relevant yielding sequence.

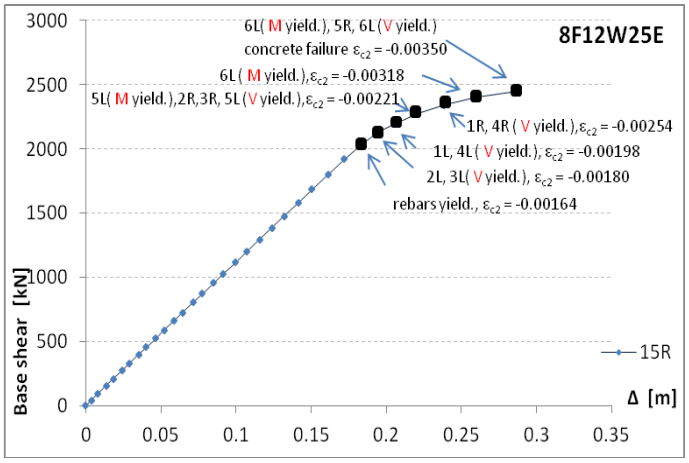


Figure 16. Pushover curve for case 8F12W25E15R and relevant yielding sequence.

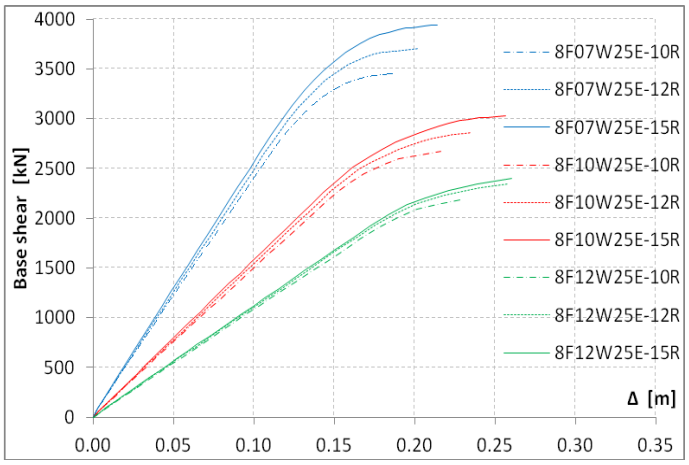


Figure 17. Pushover curves – global comparison.

5.4 ULS and DLS verifications

Outcomes in terms of pushover curves presented in section 4.3 can be analyzed with respect to different ULS and DLS criteria. This allows in particular the calculation of specific performance points associated the activation with different limit states and hence, based on the N2 method proposed in Annex B of Eurocode 8, the calculation of the acceleration level

corresponding to these performance points. In the present contribution, only preliminary assessments are given. The outcomes will be more deeply investigated in the next publications on the INNO-HYCO project. Three different limit states are taken into consideration:

- *ULS1: Maximum compressive strain reached in the concrete shear wall*. No confinement is conservatively taken into account. Accounting for the confining effect by imposing rules similar to those prescribed by EC8 for reinforced concrete walls could certainly improve the global behaviour of the system.
- *ULS2: Maximum rotation of the steel links*. In this preliminary assessment, indicative conservative values of the maximum possible rotation capacity are estimated according to the criteria proposed by FEMA 356 for seismic links in eccentrically braced structures. The values must be adjusted in a next stage on the base of experimental test results to be carried out in the context of the INNO-HYCO project.
- *DLS: Maximum allowable inter-storey drift.* Associated values of the acceleration should be referred to acceleration level for DLS, smaller than the reference design value of 0.25g.

Results are provided in table 6 in terms of maximum acceleration for the 4-storey and 8-storey cases. Additionally, table 7 gives the values of the behaviour factor estimated from an equivalent bilinear curve on the base of the ductility.

ID step1	ULS1	ULS2	DLS
4F07W25E – 10R	0.22	0.19	0.11
4F07W25E – 12R	0.23	0.18	0.11
4F07W25E – 15R	0.26	0.14	0.07
4F10W25E – 10R	0.18	0.18	0.11
4F10W25E – 12R	0.18	0.18	0.09
4F10W25E – 15R	0.15	0.14	0.06
4F12W25E – 10R	0.14	> 0.14	0.08
4F12W25E – 12R	0.14	> 0.14	0.08
4F12W25E – 15R	0.13	> 0.13	0.06
8F07W25E – 10R	0.27	0.24	0.14
8F07W25E – 12R	0.3	0.25	0.15
8F07W25E – 15R	0.35	0.29	0.18
8F10W25E – 10R	0.24	0.24	0.11
8F10W25E – 12R	0.26	0.25	0.12
8F10W25E – 15R	0.29	0.26	0.12
8F12W25E – 10R	0.21	>0.24	0.10
8F12W25E – 12R	0.24	0.24	0.10
8F12W25E – 15R	0.25	0.25	0.10

Table 6. Maximum sustainable accelerations from pushover curves and ULS/DLS criteria [in g].

ID step1	10R	12R	15R
4F07W25E	2.77	2.59	2.30
4F10W25E	2.81	2.94	2.55
4F12W25E	1.86	2.15	1.97
8F07W25E	1.30	1.28	1.41
8F10W25E	1.22	1.23	1.24
4F12W25E	1.17	1.21	1.19

Table 7. Behaviour factors at ag = 0.25g.

6 CONCLUSIONS

A selection of results involving an innovative steel-concrete hybrid coupled shear wall systems developed under the European research project INNO-HYCO was briefly illustrated.

The analysis of the case studies designed according to the adoption of existing rules in the Eurocodes has highlighted the potentialities of the proposed innovative HCSW systems, namely: it is actually possible to develop a ductile behaviour where plastic deformation are attained in the steel links and limited damage occurs in the reinforced concrete wall; the interstorey drifts up to collapse are quite regular regardless of the non-simultaneous activation of the plastic hinges in the steel links and/or in the reinforced concrete wall; the adopted design approach based on well-known concepts and procedures already available in the Eurocodes gives a promising starting design solution, although it appears that using the behaviour factor proposed by Eurocode 8 for composite walls overestimates the deformation capacity of the HCSW, in particular for short walls. On the other hand, the following issues have been encountered: the designed solutions require additional studies to clarify the relationships between wall and links in order to provide additional design recommendations as integration of the Eurocodes; the slenderness of the HCSW systems needs to be better controlled in order to limit the negative effects of geometric nonlinear effects and improve the behaviour at the damage limit states. However, the sensitivity of the response to rotation capacity of the links and to confinement of the concrete needs also to be deeper studied, including in the context on time-history analysis. Capacity design of connections will be confirmed by experimental results. The upcoming developments of this research work involve the definition of a design procedure compatible with the current Eurocode 8 recommendations and in-depth experimental studies on the connections between reinforced concrete wall and replaceable dissipative steel links.

ACKNOWLEDGEMENT

Support for this research from the European Commission, Research Fund for Coal and Steel, Steel Technical Group TGS 8 "Steel products and applications for building, construction and industry", is gratefully acknowledged

REFERENCES

[1] AISC, Seismic Provisions for Structural Steel Buildings, ANSI/AISC 360-05, American Institute for Steel Construction, 2010.

[2] ASCE, Recommendations for seismic design of hybrid coupled walls, ASCE Composite Construction Committee, 2009.

[3] COP software webpage: http://cop.fw-ing.de/en/download/free/ame

[4] El-Tawil, S., et al, Seismic design of hybrid coupled wall systems: state of the art. *Journal of Structural Engineering*, **136**, 755-769, 2010.

[5] Eurocode 4 - Design of composite steel and concrete structures. Part 2: General rules and rules for bridges, 2005.

[6] Eurocode 8 - Design of structures for earthquake resistance – Part 1: general rules, seismic actions and rules for buildings, 2004.

[7] FEMA356: Guideline for seismic rehabilitation of buildings, Federal Emergency Management Agency, 2002.

[8] O Dall'Asta, A., Leoni, G., Zona, A., INNO-HYCO INNOvative HYbrid and COmposite steel-concrete structural solutions for building in seismic area, First Anual Report, 2011.

[9] O Dall'Asta, A., Leoni, G., Zona, A., INNO-HYCO INNOvative HYbrid and COmposite steel-concrete structural solutions for building in seismic area, Mid-term Report, 2011.

[10] Paulay, T., Priestley, M.J.N., Seismic design of reinforced concrete and masonry Buildings, Wiley, 1992.

[11] Zona A., Leoni, G. Dall'Asta, A., Braham, C., Bogdan, T., Degée, H., 2012. Behaviour and design of innovative hybrid coupled shear walls for steel buildings in seismic areas. *15th World Conference on Earthquake Engineering*, 24-28 September, Lisbon, Portugal.

[12] Zona, A., Braham, C., Degée, H., Leoni, G., Dall'Asta, A., 2011. Innovative hybrid coupled shear walls for steel buildings in seismic areas. *XXIII Italian Steel Structure Conference (CTA)*. 9-12 October, Ischia, Italy.

COMPDYN 2013
4th ECCOMAS Thematic Conference on
Computational Methods in Structural Dynamics and Earthquake Engineering
M. Papadrakakis, N.D.Lagaros, V. Plevris (eds.)
Kos Island, Greece, 12–14 June 2013

HIGH-PRECISION FINITE-ELEMENT ANALYSIS OF RUBBER BEARING FOR BASE-ISOLATION OF BUILDING STRUCTURES

Makoto Ohsaki[1*], Tomoshi Miyamura[2], Masayuki Kohiyama[3], Takuzo Yamashita[4], Masashi Yamamoto[5], Naohiro Nakamura[5]

[1]Department of Architecture, Hiroshima University
1-4-1 Kagamiyama, Higashi-Hiroshima 739-8527, Japan
ohsaki@hiroshima-u.ac.jp

[2]Department of Computer Science, College of Engineering, Nihon University
1 Nakagawara, Tokusada, Tamura, Koriyama 963-8642, Japan
miyamura@cs.ce.nihon-u.ac.jp

[3] Department of System Design Engineering, Keio University
3-14-1 Hiyoshi, Kohoku, Yokohama 223-8522, Japan
kohiyama@sd.keio.ac.jp

[4] Hyogo Earthquake Eng. Res. Center, National Res. Inst. for Earth Science and Disaster Prevention
1501-21 Nishikameyama, Mitsuta, Shijimi, Miki 673-0515, Japan
tyamashi@bosai.go.jp

[5]Construction Technology Department, Takenaka Research & Development Institute
1-5-1 Ohtsuka, Inzai 270-1395, Japan
{yamamoto.masashia, nakamura.naohiro}@takenaka.co.jp

Keywords: Rubber Bearing, Finite Element Analysis, Building Frame, Seismic Response, Hyper-Elasticity, Parallel Computing.

Abstract. *Seismic response analysis is carried out for a base-isolated frame. The RC-frame members as well as the rubber bearings are discretized into hexahedral finite elements. The material properties of rubber are represented by the Ogden model, and the frame is assumed to remain in elastic range. The seismic response analysis of the frame, which has more than 3 million degrees of freedom is carried out using the E-Simulator, which is under development at E-Defense, Japan, based on a software package called ADVENTURECluster. It is shown that the global and local responses can be simultaneously evaluated through a high-precision finite element analysis.*

1 INTRODUCTION

Finite element (FE) analysis of laminated rubber bearing is not a well-established field of research. Analysis of rubber material is very difficult because of its incompressibility that leads to constitutive relation using hyper-elastic model. Matsuda *et al*. [1] investigated vertical and lateral stiffnesses of a rubber bearing using FE-analysis. The Mooney-Rivlin model is used for rubber material. Gracia *et al*. [2] developed an overlay model for simulating hyper-elastic and viscoelastic behavior of rubber material. Lejeunes *et al*. [3] presented a numerical reduction model to reduce the computational cost for a thin rubber sheet.

This study is a part of the project called Earthquake Simulator (E-Simulator) at Hyogo Earthquake Engineering Research Center (E-Defense), which belongs to National Research Institute for Earth Science and Disaster Prevention (NIED), Japan. Ohsaki *et al*. [4] demonstrated that seismic responses of an FE-model of a super-highrise steel building frame with more than 70 million DOFs can be evaluated using the E-Simulator, which is based on a parallel FE-analysis software package called ADVENTURECluster (ADVC) [5].

In this study, FE-analysis is carried out for a base-isolated frame utilizing rubber bearing. The rubber sheets and steel plates are discretized into linear hexahedral solid elements. The hyper-elastic constitutive relation is modeled using the Ogden model. It is demonstrated that the experimental results of the laminate rubber bearing under cyclic static deformation can be accurately simulated using the specified material parameters.

The rubber bearings are next attached at the base of a 10-story frame. A horizontal seismic motion is applied to the base-isolated frame, and the interaction between the base and the rubber bearing as well as the detailed local deformation of the isolator is investigated. This way, the details of local and global behavior of the base-isolated building frame can be evaluated simultaneously using a high-precision FE-analysis.

2 RUBBER BEARING MODEL

Consider a rubber bearing model as shown in Fig. 1. The radius of the rubber is 350 mm, and there exists a hole with the radius 7.5 mm at the center. Therefore, the area of rubber is 3.847×10^5 mm^2. The covering rubber on the circumferential surface is neglected.

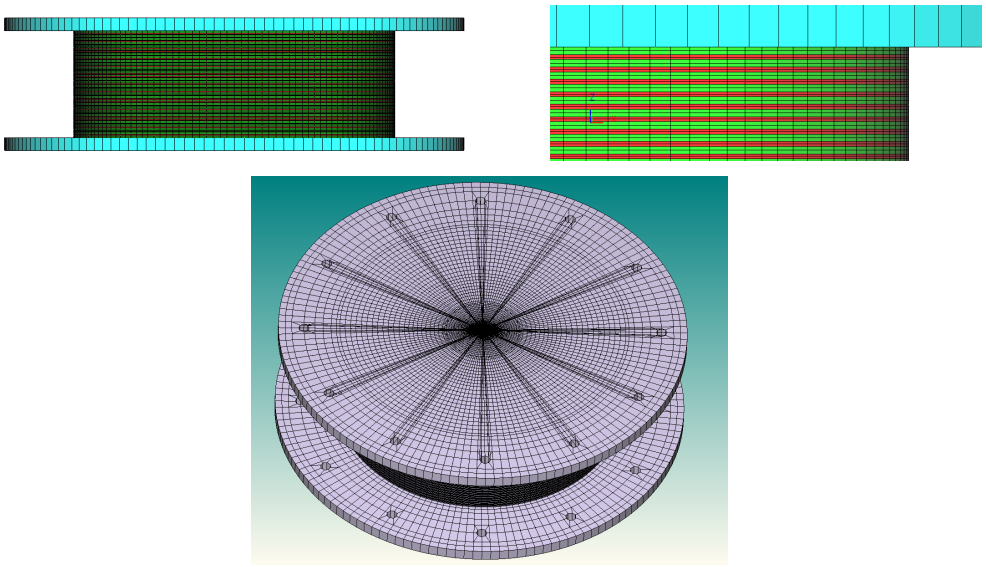


Figure 1: A rubber bearing model.

The rubber bearing has 30 sheets of rubber separated by steel plates. The thicknesses of rubber sheets and steel plates are 4.7 mm and 3.1 mm, respectively. The total height of rubber sheets and steel plates is 230.9 mm. The isolator has top and bottom steel plates called flange with radius 500 mm attached to the rubber/steel plates.

Each rubber sheet is discretized into two layers of hexahedral elements, while each steel plate including flange has only one layer. The numbers of nodes and elements are 502,980 and 486,240, respectively. The number of degrees of freedom is 1,525,002 including the control node defined in Sec. 4.1.

The Ogden model, which is categorized as hyper-elastic material, is used for the natural rubber. The strain energy density function is defined as

$$U = \sum_{n=1}^{2} \frac{\mu_n}{\alpha_n} (\bar{\lambda}_1^{\alpha_n} + \bar{\lambda}_2^{\alpha_n} + \bar{\lambda}_3^{\alpha_n} - 3) + 4.5K(J^{1/3} - 1)^2 \tag{1}$$

where the bulk modulus K is 1000 MPa, and other parameters are $\alpha_1 = 1.6$, $\alpha_2 = 6.2$, $\mu_1 = 0.41$ MPa, and $\mu_2 = 0.0012$ MPa. The variables $\bar{\lambda}_1$, $\bar{\lambda}_2$, $\bar{\lambda}_3$, and J are defined by the left stretch tensor of deformation. The mass density of rubber is 2.00×10^3 kg/m^3. The steel is assumed to be elastic with Young's modulus 205 GPa, Poisson's ration 0.3, and mass density 7.86×10^3 kg/m^3.

A fully integrated linear hexahedral element with eight integration points is used, and geometrical nonlinearity is incorporated using the updated Lagrangian formulation.

3 BASE-ISOLATED FRAME MODEL

Consider a 10-story frame as shown in Fig. 2. The distance between the centers of two rubber bearings is 7000 mm, and the story height is 3500 mm. The upper frame consists of reinforced concrete (RC) columns and beams, which are assumed to remain in elastic range, where Young's modulus is 24 GPa, Poisson's ratio is 0.2, and mass density is 2.3×10^3 kg/m^3. The frame is supported by two rubber bearings that have the same geometry and material properties as Sec. 2.

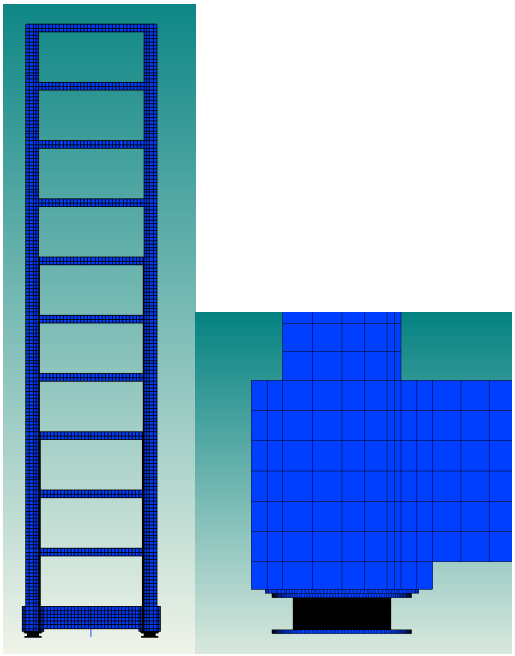


Figure 2: A 10-story base-isolated frame model.

The member sections are listed in Table 1. The height of each footing is 1500 mm. Note that all members have 3-dimensional property although we consider an in-plane deformation. Thus, the out-of-plane displacements of nodes on the plane of symmetry are constrained. The upper surface of flange and the lower surface of footing are connected by contact with sticking condition, i.e., no penetration, gap, or friction is considered.

The weight of RC frame is 1,741 kN, and the total weight including the bases is 1,755 kN. In this case, the mean pressure of the rubber is 2.26 MPa, which is too small. Therefore, considering the loads due to the slab and live loads, the mass density of beams and columns are scaled by the factor 6, which leads to the total weight 10,460 kN and the mean pressure 13.41 MPa.

Table 1: List of member sections.

Column		Beam	
Story	Size	Floor	Size
7 – 10	750×750	7 – Roof	450×750
4 – 6	800×800	4 – 6	450×800
1 – 3	850×850	1 – 3	450×850
		Base	700×1300

4 FINITE ELEMENT ANALYSIS

4.1 Static analysis of rubber bearing

We first carry out cyclic static analysis of single rubber bearing in order to investigate its mechanical properties. The lower surface of the bottom flange is fixed, and the control node is placed at the center of the upper surface of the upper flange. The control node is connected to the nodes on the flange by rigid beams that are represented by multipoint constraints (MPCs), and its rotations along three axes are fixed. The self-weight is first applied, and vertical pressure of 14 MPa is next applied.

Finally, a forced cyclic horizontal displacement is assigned at the control node. The history of displacement (mm) is given as $0 \rightarrow 450 \rightarrow 0 \rightarrow -450 \rightarrow 0$, which is divided into 25 incremental steps in total. The relation between horizontal force and displacement is plotted in solid line in Fig. 3. The curve is close to the experimental result in Ref. [6], which is plotted in dashed lines.

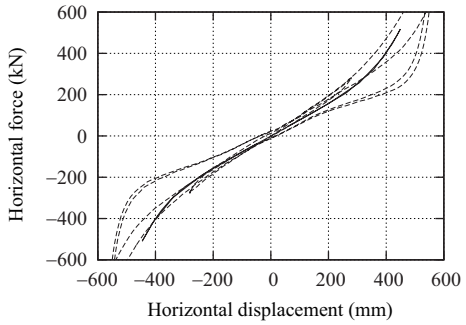
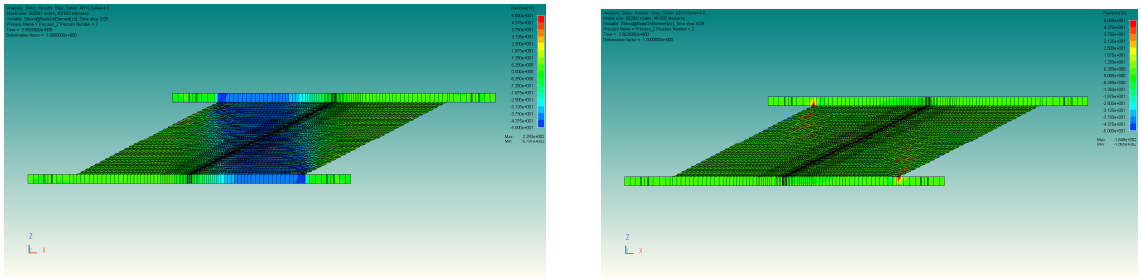


Figure 3: Relation between horizontal force and displacement under pressure of 14 MPa; solid line: numerical result, dashed line: experimental result [6].

The total computational time using 16 cores of Intel Xeon E5-2687W 3.10GHz×2 is 13,487 sec (3.75 hrs); i.e., the average time for single step is 539 sec (8.99 min).



(a) (b)

Figure 4: Stresses at maximum displacement; (a) vertical stress, (b) shear stress.

The vertical and shear stresses at the maximum deformation are shown in Fig. 4 on the section of symmetry. The non-uniform distribution of vertical stress can be clearly seen in Fig. 4(a). By contrast, Fig. 4(b) shows almost uniform distribution of shear stress.

Fig. 5 shows the distribution of normal stress between the upper surface of the top rubber sheet and the lower surface of the upper flange.

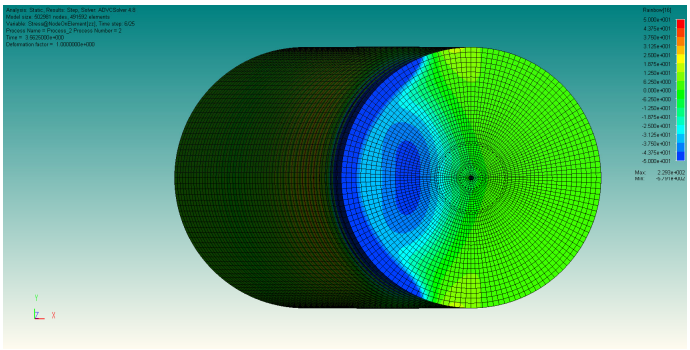


Figure 5: Normal stress between upper flange and rubber.

4.2 Static analysis of base-isolated frame

Horizontal static load, which is proportional to the mass density, is applied incrementally to find horizontal stiffness of the base. The horizontal stiffness obtained by finite difference approximation is plotted in Fig. 6 with respect to the horizontal displacement. As seen from the figure, the stiffness increases, due to material nonlinearity, as displacement is increased.

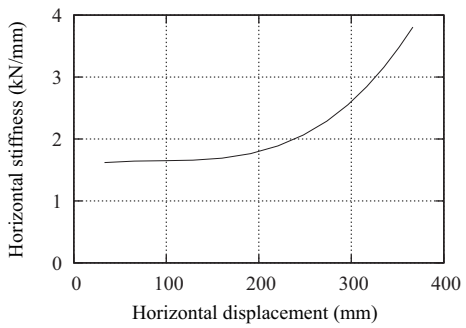


Figure 6: Relation between horizontal displacement and horizontal stiffness of the base.

4.3 Seismic response analysis

A viscous damper is attached between the center of base beam and the ground to incorporate practical situation. If we assume the stiffness 2.5 kN/mm in the displacement range around 300 mm in Fig. 6, and also assume that the upper frame is a rigid body, the first natural period is 4.103 s. Then, the damping coefficient corresponding to the damping factor of 0.15 for the first mode is 489 kN s/mm. The stiffness-proportional damping of 0.03 is given for the upper frame, although the deformation of the upper frame is very small.

The self-weight of the building are first applied. Then, time-history dynamic analysis is carried out to simulate seismic responses of the base-isolated structure. The frame is subjected to the Level-2 design ground motion in Japan, as shown in Fig. 7, which is called BCJ-L2 wave.

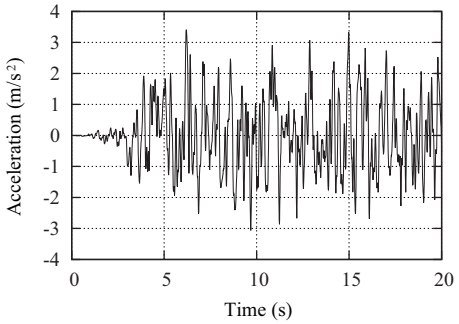


Figure 7: Seismic acceleration (BCJ-L2).

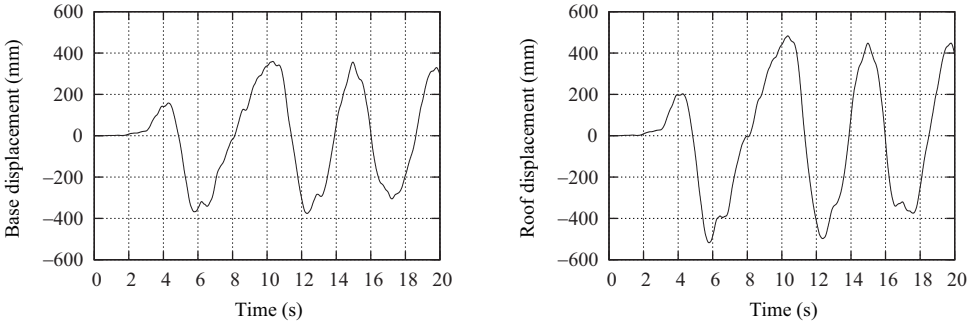


Figure 8: Displacement responses; (a) upper face of rubber bearing, (b) roof.

The total computational time using 16 cores of Intel Xeon E5-2687W 3.10GHz×2 is 1.5811×10^6 sec (18 days and 7.19 hrs) for 2,020 time steps including the initial static analysis for application of gravity; i.e., the average time for single step is 783 sec (about 13.0 min).

Figure 8(a) and (b) show the time histories of relative horizontal displacements at the top of isolator and roof of the frame, respectively. As observed in these figures, the deformation of the frame is very small, and the frame moves as a rigid body with small rocking behavior.

The horizontal and vertical reaction forces are plotted in Fig. 9(a) and (b), respectively. As seen from Fig. 9(b), the vertical reaction force is always positive; i.e., the rubber bearing does not exhibit tensile deformation.

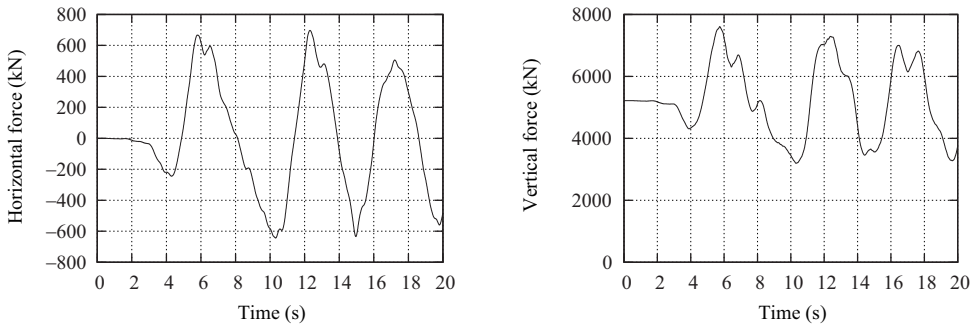
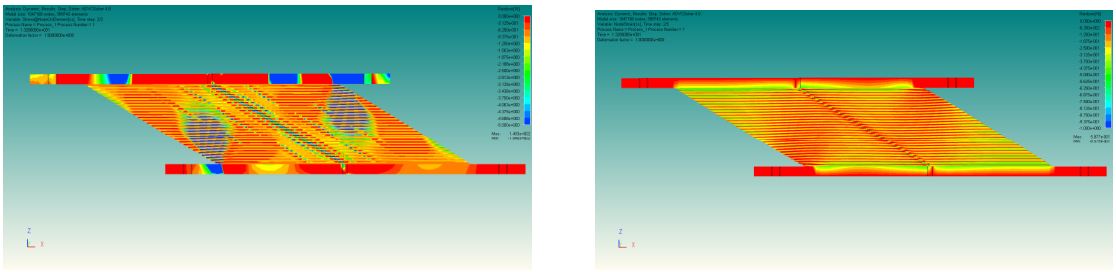


Figure 9: Force responses; (a) horizontal reaction force at fixed supports (base shear force), (b) vertical reaction force at left support.

The maximum and minimum response displacements and reaction forces are listed in Table 2, which confirms that the vertical reaction forces are positive, and the maximum base shear force is about 6.66% of the total weight of the structure. Note that the maximum displacement of the roof relative to the top of the isolator is 149.72 mm, which corresponds to a 0.406%.

Table 2: Maximum dynamic responses

	Disp. of upper-face of isolator	Roof disp.	Horizontal reaction	Vertical reaction (left)	Vertical reaction (right)
Maximum value	359.51	482.95	6.9685×10^5	7.6069×10^6	7.2730×10^6
(Time)	10.33	10.35	12.31	5.74	10.36
Minimum value	−375.84	−517.62	-6.4324×10^5	3.1955×10^6	2.8629×10^6
(Time)	12.28	5.79	10.32	10.31	5.70

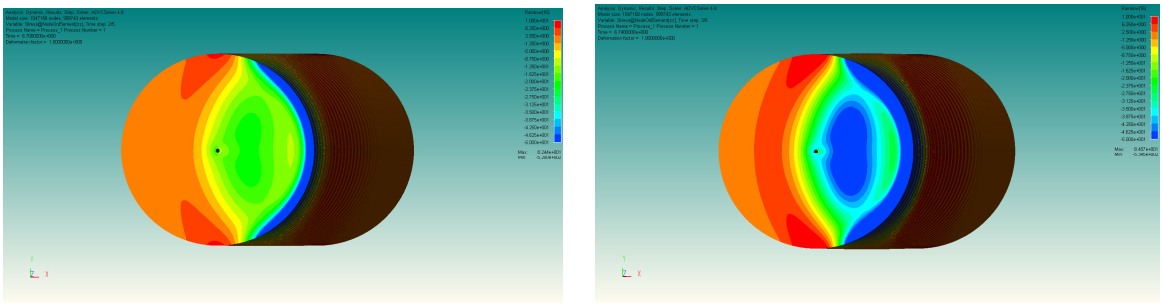


(a) (b)

Figure 10: Shear stress and strain at t = 12.28; (a) stress, (b) strain.

The shear stress and strain are shown in Fig. 10(a) and (b), respectively, at t = 12.28 s, when the absolute value of displacement at the upper-face of isolator becomes maximum. In contrast to the case of static analysis, the shear stress is not uniformly distributed.

The distributions of normal stress due to contact between the upper flange and the rubber at t = 12.28 s and 5.74 s are shown in Fig. 11, respectively. We can confirm that the normal stress is non-uniformly distributed on the surface. The maximum contact stress at t = 12.28 s is 482.6 MPa, which is very large; however, it is located at the edge, and maximum contact stress at nodes next to the edge is 203.2 MPa, which is less than the yield stress of steel. Therefore, a large stress at the edge may be due to coarse mesh division.



(a) (b)

Figure 11: Normal stress due to contact between upper flange and rubber;
(a) right isolator at t = 12.28 s, (b) left isolator at t = 5.74 s.

5 CONCLUSION

Static and dynamic analyses have been carried out for a 10-story plane frame supported by rubber bearings. It has been demonstrated that the hardening characteristics of the natural rubber are successfully simulated using the Ogden model and fine FE mesh with solid elements.

FE-analysis enables us to investigate simultaneously the global and local responses including the pressure between the layered rubbers and flanges, the distribution of vertical stress in the isolator during cyclic deformation, etc. The computational time for time-history analysis of FE-model with more than 3 million DOFs remains in a practically admissible range using a high-performance PC.

ACKNOWLEDGEMENTS

This study is a part of E-Defense Seismic Experimental Study and Simulation System Development Project conducted by E-Simulator Production Committee (Leader: Prof. Muneo Hori, The University of Tokyo). The authors acknowledge the valuable contribution from the committee members, and the financial support by NIED. The contribution by Dr. Tomonobu Ohyama and Mr. Kiyoshi Yuyama of Allied Engineering Corporation for computation and mesh generation is also acknowledged.

REFERENCES

[1] A. Matsuda, Y. Ohtori, S. Yabana and K. Hirata, Numerical simulation of the loading tests of laminated rubber bearings, *JSME Int. J., Ser. A*, **44**(1), 160-166, 2001.

[2] L. A. Garcia, E. Liarte, J. L. Pelegay and B. Calvo, Finite element simulation of the hysteretic behavior of an industrial rubber. Application to design of rubber components, *Finite Elements in Analysis and Design*, **46**(4), 357-368, 2010.

[3] S. Lejeunes, A. Boukamel and B. Cochelin, Analysis of laminated rubber bearings with a numerical reduction model method, *Arch. Appl. Mech.*, **76**(5-6), 311-326, 2006.

[4] M. Ohsaki, T. Miyamura, M. Kohiyama, M. Hori, H. Noguchi, H. Akiba, K. Kajiwara and T. Ine, High-precision finite element analysis of elastoplastic dynamic responses of super-highrise steel frames, *Earthquake Engineering and Structural Dynamics*, **38**(5), 635-654, 2009.

[5] Allied Engineering Corporation, http://www.alde.co.jp/english/advc/index.html, as of Feb. 13, 2013.

[6] S. Minewaki, M. Yamamoto, M. Higashino, H. Hamaguchi, H. Kyuke, T. Sone, H. Yoneda and A. Wada, Performance tests of full size isolators for super high-rise isolated buildings, *J. Struct. Eng.*, Architectural Inst. Japan, **55B**, 469-477, 2009. (in Japanese)

COMPDYN 2013
4th ECCOMAS Thematic Conference on
Computational Methods in Structural Dynamics and Earthquake Engineering
M. Papadrakakis, N.D.Lagaros, V. Plevris (eds.)
Kos Island, Greece, 12–14 June 2013

DYNAMIC COLLAPSE ANALYSIS OF FOUR-STORY STEEL FRAME USING E-SIMULATOR

Tomoshi Miyamura[1*], Makoto Ohsaki[2], Takuzo Yamashita[3], Daigoro Isobe[4], Masayuki Kohiyama[5]

[1]Department of Computer Science, College of Engineering, Nihon University
1 Nakagawara, Tokusada, Tamura, Koriyama 963-8642, Japan
miyamura@cs.ce.nihon-u.ac.jp

[2]Department of Architecture, Hiroshima University
1-4-1 Kagamiyama, Higashi-Hiroshima 739-8527, Japan
ohsaki@hiroshima-u.ac.jp

[3]Hyogo Earthquake Eng. Res. Center, National Res. Inst. for Earth Science and Disaster Prevention
1501-21 Nishikameyama, Mitsuta, Shijimi, Miki 673-0515, Japan
tyamashi@bosai.go.jp

[4]Division of Engineering Mechanics and Energy, University of Tsukuba
1-1-1 Tennodai, Tsukuba-shi, Ibaraki 305-8573, Japan
isobe@kz.tsukuba.ac.jp

[5]Department of System Design Engineering, Keio University
3-14-1 Hiyoshi, Kohoku, Yokohama 223-8522, Japan
kohiyama@sd.keio.ac.jp

Keywords: Finite Element Analysis, Steel Building Frame, Seismic Response, Parallel Computing.

Abstract. *Dynamic collapse analyses of a 4-story steel building frame modeled by solid elements are performed using the E-Simulator, which is a parallel finite element analysis software package for civil and building structures. Code verification, calculation verification, and validation of the numerical codes (V&V) are conducted by comparing the results obtained by the E-Simulator, those obtained by a beam element analysis code, and the experimental results obtained by the 3-D full-scale earthquake testing facility, the E-Defense at NIED. The seismic response analyses under 60% or 100% of the JR Takatori seismic wave of the 1995 Hyogoken-Nanbu earthquake are performed. The shear forces and interstory drift angles of the 1st story obtained by the E-Simulator simulation and the E-Defense full-scale test have good agreement. Both response of the whole frame and local deformation due to plastic buckling are simulated in the analysis using the E-Simulator.*

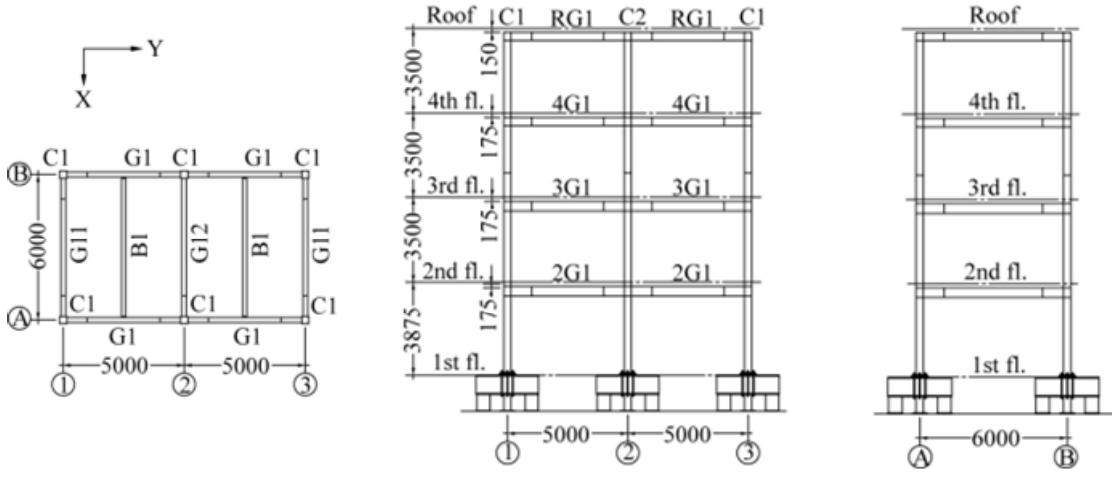
1 INTRODUCTION

The E-Simulator is a parallel finite element analysis software package for precise seismic response analysis of civil and building structures using solid elements [1]-[3]. The E-Simulator is under development in Hyogo Earthquake Engineering Research Center at National Research Institute for Earth Science and Disaster Prevention (NIED), Japan. A full-scale shake-table test for a 4-story frame (Fig. 1) was conducted using a 3-D full-scale earthquake testing facility, the E-Defense at NIED [5]. In this study, dynamic collapse analyses of the 4-story steel building frame modeled by solid elements are conducted using the E-Simulator. The seismic response analyses under 60% or 100% of the JR Takatori record of the 1995 Hyogoken-Nanbu earthquake are performed.

Validation of the E-Simulator is carried out by comparing the results obtained by the E-Simulator and the experimental results obtained by the E-Defense. The analyses using the ASI-Gauss code, which is a beam element analysis code, are also performed for the same frame and the both two codes are verified by comparing their results.

Tada et al. [6] conducted 3D analyses of the 4-story frame and compared the results with those by a full-scale shake-table test. Nam and Kasai [7] conducted 3D analyses of the 4-story frame using a fiber element method in which the effect of local buckling at the column ends is taken into account. The authors simulated the test of the 4-story steel frame using the E-Simulator [3]. Isobe et al. [8] performed analyses of the frame using an adaptive finite element code, the ASI-Gauss code, which is based on the beam element. They compared the results with those obtained by the E-Simulator [3] and the experimental results of the E-Defense test.

The analysis model used in the previous study [3] is improved in this study, that is, the stud bolts connecting the slabs and beams are considered to be rigid beams, the column bases are modeled precisely using solid elements and rigid beams, the Drucker–Prager yield criterion is introduced for concrete material used in the slabs, and a piecewise-linear combined isotropic-kinematic hardening model is introduced for the steel material.



(a) Plan (1st Floor) (b) Y-elevation (c) X-elevation

Figure 1: 4-story steel frame [4].

2 E-SIMULATOR

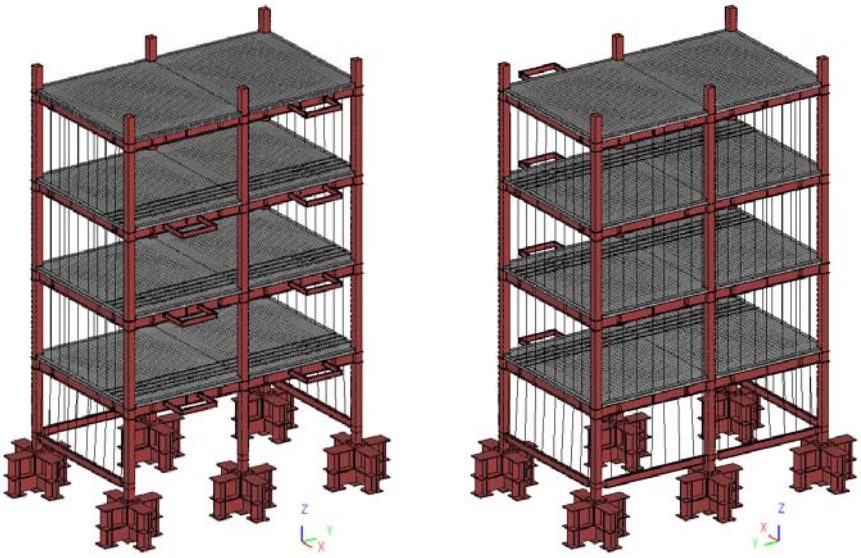
The E-Simulator is a parallel finite element structural analysis code for virtual shaking-table tests of civil or architectural structures. It enables large-scale analysis to be performed with a very fine mesh of solid elements. The main core of the E-Simulator is the commercial software package ADVENTURECluster [9, 10], which has been extended from the open source version, ADVENTURE [11]. These packages use the domain decomposition method for parallel implementation. The structural analysis code in the ADVENTURE system adopts the balancing domain decomposition (BDD) method, which is a substructuring-based linear iterative method with a Neumann-Neumann preconditioner combined with coarse grid correction. On the other hand, the Coarse Grid Conjugate Gradient (CGCG) method [10] has been developed originally for the ADVENTURECluster. The CGCG method is a conjugate gradient method combined with domain decomposition. It is preconditioned by motion of the decomposed subdomains. This idea is similar to the coarse grid correction used in the BDD method. However, the CGCG method is not a substructuring-based iterative method, and the computation cost for static condensation in each subdomain is reduced. The ADVENTURE-Cluster can be operated in a massively parallel computer; indeed, it was implemented on Blue Gene/L in 2006 and the work was selected as a finalist in the 2006 Gordon Bell Prizes [10].

3 ANALYSIS MODEL FOR E-SIMULATOR

The FE model for the 4-story frame shown in Fig. 1 is generated using the data and documents distributed for the blind analysis contest [12]. In this study, the analysis model used in the previous study [3] is improved. All the members and the floor slabs are modeled by 8-node hexahedral solid elements; i.e., the DOFs of each node correspond to three translational displacements, and the displacements in the elements are interpolated by linear shape functions and incompatible modes. Figure 2 shows the FE mesh used in the present study.

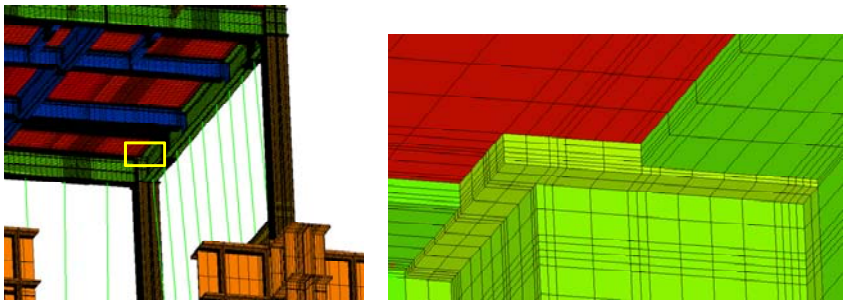
The FE mesh made by the Noguchi Laboratory at Keio University, Japan, is used as the prototype. The final mesh has 4,532,742 elements, 6,330,752 nodes, and 18,992,256 DOFs. Plates such as the flanges and webs of beams are divided into at least two layers of solid elements (Fig. 2(b)) . Each floor slab is also divided into solid elements with two layers. Studs connecting the flange and the slab are modeled using rigid beam elements that are represented by a set of multi-point constraints as shown in Fig. 2(c). Steel bars in the slab are modeled by solid elements as shown in Fig. 2(c). The cross-section of these bars is represented approximately by rectangular shape. The column bases are modeled precisely using solid elements and rigid beam elements. The size of each element in the longitudinal direction of a beam or a column is approximately 13 mm near the connections, where severe plastic deformation is expected, while a coarser mesh is used for elements located far from the connections. The exterior walls are modeled by elastic-plastic shear springs. A piecewise-linear combined isotropic-kinematic hardening model [13] is introduced in the constitutive model for the steel material, and its parameters are determined from the uniaxial test results distributed for the blind analysis contest. The Drucker–Prager yield criterion is introduced for concrete material used in the slabs.

The self-weight of the steel is computed based on a mass density of 7.86×10^3 kg/m^3. In contrast, the mass density of 2.3×10^3 kg/m^3 of the slab is increased appropriately to include the weights of nonstructural components, anti-collapse frames and stair landings installed in the experimental model. Five lowest natural periods for the analysis model are shown in Table 1. The Rayleigh damping with coefficients of $\alpha = 0.251$ and $\beta = 0.118 \times 10^{-3}$ is applied. These coefficients correspond to a damping factor of 0.02 for the 1st and 4th modes obtained by the eigenvalue analysis, which are the two lowest modes in the X-direction.



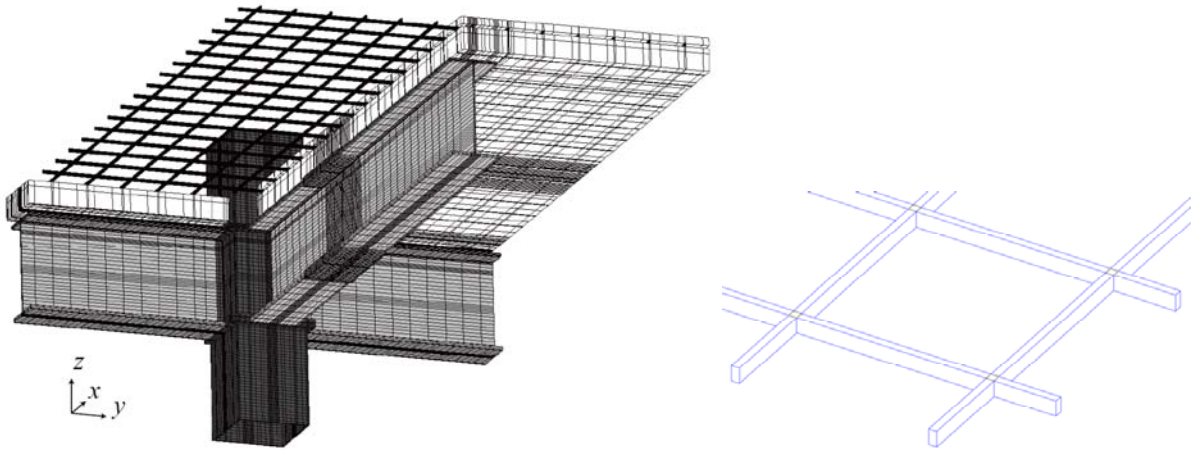
(a) Whole frame

(b)



(c) Close-up view

(d)



(e) Modeling of studs connecting the flange and the slab, and steel bars in the slab

Figure 2: Mesh of 4-story steel frame.

Table 1: Five lowest natural periods for analysis model and experimental model.

Model	Natural period				
	1st	2nd	3rd	4th	5th
Analysis model	0.8262	0.8081	0.5418	0.2660	0.2611
Experiment [5]	0.82	0.74–0.78	---	---	---

4 ANALYSIS MODEL FOR ASI-GAUSS CODE

For verifying the E-Simulator code, the analysis using the beam elements based on the ASI-Gauss technique is also performed. The ASI-Gauss technique proposed by Lynn and Isobe [14] is an improved version of the adaptively shifted integration (ASI) technique developed by Toi and Isobe [15]. These two are adaptive finite element methods using beam elements and can be applied to the seismic response analysis of framed structures that exhibit collapse sequences to obtain highly accurate solutions with a small computational cost. In the ASI-Gauss technique, the accuracy of solutions is improved particularly in the elastic range compared to the ASI technique.

Figure 3 shows the beam element model for the ASI-Gauss code, which consists of 1,388 elements, 995 nodes and 5,970 DOFs. Each column and beam in the structure is modeled with two Timoshenko beam elements per member. Instead of considering the composite beam effect, the floor slabs in the structure are modeled as a braced truss with stiffnesses and weights approximated to actual values. Offsets of the positions of the slabs from the beams are considered by imposing appropriate vertical beams. The structural strengths of the stairs and the exterior walls are ignored, and only their masses are taken into account as a dead load. The bases are completely fixed to the ground, and the stiffness of the lowest columns are increased appropriately to match the experimental model. In the original calculation process of the ASI-Gauss technique, the bending moments are estimated at the exact locations of the nodes, that is, intersections of the center lines of the beams and columns. However, in the analysis performed in this study, the bending moments are estimated at the face of the connections to reduce the modeling error. Bilinear isotropic hardening is used in the constitutive model of the steel material, and its parameters are determined from uniaxial test results distributed in the blind analysis contest [12]. A mass proportional damping with a coefficient of $\alpha = 0.2284$ is applied.

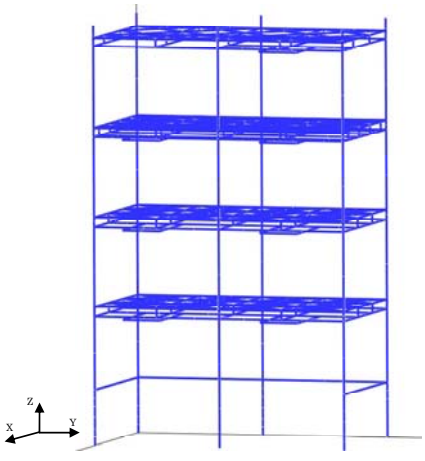


Figure 3: Beam element model of the four-story steel frame for the ASI-Gauss code.

5 RESULTS OF NUMERICAL SIMULATION

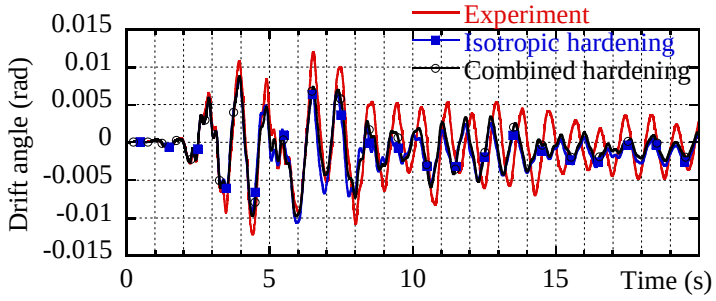
5.1 Seismic response analyses under 60% of the JR Takatori seismic wave

A 20-second segment of the JR Takatori wave is used as an input ground motion for the experiment performed in the E-Defense. The acceleration measured on the shaking table during the full-scale test under the 60 % of the JR Takatori wave is used for the input ground motion for both analyses using the E-Simulator and the ASI-Gauss code. The computational time using the E-Simulator took approximately one month using an SGI Altix 256-core computer, and the ASI-Gauss code took approximately 150 minutes using an Intel Core i7 2.93 GHz personal computer.

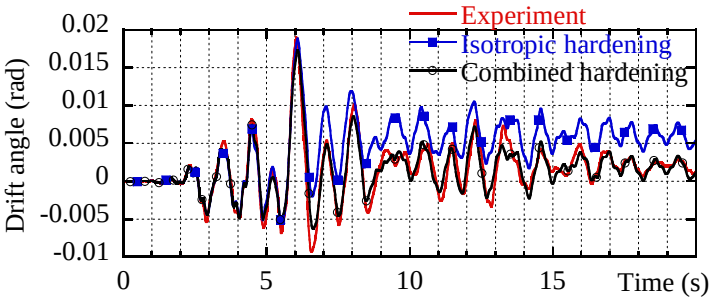
Figures 4 and 5 show the comparisons of the time histories of the interstory drift angle and the shear force of the 1st story, respectively, which are obtained by the E-Simulator and the E-Defense full-scale experiment [4]. For the E-Simulator, the results obtained by the combined hardening model for the steel material and those obtained by the isotropic hardening model are shown. The interstory drift angle is calculated from the lateral displacements at the center of the second floor. The shear force is calculated as the summation of the concentrated mass multiplied by the acceleration at the center of gravity of each floor. The interstory drift angle along the X-axis obtained by the E-Simulator, as shown in Fig. 4 (a), agrees well with the experiment until approximately 7 s. However, the differences in the phase and the amplitude become larger after 7 s, where the amplitude of the input ground motion decreases. The interstory drift angle along the Y-axis obtained by the E-Simulator, as shown in Fig. 4(b), shows a good resemblance to the experimental result when the combined hardening model is used. The interstory drift angle remains in the positive region in the later part of the time history when the isotropic hardening model is used. The time histories of the shear force shown in Fig. 5 seem to show similar tendencies as those of the interstory drift angle in Fig. 4.

Figures 6 and 7 show the comparisons of the time histories that are obtained by the E-Simulator, the ASI-Gauss code, and the E-Defense full-scale experiment. For the E-Simulator, only the results for the combined hardening model are shown. As described previously, the differences in the phase and the amplitude of the interstory drift angle along the X-axis obtained by the E-Simulator and the E-Defense become larger after approximately 7 s as shown in Fig. 6(a). The results obtained by the ASI-Gauss code, on the other hand, show good agreement with the experimental results in both the phase and the amplitude. However, the ASI-Gauss code has smaller peak values near 6 s. The time histories of the shear force shown in Fig. 7 seem to show similar tendencies as those of the interstory drift angle. It is noted that the asymmetrical drift in the positive direction in the later part of the time history of the interstory drift angle in the X-direction is not observed in the result obtained by the ASI-Gauss code though the isotropic hardening model is used in the analysis.

Figures 8 and 9 show the deformations and the distributions of the plastic region obtained by both analyses at 6.0 s. The deformation is magnified 10 times, and the colors represent the distribution of the equivalent stresses in Fig. 8 and the distribution of the yield function values in Fig. 9. The yield function values are linearly interpolated using the values at the both ends of the elements. Figure 8 shows that the plastic regions around connections are localized and the positions of the plastic regions are the same as the positions of the plastic hinges (indicated with red color) that are shown in Fig. 9. Therefore, the use of the plastic hinge model must be a good approximation of the plastic behavior obtained by the E-Simulator model. A torsional deformation can be clearly identified in the E-Simulator model, whereas less torsional deformation is observed in the ASI-Gauss model. The torsional deformation is not clearly observed in the full-scale experiment. Therefore, the stiffness of the shear spring used in the E-Simulator model for representing the exterior walls may be too large.

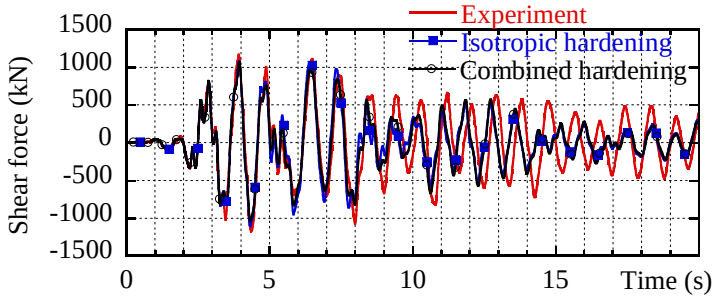


(a) X-direction

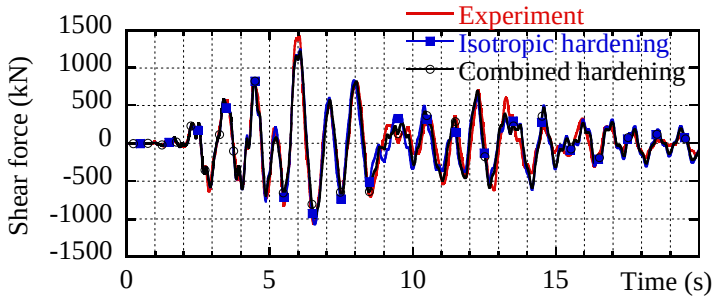


(b) Y-direction

Figure 4: Comparison of time-histories of interstory drift angle of the 1st story obtained by the E-Simulator and the E-Defense full-scale experiment.

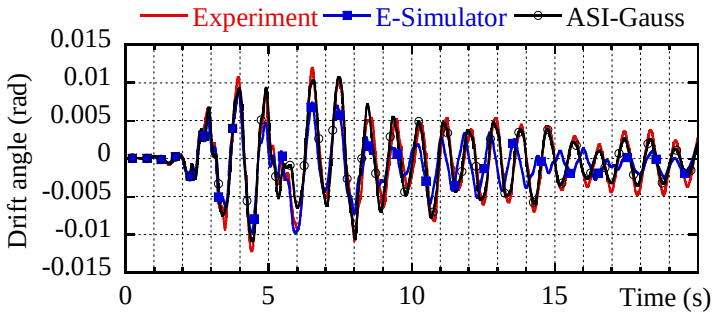


(a) X-direction

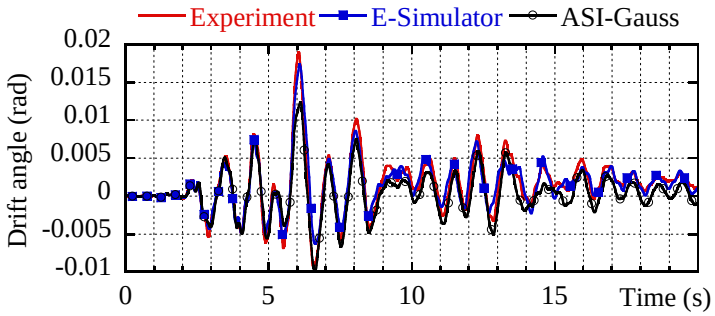


(b) Y-direction

Figure 5: Comparison of time-histories of shear force of the 1st story obtained by the E-Simulator and the E-Defense full-scale experiment.

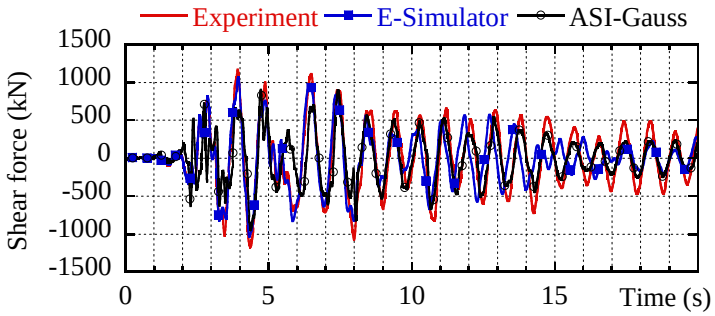


(a) X-direction

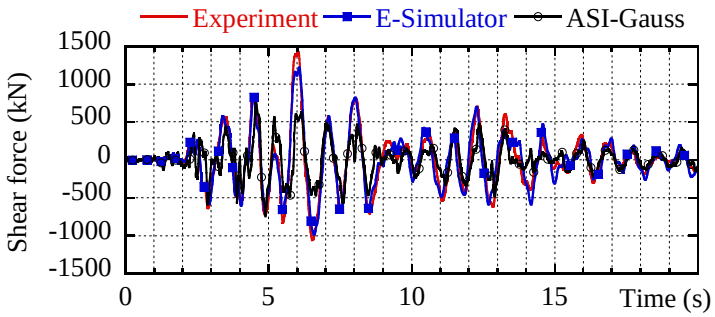


(b) Y-direction

Figure 6: Comparison of time-histories of interstory drift angle of the 1st story obtained by the E-Simulator and the ASI-Gauss code.



(a) X-direction



(b) Y-direction

Figure 7: Comparison of time-histories of shear force of the 1st story obtained by the E-Simulator and the ASI-Gauss code.

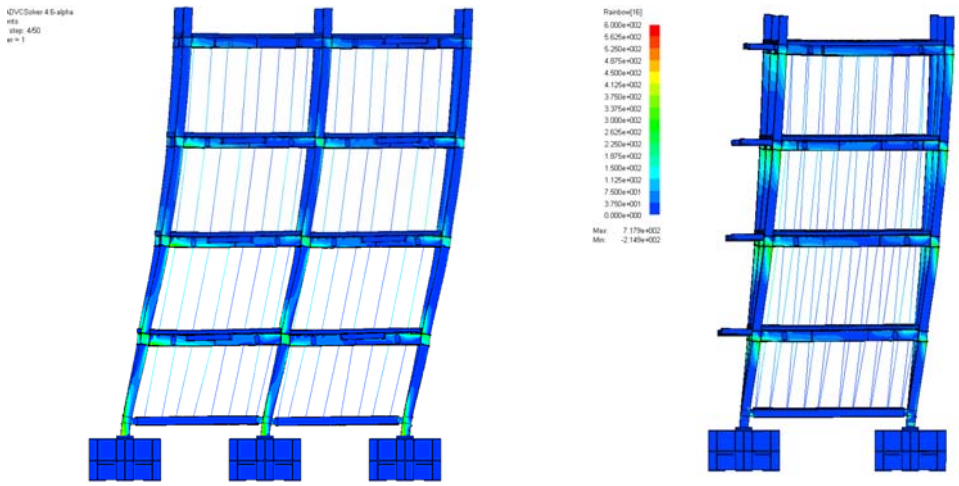


Figure 8: Deformation (magnified 10 times) and distribution of the equivalent stress at 6.08 s obtained by the E-Simulator.

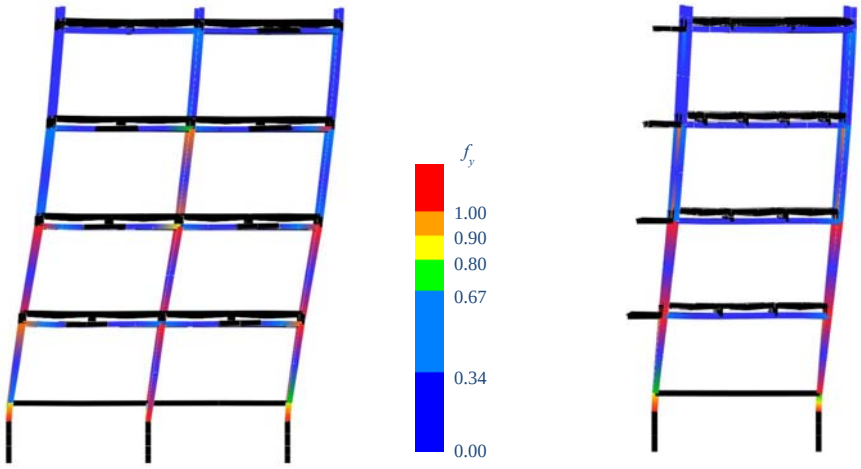
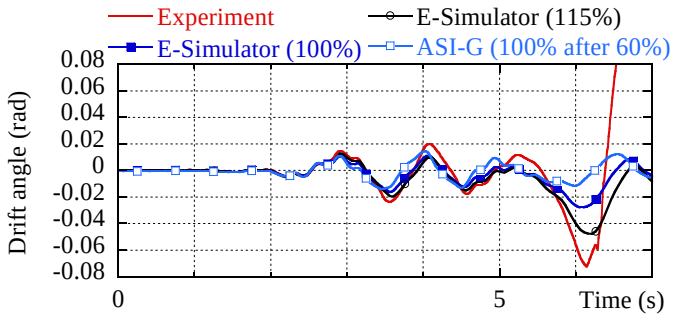


Figure 9: Deformation (magnified 10 times) and distribution of the yield function value at 6.0 s obtained by the ASI-Gauss code.

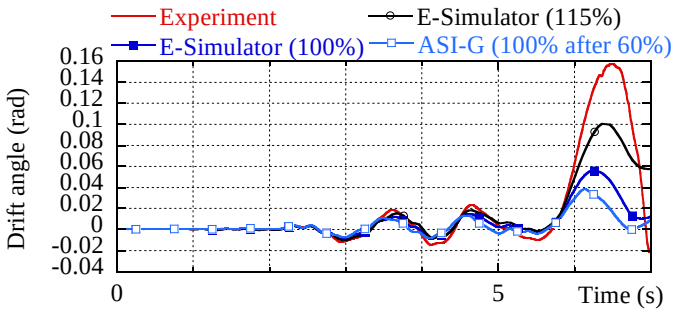
5.2 Seismic response analyses under 100% of the JR Takatori seismic wave

The acceleration measured on the shaking table during the full-scale test under the 100 % of the JR Takatori wave is used for the input ground motion in both analyses using the E-Simulator and the ASI-Gauss code. In the experiment, the shake-table test for 60% of the JR Takatori seismic wave is conducted before the test for the 100% of the wave is performed. Therefore, plastic deformation due to the preceding test remains in the specimen. In the simulation by the E-Simulation, however, the initial plastic deformation is not considered. In the simulation by the ASI-Gauss code, on the other hand, the preceding analysis for the 60% is performed. Figures 10 and 11 show the comparisons of the time histories of the interstory drift angle and the shear force of the 1st story, respectively, which are obtained by the E-Simulator, the ASI-Gauss code, and the E-Defense full-scale experiment. The simulation under 115% of the seismic wave is also conducted for the E-Simulator analysis model.

The frame collapsed after 6 s in the experiment and the interstory drift angle in the X-direction increased monotonically. Figure 12 shows deformation and distribution of the equivalent stress at 6.36 s obtained by the E-Simulator under 115% of the seismic wave. However, the frame is not fully collapsed in the analysis.

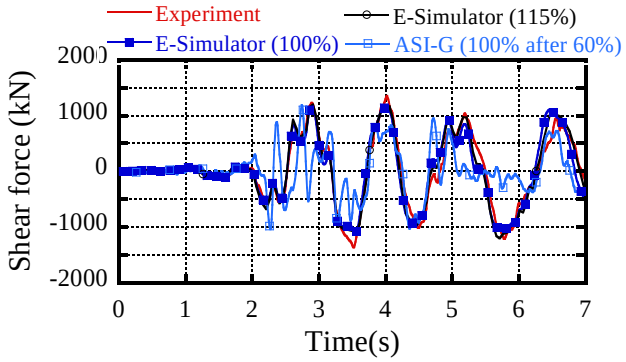


(a) X-direction

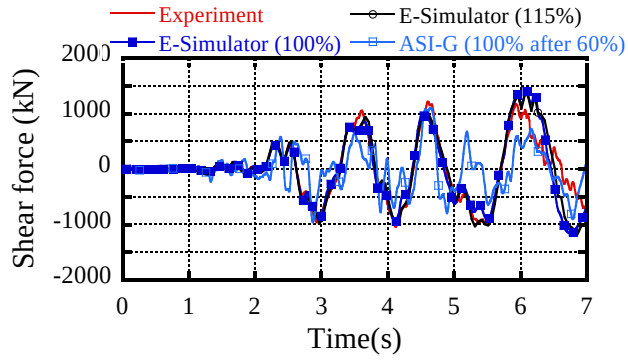


(b) Y-direction

Figure 10: Comparison of time-histories of interstory drift angle of the 1st story obtained by the E-Simulator and the ASI-Gauss code.



(a) X-direction



(b) Y-direction

Figure 11: Comparison of time-histories of shear force of the 1st story obtained by the E-Simulator and the E- the ASI-Gauss code.

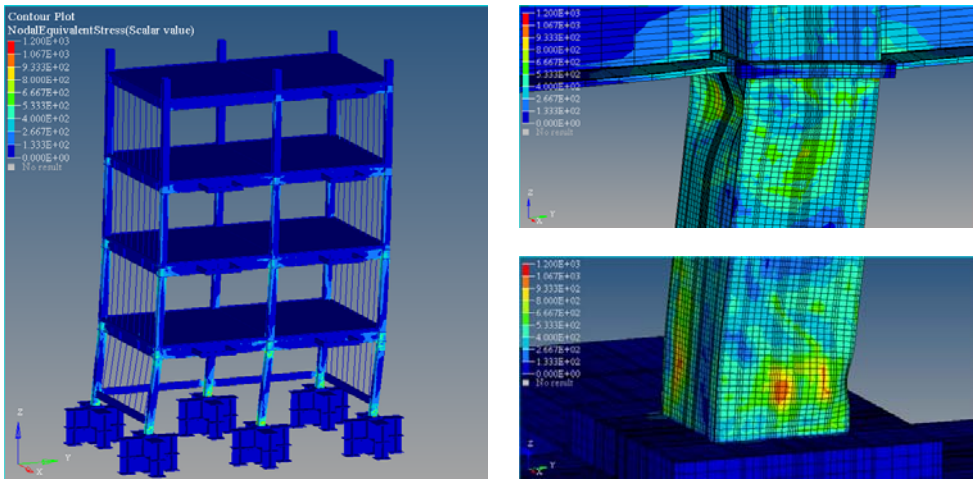


Figure 12: Deformation (not magnified) and distribution of the equivalent stress at 6.36 s obtained by the E-Simulator under 115% of the JR Takatori wave.

6 CONCLUDING REMARKS

Dynamic collapse analyses of the 4-story steel building, for which the full-scale shake table test was conducted at the E-Defense, are performed using the E-Simulator, which is parallel finite element analysis software for civil and building structures. The frame is modeled by solid elements. The analyses using the ASI-Gauss code, which is a kind of a beam element analysis code, are also conducted for the same steel frame.

In the analysis under the 60 % of the JR Takatori wave, the time histories of the interstory drift angle obtained by the E-Simulator show good agreement with the experimental results especially when the combined hardening model is used. However the differences in the phase and the amplitude of the time history of the interstory drift angle in the X-direction become larger after 7 s, where the amplitude of the input ground motion decreases. On the other hand, the results obtained by the ASI-Gauss code show good agreement with the experimental results in both the phase and the amplitude; however, it leads to smaller peak values near 6 s. In the analysis under the 100 % of the JR Takatori wave, both response of the whole frame and local deformation due to plastic buckling are simulated in the analysis using the E-Simulator.

ACKNOWLEDGEMENTS

This study is a part of E-Defense Seismic Experimental Study and Simulation System Construction Project conducted by E-Simulator Development Committee (Leader: Prof. Muneo Hori, The University of Tokyo). The authors acknowledge the valuable contribution from the committee members, and the financial support by NIED. The contribution of Dr. Tomonobu Ohyama and Mr. Kiyoshi Yuyama of Allied Engineering Corporation for computation and mesh generation is acknowledged. This work was also supported by JSPS KAKENHI Grant Numbers 24560080 and 23360248.

REFERENCES

[1] M. Hori, H. Noguchi, T. Ine, Project report of development of numerical shaking table coping with E-defense. *JSCE Journal Earthquake Engineering*, **29**, 1420-1425, 2007 [in Japanese].

[2] M. Ohsaki, T. Miyamura, M. Kohiyama, M. Hori, H. Noguchi, H. Akiba, K. Kajiwara, T. Ine, High-precision finite element analysis of elastoplastic dynamic responses of su-

per-highrise steel frames. *Earthquake Engineering and Structural Dynamics*, **38**(5), 635-654, 2009.

[3] T. Miyamura, M. Ohsaki, M. Kohiyama, D. Isobe, K. Onda, H. Akiba, M. Hori, K. Kajiwara, T. Ine, Large-scale FE analysis of steel building frames using E-Simulator. *Progress in Nuclear Science and Technology*, **2**, 651-656, 2011.

[4] Website of ASEBI at E-Defense, NIED, Project "E-Defense Tests on Full-Scale Four-Story Steel Building", https://www.edgrid.jp/data/, as of 28/2/2013.

[5] S. Yamada, K. Suita, M. Tada, K. Kasai, Y. Matsuoka, Y. Shimada, Collapse experiment on 4-story steel moment frame: Part 1 outline of test results. *Proceedings of the 14th World Conference on Earthquake Engineering* (DVD), Paper ID: S17.1.4, Beijing, China, 2008.

[6] M. Tada, H. Tamai, K. Ohgami, S. Kuwahara, A. Horimoto, Analytical simulation utilizing collaborative structural analysis system. *Proceedings of the 14th World Conference on Earthquake Engineering* (DVD), Paper ID: S17.1.5, Beijing, China, 2008.

[7] T.T. Nam, K. Kasai, Dynamic analysis of a full-scale four-story steel building experimented to collapse using strong ground motions, *Proceedings of International Symposium on Disaster Simulation and Structural Safety in the Next Generation 2011 (DS'11)*, 311-318, Kobe, Japan, 2011.

[8] D. Isobe, W.S. Han and T. Miyamura, Verification and validation of a seismic response analysis code for framed structures using the ASI-Gauss technique. *Earthquake Engineering and Structural Dynamics* (accepted).

[9] Website of Allied Engineering Corporation,

http://www.alde.co.jp/english/advc/index.html, as of 28/2/2013.

[10] H. Akiba et al., Large scale drop impact analysis of mobile phone using ADVC on Blue Gene/L. *Proceedings of the International Conference on High Performance Computing Networking and Storage (SC06)*, Tampa, USA, 2006.

[11] S. Yoshimura, R. Shioya, H. Noguchi, T. Miyamura, Advanced general-purpose computational mechanics system for large scale analysis and design. *Journal of Computational and Applied Mathematics*, **149**(1), 279-296, 2002.

[12] M. Ohsaki, K. Kasai, Y. Matsuoka, J.Y. Zhang. Results of recent E-Defense tests on full-scale steel building: Part 2, Collapse simulation and blind analysis contest. *Proceedings of the Structures Congress 2008, ASCE*, Vancouver, Canada, 2008.

[13] M. Ohsaki, J.Y. Zhang, T. Miyamura, A heuristic algorithm for parameter identification of steel materials under asymmetric cyclic elastoplastic deformation. *Proceedings of the 7th China-Japan-Korea Joint Symposium on Optimization of Structural and Mechanical Systems (CJK-OSM7)* (CD-ROM), Huangshan, China, 2012.

[14] K.M. Lynn, D. Isobe, Finite element code for impact collapse problems of framed structures. *International Journal for Numerical Methods in Engineering*, **69**(12), 2538-2563, 2007.

[15] Y. Toi, D. Isobe, Adaptively shifted integration technique for finite element collapse analysis of framed structures. *International Journal for Numerical Methods in Engineering*, **36**(14), 2323-2339, 1993.

COMPDYN 2013
4th ECCOMAS Thematic Conference on
Computational Methods in Structural Dynamics and Earthquake Engineering
M. Papadrakakis, V. Papadopoulos, V. Plevris (eds.)
Kos Island, Greece, 12–14 June 2013

DESIGN OF DISSIPATIVE BRACES FOR AN EXISTING STRATEGIC BUILDING WITH A PUSHOVER BASED PROCEDURE

A. V. Bergami[1], C. Nuti

[1] University of Roma Tre – Department of Structures
Via C. Segre, 6 - 00146 Rome (Italy)
alessandro.bergami@uniroma3.it

[2] University of Roma Tre – Department of Structures
Via C. Segre, 6 – 00146 Rome (Italy)
c.nuti@uniroma3.it

Keywords: Dissipative braces, earthquake engineering, energy dissipation, seismic retrofitting.

Abstract. *The research presented in this paper deals with the seismic protection of existing frame structures by means of passive energy dissipation. An iterative displacement-based procedure, based on capacity spectrum, to design dissipative bracings for seismic retrofitting of frame structures is described and some applications are discussed. The procedure can be used with any typology of dissipative device and for different performance targets. In this work the procedure has been applied, with both traditional pushover (load profile proportional to first mode) and multimodal pushover, to an existing r.c. frame building. In the application presented the buckling restrained braces have been used in order to prevent damages to both the structure and non structural elements. The use of multimodal pushover proves to be more effective than pushover based on single mode in case of medium rise r.c. frame building (higher than 30 metres) but, once this building is retrofitted, and therefore regularized, with a bracing system, the difference between using monomodal or multimodal pushover becomes not significant.*

1 INTRODUCTION

The use of dissipative bracings, though it seems conceptually clear and simple, requires a more complex design procedure than other retrofitting methods like base isolation. This greater complexity derives from the non linear behaviour of the dissipative devices and therefore of the final retrofitted structure. Despite that, during the last years, many design procedure has been published and, between those, the most useful for practical use seem to be those that are based on the capacity spectrum method. In fact with this approach non linear dynamic analyses can be skipped in favour of static non linear analyses that are simpler to be managed. Otherwise, also within those procedures, many have a theoretical approach that can be difficulty associated with a widespread professional use. In fact, frequently, the characteristics of an existing building (e.g. non regular distribution of masses and stiffness, presence of a soft story) can compromise the effectiveness of procedures that impose a predefined loading pattern during pushover analyses. As discussed in Bergami & Nuti (2012), the design of dissipative devices have two main goals: improve dissipation and regularize strength end stiffness distribution (this can be done adopting an adequate criteria to distribute the braces along the elevation and inside the plan of the building). Moreover, in case of medium rise building (quite widespread in Italy), it is a matter of fact that the relevance of higher modes depends not only on their level of irregularity but it is also related to the quite high number of stories. To check such hypothesis the design procedure has been tested on a medium rise irregular existing building. The necessity of using a multi modal pushover (Goel & Chopra, 2004) instead of the standard single mode pushover procedure has been investigated performing multimodal pushover and non linear dynamic analysis on both the existing and retrofitted building.

2 DISSIPATIVE BRACINGS POSITIONING: STRUCTURAL EFFECTS

The insertion of dissipative braces into the structural frame involves significant effects that can be grouped in two categories: effects on structural response and effects on the architecture of the building. Concerning the former the braces increase both stiffness and strength and consequently, as usually happens, both modal shapes and the capacity curve of the structure are modified. Moreover, for a given top displacement, these improve damping and, therefore, reduce demand. In this respect stiffness increase could render less efficient, or even useless, the increase of dissipation. Therefore a careful mix of stiffness and dissipation is requested: this subject is discussed in the following.

The bracing system has to be compatible with the architecture of the building: therefore spatial distribution of the braces descents from a compromise between the optimization of the dissipative system and the functionality of the building.

Although braces distribution should be analyzed case by case some general considerations can be made: braces should reduce or eliminate eventual translation-rotation coupling effects, induce constant interstorey drifts, exclude soft storey behavior and maximize damping for a given top displacement.

Different criteria to distribute the additional stiffness are proposed in scientific literature: constant at each story, proportional to story shear, proportional to interstorey drifts of the original structure. In this work the latter is assumed and therefore, given the interstorey drift δ_j, the stiffness $K'_{b,j}$ corresponding to each storey of the bracing system is:

$$K'_{b,j} = K_{global} c_{b,j} \tag{1}$$

where:

$$c_{bj} = \frac{\delta_j}{\max_j \{\delta_j\}} \tag{2}$$

Each brace is a composite element realized coupling an elastic element (usually a steel profile) with a dissipative device in series. The latter will determines the desired yielding force whereas the former will be designed to assure the desired stiffness of the series.

3 EVALUATION OF THE EQUIVALENT VISCOUS DAMPING

A specific energy dissipated by the structure and the braces corresponds to each deformation reached by the structure, be it with or without dissipative braces; the dissipated energy can be expressed in terms of equivalent viscous damping. Referring to the formula proposed by A.K. Chopra (2001), the equivalent viscous damping of the structure $\nu_{eq,S}$ at the generic displacement *D* can be expressed as follows:

$$\nu_{eq,S} = \frac{1}{4\pi}\frac{E_{D,S}}{E_{S,S}} \tag{3}$$

All the parameters of the Eq. (3) can be easily determined from the capacity curve: $E_{D,S}$ is the energy dissipated in a single cycle of amplitude *D* and $E_{S,S}$ is the elastic strain energy corresponding to the displacement *D*. Referring to an equivalent bilinear capacity curve (it can be determined from the capacity curve using one of the methods available in literature) terms of Eq. (3), considering an ideal elasto-plastic hysteretic cycle, can be determined as follow:

$$E_{D,S}^{bilinear} = 4\left(F_{sy}D - D_{sy}F_s(D)\right) \tag{4}$$

$$E_{S,S} = \frac{1}{2}DF_s(D) \tag{5}$$

with:

D	the displacement reached from the structure
$F_s(D)$	the force corresponding to D (the force is the base shear)
D_{sy}	displacement at yielding
F_{sy}	the yielding force (base shear at yielding)

It is well known that the hysteretic cycle of a real structure differs from the ideal cycle, therefore this difference can be taken into account adopting a corrective coefficient χ_S for the structure and χ_B for the braces (χ =1 for the ideal elasto-plastic behaviour). Therefore:

$$E_{D,S} = \chi_S E_{D,S}^{bilinear} \tag{6}$$

$$E_{D,B} = \chi_B E_{D,B}^{bilinear} \tag{7}$$

with $E_{D,B}^{bilinear}$ the energy dissipated by the ideal hysteretic cycle of the dissipative brace.

For the applications discussed in this paper the parameter χ_S has been determined referring to the provisions of *ATC40 [1996]*. For the braces the assumption of $\chi_B \approx 1$ has been considered reasonable: in fact, according to *AISC/SEAOC – Recommended Provisions for Buckling-Restrained Braced Frames [2005]*, the force-displacement relationship of a *BRB* can be ideal-

ized as a bilinear curve. However different values can be adopted, if the case, with no difference in the procedure. Authors have assumed a bilinear curve characterized by a yielding force equal to the yielding traction force (the maximum compressive strength of *BRBs* is slightly larger than the maximum tensile strength due to the confining effect of the external tube): the hysteretic cycle obtained is elasto-plastic but precautionary smaller than the real one. Than the evaluation of the equivalent viscous damping of the braced structure $\nu_{eq,S+B}$, to be added to the inherent damping ν_I (usually ν_I=5% for r.c. structures and ν_I=2% for steel ones), can be obtained using the following expression:

$$\nu_{eq,S+B} = \frac{1}{4\pi}\frac{E_{D,S+B}}{E_{S,S+B}} = \frac{1}{4\pi}\left[\frac{\chi_S E_{D,S}^{bilinear}}{E_{S,S+B}} + \frac{\chi_B \sum_j E_{D,B,j}^{bilinear}}{E_{S,S+B}}\right] \tag{8}$$

$$\nu_{eq,S} = \chi_S \frac{1}{4\pi}\frac{E_{D,S}^{bilinear}}{E_{S,S+B}}; \nu_{eq,B} = \chi_B \frac{1}{4\pi}\frac{\sum_j E_{D,B,j}^{bilinear}}{E_{S,S+B}} \tag{9}$$

where $E_{D,B,j}^{bilinear}$ is the energy dissipated by the dissipative braces placed at level *j*.

Eq. (8) can be generalized assuming that $E_{D,B,j}^{bilinear} = \sum_i E_{D,B,i}^{bilinear}$ with $E_{D,B,i}^{bilinear}$ the energy dissipated by the *i* braces placed at level *j*. Note that $\nu_{eq,S}$ and $\nu_{eq,B}$ are obtained dividing the dissipated energy, determined from the capacity curve of *S* or *B* respectively, by the elastic strain energy of the braced structure, determined from the curve of *S+B*.

4 THE DESIGN PROCEDURE: MAIN STEPS

The design procedure can be applied using every typology of pushover because it requires the only definition of capacity curve and interstorey drift distribution. Therefore the use of the multimodal procedure doesn't modify the proposed procedure that can be summarized in the following steps:

1. **Define the seismic action**: the seismic action is defined in terms of elastic response acceleration spectrum (T-S_a).

2. **Select the target displacement**: the target displacement is selected (for example the top displacement D_t^*) according to the performance desired (limit state).

3. **Define the capacity curve**: the capacity curve of the braced structure *S+B*, in terms of top displacement and base shear (D_t-V_b), is determined via pushover analysis. The pushover analysis can be easily performed using a software for structural analysis: many different force distributions can be adopted selecting the best option for the specific case (*e.g.* modal shape load profile).
If a modal shape load profile has been selected it is important to underline that the modal shape is influenced by the bracing system and consequently, at each iteration, the load profile has to be updated to the modal shape of the current braced structure.
Notice that, at the first iteration, the structure without braces is considered and therefore the capacity curve obtained will be fundamental for the evaluation of the contribution offered by the existing structure to the braced structure of the subsequent iterations.

4. **Define the equivalent bilinear capacity curve**: the capacity curve is approximated by a simpler bilinear curve D_t-F_{s+b} that is completely defined by the yielding point ($D_{s+b,y}$, $F_{s+b,y}$) and the hardening ratio β_{s+b} (at the first iteration the parameters correspond to $D_{s,y}$, $F_{s,y}$, β_s of the existing building).

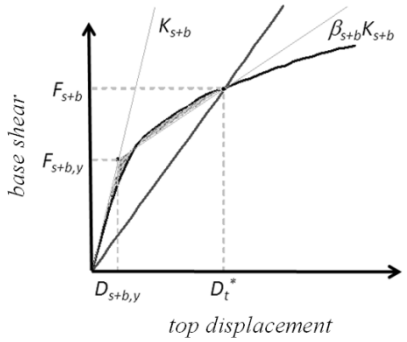


Figure 1: Evaluation of the equivalent bilinear capacity curve

5. **Define equivalent single degree of freedom**: MDOF system is converted in a SDOF system by transforming the capacity curve into the capacity spectrum (S_{dt}-S_{ab})

$$S_{dt} = \frac{D_t}{\Gamma\phi_t}; S_a = \frac{F_{S+B}}{\Gamma \cdot L} \tag{10}$$

where Γ is the participation factor of the modal shape ϕ ($\Gamma=(\phi^T MI)/(\phi^T M\phi)$) and $L=\phi^T MI$. The modal characteristics of the braced structure may change at every iteration due to new brace characteristics. Therefore ϕ, Γ and L have to be updated with the current configuration

6. **Evaluate the required equivalent viscous damping**: the equivalent viscous damping $\nu^*_{eq,S+B}$ of the braced structure to meet the displacement of the equivalent SDOF system and the target spectral displacement $S_{dt}^*=D_t^*/(\Gamma\phi^T)$ is determined.
According to the Capacity Spectrum Method the demand spectrum is obtained reducing the 5% damping response spectrum by multiplying for the damping correction factor η that is function of ν_{tot}

$$\eta = \sqrt{\frac{10}{5+\nu_{tot}\cdot 100}} = \frac{S_{\nu_{eff}}}{S_{5\%}} \tag{11}$$

From Eq. (11) one obtain ν^*_{tot} the damping needed to reduce displacement up to the target S_{dt}^*.

$$\nu^*_{tot} = 0.1\left(\frac{S_{5\%}}{S^*_{dt}}\right)^2 - 0.05 \tag{12}$$

7. **Evaluate the equivalent viscous damping contribution due to the naked structure**: the contribute to damping of the structure $\nu^*_{eq,S}(D_t^*)$ can be determined from Eq. (3.12) being D_t^* the top displacement corresponding to $E^{bilinear}_{D,S}$ and $E_{S,S+B}$ that are the energy dissipated by S and the elastic strain energy of $S+B$ ($E^{bilinear}_{D,S}$ and $E_{S,S+B}$ are determined from the capacity curve of S and $S+B$ respectively).
8. **Evaluate the additional equivalent viscous damping contribution due to braces**: given

ν^*_{tot} from Eq. (12) the equivalent viscous damping needed to be supplied by the braces $\nu^*_{eq,B}(D^*_t)$ is evaluated from Eq. (3.11) and Eq. (4.1) as follows:

$$\nu^*_{eq,B}(D^*_t) = \nu^*_{tot}(D^*_t) - \nu^*_{eq,S}(D^*_t) - \nu_I \tag{13}$$

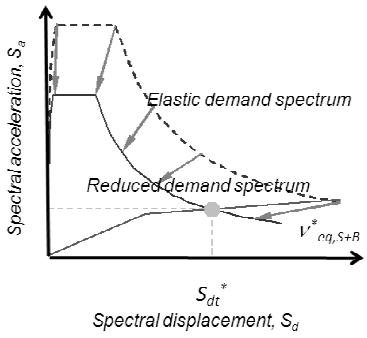


Figure 2: Evaluation of the equivalent viscous damping needed to achieve the target performance point

9. **Dimensioning of the braces**: once the required equivalent viscous damping $\nu^*_{eq,B}(D^*_t)$ has been evaluated from Eq. (13), axial stiffness and yielding strength required to achieve the desired additional damping can be determined with the same procedure previously adopted for the structure (step 7).
The energy dissipated by the braces inserted at each j_{th} level can be expressed as:

$$E^{bilinear}_{D,B} = \sum_{j=1}^{n} 4\left(F'_{by}\delta'_j - \delta'_{y,j}F'_{b,j}(\delta'_j)\right) \tag{14}$$

being δ'_j the component of the interstory drift δ_j at j_{th} of the n floors along the axe of the brace ($\delta'_{y,j}$ is the axial displacement corresponding to yielding of the device).

The axial displacement of the damping brace at the j_{th}-floor δ'_{bj} can be determined from its inclination angle $\theta_{b,j}$ and interstorey drift $\delta_j = D_j - D_{j-1}$: therefore $\delta'_{b,j} = \delta_j \cos\theta_{bj}$.

The dissipative brace is usually constituted by a dissipative device (*e.g.* the *BRB*) assembled in series with an extension element (*e.g.* realized with a steel profile) in order to connect the opposite corners of a frame (Fig. 3).

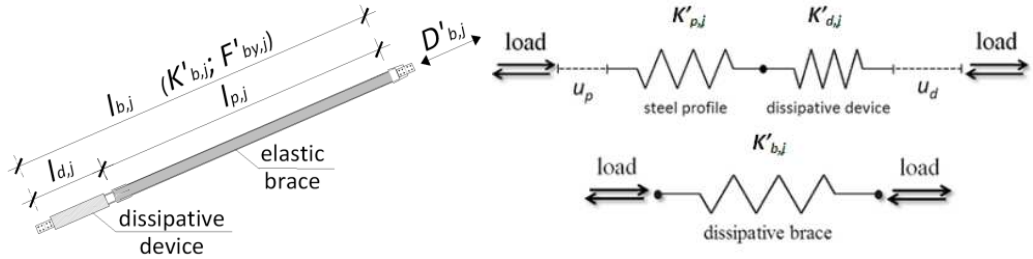


Figure 2: Dissipative device "j" assembled in series with an extension element (e.g. a steel profile): equivalent model of springs in series ($K'_{d,j}$; $K'_{p,j}$) and equivalent single spring model ($K'_{b,j}$)

Therefore, being $K'_{b,j}$ and $K'_{by,j}$ the equivalent stiffness of the spring series in the elastic and plastic range respectively, $\alpha = K'_{p,j}/K'_{d,j}$ the ratio between elastic stiffness of the steel profile and of the device and $\beta_{d,j}$ the ratio between stiffness after and before yielding of the dissipa-

tive device, the following expression can be derived:

$$K_{b,j}^{'} = \frac{K_{d,j}^{'}}{\frac{1}{\alpha_j}+1};\ K_{by,j}^{'} = \frac{\beta_{b,j}K_{d,j}^{'}}{\frac{\beta_{b,j}}{\alpha_j}+1};\ \alpha_j = \frac{K_{p,j}^{'}}{K_{d,j}^{'}} \tag{15}$$

Therefore:

$$F_{b,j}^{'} = F_{by,j}^{'} + (\delta_j^{'} - \delta_{y,j}^{'})\frac{\beta_{b,j}K_{d,j}^{'}}{\frac{\beta_{b,j}}{\alpha_j}+1} \tag{16}$$

$$\delta_{y,j}^{'} = \frac{F_{by,j}^{'}}{K_{b,j}^{'}} = \frac{F_{by,j}^{'}}{K_{d,j}^{'}}(\frac{1}{\alpha_j}+1) \tag{17}$$

Consequently, if there is one brace per direction and per floor, substituting Eq. (16) into Eq. (14), $v^{*}_{eq,B}(D_t^{*})$ can be expressed in the following way:

$$v^{*}_{eq,B}(D_t^{*}) = \chi_B \frac{2}{\pi} \frac{\sum_{j=1}^{n}\left\{F_{by,j}^{'}\delta_j^{'} - \delta_{y,j}^{'}\cdot\left[F_{by,j}^{'} + (\delta_j^{'} - \delta_{y,j}^{'})\frac{\beta_{d,j}K_{d,j}^{'}}{\frac{\beta_{d,j}}{\alpha_j}+1}\right]\right\}}{F_{S,S+B}(D_t^{*})\cdot D_{S,S+B}^{*}} \tag{18}$$

$\delta_j^{'}$ are determined from the pushover analysis for the top displacement D_t and $\delta_{y,j}^{'}$, that is the yielding displacement of devices, can be reasonable assumed as $\delta_{y,j}^{'} \le \delta_j^{'}/4$.

$F_{y,j}^{'}$ is, for each direction, the yielding force of the floor brace: once $\delta_{y,j}^{'}$ has been defined $F_{y,j}^{'}$ is consequently determined Eq. (17). Thus, according to Eq. (15), $K_{d,j}^{'}$ can be expressed as follows:

$$K_{d,j}^{'} = K_{global}\cdot c_{b,j}\cdot(\frac{1}{\alpha_j}+1) \tag{19}$$

Therefore substituting Eq. (19) into Eq. (18), K_{global} can be determined as follows:

$$K_{global} = \frac{\pi\cdot v^{*}_{eq,B}(D_t^{*})\cdot F_{S,S+B}(D_t^{*})\cdot D_{S,S+B}^{*}}{2\cdot\chi_B\cdot C_1} \tag{20}$$

with:

$$C_1 = \sum_{j=1}^{n} c_{b,j} \left\{ \delta'_{y,j} \cdot \delta'_j - \delta'_{y,j} \left[\delta'_{y,j} + (\delta'_j - \delta'_{y,j}) \frac{\beta_{b,j}(\frac{1}{\alpha_j}+1)}{\frac{\beta_{b,j}}{\alpha_j}+1} \right] \right\} \tag{21}$$

A value of α_j>3 is usual in applications, therefore $K'_{b,j}$>3/4$K'_{d,j}$, while the steel profile must be stronger (neither yielding nor buckling) than the device: for a given interstorey drift the larger is α_j the larger are device displacements and hysteretic cycles. At this point all terms of Eq. (20) are known so, from Eq. (19) and Eq. (15) , the floor brace stiffnesses $K'_{b,j}$ can be defined (the yielding force $F'_{by,j}$ can be directly derived since the stiffness $K'_{b,j}$ and the yielding displacement $\delta'_{y,j}$ have been defined). Though in this paper the procedure is discussed referring to Eq. (18) it is important to underline that, in a general case, one can have *m* different braces for each level *j*. In fact, at the same level, each brace *i* can be characterized by its specific properties as a consequence, for example, of the geometry of the bays of the structural frame. Consequently Eq. (18) can be generalized as follows.

$$v^*_{eq,B}(D_t^*) = \frac{2}{\pi} \frac{\sum_{j=1}^{n}\sum_{i=1}^{m} \chi_{B,i} \left\{ F'_{by,j,i}\delta'_j - \delta'_{y,j,i} \cdot \left[F'_{by,j,i} + (\delta'_j - \delta'_{y,j,i}) \frac{\beta_{d,j,i} K'_{d,j,i}}{\frac{\beta_{d,j,i}}{\alpha_{j,i}}+1} \right] \right\}}{F_{S,S+B}(D_t^*) \cdot D^*_{S,S+B}} \tag{22}$$

10. **Check convergence**: one must repeat steps from 3 to 9 until the performance point of the braced structure converges to the target displacement with adequate accuracy.

5 APPLICATION ON AN EXISTING BUILD

It is well known that results from a non linear static analysis are influenced by: pushover loading profile, characteristics of the numerical models. The loading profile determines loads distribution and deformed shape of the building and, consequently, the plastic distribution of forces and displacements (interstorey drift can be strongly influenced). The most common loading profiles are: proportional to masses, proportional to first mode shape (monomodal), proportional to acceleration, multimodal. The procedure presented in the previous chapter is generally applied using a “standard” monomodal pushover where the structure is subjected to monotonically increasing lateral forces, with an invariant spatial distribution (fundamental mode based), until collapse displacement is reached. This fundamental mode based force distribution doesn’t account for higher mode contribution, which can be relevant, and therefore this limits the applicability of this approach to cases where the fundamental mode is dominant. Anyway it has to be highlighted that braces, if well designed, regularize the structure that can become strongly fundamental mode dependent. As discussed in the following has been analyzed, with a specific case study, if the use of the simple monomodal approach can be considered efficient. Therefore the proposed design procedure has been applied to retrofit

an existing r.c. frame structure (Fig. 4-5) designed to resist vertical loads only: it is a strategic building, situated in a seismic area of Italy, that has been designed and built in the 1970*s* without seismic details.

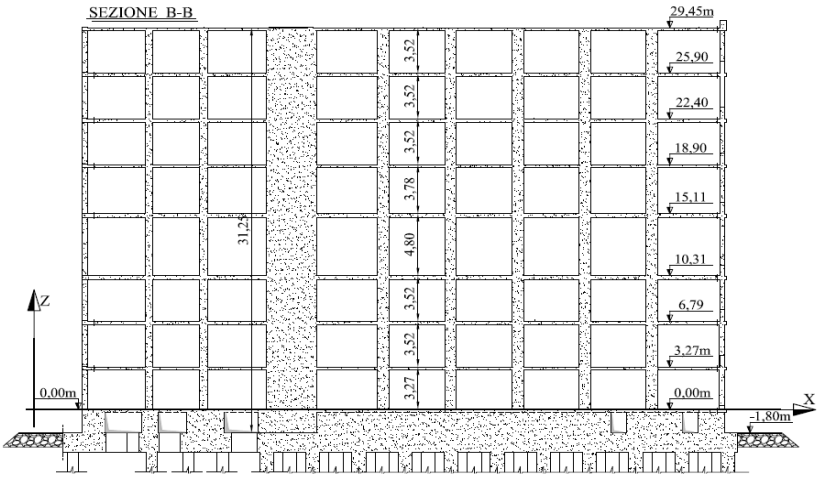


Figure 4: Longitudinal sections of the building

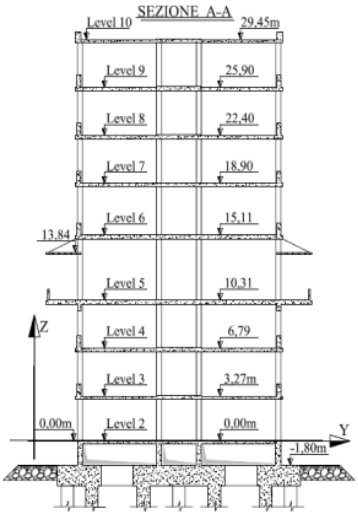


Figure 5: Transverse section of the building

For brevity, in this paper, only results from longitudinal analysis are described: the design process has been performed considering the real 3D structure. The procedure has been applied in order to retrofit the building referring to a seismic action evaluated using the technical code currently in force in Italy (*p.g.a.* 0.25g; return period 949 years). The capacity curve has been derived considering a loading profile proportional to the first mode shape. In addition both the existing structure and the retrofitted structure have been studied using the multimodal push-over (Chopra & Goel, 2002) in order to evaluate the effectiveness of the ”standard” procedure and therefore the advantages on using the monomodal pushover for such a building: in this case the effectiveness of the procedure has been confirmed and, comparing results from monomodal and multimodal pushover applied on the retrofitted structure, the use of multimodal pushover can be considered not substantial for the design process applied on this typology of building. The performance point of the existing structure in terms of base shear and top

displacement is V_S =9908 kN and $D_{t,S}$=133 mm. Then, the selected performance objective was to reduce displacement in order to avoid damage on both r.c. elements and masonry panels. Therefore the target displacement has been selected adopting the following parameters: reducing the top displacement of about 50% ($D_{t,S,targ}$=66 mm) and limiting the interstorey drift to 2‰ at whichever level. Convergence to the desired values has been obtained with three iterations and the final result (performance point, iter 3) is the base shear V_{S+B}=12105 kN, with a 19% increase with respect to the original building, and the top displacement $D_{t,S+B}$=61 mm (practically coincident with the target, see Fig. 6).

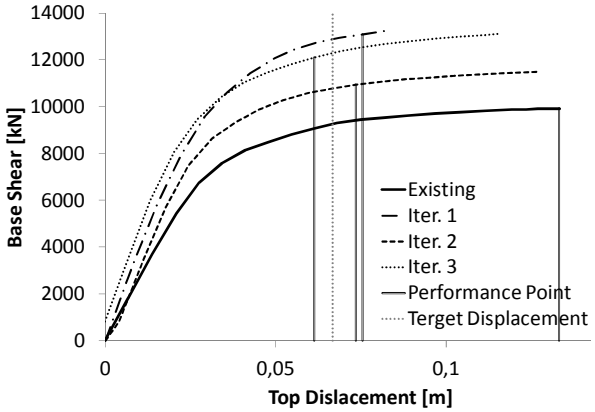


Figure 6: Capacity curves from pushover analysis along the longitudinal direction (Existing structure and braced structure at each iter from 1 to 3)

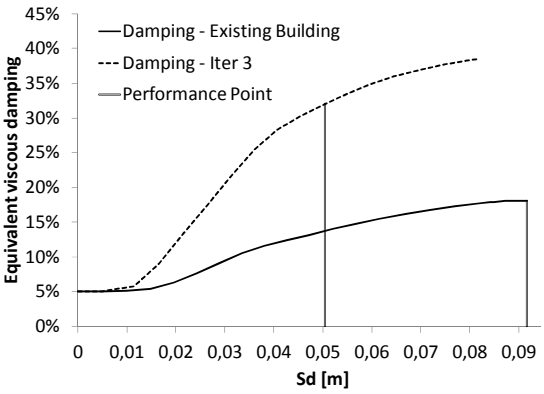


Figure 7: Variation of the total equivalent viscous damping with the spectral displacement S_d. At the p.p. $\nu_{eq,S+B}$=32% for the retrofitted structure and $\nu_{eq,S}$=14% for the existing building.

The contribution to dissipation offered by the dissipative system is ν_{eqB}=20% (ν_{eqS}=12%, ν_I=5%). In the final configuration the interstorey drift of each level has been significantly reduced to values lower than 2‰ and all the dissipative braces are in their plastic range (Fig. 8). The braced structure, if the distribution of interstorey drift is analyzed, is strongly characterized by a dominat first mode and consequently the multimodal analysis can be considered unnecessary: the two approaches differ of less than 1.5% (Fig. 9).

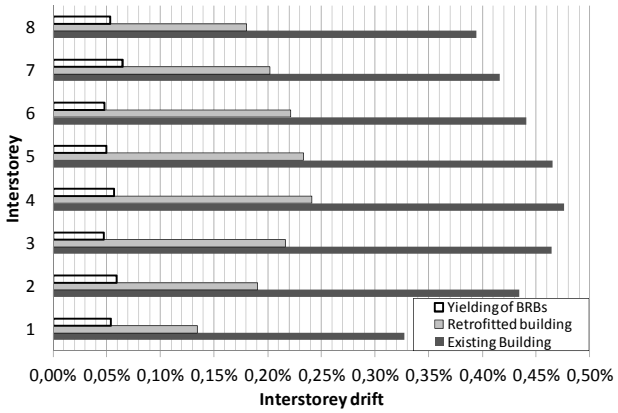


Figure 8: Interstorey drift (longitudinal) distribution for the existing building and the retrofitted building (longitudinal direction). In the graph is also indicated the drift corresponding to the yielding of the BRBs

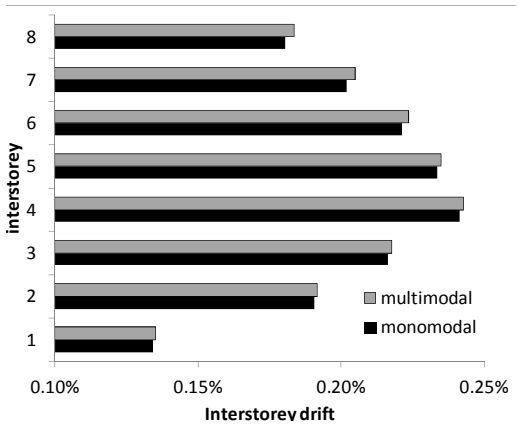


Figure 9: Interstorey drift (longitudinal) distribution in the retrofitted building obtained using the monomodal and the multimodal pushover. Differences are lower than 1,5%

6 CONCLUSIONS

A procedure for design of retrofitting of building structures using dissipative braces has been presented. The procedure, that in previous works has been applied to retrofit building up to four stories (Bergami & Nuti, 2012), has been updated with the use of the multimodal pushover and successfully applied to a structure having eight floors (30 m height). The target displacement has been determined, both in longitudinal and transverse direction, in order to limit both interstory drifts and ductility demand on existing structural elements. The final configuration obtained (the building braced along both the directions) has been tested performing pushover analyses proportional to the most relevant mode shapes (along both the longitudinal and transverse direction) of the building fully braced. Afterwards, results obtained from the application of monomodal pushover have been compared with results from multimodal pushover: the effectiveness of the procedure has been proved. Moreover, from this comparison, has been observed that, in terms of drifts and displacements, the multimodal pushover can be considered not relevant for the design procedure for dissipative braces proposed by Bergami and Nuti (2012) if it is applied on structures such as the one analyzed (midrise r.c. frame building).

REFERENCES

[1] Applied Technology Council. (1996). Seismic evaluation and retrofit of concrete buildings. Report ATC-40, Redwood City, California.

[2] Bergami A.V., Nuti C. (2013). A design procedure of dissipative braces for seismic upgrating structures. *Earthquakes and Structures,* Vol. **4**, No. 1, 85-108.

[3] Bergami A.V., Nuti C. (2011). Seismic retrofit of r.c. structures with dissipative braces, design and sustainability. fib Symposium 2011, Prague, Czech Republic.

[4] FEMA-274, (1997). "NEHRP Commentary on the Guidelines for the Seismic Rehabilitation of Buildings". Federal Emergency Management Agency Publication, U.S.A., 274.

[5] FEMA – ASCE 356 (2000). "Prestandard and Commentary for the Seismic Rehabilitation of Buildings". Washington, DC, 2000.

[6] Chopra, A. K., and Goel, R. K., 2002. Modal pushover analysis procedure for estimating seismic demands for buildings, Earthquake Eng. Struct. Dyn. 31 (3), 561–582.

COMPDYN 2013
4th ECCOMAS Thematic Conference on
Computational Methods in Structural Dynamics and Earthquake Engineering
M. Papadrakakis, V. Papadopoulos, V. Plevris (eds.)
Kos Island, Greece, 12–14 June 2013

HEURISTIC APPROACH IN STRUCTURAL STRENGTH EVALUATION AND RETROFITTING OF EXISTING BUILDINGS IN SEISMIC AREAS

Gluck N.[1], Farhat R.[1], Eid R.[1], Tzadka U.[1]

[1] Shamoon College of Engineering
Reh. Bialic 56, 84100 Beer Sheva, Israel
e-mail: mikig@sce.ac.il

{rinaf,rameid,uriz}@sce.ac.il

Keywords: Reinforced Concrete, Codes, Structural Analysis, Linear and Nonlinear FEM, Heuristic Evaluation.

Abstract. *The migration of the population, to developed areas, lead to birth of overcrowded areas with claim for residences, financial, administrative, cultural and industrial facilities. The density augmentation of the population required sophisticated solutions from the authorities to ensure adequate environmental state suited for the 21th century. Due to the huge demand of the facilities significant number of buildings must be strengthened and modified to be suitable to the new demands. This change claims increase of surfaces and storey addition. This trend leads to the hazard of the new urban agglomerations versus natural causes as flood, fire and earthquake.*

The present paper is devoted to structures which were built before the implementation of any code or obsolete ones for the seismic design. Strengthening and retrofitting of existent buildings is a major interest of the actual engineering effort to provide the suitable structures to the new demands and to be stable under seismic loads. Each seismic event is accompanied by damages that better design and execution would have prevented. In general, severe earthquakes are followed by intense research of the causes which damaged structures. In some cases the code is changed due to the short comes which were observed.

This means that each experiment including earthquakes is followed by a learning process that provides new solutions, use of new materials and new design strategies. This process must be a heuristic process according the abilities of evaluation and implementation.

1 INTRODUCTION

One of the ways to solve problems is to use a heuristic process**.** The idea to solve problems is not a new one but it was promoted by G. Polya [1] as a method of teaching mathematics at Princeton University. There is thorough link between heuristics and artificial intelligence. The former involves human involvement at each step of the solving process. Heuristics developed in various fields of activities. Jakob Nielsen [2] developed a series of guidelines to be followed during the task solving. There are a lot of domains which are prone to this process. The aim of our work is to use heuristics for the field of civil engineering with stress upon the seismic design and retrofitting of structures.

Significant example is provided by the effort to strengthen buildings (churches) before L'Aquila earthquake. In [3] Lagomarsino presents the damages of the historical buildings as consequence of the L'Aquila earthquake with detailed description of the damages of a series of buildings. Among the buildings which were damaged there were two churches that went under a strengthening process by modern techniques, such as substitution of the original timber roof with stiff r.c. slabs. Unfortunately this is not the single example where application of the codes may provoke unwanted accidents of the strengthened buildings.

Usability guidelines, or heuristics involve the existence of the problems evaluated by a certain number of evaluators to get the best solution. There are certain guidelines promoted by different experts in heuristics. For exemplification the Nielsen's 10 principles will be used. These principles are the following:

1. Match the Real World
2. Consistency and Standards
3. Help and Documentation
4. User Control and Freedom
5. Visibility and System Status
6. Flexibility and Efficiency
7. Error Prevention
8. Recognition, Not Recall
9. Error Reporting, Diagnosis, and Recovery
10. Aesthetic and Minimalist Design

During the evaluation session, the evaluator goes through the solution several times and inspects it by comparing the list of the usability principles.

In the case of seismic design civil engineers learnt to design earthquake resistant structures in time. At the actual stage typical code deals with the environmental conditions, the structure per se, the solution to be adapted to achieve the structure and the solution to retrofit an existent structure.

We get continuous updating about the seismic risk the area of interest is prone to. We get information about the faults that might become active in a certain area. Sometimes a fault reveals itself and in that case it may be too late as the seismic event already occurred such as in Haiti in 2010, in Japan 2011 etc.

The prognosis of the seismic intensity affecting a certain region must be estimated as precisely as possible. The spectral acceleration has to be indicated in the region we do design for. Erroneous assumption of this information leads to severe damages and even failure like in 1977 during the Romanian (Vrancea) earthquake where the code was built upon an acceleration spectrum which suited the Californian earthquakes with period of 0.4sec instead of 0.8-1.2 sec as it occurred during this specific earthquake. As a consequence tall buildings went under resonance during the seismic event.

The structural characteristics must be indicated according the destination and the importance of the structure to be designed or retrofitted. The destination of the designed building is in thorough link with the importance of the building. A building which has to provide housing and services immediate after the seismic event occurred is categorized as important. Such buildings must resist the seismic load without significant damages in spite the fact that the earthquake may be severe. The ability to dissipate the energy induced into the building is provided by the ductility level to which the building was designed.

Ductility abilities may be achieved through certain strategies indicated by the design recommendations of the code. Examples of increased ductility abilities belong to design strategies and control implementation.

For structures achieved from reinforced concrete special care must be placed upon achievement the concrete confination by means of closer stirrups or by applying FRP textiles by gluing procedures.

Steel structures must be carefully welded or ensembled by means of special screws to ensure the ductility abilities of the structure.

Other materials used to achieve structures are ceramics, glass, wood, aluminum, fiberglass profiles, plastics etc.

Each material must be used according the codes which have been developed based upon tests and careful analysis according the recommendations provided by the available codes.

A great step ahead was achieved in the field of structural control of structures prone to dynamic loads like wind, earthquake, blasts, etc.

Among controlled buildings the base isolated solutions have been implemented and applied for actual structures. Base isolation is not a new idea. In China it was used from ancient times as the upper structure of a building was placed on a layer of sand which, permitted its movement during earthquake excitations due to inertial forces. A range of new solutions was developed to ensure the base isolation of structures in what concerns the gap between the upper structure and its foundation. Among the best known solution it is worth to mention the use of rolls, Teflon layers, rubber cushions with and without led core, inverse pendulum, etc. Partly the codes refer to these solutions. To use them one must understand the physics behind the solution and to be able to perform the analysis which provides the solution.

On the other hand, controlled solutions may be achieved by means of devices that dissipate the energy induced into the structure and avoid the structural elements to be loaded over their strength abilities. Some of these solutions are the tuned mass dampers (TMD), the liquid tuned mass dampers, the viscous dampers, the friction dampers etc. In spite of the fact that these devices have been implemented and proved their efficiency in the case of severe earthquakes there are few code provision for their design and application.

There is still o lot of work to implement all the above specifications into reliable codes to be used for an entire range of loads which may occur due to an earthquake. We have to learn how to use the experimental data and the analysis allowable in the FEM routines. We must learn to use the results provided by such programs in order to apply them into the design process. Since the abilities of computer memories augmented to very large scales giga, terra, peta (soon) the interpretation of the results will be the main intricacy to be solved by the software users. It means that the designer must understand the data to be input into the computer and to be able to use the results in the designing process. The heuristics developed for the achievement of seismic resistant structures must be kept clear and available to the great mass of the designers whose task will be to achieve structures able to stand seismic loads. A short exemplification will clarify the principles to be used for achieving true, clear and easy use of codes and analysis results.

2 THE ENVIRONMENTAL CHARACTERISTICS

The code must provide for each area the environmental characteristics which will lead to the estimation of the loads acting upon the designed structure. The code must give the assumed peak ground acceleration which is due to occur in a specific area. Amplification phenomena have to be taken into account if there is any possibility to take place. It means that micro-zonation must be done in order to avoid unsatisfactory structural behavior of the designed or of the retrofitted structure.

The soil characteristics, at the building site have to be chosen according the existent conditions. The values to be taken into account for the determination of the seismic coefficients have to be chosen and explained thoroughly. According the intensity at the situ and the soil characteristics the acceleration spectrum is built.

The structural characteristics have to be taken into account. The importance of the building must be established carefully. Buildings are ranged according their importance, the highest coefficient is chosen for the most important building. The designer must decide the ductility of the building according the ability of energy absorption as product between force multiplied by the sway that does not damage the building

3 THE STRUCTURAL CHARACTERISTICS

The structural characteristics have to be taken into account. The importance of the building must be established carefully. Buildings are ranged according their importance, the highest coefficient is chosen for the most important building. The designer must decide the ductility of the building according the ability of energy absorption as product between the force multiplied by the sway that does not damage the building.

The response period of the structure is determined according the code provisions or by careful analysis by computer software. Usually it is compulsory to compute the fundamental period of oscillation of the structure for the static equivalent method but structural dissymmetry claims the modal method of analysis to be used.

The seismic analysis is achieved following the static analysis made by the limit state approach.

3.1 Results

The results must be carefully treated as the combination of the loads taken into account as dead, live, earthquake such as according the code provision to get the greatest load possible.

The analysis may be performed linearly or according non-linear approaches. Since new methodologies have been proposed such as the performance analysis through the pushover behavior of the structure superposed to the acceleration spectrum exciting the structure the capacity vs. demand is promoted. The structure is judged according the difference between its capacity, illustrated by the pushover ability and the demand visualized by the acceleration spectrum normalized to force. Great attention must be paid when this method is used to take into account the entire range of loads which act upon the building.

4 RETROFITTING OF EXISTENT STRUCTURES

4.1 Generalities

Existent structures must be maintained and in majority of cases must be strengthened to resist the prognosis of the loads which might affect them during their service life. The design of these buildings took into account mainly the loads of gravity which act vertically. The ho-

rizontal loads and the loads which affect dynamically these buildings were not been taken into account. It means that this kind of loads might affect this building in a very severe manner.

The categories of buildings which have to be strengthened refer to residential, public and industrial ones. Among these buildings there are some which are considered "Historic Monuments" and their architecture is characteristic to the town and this value must be protected to keep the historical heritage of the area. The aspect of these buildings must be preserved and the strengthening has to be achieved without any change that will affect the architecture externally or internally. The main solutions which are recommended refer to use same kind of materials which have used initially or to strengthen elements by injection of efficient gluing products (epoxy, or other). Steel profiles, FRP textiles must be avoided mainly due to aesthetic reasons. The range or the mass distribution of this kind of buildings must be maintained in spite of any advantage that some change may ensure.

Building which are not considered "Historic Monuments" may be completed by annexes which are added horizontally or vertically, by supplementary areas or stories. This solution is considered in Israel a win win situation since the entrepreneur achieves the work with money he obtains from selling the supplementary flats he builds. It means that the investment is covered by the money obtained by selling the added residences.

4.2 Rehabilitation requirements

According most of the codes, dealing with the rehabilitation of existing buildings a series of requirements have been established to be successful in the ensuring the features of the buildings to resist seismic effects. The design and execution of the retrofitting is the result of a lengthy learning process - a heuristic approach with a range of requirements to achieve a resistant, efficient and esthetic structure.

The main requirements refer to:

- Rehabilitation methods
- Analysis procedures
- Rehabilitation procedures
- General design requirements
- Foundation and geologic hazards
- Acceptance criteria

Each stage of the documentation must follow the principles of heuristics for achieving the task of clarity and efficiency (see table No. 1)

Principles	
1. Match the real world	The necessity to execute the retrofitting should be clearly explained and motivated
2. Consistency and standards	The physical phenomena which may occur and their link to the actual codes
3. Help and documentation	Clear documentation and motivation must be emphasized
4. User control @ Freedom	The multiple choices which were made by the designer should be presented and motivated
5. Visibility and system status	The stages of the retrofitting should be thoroughly defined
6. Flexibility and efficiency	Documentation should be elaborated for frequent use of certain solutions
7. Error prevention	Error prevention must be ensured
8. Recognition not recall	All information should be available
9. Error reports. Diagnosis and recovery	Error that occurred must be described
10. Aesthetic and minimalist design	The design should be simple and straight

Table 1: The principles of the heuristic approach for structural retrofitting

The application of the upper principles must achieve a very straight design and a project which enables the authorities to get a very clear image about the stage of the work and to avoid faults which can lead to damages or to undesired structural behavior.

5 RETROFITTING BY TAMA 38

TAMA 38 is the methodology which was developed and accepted in Israel to achieve the retrofitting and strengthening of structures built before 1980 according codes, almost neglecting the horizontal dynamic effects. Since majority of the population live in such buildings the risk of collapse of these buildings is high leading to economic and human life loss in case of an earthquake. The development of new approaches and production of new efficient materials together with the economic needs lead to special strengthening solutions. This approach is feasible in areas were the need of hosing is high. The TAMA 38 is not implementable in areas where there is no housing need. In these areas the retrofitting must be supported by money from taxes and seldom will consist from adding any structural annexes. The strengthening solutions will be simpler and more efficient.

5.1 Environmental conditions

The strengthening process will take into account the seismic intensity of the area the structure is placed. The expected seismic intensity is provided by the code and it may be refined by the use of the micro-zoning maps. Besides the seismic intensity the designer must be aware about the geological characteristics of the area which can provide information about the amplifications that may occur during seismic excitations in a certain area.

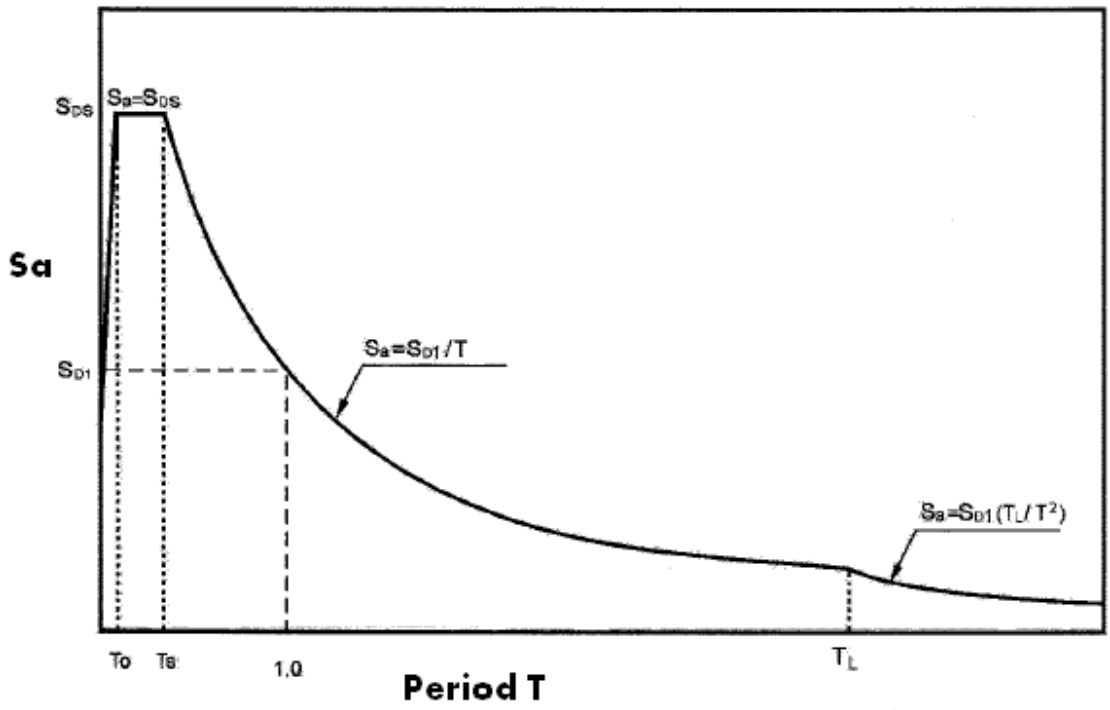


Fig. 1 The Spectral Acceleration Response

5.2 The structural characteristics

The main characteristic of an existent structure is its period of oscillation. Since majority of the retrofitted structures have less than 10 storey the main energy is introduced into the structure by means the first mode of oscillation through the fundamental period of vibration. This value can be approximately established only due to limited knowledge of the materials and both the initial design and the modification done along the structures' life. Destructive phenomena as concrete carbonation and steel corrosion change this characteristic either.

According recent research and studies the importance of ductile structural behavior was emphasized and design strategies changed accordingly. In case of reinforced concrete due to closer stirrups concrete behaves as a confined entity with increased stress – strain abilities. But in case of existent buildings we cannot take into account abilities of ductility (see fig. 1).

For existent buildings we cannot take into account any information about the used material (Fig. 2) we can assume and check the structural behavior by using micro-tremors. Since

many of these buildings suffered severe loads and modification during their life time the model we use must be thoroughly tuned according the actual structural state.

5.3 The structural retrofitting

According the recently developed approach – the structural performance analysis – the structural capacity and the demand due to the load have to be compared. The capacity is established through the pushover approach while the demand is defined by changing the acceleration spectrum of the area into a spectral force – displacement diagram. The intersection between the capacity and the demand curves defines the performance point and provides information about the structural stability. This procedure can be applied by means of the finite element method. One of the routines which may be applied for this analysis is SAP2000 developed at Berkeley California.

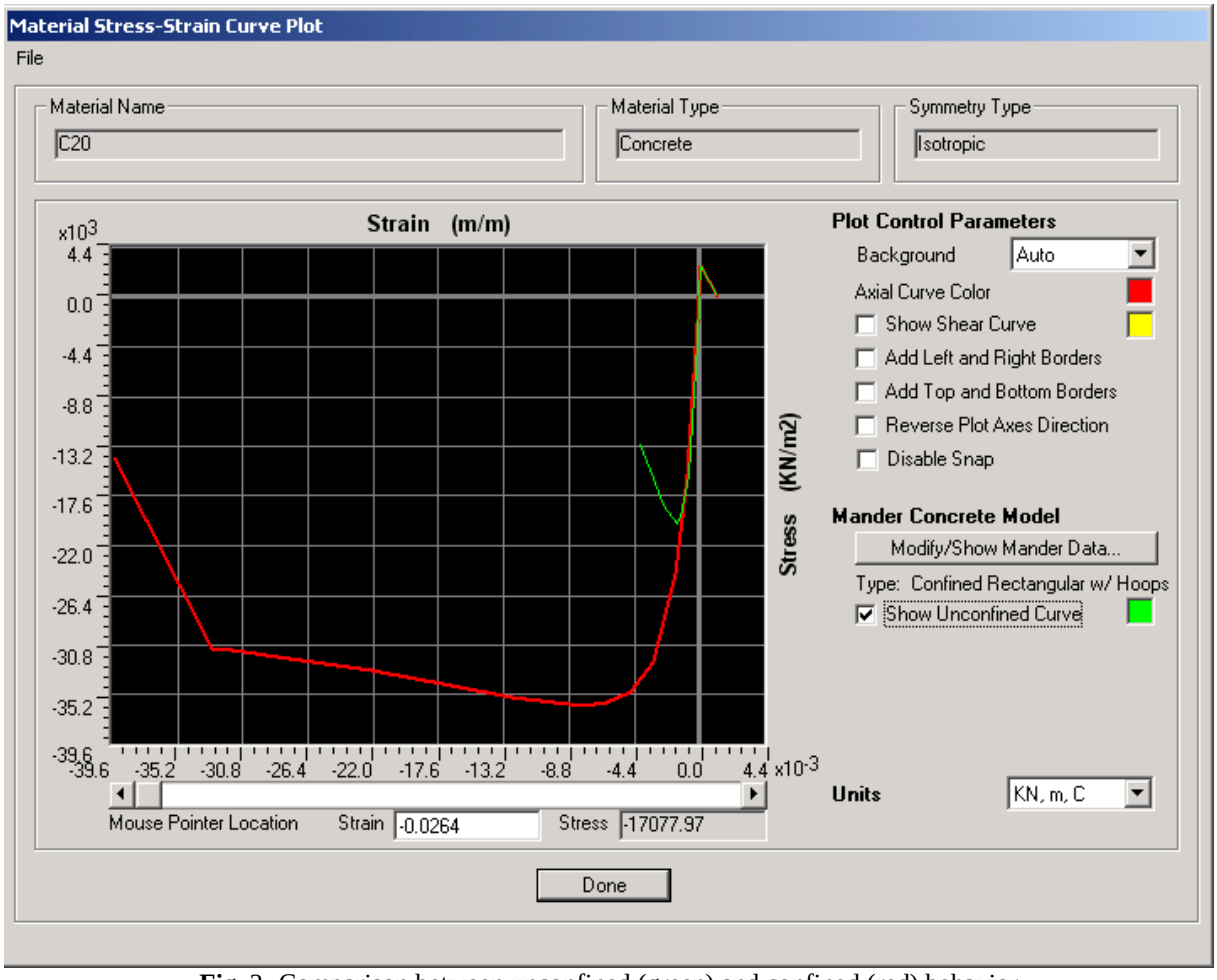


Fig. 2- Comparison between unconfined (green) and confined (red) behavior

5.4 Retrofitting Case

A specific case will be treated to exemplify the strengthening of a residential building. The building presented in Fig. 3 is a typical building built before 1980. It was designed as a

framed five storey structure without proper rigidity against horizontal loads. The frame was made of reinforced concrete without any confination at the zones prone to turn into plastic hinges.(see Fig.3)

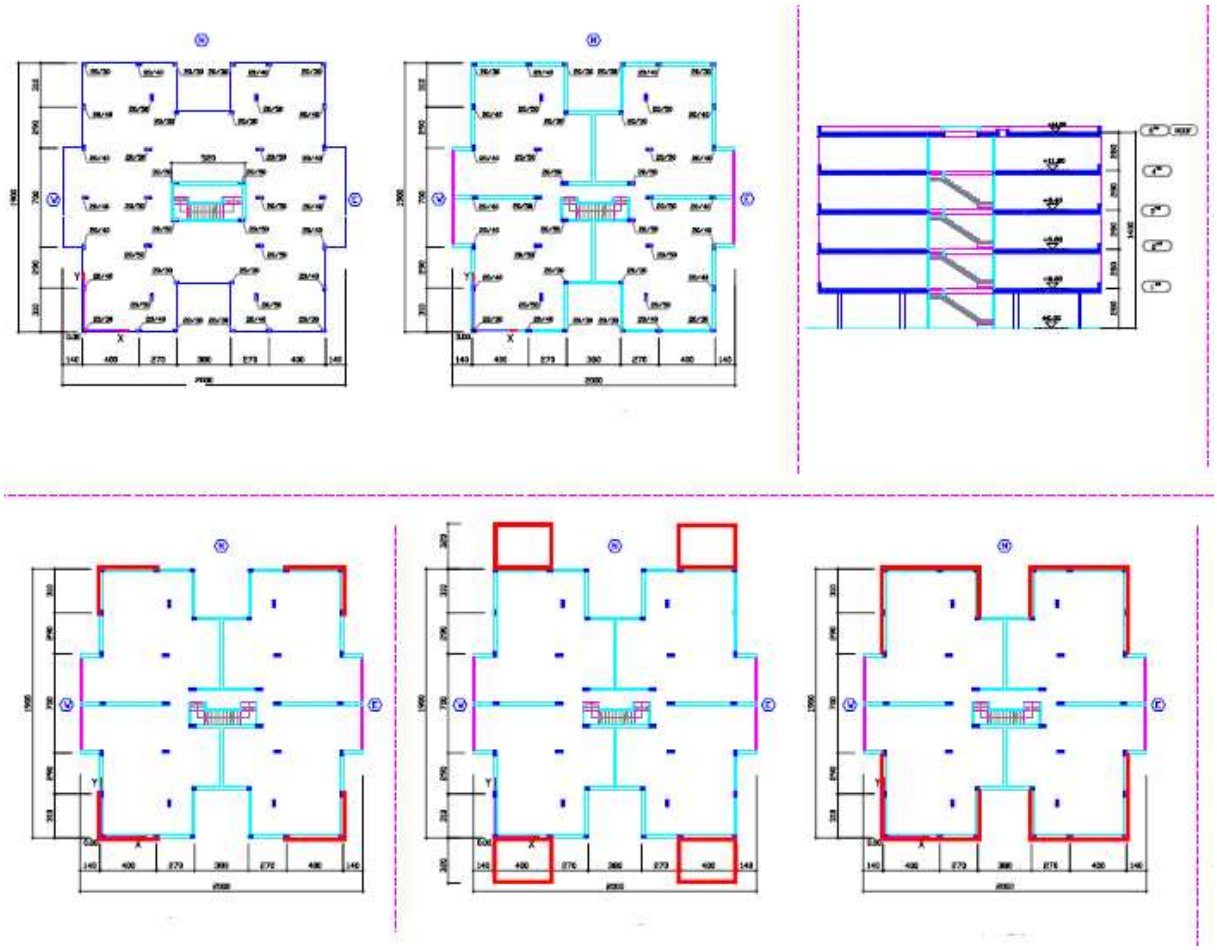


Fig. 3 The Retrofitting Case. Three Solutions of Strengthening

Three strengthening solutions have been indicated in Fig. 3:

1- Partial R.C. shear wall added at the corners of the structure
2- Four R.C. boxes built from shear walls
3- R.C. shear walls cast along the perimeter of the building.

The strengthening walls have been reinforced according to confining demands to increase the ductility of the entire structure.

The analysis for the initial structure and for the strengthened solutions was made by means the SAP2000 routine according the performance method. One of the strengthened solutions is visualized in Fig. 4.

The initial structure, according the performance analysis proved to be unsuited for the considered excitation with no performance point to show the intersection between the capacity and the demand. This analysis leads to the conclusion that it is necessary to strengthen the structure against the horizontal load which according the statistics may occur soon. The result of the performance analysis is given in Fig. 5 where it may be seen the fact that the demand is greater than the structural capacity. Fig. 6 stands for the analysis of one of the strengthened solutions. As result of the analysis one may remark that the demand and the capacity curves intersect at the performance point proving the stability of the strengthened structure.

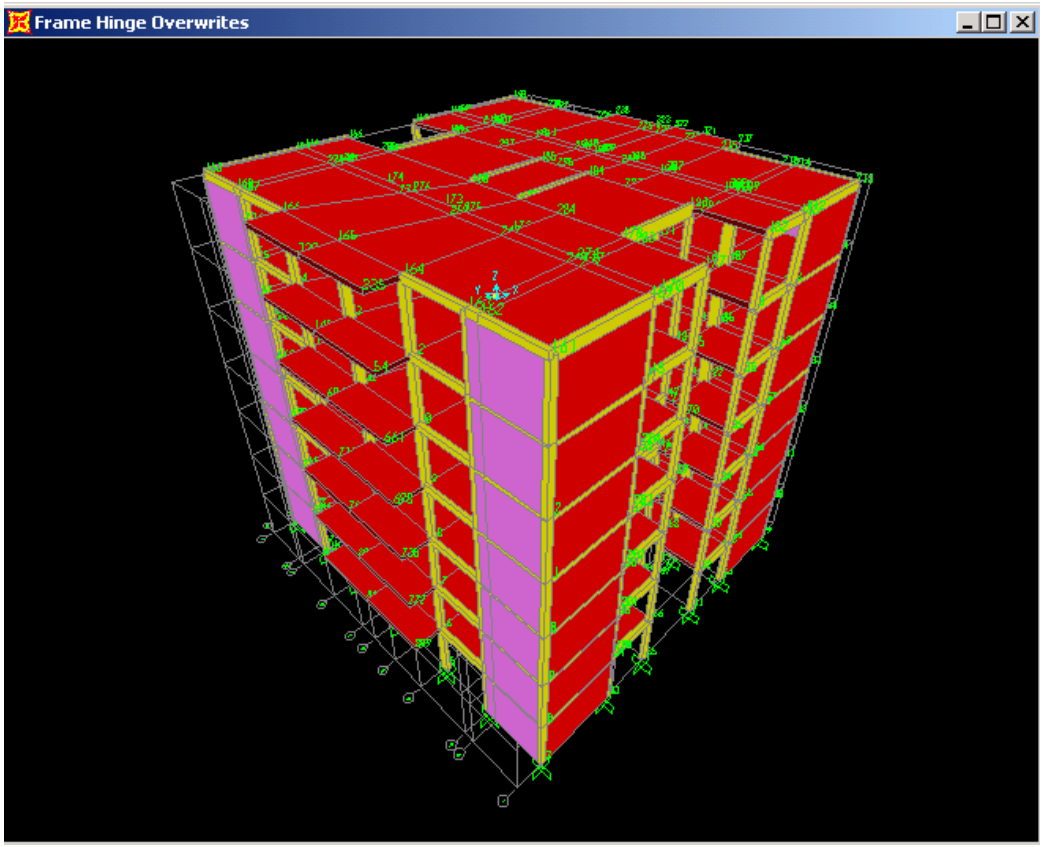


Fig. 4 Solution with shear walls at the corners

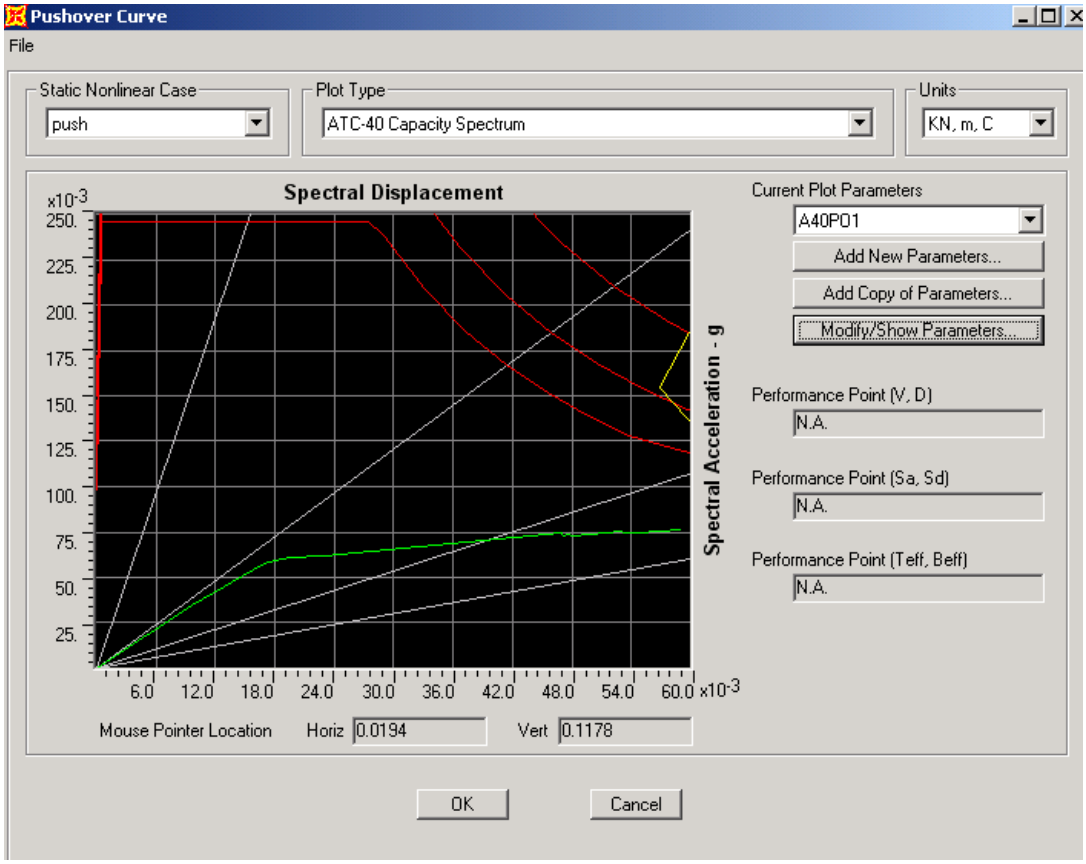


Fig - 1Performance analysis of the initial structure

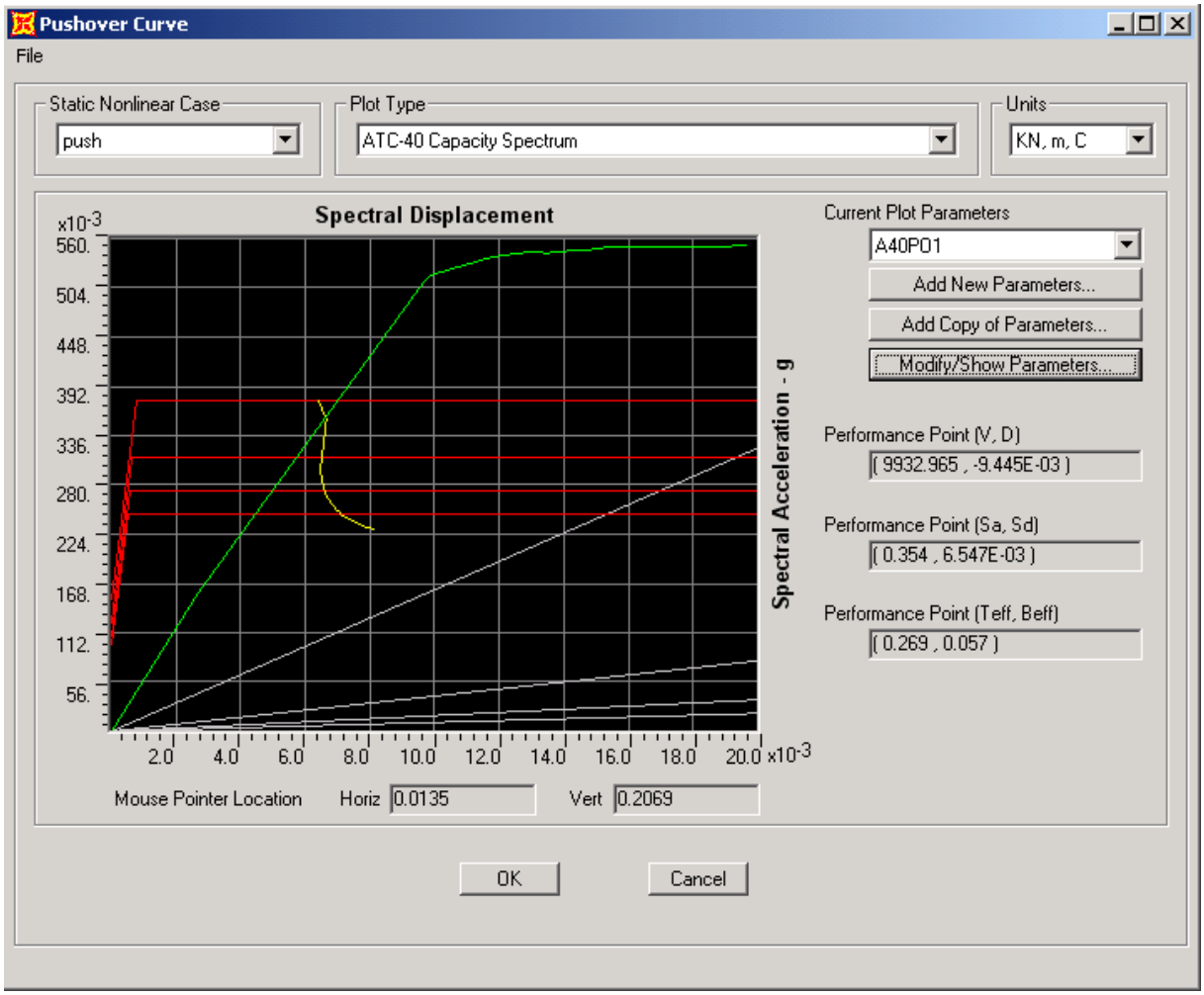


Fig. -6 The strengthened solution performance analysis

The performance point indicates the values of the base share (V= 9932kN), the top displacement (D=9.45mm), the effective oscillation period of the structure (T=0.269sec) and the considered effective damping (B=0.057).

This method is defined as NLSA – Non-Linear Static Analysis and gives an indication about both the behavior of the initial un-strengthened structure and the performance of the structure to be strengthened.

More exactly, the behavior of these two stages may be visualized by means of the R.H.A. (Response History Analysis) which is a lengthy and intricate process with results that are more exact but require intense search. This analysis is required in case of the implementation of a certain solution which was chosen by means of the N.L.S.A.

6. STRUCTURAL RETROFITTING BY THE HEURISTIC APPROACH

Heuristic approach means that the optimal solution is found by means of a learning process. This is the reason that huge efforts are made to improve the existent codes and the analysis methods. Books, scientific papers, conferences aim improvements in the design process. Each major destructive event, natural or manmade is followed by intense research to study the causes and to find the best defense against the loss. The topics of most of the conferences refer to:

- Lessons from Damaging Earthquakes
- Engineering Seismology
- Geotechnical Earthquake Engineering
- Dynamic Analysis of Structures and Seismic Codes
- Experimental Mechanics, Control of Structures and Structural Health Monitoring
- Seismic Retrofit of Structures and Protection of Historic Buildings
- Societal, Economical and Managerial Aspects

Heuristic approach leads to the optimal solution by conducting an evaluation of the proposed solution. A series of principles have been defined and their application leads to the project improvement for finding the best solution. Some of the principles were defined by Jakob Nielsen. These principles may be very general for a specific field like structural engineering or struchese principles may be very general for a specific field like structural engineering or structural retrofitting the evaluation must be more specific. The main usability problems may refer to:

- The definition of the expected earthquake
- Closeness to the active fault (distance to the Hypocenter)
- The geological characteristics of the soil
- The structural features of the analyzed building
- Use of the existent codes or proposals of improvement
- Soil Structure Interaction issues.
- Etc
- Not last the esthetics of the new or the retrofitted buildings.

7. CONCLUSIONS

This method is not new, it leads to a solution during a learning process.

The found solution may be analyzed by evaluators while the shortcomings can be reveled.

Evaluators can belong to various fields of activity but their findings can lead to significant improvements.

Heuristics is based upon experience, artificial intelligence, brain storming for solving the problem.

The need of the best solution justifies use of a variety of strategies, heuristics among them.

8. REFERENCES

[1] G. Polya, How to Solve It, Princeton University Press 1945
[2] J. Nielsen, Usability Engineering, Morgan Kaufmann, San Francisco, 1993
[3] S. Lagomarsino, Damage assessment of churches after L'Aquila earthquake(2009), Bull. Earthquake Eng. (2012), Springer
[4] ASCE/SEI 41-06, Seismic Rehabilitation of Existing Buildings, ASCE 2007
[5] SI-413, Seismic Design of Structures, the Standards Institution of Israel.
[6] SI-2413, Guidelines for Seismic Resistance Assessment and for Strengthening of Existing Structures, the Standards Institution of Israel.

COMPDYN 2013
4th ECCOMAS Thematic Conference on
Computational Methods in Structural Dynamics and Earthquake Engineering
M. Papadrakakis, V. Papadopoulos, V. Plevris (eds.)
Kos Island, Greece, 12–14 June 2013

EVALUATION OF DAMAGE IN REINFORCED CONCRETE COLUMNS UNDER BIAXIAL LOADING

Hugo Rodrigues[1,2*], António Arêde[3], Humberto Varum[1], Aníbal Costa[1]

[1] Civil Engineering Department, University of Aveiro, Portugal
hrodrigues@ua.pt, hvarum@ua.pt, agc@ua.pt

[2] Faculty of Natural Sciences, Engineering and Technology
Oporto Lusophone University

[3] Civil Engineering Department, Faculty of Engineering, University of Porto
aarede@fe.up.pt

Keywords: Column, Experimental study, Biaxial bending, Damage, Damage index.

Abstract. *The present study is focused on the analysis of damage evolution observed in an experimental campaign on 24 RC columns tested under uniaxial and biaxial loading. The observed damage evolution and damage states are compared for uniaxial and biaxial loading conditions. The test results show that for biaxial loading conditions each damage limit state occurs for lower drift demands when compared with the corresponding test for uniaxial demand (a reduction of 50–75% was found). The deformation demand associated with each damage state is compared with performance objectives proposed in international guidelines. Finally, and based on the philosophy of the Park & Ang uniaxial damage index, two new expressions are proposed for the evaluation of damage in RC elements under biaxial loading. These expressions are calibrated against the experimental results obtained with the tests on columns based on a scoring process to choose the best DI estimator.*

1 INTRODUCTION

The response of reinforced concrete (RC) members loaded by biaxial bending moment reversals with constant or variable axial force is recognized as an important research topic for building structures in earthquake prone regions. This is justified by, at least, the two following major reasons: i) the actual behavior of RC building columns under earthquake actions is strongly related to the random characteristics of the seismic event, the building's three-dimensional (3D) response characteristics and structural irregularities; ii) the biaxial bending moment cyclic demands applied to a given RC column tend to reduce its capacity and to foster the stiffness and strength deterioration process during successive load reversals [1, 2].

However, experimental research work on the inelastic response of RC members under compression axial force and biaxial lateral cyclic bending loading conditions is currently very limited, which may be justified by the uncertainties concerning the relation and combination of the two orthogonal horizontal load paths, as well as the complexity of the experimental set-up required to perform appropriate tests. Consequently, current knowledge on the inelastic response of RC columns under biaxial cyclic moments is still very much behind the present understanding of the 1D cyclic bending behavior with compressive axial load [1, 3-5].

In general, most research findings agree that, besides the expected significant influence of axial loads on the hysteretic response of columns, the 2D transversal load cycles are responsible for increasing the stiffness and strength degradation, when compared to the 1D response. In addition, the failure mechanism of RC columns is found to be highly dependent of the load path, which greatly affects both the ductility and energy dissipation capacity of the columns. On the other hand, there is some experimental evidence that plastic hinge lengths tend to be stable at around their theoretical values and are not greatly affected by 2D loading [1].

The present study is focused on the analysis of damage evolution observed in an experimental campaign on 24 RC columns tested under uniaxial and biaxial loading. The observed damage states are compared for uniaxial and biaxial loading conditions. The deformation demand associated with each damage state is compared with proposed performance objectives in international guidelines (FEMA 356 [6] and VISION 2000 [7]). Finally, analytical expressions based on the Park & Ang damage index [8, 9] are proposed and their accuracy in estimating damage is tested by a comparison with the observed experimental results.

2 EXPERIMENTAL CAMPAIGN

An experimental campaign was carried out on 24 RC columns, tested under uniaxial and biaxial cyclic loading. The specimens consisted of RC columns built as a cantilever cast in a heavily reinforced foundation. The columns were subjected to a constant axial load and cyclic lateral actions under displacement controlled conditions. The general characteristics of the specimens and testing conditions are summarized in Figure 1 and Table 1.

For each column specimen test, the following general designation "PB$$-N##" was adopted, where:

- $$ takes the value "01" for uniaxial test on the strong direction (X direction), the value "02" for uniaxial tests on the weak direction (Y direction) and the value "12" for biaxial tests;
- ## represents the reference number of the column specimen.

A more detailed description of the columns' geometry, material properties, reinforcement details and test results is reported in [10]. The materials used in the specimen design phase were regular concrete, (see compressive strength in Table 1). These values are below than the expected ones for to the ordered concrete, but this fact was duly taken into account in the re-

sult analysis so as to not affect the main objectives of the present study. The reinforcement presents a mean yielding strength of 450MPa and ultimate strength around 477MPa.

In order to characterize the response of the column specimens, cyclic lateral displacements were imposed at the top of the column with steadily increasing demand levels. For the biaxial tests four different patterns for the demands history were considered, namely one in which the displacement cycles are applied alternately in the two horizontal directions (cruciform path), one with an expanding rhombus shape, one expanding square centred in the origin and finally a circular load path.

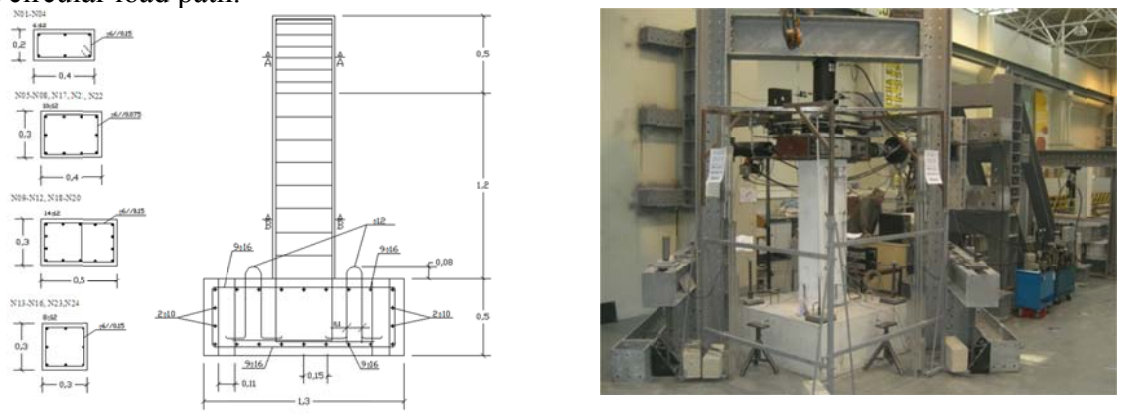


Figure 1 – Testing setup: a) RC column specimen dimensions and reinforcement detailing; b) General view of the testing set-up

Three cycles were repeated for each lateral deformation demand level. This procedure allows for the understanding of the column's behaviour and a comparison between different tests. It provides information for the development and calibration of numerical models; in this case, the following nominal peak displacement levels were considered in the directions of loading (x and y) - (displacement in mm, and corresponding drift in percentage): 3, 5, 10, 4, 12, 15, 7, 20, 25, 30, 35, 40, 45, 50, 55, 60, 65, 70, 75, 80 [10, 11]. For all the tests, the first branch of the load path is imposed in the direction (X) of the column.

Due to the large number of tests, only an example of the global results are presented in terms of shear-drift curves (along the X and Y axes) in Figure 2, but analysis of the results for the complete testing program [10] yields these main findings:

- For columns tested with the same axial load ratio, the initial column stiffness in each directions was not significantly affected by the biaxial load path;
- As expected in the uniaxial tests, the shear-drift curves showed four main branches, corresponding to pre-cracking response, post-cracking until the reinforcing steel yields, a plateau or post-yield hardening zone, and a softening phase. However, in the biaxial tests the plateau tended to be shorter and the softening was more pronounced, i.e., a more abrupt decay of the column strength was observed with increasing lateral deformation demands;
- As expected, the maximum strength values in one specific direction of the columns were lower for all biaxial tests compared with those for the corresponding uniaxial tests. Biaxial loading induced a 20–30% reduction in the maximum strength of the columns in their weak direction, Y, and an 8–15% reduction in the stronger direction, X;
- The ultimate ductility was significantly reduced in columns subjected to biaxial load paths;

- The strength degradation was practically zero in the first loading cycles, increasing after displacement ductility demands of about 3. From the strength degradation analysis, more pronounced strength degradation was observed for biaxial tests when compared with the corresponding uniaxial tests.
- It was observed that the equivalent global damping for columns tested biaxially is clearly dependent on the load path. Comparing the results obtained for uniaxial and biaxial load paths, the cruciform and rhombus paths present similar equivalent global damping. However, the quadrangular and circular paths present higher levels of damping when compared to that obtained for similar demands in the uniaxial tests. For example, for ductility factor of 6 in the columns tested under uniaxial load conditions an equivalent damping of around 20% was reached, while for the quadrangular load path it was reached an equivalent damping of approximately 30% [5].

Table 1 – Specimen specifications and loading characteristics

Series	Column	Cross-Section Dimensions [cm x cm]	f_{cm} [MPa]	N [kN]	ν $N/(A_c \cdot f_{cm})$	Displacement path type
1	PB01-N01	20 x 40	48.35	170	0.04	Uniaxial Strong
	PB02-N02					Uniaxial Weak
	PB12-N03					Cruciform
	PB12-N04					Rhombus
2	PB01-N05	30 x 40	21.40	300	0.12	Uniaxial Strong
	PB02-N06					Uniaxial Weak
	PB12-N07					Rhombus
	PB12-N08					Quadrangular
	PB12-N17		36.30	510		Circular
3	PB01-N09	30 x 50	24.39	300	0.08	Uniaxial Strong
	PB02-N10					Uniaxial Weak
	PB12-N11					Rhombus
	PB12-N12					Quadrangular
	PB12-N18		36.30	440		Circular
4	PB01-N13	30 x 30	21.57	210	0.1	Uniaxial
	PB12-N14					Rhombus
	PB12-N15					Quadrangular
	PB12-N16					Circular
5	PB12-N19	30 x 50	43.14	300	0.045	Rhombus
	PB12-N20			600	0.09	Rhombus
6	PB12-N21	30 x 40	43.14	620	0.12	Rhombus
	PB12-N22					Quadrangular
7	PB12-N23	30 x 30	36.30	650	0.2	Rhombus
	PB12-N24					Quadrangular

f_{cm}: Mean concrete compressive strength

N: Axial load

$\nu = N/(A_c \cdot f_{cm})$: Axial load ratio

A_c: Area of the column cross section

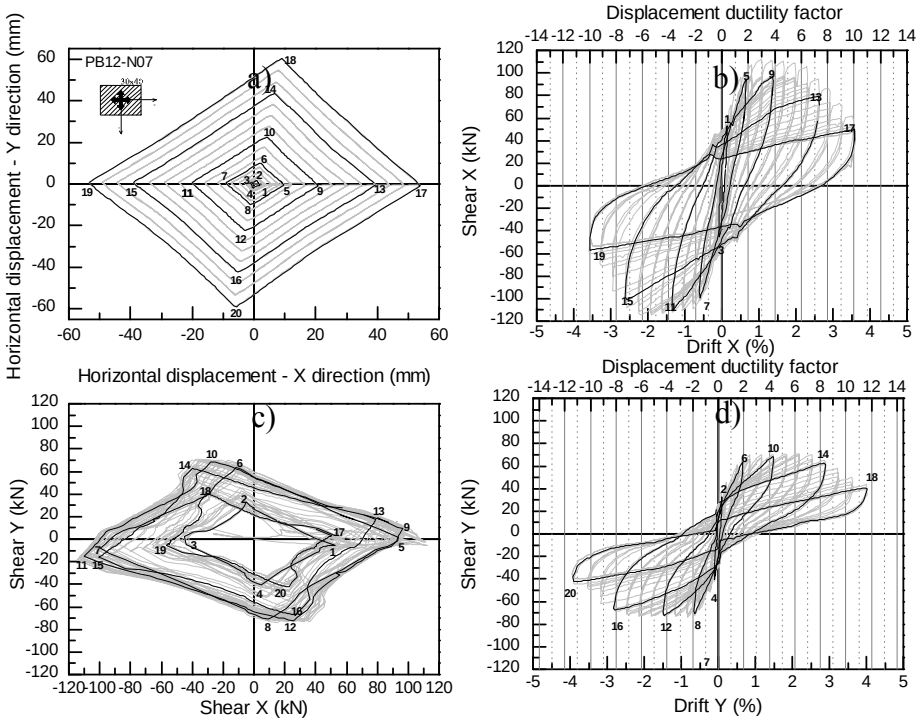


Figure 2 –Global results of rectangular column PB12-N07 for rhombus load path

3 BIAXIAL DAMAGE INDEX

The structural damage induced by earthquakes can be quantified in order to assess the structure relative to a pre-defined set of limit states [12].

Damage indices (DIs) are generally divided into two categories: local and global. Local indices are calibrated for a specific structural member. Global indices, on the other hand, are used to predict the failure of a complete structure, and are usually computed as a weighted combination of local damage indices of individual members [13].

A good damage assessment method should have general applicability, i.e., it should be valid for a variety of structural systems; it should be based on a simple formulation, be easy to use and generate easily interpretable results [14, 15].

Damage indices can be classified as cumulative or noncumulative. Noncumulative indices relate the state of damage to peak response quantities and do not account for cyclic loading effects. Cumulative indices include part or all of the loading history to predict the capacity reduction due to cyclic repetitive loading [13]. Different authors have performed extensive reviews of the DIs proposed in the literature [16-19].

The formulation used in this study for the damage index estimation is based on the methodology proposed by Park & Ang [9]. In the following section, this index and the corresponding results for the columns tested uniaxially are presented. Also, different combinations of the original Park & Ang methodology are adopted and applied to columns tested biaxially.

3.1 Original Park & Ang damage index

The damage index (DI) proposed by Park & Ang [8, 9] is defined by a linear combination of the normalized maximum deformation and the normalized dissipated hysteretic energy resulting from cyclic loading. The Park & Ang DI is therefore expressed by:

$$DI = \frac{d_{max}}{d_u} + \beta \frac{\int dE}{F_y \cdot d_u} \quad (1)$$

where d_{max} is the maximum displacement of the structural member, d_u is the ultimate curvature displacement, $\int dE$ is the dissipated hysteretic energy and F_y is the yielding strength of the structural member; β is a degradation parameter which represents the influence of cyclic response on column damage and can be estimated with empirical expressions based on structural parameters. The damage index typically ranges from 0 to 1, although the unitary upper bound is just a conventional threshold based on the assumption that total damage (failure) is reached when DI ≥ 1.

Several empirical expressions based on experimental results can be found in the literature to estimate the strength degradation parameter (β). A typical value of 0.05 is often adopted [20]. Expression (2) was proposed by Kunnath et al. [21] and is one of the most used expressions to estimate the parameter β.

$$\beta = 0.9^{100e\rho_w}(0.37\ max\{\nu; 0.05\} + 0.5.(\omega_t - 0.17)^2) \quad (2)$$

where ρ_w is the volumetric confinement ratio (volume of closed stirrups divided by the volume of confined concrete core), υ is the normalized axial stress (taken as positive for compression), and ω_t is the mechanical ratio of tensile longitudinal reinforcement.

Concerning the ultimate deformation capacity, some expressions have been proposed based on experimental tests performed up to failure on beams and columns. Park et al. [8] suggested expression (3) to estimate the ultimate displacement. According to the study performed by Fardis et al. [19], it was concluded that this equation leads to the best agreement of the Park & Ang index with several experimental results analyzed.

$$R_u(\%) = 1.958t\left(\frac{l}{d}\right)^{0.93} \cdot \rho^{-0.27} \cdot \rho_w^{0.48} \cdot \nu^{-0.48} \cdot f_c^{-0.15} \quad (3)$$

$$R_u(\%) = \frac{\delta_u}{l};\ \rho = \rho_l \cdot \frac{f_y}{f_c};\ \nu = \frac{N}{b \cdot d \cdot f_c} \quad (4, 5, 6)$$

$R_u(\%)$ is the ultimate rotational capacity (in percentage); δ_u is the ultimate horizontal displacement capacity; $\frac{l}{d}$ is the shear span ratio; ρ is the normalized steel ratio; ρ_l is the volumetric ratio of longitudinal steel; ρ_w is the confinement ratio (in percentage and taken as 0.4% if ρ_w < 0.4%); ν is the normalized axial stress (taken as 0.05 if ν < 0.05); N is the axial load (in kN); b is the cross-section width; d is the effective depth of the cross-section; f_c is the concrete strength (in kPa); and f_y is the yielding strength of steel reinforcement (in kPa).

In order to establish a correspondence between the calculated DI values and the experimentally observed damage, Table 2 presents the DI ranges for each damage degree, based on post-earthquake damage reports [14].

Table 2 – Calculated damage index vs. observed damage

Damage inspection		Calculated local damage index
Degree of damage	Physical appearance	
Collapse	Total or partial building collapse	>1.00
Severe	Extensive crushing of concrete; disclosure of buckled reinforcements	0.75–1.00
Moderate	Extensive large cracks; spalling of concrete in weaker elements	0.35–0.75
Minor	Minor cracks throughout building; partial crushing of concrete columns	0.10–0.35
Slight	Sporadic occurrence of cracking	0.00–0.10

3.2 Application of the Park & Ang damage index to the uniaxial test results

The Park & Ang DI was computed from the uniaxial test results using expressions (2) and (3) to estimate β and the ultimate displacement d_u, respectively, for each direction of RC columns. The obtained results (for each direction) are summarized in Table 3.

Table 3 – Estimated parameters for RC column damage index calculations

Column	Geometry [cm x cm]	direction	β	δ_u *(mm)*
PB01-N01	20x40	Strong (X)	0.038	92.94
PB01-N05	30x40	Strong (X)	0.047	80.22
PB02-N06	30x40	Weak (Y)	0.033	142.44
PB01-N09	30x50x	Strong (X)	0.038	73.46
PB02-N010	30x50	Weak (Y)	0.038	120.56
PB01-N13	30x30	Strong (X)	0.043	108.84

The results are plotted in Figure 3 in terms of DI evolution during the cyclic tests. For each DI curve, the drift value corresponding to each damage state observed during the tests is plotted with a specific marker, which can be compared with the ranges of damage degree described in the previous section.

Based on the results obtained in terms of DI evolution (and associated damage description) for the six columns uniaxially tested, it can be concluded that good agreement is found between DI quantification and the physical damage observed in the tested columns.

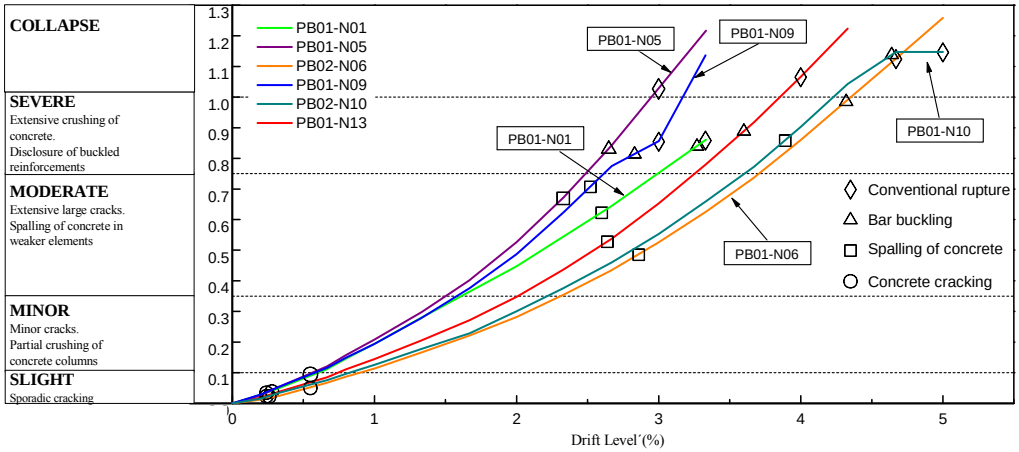


Figure 3 – Damage index evolution for uniaxial tests

3.3 Damage index for RC columns under biaxial loading conditions

As discussed previously, RC elements biaxially loaded go through given damage states for earlier levels of drift demand when compared with uniaxially loaded elements. Since the damage indices for RC elements available in the literature (such as the Park & Ang index, for example) were mainly developed and calibrated for elements under uniaxial loading conditions, this study focused on the adequacy of recent proposals of DI formulations for columns under biaxial loading, including also new formulations proposed by the authors of this paper.

All these proposals are based on the philosophy of the original Park & Ang DI model, i.e. the combination of one component for the maximum deformation demand with another for the dissipated energy. The proposals are validated against test results of columns biaxially loaded and their accuracy is discussed concerning the representativeness of damage evolution of RC elements under biaxial loading.

Expressions 7 to 10 for the evaluation of the DI of RC columns under biaxial loading ($DI_{biaxial}$) were previously studied by Qiu et al. [22]. Thus, the present study focus on the assessment and comparison the DIs given by those expressions as well as by three other expressions (11) to (13) herein proposed. In all these expressions, $DI_{biaxial}$ is the biaxial damage index, DI_x and DI_y refer to the damage indices calculated for each independent direction, E_x and E_y are the cumulative dissipated energy calculated for each independent direction, and λ is a constant parameter experimentally calibrated.

Note that in expression (13), the $DI_{biaxial}$ value is based on the calculation of the resultant displacements and total energy, rather than the sum of DIs for each direction. Thus, for each step the maximum resultant displacement ($d_{max,res}$) is calculated and, for this resultant direction, the ultimate displacement ($d_{u,res}$) and the equivalent resultant yielding force ($F_{y,res}$) are estimated. For each step, the total energy is simply calculated as the sum of the dissipated energy associated with each direction.

The $d_{u,res}$ and $F_{y,res}$ values (for each analysis) are calculated for the loading direction (α), based on a resultant interaction curve with an assumed shape. Four different shape types were tested for this curve, namely one linear, two elliptical and one parabolic, as depicted in Figure 4. From the four curves studied, the strategy based on the parabolic one gives the best results, and so this surface was adopted for the comparisons developed in the next section.

$$DI_{biaxial} = DI_x + DI_y - \lambda \cdot min(DI_x, DI_y) \quad (7)$$

$$DI_{biaxial} = max(DI_x, DI_y) + \frac{E_x \text{ or } E_y}{E_x + E_y} \cdot min(DI_x, DI_y) \quad (8)$$

$$DI_{biaxial} = max(DI_x, DI_y) + \frac{DI_x \text{ or } DI_y}{DI_x + DI_y} \cdot min(DI_x, DI_y) \quad (9)$$

$$DI_{biaxial} = \begin{cases} \frac{d_{max,x}}{d_{u,x}} + \beta \frac{E_x + E_y}{F_{y,x} \cdot d_{u,x}} & (d_{max,x} > d_{max,y}) \\ \frac{d_{max,y}}{d_{u,y}} + \beta \frac{E_x + E_y}{F_{y,y} \cdot d_{u,y}} & (d_{max,y} > d_{max,x} \end{cases} \quad (10)$$

$$DI_{biaxial} = DI_x + DI_y \quad (11)$$

$$DI_{biaxial} = \sqrt{DI_x{}^2 + DI_y{}^2} \quad (12)$$

$$DI_{biaxial} = \frac{d_{max,res}}{d_{u,res}} + \beta \frac{E_x + E_y}{F_{y,res} \cdot d_{u,res}} \quad (13)$$

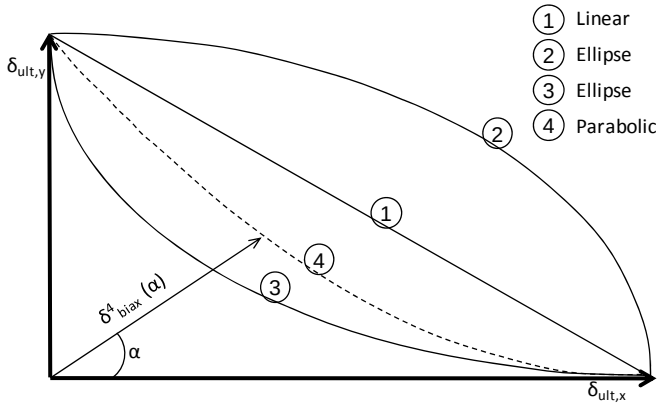


Figure 4 – Interaction curves assumed for the evaluation of the ultimate resultant displacement and equivalent yielding force

3.4 Analysis of the obtained results

The accuracy of each expression presented in the previous section for the estimation of damage in RC columns under biaxial loading conditions is evaluated based on a scoring procedure. For each of the four damage states defined based on visual inspection, the DIs calculated by each expression are assessed by assigning a given score. Thus, if the DI calculated (with a certain expression for each damage state) yields a value within the range presented in Table 4, then it is assigned a score of one; otherwise it is assigned zero. Therefore, for each column the score may vary between 0 and 4. Based on the results of the work carried out by Park et al. [8], where DIs' boundaries for each damage degree observed after earthquake events were adapted to the observed damage states as reported in previous sections, Table 4 includes proposals of DI ranges for each damage state.

Table 4 – Damage index ranges for each damage state adopted in the scoring procedure

Damage state	DI range
Conventional rupture	> 0.80
Reinforcing steel bar buckling	0.55–0.80
Concrete spalling	0.30–0.70
Cracking	0.00–0.10

The DI was computed for each biaxial test using expressions (7) to (13), whilst expressions (2) and (3) were adopted to estimate the parameter β and the ultimate displacement (for each RC column direction). The corresponding results are summarized in Table 5.

Table 5 – Estimated parameters for the damage index calculations

Colum	β	$\delta_{u,Strong}$ (mm)	$\delta_{u,Weak}$ (mm)
PB12-N03 PB12-N04	0.038	92.9	167.4
PB12-N07 PB12-N08	0.047	80.2	142.4
PB12-N11 PB12-N12	0.038	73.5	120.6
PB01-N14 PB01-N15 PB01-N16	0.043	108.8	
PB12-N17	0.055	62.1	98.2
PB12-N18	0.042	77.5	113.7
PB12-N19	0.032	97.6	143.3
PB12-N20	0.049	69.9	102.7
PB12-N21 PB12-N22	0.059	59.3	93.7
PB12-N23 PB12-N24	0.083	66.7	

For the DI calculations using expression (7), the parameter λ proposed by Qiu et al. [22] is taken equal to 0.5. However, for the experimental results analyzed in this work, the option by λ = 0.85 was seen to provide the highest score.

As for the proposal presented in expression (13), the best results are obtained using the parabolic curve, given by expressions (14) and (15), which depend on the parameter P. By comparing the obtained DI results with the experimental observation, the value P = -1.8 was found to yield the best score.

$$y = K + \frac{1}{4P} * (x - H)^2 \tag{14}$$

where

$$K = \frac{1}{4}\left(4 * \delta_{ult,y} - \frac{\left(\delta_{ult,x}^2 + 4 \cdot \delta_{ult,y} \cdot P\right)^2}{4 \cdot \delta_{ult,x}^2 \cdot P}\right) \text{, and } H = \frac{1}{4}\left(\frac{\delta_{ult,x}^2 + 4 \cdot \delta_{ult,y} \cdot P}{2 \cdot \delta_{ult,x}}\right) \tag{15}$$

The DIs estimated using the different expressions are summarized in Table 6, where the adequacy of each expression in representing the damage evolution is finally assessed, summing up the scores for each of the fifteen columns studied.

Table 6 – Scores obtained for each column with the different biaxial DI expressions

	Expression						
Column	(7)	(8)	(9)	(10)	(11)	(12)	(13)
PB12-N07	4	4	4	2	3	4	2
PB12-N08	4	3	3	3	1	3	4
PB12-N11	3	4	4	2	3	4	2
PB12-N12	3	3	3	2	2	3	4
PB12-N14	3	1	1	2	1	2	3
PB12-N15	4	2	2	2	1	2	4
PB12-N16	4	4	4	4	2	4	4
PB12-N17	4	3	2	2	2	4	2
PB12-N18	3	3	3	3	4	3	2
PB12-N19	2	4	4	2	4	2	1
PB12-N20	3	2	2	2	1	2	4
PB12-N21	2	2	2	2	2	2	3
PB12-N22	3	2	2	3	1	2	2
PB12-N23	3	2	2	3	1	2	2
PB12-N24	2	1	1	1	1	1	3
Total	**47**	**40**	**39**	**35**	**29**	**40**	**42**

Table 6 shows that expressions (7) and (13) yielded the best total scores and, therefore, Figure 5 and 6 include (for each of the RC columns' biaxial tests) the evolution of the DIs calculated with expressions (7) and (13), respectively. The plots evidence the damage states observed in the tests (cracking, concrete spalling, bar buckling and conventional failure) and it can be seen that both expressions give DIs that agree well with the physical damage evolution observed in the columns during the cyclic tests.

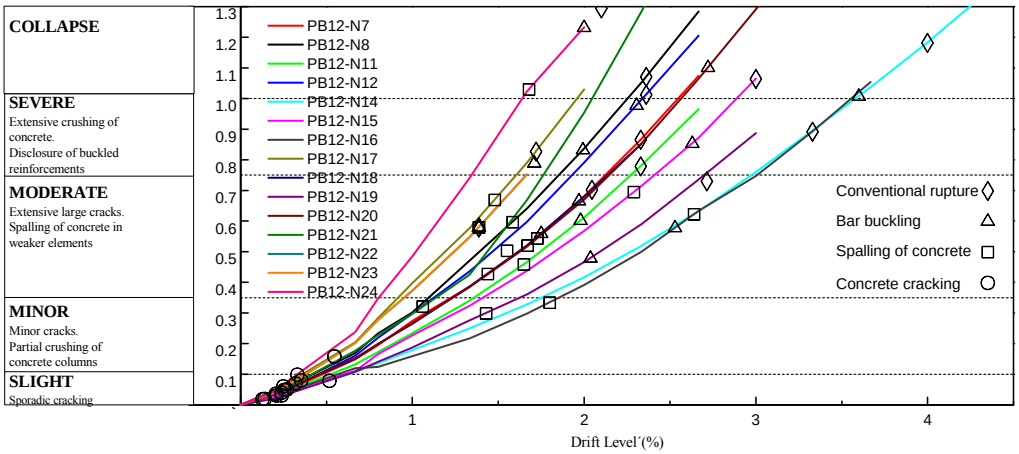


Figure 5 – Evolutions of damage index, calculated with expression (7), for each biaxial test

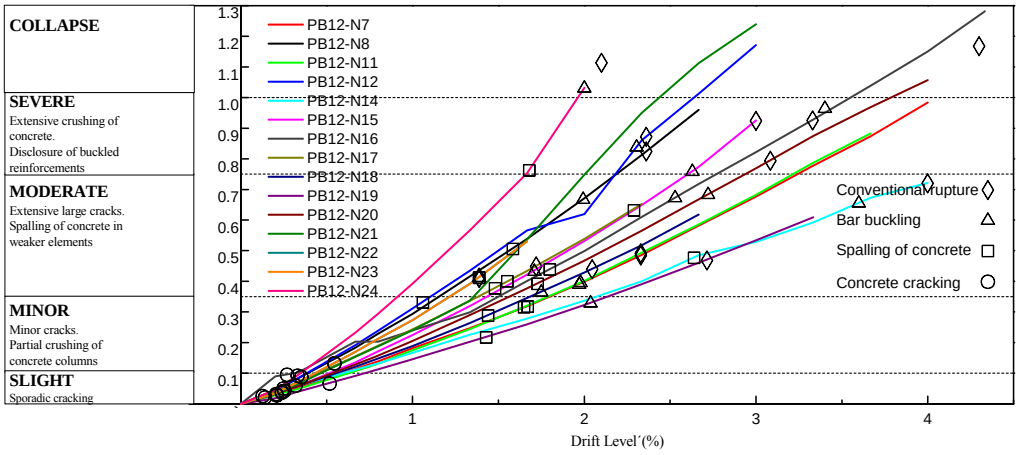


Figure 6 – Evolutions of damage index, calculated with expression (13), for each biaxial test

4 CONCLUSIONS

Even though it is recognized that RC elements under biaxial earthquake loading can experience higher levels of damage than elements under uniaxial loading conditions, the quantification of these reductions is not fully developed. This paper is therefore focused on the damage evolution in RC columns under uniaxial and biaxial horizontal loading conditions with constant axial load, further proposing new expressions for the damage quantification of columns under biaxial loading.

A large number of questions are still open concerning the biaxial behavior of RC columns, especially regarding the description and evaluation of the damage based on damage indices. In the present work, several expressions (based on the concepts inherent to the well known Park & Ang uniaxial damage index) were tested and the proposal giving better results was calibrated with the columns' test results. However, these expressions need to be checked against other experimental results and especially with results of tests on building structures subjected to bidirectional loading demands. Even so, the research work reported is expected to contribute towards a better understanding of the biaxial response of RC columns.

ACKNOWLEDGMENTS

This paper reports research developed under financial support provided by "FCT - Fundação para a Ciência e Tecnologia", Portugal, namely through the PhD grants of the first author with reference SFRH/BD/63032/2009, and through the research project PTDC/ECM/102221/2008.

REFERENCES

[1] CEB, "RC frames under earthquake loading," Lausanne Bulletin 220, 1996.
[2] H. Takizawa, M. Aoyama, and . "Biaxial effects in modelling earthquake response of RC structures," Earthquake Engineering and Structural Dynamics, vol. V. 4, pp. 523-552, 1976.
[3] M. E. Marante and J. Flórez-López, "Model of damage for RC elements subjected to biaxial bending," Engineering Structures, vol. 24, pp. 1141-1152, 2002.
[4] T. Paulay and M. J. N. Priestley, Seismic design of RC and masonry buildings - John Wiley - ISBN 0-471-54915-0, 1992.
[5] Y. J. Park, Y. K. Wen, and A. H.-S. Ang, "Random vibration of hysteretic systems under bi-directional ground motions," Earthquake Engineering and Structural Dynamics, vol. 14, pp. 543-557, 1986.
[6] FEMA356, "Prestandard and commentary for the seismic rehabilitation of buildings," ed: Federal Emergency Management Agency, Washington (DC), 2000.
[7] SEAOC-Vision2000, "Performance based seismic engineering of buildings, vols. I and II: Conceptual framework," ed: Structural Engineers Association of California, Sacramento (CA), 1995.
[8] Y. J. Park, A. H. S. Ang, and Y. K. Wen, "Damage-limiting aseismic design of buildings," Earthquake Spectra, vol. 3, No. 1, 1987.
[9] Y. J. Park and H. S. Ang, "Seismic Damage Model for Reinforced Concrete," ASCE - J Struct Eng, vol. 111(4), pp. 722-739, 1985.
[10] H. Rodrigues, A. Arêde, H. Varum, and A. G. Costa, "Experimental study on the biaxial bending cyclic behaviour of RC columns," presented at the 14th European Conference on Earthquake Engineering Ohrid, Republic of Macedonia, 2010.
[11] H. Rodrigues, H. Varum, A. Arêde, and A. Costa, "A comparative analysis of energy dissipation and equivalent viscous damping of RC columns subjected to uniaxial and biaxial loading," Engineering Structures, vol. 35, pp. 149-164, 2012.
[12] A. Arêde, "Seismic assessment of reinforced concrete frame structures with a new flexibility based element," PhD Thesis, Faculdade de Engenharia, Universidade do Porto, Porto, 1997.
[13] M. M. Hachem, S. A. Mahin, and J. P. Moehle, "Performance of Circular Reinforced Concrete Bridge Columns under Bidirectional Earthquake Loading," PEER 2003/06 - UCB/ENG-9374, University of California, Berkeley, 2003.
[14] H. Varum, "Seismic assessment, strengthening and repair of existing buildings," PhD Thesis, Civil Engineering Department, University of Aveiro, Aveiro, 2003.
[15] J. E. Stephens and J. P. T. Yao, "Damage assessment using response measurements," ASCE Journal of Structural Engineering, vol. 113, pp. 787-801, 1987.
[16] E. Coelho, "Comportamento sísmico de estruturas em pórtico de betão armado - Avaliação da resposta não-linear histerética," PhD Thesis, IST, Lisbon, 1992.

[17] M. S. Williams and R. G. Sexsmith, "Seismic Damage Indices for Concrete Structures: A State-of-the-Art Review," Earthquake Spectra, vol. 11, pp. 319-349, 1995.
[18] Y. S. Chung, C. Meyer, and M. Shinozuka, "Seismic damage assessment of reinforced concrete members," NCEER-87-0022, National Center for Earthquake Engineering Research, Buffalo, N.Y., 1987.
[19] M. N. Fardis, S. N. Economu, A. N. Antoniou, P. J. Komodromos, and M. G. Sfakianakis, "Damage Measures and Failure Criteria - Part I," Contribuition of University of Patras, Final Report of Cooperative Research on the Seismic Response of Reinforced Concrete Structures - 2nd Phase, LNEC, Lisboa, 1993.
[20] R. Bento, "Assessment of the Seismic Behaviour of Reinforced Concrete Framed Structures: An Approach Based on Damage Indices," PhD, IST, Lisbon, 1996.
[21] S. K. Kunnath, A. M. Reinhorn, and Y. J. Park, "Analytical modelling of inelastic seismic response of RC structures," ASCE, Journal of Structural Engineering, vol. 116, Nº4, 1990.
[22] F. Qiu, W. Li, P. Pan, and J. Qian, "Experimental tests on RC columns under biaxial quasi-static loading," Engrg Structures, vol. Vol. 24, pp. pp. 419-428, 2002.

COMPDYN 2013
4th ECCOMAS Thematic Conference on
Computational Methods in Structural Dynamics and Earthquake Engineering
Kos Island, Greece, 12–14 June 2013

EXPERIMENTAL AND NUMERICAL STUDY OF RC COLUMNS UNDER BIAXIAL LOADING: AS BUILT

J. P. Silva[1*], H. Rodrigues[2,3], A. Arêde[1], P. Rocha[4], A. Monteiro[1]

[1] Department of Civil Engineer, Faculty of Engineering of University of Porto, Portugal

Rua Doutor Roberto Frias, s/n. Porto

jpsilva@fe.up.com
[2] Faculty of Natural Sciences, Engineer and Tecnologies – U. Lusófona of Porto, Portugal
[3] Department of Civil Engineer, University of Aveiro, Portugal
[4] Superior School of Technology and Management of Polytechnic Institute of Viana do Castelo, Portugal

Keywords: RC Columns, Uniaxial and Biaxial Bending, Monotonic Response, Cyclic Response.

Abstract. During last decades, have been made many studies about RC columns under uniaxial and biaxial horizontal cyclic loading , however, the knowledge about biaxial behavior is far of uniaxial behavior knowledge. Due to testing difficulties and because there are still open questions regarding the cyclic behavior both in 2D bending with constant axial force, very few experimental studies have, as yet, tackled the more general problem of 2D bending on repaired and retrofitted columns.

In this work is presented the results of an experimental study about behavior under uniaxial and biaxial bending, with constant axial load of as built RC columns. Six columns were tested, three under monotonic loading and three under biaxial cyclic loading with diagonal loading path on as built specimens. After experimental work, was made a numerical nonlinear analysis to evaluate the accuracy of existent models in the representation of the RC columns behavior during a seismic event.

1 INTRODUCTION

Seismic behavior of RC structures is a widely studied theme in the last decades however, the present study had been focused on the behavior of RC columns under biaxial horizontal loading [1,2, 6, 9, 11].

However, many difficulties are still recognized for this analysis approach and, therefore, research must be pursued addressing the biaxial behaviour of RC building columns, bearing in mind that: i) only sophisticated non-linear behaviour models can provide accurate representation of the real structural cyclic response of a given building and, ii), these non-linear hysteretic models have to be calibrated and validated with experimental results obtained from bidirectional tests on RC columns [3]

Experimental research work on the inelastic response of RC members under compression axial force and biaxial lateral cyclic bending loading conditions is currently very limited. Uncertainties concerning the relationship and combination of the two orthogonal horizontal loading paths, associated to the complexity of the experimental set-up, certainly justified this lacuna [4].

From the authors who have studied the biaxial load stand out Bousias et al 1995 [8], with a vast study of biaxial load with constant and variable axial load, other authors began a few years earlier the study of biaxial models as Abrams et al (1987)[13] and Saatcioglou et al (1989)[10]. Tsuno and Park [2004] [7] tested a series of five columns with square section and designed by Japanese rules, from this job resulted two important conclusions, which are the plastic hinge length tends to stabilize by theoretical values, after some cyclic loads and this is indifferent to biaxial load [7] High displacements in the beginning of test cause high degradation and low dissipation of energy, however, if the displacements amplitude begins low and increasing slowly, as standard model of Park, [7,15] the energy capacity of column until ultimate state are the same to uniaxial and biaxial loading.

Low and Moehle [1987] [12] made some tests using rectangular cross section, with different stiffness and strength in each direction. They used three specimens, one tested uniaxially (1) and two biaxially (2 and 3). The specimen 2 was tested with a load 7,5º by diagonal of section and 45º of inclination to lower inertia direction, they got similar results of series D of Saatcioglu (1984)[5]. The third test followed a cloverleaf path, this test allowed conclude that in the major inertia direction, the dissipated energy in the orthogonal direction was the double than with regular square path and in the lower inertia direction happened the same.

Finally Rodrigues et al. [15, 16] tested 17 RC rectangular columns with four types of full-scale quadrangular building columns tested for different loading histories. The horizontal loading patterns considered were Cruciform, diamond, expanding quadrangular and Circular. In this study the comparison of the biaxial results is performed with similar columns under uniaxial load. Based on the obtained results, it was verified that: i) The initial column stiffness in both directions it is not significantly affected by the biaxial load path, ii) when comparing the maximum strength in one specific direction of the columns for each biaxial test against the corresponding uniaxial test, lower values were obtained for all biaxial tests than uniaxial ones. The biaxial loading induces a 20-30% reduction of the maximum strength of the columns in their weak direction, Y, while reductions from 8-15% for the stronger direction, X, iii) the ultimate ductility is significantly reduced in columns subjected to biaxial load paths, iv) The strength degradation is practically zero, in the first loading cycles, increasing after displacement ductility demands of about 3. From the strength degradation analysis, more pronounced strength degradation was observed for biaxial tests when compared with corresponding uniaxial tests, v) the biaxial loading can introduce higher energy dissipation

(circular, rhombus and cruciform load paths) than uniaxial loading, as previously recognised by other authors. It was confirmed that the energy dissipation also depends on the column's geometry; vi) The viscous damping highly depends on the biaxial load path. The repetition of cycles, for the same maximum displacement level, has practically no influence on the equivalent damping.

2 EXPERIMENTAL SETUP

2.1 Test Specimens

On this campaign were used cantilever columns, the system were composed by a footing with1.30x1.30x0.50 meters and column with 0.30x0.50x1.70 meters. The reinforcement arrangement is the same at all specimens. At Figure 1 are present a reinforcement arrangement and two of the tested specimens.

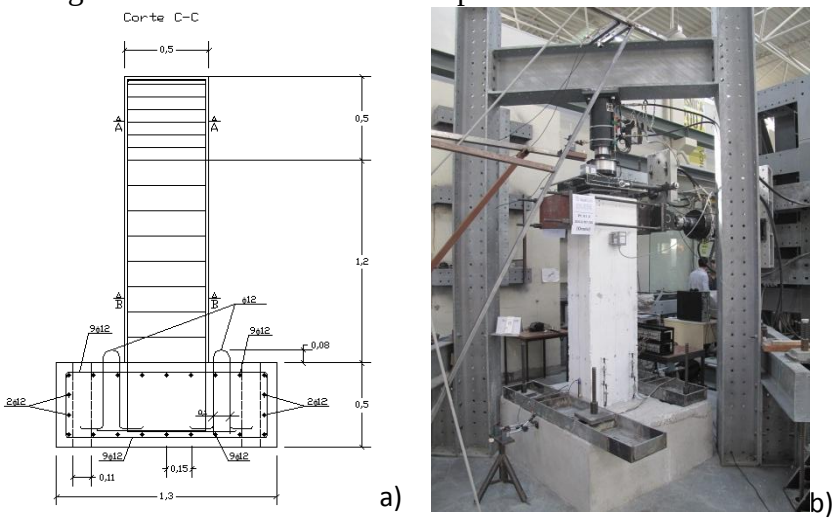


Figure 1 a) Reinforcement detailing; c) Column PC_01_N02

2.2 Testing Setup

The setup shown in Figure 3 was adopted in the experimental campaign. The system includes two, 500 and 200 kN actuator to apply lateral loads with ±100 mm stroke and a 750 kN actuator to impose axial loads, using two reaction frames (lateral and vertical). Both the specimen and the reaction frames are bolted to the strong floor with high strength prestressed rods. In the tests described below, a constant axial load was applied while the lateral loading was cycled under displacement controlled conditions. Since the axial load remains in the same position while the specimen deflects, a special sliding device is used in order to minimize spurious friction effects.

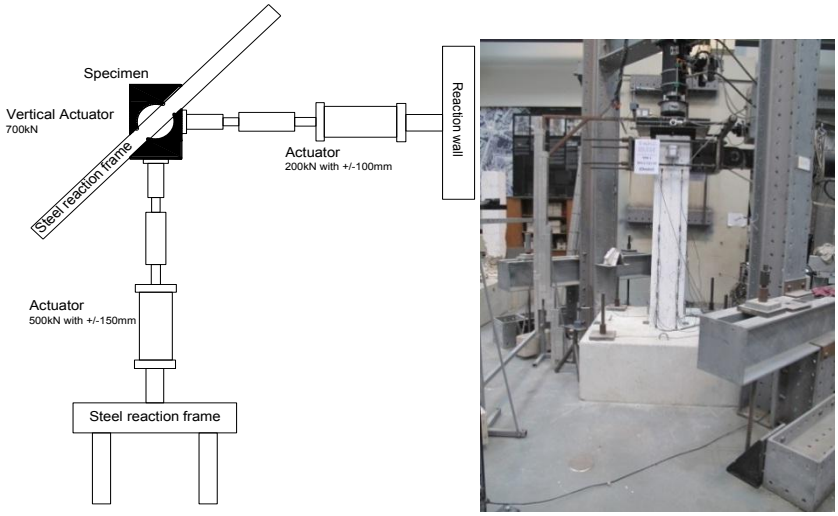
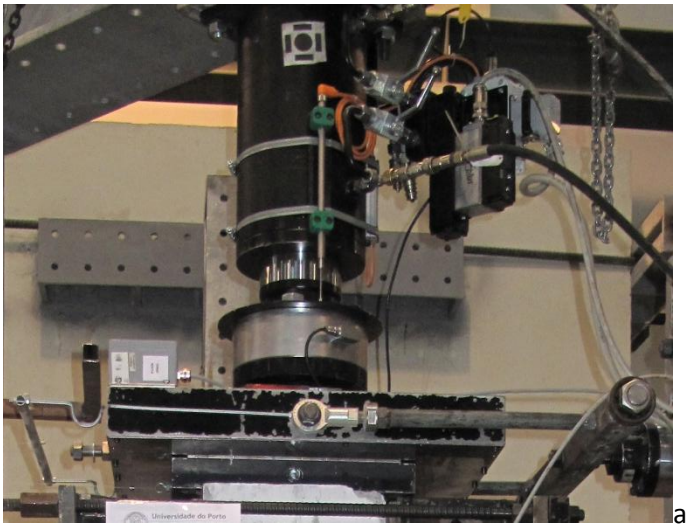


Figure 2 Test setup at LESE laboratory. a) Schematic layout. b) General view


a)


b)

Figure 3 Details of testing setup: a) The axial load sliding device; b) LVDTs

As shown in Fig. 4a, the device consists of two steel plates, the lower one bonded to the specimen top section and the top plate hinged to the vertical actuator, allowing top displacements and rotations on the specimen to occur when lateral loading is imposed. The upper plate is connected to a load cell reacting against the lateral frame in order to measure the residual frictional force between the two plates. This force is then subtracted to the horizontal actuator load, in order to obtain the correct force imposed to the specimen. The hydraulic system of the vertical actuator was designed to keep the oil pressure constant, thus ensuring a constant axial force during the tests. Data acquisition and signal conditioning cards provide direct readings from strain gauges, load cells, LVDTs (Linear Variable Displacement Transformer) and other types of amplified analogical or digital sensors as illustrated in Fig. 4b.

3 NUMERICAL ANALYSIS

Several numerical analyses were performed, using a continuum damage model (Faria and Oliver (1993)) [17] to represent the columns' concrete behavior. That model was initially

developed for the characterization of mass concrete structures, such as dams, but has already been used with very good results on the scope of simulating the seismic behavior of reinforced concrete columns (Vila Pouca (2001)[20], Faria *et al.* (2004)[18]). It relates the evolution of the strength degradation and, thus, the damage experienced by the material, with the increase in two internal variables, controlling the performance on tension and compression independently. This model was used in conjunction with a solid element FE mesh (20 node cube elements), refined accordingly to respect the specimen geometry and rebar disposition. As for the rebars, the well-proven Menegotto-Pinto model [19] was adopted as the constitutive behavior controlling the 2 node bar elements responsible for modeling the steel reinforcement. All these models are implemented in the aforementioned Cast3m software.

The numerical load was a simple monotonic biaxial law, calibrated for three different situations, representing different angles between the load axis and the column section's strong direction. The previously mentioned values were 30º, 45º and 60º.

4 RESULTS ANALYSIS

The evaluations of the experimental campaign results were made mostly by comparison with the numerical results. At this stage of the work, it was considered avoid the calibration of parameters needed on cyclic biaxial simulation models and adopt the monotonic model that mostly uses the knowledge of the characteristics of the materials obtained experimentally.

The ultimate displacement allowed by the test setup is 100mm for each side, given by the maximum stroke of hydraulic jack.

Both results, experimental and numerical, are presented at following figures 4 to 10

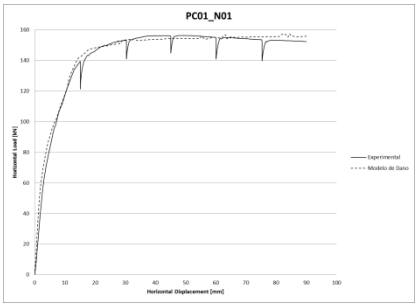


Figure 4 Monotonic Test: Experimental Vs Numerical at strong direction

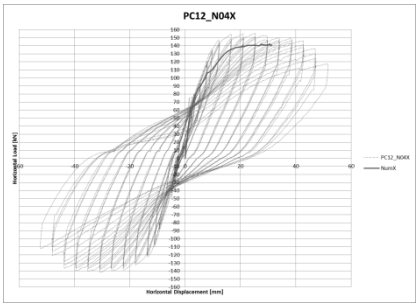


Figure 5 Biaxial Experimental Test Vs Monotonic Numerical Test 30º Test at Strong Direction

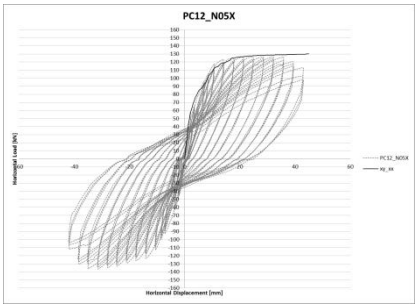


Figure 6 Biaxial Experimental Test Vs Monotonic Numerical Test 45^{o} Test at Strong Direction

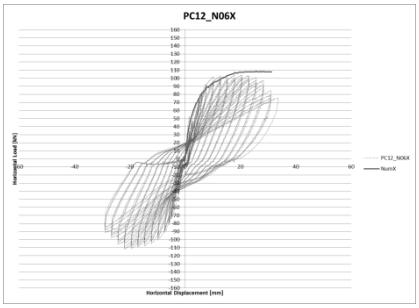


Figure 7 Biaxial Experimental Test Vs Monotonic Numerical Test 60^{o} Test at Strong Direction

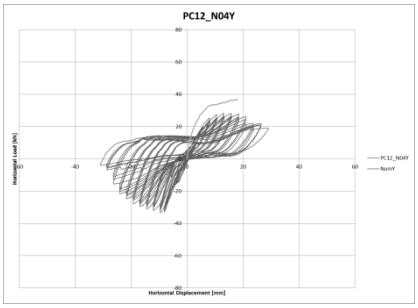


Figure 8 Biaxial Experimental Test Vs Monotonic Numerical Test 30^{o} Test at Weak Direction

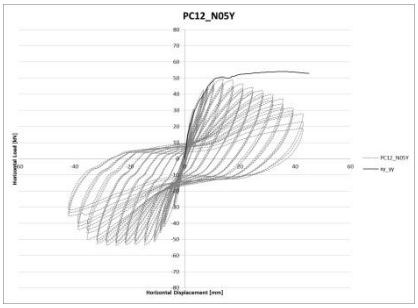


Figure 9 Biaxial Experimental Test Vs Monotonic Numerical Test 45^{o} Test at Weak Direction

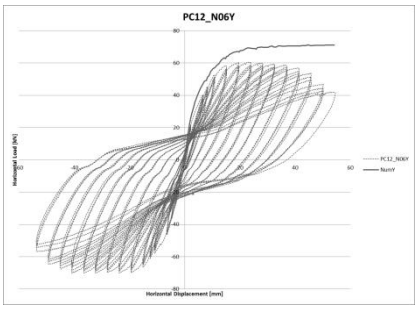


Figure 10 Biaxial Experimental Test Vs Monotonic Numerical Test 60^{o} Test at Weak Direction

The numerical unidirectional monotonic test on strong direction (Figure 4) has a perfect match with similar behavior comparing with experimental test: same displacement for same maximum horizontal load. The same conclusion is valid for same direction at most of the loading path on bidirectional cases: PC12_N05X and PC12_N06X (Figure 6 and 7). The final part of numerical test didn't follow the same levels of strength degradation.

Only with PC12_N04X the maximum strength wasn't achieved, but it has a similar initial stiffness. This experimental test of specimen PC12_N04 did not have an expected behavior,

on weak direction. The result is not good, if evaluated the low level of energy dissipation, stiffness and the asymmetric result.

This test was the first of that series and because of that had some problems at the beginning, which had some involuntary and not foreseen movement that cause some stiffness changes. Another consequence is the asymmetric behavior that also couldn't be represented at numerical simulation.

In all cases, on weak direction, the numerical tests have a higher strength capacity and any strength degradation.

4.1 Damage comparison

This analysis pretend to compare the damage and the levels of strain and tensions observed in numerical analysis and compare them with the degradation observed on experimental test. In figures 11 to 14 are present: the observed damage at the tested columns; the concentration of damage at the compression zone; the level of tension at steel rods; and the damage extension in columns height.

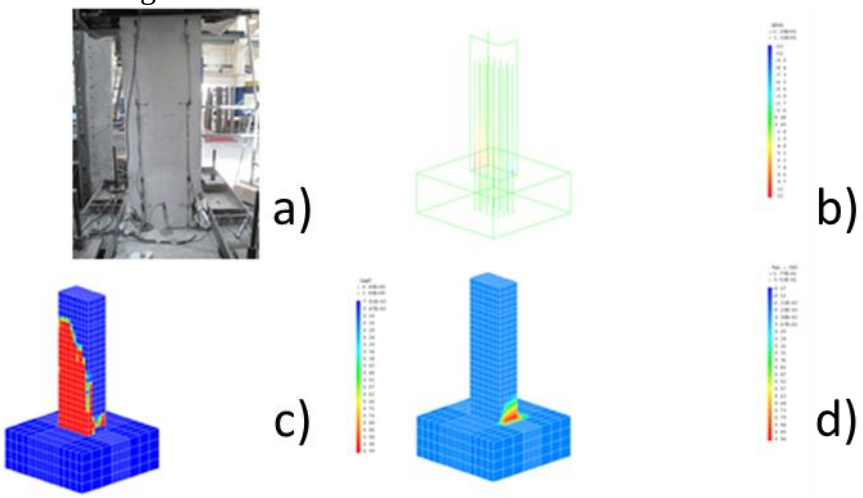


Figure 11: Column PC12_N04 - a) Experimental test; b) Tension at steel bars; c) Damage evolution; d) Compression damage

As shown at figure 11a), the damage caused by concrete compression is concentrated at the base of the column and similar to the damage observed at the experimental test. The figure 11b) shows the tensile deformation that is similar to the experimental test and also the corner bar has a higher tension.

In numerical analysis the damage spread, figure 11c), seems to be exaggerated thought column height.

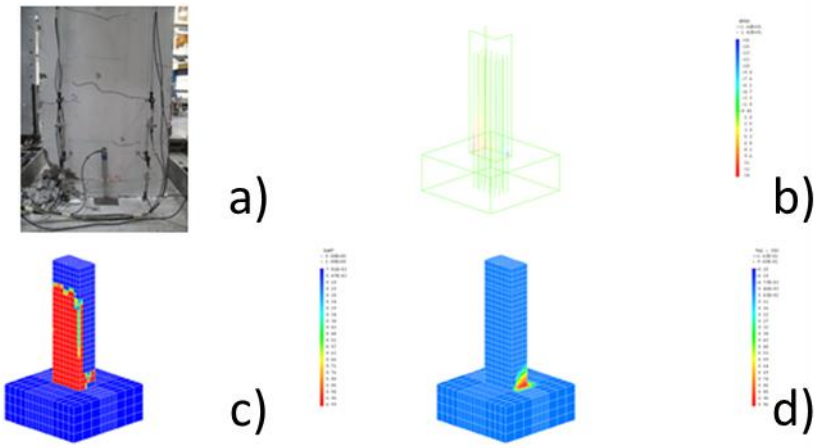


Figure 12: Column PC12_N05 - a) Experimental test; b) Tension at steel bars; c) Damage evolution; d) Compression damage

The PC12_N05 the damage extension is overestimated, figure 12c). As in the previous test the damage is concentrated at plastic hinge region. The figure 12b) has a concentration of traction at longitudinal bars similar to the experimental test, the damage is concentrated at 3 bars of the corner SE, the middle bar of the strong direction does have a soft observed damage as it seen at experimental test. At the compression the damage is highly concentrated at the NW corner, which is shown at figure 12d), the numerical analysis has a similar result of experimental test.

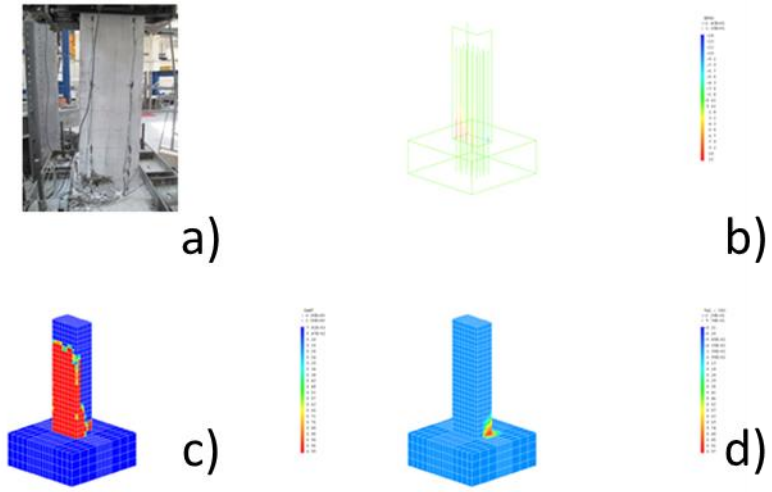


Figure 13: Column PC12_N06 - a) Experimental test; b) Tension at steel bars; c) Damage evolution; d) Compression damage

The test PC12_N06 has a problem with asymmetric cover at all section caused by experimental asymmetric initial damage. Although the numerical analysis cover the principal observed damages, the longitudinal bars with higher tension are the 3 corner bars, figure 13b).

The damage concentration in corner is more visible at this test when compared with previous. Numerical analysis closely approached the damage concentration, figures 13a), 13c) and 13d).

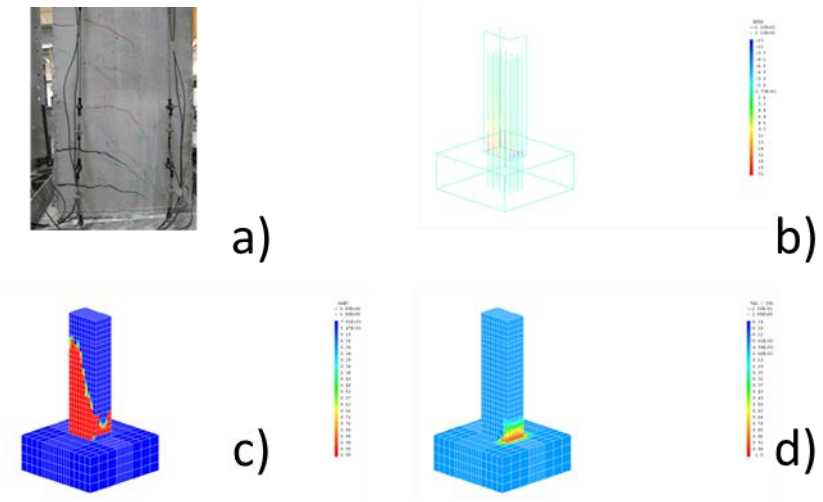


Figure 14: Column PC12_N01 - a) Experimental test; b) Tension at steel bars; c) Damage evolution; d) Compression damage

The uniaxial monotonic test has a wide range of bar deformation at the experimental test. All bars was damaged and, at the end of the test, was visible steel bars buckling.

The numerical analysis, has a good approach of tension at longitudinal bars, the compression is distributed by the total length of weak direction section, at this test wasn't visible a concentrated damage in the corner as happen at biaxial tests. The damage height spread is not realistic.

In all numerical tests the major tensions and strains was observed at steel rods, Figure 11b), 12b), 13b) and 14b), like happened with experimental tests. Due to the observation of steel rods under higher tension, some has buckling phenomena and some broke during the experimental test.

5 CONCLUSIONS

The experimental work allowed to conclude that uniaxial load tests have an higher level of strength capacity and didn't present any strength degradation. This behavior is consistent with the characteristics of biaxial cyclic degradation compared with the monotonic uniaxial degradation. The capacity required for biaxial load tests is higher, due to have strength degradation in both direction, and require a higher deformation capacity.

The numerical model is not sensitive to the experimental conditions, because it couldn't predict a faster strength properties degradation to one side when the opposite side still with full strength capacity. For example, if appear spalling in one direction and do not appear in the opposite direction, the model can't compensate that difference and that create difficulties to validate numerical proposal.

The numerical model can predict effectively the strength capacity with a small margin of error, which can ensure a good capacity prediction to real structures.

The numerical model produced acceptable results to damage analysis however it is overestimate the damage extension at column height.

The model can achieve the concentrated damage at the section corner to used biaxial load patterns.

6 REFERENCES

[1] Rodrigues H. Biaxial seismic behaviour of reinforced concrete columns. University of Aveiro Civil Engineering Department, PhD thesis. 2012

[2] Rocha P. Reforço E Reparação De Pilares De Edifícios De Betão Armado Em Zonas Sísmicas. Faculdade de Engenharia da Universidade do Porto, PhD. 2010

[3] Rodrigues, H.; Arêde, A.; Varum, H.; Costa, A. – "Behaviour of RC building columns under cyclic loading: experimental study" - Journal of Earthquake and Tsunami, JET, World Scientific Publishing - Volume 6, No. 4, DOI: 10.1142/s1793431112500261, pp. 1250026-1- 1250026-42.

[4] H. Rodrigues, H. Varum, A. Arede and A. Costa, "Behaviour of reinforced concrete column under biaxial cyclic loading---state of the art" International Journal of Advanced Structural Engineering, vol. 5, p. 4, 2013

[5] CEB. RC frames under earthquake loading. Bulletin no.231, Comité Euro-International du Béton 1996.

[6] Takizawa H, Aoyama M. Biaxial effects in modelling earthquake response of RC structures. Earthquake Engineering and Structural Dynamics 1976; 4:523–552.

[7] Tsuno K. and Park R. Experimental study of reinforced concrete bridge piers subjected to bi-directional quasi-static loading. JSCE, Vol. 21 2004.

[8] S. N. Bousias, G. Verzeletti, M. N. Fardisand E. Gutierrez, "Load-path effects in column biaxial bending with axial force" *Journal of Engineering Mechanics*, pp. 596-605, 1995.

[9] S. Otani, V. W. T. Cheungand S. S. Lai, "Reinforced concrete columns subjected to biaxial lateral load reversals" presented at the 7th World Conf. on Earthq. Engrg V. 6, 525-532., 1980.

[10] M. Saatcioglu and G. Ozcebe, "Response of reinforced concrete columns to simulated seismic loading" *ACI Structural Journal,* vol. no. 86-S1, 1989.

[11] S. N. Bousias, G. Verzelleti, M. N. Fardisand G. Magonette, "RC columns in cyclic biaxial bending and axial load" presented at the 10th World Conf. on Earthq. Engrg, 3041-3046, Madrid, 1992.

[12] S. Low and J. P. Moehle, "Experimental study of reinforced concrete columns subject to multiaxial cyclic loading" *Earthq. Engrg. Res. Center,* vol. Rep. No UCB/EERC 87-14, Univ. of California, Berkeley, Ca., 1987.

[13] D. Abrams, "Influence of axial force variation on flexural behavior of reinforced concrete columns" *ACI Struct. J.*, vol. 84, pp. 246-254, 1987.

[14] Park R. Evaluation of ductility of structures and structural assemblages from laboratory testing. Bulletin of the New Zealand National Society for Earthquake Engineering 1989; 22(3):155-166.

[15] H. Rodrigues, H. Varum, Arêde, A. and A. Costa (2012) "A comparative analysis of energy dissipation and equivalent viscous damping of RC columns subjected to uniaxial and biaxial loading",Engineering Structures, Volume 35, February 2012, Pages 149-164, ISSN 0141-0296, 10.1016/j.engstruct.2011.11.014.

[16] .Rodrigues, H., Arêde, A., Varum, H. and Costa, A. G. (2012), "Experimental evaluation of rectangular reinforced concrete column behaviour under biaxial cyclic loading". Earthquake Engineering & Structural Dynamics.. doi: 10.1002/eqe.2205

[17] Faria, R. and Oliver, J. (1993). "A rate dependent plastic-damage constitutive model for large scale computations in concrete structures.". CIMNE Monograph. Barcelona. 17.

[18] Faria, R., Pouca, N. V. and Delgado, R. (2004). "Simulation of the cyclic behaviour of R/C rectangular hollow section bridge piers via a detailed numerical model." Journal of Earthquake Engineering 8(5): 725-748.

[19] Menegotto, M. and Pinto, P. (1973). "Method of analysis for cyclically loaded reinforced concrete plane frames including changes in geometry and non-elastic behaviour of elements under combined normal force and bending.". Resist. Ultimate Deform. of Struct. Acted on by Well-Defined Repeated Loads, Final Report.IABSE Symposium. Lisbon.

[20] Vila Pouca, N. (2001). *"Simulação Numérica da Resposta Sísmica de Elementos Laminares em Betão Armado"*. Porto, Faculdade de Engenharia da Universidade do Porto.

COMPDYN 2013
4th ECCOMAS Thematic Conference on
Computational Methods in Structural Dynamics and Earthquake Engineering
M. Papadrakakis, V. Papadopoulos, V. Plevris (eds.)
Kos Island, Greece, 12–14 June 2013

ESTIMATING ROOF-LEVEL ACCELERATION SPECTRA FOR SINGLE STOREY BUILDINGS

Timothy J. Sullivan[1] Paolo M. Calvi[2], David P. Welch[3],

[1] Department of Civil Engineering & Architecture, University of Pavia
1 Via Ferrata, Pavia, PV, Italy, 27100
timothy.sullivan@unipv.it

[2]University of Toronto
35 St. George Street, Toronto, Canada, ON M5S 1A4
paolo.calvi@mail.utoronto.ca

[3] ROSE Programme, UME School, IUSS Pavia
1 Via Ferrata, Pavia, PV, Italy, 27100
david.welch@umeschool.it

Keywords: Floor spectra, Non-structural elements, Seismic Assessment, Elastic Damping

Abstract. *The performance of both structural and non-structural elements should clearly be considered when assessing the seismic safety and performance of a building. The performance of non-structural elements tends to be dependent on storey drift demands, acceleration demands or both. However, a simplified reliable means of estimating the acceleration demands on non-structural elements appears to be lacking, particularly for non-structural elements characterized by an elastic damping ratio that is not equal to 5% critical damping. As such, this paper presents a simplified means of predicting roof level acceleration spectra for single storey buildings. Such spectra should be useful in assessing the response of parapets or relatively lightweight appendages such as antennae, ceilings or mechanical services attached to the roof of single-storey buildings. As the procedure is formulated using concepts of mechanics and dynamics it is applicable to single-storey buildings that respond either in the linear or non-linear range, and is able to be adjusted for a wide range of elastic damping values. To gauge the performance of the procedure, spectra obtained from the approach are compared to those obtained from non-linear time-history analyses of a single storey building subject to ten ground motions scaled to various levels of intensity. The results demonstrate that the simplified approach for estimating roof level acceleration spectra works well and the possibility of extending it to multi-storey buildings should be explored as part of future research.*

1 INTRODUCTION

Past earthquakes have highlighted the need to consider both structural and non-structural elements when assessing seismic risk, both in terms of likely financial losses and safety of human lives. Events such as the Northridge earthquake [1] and the recent Darfield (New Zealand) earthquake of September 2010 [2] have indicated that financial losses from damage to non-structural components can far exceeded losses from structural damage. Moreover, the failure of non-structural building components can become a safety hazard and hamper the safe movement of occupants as they evacuate or rescuers as they enter the building [3], [4]. Furthermore, non-structural damage can severely limit the functionality of critical facilities such as hospitals, as demonstrated in the 1994 Northridge earthquake [5] and the 2006 Kiholo Bay and Hawi, Hawaii earthquakes [6].

Clearly, in order to reliably assess the safety of a building system, one should take steps to assess the risk posed by both structural and non-structural elements. Tools for the assessment of risk to structural elements are fairly well developed, as is illustrated by the numerous provisions provided in building codes. Indications for the assessment of non-structural elements are, however, somewhat limited. The critical type of loading for non-structural elements varies from one type of non-structural element to another. Lightweight partition walls are likely to be drift-sensitive whereas ceilings are expected to be acceleration sensitive [4],[7]. Figure 1 illustrates some of the damage to an acceleration-sensitive ceiling observed in the recent Darfield (N.Z.) earthquake [2].



Figure 1: Elevation view of case study building (reproduced from [2])

In order to permit reliable assessment of ceiling systems and other acceleration sensitive elements, one requires a means of estimating the acceleration demands on the element. This is not a trivial task since, aside from the uncertainty related to the ground motion arriving at the base of the building, it is expected that the acceleration demands vary up the height of a structure, being filtered and amplified according to the dynamic characteristics of the main structural system. This implies that an acceleration spectrum recorded at the roof of a building is likely to be very different from that at the base of the building, as illustrated in Figure 2. This paper demonstrates how a recently proposed procedure for the estimation of floor spectra [8] can be used to provide improved estimates of roof-level acceleration demands in single-storey buildings.

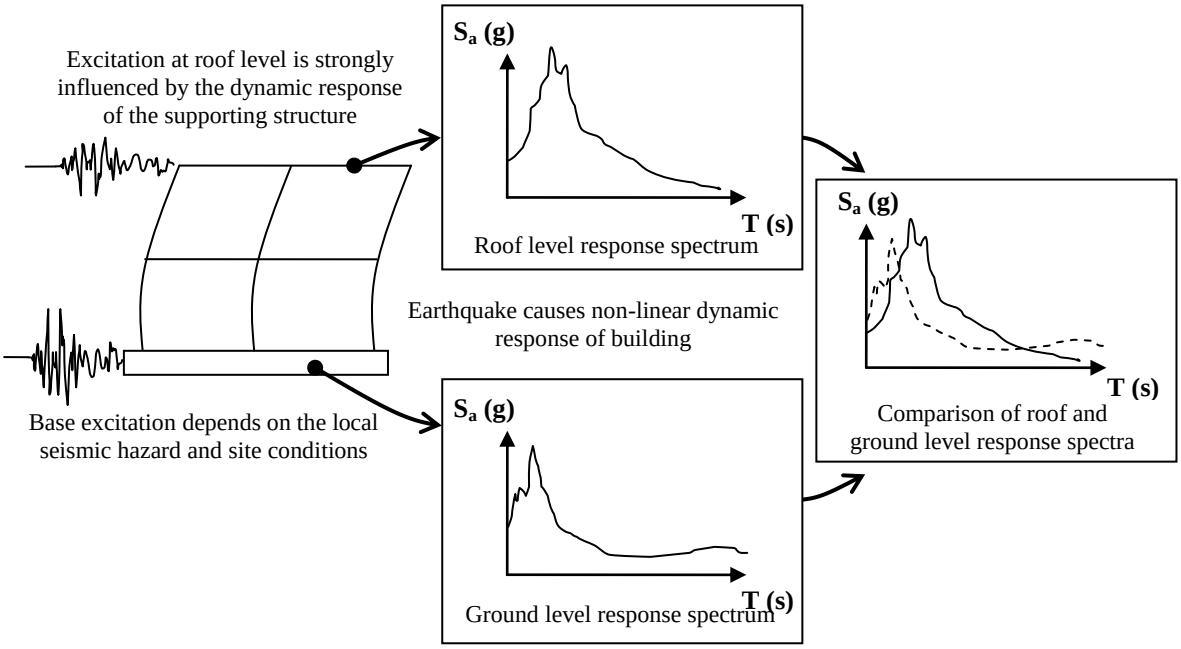


Figure 2: Elevation view of case study building (adapted from [8])

2 CODE METHODS FOR THE PREDICTION OF ACCELERATION DEMANDS

Current code approaches for the prediction of acceleration demands on non-structural elements up the height of buildings vary quite significantly, suggesting that there is considerable uncertainty as to the best methodology. In Europe [9], the acceleration demand, S_a, acting on a non-structural element of a building can be estimate as:

$$S_a = a_g.S.\left(\frac{3(1+z/H)}{1+(1-T_a/T_n)^2}-0.5\right) \geq a_g.S \quad (1)$$

where z is the height of the non-structural element above the ground level, H is the total height of the building, a_g is the design ground acceleration (units of g) for a rock site, S is a modification factor to account for other soil site conditions, T_a is the period of the non-structural element and T_n (shown as T_1 in EC8 [9]) is the natural (first-mode) period of the building in the relevant direction of excitation.

Equation 1 suggests that at roof level, when the period of the non-structural element corresponds to that of the structural system, the element could be subjected to an acceleration 5.5 times the peak ground acceleration (PGA) at the site. In contrast, using the ASCE7-05 [10] approach in the U.S. one could predict a maximum acceleration demand of 7.5 times the PGA but the code does limit the maximum design force for non-structural elements such that the peak acceleration demand is anticipated to be approximately 4.0 times the PGA. In New Zealand [11] the maximum acceleration on non-structural elements at roof level could be predicted as 6.0 times the PGA, which is not far from the EC8 estimate. However, the New Zealand approach only depends on the period of the non-structural element (and adopts maximum values for periods up to 0.75s) and does not depend on the period of the supporting structure.

In order to illustrate the potential of the different code approaches, Figure 3 compares the acceleration spectra recorded at the roof level of an 8-storey RC wall structure subject to non-

linear time-history analyses by Sullivan et al. [8] using accelerograms spectrum-compatible with the EC8 spectrum constructed at a PGA of 0.2g. The spectra are constructed for 2% and 5% elastic damping in order to illustrate how acceleration demands can be affected by the damping of the supported element. Note that none of the code approaches appear to modify acceleration demands to account for differences in element damping even though it should certainly be expected that some non-structural elements will possess considerably different damping values than others [8].

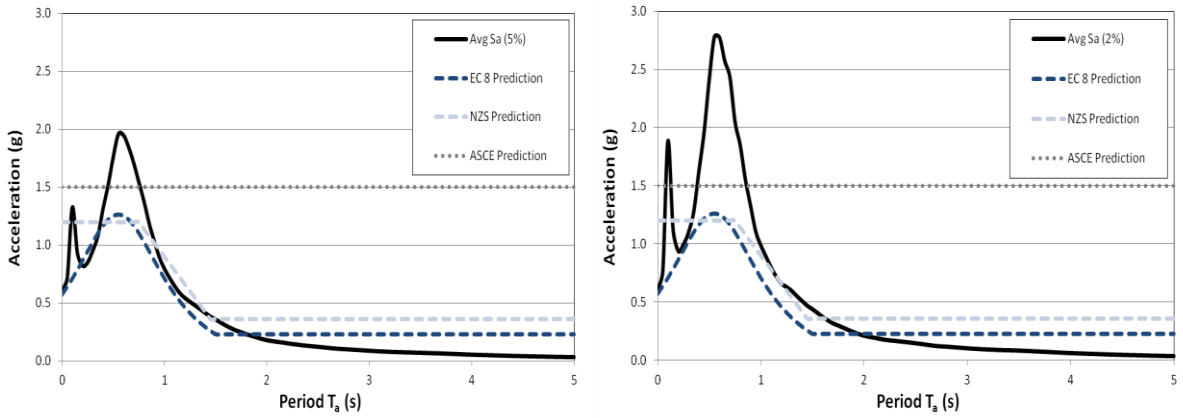


Figure 3: Comparison of roof level acceleration spectra at 5% damping (left) and 2% damping (right) as predicted via different code approaches and from non-linear time-history analyses of an 8-storey case study building (adapted from [8]).

From the comparison provided in Figure 3 it is apparent that the elastic damping of the non-structural element has a very significant influence on the peak acceleration demands and should be considered in seismic assessment. In addition, note that all of the code methods underestimate the peak acceleration demands. One can also observe the presence of two peaks in the floor spectra; the main peak is associated with amplification of demands at the fundamental period of the structure whereas the peak at short periods is related to amplification of demands due to resonance with the 2nd mode of vibration of the building. Such higher mode amplification is not considered at all in the Eurocode approach and merits further investigation but this is outside the scope of this paper. Instead, the next section presents an alternative means of predicting the acceleration that takes account of the elastic damping characteristic of the supported element as well as the possible effects of non-linear response of the supporting structure.

3 ALTERNATIVE PROCEDURE FOR THE ESTIMATION OF ROOF LEVEL ACCELEARTION SPECTRA

3.1 Conceptual Considerations

Any alternative means of predicting acceleration spectra at various levels of a structure should recognize the following points (discussed in Sullivan et al. [8]):

- Acceleration demands are affected by the ratio β of the period of the forcing function to the period of the structure (i.e. the period of the supporting element divided by the period of the supported element).
- Acceleration demands are affected by the elastic damping of the supported element.

- The forcing function period cannot typically be considered as a single constant value during an earthquake because of the participation of different modes of vibration in structural response and because of the period lengthening that occurs as the supporting structure yields and responds non-linearly.
- The peak acceleration demands at the roof of a SDOF structure are physically limited by the lateral resistance of the structure itself (provided that the roof behaves like a rigid diaphragm).

Considering the first of these points, many texts on structural dynamics (e.g. [12]) have shown that the dynamic amplification, *DAF*, (i.e. the ratio of the peak acceleration to the acceleration of the forcing function) of a system subject to harmonic excitation can be estimated from Equation 2:

$$DAF = \frac{\ddot{u}_{\max}}{\ddot{u}_0} = \frac{\beta}{\sqrt{(1-\beta^2)^2 + (2\beta\xi)^2}} \tag{2}$$

Where β is the ratio of the forcing function period to the structure's period of vibration and ξ is the elastic damping of the (supported) structure.

This expression would imply that the peak dynamic amplification, $DAF_{\max,harm}$, that could be expected (for $\beta = 1.0$) is a function of the elastic damping, and is given by:

$$DAF_{\max,harm} = \frac{1}{2\xi} \tag{3}$$

Unfortunately, however, as pointed out in [8] this equation cannot strictly be applied to earthquake engineering because real earthquakes do not impose harmonic excitation. Instead, Sullivan et al. [8] established the following empirical expression for the peak dynamic amplification (expected at $\beta = 1.0$) that is again only a function of the elastic damping on the supported element:

$$DAF_{\max} = \frac{1}{\sqrt{\xi}} \tag{4}$$

The difference between Equations 3 and 4 could be considered a reflection of the difference is the number of significant cycles of excitation imposed around the peak response. This would in turn suggest that the expression could be strongly dependent on the characteristics of the earthquake motion, possibly varying greatly for pulse-type or long duration earthquakes. However, Sullivan et al. [8] found that this may not be the case and that the significant number of cycles for dynamic amplification may in fact be rather constant for a wide range of ground motions.

The third bullet point above relates to the period of the forcing function. As demonstrated in the previous section, for multi-degree-of-freedom systems higher modes of vibration could provoke significant amplification of acceleration demands on non-structural elements. The third bullet point additionally states though, that period lengthening may occur as the supporting structure yields and responds non-linearly. This concept is illustrated in Figure 4 for a SDOF system. The figure is annotated to illustrate how the stiffness, K, reduces with the development of yielding and inelastic response and it also includes equations showing how an effective period can be related to the effective stiffness at any point of the non-linear force-displacement curve.

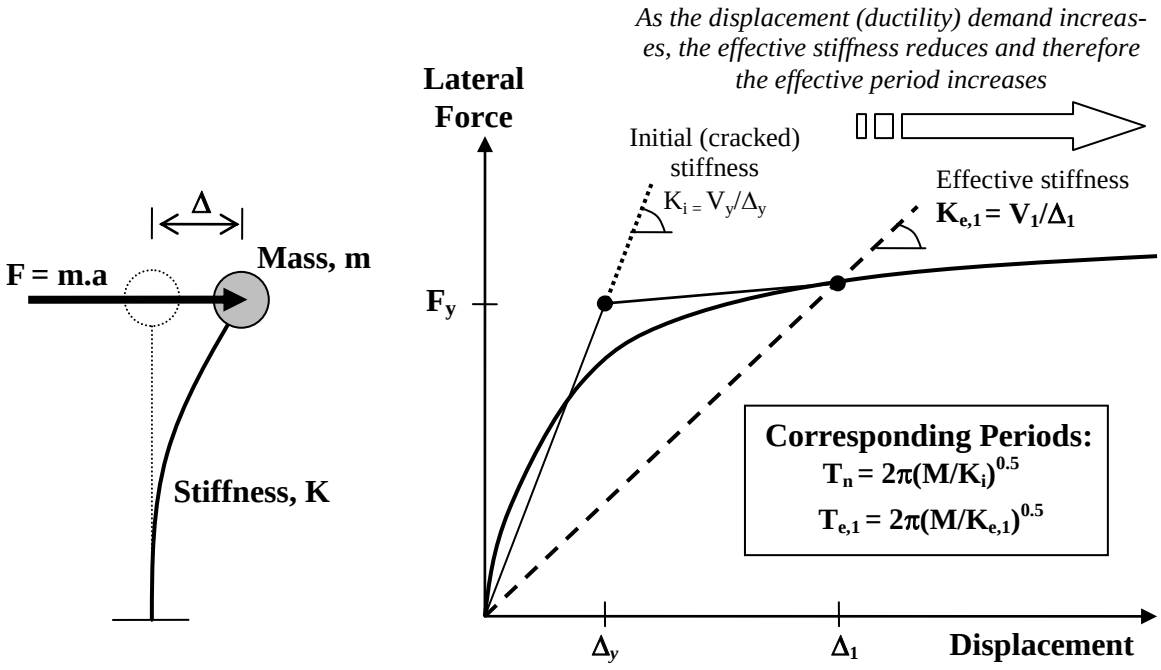


Figure 4: Force-displacement response of a SDOF structure, annotated to illustrate concept of the effective stiffness and effective period at a displacements of Δ_1 (adapted from [8]).

The fourth bullet point above states that the peak acceleration demands at the roof of a SDOF structure are physically limited by the lateral resistance of the structure itself. This concept is also illustrated in Figure 4 since it is shown that, according to Newton's second law, force is equal to mass times acceleration and given that the maximum force in the SDOF system is limited by the strength (resistance) of the system itself, so too will be the maximum acceleration of the mass. This implies that the maximum acceleration of the SDOF supporting system is given by:

$$a_{\max} = \frac{V_b}{M} = \frac{V_y\left[1 + r(\mu - 1)\right]}{M} \tag{5}$$

where V_b is the base shear resistance, M is the mass of the supporting structure, V_y is the base shear at yield, r is the post-yield strain hardening factor (typically 0.05 for RC structures) and μ is the displacement ductility demand.

Reflecting for a moment on current code methods, it is apparent that none of the existing approaches account for all the points raised above. The Eurocode accounts for the period ratio but not the other points. The New Zealand approach could arguably be interpreted as recognizing period lengthening and multiple forcing frequencies by rendering the amplification independent of the period ratio. However, even this approach risks underestimating the peak demands, particularly if the elastic damping of the non-structural element is low.

3.2 Proposed Methodology

As explained in the introduction, Sullivan et al. [8] have recently proposed a method for the prediction of floor spectra in SDOF systems that accounts for all the conceptual issues identified in the previous subsection. In the approach, the acceleration spectrum at the roof of a SDOF supporting system can be computed using the following equations:

$$a_m = \frac{T_a}{T_n}.\left[a_{\max}\left(DAF_{\max} - 1\right)\right] + a_{\max} \qquad \text{for} \quad T_a < T_n$$

$$a_m = a_{\max} DAF_{\max} \qquad \text{for} \quad T_n < T_a < T_e \qquad (6)$$

$$a_m = \frac{a_{\max}}{\sqrt{\left(1 - \frac{1}{\beta}\right)^2 + \xi}} \qquad \text{for} \quad T_a > T_e$$

where a_m is the acceleration spectral coordinate for a supported element of period T_a, $a_{\max}$ is the maximum acceleration of the mass of the supporting structure (given by Eq.5), T_n is the natural (initial) period of the supporting structure, T_e is the effective period of the supporting structure (refer Figure 4) and $DAF_{\max}$ is the maximum expected dynamic amplification obtained from Eq.(4) as a function of the elastic damping, ξ.

3.3 Performance of the method

In order to illustrate the performance of this method, Equation 6 is used to estimate acceleration spectra at the roof level of a single-storey case study building. The case study building taken into consideration here is an existing precast reinforced concrete frame industrial building, with a lateral load resisting system provided by cantilever columns and with a (cracked) fundamental period of T_n=1.33s. The structure has a ratio of yield strength to building weight of 15%. The long period is a reflection of the low stiffness provided to such existing structures, similar to those recently damaged in the Emilia (Italy) earthquake. A non-linear model of the structure is developed for non-linear time-history (NLTH) analyses in Ruaumoko (refer [13]) and is provided with Takeda-thin hysteretic properties following recommendations in [14]. The structure is subject to a series of real accelerograms (taken from [15]) that were scaled to be spectrum compatible with the EC8 type 1 spectrum on soil type A. The analyses are run at three different intensity levels corresponding to a peak ground acceleration demand of 0.2g, 0.4g and 0.8g in order to illustrate the effect of intensity on roof level acceleration spectra. The ductility demand on the case study building at each of these intensities levels could have been estimated a variety of ways, including traditional structural assessment techniques in current codes or the displacement-based assessment method of [14]. However, in this case study the mean ductility demands on the system are computed directly from the results of the non-linear time history analyses as 1.20 for 0.2g, 2.35 for 0.4g and 5.52 for the 0.6g intensity level. The roof level acceleration spectra are then computed using Equation 6 and are compared to the mean of the spectra obtained for the case study building in Figure 5. Comparisons are made for acceleration spectra developed at 2%, 5% and 10% elastic damping. Note that the roof level acceleration spectra are predicted quite well (being on slightly conservative in some instances) in all cases.

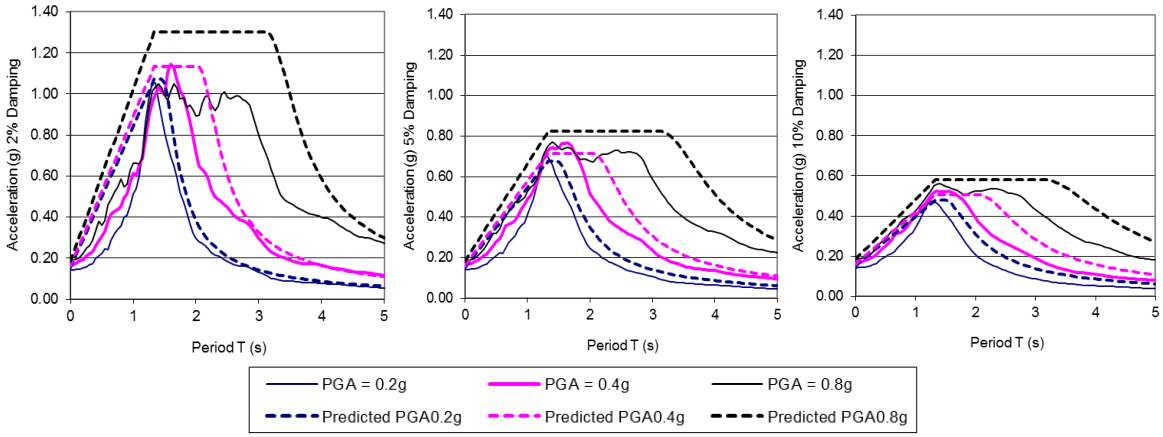


Figure 5: Mean roof level acceleration spectra obtained for the case study structure via NLTH analyses at three different intensity levels compared with those predicted using Equation 6, for 2% (left), 5% (middle) and 10% (right) elastic damping.

4 CONCLUSIONS

Previous earthquakes have illustrated that seismic safety depends on the adequate performance of both structural and non-structural elements. Non-structural elements can typically be grouped into drift-sensitive or acceleration sensitive elements, with suspended ceilings being a good example of an acceleration-sensitive non-structural element. In order to adequate assess the risk posed by acceleration-sensitive non-structural elements it has been shown that improvements methods of predicting acceleration spectra are required, particularly for non-structural elements characterized by an elastic damping ratio that is not equal to 5% critical damping. As such, this paper has presented a simplified means of predicting roof level acceleration spectra for single storey buildings. As the procedure is formulated using concepts of mechanics and dynamics it is applicable to single-storey buildings that respond either in the linear or non-linear range, and is able to be adjusted for a wide range of elastic damping values. To gauge the performance of the procedure, spectra obtained from the approach have been compared to those obtained from non-linear time-history analyses of a single storey building subject to ten ground motions scaled to various levels of intensity. The results have demonstrated that the simplified approach for estimating roof level acceleration spectra works well and the possibility of extending it to multi-storey buildings should be explored as part of future research.

ACKNOWLEDGEMENT

This research is developed as part of research line AT1-2 of the 2010-2013 RELUIS project. As such, the financial support of the RELUIS consortium (www.reluis.it) is gratefully acknowledged for this research.

REFERENCES

[1] R. Villaverde, Seismic design of secondary structures: state of the art, *Journal of Structural Engineering ASCE*, 123(8), pp.1011-1019, 1997.

[2] R.P. Dhakal, Damage to Non-structural Components and Contents in the 2010 Darfield earthquake, *Bulletin of the New Zealand Society for Earthquake Engineering*, Vol.43, No.4, pp. 404-411, 2010.

[3] R. Villaverde, "Seismic analysis and design of non-structural elements" in Earthquake engineering from engineering seismology to performance-based design, (Eds) Y. Bozorgnia, V.V. Bertero, CRC Press, pp.19-48, 2004.

[4] A. Charleson, *Architectural Design for Earthquakes – A guide to the design of non-structural elements*, Published by the New Zealand Society for Earthquake Engineering (NZSEE), Second edition revised and updated by Andrew Charleson, 2007.

[5] G. McGavin, H. Patrucco, Survey of Non Structural Damage to Healthcare Facilities in the January 17, 1994 Northridge Earthquake, Ontario, Canada: HMC Group, 1994.

[6] I.N. Robertson, P.G. Nicholson, H.G. Brandes, Reconnaissance Following the October 15th, 2006 Earthquakes on the Island of Hawai'i. University of Hawaii Dept. Civil and Environmental Eng. Research Report UHM/CEE/06-07 (http://www.cee.hawaii.edu/), 2006.

[7] Federal Emergency Management Agency (FEMA), "Reducing the Risks of Nonstructural Earthquake Damage – A Practical Guide," *FEMA E-74*, Prepared by ATC for FEMA, January 2011, Washington, D.C., 2011.

[8] T.J. Sullivan, P.M. Calvi, R. Nascimbene, Towards Improved Floor Spectra Estimates for Seismic Design, *Earthquakes and Structures*, Vol.4, No.1, 2013.

[9] CEN EC8, *Eurocode 8 – Design Provisions for Earthquake Resistant Structures*, EN-1998-1:2004: E, Comite Europeen de Normalization, Brussels, Belgium, 2004.

[10] ASCE/SEI 7-05, *Minimum Design Loads for Buildings and Other Structures*, American Society of Civil Engineers, 388pages, 2005.

[11] NZS1170.5:2004, Structural *Design Actions Part 5: Earthquake actions – New Zealand*, Standards Council of New Zealand, 2004.

[12] W.T. Thomson, M.D. Dahleh, *Theory of Vibration with Applications Fifth Edition*, Prentice Hall, Upper Saddle River, New Jersey 07458, U.S., 524 pages, 1998.

[13] A.J. Carr, Ruaumoko3D – A program for Inelastic Time-History Analysis, Department of Civil Engineering, University of Canterbury, New Zealand, 2009.

[14] M.J.N. Priestley, G.M. Calvi, M.J. Kowalsky, *Direct Displacement-Based Seismic Design*, IUSS Press, Pavia, Italy, 2007.

[15] T.J. Maley, T.J. Sullivan, A. Lago, R. Roldan *Characterising the Seismic Behaviour of Steel MRF Structures*, ROSE Research Report, IUSS Press, Pavia, Italy, *in press*.

COMPDYN 2013
4th ECCOMAS Thematic Conference on
Computational Methods in Structural Dynamics and Earthquake Engineering
M. Papadrakakis, N.D.Lagaros, V. Plevris (eds.)
Kos Island, Greece, 12–14 June 2013

A CASE STUDY OF COLLAPSE DURING THE 2009 L'AQUILA (ITALY) EARTHQUAKE

Maria G. Mulas[1], Luca Martinelli[2], and Federico Perotti[2]

[1] 1Department of Civil and Environmental Engineering, Politecnico di Milano
P.zza L. da Vinci, 32 – 20133 Milano, Italy
e-mail: mariagabriella.mulas@polimi.it

[2] 1Department of Civil and Environmental Engineering, Politecnico di Milano
P.zza L. da Vinci, 32 – 20133 Milano, Italy
luca.martinelli@polimi.it, federico.perotti@polimi.it

Keywords: case study; soft-story mechanism; partial collapse; non-ductile reinforced concrete frame; captive-beam mechanism.

Abstract. *A number of masonry and reinforced concrete (RC) buildings suffered failure during the magnitude Mw 6.3 earthquake that struck the city of L'Aquila (Italy) on April 6 2009. Many of the RC buildings were designed and built between the late fifties and the early seventies. The partial collapse of the "Casa dello Studente" (Student House) building in L'Aquila, with its high death toll of eight students killed and one suffering serious injury, is paragdimatic on one hand of the possible fragility of reinforced concrete construction of that period, on the other hand of failure due to an adverse sequence of events.*

The legal authority appointed a forensic team, lead by the first author, for investigating the causes and the mechanism of the collapse. During a six-months period, the team had a unique chance to analyze in a thorough way the collapse causes. The joint efforts of the forensic team led to a complete explanation of the collapse and highlighted the sequence of missed opportunities that let this happen. Collapse took place within part of the North wing trough a twofold mechanism: a weak-story mechanism, which involved collapse of all the columns at the first story, and the complete collapse of three columns located close to the floor center. The two mechanisms were due to an initial design error, never discovered during the subsequent renovations of the building, whose effects were adversely amplified by a non-structural fire-proof wall inserted in recent times to comply with fire safety requirements. This imposed unforeseen strength and ductility requirements on members not specifically designed for this.

This paper presents some of the result of the studies that, not strictly necessary for legal reasons, were only performed after completing the report for the legal authority. Nonlinear analyses are adopted to highlight the role of each of the factors listed above which lead to the structural failure.

1 INTRODUCTION

On April 6th 2009 at 3.32 am a magnitude Mw 6.3 earthquake struck Central Italy, with devastating effects in the city of L'Aquila and the surrounding area. Several reinforced concrete (RC) buildings in the urban area failed. Among them, the "Casa dello Studente" building (CdS, in the following), located at about 6 km from the epicenter, suffered a partial collapse. The death toll was very high, with eight students killed.

The CdS building was a seven-story RC building hosting a University dorm ("Casa dello Studente" means Student House, in Italian). It was designed in 1965, following the Italian Seismic Codes of 1937 [1] and 1962 [2], for a mixed use (residential/commercial). The plan of the residential part, in the upper four stories, was subdivided in three wings, connected through the stairwell, with an apartment in each wing. Ground floor and basement were common to all the wings; a second underground level was only present below the South wing. The ground floor and the underground levels were originally designed for offices and laboratories of a pharmaceutical company. In 1979 the building was bought by a University Institution to be used as student house. A minor refurbishment work took place at the ground floor and at the two underground floors, where a library, offices and a cafeteria for students were located. Subsequently, in 1982, the building became a property of the Abruzzo Region, in force of State and Region Laws. The second change of property did not affect the usage of the building as a student house. A wide refurbishment intervention, not covering the structural system, was performed during the years 1999-2002. The plans of the upper floors were deeply transformed to make the building more apt to its actual usage (Figure 2).



Figure 1. Aerial view of the building in the configuration at the date of the 2009 seismic event.

The partial collapse of the building was limited to the North wing (see Figure 1). Within this wing two distinct collapse zones were detected, from both pictures of the collapsed part (Figure 3) and on-site observations: the failure of all the columns at the ground floor, with a

soft/weak story mechanism, and that of three columns (21, 25 and 29, see Figure 4) along the height of the building, at the interface between the North wing and the remaining ones. Previous studies, reported in [3, 4], performed for legal reasons, showed that neither the poor quality of material properties nor the ground motion at the building site could be considered – from the Italian laws viewpoint – among the causes of the collapse. The most likely collapse sequence was established by crossing the design criteria adopted in 1965, the results of modal analyses of the building in its original configuration and after refurbishment, and all the experimental data coming from the analysis of damage in the part of building that survived the earthquake. The lack of flexural strength of ground story columns was detected as the main mechanical cause of the collapse itself.

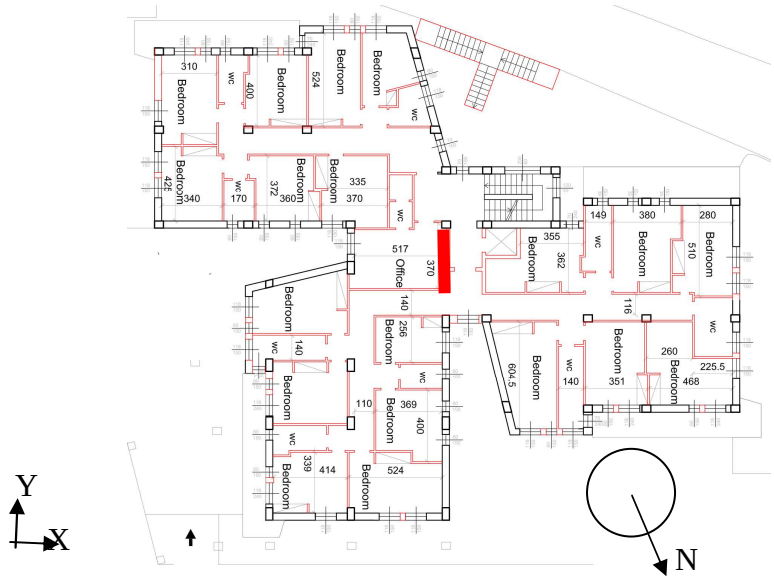


Figure 2. Plan of the typical building floor after refurbishment in 2000. The thick line marks the position of a fire resistant wall on Beam 18-29 which triggered the collapse of this beam at several levels.

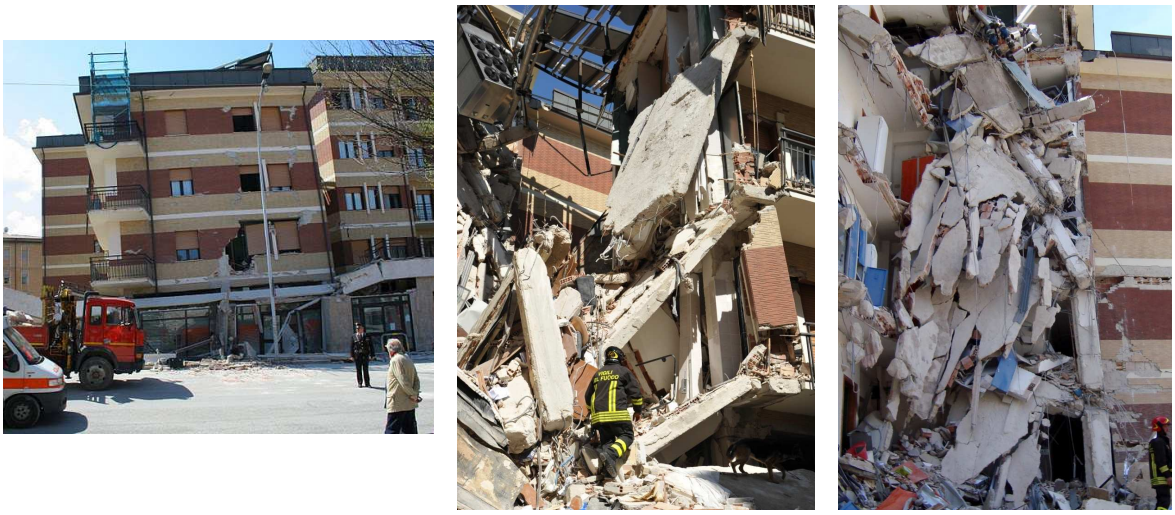


Figure 3. The partial collapse of the building. Left, the soft story of North wing, view from XX September Street. Center, the collapse of the columns at the interface between the North wing and the remaining wings. Right, the remaining of column 29 after demolition of the collapsed region

Starting from the previous results, the collapse sequence has been investigated further in this study. The availability of data on the geometry of the reinforcement has allowed the derivation of a complete and refined numerical model. Non linear static analyses are performed to compute the capacity curve of the structure, with the aim to further investigate on the disproportioned effect that arose by the partial soft-story collapse at ground floor. The results obtained help to clarify the role played by the lack of shear strength of a beam at floors 1-4 on the collapse of the three columns along the height of the building.

2 THE BUILDING: STRUCTURAL DESIGN AND RENOVATION WORKS

The CdS building is a 7-story (including two under-ground floors) RC framed structure (see [4]) having an irregular T-shaped plan composed by three nearly rectangular "wings", two roughly oriented in the East-West direction and one in the North-South direction (Figures 1, 2, 4). The code adopted in the structural design was the Italian Seismic Code [1] of 1937, even though newer provisions were enforced by the Seismic Code [2] of 1962.

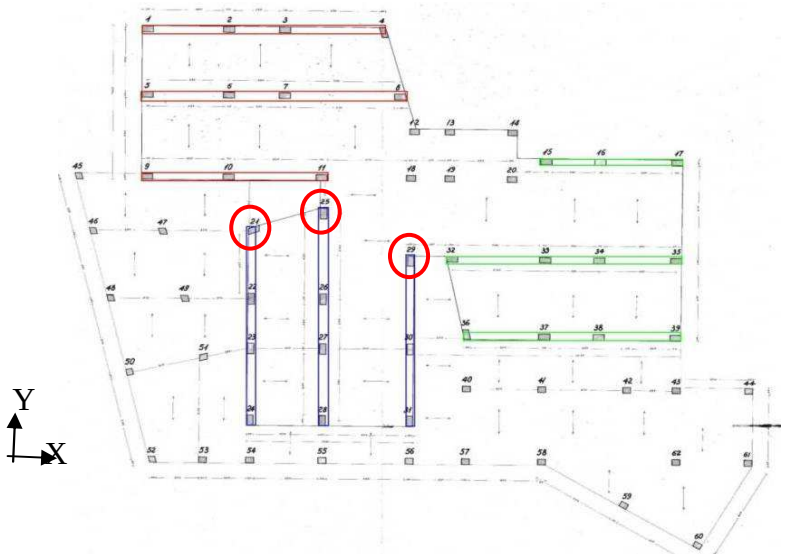


Figure 4. Layout of the vertical members. The colored lines highlight the positions of the main frames within the three wings; circles show the collapsed columns # 21, 25 and 29.

The design principles of both Codes were based on the application, at the centre of mass of each floor, of a set of equivalent static forces, equal to 5% or 7% (according to the 1937 and 1962 Code, respectively) of permanent loads plus 1/3 of variable loads. The 7% value was actually adopted in design. These static forces should have been applied both in transverse and longitudinal directions according to the 1937 Code, and in any horizontal direction according to the 1962 Code. Vertical loads had to be computed as the maximum between:

a) 1.25 times the sum of permanent loads and 1/3 of variable loads,

b) the sum of permanent loads and variable loads.

These criteria were used for designing the main lateral load resisting system, i.e. the three longitudinal moment-resisting RC frames located in each wing (Figure 4). There was no provision for transverse frame within each wing, with the only exception of elements along the short sides of the almost rectangular wings. The evaluation of horizontal loads acting on each frame was apparently performed according to tributary areas. Given the building plan con-

figuration, the procedure led to substantial underestimation of seismic forces in the North-South (NS) direction encompassing only three longitudinal frames. In addition, the contribution of perimeter walls was not included; and during construction a 5 cm thick non-structural slab was placed at all floors, that was not accounted for in the structural design. These two facts further increased the underestimation of horizontal forces.

In analyzing the structural configuration and performance it can be also observed that the stiffness and resistance of the floor assemblage have proven to be sufficient to perform adequate membrane action but the detailing of the transverse frames located, in each wing, on the facades of the short sides, was not suitable for absorbing in-plane horizontal forces. In addition, the RC frame supporting the staircase mostly contributes to strength and stiffness in the EW direction.

A wide refurbishment intervention, not covering the structural system, was performed during the years 1999-2002. The layout of the internal partitions was changed to better adapt the building to its use as a university dormitory (Figure 2). To comply with fire safety regulations, a fire resistant wall (denoted, from the French acronym, as "REI wall" in the following) composed of lightweight concrete hollow blocks, 20 cm thick, was placed at floors from the first to the fourth (thick red line in Figure 2), supported by but not connected to the underlying beam This wall spans from column 18 on roughly half of the beam 18-29, that in turn is part of the beam that connects columns 18, 29, 30, and the corner column 31 (beam 18-29-30-31).

The role that this non-structural element, inserted in a non-engineered way, had on the collapse will be investigated in the following.

3 EARTHQUAKE GROUND MOTION AT THE BUILDING SITE

The ground motion at the CdS site was estimated according to the procedure described in [4], based on considerations on both the actual ground motion recorded at the nearby station named AQK and the soil properties at these two sites. The resulting elastic response spectra along the principal directions of the CdS building (namely: N23°E and E23°S; directions Y and X, respectively in Fig. 3) are plotted for a 5% damping ratio in Figure 5. The prevailing amplitude of the N23°E component at the longer periods is a consequence of the directionality of earthquake ground motion in L'Aquila records along the fault normal direction, as pointed out by different studies (e.g., [5]). The estimated motion has been deemed compatible with the magnitude of the static horizontal forces [4], equal to 7% of gravity loads, prescribed by the 1962 Code [2] in a design process based on a working stress approach.

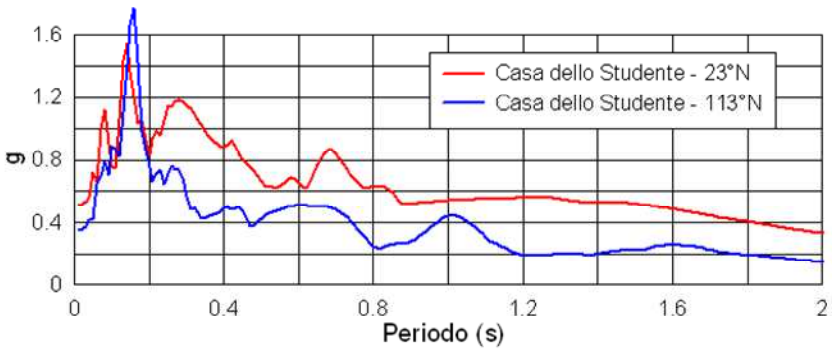


Figure 5. Estimated response spectra along the principal directions of the building, 5% damping [3].

A ratio close to 3 to 1 can be assumed for the spectral ordinates in the likely ranges of period (0.83-1.63s and 0.81-1.45s, respectively), estimated in [4] for the first and the second mode. This is confirmed by the ratio of the extreme values of ground acceleration: the acceleration in direction E23°S was 35% of that in direction N23°E. This fact will be accounted for in the direction the capacity curves are computed.

The wide period ranges depend on the boundary conditions assumed for the model, on the amount of reduction of member stiffness and on the presence of the added fire resistant wall. The boundary conditions addressed the action of the basement wall towards XX Settembre street.

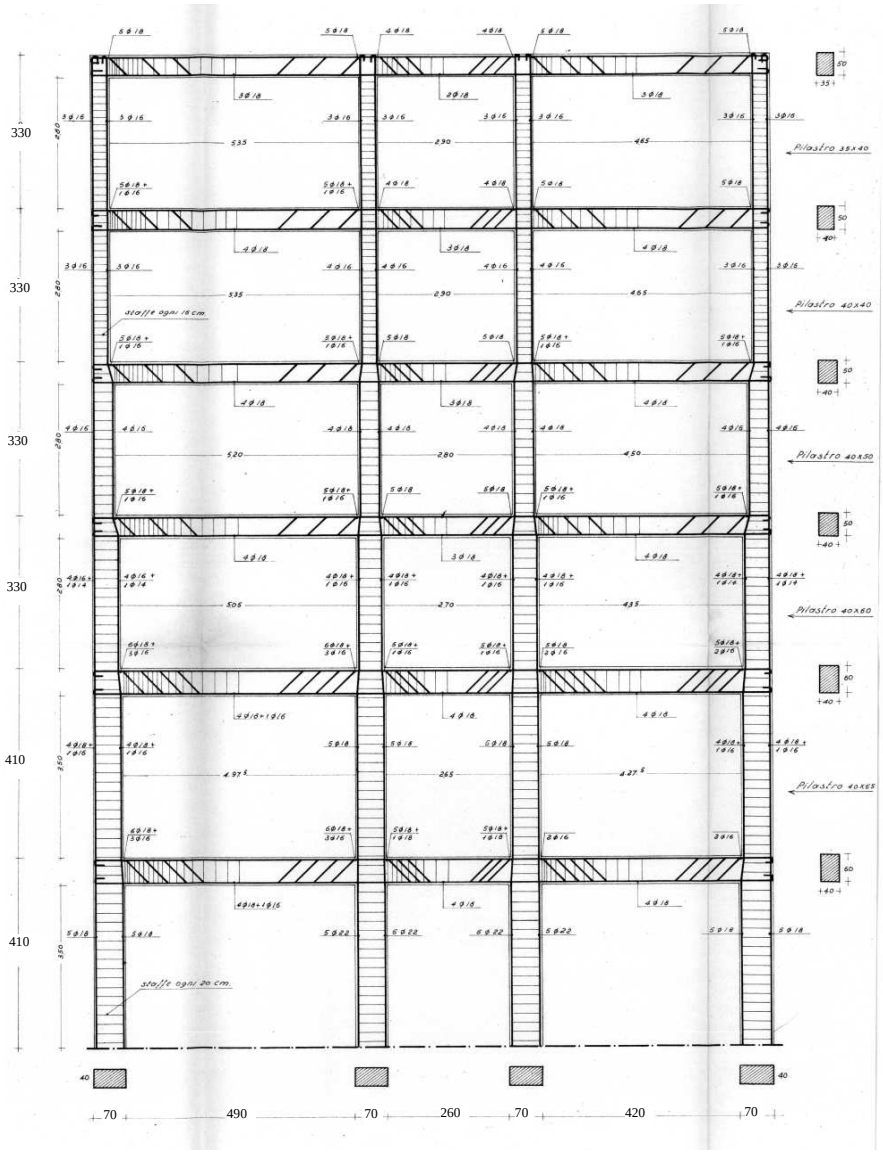


Figure 6. Dimensions of the typical frame and distribution of the reinforcement.

4 NUMERICAL MODEL FOR NONLINEAR ANALYSES

In previous studies, as reported in [3, 4], a comprehensive model was developed to achieve an accurate representation of the geometry and masses of structural and non-structural elements, and of the stiffness of the structural ones. A modification of this model was derived for the static non-linear analyses.

The geometry of the structural elements (beam, columns and floor slabs) derives from both the results of on site surveys and the blueprints recovered by State and County archives damaged by the April 6th, 2009 earthquake. Blueprints describes both the original design and the renovations of the building. As an example, Figure 6 depicts the reinforcement distribution and details of the typical central frame of each building "wing" (colored lines in Fig. 4).

The model derived for the static non-linear analyses reduces the number of degrees of freedom by eliminating the description of the balconies from the model. In the new model, then, the stiffness of the balconies is disregarded but their weight and mass have been applied to the perimeter beams. Moreover, the floor system is considered to be sufficiently rigid in its plane to act as a diaphragm. A view of the solid model is depicted in Figure 6. The new model has been validated by comparison with the previous one in terms of modal periods and correlation of the modal shapes. As in the linear models, the REI wall on beam 18-29 is modeled through 2D quadrilateral and triangular plane-stress (membrane) elements.

The boundary conditions of the model come from in situ observations. All the vertical elements are considered to be fully restrained at their base, since no evidence of movements was detected at the level of the foundations. The perimeter columns on the North and East side are connected to a basement wall.

A static non linear analysis, involving non linear material behavior, requires that beams and columns undergoing non linear response be properly discretized to avoid strain localization effects. In this work beams and columns were discretized in elements of length 20cm and 40 cm, near the members ends and elsewhere respectively. The computer code SISMICAD v.12 [6] is used in the static non linear analyses. This codes discretizes the cross-sections in rectangular sub-domains, here having the longest side less than 7 cm (see Figure 8a). The code assigns 9 Gauss points per sub-domain to follow locally the stress-strain law of the concrete material. A single Gauss point is assumed at the location of a reinforcing bar, as well as perfect bond between concrete and reinforcement. Concrete follows different laws depending on the confinement (confined or unconfined concrete). The elements behave nonlinearly for axial force and bending, being elastic in shear. To avoid spuriously enhancing the bending strength due to moment-axial force interaction, the axial force has been released at one end for all members having both nodes belonging to the same diaphragm or "rigid floor".

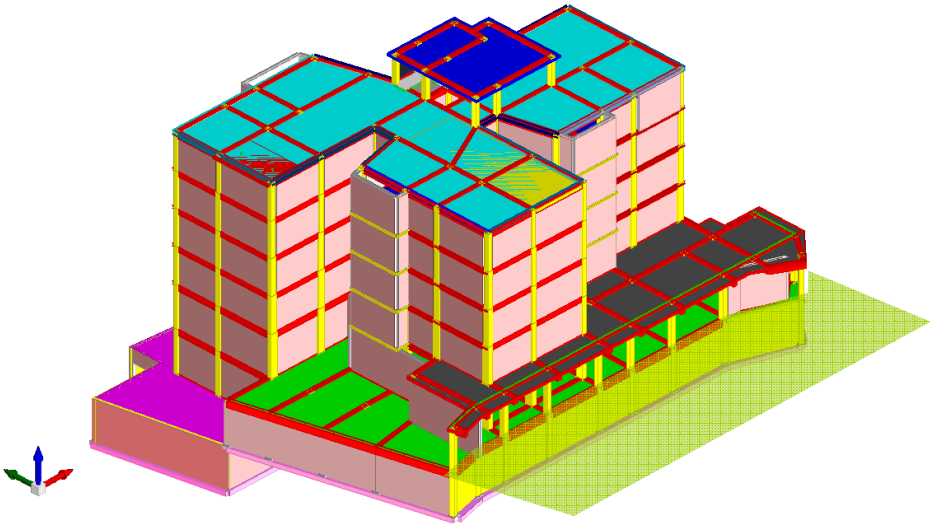


Figure 7. Geometrical model (cantilevered balconies have been disregarded in the modeling).

4.1 Concrete and steel reinforcement models

Concrete has no strength in tension and follows (Fig. 8b) a parabola-rectangle law in compression up to a strain value ε_{c0}. Compression failure is attained at a strain value ε_{cu}. Unconfined concrete has the design nominal values of strength and strain f_{ck} = 16MPa, ε_{c0} = 0.2%, ε_{cu}=0.35%. Confinement has a small effect, due to the low amount of stirrups in columns and in beams, and to a larger extent to the lack of longitudinal reinforcement along the long sides of the rectangular cross-sections. Confinement effectiveness, estimated on a sample column cross-section, accounts for the following values of strength and deformation: $f_{ck.c} = 1.033 f_{ck}$, $\varepsilon_{c2,c} = 1.067\varepsilon_{c2}$ and $\varepsilon_{cu2,c} = \varepsilon_{cu2} + 0.13\%$.

Steel reinforcement follows an elastic-perfectly plastic law (Fig. 8c) symmetric in tension and compression, and has nominal strength and Young's modulus values f_{yk} = 380 MPa, E_s = 2.6 GPa.

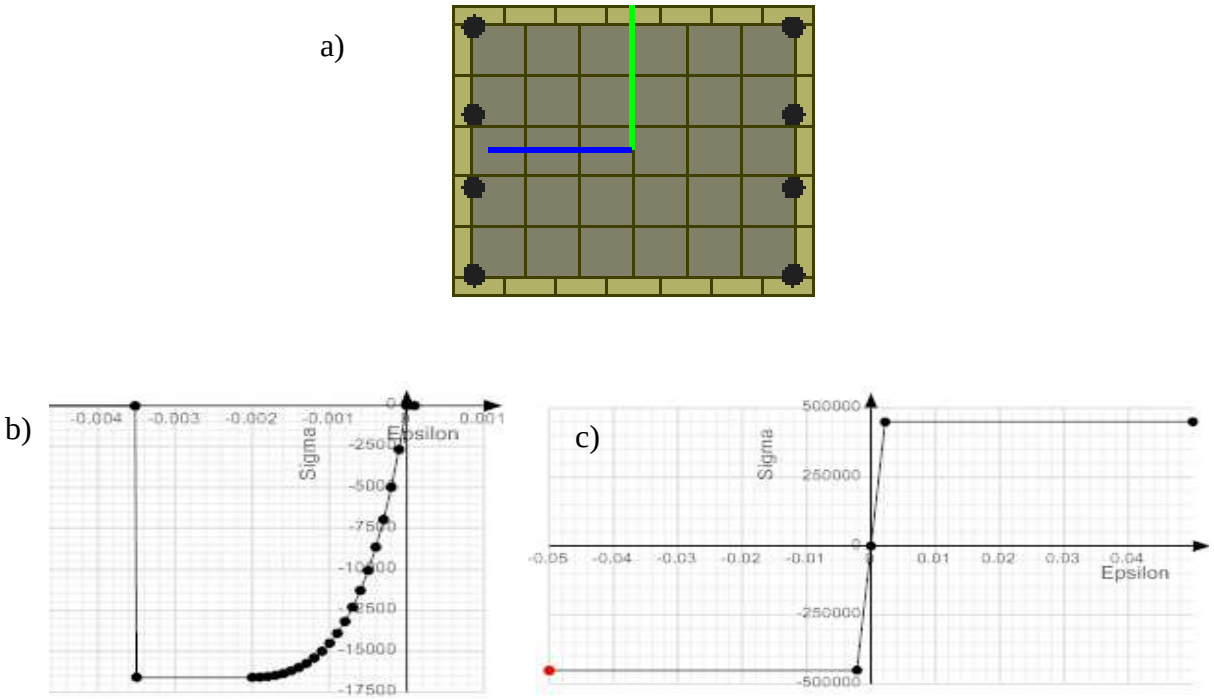


Figure 8. (a) Sample of cross-section discretization for the static non-linear analyses; a lighter color denotes unconfined concrete. Constitutive laws adopted for (b) concrete and (c) steel reinforcement.

The numerical analyses were carried out with both the nominal design values of the mechanical parameters and the average values coming from on-site and laboratory material testing: concrete average compression strength f_{cm} =13.3 MPa, steel average yielding strength f_{ym} =388 MPa. While the yielding strength of the steel reinforcement corresponds to the prescribed value, the one of the concrete is far lower than its prescribed value and corresponds to a concrete of class C8/10, instead of C16/20, according to the classification in the Italian code D.M. 14.01.2008 [8].

4.2 Layout of reinforcement

The reinforcement geometry and layout were derived for the members of the primary frames (colored lines in Figure 4) from design drawings recovered form State archives (e.g. the drawing in Figure 6). The reinforcement distribution was checked during on-site surveys which allowed also to gather further details. Finally, were appropriate, reinforcement details in manuals in widespread use at the time of the design of the structure have been assumed.

As an example of the level of detail with which the reinforcement has been described inside the numerical code, Figure 9 depicts the reinforcement considered for the critical beam 18-31 in the span that supports the REI wall. This span failed in shear at the location of the REI wall.

Bending reinforcement at mid-span is 4ϕ18 mm + 1ϕ16 mm in the lower part of the cross-section, 3ϕ18 + 1ϕ6 in the upper part. In these indications, the symbol ϕ denotes the bar diameter, the first number denotes the number of equal diameter bars, the second number the diameter of the bar in mm. At the supports the upper bending reinforcement is 6ϕ18 + 3ϕ16 while the lower one is 2ϕ18. Shear reinforcement is provided by ϕ6 stirrups at a variable spacing: 240 mm in the central part of the beam and in between 50 to 75 mm at the supports.

Table 1 lists the geometry, at ground floor, of the cross-sections of the columns of the North Wing. The reinforcement is located along each short side of the rectangular cross-section of the columns (see Figure 8a). Shear reinforcement for the columns is provided by 6 mm diameter closed stirrups. On average, the stirrups spacing is 200 mm for most of the columns, without provisions for closer spacing at the ends.

Column	Cross-section dimensions (cm)	Number of bars along short side	Bar Diameter (mm)
21	65x40	5	18
22	40x65	4	18
23	40x65	4	18
24	40x65	4	18
25	40x65	5	18
26	40x65	5	18
27	40x65	5	18
28	40x65	5	18
29	40x65	5	18
30	40x65	4	18
31	40x65	4	18
1	65x40	4	18
9	65x40	4	18
17	65x40	4	18
39	65x40	4	18

Table 1: Cross-section dimensions and reinforcement at ground floor in columns belonging to the North Wing.

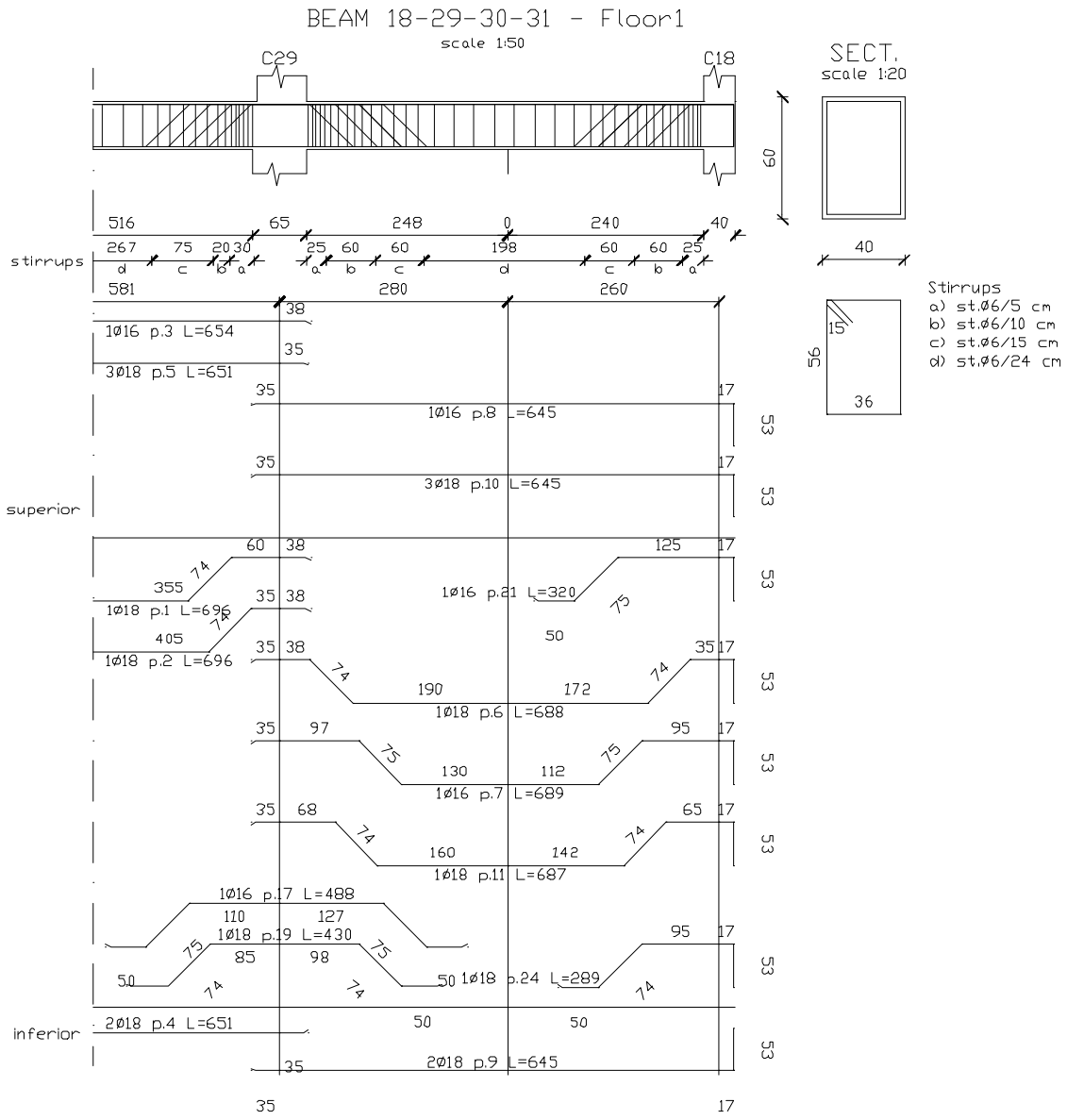


Figure 9. Detail of the reinforcement in beam 18-31 at first floor.

5 NONLINEAR ANALYSES

The non linear static analysis procedure in the present Italian Code NTC 2008 [7] has been adopted to compute the capacity curves for the CdS building. Aim of the analyses it to gain a better insight on the disproportioned effect that arose by the partial soft-story collapse at ground floor. In [7] the nonlinear static analysis, or pushover analysis, has to be performed applying to the structure first the gravity loads and then, for the considered direction of the seismic action, a fixed pattern of horizontal forces proportional to the inertia forces and having as resultant (base shear) the force F_b. The horizontal forces, acting at the floors, are increased monotonically up to the condition of local or global collapse. The horizontal displacement d_c of a control point, located at the center of mass of the last level, is monitored and the curve F_b-d_c is the capacity curve of the structure.

According to NTC2008, this analysis has to be performed with two different distributions of horizontal forces, named primary (Group 1, GR1), and secondary (Group 2, GR2) force distribution. The force distributions relate to the largest value of participating mass of the natural modes for a chosen direction of the seismic action.

Whenever the largest participating modal mass is less than 75% of the building mass in the seismic configuration and the period of the first mode is larger than the corner period T_c between the constant–spectral–acceleration and the constant–spectral–pseudo–velocity ranges of the response spectrum, as it is the case here, the GR1 force distribution is derived from the seismic floor shears calculated in a linear dynamic analysis for the chosen direction of the seismic action. The Group 2 adopts a uniform distribution of forces, that would correspond to a uniform distribution of accelerations along the height of the building.

5.1 Structural configurations at study

Two structural configurations were analyzed, namely: with and without the REI wall on beam 18-29. In addition, two sets of material parameters were considered, derived either from design specifications or from material testing. For each structural configuration and set of material parameters, several push-over analyses were carried out applying the seismic action in different directions. The floor forces were obtained from linear dynamic analyses with the response spectrum in [7], combining the effects of the seismic action in the X (East-West) and Y (North-South) direction (see Figure 4) as it follows ±X, ±Y, ±0.3X, ±0.3Y. The most severe combination turned out to be -0.30X-Y. This combination is very close to that corresponding to the extreme values of the ground acceleration at the site, characterized by an X-acceleration that is 35% of the Y-acceleration. For this ratio of seismic actions the effects of accidental eccentricities equal to 5% of the floor X and Y dimensions were also introduced.

5.2 Results of the pushover analyses

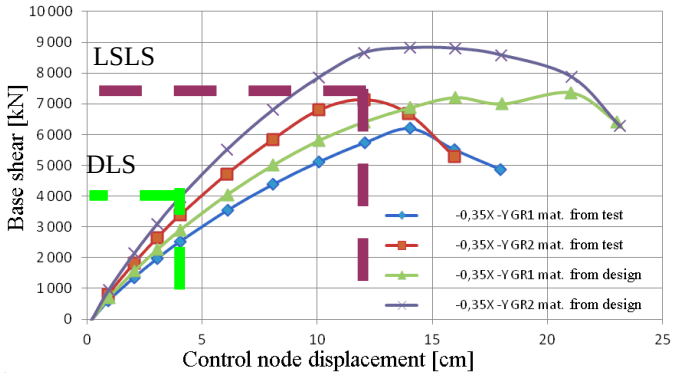
For the sake of brevity, only the results obtained for the direction -0.35X-1.0Y of the seismic action will be presented in the following. Figure 10 depicts the capacity curves of the structure, for GR1 forces distribution, as well as the estimate of the displacement demands at the Damage Limit State (DLS) and the Life Safety Limit State (LSLS). The last one corresponds to the ultimate limit state for seismic loading in EN 1998-1:2005 [8]. Figure 11 shows the deformed configurations with and without the REI wall for a displacement of the control node d_c = 23 cm.

The estimated displacement demands in Figure 10 (4.0 cm at the DLS, 11.8 cm at the LSLS obtained with the response spectrum in [7] evaluated at the CdS) clearly highlight that also the original configuration, without the REI wall, would probably have collapsed under the earthquake of April 6th, 2009. The activation of a soft/weak-story mechanism is clearly visible in both the original and renovated configuration. In the second configuration the mechanism is more apparent, so that it would seem the insertion of the REI wall has adversely affected also the ground-story performance.

From the analysis of the sequence of local collapses, it can be observed that, when the REI wall is included, the beam 18-29 fails in shear at the first floor for a displacement of the control node $3 \le d_c \le 4$ cm, then at the upper stories for $4 \le d_c \le 6$ cm. The collapse of the North wing columns at ground floor starts at $4 \le d_c \le 6$ cm with failure in shear of column #29. The structural configuration without the REI wall sees the first collapse at a larger value of the displacement of the control node, $6 \le d_c \le 8$ cm, when some of the North wing columns at ground floor fail in shear. Whatever the material properties, the force distribution and the con-

figuration (original or renovated) considered, the elements reaching failure are the same, and coincide with those that actually experienced the collapse during the 6 April 2009 earthquake.

a)



b)

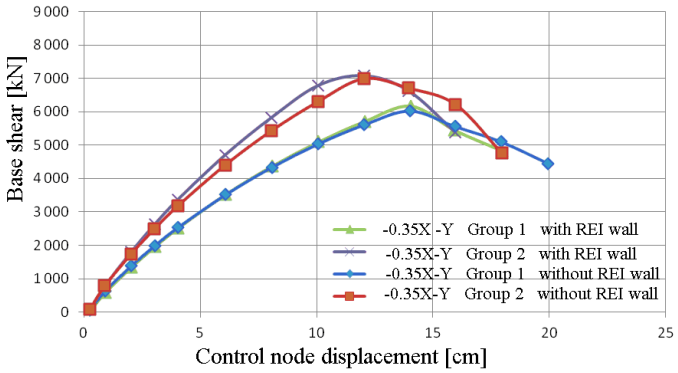


Figure 10. Capacity curves for Group 1 and Group 2 forces distributions: (a) REI wall included and material parameters from design and from tests; (b) with and without the REI wall, material parameters from tests.

The effect of the material properties is investigated in Figure 10a, where the results for the different materials are compared for the two force distributions considered. The poor quality of the materials affects more the base shear capacity of the structure than its ductility. The final value of the displacement under GR1 force distribution is practically the same, regardless the material properties adopted.

The effect of the REI wall is investigated in the Fig. 10b. The wall tends to exacerbate formation of a soft story at the ground floor and induces early failure in shear of beam 18-29. The failure of this beam accounts for the collapse of portion of the floor system in the zone from the end of the REI wall to column #29. This failure can be clearly detected at several floor in the pictures taken immediately after the seismic event of April 6th, before the remains of the North wing were taken down (see for example Figure 3 right). The collapse of column #29 can be ascribed to the increased shear force at the beam interface, causing ultimately the collapse of the column joints in shear and the loss of support of the beam 29-30. The wall plays an adverse role for this column too.

The detected shear failure of beams and columns may depend on the formula adopted for the computation of the shear strength of these members. The sequence of failures, however, do not change if one adopts a standard ideal truss with 45° struts or the more generous (in terms of shear strength) variable inclination strut method in [8].

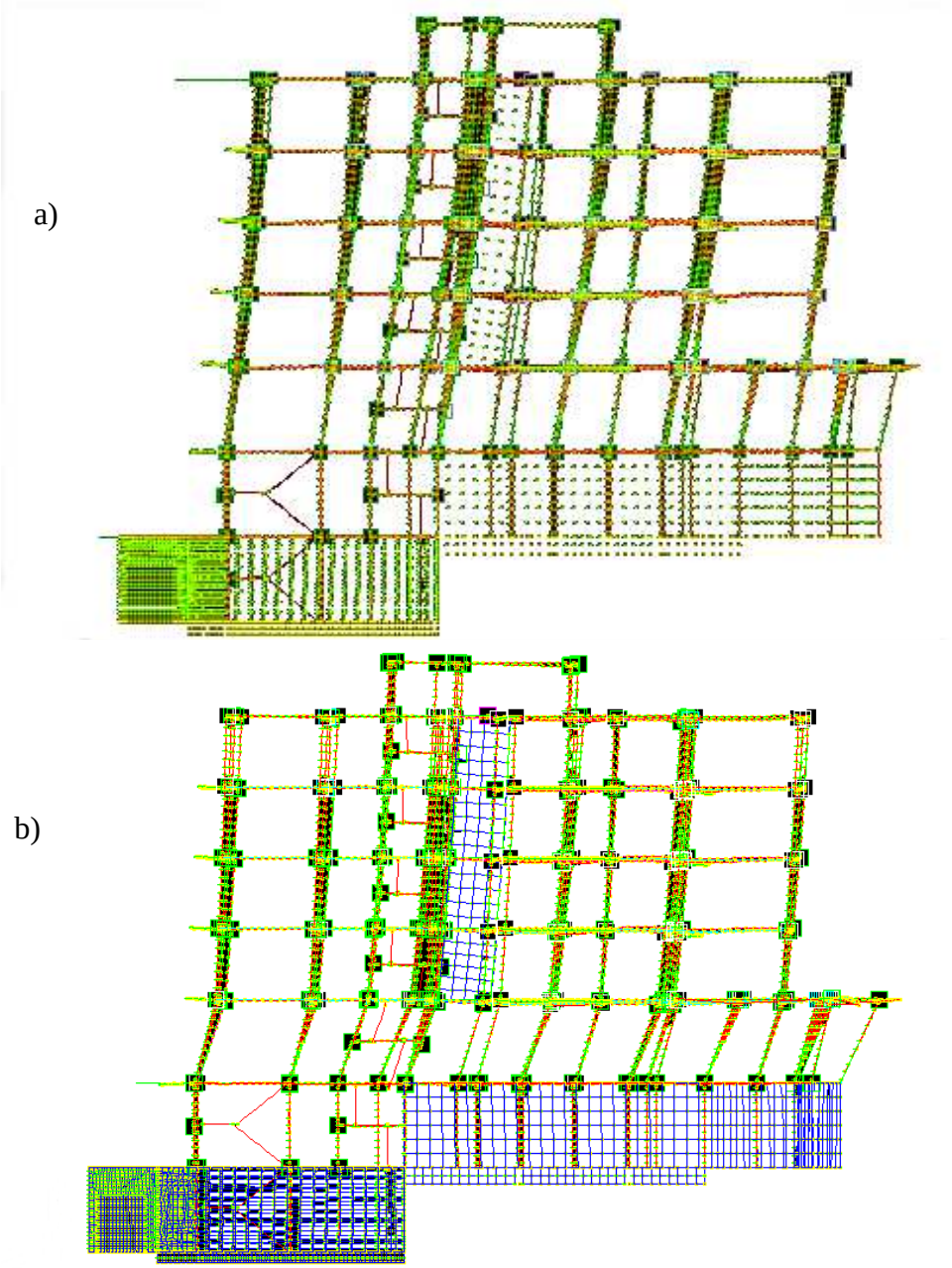


Figure 11. Displaced structure for Group 1 forces distribution and seismic action -0.35X-1.0Y (a) without the REI wall (b) with the REI wall. The control node displacement is 23 cm in both cases.

6 CONCLUSIONS

The results of the pushover analyses confirm the activation of a partial collapse mechanism, restricted to the part of the building where it actually took place, as already found from linear analyses and simple hand computation in [4]. The numerical analysis predicts well also the

elements that fail during earthquake; if performed before the earthquake, could have issued a warning about the inadequacy of the building at study to sustain the design earthquake.

From the numerical results here presented the effects that the REI wall, inserted during refurbishment works, had on the structural behavior are well highlighted. The collapse sequence points out that the combined effect of the REI wall and of the lack of shear strength of beam 18-29 is responsible for the collapse of one of the three failed columns, column #29. For the other two, the collapse can be ascribed to the soft/weak story mechanism at the ground floor, in turn triggered by shear failure of the columns. A partial soft story collapse would have taken place also in the original configuration of the building.

The numerical code here adopted detects a shear failure according to the rules of the Italian Code [7], and accounts for a linear behavior in shear even after detecting a failure. Further analyses with a research oriented code are underway, aimed to better describe the collapse sequence.

DISCLAIMER AND ACKNOWLEDGEMENTS

The content of the paper reflects the Authors opinion and does not intend to anticipate any legal conclusion. Andrea Iadanza e Matteo Rossato performed the numerical analyses as a part of their MS thesis in Civil Engineering under the guidance of the second Author. The educational license of SISMICAD is gratefully acknowledged.

REFERENCES

[1] Regio Decreto Legge n. 2105, 22 November 1937. Nuove norme tecniche di edilizia per tutti i comuni del regno e speciali norme tecniche di edilizia asismica per i paesi colpiti da terremoti. 1937 (in Italian).

[2] Legge n. 1684, 25 November 1962. Provvedimenti per l'edilizia, con particolari prescrizioni per le zone sismiche, 1962 (in Italian).

[3] M.G. Mulas, D. Coronelli, L. Martinelli, R. Paolucci, F. Perotti, A. Pavesi. Analysis of the "Casa dello Studente" collapse during the L'Aquila 6th April 2009 earthquake. *15th World Conference on Earthquake Engineering (15th WCEE)*, Lisboa, Portugal, 24-28 September 2012. Paper #5833.

[4] M.G. Mulas, F. Perotti, D. Coronelli, L. Martinelli, R. Paolucci. The partial collapse of ''Casa dello Studente'' during L'Aquila 2009 earthquake. *Engineering Failure Analysis*, http://dx.doi.org/10.1016/j.engfailanal.2013.02.031, 2013 (in press).

[5] R. Paolucci, C. Smerzini. Strong ground motion in the epicentral region of the MW 6.3, Apr 6 2009, L'Aquila earthquake, Italy. *5th International Conference on Recent Advances in Geotechnical Earthquake Engineering and Soil Dynamics*, San Diego, CA, May 24-29 2010, paper EQ4.

[6] SISMICAD v.12, Concrete S.r.L., Padova, Italy, 2012.

[7] D.M. 14 January 2008. Nuove norme tecniche per le costruzioni, 2008 (in Italian).

[8] EN 1998-1:2005 Design of structures for earthquake resistance – Part 1: general rules, seismic actions and rules for buildings. Bruxelles, Belgium: European Committee for Standardization, 2005.

COMPDYN 2013
4th ECCOMAS Thematic Conference on
Computational Methods in Structural Dynamics and Earthquake Engineering
M. Papadrakakis, V. Papadopoulos, V. Plevris (eds.)
Kos Island, Greece, 12–14 June 2013

EXPERIMENTAL CYCLIC TESTS OF HOLLOW PIERS WITH DIFFERENT RETROFIT STRATEGIES

Pedro Delgado [1], Patrício Rocha[1], António Arêde [2], Nelson Vila Pouca[2], Aníbal Costa[3] and Raimundo Delgado[2]

[1]Instituto Politécnico de Viana do Castelo
Apartado 574, 4901-908 Viana do Castelo, Portugal
pdelgado@estg.ipvc.pt, procha@estg.ipvc.pt

[2]Faculdade de Engenharia da Universidade do Porto
R. Dr. Roberto Frias, s/n 4200-465 Porto, Portugal
aarede@fe.up.pt, nelsonvp@fe.up.pt, rdelgado@fe.up.pt

[3]Departamento de Engenharia Civil, Universidade de Aveiro
Campus Universitário de Santiago, 3810-193 Aveiro, Portugal
acosta@civil.ua.pt

Keywords: experimental tests, retrofit strategies, RC hollow piers.

Abstract. *An experimental cyclic campaign of RC hollow piers has being carried out in the Laboratory for Earthquake and Structural Engineering (LESE) of the Faculty of Engineering of University of Porto (FEUP), aiming to establish, among other purposes, a strategy to retrofit RC hollow piers subjected to horizontal cyclic actions with axial load. The retrofit techniques intend to increase the shear strength and the ductility capacity through the application of CFRP sheets. The main objective of this paper is to evaluate and calibrate the efficiency of several retrofit solutions. The design criteria for the piers retrofit solutions and the different strategies for the practical application are presented, namely, the CFRP sheets for shear retrofit and CFRP base strip, with or without steel bars applied inside the hollow box, for ductility improvement, being the different types of retrofit grouped out in order to understand the main benefits of each one. Results of the experimental campaign allow to discuss and conclude about the efficiency of each retrofit solution, explicitly regarding the improvement of the shear strength and the ductility capacity.*

1 INTRODUCTION

Reinforced concrete hollow section piers are usually one type of structures that sustain seriously damage, as clearly demonstrated in several reports of recent earthquakes. In comparative terms, these consequences of bridge piers vulnerability are found greater than those observed in building structures and, in most cases, the bridge safety is limited and conditioned by pier capacities. Several studies and works have been carried out on solid piers and can be applied to building structures; however, for hollow piers much less research is found in the literature. Usually, hollow piers have large section dimensions, with reinforcement bars spread along both wall faces, and unlike common solid section columns, quite often the shear effect has great importance on the pier behavior. Thus, special attention should be given to this issue when the assessment and retrofit of such type of section piers is envisaged.

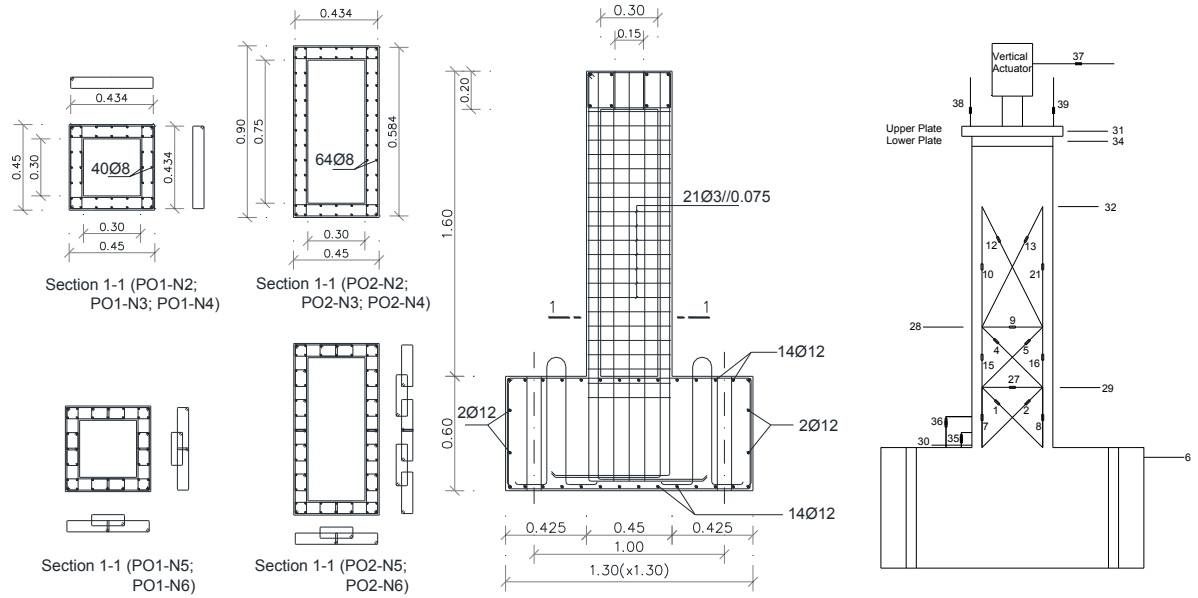
In line with this concern, an experimental campaign has been carried out at LESE – FEUP (Laboratory of Earthquake and Structural Engineering of the Faculty of Engineering of University of Porto), on a set of RC piers. The test setup characteristics and more detailed results are available in previous reports [1-4]. This set of specimens was based on square piers tested at the Laboratory of Pavia University, Italy [5,6], consisting on hollow section RC piers with 450mm x 450mm exterior dimensions and 75mm thick walls, and is being tested in order to understand the influence of the cross section geometry of rectangular hollow piers on the cyclic behavior, bearing in mind the purpose of assessing retrofitting solutions.

2 HOLLOW PIERS CHARACTERISTICS

Ten prototypes with square and rectangular hollow section (see Table 1 and Fig 1) were tested with different transverse reinforcement details, namely: piers N2, N3 and N4 - simple stirrups with 2 legs (representative of the old bridge construction); piers N5 - more detailed transverse reinforcement with 2 legs, with EC8 type, and piers N6 - also detailed stirrups (like piers N5), but with 4 legs (twice cross section area of transverse reinforcement). The unconfined concrete compressive strength (f_c) is 28 MPa and the longitudinal and transversal reinforcement yielding strengths (f_{sy} and f_{swy}) are represented in Table 1. The model schemes shown in Fig. 1a correspond to ¼ scale representations of bridge piers with square and rectangular hollow section, herein referred to as PO1 and PO2. Instrumentation to measure curvature and shear deformations was included along the pier height, because important shear deformations were expected in these tests. The LVDT configuration used in both specimens is shown in Fig. 1b.

Designation	Geometry	Concrete	Long. Reinf.		Transv. Reinf.		
		f_c (MPa)	area	f_{sy} (MPa)	ϕ (mm)	f_{swy} (MPa)	type
PO1-N2	Square	28	40ϕ8	435	2.6	440	2 legs
PO1-N3	Square	28	40ϕ8	435	2.6	440	2 legs
PO1-N4	Square	28	40ϕ8	560	2.6	440	2 legs
PO1-N5	Square	28	40ϕ8	560	2.6	440	2 legs (EC8)
PO1-N6	Square	28	40ϕ8	560	2.6	440	4 legs (EC8)
PO2-N2	Rectangular	28	64ϕ8	435	2.6	440	2 legs
PO2-N3	Rectangular	28	64ϕ8	435	2.6	440	2 legs
PO2-N4	Rectangular	28	64ϕ8	560	2.6	440	2 legs
PO2-N5	Rectangular	28	64ϕ8	560	2.6	440	2 legs (EC8)
PO2-N6	Rectangular	28	64ϕ8	560	2.6	440	4 legs (EC8)

Table 1: Resume of hollow piers characteristics.



a) b)

Figure 1: Hollow RC piers: a) geometry of specimen and b) lateral LVDT layout.

To define the values of Table 2, simple calculation were carried out for the cross section to compute the flexural capacity, while to evaluate the shear capacity the methodology suggested by Priestley [7] was adopted, usually referred in the bibliography as original UCSD shear model [8], being the shear strength (V_d) obtain for these piers through Eqn. 1.1:

$$V_d = V_c + V_s + V_p \qquad (1.1)$$

where V_c, V_s and V_p are the shear force components accounting, respectively, for the nominal strength of concrete (which depends on the pier displacement ductility), the transverse reinforcement shear resisting mechanism and the axial compression force. These values were obtained for an axial load of 250 kN (except pier PO2-N3 with 440kN) that corresponds to a normalized axial force of 0.08 and 0.05, respectively, for the square and rectangular pier cross sections [4].

Designation	Geometry	Flexural Capacity (kN)		Shear Capacity (kN)	
		yielding	ultimate	ductility of 2	ductility of 8
PO1-N2	Square	155	180	170	105
PO1-N3	Square	155	180	170	105
PO1-N4	Square	185	215	170	105
PO1-N5	Square	185	215	170	105
PO1-N6	Square	185	215	220	160
PO2-N2	Rectangular	230	265	170	105
PO2-N3	Rectangular	255	290	200	135
PO2-N4	Rectangular	280	320	170	105
PO2-N5	Rectangular	280	320	170	105
PO2-N6	Rectangular	280	320	220	160

Table 2: Resume of flexural and shear capacities.

The damage on the flange walls (face north and south) exhibited mainly horizontal cracking along the pier height. On the other hand it becomes clear that the pier webs (lateral faces east and west) were the most damaged zones of all specimens, exhibiting inclined cracking and concrete spalling on extensive zones (Fig. 2). Generally, these damage patterns are associated with shear mechanisms, revealing insufficient shear capacity provide by transverse reinforcement. However, some square piers have shear capacity slightly above the flexural capacity (see Table 2), which have resulted on a mixed collapse mechanism, bending/shear.



(a) square – flange (b) square – web (c) rectangular – flange (d) rectangular – web

Figure 2: Typical final damage on the webs and flange for square and rectangular cross sections piers.

For illustration purpose the cyclic response of two piers (PO1-N4 and PO1-N6) are shown in Fig. 3, where it is also included the shear capacity lines for both piers, [7]. Since both piers have the same maximum flexural force of about 200kN, associated with the yielding of the longitudinal reinforcement, premature shear failure was found for pier PO1-N4. On the other hand, pier PO1-N6 achieved the maximum flexural force, but with a moderately low ductility capacity and finally failing with shear mechanism.

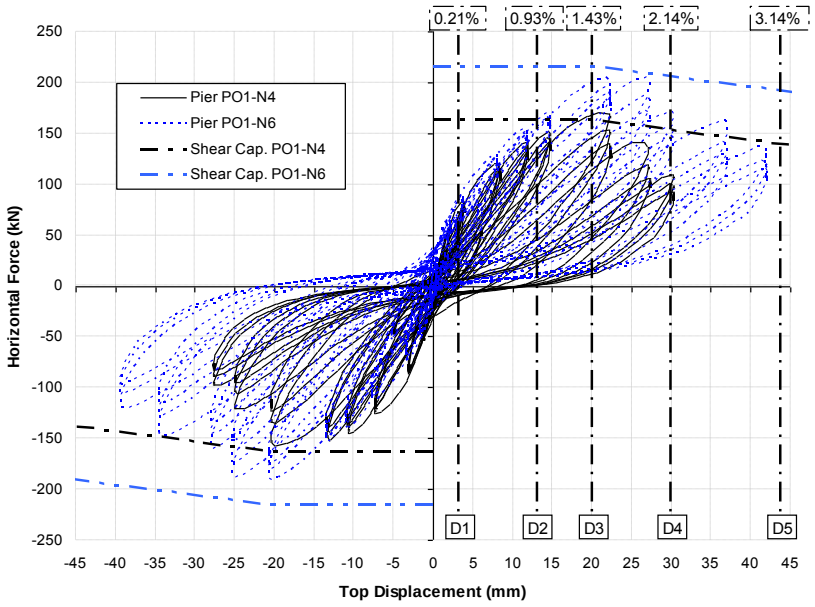


Figure 3: Experimental results comparison – PO1-N4 vs. PO1-N6.

In the Table 3 is presented a summary of shear and flexural capacities, the values of experimental results, as well as the collapse mechanism. The definition of collapse displacement corresponds to the value when the horizontal force applied to the pier reached 80% of the maximum force. For almost all the piers the shear capacity is clearly below the flexural capacity, being the maximum experimental force closer to the numerical estimation of shear strength, although in some cases the experimental response has reached a peak force slightly above the expected values.

Piers	Numerical Flexural Cap. (kN)	Numerical Shear Cap. (kN)	Experimental Max. Force (kN)	Experimental Collapse Displ. (mm)	Collapse mechanism
PO1-N2	155 / 180	170 / 105	130	33	Flexural / Shear
PO1-N3	155 / 180	170 / 105	130	33	Flexural / Shear
PO1-N4	185 / 215	170 / 105	170	25	Shear
PO1-N5	185 / 215	170 / 105	170	25	Shear
PO1-N6	185 / 215	220 / 160	210	30	Shear
PO2-N2	230 / 265	170 / 105	190	25	Shear
PO2-N3	255 / 290	200 / 135	220	25	Shear
PO2-N4	280 / 320	170 / 105	190	30	Shear
PO2-N5	280 / 320	170 / 105	200	30	Shear
PO2-N6	280 / 320	220 / 160	250	40	Shear

Table 3: Resume of forces and collapse mechanism for square and rectangular cross section piers.

3 DESIGN OF THE SEISMIC RETROFIT

After the original specimen cyclic tests, piers were repaired and retrofitted by an external contractor (S.T.A.P.) according to the following steps: 1) delimitation of the repair area; 2) removal and cleaning of the damaged concrete; 3) inside retrofit with transversal steel bars (only in some cases); 4) alignment or replacement of the longitudinal rebars; 5) application of formwork and new concrete (Microbeton, a pre-mixed micro concrete, modified with special additives to reduce shrinkage in the plastic and hydraulic phase); 6) outside retrofit with the CFRP sheets. In order to provide a general idea of the pier damage and of the retrofit process, the following pictures show the piers during repair and after retrofit with CFRP sheet jacketing (Fig. 4).

In order to design the outside shear retrofit with CFRP jackets, the methodology suggested by Priestley [7] was adopted to evaluate the thickness of the rectangular hollow pier jacket for increasing the shear strength above the maximum flexural force while keeping the initial section conditions. According to this methodology the shear strength can be conveyed by equation 1:

$$V_d = V_c + V_s + V_p + V_{sj} \tag{1}$$

where V_c, V_s and V_p are the shear force components accounting, respectively, for the nominal strength of concrete, the transverse reinforcement shear resisting mechanism and the axial compression force; the term V_{sj} corresponds to the possible retrofit contribution with CFRP or metal jackets and can be estimated according to equation 2:

$$V_{sj} = \frac{A_j}{s} f_j \cdot h \cdot \cot\theta \tag{2}$$

where h is the overall pier section dimension parallel to the applied shear force, f_j is the adopted design jacket stress, A_j is the transverse section area of the jacket sheets spaced at distance s and inclined of the angle θ relative to the member axis.



Figure 4: Hollow piers before and after the shear retrofitting with CFRP sheet.

Therefore, using equation 1 in order to increase the shear capacity of specimens, the number of 0.117mm thick CFRP strip layers was estimated. On some specimens, this retrofit was doubled near the foundation for improving the concrete confinement of the pier base and, therefore, the overall pier ductility.

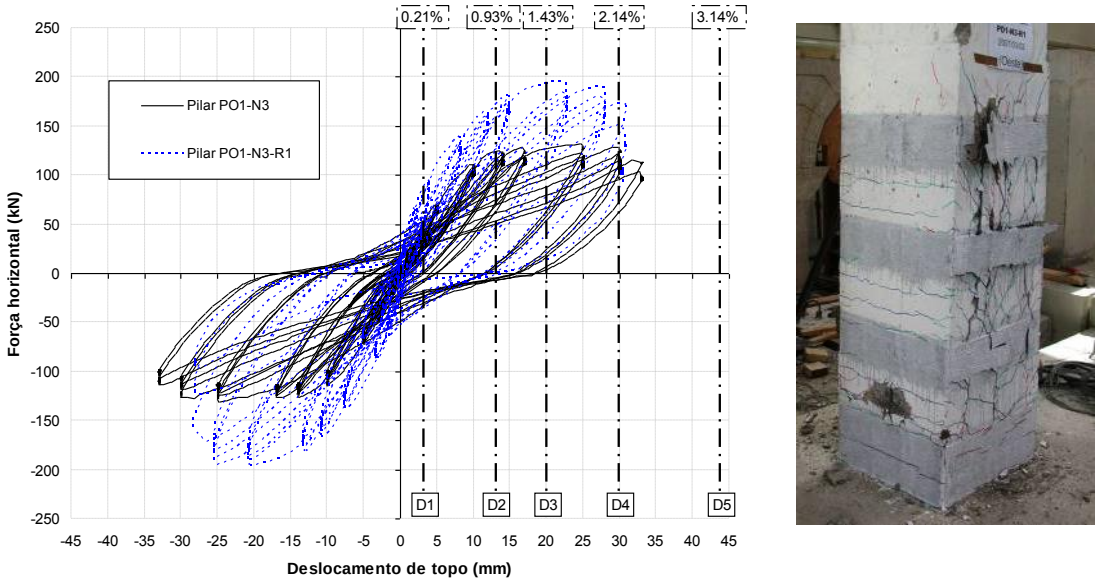
4 RETROFIT SOLUTIONS STRATEGIES

The retrofitted piers have been tested following the same cyclic displacement history of the original specimens, but with additional cycles when necessary. Experimental results for the piers are included in the following sections and fully described in [4].

4.1 Low level of retrofit

The objective of this retrofit was to achieve the shear capacity with the same (or slightly above) the maximum force that can be mobilized for bending. Therefore, for the square pier PO1-N3 one strip layer of CFRP sheet were adopted with 0.117mm thickness by 100mm width and spaced at 200mm along the pier height, at the pier base the first strip layer was considered with a 200mm wide.

This retrofit exhibited earlier cracking between CFRP strips and the pier failure was achieved after the collapse of the first carbon strip (see Fig. 5). By comparing with the original piers, at least 25% increase was obtained for the maximum force, but without significant increase on the maximum displacement, therefore this retrofit strategy has demonstrated to be insufficient to allow a satisfactory ductility behavior.

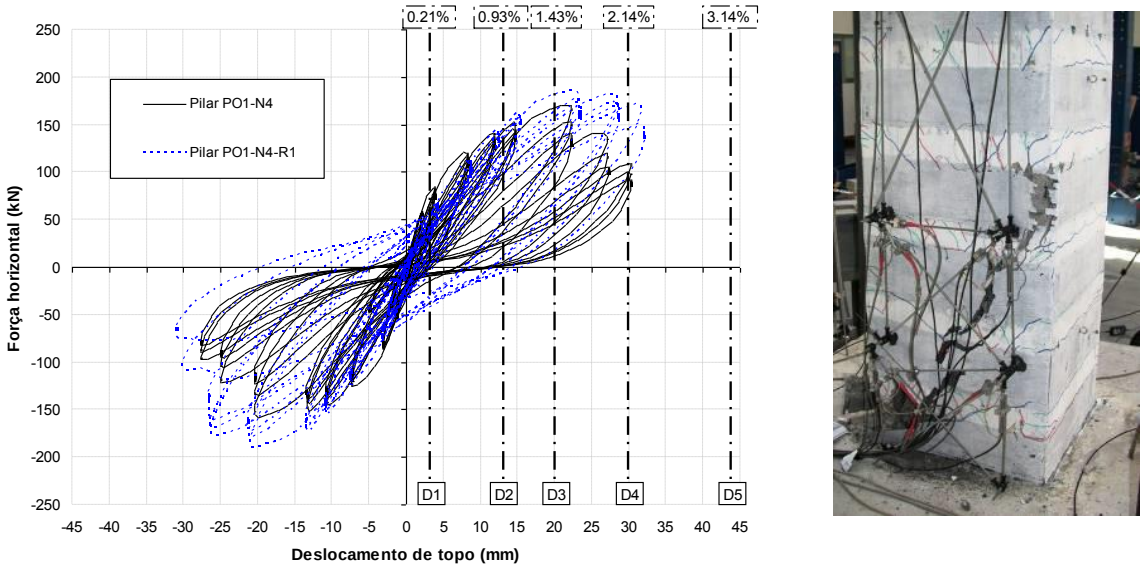


a) Comparison before and after retrofit b) Final damage

Figure 5: Experimental results of pier PO1-N3-R1.

4.2 Optimized level of retrofit

For these piers it was intended to optimize the shear retrofit, corresponding to an increase of 40% in comparison to the maximum force that can be mobilized for bending. Therefore, for the square piers PO1-N4 and PO1-N6, one strip layer of CFRP sheet were adopted with 0.117mm thickness by 100mm width and spaced at 100mm along the pier height in order to increase the shear capacity. The comparison between the original and retrofitted pier (PO1-N4 and PO1-N4-R1) is illustrated in Fig. 6, where a slightly improvement on the maximum horizontal force was reached (approximately 10%) and also a slightly increase on the maximum displacement was achieved.

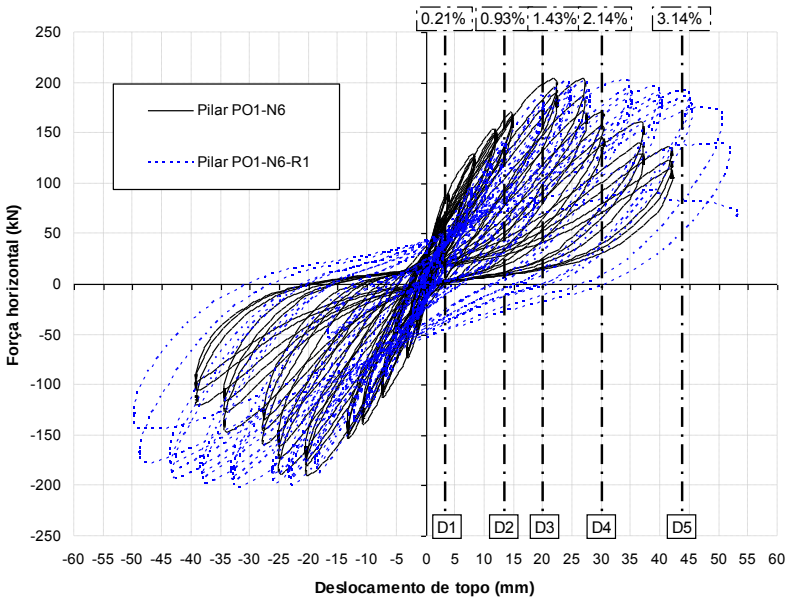


a) Comparison before and after retrofit b) Final damage

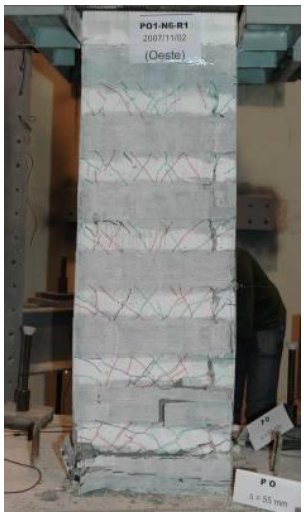
Figure 6: Experimental results of pier PO1-N4-R1.

This CFRP retrofit design evidenced benefits on the pier behavior (see Fig. 6) since it allowed mobilizing a flexure mechanism with plastic hinge at the pier base. However the pier failure was achieved after the rupture of the first CFRP strip, revealing a premature shear failure.

At this stage is worthy to recall that shear capacity of original pier PO1-N6 higher than pier PO1-N4, once the quantity of transverse reinforcement was doubled (see Table 1 and 2). In Fig. 7, the comparison between the original and retrofitted pier (PO1-N6 and PO1-N6-R1) is illustrated, where the maximum horizontal force reached in both piers was almost identical, confirming that in the original pier the maximum yielding force associated with bending behavior was achieved.



a) Comparison before and after retrofit



b) Final damage

Figure 7: Experimental results of pier PO1-N6-R1.

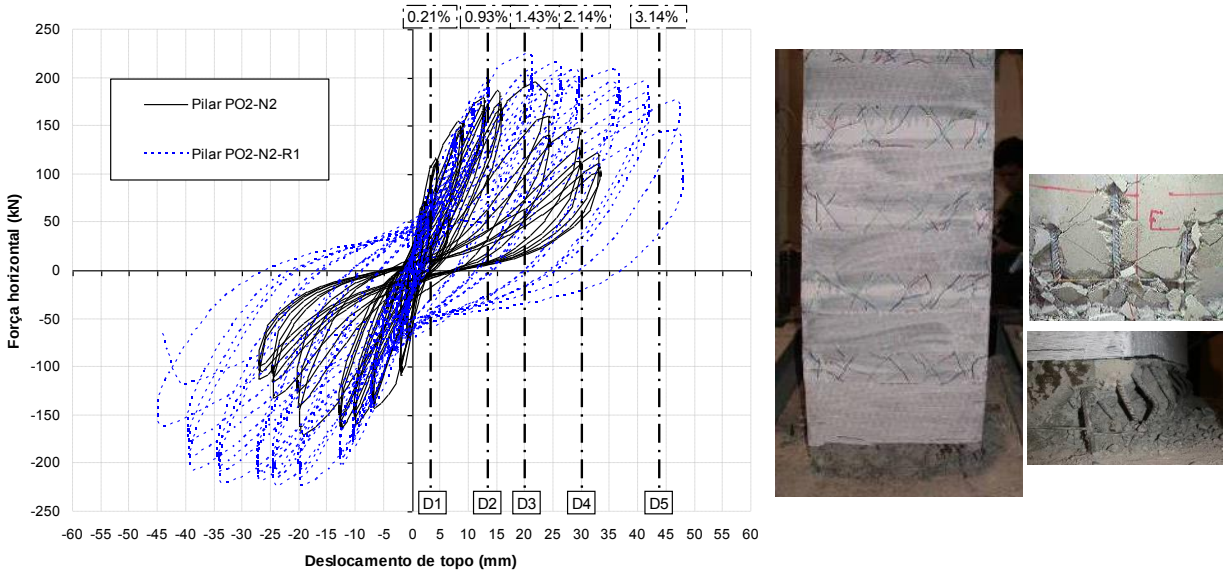
Due to the shear failure prevention provided by the CFRP strips, significant increase on the maximum displacement was achieved (see Fig. 7), corresponding to a displacement ductility capacity of about 3. Therefore, for this pier with double transverse reinforcement area, the CFRP retrofit carried out evidenced significant benefits on its behavior) since it allowed mobilizing a flexure mechanism with plastic hinge at the pier base and satisfactory ductility achieved

4.3 High level of retrofit

For these piers it was intended to obtain the shear retrofit with a significant level of safety, more than 100% in comparison to the maximum force that can be mobilized for bending. Therefore, for the pier PO2-N2, two strip layers of CFRP sheet were adopted with 0.117mm thickness by 100mm width and spaced at 100mm along the pier height in order to increase the shear capacity. The retrofit was doubled at the pier base, leading to a first strip layer 300mm wide.

For this pier, the CFRP retrofit evidenced excellent benefits on the piers behavior (see Fig. 8) since it avoided the shear collapse and allowed mobilizing a flexure mechanism with plastic hinge at the pier base (longitudinal reinforcement bucking). By comparing with the origi-

nal one, this retrofitted pier reached a significant improvement on the horizontal force capacity and maximum displacement achieved, with level of displacement ductility of 4.



a) Comparison before and after retrofit b) Final damage - inside / base

Figure 8: Experimental results of pier PO2-N2-R1.

5 CONCLUSIONS

For original piers, the damage observed in the flanges was considerably low, mainly horizontal cracking along the pier height, but significant damaged was achieved in the webs, exhibiting inclined cracking and concrete spalling on extensive zones. Therefore, generally, these damage patterns were associated with shear mechanisms, revealing insufficient shear capacity provided by transverse reinforcement, however, for some square piers a mixed shear-flexure mechanism was observed. It was also possible to verify and justify the mechanisms of shear failure, by means of simple evaluations on flexural and shear capacities.

For the retrofitting with shear capacity slightly above the maximum flexural force, tests have shown that such strategy is insufficient to allow satisfactory ductility behavior, since cracks started developing earlier between CFRP strips and pier failure was achieved after the first strip collapse. Even so, the peak force increased to 25% over the flexural force.

Pursuing the objective of retrofitting for an ideal shear design, with 40% increase over the maximum flexural force, tests have shown that such strategy is adequate to allow satisfactory ductility behavior. The failure of these piers was achieved after the first strip of CFRP collapse.

The CFRP retrofit design with overestimated level showed excellent benefits on piers behavior since the shear collapse was avoided and a flexure mechanism with plastic hinge at the pier base was achieved. A significant improvement on the horizontal force capacity and maximum displacement was achieved for retrofitted piers.

AKCNOWLEDGEMENT

The authors wish to acknowledge the “Irmãos Maia, Lda” company, for the construction of the tested piers and S.T.A.P.- Reparação, Consolidação e Modificação de Estruturas, S. A. company for the repair and retrofit works. Final acknowledgements to the laboratory staff, mainly Mr. Valdemar Luís, for all the care on the test preparation. This study was performed with the financial support of the “FCT- Fundação para a Ciência e Tecnologia" through the Project PTDC/ECM/72596/2006, ”Seismic Safety Assessment and Retrofitting of Bridges”.

REFERENCES

[1] Delgado, P. Rocha, P. Pedrosa, J. Arêde, A. Pouca, N.V. Santos, M. Costa, A. and Delgado, R. Retrofitting of Bridge Hollow Piers with CFRP. *ECCOMAS Thematic Conference on Computational Methods in Structural Dynamics and Earthquake Engineering*, Rethymno, Crete, Greece, 13-16 July, 2007.

[2] Delgado, P. Rocha, P. Santos, M. Pedrosa, J. Arêde, A. Pouca, N. V. Costa, A. and Delgado, R. Experimental and Analytical Cyclic Tests of RC Hollow Section Piers Retrofitted with CFRP. *FRPRCS-8, 8th International Symposium on Fiber Reinforced Polymer Reinforcement for Concrete Structures.* Patras, Greece, 2007.

[3] Delgado, R., Delgado, P., Vila Pouca, N., Arêde, A., Rocha, P. and Costa, A. Shear effects on hollow section piers under seismic actions: experimental and numerical analysis, *Bulletin of Earthquake Engineering*, **7**, 377-389, 2009 (DOI: 10.1007/s10518-008-9098-x).

[4] Delgado, P. Avaliação da Segurança Sísmica de Pontes. PhD Thesis, FEUP, Porto, 2009. (in Portuguese) (http://ncrep.fe.up.pt/web/artigos/PDelgado_PhD_Thesis.pdf)

[5] Calvi, G..M. Pavese, A. Rasulo, A. and Bolognini, D. Experimental and Numerical Studies on the Seismic Response of R.C. Hollow Bridge Piers, *Bulletin of Earthquake Engineering*, **3:3**, 267-297, 2005.

[6] Pavese, A. Bolognini, D. Peloso, S. FRP seismic retrofit of RC square hollow section bridge piers, *Journal of Earthquake Engineering*, **1 SPEC. ISS.**, 225-250, 2004.

[7] Priestley, M.J.N. Seible, F. Calvi, G..M. Seismic Design and Retrofit of Bridges, John Wiley & Sons, New York, 1996.

[8] Kowalsky, M. J. e Priestley, M. J. N. Improved Analytical Model for Shear Strength of Circular Reinforced Concrete Columns in Seismic Regions, *ACI Structural Journal*, **97:3**, 388-396, 2000.

COMPDYN 2013
4th ECCOMAS Thematic Conference on
Computational Methods in Structural Dynamics and Earthquake Engineering
M. Papadrakakis, V. Papadopoulos, V. Plevris (eds.)
Kos Island, Greece, 12–14 June 2013

EXPERIMENTAL EVALUATION OF THE OUT-OF-PLANE BEHAVIOUR OF TRADITIONAL STONE MASONRY BUILDINGS IN AZORES, PORTUGAL

Arêde, António[1], Costa, Aníbal[2], Costa, Alexandre[3*], Ferreira, Tiago[2], Gomes, Ana[1] and Varum, Humberto[2]

[1] University of Porto, Faculty of Engineering
R. Dr. Roberto Frias, s/n, 4200-465, Porto, Portugal
e-mail: {aarede,anazgomes}@fe.up.pt

[2]University of Aveiro
Campus Universitário de Santiago, 3810-193, Aveiro, Portugal
e-mail: {agc,tmferreira,hvarum}@ua.pt

[3] School of Engineering, Polytechnic of Porto
R. Dr. António Bernardino de Almeida, 431, 4200-072, Porto, Portugal
e-mail: alc@isep.ipp.pt

Keywords: Stone Masonry, In-situ Tests, Seismic Behaviour, Out-of-plane, Strengthening.

Abstract. *Recent earthquakes around the world, particularly those that have recently occurred in the southern regions of Europe, have provoked extensive damages in many traditional masonry structures calling into question the preservation and the safeguard of this heritage. This fact has driven the concern of the scientific community which has been undertaking several studies focused on the seismic vulnerability assessment of this type of structures, particularly in view of their rehabilitation and seismic strengthening/retrofitting.*

In this context, this paper aims at presenting an in situ experimental test campaign recently carried out on an existing building abandoned after the 1998 Azores earthquake, in order to characterize the out-of-plane behavior of traditional masonry constructions. For testing purposes, an experimental test setup based on a self-equilibrated airbags system was used in the out-of-plane test of masonry piers under distinct conditions: original, retrofitted and strengthened.

An overall and brief discussion is included concerning the used test setup, in order to highlight their advantages and shortcomings. The system was found to be efficient for in-situ out-of-plane testing of this type of thick (and massive) stone masonry walls, by applying distributed lateral loads which are agree better with actual inertia forces during seismic occurrence rather than top applied forces. The obtained results are presented and discussed focusing on the effectiveness of the retrofitting and/or strengthening solutions applied during the 1998 Azores reconstruction process. By comparing the results from the tested panels, such solutions were found to significantly increase the walls strength and energy dissipation capacity although not that much for the ultimate displacement.

1 INTRODUCTION

Stone masonry is one of the oldest building techniques used worldwide. Plus, if it is true that it can be considered as the simplest type of structure system concerning its assemblage, it is undeniable that, at the same time, it is one of the most complex construction materials in terms of mechanical properties and behaviour assessment. As a matter of fact, the behaviour of masonry structures under seismic excitations is clearly poor, calling into question the preservation of a valuable heritage which should be protected and safeguard.

Experimental studies are widely recognized as fundamental contributions for a correct characterization of structural components taking into account, for example, its constitution, behaviour, mechanical characteristics and so far. However, and despite the already mentioned value of this heritage, traditional stone masonry still remains with important lack of experimental characterization, particularly concerning its out-of-plane behaviour which is simultaneously one of the most common and most life-threatening collapse mechanisms.

In this context, the work herein presented aims at describing an experimental test campaign recently carried out in order to characterize the out-of-plane behaviour of traditional stone masonry constructions. Taking advantage of the abandon of some traditional masonry buildings after the earthquake that hit the Portuguese archipelago of Azores in 1998, three in-situ test were defined and performed with the application of quasi-static surface loads resorting to a self-equilibrated airbags' system. Bearing in mind the analysis of the retrofitting and/or strengthening solutions applied during the 1998 Azores reconstruction process, in terms of their real effectiveness, three masonry piers, under three distinct conditions: original, retrofitted and strengthened.

It is worth mentioning that this work arises in the sequence of some previous in-situ tests carried out by this research team on the study of the out-of-plane seismic resistance of traditional masonry structures (see [1, 2, 3]).

2 IN-SITU EXPERIMENTS

It is known that one of the main problems in testing existing masonry structures under laboratory-controlled environment lies on the correct reproduction of materials and assemblages. Despite this fact, vary few experimental works under in-situ conditions have been presented to date. In addition, most of the actual in-situ test setup do not guaranty that real service conditions are correctly reproduced (e.g. boundary conditions, acting loads, etc.). Therefore, the key issue of this work consisted on the definition and validation of an in-situ testing scheme that could be used on real masonry constructions, in a reliable way, according with three base requirements:

- Straightforward implementation;
- Reduced time for each test including a light and portable system;
- Possible to be used on the assessment of existing buildings under rehabilitation/strenghtening interventions.

2.1 Description of the testing scheme

The testing system used in this work was idealized to operate with simple and light components, avoiding external reaction elements. Thus, this test setup is based on a self-equilibrated action/reaction scheme making use of the existing elements in the main structure. The reaction frame used is composed by steel hollow rectangular elements and tubular steel elements with

60 mm of diameter to provide the connection between the reaction wall and the reaction frame. At the back of the airbag system and connected to the steel reaction frame, marine plywood planks were used (see Figure 1).



Figure 1: In-situ implementation for out-of-plane tests

Concerning the surface load, it was applied by means of six nylon airbags placed in two levels. The airbags are connected to an air compressor through a series of pipes (ϕ =8 mm and ϕ =14 mm), which gradually inflated the airbags according to the loading history presented in Figure 2. During the tests, the pressure inside the airbags and the displacements of the masonry pier are monitored with pressure and displacement transducers (Linear Variable Displacement Transformers) properly connected to a portable data acquisition system.

It is worth noting that the application of distributed load resorting to an airbags system is not new (see for instance [4, 5]), However, the way how the test setup is implemented in this experimental campaign, associated with the original configuration of the reaction structure, which permits larger displacement levels, could constitute a step forward in the out-of-plane in-situ testing of full-scale masonry structures. Moreover, the capacity of this loading system to apply cyclic loads should also be highlighted.

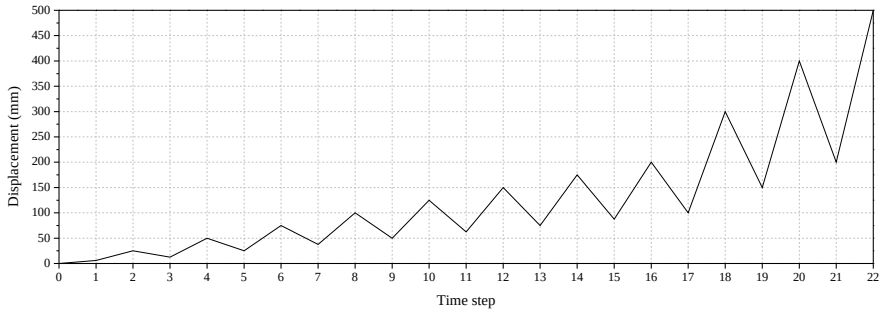


Figure 2: Loading history used in the airbag tests

2.2 Characterization of the test elements

As was already mentioned, a series of out-of-plane tests resorting to quasi-static surface loads was performed on three traditional masonry piers (*sacco* masonry), under different conditions: original, retrofitted and strengthened. Through this variation on the specimens' initial conditions, it was intended, not only to characterise their out-of-plane behaviour, but also to investigate the efficiency of some of the retrofitting and/or strengthening solutions that were widely applied after the 1998 earthquake that hit the Azores archipelago. According to this, the out-of-plane tests took place in an one-storey building, named herein as "Casa Nove", which

can be considered representative of the traditional masonry construction in Portugal. Figure 3 presents an external view of the building as well as a schematic layout in which the three piers tested are highlighted. As can be seen in the figure, for presentation purposes, the masonry piers were named as CN-02S, CN-03R and CN-04 where "R" stands to retrofit and "S" means strength.

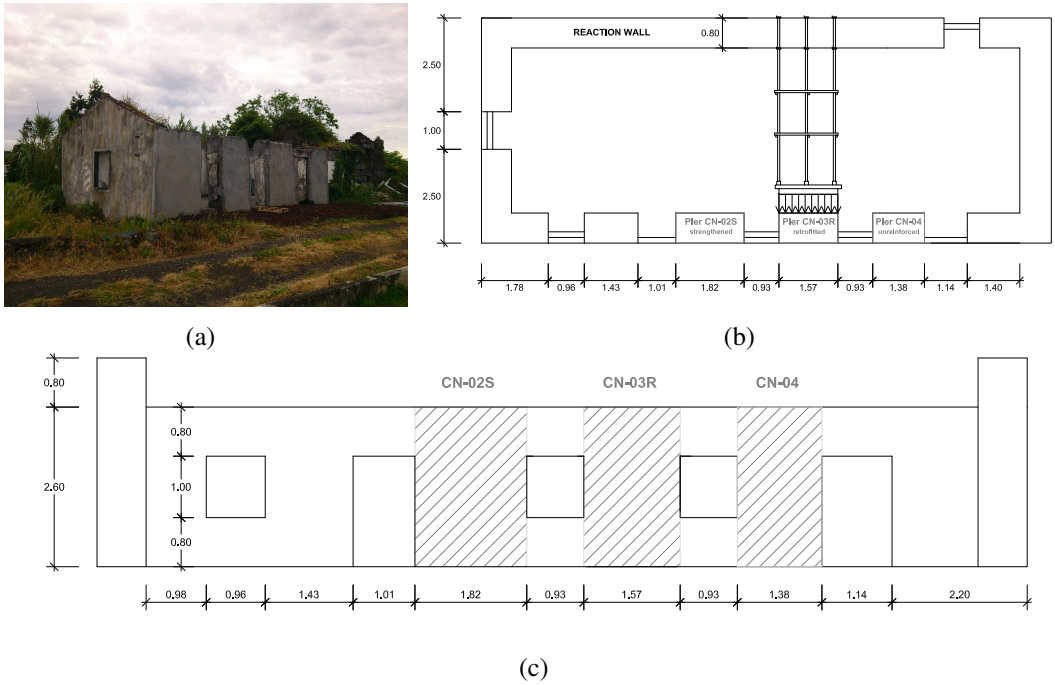


Figure 3: Building "Casa Nove": (a) external view of the building; (b) plan view; and (c) elevation

3 STRENGTHENING AND RETROFITTING TECHNIQUES

Developed in accordance with the recommendations of Carvalho et al. (1998)[6] and supported by Costa and Arêde (2006)[7], the strengthening scheme applied is based on the improvement of the connection between the two leafs that composes the walls section. Such improvement is achieved through the application of a reinforced plaster at both faces of the wall, properly connected by means of mechanical connectors. Figure 4 presents a section of the reinforced section as well as a picture of the moment when the application of the reinforcement was executed.

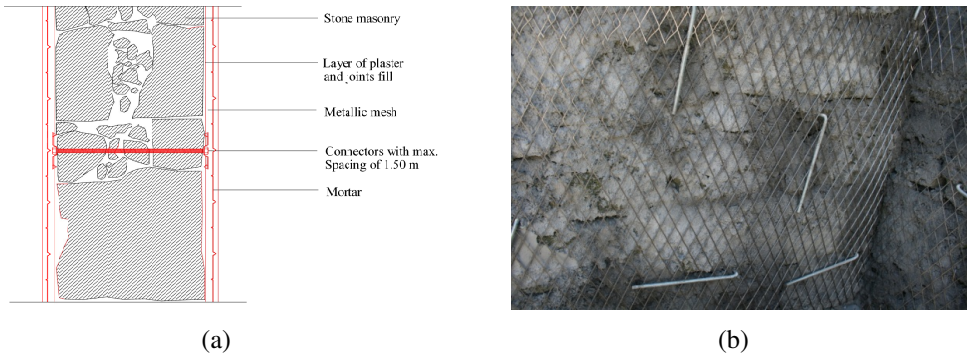
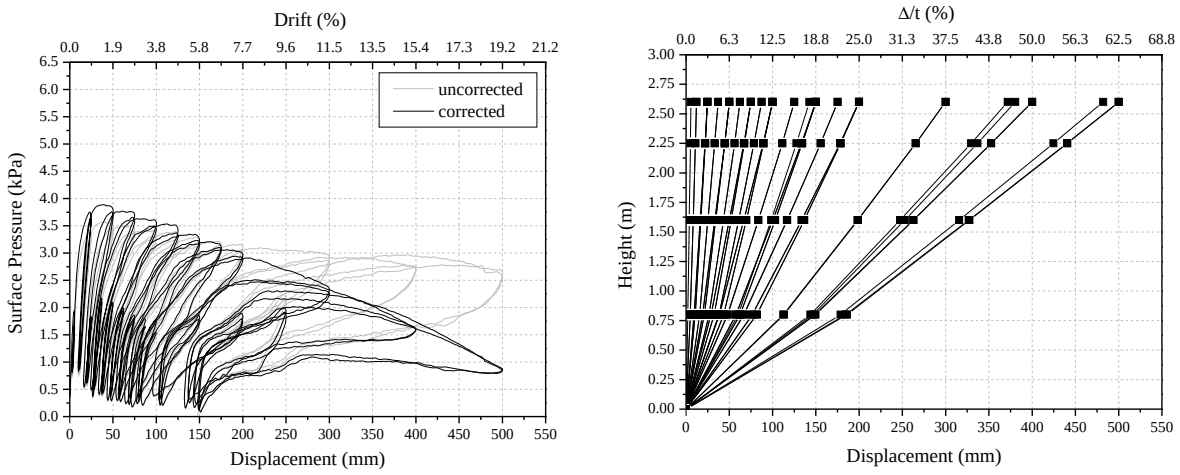


Figure 4: Wall strengthened with reinforced steel mesh: (a) schematic representation; and (b) execution of the reinforcement technique

When this technique is applied prior to the earthquake (or damage due to the experimental test), it is considered as a strengthening scheme (CN-02S). However, if this technique is applied after the earthquake (or applied in a damaged specimen) it can be called as a retrofitting technique (CN-03R).

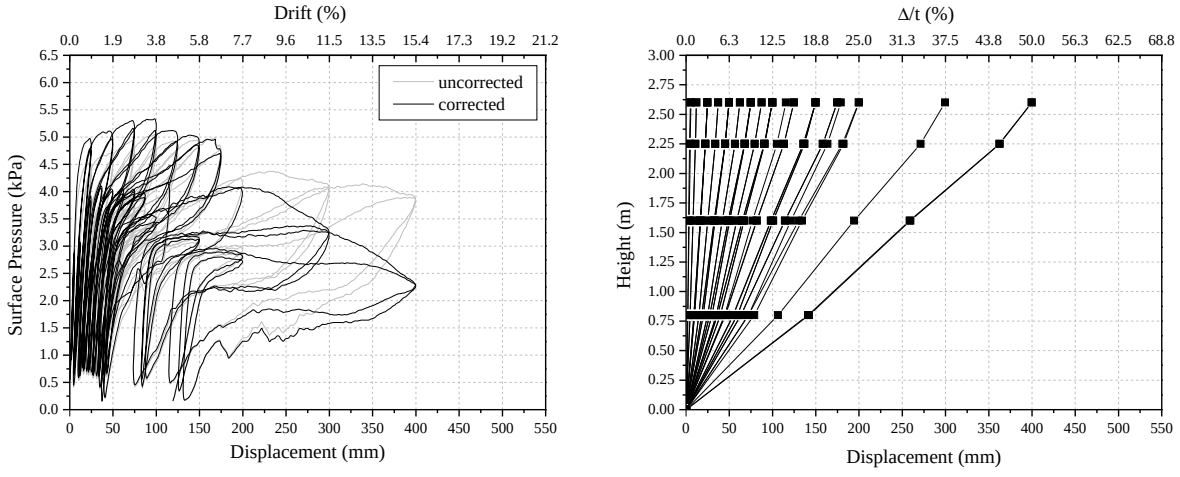
4 RESULTS AND DATA INTERPRETATION

The experimental data is presented on next in the form of load-displacement curves (Figures 7(a)-5(a)), with key points from data summarized in Table 1. It is worth mentioning that the following results were corrected by a correction factor which takes into account the effective pressure, correlated to the airbags' "opening". It is evident from the analysis of the figures, that such correction is particularly important in the range of large displacements. However, despite the importance of this aspect, its discussion is not within the scope of this paper (further considerations can be found in [2]).



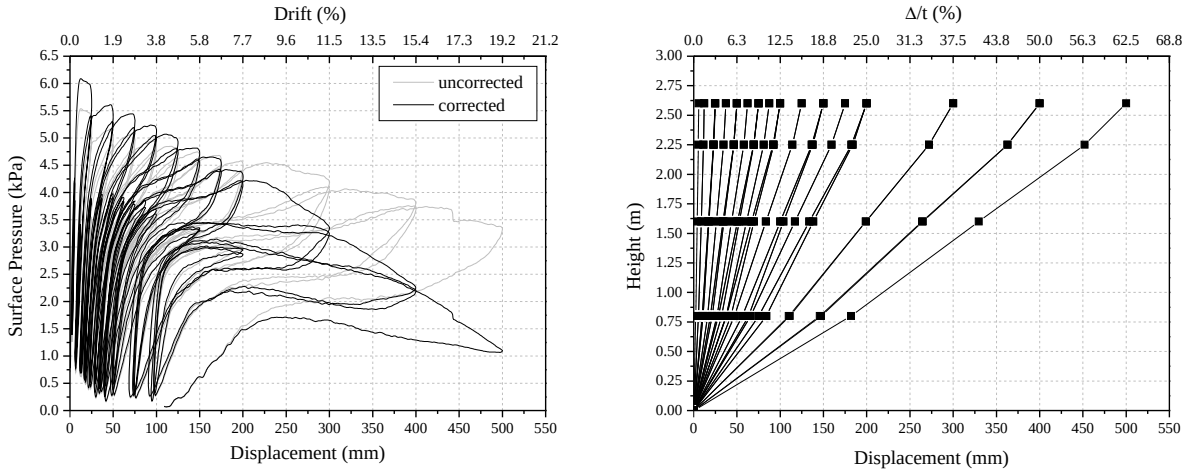
(a) (b)

Figure 5: Wall CN-04: (a) Surface pressure vs displacement results; (b) height wise profiles of out-of-plane displacements



(a) (b)

Figure 6: Wall CN-03R: (a) Surface pressure vs displacement results; (b) height wise profiles of out-of-plane displacements



(a) (b)

Figure 7: Wall CN-02S: (a) Surface pressure vs displacement results; (b) height wise profiles of out-of-plane displacements

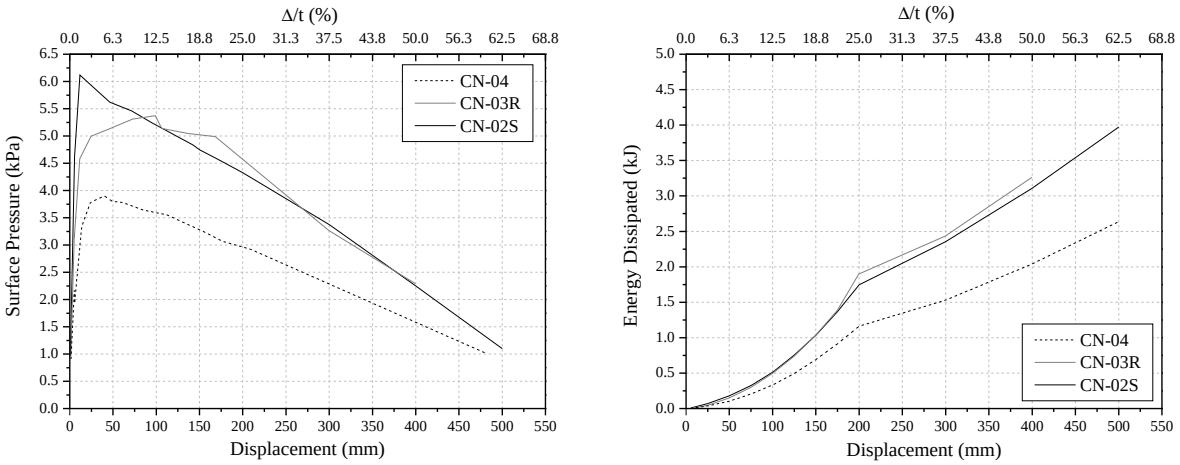
As can be observed in Figure 7(a), the maximum strength of strengthened wall CN-02S was 6.12 kPa which was reached at a displacement of Δ =11.76 mm. This maximum strength value corresponds to an increase of about 14% when compared to the maximum strength obtained for the retrofitted wall CN-03R, with 5.37 kPa, and of about 57% in comparison with the value obtained for the unreinforced wall CN-04, with 3.90 kPa at a displacement of Δ =39.82 mm (see Table 1).

Figures 7(b)-5(b) present the height wise out-of-plane displacements' profiles obtained from the test. In general terms, its analysis shows that the test setup used was able to globally mobilize the out-of-plane response of the walls, which presented a flexural/rocking behaviour. As expected, and conditioned by the test setup which mobilizes the full height of the walls, the displacement profiles are quite similar among the three experimental tests. However, and as presented in Table 1, the displacement achieved at maximum strength is significantly different between the three experiments due to the adopted strengthening/retrofitting technique.

Wall	**At Maximum Strength**				**At Maximum Displacement**			
	Surface Pressure (kPa)	Δ (mm)	Drift (%)	Δ/t (%)	Surface Pressure (kPa)	Δ (mm)	Drift (%)	Δ/t (%)
CN-02S	6.12	11.76	0.45	1.47	1.09	500	19.23	62.50
CN-03R	5.37	98.84	3.80	12.36	2.26	400	15.38	50
CN-04	3.90	39.82	1.53	4.98	0.86	500	19.24	62.5

Table 1: Summary of the surface pressure versus displacement results

Finally, Figure 8(a) presents the envelope curves referring to the three experiments and Figure 8(b) includes the curves of displacement versus energy dissipation reached during the tests. From both results, it is clear that walls CN-02S and CN-03R present better energy dissipation capacity than the unreinforced wall CN-04. In fact, as can be seen in Figure 8(b), the strengthening technique used led to an increase of about 50% on energy dissipation capacity. Moreover, it can be observed a clear change of the energy curve trend at about 200mm, in accordance with the experimental results, which may be explained by a pure rigid body rotation around the base for this displacement level.



(a) (b)

Figure 8: Comparison between experimental results: displacement vs (a) surface pressure; and (b) energy dissipated

It can be also highlighted that the three envelope curves trend to the same ultimate displacement for zero force, meaning that the strenthening/retrofit techniques may be more important for maximum strength and initial wall's behaviour rather than for ultimate displacement (for the wall's typology presented herein).

5 FINAL REMARKS

This work included a general overview of different topics focused on the experimental characterization of the out-of-plane behaviour of traditional stone masonry walls. Within this scope, an in-situ test setup was presented and validated through experimental data obtained from three in-situ tests performed in three stone masonry walls, under different conditions: original, retrofitted and strengthened. From the analysis of the results presented herein, two main conclusions can be pointed out:

(i) the test setup developed in the scope of this experimental campaign proved to be efficient on the in-situ out-of-plane testing of stone masonry walls;

(ii) the strengthening technique applied in two of the specimens, which consisted on the application of a reinforced plaster in both wall surfaces, led to a significative increase on the walls' strength and energy dissipation capacity.

ACKNOWLEDGEMENTS

This work refers to research made with a financial contribution of the Portuguese Foundation for Science and Technology (FCT). The authors' also knowledge the support of the Regional Government of Azores, through its Regional Secretariat for Tourism and Transport (RSTT), and the work of the technicians of the Laboratory of Earthquake and Structural Engineering (LESE) in the experimental activity reported.

REFERENCES

[1] Costa AA, Arêde A, Costa A, Oliveira C. In situ cyclic tests on existing stone masonry walls and strengthening solutions. *Earthquake Engineering & Structural Dynamics* 2011;

40(4):449–471, doi:10.1002/eqe.1046. URL `http://dx.doi.org/10.1002/eqe.1046`.

[2] Costa A, Costa AA, Arêde A, Garcia F, Ferreira T, Varum H. Out-of-plane in situ cyclic testing of unreinforced stone masonry walls with distributed loads. *15th IB2MaC, International Brick and Block Masonry Conference* 2012; :17.

[3] Ferreira T, Vicente R, Varum H, Costa A, Costa AA. Out-of-plane seismic response of stone masonry walls: Experimental and analytical study of real piers. *Proc. of the 15th World Conference on Earthquake Engineering*, Lisbon, Portugal (CD-ROM), 2012.

[4] Griffith M, Vaculik J, Lam N, Wilson J, Lumantarna E. Cyclic testing of unreinforced masonry walls in two-way bending. *Earthquake Engineering & Structural Dynamics* 2007; **36**(6):801–821.

[5] Dizhur D, Derakhshan H, Ingham J, Griffith M. In-situ out-of-plane testing of an unreinforced masonry partition walls. *11th Canadian Masonry Symposium, Toronto*, 2009.

[6] Carvalho E, Oliveira C, Fragoso M, Miranda V. Regras gerais de reabilitação e reconstrução de edifícios correntes afectados pela crise sísmica do faial, pico e s. Jorge iniciada pelo sísmo de 9 de Julho de 1998. *Technical Report*, Lisboa 1998.

[7] Costa A, Arêde A. Strengthening of structures damaged by the Azores earthquake of 1998. *Construction and Building Materials* 2006; **20**(4):252–268, doi:10.1016/j.conbuildmat.2005.08.029.

COMPDYN 2013
4th ECCOMAS Thematic Conference on
Computational Methods in Structural Dynamics and Earthquake Engineering
M. Papadrakakis, V. Papadopoulos, V. Plevris (eds.)
Kos Island, Greece, 12–14 June 2013

STUDY ON THE DEFINITION OF ANALYTICAL FRAGILITY FUNCTIONS FOR CONCRETE BUILDINGS

Mário Marques[1], Epiphanie Amorim[1], Luís Martins[1], Miguel Araújo[1] and Raimundo Delgado[1]

[1] Faculty of Engineering of the University of Porto
Rua Dr. Roberto Frias, s/n, 4200-465 Porto, Portugal
e-mail: mariom@fe.up.pt; ec10310@fe.up.pt, dec11007@fe.up.pt, maraujo@fe.up.pt, rdelgado@fe.up.pt

Keywords: Fragility, reinforced concrete building, seismic risk, limit states, pushover analysis, incremental dynamic analysis.

Abstract. *Development of earthquake risk mitigation strategies is a major concern of the seismology and seismic engineering communities with the main purpose to evaluate the impact of future earthquakes on society and to be able to define appropriate measures to protect citizens and the built heritage. In this way, seismic risk has been defined as the probability of losses, from human, social or economic, due to earthquake scenarios. The assessment of the vulnerability features of the built environment is a key component of a loss model in order to establish the probability of a given level of damage to a given type of structure, and associated with a specific seismic scenario. Within this evaluation, the use of fragility functions is very important since gather the information of the relationships between building performance and ground motions. This study addresses the analysis of different aspects for the definition of the fragility functions, such as: the intensity measure levels, the type of nonlinear analysis to assess the structural performance, the local and global engineer demand parameters (EDP) to characterize the behaviour of the structure and the damage state thresholds. Herein were considered the recommended provisions for seismic risk and safety assessment of structures, included in Hazus [1], FEMA 356 [2] and Eurocode 8 [3] documents and past research works. A comprehensive comparison on the aforementioned parameters and provisions is followed so as to understand how the accuracy of the derivation of the fragility functions relies on such aspects. Therefore, a three-storey gravity designed reinforced concrete building is considered on behalf of its fragility assessment, including a set of 10 real gound motion records homogenized to match the NEHRP design spectrum, defined with a 10% probability of exceedance in 50 years for Los Angeles, scaled by peak (PGA) and spectral (at the fundamental period of the structure, Sa (Te)) accelerations for 36 intensities. Nonlinear incremental dynamic and nonlinear pushover analyses, with the N2 static procedure, are used and the fragility of the building is defined using three global and local quantities: the maximum interstorey drift, the global drift, and the chord rotation of columns and beams.*

1 INTRODUCTION

The current strategies for seismic risk assessment try to replicate in their models the most complete information existent at the site of analysis, so as to ensure that, in the end, the potential damages induced by an earthquake are accurately estimated.

Thus, in general, we may consider three components of the seismic risk [1]: the hazard, the exposure and the vulnerability. When modelling the seismic hazard one should take into consideration several issues, such as the location, intensity or frequency of the events, with the aim to get the values of probability of exceeding a given level of ground shaking intensity within a given time span [2]. Concerning the exposure, a comprehensive survey on the elements that are potentially subjected to losses in hazard zones (known as assets) is sought [1]. Herein, a good exposure model has to describe the distribution of a set of assets, for example in terms of population or structures, grouped by their similar features (location, taxonomy and value). Finally, in what regards to vulnerability, it is expected that this model depicts in a proper way the characteristics of each asset that make it susceptible to the damaging effects of the hazard. When focusing on the physical side of the vulnerability it is deemed crucial to describe the variation in the distribution of loss with increasing intensity measure levels. Social, economic and political factors should also be catered in a seismic risk assessment [3].

Notwithstanding the large number of studies concerning the aforementioned main individual components of a risk analysis [4-6], due to all the uncertainty sources and difficulties to extend to different geographical, tectonic and construction conditions, there is still a wide effort to be undertaken towards the definition of more truthful risk models.

In line with these observations for seismic risk purposes one may also point out that in what seismic assessment and design activities is concerned it is not difficult to find several issues to enhance its consistency regarding the definition and modelling of the same hazard, exposure and vulnerability components, even within code provisions [7].

For risk and performance analyses it is considerably important to analyse the influence of aspects inherent to the fragility of the exposed assets (mainly structural), such as the definition of criteria for the selection of the seismic input, the considered intensity measure quantity that best correlates to the damage, the levels of acceptance of damages, the engineering demand parameter to characterize the structural behaviour or the thresholds for each change on the state conditions of the structures.

Therefore, this work tries to enforce these concerns following a comparative study on previous proposals. The most up to date and commonly used in Europe and United States seismic code provisions and reports are also assessed in the light of providing a clear overview of its expected outcomes.

2 FRAGILITY FUNCTIONS

2.1 Introduction

The distribution of structural and non-structural losses due to the seismic action effects (usually referred as vulnerability functions) is commonly derived from an initial combination of fragility functions and consequence functions. The latter are generally derived empirically and represent the distribution of loss, given a performance level, while fragility functions are essential tools under seismic loss estimations and describe the probability of exceeding a damage state level for a given structure [8, 9]. Limit states are herein perceived as damage or injury performance levels.

In this respect, one may follow three broad approaches for the definition of fragility functions: empirical, expert opinion and analytical.

Empirical fragility assessment relies on collecting damage data for different building typologies due to past historic earthquake events or following an earthquake, wherein this observation of damage under different levels of ground shaking hazard allows to create motion-damage relationships and extend these findings for structures under similar conditions, from regional to performance ones. The empirical approach is in fact often done for reasons of rapid safety evaluations of structures in the aftermath of an earthquake; for detail damage evaluation of a subset of the total number of buildings; or for detailed post-earthquake surveys undertaken by reconnaissance teams on small samples of the buildings [10, 11], Figure 1.

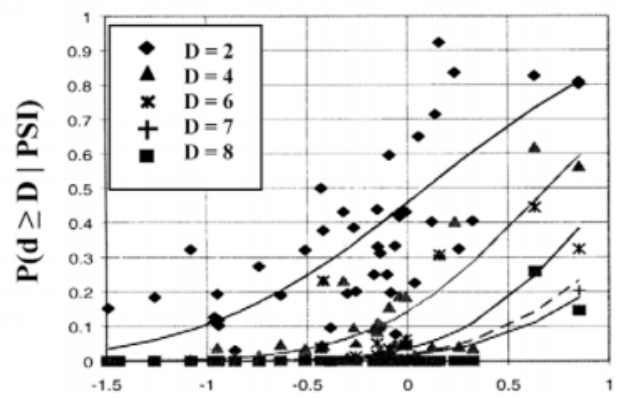


Figure 1: Example of empirical fragility functions for a class of building [12].

Notwithstanding the ease of derivation and the valuable and realistic information gathered from this approach, there are a number of drawbacks [13]. Aspects such as the relatively small number of adequate data points, bias towards damaged buildings or the need to predict the level of ground shaking and its consequent uncertainty, may pretermit the use of empirical fragility functions.

Although less common, the use of expert opinion fragility functions can also be found in literature [14, 15]. The results of this approach are expressed in terms of damage probability matrices and mean damage factor functions. These outcomes describe qualitative the proportion of buildings belonging to each damage grade for different levels of intensity, Table 1.

CLASS A		DAMAGE GRADE					
		0	1	2	3	4	5
INTENSITY DEGREE	V		Few				
	VI		Many	Few			
	VII			Many	Few		
	VIII				Many	Few	
	IX					Many	Few
	X						Many
	XI						Most
	XII						All

Table 1: Example of a damage probability matrix for vulnerability class A [16].

Shortcomings in this methodology are addressed to the vagueness of the matrices, since they are described qualitatively, and to the lack of information for all damage grades for a given level of intensity. To tackle this limitation authors [16] have proposed the use of the Fuzzy Set Theory.

Although the inclusion of real damage data and the experience attained from past seismic events, due to its limitations, the regular use of the aforementioned approaches is arguable

when deriving fragility functions for economic and casualty loss estimations. Thus, also a result of the evolution on the computational capacity, the analytical derivation of the fragility of structures is seen as the most interesting, straightforward and thorough alternative. Herein, structures are modelled through numerical models, duly calibrated to include several material, seismic load and geometric phenomena, in order to relay an adequate and realistic behaviour of a structure or class of structures.

2.2 Analytical fragility functions

Analytical methods have often been used to develop building fragility curves, wherein the structural demands and capacities used may be estimated from elastic spectra, nonlinear static and nonlinear dynamic analyses [17]. As it is understandable the accuracy on the definition of the fragility functions is highly dependent on the quality of the structural analysis, so as to reproduce its real behaviour. Consequently, nonlinear material approaches should be undertaken preferably.

2.2.1 Methods for nonlinear analysis

Two main categories of analysis are tacitly seen as the most valuable methods for fragility and performance assessment, due to its exactitude or simplicity, respectively: the nonlinear time-history and the nonlinear pushover analyses.

Nonlinear time-history is the most accurate procedure to capture the behaviour of the structures beyond their elastic capacity [18], which is evident to occur in fragility assessment. Moreover, code provisions governing seismic design and assessment of structures have included for over two decades the use of dynamic analysis [19]. The seismic load is herein introduced by means of a sufficiently large set of ground motion records at the base of the model, in such a way that enables an amply and direct evaluation of the seismic source mechanisms and of the record-to-record variability in structural responses, Figure 2.

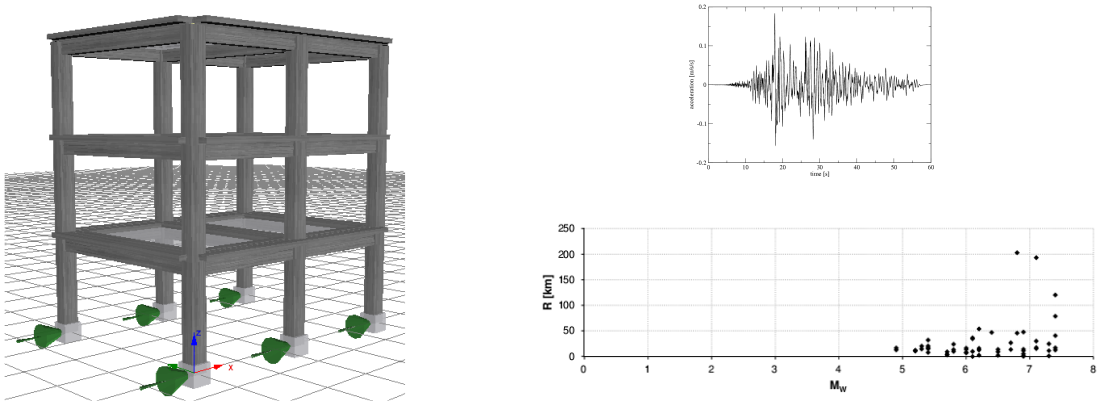


Figure 2: Example of a 3D building modelling for a nonlinear time-history analysis.

Introduced by Vamvatsikos and Cornell [20], the recently emerged Incremental Dynamic Analysis (IDA) is widely used to analyse the structural behaviour under different performance levels to seismic excitations. This method consists in a sequence of nonlinear response history analysis of the structure for a continuously intensity scaled ensemble of ground motions, to cover the entire range, from elastic behaviour to global dynamic instability, of structural response.

However, one of the major drawbacks in both dynamic and incremental dynamic history analyses is the sensitivity of the results obtained to the characteristics of the selected seismic

input, in addition to the higher level of complexity, computational demand and the significant required modelling knowledge, besides the appearance of numerically unstable solutions.

Thereby, nonlinear static pushover analysis has appeared as an interesting alternative approach, due to its simplicity and expeditious, guaranteeing also accurate results. Static analysis caters for the global response of the structures by means of a relationship between the total base shear and the displacement of a control node (usually at the top of the building). This capacity curve expresses an envelope of the equivalent outputs of the dynamic analysis by imposing a lateral load pattern in height (at each storey level) to laterally displace the structure stemming the change on its modal properties.

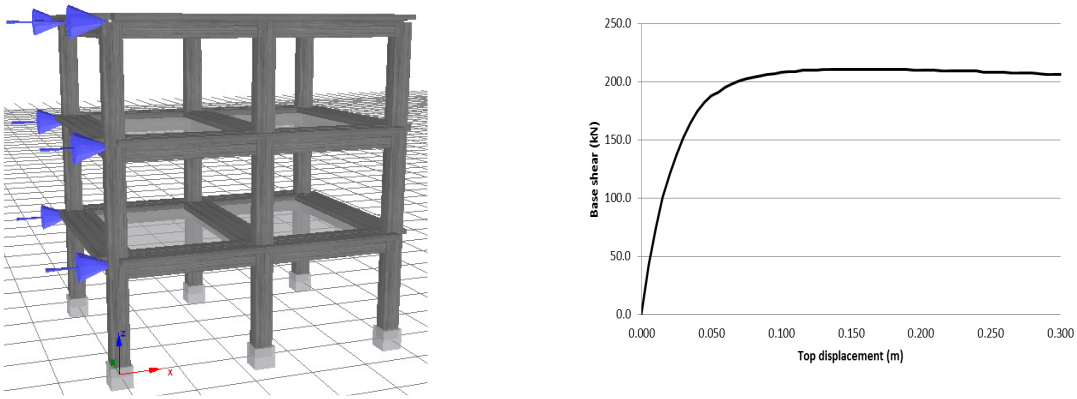


Figure 3: Example of a 3D building modelling for a nonlinear pushover analysis and capacity curve.

Different and enhance approaches haven been proposed concerning assumptions on behalf of the application of the lateral load pattern, thus distinguishing two main proposals: the conventional pushover and the adaptive pushover. The former ones apply a continuously incremented pattern that may follow a uniform, triangular or first mode proportional shape, while on the latter the load shape is changed in each step in accordance to the change on the modal properties of the structure.

Notwithstanding the global structural capacity information given by capacity curves, one may compute the performance of the structure when subjected to a specific intensity level of the seismic input. Therefore, there are a number of nonlinear static procedures (NSP) to estimate the response, among which the main ones are N2 [21], Capacity Spectrum Method [22], Modal Pushover Analysis [23] and Adaptive Capacity Spectrum Method [24]. Herein, the seismic action is introduced by an elastic response spectrum (preferably a code spectrum to vanish potential irregularities on real spectrum). These NSPs diverge on the amount of reducing the elastic response spectrum in order to account for hysteretic degrading effects, on the strategy to reduce the real structure to an equivalent single-degree-of-freedom (SDOF) one and on how *"intersect"* the demand spectra to the capacity behaviour of the structure.

Nonlinear pushover are thus appealing tools, turning into key elements when dealing with massive structural calculations (which is the case when deriving analytical fragility curves), mainly because of their less computational demanding and numerical stability, although its applicability has relevant limitations for irregular structures and do not account for the dynamic effects inherent of the seismic action, moreover one needs to use additional procedures for computing the performance of structures to specific levels of a seismic load.

2.2.2 Damage response measures and limit states

In order to quantify the damage in structures due to the seismic action one may define a specific measure. This is indeed a key stage for the final derivation of the fragility functions and towards this many proposals have been ever since appeared in literature, as well as, in code provisions.

Generally, a division in terms of displacement-based, energy-based and hybrid response quantities is made regarding to the referred damage measures [25]. Likewise, separating these parameters bearing in mind if they represent global or local quantities is also possible.

In light of the most common and reliable damage measures one should point out, for the case of global parameters, the maximum interstorey-drift proposed in FEMA 356 [26] or the global-drift that is used in HAZUS [27]. Herein, interstorey-drift is computed as the relative lateral displacement between floors and is expressed as a percentage of the storey height. On the other hand global-drift appears as the top displacement as a percentage of the building height.

The building performance is evaluated at specific damage levels, also mentioned as limit states, which are function of the referred drifts. In this sense, FEMA 356 proposes three damage performance levels: Immediate Occupancy (IO), Life Safety (LS) and Collapse Prevention (CP). HAZUS itself suggests four limit states: Slight Damage (SD), Moderate Damage (MD), Extensive Damage (ED) and Complete Damage (CD).

These documents albeit initially including a qualitative description for the aforementioned performance levels, suggest rendering to the class of structure in analysis quantitative threshold values, based on comprehensive review of past works and real damages experienced in structures from past seismic events. For the sake of further application in the present work one presents for a reinforced concrete moment frame class the threshold values of FEMA 356, Table 2, and for a reinforced concrete moment frame, Low-rise, Pre-code design level class the threshold values of HAZUS, Table 3.

Classification	**Structural damage states**		
	Immediate Occupancy	**Life Safety**	**Collapse Prevention**
Reinforced Concrete moment frame	0.010	0.020	0.040

Table 2: Maximum interstorey-drift threshold values suggested in FEMA 356.

Classification	**Structural damage states**			
	Slight	**Moderate**	**Extensive**	**Complete**
Reinforced concrete moment frame, Low-rise, Pre-code design level	0.002	0.005	0.012	0.028

Table 3: Global-drift threshold values suggested in HAZUS.

In what concerns to local quantities, a number of research studies have appeared with proposals to quantify the damage of structural elements when the structures are subjected to earthquake loadings [28, 29]. These works had been catered on seismic codes, endorsing chord-rotations as good estimators of the structural damage in ductile elements. FEMA 356 and Eurocode 8 recall on this parameter, proposing the threshold values for beams and columns presented in Table 4, and the performance Equations 1 and 2 for Slight Damage (LS1)

and Near Collapse (LS3) thresholds, while Significant Damage (LS2) limit state is quantified by 75% of the LS3, respectively.

Classification		Structural damage states		
		Immediate Occupancy	Life Safety	Collapse Prevention
Reinforced Concrete moment frame	Beams	0.0015	0.002	0.003
	Columns	0.0050	0.015	0.020

Table 4: Chord-rotation threshold values suggested in FEMA 356.

$$\theta_y = \phi_y \cdot \frac{L_v}{3} + 0.0013 \cdot \left(1 + 1.5 \cdot \frac{h}{L_v}\right) + 0.13 \cdot \phi_y \cdot \frac{d_b \cdot f_y}{6\sqrt{f_c}} \quad (1)$$

Where,

$\phi_y = \frac{\varepsilon_y}{h}$ Yield curvature of the end section;

$\varepsilon_y = \frac{f_y}{E_s}$ Yield strain;

d_b Mean diameter of the tension reinforcement;

h Depth of cross-section;

f_y Steel yield strength, in MPa;

f_c Concrete strength, in MPa;

$L_v = \frac{M}{V}$ Ratio moment/shear at the end section.

$$\theta_u = \frac{1}{\gamma_{el}} \cdot \left(\theta_y + \left(\phi_u - \phi_y\right) \cdot L_{pl} \cdot \left(1 - \frac{0.5 \cdot L_{pl}}{L_v}\right)\right) \quad (2)$$

Where,

γ_{el} Is equal to 1.5 for primary seismic elements and to 1.0 for secondary seismic elements;

$\phi_u = \frac{\varepsilon_{cu} + \varepsilon_{su}}{h}$ Ultimate curvature at the end section;

ε_{cu} Ultimate strain of the extreme fiber of the compression zone;

ε_{su} Ultimate strain steel;

$L_{pl} = 0.1 \cdot L_v + 0.17 \cdot h + 0.24 \cdot \frac{d_b \cdot f_y}{\sqrt{f_c}}$ Length of the plastic hinge.

2.2.3 Procedure for the generation of fragility functions

The analytical approach concerning the generation of fragility function is in general established for classes of structures, where the required simulation effort is very considerable, even for a limited number of random variables. However, the aim of the present study is to assess, following a comparative analysis, the fragility of an individual building in regards to the most important steps and parameters and to depict their influence on the derivation of these curves.

Therefore, the key steps on the generation of fragility functions are, as follows:

- the selection of strong ground-motion records consistent with former seismic hazard analyses, in addition to the included intensity demand measure level that best correlates to the conditional probability of damage, usually expressed in terms of peak ground accelerations (PGA) or spectral accelerations at the fundamental period of the structure (Sa(T));
- the definition of the capacity model of the structure, using one of the previously mentioned methods for nonlinear analysis and assessing the response of the structure given shaking hazard;
- the performance damage analysis, estimating through eligible engineering demand parameters the aftermath of the global behaviour of the structure at several seismic intensities;
- the computation of conditional probabilities of the seismic demand (D) placed upon the structure exceeding its capacity (C) for a given level of ground motion intensity (IM) and for a determined performance level;
- the fit of a function to the cumulative conditional probability points referenced to a single limit state (LS). According to Cornell et al [30], a lognormal cumulative distribution function (CDF) is a reasonable assumption for the statistical distribution of the response of the building, as expressed in Equation 3 in terms of an earthquake intensity measure. Hence, one needs to compute along the *x* intensity measure quantity the median (μ) and the standard-deviation (β) parameters of the CDF, from the Maximum Likelihood Estimation method.

$$P_i\left(LS_i \mid IM\right) = F_i\left(x\right) = \Phi\left[\frac{1}{\beta}\cdot \ln\left(\frac{x}{\mu}\right)\right] \tag{3}$$

3 CASE STUDY

3.1 Objectives

The methodology presented above will be applied for the fragility assessment of a reinforced concrete building, illustrating further details on key aspects of the approach through a comparative study addressed to:

- the use of PGA and Sa(T) scaling intensity measures;
- the application of nonlinear pushover or time-history nonlinear methods;
- the global and local engineering demand parameter to quantify the structural demand;
- the performance damage limit states proposed in FEMA 356, HAZUS and Eurocode 8 [31].

3.2 Building model

The seismic fragility assessment of a real reinforced concrete frame building, representative of the European construction, is performed following the procedure already presented in the above sections.

This structure, located in Italy, is a typical construction of the pre-seismic code period, which has been designed for resisting vertically-acting gravity loads. This model, herein called *mod4*, is an asymmetric three-storey RC regular frame structure without masonry infill walls, with a total height of 9.05 m and with three bays of 4.05 m, 3.0 m and 3.5 m length each, illustrated in Figure 4.

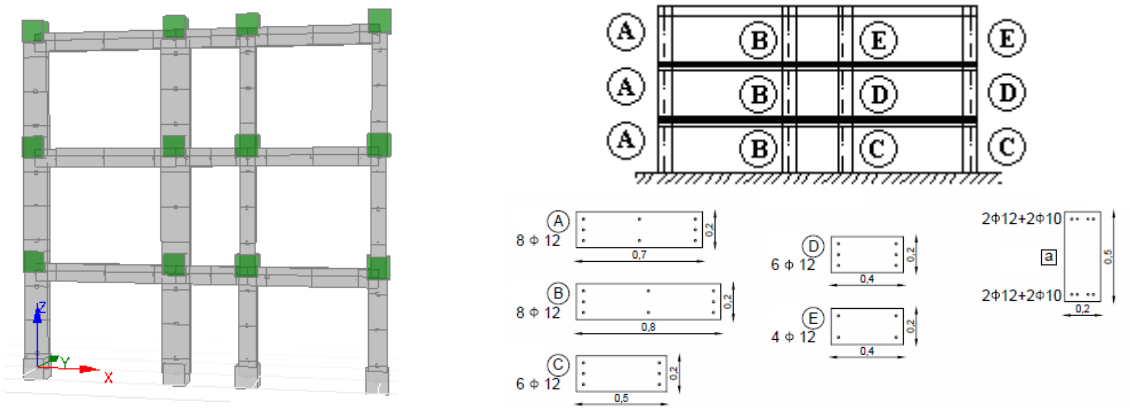


Figure 4: Structural model of mod4 frame building.

Five column sections were modelled so as to truthfully represent the disposition of the longitudinal reinforcement bars along the elements length. Whilst, a single cross section was considered for beams. A lumped mass distribution at each beam-column joint was assumed in the structural model. Moreover, soil-structure interaction effects were not taken into consideration for this study and 2% tangent stiffness proportional viscous damping was considered in the dynamic analyses.

Structural analyses were carried out using SeismoStruct [32], a finite element software capable of predicting the large displacements behaviour of space frames under static or dynamic loading, taking into account geometric nonlinearities and material inelasticity. The nonlinear material behaviour of the structure was captured using a fibre-based model where the inelasticity is considered distributed along the elements length. Modal analysis have concluded that *mod4* is mainly governed by its first mode of vibration, with a fundamental period of T=0.34s and an effective modal mass of 78% of the total mass of the structure.

3.3 Strong ground motion records

The seismic input for deriving fragility functions consists of an ensemble of ten records selected from a suite of historical earthquakes scaled to match the 10% probability of exceedance in 50 years (475 years return period) uniform hazard spectrum for Los Angeles [33].

The ground motions were obtained from California earthquakes with a magnitude (Mw) range of 6-7.3 recorded on firm ground at distances (D) of 13-30 km; their significant duration (Bommer and Martinez-Pereira, 1999) ranges from 5 to 25 seconds, whilst the PGA (for intensity 1) varies from 0.23 to 0.99g, which effectively implies a minimum of 0.11g (when intensity level is 0.5) and a maximum of 3.5g (when intensity level is 3.5), Table 5.

Label	Record	Mw	D (Km)	Duration (s)	Significant Duration (s)	PGA (cm/s^2)	Sa(T) (cm/s^2)
LA02	El Centro, 1940	6.9	10.0	53.48	24.52	663	1309
LA04	Imperial Valley, 1979	6.5	4.1	39.38	7.09	479	1510
LA06	Imperial Valley, 1979	6.5	1.2	39.09	11.22	230	622
LA08	Landers, 1992	7.3	36.0	79.98	22.24	417	1103
LA10	Landers, 1992	7.3	25.0	79.98	20.72	353	877
LA12	Loma Pietra, 1989	7.0	12.0	39.98	6.40	951	1791
LA14	Northridge, 1994	6.7	6.7	59.98	5.52	644	1824
LA16	Northridge, 1994	6.7	7.5	14.945	7.04	569	1331
LA18	Northridge, 1994	6.7	6.4	59.98	5.30	801	2711
LA20	North Palm Springs, 1986	6.0	6.7	59.98	6.78	968	2311

Table 5: Employed set of records.

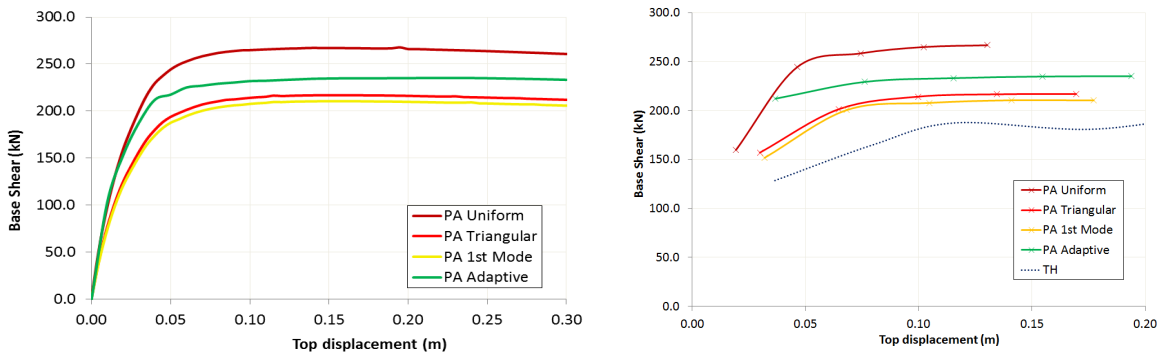
3.4 Background on performance assessment

In the current endeavour two stages were considered regarding the scaling of the ground motion records.

The former admits for the set of ground-motion records and respective spectra five intensity levels, linearly proportional by a factor of 0.25, 0.5, 0.75, 1.0 and 1.25, performing both nonlinear pushover and dynamic approaches, in a total of 50 analyses. This preliminary study enables the comparison between PGA and Sa(T) without introducing additional bias into the study due to individually scaling each record to a target intensity level.

For the second study records are scaled in terms of PGA to 36 intensities levels, considering a maximum acceleration of 2000 cm/s^2.

An initially analysis concerning the performance of pushover analyses (PA) has revealed that no major differences are depicted from adaptive and conventional triangular and first mode proportional load patterns, Figure 5. Likewise, their differences to the median structure responses captured by dynamic time-histories (TH) are identical, and justified to the use of the first version of the N2 method, that disregards the influence of the energy dissipation to the hysteretic damping in the reduction of the elastic spectra.



A) Capacity curves B) Performance assessment

Figure 5: Structure response.

From this point, further pushover analyses are performed admitting an adaptive load pattern.

3.5 Fragility assessment – intensity measures analysis

The fragility curves produced in this preliminary analysis try to call attention to the importance of the intensity measure used for the derivation of these functions. Furthermore the absence of a target intensity level to match each record is also assessed, using solely the original ten ground-motions linearly scaled by five proportional factors.

Hence, these 50 records are sorted according to their PGA and Sa(T) intensity values, and then grouped in sets of 10 elements in terms of ascending intensities. Each new set is considered for deriving the fragility functions, assuming an intensity level equal to the median of the group of records, Table 6.

Set 1		Set 2		Set 3		Set 4		Set 5	
PGA	**Sa(T)**	**PGA**	**Sa(T)**	**PGA**	**Sa(T)**	**PGA**	**Sa(T)**	**PGA**	**Sa(T)**
131	330	241	659	409	990	583	1368	890	2260

Table 6: Set of records and its median PGA and Sa(T) intensities, in cm/s^2.

The performance levels proposed in HAZUS and already presented in section 2.2.2, which consider the global drift measure the engineering demand parameter, are used to develop the fragility functions of the frame. A statistical treatment on the exceedance of each limit state is carried out, as illustrated for the case of pushover analysis in Figure 6, and thereby derived the fragility of the structure.

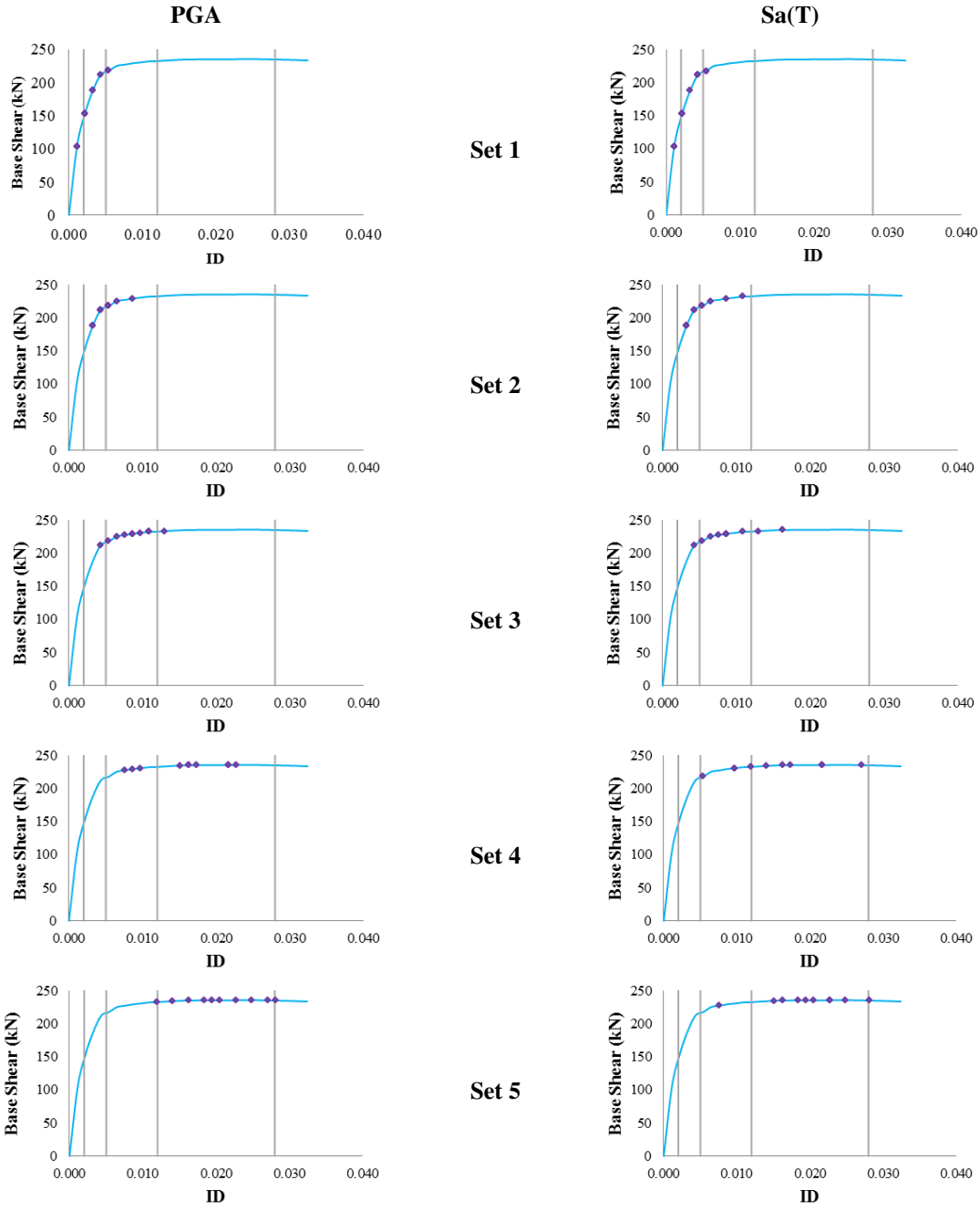


Figure 6: Pushover analysis performance points.

Figure 6 represents the performance of the structure using pushover analysis in regards to the global-drift and total base shear relationship, for each of the 10 ground-motion records contained to each ensemble. From this comparison it is attained the quite close behaviour of the building disclosed for both PGA and Sa(T) measures.

A meaningful comparison regarding the influence of the nonlinear method of analysis is needed for assessing the fragility of the structure with this approach.

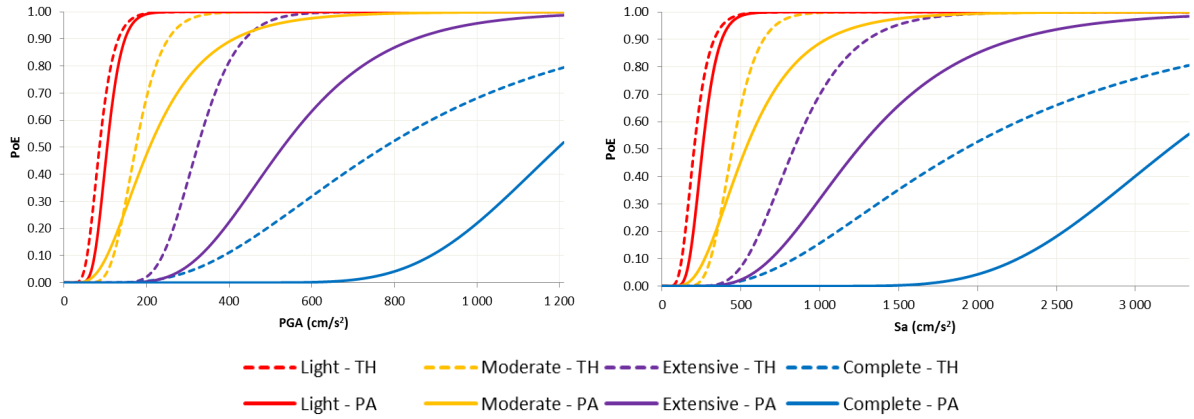


Figure 7: Fragility functions for HAZUS thresholds.

Comparing the fragility curves generated in terms of PGA or Sa(T) no major differences are identified for all the limit states of damage, Figure 7, either in the case of pushover analysis or in the dynamic analysis. Theses outcomes are explained with the similar performance responses of the structure already pointed out (Figure 6), which is a promising conclusion since one of the concerns in seismic risk evaluations is indeed the type of scaling of the seismic input. Although, this statement has to be validated through an extensive analysis, considering a wide set of ground-motion records, intensities and structures.

The conclusions drawn for the intensity measures are not extended to the analysis of the fragility functions derived from the two nonlinear methods – pushover and time-history. Notwithstanding being depicted in Figure 7 a very close fragility behaviour of the frame building for the Light and Moderate limits, it also shows that for high demanding levels both techniques diverge, with a lower fragility being obtained from pushover analyses. This is justified because the nonlinear static procedure used in this assessment, herein the N2 method, has limitations in considering the effects of the hysteretic energy dissipation, likewise the impossibility of the pushover methods to account for the cyclic behaviour effects of the seismic action.

3.6 Fragility assessment – limit states analysis

The aim of the study performed in the current section is to appraise the results of the fragility functions generated from global and local performance levels, at the same that it intends to confirm the aftermath of the preliminary study on behalf of the validation of the conclusions yielded from the nonlinear methods of analysis. Henceforth the 10 real ground motion records are scaled to reach 36 target PGA levels, not exceeding 2000 cm/s^2.

The study begins with a comparison on the aforementioned aspects devoted individualy to the HAZUS global-drift thresholds, Figure 8.

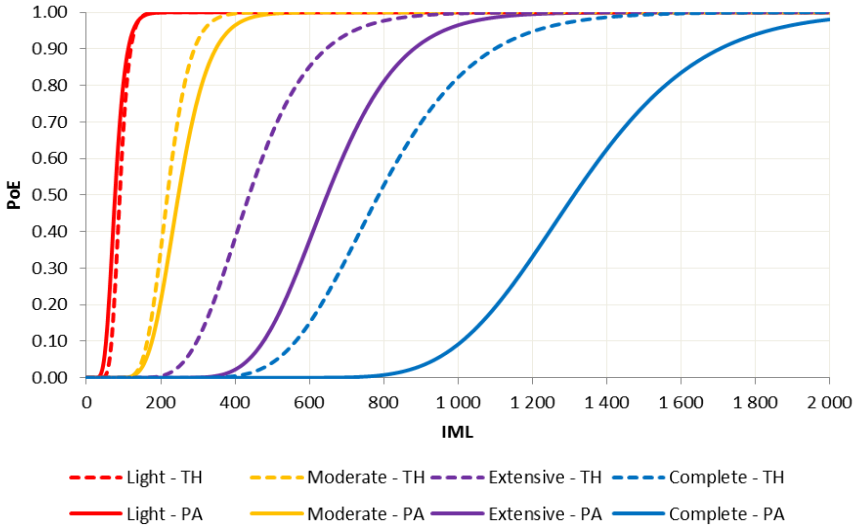


Figure 8: Fragility functions using HAZUS thresholds.

It is also observed that once the structure is responding at more demanding performance levels (extensive and complete limit states) the fragility functions derived from pushover and time-history analysis diverge. This has already been stated in the former section albeit the difficulties to fit a fragility distribution to the five points of probability of exceedance, and is justified by the loss of accuracy of the static analysis for high inelastic demands. Thus no additional comparisons regarding the use of pushover or time-history methods are made since the former seem to be only valid up to global-drift values close to the ones defined at the moderate performance level. Further assessments are only concerned on dynamic analyses of the structure.

The next analysis focus on the derivation of the fragility functions following the limit states proposed by HAZUS, FEMA and Eurocode 8. A straightforward approach is conducted, assembling the results by their structural quantities (drifts and chord-rotations).

The initial analysis on the structural fragility of the model is devoted to the drift-based thresholds of the HAZUS and FEMA 356 documents, illustrated in Figure 9 with continuous and dashed lines, respectively.

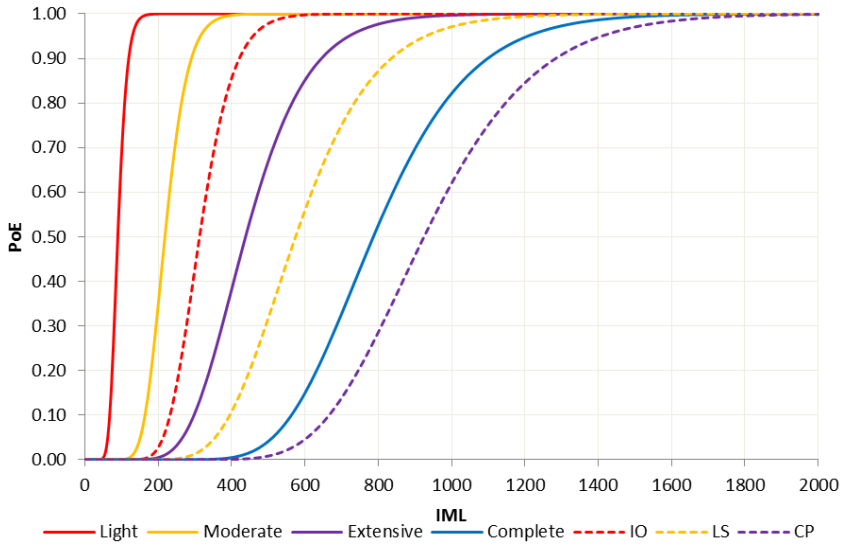


Figure 9: Fragility functions using HAZUS and FEMA drift-based thresholds.

It is noteworthy that fragility functions derived with HAZUS global-drift thresholds are far conservative than the ones obtained for the FEMA 356 maximum interstorey-drift. These differences might be explained with the evolution on the failure mechanism of the structure, which is typical of a soft storey one, and then the expected agreement between maximum inter-storey drift and global drift is not attained. Notwithstanding one may say that the Moderate, Extensive and Complete damage levels of HAZUS are comparable to the respective IO, LS and CP limit states of FEMA.

Moving forward to the analysis of local engineering demand parameters, the impact of the chord rotation thresholds is assessed for the limits proposed in Eurocode 8 and FEMA. This assessment is performed in terms of the first vertical element that reaches the limit values (Figure 10 A) or neglecting the type of structural element (Figure 10 B)

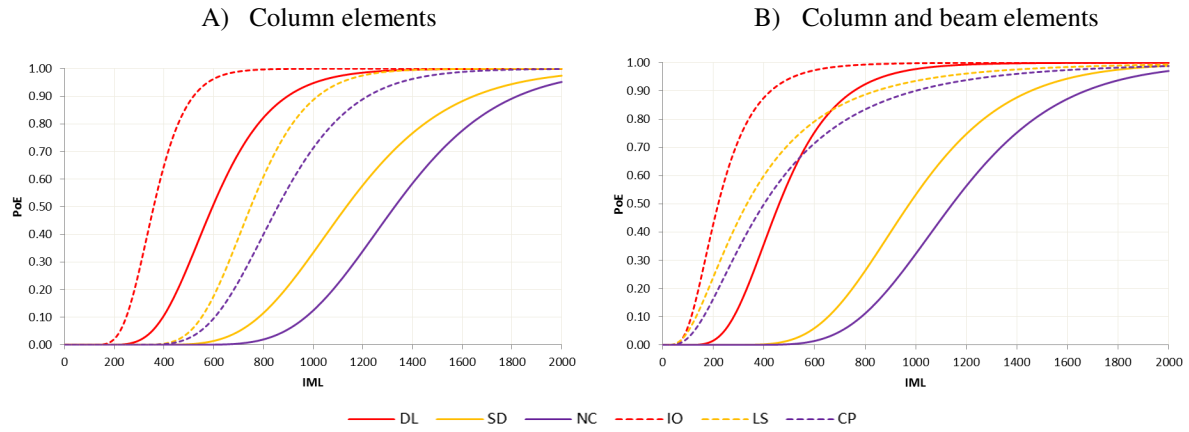


Figure 10: Fragility functions using Eurocode 8 and FEMA chord rotation-based thresholds.

The fragility functions defined in what regards only to column elements are noticeably less demanded, especially for the first limit state, because beams are the first structural elements to yield, even for this pre-coded building. In any case, if FEMA or Eurocode 8 provisions are to be applied one should neglect the type of element. However the most realistic approach bears in mind with the importance of the structural elements for the specific limit states, though if a collapse level is evaluated one should consider for example the first column or entire storey beams that surpass their limit values.

It is also depicted from Figure 10 that FEMA limits lead to more conservative fragility functions. This may be linked to the way how these limit states are established: while FEMA addresses specific values collected from an extensive review in former works, as a function of the structural class but neglecting additional information such as the materials and the dimensions of the elements, Eurocode 8 presents equations 1 and 2 that compute those thresholds at each element according to a set of parameters of the section.

Analysing Figures 9 and 10 it is conspicuously seen that global-based quantities correspond to more restrictive thresholds and high demanded structures. In this sense, HAZUS is the more conservative proposal. Besides considering 4 limit states of damage, the first level of HAZUS has no agreement with the other documents in analysis.

4 CONCLUDING REMARKS

The evaluation and comparison of the methodologies for derivation of fragility functions has been carried out for a pre-coded reinforced concrete frame building. A comparison has been established on the influence of the nonlinear methods of analysis, scaling techniques for

the seismic input, intensity measure parameters, engineering demand parameters for the fragility performance levels and thresholds of damage.

The study was separated into two stages concerning: the intensity measures analysis and the limit states analysis.

In general, results have indicated that:

- The fragility functions are not affected by the choice of the intensity measures.
- For more demanding limit states and higher intensity levels the use of pushover analysis, at least with the N2 method for performance assessment, has revealed to be less conservative than dynamic analysis.
- From the above assessed documents, the Eurocode 8 is the one that leads to lower fragility. On the other hand, the use of HAZUS thresholds is reflected in a higher fragility of the structure.

Although several relationships were outlined in the study an extensive number of analyses should be carried, increasing the number of buildings and records. In addition it would be interesting, for the sake of comparison to the observed trens, considering empirical fragility functions for the assessed class of buildings.

ACKNOWLEDGMENTS

Financial support to the first, third and fourth authors is provided by the Portuguese Science and Technology Foundation (FCT – Fundação para a Ciência e a Tecnologia), under the QREN - POPH programme.

REFERENCES

[1] Crowley, H. and J. J. Bommer (2006). "Modelling seismic hazard in earthquake loss models with spatially distributed exposure." Bulletin of Earthquake Engineering 4(3): 249-273.

[2] McGuire, R. K. (1995). "Probabilistic seismic hazard analysis and design earthquakes: closing the loop." Bulletin of the Seismological Society of America 85(5): 1275-1284.

[3] Carreño, M.-L., et al. (2007). "Urban seismic risk evaluation: a holistic approach." Natural Hazards 40(1): 137-172.

[4] Erdik, M., et al. (2003). "Earthquake risk assessment for Istanbul metropolitan area." Earthquake Engineering and Engineering Vibration 2(1): 1-23.

[5] Giovinazzi, S. and S. Lagomarsino (2003). Seismic risk analysis: a method for the vulnerability assessment of built-up areas. Proceedings, European Safety & Reliability Conference, Maastricht.

[6] Lupoi, G., et al. (2002). "Seismic risk assessment of RC structures with the" 2000 SAC/FEMA" method." Journal of earthquake engineering 6(04): 499-512.

[7] Liel, A. B., et al. (2009). "Incorporating modeling uncertainties in the assessment of seismic collapse risk of buildings." Structural Safety 31(2): 197-211.

[8] Porter, K., et al. (2007). "Creating fragility functions for performance-based earthquake engineering." Earthquake Spectra 23(2): 471-489.

[9] Shinozuka, M., et al. (2000). "Statistical analysis of fragility curves." Journal of Engineering Mechanics 126(12): 1224-1231.

[10] Jaiswal, K., et al. (2011). "Developing empirical collapse fragility functions for global building types." Earthquake Spectra 27(3): 775-795.

[11] Rossetto, T. and A. Elnashai (2003). "Derivation of vulnerability functions for European-type RC structures based on observational data." Engineering structures 25(10): 1241-1263.

[12] Orsini, G. (1999). "A model for buildings' vulnerability assessment using the parameterless scale of seismic intensity (PSI)." Earthquake Spectra 15(3): 463-483.

[13] King, S., et al. (2004). Application of empirical fragility functions from recent earthquakes. 13th world conference on earthquake engineering, Vancouver, BC, Canada.

[14] Mosleh, A. and G. Apostolakis (1986). "The assessment of probability distributions from expert opinions with an application to seismic fragility curves." Risk Analysis 6(4): 447-461.

[15] Ouchi, F. (2004). A literature review on the use of expert opinion in probabilistic risk analysis, World Bank Washington, DC.

[16] Lagomarsino, S. and S. Giovinazzi (2006). "Macroseismic and mechanical models for the vulnerability and damage assessment of current buildings." Bulletin of Earthquake Engineering 4(4): 415-443.

[17] Padgett, J. E. and R. DesRoches (2008). "Methodology for the development of analytical fragility curves for retrofitted bridges." Earthquake Engineering & Structural Dynamics 37(8): 1157-1174.

[18] Shome, N. and C. Cornell (2000). Structural seismic demand analysis: Consideration of collapse. Proceedings of the 8th ASCE Specialty Conference on Probabilistic Mechanics and Structural Reliability.

[19] Naeim, F., et al. (2004). "Selection and scaling of ground motion time histories for structural design using genetic algorithms." Earthquake Spectra 20(2): 413-426.

[20] Vamvatsikos, D. and C. A. Cornell (2002). "Incremental dynamic analysis." Earthquake Engineering & Structural Dynamics 31(3): 491-514.

[21] Fajfar, P. and P. Gašperšič (1996). "The N2 method for the seismic damage analysis of RC buildings." Earthquake Engineering & Structural Dynamics 25(1): 31-46.

[22] Freeman, S. A. (1998). The capacity spectrum method as a tool for seismic design. Proceedings of the 11th European conference on earthquake engineering.

[23] Chopra, A. K. and R. K. Goel (2002). "A modal pushover analysis procedure for estimating seismic demands for buildings." Earthquake Engineering & Structural Dynamics 31(3): 561-582.

[24] Casarotti, C. and R. Pinho (2007). "An adaptive capacity spectrum method for assessment of bridges subjected to earthquake action." Bulletin of Earthquake Engineering 5(3): 377-390.

[25] Park, J., et al. (2009). "Seismic fragility analysis of low-rise unreinforced masonry structures." Engineering structures 31(1): 125-137.

[26] Council, B. S. S. (2000). "Prestandard and commentary for the seismic rehabilitation of buildings." Report FEMA-356, Washington, DC.

[27] Sciences, N. I. o. B. and F. E. M. Agency (2003). Multi-hazard Loss Estimation Methodology, Earthquake Model, HAZUS® MH Technical Manual, Federal Emergency Management Agency Washington, DC.

[28] Mpampatsikos, V., et al. (2008). "A critical review of the RC frame existing building assessment procedure according to Eurocode 8 and Italian Seismic Code." Journal of earthquake engineering 12(S1): 52-82.

[29] Romão, X., et al. (2010). "Practical aspects of demand and capacity evaluation of RC members in the context of EC8 - 3." Earthquake Engineering & Structural Dynamics 39(5): 473-499.

[30] Cornell, C. A., et al. (2002). "Probabilistic basis for 2000 SAC Federal Emergency Management Agency steel moment frame guidelines." Journal of Structural Engineering 128(4): 526-533.

[31] Normalisation, C. E. d. (1998). "Eurocode 8: design of structures for earthquake resistance–Part 3: assessment and retrofitting of buildings." En 3: 2005.

[32] SeismoSoft (2013). SeismoStruct – a computer program for static and dynamic nonlinear analysis of framed structures. Version 6 Build 100.

[33] Somerville, P. G. and S. J. Venture (1997). Development of ground motion time histories for phase 2 of the FEMA/SAC steel project, SAC Joint Venture.

COMPDYN 2013
4th ECCOMAS Thematic Conference on
Computational Methods in Structural Dynamics and Earthquake Engineering
M. Papadrakakis, V. Papadopoulos, V. Plevris (eds.)
Kos Island, Greece, 12–14 June 2013

INFLUENCE OF CODE-BASED RECORD SELECTION METHODS ON THE SEISMIC ASSESSMENT OF EXISTING STEEL BUILDINGS

M. Araújo[1], L. Macedo[1], J. M. Castro[1] and R. Delgado[1]

[1] Faculty of Engineering of the University of Porto
Rua Dr. Roberto Frias, s/n 4200-465 Porto, Portugal
e-mail: maraujo@fe.up.pt

Keywords: Ground Motion Record Selection and Scaling, Nonlinear Dynamic Analysis, Existing Steel Buildings.

Abstract. *The recent concerns regarding the seismic safety of the existing building stock have placed the review of current seismic assessment procedures on the top of the agenda. Alongside with the development of more advanced commercial software tools and computational capacities, nonlinear dynamic analysis is becoming, more and more, a common and preferable procedure in the seismic assessment of existing buildings. Besides the complexity associated with the formulation of the mathematical model, major issues arise related with the definition of the seismic action, which can lead to different levels of uncertainty in terms of local and global building response. Aiming to address this issue, a comparative study of different code-based record selection methods proposed by EC8-3, ASC41-06 and NZSEE is presented herein. The various methods are employed in the seismic assessment of four steel buildings, designed according to different criteria, and the obtained results are compared and discussed. Special attention is devoted to the impact of the number of real ground motion records selected (three and seven) in the response of the buildings and the inclusion of additional selection criteria based on the control of the spectral mismatch of each individual record with respect to the reference response spectrum adopted in the seismic assessment. The results obtained indicate that the Eurocode selection procedure slightly underestimates both the local and global response of the buildings in comparison with the American and New Zealand procedures, which conversely, lead to similar results. It is also concluded that record sets incorporating the additional selection criteria significantly reduce the level of uncertainty in the response.*

1 INTRODUCTION

Nonlinear dynamic analysis is recognized as the most reliable tool to assess the seismic performance of structures, particularly in the case of irregular ones. The constant increase in computing power and the wide number of advanced structural analysis software tools available have set this type of analysis as the preferable procedure for the seismic assessment of structures, both for code-related proposes and probabilistic risk analysis. However, besides the complexity associated with the formulation of the mathematical model, major issues arise related with the definition of the ground-motion records, which can be artificial spectrum-compatible signals, simulated records or natural records [1].

From the various types of ground-motion data, natural records are known to be the ones that provide better unbiased estimates of structural seismic demands [2], although a number of issues related to the real ground motions selection and scaling procedures have been evoked in previous works [1, 3-5], which may lead to increasing levels of uncertainty in terms of local and global structural responses. It has demonstrated [6] that although material properties induce significant variability in the structural response, the latter is much smaller when compared to the ground motion variability.

The preferred current practice for record selection consists of carefully selecting the records that reflect the expected earthquake magnitude (M), source-site distance (R), rupture mechanism and soil profile of the source of the events that are in some sense most likely to attack the structure. Some previous studies have found no consistent evidence that suggested that it is required to take special care in the record selection with respect to M-R factors [1,7-9], albeit have not been shown completely conclusive [1]. In fact, [10] has demonstrated that scaling records randomly selected from an M-R bin can introduce bias in median nonlinear structural response, depending on the fundamental period of vibration of the structure, the overall strength of the structure and the sensitivity of the nonlinear structural response to higher modes of vibration.

In the context of probabilistic structural assessment, the frequency of the structure to reach a certain limit state (e.g., collapse) over a certain period of time provides an estimate of the failure probability conditional to a specific record set. As a result, the number of records in a set should be sufficient to capture with acceptable confidence the seismic response and the record-to-record variability. In other words, the computed median of structural demands is seen to be within one-sigma confidence band of 10% if $\sigma < 0.1\sqrt{N}$, where σ is the dispersion of the demand variable and N the number of records. As an example, 25 records should be necessary to ensure a standard error of the variable to measure of 10% admitting a dispersion of the variable of 0.5 [8, 11].

Generally speaking, the number of records falls in the range of seven to ten and the current practice of scaling records so that their mean ordinate matches or exceeds the target elastic spectrum is seen to be a reasonable approach. According to [1], the practice of using a small number of records, from three to six, and then taking the maximum inelastic response, should be abandoned. A more extensive study on the required number of records and the degree of bias may be found in [12], wherein it was concluded that both systematically decrease as one applies more constraint on the selection and scaling of the records.

Another source of bias induced in the response estimates is normally related to the ground motion scaling limits. Values varying from one to 10, or more, are considered acceptable within the engineering seismology community. Although [7] has found no compelling evidence that scaling up real records to match the strength of stronger records induces bias in the response estimation, [10] demonstrated otherwise and concluded that the bias is largely removed when records with spectral shape similar to the target spectrum are considered.

The existing code-based record selection methods, such as the one proposed by EC8-1 [13], have been shown to require significantly improvements regarding the selection of real records as an input for seismic performance assessment [14, 15], which may lead to large discrepancies in the structural response within a given set of records. As a result, the analyst may be discouraged to use natural records and eventually lean towards the use of artificial ones, despite their inherent disadvantages [1].

In the context of recent studies [16, 17] that have been carried out on the evaluation and calibration of the seismic safety assessment procedures proposed by EC8-3 [18] for existing steel buildings, a comparative study of different code-based record selection methods proposed in EC8-3, ASCE41-06 [19] and NZSEE [20] is presented herein. The various methods are employed in the seismic assessment of four steel buildings, designed according to different criteria, and the obtained results are compared and discussed, particularly in terms of the record-to-record variability of the response.

2 CODE-BASED RECORD SELECTION METHODS

In general, all main guidelines and codes set the ground motion records used for nonlinear dynamic analysis to groups of not less than three records, which may be obtained wither from real earthquake events or artificially simulated, although preference is given to the former. Specific conditions for spectral matching that these records should comply with are also specified in the above mentioned documents.

As referred above, most of the code-based record selection methods preconize that a first careful selection from a bin of random real signs should be carried out considering the expected magnitude, source-to-site distance, rupture mechanism and soil profile that are consistent with the seismic hazard scenario associated with the structure under analysis. When the ground motion records having these characteristics are not available, simulated data sets with equivalent duration and spectral content should be used to make up the total number required. Code prescriptions ask for matching of the average spectral ordinates of the chosen record set to the target code-based spectral shape. The set has to consist of at least seven records to consider mean response. Otherwise, if the set comprises three to six records, the maximum response obtained among all the records within the set should be considered.

The ground motion record selection and scaling methods proposed by the European, American and New Zealand standards and guidelines are presented next.

Eurocode 8

Based on EC8-1, EC8-3 establishes the following criteria for record selection:

- The mean of the zero period spectral response acceleration values calculated from the individual time histories should not be smaller than the value of $a_g S$ for the site in question, being a_g the design ground acceleration on rock ground and S the soil factor;
- In the range of periods between $0.2T_1$ and $2T_1$, where T_1 is the fundamental period of the structure in the direction where the record will be applied, no value of the mean 5% damping elastic spectrum, calculated from all time histories, should be less than 90% of the corresponding value of the 5% damping elastic response spectrum.

ASCE41

ASCE41-06 establishes, when performing bidirectional planar analysis, that the square root of the sum of the squares (SRSS) of the two principal horizontal components of the records

shall be scaled such that the average value of the set of constructed spectra does not fall below 1.3 times the 5% damping elastic spectrum for periods between $0.2T_1$ and $1.5T_1$. According to [14], matching the mean spectrum of the seven pairs of records to 90% of the target code spectrum or matching the mean spectrum of the SRSS spectra to the seven pairs of records to 1.3 times the code spectrum are numerically equivalent. For this reason, the recent version of ASCE 7-10 [21] defines the target spectrum as 1.0 times the design spectrum, recognizing that the design spectrum is now based on maximum response of the horizontal plane. The intent of ASCE 7-10 is to scale records such that the maximum responses in the horizontal plane of the scale records are, on average, equal to, but not less, the design spectrum over the defined period range [22].

New Zealand Guidelines

According to the NZSEE recommendations, based on NZS 1170.5:2004 [23], the ground motion records shall be scaled by a record scale factor k_1 and a family scaled factor k_2 applied in the time domain, i.e. the record ordinate shall be multiplied by the product $k_1 k_2$. The record scale factor k_1 is defined as the scale value which minimizes, in a least square sense, the function $log\left(k_1 SA_c / SA_t\right)$, where SA_c refers to the spectra constructed for each record component and SA_t the code target spectrum for the site given, over the period range of interest between $0.4T_1$ and $1.3T_1$, being recommended to ensure that $0.33 < k_1 < 3.0$ and that the record selected is of reasonable fit to the target spectra. The latter condition may be demonstrated by satisfying $D_1 < log\left(1.5\right)$, where:

$$D_1 = \sqrt{\frac{1}{n}\sum \left(log\left(SA_c\right) - log\left(SA_t\right)\right)^2} \tag{1}$$

The family scale factor, k_2, is defined as the maximum value of the ratio $SA_t / max\left(SA_c\right) > 1.0$ over the period range of interest for the direction under consideration, where $max\left(SA_c\right)$ is the maximum component of each record within a family at each period considered. It shall be verified that $1.0 < k_2 < 1.3$.

3 CASE STUDY DESCRIPTION

The study presented herein was conducted considering four 5-storey steel buildings composed by regular moment-resisting frames as illustrated in Figure 1. Each building was designed according to different criteria. The first building, denoted as GB, was designed according to Eurocode 3 [24] to resist gravity loads. The remaining three buildings were seismically designed according to EC8-1 assuming medium ductility (DCM class), with a behaviour factor q of 4.0, and to comply with different limits for the inter-storey drift sensitivity coefficient $\theta_{P-\Delta}$, which is defined in the code to address the treatment of second-order effects. Thus, the SB1 building was designed to comply with the criterion $0.2 < \theta_{P-\Delta} < 0.3$, according to which the second-order effects shall be directly included in the analysis. The SB2 building was designed assuming $0.1 < \theta_{P-\Delta} \leq 0.2$, being the second-order effects taken into account by multiplying the relevant seismic action effects by a factor equal to $1/\left(1-\theta_{P-\Delta}\right)$, and finally, the SB3 building was designed in order to neglect second-order ef-

fects ($\theta_{P-\Delta} \leq 0.1$). The design seismic action was set for Zone 3 of the Portuguese territory and assuming a soil type B, defined by a soil factor S of 1.29 according to the Portuguese National Annex of Eurocode 8.

The main structural characteristics of the analysed buildings are displayed in Figure 1 and Figure 2. Grade S275 was considered for the structural steel. The analyses were carried out using the open source software OpenSees [25]. Regarding the models used for nonlinear analysis, force-based beam-column elements were adopted considering 10 Gauss-Lobatto integration points along its length, which offers a superior solution to the classical Gauss integration method when it is important to include in the integration the end points of the element. Also, a cross-section discretization solution by fibers was followed and a bilinear elasto-plastic material model with 0.5% hardening was adopted for structural steel. The effect of the panel zones was neglected in this study. Special attention was given to the modelling of the viscous Rayleigh damping, having the mass proportional damping been neglected, since it does not have a real physical meaning, and a tangent-stiffness proportional damping assumed, which greatly reduces the elastic damping force when the structural stiffness drops to the post-yield level. A fraction of critical damping equal to 2% was considered.

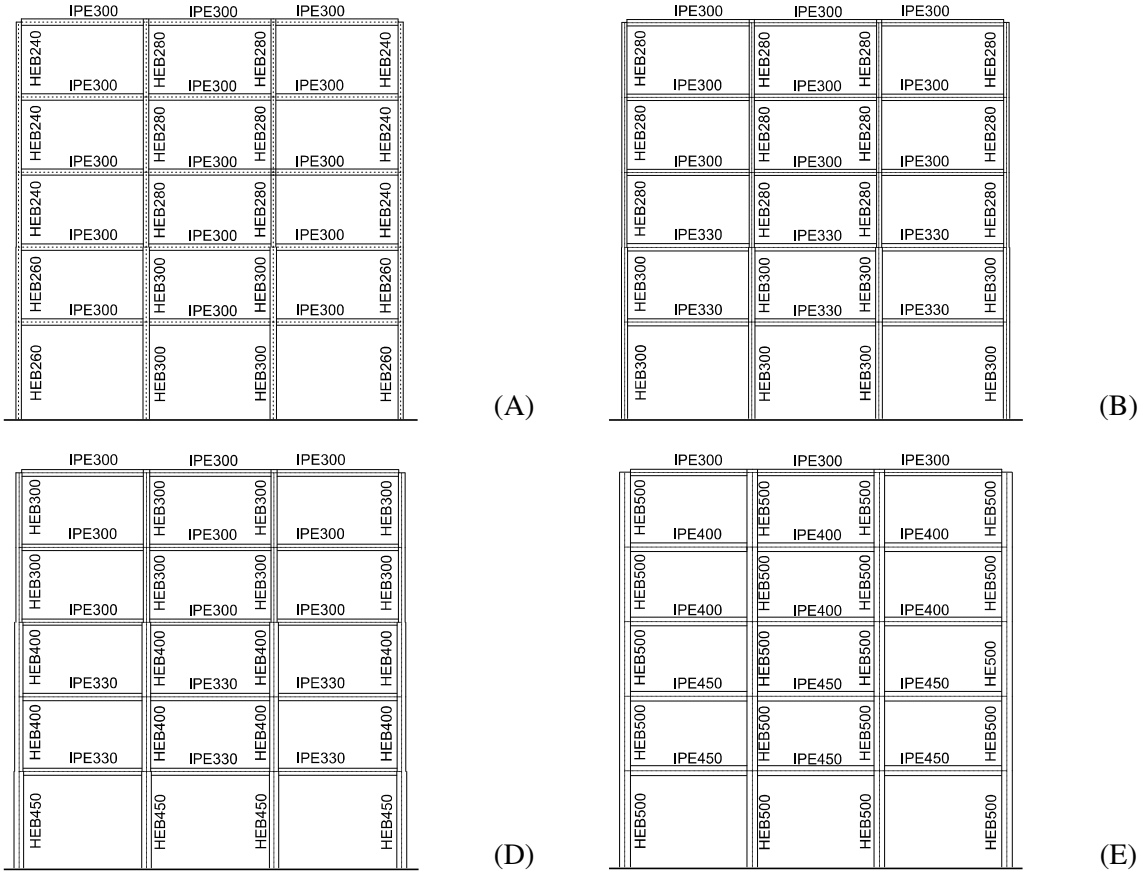


Figure 1: Plan view of the four 5-storey steel buildings studied: (A) GB building; (B) SB1 building; (C) SB2 Building; (D) and SB3 Building.

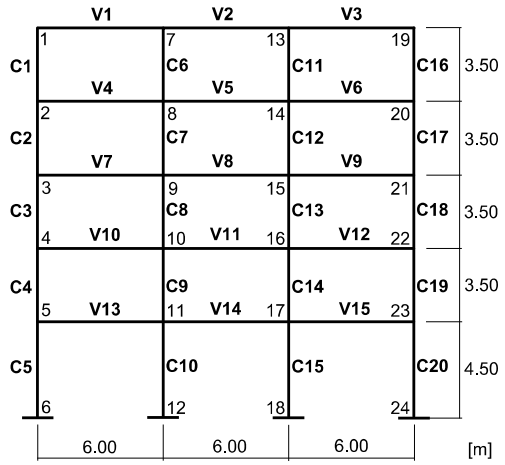


Figure 2: Frame dimensions and structural elements and nodes naming.

The gravity loading assumed in the analysis consisted of simple point loads applied at the mid-span of the beams and at each alignment of columns, which represent the vertical loads transmitted from secondary beams. On the top floor, both dead and live loads were set as $G_k = 85.5kN$ and $Q_k = 18kN$ at the inner alignment of columns and mid-span of beams and as $G_k = 42.75kN$ and $Q_k = 9kN$ at the outer alignment of columns. The dead and live loads on the remaining floors were defined as $G_k = 103.5kN$ and $Q_k = 36kN$ at the inner alignment of columns and mid-span of beams and as $G_k = 51.75kN$ and $Q_k = 18kN$ at the outer alignment of columns. The combination factor ψ_2 of the seismic combination of loads was defined as 0.0 at the top floor and 0.3 at the remaining floor levels. The masses were lumped at each node of the various floors and $P-\Delta$ effects were directly included in the numerical analysis.

Modal analysis was carried out for each frame to identify the dynamic characteristics of the buildings, which are listed in Table 1 for its first three modes of vibration.

Building	Periods of vibrations (s)			Mass Participation Ratios (%)		
	Mode 1	Mode 2	Mode 3	Mode 1	Mode 2	Mode 3
GB	1.63	0.50	0.26	85.49	9.24	3.40
SB1	1.50	0.48	0.25	83.86	10.41	3.58
SB2	1.20	0.39	0.20	78.73	12.06	5.34
SB3	0.90	0.28	0.13	80.56	13.22	4.33

Table 1: Dynamic characteristics of the buildings.

4 RECORD SETS CONSIDERED

As the Type 1 seismic action, which represents inter-plates earthquakes, was found to be the critical during the design, it served as the basis for the assessment study presented hereafter, being characterized by PGA values of 0.091g, 0.15g and 0.451g for the Damage Limitation (DL), Significant Damage (SD) and Near Collapse (NC) limit states, respectively. For the sake of convenience and since a direct correspondence between the EC8-3 limit states and the ASCE41-06 performance levels may be established, the IO, LS and CP performance levels could be henceforth referred as DL, SD and NC limit states, respectively. The real ground-motion sets were selected using SelEQ [26], which consists of a web application developed at the Faculty of Engineering of the University of Porto (FEUP) which allows the selection of

real records or groups of real records. On the basis of the seismological characteristics of the events that define the Portuguese type 1 and Zone 3 seismic action, magnitudes and epicentral distances higher than 5.5 and 20km, respectively, were assumed. Also, an interval of values of the average shear wave velocity, $v_{s,30}$, between 360m/s and 800m/s was adopted in agreement with soil type B defined in EC8-1. An additional criterion was considered in the selection of each individual record, which consisted of imposing mismatch limits relative to the target spectrum of ±50%. The aim was to reduce the record-to-record variability of each set. 15 sets of three and seven records were considered and the scaling methods proposed by the EC8-1, ASCE 7-10 and NZS 1170.5:2004 G7 used (Figure 3 and Table 2).

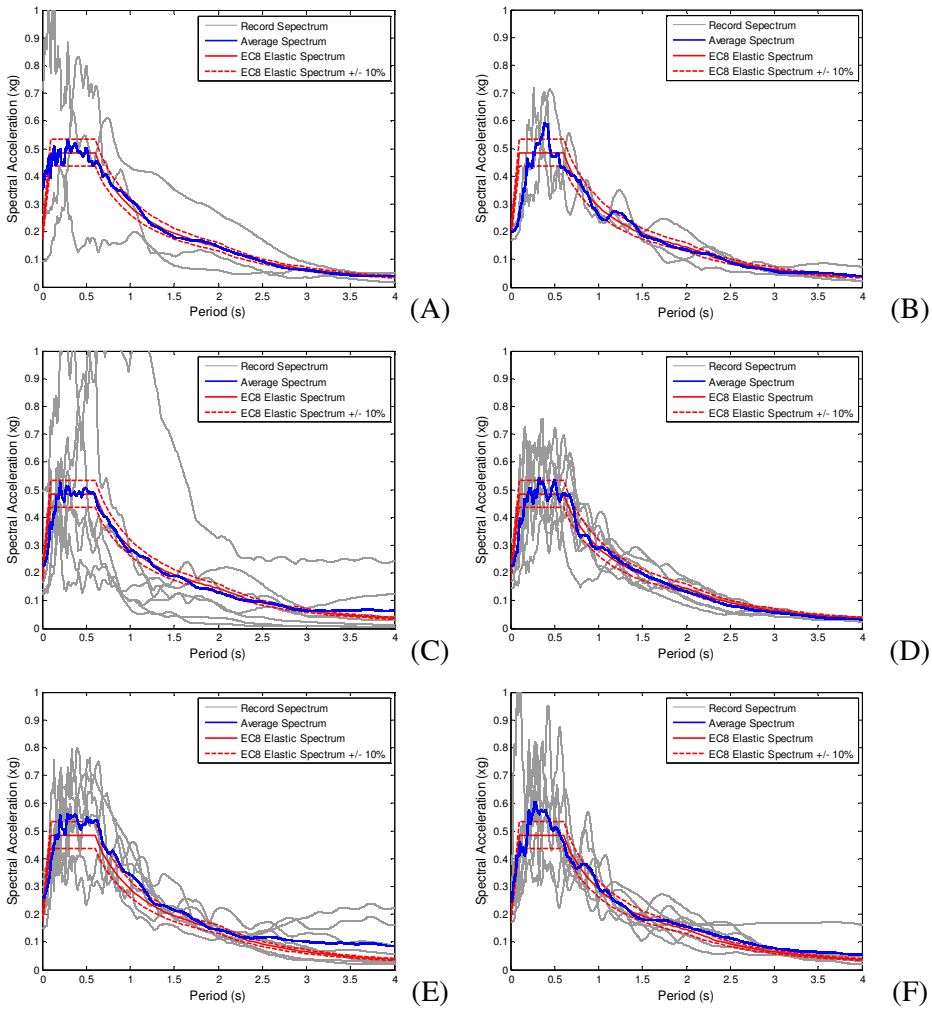


Figure 3: Matching of records with the design spectrum: (A) EC8-1 G3; (B) EC8-1 G3I; (C) EC8-1 G7; (D) EC8-1 G7I; (E) ASCE 7-10 G7I; (F) and NZS 1170.5:2004 G7.

Types of groups of records considered				
Scaling Method	Number of records / Control of mismatch relative to target spectrum			
EC8-1	3/no (G3)	3/yes (G3I)	7/no (G7)	7/yes (G7I)
ASCE7-10	3/no (G3)	3/yes (G3I)	7/no (G7)	7/yes (G7I)
NZS1170.5	3 (G3I)		7 (G7I)	

Table 2: Identification of the groups of records considered.

Regarding the scaling factors adopted, it may be referred that the records were scaled to match the SD limit state elastic spectrum, being afterwards linearly scaled to match the DL and NC limit states elastic spectra. A maximum scaling factor of approximately nine was adopted. Also, it may be noted that since NZS1170.5 already considers criteria for scaling each record individually, no control of the mismatch relative to the target spectrum was adopted in this case.

5 RESULTS

Figures 4 to 8 depict both local and global structural responses obtained in terms of mean values and respective coefficient of variation (CoV) over the 15 groups considered for each group type. The global structural responses are defined in terms of global drift ratios (i.e. displacement recorded at the top of the building divided by its height), while the local structural responses are set in terms of plastic rotation demand-to-capacity ratios (DCR), being the EC8-3 capacity limits adopted and the demands calculated by numerical integration [17]. The results are presented individually for each building, limit state (LS) and record selection method. Also, on the basis of the code prescriptions, mG3 and mG3I refers to the maximum value of response when only three records are being considered within a group set and aG7 and aG7I the average value of the response of the sets with seven records.

Hence, as already mentioned above, it may be readily concluded that the technique of taking the maximum value of response when a small number of records, from three to six, is being considered should be abandoned. In fact, by looking at the GB building results, and particularly for the NC limit state (Figures 4 and 5 (A)) values of global drift ratios and local component DCRs two times higher than the reference ones (aG7I) are observed. Thus, in the context of seismic safety verifications, while both GB and SB1 buildings verify safety according to aG7I, it fails when considering mG3. Likewise, the level of variability of the response is significantly high and beyond the acceptable, with CoV values of 60% to 40% globally and approximately 100% locally. These limitations, however, can be significantly overcome by introducing additional selection criteria based on the control of mismatch relative to target spectrum (mG3I). Not only better estimates of both local and global responses were obtained, but also building GB and SB1 are now safe according to EC8-3 and ASCE41-06.

On the other hand, as previously expected, the increase on the number of records considered in each set (aG7) significantly reduced the mean estimates and the variability of the response, although leading to some unstable results, particularly at the SD limit state of buildings GB and SB1 using ASCE41-06 (Figure 4 and Figures 5 and 6 (B)). In fact, high CoV values were observed in building GB the at SD and DL limit states mainly due to the influence a single outlier set of records, which drove to significantly higher levels of structural demands comparing to the other sets. Yet again, the adoption of alternative criteria to control the mismatch relative to target spectrum (aG7I) improved the stability of the mean values of demand, reducing its CoV to values of the order and below 30%. Moreover, it is observed that the variability of the response decreases with an increase in the demand, characterized in terms of limit states and also by the increase in the structural stiffness of the buildings. In other words, as the structural stiffness of the buildings increases, the level of demand decreases, improving the quality of results. Additionally, the stiffer building exhibits large column-to-beam capacity ratios and hence tends to develop a more stable plastic mechanism, which also contributes to reduce the variability in the demand.

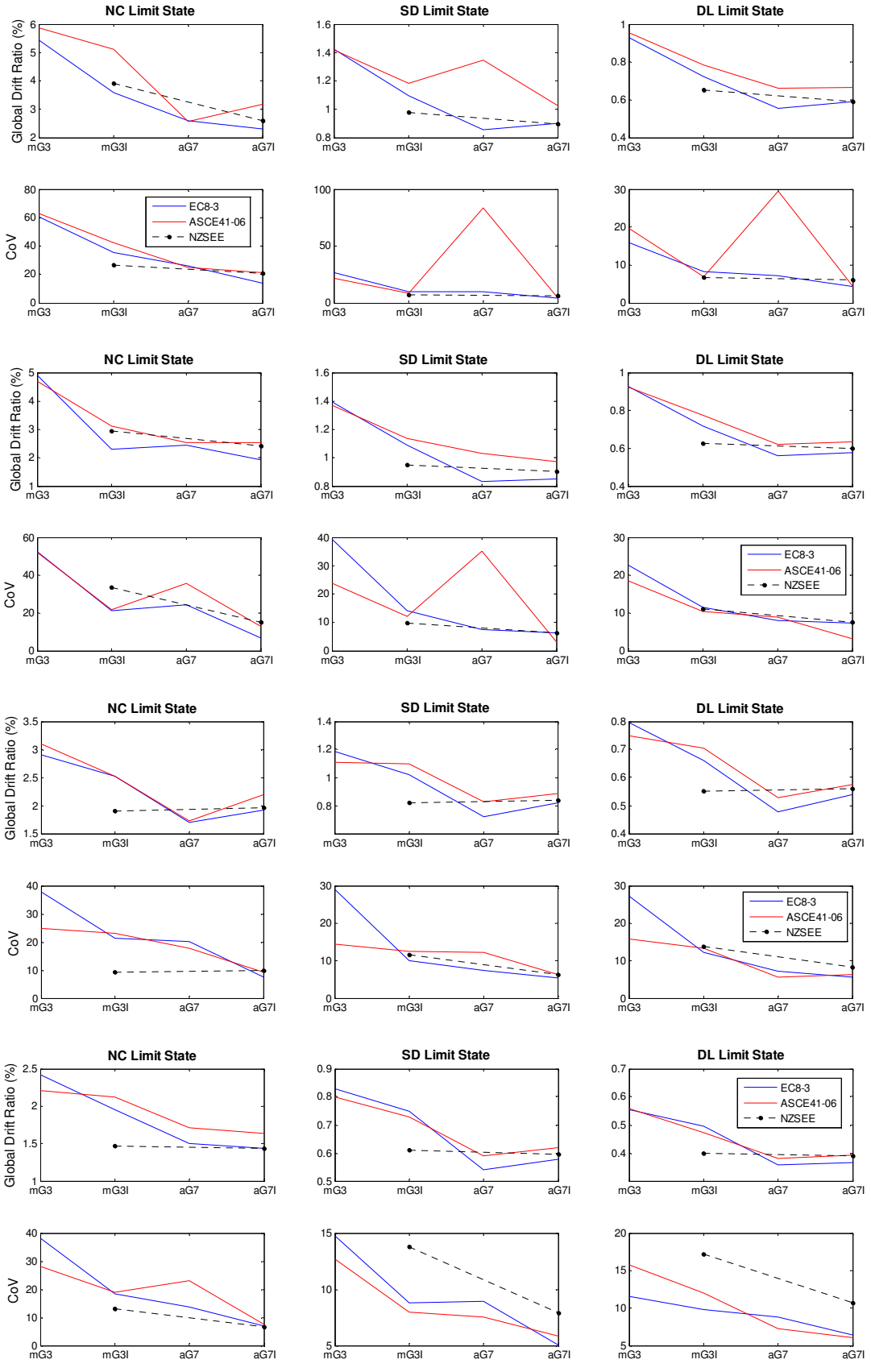


Figure 4: Mean global drift ratio results and respective CoV: (A) GB Building; (B) SB1 Building; (C) SB2 Building; (D) and SB3 Building.

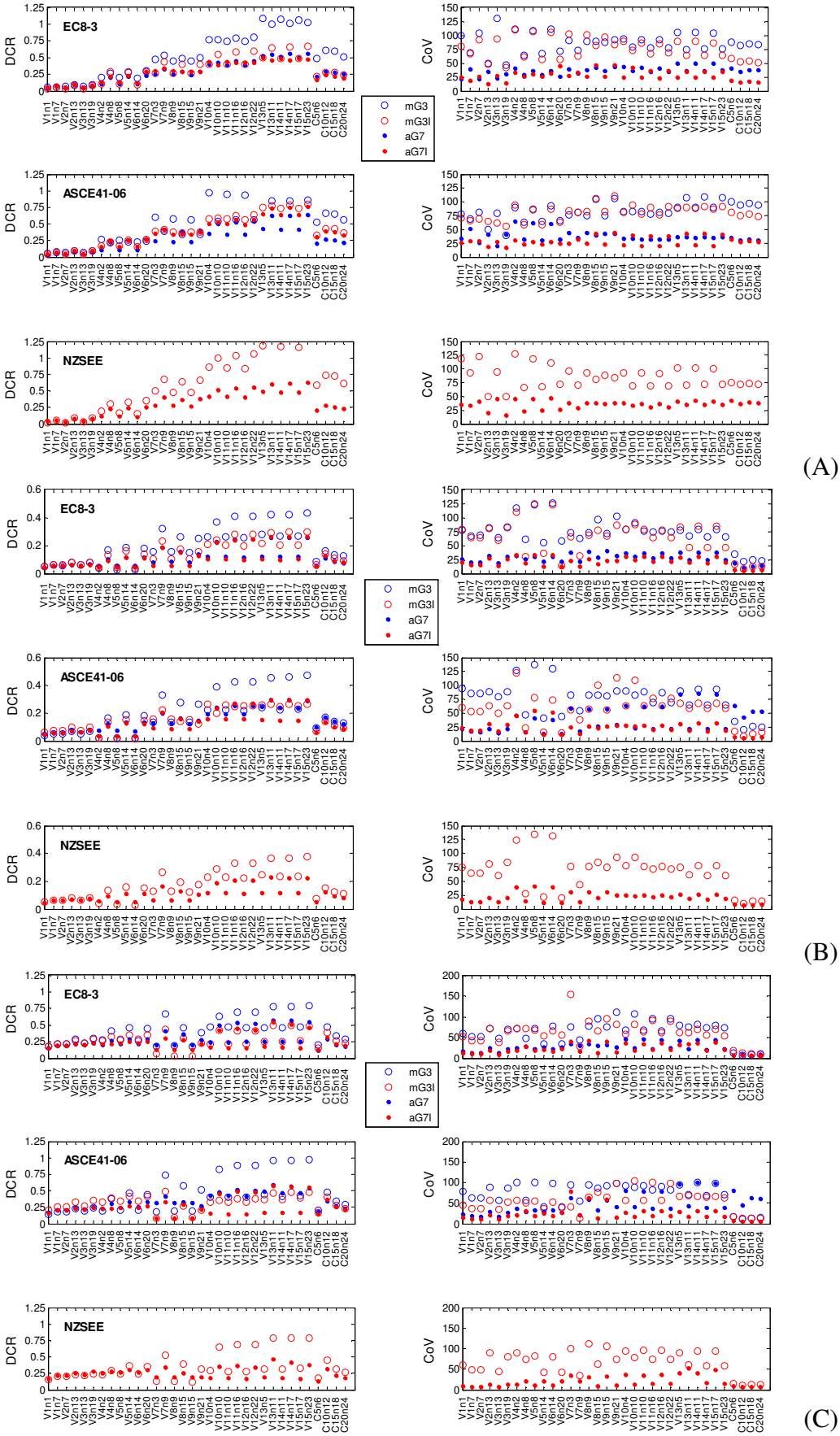


Figure 5: Mean DCR results for GB building and respective CoV: (A) NC LS; (B) SD LS; (C) and DL LS.

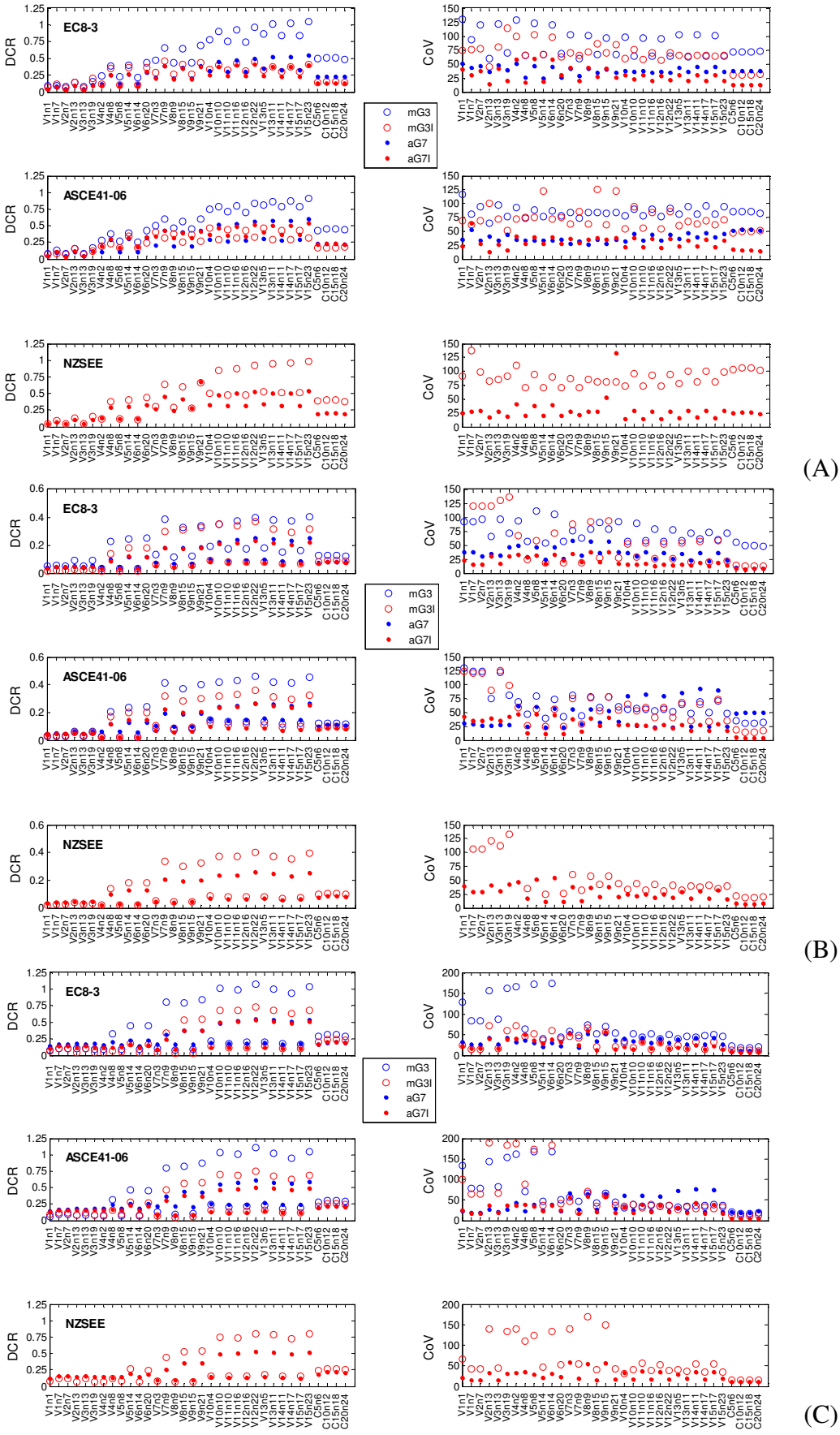


Figure 6: Mean DCR results for SB1 building and respective CoV: (A) NC LS; (B) SD LS; (C) and DL LS.

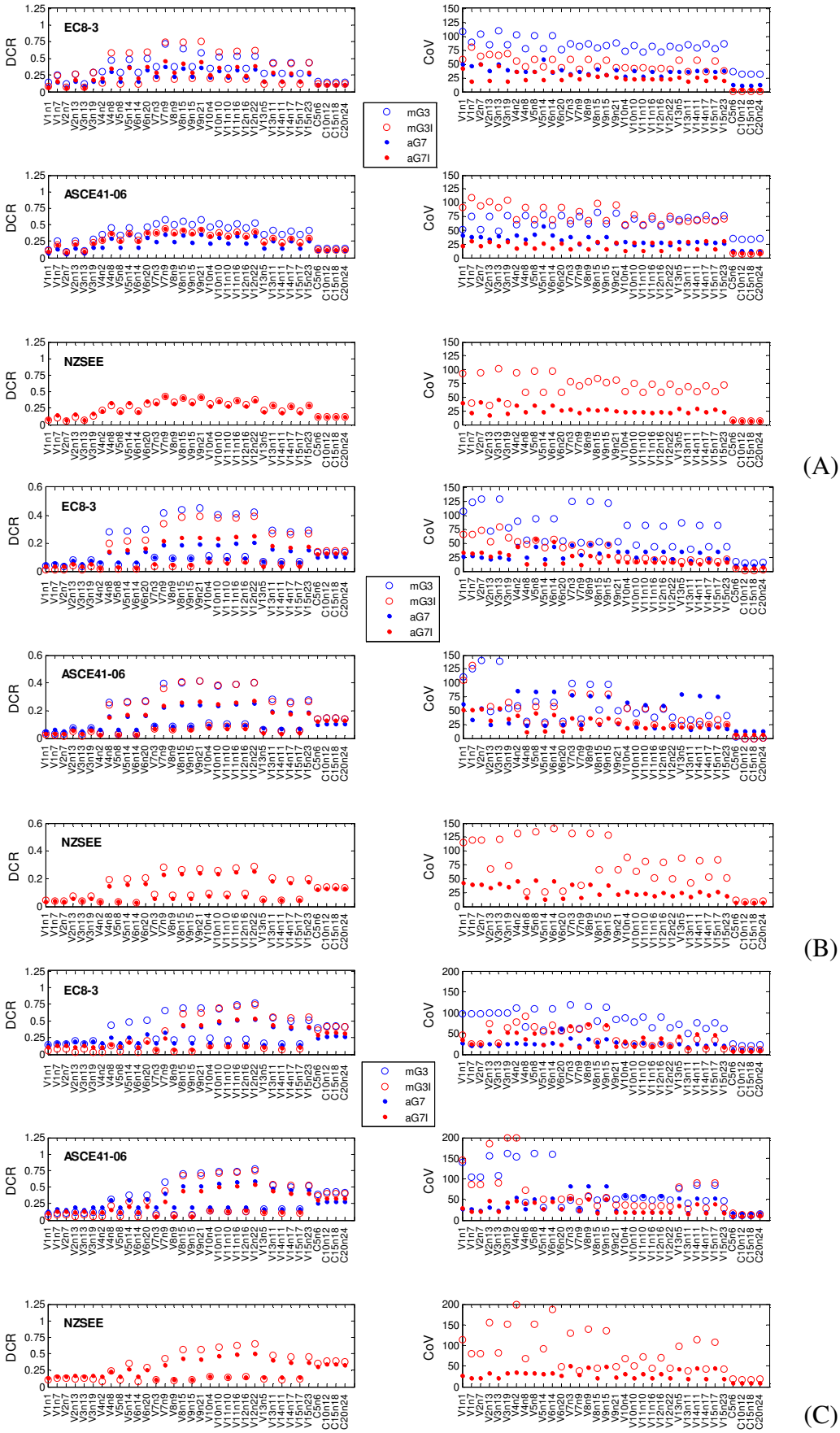


Figure 7: Mean DCR results for SB2 building and respective CoV: (A) NC LS; (B) SD LS; (C) and DL LS.

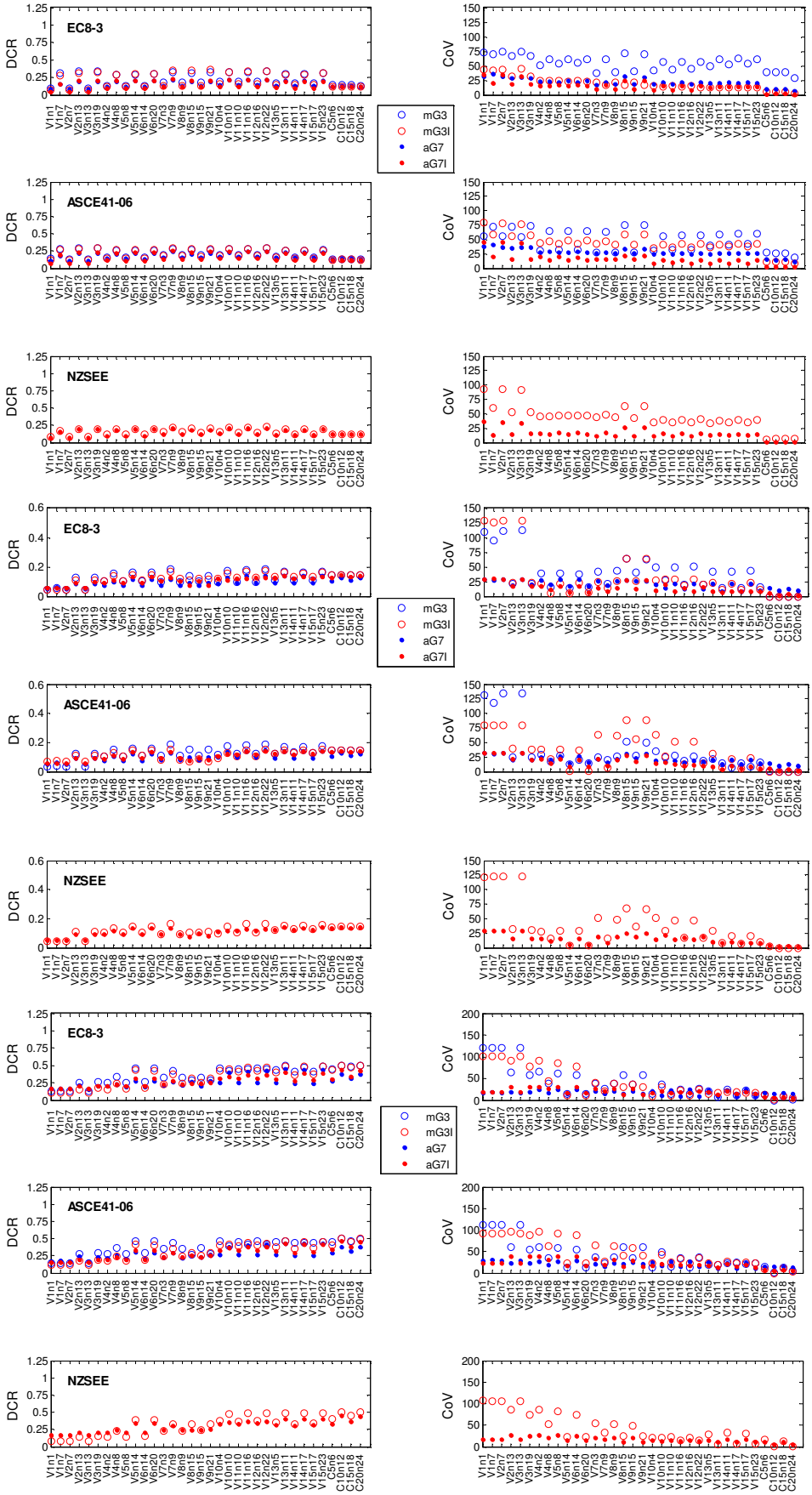


Figure 8: Mean DCR results for SB3 building and respective CoV: (A) NC LS; (B) SD LS; (C) and DL LS.

Finally, regarding the comparison between the EC8-1, ASCE 7-10 and NZS 1170.5:2004 selection and scaling methods, it may be seen that when considering the reference mG7I values EC8-3 continuously underestimates demands, particularly at the NC limit state, although its results tend to match the NZS 1170.5:2004 ones as the level of demands decreases and stiffer buildings are considered. On the contrary, ASCE 7-10 always defines an upper bound level of demand estimates, being the NZS 1170.5:2004 results in the interval defined by both European and American methods.

6 CONCLUSIONS

In this paper a comparison between the European, American and New Zealand methods for selecting and scaling real ground motion records is presented in the context of the seismic assessment of existing steel buildings. The selection techniques stipulated in the codes were discussed along with the impact of including an additional selection criterion based on the control of mismatch relative to target spectrum within a band of ±50%. Furthermore, the effects of using a minimum number of three records, as defined in all documents, in comparison to the most accepted number of seven records was discussed.

The application of the various methods to four steel buildings designed according to different criteria allowed identifying not only the limitations of using only three real records per set, and specially of having to compute the maximum value of response, but also the advantage of considering the additional selection criterion in the reduction of the level of variability of the response. Considering the comparison between the various code-based scaling methods, it was concluded that Eurocode tends to underestimate structural demands. On the other hand, the American standard always leads to higher values of seismic response.

It becomes clear from the study, as already concluded in previous works [14, 15], that further improvements should be made to the selection and scaling methods prescribed in seismic codes, particularly in terms of having to take the maximum value of response when the minimum number of three records per set is considered.

REFERENCES

[1] J. Bommer and A. Acevedo, The use of real earthquake accelerograms as input to dynamic analysis. *Journal of Earthquake Engineering*, 8, 43-91, 2004.

[2] I. Iervolino, G. Maddaloni and E. Cosenza, Eurocode 8 compliant real record sets for seismic analysis of structures. *Journal of Earthquake Engineering*, **12**, 54-90, 2008.

[3] E. I. Katsanos, A. G. Sextos and G. D. Manolis, Selection of earthquake ground motion records: a state-of-the-art review from a structural engineering perspective. *Soil Dynamics and Earthquake Engineering*, 30, 157-169, 2010.

[4] J. W. Baker and C. Cornell, Spectral Shape, epsilon and record selection. *Earthquake Engineering and Structural Dynamics*, 35, 1077-1095, 2006.

[5] A. J. Kappos and P. Kyriakakis, A re-evaluation of scaling techniques for natural records. *Soil Dynamics and Earthquake Engineering*, 20, 111-123, 2000.

[6] Oh-Sung Kwon and A. Elnashai, The effect of material and ground motion uncertainty on the seismic vulnerability curves of RC structures. Engineering Structures, 28, 289-303, 2006.

[7] I. Iervolino and A. Cornell, Record selection for nonlinear seismic analysis of structures, *Earthquake Spectra*, 21, 685-713, 2005.

[8] H. Krawinkler, R. Median and B. Alvi, Seismic drift and ductility demands and their dependence on ground motions. *Engineering Structures*, 25, 637-653, 2003.

[9] N. Shome, Probabilistic seismic demand analysis of nonlinear structures. PhD Thesis, Stanford University, 1999.

[10] N. Lucco and P. Bazzurro, Does amplitude scaling of ground motion records result in biased nonlinear drift responses? *Earthquake Engineering and Structural Dynamics*, 35, 1813-1835, 2007.

[11] I. Iervolino and G. Manfredi, A Review of ground motion record selection strategies for dynamic structural analysis. *Modern Testing Techniques for Structural Systems*, 131-163. Springer Vienna, 2008.

[12] J. Hancock, J. Bommer and P. Stafford, Numbers of scaled and matched accelerograms required for inelastic dynamic analyses. *Earthquake Engineering and Structural Dynamics*, 37, 1585-1607, 2008.

[13] CEN, ENV 1998-1 Eurocode 8: Design of structures for earthquake resistance - Part 1: eneral rules, seismic actions and rules for buildings. European Committee for Standardization, Brussels, Belgium, 2004.

[14] A. Sextos, G. Katsanos and G. Manolis, EC8-based earthquake record selection procedure evaluation: validation study based on observed damage of an irregular R/C building. *Soil Dynamics and Earthquake Engineering*, 31, 583-597, 2011.

[15] K. Beyer and J. Bommer, Selection and scaling of real accelerograms for bi-directional loadings: a review of current practice and code provisions. *Journal of Earthquake Engineering*, 11, 13-45, 2007.

[16] M. Araújo, J. M. Castro, X. Romão and R. Delgado, Comparative study of the European and American seismic safety assessment procedures for existing steel buildings. *Proceedings of the 15th World Conference of Earthquake Engineering*, Lisbon, Portugal, 2012.

[17] M. Araújo, J. M. Castro and R. Delgado, Simplified procedures for the seismic assessment of structural component demands. *Proceedings of the Vienna Congress on Recent Advances in Earthquake Engineering and Structural Dynamics*, Vienna, Austria, 2013.

[18] CEN, ENV 1998-3 Eurocode 8: Design of structures for earthquake resistance - Part 3: Assessment and retrofitting of buildings. European Committee for Standardization, Brussels, Belgium, 2005.

[19] ASCE, Seismic rehabilitation of existing buildings (ASCE/SEI 41-06). American Society of Civil Engineers, Reston, Virginia, USA, 2007.

[20] NZSEE, Assessment and improvement of the structural performance of buildings in earthquake. Recommendations of a NZSEE Study Group on Earthquake Risk Buildings. New Zealand Society for Earthquake Engineering, New Zealand, 2006.

[21] ASCE, Minimum design loads for buildings and other structures (ASCE/SEI 7-10). American Society of Civil Engineers, Reston, Virginia, USA, 2010.

[22] NEHRP, Selecting and scaling earthquake ground motions for performing response-history analyses. NIST GCR 11-917-15 report, NEHRP Consultants Joint Venture, 2011.

[23] NZS, NZS 1170.5:2004 Structural design actions. Part 5: Earthquake actions – New Zealand. New Zealand Standard, Wellington, New Zealand, 2004.

[24] CEN, ENV 1993-1 Eurocode 3: Design of steel structures - Part 1-1: General rules and rules for buildings. European Commitee for Standardization, Brussels, Belgium, 2005.

[25] PEER, OpenSees: Open system for earthquake engineering simulation. Pacific Earthquake Engineering Research Center, Universtiy of California, Berkeley, CA, 2011.

[26] L. Macedo, Improved performance-based seismic design methodologies for steel moment-resisting frames, PhD Dissertation, University of Porto, 2014 (*in preparation*).

COMPDYN 2013
4th ECCOMAS Thematic Conference on
Computational Methods in Structural Dynamics and Earthquake Engineering
M. Papadrakakis, V. Papadopoulos, V. Plevris (eds.)
Kos Island, Greece, 12–14 June 2013

CHARACTERISATION OF WALKING LOADS FROM INERTIAL MOTION TRACKING

Katrien L.N. Van Nimmen[1,2], Peter Van den Broeck[2], Geert Lombaert[1] and Guido De Roeck[1]

[1]KU Leuven, Department of Civil Engineering
Kasteelpark Arenberg 40, B-3001 Heverlee, Belgium
e-mail: katrien.vannimmen@kahosl.be

[2] KAHO Sint-Lieven, Department of Industrial Engineering
Gebroeders De Smetstraat 1, B-9000 Ghent, Belgium
e-mail: peter.vandenbroeck@kahosl.be

Keywords: human induced vibrations, 3D motion tracking, imperfect real walking.

Abstract. *A 3D inertial motion tracking technique, originating from the movement science and entertainement industry, is applied for the analysis of the walking behaviour of pedestrians. The experiments in laboratory conditions simultaneously register the ground reaction forces and the motion of the test-subject. Based on this registered motion, the main step frequency and stride-to-stride variations are identified. The ground reaction forces are subsequently simulated using a step-by-step load model available in literature. It is shown that accounting for the identified imperfect walking behaviour of the test-subject leads to a significantly improved agreement between measured and simulated ground reaction forces.*

1 INTRODUCTION

Contemporary footbridges are often designed as slender structures and tend to be susceptible to human induced vibrations [1, 2]. The mathematical load models used in the vibration assessment of these structures, are based on the traditional direct force measurements utilising a force plate and instrumented treadmill. Since human-structure interaction and pedestrian-synchronisation modify the walking behaviour and hence the pedestrian-induced forces, they are assumed only to be justifiable in case of structures which do not vibrate perceptibly [3].

More recently, visual motion tracking systems are applied to help understanding the human motion and the resulting forces. Research in biomedical sciences uses technologically advanced tools, such as VICON [4] and CODA [5]. These techniques enable to study the human motion in laboratory conditions but a remaining challenge is the analysis of the walking behaviour of pedestrians and crowds *in situ*. In view of this challenge, the authors see great potential in a 3D motion tracking technique originating from the movement science and entertainment industry. The present contribution limits itself to the demonstration of the possibilities of the technique in laboratory conditions.

The experiments are performed in the MALL (Movement & posture Analysis Laboratory Leuven) at the Department of Biomedical Kinesiology and Rehabilitation Sciences of KU Leuven [6]. The motion of the test-subject and the measured ground reaction forces are registered simultaneously. The walking behaviour is analysed and the ground reaction forces are simulated using a step-by-step load model available in literature for which the characteristics are determined based on the registered movement of the body segments.

The outline of this paper is as follows. First, the 3D motion tracking technique is presented. Second, the experiments in laboratory conditions are discussed. Third, the walking behaviour of the test-subject is analysed considering both treadmill and overground walking. The final section presents the comparison between the simulated and measured ground reaction forces.

2 3D Motion Tracking

The Xsens - MTw Development Kit measurement system consists of multiple wireless inertial units (MTw's - figure 1), incorporating 3D accelerometers, gyroscopes, magnetometers (3D compass) and a barometer (pressure sensor). The accompanied ©Awinda radio protocol ensures time synchronization among the MTw's across the wireless network. The sensors are securely fixed onto the test-subject with specially designed click-in full body straps (figure 1b). The objective is to identify the main characteristics of the walking behaviour from the motion of the pedestrian tracked by the MTw's, enabling to accurately simulate the human induced forces.

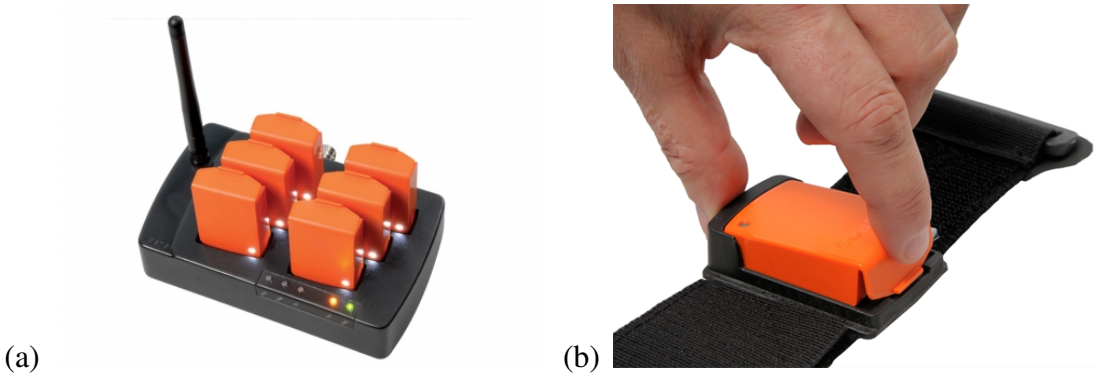


Figure 1: ©Xsens - MTw Development Kit consisting of multiple wireless inertial units (MTw's) and specially designed click-in full body straps.

3 Experiments in laboratory conditions

The experiments in laboratory conditions are considered to study the relation between the accelerations of the body segments and the measured ground reaction forces. The experiments are performed in the MALL (Movement & posture Analysis Laboratory Leuven) at the Department of Biomedical Kinesiology and Rehabilitation Sciences of the KU Leuven [6].

The positions of the MTw sensors are determined taking into account the recommendations of the manufacturer with the objective to limit the influence of skin motion artifacts which can occur with all forms of human movement measurement systems [7]. Using the click-in body straps, the Xsens MTw's are fastened tightly and robustly to the skin. Figure 2 illustrates the configuration setup applied in laboratory conditions. This setup consists of six sensors: on the lateral side of each leg, one sensor is placed close to the ankle and another on the thigh; the fifth sensor is placed as close as possible to the gravitational point of the test subject (at the small of the back) using the pelvis belt and the sixth sensor is placed at the upper back with the body strap fastened right under the armpits. The sampling frequency of the MTw's was set to 60 Hz, as recommended by the manufacturer for a configuration of 6 sensors.

The accelerations registered near the ankles of the test subject are assumed to be very strong due to the large movement of these body segments including both the impact and sway of one leg. The sensors at the lower and upper back on the other hand, will gather information about the global walking behaviour of the test subject. Analysis of the tracked motion and the corresponding registered ground reaction forces will reveal from which body segments the main characteristics of the walking behaviour can be identified.

3.1 Ground reaction forces

The experiments consider both treadmill and overground walking. The ground reaction forces are registered by an instrumented split-belt treadmill (*Forcelink*) and three *AMTI force plates* that are integrated in the walkway (Figure 3). The sampling frequency of both systems is 1 kHz.

The main advantage of the treadmill technology is that it allows identifying stride-to-stride variations [3]. The applied protocol considered a measurement time of 2 min for each walking speed which resulted in the registration of about 200 steps for each trial. The test-subject considered herself to be an experienced treadmill user and sufficient time was provided to get used to each treadmill speed. In total, 8 walking speeds were considered, varying from 2.5 up to 6.0

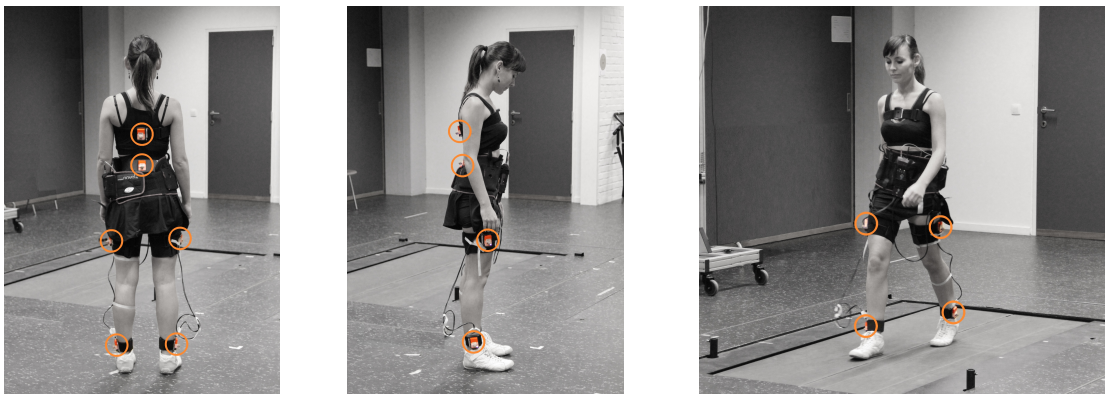


Figure 2: Configuration setup of the wireless inertial units (MTw's) in laboratory conditions.

km/h.

In case of overground walking, the different trials considered normal (self-selected), slow and fast walking. Since the laboratory floor has 3 force plates integrated in the walkway (figure 3), two successive steps could be registered for each path and at least 4 steps were taken before and after crossing the plates. In total, 24 successful steps were registered for each walking speed.

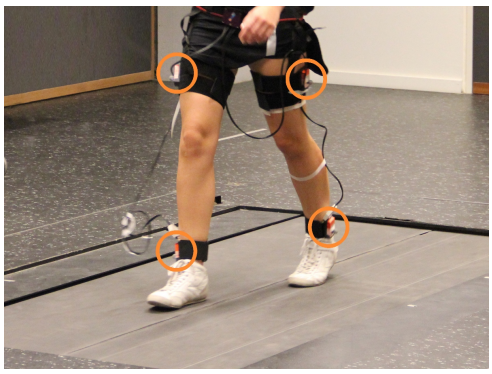
(a)  (b) 

Figure 3: Measurement of ground reaction forces (GRF's): (a) instrumented split-belt treadmill (*Forcelink*) and (b) three *AMTI force plates* integrated in the walkway (the borders of the plates are artificially accentuated).

Figure 4 presents two successive steps registered by the force plates together with the single-sided amplitude spectrum of a single step. This figure illustrates that the main frequency content of the induced forces is found below 10 Hz. Figure 5 presents the ground reaction forces registered by the instrumented treadmill. To minimise the influence of instrumental noise and moving parts of the treadmill [8], a cutoff frequency of 12 Hz is applied (figure 5b).

4 Analysis of treadmill and overground walking

In this section, the registered accelerations of the selected body segments are studied in relation to the measured ground reaction forces.

Figure 6a and 6b show that the frequency content of the sum of the vertical forces and the ones of the measured acceleration levels of the lower back respectively, are highly similar. The

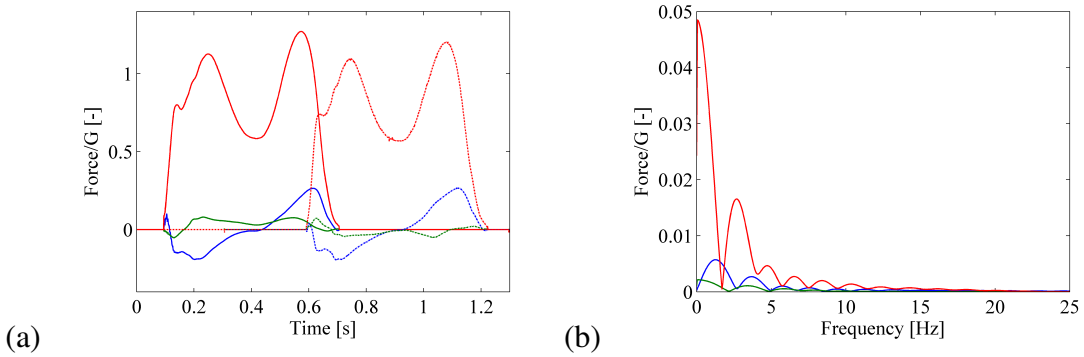


Figure 4: (a) ground reaction forces registered by the *AMTI force plates* with a sampling frequency of 1 kHz for a normal walking speed and (b) corresponding Fourier series coefficients of a single step: longitudinal (blue), lateral (green) and vertical (red) component.

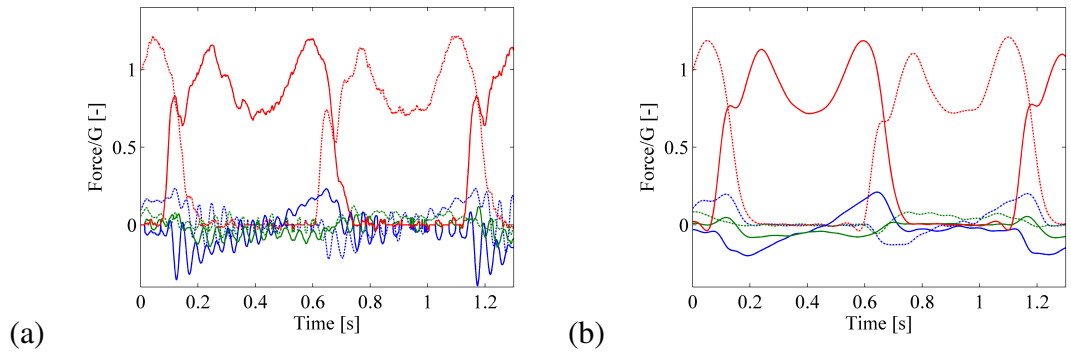


Figure 5: Ground reaction forces for a normal walking speed of 5 km/h, registered by the instrumented split-belt treadmill: (a) original signal with a sampling frequency of 1 kHz and (b) low-pass filtered using an eighth order Chebyshev type I filter with a cutoff frequency of 12 Hz: longitudinal (blue), lateral (green) and vertical (red) component.

fundamental frequency of these spectra represents the main step frequency of the test-subject during the treadmill trial. Analysis of the measured ground reaction forces and the registered lower back accelerations of all trials, covering different walking speeds, shows that the same step frequency is in this way identified up to $\pm 0.1\%$.

The accelerations measured near the ankles are very strong due to the large movement of these body segments that include both the impact and sway of one leg. Analysis showed that the magnitude of the total acceleration vector enables in this case a clear interpretation. Figures 7 and 8 present the ground reaction forces, the acceleration levels registered at the lower back and the magnitude of the total acceleration vector measured near the ankles. The signals are normalised respectively to the weight of the test-subject, the gravitational constant and the mean peak value. These figures illustrate that both the acceleration levels at the lower back and at the ankles, enable to identify the time in between two successive steps, and therefore, the pacing rate of the test-subject.

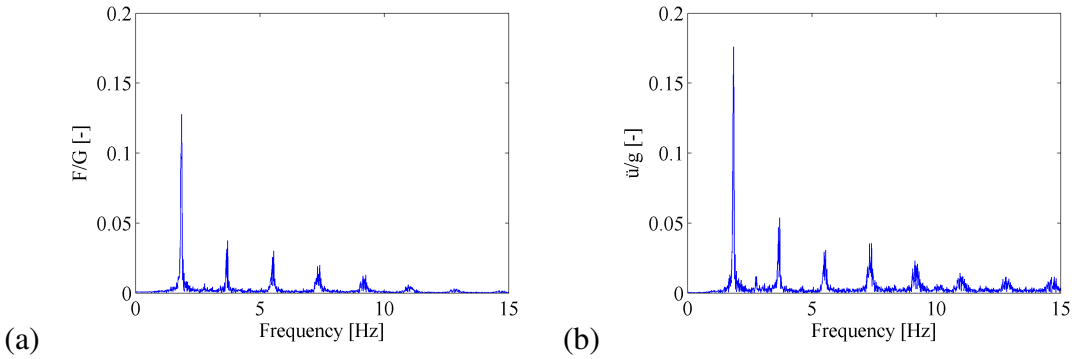


Figure 6: Fourier series coefficients up to 15 Hz of (a) the sum of the vertical ground reaction forces registered by the instrumented split-belt treadmill (*Forcelink*) for a normal walking speed of 5 km/h and (b) the corresponding measured vertical acceleration levels at the lower back.

5 Simulation of the ground reaction forces

In this section, the measured vertical ground reaction forces (GRF) are simulated using a step-by-step load model available in literature for which the characteristics are determined based on the registered movement of the body segments. To include the stride-to-stride variations of the human-induced forces, the results of the treadmill experiments are applied.

First, the mean step frequency of the test-subject is determined for the considered treadmill trial based on the analysis in the frequency domain of the accelerations measured on the lower back. This step frequency along with the static weight of the test-subject, determines the vertical single foot force F_1 [N] as defined by Li *et al.* [9]:

$$F_1(t) = G \sum_{n=1}^{5} A_n\left(f_s\right) \sin\left(\frac{\pi n}{T_c\left(f_s\right)} t\right), \qquad 0 \leq t \leq T_c\left(f_s\right) \tag{1}$$

with G [N] the static weight of the test-subject, f_s [Hz] the step frequency, $A_n\left(f_s\right)$ [-] the Fourier coefficient of the n^{th} harmonic, and $T_c\left(f_s\right)$ [s] the time duration of contact between the foot and the ground. The ratio of the cycle of the single foot force to the period during which the foot has contact with the ground is basically unchanged [10]:

$$T_c = \frac{1}{0.76 f_s} \tag{2}$$

Secondly, the accelerations measured near the ankles (or at the lower back) are applied to determine the beginning of each step in time (t_i). Subsequently, the corresponding force due to step i in time is found as:

$$F_i(t) = \kappa\left(t - t_i\right) F_1\left(t - t_i\right), \qquad \text{with} \quad \kappa\left(t\right) = \begin{cases} 1 & 0 \leq t \leq T_c \\ 0 & \text{otherwise} \end{cases} \tag{3}$$

with t [s] the general time of the considered treadmill trial. Together, this collected time information and mean step frequency, provide the necessary input to simulate the measured ground reaction forces based on the generalised vertical single foot force of Li *et al.* [9].

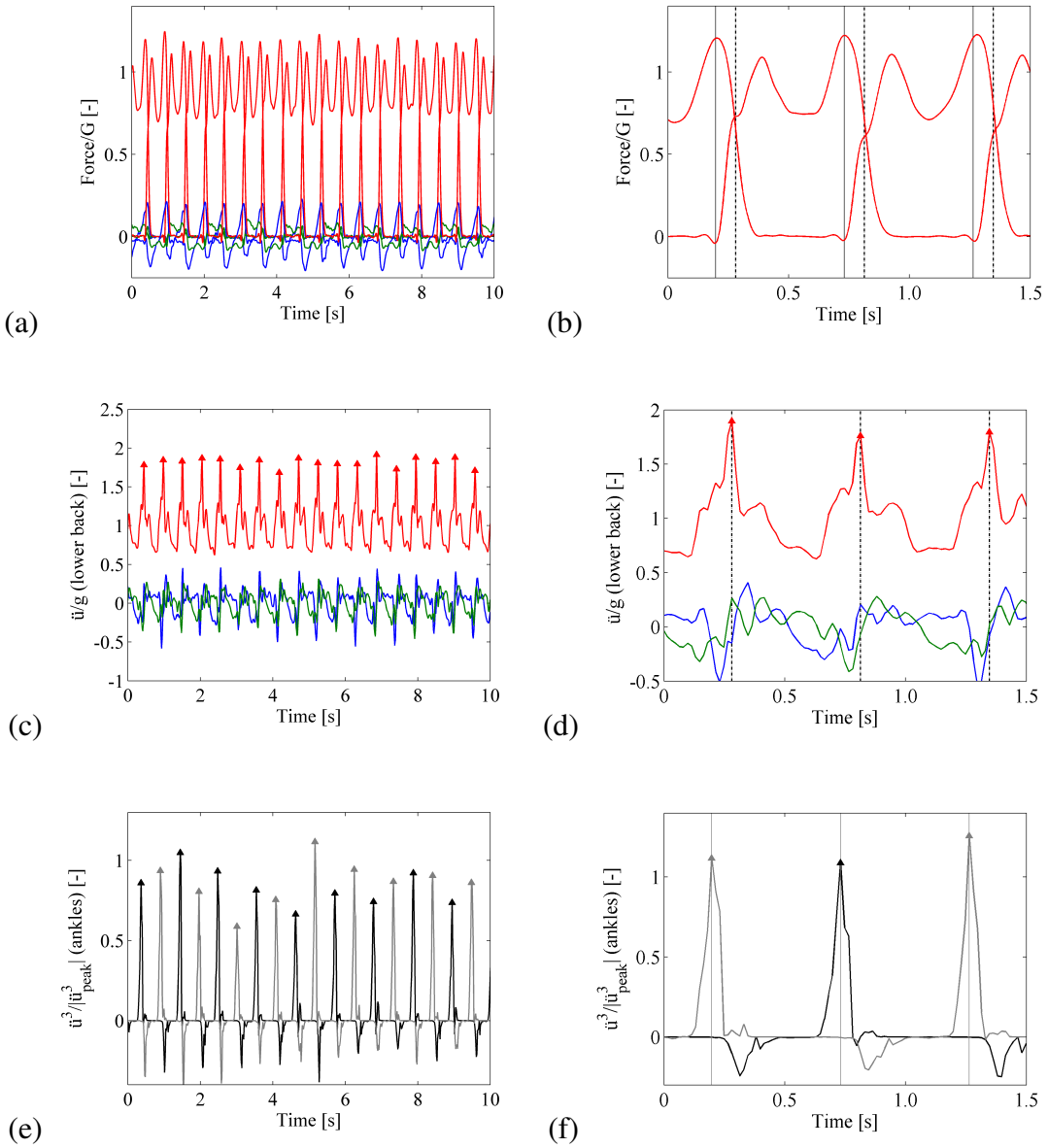


Figure 7: For a normal walking of speed of 5 km/h: (a-b) normalised ground reaction forces registered by the instrumented split-belt treadmill and (c-d) normalised measured accelerations at the lower back for the longitudinal (blue), lateral (green) and vertical (red) component. (e-f) normalised magnitude of the total acceleration vector measured near the left (black) and right (gray) ankle.

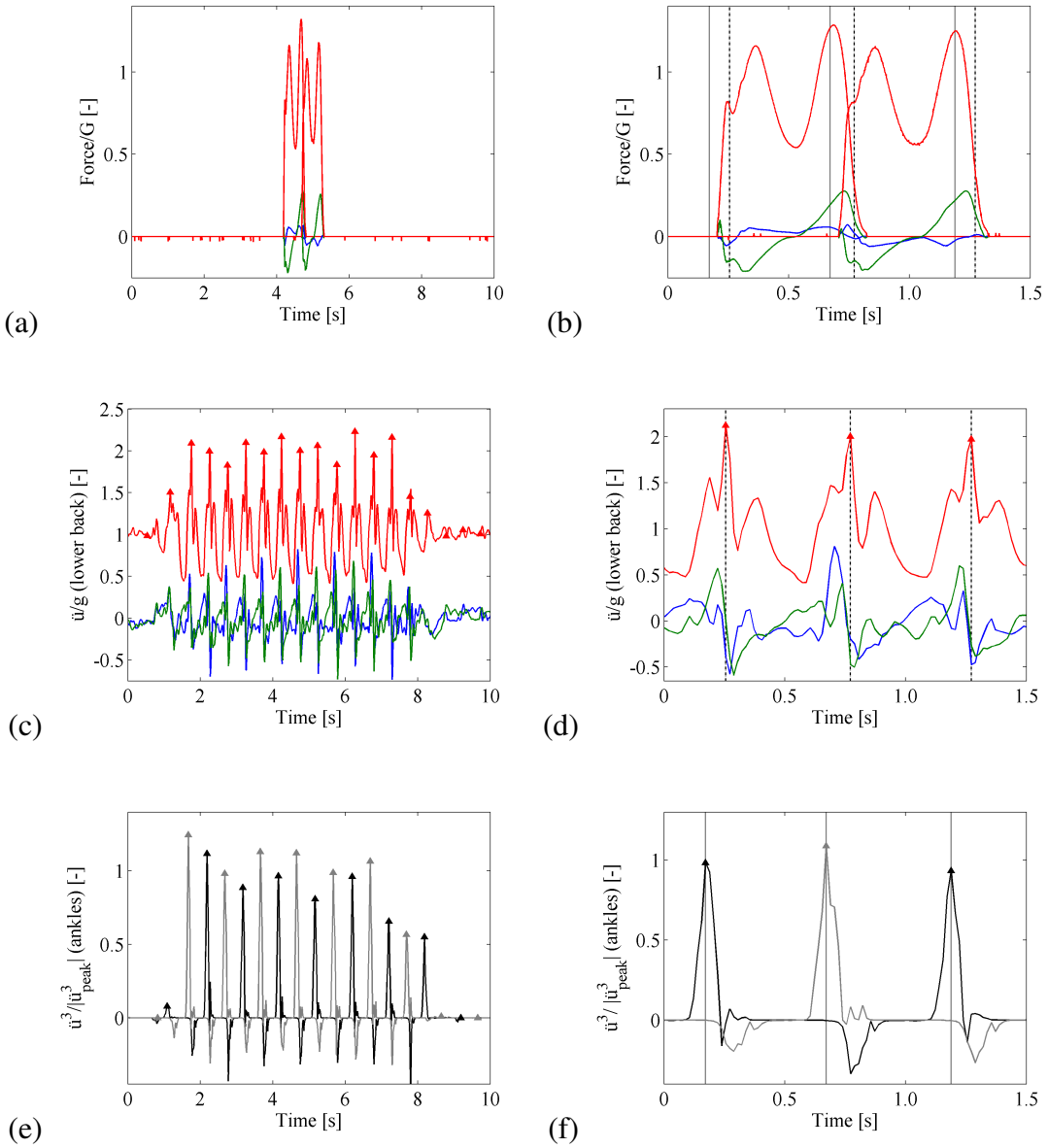


Figure 8: For a normal walking of speed: (a-b) normalised ground reaction forces registered by the *AMTI force plates* and (c-d) normalised measured accelerations at the lower back for the longitudinal (blue), lateral (green) and vertical (red) component. (e-f) normalised magnitude of the total acceleration vector measured near the left (black) and right (gray) ankle.

Figure 9 shows that there is a difference between the simulated vertical single foot force of Li *et al.* [9] and the measured forces. This difference could be minimized using the averaged vertical single foot force of the test-subject for the corresponding walking speed, however, it is expected that the simulated vibration response is more sensitive to the variations of the pacing rate for successive footfalls, than to the small variations in force amplitude or contact time, which was also observed by Middleton [11]. Figure 9 illustrates that the beginning of each step, and therefore also the pacing rate, can be accurately estimated from the measured accelerations of the ankles. The same results (with a certain time-shift) are found for the analysis based on the measured accelerations at the lower back.

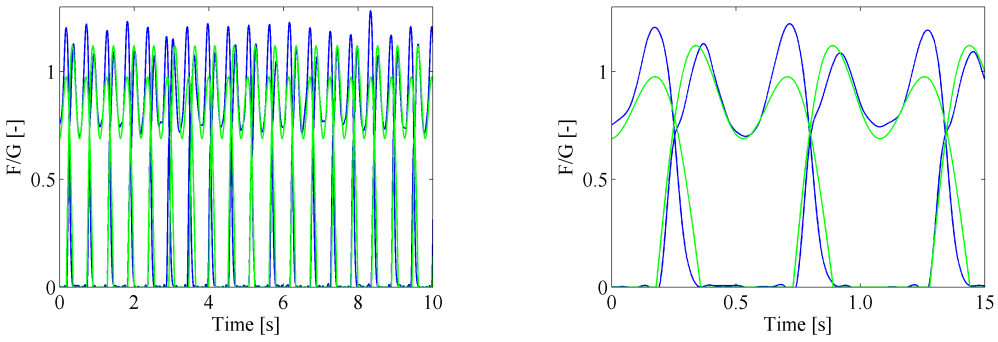


Figure 9: The measured vertical ground reaction forces for a normal walking speed of 5 km/h (blue) and the corresponding simulated vertical walking forces according to Li *et al.* [9] with step frequency and time in between two successive steps identified based on the tracked motion of the body segments of the test-subject (green).

Figure 10 presents the single-sided amplitude spectrum of the simulated and measured ground reaction forces. For the simulated forces, two cases were considered. In case 1, perfectly periodic forces are generated simply based on the identified mean step frequency. In case 2, the simulations account for the identified pacing rate. Figure 10 illustrates that the perfectly periodic forces only succeed in identifying the dominant harmonics of the walking forces. Imperfect real walking forces are however near-periodic by nature [12] and result into a distribution of forces around the dominant harmonics [13, 14]. These narrow band forces are clearly present in the measured forces but also in the simulated forces that account for the identified pacing rate. This comparison shows that simulations based on the generalised single foot force model and the in situ identified pacing rate, allow for a good approximation of the GRF in case of imperfect real walking.

6 Conclusions

A 3D motion tracking technique is presented for the analysis of the walking behaviour of pedestrians. The technique is applied in laboratory conditions and it is shown that it enables to identify the main step frequency and pacing rate of the test-subject. Applying a generalised model for the ground reaction forces available in literature, together with the weight of the test-subject and the identified pacing rate, provides a good approximation of the imperfect real walking forces.

The major advantage of the presented technique is its applicability for the in situ analysis of the walking behaviour of (groups of) pedestrians and crowd. The time synchronisation

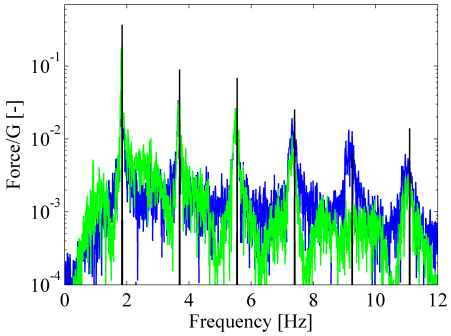


Figure 10: The Fourier series coefficients of the measured vertical ground reaction forces for a normal walking speed of 5 km/h (blue) and the corresponding simulated vertical walking forces according to Li *et al.* [9] with main step frequency f_s and pacing rated identified based on the tracked motion of the body segments of the test-subject (green) and the perfectly periodic forces with the identified main step frequency and the time in between two successive steps equal to $1/f_s$ (black).

among the inertial sensors will also enable to study the synchronisation rate among the different test-subjects. The application in situ and the simultaneous registration of the movement of pedestrians and the structure, will contribute to a better understanding of the normal walking behaviour, the resulting forces and the observed crowd-structure interaction phenomena.

7 Acknowledgements

We thank Prof. I. Jonkers and Prof. B. Vanwanseele for the cooperation and the support in the framework of the interdepartmental research laboratory (MALL) at Faber (Faculty of Kinisiology and Rehabilitation Sciences) at KU Leuven.

This research is funded by the Agency for Innovation by Science and Technology in Flanders (IWT). Their financial support is gratefully acknowledged.

REFERENCES

[1] J. Brownjohn, P. Fok, M. Roche, and P. Moyo, "Long span steel pedestrian bridge at Singapore Changi Airport - part 1: Prediction of vibration serviceability problems," *The Structural Engineer*, vol. 82, no. 16, pp. 21–27, 2004.

[2] S. Živanović, A. Pavic, and P. Reynolds, "Vibration serviceability of footbridges under human-induced excitation: a literature review," *Journal of Sound and Vibration*, vol. 279, no. 1-2, pp. 1–74, 2005.

[3] V. Racic, A. Pavic, and P. Reynolds, "Experimental identification and analytical modelling of walking forces: a literature review," *Journal of Sound and Vibration*, vol. 326, pp. 1–49, 2009.

[4] Vicon Motion Systems, *Vicon Motion Systems Product Manuals*. Movement & posture Analysis Laboratory Leuven (MALL) Interdepartmental research laboratory at the Faculty of Kinisiology and Rehabilitation Sciences - KU Leuven.

[5] CODAmotion, *Technical dat sheet*. Charnwood Dynamics.

[6] J. Duysens, I. Jonkers, and S. Verschueren, *MALL: Movement & posture Analysis Laboratory Leuven*. Interdepartmental research laboratory at the Faculty of Kinisiology and Rehabilitation Sciences - KU Leuven.

[7] Xsens Technologies B.V., *MTw User Manual*, 2010.

[8] G. Paolini, U. Croce, P. Riley, F. Neuwton, and D. Kerrigan, "Testing of a tri-instrumented-treadmill unit for kinetic analysis of locomotion tasks in static and dynamic loading conditions," *Medical Engineering and Physics*, no. 29, pp. 404–411, 2007.

[9] Q. Li, J. Fan, J. Nie, Q. Li, and Y. Chen, "Crowd-induced random vibration of footbridge and vibration control using multiple tuned mass dampers," *Journal of Sound and Vibration*, no. 329, pp. 4068–4092, 2010.

[10] A. Ebrahimpour, A. Hamam, R. Sack, and W. Patten, "Measuring and Modeling Dynamic Loads imposed by Moving Crowds," *Journal of Structural Engineering*, no. 122, pp. 1468–1474, 1996.

[11] C. Middleton, *Dynamic Performance of High Frequency Floors*. PhD thesis.

[12] V. Racic, A. Pavic, and P. Reynolds, "Mathematical model to generate near-periodic human jumping force signals," *Mechanical Systems and Signal Processing*, vol. 24, pp. 138–152, 2010.

[13] V. Racic and J. Brownjohn, "Mathematical modelling of random narrow band lateral excitation of footbridges due to pedestrians walking," *Computers and Structures*, vol. 90-91, pp. 116–130, 2012.

[14] E. Ingolfson, C. Georgakis, F. Ricciardelli, and J. Jonsson, "Experimental identification of pedestrian-induced lateral forces on footbridges," *Journal of Sound and Vibration*, vol. 330, pp. 1265–1284, 2011.

COMPDYN 2013
4th ECCOMAS Thematic Conference on
Computational Methods in Structural Dynamics and Earthquake Engineering
M. Papadrakakis, N.D.Lagaros, V. Plevris (eds.)
Kos Island, Greece, 12–14 June 2013

ANALYTICAL AND NUMERICAL ESTIMATE OF FOOTBRIDGES' MAXIMUM DYNAMIC RESPONSE TO UNRESTRICTED PEDESTRIAN TRAFFIC

Federica Tubino [1] **and Giuseppe Piccardo** [1]

[1] DICCA, Polytechnic School, University of Genoa
Via Montallegro 1, 16145 Genova
e-mail: federica.tubino, giuseppe.piccardo@unige.it

Keywords: Dynamics, Footbridges, Maximum dynamic response, Random processes, Serviceability, Unrestricted pedestrians.

Abstract. *The assessment of footbridge vibrations due to normal unrestricted pedestrian traffic is a topical problem in the serviceability analysis of these structures. Based on a probabilistic model of the parameters involved, the authors of the present paper have analytically derived an equivalent spectral model for the loading induced by pedestrian groups, modeled as a stationary random process, and simple closed-form expressions for the evaluation of the mean value of the maximum dynamic response. This paper provides a complete assessment of the random walking parameters which mainly influence the serviceability analysis of footbridges, and a comparison between the analytical predictions provided by the simple expressions for the estimate of the maximum dynamic response and the results of Monte Carlo simulations.*

1 INTRODUCTION

Modern footbridges can be very sensitive to walking-induced vibrations because of their increasing slenderness and flexibility. The assessment of footbridge vibrations due to normal unrestricted pedestrian traffic is a topical problem in the serviceability analysis of these structures (see, e.g., [1]). Real pedestrian traffic conditions should be modeled probabilistically, considering several sources of randomness among which pedestrian arrivals, step frequencies and velocities, force amplitudes and pedestrian weights. Based on a probabilistic model of the involved parameters, the authors have derived analytically an equivalent spectral model for the loading induced by pedestrian groups, modeled as a stationary random process under suitable simplifying assumptions ([2], [3]). Furthermore, starting from the assumption that the footbridge dynamic response is a narrow-band random process, simple closed-form expressions for the evaluation of the mean value of the maximum dynamic response have been provided [3]. According to the proposed spectral model, the main force parameter affecting the structural response is the probability distribution of the pedestrian step frequency, in terms of mean value and coefficient of variation: pedestrian arrivals, walking velocity, dynamic load factor and pedestrian weight may be assumed as deterministic and coincident with their mean value. The statistical characterization of these loading parameters is possible through experimental measurements available in the scientific literature, which furnish information concerning the statistical distribution of the step frequency ([1], [4]-[9]).

The present paper has three main objectives: the complete assessment of the random walking parameters which mainly influence the serviceability of footbridges to normal unrestricted pedestrian traffic, a full validation of the simple expressions proposed in [3] for the estimate of the maximum dynamic response, and the analysis of the influence of the variability of walking random parameters on the maximum footbridge acceleration.

Monte Carlo simulations are performed in order to deal with the first two aspects. At first, the variability of all the involved random parameters is analyzed in order to verify the effective role of the parameters that the proposed spectral model assumes as deterministic: the influence of the randomness of walking velocity, dynamic load factor and pedestrian weight on the maximum dynamic response is analyzed. After this first step, extensive analyses are carried out for different values of the relevant statistical parameters, i.e. the non-dimensional mean step frequency and its coefficient of variation: the results of Monte Carlo simulations are compared with the analytical estimate of the mean value of the maximum dynamic response provided by the model proposed by the authors in [3]. The reliability of the formulation adopted for the statistical characterization of the maximum response, based on the narrow band assumption, is assessed through the analysis of the mean maximum dynamic response and its probability density function.

Finally, the role of the main parameters on footbridge serviceability assessment is investigated through extensive parametric analyses. The closed-form expression for the maximum structural response in free pedestrian traffic conditions allows to perform such analysis without the need to carry out burdensome Monte Carlo simulations. Furthermore, the use of the spectral approach allows a synthetic description of the maximum dynamic response as a function of its relevant parameters; its use appears very appropriate for technical purposes.

2 LOAD MODELLING AND MAXIMUM DYNAMIC RESPONSE

2.1 Probabilistic loading model

Dealing with pedestrian traffic on footbridges, a realistic loading scenario is characterized by pedestrians arriving in a random way and able to move undisturbed, each of them with

their own characteristics in terms of loading amplitude, frequency, velocity and phase. In such a case, focusing attention only on the first walking harmonic for each pedestrian, the force induced by N_p pedestrians can be expressed as:

$$f(x,t) = \sum_{i=1}^{N_p} \alpha_i G_i \sin\left(\Omega_i (t-\tau_i) + \Psi_i\right) \delta\left[x - c_i (t-\tau_i)\right] \left[H(t-\tau_i) - H\left(t-\tau_i - \frac{L}{c_i}\right)\right] \quad (1)$$

where $\delta(\bullet)$ and $H(\bullet)$ are the Dirac function and the Heaviside function, respectively; furthermore, F_i ($=\alpha_i G_i$), Ω_i, Ψ_i, c_i and τ_i are, respectively, the force amplitude, the step circular frequency, the phase-angle, the walking speed and the arrival time of the i-th pedestrian, while α_i and G_i are the DLF and the weight of the i-th pedestrian. All these quantities have to be probabilistically modeled in order to consider the inter-subject variability in walking forces induced by different pedestrians. In particular, the step circular frequency Ω, the pedestrian weight G, the DLF α and the walking velocity c can be considered as random Gaussian variables. Table 1 reports the results of some experimental tests for the statistical characterization of the step frequency.

References	People tested	Type of event	f_{pm} (Hz)	σ_{fp} (Hz)	V_{fp}
[4]	505	Free field, normal traffic	2	0.173	0.09
[5]	251	Laboratory	1.82	0.12	0.07
[6], [1] Podgorica Bridge	1976	Free field, normal traffic	1.87	0.186	0.1
[1] Reykjavik City Footbridge	38	Free field, normal traffic	1.95	0.15	0.08
[7]	227	Laboratory	1.92		0.07
[8]	400	Free field, normal traffic	1.8	0.11	0.06
[9]	116	Laboratory	1.835	0.172	0.09

Table 1: Statistical characterization of the step frequency.

Starting from the probabilistic characterization of all the parameters involved in Eq. (1), the footbridge dynamic response to unrestricted pedestrian traffic may be numerically determined through Monte Carlo simulations (e.g. [10]).

The authors recently proposed an equivalent spectral model of pedestrian-induced loads, which permits a closed-form estimate of the maximum acceleration due to unrestricted pedestrian traffic [3], without the need to carry out numerical simulations.

Considering a structure with linear behavior and classical damping, the equation of motion of the j-th non-dimensional principal coordinate $\tilde{p}_j$ can be expressed in the following non-dimensional form:

$$\ddot{\tilde{p}}_j(\tilde{t}) + 2\xi_j \dot{\tilde{p}}_j(\tilde{t}) + \tilde{p}_j(\tilde{t}) = \tilde{F}_j(\tilde{t}) \quad (2)$$

where ξ_j is the j-th modal damping ratio, and the non-dimensional quantities $\tilde{t}$, $\tilde{p}_j$, $\tilde{F}_j$ read [3]:

$$\tilde{t} = \omega_j t, \quad \tilde{p}_j = \frac{p_j}{p_{js}} = \frac{p_j M_j \omega_j^2}{\alpha_m G_m}, \quad \tilde{F}_j(\tilde{t}) = \int_0^1 \tilde{f}(\tilde{x},\tilde{t})\,\varphi_j(\tilde{x})\,\mathrm{d}\tilde{x}$$
$$\tilde{f}(\tilde{x},\tilde{t}) = \frac{f(x,t)L}{\alpha_m G_m}, \quad \tilde{x} = \frac{x}{L} \tag{3}$$

t being the time, x the abscissa along the structure, L the length of the structure, ω_j and M_j the j-th natural circular frequency and modal mass, α_m the mean dynamic loading factor, G_m the mean pedestrian weight, φ_j the j-th mode shape.

The non-dimensional modal force due to a probabilistically-modeled group of pedestrians is obtained substituting Eq. (1) into Eq. (3), and is given by [2]:

$$\tilde{F}_j(\tilde{t}) = \sum_{i=1}^{N_p} \tilde{\alpha}_i \tilde{G}_i \sin\left(\tilde{\Omega}_i(\tilde{t}-\tilde{\tau}_i)+\Psi_i\right)\varphi_j\left(\tilde{\Omega}_{ci}(\tilde{t}-\tilde{\tau}_i)\right)\left[H(\tilde{t}-\tilde{\tau}_i)-H\left(\tilde{t}-\tilde{\tau}_i-\frac{1}{\tilde{\Omega}_{ci}}\right)\right] \tag{4}$$

where the following non-dimensional parameters are introduced:

$$\tilde{\alpha}_i = \frac{\alpha_i}{\alpha_m}, \quad \tilde{G}_i = \frac{G_i}{G_m}, \quad \tilde{\Omega}_i = \frac{\Omega_i}{\omega_j}, \quad \tilde{\Omega}_{ci} = \frac{c_i}{\omega_j L}, \quad \tilde{\tau}_i = \omega_j \tau_i \tag{5}$$

2.2 Equivalent spectral model

Considering the particular case in which the structural mode shape is sinusoidal, $\varphi_j(\tilde{x}) = \sin(\pi\tilde{x})$, focusing attention only on the randomness of the step frequency and under the assumption that $\tilde{\Omega}_{cm}$ is very small compared with $\tilde{\Omega}_i$, the following expression for the psdf of the non-dimensional modal force is obtained [3]:

$$S_{\tilde{F}_j}(\tilde{\Omega}) \simeq \frac{N_p}{4} p_{\tilde{\Omega}}(\tilde{\Omega}) \tag{6}$$

In Eq. (6), $p_{\tilde{\Omega}}(\tilde{\Omega})$ is the probability density function of the non-dimensional circular step frequency $\tilde{\Omega} = \omega/\omega_j$.

The psdf of the j-th non-dimensional principal coordinate is supplied by:

$$S_{\tilde{P}_j}(\tilde{\Omega}) = \left|H_{\tilde{P}_j}(\tilde{\Omega})\right|^2 S_{\tilde{F}_j}(\tilde{\Omega}) \tag{7}$$

where $H_{\tilde{P}_j}(\tilde{\Omega})$ is the complex frequency response function of the j-th non-dimensional principal coordinate:

$$H_{\tilde{P}_j}(\tilde{\Omega}) = \frac{1}{1-\tilde{\Omega}^2 + 2\mathrm{i}\xi_j\tilde{\Omega}} \tag{8}$$

i being the imaginary unit.

Finally, the psdf of the acceleration of the j-th non-dimensional principal coordinate $\tilde{p}_j$, $S_{\ddot{\tilde{P}}_j}(\tilde{\Omega})$, is:

$$S_{\ddot{\tilde{P}}_j}(\tilde{\Omega}) = \tilde{\Omega}^4 S_{\tilde{P}_j}(\tilde{\Omega}) \tag{9}$$

2.3 Maximum dynamic response

Starting from the proposed equivalent spectral model of the modal force, the maximum value of the acceleration of the *j*-th non-dimensional principal coordinate $\tilde{p}_j$ can be expressed as follows:

$$\ddot{\tilde{p}}_{j\max} = g_{\ddot{\tilde{p}}_j} \sigma_{\ddot{\tilde{p}}_j} \tag{10}$$

where $\sigma_{\ddot{\tilde{p}}_j}$ and $g_{\ddot{\tilde{p}}_j}$ are, respectively, the standard deviation and the so-called peak factor of $\ddot{\tilde{p}}_j$.

If the non-dimensional mean step frequency is close to a unit value (i.e. the bridge is prone to pedestrian excitation), the dynamic response may be considered as mainly resonant. In such a case, the standard deviation is given by the following simple approximate formula [3]:

$$\sigma^2_{\ddot{\tilde{p}}_j} \cong \frac{\pi}{4\xi_j} S_{\tilde{F}_j}(1) \tag{11}$$

According to Davenport formulation, [13], the peak factor can be expressed as:

$$g_{\ddot{\tilde{p}}_j} = \sqrt{2\ln\left(2\nu_{\ddot{\tilde{p}}_j}\tilde{T}\right)} + \frac{0.5772}{\sqrt{2\ln\left(2\nu_{\ddot{\tilde{p}}_j}\tilde{T}\right)}} \tag{12}$$

where $\tilde{T}$ is the non-dimensional time duration over which the maximum response is estimated, and $\nu^e_{\ddot{\tilde{p}}_j}$ is the non-dimensional expected frequency of $\ddot{\tilde{p}}_j$. They can be given by [13]:

$$\tilde{T} = \omega_j \frac{NL}{c_m} = \frac{N}{\tilde{\Omega}_{cm}} \qquad \nu_{\ddot{\tilde{p}}_j} \simeq \tilde{n}_j = \frac{1}{2\pi} \tag{13}$$

N being the number of consecutive pedestrian groups to be considered in the serviceability analysis in order to satisfy the stationarity hypothesis (a reasonable value seems to be around 10 [3]), $\tilde{\Omega}_{cm}$ being the non-dimensional mean walking velocity, given by Eq. (5) with $c_i = c_m$.

The Davenport expression for the peak factor [11] is based on the assumption that threshold upcrossings are Poisson events. As discussed in [13], a conventional peak factor formula on the basis of the Poisson assumption may still be a reasonable choice because of its conservative nature. This aspect will be analyzed in Section 3.2.

The maximum acceleration of the *j*-th non-dimensional principal coordinate $\tilde{p}_j$ can thus be obtained by considering Eqs. (6), (10) and (11):

$$\ddot{\tilde{p}}_{j\max} = \sqrt{\frac{N_p}{\xi_j}} g_{\ddot{\tilde{p}}_j} \frac{\sqrt{\pi}}{4} \sqrt{p_{\tilde{\Omega}}(1)} \tag{14}$$

Eq. (14) shows that, according to the equivalent spectral model proposed by the authors in [3], the maximum non-dimensional principal coordinate is a function of the non-dimensional mean walking speed $\tilde{\Omega}_{cm}$ through the peak factor; furthermore, it is a function of N_p, ξ_j and of the probability density function of the non-dimensional step circular frequency $p_{\tilde{\Omega}}$, estimated for $\tilde{\Omega}$=1.

The maximum structural acceleration in dimensional form can finally be obtained considering Eqs. (3) and (14) together, and is given by:

$$\ddot{q}_{\max} = \ddot{p}_{j_{\max}} = \frac{\alpha_m G_m}{M_j} \ddot{\tilde{p}}_{j_{\max}} = \frac{\alpha_m G_m}{M_j} \sqrt{\frac{N_p}{\xi_j}} g_{\ddot{\tilde{p}}_j} \frac{\sqrt{\pi}}{4} \sqrt{p_{\tilde{\Omega}}(1)} \tag{15}$$

3 MONTE CARLO SIMULATIONS

Monte Carlo simulations are performed with two main objectives. The first goal is an analysis of the influence of the variability of all the statistical parameters involved on the mean value of the maximum dynamic response in order to verify the effective role of the parameters that the spectral model assumes as deterministic. In particular, walking speed, dynamic load factor and pedestrian weight are analyzed (Section 3.1). The second aim is an assessment of the reliability of the proposed formulation for the statistical characterization of the maximum response. The results of Monte Carlo simulations are compared with the analytical evaluation of the mean value of the maximum dynamic response provided by the spectral model (Section 3.2).

In order to obtain general results without the need to focus on a particular structure, Monte Carlo simulations are performed starting from the non-dimensional expression of the modal force in Eq. (4). The non-dimensional form of the equation of motion of the *j*-th principal coordinate, Eq. (2), is numerically solved and the maximum acceleration of the non-dimensional principal coordinate is extracted from each simulation. For every case analyzed, the mean value of the maximum acceleration is estimated from 10^4 simulations. All simulations are performed assuming N_p=10, ξ_j= 0.005, V_α=0.1.

3.1 Statistical parameters affecting dynamic response

The equivalent spectral model of pedestrian loading, described in Section 2, has been obtained under the assumption that the pedestrian weight, the dynamic loading factor, the walking speed and the pedestrian arrivals could be considered as deterministic and coincident with their mean value: only the randomness of the step frequency has been taken into account. In the following, the influence of the parameters' statistical representation on the maximum structural acceleration is investigated through fully probabilistic simulations. In particular, numerical simulations are performed with the aim of verifying the secondary role of the randomness of the parameters that are assumed as deterministic; moreover, an assessment of the influence of the step frequency statistical distribution on the maximum dynamic response is performed.

The role of the probabilistic distribution of the body weight and of walking speed is analyzed by performing fully probabilistic simulations with different values of the coefficients of the two random variables. Fully-probabilistic Monte Carlo simulations are performed assuming $\tilde{\Omega}_m$=1.

Figure 1 plots the mean value of the maximum acceleration of the principal coordinate for different values of the coefficient of variation of pedestrian weight V_W (Fig. 1a, V_Ω = 0.09, V_c = 0.11) and of the walking speed (Fig. 1b, V_Ω = 0.09, V_W = 0.17). The maximum acceleration of the principal coordinate is almost independent of the variation coefficient of the pedestrian weight and of the walking speed. Thus, the probabilistic distribution of the body weight and of the walking speed practically do not affect the footbridge serviceability: assuming the pedestrian weight and the walking speed as deterministic and coincident with their mean value provides an accurate estimate of the maximum structural acceleration.

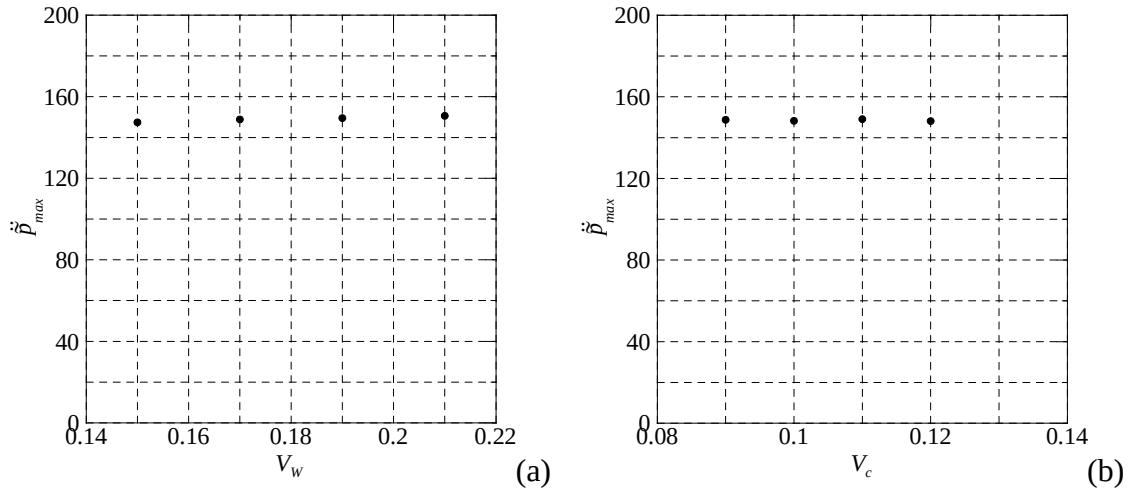


Figure 1: Influence of the probability distribution of the body weight (a) and of the walking speed (b) on the mean value of the maximum acceleration.

Finally, the role of the statistical distribution of the pedestrian step frequency is analyzed. Monte Carlo simulations are performed assuming fixed values for V_c and V_w (V_c = 0.11, V_W=0.17), whereas the coefficient of variation of pedestrian step frequency V_Ω is varied between 0.06 and 0.1, and the non-dimensional mean step frequency $\tilde{\Omega}_m$ between 0.8 and 1.2. Figure 2(a) plots the mean value of the maximum acceleration of the non-dimensional principal coordinate as a function of the variation coefficient of the step frequency V_Ω, for a unitary non-dimensional mean step frequency ($\tilde{\Omega}_m$=1); Figure 2(b) plots the mean value of the maximum acceleration of the non-dimensional principal coordinate as a function of the mean value of the non-dimensional step frequency $\tilde{\Omega}_m$, for V_Ω=0.09. From Figures 3(a) and 3(b) it is evident that the probabilistic distribution of the step frequency has a strong influence on the maximum dynamic response: both the coefficient of variation and the mean value of the non-dimensional step frequency cause remarkable variations of the maximum dynamic response.

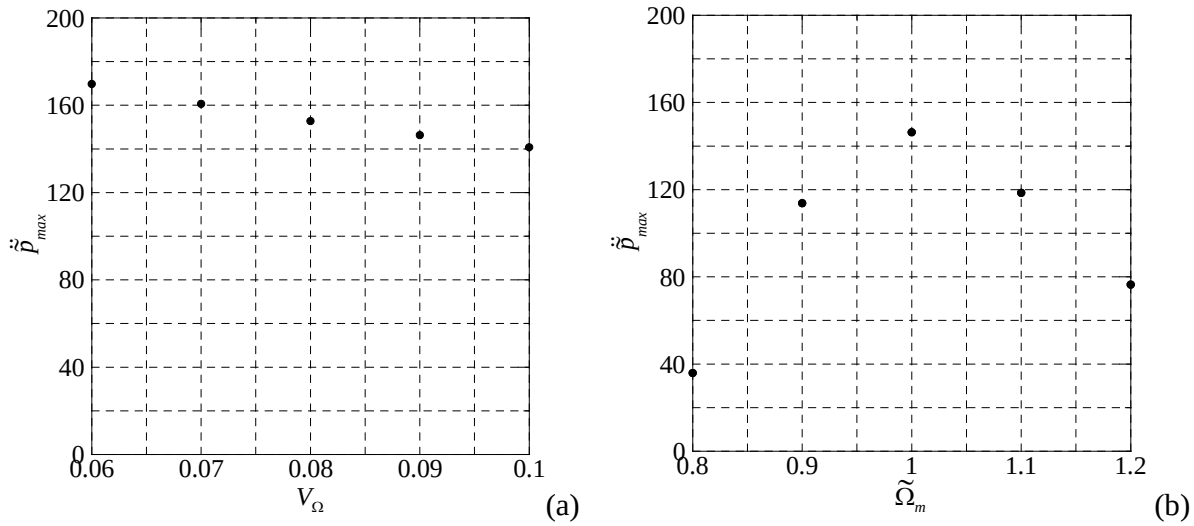


Figure 2: Influence of the probability distribution of the step frequency on the mean value of the maximum acceleration: (a) dependence on V_Ω ($\tilde{\Omega}_m$=1), (b) dependence on $\tilde{\Omega}_m$ (V_Ω=0.09).

In conclusion, the Monte Carlo simulations presented in this Section have shown that the maximum dynamic response is mainly governed by the probability distribution of the pedestrian step frequency in terms of its mean value and standard deviation. The basic assumption of the spectral model (to adopt the pedestrian weight, the walking speed and the dynamic loading factor as deterministic) appears totally reliable.

3.2 Validation of the proposed expression for the maximum dynamic response

In this Section, Monte Carlo simulations are performed with the aim of validating the proposed closed-form expression in order to estimate the maximum dynamic response, by comparing numerical results with the closed-form expression, Eq. (10).

Monte Carlo simulations are performed assuming fixed values for the variation coefficients of the walking speed, of the dynamic loading factor and of the pedestrian weight (V_c = 0.11, V_α = 0.1, V_W=0.17), whereas the coefficient of variation of pedestrian step frequency V_Ω is varied between 0.06 and 0.1 and the non-dimensional mean step frequency $\tilde{\Omega}_m$ between 0.8 and 1.2.

Figure 3 plots the mean value of the maximum non-dimensional acceleration as a function of the coefficient of variation of the step frequency V_Ω; the different curves correspond to different values of the non-dimensional mean step frequency $\tilde{\Omega}_m$. The results of numerical simulations (symbols) are compared with the closed-form expression (solid and dashed lines). It can be observed that the closed-form expression of the maximum acceleration provides an overestimation of the numerical results when the non-dimensional mean step frequency is approximately one. However, the proposed expession provides a better approximation of the numerical results when the non-dimensional mean step frequency is lower than 0.95 or higher than 1.05: in such cases, the analytical expression slightly overestimates the numerically estimated maximum acceleration.

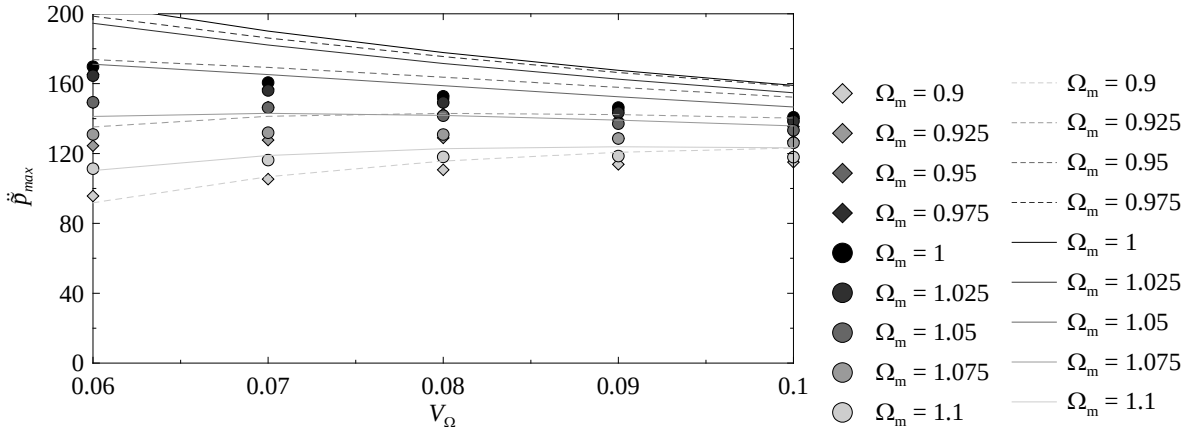


Figure 3: Mean value of the maximum non-dimensional acceleration: comparison between numerical simulations and closed-form expression.

In order to have a better insight into the problem, Figure 4 compares the numerically-estimated probability density function of the maximum non-dimensional acceleration (bar plot) with the one based on Davenport (solid lines) theory, for two different values of the non-dimensional mean step frequency, (a) $\tilde{\Omega}_m$=1 and (b) $\tilde{\Omega}_m$=1.1. Both figures show that the distribution of the maximum obtained from a Monte Carlo simulation (bar plot) is much wider than the one predicted by the Davenport theory, that is very far from the one obtained from

Monte Carlo simulations. Numerical distributions are in fact wide and identifying the maximum response with its mean value may be difficult and, sometimes, unsafe. In any case, due to the width of the numerically-estimated maximum distribution, adopting the Davenport theory may be a good choice for all possible technical values of the non-dimensional mean step frequency: it implies identifying the maximum structural response with a value characterized by a small probability of exceedance.

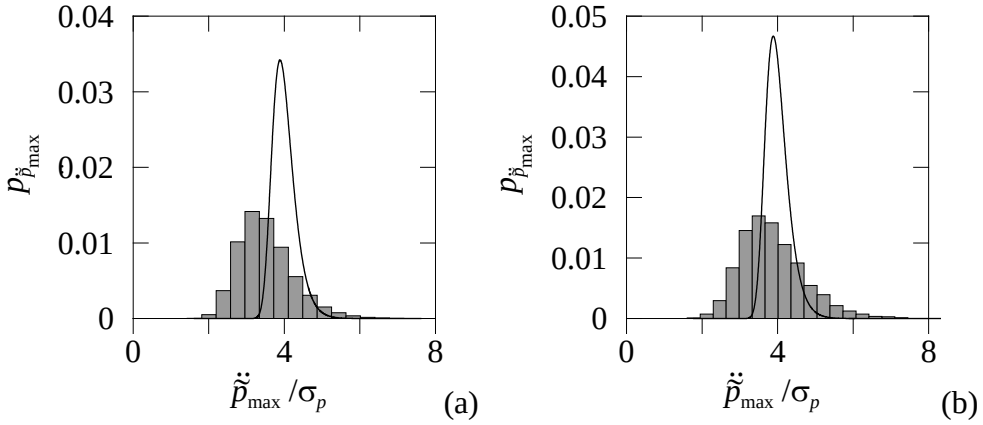


Figure 4: Probability density function of the maximum non-dimensional acceleration: comparison between numerical simulation and analytical model (a) $\tilde{\Omega}_m$ =1, (b) $\tilde{\Omega}_m$ =1.1.

4 PARAMETRIC ANALYSIS

The non-dimensional formulation in Section 2.1 allows a critical analysis of the essential parameters governing footbridge serviceability that have been developed throughout Section 3. Then, the main parameter affecting the dynamic response is the probability density function of the non-dimensional step frequency, which is essentially governed by two parameters: the non-dimensional mean step frequency (i.e. the ratio between the mean step frequency and the structural natural frequency) and the coefficient of variation (i.e. the ratio between the standard deviation of the step frequency and its mean value). In the literature, a variability of such parameters has been observed in real cases (Table 1). In this Section, a parametric analysis is performed starting from the equivalent spectral model of the loading, in order to assess the effective role of the statistical distribution of the step frequency on the maximum footbridge acceleration.

A quantitative estimate of the influence of the stochastic walking parameters on the maximum footbridge acceleration may be obtained by adopting the closed-form solution for the evaluation of the maximum acceleration, Eq. (14). In order to obtain general results without the need to set any value of the structural damping ratio ξ_j and of the pedestrian number N_p, a normalized value $\ddot{\tilde{p}}_{j_{\text{norm}}}$ of the maximum acceleration of the non-dimensional principal coordinate $\ddot{\tilde{p}}_{j_{\max}}$ is defined as follows:

$$\ddot{\tilde{p}}_{j_{\text{norm}}} = \ddot{\tilde{p}}_{j_{\max}} \sqrt{\xi_j / N_p} \tag{16}$$

Substituting Eq. (14) into Eq. (16), $\ddot{\tilde{p}}_{j_{\text{norm}}}$ is given by:

$$\ddot{\tilde{p}}_{j_{\text{norm}}} = g_{\ddot{\tilde{p}}_j} \frac{\sqrt{\pi}}{4} \sqrt{p_{\tilde{\Omega}}(1)} \tag{17}$$

Eq. (17) shows that the normalized maximum non-dimensional acceleration only depends on the peak factor $g_{\ddot{\tilde{p}}_j}$ and on the probability density function of the non-dimensional step frequency, estimated for $\tilde{\Omega}$=1. The peak factor essentially depends on $\tilde{\Omega}_{cm}$; thus it does not depend on the probabilistic distribution of the step frequency. Furthermore, $\tilde{\Omega}_{cm}$ is certainly a small parameter for real footbridges [3]. For bridges having a span length greater than 30 m, assuming a mean walking speed $c_m = 0.9\tilde{\Omega}_{cm}/(2\pi)$, it is lower than 0.006. The peak factor being a decreasing function of $\tilde{\Omega}_{cm}$, the following evaluations are carried out assuming, on the safe side, $\tilde{\Omega}_{cm}$=0.001.

Figure 5 plots $\ddot{\tilde{p}}_{j\text{norm}}$, estimated from Eq. (17), as a function of the non-dimensional mean step frequency and of the coefficient of variation of the step frequency. The peak factor is set $g_{\ddot{\tilde{p}}_j}$=4.16, corresponding to $\tilde{\Omega}_{cm}$=0.001. Fig.5(a) provides a surface plot representation, Fig.5(b) provides the variation of the maximum acceleration of the non-dimensional principal coordinate as a function of the non-dimensional mean step frequency, for different values of the coefficient of variation. Figure 5 clearly shows the combined effect of the two parameters governing the maximum dynamic response. The non-dimensional mean step frequency strongly modifies the maximum value in the plot, but also the coefficient of variation considerably influences the shape of the response curves. Concerning the effect of the mean step frequency, it is evident from Figs. 5(a) and (b) (and also trivial from a theoretical point of view) that the worst situation occurs when the pedestrians' mean step frequency coincides with a natural frequency of the structure (a maximum is always detectable for $\tilde{\Omega}_m$=1). From Fig. 5(b) it can be observed that the influence of the coefficient of variation depends on the value of $\tilde{\Omega}_m$: for $\tilde{\Omega}_m$ close to a unit value, $\tilde{\Omega}_m$ = [0.95 - 1.05], the dynamic response decreases on increasing V_Ω; for $\tilde{\Omega}_m$ far from the unit value ($\tilde{\Omega}_m$ < 0.9, $\tilde{\Omega}_m$ > 1.1), the dynamic response increases on increasing V_Ω. For intermediate values of $\tilde{\Omega}_m$ ($\tilde{\Omega}_m$ ~ 0.93, $\tilde{\Omega}_m$ ~ 1.08), the dynamic response is almost independent of the coefficient of variation.

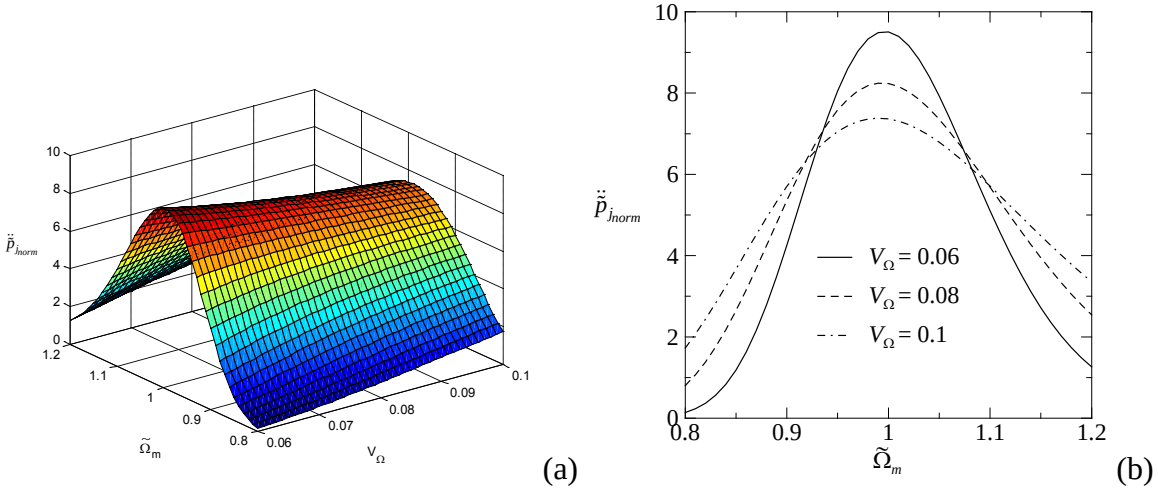


Figure 5: Influence of the of the step frequency distribution on the maximum structural response.

From these observations it can be deduced that, as schematized in Figure 6, if a footbridge has a natural frequency included between 1.8 Hz and 2 Hz (the values observed for the mean step frequency, Table 1), it is recommended to perform the serviceability analysis assuming a

mean step frequency coincident with the natural frequency of the footbridge ($\tilde{\Omega}_m = 1$): in such a case, the worst condition is achieved assuming a small value for the coefficient of variation of the pedestrian step frequency (V_Ω=0.06). If the footbridge natural frequency is not in the interval 1.8 Hz - 2 Hz, assuming a mean step frequency coincident with the structural natural frequency could be too conservative. In such a case, it is recommended to assume a mean step frequency which is closer to the footbridge natural frequency, and to assume a low coefficient of variation (e.g. 0.06, Fig. 6) if $\tilde{\Omega}_m$ is close to 1, a large coefficient of variation (e.g., 0.1, Fig. 6) if $\tilde{\Omega}_m$ is far from 1.

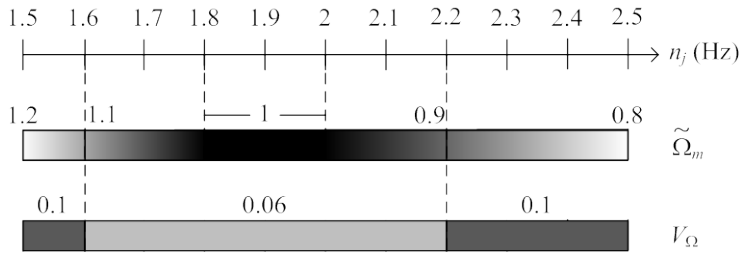


Figure 6: Recommended values of statistical parameters of non-dimensional step frequency.

The clarity and simplicity of the spectral approach allows an approximate, conservative direct estimation of footbridge maximum acceleration by Eq. (15) as a function of the main parameters governing the response. The load effect emerges through the statistical properties of the step frequency, in addition to the number of pedestrians (which is only a magnification factor of the response). The structural parameters (here assumed deterministic) are represented by the modal mass and the damping ratio (in addition to the natural frequency, which influences the assumption of the $\tilde{\Omega}_m$ value). Figure 7 plots the ratio $\ddot{q}_{\max}/\sqrt{N_p}$ as a function of the product $M_j\sqrt{\xi_j}$, setting a classic value for the average weight of pedestrians $\alpha_m G_m$ = 280 N. The different curves correspond to different values of the non-dimensional mean step frequency $\tilde{\Omega}_m$ ($\tilde{\Omega}_m$ is assumed in the range 0.8-1.2); in each case the worst coefficient of variation is selected according to Figure 6 (V_Ω=0.06 for $\tilde{\Omega}_m$ =0.9-1.1, V_Ω=0.1 for $\tilde{\Omega}_m$ outside this interval).

The response curves seem almost linear in a bi-logarithmic scale making the role of the different parameters explicit. Both the non-dimensional mean step frequency $\tilde{\Omega}_m$ and the product $M_j\sqrt{\xi_j}$ strongly affect the maximum structural acceleration, and thus footbridge serviceability. The graph quantifies the well-known beneficial effect on the dynamical behavior due to the increase of the modal mass and of the damping ratio. Moreover, the maximum structural acceleration greatly increases as the non-dimensional mean step frequency $\tilde{\Omega}_m$ moves closer to 1. Bridges characterized by $\tilde{\Omega}_m$ in the neighborhood of unity (0.9-1.1) appear to be very sensitive to vibrations; on the contrary, very small accelerations are expected only for small $\tilde{\Omega}_m$, such as $\tilde{\Omega}_m$ =0.8 (i.e. when the natural frequency of the bridge is much larger than the mean step frequency). Finally, it should be noted that values of 1 m/s^2 on the ordinate of Figure 7 are clearly out-of-comfort as regards any possible criteria (e.g. [12]), since the maximum acceleration caused by N_p pedestrians is obtained by multiplying the ordinate value

by $\sqrt{N_p}$ (N_p being in general a number greater than 5). Bridges that exceed this limit are poorly designed from a dynamic point of view.

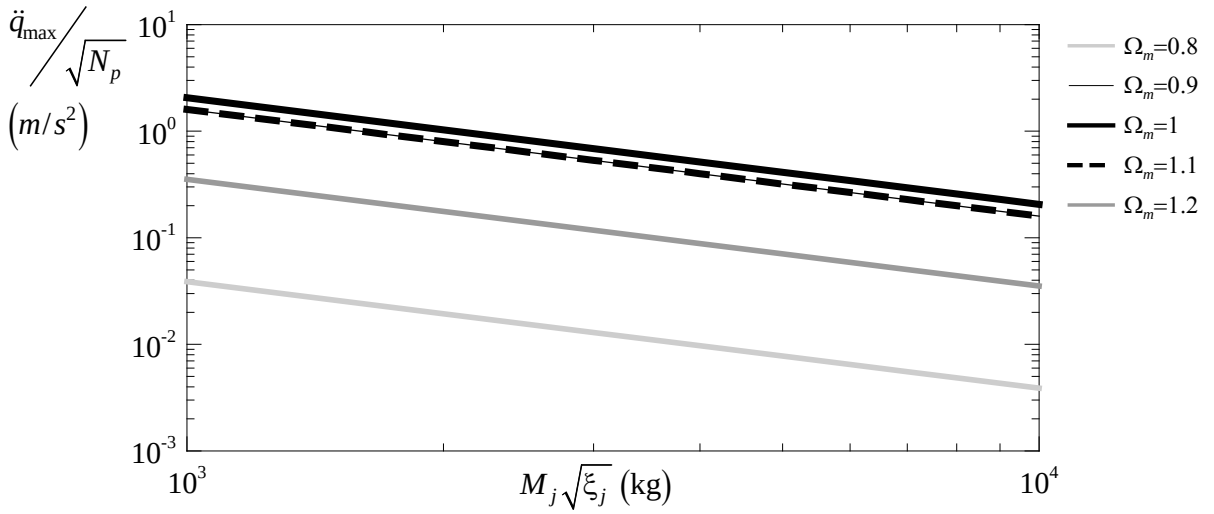


Figure 7: Estimate of the maximum structural acceleration.

5 CONCLUSIONS

In this paper, normal unrestricted pedestrian traffic has been analyzed adopting an equivalent spectral loading model that has been introduced by the authors in [3], starting from a complete probabilistic representation of pedestrians. With the aim of studying the dynamic response of lively footbridges, characterized by a vibration mode with a natural frequency close to the mean step frequency, attention is focused on the effect of the first walking harmonic only; higher walking harmonics are neglected.

Based on the proposed spectral model, the main force parameter affecting the structural response is the statistical characterization of the pedestrian step frequency, in terms of mean value and coefficient of variation. The comparison between the mean value of the maximum structural response estimated from numerical simulations and the analytical estimate has highlighted that the closed-form expression provides a slight overestimate of the numerical maximum. In any case, since the maximum structural response is characterized by a wide probability density function, the closed-form expression provides a safe estimates of the maximum structural response.

Extensive parametric analyses have been carried out in order to investigate the role of the probabilistic distribution of the step frequency on footbridge serviceability assessment. The analysis of the shape of the power spectral density function, structural acceleration and maximum dynamic response points out the two parameters governing the footbridge dynamic sensitivity: the non-dimensional mean step frequency (i.e. the ratio between the mean step frequency and the natural frequency of the structure) and the coefficient of variation of the step frequency (which becomes particularly important when the mean step frequency is not in resonance with a structural mode of vibration). From the analyses performed it can be deduced that, if a footbridge has a natural frequency included between 1.8 Hz and 2 Hz (the values observed for the mean step frequency), it is recommended to check the serviceability assuming a mean step frequency coincident with the natural frequency of the footbridge: in such case, the worst condition is achieved assuming a small value for the coefficient of variation of the pedestrian step frequency. If the footbridge natural frequency is not in the interval 1.8 Hz - 2 Hz, assuming a mean step frequency coincident with the structural natural frequen-

cy may even be too conservative. In this latter case, it is recommended to assume a mean step frequency which is closer to the footbridge natural frequency, and to assume a low coefficient of variation if the non-dimensional mean step frequency is close to 1, a high coefficient of variation if the non-dimensional mean step frequency is far from 1.

Finally, it is possible to summarize the results obtained from the spectral approach in a very synthetic way, as a function of mechanical damping and structural modal mass. Using the proposed conservative criterion on the choice of the step frequency variation coefficient, it is thus possible to obtain simple graphs which permit a direct and simple evaluation of footbridge maximum acceleration. These results seem of interest also from a technical point of view, and might apply to codes and guidelines for the evaluation of footbridge serviceability subjected to unrestricted pedestrian traffic.

ACKNOWLEDGMENTS

This work has been partially supported by the Italian Ministry of Education, Universities and Research (MIUR) through the PRIN funded program 'Dynamics, Stability and Control of Flexible Structures' [grant number 2010MBJK5B].

REFERENCES

[1] S. Zivanovic, A. Pavic, ET. Ingolfsson. Modeling spatially unrestricted pedestrian traffic on footbridges. Journal of Structural Engineering, ASCE 136 (2010) 1296-1308.

[2] F. Tubino, G. Piccardo. A spectral model for pedestrian loading of footbridges. Proceedings of the VIII European Conference on Structural Dynamics, EURODYN 2011, Leuven, Belgium, 2011.

[3] G. Piccardo, F. Tubino. Equivalent spectral model and maximum dynamic response for the serviceability analysis of footbridges. Engineering Structures 40 (2012) 445-456.

[4] Y. Matsumoto, T. Nishioka, H. Shiojiri, K. Matsuzaki. Dynamic design of footbridges. IABSE Proceedings 17/78 (1978) 1-15.

[5] C. Sahnaci, M. Kasperski. Random loads induced by walking. Proceedings of the VI European Conference on Structural Dynamics, EURODYN 2005, Paris, France, 2005, pp. 441-446.

[6] S. Zivanovic, A. Pavic, P. Reynolds. Probability-based prediction of multi-mode vibration response to walking excitation. Engineering Structures 29 (2007) 942-954.

[7] C. Sahnaci, M. Kasperski. Simulation of random pedestrian flow. Proceedings of the VIII European Conference on Structural Dynamics, EURODYN 2011, Leuven, Belgium, 2011.

[8] A. Pachi, T. Ji. Frequency and velocity of people walking. The structural Engineer 83 (2005) 36-40.

[9] F. Ricciardelli, C. Briatico, ET Ingolfsson, CT Georgakis. Experimental validation and calibration of pedestrian loading models for footbridges. Proceedings Experimental Vibration Analysis for Civil Engineering Structures, EVACES 2007, Porto, Portugal, 2007, pp. 219-225.

[10] G. Piccardo, F. Tubino. Simplified procedures for the vibration serviceability analysis of footbridges subjected to realistic walking loads. Computers and Structures 87 (2009) 890-903.

[11] AG. Davenport. Note on the distribution of the largest value of a random function with application to the gust loading. Proc. Inst. Civ. Eng. 28(2) (1964) 187-196.

[12] SETRA. Footbridges - Assessment of vibrational behaviour of footbridges under pedestrian loading. Paris: Technical Department for Transport, Roads and Bridges Engineering and Road Safety, Ministry of Transport and Infrastructure, 2006.

[13] F. Tubino, G. Piccardo. The role of random walking parameters in the serviceability assessment of footbridges. *Journal of Sound and Vibration*, submitted.

COMPDYN 2013
4th ECCOMAS Thematic Conference on
Computational Methods in Structural Dynamics and Earthquake Engineering
M. Papadrakakis, V. Papadopoulos, V. Plevris (eds.)
Kos Island, Greece, 12–14 June 2013

AN OPTICALLY BASED ASSESSMENT OF PEDESTRIAN BALANCE BEHAVIOUR WHILE WALKING ON A LATERALLY OSCILLATING TREADMILL

Seán P. Carroll, John S. Owen, and Mohammed F.M. Hussein

Centre for Structural Engineering and Construction (CSEC)
University of Nottingham
University Park
Nottingham
NG7 2RD, UK
e-mail: sean.carroll@nottingham.ac.uk
john.owen@nottingham.ac.uk
mohammed.hussein@nottingham.ac.uk

Keywords: Human-Structure Interaction, Human-Induced Vibration, Biomechanics, Amplitude Modulation, Motion Capture, Inverted Pendulum

Abstract. *This paper reports findings from an experimental campaign in which subject balance behaviour while walking on a laterally oscillating treadmill was recorded. A 3-dimensional motion capture camera system was used to track the position of 31 active markers, placed on each subject during walking tests. A range of deck oscillation frequencies and amplitudes were tested. The campaign was executed with the aim of identifying the interaction mechanism by which pedestrians produce force harmonics, that resonate with the oscillating structure on which they walk. These so-called self-excited forces have been experimentally identified by others but the underlying reason for their existence has remained an open question.*

Analysis has revealed that subject balance response to sinusoidal base motion is dominated by periodic alteration of foot placement position. This results in amplitude modulation of the lateral component of the ground reaction force (GRF). The frequency of modulation was found to be equal to the modulus of the difference between the lateral forcing and deck oscillation frequencies. This is consistent with the identification of interaction force harmonics as frequency sidebands. The underlying reason for gait width modulation was revealed by examining the subject's CoM oscillation and recognising the influence of a sinusoidally varying inertia force experienced by the subject. Furthermore, the degree to which the subject alters their gait is determined by the degree to which their frontal plane stability is impaired by deck motion. Thus the link between frontal plane balance behaviour and the generation of the self-excited component of the lateral GRF is established.

Further analysis suggests that subject centre of mass (CoM) motion while walking on a laterally oscillating deck is predominantly passive. The simple inverted pendulum model is thus an excellent model of pedestrian CoM motion in the frontal plane during the single stance gait phase. This was established by comparison between simulated and observed CoM motion.

1 INTRODUCTION

The process of step synchronisation between pedestrians and an oscillating bridge deck is now thought to be preceded by a more subtle interaction [1, 2]. This human-structure interaction (HSI) (as opposed to human-structure synchronisation) results in force harmonics within the GRF spectrum, that resonate with the bridge deck oscillation [3, 4]. Fundamental to the production of these resonant force harmonics is the pedestrian's balance response to base motion. As such, to further understand HSI, one must first consider pedestrian stability and balance behaviour during locomotion.

To this end, an experimental campaign was designed in which test subjects walk individually on a laterally oscillating treadmill. A range of tests were carried out, with varying oscillation frequencies and amplitudes imposed on the deck. GRFs were directly measured using deck mounted load cells. In addition, each subject was instrumented with 31 active visual markers in order to record 3-dimensional whole body motion.

The experimental campaign was carried out between March and May of 2012, in the Human Performance Laboratory, at the University of Nottingham. The test protocol received ethical approval from the Faculty (of Engineering) Research Ethics Committee within the University of Nottingham. The test protocol for an individual subject was as follows;

- The subject was familiarised with the oscillating treadmill rig and all safety procedures.
- The subject was instrumented with gait analysis wands and visual markers.
- The subject had a further unrecorded period of familiarisation walking on the treadmill without lateral motion, lasting approximately 10 minutes. During this time a comfortable walking speed was selected by the subject
- The subject was then recorded walking without lateral motion imposed on the deck. This data served as a baseline for the subject's walking behaviour.
- After baseline tests were completed, the subject was recorded walking while lateral oscillations were imposed on the deck, referred to hereafter as dynamic tests.
- Rest breaks were imposed every 2-3 minutes during the course of the test session.

During each test, the lateral GRF was measured directly via 4 deck mounted Zemic bending beam load cells (490 N capacity each). For the duration of each dynamic test, the lateral deck displacement and acceleration were also recorded via a linear variable differential transformer (LVDT) and Schaevitz linear servo accelerometer. A sampling rate of 250 Hz was selected for all treadmill-borne data to provide good time domain resolution. A National Instruments SCXI-1000 chassis, housing a SCXI-1100, 32 channel multiplexer amplifier (receiving LVDT and accelerometer signals) and SCXI-1520 strain bridge (receiving load cell signals) was used to coordinate data logging and signal conditioning. The chassis was also used to trigger simultaneous logging of the marker data. All marker data was sampled at 100 Hz using a CODA ActiveHub computer from Charnwood Dynamics Ltd.

Five oscillation amplitudes were tested, 5 mm, 10 mm, 20 mm, 35 mm and 50 mm. Within each amplitude, 9 oscillation frequencies were tested ranging from 0.3 Hz to 1.1 Hz in 0.1 Hz increments, resulting in a 45 point test matrix.

Ten subjects took part in the test campaign. The age, height and weight of all participants is shown in table 1. The majority of anthropometric data in the literature has been obtained from

male subjects. In order to utilise this data as effectively as possible only male subjects were recruited for this campaign. This is justifiable when one considers that there is no reason to suspect that male subjects will behave (statistically) significantly differently to female subjects. It is therefore assumed (until proven otherwise) that the behaviours observed and conclusions drawn are equally applicable to both sexes.

Table 1: Test subject data.

Subject	Height (m)	Mass (kg)	Age (Years)
1	1.73	82.05	28
2	1.82	96.20	30
3	1.74	63.05	27
4	1.84	98.95	28
5	1.68	85.45	34
6	1.88	90.95	21
7	1.82	87.20	26
8	1.61	75.00	31
9	1.80	74.05	28
10	1.76	82.70	34
Mean	1.77	83.11	28.7

2 OSCILLATING TREADMILL

The design of the treadmill test rig, Fig. 1 (a), is similar to that originally constructed by Pizzimenti [5] and used more recently by Ingólfsson [4]. What marks this test campaign as a further development of what has gone before is the use of motion capture techniques and the focus on the biomechanical behaviour that is ultimately responsible for GRF generation.

2.1 Construction

The treadmill structure consists of three steel frames arranged as follows (refer to Fig. 2):

1. The base frame is the lowermost frame and remains stationary. The motor providing lateral motion is connected to this frame.

2. The chassis frame sits on 4 carriages that travel along linear guide rails fixed to the base frame. The chassis frame is driven laterally by a drive arm connected to the motor, see Fig. 1 (b). Thus rotational motion, provided by the motor is converted, through the drive arm, to sinusoidal reciprocating motion.

3. The uppermost treadmill frame is suspended from the chassis frame by 4 hangers, Fig. 1 (c). The self-weight of the treadmill frame and any vertical imposed loads are resisted by the hangers. The treadmill frame is restrained laterally by 4 bending beam load cells, the means through which the lateral GRF is recorded. The treadmill belt is driven by a second motor mounted on the chassis frame.

The chassis frame is driven laterally by a Nordbloc 0.55 kW geared motor. A specifically designed coupling is used to allow the drive arm to be fitted at different radii from the motor

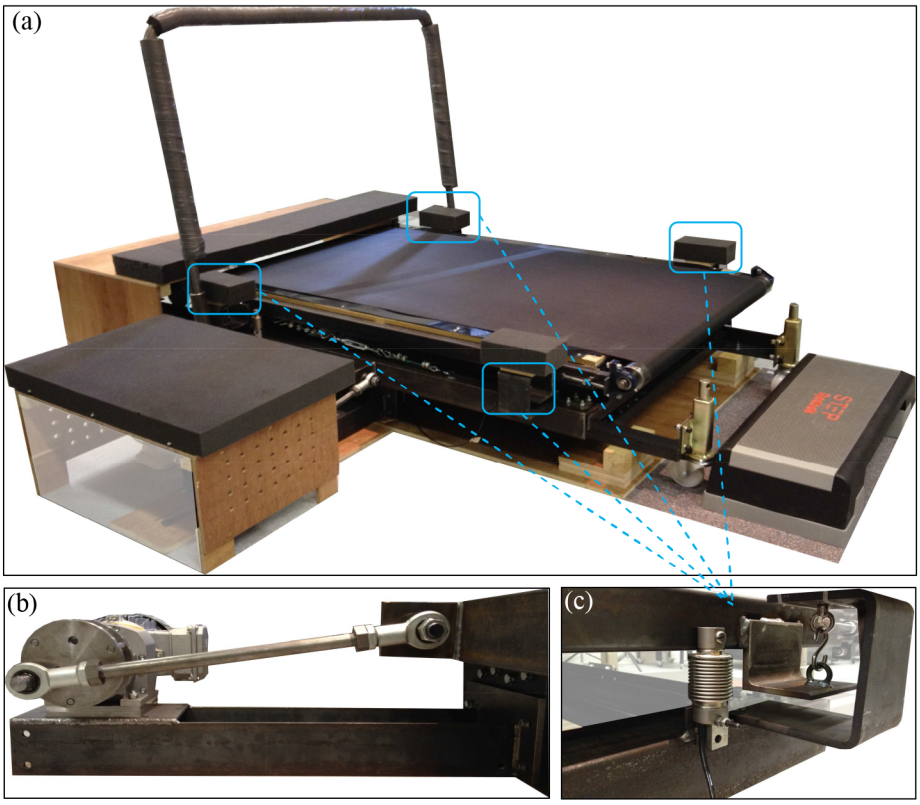


Figure 1: (a) Oscillating treadmill test rig, (b) Motor and lateral drive arm producing reciprocating sinusoidal motion from rotary motion, (c) Hanger and load cell arrangement (1 of 4), the treadmill deck is supported vertically by hangers and restrained laterally by bending beam load cells.

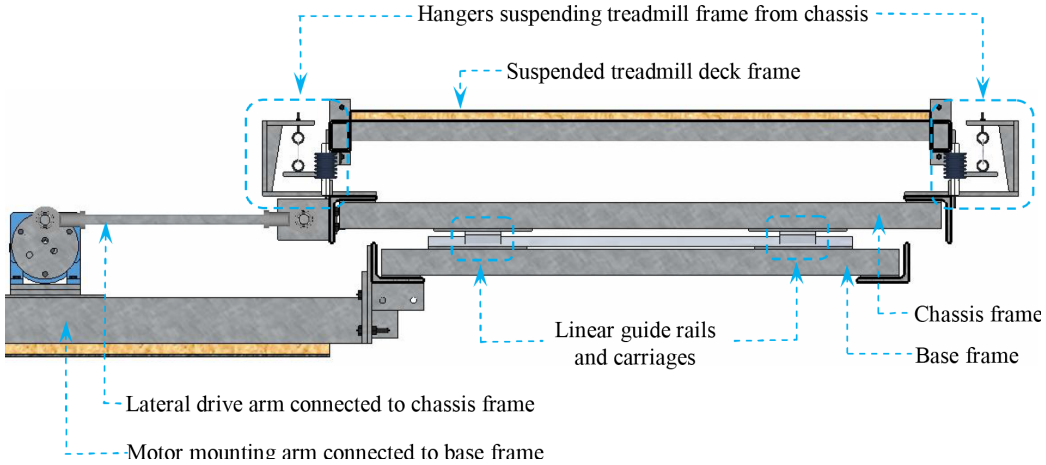


Figure 2: Section through treadmill rig showing three constituent frames (base, chassis and treadmill deck), lateral drive system, and lateral restraint of treadmill deck frame against chassis frame.

shaft, allowing variability in the deck oscillation amplitude. The treadmill belt is itself belt driven by a Nordbloc 0.75 kW geared motor. The speed of both motors is controlled via 2 Siemens G110 inverters.

The deck walking area measures 1 m wide $\times$ 1.5 m long. A horizontal bar/handle was placed across the front of the treadmill to provide extra stability should a test subject feel particularly unstable. Subjects were instructed not to touch the bar unless absolutely necessary, after which

the test data was discounted. The front-mounted bar is obviously not in keeping with what one would experience on a real bridge, however side rails could not be provided without obscuring marker visibility.

2.2 Data acquisition and rig validation

The accelerometer and LVDT recording deck motion were digitally low pass filtered with 4th order Butterworth (BW4) filters with cutoff frequencies of 5 Hz and 2 Hz respectively. The load cells were digitally low pass filtered at 6 Hz (BW4). The lateral GRF obtained from the treadmill rig shall be referred to as the measured GRF, $F_{L,meas}$, and is calculated as,

$$F_{L,meas} = \left(\sum_{i=1}^{4} F_{c,i} \right) - m_d \, \ddot{U}_d \tag{1}$$

in which $F_{c,i}$ is the load imposed on the i^{th} load cell, m_d is the mass of the treadmill deck and associated suspended structure and $\ddot{U}_d$ is the lateral acceleration of the treadmill deck. $F_{L,meas}$ was validated against GRFs recorded from independently calibrated Kistler force plates (in-situ in the Human Performance Lab). It is obviously not possible to directly compare forces from the same footstep, therefore the modified force plate record is compared against the phase-averaged cycle obtained from the treadmill, Fig. 3. Further discussion of rig force data processing can be found in [6]. Allowing for the time domain effects of intra-subject variability, good agreement is observed between treadmill and force plate data. This provides confidence that GRFs are being extracted from the test rig with acceptable accuracy.

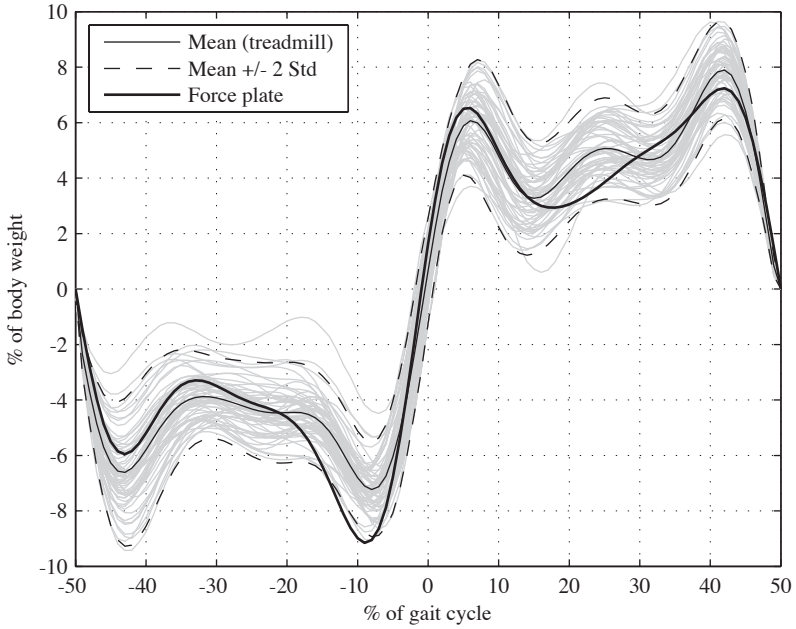


Figure 3: Comparison between the resultant lateral GRFs determined from the treadmill and from the laboratory force plates. Treadmill GRFs from multiple gait cycles are plotted along with the sample mean and $\pm$ 2 standard deviation boundaries.

3 MOTION CAPTURE SYSTEM

A Coda mpx30 general-purpose 3D motion tracking system was used. The system consists of 2 measurement units, each containing 3, pre-aligned cameras, wall mounted on either side

of the treadmill deck. The cameras track the position of active markers (infra-red LEDs) in the measurement volume, achieving a position resolution of 0.1 mm horizontally and vertically and a distance resolution of 0.3 mm. Each subject was instrumented with 31 active markers, placed directly on the skin (over bony landmarks) and attached to gait analysis wands strapped to the body, Fig. 4. The use of gait analysis wands improves marker visibility and facilitates the calculation of joint centres and body segment embedded vector bases (EVB).

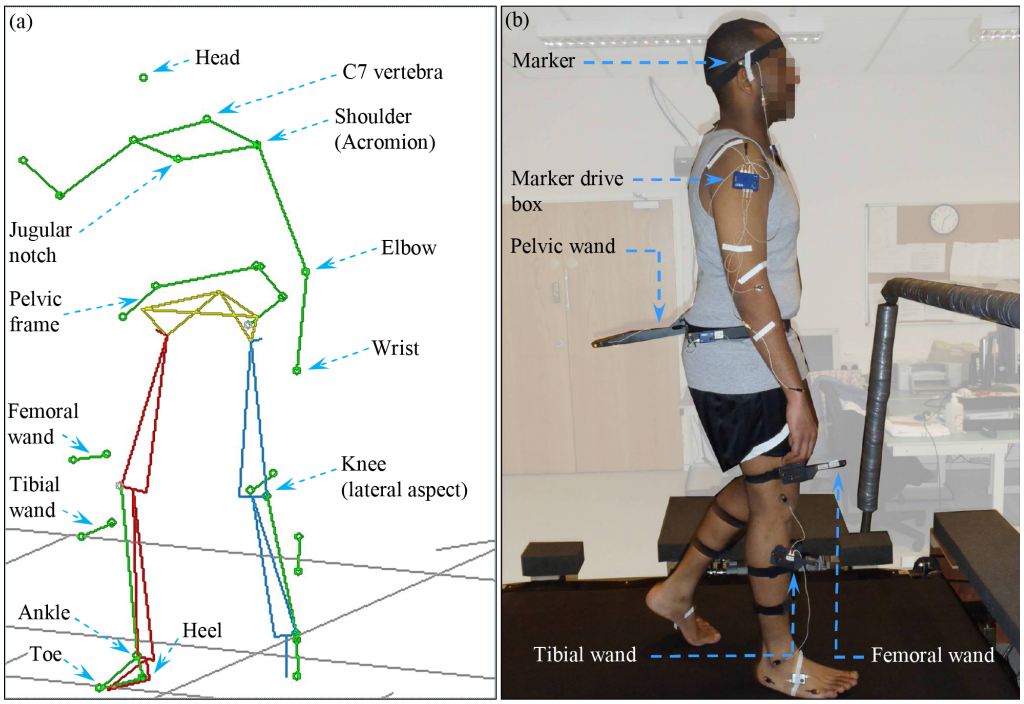


Figure 4: (a) Marker arrangement showing locations of 31 active markers, (b) Test subject instrumented with markers and gait analysis wands.

3.1 Marker placement

During testing subjects wore a sleeveless shirt and shorts, Fig. 4 (b). Subjects were not permitted to wear any form of footwear. This may at first appear odd as pedestrians walking on a bridge rarely walk barefoot. However, the emphasis in this campaign is on understanding biomechanical response in the face of lateral deck motion. The somatosensory information received through the sole of the foot is undoubtedly altered if a person wears shoes. Whether or not this information is altered to the extent that it has an influence on the actual balance behaviour is less certain. It was therefore decided to remove any potential variability introduced by footwear.

The positioning of all markers placed at or below hip level was determined by the marker placement protocol set out in the Coda mpx30 user guide [7]. Hip, knee and ankle joint centres are calculated relative to marker positions as per the procedure set out in [7]. Markers placed on the upper torso, arm and head were placed based on the specific requirements of this test campaign; to allow quantification of upper torso rotation and head and arm movement allowing accurate calculation of the CoM trajectory.

More specifically, markers were positioned at the heel, at the end of the 5^{th} metatarsal (toe), both facing laterally, at the lateral malleolus (ankle) and on the lateral aspect of the medio-lateral

knee axis. Tibial and femoral wands, containing two additional markers each, were strapped to the subject's lower leg and thigh.

A pelvic frame containing 6 markers allows a pelvis EVB to be constructed. Two markers were positioned such that they formed an imaginary line passed through the anterior superior iliac spine (ASIS markers), two more were positioned similarly for the posterior superior iliac spine (PSIS markers). Two more were placed on either side of a wand extended from the sacrum.

Four markers were placed to allow the construction of an EVB for the upper torso; one on each acromion (shoulder), one over the C7 vertebra at the back of the neck and one over the jugular notch. An additional marker was also placed just above the ear, at eye level. Finally, a marker was placed on the lateral aspect of each elbow and wrist in order to record arm movement.

4 GAIT BEHAVIOUR AND THE SELF-EXCITED FORCE

The self-excited (SE) force and its equivalent mass and damping effects have been investigated previously. However, the biomechanical behaviour resulting in the GRF, of which the SE force is a part, has not been sufficiently explored. The equipment and techniques employed in this investigation allow whole body behaviour of the test subject to be observed. As such, a more complete picture of HSI is obtained.

The following two figures detail the behaviour of subject 1 during individual dynamic tests and demonstrate the salient behaviours observed. Further discussion of this data can be found in [6]. The imposed deck oscillation amplitude is 10 mm and deck oscillation frequencies are 0.7 Hz and 0.9 Hz. In both cases the subject maintained a constant pacing frequency of 1.8 Hz, resulting in a lateral forcing frequency of 0.9 Hz throughout the tests.

Figure 5 (a) shows the subject's CoM oscillation relative to the moving deck (solid black line and left scale), the corresponding deck oscillation is also shown (solid grey line and right scale). The underlying deck motion has been removed from all marker data, thus all reported subject motion is relative to the moving deck. Markers on the lateral aspect of the foot, at the heel and toe have been used to determine the position of the foot for each footstep (intermittent black lines), the position is calculated as the median point between both markers. The circle at each foot position, marks the average foot position for the duration of the footstep.

Plot (b) shows the step widths for successive steps, defined as the lateral distance between the mean foot position marks. The x-axis position of each vertical stem is determined as the mid-time between the foot positions used to calculate that step width. Plot (c) shows the directly measured GRF, $F_{L,meas}$, and plot (d) shows its harmonic components.

The most striking feature of the subject's behaviour is the alteration of their gait width. Closer inspection of plot (a) reveals that if the subject steps to the left in time with the rig's maximum leftward displacement (and vice versa on the right), the CoM oscillation amplitude is a minimum. Conversely, when the subject steps in a direction opposite to the deck's motion and in time with the peak deck displacement, the CoM amplitude is at a maximum. This is a direct result of the sinusoidally varying inertia force experienced by the subject due to the base acceleration. Owing to the different pacing and oscillation frequencies, this results in a periodic modulation of the CoM oscillation amplitude. Coincident with this, is a narrowing and widening of the subject's gait and as a result, modulation of the GRF occurs.

When the whole body behaviour responsible for the GRF is examined, it becomes apparent that the gait width and therefore the GRF is being modulated at a fixed frequency equal to the modulus of the difference between the lateral forcing frequency and the base oscillation

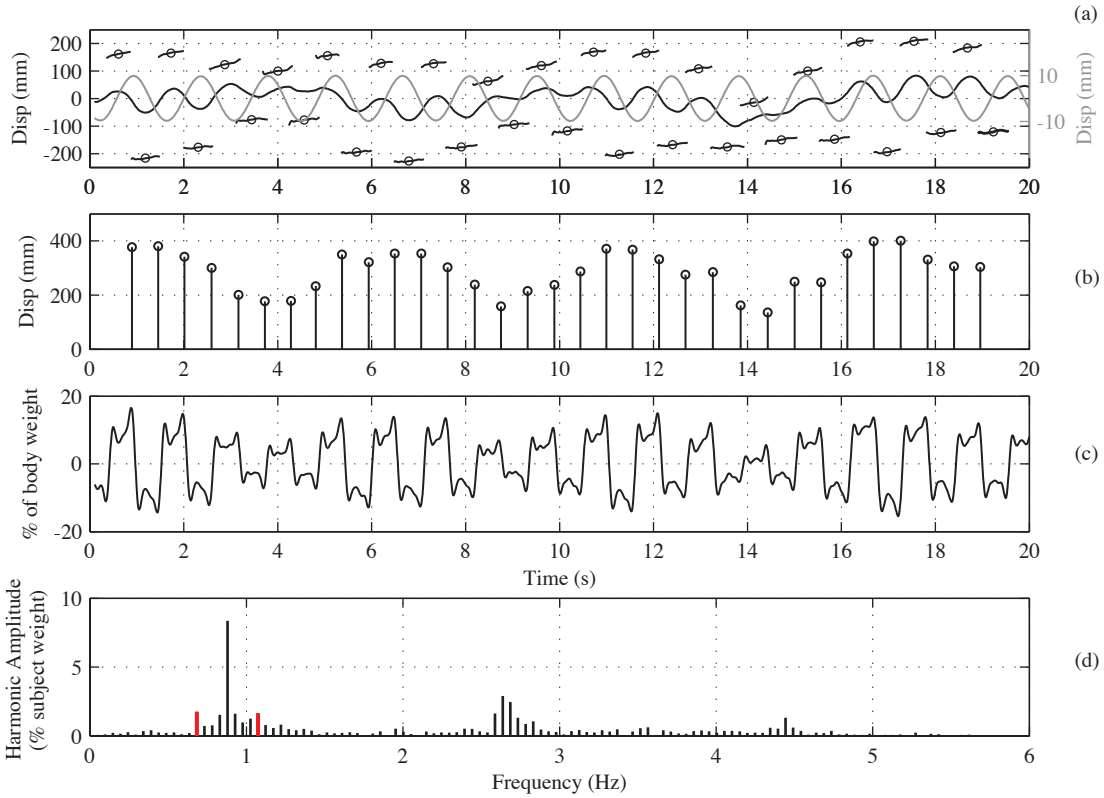


Figure 5: Deck oscillation amplitude = 10 mm, frequency = 0.7 Hz. (a) CoM oscillation (continuous black line and left scale), deck oscillation (continuous grey line and right scale) and lateral foot position (intermittent black line), (b) step widths, (c) directly measured GRF, (d) harmonic components of the directly measured GRF (interaction forces shown in red).

frequency, in this case approximately 0.2 Hz or every 5 seconds. The gait width modulation is quantified through the percentage modulation depth, MD, where:

$$\text{MD} = 100 \times \frac{\text{wave peak} - \text{wave trough}}{\text{wave peak} + \text{wave trough}} \tag{2}$$

The wave peak was determined by discarding the maximum value of gait width and obtaining the average of the next two largest values. The corresponding procedure was applied to the minimum gait widths to determine the wave trough. In the case of Fig. 5, MD $= 42\%$

Plot (d) shows the harmonic components of the GRF, the interaction force harmonics are shown in red. Notably, these are also spaced approximately 0.2 Hz on either side of the fundamental force harmonic, a measure predicted by the biomechanical behaviour described above.

In Fig. 6, the base oscillation amplitude is 10 mm but the frequency is increased to 0.9 Hz, synchronised with the lateral forcing frequency imposed by the subject. The alterations in gait width previously observed are notably absent, plot (a) and (b). CoM oscillation amplitude, gait width and GRF amplitude all remain relatively stable during the test. Due to the constant phase relationship between the subject's lateral forcing frequency and the deck oscillation frequency, the inertia force experienced by the subject remains the same from gait cycle to gait cycle. This eliminates the need to periodically alter foot placement position to maintain frontal plane stability, instead, the subject adopts a wider gait sufficient to deal with the imposed inertia force, leading to a scale increase in the GRF.

To investigate the generality of this frequency relationship, the factor β is defined as the ratio

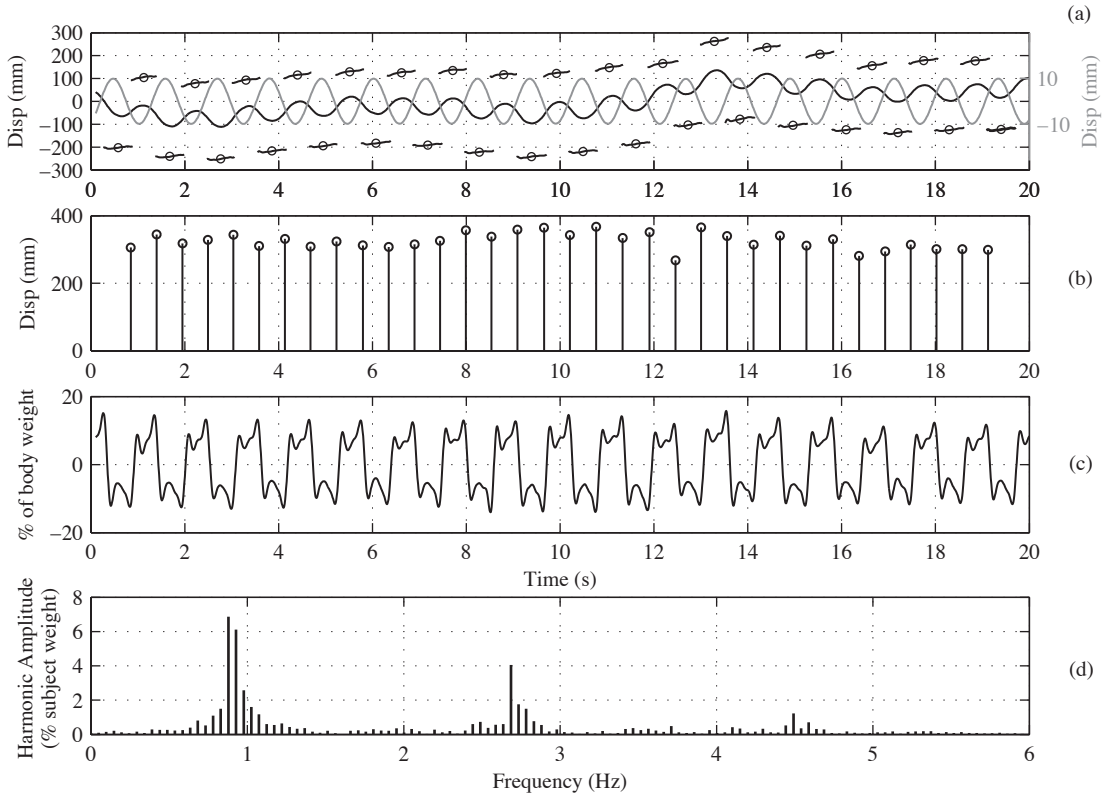


Figure 6: Deck oscillation amplitude = 10 mm, frequency = 0.9 Hz. (a) CoM oscillation (continuous black line and left scale), deck oscillation (continuous grey line and right scale) and lateral foot position (intermittent black line), (b) step widths, (c) directly measured GRF, (d) harmonic components of the directly measured GRF.

of observed modulation frequency to the modulation frequency predicted by the base oscillation and forcing frequency relationship:

$$\beta = \frac{\text{Observed modulation frequency}}{|f_{\text{base}} - f_{\text{subject}}|} \tag{3}$$

where f_{base} is the base oscillation frequency and f_{subject} is the frequency of the lateral GRF imposed by the subject (0.9 Hz). Figure 7 show the ratio β calculated for each test completed by subject 1. Note that β values for which $f_{\text{base}} \approx f_{\text{subject}}$ have been omitted as the parameter is not applicable under this frequency regime.

It can be seen that in the majority of cases $\beta \approx 1$, indicating that a periodic gait width modulation is generally occurring at a frequency equal to $|f_{\text{base}} - f_{\text{subject}}|$. The biomechanical motivation for alteration of foot position has been identified as being a response to a sinusoidally varying inertia force. Furthermore, the frequency of the SE force harmonic is also identified as $f_{\text{subject}} \pm |f_{\text{base}} - f_{\text{subject}}|$. Therefore, Fig. 7, in which β is predominantly equal to one, establishes the link between pedestrian balance behaviour and the generation of a SE force harmonic.

Note that for the lowest frequency test during 5 mm and 10 mm amplitude oscillations, Fig. 7 plots (a) and (b), $\beta \approx 0$. This is due to the gait width modulation not being sufficiently well defined for a dominant harmonic to be extracted. In both cases the peak lateral acceleration experienced by the subject < 0.04 m/s^2 and resulted in only a minor influence on gait width. However as the strength of external stimulus grows, periodic modulation is quickly established.

The percentage MD and normalised average gait width have been determined for each test completed by subject 1, Fig. 8. The average gait width has been normalised by the average

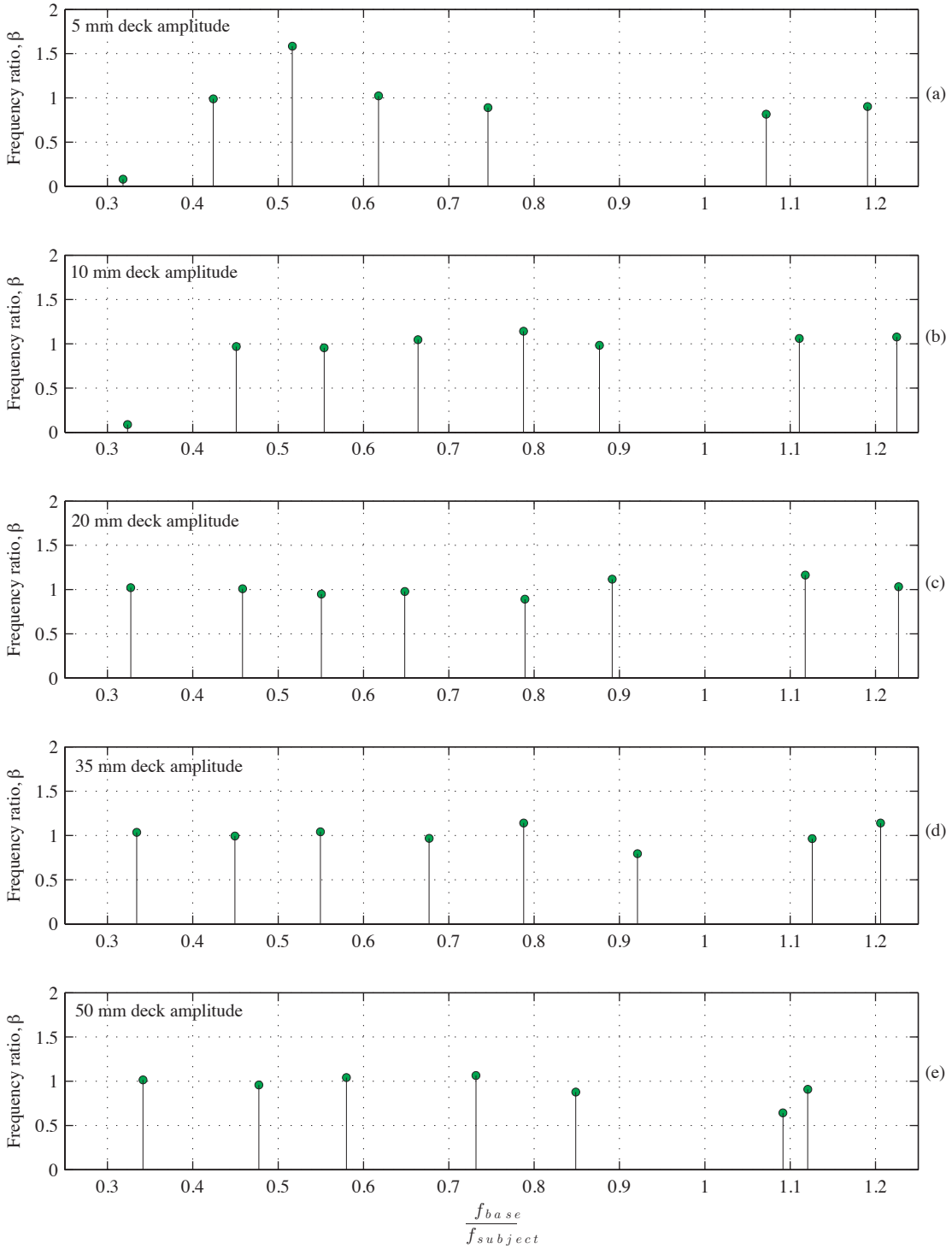


Figure 7: The ratio of observed gait width modulation frequency to that predicted by the expression, $|f_{\text{base}} - f_{\text{subject}}|$. Data shown for 5 mm (a), 10 mm (b), 20 mm (c), 35 mm (d) and 50 mm (e) amplitude tests, completed by test subject 1.

obtained for the subject during static (treadmill) tests.

During 5 mm amplitude tests, Fig. 8 (a), MD is relatively low ($< 20\ \%$), although this increases as the deck oscillation frequency increases imposing higher amplitude oscillations on the subject. Interestingly, despite the low oscillation amplitude, the mean gait width is

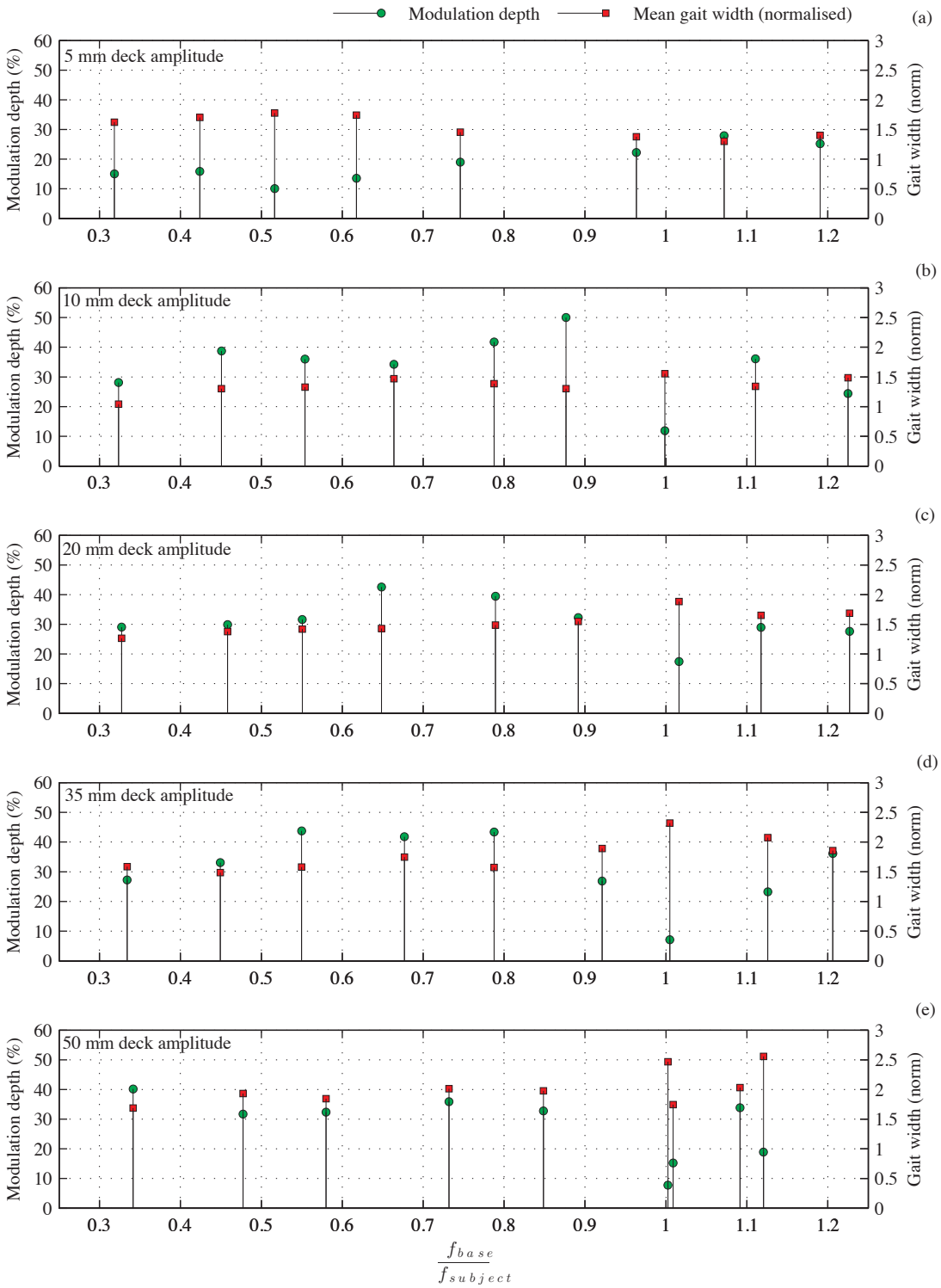


Figure 8: The percentage MD and normalised average gait width for each test completed by subject 1. Data shown for 5 mm (a), 10 mm (b), 20 mm (c), 35 mm (d) and 50 mm (e) amplitude tests.

approximately 50% greater than that observed during static tests. This underlines the subject's sensitivity to frontal plane motion.

During larger amplitude oscillations, MD increases and is generally in excess of $30\,\%$ and in some cases $40\,\%$. The gait width ratio remains stable at approximately 1.5 for 5 mm, 10 mm

and 20 mm tests. However it increases significantly for 35 mm and 50 mm tests.

The stabilisation of gait width discussed previously is clearly seen for cases when the subject is synchronised with the deck. In all cases when $(f_{\text{base}}/f_{\text{subject}}) \approx 1$, MD is reduced significantly. In such cases the average gait width is typically wider than for unsynchronised walking. Figures 7 and 8 have demonstrated that the detailed discussion presented above for subject 1 does indeed represent typical gait behaviour for that subject. Furthermore, the behaviour identified above, was found to be typical across all test subjects, although there was significant quantitative inter-subject variability.

5 PASSIVE VERSUS ACTIVE CoM MOTION

To investigate subject CoM motion (in the presence of the deck-induced inertia force), a simple comparison between observed subject behaviour and that predicted by an equivalent passive inverted pendulum (IP) model was considered, Fig. 9. Data relating to subject number 4 is discussed in detail herein.

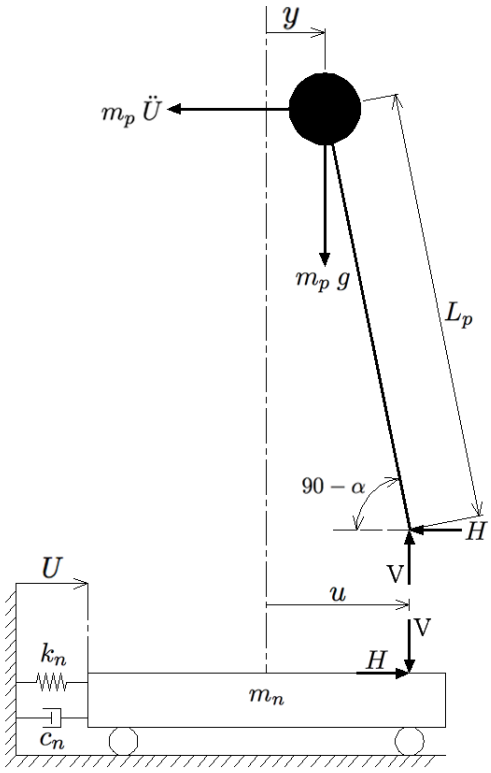


Figure 9: Biomechanical IP model on a laterally moving structure.

To facilitate the comparison, an IP model equivalent to the subject in question was established. The IP length was determined as the vertical distance to the subjects CoM (based on marker data and de Leva's body model [8]), while the IP mass was equal to the subject's body mass. The IP walking model, stabilised by the support placement law given by Eq. (4) [9], was subjected to the same base motion experienced by the subject. Its motion was them compared with the subject's observed CoM motion, reproduced from marker data.

$$u = y_0 + \frac{\dot{y}_0}{\omega} \pm b_{min} \tag{4}$$

IP support position, u, is determined by the IP mass position, y_0, and velocity, $\dot{y}_0$, immediately before the 'foot' is placed. The IP biomechanical model and its implementation as a pedestrian model in the study of HSI is discussed in detail in [10, 11, 12, 13], to which the reader is referred for further IP model background information.

5.1 IP-subject comparison: Stationary deck

The IP was first tuned to match the subject's observed behaviour during a stationary test in which no treadmill oscillation was imposed. IP initial mass position, velocity and support position were chosen to match the subject at the beginning of the simulation. In order to tune the IP behaviour to match the subject, the minimum stability margin, b_{min} from Eq. (4) was used as a tuning parameter.

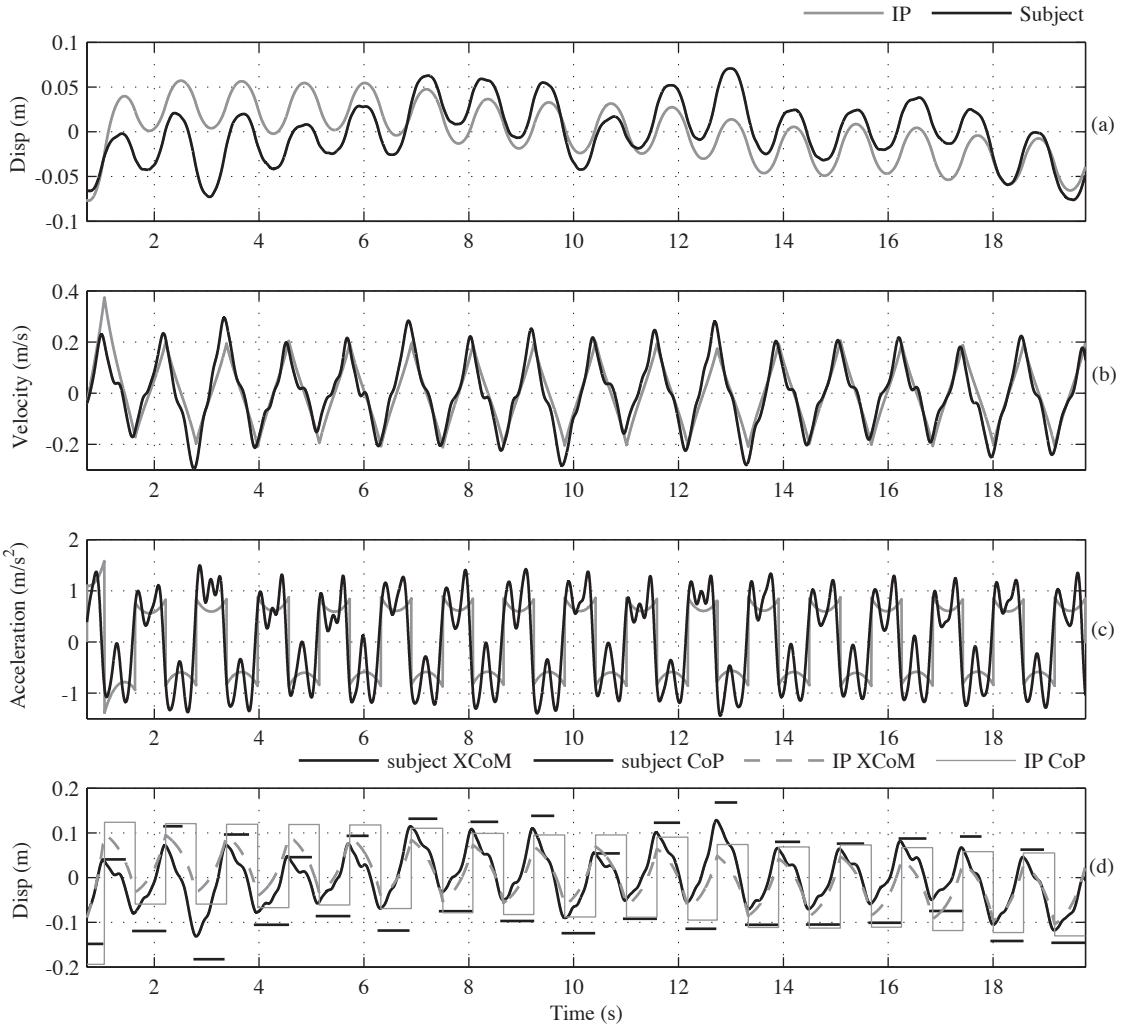


Figure 10: Comparison between subject and equivalent IP, (a) CoM position (correlation coefficient, CC = 0.55, slope of the linear regression line, m$_{reg}$= 0.51), (b) CoM velocity (CC/m$_{reg}$ = 0.93/0.77), (c) CoM acceleration (CC/m$_{reg}$ = 0.81/0.66) and (d) XCoM and CoP position.

The cumulative area under the (absolute) GRF time history was compared for the IP and subject and b_{min} altered until the difference in areas was a minimum. Note that the subject's measured rather than reproduced GRF was considered. Figure 10 shows the result of this tuning

process for CoM position, velocity and acceleration, plots (a) to (c). Plot (d) shows a comparison between extrapolated centre of mass (XCoM) and centre of pressure (CoP) position for the subject and IP.

The initial drift in IP CoM trajectory results from a discrepancy between the IP and subject's (assumed) initial CoP position. The influence of this discrepancy is dissipated within the first two steps and has no bearing on the comparison thereafter. To facilitate the comparison, the mean value offset (determined after the first two steps have occurred) has been removed from both sets of data in plot (a). This removes the influence of the initial drift in simulated CoM motion, arising due to the initial CoP position inaccuracy. The same offsets have also been removed from the simulated and observed data in plot (d).

Considering the CoM position, velocity and acceleration comparisons in plots (a), (b) and (c), the IP appears to simulate the CoM trajectory quite well, particularly in the case of the CoM velocity, plot (b). With reference to plot (a), it is apparent that the IP model is unable to simulate 'atypical' CoM oscillations such as arise from the subject drifting across the treadmill deck as they walk. Nevertheless, the general character of the oscillatory behaviour agrees quite well. The CoM accelerations in plot (c) show good amplitude agreement (ensured by the b_{min} tuning process), although the subject's acceleration during the mid-stance deviates significantly from the smooth trajectory simulated by the IP.

Plotting the simulated versus observed behaviour for position, velocity and acceleration data, the correlation coefficient (CC) is used as a quantitative measure of the linearity between simulated and observed behaviour. In this way, linearity is used as the measure of similarity. These were calculated as 0.55, 0.93 and 0.81 for position, velocity and acceleration respectively. However, this measure is independent of any scaling difference between simulated and observed trajectories. This is quantified by the slope of the line of linear regression, m_{reg}, between observed and simulated behaviour. These are calculated as 0.51, 0.77 and 0.66, all identifying that the magnitude of position, velocity and acceleration is underestimated by the IP model. In this way, the simulated versus observed comparison (averaged for the duration of the comparison) is represented by two parameters, CC, representing linearity and m_{reg}, representing purely scale differences.

Plot (d) shows the XCoM and CoP positions for the subject and IP. A constant medial offset of 35 mm has been applied to the recorded foot position to approximate the average position of the subject's CoP. Again, with the exception of anomalous steps, eg. at t = [3, 5, 13] s, the IP approximates the subject's behaviour well. Considering the complexity of human locomotion and the comparative simplicity of the biomechanical model, the general agreement seen in Fig. 10 is encouraging. Particularly considering the IP model's prevalence in the study of HSI.

5.2 IP-subject comparison: Oscillating deck

Having tuned the IP model to the specific subject under consideration, the comparison is now repeated for dynamic tests. If the model performs well, it can be concluded that subject CoM oscillation is predominantly passive and any active balance control in response to deck motion can be discounted. However, if there is a divergence in the predicted and observed balance behaviour, the alternative conclusion can be drawn, i.e. that there is some form of additional active control causing the subject to behave differently to the passive pendulum.

Figures 11 and 12 represent two dynamic test comparisons which indicate the IP model's performance. In both cases the subject's lateral forcing frequency was approximately 0.9 Hz. When determining the IP support placement position from Eq. (4), the CoM velocity relative to the moving deck was found to be appropriate.

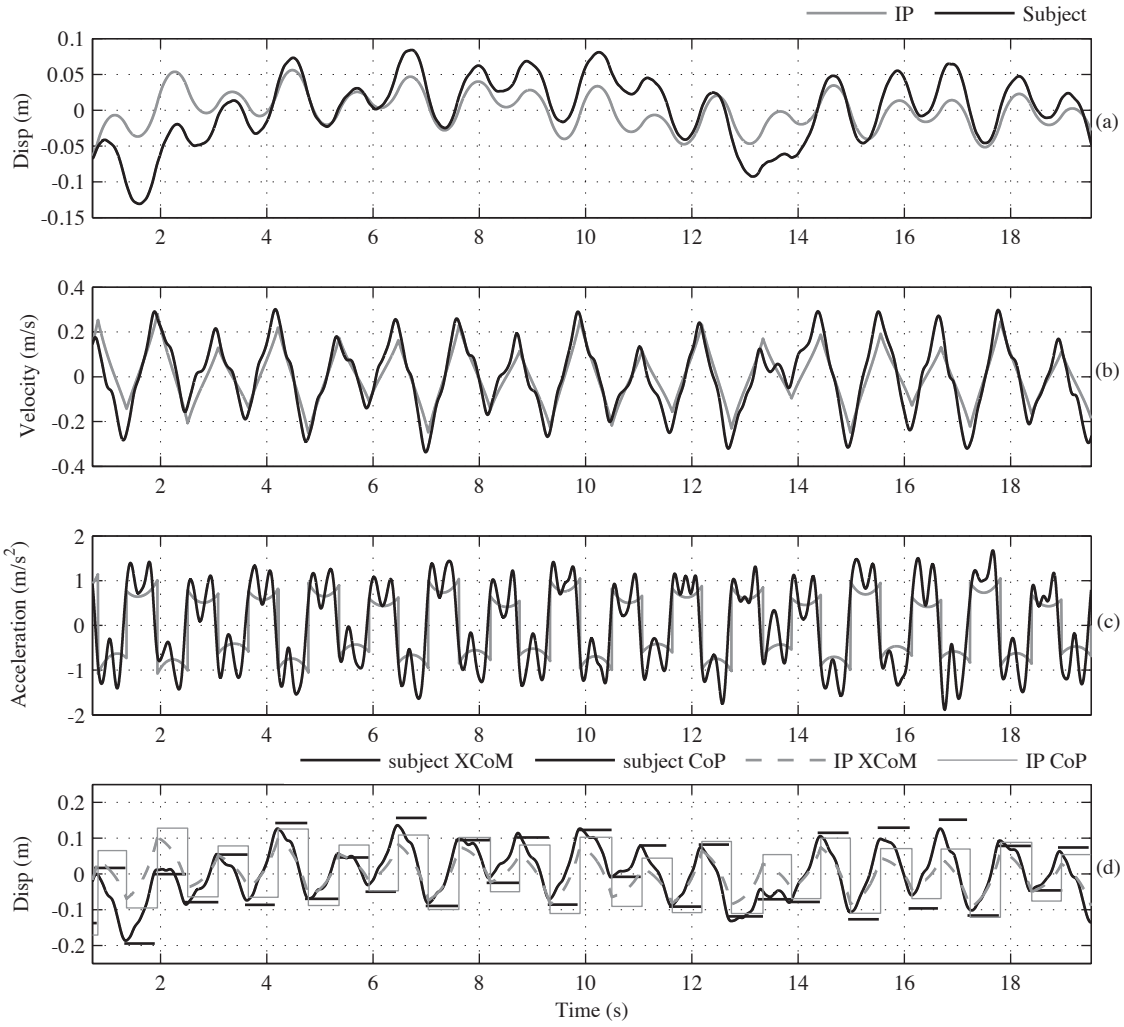


Figure 11: Comparison between subject and equivalent IP, deck oscillation 10 mm amplitude at 0.5 Hz. (a) CoM position (CC/m$_{reg}$ = 0.64/0.34), (b) CoM velocity (CC/m$_{reg}$ = 0.93/0.66), (c) CoM acceleration (CC/m$_{reg}$ = 0.81/0.59) and (d) XCoM and CoP position.

Figure 11 shows the comparison during lateral oscillations of 10 mm amplitude at a frequency of 0.5 Hz. The passive dynamics of the IP appear to predict reasonably well the subject's oscillatory behaviour in the presence of deck motion. This is particularly the case between $4s <= t <= 12s$, during which position, velocity and acceleration are well predicted. However atypical behaviour, e.g. between $13s <= t <= 14s$ obviously cannot be predicted by the IP. The correlation and regression data was calculated as CC/m$_{reg}$ = 0.64/0.34 (pos), 0.93/0.66 (vel) and 0.81/0.59 (acc). It can be seen in plot (d) that the support placement law, Eq. (4), also results in modulation of the simulated gait with, broadly in line with the subject's behaviour.

Figure 12 shows the IP performance when the lateral forcing and deck oscillation frequencies coincide. The oscillation amplitude and frequency are 20 mm and 0.9 Hz respectively. Exceptionally good agreement is observed between the subject and IP behaviour, quantified by the correlation and regression data, CC/m$_{reg}$ = 0.89/0.78 (pos), 0.97/0.93 (vel) and 0.88/0.89 (acc).

As already discussed in relation to test subject 1, Fig. 6, there is a constant phase relationship between the lateral forcing and deck oscillation frequencies. As a result the inertia force experienced by the subject and IP, at the time of support placement, remains constant from gait

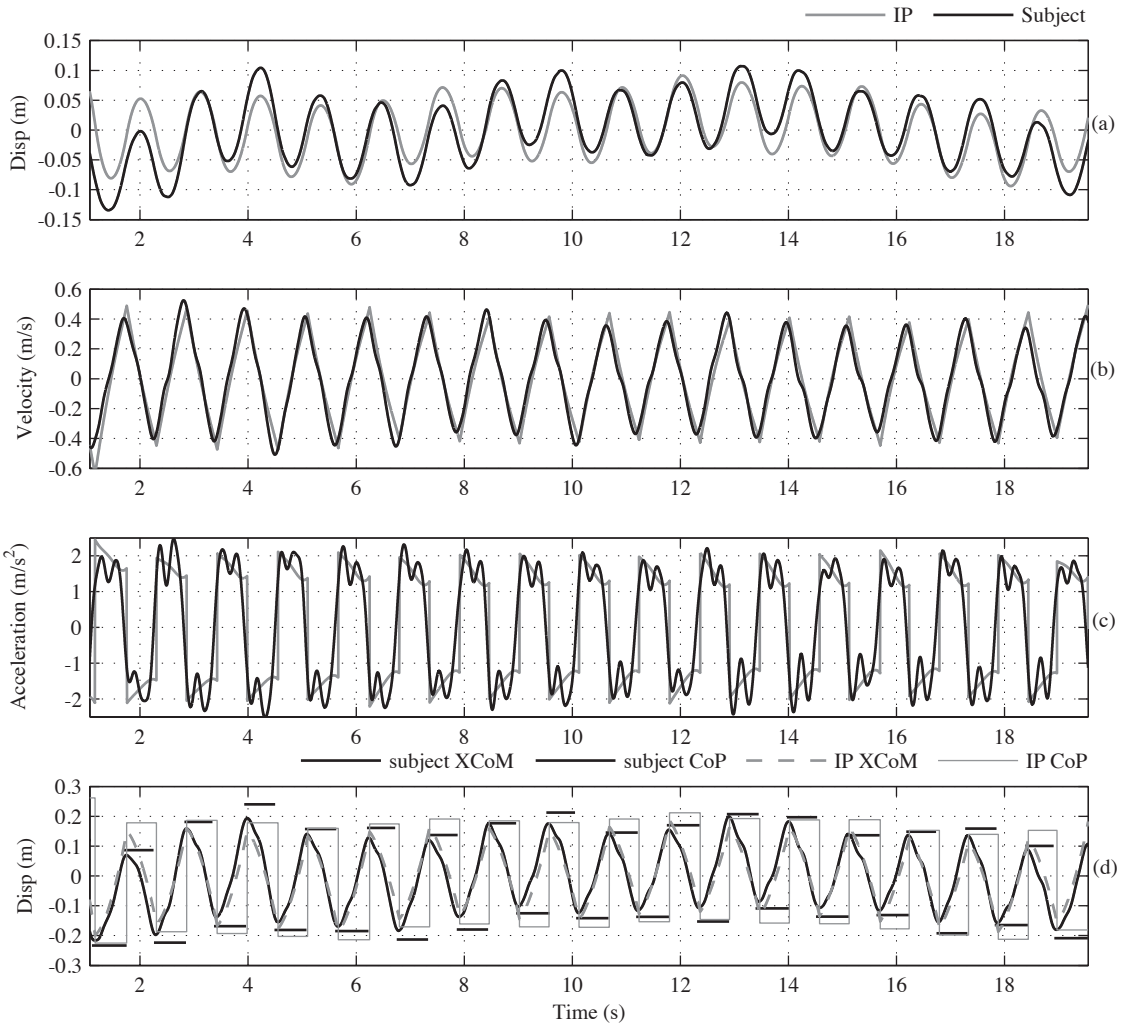


Figure 12: Comparison between subject and equivalent IP, deck oscillation 20 mm amplitude at 0.9 Hz. (a) CoM position (CC/m$_{reg}$ = 0.89/0.78), (b) CoM velocity (CC/m$_{reg}$ = 0.97/0.93), (c) CoM acceleration (CC/m$_{reg}$ = 0.88/0.89) and (d) XCoM and CoP position.

cycle to gait cycle and there is no modulation of gait width. In this particular case, the CoP position is well predicted by the balance law, Eq. (4), and as a result the CoM position, velocity and acceleration are also well predicted.

Not withstanding the inaccuracies in support placement position, exemplified by Fig. 11, Fig. 12 further confirms the suitability of a passive model for CoM oscillatory behaviour. It is at least reasonable to suggest that the passive nature of the IP model is sufficient to describe the subject's CoM oscillation in the presence of lateral deck motion. That is to say, the addition of a further active control element on CoM motion does not appear to be warranted. On this basis (and considering that similar behaviour is observed across all subject comparisons), it can be tentatively concluded that while active balance control certainly plays a role in maintaining stability during locomotion on a laterally oscillating deck, the CoM behaviour is adequately described by the dynamics of a passive IP.

A limitation of the CoP placement law, becomes apparent as the magnitude of deck velocity experienced by the IP grows. According to Eq. (4), the lateral position of the CoP contains a term proportional to CoM velocity, $\frac{\dot{y}_0}{\omega}$, and the additional stability margin, b_{min}. In the event that the IP and deck have global velocities (velocities measured in the stationary global reference

frame) in the same direction but the deck velocity magnitude is greater than the absolute velocity of the IP, the velocity of the IP relative to the deck will be in the medial direction. As a result, the term $\frac{\dot{y}_0}{\omega}$ will be opposite in sign to b_{min}. As deck velocity magnitude increases, b_{min} is effectively eroded by $\frac{\dot{y}_0}{\omega}$ and a 'crossover' step occurs. A crossover step describes the situation in which the IP CoP is placed on the 'wrong' side of the CoM for the imminent step. This behaviour, although ensuring IP stability, signals the breakdown of the balance law as the IP behaviour no longer resembles human locomotion. For this reason, comparisons have not been presented for 35 mm and 50 mm amplitude tests.

5.3 IP-subject comparison: 5 mm, 10 mm and 20 mm tests

Comparison data from all tests for subject 4 can be seen in Fig. 13 which show the subject versus equivalent IP behaviour for CoM position (plot a, d, g), velocity (plot b, e, h) and acceleration (plot c, f, i). All comparison data has been combined for 5mm tests (plots a - c), 10mm tests (plots d - f) and 20mm tests (h - i). As above, IP CoP placement is based on CoM velocity in the moving treadmill (local) reference frame.

Figure 4 demonstrates that the behaviours and level of agreement discussed above are typical for the entire text matrix for subject 4. In all cases the slope of the regression lines show that the magnitude of CoM motion is underestimated by the IP model, however in the case of velocity and acceleration, all CCs are ≥ 0.77 indicating strong linearity. CoM position however shows weaker linearity with CC between 0.36 and 0.42. This is due to the tendency for the subject (and IP) to drift laterally on the deck during testing (simulation) whereas the velocity and acceleration data is zero-centred throughout the test.

6 CONCLUSIONS

In this experimental investigation, subject balance behaviour while walking on both a stationary and laterally oscillating treadmill was investigated with the aid of a 3D motion tracking camera system. The objective was to obtain a better understanding of the root cause or source of the SE GRF, identified in Fig. 5 (d). The approach in this campaign was to investigate the behaviour of a relatively small number of subjects, but in greater detail than has typically been the case in the literature thus far.

The subject's balance response to deck oscillation is dominated by changes to lateral foot placement position. Amplitude modulation from the field of communication theory has been identified as a mathematical analogue for the biomechanical behaviour observed. It has been confirmed that the interaction forces arise directly as a result of the foot placement position, which itself is a function of pedestrian stability. The frequency of gait width modulation was identified as the modulus of the difference between the lateral forcing and deck oscillation frequencies. The underlying reason for this was revealed by examining the subject's CoM oscillation and recognising the influence of a sinusoidally varying inertia force induced by deck motion. Furthermore, the degree to which the subject alters their gait is determined by the degree to which their frontal plane stability is impaired by deck motion. Thus the link between frontal plane balance behaviour and the generation of the SE component of the lateral GRF has been established. Although there is a large degree of ISV, the fundamental HSI mechanism identified, namely periodic gait width modulation resulting in AM of the GRF, can be considered typical for the full test population.

Subject's CoM motion was also found to be well described by the passive dynamics of the IP biomechanical model. Thus active balance control in response to deck motion, (based on

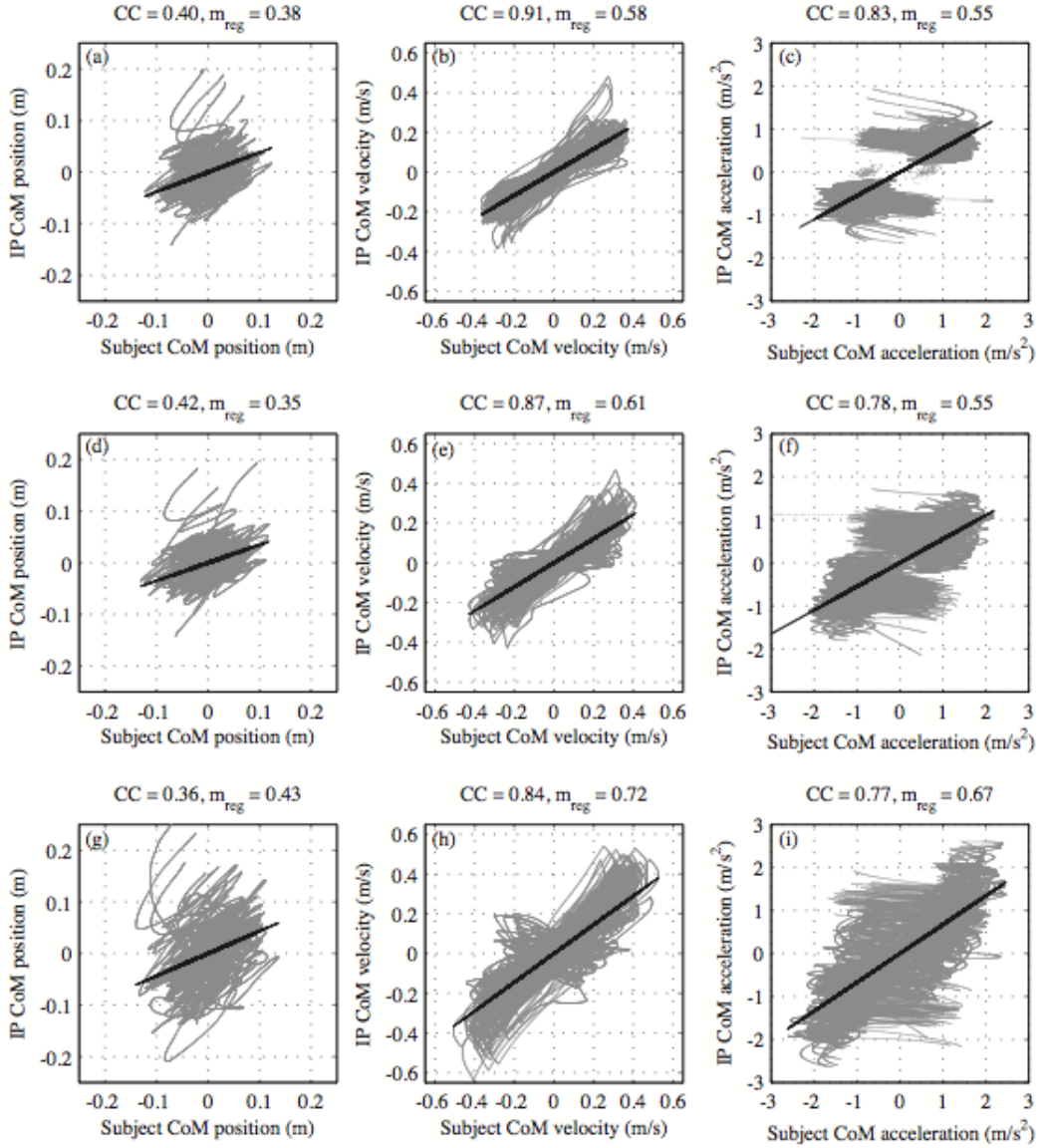


Figure 13: Plot of subject (No. 4) versus equivalent IP behaviour for CoM position (plot a, d, g), velocity (plot b, e, h) and acceleration (plot c, f, i). Plots (a - c) contain all data relating to 5 mm amplitude tests, plots (d - f) contain all data relating to 10 mm amplitude tests and plots (h - i) contain all data relating to 20 mm amplitude tests. Corresponding correlation coefficients are shown above the relevant plot. IP CoP placement based on local CoM velocity.

sensory feedback) does not appear to contribute significantly to the observed CoM motion. In the context of human-induced vibration, the raison d'être of the IP model is to generate GRFs consistent with HSI. In light of the discussion above it can be stated that the gait behaviour simulated is consistent with HSI, i.e. SE forces are simulated through the modulation of IP gait width, Figs. 11. The same mechanism has been confirmed in test subjects under the influence of the identical deck motion.

REFERENCES

[1] J.G.H. Macdonald, Pedestrian-induced vibrations of the Clifton Suspension Bridge, UK, *Proceedings of the ICE - Bridge Engineering*, **161**, 69-77, 2008.

[2] J. Brownjohn, P. Fok, M. Roche, P. Omenzetter, Long span steel pedestrian bridge at Singapore Changi Airport part 2: Crowd loading tests and vibration mitigation measures, *The Structural Engineer*, **82**, 28-34, 2004.

[3] F. Ricciardelli, A. Pizzimenti, Lateral walking-induced forces on footbridges, *Journal of Bridge Engineering*, **6**, 677-688, 2007

[4] E.T. Ingölfsson, C.T. Georgakis, F. Ricciardelli, J. Jönsson, Experimental identification of pedestrian-induced lateral forces on footbridges, *Journal of Sound and Vibration*, **330**, 1265-1284, 2011.

[5] A. Pizzimenti, Analisi sperimentale dei meccanismi di eccitazione laterale delle passerelle ad opera dei pedoni (experimental analysis of the lateral pedestrian-induced mechanism of excitation of footbridges), *Ph.D Thesis*, Department of Civil and Environmental Engineering, University of Catania, 2003

[6] S.P. Carroll, J.S. Owen, M.F.M Hussein, Reproduction of lateral ground reaction forces from visual marker data and analysis of balance response while walking on a laterally oscillating deck, *Engineering Structures*, **49**, 1034-1047, 2013

[7] Charnwood Dynamics Ltd, Leicestershire, UK Coda mpx30 User Guide,

[8] P. deLeva Adjustment to Zatsiorsky-Seluyanov's segment inertia parameters, *Journal of Biomechanics*, **29**, 1223-1230, 1996

[9] A. Hof, M. Gazendam, W. Sinke, The condition for dynamic stability, *Journal of Biomechanics*, **38**, 1-8, 2005.

[10] J.G.H. Macdonald, Lateral excitation of bridges by balancing pedestrians, *Proceedings of the Royal Society a-Mathematical Physical and Engineering Sciences*, **465**, 1055-1073, 2009.

[11] S.P. Carroll, J.S. Owen, M.F.M Hussein, Crowd-bridge interaction by combining biomechanical and discrete element models, In: *Proceedings of the 8th international conference on structural dynamics*, Leuven, 2011

[12] M. Bocian, J.G.H. Macdonald, J. Burn Biomechanically inspired modelling of pedestrian-induced forces on laterally oscillating structures, *Journal of Sound and Vibration*, **331**, 3914-3929, 2012.

[13] S.P. Carroll, J.S. Owen, M.F.M Hussein, A coupled biomechanical/discrete element crowd model of crowd-bridge dynamic interaction & application to the Clifton Suspension Bridge, *Engineering Structures*, **49**, 58-75, 2013

COMPDYN 2013
4th ECCOMAS Thematic Conference on
Computational Methods in Structural Dynamics and Earthquake Engineering
M. Papadrakakis, V. Papadopoulos, V. Plevris (eds.)
Kos Island, Greece, 12–14 June 2013

HUMAN INDUCED VIBRATIONS IN A PEDESTRIAN TIMBER BRIDGE

Sara Casciati[1], Lucia Faravelli[2], and Daniele Bortoluzzi[2]

[1] Dept. DICA, Dipartimento di Ingegneria Civile e Ambientale, School of Architecture, University of Catania at Siracusa, Piazza Federico di Svevia, 96100 Siracusa, Tel.: (+39) 338 5953658
e-mail: saracasciati@msn.com

[2] Department of Civil Engineering and Architecture, University of Pavia, via Ferrata 1, 27100 Pavia, Italy, Tel: (+39) 0382 985459

lucia@dipmec.unipv.it; daniele.bortoluzzi@unipv.it

Keywords: Condition monitoring; Fatigue damage; Structural health monitoring; Structural integrity.

Abstract. *The mountain landscape fits well with slender timber structures. Among them timber bridges are becoming very popular, and the designers are extending the span toward the hundred meters threshold. For a long pedestrian timber bridge in the Italian Alps, the authors had the chance to acquire measurements of the structural response which were collected for periods of few days and repeated in different seasonal weather conditions. A previously developed elaboration of the collected data leads to the validation of a numerical model. In this paper, the numerical model is used to investigate the dynamic response of the structural system which, according to the current structural code, can be ignored along the design process.*

1 INTRODUCTION

The designer of pedestrian bridges is allowed to work in the static context. It is therefore quite frequent, that after the construction of the bridge, the crossing pedestrians feel vibrations, a structural monitoring program starts and, eventually, damping devices are added "a posteriori".

Despite the objective fact that the bridge damping properties are difficult to be foreseen "a priori", a few further steps in the design process could avoid such a negative post-construction duty. There is no problem in claiming for the availability of a numerical tool able to analyze the dynamic structural response; it will be generally based on a finite element discretization. But, the model itself offers serious areas of uncertainties, mainly in the modeling of the joint behavior and, as said, in the definition of the damping contribution of materials and links.

The next two steps, however, are even more critic in view of a successful design accounting for the expected vibration:

1) an accurate description of the load-cases causing vibration;
2) an adequate definition of the associated limit state.

The two items listed above are discussed in the next section. Then, a further section is devoted to the illustration of a case study in the Italian Alps. The results of the numerical analyses follow.

2 GOVERNING RELATIONS

2.1 Dynamic excitations

A pedestrian bridge is entering vibrations as a consequence of environmental and man-made excitation characterized by a variability in time and space of the load intensity.

The environmental actions are mainly those associated with wind and earthquake but this paper is focused on the man-made excitation which can be categorized into three types:

1) single or couple of persons running across the bridge;
2) people covering the whole deck and progressing along the bridge;
3) the passage of a service car associated to the maintenance plan (of course this last action will only be possible when a direct access exists, i.e., the bridge can be accessed by ramps and not by stairs and/or elevator).

2.2 Limit state

An overview of the proposed strategies introduced to limit the vibration amplitudes in pedestrian bridges is reported in the books [1, 2]. Among these suggestions, the most appealing one is extracted from book [2] and can be summarized as it follows.

One considers a harmonic component of the motion:

$$x(t) = X \cos(2\pi f t)$$

where X denotes the amplitude of the vibration and f its frequency. It is well known that the amplitude of the associated acceleration is $X(2\pi f)^2$ from which one derives the quantity:

$$Z = [X(2\pi f)^2]^2 / f = 16\,\pi^4 X^2 f^3$$

which can be made dimensionless by dividing it by the reference value of $Z_0 = 10$ mm^2/sec^3.

A dimensionless vibration measure is then introduced as:

$$S = 10 \log (Z/Z_0) = 22 \log (X^2 f^3)$$

which is the logarithm of a dimensionless quantity; for the sake of specification, one introduces a fictitious unit called "vibrar".

By plotting a log-log diagram in the frequency-amplitude plane, the lines of constant $X^2 f^3$ are straight lines oriented as in Figure 1. It is a praxis to give evidence to the lines/domains corresponding to:

a) S= 17.5 vibrar: the domain from the origin to this line is regarded as a no-damage domain;
b) S= 40 vibrar: when in this layer, minor damage (e.g., plaster cracks) is detected;
c) S= 72.5 vibrar: when in this layer, damage to load-bearing parts is detected;
d) the outer domain is associated to the bridge destruction event.

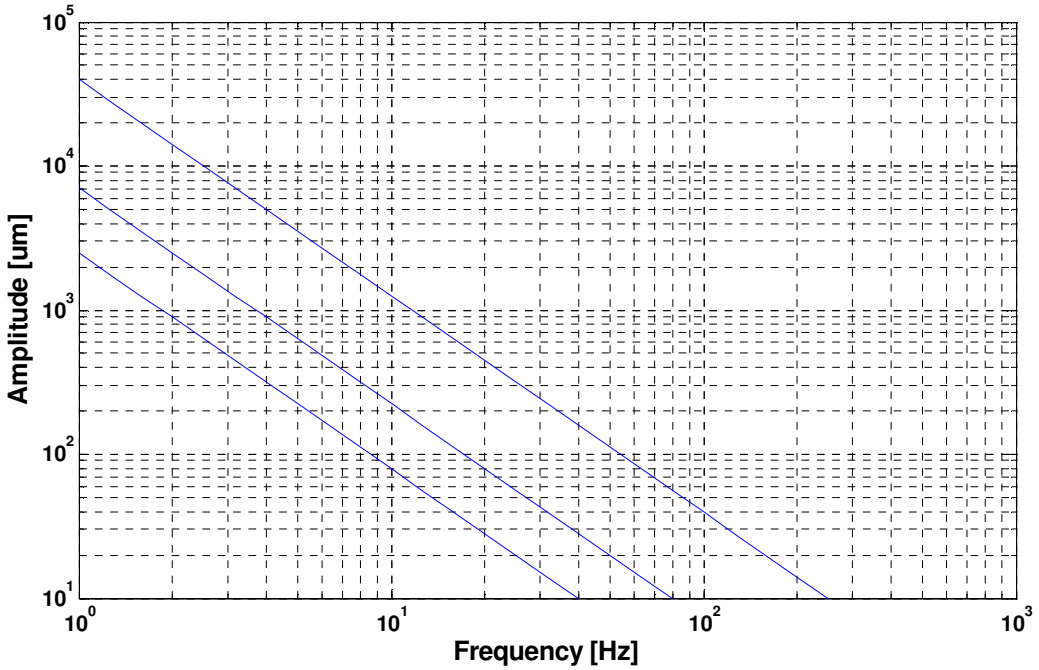


Figure 1 – The frequency vibration plot, with emphasis on the 4 damage zones: I – the no-damage zone contains the left-bottom corner; II – the straight line at 17.5 vibrar limits the possible plaster cracks area; III - the straight line at 40 vibrar limits the zone of possible damage to load bearing structural parts; IV - the straight line at 72.5 vibrar limits the zone of damage to load bearing structural parts

3 THE CASE STUDY

Earthquake engineers are familiar with the word "Tolmezzo", the name of a large village in Italy, where earthquake records were collected during the seismic events of spring and late summer in 1976. Nearby there is the largest natural lake in the area called the "Lake of the three municipalities" (or, simpler, the "Cavazzo Lake") with an emissary channel which was a barrier for the jogging activity across the surrounding park. Thus the two sides were linked by a pedestrian bridge assembling steel and timber components (Figure 2 and 3) to be harmonized with the surrounding environment. Instead, reinforced concrete was limited to the foundation components.



Figure 2 – A general view of the bridge which represents the case study of this manuscript.

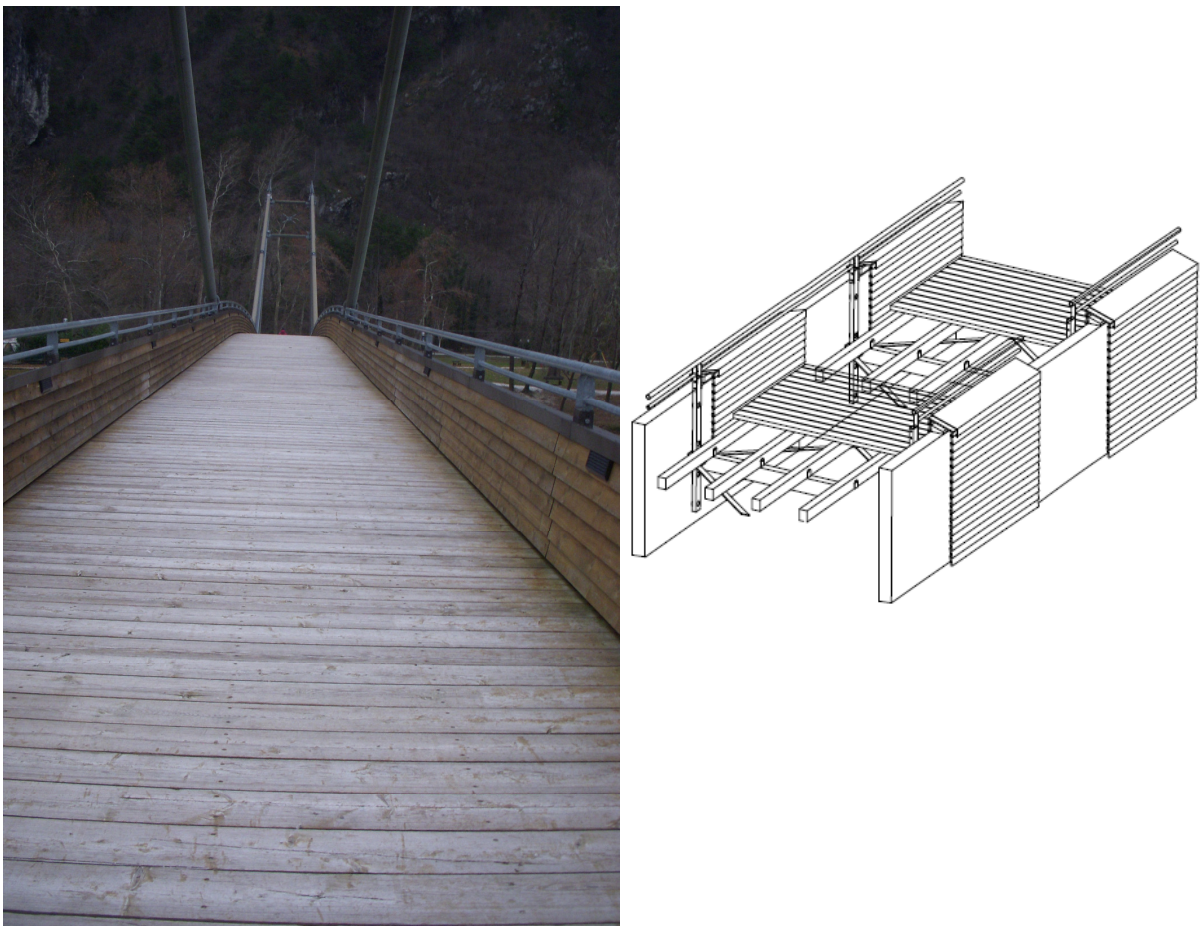


Figure 3 – Details of the walking path across the bridge.

Despite the bridge seems to be of a cable-stayed type, there are no cables. The static scheme consists of a vertical antenna on both ends of the bridge supporting the deck at one third of the span (from each side) by tubular steel elements. The span is 83 m and the double-beam deck width is 4 m, of which 3.22 m represents the free crossing width.

Glued laminated timber of high strength GL28c is adopted for all structural elements, except for the lateral cladding, made by larch, and the walking deck, which is made by glued laminated timber of type GL24c [3-4].

Two lateral curved beams of section 20 by 194.1 cm (Figure 3), with neoprene supports at the ends, are linked by a sequence of H-shaped, transversal tubular steel elements of type S355JR. The transversal elements of length 3.64m are braced and support five timber beams on which the walking platforms are mounted.

The beams are anchored at the thirds to the steel antennas on the two sides. The height of the antennas is 15 m, and they are made by elements of tubular steel section of external diameter 457. mm and thickness 14.2 mm. The link antenna-beam is made by elements of tubular steel section of external diameter 273 mm and thickness 8 mm.

The pedestrian bridge is regarded as category 3, which means that two live loads have to be considered:

- $q_{1.d}$ = isolated load of 10kN over an area of 70 by 70cm;
- $q_{1.e}$ = distributed load of 4.0 kN/m^2 resulting from a dense crowd.

In addition, the effects of snow, wind and earthquake are taken into account.

In order to have a numerical model of the system, a finite element model was created within the software environment Mentat-Marc [5], by paying particular attention to the wood material modelling [6]. The behavior of the link between the longest oblique elements and the deck is not a priori known, and for this reason a preliminary model of the steel portal was implemented to clarify this aspect. The numerical model of the whole bridge is shown in Figure 4.

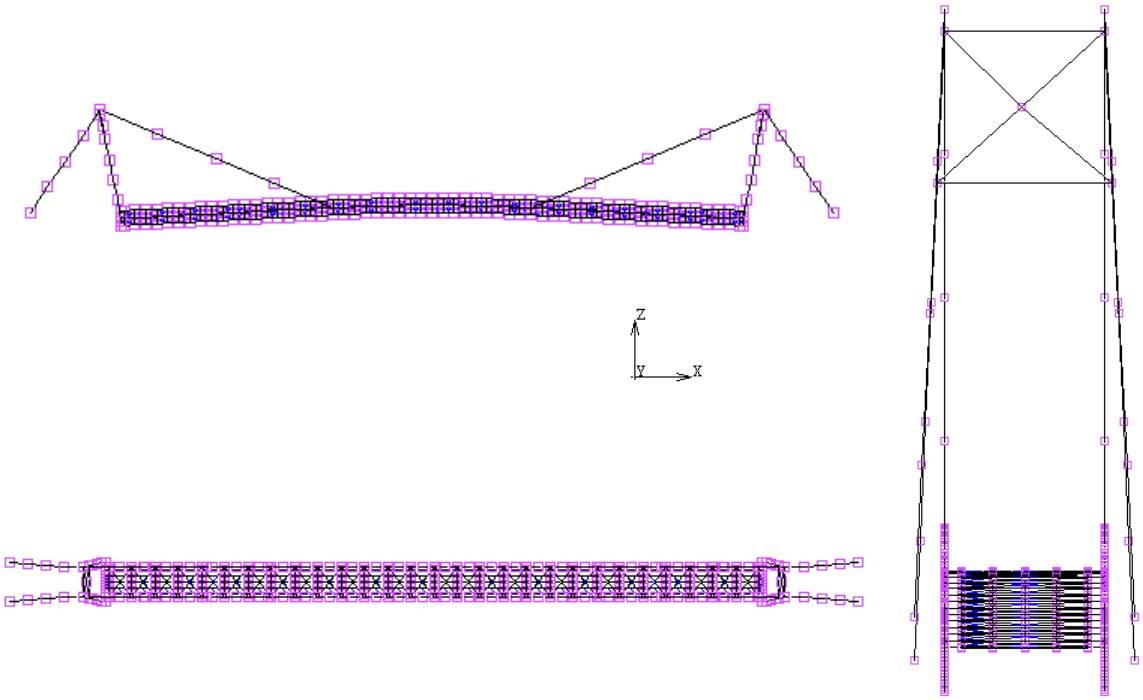


Figure 4 – Beam elements and shell elements used to discretize the pedestrian bridge.

4 SELECTED RESULTS FROM THE DYNAMIC ANALYSES

The results of the analyses reported in this section pursue the goal of showing the feasibility of the simulation. A deeper study on the damping properties would be required in order to produce more realistic time histories of the response.

First, the analysis is conducted by considering the crossing of a car of mass 2 t along the bridge at a speed of 10m/s. The load case is a sequence of pulses at 29 different positions along the bridge. Moving masses are also added to refine the dynamic analysis. Just for sake of illustration, the single pulse in position 12 would produce the response summarized in Figure 5.

The dynamic analysis is conducted in 1000 steps, with a time step of 0.18 sec. The response in terms of vertical displacement time history is plotted in Figure 6 for the node 101, the one of the maximum deflection under pulse 12.

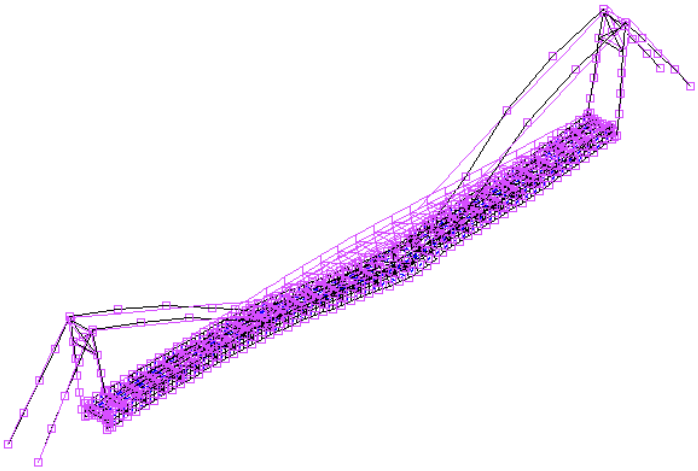


Figure 5 – The bridge response under the action of pulse 12, in a global sequence of 29 by which the crossing of a car is simulated.

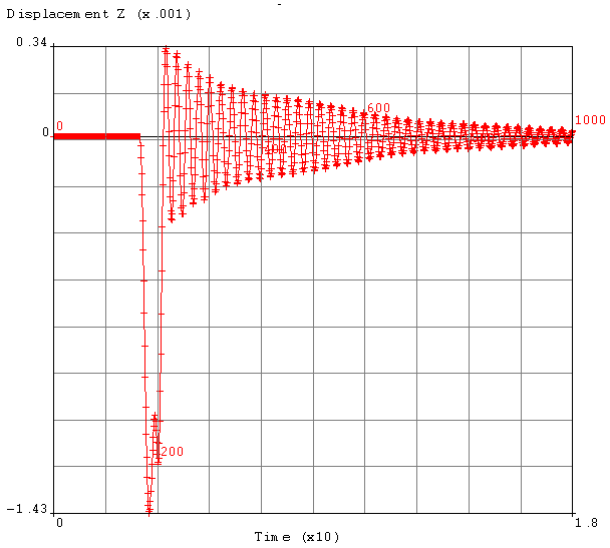


Figure 6 – Time history of the vertical displacement (in meters) of the bridge node (labeled 101) of maximum deflection in Figure 5, under the action of pulse 12 (with time expressed in seconds).

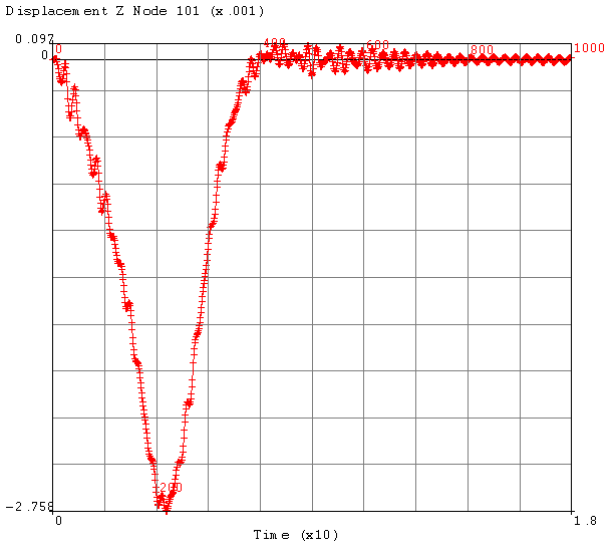


Figure 7 – Time history of the vertical displacement (in meters) of the bridge node 101 during the car crossing (with time expressed in seconds).

The car crossing analysis, i.e., the response to the entire sequence of 29 pulses, is summarized, again for node 101, in Figure 7. It is seen that, after a peak of 2.75 mm, a free oscillation of 0.1 mm amplitude starts and then decays with a damping of 1%, which was introduced as default in the model. A comparison with experimental data will then allow a more realistic simulation. The mode associated with this free oscillation is provided in Figure 8; it corresponds to a natural frequency of 2.7 Hz. The amplitude of the free oscillation is marked in the diagram of Figure 1 by a cross as shown in Figure 9.

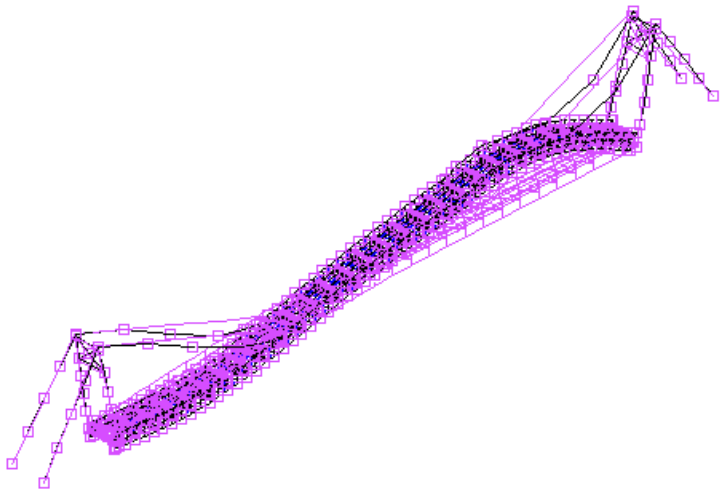


Figure 8 – The damped free oscillation after the car crossing: frequency 2.7 Hz. and damping 1%.

It is worth noticing that apart from the fact that the masses are one tenth of the one of the car, the car crossing load is also a rough representation of two persons running along the bridge (since the walking kinematics is ignored). Thus, such a passage would generate a free oscillation of amplitude 0.01 mm, as from Figure 7 after dividing by 10.

The case of people clustering on the bridge and moving along the same direction required a fully different analysis whose results are summarized in Figures 10 and 11. A second point is

then added by this analysis in Figure 9. The walking is simulated by a moving half of the weight from the left to the right node and vice versa with frequency 1Hz. This also gives rise to an external horizontal component of 0.1 time the weight in the overloaded node.

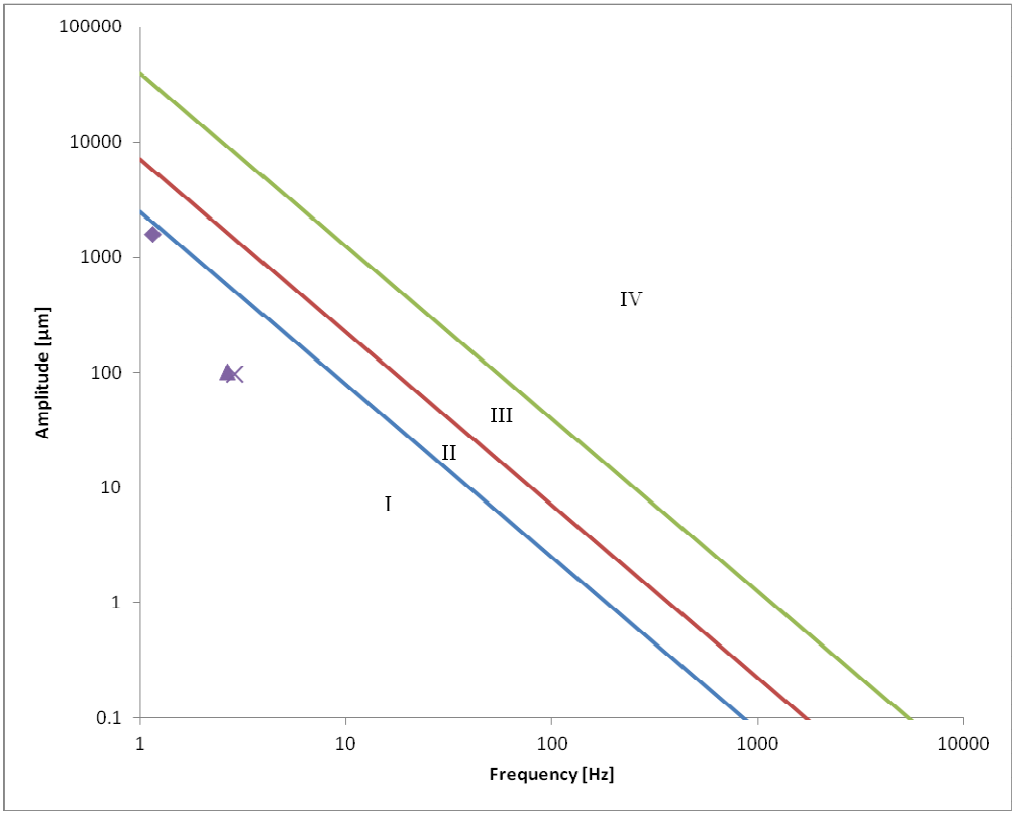


Figure 9 – Free oscillations induced by car and persons crossing: representations in the diagram introduced as Figure 1. Triangle and cross correspond to the car crossing and a vibrodine test simulation: the vibration is along the vertical axis. The third mark corresponds to the dense clustering of people and reports the vibration along the transversal axis.

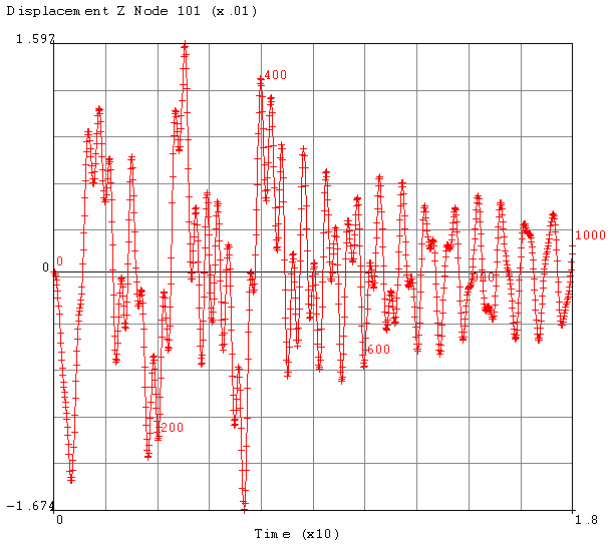


Figure 10 – The vertical displacement (in meters) of the bridge node labeled 101 during the dense clustering of people crossing (time expressed in seconds) for one half of the time history and then at rest on the bridge.

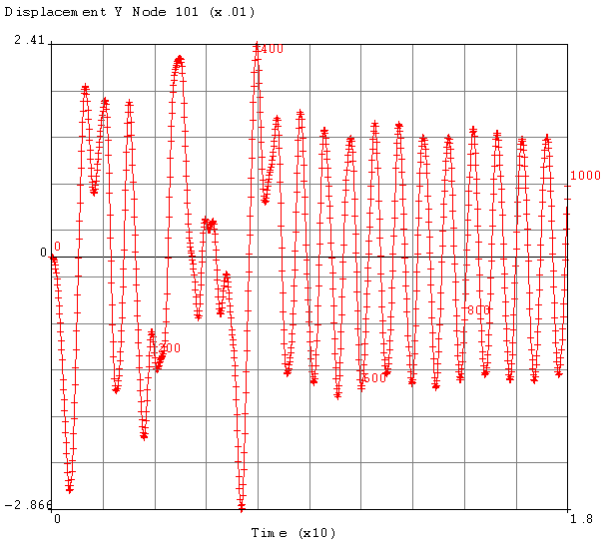


Figure 11 – The horizontal displacement (in meters) of the bridge node (say 101) during the dense clustering of people crossing (time expressed in seconds) for one half of the time history and then at rest on the bridge. This response, scaled by 10, is used to add the corresponding mark in Figure 9.

The result of the analysis, carried out without fixing the damping which is quite low, is exploiting many of the resource of the structural system, but one is moving 1000 persons along the bridge in a very aggressive way, both in terms of vertical load variation and of horizontal action.

The points representative of this situation of distributed crowd is first scaled to one tenth and then plotted (by a diamond) in the diagram of Figure 1, as shown in Figure 9. A third point obtained as free vibration after the numerical simulation of a vibrodine test (in the vertical direction) is also plotted by a triangle.

5 CONCLUSIONS

On a numerical model calibrated by the available experimental data, two design steps, additional to the static procedure required by structural codes in Europe, are discussed. The first one sees the development of a dynamic analysis; the second one the translation of the dynamic analysis results into a diagram of expected performance.

In this paper, one investigates the feasibility of a procedure whose goal is to avoid that feeling vibration when crossing the realized bridge statically designed results in the designer being obliged to a costly experimental campaign. A preliminary estimation of the expected vibration levels would immediately classify the performance as allowable or non-allowable.

It is worth noticing however that in this process the calibration of the model parameters and mainly of the damping properties [7-9] will always suggest a dynamic testing of the bridge at the proofing stage.

ACKNOWLEDGEMENTS

The authors are indebted with the bridge designer, Ing. Stefano Boranga, and the timber elements producer Rubner Holzbau S.p.A., of Bolzano, Italy, for providing them access to the technical documents.

Moreover, the authors acknowledge the cooperation of Elena Chiapparoli and Marco Savini who developed the numerical analyses as partial fulfillment of their duties toward the Master in Civil Engineering at the University of Pavia.

REFERENCES

[1] H. Wenzel, *Health monitoring of bridges*, John Wiley & sons, Chichester, 2009

[2] C.F. Beards, *Structural vibration: analysis and damping*, Arnold, London, 1996.

[3] G. Giordano, A. Ceccotti and L. Uzielli, *Tecnica delle Costruzioni in Legno* [in Italian], Hoepli, Milano, Italy , 1999.

[4] M. Piazza, R. Tomasi and R. Modena, *Strutture in Legno* [in Italian]. Hoepli, Milano Italy, 2005.

[5] http://www.mscsoftware.com.

[6] S. Casciati and M. Domansechi, Random imperfection fields to model the size effect in laboratory wood specimens, *Structural Safety*, 29 (4), 2007, 308-321.

[7] Sétra, *Passerelles piétonnes - Evaluation du comportement vibratoire sous l'action des piétons* [in French] , 2006.

[8] C. Moutinho, A. Cunha and E. Caetano, Analysis and Control of Vibration in a Stress-ribbon Footbridge, *Structural Control and Health Monitoring*, 18, 2011, 619–634

[9] C.M. Casado, I.M. Diaz, J. de Sebastian, A.V. Poncela and A. Lorenzana, Implementation of Passive and Active Vibration Control on an In-service Footbridge, *Structural Control and Health Monitoring*, 20,2013, 70-87.

COMPDYN 2013
4th ECCOMAS Thematic Conference on
Computational Methods in Structural Dynamics and Earthquake Engineering
M. Papadrakakis, N.D.Lagaros, V. Plevris (eds.)
Kos Island, Greece, 12–14 June 2013

DYNAMIC LOADING FACTORS OF INDIVIDUAL JOGGING FORCES

Vitomir Racic, James M.W. Brownjohn, Aleksandar Pavic

[1] University of Sheffield
Department of Civil and Structural Engineering
Sir Frederick Mappin Building
Mappin Street, Sheffield, S1 3JD
e-mails: v.racic@sheffield.ac.uk
a.pavic@sheffield.ac.uk
james.brownjohn@sheffield.ac.uk

Keywords: human-induced vibrations, footbridges, running, dynamic loading.

Abstract. *With increasingly popular marathon events in urban environments, such as in London and New York City, structural designers are faced with a great deal of uncertainty when assessing dynamic performance of bridges occupied and dynamically excited by people running. While the dynamic loads induced by people walking have been intensively studied since the infamous lateral sway of the London Millennium Bridge in 2000, reliable and practical descriptions of running excitation are still very rare and limited.*

This paper makes a step forward by bringing together a unique database of individual jogging force records and their simple mathematical model which can be used in everyday design practice. The forcing data has been collected in Vibration Engineering Section Laboratory in the University of Sheffield using a state-of-the-art instrumented treadmill, which is commonly used in clinical studies of human gait and sports biomechanics. The modelling strategy featuring Fourier harmonics of measured jogging force-time histories is adopted from a popular design guidelines for human walking excitation of structures.

The results show a great scatter in the DLF data and no strong link with jogging footfall rate, which is the case with walking forces. This clearly suggests that traditional deterministic Fourier based approach is not the best modelling strategy for jogging loading. Uncertainty and inter-personal randomness of the force amplitudes indicate that stochastic - rather than deterministic models of jogging forces should provide more reliable predictions of the bridge dynamics. These forces could be modeled in a similar fashion as other key dynamic loading of structures characterized by great randomness and uncertainty, such as wind and earthquake.

1 INTRODUCTION

In the last fifteen years substantial developments in workmanship and structural materials have enabled bridge engineers to promote much more slender designs than ever. As a result, modern bridges are at a considerable risk of developing resonance when occupied and dynamically excited by people moving during ordinary activities, such as walking, jumping and running [1]. Excessive dynamic responses recorded worldwide on at least a dozen bridges of different structural forms and sizes under groups and crowds of active people clearly prove the point [2].

While the loads induced by walking [3-7] and jumping [8-9] have been intensively studied, reliable and practical descriptions of jogging forces are still very rare and limited [10-12]. In the context of this paper, jogging refers to running at a slow or leisurely pace, usually slower than 10 km/h. Jogging is common in urban environments, hence brings a potential hazard to vibration serviceability performance of bridge structures.

Much research into jogging forces has been in the domain of biomechanics as the contact forces between the feet and supporting ground (thus generally called 'ground reaction forces' - GRFs) provide useful diagnostics for medical and sports applications [13]. Medics introduced instrumented force measuring treadmills which can be used to carry out even high-speed running studies in very small laboratories [14]. However, no database of jogging forces in the form of continuously recorded signals has yet been found that can be used for development of their statistically reliable analytical model for application in the civil engineering context.

The lack of fundamental forcing data and their reliable mathematical models has resulted in a total lack of formal design guidance regarding jogging/running excitation of bridges. The present study aims to change this situation by bringing together: (1) a comprehensive database of continuously measured vertical jogging loads generated by individuals on flat stationary surfaces, and (2) a simple mathematical characterisation of the measurements motivated by the Fourier-based modelling approach adapted from a popular design guideline for walking loading [15]. The models could be applied to cases of incipient instability, i.e. when vertical bridge motion is still not significantly perceptible to the jogger, and is ideally suited for considering cases of multiple joggers in a group or crowd.

2 EXPERIMENTAL DATA COLLECTION

The tests were carried out in the Vibration Engineering Section Laboratory in the University of Sheffield (UK). Continuously measured individual force records were collected on a state-of-the-art instrumented treadmill ADAL3D-F (Figure 1).

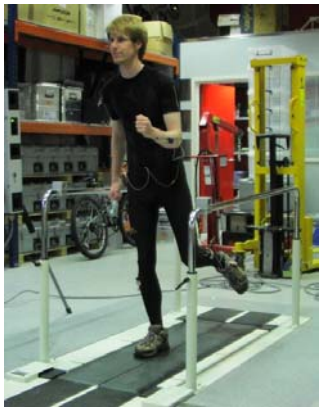


Figure 1: Experimental setup.

Speed of the belt rotation (here also called 'treadmill speed') can be controlled and monitored remotely either with a control panel or with bespoke software, run from the data acquisition PC. Similar to fitness treadmills, the remote control panel and the treadmill itself are equipped with a safety stop switch. Rotational speed of ADAL3D-F belts is in the range 0.1-10 km/h.

All participants wore comfortable running footwear. Those who had no experience with treadmill jogging were given a brief training prior to the force collection supervised by a qualified instructor. During each individual test, participants were asked to jog on the treadmill at a fixed speed. Pacing rate was not prompted by any stimuli such as a metronome, and it was determined only from subsequent analysis of the generated force signals (see Section 3). Each test was completed when at least 64 successive footfalls were recorded. Rests were allowed between successive tests.

Acquisition of the force records started at the slowest self-selected speed at which jogging, rather than walking, is more comfortable. In 95% of test subjects processed, this speed was 6.5 km/h. In each following test the running speed was increased by 0.5 km/h, until it added up to 10 km/h.

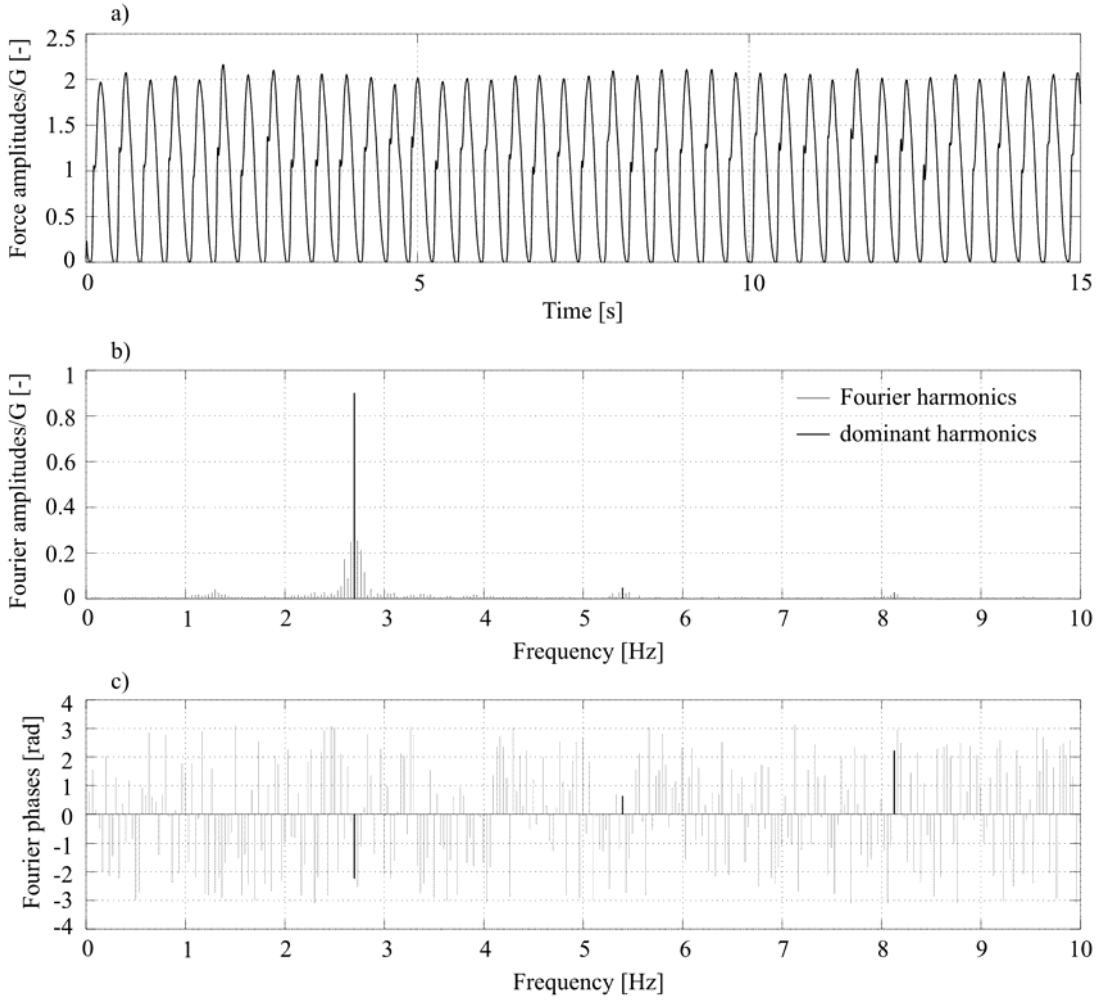


Figure 2: An example of measured force signal: (a) force-time history and its Fourier (b) amplitude and (c) phase spectra calculated from 64 successive footfalls.

In total, 24 volunteers (18 males and 6 females, body mass 68.3±12.2 kg, height 167.2± 7.1 cm, age 24.2±7.6 years) were drawn from students, academics and technical staff of the Uni-

versity of Sheffield. All together they generated 181 vertical jogging force-time histories of kind illustrated in Figure 2. In the remaining part of the paper, this unique database is used to provide their mathematical representation based on the Fourier series.

3 DATA ANALYSIS AND MODELLING

Measured force-time histories of human-induced loading are invariably near-periodic [1], indicating their narrow band nature (Figure 2b). However, to simplify their mathematical representations for design purposes, they are usually assumed perfectly periodic, deterministic and presentable via Fourier series [15]:

$$F(t) = G\sum_{j=1}^{m} \alpha_i \sin\left(2\pi f_r t - \varphi_i\right) \tag{1}$$

Here F(t) represents the total force at time t, with G representing the body weight in the same unit. A total of m harmonics are considered, capturing peaks α_i from the Fourier amplitude spectrum (Figure 2) at integer multiples of the footfall rate f_j. In the literature, α_i coefficients are commonly known as 'dynamic load(ing) factors' (DLFs). On the other hand, values of the phase angles φi have never been publicised in detail and are usually ignored in Equation (1).

Fitting Equation (1) to the numerous database of jogging force records established in the previous section can provide a valuable insight into their inter-subject variability. Shapes of the histograms shown in Figure3a suggest that jogging footfall rate is not a normally distributed as in case of walking [7,16-18]. The normal probability plots in Figure 3b further proves the point. Moreover, fitting a wide range of other probability density functions, such as the family of skewed distributions [19], showed a lack of statistical significance.

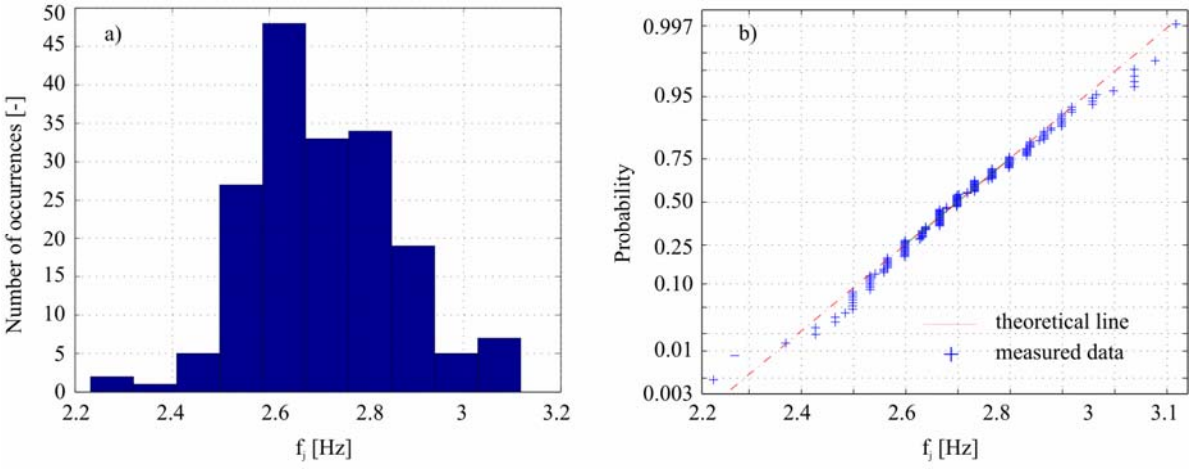


Figure 3: (a) Histogram of footfall rates and (b) the corresponding normal probability plot.

Apart from the linear trend between jogging speed and footfall rate (ρ=0.39), Figure 4 illustrates a large scatter of the running frequencies at fixed running speeds, and vice versa. This observation can play a key role in simulating reliably jogging excitation of bridges due to dense crowd situations (e.g. marathon events) where jogging speed of individuals in a crowd can be controled by spatial constrains and the crowd flow.

Graphs shown in Figure 5 indicate that jogging force amplitudes generally increase as people increase their footfall rate. Due to the apparently large scatter of the DLF values at a fixed

running frequency, their relationship cannot be described reliably as a deterministic function, such as the linear and polynomial curve fits suggested for vertical walking loads elsewhere [15,20]. Moreover, histograms of DLFs corresponding to a narrow range 0.1 Hz around the most frequent footfall rate in the sample f_j =2.7 Hz do not resemble any known probability density function (Figure 6), which is a key condition for probabilistic curve fitting [19]. Also, there is no strong link between the fundamental DLF1 and DLF_i ($i \geq 2$) of higher harmonics, as shown in Figure 7.

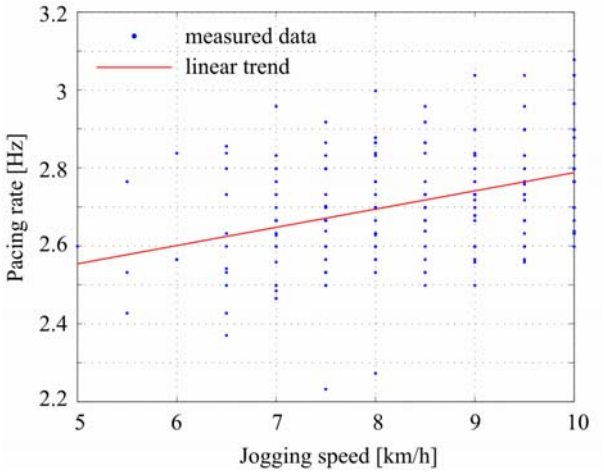


Figure 4: Jogging speed vs. footfall rate.

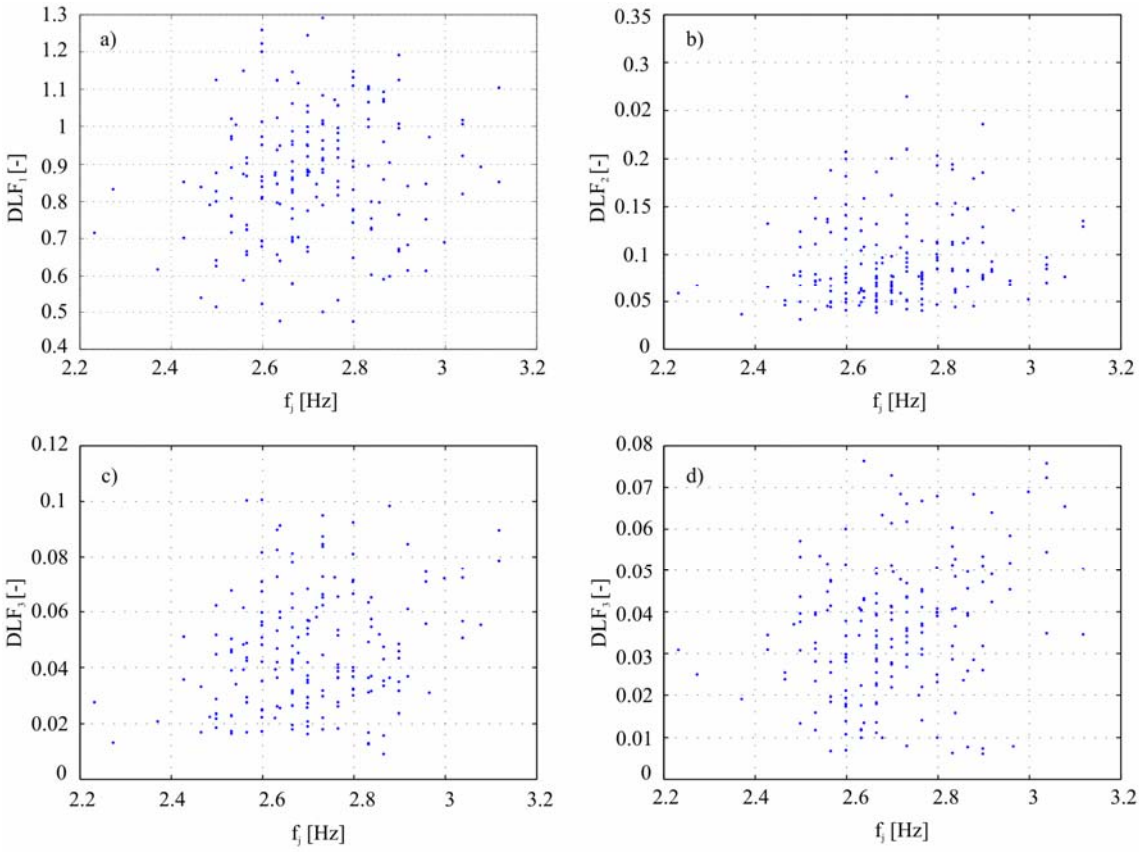


Figure 5: DLFs of the first four dominant harmonics vs. footfall rate.

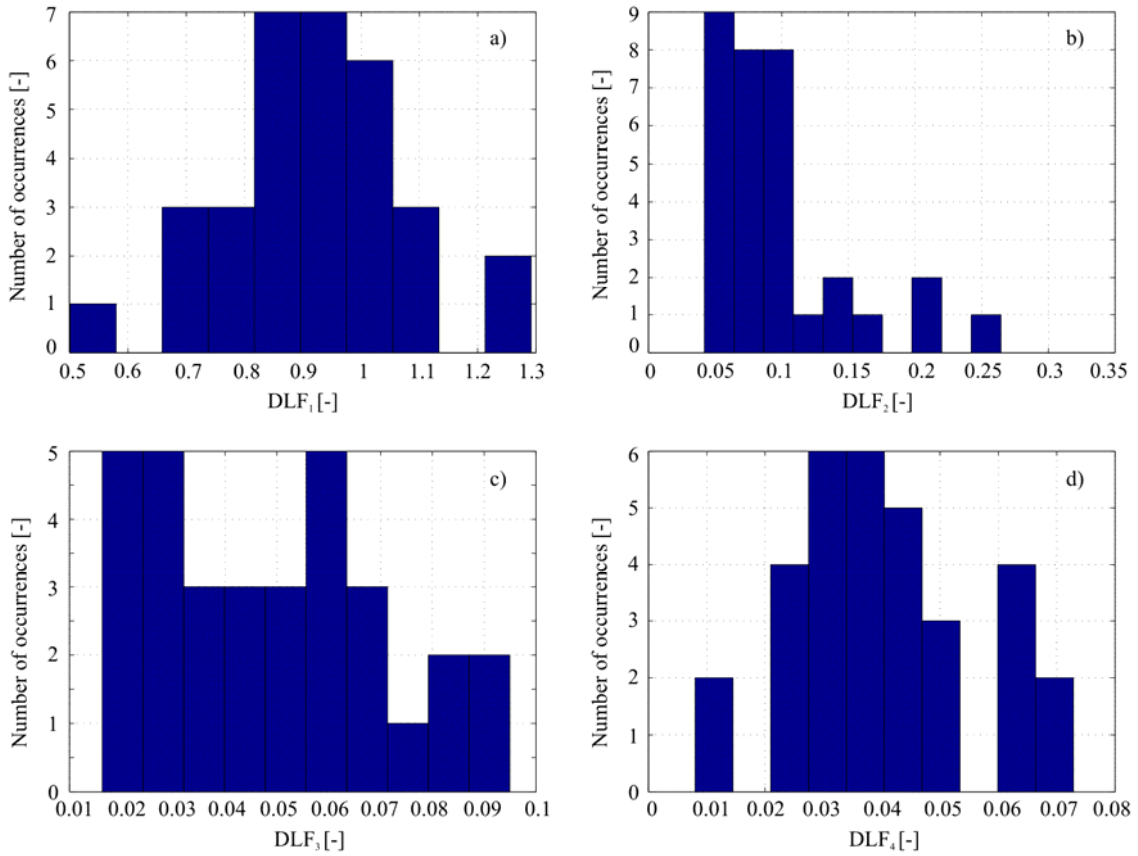


Figure 6: Histograms of DLFs corresponding to the most frequent footfall rate fj=2.7 Hz.

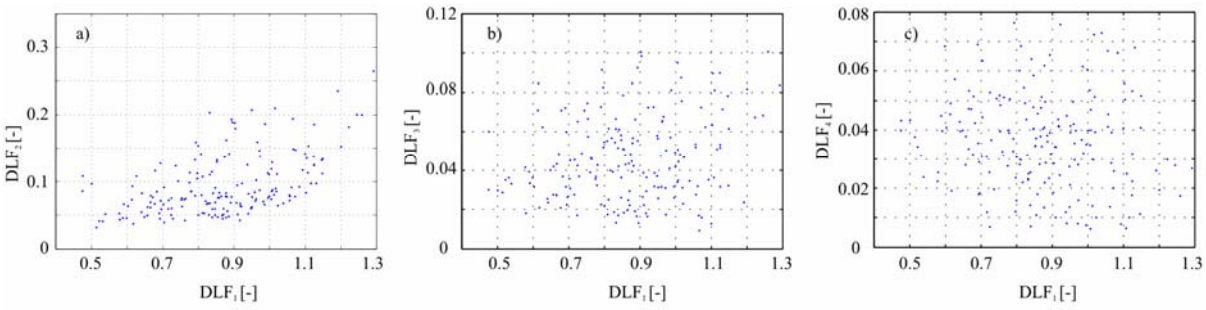


Figure 7: Fundamental DLF1 vs. (a) DLF_2, (b) DLF_3 and (c)DLF_4.

f_j [Hz]	DLF_1 [-]	DLF_2 [-]	DLF_3 [-]	DLF_4 [-]
<2.5	[0.514, 1.125]	[0.031, 0.132]	[0.013, 0.062]	[0.013, 0.057]
[2.5, 2.6)	[0.476, 1.245]	[0.039, 0.200]	[0.016, 0.091]	[0.010, 0.076]
[2.6, 2.7)	[0.475, 1.292]	[0.040, 0.264]	[0.018, 0.095]	[0.008, 0.068]
[2.7, 2.8)	[0.591, 1.191]	[0.044, 0.236]	[0.009, 0.098]	[0.006, 0.068]
[2.8, 2.9)	[0.613, 0.971]	[0.052, 0.146]	[0.031, 0.085]	[0.008, 0.069]
[2.9, 3)	[0.820, 1.012]	[0.070, 0.097]	[0.051, 0.076]	[0.035, 0.076]
≥3	[0.820, 1.104]	[0.070, 0.135]	[0.051, 0.090]	[0.035, 0.076]

Table 1: Lower and upper bands of DLF values for the given range of jogging rate f_j.

All these results have demonstrated large inter-subject randomness of jogging forces which cannot be modelled reliably using the popular deterministic Fourier series approach. There-

fore, this study suggests randomization of DLF values in Equation (1). For the given footfall rate, DLF amplitudes are calculated randomly and equally likely using parameters of uniform distributions summarised in Table 1.

4 DISCUSSIONS AND CONCLUSIONS

The lack of fundamental forcing data and their reliable mathematical characterisation are the key reasons for a total lack of a formal design guidance regarding jogging excitation of bridges. To change this situation, this interdisciplinary study first established a unique database comprising 181 individual force signals collected from 24 individuals running on a biomedical instrumented treadmill at a wide range of speeds. The measurements are then fitted to the Fourier series model transferred and adopted from a popular contemporary design guideline on dynamic loads due to pedestrians walking. However, deterministic modelling approach was shown to be unreliable since the extracted force parameters are characterised by significant randomness. Therefore, the force parameters are described here using simple statistics.

Being derived from the force data recorded on a stiff ground (i.e. treadmill), the current version of the model represents only jogging excitation of structures which do not vibrate perceptibly, i.e. cases when they are not significantly affected by the structural vibrations. However, perceptible motion of the structure is just one type of cue or stimulus among several others affecting human-induced loads, such as different auditory, visual and tactile stimuli. To include all these parameters in the model, DLFs and footfall rate should be modelled as a function of bridge dynamic response, human perception to vertical vibrations and different external stimuli. To the best knowledge of the authors, experimental data necessary to accomplish this challenge is currently not available anywhere in the world.

5 REFERENCES

[1] V. Racic, A. Pavic, J.M.W. Brownjohn, Experimental identification and analytical modelling of human walking forces: Literature review. *Journal of Sound and Vibration*, **326**, 1-49, 2009.

[2] S. Zivanovic, A. Pavic, P. Reynolds, Vibration serviceability of footbridges under human-induced excitation: a literature review. *Journal of Sound and Vibration*, **279**, 1-74, 2005.

[3] S. Zivanovic, A. Pavic, P. Reynolds, Human-structure dynamic interaction in footbridges. *Bridge Engineering* **158 (BE4)**, 165-177, 2005.

[4] F. Venuti, L. Bruno, The synchronous lateral excitation phenomenon: modelling framework and an application. *Comptes Rendus Mecanique*, **335**, 739-745, 2007.

[5] J.H.G. Macdonald, Lateral excitation of bridges by balancing pedestrians. *Proceedings of the Royal Society A*, 16 December 2008.

[6] M. Kasperski, C. Sahnaci, Serviceability of pedestrian structures exposed to vibrations during marathon events. In: *Proceedings of IMAC XXVI*, Orlando, Florida, USA, 4-7 February, 2008.

[7] E.T. Ingólfsson, C.T. Georgakis, F. Ricciardelli, J. Jönsson, Experimental identification of pedestrian-induced lateral forces on footbridges. Journal of Sound and Vibration **330(6)**, 1265-1284, 2011.

[8] E. Caetano, A. Cunha, C. Moutinho, Vandal loads and induced vibrations on a footbridge. *ASCE Journal of Bridge Engineering,* **16(3)**, 375-382, 2011.

[9] V. Racic, A. Pavic, Stochastic approach to modelling near-periodic jumping force signals. *Mechanical Systems and Signal Processing,* **24**, 3037-3059, 2010.

[10] Galbraith F.W., Barton M.V. (1970) Ground loading from footsteps. *Journal of Acoustic Society of America* 48 (5), 1288-1292.

[11] J.H. Rainer, G. Pernica, D.E. Allen, Dynamic loading and response of footbridges. Canadian Journal of Civil Engineering 15 (1988) 66-71.

[12] C. Sahnaci, M. Kasperski, Excitation of buildings and pedestrian structures from walking and running. In: *Proceedings of EVACES07*, Porto, Portugal, 24-26 October, 2007.

[13] K. Sabri, M.E. Badaoui, F. Guillet, A. Belli, G. Millet, J.B. Morin, Cyclostationary modeling of ground reaction force signals. *Signal Processing*, **90(4)**, 1146-1152, 2010.

[14] A. Belli, P. Bui, A. Berger, A. Geyssant, J.R. Lacour, A treadmill ergometer for three-dimensional ground reaction forces measurement during walking. *Journal of Biomechanics*, **34(1)**, 105-112, 2001.

[15] A. Pavic, M. Willford, Vibration serviceability of post-tensioned concrete floors, Appendix G. In *Post-tensioned concrete floors design handbook*, technical report 43, 99-107, 2005.

[16] Y. Matsumoto, T. Nishioka, H. Shiojiri, K. Matsuzaki, Dynamic design of footbridges. In: *Proceedings of IABSE*, No. P-17/78, 1-15, 1978.

[17] S. Zivanovic, A. Pavic, P. Reynolds, Probability-based prediction of multi-mode vibration response to walking excitation. *Engineering Structures*, **29(6)**, 942-954, 2007.

[18] V. Racic, J.M.W. Brownjohn, Stochastic model of near-periodic vertical loads due to humans walking. *Advanced Engineering Informatics*, **25(2)**, 259-275, 2011.

[19] C. M. Bishop, *Pattern recognition and machine learning.* Springer, New York, USA, 2006.

[20] P. Young, Improved floor vibration prediction methodologies. *ARUP Vibration Seminar*, 4 October, London, UK, 2001.

COMPDYN 2013
4th ECCOMAS Thematic Conference on
Computational Methods in Structural Dynamics and Earthquake Engineering
M. Papadrakakis, V. Papadopoulos, V. Plevris (eds.)
Kos Island, Greece, 12–14 June 2013

DYNAMIC ANALYSIS OF STEEL-CONCRETE COMPOSITE TUBULAR FOOTBRIDGES SUBMITTED TO HUMAN WALKING

Gilvan L. Debona[1], José G. S. da Silva[2*] and Ana C. C. F. Sieira[2]

[1] Civil Engineering Post-graduate Programme, PGECIV, State University of Rio de Janeiro, UERJ
São Francisco Xavier St., 524, Maracanã, 20550-900, Rio de Janeiro, RJ, Brazil
e-mail: gilvanld@yahoo.com.br

[2] Structural Engineering Department, ESTR, State University of Rio de Janeiro, UERJ
São Francisco Xavier St., 524, Maracanã, 20550-900, Rio de Janeiro, RJ, Brazil
e-mail: jgss@uerj.br; sieira@eng.uerj.br

Keywords: Dynamic Analysis, Human Comfort, Structural Dynamics, Steel-concrete Composite Tubular Footbridges, Design Codes, Finite Element Modelling.

Abstract. *The increasing incidence of footbridges excessive vibration problems due to human walking induced loads led to an increase in the number of complaints arising from annoying human-induced vibrations in new footbridge structures. Based on the improvements in design methods, structural engineers seem to continuously move the safety border to increase slenderness and lightness of their footbridges using more slender structural designs. Considering all aspects mentioned before, this was the main motivation for the development of a finite element modelling of the dynamic behaviour of steel-concrete composite tubular footbridges, when subjected to human walking vibrations. The investigated structural system was based on a steel-concrete composite tubular footbridge spanning 82.5 m. The structural model consists of tubular steel sections and a concrete slab. This investigation is carried out based on correlations between the experimental results related to the footbridge dynamic response and those obtained with finite element modelling. The finite element model enabled a complete dynamic evaluation of the composite tubular footbridge in terms of human comfort and its associated vibration serviceability limit states. The peak accelerations found in the present analysis indicated that the investigated footbridge presented problems related with human comfort. Hence it was detected that this type of structure can reach high vibration levels that can compromise the footbridge user's comfort.*

1 INTRODUCTION

The increasing incidence of footbridges excessive vibration problems due to human walking induced loads led to an increase in the number of complaints arising from annoying human-induced vibrations in new footbridge structures. Based on the improvements in design methods, structural engineers seem to continuously move the safety border to increase slenderness and lightness of their footbridges using more slender structural designs.

This was the main motivation for the development of a design methodology centred on the dynamic response of steel-concrete composite tubular footbridges subjected to human walking induced vibrations. On the other hand, tubular hollow sections are increasingly used in off-shore structures, highway bridges, pedestrian footbridges, large-span roofs and multi-storey buildings due to their excellent properties and the associated advances in fabrication technology. The intensive use of tubular structural elements in Brazil, such as the example depicted in Figure 1, mainly due to its associated aesthetical and structural advantages, led designers to be focused on their technologic and design issues.



Figure 1: Example of a tubular steel pedestrian footbridge in Rio de Janeiro, Brazil.

Steel and composite tubular footbridges are currently subjected to dynamic actions with variable magnitudes due to the pedestrian crossing on the concrete deck. These dynamic actions can generate the initiation of fractures or even their propagation in the structure. Depending on the magnitude and intensity, these adverse effects can compromise the structural system response and the reliability which may also lead to a reduction of the expected footbridge service life [1-3].

The use of circular hollow section members as part of the structure of pedestrian footbridges is a relatively new constructional concept. During the last couple years several steel-concrete composite footbridges had been constructed in Brazil, as illustrated in Figure 1. The typical cross-section of this type of pedestrian footbridge generally consists of a tubular spatial truss girder carrying the concrete deck slab, as presented in Figure 1. The deck slab is connected directly to the steel structure by either shear studs, concrete dowels or in some cases where no top chord exists. At the bottom chord of the tubular space truss four brace members have to be connected to the continuous bottom chord. This type of joint is usually named K-joint, as depicted in Figure 2 [2].

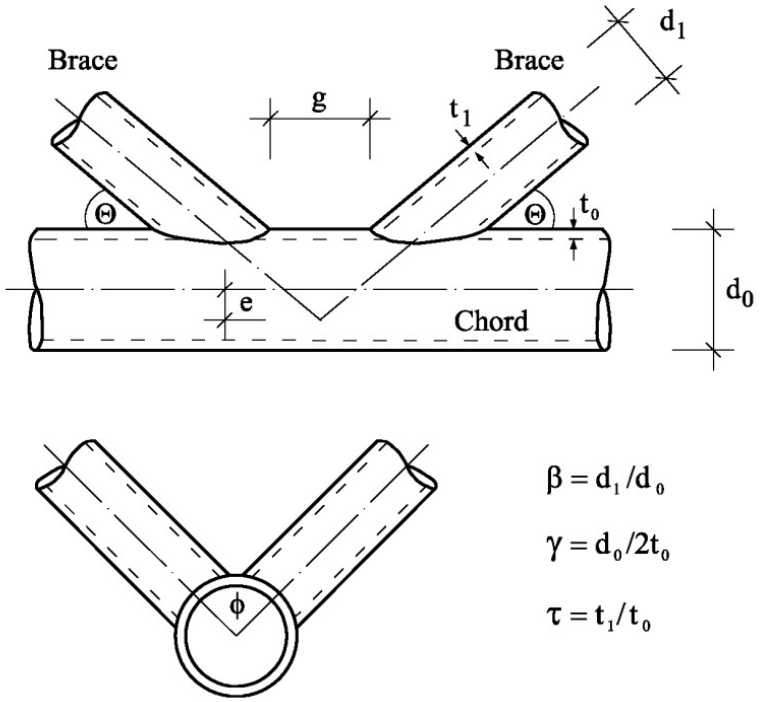


Figure 2: Typical multiplanar K-joint with notations.

The structural engineers experience and knowledge allied by the use newly developed materials and technologies have produced tubular steel and composite (steel-concrete) foot-bridges with daring structures. This fact have generated very slender tubular steel and composite (steel-concrete) pedestrian foot-bridges and consequently changed the serviceability and ultimate limit states associated to their design. A direct consequence of this design trend is a considerable increase of structural vibrations [3-12].

Considering all aspects mentioned before, the main objective of this investigation is to present the finite element modelling of the dynamic behaviour of tubular composite (steel-concrete) footbridges submitted to human walking vibration. Based on the results obtained in this study, a fatigue assessment will be performed, in order to evaluate the tubular footbridges service life. Further research in this area is currently being carried out.

The investigated structural model was based on a tubular composite (steel-concrete) foot-bridge, spanning 82.5 m. The structure is composed by three spans (32.5 m, 17.5 m and 20.0 m, respectively) and two overhangs (7.50 m and 5.0 m, respectively). The structural system consists of tubular steel sections and a concrete slab and is currently used for pedestrian crossing [6, 12].

The proposed computational model adopted the usual mesh refinement techniques present in finite element method simulations, based on the ANSYS program [13]. The finite element model has been developed and validated with the experimental results. This numerical model enabled a complete dynamic evaluation of the investigated tubular footbridge especially in terms of human comfort and its associated vibration serviceability limit states [6, 12].

This investigation is carried out based on correlations between the experimental results related to the footbridge dynamic response and those obtained with finite element models. The proposed computational model adopted the usual mesh refinement techniques present in finite element method simulations. The structural system dynamic response, in terms of peak accelerations, was obtained and compared to the limiting values proposed by several authors and design standards [8, 14].

The peak acceleration values found in the present investigation indicated that the analysed tubular footbridge presented problems related with human comfort. Hence it was detected that this type of structure can reach high vibration levels that can compromise the footbridge user's comfort and especially its safety.

2 HUMAN WALKING MODELLING

The present investigation was carried out based on a more realistic loading model developed to incorporate the dynamic effects induced by people walking on the footbridge. The loading model considered the ascent and descending movement of the human body effective mass at each step and the position of the dynamic load (human walking load) was also changed according to the individual position on the structure. This dynamic loading model considered a space and time variation of the human walking dynamic action over the footbridge. Additionally, also incorporates the transient effect due to the human heel impact, as presented in Equations (1) to (4) [11].

$$F(t) = \begin{cases} \left(\dfrac{f_{mi} F_m - P}{0.04 T_p}\right) t + P & if \;\; 0 \le t < 0.04 T_p \\ f_{mi} F_m \left[\dfrac{C_1 \left(t - 0.04 T_p\right)}{0.02 T_p} + 1\right] & if \;\; 0.04 T_p \le t < 0.06 T_p \\ F_m & if \;\; 0.06 T_p \le t < 0.15 T_p \\ P + \sum_{i=1}^{nh} P \alpha \, sen\left[2\pi i f_p \left(t + 0.1 T_p\right) + \phi_i\right] & if \;\; 0.15 T_p \le t < 0.90 T_p \\ 10\left(P - C_2\right)\left(\dfrac{t}{T_p} - 1\right) + P & if \;\; 0.90 T_p \le t < T_p \end{cases} \quad (1)$$

$$F_m = P\left(1 + \sum_{i=1}^{nh} \alpha_i\right) \quad (2)$$

$$C_1 = \left(\frac{1}{f_{mi}} - 1\right) \quad (3)$$

$$C_2 = \begin{cases} P\left(1 - \alpha_2\right) & if \; nh = 3 \\ P\left(1 - \alpha_2 + \alpha_4\right) & if \; nh = 4 \end{cases} \quad (4)$$

Where:

F_m : maximum Fourier series value, given by Equation (2);
f_{mi} : human heel impact factor;
T_p : step period;
f_s : step frequency;
Φ : harmonic phase angle;
P : person's weight;
α_i : dynamic coefficient for the harmonic force;
i : harmonic multiple (i = 1,2,3…,n);
t : time;
C_1 and C2 : coefficients given by Equations (3) and (4).

The proposed mathematical model used to represent the dynamical actions produced by people walking on the floor slabs is not simply a Fourier series, due to the fact that the mentioned equations also incorporate the human heel impact effect [10, 11]. The present investigation used a heel impact factor equal to 1.12 (f_{mi} = 1.12). However, it must be emphasized that this value can vary substantially from person-to-person [6, 10].

The pedestrian motion on the tubular footbridge was modelled based on the Equations (1) to (4) and four harmonics were used to generate the dynamic forces produced by human walking. Figure 3 illustrates the dynamic load function for an individual walking at a step frequency of 2.0 Hz (f_s = 2.0 Hz).

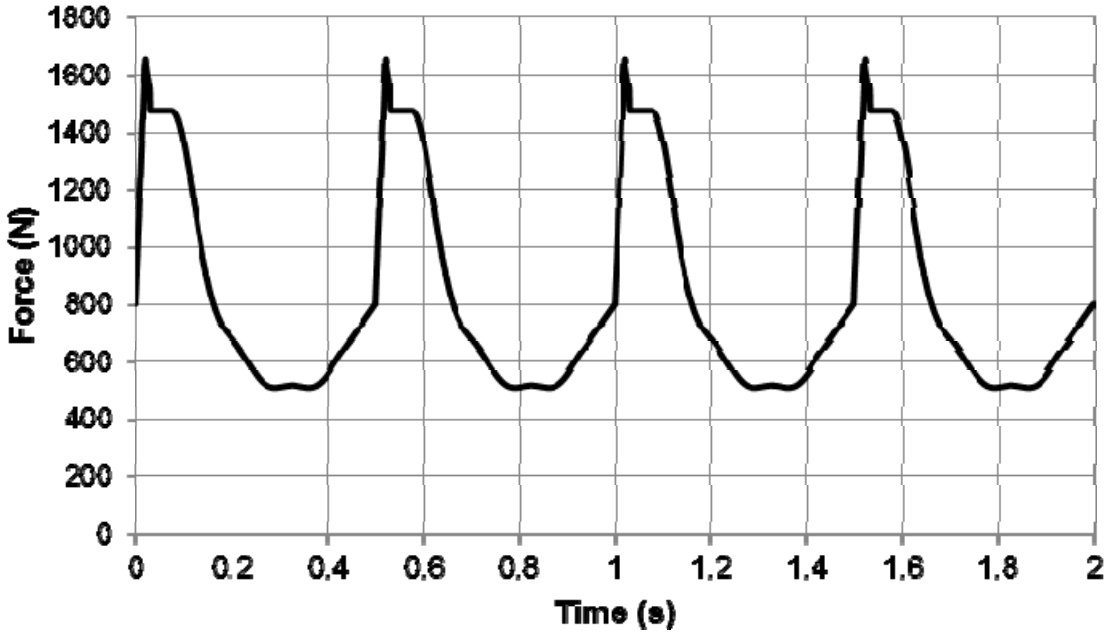


Figure 3: Dynamic load function for one person walking (f_s = 2.0 Hz). Resonant harmonic of the walking load (3rd harmonic: 3 x 2.0 Hz = 6.0 Hz).

Considering the investigated tubular footbridge, the third harmonic with step frequency equal to 2.0Hz (f_s = 2.0 Hz) was considered the resonant harmonic of the walking load (3 x 2.0 Hz = 6.0 Hz). In this situation, the finite element mesh has to be very refined and the contact time of application of the dynamic load over the structure depends of the step distance and step frequency, see Table 1.

The following strategy was adopted in this study: a step distance equal to 0.75 m corresponding to the third harmonic with a step frequency of 2.0 Hz was used, see Table 1. The step period is equal to $1/f_s$ = 1/2.0 Hz = 0.50 s, corresponding to a distance of 0.75 m. This way, the adopted strategy considered three forces to model one human step and each of the dynamic loads P1, P2 and P3 were applied to the steel-concrete tubular footbridge during 0.50/3 = 0.1667 s, corresponding to the contact time of each dynamic load.

Harmonic i	f_s	α_i	ϕ_i
1	1.6-2.2	0.50	0
2	3.2-4.4	0.20	$\pi/2$
3	4.8-6.6	0.10	π
4	6.4-8.8	0.05	$3\pi/2$

Table 1: Forcing frequencies (f_s), dynamic coefficients (α_i) and phase angles ϕ_i [4, 8].

However, the dynamic forces were not simultaneously applied. The load application begins with the first human step where the first load, P1 is applied for 0.1667 s, see Equations 1 to 4. At the end of this time period, the load P1 becomes zero while the load P2 is subsequently applied for 0.1667 s. The process continues with the application of the other load P3, based on the same procedure previously described, until the end of the first step. At this point, the load P3 from the first step is made equal to the load P1 of the second step. This numerical process continues with subsequent step applications until all dynamic loads are applied along the entire structure length.

3 INVESTIGATED STRUCTURAL MODEL

The structural model consists of tubular steel sections and a 100 mm concrete slab and is currently submitted to human walking loads. The structure was based on a steel-concrete tubular composite footbridge, spanning 82.5 m. The structure is composed by three spans (32.5 m, 17.5 m and 20.0 m, respectively) and two overhangs (7.50 m and 5.0 m, respectively), as illustrated in Figure 4.



Figure 4: Investigated structural model.

The steel sections used were welded wide flanges (WWF) made with a 300 MPa yield stress steel grade. A 2.05 x 10^5 MPa Young's modulus was adopted for the tubular footbridge steel beams and columns. The concrete slab has a 20 MPa specified compression strength and a 2.13 x 10^4 MPa Young's Modulus.

4 FINITE ELEMENT MODELLING

The developed finite element model adopted the usual mesh refinement techniques present in finite element method simulations, based on the ANSYS program [13]. The finite element model has been developed and validated with the experimental results [12]. This model enabled a complete dynamic evaluation of the investigated steel-concrete composite tubular footbridge, especially in terms of human comfort and its associated vibration serviceability limit states [6], as presented in Figure 5.

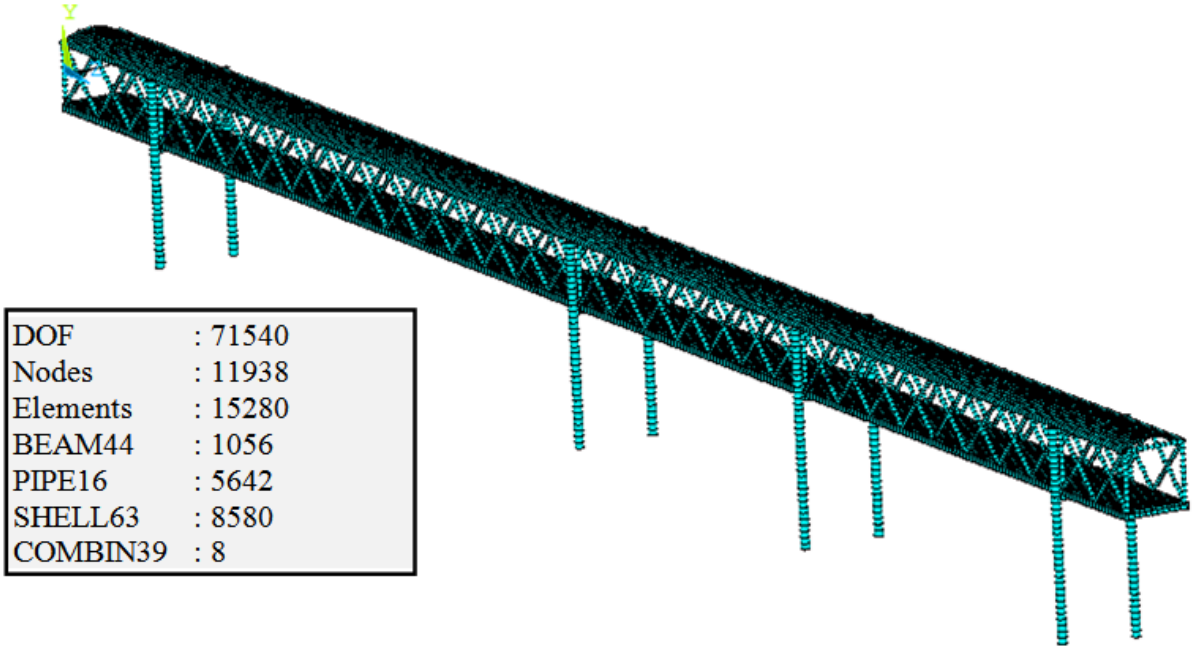


Figure 5: Tubular footbridge finite element model.

In this computational model, all steel tubular sections were represented by three-dimensional beam elements (PIPE16 and BEAM44) with tension, compression, torsion and bending capabilities. These elements have six degrees of freedom at each node: translations in the nodal x, y, and z directions and rotations about x, y, and z axes.

On the other hand, the reinforced concrete slab was represented by shell finite elements (SHELL63). This finite element has both bending and membrane capabilities. Both in-plane and normal loads are permitted. The element has six degrees of freedom at each node: translations in the nodal x, y, and z directions and rotations about the nodal x, y, and z axes.

The footbridge pier bearings were represented by a non-linear rotational spring element (COMBIN39). This element is a unidirectional element with nonlinear generalized force-deflection capability that can be used in any analysis.

The finite element model presented 71540 degrees of freedom, 11938 nodes and 15280 finite elements (BEAM44: 1056; PIPE16: 5642; SHELL63: 8580 and COMBIN39: 8), see Figure 5. It was considered that both structural elements (steel tubular sections and concrete slab) have total interaction with an elastic behaviour.

5 VIBRATION ANALYSIS

Initially, the tubular composite (steel-concrete) footbridge natural frequencies, vibration modes and peak accelerations were determined based on experimental tests [12]. The peak acceleration values were obtained considering three types of human walking: slow walking, regular walking and fast walking [12].

In a second phase, the tubular composite (steel-concrete) footbridge natural frequencies vibration modes and peak accelerations were determined with the aid of the numerical simulations, based on the finite element method using the ANSYS program [13].

It can be clearly noticed that there is a very good agreement between the structural model natural frequency values calculated using finite element simulations and the experimental results, see Table 2. Such fact validates the finite element model here presented, as well as the results and conclusions obtained throughout this investigation. The vibration modes of the tubular footbridge are depicted in Figures 6 to 8.

Natural frequencies (Hz)	f_{01}	f_{02}	f_{03}
Finite element modelling	1.61	2.12	5.39
Experimental results	1.56	2.34	5.08
Error (%)	3.20	9.40	6.10

Table 2: Tubular footbridge natural frequencies.

When the tubular footbridge freely vibrates in a particular mode, it moves up and down with a certain configuration or mode shape. Each footbridge natural frequency has an associated mode shape. It was verified that longitudinal amplitudes were predominant in the fundamental vibration mode (f_{01} = 1.61 Hz), see Figure 6. In the second mode shape lateral displacements were predominant (f_{02} = 2.12 Hz), see Figure 7. On the other hand, in the third vibration mode (f_{03} = 5.39 Hz), the flexural effects were predominant, see Figure 8.

The finite element modelling follows with the evaluation of the footbridge performance in terms of vibration serviceability due to dynamic forces induced by people walking. The first step of this investigation concerned in the determination of the tubular footbridge peak accelerations, based on a linear time-domain dynamic analysis.

The dynamic loading related to one person crossing the tubular footbridge on the concrete slab centre, as presented in Figure 3, was applied over 55.0 s and an integration time step of $2x10^{-3}$ s ($\Delta t = 2x10^{-3}$ s) was adopted in this investigation. The peak accelerations were obtained at seven sections of the analysed structural model, as presented in Figure 9. These maximum accelerations were compared to the limits recommended by design codes [8, 14].

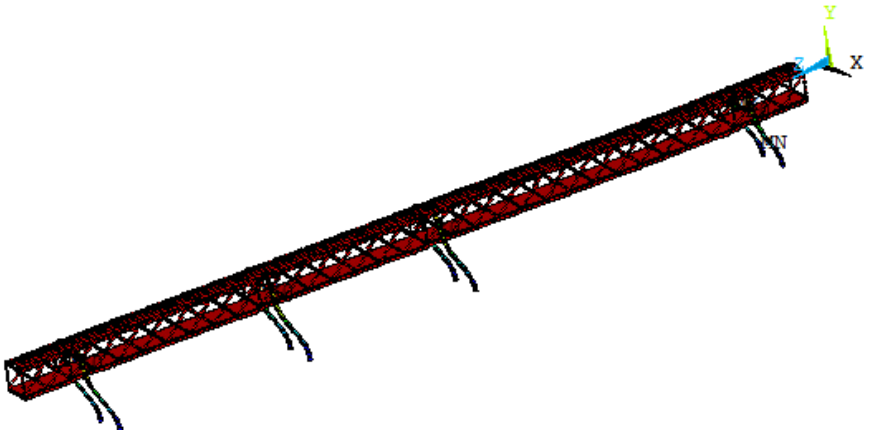


Figure 6. Vibration mode associated with the 1st footbridge natural frequency (f_{01}=1.61 Hz).

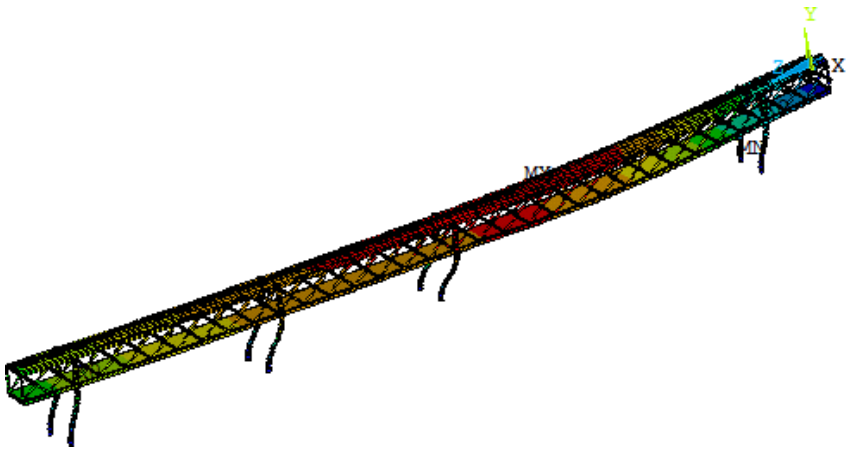


Figure 7. Vibration mode associated with the 2nd footbridge natural frequency (f_{02} = 2.12 Hz).

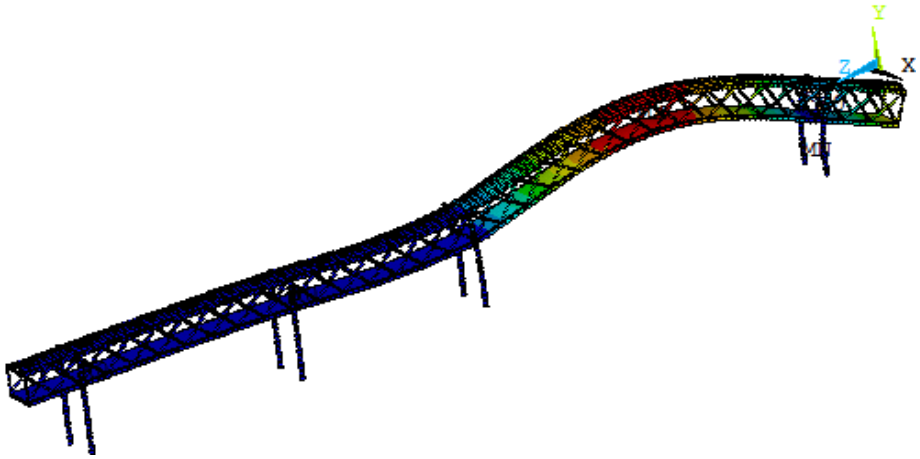


Figure 8. Vibration mode associated with the 3rd footbridge natural frequency (f_{03} = 5.39Hz).

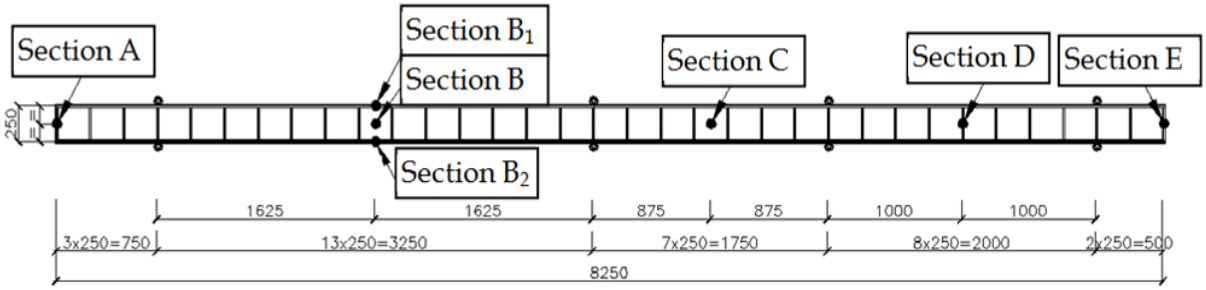


Figure 9. Tubular composite (steel-concrete) footbridge investigated sections.

In sequence, Figure 10 illustrates the tubular footbridge dynamic response, along the time, related to the section B (see Figure 9), when one pedestrian crosses the footbridge in regular walking (resonance condition).

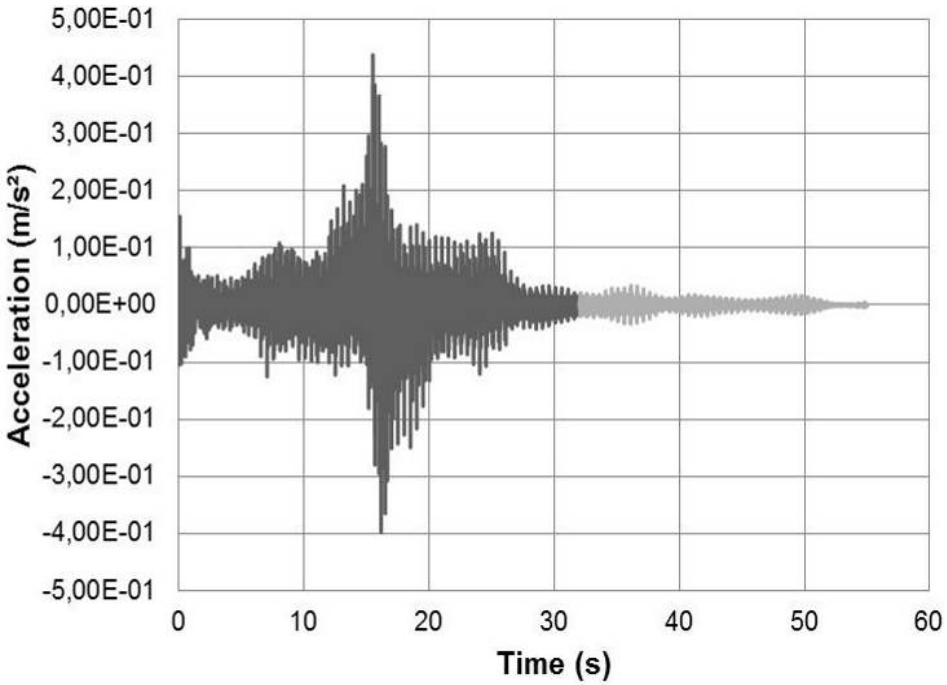


Figure 10. Tubular footbridge acceleration response at section B. One pedestrian crossing over the concrete slab centre at resonance. Regular walking.

Figure 10 presents the vertical acceleration versus time graph for the tubular footbridge at section B (see Figure 9). This figure shows that the vertical acceleration gradually increase with time. In this particular case, the third harmonic with a 2.0 Hz step frequency (f_s = 2.0 Hz), was the walking load resonant harmonic.

The maximum acceleration value found at section B (see Figure 9) was equal to 0.44 m/s^2. Figure 10 also indicates that from the moment that the pedestrian leaves the footbridge span (Section B, see Figure 9), when the time is approximately equal to 26 s, the structural damping minimizes the dynamic structural model response, as presented in Figure 10. This assertive occurs in dynamic loading models that consider the load spatial variation.

The peak acceleration analysis was focused in three types of human walking: slow walking, regular walking and fast walking. Table 3 presents the maximum accelerations (peak accelerations: a_p in m/s^2), related to seven sections of the investigated footbridge (A, B, B_1, B_2, C, D and E), as illustrated in Figure 9.

Tubular footbridge peak accelerations (a_p in m/s^2)							
S	slow walking						
R	regular walking						
F	fast walking						
Walking	A	B_1	B	B_2	C	D	E
S	1.15	0.22	0.57	0.22	0.67	0.54	0.94
R	1.00	0.16	0.44	0.16	0.38	0.33	0.78
F	**1.41**	0.18	**0.62**	0.18	**0.75**	**0.54**	**1.58**
*a_{lim} = 1.5%g = 0.15 m/s^2: indoor footbridges							
*a_{lim} = 5.0%g = 0.49 m/s^2: outdoor footbridges							

Table 3: Structural model peak accelerations corresponding to individual walking.

The maximum acceleration values (peak accelerations) are respectively equal to 1.41 m/s^2 (Section A), 0.62 m/s^2 (Section B), 0.75 m/s^2 (Section C), 0.54 m/s^2 (Section D) and 1.58 m/s^2 (Section E), see Table 3. These peak accelerations presented in Table 7 are related to a pedestrian fast walking situation. It must be emphasized that the limit acceleration value is equal to 0.49 m/s^2, when outdoor footbridges are considered in the analysis [8, 14].

Based on the finite element modelling of the tubular composite (steel-concrete) footbridge dynamic behaviour, the numerical results presented in Table 3 indicated that the dynamic actions produced by human walking led to peak accelerations higher than the limiting values present in design code recommendations (Outdoor footbridges: 5%g = 0.49 m/s²), [8, 14], as depicted in Table 3.

6 CONCLUSIONS

This contribution covers the application of tubular structural elements in pedestrian footbridge design and tries to give an overview about the evaluation of steel-concrete composite tubular footbridges dynamic behaviour, objectifying to help practical structural engineers to deal with this kind of problem and to allow for a further application of tubular structural elements in pedestrian footbridge design.

The present study was carried out based on a more realistic loading model developed to incorporate the dynamic effects induced by people walking. The loading model considered the ascent and descending movement of the human body effective mass at each step and the position of the dynamic load (human walking load) was also changed ac-cording to the individual position. Additionally, also incorporates the transient effect due to the human heel impact.

The proposed analysis methodology considered the investigation of the dynamic behaviour, in terms of serviceability limit states, of a tubular composite (steel-concrete) footbridge, spanning 82.5 m. The structure is composed by three spans (32.5 m, 17.5 m and 20.0 m, respectively) and two overhangs (7.50 m and 5.0 m, respectively). The structural system consists of tubular steel sections and a concrete slab and is currently used for pedestrian crossing.

A computational model, based on the finite element method, was developed using the ANSYS program. This model enabled a complete dynamic evaluation of the investigated tubular footbridge especially in terms of human comfort and its associated vibration serviceability limit states.

The results found throughout this investigation have indicated that the dynamic actions produced by human walking could generate peak accelerations that surpass design criteria limits developed for ensuring human comfort. Hence it was detected that this type of structure can reach high vibration levels that can compromise the footbridge user's comfort and especially its safety.

The analysis methodology presented in this paper is completely general and is the author's intention to use this solution strategy on other pedestrian footbridge types and to investigate the fatigue problem. The fatigue problem is a relevant issue and certainly much more complicated and is influenced by several design parameters and footbridge types. Further research in this area is currently being carried out.

7 ACKNOWLEDGEMENTS

The authors gratefully acknowledge the financial support for this work provided by the Brazilian Science Foundation's CAPES, CNPq and FAPERJ.

REFERENCES

[1] Eurocode 3: *Design of steel structures. Part 1.9: General rule - Fatigue.* European Committee for Standardisation, 2005.

[2] Kuhlmann, U., H.-P. Günther, Saul, R., Häderle, M.-U. *Welded circular hollow section (CHS) joints in bridges.* ISTS 2003: Proceedings of the 10th International Symposium on Tubular Structures, Madrid, Spain, 2003.

[3] Leitão, F.N., Silva, J.G.S. da, Vellasco, P.C.G. da S., Lima, L.R.O. de, Andrade, S.A.L. de. *Composite (steel-concrete) highway fatigue assessment.* Journal of Constructional Steel Research, 67(1): 14-24, 2011.

[4] Bachmann, H. & Ammann, W. *Vibrations in structures induced by man and machines,* Structural Engineering Document 3e, International Association for Bridges and Structural Engineering, 1987.

[5] Chen, Y. *Finite element analysis for walking vibration problems for composite precast building floors using ADINA: modelling, simulation and comparison.* Computer & Structures, 72:109-126, 1999

[6] Debona, G.L. *Modelagem do comportamento dinâmico de passarelas tubulares em aço e mistas (aço-concreto) (Modelling of the dynamic behaviour of composite (steel-concrete) tubular footbridges),* MSc Dissertation (in Portuguese), Civil Engineering Post-Graduate Programme, PGECIV, State University of Rio de Janeiro, UERJ, Rio de Janeiro, Brazil, pp. 1-152, 2011.

[7] Figueiredo, F.P., Silva, J.G.S. da, Vellasco, P.C.G. da S., Lima, L.R.O. de, Andrade, S.A.L. de. *A parametric study of composite footbridges under pedestrian walking loads.* Engineering Structures, 30: 605-615, 2008.

[8] Murray, T.M., Allen, D.E., Ungar, E.E. *Floor vibrations due to human activity,* Steel Design Guide Series, American Institute of Steel Construction, AISC, Chicago, USA, 2003.

[9] Pimentel, R.L., Pavic, A., Waldron, P. *Evaluation of design requirements for footbridges excited by vertical forces from walking.* Canadian Journal of Civil Engineering, Vol. 28(5), 769-776, 2001.

[10] Silva, J.G.S. da, Vellasco, P.C.G. da S., Andrade, S.A.L. de, Lima, L.R.O. de, Figueiredo, F.P. *Vibration analysis of footbridges due to vertical human loads.* Computers & Structures, 85: 1693-1703, 2007.

[11] Varela, W.D. *Modelo teórico-experimental para análises de vibrações induzidas por pessoas caminhando sobre lajes de edifícios (Theoretical-experimental model to analyse vibrations induced by people walking on floor slabs of buildings)*, PhD Thesis (in Portuguese), Federal University of Rio de Janeiro, Civil Engineering Department, COPPE/UFRJ, Rio de Janeiro, Brazil, pp. 1-309, 2004.

[12] Zúñiga, J. E. V. *Análise da resposta dinâmica experimental de uma passarela tubular mista, aço-concreto, submetida ao caminhar humano (Dynamic experimental analysis of a composite (steel-concrete) tubular footbridge submitted to human walking)*, MSc Dissertation (in Portuguese), Civil Engineering Post-Graduate Programme, PGECIV, State University of Rio de Janeiro, UERJ, Rio de Janeiro, Brazil, pp. 1-135, 2011.

[13] ANSYS. *Swanson Analysis Systems*, Inc. P.O. Box 65, Johnson Road, Houston, PA, 15342-0065, Version 10.0, Basic analysis procedures, Second edition, 2003.

[14] International Standard Organization / ISO 2631-2. 1989. *Evaluation of human exposure to whole-body vibration, Part 2: Human Exposure to Continuous and Shock-Induced Vibrations in Buildings (1 to 80Hz)*, International Standard.

COMPDYN 2013
4th ECCOMAS Thematic Conference on
Computational Methods in Structural Dynamics and Earthquake Engineering
M. Papadrakakis, V. Papadopoulos, V. Plevris (eds.)
Kos Island, Greece, 12–14 June 2013

QUANTIFICATION OF THE STRUCTURAL RESPONSE OF A STAIRCASE DAMPED BY THE PRESENCE OF PEOPLE: NUMERICAL MODEL AND EXPERIMENTAL TESTS

A. Cappellini[1], **S. Manzoni**[1], **M. Vanali**[2]

[1] Dipartimento di Meccanica, Politecnico di Milano
Via La Masa, 1 20156 Milano Italy
anna.cappellini@mail.polimi.it
stefano.manzoni@polimi.it

[2] Università degli Studi di Parma
Parco Area delle Scienze, 181/A, 43124 PARMA Italy
marcello.vanali@unipr.it

Keywords: Human-Structure interaction, modal analysis, damping, serviceability.

Abstract. *People acting on a structure such as a footbridge or a staircase are a source of excitation but can also affect the dynamic behavior of the structure they occupy. Particularly, considerable damping ratio value changes are often experienced. If this phenomenon occurs, considering the dynamic properties of the structure when empty for estimating the structural response can lead to significant overestimation of the amplitudes of vibration.*
In this paper this problem is faced considering the case of a lightly damped steel staircase. The structure was tested with and without the presence of people. A model, able to describe people effect on a structure, is used to predict the changes of the modal properties due to the presence of people. It is finally proposed a comparison between the amplitudes of vibration measured experimentally and those predicted starting from the model of the structure when empty and the model of the structure with people respectively. Results highlight how the correctly estimated damping values leads to a significant increase in the overall in service vibration level prediction accuracy.

1 INTRODUCTION

People acting on a pedestrian structure, such as a footbridge or a staircase, behave as dynamical systems capable of modifying the dynamics of the structure itself as well as of introducing a load. At present, however, the knowledge of this phenomenon, known as Human Structure Interaction (HSI), is still limited. Therefore, although the experimental evidence suggests that appropriate dynamic models of human occupants should be used in order to obtain an accurate description of human-structure interaction [1], at the design stage, it is common practice to consider people interacting with a structure as a source of force only [2], [3], [4]. This approach, however, may lead to an erroneous estimation of the vibration levels at the design stage as evidenced in some striking cases, such as the Millennium Bridge [5]. This work focuses on the analysis of vertical vibrations of a slender structure. As regards vertical vibrations, the experimental evidence suggests that people interacting on a structure are a source of added damping [6], [7], [8]. If considerable damping ratio value changes are experienced, considering the dynamic properties of the structure when empty for estimating the structural response can lead to significant overestimation of the amplitudes of vibration. To the purpose of obtaining an accurate prediction of the structural response, a model capable of accounting for the phenomenon of HSI is used. This model [9] was proved to be effective to predict the effect of passive people on the modal properties of a slender structure. In Section 2 the model and a possible extension to the case of moving people are presented. To the purpose of a first verification of the possibility of extending the proposed model to the case of moving people, the simple case of a subject marching on a defined point of the structure is considered. In Section 3 the experimental tests performed to verify the effectiveness of the model are presented. A comparison between the test results and the prediction obtained with the model are reported in Section 4. The performed tests allowed to show the suitability of the proposed model and to show how to treat people as a source of forcing only can lead to significant errors in the estimation of the structural response.

2 NUMERICAL MODEL

To obtain an accurate prediction of the structural response, a method to account for the phenomenon of HSI is proposed. This method is based on a model [9] that was proved to be effective to predict the effect of passive people on the modal properties of a slender structure. Using the method proposed in [9], starting from the transfer functions of the empty structure and introducing each passive subject separately, it is possible to obtain the transfer functions of the Human+Structure system with high accuracy. The model is rigorous for the case of passive people. For the case of moving people, experimental evidence suggested that their action could be modeled through a set of static positions, as explained in the next section. Therefore, the proposed method to extend the static model proposed in [9] to the case of moving people consists in a two steps approach:

1. obtaining an equivalent static model capable of accounting for the average effect of moving people
2. introducing, on the modified model, the load induced by people on the structure.

This approach allows obtaining an approximate description of the HSI phenomenon that can provide useful information on the behaviour of the Human+Structure system.

In this section the method used to extend the results to the case of moving people is presented while the fundamentals of the model proposed in [9] are recalled.

2.1 Equivalent dynamic model for a moving subject

In the proposed approach each subject is introduced on the empty structure through a bio-mechanical model. In particular, subjects were modelled with their so called apparent mass. To this purpose the work of Mastumoto and Griffin [10], who proposed mathematical models to represent the dynamic behaviour of standing subjects, was employed.

In their work the authors proposed the results of several tests conducted with different subjects in different postures. In particular, tests on 12 subjects were performed and the experimental data were fitted using lumped parameter models. The model considered in this work is 2 degrees of freedom and is referred to as model 2a in [10]. Figure 1 shows the model used in this study, while the corresponding analytical expression of the apparent mass is reported in Equation (1).

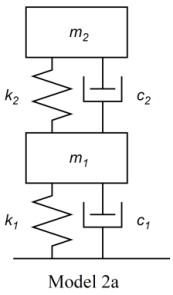


Figure 1: Mechanical model (2a) of a standing person proposed by Matsumoto and Griffin

$$M_{2a}(\omega) = \frac{(ic_1\omega + k_1)\{m_1(-m_2\omega^2 + ic_2\omega + k_2) + m_2(ic_2\omega + k_2)\}}{\{-m_1\omega^2 + i(c_1 + c_2) + (k_1 + k_2)\}(-m_2\omega^2 + ic_2\omega + k_2) - (ic_2\omega + k_2)^2} \quad (1)$$

The authors propose the optimized model parameters (m_1, m_2, c_1, c_2, k_1, $k_{2)}$ obtained using the mean normalized apparent mass ($m_{2a}=M_{2a}/m$, where m is the static weight of the subject) of 12 male subjects involved in the tests. Different postures (standing, one leg, bent legs) were investigated.

In this work the case of a subject marching on a fixed point of the structure was considered. Experimental tests were performed to get information on the posture of some subjects while performing this action. If T is the time elapsing between two touches on the ground of the same foot (1 cycle), a subject, during 1 cycle, was seen to stand on two legs for a time of about 5-15% of T and on one leg (left or right) for the remaining time.

Therefore, in order to get en equivalent model of a marching subject, the apparent masses proposed by Matsumoto and Griffin for the cases of standing and on one leg subjects were considered.

Figure 2 shows the mean normalized apparent mass of standing and on one leg subjects according to model 2a while the corresponding parameters are reported in Table 1.

	Stiffness (Nm-1kg-1)		Damping (Nsm-1kg-1)		Mass (no unit)	
Case	k1	k2	c1	c2	m1	m2
Model 2a (standing)	4.39·103	5.53·102	3.71·101	1.18·101	5.74·10-1	3.94·10-1
Model 2a (one leg)	6.66·102	6.07·102	2.90·101	8.81·100	5.13·10-1	4.22·10-1

Table 1: Modal parameters for the mean normalized apparent mass of standing subjects

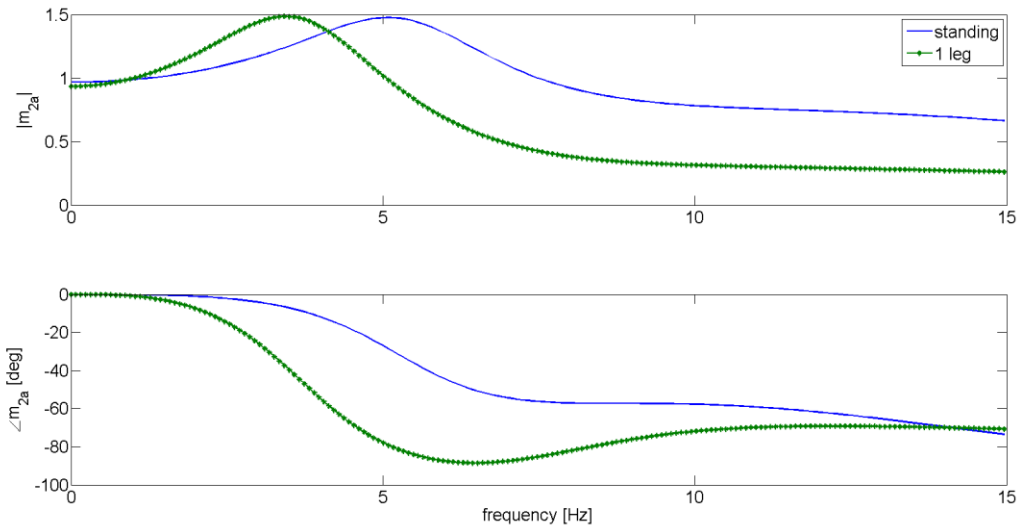


Figure 2: Mean normalized apparent mass, model 2a

The equivalent apparent mass for a marching subject was then obtained as in Equation (2).

$$m_{2a(marching)} = 0.1 \cdot m_{2a(standing)} + 0.9 \cdot m_{2a(one\ leg)} \quad (2)$$

The so determined apparent mass was used to assess the equivalent effect of a subject marching on a fixed point of the structure.

2.2 Model of the Human-Structure system

The model to account for the presence of people relies on a modal model of the empty structure. The model proposed in [9] was employed. This model is based on the approach proposed by Krenk [11]. The same model was then used to introduce people. One of the advantages of this model is the possibility to introduce each person individually.

The model starts from the frequency response function $\mathbf{G}(\omega)$ of the empty structure, expressed in Equation (3)

$$\mathbf{G}(\omega) = \sum_{\mathbf{j=1}}^{\mathbf{n}} \frac{\boldsymbol{\phi}_\mathbf{j}\boldsymbol{\phi}_\mathbf{j}^\mathbf{T}}{\omega_j^2 - \omega^2 + 2j\zeta_j\omega\omega_j} \quad (3)$$

where $\boldsymbol{\phi}_\mathbf{j}$ is the jth unit modal mass scaled mode shape vector, ω_j is the natural frequency of the jth mode and ζ_j is the jth non-dimensional damping ratio. The dynamic behaviour of the structure is expressed as in Equation (4)

$$\mathbf{x}(\boldsymbol{\omega}) = \mathbf{G}(\omega)\mathbf{f}(\omega) \quad (4)$$

being $\mathbf{x}(\omega)$ the displacement vector and $\mathbf{f}(\omega)$ the generic force vector

As detailed in [9], the force exerted by each static person is modelled through its apparent mass, as in Equation (5)

$$\boldsymbol{f_i^{Human}}(\omega) = -\boldsymbol{M_{2a}}(\omega)\boldsymbol{\omega^2}\boldsymbol{x_i}(\omega) = \boldsymbol{H}(\omega)\boldsymbol{x_i}(\omega) \quad (5)$$

The model allows then to obtain an estimate of the frequency response function of the subjects+structure system, as expressed in Equation (6), (7) and (8)

$$\mathbf{G^{-1}}(\omega)\mathbf{x}(\omega) = \mathbf{f}(\omega) - \mathbf{f^{Human}}(\omega) = \mathbf{f}(\omega) - \mathbf{WH}(\omega)\mathbf{W^T}\mathbf{x} \quad (6)$$

$$\mathbf{G_H}(\omega) = [\mathbf{G}(\omega)^{-1} + \mathbf{WH}(\omega)\mathbf{W^T}]^{-1} \quad (7)$$

$$\mathbf{G_H}(\omega)^{-1}\mathbf{x}(\omega) = \mathbf{f}(\omega) \quad (8)$$

where $\mathbf{W} = [\mathbf{w_1}, \dots, \mathbf{w_m}]$ represents the connection of m elements, **H** is the (diagonal) transfer function matrix, containing the mechanical impedance of all the subjects, and $\mathbf{G_H}$ represents the new transfer function of the people-structure system.

The new frequency response function can be expressed explicitly in terms of the frequency response function $\mathbf{G}(\omega)$ by the Woodbury matrix identity.

$$(\mathbf{A} + \mathbf{UCV})^{-1} = \mathbf{A^{-1}} - \mathbf{A^{-1}U}(\mathbf{C^{-1}} + \mathbf{VA^{-1}U})^{-1}\mathbf{VA^{-1}} \quad (9)$$

as

$$\begin{aligned}\mathbf{G_H}(\omega) &= [\mathbf{G}(\omega)^{-1} + \mathbf{WH}(\omega)\mathbf{W^T}]^{-1} \\ &= \mathbf{G}(\omega) - \mathbf{G}(\omega)\mathbf{W}(\mathbf{H}(\omega)^{-1} + \mathbf{W^T}\mathbf{G}(\omega)\mathbf{W})^{-1}\mathbf{W^T}\mathbf{G}(\omega)\end{aligned} \quad (10)$$

This simple equation allows calculating the transfer function of the new human+structure system. This model allows evaluating the local effect due to the presence of each subject separately. This effect is a function of the subject characteristics, posture and the point where the subject is located (i.e. mode shape components relating to that point). In the next section the tests performed to verify the effectiveness of the proposed model are presented.

3 EXPERIMENTAL TESTS

A slender staircase was used to verify the effectiveness of the proposed model. The staircase was instrumented with 12 accelerometers in the vertical direction. At first an experimental modal analysis was performed. To this purpose an electrodynamic shaker was used to force the staircase in order to obtain a modal model of the empty structure. Once estimated the experimental FRFs of the empty structure, a dynamometric plate was added in order to measure the force induced by one subject in a fixed point. Figure 3 shows the considered staircase and a scheme of the used sensors.

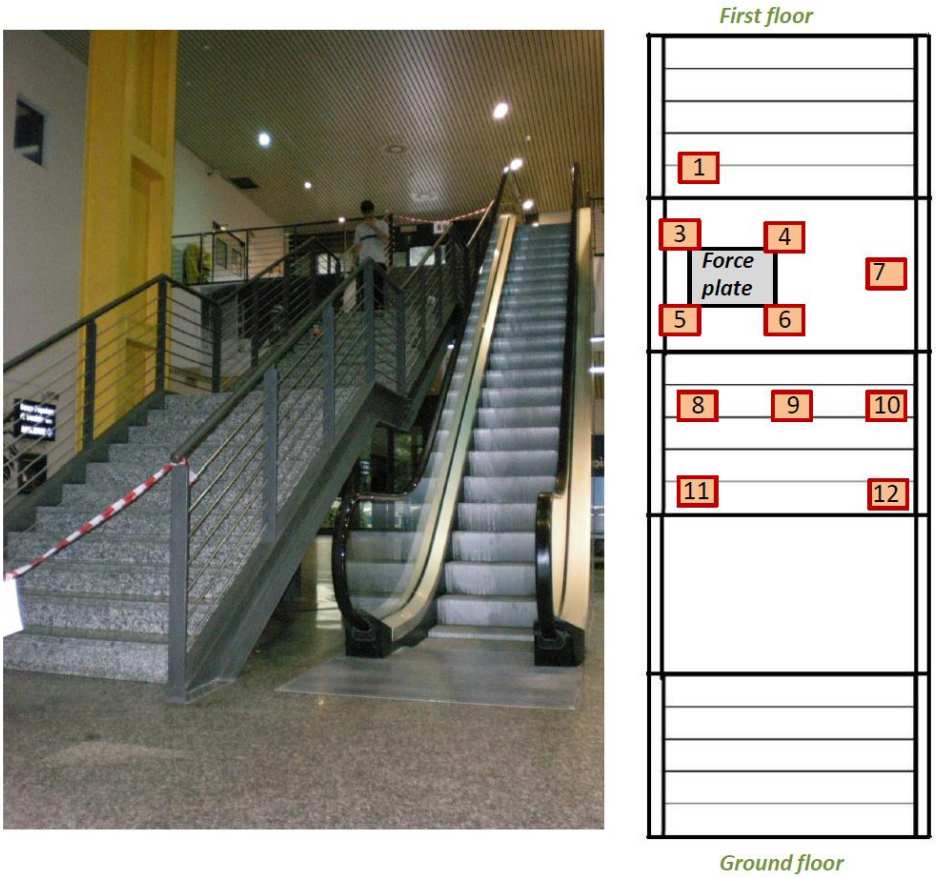


Figure 3: Structure under test and experimental setup

The considered structure has two dominant modes around 8 Hz and 9 Hz. The modes at a higher frequency, being little forced by human walking, are not considered in this study.

Figure 4 shows an example of FRF of the empty structure while Table 2 shows the associated modal parameters.

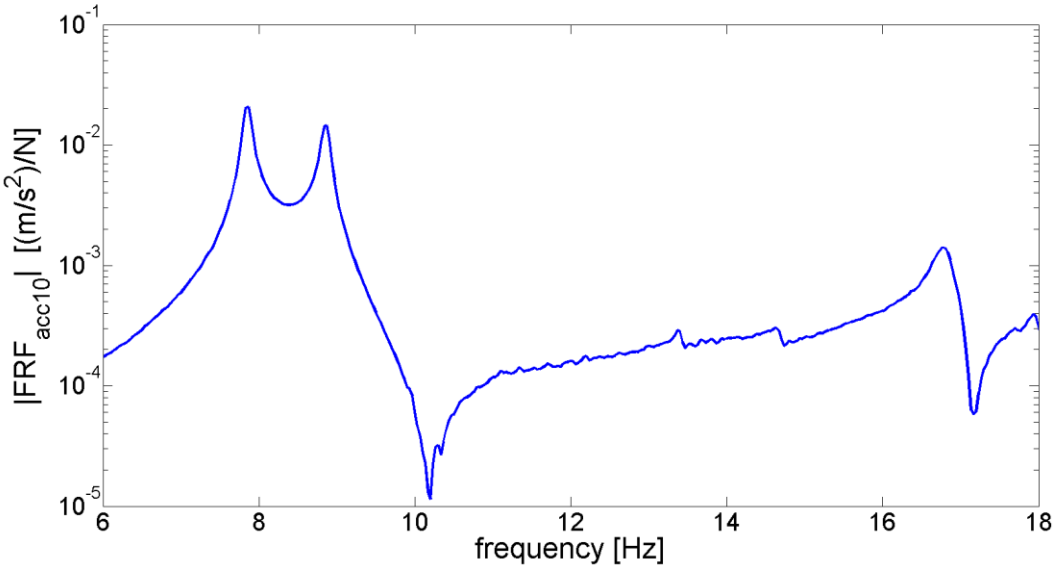


Figure 4: Experimental FRF – accelerometer 10

f_n [Hz]	ζ [%]
7.85	0.48
8.86	0.50

Table 2: Modal parameters of the empty staircase

Once obtained a modal model of the empty staircase, the structure was tested in different conditions. In particular two different kinds of tests were performed:

1. A single subject marching on the force plate
2. A subject marching on the force plate plus an additional subject standing on a different point of the structure

The second case was chosen to increase the damping introduced by people on the structure

For what concern the type of forcing, two cases were considered:

1. Subject free to march at his own frequency
2. Subject forced to march at a frequency of 1.95 Hz

The last frequency was chosen to concentrate the introduced energy in correspondence of the first natural frequencies of the structure. The fourth harmonic of the forcing thus introduced indeed falls in the vicinity of the first resonance peak

In the following section the experimental results of two tests, one corresponding to case 1 and one corresponding to case 2, are reported. In addition a comparison among these results and those obtained starting from the model of the empty structure and the model of the human+structure system are presented. For the last two cases the accelerations were obtained using the transfer functions of the empty structure $G(\omega)$ and of the Human+ Structure system $\mathbf{G_H}(\omega)$**,** as in Equation (4) and (8), and the force $f(\omega)$ introduced by the subject marching on the force plate.

4 EXPERIMENTAL AND NUMERICAL RESULTS

In this section the results of two significant tests are proposed. In the first test one subject was asked to march at his own frequency on the force plate. This condition is more disadvantageous for our purposes since the damping introduced by a single subject is not very high and an average model was used to model the human body. The modal parameters predicted for the case of a single subject (75 kg) marching on the force plate are reported in Table 3.

f_n [Hz]	ζ [%]
7.84	0.95
8.85	0.85

Table 3: Modal parameters predicted with 1 subject marching on the force plate (test 1)

Figure 5 shows, for the case of test 1, accelerometer 10, a comparison among the power-spectrum of the measured acceleration and the power-spectrum of the acceleration predicted using the force measured with the dynamometric plate (power spectrum in Figure 6) and the

model of the empty structure and subject+structure respectively. As shown in Figure 6 and Figure 5**,** the force induced by the subject on the structure is capable of introducing energy at the first two resonances of the structure. The RMSs of all the accelerations in a frequency band of 0-10 Hz are reported in Table 4 with the corresponding relative errors estimated as in Eq. (11) and Eq. (12).

$$\boldsymbol{Error\ \%\ empty} = \frac{(\boldsymbol{RMS\ empty}) - (\boldsymbol{RMS\ experimental})}{(\boldsymbol{RMS\ experimental})} \quad (11)$$

$$\boldsymbol{Error\ \%\ H+S} = \frac{(\boldsymbol{RMS\ H+S}) - (\boldsymbol{RMS\ experimental})}{(\boldsymbol{RMS\ experimental})} \quad (12)$$

where (RMS empty) is the RMS of the acceleration estimated using the model of the empty structure, (RMS H+S) is the RMS of the acceleration estimated using the model of the Human+Structure system and (RMS experimental) is the RMS of the measure acceleration.

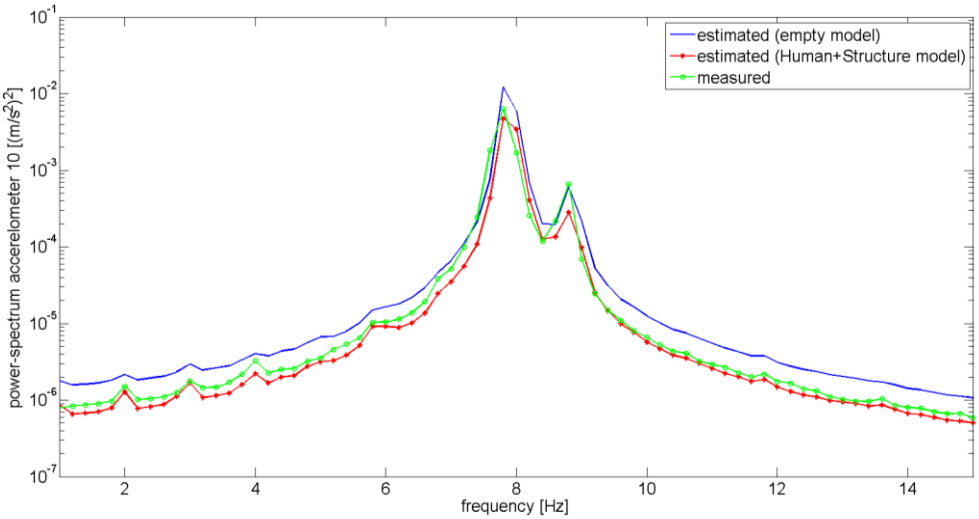


Figure 5: Test 1 – power-spectrum accelerometer 10

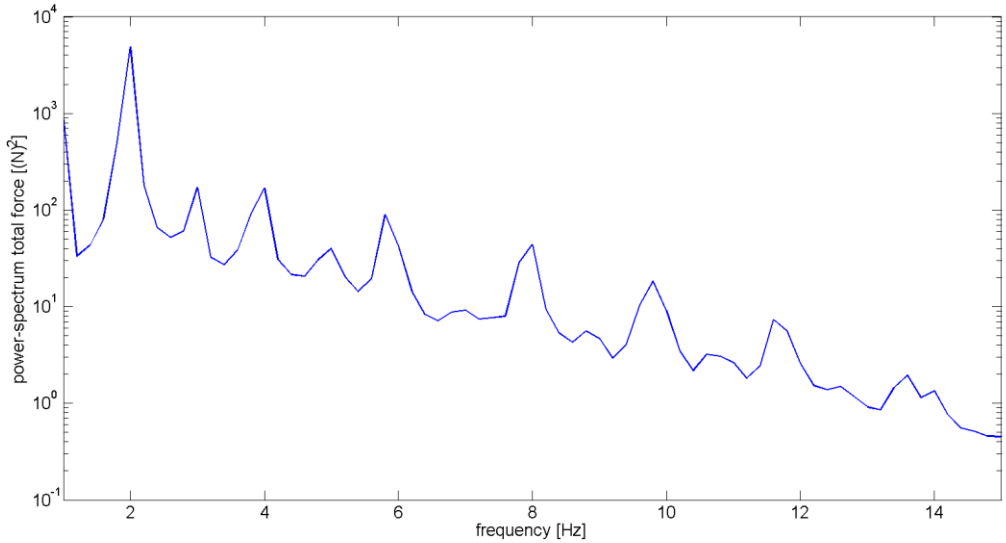


Figure 6: Test 2 – power-spectrum total force

	A1	**A2**	**A3**	**A4**	**A5**	**A6**	**A7**	**A8**	**A9**	**A10**	**A11**	**A12**
RMS meas (m/s^2)	0.065	0.091	0.075	0.078	0.077	0.081	0.112	0.0790	0.084	0.109	0.057	0.081
RMS empty (m/s^2)	0.087	0.125	0.101	0.111	0.105	0.117	0.153	0.105	0.120	0.147	0.074	0.108
Error % Empty	35.1	37.2	34.9	42.6	36.7	43.5	35.9	33.4	43.1	35.4	29.0	33.3
RMS H+S (m/s^2)	0.061	0.085	0.070	0.075	0.073	0.080	0.104	0.074	0.081	0.100	0.0520	0.074
Error % H+S	-6.1	-6.7	-6.4	-2.9	-5.1	-2.2	-7.5	-6.7	-2.7	-7.8	-8.9	-9.1

Table 4: Test 1 – RMS and relative errors

As might be expected, the use of the model of the empty structure led to an overestimation of the results. In this particular case, using a model of the subject+structure a light underestimation of the results was obtained. The agreement between the experimental data and the predicted is, however, much better in the latter case.

In the second test a subject was asked to march at a frequency of 1.95 Hz on the force plate while another subject was standing still in correspondence of point 9. This condition is more advantageous for the purpose since the damping introduced in this case is much higher, as reported in Table 5.

f_n [Hz]	ζ [%]
7.77	2.34
8.84	0.90

Table 5: Modal parameters predicted with 1 subject marching on the force plate + 1 subject in point 9 (test2)

Figure 7 and Table 6 show the results obtained for the case of test 2.

In this case the results obtained using the model of the empty structure greatly overestimate the structural response while there is a very good agreement between the experimental results and those predicted with the model of the human+structure system.

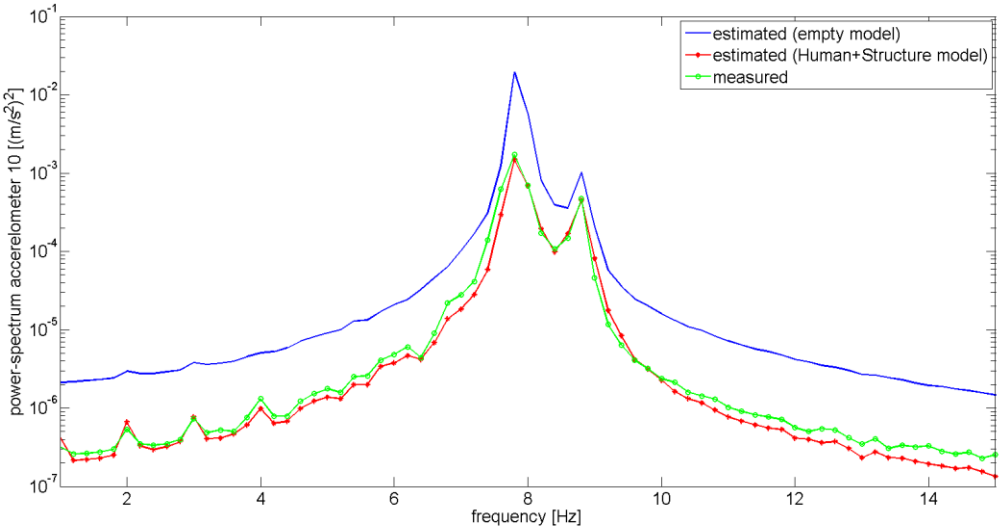


Figure 7: Test 2 – power-spectrum accelerometer 10

	A1	A2	A3	A4	A5	A6	A7	A8	A9	A10	A11	A12
RMS meas (m/s^2)	0.043	0.054	0.049	0.045	0.051	0.047	0.067	0.055	0.048	0.066	0.041	0.050
RMS empty (m/s^2)	0.105	0.148	0.121	0.132	0.127	0.140	0.181	0.127	0.143	0.174	0.088	0.128
Error % empty	145.4	174.5	147.9	194.1	148.0	194.6	169.4	132.0	195.0	165.6	115.4	155.4
RMS H+S (m/s^2)	0.044	0.050	0.049	0.044	0.052	0.046	0.062	0.056	0.046	0.060	0.043	0.046
Error % H+S	1.9	-7.5	1.1	-2.9	2.9	-2.3	-8.0	3.2	-5.0	-8.9	4.6	-7.5

Table 6: Test 2 – RMS and relative errors

In addition, another important consideration regards the mode shapes of the considered structure. The empty structure has nearly real mode shapes. Due to people presence the mode shapes become increasingly complex. In the case of just one or two people on the structure the complexity of the mode shapes is still low and so, in this particular case, the use of real or complex mode shapes to simulate the structural response leads to similar results. With an increasing number of people acting on the structure these differences could become important. Therefore all the modifications in the dynamic properties should be considered when predicting the response of a structure occupied by people.

5 CONCLUSIONS

This work aimed at presenting the results of a model capable of accounting for the effect of people on the modal properties of a structure they are interacting with. The idea behind this model is that of finding and equivalent model capable of accounting for the effects of moving people in terms of changing of modal parameters. Starting from the transfer functions of the empty structure, a new set of transfer functions accounting for people is obtained. The load induced by people on the structure is then introduced on this modified model. To the purpose of verifying the effectiveness of the proposed approach, a slender staircase was used. Tests were performed by asking a subject to march on a fixed point and measuring the corresponding load on the structure and the structural response. The experimental results, in terms of amplitudes of vibration of the structure, were compared with those obtained starting from the measured force and using the model of the empty structure and the model of the subjects+structure respectively. In all the considered cases the use of the model of the empty structure to simulate the structural response caused an overestimation of the amplitudes of vibration, while using the proposed model the results were always compatible with the experimental ones. The results are even more satisfactory since people were introduced using average model and the tests involved a maximum of two subjects on the structure.

The proposed approach was verified for the case of subjects marching on a fixed point. The performed tests were useful to verify the possibility of applying the proposed model but require additional development in order to be used in practice. Further work aims at extending the proposed model to the case of people walking freely on a generic structure.

REFERENCES

[1] R. Sachse, A. Pavic, P. Reynolds, Human-structure dynamic interaction in civil engineering dynamics: A literature review, Shock and Vibration Digest, Vol. 35, No. 1, pp. 3-18, January 2003
[2] EN 1990 - Eurocode, Basis of structural design, 2002.
[3] International Organization for Standardization ISO 10137, Bases for design of structures - Serviceability of buildings and walkways against vibration, 2007
[4] Sètra, Technical Guide - Assessment of vibrational behaviour of footbridges under pedestrian loading, Service d'Etudes techniques des routes et autoroutes, Paris, 2006
[5] P. Dallard, T. Fitzpatrick, A. Flint, A. Low, R. R. Smith, M. Willford, M. Roche, London Millennium bridge: Pedestrian-induced lateral vibration, Journal of Bridge Engineering, v 6, n 6, p 412-417, November/December 2001
[6] J.M.W. Brownjohn, Energy dissipation from vibrating floor slabs due to human-structure interaction, Shock and Vibration 8(6): 315-23, 2001.
[7] J.M.W. Brownjohn, X. Zheng, The effects of human postures on energy dissipation from vibrating floors, in Chau, F.S. and Quan, C. (eds). Second International Conference on Experimental Mechanics. Proceedings of SPIE, Vol. 4317: 489-93. 2001.
[8] P. Reynolds, A. Pavic, Z. Ibrahim, Changes of modal properties of a stadium structure occupied by a crowd, Proceedings of XXII International Modal Analysis Conference, Orlando, Fl, USA, 2004.
[9] A. Cappellini, S. Manzoni, M. Vanali, Quantification of Damping Effect of Humans on Lightly Damped Staircases, Proceedings of XXXI International Modal Analysis Conference, Garden Grove (California, USA), February 11-14, 2013
[10] Y. Matsumoto, M.J. Griffin, Mathematical models for the apparent masses of standing subjects exposed to vertical whole-body vibration. Journal of Sound and Vibration 260 (2003) 431-451.
[11] S. Krenk, Lectures presented at 'Semi–Active Vibration Suppression – The Best from Active and Passive Technologies', CISM, Udine, October 1–5, 2007

COMPDYN 2013
4th ECCOMAS Thematic Conference on
Computational Methods in Structural Dynamics and Earthquake Engineering
M. Papadrakakis, V. Papadopoulos, V. Plevris (eds.)
Kos Island, Greece, 12–14 June 2013

3-D CONVOLUTIONAL PERFECTLY MATCHED LAYER MODELS FOR DYNAMIC SOIL-STRUCTURE INTERACTION ANALYSIS IN THE FINITE ELEMENT TIME-DOMAIN

Bo-Qing Xu[1], Hing-Ho Tsang[2], and S. H. Lo[3]

Department of Civil Engineering, The University of Hong Kong
Pokfulam Road, Hong Kong

[1] xuboqing@hku.hk, [2] tsanghh@hku.hk, [3] hrcclsh@hku.hk

Keywords: Perfectly Matched Layer, Finite Element Method, Seismic Isolation, Dynamic Soil-Structure Interaction, Boundary Conditions.

Abstract. *The perfectly matched layer (PML) has been employed as a very efficient absorbing boundary condition for solving elastodynamic problems in bounded domains by using the finite difference method. However, in the finite element time domain (FETD), the application of PML formulations usually involves a mixed scheme with velocity/displacement and stresses as unknowns to avoid temporal convolution operations, which could lead to an increase in computational costs especially when three-dimensional (3-D) simulations are used. This paper presents the preliminary research on 3-D convolutional PML models for dynamic soil-structure interaction (SSI) analysis in FETD with displacements as the only unknowns. The variational formulation is derived for the use of finite element method (FEM) to discretize the problem domain, which avoids tricky coordinate transformation and requires minor modification of existing displacement-based finite element software. The stability and efficiency of the proposed formulation are first demonstrated by relevant 3-D benchmark examples even with small bounded domains. Numerical results are also presented for the classical SSI problem of a building with rigid footing on layers on a half-space.*

1 INTRODUCTION

A PML is an artificial absorbing layer for wave equations, commonly used to truncate computational regions in numerical methods to simulate problems with open boundaries [1]. The key property of a PML that distinguishes it from an ordinary absorbing material is that it is designed so that wave incident upon the PML from a non-PML medium does not reflect at the interface. This property allows the PML to strongly absorb outgoing waves from the interior of a computational region without reflecting them back into the interior.

The concept of a PML was first introduced to electromagnetic waves by Berenger [2] for the finite-difference time-domain (FDTD) method [3]. After the introduction of this idea, extensive research has been conducted on various aspects of PMLs for electromagnetic waves; this is mentioned without references because a review of electromagnetic PMLs is beyond the scope of this study. Most of the applications regarding PMLs are connected to FDTD, but PML has also been used in the frequency-domain finite-element method [4, 5] and more recently in the FETD method [6, 7].

PMLs have also been found applicable to other linear wave equations, for example, the Helmholtz equation [8-10], the linearized Euler equations [11], the wave equation for poroelastic media [12] and the elastodynamic wave equation [13]. The first real applications of PMLs to elastic waves were based on the split-field, velocity-stress formulation [13, 14], later extended to cases involving anisotropic media [15]. A non-splitting velocity-stress or displacement-stress approach has been suggested in which an effective recursive update strategy [16] is applied to resolve the expensive temporal convolution operations. This is known as the convolutional PML (C-PML) including the option for complex frequency shifted (CFS) [17] coordinate stretching that improves the performance of the discrete PML for near-grazing waves [18]. In the studies aforementioned, the spatial operators are approximated by finite differences. In the FETD or spectral element time-domain (SETD), the application of both split-field [19] and non-split PML [20] formulations usually involves a mixed scheme with velocity/displacement and stresses as unknowns to avoid temporal convolution operations. However, these formulations could lead to an increase in computational costs, since, apart from displacements, stresses additionally become unknowns. Since existing software for FE modeling of solid mechanics and elasticity problems usually solves for displacements only, there is a need for a PML formulation of FETD with only displacements as unknowns for the elastic second-order wave equation.

To the author's knowledge, more than four attempts to solve the above challenge have been reported. Komatitisch and Tromp [21] manage to eliminate the stress terms at the cost of splitting the displacement field into four components. Basu almost established an FE discretized second-order wave equation for the displacement in [22] although the formulation involves tricky coordinate transformations of the displacement gradients to compute the strains and the implicit time integration has to be replaced by an explicit scheme [23] to enhance the computational efficiency. Recent work by Li and Matar [24] demonstrates a C-PML model for the second-order wave equation using auxiliary memory variables to avoid the convolution operators. However in reality, each memory variable in this scheme is governed by an additional equation of first-order in which the stresses are needed. The common outcome of these formulations is rather complex implementations that necessitate fundamental re-structuring of existing FE codes. Another recent work in [25] suggests a non-split variational formulation of the C-PML for the elastic-second order wave equation with displacement as the single unknown. It shows the possibility of FE implementation of an efficient CPML to existing displacement-based FE codes to solve open-region elastic wave propagation problems.

The second section of this paper developed the 3-D C-PML formulation for FETD method and implement in the model for dynamic SSI analysis. Relevant benchmark example with small bounded domains is demonstrated in the third section to show the stability and efficiency of the proposed formulation. An interesting application of this technique can also be found about the classical SSI problem of a building with rigid footing on layers on a half-space. The conclusions are discussed in the last section.

2 3-D C-PML MODEL AND FORMULATION

2.1 Concepts of Standard PML and C-PML

The key concept of the PML is a complex frequency coordinate stretching, which maps the spartial variables onto a complex space by a complex coordinate stretching function. In a 3-D space, this function can be defined as [26]

$$x_i' = \int_0^{x_i} s_i(\tilde{x}_i, \omega)\, \mathrm{d}\tilde{x}_i, \qquad i = 1, 2, 3 \tag{1}$$

The apostrophe $(\bullet)'$ indicates the stretched version of the function, ω is the angular frequency and s_i $(i = 1, 2, 3)$ are the complex frequency shifted stretched coordinate metrics proposed by Kuzuoglu and Mittra [17]

$$s_i(x_i, \omega) = \kappa_i(x_i) + \frac{\beta_i(x_i)}{\alpha_i(x_i) + j\omega}, \qquad i = 1, 2, 3 \tag{2}$$

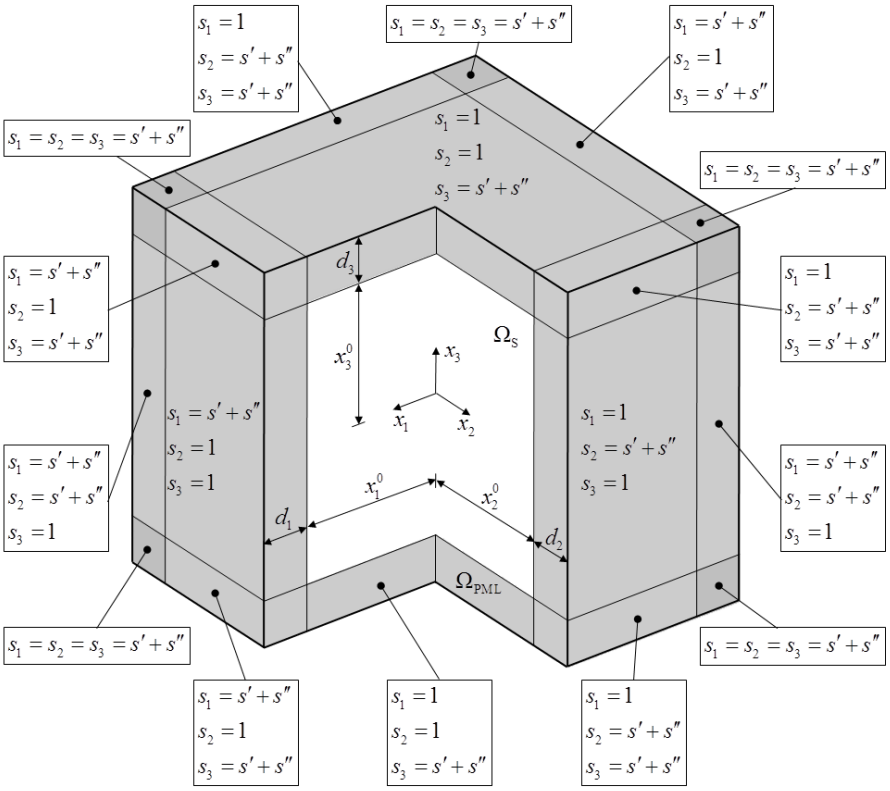


Figure 1: Computational domain truncated by Convolutional PML.

where j is the imaginary unit and κ_i, α_i and β_i are the coordinate-wise non-negative real function that controls the attenuation of the propagating waves. At the interface of the computational domain and PML, $\kappa_i = 1$ and $\beta_i = 0$. For standard PML, $\kappa_i = 1$ and $\alpha_i = 0$ in Equation (2). For the complex frequency shifted C-PML with the interface located at $x_i = x_i^0$, see Figure 1, the attenuation of the wave occurs over the PML width d_i, and continues after the remainder of the wave has been reflected from the PML boundary at $x_i = x_i^0 + d_i$. The real function $s' = \kappa_i \geq 1$ and the imaginary function $s'' = \beta / (\alpha + j\omega)$ serve to enhance attenuation of evanescent and near-grazing waves.

2.2 C-PML Equations

This paper aims at combining the 3-D C-PML model in dynamic SSI analysis. For simplicity, we consider a linear elastic medium with an open 3-D domain $\Omega = \Omega_S \cup \Omega_{PML}$, such as the one in Figure 1, in which the wave propagation is governed by

$$\text{Equation of motion: } \nabla \cdot \boldsymbol{\sigma} + \rho \mathbf{p} = \rho \ddot{\mathbf{u}} \tag{3}$$

$$\text{Strain-displacement equations: } \boldsymbol{\varepsilon} = \frac{1}{2}[\nabla \mathbf{u} + (\nabla \mathbf{u})^T] \tag{4}$$

$$\text{Constitutive equations: } \boldsymbol{\sigma} = \mathbf{C} : \boldsymbol{\varepsilon} \tag{5}$$

where $\boldsymbol{\sigma}$, $\boldsymbol{\varepsilon}$ and $\mathbf{C}$ are the stress, strain and stiffness tensors, respectively, ρ is the mass density, $\mathbf{u} = (u_1, u_2, u_3)^T$ and $\mathbf{p} = (p_1, p_2, p_3)^T$ are the displacement and body force vectors, respectively. $\nabla \cdot (\bullet)$ is the divergence operator, $\nabla (\bullet)$ represents the gradient operator and $(\bullet)^T$ represents a transpose and $(\ddot{\bullet})$ represents the second derivative with respect to time.

By introducing the complex stretched function of Equation (1) into the frequency-domain counterparts of the above governing equations and then applying the inverse Fourier transform, we can get the time-domain equation of motion and the displacement-based constitutive equations for the C-PML domain as follows

$$\nabla \cdot \boldsymbol{\sigma}' + \rho \mathbf{p} = \Psi_0(t)\mathbf{u} \tag{6}$$

$$\boldsymbol{\sigma}' = \mathbf{C}' \partial \mathbf{u} \tag{7}$$

with

$$\mathbf{C}' = \Psi_1(t)\mathbf{C}_1 + \Psi_2(t)\mathbf{C}_2 + \Psi_3(t)\mathbf{C}_3 + \Psi_4(t)\mathbf{C}_4 + \Psi_5(t)\mathbf{C}_5 + \Psi_6(t)\mathbf{C}_6 \tag{8}$$

In Equation (8), the six matrices $\mathbf{C}_i$ $(i = 1, 2, \cdots, 6)$ are given in Appendix. In Equations (6) and (8), the operators $\Psi_i(t)$ $(i = 0, 1, \cdots, 6)$ are generated by the process of the inverse Fourier transform, which are respectively given by

$$\begin{aligned} \Psi_0(t) = {} & P_0 \frac{\partial^2}{\partial t^2} + P_1 \frac{\partial}{\partial t} + P_2 + \alpha_1^2 \beta_1 P_{3,12} P_{3,13} e^{-\alpha_1 t} H(t) * \\ & + \alpha_2^2 \beta_2 P_{3,21} P_{3,23} e^{-\alpha_2 t} H(t) * + \alpha_3^2 \beta_3 P_{3,31} P_{3,32} e^{-\alpha_3 t} H(t) * \end{aligned} \tag{9}$$

$$\Psi_1(t) = \kappa_1 + \beta_1 e^{-\alpha_1 t} H(t) * \tag{10}$$

$$\Psi_2(t) = \kappa_2 + \beta_2 e^{-\alpha_2 t} H(t) * \tag{11}$$

$$\Psi_3(t) = \kappa_3 + \beta_3 e^{-\alpha_3 t} H(t) * \tag{12}$$

$$\Psi_4(t) = \frac{\kappa_1\kappa_2}{\kappa_3} + \beta_1 P_{3,12} P_{3,13}^{-1} e^{-\alpha_1 t} H(t) * + \beta_2 P_{3,21} P_{3,23}^{-1} e^{-\alpha_2 t} H(t) * - \frac{\beta_3}{\kappa_3^2} P_{4,31} P_{4,32} e^{-(\kappa_3\alpha_3+\beta_3)t/\kappa_3} H(t) * \tag{13}$$

$$\Psi_5(t) = \frac{\kappa_1\kappa_3}{\kappa_2} + \beta_1 P_{3,13} P_{3,12}^{-1} e^{-\alpha_1 t} H(t) * + \beta_3 P_{3,31} P_{3,32}^{-1} e^{-\alpha_3 t} H(t) * - \frac{\beta_2}{\kappa_2^2} P_{4,21} P_{4,23} e^{-(\kappa_2\alpha_2+\beta_2)t/\kappa_2} H(t) * \tag{14}$$

$$\Psi_6(t) = \frac{\kappa_2\kappa_3}{\kappa_1} + \beta_2 P_{3,23} P_{3,21}^{-1} e^{-\alpha_2 t} H(t) * + \beta_3 P_{3,12} P_{3,13}^{-1} e^{-\alpha_3 t} H(t) * - \frac{\beta_1}{\kappa_1^2} P_{4,12} P_{4,13} e^{-(\kappa_1\alpha_1+\beta_1)t/\kappa_1} H(t) * \tag{15}$$

where $H(t)$ is the Heaviside step function, $*$ denotes the temporal convolution and P_0, P_1, P_2, $P_{3,i}$, $P_{4,i}$ $(i = 1, 2, 3)$ are the spatially varying functions which are introduced as follows

$$P_0 = \kappa_1\kappa_2\kappa_3 \tag{16}$$

$$P_1 = \kappa_2\kappa_3\beta_1 + \kappa_1\kappa_3\beta_2 + \kappa_1\kappa_2\beta_3 \tag{17}$$

$$P_2 = \kappa_1\beta_2\beta_3 + \kappa_2\beta_1\beta_3 + \kappa_3\beta_1\beta_2 - \alpha_1\kappa_2\kappa_3\beta_1 - \alpha_2\kappa_1\kappa_3\beta_2 - \alpha_3\kappa_1\kappa_2\beta_3 \tag{18}$$

$$P_{3,ij} = \frac{\kappa_j(\alpha_i - \alpha_j) - \beta_j}{\alpha_i - \alpha_j} \quad (i, j = 1, 2, 3 \text{ and } i \neq j) \tag{19}$$

$$P_{4,ij} = \frac{\kappa_i\kappa_j(\alpha_i - \alpha_j) + \kappa_j\beta_i - \kappa_i\beta_j}{\kappa_i(\alpha_i - \alpha_j) + \beta_i} \quad (i, j = 1, 2, 3 \text{ and } i \neq j) \tag{20}$$

Note that in the computational domain Ω_S, $\kappa_i = 1$ and $\alpha_i = \beta_i = 0$ $(i = 1, 2, 3)$, herein $P_0 = 1$ and other functions in Equations (17-20) vanish. In the corner and edge regions of the C-PML, when $\alpha_i = \alpha_j$, $P_{3,ij}$ can be simplified to κ_j. By carefully choosing the spatial parameters κ_i, α_i and β_i, the singularities of $P_{4,ij}$ can be avoided. These parameters of the C-PML in the x_i direction can be chosen as suggests [20, 27, 28]

$$\kappa_i = 1 - \frac{20\Delta x_i \log_{10}(R_0)}{d_i}\left(\frac{x_i - x_i^0}{d_i}\right)^3 \tag{21}$$

$$\alpha_i = \pi\left(\frac{d_i - x_i + x_i^0}{d_i}\right) \tag{22}$$

$$\beta_i = -\frac{2v_p \log_{10}(R_0)}{d_i}\left(\frac{x_i - x_i^0}{d_i}\right)^3 \tag{23}$$

where R_0 is the theoretical reflection coefficient at normal incidence, Δx_i is the element size, v_p the longitudinal wave velocity, and x_i^0 and d_i as stated in the first part of this section are the starting location and the thickness of the C-PML, respectively.

2.3 Finite element implementation and time integration

To find a displacement-based FE solution, Equations (6-8) should be written into the weak form by using the principle of virtual work over the domain Ω with the boundary Γ

$$\int_\Omega (\delta \mathbf{u})^T \rho \Psi_0 \mathbf{u} \, \mathrm{d}\Omega + \int_\Omega (\partial \delta \mathbf{u})^T \boldsymbol{\sigma}' \, \mathrm{d}\Omega - \int_\Omega (\delta \mathbf{u})^T \mathbf{p} \, \mathrm{d}\Omega - \int_\Omega (\delta \mathbf{u})^T \mathbf{T} \, \mathrm{d}\Gamma = 0 \tag{24}$$

If we assume a free-surface boundary condition on Γ, then the contour integral in Equation (24) vanishes. By separating the convolution terms in the operators $\Psi_i(t)$, adding the external load and expanding the displacement field using FEM, we can obtain the ordinary differential equation

$$\mathbf{M}\ddot{\mathbf{d}} + \mathbf{D}\dot{\mathbf{d}} + \mathbf{K}\mathbf{d} = \mathbf{f} + \mathbf{h} + \mathbf{g} \tag{25}$$

In Equation (25), the external force vector $\mathbf{f}$ can be expressed as $\mathbf{f}(t) = -\mathbf{M}\ddot{\mathbf{d}}_{\mathrm{in}}(t)$, when there is a time-dependent input acceleration. $\mathbf{K}$, $\mathbf{M}$, and $\mathbf{D}$ are the global stiffness, mass and damping matrices, which are assembled from the respective element matrices $\mathbf{K}^e$, $\mathbf{M}^e$, and $\mathbf{D}^e$, with the matrix entries given by

$$\begin{aligned}
\mathbf{K}_{ij}^e &= \int_{\Omega^e} \mathbf{B}_i^T \left(\kappa_1 \mathbf{C}_1 + \kappa_2 \mathbf{C}_2 + \kappa_3 \mathbf{C}_3 + \frac{\kappa_1 \kappa_2}{\kappa_3} \mathbf{C}_4 + \frac{\kappa_1 \kappa_3}{\kappa_2} \mathbf{C}_5 + \frac{\kappa_2 \kappa_3}{\kappa_1} \mathbf{C}_6 \right) \mathbf{B}_j \, \mathrm{d}\Omega \\
&\quad + \int_{\Omega^e} \rho P_2 \mathbf{N}_i^T \mathbf{N}_j \, \mathrm{d}\Omega \\
\mathbf{M}_{ij}^e &= \int_{\Omega^e} \rho P_0 \mathbf{N}_i^T \mathbf{N}_j \, \mathrm{d}\Omega \\
\mathbf{D}_{ij}^e &= \int_{\Omega^e} \rho P_1 \mathbf{N}_i^T \mathbf{N}_j \, \mathrm{d}\Omega
\end{aligned} \tag{26}$$

Here, $\mathbf{B}_j = \partial \mathbf{N}_i$ denotes the strain-displacement matrix and $\mathbf{d}$, $\dot{\mathbf{d}}$ and $\ddot{\mathbf{d}}$ are the unknown displacement, velocity and acceleration vectors, respectively. The $\mathbf{B}_j$ matrix for 3-D C-PML now reads as

$$\mathbf{B}_j = \begin{bmatrix}
N_{j,1} & 0 & 0 \\
0 & N_{j,2} & 0 \\
0 & 0 & N_{j,3} \\
N_{j,2} & N_{j,1} & 0 \\
N_{j,3} & 0 & N_{j,1} \\
0 & N_{j,3} & N_{j,2} \\
N_{j,2} & -N_{j,1} & 0 \\
N_{j,3} & 0 & -N_{j,1} \\
0 & N_{j,3} & -N_{j,2}
\end{bmatrix} \tag{27}$$

which is different from that of element inside the computational domain because the complex coordinate stretching has alternated the C-PML into an anisotropic material model. The global body force vector $\mathbf{h}$ and the global convolution vector $\mathbf{g}$ are also assembled from their respective element-level sub-vectors

$$\mathbf{h}^e = \int_{\Omega^e} \mathbf{N}^T \mathbf{p} \, \mathrm{d}\Omega \tag{28}$$

$$\begin{aligned}
\mathbf{g}^e = & -\int_{\Omega^e} \rho \mathbf{N}^T \mathbf{N} \begin{pmatrix} \alpha_1^2 \beta_1 P_{3,12} P_{3,13} e^{-\alpha_1 t} H(t) * + \alpha_2^2 \beta_2 P_{3,21} P_{3,23} e^{-\alpha_2 t} H(t) * \\ + \alpha_3^2 \beta_3 P_{3,31} P_{3,32} e^{-\alpha_3 t} H(t) * \end{pmatrix} \mathbf{d}^e \, \mathrm{d}\Omega \\
& - \sum_{k=1}^{3} \int_{\Omega^e} \mathbf{B}^T \mathbf{C}_k \mathbf{B} \; \beta_k e^{-\alpha_k t} H(t) * \mathbf{d}^e \, \mathrm{d}\Omega \\
& - \int_{\Omega^e} \mathbf{B}^T \mathbf{C}_4 \mathbf{B} \begin{pmatrix} \beta_1 P_{3,12} P_{3,13}^{-1} e^{-\alpha_1 t} H(t) * + \beta_2 P_{3,21} P_{3,23}^{-1} e^{-\alpha_2 t} H(t) * \\ - \beta_3 \kappa_3^{-2} P_{4,31} P_{4,32} e^{-(\kappa_3 \alpha_3 + \beta_3) t / \kappa_3} H(t) * \end{pmatrix} \mathbf{d}^e \, \mathrm{d}\Omega \\
& - \int_{\Omega^e} \mathbf{B}^T \mathbf{C}_5 \mathbf{B} \begin{pmatrix} \beta_1 P_{3,13} P_{3,12}^{-1} e^{-\alpha_1 t} H(t) * + \beta_3 P_{3,31} P_{3,32}^{-1} e^{-\alpha_3 t} H(t) * \\ - \beta_2 \kappa_2^{-2} P_{4,21} P_{4,23} e^{-(\kappa_2 \alpha_2 + \beta_2) t / \kappa_2} H(t) * \end{pmatrix} \mathbf{d}^e \, \mathrm{d}\Omega \\
& - \int_{\Omega^e} \mathbf{B}^T \mathbf{C}_6 \mathbf{B} \begin{pmatrix} \beta_2 P_{3,23} P_{3,21}^{-1} e^{-\alpha_2 t} H(t) * + \beta_3 P_{3,12} P_{3,13}^{-1} e^{-\alpha_3 t} H(t) * \\ - \beta_1 \kappa_1^{-2} P_{4,12} P_{4,13} e^{-(\kappa_1 \alpha_1 + \beta_1) t / \kappa_1} H(t) * \end{pmatrix} \mathbf{d}^e \, \mathrm{d}\Omega
\end{aligned} \tag{29}$$

where $\mathbf{d}^e$ is the element displacement vector.

In order to solve the differential equation for arbitrary variation of forcing function as a function of time, the most widely used methods of numerical integration in earthquake engineering are the Newmark family methods. Here we adopt one of the members of the Newmark family methods, for example, the average acceleration method, which is unconditionally stable and in the second order of accuracy. The following equation is derived for solving the displacement, velocity and acceleration at each time step Δt:

$$\begin{aligned}
\left(\frac{1}{4}\mathbf{K} + \frac{1}{\Delta t^2}\mathbf{M} + \frac{1}{2\Delta t}\mathbf{D} \right) \mathbf{d}_{t+\Delta t} = & -\left[\frac{1}{2}\mathbf{K} - \frac{2}{\Delta t^2}\mathbf{M} \right] \mathbf{d}_t - \left(\frac{1}{4}\mathbf{K} + \frac{1}{\Delta t^2}\mathbf{M} - \frac{1}{2\Delta t}\mathbf{D} \right) \mathbf{d}_{t-\Delta t} \\
& + \frac{1}{4}\mathbf{f}_{t+\Delta t} + \frac{1}{2}\mathbf{f}_t + \frac{1}{4}\mathbf{f}_{t-\Delta t} + \frac{1}{4}\mathbf{h}_{t+\Delta t} + \frac{1}{2}\mathbf{h}_t + \frac{1}{4}\mathbf{h}_{t-\Delta t} + \frac{1}{4}\mathbf{g}_{t+\Delta t} + \frac{1}{2}\mathbf{g}_t + \frac{1}{4}\mathbf{g}_{t-\Delta t}
\end{aligned} \tag{30}$$

3 NUMERICAL EXPERIMENTS

3.1 Experiment 1

To demonstrate the excellent absorbing properties of the C-PML suggested, we first attach the C-PML to five of the six faces of a cubic domain, which involves an explosive point-source residing inside the domain, see Figure 2. For the sake of simplicity, we assume the materials are homogeneous, with the density $\rho = 16500 kg/m^3$, the primary wave velocity $v_p = 100 m/s$, and the shear wave velocity $v_s = 58 m/s$. The elastic medium of 500m×500m×500m is surrounded by C-PML with the thickness of 70m. The source is located at the center of the solution domain, which is defined by

$$p(t) = 2 \times 10^7 \pi^2 (t - t_0) e^{-\pi^2 (t - t_0)} \tag{31}$$

where t_0 is the delay time. We record the horizontal and vertical displacement response in two positions R_1 and R_2 located at (-250m, 250m, 250m) and (250m, 250m, -250m), respectively. To make it convenient to compare the results to the analytical solution, we choose the direction of the source to be vertical. The FORTRAN code TI_anlytical_3D written by Dimitri Komatitsch can be used to compute the analytical solution for 3D transversely isotropic homogeneous material due to a point force source.

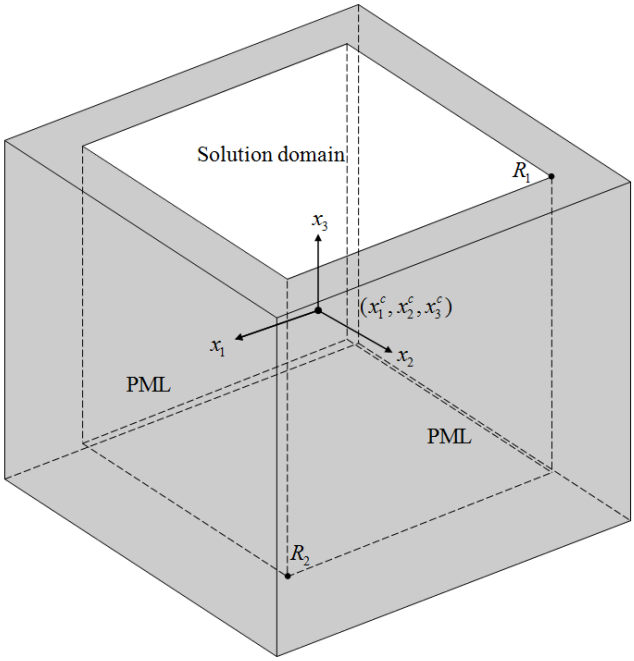


Figure 2: C-PML-truncated domain in three dimensions subjected to a point-source located at (x_1^c, x_2^c, x_3^c). R_1 and R_2 are two receivers at which the respective response is recorded.

The results of simulation with C-PML are shown in Figure 3 and Figure 4, which are compared to that of standard PML with $\alpha_i = 0$ and $\kappa_i = 1$ and the analytical solution. From all the plots, we can see the C-PML behaves perfectly in accordance with the analytical solution. Figure 5 shows some snapshots of the displacement field in the cross section of $x_1 = 0$. The displacement field magnitude here is defined as the norm $\|\mathbf{u}\| = \sqrt{u_1^2 + u_2^2 + u_3^2}$. From Figure 4, we can see that the C-PML absorbs the waves well, while the reflection of the waves from the top free surface is quite obvious after 2.0s.

3.2 Experiment 2

Typical soil-structure interaction model is used in this example as shows in Figure 6. The building structure on a 2m thick concrete foundation has a height of 24m. It is 8m in both of the other two dimensions. The superstructure is modeled by an assembly of three-dimensional frame elements. For the foundation and subsoil materials, eight-node solid elements are used in the modeling.

In order to simulate the non-reflective effects of the infinite soil transmitting half-space, the model of C-PML has been used as the boundary of the computational domain. The

numerical analysis is conducted by reducing the soil system to a 32m×32m×12m computational domain surrounded by 10m thick C-PML.

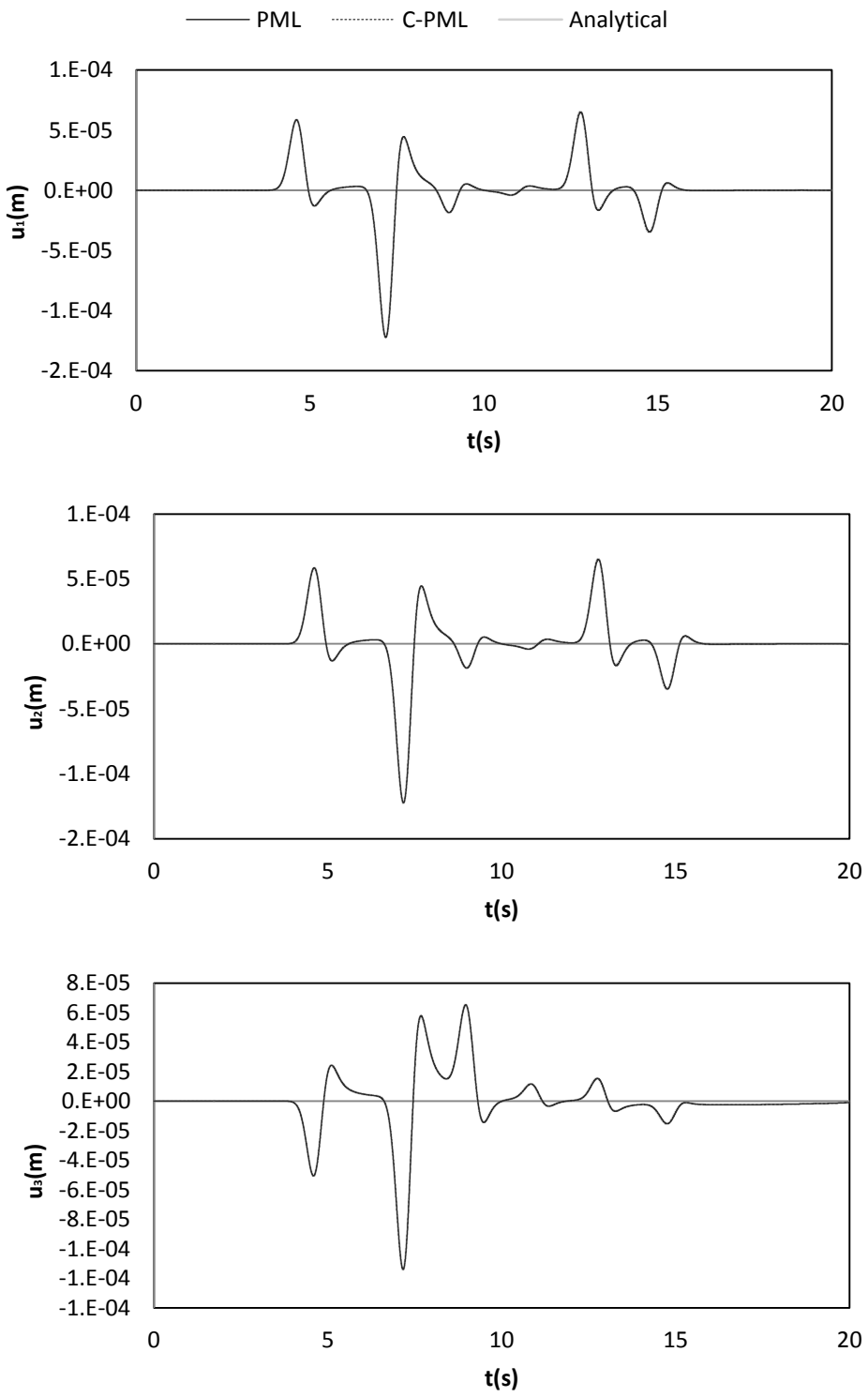


Figure 3: Comparison of the results at the receiving position R_1

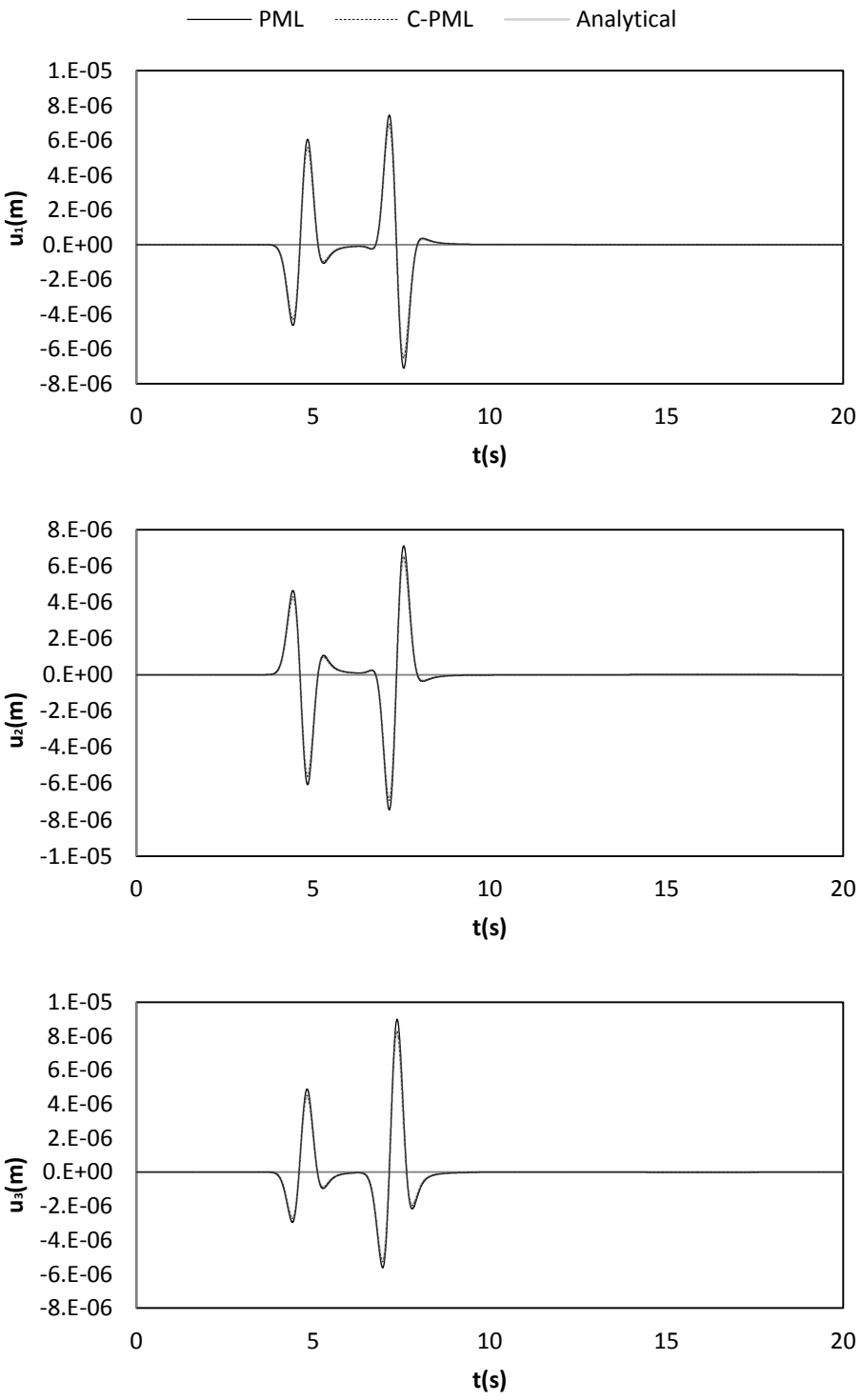
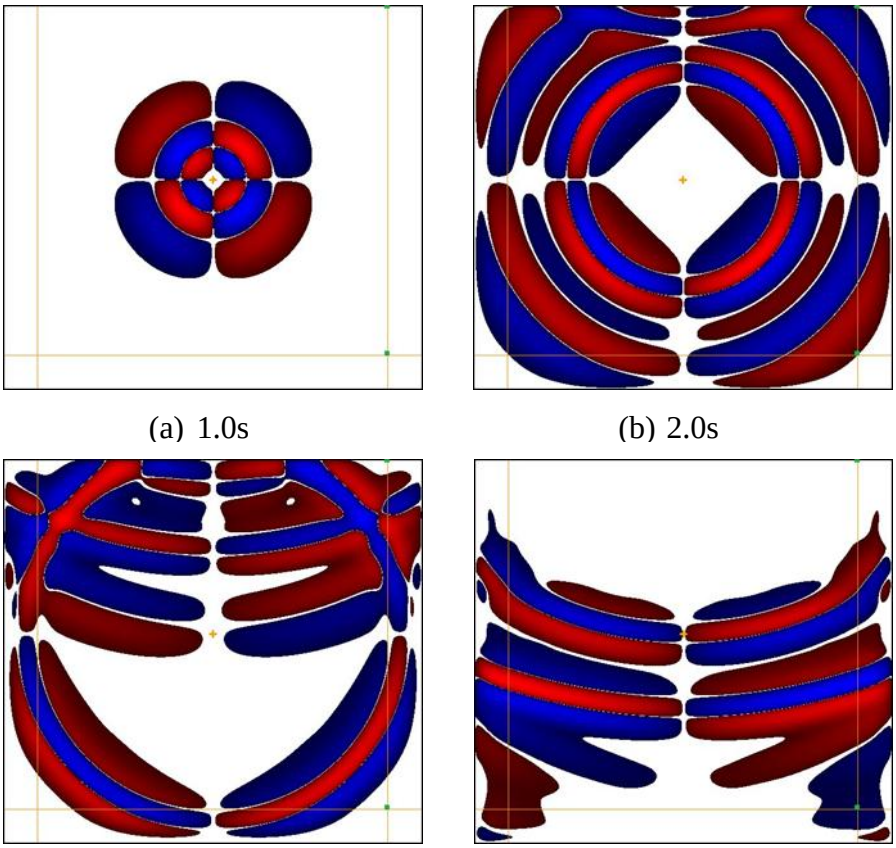


Figure 4: Comparison of the results at the receiving position R_2



(a) 1.0s (b) 2.0s

(c) 3.0s (d) 4.0s

Figure 5: Snapshots of the displacement field magnitude of Experiment 1

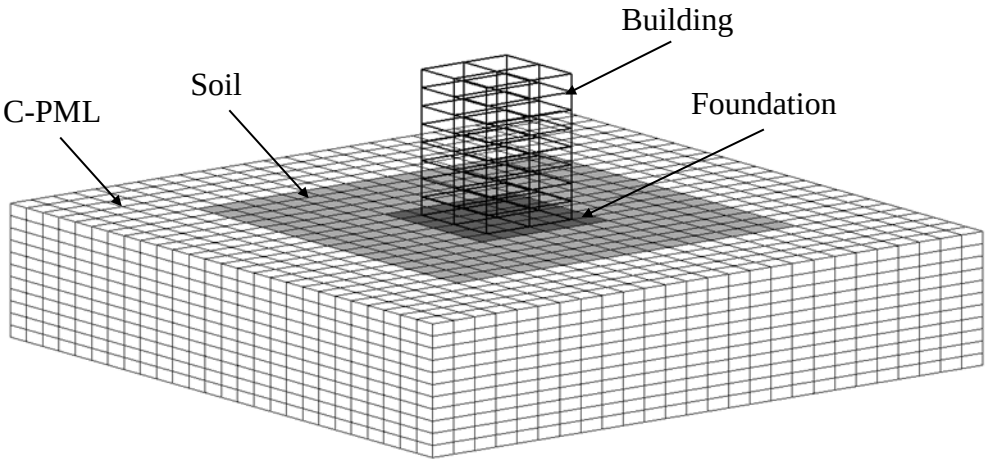


Figure 6: Finite element model of the soil-foundation-structure system with C-PML

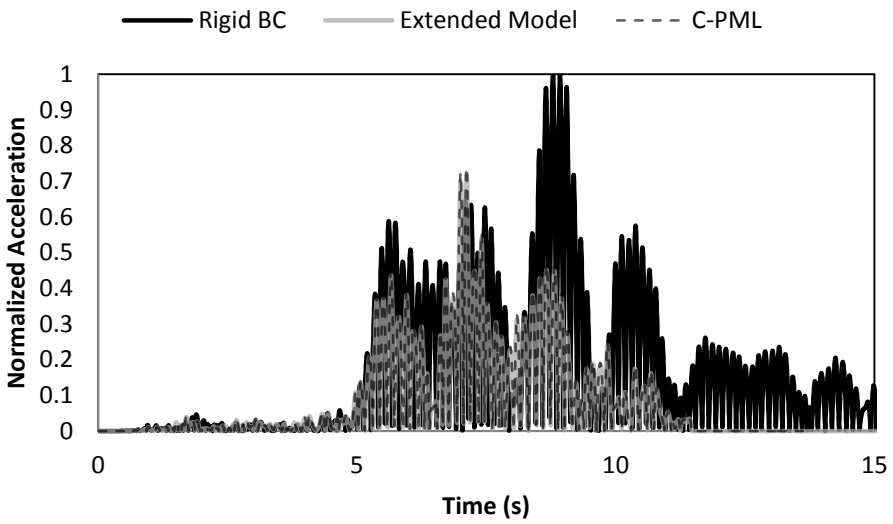


Figure 7: Footing horizontal motion

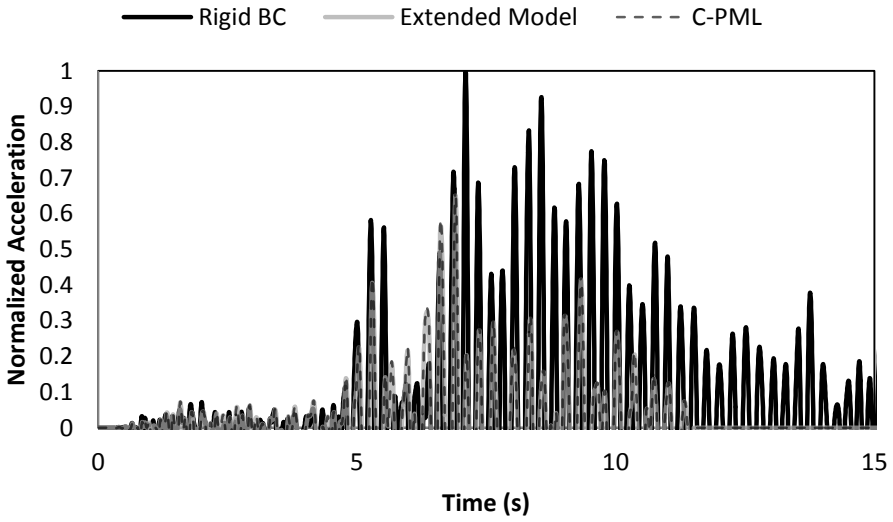


Figure 8: Roof horizontal motion

An earthquake ground motion time histories is applied at the depth of 10m. The results are compared to those from an extended model of 320m×320m×120m and those from a model with rigid boundary. Figure 7 shows the response of the center of the footing and Figure 8 shows the response of the roof. We use the norm $\ddot{u}_h = \sqrt{\ddot{u}_1^2 + \ddot{u}_2^2}$ to indicate the amplitude of horizontal motion. The results from the C-PML model are quite close to those from the extended model.

4 CONCLUSIONS

Efficient 3D C-PML models have been developed for application to dynamic soil-structure interaction analyses in time domain. It is demonstrated by numerical examples that the accuracy of the developed models is quite high. The primary purpose of this paper is to show how to implementation an efficient C-PML model to the analyses of SSI problems, when existing displacement based finite element codes need to be used to handle open-region or larger domain.

REFERENCES

[1] J.-P. Bérenger, "Perfectly Matched Layer (PML) for Computational Electromagnetics," *Synthesis Lectures on Computational Electromagnetics,* vol. 2, pp. 1-117, 2007/01/01 2007.

[2] J. P. Berenger, "A Perfectly Matched Layer for the Absorption of Electromagnetic-Waves," *Journal of Computational Physics,* vol. 114, pp. 185-200, Oct 1994.

[3] A. Taflove and S. C. Hagness, *Computational electrodynamics : the finite-difference time-domain method*, 3rd ed. Boston: Artech House, 2005.

[4] J. Y. Wu, D. M. Kingsland, J. F. Lee, and R. Lee, "A comparison of anisotropic PML to Berenger's PML and its application to the finite-element method for EM scattering," *Ieee Transactions on Antennas and Propagation,* vol. 45, pp. 40-50, Jan 1997.

[5] M. Kuzuoglu and R. Mittra, "Investigation of nonplanar perfectly matched absorbers for finite-element mesh truncation," *Ieee Transactions on Antennas and Propagation,* vol. 45, pp. 474-486, Mar 1997.

[6] D. Jiao, J. M. Jin, E. Michielssen, and D. J. Riley, "Time-domain finite-element simulation of three-dimensional scattering and radiation problems using perfectly matched layers," *Ieee Transactions on Antennas and Propagation,* vol. 51, pp. 296-305, Feb 2003.

[7] T. Rylander and J. M. Jin, "Perfectly matched layer in three dimensions for the time-domain finite element method applied to radiation problems," *Ieee Transactions on Antennas and Propagation,* vol. 53, pp. 1489-1499, Apr 2005.

[8] Q. A. Qi and T. L. Geers, "Evaluation of the perfectly matched layer for computational acoustics," *Journal of Computational Physics,* vol. 139, pp. 166-183, Jan 1 1998.

[9] E. Turkel and A. Yefet, "Absorbing PML boundary layers for wave-like equations," *Applied Numerical Mathematics,* vol. 27, pp. 533-557, Aug 1998.

[10] I. Harari, M. Slavutin, and E. Turkel, "Analytical and numerical studies of a finite element PML for the Helmholtz equation," *Journal of Computational Acoustics,* vol. 8, pp. 121-137, Mar 2000.

[11] F. Q. Hu, "On absorbing boundary conditions for linearized Euler equations by a perfectly matched layer," *Journal of Computational Physics,* vol. 129, pp. 201-219, Nov 1996.

[12] Y. Q. Zeng, J. Q. He, and Q. H. Liu, "The application of the perfectly matched layer in numerical modeling of wave propagation in poroelastic media," *Geophysics,* vol. 66, pp. 1258-1266, Jul-Aug 2001.

[13] W. C. Chew and Q. H. Liu, "Perfectly matched layers for elastodynamics: A new absorbing boundary condition," *Journal of Computational Acoustics,* vol. 4, pp. 341-359, Dec 1996.

[14] Q. H. Liu and J. P. Tao, "The perfectly matched layer for acoustic waves in absorptive media," *Journal of the Acoustical Society of America,* vol. 102, pp. 2072-2082, Oct 1997.

[15] F. Collino and C. Tsogka, "Application of the perfectly matched absorbing layer model to the linear elastodynamic problem in anisotropic heterogeneous media," *Geophysics,* vol. 66, pp. 294-307, Jan-Feb 2001.

[16] R. J. Luebbers and F. Hunsberger, "Fdtd for Nth-Order Dispersive Media," *Ieee Transactions on Antennas and Propagation,* vol. 40, pp. 1297-1301, Nov 1992.

[17] M. Kuzuoglu and R. Mittra, "Frequency dependence of the constitutive parameters of causal perfectly matched anisotropic absorbers," *Ieee Microwave and Guided Wave Letters,* vol. 6, pp. 447-449, Dec 1996.

[18] J. A. Roden and S. D. Gedney, "Convolution PML (CPML): An efficient FDTD implementation of the CFS-PML for arbitrary media," *Microwave and Optical Technology Letters,* vol. 27, pp. 334-339, Dec 5 2000.

[19] E. Becache, P. Joly, and C. Tsogka, "Fictitious domains, mixed finite elements and perfectly matched layers for 2-D elastic wave propagation," *Journal of Computational Acoustics,* vol. 9, pp. 1175-1201, Sep 2001.

[20] S. Kucukcoban and L. F. Kallivokas, "Mixed perfectly-matched-layers for direct transient analysis in 2D elastic heterogeneous media," *Computer Methods in Applied Mechanics and Engineering,* vol. 200, pp. 57-76, 2011.

[21] D. Komatitsch and J. Tromp, "A perfectly matched layer absorbing boundary condition for the second-order seismic wave equation," *Geophysical Journal International,* vol. 154, pp. 146-153, Jul 2003.

[22] U. Basu and A. K. Chopra, "Perfectly matched layers for transient elastodynamics of unbounded domains," *International Journal for Numerical Methods in Engineering,* vol. 59, pp. 1039-1074, Feb 28 2004.

[23] U. Basu, "Explicit finite element perfectly matched layer for transient three-dimensional elastic waves," *International Journal for Numerical Methods in Engineering,* vol. 77, pp. 151-176, Jan 8 2009.

[24] Y. F. Li and O. B. Matar, "Convolutional perfectly matched layer for elastic second-order wave equation," *Journal of the Acoustical Society of America,* vol. 127, pp. 1318-1327, Mar 2010.

[25] R. Matzen, "An efficient finite element time-domain formulation for the elastic second-order wave equation: A non-split complex frequency shifted convolutional PML," *International Journal for Numerical Methods in Engineering,* vol. 88, pp. 951-973, Dec 9 2011.

[26] W. C. Chew and W. H. Weedon, "A 3d Perfectly Matched Medium from Modified Maxwells Equations with Stretched Coordinates," *Microwave and Optical Technology Letters,* vol. 7, pp. 599-604, Sep 1994.

[27] G. Festa and J. P. Vilotte, "The Newmark scheme as velocity-stress time-staggering: an efficient PML implementation for spectral element simulations of elastodynamics," *Geophysical Journal International,* vol. 161, pp. 789-812, Jun 2005.

[28] F. Collino and P. B. Monk, "Optimizing the perfectly matched layer," *Computer Methods in Applied Mechanics and Engineering,* vol. 164, pp. 157-171, Oct 2 1998.

APPENDIX

$$\mathbf{C}_1 = \begin{bmatrix} 0 & 0 & 0 & 0 & 0 & 0 & 0 & 0 & 0 \\ 0 & 0 & \lambda & 0 & 0 & 0 & 0 & 0 & 0 \\ 0 & \lambda & 0 & 0 & 0 & 0 & 0 & 0 & 0 \\ 0 & 0 & 0 & 0 & 0 & 0 & 0 & 0 & 0 \\ 0 & 0 & 0 & 0 & 0 & 0 & 0 & 0 & 0 \\ 0 & 0 & 0 & 0 & 0 & \frac{\mu}{2} & 0 & 0 & 0 \\ 0 & 0 & 0 & 0 & 0 & 0 & 0 & 0 & 0 \\ 0 & 0 & 0 & 0 & 0 & 0 & 0 & 0 & 0 \\ 0 & 0 & 0 & 0 & 0 & 0 & 0 & 0 & -\frac{\mu}{2} \end{bmatrix}, \tag{32}$$

$$\mathbf{C}_2 = \begin{bmatrix} 0 & 0 & \lambda & 0 & 0 & 0 & 0 & 0 & 0 \\ 0 & 0 & 0 & 0 & 0 & 0 & 0 & 0 & 0 \\ \lambda & 0 & 0 & 0 & 0 & 0 & 0 & 0 & 0 \\ 0 & 0 & 0 & 0 & 0 & 0 & 0 & 0 & 0 \\ 0 & 0 & 0 & 0 & \frac{\mu}{2} & 0 & 0 & 0 & 0 \\ 0 & 0 & 0 & 0 & 0 & 0 & 0 & 0 & 0 \\ 0 & 0 & 0 & 0 & 0 & 0 & 0 & 0 & 0 \\ 0 & 0 & 0 & 0 & 0 & 0 & 0 & -\frac{\mu}{2} & 0 \\ 0 & 0 & 0 & 0 & 0 & 0 & 0 & 0 & 0 \end{bmatrix}, \tag{33}$$

$$\mathbf{C}_3 = \begin{bmatrix} 0 & \lambda & 0 & 0 & 0 & 0 & 0 & 0 & 0 \\ \lambda & 0 & 0 & 0 & 0 & 0 & 0 & 0 & 0 \\ 0 & 0 & 0 & 0 & 0 & 0 & 0 & 0 & 0 \\ 0 & 0 & 0 & \frac{\mu}{2} & 0 & 0 & 0 & 0 & 0 \\ 0 & 0 & 0 & 0 & 0 & 0 & 0 & 0 & 0 \\ 0 & 0 & 0 & 0 & 0 & 0 & 0 & 0 & 0 \\ 0 & 0 & 0 & 0 & 0 & 0 & -\frac{\mu}{2} & 0 & 0 \\ 0 & 0 & 0 & 0 & 0 & 0 & 0 & 0 & 0 \\ 0 & 0 & 0 & 0 & 0 & 0 & 0 & 0 & 0 \end{bmatrix}, \tag{34}$$

$$\mathbf{C}_4 = \begin{bmatrix} 0 & 0 & 0 & 0 & 0 & 0 & 0 & 0 & 0 \\ 0 & 0 & 0 & 0 & 0 & 0 & 0 & 0 & 0 \\ 0 & 0 & 2\mu+\lambda & 0 & 0 & 0 & 0 & 0 & 0 \\ 0 & 0 & 0 & 0 & 0 & 0 & 0 & 0 & 0 \\ 0 & 0 & 0 & 0 & \frac{\mu}{4} & 0 & 0 & -\frac{\mu}{4} & 0 \\ 0 & 0 & 0 & 0 & 0 & \frac{\mu}{4} & 0 & 0 & -\frac{\mu}{4} \\ 0 & 0 & 0 & 0 & 0 & 0 & 0 & 0 & 0 \\ 0 & 0 & 0 & 0 & -\frac{\mu}{4} & 0 & 0 & \frac{\mu}{4} & 0 \\ 0 & 0 & 0 & 0 & 0 & -\frac{\mu}{4} & 0 & 0 & \frac{\mu}{4} \end{bmatrix}, \tag{35}$$

$$\mathbf{C}_5 = \begin{bmatrix} 0 & 0 & 0 & 0 & 0 & 0 & 0 & 0 & 0 \\ 0 & 2\mu+\lambda & 0 & 0 & 0 & 0 & 0 & 0 & 0 \\ 0 & 0 & 0 & 0 & 0 & 0 & 0 & 0 & 0 \\ 0 & 0 & 0 & \frac{\mu}{4} & 0 & 0 & -\frac{\mu}{4} & 0 & 0 \\ 0 & 0 & 0 & 0 & 0 & 0 & 0 & 0 & 0 \\ 0 & 0 & 0 & 0 & 0 & \frac{\mu}{4} & 0 & 0 & \frac{\mu}{4} \\ 0 & 0 & 0 & -\frac{\mu}{4} & 0 & 0 & \frac{\mu}{4} & 0 & 0 \\ 0 & 0 & 0 & 0 & 0 & 0 & 0 & 0 & 0 \\ 0 & 0 & 0 & 0 & 0 & \frac{\mu}{4} & 0 & 0 & \frac{\mu}{4} \end{bmatrix}, \tag{36}$$

$$\mathbf{C}_6 = \begin{bmatrix} 2\mu+\lambda & 0 & 0 & 0 & 0 & 0 & 0 & 0 & 0 \\ 0 & 0 & 0 & 0 & 0 & 0 & 0 & 0 & 0 \\ 0 & 0 & 0 & 0 & 0 & 0 & 0 & 0 & 0 \\ 0 & 0 & 0 & \frac{\mu}{4} & 0 & 0 & \frac{\mu}{4} & 0 & 0 \\ 0 & 0 & 0 & 0 & \frac{\mu}{4} & 0 & 0 & \frac{\mu}{4} & 0 \\ 0 & 0 & 0 & 0 & 0 & 0 & 0 & 0 & 0 \\ 0 & 0 & 0 & \frac{\mu}{4} & 0 & 0 & \frac{\mu}{4} & 0 & 0 \\ 0 & 0 & 0 & 0 & \frac{\mu}{4} & 0 & 0 & \frac{\mu}{4} & 0 \\ 0 & 0 & 0 & 0 & 0 & 0 & 0 & 0 & 0 \end{bmatrix}. \tag{37}$$

COMPDYN 2013
4th ECCOMAS Thematic Conference on
Computational Methods in Structural Dynamics and Earthquake Engineering
M. Papadrakakis, V. Papadopoulos, V. Plevris (eds.)
Kos Island, Greece, 12–14 June 2013

APPLICABILITY OF TOTAL STRESS SEISMIC GROUND RESPONSE ANALYSIS UNDER LARGE EARTHQUAKES

Nozomu Yoshida [1]

[1] *Department of Civil and Environmental Engineering, Tohoku Gakuin University*
Chuo 1-13-1, Tagajo, Miyagi, Japan
yoshidan@tjcc.tohoku-gakuin.ac.jp

Keywords: Total stress analysis, Equivalent linear analysis, Effective stress analysis, earthquake motion index

Abstract. *Equivalent linear and truly nonlinear analyses, and total stress and effective stress analyses are compared at 268 sites under 11 earthquake motions in order to grasp general feature of the applicability of the equivalent linear method and total stress analysis. SHAKE and YUSAYUSA are used for equivalent linear and truly nonlinear methods, respectively. SHAKE shows larger peak acceleration and smaller peak displacement than YUSAYUSA (total stress analysis), but other indices such as instrumental seismic intensity, peak velocity, and spectral intensity are nearly same to each other. Therefore, it is applicable when truly nonlinear analysis is applicable. All earthquake motion indices are overestimated by the total stress analysis at the liquefiable sites. Therefore, it is recommended to use effective stress analysis at these sites. However, as indices are overestimated, use of the total stress can be said to result in conservative design. It is also noted that displacement or shear strain is underestimated in the total stress analysis.*

1 INTRODUCTION

Static analysis based on the seismic coefficient has been made long time. Recently, however, seismic response analysis becomes a powerful tool for the design of structures. There are several reasons that the seismic response analysis becomes important. One of the big reasons is that the input earthquake motion becomes large, under which design based on the static analysis frequently results in too conservative. In order to make the design based on the seismic response analysis, seismic response analysis of ground also becomes important as a tool to obtain the input earthquake motions to the structure.

Input earthquake motion was increased significantly in Japan, especially after the 1995 Kobe earthquake and more after the 2007 Niigataken-chuetsu-oki earthquake. Magnitude of the design earthquake motion, for example, exceeds 1 G in the design of nuclear power plants. Design input earthquake motions with maximum acceleration more than 0.5 m/s^2 is not an extraordinary case, but frequently appears in the practical design of civil and building structures. In these situations, maximum shear strain frequently reaches a few percent or more.

Various methods and computer programs have been proposed for the seismic response analysis of ground.

One of the frequently used computer programs is SHAKE [2], which employs an equivalent linear technique. The name SHAKE is now used as if it is a common noun, and it is also used as common noun in this paper. Unlike the name "equivalent", however, it is an approximate method. Therefore, it is believed that it cannot be applied at large strains. For example, Ishihara [3] suggests constitutive models and methods of the seismic response analysis related to different shear strain ranges and soil properties as shown in Figure 1. If maximum shear strain yields several percent, therefore, it is recommended to use the truly nonlinear method because the equivalent linear method is not applicable. However, engineers have a tendency to use SHAKE partly because of its easy handling compared with the truly nonlinear method, and partly because of the huge accumulation of experience to use the equivalent linear analysis.

Next problem is soil liquefaction. Considering that the definition of the soil liquefaction by means of shear strain is usually 5 % double amplitude axial strain under the tri-axial test condition, which corresponds to 3.75 % shear strain, effective stress analysis considering the excess porewater pressure generation is necessary if maximum strain comes several percent. However, use of the effective stress analysis is more difficult than that of total stress analysis. Therefore, total stress analysis is frequently carried out even when shear strain becomes very large.

There were not a few reports that compares various analytical method, and some reported that, for example, SHAKE is applicable, some does not. There seem at least two reasons to make this conflict. The one is that comparison is made on very few number of case studies, usually one or two, in which case obtained conclusion can be accidental except that the mechanism is clearly explained such

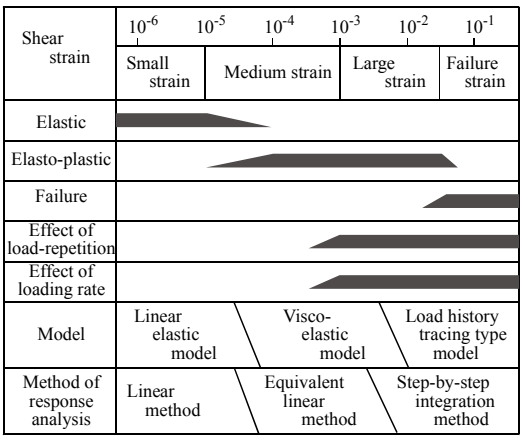


Figure 1 Change in soil properties with shear strain and corresponding modelling principle and method of response analysis [1]

as ref. [4] which shows two shortages of SHAKE and solution against them. The second reason is that there is no common method to evaluate accuracy of the result of the seismic response analysis.

Looking at past researches to show applicability of the seismic response analysis, one of the indices such as agreement of the maximum acceleration, similarity of waveforms, etc. has been used. Now it is well known that maximum acceleration is not a good ground motion index for long period structures. Detailed investigation is difficult only from the similarity of the waveform. Applicability must be evaluated by using objective and effective ground motion indices.

In this paper, accuracy of the total stress analysis by equivalent linear and truly nonlinear methods is evaluated by comparing the effective stress analysis for more than 250 sites and under various types of input earthquake motions.

2 ANALYZED SITES AND MODELING OF MECHANICAL PROPERTIES

Figure 2 shows soil profiles and SPT-*N* value of the ground used in this paper; in total, 268 sites are used. These sites were the sites used to evaluate applicability of the conventional method to evaluate onset of identification during the 1995 Kobe earthquake [5]. Many sites in Japan are included here.

Soils are classified into 6 categories, i.e., sand, silt, clay, gravel, humus, and others. Here, others include concrete and cobble, etc. In the modeling in this paper, humus soil are treated same as clay, and others are neglected by replacing them by the soil below it. The SPT-*N* values are averaged in the same soil layer. If there is no *N* value data in a layer, it is set same with the one below the layer. These modeling may not be good if actual behavior of the ground is investigated, but are not because the purpose of this paper is to investigate different ground model.

Unit weight of each layer was included in the original data. The shear wave velocity V_s is evaluated based on the specifications for highway bridges [6], i.e.,

$$\begin{aligned} V_s &= 100N^{1/3} \quad \text{(clayey soil)} \\ V_s &= 80N^{1/3} \quad \text{(sandy soil, other soils)} \end{aligned} \tag{1}$$

Shear strength of the clayey soil is evaluated as an average value suggested by JGS [7]

$$\tau_f = 19N \quad \text{(kPa)} \tag{2}$$

On the other hand, the internal friction angle ϕ is evaluated based on Hatanaka and Uchida [8] as

$$\phi = 20 + \sqrt{20N_1} \quad \text{(degree)} \tag{3}$$

where N_1 is corrected *N* value considering the effective over burden stress, and is evaluated as [6]

$$N_1 = \frac{170N}{\sigma'_v + 100} \quad (\sigma'_v \text{ in kPa}) \tag{4}$$

The hyperbolic model

$$\tau = \frac{G_0 \gamma}{1 + \tau_f \gamma / G_0} \tag{5}$$

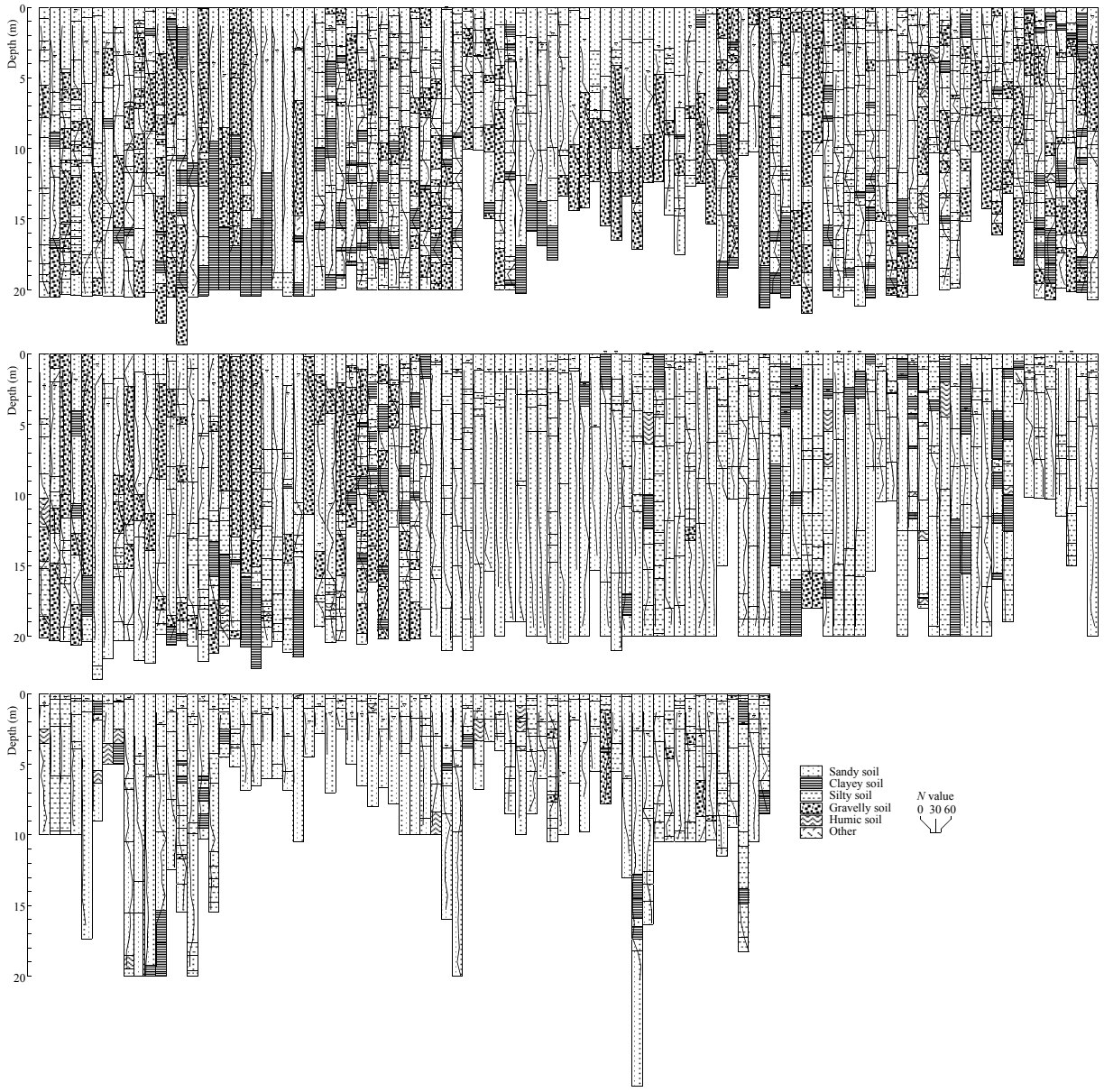


Figure 2 Soil profiles

is used for shear stress τ - shear strain γ relationships, and the Masing's rule is used to obtain damping characteristics, where G_0 is an elastic shear modulus.

Liquefaction strength of the sandy soils is evaluated based on the design specification of road bridges [6]. Shear stress ratio R_L is calculates as

$$R_L = \begin{cases} 0.0882\sqrt{N_a/1.7} & (N_a < 14) \\ 0.0882\sqrt{N_a/1.7} + 1.6\times10^{-6}(N_a - 14)^{4.5} & (N_a \geq 14) \end{cases} \tag{6}$$

where N_a is corrected SPT-N value considering fines contents F_c as

$$N_a = C_1 N_1 + C_2 \tag{7}$$

where

$$C_1 = \begin{cases} 1 & (0\% \le F_c < 10\%) \\ (F_c + 40)/50 & (10\% \le F_c < 60\%) \\ F_c/20 - 1 & (60\% \le F_c \le 100\%) \end{cases}, \quad C_2 = \begin{cases} 0 & (0\% \le F_c < 10\%) \\ (F_c - 10)/18 & (10\% \le F_c \le 100\%) \end{cases} \tag{8}$$

and N_1 is corrected SPT-N value considering the effective overburden stress obtained from Eq. (4).

This shear stress ratio (liquefaction strength) corresponds to 20 cycles of loading. Shear stress ratio at other cycles of loading is evaluated based on Seed et al. [9].

3 EARTHQUAKE MOTIONS

Input earthquake motion must have various and typical natures in order to obtain the general feature of the response. Eleven recorded earthquake motions which have different characteristics are employed so as to satisfy this requirement. They are as follows.

1) Inland earthquake
   Port Island GL-33 m, NS, 1995 Kobe eq.
   JMA Kobe, NS, 1995 Kobe eq.
   Hakuta, NS, 1999 Tottoriken-seibu eq.
   JMA Kawaguchi, EW, 2004 Niigataken-chuetsu eq.
   TEPCO Kashiwa-Kariwa Service hole SG1, NS, 2007 Niigataken-chuetsu-oki eq.
   Ichinoseki-nishi, EW, 2008 Iwate-Miyagi-nairiku eq.
2) Ocean trench earthquake
   Kaihoku bridge EW, 1978 Miyagiken-oki eq.
   Akita port, 1983 Nihonkai-chubu eq.
   Hachinohe office, EW, 1994 Sanriku-haruka eq.
   Hanasaki, EW, 1994 Hokkaido-toho-oki eq.
   Taiki, EW, 2003 Tokachi-oki eq.

These waves are applied as the earthquake motion of the outcropped base. Layers with V_s=300 m/s is added at the bottom of the ground in Figure 2. The shear wave velocity of the base layer is confirmed not to affect the behavior in the subsoil [10].

Waveforms of the input motion are shown in Figure 3. Generally speaking, duration of the earthquake is shorter in the inland earthquakes, but intensity is larger. Figure 4 shows response spectra of the input motions under 5% damping.

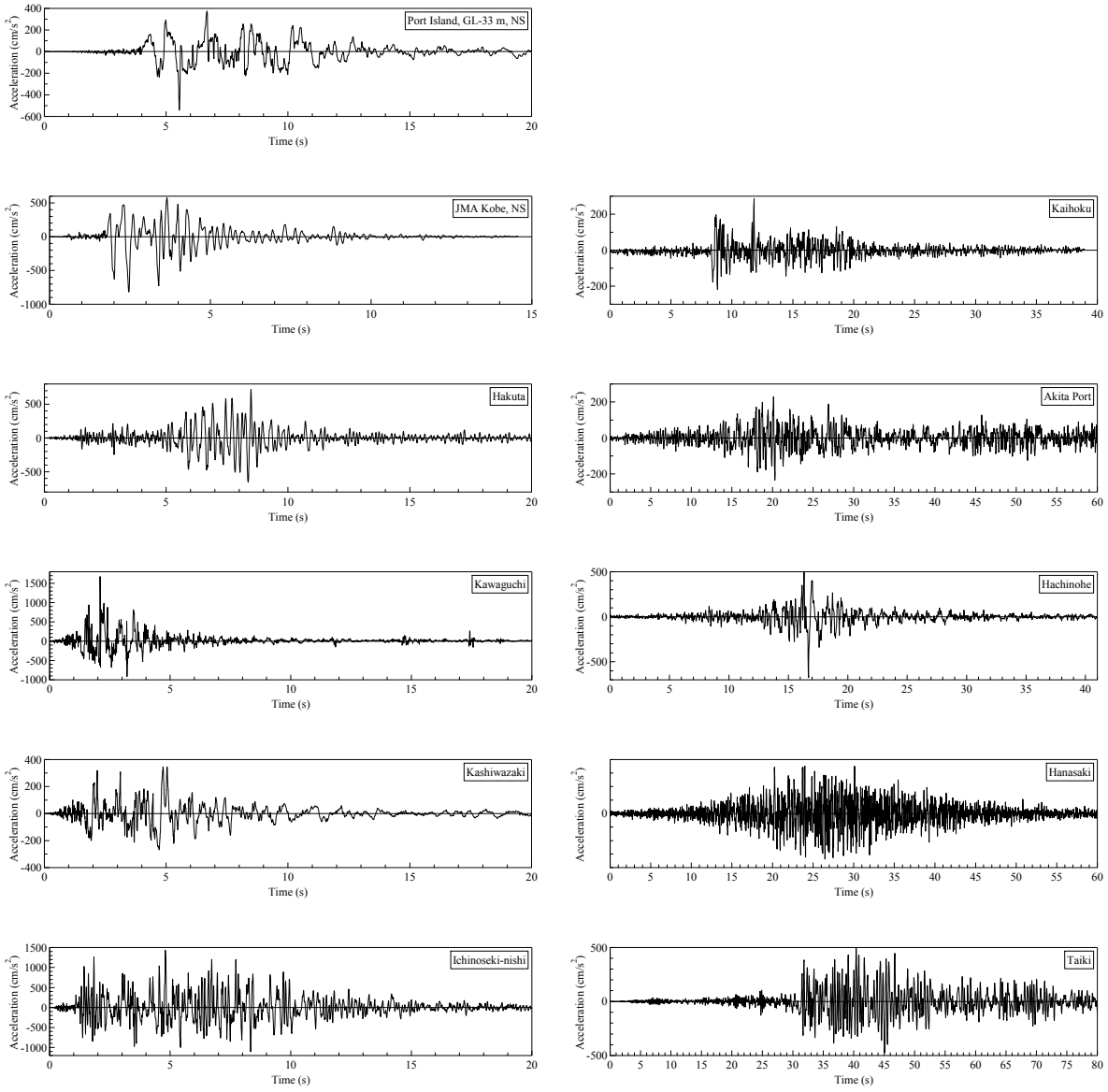
4 METHOD OF ANALYSIS AND ITS CHARACTERISTICS

Two different total stress analyses, equivalent linear method and truly nonlinear method, and one effective stress analysis are used. A computer program DYNEQ [11] is used for the equivalent linear analysis. DYNEQ is an open source program that has various functions based on complex moduli method, among which technique same with SHAKE is used in the calculation, and is referred as SHAKE. A computer program YUSAYUSA-2 [12], which is also an open source program, is used for the truly nonlinear and effective stress analyses. It will be referred as YUSAYUSA in the followings.

These two programs are examined under the same condition, i.e., the same ground model and the same stress-strain relationships. The only difference is that velocity proportional damping is considered in YUSAYUSA for the stability of numerical integration. Since the Rayleigh damping is employed, viscous coefficient matric [c] is calculated from the mass matrix [m] and stiffness matrix [k] as

$$[c]=\alpha[m]+\beta[k] \tag{9}$$

where α and β are constants and are set 0.090 and 0.00091, respectively, so that average



(a) Inland earthquakes (b) Ocean trench earthquakes

Figure 3 Input earthquake motions

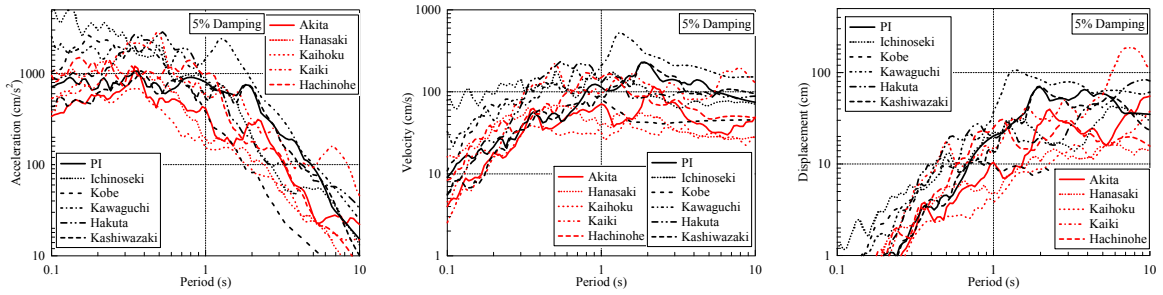


Figure 4 Response spectra of input motion

damping ratio between 0.5 Hz and 6 Hz becomes 1.43 % (Q=35)

Method of each analysis is briefly explained in the followings.

4.1 SHAKE

SHAKE [2] is based on the multiple reflection theory; equation of motion is solved in the frequency domain. Equivalent linear method is used in order to consider nonlinear behavior, in which stiffness and damping ratio at the effective stress γ_{eff} are used in whole analysis. The effective stress is evaluated from the maximum strain γ_{max} as

$$\gamma_{eff} = \alpha\gamma_{max} \tag{10}$$

where α is an adjusting parameter and 0.65 is usually used.

Two shortages are known in SHAKE [4] in addition to the fact that it cannot express the accurate stress-strain behavior because it is produced by the complex moduli.

The first shortage of SHAKE is overestimation of the maximum acceleration. The mechanism is shown in Figure 5. Since stress-strain relationships is a linear line passing the point A (γ_{eff}, τ=$G\gamma_{eff}$), maximum stress at γ=γ_{max} (τ_1 at point C) is larger than the actual stress (τ_2 at point B), which overestimation of the maximum shear stress result in overestimation of the maximum acceleration (See section 6.2 on the mechanism).

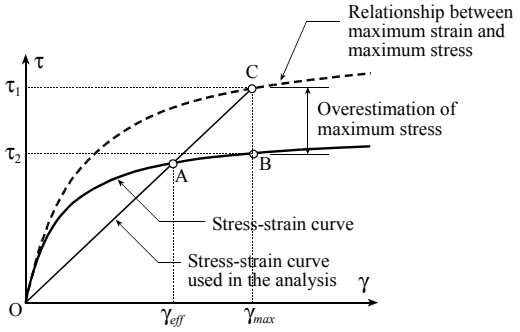


Figure 5 Mechanism of overestimation of maximum shear stress [4]

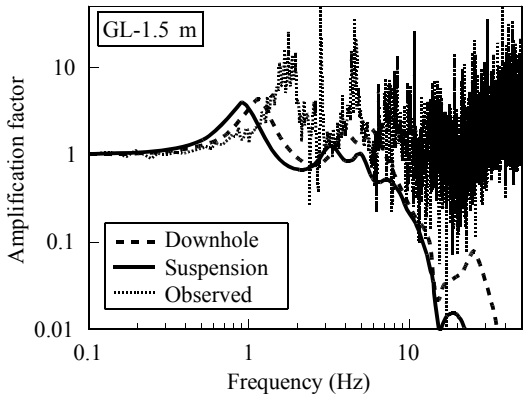


Figure 6 Underestimation of amplification at high frequencies [4]

The second shortage is typically seen in Figure 6. Amplification is significantly underestimated at high frequency. Maximum acceleration is underestimated by this mechanism.

These two factors work in the opposite way. The first mechanism overestimates maximum acceleration and the second mechanism underestimates maximum acceleration. Degree of effects depends on the degree of nonlinearity. This may be one of the reasons why evaluations of SHAKE scatter.

4.2 YUSAYUSA

YUSAYUSA [12] is a truly nonlinear seismic response analysis program. It uses hyperbolic model, Eq. (5), for backbone curve and the Masing's rule is used to develop hysteresis curve. Both total and effective stress analysis can be made. Excess porewater pressure generation is evaluated in the effective stress analysis by specifying the stress paths in the shear stress-effective overburden stress plane as shown in Figure 7, where B_p and B_u are parameters to control excess porewater pressure generation. They are evaluated so that R_{20} and R_5 coincide with the liquefaction strength defined in chapter 2.

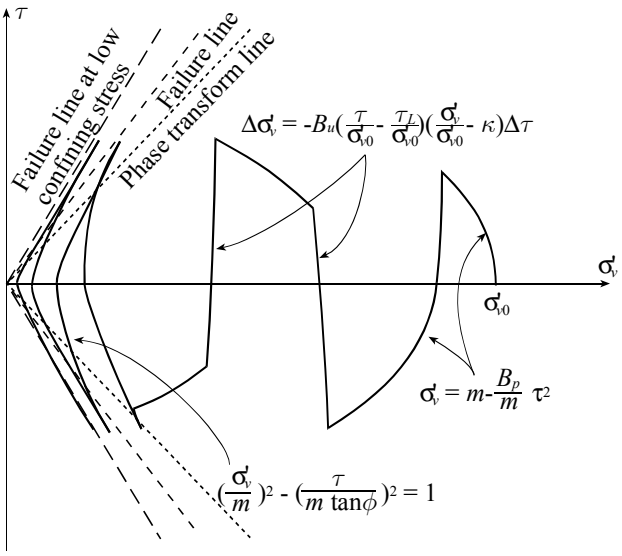


Figure 7 Stress-path model in YUSAYUSA

5 EARTHQUAKE MOTION INDEX

Many earthquake motion indices have been proposed, which indicates difficulty to express the intensity of the ground motion in one index. In this paper, several frequently used indices are used.

1) Peak acceleration

Peak acceleration is the most frequently used index because it directly related to inertia force of the structure. However, it is sometimes too sensitive.

2) Peak velocity

Applicability of the peak acceleration as an earthquake motion index becomes less for longer period structure. Instead of it, peak velocity becomes a good index. Here, this velocity is absolute velocity, but not relative velocity from the base although relative velocity is frequently used as outputs because it is directly obtained by solving the equation of motion.

3) Peak displacement

Displacement is a very important index for the design of the underground structures. Comparison of the relative displacements with recorded one is very difficult because vertical array records are necessary and because it depends on the method of integration as will be seen in in Figure 12. However, it can be done between analyses.

4) Instrumental seismic intensity

Seismic intensity has been used to express the degree of damage or ground shaking. Because of its nature, it takes time to evaluate the seismic intensity. After the 1995 Kobe earthquake, Japan Meteorological Agency made an seismic intensity which can be calculated from the acceleration time history and which is consistent with traditional JMA seismic intensity [13]. Evaluation of the seismic intensity can be done very quickly. Instrumental seismic intensity I_{JMA} is evaluated as

$$I_{JMA} = 2\log a_0 + 0.94 \tag{11}$$

where a_0 is the acceleration in cm/s^2 ; sum of the duration where acceleration exceeds a_0 is just 0.3 s in the filtered acceleration-time history. It is defined by using three directional components, but only one-directional component is used in this paper.

5) Spectral Intensity

Spectral intensity *SI* is first proposed by Housner [14] by integrating the response spectrum from 0.1 s to 2.5 s. It is modified to divide 2.4 s in order to make the dimension of the seismic intensity to be same with velocity. Then it is calculated as

$$SI = \frac{1}{2.4}\int_{0.1}^{2.5} S_{v,0.2}\,dt \tag{12}$$

where $S_{v,0.2}$ is a velocity response spectrum under 20 % damping. Equation (12) indicates that *SI* is an average of the velocity spectrum between 0.1 and 2.5 s. Pseudo velocity spectrum is sometimes used instead of velocity spectrum, but velocity spectrum is used in this paper.

6 COMPARISON AND DISCUSSION

6.1 Equivalent linear vs. truly nonlinear

Result under 11 earthquake motions are shown in one figure in the followings, in which result of each earthquake motion is distinguished by the symbols shown in Figure 8.

Figure 9 compares *PGA*s by all analyses, where subscript *EQ* indicates equivalent linear method (SHAKE) and *NL* indicates truly nonlinear method (YUSAYUSA). Two lines are drawn in the figure whose gradients are 1:1 and 1.5:1. *PGA* by SHAKE is always larger than that by YUSAYUSA except only several cases. *PGA* is overestimated more than 1.5 times in SHAKE in many cases which agrees with the discussion in Ref. [4] and Figure 5.

Figure 10 shows ratio of *PGA* in each soil profile. The same symbols seem to lie nearly horizontally although *PGA* scatters widely as seen in Figure 9.

Peak ground velocity, *PGV*, is compared in Figure 11. Both *PGV*s are nearly the same although that by the equivalent linear method seems to be a little larger than that by the nonlinear analysis. There are, however, two exceptions. *PGV* by nonlinear method shows much larger value than that of equivalent linear method under Kawaguchi (△) and Kaihoku (▼). This is not caused from the difference of the analytical methods but other reason.

Input earthquake motions are integrated to obtain absolute velocity by Fourier transform in SHAKE and Newmark's β method (β=0.25) in YUSAYUSA, respectively. Zero-th order or constant term is neglected in SHAKE, but is also integrated in YUSAYUSA. Figure 12 compares maximum velocity integrated by the Fourier transform and by the Newmark's β method. Almost all earthquake motion shows the same maximum velocity in two methods, but maximum velocity by the Newmark's β method is much larger than that by Fourier transform for Kaihoku and JMA Kawaguchi, which is the reason why *PGV*s by YUSAYUSA are much larger than those by SHAKE in Figure 11.

Considering these it can be concluded that *PGV*s are nearly the same for both SHAKE and YUSAYUSA although those by SHAKE is a little larger than those by YUSAYUSA.

Figure 13 compares displacements at the ground surface relative to base, *PGD*. *PGD* by SHAKE is in general smaller than that by YUSAYUSA. This behavior can be explained by the mechanism in Figure 5, too. Since stiffness is estimated large in SHAKE, resulting stress becomes small. It is also seen that degree of difference depends on the earthquakes as the same symbol shows similar tendency. Both analyses, for example, show similar PDG under Kaihoku. PDGs under Hachinohe also seem similar although *PGD* by SHAKE becomes

smaller when PDG becomes larger than 0.1 m. In addition, agreement is better under the ocean type earthquake than under the inland earthquake, except under Taiki.

Figures 14 and 15 compare JMA seismic intensity I_{JMA} and spectral intensity SI, respectively. Same with PGV, both indices are nearly the same although those by SHAKE are a little larger than that by YUSAYUSA. It is also pointed out that data under the same earthquake

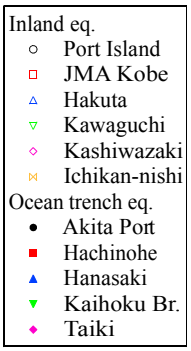


Figure 8 Legend to distinguish input earthquake

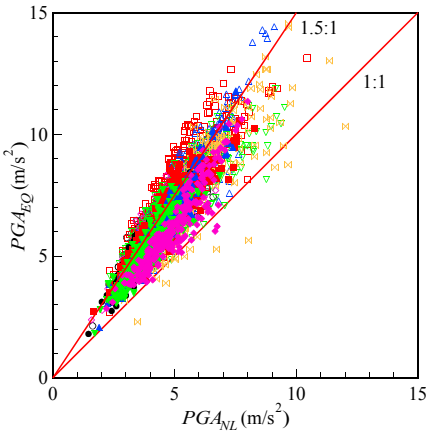


Figure 9 Comparison of peak ground accelerations

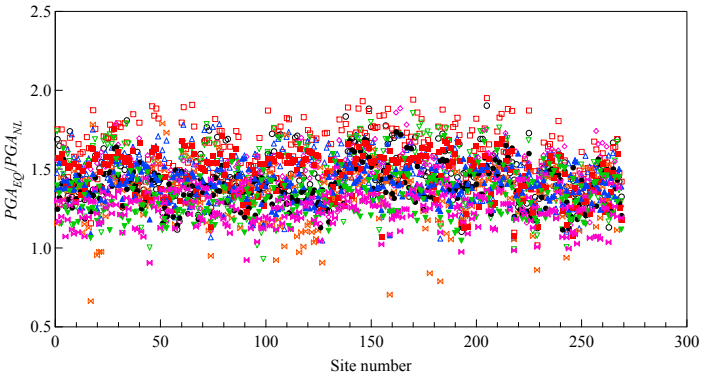


Figure 10 Acceleration ratios (SHAKE/YUSAYUSA)

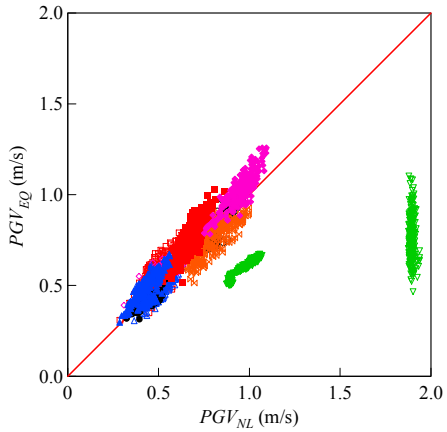


Figure 11 Comparison of peak ground (absolute) velocity

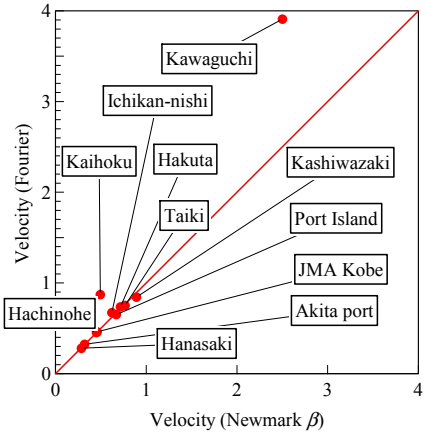


Figure 12 Maximum velocity of input earthquake motions

motion show similar characteristics

Figure 16 shows comparison of the maximum stresses by both methods. Here, the largest strain in each ground is used as the maximum strain. Therefore, it may not be the same layer. If the mechanism shown in Figure 5 works, the shear strain by SHAKE is smaller than that by YUSAYUSA. Validity of this mechanism was confirmed through Figure 5 and Figure 13 in general. However, there are many data that strains by SHAKE are larger than those by YUSAYUSA. It may indicate that vibration modes are different under each analysis.

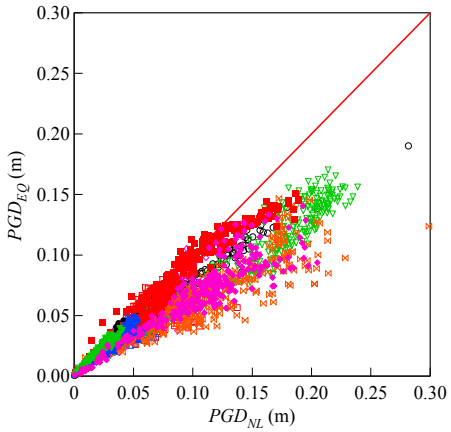


Figure 13 Comparison of *PGD*

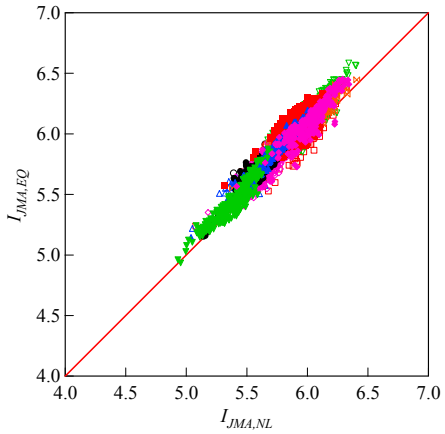


Figure 14 Comparison of JMA seismic intensity

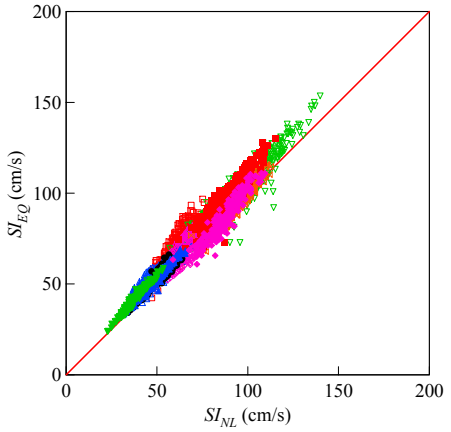


Figure 15 Comparison of *SI* value

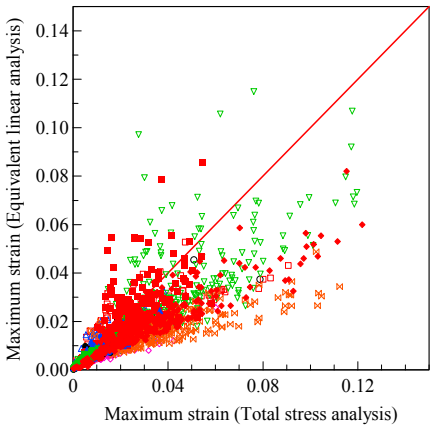


Figure 16 Comparison of maximum strains

6.2 Total stress vs. effective stress

Effective stress analysis and total stress truly nonlinear analysis are compared here. Both calculations are made by YUSAYUSA; the only difference is consideration of excess porewater pressure generation or not. The subscript *EF* and *NL* indicate effective stress and total stress analyses, respectively.

The peak ground acceleration *PGA* is compared in Figure 17. Many data lie on the line $PGA_{EF} = PGA_{NL}$. They are the case where there is no liquefiable layer, in which case results becomes identical. Beside these data, *PGA* by effective stress analysis is smaller than that by total stress analysis. Sometimes it reaches 1/3 or less, which can be seen in Figure 19.

The peak ground velocity *PGV* is compared in Figure 18. Again magnitude by the effective stress analysis is much smaller than that by the total stress analysis. This is quite different feature compared with the comparison between equivalent linear and truly nonlinear analyses in Figure 11, in which *PGV*s are similar.

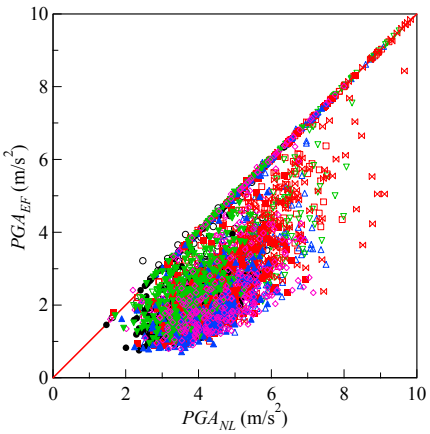


Figure 17 Comparison of *PGA*

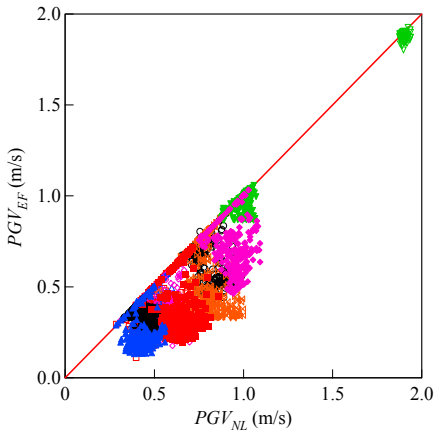


Figure 18 Comparison of *PGV*

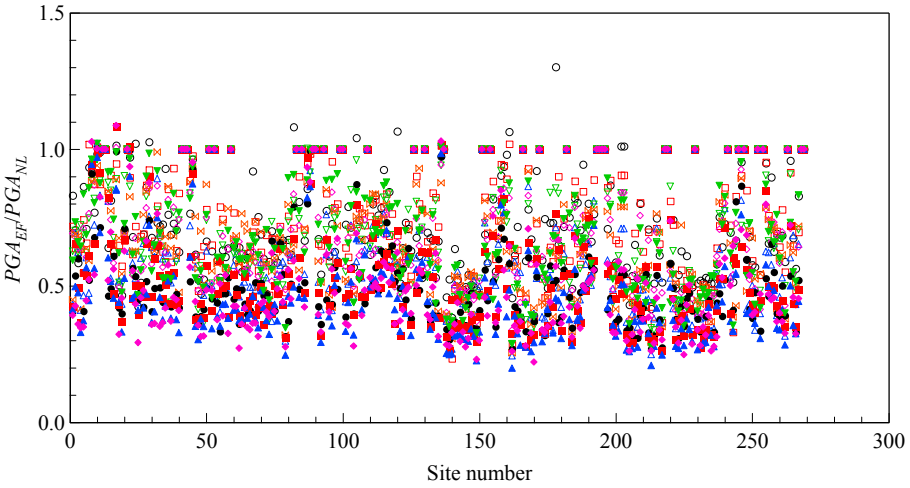


Figure 19 Acceleration ratios (Effective stress/Total stress)

Instrumental seismic intensity I_{JMA} is compared in Figure 20 and *SI* is compared in Figure 21. Similar with *PGA* and *PGV*, those by the effective stress analysis are frequently much smaller than those by the total stress analysis. These observations can be explained by considering the upper bound ground motion caused by the nonlinear behavior [15].

Left side of Figure 22 shows equilibrium of a infinitesimally small element, from which equation of motion or equation of wave motion can be derived. On the other hand, right side of Figure 22 shows equilibrium of a soil column above the weak layer. If shear stress of the weak layer reaches shear strength, average acceleration above this layer reaches upper bound. This mechanism can explain the reason why *PGA* by the effective stress analysis is smaller than that by the total stress analysis.

There are also upper bounds on I_{JMA} and *SI* values, but the mechanism is somewhat different from the upper bound of *PGA*. I_{JMA} uses frequency between 0.5 to 8 Hz and *SI* uses period between 0.1 to 2.5 s. Period of the wave become longer as nonlinear behavior becomes signif-

icant, and if period becomes longer than the period that is used in these indices, earthquake motion does not contribute these indices. Indices by the effective stress analysis are sometimes much smaller than that by the total stress analysis, which indicates that nonlinear behavior is significant when liquefaction occurs.

Peak ground displacements are compared in Figure 23 and maximum shear strains are compared in Figure 24. Those by the effective stress analysis are sometimes much larger than those by the total stress analysis, which also suggests significant nonlinear behavior.

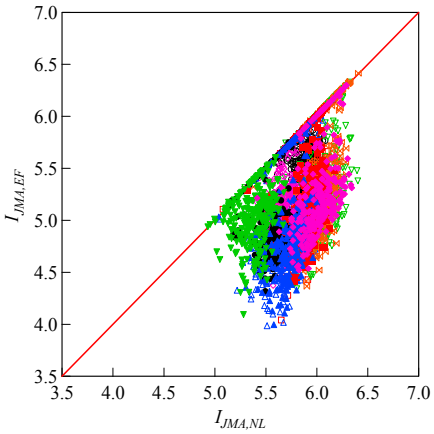


Figure 20 Comparison of I_{JMA}

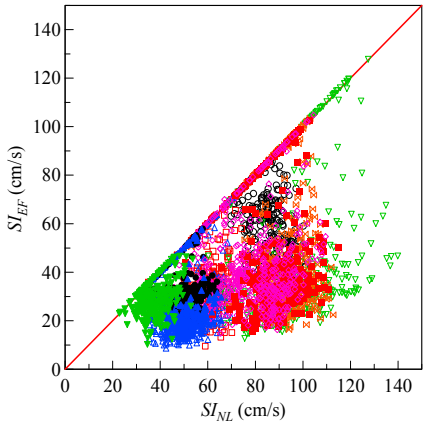


Figure 21 Comparison of SI value

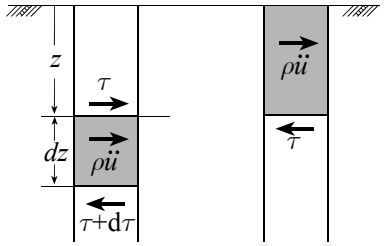


Figure 22 Equilibrium of soil column

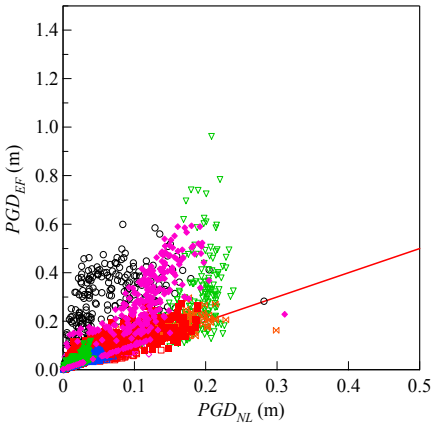


Figure 23 Comparison of *PGD*

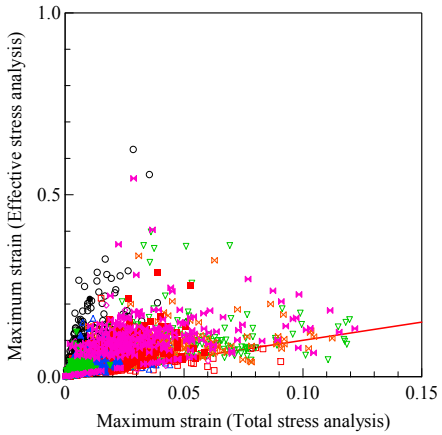


Figure 24 Comparison of maximum shear strain

7 CONCLUDING REMARKS

Applicability of the equivalent linear analysis (SHAKE) and total stress analysis under large earthquakes are examined by using more than 250 sites and 11 earthquakes. Since typical grounds and earthquake motions are included, the conclusions obtained here shows general feature of the analysis. The following conclusions are obtained.

1) *PGA* is overestimated by the equivalent linear method. Sometimes, it is more than 1.5 times larger than that by the truly nonlinear method.
2) *PGD* is underestimated by the equivalent linear method. It is frequently less than a half compared with that by the truly nonlinear method.
3) Other indices such as *PGV*, seismic intensity, and spectral intensity are nearly the same between the equivalent linear method and truly nonlinear method although evaluation by the equivalent linear method is a little larger than that by the truly nonlinear method.
4) All earthquake motion indices become significantly small when soil liquefaction occurs, except PGD and the maximum shear strain which becomes large.

Considering these, it is recommended to use effective stress analysis at the liquefiable site, but total stress analysis may be applicable because it results in larger earthquake motion to the structures. However, as predominant period of the wave becomes long, it may affect the structure with long natural period. It is also noted that shear strain and relative displacement is underestimated in the total stress analysis, which affects the design of underground structures such as pipe and pile lines.

Equivalent linear method is applicable in many fields if liquefaction does not occur because it shows a little conservative result, except the case that maximum displacement and maximum acceleration are interested at.

REFERENCES

[1] Ishihara, K. (1982): Evaluation of soil properties for use in earthquake response analysis, Proc., 9th International Symposium on Numerical Models in Geomechanics, Zurich, pp. 237-259

[2] P.B. Schnabel, J. Lysmer, H. B. Seed, SHAKE A Computer program for earthquake response analysis of horizontally layered sites, *Report No. EERC72-12, University of California, Berkeley*, 1972.

[3] K. Ishihara, Evaluation of soil properties for use in earthquake response analysis, *9th International Symposium on Numerical Models in Geomechanics*, Zurich, 237-259, 1982.

[4] N. Yoshida, S. Kobayashi, I. Suetomi, K. Miura, Equivalent linear method considering frequency dependent characteristics of stiffness and damping, *Soil Dynamics and Earthquake Engineering*, **22**, 3, 205-222, 2002.

[5] Report on accuracy of method to identify liquefaction during the Hyogoken-nambu earthquake, *Public Work Research Institute*, 1996. (in Japanese)

[6] Specifications for highway bridges, Part V (seismic design), *Japan Road Association*, 2012. (in Japanese)

[7] Japanese standards for geotechnical and geoenvironmental investigation methods -standards and explanations-,Japanese Geotechnical Society, 2004. (in Japanese)

[8] M. Hatanaka, A. Uchida, Empirical correlation between penetration resistance and internal friction angle of sandy soils, *Soils and Foundations*, **36**, 4, 1-9, 1996.

[9] H. B. Seed, I. M. Idriss, I Arango, Evaluation of liquefaction potential using field performance data, *J, of GT*, *ASCE*, **109**,3, 458-482, 1981.

[10] Y. Usami, T. Sasaki, N. Yoshida, Effect of velocity structure under seismic base layer on earthquake response, *Annual Meeting of Tohoku Branch of JSCE*, 317-318, 2009. (in Japanese)

[11] N. Yoshida, A computer program for DYNamic response analysis of level ground by EQuivalent linear method, Revised in 2004 (version 3.25), *Tohoku Gakuin University*; *http://www.civil.tohoku-gakuin.ac.jp/yoshida/computercodes/eqcode.html*, 1995.

[12] N. Yoshida, I. Towhata, YUSAYUSA-2 and SIMMDL-2, theory and practice, revised in 2003 (version 2.1), *Tohoku Gakuin University and University of Tokyo; http://www.civil.tohoku-gakuin.ac.jp/yoshida/computercodes/eqcode.html*, 1991.

[13] I. Muramatsu, On JMA instrumental seismic intensity, *JSEEP NEWS*, 150, 27-36, 1996, (in Japanese)

[14] G. W. Housner, Intensity of earthquake ground shaking near the causative fault, *3WCEE*, **I**, III-94-III-115, 1965.

[15] N. Yoshida, Large earthquake motion and ground -nonlinear problem-, Jishin Journal, Association for Development of Earthquake Prediction, 28, 66-74, 1999. (in Japanese)

COMPDYN 2013
4th ECCOMAS Thematic Conference on
Computational Methods in Structural Dynamics and Earthquake Engineering
M. Papadrakakis, V. Papadopoulos, V. Plevris (eds.)
Kos Island, Greece, 12–14 June 2013

THE STABILITY OF THE GENERALISED-A METHOD IN SOIL-PORE FLUID COUPLED FORMULATION

Bo Han[1], **Lidija Zdravković**[1], **Stavroula Kontoe**[1]

[1] Department of Civil and Environmental Engineering, Imperial College, London SW7 2AZ
e-mail: b.han10@imperial.ac.uk
l.zdravkovic@imperial.ac.uk
stavroula.kontoe@imperial.ac.uk

Keywords: stability condition, CH method, dynamic analysis, finite element method, coupled formulation

Abstract. *This paper investigates the stability of the Generalised-α time integration method (the CH method) for a fully coupled solid-pore fluid formulation. Theoretical stability conditions are derived, which are shown to simplify to the existing ones of the CH method for the one–phase formulation when the solid-fluid coupling is ignored. Finite Element (FE) analyses considering a range of loading conditions are conducted to validate the analytically derived stability condition, showing that the numerical results are in agreement with the theoretical investigation. The CH method is a generalisation of a number of other time integration schemes and hence the derived stability conditions are relevant for most of the commonly utilised time integration methods for fully coupled two-phase formulation.*

1 INTRODUCTION

In dynamic Finite Element (FE) analysis, the time integration method has been widely and successfully used to solve the second order governing equation of motion, due to its ability of reproducing both material and geometric nonlinearities. Since 1950s, various time integration methods have been proposed, like the Newmark method [16] and the Generalised-α method (CH method) of Chung & Hulbert [6], which have been widely implemented into FE programs and successfully utilised to solve numerically the equation of motion for one-phase materials. The CH method satisfies the main requirements for an efficient time marching algorithm, which include unconditional stability for linear problems, second order accuracy and controllable numerical dissipation in the high frequency range [11]. The role of numerical damping is to eliminate spurious high frequency oscillations that are introduced into the solution due to poor spatial representation of the high-frequency modes.

Depending on the soil permeability, the rate of loading and the hydraulic boundary conditions, it is often necessary to employ coupled analysis to accurately model the two phase behaviour of the soil. Dynamic analyses are further complicated by the presence of the inertia forces of the different phases (i.e. solid skeleton and pore water) and the coupling between them. Hence, the formulation of the CH method was extended by Kontoe [13] and Kontoe et al [14] to enable the solution of dynamic coupled consolidation problems and was then implemented in the FE program ICFEP (Imperial College Finite Element Program) [17]. The key feature of unconditional stability of this method has been comprehensively investigated by previous studies, both analytically and numerically, but only for the one-phase formulation. The two-phase coupled FE formulation requires an additional equation (the dynamic consolidation equation) and an additional unknown (pore water pressure). Aiming to solve two dynamic coupled equations (i.e. the equation of motion and the consolidation equation), the time integration method is applied to both equations. This not only increases the complexity of the implementation, but it also changes the numerical features of the time integration method. Therefore, the numerical stability of the CH method needs to be investigated rigorously for two-phase coupled problems.

In this paper, the stability of the CH method for the coupled formulation is analytically investigated and the corresponding theoretical stability conditions are derived. The analytically derived stability conditions are validated by various FE analyses considering a range of loading conditions. Furthermore, since the CH method is a generalisation of the Newmark [16], HHT [10] and WBZ [19] methods, the stability investigation of the CH method for the two-phase coupled formulation is relevant for most of the commonly used time integration methods.

2 THE CH METHOD FOR THE COUPLED DYNAMIC FORMULATION

The coupled FE formulation for saturated porous materials is based on Biot's consolidation theory, proposed in 1956 and 1962 [2][3][4], which was firstly implemented numerically by Ghaboussi and Wilson [8]. Zienkiewicz and Shiomi [20] identified three categories of dynamic coupled formulations, namely the u-p formulation, the u-p-w formulation and the u-U formulation, where u, w, U and p denote the solid displacement, the fluid velocity relative to the solid component, the fluid displacement and the pore water pressure respectively. According to Zienkiewicz and Shiomi [20], the fluid acceleration relative to the solid and its convective terms are insignificant in the frequency range that is of concern in earthquake engineering problems. Therefore, by ignoring the relative fluid acceleration and its convective terms, Biot's theory can be simplified to the u-p formulation. In ICFEP, the u-p formulation was

adopted by Potts and Zdravkovic [17] and was later extended to deal with dynamic loading by Hardy [9] and Kontoe [13].

The principle of the CH method is that the acceleration, velocity, displacement and pore water pressure terms are evaluated at different instants within the time step, controlled by integration parameters α_m and α_f (shown in Equation (1)). The variations of velocity and displacement within the time step for the CH method are approximated by Newmark's equations, governed by the integration parameters α and δ (shown in Equation (2)). Kontoe [13] and Kontoe et al [14] showed that the final dynamic FE coupled consolidation formulation for the CH method can be described by Equation (3), where five integration parameters, α_m, α_f, α, δ and β, are involved. It should be noted that β is the integration parameter of a time marching scheme which is employed in ICFEP to solve the integrals of the consolidation equation, which are shown in Equation (4).

$$\left\{\begin{array}{l} \ddot{u}_{t_{k+1-\alpha_m}} = (1-\alpha_m)\ddot{u}_{t_{k+1}} + \alpha_m \ddot{u}_{t_k} \\ \dot{u}_{t_{k+1-\alpha_f}} = (1-\alpha_f)\dot{u}_{t_{k+1}} + \alpha_f \dot{u}_{t_k} \\ u_{t_{k+1-\alpha_f}} = (1-\alpha_f)u_{t_{k+1}} + \alpha_f u_{t_k} \\ p_{t_{k+1-\alpha_f}} = (1-\alpha_f)p_{t_{k+1}} + \alpha_f p_{t_k} \\ t_{k+1-\alpha_m} = (1-\alpha_m)t_{k+1} + \alpha_m t_k \\ t_{k+1-\alpha_f} = (1-\alpha_f)t_{k+1} + \alpha_f t_k \end{array}\right\} \tag{1}$$

$$\begin{aligned} \Delta\dot{u} &= \frac{\delta}{\alpha\Delta t}\Delta u - \frac{\delta}{\alpha}\dot{u}_{t_k} + \left(1-\frac{\delta}{2\alpha}\right)\Delta t\ddot{u}_{t_k} \\ \Delta\ddot{u} &= \frac{1}{\alpha\Delta t^2}\Delta u - \frac{1}{\alpha\Delta t}\dot{u}_{t_k} - \frac{1}{2\alpha}\ddot{u}_{t_k} \end{aligned} \tag{2}$$

$$\begin{bmatrix} \left(\frac{1-\alpha_m}{\alpha\Delta t^2}\right)[M] + \left(\frac{(1-\alpha_f)\delta}{\alpha\Delta t}\right)[C] + (1-\alpha_f)[K] & (1-\alpha_f)[L] \\ \frac{(1-\alpha_m)\beta}{\alpha\Delta t}[G] + (1-\alpha_f)[L]^T & (1-\alpha_f)(-\beta\Delta t[\phi] - [S]) \end{bmatrix} \begin{bmatrix} \{\Delta u\} \\ \{\Delta p\} \end{bmatrix} = \begin{bmatrix} \Delta\overline{R} \\ \Delta\overline{F} \end{bmatrix} \tag{3}$$

$$\begin{aligned} \int_{t_k}^{t_k+\Delta t} \{p\}dt &= \left[\{p_{t_k}\} + \beta\{\Delta p\}\right]\Delta t \\ \int_{t_k}^{t_k+\Delta t} \{\ddot{u}\}dt &= \left[\{\ddot{u}_{t_k}\} + \beta\{\Delta\ddot{u}\}\right]\Delta t \end{aligned} \tag{4}$$

The coupled dynamic formulation (Equation (3)) was derived based on the dynamic equilibrium of the solid-fluid mixture, the continuity equation of the pore fluid flow and the generalised Darcy's law. In the above equations, $[M]$, $[C]$, $[K]$, $[L]$, $[\phi]$ and $[S]$ are the global mass, damping, stiffness, coupling, permeability and water compressibility matrices respectively, and $\ddot{u}$, $\dot{u}$, u and p represent the nodal acceleration, velocity, displacement and pore water pressure variables respectively. It should be noted that the matrix $[G]$ in Equation (3) represents the impact of the inertia of the solid on the pore water pressure. It has been though suggested that the influence of the matrix $[G]$ on the dynamic response is insignificant for the frequency range within which the "u-p" formulation is valid [5]. Therefore, the matrix $[G]$ is not taken into account in the dynamic coupled formulation for the work presented herein. Fur-

thermore, the matrices and the right hand side terms of Equation (3) are detailed in the Appendix.

3 STABILITY ANALYSIS OF THE CH METHOD FOR THE COUPLED FORMULATION

A time integration method is considered stable when it produces a numerical solution which remains always bounded [1]. The fundamental assumption of a time integration method is that the acceleration, velocity and displacement at a specific increment can be expressed as a function of these variables at previous increments, as follows:

$$\begin{Bmatrix} \ddot{u}_{t_{k+1}} \\ \dot{u}_{t_{k+1}} \\ u_{t_{k+1}} \end{Bmatrix} = [A] \begin{Bmatrix} \ddot{u}_{t_k} \\ \dot{u}_{t_k} \\ u_{t_k} \end{Bmatrix} \tag{5}$$

where $[A]$ is the amplification matrix controlling the stability, accuracy and other numerical features of the considered time integration method. Based on the definition of numerical stability, for a time integration method to be stable, the matrix $[A]$ should be bounded. Therefore, the modulus of the eigenvalues of matrix $[A]$ should be less than one, expressed by the following equation:

$$\rho(A) = \max\{|\lambda_1|, |\lambda_2|, |\lambda_3|\} \leq 1 \tag{6}$$

where ρ is the spectral radius of the matrix $[A]$, and λ_1, λ_2 and λ_3 are the eigenvalues of the matrix $[A]$.

Considering the above-mentioned stability condition, Routh [18] and Hurwitz [12] suggested that, if λ is substituted by a complex number z (as shown in Equation (7)), the condition of $|\lambda| \leq 1$ can be converted to the condition of $\mathrm{Re}(z) \leq 0$.This indicates that the real part of z should be less or equal to zero in order to satisfy the stability condition.

$$\lambda = \frac{1+z}{1-z} \tag{7}$$

Furthermore, for a general polynomial of the form shown in Equation (8) to satisfy the condition of $\mathrm{Re}(z) \leq 0$, the conditions of Equation (9) should be also satisfied. Therefore, the stability condition of $|\lambda| \leq 1$ is finally converted to the condition given by Equation (9) which will be utilised for the following stability analysis of the CH method.

$$a_0 z^n + a_1 z^{n-1} + a_2 z^{n-2} + \ldots . a_n = 0 \tag{8}$$

$$a_0 > 0 \quad and \quad a_i \geq 0 \quad for \quad i > 0 \tag{9}$$

Expressing the acceleration, velocity, displacement and pore water pressure at time increment t_{k+1} as a function of their historic values and employing the Routh-Hurwitz condition results to:

$$\begin{Bmatrix} \ddot{u}_{t_{k+1}} \\ \dot{u}_{t_{k+1}} \\ u_{t_{k+1}} \\ p_{t_{k+1}} \end{Bmatrix} = \frac{1+z}{1-z} \begin{Bmatrix} \ddot{u}_{t_k} \\ \dot{u}_{t_k} \\ u_{t_k} \\ p_{t_k} \end{Bmatrix} \tag{10}$$

In addition, by employing Newmark's expressions (Equation (2)) and the CH method (Equation (1)), the acceleration, velocity, displacement and pore water pressure at different instants within a time step can be expressed as follows:

$$\begin{Bmatrix} \ddot{u}_{t_{k+1-\alpha_m}} \\ \dot{u}_{t_{k+1-\alpha_f}} \\ u_{t_{k+1-\alpha_f}} \\ p_{t_{k+1-\alpha_f}} \end{Bmatrix} = \begin{Bmatrix} \dfrac{(1-2\alpha_m)z+1}{2z}\Delta\ddot{u} \\ \dfrac{(2\delta-1)(1-2\alpha_f)z^2+(2\delta-2\alpha_f)z+1}{4z^2}\Delta\ddot{u}\Delta t \\ \dfrac{(4\alpha-2\delta)(1-2\alpha_f)z^3+(4\alpha-4\delta\alpha_f+2\alpha_f-1)z^2+(2\delta-2\alpha_f)z+1}{8z^3}\Delta\ddot{u}\Delta t^2 \\ \dfrac{(1-2\alpha_f)z+1}{2z}\Delta p \end{Bmatrix} \tag{11}$$

Equation (11) can be then substituted into the scalar forms of the coupled dynamic FE formulation (Equations (12) and (13)). This allows the equation of motion and the dynamic consolidation equation to be expressed in terms of only two unknowns ($\Delta\ddot{u}$ and Δp) as shown in Equations (14) and (15).

$$m\ddot{u}_{t_{k+1-\alpha_m}} + c\dot{u}_{t_{k+1-\alpha_f}} + ku_{t_{k+1-\alpha_f}} + lp_{t_{k+1-\alpha_f}} = 0 \tag{12}$$

where m, c, k and l are the scalar forms of the matrices $[M]$, $[C]$, $[K]$ and $[L]$ respectively.

$$-(1-\alpha_f)\varphi(p_k+\beta\Delta p)-(1-\alpha_f)s\frac{\Delta p}{\Delta t}+(1-\alpha_f)l^T\frac{\Delta u}{\Delta t}=0 \tag{13}$$

where φ and s are the scalar forms of the matrices $[\phi]$ and $[S]$ respectively.

$$\begin{Bmatrix} \left[4m(1-2\alpha_m)+2c\Delta t(2\delta-1)(1-2\alpha_f)+k\Delta t^2(4\alpha-2\delta)(1-2\alpha_f)\right]z^3 \\ +\left[4m+2c\Delta t(2\delta-2\alpha_f)+k\Delta t^2(4\alpha-4\delta\alpha_f+2\alpha_f-1)\right]z^2 \\ +\left[2c\Delta t+k\Delta t^2(2\delta-2\alpha_f)\right]z \\ +k\Delta t^2 \end{Bmatrix}\Delta\ddot{u} + \begin{Bmatrix} 4l(1-2\alpha_f)z^3 \\ +(4l)z^2 \end{Bmatrix}\Delta p = 0 \tag{14}$$

$$\begin{Bmatrix} l^T\Delta t(4\alpha-2\delta)(1-\alpha_f)z^2 \\ +l^T\Delta t(2\delta-1)(1-\alpha_f)z \\ +l^T\Delta t(1-\alpha_f) \end{Bmatrix}\Delta\ddot{u} - \begin{Bmatrix} \varphi(4\beta-2)(1-\alpha_f)+4\dfrac{s}{\Delta t}(1-\alpha_f)z^2 \\ +2\varphi(1-\alpha_f)z \end{Bmatrix}\Delta p = 0 \tag{15}$$

For convenience, applying A, B, C and D to represent the multipliers in front of $\Delta\ddot{u}$ and Δp, Equations (14) and (15) can be written as the following Equation (16):

$$\begin{bmatrix} A & B \\ C & -D \end{bmatrix}\begin{Bmatrix} \Delta\ddot{u} \\ \Delta p \end{Bmatrix} = 0 \tag{16}$$

For a non-trivial solution, the determinant of matrix $\begin{bmatrix} A & B \\ C & -D \end{bmatrix}$ must be zero which leads to a polynomial of z expressed by Equation (17):

$$F(z)=\begin{vmatrix} A & B \\ C & -D \end{vmatrix} = A(-D)-BC=0 \tag{17}$$

where $F(z)$ is the polynomial of z. After substituting the original forms of A, B, C and D into Equation (17), $F(z)$ is expressed by the following equation:

$$F(z)=a_0 z^5 + a_1 z^4 + a_2 z^3 + a_3 z^2 + a_4 z = 0 \tag{18}$$

where

$$\begin{aligned} a_0 &= (a+b+c)(o+p)+lj \\ a_1 &= (a+b+c)q+(d+e+f)(o+p)+lk+mj \\ a_2 &= (d+e+f)q+(g+h)(o+p)+mk+nj \\ a_3 &= (g+h)q+i(o+p)+nk \\ a_4 &= iq \end{aligned}$$

where a, b, …,q are illustrated in Figure 1.

$$\left\{\begin{matrix} a \\ [4m(1-2\alpha_m)+2c\Delta t(2\delta-1)(1-2\alpha_f)+k\Delta t^2(4\alpha-2\delta)(1-2\alpha_f)]z^3 \\ d \\ +[4m+2c\Delta t(2\delta-2\alpha_f)+k\Delta t^2(4\alpha-4\delta\alpha_f+2\alpha_f-1)]z^2 \\ g \\ +[2c\Delta t+k\Delta t^2(2\delta-2\alpha_f)]z \\ i \\ +k\Delta t^2 \end{matrix}\right. \begin{matrix} b \\ e \\ h \end{matrix} \left.\begin{matrix} c \\ f \end{matrix}\right\} \Delta ii + \left\{\begin{matrix} j \\ 4l(1-2\alpha_f)z^3 \\ k \\ +(4l)z^2 \end{matrix}\right\} \Delta p = 0$$

$$\left\{\begin{matrix} l \\ l^T\Delta t(4\alpha-2\delta)(1-\alpha_f)z^2 \\ m \\ +l^T\Delta t(2\delta-1)(1-\alpha_f)z \\ n \\ +l^T\Delta t(1-\alpha_f) \end{matrix}\right\} \Delta ii - \left\{\begin{matrix} o & p \\ \varphi(4\beta-2)(1-\alpha_f)+4\frac{s}{\Delta t}(1-\alpha_f)z^2 & \\ q & \\ +2\varphi(1-\alpha_f)z & \end{matrix}\right\} \Delta p = 0$$

Figure 1: Illustration of the parameters in the characteristic polynomial

Based on the Routh-Hurwitz condition for stability, in order for the CH method to be stable, the coefficients in Equation (18) should obey the conditions of $a_0 > 0$ and $a_i \geq 0$ for $i > 0$. However, based on the expressions of a_0 to a_4, the time step Δt is included in the terms a_0 to a_4, which means that the stability conditions depend on the time step and therefore the CH method is only conditionally stable. In order to obtain unconditional stability for the CH method, the time step should be separated from the stability conditions. Hence, every single term of a_0 to a_4 (i.e. a, b, …,q) should be equal or larger than zero, which leads to the following unconditional stability conditions for the CH method:

$$a, b, ..., q \geq 0 \tag{19}$$

Based on Chung and Hulbert [6], the CH method achieves second accuracy and maximum high frequency dissipation when $\delta = 0.5 - \alpha_m + \alpha_f$ and $\alpha = 0.25(1 - \alpha_m + \alpha_f)^2$. These two expressions for δ and α are employed herein to derive the unconditional stability condi-

tions only in terms of α_m, α_f and β. Hence, after substituting the two expressions into Equation (19), the final unconditional stability conditions of the CH method for the coupled formulation are expressed by Equation (20).

$$\alpha_m \leq \alpha_f \leq 0.5 \quad and \quad \beta \geq 0.5 \tag{20}$$

In the proposed stability conditions, the former condition is based on the equation of motion and the latter one is based on the dynamic consolidation equation. It is obvious that the stability conditions can reduce to $\alpha_m \leq \alpha_f \leq 0.5$ by ignoring the hydraulic coupling, which are identical to the unconditional stability conditions of the CH method for the one-phase formulation proposed by Chung and Hulbert [6].

4 VALIDATION OF STABILITY CONDITIONS

A one-dimensional (1-D) soil column, assuming linear elastic soil behaviour and plane strain conditions, is analysed considering a range of dynamic loading conditions. The CH method is utilised for the simulations and the numerical results are firstly compared with either a closed form solution or an existing numerical investigation. Furthermore, parametric studies of varying integration parameters are conducted, in order to validate the proposed stability conditions. It should be noted that zero material damping is employed for all the numerical simulations in this paper, for the consistency with the assumptions of the theoretical stability analysis.

4.1 1-D Column Subjected to Step Loading

The first example concerns a soil column subjected to step loading. The finite element mesh (consisting of 500 4-noded elements) and the boundary conditions are shown in Figure 2. For the hydraulic boundary conditions, pore water pressure is prescribed as zero at the top of the mesh and the remaining boundaries are considered to be impermeable. Furthermore, a uniformly distributed load is applied on the top boundary as illustrated in Figure 3. The soil properties are shown in Table 1. Lastly, the values for the integration parameters of the CH method are listed in Table 2, which satisfy the proposed unconditional stability conditions.

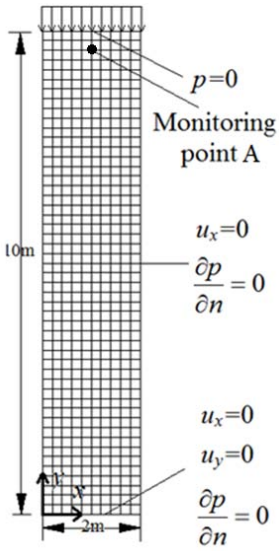


Figure 2: Finite element model for 1-D column analysis subjected to step loading

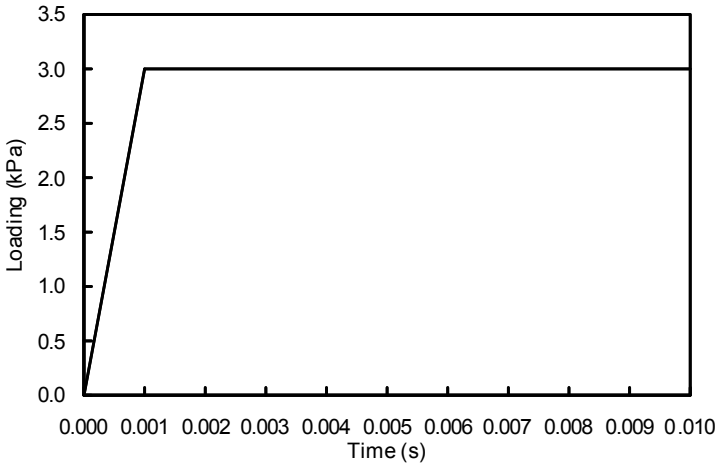


Figure 3: The loading history for 1-D column analysis subjected to step loading

Table 1 Soil properties for 1-D column analysis subjected to step loading

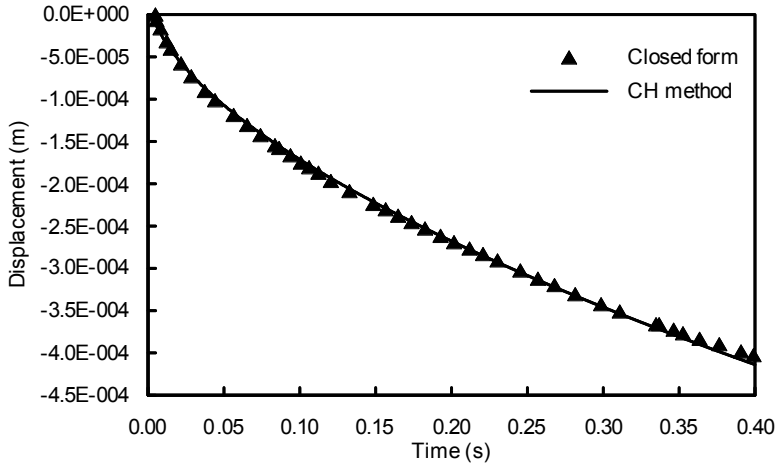
Parameter	**Value**
Yong's modulus E (kPa)	3.0E+04
Density ρ (g/cm^3)	1.67
Poisson ratio ν	0.2
Void ratio e	0.5
Permeability k (m/s)	1.0E-02
Time step Δt (s)	1.0E-03

Table 2 Integration parameters for the CH method

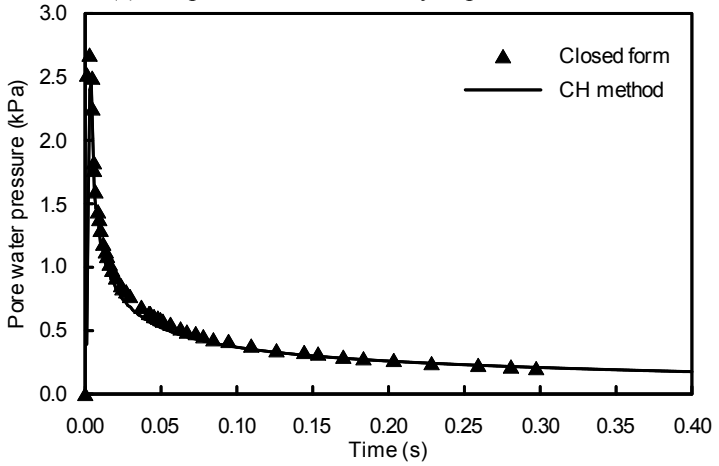
Parameter	**δ**	**α**	**α_m**	**α_f**	**β**
CH method	0.6	0.3025	0.35	0.45	0.8

The displacement and pore water pressure time histories[a] are calculated at a monitoring point A (0.4m below the top boundary as shown in Figure 2). These two sets of results are compared with a closed form solution, which was proposed by de Boer et al. [7] to simulate the dynamic response of saturated porous media. Figure 4 shows the comparison between numerical analysis results and the closed form solution. It can be seen that both the displacement and pore water pressure time histories are accurately predicted by the numerical analysis.

a: Downward displacements are shown as negative values and compressive pore water pressures are shown as positive values in the results of this paper.



(a): Displacement time history at point A

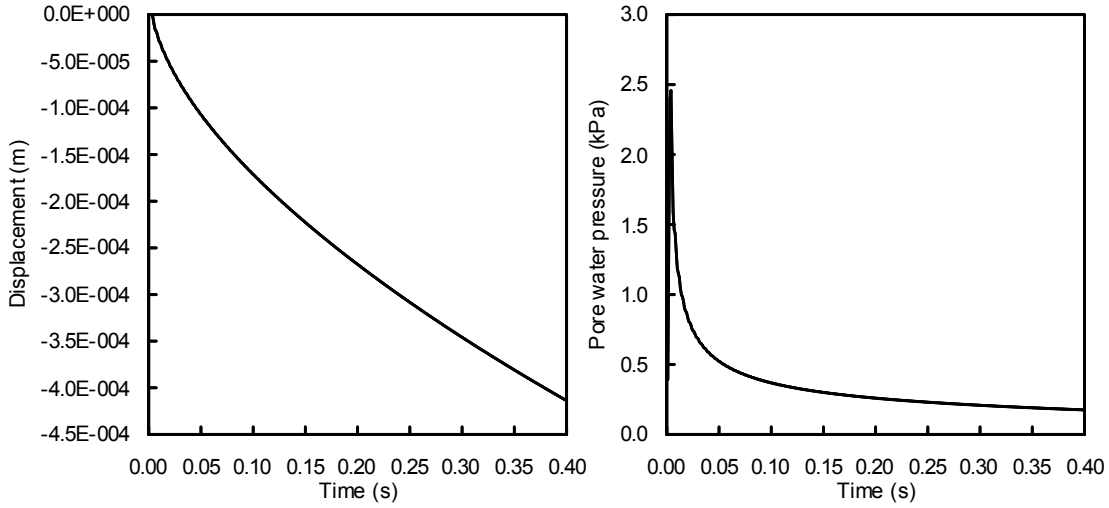


(b): Pore water pressure time history at point A

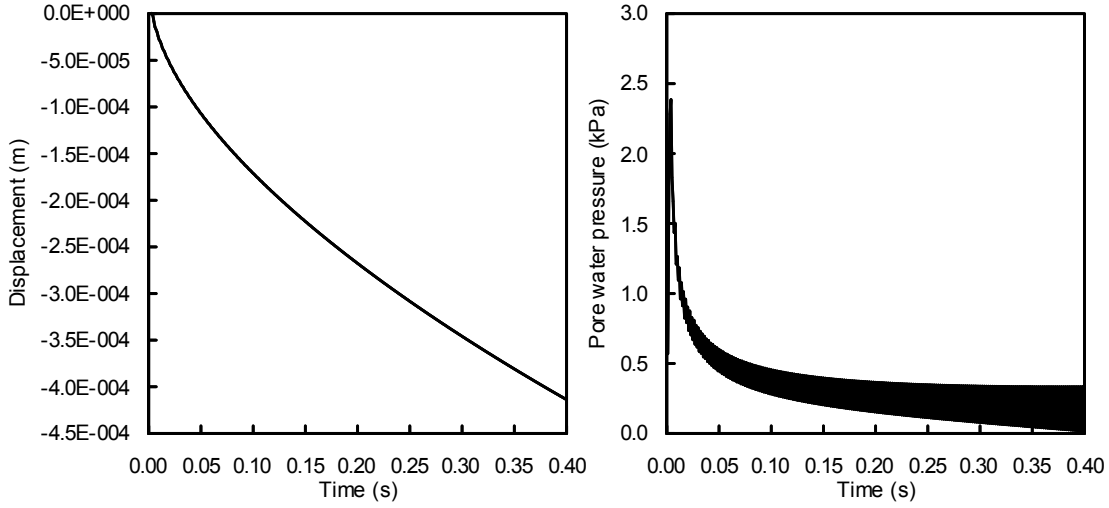
Figure 4: Comparison of numerical results and the closed form solution of de Boer at al.

In the following analyses, the integration parameters are varied parametrically, in order to validate the stability conditions introduced in the previous section. As it was mentioned before, the parameters α_m, α_f and β govern the stability conditions for the CH method, which are $\alpha_m \leq \alpha_f \leq 0.5 \; and \; \beta \leq 0.5$. Since the stability of the CH method for the one-phase formulation has been previously thoroughly checked by other studies, the focus of the present investigation is only on the stability for the coupled formulation. Therefore, for the following validation analyses, only the effect of parameter β is examined. In particular, β is gradually reduced in order to reach numerically the stability limit for the CH method.

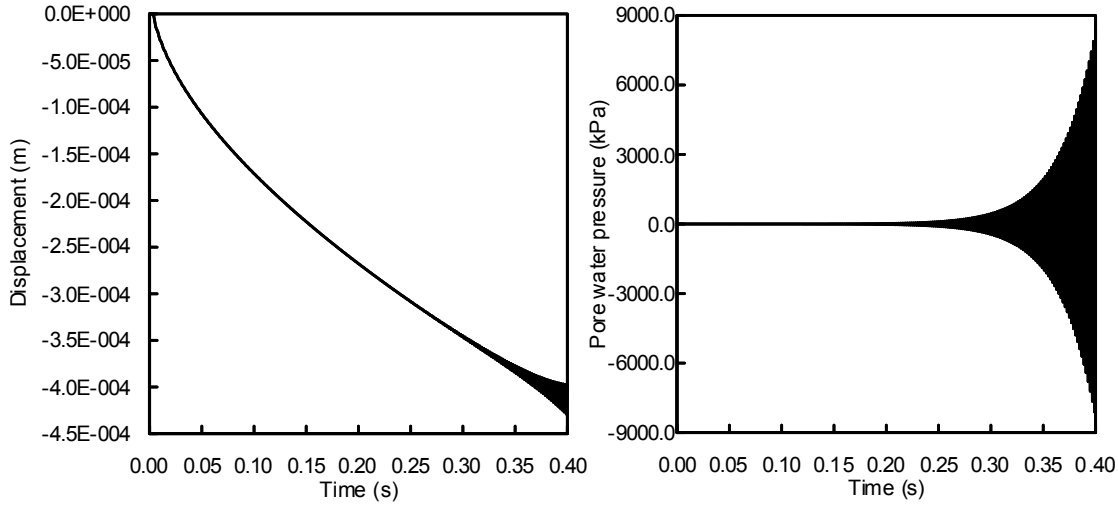
Figure 5 shows the displacement and pore water pressure time histories recorded at the monitoring point A for various values of β. Clearly, when β =0.8 (Figure 5a), both the displacement and pore water pressure responses are stable. When, however, β is reduced to a value slightly less than 0.5 (0.499), an instability in the pore water pressure response is observed immediately. Nevertheless, the displacement still remains stable (Figure 5b). Finally, when β is reduced further to 0.492 , the instability in terms of pore water pressure aggravates, while the displacement response also starts to be unstable (Figure 5c). Consequently, based on this example, in order to ensure stability of the numerical solution when using the CH method, β should be equal or larger than 0.5, which is in agreement with the proposed theoretical unconditional stability conditions. Furthermore, the pore water pressure response seems to be more sensitive to the β value than the displacement response.



(a): Displacement and pore water pressure time histories (β=0.8)



(b): Displacement and pore water pressure time histories (β=0.499)



(c): Displacement and pore water pressure time histories (β=0.492)

Figure 5: Displacement and pore water pressure time histories at point A for various β values

4.2 1-D Column Subjected to Harmonic Loading

To validate the stability conditions of the CH method when subjected to more complicated loading, 1-D soil column analyses under harmonic loading are carried out in this part. The finite element mesh (consisting of 80 8-noded elements) and the boundary conditions are shown in Figure 6. The displacement and hydraulic boundary conditions are identical to the ones used in the previous section. Furthermore, a uniformly distributed sinusoidal load is applied on the top boundary of the model, which is described by Equation (21) and is illustrated in Figure 7. Lastly, the soil properties of the model are listed in Table 3.

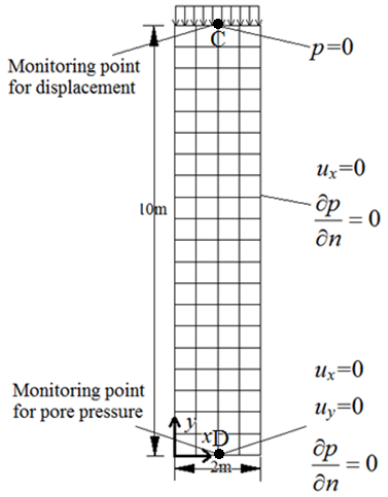


Figure 6: Finite element model for 1-D column analysis subjected to harmonic loading

$$q=\begin{cases} t/0.02 & 0\le t\le 0.02s \\ 1+0.25\sin 20\pi(t-0.02) & t>0.02s \end{cases} \tag{21}$$

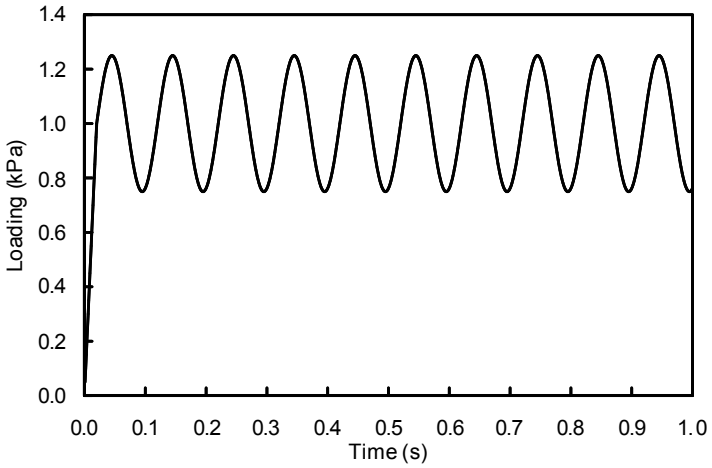


Figure 7: The loading history for 1-D column analysis subjected to harmonic loading

Table 3 Soil properties for 1-D column analysis subjected to harmonic loading

Parameter	Case1
Yong's modulus E (kPa)	1.0E+04
Density ρ (g/cm^3)	2.0
Poisson ratio ν	0.2
Void ratio e	0.538
Permeability k (m/s)	1.0E-15
Time step Δt (s)	1.0E-03

Firstly, the numerical predictions of this study are compared with the results presented by Li et al. [15], where an iterative stabilised fractional step algorithm was used. It should be noted that an impermeable soil column was simulated by Li et al. In the present study, a very low permeability value (k=1.0E-15 m/s) is adopted to represent an impermeable material but still utilise the two-phase coupled formulation. Figure 8 shows the comparison of the pore water pressure time history at the point D, which shows good agreement between the numerical prediction and Li et al.'s results.

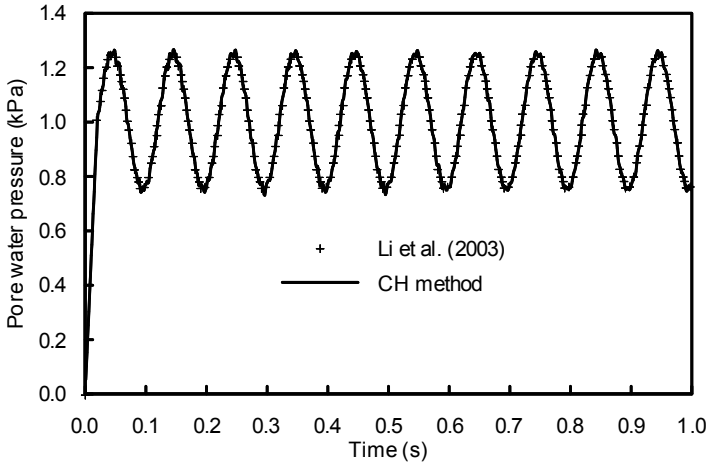
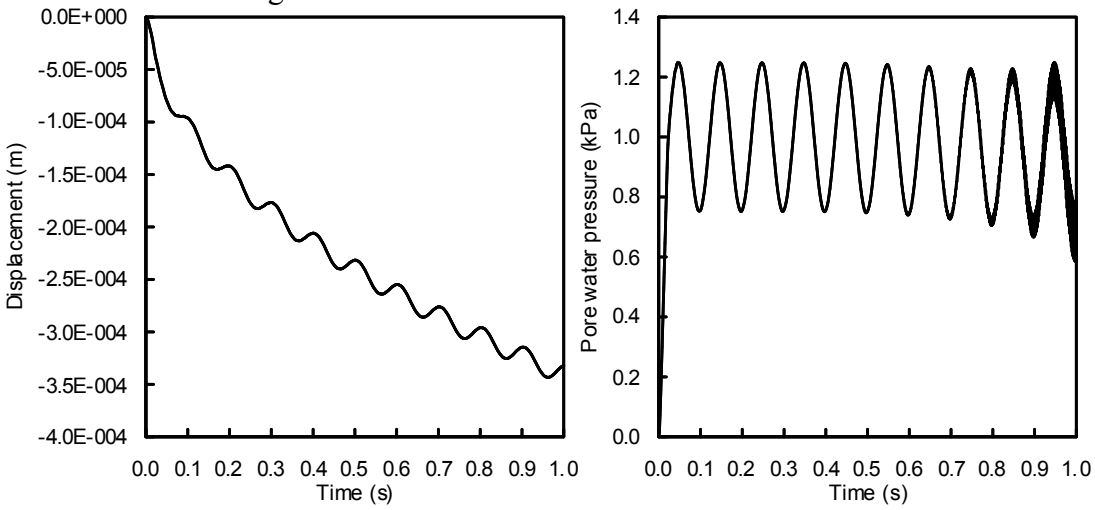
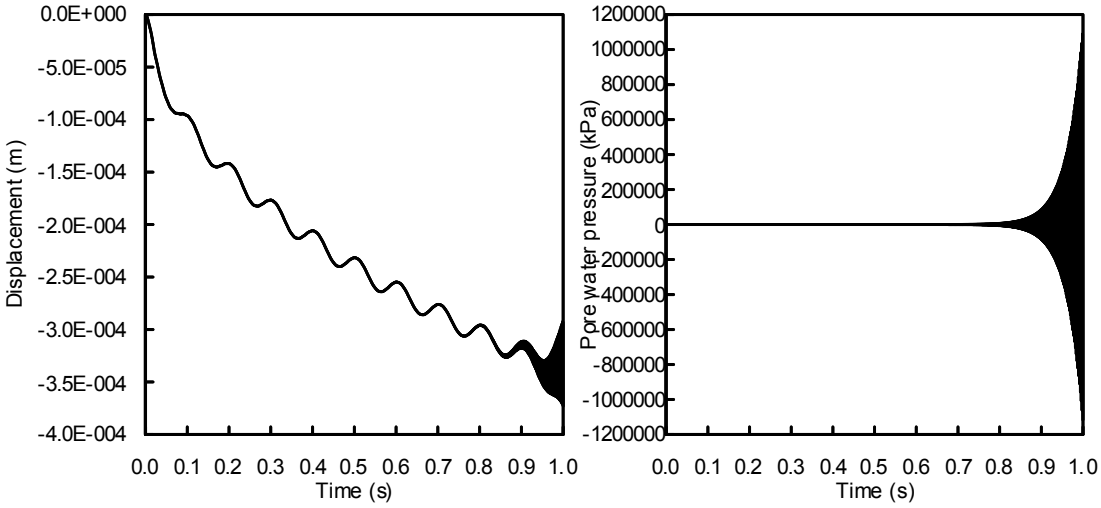


Figure 8: Comparison of the pore water pressure time history at point D

In order to highlight the effect of the parameter β on the stability, a higher permeability value (k=1.0E-2 m/s) is adopted for the soil column in the following parametric investigations. Similar to the analyses conducted in the previous section, β is gradually reduced to reach numerically the stability limit. The analysis results in terms of displacement (at point C) and pore water pressure (at point D) time histories are shown in Figure 9. It is obvious that when β is reduced to 0.497, the pore water pressure response starts to be unstable immediately, while the displacement response is still stable (Figure 9a). Furthermore, when β is reduced to 0.493, the instability of the pore water pressure aggravates and this triggers the instability of the displacement response (Figure 9b). Therefore, good agreement is observed between the numerical results and the theoretical stability conditions for the 1-D column analysis subjected to harmonic loading.



(a): Displacement and pore water pressure time histories (β=0.497)



(b): Displacement and pore water pressure time histories (β=0.493)

Figure 9: Displacement (at point C) and pore water pressure (at point D) time histories for various β values

5 CONCLUSIONS

The stability of the CH method for a fully coupled dynamic consolidation formulation is analytically investigated and unconditional stability conditions are proposed. It is observed that the proposed stability conditions can simplify to the ones of the CH method for the one-phase formulation by ignoring the hydraulic coupling. In addition, since the CH method is a generalisation of the Newmark, HHT and WBZ methods, the proposed stability conditions are relevant for most of the commonly used time integration methods for two-phase coupled formulation.

The analytically derived stability conditions are validated with FE analyses considering a range of loading conditions. According to the numerical results, in order to ensure the stability for the coupled dynamic analysis, the integration parameter for the hydraulic coupling formulation, β, should be equal or larger than 0.5, which agrees with the proposed theoretical unconditional stability conditions of the CH method for the solid-pore fluid coupled formulation.

REFERENCES

[1] Bathe, K. J., *Finite element procedures in engineering analysis*. Prentice Hall, 1996.

[2] Biot, M. A., Theory of propagation of elastic waves in a fluid saturated porous solid 1: Low-frequency range. *Journal of the Acoustical Society of America*, **28**(2), 168-178, 1956.

[3] Biot, M. A., Theory of propagation of elastic waves in a fluid saturated porous solid 2: Higher-frequency range. *Journal of the Acoustical Society of America*, **28**(2), 179-191, 1956.

[4] Biot, M. A., Mechanics of deformation and acoustic propagation in porous media. *Journal of Applied Physics*, **33**(4), 1482-1498, 1962.

[5] Chan, A. H. C., A unified finite element solution to static and dynamic problems of geomechanics. PhD thesis, Swansea University, 1988.

[6] Chung, J. and Hulbert, G. M., A time integration algorithm for structural dynamics with improved numerical dissipation : the generalized-α method. *Journal of Applied Mechanics*, **60**(2), 371-375, 1993.

[7] de Boer, R., Ehlers, W. and Liu, Z., One-dimensional transient wave propagation in fluid- saturated incompressible porous media. *Archive of Applied Mechanics*, **63**(1), 59-72, 1993.

[8] Ghaboussi, J. and Wilson, E. L., Flow of compressible fluid in porous elastic media. *International Journal for Numerical Methods in Engineering*, **5**(3), 419-442, 1973.

[9] Hardy, S., The implementation and application of dynamic finite element analysis to geotechnical problems. PhD thesis, Imperial College London, 2003.

[10] Hilber, H. M., Hughes, T. J. R. and Taylor, R. L., Improved numerical dissipation for time integration algorithms in structrual dynamics. *Earthquake Engineering and Structural Dynamics*, **5**(3), 283-292, 1977.

[11] Hughes, TJR, Hilber, H. M., Collocation, dissipation and overshoot for time integration schemes in structural dynamics. *Earthquake Engineering & Structural Dynamics*, **6**, 99-117, 1978.

[12] Hurwitz, A., Uber die Bedingungen, unter welchen eine Gleichung nur Wurzeln mit negativen reellen Teilen bestzt. *Mathematische Annalen*, **46**, 273-284, 1895.

[13] Kontoe, S., Development of time integration schemes and advanced boundary conditions for dynamic geotechnical analysis. PhD thesis, Imperial College London, 2006.

[14] Kontoe, S., Zdravkovic, L. and Potts, D. M., An assessment of time integration schemes for dynamic geotechnical problems. *Computers and Geotechnics*, **35**(2), 253-264, 2008.

[15] Li, X., Han, X. and Pastor, M., An iterative stabilized fractional step algorithm for finite element analysis in saturated soil dynamics. *Computer Methods in Applied Mechanics and Engineering*, **192**(35-36), 3845-3859, 2003.

[16] Newmark, N. M., A method of computation for structural dynamics. *Journal of Engineering Mechanics, ASCE* **85**, 67-94, 1959.

[17] Potts, D. M. and Zdravkovic, L., *Finite element analysis in geotechnical engineering: Theory*. Thomas Telford, 1999.

[18] Routh, E. J., *A treatise on the stability of a given state of motion*. Macmillan, 1877.

[19] Wood, W. L., Bossak, M. and Zienkiewicz, O. C., An alpha modification of Newmark's method. *International Journal for Numerical Methods in Engineering*, **15**(10), 1562-1566, 1981.

[20] Zienkiewicz, O. C. and Shiomi, T., Dynamic behaviour of saturated porous media; The generalized Biot formulation and its numerical solution. *International Journal for Numerical and Analytical Methods in Geomechanics*, **8**(1), 71-96, 1984.

APPENDIX

$$[M]=\sum_{i=1}^{N}\left(\int_{Vol}[N]^T\rho[N]dVol\right)$$

$$[C]=\sum_{i=1}^{N}\left(\int_{Vol}[N]^T c[N]dVol\right)$$

$$[K]=\sum_{i=1}^{N}\left(\int_{Vol}[B]^T[D][B]dVol\right)$$

$$[L]=\sum_{i=1}^{N}\left(\int_{Vol}\{m\}[B]^T[N_p]dVol\right)$$

$$\{m\}^T=\{1\quad 1\quad 1\quad 0\quad 0\quad 0\}$$

$$[\phi]=\sum_{i=1}^{N}\left(\int_{Vol}\frac{1}{\gamma_f}[E]^T[k][E]dVol\right)$$

$$[G]=\sum_{i=1}^{N}\left(\int_{Vol}\frac{1}{g}[N]^T[k][E]dVol\right)$$

$$[S]=\sum_{i=1}^{N}\left(\int_{Vol}\frac{n}{K_f}[N_p]^T[N_p]dVol\right)$$

$$[n]=\sum_{i=1}^{N}\left(\int_{Vol}[E]^T[k]\{i_G\}dVol\right)$$

$$[E]=\left[\frac{\partial N_p}{\partial x}\quad\frac{\partial N_p}{\partial y}\quad\frac{\partial N_p}{\partial z}\right]^T$$

$$\Delta\overline{R}=(1-\alpha_f)\{\Delta R\}+(1-\alpha_m)[M]\left(\frac{1}{\alpha\Delta t}\{\dot{u}_{t_k}\}+\frac{1}{2\alpha}\{\ddot{u}_{t_k}\}\right)+(1-\alpha_f)[C]\left(\frac{\delta}{\alpha}\{\dot{u}_{t_k}\}-\left(1-\frac{\delta}{2\alpha}\right)\Delta t\{\ddot{u}_{t_k}\}\right)+\{\Delta R\}_{t_k}$$

$$\Delta\overline{F}=(1-\alpha_f)\Delta t\left(-[n]-\{Q\}+[\phi]\{p_{t_k}\}-[G]\{\ddot{u}_{t_k}\}\right)+(1-\alpha_m)\beta\Delta t[G]\left(\frac{1}{\alpha\Delta t}\{\dot{u}_{t_k}\}+\frac{1}{2\alpha}\{\ddot{u}_{t_k}\}\right)+\{\Delta F\}_{t_k}$$

where $[N]$ is the shape function matrix, $[B]$ is the derivative matrix of the shape function, $[D]$ is the constitutive relation matrix, $[N_p]$ *is* the shape function matrix for the pore fluid, ρ and c are the material density and damping ratio of the material, $[k]$ is the permeability matrix, n and K_f are the porosity of the soil and the bulk modulus of the pore fluid, i_G are the unit vectors, which is opposite to the gravity, γ_f is the bulk unit weight for the pore fluid, Q is any sink or/and sources, and $\{\Delta R_{t_k}\}$ and $\{\Delta F_{t_k}\}$ are the out-of-balance force at the previous time increment, which ideally should be zero.

COMPDYN 2013
4th ECCOMAS Thematic Conference on
Computational Methods in Structural Dynamics and Earthquake Engineering
M. Papadrakakis, V. Papadopoulos, V. Plevris (eds.)
Kos Island, Greece, 12–14 June 2013

EFFECTS OF ARTIFICIAL LANDFORM CHANGE TO WATER PIPELINE DAMAGE IN SENDAI CITY DURING THE 2011 TOHOKU OFFSHORE JAPAN EARTHQUAKE

Kazue Wakamatsu [1], Shigeru Nagata[2], and Yoshihisa Maruyama[3]

[1] Kanto Gakuin University
Mutsuura-higashi 1-50-1, Kanazawa, Yokohama, 236-8501, JAPAN
e-mail: wakamatu@kanto-gakuin.ac.jp

[2] Kajima Corporation
Tobitakyu 2-19-1, Chofu, Tokyo, 182-0036, JAPAN
nagata-shigeru@kajima.com

[3]Chiba University
Yayoi-cho 1-33, Inage-ku, Chiba, 263-8522, JAPAN
ymaruyam@tu.chiba-u.ac.jp

Keywords: Water supply pipe, Earthquake damage, The 2011 Tohoku Offshore Japan Earthquake.

Abstract. *Sendai City was severely affected by the Mw9.0 Tohoku Offshore Earthquake of March 11th, 2011. A system of 4458-km water supply network in the city had extensive damage, with 1064 locations seriously affected, resulting in cuts off water supply of 2.3 hundred thousand houses just after the earthquake. About 60 percent of locations of the damaged pipelines were found to be located not on low-lying land consisting of soft soils but on hilly residential lands developed by cutting and leveling the hills and then filling the valleys for the past several ten years. In this study, the old topographic maps surveyed before the land development were digitized and normalized for superimposing on locations of pipeline damage to analyze the effects of landform change to pipelines damage. As a result, the followings were reached: more than a half of pipe breaks in the developed areas occurred in the former hillside slope and one third of the breaks occurred in the former valleys in the hill; The heaviest concentration of the pipe breaks observed within the boundary area between cutting and filling with a thickness ranging from -2.5 m to 2.5 m; and the higher concentration of pipe breaks is found in the area of ground failures but the greater numbers of breaks also occurred outside of the areas.*

1 INTRODUCTION

Sendai City is the most densely-inhabited city in the Tohoku region, northern part of Japan's main island, Honshu, which was severely affected by the M_W 9.0 Tohoku Offshore Japan Earthquake of March 11th, 2011. A system of 4458-km water supply network in the city had extensive damage, with 1064 locations seriously affected, resulting in cuts off water supply of approximately 2.3 hundred thousand households just after the earthquake. The damage to water supply network includes 437 of transmission and distribution pipes, 522 of water supply pipes, and 105 of auxiliary equipment, i.e. air valve, hydrant, pressure reducing valves, etc. About 60 percent of locations of the damaged pipelines were found to be located not on low-lying land consisting of soft soils but on hilly residential lands developed by cutting and leveling the hills and then filling the valleys for the past several ten years. There is no precedent for so many pipelines damaged in hilly land in Japan, possibly no other country in the world. It is important to analyze the conditions at the damaged sites especially effects of the artificial landform change and relation with occurrence of ground failures to prepare for future earthquakes, because there are great many similar residential lands in Tokyo and its suburbs, and other metropolitan areas in Japan such as Nagoya and Osaka.

In this study, the old topographic maps surveyed in 1928 and 1964 before the land development were digitized and normalized for superimposing on the locations of pipeline damage to analyze the effects of landform change to pipelines damage.

2 IMPACT OF THE 2011 TOHOKU OFFSHORE JAPAN EARTHQUAKE ON THE SENDAI WATER SUPPLY DISTRIBUTION NETWORK

The City of Sendai with a population of over one million and with an area of approximately 78,800 hectares is the biggest city in the Tohoku region, Japan. About 66% of the total area of the city is land covered with forests and farmland and only 16% of the area is used for residential land [1].

On March 11, 2011 at 2:46 PM local time a M_W 9.0 earthquake struck along the subduction zone interface plate boundary between the Pacific and North America plates. The earthquake was immediately followed by a large tsunami that inflicted wide-spread damage to modern urban infrastructure extending from northern Tohoku to southern Kanto regions including Sendai and Tokyo.

Recorded horizontal ground motion accelerations ranged from 254 to 1869cm/s^2 and velocities ranged from 31 to 145cm/s with JMA Intensities reaching 5 upper and 6 minor over large populated areas in Sendai [2], [3]. Water supply was suspended to approximately 2.3 hundred thousand households (affected populations of 5 hundred thousand and 50% of water outage rate) in Sendai: it required eighteen days to restore water to all habitable service areas except tsunami- and severe ground failure-affected areas [4]. This is a relatively short recovery-period in the earthquake-affected areas.

The Sendai water system is consists of eight water treatment plants and fourteen water distribution plants, two pumping stations and 4458-km water pipeline network. Although there was considerable damage to drainage facilities and civil engineering facilities such as retaining walls and slopes in the yards, there was a little functional damage at two water distribution plants [4].

In contrast, there was significant damage to water distribution pipelines. Figure 1 shows the locations of water pipe breaks in Sendai following the 2011Tohoku Offshore Japan Earthquake, which is overlaid to the map of the water distribution network. A system of 4458-km water pipeline network in the city had extensive damage, with 1064 locations seriously affected: the damage to the pipeline network includes 437 of transmission and distribution pipes

(Photo 1), 522 of water supply pipes, and 105 of auxiliary equipment. No damage was found in ductile cast-iron: pipes with earthquake-proofing joint (Photo 2).

Table 1 presents summary of damage to transmission and distribution pipes and water supply pipes, and auxiliary equipment, showing that more than 90% of the breaks for the water pipes were in pipelines of VP and DIP with a diameter less than 150mm, and approximately 99% of the breaks for the water supply pipes addressed damage to VP, LP, PP and GP with a diameter less than 75mm [4].

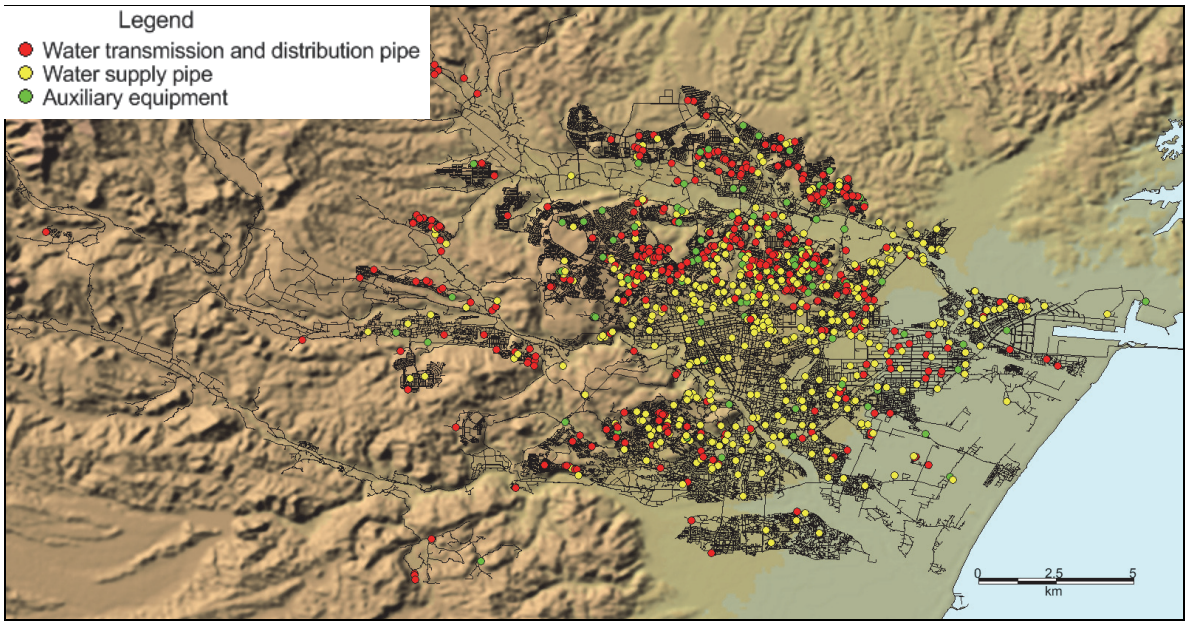


Figure 1: Locations of water pipeline breaks in Sendai following the March 11th 2011 Tohoku Offshore Japan Earthquake



Photo 1: Repair of water distribution pipe with a diameter of 800mm [4]



Photo 2: Earthquake-proofing water pipe with a diameter of 150 mm survived the tsunami [4]

Table 1: Summary of pipeline damage in Sendai water supply distribution network [4]

	Diameter (mm)	Pipe material and number of Breaks							Total	Length (km)	breaks/km
		CIP	DIP	SP/SU	VP	LP	PP	GP			
Water transmission and water distribution pipes	<ϕ75	0	0	3	147	2	3	6	161	695.6	0.23
	ϕ75	0	17	1	77	–	–	–	95	439.1	0.22
	ϕ100-150	0	74	6	73	–	–	–	153	2236.4	0.07
	ϕ200-450	0	23	1	–	–	–	–	24	861.6	0.03
	ϕ500≤	0	3	1	–	–	–	–	4	225.5	0.02
	Subtotal	0	117	12	297	2	3	6	437	4458.0	
Water supply pipes	<ϕ75	0	0	11	113	249	97	45	515	164.57	3.13
	ϕ75	0	1	0	5	0	0	0	6	6.70	0.90
	ϕ100-150	0	0	0	1	0		0	1	4.54	0.22
	Subtotal	0	1	0	119	249	97	45	522	175.81	
Auxiliary equipment	Fire hydrant	0	4	0	3	0	0	0	7		
	Air valve	0	38	16	2	0	0	0	56		
	Sluice valve	0	6	2	11	0	0	0	19		
	Diversion valve	0	12	0	10	0	0	0	22		
	Water shutoff valve	0	0	0	1	0	0	0	1		
	Subtotal	0	60	18	27	0	0	0	105		

CIP: Cast-iron; DIP: Ductile cast-iron; SP: Steel; SU: Stainless-steel; VP: Vinyl chloride; LP: Lead; PP: Polyethylene; GP: Galvanized-iron plating

Table 2 represents number of breaks, length and break rate (breaks/km) in Sendai water distribution network differentiated per pipe material. Figure 2 shows the break rate for water distribution network to different pipe material. The break rate for GP is the highest among the other material and followed by LP, whereas no damage was found in CIP. The break rate for DIP is fairly-low although it has the longest pipe length of 2723.1km, which corresponds to 61% of the total length of the overall water pipes.

Table 2: Number of breaks, length and break rate (breaks/km) in Sendai water supply distribution network to different pipe material [4]

Material	N. of breaks	Length(km)	Break rate
Cast-iron	0	14.4	0
Ductile cast-iron	117	2723.1	0.04
Steel/ Stainless-steel	12	137.3	0.09
Vinyl chloride	297	1514.5	0.20
Lead	2	3.4	0.59
Polyethylene	3	52.7	0.06
Galvanized-iron plating	6	4.9	1.22
Total	437	4458.0	0.10

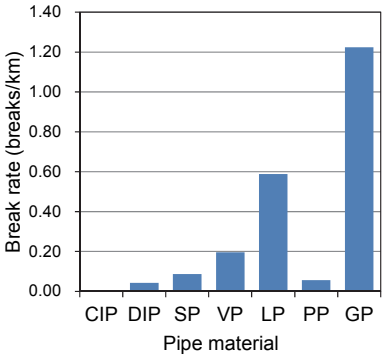


Figure 2: Break rate for water distribution network to different pipe material [4]

3 RELATIONSHIP BETWEEN GEOMORPHOLOGIC CONDITION AND LOCATIONS OF PIPE BREAKS

Figure 3 shows locations of pipe breaks and the water distribution network superimposed on the 7.5-sec Japan Engineering Geomorphologic Land Classification Map (JEGM) which is a nationwide site-condition map based on geomorphologic classification for various kinds of hazard mapping [5]. The damage to pipes was spread across hill (moss green), gravelly terrace (orange) and lowlands such as alluvial fan (yellow-green), delta and coastal lowlands (sky blue).

Figure 4 shows the break rate (breaks/km) for the Sendai water pipelines according to the geomorphological units in Figure 3, in which the units for lowlands such as alluvial fan, natural levee, back marsh and delta and coastal lowlands are combined into ”lowland”. The break rate for the pipes installed in “hill” is the highest among all geomorphologic units, which is more than 1.7 times than that for “other lowlands”. This implies that the pipe break rate is higher in steep and hard ground than that in relatively flat ground containing soft soils. In order to investigate the causes of the concentration of the damage on the steeper hillsides, the history of land reclamation and former landform before the development in Sendai was investigated using old topographic maps.

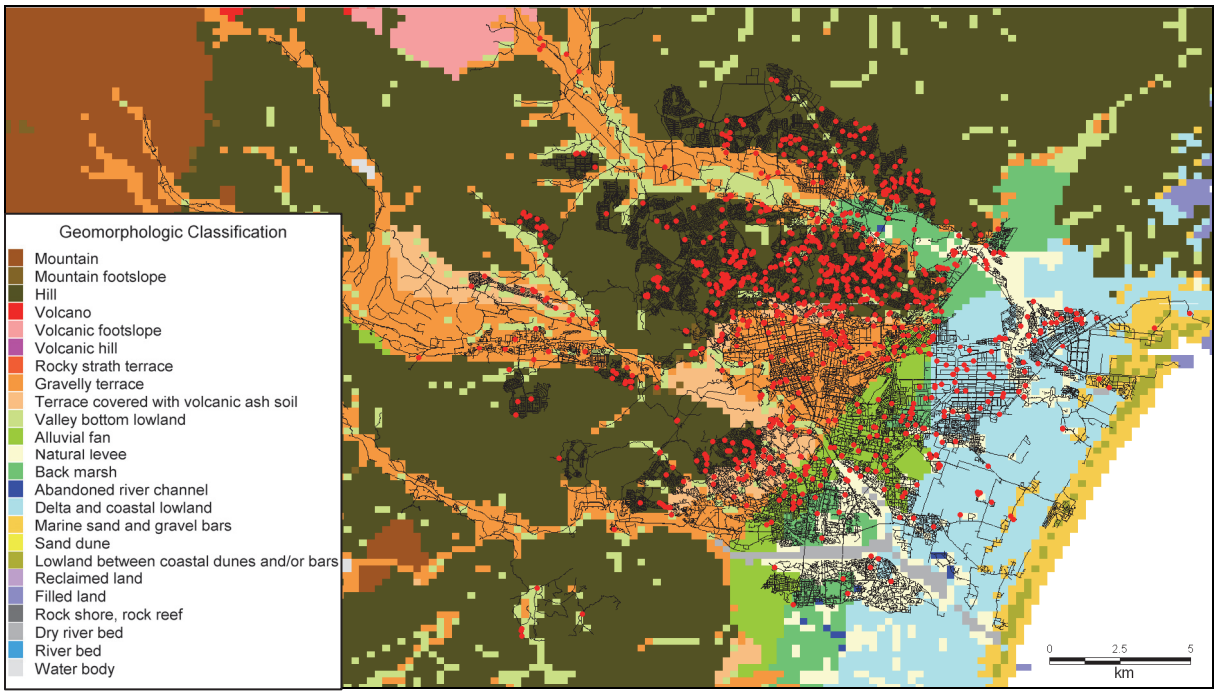


Figure 3: Locations of pipe breaks (red dots) and the water distribution network (black lines) superimposed on the 7.5-sec Japan Engineering Geomorphologic Classification Map

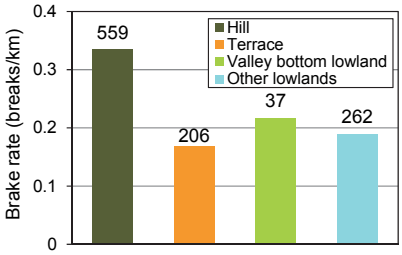


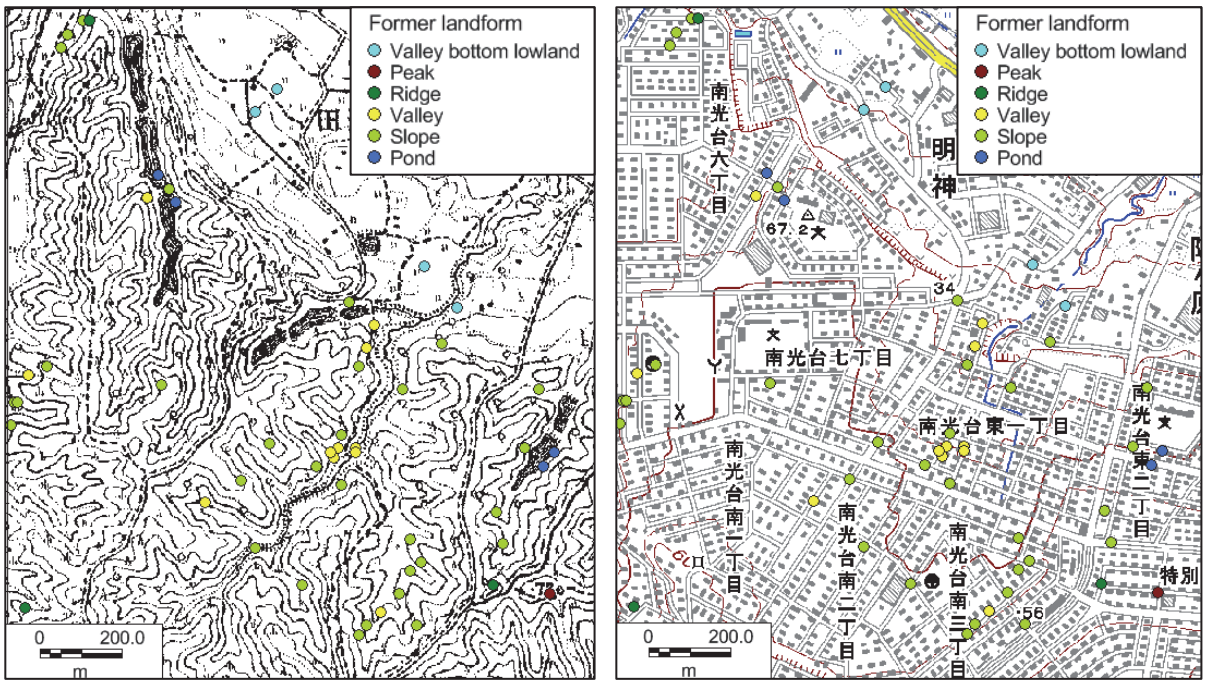
Figure 4: Break rate for water distribution network differentiated per geomorphologic land classification shown in Figure 3 (number on the bar graph shows the number of pipe breaks)

4 EFFECTS OF THE ARTIFICIAL LANDFORM CHANGE TO PIPE DAMAGE

Figure 5(a) is an old topographic map surveyed in 1928. It should be noted that the hill is dissected by many small valleys and streams in the hill. The development of the hills started in the early 1950s and gradually extended toward surrounding areas of the old urban district of Sendai. Figure 5(b) shows the topographic map after the land development for housing. The area was developed typically by cutting and leveling the hill and then filling the valleys with soils from the excavated areas in the hill. Therefore there are two general types of subsurface conditions in hilly land in Sendai: 1) natural soils of the original or excavated surface of the hill; it associated with the volcanic pumice flow deposit overlying Neocene sedimentary or volcanic bedrocks and 2) fills consisting mainly with the volcanic pumice flow deposit placed on the valleys and hollow parts in the hill. Areas underlain by these different profiles might to behave differently during the earthquakes.

In this study, we interpreted whether the landform change was done or not for the locations of the 1064 pipe breaks by comparing the present topographic maps with old maps before land development. Then, surface elevation before land development was evaluated by reading out of the counter lines in the old topographic maps, as well as interpreting of the former landforms: peak, ridge, slope, valley, pond and valley bottom lowland by means of interpretation of the old topographic maps.

Figure 6 presents pie chart of the percentages of landform change for the locations of a total of 1064 pipe breaks, indicating that more than 60% of the pipe breaks took place in the pipelines installed in the developed areas where landform change was done by cutting and filling. Figure 7 shows pie chart of the percentages of geomorphological units for 663 pipe break points where landform change was done. More than 80 % of the pipe breaks occurred in the pipelines installed hill. Consequently the two figures suggest that about 60% of the 1064 pipe breaks occurred within developed land of hill or terrace.



(a) Before land development (1964) (b) After land development (2008)

Figure 5: Locations of pipe breaks (red dot) superimposed on 1:25,000-scale topographic map set surveyed before and after land development in Sendai

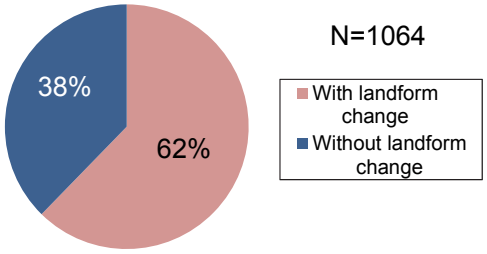


Figure 6: Percentage of pipe breaks according to landform change for all 1064 location

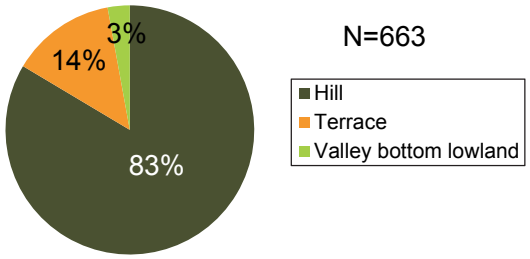


Figure 7: Percentage of pipe breaks according to geomorphologic land classification for 663 pipe break points located on the developed area

5 EFFECTS OF THE FORMER LANDFORM BEFORE LAND DEVELOPMENT TO PIPE DAMAGE

Figure 8 presents pie chart of the percentages of pipe breaks according to former landform before development. More than a half of the pipe breaks occurred in slope (yellow green in Figure 8) and one third of the breaks occurred in valleys in hillside (yellow). It should be noted that the breaks were found within former ponds (blue) although the numbers are small.

Figures 9 and 10 present bar charts summarizing the number of water pipe breaks of different pipe materials and different failure mode to different landforms before development, respectively. Figure 9 shows similar trends for different pipe materials: the percentages of slope are roughly 55-60% in spite of different types of pipe material and those of valley are around 30%, although number of the breaks for Vinyl chloride (VP) is the largest. The same trends with Figure 9 are found in Figure 10: the percentages of slope roughly 55-60% and those of valley are approximately 25-30% in spite of different failure mode, although number of pipe break with failure of pipe body is the largest.

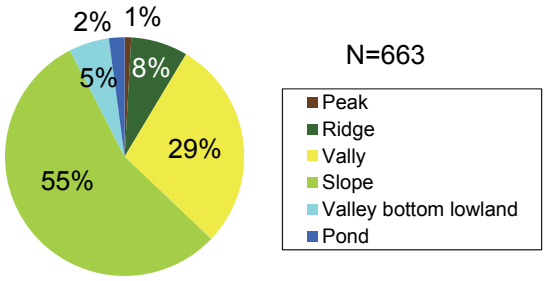


Figure 8: Percentage of pipe breaks according to former landform before land development

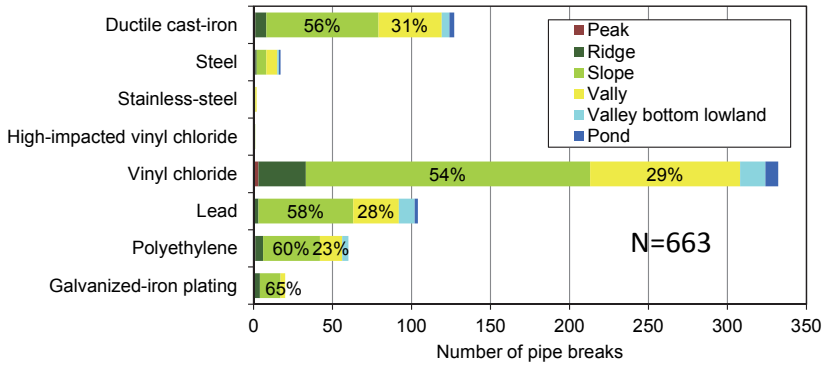


Figure 9: Number of water pipe breaks of different pipe materials to different landforms before development

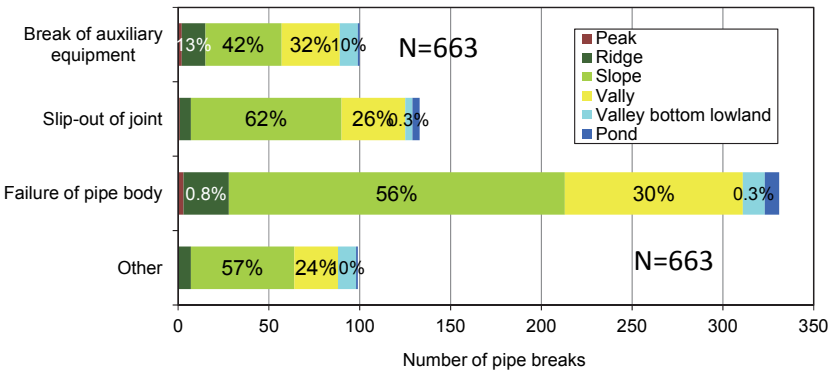


Figure 10: Number of water pipe breaks of different failure mode to different landforms before development

6 EFFECTS OF FILL THICKNESS TO PIPE DAMAGE

Subsurface ground conditions in the developed areas of the hilly land are primarily depend on whether the site was developed by filling the relatively low area such as valley or cutting and leveling the relatively high area such as hill ridge. Therefore, thickness of the cutting and filling at a total of 663 locations of pipe breaks was investigated in the developed area.

The surface elevation before land development was evaluated by reading out of the counter lines in the old topographic maps based on aerial photographic survey and current one was obtained from 5-m grid digital elevation model based on aerial laser survey [6]. In general, the leveling accuracy for this type of survey is roughly ±3 m and ±15 cm, respectively. The locations where current elevation is higher than that before the land development were considered to be fill areas in the hill, whereas the locations where it is lower than that before the development were considered to be cut areas. Thus the thickness of the filling and cutting were estimated by the difference of surface elevations between before and after the development.

Figure 11 shows relationship between thickness of the cut and fill and number of pipe breaks to different original (before-development) landforms, in which minus values represent thickness of cutting and plus values represent that of filling. In this figure, the number of pipe breaks is plotted according use of pipelines. It can be seen from the figure the heaviest concentration of the damage observed within the boundary area between cutting and filling with a thickness ranging from -2.5 m to +2.5 m. Damage to pipelines, in general, is observed many in fill areas whose original landforms are mainly slope or valley but very small number in cut areas whose original landforms are mainly slope and ridge, which implies that the performance of the fills placed on the natural ground of hilly areas is directly concern of the pipeline damage.

Figure 12 represents relationship between thickness of the cut and fill and number of pipe breaks to different type of pipe material. There are higher concentration within the boundary area between cutting and filling and fill areas regardless of the type of pipe material.

Figure 13 shows relationship between thickness of the cut and fill and number of pipe breaks to different failure mode. The breaks with every failure modes can be seen in the boundary area between cutting and filling and fill areas.

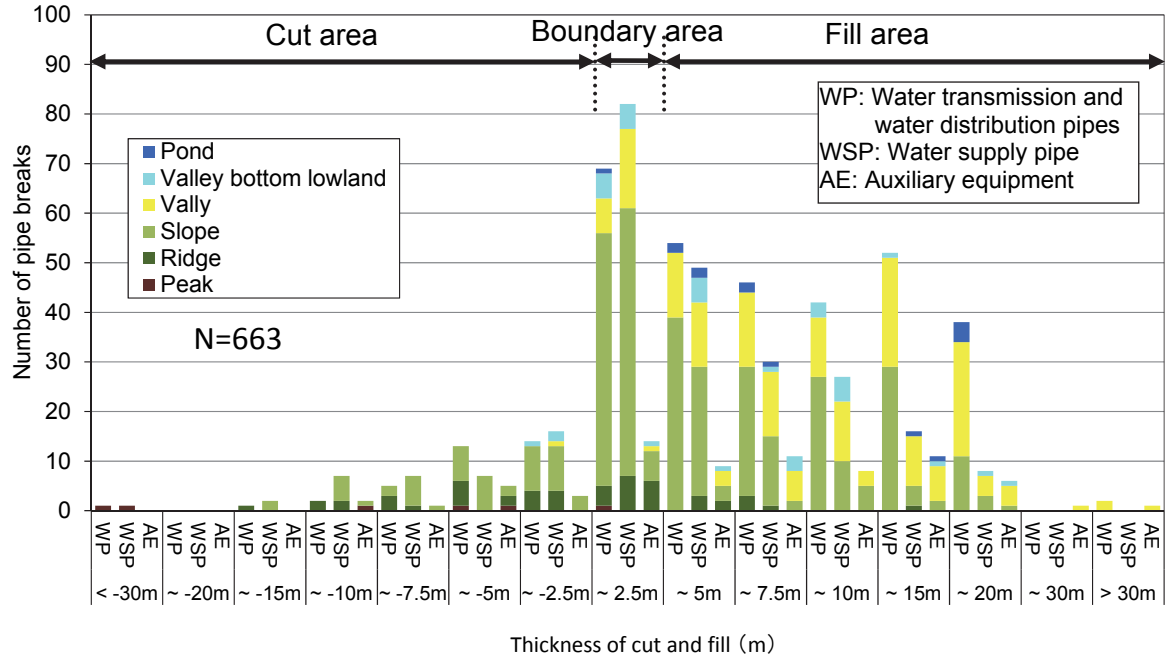


Figure 11 Relationship between thickness of the cut and fill and number of pipe breaks to different landforms before land development

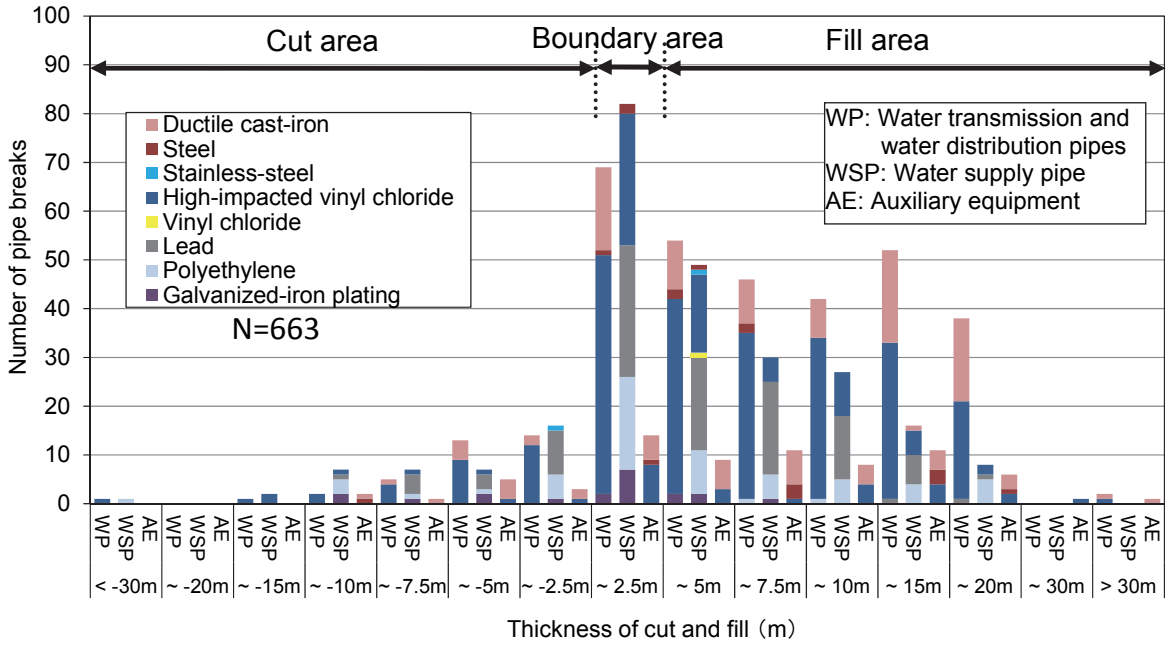


Figure 12 Relationship between thickness of the cut and fill and number of pipe breaks to different type of pipe material

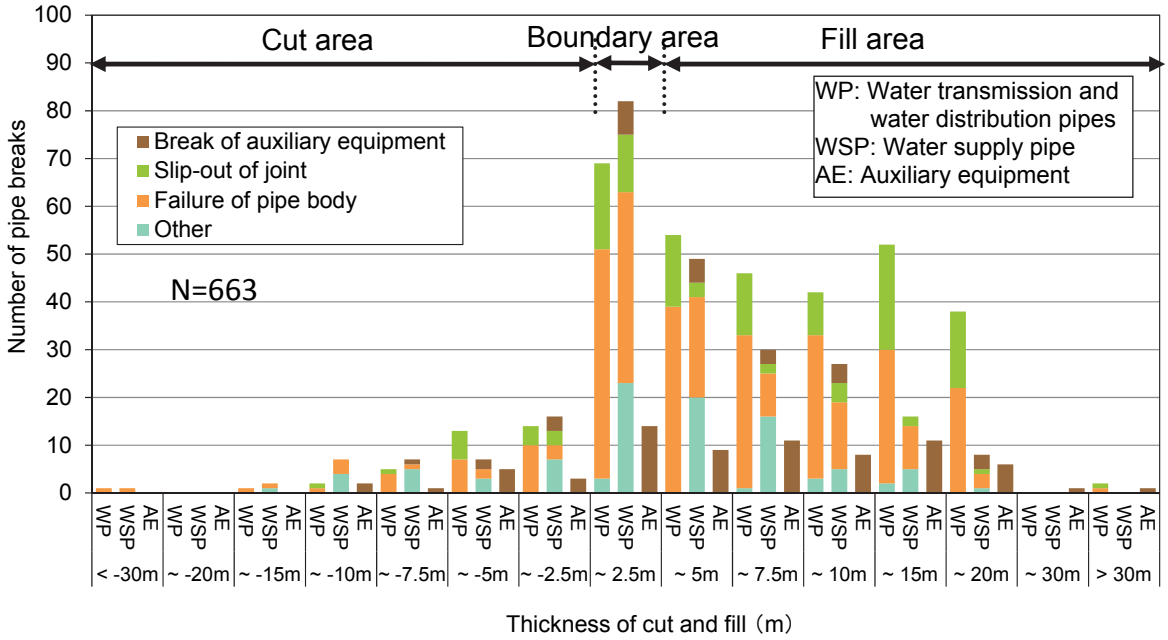


Figure 13 Relationship between thickness of the cut and fill and number of pipe breaks to different failure modes

7 EFFECTS OF GROUND FAILURES TO PIPE DAMAGE

Significant ground failures occurred in many place in developed areas in hilly land in Sendai: ground failures include landslide, slope failure, collapse of retaining wall and liquefaction-induced lateral spreading (Photos 3 and 4). The number of damaged lots due to ground failures reached 5080 [7]. Figure 14 shows the locations of water pipeline breaks and superimposed on a map of ground failures. The higher concentration of pipe breaks is found in the area of ground failures but the greater numbers of breaks are also plotted outside of the areas.

Photo 5 shows an example of pipe break location where no ground failure was reported. The current surface elevation is around 60 m from the sea level and thickness of the fill was estimated to be 70 cm. A vinyl chloride pipe with a 75-mm-diameter for water distribution pipelines was broken along the street in the photo. The ground surface is gently sloping and wavy deformation was found when we visited (one and a half years after the earthquake) as



Photo 3 Large crack due to landslide in Midorigaoka (courtesy of Sendai City)



Photo 4 Collapse of retaining wall in Asahigaoka

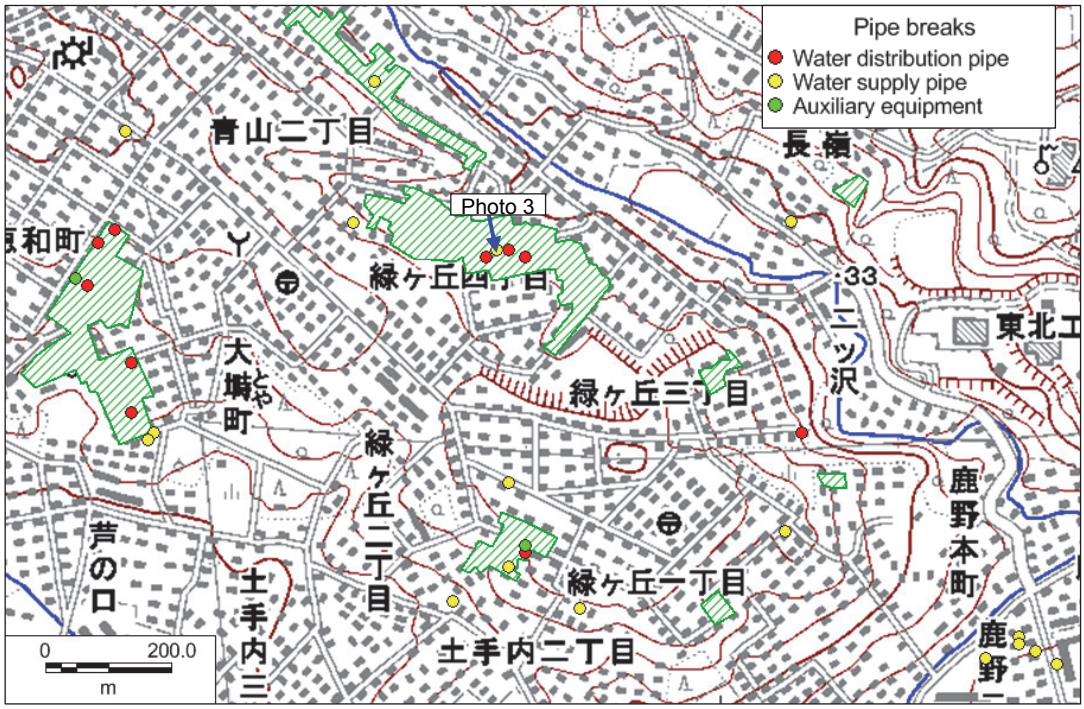


Figure 14 Locations of water pipeline damage and areas of ground failures (green polygons) caused by the 2011 Tohoku Offshore Japan Earthquake (areas of ground failure is adapted from [8] and geographic map is adapted from [9])



Photo 5 Location of pipe break in Anyouji

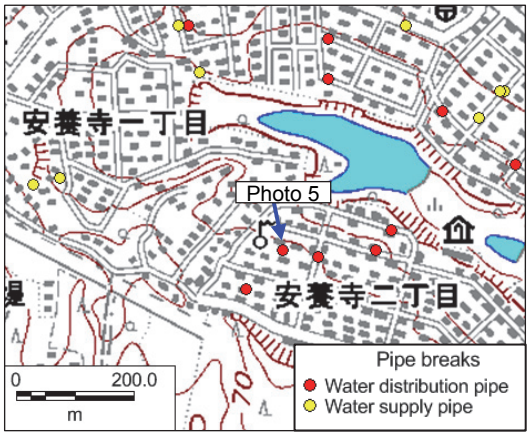


Figure 15 Map of pipe break locations in Anyouji (geographic map is adapted from [9])

shown in the photo. The pattern of ground deformation suggests that lateral spreading of the fill took place. The pipeline along the road was assumed to be ruptured in tension and compression in the tensile and compressive ground deformation zones.

8 CONCLUDING REMARKS

Based on an analysis of the damage to water pipelines in Sendai City associated with the 2011 Tohoku Offshore Japan earthquake, focusing on the landform change in the developed area of hilly land, the following conclusions have been reached:

- The break rate according to different geomorphologic units is the highest for pipes installed in “hill”, which is more than 1.7 times than that for “lowland”.
- Approximately 60% of the 1064 pipe breaks occurred within developed land of hill or terrace where landform change was done by cutting and filling.
- More than a half of pipe break in the developed areas occurred in the former hillside slope and one third of the breaks occurred in the former valleys in the hill.
- Concerning thickness of the cutting and filling in the developed land, the heaviest concentration of the pipe breaks observed within the boundary area between cutting and filling with a thickness ranging from -2.5 m to +2.5 m.
- The higher concentration of pipe breaks is found in the area of ground failures but the greater numbers of breaks also occurred outside of the areas.

ACONOWLEGEMENT

The authors wish to thank Mr. Masao Nishino and Seiichi Suzuki of the Sendai Waterworks Department, who provided the damage database of Sendai water supply network associated with the 2011 Tohoku Offshore Japan Earthquake.

REFERENCES

[1] Sendai City, *Data Sendai 2012*, http://www.city.sendai.jp/kikaku/seisaku/yoran/data_ sendai/index.html, 2012 (in Japanese)

[2] National Research Institute for Earth Science and Disaster Prevention, *Strong-motion Seismograph network (K-NET)*, http://www.kyoshin.bosai.go.jp, 2011.

[3] Tohoku Institute of Technology, *Strong-Motion Records Obtained by Small-Titan of Tohoku Institute of Technology During the 2011 Great East Japan Earthquake*, http://smweb.tohtech.ac.jp/smalltitan/english/, 2011.

[4] Waterworks Department, Sendai City, *Restoration Record on Water Service in Sendai City Associated with the Great East Japan Earthquake*, http://www.suidou.city.sendai.jp/06_bousai/jisin7.html, 2012 (in Japanese).

[5] Wakamatsu, K. and Matsuoka, M., Developing a 7.5-sec Site-condition Map for Japan based on Geomorphologic Classification, *Earthquake Resistant Engineering Structures* VIII, 101-112, WITT Press, 2011.

[6] Geospatial Information Authority of Japan, *5-m Grid Digital Elevation Model*, http://fgd.gsi.go.jp/download/, [Cited 2013.1.31]

[7] Sendai City, *Map of Damaged Housing Lots*, http://www.city.sendai.jp/jutaku/ takuchihisai_010.html [Cited 2012.7.20] (in Japanese)

[8] Sendai City, *Current State of District Examined for Public Work Project,* http://www.city.sendai.jp/jutaku/takuchihisai_020.html [Cited 2013.1.31] (in Japanese)

[9] Geospatial Information Authority of Japan, *1/25,000 Digital Topographic Maps of Sendai*, CD-ROM, 2010.

COMPDYN 2013
4th ECCOMAS Thematic Conference on
Computational Methods in Structural Dynamics and Earthquake Engineering
M. Papadrakakis, V. Papadopoulos, V. Plevris (eds.)
Kos Island, Greece, 12–14 June 2013

BEHAVIOUR OF A GEOSYNTHETIC REINFORCED STEEP SLOPE CONSTRUCTED WITH COHESIVE BACKFILL UNDER EARTHQUAKE LOADING

Castorina Silva Vieira[1] **and Maria de Lurdes Lopes**[1]

[1] University of Porto – Faculty of Engineering – Civil Engineering Department
R. Dr Roberto Frias, s/n 4200-465 Porto, Portugal
cvieira@fe.up.pt; lcosta@fe.up.pt

Keywords: Geosynthetics, Reinforced soil, Cohesive Soil, Numerical modelling, Earthquake loading

Abstract. *The use of geosynthetics as reinforcement elements of granular backfills has been widely used and their behaviour either during the service life or under seismic loading has been studied by several authors [1, 2]. However the use of fine grained soils, often referred as marginal fills, are not strongly implemented and, since they are susceptible for pore water pressure, not recommended by some international guidelines and standards. The use of soils locally available has cost benefits and sustainable gains. Therefore it is important to study the behaviour of geosynthetic reinforced steep slopes constructed with cohesive backfills.*

In this work the two-dimensional finite difference program Fast Lagrangian Analysis of Continua (FLAC) was used to model the seismic behaviour of an 8.4 m high geogrid-reinforced steep slope. The embankment was reinforced with 14 horizontal reinforcement layers and its face is inclined of 60º. The seismic behaviour of the structure constructed with cohesive backfill was compared to its behaviour if a granular material was selected.

Two constitutive models were used to model the cohesive backfills: the Mohr-Coulomb model and a Strain-Softening model.

In order to investigate the influence of input motion on the seismic behaviour of the structure, two earthquake ground motions artificially generated and two variable amplitude harmonic motions were considered.

The numerical simulations of the structure behaviour under seismic loading showed that the possible decrease of the backfill shear strength properties with the shear strain during cycling is an important issue. Even so, it could be concluded that a well compacted and drained cohesive soil can be used as backfill material in geosynthetic reinforced steep slopes.

1 INTRODUCTION

The use of geosynthetics as reinforcement elements of granular backfills has been widely used and their behaviour either during the service life or under seismic loading has been studied by several authors [1, 2]. However the use of fine grained soils, often referred as marginal fills, are not strongly implemented and not recommended by international guidelines and standards [3] since they are susceptible for pore water pressure.

Although there are several reasons for requiring good quality granular soils as backfill materials of reinforced earth structures, this specification could limit the use of these structures when these materials are not available near the site construction.

The use of poorly draining soils as backfill materials in geosynthetic reinforced structures brings some concerns, namely [4]:

- The pore water pressures induced during construction may reduce the backfill strength. Furthermore, the drained frictional strength of cohesive soils is lower than that of cohesionless soils;
- Post-construction movements may occur under sustained stresses as a result of the higher creep potential of poorly draining soils;
- Poorly draining soils are usually more difficult to compact.

These concerns may be mitigated since in many cases, the excess pore water pressures can be reduced by adopting suitable construction techniques and drainage systems. Some studies [5, 6] have shown that in many cases pore water pressure excesses are not generated and when the fill is compacted close to the optimum moisture content, the reinforced soil structure contains significant suctions (negative pore water pressures). Moreover, the use of some geosynthetics such as nonwoven geotextiles sheets has been reported to allow better compaction of cohesive soils [4, 7].

The use of soils locally available has cost benefits and sustainable gains. Therefore it is important to study the behaviour of geosynthetic reinforced steep slopes constructed with cohesive backfills.

The work herein presented is a preliminary study of the behaviour of geosynthetic reinforced steep slopes constructed with cohesive backfill. The effect of water content and pore water pressures will not be analyzed in this paper. The influence of some parameters, such as soil constitutive model, reinforcement stiffness and seismic input motion will be presented.

2 BRIEF DESCRIPTION OF FLAC CODE AND SEISMIC LOADING INPUT

FLAC is an explicit finite difference program that performs a Lagrangian analysis. The finite difference method is perhaps the oldest numerical technique used for the solution of sets of differential equations, given initial values and/or boundary values [8]. For dynamic analyses the full equations of motion are solved using lumped gridpoint masses derived from the real density of surrounding zones (rather than fictitious masses used for static solution). Each triangular sub-zone contributes one-third of its mass (computed from zone density and area) to each of the three associated gridpoints. The final gridpoint mass is then divided by two in the case of a quadrilateral zone that contains two overlays. In finite-element terminology, FLAC uses lumped masses and a diagonal mass matrix [8].

In FLAC, the dynamic input can be applied as an acceleration history, as a velocity history, as a stress (or pressure) history or as a force history. Dynamic input can be applied either in the x or y directions corresponding to the xy axes for the model, or in the normal and shear directions to the model boundary.

Two types of seismic action were considered in this study: two earthquake ground motions artificially generated and variable amplitude single frequency harmonic motions with identical peak ground acceleration. Two values of frequency were analyzed for the variable amplitude harmonic acceleration: 3 Hz, close to the fundamental frequency of the structure and 4 Hz.

Figure 1(a) presents one of the earthquake ground motions artificially generated [9] according to Portuguese National Annexes (PNA) of Eurocode 8 [10] for the greatest seismicity area of Portugal, considering seismic action type 2 (earthquake with moderate magnitude and small focal distance – close earthquake) and ground type B (deposits of very dense sand, gravel or very stiff clay). According to the PNA of Eurocode 8 [10] for the greatest seismicity area, the peak ground acceleration on type B ground is 2.7m/s^2 for a close earthquake (seismic action type 2). The duration of the stationary part of the accelerograms is equal to 10 seconds. The Fourier spectrum for the accelerogram presented in Figure 1(a) is plotted in Figure 1(b). This graph indicates that the highest frequency is less than approximately 20 Hz and that the majority of the frequencies are less than 13 Hz. Even so, before applying the seismic input motions, they were filtered to remove frequencies above the maximum frequency that can be modelled accurately.

Figure 2 illustrates the variable amplitude single frequency harmonic motions with frequency of 3 Hz.

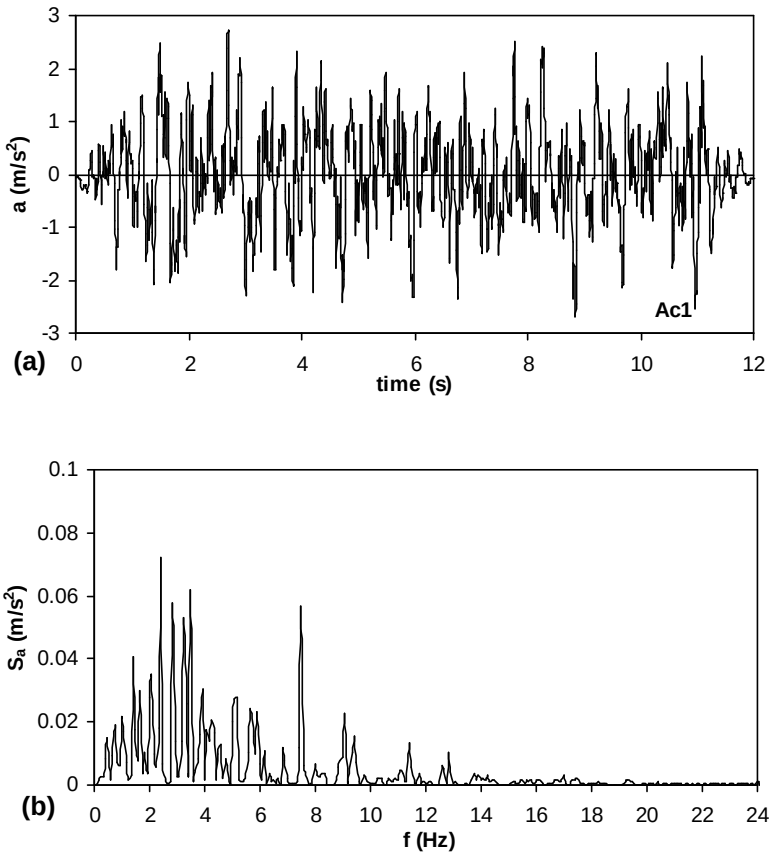


Figure 1: One seismic input motion used in this study: a) artificial accelerogram; b) Fourier spectrum.

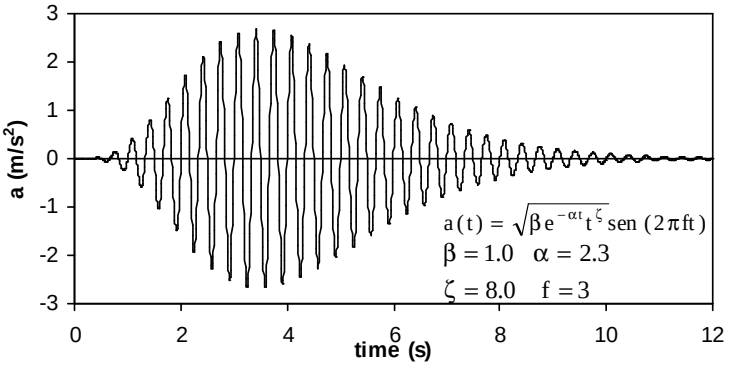


Figure 2: Variable amplitude single frequency harmonic motion (f = 3Hz).

In the analyses presented in this paper, two constitutive models were used: the *Mohr-Coulomb* model and a *Strain-Softening* model.

In the implementation of the *Mohr-Coulomb* model in FLAC, principal stresses σ_1, σ_2, σ_3 are used, being the out-of-plane stress, σ_{zz}, recognized as one of these. With the ordering convention $\sigma_1 \leq \sigma_2 \leq \sigma_3$ (compressive stresses are negative), the failure criterion for this model is represented in the plane (σ_1, σ_3) as illustrated in Figure 3.

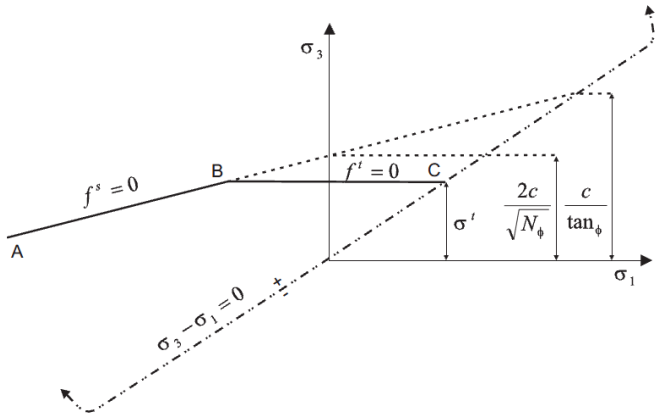


Figure 3: Mohr-Coulomb failure criterion in FLAC [8].

The failure envelope is defined from point A to point B (Figure 3) by the *Mohr-Coulomb* yield function:

$$f^s = \sigma_1 - \sigma_3 N_\phi + 2c\sqrt{N_\phi} \tag{1}$$

and from B to C by a tension yield function of the form:

$$f^t = \sigma^t - \sigma_3 \tag{2}$$

where ϕ is the soil friction angle, c is the cohesion, σ^t is the tensile strength and N_ϕ is defined as:

$$N_\phi = \frac{1+\sin\phi}{1-\sin\phi} \tag{3}$$

The tensile strength of the material, σ^t, cannot exceed the maximum value given by:

$$\sigma^t_{max} = \frac{c}{\tan\phi} \tag{4}$$

The *Strain-Hardening/Softening* model is based on the *Mohr-Coulomb* model with non-associated tension flow rules. The difference lies in the possibility that cohesion, friction, dilatation and tensile strength may harden or soften after the onset plastic yield [8]. The user can define the variation of the cohesion, friction and dilation as a function of the plastic shear strain. The variation of the tensile strength can also be prescribed in terms of plastic tensile strength. The code measures the total plastic shear and tensile strains at each timestep and causes the model properties to conform to the user-defined functions.

More details about these models and their implementation can be found in the manual of the software [8].

3 NUMERICAL GRID AND MATERIAL PROPERTIES

The geosynthetic reinforced embankment is 8.4 m high, reinforced with 14 horizontal reinforcement layers of length 6.8 m (L ≈ 0.8H) uniformly spaced and supported by a stiff foundation. The slope face is inclined of 60º. The geometry of the model and the numerical grid is illustrated in Figure 4.

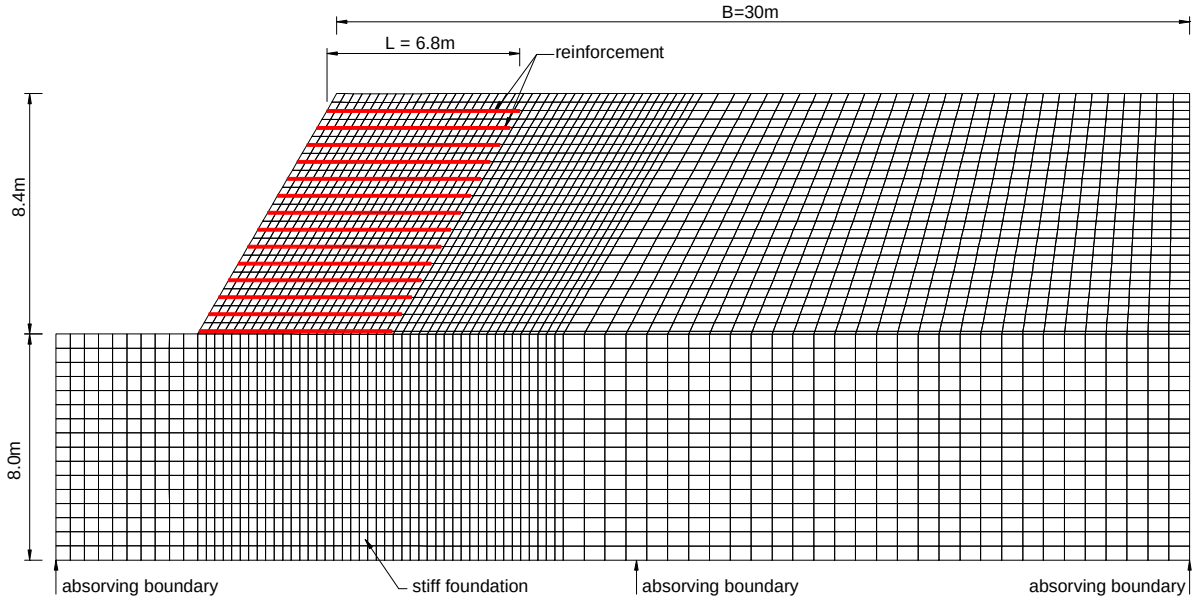


Figure 4: Geometrical properties and numerical grid.

The reinforcement layers were modelled using linear elasto-plastic cable elements with negligible compressive strength. The tensile yield strength was taken equal to 50 kN/m corresponding to the long term design strength (120 years) of a high strength composite geotextile, with nominal strength of 100 kN/m. The linear elastic stiffness of the reinforcement depends on the reinforcement strength and strain level. The reinforcement stiffness was taken equal to 1000 kN/m (approximately the stiffness value corresponding to 2% of strain). The influence of the reinforcement stiffness on the seismic behaviour of the structure is also analysed in this study.

The interface between the reinforcement and the soil was modelled by a grout material. The interface shear strength was considered dependent of the backfill shear strength.

A granular and two cohesive soils were considered as backfill material. Table 1 summarizes the soil properties. The granular soil was modelled as a purely frictional elasto-plastic material, with a *Mohr-Coulomb* yield function and a non-associated flow rule ($\psi = 0^o$). Two constitutive models were used to model the behaviour of the cohesive backfills: *Mohr-Coulomb* model and *Strain-Softening* model.

	Foundation	Granular Backfill	Cohesive Backfill "I"	Cohesive Backfill "II"
Unit weight, γ (kN/m^3)	22	17.5	16	16
Elasticity modulus, E (kN/m^2)	200×10^3	60×10^3	30×10^3	30×10^3
Poisson ratio, υ	0.30	0.30	0.30	0.30
Shear modulus, G (kN/m^2)	76.9×10^3	23.1×10^3	11.5×10^3	11.5×10^3
Cohesion, c (kN/m^2)	50	0	20	20
Internal friction angle, ϕ (^{o})	45	35	27	10

Table 1: Soil properties.

Figure 5 presents the variation of the internal friction angle and cohesion of the cohesive backfill "I", with the shear plastic strain, assumed in the *Strain-Softening* model. The values remain constant for shear plastic strains greater than 1%.

To analyze the importance of the backfill cohesion in the seismic behaviour of the reinforced embankment, a second situation was admitted: no variation of the backfill cohesion with shear plastic strain (thin line in Figure 5b - *Strain-Softening_f*) and the variation of the backfill friction angle shown in Figure 5(a).

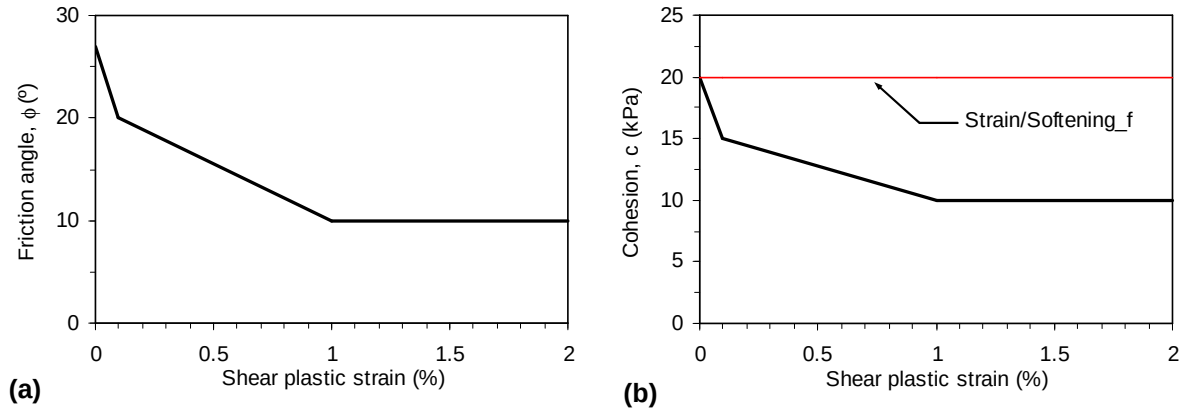


Figure 5: Decrease of backfill properties with shear plastic strains in the *Strain-Softening* model (cohesive backfill "I"): (a) internal friction angle, ϕ; (b) cohesion, c.

4 EFFECT OF BACKFILL SOIL

4.1 Influence of the constitutive model for cohesive backfill

After the simulation of the embankment construction with the cohesive backfill "I" (see Table 1) considering the *Strain-Softening* model and the shear strength decrease plotted in Figure 5, the structure was submitted to the artificial accelerogram plotted in Figure 1(a).

Based on the elastic properties of the soil and the mesh size, the maximum frequency that could be modelled accurately was 11.3Hz. So, before applying the seismic input, the frequencies above 10 Hz were removed. The filtered accelerogram was checked for the baseline drift (i.e., continuing residual displacement after the motion has finished) and a baseline correction was carried out [2].

Figure 6 shows the contours of horizontal displacements at the end of the seismic motion considering the embankment constructed with the cohesive backfill "I" and the *Strain-Softening* model (Figure 5). This figure indicates the imminent failure of the structure. The potential failure surface has developed in the retaining soil, i.e., behind the reinforced soil mass. The potential failure surface is also clear in Figure 7, where the maximum shear strain increments at the end of the seismic motion are represented.

Figures 6 and 7 show that if the backfill shear strength decreases significantly during the seismic motion, the stability of the reinforced embankment can be compromised.

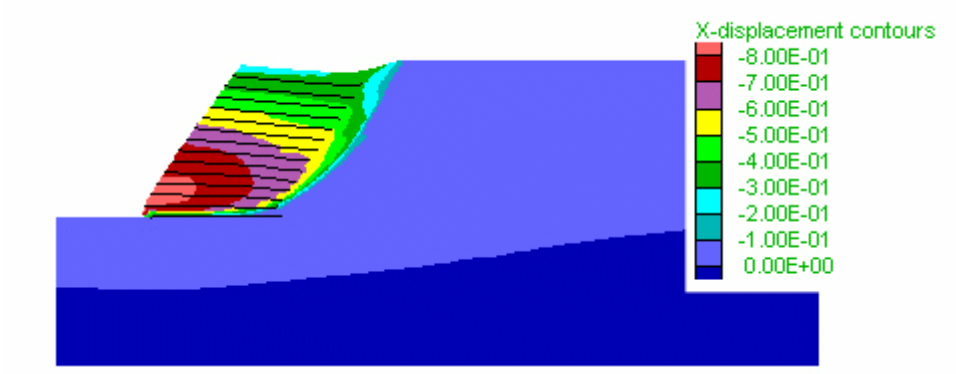


Figure 6: Contours of horizontal displacements at the end of the seismic motion considering the *Strain-Softening* model (cohesive backfill "I").

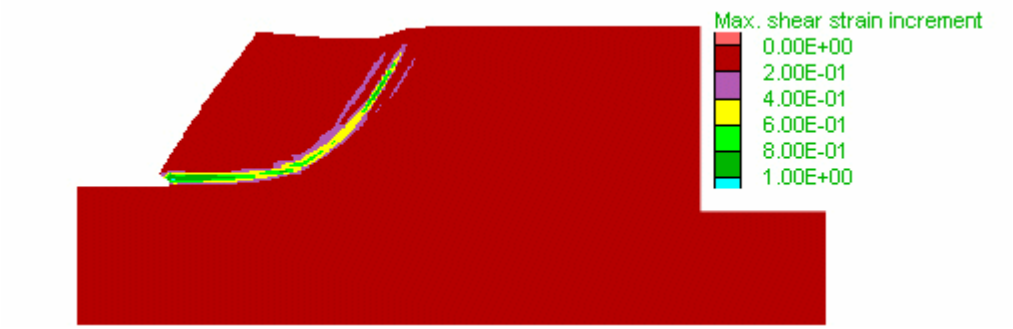


Figure 7: Maximum shear strain increments at the end of the seismic motion considering the *Strain-Softening* model (cohesive backfill "I").

As mentioned previously, to isolate the effect of the cohesive component it was performed an analysis in which only the backfill friction angle decreased with shear plastic strain. This analysis was referred as *Strain-Softening_f*. As expected, since the backfill shear strength is higher, this analysis has shown that at the end of the seismic motion the embankment deformation will be smaller. However, so large differences were not expected. For example, the decrease in the maximum residual horizontal displacement of the slope face was 95% and the maximum reinforcement tensile force decreases 68%.

Figure 8 compares the residual horizontal displacements of the slope face and the residual surface settlements at the end of the seismic motion, when the cohesive backfill was modelled by *Mohr-Coulomb* and *Strain-Softening* models. In the *Mohr-Coulomb* model the backfill shear properties are kept constant during the ground motion, so the embankment deformation is much smaller. It should be noted that in the *Strain-Softening* model only the decrease of the backfill friction angle was considered (model *Strain-Softening_f*).

Figure 8(a) evidences that when the *Strain-Softening* model was considered, the pattern of the horizontal displacements of the slope face underwent some changes. The displacements near the slope base tend to increase significantly.

The maximum reinforcement tensile loads obtained with the two models are illustrated in Figure 9. The differences in the reinforcement tensile loads are more significant in the lower half height of the embankment.

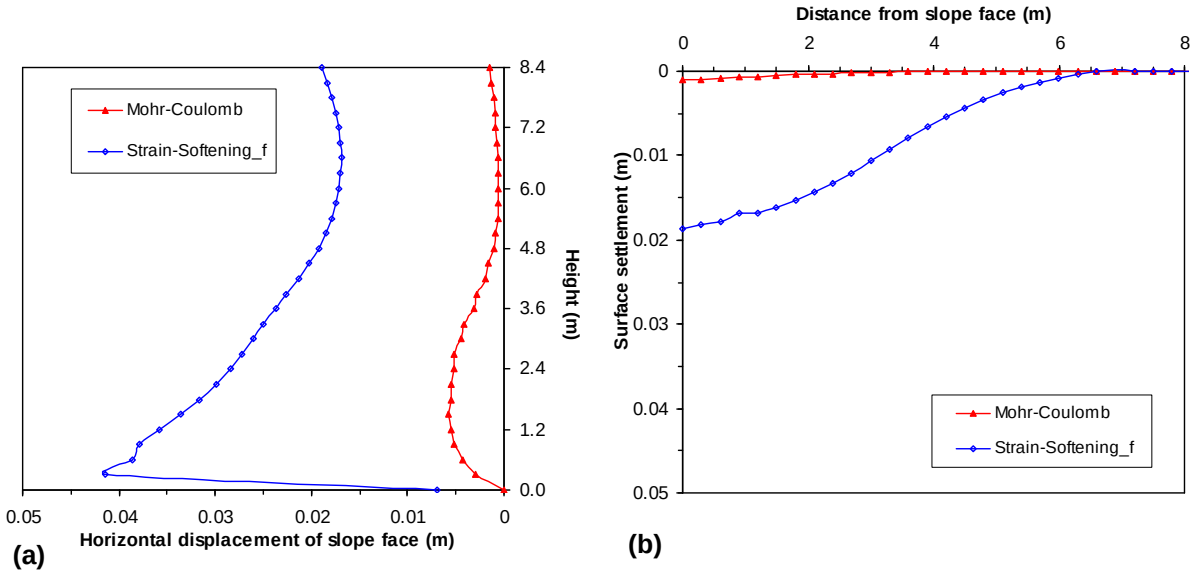


Figure 8: Effect of the backfill constitutive model on: (a) horizontal displacements of the slope face; (b) surface settlements.

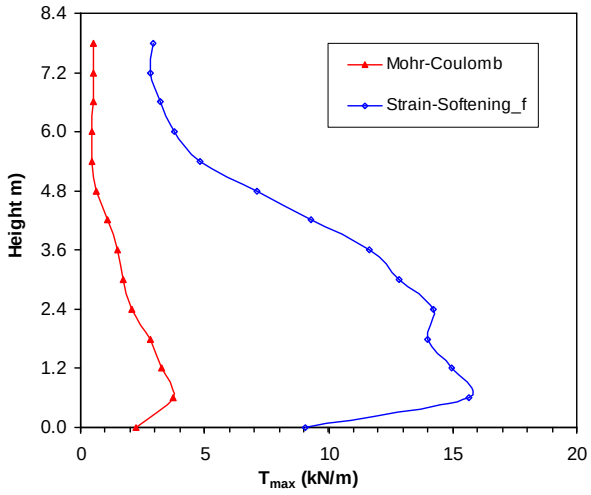


Figure 9: Effect of the backfill constitutive model on the maximum reinforcement tensile loads.

Figures 8 and 9 show that the decrease of the backfill friction angle with the shear strain (Figure 5a) is an important factor in the seismic behaviour of the structure. The conclusions presented by some researchers regarding the good behaviour of reinforced soil walls constructed with cohesive backfills should be regarded with some reserves.

The cohesive backfill "II" was selected to have the same shear strength properties of the backfill "I" when the *Strain-Softening_f* is assumed and the shear plastic strain exceeds 1% (see Table 1 and Figure 5).

Figure 10 compares the residual horizontal displacements of the slope face and the maximum reinforcement tensile loads obtained for the cohesive backfill "I", modelled with the *Strain-Softening_f* model, with the results obtained for the cohesive backfill "II", analyzed with the *Mohr-Coulomb* model.

Taking into consideration that the cohesive component is equal for both backfills, Figure 10 illustrates the influence of the frictional component of the backfill. Note that the friction angle is also the same for shear plastic strains greater than 1%.

For the cohesive backfill "II", the friction angle is equal to 10º throughout the numerical simulation so, greater residual deformations were expected. However, Figure 10(b) shows that the differences in the maximum reinforcement tensile loads were not very significant. Greater reinforcement tensile loads were achieved for most of the layers when cohesive backfill "I" was admitted.

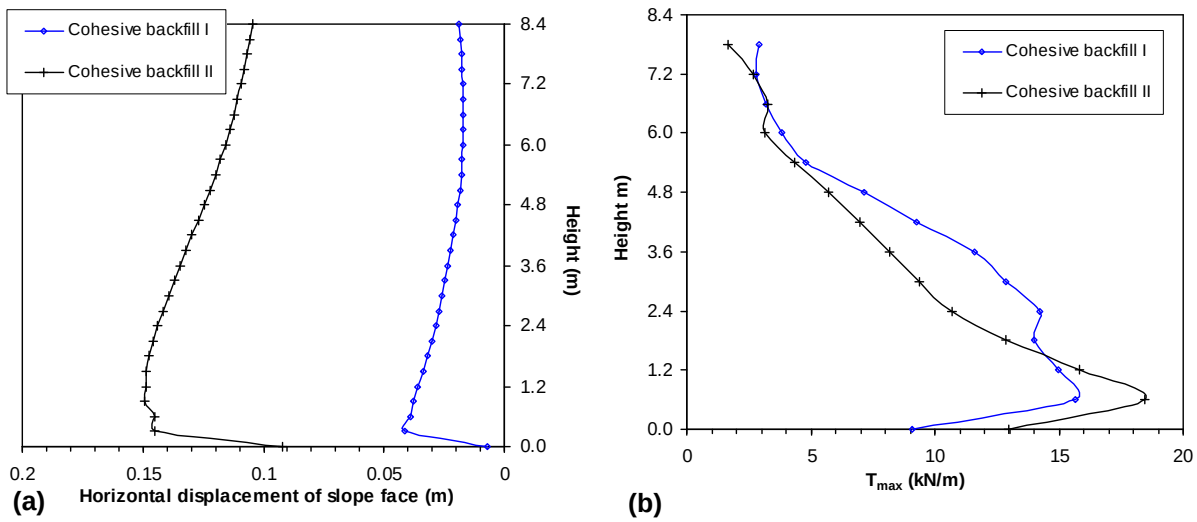


Figure 10: Influence of the frictional component of the backfill on: (a) horizontal displacement of the slope face; (b) the maximum reinforcement tensile loads.

4.2 Effect of backfill soil type

The influence of the backfill soil properties on the residual horizontal displacements of the slope face and maximum reinforcement tensile loads is illustrated in Figure 11. The granular backfill and the cohesive backfill "II" were analyzed with the *Mohr-Coulomb* model. The cohesive backfill "I" was modelled by the *Strain-Softening_f* model (see Figure 5).

The theoretical distribution of the reinforcement tensile forces considering the granular backfill, the horizontal seismic coefficient, k_h, equal to 0.27 and the seismic earth pressure coefficients estimated by the equation proposed by [11] is also plotted in Figure 11(b).

Figure 11(a) shows that the residual horizontal displacements of the slope face for the embankment constructed with the granular backfill are, in general, between the values achieved for the cohesive backfills. As mentioned, the displacements near the slope base increase when the *Strain-Softening* model is used.

For the same constitutive model (*Mohr-Coulomb*), greater reinforcement tensile loads were achieved in the embankment constructed with the granular backfill (with exception of the 3 lower reinforcement layers). If the embankment has been constructed with the cohesive backfill "I" and modelled with the *Strain-Softening_ f* model, the maximum reinforcement tensile loads in the lower half of the embankment height exceed the tensile loads achieved for the granular backfill (Figure 11b).

For the granular backfill, the maximum reinforcement tensile loads for the layers located in the upper half height of the embankment are very close to those estimated by the theoretical distribution (with the exception of the top layers, where the theoretical distribution underestimates the reinforcement tensile loads). The theoretical distribution overestimates the reinforcement tensile loads for the reinforcement layers located in the lower half of the embankment height.

It can be seen in Figure 11(b) that the maximum reinforcement tensile load recorded in the 4th reinforcement layer was not very different when distinct backfill materials were used. Notwithstanding, the distribution of the tensile forces (and consequently, the axial strain) through the reinforcement length can be different. Figure 12 illustrates the axial strains through the reinforcement length of the 4th layer obtained for the three backfill materials.

The sudden decrease of the axial strain near the end of the reinforcement for the cohesive backfill "II" suggests that the reinforcement length could not be the appropriate. Even if the maximum axial strain reached in the three simulations has been similar, the axial strain distribution when the *Strain-Softening_ f* model was used (cohesive backfill "I") was significantly distinct from those achieved with the *Mohr-Coulomb* model.

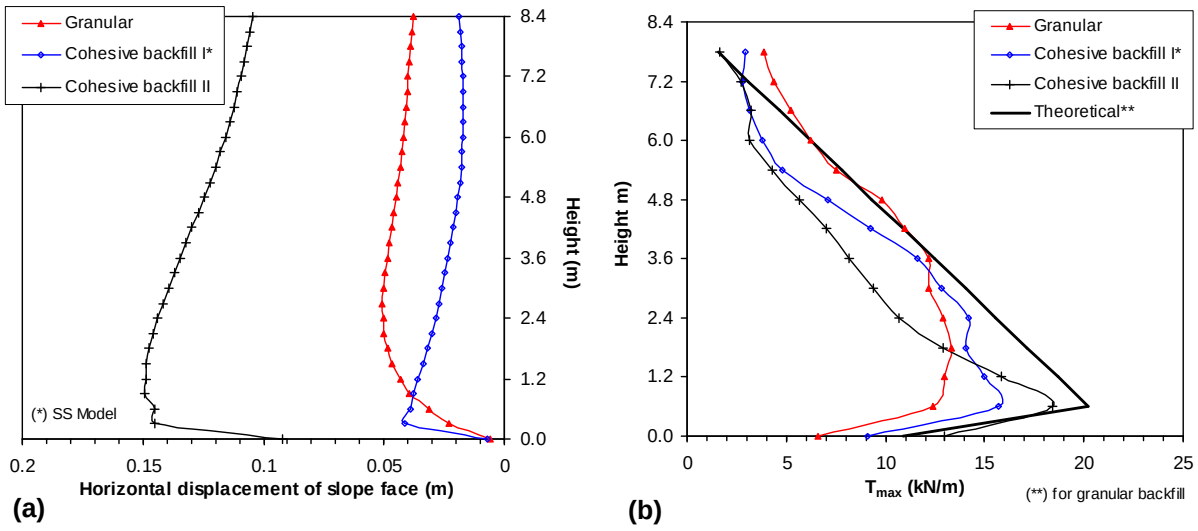


Figure 11: Influence of the backfill soil properties on: (a) horizontal displacement of the slope face; (b) the maximum reinforcement tensile loads.

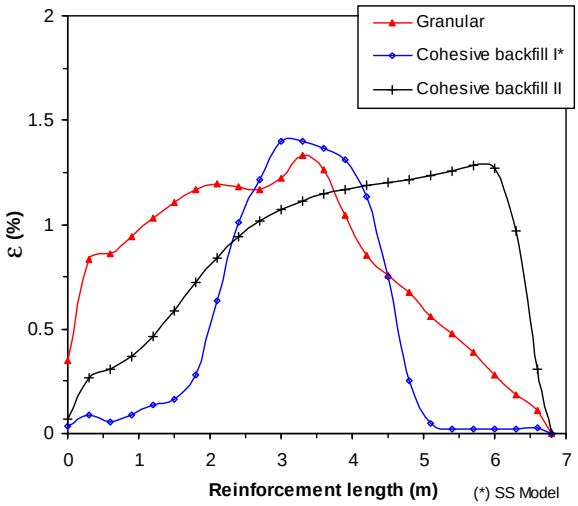


Figure 12: Influence of the backfill soil properties on the axial strain through the 4th reinforcement layer.

5 INFLUENCE OF INPUT MOTION

In order to investigate the influence of the input motion on seismic behaviour of the structure, as it was referred in section 2, four input motions were considered: two earthquake ground motions artificially generated and two variable amplitude single frequency harmonic motions, with frequencies of 3Hz (close to the fundamental frequency of the structure) and 4 Hz.

Figure 13 presents the effect of the seismic input motion on the residual horizontal displacements of the slope face and on the maximum reinforcement tensile loads. The variable amplitude harmonic motion with frequency of 3 Hz induces, not unexpectedly, very large lateral displacements and reinforcement tensile loads. It should be remembered that this frequency is close to the fundamental frequency of the structure. This input motion is much more aggressive to the structure than the earthquake loadings. On the other hand, the residual deformations recorded at the end of the harmonic motion with frequency of 4 Hz are not significantly different from those obtained with the earthquake loadings.

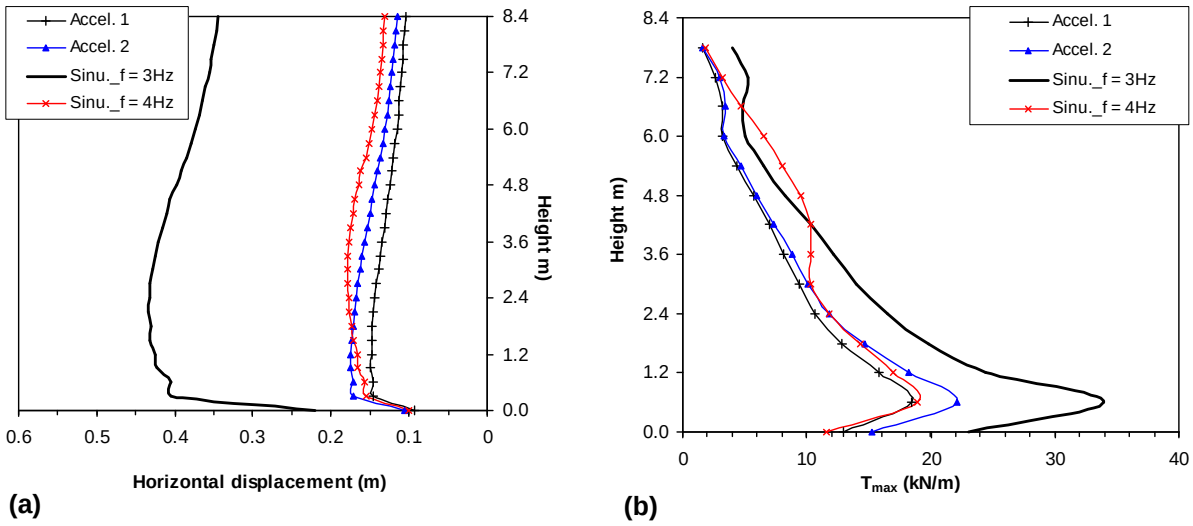


Figure 13: Influence of the seismic input motion on: (a) horizontal displacement of the slope face; (b) the maximum reinforcement tensile loads.

Figure 14 illustrates the time histories of the tensile load recorded 2 m from the slope face in the 2nd reinforcement layer. This graph shows that, for the harmonic motion with f = 3Hz the tensile load increased almost fourteen times, when compared to the value installed at begin of the input motion. In particular for the harmonic motions, the tensile load variation after 6 seconds was very small. The variations induced by the earthquake motions were gentler.

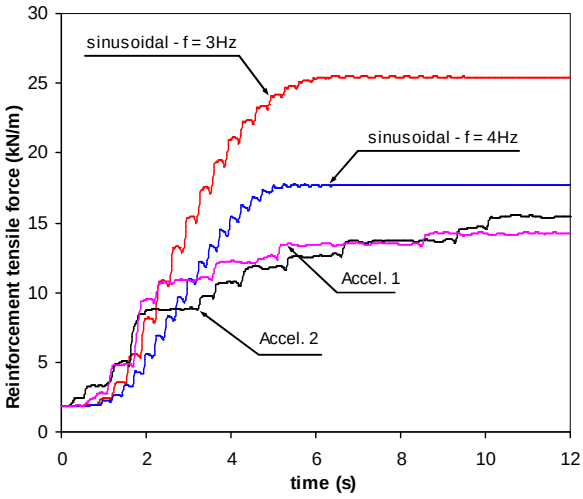


Figure 14: Time histories of the tensile loads recorded at 2 m from the slope face in the 2nd reinforcement layer.

6 EFFECT OF REINFORCEMENT STIFFNESS

The effect of the reinforcement stiffness on the seismic behaviour of the reinforced embankment constructed with the cohesive backfill "II" was analyzed. Figure 15 shows the residual horizontal displacements of the slope face and reinforcement tensile loads for three geosynthetics: a geotextile (J = 250 kN/m), a low strength geogrid (J = 500kN/m) and a medium strength geogrid or a high strength composite geotextile (J = 1000kN/m). These values were estimated for 2% of strain.

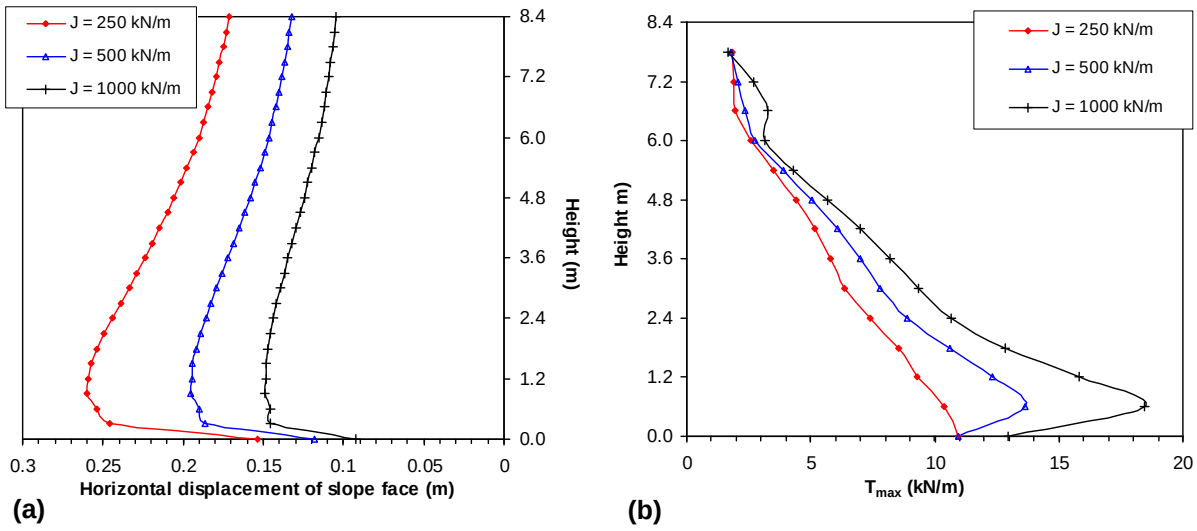


Figure 15: Influence of the reinforcement axial stiffness on: (a) horizontal displacement of the slope face; (b) the maximum reinforcement tensile loads.

Not unexpectedly, the residual deformations of the slope face increased with the decrease of the reinforcement stiffness (Figure 15a).

The stiffer reinforcements have been subjected to greater reinforcement tensile loads. For the lower value of the reinforcement stiffness, the restraining effect of the foundation (which causes small tensile load in the lower reinforcement layer) disappeared (Figure 15b).

7 CONCLUSIONS

The use of soils locally available has cost benefits and sustainable gains. Therefore it is important to study the behaviour of geosynthetic reinforced steep slopes constructed with cohesive backfills.

This numerical study carried out allows drawing the following main conclusions:

- If the backfill shear strength decreases significantly during the seismic motion, the stability of the reinforced embankment can be compromised.
- When the *Strain-Softening* model was used, the residual displacements near the slope base tended to increase significantly.
- The decrease of the backfill friction angle with the shear strain is an important factor in the seismic behaviour of the structure. The conclusions presented by some researchers regarding the good behaviour of reinforced soil walls constructed with cohesive backfills should be regarded with some reserves.
- Single frequency harmonic motions may be useful to analyse the dynamic response of reinforced soil structures, however the magnitude of the response might be excessive when compared to artificial (or real) earthquake ground motions.

The numerical study herein presented has some limitations, namely, neglecting the effect of water content and pore water pressures. Even so, the achieved results indicate that the use of cohesive soils as backfill material of geosynthetic reinforced steep slopes can have advantages and encourage further research.

ACKNOWLEDGMENTS

The authors would like to thank the financial support of Portuguese Science and Technology Foundation (FCT) and FEDER, Research Project FCOMP-01-0124-FEDER-009750 - PTDC/ECM/100975/2008.

REFERENCES

[1] Bathurst, R.J., Hatami, K. Seismic response analysis of a geosynthetic-reinforced soil retaining wall. *Geosynthetics International*, **5**(1-2), pp. 127-166, 1998.

[2] Vieira, C.S., Lopes, M.L., Caldeira, L.M. Numerical modelling of a geosynthetic reinforced steep slope subjected to seismic loading. *Proc. of 3rd Computational Methods in Structural Dynamics and Earthquake Engineering - COMPDYN 2011*, Corfu, Greece, 2011.

[3] BS 8006. Code of practice for strengthened/reinforced soils and other fills, in British Standard Institution, 260p, 2010.

[4] Zornberg, J.G., Mitchell, J.K. Reinforced soil structures with poorly draining backfills. Part I: reinforcement interactions and functions. *Geosynthetics International*, **1**(1), pp. 103–147, 1994.

[5] Liu, Y., Scott, J.D., Sego, D.C. Geogrid reinforced clay slopes in a test embankment. *Geosynthetics International*, **1**(1), pp. 67-91, 1994.

[6] Dobie, M. Practical use of clay fills in reinforced soil structures. *Development of Geotechnical Engineering in Civil Works and Geo-Environment*, Yogyakarta, December 2010.

[7] Mitchell, J.K., Zornberg, J.G. Reinforced soil structures with poorly draining backfills. Part ii: case histories and applications. *Geosynthetics International*, **2**(1), pp. 265–307, 1995.

[8] Itasca. FLAC - Fast Lagrangian Analysis of Continua, Version 5.00, Itasca Consulting Group, Inc., USA, 2005.

[9] Gasparini, D., Vanmarcke, E. SIMQKE - A computer program for artificial motion generation, in User's Manual and Documentation, Department of Civil Engineering, Massachusetts Institute of Technology, 1976.

[10] [NP-ENV 1998-1-1. Eurocode 8: Design provisions for earthquake resistance of structures. Part 1-1: General rules – Seismic actions and general requirements for structures. Portuguese NAD, 2010.

[11] Vieira, C.S., Lopes, M.L., Caldeira, L.M. Earth pressure coefficients for design of geosynthetic reinforced soil structures. *Geotextiles and Geomembranes*, **29**(5), pp. 491-501, 2011.

COMPDYN 2013
4th ECCOMAS Thematic Conference on
Computational Methods in Structural Dynamics and Earthquake Engineering
M. Papadrakakis, V. Papadopoulos, V. Plevris (eds.)
Kos Island, Greece, 12–14 June 2013

SITE RESPONSE ANALYSIS FOR VERTICAL GROUND MOTION

S Kontoe[1], A. Christopoulos[2] and R. May[3]

[1]Lecturer
Department of Civil & Environmental Engineering, Imperial College, London UK, SW7 2AZ
stavroula.kontoe@imperial.ac.uk

[2]Civil Engineer, SAIPEM
christopantonis@gmail.com

[3]Head of Technology – Geotechnics
Atkins Ltd, Rob.May@atkinsglobal.com

Keywords: Vertical ground motion, dynamic coupled consolidation analysis, permeability.

Abstract. *This study initially considers a uniform soil layer subjected to vertically propagating harmonic P-waves. The response of the layer is calculated analytically, considering one-dimensional propagation, and numerically employing time domain coupled consolidation Finite Element analysis for a range of input frequencies. The computed amplification function is shown to significantly depend on the modelling of the fluid phase and the soil permeability. Subsequently, a ground profile corresponding to a downhole array in Dahan (Taiwan) is examined assuming undrained, drained and coupled consolidation behaviour. The numerical predictions are compared with the vertical recorded response during the 1999 Chi-Chi earthquake demonstrating a very good agreement for the coupled consolidation analysis and highlighting the limitations of the other two approaches (i.e. drained and undrained analyses).*

1 INTRODUCTION

Site response analysis is commonly performed to account for local site effects on ground motion propagation during an earthquake. Most site response analyses involve horizontal ground motion, considering vertically propagating shear waves in horizontally layered systems. In reality, the ground is simultaneously subjected to shaking in both the horizontal and vertical directions during an earthquake, but the vertical response has generally received limited attention in the literature. Field evidence from various recent earthquakes indicates though that damage of concrete buildings and bridges can be attributed to high vertical ground motion (e.g. [4]). Therefore there is a need for better establishing the site response to vertical ground motion.

It is widely believed that vertical ground response is dominated by the propagation of compression waves (P-waves) and has been found to depend on the pore-fluid compressibility, permeability, soil stiffness and porosity ([1], [9]). Saturated soils are two-phase materials consisting of a solid phase (soil skeleton) and a fluid phase (pore water filling the voids). Depending on the soil permeability, the rate of loading and the hydraulic boundary conditions, it is often necessary to employ coupled analysis to accurately model the two phase behaviour of soils. This is in particular the case when the response to vertical motion is considered.

This study examines first the response of a uniform soil layer subjected to harmonic P-waves analytically and numerically, with dynamic coupled consolidation Finite Element (FE) analysis, aiming to highlight the importance of appropriately modelling the fluid-phase when vertical ground motion is considered. This is further emphasised in the second part of this study where the vertical seismic response of a ground profile is computed with different assumptions regarding the pore fluid compressibility (drained, undrained and coupled consolidation) and the results are compared with field measurements.

2 UNIFORM SOIL LAYER ON RIGID BEDROCK

The solution of the wave equation for a uniform soil layer on rigid bedrock (see Figure 1) subjected to vertically propagating harmonic P-waves is a vertical displacement of the form:

$$v(z,t) = Ae^{i(\omega t + k^* z)} + B\, e^{i(\omega t - k^* z)} \tag{1}$$

where ω is the circular frequency of the input pulse, k* is the complex wave number ($= \frac{\boldsymbol{\omega}}{V_p^*}$) and A and B are the amplitudes of waves traveling in the upward and downward directions respectively. Considering the equilibrium of stresses at the ground surface and the compatibility of displacements at the soil-rock interface, similarly to the case of vertically propagating shear waves [6], it can be shown that the transfer function between the top and the bottom of the soil layer is given by:

$$F(\omega) = \frac{1}{cos(\omega H / V_p^*)} \tag{2}$$

where H is the thickness of the soil layer and the complex P-wave velocity is given by:

$$V_p^* = \sqrt{\frac{D}{\rho}}(1 + i\xi) = V_p\ (1 + i\xi) \tag{3}$$

where D, ρ and ξ are the constrained modulus, mass density and damping respectively of the soil. For a fully saturated deposit the expression for the P-wave velocity becomes:

$$V_p^* = \sqrt{\frac{D+\frac{K_f}{n}}{\rho}}(1+i\xi) = V_p\ (1+i\xi) \quad (4)$$

where K_f is the bulk modulus of the pore fluid and n is the porosity. Based on Equations (2) & (4) the vertical site response depends significantly on the pore fluid stiffness. This is clearly demonstrated in Figure 2 which plots the transfer function for a typical soil layer for ideal undrained conditions with undrained Poisson's ratio equal to 0.5 and K_f=∞, drained (K_f=0) and for K_f=2.2GPa, which is the value of the bulk modulus of water. Assuming undrained behaviour results in no amplification, while employing the bulk modulus of the water shifts the response to higher frequencies without though affecting the amplitude of the transfer function with respect to the drained case.

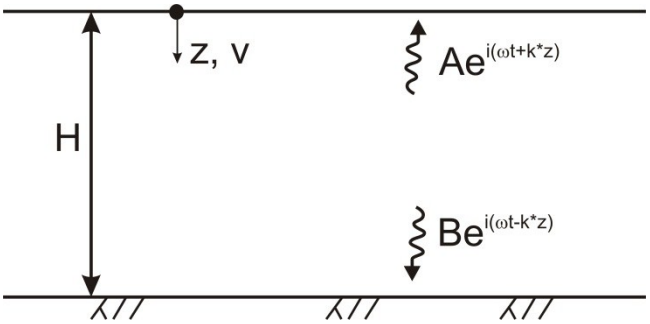


Figure 1: Uniform soil layer of thickness H underlain by rigid bedrock.

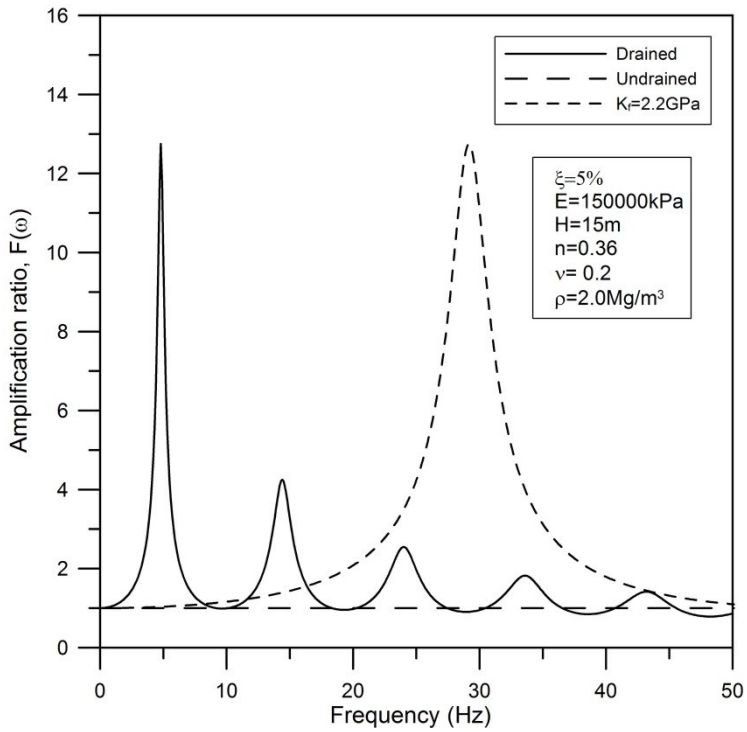


Figure 2: Transfer functions for a uniform elastic soil layer underlain by rigid bedrock for various values of the pore fluid bulk modulus

3 DYNAMIC COUPLED CONSOLIDATION ANALYSIS OF A UNIFORM SOIL LAYER

The simple analysis of the previous section, which is based on one dimensional wave propagation within a one-phase material, gives some insight into the layer response, but it cannot account for the coupling in the dynamic response between the solid and the fluid phase. In order to investigate the effect of the solid-fluid interaction on the vertical ground response, dynamic coupled consolidation analyses are carried out with the Finite Element method in this section.

3.1 Analysis arrangement

To analyse the response of the uniform soil layer illustrated in Figure 1, a 15m high soil column of was analysed in plane strain conditions with the Imperial College Finite Element program ICFEP [7]. In all analyses full coupling of the fluid and solid phases was considered by a adopting a "u-p" formulation, in which the primary unknowns are the solid phase displacements and the pore fluid pressure. The FE mesh comprised of 60 8-noded quadrilateral elements (1m wide and 0.5m high). The water table assumed to be at the ground surface and the soil was treated as fully saturated with hydrostatic pore water pressure distribution. The column was subjected to a set of harmonic pulses of unit amplitude which were applied as a vertical acceleration along the base of the mesh. The tied degrees of freedom boundary condition was applied along the vertical boundaries to ensure one-dimensional propagation and the horizontal movement was restricted along the bottom boundary. The ground surface was treated as a free draining boundary, while the bottom and side boundaries were treated as impermeable ones. A target damping ratio of 5% was adopted using the Rayleigh damping formulation. The time integration was performed with the generalised-α method ([3], [5]) which is an unconditionally stable implicit method, with second order accuracy and controllable numerical damping. The remaining material properties are listed in Table 1. The time step of each analysis was taken as a fraction ($\Delta t = T/40$) of the pulse period. The soil layer was subjected to 13 harmonic pulses which covered a wide range of frequencies (f=5,10,15,20,25,27,28,29,30,40,45,50 Hzs) and each set of analyses was repeated for the four permeability values listed in Table 1.

Table 1: Material Properties

Parameter	Value
Young's modulus, E (MPa)	150.0
Mass density, ρ (Mg/m3)	2.0
Poisson's ratio, ν	0.2
Bulk modulus of water (MPa)	2.2E3
Porosity	0.36
Permeability, k (m/sec)	Varied, 10^{-6}, 10^{-4}, 10^{-3}, 10^{-2}

3.2 Results

The steady-state response at the ground surface was established for each considered pulse by examining a large number of cycles. The amplitude of the steady-state response normalised by the amplitude of the input motion for the four permeability values is plotted in Figure 3. The computed amplification ratios are also compared with the analytical transfer functions. The analyses for the very impermeable soil layer ($k=10^{-10}$m/sec) compare very well with the analytical transfer function with K_f=2.2GPa for the entire frequency range. For such a low

value of permeability there is no relative movement between the solid and the fluid phase and hence the main effect of the fluid phase in the elastic response is to increase the stiffness of the soil layer in compression. It should be noted that the numerical analyses slightly overestimate the amplification close to resonance (f=29Hz), which is probably due to inability of the Rayleigh damping to maintain the target damping ratio constant across the entire frequency range. It is interesting to note that for the range of frequencies which are close to the natural frequency (f_o=29.14Hz) of the layer, the amplification ratio decreases as the permeability increases. This is more pronounced for the highest value of permeability (k=10^{-2} m/sec). Keeping in mind that all analyses were conducted for the same value of damping ratio (ξ=5%), the additional damping in the response results from the relative movement between the solid and the fluid phases which is more evident for the analyses with the higher permeability values. Bardet [1] also concluded that the solid-fluid damping within fully saturated sands can be comparable in magnitude to damping developed by hysteresis.

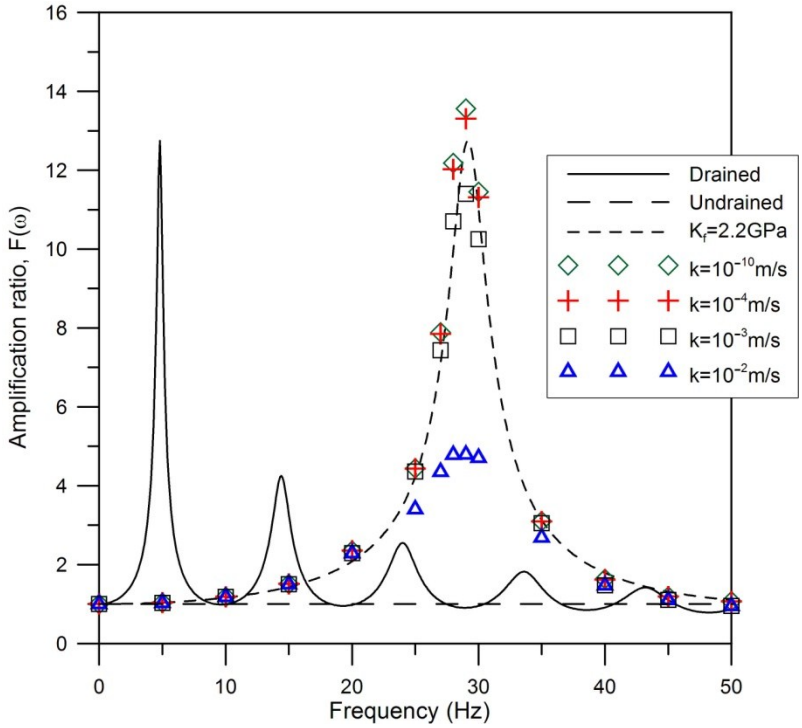


Figure 3: Amplification ratio for various values of permeability.

4 DAHAN DOWNHOLE ARRAY

4.1 Ground profile and analysis arrangement

In this section, acceleration time histories from the 1999 Chi–Chi earthquake in Taiwan recorded at the Dahan downhole array site [2], are used to validate the numerical model. The Dahan downhole array is part of the SMART-2 strong-motion array, located at a distance of about 80 km from the epicentre, and consists of three accelerometers at the depths of 50m, 100m and 200m and one at the ground surface. In this study, only the upper 50m of the stratigraphy were considered. The vertical acceleration time history recorded during the main shock of the Chi–Chi earthquake at a depth of 50m (Figure 4) was used as the input motion for the numerical model and the computed response at the ground surface is compared with the actual recording.

The Dahan site consists of alluvial deposits of silty sands, gravels and silty clays. The profile described in Table 2 was adopted based on information provided by the National Centre for Research on Earthquake Engineering (NCREE) and the Central Weather Bureau (CWB) in Taiwan. Rontogianni [8] performed equivalent linear analysis for the same site and examined its response to the horizontal components of the Chi-Chi earthquake. The converged values of stiffness and damping ratio for each layer obtained from the equivalent linear analysis of [8] were used in the analyses of this section and are also listed in Table 2 (denoted as E_{eq} and ξ_{eq} respectively). The water table was taken at 2m below the ground surface and the Poisson ratio was assumed to be 0.3 for all layers. The acceleration time history illustrated in Figure 4a was applied in the vertical direction along the base of the mesh with a time step, Δt=0.01sec. All other boundary conditions and analysis details are identical to the ones described in the previous section.

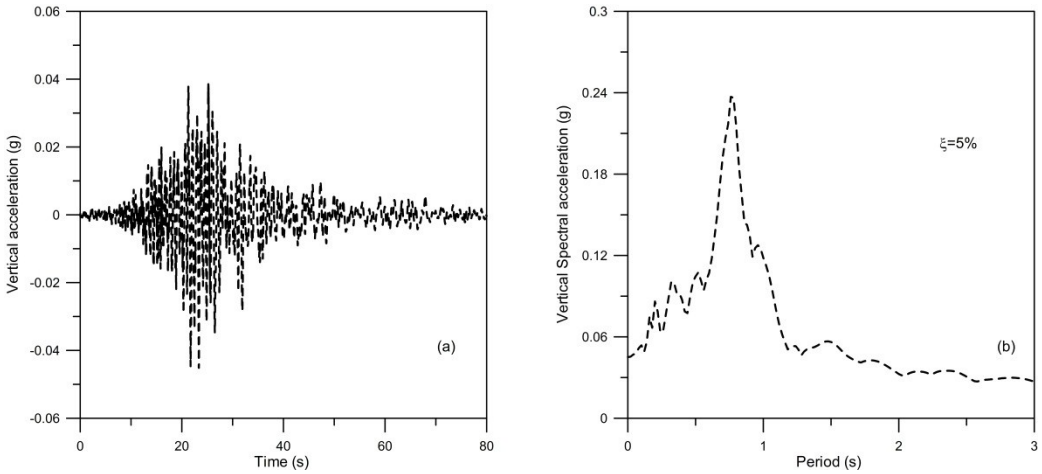


Figure 4: Acceleration time history (a) and the corresponding response spectrum (b) recorded at a depth of 50m at the Dahan site during the main shock of the Chi-Chi earthquake (Chiu [2]).

Table 2: Material properties assumed for the Dahan profile

Soil layer thickness (m)	ρ (Mg/m^3)	E (MPa)	E_{eq} (MPa)	ξ_{eq} (%)	k (m/s)
6	1.76	531.0	480.0	3	5.5E-5
2	1.82	1621.0	1516.0	3	1.5E-4
6	2.1	2333.0	2189.0	3	6.4E-5
4	2.1	1641.0	1467.0	3	6.4E-5
12	1.95	594.0	414.0	3	4.4E-5
20	1.95	670.0	496.0	3	2.0E-6

4.2 Numerical results

Figure 5 compares the recorded surface acceleration in the vertical direction against the computed ones, for undrained, drained and coupled consolidation analyses. The undrained analysis underestimates the ground motion and gives a response which is very similar to the input acceleration of Figure 4a. Since the water table is very close to the ground surface, most of the layers respond in an undrained manner and therefore, based on the transfer function of Figure 2, they do not amplify the response. On the other hand the drained analysis significantly overestimates the ground motion as it amplifies the lower frequencies of the input excita-

tion. The coupled consolidation analysis gives the best prediction out of the three analyses and is in very good agreement with the recorded motion.

Figure 6 compares the computed vertical acceleration response spectra (by undrained, drained and coupled consolidation analyses) at the ground surface with the spectrum of the recorded motion. The undrained analysis significantly underestimates the high-frequency part of the response, but it predicts correctly the main peak of the spectrum. The drained analysis overestimates the response in the medium to low frequency range, while the spectrum of the coupled consolidation analysis compares very favourably with the spectrum of the actual record.

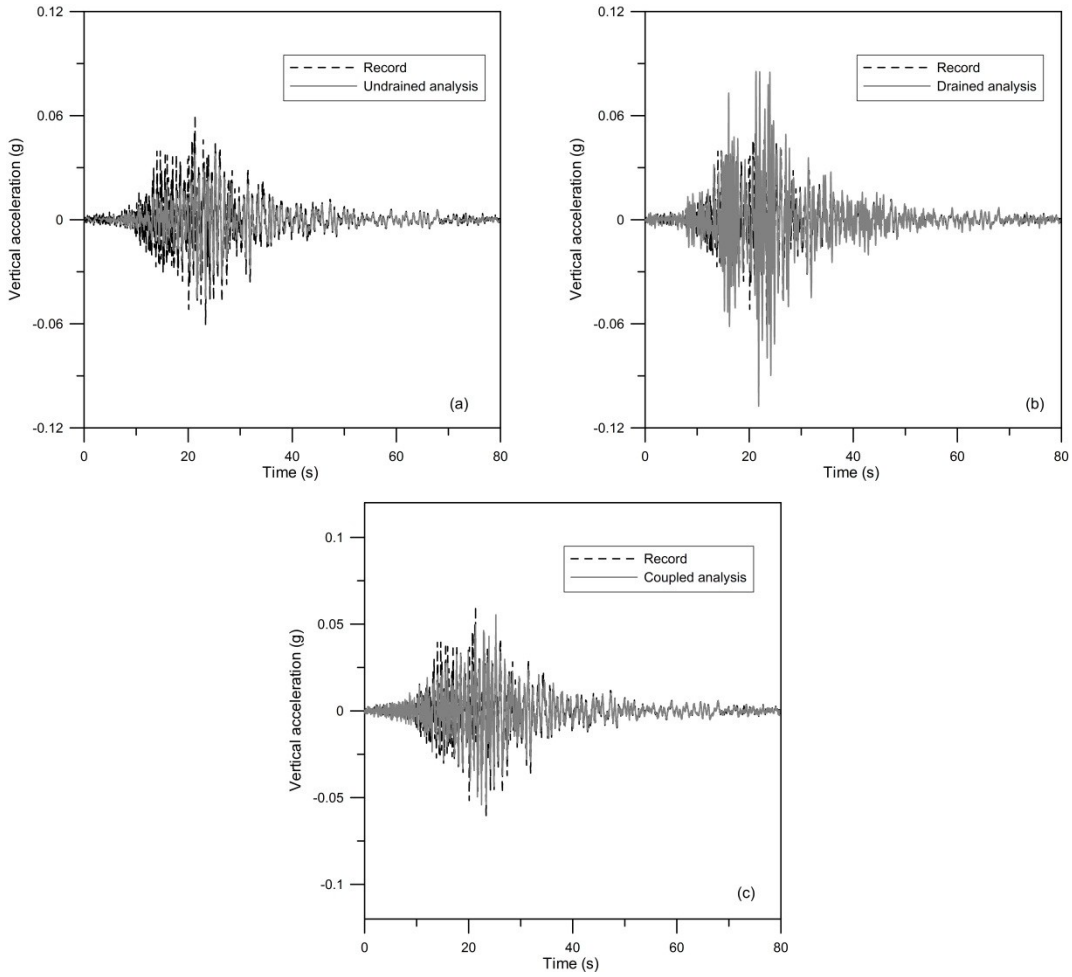


Figure 5: Comparison of the computed acceleration time histories at the ground surface with the recorded one for (a) undrained, (b) drained and (c) coupled analyses.

5 CONCLUSIONS

This study first examined the response of a uniform soil layer subjected to harmonic P-waves analytically, based on one dimensional wave propagation within a one-phase material and numerically, with dynamic coupled consolidation FE analysis. The analytical investigation showed that assuming undrained behaviour results in no amplification of the vertical ground motion, while employing the bulk modulus of the water shifts the response to higher frequencies without though affecting the amplitude of the transfer function with respect to the corresponding drained case. The numerical results showed that the transfer function depends

also on the soil permeability and that for high permeability values (greater than $k=10^{-4}$ m/sec) there is evidence of additional non-hysteretic damping in the response which results from the relative movement between the solid and the fluid phases.

In the second part of this study, the vertical seismic response of a ground profile was computed with different assumptions regarding the pore fluid compressibility (drained, undrained and coupled consolidation) and the results were compared with field measurements. The undrained analysis underestimated the ground motion and gave a response which was very similar to the input acceleration. On the other hand the drained analysis significantly overestimated the ground motion as it amplified the lower frequencies of the input excitation, while the results of the coupled consolidation analysis were in very good agreement with the measured ground motion.

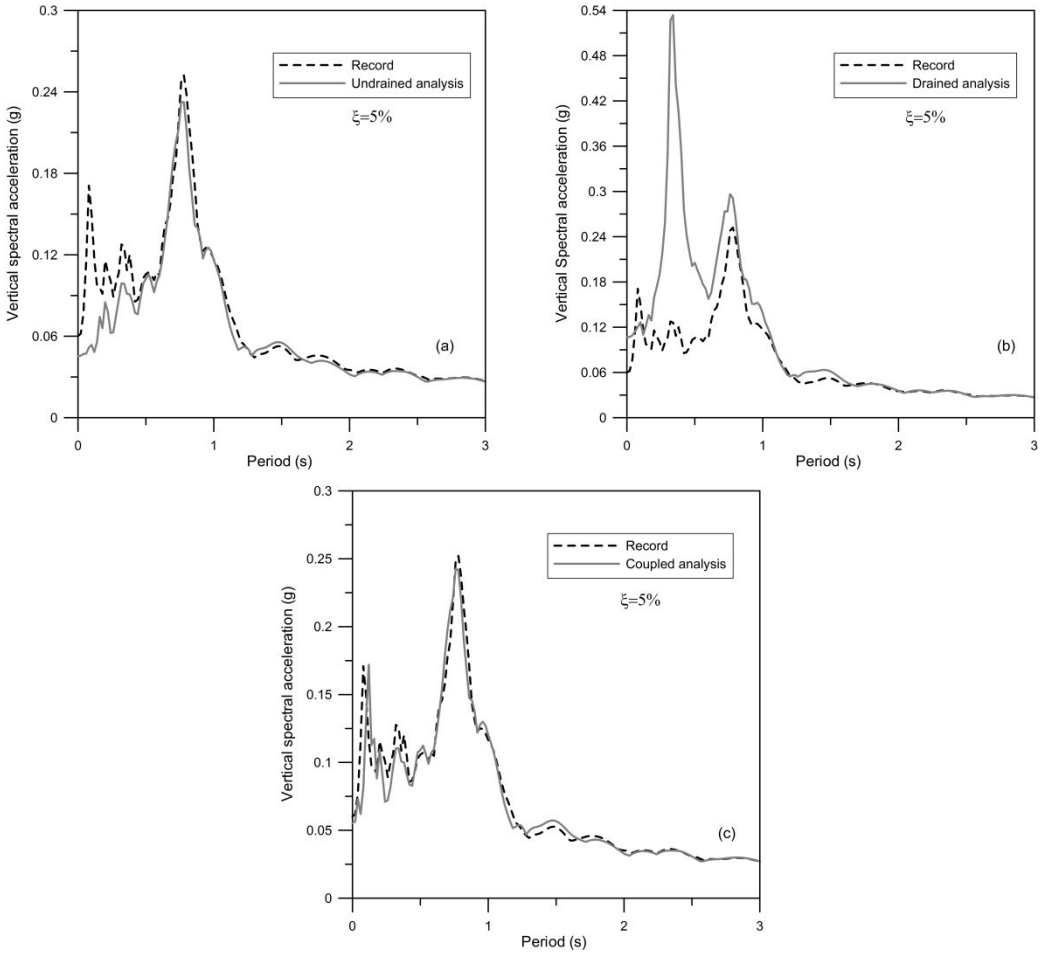


Figure 6: Comparison of the computed acceleration response spectra at the ground surface with the spectrum of the surface record for (a) undrained, (b) drained and (c) coupled analyses.

6 REFERENCES

[1] J.P. Bardet "The damping of saturated poroelastic soils during steady-state vibrations", Applied Mathematics and Computation, 67, 3-31, 1995.

[2] H. Chiu Data files from the SMART-2 strong-motion array for the Chi-Chi earthquake. Bulletin of the Seismological Society of America. 91 (5), 1391-1392, 2001.

[3] J. Chung & G.M. Hulbert "A time integration algorithm for structural dynamics with improved numerical dissipation: the generalized-α method", Journal of Applied Mechanics, Vol. 60, pp. 371–375, 1993.

[4] Hashash, Y. M. A., Phillips, C. & Groholski, D. R. "Recent advances in non-linear site response analysis". 5th International Conference in Recent Advances in Geotechnical Earthquake Engineering and Soil Dynamics, 2010.

[5] S. Kontoe, L. Zdravkovic & D.M. Potts D.M, An assessment of time integration schemes for dynamic geotechnical problems, Computers and Geotechnics, **35** (2), 253-264, 2008.

[6] S.L. Kramer, Geotechnical earthquake engineering, Prentice Hall, New Jersey, 1996.

[7] D.M. Potts & L. Zdravkovic, Finite element analysis in geotechnical engineering: theory, Thomas Telford, London, 1999.

[8] A. Rontogianni, "Numerical modelling of site response". MSc Dissertation. Department of Civil Engineering, Imperial College London, 2012.

[9] J. Yang & T. Sato "Interpretation of seismic vertical amplification observed at an array site". Bulletin of the Seismological Society of America. 90 (2), 275-285, 2000.

COMPDYN 2013
4th ECCOMAS Thematic Conference on
Computational Methods in Structural Dynamics and Earthquake Engineering
M. Papadrakakis, V. Papadopoulos, V. Plevris (eds.)
Kos Island, Greece, 12–14 June 2013

OPTIMUM DESIGN OF CANTILEVER WALLS RETAINING LINEAR ELASTIC BACKFILL BY USE OF GENETIC ALGORITHM

George Papazafeiropoulos, Vagelis Plevris, and Manolis Papadrakakis

National Technical University of Athens
Institute of Structural Analysis and Antiseismic Research
Zografou Campus, Athens 15780, Greece

gpapazafeiropoulos@yahoo.gr, {vplevris, mpapadra}@central.ntua.gr

Keywords: Genetic Algorithm, dynamic soil-structure interaction, linear elastic soil response, retaining wall.

Abstract. *Retaining walls are used in many geotechnical engineering applications, e.g. supporting deep excavations, bridge abutments, harbor-quay walls, anchored retaining walls, etc. Although they are generally simple structures, their static and dynamic interaction with the supporting and/or retained soil is a subject of ongoing research. Apart from this, seismic design of retaining walls is primarily based on rules of thumb and the designer's experience, in order to set the initial dimensions and make the necessary checks to comply with the design codes. In addition, the calculation of the seismic earth pressures is done in a rather simplistic way which may lead to either conservative or unsafe designs. In the present study, after a comprehensive literature review, optimum design is performed for cantilever walls retaining soil layers of two different heights, using numerical two-dimensional simulations and a genetic algorithm. Numerical simulations are performed using the finite element code ABAQUS [1] whereas for optimization purposes, the genetic algorithm provided with MATLAB [2] is utilized. For the calculation of the seismic earth pressures, linear elastic soil, retaining wall stem and wall foundation are assumed. The optimization procedure involves four design variables that have to do with the wall geometry, while the soil and wall material parameters and the frequency range of interest are kept fixed. Structural and geotechnical constraints as well as upper and lower bounds for the design variables are imposed to ensure technical feasibility of the solutions. The results on the optimum solutions are presented and comparisons are made with the corresponding results according to conventional seismic design methods. The numerical results of the study provide a clear indication of the direct dynamic interaction between the retaining wall and the surrounding soil, whereas the complexity of the optimization problem itself is evident. This justifies the necessity for a more elaborate consideration of the optimum design of retaining walls, especially if material and geometric non-linearities are taken into account.*

1 INTRODUCTION

Cantilever retaining walls are among the simplest and most common geotechnical structures intended to support earth backfills. Their main representatives are retaining walls supporting deep excavations, bridge abutments, harbor-quay walls, anchored retaining walls, etc. Their design must satisfy two major requirements: internal and external stability. The former ensures the structural integrity of the various parts of the retaining wall; the latter ensures that the wall – soil system formed after construction will remain in equilibrium, except for some displacements of affordable magnitude.

Retaining walls have to satisfy constraints imposed by the norms, assumptions, preferences and the target to be accomplished, and simultaneously have to be as economical as possible. The design is based on a trial-and-error procedure, which renders the experience of the designer an important factor to reach a cost-effective design. This manual research for the optimum design may be very time-consuming and tedious, while it is not ensured that the final result will be the optimum possible. This necessitates the need for application of various optimization procedures in order to achieve the optimum design.

Relevant optimization methods range from relatively simple mathematical programming based (exact) methods to novel heuristic search techniques. The methods belonging to the first category are very efficient for cases with a few design variables. Representative studies of this category are conducted in [3-6]. In [3] a design aid is compiled from results of an exhaustive search, with which simple rules of thumb were developed to provide for minimum cost design of cantilever retaining walls. In [4] optimization of reinforced concrete cantilever retaining walls is performed and the optimum design problem is posed as a constrained non-linear programming problem with seven design variables. Cost and weight of the walls were used as objective functions and overturning failure, sliding failure, no tension condition in the foundation base, shear and moment capacities of toe slab, heel slab, and stem of wall as constraints. In [5] the problem of optimal cost design of cantilever retaining walls is formulated as a non-linear programming problem and a sequential unconstrained minimization technique is adopted. In [6] optimum reliability-based design of cantilever retaining walls was presented by considering the parameter uncertainties and evaluating the safety in terms of reliability index and not merely by calculating the safety factor.

However, exact methods require large computational effort when the number of design variables increases, and apart from this, they require gradient information and seek to improve the solution in the neighborhood of a starting point. So, in order to attain an optimum design, one has to resort to more robust optimization techniques, which are capable of searching effectively the whole design variable domain and not being trapped into local optima. Recently developed heuristic methods, such as genetic algorithms, simulated annealing, threshold accepting, tabu search, ant colonies, particle swarm, etc. provide more attractive alternatives. Although these methods use simple algorithms, they require great computational effort. Representative studies of optimum design of retaining walls by use of heuristic methods are those presented in [7-16]. In [7] an application of a simulated annealing algorithm is reported to minimum cost design of reinforced concrete cantilever retaining walls that are required to resist a combination of earth and hydrostatic loading by using only geometric design variables, whereas in [8] simulated annealing for optimum design of RC cantilever retaining walls used in road construction is utilized, by using more design variables, effectively leading to more detailed simulations. In [9] and [10] a modified particle swarm optimization (MPSO) based on PSO with passive congregation is proposed, to find the optimum cost design of a cantilever RC retaining wall. In [11] an Ant Colony Optimization (ACO) algorithm is applied to arrive at optimal design of a RC retaining wall (designed as a gravity wall, i.e. structural integrity is

not taken into account while imposing the constraints). In [12] a bacterial foraging optimization algorithm is presented whereas harmony search based algorithms were proposed in [13]. In [14] a genetic algorithm is applied to reach minimum cost design of three types of retaining walls: cantilever retaining wall, counterfort retaining wall and retaining wall with relieving platforms. In [15] a random direction search complex method is applied and three heuristic algorithms (genetic algorithm, particle swarm optimization and simulated annealing) are used to obtain the minimum cost design of a reinforced concrete cantilever retaining wall. Finally, in [16] optimum design of gravity retaining walls subject to dynamic loading was performed using a charged system search algorithm, while the Mononobe-Okabe method was used to determine the dynamic earth pressures.

Common feature of all the aforementioned studies is the fact that for the design of the retaining wall, dynamic earth pressures are ignored (except for [16] in which they are taken into account in a simplistic way through a pseudostatic approach). In addition, the static earth pressures (resulting from gravity and/or surcharge load) are calculated according to Rankine or Coulomb earth pressure theories which assume that a state of plastic equilibrium is developed in the retained backfill. Moreover, to the authors' knowledge, no suitable constraint has been imposed to any retaining wall optimum design case to ensure that the deformations of the retaining wall and the backfill are within acceptable limits. In most studies, this is ensured implicitly by avoiding the possibility of overturning and sliding, by controlling the stresses within allowable limits and by securing the stability of the retaining wall – retained soil system.

Apart from these, the seismic response of retaining systems is still a matter of ongoing experimental, analytical and numerical research. The dynamic interaction between a wall and a retained soil layer makes the response complicated. The dynamic analysis becomes much more complex, as usually material and/or geometry non-linearities have to be taken into account [17, 18]. Depending on the expected material behavior of the retained soil and the possible mode of the wall displacement, there exist two main categories of analytical methods used in the design of retaining walls against earthquakes: (a) the pseudo-static limiting-equilibrium solutions which assume yielding walls resulting in plastic behavior of the retained soil [19-21], and (b) the elasticity-based solutions that regard the retained soil as a viscoelastic continuum [22-24]. In most studies presented so far, in order to perform optimum design of retaining walls, the assumption of pseudo-static limiting equilibrium is made; therefore the design is performed in a simplistic way, ignoring the possibility of a linear elastic or viscoelastic soil backfill.

This study is concerned with the optimum design of cantilever retaining walls which are subject to earthquake loading and are responding in a linear elastic way. The objective function which is optimized is the weight of the retaining wall. This is roughly proportional to its construction cost, as the latter is generally an increasing function of the weight of the material used. This function is minimized subject to design constraints. Apart from the usual constraints imposed in most optimization studies, in this study a direct design constraint is imposed which controls the rocking response of the retaining wall. The optimization analysis is conducted via the use of a genetic algorithm, since in [15] it is shown that GA can be successfully applied for the optimal solution of structural optimization problems with many design variables and complex constraints. Two numerical examples are presented, in which optimum designs are performed for two values of the height of the soil layer to be retained.

2 NUMERICAL MODELING

In this section the numerical model used to simulate the dynamic response of a cantilever retaining wall is described. This model consists of an infinite soil layer with horizontal base and

free surface which is at higher elevation towards $+\infty$ than $-\infty$. These two elevations result in the existence of a vertical slope of height H which is retained by a cantilever wall. The wall's foundation is at a depth equal to h_{emb}, relative to the downstream soil surface. Consequently, the overall height of the retaining wall stem is $H+h_{emb}$. The retaining wall is considered to rest on a strip foundation which consists of the toe, which is the portion of the foundation extending downstream from the wall, and of the heel, extending in the opposite direction (upstream). The depth of the rigid bedrock from the foundation of the wall is $1.5 \cdot H$, where H is the thickness of the horizontal layer to be retained, as seen schematically in Figure 1. The distance from the wall toe tip to the far field (downstream) vertical boundary of the model is $10 \cdot H$; the same happens with the distance from the wall heel tip to the far field boundary of the model in the upstream direction. Shown in Figure 1 is also the local coordinate system to which the graphs showing the internal forces and stress distributions along the wall or its components in later sections refer. Text in bold denotes the design variables whereas the others either denote the variables which are dependent on the design variables or are problem parameters which remain fixed during optimum design.

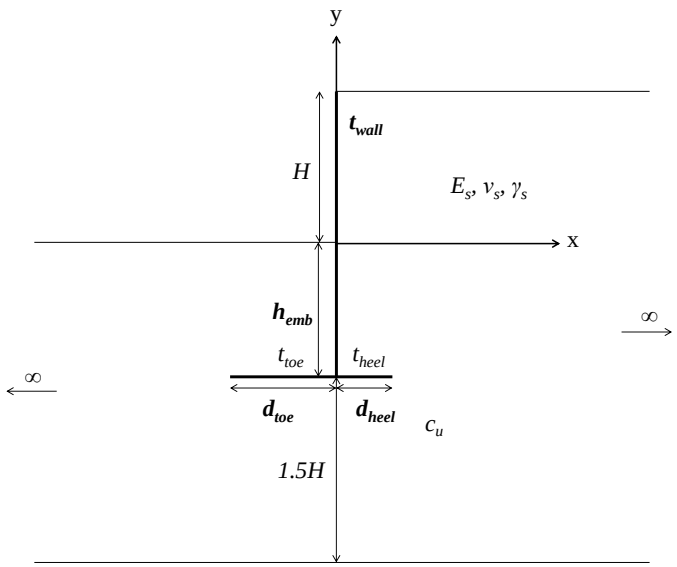


Figure 1: Cantilever reinforced concrete retaining wall model considered in this study.

The soil layer is fixed on rigid bedrock and along the soil – rock interface horizontal and vertical fixity is imposed. In order to simulate sufficiently the one dimensional dynamic soil response, vertical kinematic constraints were used at the two vertical ends of the model. These constraints are different from the corresponding kinematic constraints imposed for gravity loading at the same boundaries, which were in the horizontal direction to simulate one dimensional compression. The two vertical boundaries of the model were placed relatively far from the wall to minimize the influence of the difference between the model response in these regions and one dimensional soil response. The whole model is considered to respond in plane strain condition, an assumption fairly accurate for cantilever retaining walls with length much higher than their width, height and thickness. The wall – soil and the foundation – soil interfaces are considered to be tied, an assumption generally valid for cohesive soils. This means there is no separation or relative slip along these interfaces. Initially, gravity acceleration (body force) is applied to the whole model and in a second step of the analysis, the transverse ground acceleration record recorded during the December 11, 1967 Koyna earthquake, which

was of magnitude 6.5 on the Richter scale, is imposed along the base of the soil layer. The time history graph of this record is shown in Figure 2.

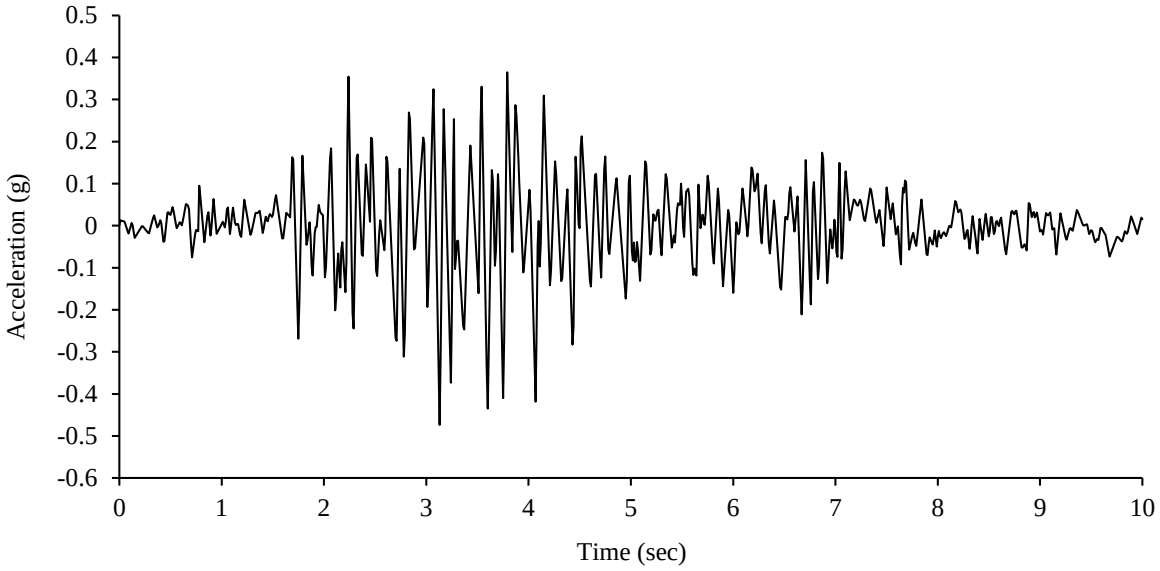


Figure 2: Transverse acceleration time history record of the December 11, 1967 Koyna earthquake, of magnitude 6.5 on the Richter scale.

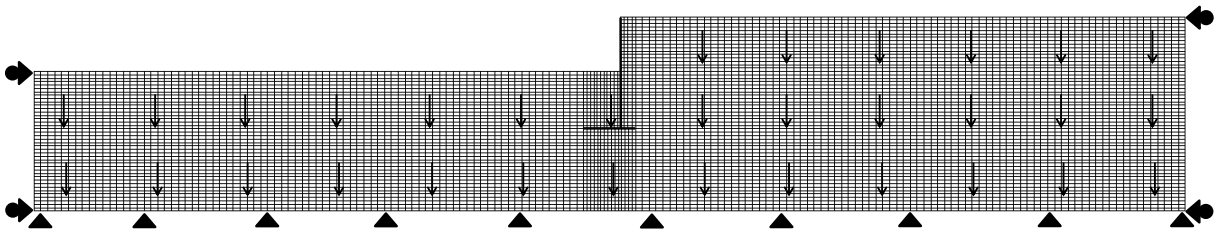


Figure 3: Numerical model analyzed for the 1st case (H=8m). Loading and boundary conditions for the initial gravity step are shown.

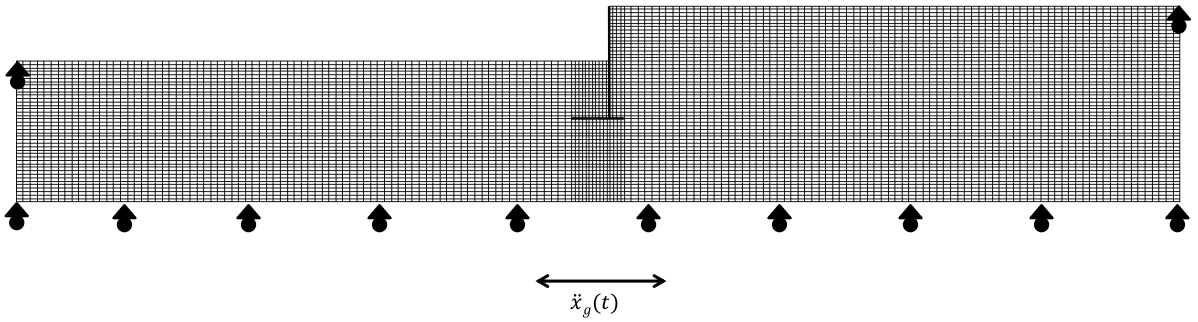


Figure 4: Numerical model analyzed for the 1st case (H=8m). Loading and boundary conditions for the main dynamic time – history analysis step are shown.

In this study, in order to minimize the weight of the retaining wall, two-dimensional numerical simulations were performed for the wall-soil systems depicted in Figures 3 and 4, utilizing the finite element software ABAQUS [1]. The soil layer is discretized with 8-node

biquadratic plane strain solid elements (CPE8). 3-node quadratic interpolation beam elements in plane (B22) are used for modeling the retaining wall and its foundation. These elements allow for transverse shear deformation according to Timoshenko theory and in their shear flexible formulation it is assumed that the transverse shear behavior is linear elastic with a fixed shear modulus and, thus, independent of the response of the beam section to axial stretch and bending. For Timoshenko beam elements a lumped mass formulation with a 1/6, 2/3, 1/6 distribution is used. The mesh gets coarser for the part of the soil layer which is left and right of the wall (the horizontal dimension of the elements is double). This is apparent in Figures 3 and 4.

The eigenmodes used for the modal dynamic analysis are extracted in a previous frequency step, in which the Lanczos eigensolver is used, which is a powerful tool for extraction of the extreme eigenvalues and the corresponding eigenvectors of a sparse symmetric generalized eigenproblem. For the Lanczos eigensolver, the minimum and maximum frequencies of interest are specified and all eigenmodes with eigenfrequencies falling in this range are extracted. These modes are subsequently used for the calculation of the dynamic response during the modal dynamic analysis. Energy dissipation due to damping mechanisms is not modeled explicitly as a material property (e.g. through the simplistic Rayleigh damping approximation), but it is specified as a fraction of critical damping assigned at all eigenmodes included for the calculation of the dynamic response, equal to 5%. Thus the damping fraction remains constant along the frequency range of interest and energy dissipation is of the same intensity for lower and higher frequencies.

3 FORMULATION OF THE OPTIMIZATION PROBLEM

In this section the optimization problem to be solved is explained in detail. The design variables, the parameters, the constraints, the objective function and the optimum design process are presented.

3.1 Design variables

The design variables of the problem are shown in bold in Figure 1. These are the depth of the wall embedment denoted by h_{emb}, the width of the toe denoted by d_{toe}, the width of the heel denoted by d_{heel} and the thickness of the wall stem denoted by t_{wall}. The thickness of the wall toe and heel (t_{toe} and t_{heel} respectively) are selected to be the same and equal to the minimum between the wall stem thickness t_{wall} and one tenth of the corresponding widths (d_{toe}/10 and d_{heel}/10), so that beam modeling for these components is reasonable.

Design variable	Lower limit (m)	Upper limit (m)
h_{emb}	0.2	16
d_{toe}	2	12
d_{heel}	2	12
t_{wall}	0.2	2.5

Table 1: Design variables of the optimization problem and their lower and upper bounds.

In the aforementioned design variables upper and lower limits are set, in order to prevent the algorithm from giving technically infeasible solutions. Table 1 shows the design variables and their corresponding upper and lower limits.

3.2 Parameters

The parameters of the wall-soil layer system are all the quantities that remain fixed during a particular optimization search. The parameters of the problem are summarized in Table 2. These are the physical properties of the soil and the wall. All materials involved in the model are linear elastic, leading thus to a linear dynamic response. The soil has density γ_s=1800 kg/m^3, modulus of elasticity E_s=100 MPa and Poisson's ratio ν_s=0.3. The retaining wall is modeled as a reinforced concrete beam with a general section, density γ_w=2500 kg/m^3, and modulus of elasticity E_w=30.5 GPa which corresponds to C25/30. Although the retaining wall has the inertial and stiffness characteristics of concrete, it deforms in a linear elastic way, which implies that its stiffness in tension and compression is equal. Another parameter of the problem is the frequency range used for the modal dynamic analysis; this is selected to be in the range [0.01 Hz, 29 Hz]. The lower limit is selected so that the very low frequency spurious eigenmodes are excluded from the analysis; these are associated with very large modal mass. The higher limit is selected based upon the fact that the lowest wavelength of the waves propagating into the soil (lowest velocity of propagation and highest frequency) has to be at least ten times the internodal interval of the mesh; this is approximately the distance between adjacent nodes, and it increases as the mesh gets coarser.

Parameter	Assigned value
γ_s	1800 kg/m^3
E_s	100 MPa
ν_s	0.3
γ_w	2500 kg/m^3
E_w	30.5 GPa
f_{min}	0.01 Hz
f_{max}	29 Hz

Table 2: Parameters of the optimization problem and their fixed values.

3.3 Constraints

The constraints of the optimization problem at hand are divided into structural constraints and geotechnical constraints. The satisfaction of the former ensures that the retaining wall does not fail as regards its structural integrity, whereas the latter ensures that the soil retained by and supporting the wall does not fail. The constraints are shown in Table 3, which includes the formulas for the calculation of the limiting quantities and the constraint inequalities imposed for the optimization problem. As far as the structural constraints are concerned, the maximum tensile (and the minimum compressive) stress which develop due to axial force and bending moment at the wall stem, toe and heel must not be higher than (respectively lower than) the material strength. For concrete C25/30 this is 25 MPa by definition, without taking into account the partial safety factor for concrete strength [25]. The material model used for the wall in this study is linear elastic and this leads to the essential assumption that the distribution of strains and stresses along the section of the wall and its foundation is linear which results in the presence of "theoretical" tensile stresses which are not present in practice. In practice, there are no tensile concrete stresses and the necessary tensile forces for the equilibrium of the section are provided by the steel reinforcement. In any case, the tensile stress constraint is not active in the final optimum design, as will be described in detail later. Shear stiffness is ignored since shear strength of reinforced concrete cannot be calculated in a theoretically sound basis; the procedure of calculation and the final result is very norm specific in

general. Except for this, it depends highly on the reinforcement and its distribution into the beam. Concerning the geotechnical constraints, the following are specified:

a) It is ensured that the normalized displacement at the top of the wall stem θ does not exceed 0.33%. The normalized displacement is given by the ratio of the horizontal displacement at the top of the wall due to tilting or horizontal translation, divided by the height of its stem including embedded part ($H+h_{emb}$). The above inequality is specified to prevent the development of a limit state or the initiation of a failure plane in the retained soil [26]. In the opposite case the assumption of a linear elastic soil would not be accurate. It is assumed in this study that, as far as its strength is concerned, the supporting and retained soil behaves like compacted clay. According to [26] the values of normalized displacement required to reach active and passive earth pressure conditions are 1% and 5% respectively. By ensuring that the normalized displacement is lower than 0.33% (conventionally taken as one third of the normalized displacement required for active conditions) neither active nor passive states will develop in the soil.

Quantity	Formula	Constraint
Normalized displacement of wall stem	$\theta=\max[\text{abs}\{Displ_{top}/(H+h_{emb})\}]$	$\theta\leq 0.33\%$
Undrained shear strength	$c_u=E_u/850=3\cdot E_s/\{2\cdot(1+\nu_s)\}/850=136$ kPa	$\max(\tau)\leq c_u$ $\min(\tau)\geq -c_u$
Soil bearing capacity	$q_u=5.14c_u+\gamma_s\cdot h_{emb}$	$-\min(\sigma_{yy})\leq q_u$
Foundation uplift		$\max(\sigma_{yy})\leq 0$
Max bending stress*	$\sigma_{max}=\max(N/t+6M/t^2)$	$\sigma_{max}\leq 25$ MPa
Min bending stress*	$\sigma_{min}=\min(N/t-6M/t^2)$	$\sigma_{min}\geq -25$ MPa

* For the wall stem, toe and heel. t denotes t_{stem}, t_{toe} and t_{heel}.

Table 3: Constraints of the optimization problem.

b) Regarding its strength, the soil is assumed to behave as a cohesive soil in undrained conditions. So, its shear strength in terms of total stresses is equal to its undrained shear strength c_u, i.e. the $\varphi=0$ approach is followed. Thus, it is specified that the maximum and minimum shear stress along the wall foundation must not exceed the undrained shear strength of the underlying soil, equal to 136 kPa. This value is calculated as follows: the undrained modulus of elasticity E_u of the soil is calculated according to Table 3 to be E_u=115.38 MPa. The fraction E_u/c_u according to data available in the literature [27, 28], is selected to be roughly 850.

c) The bearing capacity of the soil underlying the foundation must not be surpassed. For this purpose, the bearing capacity under undrained loading ($c = c_u$, $\varphi = 0$) is calculated according to the Meyerhof formula for vertical and central loading of horizontal strip foundation at a depth equal to h_{emb}. The maximum vertical normal stress at the lower interface of the wall foundation must not get larger than this value.

d) Along the interface where constraint (c) is imposed, there must also be no tension, otherwise there would be foundation uplift which would render the dynamic response of the retaining wall geometrically non-linear.

The approach followed to impose the constraints is the penalty method. Penalty methods add a penalty to the objective function to decrease the quality of infeasible solutions. The penalty quantities that are added are virtually the product of the constraint violation and a penalty factor which is fixed for each constraint and adjusted to take into account the relative importance of the constraint violations.

3.4 Objective function

The objective function to be minimized is the volume of the retaining wall per meter in the longitudinal direction. This is proportional to its weight and indirectly related to its cost of construction. The fitness function which is minimized by the genetic algorithm used in this study results from the objective function after the application of the penalties due to constraint violations, if any.

4 GENETIC ALGORITHM USED FOR OPTIMIZATION

The Genetic Algorithm (GA) is a stochastic global search optimization method that emulates natural biological evolution. GAs apply on a population of potential solutions the principle of survival of the fittest to produce better approximations to a solution. At each generation, a new set of approximations is created by the process of selecting individuals according to their level of fitness in the problem domain and breeding them together using operators borrowed from natural genetics (crossover, mutation, etc.). This process leads to the evolution of individuals that are better suited to their environment than the individuals that they were created from, just as in natural evolution process. In order to minimize the objective function, the genetic algorithm implemented in MATLAB software [2] was used.

The encoding strategy followed is real-valued representation. The use of real-valued genes in GAs offers a number of advantages in numerical function optimization over binary encodings: (a) efficiency of the GA is increased as there is no need to convert chromosomes to phenotypes before each function evaluation, (b) less memory is required as efficient floating point internal computer representations can be used directly, (c) there is no loss in precision by discretization to binary or other values and (d) there is greater freedom to use different genetic operators.

The population size (number of individuals in each generation) is equal to 20. The initial population with which the GA begins is created as a random initial population with uniform distribution. Fitness scaling was implemented by using a rank function, which scales the raw scores based on the rank of each individual instead of its score. The rank of an individual is its position in the sorted scores. An individual with rank r has scaled score proportional to $r^{-1/2}$. Rank fitness scaling removes the effect of the spread of the raw scores. The square root makes poorly ranked individuals more nearly equal in score, compared to rank scoring.

Regarding the basic genetic operators, stochastic uniform selection is used for the selection process. In this function each parent corresponds to a section of the line of length proportional to its scaled value. The algorithm moves along the line in steps of equal size. At each step, the algorithm allocates a parent from the section it lands on. The first step is a uniform random number less than the step size. For reproduction, the number of individuals that are guaranteed to survive to the next generation (elite children) is 2 and the fraction of the next generation, other than elite children, that is produced by crossover (crossover fraction) is equal to 0.8. The mutation function used is Gaussian, which adds a random number taken from a Gaussian distribution with mean 0 to each entry of the parent vector. For the combination of parents to produce the next generation offspring (crossover), scattered crossover is used, which applies in problems without linear constraints. It creates a random binary vector and selects the genes where the vector entry is 1 from the first parent, and the genes where the vector entry is 0 from the second parent, and combines the genes to form the child. In the GA no migration occurs, as there are no subpopulations.

As stopping criteria for the algorithm the following were specified: (a) the maximum number of iterations for the genetic algorithm to perform is equal to 100, (b) the algorithm stops if

the weighted average relative change in the best fitness function value over 50 generations is less than or equal to the function tolerance (equal to 10^{-6}).

The following outline summarizes how the GA procedure works:

a) The algorithm begins by creating a random initial population.

b) The algorithm then creates a sequence of new populations. At each step, the algorithm uses the individuals in the current generation to create the next population. To create the new population, the algorithm performs the following steps:

1. Scores each member of the current population by computing its fitness value.
2. Scales the raw fitness scores to convert them into a more usable range of values.
3. Selects members, called parents, based on their fitness.
4. Some of the individuals in the current population that have better fitness are chosen as elite. These elite individuals are passed to the next population.
5. Produces offspring from the parents. Offspring are produced either by making random changes to a single parent (mutation) or by combining the vector entries of a pair of parents (crossover).
6. Replaces the current population with the offspring to form the next generation.

c) The algorithm stops when one of the stopping criteria is met.

The GA optimizer is properly coupled with the analysis solver in order to take the modal dynamic analysis results. This is done inside the objective function in which the analysis solver is called to perform the necessary analyses. Except for this, suitable functions are called to create the necessary input (*.inp) files to conduct the analyses and read the results of the analyses from the corresponding results (*.fil) files. While the analysis solver is running the optimizer is halted and its execution is continued after the lock (*.lck) file has been deleted. Constraint enforcement is applied through an advanced penalty method and not by the default constraint handlers developed in MATLAB.

5 CONVENTIONAL SEISMIC DESIGN OF CANTILEVER RETAINING WALLS

Conventional seismic design of cantilever reinforced concrete retaining walls is achieved with use of the well-known Mononobe-Okabe (M-O) theory of seismic earth pressures [19, 20]. Design is performed regarding the wall stability (sliding and overturning about the tip of its toe), and the design variables are the wall embedment (h_{emb}), the width of the wall toe (d_{toe}) and the width of the wall heel (d_{heel}). The thickness of the wall stem and foundation (toe and heel) are selected based on general guidelines for initial wall dimension proportioning, i.e. they are set equal to 1/10 of the total wall height ($H+h_{emb}$). According to the dimension proportioning practice, the inequality $0.3\cdot(H+h_{emb}) \leq d_{heel} \leq 0.5\cdot(H+h_{emb})$ must hold for the width of the wall heel. The minimum values of the wall embedment, toe width and heel width are set equal to 0.2 m, 2 m and 2 m respectively. The conventional seismic design method implemented in this study involves also some kind of optimization procedure which leads to the minimum total weight of the wall by strict abidance by all of the constraints mentioned above.

A necessary step during the design process is the evaluation of the soil internal friction angle φ and the soil – wall interface friction angle δ. These are set to the following typical values: $\varphi=30^o$, $\delta=18^o$. The horizontal acceleration coefficient is taken as $k_h=0.48$ (resulting from the maximum acceleration of the earthquake record which is 0.48g). These properties are assigned to the soil lying over the wall foundation. For the soil under the wall foundation undrained response is assumed, namely its internal friction angle is taken equal to zero and its undrained shear strength c_u is the one specified in section 3 of this study. The inertial forces and moments of the wall are also taken into account for the design whereas, regarding overturning checks, only the upstream and downstream soil portions lying over the wall foundation are considered to contribute to the wall stability.

6 NUMERICAL RESULTS

Two retaining wall weight optimization cases were examined in this study: in the first case (Case 1) the height of the soil layer to be retained by the wall is equal to 8 m and in the second case (Case 2) the height is 12 m. The results of the GA optimization procedure as analyzed in the previous sections are shown in Table 4. It is observed in general that the embedment and foundation dimensions required to retain the soil layer with greater height (Case 2) are larger than those in Case 1. The optimum value of the objective function increases as well. In both cases, the length of the wall heel (d_{heel}) which leads to optimum design is the minimum possible, i.e. its lower bound. This means that for the parameter values and earthquake record considered in this study the heel does not contribute significantly to the retaining wall stability and/or structural integrity. The thickness of the heel is constrained by the requirement that it is not more than one tenth of its length (to justify its modeling as a beam), whereas the thicknesses of the other components (stem and toe) are equal.

	Case 1 (H=8m)	Case 2 (H=12m)
Design variables		
h_{emb} (m)	7.76	7.16
d_{toe} (m)	4.57	6.57
d_{heel} (m)	2.00	2.00
t_{wall} (m)	0.20	0.22
t_{toe} (m)	0.20	0.22
t_{heel} (m)	0.20	0.20
Constraint quantities		
θ	**0.328%**	0.246%
maxτ (kPa)	78.42	88.46
minτ (kPa)	-131.96	**-135.73**
minσ_{yy} (kPa)	-505.98	-592.45
maxσ_{yy} (kPa)	-122.07	-124.53
$\sigma_{b,s,max}$ (kPa)	22570.73	21476.85
$\sigma_{b,t,max}$ (kPa)	4265.33	1183.35
$\sigma_{b,h,max}$ (kPa)	2029.97	2180.68
$\sigma_{b,s,min}$ (kPa)	-23795.84	-23385.15
$\sigma_{b,t,min}$ (kPa)	-7336.37	-8128.82
$\sigma_{b,h,min}$ (kPa)	-2176.36	-2501.06
Algorithm details		
Min. value of obj. fun. (m^2)	4.47	6.12
Number of generations	73	64
Number of fun. evaluations	1480	1300

Table 4: Results of the optimization procedure of the two retaining wall cases considered in this study.

Table 5 shows the results of the conventional seismic design according to the M-O method. It is observed that the conventional design which is adopted in most seismic norms worldwide leads to larger weight of the retaining wall. Although the two methods stem from essentially different assumptions, their comparison shows clearly the fact that more economical and simultaneously safe designs can be achieved by applying detailed optimization methods for the seismic design of retaining walls; current seismic code practices can lead to unreasonably conservative designs.

	Case 1 (H=8m)	Case 2 (H=12m)
h_{emb} (m)	0.20	0.20
d_{toe} (m)	5.58	8.43
d_{heel} (m)	4.10	6.10
t_{wall} (m)	0.73	1.32
t_{toe} (m)	0.73	1.32
t_{heel} (m)	0.73	1.32
Area (m^2)	13.05	35.28

Table 5: Results of the conventional seismic design of the two retaining wall cases considered in this study.

As far as the constraints are concerned, the maximum and minimum normal stresses of the heels of the two walls do not differ much. On the contrary, the maximum normal stress of the toe differs by a factor greater than 2 between the two wall cases. Furthermore, the minimum shear stress along the lower interface between the wall foundation and the supporting soil is roughly the same for the two wall cases. This observation implies that minimum shear stress along the lower interface of the wall foundation is independent of the wall height. Furthermore, the constraint imposed for this quantity is active in Case 2. The above may provide a hint for controlling the optimization process. To investigate more thoroughly the dynamic response of the retaining wall and the surrounding soil, the internal forces of the wall and the shear stress distributions along the wall foundation – soil lower interface are shown in the following sections.

7 DYNAMIC RESPONSE OF THE RETAINING WALL

In this section the dynamic response of the retaining wall in the two cases examined in this study is considered. Internal force distributions as well as normalized displacement at the wall top are presented. In Figure 5 the axial force distribution along the stem of the wall (including embedment) is shown for the case 1. This distribution refers to its optimum design with design variable values set as shown in case 1 of the previous section. The vertical axis (y) is associated with the Cartesian coordinate system shown in Figure 1. At the elevation of the downstream soil surface the y axis becomes zero, namely the horizontal axis of the diagrams coincides with the aforementioned soil surface. The two curves shown in Figure 5 show the maximum and minimum values respectively for each point of the wall stem. The two distributions presented do not occur in a specific instance during the earthquake loading; they are rather the two envelope curves which incorporate all the axial force distributions which occur over the whole time history during the dynamic response. The respective axial force distribution for the second case (H=12 m) is shown in Figure 6. It is apparent that the retaining wall

in both cases is subject to compression, which originates primarily from the gravity loading. In addition, the two envelope distributions have the same configuration, which advocates over this observation.

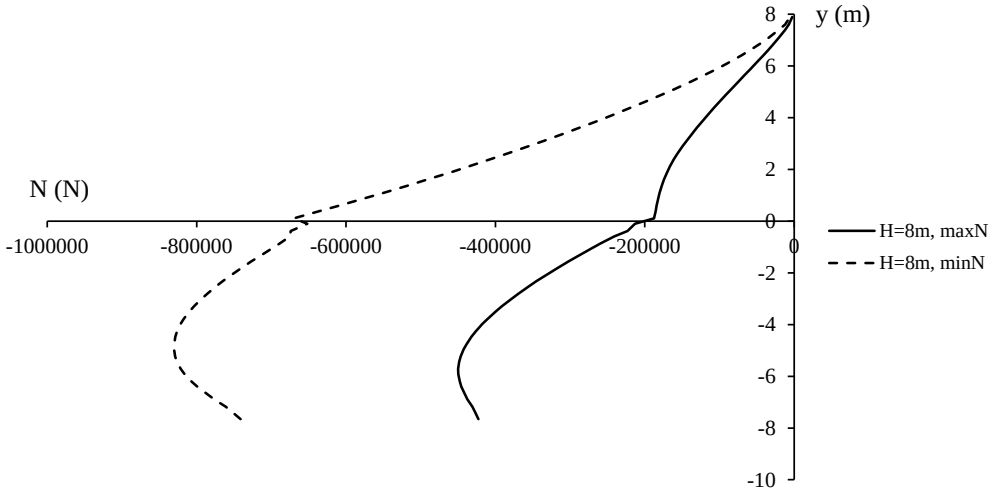


Figure 5: Maximum and minimum axial force distributions along the retaining wall stem for case 1 (H=8m).

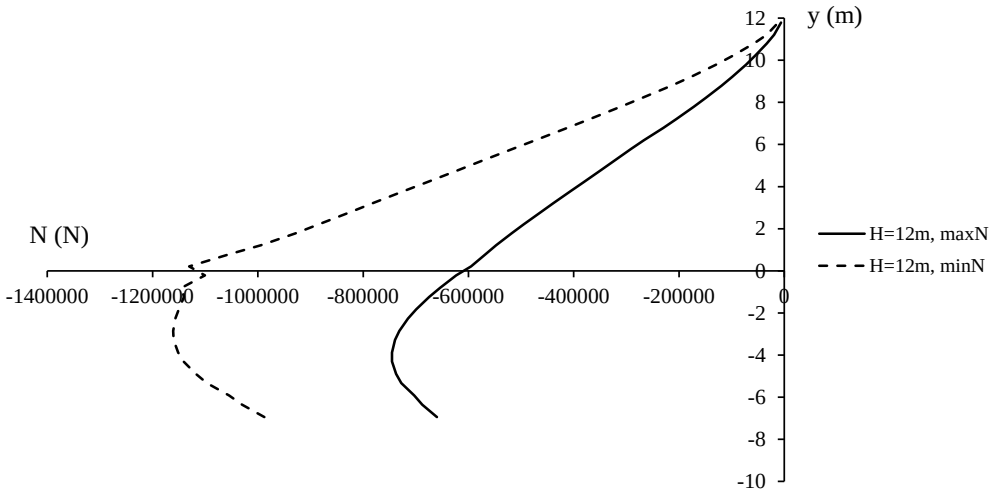


Figure 6: Maximum and minimum axial force distributions along the retaining wall stem for Case 2 (H=12m).

In Figure 7 and Figure 8 the maximum and minimum shear force distributions are shown for cases 1 (H=8m) and 2 (H=12m) respectively. It is observed that in case 1 the minimum and maximum distributions are approximately symmetric about the vertical axis (the stem of the wall). Since the fundamental eigenfrequencies of the upstream and downstream soil layers in case 1 are essentially higher than those in Case 2 (due to the fact that the layer thickness in case 1 is smaller than that in Case 2), it is more possible that the eigenfrequencies of the wall – soil system in case 1 lie within the dominant frequency range of the earthquake record. Thus, it is anticipated that the system of case 1 will exhibit more pronounced dynamic response, which stems from its kinematic and inertial dynamic interaction. Thus the rough symmetry between the two graphs is explained. On the contrary, in Case 2, where the eigenfrequencies are lower, the wall – soil system response is inertial for its most part, due to the lower frequency content. This result can be drawn also from the configuration of the shear force distri-

butions; they are positive near the surface of the downstream soil layer, become negative for lower elevation and get again positive at the foundation. This shows a quasi-static response.

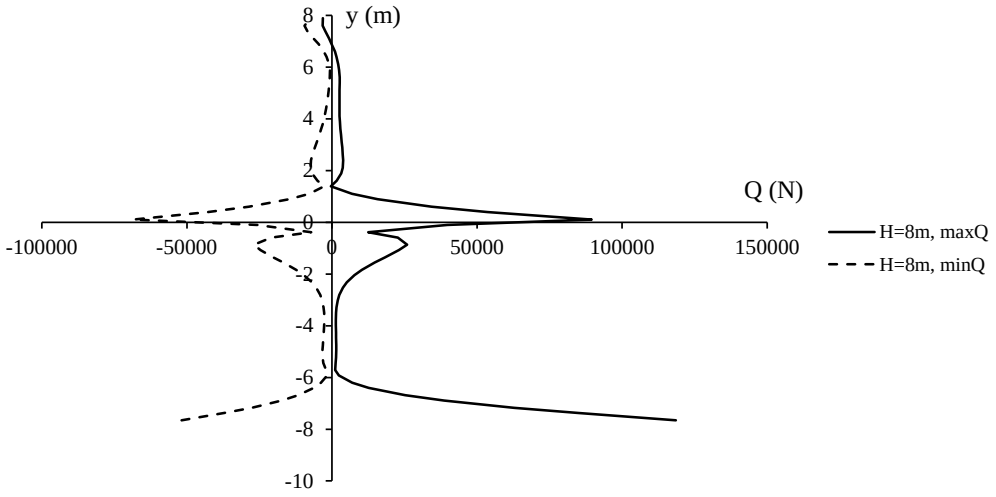


Figure 7: Maximum and minimum shear force distributions along the retaining wall stem for case 1 (H=8m).

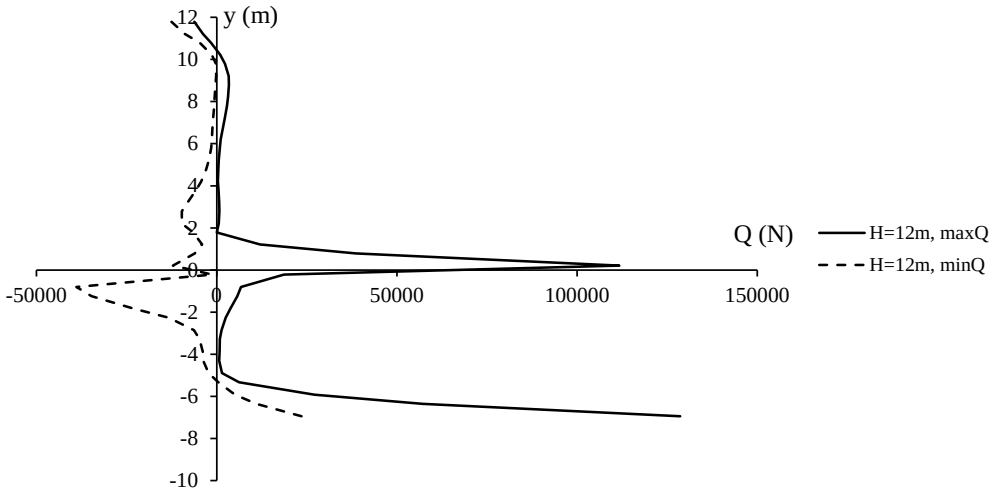


Figure 8: Maximum and minimum shear force distributions along the retaining wall stem for Case 2 (H=12m).

In both Figures 7 and 8 the shear force distributions display some common characteristics. They take local maxima (in terms of absolute values) at the wall foundation and at the surface of the downstream soil layer. The reason for the occurrence of the local maximum at the downstream soil layer surface is apparent; there is the point where passive soil pressures start, virtually relieving the distress due to soil pressures from the upstream soil layer. In the lower part of the wall stem shear forces from the foundation are transmitted. At the upper part of the wall shear forces are much lower and they depend highly on the wall compliance.

In Figures 9 and 10 the maximum and minimum bending moment distributions are shown for cases 1 (H=8m) and 2 (H=12m) respectively. Similar trends with the corresponding shear force diagrams are observed, i.e. the pronounced response of the wall in case 1 and the quasi-static response noted in Case 2. Along the part of the wall stem lying over its embedded part bending moments are mainly positive, as this part of the wall essentially retains the upstream soil layer. Bending moments show local optima at the same positions with the local optima of shear forces.

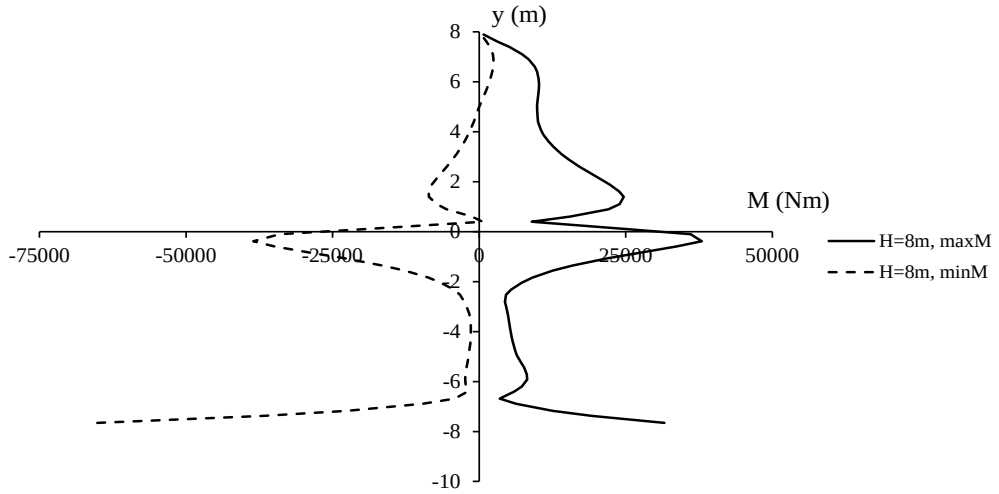


Figure 9: Maximum and minimum bending moment distributions along the retaining wall stem for case 1 (H=8m).

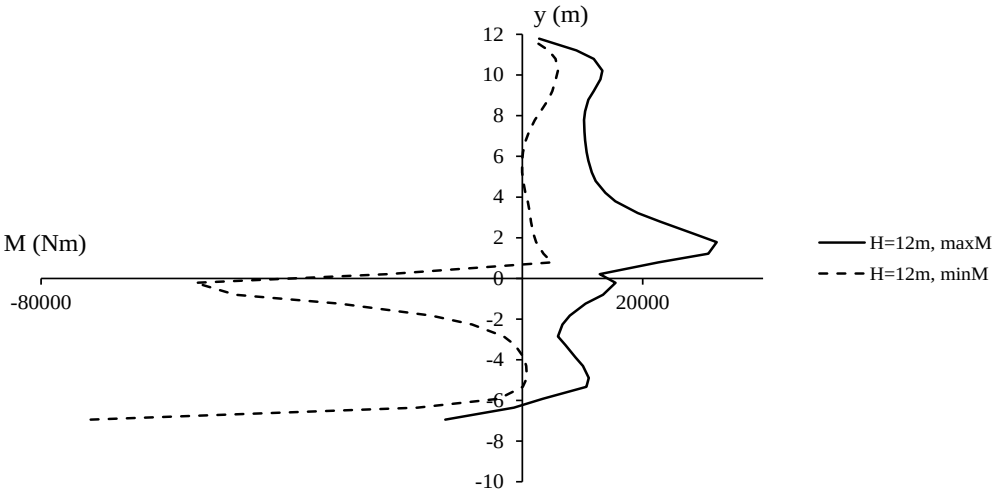


Figure 10: Maximum and minimum bending moment distributions along the retaining wall stem for Case 2 (H=12m).

In Figure 11 the variation in time history of the normalized displacement at the wall top is shown for cases 1 (H=8 m) and 2 (H=12 m). Firstly, it is noted that the dynamic response of the wall in the 1st case (H=8 m) is more pronounced than that in Case 2 (H=12 m). This agrees with the explanation given previously to interpret the dynamic nature of the response in case 1. However, although the maximum normalized displacement occurs for the 1st case, this does not entail that the response for this case is larger than that in Case 2 for the whole time history. Another observation to be made is that in case 1 the constraint affecting the

normalized displacement at the top of the retaining wall is active, i.e. controls the optimization process. This is expected, since the pronounced dynamic response in Case 1 leads to increased normalized displacement which eventually after the constraint imposition controls the optimization process.

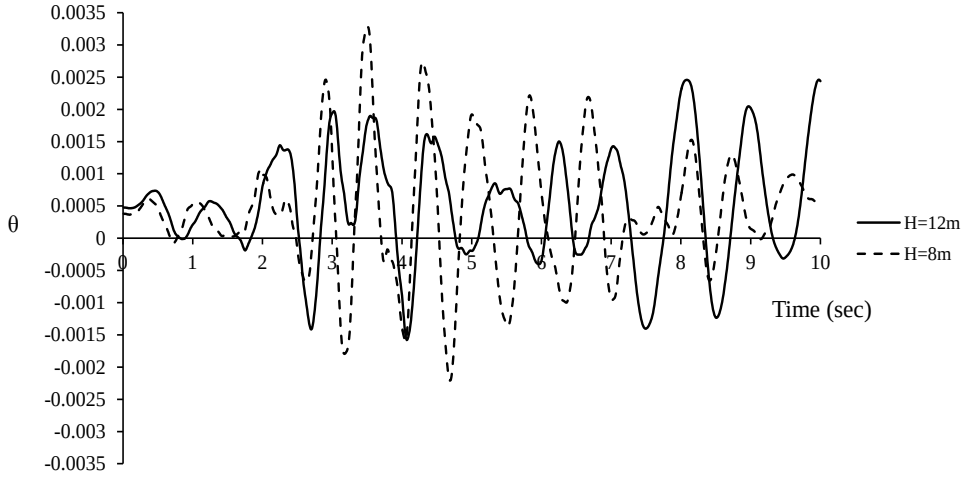


Figure 11: Normalized displacement at the top of the retaining wall for both cases considered in this study.

8 DYNAMIC SHEAR DISTRESS OF SUPPORTING SOIL

In this section the dynamic distress of the soil supporting the retaining wall is presented in terms of shear stresses. Especially, since shear stress is the primary factor affecting the stiffness and strength exhibited by soils in general, this quantity will be investigated. The region of the soil supporting the wall foundation which experiences the most intense shear stress is its interface with the lower horizontal boundary of the wall toe and heel. Plots of shear stress distributions developed along the wall foundation are shown in Figures 12 and 13 for the two cases examined in this study.

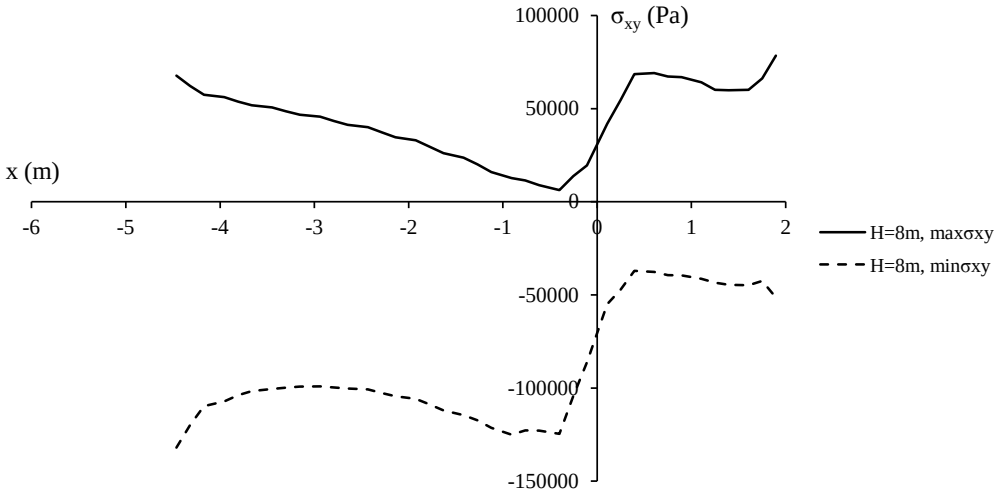


Figure 12: Maximum and minimum shear stress distributions along the retaining wall foundation (toe & heel) for case 1 (H=8m).

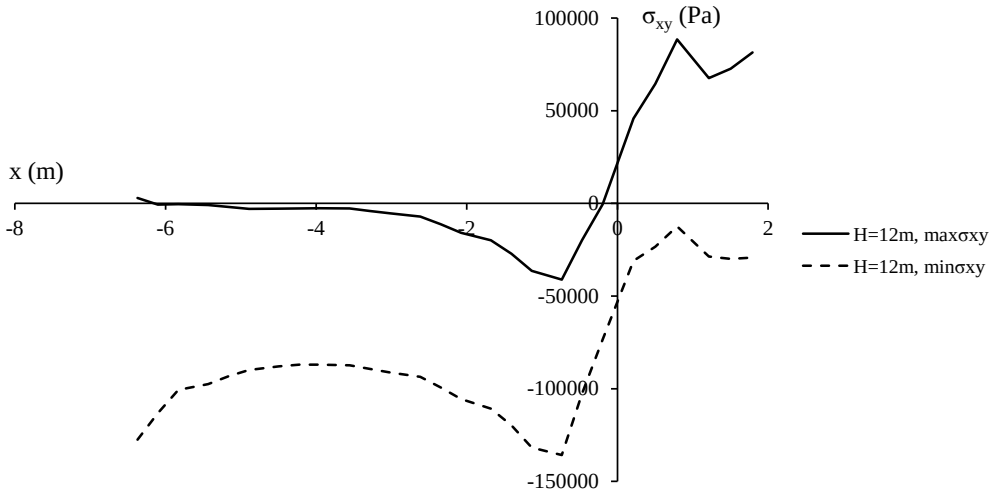


Figure 13: Maximum and minimum shear stress distributions along the retaining wall foundation (toe & heel) for Case 2 (H=12m).

The horizontal axis of these diagrams coincides with the wall foundation: its negative part shows the distribution along the wall toe and its positive part shows the distribution along the wall heel. Therefore, the vertical axis is in the same way coincident with the retaining wall stem. Its substantial difference from the horizontal axis is that it does not show vertical distance along the wall stem.

A major difference noted by comparing the two figures is that in Case 1 shear stresses may be positive (occurring when the retaining wall foundation is displaced towards the upstream soil layer) or negative (occurring when the retaining wall foundation is displaced towards the downstream soil layer). On the contrary, in Case 2, shear stresses along the wall toe are for the most part negative (since the distribution of the maximum shear stresses lies very close to the horizontal axis). This observation can be used as a hint to govern the optimization process. In both figures, along the wall heel the shear stress range tends to be generally higher than that along the wall toe.

9 CONCLUSIONS

- Unlike most optimization studies regarding retaining wall optimum design, two major features are examined in this study, i.e. optimum design for (a) seismic loading implemented through modal dynamic analysis with a rigorous time history integration procedure and (b) retaining wall – soil system responding linearly elastically.
- From the values of the design variables leading to retaining wall weight minimization it can be inferred that the length of the wall heel does not affect much its stability.
- Soil layers with increased thickness (and the same shear modulus and density) lead to systems with decreased eigenfrequencies. As a result, there is a greater possibility that their response to specific seismic loading is of more quasi-static nature, as is the 2nd case examined in the present study. The opposite happens with soil layers with decreased thickness; they show: (a) more pronounced dynamic response and (b) upper and lower internal force envelopes which tend to be more "symmetric".
- For systems with increased dynamic response (such as Case 1 of this study) the constraints which control displacements (or their derivatives) are more likely to be active

during the optimization process, whereas for systems with quasi – static response (such as Case 2 of this study) the constraint controlling the shear stress along the wall foundation – supporting soil interface is more likely to be active.

- As far as the soil shear distress is concerned, in the quasi-static case (H=12 m) it is generally negative under the retaining wall toe.
- Conventional seismic design methods (M-O), even if they are applied in an optimal way, can lead to conservative designs by increasing the required material compared with more refined design methods such as the optimum design implemented in this study.
- Last but not least, it has to be mentioned that the genetic algorithm used for the optimization process in this study is efficient and robust, since it leads to the optimum solutions with a relatively low number of function evaluations and not being trapped in local minima.

REFERENCES

[1] ABAQUS, *Analysis User's Manual Version 6.11*, Dassault Systèmes Simulia Corp., Providence, Rhode Island, USA.

[2] MATLAB, *Global Optimization Toolbox Version 8 (R2012b)*, The MathWorks Inc., Natick, MA, USA.

[3] E.J. Rhomberg, W.M. Street, Optimal design of retaining walls. *Journal of Structural Division, ASCE,* **107**, 992-1002, 1981.

[4] A. Saribas, F. Erbatur, Optimization and sensitivity of retaining structures. *ASCE Journal of Geotechnical Engineering*, **122(8)**, 649–656, 1996.

[5] P.K. Basudhar, B. Lakshman, A. Dey, Optimal cost design of cantilever retaining walls. *IGC 2006*, Chennai, India, December 14-16, 2006.

[6] G.L. Sivakumar Babu, B. Munwar Basha, Optimum design of cantilever retaining walls using target reliability approach. *International Journal of Geomechanics, ASCE,* **8(4)**, 240-252, 2008.

[7] B. Ceranic, C. Fryer, R.W. Baines, An application of simulated annealing to the optimum design of reinforced concrete retaining structures. *Computers and Structures*, **79**, 1569–1581, 2001.

[8] V. Yepes, J. Alcala, C. Perea and F. González-Vidosa, A parametric study of optimum earth retaining walls by simulated annealing. *Engineering Structures*, **30(3)**, 821-830, 2008.

[9] M. Khajehzadeh, M. Raihan Taha, A. El-Shafie, M. Eslami, Economic Design of Retaining Wall Using Particle Swarm Optimization with Passive Congregation. *Australian Journal of Basic and Applied Sciences*, **4(11)**, 5500-5507, 2010.

[10] M. Khajehzadeh, M. Raihan Taha, A. El-Shafie, M. Eslami, Modified particle swarm optimization for optimum design of spread footing and retaining wall. *Journal of Zhejiang University-SCIENCE A (Applied Physics & Engineering),* **12(6)**, 415-427, 2011.

[11] M. Ghazavi, S. Bazzazian Bonab, Optimization of Reinforced Concrete Retaining Walls Using Ant Colony Method. *3rd International Symposium on Geotechnical Safety and Risk (ISGSR)*, 2011.

[12] M. Ghazavi, V. Salavati, Sensitivity analysis and design of reinforced concrete cantilever retaining walls using bacterial foraging optimization algorithm. *3rd International Symposium on Geotechnical Safety and Risk (ISGSR)*, 2011.

[13] A. Kaveh, A.S.M. Abadi, Harmony Search Based Algorithm for the Optimum Cost Design of Reinforced Concrete Cantilever Retaining Walls. *International Journal of Civil Engineering*, **4(8)**, 336-357, 2010.

[14] S. Donkada, D. Menon, Optimal design of reinforced concrete retaining walls. *The Indian Concrete Journal*, 9-18, 2012.

[15] Y. Pei, Y. Xia, Design of Reinforced Cantilever Retaining Walls using Heuristic Optimization Algorithms. *2012 International Conference on Structural Computation and Geotechnical Mechanics, Procedia Earth and Planetary Science* **5,** 32 – 36, 2012.

[16] S. Talatahari, R. Sheikholeslami, M. Shadfaran, M. Pourbaba, Optimum Design of Gravity Retaining Walls Using Charged System Search Algorithm. *Mathematical Problems in Engineering*, Vol. 2012, Article ID 301628.

[17] S. Kramer, *Geotechnical Earthquake Engineering*, Prentice Hall, 1996.

[18] G. Wu, W.D.L. Finn, Seismic lateral pressures for design of rigid walls. *Canadian Geotechnical Journal*, **36(3)**, 509-522, 1999.

[19] S. Okabe, General theory of earth pressures. *Journal of the Japan Society of Civil Engineering*, **12(1)**, 1926.

[20] N. Mononobe, H. Matsuo, On the determination of earth pressures during earthquakes. *Proceedings of the World Engineering Congress*, Tokyo, Japan, Vol. 9, Paper 388, 1929.

[21] H.B. Seed, R.V. Whitman, Design of earth retaining structures for dynamic loads. *Proceedings of the ASCE Special Conference on Lateral Stresses in the Ground and Design of Earth Retaining Structures*, 103–147, 1970.

[22] A.S. Veletsos, A.H. Younan, Dynamic Response of Cantilever Retaining Walls. *ASCE Journal of Geotechnical and Geoenvironmental Engineering*, **123(2)**, 161–172, 1997.

[23] R.F. Scott, Earthquake induced pressures on retaining walls. *Proceedings of the 5th World Conference on Earthquake Engineering*, **2**, 1611–1620, 1973.

[24] J.H. Wood, Earthquake – Induced Pressures on a Rigid Wall Structure. *Bulletin of New Zealand National Earthquake Engineering*, **8**, 175–186, 1975.

[25] EC2, Eurocode 2: Design of concrete structures - Part 1-1: General rules and rules for buildings. *European standard CEN-EN-1992-1, European Committee for Standardization*, Brussels, 2004.

[26] G.W. Clough, J.M. Duncan, Earth pressures. *Foundation Engineering Handbook, ed. H-Y. Fang*, 224–235, Van Nostrand Reinhold, New York, 1991.

[27] M. Jamiolkowki, R. Lancellotta, S. Marchetti, R. Nova, E. Pasqualini, Design Parameters for Soft Clays. *Proc. 7th Eur. Conf. on Soil Mech. Found. Engrg.*, **5**, 21-54, Brighton, 1979.

[28] R.J. Jardine, N.J. Brooks, P.R. Smith, The use of electrolevel gauges in triaxial tests on weak rock. *Int. J. Rock Mech. Min. Sci. and Geomech.*, **22(5)**, 331-337, 1985.

COMPDYN 2013
4th ECCOMAS Thematic Conference on
Computational Methods in Structural Dynamics and Earthquake Engineering
M. Papadrakakis, V. Papadopoulos, V. Plevris (eds.)
Kos Island, Greece, 12–14 June 2013

A NEW PERFORMANCE-BASED DESIGN METHODOLOGY FOR CONTROLLED ROCKING STEEL FRAMES

Lydell Wiebe[1], **Constantin Christopoulos**[1]

[1] Department of Civil Engineering, University of Toronto
35 St. George Street, Toronto, ON, Canada, M5S 1A4
e-mail: lydell.wiebe@mail.utoronto.ca
e-mail: c.christopoulos@utoronto.ca

Keywords: Controlled rocking steel frames, self-centering systems, higher mode effects, multiple force-limiting mechanisms, performance-based design, capacity design.

Abstract. *The damage caused by recent earthquakes has highlighted the limitations of current seismic force resisting systems and design methodologies, which limit seismic forces by accepting structural damage. Controlled rocking steel frames have been proposed as an alternative system that can limit seismic forces while minimizing structural damage. This paper proposes a new performance-based design methodology for controlled rocking steel frames. In the first step of this methodology, post-tensioning and energy dissipation are designed to achieve target peak displacements at multiple seismic hazard levels. In the second step, the peak force demands on the frame members are estimated using a procedure that is based on the modal properties of cantilever beams with uniformly distributed mass and elasticity. These demands can either be satisfied through elastic design or reduced by using multiple force-limiting mechanisms.*

The proposed design methodology is demonstrated by application to a twelve-storey structure in California. The results of nonlinear time history analyses show that the methodology leads to a design that satisfies the displacement limits, and that it provides good estimates of the peak force demands on the frame members. The methodology also captures the reduction in forces that is achieved by using multiple mechanisms to control the higher mode effects.

1 INTRODUCTION

Events like the 2011 Canterbury earthquake sequence have demonstrated how costly it is to recover from the damage that major earthquakes cause to code-compliant conventional structural systems. Controlled rocking systems (CRS) show great promise for avoiding expensive repairs and lost building use after major earthquakes. These systems exhibit the characteristic flag-shaped hysteresis that is shown in Figure 1, which is defined by an initial stiffness k_0, linear limit f_y, nonlinear stiffness ratio α, and energy dissipation parameter β. Systems with this self-centering hysteresis can be designed to achieve similar peak displacements as conventional systems, while also avoiding residual displacements [1].

In a controlled rocking steel frame, the columns of a frame are allowed to uplift from the foundation, while post-tensioning and energy dissipation devices are used to control the response. Rocking steel frames were first tested in the 1970s [2-4], and recent tests of systems with energy dissipation and post-tensioning have further validated the system [e.g. 5-11]. However, numerical analyses of controlled rocking steel frames have demonstrated that the peak forces are not limited by rocking in the way that would be expected for capacity design [12-14]. Instead, the forces continue to increase as the system rocks because of higher mode effects. This behaviour has recently been demonstrated by large-scale shake table testing [11].

To mitigate the effects of the higher modes, Wiebe et al. [15] proposed using multiple mechanisms to limit the peak seismic forces. Two mechanisms were proposed: designing for rocking to occur at multiple locations over the height of the structure, and designing nonlinear braces at one or more levels to limit the storey shears. Shake table testing demonstrated that both proposals reduce the peak forces with only minor increases in peak displacements [11]. Furthermore, these mechanisms make numerical models more reliable because they reduce the sensitivity to the assumed inherent damping [16].

The purpose of this paper is to give an overview of a new methodology that enables designers to make use of these recent advances in controlled rocking steel frames. Numerical results that validate the methodology will also be presented.

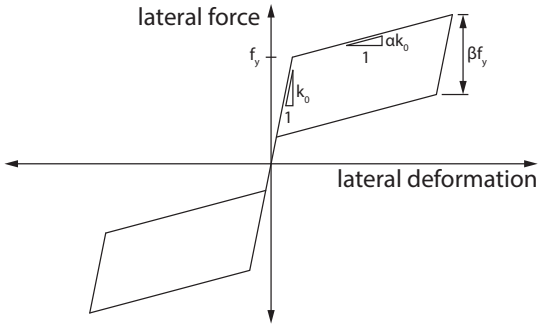


Figure 1: Flag-shaped hysteresis: definition of terms.

2 DESIGN METHODOLOGY

2.1 Overview

Other researchers have proposed designing controlled rocking steel frames with force reduction factors that are similar to the maximum factors in current codes [13-14, 17]. This paper proposes a performance-based design methodology, which is based on two discrete performance levels that are defined following the seismic rehabilitation guidelines of ASCE 41-06 [18]. The first considered performance level is Immediate Occupancy (IO), in which a

building is safe to occupy, although some non-structural repairs may be necessary. The second considered performance level is Collapse Prevention (CP), in which any level of structural damage is accepted except for collapse. In the proposed methodology, these performance levels are associated with the design basis earthquake (DBE, probability of exceedance of 10% in 50 years) and the maximum considered earthquake (MCE, probability of exceedance of 2% in 50 years) levels, respectively. Based on recent events [19], this is considered to be a better reflection of societal expectations than what is currently codified [20-21]. However, these performance targets could be adjusted without affecting the underlying methodology.

Figure 2 summarizes the steps of the proposed design methodology, together with significant limit states for controlled rocking steel systems. The hierarchy of limit states may vary from one CRS to another, depending on the design. The proposed methodology follows the same steps as the design of conventional seismic force resisting systems. Before beginning design, it is necessary to establish the design parameters, such as the seismic hazard, site class, structural layout, and preliminary locations and dimensions of seismic force resisting systems.

With this information, the first step is to proportion the base rocking joint by selecting the amount and location of post-tensioning and energy dissipation, as well as what gravity loads the CRS will carry. Section 2.2 describes a performance-based method for doing this, but other methods could be used without affecting the other steps of the methodology. Higher mode effects and mitigation are not considered in this step because the displacement response of the CRS is intended to be dominated by the base rocking behaviour.

The second step is to capacity design all other elements for elastic response under the maximum expected loads. Because of higher mode effects, these loads cannot be estimated using the properties of the first mode alone. A method for estimating the higher mode effects, which is based on the theoretical modal properties of cantilevered beams with uniformly distributed mass and elasticity, is proposed in Section 2.3. However, other capacity design methods [e.g. 12-14] could be used without affecting the other steps of the methodology. If higher mode effects have a pronounced influence on the capacity design forces, these effects can be mitigated by using multiple force-limiting mechanisms, as will be discussed in Section 2.4.

The third step of the design is to detail the connections. Because of the variability associated with the peak member forces, a double capacity design approach is proposed, with the connections designed for the maximum likely member strengths. Although no capacity-designed elements of the CRS are intended to yield, this step ensures some reserve of ductility by confining any unintentional yielding to the members, rather than the connections.

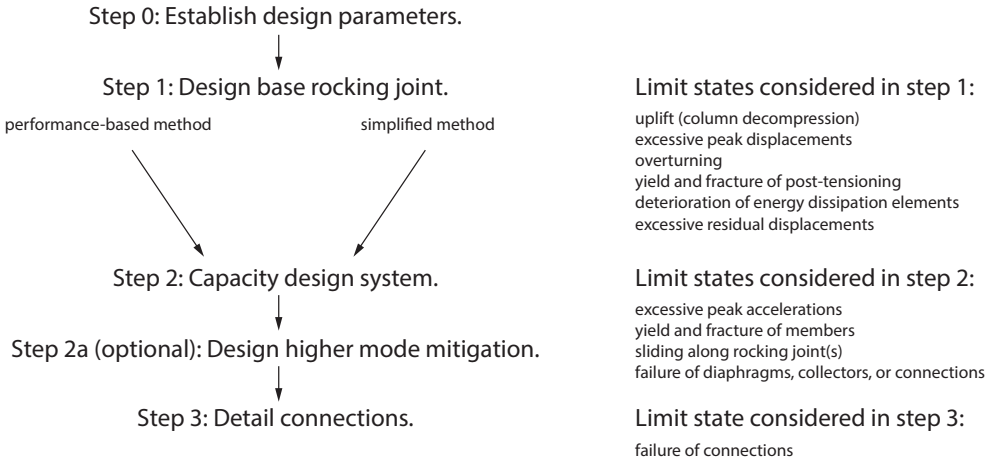


Figure 2: Steps of proposed design methodology.

2.2 Step 1: Design of base rocking joint for displacement-based limit states

To achieve IO at a seismic hazard level, it is necessary to limit the displacements to avoid both non-structural and structural damage. Priestley et al. [22] suggest that peak interstorey drifts of 1.2% could be permitted with proper detailing of non-structural elements. Yielding of the post-tensioning and deterioration of any energy dissipation devices should be prevented at this level. Residual deformations must also be limited to 0.5% [23].

To achieve CP at a seismic hazard level, it is necessary to limit the displacements to avoid failure of the gravity load system and the CRS components. The National Building Code of Canada [21] limits the peak interstorey drifts to 2.5% for most structures under MCE-level ground motions. The maximum expected displacement demands on the post-tensioning and energy dissipation elements must not cause them to fail. P-Δ effects at the maximum expected system displacement must not cause overturning of the CRS.

The above requirements are used to compute maximum allowable interstorey drifts and base rotations at the IO and the CP performance levels. Because the displacements of a CRS are intended to be dominated by the base rocking behavior, the peak interstorey drift is assumed for design to be approximately equal to the peak base rotation, $\theta_{\max}$. At each performance level, this rotation is used to compute the target displacement demand at the effective height of a single-degree-of-freedom (SDOF) model:

$$\Delta_{des} = \theta_{\max} \frac{\sum_{i=1}^{n}\left(m_i h_i^2\right)}{\sum_{i=1}^{n}\left(m_i h_i\right)} \tag{1}$$

where m_i is the tributary seismic mass at storey i, h_i is the height of that storey above the base rocking joint, and n is the number of storeys. The initial period of the system is estimated using approximately 1.4-1.5 times the period given by building codes [20-21]:

$$T_1 = 0.07 h_n^{0.75} \tag{2}$$

where h_n is the height of the structure in meters.

Having determined the target displacement demand and estimated T_1, the next step is to choose hysteretic parameters (f_y, α, and β) that will achieve Δ_{des}. These hysteretic parameters may be chosen using design charts based on the response of SDOF systems with flag-shaped hystereses. Figure 3 shows one such chart, which is based on the median response to the suite of 44 ground motions that was developed for FEMA P695 [24] and scaled to match the maximum MCE-level spectrum in Seismic Design Category D between periods of 0.1 s and 2.0 s. For each ground motion, linear elastic systems with 11 different initial periods were analyzed to determine the peak force demands, and each median demand was divided by a force reduction factor (R) to determine the linear limit (f_y) for an SDOF system with a flag-shaped hysteresis and the same initial period. All of the systems represented in Figure 3 have zero energy dissipation ($\beta = 0$). The nonlinear stiffness ratio, $\alpha = \left(0.1\,\mathrm{s}^{-2}\right)\left(T_1/2\pi\right)^2$, varies with the initial period so that the post-uplift stiffness (αk_0) is independent of the initial period. The post-uplift stiffness can be targeted when designing the base rocking joint, whereas α depends on the initial stiffness, which is known only after the members have been designed. Design charts for other values of α and β are given elsewhere [25].

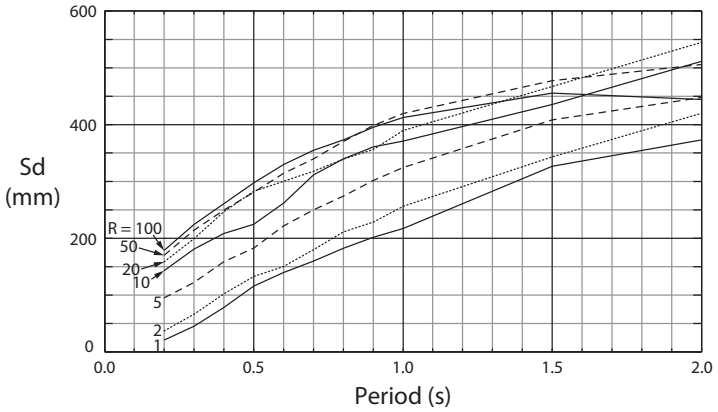


Figure 3: Median peak displacements under MCE-level ground motions: SDOF systems with flag-shaped hysteresis, $\beta = 0$, and $\alpha = \left(0.1\,\mathrm{s}^{-2}\right)\left(T_1/2\pi\right)^2$.

Figure 3 shows an increase in peak displacements with increasing initial period. The peak displacements also tend to increase as the linear limit decreases, but this effect reduces when R is increased beyond about 10. In this range, the peak displacements at some periods reduce when R is increased. This is believed to be because of the statistical error that comes from the limited set of ground motions, and because much of the response of these systems occurs in the nonlinear range, where the instantaneous natural frequency is in the range that is filtered out of the recorded ground motion.

Having selected the force reduction factor, the design base rocking moment is calculated as:

$$M_{b,rock} = \frac{S_a(T_1)}{R} \frac{\left[\sum_{i=1}^{n}(m_i h_i)\right]^2}{\sum_{i=1}^{n}(m_i h_i)} \tag{3}$$

where $S_a(T_1)$ is the design spectral acceleration at the estimated initial period (see equation 2). It is not proposed to allow uplift under any considered level of wind loading. However, it is expected that this requirement could be relaxed if it was shown that many small-amplitude cycles of uplift would not damage the post-tensioning and energy dissipation elements.

Next, the base rocking joint is proportioned to provide the required moment resistance. The contribution from the self-weight on the CRS is calculated first. It is not recommended to have the CRS carry any gravity load other than its self-weight, so as to avoid column force amplification due to impact [26] and to provide better control over the rocking moment in order to minimize the capacity design forces. For preliminary design, the contribution of the frame self-weight can be estimated as 5% of $M_{b,rock}$.

The contribution to the base overturning moment resistance from the energy dissipation, M_{ED}, is designed to achieve the target level of energy dissipation:

$$M_{ED} = M_{b,rock}\left(\frac{\beta}{2}\right) \tag{4}$$

The post-tensioning is selected to provide the remainder of $M_{b,rock}$. The post-uplift stiffness ratio, which was assumed when selecting which design chart to use, must also be verified:

$$\alpha = \frac{\left(A_{PT} E_{PT} / L_{PT}\right) d_{PT}^2 - W_{trib} H_W}{\sum_{i=1}^{n} \left(m_i h_i^2\right)} \left(\frac{T_1}{2\pi}\right)^2 \tag{5}$$

where A_{PT}, E_{PT}, and L_{PT} are the area, modulus of elasticity, and unbonded length of the post-tensioning, respectively, d_{PT} is the horizontal distance from the rocking toe to the location of the post-tensioning, and W_{trib} and H_W are the total tributary seismic weight and the height of its centroid. The peak displacement is not sensitive to the post-uplift stiffness, so it can usually be verified that the value of R that was chosen using an assumed value of α is also adequate when α is determined using equation 5. The energy dissipation and post-tensioning must both be designed to avoid failure at the maximum expected base rotation at the CP performance level (2.5%, unless a different value is used in equation 1). The energy dissipation and post-tensioning are also designed to avoid damage at the maximum expected base rotation at the IO level.

Once the base rocking joint has been designed, the resistance to overturning is checked at the maximum expected base rotation at the CP performance level. To provide an added measure of safety for very large earthquakes, it is recommended that the rocking joint be designed with a slotted connection that causes it to lock up at the maximum expected base rotation. For demands beyond this point, it is expected that the frame would respond similarly to a conventional braced frame, but with an additional rigid body rotation that would reduce the ductility demand. A similar concept for post-tensioned steel frames, in which the connections are capacity designed to confine yielding to the beams, has been experimentally validated [27].

2.3 Step 2: Capacity design of frame for acceleration-based limit states

Because the peak force demands in a CRS are strongly influenced by higher mode effects, these effects must be estimated during design. A method for calculating the design forces has been developed based on the modal properties of cantilever beams with uniformly distributed mass and elasticity, and this method has been calibrated through extensive time history analyses [25]. The method does not require a structural model of the CRS because the equations use only the overstrength base overturning moment resistance ($M_{b,\max}$), the height of each storey above the base (z), the height of the CRS (H), the tributary seismic mass (W_{trib}/g), and the five-percent-damped spectral accelerations at one third and one fifth of the fundamental period ($S_a\left(T_1/3\right)$ and $S_a\left(T_1/5\right)$). Table 1 lists the equations that are used for the modal contributions to the shear force and overturning moment envelopes ($V_{\max}$ and $M_{\max}$, respectively). To account for uncertainties in the ground motion, the acceleration spectrum is multiplied by a demand factor $\alpha_i \geq 1$. It is proposed that this factor be taken as the ratio of the median-plus-standard-deviation acceleration spectrum to the median spectrum, which is approximately 1.5 for the suite of FEMA P695 records [24] at periods of less than 2 s.

Using the first three modes, the modal contributions are combined by assuming that the peak response is reached in the first mode and sustained, and that the higher modes are superimposed on that first-mode response:

$$V_{\max}(z) = V_{1,\max}(z) + \sqrt{\left(V_{2,\max}(z)\right)^2 + \left(V_{3,\max}(z)\right)^2} \tag{6}$$

$$M_{\max}(z) = M_{1,\max}(z) + \sqrt{\left(M_{2,\max}(z)\right)^2 + \left(M_{3,\max}(z)\right)^2} \tag{7}$$

description	equation
storey shear	
first mode	$V_{1,\max}(z) = \frac{3}{2}\left(\frac{M_{b,\max}}{H}\right)\left[1-\left(\frac{z}{H}\right)^2\right]$
second mode	$V_{2,\max}(z) = 0.1265\left[\alpha_i S_a(T_1/3)\right]\left(\frac{W_{trib}}{g}\right)\left\lvert\cos 4.49\left(\frac{z}{H}\right)+0.217\right\rvert$
third mode	$V_{3,\max}(z) = 0.0297\left[\alpha_i S_a(T_1/5)\right]\left(\frac{W_{trib}}{g}\right)\left\lvert\cos 7.73\left(\frac{z}{H}\right)-0.1283\right\rvert$
overturning moment	
first mode	$M_{1,\max}(z) = M_{b,\max}\left[1-\frac{3}{2}\left(\frac{z}{H}\right)+\frac{1}{2}\left(\frac{z}{H}\right)^2\right]$
second mode	$M_{2,\max}(z) = 0.0282\left[\alpha_i S_a(T_1/3)\right]\left(\frac{W_{trib}}{g}\right)H\left\lvert\sin 4.49\left(\frac{z}{H}\right)+0.976\left(\frac{z}{H}\right)\right\rvert$
third mode	$M_{3,\max}(z) = 0.00384\left[\alpha_i S_a(T_1/5)\right]\left(\frac{W_{trib}}{g}\right)H\left\lvert\sin 7.73\left(\frac{z}{H}\right)-0.991\left(\frac{z}{H}\right)\right\rvert$

Table 1: Summary of modal contributions to design envelopes.

At each storey level, the brace elements are designed to carry the larger of the shear force demands at the top and bottom of that level. Similarly, each pair of vertical elements is designed to carry the larger of the overturning moment demands at the top and bottom of each storey level. In addition, local effects from post-tensioning and energy dissipation anchorages, as well as from rocking, must be considered.

2.4 Step 2a: Design of upper rocking joint to control acceleration-based limit states

If the design envelopes calculated as described in Section 2.3 are dominated by the higher modes, it may be desirable to use additional mechanisms to better control the response. For such mechanisms to be effective, they must activate at a low enough load to limit the response in the higher modes, but they must not activate at too low a load, or else the deformation demand for the system will concentrate at the higher mode mitigation mechanisms. It is proposed that any upper rocking joint be designed to activate at a moment that is at least as large as the moment associated with rocking at the base, assuming a first-mode distribution of lateral loads, and to have an energy dissipation parameter β that is at least as large as at the base joint. Proposals for the design shear force and overturning moment envelopes, as well as for the design of nonlinear braces, are given elsewhere [25].

3 DESIGN AND MODELLING OF 12-STOREY FRAMES

The proposed methodology was used to design a 12-storey structure. The floor plan and storey heights, which are shown in Figures 4a and 4c, have also been used in a recent study to evaluate the FEMA P695 methodology [28]. The acceleration design spectrum is shown in Figure 4b, together with the spectra of the 44 MCE-level ground motions that were scaled to the design spectrum. Figure 4c shows the structural layout of the CRS, which is designed to fit between the gravity columns. Placing the post-tensioning at the edges of the frame and anchoring it at the sixth storey level provided sufficient elongation capacity to reach base rota-

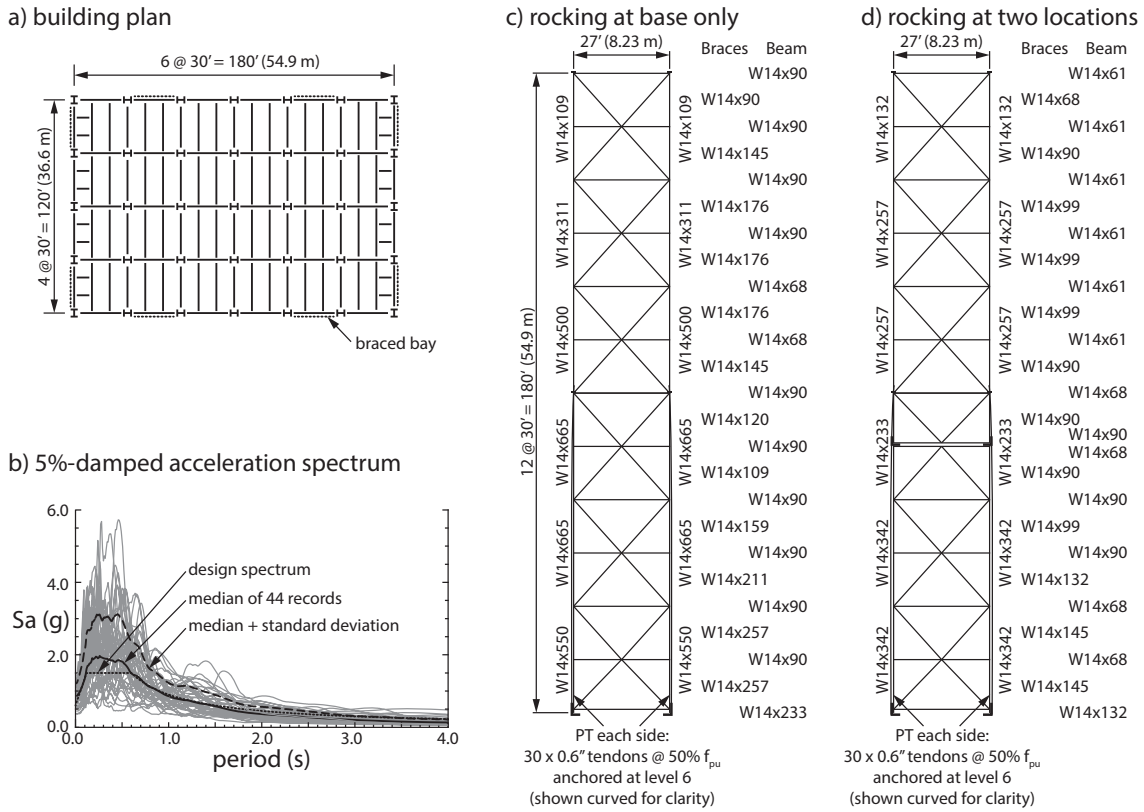


Figure 4: Example design: (a) building plan; (b) 5%-damped acceleration spectrum; (c) summary of design with rocking at base only (US section sizes); (d) summary of design with rocking at two locations (US section sizes).

tions of 1.2% and 2.5% without yield and failure of the post-tensioning, respectively. Therefore, it was not necessary to extend the post-tensioning over the full height of the frame. The target displacement at the CP performance level was calculated using equation 1 as 928 mm, and the fundamental period of the structure was estimated using equation 2 as 1.41 s. At this period, Figure 3 shows that the peak displacement of an SDOF system under the MCE-level suite of ground motions is much less than the maximum allowable displacement, even using a force reduction factor of $R = 100$ and no energy dissipation. Therefore, the CRS is designed with enough post-tensioning to avoid uplift under wind loading, which corresponds to $M_{b,rock} = 32\,800$ kN-m (equivalent to $R = 20.9$) for each frame according to the Directional Procedure of ASCE 7-10 [20].

The capacity design method of Section 2.3 was used to estimate the demands on the frame members, using the median-plus-standard-deviation acceleration spectrum with $\alpha_i = 1$ instead of multiplying the median spectrum by $\alpha_i = 1.5$. As shown in Figure 5, the higher modes dominated the design shear force and overturning moment envelopes. Therefore, an alternative design was considered, in which rocking is allowed not only at the base, but also at the fifth storey. This location was chosen because it is where the estimated second-mode contribution to the overturning moment is largest. No change to the post-tensioning was necessary because of this additional joint, but the member design forces were greatly reduced. The resulting design is shown in Figure 4d; this frame uses 40% less steel than the design with rocking only at the base. An alternative with SCED braces at the first storey was also considered [25] but is not discussed here.

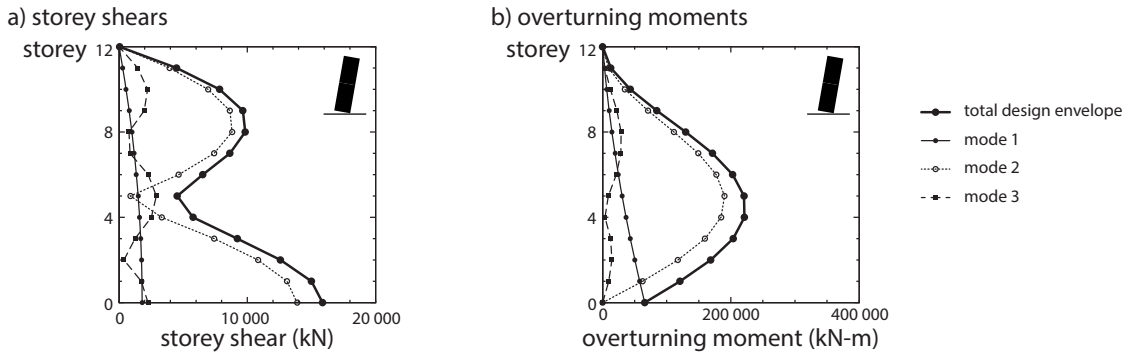


Figure 5: Design envelopes for frame with rocking only at base: (a) storey shears; (b) overturning moments.

Both frames were modelled using OpenSees [29]. The frame members were modelled as linear elastic, but yielding of the post-tensioning elements was modelled with Steel02 elements. The tributary seismic mass was modelled using leaning columns, and the horizontal displacement of the centre node of the frame at each level was slaved to the horizontal displacement of the leaning column at the same level. Five percent tangent stiffness-proportional Rayleigh damping was assigned in the first two modes. The first-mode periods of the frames with rocking only at the base and with two rocking joints were calculated as 1.69 s and 2.24 s, respectively. These periods are larger than the original design estimate of 1.41 s.

4 RESPONSE OF FRAMES TO MCE-LEVEL GROUND MOTIONS

4.1 Peak displacements

To evaluate the ability of the first step of the methodology to target the desired peak displacements at the CP performance level, Figure 6 shows the peak interstorey drifts for both frames during the suite of MCE-level records. The median and median-plus-standard-deviation responses are shown in each figure, both calculated assuming a lognormal distribution. As expected, the median peak interstorey drifts are less than the design limits for both frames, despite the low rocking load that was assigned. Additional analyses confirmed that the displacement response at the IO performance level was also less than the design target [25]. For the frame with an upper rocking joint, one record caused instability in the numerical model after attaining a roof displacement of approximately 10%. This is because the recommended lock-up device, which is intended to prevent collapse under extreme ground motions, was not included in the numerical model.

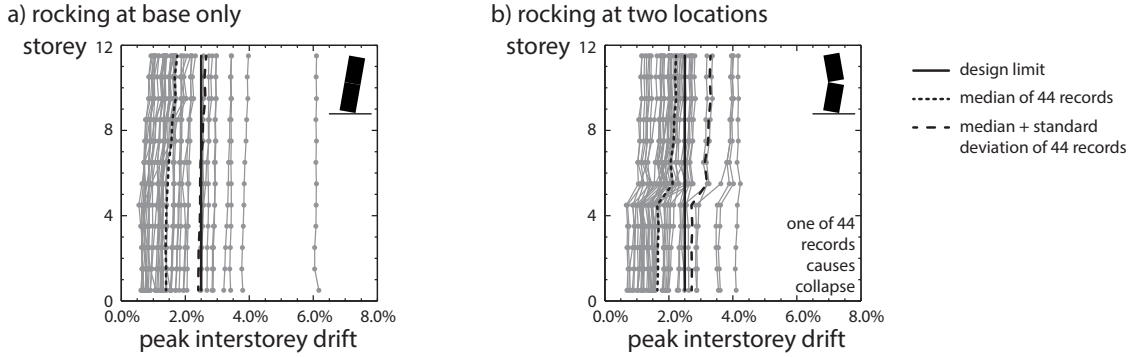


Figure 6: Peak interstorey drifts: (a) rocking at base only; (b) rocking at two locations.

For both frames, the residual displacements were zero after nearly all records. For two MCE-level records, yielding of the post-tensioning reduced the self-centering ability of both frames enough that P-Δ effects caused residual displacements. Nevertheless, this still satisfied the design objectives of IO after a DBE-level record and CP after an MCE-level record.

4.2 Peak forces

To evaluate the ability of the second step of the methodology to capacity design the frame members, Figure 7a shows the peak brace compression demands for the frame with rocking only at the base and Figure 7b shows the peak column compression demands. The design estimates of the peak brace forces are in very good agreement with the median-plus-standard-deviation results from the analyses. The design estimates of the peak column compression demands are good for the upper half of the frame but more conservative than desired for the lower half of the frame. Considering the consequences of member failure and the simplicity of the proposed design method, this extra conservatism is considered acceptable.

Figures 7c-d show the peak brace and column compression demands for the frame with two rocking joints. The median peak forces are substantially reduced by the upper joint. Moreover, the record-to-record variability in the peak response is much less than it was with rocking only at the base because of the increased control provided by the upper joint. The capacity design method produces reasonably good estimates of the peak forces in the braces in the lower half of the frame. As was observed for the frame with rocking only at the base, the design method is more conservative than desired for the columns. However, the method still captures the reduction in force demands for this frame relative to the one with rocking only at the base.

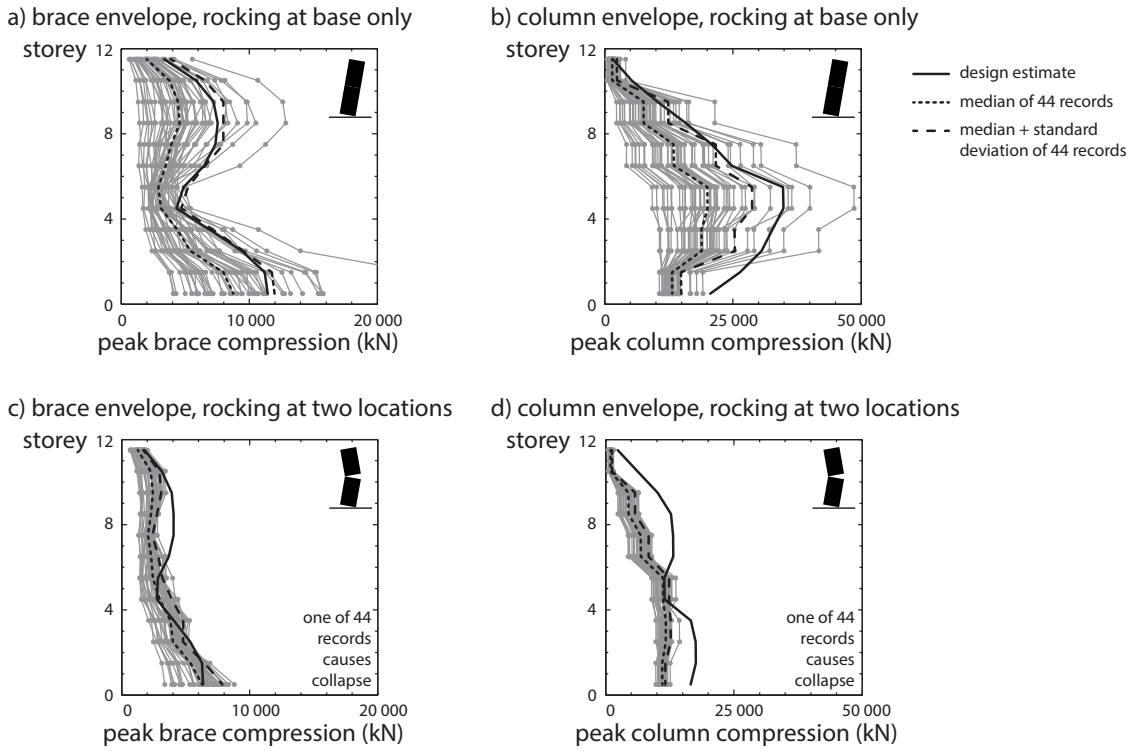


Figure 7: Member compressive force envelopes: (a) braces, rocking at base only; (b) columns, rocking at base only; (c) braces, rocking at two locations; (d) braces, rocking at two locations.

5 CONCLUSION

A new design methodology has been proposed for controlled rocking steel frames. In the first step of the methodology, the base rocking joint is designed to target the desired peak displacements. The proposed method uses an SDOF representation of the system, together with design charts. The method does not require iteration, although an improved response prediction could be obtained by replacing the estimated first-mode period with a period from a structural model. In the second step of the methodology, the frame members are capacity designed for the maximum expected forces, including the effects of the higher modes. Equations were presented that allow these forces to be estimated using only properties that are known during preliminary design.

Two 12-storey frames were designed, one with rocking only at the base and the other with two rocking joints. Nonlinear time history analyses of these frames confirmed that the methodology resulted in designs that achieved the displacement targets. The peak member forces were estimated well or slightly conservatively. The beneficial effect of adding an upper rocking joint was captured by the design method.

This paper has presented a simple and effective way for designers to apply the beneficial effects of controlled rocking. Forthcoming papers will discuss the development and validation of this design methodology more fully. Ongoing research seeks to further refine the methodology, to extend it to other structural systems, and to develop improved details for controlled rocking steel frames.

REFERENCES

[1] C. Christopoulos, A. Filiatrault, B. Folz. Seismic response of self-centring hysteretic SDOF systems. *Earthquake Engineering and Structural Dynamics*, **31**, 1131-1150, 2002.

[2] J.M. Kelly, D.F. Tsztoo. Earthquake simulation testing of a stepping frame with energy-absorbing devices. *Report UCB/EERC-77/17*. Earthquake Engineering Research Center, University of California, Berkeley, 1977.

[3] R.W. Clough, A.A. Huckelbridge. Preliminary experimental study of seismic uplift of a steel frame. *Report UCB/EERC-77/22*, Earthquake Engineering Research Center, University of California, Berkeley, 1977.

[4] A.A. Huckelbridge. Earthquake simulation tests of a nine story steel frame with columns allowed to uplift. Report *UCB/EERC-77/23*, Earthquake Engineering Research Center, University of California, Berkeley, 1977.

[5] M. Midorikawa, T. Azuhata, T. Ishihara, A. Wada. Shaking table tests on seismic response of steel braced frames with column uplift. *Earthquake Engineering and Structural Dynamics*, **35**, 1767-1785, 2006.

[6] R. Tremblay, L.-P. Poirier, N. Bouaanani, M. Leclerc, V. Rene, L. Fronteddu, S. Rivest. Innovative viscously damped rocking braced frames. *Proceedings of the 14th World Conference on Earthquake Engineering*, Beijing, China, October 12-17, 2008.

[7] M. Eatherton, J. Hajjar, G. Deierlein, X. Ma, H. Krawinkler. Hybrid simulation testing of a controlled rocking steel braced frame system. *Proceedings of the 9th US and 10th Canadian Conference on Earthquake Engineering*, Toronto, ON, July 25-29, 2010.

[8] X. Ma, G. Deierlein, M. Eatherton, H. Krawinkler, J. Hajjar, T. Takeuchi, K. Kasai, M. Midorikawa, T. Hikino. Large-scale shaking table test of steel braced frame with controlled rocking and energy dissipating fuses. *Proceedings of the 9th US and 10th Canadian Conference on Earthquake Engineering*, Toronto, ON, July 25-29, 2010.

[9] R. Sause, J.M. Ricles, D.A. Roke, N.B. Chancellor, N.P. Gonner. Seismic performance of a self-centering rocking concentrically-braced frame. *Proceedings of the 9th US and 10th Canadian Conference on Earthquake Engineering*, Toronto, ON, July 25-29, 2010.

[10] M. Pollino, M. Bruneau. Seismic testing of a bridge steel truss pier designed for controlled rocking. *Journal of Structural Engineering*, **136**, 1523-1532, 2010.

[11] L. Wiebe, C. Christopoulos, R. Tremblay, M. Leclerc. Mechanisms to limit higher mode effects in a controlled rocking steel frame. 2: Large-amplitude shake table testing. *Earthquake Engineering and Structural Dynamics*, Early View, DOI 10.1002/eqe.2258, 2012.

[12] D. Roke, R. Sause, J.M. Ricles, N. Gonner. Damage-free seismic-resistant self-centering steel concentrically braced frames. *Proceedings of the 6th International Conference on Behaviour of Steel Structures in Seismic Areas (STESSA 2009)*, Philadelphia, PA, August 16-20, 2009.

[13] M. Eatherton, J. Hajjar. Large-scale cyclic and hybrid simulation testing and development of a controlled-rocking steel building system with replaceable fuses. *NSEL Report NSEL-025*, Department of Civil and Environmental Engineering, University of Illinois at Urbana-Champaign, 2010.

[14] X. Ma. Seismic design and behavior of self-centering braced frame with controlled rocking and energy-dissipating fuses. *PhD Dissertation*. Stanford University, 2010.

[15] L. Wiebe, C. Christopoulos, R. Tremblay, M. Leclerc. Mechanisms to limit higher mode effects in a controlled rocking steel frame. 1: Concept, modelling, and low-amplitude shake table testing. *Earthquake Engineering and Structural Dynamics*, Early View, DOI 10.1002/eqe.2259, 2012.

[16] L. Wiebe, C. Christopoulos, R. Tremblay, M. Leclerc. Modelling inherent damping for rocking systems: results of large-scale shake table testing. *Proceedings of the 15th World Conference on Earthquake Engineering*, Lisbon, Portugal, September 24-28, 2012.

[17] D.A. Roke. Damage-free seismic-resistant self-centering concentrically-braced frames. *PhD Dissertation*. Lehigh University, 2010.

[18] American Society of Civil Engineers. *Seismic rehabilitation of existing buildings*. ASCE Standard ASCE/SEI 41-06. American Society of Civil Engineers, 2007.

[19] Canterbury Earthquakes Royal Commission. *Final Report, Volume 3: low-damage building technologies*. Royal Commission of Inquiry into Building Failure Caused by the Canterbury Earthquakes, 2012.

[20] American Society of Civil Engineers. *Minimum design loads for buildings and other structures*. ASCE Standard ASCE/SEI 7-10. American Society of Civil Engineers, 2010.

[21] National Research Council Canada. *National building code of Canada, 13th ed*. National Research Council of Canada, 2010.

[22] M.J.N. Priestley, G.M. Calvi, M.J. Kowalsky. *Displacement-based seismic design of structures*. IUSS Press, 2007.

[23] J. McCormick, H. Aburano, M. Ikenaga, M. Nakashima. Permissible residual deformation levels for building structures considering both safety and human elements. *Proceedings of the 14th World Conference on Earthquake Engineering*, Beijing, China, October 12-17, 2008.

[24] Federal Emergency Management Agency. Quantification of building seismic performance factors. *Report FEMA P695*. Federal Emergency Management Agency, 2009.

[25] L.D.A. Wiebe. Design of controlled rocking steel frames to limit higher mode effects. *PhD Dissertation*. University of Toronto, 2013.

[26] M. Pollino, M. Bruneau. Dynamic seismic response of controlled rocking bridge steel-truss piers. *Engineering Structures*, **30**, 1667-1676, 2008.

[27] H.-J. Kim, C. Christopoulos. Friction damped posttensioned self-centering steel moment-resisting frames. *Journal of Structural Engineering*, **134**, 1768-1779, 2008

[28] National Institute of Standards and Technology. Evaluation of the FEMA P-695 methodology for quantification of building seismic performance factors. *Report NIST GCR 10-917-8*. National Institute of Standards and Technology, 2010.

[29] OpenSees. Open system for earthquake engineering simulation (OpenSees), v2.3.2. Pacific Earthquake Engineering Research Center, 2011.

COMPDYN 2013
4th ECCOMAS Thematic Conference on
Computational Methods in Structural Dynamics and Earthquake Engineering
M. Papadrakakis, V. Papadopoulos, V. Plevris (eds.)
Kos Island, Greece, 12–14 June 2013

ROCKING RESPONSE AND STABILITY ANALYSIS OF AN ARRAY OF FREE-STANDING COLUMNS CAPPED WITH A FREE-STANDING RIGID BEAM

Nicos Makris[1] **and Michalis F. Vassiliou**[2]

[1] University of Patras, Department of Civil Engineering,
Division of Structures, Patras, GR-26500, Greece
e-mail: nmakris@upatras.gr

[2] ETH Zürich,
IBK, Wolfgang-Pauli-Strasse 15, CH-8093
vassiliou@ibk.baug.ethz.ch

Keywords: Rocking Frame, Seismic Isolation, Ancient Temples, Prefabricated Bridges, Earthquake Engineering

Abstract. *This paper investigates the planar rocking response of an array of free-standing columns capped with a freely supported rigid beam in an effort to explain the appreciable seismic stability of ancient free-standing columns which support heavy epistyles together with the even heavier frieze atop. Following a variational formulation the paper concludes to the remarkable result that the dynamic rocking response of an array of free-standing columns capped with a rigid beam is identical to the rocking response of a single free-standing column with the same slenderness; yet with larger size—that is a more stable configuration. Most importantly, the study shows that the heavier the freely supported cap-beam is (epistyles with frieze atop), the more stable is the rocking frame regardless the rise of the center of gravity of the cap-beam; concluding that top-heavy rocking frames are more stable than when they are top-light. This "counter intuitive" finding renders rocking isolation a most attractive alternative for the seismic protection of bridges with tall piers; while its potential implementation shall remove several of the concerns associated with the seismic connections of prefabricated bridges.*

1 INTRODUCTION

Under base shaking slender objects and tall rigid structures may enter into rocking motion that occasionally results in overturning. Early studies on the seismic response of a slender rigid block were presented by Milne [1]; however, it was Housner [2] who uncovered a size-frequency scale effect which explained why: (a) the larger of two geometrically similar blocks can survive the excitation that will topple the smaller block; and (b) out of two same acceleration amplitude pulses, the one with the longer duration is more capable to induce overturning. Following Housner's seminal paper a number of studies have been presented to address the complex dynamics of one of the simplest man-made structures—the free standing rigid column.

Yim et al. [3] conducted numerical studies by adopting a probabilistic approach, Aslam et al.[4] confirmed with experimental studies that the rocking response of rigid blocks is sensitive to system parameters; while Psycharis and Jennings [5] examined the uplift of rigid bodies supported on viscoelastic foundation. Subsequent studies by Spanos and Koh [6] investigated the rocking response due to harmonic steady-state loading and identified "safe" and "unsafe" regions together with the fundamental and suharmonic modes of the system. Their study was extended by Hogan [7],[8] who further elucidated the mathematical structure of the problem by introducing the concepts of orbital stability and Poincare sections. The transient rocking response of free-standing rigid blocks was examined in depth by Zhang and Makris [9] who showed that there exist two modes of overturning: (a) by exhibiting one or more impacts; and (b) without exhibiting any impact. The existence of the second mode of overturning results in a safe region that is located on the acceleration-frequency plane above the minimum overturning acceleration spectrum. The fundamental differences between the response of a rocking rigid column (inverted pendulum) and the response of the linear elastic oscillator (regular pendulum) led to the development of the rocking spectrum (Makris and Konstantinidis [10]). More recent studies pertinent to the rocking response of rigid columns have focused on more practical issues such as representation of the impact (Prieto et al. [11]), the effect of the flexibility-yielding of the supporting base (Apostolou et al. [12], Palmeri and Makris [13]) or the effect of seismic isolation (Vassiliou and Makris [14]).

In this paper we investigate the planar rocking response of an array of free-standing columns capped with a freely supported rigid beam as shown schematically in Figure 1. Herein we use the term "rocking frame" for the one degree of freedom structure shown in Figure 1. Sliding does not occur either at the pivot points at the base or at the pivot points at the cap-beam. Our interest to this problem was partly motivated from the need to explain the remarkable seismic stability of ancient free-standing columns which support heavy free standing epistyles together with the even heavier frieze atop. As an example, Figure 2 shows the entrance view of the late archaic temple of Aphaia in the island of Aegina nearby Athens, Greece. Dates ranging from 510BC to 470BC have been proposed for this temple. All but three of the 32 outer columns of the temple are monolithic and they have been supporting for 2.5 millennia the front and back epistyles together with the heavy frieze (triglyph and metope).

The understanding of the rocking response and stability of the configuration shown in Figure 1 is also pertinent to the growing precast bridge construction technology where bridge piers supporting heavy decks are allowed to rock atop their foundation in order to achieve re-centering of the bridge bent after a seismic event.

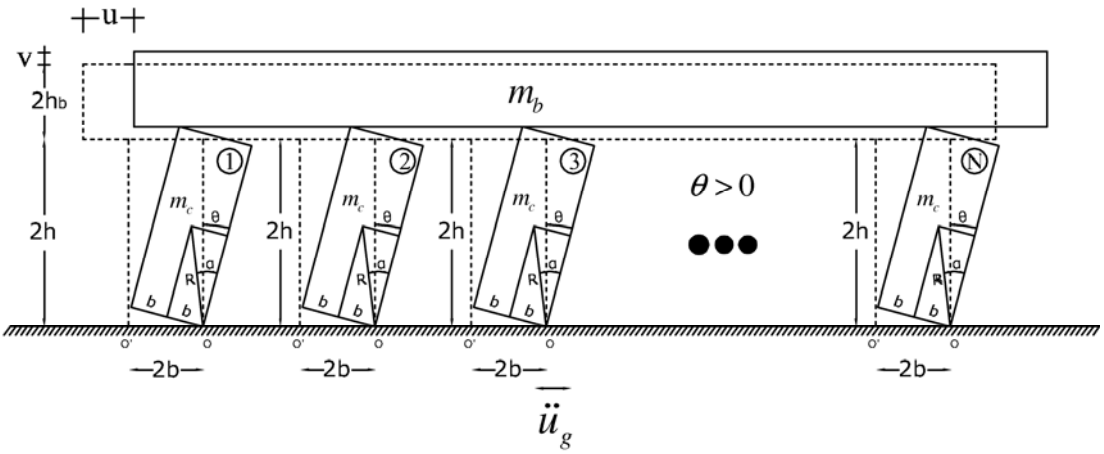


Figure 1: Rocking array of free-standing columns capped with a freely supported rigid beam.

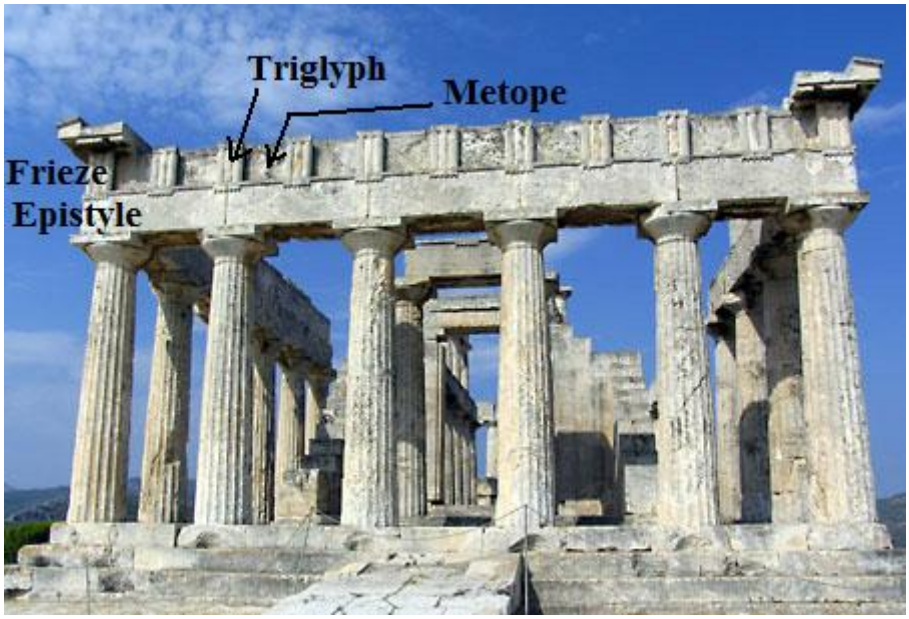


Figure 2: View of the Temple of Aphaia, in Aegina, Greece. Its monolithic, free-standing columns support massive epistyles and the frieze atop and the entire rocking frame remains standing for more than 2500 years in a region with high seismicity.

2 GENERAL SPECIFICATIONS

With reference to Figure 3 and assuming that the coefficient of friction is large enough so that there is no sliding, the equation of motion of a free standing block with size $R = \sqrt{h^2 + b^2}$ and slenderness α=atan(b/h) subjected to a horizontal ground acceleration, $\ddot{u}_g(t)$, when rocking around O and O' respectively is (Yim et al. [3], Hogan [7], Makris and Roussos [15] , Zhang and Makris [9] among others)

$$I_o\ddot{\theta}(t) + mgR\sin\left[-\alpha - \theta(t)\right] = -m\ddot{u}_g(t)R\cos\left[-\alpha - \theta(t)\right], \quad \theta(t) < 0 \tag{1}$$

$$I_o\ddot{\theta}(t) + mgR\sin\left[\alpha - \theta(t)\right] = -m\ddot{u}_g(t)R\cos\left[\alpha - \theta(t)\right], \quad \theta(t) > 0\,. \tag{2}$$

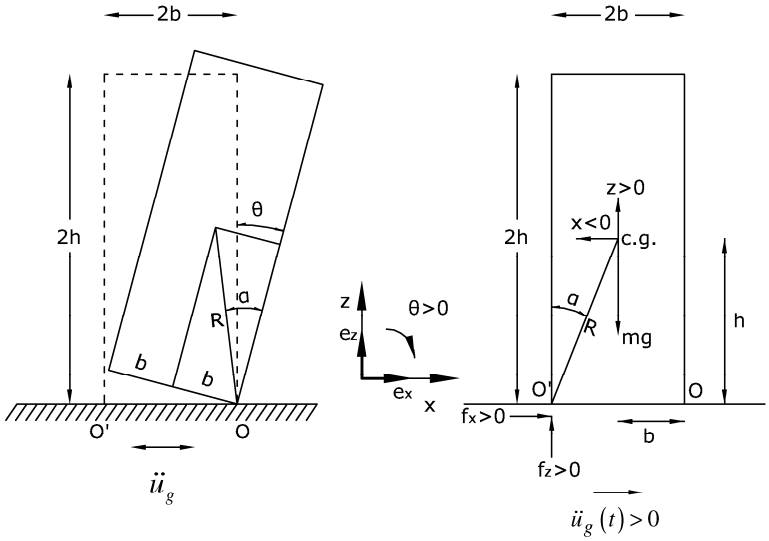


Figure 3: Left: Geometric characteristics of the model considered. Right :Free-body diagram of a free-standing block at the instant that it enters rocking motion.

In order for rocking motion to be initiated, $\ddot{u}_g(t) > g\tan\alpha$ at some time of its history. For rectangular blocks, $I_o = (4/3)mR^2$; and the above equations can be expressed in the compact form

$$\ddot{\theta}(t) = -p^2\left\{\sin\left[\alpha\,\mathrm{sgn}\left(\theta(t)\right)-\theta(t)\right]+\frac{\ddot{u}_g}{g}\cos\left[\alpha\,\mathrm{sgn}\left(\theta(t)\right)-\theta(t)\right]\right\}. \qquad (3)$$

The oscillation frequency of a rigid block under free vibration is not constant, because it strongly depends on the vibration amplitude (Housner [2]). Nevertheless, the quantity $p=\sqrt{\frac{3g}{4R}}$ is a measure of the dynamic characteristics of the block. For the 7.5m×1.8m free-standing column of the Temple of Appolo in Corinth, *p =1.4 rad/s*, and for a household brick, $p \approx 8$ *rad/s*.

Figure 4 shows the moment-rotation relationship during the rocking motion of a free-standing block. The system has infinite stiffness until the magnitude of the applied moment reaches the value $mgR\sin\alpha$, and once the block is rocking, its restoring force decreases monotonically, reaching zero when $\theta = \alpha$. This negative stiffness, which is inherent in rocking systems is most attractive in earthquake engineering given that such systems do not resonate.
During the oscillatory rocking motion of a free-standing rigid column, the moment-rotation curve follows the curve shown in Figure 4 without enclosing any area. Energy is lost only during impact, when the angle of rotation reverses. When the angle of rotation reverses, it is assumed that the rotation continues smoothly from points *O* to *O'* and that the impact force is concentrated at the new pivot point, *O'*. With this idealization, the impact force applies no moment around *O'*, hence the angular momentum around *O'* is conserved. Conservation of angular momentum about point *O'* just before the impact and right after the impact gives

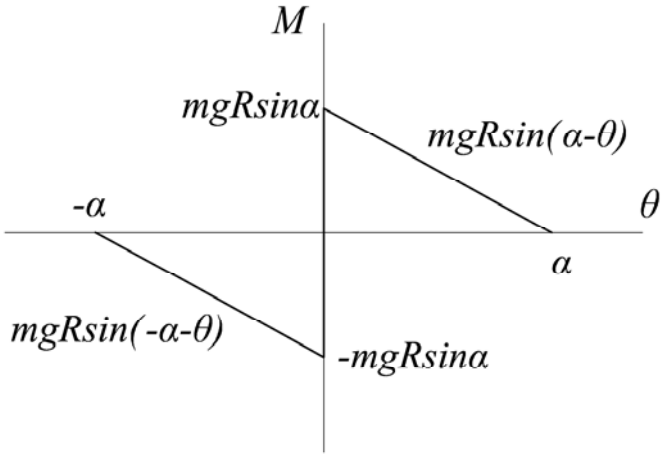


Figure 4: Moment rotation diagram of a rocking object

$$I_o\dot{\theta}_1 - m\dot{\theta}_1 2bR\sin(\alpha) = I_o\dot{\theta}_2 \tag{4}$$

where $\dot{\theta}_1$ = angular velocity just prior to the impact; and $\dot{\theta}_2$ = angular velocity right after the impact. The ratio of kinetic energy after and before the impact is

$$r = \frac{\dot{\theta}_2^2}{\dot{\theta}_1^2} \tag{5}$$

which means that the angular velocity after the impact is only $\sqrt{r}$ times the velocity before the impact. Substitution of (4) into (5) gives

$$r = [1 - \frac{3}{2}\sin^2\alpha]^2 \tag{6}$$

The value of the coefficient of restitution given by (6) is the maximum value of r under which a free-standing rigid block with slenderness α will undergo rocking motion. Consequently, in order to observe rocking motion, the impact has to be inelastic. The less slender a block (larger α), the more plastic is the impact, and for the value of $\alpha = \sin^{-1}\sqrt{2/3} = 54.73^o$, the impact is perfectly plastic. During the rocking motion of slender blocks, if additional energy is lost due to the inelastic behavior at the instant of impact, the value of the true coefficient of restitution r will be less than the one computed from equation (6).

3 EQUATION OF MOTION OF THE ROCKING FRAME

The free standing rocking frame shown in Figure 1 is a single-degree-of-freedom structure with size $R = \sqrt{h^2 + b^2}$ and slenderness $\alpha = atan(b/h)$. The only other parameter that influences the dynamics of the rocking frame is the ratio of the mass of the cap-beam, m_b, to the mass of all the N rocking columns, m_c, $\gamma = \frac{m_b}{Nm_c}$. For the temple of Apollo in Corinth where the frieze is missing, γ is as low as 0.3; whereas in prefabricated bridges γ>4. As in the case of the single rocking column, the coefficient of friction is large enough so that sliding does not occur at the pivot point at the base and at the cap-beam. Accordingly, the horizontal translation displacement $u(t)$ and the vertical lift $v(t)$ of the cap-beam are functions of the single degree of freedom $\theta(t)$. For a positive horizontal ground acceleration (the ground is accelerating

to the right), the rocking frame will initially rock to the left ($\theta(t)<0$). Assuming that the rocking frame will not topple, it will recenter, impacts will happen at the pivot points (at the base and at the cap-beam) and subsequently it will rock to the right ($\theta(t)>0$). During rocking the dependant variables $u(t)$, $v(t)$ and their time derivatives are given for $\theta(t)<0$ and $\theta(t)>0$ by the following expressions.

$$u = \mp 2R\left(\sin\alpha - \sin\left(\alpha \pm \theta\right)\right) \tag{7}$$

$$\dot{u} = 2R\cos\left(\alpha \pm \theta\right)\dot{\theta} \tag{8}$$

$$\ddot{u} = 2R\left(\mp\sin\left(\alpha \pm \theta\right)\left(\dot{\theta}\right)^2 + \cos\left(\alpha \pm \theta\right)\ddot{\theta}\right) \tag{9}$$

and

$$v = 2R\left(\cos\left(\alpha \pm \theta\right) - \cos\alpha\right) \tag{10}$$

$$\dot{v} = \mp 2R\sin\left(\alpha \pm \theta\right)\dot{\theta} \tag{11}$$

$$\ddot{v} = -2R\left(\cos\left(\alpha \pm \theta\right)\left(\dot{\theta}\right)^2 + \sin\left(\alpha \pm \theta\right)\ddot{\theta}\right) \tag{12}$$

In the equations above, whenever there is a double sign (say $\pm$) the top sign is for $\theta(t)<0$ and the bottom sign is for $\theta(t)>0$.

During rocking motion Langrange's equation must be satisfied,

$$\frac{d}{dt}\left(\frac{dT}{d\dot{\theta}}\right) - \frac{dT}{d\theta} = Q\,. \tag{13}$$

In equation (13), T is the kinetic energy of the system and Q is the generalized force acting on the system

$$Q = -\frac{dW}{d\theta} \tag{14}$$

in which W is the work done by the external forces acting on the rocking frame during an admissible rotation $\delta\theta$. During this admissible rotation $\delta\theta$, the variation of work is

$$\delta W = \frac{dW}{d\theta}\delta\theta \tag{15}$$

In either case were $\theta(t)<0$ or $\theta(t)>0$ the kinetic energy of the system is

$$T = N\frac{1}{2}I_o\left(\dot{\theta}\right)^2 + \frac{1}{2}m_b\left(\left(\dot{u}\right)^2 + \left(\dot{v}\right)^2\right) \tag{16}$$

Using equations (8) and (11), equation (16) reduces to

$$T = \left(\frac{N}{2}I_o + 2m_bR^2\right)\left(\dot{\theta}\right)^2 \tag{17}$$

Our analysis proceeds by first investigating the rocking motion of a free-standing frame subjected to a horizontal ground acceleration $\ddot{u}_g\left(t\right)$ when $\theta(t)<0$. During this segment of the motion the variation of the work, W, is

$$\delta W = \left(m_b + \frac{N}{2} m_c \right) \left(\ddot{u}_g \delta u + g \delta v \right) \tag{18}$$

or

$$\delta W = \left(m_b + \frac{N}{2} m_c \right) \left(\ddot{u}_g \frac{du}{d\theta} + g \frac{dv}{d\theta} \right) \delta\theta \tag{19}$$

The combination of equations (15) and (19) gives

$$\frac{dW}{d\theta} = \left(m_b + \frac{N}{2} m_c \right) \left(\ddot{u}_g \frac{du}{d\theta} + g \frac{dv}{d\theta} \right) \tag{20}$$

which simplifies to

$$\frac{dW}{d\theta} = 2R \left(m_b + \frac{N}{2} m_c \right) \left(\ddot{u}_g \cos\left(\alpha + \theta\right) - g \sin\left(\alpha + \theta\right) \right), \tag{21}$$

after using the expression given by (7) and (10).

The substitution of equations (17) and (21) into Lagrange's equation given by (13) results to the equation of motion of the rocking frame for $\theta(t)<0$.

$$\left(\frac{\frac{I_o}{2m_c R} + 2\gamma R}{\left(\gamma + \frac{1}{2}\right) g} \right) \ddot{\theta} = \sin\left(a + \theta\right) - \frac{\ddot{u}_g}{g} \cos\left(\alpha + \theta\right), \tag{22}$$

where $\gamma = \dfrac{m_b}{N m_c}$ is the ratio of the mass of the cap-beam (epistyle), m_b, to the mass of all the N columns= $N m_c$.

For the case where the rotation is positive $\theta(t)>0$ the variation of the work is

$$\delta W = \left(m_b + \frac{N}{m_c} m_c \right) \left(\ddot{u}_g \delta u + g \delta v \right) \tag{23}$$

and equation (14) takes the form

$$\frac{dW}{d\theta} = 2R \left(m_b + \frac{N}{2} m_c \right) \left(\ddot{u}_g \cos\left(\alpha + \theta\right) + g \sin\left(\alpha + \theta\right) \right). \tag{24}$$

The substitution of equation (17) and (24) into Lagrange's equation given by (13) offers the equation of motion of the rocking frame for $\theta(t)>0$.

$$\left(\frac{\frac{I_o}{2m_c R} + 2\gamma R}{\left(\gamma + \frac{1}{2}\right) g} \right) \ddot{\theta} = -\sin\left(a - \theta\right) - \frac{\ddot{u}_g}{g} \cos\left(\alpha - \theta\right). \tag{25}$$

For rectangular columns $I_o=(4/3)mR^2$; and equations (22) and (25) can be expressed in a single compact form

$$\ddot{\theta} = -\frac{1+2\gamma}{1+3\gamma} p^2 \left(\sin\left[a\,\mathrm{sgn}\left(\theta(t)\right) - \theta(t) \right] + \frac{\ddot{u}_g(t)}{g} \cos\left[a\,\mathrm{sgn}\left(\theta(t)\right) - \theta(t) \right] \right) \tag{26}$$

Equation (26) which describes the planar motion of the free-standing rocking frame is precisely the same as equation (3) which describes the planar rocking motion of a single free-standing rigid column with the same slenderness α, except that in the rocking frame the term p^2 is multiplied with the factor $\frac{1+2\gamma}{1+3\gamma}$. Accordingly, the frequency parameter of the rocking frame, $\hat{p}$, is

$$\hat{p} = \sqrt{\frac{1+2\gamma}{1+3\gamma}}\, p \tag{27}$$

where $p = \sqrt{\frac{3g}{4R}}$ is the frequency parameter of the rocking column and $\gamma = \frac{m_b}{N m_c}$ is the mass of the cap-beam to the mass of all N columns.

For a light cap-beam ($\gamma = \frac{m_b}{N m_c} \to 0$), the multiplication factor $\frac{1+2\gamma}{1+3\gamma} \to 1$ and the array of free standing columns coupled with a light epistyle exhibit precisely the dynamic rocking response of the solitary free-standing column. On the other hand, as the mass of the epistyle increases

$$\lim_{\gamma \to \infty} \frac{1+2\gamma}{1+3\gamma} = \frac{2}{3}. \tag{28}$$

Accordingly, the dynamic behavior of a rocking frame with a very heavy cap-beam supported on columns with slenderness α and frequency parameter, $p = \sqrt{\frac{3g}{4R}}$, is identical to the dynamic rocking response of a single rigid column with slenderness α and frequency parameter $\hat{p} = \sqrt{\frac{2}{3}}\, p$ – that is a smaller frequency parameter; therefore a larger, more stable column.

This remarkable result offered by equation (26) – that the heavier the cap-beam is, the more stable is the free standing rocking frame despite the rise of the center of gravity of the cap-beam – has been also confirmed by obtaining equation (26) for a pair of columns with the algebraically-intense direct formulation after deriving the equations of motion of the two-column frame through dynamic equilibrium.

According to equation (26) the rocking response and stability analysis of the free-standing rocking frame with columns having slenderness, α, and size R, is described by all the past published work on the rocking response of the free-standing single block ([2], [3], [4], [6], [9], [10], [14] among others), where the block has the same slenderness, α, and a larger size $\hat{R}$ given by

$$\hat{R} = \frac{1+3\gamma}{1+2\gamma} R = \left(1 + \frac{\gamma}{1+2\gamma} \right) R \tag{29}$$

Figure 5 plots the value of $\hat{R}$ as a function of the mass ratio $\gamma = \dfrac{m_b}{Nm_c}$. When replacing the rocking frame with the larger-size, equal slenderness solitary column, the maximum coefficient of restitution is given by equation (43)

4 MINIMUM ACCELERATION NEEDED TO INITIATE UPLIFT OF A ROCKING FRAME

With reference to Figure 1 during an admissible rotation $\delta\theta$, the application of the principle of virtual work gives:

$$m_b \ddot{u}_g \delta u + N m_c \ddot{u}_g R\left(\cos\alpha\right)\delta\theta = m_b g \delta v + N m_c g R\left(\sin\alpha\right)\delta\theta \tag{30}$$

where

$$\delta u = \frac{du}{d\theta}\delta\theta \quad \text{and} \quad \delta v = \frac{dv}{d\theta}\delta\theta \tag{31}$$

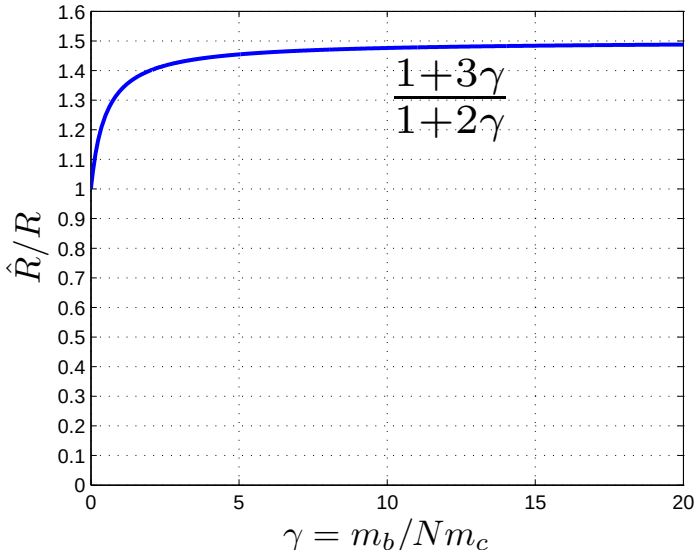


Figure 5: Values of the semidiagonal $\hat{R}$ of a free-standing rigid column with slenderness α that has identical dynamic properties and response as the free-standing rocking frame with N columns having slenderness α, semi-diagonal R, and mass m_c, supporting a cap-beam with mass m_b.

Without loss of generality we assume that the rocking frame undergoes positive rotations ($\theta(t)>0$); and according to equations (7) and (10) with their bottom signs

$$\delta u = 2R\cos\left(\alpha-\theta\right)\delta\theta \tag{32}$$

$$\delta v = 2R\sin\left(\alpha-\theta\right)\delta\theta \tag{33}$$

Substitution of equations (32) and (33) into equation (30) and after cancelling the admissible rotation $\delta\theta$ one obtains

$$m_b \ddot{u}_g 2\cos\left(\alpha-\theta\right) + N m_c \ddot{u}_g \cos\alpha = m_b g 2\sin\left(\alpha-\theta\right) + N m_c g \sin\alpha \tag{34}$$

At the initiation of uplift, θ=0, and equation (34) simplifies to

$$\left(2m_b + Nm_c\right)\ddot{u}_g^{up}\cos\alpha = \left(2m_b + Nm_c\right)g\sin\alpha \tag{35}$$

which shows that the minimum acceleration needed to initiate uplift of a rocking frame is

$$\ddot{u}_g^{up} = g\tan\alpha\,. \tag{36}$$

According to equation (36) the minimum uplift acceleration of the rocking frame depends solely on the slenderness of its columns and is entirely independent of the mass of the cap-beam (epistyles and frieze atop). This result was expected from the previous analysis on the rocking motion of the free-standing frame (see equation 26) which showed that its dynamic rocking response is identical to the rocking response of a single column which has the same slenderness, α, as the columns of the rocking frame, but larger size, $\hat{R} = \dfrac{1+3\gamma}{1+2\gamma}R$ (see Figure 5).

5 MAXIMUM COEFFICIENT OF RESTITUTION

The maximum coefficient of restitution of the rocking frame during the impact which happens when the rotation $\theta(t)$ alternates sign is calculated by applying the angular momentum-impulse theorem on one column of the frame before and after the impact. As in the case of the solitary rocking column, the angular momentum of one column of the rocking frame with respect to the imminent pivot point O' (see Figure 6) is

$$H_1 = \left(I_o - 2m_c bR\sin\alpha\right)\dot{\theta}_1\,, \tag{37}$$

where $\dot{\theta}_1$ is the angular velocity of the rocking column just before the impact. Upon impact, the angular momentum of the column with respect to the new pivot point O' is

$$H_2 = I_o\dot{\theta}_2 \tag{38}$$

where $\dot{\theta}_2$ is the angular velocity of the rocking column immediately after the impact.

The main difference between the conservation of angular momentum before and after the impact of the free-standing rocking frame with a freely supported cap-beam and the rocking of a free-standing solitary column, is that, upon impact happens, additional forces are acting on the columns of the rocking frame which were absent in the solitary column. These forces appear when the reactions of the cap-beam (epistyle) shift from point P' to point P as the pivot points at the base shift from point O to O' (see Figure 6)

Given that the cap-beam is rigid and that during the rocking motion of the frame, the motion of the cap-beam is only a translation (no rotations), it is assumed that the impact forces at all columns are equal. Accordingly, the change of the linear momentum of the cap-beam in the horizontal and vertical direction before and after the impact is

$$N\int\limits_{\substack{duration\\ of\ impact}} F_{xI}\,dt = 2m_b R\cos\alpha\left(\dot{\theta}_1 - \dot{\theta}_2\right) \tag{39}$$

and

$$N \int_{\substack{duration\\ of\ impact}} F_{zI}\,dt = 2m_b R \sin\alpha \left(\dot{\theta}_1 + \dot{\theta}_2\right) \tag{40}$$

Application of the angular momentum – impulse theorem before and after the impact gives

$$H_1 - 2b \int_{\substack{duration\\ of\ impact}} F_{zI}\,dt + 2h \int_{\substack{duration\\ of\ impact}} F_{xI}\,dt = H_2 \tag{41}$$

After substituting equation (37)-(40) into (41) and using that $I_o=4/3m_cR^2$ one obtains

$$\left(\frac{4}{3}m_c - 2m_c \sin^2\alpha - \frac{4}{N}m_b \sin^2\alpha + \frac{4}{N}m_b \cos^2\alpha\right)\dot{\theta}_1 = \left(\frac{4}{N}m_b + \frac{4}{3}m_c\right)\dot{\theta}_2 . \tag{42}$$

Further simplification of equation (42) gives that the ratio of kinetic energy of the rocking frame after and before the impact is

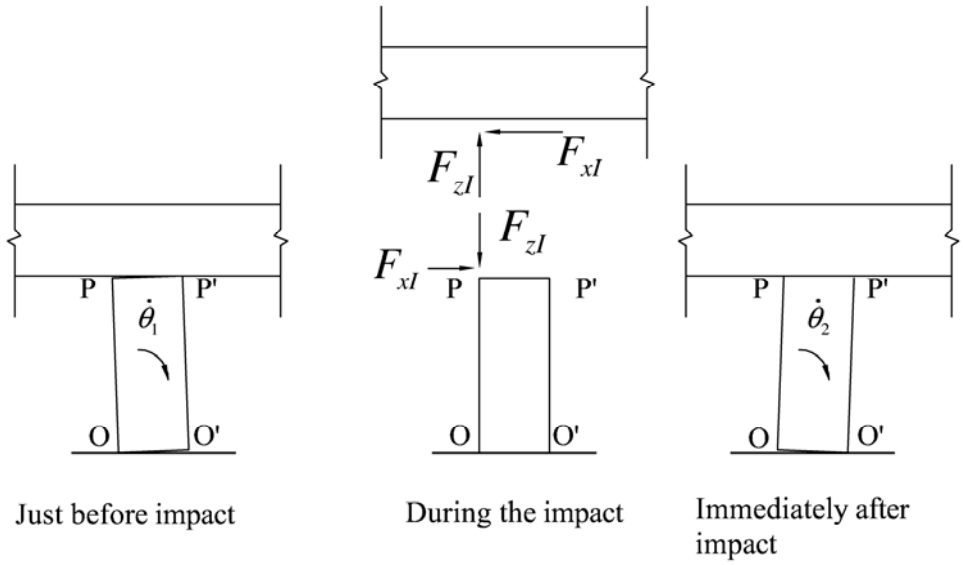


Figure 6: Configuration of the rocking column of the free standing frame just before and immediately after the impact together with the impact forces which develop at point P as the pivoting transfers to point O'.

$$r = \left(\frac{\dot{\theta}_2}{\dot{\theta}_1}\right)^2 = \left(\frac{1 - \frac{3}{2}\sin^2\alpha + 3\gamma\cos 2a}{1+3\gamma}\right)^2 . \tag{43}$$

Equation (5.6) indicates that the angular velocity of the rocking frame after the impact is only $\sqrt{r}$ times the velocity before the impact. Figure 7 plots the value of the minimum coefficient of restitution $\sqrt{r} = \dfrac{1 - \frac{3}{2}\sin^2\alpha + 3\gamma\cos 2a}{1+3\gamma}$ as a function of the slenderness α for different values of the mass ratio $\gamma = \dfrac{m_b}{Nm_c}$.

Figure 7 indicates that the maximum coefficient of restitution $\sqrt{r}$ of the rocking frame is always smaller than the maximum coefficient of restitution of the solitary column $=1-\frac{3}{2}\sin^2\alpha$, indicating that when a free-standing frame engages into rocking motion, it dissipates more energy than the equal slenderness equivalent solitary free-standing column with size $\hat{R}$ due to the aaditional impacts that happen between the columns and the cap-beam (epistyles and frieze)

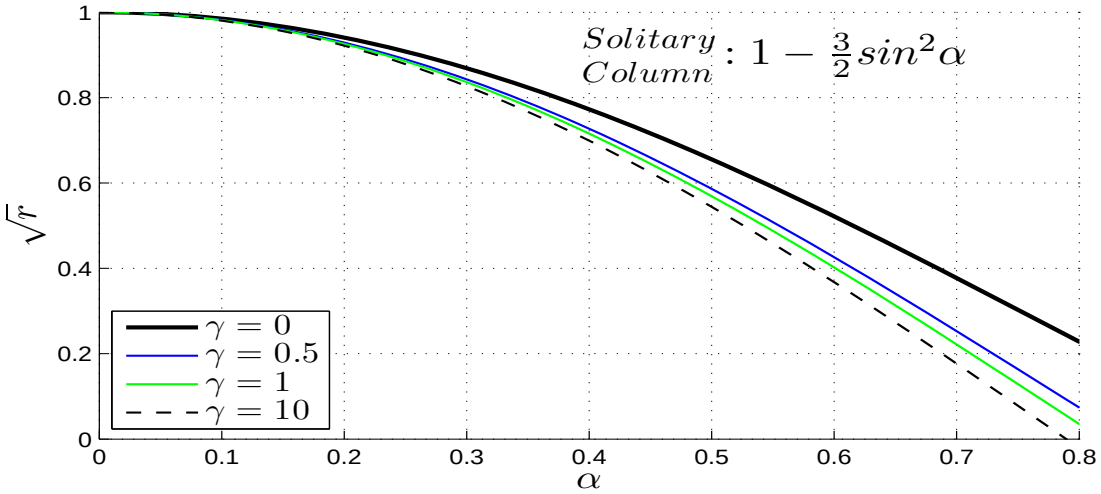


Figure 7: Values of the maximum coefficient of restitution as a function of the slenderness, α of the columns of the rocking frame for different values of the mass ratio $\gamma = \frac{m_b}{Nm_c}$.

6 OVERTURNING SPECTRA – SELF SIMILAR RESPONSE

The relative simple form yet destructive potential of near source ground motions has motivated the development of various closed form expressions which approximate their dominant kinematic characteristics. The early work of Veletsos et al. [16] was followed by the papers of Hall et al. [17], Makris [18], Makris and Chang [19], Alavi and Krawinkler [20] and more recently by the papers of Mavroeidis and Papageorgiou [21] and Vassiliou and Makris [22]. Physically realizable pulses can adequately describe the impulsive character of near-fault ground motions both qualitatively and quantitatively. The minimum number of parameters of the mathematical pulse is two, which are the acceleration amplitude, a_p and the duration T_p. The more sophisticated model of Mavroeidis and Papageorgiou [21] involves 4 parameters which are the pulse period, the pulse amplitude, the pulse phase and the number of half cycles. Recently, Vassiliou and Makris [22] used the Mavroeidis and Papageorgiou model [21] in association with wavelet analysis to develop a mathematically formal and objective procedure to extract the time scale and length scale of strong ground motions.

The current established methodologies for estimating the pulse characteristics of a wide class of records are of unique value, since the product, $a_pT_p^2=L_p$ is a characteristic length scale of the ground excitation and is a measure of the persistence of the most energetic pulse to generate inelastic deformation (Makris and Black [23],[24]). It is emphasized that the persistence of the pulse, $a_pT_p^2=L_p$, is a different characteristic than the strength of the pulse which is measured with the peak pulse acceleration, a_p. The reader may recall that among two pulses with different acceleration amplitude (say $a_{p1}>a_{p2}$) and different pulse durations (say $T_{p1}<T_{p2}$)

the inelastic deformation does not scale with the peak pulse acceleration (most intense pulse) but with the strongest length scale (larger $a_p T_p^2$ = most persistent pulse), (Makris and Black [23][24], Karavassilis et al. [25])

The heavy dark line in Figure 8 (Top) which approximates the long-period acceleration pulse of the NS component of the 1992 Erzincan, Turkey, record is a scaled expression of the second derivative of the Gaussian distribution, $e^{-t^2/2}$, known in the seismological literature as the symmetric Ricker wavelet (Ricker [26][27])

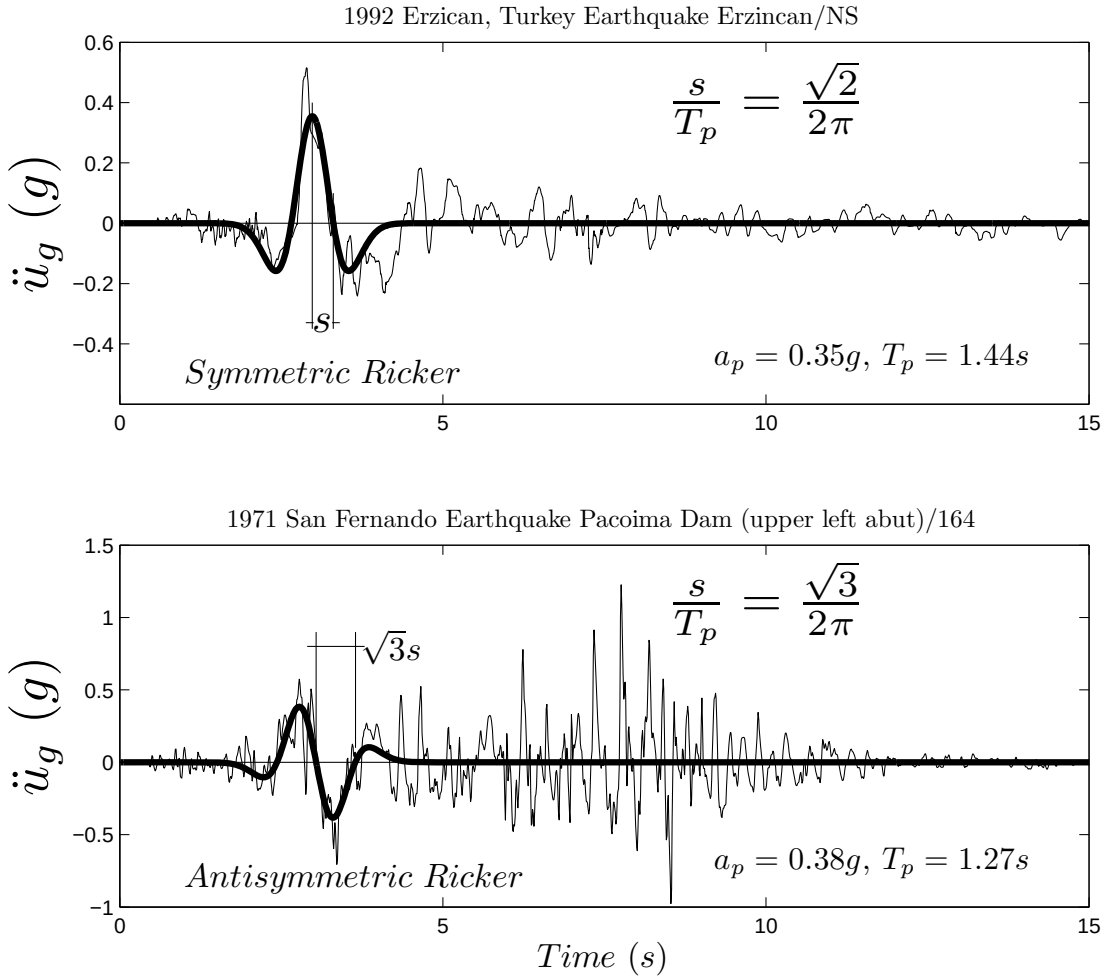


Figure 8: Top: North-South components of the acceleration time history recorded during the 1992 Erzican, Turkey earthquake together with a symmetric Ricker wavelet . Bottom: Fault-normal component of the acceleration time history recorded during the 1971 San Fernando earthquake, together with an antisymmetric Ricker wavelet.

$$\psi(t) = a_p\left(1 - \frac{2\pi^2 t^2}{T_p^2}\right)e^{-\frac{1}{2}\frac{2\pi^2 t^2}{T_p^2}} \tag{44}$$

The value of $T_p = \dfrac{2\pi}{\omega_p}$, is the period that maximizes the Fourrier spectrum of the symmetric Ricker wavelet. Similarly, the heavy dark line in Figure 7 (Bottom) which approximates the long-period acceleration pulse of the Pacoima Dam motion recorded during the February 9,

1971 San Fernando, California earthquake is a scaled expression of the third derivative of the Gaussian distribution $e^{-\frac{t^2}{2}}$.

$$\psi(t) = \frac{a_p}{\beta}\left(\frac{4\pi^2 t^2}{3T_p^2} - 3\right) t e^{-\frac{1}{2}\frac{4\pi^2 t^2}{3T_p^2}} \tag{45}$$

in which β is a factor equal to 1.3801 that enforces the above function to have a maximum equal to a_p.

The choice of the specific functional expression to approximate the main pulse of pulse–type ground motions has limited significance in this work. What is important to recognize is that several strong ground motions contain a distinguishable acceleration pulse which is responsible for most of the inelastic deformation of structures (Hall et al. [17], Makris and Chang [19], Alavi and Krawinkler [20], Makris and Psychogios [28], Karavassilis et al. [23] among others). A mathematically rigorous and easily reproducible methodology based on wavelet analysis to construct the best matching wavelet has been recently proposed by Vassiliou and Makris [22].

Consider the free-standing rocking frame shown in Figure 1 that is subjected to an acceleration pulse (like those shown in Figure 8) with acceleration amplitude a_p and pulse duration, $T_p = \frac{2\pi}{\omega_p}$. From equation (26) it results that the response of a free-standing rocking frame subjected to an acceleration pulse is a function of six variables

$$\theta(t) = f\left(p, \alpha, \gamma, g, a_p, \omega_p\right) \tag{46}$$

The seven variables appearing in equation (46) involve only two reference dimensions; that of length [L] and time [T]. According to Buckingham's Π-Theorem, the number of dimensionless products with which the problem can be completely described is equal to [number of variables = 7] – [number of reference dimensions = 2]=5. Herein we select as repeating variables the characteristics of the pulse-excitation, a_p and ω_p and the five independent Π-products are: $\Pi_\theta=\theta$, $\Pi_\omega=\omega_p/p$, $\Pi_\alpha=\tan\alpha$, $\Pi_\gamma=\gamma$ and $\Pi_g=a_p/g$. With these five dimensionless Π-products, equation (46) reduces to

$$\theta(t) = \varphi\left(\frac{\omega_p}{p}, \tan\alpha, \gamma, \frac{a_p}{g}\right) \tag{47}$$

The rocking response of the free-standing frame shown in Figure 1 when subjected to a horizontal base acceleration history $\ddot{u}_g(t)$ is computed by solving equation (26) in association with the minimum energy loss expression given by equation (43) which takes place at every impact.

Figure 9 shows the minimum overturning acceleration spectra of a free-standing rocking frame when subjected to a symmetric Ricker pulse (left) and an antisymmetric Ricker pulse (right) for different values of the mass ratio $\gamma = \frac{m_b}{Nm_c}$. The top plots are for values of the column slenderness $\alpha=10^o$ and the bottom plots are for $\alpha=14^o$.

In constructing Figure 9, the frequency parameter p is the frequency parameter of the columns of the frame (not $\hat{p}$) and the enhanced stability of the rocking frame due to (a) the cor-

responding larger size, $\hat{p} = \sqrt{\frac{1+2\gamma}{1+3\gamma}}\, p$, and (b) the reduced coefficient of restitution (see equation (43)) is given by the curves for each given value of γ.

Figure 9 indicates that up to values of ω_p/p=4 the additional stability of the rocking frame versus the stability of the equal slenderness solitary column is marginal.

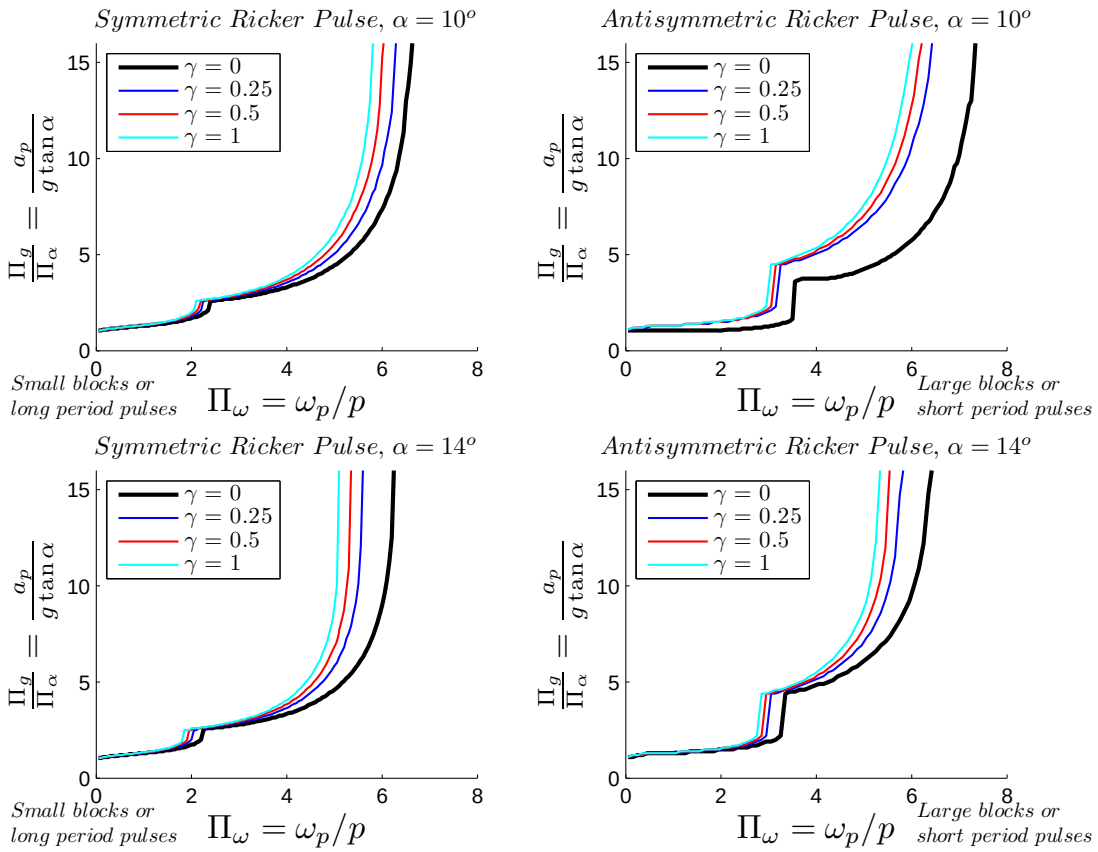


Figure 9: Minimum overturning acceleration spectra of the free-standing rocking frame shown in Figure 1 when subjected to a symmetric Ricker pulse (left) and an antisymmetric Ricker pulse (right) for different values of the mass ratio $\gamma = \frac{m_b}{N m_c}$. Top: α=10°, Bottom α=14°. The values of the coefficient of restitution are give by equation (43).

For values of ω_p/p>4 (larger columns or shorter period pulses) the minimum acceleration overturning spectra of the rocking frame are higher than the corresponding spectrum of the solitary rocking column showing the enhanced seismic stability of the top-heavy rocking frame. This enhanced seismic stability is indifferent to the height of the center of gravity of the cap-beam .

7 SEISMIC STABILITY OF ANCIENT COLUMNS SUPPORTING EPISTYLES AND THE FRIEZE ATOP.

In ancient Greek temples the epistyles are positioned from the vertical axis of one column to the vertical axis of the neighboring column; therefore, the joint of the epistyles are along the vertical axis of the column (see Figure 2). With this configuration during lateral loading of the peristyle of the temple, each epistyle in addition to the horizontal translation, u, shown in

Figure 1 it will also experience a small rotation. Nevertheless, the tendency of the epistyle to rotate is partially prevented from the presence of the neighboring high-profile epistyle and the heavy stone of the frieze atop which goes over the joint of the epistyles. According to this construction pattern with very tight joints the ancient builders constructed a nearly continuous and massive structure atop the columns which according to this study enhanced appreciably the seismic-rocking stability of the peristyle of the temples.

Two of the strongest ground motions recorded in Greece are the 1973 Lefkada record and the 1995 Aigion record (Vassiliou and Makris [22]). Both records exhibit distinguishable acceleration pulses with durations $T_p \approx 0.6$s. We concentrate on the Temple of Apollo in Corinth where its 7.5m×1.8m monolithic columns remain standing since 540BC in an area with high seismicity. The dimensions of its columns yield a frequency parameter $p = \sqrt{\frac{3g}{4R}} = 1.4 rad/s$ and a slenderness $\alpha = \tan^{-1}(b/h) = 13.5^{\circ}$. By taking the pulse duration T_p=0.6s of the nearby Aigion record, the dimensionless term Π_ω assumes the value $\frac{\omega_p}{p} = \frac{2\pi}{pT_p} = 7.5$. For such large value of $\omega_p/p \approx 7.5$ the bottom plots of Figure 9 give for the solitary free-standing column (γ=0 line) an overturning ground acceleration $a_p > 15g\tan\alpha = 15g \times 0.24 = 3.6g$ – which is an unrealistically high acceleration. Consider now the extreme situation for Greece, where the predominant pulse of the ground shaking exhibits a period T_p=0.9s. A pulse period T_p=0.9s may be a rare event for the fault size and earthquake magnitude that prevail in Greece; nevertheless, it helps one understanding the appreciable seismic stability of rocking structures.

With $T_p = 0.9s$ and $p = 1.4 rad/s$, ω_p/p=5 and according to the bottom plots of Figure 9 which are for slenderness $\alpha = 14^{\circ}$, the minimum overturning acceleration of a rocking frame with γ=0.25 exceeds the value of $a_p \approx 5g \times 0.24 = 1.2g$. This analysis shows that the free-standing peristyles of ancient temples can survive acceleration pulses as long as 0.9s and as intense as 1.2g. While this is a physically realizable pulse (Loh et al. [26]), it is an unlikely strong shaking for the seismicity of Greece that apparently never happened over the 2500 years of the lifespan of the temple shown in Figure 2.

8 ROCKING ISOLATION OF BRIDGES – PROOF OF CONCEPT

The concept of allowing the piers of bridges to rock in not new. For instance, the beneficial effects that derive from uplifting and rocking have been implemented since the early 1970s in the South Rangitikei bridge in New Zealand (Beck and Skinner [30]). During the last decade, the benefits /challenges associated with the rocking of bridge piers have been receiving increasing attention partly because of growing interest in the prefabricated bridge technology (Wacker et al. [31], Pang et al. [32], Cohagen et al. [33] and references reported therein) and partly because of the need for the bridge structure to recenter after a strong seismic event (Sakai et al. [34], Cheng [35] among others).

In the prefabricated bridge technology the bridge piers and the deck are not free standing. The structural system is essentially a hybrid system (see Wacker et al. [31], Cheng [35]) where the bridge pier is connected to its foundation and at the deck with a post-tensioned tendon that passes through the axis of the column together with longitudinal mild steel reinforcement running near the circumference of the column. During earthquake loading the majority of deformation is concentrated at the pier-foundation and pier-cap-beam interfaces and the overall deformation pattern of the post-tensioned pier-cap-beam system resembles the deformation pattern of the free-standing rocking frame that is under investigation in this study.

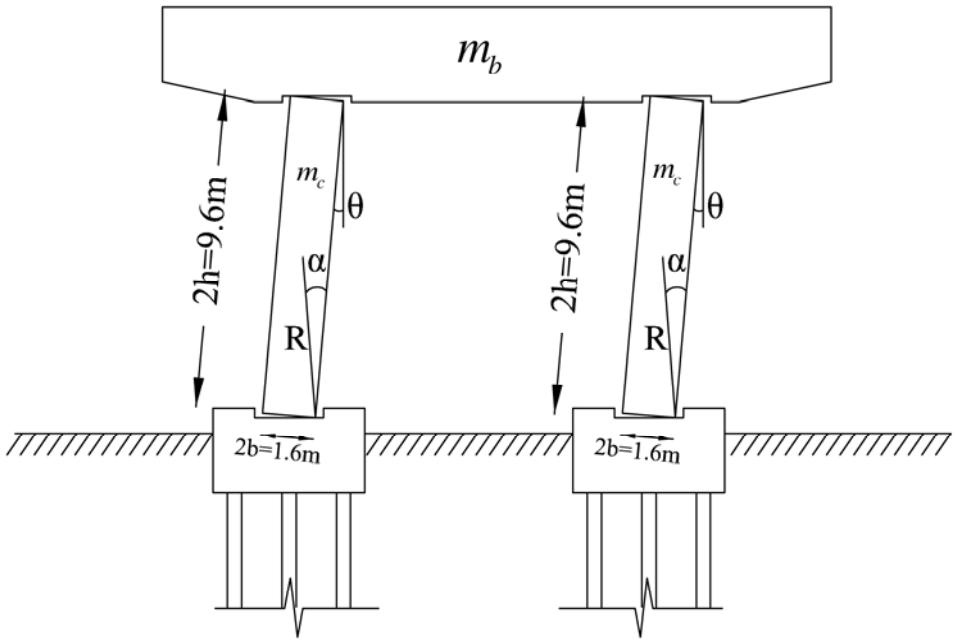


Figure 10: Free Standing rocking bridge bent. Potential sliding during impact is prevented with the recess shown. No vertical post-tensioning, no continuation of the longitudinal reinforcement of the columns through the rocking interfaces at the pile-caps and the cap-beam.

Nevertheless, the post-tensioning tendons and the mild-steel longitudinal reinforcement that extends into the foundation and the cap-beam contributes appreciably to the lateral moment capacity of the system and in most prefabricated bridge applications, the moment-rotation curve of the hybrid systems follows a positive slope.

Within the context of a proof-of-concept, in this study we present the planar rocking response of a free-standing two-column bridge bent where its moment rotation curve follows a negative slope given that the frame is entirely free to rock (see Figure 4). Figure 10 shows schematically the free-standing two-column bridge bent of interest in its deformed configuration. Sliding at the pivot point during impact is prevented with a recess at the pile-cap an the cap-beam as shown in Figure 10. In this numerical application the cylindrical piers of the free-standing bridge bent are 9.6m tall with a diameter $d=2b$=1.6m. These are typical dimensions of bridge piers for highway overpasses and other bridges in Europe and USA. Taller bridge piers will result to even more stable configurations. With $2h$=9.6m and $2b$=1.6m, the slenderness of the bridge pier is $\tan\alpha = \frac{1}{6} = 0.166$ and its frequency parameter p=1.23.

Depending on the length of the adjacent spans and the per-length weight of the deck, the mass ratio $\gamma = \frac{m_b}{2m_c}$ assumes values from 4 and above (γ>4). The larger the value of γ (heavier deck), the more stable is the free standing rocking frame (see Figure 9). The seismic response analysis of the rocking frame has been studied until this section by using as ground excitation acceleration pulses described either by symmetric or the antisymmetric Ricker wavelets. The acceleration amplitude, a_p, and the duration, T_p, of any distinct acceleration pulse allow the use of the dimensional analysis presented in this work and the derivation of the associated Π-products which improve the understanding of the physics that govern the problem together with the organization and presentation of the response. Nevertheless, in order to stress the main finding of this study – that top-heavy free-standing rocking frames enjoy ample seismic

stability – we examine the planar seismic response of the free standing two column bridge bent shown in Figure 10 when subjected to six strong-motion historic records listed in Table 1. The values of the acceleration amplitude, a_p, and pulse period, T_p, shown in last two columns of Table 1 have been determined with the extended wavelet transform (Vassiliou and Makris [22]).

Figure 11 plots the time histories of the normalized rotation, θ/α, together with the vertical uplift, $v(t)$, and the horizontal drift, $u(t)$, of the free standing rocking bridge bent shown in Figure 10 with $\gamma = \dfrac{m_b}{2m_c} = 4$. Note that for all six strong ground motions selected in this analysis the frame rotation, θ, is less than 1/3 of the slenderness, α, of the columns (θ/α<0.33); therefore the free-standing rocking frame exhibits ample seismic stability.

The peak horizontal displacement $u_{\max}$ ranges from 20cm to 50 cm; while the vertical uplift is as high as 5cm. The evaluation of these response quantities shall be conducted in association with the equivalent response quantities from vertically post-tensioned hybrid frames (Wacker et al. [31], Pang et al. [32], Cheng [35]) and seismically isolated decks (Constantinou et al. [36], Makris and Zhang [37], Buckle et al. [38] among others) after considering the effects of the end-conditions of the deck at the abutments. This comparison/evaluation is the subject of an ongoing study which also examines other practical issues such as the effect of the crushing of the pivoting points of the columns (Roh and Reinhorn [39], [40]) and the accommodation of the deck uplift at the end-abutments.

The main conclusion of this study is that heavy decks freely supported on free-standing piers exhibit ample seismic stability and that the heavier is the deck (even if the center of gravity rises) the more stable is the rocking frame. This conclusion may eventually lead to the implementation of the free-standing rocking frame – a structural configuration where all the issues associated with seismic connections such as buckling and fracture of the longitudinal reinforcing bars or spalling of the concrete cover [31-35] are removed as they are not an issue in the ancient temple shown in Figures 2.

Earthquake	Record	Magnitude (Mw)	Epicentral Distance (km)	PGA (g)	PGV (m/s)	a_p (g)	T_p (s)
1966 Parkfield	CO2/065	6.1	0.1	0.48	0.75	0.41	0.6
1971 San Fernando	Pacoima Dam/164	6.6	11.9	1.23	1.13	0.38	1.27
1986 San Salvador	Geotech Investig. Center	5.4	4.3	0.48	0.48	0.34	0.8
1992 Erzican,	Erzincan/EW	6.9	13	0.50	0.64	0.34	0.9
1994 Northridge	Jensen Filter Plant/022	6.7	6.2	0.57	0.76	0.39	0.5
1995Kobe	Takarazuka/000	6.9	1.2	0.69	0.69	0.50	1.1

Table 1: Earthquake records used for the seismic response analysis of the free-standing rocking bridge bent.

9 CONCLUSIONS

This paper investigated the planar rocking response of an array of free-standing columns capped with a freely supported rigid beam. Following a variational formulation, the paper concludes to the remarkable result that the dynamic rocking response of an array of free

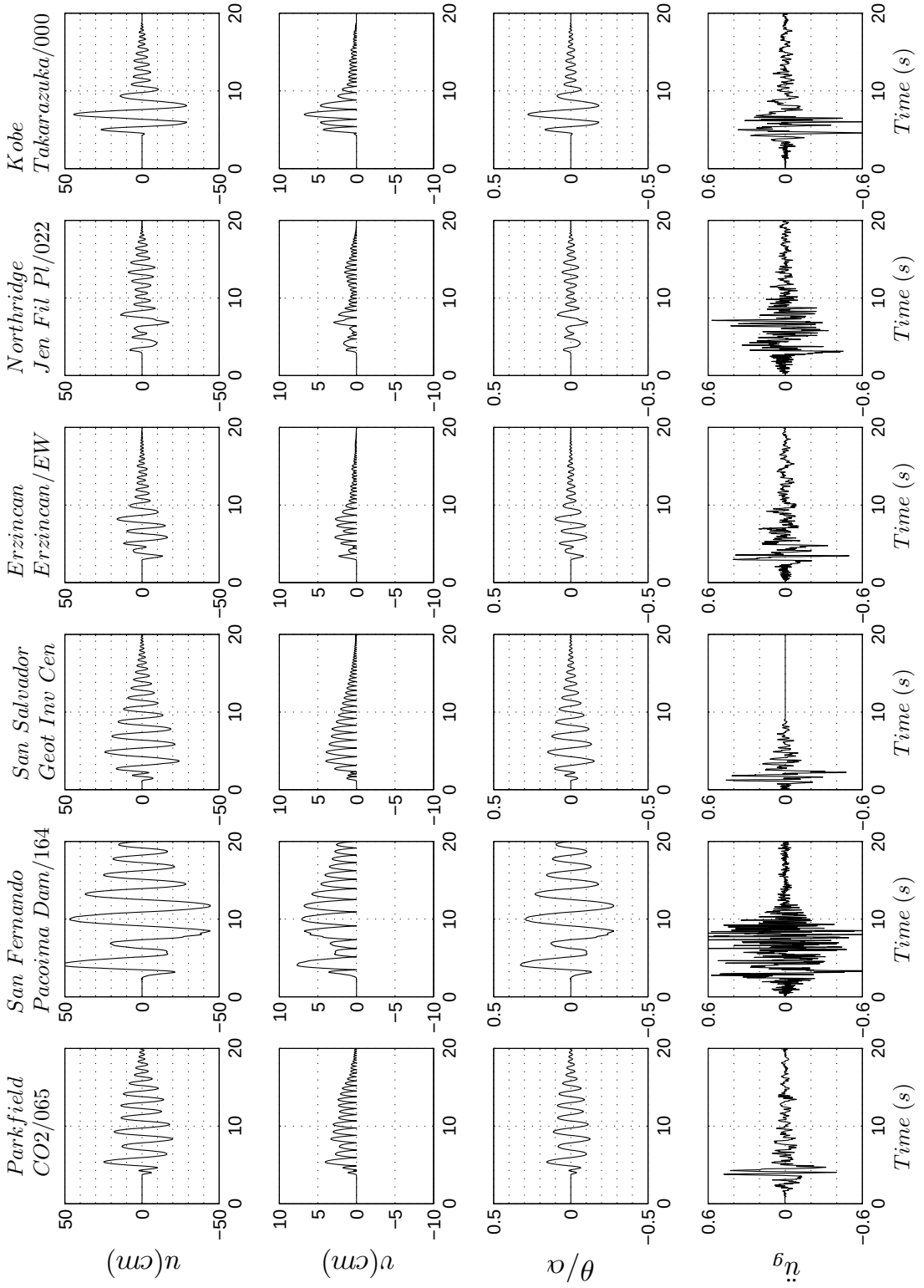


Figure 11: Rotation, vertical and horizontal displacement histories of the free standing rocking frame shown in Figure 10 (p=1.23, tanα=1/6, γ=4) when subjected to the recorded ground motions listed in Table 1.

standing columns capped with a rigid beam is identical to the rocking response of a single free standing column with the same slenderness as the slenderness of the columns of the rocking frame; yet with larger size and more energy loss during impacts. A larger size rocking column

corresponds to a more stable configuration; therefore, the presence of the freely supported cap-beam renders the rocking frame more stable despite the rise of the center of gravity.

Most importantly, the study shows that the heavier the freely supported cap-beam is, the more stable is the rocking frame concluding that top-heavy rocking frames are more stable than when they are top-light. The stability of the rocking frame is independent to the number of columns and depends only on the ratio of the weight that is transferred to the column to the weight of the column together with the size and the slenderness of the columns.

The acceleration needed to create uplift of the rocking frame is independent to the mass and the height of the center of gravity of the cap-beam and depends only on the slenderness, α, of the columns ($u_g^{up} = g \tan\alpha$).

The findings above render rocking isolation a most attractive alternative for the seismic protection of bridges given that the heavier is the deck the more stable is the rocking bridge. The future implementation of a truly rocking frame where there is neither post-tensioning nor continuation of the longitudinal reinforcement through the rocking interfaces shall remove several of the concerns associated with the seismic connections of prefabricated bridges such as buckling and fracture of the longitudinal reinforcing bars or spalling of the concrete cover.

10 ACKNOWLEDGEMENTS

Partial financial support for this study has been provided to the first author by the Alexander S. Onassis Public Benefit Foundation and by the EU research project "DARE" ("Soil-Foundation-Structure Systems Beyond Conventional Seismic Failure Thresholds: Application to New or Existing Structures and Monuments"), which is funded through the 7th Framework Programme "Ideas", Support for Frontier Research – Advanced Grant, under contract number ERC-2—9-AdG 228254-DARE to professor G. Gazetas.

REFERENCES

[1] Milne, J. (1885). Seismic experiments. *Trans. Seism. Soc. Japan*, 8, 1–82.

[2] Housner, G. W. The behaviour of inverted pendulum structures during earthquakes. *Bulletin of the Seismological Society of America.* 1963; **53(2)**: 404–417.

[3] Yim CS, Chopra AK, Penzien J. Rocking response of rigid blocks to earthquakes. *Earthquake Engineering and Structural Dynamics* 1980; **8**(6):565–587.

[4] Aslam, M., Scalise, D. T., and Godden, W. G. (1980). ''Earthquake rocking response of rigid bodies.'' *J. Struct. Div.,* ASCE, 106(2), 377–392.

[5] Psycharis, I. N. and Jennings, P. C. (1983), Rocking of slender rigid bodies allowed to uplift. *Earthquake Engineering & Structural Dynamics*, 11: 57–76. doi: 10.1002/eqe.4290110106

[6] Spanos, P. D., and Koh, A. S. (1984). Rocking of rigid blocks due to harmonic shaking. *Journal of Engineering Mechanics*., ASCE, 110(11), pp1627–1642.

[7] Hogan, S. J. (1989). On the dynamics of rigid-block motion under harmonic forcing. *Proceedings of the Royal Society*., London, A425, 441–476.

[8] Hogan, S. J. (1990). The many steady state responses of a rigid block under harmonic forcing. *Earthquake Engineering and Structural Dynamics*, 19(7), 1057–1071.

[9] Zhang J, Makris N. Rocking response of free-standing blocks under cycloidal pulses. *Journal of Engineering Mechanics*, ASCE 2001; 127(5):473–483.

[10] Makris, N. and Konstantinidis, D. (2003), The rocking spectrum and the limitations of practical design methodologies. *Earthquake Engineering & Structural Dynamics*, 32, pp265–289.

[11] Prieto, F., Lourenço, P. B. and Oliveira, C. S. (2004), Impulsive Dirac-delta forces in the rocking motion. *Earthquake Engineering & Structural Dynamics*, 33: 839–857. doi: 10.1002/eqe.381

[12] Apostolou M, Gazetas G, Garini E. Seismic response of slender rigid structures with foundation uplift. *Soil Dynamics and Earthquake Engineering* 2007; 27:642-654

[13] Palmeri, A. and Makris, N. (2008), Response analysis of rigid structures rocking on viscoelastic foundation. *Earthquake Engineering & Structural Dynamics*, 37: 1039–1063. doi: 10.1002/eqe.800

[14] Vassiliou, M. F. and Makris, N. (2011), Analysis of the rocking response of rigid blocks standing free on a seismically isolated base. *Earthquake Engineering & Structural Dynamics*. doi: 10.1002/eqe.1124

[15] Makris N, Roussos Y. Rocking response of rigid blocks under near-source ground motions. *Geotechnique* 2000; **50**(3):243–262.

[16] Veletsos AS, Newmark NM, Chelepati CV. Deformation spectra for elastic and elastoplastic systems subjected to ground shock and earthquake motions. *Proceedings of the 3rd World Conference on Earthquake Engineering*, vol. II, Wellington, New Zealand, 1965; 663–682.

[17] Hall JF, Heaton TH, Halling MW, Wald DJ. Near-source ground motion and its effects on flexible buildings. *Earthquake Spectra* 1995; **11**(4):569 –605.

[18] Makris N. Rigidity–plasticity–viscosity: can electrorheological dampers protect base-isolated structures from near-source ground motions? *Earthquake Engineering and Structural Dynamics* 1997; **26**:571–591.

[19] Makris N, Chang S-P. Effect of viscous, viscoplastic and friction damping on the response of seismic isolated structures. *Earthquake Engineering and Structural Dynamics 2000*; **29**(1):85–107.

[20] Alavi B, Krawinkler H. Effects of near-source ground motions on frame-structures. *Technical Report No. 138*, The John A. Blume Earthquake Engineering Center, Stanford University, 2001.

[21] Mavroeidis GP, Papageorgiou AS. A mathematical representation of near-fault ground motions. *Bull. Seism. Soc. Am. 2003;* **93**(3):1099 –1131.

[22] Vassiliou MF, Makris N, Estimating Time Scales and Length Scales in Pulse-Like Earthquake Acceleration Records with Wavelet Analysis, *Bulletin of the Seismological Society of America.* April 2011.

[23] Makris N, Black CJ. Dimensional analysis of rigid-plastic and elastoplastic structures under pulse-type excitations. *Journal of Engineering Mechanics* (ASCE) 2004; **130**(9):1006–1018.

[24] Makris N, Black CJ. Dimensional Analysis of Bilinear Oscillators under Pulse-Type Excitations *Journal of Engineering Mechanics* (ASCE) 2004 **130**(9) 1019-1031.

[25] Karavasilis, T. L., Makris, N., Bazeos, N., and Beskos, D. E. (2010). "Dimensional response analysis of multistory regular steel MRF subjected to pulselike earthquake ground motions." *J. Struct. Eng*., 136(8), 921–932.

[26] Ricker N. Further developments in the wavelet theory of seismogram structure. *Bulletin of the Seismological Society of America* 1943; **33,** 197-228.

[27] Ricker N. Wavelet functions and their polynomials, *Geophysics* 1944 **9,** 314–323.

[28] Makris N. and C. Psychogios (2006) Dimensional response analysis of yielding structures with first-mode dominated response. *Earthquake Eng. Struct. Dyn*, 35, 1203–1224

[29] Loh, C.-H., Lee, Z.-K., Wu, T.-C. and Peng, S.-Y. (2000), Ground motion characteristics of the Chi-Chi earthquake of 21 September 1999. *Earthquake Engineering & Structural Dynamics*, 29: 867–897.

[30] Beck, J. L. and Skinner, R. I. (1974), The seismic response of a reinforced concrete bridge pier designed to step. *Earthquake Engineering & Structural Dynamics*, 2, 343–358.

[31] Wacker, JM, Hieber, D.G, Stanton JF and Eberhard, MO 2005 "Design of Precast Concrete piers for Rapid Bridge Construction in Seismic Regions", *Research Report*, Federal Highway Administration

[32] Pang, JBK, Stenk KP, Cohagen L, Stanton JF and Eberhard, MO, 2008 "Rapidly Constructible Large-Bar precast Bridge-Bent Seismic Connection", *Research Report WA-RD684.2*, Washington State Department of Transportation

[33] Cohagen L., Pang JBK, Stanton JF and Eberhard MO, 2008 "A precast Concrete Bridge Bent Designed to Recenter after an Earthquake", *Research Report*, Federal Highway Administration

[34] Sakai J, Hyungil J, Mahin S, 2006, "Reinforced concrete bridge columns that re-center following earthquakes", *Proceedings of the 8th US National Conference on Earthquake Engineering*, April 18-22, 2006 San Francisco, California, USA

[35] Cheng CT, 2008 "Shaking table tests of a self-centering designed bridge substructure". *Engineering Structures*, (30) 3426-3433

[36] Constantinou MC, Soong TT and Dargush GF 1998, "Passive energy dissipation Systems for Structural Design and Retrofit", *Monograph Series*, MCEER, University of Buffalo, NY

[37] Makris N, J Zhang, 2004, "Seismic response analysis of Highway Overcrossings Equipped with Elastomeric Bearings and Fluid Dampers", *Journal of Structural Engineering*, ASCE, Vol. 130, No.6, 2004, pp.830-845

[38] Buckle IG, Constantinou MC, Diclali M and Chasemi H. 2006 "Seismic Isolation of Highway Bridges", *Research Report MCEER-06-SP07*, MCEER, University of Buffalo, NY.

[39] Roh H, Reinhorn A, 2010 Nonlinear Static Analysis of Structures with Rocking Columns, *Journal of Structural Engineering,* ASCE Vol. 136, No. 5, pp. 532-542

[40] Roh H, Reinhorn A, 2010 "Modeling and seismic response of structures with concrete rocking columns and viscous dampers". *Engineering Structures*, (32) 2096-2107

COMPDYN 2013
4th ECCOMAS Thematic Conference on
Computational Methods in Structural Dynamics and Earthquake Engineering
M. Papadrakakis, V. Papadopoulos, V. Plevris (eds.)
Kos Island, Greece, 12–14 June 2013

ROCKING RESPONSE OF SLENDER, FLEXIBLE COLUMNS UNDER PULSE EXCITATION

Michalis F. Vassiliou[1], Kevin R. Mackie[2] and Božidar Stojadinović[1]

[1]Institute of Structural Engineering (IBK), Swiss Federal Institute of Technology (ETHZ),
Wolfgang-Pauli-Strasse 15, 8093, Zürich, Switzerland
email: vassiliou@ibk.baug.ethz.ch and stojadinovic@ibk.baug.ethz.ch

[2]University of Central Florida,
Civil Environmental and Construction Engineering Department, Engr II 402, 4000 Central Florida Blvd., Building 91, Suite 211, Orlando, Florida 32816-2450
email: kmackie@mail.ucf.edu

Keywords: Rocking, Earthquake Engineering, Seismic Isolation

Abstract. *Early studies of the response of rigid blocks allowed to uplift and rock under seismic motion have shown a scale effect that characterizes the response of rocking blocks subjected to a ground motion. Namely; larger objects need a larger ground acceleration to overturn; and longer dominant period earthquakes have a larger overturning capability than shorter period ones. This is why it has been proposed that rocking can be used as an isolation strategy. However, actual structures are not rigid: structural elements where rocking is expected to occur are often slender and flexible. Modeling rocking of flexible bodies is a challenging task. A finite element model of a rocking elastic body that does not involve explicit modeling of impact is presented in this paper. This model was validated by comparing its response to pulse excitation with an analytical solution. It is concluded that the extensively studied rigid rocking block model provides a good approximation of the seismic response of an elastic rocking column for small-size columns and that it provides a conservative response estimate for larger columns. Guidance for development of rocking column models in ordinary finite element software is provided.*

1 INTRODUCTION

Early studies of the response of rigid blocks allowed to uplift and rock under seismic motion have been presented by Milne [1]. Housner [2] has shown a scale effect that characterizes the response of rocking blocks subjected to a ground motion: a) Larger objects need a larger ground acceleration to overturn b) Longer period earthquakes have a larger overturning capability than shorter period ones. For pulse-like records, the above results are presented in the form of rocking spectra in the papers by Zhang and Makris [3] and Makris and Konstantinidis [4]. In the latter paper it is shown that the representation of a rigid rocking block as a SDOF linear elastic system, a representation adopted by building codes (FEMA 356) is fundamentally flawed. In the present paper, it is shown that rigid rocking blocks can be modeled as SDOF nonlinear-elastic viscously-damped systems. This modeling makes possible the use ordinary FEM software equipped with nonlinear elastic elements and with nonlinear geometry capabilities to model the rocking response not only of rigid but of flexible blocks as well. Hence it can be used to study the influence of flexibility on the response of rocking structures, a phenomenon that has been examined by Psycharis [5], Olivetto et al. [6], Apostolou et al. [7] and recently by Acikgoz and DeJong [8]. The interest on the influence of the flexibility of structures on their rocking behavior originates from the studies on the feasibility of using rocking as an isolation technique with small residual displacements (Apostolou et al. [7], Gelagoti et al [9], Makris and Vassiliou [10]). It is worth mentioning that a bridge that uses rocking as an isolation technique has already been built in the Rangitikei river in New Zealand in 1981 (Beck and Skinner [11]). Moreover, it has been shown that ancient columns have survived earthquakes for more than 2,500 years due to their ability to sustain rocking motion without overturning (Konstantinidis and Makris [12])

2 REVIEW OF THE ROCKING RESPONSE OF A RIGID BLOCK.

With reference to Figure 1 (top left) and assuming there is no sliding, the equation of motion of a free standing block with size $R=\sqrt{h^2+b^2}$ and slenderness α=atan(b/h) subjected to a horizontal ground acceleration $\ddot{u}_g(t)$, when rocking around O and O' respectively is (Yim et al. [13], Makris and Roussos [14], Zhang and Makris [3], among others)

$$I_o\ddot{\theta}(t)+mgR\sin\left[\alpha\,\mathrm{sgn}\,\theta(t)-\theta(t)\right]=-m\ddot{u}_g(t)R\cos\left[\alpha\,\mathrm{sgn}\,\theta(t)-\theta(t)\right] \tag{1}$$

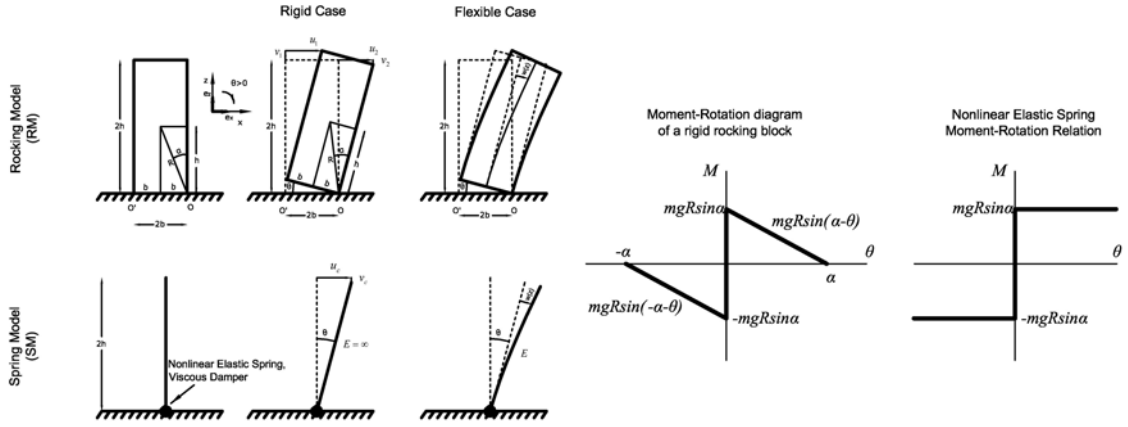


Figure 1. Left: Original Rocking Model (RM) and proposed Spring Model (SM). Right: Moment-rotation diagram of a rigid rocking block with slenderness α and size R; and Moment-Rotation relationship of the non linear elastic spring (unloads on the same path) used in the Spring Model.

For rectangular blocks, $I_o = (4/3)mR^2$ and the above equations can be expressed in the compact form

$$\ddot{\theta}(t) = -p^2 \left\{ \sin\left[\alpha \operatorname{sgn}\left(\theta(t)\right) - \theta(t)\right] + \frac{\ddot{u}_g}{g} \cos\left[\alpha \operatorname{sgn}\left(\theta(t)\right) - \theta(t)\right] \right\} \tag{2}$$

where $p = \sqrt{3g/4R}$.

Figure 1 (Right) shows the moment-rotation relationship during the rocking motion of a free-standing block. The system has infinite stiffness until the magnitude of the applied moment reaches the value $mgR\sin\alpha$, and once the block is rocking, its restoring force decreases monotonically, reaching zero when $\theta = \alpha$. This negative stiffness, which is inherent in rocking systems is most attractive in earthquake engineering in terms of keeping base shears and moments low (Makris and Konstantinidis [4]) provided that the rocking block remains stable.

During the oscillatory rocking motion, the moment-rotation curve follows the curve shown in Figure 1 (Right) without enclosing any area. Energy is lost only during impact, when the angle of rotation reverses. Conservation of angular momentum an instant before the impact and immediately after the impact gives:

$$r = \frac{\dot{\theta}_2^2}{\dot{\theta}_1^2} = [1 - \frac{3}{2}\sin^2\alpha]^2 \tag{3}$$

3 SDOF NONLINEAR ELASTIC VISCOUSLY DAMPED RIGID EQUIVALENT SYSTEM

Equations (2) and (3) can be easily solved with a numerical computing package (e.g. MATLAB [15]). However, the equations of more complex rocking structures or flexible rocking structures become much more complicated and their solution becomes cumbersome. Therefore, an equivalent SDOF nonlinear elastic viscously damped Spring Model (SM) is proposed (Figure 1). In this section the proposed Spring Model will be tested via a comparison with rigid rocking blocks and in the next section it will be used to examine the rocking behavior of finite stiffness columns.

The proposed model consists of a cantilever vertical column with crossection identical to the crossection of the rocking block connected to a nonlinear elastic spring (that unloads on the same path that it loads) with yield moment equal to *mgRsin(α)*, yield rotation tending to zero and zero post yielding stiffness (Figure 1) in parallel with a viscous damper with damping coefficient *c*. Note that in order for the two models to be equivalent (softening moment-rotation behavior after yield) *P-Δ* effects and large displacements should be taken into account. When the Spring Model is tested against the Rocking Model (RM) (i.e. the numerical solution of equation (2)), the young modulus, *E*, of the column material is taken very large so that the column does not bend.

The proposed Spring Model can be easily implemented in FEM software like OpenSees [16] or commercial products.

3.1 Comparison of the equations of motion

The equation of motion of the Spring Model (not taking into account damping) is

$$I_o'\ddot{\theta}(t) + mgR\left(\sin\alpha \operatorname{sgn}\theta - \cos\alpha \sin\theta\right) = -m\ddot{u}_g R\cos\alpha\cos\theta \tag{4}$$

where

$$I_o' = \frac{4}{3} mR^2 \cos^2 \alpha \tag{5}$$

Assuming $\cos\theta \simeq 1$ and $\sin\alpha \sin\theta \ll 1$, the equation of motion of a rigid rocking block (equation (1)) reduces to

$$I_o \ddot{\theta}(t) + mgR\left(\sin\alpha \operatorname{sgn}\theta - \cos\alpha \sin\theta\right) = -m\ddot{u}_g R \cos\alpha \cos\theta \tag{6}$$

If α is small, $\cos^2 \alpha \to 1$ and equations (4) and (6) become identical.

The moment of inertia appearing in equation (1) refers to rotational moment around the pivot point ($I_o = \frac{4}{3} mR^2$). However, assigning just translational masses in the FEM implementation of the spring model, give a moment of inertia given by equation (5). For this reason the Spring Model is enhanced by evenly distributing the difference $\Delta I_o = \frac{4}{3} mR^2 \left(1 - \cos^2 a\right)$ between all the rotational degrees of freedom of the vertical column. Initially assuming zero damping for both models, Figure 2 (left) plots time histories (obtained with OpenSees) of the response of a rigid (E=10^{11}kPa) block with height 2h=10m, and tanα=0.1, 0.2 and 0.3, when excited by a symmetric Ricker [17] pulse excitation with a_p = 4$g$tanα and ω_p=2π rad/s (Figure 2 – bottom). No damping is included in either of the models. The results show good agreement of the two methods.

3.2 Treatment of energy dissipation

Energy dissipation in rocking blocks takes place instantaneously at each impact. On the contrary the proposed model is equipped with a viscous damper at its base, a damping mechanism that dissipates energy continuously. However, viscous damping models are widely used to describe different kinds of energy dissipation (as long as it is not large). For example, the opening and closing of cracks in concrete, an energy dissipation mechanism that is similar to the mechanism of rocking, is widely modeled with viscous damping. This is why even though these two energy dissipation mechanisms act differently, this paper attempts to match the two dissipating mechanisms in terms of maximum rotation of the system.

In order determine the appropriate value of the viscous damping coefficient and assuming that it would not strongly depend on the column flexibility (an assumption that needs to be verified either experimentally or by more sophisticated numerical models), energy loss during the free vibration both of the Rocking Model and of the Spring Model will be studied.

In the case of the Rocking Model the energy dissipation per cycle of free vibration is independent of the amplitude of vibration and is described by the restitution factor r. The ratio of the energy after one complete cycle, E, to the initial energy, E_o, is

$$\frac{E}{E_o} = r^2 = \left(1 - \frac{3}{2}\sin^2 \alpha\right)^4 \tag{7}$$

Accordingly, for the Spring Model and for initial conditions $\theta(0) = \theta_o$ and $\dot{\theta}(0) = 0$ the corresponding ratio, ξ, is a function of 6 variables:

$$\frac{E}{E_o} = \xi = f\left(m, \alpha, R, g, \theta_o, c\right) \tag{8}$$

Each term of equation (8) includes only 3 reference dimensions ($\xi \doteq []$, $\alpha \doteq []$, $R \doteq [\mathrm{L}]$, $g \doteq [\mathrm{LT}^{-2}]$, $\theta_o \doteq []$,$c \doteq [\mathrm{ML}^2\mathrm{S}^{-1}]$). Hence, according to Buckinghams's Π theorem of dimensional analysis [18], equation (8) can be transformed into

$$\frac{E}{E_o} = \xi = \varphi\left(\frac{\theta}{\alpha}, \alpha, \frac{c}{mg^{0.5}R^{1.5}}\right) \tag{16}$$

Figure 3 plots Equation (9) for $0<\theta/\alpha<1$, $\tan\alpha = 0.1$, 0.2 and 0.3, and $\frac{c}{mg^{0.5}R^{1.5}}$=0.02, 0.08 and 0.18 respectively. The plot shows that a) The value of α is immaterial to ξ and b) that for $\theta/\alpha>0.5$, ξ only lightly depends on θ/α. Hence for $\theta/\alpha>0.5$ and $\alpha<0.3$, equation (16) reduces to

$$\frac{E}{E_o} = \xi = \varphi\left(\frac{c}{mg^{0.5}R^{1.5}}\right) \tag{10}$$

Equations (7) and (10) indicate that by equating the energy loss in a free vibration, a relation between $\frac{c}{mg^{0.5}R^{1.5}}$ and α can be determined so that the energy losses during a free vibration cycle of the two models is the same (at least for $\theta/\alpha>0.5$). Based on Figure 3, an analytical approximation would be

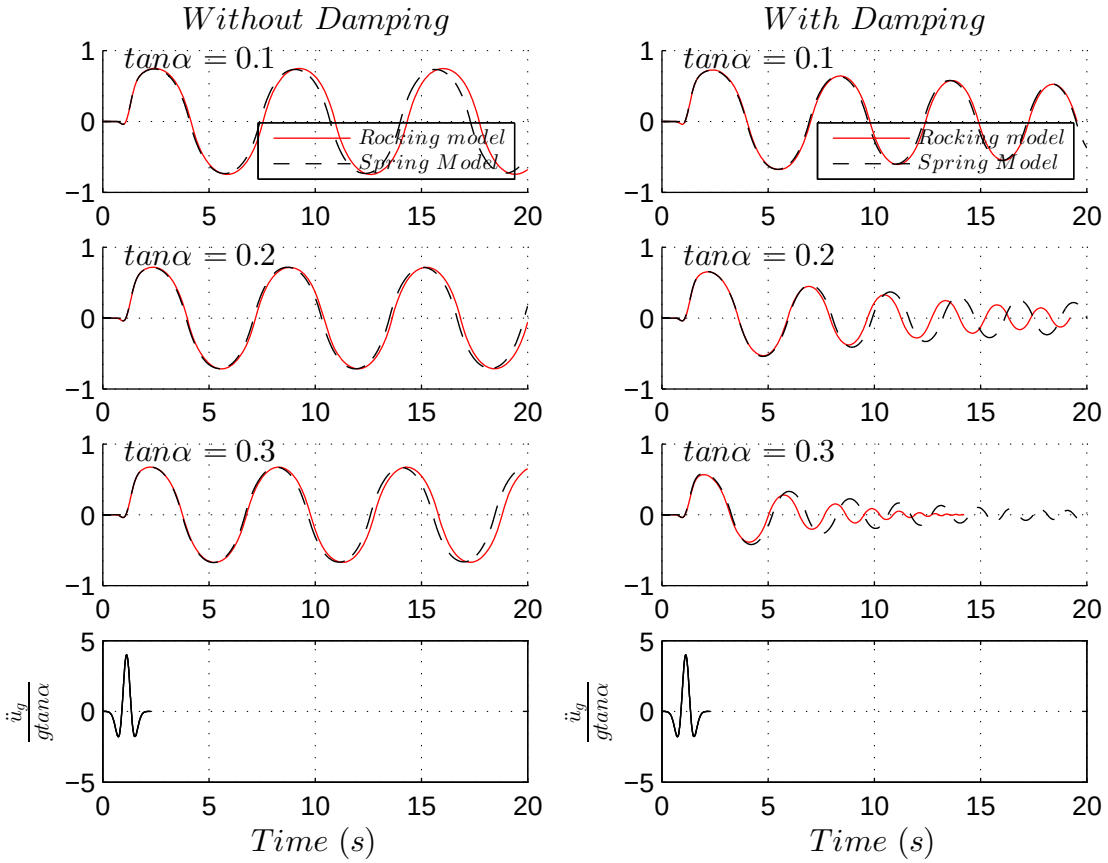


Figure 2. Time histories of the response of a rigid block with height 10m and slenderness tanα=0.1, 0.2 and 0.3 (top 3 rows), when excited by a symmetric Ricker pulse excitation with $a_p = 4g\tan\alpha$ and $\omega_p=2\pi$ rad/s (bottom row). The response was computed with the Rocking Model (RM) and the Spring Model (SM).

$$\frac{c}{mg^{0.5}R^{1.5}} = 0.02\left(\frac{\alpha}{0.1}\right)^2 \tag{11}$$

ElGawady et al. [19] have shown that the energy dissipation at every impact not only depends on slenderness, α, but it strongly depends on the interface material as well. Therefore the exact correlation of the damping of the two models is inherently non feasible and further investigation should be performed to correlate the damping coefficient to the real model taking into account the interface material.

Figure 2 (right) plots time histories of the response to a symmetric Ricker [17] pulse excitation (damping included). In all cases the proposed model is able to accurately predict the maximum rotation of the base. For the most slender case ($\tan\alpha$=0.1) it is able to predict accurately the whole time history. Its inability to predict the whole time history for the least slender case ($\tan\alpha$=0.3) is due to the inherently sensitive highly nonlinear nature of the rocking problem: The period of free vibration depends on the amplitude of the motion. Hence a small error in the estimation of the amplitude leads to error in the prediction of the phase of the motion. Accordingly, Figure 4 plots the overturning spectra for the two models demonstrating the ability of the Spring Model (SM) to approximate well the results of the Rocking Model (RM).

4 EXTENTION TO FLEXIBLE SYSTEMS

Even though rocking of rigid structures has been studied extensively relatively few studies have been carried on the influence of the flexibility of a structure on its rocking behavior. This section attempts to shed light on the interaction of elasticity and rocking of flexible blocks and to examine the limits of the validity of the rigid block assumption. This is accomplished by extending the method developed in the previous section to study the behavior of flexible rocking columns. The model examined is shown in Figure 1. It is an Euler-Bernoulli beam (made out of a material with young modulus E and density ρ) that is allowed to uplift. Roh and Reinhorn [20] performed experiments on rocking concrete columns and proved that, for low values of axial force, spalling of concrete does not occur when the column uplifts. Therefore, it is reasonable to assume that, in the column examined in this section, the axial

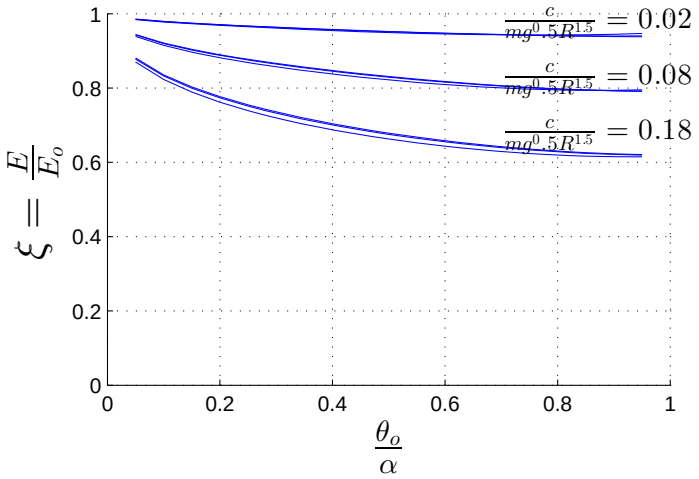


Figure 3 Damping ratio, ξ, plotted against the normalized initial angle of rotation θ_o/α for free vibrations of the Spring Model for different values of α and $\frac{c}{mg^{0.5}R^{1.5}}$.

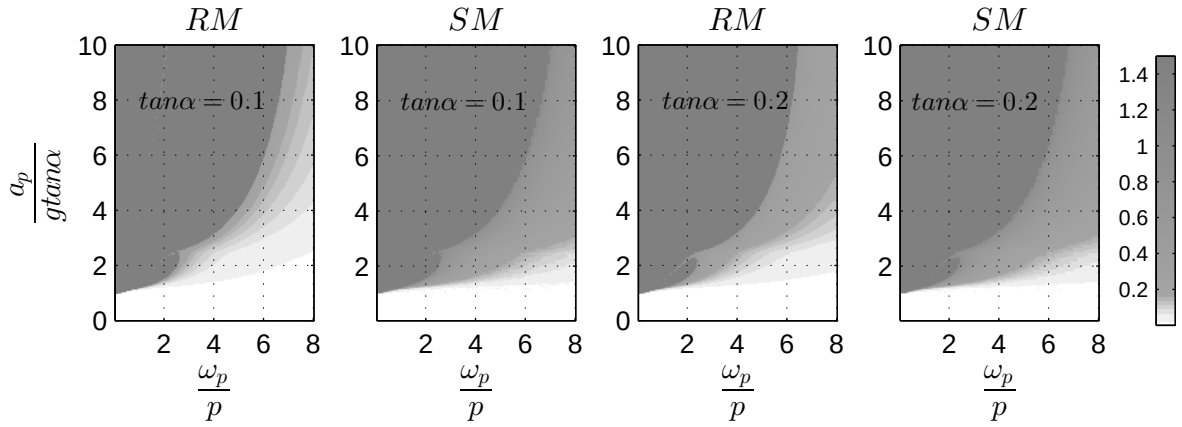


Figure 4 Contour plots of the maximum rotation of rigid blocks subjected to a symmetric Ricker pulse.

force of which is only due to its self weight, no spalling will occur and the column will rotate around points O and O'. Moreover, since the axial force is small, it is assumed that the curvature at the base of the column when rocking initiates will be negligible. In the presence of extra axial load this curvature might not be negligible and the yield rotation of the Spring Model should be adjusted accordingly. The damping ratio, ζ, is the damping ratio of the column prior to its uplift, i.e. The damping ratio for a fixed cantilever column.

4.1 Dimensional analysis of the system

The overturning instability of a flexible rocking column subjected to a symmetric Ricker pulse is described by its base rotation and is a function of 7 variables.

$$\theta(t) = f\left(a_p, \omega_p, g, R, \alpha, \zeta, \rho, E\right) \tag{12}$$

Each term of equation (12) includes only 3 reference dimensions ($a_p \doteq [\,LT^{-2}]$, $\omega_p \doteq [T^{-1}]$, $g \doteq [LT^{-2}]$, $R \doteq [L]$, $\alpha \doteq []$, $\zeta \doteq []$, $\rho \doteq [ML^{-3}]$, $E \doteq [ML^{-1}S^{-2}]$). Hence, according to Buckinghams's Π theorem of dimensional analysis [18], equation (12) can be transformed into

$$\theta(t) = \varphi\left(\frac{a_p}{g\tan\alpha}, \frac{\omega_p}{p}, \alpha, \zeta, \frac{E}{\rho g R}\right) \tag{12}$$

From the above equation it can be seen that the response of the column depends on the ratio *E/R*. Hence, it is expected that the flexibility of the columns will have a more significant effect on larger columns. Moreover, since for a specified material, the Young modulus, *E*, and the density, ρ, are constant, the dimensionless flexibility $\frac{E}{\rho g R}$ solely depends on the size of the column.

It is worth noting that, for specified material properties, *E* and ρ, and slenderness α, the first eigenperiod of the column before uplift depends only on its size

$$T_1 = 12.38\sqrt{\frac{\rho}{E}}\frac{h}{\tan\alpha} \tag{13}$$

The flexible rocking column is studied via the proposed FEM model by using a material with finite stiffness. Energy dissipation due to impact is modeled by the same type of viscous damper that was used for the rigid case. Energy dissipation inside the column is modeled by

applying Rayleigh damping only at the nodes of the column (an option available in OpenSees). This is because applying Rayleigh Damping to the whole the model would result in excessive overall damping due to the very large pre yielding stiffness of the spring used to model the rocking behavior.

Figure 5 plots the contour plots of the maximum rotation over slenderness, θ/α, at the base of a concrete column with Young modulus E=30GPa and density ρ=2.5Mg/m^3 subjected to a symmetric Ricker pulse of amplitude a_p and cyclic frequency ω_p. Since most of the energy dissipation occurs at the base of the rocking column, the damping ratio, ζ, of the cantilever column was set to 0.01. The response was computed using the Spring Model implemented in OpenSees.

Figure 6 plots the minimum overturning acceleration spectra (i.e. the minimum acceleration required to overturn the concrete column) for several values of slenderness and height. It also shows the acceleration required to uplift the column. The plots show that for columns with tanα>0.2, the flexibility of the column is immaterial to the overturning stability and the rigid model gives accurate results.

For smaller values of tanα, Figure 6 indicates that the flexibility of the concrete column decreases the acceleration needed to cause uplift to values less than $g$tanα. This is because, for the range of ω_p/p plotted, the eigenperiods of the concrete column fall in the spectral region where the spectral acceleration is larger than PGA. Concerning the minimum acceleration to overturn the column, Figure 6 shows that for ω_p/p<4.5 the concrete column is less stable than the rigid column while for ω_p/p>4.5 the concrete column exhibits superior stability. It is worth noting that for columns large enough for their flexibility to influence their rocking response, small values ω_p/p correspond to pulses with unrealistically large periods. Hence, flexibility becomes important only for the region where it is beneficiary to the response. Therefore it is concluded that the results of solitary rigid columns analysis are applicable to solitary concrete columns because they are either accurate (for small size columns) or at the safe side (for larger size columns).

In an attempt to examine the interaction of elasticity and rocking, Figure 7 plots the response of a rigid and a concrete column with dimensions $2h$=$50m$ and $2b$=$5m$ when excited by symmetric Ricker pulses with ω_p/p=3 (T_p=3.87s) and ω_p/p=6 (T_p=1.93s) and acceleration amplitude a_p/gtanα=2.6 (a_p=2.55m/s^2) and a_p/gtanα=5.85 (a_p=5.74m/s^2). The first row plots the normalized rotation at the base of the column, θ/α and the second row plots the flexural deformation at the top of the column, w, i.e. the difference between the total top displacement and the top displacement due to base rotation. The plot indicates that at each impact the deformation at the top caused by flexure reverses. This reversal generates flexural vibration at the column. Hence, part of the rotational kinetic energy of the column is transformed into high frequency flexural vibration energy, which cannot cause the column to overturn. This transformation is the reason for which the concrete is more stable than the rigid column for ω_p/p=6 (left). On the contrary, for the case where ω_p/p=3 (right) the pulse has a smaller amplitude and the first part of it only slightly lifts the column. Therefore, the flexural vibration caused by the impact is less intense and most of the rotation kinetic energy is conserved.

Note that the flexural vibration has a much higher frequency than the column's eigenfrequency and is more heavily damped than what ζ=0.01 would indicate. This behavior is in accordance to the findings of Acikgoz and DeJong [8] for a SDOF oscillator able to uplift.

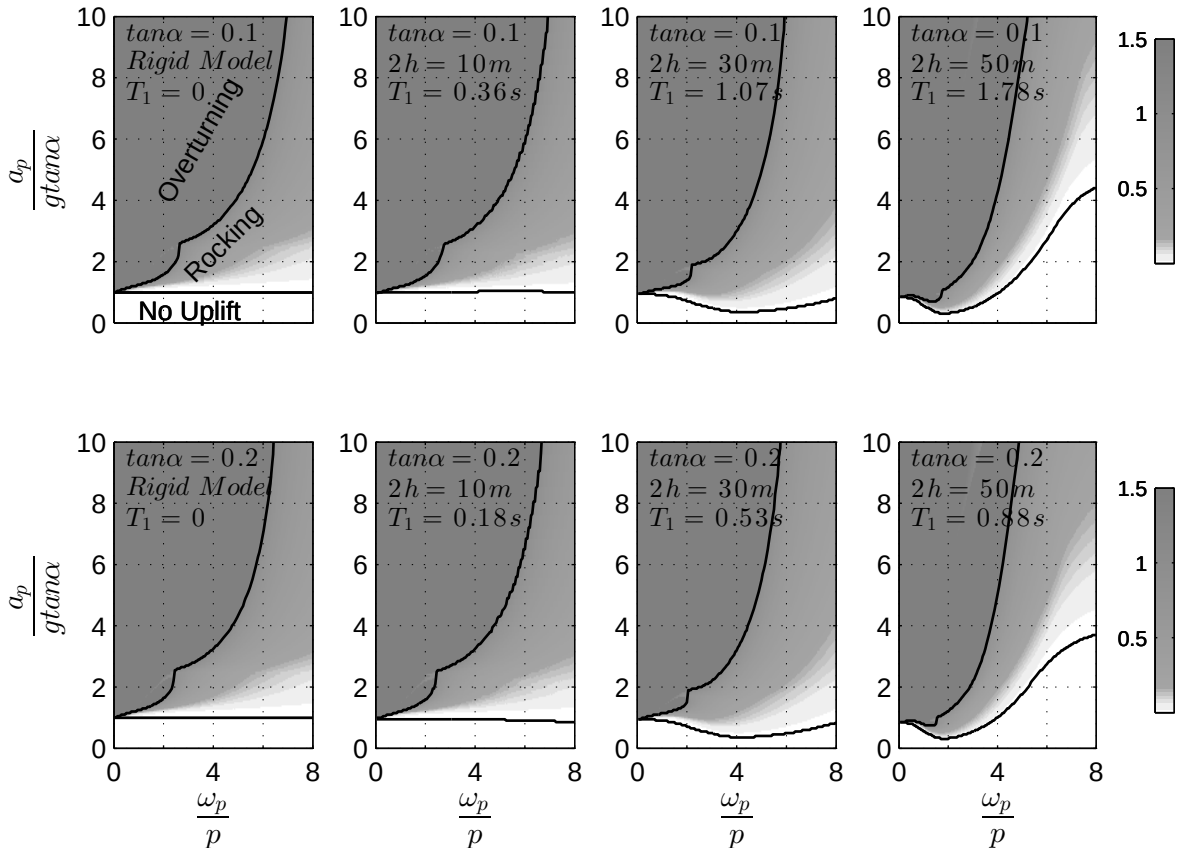


Figure 5 Contour plots of the normalized rotation, θ/α, of concrete (E=30GPa, ρ=2.5Mg/m^3) columns with height 2h and slenderness α when subjected to a symmetric Ricker acceleration pulse with amplitude a_p and cyclic frequency ω_p. The bold lines define the margin between uplift and no-uplift regions as well as the minimum acceleration to cause overturn.

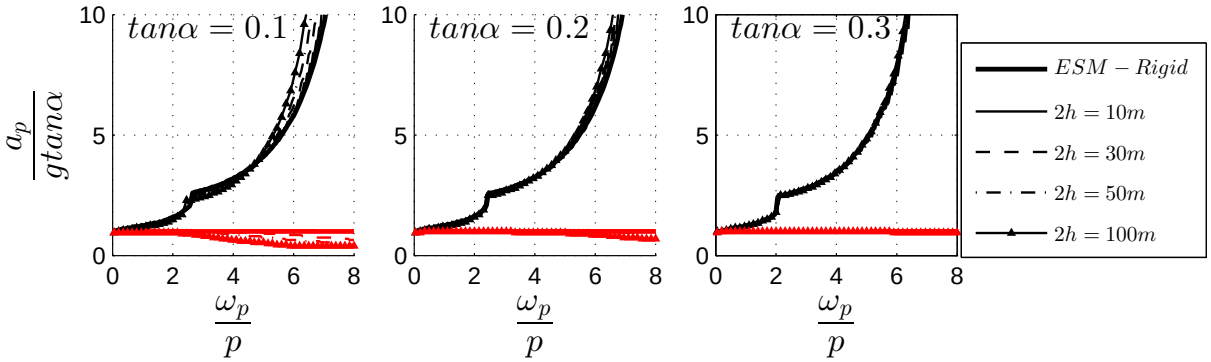


Figure 6 Minimum uplift and overturning acceleration spectra of concrete (E=30GPa, ρ=2.5Mg/m^3) columns with height 2h and slenderness α when subjected to a symmetric Ricker acceleration pulse with amplitude a_p and cyclic frequency ω_p.

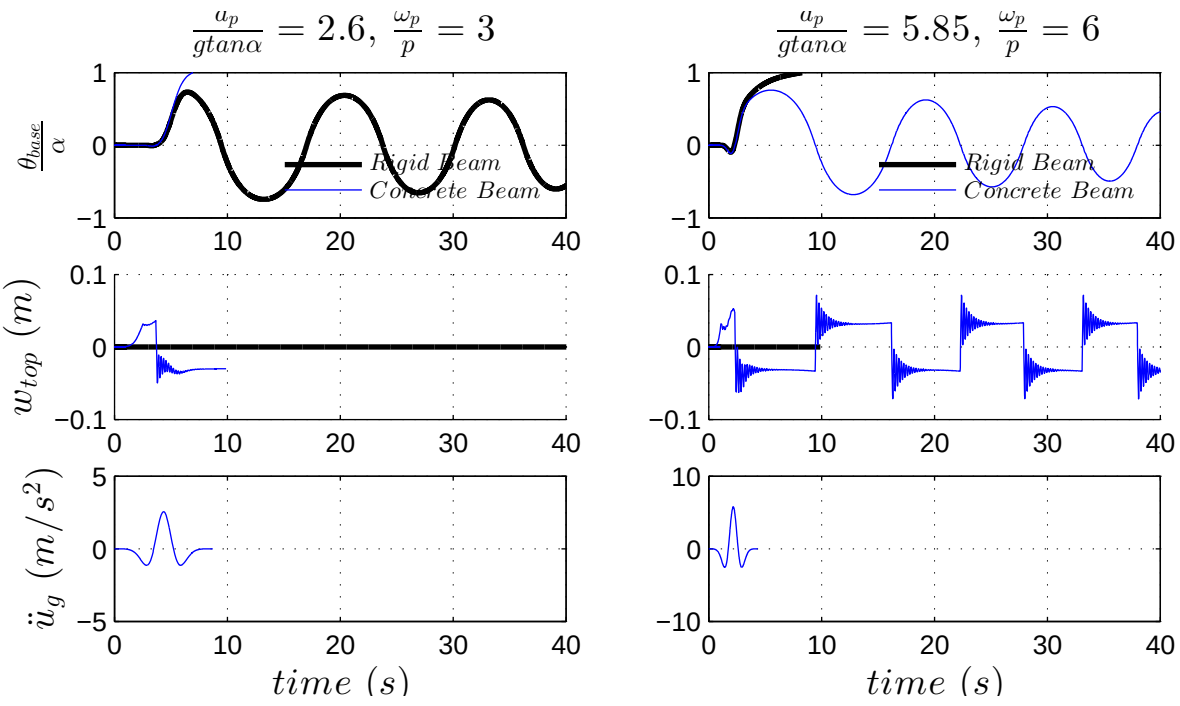


Figure 7 Comparison of time histories of the response of a rigid and a concrete beam of slenderness α and frequency parameter p, when subjected to a symmetric Ricker pulse with amplitude a_p and cyclic frequency ω_p. First row: normalized base rotation; Second row: top displacement due to bending; Third row: Ground acceleration

5 ROCKING OF COLUMNS OF FINITE STIFFNESS ON A RIGID BASE

In the usual design approach the column dimensions are based on their section forces capacity – not on their rocking stability. The latter is ensured by monolithically connecting the column to a large enough foundation. The foundation is designed so that no uplift occurs. This constraint often requires a very large foundation that makes the column behave like a fixed base one, thus transmitting large forces to the structure. It has been proposed [9, 20-23] that the foundation should be allowed to uplift or that the ground should be allowed to reach its bearing capacity so that the forces transmitted to the structure become smaller. This approach leads to lighter structures but the mobilization of all the soil strength often leads to large residual displacements, which is an undesirable performance. Makris and Vassiliou [10] have shown that frames consisting of unconnected assemblies of rigid bodies experience remarkable stability with zero residual deformations and suggested that uplift and rocking can be used as seismic isolation strategy strategies. When it comes to applying this concept to a sole rocking column (e.g. a tall chimney) the foundation and the column can be designed based on the ground acceleration that the designer would choose to cause uplift. In this section, the response of flexible rocking columns connected to a rigid foundation able to uplift is studied. It is investigated whether the increase in the flexural deformation prior to uplift due to the presence of the foundation makes the flexibility of the column influence the response of the system. The system that is studied is shown in Figure 8.

The equation of motion for the case where the column is rigid is

$$\ddot{\theta}(t) = -p'^2 \left\{ \sin\left[\alpha' \operatorname{sgn}\left(\theta(t)\right) - \theta(t)\right] + \frac{\ddot{u}_g}{g} \cos\left[\alpha' \operatorname{sgn}\left(\theta(t)\right) - \theta(t)\right] \right\} \tag{14}$$

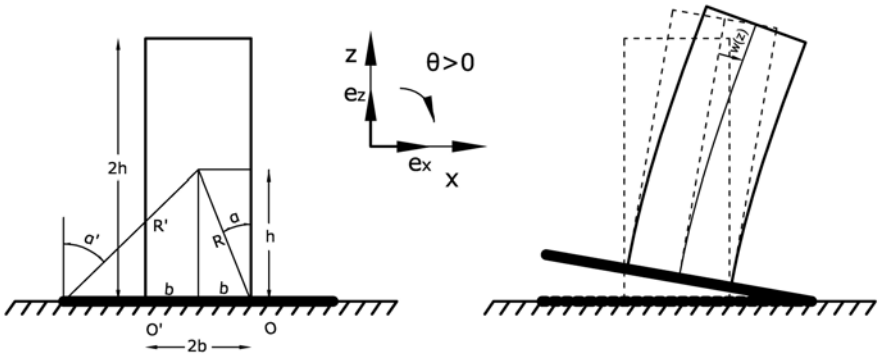


Figure 8 Flexible beam monolithically connected to a rigid base.

where

$$p'^2 = \frac{mgR'}{I'_o} \tag{15}$$

where α' and R' are defined in Figure 8 and I'_o is the moment of inertia of the rocking system around the pivot point and is equal to

$$I'_o = \frac{1}{3}mR^2 + mR^2\frac{\cos\alpha}{\cos a'} \tag{16}$$

Equations (15) and (16) give

$$p'^2 = p^2\frac{4\cos\alpha}{3\cos\alpha + \cos\alpha'} \tag{17}$$

that gives $p \simeq p'$ for small α and α'.
The uplift acceleration is

$$\ddot{u}_g^{uplift} = g\tan\alpha' \tag{18}$$

and the restitution coefficient is

$$r' = \left(1 - \frac{3}{2}\sin^2 a'\frac{\cos^2\alpha}{\cos\alpha'}\frac{4}{\cos\alpha' + 3\cos\alpha}\right)^2 \tag{19}$$

that gives $r' \simeq r = \left(1 - \frac{3}{2}\sin^2\alpha\right)^2$ for small α and α'.
Hence, if the column is rigid enough and for small α', columns with equal footing, $2b'$, and height, $2h$, behave the same, no matter what their width, $2b$, is.

In order for the Spring Model to be used to model this system in an ordinary FEM software the elastic nonlinear spring used at the base of the column should have a yield moment equal to $mgR'\sin\alpha'$. The extra rotational mass that should be distributed to the nodes of the model is $\Delta I = mR^2\left(\frac{1}{3} + \frac{\cos\alpha}{\cos\alpha'} - \frac{4}{3}\cos^2\alpha\right)$.

Extending equation (12), the overturning stability of a flexible column connected to rigid base is given by

$$\theta(t) = \varphi\left(\frac{a_p}{g \tan\alpha}, \frac{\omega_p}{p}, \alpha, \zeta, \frac{E}{\rho g R}, \alpha' \right) \tag{20}$$

Figure 9 plots the contour plots of the normalized maximum rotation, θ/α', at the base of a concrete column with Young modulus E=30GPa and density ρ=2.5Mg/m^3 subjected to a symmetric Ricker pulse of amplitude a_p and cyclic frequency ω_p. The response was computed using the Spring Model implemented in OpenSees. Figure 10 plots the overturning and uplifting minimum acceleration spectra for the same columns. Even in this case, where the developed moments are larger than in the column without a base, the effect of column flexibility is negligible for tanα>0.2. For columns with tanα=0.1, the flexibility of the column influences the response only for columns taller than 50m and for ω_p/p smaller than 4. For this size of columns, these values of ω_p/p correspond to unrealistic pulses with periods larger than 5 seconds. Therefore, it is concluded that Housnser's rigid model can be used to describe the rocking motion of columns with a slenderness as low as tanα=0.1 and a height of 100m, connected to a base 3 times larger than their width.

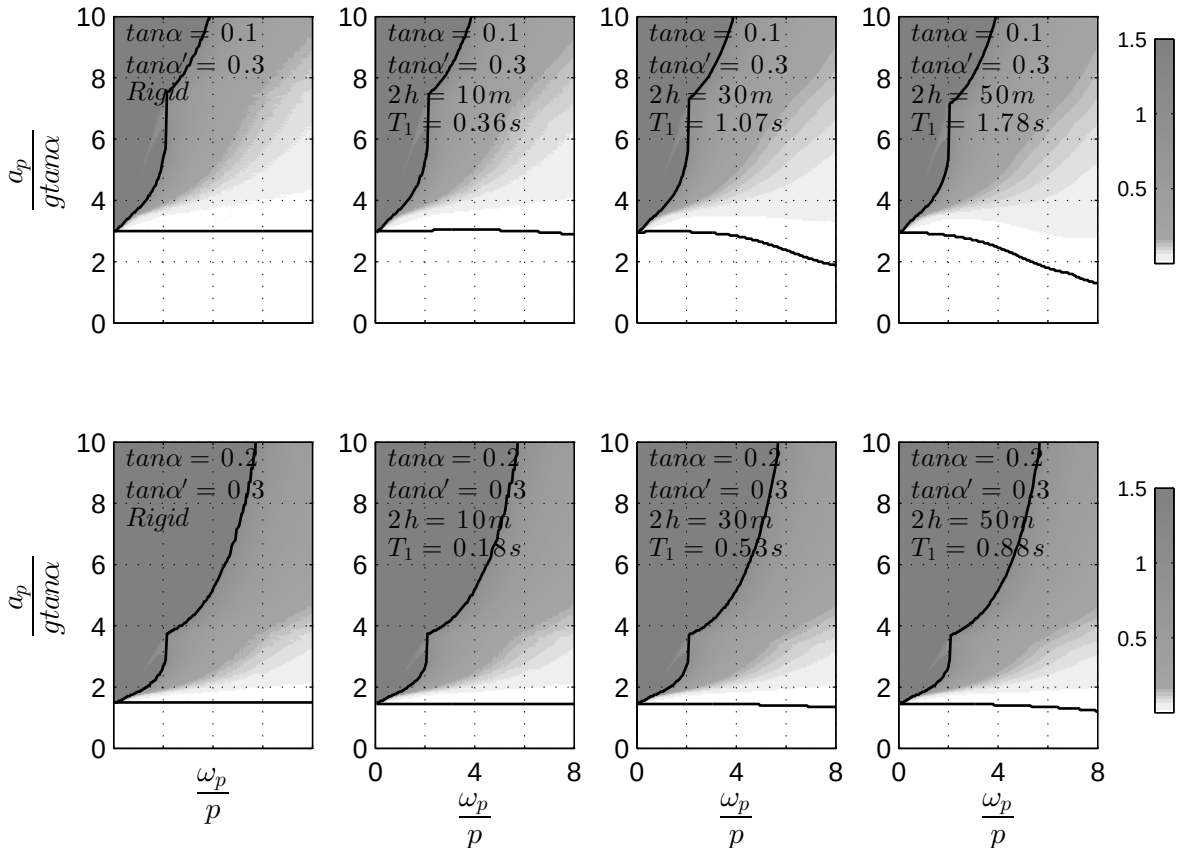


Figure 9 Contour plots of the normalized rotation, θ/α, of concrete (E=30GPa, ρ=2.5Mg/m^3) columns with height $2h$ and slenderness α connected to a rigid base with $\tan\alpha' = 0.3$, when subjected to a symmetric Ricker acceleration pulse with amplitude a_p and cyclic frequency ω_p. The bold lines define the margin between uplift and no-uplift regions as well as the minimum acceleration to cause overturn.

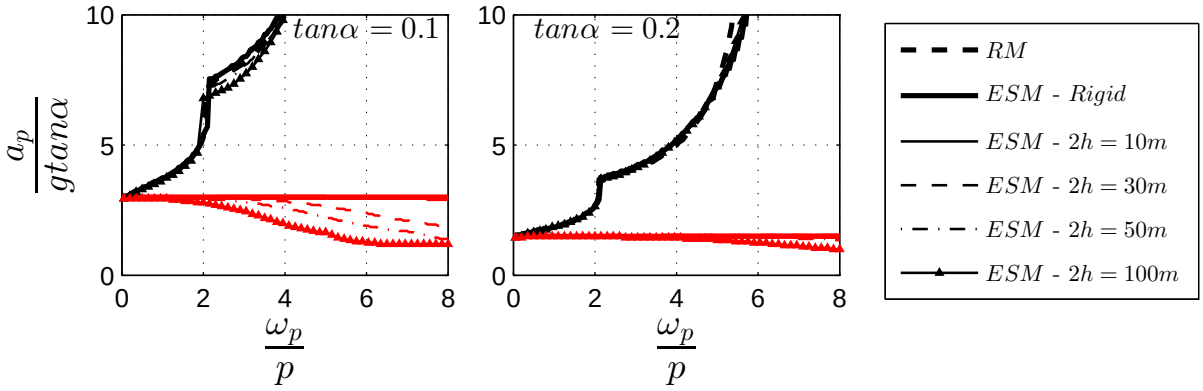


Figure 10 Minimum uplift and overturning acceleration spectra of concrete (E=30GPa, ρ=2.5Mg/m^3) columns with height $2h$ and slenderness α connected to a rigid base with $\tan\alpha' = 0.3$, when subjected to a symmetric Ricker acceleration pulse with amplitude a_p and cyclic frequency ω_p.

6 APPLICATION ON A ROCKING CHIMNEY

The use of rocking structures in construction dates back to ancient times. However, there is no historical evidence that ancient engineers actually designed rocking structures having in mind their rocking behavior during an earthquake. To the authors' knowledge, the first conscious uses of rocking as a seismic response modification mechanism were for a bridge across the Rangitikei river in New Zealand in 1981 (Beck and Skinner [11]) and for rocking chimney at the Christchurch airport (Sharpe and Skinner [24]).

The latter is a 33m tall chimney of cruciform cross section on a 7.5m×7.5m base. The chimney is designed so that it can rock during large earthquakes. Extra energy dissipation is provided by two steel hysteretic dampers. The chimney is equipped with an original system that allows the rocking motion, while preventing the chimney from walking off the foundation. Sharpe and Skinner mention that the chimney's "freedom to rock gives it the ability to withstand very large earthquakes without requiring the substantial repairs that most reinforced concrete structures would need".

In order to test the application of rocking motion as an isolation technique, the chimney is excited by the NS component of the ElCentro 18/5/1940 ground motion, which was used in the original paper by Sharpe and Skinner. To demonstrate the effectiveness of rocking, the chimney is modeled without the extra steel hysteretic dampers. For simplicity the cross section is modeled as constant across the height of the column with I_{xx}=I_{yy}=2.99m^4 and A=1.74m^2. Figure 11 plots the response histories of the chimney based a) on the original foundation and b) on a foundation large enough so that the chimney does not uplift: The rocking chimney develops a maximum base moment (M_{base}) of 7327 kNm while the fixed base one a maximum of 33200 kNm.

Hence the chimney and the foundation can be designed with less than a quarter of the moment that would develop if the column was designed not to uplift. The maximum rotation of the rocking column is as small as $0.036\,a'$ (i.e. less than 4% of the rotation that would cause overturning). Note that the second plot of Figure 11 shows that flexural deformation cannot be neglected and that modeling the chimney as a rigid block would give large error. This is due to the small radius of gyration (I/A) of the cruciform cross section.

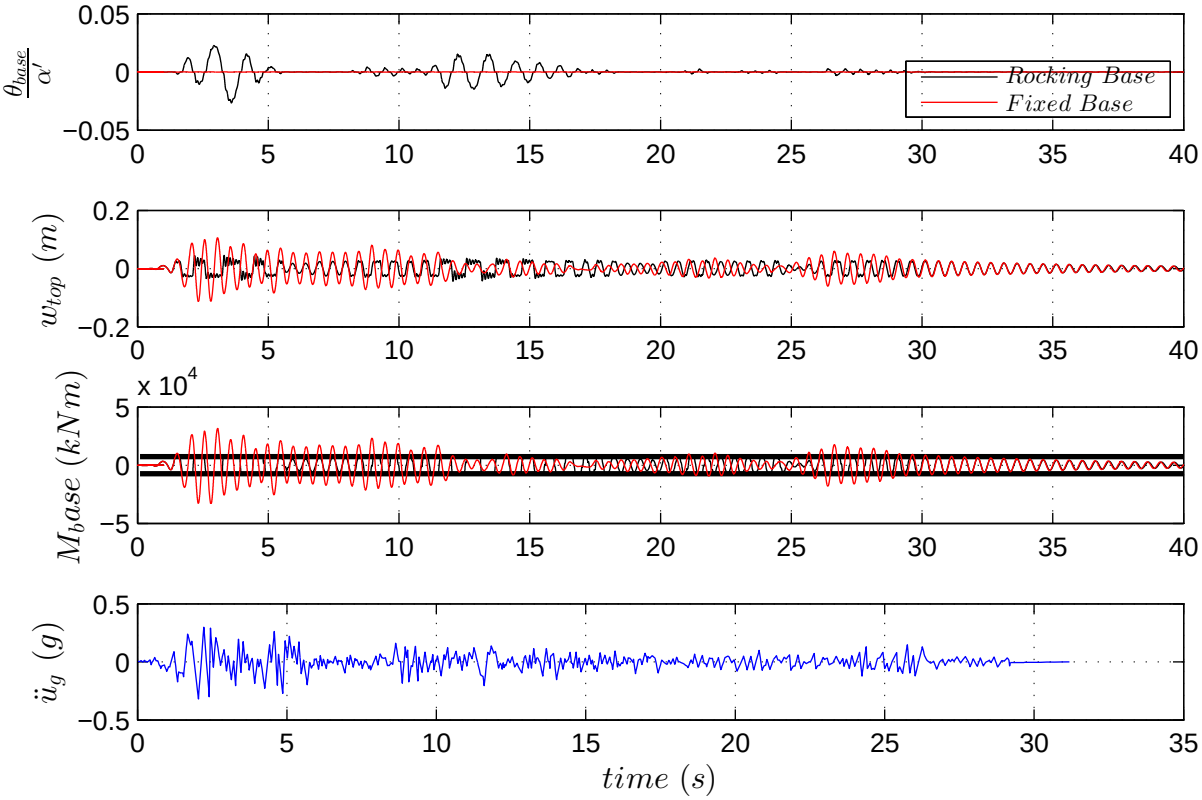


Figure 11 Response time histories of Sharpe and Skinner's chimney based a)on the original foundation and b) on a foundation large enough not to uplift First row: normalized base rotation; Second row: top displacement due to bending; Third row: Base moment Forth row: Ground acceleration (El Centro 18/5/1940 ground motion, NS Component)

7 CONCLUSIONS

A simple model for the description of rocking structures has been proposed. The model can be implemented in any FEM software that can handle large displacements, P-Δ effects and nonlinear elastic elements. Due to its simplicity, it takes so little computational time that it was able to produce rocking spectra. The model has been enhanced with extra rotational masses to take into account the minor effect of the fact that the real columns do not rotate around the center of their base but around its edge. The model was tested against the numerical solution of Housner's equation for rigid blocks with excellent results. Subsequently, it was used to study the effect of the flexibility of rocking solitary columns (with or without a base). It is concluded that for concrete rectangular columns the effect of their flexibility in their rocking response is negligible for columns up to 30m tall and on the safe side for taller columns. The latter is a result of the transformation of rotational kinetic energy to bending vibration at each impact. Finally the model was used to test the performance of an existing rocking chimney equipped with extra dissipation. It is concluded that the rocking chimney would exhibit remarkable stability even without the extra damping.

REFERENCES

1.Milne, J. (1885). ‘‘Seismic experiments.’’ *Trans. Seism. Soc. Japan*, 8, 1–82.

2.Housner, G. W. The behaviour of inverted pendulum structures during earthquakes. *Bulletin of the Seismological Society of America.* 1963; **53(2)**: 404–417.
3.Zhang J, Makris N. Rocking response of free-standing blocks under cycloidal pulses. *Journal of Engineering Mechanics*, ASCE 2001; 127(5):473–483.
4.Makris, N. and Konstantinidis, D. (2003), The rocking spectrum and the limitations of practical design methodologies. *Earthquake Engineering & Structural Dynamics*, 32, pp265–289.
5.Psycharis, I. N. and Jennings, P. C. (1983), Rocking of slender rigid bodies allowed to uplift. *Earthquake Engineering & Structural Dynamics*, 11: 57–76. doi: 10.1002/eqe.4290110106
6. Oliveto, G., Caliò, I. and Greco, A. (2003), Large displacement behaviour of a structural model with foundation uplift under impulsive and earthquake excitations. *Earthquake Engng. Struct. Dyn*., 32: 369–393.
7. Apostolou M, Gazetas G, Garini E. (2007) Seismic response of slender rigid structures with foundation uplifting, *Soil Dynamics and Earthquake Engineering*, 27(7), 642-654,
8. Acikgoz, S. and DeJong, M. J. (2012), The interaction of elasticity and rocking in flexible structures allowed to uplift. *Earthquake Engng. Struct. Dyn*.. doi: 10.1002/eqe.2181
9. Gelagoti, F., Kourkoulis, R., Anastasopoulos, I. and Gazetas, G. (2012), Rocking isolation of low-rise frame structures founded on isolated footings. *Earthquake Engng. Struct. Dyn*., 41: 1177–1197.
10. Makris N. and Vassiliou M.F. (2012), Planar rocking response and stability analysis of an array of free standing columns capped with a freely supported rigid beam (2012) *Earthquake Engng. Struct. Dyn* (accepted for publication).
11. Beck, J. L. and Skinner, R. I. (1973), The seismic response of a reinforced concrete bridge pier designed to step. *Earthquake Engng. Struct. Dyn*., 2: 343–358.
12. Konstantinidis, D. and Makris, N. (2005), Seismic response analysis of multidrum classical columns. *Earthquake Engng. Struct. Dyn*., 34: 1243–1270.
13. Yim CS, Chopra AK, Penzien J. Rocking response of rigid blocks to earthquakes. *Earthquake Engineering and Structural Dynamics* 1980; **8**(6):565–587.
14. Makris N, Roussos Y. Rocking response of rigid blocks under near-source ground motions. *Geotechnique* 2000; **50**(3):243–262
15. MATLAB Version 2011b. The Language of Technical Computing. The Mathworks, Inc.: Natick, MA, 1999.
16. OpenSEES (Open System for Earthquake Engineering Simulation), opensees.berkeley.edu
17. Ricker N. Further developments in the wavelet theory of seismogram structure (1943). *Bulletin of the Seismological Society of America*; 33:197–228.
18. Barenblatt, G. I. (1996), Scaling, self-similarity, and intermediate asymptotics, Cambridge University Press, Cambridge, U.K
19. ElGawady, M. A., Ma, Q., Butterworth, J. W. and Ingham, J. (2011), Effects of interface material on the performance of free rocking blocks. *Earthquake Engng. Struct. Dyn*., 40: 375–392.
20. Roh H., Reinhorn A., (2010) Modeling and seismic response of structures with concrete rocking columns and viscous dampers, *Engineering Structures*, 32(8), 2096-2107,
21. Pecker A, Pender MJ. (2000) Earthquake resistant design of foundations: new construction. Invited paper. GeoEng Conference, Melbourne 2000, 1:313–332.
22. Kawashima K, Nagai T, Sakellaraki D. (2007) Rocking seismic isolation of bridges supported by spread foundations. *Proc.of 2nd Japan-Greece Workshop on Seismic Design, Observation, and Retrofit of Foundations*, Tokyo, Japan 2007; 1:254–265.

23. Anastasopoulos I, Gazetas G, Loli M, Apostolou M, Gerolymos N. (2010) Soil failure can be used for earthquake protection of structures. *Bulletin of Earthquake Engineering*; 8:309–326.
24. Sharpe RD, Skinner RI, The seismic design of an industrial chimney with rocking base, (1983) *Bulletin of the New Zealand National Society for Earthquake Engineering* 16(2):98-106

COMPDYN 2013
4th ECCOMAS Thematic Conference on
Computational Methods in Structural Dynamics and Earthquake Engineering
M. Papadrakakis, V. Papadopoulos, V. Plevris (eds.)
Kos Island, Greece, 12–14 June 2013

TOWARDS A UNIFIED DESCRIPTION OF ROCKING STRUCTURES

Matthew J. DeJong[1], **Elias G. Dimitrakopoulos**[2]

[1] University of Cambridge
Department of Engineering, Trumpington Street, Cambridge, CB2 1PZ, United Kingdom
e-mail: mjd97@cam.ac.uk

[2] Hong Kong University of Science and Technology
Department of Civil and Environmental Engineering, Kowloon, Clear Water Bay, Hong Kong
ilias@ust.hk

Keywords: rocking, self-centering, rocking spectra, analytical dynamics, equivalent systems.

Abstract. *Numerous studies on the rigid rocking block have generated a wealth of knowledge about rocking behavior. However, evaluation of more complex rocking systems requires the derivation and solution of complicated equations of motion. This paper investigates the possibility of a unified description of several rocking systems through investigation of rocking mechanisms which describe the masonry wall and the masonry arch. Effective rocking parameters are derived for each of these structures, and the similarity of the rocking behavior is discussed. The error of the proposed approximation, which defines the limitations for this approach, is quantified for the example structures considered. Where appropriate, a unified description of rocking would allow the use of rocking spectra, which would be useful to readily predict the response of a wide array of rocking structures.*

1 INTRODUCTION

The concept of re-centering structures, which use some degree of rocking motion to isolate a structure from the stresses induced by earthquakes, is becoming increasingly investigated as a modern seismic design alternative. Anecdotally, this beneficial isolating effect has been proposed as an explanation for the ability of some monumental masonry structures to survive large earthquake events. Despite these claims, the assessment of existing masonry structures which may be susceptible to rocking overturning collapse during earthquakes remains a difficult task.

This paper describes continued investigations regarding the use of rocking spectra, derived by considering the response of a single rigid rocking block, to predict the maximum response of a much wider range of structures. In order for this to be possible, equivalent rocking blocks must be defined for a range of more complex rocking mechanisms.

In this paper, rocking structures which have already been demonstrated to exhibit direct equivalence with a single rigid block are first reviewed. For these structures, the use of rocking spectra to predict response is more obvious. Subsequently, two rocking mechanisms will be considered which exhibit more complex kinematics. Equivalence between these structures and a single rigid block is sought. In this context, the error associated with required simplifying assumptions is quantified. In the process, the equations of motion are presented in general form in order to provide a more unified description of complicated rocking structures.

2 REVIEW OF SIMPLE ROCKING STRUCTURES

This section briefly reviews the equations of motion governing the response of the single rigid rocking block and discusses other rocking structures which are dynamically equivalent.

2.1 The rocking block

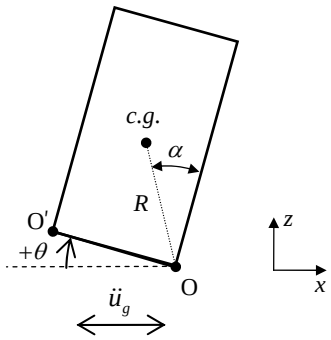


Figure 1: Geometry of the rocking block.

The equation of motion for positive rotation of the rocking block shown in Fig. 1 can be written [1]:

$$\ddot{\theta} = p^2 \left(-\sin\left(\theta_{cr} - \theta\right) - \frac{\ddot{u}_g}{g} \cos\left(\theta_{cr} - \theta\right) \right) \tag{1}$$

where $p^2 = 3g/4R$, $\theta_{cr} = \alpha$, and $\ddot{u}_g$ is the horizontal acceleration of the ground. According to Eqn. (1), the ground motion ($\ddot{u}_g / g$) required to initiate rocking motion is $\lambda = \tan\alpha$. When

the block returns to its initial position, impact occurs causing a dissipation of energy which can be approximated by a coefficient of restitution:

$$\eta = \dot{\theta}^{+} / \dot{\theta}^{-} \tag{2}$$

where $\dot{\theta}^{-}$ and $\dot{\theta}^{+}$ are the angular velocity before and after impact respectively. Conservation of momentum equations are often used to estimate the coefficient of restitution [1], but it will be left as an independent parameter in this paper. An equation similar to (1) can then be used for negative rotations ($\theta_{cr} = -\alpha$) about the point O′ in Fig. 1 [1].

While Eqn. (1) can be solved numerically, it is convenient to linearize it about the point of unstable equilibrium (θ_{cr}), yielding:

$$\ddot{\theta} = p^2 \left(\theta_{cr} - \theta - \frac{\ddot{u}_g}{g} \right) \tag{3}$$

According to Eqn. (3), the ground acceleration ($\ddot{u}_g / g$) required to initiate rocking motion of the linearized system is $\lambda_{lin} = \alpha$.

The error in predicting the rocking response using Eqn. (3) as opposed to Eqn. (1) increases as the slenderness decreases. Generally, the assumed analytical model is only reasonable for relatively slender blocks where sliding and bouncing can be neglected. For these same slender geometries, the errors associated with linearization are small when compared to the uncertainty involved in predicting expected ground motions, so Eqn. (3) is practically useful.

2.2 Equivalent rocking structures

The analytical model presented in §2.1 has been extensively used to study the response of the rigid rocking block to a wide variety of ground motions (e.g. harmonic [2], pulses [3], real earthquake time histories [4], synthetic earthquake time histories [1,5]). These studies have yielded a wealth of knowledge regarding the behavior of rocking structures. However, application of this knowledge to more complicated structures has been relatively limited.

Clearly, any single rigid body which rocks about alternating corners can be described by Eqns. (1) or (3) by deriving appropriate expressions for p, θ_{cr} and λ. Derivation of these parameters is trivial for some structures, but tedious for others. Regardless, if these parameters can be derived, then rocking response spectra, which predict the maximum response of a single rocking block to a given ground motion, could be used to predict the maximum response. For example, rocking spectra for pulse ground motions (e.g. [6]) are generally applicable to all single rigid bodies.

While the use of rocking spectra for single block structures may seem trivial, these spectra are particularly useful for masonry structures composed of multiple blocks where numerous displacement mechanisms could form. For example, when considering the rocking collapse of masonry spires [7], numerous possible collapse mechanisms were rapidly considered using pulse-based rocking spectra, in order to predict the mechanism which is dynamically most vulnerable to overturning collapse. It should be noted that the governing mechanism is dependent on the pulse characteristics, and is generally different than the mechanism predicted using static methods [7]. Further, single block rocking spectra results compared well with results from detailed computational and experimental models involving numerous blocks [8].

The application of rocking spectra to multiple block rocking mechanisms is the primary focus of this paper. The symmetric three-block frame considered by Makris and Vassiliou [9]

provides a unique example of a multiple block mechanism which has direct equivalence with the rocking block. More general rocking mechanisms are considered in the following section.

3 ROCKING MECHANISMS

In general, the large displacement response of multiple-member kinematic mechanisms is highly nonlinear, and differs between configurations. However, for many structures, the rotation required to reach a point of unstable equilibrium (θ_{cr}), and therefore possible overturning, is relatively small. Thus, the aim of this section is to investigate an approximate equivalence between multiple-member mechanisms and the single rocking block.

3.1 The masonry wall

An example of mechanism that may rock during earthquake excitation is shown in Fig. 2. Several researchers (e.g. [10,11]) have studied the out of plane behavior of masonry walls using a similar model. A static analysis of the wall yields a relatively small lateral resistance to seismic loading because walls are generally slender. While this static analysis may be appropriate for design, it may be overly conservative for assessment. Instead, a simple procedure which accounts for the 'reserve capacity' resulting from the dynamics of the system [10] is desired.

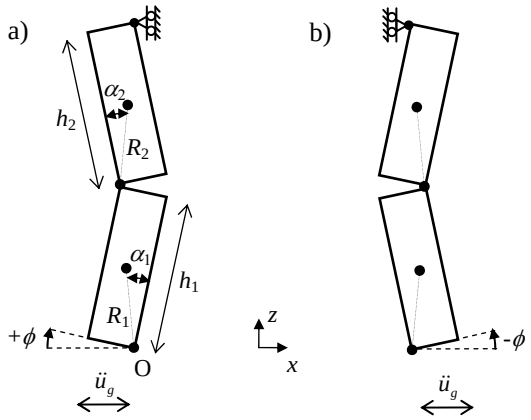


Figure 2: Geometry of the rocking masonry wall for (a) positive and (b) negative rotations.

Wall with mid-height hinge

Initially, it is assumed that a hinge forms at the mid-height of the wall ($\alpha_1 = \alpha_2 = \alpha$, $R_1 = R_2 = R$). The equation of motion of the resulting three-hinge mechanism shown in Fig. 2(a) is:

$$\left(\frac{I_O}{2mR} + 6R\sin^2(\alpha-\phi)\right)\ddot{\phi} - 3R\sin 2(\alpha-\phi)\dot{\phi}^2 + \sin(\alpha-\phi)g = -\frac{1}{2}\ddot{u}_g\cos(\alpha-\phi) \qquad (4)$$

where I_O is the moment of inertia of the bottom block about point O, m is the mass of a single block, and ϕ is the rocking rotation, for which the positive direction is shown in Fig. 2(a). A similar equation could be written for the negative rotation shown in Fig. 2(b). More generally, Eqn. (4) can be written as:

$$I_{nl}(\phi)\ddot{\phi} + J_{nl}(\phi)\dot{\phi}^2 - G_{nl}(\phi)g = -B_{nl}(\phi)\ddot{u}_g \qquad (5)$$

where:

$$
\begin{aligned}
I_{nl} &= \frac{I_O}{2mR} + 6R\sin^2\left(\alpha - \phi\right) \\
J_{nl} &= 3R\sin 2\left(\alpha - \phi\right) \\
G_{nl} &= \sin\left(\alpha - \phi\right) \\
B_{nl} &= 0.5\cos\left(\alpha - \phi\right)
\end{aligned}
\tag{6}
$$

Note that the ground acceleration ($\ddot{u}_g / g$) which causes initiation of rocking is:

$$
\lambda = \left.\frac{G_{nl}}{B_{nl}}\right|_{\phi=0} \tag{7}
$$

For the rocking wall in question, $\lambda = 2\tan\alpha$, which is twice the value of free standing block with equal dimensions as one of two blocks composing the wall.

Equation (5) could be solved directly to find the response of the wall to dynamic loading. However, the objective here is to define an equivalent block which can be used to predict the response of the more complicated wall mechanism. Clearly Eqn. (5) is different than Eqn. (1) due to the mechanism kinematics which involve centripetal and Coriolis accelerations. Thus, it is useful to linearize the equation of motion to allow comparison with the rocking block. Linearization of Eqn. (4) about the point of unstable equilibrium ($\phi = \phi_{cr} = \alpha$) yields:

$$
\frac{2R}{3}\ddot{\phi} + \left(\phi - \phi_{cr}\right) g = -\frac{1}{2}\ddot{u}_g \tag{8}
$$

More generally, Eqn. (8) can be written as:

$$
I_{eq}\ddot{\phi} + G_{eq}\left(\phi - \phi_{cr}\right) g = -B_{eq}\ddot{u}_g \tag{9}
$$

where $I_{eq} = 2R/3$, $G_{eq} = 1$, and $B_{eq} = 0.5$ for the wall under consideration. Rearranging Eqn. (9) yields:

$$
\ddot{\phi} = p_{eq}^2\left(\phi - \phi_{cr} - a_{sc}\frac{\ddot{u}_g}{g}\right) \tag{10}
$$

where:

$$
p_{eq} = \sqrt{\frac{gG_{eq}}{I_{eq}}} \quad ; \quad a_{sc} = \frac{B_{eq}}{G_{eq}} \tag{11}
$$

which yields $p_{eq} = \sqrt{3g/2R} = \sqrt{2}p_{block}$ and $a_{sc} = 0.5$ for the wall under consideration. The ground acceleration ($\ddot{u}_g / g$) required to initiate rocking of the linearized system is:

$$
\lambda_{lin} = \frac{G_{eq}}{B_{eq}}\phi_{cr} \tag{12}
$$

which yields $\lambda_{lin} = 2\alpha$ for the wall under consideration. If the difference between λ and λ_{lin} is small, then the definition of a_{sc} above may be sufficient. However, if the difference is large, then an alternate definition of a_{sc} which preserves the actual uplift acceleration of the nonlinear system may be useful:

$$a_{sc,alt} = \frac{\phi_{cr}}{\lambda} \tag{13}$$

In general, Equation (10) is now similar to Eqn. (3) apart from the a_{sc} term. Thus, the response of a single block can be used to predict the response of the wall mechanism, provided that the acceleration input is scaled by a_{sc}.

While the simplification of the wall to an equivalent block is advantageous, the accuracy of the linear approximation must be evaluated. It is useful to first consider the accuracy under free vibration, where a_{sc} has no effect, and the accuracy is primarily dependent on the estimation of p_{eq}, which results in an effective natural rocking period. It is well documented [1] that the natural rocking period varies with the amplitude of the rocking motion. Thus, the error in the natural rocking period predicted by the equivalent block versus the actual wall ($T_{n,blockeq}$ / $T_{n,wall}$) is plotted in Fig. 3(a) as a function of rocking amplitude (ϕ/ϕ_{cr}). For slender blocks, the error is small, while for stockier blocks the error increases, as expected. In addition, the error is greater for smaller angles of rocking, which results from the linearization about the unstable point of equilibrium ($\phi/\phi_{cr} = 1$). Subsequently, the error associated with a_{sc}, which is directly related to the difference between λ and λ_{lin}, was also considered. The error in the uplift acceleration (λ_{lin}/λ) is plotted in Fig. 3(b), and is generally small.

Finally, the error due to forced vibration was evaluated by considering the time required (t_{over}) for the block to reach the unstable equilibrium position under a constant ground acceleration. The ratio of the overturning time for the linearized system compared to the nonlinear system ($t_{over,blockeq} / t_{over,wall}$) is plotted in Fig. 4, for the values of a_{sc} defined in Eqns. (11) and (13). Again, for slender blocks, the error is relatively small. Further, the effect of using a_{sc} versus $a_{sc,alt}$ is small, and is proportional to the error in uplift acceleration shown in Fig. 3(b), as expected. Thus, either definition of a_{sc} is sufficient for the wall under investigation.

Generally, Figs. 3 and 4 quantify the error associated with the linearization, providing a measure of the confidence with which an equivalent block could be used describe the rocking of a symmetric wall mechanism of a given slenderness.

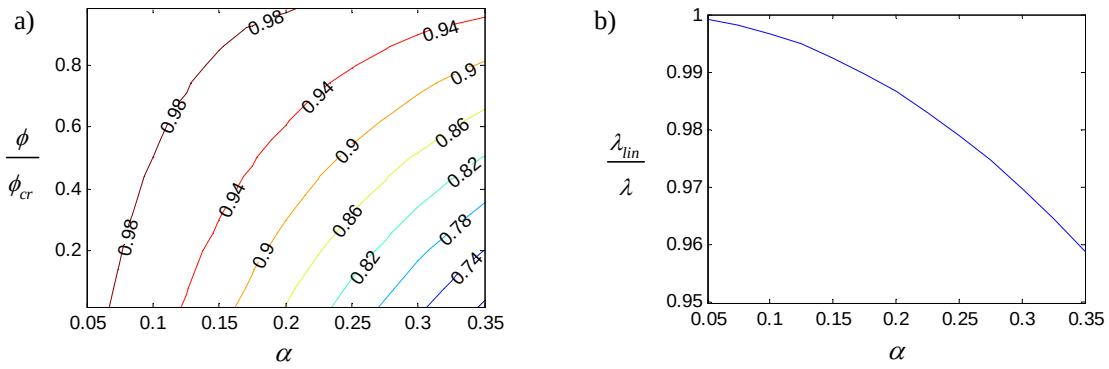


Figure 3: Linearization errors for the masonry wall: (a) natural frequency $T_{n,blockeq} / T_{n,wall}$, (b) uplift acceleration λ_{lin}/λ.

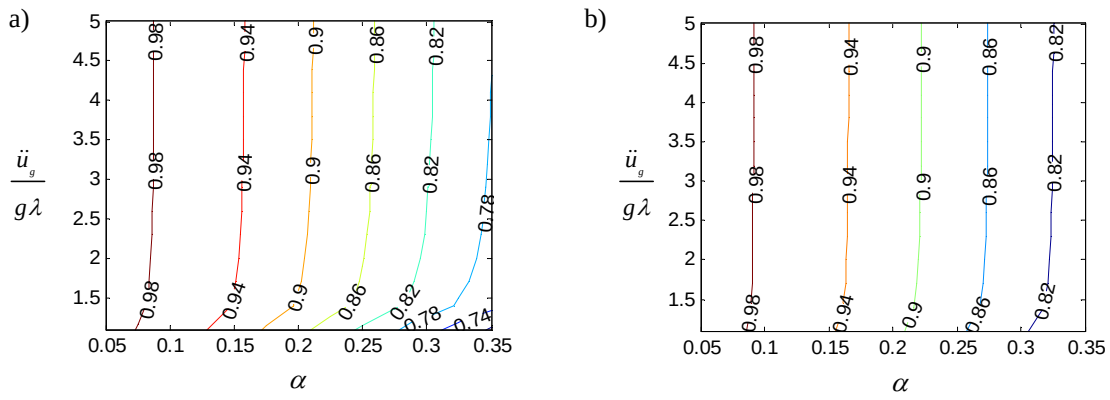


Figure 4: Linearization errors for overturning time ($t_{over,blockeq} / t_{over,wall}$) of the masonry wall due to a constant acceleration of amplitude of $\ddot{u}_g / g\lambda$: (a) a_{sc} , (b) $a_{sc,alt}$.

Wall with arbitrary hinge

If the hinge is not assumed to form at the mid-height of the wall, the equation of motion can still be described by Eqn. (5), but it becomes considerably more complicated than Eqn. (4). Regardless, linearization of the equation of motion about the unstable point of equilibrium ($\phi = \phi_{cr} = \alpha_1$) still yields Eqn. (10), and the equivalent block parameters become:

$$p_{eq} = \sqrt{\frac{3g}{4R_1}\frac{1+2\frac{h_2}{h_1}+\frac{h_2}{h_1}\frac{R_1}{R_2}}{1+\frac{h_2}{h_1}\left(\frac{R_2}{R_1}\right)^2}}$$
$$a_{sc} = 0.5 \tag{14}$$
$$\lambda_{lin} = 2\alpha_1$$

Remarkably, a_{sc} is unaffected by the change in position of the central hinge, while p_{eq} and λ_{lin} vary. In general, smaller scale structures, which correspond to larger values of p_{eq}, are more vulnerable to overturning during an earthquake [1]. For Eqn. (14), p_{eq} is maximum for $h_2/h_1 = 0.74$. However, the initiation of rocking decreases with the height of the central hinge, so an unrealistic structure with $h_2/h_1 = 0$ would be least resistant to rocking initiation. The central hinge height which would be most vulnerable to overturning would therefore be dependent on the ground motion input. For pulse type motions, response spectra [6] could then be used to predict the response for each possible location of the central hinge. Using a similar procedure to previous investigations of masonry spires [7], these spectra could then be used to create a governing response envelope based on all possible mechanisms.

3.2 The masonry arch

Numerous previous studies have used the rigid body mechanism shown in Fig. 5 to analytically describe the dynamic response of the free standing masonry arch. In these studies, the initial hinge locations were found by static analysis, and were then assumed to reflect when the arch returns to its initial position. Despite being a single degree of freedom mechanism, the analytical model proved to effectively predict global collapse when compared to both

computational discrete element modeling [12] and experimental [13] results. Regardless, the aim of this study is again to determine if this complicated four-hinge mechanism can be effectively described by an equivalent single rocking block.

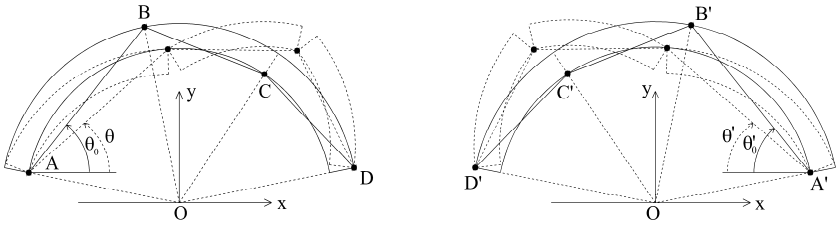


Figure 5: Geometry of the rocking arch.

The equation of motion of the arch in Fig. 5 was derived by Oppenheim [14], and is of the same form as Eqn. (5). The ground acceleration ($\ddot{u}_g / g$) required to uplift the nonlinear system is again described by Eqn. (7). Just as for the two-block rocking wall, the equation of motion can be linearized, resulting in Eqn. (9), and the ground acceleration ($\ddot{u}_g / g$) required for uplift of the linearized system is described by Eqn. (12).

Again it is useful to quantify the error associated with the linearization, which is done using the procedures described in §3.1. For a semi-circular arch (inclusion angle of 180 degrees), the error in natural rocking period ($T_{n,blockeq}$ / $T_{n,arch}$) caused by the linearization is shown in Fig. 6(a) for a range of reasonable thickness to radius ratios (t_a / r). The error is relatively small, and increases as the arch becomes thicker, or less slender, as expected. For the same range of geometries, the error associated with the acceleration which initiates rocking (λ_{lin} / λ) is shown in Fig. 6(b). The error is nearly zero for extremely thin arches, but increases significantly with arch thickness.

To evaluate forced vibration, the error in overturning time ($t_{over,blockeq}$ / $t_{over,arch}$) is shown in Fig. 7, again for the values of a_{sc} defined in Eqns. (11) and (13). Unlike for the wall, the arch results are significantly affected by the definition of a_{sc} due to the kinematics of the mechanism. The error is larger for a_{sc}, but the prediction of maximum response is conservative. The error is smaller for $a_{sc.alt}$, but the prediction of maximum response is unconservative. As a compromise, an average value of a_{sc} could be taken to provide a conservative prediction with reduced error.

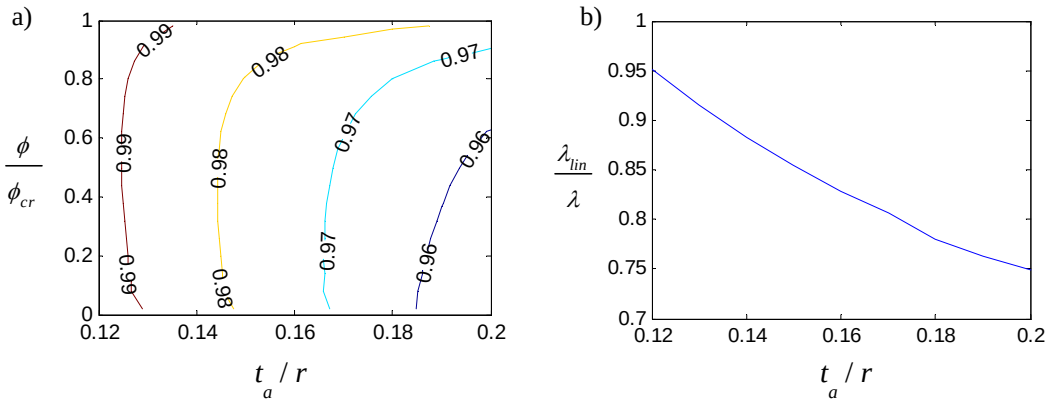


Figure 6: Linearization errors for a semi-circular masonry arch: (a) natural frequency $T_{n,blockeq}$ / $T_{n,wall}$, (b) uplift acceleration λ_{lin} / λ.

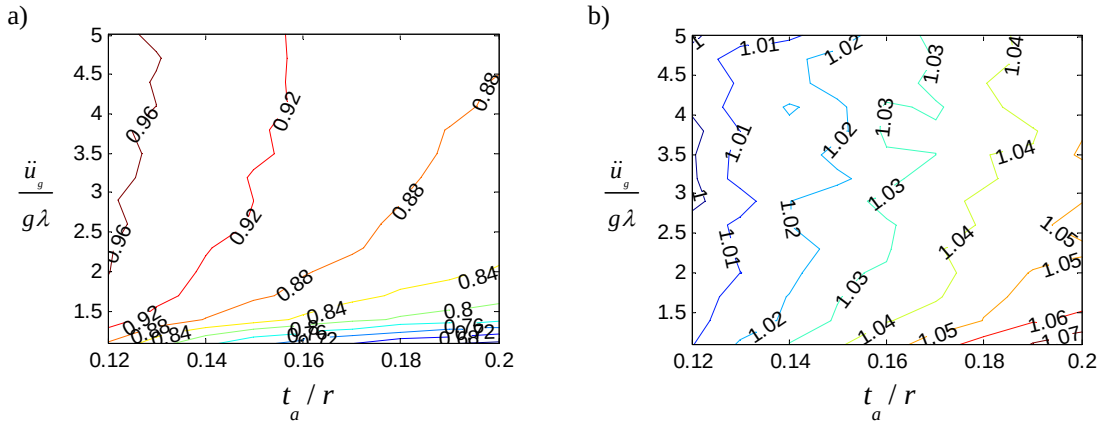


Figure 7: Linearization errors for overturning time ($t_{over,blockeq} / t_{over,wall}$) of a semi-circular masonry arch due to a constant acceleration of amplitude of $\ddot{u}_g / g\lambda$: (a) a_{sc} , (b) $a_{sc,alt}$.

4 EXAMPLE

To exemplify the utility of the equivalence derived in the previous section, the response of an arch (Fig. 8(a)) to the pulse-type Northridge-Rinaldi earthquake record (Fig. 8(b)) will be considered. Rocking response spectra could be produced for the entire earthquake record and used to predict the maximum response of the arch, although this would be computationally intensive. Instead, the primary sinusoidal acceleration pulse within the earthquake (Fig. 8(b)) will be considered alone for prediction purposes.

An approximate closed-form solution [6] for the maximum response of the single rocking block to a single sinusoidal pulse is:

$$\frac{\phi_{max}}{\phi_{cr}} = 1 - \sqrt{1 - \eta^2 \left(1 - D_0^*\right)} \tag{15}$$

where:

$$D_0^* = \left(\frac{\omega}{\omega^2 + 1}\right)^2 \left\{\omega^2 - 2a^2 + 1 + \left(\sqrt{a^2 - 1} + \omega\right) a e^{-\left(2\pi - \sin^{-1}(1/a)\right)/\omega} + \left(\sqrt{a^2 - 1} - \omega\right) a e^{\left(2\pi - \sin^{-1}(1/a)\right)/\omega}\right\} \tag{16}$$

where $a = a_g / (g\lambda)$, $\omega = \omega_g / p$, and a_g and ω_g are the amplitude and circular frequency of the acceleration pulse, respectively. The equivalence derived in §3.2 allows the maximum response of the rocking arch to also be predicted with Eqns. (15) and (16) by using Eqns. (7) and (11) to calculate λ and p.

The predicted maximum response using Eqn. (15) is compared to the full dynamic response predicted using Eqn. (5) in Fig. 8(c,d) for two different geometric scales. In this case, the pulse is dominant, and the maximum response predicted by the two methods is nearly identical. The accuracy of this approach is clearly dependent on whether the pulse dominates the earthquake motion. However, that is true for the single block as well as the arch, and is beside the point of the current paper. Instead, when the pulse does dominate, the results exemplify that the response of a single block can be directly used to predict the response of more complicated structures using the equivalence derived in §3.

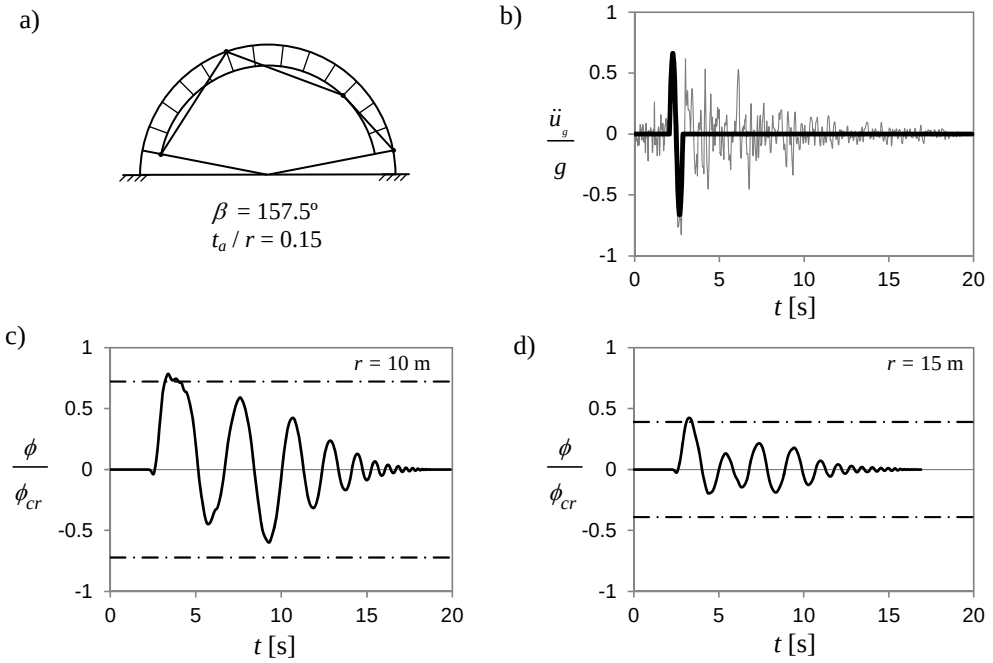


Figure 8: Response of the arch to earthquake motion: (a) arch geoemetry, (b) Northridge-Rinaldi earthquake record with primary impulse highlighted, (c,d) comparison of the arch response calculated using Eqn. (5) (solid line) with the maximum response predicted by Eqn. (15) (dash-dot line) for two different scales (r = 10 m, 15 m).

5 CONCLUSIONS

The objective of this work was to derive an equivalence between the rocking block and a variety of rocking mechanisms in order to develop a unified method for predicting the maximum response of rocking structures during earthquakes. Linearization of the governing equations of motion about the unstable point of equilibrium provided the desired equivalence, although approximate. The error associated with the approximate equivalence was quantified. The results indicate that kinematics complicate the response of the arch, but an alternate scaling relation proved effective in reducing the error caused by linearization. Regardless, the error may be acceptable for seismic assessment where the uncertainty involved in predicting expected ground motions is large.

REFERENCES

[1] G.W. Housner, The behavior of inverted pendulum structures during earthquakes, *Bulletin of the Seismological Society of America*, **53**(2), 403-417, 1963.

[2] P.D. Spanos, A. Koh, Rocking of rigid blocks due to harmonic shaking, *Journal of Engineering Mechanics (ASCE)*, **110**(11), 1627-1642, 1984.

[3] J. Zhang, N. Makris, Rocking response of free-standing blocks under cycloidal pulses, *Journal of Engineering Mechanics (ASCE)*, **127**(5), 473–483, 2001.

[4] M.J. DeJong, Amplification of rocking due to horizontal ground motion, *Earthquake Spectra*, **28**(4), 1405-1421, 2012.

[5] C. Yim, A.K. Chopra, J. Penzien, Rocking response of rigid blocks to earthquakes, *Earthquake Engineering and Structural Dynamics*, **8**(6), 565-587, 1980.

[6] E.G. Dimitrakopoulos, M.J. DeJong, Revisiting the rocking block: Closed form solutions and similarity laws, *Proceedings of the Royal Society A*, **468**(2144), 2294-2318, 2012.

[7] M.J. DeJong, Seismic response of stone masonry spires: Analytical Modeling, *Engineering Structures*, **40**, 556-565, 2012.

[8] M.J. DeJong, C. Vibert, Seismic response of stone masonry spires: Computational and Experimental Modeling, *Engineering Structures*, **40**, 566-574, 2012.

[9] N. Makris, M.F. Vassiliou, Planar rocking response and stability analysis of an array of free-standing columns capped with a freely supported rigid beam, *Earthquake Engineering and Structural Dynamics*, **42**(3), 431–449, 2013.

[10] K. Doherty, M.C. Griffith, N. Lam, J. Wilson, Displacement-based seismic analysis for out-of-plane bending of unreinforced masonry walls, *Earthquake Engineering and Structural Dynamics*, **31**, 833–850, 2002.

[11] D. Ciancio, C. Augarde, Capacity of unreinforced rammed earth walls subject to lateral wind force: elastic analysis versus ultimate strength analysis, *Materials and Structures*, doi: 10.1617/s11527-012-9998-8, 2013.

[12] L. De Lorenzis, M.J. DeJong, J. Ochsendorf, Failure of masonry arches under impulse base motion, *Earthquake Engineering and Structural Dynamics*, **36**, 2119-2136, 2007.

[13] M.J. DeJong, L. De Lorenzis, S. Adams, J.A. Ochsendorf, Rocking stability of masonry arches in seismic regions, *Earthquake Spectra*, **24**(4), 847-865, 2008.

[14] I.J. Oppenheim, The masonry arch as a four-link mechanism under base motion, *Earthquake Engineering and Structural Dynamics*, **21**(11), 1005-1017, 1992.

COMPDYN 2013
4th ECCOMAS Thematic Conference on
Computational Methods in Structural Dynamics and Earthquake Engineering
M. Papadrakakis, V. Papadopoulos, V. Plevris (eds.)
Kos Island, Greece, 12–14 June 2013

ROCKING RESPONSE OF FREE-STANDING FURNITURES UNDER EARTHQUAKE FLOOR MOTIONS

M. Chiriatti[1*], G. P. Cimellaro[2]

[1]Graduate Research Assistant, Department of Structural, Building & Geotechnical Engineering (DISEG) Politecnico di Torino, Corso Duca degli Abruzzi 24
marco.chiriatti@studenti.polito.it

[2]Assistant Professor, Department of Structural, Building & Geotechnical Engineering (DISEG) Politecnico di Torino, room7, Corso Duca degli Abruzzi 24
gianpaolo.cimellaro@studenti.polito.it

Keywords: Overturning, Rocking Motion, Floor Response, Furniture, Non-structural Element.

Abstract. *Over the last decade the amount of population injured by accident furniture overturning is increased and this trend is expected to continue. Non anchored body motion can be categorized in 6 basic types: rest, slide, rock, slide-rock, free flight and impact. The aim of this research is to analyze through numerical analysis the behavior of a free-standing rigid body during the phase of rocking motion under dynamic load. The model of free body rocking motion was proposed by G. W. Housner in 1963 first. Later a number of alternative models have been developed opportunely change the original assumption in order to and obtain more realistic results.*

In this research different models are compared with numerical simulations, using different excitation input and results are shown in the acceleration-frequency plane. These results confirmed the importance of the geometrical shape of the rigid block and the necessity to individuate the risk factors that can cause overturning phenomena. Nonlinear time history analysis using real earthquake floor motions recorded in a real time monitored building in California are used to simulate the behavior of a furniture located inside a multi-story building. Sensitivity analysis is performed in order to find the optimal location of the furniture inside the building.

The research goal is to establish how to reduce the risk of overturning during an earthquake in real structures and to propose a simple and practical procedure to locate the risk area in the building where slender furniture can overturn. Prevention actions are proposed by changing the shape of the furniture, the friction coefficient or by using some appropriate devices.

1 INTRODUCTION

Although a strong earthquake motion does not always cause severe damage of structures, there may be the possibility that a lot of people are injured by an overturning accident of furniture inside structures. A fundamental topic in the seismic protection is to limit the excessive motion of non-anchored bodies. It can be partitioned in 6 basic conditions: rest, slide, rock, slide-rock, free flight and impact. These motions have been analysed by different authors (Ishiyama, Housner, Shenton, Yim). The purpose of this study is to analyze the behavior of a rigid body under different geometric pulse.

As demonstrated by the analysis, after the input excitation, a rigid body can have different behaviors depending on the system parameters. In particular we can distinguish if a rigid body starts a rocking motion but it doesn't overturn or if it overturns with distinct modes: by exhibiting one or more impacts, and without exhibiting any impact. The results obtained are shown in the acceleration-frequency plane that can be developed for any geometry, in which there are two main areas: a safe zone where the free-standing block doesn't overturn and the other one where the rigid body overturns whether exhibiting impacts or without exhibiting any impact.

Nonlinear time history analysis using real earthquake floor motions recorded in a real time monitored building in California are used to simulate the behavior of a furniture located inside a multi-story building. Sensitivity analysis is performed in order to find the optimal location of the furniture inside the building. Prevention actions are proposed by changing the shape of the furniture, the friction coefficient or by using some appropriate devices.

2 ROCKING RESPONSE OF FREE-STANDING BLOCK

Consider the model shown in Figure 1, which can oscillate about the centres of rotation *O* and *O'* when it is set to rocking. Its center of gravity coincides with the geometric center, which is at a distance *R* from any corner. The angle α of the block is given by $tan(\alpha) = b/h$.

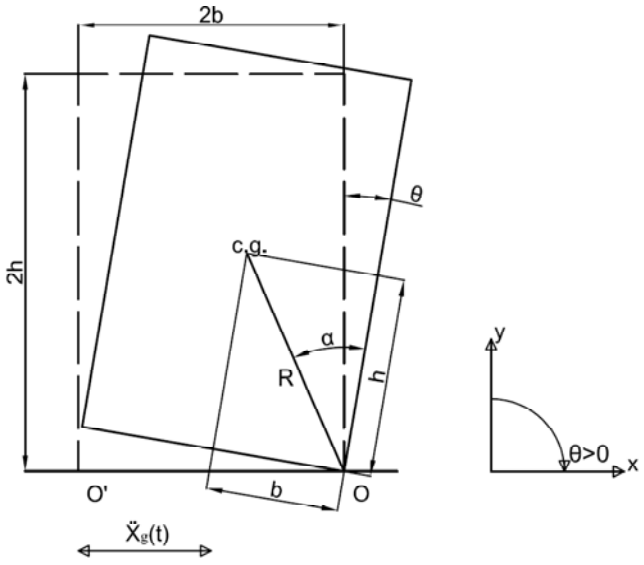


Figure 1 : Schematic of rocking block

Depending on the value of the ground acceleration and the coefficient of friction μ, the block may translate with the ground; enter in a rocking motion or a sliding motion. A necessary condition for the block to enter in a rocking motion is $\mu > b/h$ (Aslam et al. 1980, Scalia and Sumbatyan 1996). The possibility for a block to slide during the rocking motion has been investigated by Zhu and Soong (1997), and Pompei et al. (1998). In this study, it is assumed that the coefficient of friction between the block and its base is sufficiently large to prevent sliding at any instant in the rocking motion.

Under a positive horizontal ground acceleration, $\ddot{u}_g$, the block will initially rotate with a negative rotation, $\theta<0$, and, if it does not overturn, it will eventually assume a positive rotation and so forth. Assuming zero vertical base acceleration ($\ddot{v}_g(t) = 0$), the equations of motion are

$$I_0\ddot{\theta} + mgR\sin(-\alpha-\theta) = -m\ddot{u}_g R\cos(-\alpha-\theta) \qquad \theta < 0 \tag{1}$$

and

$$I_0\ddot{\theta} + mgR\sin(\alpha-\theta) = -m\ddot{u}_g R\cos(\alpha-\theta) \qquad \theta > 0 \tag{2}$$

Where, for rectangular blocks, can be assumed:

$$I_0 = \frac{4}{3}mR^2 \tag{3}$$

The equations (1) and (2) can be expressed in the compact form

$$\ddot{\theta}(t) = -p^2\left\{\sin\left(\alpha\ sgn\left[\theta(t)\right]-\theta(t)\right)+\frac{\ddot{u}_g}{g}\cos(\alpha\ sgn\left[\theta(t)\right]-\theta(t))\right\} \tag{4}$$

Where

$$p = \sqrt{\frac{3g}{4R}} \tag{5}$$

is a quantity with units in rad/sec.

The oscillation frequency of a rigid block under free vibration is not constant, since it strongly depends on the vibration amplitude (Housner, 1963). Nevertheless, the quantity p is a measure of the dynamic characteristics of the block.

When the block is rocking, it is assumed that the rotation continues smoothly from point O to O' and there is no loss of energy during the rocking motion.

Considering the non linear nature of the problem, for evaluating the various overturning boundaries conditions, equation (4) must be rewritten in a system:

$$\left\{y(t)\right\} = \begin{Bmatrix}\theta(t)\\ \dot{\theta}(t)\end{Bmatrix} \tag{6}$$

and the time-derivate vector is

$$f(t) = \left\{\dot{y}(t)\right\} = \begin{Bmatrix}\dot{\theta}(t)\\ -p^2\left[\sin\left[\alpha\ sgn\left[\theta(t)\right]-\theta(t)\right]+\frac{\ddot{u}_g(t)}{g}\cos\left[\alpha\ sgn\left[\theta(t)\right]-\theta(t)\right]\right]\end{Bmatrix} \tag{7}$$

This system can be solved by a numerical integration. One way for performing this integration is to use the standard Ordinary Differential Equation (ODE45) solver available in

MATLAB®, therefore equation (7) was implemented in Matlab, and results found for a given geometry have been shown in the acceleration-frequency plane.

The results are functions of the geometrical shape of the rigid body, in fact it determines the dynamic characteristics p and the angle α which can be considered the limit not to be exceeded to prevent overturning. The ground accelerations are expressed by $\ddot{u}_g$. It can be a real accelerogram or a geometrical pulse creates to simulate the behaviour of the rigid body.

The results obtained shown the variation of the position of the center of gravity, and consequently the variation of the angle θ. During this phase the rocking response is determined by the ratio between the angle θ and angle α. If the ratio is smaller than *1* the rigid body is in a condition of rocking but if the ratio becomes bigger than *1,* the centre of gravity is out of the base of the rigid body, consequently the equilibrium is not satisfied and the object overturns

This type of problem is independent from the mass of the rigid body (the mass m is present in all the terms of equation (1) and (2), and consequently results are equally valid for each rigid body with this particular geometry).

The geometry of the rigid body is very important. In fact, a slender body will have more chances to overturn than a stubby one. This statement is justified by the position of the center of gravity. If the rigid body has a small base and is tall, the center of gravity will have a larger lever arm when it will be subjected to dynamic actions, therefore the possibility of overturning will be more.

3 ROCKING RESPONSE UNDER GEOMETRICAL PULSE

The analysis presented in this section focuses on the overturning potential of some geometrical pulse used to simulate the ground acceleration.

This problem is governed by three major variables: the geometric nature of the system, the acceleration and the frequency of the input. The behavior of a free standing body can be defined after setting these variables.

Once it has been fixed the geometry of the rigid body the acceleration-frequency plane is the most convenient way to show the results. This plane represents all the waves that have been used in the simulation of the behavior of the rigid body. If a specific acceleration and a given frequency will cause the overturning of the rigid body an appropriate sign on the plane will mark this event. The collection of all these accelerations and frequencies that cause the overturning will form the non-secure area of the acceleration-frequency plane. In fact, a line will be the boundary that divides the safe area from the unsafe one.

In order to obtain results is necessary to determine the geometry of the problem. We consider a slender block, then can be assumed $\alpha=0.25\ rad$. This means that the value of the measure of the dynamic characteristics of the block is $p = 2.14\ rad/s$.

Then the other two variables (acceleration and frequency) that govern the system are ranged and results are summarized in the acceleration-frequency plane.

3.1 One-sine Pulse

The ground acceleration used for this analysis is represented by a sine wave like the one in Figure 2:

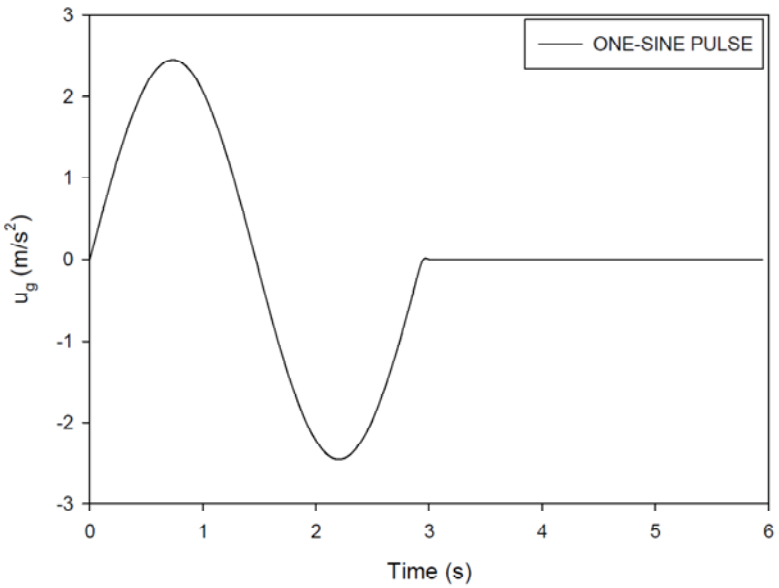


Figure 2 : Ground acceleration one sine pulse

It can be expressed by the following expression:

$$\ddot{u}_g(t) = a_p \sin(\omega_p t) \tag{8}$$

Where a_p is responsible of the maximum acceleration while ω_p is the frequency of the input; changing these terms one can explore the whole acceleration-frequency plane.

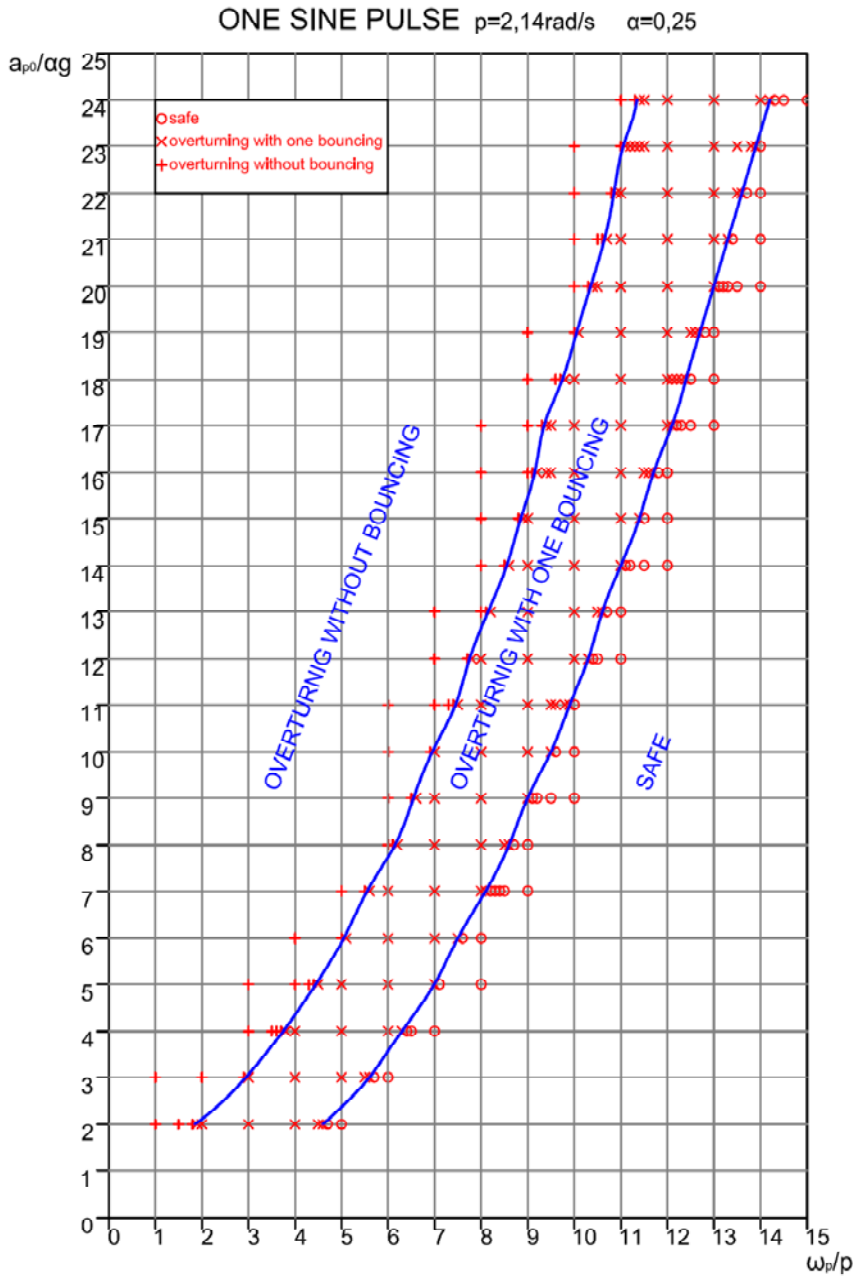


Figure 3 : Acceleration-frequency plane for one-sine pulse.

The results obtained can be grouped into several classes: (i) overturning without bouncing, (ii) overturning with one bouncing, (iii) no overturning.

Overturning without bouncing: in this case the input doesn't enable the rocking motion of the rigid body and the absolute value of the ratio θ/α quickly becomes greater than 1. This means that the rigid body overturns because the equilibrium is not satisfied. A cross is placed in the acceleration-frequency plane where overturning occurs.

Overturning with bouncing: in this case rigid body bounces on a vertex then changes direction of motion and overturns on the other side. This behavior occurs in a specific area of the acceleration-frequency plane, between the previous zones where the reversal occurs and a safe zone where the rigid body doesn't overturn.

No overturning: in this case the rigid body starts a rocking motion and the absolute value of the ratio θ/α remains always less than one, therefore the rigid body does not overturn. It happens in the third main area of the acceleration-frequency plane. This behavior is represented in the plane by a little circle.

3.2 One-cosine Pulse

The ground acceleration used for this analysis is represented by a sine wave like the one in Figure 4:

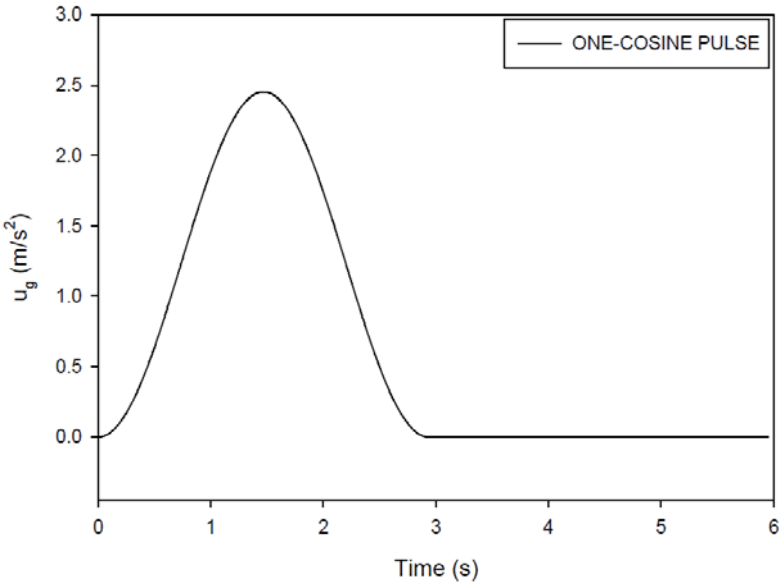


Figure 4: Ground acceleration one sine pulse.

It can be expressed by the following expression:

$$ii_g(t) = \left(\left(a_p - a_p \cos\cos\left(\omega_p t\right)\right)/2\right) \tag{9}$$

The results obtained with this input can be grouped into two classes: overturning without bouncing and no overturning.

The safe area of the acceleration-frequency plane is smaller than the previous case and one can notice the absence of overturning with bouncing this time.

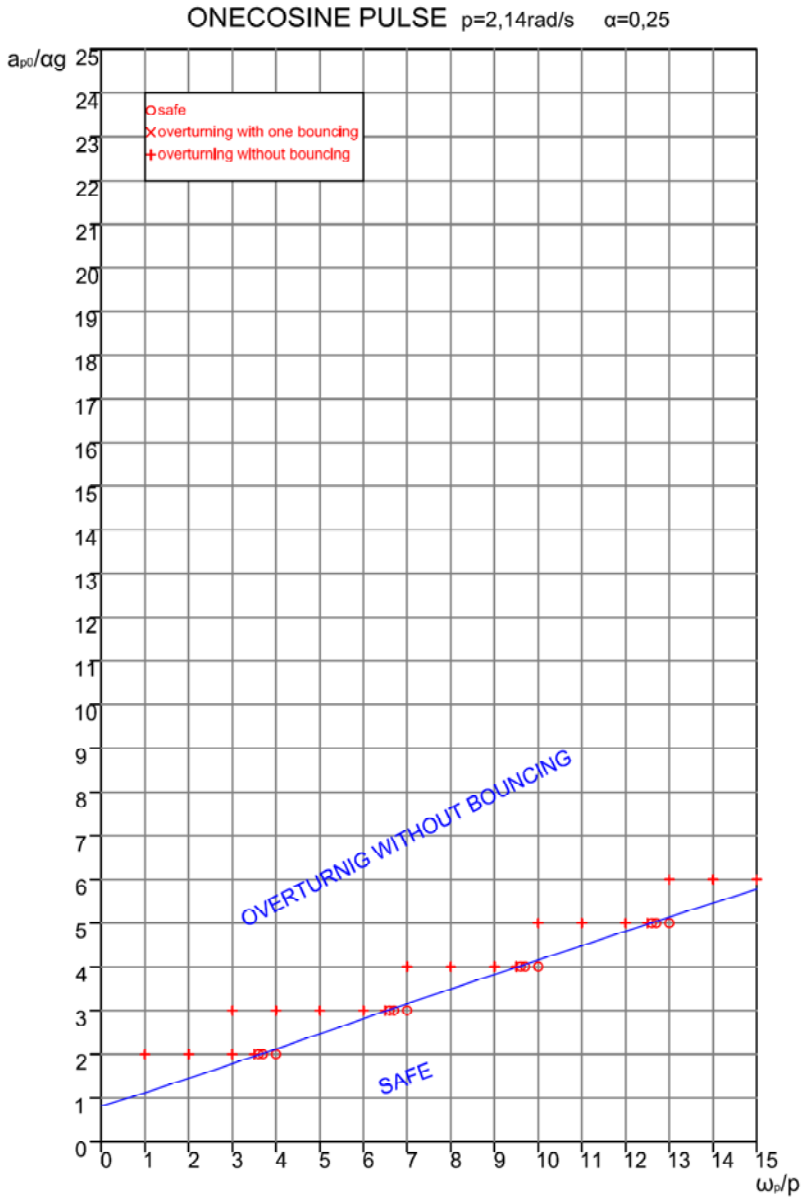


Figure 5: Ground acceleration one cosine pulse.

3.3 Half-sine Pulse

The ground acceleration used for this analysis is represented by a sine wave like the one in Figure 6:

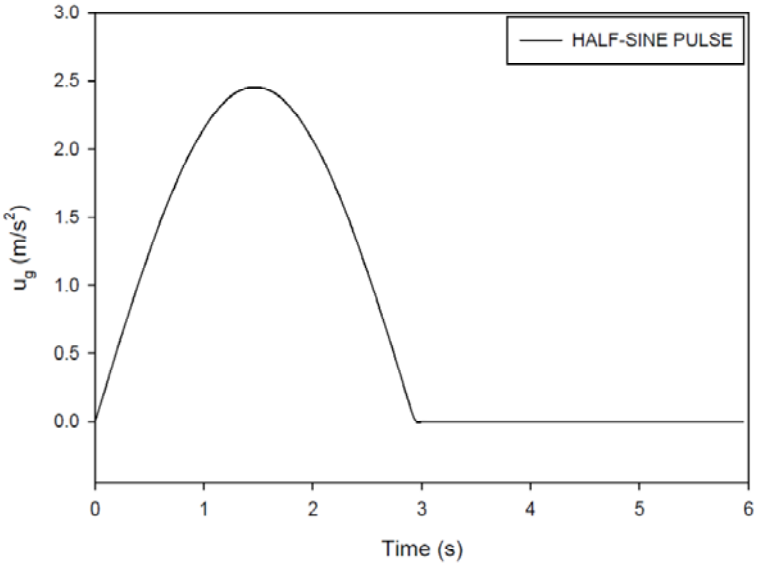


Figure 6: Ground acceleration half sine pulse.

It can be expressed by the following expression:

$$\ddot{u}_g(t) = a_p \sin\left(\left(\omega_p t\right)/2\right) \tag{10}$$

The results obtained with this input can be grouped into two classes: overturning without bouncing and no overturning.

The results obtained are very similar to the previous one obtained for the cosine pulse, but the safe-area is slightly smaller than the previous.

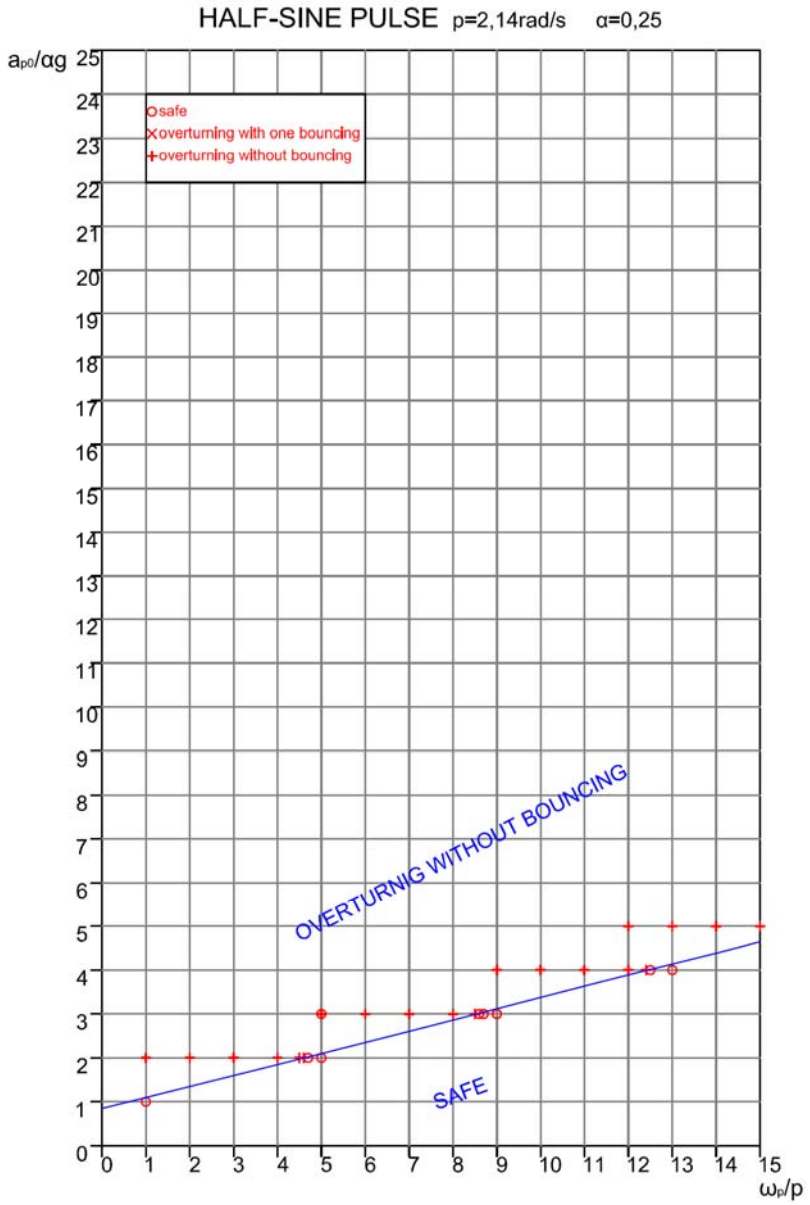


Figure 7: Ground acceleration half-sine pulse.

4 CASE STUDY: TYPICAL STEEL BUILDING IN CALIFORNIA

In this section the overturning potential of one piece of furniture is calculated with real floor acceleration and considering a common piece of furniture.

4.1 Floor motion data

The following table lists real time monitored buildings in California. The geometry of these structures is very different, but they are all made of stainless, they have different floor shape and different number of story. For every building some sensors have been placed in specific place at different height of the structure and with different orientation. Every sensor during a seismic event has recorded the floor acceleration. The total number of floor motion

used for the following analysis is 436, some records were discarded because the signal was not clean.

Table-1 Floor motion data

ID	Station	No. of Stories	Height (in.)	Earthquake	PGA (g) Transverse	PGA (g) Longitudinal
001	Pasadena	12	2016	Northridge 17Jan1994	0.135	0.234
002	Burbank	6	990	Whittier87	0.17	0.23
003	San Jose	3	594	LomaPrieta 17Oct1989	0.18	0.2
004	Palm Springs	4	954	PalmSprings86	0.16	0.19
005	South San Francisco	4	726	LomaPrieta 17Oct1989	0.16	0.14
006	Richmond	3	554	LomaPrieta 17Oct1989	0.11	0.08
007	San Jose	13	2527	LomaPrieta 17Oct1989	0.087	0.098
008	San Bernardino	3	496	Landers92	0.11	0.08
009	Burbank	6	990	SierraMadre91	0.11	0.12
010	San Rafael	5	1110	Bolinas99	0.107	0.082
011	Pasadena	12	2016	WhittierNarrows 16Mar2010	0.045	0.11
012	San Bernardino	3	496	San Bernardino 08Jan2009	0.1	0.08
013	San Bernardino	9	1411	Landers92	0.068	0.088
014	Pasadena	12	2314	Northridge 17Jan1994		
015	Pasadena	12	2016	ChinoHills 29Jul2008	0.08	0.06
016	San Bernardino	5	828	Northridge 17Jan1994	0.046	0.057
017	Redlands	7	1253	Landers92	0.06	0.07
018	San Bernardino	5	828	Landers92	0.08	0.08
019	Lancaster	5	942	Landers92	0.08	0.05
020	Chatsworth	2	482	ChinoHills 29Jul2008	0.07	0.04
021	Long Beach	7	1248	Whittier87	0.07	0.04
022	Lancaster	5	942	Landers92	0.055	0.07
023	San Bernardino	5	828	BigBear92	0.06	0.07
024	Los Angeles	32	4214	ChinoHills 29Jul2008	0.065	0.06
025	Long Beach	15	3456	Whittier87	0.055	0.041
026	Long Beach	15	3456	Inglewood 17May2009	0.059	0.043
027	San Bernardino	3	496	ChinoHills 29Jul2008	0.052	0.047
028	Chatsworth	2	482	Chatsworth 09Aug2007	0.04	0.046
029	San Jose	13	2527	MorganHill84	0.039	0.036
030	San Jose	3	594	AlumRock 30Oct2007	0.034	0.027
031	Palm Springs	4	954	Calexico 04Apr2010	0.04	0.02
032	San Bernardino	5	828	ChinoHills 29Jul2008	0.0265	0.036
033	San Bernardino	3	496	LakeElsinore 02Sep2007	0.036	0.031
034	San Diego	22	3804	Calexico 04Apr2010	0.034	0.026
035	Palm Springs	4	954	BorregoSprings 07Jul2010	0.03	0.03
036	Los Angeles	32	4214	WhittierNarrows 16Mar2010	0.028	0.033
037	Redlands	7	1253	Redlands 13Feb2010	0.0255	0.026
038	San Bernardino	3	496	Whittier87	0.029	0.024
039	South San Francisco	4	726	MorganHill84	0.03	0.02
040	Burbank	6	990	ChinoHills 29Jul2008	0.028	0.029
041	San Bernardino	5	828	BigBearCity 22Feb2003	0.0125	0.023

042	San Bernardino	3	496	Calexico 04Apr2010	0.0221	0.0179
043	Long Beach	15	3456	ChinoHills 29Jul2008	0.013	0.021
044	San Bernardino	3	496	BorregoSprings 07Jul2010	0.0179	0.0169
045	Lancaster	5	942	BigBearCity 22Feb2003	0.009	0.008
046	San Diego	22	3804	BorregoSprings 07Jul2010	0.0155	0.0157
047	Los Angeles	32	4214	Inglewood 17May2009	0.008	0.0155
048	Gilroy	2	372	San Martin 15Jun2006	0.016	0.012
049	Richmond	3	554	Piedmont 20Jul2007	0.015	0.013
050	Redlands	7	1253	Calexico 04Apr2010	0.0112	0.0125

4.2 Geometrical dimension of furniture

For the analysis we can consider a piece of furniture like the one shown in the following figure with the following characteristic:

- Width = 0,91 m
- Depth = 0,54 m
- Height = 1,90 m

Obviously the risk of overturning is higher in the shortest side of the furniture.

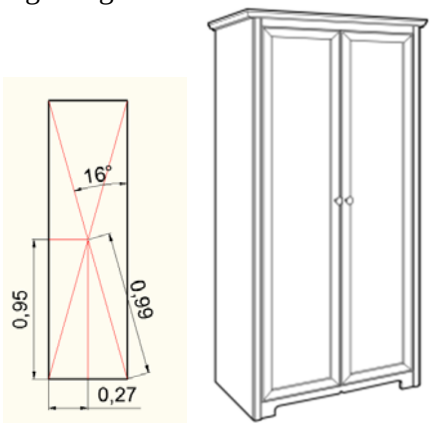


Figure 8 : Geometrical shape of the piece of the furniture.

4.3 Overturning risk

4.3.1. Kaneko risk estimation

Kaneko in 2004 proposed a simplified formula to estimate the risks of the overturning of furniture:

$$R = \begin{cases} \alpha \cdot \phi\left(\left(\ln Acc_f - \lambda_A\right)/\zeta_A\right), F_f \le F_b \\ \alpha \cdot \phi\left(\left(\ln Vel_f - \lambda_V\right)/\zeta_V\right), F_f > F_b \end{cases}$$
$$\lambda_A = \ln\left(\left(B/H\right) g \cdot \left(1 + B/H\right)\right) \quad (11)$$
$$\lambda_V = \ln\left(10B/\sqrt{H} \cdot \left(1 + B/H\right)^{2.5}\right)$$

Where Acc_f [cm/sec^2] is the maximum acceleration and Vel_f [cm/sec] is the maximum velocity floor response, ϕ is the normal distribution function with mean value λ_A or λ_V and standard deviation ζ_A or ζ_V, which is assumed to be 0.2 or 0.3 for an individual piece of furniture. H [cm] and B [cm] are the height and the depth of furniture, g is the acceleration of

gravity, F_f [Hz] is the equivalent frequency of floor, F_b [Hz] is the boundary frequency of furniture given by

$$F_f = Acc_f / \left(2\pi Vel_f\right)$$
$$F_b = 15.6 / \sqrt{H} \cdot \left(1 + B / H\right)^{-1.5} \tag{12}$$

α is the slide resistant coefficient which ranges from 0 to 1and is determinate by considering the ratio B/H and the friction coefficient between floor and furniture. In this study, it is assumed that the coefficient of friction between the block and its base is sufficiently large to prevent sliding at any instant in the rocking motion, therefore α=1.

The results obtained from the equation (11) are a measure of the risk of overturning. If the value of R is bigger than 0,7 then the risk will be very high.

The equation (11) has been implemented on matlab in order to estimate the overturning risk for the signals recorded in the considerate building.

The results obtained are shown in Figure 9, and show that the risk of overturning is very high in only three buildings. These buildings are the station San Jose during the earthquake of Lomapietra (17Oct1989) ID 003; the station Palm Springs ID 004 during the earthquake PalmSprings86 and the station South San Francisco ID 005 during the earthquake of Lomapietra (17Oct1989).

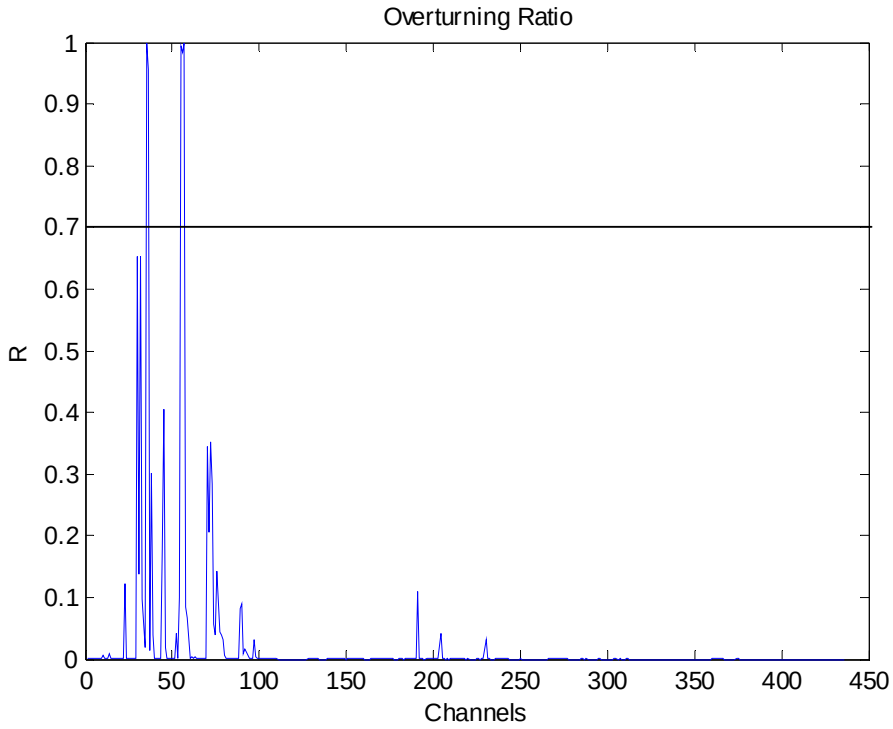


Figure 9 : Overturning risk

The following table summarizes the result obtained with the Kaneko formulation for the three buildings where the risk of overturning is high. In all this building the higher risk is in last floor of the structure, but sometimes the differences between two signals located in the same floor are very large.

Table-2 Overturning risk for Kaneko

ID	story	CHANNEL	R [%]
003	1	ACCCHAN2	0%
	1	ACCCHAN3	0%
	1	ACCCHAN4	0%
	3	ACCCHAN5	65%
	3	ACCCHAN6	14%
	3	ACCCHAN7	65%
	4	ACCCHAN8	10%
	4	ACCCHAN9	2%
	4	ACCCHAN10	100%
004	5	ACCCHAN2	96%
	5	ACCCHAN3	1%
	5	ACCCHAN4	30%
	3	ACCCHAN5	4%
	3	ACCCHAN6	0%
	2	ACCCHAN7	0%
	2	ACCCHAN8	0%
	5	ACCCHAN10	18%
	3	ACCCHAN11	41%
	2	ACCCHAN12	2%
005	1	ACCCHAN4	0%
	1	ACCCHAN5	0%
	2	ACCCHAN6	4%
	2	ACCCHAN7	0%
	2	ACCCHAN8	10%
	5	ACCCHAN9	99%
	5	ACCCHAN10	98%
	5	ACCCHAN11	100%

For example, the results obtained for the record 003 shows a strange conduct in the last floor because for one signal the risk of overturning is very high while for the other two signals on the same floor the risk is negligible. Even if the accelerations of the floor of the structure are different in different point where the signals are recorded these differences are too marked for a single floor response. The same consideration can be done for the building 004 while for the building 005 all the signals on the last floor show high risk of overturning phenomena.

4.3.2. Housner risk estimation

A safety factor for the overturning phenomena has been evaluated also with the Housner formulation Equation(7), considering the floor time history and the same piece of furniture used with Kaneko. This kind of analysis is very expensive in terms of calculation time, in fact for every channel is necessary to solve the differential equation and the computing time can last for several hours. For this reason the analysis has been done only with the three buildings that have shown overturning phenomena with the Kaneko formulation.

The results obtained are shown in the Table 3.

Table 3 : Overturning risk for Housner formulation

ID	story	CHANNEL	[%]
003	1	ACCCHAN2	29%
	1	ACCCHAN3	37%
	1	ACCCHAN4	36%
	3	ACCCHAN5	48%
	3	ACCCHAN6	53%
	3	ACCCHAN7	71%
	4	ACCCHAN8	83%
	4	ACCCHAN9	100%
	4	ACCCHAN10	99%
004	5	ACCCHAN2	100%
	5	ACCCHAN3	100%
	5	ACCCHAN4	71%
	3	ACCCHAN5	77%
	3	ACCCHAN6	59%
	2	ACCCHAN7	37%
	2	ACCCHAN8	40%
	5	ACCCHAN10	100%
	3	ACCCHAN11	77%
	2	ACCCHAN12	56%
005	1	ACCCHAN4	42%
	1	ACCCHAN5	45%
	2	ACCCHAN6	59%
	2	ACCCHAN7	50%
	2	ACCCHAN8	71%
	5	ACCCHAN9	100%
	5	ACCCHAN10	77%
	5	ACCCHAN11	100%

With this model the risk of overturning phenomena within the same floor does not exhibit excessive difference. One can notice higher possibility of overturning in the fourth floor of the building 003 as well as on the fifth floor of the building 004.

This analysis however show higher risk of overturning phenomena compared to the previous one.

5 PROPOSED FORMULATION

The followings formulas have been developed to avoid long calculation times. They have a structure similar to the Kaneko formula but with some new coefficients and some new parameters minimize the differences between the two methods. Therefore the aim of this formula is to avoid the excessive differences between signals on the same floor.

The proposed formula is:

$$OR = \phi\left(\left(\ln Acc_f - \lambda_A\right)/X_1\right) + X_2 \cdot T_1 \cdot \left(\frac{Acc_f}{Vel_f}\right) + X_3 \cdot \left(\frac{H_m}{Dis_f}\right) \cdot \left(B/H\right) \tag{13}$$

Where Acc_f [cm/sec^2] is the maximum acceleration and Vel_f [cm/sec] is the maximum velocity floor response and Dis_f [cm] is the maximum displacement floor response. ϕ is the

normal distribution function with mean value λ_A and standard deviation X_1. H [cm] and B [cm] are the height and the depth of furniture. H_m expresses the height from the ground where the furniture is located.

T_1 is the main period of the structure calculate with the approximate formulas proposed by the Italian NTC2008 – Norme tecniche per le costruzioni – D.M. 14 gennaio 2008.

$$T_1 = C_1 \cdot H^{3/4} \tag{14}$$

Where $C_1$is a constant equals to 0,085 for steel frame building and H is the height in meter of the structure.

The coefficient: X_1, X_2, X_3 have been evaluated minimizing the differences between the results of the three building considering only the signals in the last floor of every structure.

X_1 = 0.1104
X_2 = 0.0141
X_3 = -0.0890

The results obtained are shown in the following table:

Table 4 Overturning risk for proposed formulation

ID	story	CHANNEL	[%]
003	1	ACCCHAN2	11%
	1	ACCCHAN3	8%
	1	ACCCHAN4	10%
	3	ACCCHAN5	80%
	3	ACCCHAN6	9%
	3	ACCCHAN7	81%
	4	ACCCHAN8	100%
	4	ACCCHAN9	95%
	4	ACCCHAN10	100%
004	5	ACCCHAN2	100%
	5	ACCCHAN3	98%
	5	ACCCHAN4	13%
	3	ACCCHAN5	6%
	3	ACCCHAN6	7%
	2	ACCCHAN7	10%
	2	ACCCHAN8	10%
	5	ACCCHAN10	100%
	3	ACCCHAN11	41%
	2	ACCCHAN12	9%
005	1	ACCCHAN4	6%
	1	ACCCHAN5	9%
	2	ACCCHAN6	6%
	2	ACCCHAN7	7%
	2	ACCCHAN8	8%
	5	ACCCHAN9	100%
	5	ACCCHAN10	100%
	5	ACCCHAN11	100%

The number of overturning phenomena evaluated with this formula is consistent with the previous one and the behaviour of furniture located in the same plane seems to be improved, as shown in the following figure that summarize all the signal.

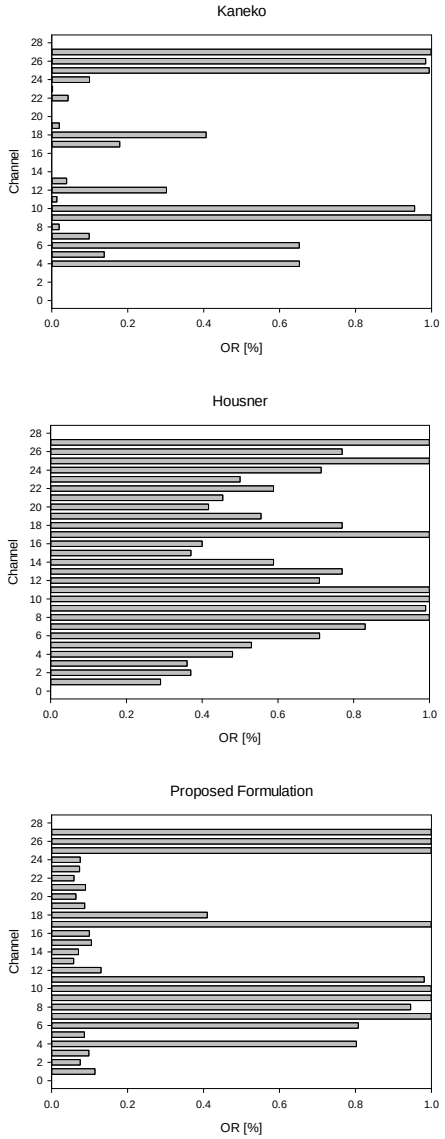


Figure 10 : Overturning ratio for the different formulation

6 CONCLUDING REMARKS

The aim of this study is to establish an easy way to locate the area for overturning risk inside a generic building. The problem is complex but the proposed formulas provide an important support to establish the floor on which are greater the chances of a reversal.

As shown in the Figure 10, all the results clearly indicate that there is the possibility of overturning phenomena in these buildings for some determinate acceleration value e specific furniture geometry. The proposed formulation has the main benefit of the two method used in this research, it is easy to use and the results are homogeneous in specific floor of the structure.

Developments of this research are now directed to give a bigger importance at the shape of the object. The slenderness of the furniture plays an important role in overturning phenomena, therefore the coefficientsX_1, X_2, X_3 must be re-setting using different geometry of the furniture. For example using a bigger base of the furniture one can reduce the lever arm of the rigid body subjected to dynamic actions, this means that the possibility of overturning phenomena will be smaller.

REFERENCES

[1] A. Pompei, A. Scalia and M. A. Sumbatyan, "Dynamics of rigid block due to horizontal ground motion", Journal of Engineering Mechanics, ASCE, Vol. 124, 713-717, (1998).

[2] A. Scalia and M. A. Sumbatyan, "Slide rotation of rigid bodies subjected to a horizontal ground motion", Earthquake Eng. and Str. Dynamics, Vol. 25, 1139-1149, (1996).

[3] Housner GW. (1963)The beaviour of inverted pendulum structures during earthquakes.*Bulletin of the Seismiological Society of America,* **53(2)**,403-417.

[4] Ishiyama Y. (1982). Motions of Rigid Bodies and Criteria for Overturning by Earthquake Excitations. Earthquake Engineering and Structural Dinamics, Vol.10, 635-350.

[5] Kaneko Mika, Hayashi Yasuhiro (2004). A proposal for simple equations to express a relation between overturning ratios of rigid bodies and input excitation.

[6] Makris Nicos, Yiannis Roussos (1998) Rocking response and overturning of equipment under horizontal pulse type motion.

[7] P. D. Spanos and A. S. Koh, "Rocking of rigid blocks due to harmonic shaking", Journ. Engrg.Mech. Div. ASCE 110, 1627-1642, (1984).

[8] Shenton, H.W. (1995)"Criteria for Initiation of Slide, Rock, and Slide-Rock Rigid-Body Modes. *Journal of engineering mechanics, 690-693.*

[9] Yim, Chopra, Penzien.(1980). Rocking response of rigid block to earthquake. Earthquake Engineering and Structural Dinamics, Vol. 8, 565-587.

[10] Zhang Jian, Makris Nicos (2001). Rocking respone of free-standing blocks under cycloidal pulses.*Journal of engineering mechanics, 473-481.*

COMPDYN 2013
4th ECCOMAS Thematic Conference on
Computational Methods in Structural Dynamics and Earthquake Engineering
M. Papadrakakis, N.D.Lagaros, V. Plevris (eds.)
Kos Island, Greece, 12–14 June 2013

FINITE ELEMENT MODELING OF "ROCKING WALLS"

Andrea Belleri[1], Mauro Torquati[1], and Paolo Riva[1]

[1] Department of Engineering, University of Bergamo
Viale Marconi 5, 24044 Dalmine – Bergamo, Italy
e-mail: andrea.belleri@unibg.it; mauro.torquati@unibg.it; paolo.riva@unibg.it

Keywords: Rocking Walls; Nonlinear Static Analyses; Nonlinear Time History Analyses; Rayleigh Damping; Acceleration Spikes.

Abstract. *Rocking walls represent an emerging solution for lateral force resisting systems in low to medium seismicity sites. The main features of these systems are the self-centering capacity after a seismic event provided by unbonded post-tensioned tendons connecting the top of the wall to the foundation and the low damage, compared to traditional reinforced concrete shear walls, being the rocking wall placed on top of the foundation with no longitudinal reinforcing bar crossing the wall-foundation joint, thus avoiding tension in concrete. These systems accommodate displacement seismic demand by the development of a concentrated gap opening between the wall and the foundation instead of an extended plastic hinge as in traditional shear walls.*

The aim of the present paper is the comparison of different rocking wall finite element modeling techniques, by means of nonlinear static and dynamic analyses, in order to highlight the influence of the system damping choice on the numerical response and the differences in terms of lateral and vertical wall displacements, base shear, neutral axis variation and compressive strain at the wall toe. The finite element models considered herein are based on nonlinear brick and plane-stress plate elements, fiber beam elements, compression only springs and concentrated rotational springs.

1 INTRODUCTION

Precast concrete structures have been successfully adopted worldwide as lateral force resisting systems of buildings in low to high seismicity areas. In the case of one to two story industrial and commercial buildings, in low to moderate seismicity areas, the structural layout is typically a hinged frame and the lateral force resistance is provided by cantilever columns connected at the base to isolated footings through mechanical connectors, pocket foundations or grouted sleeve solutions [1-3].

For higher buildings and higher seismicity levels the lateral force resistance is provided by precast concrete structures emulating cast in place reinforced concrete [4] or by jointed ductile precast concrete connections which, by means of prestressed or post-tensioned elements, eliminate or reduce the residual structural displacement and rotations after a seismic event and provide energy dissipation by means of specific details [5].

As an alternative to traditional reinforced concrete walls as lateral force resisting system, a possible precast solution, suitable for medium rise buildings in low seismicity areas, consists of precast wall panels placed on top of the foundation without providing continuity to longitudinal rebars at the foundation-wall interface; the overturning moment capacity and self-centering capability is provided by gravity loads supplemented with unbonded post-tensioned tendons. This solution is referred to as "rocking wall" and is an extension of the hybrid coupled wall system developed under the PRESSS program [5]. In this system the wall horizontal displacement demand is accommodated by the development of a single gap opening at the wall-foundation interface with no concrete in tension compared to extended cracking in the plastic hinge region at the wall base in traditional reinforced concrete walls.

During a seismic event the wall rocks at its toes, providing appropriate compressive concrete resistance in the toe region by confinement and appropriate self-centering capacity by unbonded post-tensioned tendons, exhibiting a nonlinear elastic response with a distinct stiffness reduction associated to uplift of the wall base. Due to the lack of energy dissipation, limited to the hysteresis in the concrete at the compressed toes, rocking wall systems are suitable only for low seismicity areas. For higher seismic demand additional energy dissipators, hysteretic or viscous devices among others, could be added to the wall panels leading to the so called "hybrid wall" solutions.

Experimental research was conducted on single rocking and hybrid wall panels under both quasi-static [6-8] and dynamic loading [9] proving the good performance of these systems if detailed appropriately. The dynamic interaction between rocking and hybrid walls and the rest of the structure was investigated during the DSDM project [10] in which shake table tests were conducted on a three story half-scale precast concrete structure whose lateral force resisting system consisted entirely on rocking and hybrid walls [11, 12].

Although extensive experimental tests were carried out on rocking and hybrid walls, limited information is available, to the authors' knowledge, on how to numerically model these structures [13-15] in order to capture the typical nonlinear response associated to wall base uplift. The present paper focuses on numerical modeling of rocking walls investigating the effects of different modeling techniques in both nonlinear static and dynamic analyses. The rocking wall chosen as reference for the present study is extrapolated from the aforementioned DSDM project [11, 12]. Being the aim of the paper the investigation of finite modeling techniques, there is no interest in modeling the whole building in order to capture rocking wall and floors interaction and wall foundation influence; therefore the floors are modeled as point masses and the foundation is deliberately made rigid.

The finite element models considered herein are based on three dimensions (3D), two dimensions (2D) and one dimension (1D) elements, being the 3D and 2D nonlinear brick and

plane-stress plate elements, respectively, and the 1D fiber beam elements, compression only springs and concentrated rotational spring at the base of the wall. The comparison between the investigated modeling techniques is carried out both in global terms, as base shear, lateral displacement and vertical uplift, and in local terms, as neutral axis variation and compressive strain at the wall toe when available. The influence of the system damping choice on the numerical response is also investigated.

2 SELECTED CASE STUDY

The selected case study considers the rocking wall adopted as lateral force resisting system for a three story half-scale precast concrete structure resembling a parking garage tested on the Network for Earthquake Engineering Simulation (NEES) Large High-Performance Outdoor Shake Table at the University of California at San Diego. Detailed information on the test specimen geometry, material tests and loading sequence can be found elsewhere [11, 12].

A picture of the tested structure and wall dimensions are shown in Figure 1, while the relevant data for the finite element analyses are reported in Table 1. The total mass of each floor, taking into account the tributary mass of the columns, is 36795 kg, 38999 kg and 34230 kg for the 1st, 2nd and 3rd floor, respectively; it is worth noting that a vertical slotted connection between the wall and the floors allowed to transfer only horizontal loads.

The walls were designed to act as rocking walls for low intensity tests and as hybrid walls for moderate and high seismic hazard. In the present paper only the rocking wall configuration is considered. The input motion adopted for the selected case study represents a design basis earthquake for Knoxville (TN – USA); the pseudo acceleration spectrum is shown in Figure 2. It is worth noting that similitude law was not achieved by mass substitution but only by scaling the input ground motions, horizontal acceleration field amplified by 1.855 and ground motions time step compressed by 1.855, therefore for sake of clarity the results will be presented herein in dimensionless terms.



Figure 1: Tested structure and wall dimensions.

Unconfined concrete properties [16]	
Strength (f'_c) average of two cylinder tests	54 MPa
Elastic modulus (E_c)	37000 MPa
Strain at maximum stress (ε_{c0})	0.2%
Ultimate compressive strain	0.55%
Confined concrete properties [16]	
Confined maximum stress (f'_{cc})	80.8 MPa
Strain at maximum stress (ε_{cc})	0.67%
Ultimate compressive strain (ε_{cu})	3.77%
Unbonded prestress tendons	
Tendon set	5 x 0.5" strands
Prestressing force for each tendon set	235.75 kN
Unbonded length	8529 mm

Table 1: Rocking wall relevant properties.

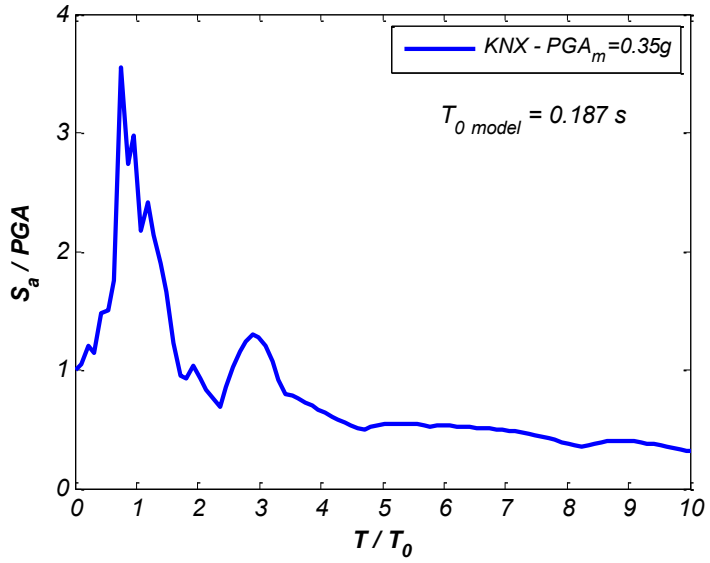


Figure 2: Pseudo acceleration spectrum (ξ = 0.05%).

3 FINITE ELEMENT MODELING

The finite element models presented herein represent a single rocking wall panel (Figure 1), being the scope of the paper the investigation of different modeling techniques with no interest on the global interaction between the wall and the building and the local influence of the foundation beam in the rocking wall response. The foundation is made deliberately rigid by increasing the concrete elastic modulus by two orders of magnitude for the 3D and 2D elements representation and it is modeled consistently in all the 1D elements models in order to achieve the same rotational stiffness. The tributary mass of each floor is modeled as lumped horizontal mass at the wall center line corresponding to the floor height. The wall mass is considered directly starting from the wall material density.

Mander model [16] is adopted to describe the material stress-strain relationship for confined and unconfined concrete, while the formulation contained in the PCI Handbook [17] is considered for the prestressing strands.

3.1 3D and 2D elements models

The 3D and 2D elements models analyses are performed with the finite element software Abaqus [18] adopting brick elements (3D elements model) and plane stress elements (2D elements model) for the wall panel and the foundation and truss elements for the prestressing tendons. The inelastic properties of the concrete are taken into account with the "concrete damaged plasticity model" available in the software package, a viscosity parameter of 0.0004 is added for convergence issues; the tendons inelastic component is modeled with a plastic isotropic material model.

The foundation, whose arbitrary chosen dimensions are 3000x500x203mm, is made to act as a rigid body increasing the concrete elastic modulus by two orders of magnitude. The connection between the wall and the foundation is modeled using a "surface to surface contact" interaction, with tangential behavior type "rough" and normal behavior type "hard contact" under compressive stress: this model allows vertical uplift and avoid horizontal slippage.

The unbounded tendons are modeled as truss elements pinned connected to the ground at the base and rigidly connected to the top of the wall by means of the "beam" type multi point constrain [18]. The vertical and horizontal reinforcing steel bars of the wall confined toe region are modeled as one-dimensional beam elements directly embedded in the concrete matrix only for the 2D elements model.

Three loading steps are created: in the first load step the boundary conditions are set and the gravity load is applied to the model; in the second load step prestressing force is applied to each tendon; in the third load step the nonlinear static or dynamic analysis is performed.

A mesh composed of quad-dominated elements with 4-node bilinear plane stress elements and reduced integration is used both for the wall and the foundation in the 2D elements model while 8-node linear bricks with reduced integration are adopted in the 3D elements model (Figure 3). The foundation element size is 100mm while the wall element size varies from 200mm, at the top of the wall, to 25mm, at the toe regions, for a better description of local effects during base joint opening. Higher order elements and a refined discretization led to similar output results and are not presented herein.

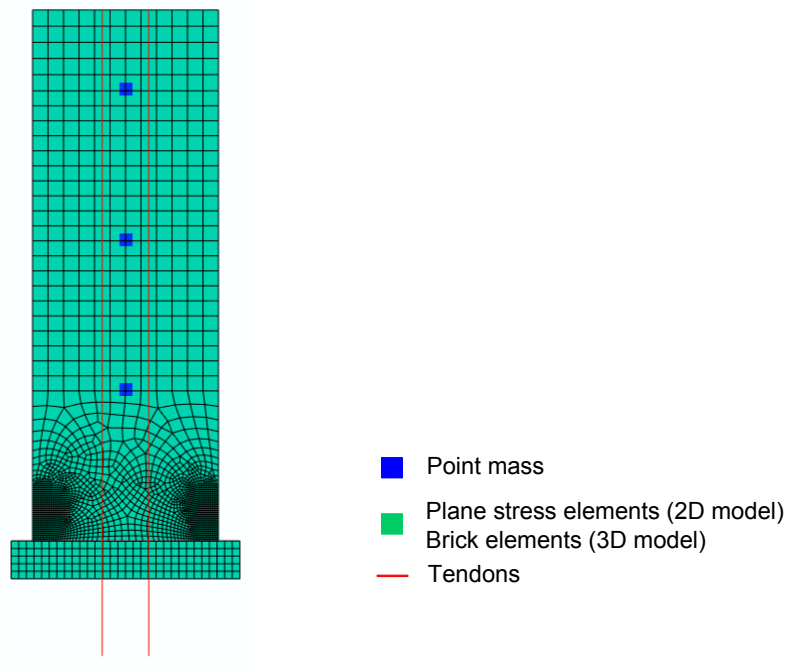


Figure 3: Representation of the 2D/3D elements models.

In the nonlinear dynamic analyses, no global damping is assigned to the model; mass proportional material damping (β=0.00623) is provided only in the wall for convergence issues.

3.2 1D elements models

Three 1D element models are considered in the paper adopting basic and advanced features of the finite element software MidasGEN [20]: fiber elements (*Fb*) model, multi-springs (*MS*) model and rotational spring (*RS*) model (Figure 4).

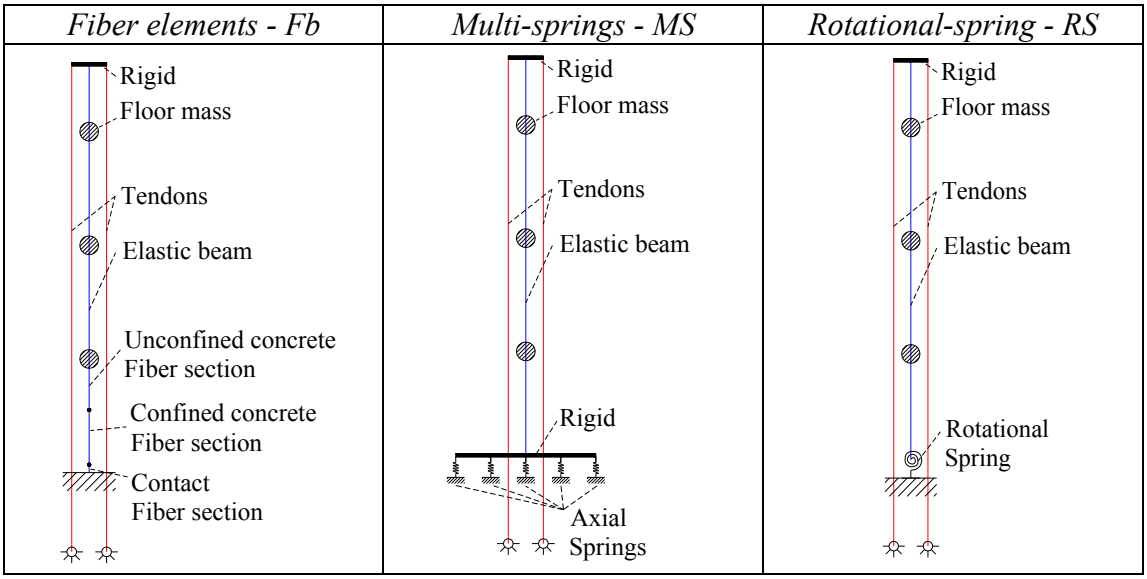


Figure 4: Representation of the 1D elements models.

In the *Fb* model (Figure 4), different fiber sections are used in order to describe the behavior of the wall and wall-foundation interaction. Regular fiber sections are adopted in the wall panel considering nonlinear stress-strain relationship for the confined and unconfined concrete and the reinforcing bars. No fiber elements are placed above the first floor being the response in that region essentially elastic. To simulate the wall-foundation interaction, a fiber section with no reinforcing bars and with no tensile strength concrete is positioned between the wall base and the ground with a stress-strain relationship consistent with the 2D elements model foundation.

The fiber elements adopted in the analyses are based on a force formulation and on the assumption of plane sections remaining plane during the analysis. This is in contrast with the actual strain distribution in the rocking wall discontinuity region which extends from the wall-foundation interface up to approximately a height equal to the wall width. Following the element formulation assumptions, the first section at the base of the wall will exhibit reinforcing bars in tension also during uplift of the wall base which clearly violates the equilibrium of the real situation. Therefore this formulation is suitable to describe rocking walls in global terms, base shear – base rotation relationship, but inappropriate for the local behavior at the wall base, contact length and strain distribution.

Prestressing tendons modeling is the same for all the three 1D elements models. Each tendon set is constituted by a truss element pinned connected at the base and rigidly connected at the top to the wall by means of a stiff beam element. The possible contact between each tendon and the relative duct during wall rotation is not considered. The inelastic behavior, in terms of force-displacement relationship, is taken into account with a normal bilinear lumped plasticity hinge.

In the *MS* model (Figure 4) the support of the wall on the foundation is schematized with a series of axial springs acting only in compression to allow separation between the wall and the foundation during rocking. The elastic stiffness of each spring is EA/H where, according to the 2D elements model foundation, E and H are respectively the elastic modulus and the height of the foundation and A is the influence area of each spring. As it will be shown in the next section, the aforementioned axial spring stiffness leads to stiffer results in the initial part of the shear-rotation relationship compared to 2D elements models. Therefore another tentative axial stiffness formulation is adopted considering the resultant stiffness of two springs in series: the first spring is the aforementioned spring simulating the foundation and the second spring takes into account somehow the wall flexibility in the contact region. To accomplish this, the latter spring stiffness is evaluated as EA/(0.15 l_w) where E is the elastic modulus of the wall concrete, A is the influence area of each spring and 0.15 l_w, being l_w the wall length, represents the wall base neutral axis value at stiffness change in the shear-rotation relationship, therefore considering the axial stiffness of a portion of the wall base with height equal to the neutral axis depth. Yielding of concrete in compression is also introduced in each axial spring with a normal bilinear model. The influence of the number of springs is also investigated taking into account four different models with 99, 25 and 15 springs respectively.

In the *RS* model (Figure 4), the simplest model presented in this paper, the wall panel is modeled with an elastic beam pin-connected to the ground, the interaction between the wall and the foundation is described by means of a nonlinear rotational spring connecting the wall base to the ground. The difficulty of this model arises from the definition of appropriate nonlinear properties of the rotational spring. A possible solution is the adoption of elastic bilinear or multilinear analytical formulations available in the literature such as the one proposed by Restrepo and Rahman [6]. For sake of clarity between the 1D elements models comparison, in the present paper the rotational spring is calibrated according to the 2D elements model adopting an elastic trilinear representation.

In all the models, especially in the simplified 1D elements models, special care must be placed in the choice of numerical damping [20-22], adopted in the dynamic analyses to take into account all the sources and mechanisms of energy dissipation not directly considered in the material hysteretic behavior. The most common and well known representation of damping is Rayleigh damping, in which the viscous damping matrix is obtained as a linear combination of the mass and stiffness matrixes:

$$\boldsymbol{C} = \alpha \boldsymbol{K} + \beta \boldsymbol{M} \tag{1}$$

In the case of rocking walls, such a formulation could lead to fictitious viscous forces at the base of the wall, especially if initial stiffness matrix is considered in the damping formulation. In fact, during rocking of the wall the base gap opens and the wall and foundation points, *Fb* and *MS* models, gain relative velocity and therefore viscous forces arises in those positions if the initial elastic stiffness is considered in damping formulation. Analogous considerations apply in the case of *RS* model, where the initial elastic rotational stiffness is significantly higher than the stiffness associated to the gap opening: when the base rotational spring reaches the yield point, it gains rotational velocity and therefore a viscous moment arises.

This fictitious forces and moments introduce unrealistic sources of resistance and viscous energy dissipation at the base of the wall and lead to a significant underestimation of the structural seismic demand. To avoid this problem tangent stiffness proportional damping must be adopted.

In the 1D element models presented in the paper, only the results of tangent stiffness proportional damping are considered, both in the case of Rayleigh damping and stiffness proportional damping. The stiffness proportional coefficient α (Eqn.1) is obtained assigning the

selected relative damping ratio to the structural first mode period. In the case of Rayleigh damping the coefficients α and β (Eqn.1) are obtained assigning the selected relative damping ratio to the structural first mode period and to the period corresponding to the shear-rotation post yield stiffness, which corresponds in the present case to 10 times the fundamental period.

4 FINITE ELEMENT ANALYSES RESULTS

In this section the results of the nonlinear static and dynamic analyses are presented. For sake of clarity, being the rocking wall representative of a scaled structure, the results are presented in dimensionless terms: the neutral axis depth is normalized to the wall length, the base shear to the model weight (621.3 kN) corresponding to half of the total weight of the tested structure, and the accelerations to the PGA (0.35g).

4.1 Nonlinear Static Analyses Results

The nonlinear static results of the 2D and 3D elements models are shown in global and local terms in Figure 5 and Figure 6 respectively. The 2D and 3D elements models considering the concrete as a linear elastic material show basically the same behavior both in global and local terms. When nonlinear concrete behavior is introduced in the wall there is, as expected, an increase in the axial compressive strains. This increase is higher in the 2D than in the 3D elements model, although these results sould be compared with actual values obtained from experimental tests to check finite element model suitability.

The implementation of the longitudinal and transverse rebars in the confined area at the base of the wall reduced both neutral axis and strain values compared to the case in which only concrete nonlinearity is considered.

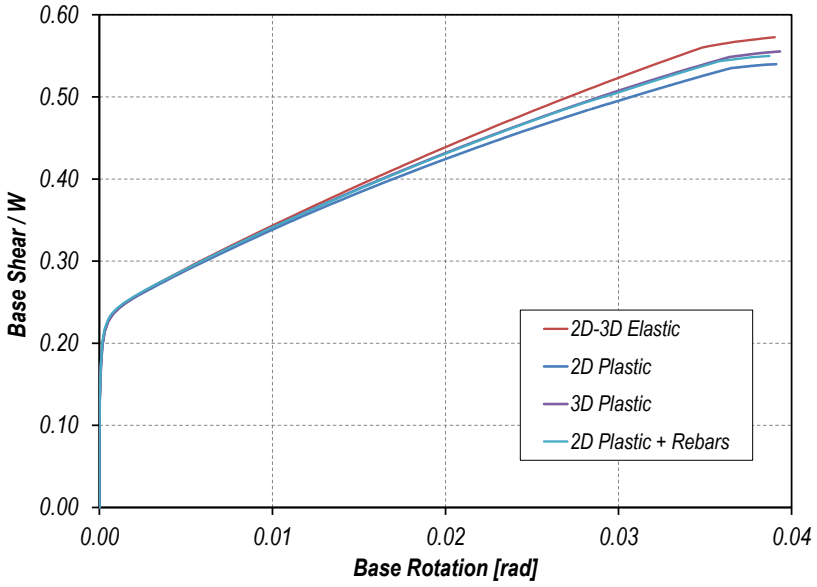


Figure 5: Base shear – base rotation 2D-3D elements models.

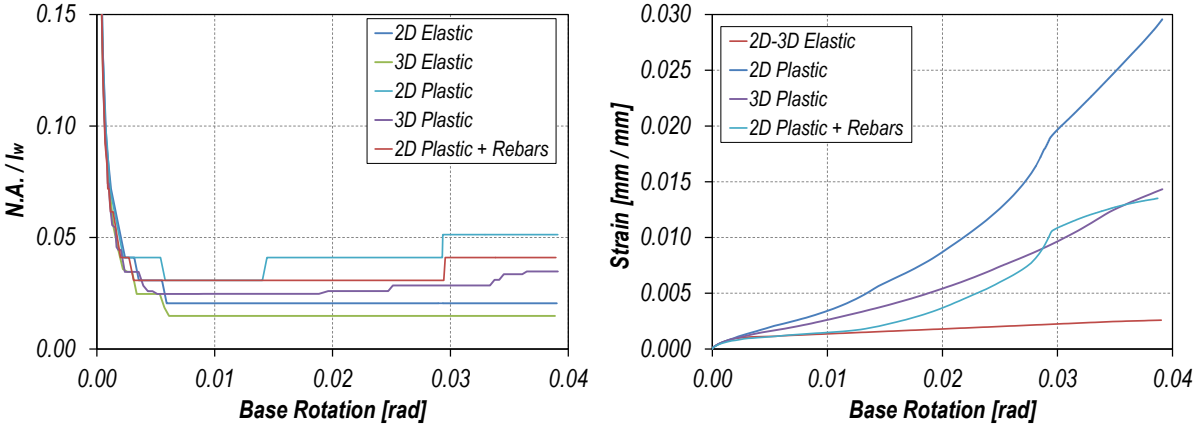


Figure 6: Neutral axis variation and concrete compressive strain 2D-3D elements models.

Regarding 1D elements models, Figure 7 shows the influence of the number of axial compression only springs in *MS* model on the base shear – base rotation response. There is basically no difference between 99 and 25 axial springs models while there is an increase in the post yield stiffness in the case of 15 springs, which is associated to the concentration of the compressive force in the last external spring. It is therefore suggested to have at least 2 springs fully in contact in the minimum expected neutral axis depth. Figure 7 shows also the stiffer response at the apparent yield point in the case of axial springs with stiffness equal to the solely foundation stiffness (*"MS_f – 99 Springs"* model).

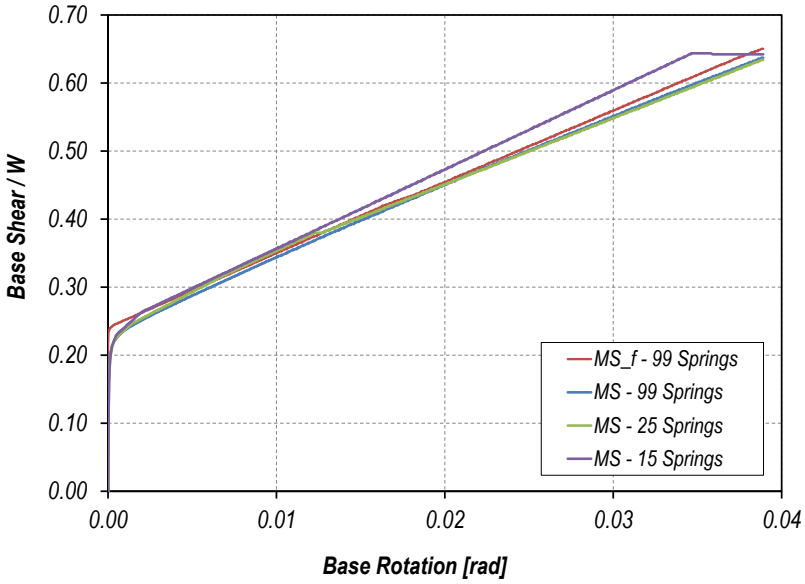


Figure 7: Base shear – base rotation MS models as a function of axial springs number.

Figure 8 compares the base shear – base rotation response of all the 1D elements models and the 2D elements model plus rebars in the confined region. The same figure contains the bilinear elastic response proposed by Restrepo and Rahman [6]. *Fb* model and Restrepo and Rahman bilinear approximation show a stiffer response in the post yield region. *Fb* and *RS* models also present an abrupt change in the apparent yield region which causes high horizontal spikes in the dynamic response as it will be shown later. Among the 1D elements models, *MS* model gives the best global response approximation.

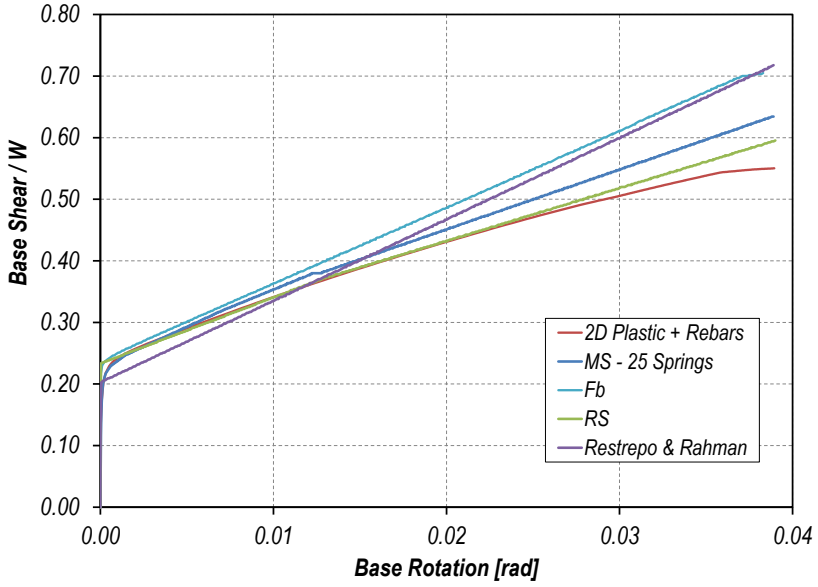


Figure 8: Base shear – base rotation 1D elements models.

Figure 9 shows the 1D elements response in local terms. Only *Fb* and *MS* models allow to determine the neutral axis variation and only *Fb* model provides concrete strains, although their values are not reliable as evident in the figure and explained before.

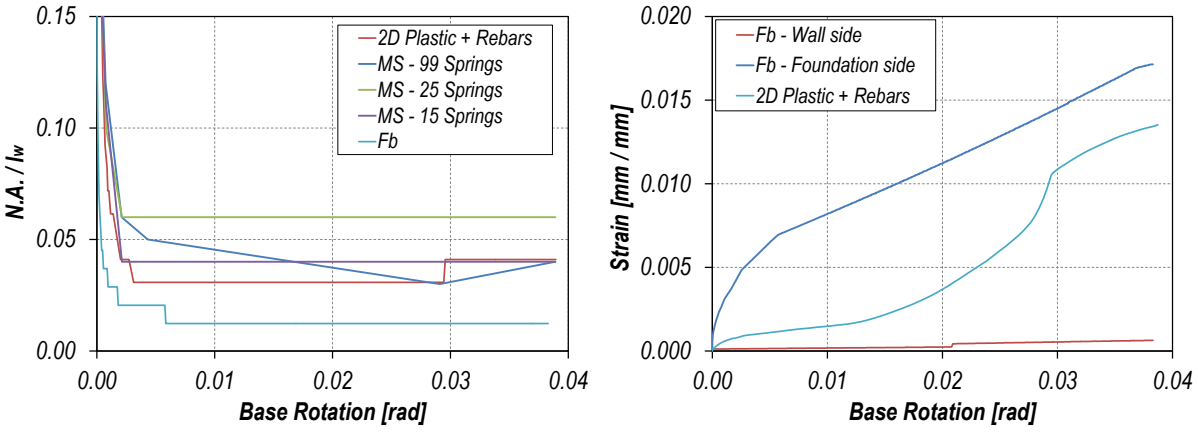


Figure 9: Neutral axis variation and concrete compressive strain 1D elements models.

Even though not presented in graphical format, another feature worth of being investigated is the vertical uplift at the wall center line which influences geometric compatibility and interaction between the wall and adjacent elements. Among the 1D elements models only the *RS* one is not able to capture the wall vertical uplift, in fact in this model wall uplift is not provided at all.

4.2 Nonlinear Time History Analyses Results

This section presents the results of nonlinear dynamic analyses. Being the seismic demand limited according to the low seismicity site chosen (Knoxville-TN), the expected base gap opening is limited to few milliradians. For these rotation values the local and global behavior of the different 2D and 3D elements models investigated is very close, therefore only the re-

sults of the 2D elements with rebars in the confined region are presented as representative of 2D and 3D elements models.

Figure 10 shows the base shear - base rotation response of the 2D elements model and the experimental test results, being the latter added only for qualitative comparison as the present paper does not intend to capture the dynamic interactions between the walls and the floors and the influence of the foundation. From the graph it is possible to see how the 2D elements model is able to describe the global rocking wall behavior and to capture base shear peaks for wall base rotations close to zero. These peaks are associated to horizontal acceleration spikes (Figure 11) arising when the wall gains horizontal lateral stiffness in the unloading phase, as explained and showed elsewhere [12, 23], which happens in proximity of zero base rotation. Figure 11 shows horizontal (a_h) and vertical (a_v, positive upward, acceleration of gravity excluded) acceleration time histories at the wall 3rd floor.

The peaks in vertical acceleration arise when the wall base gap closes [12] and show higher values compared to experimental test due to the increased stiffness of the foundation beam model compared to the actual tested structure.

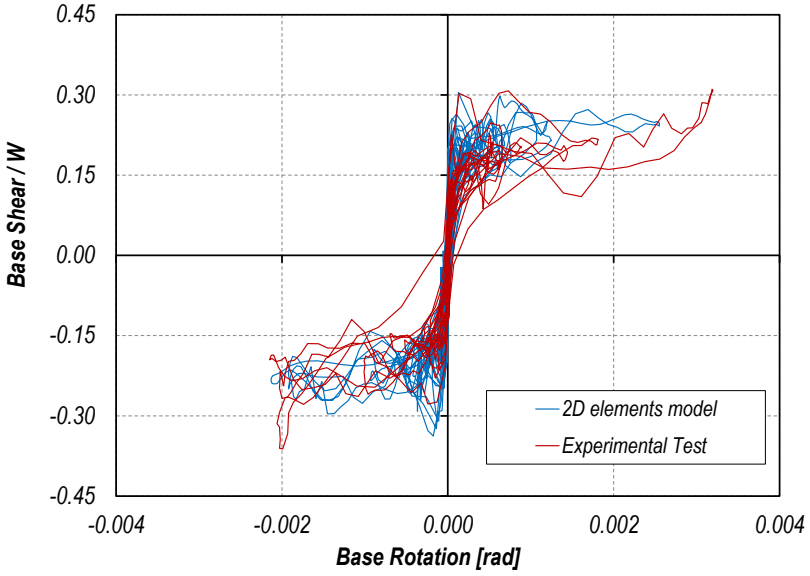


Figure 10: Base shear – base rotation for the 2D elements model and the tested structure.

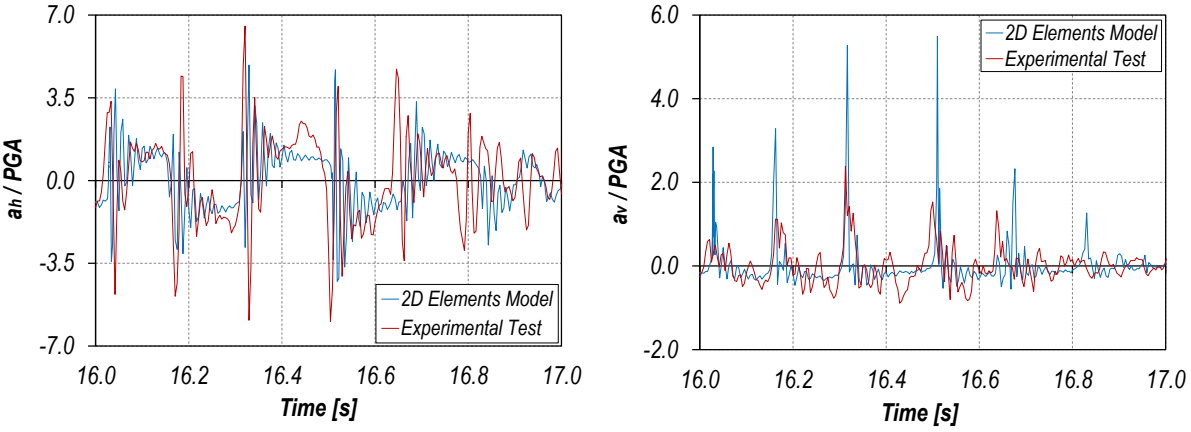


Figure 11: Horizontal (a_h) and vertical (a_v) acceleration for the 2D elements model and the tested structure.

Regarding 1D elements models, the comparison is made between two damping formulations, Rayleigh (R) damping and stiffness proportional (SP) damping, both considering tangent stiffness proportionality at each time increment in the damping matrix definition. A damping ratio of 3% is selected for each formulation in the way explained before.

Figure 12, Figure 13 and Figure 14 show, respectively, the base shear - base rotation, horizontal acceleration and vertical acceleration of the 1D elements models and the comparison with the 2D element model response.

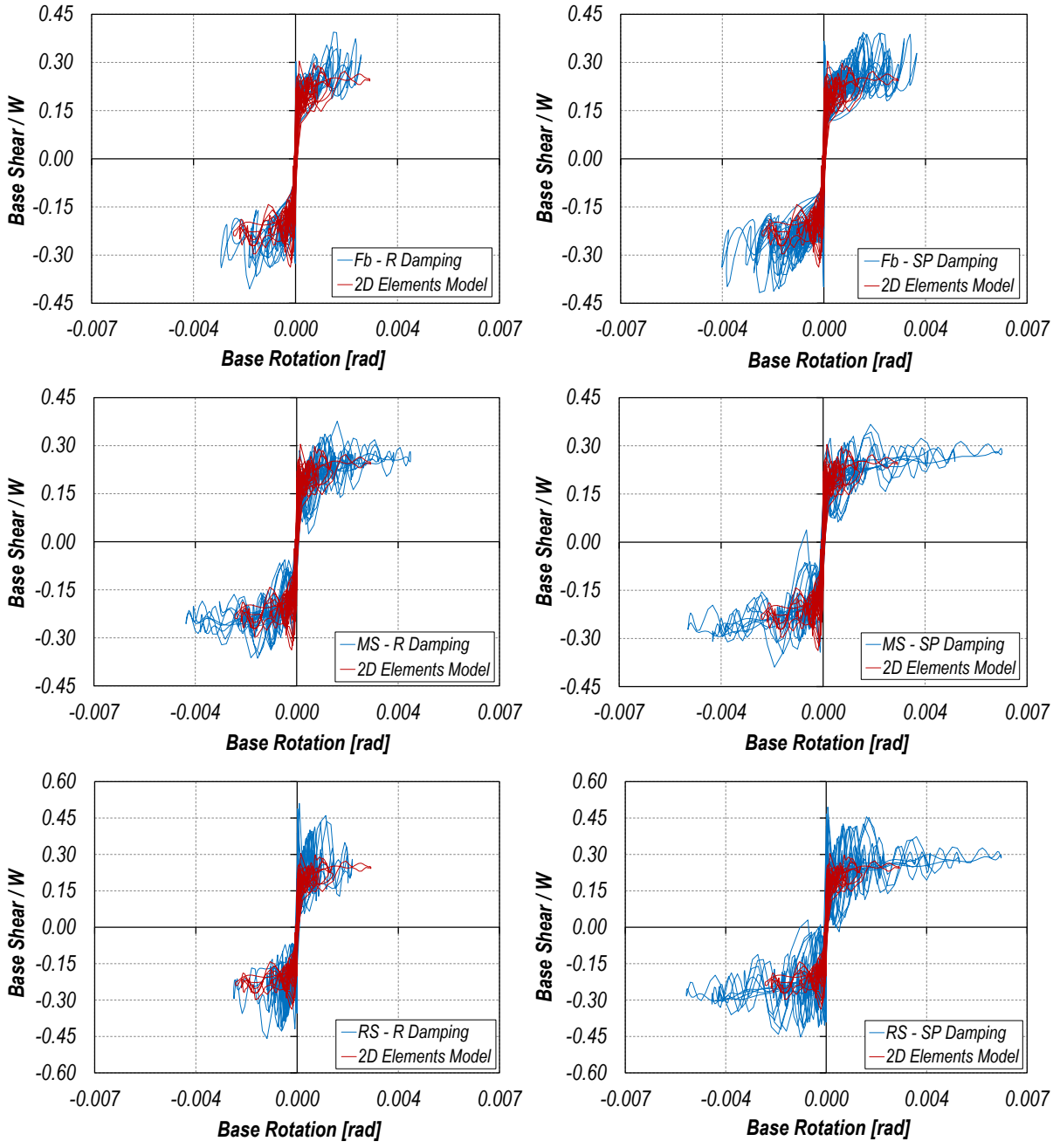


Figure 12: Base shear – base rotation 1D elements models; comparison with 2D elements model.
Note: Fb = Fiber elements; MS = Multi-Spring; RS = Rotational Spring;
R damping = Rayleigh damping; SP damping = Stiffness Proportional damping.

The results indicate how 1D elements models could significantly over-predict the structural response, both in base shear and base rotation terms, depending on the damping formulation chosen and on the selected damping ratio.

Horizontal acceleration significantly differs between the 2D elements model and the *Fb* and *MS* models. In the *RS* model horizontal acceleration spikes are qualitatively similar to 2D elements model, although, as stated before, base shear values are over-predicted.

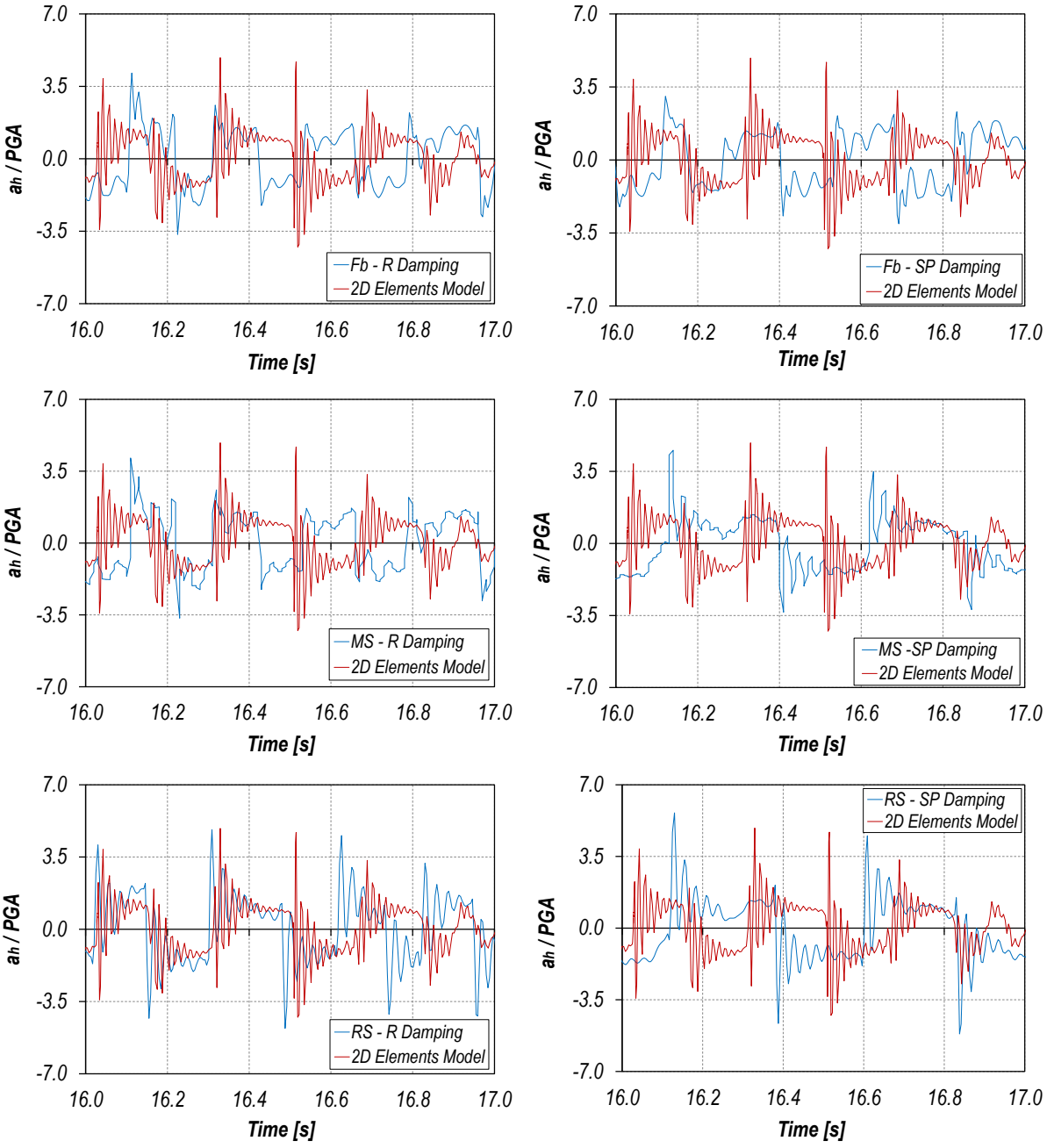


Figure 13: Horizontal acceleration 1D elements models; comparison with 2D elements model.
Note: Fb = Fiber elements; MS = Multi-Spring; RS = Rotational Spring;
R damping = Rayleigh damping; SP damping = Stiffness Proportional damping.

Vertical acceleration spikes are better captured by the *MS* model; *RS* model does not consider wall uplift and therefore the vertical acceleration (a_v) in this model is zero.

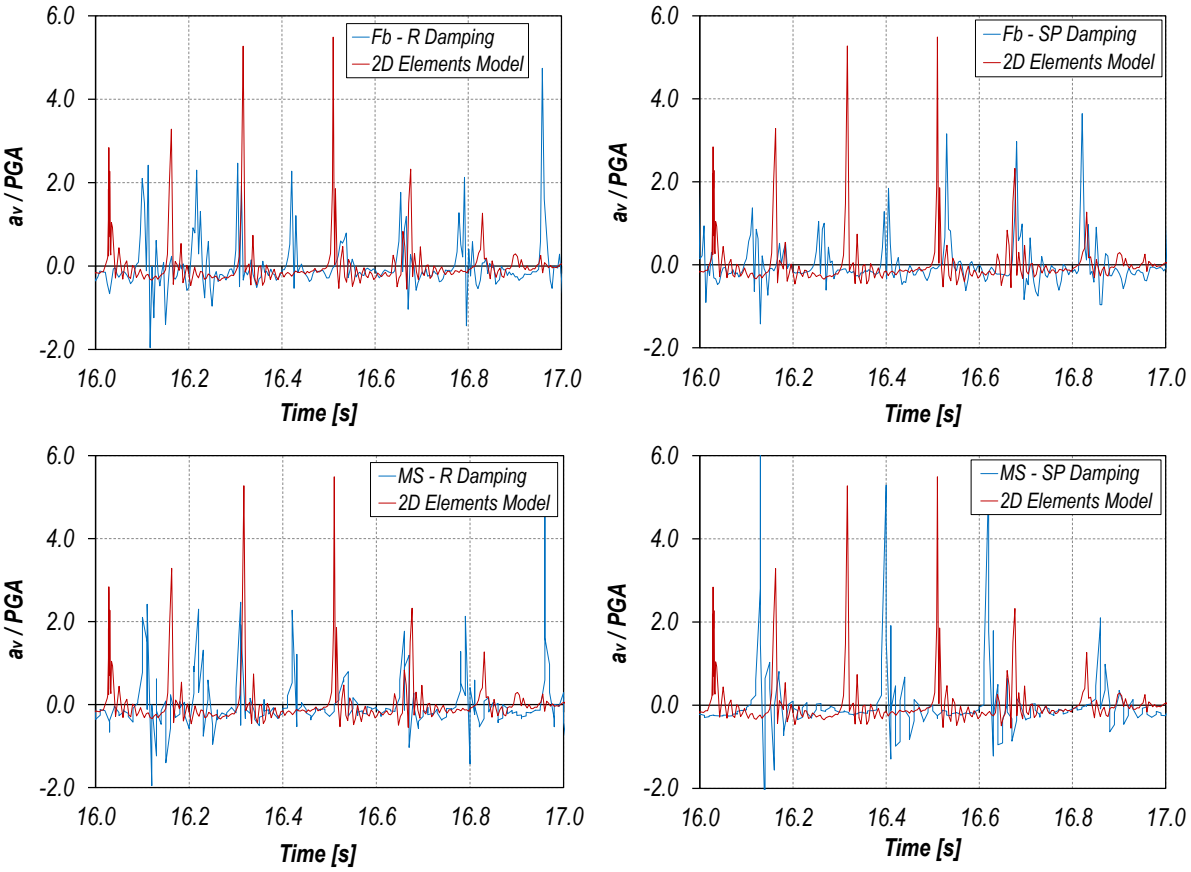


Figure 14: Vertical acceleration 1D elements models; comparison with 2D elements model.
Note: Fb = Fiber elements; MS = Multi-Spring;
R damping = Rayleigh damping; SP damping = Stiffness Proportional damping.

Figure 15 shows the results of 1D elements models after tuning the damping ratio value, in tangent stiffness proportional formulation, in order to obtain approximately the same maximum base rotation of the 2D elements model. The damping ratios chosen are 0.061, 0.144 and 0.142 for the *Fb*, *MS* and *RS* models respectively.

The results show how with the selected damping values the 1D elements models predict quite well the rocking wall behavior in global terms, although significant differences are present close to zero base rotation being the horizontal acceleration spikes, arising when the wall approaches the rest position, damped out. This could underestimate the base shear demand in those regions and causing wall horizontal slippage if relying solely on friction in the base shear transfer mechanism [12].

The vertical acceleration spikes are only slightly affected by the selected damping ratios.

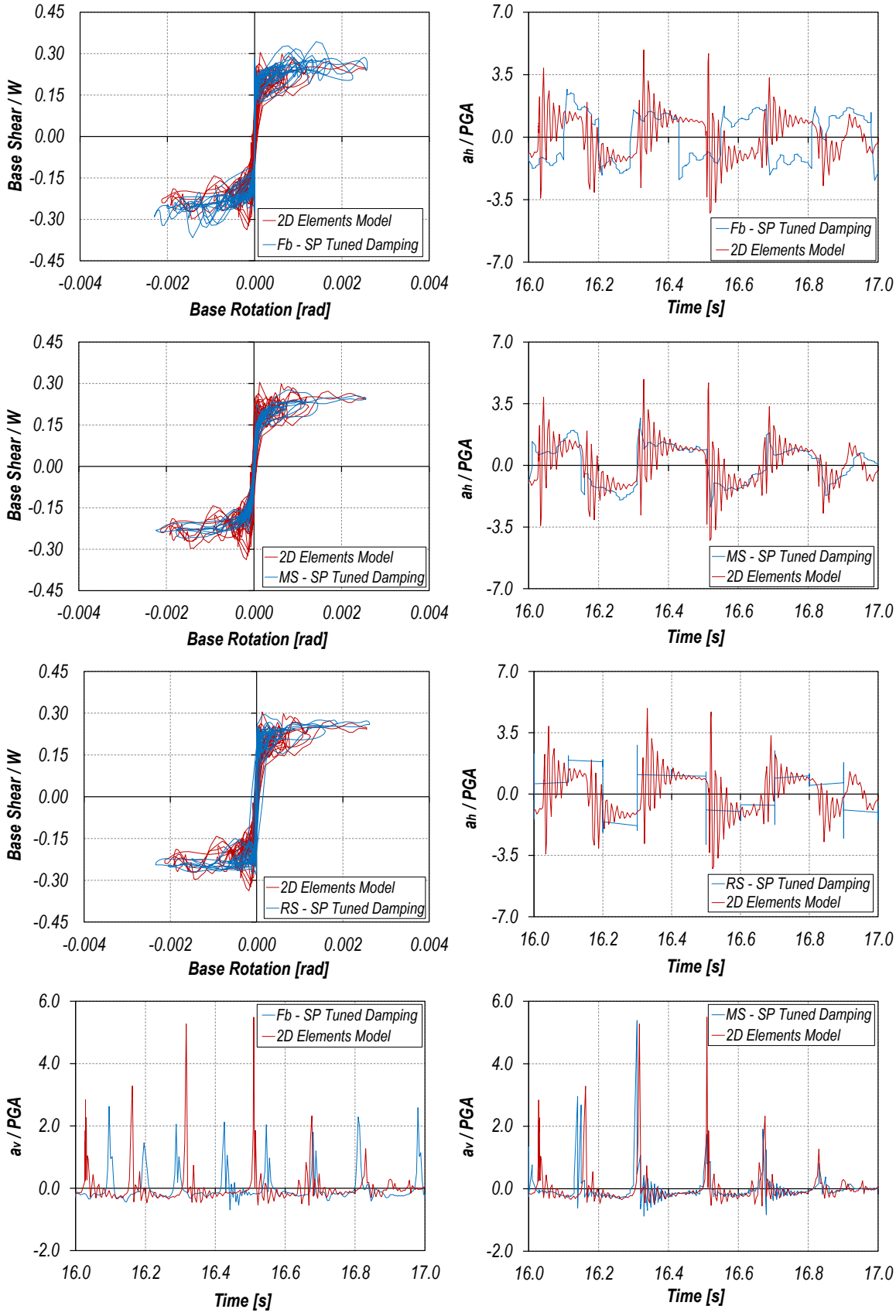


Figure 15: Base shear – base rotation, horizontal and vertical acceleration
1D elements models with tuned damping.

5 CONCLUSIONS

In the present paper the finite element modeling of rocking walls is considered in order to highlight differences between different modeling techniques comprising 3D, 2D and 1D elements. The dynamic interaction between the wall and the building and the influence of the foundation is beyond the purpose of the paper and therefore neglected in the investigation.

The results of the research show that 3D and 2D models are the only suitable to describe the rocking wall behavior in local terms, neutral axis variation and wall toe concrete compressive strains. 3D elements models considering concrete nonlinearities provide lower concrete compressive strains compared to the corresponding 2D elements models. To determine the most reliable model in terms of strain prediction, comparisons to test results are needed.

The 1D elements models considered are based on fiber elements (*Fb*), multi compression only springs (*MS*) and concentrated rotational spring (*RS*). These models allow to capture the rocking wall behavior in global terms, base shear - base rotation relationship, although differences arise in the nonlinear static analyses compared to 2D elements model results. *Fb* model and Restrepo and Rahman [6] bilinear approximation, commonly adopted in the *RS* model definition, show a stiffer response in the post yield region. *Fb* and *RS* models also present an abrupt change in the apparent yield region. Among the 1D elements models, *MS* model gives the best global response approximation in nonlinear static analyses. It is worth to note that *RS* model does not allow wall center line uplift and therefore with this model it is not possible to capture interactions between the wall and adjacent elements.

Regarding nonlinear dynamic analyses, 2D and 3D models provide results qualitatively similar to the experimental test without the addition of global damping. In the case of 1D elements models global damping was needed for convergence issues and the results are strongly influenced by the chosen damping formulation. The use of Rayleigh or stiffness proportional damping without damping matrix update, that is proportional to initial elastic stiffness, leads to unconservative results and therefore should be avoided; this is associated to the development of fictitious viscous forces (*Fb* and *MS* models), or moments (*RS* model), at the base of the wall which unrealistically increase the wall base capacity and viscous energy dissipation. Better results are obtained when damping matrix is formulated proportionally to tangent stiffness, both in the case of Rayleigh and stiffness proportional damping.

Tangent stiffness proportional damping formulation overestimates the wall response in terms of base shear and base rotation compared to Rayleigh damping. This could be overcome by increasing the damping in the former formulation although in this way there is a significant under-prediction of the horizontal acceleration spikes especially around zero base rotation. Among 1D elements models, *Fb* model gives closer results to 2D elements model with lower damping ratios compared to *MS* and *RS* models.

ACKNOWLEDGEMENTS

The authors wish to express their gratitude to the Precast/Prestressed Concrete Institute, the National Science Foundation, the Charles Pankow Foundation, and the George E. Brown Jr. Network for Earthquake Engineering Simulation and all the people involved in the DSDM project especially to Prof. R.B. Fleischman at the UA, prof. J.I. Restrepo at the UCSD and to Dr. M.J. Schoettler at the UC Berkeley. The opinions, findings, and conclusions expressed in the paper are those of the authors and do not necessarily reflect the views of the individuals and organizations involved in the DSDM project.

REFERENCES

[1] Y. Osanai, F. Watanabe, S. Okamoto, Stress Transfer Mechanism of Socket Base Connections with Precast Concrete Columns, *ACI Structural Journal*, **93**: 3, 1-11, 1996

[2] J. J. Blandón, M. E. Rodríguez, Behavior of Connections and Floor Diaphragms in Seismic- Resisting Precast Concrete Buildings, *PCI Journal*, **50**:2, 56-75, 2005.

[3] A. Belleri, P. Riva, Seismic performance and retrofit of precast grouted sleeve connections, *PCI Journal*, **57**:1, 97-109, 2012.

[4] J. I. Restrepo, R. Park, A. H. Buchanan, Design of Connections of Earthquake Resisting Precast Reinforced Concrete Perimeter Frames, *PCI Journal*, **40**:5, 68-80, 1995.

[5] M. J. N. Priestley, S. Sritharan, J. R. Conley, S. Pampanin, Preliminary Results and Conclusions from the PRESSS Five-Story Precast Concrete Test-Building, *PCI Journal*, **44**:6, 42-67, 1999.

[6] J. I. Restrepo, A. Rahman, Seismic Performance of Self-Centering Structural Walls Incorporating Energy Dissipators, *Journal of Structural Engineering*, **133**:11, 1560-1570, 2007.

[7] F. J. Pérez, R. Sause, S. Pessiki, Analytical and experimental lateral load behavior of unbonded posttensioned precast concrete walls, *Journal of Structural Engineering*, **133**:11, 1531-1540, 2007.

[8] Y. C. Kurama, Hybrid Post-Tensioned Precast Concrete Walls for Use in Seismic Regions, *PCI Journal*, **47**:5, 36-59, 2002.

[9] D. Marriott, S. Pampanin, D. Bull, A. Palermo, Dynamic Testing of Precast Post- Tensioned Rocking Walls Systems with Alternative Dissipating Solutions, *Bulletin of the New Zealand Society for Earthquake Engineering*, **41**:2, 90-103, 2008.

[10] R. B. Fleischman, C. Naito, J. Restrepo, R. Sause, S. K. Ghosh, G. Wan, M. Schoettler, L. Cao, Precast Diaphragm Seismic Design Methodology (DSDM) Project, Part 2: Research Program, *PCI Journal*, **50**:6, 14-31, 2005.

[11] M. J. Schoettler, A. Belleri, D. Zhang, J. I. Restrepo, R. B. Fleischman, Preliminary results of the shake-table testing for the development of a diaphragm seismic design methodology. *PCI Journal*; 2009; **54**(1), 100-124, 2009.

[12] A. Belleri, M. J. Schoettler, J. I. Restrepo, R. B. Fleischman, Dynamic behavior of rocking and hybrid cantilever walls in a precast concrete building. Accepted at *ACI Structural Journal*, 06/02/2013.

[13] Y. C. Kurama, R. Sause, S. Pessiki, L. Le-Wu, Lateral Load Behavior and Seismic Design of Unbonded Post-Tensioned Precast Concrete Walls. *ACI Structural Journal*, **96**:4, 622-632, 1999.

[14] B. Erkmen, A. E. Schultz, Self-Centering Behavior of Unbonded, Post-Tensioned Precast Concrete Shear Walls. *Journal of Earthquake Engineering*, **13**, 1047-1064, 2009.

[15] W. Y. Kam, S. Pampanin, A. Palermo, A. J. Carr, Self-centering structural systems with combination of hysteretic and viscous energy dissipations. *Earthquake Engineering and Structural Dynamics*, **39**, 1083-1108, 2010.

[16] J. B. Mander, M. J. N. Priestley, R. Park, Theoretical stress-strain model for confined concrete, *Journal of Structural Engineering,* **114**:8, 1804-1826, 1988.

[17] PCI Industry Handbook Committee, PCI Design Handbook: Precast and Prestressed Concrete. 6th ed. Chicago-IL, 2004.

[18] ABAQUS user's manual version 6.11. Dassault Systèmes Simulia Corp., 2011.

[19] MidasGEN 2012 (v3.1), MIDAS Information Technologies Co. Ltd.

[20] F. A. Charney, Unintended consequences of Modeling Damping in Structures, *ASCE Journal of Structural Engineering*, **134**:4, 581-592, 2008.

[21] J. F. Hall, Problems encountered from the use (or misuse) of Rayleigh damping, *Earthquake Engineering and Structural Dynamics*, 35, 525-545, 2006.

[22] L. Petrini, C. Maggi, M. J. Priestley, G. M. Calvi, Experimental Verification of Viscous Damping Modeling for Inlelastic Time History Analyzes, *Journal of Earthquake Engineering*, **12(S1)**, 125-145, 2008.

[23] L. Wiebe, C. Christopoulos, Characterizing acceleration spikes due to stiffness changes in nonlinear systems, *Earthquake Engineering and Structural Dynamics*, **39**, 2010, 1653-1670, 2010.

COMPDYN 2013
4th ECCOMAS Thematic Conference on
Computational Methods in Structural Dynamics and Earthquake Engineering
M. Papadrakakis, V. Papadopoulos, V. Plevris (eds.)
Kos Island, Greece, 12–14 June 2013

SHAKING TABLE TESTS ON UNREINFORCED LOAD-BEARING MASONRY WALLS – COMPARISON WITH SIMPLE ROCKING MODELS

Christophe Mordant[1], Matt Dietz[2], Hervé Degée[1]

[1]University of Liège
Chemin des Chevreuils, 1 – 4000 Liège (Belgium)
cmordant@ulg.ac.be / h.degee@ulg.ac.be

[2] University of Bristol
University Walk, Bristol BS8 1TR (UK)
m.dietz@bristol.ac.uk

Keywords: Unreinforced masonry walls, Rocking, Coefficient of restitution

Abstract. *Assessment of the overall seismic performances of multi-storey unreinforced masonry structures requires an appropriate characterization of the behaviour of their structural components, in particular when these are subjected to a dynamic ground motion input. In order to develop a better understanding on this issue and in a further perspective of investigating the consequences of the presence of 1 cm thick rubber elements used for improving the sound-proofing performances of the building, shaking table tests have been carried out in the framework of the European project SERIES. Four single walls were tested. These were built with high resistance thin-bed layered clay masonry with empty vertical joints. Two of them had an aspect ratio close to 1, while the other two were close to 0.4. One wall of each aspect ratio included rubber devices at its bottom and top to enable comparisons and conclusions about the influence of rubber on the wall behaviour. The test results were then partially compared to results obtained with a theoretical rocking model considering the wall as a rigid body. The results summarized in the present contribution evidence a significant rocking behaviour for the highest input acceleration levels. Characterization of this behaviour is however strongly dependent on the aspect ratio of the wall and on the presence or not of rubber devices in terms of natural frequencies, damping, dynamic amplifications and progressive damage with increasing acceleration levels. It is also showed that the theoretical rocking predictions are in good agreement with the experimental results for high acceleration levels, while the behaviour is closer to the one of a cantilever for the lower levels. It is finally evidenced that, in presence of acoustic rubber devices, amplitudes of the rocking motion are increased but with a more limited damaging of the wall because of the capacity of the rubber to absorb the impact energy. Results of this study on single walls are expected to be further extended to global masonry structures, account taken for the influence of actual boundary conditions of the wall.*

1 INTRODUCTION

1.1 General context

Unreinforced load-bearing masonry structures are traditionally used for single family houses. Nevertheless, recent improvements of their mechanical properties and better control of their global behaviour have led to the extension of their range of application to multi-storey buildings up to 5-6 levels, which are particularly used for apartments [1]. This kind of buildings generally requires a good acoustic insulation level to fulfil the standards in terms of individual comfort. A convenient and validated solution consists in placing a rubber layer at the bottom and/or top of each wall to prevent acoustic bridges (see Figure 1).



Figure 1 – Acoustic solution (Wienerberger)

The influence of this technical solution on the seismic behaviour of multi-storey unreinforced masonry structures optimized for acoustic performances is however questionable, even in the case of moderate seismic action. Indeed, the rubber layers are likely to modify the stiffness and resistance of the structural elements as well as the boundary conditions of the walls. In this perspective, shaking table tests have been carried out at the Earthquake and Large Structures Laboratory (EQUALS) of the University of Bristol, in the framework of the European project SERIES. The research program aims at a better understanding of the seismic behaviour and of the consequences of the use of rubber layers on the dynamic behaviour of the walls and hence of the global structure. This paper presents a summary of the test specimens, procedures and results, followed by a comparison of the actual experimental behaviour with respect to theoretical rocking models assuming a rigid-body behaviour of the wall. The assumptions on the criterion defining the initiation of the rocking motion and on the restitution coefficient are also discussed.

1.2 Description of the specimens



Figure 2 – View of a specimen

Studied specimens are single walls constituted by thin-bed layered clay masonry with empty vertical joints (see Figure 2). Two of them have an aspect ratio close to 1, while it is close to 0.4 for the other two. Exact dimensions of the walls are the following :

- Length x Height x Width = 2.1m x 1.8m x 0.138m (long wall)
- Length x Height x Width = 0.72m x 1.8m x 0.138m (short wall)

The block dimensions are $length\ x\ height\ x\ width = 300.0mm\,x\,188.0mm\,x\,138.0mm$

Mechanical characteristics of the units and masonry are the following ones:

- Normalised compressive strength of units (EN 772-1 Annex A)

$$f_b = 13.0\, N / mm^2$$

- Measured characteristic masonry compressive strength (EN 1052-1)

$$f_k = 5.6\, N / mm^2$$

- Characteristic compressive strength (NBN-EN 1996-1-1)

$$f_k = 3.9\, N / mm^2$$

A 5-tons mass is placed at the wall top to emulate the structural floor load, with due consideration to the shaking table capacities and to the common range of compression level in masonry structures. The instrumentation layout of the tested specimens and safety arrangements are extensively described in [2, 3].

2 DESCRIPTION AND SUMMARY OF THE TEST RESULTS

The experimental procedure includes two different types of tests. The first type is performed in order to characterize the specimen dynamic properties (natural frequency, damping) on the base of a "white noise" excitation. The second type consists in seismic test *stricto sensu*, using an artificially generated seismic input signal consistent with Eurocode 8 spectrum, with an acceleration level increased step-by-step. The PGAs measured during the seismic tests are given in Table 1. Details of the testing procedures and extensive analysis of the results are available in [2, 3]. The main information and results are summarized in the present paper and the main conclusions are recalled.

No Test	Long wall without rubber	Long wall with rubber	Short wall without rubber	Short wall with rubber
1	0.0393	0.0426	0.0413	0.0417
2	0.0777	0.0901	0.0654	0.0604
3	0.0777	0.0877	0.0635	0.0607
4	0.1583	0.1871	0.0867	0.0803
5	0.2387	0.2784	0.1356	0.1235
6	0.3230	0.3556	0.331	0.1278
7	0.4496	0.4567	0.1784	0.1709
8	0.5716	0.5692	0.1869	/
9	0.6878	0.6392	0.2336	/

Table 1 – Measured PGA [g]

In practice, for each specimen, the testing sequence starts with a "white noise" test. Then, the procedure consists in an alternation of seismic and "white noise" tests in the perspective of studying the effects of the earthquake action on the specimen in terms of degradation of the dynamic properties (natural frequency and damping).

2.1 White noise test results

White noise tests are mainly useful to characterize the specimens in terms of natural frequencies, modal shape and damping ratio. The evolutions of the natural frequencies and the damping ratio are represented respectively in Figure 3 and Figure 4. Note that seismic tests have been duplicated at selected acceleration levels to study the effects of repeated earthquakes.

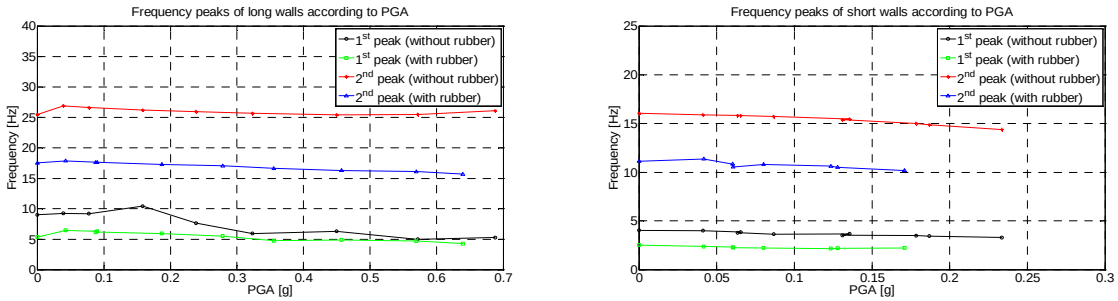


Figure 3 – Natural frequencies

Walls without rubber layers are characterized by higher values in terms of natural frequencies. The difference is about 30% to 40% for undamaged situations. When going through the testing sequence, a decrease of the natural frequency is observed for each wall. This observation can be explained by the deterioration of the specimens. Walls without rubber present however a more important frequency drop translating a higher degree of damage for a same ground acceleration level.

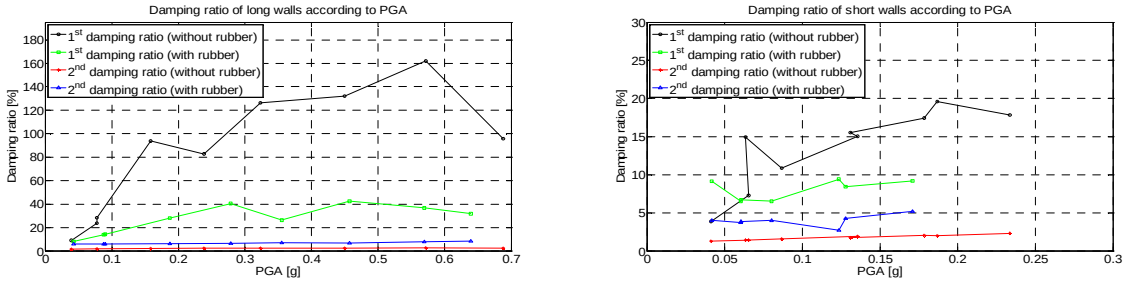


Figure 4 – Damping ratio

An increase of the acceleration level results also in an increase of the damping ratio. Although this increase occurs for each specimen, it is more important for the first mode of walls without rubber devices, especially for the longer one. Some measurements are however questionable since their values are as high as 100%. This could be explained by a poor accuracy of the procedure used to determine the damping ratio.

The influence of rubber layers can also be clearly highlighted. One can firstly think that the presence of acoustic insulation devices is unfavourable for the structure because it results in lower natural frequencies and hence in a higher flexibility and in larger displacements. Nevertheless, it appears that these devices have positive effects. Indeed, even if the seismic shakes affect the wall properties, rubber devices mitigate the frequency drop and limit the damping increase. As proposed in [3], a possible and convenient explanation is due to an essentially different behaviour. With the rubber layers, the assumption of rigid support is no more valid and the wall has to be considered as resting on an elastic foundation. Therefore, the instantaneous energy dissipation occurring when the wall passes through the vertical position is lower and the damages due to a less strong impact are thus less important.

2.2 Seismic test results

A major output of the seismic tests is the possible measurement of the compressive length, this so-called compressive length being actually the contact length at the interface between the wall and its foundation. This parameter is indeed the main one used in the design of walls and the assessment of their overturning resistance according to classical static equivalent design methodologies such as suggested by the Eurocode 6 [4].

2.2.1. Design method of Eurocode 6

The verification methodology proposed by the Eurocode 6 is a static equivalent one based on the static equilibrium of an element submitted to a combination of normal force and bending moment due to a horizontal shear. For a same loading scheme, the value of the compressive length can however be different, depending on the assumption of the shape of the normal stress distribution at the wall-foundation interface. It is indeed possible to consider for instance a constant (2,a) or a linear (2,b) stress distribution. These two assumptions respectively lead to the following formulas to estimate the compressive length L_c:

$$M = V.H \qquad e = \frac{M}{N} \tag{1}$$

$$L_c = \begin{cases} 0 & if\ e \geq L/2 \\ 2.(\frac{L}{2} - e) & if\ e \leq L/2 \wedge e \geq 0 \\ L & if\ e = 0 \end{cases} \tag{2,a}$$

$$L_c = \begin{cases} 0 & if\ e \geq L/2 \\ 3.(\frac{L}{2} - e) & if\ e \leq L/2 \wedge e \geq L/6 \\ L & if\ e \leq L/6 \end{cases} \tag{2,b}$$

2.2.2. Experimental results and comparisons

The methodology used to derive the compressive length from the direct test measurements is developed in [2] and is based on the assumption that the base section of the wall remains plane. Illustrative values are given in Table 2 and compared with values calculated according to the Eurocode procedure for selected acceleration levels. Figure 5 shows the complete evolution of the experimental compressive length according to the acceleration level.

Specimen	Acceleration level [g]	Compressive length [%]	[mm]	Assessment (linear) [%]	[mm]	Assessment (constant) [%]	[mm]
Long wall	0.04	83.20	1747.2	100.00	2100	82.86	1740
without	0.15	47.15	990.15	57.23	1201.9	35.71	750
rubber	0.66	0.03	0.5	0	0	0	0
Long wall	0.04	100.00	2100.0	/	/	/	/
with	0.19	67.20	1411.2	/	/	/	/
rubber	0.64	0.05	1.1	/	/	/	/
Short wall	0.01	77.01	554.5	100.00	720	87.50	630
without	0.02	58.70	422.6	100.00	720	75.00	540
rubber	0.15	14.37	103.5	0	0	0	0
Short wall	0.04	100.00	720.0	/	/	/	/
with	0.06	100.00	720.0	/	/	/	/
rubber	0.17	32.13	231.3	/	/	/	/

Table 2 – Illustrative values of compressive length

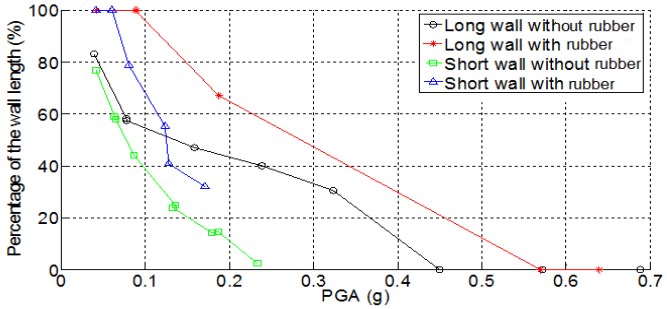


Figure 5 – Compression length

Comparison between measurements and theoretical predictions yields the following comments. For low acceleration level, the measured values are intermediate between the theoretical values obtained assuming the two different shapes of stress distribution. For higher acceleration level, the design method underestimates the compressive length. Note that, contrary to what is assumed in an equivalent static procedure, a zero value for the compressive length doesn't necessary mean a collapse of the wall, but can be associated to a rocking motion. The influence of rubber devices on the compressive length is favourable. This length is indeed larger for a same acceleration level in presence of acoustic insulation devices.

2.3 Classification of the test results

A sorting of the tests is proposed based on a comparison of the rotations measured at the bottom and top of the wall. Three different situations are identified.

The first situation appears for the seismic tests with a low level of acceleration, where a significant difference between rotations at the wall bottom and top is observed, as illustrated in Figure 6 for the first seismic test on the short wall without rubber devices. In this case, it is shown in [5] that the specimens can accurately be modelled as a cantilever beam (provided shear deformability is correctly accounted for). Among the present set of experimental results, this assumption is shown to be valid for the first three seismic tests. Comparisons between measurements and modelling results are carried out in [5]. This range and the associated modelling assumption are mainly useful for assessing damage limit states at low acceleration level.

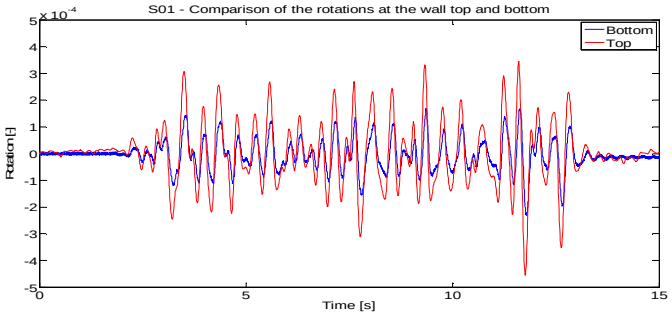


Figure 6 – Bottom and top rotations for a low level of acceleration

The second case corresponds to situations where quasi-equal rotations are measured at the top and at the bottom. This is observed when the acceleration level is rather high (tests S07, S08, S09). Figure 7 illustrates the situation for the seismic test S08 on the short wall without rubber devices. In this case, the specimen can be considered as a rigid body rocking on its support. Section 3 of this paper will focus specifically on the modelling of this situation. This range is of prime interest for the evaluation of the ultimate limit state.

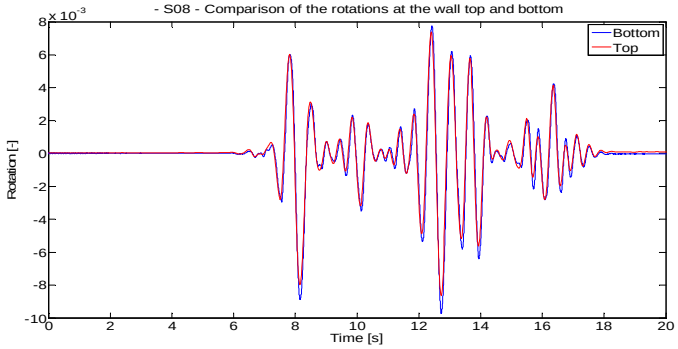


Figure 7 – Bottom and top rotations for a high level of acceleration

The third situation is a hybrid one and corresponds to tests with an intermediate acceleration level (S04, S05 and S06). A proper modelling would thus require combining a simple cantilever with a rocking model. It is felt however of a more limited practical interest.

3 DEVELOPMENT OF A THEORETICAL ROCKING MODEL AND COMPARISONS WITH TESTS RESULTS

3.1 Description of the reference theoretical model

3.1.1 Basic equations

The theoretical model used to carry out the comparisons with the experimental results is derived from the historical reference model developed by Housner [6]. This model has been initially developed to study the oscillations of a rigid body standing on a rigid support and is based on the resolution of the equation of motion deduced from the theorem of angular momentum :

$$\dot{H}_O = M_O \tag{1}$$

where H_O is the angular momentum relative to O

M_O is the resultant of moments of external forces relative to O.

In the reference version of the model, the gravity load is the specific weight of the body and is applied at its centre of gravity, as well as the inertial forces. The actual configuration of the tested specimens requires adjustments of this reference model in order to take into account the fact that :

- The specific weight of the wall can be reasonably neglected since it is less than 10% of the additional mass lying on the top of the wall;
- The main gravity load and the inertial forces are consequently acting at the top of wall.

The model considers thus a rigid body on a rigid support, with H and B being respectively the height and the length of the body. The rigid body is characterized by the angle $\alpha = \tan(B/2H)$. This angle characterizes the maximum rotation of the block beyond which the body turns over in static conditions under the effect of the gravity only. The two lower corners of the body are denoted O and O'. As it is assumed that the block and the support are both rigid, the oscillations are alternatively around O and O'. The angle between the body and the vertical is called θ and is the main kinematic unknown of the problem. θ is positive in clockwise rotation. A last assumption is to consider the coefficient of friction large enough for the risk of sliding to be neglected.

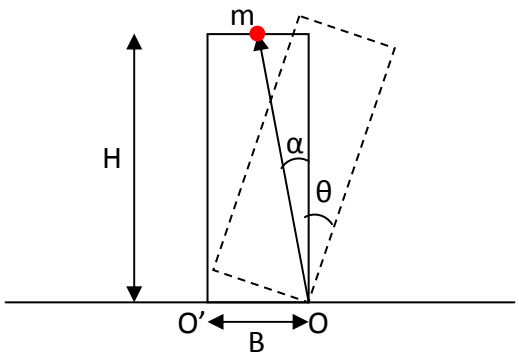


Figure 8 - Sketch of the model configuration

In Figure 8, the distance between a corner and the application point of the gravity load is denoted *R* (2).

$$R = \sqrt{H^2 + (B/2)^2} \tag{2}$$

In Equation (1), the angular momentum relative to O is the result of the multiplication of the moment of inertia I_O calculated in O by the time-derivative $\dot{\theta}$. As the contribution of the specific weight of the wall is neglected, it follows :

$$\dot{H}_O = I_O.\ddot{\theta} \tag{3}$$

$$\text{with} \qquad I_O = \rho\int_A (x^2 + y^2)dA + mR^2 = mR^2 \tag{4}$$

In presence of a seismic action, the resultant of moments of external forces relative to O, i.e. M_O, is due to the gravity load and to the inertial force, yielding :

$$M_O = -mgR\sin(\alpha.sign\theta - \theta) + m\ddot{u}_g R\cos(\alpha.sign\theta - \theta) \tag{5}$$

where m [kg] is the dead load
g [m/s²] is the gravity
$\ddot{u}_g$ [m/s²] is the seismic acceleration

3.1.2 Numerical resolution

The resolution of the equation of motion is carried out using a standard Newmark integration scheme, under the assumption of constant acceleration (β=1/4, δ=1/2). The following equations (6), (7) and (8) are thus implemented to determine the time evolution of the angle θ.

$$\ddot{\theta}_{n+1} = -\frac{mgR}{I_O}\left[\sin(\alpha.sign\theta_n - \theta_n) + \frac{\ddot{u}_{g,n+1}}{g}R\cos(\alpha.sign\theta_n - \theta_n)\right] \tag{6}$$

$$\dot{\theta}_{n+1} = \dot{\theta}_n + [(1-\delta).\ddot{\theta}_n + \delta.\ddot{\theta}_{n+1}].\Delta t = \dot{\theta}_n + 0.5[\ddot{\theta}_n + \ddot{\theta}_{n+1}].\Delta t \tag{7}$$

$$\begin{aligned}\theta_{n+1} &= \theta_n + \dot{\theta}_n.\Delta t + [(\frac{1}{2} - \beta).\ddot{\theta}_n + \beta.\ddot{\theta}_{n+1,lin}].\Delta t^2 \\ &= \frac{\theta_n + \dot{\theta}_n.\Delta t + \frac{\Delta t^2}{4}\left[\ddot{\theta}_n - \frac{mgR}{I_0}(\alpha sign\theta_{n+1} + \frac{\ddot{u}_{g,n+1}}{g})\right]}{1 - \frac{mgR}{I_0}\frac{\Delta t^2}{4}}\end{aligned} \tag{8}$$

3.1.3 Initiation of the rocking motion

The rocking motion of the wall is initiated as soon as the moment due to the inertial force is higher than the restoring force moment of the gravity load. The equilibrium is expressed with respect to the corner O or O' according to the assumption of a rigid body placed on a rigid support. Therefore, a rocking criterion *RC* can be written as follows :

$$RC = \frac{m\ddot{u}_g H}{mg\dfrac{B}{2}} > 1 \tag{9}$$

As long as the condition (9) is not verified, no rocking motion is initiated and the angle θ remains equal to zero.

3.1.4 Coefficient of restitution

When the body oscillation switches from a rotation around one of its corners to a rotation around the other one, it has to pass through its original resting vertical position. This transition is actually associated with an impact since the body hits the support. This impact obviously dissipates energy. The approach proposed by Housner to account for the dissipation is to consider the conservation of angular momentum with various assumptions (see [7]). According to this, a reduction factor *e* is defined and has to be applied to the velocity of the wall before the impact to obtain the velocity right after this impact. The reduction factor is given by :

$$e = 1 - 2\frac{mR^2}{I_O}\sin^2\alpha \tag{10}$$

where α is the angle drawn in Figure 8. In this way, the incoming velocity is reduced each time the angle θ changes its sign.

3.2 Predictions with the reference theoretical model

The theoretical model described above is first crudely applied to perform a direct simulation of the seismic tests S07, S08 and S09 for the walls without rubber layers. The input data for the theoretical prediction is the shaking table acceleration signal as measured during the test.

Figures 9, 10 and 11 shows the evolution of the Rocking Initiation Criterion calculated according to Equation (9) with the theoretical predictive model. Left-hand side and right-hand side graphs correspond respectively to the short and long walls. It is observed in Figure 9 and Figure 10 that the Rocking Criterion is never overcoming a unit value for tests S07 and S08, translating the fact that the theoretical model is predicting a non-occurrence of rocking motion. On the other hand, Figure 11 shows a criterion exceeding the unit, and thus predicting the initiation of a rocking motion, at about 4 seconds for the short wall (left) and at about 10 seconds for the long wall (right).

Together with the time-evolution of the rocking criterion, all three figures also present the time-evolution of the measured rotation of the wall illustrating the actual rocking behaviour observed during the tests, with a significant motion occurring for tests S07 and S08 although not predicted. It can thus already be concluded that a further modification of the rocking criterion is required. The impossibility of the theoretical model to predict the initiation of motion is at this stage identified as a consequence of the strong assumption of a perfectly rigid body lying on a perfectly rigid foundation and will be discussed in section 3.3.1.

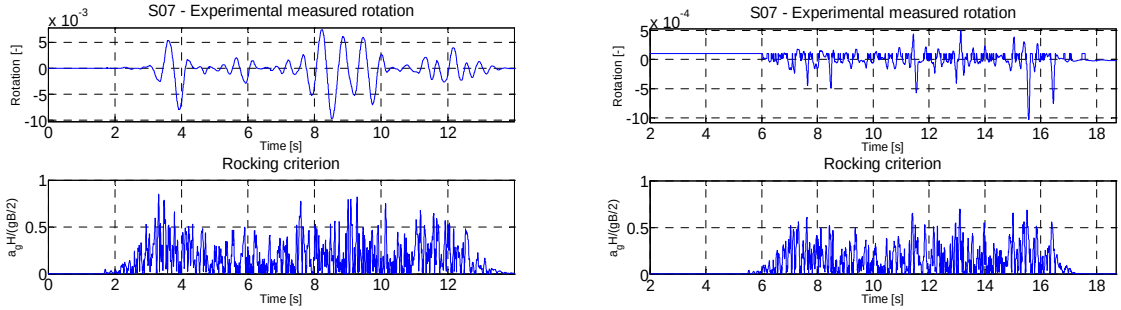


Figure 9 – Rocking criterion for short (left) and long (right) walls without rubber devices during seismic test S07

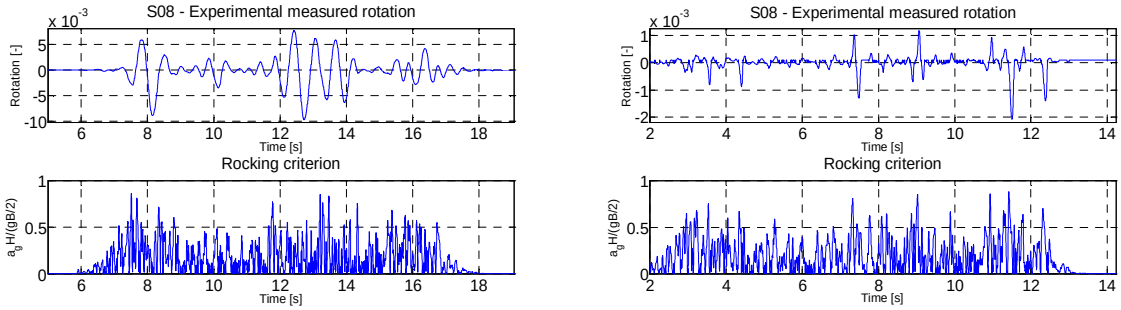


Figure 10 – Rocking criterion for short (left) and long (right) walls without rubber devices during seismic test S08

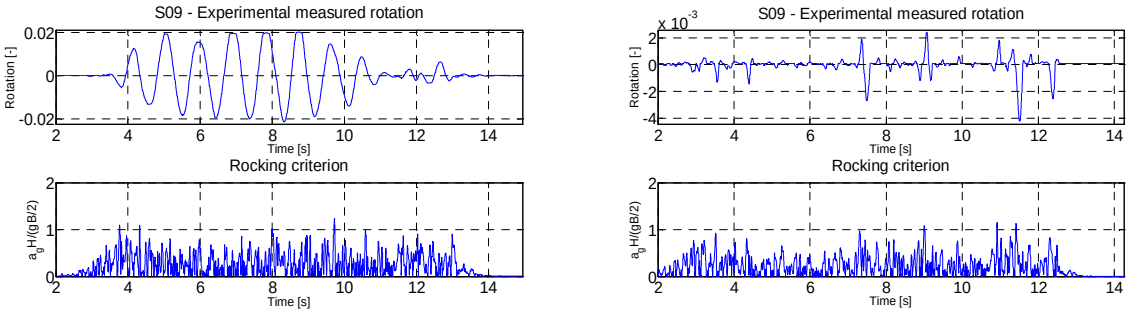


Figure 11 – Rocking criterion for short (left) and long (right) walls without rubber devices during seismic test S09

As a further comparison, Figure 12 compares the rotation calculated by the theoretical model with those observed from tests S09, for which the rocking criterion is predicted a motion. This figure evidences the two main issues faced by the theoretical model.

The first one is related with the definition of the rocking criterion. Indeed, the initiation of the motion in Figure 12 (right) occurs at about 10 seconds, whereas the measurements are catching a rotation of the wall from 2 seconds. This observation is in line with the conclusions of tests S07 and S08 about a too conservative rocking criterion.

The second issue deals with the coefficient of restitution. In Figure 12 (left), it is obvious that the model is not able to reach the level of rotation measured during the test ($t \approx 5s$), while it predicts a non-observed amplification of the oscillations at the end of the signal ($t > 10s$). These observations can be felt as due to a respectively too low or too high estimate of the coefficient of restitution.

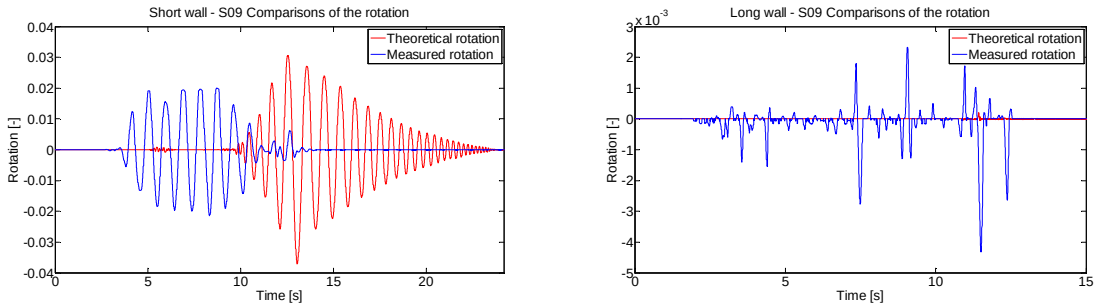


Figure 12 – Comparison between model and experimental results (S09)

3.3 Improvements of the reference model

In conclusion of the previous section, it comes out that the crude use of a basic rocking model is not suitable for walls. The two main parameters that could be adjusted to tune the model for the specific situation considered in the present study are respectively the condition initializing the rocking motion and the estimate of the restitution coefficient. Possible adjustments are proposed in the following sections.

3.3.1 Initiation of the rocking motion

As the contact between the masonry wall and its foundation cannot be considered as perfectly rigid, the assumption of a rigid body rotation around its edge considered as a single dimensionless point is certainly not valid.

It is generally assumed that masonry structural elements have no tensile strength. Thus, the equilibrium is performed according to a static equivalent method such as for instance the approach previously described in 2.2.1. This equilibrium implicitly considers that the base section of the wall remains plane, from which a strain then a stress distribution can be derived. The proposed modification of the rocking initiation criterion consists in considering that, when the motion starts, the rotation doesn't occur around the edge of the wall but around the point of zero stress, and thus zero strain, calculated according to § 2.2.1. It yields:

$$RC = \frac{m\ddot{u}_g H}{mg\left|\frac{B}{2} - L_C\right|} > 1 \tag{11}$$

where L_c is the compressive length calculated with the assumption of a linear distribution of stresses.

With this updated definition of the rocking criterion, the model is predicting the initiation of a rocking behaviour for all tests considered in the study (i.e. S07 to S09 for both aspect ratios of the walls). Figure 13 illustrates this for test S07 of the short wall. In this figure, the criterion calculated by Equation (9) remains below the motion initiation threshold, whereas the modified one calculated by Equation (11) is now sufficient to initiate the motion.

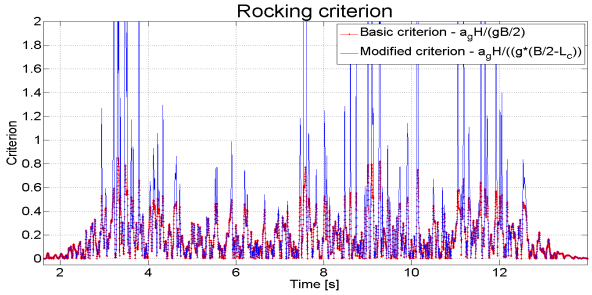


Figure 13 – Rocking criterion for short wall during seismic test S07

In order to keep a fully consistent formulation, the modification of the rocking criterion in terms of position of reference fix point also influences the constitutive equations of the model. Indeed, once the motion starts, the rotation point should now be assumed to be calculated in the same way as when estimating the rocking initiation criterion. This is also consistent with the test measurements summarized in Table 2 and showing that the compressive length generally does not reduce to a single point, even in the case of a slender wall under large acceleration level.

In practice, it implies that the rotation point is likely to vary at each time step (see Figure 14). As a consequence, the angle α is no more a constant, as well as the distance *R* or the coefficient of restitution *e*, these last two parameters being indeed function of the angle α. The values at time-step *n* are then :

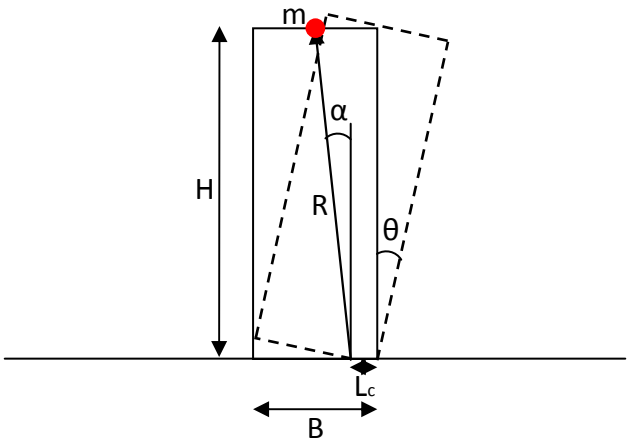


Figure 14 – Updated sketch of the model configuration

$$\tan\alpha_n = \frac{\left|\frac{B}{2} - L_{C,n}\right|}{H} \tag{12}$$

$$R_n = \sqrt{H^2 + \left|\frac{B}{2} - L_{C,n}\right|^2} = \frac{H}{\cos\alpha_n} \tag{13}$$

$$e = 1 - 2\frac{mR_n^{\,2}}{I_{O,n}}\sin^2\alpha_n \tag{14}$$

This only modification is however not sufficient alone to get accurate results, although the general trend of the calculated motion is already better in the initial stage of the simulation when compared to experimental results. This is illustrated in Figure 15, where the model with modified reference point is run for the S09 short wall.

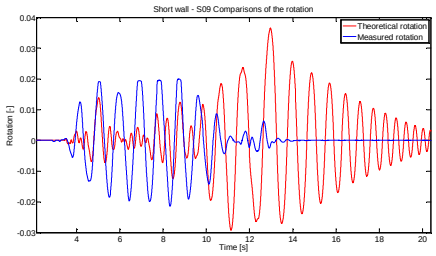


Figure 15 – Comparison between model and experimental results

3.3.2 Restitution coefficient

The formulation of the restitution coefficient used in the basic reference model is the one proposed by [7] deduced from the theory developed by Housner. An alternative formulation is however proposed by [8], also on the base of the Housner theory, that can in the present case be further simplified according to the specific expression of I_O :

$$e_n = 1 - \frac{mR_n^{\,2}}{I_{O,n}} \sin^2\alpha_n = 1 - \sin^2\alpha_n \tag{15}$$

This shows that different options are actually possible regarding the coefficient of $\sin^2\alpha$ in the expression of e_n. In the case of a real masonry wall, the restitution coefficient is very likely to be influenced by the level of degradation of the material, while this level of degradation at a given impact is also likely to depend on the amplitude of the motion during the previous oscillation. The largest is the amplitude, the stronger is the impact, the higher is the dissipation and hence the lower is the restitution coefficient. This dependency is assumed to be represented by the ratio of the maximum rotation calculated during the oscillation preceding the considered impact $\theta_{\max,n}$ normalized by the very maximum rotation calculated since the beginning of the motion $\theta_{\max,abs}$, yielding:

$$e_n = 1 - \frac{\theta_{\max,n}}{\theta_{\max,abs}} \sin^2\alpha_n \tag{16}$$

A second modification is introduced to take into account a lower level of dissipation observed as soon as the seismic input is stopped. Indeed, in case the same coefficient is used during the whole simulation, an unexpected amplification of the response is predicted right after the occurrence of the earthquake (see Figure 15). Therefore it is suggested to use two different expressions of the restitution coefficient for the forced vibration and for the free vibration motions. Eq. (16) is considered for the forced vibrations, while an empirically modified value is used for the free vibration, as suggested in Eqs. (17).

$$e_n = \begin{cases} 1 - \dfrac{\theta_{\max,n}}{\theta_{\max,abs}} \sin^2\alpha_n & \text{if } \ddot{u}_g \neq 0 \\ 1 - \dfrac{1}{2}\dfrac{\theta_{\max,n}}{\theta_{\max,abs}} \sin^2\alpha_n & \text{if } \ddot{u}_g = 0 \end{cases} \tag{17}$$

A final dependency on the wall aspect ratio is introduced on the base of the test observations in order to improve the fitting of the results for the long wall. Indeed, in this latter case, the rocking is clearly not the one of a pure rigid body, as evidenced by the higher values of the compressive length given in Table 2. It is thus assumed that, all other conditions being

identical, i.e. for similar values of the parameters in Eq. (17), the energy dissipated by the long wall should be lower than by the shorter one. A reduction factor is then introduced to account for this effect. An empirical approach by progressive fitting of the numerical results with respect to the experimental data leads to a dependency proportional to the square of the proportion of the aspect ratios, yielding Eq. (18), where A_0 is a constant to be calibrated:

$$e_n = \left(\frac{A_0}{Aspect_Ratio} \right)^2 \left(1 - \frac{\theta_{\max,n}}{\theta_{\max,abs}} \sin^2 \alpha_n \right) \tag{18}$$

3.4 Predictions of the modified theoretical model

Theoretical predictions are first compared with experimental results for the shorter wall in Figure 16, Figure 17 and Figure 18 (left). For this specimen, the model predictions and test measurements match reasonably well, in particular in terms of frequency content and prediction of the strong motions. The time-evolution is however slightly different with a relative difference of the maximum rotation equal to about 30 % in the worst case. Another discordance appears at the end of the test, once the acceleration signal comes down to zero (for t > 11s for S07 and S09, t > 14s for S08). This could be explained by the influence of the shaking table itself which modifies artificially the damping through its breaking system. Indeed, the measurements show a renewed increase of the rotation, while the theoretical results remain close to zero. Except for these observations, the most important phase of strong motion appears to be well approached by the model. This phase corresponds to the motion between the fourth and the tenth seconds for S07 and S09 tests and between the eighth and fourteenth for S08 test. In this latter, the correspondence is less good, but the measurements are actually disturbed by the specimen hitting the safety arrangements. Figure 17 (left) shows a asymmetric rocking behaviour with higher values of positive rotations, which is in accordance with the model predictions.

Comparisons for the longer wall are plotted in Figure 16, Figure 17 and Figure 18 (right). for seismic test S07, S08 and S09 respectively. The fitting of the theoretical curve with the experimental one is pretty accurate in terms of predicting the occurrences of peak rotations, although the orders of magnitude of these peaks are generally overestimated by the theoretical model.

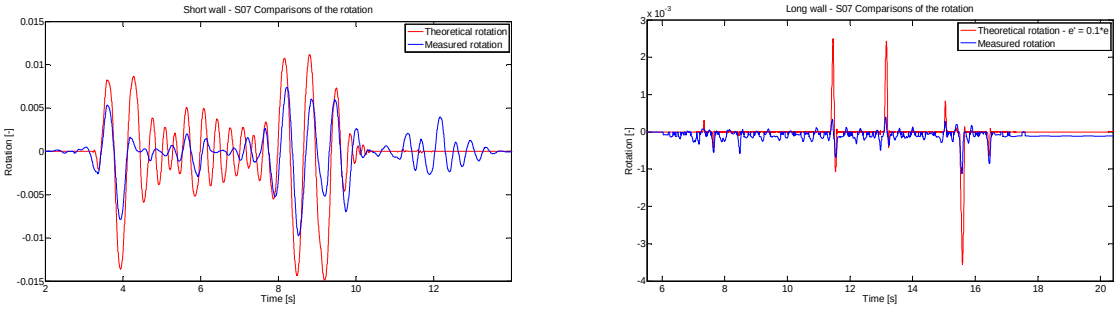


Figure 16 – Results for S07 (short wall : left – long wall right)

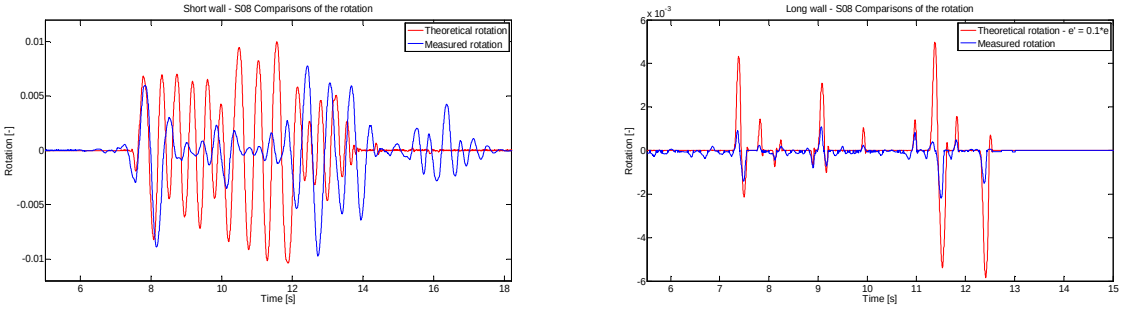


Figure 17 – Results for S08 (short wall : left – long wall right)

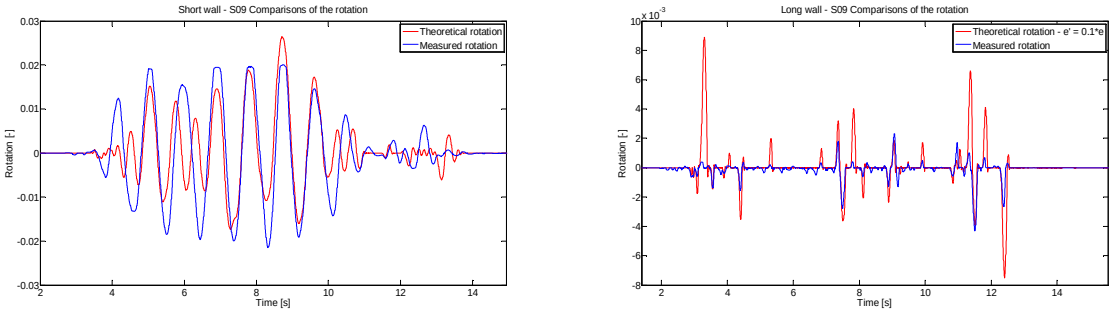


Figure 18 – Results for S09 (short wall : left – long wall right)

Results of the experimental tests and predictions of the model can also be compared in terms of the uplifting of the wall. Let's denote by "lifted length", the part of the wall which is no longer in contact with the support. Its time-evolution is drawn in Figure 19 and Figure 20 for the tests S07 and S09 respectively on short wall (left) and long wall (right). The results provided by the theoretical model assume that the wall is either straight in vertical position (lifted length equal to zero) or completely uplifted. Test and predictive values are in good agreement in the case of the short wall, especially for the seismic test S09. This latter observation was expected since the test conditions were the closest to the model assumptions in terms of measured contact length. In the case of the long wall, the correspondence of the results is not so clear and several differences are observed. Mainly, the model is not able to simulate every single uplifting of the wall. The reason may be the choice of the point of rotation, although further investigation is clearly required in this perspective.

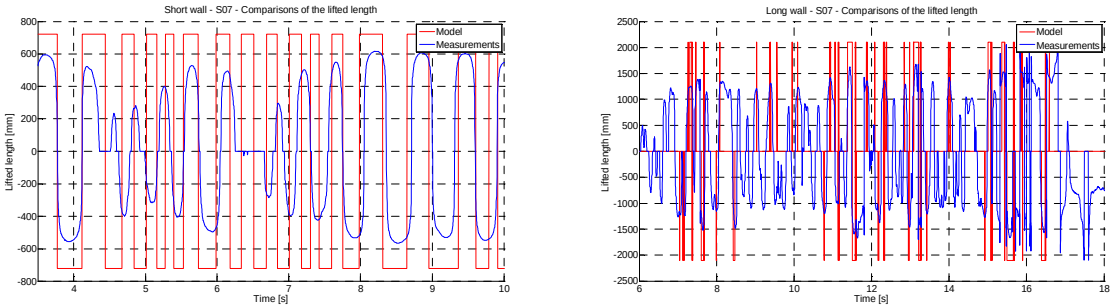


Figure 19 – Comparison of the "lifted length" for the short wall (left) and long wall (right) during seismic tests S07

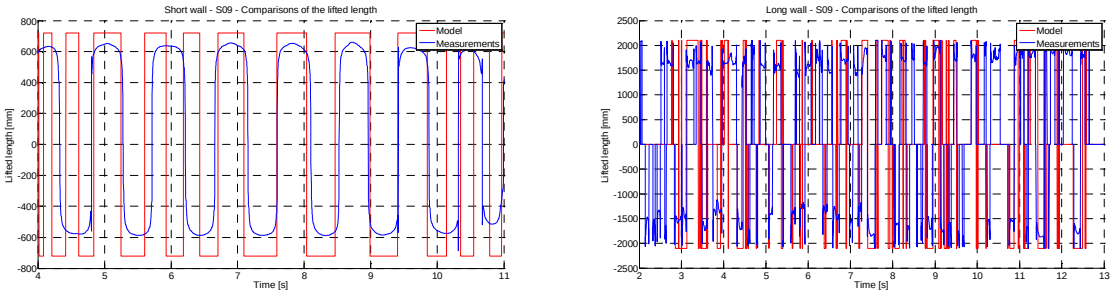


Figure 20 – Comparison of the "lifted length" for the short wall (left) and long wall (right) during seismic tests S09

4 CONCLUSIONS

The present paper describes the results of experimental tests on simple unreinforced masonry walls, with glued horizontal joints and empty vertical joints, stressed by a seismic action. In the first part, the paper presents the general test observations, including the consequences of the use of rubber elements on the global behaviour. The following observations are made:

- The natural frequencies of the element are decreased by about 30% to 40% in presence of rubber layers.
- A frequency drop and an increase of the damping ratio are observed as the acceleration level goes up. The presence of rubber reduces the drop and the increase of the damping ratio.
- The motion of the specimen can be easily characterized by its compressive length. This latter can be assessed thanks to static equivalent methods when the acceleration level remains low, but is underestimated for higher acceleration levels.
- The use of rubber layers leads to higher compressive length for a same acceleration level compared to similar walls without rubber but results in higher horizontal displacements.

In the second part of the paper, the different test results are classified in three categories. A first group is gathering the tests at a low acceleration level for which the specimen can be modelled as a cantilever beam. A second one corresponds to tests submitted to high acceleration, characterized by a significant rocking behaviour. The last group is a hybrid one, where the specimen behaviour is a mix of a cantilever-like and of a rocking behaviour.

The paper focuses then on the high acceleration levels and presents a modelling of the specimens without rubber layers with the objective of predicting their rocking behaviour. The following conclusions are made:

- Two main parameters influence the general behaviour, namely the rocking initiation criterion and the restitution coefficient.
- The rocking criterion defines the minimum acceleration required to initiate the rocking behaviour, depending on the geometry of the specimen. As the specimen cannot be considered as perfect rigid body, the criterion is a function of the actual compressive length assessed with the assumption of a linear distribution of stresses along the compressive length.
- Modifications of the restitution coefficient have been empirically derived depending on several factors, such as the number of impacts, the amplitude of the rocking motion, the geometry of the specimen and excitation.

Further perspectives cover the investigation of the modelling and behaviour of walls with rubber and the globalization of the theoretical model to study entire buildings composed by walls likely to exhibit a rocking behaviour.

ACKNOWLEDGEMENTS

The research leading to these results has received funding from the European Union Seventh Framework Programme (FP7/2007-2013) under grant agreement n° 227887, SERIES. H. Degée also acknowledges the direct support received from F.R.S.-FNRS (Belgian Fund for Research).

REFERENCES

[1] Stuerz, ESECMaSE - Enhanced Safety and Efficient Construction of Masonry Structures in Europe. *Retrieved May 2012, from ESECMaSE*: http://www.esecmase.org

[2] C. MORDANT, Contribution to experimental tests on the seismic behaviour of masonry structural elements. *Master dissertation,* University of Liège, 2012.

[3] C. MORDANT, M. DIETZ, C. TAYLOR, A. PLUMIER, H. DEGEE, Seismic behaviour of thin-bed layered unreinforced clay masonry shear walls including soundproofing elements, *Seismic Evaluation and Rehabilitation of Structures: SERIES Workshop. Geotechnical, Geological and Earthquake Engineering series (chapter 6).* Alper Ilki and Michael N. Fardis (eds), Springer (in press), 2013

[4] Eurocode 6 : Design of masonry structures – Part 1.1 : Common rules for reinforced and unreinforced masonry structures, 2004

[5] C. MORDANT, M. DIETZ, H. DEGEE, Shaking table tests on unreinforced load-bearing masonry walls – comparison with simple cantilever model, *University of Liege internal report,* 2013

[6] G. W. HOUSNER, « The behavior of inverted pendulum structures during earthquakes », *Bulletin of the Seismological Society of America,* Vol. 53, No. 2, February 1963, p.403-417.

[7] L. SORRENTINO, O. ALSHAWA, L.D. DECANINI, The relevance of energy damping in unreinforced masonry rocking mechanisms. Experimental and analytic investigations, *Bull Earthquake Eng* **9**:1617-164, 2011

[8] A. PALMERI, N. MAKRIS, Response analysis of rigid structures rocking on viscoelastic foundation, *Earthquake Engng and Struct. Dyn*. **37**:1039-1063, 2008.

COMPDYN 2013
4th ECCOMAS Thematic Conference on
Computational Methods in Structural Dynamics and Earthquake Engineering
M. Papadrakakis, V. Papadopoulos, V. Plevris (eds.)
Kos Island, Greece, 12–14 June 2013

SEISMIC RESPONSE OF POST-TENSIONED STEEL ROCKING CONCENTRICALLY BRACED FRAMES WITH VARIOUS ASPECT RATIOS

N. Brent Chancellor[1], Richard Sause[1], James M. Ricles[1], Ebrahim Tahmasebi[1], and Tugce Akbas[1]

[1] Lehigh University
117 ATLSS Drive, Bethlehem, PA 18015, USA
{nbc208, rs0c}@lehigh.edu

Keywords: Self-Centering, Rocking, Steel, Concentrically-Braced Frames.

Abstract. *Post-tensioned, steel, rocking concentrically braced frames (also known as self-centering concentrically braced frames or SC-CBFs) are a new type of seismic lateral force resisting system that reduces or eliminates the damage and residual drift often associated with conventional concentrically-braced frames (CBFs) under design level earthquakes. The SC-CBF is made up of a CBF whose column bases are not anchored to the foundation (they are free to uplift), post-tensioning steel that runs vertically over the height of the SC-CBF to prestress the SC-CBF to the foundation and some sort of energy dissipation device. The SC-CBF eliminates the damage to the CBF members under design level earthquakes by limiting the base overturning moment that can develop and then keeping the members nominally elastic. The maximum base overturning moment is limited by allowing the SC-CBF to rock on its foundation and yielding of the post-tensioning steel. The residual drift is reduced or eliminated under design level earthquakes by a prestressing force from the post-tensioning steel running vertically over the height of the SC-CBF. The prestressing force provides a restoring overturning moment that returns the SC-CBF to its original undisplaced state after the earthquake.*

One of the key aspects and assumptions of the SC-CBF system is that the member forces are controlled by limiting the base overturning moment that can develop. Generally, base overturning moment is considered to be a first mode response, but as the aspect ratio increases this assumption becomes less valid. This means that the member forces may not be as well controlled as thought by limiting the base overturning moment. This paper studies the seismic response of six SC-CBFs across a range of aspect ratios through nonlinear time-history analysis and shows how the performance of the SC-CBF changes with aspect ratio.

1 INTRODUCTION

Steel Self-Centering Concentrically-Braced Frames (SC-CBFs) are a new type of seismic lateral force resisting system that are intended to reduce or eliminate the damage and residual drift often associated with conventional concentrically braced frames (CBFs) under the design basis earthquake (DBE) [1, 2]. The SC-CBF system increases the drift capacity of the CBF by allowing the CBF to rock on its foundation. Post-tensioning (PT) bars run vertically over the height of the CBF and provide a restoring overturning moment at the base to self-center the SC-CBF so that there is little or no residual drift. Energy dissipation in an SC-CBF is provided by lateral load bearings with friction at each floor level and/or supplemental energy dissipation devices. Damage to the braces and other members is not a significant energy dissipation mechanism in the SC-CBF, which is in contrast to conventional CBFs which dissipate energy through yielding and buckling of the braces and connecting elements. The hysteretic behavior of the entire SC-CBF seismic lateral force resisting system is characterized by flag shaped hysteresis loops [1]. A schematic of hysteresis loops for an SC-CBF using lateral load bearing with friction for energy dissipation is shown in Figure 1.

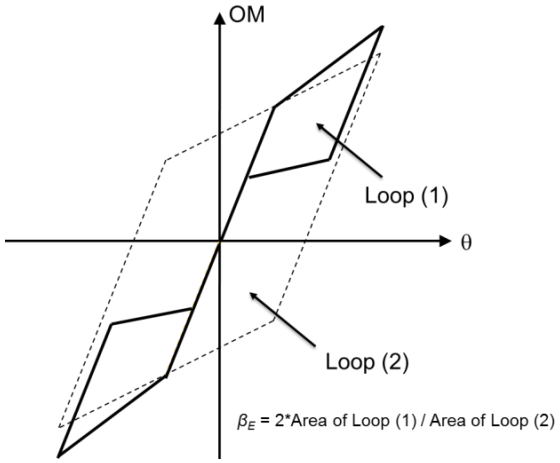


Figure 1: Schematic base overturning moment versus roof drift hysteresis loops for an SC-CBF (Loop 1) and an equivalent bilinear elastic-plastic system (Loop 2). Also shown is a graphical demonstration of the definition of the energy dissipation ratio (β_E).

One of the key aspects and assumptions of the SC-CBF system is that the member forces are controlled by limiting the base overturning moment that can develop. Generally, base overturning moment is considered to be a first mode response, but as the aspect ratio of the SC-CBF increases this assumption becomes less valid. As a result, the member forces may not be controlled as intended by limiting the base overturning moment. This paper studies the seismic response of several SC-CBFs with various heights subjected to design level earthquakes. First the SC-CBF system and its behavior are outlined. Then the designs of the archetype SC-CBFs studied in this paper are described. Details of the numerical model used in time-history analyses are given, followed by details about the ground motion set used in time-history analyses. Results from the time-history analyses are described. Finally, the behavior of the archetype SC-CBFs at various aspect ratios is studied to show how the performance of the SC-CBF system changes with aspect ratio.

2 SC-CBF SYSTEM AND BEHAVIOR

An SC-CBF is similar to a conventional CBF in that it is made up of beams, columns and braces connected together in such a manner that the applied external forces are resisted primarily through axial forces in the members. However, a few changes to the conventional CBF provide the SC-CBF with larger drift capacity and self-centering behavior after a significant earthquake [1, 2]. The first significant change is that the SC-CBF column bases are not vertically anchored to the foundation; they are free to uplift and allow the SC-CBF to rock at its base during the earthquake. The SC-CBF is restrained in the horizontal direction at the base level. The SC-CBF has post-tensioning (PT) steel which runs vertically over the height of the SC-CBF. This PT steel is prestressed and clamps the SC-CBF to its foundation. The purpose of the PT steel is to provide an initial base overturning moment resistance as well as a restoring base overturning moment so that the SC-CBF will return to its plumb condition. A third difference is that the SC-CBF system includes an extra gravity column adjacent to each SC-CBF column. This extra gravity column allows the floor diaphragm to be separated from the SC-CBF so that it will not be damaged when the SC-CBF columns uplift during an earthquake. A lateral load bearing is located between the SC-CBF column and the adjacent gravity column. The lateral load bearing transfers the lateral forces from the floor diaphragm (attached to the gravity column) to the SC-CBF while still allowing the SC-CBF columns to uplift, preventing floor diaphragm damage. The lateral load bearings also act as passive energy dissipation devices due to the normal force and frictional force that develops in the bearing from the lateral loads and the relative vertical motion between the SC-CBF column and the adjacent gravity column. An SC-CBF also includes a horizontal base strut between the bases of the SC-CBF columns to transfer base shear from the uplifted SC-CBF column to the SC-CBF column in contact with the foundation. A vertical "distribution" strut in the upper stories of the SC-CBF at the center of the bay is included to distribute the large vertical force from the PT steel to braces in the upper stories of the SC-CBF. A typical SC-CBF with adjacent gravity columns and lateral load bearings with friction is shown in Figure 2a.

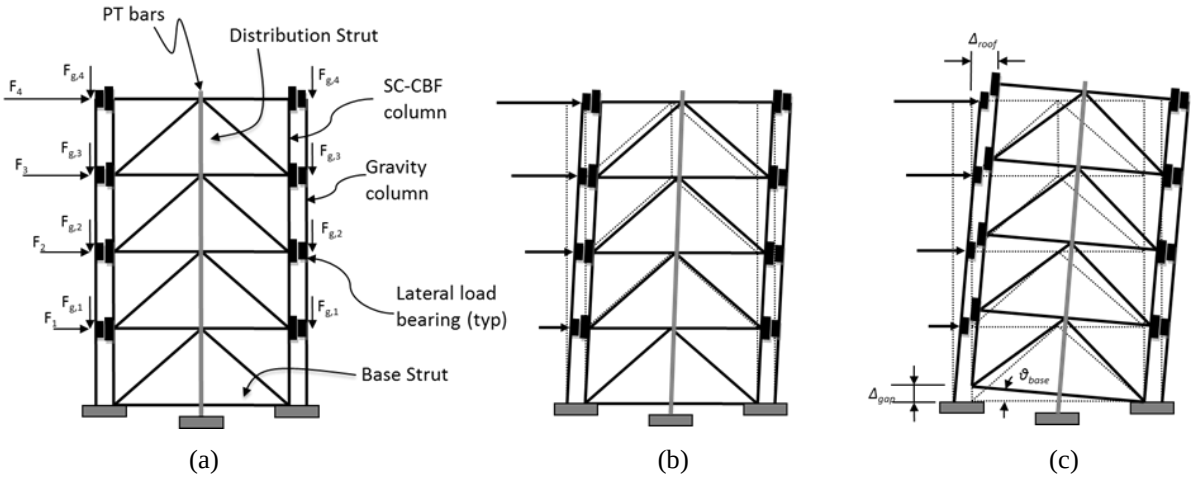


Figure 2: Lateral load behavior of SC-CBF: (a) layout of typical SC-CBF with gravity and lateral forces; (b) elastic response of SC-CBF frame before SC-CBF "tension" column decompresses and lifts up; (c) rigid body rocking of frame on foundation.

As lateral force is applied to the SC-CBF (shown in Figure 2a) the SC-CBF will deform elastically (Figure 2b) similar to a conventional CBF. However, after the applied base overturning moment becomes large enough to overcome the initial overturning moment resistance

provided by the prestress force in the PT bars, the SC-CBF weight and the friction in the lateral load bearings, one column will uplift or "decompress" and the SC-CBF will begin to rock on its foundation (Figure 2c). As the lateral force is reduced, the force in the PT bars provides a restoring overturning moment to return the SC-CBF to its plumb, upright position.

The internal forces that can develop in the members of the SC-CBF are intended to be limited by the rocking action of the SC-CBF (and yielding of the PT bars if the lateral drift demand is large enough). After decompression, the stiffness of the SC-CBF system is primarily controlled by the area and location of the PT bars.

An experimental study of a 4-story, 0.6 scale SC-CBF was performed at Lehigh University to validate the SC-CBF lateral force resisting system concept. The results of this study are covered extensively in references [2, 3, 4]. The testing program used the hybrid simulation technique [5] and simulations were performed pseudo-dynamically. Simulations were performed at the DBE and maximum considered earthquake (MCE) demand levels. Thirty one successful simulations were performed showing that large ductility without damage or residual drift can be achieved for SC-CBFs.

Most studies of the SC-CBF concept or variants of the concept are limited to structures 6-stories or less in height [1, 2, 6, 7, 8, 9, 10]. This paper addresses the behavior of SC-CBFs at many aspect ratios, including structures up to 18 stories.

3 DESIGN OF ARCHETYPE SC-CBF STRUCTURES

3.1 Floor Plan and Elevation Layouts

All of the archetype SC-CBFs studied in this paper were designed using a performance-based design procedure from reference [1] with a few modifications. Schematics for the floor plan and elevation layouts for the archetype SC-CBFs structures studied in this paper are shown in Figure 3. The structure is symmetric in two directions and eight SC-CBFs are distributed around the perimeter of the structure. This symmetry requires only a single SC-CBF for each structure to be designed.

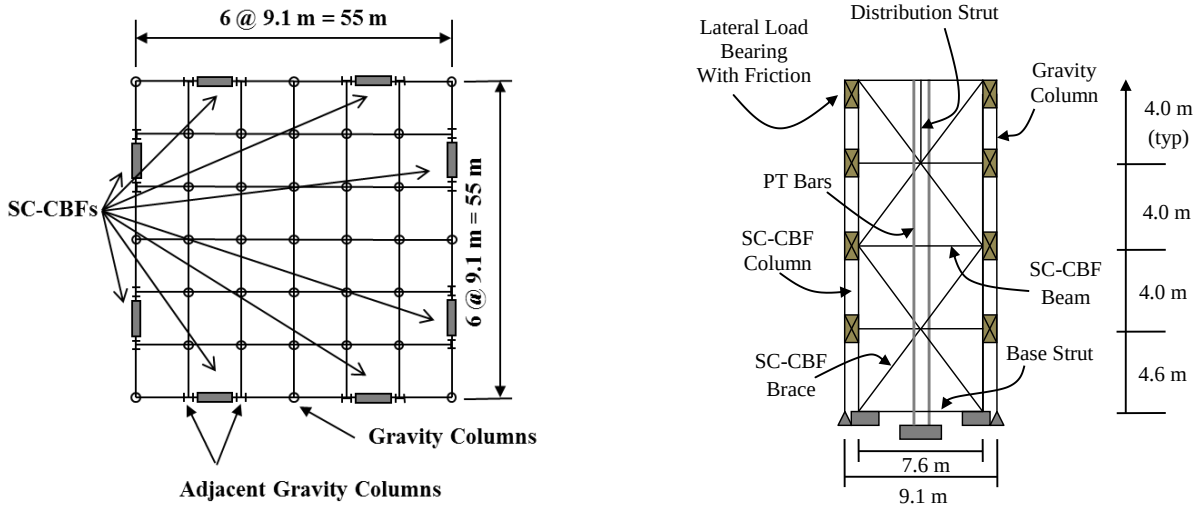


Figure 2: Lateral load behavior of SC-CBF: (a) layout of typical SC-CBF with gravity and lateral forces; (b) elastic response of SC-CBF frame before SC-CBF "tension" column decompresses and lifts up; (c) rigid body rocking of frame on foundation.

The braces of the archetype SC-CBFs studied in this paper are arranged in an x-braced configuration. A gravity column is located adjacent to each SC-CBF column. High strength, high ductility post-tensioning (PT) bars run vertically over the height of the SC-CBF at mid-bay. A vertical distribution strut is located at the center of the bay in the top one or two stories to distribute the large concentrated force from the PT bars to the braces in the top two or three stories. A horizontal base strut is located at the bottom of the SC-CBF between the SC-CBF columns to transfer base shear from the uplifted column to the column in contact with the foundation.

3.2 Loads on Archetype SC-CBFs

The dead loads for the archetype SC-CBF structures are expressed in terms of a floor pressure and are shown in Table 1. The live loads for the archetype SC-CBF structures are expressed as a floor pressure in Table 2. The structures are assumed to be office-type structures. Wind loads and other loading conditions were not considered in the design of the archetype SC-CBFs.

Dead Load (kN/m^2)	Floor 1	Middle Floors	Roof
Floor/Roof Deck	0.14	0.14	0.14
Floor/Roof Slab	2.06	2.06	0
Roofing Material	0	0	0.48
Mechanical Weight	0.48	0.48	1.20
Ceiling Material	0.24	0.24	0.24
Floor Finish	0.10	0.10	0
Structural Steel	0.72	0.72	0.48
Steel Fireproofing	0.10	0.10	0.10
Building Envelope	0.37	0.35	0.25
Total	**4.20**	**4.18**	**2.89**

Table 1: Summary of dead loads.

Live Load (kN/m^2)	Floors	Roof
Office	2.39	0
Partitions	0.72	0
Roof (unreduced)	0	0.96
Total	**3.11**	**0.96**
Live Load Included in Seismic Mass	0.72	0

Table 2: Summary of live loads.

3.3 Archetype SC-CBF Designs

All of the SC-CBF members were designed using wide-flange shapes that meet the seismic compactness requirements of ANSI/AISC 341-05 [11]. The specified yield strength of the steel for the SC-CBF and CBF members was 0.35 kN/mm^2 and the modulus of elasticity was 200 kN/mm^2. The yield strength for the PT bars for the SC-CBF was assumed to be 0.83 kN/mm^2 and the modulus of elasticity was assumed to be 205 kN/mm^2.

The seismic design category for the SC-CBF and CBF was Category D [12]. The short period spectral acceleration used in design (S_S) was 1.5g and the 1 sec period spectral acceleration used in design (S_1) was 0.6g. The site class was assumed to be Site Class D [12].

Six archetype SC-CBFs were designed (4, 6, 9, 12, 15, and 18-stories). Table 4 lists important parameters for each archetype SC-CBF design. The aspect ratio is the height of the archetype SC-CBF divided by the width of the SC-CBF, T_1 is the first mode period of the SC-CBF calculated using a fixed base linear numerical model, θ_{DBE} is the predicted roof drift un-

der the DBE, β_E is the energy dissipation ratio (ratio of the area of idealized SC-CBF hysteresis loops to an equivalent bilinear elastic plastic system, see Figure 1), β_{SC} is a measure of the self-centering capability of the archetype SC-CBF (β_{SC} must be less than 0.50 to ensure self-centering behavior), and R_A is similar to the response modification coefficient, *R*, used in building codes for seismic design of structures and will be explained further later. Table 4 also lists the parameters that strongly influenced the design of the archetype SC-CBFs. *AMS* indicates that the available member sizes influenced the design of the archetype SC-CBF, and θ_{DBE} indicates that drift influenced the design. Some archetype SC-CBF designs required members larger than the typical column sections listed in the 13th Edition of the AISC Steel Construction Manual [13].

The aspect ratio for the archetype SC-CBFs varies from approximately 2 for the 4-story SC-CBF to approximately 10 for the 18-story. The first mode period varies from 0.48 sec to 3.30 sec. The predicted roof drift (θ_{DBE}) is approximately 1.5% radians for most of the archetype SC-CBFs. The roof drift values are calculated using ductility-response modification coefficient-period (μ-*R*-*T*) relationships developed by Seo [14] for self-centering systems.

The energy dissipation ratio (β_E) decreases with increasing aspect ratio, but the lateral load bearings still allow the SC-CBF columns to uplift without damaging the floor system. Additional energy dissipation devices, such as yielding elements, can be added to increase β_E, but were not used for the archetype SC-CBFs studied in this paper. Additional energy dissipation can reduce the required amount of PT steel, which in turn will reduce the SC-CBF member sizes. β_{SC} for the archetype SC-CBFs was intentionally kept below 0.50 to ensure that the SC-CBFs will self-center. If β_{SC} is greater than 0.50, the hysteresis loops for the SC-CBF will extend into the second and fourth quadrants on a plot of the hysteresis loops and self-centering is not guaranteed.

Archetype	**Aspect Ratio (height/width)**	***T*$_1$ *(sec)***	**θ_{DBE} (% rad)**	**β_E**	**β_{SC}**	**R_A**	***SC-CBF Weight (kN)***	***Parameter Controlling Design***
4-story	2.16	0.48	1.02	0.51	0.35	7.45	205	-----
6-story	3.20	0.84	1.51	0.36	0.23	13.2	326	θ_{DBE}
9-story	4.76	1.32	1.52	0.20	0.16	12.7	700	θ_{DBE}
12-story	6.32	1.78	1.51	0.14	0.12	10.2	1236	θ_{DBE}
15-story	7.88	2.39	1.51	0.11	0.096	7.84	1992	θ_{DBE},*AMS**
18-story	9.44	3.30	1.66	0.086	0.080	5.82	2760	θ_{DBE},*AMS**

Table 3: Summary of design parameters for archetype SC-CBFs.

R_A is a parameter similar to the response modification coefficient, *R*, in ASCE 7-05 (ASCE 2005) and ASCE 7-10 (ASCE 2010). R_A is calculated as follows:

$$R_A = \frac{OM_{elastic}}{OM_D} \tag{1}$$

where, $OM_{elastic}$ is the base overturning moment calculated using the equivalent lateral forces from ASCE 7 with *R*=1 and OM_D is the overturning moment when the SC-CBF uplifts and rocking begins. The calculation of OM_D is explained further in Roke et al. [2]. The values of $OM_{elastic}$ and OM_D are shown in Table 5 for each archetype SC-CBF studied in this paper. Also in Table 5 are the base overturning moment at yield of the PT steel and the peak overturning moment predicted for the design basis earthquake, which is based on estimated drift.

The area of PT steel used in each archetype SC-CBF design along with the initial prestress ratio (initial prestress force/yield force) is summarized in Table 5. The amount of PT steel

can be reduced if added energy dissipation devices are used, because additional PT steel is used to help control the "*R*" parameter used to predict the drift demand. Increasing OM_D reduces the "*R*" parameter used in the drift prediction and reduces the expected roof drift under the DBE (θ_{DBE}). Added energy dissipation devices also increase β_E, which also reduces θ_{DBE}.

Archetype	Area of PT Steel (cm^2)	Initial Prestress Ratio (% of Yield Force)	OM_D (MN-m)	OM_Y (MN-m)	$OM_{elastic}$ (MN-m)	OM_{DBE} (MN-m)
4-story	81	0.50	20.6	40.0	153.6	40.6
6-story	102	0.47	21.3	43.5	281.6	43.6
9-story	169	0.55	37.9	66.4	480.4	60.4
12-story	237	0.75	68.7	89.9	703.1	90.4
15-story	403	0.80	120.6	148.7	945.3	146.9
18-story	671	0.85	206.8	241.3	1205	236.8

Table 4: Summary of additional design parameters for archetype SC-CBFs.

A key assumption about the behavior of an SC-CBF under earthquake load is that the base overturning moment is primarily a first mode response and that rocking behavior of the SC-CBF will limit the overturning moment that can develop. If this assumption is violated, the braces and other members of the SC-CBF must be designed for larger forces or, damage to the members must be accepted by the performance criteria. To assess the contributions of each mode to the base overturning moment, the modal overturning moment at the base of the archetype SC-CBFs were calculated and then normalized by dividing by the sum of the absolute values of the modal base overturning moments for all of the modes. The contribution of the modal base overturning moment for the first two modes to the sum of the absolute value of the base overturning moment for all of the modes is shown in Figure 4.

In Figure 4, as the number of stories increases up to 12-stories, the normalized first mode base overturning moment decreases rapidly while the normalized second mode overturning moment increases rapidly. The first mode and second mode base overturning moment are about the same for the 12, 15, and 18-story archetypes. Figure 4 indicates that the SC-CBF system may be more effective for structures with fewer stories or smaller aspect ratios. The results from time-history analyses of the archetype SC-CBFs will be used to study this issue further.

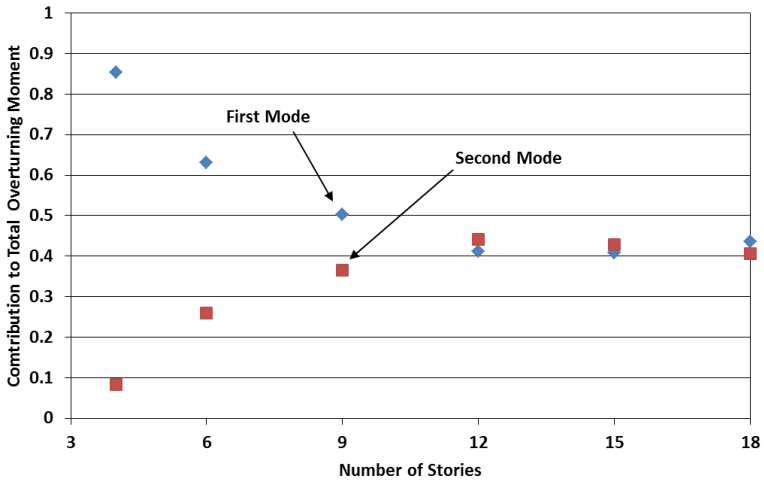


Figure 4: Plot of modal overturning moment contributions for the 4, 6, 9, 12, 15, and 18-story SC-CBFs.

4 EVALUATION OF ARCHETYPE SC-CBFS USING TIME-HISTORY ANALYSES

4.1 Modeling of Archetype SC-CBFs for Time-History Analyses

Nonlinear numerical models for the archetype SC-CBFs were created in OpenSees [15]. OpenSees is an open source nonlinear dynamic analysis software package. The numerical model was a two dimensional (planar) model. The braces in the numerical model form an "x" configuration with the bottom end of the first story braces attaching to the columns. A schematic of the numerical model is shown in Figure 5. There is a gravity column located adjacent to each SC-CBF column. A lean-on column is connected to the adjacent gravity columns and models the gravity system tributary to the SC-CBF. Lateral load bearings are located at each floor between the SC-CBF columns and the adjacent gravity columns.

All of the archetype SC-CBF members are modeled using beam-column elements with an elastic material model. An elastic material model was used because the design procedure intends to keep the members elastic under DBE level design forces. The nonlinearity in the SC-CBF is expected to be from rocking action and yielding of the PT steel. The lateral load bearings are modeled using a friction-contact-gap element. The friction-contact-gap element models friction behavior using a slightly modified Mohr-Coulomb friction model to account for the contact and friction stiffness. A small, initial gap in the lateral load bearings is modeled.

The steel post-tensioning (PT) bars used in the design of the archetype SC-CBFs are represented in the numerical models by a beam-column element with section and material properties such that the total axial yield force of the PT bars is the same as that in the model. The material model for the PT bars was bilinear elastic-plastic with a 2% post-yield slope. The yield strength of the PT bars was modeled as 0.83 kN/mm^2. The PT bars in the numerical model are anchored at a node located at the center of the SC-CBF at the roof level and at a node 0.91 m below the base level. The 0.91 m of PT bar length below the base level is intended to represent the additional free length of PT bar that would be present in the anchorage in the foundation. At the node where the PT steel is anchored there is a zero-length element. The zero-length element is used to modify the PT steel model so that the PT steel can only carry tension loads and allow for "slack" or gap condition to form at the base of the PT bars if the permanent deformation in the PT bars becomes large enough.

The model has six locations where boundary conditions are applied. These locations include: the base of the lean-on column, the base of each gravity column adjacent to the SC-CBF columns, the base of each SC-CBF column, and one location at the anchorage of the PT bars. The boundary condition at the base of the lean-on column is a "pin" condition where the vertical and horizontal displacement are restrained, but the rotation is not. The base of each gravity column (adjacent to the SC-CBF columns) has a pinned condition. The boundary condition at the base of each SC-CBF column models the vertical and horizontal gap and contact condition. Two zero-length elements are used at each SC-CBF column base. One zero-length element models the vertical gap and contact condition while the other zero-length element models the horizontal gap and contact condition. The material/behavior model for the zero length elements at the SC-CBF column base has a positive stiffness as the column is displaced towards the foundation while the stiffness in the other direction is very small, creating a linear elastic-gap model. The element that connects the zero-length element at the base of the PT bars to the foundation is restrained so that only axial deformation is possible. Figure 6 shows a schematic of the boundary conditions of numerical model.

The lateral degree-of-freedom at each floor of the gravity columns (adjacent to the SC-CBF columns) is constrained to the lean-on column in the numerical model. The seismic

mass at each floor level is assigned to the horizontal degree of freedom at the lean-on column node at each respective floor level. In addition to the seismic mass applied to the lean-on column a small mass was applied to the center node of the SC-CBF or CBF at each floor. This mass was applied for numerical stability of the SC-CBF numerical model. The sum of the masses applied to the center of the SC-CBF equals the total mass of the SC-CBF. The mass at the center nodes of the SC-CBF was assigned to both the vertical and horizontal degrees-of-freedom since the SC-CBF floor center nodes may have both significant lateral and vertical motion.

Second order effects are considered in the numerical model through use of a lean-on column and a corotational geometric transformation. Inherent damping in the structure was modeled using Rayleigh damping with 2.6% damping in the first mode and 6.1% in the third mode.

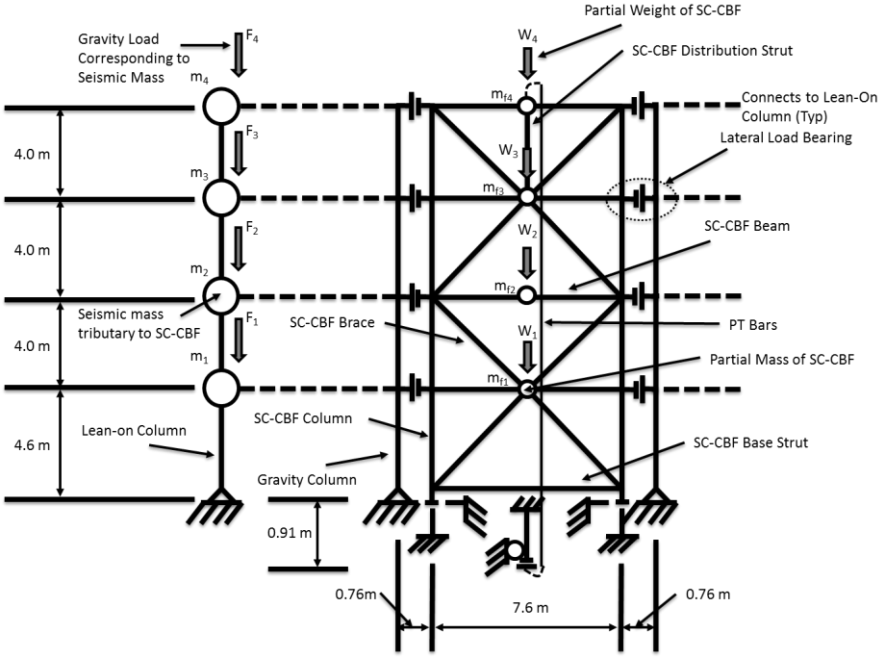


Figure 5: Schematic of numerical model layout for archetype SC-CBFs.

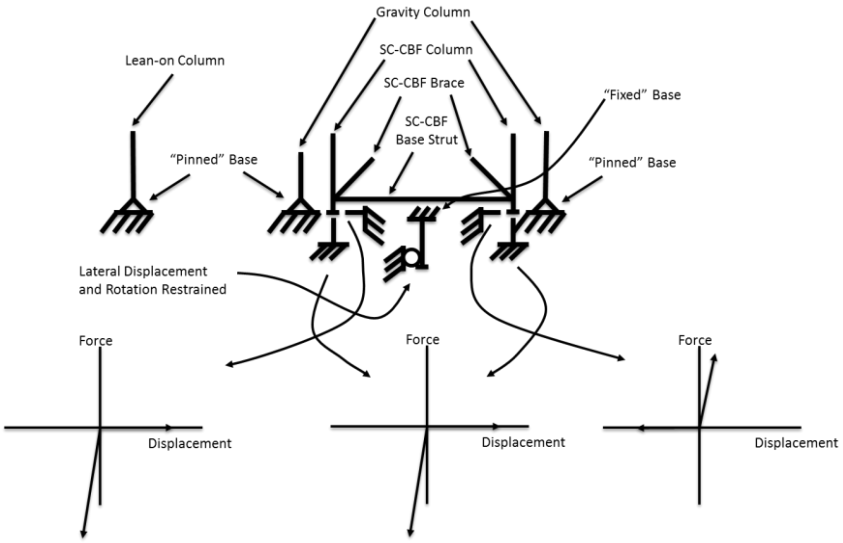


Figure 6: Numerical model boundary conditions for archetype SC-CBFs.

4.2 Ground Motions Used in Study of Archetype SC-CBF Structures

The ground motion set that was used in this study was selected to represent the design spectrum for the archetype SC-BFs over a broad period range. Eighteen ground motion pairs were selected from a subset of the filtered ground motions in the PEER-NGA database [16] meeting some special requirements. Ground motions used in the subset of the PEER-NGA database met the following criteria:

1. The lowest usable frequency of the ground motion was 0.125 Hz or less, providing seismic input to periods of 8 sec or more.
2. The ground motion was recorded on a site with NEHRP Type D soil (based on Vs30).

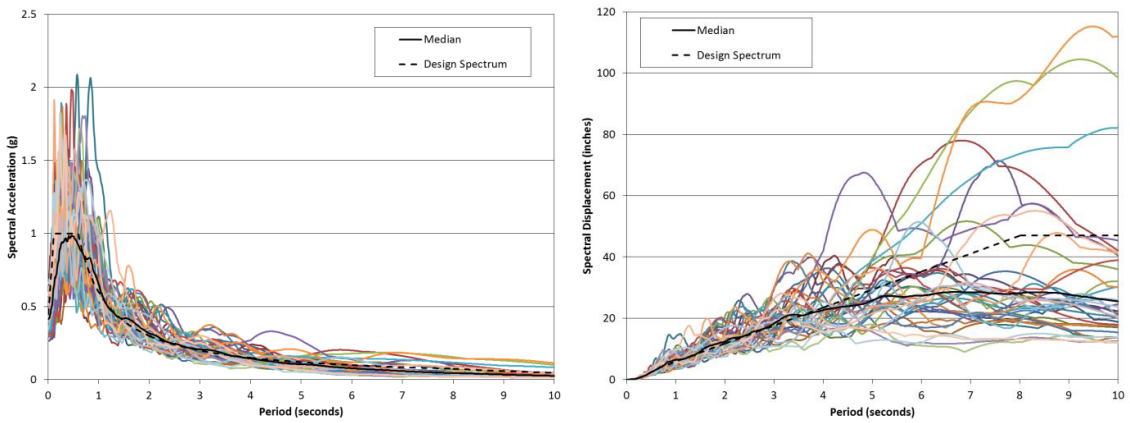
The eighteen ground motion pairs were selected and scaled to match the design spectrum for the archetype SC-CBFs over the period range of 0.1-7.0 sec. The spectral acceleration and spectral displacement for each scaled ground motion are plotted versus period in Figure 7 along with the design spectrum and the median of the ground motion set. The ground motions were scaled so that the geometric mean of spectral acceleration for the pair of records matched the design spectrum over the period range of 0.1-7.0 sec (with a period increment of 0.01 sec). A scaling method given in Baker [17] was used, which scales each ground motion so that the average spectral acceleration of the target spectrum is equal to the average of the response spectrum over the desired period range. The scale factor calculated using this method is:

$$SF_j = \frac{\sum_{k=1}^{n} SA_{TS}(T_k)}{\sum_{k=1}^{n} SA_{GM}(T_k)} \tag{2}$$

where,

SF_j is the scale factor for ground motion j in the ground motion set
T_k is the k^{th} period in a vector of n periods that will be considered
$SA_{TS}(T_k)$ is the spectral acceleration of the target spectrum at period T_k
$SA_{GM}(T_k)$ is the spectral acceleration of the ground motion being scaled at period T_k.

The scale factor for all ground motion pairs was less than 3.0.



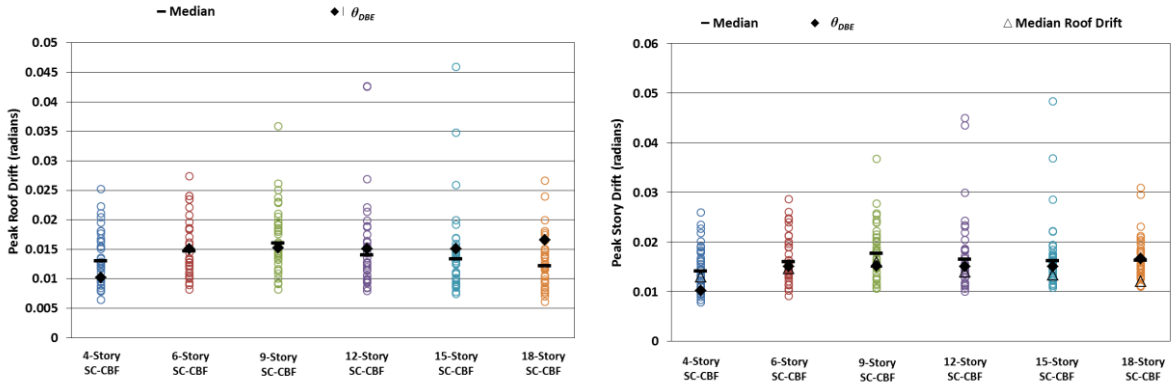
(a) (b)

Figure 7: (a) Spectral acceleration and (b) spectral displacement versus period.

4.3 Results of Time-History Analyses and Seismic Behavior of SC-CBFs

The peak roof drift demand and the peak story drift demand from the time-history analyses of the archetype SC-CBFs are shown in Figure 8. The median value of the peak response is shown with a solid bar. The median peak roof drift on the plot of peak story drifts is shown by an open triangle. The median value shown is calculated by taking the exponential of the average of the natural log of the data. The median peak roof drift predicted by the design procedure used for the archetype SC-CBFs is shown by a solid diamond. The median peak roof drift demand for the archetypes is 1.6% radians or less. Improvement in the prediction of the peak roof drift demand is needed for many of the archetype SC-CBFs and is the subject of ongoing research. The median peak story drift was 9%-34% higher than the median peak roof drift.

Two key assumptions of the behavior of SC-CBFs are that (a) rocking of the SC-CBF is primarily a first mode response and (b) that rocking of the SC-CBF and yielding of the PT steel limits the forces that can develop in the SC-CBF members. If the base overturning moment in the higher modes is significant, assumption (a) may be violated. Figure 9 compares modal overturning moment ratios calculated from time-history analysis results with design modal overturning moment ratios. The modal base overturning moments from time-history analysis were calculated by using the elastic mode shapes to decompose the restoring force vector at each time step into modal components. The result was then used to calculate modal base overturning moments. The modal base overturning moment ratio is the maximum of the absolute value of the base overturning moment for a mode divided by the sum of the maximum of the absolute value of the base overturning moment for each mode. The median value for the modal overturning moment ratio is shown with a solid bar. The median is calculated by taking the exponential of the average of the natural log of the data. The design modal overturning moment ratio for the first two modes is also shown. The plot of the modal overturning moment ratio shows that, as the height of the SC-CBFs increases, the assumption that the overturning moment response is primarily a first mode response is violated. This result raises some doubt about the effectiveness of the SC-CBF system studied herein as the height and aspect ratio increases.



(a) (b)

Figure 8: (a) Peak roof demand and (b) peak story drift demand.

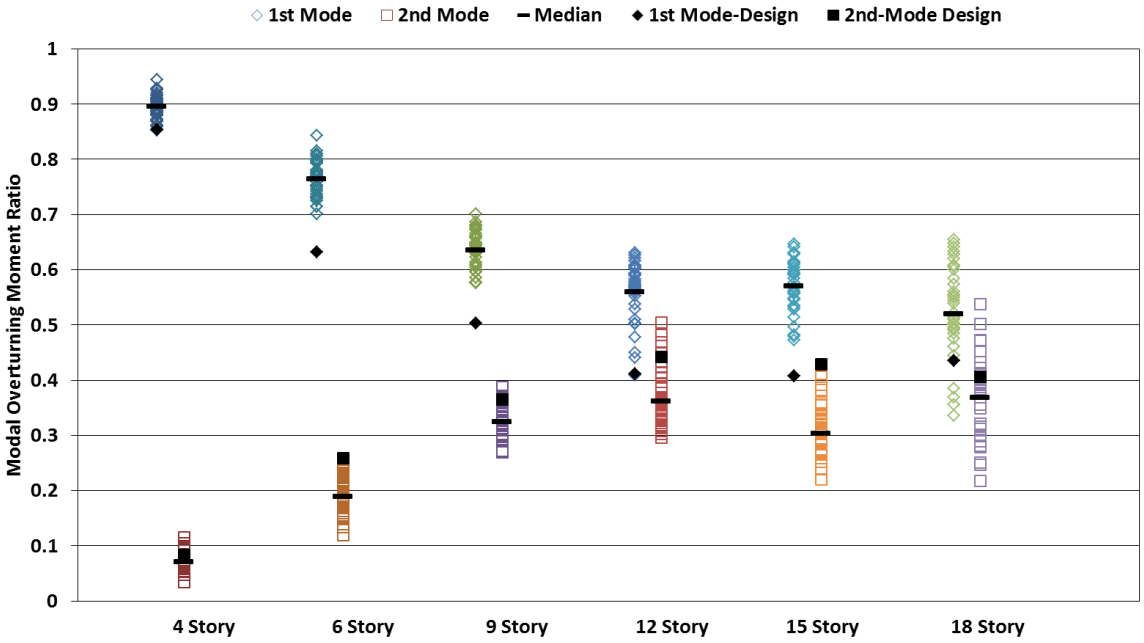


Figure 9: Modal overturning moment ratio from time-history analysis.

5 SUMMARY AND CONCLUSIONS

Steel SC-CBFs are a new type of seismic lateral force resisting system that reduces or eliminates the damage and residual drift often associated with conventional CBFs under the DBE. The SC-CBF system controls the member forces that can develop by assuming that the base overturning moment is a first mode response and then limits the base overturning moment by rocking of the SC-CBF and yielding of the PT steel. Six archetype SC-CBFs ranging from 4-stories to 18-stories were designed and subjected to design level earthquakes using time-history analysis. The median peak roof drift for the archetype SC-CBFs was 1.6% radians or less. The median peak story drift was 6% to 35% higher than the median peak roof drift. The difference between the median peak roof drift and median peak story drift generally increased with increasing aspect ratio. The first mode base overturning moment ratio generally decreased with an increase in aspect ratio while the second mode base overturning moment ratio generally increased with an increase in aspect ratio. Since the second mode base overturning moment ratio increases as the aspect ratio of the SC-CBF increases, this violates the assumed behavior and indicates that the SC-CBF member forces may not be as well controlled as thought. Methods of limiting higher mode response should be explored for SC-CBFs as the aspect ratio increases.

REFERENCES

[1] Roke, D.; Sause, R.; Ricles, J.M.; Seo, C.-Y.; and Lee, K.-S. (2006). "Self-Centering Seismic-Resistant Steel Concentrically-Braced Frames," Proceedings of the 8th U.S. National Conference on Earthquake Engineering, EERI, San Francisco, April 18-22.

[2] Roke, D.; Sause, R.; Ricles, J.M.; and Chancellor, N.B. (2010). "Damage-Free Seismic-Resistant Self-Centering Concentrically-Braced Frames." ATLSS Report 10-09, Lehigh University, Bethlehem, PA.

[3] Sause, R.; Ricles, J.M.; Roke, D.A.; Chancellor, N.B.; and Gonner, N.P. (2010a). "Seismic Performance of a Self-Centering Rocking Concentrically-Braced Frame." Proceedings of the 9th U.S. National and 10th Canadian Conference on Earthquake Engineering, EERI, Toronto, July 25-29.

[4] Sause, R.; Ricles, J.M.; Roke, D.A.; Chancellor, N.B.; and Gonner, N.P. (2010b). "Large-Scale Experimental Studies of Damage-Free Self-Centering Concentrically Braced Steel Frames Under Seismic Loading." NASCC Steel Conference/ASCE Structures Congress, Orlando, May 12-15.

[5] Hybrid Simulation: Theory, Implementation and Applications, Edited by Victor Saouma and Siva Mettupalayam, Francis and Taylor Publishers, London, England, 2008.

[6] Tremblay, R.; Poirier, L.-P.; Bouaanani, N.; Leclerc, M.; Rene, V.; Fronteddu, L.; and Rivest, S. (2008b). "Innovative Viscously Damped Rocking Braced Steel Frames," Proceedings of the 14th World Conference on Earthquake Engineering, Beijing, China, October 12-17.

[7] Eatherton, M.; Hajjar, J.; Ma, X.; Krawinkler, H.; and Deierlein, G. (2010a). "Seismic Design and Behavior of Steel Frames with Controlled Rocking – Part I: Concepts and Quasi-Static Subassembly Testing," Proceedings of the ASCE/SEI Structures Congress 2010, Orlando, FL, May 12-15.

[8] Eatherton, M.; Hajjar, J.; Deierlein, G.; Ma, X.; and Krawinkler, H. (2010b). "Hybrid Simulation Testing of a Controlled Rocking Steel Braced Frame System." Proceedings of the 9th U.S. National and 10th Canadian Conference on Earthquake Engineering, EERI, Toronto, July 25-29.

[9] Ma, X.; Eatherton, M.; Hajjar, J.; Krawinkler, H.; and Deierlein, G. (2010). "Seismic Design and Behavior of Steel Frames with Controlled Rocking – Part II: Large Scale Shake Table Testing and System Collapse Analysis," Proceedings of the ASCE/SEI Structures Congress 2010, Orlando, FL, May 12-15.

[10] Midorikawa, M.; Azuhata, T.; Ishihara, T.; and Wada, A. (2006). "Shaking Table Tests on Seismic Response of Steel Braced Frames with Column Uplift," Earthquake Engineering and Structural Dynamics, 35(14), pp 1767-1785.

[11] AISC (2005). Seismic Provisions for Structural Steel Buildings. American Institute of Steel Construction, Chicago, IL.

[12] ASCE (2005). Minimum Design Loads for Buildings and Other Structures, ASCE7-05. American Society of Civil Engineers (ASCE), Reston, VA.

[13] AISC (2005). Steel Construction Manual, 13th Edition. American Institute of Steel Construction, Chicago, IL.

[14] Seo, C.-Y. (2005). "Influence of Ground Motion Characteristics and Structural Parameters on Seismic Responses of SDOF Systems." Ph.D. Dissertation, Department of Civil and Environmental Engineering, Lehigh University, Bethlehem, PA.

[15] Mazzoni, S.; McKenna, F.; Scott, M.H.; Fenves, G.L.; et al. (2009). Open System for Earthquake Engineering Simulation (OpenSEES) User Command-Language Manual. Pacific Earthquake Engineering Research Center, University of California, Berkeley.

[16] Pacific Earthquake Engineering Research Center (PEER) (2011a). Ground motion database, http://peer.berkeley.edu/nga/earthquakes.html.

[17] Baker, J.W. (2011). "Conditional Mean Spectrum: Tool for Ground-Motion Selection," Journal of Structural Engineering, 137(3), pp 322-331.

COMPDYN 2013
4th ECCOMAS Thematic Conference on
Computational Methods in Structural Dynamics and Earthquake Engineering
M. Papadrakakis, V. Papadopoulos, V. Plevris (eds.)
Kos Island, Greece, 12–14 June 2013

COMPUTATIONAL MODELLING OF SELF-CENTERING PRECAST CONCRETE WALLS

Jonathan Watkins[1], Richard S. Henry[1], and Sri Sirtharan[2]

[1] The University of Auckland
20 Symonds Street, Auckland 1010, New Zealand
jwat133@aucklanduni.ac.nz ; rs.henry@auckland.ac.nz

[2] Iowa State University
406 Town Engineering Building, Ames, IA 50011, USA
sri@iastate.edu

Keywords: concrete wall, unbonded post-tensioned, modelling, analysis, self-centering, rocking.

Abstract. *Existing predictive models of self-centering precast concrete walls with post-tensioning are generally computationally expensive. While simplistic models have a low computational cost, they are generally incapable of simulating cyclic behavior of these walls. Hence, a new computational model suitable for characterizing cyclic response of self-centering precast concrete walls was developed with emphasis on accuracy and computational efficiency. The proposed model consisted of a bed of truss elements at the base of wall where the rocking response is expected, truss elements for the post-tensioning tendons, and an elastic beam-column element for the wall panel. To ensure the accuracy of wall response, including the quantification of residual displacements, a robust concrete hysteresis model was required in the analysis. The proposed modelling technique was verified against five experimental tests completed on self-centering precast concrete walls. In all cases, the model accurately captured the overall cyclic behavior and residual displacements of the self-centering precast concrete wall. Furthermore, the models also satisfactorily captured several local response parameters, including the wall uplift, neutral axis depth, lateral drifts at which concrete spalling and crushing occurred, and post-tensioning force for both loading and unloading cycles at all ranges of lateral drifts.*

1 INTRODUCTION

Self-centering precast concrete walls are generally designed with unbonded post-tensioned (PT) tendons. Due to their low energy dissipating ability, additional energy dissipation for these walls can be provided by supplemental energy dissipating elements. Self-centering precast concrete walls allow for safe dissipation of energy imparted to the building by an earthquake motion while incurring minimal structural damage. Previous experimental and analytical research has shown that these walls can be designed to produce excellent seismic performance [1, 2].

The prediction of self-centering precast concrete walls behavior and performance when subjected to seismic excitation is critical for their implementation into buildings. Existing computational models developed for self-centering precast concrete walls are often computationally expensive, or reduce the computational demand with model simplifications that degrade the accuracy of the analysis. A summary of available computational modeling techniques for self-centering precast concrete walls is first presented. The development of a new, efficient computational model with a capability of simulating the cyclic behavior of self-centering precast concrete walls is then reported. Finally, the proposed computational modelling technique is verified against available experimental results and the results are discussed.

2 BACKGROUND

Previous research in the modelling of cyclic behavior of self-centering precast concrete walls has led to the development of several computational techniques using the finite element method (FEM) in various forms including those based on solid brick, fiber-based, multi-spring macro and lumped plasticity elements. Lumped plasticity models, in the form of non-linear rotational springs, have a low computational demand and are the simplest computational technique. Several researchers have used this element to model self-centering precast concrete walls [e.g., 3-5]. In general, these models showed satisfactory agreement with the overall experimental response. However, two disadvantages of non-linear rotational springs were found. In most cases, the springs were limited in their ability to capture the cyclic behavior. In one case that characterized the cyclic response, the lumped plasticity models parameters were calibrated using the measured experimental results.

Multi-spring macro-models have increased computational cost but do not suffer from the deficiencies noted earlier. These models capture the wall's rocking motion with a bed of compression only axial springs at the wall-to-foundation interface, and truss elements represent the post-tensioning. This approach can explicitly account for the hysteric energy dissipation from the inelastic strains in the concrete and post-tensioning. Researchers using this model have adequately captured the cyclic behavior of self-centering precast concrete walls [5-7]. The accuracy of the wall response was increased when a greater number of axial springs were used to represent the wall-to-foundation interface.

In contrast to the previous models, fiber and solid brick models capture the spread of strains along the height of the wall. This enables all aspects of the walls to be accurately captured but the computational cost is high. Many researchers have used fiber or solid brick models to characterize the response of self-centering precast concrete walls [4, 8-14]. Overall the behavior of the wall was well captured using fiber models, with further improvements resulting from the use of models based on brick elements.

The reported differences between these models can be seen in the analyses published on the same experimental test of a self-centering precast concrete wall [5, 7, 9]. The non-linear rotational spring model failed to accurately capture the hysteretic actions, which were adequately characterized by both the multi-spring and fiber section models. These analyses ap-

pear to validate that an average strain at the wall base can be used to determine the wall's resistance and energy dissipation characteristics. The high rate of change of curvature, and therefore strain, at the wall base is thought to allow this simplification. This model can have comparable accuracy to that of fiber section models, which does not use this simplification.

3 PROPOSED COMPUTATIONAL MODEL

The proposed computational model, shown in Figure 1, is an amalgamation of the fiber section and multi-spring models. It retains the accuracy of the fiber section model and the low computational demand of the multi-spring model. The model contains three elements: a bed of truss elements representing the rocking interface, truss elements representing the post-tensioning tendons, and an elastic beam-column element representing the wall panel. The truss elements are fixed at the base and connected via rigid links to the base of the elastic beam-column element. Therefore, the deformation of the truss elements, which represents the wall uplift and toe compression, is only a function of the wall's rotation. In using this technique to model the rocking wall interface, two assumptions are made: inelastic action of the concrete wall panel is concentrated at the rocking interface, and the wall uplift and toe compression depend only on the wall panel's rotation. Henry *et al.* [13] found both experimentally and analytically that the wall panel behaved elastically a short distance above the single horizontal crack located at the wall base, and therefore using an elastic beam-column element to represent the wall panel above the wall-to-foundation interface is acceptable. As previously discussed, using an average strain at the wall base, i.e. the bed of truss elements, can adequately capture the energy dissipation of the wall panel. Perez *et al.* [11] have presented equations to calculate the height of the truss elements at the wall base, which allowed the truss elements to correctly capture the spalling and crushing of concrete at a comparable drift to experimental results.

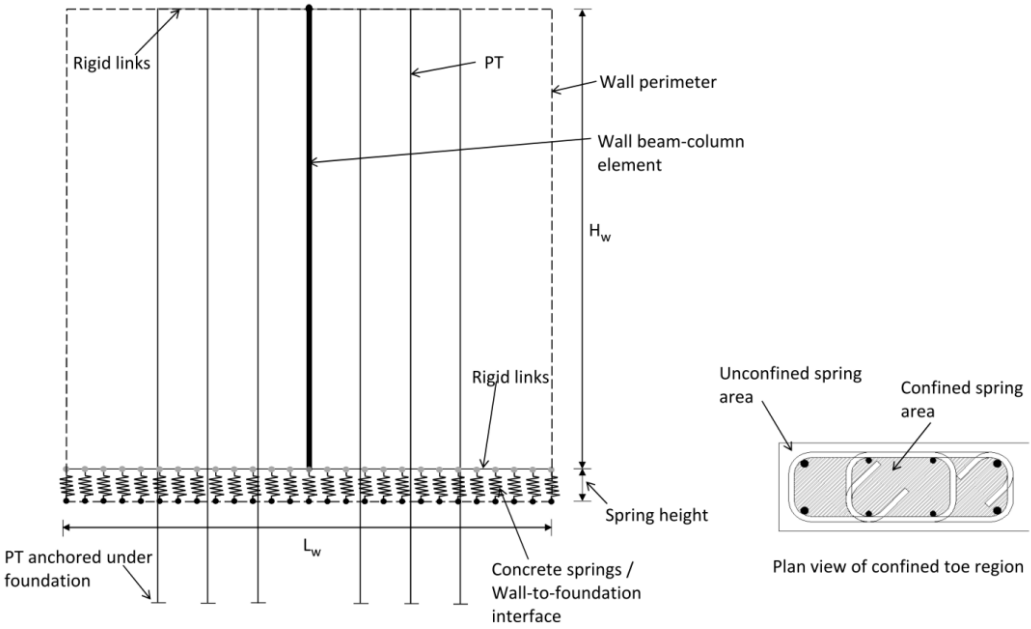


Figure 1: General layout of the proposed computational model

An analysis of several experiments on self-centering precast concrete walls showed strong evidence that the wall uplift is a function only of the rotation at the base of the wall panel [1, 12, 15]. In the self-centering precast concrete wall experiment conducted by Aaleti *et al.* [1],

LVDT's were used to measure the uplift along the base of the wall, and strain guages were used to measure the toe compression. The experimental uplift of the wall base was compared to the uplift calculated using the wall base rotation. This comparision confirmed that there was a 94.7% fit to the hypothesis that the wall uplift is a function of the wall base rotatation, and for lateral drifts greater than 0.5%, the corresponding accuracy increased and resulted in 99.6% fit. Furthermore, the analysis showed the toe compressive strains followed a triangular distribution, which is used in the proposed computational model.

For the bed of truss elements at the wall base in the proposed model the required inputs are length, area, and uniaxial material model. The element length can be calculated from recommendations by Perez *et al.* [11], where the minimum of either twice the walls' neutral axis depth at failure, or twice the width between the centerlines of toe confinement reinforcement was suggested. The area of the spring is dependent of its location. In unconfined regions, the spring's area is equal to the wall's width multiplied by the spring spacing. In the confined toe region two springs are used, one for the confined region and the other for the unconfined cover region, and the areas calculated from construction drawings as illustrated in Figure 1.

The uniaxial concrete stress-strain material model for the truss elements was established from research by Waugh [16], and Chang and Mander [17]. Waugh implemented a unidirectional cyclic concrete material model, known as Concrete07, into OpenSees [18], which was based on Chang and Mander's concrete model that is applicable to both confined and unconfined concrete. The response envelope of the Chang and Mander's model is the same as that proposed by Mander et al. [19], which has been extensively used in analytical research. The use of Waugh's uniaxial concrete material model has improved the accuracy of analytical models of experimentally tested reinforced concrete walls in comparison to other existing uniaxial concrete material models [16]. The increased accuracy was attributed to Chang and Mander's degrading unloading stiffness.

With further simplifications to Concrete07, a compression only uniaxial concrete material model was established in OpenSees, as this is more suitable for modeling concrete at the base of a rocking wall. Figure 2 shows the typical loading, unloading and reloading path of the modified Concrete07, with numbers 1 through 6 illustrating various paths. Number 1 is the Chang and Mander's envelope. When loading at strains greater than ε_{cc}, representing the strain at maximum concrete stress, there is an option to continue with Chang and Mander's envelope, or follow a user defined linear backbone by specifying (ε_u , f_u). Numbers 2 to 5 illustrate various unloading and reloading options, with the simplest definition being unloading and reloading paths with the initial stiffness E_c (i.e, 2a) or degraded stiffness E_{sec} (i.e., 2b). Unloading along the response curve and reloading with E_{sec} (2, 5) has a high computational cost due to the large number of iterations required for the model to converge. To reduce the computational cost, Waugh proposed a tri-linear approximation of the Chang and Mander unloading curve based on the initial and final stiffness of unloading (2c). The tri-linear unloading path introduced convergence errors because at large strains the final stiffness is a small fraction of the initial stiffness. Hence, a bi-linear unloading option was implemented in the modified Concrete07, illustrated by path 2d. As seen in Figure 2, the model unloads from, and reloads to the same strain, ε_{un}, whereas Chang and Mander's model reloads to a slightly greater strain. This modification was adopted by Waugh and in the modified Concrete07 to further minimize convergence errors. Paths 3 to 5 illustrate the compression only nature of the concrete model. Once the model has unloaded to a strain of ε_{pl}, there is no increase in stress until a strain greater than ε_{pl} is reached. Number 6 shows after reloading to a strain of ε_{un} the concrete model follows the envelope option previously specified. The strain ε_{sp} sets the concrete crushing strain. Once this strain is met, the concrete is assumed to provide no further resistance, returning zero stresses for all strains.

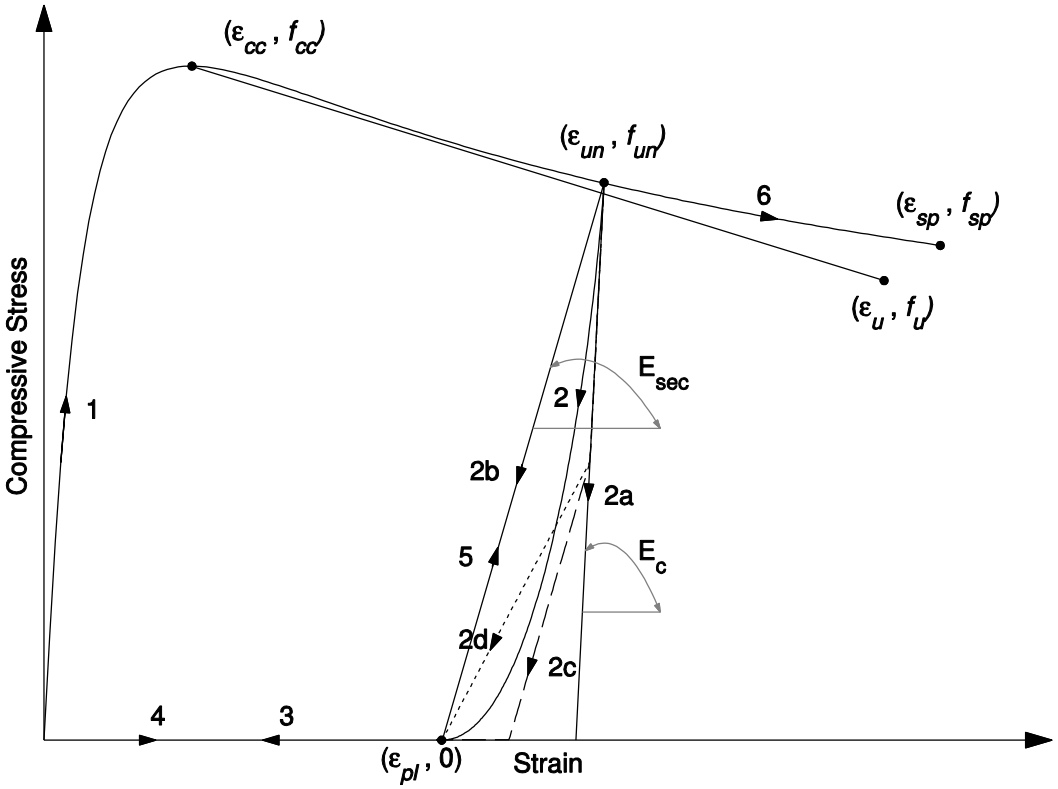


Figure 2: Stress-Strain definition of modified Concrete07 representing compression only uniaxial behavior

4 EXPERIMENTAL VALIDATION

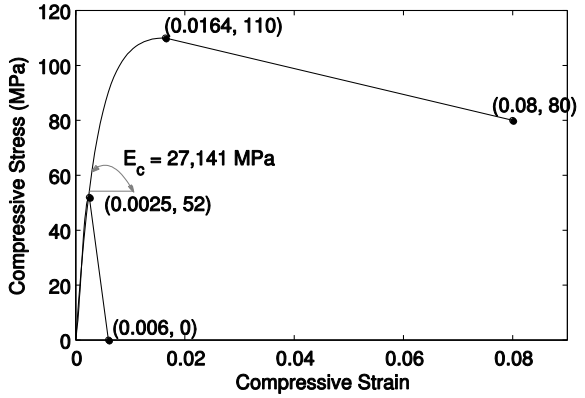
A set of experimental tests were used to validate the proposed computational model. Perez *et al.* [11, 12] conducted an experimental program into the behavior of multistory concrete walls utilizing unbonded post-tensioned tendons. The five wall tests were conducted by representing a prototype wall approximately at half scale, and included the bottom four stories of the six story wall. The test walls were subjected to quasi-static monotonic and cyclic lateral loads, and the average total gravity load was 3.7% of $f_c' A_g$. Four parameters were changed between the five test walls: type of confinement reinforcement, initial stress in the PT bars, f_{pi}, initial concrete stress due to post-tensioning, $f_{ci,p}$, and total area of the PT tendons, A_p. These parameters are summarized in Table 1 and further details are reported by Perez *et al.*

The model layout used in the analysis was shown previously in Figure 1. The lateral displacement was applied at a height of 7.23 m from the wall base, and the unbonded tendon length was 9.91 m. There were seven oversized ducts 70 mm in diameter in the wall panel and the PT was 32 mm in diameter. Elastic beam-column elements were used to represent the concrete wall panels. The material stress-strain inputs for the bed of truss elements shown in Figure 3a and 3b were based on cylinder tests conducted by Perez *et al*. A bed truss height of twice the width between the centerlines of toe confinement reinforcement was used. However, the bed truss height of TW5 was increased by 40% to prevent confined crushing occurring in the computational model, reflecting the experimental results. Confined concrete crushing did not occur in TW5 due to the smaller area of PT, which decreased the toe compressive forces. Alternatively, to match the experimental lateral drift at which concrete crushing occurred, Perez *et al's.* cyclic analysis kept the fiber's height constant, and adjusted the concrete crushing strain in the material. Given the discrepancies in capturing the lateral drift when concrete crushing occurs, further analysis is required to establish predictive equations for the truss height. In the proposed model the spacing between truss elements representing the rocking at

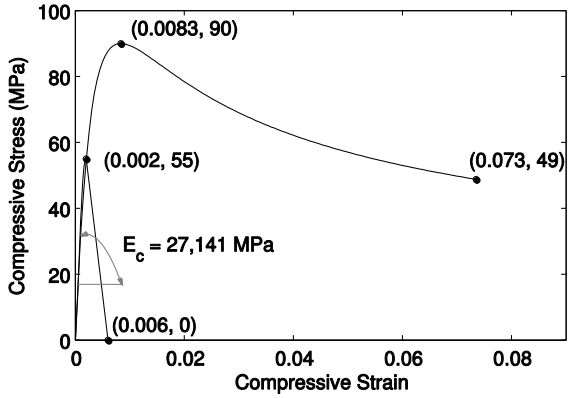
the wall base was set at L_w/1000, i.e. 2.54 mm. The relatively small spacing was required to minimize any convergence issues, which can be triggered by a reduction in a truss elements stress that cannot be redistributed to adjacent elements because of the large spacing.

Table 1: Test matrix from Perez *et al.* [11]

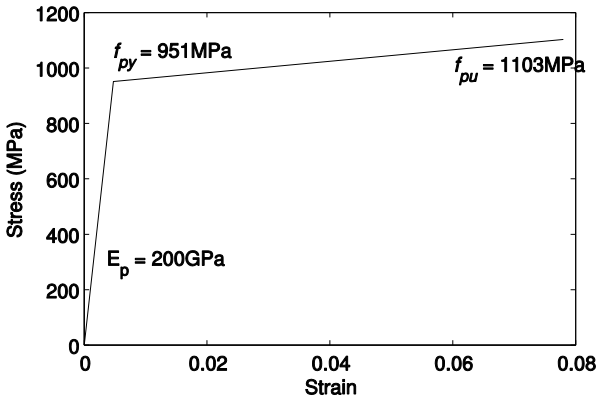
Test wall	Loading	A_p (cm^2)	f_{pi}/f_{pu}	$f_{ci,p}$ (MPa)	Confinement Type	PT bars
TW1	Monotonic	48.4	0.553	8.20	Spirals	xx xox xx
TW2	Cyclic	48.4	0.553	8.20	Spirals	xx xox xx
TW3	Cyclic	48.4	0.553	8.20	Hoops	xx xox xx
TW4	Cyclic	48.4	0.277	4.07	Hoops	xx xox xx
TW5	Cyclic	24.2	0.553	4.07	Hoops	xo oxo ox
*x = bar and o = empty duct						



a) Concrete stress-strain for TW1 & TW2



b) Concrete stress-strain for TW3-TW5



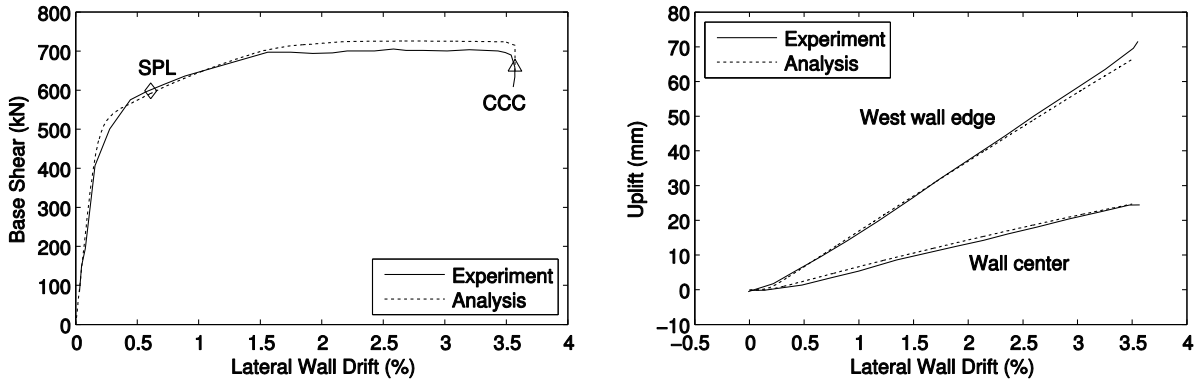
c) PT bars stress-strain

Figure 3: Material properties used for the analyses, based on experimental testing by Perez *et al.* [12]

5 RESULTS

Figures 4-9 compare the analytical results from the new model to the experimental test results for all five test walls, referred to as TW1 to TW5. Figure 4a compares the experimental results of the base shear versus lateral drift with the analytical results for TW1. This comparison shows the initial stiffness and decompression of the wall were closely matched. It also shows the spalling (SPL) and crushing of concrete (CCC) were closely captured at 0.6% and

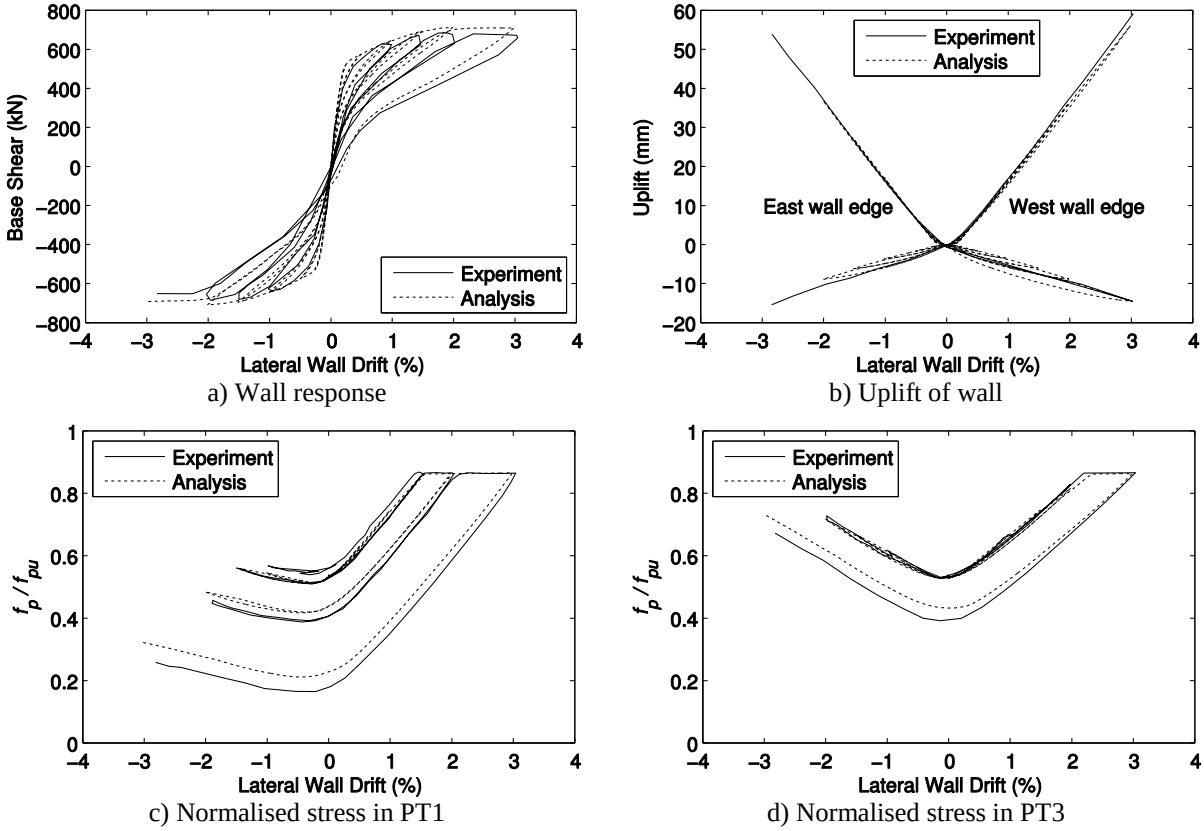
3.5% lateral drifts, respectively, so is the yielding of the PT at 1.5% lateral drift. However, the base shear is slightly overestimated after yielding of the PT steel. In addition, Figure 4b shows the analytical model closely matched the uplift of the wall at the west wall edge and at the center of the wall.



a) Wall response b) Uplift of wall

Figure 4: Comparison between experimental and analytical results for TW1

TW2 had identical parameters to TW1, except that it was subjected to cyclic loading. Figure 5a shows the analytical loading and unloading hysteresis loops are in good agreement with the experimental results. Figure 5a also shows the experimental residual drifts were well captured. Figures 5c and 5d confirm that the yielding of PT1 and PT3 which occurred at 1.5% and 2.1% drifts were accurately captured. Figure 5b also shows the analytical model closely matched the uplift of both wall ends.

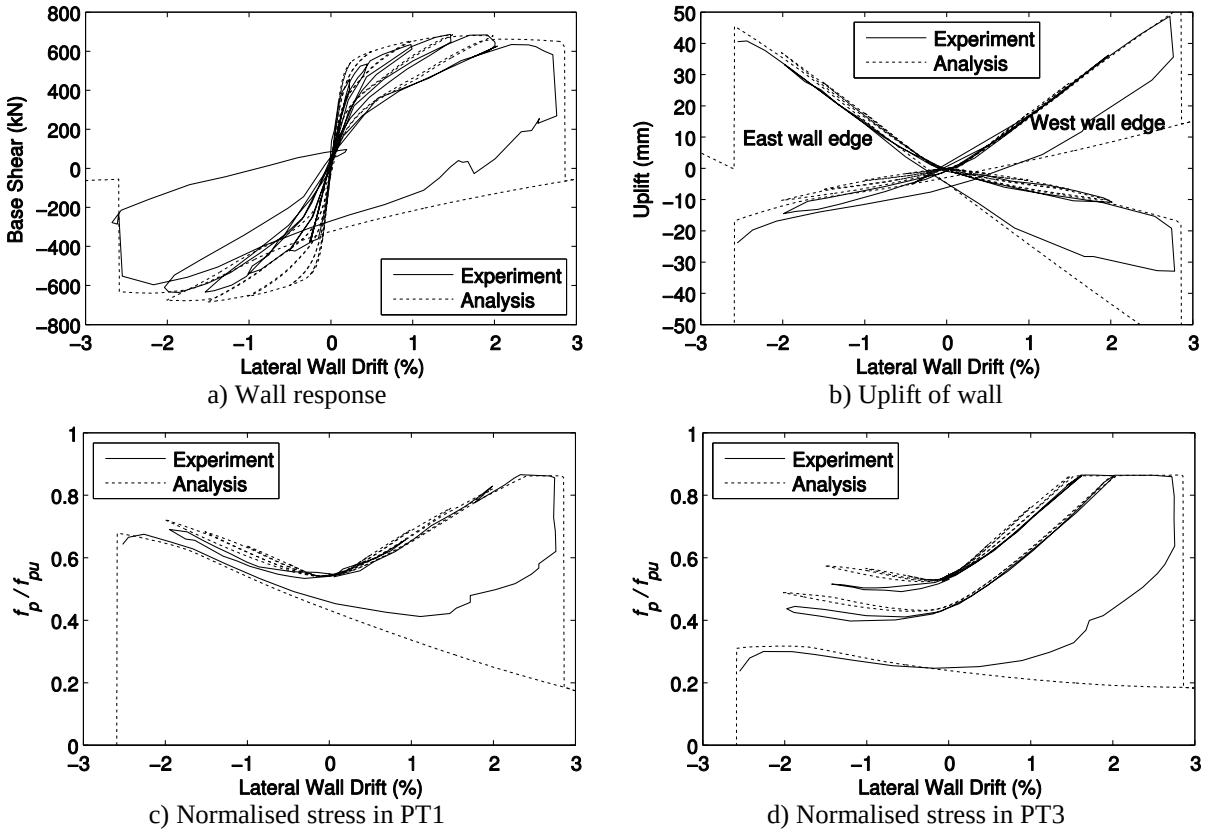


a) Wall response b) Uplift of wall

c) Normalised stress in PT1 d) Normalised stress in PT3

Figure 5: Comparison between experimental and analytical results for TW2

TW3 differed from TW2 and TW1 by using hoop rather than spiral reinforcement in the wall toe confinement region. TW3's experimental lateral load response shows early spalling of the concrete at the west wall end at 0.57% lateral drift as seen in Figure 6a, which was attributed to poor consolidation of concrete during casting [12]. Furthermore, the unsymmetrical nature of the experimental results led to an accumulated negative drift of 0.1%. The analytical results presented in Figure 6 do not reflect this behavior because the model was based on symmetrical properties of the test wall. A comparison between the experimental and analytical lateral load response of TW3, shown in Figure 6a, shows the results are generally in good agreement, and in some agreement for the hysteresis loops obtained for the east end. The comparison also shows the loss of strength in the east direction of the wall at 3% lateral drift indicating that concrete crushing was accurately captured. Convergence errors arose when crushing of the confined concrete occurred. Figures 6c and 6d show that the yielding of PT1 and PT3 were closely matched, while Figure 6b shows the wall uplift was closely captured until crushing of the confined concrete occurred.



a) Wall response

b) Uplift of wall

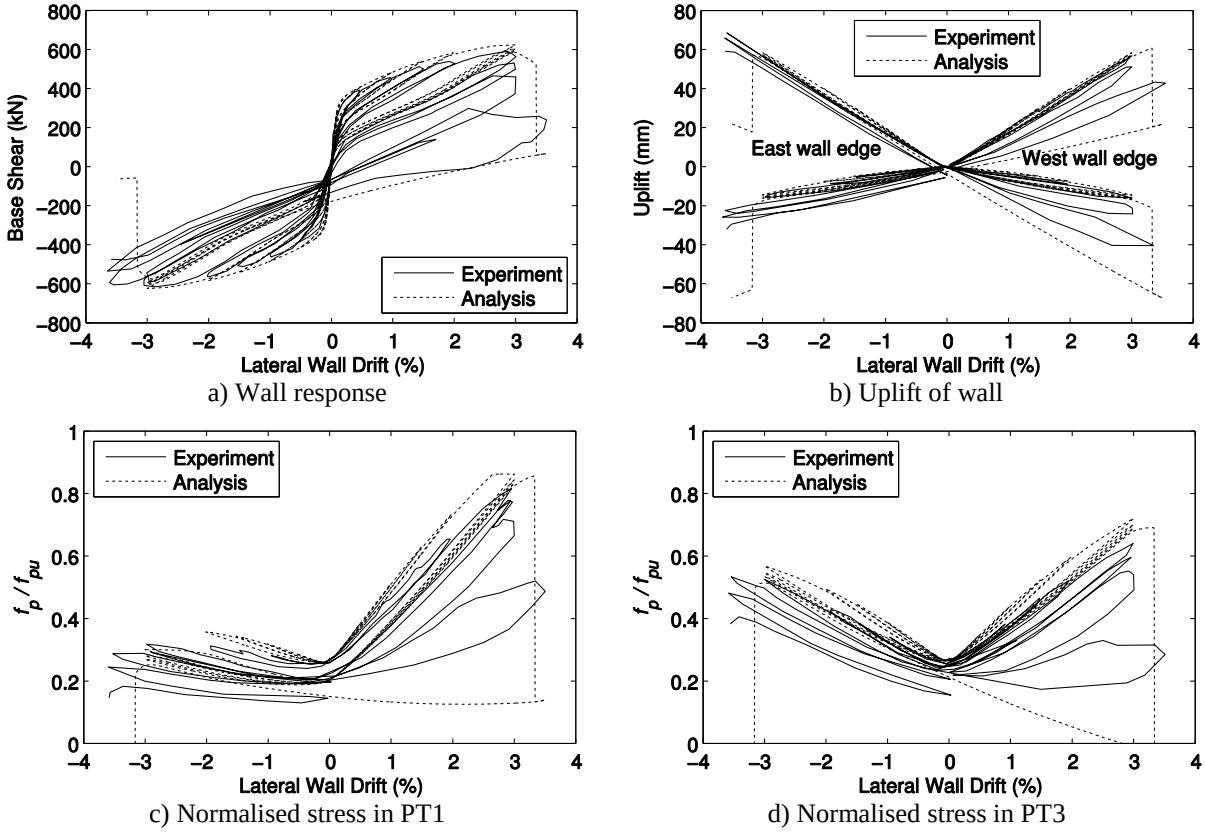
c) Normalised stress in PT1

d) Normalised stress in PT3

Figure 6: Comparison between experimental and analytical results for TW3

TW4 was intended to quantify the effect of reducing the initial stress in the PT on the wall response. Figure 7a compares the base shear versus lateral drift obtained from the test and that calculated by the analytical model for TW4. The comparison again shows good agreement until the experimental lateral resistance progressively weakened after a lateral drift of 3%. Unlike the previous walls, TW4 retained some of its lateral resisting capacity after experiencing crushing of the confined concrete, suggesting that the uniaxial concrete stress-strain model requires some modifications to capture the residual strength of the concrete after rupture of the confinement reinforcement. Figure 7b shows the wall uplift was accurately captured for

lateral drifts up to 3%; Figures 7c and 7d show generally good agreement between the analytical and experimental PT stresses for lateral drifts up to 3%.

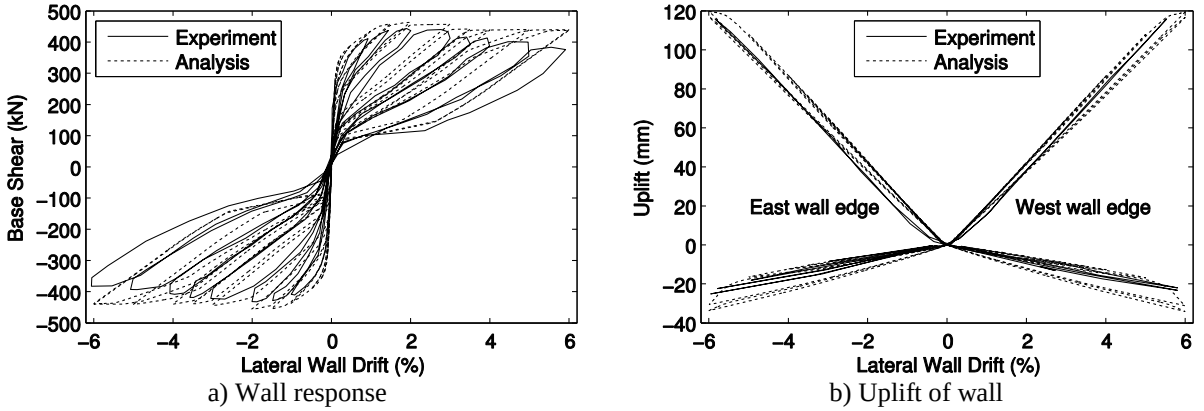


a) Wall response b) Uplift of wall

c) Normalised stress in PT1 d) Normalised stress in PT3

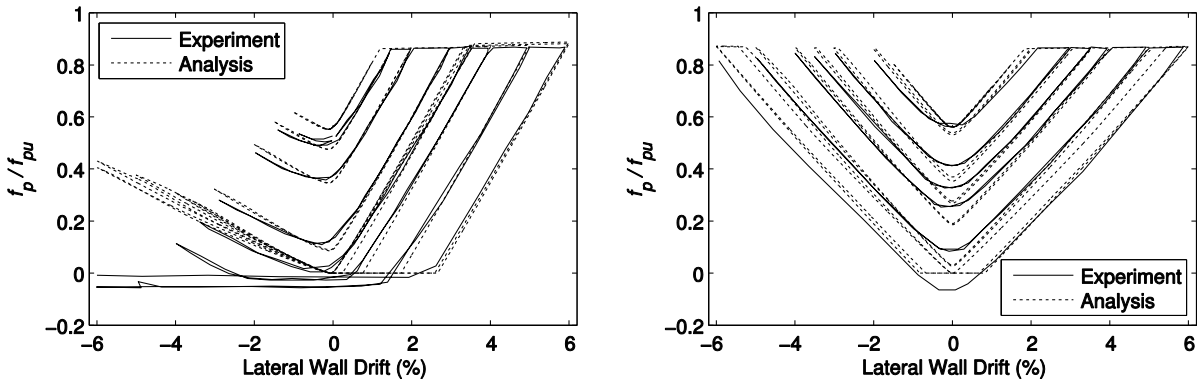
Figure 7: Comparison between experimental and analytical results for TW4

The purpose of TW5 was to quantify the effect of reducing the total area of PT steel, A_p, while maintaining the initial stress in the PT and at the wall base. During the experiment, PT1 and PT3 lost all of their initial pre-stress due to yielding occurring at a high drift of about 5%. To prevent the truss elements representing the PT from resisting compressive stresses, a tension only element was placed in series with the PT truss. Figure 8a shows very good agreement between the experimental and analytical results of the base shear versus lateral drift. Figure 8b shows the wall uplift was accurately quantified, while Figures 9a and 9b show PT stresses were closely matched, but with some discrepancy on the final cycle at 6% lateral drift.



a) Wall response b) Uplift of wall

Figure 8: Comparison between experimental and analytical results for TW5



a) Normalised stress in PT1 b) Normalised stress in PT2

Figure 9: Comparison between experimental and analytical results for TW5

6 CONCLUSIONS

After identifying lack of computationally efficient models for quantifying nonlinear cyclic behavior of self-centering precast concrete walls, a new computational model was presented. The proposed model comprised of: a bed of truss elements to capture the wall-to-foundation rocking interface, truss elements for the PT, and elastic beam-column elements for the wall panel. A robust uniaxial concrete stress-strain model was used to increase the accuracy of the analytical simulation, including accurate capture of residual displacements. The model was validated using five tests reported on self-centering precast concrete walls. The following conclusions were drawn from this investigation:

- The computational model showed very good agreement with the non-linear cyclic behavior of the self-centering precast concrete walls. The model accurately captured the inelastic energy dissipated by the rocking behavior and inelastic elongation of the post-tensioning.
- The model had a low computational cost and has the ability to predict the cyclic behavior of self-centering precast concrete walls.
- The bed of truss elements using the uniaxial concrete stress-strain material model accurately captured the wall-to-foundation rocking interface, including residual displacements. The concrete stress-strain material model allowed the computational model to closely capture the lateral drifts at which concrete spalling and confined concrete crushing occurred. A truss bed height of twice the width between the centerlines of toe confinement reinforcement is recommended.
- The model closely estimated the wall uplift and change in neutral axis. The stress in the post-tensioning was comparable to the experimental results, however, the stress was slightly over estimated in some cases.

In the process of validating the proposed model, the following areas were identified for improvements: 1) calculating the bed height and spacing of truss elements; 2) characterizing wall behavior after crushing of confined concrete; and 3) a further refinement to the estimation of PT stresses. Further research will be conducted to overcome these challenges in the proposed computational model.

7 ACKNOWLEDGEMENTS

The author acknowledges the financial support provided by the University of Auckland, Fulbright New Zealand, the Earthquake Commission of New Zealand, and Iowa State University. Support was also provided from a National Science Foundation grant NEESR-CR: *Un-*

bonded Post-Tensioned Rocking Walls for Seismic Resilient Structures (Grant No. CMMI-1041650). Any opinions, findings, and conclusions or recommendations expressed in this material are those of the authors and do not necessarily reflect the views of the sponsors.

REFERENCES

1. Aaleti, S. and S. Sritharan, *Performance Verification of the PreWEC Concept and Development of Seismic Design Guidelines*, 2011, ISU-CCEE Report 02/11 Iowa State University.
2. Priestley, M.J.N., S.S. Sritharan, J.R. Conley, and S. Pampanin, *Preliminary results and conclusions from the PRESSS five-story precast concrete test building.* PCI Journal, 1999. **44**(6): p. 42-67.
3. Rahman, M.A. and S. Sritharan, *An evaluation of force-based design vs. direct displacement-based design of jointed precast post-tensioned wall systems.* Earthquake Engineering and Engineering Vibration, 2006. **5**(2): p. 285-296.
4. Henry, R.S., *Self-centering Precast Concrete Walls for Buildings in Regions with Low to High Seismicity*, 2011, PhD Thesis, University of Auckland.
5. Palermo, A., S. Pampanin, and A.J. Carr, *Efficiency of simplified alternative modelling approaches to predict the seismic response of precast concrete hybrid systems*, in *fibSymposium 2005: "Keep Concrete Attractive"* 2005: Budapest, Hungary.
6. Conley, J., S. Sritharan, and M.J.N. Priestley, *Precast Seismic Structural Systems PRESSS-3: The Five-Story Precast Test Building Vol. 3-1: Wall Direction Response*, 2002, Report No. SSRP-99/19: University of California, San Diego.
7. Pennucci, D., G.M. Calvi, and T.J. Sullivan, *Displacement-based design of precast walls with additional dampers.* Journal of Earthquake Engineering, 2009. **13**(1): p. 40-65.
8. Kurama, Y., R. Sause, S. Pessiki, and L.W. Lu, *Lateral load behavior and seismic design of unbonded post-tensioned precast concrete walls.* ACI Structural Journal, 1999. **96**(4): p. 622-632.
9. Smith, B.J. and Y.C. Kurama. *Design of hybrid precast concrete walls for seismic regions*. in *2009 Structures Congress*. 2009. Austin, TX, United States.
10. Erkmen, B. and A.E. Schultz, *Self-centering behavior of unbonded, post-tensioned precast concrete shear walls.* Journal of Earthquake Engineering, 2009. **13**(7): p. 1047-1064.
11. Perez, F.J., R. Sause, and S. Pessiki, *Analytical and experimental lateral load behavior of unbonded posttensioned precast concrete walls.* Journal of Structural Engineering, 2007. **133**(11): p. 1531-1540.
12. Perez, F.J., *Experimental and Analytical Lateral Load Response of Unbonded Post-Tensioned Precast Concrete Walls*, 2004, PhD Thesis, Lehigh University.
13. Henry, R.S., N.J. Brooke, S. Sritharan, and J.M. Ingham, *Defining concrete compressive strain in unbonded post-tensioned walls.* ACI Structural Journal, 2012. **109**(1): p. 101-112.
14. Kurama, Y.C., *Seismic design of unbonded post-tensioned precast concrete walls with supplemental viscous damping.* ACI Structural Journal, 2000. **97**(4): p. 648-658.
15. Twigden, K.M., R.S. Henry, and Q.T. Ma, *Dynamic testing of post-tensioned rocking walls*, in *15th World Conference on Earthquake Engineering* 2012: Lisbon,Portugal.
16. Waugh, J.D., *Nonlinear analysis of T-shaped concrete walls subjected to multi-directional displacements*, 2009, PhD Thesis, Iowa State University.

17. Chang, G.A. and J.B. Mander, *Seismic Energy Based Fatigue Damage Analysis of Bridge Columns: Part 1 - Evaluation of Seismic Capacity*, 1994, State University of New York, Buffalo, NY: NCEER Tehcnical Report No. NCEER-94-006.
18. Mazzoni, S., F. McKenna, M.H. Scott, and G.L. Fenves, *Open System for Earthquake Engineering Simulation*, 2006, Pacific Earthquake Engineering Research Center, University of California, Berkeley.
19. Mander, J.B., M.J.N. Priestley, and R. Park, *THEORETICAL STRESS-STRAIN MODEL FOR CONFINED CONCRETE.* Journal of Structural Engineering New York, N.Y., 1988. **114**(8): p. 1804-1826.

COMPDYN 2013
4th ECCOMAS Thematic Conference on
Computational Methods in Structural Dynamics and Earthquake Engineering
M. Papadrakakis, V. Papadopoulos, V. Plevris (eds.)
Kos Island, Greece, 12–14 June 2013

BALANCING THE BENEFICIAL CONTRIBUTIONS OF FOUNDATION ROCKING AND STRUCTURAL YIELDING TO IMPROVE STRUCTURAL SEISMIC RESILIENCE

Weian Liu[1], Tara C. Hutchinson[1], Bruce L. Kutter[2], Manouchehr Hakhamaneshi[2], and Andreas-Gerasimos Gavras[2]

[1] Department of Structural Engineering, University of California, San Diego, USA
9500 Gilman Drive, Mail Code 0085, La Jolla, CA, USA 92093-0085
e-mail: {wel007, tara}@ucsd.edu

[2] Department of Civil and Environmental Engineering, University of California, Davis, USA
2001 Ghausi Hall, 1 Shields Avenue, Department of Civil & Environmental Engineering, University of California, Davis, CA, USA 95616
{blkutter, mhakhamaneshi, aggavras}@ucdavis.edu

Keywords: Foundation Rocking, Structural Hinging, Seismic Performance.

Abstract. *To date, numerous individual and system-level experimental studies have illustrated that the mode of foundation rocking advantageously can provide dissipation of seismic energy and re-centering of a structural system. Likewise, within the framework of performance-based earthquake engineering, structural components are strategically designed to behave inelastically. Balancing the beneficial attributes of each of these yielding systems has the potential to increase seismic resilience of the foundation-building system.*

This paper considers a balanced design strategy whereby the strength of a rocking footing is equated to the strength of inelastic structural fuses within the superstructure of a building. This balanced design concept is applied to the design of two model-building structures constructed and tested on the large geotechnical centrifuge at the University of California, Davis. Model buildings included a 3-dimensional low-rise frame-type and a 2-dimensional wall-type structure supported on shallow footings, where footing sizes were sized to encourage inelastic rocking. Two extreme hinging dominated systems, namely, a Foundation Rocking Dominated (FRD) and Structural Hinging Dominated (SHD) system were simultaneously constructed and tested as well. Experiments show that for a balanced design frame-braced configuration, the energy is well distributed between structural and footing fuses. In wall-type foundation-building systems, the FRD system observes significantly larger total roof drift, much of which is accumulated at the foundation level. Irrespective of the structure type, base shear demand in is greatly minimized when footing rocking is initiated in both the balanced design and FRD model.

1 INTRODUCTION AND SCOPE

1.1 Introduction

During a traditional building or bridge design, an engineer usually assumes that the foundation is fixed, while the superstructure carries the deformation induced during static and dynamic loading. This design concept leads to two major consequences, namely: (1) a design with unreasonably oversized foundation components to support the "fixed" condition and (2) a design which constrains plastic hinging behavior to the above-ground structural elements during a seismic event, such as at the ends of beams or at the base of shear walls, within the structural wall itself. Nonetheless, allowing the foundation to uplift at the ends has been gradually acknowledged as an effective inelastic mode to dissipate dynamic input energy. Moreover, such a mode promotes a natural re-centering tendency of the structure with the aid of the so-called "P-Δ effect". Commonly in the literature this is referred to as the *foundation rocking mechanism*. Numerous foundation-level component tests uniformly verify the advantageous seismic benefits of this mechanism.

Often cited as the earliest, most convincing work identifying such a mechanism are the field observations documented by Housner [11], who conducted field reconnaissance following the 1960 Valdivia earthquake in Chile. He observed that several lollipop structures survived, while modern structures were severely damaged. Researchers in New Zealand in the 1970s (e.g. Bartlett [3] and Wiessing [22]) subsequently conducted a series of 1-g experiments on shallow foundation-shearwall systems with footings of various sizes and vertical factors of safety (*FSv*). These experiments provided highly convincing moment-rotation hysteresis at the footing level that further substantiated the merits of the rocking footing mechanism. More recently, researchers across the United States and Europe have undertaken a variety of 1-g and centrifuge tests coupled with numerical work to investigate the mobilization of soil-foundation capacity (see e.g. Rosebrook and Kutter [17]; Gajan and Kutter [8]; Anastasopoulos et al. [1]; Deng et al. [5]; Hakhamaneshi et al. [10]; Gelagoti et al. [9]; Drosos et al. [6]). Since the centrifuge facility has the capability to create confining stress levels comparable with prototype conditions, the stress-dependent soil nonlinear behavior can thereby be reasonably captured. A common strategy in centrifuge testing has involved placing a number of simple structural assemblies, such as a shearwall-footing system or a single degree-of-freedom (SDOF) lollipop structural model supported on a shallow foundation element and subjecting the models to combined compression (N-g) and cyclic inertial or ground excitation loading. Model foundations have been designed with various geometries, FS_v, and different types of soils. In general, centrifuge tests concur that irrespective of the soil type, footings with a relatively high FS_v (~10) will result in quite reasonable moment-rotation hysteresis, which quantifiably dissipates energy, without significant settlement (Deng et al. [5]; Hakhamaneshi et al. [10]). Large-scale 1-g tests on shallow footings report similar findings (e.g. Taylor and Crewe [19], Negro et al. [15], Paolucci et al. [16] and Shirato et al. [18]).

Given the demonstrated benefits of the rocking foundation component, the merits of integrating it into the overall soil-structure system need to be studied on level playing field with other inelastic mechanisms. To the authors' knowledge, only a handful of test programs have considered the dual inelastic mechanisms of soil and structural components. For example, Chang et al. [4] examined a set of 2-dimensional physical shearwall-frame building models considering the nonlinear behavior of the footings coupled with inelastic structural fuses within the superstructure. More recently, Deng et al. [5] incorporated the foundation rocking mechanism into a bridge structural system while also accounting for a common column hinging mechanism. Trombetta et al. [21] constructed and tested a pair of 3-dimensional inelastic frame models to study the effect of building adjacency on the seismic response.

1.2 Scope of this work

Although a handful of experiments have considered the participation of both foundation and structural components to a systems seismic resistance, prior test efforts did not strategically implement a targeted design strategy. To embrace the foundation rocking mechanism within a conventional structural design paradigm, it is useful to systematically consider the systems behavior with varying levels of foundation strength. In parallel, typical earthquake-resistant structural configurations within a building system incorporate structural fuse mechanisms within the superstructure components to dissipate seismic energy; therefore such a systematic study should similarly embrace this philosophy. The question of how these two inelastic components dynamically interact with each other and share the seismic demand is still unreported and warrants a future investigation. In a research program supported by National Science Foundation (NSF), we investigate the seismic performance of this integrated inelastic foundation-building system. In this paper, we propose balancing the demands to each of these components, and apply this methodology to the design of a series of centrifuge test models. Two different building configurations are constructed at centrifuge scale, namely a 3-dimensional frame-type structure and a 2-dimensional wall-type structure. Select experimental data for these two systems are presented and compared with other models, in which the yielding of structural fuse and rocking foundation is unbalanced.

2 BALANCED DESIGN METHODOLOGY

Within the framework of performance-based earthquake engineering, structural components are encouraged to behave inelastically. For instance, a weak-beam strong-column strategy is a common inelastic mechanism adopted in the seismic design of frame-braced buildings. This strategy aims to localize the plastic behavior at the ends of beam elements, therefore ensuring that damage to beams will occur prior to column failure. Columns provide essential support for transferring gravity loads in a building; therefore their failure could result in an undesired catastrophic building collapse. For a wall-based lateral load resisting system, even with frame elements integrated within the system, the shear wall component is designed to carry the majority of the lateral load. Consequently, the plastic hinging behavior will inevitably occur at the interface between the wall and footing. Figure 1a depicts a hysteresis for a structural wall fuse, and quite comparably broad and stable hysteresis can be realized at the footing-soil interface as well (Figure 1b).

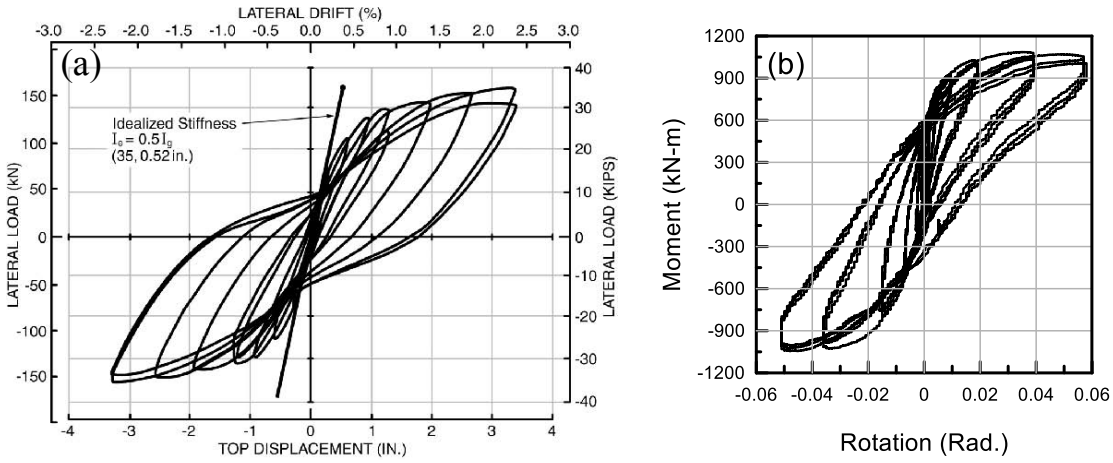


Figure 1: Hysteretic curves for concrete shear wall (test by Taylor et al. [20], adapted from Englekirk [7]) and rocking-dominated footing in prototype scale (Hakhamaneshi et al. [10]).

When the rocking footing mechanism is integrated into a building system, considering the strength difference between these two plastic behaviors, three fundamental systems could be realized. One extreme may be when the footing's load capacity is significantly larger than that of the structural fuse; the foundation component is intended to be protected during seismic events, while the structural fuse is expected to carry large inelastic demands. In this paper, we refer to this system as a **Structural Hinging Dominated** (SHD) system. Most of the existing buildings fall into this category. They are usually constructed with oversized foundations, which in turn increase the overall construction cost. If properly designed, this system could perform well during a design-level earthquake. On the other extreme, one could realize inelastic behavior solely via the mechanism of footing rocking. In this paper, we refer to this type of system as a **Foundation Rocking Dominated** (FRD) system. This is a theoretically proposed, yet unimplemented building configuration in reality. Nonetheless, the final behavior of a FRD building is akin to that observed when a building is base isolated (BI), namely nearly all shear strains are absorbed close the ground level. In contrast to the BI building, which would largely translate horizontally, an FRD building would rotate. The foundation geometry could be designed considerably smaller than an SHD system, however, superstructure components would need to be relatively strong, particularly within regions of the structure where large seismic forces cumulate (such as the ends of beams and columns). This type of system has the potential to reduce the residual displacement on the superstructure due to its inherent re-centering characteristic. However, depending on the soil stiffness, large amplitude rocking at the footing-soil interface could potentially exacerbate footing absolute or differential settlement. Adopting the beneficial attributes of both superstructure and foundation fuses by equating the strengths of both components is appealing, and in this paper we term this a **Balanced Design** (BD) system. Ultimately, some type of optimization should be considered and perhaps this does not stem from equitable strength distributions, but more careful consideration of the kinematics of the building as a system. We hypothesize that the balanced design system however provides an initial compromise to demonstrate avoidance of extreme behaviors, such as significant story drift or excessive foundation settlement. Compared with the SHD system, this configuration could not only save construction cost for foundations, but also continue to maintain the self-centering benefits of an FRD system.

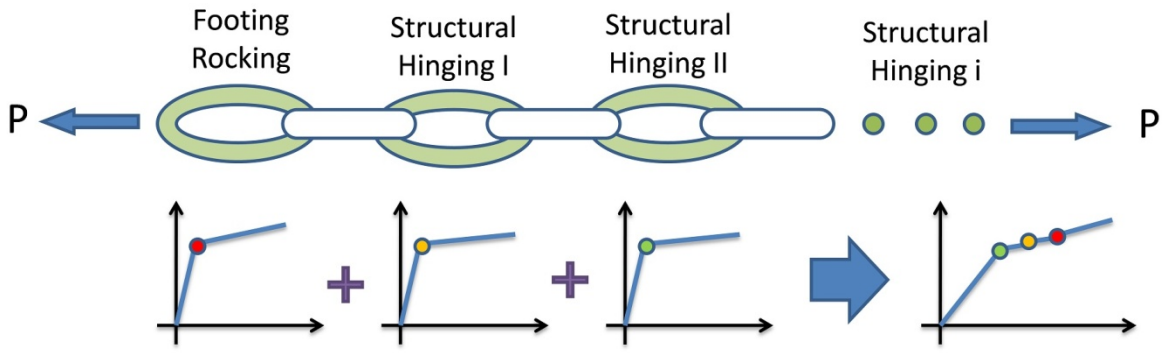


Figure 2: Illustrative Chain Analogy.

To emphasize the fundamental concept of a balanced design philosophy, a chain analogy is illustrated as shown in Figure 2. In this figure, each chain element represents a ductile component in the entire building-footing system. Footing rocking behavior certainly plays an important role in seismic energy dissipation, and thereby serves as a fundamental ductile link within the chain. In a complex structural system, structural hinging behavior is not always limited within one or two elements; therefore, it usually develops a multi-fuse mechanism

during seismic activities. When the entire system is subjected to an external force P, the link with the weakest capacity is the first element to develop nonlinear behavior. Consequently, the potential contributions from other stronger links will be limited and the system global behavior will be solely governed by the weakest part in this idealized series system. However, when all the inelastic elements are prone to yield under the same P, as illustrated in Figure 2, the hinging of one element and its triggered detrimental response could be properly avoided, and the system's global ductile behavior will be greatly improved. An implementation of this design idea could promote and reinforce the structural system's seismic resilience. It should be pointed that, fuse elements in realistic buildings are not necessarily placed in series, but rather could be in a complex arrangement of series or parallel.

Quantifying the strength of each fuse element such that a balanced design philosophy could be appropriately accomplished is the next step. First and foremost, one needs to identify the yield strength of each fuse separately. To simplify the mechanism, let us consider a shear wall supporting a heavy SDOF mass, and resting on a shallow footing on competent soil. Figure 3 displays two the two extreme fuse yielding mechanisms, namely the SHD and FRD systems.

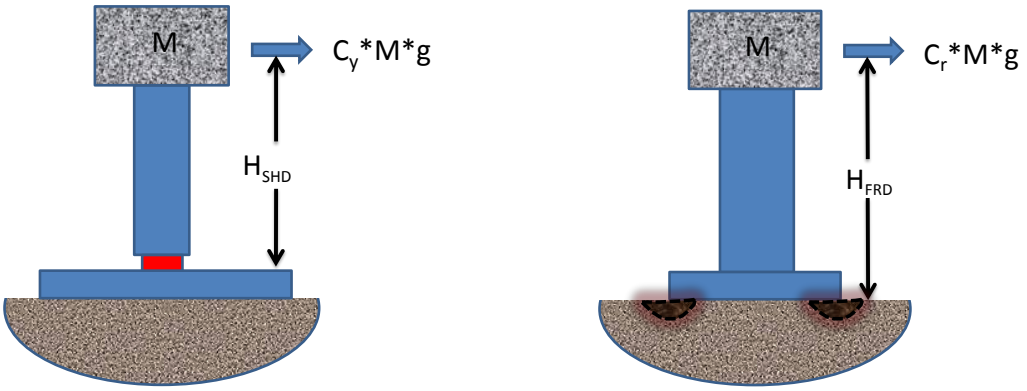


Figure 3: Schematics of SHD and FRD system.

For the structural hinging system, the moment capacity of the shear wall fuse can be correlated to the weight it must support by the following equation:

$$M_{y_fuse} = C_y * M * g * H_{SHD} \quad (1)$$

The coefficient Cy is usually known as the base shear coefficient and in this work used to defined the yield strength associated with a structural fuse. Given the details of a shear wall, its corresponding strength can be easily computed by applying flexural beam theory. For a constant supported weight, Cy is directly proportional to the strength of the shear wall fuse, therefore it serves as an index to quantify its yield strength.

Similarly, the critical bending moment required to initiate footing rocking at footing-soil interface can be also correlated to the supported mass by introducing another dimensionless parameter Cr, which we define as the foundation rocking yield coefficient. (Deng et al. [5] and Liu et al. [14])

$$M_{y_footing} = C_r * M * g * H_{FRD} \quad (2)$$

Deriving the footing rocking capacity ($M_{y_footing}$) requires knowledge of the foundation geometry, axial load acting on the footing and the properties of the surrounding soil (Gajan and Kutter [8], Deng et al. [5] and Liu et al. [14]).

It is evident that, for a combined structural hinging and footing rocking structural system, the difference between Cy and Cr will render the three abovementioned footing-building configurations. A significantly larger Cy or Cr will lean the system towards behaving more like either an FRD or SHD system. By setting up Cy and Cr being approximately equal, a balanced design condition can be achieved.

It should be noted that the structural configuration for realistic buildings or bridges, are usually much more complicated than the idealized SDOF system. Therefore, the determination of these two indices should not necessarily follow the equations above, and could be varied or adjusted based on the actual structural system setup (Liu et al. [14]).

3 APPLICATION AND TESTING OF FRAME-BRACED FOUNDATION-BUILDING SYSTEM

The strength of soil, and consequently the development of a foundation rocking fuse mechanism at the soil-footing interface are greatly affected by the confining stress acting on the surrounding soil. Consequently, during an experimental evaluation, reasonably modeling of confining stress is important to capture the footings behavior. The NEES[1] centrifuge facility at the University of California, Davis (UCD) has been well established and utilized in the field of geotechnical earthquake engineering for many years (Kutter [12]), and is able to accommodate the research goals affiliated with this topic.

Two large scale system-level centrifuge tests were conducted at the UCD NEES facility. The first involved testing of three different 3-dimensional low-rise (2-story) frame-braced building models. The models included an FRD, SHD, and a BD building structure founded on shallow footings. Figure 4 provides photographs of one corner of each of the assembled models, showing both the structural fuse and footing elements. As indicated in Figure 5, the models were supported on overconsolidated clay in a rigid container and spun up to 56 RPM to create a 30-g level gravitational acceleration at the ground surface. Three models were tested at different spins and different stations; however they were subjected to a similar sequence of motions. For more details regarding the model design process, construction, instrumentation, soil profile and motion protocol, one may refer to the experimental data report (Liu et al. [13]) or a recently accepted paper (Liu et al. [14]).

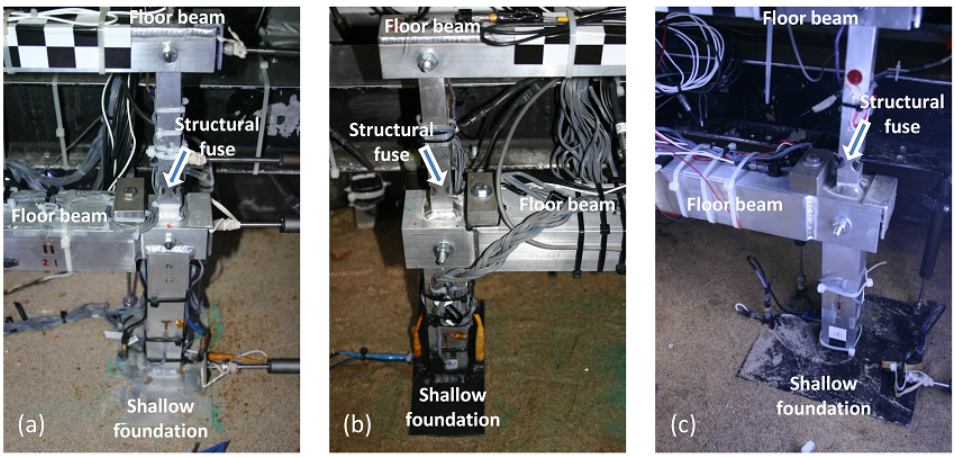


Figure 4. Photographs of: (a) BD Model; (b) FRD Model; (c) SHD Model (Liu et al. [14]).

[1] NEES is the Network for Earthquake Engineering Simulation (nees.org)

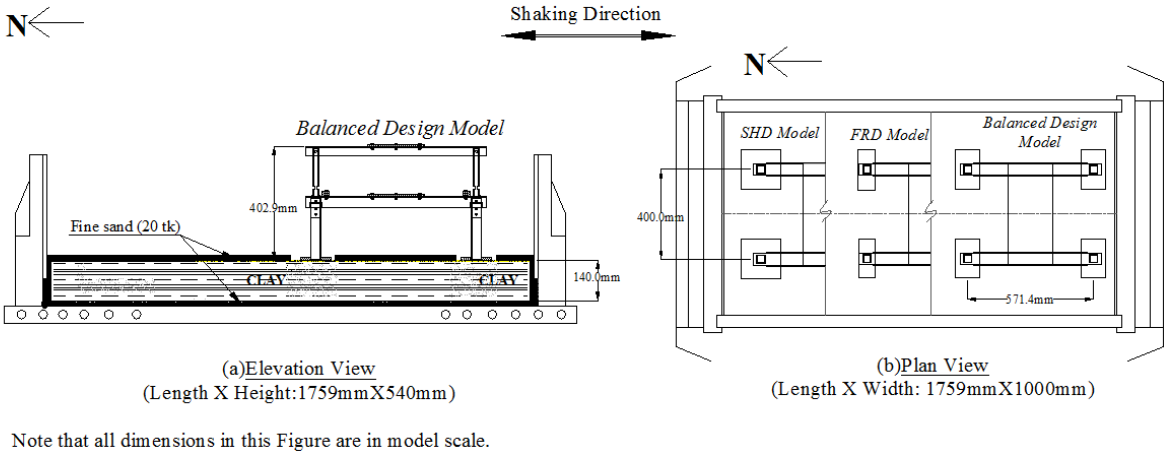


Figure 5. Model schematics and Experimental setup: (a) Elevation view; (b) Plan View.

Table 1 lists the most important system characteristics of each model, and Figure 6 shows the 5% damped elastic acceleration response spectra for each achieved input motion, overlaid with the numerically estimated first natural period of each model. Note that the intensity of the applied motion is generally gradually increased with each subsequent motion. Motions indicated by dash lines are scaled versions of recording obtained during 1971 San Fernando earthquake, while the rest plotted by solid lines are adapted from Gazli earthquake (USSR) in 1976. Unless otherwise stated, all of the results throughout this paper are expressed in prototype scale.

Parameter	Description	BD	FRD	SHD
C_r	Shallow footing rocking coefficient	0.35	0.22	0.81
C_y	Structural fuse yield coefficient	0.37	0.44	0.33
T_1 (sec)	First system natural period	0.73	0.99	0.49
T_2 (sec)	Second system natural period	0.27	0.26	0.25
FS_v	Vertical factor of safety of shallow footing	9.1	6.9	14.7
s_u	Undrained shear strength of clay	70 kPa		

Table 1: Frame-type foundation-building models' properties summary (as-built values).

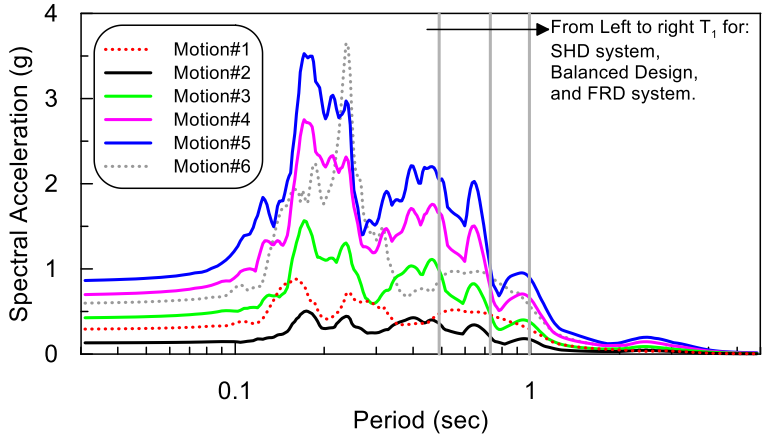


Figure 6: Input elastic spectral acceleration with 5% damping for each event.

Figure 7 displays the maximum values of selected engineering demand parameters as measured during the tests, namely the maximum roof acceleration, maximum roof drift ratio and maximum normalized base shear, for all three models. The absolute maximum roof acceleration comparison indicates that the balanced design model consistently resulted in the largest roof response. Roof acceleration is a system response and will be dictated by the strength of the foundation-building system as a whole. Total roof drift (part b) will observe contributions from both the structural fuse rotation and the footing rotation. Part (b) scatter plots reveal that the SHD system has the greatest total roof drift demand compared with the other models. In the FRD model, it has been markedly reduced in comparison with the other two models, with the exception of motion #6. Inspection of base shear coefficient indicates that system base shear demand is proportional to its footing rocking strength (Table 1). Upon moderate and intensive shaking, the SHD model is observed to have the largest base shear and the FRD has the lowest demand. Therefore, it can be concluded that implementation of relatively weaker footing element could advantageously reduce global base shear demand.

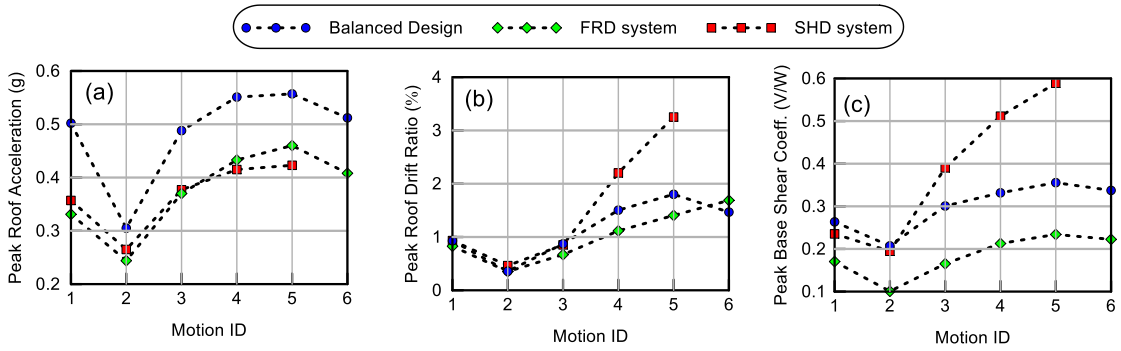


Figure 7: Selected synthesis results: (a) Peak Roof Acceleration; (b) Peak Total Roof Drift Ratio; (c) Peak Normalized Base Shear.

Figure 8 shows the dissipated energy within the fuse and footing elements, as determined using the measured moment-rotation response of the components. It is clear that the total energy is well distributed between these two elements in the balanced design configuration, irrespective of motion characteristics. For the FRD model, the foundation absorbs the majority of the input energy, which supports the fact that the structural fuse is designed to be stronger than the rocking footing element. In this case, the structural fuse behaved nearly elastically for all events. In contrast, the SHD model energy distribution is slightly sensitive to the motion amplitude and motion characteristics. Under the low amplitude motion excitation, Motion#2 for example, the foundation vibration dominates the energy absorption. While for other events, the energy is relatively well spread, but it occurred at the price of significantly higher roof drift demand, as indicated in Figure 6 (b).

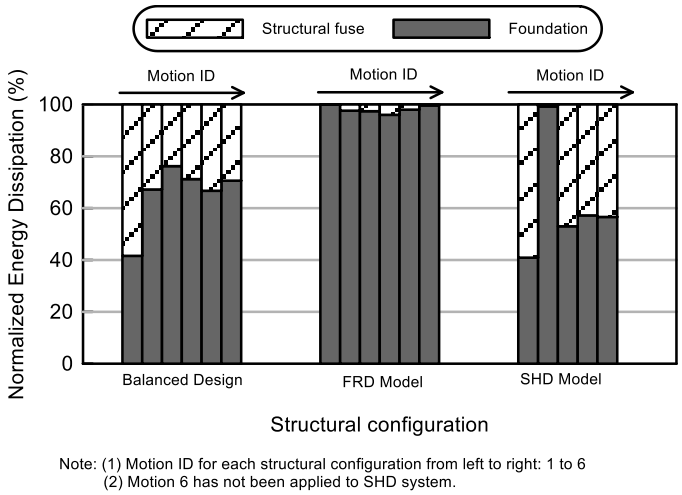


Figure 8: Normalized Energy dissipation between structural fuse and foundation element.

4 CENTRIFUGE TESTING OF WALL-BRACED FOUNDATION-BUILDING SYSTEM

The second system-level test program aims to incorporate the balanced design concept into wall-braced building system. Adopting the ASCE design guidelines (ASCE 7-10 [2]), three two-story-two-bay wall-type models were designed as planar (2-dimensional) centrifuge models. These structures represent typical low-rise segments of a building, whereby the wall component is intended to provide the majority of the lateral load resistance, yet gravity frame bays are attached and supplement not only service load carrying capacity but also inherently provide some lateral load resistance. Figure 8 shows elevation photos of each instrumented model. The simulated shear wall component was constructed by using two parallel annealed Aluminum plates (Alloy 1100-O) with a group of HDPE block spacing in between. The columns and beams were modeled by Aluminum tubing section and inverted-U channel sections, respectively. The shallow footings were designed with rectangular Aluminum block. The structural fuses were located at the base of shear wall and the ends of columns, and they were achieved via notching the edge.

Similar to the frame-braced building test objective, three different walled models were designed with a similar layout, yet with different fuse or footing geometry. In addition, the attributes of symmetry were explored by placing the wall component in the middle and at the ends of the model. This aspect is not presented in the current paper however. Parts (a) through (c) in Figure 9 displays the model of the BD, FRD and SHD building segments, respectively. Part (d) provides the overall dimensions of the models, which was consistent between the different types of structures. In addition, the sign convention adopted in subsequent plots is specified, where the (+) sign indicates that the system moves towards the exterior column and the (-) indicates movement towards the shear wall. Due to the unsymmetrical setup of the shear wall component, gravity induced load could add static moment bias at the fuse and footing level prior to dynamic shaking. This implies that shear wall fuse or footing fuse on the (+) side of the model is prone to more easily mobilize their capacity. Consequently, the response of this structural system could vary significantly in each direction, particularly when nonlinear behavior is initiated. It is desirable therefore to differentiate the direction of movement, and one should also examine the response parameters at both directions to fully understand its seismic behavior.

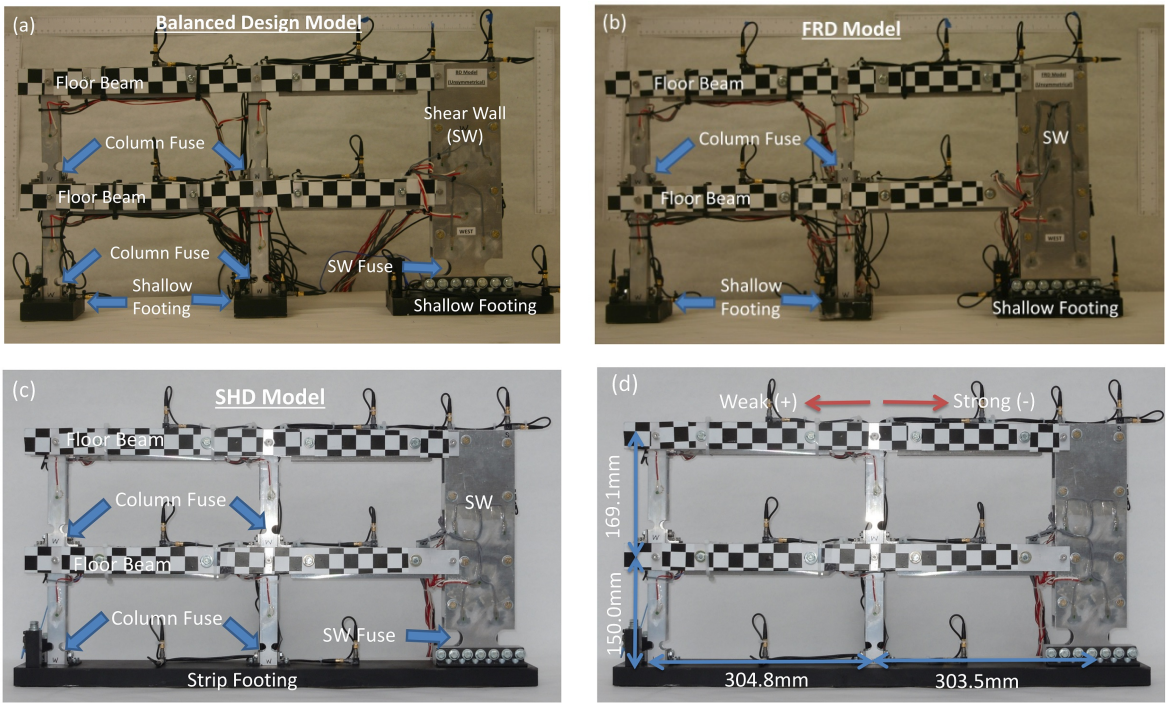
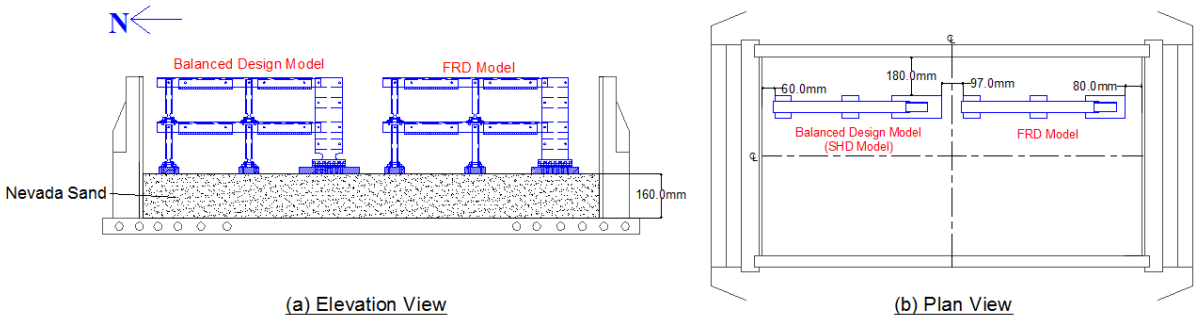


Figure 9: Elevation view of three instrumented models (a-c) and dimensional details in model scale (d).

Each model is heavily instrumented with more than 50 sensors, including accelerometers, strain gauges and linear potentiometers (Figure 9). Similar to test setup of frame models, all three wall models were supported on dry Nevada sand in a rigid container and spun up to 56 RPM to create a 30-g level gravitational acceleration at the ground surface. As indicated in Figure 10, the BD and FRD model were situated along one side of the rigid container and simultaneously subjected to a series of generally increasing amplitude motions. This arrangement could induce a more consistent input shaking for both models during the same spin. The SHD model was constructed and placed at the station where the BD had been placed following shaking of the BD and FRD model. Since the SHD model incorporates a large strip footing, any disturbance around the soil inherited from previous spins would not significantly affect its seismic response. Table 2 summarizes the most important as-built system characteristics of each model. Importantly, in contrast to the frame-braced model, the extreme cases of FRD and SHD models were able to theoretically achieve infinite Cy and Cr values when comparing with BD model.



Note that all dimensions are in model scale, and the size of the container can be referred to Figure 5.

Figure 10. Experimental setup for wall-braced models: (a) Elevation view; (b) Plan view.

Parameter	Description	BD	FRD	SHD
C_r	SW footing rocking coefficient	0.24	0.16	N/A
C_y	SW fuse yield coefficient	0.29	N/A	0.29
T_1 (sec)	First natural period	0.48	0.39	0.47
FS_v	Vertical factor of safety of SW footing	20.83	17.31	N/A
$M/(V*L)$	Moment to shear ratio of SW footing	1.26	1.61	N/A
H/L	Wall aspect ratio (total height/wall length)		3.33	
D_r	Relative density of Nevada Sand		96%	
ρ	Mass density of sand		1803 kg/m^3	

Table 2: Wall-frame building model and soil properties summary (achieved values).

The three models were also subjected to an identical sequence of eleven earthquake motions. Figure 11 provides an elastic spectral acceleration response for one accelerometer located at surface free field (FF), overlaid with the estimated first natural period of each model. Table 3 lists the achieved motion characteristics of each event. The intention of the motion protocol is to employ low amplitude motions early in the series to initiate elastic response, and then gradually increase the amplitude to trigger highly nonlinear behavior towards the end.

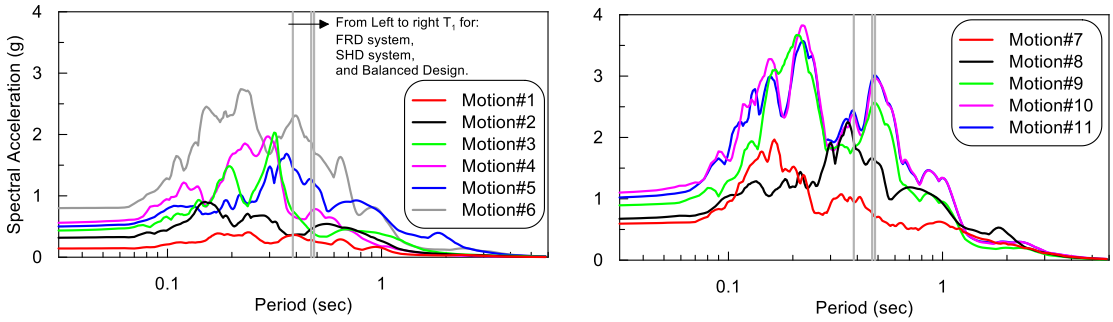


Figure 11: Elastic spectral acceleration of free field surface motion with 5% damping for all events.

Motion ID	Source Earthquake	Peak Free Field Surface Acceleration (g)	Strong Motion Duration (s)
1	Gazli, USSR, 1976	0.140	6.06
2	San Fernando, USA, 1971	0.314	6.79
3	San Fernando, USA, 1971	0.429	9.33
4	Morgan Hill, USA, 1984	0.550	3.90
5	Kobe, Japan, 1995	0.493	11.21
6	Gazli, USSR, 1976	0.797	6.06
7	Chi-Chi, Taiwan, 1999	0.586	24.11
8	Kobe, Japan, 1995	0.661	11.21
9*	Combined Morgan Step	0.882	6.86
10*	Combined Morgan Step	1.079	6.86
11*	Combined Morgan Step	1.004	6.86

*Note: these motions were an adaption of motion #4; strong motion duration is estimated by computing the time different between Arias Intensity of 95% and 5%.

Table 3: Source motion achieved characteristics.

Figure 12 compares the peak roof acceleration in (+) and (-) directions for each of the three models. The scatter plot shows that the SHD model was consistently reporting the highest roof acceleration in both the weak and strong directions, when compared with the models with footings more prone to rock. The response difference is particularly remarkable at high amplitude motions. Under motion#11, for example, the peak positive acceleration observed in the SHD model is almost double that of the FRD and BD models. However, comparing footing rocking promoted structures reveal that they have relatively similar performance at weak direction, and only moderately varying acceleration response in the strong direction, with the BD model reporting about 20% lower peak acceleration during the high intensity motions (motion #8 onward).

The peak acceleration difference observed in the wall-type structures completely deviate with the observations reported for the frame-braced models, as indicated in Figure 6 (a). This may be due to the fact that frame model is likely susceptible to higher mode effect and motion characteristics. Due to the pinned configuration at beam-column connection in frame models, second mode could either facilitate or counterbalance the movement of top story depending on the inelastic behavior development occurred within each fuse section. On the contrary, since the wall aspect ratio is relatively low, second mode contribution is very minimal for this wall-braced model.

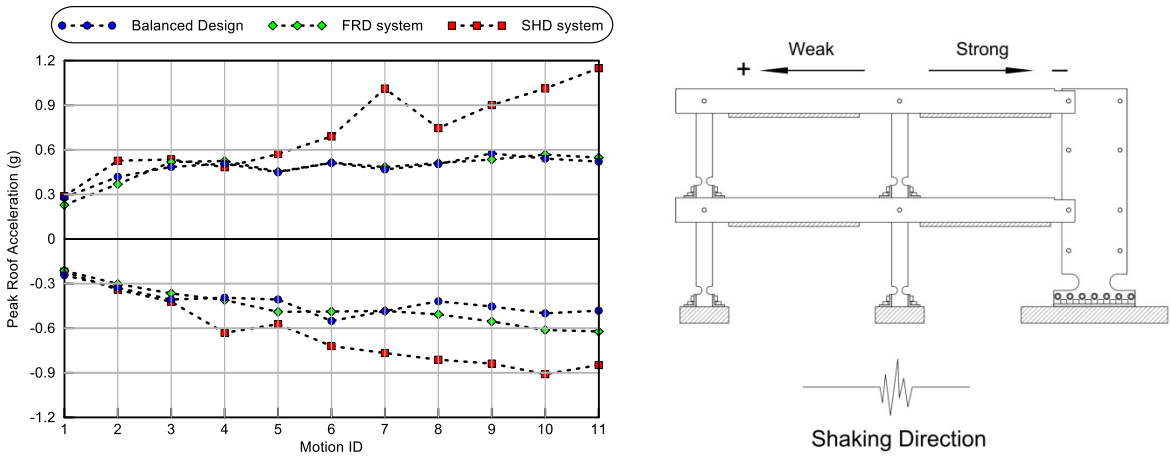


Figure 12: Peak roof acceleration comparisons at both directions.

In Figure 13, the peak roof drift demand is systematically compared among the models. The roof drift was computed by combing the high frequency component of double integration data obtained from roof accelerometer, and the low frequency component of the data recorded in LP (Deng et al. [5]). Meanwhile, this value does not account for the residual drift occurred from prior event. It is observed that the roof drift is fairly sensitive to motion characteristics. There is no definitive trend between the peak roof drift and model type for the various motions. However, comparison among the models shows that the FRD model experienced the largest roof drift, while the SHD model observes the lowest demand, and this trend is particularly pronounced in the (+) direction, i.e. towards the exterior column.

The difference in response amongst the various models also disagrees with the results generated from frame-type models. The reason for this is partially due to sectional characteristics of the dominant structural fuses, namely the column and shear wall fuses, in the frame-type and wall-type models, respectively. In the frame models, the structural fuse is dimensionally small and the entire sectional strength can be easily and fully mobilized during intense shaking, which could lead to a significant amount of sectional rotation and therefore contribute to

large roof drifts of the system. On the other hand, the shear wall fuse usually develops nonlinear behavior at its extreme fiber under a rotation of about 0.5% according to a wall component test conducted following the system tests. Upon further development, strain hardening behavior combined with the wider cross section in shaking direction will result in a significant overstrength behavior. This could minimize the total fuse rotation, and thereby the entire structural displacement. In the meantime, this behavior transmits the seismic demand from fuse level to the soil-footing interface since the footing rocking capacity is lower than the shear wall fuse initial strength. As a result, large amplitude footing rocking may be observed, and the total roof drift may be significantly increased.

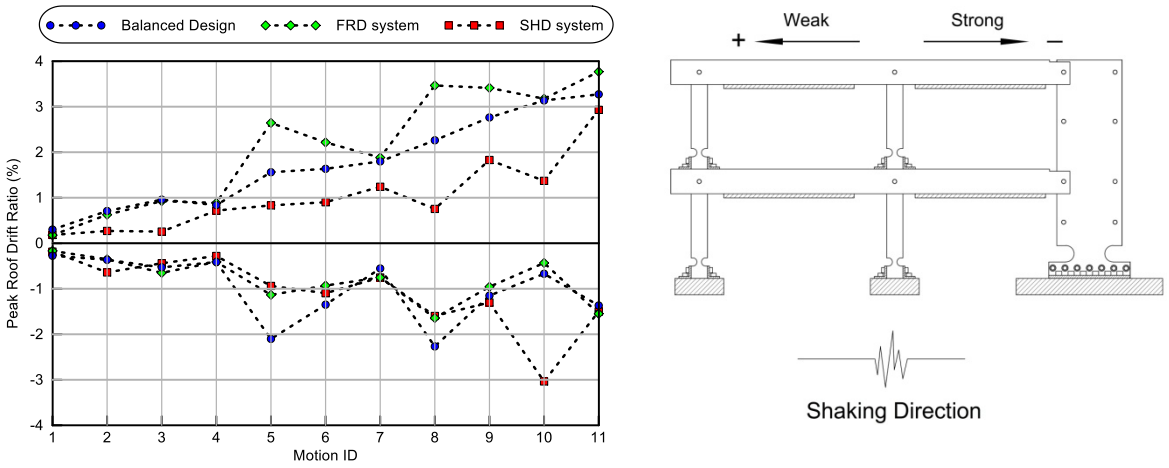


Figure 13: Peak roof drift ratio comparison at both directions.

Figure 14 plots the peak base shear demand normalized by the weight of each model (W). Similar with frame models' results, the SHD model has the largest base shear demand, regardless of motion characteristics and amplitude among the three tested models. When footing rocking is facilitated, this demand is greatly reduced as seen for the BD and FRD system. In addition, the peak base shear measured in the FRD model is less than that of balanced design. Combined with Figure 7(c), these results uniformly confirm that base shear demand is proportional to shear wall footing rocking strength. It is also notable for SHD model that the base shear demand continues to increase at high amplitude motion case despite the fact that the fuses in wall and columns have yielded at moderate motion excitation. This is directly attributed to the overstrength of the shear wall fuse.

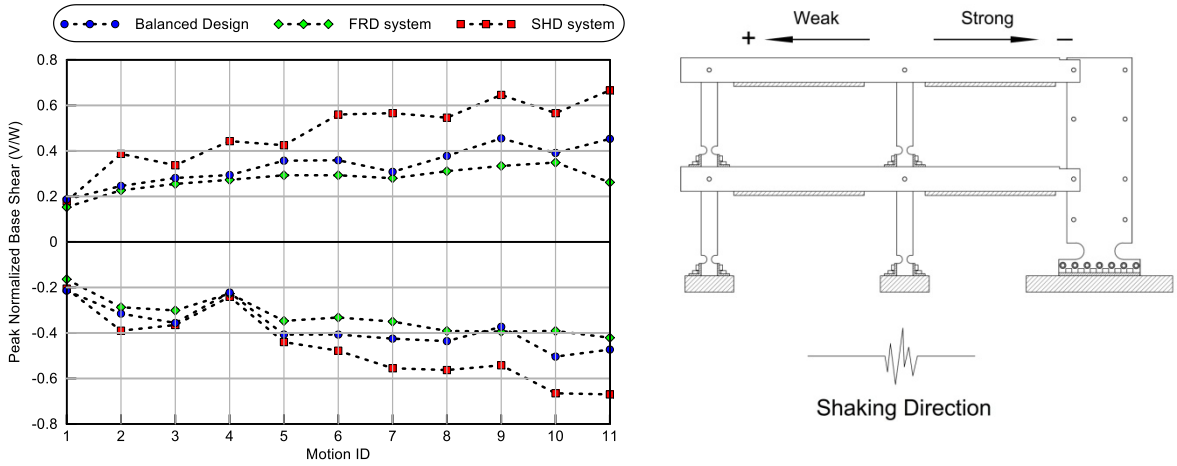


Figure 14: Peak base shear comparison at both directions.

Figure 15 documents the moment demand developed in the SW fuse and SW footing. Those demands were directly measured from the calibrated moment strain gauges. Values in the plot are the peak transient demand during shaking without considering the static load induced demand. Those values have been normalized by the respective components strength at yield (M_y). In general, the SW fuse in the SHD system experienced larger moment demands compared with the BD model. It is noted that values in excess of unity are observed around motion #4. In motion#11, for instance, the SW fuse flexural overstrength ratio reaches above 2.0 for both directions. For the SW fuse this is attributed mostly to material overstrength, whereas for the SW footing this is attributed mostly to dynamically varying axial loads, both of which modify the yield moment of the component. From motion#6 onward, the SW fuse demand in the SHD model consistently exceeds 60% of its yield strength. With footing rocking implemented (BD model), the demand to the SW fuse is reduced by at least 50%, as indicated in the blue dot line in part (a). Comparing the moment demand in the (+) and (-) directions reveals that the demand in the strong direction is larger than that of weak direction. This is due to a static moment bias in the weak direction induced by an unsymmetrical gravity load distribution.

Comparison of the footing moment demand shows that the footings of both systems likely mobilized at motion#4, and experienced an increase in moment demand upon continuing shaking. In the weak direction, the peak moment demand is about 20% greater than the theoretical yield strength at high amplitude motions. The overstrength is consistently larger in the strong direction of the shear wall, approaching 60% overstrength for each of the BD and FRD models during motion #10. Comparing the peak moment demand developed in the SW fuse and footing within the BD model indicates that the rocking foundation carries slightly more normalized moment than the shear wall fuse.

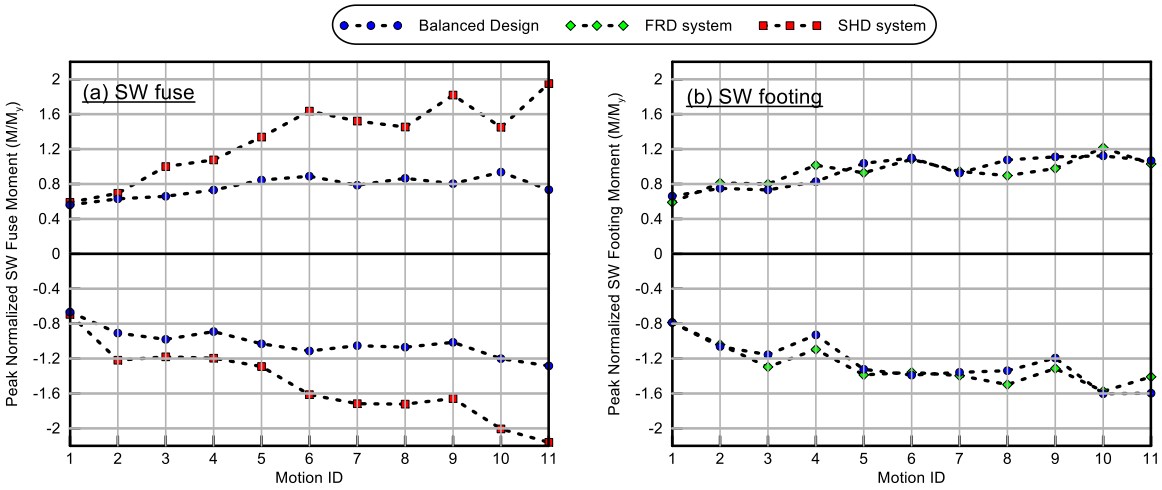


Figure 15: Peak transient moment demand comparison.

5 CONCLUSIONS

In this paper, we consider the idea of equating the rotational strength of a rocking foundation with that of conventional structural fuses and adapting this within the seismic design of a building. Three simple types of models for each of frame-braced and wall-braced types of load resisting systems used in buildings are constructed to investigate the ramification of introducing the rocking foundation as a load sharing mechanism. Models are tested at centrifuge scale considering (i) the rocking foundation and structural fuses to yield approximately simultaneously (*balanced design – BD model*), (ii) promoting only structural fuses to yield (*struc-*

tural hinging dominated – SHD model), and (iii) promoting only the foundation to yield in a mode of rocking (*foundation rocking dominated – FRD model*). Preliminary analysis of the experimental data indicates the following:

- In the frame-type building system, the balanced design model carried the largest roof acceleration compared with the FRD and SHD model. The SHD model consistently experienced the largest peak roof drift and base shear demand, while each of these responses were greatly reduced in the FRD system. In the balanced design model, the seismic energy energy dissipation was distributed between the structural fuse and rocking footing and this feature is independent of motion characteristics.
- In the unsymmetrical wall-braced systems, the SHD system has the largest peak roof acceleration demand in both the weak and strong directions, compared with the BD and FRD systems. The BD and FRD model produced a similar peak acceleration response in the weak direction. The peak roof drift is observed to be very sensitive to footing rocking. Among the three models, the FRD model consistently produced the largest total peak roof displacement. On the other hand, the SHD model reported the largest base shear force demand at the foundation level. The SW fuse in the SHD model reported large peak normalized moments, more than 50% greater than the BD model during moderate and high amplitude motions. Footings in the FRD and BD model responded with relatively consistent peak normalized moment amplitudes irrespective of the motion. Flexural overstrength is observed in both the structural fuse and rocking footing elements.

6 ACKNOWLEDGEMENTS

The research work described herein is supported by the National Science Foundation NEESR program under the award CMMI-0936503. Any opinions, findings, and conclusions expressed are those of the authors, and do not necessarily reflect those of the sponsoring organization. Special thanks go to Professor Mark Aschheim at Santa Clara University and Professor Sashi Kunnath at the University of California at Davis for their valuable suggestions and feedback during model construction and testing. Student assistants, Lijun Deng, Danielle Locklar, Kaijie Huang and Mark Stringer helped through this test program. Staff member at the UC Davis NEES facility and UCSD Powell laboratory also contributed in the program, including but not limited to: Dr. Dan Wilson, Chad Justice, Anatoliy Ganchenko, Peter Rojas and Ray Gerhard. The above support is greatly appreciated. A.G. Gavras is also grateful for the partial support provided by the Alexander S. Onassis Foundation during his M.S studies at UC Davis.

REFERENCES

[1] Anastasopoulos, I., Gazetas, G., Loli, M., Apostolou, M., and Gerolymos, N., Soil failure can be used for seismic protection of structures. *Bull. Earthq. Eng.* **8**:3, 309-326, 2010.

[2] American Society of Civil Engineers, *Minimum Design Loads for Buildings and Other Structures.* ASCE/SEI 7-10 document, ASCE, Reston, VA., 2010.

[3] Barlett, P. E., Foundation rocking on a clay soil. ME thesis, University of Auckland, *School of Engineering, Report No. 154*, Auckland, New Zealand, 1976.

[4] Chang, B. J., Thomas, J. M., Raychowdhury, P., Gajan, S., Kutter, B. L. and Hutchinson, T. C., Soil-Foundation-Structure Interaction: Shallow Foundations. Centrifuge Data Re-

port for JMT02. *University of California, San Diego, Structural Systems Research Project, Report No. SSRP-07/24*, 2007.

[5] Deng, L., Kutter, B. L., Kunnath, S., Centrifuge modeling of bridge systems designed for rocking foundations. *ASCE J. Geotech. Geoenviron. Engrg.,* **138**:3, 335-344, 2012.

[6] Drosos, V., Georgarakos, T., Loli, M., Anastasopoulos, I., Zarzouras, O. and Gazetas, G., Soil-Foundation-Structure Interaction with Mobilization of Bearing Capacity: An Experimental Study on Sand. *ASCE J. Geotech. Geoenviron. Engrg.,* **138**:11, 1369-1386, 2012.

[7] Englekirk, R. E., *Seismic design of reinforced and precast concrete buildings.* Wiley, 2003.

[8] Gajan, S., and Kutter, B. L., Capacity, settlement, and energy dissipation of shallow footings subjected to rocking. *ASCE J. Geotech. Geoenviron. Engrg*., **134**:8, 1129-1141, 2008.

[9] Gelagoti, F., Kourkoulis, R., Anastasopoulos, I. and Gazetas, G., Rocking isolation of low-rise frame structures founded on isolated footings. *Eqk. Engr. and Str. Dynamics,* **41**:7, 1177-1197, 2012.

[10] Hakhamaneshi, M., Kutter, B.L., Deng, L., Hutchinson, T.C. and Liu, W., New findings from centrifuge modeling of rocking shallow foundations in clayey ground. *ASCE 2012 Geo-congress*, Oakland, CA, Mar. 25-29, 2012.

[11] Housner, G. W., The behavior of inverted pendulum structures during earthquakes. *Bull. Seismo. Soc. Am.,* **53**:2, 403-417, 1963.

[12] Kutter, B. L., Recent advances in centrifuge modeling of seismic shaking. State-of-art paper, *Proc. 3rd Intl. Conf. on Recent Advances in Geotechnical Earthquake Engineering and Soil Dynamics,* Vol. **2**, St. Louis, 927-942, 1995.

[13] Liu, W., Hakhamaneshi, M., Kutter, B. L. and Hutchinson, T. C., Compatible soil and structure yielding to improve system performance. *Centrifuge Data Report for Test Series MAH02, Report No. UCD/CGMDR-11/07*, Center for Geotechnical Modeling, University of California, Davis, 2011.

[14] Liu,W., Hutchinson,T.C., Kutter, B.L., Hakhamaneshi, M., Aschheim, M. and Kunnath, S., Demonstration of Compatible Yielding between Soil-Foundation and Superstructure Components. *Journal of Structural Engineering, ASCE,* Posted ahead of print, April, 2012.

[15] Negro P., Paolucci R., Pedretti S., Faccioli E., Large-scale soil-structure interaction experiments on sand under cyclic loading. *Proc. 12th World Conference on Earthquake Engineering,* Auckland, New Zealand, Paper#1191, 2000.

[16] Paolucci, R., Shirato, M., and Yilmaz, M. T., Seismic behavior of shallow foundations: Shaking table experiments vs numerical modeling. *Earthquake Engineering and Structural Dynamics,* **37**, 577-595, 2008.

[17] Rosebrook, K.R., and Kutter, B.L., Soil-foundation-structure interaction: Shallow foundations. *Centrifuge Data Rep. for test series KRR01, Rep. No. UCD/CGMDR-01/09,* University of California, Davis, CA, 2001.

[18] Shirato, M., Kouno, T., Asai, R., Nakani, S., Fukui, J. and Paolucci, R., Large-scale experiments on nonlinear behavior of shallow foundations subjected to large earthquakes. *Soils and Foundations,* **48**:5, 673-692, 2008.

[19] Taylor, C.A., Crewe, A.J., Shaking table tests of simple direct foundations. *Proc. 11th World Conference on Earthquake Engineering,* Acapulco, Mexico, Paper#2048, 1996.

[20] Taylor, C. P., Cote, P. A., Wallace, J. W., Design of Slender Reinforced Concrete Walls with Openings. *ACI Structural Journal.,* **95**:4, 420-433, July-August, 1998.

[21] Trombetta, N.W., Mason, H.B., Chen, Z., Hutchinson, T.C., Bray, J.D., and Kutter, B.L., Nonlinear dynamic foundation and frame structure response observed in geotechnical centrifuge experiments. *Soil Dynamics and Earthquake Engineering*, Posted ahead of print, February, 2013.

[22] Wiessing, P. R., Foundation rocking on sand. ME thesis, University of Auckland, *School of Engineering, Report No. 203,* Auckland, New Zealand, 1979.

COMPDYN 2013
4th ECCOMAS Thematic Conference on
Computational Methods in Structural Dynamics and Earthquake Engineering
M. Papadrakakis, V. Papadopoulos, V. Plevris (eds.)
Kos Island, Greece, 12–14 June 2013

ROCKING RESPONSE OF TALLER REINFORCED CONCRETE WALLS

Marc-André Lemieux[1] **and Sanda Koboevic**[2]

[1] École Polytechnique de Monteal
Montreal (Quebec) Canada
marc-andre.lemieux @polymtl.ca

[2] École Polytechnique de Montreal
Montreal (Quebec) Canada
sanda.koboevic@polymtl.ca

Keywords: Seismic design, seismic response, rocking behavior, taller reinforced concrete walls, nonlinear analysis.

Abstract. *The study of seismic response of taller reinforced concrete shear walls with rocking foundations is carried out on the example of a 20-storey building. The building is framed by simple ductile concrete shear and located in Montreal, Canada. The location is representative of Eastern North American seismic conditions characterized by high-frequency ground motions that can exemplify the impact of higher modes on the response. The walls are designed and detailed according to the Canadian design provisions for ductile shear walls. Different options for the foundation design are considered to examine the effect of foundation size on the type of structural response. Two-dimensional nonlinear time history analyses of the wall-foundation system were performed using the OpenSees program for simulated ground motions compatible with the design spectrum. Wall inelastic behaviour and the nonlinear soil response were both represented in the model. Soil-structure interaction and uplift due to overturning are modeled using the beam-on-nonlinear-Winkler-foundation concept. The overturning moments, base shears and roof displacements are compared to those obtained assuming a fixed-base condition to quantify the impact of rocking on the superstructure. The usefulness of rocking to mitigate higher-mode effects is also evaluated. The foundation displacements and stresses in the soil are examined to assess the consequences of the rocking behaviour on the global structural response. The analyses show that the code compliant design exhibited yielding at the wall base and rocking. Reduction of foundation size increased the rocking response and eliminated the inelastic response in the superstructure. Rocking reduced the force demand on the superstructure without significantly increasing the displacements, but some permanent deformations and high bearing pressures developed in the soil under the foundation edges. Rocking did not reduce the impact of higher modes on the response.*

1 INTRODUCTION

Capacity-based approach to seismic design of buildings generally aims to confine energy dissipation in the superstructure and avoid any damage to the foundations. This design philosophy can be justified by the difficulty to conduct inspection of the foundations following an earthquake and the high cost associated with possible repairs. Conversely, such approach neglects the great potential to engage nonlinearity inherent to the foundation-soil system through foundation yielding, the mobilisation of bearing capacity failure mechanisms in supporting soil or the uplifting at foundation-soil interface which can efficiently reduce global seismic demand to the structural system [1,2,3,4].

Incorporating soil-structure interaction effects to reduce seismic design loads has been allowed to certain extent in modern building codes. Some of the related provisions imply for instance that uplift due to rocking will eventually occur during the design earthquake and thus limit seismic forces introduced into the superstructure. However, this is not the primary mechanism of energy dissipation intended in the design. In Canada, design procedures for reinforced concrete shear walls [5] favour the formation of flexural plastic hinges at the base of the structure. Foundations are sized to carry overturning moments corresponding to wall nominal bending moment capacity, the corresponding shear force and the tributary gravity loads. Design forces are limited to 50% of the elastic seismic shear which corresponds to load level at incipient rocking [6]. The latter usually applies to design foundations of overstrong walls for which minimum ductility requirements are critical.

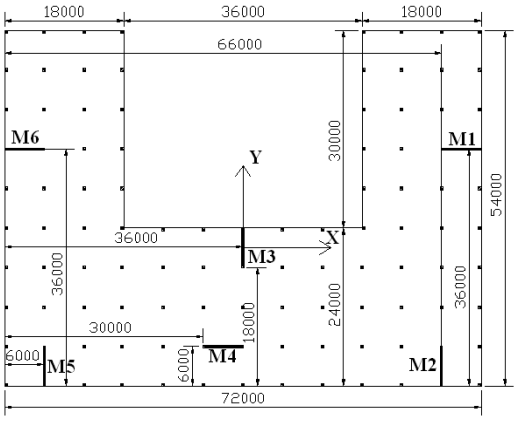
For taller buildings located in moderate seismic zones such approach generally results in excessively large foundations. Modifying design approach by favoring rocking as a principal mechanism of limiting seismic forces in the superstructure could be beneficial for such structures. Negative consequences are also possible: horizontal displacements of the structure may be increased beyond acceptable limits and permanent deformations can develop in the soil. Further studies of global structural response using adequate analytical models and experimental studies are therefore needed before such procedures can be safely implemented in the design.

The study presented in this paper was conducted with the objectives to understand better the seismic response of taller reinforced concrete shear walls with rocking foundations. A studied 20-storey building was located in Montreal and framed by simple ductile reinforced concrete shear walls. This location is representative of Eastern North American seismic conditions with characteristic high-frequency ground motions that can exemplify the impact of higher modes on the response. The walls were designed and detailed following the Canadian design provisions for ductile shear walls. Different options for foundation design were considered to examine the impact of foundation size on the structural response.

Two-dimensional nonlinear time history analyses of the wall-foundation-soil system were performed using the OpenSees program for a set of simulated ground motions compatible with the design spectrum. The model included the wall inelastic behaviour and the nonlinear soil response. Soil-structure interaction and uplift due to overturning were modeled using the beam-on-nonlinear-Winkler-foundation concept. The overturning moments, base shears and roof displacements are determined and compared to those obtained assuming a fixed-base condition to quantify the impact of rocking on the superstructure. The impact of rocking to higher-mode response is also evaluated. The foundation displacements and stresses in the soil are examined to assess the consequences of rocking behaviour on the global structural response.

2 BUILDING DESIGN

The study was conducted for 20-storey building designed for Montreal, Quebec, on a reference class C site (360m/s ≤ v_s ≤ 760m/s). Montreal is located in moderate seismic zone with spectral accelerations for reference class site varying between 0.64g and 0.048 g for 0.2 s and 2 s periods, respectively. The building floor plan is shown in Figure 1. Three ductile rectangular reinforced concrete walls, 9 m long, provide lateral resistance in each orthogonal direction. Wall thickness varies between 400mm for walls M1, M3 and M6 and 500 mm thickness for walls M2, M4 and M5. Typical storey height is 2.95 m with 3.45 m at the first storey giving a total building height, h_n = 59.5 m.



Gravity Loads

Roof:	Dead	= 6.20 kPa
	Toiture	= 1.00 kPa
	Snow	= 2.48 kPa
Floor:	Dead	= 5.20 kPa
	Partitions	= 1.00 kPa
	Live	= 1.90 kPa
Exterior walls		= 1.20 kPa

Figure 1. Layout of a typical floor (dimensions in mm) and design gravity loads

Design was performed in accordance with the provisions of NBCC 2010 [7]. Gravity loads are given in Figure 1. The 3D response spectrum analysis was employed to determine seismic load effects. NBCC 2010 does not require the inclusion of soil-structure interaction in the design, thus in the analysis the fixed-base support conditions were represented. Accidental in-plane torsion was included. To account for concrete cracking, gross section properties of the wall were reduced by 30% reflecting the axial load present at the wall base.

In order to engage 90% of the seismic mass of the building, as required by the NBCC, it was necessary to consider 9 modes. The first two modes (T_1 = 5.08 s, T_2 = 4.81 s) are predominantly flexural and mobilize 54% and 64% of the mass, respectively, while the participating mass of the third torsional mode (T_3 = 4.55 s) is 54%. This confirms that the impact of higher modes on the building response can be anticipated. In spite of the characteristic U-shape, the building was not irregular in torsion (B < 1.7), and no other irregularities were present. Thus, as permitted by NBCC 2010 for regular buildings, the seismic base shear from dynamic analysis was increased to 80% of the design base shear, V, calculated by the equivalent static method. The design base shear, V, is obtained by dividing the elastic base shear, V_e = $S(T_a)$ M_v I_E W, by the product of ductility and the overstrengh-related force modification factors, R_d and R_o. In this expression, $S(T_a)$ is the design spectral acceleration for the given site determined at the fixed-base fundamental building period, T_a, M_V is a factor accounting for higher mode effects, I_E is the importance factor, and W is the seismic weight. The fundamental periods obtained from modal analysis exceeded the code suggested empirical value by a large margin (T_{emp} = 1.07 s), and thus the maximum period permitted by NBCC for this type of structures, T_a = 2T_{emp} was used to determine V. The calculation of seismic base shear is summarized in Table 1. Because of the limitation imposed on the design fundamental period, the minimum design shear obtained for periods larger than 4.0 s did not control the design.

Seismic loads induced the largest bending moments in the shear walls M2, M5 and M4. Because of the symmetric arrangement, forces induced in walls M2 and M5 were identical. To maintain consistency with the previous study that investigated the rocking behavior of a 10-storey wall [8], further design and nonlinear time history results were carried out for these two walls. Forces considered for the design of walls M2 and M5 are shown in Table 1.

Fundamental period (s)	5.08
Design period (s) (T_a=2*T_{emp})	2.14
Spectral acceleration at the design period (g), S(T_a)	0,046 g
Higher mode effects amplification factor (M_v)	3
R_o	1.6
R_d	3.5
Seismic weight (kN)	486530
Building design base shear (kN) *	9652
Design base shear for M2 and M5 (kN)*	4355
Design bending moment for M2 and M7 (kNm)*	85319
Axial load in the wall at ground floor level (1.0D+0.5L+0.25S) (kN)	14090

* includes accidental torsion

Table 1. Seismic load calculations and design seismic forces at the wall base

The design was carried out in accordance with the seismic requirements of CAN/CSA A23.3 standard [5] for ductile shear walls. The design procedure is capacity-based and aims to achieve the formation of flexural plastic hinge only at the base of the structure and prevent brittle shear failure as well as any damage to the foundations. The compressive concrete strength, f'_c, was 30 MPa, and the yield strength of the reinforcement, F_y, was 400 MPa. Plastic hinge zone extended to the sixth floor. The design shear force in the zone of plastic hinge was set equal to the value that corresponded to the development of the probable moment capacity at the base of the wall (ϕ_c = 1.0, ϕ_s = 1.0 and 1.25f_y) because this value was smaller than the elastic shear force. Outside of this zone, the bending moments and shear forces were amplified by the ratio of the factored bending resistance of the wall at the top of the plastic hinge to the factored seismic bending moment at the same location. The required flexural reinforcement was determined using the program RESPONSE2000 [9], taking into account the tributary gravity loads. Minimum reinforcement requirements did not govern the design. Note that the selected design did not fully comply with rotational ductility requirements prescribed by [5]. This condition was not problematic in view of the seismic response observed in subsequent nonlinear time history analysis.

The size of the foundation was determined using the capacity design. According to the Canadian code, the foundations are designed for the lesser of the shear force corresponding to the development of nominal bending moment capacity at the wall base (ϕ_c = 1.0, ϕ_s = 1.0 and f_y) and 50% of the elastic seismic base shear. The latter corresponds to the force level at which the rocking movement is anticipated. Such approach recognises that the foundation rocking can occur but prioritizes energy dissipation in the superstructure. For the wall under study, development of the nominal flexural capacity of the wall base was critical suggesting that the dissipation of seismic energy should occur in the superstructure without any noticeable rocking. This level of load corresponds to elastic base shear reduced by R_oR_d = 4.74.

In order to study further the impact of the foundation dimensions on the seismic behaviour of the soil-structure system, two alternate solutions were conceived. In the first option, the

foundation was designed considering the overturning moment which corresponded to the initiation of rocking ($R_oR_d = 2$). In the second option, the foundation was designed without applying any capacity design procedure, thus the level of load was identical to that considered for the flexural design of the wall base ($R_oR_d = 5.6$). Two soil profiles, typical for the Montreal area [10], and representative of a class C site were considered to investigate the possible impact of different soil characteristics on the seismic response of the soil-structure system. The shear wave velocity of the selected profiles corresponded to the average (v_s = 550 m/s) and lower bound (360 m/s) shear wave velocity characterizing the design site. The typical properties of selected soil profiles are summarized in Table 2.

	Soil profile INF (v_s = 360 m/s)	Soil profile SUP (v_s = 550 m/s)
Standard penetration index, N_{60}	≈ 50	≈ 90
Poisson ratio, ν	0.3	0.25
Mass density, γ_t (kg/ m^3)	2100	2300
Angle of internal friction, ϕ' (°)	41	43
Young's modulus (static), E (MPa)	160	410
Young's modulus (dynamic), E' (MPa)	700	1780
Dynamic shear modulus, G_{max} (MPa)	270	710

Table 2.Characteristic properties for the selected soil profiles

The design of the foundation followed the recommendations specified in the Canadian Foundation Manual [11]. The size of the footing depends on the tributary vertical load, overturning moment and the soil bearing capacity. To obtain a realistic bottom flexural reinforcement of the foundation, the depth of the foundation, H, was determined considering that the bars should not be larger than M35 and not spaced apart more than 150 mm c/c. Identical foundation cantilever offsets, d_b and d_l were assumed in the directions parallel and perpendicular to the wall and the thickness. The soil factored bearing capacity, q_r, was taken as 50% of the ultimate bearing capacity, q_u, and it was assumed that the soil pressure due to the vertical force and the overturning moment are uniformly distributed over the length B_{eff} = L-2e. In this expression, L is the length of the footing, and e is the eccentricity of the vertical load with respect to the center of the foundation ($e = M_f/P_f$). The design parameters and the foundation dimensions obtained for soil profile INF are listed in Table 2.

Force level	P_f (kN)	M_f (kNm)	L (m)	B (m)	H (m)	q_r (kPa)	Settlement (mm)
R_oR_d = 2.0	27287	238 993	18.8	10.3	2.90	2176	9.17
R_oR_d = 4.7	14209	100 474	14.3	5.75	1.45	1292	8.35
R_oR_d = 5.6	14178	85 319	13.5	5.0	1.30	1137	8.74

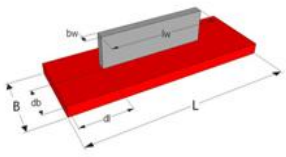


Table 3.Summary of foundation designs

3 NONLINEAR TIME HISTORY ANALYSIS

3.1 Selection of earthquake records

The seismic response of the walls was studied using 2-D nonlinear time history analysis (NHTA) for two sets of 10 ground motion records compatible with the design NBCC spectra. To compensate for the lack of historical earthquake records representative of seismic hazards in Eastern Canada, simulated records were employed. The records were selected and scaled

using the procedure described in [12]. The initial selection was done with respect to M-R scenarios that dominate seismic hazard at design locations. In Canada seismic risk desegregation is not available for the spectral accelerations, S_a at periods exceeding 2 s, so the dominant scenarios were established from data given for 2 s period. The first set was composed of 10 records selected from the ground motion records with **M**7.0 at 25 km, and the second set consisted of 5 records **M**6.0 at 15 km and 5 **M**7.0 at 25 km. In the selection process, for each candidate ground motion record, the ratio between the NBCC target spectral acceleration, SA_{targ}, and the response spectral acceleration, SA_{sim}, is first determined at every characteristic period within the period range from 1 to 5 s, and the mean and standard deviation values are calculated. This range was selected to include the periods of the modes that engage 90% of seismic mass. The final selected records have the lowest standard deviation and are scaled by the mean SA_{targ}/SA_{sim} ratio. The scaling factors varied between 0.71 and 1.02 for the first set, and 0.89 and 1.48 for the second set. These values are in line with the recommendations provided in [12].

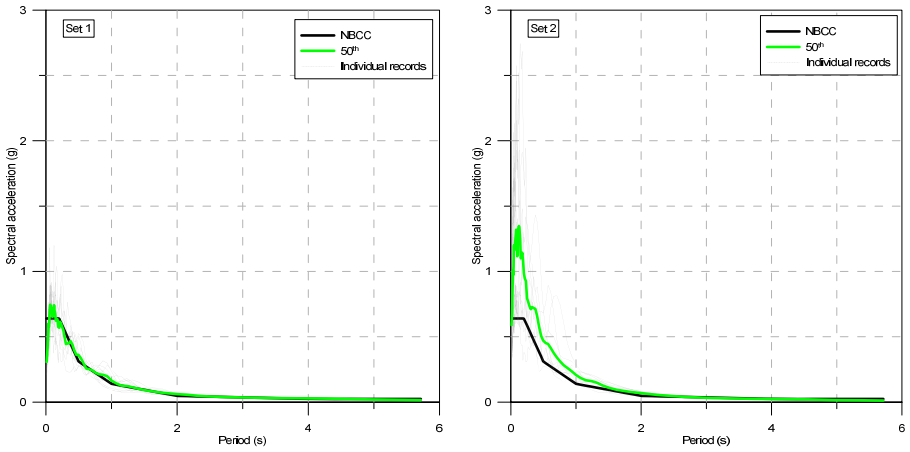


Figure 2. NBCC design acceleration spectrum and median 5% damped elastic acceleration spectra for calibrated ground motions

3.2 Modelling of the soil-foundation system

The nonlinear time history analysis of the soil-foundation-wall system was carried out in the OpenSees program [13]. The model accounts for inelastic wall behaviour and the nonlinear soil response. Nonlinear foundation response was represented using the Beam-on-Nonlinear-Winkler-Foundation concept [2,14]. The foundation is modeled as an elastic beam with a finite number of vertical nonlinear springs. Each spring is represented by a one-dimensional zero-Length element, and nonlinearity is modeled using the qzsimple1 material [15] that permits to represent uplift (geometric nonlinearity) and permanent settlement (material non-linearity). The backbone curve is unsymmetrical and is defined by an ultimate compression load and the reduced tensile strength when the foundation uplift occurs. To achieve this behaviour, three elements are connected in series: an elastic spring connected in parallel with a viscous dashpot, a rigid-plastic spring, and a gap element consisting of a bilinear elastic spring and a nonlinear spring connected in parallel. Several input parameters are required to describe the behaviour of the qzsimple1 material, namely the type of the soil, the ultimate bearing capacity, the tension capacity, the vertical stiffness, the displacement at 50% of ultimate load, suction, and viscous damping.

To characterise the springs below the foundation, it is necessary to define the stiffness, ultimate bearing capacity, and the strain at yielding. In fact, the knowledge of the appropriate

distribution of stiffness and bearing below the foundation to individual springs is essential, because of its impact on the global response of the system [3]. Figure 3 illustrates the distribution of the nonlinear springs used in this study. As recommended by [16], the foundation was divided into three zones, two end zones and a middle zone, and the springs were uniformly distributed within each zone. The length of the zones and the stiffness of the springs were calculated following the recommendations by [14]. The springs are more tightly spaced in the end zones compared to the middle zone to reflect more heavily loaded edges of the footing. Different stiffness values were assigned to the nonlinear springs in the middle and end zones to reproduce the non-uniform distribution of soil pressure under vertical loads, as well as to represent the rotational stiffness of the soil. It was assumed in the analysis that sliding cannot occur. The elastic beam used to model the foundation was considered as infinitely stiff in the middle zone to account for the presence of the wall. The elastic beam-column element, that was employed to model the structural foundation, was considered as infinitely stiff in the middle zone to account for the presence of the wall.

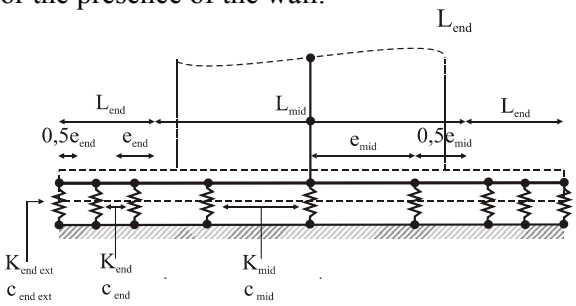


Figure 3. Characteristic parameters for the soil-foundation model

The required number of springs and their spacing was determined from the results of a parametric study. Five configurations were examined including 9,11,13,15 and 17 springs placed in each of the three zones. The response was compared by observing the first three periods of vibration, the force in the spring that is related to the bearing pressure in the soil, the vertical displacements at the center of the wall and at the foundation edge, the wall storey shears and the overturning moments as well as the horizontal displacements at roof level.

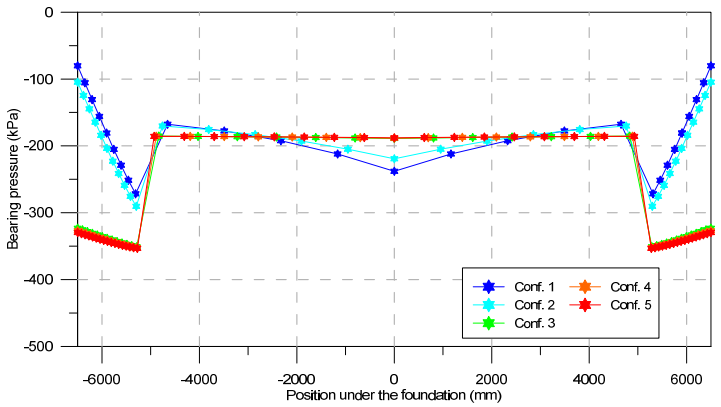


Figure 4. Soil bearing pressure distributions for various spring configurations studied

Figure 4 shows an example of the results for bearing soil pressures for different spring configurations. The anticipated soil pressure distributions were obtained for configurations with at least 13 springs per zone. Overall, for all the parameters studied, the study showed that the number of springs did not influence the response when at least 15 springs were used in each

zone. Thus, the configuration including a total of 45 springs was selected for further analyses. The values of the parameters used in the soil-foundation model for soil profile INF are summarized in Table 4.

Force level	$R_oR_d = 2.0$	M_n ($R_oR_d = 4.74$)	$R_oR_d = 5.6$
L_{end} (mm)	1465	1290	1230
e_{end} (mm)	101	89	85
$K_{end\ ext}$ (N/mm)	5.53E+04	4.73E+04	4.38E+04
K_{end} (N/mm)	1.11E+05	9.57E+04	8.76E+04
$C_{end\ ext}$ (N-mm/s)	3.04E+02	2.50E+02	1.24E+02
C_{end} (N-mm/s)	6.08E+02	2.99E+02	2.48E+02
L_{mid} (mm)	15870	11670	11040
e_{mid} (mm)	1058	778	736
K_{mid} (N/mm)	6.98E+05	4.53E+05	4.15E+05
C_{mid} (N-mm/s)	6.37E+03	2.61E+03	2.15E+03

Table 4. Values of characteristic parameters for the soil-foundation model (soil profile INF)

The study carried out by Le Bec [8] for a 10-storey reinforced concrete wall with rocking foundations showed that radiation damping had little impact on the system behaviour. Therefore, the component of radiation damping associated to foundation rotation was represented in the model, while the component associated with the vertical movement was neglected. The same approach was adopted in the present study. Le Bec also indicated that the higher suction capacity of the soil generally reduced the effects of rocking response. Because the observation of the rocking behaviour was the focus of the present study, the suction capacity of the soil was also omitted in the analysis.

3.3 Modelling of the shear wall

The studied OpenSees model of the shear wall is illustrated in Figure 5. The walls were modeled using one force-based nonlinear beam column element per floor. Based on results of the parametric study, the elements were divided into 2 vertical sections. Each section was discretized into fibers for which the nonlinear material stress-strain response was defined. Distinct fibers were defined for confined and unconfined concrete zones and for the steel reinforcement**.**

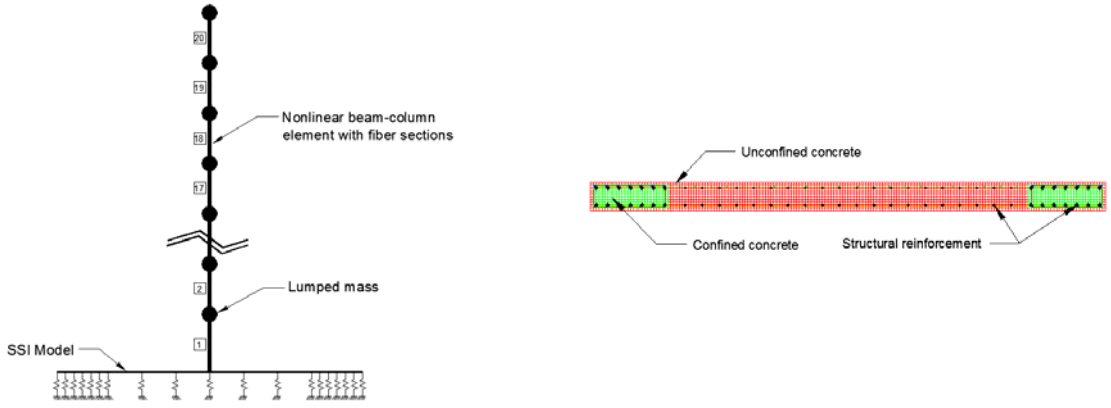


Figure 5. Shear wall model for nonlinear time history analysis with OpenSees

The fiber section model considers the bending moment and axial load interaction, but the shear-bending or shear-axial load interactions cannot be represented. Concrete behaviour was modeled using the uniaxial Kent–Scott–Park model with linear tension softening (Concrete02). The Giuffré-Menegotto-Pinto (Steel02) hysteretic material was employed to describe the inelastic behaviour of the reinforcing bars.

The parametric study was conducted for the fixed-base conditions to determine the adequate number of integration points for the analysis. After examining the structural periods, wall base shear and storey shears, overturning moments and roof displacements, three integration points per element were selected as a rational compromise offering adequate accuracy, convergence and reasonable computational time. This is in line with the practice reported in the literature [17].

3.4 Discussion of results

The response of the soil-foundation-wall system was examined by tracking the wall overturning moments and the shear forces, the horizontal wall displacements, the foundation uplift and the settlement of the soil as well as the maximal force in the nonlinear soil springs, which is indicative of the soil bearing pressure. The comparison is made for median response, but the peak and 84th percentile response values were also recorded. The results obtained for two earthquake sets were comparable. Because more important rocking response was observed for the soil profile INF, the results are presented for this soil profile.

The structure with the foundation designed to develop the nominal capacity of the wall, M_n, (R_oR_d = 4.74, design 2) and the one with the foundation conceived without implementing capacity design principles (R_oR_d = 5.6, design 3) experienced a rocking behaviour. The response of the structure with the foundation designed for the overturning moments corresponding to the incipient rocking limit (R_oR_d = 2, design 1) did not include rocking and was almost identical to that of the fixed-base structure. The rocking movement lengthened the first-mode period by 12% and 15% for design cases 2 and 3, respectively. Previous studies [3] indicate that the increase in vibration period due to soil-structure interaction is influenced by the wall aspect ratio, as well as by the relative stiffness between the structure and the soil, and that, in general, for taller structures the lengthening is usually smaller.

The occurrence of rocking modified the nature of the seismic response of the building. While for design case 1, dissipation of the energy took place exclusively in the superstructure, for two other cases, some yielding initiated at the base of the wall and was followed by rocking. The imposed curvature ductility demand at the base of the wall was much smaller than design prediction with the median value of 2. The maximum value recorded for this design case was about 5 which is still bellow the values that correspond to global ductility of 3.5 assumed in the wall design. The rocking response was the most significant for the structure with the smallest foundations (design case 3). This wall responded elastically, and the seismic energy was converted into kinetic energy associated with the rocking motion. Note that, contrary to design predictions, the rocking behaviour was observed before the overturning moment attained the nominal capacity of the wall. Although the design procedure aimed at achieving energy dissipation in the wall, the analysis showed that the structural system and the soil-foundation provided mechanisms for energy dissipation.

Foundation rocking limited the shear forces and the overturning moments that developed at the base of the wall. In turn, roof displacements increased but by a small margin. In Table 5, median results produced by the Set 1 ground motion records for three designs on soil profile INF are compared with the fixed-base case. Rocking had more impact on decreasing the overturning moments compared to base shears. A similar trend was observed in the study of the 10-storey building [8].

	Shear force (kN)		Overturning moment (kNm)		Roof displacements (mm)	
	V_{50th}	% decrease	M_{50th}	% decrease	Δ_{50th}	% increase
Fixed-base	7790		83 767		209	
$R_oR_d = 2.0$	7454	4.3	81 758	2.4	213	1.9
$R_oR_d = 4.7$	7105	8.8	71 243	14.9	222	6.2
$R_oR_d = 5.6$	6823	12.4	65 754	21.5	224	7.2

Table 5. Impact of foundation size on seismic response parameters of the shear wall: (a) seismic base shear, (b) overturning moments at the base and (c) roof displacements

For design cases 2 and 3, the maximum normalized force in the edge spring exceeded $0.3q_{ult}$, indicating an inelastic soil response. The median soil bearing pressures were larger for the structure with smaller foundation, reaching $0.59q_{ult}$. Note that for one ground motion record a peak bearing pressure of $0.78q_{ult}$ was recorded. For design case 2, with a larger foundation footprint, the mean soil bearing pressure under the edge of the foundation was approximately 30 percent lower. However, as seen in Figure 6 (a), these values are restricted to the springs at foundation edges and they quickly decrease over the end foundation zone. The impact of localised increase of bearing pressure in the soil and its impact on the overall system behaviour should be further examined in experimental and analytical studies.

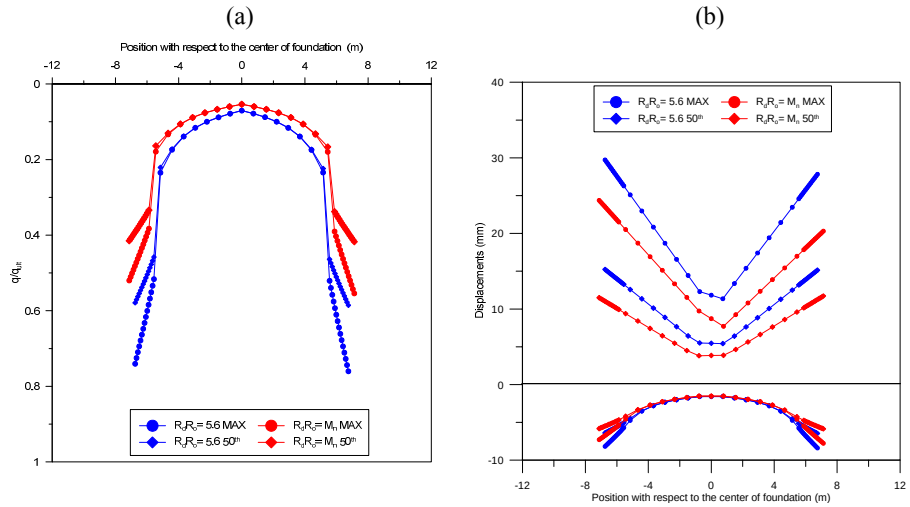


Figure 6. (a) Maximum normalized forces in springs and (b) peak foundation uplift and soil settlement (soil profile INF)

Figure 6 (b) shows the distribution of median and maximum peak foundation uplifts and settlements recorded along the length of foundation for design cases 2 and 3. Displacements were measured with respect to the initial position of the foundation under gravity loads and include elastic and inelastic components. As anticipated, higher values were recorded for the smaller foundation. Consistent with the location of the largest forces in the springs, the most important displacements were observed at the foundation edges. Inspection of the corresponding level of the force in the soil springs revealed that most of the peak displacement resulted in permanent soil deformations. However these deformations are relatively small and should not be detrimental the overall response of the system.

One of the objectives of this study was to examine if rocking can successfully mitigate higher-mode response. In Eastern Canada, shear walls are particularly prone to exhibit re-

sponse influenced by higher-mode contributions because typical ground motion excitations are particularly rich in high frequencies. Many researchers reported inadequate seismic design strength envelopes for shear walls [18,19, 20]. A more recent experimental study [21] conducted specifically for Eastern Canadian seismic conditions, showed increased flexural and shear demand in the upper storeys of the shear walls leading to the creation of second flexural plastic hinge and potential fragile shear failure.

The inspection of the time history of storey shears, bending moments, displacement profiles and rotational curvature demand confirmed that the seismic response of the studied structure is influenced by the higher modes. However, no significant difference in the distribution of response parameters over the height of the wall was observed regardless whether rocking occurred or not. For the wall under study, rocking did not result in the reduction of bending moments or shears in the upper part of the structure although it had a beneficial effect on the forces at the base of the wall. The occurrence of rocking seems to produce similar effects on the rest of the structure as the formation of the plastic hinge at the base of the structure. This similarity could be anticipated because both phenomena rely on the formation of a mechanism at the base of the wall to limit seismic response.

4 CONCLUSIONS

- Traditional seismic design procedures aim to achieve inelastic response in the superstructure and avoid any damage to the foundations. In the Canadian provisions, rocking of the shear walls on their foundations is not intended to be a principle source of seismic energy dissipation. In this study, the behavior predicted by the design procedures could not be validated using the analysis which included the soil-structure interaction effects. In code compliant design both the yielding of the superstructure and inelastic soil response occurred and contributed to dissipate seismic energy induced in the building. Permanent soil deformations were limited and peak median values of soil bearing pressure remained within the design predictions.
- The foundation footprint was significantly reduced when capacity approach was not integrated into foundation design. The response of the superstructure was elastic and more prominent rocking was observed compared to the code compliant design. Permanent soil deformations did not increase significantly, but soil bearing pressures under the edge of foundation reached high values and exceeded the factored resistance assumed in design. However these high values were localized under the edge of foundation and rapidly decreased within the end foundation zone.
- Compared to the fixed-base structure, rocking reduced seismic force demand. The reduction was more appreciable for overturning moments compared to the base shears. Rocking response increased wall roof displacements, but only by a small margin.
- Rocking response was not efficient in mitigation the impact of higher mode on seismic response of the shear wall studied.
- The study was carried out for firm soil conditions and a specific building configuration. Response of soil-foundation-structure system founded on a softer soil should be investigated as well as different building configurations before more the general conclusions can be drawn.

ACKNOWLEDGEMENTS

The authors gratefully acknowledge the financial support of the Natural Sciences and Engineering Research Council of Canada (NSERC) under the Strategic Network Grant Program. This project builds on the previous study carried out by Antoine Le Bec, Sanda Koboevic and Robert Tremblay. The contribution of Antoine Le Bec and Robert Tremblay is gratefully acknowledged.

REFERENCES

[1] G. Gazetas, Seismic design of foundations and soil-structure interaction. First European Conference on Earthquake Engineering and Seismology (ECEES), Geneva, Switzerland, September 3-8, 2006.

[2] Tarra, T. Belytschko, I. Babuska, T.J.R. Hughes, Research directions in computational mechanics. *Computer Methods in Applied Mechanics and Engineering*, **192**, 913-922, 2003.

[3] B.L. Kutter, G. Martin, T.C. Hutchinson, C. Harden, S. Gajan, J. Phalen, *Workshop on modelling of nonlinear cyclic load-deformation behavior of shallow foundations. Report no. PEER-2005/14*, Pacific Earthquake Engineering Research Center (PEER), 2006.

[4] R. Paolucci, M. Shirato, M.T. Yilmaz, Seismic behavior of shallow foundations: Shaking table experiments *vs* numerical modeling. *Earthquake Engineering and Structural Dynamics*, **37:4**, 557-595, 2008.

[5] CSA, *Design of concrete structures, Standard CAN/CSA-A23.3-04.* Canadian Standard Association, Rexdale, ON, 2004.

[6] D.L. Anderson, Effect of foundation rocking on the seismic response of shear walls. *Canadian Journal of Civil Engineering.* **30:2**, 360-365, 2003.

[7] NRCC, *National building code of Canada 2010*. National Research Council of Canada, Ottawa, ON, 2010.

[8] A. Le Bec, *Effects of rocking of shallow foundation on seismic response of reinforced concrete shear walls*. M.Sc. Thesis. CGM Dept., Ecole Polytechnique de Montréal, Montréal, QC. *(In French),* 2009.

[9] E. Bentz, P. Collins, *Response2000: reinforced concrete sectional analysis using the modified compression theory* Version 1.0.5: www.ecf.utoronto.ca/~bentz/r2k.htm, 2000.

[10] V. K. Prest, J. Hode-Keyser, Geological and engineering characteristics of surficial deposits, Montreal island and vicinity, Quebec. Geological survey of Canada, Paper 75-27, 577-595, 1977.

[11] CGS, *Canadian foundation engineering manual (4^{th} ed).* Canadian Geotechnical Society, Richmond, B.C, 2006.

[12] G.M.Atkinson, Earthquake time histories compatible with 2005 National building code of Canada uniform hazard spectrum. *Canadian Journal of Civil Engineering.* **36:6**, 991-1000, 2009.

[13] F. McKenna, G.L. Fenves, M. H. Scott, *Open system for earthquake engineering simulation: OpenSees.* Pacific Earthquake Engineering Research Center (PEER), University of California, Berkeley, 2008.

[14] C. Harden, T.C. Hutchinson, G. R.Martin, B. L Kutter, B. L, *Numerical modeling of the nonlinear cyclic response of shallow foundations. Report no. PEER-2005/04*, Pacific Earthquake Engineering Research Center (PEER), 2005.

[15] R. W. Boulanger, The QzSimple1 material. *Document for the OpenSees Platform,* 2003.

[16] ASCE (2000). *Prestandard and commentary for the seismic rehabilitation of buildings (FEMA 356)*: Federal Emergency Management Agency, Washington, D.C.

[17] Y. Boivin, P. Paultre, Seismic force demand on ductile reinforced concrete subjected to Western North American ground motions: Part 1 – parametric study. *Canadian journal of civil engineering*, **39**, 723-727, 2012.

[18] M.J.N Priestley, Does capacity do the job? Examination of higher mode effects in cantilever walls. Bulletin of New Zeeland Society fo Earthquake Engineering, **36:4**, 276-292, 2003.

[19] A. Rutenberg, E. Nsieri, The seismic shear demand in ductile cantilever wall systems and the EC8 provisions. *Bulletin of Earthquake Engineering* **4**,1–21, 2006.

[20] Y. Boivin, P. Paultre, Seismic force demand on ductile reinforced concrete subjected to Western North American ground motions: Part 1 – mew capacity design methods. *Canadian journal of civil engineering*, **39**, 738-750, 2012.

[21] I. Ghorbanirenani, R. Tremblay, P. Léger, M. Leclerc, Shake table testing of slender RC shear walls subject to Eastern North America seismic gound motions. *ASCE Journal of structural engineering*, **138:12**, 1515-1529, 2012.

COMPDYN 2013
4th ECCOMAS Thematic Conference on
Computational Methods in Structural Dynamics and Earthquake Engineering
X.L. Dang, Y. Zhou, X.L. Lu
Kos Island, Greece, 12–14 June 2013

SEISMIC PERFORMANCE OF PRE-STRESSED SHEAR WALLS WITH BOTTOM HORIZONTAL SLITS AND BUCKLING RESTRAINED REINFORCEMENT

Xiangliang Dang[1], Ying Zhou[2], Xilin Lu[2]

[1]College of Civil Engineering, Tongji University,
Shanghai 200092, China
11dangxiangliang@tongji.edu.cn

[2]State Key Laboratory of Disaster Reduction in Civil Engineering, Tongji University,
Shanghai 200092, China
yingzhou@tongji.edu.cn
lxlst@tongji.edu.cn

Keywords: Pre-stressed shear walls, bottom horizontal slits, buckling restrained reinforcement, seismic performance, cyclic loading.

Abstract. *The research on seismic behavior of rocking structures with bottom horizontal slits got increasingly attention in recent years. The rocking structures could concentrate the deformation at the bottom slits and use the unbounded pre-stressed tendon to provide self-centering ability. Thus the residual deformation is small and the main structure is protected. This paper researches on the seismic behavior of a new-type pre-stressed shear wall with buckling restrained reinforcement. ABAQUS models are built to study the performance influence of the bottom slits length, slits height, and the number of buckling restrained reinforcement under quasi-static reversed cyclic loading conditions. The comparison is made between the behavior of the new-type walls and the traditional rocking structures. All these walls display a characteristic "flag-shape" hysteretic response. And the walls with buckling restrained reinforcement exhibit higher energy-dissipating ability than the traditional rocking walls do and also higher in lateral capacity. The results indicate that the new-type walls exhibit excellent self-centering property, energy-dissipating ability and the ability of protecting the main structure from being damaged.*

1 INTRODUCTION

Pre-stressed shear walls gain their lateral strength and desirable seismic properties through the utilization of vertical unbounded post-tensioning. In-plane cyclic loading of a pre-stressed shear wall results in a horizontal crack forming at the wall-foundation interface. This leads to rocking behavior which means large drift capacity and reduction of the wall damage, with the wall returning to its original vertical alignment, known as the self-centering ability, provided that sufficient pre-stress remains in the tendons at the end of loading. Existing research on the cyclic and dynamic response of pre-stressed shear walls has demonstrated these characteristics [1,2,3].

The wall toes usually suffer drastic damage after the earthquake as undergoing highest moment and largest strain in the structure. For this reason, this paper replaces wall toes [4] of the pre-stressed shear wall with the energy dissipaters.

Energy dissipaters are frequently used in the pre-stressed shear wall systems to dissipate the seismic energy and to protect the wall from being damaged. In this paper, the buckling restrained reinforcement (BRR) is imported to act as the energy dissipater. The idea of the buckling restrained reinforcement comes from the widely use of buckling restrained brace, known as BRB, which can restrain almost the same compressive loading as well as tension loading without buckling. Results from an experiment program [5] showed that BRBs exhibit ductile, stable and repeatable hysteretic behavior and are suitable for dissipating seismic energy.

In this new type wall, rectangular slits are set at the wall toes and the BRRs are placed vertically inside the slits. There is a horizontal crack at the wall-foundation interface and pre-stressed tendons are used to provide self-centering ability. The sketch of the pre-stressed shear walls with bottom horizontal slits and BRRs is shown in Figure 1.

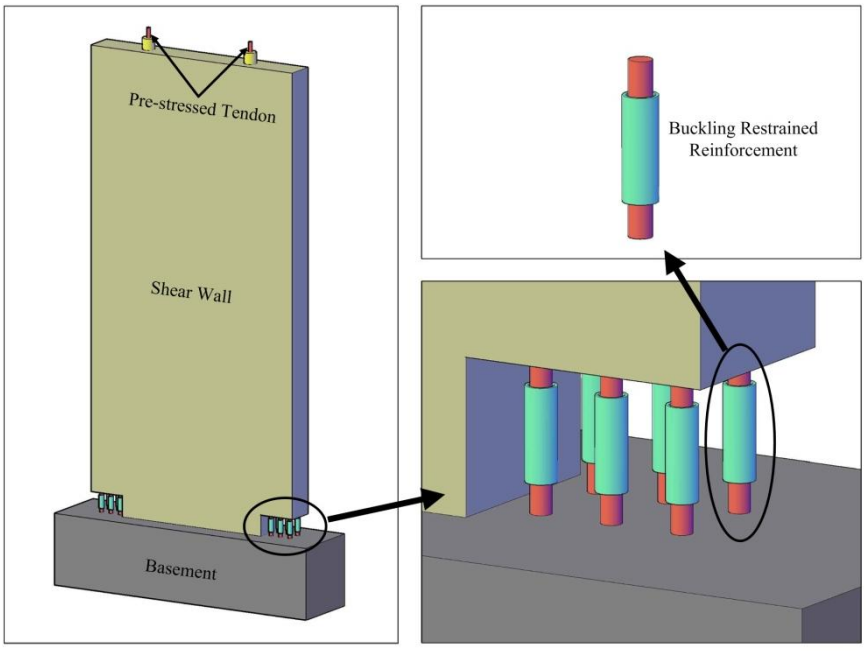


Figure 1: Sketch of the pre-stressed shear wall with bottom slits and BRRs

2 FINITE ELEMENT MODELING

2.1 Modeling method

The finite element software ABAQUS is employed here to investigate the cyclic loading behavior of the new type walls. The concrete is modeled using solid element and meshed as C3D8R while the reinforcement is modeled using truss element. Then the reinforcement mesh is embedded in the whole model to act together with the concrete material. The BRR element applies truss element as well, and end nodes of BRR are bonded to the concrete nodes.

Modeling of the horizontal joint during wall rocking is essential for pre-stressed shear wall systems. A specific contact property is used between the wall base and foundation. In the horizontal direction, it is assumed that no slip would occur between two points once in contact [6], and "hard contact" is adopted in the vertical direction.

This paper uses nonlinear spring element in the ABAQUS to simulate the unbounded post-tensioning tendon. The spring element is set by the means of spring stiffness, *K*, which is calculated as follow equation:

$$K = \frac{F}{S} = \frac{\sigma A}{\varepsilon l} = \frac{EA}{l} \tag{1}$$

Where *l*=length of the pre-stress tendon; *E*=modulus of elasticity; *A*=area of the pre-stress tendon; *F*= force in the pre-stress tendon; *S*= deformation in the pre-stress tendon.

Then the force-displacement curve of the unbounded post-tensioning tendon is obtained by knowing the yield stress and modulus of elasticity, shown in Figure 2:

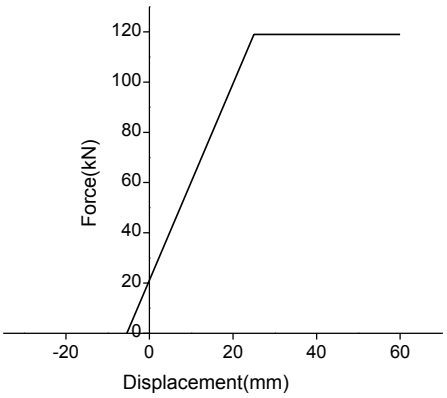


Figure 2: Displacement-force curve of a post-tensioning tendon

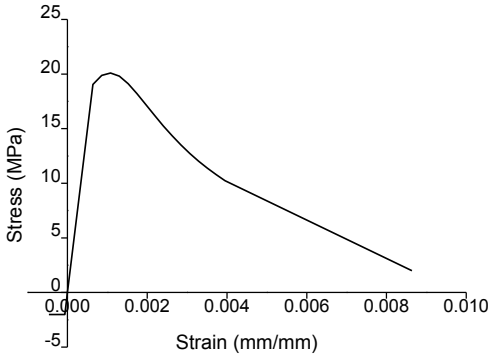


Figure 3: Uniaxial stress-strain relationship of concrete

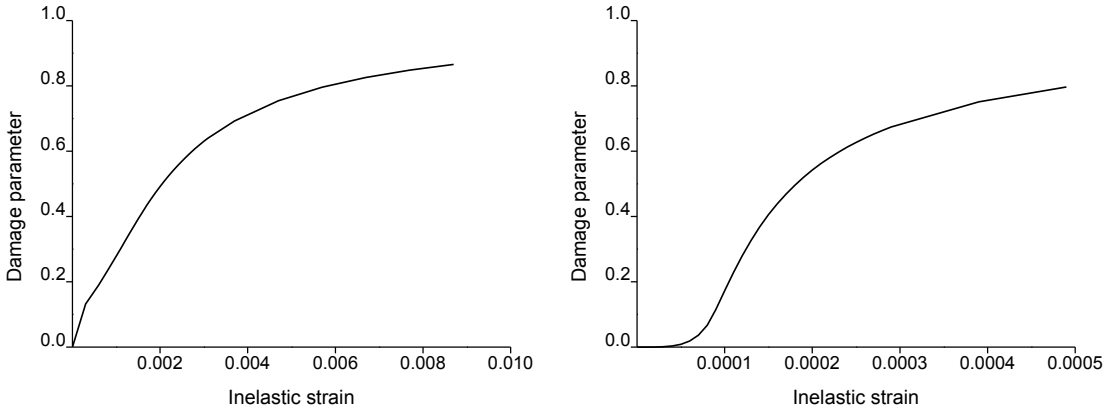
2.2 Material properties

The "concrete damaged plasticity model" is used to predict plastic concrete bebavior for axial tension or compression. Figure 3 shows the uniaxial stress-strain relationship of the concrete used in this paper with a compressive strength of 20.1MPa and tensile strength of

2.01MPa. The tensile strength is capped at the maximum value and no strain softening is permitted to prevent convergence issues [2].

Damage parameters should be defined in the "concrete damaged plasticity model", and these parameters are obtained according to "Code for design of concrete structures" [7] in China. The relationship of inelastic strain and damage parameters for compression and tension of concrete is shown in Figure 4. The damage parameter values range from 0 to 1, and larger value of parameter means more damage in concrete [8].

The steel constitutive relationship applied two-line relationship including the longitudinal steel bars and the distribution bars, with the yield stress of 335MPa. The yield stress used in the BRR element is 225MPa, and the material used in BRRs has long yield plateau which means perfect energy dissipating ability.



(a) Compression (b) Tension

Figure 4: Relationship of concrete inelastic strain and damage parameter

2.3 Model details

Eight finite element models in ABAQUS software are built to study the behavior of the walls with bottom horizontal slits and buckling restrained reinforcement. Slits length, slits height and quantity of BRRs are parameters studied in this paper. All of the walls undergo at most 3% drift, which is 96mm, in the analysis. In these models, RW1-0 is the wall without any slits or BRRs. Sectional reinforcement details are shown in Figure 5.

Model number	Slits length/mm	Slits height/mm	Quantity of BRRs
RW1-0	0	0	0
PW1-1	200	80	6
PW1-2	250	80	6
PW1-3	300	80	6
PW2-1	200	40	6
PW2-2	200	120	6
PW3-1	200	80	4
PW3-2	200	80	8

Table 1: Parameters of models

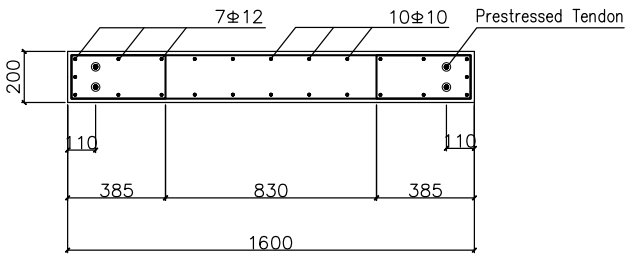


Figure 5: Reinforcement details of models

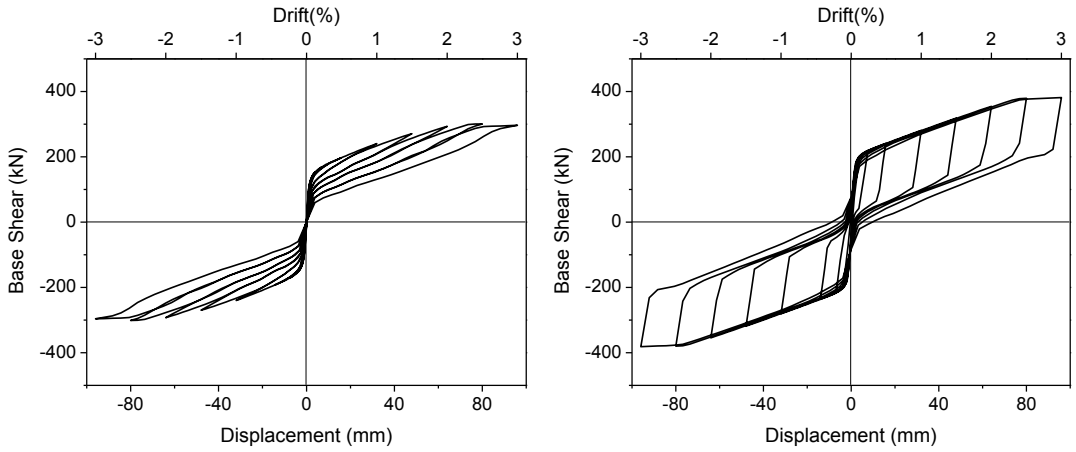
3 ANALYSIS RESULTS

Force-displacement curves under cyclic loading are obtained from the finite element analysis and displayed below. Differences could be found in these figures as the parameter changes.

3.1 Slits length

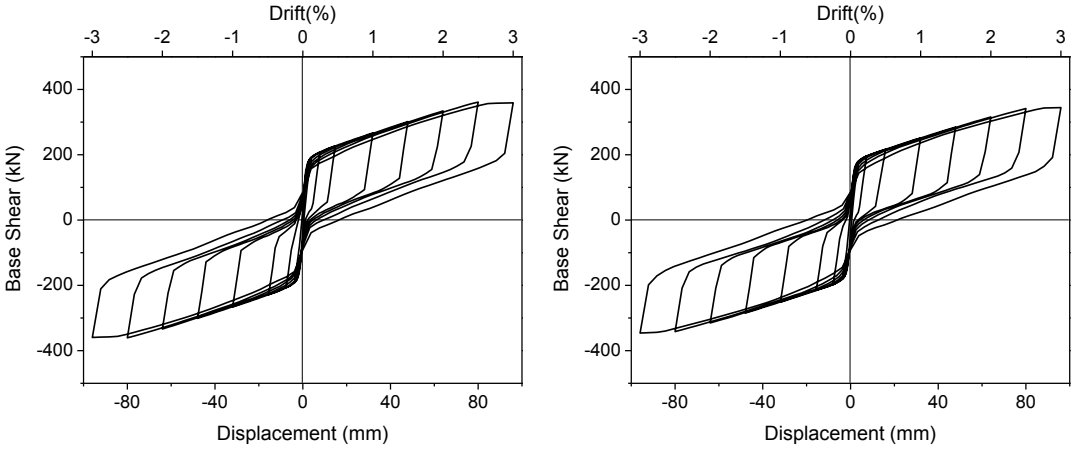
As can be seen from these force-displacement curves, all these walls display a characteristic "flag-shape" [9] hysteresis response, and the lateral capacity of the wall grows slowly when the slits length decrease except RW1-0 which has no slits or BRRs. It is because that the absence of the wall toe may reduce the resisting moment provided from wall base. The larger slits length is, the lower lateral capacity becomes. However, the lateral capacity of the rocking wall is lowest because there are no BRRs to provide extra tensile force at the wall toe.

There is obvious difference in the residual drift as the slits length changes although envelop area of the curves remains almost the same. Larger slits length results in more residual drift, which could be explained by knowing that more plastic deformation occurs in the wall base under the vertical loading when the slits length increases.



(a) RW1-0

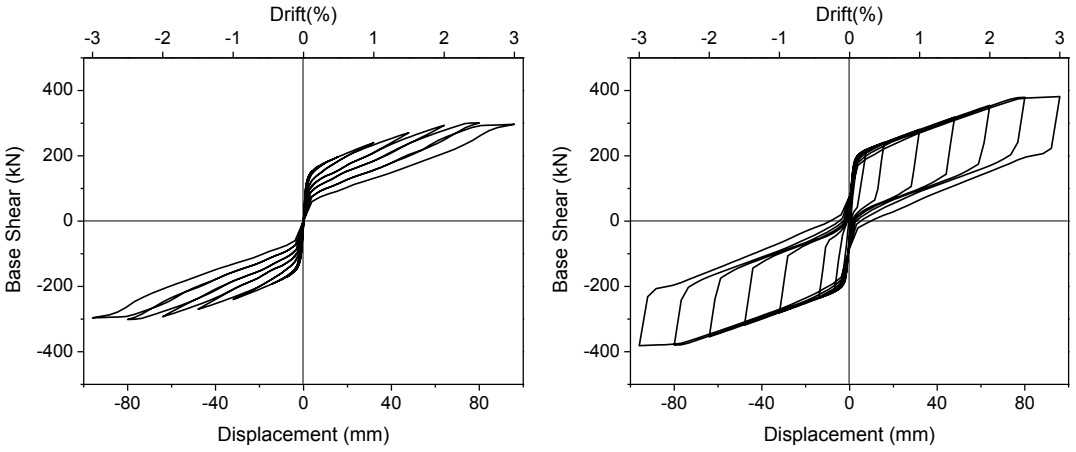
(b) PW1-1



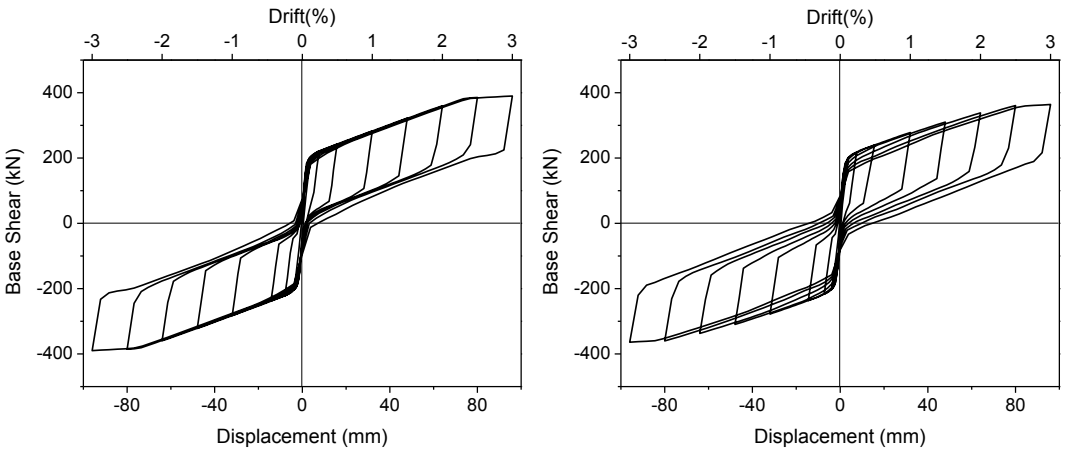
(c) PW1-2 (d) PW1-3

Figure 6: Force-displacement relationship under different slits length

3.2 Slits height



(a) RW1-0 (b) PW1-1



(c) PW2-1 (d) PW2-2

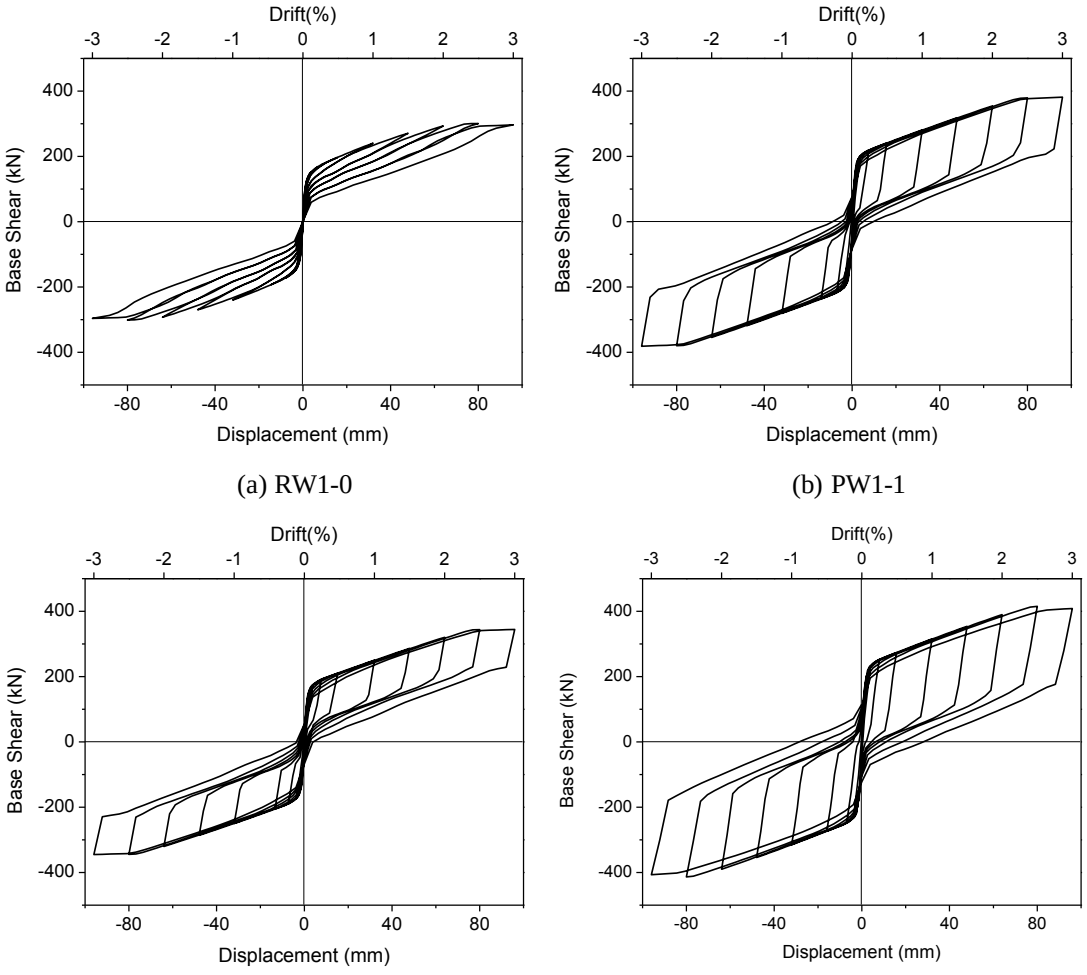
Figure 7: Force-displacement relationship under different slits height

There is no obvious difference of lateral capacity between the curves in Figure 7 when the slits height increases except that RW1-0 exhibits a little lower lateral capacity because of the absence of the wall toe. However, the residual drift become larger as the slits height grows. The reason lies that larger slits height results in more damage in the wall concrete, which causes larger residual drift in the hysteresis curves.

3.3 Quantity of BRRs

As expected beforehand, large quantity of BRRs leads to large envelope area of curves as the BRRs are main energy dissipation members in the pre-stressed shear wall systems. And high lateral capacity is benefited from BRRs because of the extra tensile force that mentioned in section 3.1.

However, use of BRRs not only results in better energy dissipation ability but also leads to larger residual drift. So the quantity of BRRs should depend on the design object of structural system.



(a) RW1-0 (b) PW1-1

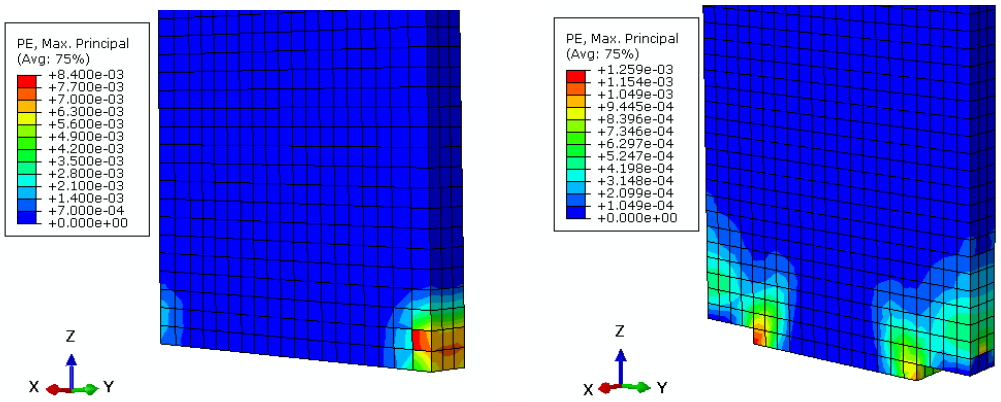
(c) PW3-1 (d) PW3-2

Figure 8: Force-displacement relationship under different quantity of BRRs

3.4 Strain in the wall toe

Two strain contours of the concrete in the walls are displayed here to ensure the contribution made from the BRRs. The wall RW1-0 and PW1-3 are chosen to represent the walls with and without slits. And the figures display the strain state at the drift of 1.5% which is 48mm.

As can be seen from the figures, the maximum plastic strain of concrete in RW1-0 is larger than that in PW1-3, which means less damage observed in the concrete of wall with bottom horizontal slits. The reason is that utilization of BRRs in the wall toe dissipate the seismic energy inputted to the wall system, thus protect the concrete material from being damage severely.



(a) RW1-0 (b) PW1-3

Figure 9: Plastic strain contour of the concrete

4 CONCLUSIONS

- Pre-stressed shear wall with bottom horizontal slits and buckling restrained reinforcements (BRRs) shows a "flag-shape" hysteretic response, which means good self-centering ability is achieved for this new type wall.
- The increase in slits length, slits height and quantity of BRRs results in the growth of residual drift for the wall under cyclic loading.
- The envelop area of the hysteresis curves is largely influenced by the quantity of BRRs. More BRRs provide better energy dissipating ability as well as increase in the lateral capacity.
- By using bottom horizontal slits and BRRs in the wall toe, plastic strains of the concrete are largely reduced and severe damage of the wall is avoided.

REFERENCES

[1]Y.C. Kurama, *Seismic analysis, behavior, and design of unbounded post-tensioned precast concrete walls*. Lehigh University, May, 1997.

[2]R.S. Henry, *Self-centering precast concrete walls for buildings in regions with low to high seismicity*. University of Auckland, June, 2011.

[3]Y. Zhou, X.L. Lu, State-of-the-art on rocking and self-centering structures. *Journal of Building Structures*, **32(9)**, 1-10,2011. (in Chinese)

[4]X.L. Lu, Y. Chen, Y.J. Mao, New concept of structural seismic design: earthquake resilient structures. *Journal of Tongji University(Natural Science)*, **39(7)**, 941-948, 2011. (in Chinese)

[5]C. Black, N. Makris, A. Ian, Component testing, seismic evaluation and characterization of buckling-restrained braces. *Journal of Structural Engineering*, **130(6)**, 880-894, 2004.

[6]G.D. Wight, J.M. Ingham, Tendon stress in unbounded posttensioned masonry walls at nominal in-plane strength. *Journal of Structural Engineering*,**134(6)**, 938-946, 2008.

[7]Ministry of Construction of the People's Republic of China, *Code for Design of Concrete Structures(GB 50010-2010)*. China Architecture & Building Press. Beijing, 2010. (in Chinese)

[8]Hibbitt, Karlsson & Sorensen,INC, *ABAQUS/Standard user's manual*. USA, 2000.

[9]B. Erkmen, A. Schultz, Self-centering behaviour of unbounded, post-tensioned precast concrete shear walls, *Journal of Earthquake Engineering*, **13(7)**, 1047-1064, 2009.

COMPDYN 2013
4th ECCOMAS Thematic Conference on
Computational Methods in Structural Dynamics and Earthquake Engineering
M. Papadrakakis, N.D.Lagaros, V. Plevris (eds.)
Kos Island, Greece, 12–14 June 2013

LOCAL EFFECTS IN THE SEISMIC DESIGN OF RC FRAME STRUCTURES WITH MASONRY INFILLS

S. Hak[1], P. Morandi[2], and G. Magenes[2]

[1] University of Pavia
Via Ferrata 1, Pavia, Italy
shak@roseschool.it

[2] University of Pavia and EUCENTRE
Via Ferrata 1, Pavia, Italy
paolo.morandi@unipv.it, guido.magenes@unipv.it

Keywords: Local Effects, RC Frames, Masonry Infills, Shear Design, Nonlinear Analyses.

Abstract. *For the prevention of local effects that may occur on the load-bearing elements of newly designed masonry infilled RC frames, additional measures are foreseen in modern seismic design codes. In particular, European code regulations impose special detailing and confinement requirements for structural elements in RC frames with adherent masonry infills. Moreover, the verification of adjacent columns for increased shear demands is required, estimated based on approximate values of horizontal shear strength of the infill, and through the application of capacity design principles along the contact length. With the aim to verify the efficiency of the current design approach and provide additional recommendations related to local effects due to the presence of masonry infills in RC frames, in this study a series of nonlinear dynamic analyses on typical newly designed building configurations with different masonry infill typologies of varying strength and stiffness properties has been performed at increasing levels of seismicity. The analyses are carried out using a simple numerical model representing the masonry infill as a single diagonal strut. Although such model cannot directly capture the local effects in the contact region, it allows, a posteriori, the calculation of effective shear demands on the columns. For a number of considered prototype buildings, a comparison of effective shear demands obtained from analyses and shear design forces required by the code has been carried out. Furthermore, a simplified procedure for the verification of columns in RC frames exposed to increased shear demands due to the presence of masonry infills as a function of expected inter-storey drift demands has been proposed. Hence, starting from existing code recommendations, the given method allows the evaluation of shear design forces in compliance with effective shear demands, accounting for different masonry infill typologies, the position of the infill along the height of the building and the seismic ground motion intensity.*

1 INTRODUCTION

The possible occurrence of local effects on structural elements of RC frames with masonry infills is widely recognized and has repeatedly been supported by field evidence from recent earthquake events in Italy. After the April 2009 earthquake in Abruzzo (L'Aquila), extensive damage has been reported on non-structural masonry infills, see *e.g.* [1]; moreover, in many cases the poor behaviour or even failure of structural elements in RC frames has been identified [2], often caused by adverse effects due to the presence of masonry infills. Also following the most recent seismic event that has stroked the region of Emilia in May 2012, examples of local effects on the structural elements of infilled frames have been reported [3, 4, 5], as illustrated in Figure 1.



Figure 1: Examples of local effects reported after the May 2012 Emilia earthquake
a) Magenes *et al.* 2012 [3]; b) Manzini and Morandi 2012 [4].

In particular, local damage and eventually brittle failure can commonly be caused on columns that are in partial contact with masonry infill walls, causing a reduction of the clear height of the column and, hence, inducing increased shear and displacement demands. As discussed in previous studies [6], the problem of laterally restrained captive columns, particularly vulnerable to seismic actions, should possibly be pursued through adequate measures in the conceptual design of new buildings. However, detrimental effects on columns of RC frame structures can be caused by the interaction with masonry infills also in the case of full contact along the height of the column, in particular when masonry infill typologies of high strength and stiffness properties are used in construction, and/or when the infill is located only on one side of the column. Specifically, additional concentrated shear demands may be imposed on the column at its ends in the region of contact with the masonry infill due to the activation of compressive diagonal strut forces. For the prevention of such local effects in newly designed structures, with infills adherent to the RC frame, additional measures are foreseen in modern seismic design codes, such as Eurocode 8 – Part 1 [7].

The application of the recommended simplified approaches to practical design cases reveals, however, the fact that increased shear design forces are imposed independently of the design conditions and of the position of the structural element in the building, even though the corresponding column shear may vary significantly. In this study the current European design provisions for RC frames have been applied to a number of prototype building configurations, including the additional measures for infilled structures by means of increased shear design forces, capacity design principles and detailing rules, in order to detect the governing design situations for different peak ground accelerations and design ductility classes. Subsequently, a

number of nonlinear time-history analyses of the RC frames with masonry infills of increasing strength and stiffness properties has been carried out, with the aim of determining effective shear demands imposed on the columns and to propose improved shear design verifications as a function of in-plane drift demands imposed on the structure.

2 DESIGN FOR THE PREVENTION OF ADVERSE LOCAL EFFECTS

2.1 Current European Design Provisions

According to current European provisions for the design of structures for earthquake resistance Eurocode 8 – Part 1 [7], besides irregularities in plan and elevation due to the presence of infills that may adversely influence the global behaviour of RC frames, possible local effects due to the frame-infill interaction need to be taken into account. Therefore, special detailing and confinement requirements for structural elements in RC frames with adherent masonry infills, as well as a verification of the adjacent columns for approximate increased shear demands are imposed. Specifically, due to the particular vulnerability of infills in the ground floor, where seismically induced irregularity may be expected, if a more precise method is not used, the entire length of all columns should be considered as critical region (Figure 2a) and consequently, the relevant confinement and detailing rules have to be satisfied. The same requirement applies in the case when infills extend over the entire column height l_t, but only on one side of the column (Figure 2b), as well as for columns which are in contact with adjacent infills along just a part of their total height l_t (Figure 2c), inducing the presence of a clear portion of the column height $l_{cl} < l_t$. In this latter case, the consequences of the decreased shear span of the column due to the horizontal restraint by the infills (Figure 3) should be covered in addition. Therefore, the shear demand has to be determined from the provided column resistance $M_{C,Rd}$ following the capacity design principle applied over the clear height l_{cl} (Equation 1), adopting an overstrength coefficient γ_{Rd} = 1.1 for ductility class medium (DCM) and γ_{Rd} = 1.3 for ductility class high (DCH).

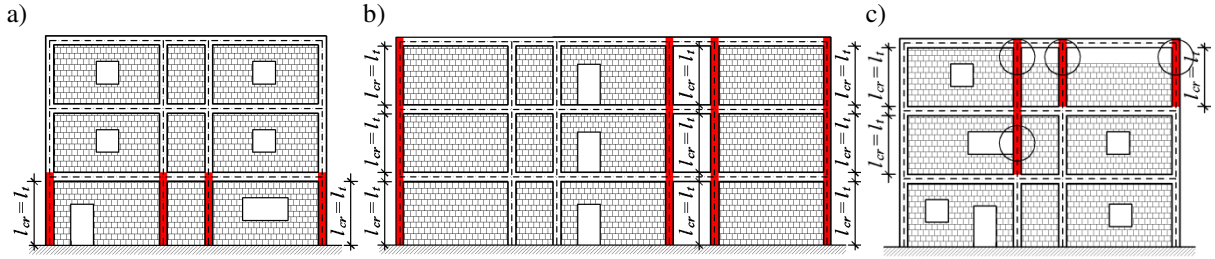


Figure 2: a) Critical length of columns in the ground floor;
b) Critical length of columns in full contact with the infill on one side;
c) Critical length of columns in partial contact with the infill.

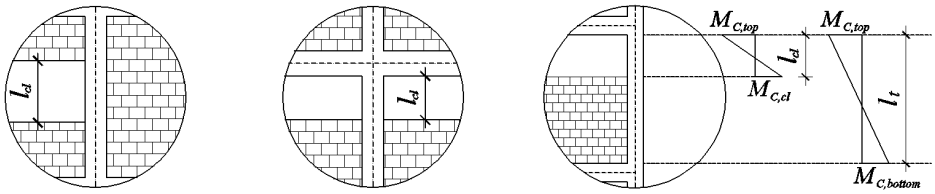


Figure 3: Decreased column shear span ratio due to partial contact with the infill

$$V_{Ed,cl} = \gamma_{Rd} \frac{2M_{C,Rd}}{l_{cl}} \tag{1}$$

Further safety verifications present in the European code regulations rely upon the common simplification of the masonry infill action based on an equivalent strut model, representing the diagonal portion of the infill by a compressive strut. The requirement that is of particular interest for this study indicates that the contact length l_c of the column, over which the diagonal strut force of the infill acts on the column causing a local pressure f_s and introducing a concentration of forces (Figure 4a), should be verified in shear for the smaller of the following two shear forces:

a) the horizontal component $F_{w,s,hor}$ of the diagonal strut force $F_{w,s}$ of the infill, that can be assumed to be equal to the shear strength of the panel;
b) the shear force $V_{C,Ed}$ determined following the capacity design principle (Equation 2), assuming that the flexural column capacity develops at the ends of the contact length l_c (Figure 4b).

$$V_{C,Ed} = \gamma_{Rd} \frac{2M_{C,Rd}}{l_c} \tag{2}$$

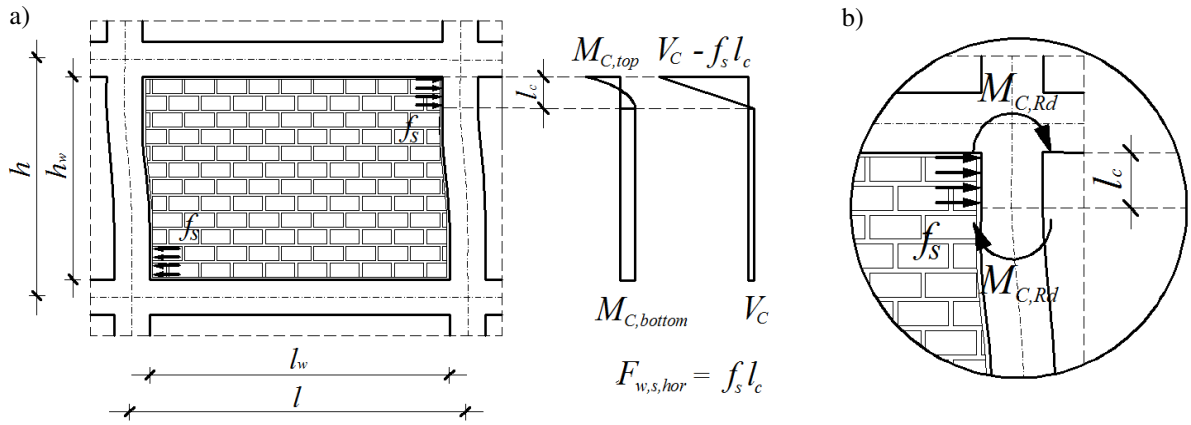


Figure 4: a) Application of the diagonal strut action on the column within the contact length; b) Flexural column capacity developed at the ends of the contact length

2.2 Interpretation of Design Requirements

According to the code, the horizontal component $F_{w,s,hor}$ of the diagonal strut force $F_{w,s}$ can be assumed to be equal to the horizontal shear strength of the panel, estimated on the basis of the shear strength of bed joints. Since no explicit recommendations related to the evaluation of the shear strength of the bed joints are specified in the code, it could be reasonable to use the expression included in the Eurocode 6 – Part 1 [8], commonly assumed for load-bearing masonry walls, considering the shear strength of the bed joints equal to the initial shear strength under zero compressive stress f_{v0}. Hence, for a masonry infill of thickness t_w, length l_w and shear strength $f_v = f_{v0}$ the corresponding horizontal strength $F_{w,s,hor,1}$ may be estimated as given in Equation 3.

$$F_{w,s,hor,1} = f_{v0} t_w l_w \tag{3}$$

A number of more refined models for the evaluation of the masonry infill strength and corresponding equivalent diagonal strut forces is available. Some of these models are able to account for different failure mechanisms typically observed on masonry panels and usually supported by experimental studies, *e.g.* as proposed by Decanini *et al.* [9] for compression at

the centre, compression at the corners, shear sliding and diagonal tension. The horizontal component of the corresponding equivalent strut strength $F_{w,s,hor,2}$ can be expressed by Equation 4, where f_m' indicates the strength associated with the critical failure mode, t_w the thickness of the infill, b_w the width and θ the inclination of the equivalent strut.

$$F_{w,s,hor,2} = f_m' t_w b_w \cos\theta \tag{4}$$

The evaluation of local shear design forces can eventually be influenced by the choice of the contact length l_c, over which the diagonal strut force of the infill acts on the column, since applying the capacity design principle given in Equation 2, for larger values of contact length lower shear demands $V_{C,Ed}$ are obtained and may be governing with respect to the horizontal strength of the panel $F_{w,s,hor}$. As specified in the code, unless a more accurate estimation is made taking into account the elastic properties and the geometry of the infill and the column, the strut width may be assumed to be a fixed fraction of the length of the panel diagonal. Paulay and Priestley have suggested that a conservatively high value of the diagonal strut width b_w equal to one quarter of the panel diagonal d_w may be assumed [10]. However, for the definition of the equivalent strut width a series of more refined approaches are available in literature. For instance, according to the model proposed by Decanini *et al.* [9], the equivalent strut width is evaluated as a function of a relative stiffness parameter to account for the interaction between the frame and the infill. A similar approach is adopted in Mainstone's model [11], suggested also in other studies, and recommended *e.g.* in the work by Fardis for the application of design provisions according to Eurocode 8 [6]. Even though it is stated in the code that the contact length should be assumed to be equal to the full vertical width of the diagonal strut of the infill b_w, this requirement should be interpreted depending on the strut model that is being adopted and the corresponding failure modes considered. Herein, the contact length has been evaluated following the model by Paulay and Priestley [10] and Decanini *et al.* [9], assuming the contact length equal to $0.5b_w/\cos\theta$ (see Figure 5a) and according to the model by Mainstone [11], assuming the contact length equal to $b_w/\cos\theta$ (see Figure 5b).

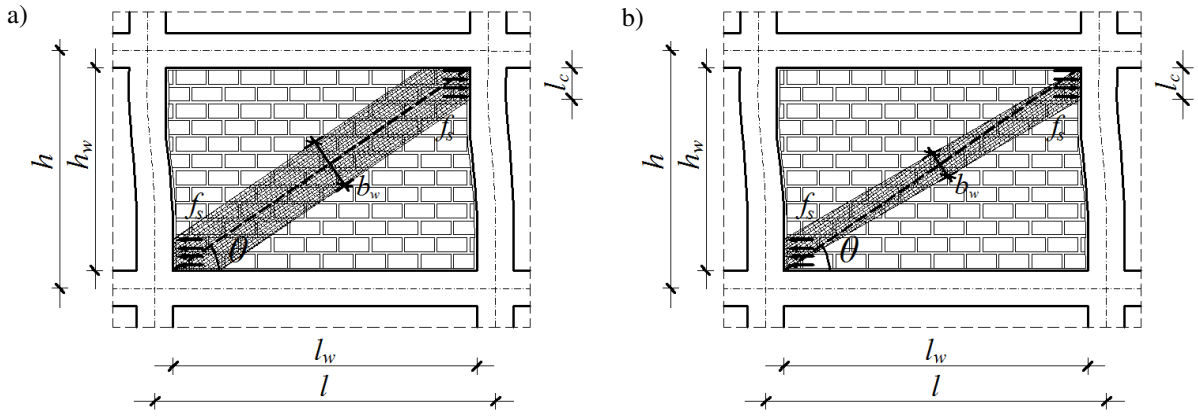


Figure 5: Evaluation of the contact length: a) $l_c = 0.5b_w/\cos\theta$; b) $l_c = b_w/\cos\theta$

3 NUMERICAL STUDY

3.1 Design and Modelling Assumptions

For the needs of this study, as part of a wider analytical campaign, a number of numerical analyses has been carried out on different typologies of RC frames, newly designed according to current European (Eurocode 8 – Part 1 [7]) and Italian national code provisions (NTC08

[12]). Specifically, 3-storey, 6-storey and 9-storey frames have been considered, designed for two different ductility classes, namely medium (DCM) and high (DCH), and five different design peak ground accelerations, *i.e.* 0.05g, 0.10g, 0.15g, 0.25g and 0.35g, resulting in 30 different bare frame configurations. A more detailed description of the frame design procedure is given in the work by Morandi *et al*. [13].

In summary, as recommended in the code provisions for the design of regular structures, the design has been carried out for bare frame configurations, based on linear analyses of elastic models, satisfying capacity design principles, strength and ductility requirements as well as displacement limitations. Subsequently, time-history analyses have been carried out on nonlinear models of the infilled frame typologies, using the structural analysis program Ruaumoko [14], adopting the concentrated plasticity modelling approach for structural elements and representing the masonry infills by a simple single-strut model. Even though in such simplified model the local effects due to the presence of masonry infills cannot be captured directly, induced effective column shear demands have been evaluated a posteriori from the diagonal strut force. In order to evaluate the strength and stiffness properties of the equivalent strut, the model proposed by Decanini *et al.* [9] has been adopted, while the hysteretic rule introduced by Crisafulli [15] has been calibrated on experimental test results and used to model the nonlinear cyclic behaviour of the infill. The local effects have been studied on the external columns of fully infilled frame typologies for three different types of masonry infills with increasing strength and stiffness properties, representing weak (T1), medium (T2) and strong infill (T3). Further details on the modelling assumptions and the considered masonry infill typologies are given in the work by Hak *et al.* [16].

3.2 Column Shear Design Forces

The shear design procedure complying with the provisions given in Eurocode 8 [7] has been applied to the columns of the considered case study frames, showing that in some cases the detailing rules, imposed to attain satisfactory local ductility in critical regions of primary seismic elements, may require transversal reinforcement amounts resulting in values of shear resistance high enough to satisfy also the recommended shear demands imposed due to local effects, evaluated from Equation 2 or Equation 3, whichever is governing. In order to represent a typical set of results, the shear demands evaluated for the external columns at the first and at the last storey of the 6-storey case study frames are summarised in Table 1. In particular, the shear demands indicated as *w/o* local effects have been evaluated for the case when only action effects obtained from linear analyses on an elastic model of the bare frame and global capacity design principles are considered, while local effects due to the presence of infills are neglected. The shear demands obtained for the case when local effects are taken into consideration following the code recommendation, determined as the minimum of the values obtained from Equation 2 and Equation 3, is indicated as *w/* local effects. The provided column shear resistance has been calculated based on shear design for obtained action effects, global capacity design verifications and local ductility requirements in the critical region of the column, as commonly performed for bare frames. The shear demand imposed due to local capacity design requirements (Equation 2) has been verified assuming the simplified approach for the evaluation of the contact length based on the strut width recommended by Paulay and Priestley [10]. The strut force of the external masonry panel has been evaluated from Equation 3, based on the values of initial shear strength f_{v0} and thickness t_w, as summarised in Table 2 for the considered masonry typologies. The length of the masonry panel l_w varies depending on the dimensions of the adjacent column and can be evaluated subtracting the column width h_c from the centreline span of the external bay of the prototype frame, *i.e.*, $l = 5.0\ m$.

	6-storey		Shear demand Local effects				Column shear resistance			Shear demand Local effects				Column shear resistance
		h_c	*w/o*		*w/*				h_c	*w/o*		*w/*		
				T1	**T2**	**T3**					**T1**	**T2**	**T3**	
PGA	DCM	[*m*]	[*kN*]	[*kN*]	[*kN*]	[*kN*]	[*kN*]	DCM	[*m*]	[*kN*]	[*kN*]	[*kN*]	[*kN*]	[*kN*]
0.05*g*		0.45	202.8	200.2	295.8	409.5	422.6		0.35	96.9	204.6	302.3	331.1	230.0
0.10*g*		0.45	202.8	200.2	295.8	409.5	422.6		0.35	96.9	204.6	302.3	331.1	230.0
0.15*g*	1st st.	0.45	202.8	200.2	295.8	409.5	422.6	6th st.	0.35	96.9	204.6	302.3	331.1	230.0
0.25*g*		0.45	202.8	200.2	295.8	409.5	422.6		0.35	96.9	204.6	302.3	331.1	230.0
0.35*g*		0.50	300.0	198.0	292.5	405.0	535.0		0.40	116.9	202.4	299.0	397.5	323.6
	DCH							DCH						
0.05*g*		0.45	249.1	200.2	295.8	409.5	422.6		0.35	123.7	204.6	302.3	406.8	237.7
0.10*g*		0.45	249.1	200.2	295.8	409.5	422.6		0.35	123.7	204.6	302.3	406.8	237.7
0.15*g*	1st st.	0.45	249.1	200.2	295.8	409.5	422.6	6th st.	0.35	123.7	204.6	302.3	406.8	237.7
0.25*g*		0.45	249.1	200.2	295.8	409.5	422.6		0.35	123.7	204.6	302.3	406.8	237.7
0.35*g*		0.45	249.1	200.2	295.8	409.5	422.6		0.35	123.7	204.6	302.3	406.8	237.7

Table 1: Column shear demands (*w/o* and *w/* local effects) and shear resistance of 6-storey prototype frames

	T1	**T2**	**T3**
f_{v0} [*MPa*]	0.44	0.25	0.30
t_w [*mm*]	0.10	0.26	0.30

Table 2: Masonry infill initial shear strength and thickness

In the case of external columns, the EC8 recommendations state that the critical region should be taken equal to the full height of the column since the infill is present only on one side. It can be noticed that in some cases a high shear resistance may be achieved due to the given detailing requirements in order to obtain the needed ductility in critical regions, or due to the choice of large cross sections required by other design issues, such as the limitation of in-plane displacement demands. Hence, the additional shear demand due to the presence of infills may not always govern the shear design, above all at the bottom storeys of taller buildings and/or in the case of high seismicity. At the same time, however, it can be observed that in the upper storeys, in particular in buildings of lower height and/or in the case of lower or intermediate seismicity, shear demands imposed due to the presence of infills may exceed significantly the values obtained from other design criteria. Following the current design procedure, shear demands induced by local effects due to the presence of infills are determined independently of different design conditions and the position of the infill along the height of the building, although the assumption of equal maximum strut forces for all verifications may not always be rational.

3.3 Nonlinear Analyses Results

In order to determine the variation of possible shear effects, imposed under seismic actions, along the height of a building as a function of the considered design parameters, *i.e.,* design peak ground acceleration, ductility class and building height, nonlinear time-history analyses of the infilled frame models have been performed at different levels of seismicity, corresponding to the considered levels of design peak ground acceleration. The analyses have been carried out for a set of ten scaled natural earthquake records selected matching the average earthquake response spectrum with the design spectrum [13]. Hence, maximum response quantities have been determined for each record and subsequently a corresponding average value has been evaluated. In particular, the maximum horizontal strut actions achieved in the external masonry panels and the maximum effective shear forces on the external columns of each storey of the fully infilled case study frames have been evaluated.

Activated Strut Forces. The average maximum horizontal component of the activated strut force $F_{w,s,hor,act}$, see Equation 5 where i indicates the i-th acceleration record, obtained from analyses for each storey of each prototype frame, for the three considered infill typologies, has been normalised, as given by Equation 6, to the corresponding horizontal resistance of the strut $F_{w,s,hor,2}$, determined from the governing failure mode according to the model by Decanini *et al.* [9] (Equation 4). The percentage of strut force activation a_w and its variation along the building height, for infills in the 6-storey frame typologies, designed for ductility class medium, is shown in Figure 6. The position of the infill along the height of the building is represented by the ratio h_n of the distance from the foundation of the building to the centre of mass of the infill h_w and the total height of the building H as given by Equation 7.

$$F_{w,s,hor,act} = \frac{1}{10}\sum_{i=1}^{10} F_{w,s,hor,\max,i} \tag{5}$$

$$a_w = \frac{F_{w,s,hor,act}}{F_{w,s,hor,2}} \cdot 100 \tag{6}$$

$$h_n = \frac{h_w}{H} \tag{7}$$

A significant reduction of the strut force amplitude can be observed in the upper quarter of the building height. Moreover, the results show clearly the considerable increase of activated strut forces with increasing ground motion intensity. Additionally, a reduction of the strut force activation can be noticed for increasing strength and stiffness properties of the considered masonry infills.

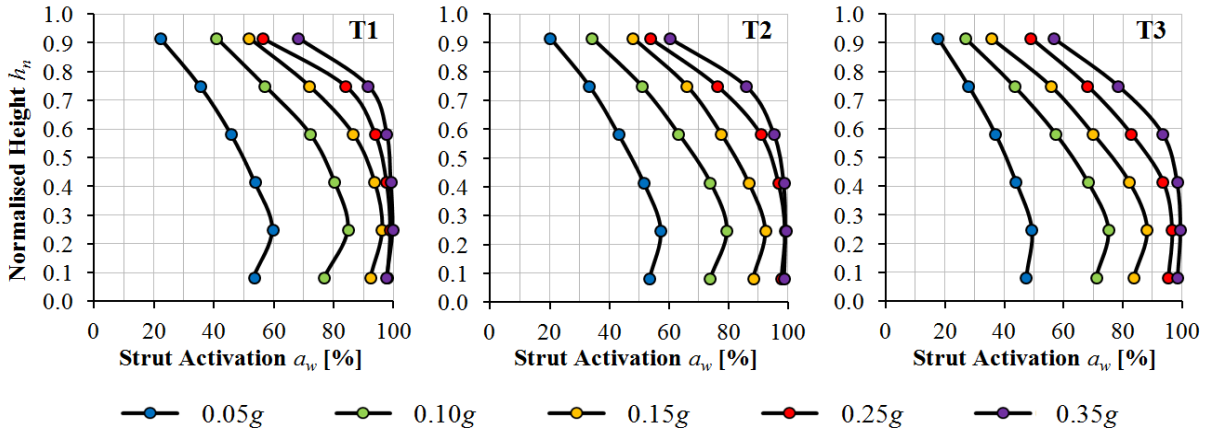


Figure 6: Strut force activation in 6-storey DCM frames

Effective Column Shear Demands. The effective shear demand $V_{w,C}$ imposed on a column due to the strut action (see Figure 4a) can be approximately evaluated a posteriori as the difference between the horizontal component of the activated strut force $F_{w,s,hor,act}$ and the corresponding shear in the column V_C, as given in Equation 8. For the considered prototype frames, the average maximum effective shear demand $V_{w,C,ref}$ imposed on each column has been evaluated from Equation 9.

$$V_{w,C} = \left| F_{w,s,hor,act} - V_C \right| \tag{8}$$

$$V_{w,C,ref} = \frac{1}{10}\sum_{i=1}^{10} V_{w,C,\max,i} \tag{9}$$

The obtained results indicate that the effective column shear demands are regularly slightly lower than the activated strut forces; hence the verification of the column for the activated strut force rather than the effective column shear demand can be considered safe-sided, but not too conservative. In fact, also the code provisions rationally require the verification of the column for the strut force action neglecting the eventual presence of shear forces in the columns, considering the strut, however, always fully activated.

Comparison: Design Shear Forces, Activated Strut Forces, Effective Shear Demands. Summarising the presented results, a comparison of the column design shear forces obtained following the code recommendations, and the shear forces obtained from nonlinear time-history analyses, for two selected case studies, namely the 6-storey fame designed for peak ground accelerations of 0.10*g* and 0.25*g* in ductility class medium, are shown in Figure 7. In particular, as summarised in Table 3, the graphs include shear design forces obtained from locally applied capacity design principles using three different models for the evaluation of the contact length, horizontal strut forces calculated following two different approaches, activated strut forces and effective shear demands from nonlinear analyses and design shear forces that would be imposed due to action effects evaluated from linear analyses and from capacity design principles, without considering any local effects.

		Column shear demand	**Description**
1	$V_{C,Ed}$	Capacity design shear force	Equation 2
		Contact length	l_c - Mainstone [11], Figure 5b
2	$V_{C,Ed}$	Capacity design shear force	Equation 2
		Contact length	l_c - Paulay and Priestley [10], Figure 5a
3	$V_{C,Ed}$	Capacity design shear force	Equation 2
		Contact length	l_c - Decanini *et al.* [9], Figure 5a
4	$F_{w,s,hor,1}$	Horizontal strut resistance (simplified)	Equation 3, Initial shear strength criterion
5	$F_{w,s,hor,2}$	Horizontal strut resistance (refined)	Equation 4, Decanini *et al.* [9]
6	$F_{w,s,hor,act}$	Activated horizontal strut force	Equation 5, from nonlinear analyses
7	$V_{w,C,ref}$	Effective shear demand	Equation 9, from nonlinear analyses
8	$V_{C,Ed,0}$	Design shear demand *w/o* local effects	From linear analysis and global capacity design

Table 3: Design and effective column shear demands

The design shear forces obtained applying the capacity design along the contact length evaluated following the simplified model proposed by Paulay and Priestley [10] vary only due to the difference in moment resistance of adjacent column elements, while the other two models considered for the evaluation of the strut width result in increasing values of shear demands for increasing masonry strength and stiffness. Due to the significant influence of the relative stiffness of frame and infill on the contact length evaluated following the model proposed by Decanini *et al*. [9], the corresponding shear forces are considerably lower compared to the other models, especially where the relative stiffness of the masonry is low compared to that of the frame, as in the case for weak masonry infills and/or in lower storeys, due to larger column dimensions. However, independently of the strut model, the capacity design shear force from Equation 2 in comparison with the simplified horizontal resistance of the strut

from Equation 3, results to be governing only for the strong infill (typology T3) in some of the upper storeys, where columns have smaller dimensions and a lower bending capacity.

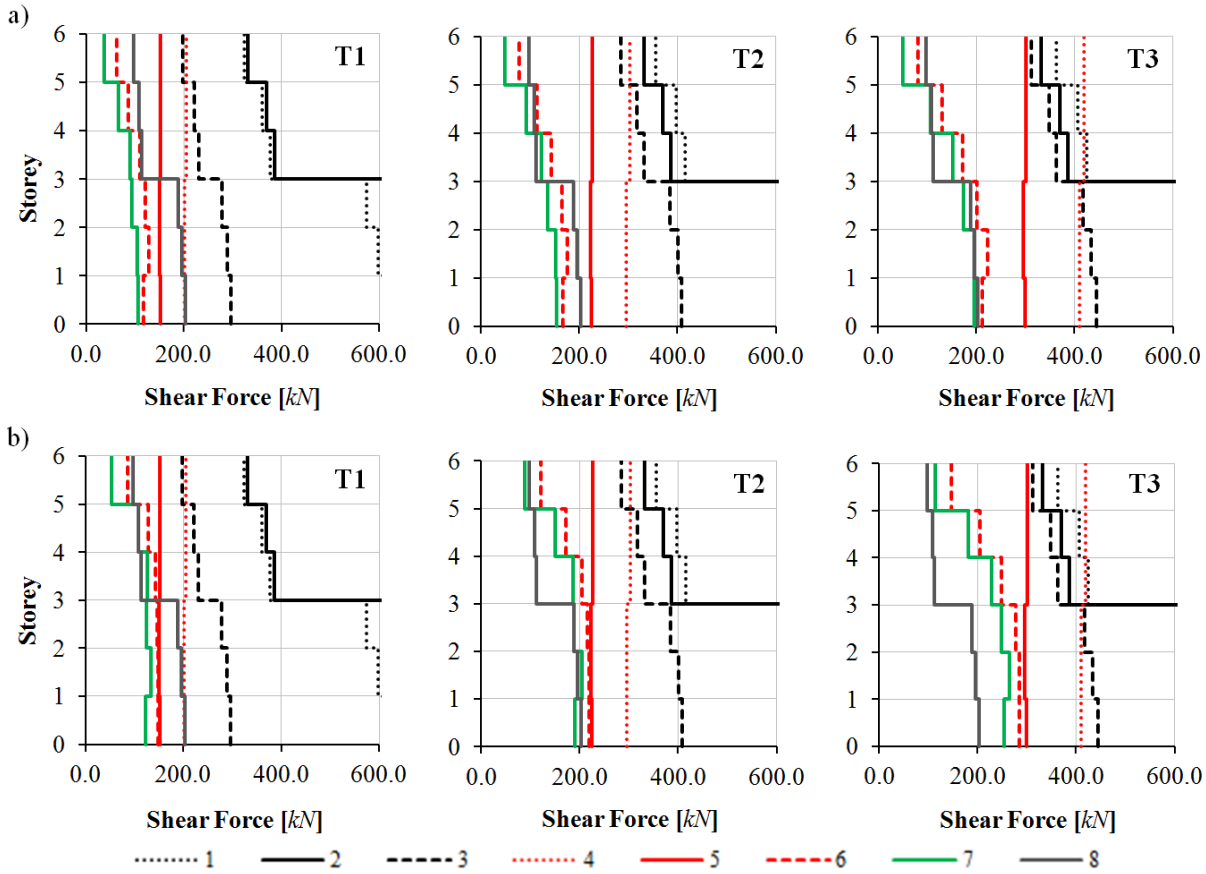


Figure 7: Design shear forces, activated strut forces and effective shear demands for 6-storey frames a) 0.10*g* DCM; b) 0.25*g* DCM

Considering a refined evaluation of the strut resistance, including the possible occurrence of different failure modes, as for example based on the model by Decanini *et al.* [9] (Equation 4), the local shear imposed due to the strut action can be identified as the governing value for all considered case studies. Besides that, such model results in 30-40 % lower values of masonry infill strength compared to the values obtained from the initial strength criterion (Equation 3), depending on the typology. Therefore, it can also be noticed that for all considered infill strength and stiffness properties, the resistance based on the initial shear strength criterion exceeds significantly the effective shear demands on the columns evaluated from time-history analyses based on the more refined infill model. This fact is particularly pronounced if the maximum strut force has been only partially activated, such as in the case of lower earthquake actions, stronger infills and in upper storeys.

4 CONCLUSIONS AND IMPLICATIONS FOR DESIGN

4.1 Shear Demands in Function of Inter-storey Drifts

Having in mind the considerable variation of shear demands imposed due to the presence of masonry infills, the application of a refined procedure for the evaluation of design forces accounting for local effects is envisaged. It can be shown that the activation of the strut force a_w in each storey of the infilled frame, as presented in Figure 6 *e.g.* for varying peak ground

accelerations and infill typologies in the case of DCM 6-storey building configurations, can be expressed as a function of a single parameter, namely the average inter-storey drift demand δ_w imposed on the infilled frame. Accordingly, the complete set of results for all considered prototype frames showing the strut activation obtained from nonlinear time-history analyses can be summarised as given in Figure 8a. The obtained relation can be represented approximately, for example, by polynomial and linear or linear segments, as shown in Figure 8b, and expressed by Equation 10 and Equation 11, respectively. Such simplified expressions may be used in the design of infilled RC frames in order to determine the expected activation of the strut action.

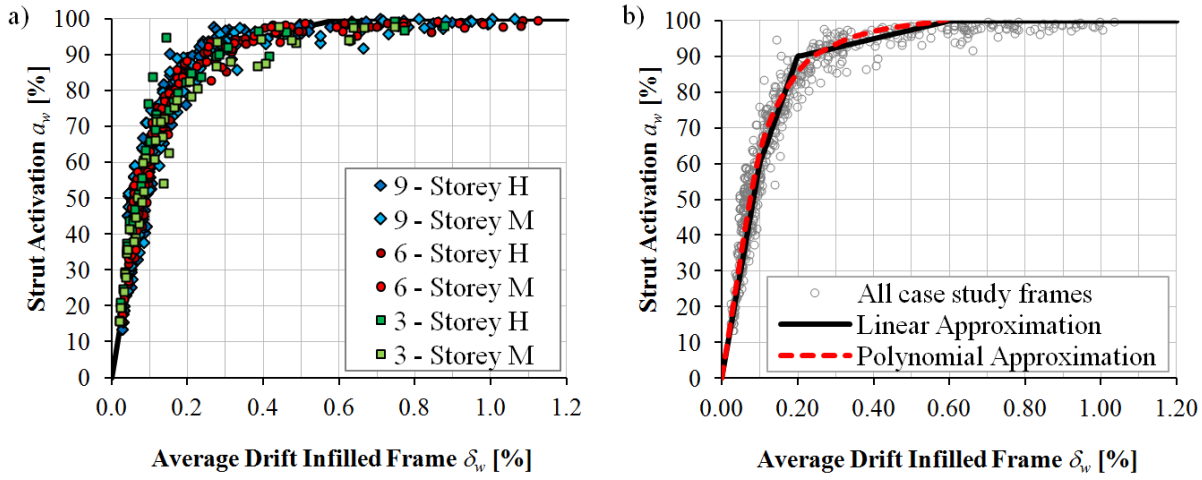


Figure 8: Strut force activation vs. average drift of the infilled frame: a) TH results; b) Possible approximations

$$a_w = \begin{cases} 62.5\delta_w^{\,5} - 126.0\delta_w^{\,4} + 102.5\delta_w^{\,3} - 43.2\delta_w^{\,2} + 9.7\delta_w, & \delta_w < 0.006 \\ 1.0, & \delta_w > 0.006 \end{cases} \tag{10}$$

$$a_w = \begin{cases} 600\,\delta_w, & \delta_w \le 0.001 \\ 300\,\delta_w + 0.30, & 0.001 < \delta_w \le 0.002 \\ 25\,\delta_w + 0.85, & 0.002 < \delta_w \le 0.006 \\ 1.0, & \delta_w > 0.006 \end{cases} \tag{11}$$

4.2 Refined Shear Design for Local Effects

Based on the presented results, a possible refinement of the current design procedure for the evaluation of local effects due to the presence of masonry infills in RC frames may be introduced, assuming that the inter-storey drifts of the infilled frame δ_w can be predicted. Hence, the corresponding expected strut force activation a_w can be evaluated from a simplified expression, such as Equation 10 or Equation 11. Given that the design of regular infilled frame structures is commonly carried out on bare frames, the evaluation of expected drifts of the infilled frame is not a straightforward task and clearly depends, besides on the design properties of the bare frame, such as the building configuration, design seismic action and ductility class, also on the typology and distribution of the masonry infill. Assuming conservatively that the maximum shear demand on the column equals the activated horizontal component of the strut force rather than the effective column shear force (see Equation 8 and Equation 9), the shear demand can be estimated as given in Equation 12.

$$V_{C,Ed} = a_w F_{w,hor} \tag{12}$$

The maximum horizontal strut force $F_{w,hor}$ should possibly be evaluated from a model accounting for different infill failure modes (Equation 4) or may be estimated following other approaches (*e.g.* such given by Equation 3). Finally, the capacity design verification has to be accomplished along the contact length in order to determine the governing shear demand. Even though different values of the contact length l_c can be obtained from different strut models, the design is not significantly influenced by this choice and the application of a simple model, such as assuming the diagonal strut width b_w equal to one quarter of the panel diagonal d_w, as suggested by Paulay and Priestley [10], can be considered satisfactory.

ACKNOWLEDGEMENTS

The research upon which this work is based is carried out at the University of Pavia and at EUCENTRE Pavia, and it is sponsored by ANDIL Assolaterizi and by the Executive Project DPC-RELUIS 2010-2013, task AT2-1.3. The financial support of these sponsors is gratefully acknowledged.

REFERENCES

[1] F. Braga, V. Manfredi, A.Masi, A.Salvatori, M. Vona, Performance of nonstructural elements in RC buildings during the L'Aquila, 2009 earthquake, *Bulletin of Earthquake Engineering*, **9**, 307–324, 2011.

[2] P. Ricci, V. Manfredi, F. De Luca, G.M. Verderame, 6th April 2009 L'Aquila earthquake, Italy: reinforced concrete building performance, *Bulletin of Earthquake Engineering*, **9**, 285–305, 2011.

[3] G. Magenes, S. Bracchi, F. Graziotti, M. Mandirola, C.F. Manzini, P. Morandi, M. Palmieri, A. Penna, A. Rosti, M. Rota, M. Tondelli, *Preliminary damage survey to masonry structures after the May 2012 Emilia earthquakes*, v.1, http://www.eqclearinghouse.org/2012-05-20-italy-it, 2012.

[4] C.F. Manzini, P. Morandi, *Rapporto preliminare sulle prestazioni ed i danneggiamenti agli edifici in muratura portante moderni a seguito degli eventi sismici emiliani del 2012*, v.1, Eucentre, http://www.eqclearinghouse.org/2012-05-20-italy/, 2012.

[5] L.D. Decanini, D. Liberatore, L. Liberatore, L. Sorrentino, *Preliminary Report on the 2012, May 20, Emilia Earthquake*, v.1, http://www.eqclearinghouse.org/2012-05-20-italy-it/, 2012.

[6] M.N. Fardis, Seismic design issues for masonry-infilled RC frames, *Proceedings of First European Conference on Earthquake Engineering and Seismology*, Geneva, Switzerland, 2006.

[7] CEN Eurocode 8 - Design of structures for earthquake resistance - Part 1: General rules, seismic actions and rules for buildings, European Committee for Standardisation, EN 1998-1:2004, Brussels, 2004.

[8] CEN Eurocode 6 - Design of masonry structures - Part 1-1: Common rules for reinforced and unreinforced masonry structures, European Committee for Standardisation, ENV 1996-1-1:2004, Brussels, 2005.

[9] L.D. Decanini, S.H. Bertoldi, C. Gavarini, Telai tamponati soggetti ad azione sismica, un modello semplificato: confronto sperimentale e numerico (in Italian). *Atti del 6 Convegno Nazionale ANIDIS*, Perugia, Italy, 1993.

[10] T. Paulay, M.J. Priestley, *Seismic design of reinforced concrete and masonry buildings*. John Wiley & Sons, USA, 1992.

[11] R.J. Mainstone, On the stiffnesses and strengths of infilled frames, *Proc. of the Institution of Civil Engineers*, **Supp.(iv)**, 57–90, 1971.

[12] NTC08 Decreto Ministeriale 14 Gennaio 2008: Norme tecniche per le costruzioni, Ministero delle Infrastrutture. S.O. n.30 alla G.U. del 4.2.2008, No. 29, 2008.

[13] P. Morandi, S. Hak, G. Magenes, Comportamento sismico delle tamponature in laterizio in telai in c.a.: analisi numeriche su edifici ed implicazioni progettuali (in Italian), *Atti del XIV convegno nazionale ANIDIS*, Bari, Italy, 2011.

[14] A.J. Carr, *Ruaumoko Manual*, University of Canterbury, Cristchurch, New Zealand, 2007.

[15] F.J. Crisafulli, Seismic behaviour of reinforced concrete structures with masonry infills, PhD Thesis, Department of Civil Engineering, University of Canterbury, New Zealand, 1997.

[16] S. Hak, P. Morandi, G. Magenes, T.J. Sullivan, Damage control for clay masonry infills in the design of RC frame structures, *Journal of Earthquake Engineering*, **16**(S1), 1–35, 2012.

COMPDYN 2013
4th ECCOMAS Thematic Conference on
Computational Methods in Structural Dynamics and Earthquake Engineering
M. Papadrakakis, V. Papadopoulos, V. Plevris (eds.)
Kos Island, Greece, 12–14 June 2013

ESTIMATION OF EFFECTIVE STIFFNESS OF INFILL PANELS AT DAMAGE LIMITATION LIMIT STATE FOR LOW- AND MID-RISE INFILLED RC FRAMES

Maria Teresa De Risi[1], Paolo Ricci[1], Gerardo M. Verderame[1], Gaetano Manfredi[1]

[1] Department of Structures for Engineering and Architecture, University of Naples Federico II

Via Claudio 21, 80125 Naples, Italy

mariateresa.derisi@unina.it, paolo.ricci@unina.it, verderam@unina.it, gaetano.manfredi@unina.it

Keywords: Effective Stiffness, Infill Panels, RC Frames, Damage Limitation, Incremental Dynamic Analysis.

Abstract. *A growing attention has been addressed to the influence of infills on the seismic behavior of Reinforced Concrete buildings, also supported by numerical and experimental analyses, and by the observation of damage to infilled RC buildings after recent earthquakes (e.g. L'Aquila 2009, Lorca 2011, Emilia 2012). In this paper, the attention is focused on the Damage Limitation Limit State (DL LS), defined as dependent on displacement capacity limit directly related to the damage to infill panels. Although inelastic (post-cracking) displacement demand in RC members at this LS can be quite low, infill behavior can be already strongly non linear, if a diffuse state of cracking has begun to arise in infill panels. Thus, based on the results of several non linear dynamic analyses, a reduction factor of the initial elastic stiffness of infills is estimated, in order to obtain an effective stiffness of infill panels to be used in a linear analysis in order to obtain a displacement demand at DL LS (i.e., maximum Interstorey Drift Ratio) which is approximately equal to the demand evaluated through non linear dynamic analysis on the same model. To this end, Incremental Dynamic Analyses (IDAs) are performed on four- and eight-storey infilled frames, designed for seismic loads according to the current Italian technical code and for gravity loads only according to an obsolete technical code. Influence of number of storeys and design typology on the obtained effective stiffness is also analyzed.*

1 INTRODUCTION

The observation of damage to infilled RC buildings after recent earthquakes (e.g. L'Aquila 2009, Emilia 2012) has demonstrated that the presence of infills in Reinforced Concrete (RC) buildings cannot be disregarded. Infills are usually assumed as partition elements without any structural function, but they have a significant influence on the increase in lateral stiffness and consequently on the reduction in period of vibration, on base shear capacity, on possible brittle failure mechanisms in joints and columns due to local interaction between panels and the adjacent structural elements, and on the building collapse mechanism.

The issue was investigated during last years supported by numerical ([1]-[9]) and experimental analyses ([11]-[19]), regarding both the influence of infills on the global seismic performance of infilled structures and "local" effects due to the interaction between infill panels and surrounding RC frames. The effect of mechanical properties of infills and RC influencing the seismic capacity of infilled RC structures has been investigated also through sensitivity analyses ([6], [8], [10]). Such analyses have shown that the rotational capacity of RC columns and concrete compressive strength have the highest influence on the seismic capacity at high level of displacement demand; whereas, as far as seismic capacity at low level of displacement demand is concerned, e.g. at Damage Limitation (DL) Limit State (LS), mechanical characteristics of infill panels have the highest influence on the response of the uniformly infilled frames ([8], [10]).

Thus, the contribution of infills to the lateral seismic response in terms of strength and stiffness significantly changes with the displacement demand: displacement and drift demand significantly decrease if infills are explicitly taken into account in the numerical model with respect to the corresponding bare frame, but such a reduction depends on strength and stiffness properties of infills and it is more significant at DL LS than at Ultimate LS (when infills are already extensively damaged). At DL LS the presence of infill panels produces a reduction in displacement capacity compared with a bare structure, due to the assumption of displacement capacity limits accounting for the damage affecting these elements; if such detrimental reduction is not counterbalanced by the beneficial increase in stiffness and strength provided by infill panels, a reduction in seismic capacity can be observed [9].

In this paper, a procedure is proposed for the estimation of an effective stiffness of infill panels to be used in linear analysis for seismic assessment at DL LS, thus allowing to explicitly include these elements also within this kind of analysis approach, which nowadays is still a widespread method, especially for seismic design of new structures. To this end, results from non linear Incremental Dynamic Analyses (IDAs) are used as a reference, and a principle of equivalence between linear and non linear analyses in terms of Interstorey Drift Ratio (IDR) demand is applied – being the demand parameter used for seismic assessment at this performance level. The influence of the number of storeys and of the design typology is investigated, too.

2 STATE OF ART AND CODE REVIEW

According to Eurocode 8 [20], the design and the construction of a structure should guarantee that, under DL LS seismic action, the costs due to the damage and the corresponding limitation of use of the structure should not be disproportionately high with respect to the cost of the whole structure. Provisions for seismic assessment of existing buildings [21] indicate that the damage occurring at this LS has to be easily and economically repaired.

As far as the infills are concerned, it can be assumed that the requirement corresponding to such a criterion is that the infill panel has not achieved the inter-storey drift corresponding to its maximum resistance, as some experimental results pointed out ([15], [17]), although at this

stage some cracks have already occurred. In literature, different assumptions can be found regarding the diffusion of this kind of damage (that is, the proportion of panels reaching the maximum resistance displacement) to be assumed as corresponding to the attainment of DL LS. As a matter of fact, according to different authors this LS occurs when the maximum resistance displacement is reached in the first infill panel ([15], [17], [22]), in 50% of the infill panels at one storey ([23]), or in all of the infill panels at one storey [4]. Based on the results of experimental studies presented in literature ([15]-[19]), it is observed that the displacement corresponding to such maximum resistance condition is strictly dependent on the mechanical properties of both RC frame and infill panel, leading to an IDR ranging from 0.1 to 0.8%.

Code provisions for seismic assessment at DL LS regarding the specific role of infills are present, but – even if some recommendations for the prevention of damage to infill panels are provided ([20], [21], [24]-[28]) – an effective design procedure has not yet been proposed. Some additional measures for masonry infilled frames are introduced at higher level of seismic demand, in order to take into account the effects of the irregularity in plan or elevation produced by the infills, or the possible local detrimental effects due to interaction between infills and the surrounding frame, and to avoid possible brittle failures or out-of-plane collapse of slender panels. In order to effectively account for the damage occurring to infill panels, a seismic assessment at DL LS should be carried out using a model that explicitly takes into account these elements, and assuming a displacement limit directly correlated to their damage.

However, when assessing seismic capacity at DL LS, technical codes ([20], [21], [24]) allow to take into account the presence of infills – if a bare numerical model, as usual, is used – by assuming a fictitious displacement capacity limit (e.g., 5‰ IDR). The Italian "Circolare Esplicativa" [25] allows to limit the maximum IDR in a RC structure to values related to masonry (e.g., 3‰ for unreinforced masonry) if infills are explicitly taken into account in the numerical model. The conservatism of such a provision – depending on the number of storeys and the design typology – have been analyzed in N2 framework and some attempts to identify an equivalent displacement limit to be adopted for a bare model at DL LS depending on the design typology, the number of storey and, above all, on the mechanical properties of infill panels have been performed [9]. Other literature studies [15] suggest to use a conservative lower bound value of IDR limit, i.e. 3‰. However, further efforts to extend the concept of drift limitations to obtained some comprehensive design criteria for RC structures, depending on strength and stiffness properties of infill panels, should be produced.

If a linear analysis approach is adopted, the choice of the stiffness assumed for structural and non-structural elements is not trivial. In linear analyses at Serviceability LSs, it should take into account the influence of first cracks which occur also for low level of seismic demand. Generally speaking, the estimation of such "effective" stiffness should depend on displacement demand on the structural elements, and thus it should be different for each element in the structure, depending on the level of displacement demand involving each of them. However, this kind of – necessarily iterative – procedure should require a computational demand which seems to be not compatible with the level of approximation that implicitly characterizes a linear analysis. Hence, for a RC structure, when an effective stiffness is employed for a linear analysis, a unique value of degradation of the elastic stiffness (pre-cracking) is usually applied to RC members.

As far as RC structural members are concerned, several indications are provided. Some authors (e.g., [29]) suggest to use the secant-to-yielding stiffness in order to predict displacement and forces demand with a good approximation with respect to a non linear analysis, as far as ultimate limit states are concerned. EC8-part 1 [20] prescribes an effective stiffness equal to one-half of the corresponding elastic one, often overestimating the secant-to-yielding

stiffness [30]; such an overestimation obviously implies a non-conservative underestimation of the displacement demand. Thus, in EC8-part 3 [21] the adoption of a secant-to-yielding stiffness is explicitly suggested for checks in terms of displacements. ASCE SEI 41/06 – Supplement I [26] suggests to use the secant-to-yielding stiffness, too, and the value of the effective stiffness for RC members depends on the kind of element and the axial load ratio. New Zealand standards [27] prescribe a value of effective stiffness which not only depends on the kind of element and the axial load ratio, but also on the considered LS, on the ductility capacity at Ultimate LS, and on the steel yield strength.

When infills are modeled for a linear analysis, the evaluation of their stiffness is a key point, but, compared with RC members, literature and code provisions regarding this issue are much more limited. Such "effective" stiffness should ideally account for stiffness degradation due to first cracks and detachments between the infill and the surrounding frame. It should be intermediate between the initial elastic (pre-cracking) stiffness and the secant-to-maximum stiffness, provided that such point is assumed as corresponding to the limit displacement capacity at DL LS. If an equivalent strut approach is adopted, the problem of evaluating the stiffness assumed for the infill panel is translated into the determination of the strut width. EC8-part 1 [20] does not provide a specific value of width-to-length ratio for the equivalent strut. Paulay and Priestley (1992) [31] suggest a value of this ratio equal to 0.25 in order to estimate the secant stiffness corresponding to a lateral load equal to 50% of the maximum load capacity of the infilled frame; in Fardis (2009) [30] a width-to-diagonal length ratio equal to 0.20 is proposed at DL LS, whereas a lower value (namely, 0.10-0.15) is suggested at Significant Damage LS.

3 NUMERICAL MODELING

3.1 Case study frames

The case study structures analyzed in this paper are infilled RC planar frames with five equal-length bays, with a bay length equal to 4.5 m and an inter-storey height equal to 3.0 m. The analyzed frames are extracted from a 3-D structure symmetric in plan, both in longitudinal and in transverse direction, with five bays in longitudinal direction and three bays in transverse direction. Slab way is always parallel to the transverse direction; dead load is equal to 7 kN/m^2 for the all stories; live load is equal to 2 kN/m^2.

Starting from different design typologies and number of storeys, four case study frames are extracted and analyzed:

- two gravity load designed (GLD) frames, a four-storey and an eight-storey frame, defined by means of a simulated design procedure according to code prescriptions and design practices in force in Italy between 1950s and 1970s ([32], [33]);
- two seismic load designed (SLD) frames, a four-storey and an eight-storey frame, designed for seismic loads according to the current Italian code [24] in Ductility Class High; hence, the principles of the Capacity Design are applied.

In each frame, infill panels are uniformly distributed along the height (see Figure 1). Panel thickness is equal to 200 mm, corresponding to a double layer brick infill (120+80) mm thick, which can be considered as typical of a non-structural infill masonry wall [34]. Presence of openings is not taken into account.

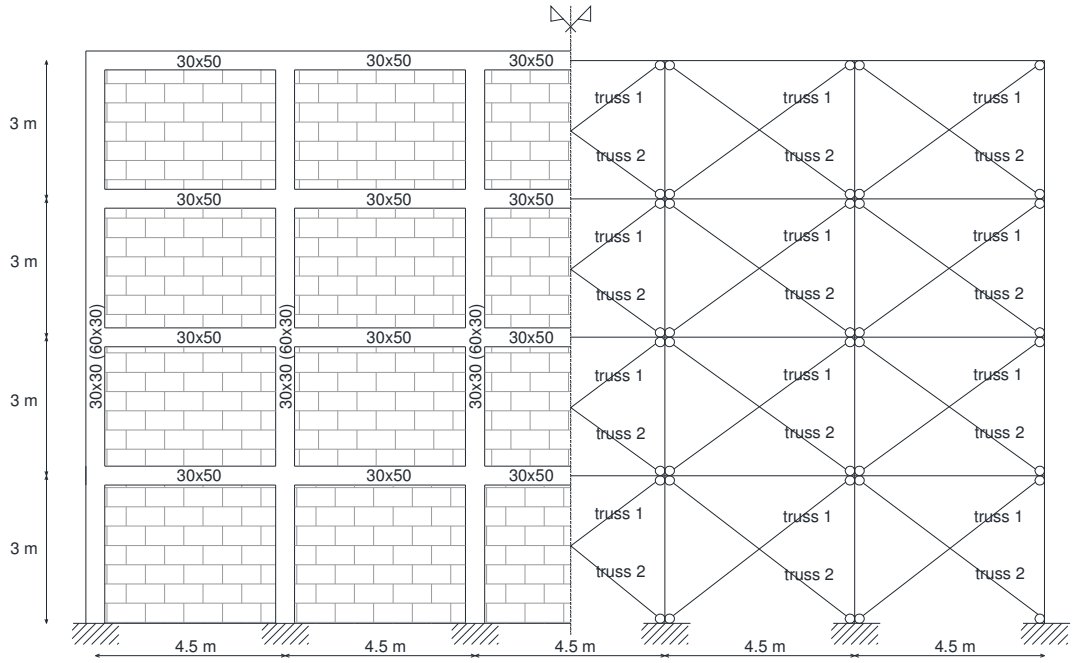


Figure 1: Four storey case-study infilled RC frame; member dimensions for GLD (and SLD) are provided.

3.2 RC and Infill modeling

Nonlinear response of RC elements is modeled by means of a lumped plasticity approach: beams and columns are represented by elastic elements with rotational hinges at the ends. A three-linear envelope is used, with cracking and yielding assumed as characteristic points. Section moment and curvature at cracking and yielding are calculated on a fiber section, for an axial load value corresponding to gravity loads. The behavior is assumed linear elastic up to cracking and perfectly-plastic after yielding. Rotation at yielding is evaluated through the formulations given in [35]. It is worth noting that displacement demand in RC members is typically low at the investigated LS, and in the analyses carried out in this paper no yielding of RC members was observed (for this reason the behavior after yielding is represented by a dashed line in Figure 2(a)). As far as the hysteretic behavior of RC members is concerned Figure 2(a)), no pinching of force and deformation is introduced, no damage due to ductility and energy, and degradation in unloading stiffness based on ductility are taken into account. Strength deterioration becomes an important factor when the structural response approaches the collapse limit state; at earlier steps of inelastic behavior, both deteriorating and non-deteriorating systems exhibit similar responses [36]. Since the inelastic demand on RC member is expected to be very low at the investigated LS, these hypotheses are not reasonably expected to introduce any significant lack of generality. Moreover, in new structures, with detailing of members for ductility, cyclic degradation of strength appears to be negligible [30].

Infill panels are modeled by means of equivalent struts. Modeling infills through single compressed struts allows to investigate the effects of the panels on the global behavior of the analyzed structure, consistently with the purpose of this study. The adopted model for the envelope curve of the force-displacement relationship is the model proposed by Panagiotakos and Fardis [37]. This force-displacement envelope is composed by four branches, as shown in Figure 2(a). The first branch corresponds to the linear elastic behavior up to cracking; the slope of this branch is the elastic stiffness of the infill panel k_{el}, and it can be expressed ac-

cording to Equation (1), being A_w is the transversal area of the infill panel, G_w the shear elastic modulus and h_w its clear height. The assumption of such a model for the elastic (pre-cracking) stiffness of infills has demonstrated to provide a good agreement between numerical analysis and dynamic behavior of infilled RC buildings [38]. If τ_{cr} is the shear cracking stress, the shear cracking strength F_{cr} can be obtained according to Equation (2).

$$K_{el} = \frac{G_w A_w}{h_w} \tag{1}$$

$$F_{cr} = \tau_{cr} A_w \tag{2}$$

The second branch continues up to the maximum strength F_{max}, which can be calculated according to Equation (3). The corresponding displacement Δ_{max} is estimated according to the hypothesis that the secant stiffness up to maximum is provided by Mainstone's formulation [39], assuming that the width of the equivalent truss b_w depends on the height and the diagonal length of the panel, h_w and d_w respectively, and on the parameter λ_h (Equation (4)); the latter parameter depends on the elastic Young modulus of the infill panel E_w and of the surrounding concrete E_c, the diagonal slope of the equivalent truss to the horizontal θ, the infill thickness t_w, the moment of inertia of the adjacent columns I_c (Equation (5)). Secant stiffness up to maximum, k_{sec}, is provided by the expression shown in Equation (6).

$$F_{\max} = 1.30 \cdot F_{cr} \tag{3}$$

$$b_w = 0.175 \left(\lambda_h h_w\right)^{-0.4} d_w \tag{4}$$

$$\lambda_h = \sqrt[4]{\frac{E_w t_w \sin(2\theta)}{4 E_c I_c h_w}} \tag{5}$$

$$K_{\sec} = \frac{E_w b_w t_w}{\sqrt{L^2 + H^2}} \cos\theta \tag{6}$$

The third branch of the envelope is a degrading branch up to the achievement of a constant branch. Due to the definition itself of DL LS, the field of behavior of the infill trusses after the peak is never reached (thus the behavior after the peak is represented by a dashed line in Figure 2(b)).

Starting from this model and noting that the infill panels are all equal, the IDR corresponding to the peak strength is about equal to 1.4‰.

As far as the response of the equivalent masonry strut due to cyclic loading is concerned, no strength and stiffness cyclic degradation is considered, as shown in Figure 2(b), basically due to lack of data leading to high uncertainties and modeling difficulties ([40]-[42]). However, further studies should also consider this degradation investigating on the influence of hysteresis rules on the seismic behavior at the analyzed LS.

The viscous damping is represented by a mass and current stiffness proportional Rayleigh model, assuming 2% damping for the first and the third modes.

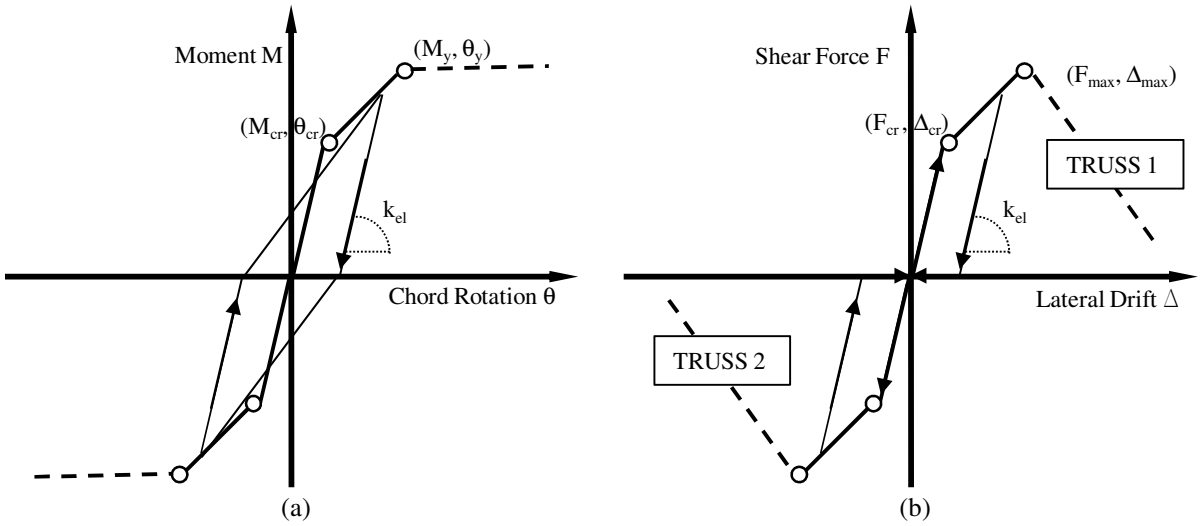


Figure 2: hysteretic behavior of RC members (a) and "simple hysteresis rule" [40] of infill panels (b)

A summary of the mechanical properties of both RC and infills is reported in Table 1.

	Mechanical property	GLD	SLD	References
RC	Concrete compressive strength, f_c	25.0 MPa	36.0 MPa	[43],[45]
	Steel yield strength, f_y	369.7 MPa	550.0 MPa	[44],[46]
Infill	Shear elastic modulus, G_w	1240 MPa		[47]
	Young elastic modulus, E_w	4133 MPa		[47]
	Shear cracking stress, τ_{cr}	0.33 MPa		[47]
	Softening-to-elastic stiffness ratio, α	1%		[37]
	Residual-to-maximum stress ratio, β	1%		[37]
	"Peak" IDR, IDR_{DL}	1.4‰		from model [37]

Table 1: Mechanical properties of RC and Infill

4 ANALYSIS METHODOLOGY

The methodology applied to search the effective stiffness for infill panels starts from Incremental Dynamic Analyses (IDA) ([48], [49]): the non-linear structural model is investigated through time history analyses under the action of a set of ground motion records; the non-linear time-history analysis is repeated increasing the scale factor of the record, for each record, thus obtaining a relationship between a ground motion intensity (spectral acceleration $S_a(T_1,5\%)$) and an engineering demand parameter (maximum IDR) for the structural model. Then, linear time-history analyses were performed, assuming a linear behavior for both RC members and infill panels.

Structural modeling and numerical analyses are performed through the "PBEE toolbox" software [50], combining MATLAB® with OpenSees [51], modified in order to include also infill elements ([52], [6]). A solution algorithm has been introduced in PBEE toolbox in order to solve non-converging problems, trying different possible solution algorithms, or reducing integration time step, or reducing tolerance as suggested in [53]. Moreover the "hunt and fill" procedure suggested in ([48], [49]) is adopted to trace IDA curves.

The definition of DL LS has to be considered still an open issue (see Section 2). In this study, this LS is conservatively assumed to occur when the maximum resistance displacement is reached in the first infill panel, thus starting to degrade. However, in the case study struc-

tures analyzed herein the clear span of each infill panel is almost the same, and all the infills at the same storey have the same displacement capacity, thus reaching their maximum resistance at same time. However, this issue could deserve further discussion in the future.

4.1 Ground motion record selection

Natural records are selected and scaled to different level of seismicity in order to obtain IDA curves. The record selection has been performed by using REXEL software [54], from the European Strong-motion Database, between earthquakes characterized by a magnitude which ranges between 6 and 7, with a source-to-site distance ranging between 0 and 30 km, and recorded on soil class A.

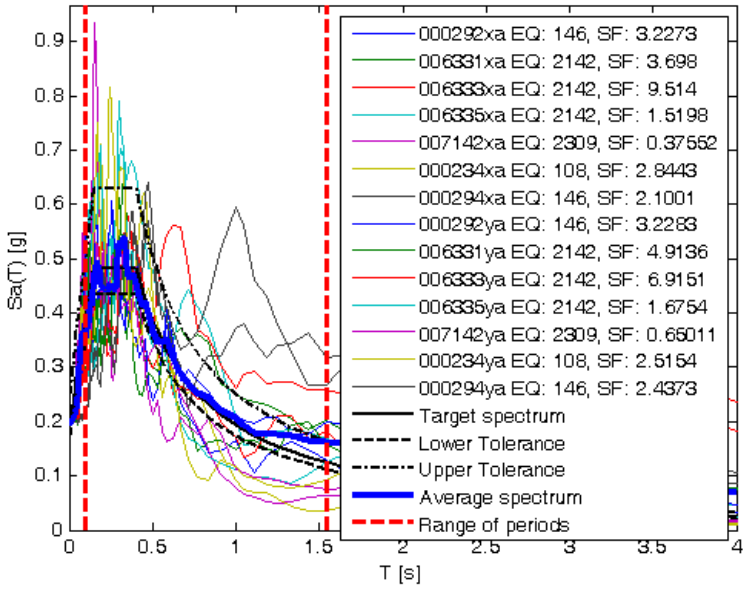


Figure 3: Selected ground motion records [54]

The average spectrum of the selected records matches the target spectrum in the range between 0.1s and 1.5s, with a lower tolerance of 10% and an upper tolerance equal to 30%. The target spectrum is the EC8 spectrum-Type 2 related to soil class A.

A summary of the main properties of the two components of the seven selected records is reported in Table 2. On the whole, 14 records are used in the dynamic analyses.

Earthquake Name	Date	M_w	Fault Mechanism	Epicentral Distance [km]	PGA_X [m/s^2]	PGA_Y [m/s^2]	EC8 Site class
Campano Lucano	23/11/1980	6.9	normal	25	0.5878	0.5876	
South Iceland	21/06/2000	6.4	strike slip	22	0.5130	0.3860	
South Iceland	21/06/2000	6.4	strike slip	28	0.1994	0.2743	
South Iceland	21/06/2000	6.4	strike slip	15	1.2481	1.1322	A
Bingol	01/05/2003	6.3	strike slip	14	5.0514	2.9178	
Montenegro	24/05/1979	6.2	thrust	30	0.6669	0.7541	
Campano Lucano	23/11/1980	6.9	normal	26	0.9032	0.7783	

Table 2: Selected ground motion records

4.2 Procedure: research of the effective stiffness of infill panels

First of all, the non-linear structural model is investigated through time history analyses under the action of the selected set of ground motion records, thus obtaining an IDA curve for each record in terms of peak IDR versus elastic spectral acceleration $S_a(T_1,5\%)$, where T_1 is the fundamental period of the infilled frame.

The attention is focused on the DL LS defined as dependent on a displacement capacity limit directly related to the damage to infill panels and, in particular, to the IDR corresponding to the achievement of the maximum strength of the infills, IDR_{DL}. As reported in Table 1, in the cases investigated in this paper, IDR_{DL} is equal to 1.4‰. Thus the median value of $S_a(T_1,5\%)$ corresponding to this IDR limit, $\eta_{Sa(T1,5\%)|IDR}$, can be evaluated from the previously obtained set of IDAs. This value of $S_a(T_1,5\%)$ is the Intensity Measure (IM) capacity at DL LS, $S_a(T_1,5\%)_{DL}$.

Then, Linear Time-History (LTH) analyses are performed, assuming a linear behavior for both RC members and infill panels, and assuming a reduction factor α of the initial elastic stiffness of all the infill trusses (evaluated according to Equation (1)).

As shown in Figure **4**, an iterative procedure is applied, varying the coefficient α between 0 (infinitely flexible infills) and 1 (infills with elastic stiffness). For each α value, LTH analyses for all of the selected records are performed, and the median value of the maximum IDR, $\eta_{IDR|Sa(T1,5\%)}$, is estimated at the IM level equal to $S_a(T_1,5\%)_{DL}$. The iterative procedure stops when the value of $\eta_{IDR|Sa(T1,5\%)}$ is equal to IDR_{DL}, i.e. 1.4‰ in our case; the corresponding α factor, $\alpha_{kel,infill}$, is the reduction factor of the initial elastic stiffness of infills providing an effective stiffness of infill panels such that a linear dynamic analysis of the infilled numerical model leads to a displacement demand in terms of maximum IDR at DL LS which is approximately equal to the maximum IDR demand evaluated through non linear dynamic analysis on the same model.

In Figure **5** a schematic example of results of the procedure explained herein is reported.

It is worth noting that, since that it is not possible to know a-priori which storey is involved in the achievement of DL LS, the reduction factor is applied to all of the infill panels. Such a procedure allows to calibrate the factor α that provides the "real" maximum IDR demand – at a certain level of intensity measure – through a linear analysis, but an error may occur in the estimation of the corresponding top displacement. This could be considered as an unavoidable approximation due to the limitation of a linear analysis itself, which is not able to capture the effects of a concentration in post-elastic displacement demand. However, this error could be considered not of a primary importance, since DL LS check is performed in terms of another displacement demand parameter, namely maximum IDR.

Non linear behavior of RC members can be considered, too, by repeating the described procedure for different value of effective stiffness of RC members. Such an effective stiffness can be estimated as a rate (α_{RC}) of the elastic (pre-cracking) stiffness of each RC member, e.g. 50% (EC8-part 3). For each value of α_{RC}, a $\alpha_{kel,infill}$ factor can be estimated.

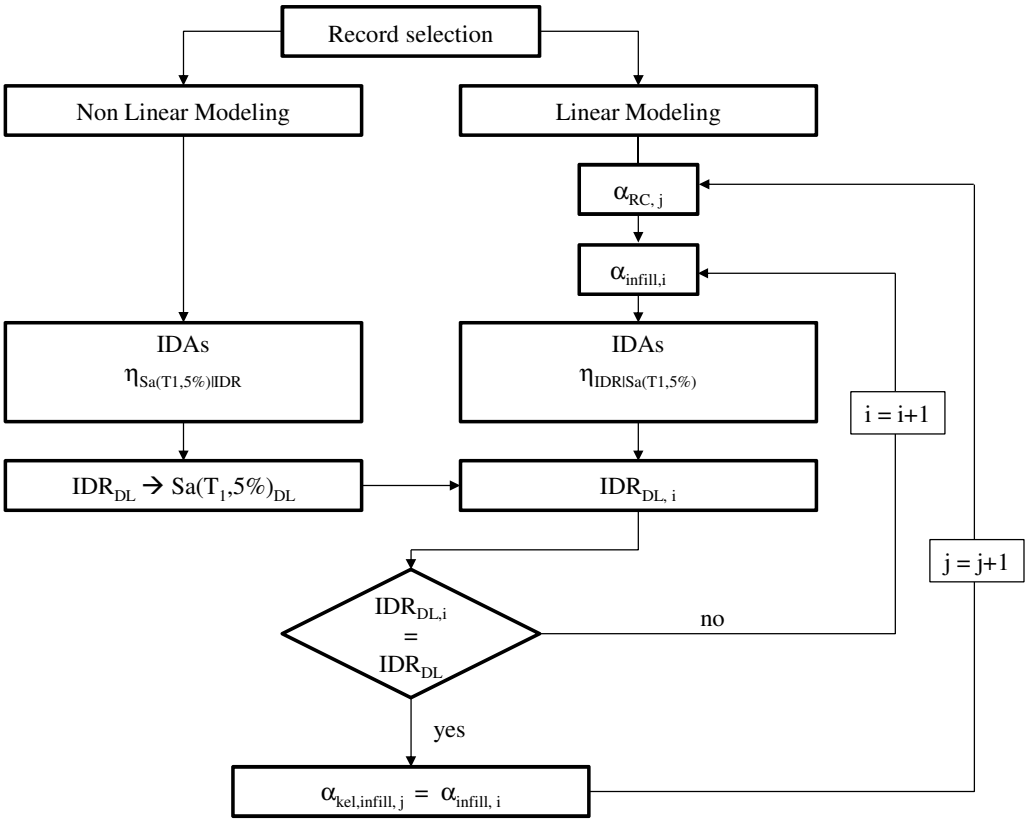


Figure 4: Steps of the procedure: research of the effective stiffness for infill panels

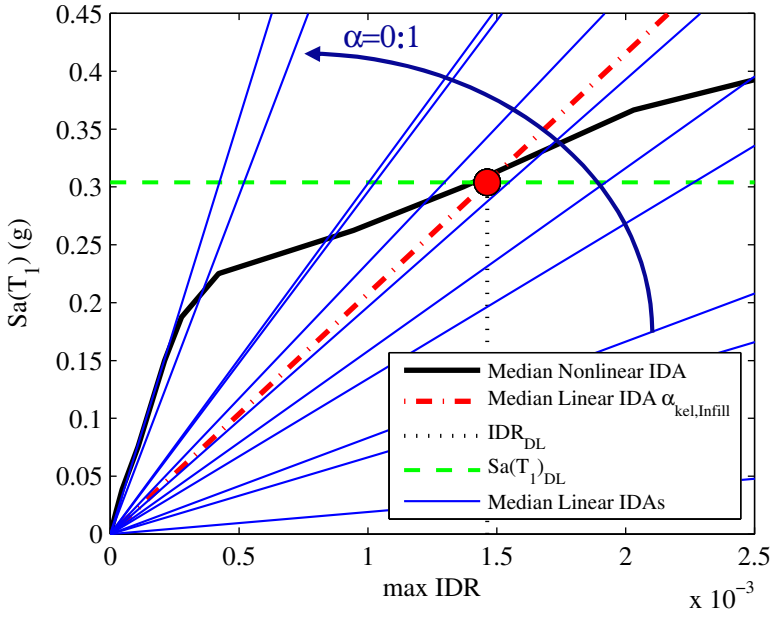


Figure 5: Schematic example of the results of the procedure

5 ANALYSIS OF RESULTS

Hence, the procedure described in the previous paragraph is applied for each of the case-study frames.

In Table 3, the first-mode periods, the PGA capacity at DL LS and $S_a(T_1,5\%)$ capacity at DL LS, respectively, are shown for each case study frame.

	GLD			SLD		
	T_1 (s)	PGA_{DL} (g)	$Sa(T_1)_{DL}$ (g)	T_1 (s)	PGA_{DL} (g)	$Sa(T_1)_{DL}$ (g)
4 storey	0.122	0.32	0.32	0.114	0.41	0.39
8 storey	0.268	0.19	0.28	0.239	0.22	0.30

Table 3: Elastic periods of infilled frames; PGA and $Sa(T_1)$ capacity at DL LS

The results of such a procedure in terms of non linear IDA curves and LTH analyses are reported in Figure 6, where $S_a(T_1,5\%)$ capacity at DL LS and the IDR corresponding to the achievement of DL LS are represented, too.

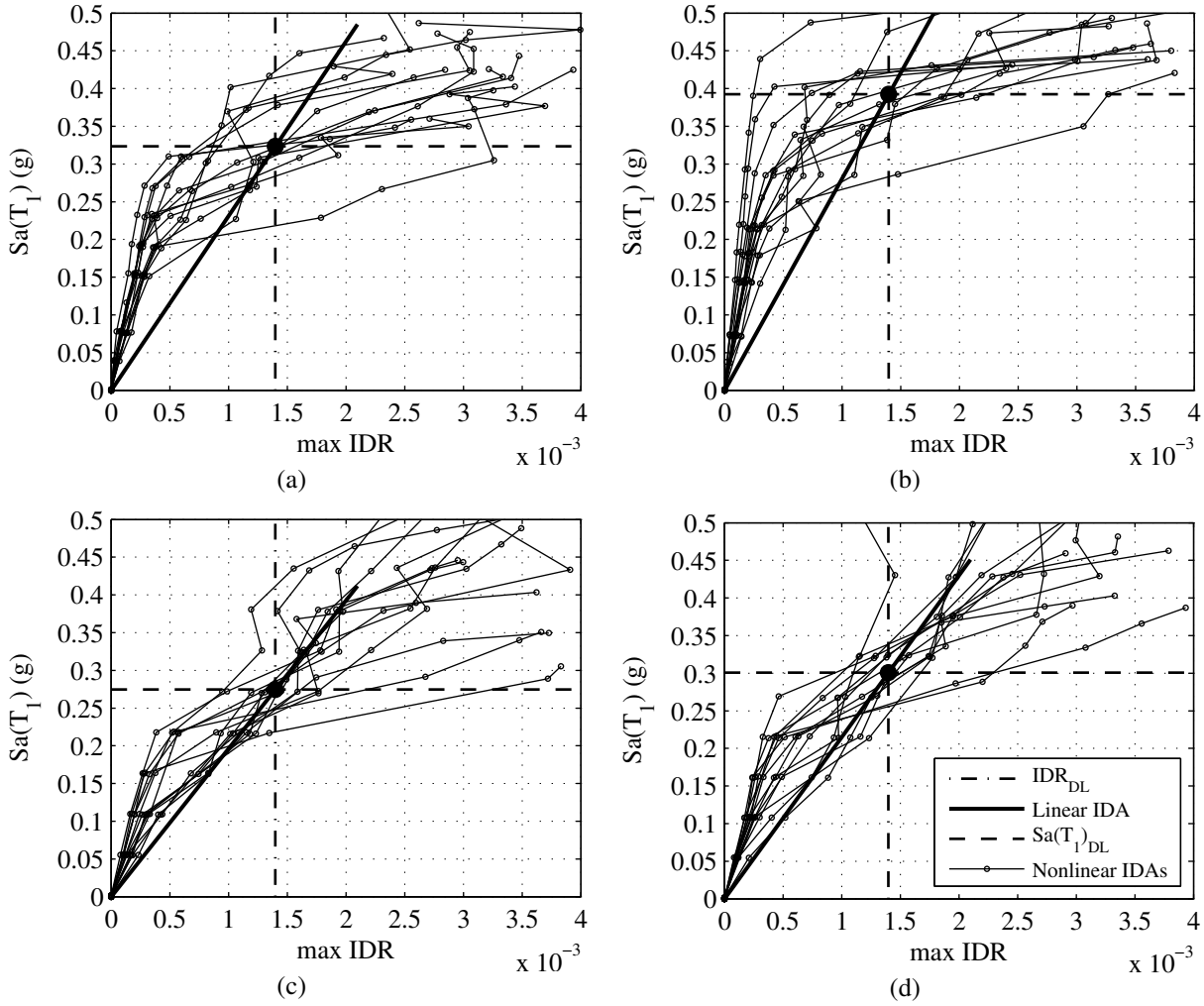


Figure 6: Non linear IDAs and Linear IDA for $\alpha_{kel,infill}$: 4-storey GLD (a) and SLD (b) frames, 8-storey GLD (c) and SLD (d) frames

The distribution of IDR demand corresponding to the achievement of DL LS can be evaluated through the non linear analyses as the median of the IDR demand at each storey for all of the records when an IM value equal to the IM capacity at DL LS is considered. A concentration of IDR demand is shown at lower storeys both for 4- and 8-storey frames, as shown in Figure 7. It is worth noting that the maximum IDR demand shown in this figure can be a bit lower than the IDR_{DL} limit because of the procedure by which it is estimated: if the IDR_{DL} is achieved at different storeys when different records are analyzed, the median value of the maximum IDR demand at each storey for all of the records will result lower than IDR_{DL}. Finally, the values obtained for $\alpha_{kel,infill}$ and the corresponding elastic periods of the case-study frames with elastic stiffness of infills reduced by $\alpha_{kel,infill}$ are reported in Table 4.

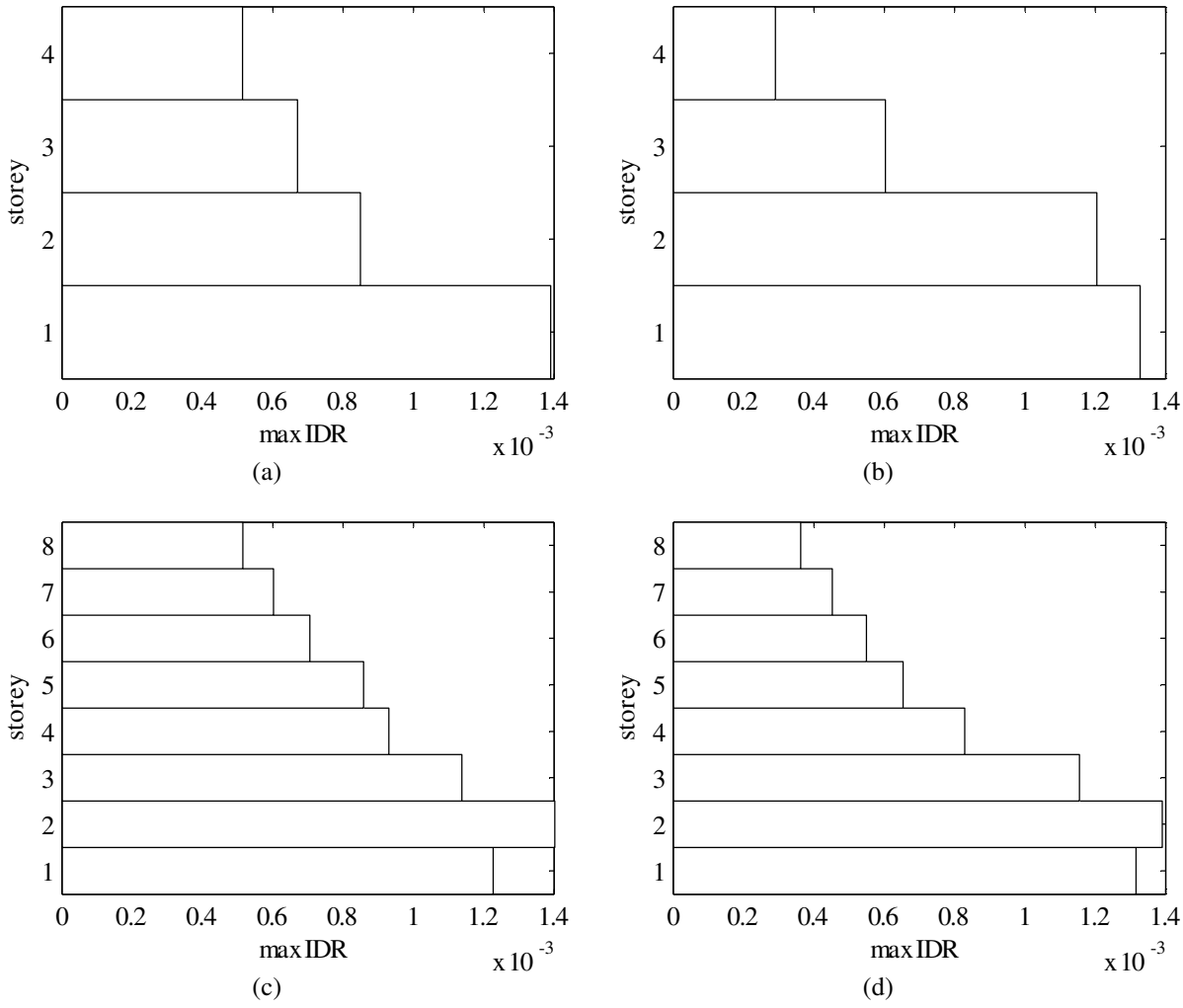


Figure 7: IDR demand at each storey: 4-storey GLD (a) and SLD (b) frames, 8-storey GLD (c) and SLD (d) frames

	GLD		SLD	
	$\alpha_{kel,infill}$	$T(\alpha_{kel,infill})$ (s)	$\alpha_{kel,infill}$	$T(\alpha_{kel,infill})$ (s)
4 storey	0.31	0.202	0.34	0.196
8 storey	0.36	0.351	0.41	0.331

Table 4: Obtained values of $\alpha_{kel,infill}$ (with α_{RC}=1) and corresponding elastic periods

When also non linear behavior of RC members is considered, by repeating the procedure for different value of effective stiffness of RC members, i.e. for different values of α_{RC}, a vector of $\alpha_{kel,infill}$ can be estimated.

In Figure 8 and in Table 5 the variation of $\alpha_{kel,infill}$ depending on the investigated values of α_{RC} is represented for each case-study frame. Figure 8 clearly shows that if α_{RC} decreases, a higher effective stiffness has to be assumed for infill panels in order to obtain the same displacement demand, as expected. However, the curves representing the variability of $\alpha_{kel,infill}$ depending on α_{RC} have a very low slope: the value of $\alpha_{kel,infill}$ is almost constant when the effective stiffness of RC members ranges between zero-stiffness and the gross elastic stiffness. This trend is more evident for the 4-storey GLD frame with respect to the 4-storey SLD frame, because of the increase in the influence of infill panels when RC members have a lower stiffness.

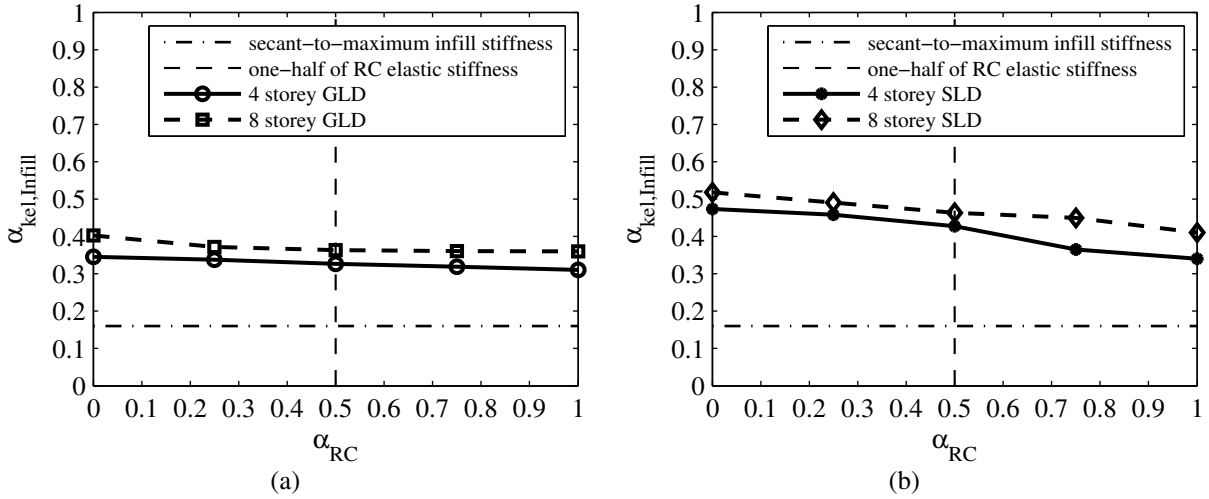


Figure 8: Variation of $\alpha_{kel,infill}$ depending on α_{RC} for GLD (a) and SLD (b) frames

	$\alpha_{kel,infill}$			
α_{RC}	4storey GLD	4storey SLD	8storey GLD	8storey SLD
0	0.35	0.47	0.40	0.52
0.25	0.34	0.46	0.37	0.49
0.50	0.33	0.43	0.36	0.46
0.75	0.32	0.36	0.36	0.45
1	0.31	0.34	0.36	0.41

Table 5: Variation of $\alpha_{kel,infill}$ depending on α_{RC}

If the same design typology is considered, $\alpha_{kel,infill}$ is higher in the case of the 8-storey frames with respect to the corresponding 4-storey frames, whichever α_{RC} is considered. From a qualitative point of view, it could be expected that the reduction in the initial elastic stiffness of infills is lower when it involves a higher number of infill panels, such as in the case of 8-storey frames, since the achievement of DL LS involves always one storey only.

If frames with the same number of storeys are considered, a stronger dependence of $\alpha_{kel,infill}$ on α_{RC} is observed for SLD frames with respect to GLD frames. For example, comparing the 4-storey SLD frame with the 4-storey GLD frame, a higher contribution to lateral strength and stiffness of RC members is present in SLD case: the higher this contribution, the

more sensitive the variation of the effective stiffness of infills with respect to the effective stiffness of RC members.

When a α_{RC} equal to 0.50 is adopted for RC members (as suggested in EC8), $\alpha_{kel,infill}$ ranges between 0.33 and 0.46 (Table 5) for the analyzed frames; since DL LS check is performed in terms of displacement, a conservative value of $\alpha_{kel,infill}$ to estimate the effective stiffness of infills is the lower value of this range, i.e. 0.33, thanks also to the quite small variation of $\alpha_{kel,infill}$ depending on α_{RC} and on the characteristics of the frame. Moreover, Figure 8 shows that effective stiffness of infills estimated through $\alpha_{kel,infill}$ is always higher than the secant-to maximum stiffness (Mainstone's stiffness), i.e. $\alpha_{kel,infill}$ equal to 0.16 in the analyzed case-studies. Hence, if an effective stiffness equal to the secant-to maximum stiffness is adopted for infills, DL LS check could be too conservative. Considering the geometrical and mechanical properties of the infill panels modeled in the case-study frames (Table 1), a $\alpha_{kel,infill}$ value equal to 0.33 implies a width-to-diagonal length ratio equal to 0.18, quite close to the value proposed in Fardis (2009) [30], where a width-to-diagonal length ratio equal to 0.20 is suggested at DL LS. The variation of that width-to-diagonal length ratio depending on α_{RC} is shown in Figure 9.

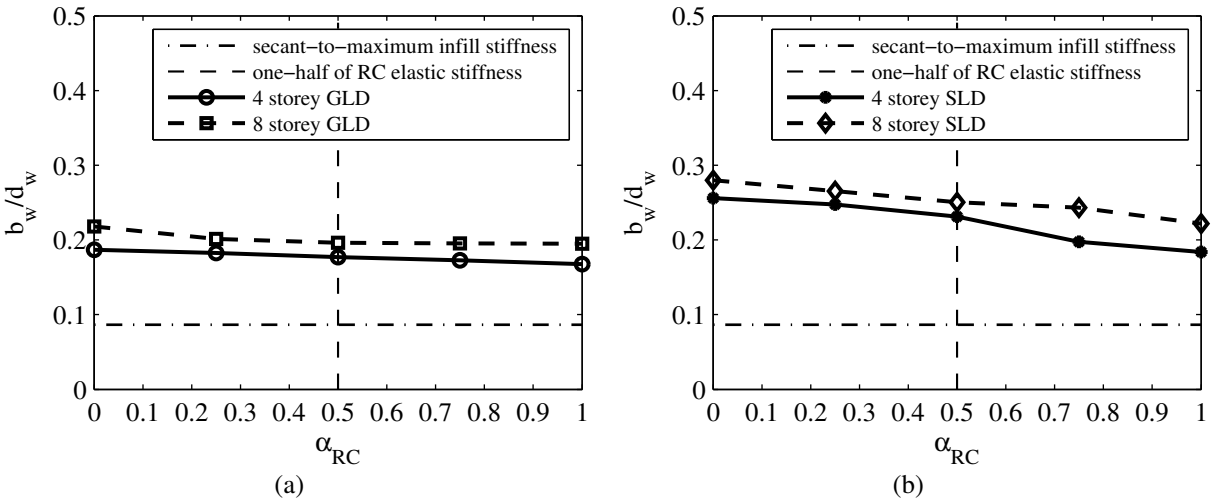


Figure 9: Variation of width-to-diagonal length ratio depending on α_{RC} for GLD (a) and SLD (b) frames

6 CONCLUSIONS AND FUTURE DEVELOPMENTS

Based on the results of several non linear dynamic analyses, a reduction factor of the initial elastic stiffness of infills has been estimated, in order to obtain an effective stiffness of infill panels such that a linear dynamic analysis of the infilled numerical model leads to a displacement demand at DL LS – in terms of maximum IDR – which is approximately equal to the demand evaluated through a non linear dynamic analysis on the same model, under the seismic demand leading to the attainment of such LS.

To this end, IDAs were performed on four- and eight-storey infilled frames, designed for seismic loads according to the current Italian technical code and for gravity loads only according to an obsolete technical code. The influence of number of storeys and design typology on the obtained effective stiffness was analyzed, depending also on the effective stiffness adopted for RC members. In particular, when an effective stiffness equal to one-half of the elastic one is adopted for RC members [20], a value of effective stiffness equal to one-third of the elastic one for infills appears to be a conservative value to perform the DL LS check in terms of displacement.

Work is ongoing to carry out a comparison between LTH results and a Response Spectrum Analysis (RSA) in order to simplify further that kind of analysis. The estimation of the effective stiffness for infills at DL LS could come from an equivalence between non linear time history and RSA analysis, since the latter is the most widespread method of analysis, especially for seismic design of new structures.

Further studies should investigate the effects of a possible variation in masonry infill characteristics, namely displacement capacity and hysteresis rules, on the estimation of the effective stiffness. The influence of the presence of openings in infill panels could be investigated, too. Moreover, RC structural types different from moment resisting frames (i.e., shear wall frames) could be considered.

REFERENCES

[1] M. Dolšek, P. Fajfar, Soft storey effects in uniformly infilled reinforced concrete frames. *Earthquake Engineering*, 5(1), 1-12, 2001.

[2] M. Dolšek, P. Fajfar, Mathematical modelling of an infilled RC frame structure based on the results of pseudo-dynamic tests. *Earthquake Engineering and Structural Dynamics*, 31(6), 1215-1230, 2002.

[3] M. Dolšek, P. Fajfar, Inelastic spectra for infilled reinforced concrete frames. *Earthquake Engineering and Structural Dynamics*, 33(15), 1395-1416, 2004.

[4] M. Dolšek, P. Fajfar, The effect of masonry infills on the seismic response of a four-storey reinforced concrete frame – a deterministic assessment. *Engineering Structures*, 30(7), 1991-2001, 2008.

[5] M. Dolšek, P. Fajfar, The effect of masonry infills on the seismic response of a four-storey reinforced concrete frame – a probabilistic assessment. *Engineering Structures*, 30(11), 3186-3192, 2008.

[6] D. Celarec, P. Ricci, M. Dolšek, The sensitivity of seismic response parameters to the uncertain modelling variables of masonry-infilled reinforced concrete frames. *Engineering Structures*, 35, 165-177, 2012.

[7] C. Dymiotis, A.J. Kappos, M.K. Chryssanthopoulos, Seismic reliability of masonry-infilled RC frames. *ASCE Journal of Structural Engineering*, 127(3), 296-305, 2001.

[8] P. Ricci, M.T. De Risi, G.M. Verderame, G. Manfredi, Influence of infill presence and design typology on seismic performance of RC buildings. Part I: sensitivity analysis. *Proceedings of the 15th World Conference on Earthquake Engineering*, Lisbon, Portugal, September 24-28, 2012.

[9] P. Ricci, M.T. De Risi, G.M. Verderame, G. Manfredi, Influence of infill presence and design typology on seismic performance of RC buildings. Part II: fragility analysis and evaluation of code provisions at Damage Limitation Limit State. *Proceedings of the 15th World Conference on Earthquake Engineering*, Lisbon, Portugal, September 24-28, 2012.

[10] P. Ricci, M.T. De Risi, G.M. Verderame, G. Manfredi, Influence of infill distribution and design typology on seismic performance of low- and mid-rise RC buildings. *Bulletin of Earthquake Engineering*, 2013. (tentatively accepted for publication)

[11] P. Negro, A. Colombo, Irregularities induced by nonstructural masonry panels in framed buildings. *Engineering Structures*, 19(7), 576-85, 1997.

[12] P. Fajfar, D. Drobnič, Nonlinear seismic analyses of the ELSA buildings. *Proceedings of the 11th European Conference on Earthquake Engineering*, Paris, France, September 6-11, 1998.

[13] P. Negro, G. Verzeletti, Effect of infills on the global behaviour of R/C frames: energy considerations from pseudodynamic tests. *Earthquake Engineering and Structural Dynamics*, 25(8), 753-773, 1997.

[14] A.V. Pinto, G. Verzeletti, J. Molina, H. Varum, E. Coelho, Pseudodynamic tests on non-seismic resisting RC frames (infilled frame and infill strengthened frame tests). Report EUR, EC, Joint Research Centre, Ispra, Italy, 2002.

[15] S. Hak, P. Morandi, G. Magenes, T. J. Sullivan, Damage Control for Clay Masonry Infills in the Design of RC Frame Structures, *Journal of Earthquake Engineering*, 16:sup1, 1-35, 2012.

[16] A.B. Mehrabi, P.B. Shing, M.P. Schuller, J.L. Noland, Performance of masonry infilled R/C frames under in-plane lateral loads, Report No. CU/SR-94/6. Department of Civil, Environmental, and Architectural Engineering, University of Colorado at Boulder, Boulder, CO, USA, 1994.

[17] F. Colangelo, A simple model to include fuzziness in the seismic fragility curve and relevant effect compared with randomness. *Earthquake Engineering and Structural Dynamics*, 41(5), 969-986, 2012.

[18] F. Colangelo, Pseudo-dynamic seismic response of reinforced concrete frames infilled with non-structural brick masonry, *Earthquake Engineering and Structural Dynamics* 34(10), 1219-1241, 2005.

[19] F.J. Crisafulli, Seismic behaviour of reinforced concrete structures with masonry infills. Ph.D. Thesis, University of Canterbury, Christchurch, New Zealand, 1997.

[20] CEN. European Standard ENV 1998-1-1/2/3. Eurocode 8: Design provisions for earthquake resistance of structures – Part I: General rules. Technical Committee 250/SC8, Comité Européen de Normalisation, Brussels, 1995.

[21] CEN. European standard EN 1998-3. Eurocode 8: design provisions for earthquake resistance of structures – Part 3: assessment and retrofitting of buildings. European Committee for Standardisation, Brussels, 2005.

[22] M. Dolšek, P. Faifar, Simplified seismic assessment of infilled reinforced concrete frames, *Proceedings of the First European Conference on Earthquake Engineering and Seismology*, Geneva, Switzerland, 3-8 September 2006. Paper Number 888, 2006.

[23] D. Celarek, M. Dolšek, Practice-oriented probabilistic seismic performance assessment of infilled frames with consideration of shear failure of columns, *Earthquake Engineering and Structural Dynamics*, DOI: 10.1002/eqe.2275, 2012.

[24] Decreto Ministeriale del 14/1/2008. Approvazione delle nuove norme tecniche per le costruzioni. G.U. n. 29 del 4/2/2008, 2008. (in Italian)

[25] Circolare del Ministero dei Lavori Pubblici n. 617 del 2/2/2009. Istruzioni per l'applicazione delle "Nuove norme tecniche per le costruzioni" di cui al D.M. 14 gennaio 2008. G.U. n. 47 del 26/2/2009, 2009. (in Italian)

[26] ASCE/SEI 41, Seismic rehabilitation of existing buildings. American Society of Civil Engineers, Reston, VA, USA, 2007.

[27] NZS 3101:2006, Commentary on the Concrete Design Standard, Part 2. Standards Association of New Zealand, Wellington, New Zealand, 2006.

[28] NZS 4230:2004, New Zealand Standard, Design of Reinforced Concrete Masonry Structures, 2004.

[29] T.B. Panagiotakos, M.N. Fardis, Estimation of inelastic deformation demands in multistorey RC frame buildings. *Earthquake Engineering and Structural Dynamics*, 28(5):501-528, 1999.

[30] M.N. Fardis, Seismic design, assessment and retrofitting of concrete buildings based on EN-Eurocode 8, Springer, 2009.

[31] T. Paulay, M.J.N Priestley, Seismic design of reinforced concrete and masonry buildings. John Wiley & Sons, New York, USA, 1992.

[32] Regio Decreto Legge n. 2229 del 16/11/1939. Norme per la esecuzione delle opere in conglomerate cementizio semplice od armato. G.U. n. 92 del 18/04/1940. (in Italian)

[33] G.M. Verderame, M. Polese, C. Mariniello, G. Manfredi, A simulated design procedure for the assessment of seismic capacity of existing reinforced concrete buildings. *Advances in Engineering Software*, 41(2), 323-335, 2010.

[34] I.E. Bal, H. Crowley, R. Pinho, F.G. Gulay, Structural characteristics of Turkish RC building stock in Northern Marmara region for loss assessment applications. ROSE Research Report No. 2007/03, IUSS Press, Pavia, Italy, 2007.

[35] D.E. Biskinis, M.N. Fardis, Flexure-controlled ultimate deformations of members with continuous or lap-spliced bars. *Structural Concrete*, 11(2), 93-108, 2010.

[36] L.F. Ibarra, R.A. Medina, H. Krawinkler, Hysteretic models that incorporate strength and stiffness deterioration. *Earthquake Engineering and Structural Dynamics*, 34(12), 1489-1511, 2005.

[37] T.B. Panagiotakos, M.N. Fardis, Seismic response of infilled RC frames structures. *11th World Conference on Earthquake Engineering*, Acapulco, México, June 23-28. Paper No. 225, 1996.

[38] P. Ricci, G.M. Verderame, G. Manfredi, Analytical investigation of elastic period of infilled RC MRF buildings. *Engineering Structures*, 33(2), 308-319, 2011.

[39] R.J. Mainstone, On the stiffnesses and strengths of infilled frames. *Proceedings of the Institution of Civil Engineering*, Supplement IV, 57-90, 1971.

[40] P. Fajfar, M. Dolšek, R. Žarnić, S. Gostič, Development of numerical methodologies for infilled frames. *Towards European integration in seismic design and upgrading of building structures, Euroquake-project,* Final report, 2001.

[41] R. Žarnić, S. Gostič, Masonry infilled frames as an effective structural sub-assemblage. In: Fajfar, Krawinkler, Ed. Seismic design methodologies for the next generation of codes. Rotterdam: Balkema, 335-46, 1997.

[42] S. Sattar, A.B. Liel, Seismic Performance of Reinforced Concrete Frame Structures With and Without Masonry Infill Walls. *9th US National and 10th Canadian Conference on Earthquake Engineering,* Toronto, Canada, 2010.

[43] G.M. Verderame, G. Manfredi, G. Frunzio, Le proprietà meccaniche dei calcestruzzi impiegati nelle strutture in cemento armato realizzate negli anni '60. *Atti del X congresso nazionale ANIDIS "L'ingegneria Sismica in Italia"*, Potenza-Matera, Italy, September 9-13, 2001. (in Italian)

[44] G.M. Verderame, P. Ricci, M. Esposito, G. Manfredi, STIL v1.0 – Software per la caratterizzazione delle proprietà meccaniche degli acciai da c.a. tra il 1950 e il 2000, available at http://www.reluis.it/, 2012.

[45] E. Cosenza, C. Galasso, G. Maddaloni, Resistenza del calcestruzzo: modellazione probabilistica e risultati sperimentali, *Atti del XXV Convegno Nazionale AICAP "La progettazione e l'esecuzione delle opere strutturali nell'ottica della sostenibilità"*, Pisa, Italy, May 14-16. Paper No. 59, 2009. (in Italian)

[46] E. Cosenza, C. Galasso, G. Maddaloni, Analisi statistica delle caratteristiche sismiche degli acciai da cemento armato, *Atti del XXV Convegno Nazionale AICAP "La progettazione e l'esecuzione delle opere strutturali nell'ottica della sostenibilità"*, Pisa, Italy, May 14-16. Paper No. 57, 2009. (in Italian)

[47] M.N. Fardis, Experimental and numerical investigations on the seismic response of RC infilled frames and recommendations for code provisions. Report ECOEST-PREC8 No. 6. Prenormative research in support of Eurocode 8, 1997.

[48] D. Vamvatsikos, C.A. Cornell, Incremental dynamic analysis. *Earthquake Engineering and Structural Dynamics*, 31(3), 491-514, 2002.

[49] D. Vamvatsikos, C.A. Cornell. Applied incremental dynamic analysis. *Earthquake Spectra*, 20(2), 523-553, 2004.

[50] M. Dolšek, Development of computing environment for the seismic performance assessment of reinforced concrete frames by using simplified nonlinear models. *Bulletin of Earthquake Engineering*, 8(6), 1309-1329, 2010.

[51] F. McKenna, G.L. Fenves, M.H. Scott, OpenSees: Open System for Earthquake Engineering Simulation. Pacific Earthquake Engineering Research Center. University of California, Berkeley, CA, USA. http://opensees.berkeley.edu, 2004.

[52] P. Ricci, Seismic vulnerability of existing RC buildings. Ph.D. Thesis, University of Naples Federico II, Naples, Italy, 2010.

[53] C.B. Haselton, A.B. Liel, G.G. Deierlein, Simulating structural collapse due to earthquakes: model idealization, model calibration, and numerical solution algorithms. M. Papadrakakis, N.D. Lagaros, M. Fragiadakis eds. *ECCOMAS Thematic Conference on Computational Methods in Structural Dynamics and Earthquake Engineering (COMPDYN 2009),* Rhodes, Greece, June 22–24, 2009.

[54] I. Iervolino, C. Galasso, E. Cosenza, REXEL: computer aided record selection for code-based seismic structural analysis, *Bulletin of Earthquake Engineering*, 8(2), 339-362, 2010.

COMPDYN 2013
4th ECCOMAS Thematic Conference on
Computational Methods in Structural Dynamics and Earthquake Engineering
M. Papadrakakis, V. Papadopoulos, V. Plevris (eds.)
Kos Island, Greece, 12–14 June 2013

ANALYSIS OF LOCAL SHEAR EFFECTS IN BRICK MASONRY INFILLED RC FRAMES

L. Cavaleri, F. Di Trapani, M. Papia
Dipartimento di Ingegneria Civile, Ambientale, Aerospaziale e dei Materiali (DICAM).
University of Palermo, Viale delle Scienze – 90128 Palermo, ITALY
liborio.cavaleri@unipa.it

Keywords: infilled RC frames, equivalent strut, micromodel, brick masonry, local shear effects.

Abstract. *Masonry infills panels placed among framed structures meshes have a relevant influence in presence seismic actions in terms of strength stiffness and global displacement capacity. In the case of RC structures, the modifications of internal forces due to infill-frame interaction may be not compatible with surrounding frame members strength especially considering additional shear forces arising at the ends of beams and columns in contact with the panel under lateral actions. Such effects may be in many cases the cause of unexpected brittle collapse mechanisms which compromise the safety of the entire structure. In this paper by means of a double (micromodeling and macromodeling) procedure regarding RC meshes infilled with hollow brick masonry, a parametric study is provided defining a connection between local shear forces in critical frame regions and axial force on diagonal pin jointed strut. Proposed strategy allows to predict effective local shear forces using the simple macromodeling approach to reproduce the effect of masonry infills in models.*

1 INTRODUCTION

Masonry infill panels are largely diffused in the common building practice of framed structures even if they are usually considered as non-structural elements. By the observation of seismic damage on infilled frames structures and as largely documented by several analytical and experimental studies in the last decades, it is clear that frames and infills have a strong interaction under seismic load that is not always possible to consider as beneficial for structural safety.

The infilled meshes show, respect to bare ones, a significant increasing of lateral strength and stiffness. However global predictions extended to a whole structural complex are not easy to perform without specific analyses because these depend on the effective distribution of infills among structural meshes.

If planar distribution is regular and approximately symmetric, the contribution given by infill panels is generally beneficial especially in the case of buildings designed to resist to gravity loads only. Conversely irregular planar or elevation distributions are potentially dangerous being often the cause of additional torsional effects and soft story mechanisms activation respectively.

Another relevant aspect to consider in frame-infill interaction regards the modification of internal forces caused by the infills on the adjacent RC members and constitutes the central topic of this paper. As well known, in presence of lateral actions, the panel has a detachment from the infill, remaining in contact with this only in correspondence of the two opposite corners (Fig. 1).

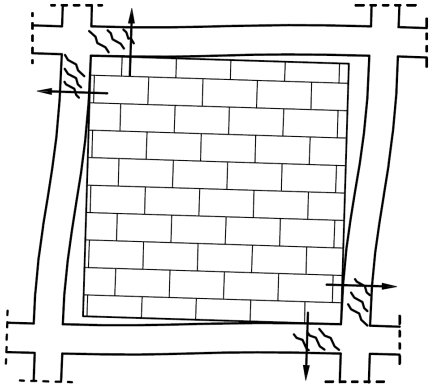


Figure 1. Transmission of local shear forces in infilled frames nodal regions in presence of seismic actions.

Lateral force increasing that occurs on infilled frames because of their higher stiffness is however allowable if RC members adjacent to panels (beams, columns and joints) have sufficient shear strength to avoid local failures.

Especially in the cases of strong infills combined with low shear reinforced frames, local collapse mechanisms are possible to activate compromising global capacity and safety of the entire structure. In Fig. 2 some examples of local shear failure mechanisms due to interaction with infills are reported.

Several authors proposed strategies to reproduce infills effects in structural models. Among these the most employed refer to the macromodel approach which is based on the substitution of the infill by means of an equivalent diagonal concentric pin jointed strut. Such approach, introduced for the first time by Holmes (1961) [1] and suddenly developed by other researchers Stafford Smith (1966) [2], Stafford Smith and Carter (1969) [3], Mainstone (1974) [4], Angel et al. (1994) [5], Papia et al. (2003) [6], has a good reliability in modelling of stiffening

effects produced by panels but is unable to provide any prediction about infill – frame interaction effects in nodal regions.

More complex macromodels, able to reproduce these aspects by means of two or three diagonal struts were also developed by Crisafulli et al. (2000) [7], Crisafulli and Carr (2007) [8], Fiore et al. (2012) [9]. Anyway the identification of mechanical properties to attribute to single struts is quite difficult to accomplish since this depends not only on mechanical features of masonry but also on infill – frame stiffness and geometrical ratios. Such difficulties in identification are more relevant when nonlinear analyses should be performed and the attribution of monotonical or cyclic nonlinear laws for multiple struts is required.



Figure 2. Local shear failures of frames due to interaction with infills under seismic loads.

Conversely to above mentioned methods, others authors Mallik and Severn (1969) [10], Mehrabi and Benson Shing (1997) [11], Benson Shing et al. (2002) [12], Gosh et al. (2002) [13], Asteris (2008) [14], Koutromanos et al. (2011) [15] adopted micromodeling approach to reproduce infill – frame interaction. In these cases panel and frames are modelled using planar shell finite elements while infill – frame contact regions are governed by means of interface elements able to reproduce frictional effects and infill – frame detachment. This kind of approach, that is surely more accurate, gives the best results in terms of local effects and global internal force distribution but, also in this case, the calibration of models and the attribution of interface laws is not easy to accomplish being often not well known all mechanical properties of infill masonries that depend moreover on manufacturing and constructive modalities. Besides the analyses of framed structures which involve micromodels require a so high computational effort to be unacceptable for practical engineering uses.

Interaction between infills and RC frames is also treated by technical codes. Eurocode 8 [16] in the section devoted to modelling in structural analysis prescribes that infill walls which contribute significantly to the lateral stiffness and resistance of building should be taken into account. Then, in the section regarding irregularities in plan, it is stated that infills should be included in the model and a sensitivity analysis regarding the position and the properties of the infills should be performed. Then, with reference to non-uniform distribution of infills in elevation, if a more accurate model is not used, one can calculate the seismic action effects on columns by amplifying them by the magnification factor η calculated as:

$$\eta = 1 + \frac{\Delta W_{Rw}}{\Delta W_{Sd}} \tag{1}$$

where ΔW_{Rw} is the strength reduction of considered storey respect to the upper infilled one and ΔW_{Sd} is the sum of the seismic shear forces acting at the top of considered storey.
Although many times the use of a reliable model is recommended, no models for the infill are included in Eurocode 8 as a support for practical applications, leaving designers free in choosing a criterion for modelling infills and identifying the complex frame-infill interactions.

In a similar way Italian technical code, D.M. 14/01/2008 [17], suggest to amplify forces in potentially soft storeys multiplying by a magnification factor which have a fixed value of 1.4 but also in this case no modelling criteria are given.

Unlike Eurocode 8 and Italian codes, the Federal Emergency Management Agency (FEMA) code 356 [18] explains clearly enough how to take infills into account: the effect of infills has to be considered by a FEM analysis or, alternatively, by introducing a diagonal pin-jointed strut equivalent to the infill. For the first option no more is said, unlike according the second one is specified that the equivalent strut should have the same thickness and modulus of elasticity as the infill panel (but it is not clear along which direction the modulus of elasticity must be calculated) while the width w is given by the following equation:

$$w = 0.175 \left(\lambda_1 h'\right)^{-0.4} d \tag{2}$$

where, with reference to Fig. 3, h' is the height of the frame, measured between the centrelines of the beams, d is the measure of the diagonal dimension of the infill and λ_1 is given by the equation:

$$\lambda_1 = \left[\frac{E_d t \sin 2\theta}{4 E_f I_c h} \right]^{\frac{1}{4}} \tag{3}$$

in which t is the thickness of the infill, h and ℓ are its height and length, respectively, $\theta = atan(h/\ell)$, I_c is the moment of inertia of the columns, E_d and E_f are Young's modulus of the infill and of the material constituting the frame, respectively.

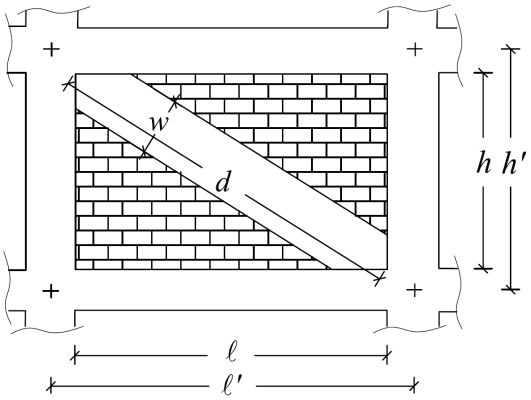


Figure 3. Geometrical features of infill-frame system for the identification of equivalent diagonal strut.

The FEMA code also specifies that beams and columns adjacent to infills should have sufficient strength to support local shear effects arising from the infill – frame interaction in presence of lateral actions. When more accurate analyses are not performed FEMA code states that flexural and shear strength of beams and columns in nodal regions should exceed

the internal forces evaluated by the application, at a specified length (Eqs. 3-4), of the horizontal and vertical components of the axial force in equivalent struts (Fig.4).

$$l_{ceff} = \frac{w}{\cos\theta_c}; \quad \tan\theta_c = \frac{h - l_{ceff}}{\ell} \tag{4}$$

$$l_{beff} = \frac{w}{\sin\theta_b}; \quad \tan\theta_b = \frac{h}{\ell - l_{beff}} \tag{5}$$

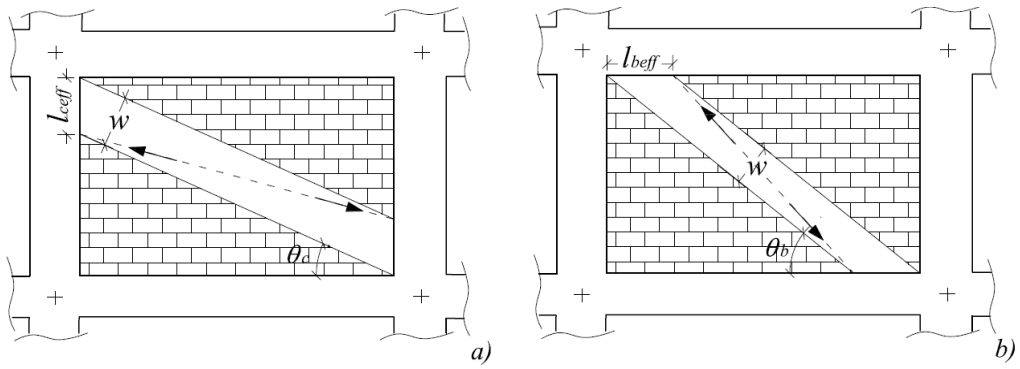


Figure 4. Schemes for evaluation of local effect according to FEMA 356: a) on columns; b) on beams.

A second condition should be verified calculating shear request in the case of formation of a possible ductile mechanism which originates by the activation of plastic hinges at the ends of the reduced lengths l_{ceff} and l_{beff}.

Despite the question of local failure of RC members adjacent to infills is treated in FEMA 356 more the other codes do, the modalities suggested for the evaluation of local effects do not derive form an effective evaluation on the model and may lead to possible overestimations of additional local effects to consider.

Taking into account what above mentioned, a strategy for the evaluation of effective local shear effects when single equivalent strut macromodels are used is developed in this paper.

Masonry typology constituting infill panels which is object of the actual study is hollow brick masonry as defined in ASTM C652 REV A [19].

Infilled meshes which are object of investigation are reproduced by means of two equivalent models in order to compare results: the first one (M1) which provides the use an equivalent concentric braced strut, the second (M2), which makes use of plane shell elements to model infills, nonlinear beam elements to model beams and columns and multilinear elastic links (*MElink*) resisting to compression only to model infill – frame interfaces. Comparisons are carried out varying mechanical features, geometry and stiffening ratios between frame and infill, evaluating for fixed interstorey drifts, the relationship between the axial force evaluated on equivalent strut in M1 model and shear forces evaluated in critical sections of beams and columns in M2 model. The final scope is the definition of a tool which permits to use the simple equivalent concentric strut approach as reference model for the analysis, being able to provide adequate correction coefficients for local shear forces arising in nodal regions.

2 FEM MODELLING

2.1 Models definition

As above mentioned the results of this work are based on the comparison between two different approaches to model same structural system. Referring to a generic infilled mesh, hav-

ing geometrical features indicated in Fig. 5, the responses for a fixed interstorey drift are compared for both M1 and M2 modelling approaches. The M1 model (Fig. 6a), based on the identification of an equivalent diagonal concentric strut replacing panel has a better performance in term of required computational effort. Nevertheless local shear effects on the RC members adjacent to the panel are not evaluable by means of this model. The M2 model (Fig. 6b) requires conversely a higher computational effort but it allows to determine the effective internal forces distribution on RC members trough micromodeling of panels, which are connected to beams and columns trough interfaces elements.

The two models are considered equivalent and comparable when they exhibit the same stiffness both in linear and nonlinear field. More generally stiffness equivalence is defined as function of interstorey drift (d_r) and expressed by the equation:

$$K_{M1}(d_r) = K_{M2}(d_r) \tag{6}$$

$K_{M1}(d_r)$ and $K_{M2}(d_r)$ being the lateral stiffness of M1 and M2 model for assigned d_r.

The identification of M1 and M2 models is afterward exposed while comparing procedures and results are discussed in the subsequent sections.

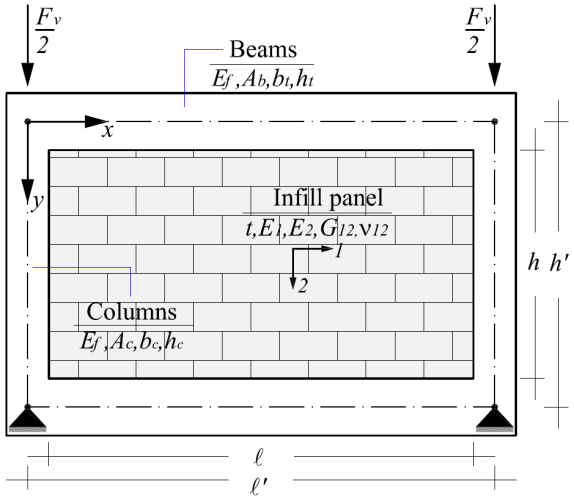


Figure 5. Generic features for an infilled mesh.

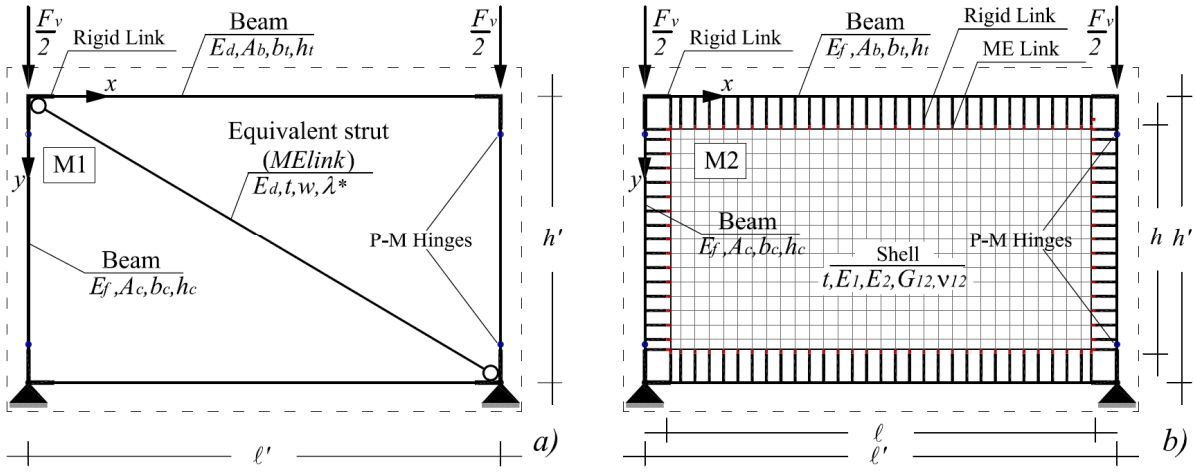


Figure 6. Modelling of infilled mesh: a) M1 model; b) M2 model.

2.2 M1 Model

The M1 model, represented in Fig. 6a, simulates RC infilled mesh having geometrical and mechanical characteristics reported in Fig. 5, in which b_t and h_t are width and depth of beams cross sections respectively and A_b the resultant area while b_c and h_c are width and depth of columns cross sections respectively and A_c the resultant area. The elastic Young modulus of concrete is indicated as E_f. Masonry infills are mechanically characterized by the parameters E_1, E_2, G_{12}, ν_{12} which are respectively the elastic Young modulus, shear modulus and Poisson ratio referred to directions 1 and 2. Equivalent diagonal strut cross section height w is identified through the below reported expression [6]:

$$w = d\,\kappa\frac{c}{z}\,\frac{1}{(\lambda^*)^{\beta}} \tag{7}$$

in which coefficients c and β depends on Poisson ratio ν_d along the diagonal direction and are defined by the below reported equations.

$$c = 0.249 - 0.0116\,\nu_d + 0.567\,\nu_d^{\,2} \tag{8}$$

$$\beta = 0.146 + 0.0073\,\nu_d + 0.126\,\nu_d^{\,2} \tag{9}$$

while the coefficient z depends on panels shape and is evaluable as:

$$z = 1 + 0.25(\ell / h - 1) \tag{10}$$

In Eq.(7) the coefficient k takes into account the effect of the vertical loads involving infill panels. This can be obtained as function of the vertical deformation on columns ε_v due to compressive load F_v (Amato et al. (2008) [20]) through the equation

$$\kappa = 1 + (18\lambda^* + 200)\varepsilon_v : \tag{11}$$

ε_v being evaluated as:

$$\varepsilon_v = \frac{F_v}{2A_cE_f} \tag{12}$$

The parameter λ^* (Eqs. (7) and (11)), which characterize stiffness ratios between infill and frame is finally defined as:

$$\lambda^* = \frac{E_d}{E_f}\frac{t\,h'}{A_c}\left(\frac{h'^2}{\ell'^2} + \frac{1}{4}\frac{A_c}{A_b}\frac{\ell'}{h'}\right) \tag{13}$$

Masonry elastic Young modulus E_d and Poisson ratio ν_d along diagonal direction can be expressed as function of the above defined mechanical parameter (E_1, E_2, G_{12}, ν_{12}) as suggested in Cavaleri et a. (2013) [21].

The equivalent strut constitutive law is defined by a trilinear force-displacement compressive diagram with no tensile strength (Fig. 6). The initial elastic stiffness K_1 evaluated as:

$$K_1 = \frac{E_d t w}{d} \tag{14}$$

while strength at elastic limit F_1 is defined as function of α parameter as follow:

$$F_1 = \alpha F_2 \tag{15}$$

Stiffness in post elastic branch K_2 is instead related to the parameter β as:

$$K_2 = \beta K_1 \tag{16}$$

Elastic limit and peak strength displacements are therefore directly identified:

$$\delta_1 = F_1 / K_1; \qquad \delta_2 = \delta_1 + (F_2 - F_1) / K_2 \tag{17}$$

The softening branch is linearized by connecting points F_2-δ_2 and F_3-δ_3, since F_3=0.7S_2 and δ_3 is obtained by the following expression (Cavaleri *et al*. (2005) [22]):

$$\delta_3 = \frac{1}{\zeta} ln\left[\frac{S_2}{S_3} exp(\zeta\delta_2)\right] \tag{18}$$

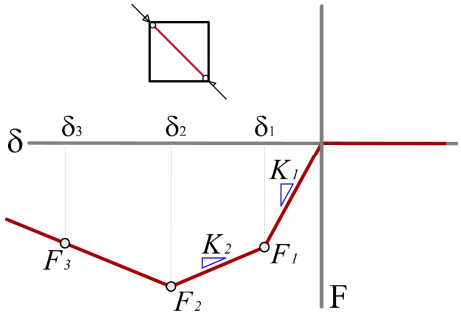


Figure 6. Force – displacement law for equivalent diagonal strut.

Peak strength F_2 of equivalent strut is determined as function of mean shear strength of the panel f_{v0m} as follow:

$$F_2 = f_{v0m} t \tilde{d} \tag{19}$$

in which $\tilde{d}$ represent the ideal diagonal dimension of the panel and is introduced in order to take into account a shear strength reduction due to its aspect ratio. The ideal dimension $\tilde{d}$ is calculated as a fraction of the effective diagonal length d of the panel as shown by means of the reduction factor ψ (Eq. (20)).

$$\tilde{d} = \psi d \tag{20}$$

ψ being obtained as:

$$\psi = \frac{h\sqrt{2}}{\sqrt{(h^2 + \ell^2)}} \tag{21}$$

Table 1 shows $\tilde{d}$ values calculated by substituting Eq. (21) in Eq. (20) for ℓ/h ratios *1, 1.5* and *2*.

ℓ/h	$\tilde{d}$
1.0	d
1.5	0.78 d
2.0	0.63 d

Table 1. Equivalent diagonal length dimensions for different ℓ/h ratios.

The case of collapse for crushing of the corners units in contact with the frame is conservatively here not considered.

The frame mechanical nonlinearities are introduced by means of 4 interacting axial force – bending moment plastic hinges (P-M) defined considering the effective cross section rein-

forcement and geometrical dimensions. Nodal regions at the intersections between beams and columns are modelled as rigid links.

Values adopted for parameters α, β and ζ, defining constitutive law shape for the equivalent diagonal strut, are the same of those proposed in Cavaleri et al. (2012) [23] for hollow brick masonry infills. Besides, basing on results reported in [22], is assumed that the elastic Young modulus ratio $\gamma=E_1/E_2$ is equal to *0.75*, shear modulus $G_{12}=0.4E_2$, Poisson's ratio $\nu_d \cong \nu_{12}=0.1$ while shear strength f_{v0m} of panels is *1.07 MPa* as noticeable by the experimental tests. The above mentioned parameters governing equivalent strut compressive law are summarized in Table 2.

α	β	ζ	f_{v0m} [Mpa]
0.4	0.15	0.02	1.07

Table 2. Parameters defining equivalent diagonal strut constitutive law.

2.3 M2 Model

Referring to the generic infilled mesh (Fig. 5a), the M2 model was also defined (Fig. 5c) providing micromodeling of infill panel by means of orthotropic elastic shell elements identified by the elastic Young moduli E_1 and E_2 along the two orthogonal directions, shear modulus G_{12} and Poisson ration ν_{12}. Modelling of RC beams and columns and plastic hinges is the same of M1 model. The distance between infill panel and surrounding frame beam elements is covered by means of null weight rigid links while mortar joint are modelled as interface elements. Rigid links have the unique function to transmit at each joint the mutual interface infill – frame forces. A similar approach is also proposed in Doudomins (2007) [24]. Interface elements are modelled using *multilinear elastic link* elements having only axial stiffness, no tensile strength and a constitutive law that is assumed elastic in compression. As above mentioned the interface elements are used to simulate mortar joints between masonry infills and RC frames. Taking into account the high manufacturing variability affecting the realization of these interface joints, a conventional elastic Young modulus $E_m=3000$ *MPa* and a conventional joint thickness $h_m=20$ *mm* is fixed. Considering that under lateral loads the infill – frame contact lengths are strongly reduced and mortar interface joints undergo a significant damaging, frictional effects are not included in the model. Moreover other studies (e.g. [9]) demonstrate that friction arising in interfaces is not decisive on the overall response.

Nonlinearity of shell elements, used to model infill panels, is introduced by iteratively modulating an equivalent thickness of masonry. The latter corresponds to the ideal thickness which allows to gain for M2 model, the same lateral stiffness exhibited by M1 model for a fixed interstorey drift.

The M2 model furnishes more detailed results being able to simulate both interface detachment and local shear effects on RC members ends.

3 PARAMETRIC ANALISYS

3.1 Models comparison procedure

As defined in section 2.1, the comparability of the models is possible when they exhibit the same stiffness at a generically assigned interstorey drift. The steps that make up the procedure used to evaluate local shear effects produced by infill panels on RC surrounding frames are below exposed: *a)* assignment of the mechanical properties and geometry of infilled mesh; *b)* choice of a reference interstorey drift (d_r); *c)* definition of M1 equivalent strut macromodel; d) definition of M2 micromodel in which thickness (t) of infill is initially set equal to the real thickness; *e)* identification of the level of damage in M2 model (iteratively reducing infill

thickness) restituting the same secant stiffness exhibited by M1 model (the damage of the frame is uniquely defined by assigning the drift ratio)*; f)* evaluation of effective RC frame internal forces on M2 model.

3.2 Experimental validation of models

In order to verify reliability of the models used to accomplish analyses, an experimental/analytical validation is preliminary performed on the basis of experimental results proposed by Cavaleri et. al (2012) [23], who investigated on the cyclic behaviour of hollow brick masonry infilled frames (Fig. 7). Experimental secant stiffness shown by specimens in cyclic tests are compared, for different drift levels, with those exhibited models M1 and M2 at the same drifts. Geometrical and mechanical characteristics of specimens are reported in Table 3.

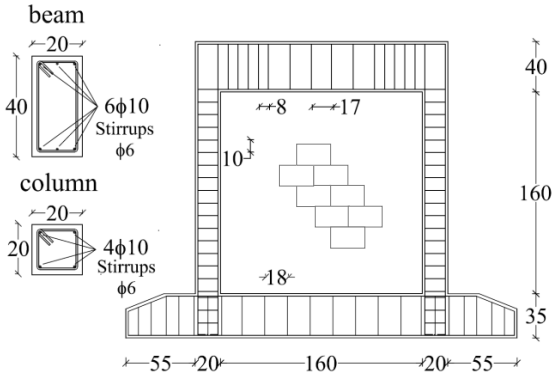


Figure 7. Hollow brick masonry infilled frame specimens details (Cavaleri et. al., 2012 [23]).

h_c [mm]	b_c [mm]	h_t [mm]	b_t [mm]	h [mm]	h' [mm]	ℓ [mm]	ℓ' [mm]
200	200	200	200	1600	1800	1600	1800
t [mm]	f_{v0m} [Mpa]	E_1 [Mpa]	E_2 [Mpa]	G_{12} [Mpa]	ν_{12}	E_f [Mpa]	F_v [kN]
150	1.07	6401	5038	2550	0.07	25000	400

Table 3. Geometrical and mechanical features of hollow brick masonry infilled frames specimens (Cavaleri et al., 2012 [23]).

Interstorey drifts selected for validation of M1 and M2 models are representative of three fundamental conditions of the overall response of the system: elastic phase (d_r*=0.03%*), post-elastic phase (d_r*=0.1%*) and peak strength (d_r*=0.6%*). The comparison between the experimental medium K_{SPM} secant stiffness of tested specimens and numerical secant stiffness K_{M1} and K_{M2} exhibited by models, provided the results reported in Table 4 for the previously defined interstorey drifts.

d_r [%]	K_{spm} [kN/mm]	K_{M1} [kN/mm]	K_{M2} [kN/mm]
0.03	125	130	112.6
0.1	62.50	66.1	67.2
0.6	17.6	16.64	16.55

Table 4. Comparison between experimental medium secant stiffness of specimens (Cavaleri et al., 2012 [23]) and M1, M2 models stiffness for different drift levels.

3.3 Parametric analysis

Parametric analyses afterwards discussed are carried out to evaluate the responses, for assigned damage level (identified by interstorey drift ratio), of infilled systems modelled by means of both the above described approaches. Geometrical and mechanical properties of frames and infills are varied in order to evaluate their influence on the distribution of shear forces occurring on beams and columns ends in contact with infills.

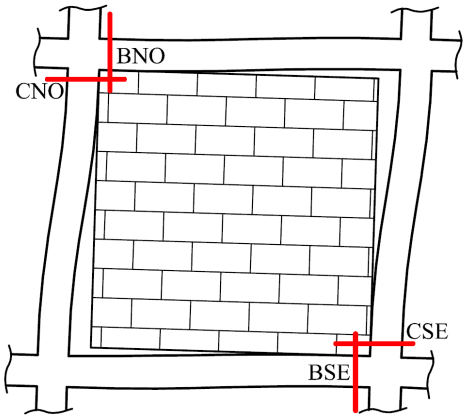


Figure 8. Critical section on RC frame.

With reference to Fig. 8, four critical sections can be identified as the most affected by local shear effects due to infill – frame interaction: BNO (Beam Northwest), BSE (Beam Southeast), CNO (Columns Northwest), CSE (Columns Southeast).

For each considered infilled mesh M1 and M2 models were generated and compared for a fixed drift by means of the previously described procedure. The below reported dimensionless quantities can be thus evaluated:

$$\alpha_{BNO} = \frac{V_{BNO}^{(M_2)}}{N_p^{(M_1)}}; \alpha_{BSE} = \frac{V_{BSE}^{(M_2)}}{N_p^{(M_1)}} \tag{22}$$

$$\alpha_{CNO} = \frac{V_{CNO}^{(M_2)}}{N_p^{(M_1)}}; \ \alpha_{CSE} = \frac{V_{CSE}^{(M_2)}}{N_p^{(M_1)}} \tag{23}$$

in which $N_P^{(M_1)}$ is the axial force on the equivalent diagonal strut evaluated in M1 model while $V_{BNO}^{(M_2)}$, $V_{BSE}^{(M_2)}$, $V_{CNO}^{(M_2)}$, $V_{CSE}^{(M_2)}$ are shear forces in critical sections evaluated in model M2.

In this way, the coefficients α_{BNO}, α_{BSE}, α_{CNO}, α_{CSE} define the relationship existing between shear forces on frame critical sections and axial force on the equivalent strut. If their prediction is possible a priori, they become a useful tool to evaluate the effective shear forces on frame sections as a quote of equivalent strut axial force for all cases in which modelling is performed by means of concentric equivalent strut models. The analyses are executed for two different fixed drift levels, which are representative (taking also into account the experimental evidence) of medium damage and peak strength damage (respectively d_{r1}= 0.1% and d_{r2} = 0.6%).

For d_{r1} analyses the parameter λ^* (Eq. (13)) was chosen as representative of the infill – frame system since it takes into account geometrical and stiffness ratios, while for d_{r2} analyses the product $\xi\lambda^*$ was adopted, being $\xi = h_f/h_c$. This difference on the choice of parameters identifying the infilled mesh is due to the fact that the term λ^* is determined by means of an elastic

approach not taking into account the strength ratios between beams and columns. The latter significantly affects coefficients α_{BNO}, α_{BSE}, α_{CNO} and α_{CSE} when high drift levels occur, especially with regard to plastic hinges formation. The term ξ does not exactly define the flexural strength ratio between beams and columns, however is closely related to it as it is defined.

Two sets of numerical specimens, having different infill aspect ratios (*ℓ/h=1.0* and *ℓ/h=2.0*) were analyzed. The geometrical dimensions are indicated in Tables 5-6 together with the terms λ^*, $\xi\lambda^*$ and *w*. Elastic properties are the same of those indicated in §2.1 while reinforcement geometrical ratio is 1% for all columns sections. It was furthermore assumed that beams have a higher flexural strength respect to columns as in the case of structures designed to resist to gravity loads only. Finally a dimensionless axial force *n=0.2* is assigned on columns.

Case	b_c [mm]	h_c [mm]	b_t [mm]	h_t [mm]	h [mm]	ℓ [mm]	λ^*	$\xi\lambda^*$	w [mm]
C1A	200	200	200	400	1600	1600	1.70	3.40	623
C2A	200	200	200	400	1600	1600	3.40	6.80	565
C3A	250	400	250	500	2700	2700	0.85	1.06	1190
C4A	250	400	250	500	2700	2700	1.30	1.63	1190
C5A	250	400	250	500	2700	2700	2.60	3.25	1034
C6A	250	400	250	500	2700	2700	3.00	3.75	1012
C7A	250	400	250	500	2700	2700	2.05	2.56	1067
C8A	600	300	300	500	2700	2700	0.82	1.37	1192
C9A	600	300	300	500	2700	2700	3.00	5.00	1054

Table 5. Numerical models features - *ℓ/h=1*.

Case	b_c [mm]	h_c [mm]	b_t [mm]	h_t [mm]	h [mm]	ℓ [mm]	λ^*	$\xi\lambda^*$	w [mm]
C1B	200	200	200	400	1600	3200	1.10	2.20	757
C2B	200	200	200	400	1600	3200	2.82	5.64	707
C3B	200	400	200	500	2700	5400	1.30	1.63	1362
C4B	200	400	200	500	2700	5400	2.00	2.50	1368
C5B	200	400	200	500	2700	5400	2.80	3.50	1121
C6B	200	400	200	500	2700	5400	0.85	1.06	1450
C7B	200	400	200	500	2700	5400	3.25	4.06	1200
C8B	600	300	300	500	2700	5400	0.82	1.37	1453
C9B	600	300	300	500	2700	5400	2.14	3.57	1293

Table 6. Numerical models features - *ℓ/h=2*.

Results of analyses are reported in Figs. 9-12 and show the relationship between the quantities λ^* and $\xi\lambda^*$ and coefficients α_{BNO}, α_{BSE}, α_{CNO}, α_{CSE} for drift levels d_{r1} and d_{r2}. Analytical best fitting functions are also provided.

It can be observed that for both considered drift levels α – coefficients undergo a reduction when increasing values λ^* and $\xi\lambda^*$. This trend expresses the general tendency of RC frames to receive shear forces quotes on critical sections that are much relevant as higher is frame stiffness with respect to the panel one. Results also show that the influence of panels' aspect ratio (*ℓ/h*) has a relevant role only for significant drift levels (d_{r2}). In these cases, when horizontal dimension ℓ prevails on height *h*, local shear effects are significantly more relevant on columns respect to beams.

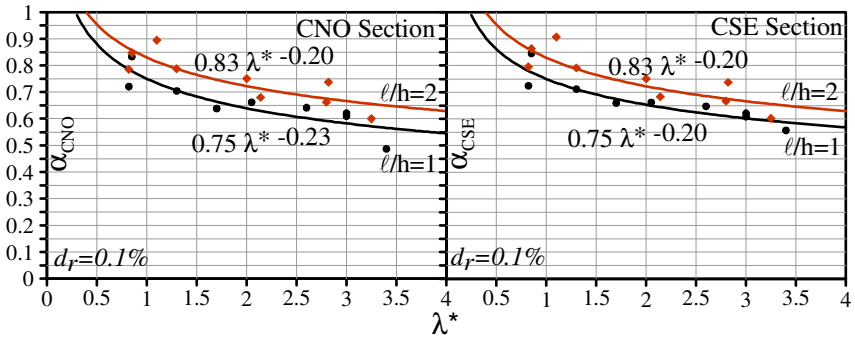


Figure 9. α_{CNO} - α_{CNE} vs. λ^* parametric analysis at d_r=0.1% and best fitting functions.

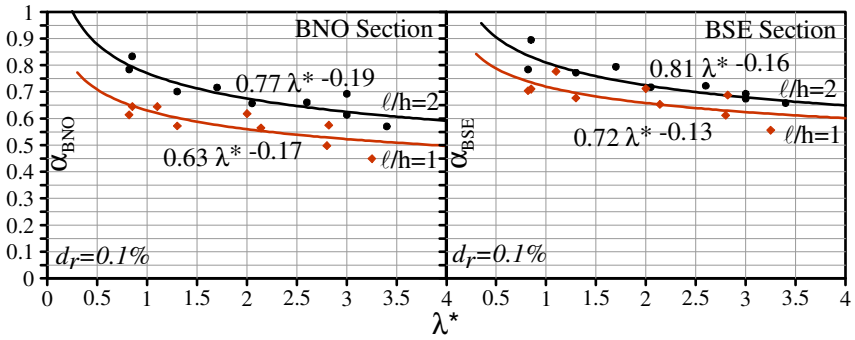


Figure 10. α_{BNO} - α_{BNE} vs. λ^* parametric analysis at d_r=0.1% and best fitting functions.

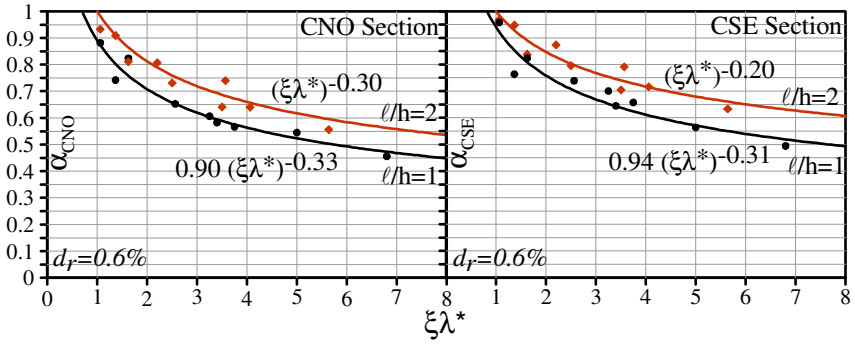


Figure 11. α_{CNO} - α_{CNE} vs. $\xi\lambda^*$ parametric analysis at d_r=0.6% and best fitting functions.

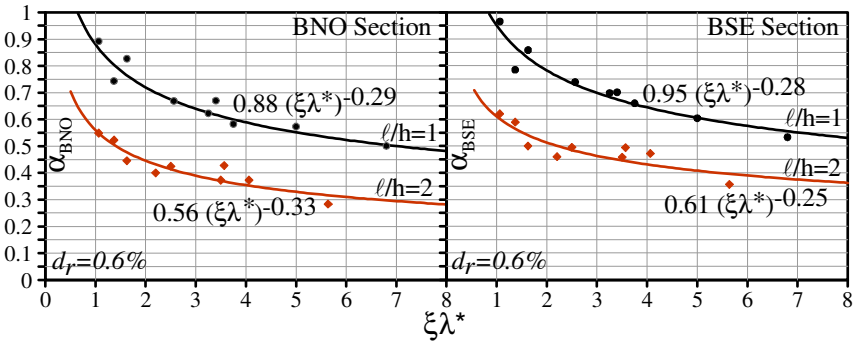


Figure 11. α_{BNO} - α_{BNE} vs. $\xi\lambda^*$ parametric analysis at d_r=0.6% and best fitting functions.

In Fig. 10 a comparison between the response exhibited by models M1 and M2 for a fixed drift is reported in terms of deformed shapes and internal shear forces distribution on RC

frame members evidencing also the strong relevance of local shear effects on critical sections determined by means of M2 model with respect to M1.

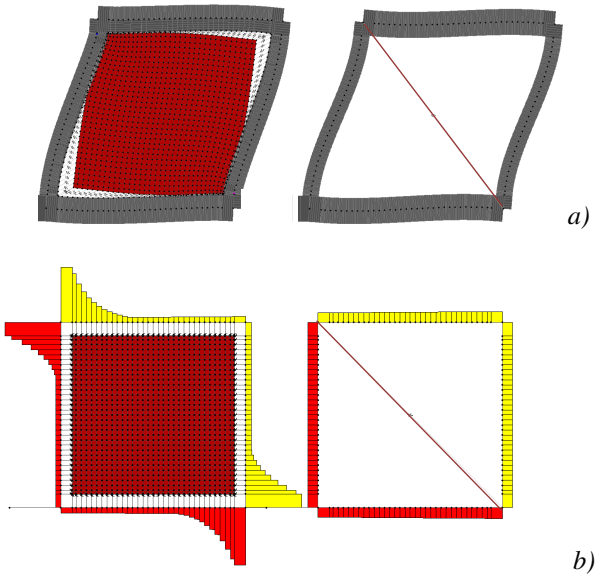


Figure 10. Comparison between M1 and M2 models responses: a) deformed shape; b) shear distribution.

Results of the above reported analyses can be used for verification RC members capacity when linear or nonlinear analyses are performed by means of equivalent concentric strut models. The suggested verification procedure provides first the evaluation of damage level by simply identifying the occurring interstorey drift ratio, the evaluation of the axial force on equivalent strut and subsequently the identification of parameters λ^* and $\xi\lambda^*$ for the reference infilled mesh. Once panel ℓ/h ratio is assigned, coefficients α_{BNO}, α_{BSE}, α_{CNO} and α_{CSE} are univocally identified through the analytical interpolating functions. Shear demand to be considered for verification of critical section V_{BNO}, V_{BSE}, V_{CNO}, V_{CSE} is thus evaluable by means of the following expressions:

$$V_{BNO} = V_0 + \alpha_{BNO} N_P \; ; \; V_{BSE} = V_0 + \alpha_{BSE} N_P \tag{24}$$

$$V_{CNO} = \alpha_{CNO} N_P \; ; \; V_{CSE} = \alpha_{CSE} N_P \tag{25}$$

V_0 being shear force due to the vertical loads on the beams and N_p the axial load on equivalent strut.

4 CONCLUSIONS

The present paper provides a tool for the evaluation local shear forces acting at the ends of beams and columns of hollow brick infilled frames in presence of lateral loads when adopting equivalent concentric strut macromodels.

By means of a parametric analysis, in which the mechanical characteristics of infill – frame systems are varied with the parameter λ^*, α- coefficients are evaluated providing also analytical best fitting functions. The latter permit to express local shear forces on critical sections of beams and columns as a fraction of axial load evaluated on the equivalent strut.

Once verified the substantial dependence of these coefficients on stiffness infill – frame ratio in linear and nonlinear phases, the latter become a predictive tool that is useful to asses

shear demand on RC members critical sections which is otherwise undetectable by means of simple equivalent concentric strut models.

The proposed tool was obtained by considering the mechanical properties of hollow brick masonry infills and primary structure configurations representative of RC frames designed to resist to vertical loads only. The study can be surely improved including the cases of masonry infills having different mechanical properties and seismic designed frames. It is however here possible to point out that a more accurate assessment of local shear effects is achievable even if high detailed and onerous models are not used to perform analyses. Moreover, the procedure here developed, may represent a supplementary instrument to technical codes prescriptions which may be often cause overestimations in evaluation of local infill – frame interaction effects.

AKNOWLEDGEMENTS

This study was sponsored by ReLUIS, Rete di Laboratori Universitari di Ingegneria Sismica, Linea 2, Obiettivo 5: Influenza della Tamponatura sulla Risposta Strutturale.

REFERENCES

[1] M. Holmes, Steel frames with brickwork and concrete infilling, *Proc. of Institution of Civil Engineers*, Paper No.6501:473-478,1961.

[2] B. Stafford Smith, Behaviour of the square infilled frames. *J. Struct. Div. (ASCE)*, **92**(1), 381-403, 1966.

[3] B. Stafford Smith, C. Carter, A method for analysis for infilled frames. *Proc. of Institution of Civil Engineers*, Paper No.7218, 31-48, 1969.

[4] R.J. Mainstone, Supplementary note on the stiffness and strength of infilled frames. *Building Research Station*, UK, Current Paper CP 13/74, 1974.

[5] R. Angel, D. Abrams, D. Shapiro, J. Uzarski, M. Webster, Behavior of Reinforced Concrete Frames with Masonry Infills. *Civil Engrg. Studies, Structural Research Series*. No. 589, UILU-ENG-94-2005, Dept. of Civil Engineering, University of Illinois at Urbana Champaign, 1994.

[6] M. Papia, L. Cavaleri, M. Fossetti, Infilled frames: developments in the evaluation of the stiffening effect of infills. *Struct. Eng. and Mech.*, **16**(6), 675-93, 2003.

[7] F.J. Crisafulli, A.J. Carr, R. Park, Analytical modelling of infilled frames structures –a general review. *Bull. NZ Soc. Earth. Eng.*, **33**(1), 30–47, 2000.

[8] F.J. Crisafulli, A.J. Carr, Proposed macro-model for the analysis of infilled frame structures. *Bull. New Zealand Soc. Earth. Eng.*, **40**(2), 69–77, 2007.

[9] A. Fiore, A. Netti, P. Monaco, The influence of masonry infill on the seismic behavior of RC frame buildings. *Eng. Struct.* , **44,** 133-45, 2012.

[10] D.V. Mallick, R.T. Severn, The behaviour of infilled frames under static loading. *Proc. Inst. Civ. Eng.*, **38**, 639-56, 1967.

[11] A.B. Mehrabi, P.B. Shing, Finite element modelling of masonry-infilled RC frames. *J. Struct. Eng.*, **123**(5), 604-13, 1997.

[12] P.B. Shing, A.B. Mehrabi, Behaviour and analysis of masonry-infilled frames. *Prog. Struct. Eng. Mater.*, **4**(3), 320–31, 2002.

[13] A.K. Ghosh, A.M. Made, Finite element analysis of infilled frames. *J. Struct. Eng.*, **128**(7), 881–89, 2002.

[14] P.G. Asteris, Finite element micro-modeling of infilled frames, *Electronic J. of Struct. Eng.*, **8**, 1-11, 2008.

[15] I. Koutromanos, A. Stavridis, P. Benson Shing, K. Willam, Numerical modeling of masonry-infilled RC frames subjected to seismic loads. *Computers and Structures*, **89**(11-12), 1026-37, 2011.

[16] Eurocode 8, 2004. Design of structures for earthquake resistance - Part 1: General rules, seismic actions and rules for buildings.

[17] D.M. LL. PP. 14 Gennaio 2008, Nuove norme tecniche per le costruzioni.

[18] FEMA 356, 2000. Prestandard and commentary for the seismic rehabilitation of buildings.

[19] ASTM C652 REV A, Standard Specification for Hollow Brick (Hollow Masonry Units Made From Clay or Shale), 2012.

[20] G. Amato, M. Fossetti, L. Cavaleri, M. Papia, An updated model of equivalent diagonal strut for infill panels. *Eurocode 8 perspectives from Italian standpoint, workshop*; Napoli, Italy, 2008.

[21] L. Cavaleri, F. Di Trapani, G. Macaluso, M. Papia, P. Colajanni, Definition of diagonal Poisson's ratio and elastic modulus for infill masonry walls. *Mat. and Struct.* DOI 10.1617/s11527-013-0058-9, 2013.

[22] L. Cavaleri, M. Fossetti, M. Papia, Infilled frames: developments in the evaluation of cyclic behavior under lateral loads. *Struct. Eng. and Mech.*, **21**(4), 469-94, 2005.

[23] L. Cavaleri, F. Di Trapani, M. Papia, Strutture intelaiate e tamponate in c.a.: sperimentazione e sviluppi nella modellazione analitica e numerica. *19° Congresso CTE*, Bologna, Itay, November 8-10, 2012.

[24] I.N. Doudoumis, Finite element modelling and investigation of the behaviour of elastic infilled frames under monotonic loading, *Eng. Struct.*, **29**(6), 1004–24, 2007.

COMPDYN 2013
4th ECCOMAS Thematic Conference on
Computational Methods in Structural Dynamics and Earthquake Engineering
M. Papadrakakis, V. Papadopoulos, V. Plevris (eds.)
Kos Island, Greece, 12–14 June 2013

VALIDATION OF ANALYTICAL MODELS FOR THE ASSESSMENT OF BRICK-INFILLED RC FRAMES STRENGTHENED WITH FRPS

Constantine C. Spyrakos[1], Charilaos A. Maniatakis[1], Ioannis N. Psycharis[1], Eleni Smyrou[1], and Panagiotis G. Asteris[2]

[1] Laboratory for Earthquake Engineering, School of Civil Engineering, National Technical University of Athens
Iroon Polytecheiou Str., Zografou Campus, GR 15780, Athens, Greece
cspyrakos@central.ntua.gr; chamaniatakis@gmail.com; ipsych@central.ntua.gr; smiroulena@gmail.com

[2] Computational Mechanics Laboratory, School of Pedagogical & Technological Education
Heraklion GR 14121, Athens, Greece
asteris@aspete.gr

Keywords: Brick-infilled Reinforced Concrete Frames, FRP Composites, Retrofit of Structures.

Abstract. *Numerous modern seismic codes including Eurocode 8 provide rules to avoid possible adverse impact of the presence of masonry infills in concrete buildings or unbraced steel or composite structures. These adverse effects include damage of columns in contact with strong infills, reduction of the clear column height because of partial contact with masonry along height, planwise and heightwise irregularity. However, codes emphasize on the design of new structures, while little information is provided on modeling of masonry infills. Conversely, when the seismic upgrading of existing structures is performed with those methods that have received wider application in engineering practice, i.e., strengthening of columns and beams with reinforced concrete (RC) jackets or Fiber Reinforced Polymers (FRPs), construction of additional RC shear walls and construction of diagonal steel elements, any beneficial effect of masonry infills is usually ignored. The present research examines the effectiveness of strengthening existing RC frames with the application of FRP sheets on their brick-infill walls. This recently proposed method uses the advantageous mechanical properties of FRPs and is characterized by relatively low cost and ease of implementation compared to other aforementioned available retrofit schemes. A multi-strut masonry panel element is used to simulate the nonlinear response of the infill wall, while the FRP contribution to the response is modeled with a tension tie. Experimental results available in the literature for a scaled reinforced concrete frame are used to calibrate the parameters of the numerical model. Comparisons are made between the analytically and the experimentally derived results, and the effectiveness of the retrofit scheme is assessed. Also a simple method to modify the lateral stiffness of masonry infills to account for the presence of openings is addressed.*

1 INTRODUCTION

The modelling of masonry infills in reinforced concrete (RC) structures has received less attention from design codes, since non-structural masonry infills are usually considered as a beneficial second line of defence for the structure, provided that they are effectively confined by the surrounding frame and properly placed. The current Eurocode 8 [1], following this concept, does not provide detailed guidance on modelling masonry infill panels, except for the case of solid infill panels, while it provides appropriate rules to avoid possible adverse impact of the presence of masonry infills in concrete buildings or unbraced steel or composite structures. These adverse effects include [2]:

(i) Possible damage of columns in contact with strong infills; the presence of infills is considered in the shear design of RC columns of the surrounding frame.
(ii) Reduction of the clear column height because of partial contact with masonry along height ('short column' effect); in that case, pre-emptive brittle failure of the surrounding is possible.
(iii) Plan-wise or height-wise irregularity; an asymmetric distribution of infills in plan may cause significant torsional response, while a soft or weak storey may cause an unexpected concentration of damage.

Ignoring infills in design is also attributed to the lack of ductile behaviour, their complex dynamic behaviour, the uncertainty and large variability of critical parameters, the lack of sufficient experimental data, and the difficulty in modelling many of the failure modes because of the interaction of masonry with the frame members [3].

A large number of reinforced concrete (RC) structures with masonry infills were severely damaged or even collapsed during recent earthquakes. Existing brick-infilled RC buildings often present common weaknesses attributed to their design or construction that explain their high seismic vulnerability, e.g. existence of soft first or intermediate storey, application of the strong-beam and weak-column design approach, use of low-strength concrete, and lack of adequate reinforcement detailing.

Usually, upgrading of existing RC structures is related with extensive interventions, aesthetical modifications, and significant cost or even operational interruptions. Common retrofit schemes include construction of new reinforced concrete shear walls, precast elements or steel diagonal struts, and the use of RC jackets. In this sense, the consideration of the contribution in strength and stiffness of masonry infills might be beneficial in providing a most effective retrofit scheme. The present research studies the efficiency of upgrading existing masonry-infilled RC frame structures with the use of Carbon Fibre Reinforced Polymers (CFRP). The fibre reinforced polymers are characterized by small thickness and weight, relative ease of application, resistance to environmental conditions and high strength compared to conventional materials. Their application results in significant increase in strength with very little modification of mass and stiffness; thus, slightly modifying the design seismic loads that are expected for the retrofitted structure [4-6].

Under small lateral loading, the RC frame and the infill masonry operate uniformly as a single body, while the increase of lateral load leads to a highly non-linear behaviour [7]. The contribution of infill walls to lateral stiffness depends on the type of loading and is drastically reduced under reversed cycling loading [8]. In engineering practice, infill walls are usually modelled as a combination of diagonal struts following a macro-modelling approach [9, 10] while more complex models exist that implement constitutive relations available in the literature to account for the non-linearity of the response [11-14].

In infilled RC frames with no openings, the orbits of compressive and tensile stresses follow the two diagonal paths. Therefore, the infill wall behaves as a strut in the diagonal that is

under compression, while detachment from the surrounding frame is observed at the other diagonal. The placement of CFRP along the two main diagonals allows the wall to undertake tensile stresses along the tensile diagonal, limiting the deformation of the frame and increasing the resistance to lateral loads [15, 16]. Several efforts have been made recently to understand the in-plane and out-of-plane behaviour of FRP infilled RC frames [5, 15-18] that resulted in the identification of two main failure modes for this retrofit method: (a) anchor failure; and (b) debonding. Since widespread dispersion in the mechanical characteristics of masonry is observed, the most possible accurate knowledge of these values is important for the effective application of this retrofit scheme.

The present research attempts to validate analytically the effectiveness of the FRP application on brick infilled RC frames using the experimental results of Akgüzel [19] and Özden & Akgüzel [18]. The nonlinear response of the brick infill wall is modelled applying the four node masonry panel element developed by Crisafulli [10], available in SeismoStruct [20], a fibre-based finite element software package for static and dynamic analyses, that takes into account both geometric and material nonlinearities.

2 DESCRIPTION OF SPECIMENS AND LOADING

The research of Akgüzel [19] includes experiments on five identical two-storey scaled frames named U_i (i=1, 2, …, 5), that exhibit structural shortcomings, i.e., lack of sufficient anchorage length of the longitudinal reinforcement, low concrete strength, insufficient column lap splice length and poor confinement: (1) U_1 frame was a bare frame without infills; (2) U_2 frame was identical to U_1 with brick-infills without FRP strengthening; (3) U_3 frame was identical to U_2 with CFRP sheets of inadequate bond length along the two main diagonals on both stories; (4) U_4 frame was identical to U_3 with rather sufficient bond length on the masonry surface; (5) U_5 frame was identical to U_3 and U_4 but the appropriate anchorage of the FRPs was achieved by extending the sheets outside the diagonals of the infills on the columns of the frame. All the experiments were conducted in the Structures Laboratory of Boğaziçi University. Only the first three frames U_1, U_2 and U_3 are considered in the present research.

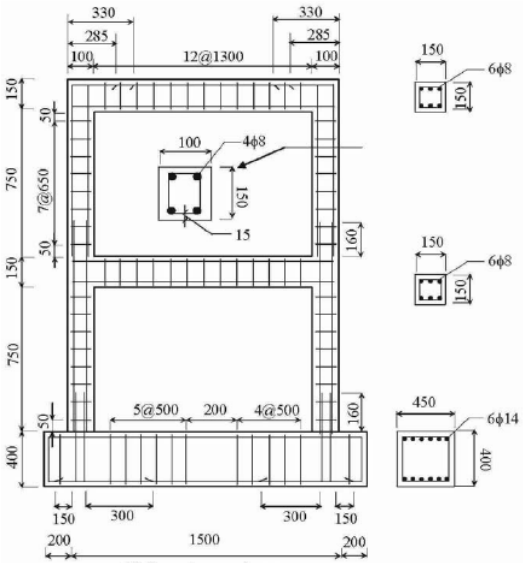


Figure 1: Bare frame U_1 tested in the Boğaziçi University, Structures Laboratory (dimensions in mm) - reproduced from [19].

The two-storey, one-bay plane frame with a 0.90 m typical storey height and 1.50 m typical bay length is shown in Fig. 1. Orthogonal sections of 100 mm × 150 mm and 150 mm × 150 mm were used for the columns and the beams, respectively, as shown in Fig. 1, with the small dimension of the columns' section being in-plane with the frame. The compressive strength of the concrete was slightly varying between the frames, with an average value of f_c = 15.4 MPa and reinforcement with yield strength f_y = 241 MPa was used for the columns and the beams. Bricks, with dimensions: 70 mm (height, put in the vertical direction), 90 mm (width) and 85 mm (length), were used for the construction of infill walls in frames U_2 to U_5. Low strength mortar was used between the brick connection and for the plaster. The CFRP sheets were applied at both sides of the masonry using epoxy resin. In all specimens, the material was applied in layers of 200 mm, in such a way that could operate along the two main diagonals of the wall. The tensile strength and the modulus of elasticity of the fibres were f_{fib} = 3500 MPa and E_{fib}=230000 MPa, respectively. The tensile strength and the modulus of elasticity of the epoxy were f_m = 30 MPa and E_m=3800 MPa, respectively. For more information on the material properties one should refer to [18, 19].

Cyclic loading was applied to the specimens in two phases: firstly, the frames were pushed under lateral cyclic forces with a triangular pattern along their height, until the first yield occurred; then, a cyclic loading phase was following till failure. The loading history for U_1 frame is shown in Fig. 2.

3 MODELING OF THE SPECIMENS

As mentioned, three types of RC frames were studied: the bare frame U_1 and two infilled frames, the un-strengthened frame U_2 and the CFRP strengthened frame U_3. The numerical models for the bare frame and the infilled ones had the same geometry with the typical section details shown in Fig. 1. The frame structure was modelled using inelastic fibre elements for the beams and the columns, which were calibrated from the experiments [19]. The steel model proposed by Menegotto and Pinto [21, 22] and the nonlinear constant confinement concrete model of Mander *et al.* [23] were applied for the reinforcement bars and the concrete, respectively.

The masonry panel element model used in the present study was originally developed by Crisafulli [10] and calibrated by Smyrou [24]. Each panel element contained six elements: two struts parallel to each diagonal that transferred the axial load between the two diagonal

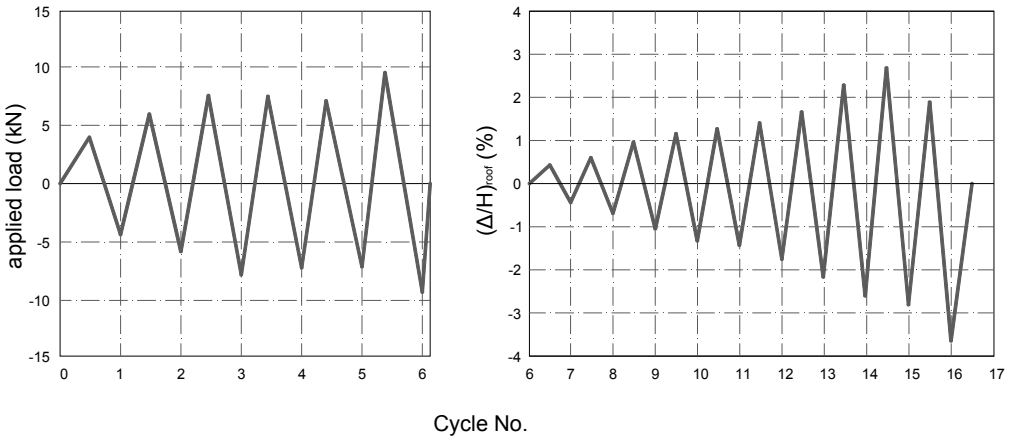


Figure2 : Loading history for cyclic analysis of the bare frame U_1 [19].

nodes and a pair of springs related to each diagonal (one for each direction of loading) that transferred the shear load from the top of the wall to the base. Each one of the latter was activated if the corresponding diagonal at which it belonged was compressed; thus its activation was directly dependent on the deformation level of the masonry.

A simple uniaxial tri-linear model that acts only under tension was used to simulate the CFRP. The main parameters that determine the response of this element are: (i) the tensile strength, f_t; (ii) the initial stiffness, E_1; (iii) the post-peak stiffness, E_2; and (iv) the specific weight, γ. The main parameters needed to describe the constitutive laws of the models implied are shown in Table 1. The selected values result from either the characteristics of the materials used for the specimens' construction [19] or the parametric analyses that follow. The range of values and the default values described in Table 1 are indicative and are based on the literature included in the development of the Seismostruct code [20]. When a value is not included in the "common range of values" column, either the range is extremely wide or there are insufficient experimental data to determine a reasonable range for this parameter. In several cases the parameter is calculated analytically, so the determination of a strict range is of no point. In the following, a brief discussion on these main parameters is made.

As discussed previously the model proposed by Crisafulli [10] uses two pairs of diagonal struts that act mainly under compression and a pair of shear springs that transfer shear loads

Model	Parameter name	Default value in Seismostruct	Common range of values	Selected value
Concrete model - Mander *et al.* [23]	Compressive strength - f_c	30.0 MPa	15 ~ 45 MPa	15.4 MPa
	Tensile strength - f_{tc}	0.0 MPa	0.50 ~ 0.75 MPa	0.0 MPa
	Strain at peak stress -ε_c	0.002 mm/mm	0.002 ~ 0.0022 mm/mm	0.002 mm/mm
Steel model - Menegotto & Pinto [21, 22]	Modulus of elasticity - E_s	200 GPa	200 ~ 210 GPa	195 GPa
	Yield strength - f_y	500 MPa	230 ~ 650 MPa	200 MPa
	Strain hardening parameter - μ_s	0.005	0.005 ~ 0.015	0.005
	Transition curve initial shape parameter - R_0	20.0		19.0
	Transition curve shape calibrating coefficient - a_1	18.5		18.7
	Transition curve shape calibrating coefficient - a_2	0.15	0.05 ~ 0.15	0.15
Masonry Panel Model - Crisafulli [10]	Initial Young modulus - E_{mas}	1.6 GPa		1.7 GPa
	Compressive strength - f_{mas}	1 MPa		1.65 MPa
	Tensile strength - $f_{t,mas}$	0.575 MPa		0.575 MPa
	Strut Area 2 - A_2	40 %		15 %
	Strain at maximum stress - $e_{m,mas}$	0.0012 mm/mm	0.001 ~ 0.005 mm/mm	0.0014 mm/mm
	Utimate strain - $e_{u,mas}$	0.024 mm/mm		0.012 mm/mm
	Closing strain - $e_{cl,mas}$	0.003 mm/mm	0 ~ 0.003 mm/mm	0.003 mm/mm
	Strut area reduction strain – e_1	0.0006 mm/mm	0.0003 to 0.0008 mm/mm	0.0006 mm/mm
	Residual strut area strain – e_2	0.001 mm/mm	0.0006 ~ 0.016 mm/mm	0.002 mm/mm
	Shear bond strength – τ_0	0.3 MPa	0.1 ~ 1.5MPa	0.7 MPa
	friction coefficient - μ_{mas}	0.3	0.1 ~ 1.2	1.2
	Maximum shear strength - τmax	0.6 MPa		1.2 MPa
	Starting unloading stiffness factor - γ_{un}	1.5	1.5 ~ 2.5	1.5
	Strain reloading factor - α_{ch}	0.2	0.2 ~ 0.4	0.2
	Plastic unloading stiffness factor - e_{x1}	3.0	2.0 ~ 3.0	3.0
Trilinear CFRP model	Tensile strength - f_t	3000 MPa	1900 ~ 4800 MPa	953 MPa
	Initial stiffness - E_1	300 GPa	70 ~ 700 GPa	130 GPa
	Post-peak stiffness - E_2	500 GPa		130 GPa

Table 1: Main model parameters.

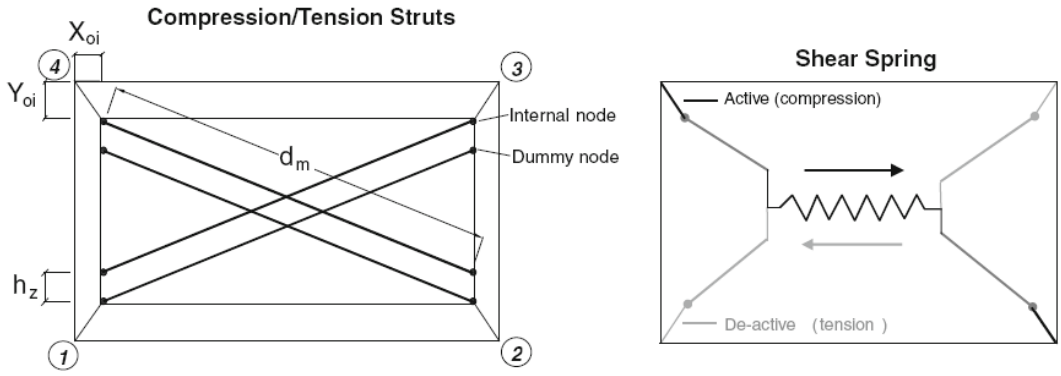


Figure 3: Four-node panel element model used in this study - reproduced from [25].

from the top to the bottom of the panel element across the diagonal under compression. Two different hysteretic rules apply for the total representation of the infill response: (i) a masonry strut hysteresis model for the diagonal struts; and (ii) a bilinear hysteresis rule for the shear springs. In Fig. 3, the two parallel struts per diagonal direction and the two shear strings (one per each diagonal direction) are shown (reproduced from Crisafulli & Carr [25]). The four dummy nodes shown in Fig. 3 are introduced to account for the contact length between the frame and the infill panel.

A relatively simple tri-linear uniaxial model is implemented for the FRP material. This model is fully described by four parameters: (i) tensile strength, f_t; initial stiffness, E_1; post-peak stiffness, E_2; and specific weight. The FRP material looses its strength very sharply upon rupture; however, a finite value is usually assigned to the post-peak stiffness E_2 to avoid numerical instability of the analyses. Since bond failure is difficult to model without the application of a more sophisticated procedure, the tensile strength f_t of the FRP was determined so that the failure occurs for the same axial deformation with the experiment; thus, in the analytical model the CFRP reaches its full tensile strength that is smaller than the original.

4 ANALYTICAL RESULTS

Two types of analyses were contacted, namely: (a) static non-linear analysis; and (b) quasi-static (cyclic) analysis, in order to: (i) compare with the experimental results; and (ii) determine "critical parameters" for the analysis.

The static non-linear analysis consisted of a Load Control phase and a subsequent Displacement Control phase and aimed to determine the capacity curve of the frames under lateral loads. A triangular load distribution was selected during the first phase, so that the load at the second floor level was always twice the load applied at the first floor. For U_1 frame, loading at the level of the second floor only was considered, as was the case during the experiment [19]. Subsequently, a Displacement Control phase followed till the desired roof displacement was reached. The load factor and the total number of steps for the two phases were different for each frame.

The second type of analysis was identical in terms of conditions and loading protocol to the experiments performed by Akgüzel [19]. A pseudo-dynamic analysis was performed, modelling the cyclic loading of the experiments. More specifically, cyclic forces were imposed at both storey levels up to yield and then displacements were imposed till failure occurred, with the exception of the bare frame where only the second floor was loaded as mentioned above. The experimental results were used to estimate the values of critical parameters of the analytical models. This assessment was made by comparing the capacity curves that resulted from the non-linear static analyses for several values of these parameters

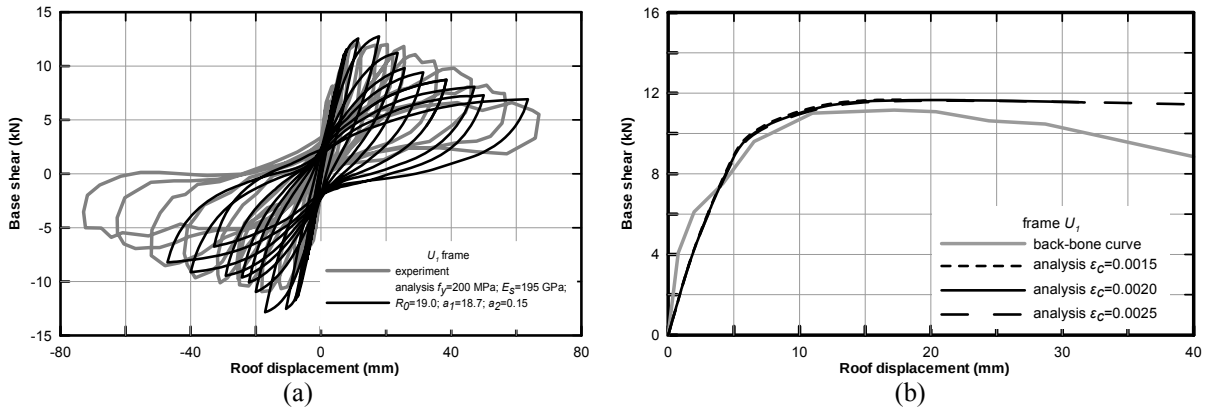
with the corresponding backbone curves that resulted as envelopes of the lateral load–displacement hysteretic curves obtained from the experiments.

4.1 Validation of U_1 frame

The characteristic parameters of the concrete and the steel of the reinforcement were determined to account thoroughly for the response of the bare frame U_1. The lateral load–displacement curve for the cyclic test is shown in Fig. 4a, while the backbone curve was obtained after connecting the points of maximum force and displacement for each cycle.

Since the strength and the modulus of elasticity of the materials were already known [19], the following parameters had to be calibrated from the comparison with the experimental results: (i) the strain hardening parameter, μ; and (ii) the strain of concrete at peak stress, ε_c [20]. The overlap length of the longitudinal bars of the reinforcement at the base of each floor was inadequate (equal to 160 mm, twenty times the diameter of bars). Therefore, it was expected that bond slip would occur prior to yielding of the reinforcement. An accurate modelling of the bond slip would require the use of a more sophisticated model, which was out of the scope of the present research. On the other hand, the assumption that no bond slip occurs allows the reinforcement to develop its full strength, which was not the case in the experiments, thus differences from the experimental data were expected. In order to reduce the error, we assumed full bond of the rebars and reduced yield strength of the steel. It was found that a value of f_y = 165 MPa resulted in an acceptable fit; thus, a reduction of f_y to ~45% of its nominal value was applied to account for the inadequate bond. Such an approximation is valid, since the primary objective of this research was to focus on the CFRP effects and on the modelling of infilled frames. A similar investigation was performed in order to determine the strain hardening parameter μ. As expected, this parameter affected the inelastic response of the frame structure and the most acceptable value resulted to be μ=0.00.

In Fig. 4a, the static pushover curve for the finally selected values for all the basic parameters is compared with the curve corresponding to the experimental results. It is observed that, for the selected values of the critical parameters f_y and μ, a very satisfying match is achieved between the analytical results of static pushover analysis and the envelope of the experimental results for lateral load and displacement. The inelastic and plastic behaviour of the frame is simulated with acceptable accuracy regarding the shape and the maximum values. In the experiment, the maximum base shear was 11.16 kN and corresponded to roof displacement 17.2 mm, while the corresponding value of the analytical model was 11.07 kN at 20.3 mm roof displacement.



(a) (b)

Figure 4: Comparison of the experimentally and the analytically derived load-displacement curves for U_1 frame: (a) cyclic loading, and (b) monotonic loading. The parameters used in the analytical model are; f_y = 200 MPa; E_s = 195 GPa; μ_s = 0.005; f_c = 15.40 MPa; ε_c = 0.002; R_0 = 19.0; a_1 = 18.7; a_2 = 0.15.

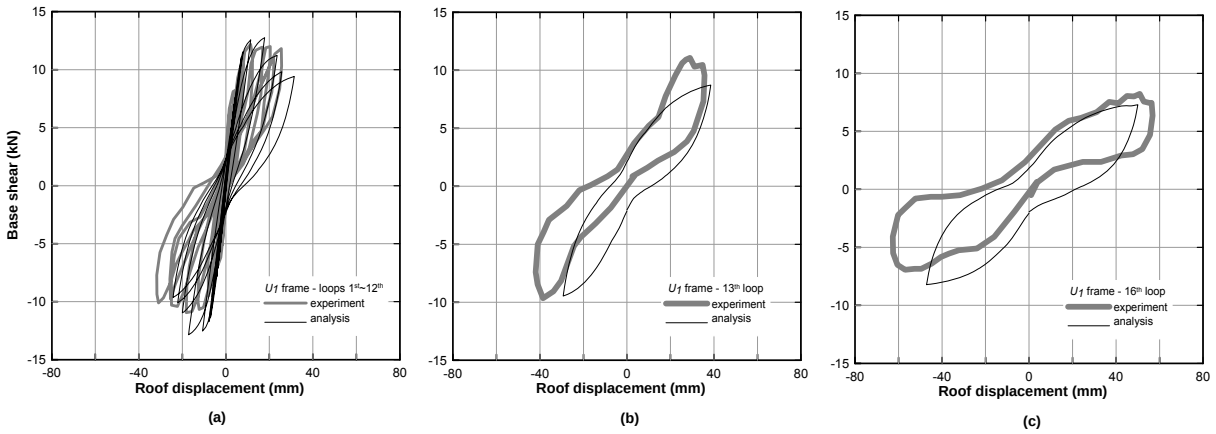


Figure 5: Comparison of the experimentally and the analytically derived load-displacement curves for U_1 frame: (a) force-displacement loops 1 to 12; (b) 13th force-displacement loop; (c) 16th force-displacement loop.

The final results of the cyclic analysis are presented in Fig. 4b and are compared with the experimentally derived curves. It is seen that the maximum base shear at each cycle and the corresponding rood displacement of the analytical model are similar to those of the experiment. In the experiment, the stiffness during unloading was decreasing progressively and the loops were narrower around the origin. This phenomenon, known as pinching, is attributed to bond slip at the overlap regions and is controlled by the parameter R and the coefficients a_1 and a_2 of the Menegotto & Pinto steel model [21]. Modifying the values of these quantities through a parametric evaluation, a better fit of the analytical and experimental results was achieved, as shown in Fig. 4b. However, a slight deviation from the analytical results still remained because full bond of the rebar was considered and the effect of the bond slip was taken under consideration with the reduction of the yield stress, as described above. This approximation slightly affected the response of the frames with infill walls, as will be shown in the following sections.

In Figs 5, the analytically derived base shear – roof displacement loops are compared with the experimental results to further confirm the applicability of the procedure. In Fig. 5a, the first twelve loops, where the maximum resistance is reached, are shown, while in Figs 5b and 5c the 13th and the 16th loops are compared, respectively, where pure inelastic response is noticed. Both the shape and the maximum values of the loops that are obtained by the analysis present acceptable accuracy.

4.2 Validation of U_2 frame

In the development of U_2 frame model, the values of the parameters for concrete and steel determined for U_1 frame were used. The applied loading protocol was similar to the one applied to the U_1 frame. The experimental results for base shear and the roof displacement for the cyclic loading and the corresponding backbone curve are shown in Fig. 6. In this case, the comparison of analytical with experimental results was used to calibrate the parameters of the Crisafulli [10] masonry panel element that was used.

For a detailed presentation of the parameters characterising the model developed by Crisafulli [10] and their effects on the overall response of masonry, the reader is referred to the work of Smyrou *et al.* [26]. Some of the parameters of the numerical model can be directly evaluated from the known geometrical characteristics of the masonry wall [19], e.g. the panel thickness. The parameters of the model that cannot be determined from the available data are the following: (i) the compressive strength, f_{mas}, and the modulus of elasticity, E_{mas}, of the masonry; (ii) the residual strut area strain, e_2; (iii) the friction coefficient of the masonry, μ_{mas};

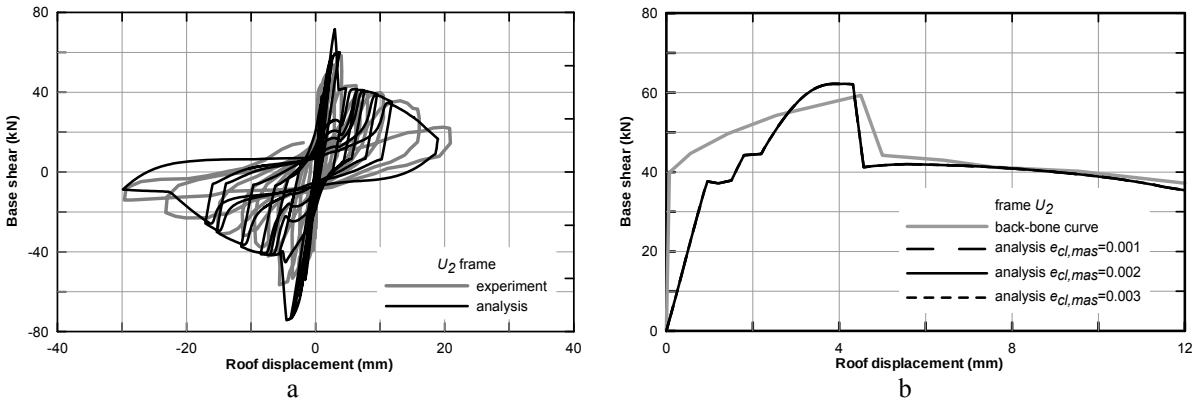


Figure 6: Comparison of the experimentally and the analytically derived load-displacement curves for U_2 frame: (a) cyclic loading, and (b) monotonic loading. The parameters used in the analytical model are; f_{mas} = 1.65 MPa; E_{mas} = 1700 MPa; e_2 = 0.002; μ_{mas} = 1.20; τ_0 = 700 kPa; τ_{max} = 1200 kPa; A_2 = 15%; $e_{u,mas}$ = 0.012; $e_{m,mas}$ = 0.0014; $e_{cl,mas}$ = 0.003.

(iv) the shear bond strength τ_0 and the maximum shear strength τ_{max}; (v) the residual strut area, A_2; (vi) the ultimate strain, $e_{u,mas}$; (vii) the strain at maximum stress $e_{m,mas}$; (viii) the closing strain $e_{cl,mas}$. The basic mechanical properties, usually determined by simple test series, were not available from the experimental data [19]; thus, their determination was based also on the parametric analyses conducted, starting from reasonable assumptions.

Various combinations of f_{mas} and E_{mas} that satisfy the relationship proposed by Paulay and Priestley [27], i.e. $E_{mas} = 1000 \times f_{mas}$ have been examined in order to achieve an acceptable fit between the analytical results with the experimental data. The optimum fit was achieved for f_{mas} = 3.5 MPa and E_{mas} = 3500 MPa; however, a perfect match could not be obtained, especially regarding the displacements at which the maximum shear was attained and the horizontal branch of the pushover curve started. The calibration of the other parameters, and especially of the residual strut area strain e_2, aimed to correct the mismatch and to lead to a better assessment of the cyclic behaviour. The area of the equivalent strut strain e_2 successively reduces with the increase of the lateral displacement and the development of the cracking. The strain e_2 characterises the end of the strut section reduction, so it is related to the strain at which the frame reaches its maximum resistance.

It is observed that an increase in the deformation e_2 results in an increase in the displacement at which the frame reaches its ultimate resistance and also causes a strong amplification of the resistance itself. This happens because a larger value of e_2 delays the reduction of the strut cross section, so it amplifies the deformation and the roof displacement that correspond to the maximum resistance. Moreover, due to the lesser reduction of its cross section, the strut can resist with larger force for the same roof displacement, which explains the increased lateral resistance of the infill frame.

The final comparison of the obtained pushover curve with the backbone curve for specimen U_2 is shown in Fig. 6b. It is seen that the analytical model can capture satisfactorily the shape of the backbone curve and can describe the overall behaviour of the infill frame with acceptable accuracy for both the elastic and the inelastic ranges of deformation. In the experiment, the maximum recorded base shear was 59.64 kN and occurred at roof displacement equal to 3.74 mm. The corresponding values of the pushover analysis with the proposed model were quite similar, specifically, base shear 62.64 kN at roof displacement equal to 3.71 mm. Also, the residual resistance was similar: 40.22 kN for both the analytical and the experimental results with a small difference in the roof displacement at which the final plateau

starts. Note that the two horizontal plateaus in the ascending branch of the pushover curve of the analytical model correspond to axial failure of the tensile struts, as mentioned above.

Based on the response for various combinations of f_{mas}, E_{mas} and e_2 the finally selected values were: f_{mas} = 1.65 MPa, E_{mas} = 1700 MPa and e_2 = 0.002. The value of f_{mas} (compressive strength of the masonry) suggests very low resistance, which should not be considered as unusual for existing structures, especially those with poor mechanical properties of mortar [28]. Note that in the ascending branch of the pushover curve for the selected parameters, shown in Fig. 6b, two small horizontal plateaus are observed: the first one corresponds to base shear approximately equal to 38 kN and the second one to base shear about 45 kN. This response is attributed to failures in the diagonal struts that simulate the small tensile resistance of the masonry. When tensile failure of masonry is observed an almost instantaneous redistribution of forces takes place, i.e., the axial forces in the compressive struts and the shear loads in the frame columns suddenly increase at a nearly constant overall shear load. The first horizontal plateau corresponds to the failure of the tensile struts in the first floor and the second one to the failure of the tensile struts in the second floor.

The friction coefficient of the masonry model, μ_{mas}, the shear bond strength, τ_0, and the maximum shear strength, τ_{max}, do not significantly affect the pushover curve and the cyclic behaviour. A parametric study on the friction coefficient revealed that an increase in μ_{mas} results in trivial modification of the resistance; thus, the maximum value, μ_{mas} =1.20, was selected as most appropriate, as also suggested in the literature [27]. Similarly, the response of the frame was practically unaffected from the variation of the parameters τ_0 and τ_{max} within the limits of acceptable values; therefore, values consistent with the selected friction coefficient were considered: τ_0 = 700 kPa and τ_{max} = 1200 kPa. The residual strut area A_2 had a more significant effect on the structural response, as expected. The value A_2 = 15% was selected, which implies that the final section of the strut was equal to 15% of the original.

The ultimate strain ε_{ult} affects the response of the frame exclusively at large deformations. The value $e_{u,mas}$ = 0.012 was chosen, because it leads to results closest to the experimental data. A similar investigation on the effect of the peak strain at maximum stress $e_{m,mas}$ revealed that the ultimate lateral resistance of the frame decreases with $e_{m,mas}$, while the roof displacement that corresponds to the maximum lateral force increases. This occurs because the reduction in the strut sectional area begins before the masonry model develops its total strength. The selected value for $e_{m,\,mas}$ was 0.0014.

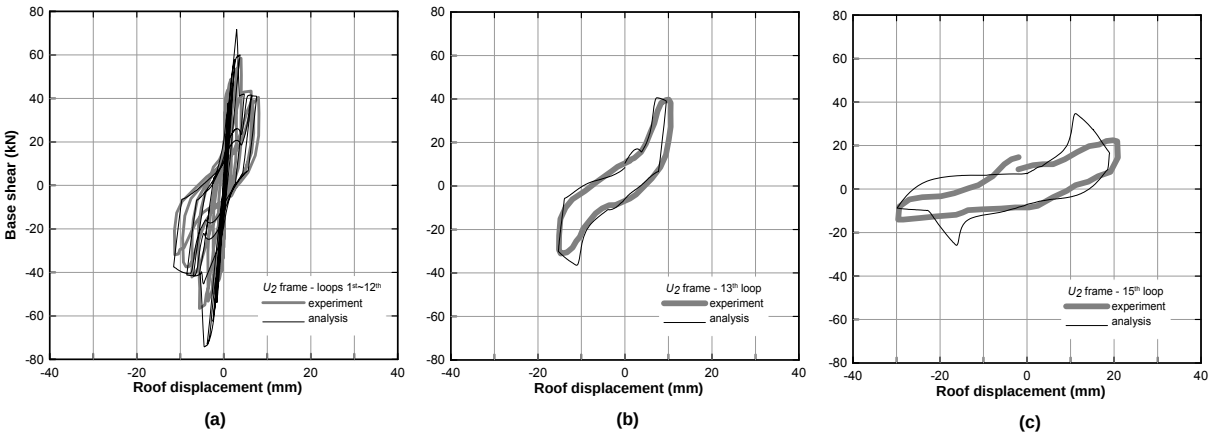


Figure 7: Comparison of the experimentally and the analytically derived load-displacement curves for U2 frame: (a) force-displacement loops 1 to 12; (b) 13th force-displacement loop; (c) 15th force-displacement loop.

Regarding the determination of the strain $e_{cl,mas}$ after which the cracks partially close allowing for compression stresses to develop, the default value of $\varepsilon_{cl,max} = 0.003$ was used, since this parameter does not seem to affect the response of the model.

Very good fit was also achieved for the cyclic loading. The maximum base shear of each cycle and the corresponding roof displacement according to the experiment and the analytical model nearly coincide, as shown in Fig. 6a. The analytical model can also predict the shape of the hysteretic loops, capturing very well the sequence of failures in the test specimen. This is more clearly depicted in Fig. 7 where individual hysteretic loops obtained analytically are compared to the experimental data. It is shown that for both nearly elastic behaviour that is identified for the first twelve loops as shown in Fig. 7a and for pure inelastic response as shown in Fig. 7b and 7c for the 13th and the 15th loop, respectively, an acceptably accurate fit is achieved by the analysis, validating the procedure applied.

4.3 Validation of U_3 frame

In the third model U_3, the parameters defined for the concrete, the steel and the masonry from the calibration of the analytical model with the experimental data for the specimens U_1 and U_2 were retained and the parametric investigation was focused on the calibration of the parameters for the FRP. Specifically, the parameters used for the frame and the infill masonry were: f_y = 165 MPa; μ = 0.00; ε_c = 0.00128; f_{mas} = 1.65 MPa; E_{mas} = 1700 MPa; e_2 = 0.002; μ_{mas} = 1.20; τ_0 = 700 kPa; τ_{max} = 1200 kPa; A_2 = 15%; $e_{u,mas}$ = 0.012; $e_{m,mas}$ = 0.0014; $e_{cl,mas}$ = 0.003. The loading protocol applied in specimen U_3 was similar to that for the other two specimens, consisting of a force-based phase followed by a displacement-based phase, as described earlier. In Fig. 8a, the cyclic response and its backbone envelope are shown.

The difference of specimen U_3 from specimen U_2 concerns only the strengthening with the CFRP. The parameters that define the response of the FRP are: (i) the tensile strength, f_t; (ii) the initial modulus of elasticity, E_1; and (iii) the post-peak modulus of elasticity, E_2. According to Akgüzel [19], debonding of the FRP was observed due to insufficient anchorage of CFRP sheets on the frame-wall structure.

In order to accurately account for this type of failure, and since a more complex model was not used, the selection of the parameters was made so that the FRP had smaller ultimate tensile strength than the one measured during the experiments, which was defined from the maximum axial strain developed at debonding. The modulus of elasticity was evaluated as the volumetric average of the moduli of the individual materials, i.e. the fibres and the epoxy, resulting in f_t = 953 MPa and E_1 = 130000 MPa. The post-peak modulus of elasticity was set equal to the initial modulus $E_2 = E_1$, since it was found that the response was practically unaffected by this parameter because the post-peak stiffness affected the response of the FRP at displacements greater than the displacements imposed on the test specimen. Using these values for the parameters, the comparison of the analytically predicted response with the experimental data for the FRP strengthened RC brick infilled frame are presented in Figs 8a and 8b for monotonic and cyclic loading, respectively.

Regarding the monotonic behaviour, good agreement was achieved concerning the ultimate resistance to lateral loading: in the experiment, this value was 76.23 kN and occurred at roof displacement equal to 4.87 mm, while the corresponding value of the analytical model was 71.55 kN at 4.26 mm roof displacement. However, significant discrepancy of the analytical results from the experimental data appears for large displacements, specifically for roof displacement larger than 15 mm, as shown in Fig. 8b. The difference is attributed to the different way in which the loading was implemented: in the experiment, the test specimen was partially blocked in order to follow the imposed displacement at each step [19], while the analytical model under monotonic loading was free under lateral deformations till collapse.

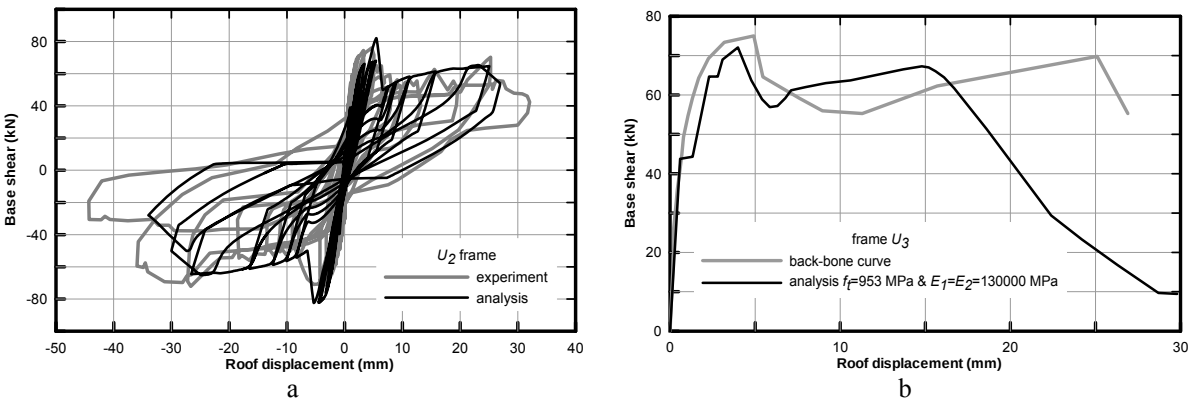


Figure 8: Comparison of the experimentally and the analytically derived load-displacement curves for U_3 frame: (a) cyclic loading, and (b) monotonic loading. The parameters used in the analytical model are; f_t = 953 MPa; E_1 = E_2 = 130000 MPa.

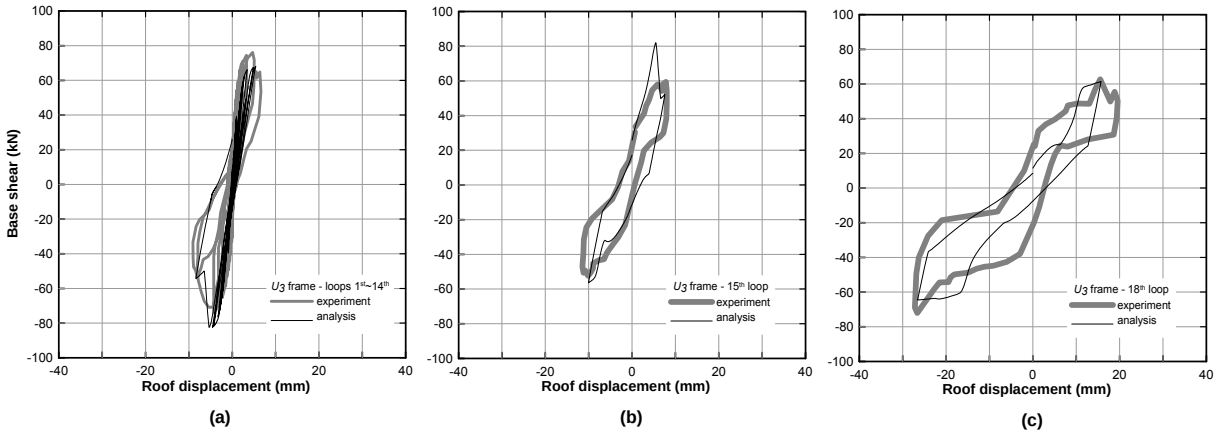


Figure 9: Comparison of the experimentally and the analytically derived load-displacement curves for U_3 frame: (a) force-displacement loops 1 to 14; (b) 15th force-displacement loop; (c) 18th force-displacement loop.

The predicted cyclic response was also very good, as evident from the comparison with the experimental data depicted in Fig. 8a. Some differences between the analytical results and the load-displacement loops obtained from the experiment, that occurred during the few last cycles, are attributed to the fact that the test the specimen was allowed to deform beyond the displacement that corresponded to the loading protocol. Thus, there was a mismatch between the assumed imposed displacements according to the loading history and the measured ones, as depicted in the cyclic loops [19]. In the numerical analysis, the loading protocol was followed, thus the displacements were smaller. Apart of this difference, the prediction of the analytical model is quite good, with the maximum base shear of each cycle and the corresponding roof displacement displaying acceptable agreement with the experimental data. This is also depicted in Fig. 9, where analytically derived base shear – roof displacement loops are compared with the experimental data. For the first fourteen loops the response is nearly elastic, as shown in Fig. 9a, and small deviations from the real behaviour are noticed. The first completely inelastic loop, which is the 15th as shown in Fig. 9b, presents smalls deviations regarding the maximum base shear. The 18th hysteretic loop is shown in Fig. 9c, where more deviations may be observed, mainly regarding the shape of the loop; however, acceptable accuracy is achieved in the maximum values of force and displacement.

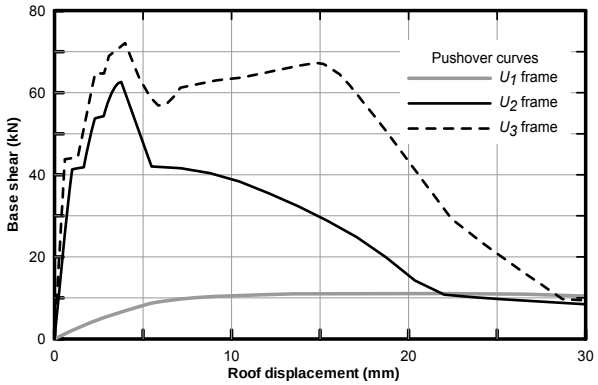


Figure 10: Load-displacement pushover curves for frames U_1, U_2 and U_3.

4.4 Comparison of the behaviour for the three frames

In order to compare the difference in strength and stiffness characteristics of the three alternative frame models U_1, U_2 and U_3, the corresponding pushover curves are drawn in Fig. 10. It is reminded that U_1 corresponds to the bare frame, U_2 was the same frame with the addition of infill masonry walls and U_3 was similar to U_2 but the infill walls were strengthened with CFRP.

It is evident that the successive upgrading of the structure, from the bare frame to a brick infilled masonry frame and to the addition of the FRP on the masonry, resulted in successive increase in the lateral resistance. The addition of the infill walls resulted in substantial increase in the stiffness, which was moderately affected by the addition of the FRP. Specifically, the maximum lateral resistance of frame U_1 was 13.75 kN, while the corresponding value for frame U_2 was 62.64 kN, demonstrating an increase of 355%. In frame U_3, the strengthening with FRP lead to further increase in the resistance by 14%, to a value of 71.55 kN. Concerning the stiffness, the initial elastic stiffness for frame U_1 was only 2.55 kN/mm, while for frames U_2 and U_3 it was 63.53 kN/mm.

Significant difference was also observed in the displacement that corresponded to the maximum base shear: frame U_1 reached its maximum resistance when the roof displacement was 18.1 mm, U_2 when it was 3.71 mm and U_3 when it was 4.26 mm.

The ductility capacity of the three frames was also significantly different. Frame U_1 showed that it could be deformed to large post-yield displacements, more than four times the yield displacement, without significant loss of strength. On the contrary, the behaviour of frame U_2 was characterized by a sharp drop of resistance after the maximum base shear was attained, evidently due to damage in the infill walls, showing a practically "brittle" response. However, the strengthening of the masonry with FRP in frame U_3 improved the response significantly, providing a relatively smooth maintenance of the resistance up to ductility around 4.0; for larger displacements, the resistance decreased sharply but remained always greater than that of U_2 without the FRP. It seems, therefore, that strengthening of the masonry with FRP improves significantly the response, as can also be seen comparing the cyclic response of frames U_2 and U_3 shown in Figs. 6a and 8a: the behaviour of U_3 was more stable and retained its resistance for a relatively large number of loops.

5 EFFECT OF OPENINGS IN THE LATERAL STIFFNESS OF INFILL WALLS

Although infill walls usually have oversized openings, recent research has mainly focused on the simple case of infill wall without openings. Research on infill walls with openings is mostly analytical, restricted to special cases, and as such cannot provide rigorous comparison to actual cases because of its focus on specific materials used and specific types of openings.

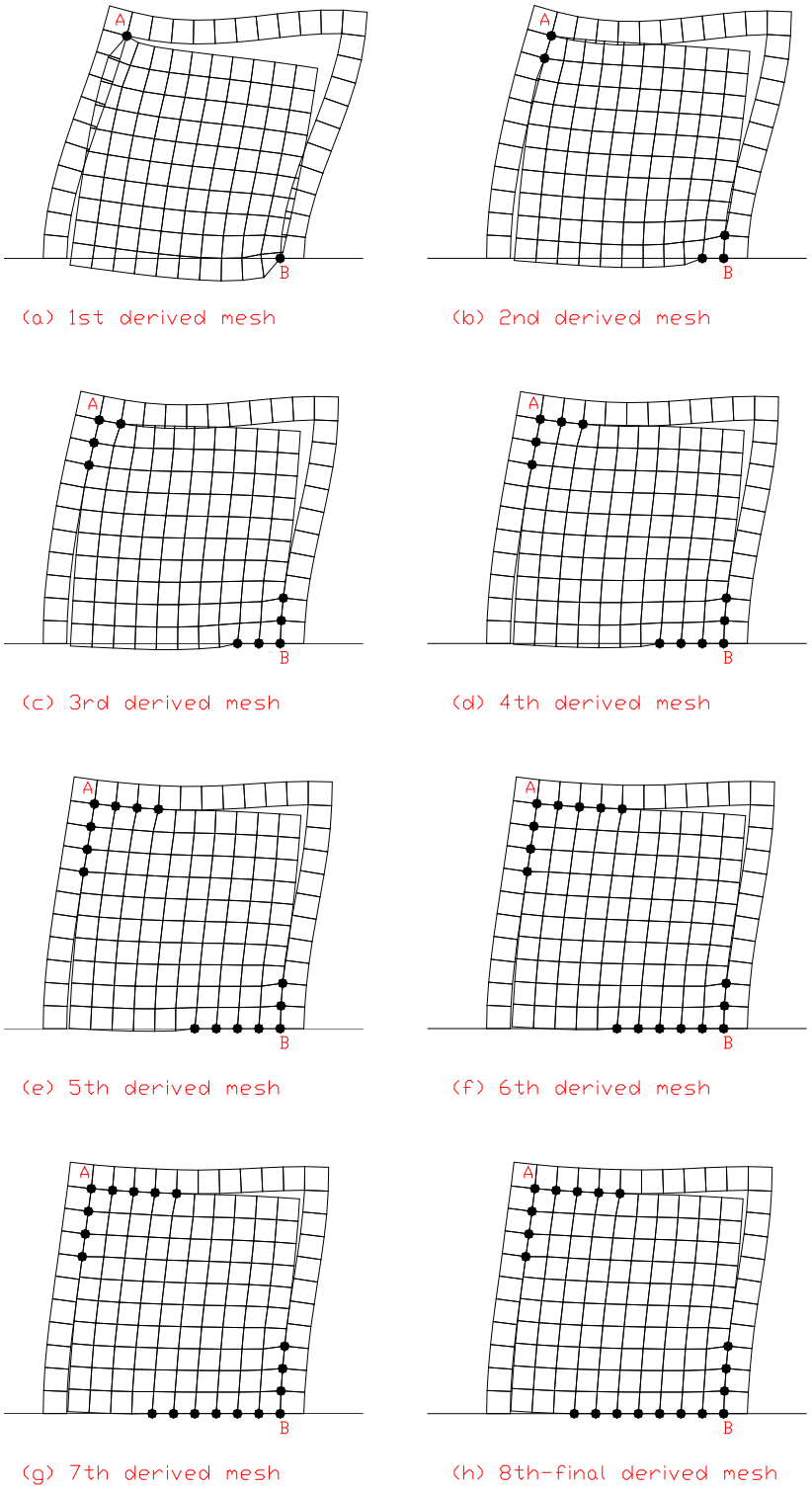


Figure 11: Deformed meshes of a one-storey, one-bay infilled frame using the finite element technique proposed by Asteris [29, 30].

It is worth noting that the contribution of the infill wall to the frame lateral stiffness is much reduced when the structure is subjected to reverse cyclic loading, as is the case in real structures under earthquake conditions.

In order to investigate the effect of openings in the lateral stiffness of masonry infill walls, the finite element technique proposed by Asteris [29, 30] can be applied. The basic characteristic of this analysis is that the infill – frame contact lengths and the contact stresses are estimated as an integral part of the solution, and are not assumed in an ad-hoc way.

In brief, according to this technique, the infill finite element models are considered to be linked to the surrounding frame finite element models at two corner points (only), at the ends of the compressed diagonal of the infill (points A and B in Fig. 11a). Then, the nodal displacements are computed and checked whether the infill model points overlap the surrounding frame finite elements. If the answer is positive, the neighbouring points (to the previous linked) are also linked and the procedure is repeated. If the answer is negative, the procedure stops and the derived deformed mesh is the determined one (Fig. 11h).

Using this technique, analytical results are presented on the influence of the opening size on the seismic response of masonry infilled frames. Figure 12 shows the variation of the λ factor as a function of the opening percentage (opening area/infill wall area), for the case of an opening on the compressed diagonal of the infill wall (with the same aspect ratio for the opening and the infill). As expected, the increase in the opening percentage leads to a decrease in the frame's stiffness. Specifically, for an opening percentage greater than 50% the stiffness reduction factor tends to zero. The findings of the present parametric study using the finite-element method, lead to the following relationship for the infill wall stiffness reduction factor λ:

$$\lambda = 1 - 2 \cdot \alpha_w^{0.54} + \alpha_w^{1.14} \tag{1}$$

in which α_w is the infill wall opening percentage (area of opening to the area of infill wall).

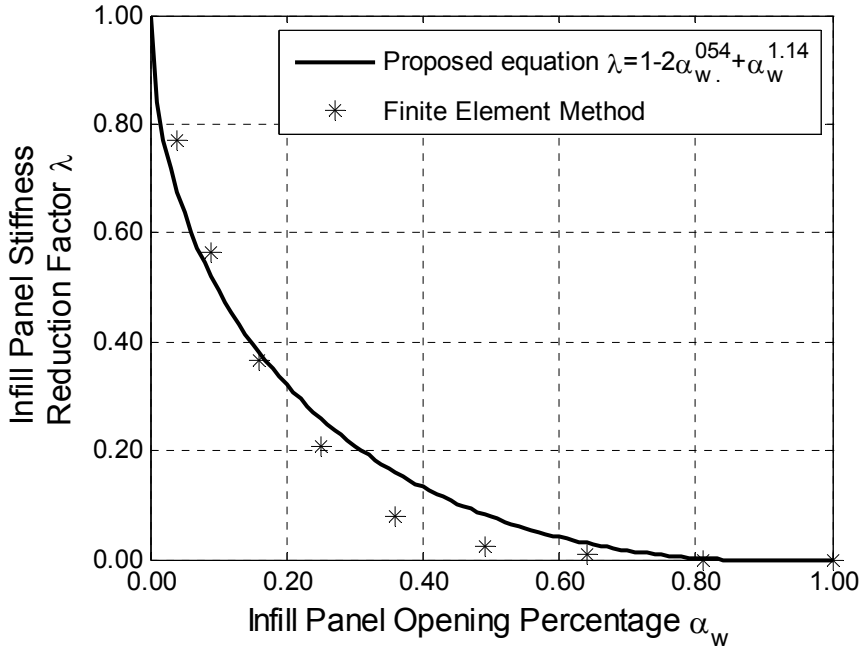


Figure 12: Infill panel stiffness reduction factor in relation to the opening percentage.

The above coefficient could be applied to find the equivalent width of a strut for the case of an infill with opening, modifying the equations of the Crisafulli model [10], which has been used in the present research.

6 DISCUSSION AND CONCLUSIONS

The research presented in this paper aims to assess the effectiveness of CFRP strengthening of brick infilled RC frame structures, typical of past design concepts. Three types of two-storey, one-bay frames were analysed with models that were validated against experimental data available in the literature [18, 19]: (i) bare frame U_1; (ii) brick infilled frame U_2; and (iii) FRP strengthened brick infilled frame U_3. The calibration of the parameters of the models was performed using experimental data for specimens that were imposed to cyclic loading and was based on the comparison of the analytical with the experimental response for the same type of loading and additionally on the comparison of analytical pushover curves with backbone curves derived from the envelopes of the cyclic response of the test specimens. For more extensive details on the material models used herein and the explanation of their critical parameters the reader is referred to [4]. In view of the present research the following conclusions can be drawn:

- The analytical model for the masonry panel element developed by Crisafulli [10] could estimate effectively the response of the brick-infilled frames that were investigated experimentally.
- Comparisons of analytically derived pushover curves with backbone curves from cyclic tests can be used to calibrate the parameters of the numerical models. Caution should be paid to the use of this method on multi-storey structures, where the results of the pushover analysis might diverge significantly from the dynamic response, being sensitive to several parameters including the pattern of the lateral load distribution, higher mode effects and special characteristics of strong ground motion [31, 32].
- Relatively small deviations were observed between the experimental and analytical results not only comparing the overall response but also comparing individual force-displacement hysteretic loops.
- The role of the masonry walls on the response is significant since they increase the resistance and the stiffness. However, the overall behaviour is rather brittle, which justifies why, in seismic design, masonry walls are not included in the assessment of the structural strength. The most critical parameters that affect the response of the masonry panel element were found to be the compressive strength f_{mas}, the modulus of elasticity E_{mas} and the residual strut area strain e_2.
- The effectiveness of the proposed retrofit scheme for brick infills was re-confirmed. Strengthening of masonry with FRP significantly increased the ductility capacity of the structure and improved its resistance. Therefore, this technique could be used to lessen the vulnerability of existing structures in earthquake-prone regions.
- The effect of openings in the response of masonry infills is an issue that deserves further analytical and experimental research. A simple method is suggested to account for the modification of lateral stiffness due to the presence of openings in masonry.

7 ACKNOWLEDGEMENTS

The authors are most grateful to Umut Akgüzel who kindly provided the experimental results used in the present research. Also the valuable contribution of A. Kafkas and Ch. Klidis, who performed preliminary parametric analyses, is gratefully acknowledged.

REFERENCES

[1] Comité Européen de Normalisation CEN. Eurocode 8 - Design of structures for earthquake resistance, Part – 1. General rules, seismic actions and rules for Buildings. Brussels: European Committee for Standardization; 2004.

[2] M.N. Fardis, E. Carvalho, A. Elnashai, E. Faccioli, P. Pinto, A. Plumier, *Designers' Guide to EN 1998-1 and 1998-5. Eurocode 8: Design Provisions for Earthquake Resistant Structures*, Series Editor: H. Gulvanessian, Thomas Telford Ltd, London 2005.

[3] A.B. Mehrabi, P.B. Shing, M. Schuller, J. Noland, Experimental Evaluation of Masonry-Infilled RC Frames, *ASCE Journal of Structural Engineering*, **122**(3), 228-237, 1996.

[4] C.C. Spyrakos, Ch.A. Maniatakis, E. Smyrou, I.N. Psycharis, FRP strengthened brick-infilled RC frames: An approach for their proper consideration in design. *Open Construction and Building Technology Journal*, **6**(SPEC. ISS. 1), 306-324, 2012.

[5] Fédération Internationale du Béton (FIB), *Retrofitting of Concrete Structures by Externally Bonded FRPs With Emphasis on Seismic Applications*, Bulletin 35, Lausanne, Switzerland 2006.

[6] C.C. Spyrakos, *Strengthening of Structures for Seismic Loads*, Technical Chamber of Greece Editions, 2004. (in Greek)

[7] M. Tomaževič, *Earthquake-resistant design of masonry buildings*, Imperial College Press, 1999.

[8] E. Vintzileou, T.P. Tassios, Seismic Behaviour and Design of Infilled R.C. Frames, *International Journal of Earthquake Engineering and Engineering Seismology*, **3**(2), 22–28, 1989.

[9] B. Stafford-Smith, C. Carter, A Method of Analysis for Infilled Frames, *Proceedings of the Institution of Civil Engineers*, **44**(1), 31–48, 1969.

[10] F.J. Crisafulli, *Seismic Behaviour of Reinforced Concrete Structures with Masonry Infill*, Ph. D. thesis, University of Canterbury, New Zealand, 1997.

[11] J.R. Riddington, B. Stafford-Smith, Analysis of Infilled Frames Subject to Racking With Design Recommendations, *The Structural Engineer*, **55**(6), 263–268, 1977.

[12] I. Koutromanos, A. Stavridis, P.B. Shing, K. Willam, Numerical Modeling of Masonry-Infilled RC Frames Subjected to Seismic Loads, *Computers and Structures*, **89**(11-12), 1026-1037, 2011.

[13] P.G. Asteris, S.T. Antoniou, D.S. Sophianopoulos, C.Z. Chrysostomou, Mathematical Macromodeling of Infilled Frames: State of the Art, *ASCE Journal of Structural Engineering*, **137**(12), 1508-1517, 2011.

[14] I.N. Doudoumis, Finite element modelling and investigation of the behaviour of elastic infilled frames under monotonic loading, *Engineering Structures*, **29**, 1004–1024, 2007.

[15] I. Erdem, U. Akyuz, U. Ersoy, G. Ozcebe, An Experimental Study on Two Different Strengthening Techniques for RC Frames, *Engineering Structures*, **28**(13), 1843–1851, 2006.

[16] S. Altin, O. Anil, M.E. Kara, M. Kaya, An Experimental Study on Strengthening of Masonry Infilled RC Frames Using Diagonal CFRP Strips, *Composites: Part B*, **39**, 680–693, 2008.

[17] G. Ozcebe, U. Ersoy, T. Tankut, E. Erduran, R.S. Keskin, H.C. Mertol, Strengthening of Brick-Infilled RC Frames With CFRP, Ankara: SERU – Structural Engineering Research Unit, TUBITAK – METU, 2003.

[18] Ş. Özden, U. Akgüzel, CFRP Overlays in Strengthening of Frames with Column Rebar Lap Splice Problem. S.T. Wasti, G. Ozcebe eds. *Advances in Earthquake Engineering for Urban Risk Reduction*, NATO Science Series, Earth and Environmental Sciences, Springer, **66**, 455–71, 2006.

[19] U. Akgüzel, *Seismic Retrofit of Brick Infilled R/C Frames with Lap Splice Problem in Columns*, M.Sc. thesis, Department of Civil Engineering, Bogazici University, Istanbul, Turkey, 2003.

[20] SeismoSoft, SeismoStruct v5.2.5 - A Computer Program for Static and Dynamic Nonlinear Analysis of Framed Structures, 2011. [Online] Available; URL:http://www.seismosoft.com [Accessed Jan. 2012].

[21] M. Menegotto, P.E. Pinto, Method of Analysis for Cyclically Loaded R.C. Plane Frames Including Changes in Geometry and Non-Elastic Behaviour of Elements Under Combined Normal Force and Bending. International Association for Bridge and Structural Engineering. *Symposium on the Resistance and Ultimate Deformability of Structures Acted on by Well Defined Repeated Loads*, Zurich, Switzerland, 15-22, 1973.

[22] F.C. Filippou, E.P. Popov, V.V. Bertero, Modelling of R/C Joints Under Cyclic Excitations, *ASCE Journal of Structural Engineering*, **109**(11), 2666-2684, 1983.

[23] J.B. Mander, M.J.N. Priestley, R. Park, Theoretical Stress-Strain Model for Confined Concrete, *Journal of Structural Engineering*, **114**(8), 1804-1826, 1988.

[24] E. Smyrou, *Implementation and Verification of a Masonry Panel Model for Nonlinear Dynamic Analysis of Infilled RC Frames*, M.Sc. Dissertation, European School for Advanced Studies in Reduction of Seismic Risk (ROSE School), Pavia, Italy 2006. [Online] Available; www.roseschool.it [Accessed Jan. 2012].

[25] F.J. Crisafulli, A.J. Carr, Proposed Macro-Model for the Analysis of Infilled Frame Structures, *Bulletin of the New Zealand Society for Earthquake Engineering*, **40**(2), 69–77, 2007.

[26] E. Smyrou, C. Blandon, S. Antoniou, R. Pinho, F. Crisafulli, Implementation and Verification of a Masonry Panel Model for Nonlinear Dynamic Analysis of Infilled RC Frames, *Bulletin of Earthquake Engineering*, **9**(5), 1519-1534, 2011.

[27] T. Paulay, M.J.N. Priestley, *Seismic Design of Reinforced Concrete and Masonry Buildings*, John Wiley & Sons Inc., 1992.

[28] I.E. Bal, H. Crowley, R. Pinho, F.G. Gulay, Detailed Assessment of Structural Characteristics of Turkish RC Building Stock for Loss Assessment Models, *Soil Dynamics and Earthquake Engineering*, **28**(10–11), 914–932, 2008.

[29] P.G. Asteris, Lateral stiffness of brick masonry infilled plane frames, *Journal of Structural Engineering, ASCE*, **129**(8), 1071-1079, 2003.

[30] P.G. Asteris, Finite Element Micro-Modeling of Infilled Frames, *Electronic Journal of Structural Engineering*, **8**, 1-11, 2008.

[31] C.C. Spyrakos, Ch.A. Maniatakis, J. Taflambas, Evaluation of near-source seismic records based on damage potential parameters. Case study: Greece. *Soil Dynamics and Earthquake Engineering*, **28**(9), 738-753, 2008.

[32] Ch.A. Maniatakis, C.C. Spyrakos, A new methodology to determine elastic displacement spectra in the near-fault region. *Soil Dynamics and Earthquake Engineering*, **35**, 41-58, 2012.

COMPDYN 2013
4th ECCOMAS Thematic Conference on
Computational Methods in Structural Dynamics and Earthquake Engineering
M. Papadrakakis, V. Papadopoulos, V. Plevris (eds.)
Kos Island, Greece, 12–14 June 2013

SEISMIC ANALYSIS OF MASONRY ARCH STRUCTURES THROUGH THE FINITE ELEMENT MODEL "BLOCK-JOINT"

Francesco Pugi[1]

[1] AEDES Software
San Miniato Basso 56028, Pisa, Italy
e-mail: info@aedes.it

Keywords: historic masonry structure, limit analysis, nonlinear analysis, macroelements, block-joint.

Abstract. *In monumental buildings vaulted structures and arches are structures of great importance. The traditional approach with the analysis of a rigid-brittle model constitutes a reference method but it is affected by some operational limits, such as, the use of a planar model which cannot represent effectively spatial systems which include adjacent structures (walls, pillars). Moreover, disregarding elasticity, modal analysis cannot be performed. An alternative methodology is proposed. Using simple one-dimensional finite element (blocks - joints) the collapse mechanism is obtained through an incremental elastic-brittle analysis. The method easily finds a balanced solution compatible with the mechanical characteristics of the material. Also, considering the tensile stress of the mortar joints, it is possible to evaluate more accurately the effective seismic resistance of the structure. The proposed method is applied to study an important religious monument.*

1 INTRODUCTION

Under seismic loading, the existing masonry buildings and historic structures are frequently affected by partial collapses due to loss of equilibrium of portions of the structure. Local mechanisms occur in masonry walls because of out-of-plane actions, and in case of arches also under in-plane actions. In order to assess the seismic safety of the structure, the verifications in terms of local collapse mechanisms can be carried out by means of limit analysis following the kinematic approach proposed by the current standards [1-3].

The most common method of analysis, also described in the standards [3], is based on the evaluation of the horizontal action that activates the collapse mechanism selected a priori. The relevant collapse mechanisms can be assumed on the base of the seismic behaviour of similar structures or defined according to the state of damage of the structure.

In this approach, however, the selection a priori of a proper collapse mechanism is not an easy task given the wide variety of the cases that can be examined. For example, not all the arches are symmetric or have symmetrical loads; some structures may differ significantly from the reference models as in the case of complex vaults set on walls or pillars or in the case of walls with an irregular layout of the openings.

Therefore, an accurate modelling of the monumental structures requires the adoption of methodologies capable to determine the collapse mechanism avoiding the uncertainties of the selection a priori. For this reason specific methods have been developed for some important structural typologies.

Algorithms able to define the collapse mechanism of arches and vaults under seismic action [4] were developed following the Heyman theory and an approach based on rigid-brittle elements. This methodology is described in section 2.

However, the definition of the collapse mechanism, or more properly the seismic action that activates the mechanism, can also be pursued with traditional finite element methods, according to nonlinear procedures that take into account the progressive damage of the structures. At first, the structure, generally strongly hyperstatic, is analysed under vertical loads in the elastic range. The application of increasing horizontal forces leads to a gradual loss of hyperstaticity, until the structure becomes isostatic and at last unstable: at that point the collapse mechanism occurs. This type of incremental analysis, proposed as an alternative to limit analysis in recent standards [3], is described in section 3.

The result of the nonlinear static analysis is a force-displacement diagram (the capacity curve) that shows the relation between the increasing base shear and the control displacement that can be assumed at the centroid of the active masses.

In both approaches the maximum sustainable value of the horizontal action is pursued. In the kinematic approach (limit analysis) the action is obtained as the minimum force able to activate the mechanism, while in the static approach (static nonlinear analysis) the action pursued is the maximum force for which the structure remains in equilibrium. The horizontal force is due to the seismic action, therefore it is an inertial force and it corresponds to a mass multiplier. The collapse multiplier λ is defined dividing the force by the corresponding inertia.

Both the above mentioned methods aim to evaluate the collapse multiplier: its value can be assumed as a characteristic of the examined structures for given geometry, restraints, materials and applied loads.

The following paragraphs describe the two alternative methodologies for the definition of the collapse multiplier of arches and vaults.

2 LIMIT ANALYSIS

For masonry structures subjected to horizontal actions, the research of the collapse multiplier can be conducted through limit analysis using equilibrium conditions.

Limit analysis evaluates the condition of equilibrium of an unstable structure, such as an assembly of rigid wall parts in order to asses if the structure is statically determined under the applied loads. The deformation, which cannot be determined through limit analysis, is neglected assuming that the structure is still in equilibrium even in the deformed shape. However it should be considered that, dealing with existing structures, the geometrical configuration measured through geometrical survey is already the deformed one, therefore the limit analysis is capable to evaluate the actual safety level of the structure.

As said before, limit analysis methodologies are of two types: the ones based on a priori selected mechanisms, and the ones which try to determine the collapse mechanisms through calculations.

As far as the a priori selected mechanism, the recent Italian standards on monumental buildings [3] propose an abacus of different collapse mechanisms derived from the observation of the damages caused by mayor earthquakes.

In this paragraph, a limit analysis method that does not require the a priori selection of the collapse mechanism is presented. The method refers to the kinematic analysis of arches according to a rigid-brittle model [4], elaborated from Heyman's studies [5-6]. This approach, largely used in engineering practice [7], constitutes a solid reference for the calibration of alternative procedures.

Assuming that the arch is made of rigid blocks, each one able to transfer to the next one only shear and compression, the method searches – if exists – a thrust line which, under the applied load and with the structure in equilibrium, is defined within the geometric shape of the arch.

Where tensile forces occur, a hinge develops at the correspondent block interface and the thrust line at that point is tangent to the arch profile (at extrados or intrados). If necessary, a maximum of three hinges may be considered, after that a mechanism occurs. If it was possible to find an equilibrate solution under the given boundary conditions, the arch is stable.

Therefore, starting from a configuration in equilibrium under vertical loads, a system of horizontal forces is applied to the structure. Such forces are proportional to the vertical loads, that is, derived from the latters by applying a multiplier. Assessing the arch stability under increasing values of the horizontal forces, it is possible to determine the collapse multiplier, that is the maximum value of the multiplier for which the structure is still in equilibrium.

The rigid-brittle model presented in Figure 1 ignores the elasticity and the resistance of the materials. The procedure represents an important step forward with respect to traditional methods (such as the Méry method) where the position of the hinges is selected a priori. With this method instead, the hinges – if they develop – are considered in the actual position resulting from the analysis under the applied loads.

The original formulation of the procedure is for plane structures and can be used for the analysis of single arches and barrel vaults. Extensions of this procedure make possible its application even for cross vaults [7]. In general, these methodologies consider an infinite compressive strength and zero tensile strength.

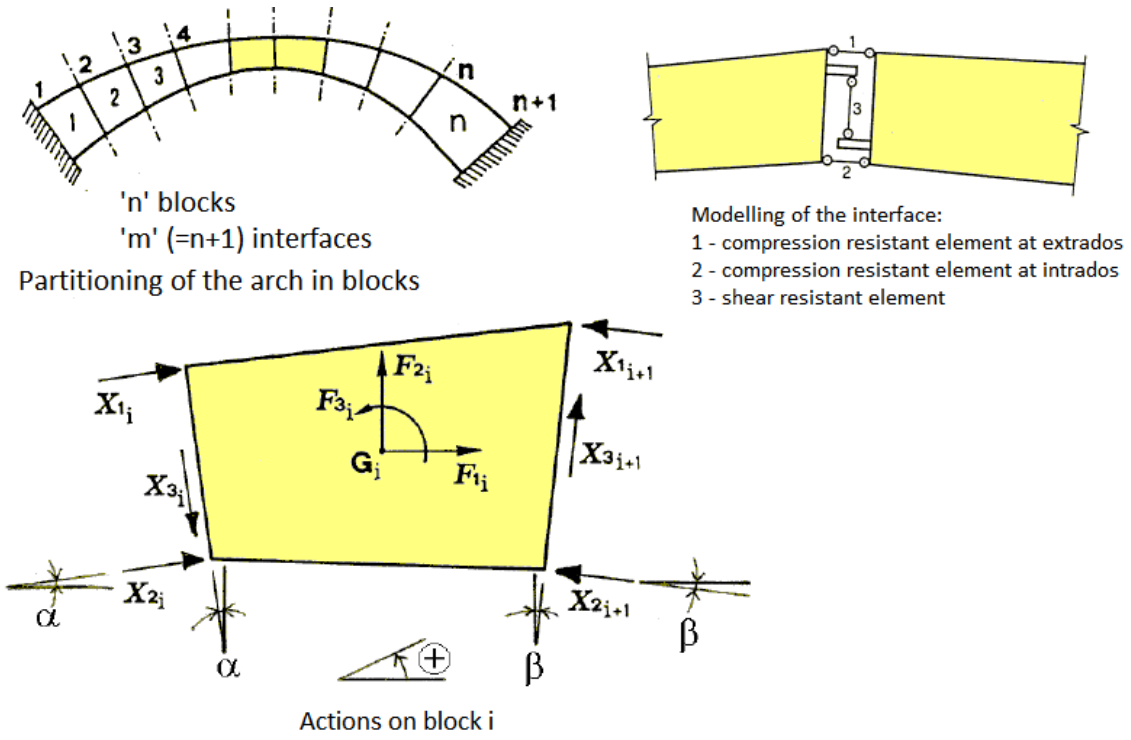


Figure 1. Rigid-brittle modelling of arch structures

3 NONLINEAR STATIC ANALYSIS: THE "BLOCK-JOINT" MODEL

As described above, according to the limit analysis approach the arch can be evaluated as a rigid-brittle system. However, the application of this method is subjected to important limits:
a) the tensile strength is considered to be null; thus, neglecting the real capacity of the mortar joints. In this way the collapse multiplier can be significantly underestimated and, although it would appear in favour of safety, this could lead to excessive strengthening interventions. The safety evaluation, in fact, should assess as close as possible the real behaviour of the structure in order to adequately design the interventions and avoid oversizing;
b) the formulation for plane structures does not allow evaluating the out-of-plane behaviour of the arches: for this purpose it is necessary to extend the method adopting more elements (at least 8) in order to correctly account for the axial force and the shear at the interface;
c) the structural scheme can be hardly generalized in case of systems of arches or structures that besides the arches include the adjacent structure or the supports (such as walls or piers);
d) the original formulation, based on a rigid-brittle behaviour, ignores elasticity; therefore, modal analysis cannot be performed.

Some of these issues can be overcome through a series of generalizations; however, finite element models and static nonlinear analyses already provide similar techniques, simple in their approach but just as effective and easily reproducible. The model proposed in this paper uses two types of finite elements, "blocks" and "joints", under the assumption of an initial elastic behaviour of the structure.

Both blocks and joints are frame elements: the blocks have the mechanical properties of the stone and their cross section is the effective cross section of the arch, the joints represent the mortar between the blocks. Four joints for each block are used; therefore, the joint cross section is ¼ of the arch cross section. The joints have a pin-end and a fixed-end, the fixed-end provides continuity with the previous block, the pin-end transfers shear and axial force to the

next block, while the joints are connected to the block ends through rigid links; in this manner the system transfers moment, shear and axial force from one block to another.

Performing a pushover analysis the system is subjected to an increasing horizontal force. At each step an axial force verification is applied to the joints: if tensile stresses occur, the internal axial force is released and the fixed-end is turned to pin so that the element loses any stiffness and the internal action remain constant at the value reached so far. As the analysis continues, the progressive deterioration of the joints lead to an unstable configuration that define the end of the pushover curve.

Assuming that the internal actions remain constant after deterioration of the joints, this procedure is capable to find easily a balanced solution compatible with the mechanical characteristics of the materials. The procedure can be applied considering or not a limited tensile strength of the material: if the tensile strength is assumed to be null a comparison with the rigid-brittle limit analysis is feasible. Passing from the rigid-brittle model to the elastic one, the collapse multiplier can either decrease or increase. However, in the elastic model, the adoption of a limited tensile strength (f_{tk}) surely leads to an increase of the collapse multiplier in comparison to the case in which it is considered to be null; thus, avoiding underestimation of the seismic capacity of the structure.

The block-joint system has the great advantage of adopting only one-dimensional elements; thus, it is easily implemented with any finite element solver.

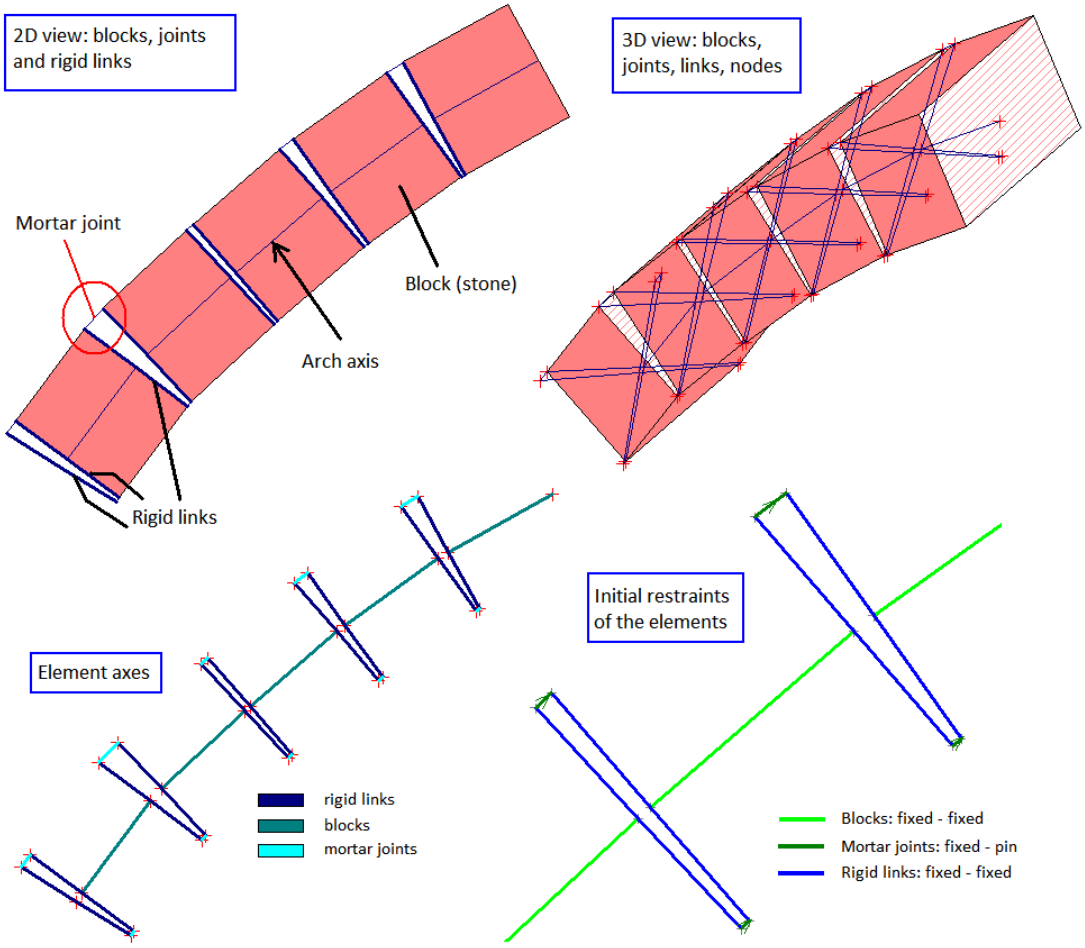


Figure 2. The finite element model block-joint

In the following several comments and remarks regarding the method are presented.

I. If excessive tensile stress occur at the joints, it is possible to intervene on the initial model modifying the internal restraints of the elements in traction. In fact, for a correct application of the nonlinear procedure, an equilibrate initial configuration is considered essential. For certain geometries and under certain loads an equilibrate static solution may not exist, this situation represents the maximum vulnerability since the system cannot withstand any horizontal seismic action. In this cases, immediate strengthening measures should be taken beyond the seismic issue.

II. As for the limit analysis procedure (cfr. Paragraph 2), the subdivision into blocks can be physical or mathematical; applications of the method show that the solution can be achieved even without a very dense subdivision. Therefore, an effective matching is not necessary between the frame elements and the real dimension of the blocks.

III. Being the modulus of elasticity of the stone much larger than the one of the mortar, the deformation is concentrated in the joints, while the blocks behave practically as rigid elements. For this reason the compression force verification is not applied to the blocks, while the tensile force verification is still applied. The linear dilatation of the block is

$$\Delta l = l_s - l_i$$

where l_s is the length of the deformed block, l_i is the original length. The linear deformation is given by

$$\varepsilon = \Delta l / l_i$$

If $\Delta l > 0$, the block is in elongation and the tensile stress is

$$\sigma_t = E \cdot \varepsilon$$

where E is the modulus of elasticity of the material. If the tensile stress exceeds the resistance of the stone, the internal restraints of the block are released as it happens for the joint elements. The deterioration of the block contributes to the mechanism affecting the value of the maximum horizontal force sustainable by the system.

IV. Since the blocks are modelled as one-dimensional prismatic elements, the joints assume a trapezoidal shape which at the extrados of the arches may be larger than the real one, especially if the arch is modelled with a limited number of blocks. This configuration, given the high deformability of the mortar, can lead to thrust lines not always coincident with the ones obtained with a rigid-brittle model; a series of comparative examples has proved that the difference is due to the internal distribution of the stresses. There are some adjustments that can be made in order to improve the block-joint model; for example, the blocks may be modelled with non-prismatic elements or the modulus of elasticity may be increased for the joints that are longer than the real ones. However, in order to preserve the ease of understanding and the repeatability of the modelling, a version of the block-joint model which disregards such adjustments has been adopted in this work.

4 CASE STUDY

The structure analysed is a great arch located in the Basilica of the Holy Sepulchre in Jerusalem. The church has been recently studied in order to evaluate its seismic vulnerability [8]. Among the several transformations undergone by the monumental building, in the period 1099-1167, the Crusaders after conquering Jerusalem rebuilt the church that was largely destroyed and they also built a new Choir (Figure 3) that remained essentially the same until today. The Crusaders created in this way a structure that still connect the Rotunda to the area of the Calvary.



Figure 3. Floor plan of the monument: Constantinian period (4th century) in black, restoration of Constantine Monomachos (11th century) in blue, structures built by the Crusaders (12th century) in red.

The floor plan of the Choir has a rectangular shape of about 12.5x24m, the apse is semi-circular with an external ray of 6.5m. The main arch that separates the Choir from the apse has an imposing size and outline the half dome on top of the apse. In recent studies [8] the apse was analysed together with the great arch; in this paper, however, we focus on the application of the finite element block-joint model only to the great arch, in order to provide a direct comparison with the rigid-brittle approach that would not be feasible dealing with a more complex structure.

Figure 4 shows the vertical section of the arch and the apse developed in 1955 by the Architects Rolando, Coupel, Antonian [10].



Figure 4. Vertical section of the apse

Figure 5 is a photo of the actual state of the structure. From left to right: (i) the half dome above the apse set on ten arches radially arranged; (ii) the great arches between the Choir and the apse analysed in this paper; (iii) the cross vault of the Choir. The great pointed arch between the Choir and the apse presents a large depth (166cm). Its thickness that at first sight appear quite large, due to the ventilation holes located above the keystone, cannot be assumed larger than 30cm. Above the arch sets a masonry wall having the same depth (166 cm) and a height over the keystone of about 160cm.



Figure 5. Internal view of the top of the apse

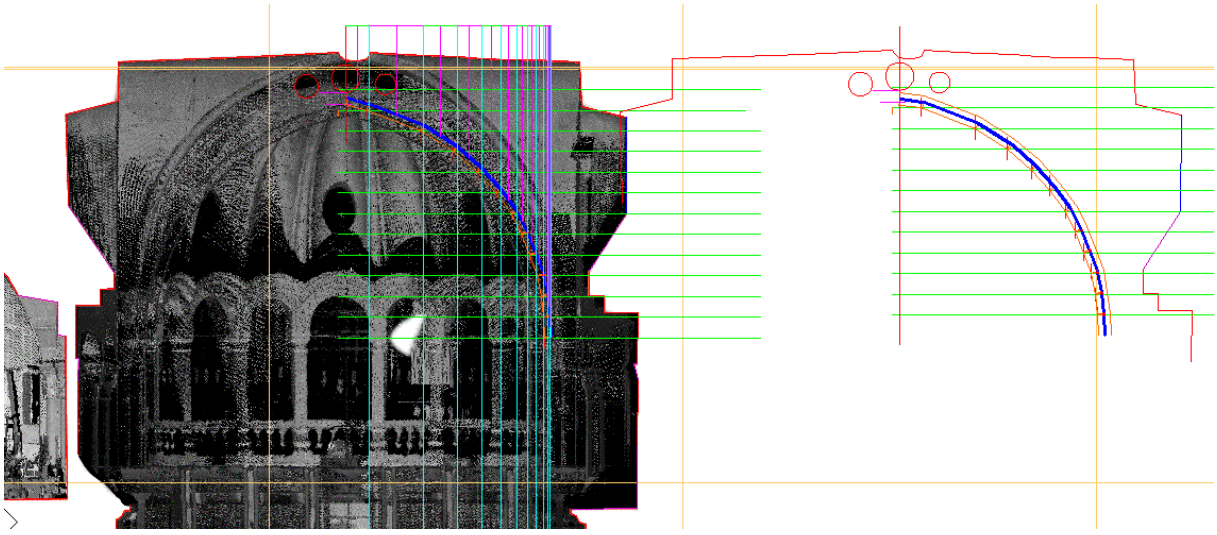


Figure 6. Study of the great arch between Choir and apse

Two structural models of the arch were analysed, the first according to the rigid-brittle approach (§4.1) and the second with the elastic nonlinear approach (§4.2) proposed in this paper.

4.1 Rigid-brittle model. Limit Analysis

The rigid-brittle model featuring zero tensile strength is presented in Figure 7. The arch was divided in blocks with a length of about 15cm.

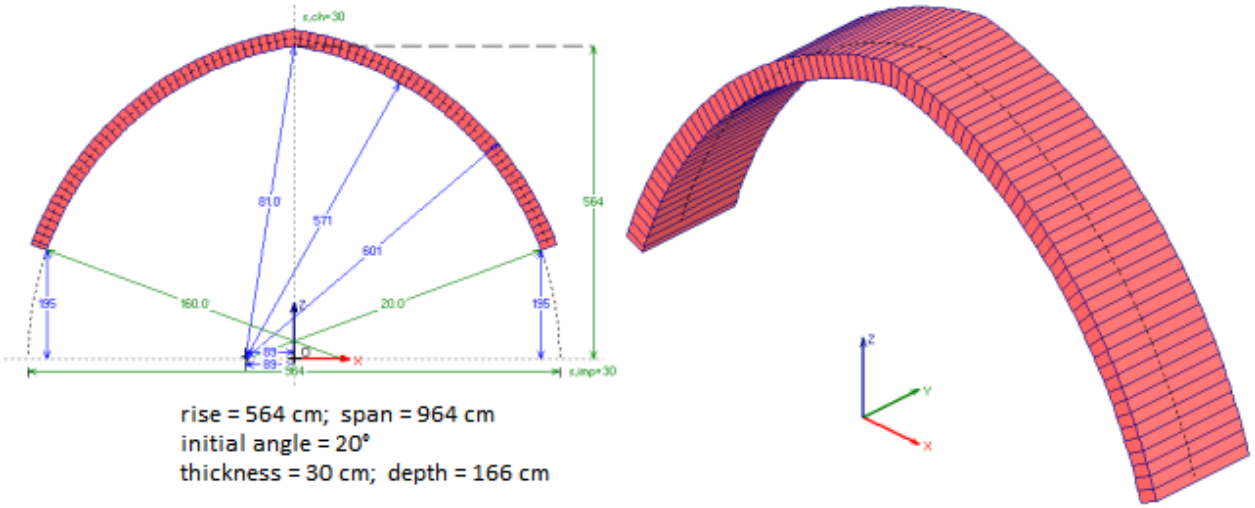


Figure 7. Rigid-brittle model of the arch

The characteristic aspects of the analysis are the following:

a) Mechanical characteristics
   - *Behaviour:* Rigid-brittle
   - *Tensile strength:* null
   - *Modulus of elasticity:* irrelevant

b) Analysis type and verifications
   - Limit analysis with analysis-determined collapse mechanism.
   - Equilibrium verification under static load and increasing seismic loads.
   - Calculation of the collapse multiplier for horizontal actions.
   - Definition of the reactions at the impost of the arch.

c) Model characteristics
   - *Geometry*: pointed arch with constant thickness and initial angle equal to 20°.
   - *Load patterns*: the self-weight and the other vertical loads are considered within the same load pattern.
   - *Restraints*: the arch is fixed at the imposts. The blocks are rigid and each block transfers to the next one only compressive stress. The joints are modelled with three frame element located at the block interfaces.
   - *Load combinations*: (i) static, with self-weight and vertical loads; (ii) seismic, with static loads and horizontal forces defined applying a multiplier to the each weight. The seismic analysis is performed for increasing values of the multiplier until the collapse mechanism occurs.

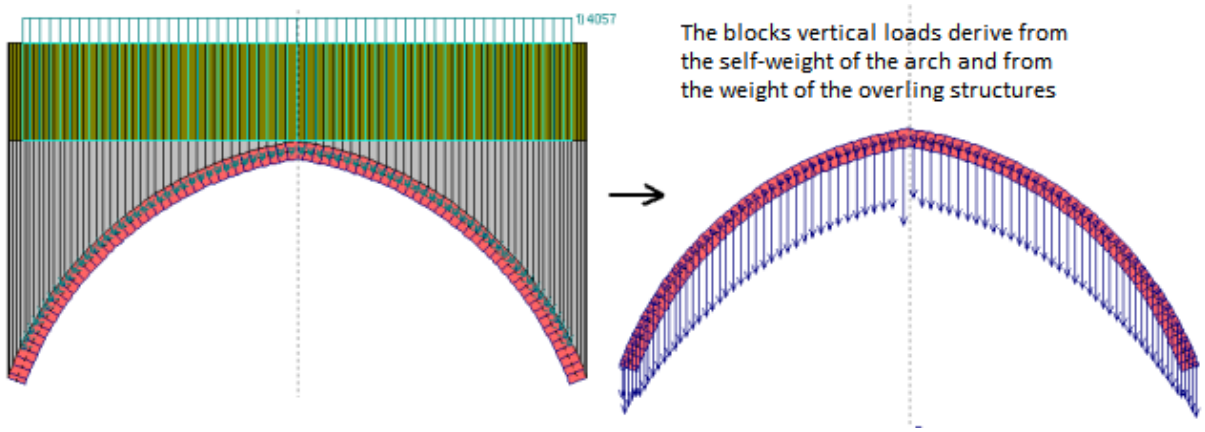


Figure 8. Loads acting on the arch

The structural analysis was performed with the aid of the software Aedes©SAV [7] according to the methods described in §2. Figure 9 presents the results of the static analysis. The arch is stable and under static load retains 3 degrees of hyperstaticity. The reaction at the impost are:

$$F_V = 839.29\ kN$$

$$F_H = 441.29\ kN$$

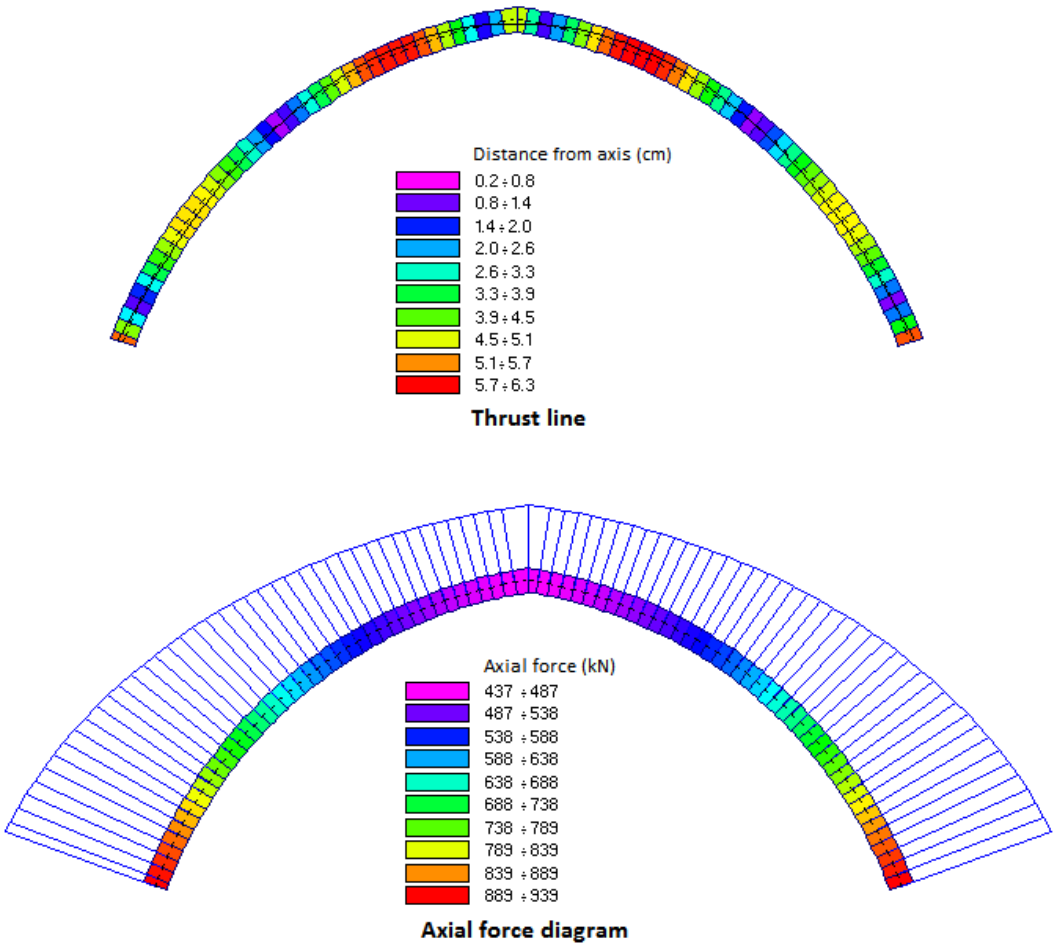


Figure 9. Static analysis results

The results of seismic analysis are provided in Figure 10.

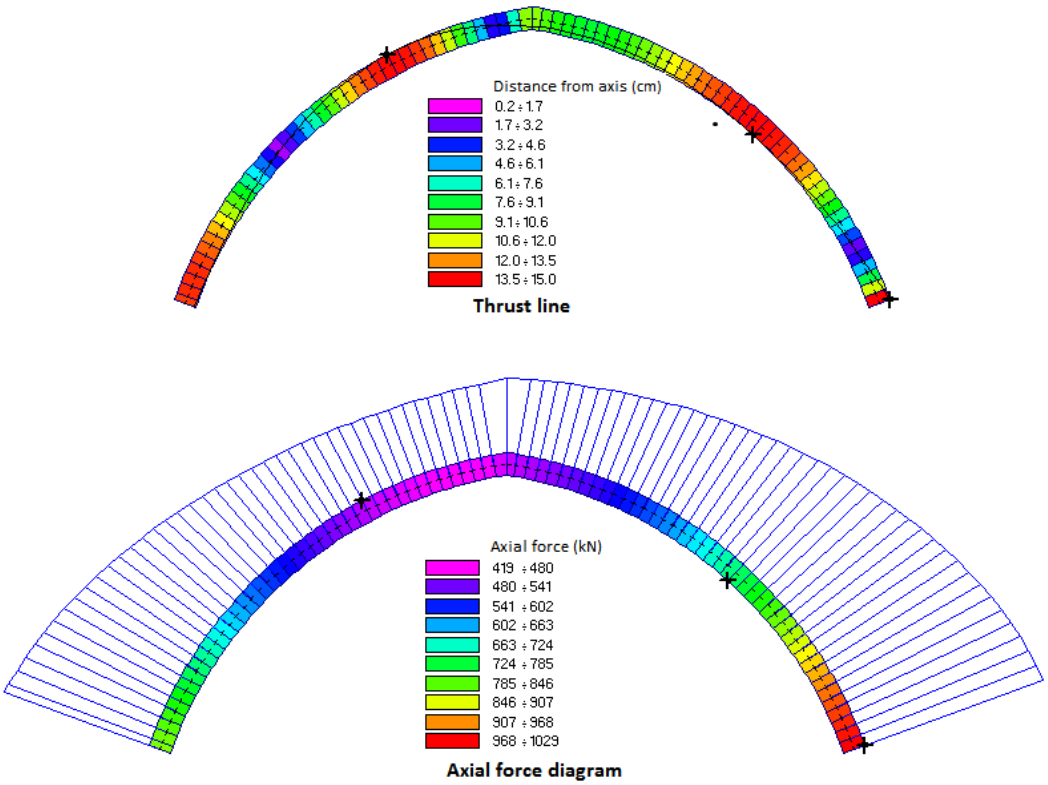


Figure 10. Seismic analysis results

The collapse multiplier is equal to 0.173; that is, the collapse mechanism shown in Figure 11 was activated applying a system of horizontal forces each one equal to the 17.3% of the corresponding weight. In the last configuration in equilibrium the arch was isostatic and presented three active hinges. A further increment of the horizontal loads led to the development of the fourth hinge at the upwind impost, then the collapse mechanism occurred. In the last configuration the reactions at the upwind (L) and at the downwind (R) imposts were

$$F_{V,L} = 794.81\ kN, \quad F_{H,L} = 293.30\ kN$$

$$F_{V,R} = 883.58\ kN, \quad F_{H,R} = 583.66\ kN$$

Therefore, for a multiplier $\lambda = 0.173$ the vertical reaction at the downwind impost increased by 6% while the horizontal reactions increased by 32%. Obviously the seismic event will provoke the thrust increment alternately at each impost.

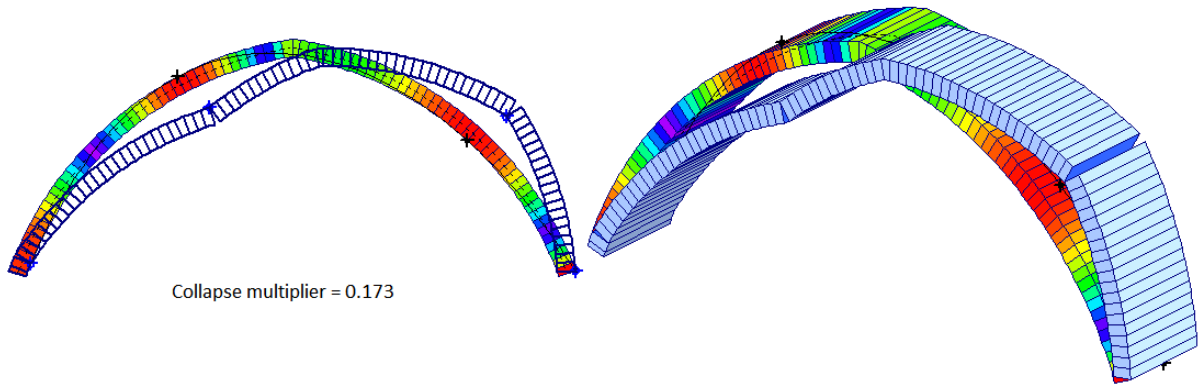


Figure 11. Collapse mechanism for seismic action

4.2 Block-joint model. Nonlinear static analysis

The analysis with the nonlinear elastic model, according to the method proposed in this paper, is able to assess the collapse multiplier taking into account the tensile strength of the mortar joints. In the structural model shown in Figure 12, first the mortar joints were considered to have zero tensile strength for a direct comparison with the rigid-brittle model results, then a tensile strength of 0.25 MPa was considered.

The characteristic aspects of the analysis are the following:

a) Mechanical characteristics
   - *Behaviour:* nonlinear elastic
   - *Tensile strength:* 0.00/0.25 MPa for the mortar joints, 3.50 MPa for the blocks
   - *Modulus of elasticity:* 660 MPa for the mortar joints, 50000 MPa for the blocks

b) Analysis type and verifications
   - Modal analysis. Static analysis.
   - Seismic static nonlinear analysis. Collapse mechanism due to the achievement of an unstable configuration after development of hinges.
   - Equilibrium verification under static load and increasing seismic loads.
   - Calculation of the collapse multiplier for horizontal actions.

c) Model characteristics
   - *Geometry:* arch modelled with block-joint system
   - *Load patterns:* (i) self-weight of the arch, (ii) weight of the overlying wall, (iii) weight of the fence on top.
   - *Load combinations:* (i) static, with self-weight and vertical loads; (ii) seismic, with static loads and increasing horizontal forces defined by predefined distributions of the total base shear.

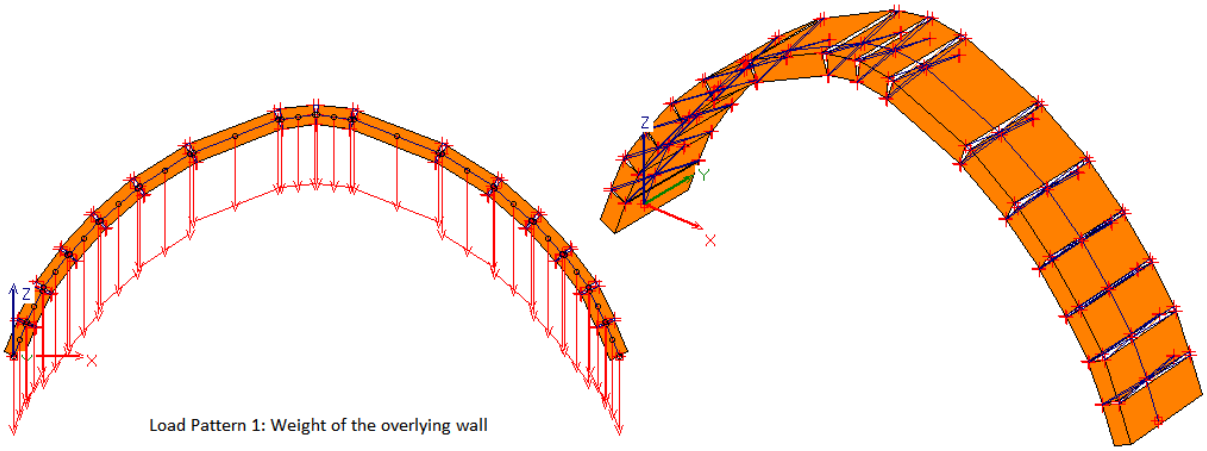


Figure 12. Nonlinear elastic model

The software Aedes©PCM [7] was used to perform the analysis.

Modal analysis is particularly significant in monumental buildings and the application to the arch proves the potential of a static approach. The knowledge of the modal characteristics allows to validate the structural model on the base of ambient vibration testing measurements and to evaluate the interaction with the adjacent macroelements.

The block-joint method allows to consider a dense distribution of the masses concentrated in the nodes which represents the real object well.

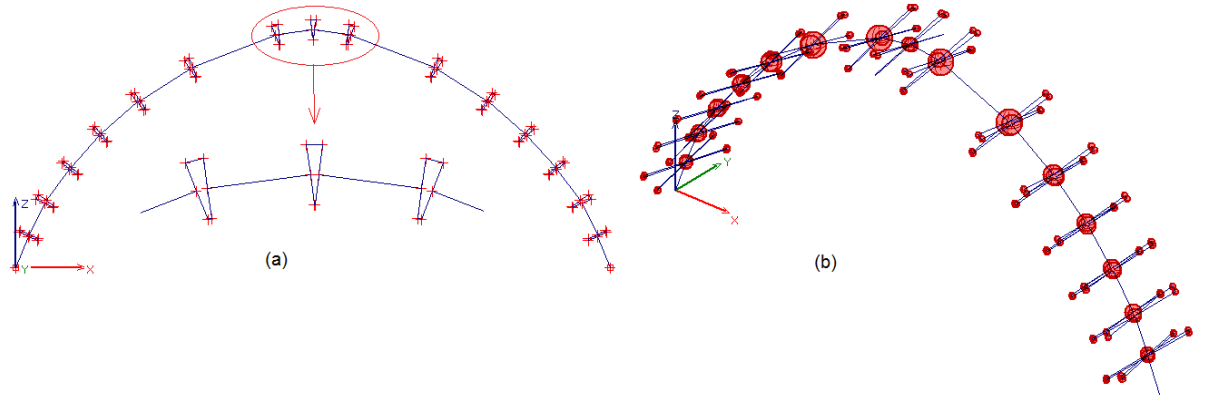


Figure 13. a) Structural model (frame elements and nodes). b) Active masses obtained from the weights applied to each node. The size of the sphere is proportional to the mass.

Given the modelling of the joints, the structure is not plane; thus, the model features 300 degrees-of-freedom and the masses are free to move in-plane and out-of-plane. Considering the in-plane behaviour (XZ plane), the first mode of vibration with a period of 0.197s (5.07 Hz) features a participating mass larger than the 85% of the total mass. Figure 14 shows the modal deformed shape.

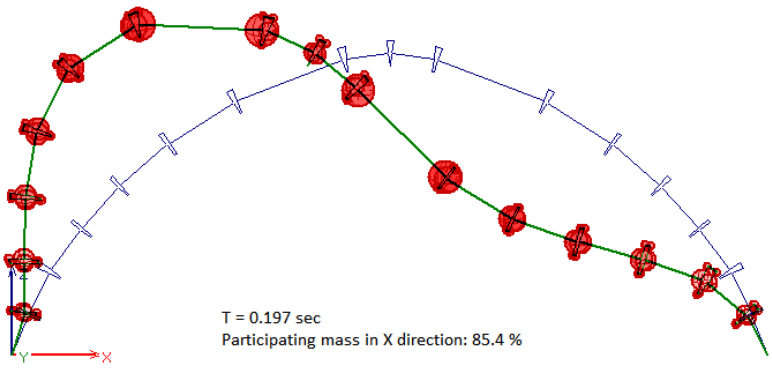


Figure 14. Modal analysis

According to the results of the non-seismic static analysis, the arch is stable and under the static loads it retains three degrees of hyperstaticity.

The nonlinear static analysis, performed applying to the structure increasing horizontal forces, allows to determine the collapse multiplier and to evaluate the capacity of the structure in terms of ground acceleration. The seismic verification that, beyond the collapse multiplier, takes into account the participating mass and the seismic action at the exact location of the structure, is independent from the model used to perform the analysis and is not presented in this paper. Attention will be paid, instead, to the calculation of the collapse multiplier with the two alternative approaches.

The nonlinear static analysis was performed applying two distributions of horizontal forces: (A) a linear distribution proportional to mass and height, that well represents the initial elastic behaviour of the structure; (E) a distribution proportional to mass and independent from height, that well represents the post-elastic phase.

The maximum sustainable force is assumed as the smallest of the ones obtained with the two distributions. The nonlinearity, that is, the non-proportionality between forces and displacements, depends on the variation of the structural model during the incremental analysis. At each step, a verification is applied to the structural elements and their mechanical characteristic and restraints are updated. In the block-joint model particularly significant is the tensile stress verification applied to the joints.

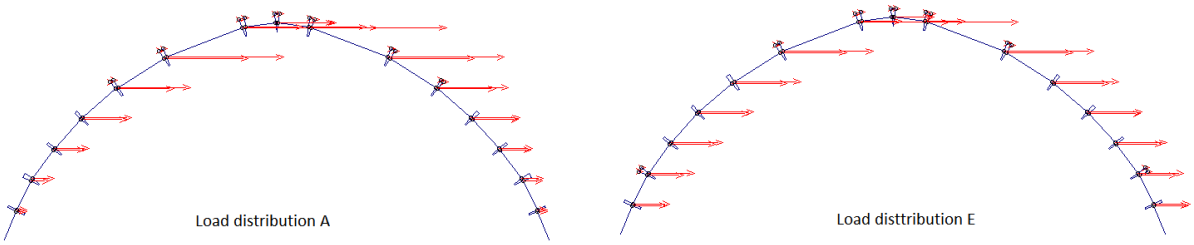


Figure 15. Load distributions in nonlinear static analysis

The total weight of the structure is 1670 kN, while the seismic active weight is 1611 kN. The nonlinear static analysis was performed with a base shear increment of 5 kN, considering first zero tensile strength of the joints and then a tensile strength equal to 0.25 MPa.

Table 1 shows the results obtained with zero tensile strength of the joints, for the two load distributions.

Distribution	Maximum force	Collapse multiplier
A	340 kN	0.211
E	415 kN	0.258

Table 1. Analysis results with zero tensile strength

The results obtained with distribution E (forces proportional to the masses), may be directly compared with the ones of the rigid-brittle model examined in §4.1; in fact, the reference software (SAV) uses the same load distribution. Compared to the rigid-brittle model, the collapse multiplier increased due to the effects of elasticity; the nonlinear curve (Figure 16) shows the end of the elastic range for a force of 360 kN and a multiplier of 0.223, that is, with an increment of 29% compared to the one obtained with the rigid-brittle model.

Figure 16 shows the deformation of the structure at the last step of the incremental analysis, when the collapse mechanism occurs: with the aid of the software [8] it is possible to visualize step-by-step the deformation process and the failures of the joints. It is worth noting that the collapse mechanism is equivalent to the one obtained with limit analysis (Figure 11) although they correspond to different values of the collapse multiplier.

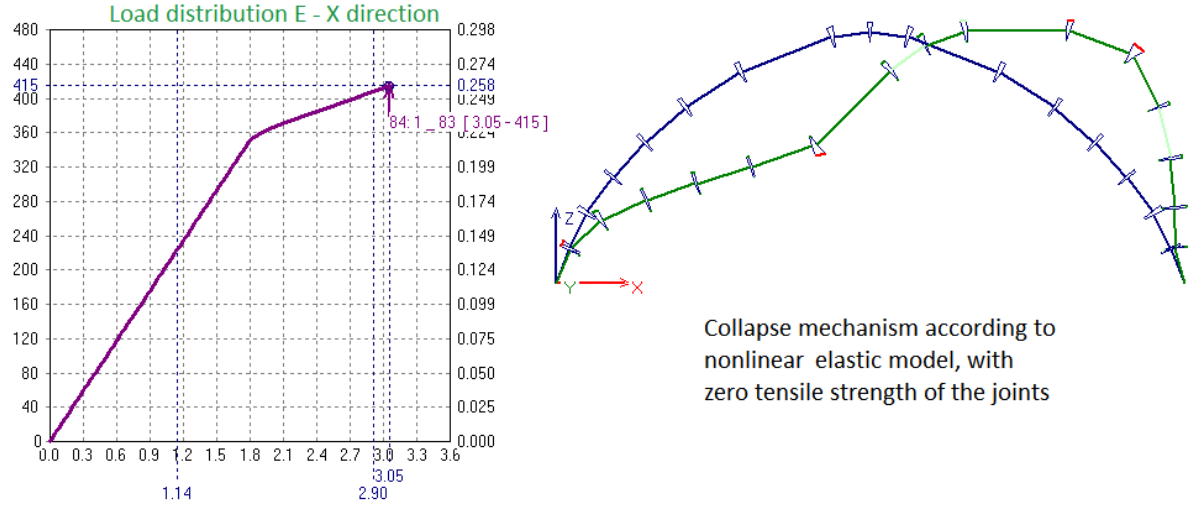


Figure 16. Nonlinear static analysis with zero tensile strength

The results of the analysis with a tensile strength of the joints equal to 0.25 MPa are shown in Table 2.

Distribution	Maximum force	Collapse multiplier
A	400 kN	0.249
E	495 kN	0.308

Table 2. Analysis results with tensile strength equal to 0.25 MPa

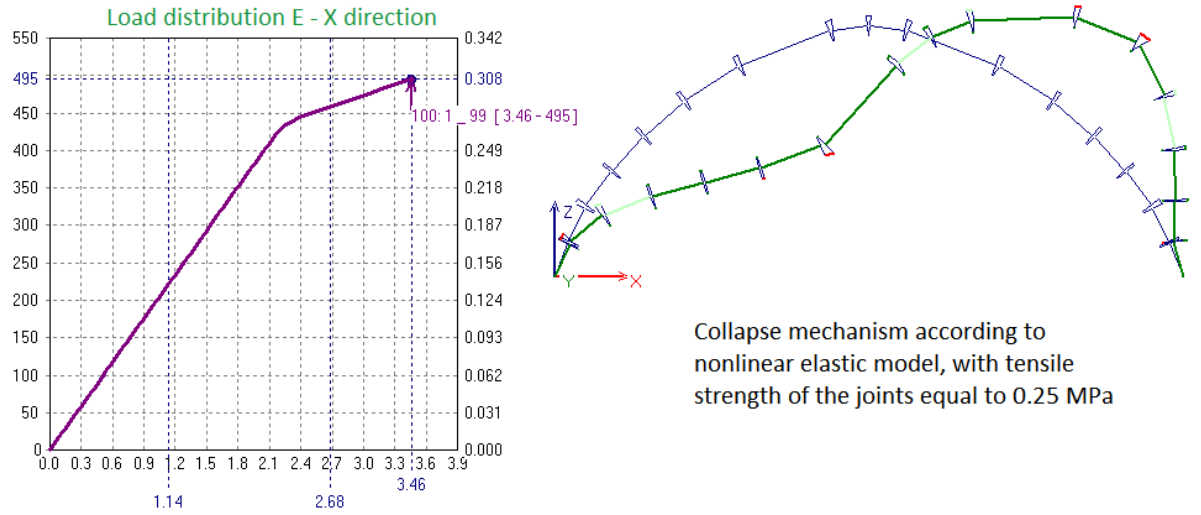


Figure 17. Nonlinear static analysis with tensile strength equal to 0.25 MPa

Due to the tensile strength of the joints, the collapse multiplier increased from 0.211 to 0.249. Finally, the application of the block-joint method led to:

- the fundamental period of the structure, equal to 0.197s,
- an increment of the collapse multiplier from 0.173 (rigid-brittle model) to 0.249 (nonlinear elastic model).

5 CONCLUSION

A new finite element model for the analysis of arch systems is proposed in this paper. The method assesses the maximum sustainable horizontal force, and thus the collapse multiplier, through an incremental procedure typical of nonlinear analysis. The ease of the approach was pursued, so that it could be performed with any finite element program that deals with one-dimensional elements. Compared to the rigid-brittle model, the new approach provides higher collapse multipliers, basically due to the possibility of taking into account the mortar tensile strength. This is favourable in order to avoid oversizing of the strengthening interventions.

The case of an arch structure located in an important monumental complex was examined; the new method was applied considering several distribution of the horizontal forces.

It is the intent of the author to further investigate the block-joint method especially regarding the following aspects: (i) curved axis blocks, in order to ensure the correct modelling of the joints avoiding excessive thickness at the extrados; (ii) calibration of the tensile strength of the joints according to their length; (iii) comparison between the nonlinear elastic and the rigid-brittle model in order to qualitatively understand the variation of the collapse multiplier according to the geometry of the structure and the applied loads.

AKNOWLEDGMENTS

The author thanks Prof. Piergiorgio Malesani, director of CABeC (Università degli Studi di Firenze) and coordinator of the research carried out on behalf of the Franciscan Custody of the Holy Land, who granted the publication of an extract of the work [8]. Moreover, the author thanks Dr. Alessio Francioso for his support in the translation of this paper.

REFERENCES

[1] Ministero delle Infrastrutture e dei Trasporti, *Decreto 14 gennaio 2008. Approvazione delle nuove norme tecniche per le costruzioni*, §8.7.1, Gazzetta Ufficiale della Repubblica Italiana n. 29 del 4 febbraio 2008, Supplemento ordinario n.29. (in Italian)

[2] Ministero delle Infrastrutture e dei Trasporti, *Circolare. n. 617 del 02 febbraio 2009. Istruzioni per l'applicazione delle Nuove Norme Tecniche per le costruzioni*, §C8A.4, Gazzetta Ufficiale della Repubblica Italiana n. 47 del 26 febbraio 2009, Supplemento ordinario *n.27.* (in Italian)

[3] Direttiva del Presidente del Consiglio dei Ministri, 9 febbraio 2011: *Valutazione e riduzione del rischio sismico del patrimonio culturale con riferimento alle Norme tecniche per le costruzioni di cui al decreto del Ministero delle infrastrutture e dei trasporti del 14 gennaio 2008*, §All.B-§All.C-§5.4.2, Gazzetta Ufficiale della Repubblica Italiana n. 47 del 26 febbraio 2011, Supplemento ordinario n.54. (in Italian)

[4] M. Paradiso, G. Tempesta, S. Galassi, F. Pugi, *Sistemi Voltati in Muratura. Teoria e Applicazioni*, DEI Tipografia del Genio Civile, Roma, 2007. (in Italian)

[5] J. Heyman, *The Masonry Arch*, Chichester, West Sussex, England: Hellis Horwood Ltd., 1982.

[6] J. Heyman, *The Stone Skeleton*, Cambridge: Cambridge University Press, 1995.

[7] AEDES Software: "SAV": *Stabilità di Archi e Volte in muratura, "SVM": Sistemi Voltati in Muratura, software per il calcolo strutturale dei sistemi voltati, Ia edizione: 2000; "PC.M-PC.E": Progettazione di Costruzioni in Muratura, con solutore ad Elementi finiti*, I edizione: 1997, www.aedes.it

[8] F. Pugi, *Valutazione struttuale della vulnerabilità sismica, in: "Seismic vulnerability of the Church of the Holy Sepulchre in Jerusalem*", Research performed by CABeC (Centro di Ateneo per i Beni Culturali, Università degli Studi di Firenze) on behalf of: Greek Orthodox Patriarchate of Jerusalem, Franciscan Custody of the Holy Land, Armenian Patriarchate of Jerusalem, 2009.

[9] P.Virgilio C.Corbo, *Il Santo Sepolcro di Gerusalemme. Aspetti archeologici dalle origini al periodo crociato*, I-III, Studium Biblicum Franciscanum, Gerusalemme, 1981. (in Italian)

[10] Archive of the Franciscan Custody of the Holy Land

COMPDYN 2013
4th ECCOMAS Thematic Conference on
Computational Methods in Structural Dynamics and Earthquake Engineering
M. Papadrakakis, V. Papadopoulos, V. Plevris (eds.)
Kos Island, Greece, 12–14 June 2013

SEISMIC EVALUATION OF THE HISTORIC CHURCH OF ST.NICHOLAS IN PIRAEUS BEFORE AND AFTER INTERVENTIONS

Constantine C. Spyrakos[1], Alessio Francioso[1], Panagiotis Kiriakopoulos[1], and Stavros Papoutsellis[1]

[1] Laboratory for Earthquake Engineering, School of Civil Engineering
National Technical University of Athens
Zografos 15700, Athens, Greece
e-mail: cspyrakos@central.ntua.gr

Keywords: historic masonry structure, in-situ testing, non-linear analysis, macroelements, strengthening interventions.

Abstract. *The construction of the church of St. Nicholas located in Piraeus dates back to 1839. Over the years the building has undergone several interventions until recent earthquakes caused serious damages to the structure. The damages are mainly attributed to the absence of particular provisions to sustain seismic loads. A detailed in-situ and laboratory testing of the masonry structure was carried out in order to search its geometry, the constructions details and the mechanical characteristics of the materials. Also, finite element analyses were performed in order to assess the current condition of the structure and its dynamic behavior. The capacity of the church was determined through linear global analysis and non-linear analysis with macroelements. Based on the results, strengthening interventions were proposed, using a combination of masonry consolidation techniques, carbon fiber reinforced materials (CFRP) and steel tie rods. The effectiveness of the strengthening is assessed through comparison of the analysis results before and after interventions.*

1 INTRODUCTION AND DESCRIPTION OF THE STRUCTURE

The construction of the church of St. Nicholas located in Piraeus dates back to 1839. It belongs to the type of cruciform temples with a form that follows the standards of the neoclassical style, distinguished by three monumental propylaea on the west, the north and south side, resembling the type of an ancient Corinthian temple [1].



Figure 1. a) West façade and b) North façade of the church

The dimensions of the temple are 33.75m (depth) by 26.00m (length of the facade). The height of the walls is 16.52m. The height at the base of the dome reaches the 28m, while at the top the dome rises to 30m. The perimeter walls of the temple consist of three strata with a width of 1.30m. Generally the construction materials found in the building are stone, marble and tile.

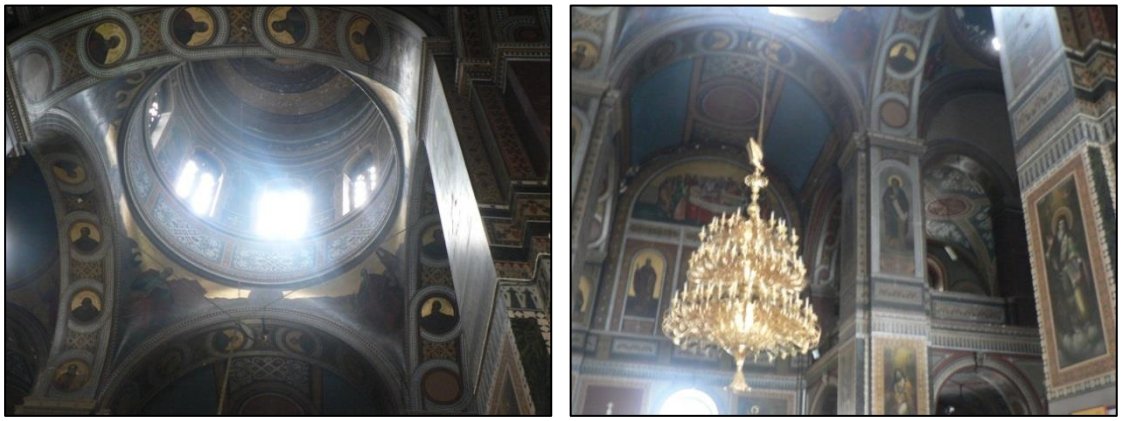


Figure 2. a) Internal view of dome. b) Internal view over the temple

Over the years the building has undergone several modifications until recent earthquakes (the Alkyonides 1981 and the Athens 1999) caused serious damages to the structure. The damages are mainly attributed to the fact that no special consideration was given in the initial design for seismic loads. Cracks appear in many parts of the masonry structure and mainly at the intrados of arches and vaults in the longitudinal and transverse directions.

Because of its neighboring with the Piraeus harbor, just 100m away, the walls have suffered extensive weathering damage.

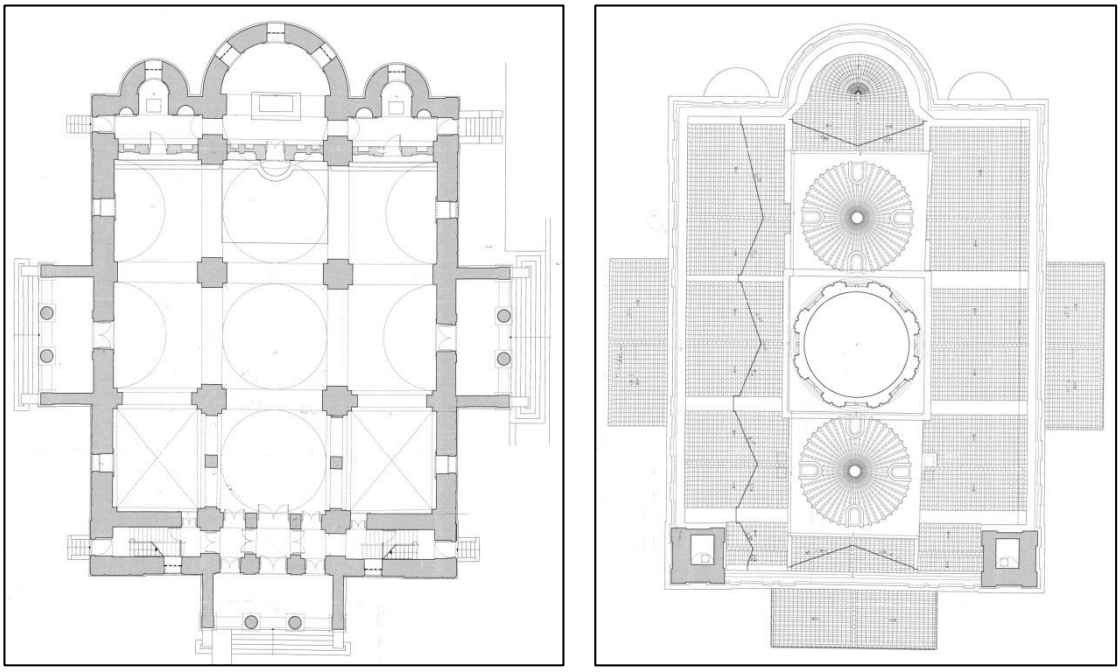


Figure 3. a) Ground floor plan. b) Roof plan



Figure 4. a) Through crack and detachment of lower drum at the southern part of the structure. b) Sliding of drum of a marble pillar caused by bombardment

2 IN SITU AND LABORATORY TESTING

Several tests were carried out in order to assess the mechanical characteristics of the masonry walls and the piers of the church. In-situ testing was performed at several locations

of the structure. Based on the collected measurements, the compressive strength of the stones was estimated to be:

$$f_{bc} = 40MPa$$

Drilled holes were opened in order to investigate by means of an endoscope the composition of the masonry walls along their thickness (Figure 5). The inspections revealed that the masonry walls were made of three-leaf masonry.



Figure 5. a) Area without plaster for inspection with endoscope. b) View inside the drilled hole

Mortar samples were analyzed following a three-step procedure: natural separation of mortar-stone, X-Ray diffraction and thermal analysis TG-DTG (Figure 6).

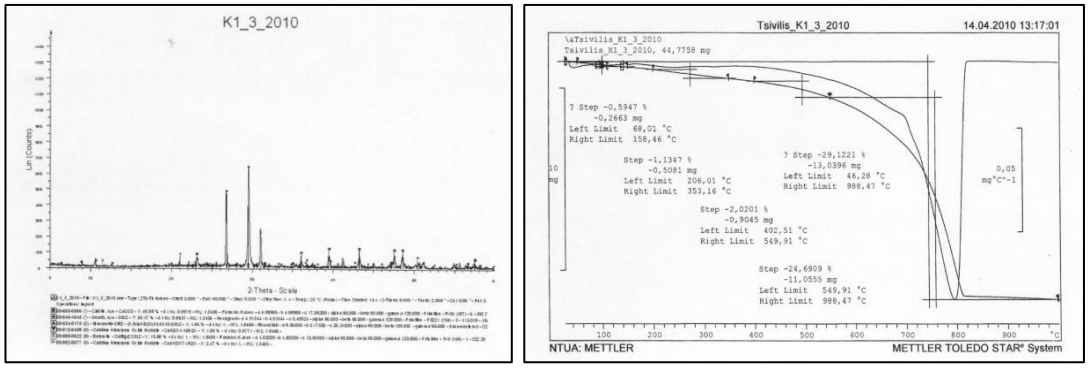


Figure 6. a) X-Ray analysis results. b) Thermal analysis results

The measurements and their analysis showed that: (i) the mortar contains natural hydraulic lime; (ii) the aggregate is a mixture of limestone, dolomitic and silica sands; (iii) the mortar contains muscovite.

The compressive strength of the mortar was estimated to be $f_{mc} = 1MPa$.

Ambient vibration tests were performed in order to measure the modes and natural frequencies of the church at its current state. The measurements were taken at three distinct positions: ground floor, mezzanine and dome level, along the principal directions of the church.

The analyses were performed using appropriate software that calculated transfer functions and Fourier spectra at different positions.

Table 1 presents the peaks of the Fourier spectra (see Figure 7) obtained from the ambient testing measurements.

	Mode	Modal period (s)
Transverse direction X (N-S)	1	0.357
	2	0.187
Longitudinal direction Y (E-W)	1	0.329
	2	0.187

Table 1. Modal periods of the church

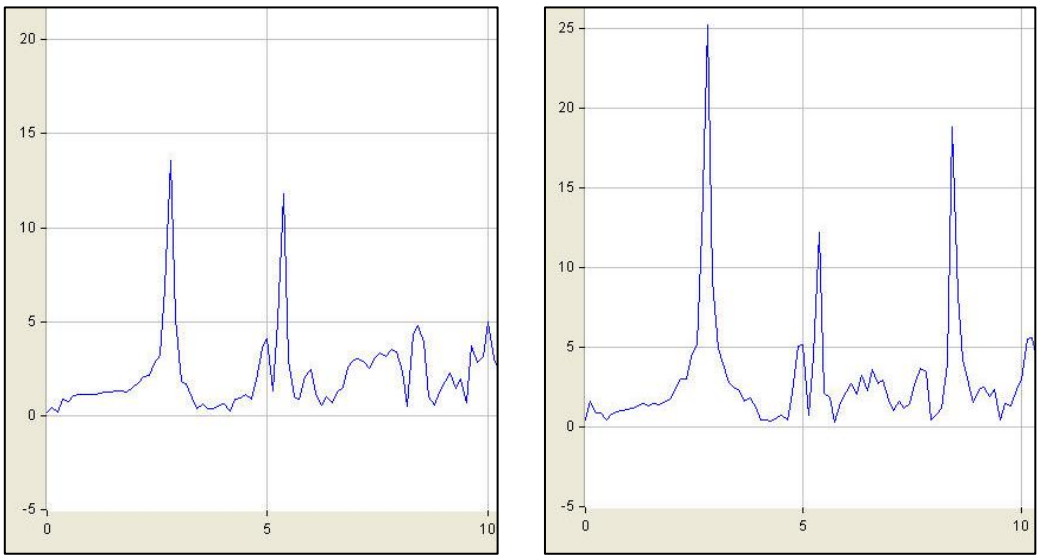


Figure 7. Transverse direction X (N-S): a) at mezzanine; b) at dome level

3 ANALYSIS OF THE CHURCH AT ITS CURRENT STATE

Two types of analyses were performed: a) global and b) local. With global analysis the structural response is studied with the aid of a finite element model considering that the structure behave as a whole, that is without developing any local mechanisms of failure.

The local analysis is performed only for the transversal frame that is directly loaded by the central dome; thus, one of the most vulnerable local load bearing systems of the church.

In order to calculate the compressive strength of the stone masonry, the following expression was used [2]:

$$f_{wc} = \frac{2}{3}\sqrt{f_{bc}} - a + \beta f_{mc} \tag{1}$$

where:

f_{bc} is the compressive strength of the stones;
f_{mc} is the compressive strength of the mortar;
α is a reduction factor (for masonry made of natural stone $\alpha = 1$);
β is a factor that accounts for the mortar contribution on the masonry strength (for stone masonry $\beta = 0.5$).

The tensile strength and the modulus of elasticity were obtained from the masonry compressive strength according to the following expressions:

$$f_t = f_c/10 \tag{2}$$

$$E = 1000 f_c \tag{3}$$

Table 2 presents the data used, as well as the results obtained from Equations (1 - 3).

Stones	Compressive strength	f_{bc}	40	N/mm^2
Mortar	Compressive strength	f_{mc}	1	N/mm^2
Masonry	Compressive strength	f_c	3.71	N/mm^2
	Tensile strength	f_t	0.37	N/mm^2
	Modulus of Elasticity	E	3710	N/mm^2
	Specific weight	W	22	kN/m^3

Table 2. Mechanical characteristics of masonry

3.1 Global analysis

The structural model and the global analysis of the structure were performed with the finite element software SAP2000 v.15 [3]. The stone masonry and marble elements were modeled with eight node solid elements with three degrees-of-freedom per node, while four-node shell elements were used to model the central dome. Frame elements were used for the proper connection and collaboration of solid and shell elements [4]. The final model consists of 42180 solids, 3350 shells, 96 frame elements and 63580 nodes, see Figure 8.

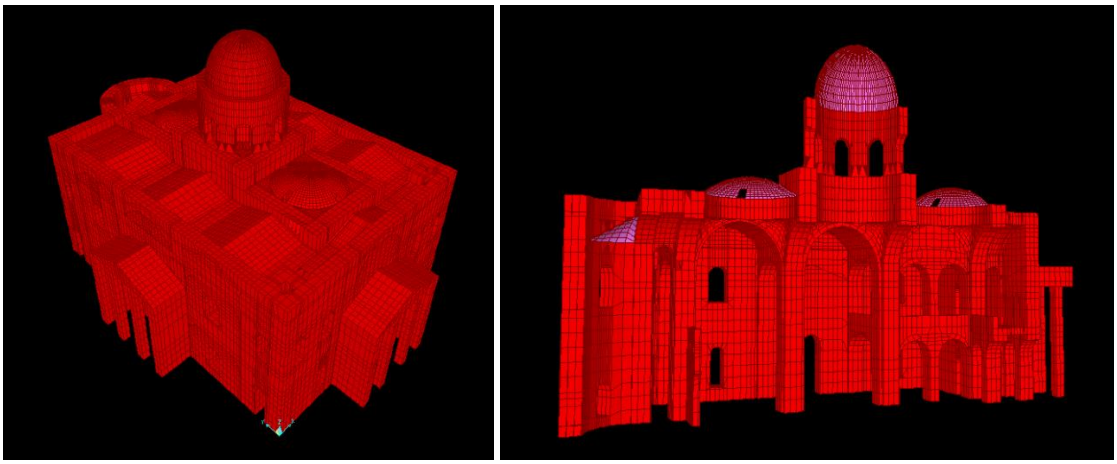


Figure 8. Three dimensional model: a) N-W view b) E-W section

The static and seismic analyses were performed applying the following loads:

a) the dead load of the masonry walls and the dome were automatically calculated by the program based on the dimensions of the structure and the specific weight. The tiles of the roof were considered as an additional weight equal to 0.9 kN/m^2
b) the live loads at the mezzanine were 5.0 kN/m^2.

A response spectrum analysis was performed according to Eurocode 8 [5, 6]. For the horizontal components of the seismic action the design response spectrum $S_d(T)$ is defined by the following expressions:

$$a_g = \gamma_I \cdot a_{gR} \tag{4}$$

$$0 \le T \le T_{\mathrm{B}}: \; S_{\mathrm{d}}(T) = a_{\mathrm{g}} \cdot S \cdot \left[\frac{2}{3} + \frac{T}{T_{\mathrm{B}}} \cdot \left(\frac{2{,}5}{q} - \frac{2}{3} \right) \right] \tag{5}$$

$$T_{\mathrm{B}} \le T \le T_{\mathrm{C}}: \; S_{\mathrm{d}}(T) = a_{\mathrm{g}} \cdot S \cdot \frac{2{,}5}{q} \tag{6}$$

$$T_{\mathrm{C}} \le T \le T_{\mathrm{D}}: \; S_{\mathrm{d}}(T) \begin{cases} = a_{\mathrm{g}} \cdot S \cdot \dfrac{2{,}5}{q} \cdot \left[\dfrac{T_{\mathrm{C}}}{T} \right] \\ \ge \beta \cdot a_{\mathrm{g}} \end{cases} \tag{7}$$

$$T_{\mathrm{D}} \le T: \quad S_{\mathrm{d}}(T) \begin{cases} = a_{\mathrm{g}} \cdot S \cdot \dfrac{2{,}5}{q} \cdot \left[\dfrac{T_{\mathrm{C}} T_{\mathrm{D}}}{T^2} \right] \\ \ge \beta \cdot a_{\mathrm{g}} \end{cases} \tag{8}$$

where T is the vibration period in sec, $a_{gR} = 0.16g$ is the design ground acceleration on soil type A, $\gamma_I = 1.2$ is the importance factor, $T_B = 0.15\ s$ is the lower limit of the period of the constant spectral acceleration branch, $T_C = 0.50\ s$ is the upper limit of the period of the constant spectral acceleration branch, $T_D = 2.00\ s$ is the value defining the beginning of the constant displacement response range of the spectrum, $S = 1.2$ is the soil factor, $\eta = 1$ is the damping correction factor, $q = 1.5$ is the behavior factor, $\beta = 0.2$ is the lower bound factor for the horizontal design spectrum.

For the vertical component of the seismic action the design response spectrum $S_d(T)$ is defined by Equations (4 - 8) replacing a_g with $a_{vgR} = 0.144g$ and adopting $T_B = 0.05\ s$, $T_C = 0.15\ s$, $T_D = 1.00\ s$, $S = 1$, respectively.

Table 3 presents the results of modal analysis for the first three modes as well as the corresponding modal participating mass ratios. A good correlation between the measured and calculated modal periods is observed, a fact that validates the adequacy of the structural model at least for static and small intensity dynamic loads.

Mode	Period (sec)	Ux	Uy	Uz	Rx	Ry	Rz
1st	0,290(0.357)	0,73	1,845E-05	0,00012	0,0001	0,32	0,357
2nd	0,263(0.329)	8,18E-08	0,78	0,00071	0,26612	3,9E-04	0,182
3rd	0,196	0,00861	0,00024	7,16E-06	3,82E-06	2,66E-03	0,200

Table 3. Modal periods and participating mass ratios for displacement (U) and rotation (R). In parentheses the corresponding measured values

The representative Figure 9 shows the stress distribution for a seismic combination. Deep blue (darkest color) indicates the areas where the developed stresses are greater than the tensile strength of masonry. A detailed presentation of the results and the corresponding figures are provided in [7]. It is worth noting that the analysis identified with good accuracy the areas where critical damages were identified from the visual inspection.

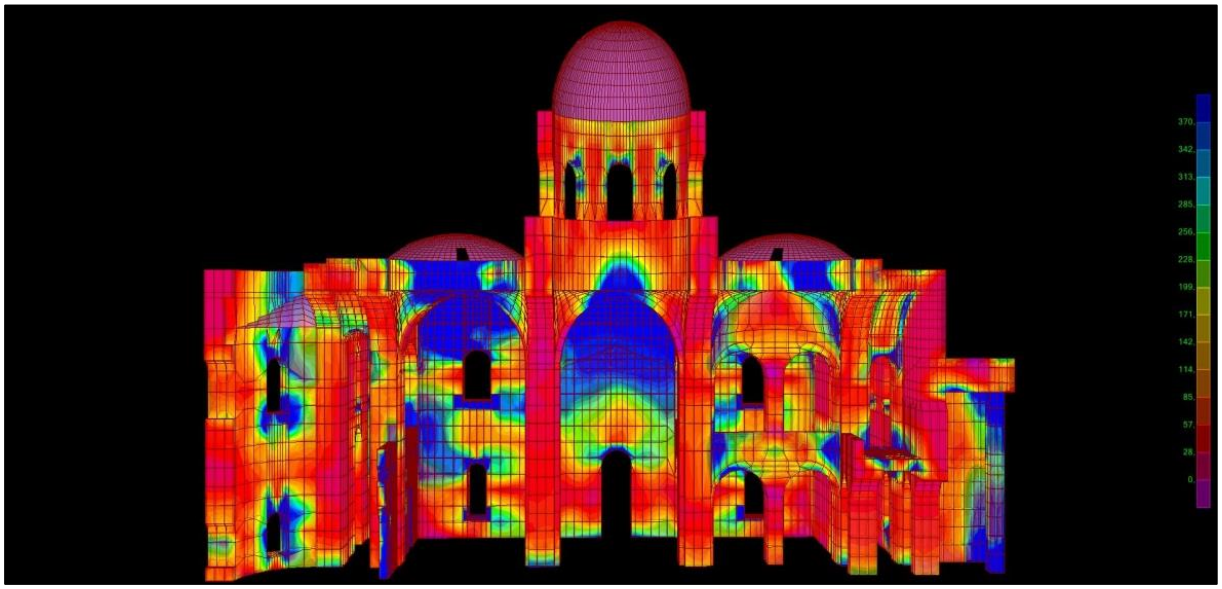


Figure 9. Stress distribution S22 for the $E_x+0.3E_y+0.3E_z$ combination

3.2 Local Analysis

The observation of the damages on churches struck by major earthquakes has revealed that this type of structures can be analyzed as a set of architectural parts characterized by a structural response basically independent from the church as a whole. These parts, referred to as macroelements, can be identified depending on the architectural and structural features of a church, such as the façade, the apse, the bell tower, the dome, the triumphal arch, etc. [8].

For each macroelement, a kinematic limit analysis is performed. Dealing with damaged churches, the uncertainties in choosing, a priori, the collapse mechanism are usually very small, since an accurate survey of the damages can lead to an "understanding" of their structural behavior. Moreover, a systematic analysis of the construction details, such as the masonry typology or the presence of earthquake-resistant elements, can help to identify the macroelements and to forsee which collapse mechanism is more likely to develop.

In addition to the kinematic approach, another feasible way to evaluate the seismic resistance of a macroelement, without choosing a priori the collapse mechanism, is to perform a non-linear static analysis by means of a finite element model.

A realistic approach to analyze these systems is to model the arches as a set of blocks and joints. The approach is known as the "blocks and joints" method [9]. As shown in Figure 10, both blocks and joints are frame elements: the blocks have the mechanical properties of the stone and their cross section is the effective cross section of the arch, the joints represent the mortar between the blocks. Four joints for each block are used; therefore, the joint cross section is ¼ of the arch cross section. The joints have a pin-end and a fixed-end, the fixed-end provides continuity with the previous block, the pin-end transfers shear and axial force to the next block, while the joints are connected to the block ends through rigid links; in this manner the system transfers moment, shear and axial force from one block to another.

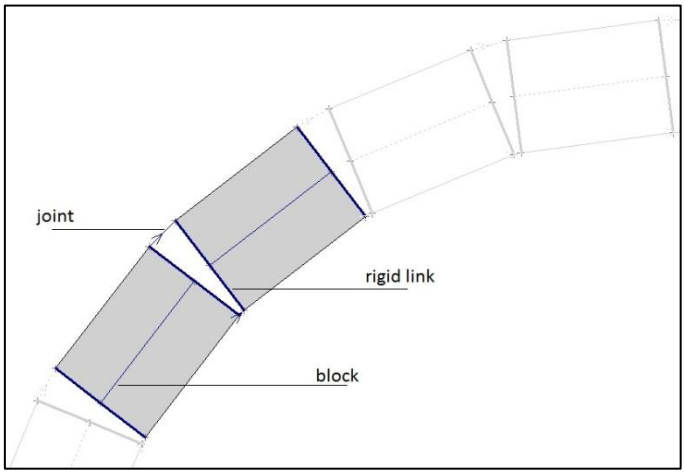


Figure 10. Structural model of an arch

When performing a pushover analysis, an axial force verification is applied to the joints, that is: if the tensile stresses exceed resistance, the fixed-end is turned to pin and the axial force is released so that the element loses any stiffness and the internal actions remain constant at the value reached so far. As the analysis continues, the progressive deterioration of the joints lead to an unstable configuration that define the end of the pushover curve.

The pillars are also divided into blocks and modeled with frame elements. At each step of the pushover analysis, the blocks are subjected to verification in terms of compression, that is examination of the thrust line position. If the thrust line comes out of the section of the block, a plastic hinge develops at the relevant node. The incremental analysis continues until the structure becomes unstable determining the maximum lateral force that the system can sustain.

The aim of non-linear static analysis applied to a *"blocks and joints"* system and to the masonry pillars is to determine the collapse multiplier α_0, that is given by

$$\alpha_0 = \frac{F_{max}}{W} \tag{9}$$

where F_{max} is the maximum lateral force that the structure can sustain and W is the total weight of the structure.

It should be pointed out that the "blocks and joints" analysis resembles to a kinematic analysis; however, the collapse multiplier is pursued as the maximum static multiplier instead of the minimum kinematic multiplier.

The spectral acceleration that activates the mechanism can be calculated as follows:

$$\alpha_0^* = \frac{\alpha_0 \cdot g}{e^* \cdot CF} \tag{10}$$

where g is the gravity acceleration, e^* is the participating mass ratio, CF is the confidence factor related to a limit knowledge level (KL1): thus equal to 1.35 [10, 11].

The participating mass and the participating mass ratios can be obtained from the following formulas considering the virtual displacement of the nodes where the weight is applied

$$M^* = \frac{(\sum P_i \delta_{x,i})^2}{g \cdot \sum P_i \delta_{x,i}^2} \tag{11}$$

$$e^* = \frac{g \cdot M^*}{\sum P_i} \tag{12}$$

where P_i is the weight applied to node i of the structure, $\delta_{x,I}$ is the virtual horizontal displacement of node i at the ultimate limit state.

The analyzed macroelement consists of three arches and four piers arranged along an alignment in the transverse direction of the church. The model and the analysis were performed with the aid of the software Aedes PC.E [9]. The model shown in Figure 11 consists of 604 frame elements and 488 nodes. For each node the rotation around the vertical Z axis is restrained, while the nodes at the base of the piers are fully fixed.

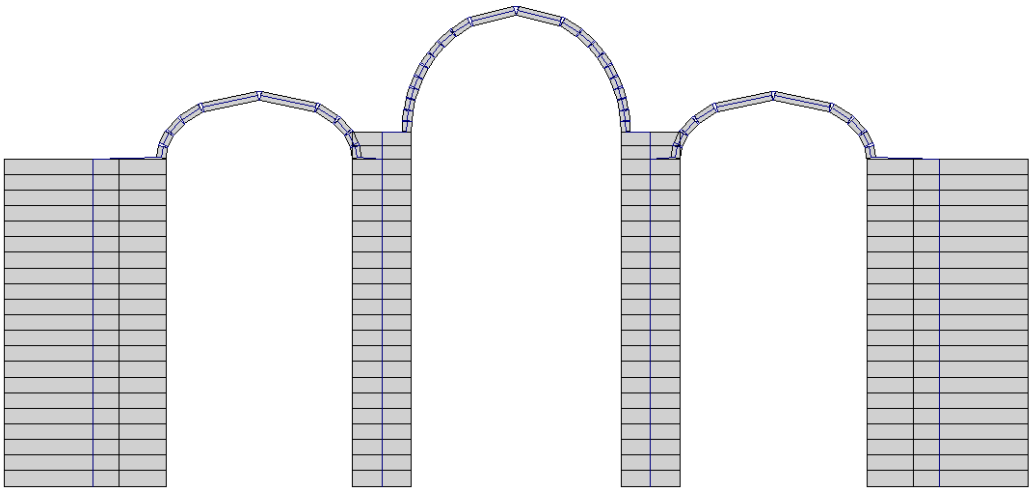


Figure 11. Structural model of the analyzed macroelement

To account for the weight of the structure that was not included in the model, vertical point loads have been applied at the top nodes of the piers. Their values were calculated in order to cause a vertical reaction at the base of the pier equal to the one found with the global model of the church; thus, vertical loads of *1890 kN* and *1570 kN* were applied on a lateral pier and a central one, respectively. The total weight of the structure is $W = 11105$ *kN*.

Figure 12 shows the deformed shape of the first mode of vibration, with the red spheres representing the mass associated to each node. The fundamental period of the structure is *0.544s* and the associated participating mass is *58%* as obtained from modal analysis.

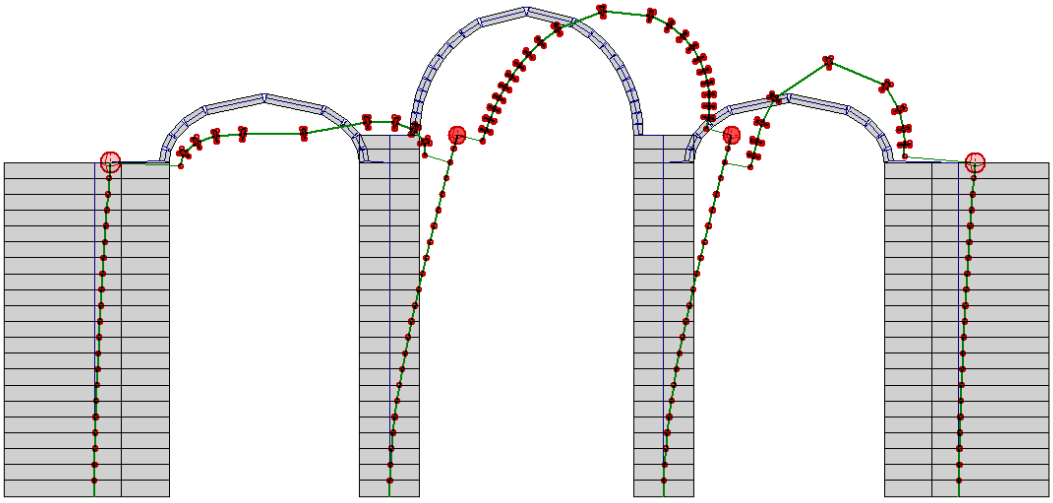


Figure 12. Deformed shape of the fundamental mode of vibration

The pushover analyses were performed using two lateral load distributions: (i) a "triangular" distribution (A) with lateral forces proportional to mass and elevation; and (ii) a "uniform" distribution (B) with lateral forces proportional to mass regardless of elevation.

Figure 13 shows the capacity curves of the structure at the initial state, obtained for the load distributions A and B. In the first case the structure reaches an unstable configuration for a lateral force equal to 600 kN, while with the load distribution B the maximum lateral force the structure can sustain is 750 kN.

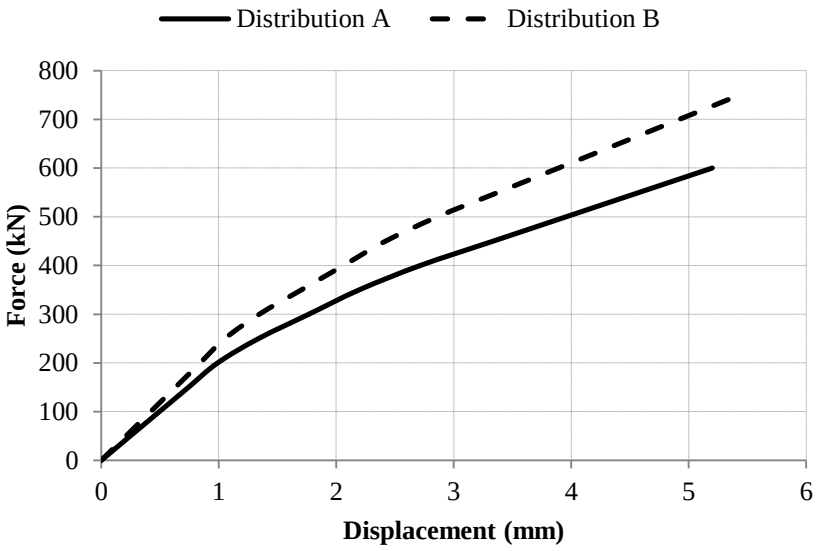


Figure 13. Capacity curves of the structure at initial state

The results from the "triangular" distribution of the lateral forces, being more severe, will be used for safety evaluation of the structure. Figure 14 shows the deformed shape and the position of the pressure curve at the last step of the pushover analysis for the distribution A.

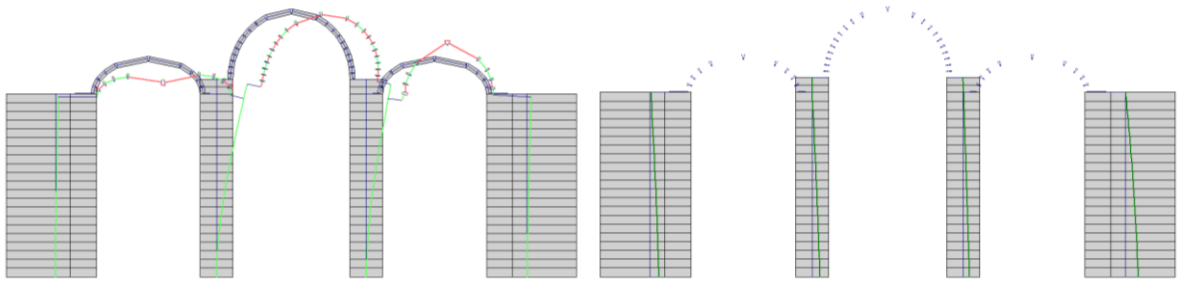


Figure 14. a) Deformed shape and b) pressure curve at last step of curve A

The deformed shape reveals the position of the plastic hinges that developed in the arches for joint degradation between the blocks. The pressure curve remains internal to the cross section of the piers; therefore, no plastic hinges develop in that area.

The collapse multiplier obtained from the analysis is

$$\alpha_0 = \frac{F_{max}}{W} = \frac{600}{11105} = 0.054 \tag{13}$$

The participating mass ratio was calculated from Equation (12) to be *e*=0.487*. Therefore, use of Equation (10) led to the acceleration that activates the mechanism

$$\alpha_{0,1}^{*} = \frac{\alpha_0 \cdot g}{e^{*} \cdot CF} = \frac{0.054}{0.487 \cdot 1.35} \cdot g = 0.082\ g \tag{14}$$

The ultimate limit state is reached if the spectral acceleration

$$\alpha_0^{*} \geq \frac{\alpha_g \cdot S}{q} = \frac{0.16g \cdot 1.2}{1.5} = 0.128\ g \tag{15}$$

where $a_g = 0.16g$ is the design ground acceleration for ground type A, $S = 1.2$ is the soil factor and $q = 1.5$ is the behavior factor.

For the structure at the initial state, $\alpha_{0,1}^{*}$ calculated from Equation (14) does not satisfy Equation (15); therefore, the structure does not reach the ultimate limit state. The maximum ground acceleration that it can sustain is

$$\alpha_{g,max,1} = \alpha_{0,1}^{*} \cdot q/S = 0.103g \tag{16}$$

4 RETROFIT AND STRENGTHENING MEASURES

According to the results of the analysis and the architectural restrictions imposed by the authorities that require minimum intervention to the structural configuration of the historic building and its decorated walls, the rehabilitation and strengthening of the church was based on a combined scheme using (a) grout injections, (b) CFRP and (c) steel tie-rods that complied with all limitations [12, 13]. The scheme is briefly described in the following.

According to international practice for seismic strengthening of three-leaf masonry walls, consolidation of masonry walls can be accomplished with grout injection characterized by grouts with a compressive strength in the range of 10 MPa. A compressive strength of 10 MPa was used in the analysis for the injected material which, combined with strength of the stones, determined the strength of the wall according to [14]

$$f_{wc,s} = f_{wc,0} + 0{,}31(V_{\text{inf}}/V)\, f_{gr}^{1{,}18} \tag{17}$$

where $f_{wc,S}$ is the compressive strength before grout injection, $f_{wc,0}$ is the compressive strength before grout injection, V_{inf}/V is ratio of grout volume to masonry volume, f_{gr} is the compressive strength of the grout. Application of Equation (17) led to Table 4.

		At initial state	After interventions	
Modulus of Elasticity	E	3710	5600	N/mm^2
Compressive strength	f_c	3.71	5.60	N/mm^2
Tensile strength	f_t	0.37	0.56	N/mm^2

Table 4. Mechanical characteristics of masonry

The tensile strength and stiffness of the exterior surface of the roof, as well as parts of the interior surfaces of certain vaults that are not decorated with historic paintings, was increased by applying sheets of carbon fiber impregnated with inorganic resins [15]. Specifically either three or two-plies of carbon fiber sheets (CFRP), with carbon sheet thickness of 0.17 mm per ply, were selected. The mechanical properties of the carbon fiber are: modulus of elasticity $E_c = 240\ GPa$ and ultimate strength $f_j = 3500\ MPa$.

Also stainless steel tie-rods F430 with a diameter of 40mm were placed at the upper part of the arches in the interior of the church. The mechanical properties of the tie-rods are: modulus of elasticity $E_c = 200\ GPa$, yield strength $f_y = 379\ MPa$ and ultimate strength $f_u = 552\ MPa$.



Figure 15. Position of the steel tie-rods

The results of modal analysis for the first three modes of the strengthened structure and the modal participating mass ratios are listed in Table 5.

Mode	Period (sec)	Ux	Uy	Uz	Rx	Ry	Rz
1st	0,186	7,508E-07	0,594	0	0,875	1,102E-6	0,206
2nd	0,186	0,594	7,508E-07	0	1,102E-6	0,875	0,205
3rd	0,124	2,561E-09	2,554E-09	0	3,736E-09	3,745E-09	0,189

Table 5. Modal periods and participating mass ratios from global modal analysis

Comparison between Table 3 and Table 5 clearly indicates the decrease of the modal periods after the interventions. According to the results of response spectrum analysis applied to the strengthened structure, it was observed that excess of the tensile strength (10% of the compressive strength of masonry) is limited at "secondary" places of the masonry walls for the seismic load combinations. Figure 16 showing the stresses after interventions corresponds to Figure 9.

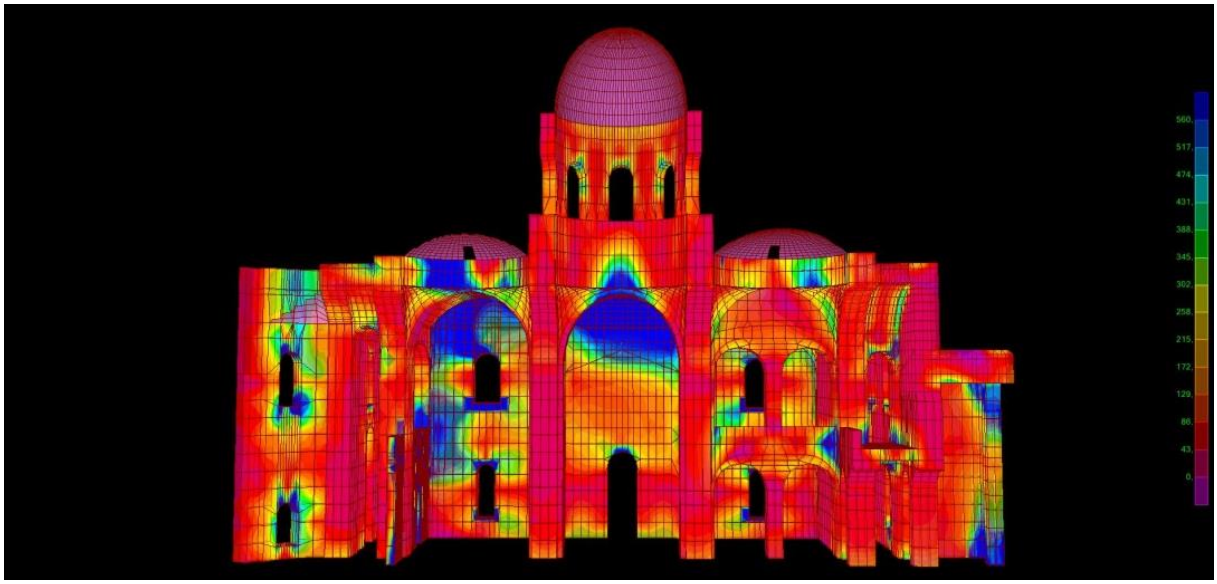


Figure 16. Stress distribution S22 for the E_x+0.3E_y+0.3E_z combination

Local analysis provided that after the interventions the collapse multiplier is

$$\alpha_0 = \frac{F_{max}}{W} = \frac{1200}{11105} = 0.108 \tag{18}$$

The participating mass ratio calculated according to Equation (12) is $e^* = 0.657$. Therefore, the acceleration that activates the mechanism, calculated from Equation (10) is

$$\alpha_{0,2}^* = \frac{\alpha_0 \cdot g}{e^* \cdot CF} = \frac{0.108}{0.465 \cdot 1.35} \cdot g = 0.172\ g \tag{19}$$

Since $\alpha_{0,2}^*$ satisfy Equation (15), the structure reaches the ultimate limit state and the maximum ground acceleration that it can sustain is:

$$\alpha_{g,max,1} = \alpha_{0,2}^* \cdot q/S = 0.175g \tag{20}$$

5 CONCLUSIONS

A series of tests were performed to the historic church of St. Nicholas in Piraeus. Besides the visual inspections, in-situ and laboratory testing as well as ambient vibration testing provided the mechanical characteristics of the materials and the dynamic characteristics of the church as a whole.

Three types of analysis were conducted: (i) modal analysis that was validated through ambient vibration measurements; (ii) response spectrum analysis based on the current Eurocode provisions; (iii) local analysis using a “block and joints” model. All analyses were performed in order to evaluate the response of the structure prior and after interventions.

It was ascertained: (i) the seismic risk of the church prior to interventions, and (ii) the effectiveness of the proposed strengthening measures, that is, consolidation of the walls through grouting, use of CFRP with inorganic resins and steel tie-rods.

Combination of the intervention technics dramatically enhanced the seismic safety of the structure and fulfilled the historic preservation mandates.

REFERENCES

[1] Σ.Γ. Μαλικούτη, *Πειραιάς 1834-1912. Λειτουργική συγκρότηση και πολεοδομική εξέλιξη*. Πολιτιστικό Ίδρυμα Ομίλου Πειραιώς, Αθήνα, 2004. (in Greek)

[2] Θ.Π. Τάσιος, Μ.Π. Χρονόπουλος, *Παθολογικά Αίτια και Μηχανική των Βλαβών της Τοιχοποιίας*. Υ.ΠΕ.ΧΩ.ΔΕ. Εργ. Ωπλ. Σκυροδέματος Ε.Μ.Π., Αθήνα, 1986. (in Greek)

[3] SAP2000, 14.0.0, Computers and Structures Inc, Berkeley, California, 2009.

[4] C.C. Spyrakos, *Finite Element Modeling in Engineering Practice*. Algor Publishing Division, Pittsburg, PA, USA, 1995.

[5] EN 1998-1:2005. Eurocode 8: Design of structures for earthquake resistance - Part 1: General rules, seismic action and rules for buildings, CEN, 2005.

[6] EN 1998-3:2005. Eurocode 8: Design of structures for earthquake resistance - Part 3: Assessment and retrofitting of buildings, CEN, 2005.

[7] Σ. Παπουτσέλης, *Δομική Αποκατάσταση και Στατική Στερέωση του Ιερού Ναού Αγίου Νικολάου Πειραιώς*, Σχολή Πολιτικών Μηχαωικών, Εθνικό Μετσόβιο Πολυτεχνείο, 2012. (in Greek)

[8] D.P.C.M 9 febbraio 2011. Linee guida per la valutazione e la riduzione del rischio sismico del patrimonio culturale con riferimento alle Norme tecniche per le costruzioni di cui al D.M. 14/01/2008, 2011. (in Italian)

[9] PC.E, 2012.04.1, Aedes Software snc, Pisa, 2012.

[10] Circolare 2 febbraio 2009, n. 617. Istruzioni per l'applicazione delle "Nuove norme tecniche per le costruzioni" di cui al D.M. 14 gennaio 2008, 2009. (in Italian)

[11] D.M. 14 gennaio 2008. Nuove norme tecniche per le costruzioni, 2008. (in Italian)

[12] Κ. Σπυράκος, *Ενίσχυση Κατασκευών για Σεισμικά Φορτία*. Τεχνικό Επιμελητήριο Ελλάδας, Αθήνα, 2004. (in Greek)

[13] P. Foraboschi, Strengthening of masonry arches with fiber-reinforced polymer strips. *Journal of Composites for Construction*, **8**, 191-202, 2004.

[14] M.R. Valluzzi, F. Da Porto, C. Modena, Behavior and modeling of strengthened three-leaf stone masonry walls. *Materials and Structures/Materiaux et Constructions*, **37**, 184-192, 2004.

[15] L. Credali, G. Ussia, Composite Materials Technologies in Constructions Structural Retrofitting: New Developments and Applications in Historical Buildings and Applications in Seismic Zone. *COMPDYN 2011 3rd International Conference on Computational Methods in Structural Dynamics and Earthquake Engineering*, Corfu, Greece, May 25-28, 2011.

[16] C.C. Spyrakos, P.D. Kiriakopoulos, E. Smyrou, Seismic Strengthening of the Historic Church of Sts Helen and Constantine in Piraeus. *COMPDYN 2011 3rd International Conference on Computational Methods in Structural Dynamics and Earthquake Engineering*, Corfu, Greece, May 25-28, 2011.

[17] F. Pugi, *Edifici in Muratura e nuova Normativa Sismica: l'Analisi Pushover come evoluzione del Metodo Por*. Alinea, Firenze, 2006. (in Italian)

[18] P. Lenza, A. Ghersi, B. Calderoni, *Edifici in muratura alla luce della nuova normativa sismica*. D. Flaccovio, Palermo, 2011. (in Italian)

[19] M. Corradi, A. Borri, A. Vignoli, Strengthening techniques tested on masonry structures struck by the Umbria–Marche earthquake of 1997–1998. *Construction and Building Materials*, **16**, 229-239, 2002.

[20] P.B. Lourenço, Assessment, diagnosis and strengthening of Outeiro Church, Portugal. *Construction and Building Materials*, **19**, 634-645, 2005.

COMPDYN 2013
4th ECCOMAS Thematic Conference on
Computational Methods in Structural Dynamics and Earthquake Engineering
M. Papadrakakis, V. Papadopoulos, V. Plevris (eds.)
Kos Island, Greece, 12–14 June 2013

OPTIMAL CONTROL DESIGN BY ADJOINT-BASED OPTIMIZATION FOR ACTIVE MASS DAMPER WITH DRY FRICTION

Domenico Guida[1], **Fabio Nilvetti**[1], **and Carmine M. Pappalardo**[1]

[1]University of Salerno
via Ponte don Melillo - 84084 - Fisciano (SA) - Italy
e-mail: {guida,fnilvetti,cpappalardo}@unisa.it

Keywords: Optimal Control, Adjoint-Based Optimization, Active Mass Damper, Dry Friction.

Abstract. *The goal of our research is to set up an effective procedure to design control laws of Hybrid Mass Dampers (HMDs) in order to mitigate structural vibration. The system under test is a two-storey frame equipped with an active vibration absorber located on the top of it. The vibration absorber is subjected to dry friction and is driven by a control force. The two-storey frame is subjected to a base excitation whose harmonic content is close to the system natural frequencies. The control actuator is located between the second floor and the mass damper. The control law is obtained using optimal control theory and is calculated solving a constrained minimization problem. The cost function penalizes the control effort and the state deviation from a reference position. Since the system model is non-linear, the optimal control problem is to be solved numerically. The numerical algorithm used in the proposed procedure is an iterative adjoint-based optimization method. This method combines the non-linear conjugate gradient algorithm with adjoint-based gradient computation.*

In this paper authors propose an analytical model of the dry friction force which describes the interaction between the absorber and structure. Simulations show that the designed control law significantly reduces the structural vibration caused by the base excitation.

1 INTRODUCTION

Dynamic Vibration Absorbers (DVAs) or Tuned Mass Dampers (TMDs) are mechanical devices capable of reducing potentially dangerous vibrations of structural systems [1]. The basic configuration of DVAs comprises inertia, stiffness and damping elements which can be properly designed to absorb the vibratory energy of the mechanical system to be protected. Since DVAs operate without using an external energy supply, they are passive control systems. On the other hand, Active Control Systems (ACSs) are electro-mechanical devices which can modify the motion of the structure to be protected through the action of external forces [2]. The fundamental scheme for ACSs consists of four parts: 1) the mechanical system to be preserved, 2) sensors located on the system to measure structural vibrations and external excitations, 3) a control unit necessary to process the measured information, to compute the control actions according to a dedicated control algorithm and to drive the actuators, 4) actuators necessary to provide the required forces. Active Vibration Absorbers (AVAs) or Hybrid Mass Dampers (HMDs) are a natural evolution of DVAs, TMDs and ACSs [3]. They combine the advantages of passive vibration absorbers with the versatility of active controllers. AVAs or HMDs are designed to work as DVAs or TMDs but are subjected to control forces delivered by control actuators. The performances of AVAs or HMDs can be considerably improved introducing dry friction dampers in the system [4]. The dynamic properties of vibration absorbers subjected to dry friction forces significantly differ from those of linear viscous absorbers. Indeed, the introduction of dry friction dampers complicates the system model, which becomes nonlinear, and therefore the control actions cannot be computed using classical control algorithm. In this paper authors propose the development of a new control scheme for a two-storey system equipped with a vibration absorber subjected to a dry friction force.

2 SYSTEM MODEL

2.1 System Description

The system being analysed is showed in figure 1. All system data are reported in table 1.

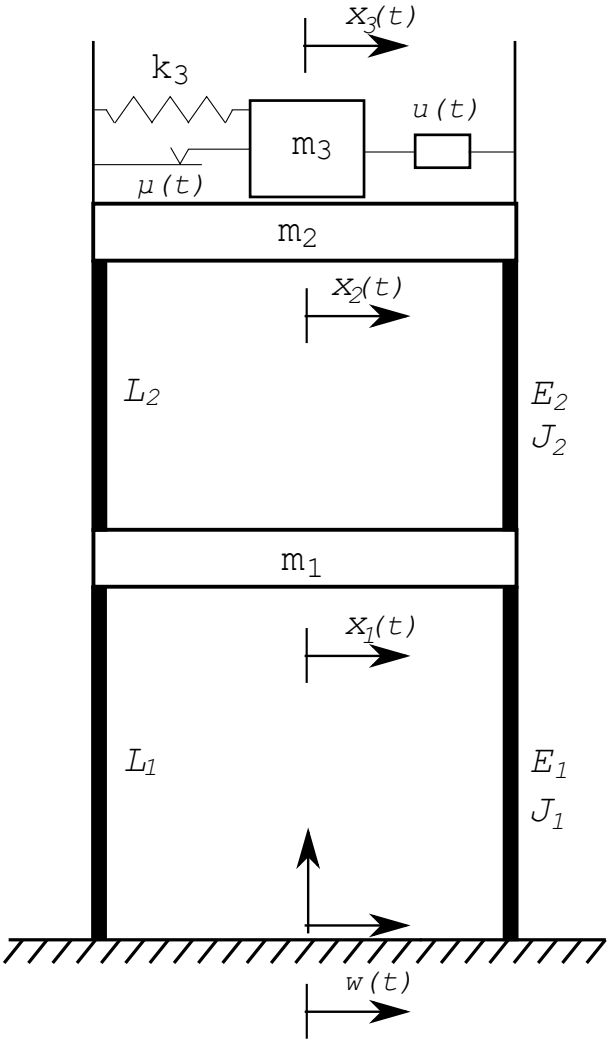


Figure 1: Two-Storey Building with Controlled Friction Absorber

The system is essentially a two-storey building with an absorber located on the second floor [5], [6]. The frequency range of interest encompasses frequencies below $15[Hz]$. The two-storey frame is modelled as a two degrees of freedom system. The system floors were modelled as bulky elements with mass m_1 and m_2. The supporting beams are of length L_1 and L_2 with a second moment of area equal to J_1 and J_2 and are made of steel with elastic modulus E_1 and E_2. The flexible elements provide the stiffness k_1 and k_2 which can be computed assuming a clamped-clamped beam configuration. The system natural frequencies are respectively equal to $f_{n,1} = 3.23[Hz]$ and $f_{n,2} = 6.82[Hz]$. The two-storey frame is subjected to proportional damping with coefficients α and β [7]. The absorber is located on the second floor, has a mass m_3 and is connected to the second floor with a spring of stiffness k_3. The absorber can slide on

the second floor and is subjected to a dry friction force with a friction coefficient μ_0. Friction force was smoothed to facilitate the computation [8] according to two different models: $\eta_1(t)$ for Coulomb friction and $\eta_2(t)$ for Stribeck friction. The first approximated friction model can be written as follows:

$$\mu(t) = \mu_0 \eta_1(t) = \mu_0 D_1 \left(1 - \frac{2}{e^{2D_2(\dot{x}_3(t) - \dot{x}_2(t))} + 1}\right) \tag{1}$$

where μ_0 is the dry friction coefficient and $\eta_1(t)$ is the function which approximates the Coulomb friction model. The friction model (1) is showed in figure 2. This is a smoothed

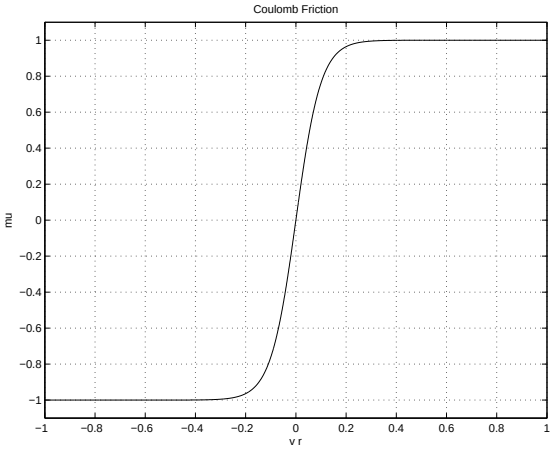


Figure 2: $\eta_1(t)$ - Approximated Friction Model 1

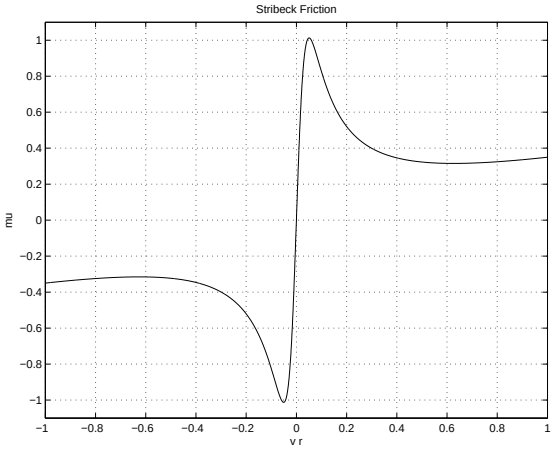


Figure 3: $\eta_2(t)$ - Approximated Friction Model 2

version of the Coulomb friction model which approaches the discontinuous model when the parameter D_2 tends to infinity. The second approximated friction model can be written as follows:

$$\mu(t) = \mu_0 \eta_2(t) = \mu_0 \left(\frac{C_1(\dot{x}_3(t) - \dot{x}_2(t))}{C_2 + C_3(\dot{x}_3(t) - \dot{x}_2(t))^2} + C_4(\dot{x}_3(t) - \dot{x}_2(t))\right) \tag{2}$$

where μ_0 is the dry friction coefficient and $\eta_2(t)$ is the function which approximates the Stribeck friction model. The friction model (2) is showed in figure 3. This smoothed version of the dry friction model approaches the discontinuous model when the parameter C_3 tends to infinity. On the other hand, the control actuator is interposed between the absorber and the second floor. The whole system is excited by a ground motion $w(t)$. Considering a worst-case scenario, the ground motion $w(t)$ is assumed as a superposition of two harmonic displacements whose excitation frequencies are close to the two-storey frame natural frequencies. Indeed:

$$w(t) = W_1 \sin(2\pi f_1 t) + W_2 \sin(2\pi f_2 t) \tag{3}$$

where W_1 and W_2 are the ground motion amplitudes whereas f_1 and f_2 are the ground motion excitation frequencies.

2.2 Equations of Motion

The configuration of the system can be described by a set of $n_2 = 3$ generalised coordinates which can be grouped into a vector $q(t)$ as:

$$q(t) = \begin{bmatrix} x_1(t) \\ x_2(t) \\ x_3(t) \end{bmatrix} \tag{4}$$

The Lagrangian coordinates $x_1(t)$ and $x_2(t)$ represent the displacements of each floor whereas the Lagrangian coordinate $x_3(t)$ represent the displacement of the absorber. The system model encompasses three degrees of freedom and is non-linear because of the dry friction force. In general, the matrix form of a non-linear dynamic system model can be written as follows:

$$M(t)\ddot{q}(t) = Q(t) \tag{5}$$

where $M(t)$ represents system mass matrix and $Q(t)$ denotes the total generalised forces acting on the system. This is a set of $n_2 = 3$ ordinary differential equations which requires a set of $2n_2 = 6$ initial conditions $q(0) = q_0$ and $\dot{q}(0) = p_0$. For the system being analysed, the mass matrix $M(t)$ and the vector of generalised forces $Q(t)$ can be derived using Lagrangian Dynamics to yield:

$$M(t) = \begin{bmatrix} m_1 & 0 & 0 \\ 0 & m_2 & 0 \\ 0 & 0 & m_3 \end{bmatrix} \tag{6}$$

$$Q(t) = \begin{bmatrix} -k_1(x_1(t) - w(t)) - k_2(x_1(t) - x_2(t)) + \\ -r_1(\dot{x}_1(t) - \dot{w}(t)) - r_2(\dot{x}_1(t) - \dot{x}_2(t)) \\ \\ -k_2(x_2(t) - x_1(t)) - k_3(x_2(t) - x_3(t)) + \\ -r_2(\dot{x}_2(t) - \dot{x}_1(t)) - r_3(\dot{x}_2(t) - \dot{x}_3(t)) + m_3 g\mu(t) \\ \\ -k_3(x_3(t) - x_2(t)) - m_3 g\mu(t) \end{bmatrix} \tag{7}$$

If a control action $Q_c(t)$ is introduced on the system, the matrix form of system equations of motion becomes:

$$M(t)\ddot{q}(t) = Q(t) + Q_c(t) \tag{8}$$

In the case of the system under test, the control action is interposed between the second floor and the mass damper:

$$Q_c(t) = B_2(t)u(t) \tag{9}$$

where $u(t)$ is the control input and $B_2(t)$ is a Boolean matrix defined as follows:

$$B_2(t) = \begin{bmatrix} -1 \\ 1 \end{bmatrix} \tag{10}$$

System equations of motion can be used as an analytical model to design a controller whose objective is to reduce structural vibration.

2.3 State-Space Model

The preliminary step to design a control system consists in rewriting system equations of motion (8) in the state-space form. The system state can be represented using a state vector of dimension $n = 2n_2 = 6$ defined as:

$$z(t) = \begin{bmatrix} q(t) \\ \dot{q}(t) \end{bmatrix} \tag{11}$$

The system equations of motion (8) can be rewritten in term of the state vector as follows:

$$\dot{z}(t) = f(t) + B_c(t)u(t) \tag{12}$$

where $f(t)$ is a non-linear state function and $B_c(t)$ is the state influence matrix which can be respectively computed as:

$$f(t) = \begin{bmatrix} \dot{q}(t) \\ M^{-1}(t)Q(t) \end{bmatrix} \tag{13}$$

$$B_c = \begin{bmatrix} O \\ M^{-1}(t)B_2(t) \end{bmatrix} \tag{14}$$

This is the state-space form of system equations of motion namely a set of $n = 2n_2 = 6$ first-order differential equations which constitute the system state-space model. The initial state $z(0) = z_0$ required to solve the state-space equations can be derived from system initial conditions $q(0) = q_0$ and $\dot{q}(0) = p_0$.

3 CONTROL STRATEGY

3.1 Optimal Control

In general, the raison d'etre of a control system is to influence the dynamics of a mechanical system in order to make it behave in a desirable manner. An approach to design a control system is to use optimal control methods. Optimal control consists in implementing mathematical optimization methods for deriving control laws [9]. The essence of optimal control theory can be summarised as follows. The key idea is to find the control action $u(t)$ which minimizes a cost function J_c. The cost function or performance index is a quantitative expression which can be used to determine how well a particular control law meets the design goals. A general cost functional can be written as:

$$J_c = h(T) + \int_0^T g(t)dt \tag{15}$$

where $h(T)$ and $g(t)$ are two analytical functions which, in the case of a quadratic cost index, are defined as follows:

$$h(T) = \frac{1}{2}(z(T) - \bar{z}(T))^T Q_T (z(T) - \bar{z}(T)) \tag{16}$$

$$g(t) = \frac{1}{2}(z(t) - \bar{z}(t))^T Q_z (z(t) - \bar{z}(t)) + \frac{1}{2}(u(t) - \bar{u}(t))^T Q_u (u(t) - \bar{u}(t)) \tag{17}$$

where $\bar{z}(t)$ and $\bar{u}(t)$ are respectively the reference trajectory and the reference control action used in tracking problems whereas Q_T, Q_z and Q_u are positive semi-definite weight matrices. The definition of the weight matrices Q_T, Q_z and Q_u represents a crucial step in the design process which drastically influences the resulting control law. In regulation problems the reference functions $\bar{z}(t)$ and $\bar{u}(t)$ are set equal to zero. The system equations of motion (12) represent a set of dynamic constraints for the minimization problem. An approach to solve this problem consists in employing calculus of variation techniques in order to obtain the necessary conditions which minimize the cost functional [9]. The first step consists in defining the Hamiltonian function as:

$$H_c(t) = g(t) + \lambda^T(t)(f(t) + B_c(t)u(t)) \tag{18}$$

where $\lambda(t)$ is a co-state vector which contains the Lagrange multipliers that arise from adjoining the state-space equations of motion (12) to the cost functional (15). Thus, the resulting optimal conditions can be computed from the Hamiltonian function (18) as follows:

$$\dot{z}(t) = (\frac{\partial H_c(t)}{\partial \lambda(t)})^T = f(t) + B_c(t)u(t) \tag{19}$$

$$\dot{\lambda}(t) = -(\frac{\partial H_c(t)}{\partial z(t)})^T = -Q_z(z(t) - \bar{z}(t)) - A_c^T(t)\lambda(t) \tag{20}$$

Where $A_c(t)$ is a state matrix derived from the linearization of the state function $f(t)$ around the reference functions $\bar{z}(t)$ and $\bar{u}(t)$. The fist set of equations (19) is exactly the state-space form of system equations of motion whereas the second set of equations (20) represents the co-state equations or adjoint equations. The adjoint equations (20) require a set of terminal conditions which can be computed as:

$$\lambda(T) = (\frac{\partial h(T)}{\partial z(T)})^T = Q_T(z(T) - \bar{z}(T)) \tag{21}$$

The resulting equations are necessary to solve the constrained minimization problem and form a two-point boundary-value problem. Indeed, the set of system equations of motion (12) and adjoint equations (20) constitutes a coupled non-linear problem which can be solved numerically by using non-linear optimization techniques.

3.2 Iterative Adjoint-Based Optimization

A method to solve the two-point boundary-value problem (12), (20) resulting from the minimization of the cost function (15) consists in using an iterative adjoint-based optimization approach. The key idea of the iterative adjoint-based optimization method is to exploit the knowledge of the cost functional gradient to solve the minimization problem [10], [11]. Indeed, the gradient of the performance index can be derived from the Hamiltonian function (18) as follows:

$$G_c(t) = (\frac{\partial H_c(t)}{\partial u(t)})^T = Q_u(u(t) - \bar{u}(t)) + B_c^T(t)\lambda(t) \tag{22}$$

The gradient (22) is readily determined once that the adjoint state $\lambda(t)$ is known solving the adjoint equations (20) and it can be used in an iterative gradient-based optimization algorithm in order to gradually improve the approximated solution towards the cost function minimum. Typically, to accomplish this task a line search method is used, such as the steepest descent method or the non-linear conjugate gradient method [12]. Algorithms based on the line search strategy use a descent direction e_k and search the minimum along this direction from the current solution u_k to the next solution u_{k+1} corresponding to a lower cost index. Indeed, using a line search method the control input can be iteratively calculated as:

$$u_{k+1} = u_k + \alpha_k e_k \tag{23}$$

where α_k is a line parameter which represents the step length corresponding to the current iteration. The minimization algorithms based on a line search strategy differ from each other with the selection of the descent direction e_k. The steepest descent method sets the descent direction equal to the cost function gradient:

$$e_k = -G_{c,k} \tag{24}$$

The basic idea is to perform the line search of the minimum along the direction where the cost function decreases the most rapidly. This method can be very slow in some problems because the choice of the descent direction is too rigid. On the other hand, the non-linear conjugate gradient method defines the descent direction as follows:

$$e_k = -G_{c,k} + \beta_k e_{k-1} \tag{25}$$

where β_k is a parameter which ensures that the descent direction e_{k-1} and e_k are conjugate [10], [12]. Three of the best known formulas for β_k are titled Fletcher-Reeves, Polak-Ribiere and Hestenes-Stiefel after their developers [10], [12]. These formulae can be respectively written as follows:

$$\beta_k^{FR} = \frac{G_{c,k}^T G_{c,k}}{G_{c,k-1}^T G_{c,k-1}} \tag{26}$$

$$\beta_k^{PR} = \frac{G_{c,k}^T (G_{c,k} - G_{c,k-1})}{G_{c,k-1}^T G_{c,k-1}} \tag{27}$$

$$\beta_k^{HS} = -\frac{G_{c,k}^T (G_{c,k} - G_{c,k-1})}{e_k^T (G_{c,k} - G_{c,k-1})} \tag{28}$$

where β_k^{FR} is Fletcher-Reeves parameter, β_k^{PR} is Polak-Ribiere parameter and β_k^{HS} is Hestenes-Stiefel parameter. Once that the descent direction has been set, the solution can be found with a minimum search algorithm such as Brent method or golden section method [10], [11]. The overall procedure to implement an iterative adjoint-based optimization of the control action can be summarized as follows:

- Step 1) Select an initial control input u_k;

- Step 2) Use the control input u_k to solve numerically system state equations (12) in order to obtain the system state z_k;

- Step 3) Use the system state z_k to solve numerically adjoint equations (20) in order to obtain the adjoint state λ_k;

- Step 4) Use the control input u_k and the adjoint state λ_k to compute the cost function gradient $G_{c,k}$ by using equations (22);

- Step 5) Use the cost function gradient $G_{c,k}$ to compute the descent direction e_k by using equations (25);

- Step 6) Use the descent direction e_k in order to obtain numerically the line parameter α_k by a line search numerical method;

- Step 7) Use the line parameter α_k to update the control input u_{k+1} by using equations (23);

- Step 8) Restart from step 1 if the chosen stopping criteria is not satisfied;

To solve numerically the state equations and the adjoint state equations Runge-Kutta methods are adequate. To stop the algorithm a tolerance on the cost function variation can be assigned, namely when no progress are made the iteration must stop.

4 RESULTS AND DISCUSSION

4.1 Control Design

A controller was designed using the iterative adjoint-based optimization method described in the preceding section. The penalty matrices were chosen as follows:

$$Q_T = diag(10^4, 10^4, 10^4, 10^4, 10^4, 10^4) \tag{29}$$

$$Q_z = diag(10^4, 10^4, 10^4, 10^4, 10^4, 10^4) \tag{30}$$

$$Q_u = 10^{-4} \tag{31}$$

The weight matrices Q_T and Q_z drastically penalise the displacements and the velocities of each system floor and of the absorber. On the other hand, the control effort is relatively less penalised by the weight matrix Q_u. Two different case study has been analysed and two different control law has been designed. The two case study differ for the friction model utilised. In the first case study the friction model utilised is a smoothed version of Coulomb friction (1) whose model is showed in figure 2 whereas in the second case study the friction model utilised is a smoothed version of Stribeck friction (2) whose model is showed in figure 3.

4.2 Case Study 1

In this case study the friction model (1) was used. First the system motion without the controller has been analysed. The displacements of system floors in the case of the uncontrolled motion are represented in figure 4 and 6 whereas the displacements of system floors in the case of the controlled motion are represented in figure 5 and 7. The displacement of the absorber in

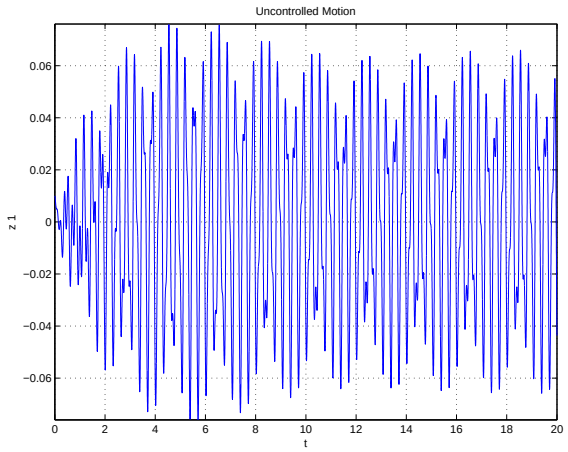


Figure 4: $x_1(t)$ - Uncontrolled Motion - Case Study 1

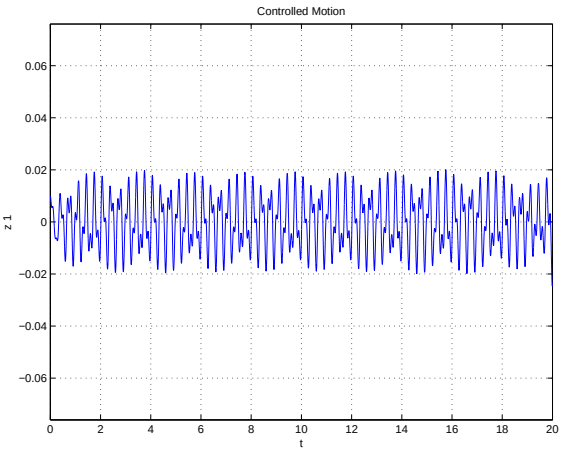


Figure 5: $x_1(t)$ - Controlled Motion - Case Study 1

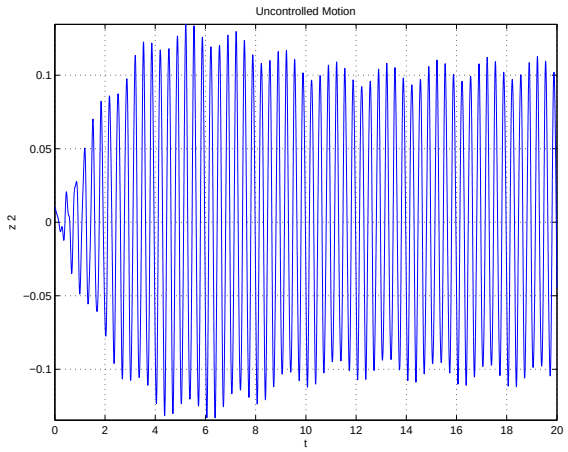


Figure 6: $x_2(t)$ - Uncontrolled Motion - Case Study 1

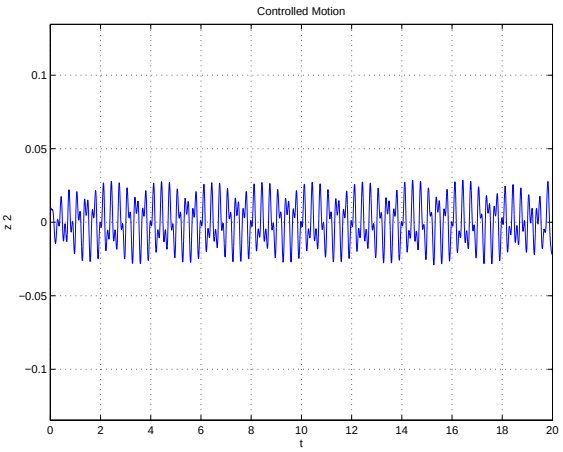


Figure 7: $x_2(t)$ - Controlled Motion - Case Study 1

the case of the uncontrolled motion is represented in figure 8 whereas the displacement of the absorber in the case of the controlled motion is represented in figure 9. The velocities of system floors and of the absorber in the case of the controlled motion exhibit an amplitude reduction qualitatively similar to that of their respective displacements. The iterative decrease of the cost function is represented in figure 10. The resulting controller is represented in figure 11. As can be seen from the preceding figures, the introduction of the controller drastically reduces the magnitudes of system displacements and velocities. This reduction can be quantified comparing the maximum amplitudes of system motion with and without the controller. Indeed:

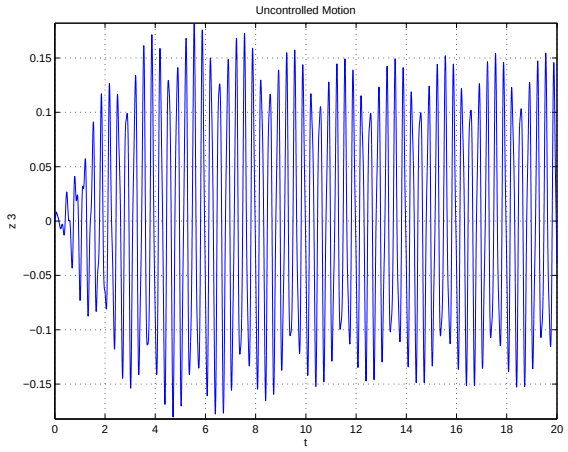


Figure 8: $x_3(t)$ - Uncontrolled Motion - Case Study 1

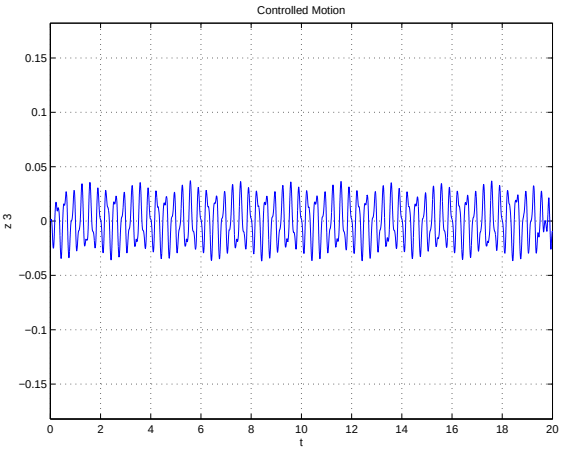


Figure 9: $x_3(t)$ - Controlled Motion - Case Study 1

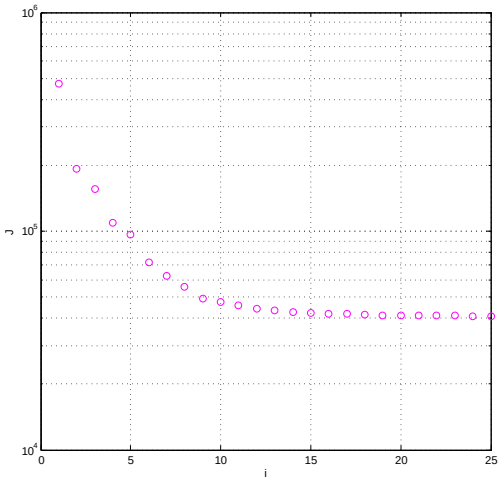


Figure 10: J_c - Performance Index - Case Study 1

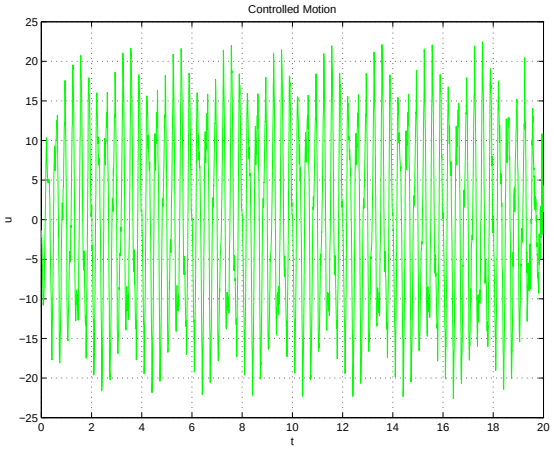


Figure 11: $u(t)$ - Control Action - Case Study 1

$$\varepsilon_{r,x_i} = \frac{\max\limits_{t\in[0,T]}(\mathrm{abs}(x_{i,uncontrolled}(t))) - \max\limits_{t\in[0,T]}(\mathrm{abs}(x_{i,controlled}(t)))}{\max\limits_{t\in[0,T]}(\mathrm{abs}(x_{i,uncontrolled}(t)))} = \begin{cases} 0.6770 \\ 0.7852 \\ 0.7968 \end{cases} \tag{32}$$

$$\varepsilon_{r,\dot{x}_i} = \frac{\max\limits_{t\in[0,T]}(\mathrm{abs}(\dot{x}_{i,uncontrolled}(t))) - \max\limits_{t\in[0,T]}(\mathrm{abs}(\dot{x}_{i,controlled}(t)))}{\max\limits_{t\in[0,T]}(\mathrm{abs}(\dot{x}_{i,uncontrolled}(t)))} = \begin{cases} 0.7081 \\ 0.7090 \\ 0.7495 \end{cases} \tag{33}$$

The magnitude reductions of floors and absorber displacements are greater than the 67% whereas the magnitude reductions of floors and absorber velocities are greater than the 70%.

4.3 Case Study 2

In this case study the friction model (2) was used. First the system motion without the controller has been analysed. The displacements of system floors in the case of the uncontrolled motion are represented in figure 12 and 14 whereas the displacements of system floors in the case of the controlled motion are represented in figure 13 and 15. The displacement of the

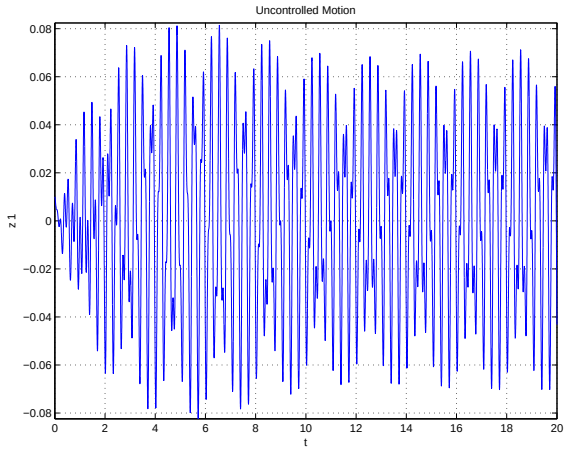


Figure 12: $x_1(t)$ - Uncontrolled Motion - Case Study 2

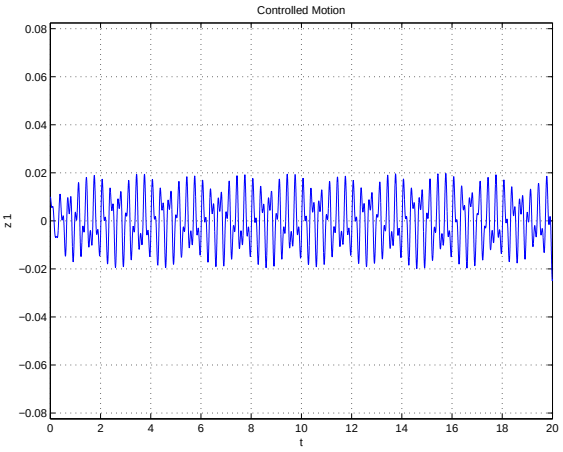


Figure 13: $x_1(t)$ - Controlled Motion - Case Study 2

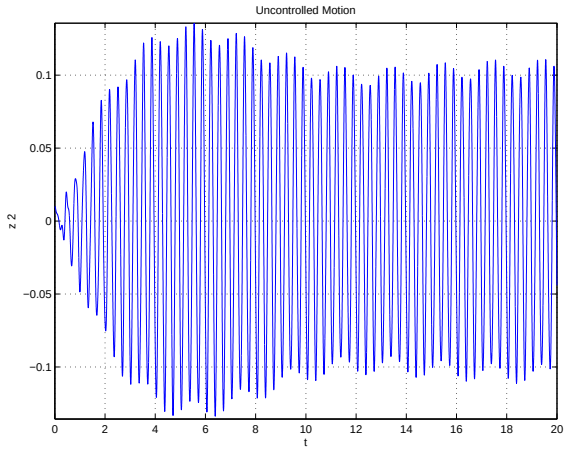


Figure 14: $x_2(t)$ - Uncontrolled Motion - Case Study 2

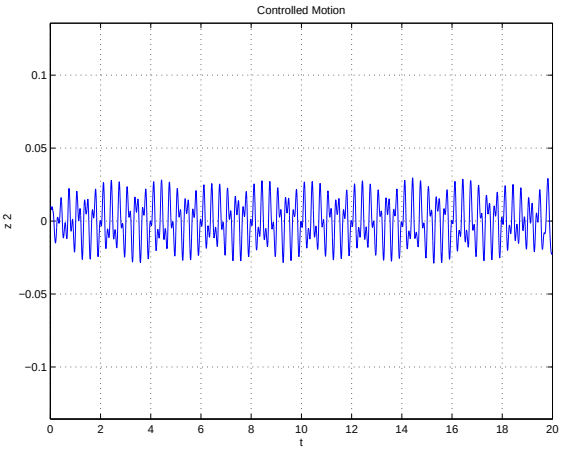


Figure 15: $x_2(t)$ - Controlled Motion - Case Study 2

absorber in the case of the uncontrolled motion is represented in figure 16 whereas the displacement of the absorber in the case of the controlled motion is represented in figure 17. The velocities of system floors and of the absorber in the case of the controlled motion exhibit an amplitude reduction qualitatively similar to that of their respective displacements. The iterative decrease of the cost function is represented in figure 18. The resulting controller is represented in figure 19. As can be seen from the preceding figures, the introduction of the controller drastically reduces the magnitudes of system displacements and velocities. This reduction can be

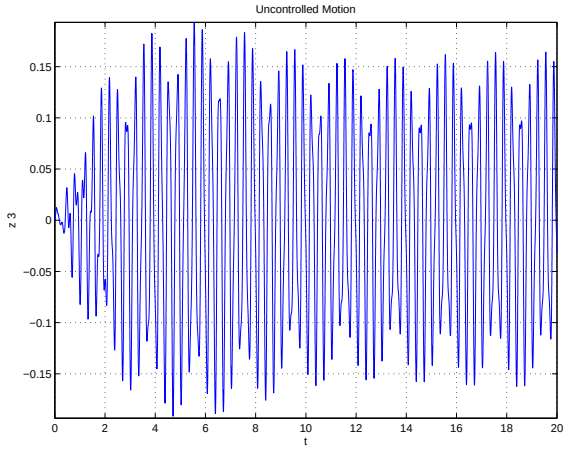


Figure 16: $x_3(t)$ - Uncontrolled Motion - Case Study 2

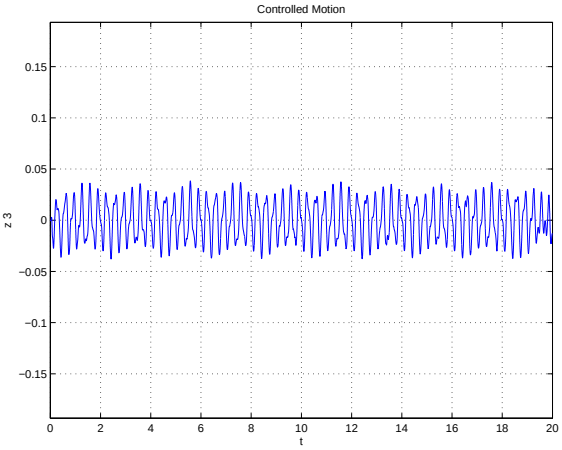


Figure 17: $x_3(t)$ - Controlled Motion - Case Study 2

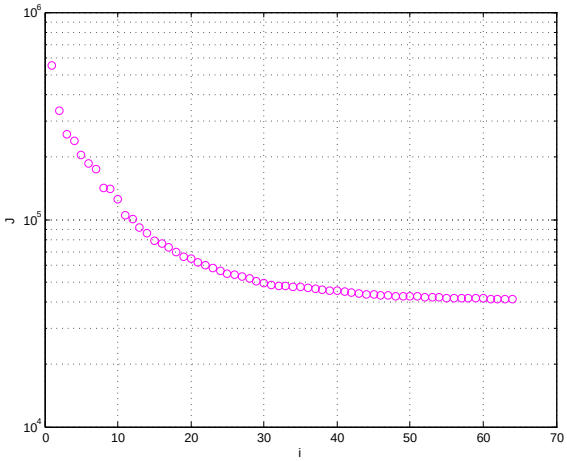


Figure 18: J_c - Performance Index - Case Study 2

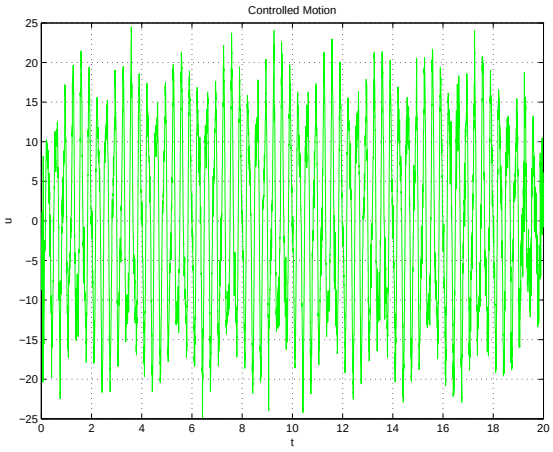


Figure 19: $u(t)$ - Control Action - Case Study 2

quantified comparing the maximum amplitudes of system motion with and without the controller. Indeed:

$$\varepsilon_{r,x_i} = \frac{\max\limits_{t\in[0,T]}(\mathrm{abs}(x_{i,uncontrolled}(t))) - \max\limits_{t\in[0,T]}(\mathrm{abs}(x_{i,controlled}(t)))}{\max\limits_{t\in[0,T]}(\mathrm{abs}(x_{i,uncontrolled}(t)))} = \begin{cases} 0.6979 \\ 0.7824 \\ 0.8014 \end{cases} \tag{34}$$

$$\varepsilon_{r,\dot{x}_i} = \frac{\max\limits_{t\in[0,T]}(\mathrm{abs}(\dot{x}_{i,uncontrolled}(t))) - \max\limits_{t\in[0,T]}(\mathrm{abs}(\dot{x}_{i,controlled}(t)))}{\max\limits_{t\in[0,T]}(\mathrm{abs}(\dot{x}_{i,uncontrolled}(t)))} = \begin{cases} 0.7375 \\ 0.6989 \\ 0.7600 \end{cases} \tag{35}$$

The magnitude reductions of floors and absorber displacements are greater than the 69% whereas the magnitude reductions of floors and absorber velocities are greater than the 69%.

5 CONCLUSIONS

In this paper authors propose the development of an efficient control method for nonlinear mechanical systems. The system analysed is a two-storey building model coupled with an active vibration absorber. The active vibration absorber considered is a hybrid mass damper subjected to a dry friction force. The control actuator is located between the second floor and the mass damper. Two approximated model for the dry friction force has been considered in order to facilitate the numerical integration procedure. For each friction model the control law has been obtained using optimal control theory and has been computed solving a constrained minimization problem by using an iterative adjoint-based optimization method. The effectiveness of the proposed algorithm has been tested in the worst-case scenario in which the system is excited by a ground motion whose harmonic content is close to the first two system natural frequencies. From the simulation results it is clear that the designed controller drastically reduces the amplitude of displacements and velocities relative to each system floor even in the considered worst-case scenario.

DESCRIPTION	SYMBOL	DATA [UNITS]
Length of Structural Element 1	L_1	$23 \cdot 10^{-2}[m]$
Length of Structural Element 2	L_2	$28 \cdot 10^{-2}[m]$
Second Moment of Area of Structural Element 1	J_1	$2.92 \cdot 10^{-12}[m^4]$
Second Moment of Area of Structural Element 2	J_2	$2.92 \cdot 10^{-12}[m^4]$
Mass of Floor 1	m_1	$1.3[kg]$
Mass of Floor 2	m_2	$0.8[kg]$
Mass of Absorber	m_3	$0.2[kg]$
Elastic Modulus of Structural Element 1	E_1	$207 \cdot 10^9[kg \cdot m^{-1} \cdot s^{-2}]$
Elastic Modulus of Structural Element 2	E_2	$207 \cdot 10^9[kg \cdot m^{-1} \cdot s^{-2}]$
Equivalent Stiffness of Structural Element 1	k_1	$1.19 \cdot 10^3[kg \cdot s^{-2}]$
Equivalent Stiffness of Structural Element 2	k_2	$660[kg \cdot s^{-2}]$
Stiffness of Absorber	k_3	$400[kg \cdot s^{-2}]$
Proportional Damping Coefficient of Mass Matrix	α	$1[s]$
Proportional Damping Coefficient of Stiffness Matrix	β	$3 \cdot 10^{-4}[s^{-1}]$
Ground Motion Amplitude 1	W_1	$5 \cdot 10^{-3}[m]$
Ground Motion Amplitude 2	W_2	$5 \cdot 10^{-3}[m]$
Ground Motion Frequency 1	f_1	$3[s^{-1}]$
Ground Motion Frequency 2	f_2	$6.5[s^{-1}]$
Dry Friction Coefficient	μ_0	$0.3[\backslash]$
Friction Model 1 Coefficient 1	D_1	$1[\backslash]$
Friction Model 1 Coefficient 2	D_2	$10[m^{-1} \cdot s]$
Friction Model 2 Coefficient 1	C_1	$40[kg \cdot s^{-1}]$
Friction Model 2 Coefficient 2	C_2	$1[\backslash]$
Friction Model 2 Coefficient 3	C_3	$400[kg^{-2}s^2]$
Friction Model 2 Coefficient 4	C_4	$0.25[kg \cdot s^{-1}]$
Initial Displacement of Floor 1	$x_{1,0}$	$1 \cdot 10^{-2}[m]$
Initial Displacement of Floor 2	$x_{2,0}$	$1 \cdot 10^{-2}[m]$
Initial Displacement of Absorber	$x_{3,0}$	$0[m]$
Initial Velocity of Floor 1	$v_{1,0}$	$0[m \cdot s^{-1}]$
Initial Velocity of Floor 2	$v_{2,0}$	$0[m \cdot s^{-1}]$
Initial Velocity of Absorber	$v_{3,0}$	$0[m \cdot s^{-1}]$
Time Span	T	$20[s]$
Time Step	Δt	$10^{-3}[s]$

Table 1: System Data

REFERENCES

[1] B. G. Korenev, L. M. Reznikov, Dynamic Vibration Absorbers: Theory and Technical Applications. *John Wiley and Sons*, ISBN: 047192850X.

[2] A. V. Srinivasan, D. M. McFarland, Smart Structures: Analysis and Design. *Cambridge University Press*, ISBN: 0521659779.

[3] D. J. Ewins, S. S. Rao, S. G. Braun, Encyclopedia of Vibration. *Academic Press*, ISBN: 0122270851.

[4] A. Hartung, H. Schmieg, P. Vielsack, Passive Vibration Absorber with Dry Friction. *Archive of Applied Mechanics*, Volume: 71, Issue: 6-7, July 2001, pp. 463 - 472.

[5] F. Nilvetti, C. M. Pappalardo, Experimental Investigation of a Virtual Passive Absorber For Structural Vibration Control. *International Journal of Mechanical Engineering and Industrial Design (JMEID)*, ISSN: 2280-6407, volume 1, 2012, 1(5): 83-90.

[6] D. Guida, F. Nilvetti, C. M. Pappalardo, Experimental Investigation of an Active Structural Control Device. *International Journal of Mechanical Engineering and Industrial Design (JMEID)*, ISSN: 2280-6407, Volume 1, 2012, 1(6): 91-96.

[7] D. Guida, F. Nilvetti, C. M. Pappalardo, Modelling, Identification and Control of a Three-Story Building System. *International Journal of Mechanical Engineering and Industrial Design (JMEID)*, ISSN: 2280-6407, Volume 1, 2012, 1(3): 36-60.

[8] D. Guida, F. Nilvetti, C. M. Pappalardo, Dry Friction Influence on Cart Pendulum Dynamics. *International Journal of Mechanics*, ISSN: 1998-4448, Issue 2, Volume 3, 2009, Pages 31-38.

[9] A. E. Bryson, Y. C. Ho, Applied Optimal Control: Optimization, Estimation and Control. *Taylor and Francis*, ISBN: 0891162283

[10] T. R. Bewley, Numerical Renaissance: Simulation, Optimization and Control. *Renaissance Press*, To be published.

[11] T. R. Bewley, A Linear Systems Approach to Flow Control. *Annual Review of Fluid Mechanics*, 39:383417, 2007.

[12] W. H. Press, S. A. Teukolsky, W. T. Vetterling, B. P. Flannery, Numerical Recipes: The Art of Scientific Computing. *Cambridge University Press*, ISBN: 0521880688

COMPDYN 2013
4th ECCOMAS Thematic Conference on
Computational Methods in Structural Dynamics and Earthquake Engineering
M. Papadrakakis, V. Papadopoulos, V. Plevris (eds.)
Kos Island, Greece, 12–14 June 2013

BASIC DISPLACEMENT FUNCTIONS IN DYNAMIC ANALYSIS OF AN ARCH DAM AS A CURVED BEAM RESTING ON A CONTINUES ELASTIC FOUNDATION

Ashkan Hashemi[1], Reza Attarnejad[2], Shermineh Zarinkamar[3]

[1] MSc Graduate, School of Civil Engineering, University of Tehran
Tehran, Iran.
bu.hashemi@gmail.com

[2] Associate Professor, School of Civil Engineering, University of Tehran
Tehran, Iran
attarnjd@ut.ac.ir

[3] MSc Student, Computer & Information Technology Department, Amirkabir University of Technology
Tehran, Iran
sh.zarinkamar@gmail.com

Keywords: Basic Displacement Functions, Curved beam, Differential transform, Dynamic Stiffness Matrix, Non-prismatic, Elastic foundation.

Abstract. *In recent years several researches have been done on different ways of analyzing and designing arch dams but most of them were involved with cumbersome calculations and heavy loads of computations. In this paper a novel approach for dynamic analysis of arch dams is presented. The most commonly accepted method for analyzing arch dams assumes that the horizontal water load is divided between arches and cantilevers so that the arch and cantilever deflections are equal at conjugate points in all parts of structure. In this the arch dam is modeled as non-prismatic curved beam resting on continues elastic foundation. Based on structural and mechanical principals, a flexibility based method is used to evaluate exact structural matrices and by introducing the concept of basic displacement functions (BDFs), it is shown that dynamic shape functions are derived in terms of BDFs. The flexibility basis ensures the true satisfaction of equilibrium equations at any interior point of the curved element. Dynamic stiffness matrix is evaluated by solving the governing equation of motion. Differential Transform method, a powerful numerical tool in solving of ordinary differential equations, is used for this purpose. The method is capable of modeling any curved element whose cross-sectional area and moment of inertia vary along beam with any two arbitrary functions and any type of cross-section with just few numbers of elements so that it can be used in most of engineering applications concerning non-prismatic curved beams and arch dams in particular. In order to verify the competency of the method, a numerical example are presented and the results and convergence of them are compared with other methods in the literature.*

1 INTRODUCTION

An arch dam is a curved dam which carries a major part of its water load horizontally to the abutments by the arch action, the part so carried being primarily dependent on the amount of curvature. The most commonly accepted method of analyzing arch dams assumes that the horizontal water load is divided between arches and cantilevers so that the arch and cantilever deflections are equal at conjugate points in all parts of the structure. In this study this theory is used and the arches are modeled as a non-homogeneous elastic foundation which prevents mentioned cantilevers from free displacements so the structure is modeled as a Non-prismatic curved beam resting on a non-homogeneous continuous elastic foundation. Moreover, in this study a new formulation for non-prismatic curved beams is derived which is based on flexibility method and respectively a new series of dynamic shape functions are obtained which also are based on applied load's frequency and finally new elements for analyzing curved beams are generated. Correspondingly, the stiffness and consistent mass matrices have been derived. The results show the efficiency and accuracy of the presented formulation in comparison with the methods in the technical literature. By using the method for modeling and analyzing of arch dams with simply employing just one element, same results are almost achieved comparing to using numerous normal elements. Flexibility basis ensures the true satisfaction of equilibrium equations at any interior point of the element in analyzing these types of structures. The accuracy and competency of this method is proven through a numerical example.

2 SHAPE FUNCTIONS FOR STATIC ANALYSIS

In this paper a novel method for analyzing and modeling of arch dams (Such as single curvature arch dams, double curvature arch dams or multiple arch dams) is proposed which is based on flexibility concept. Assume that a non-prismatic curved beam has two fix ends and subjected to arbitrary distributed load. This curved beam can be modeled with two cantilever beams which one is subjected to the arbitrary distributed load and the second beam is subjected to reactions (Figure 1 and 2).

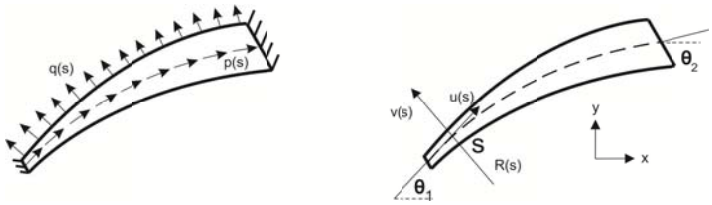


Figure 1: Non-Prismatic Curved Beam

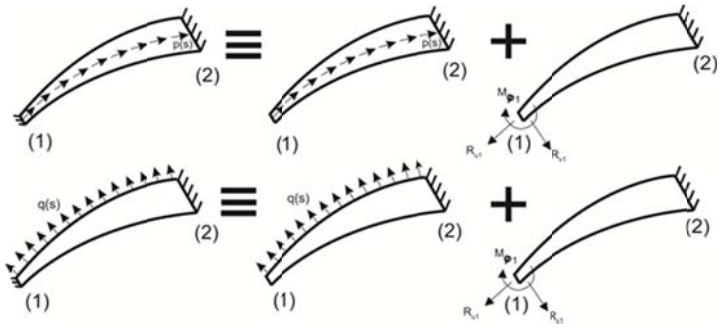


Figure 2: Non-Prismatic Curved Beam Modeling

With Regard to Figure 1, support reactions are obtained as equation (1).

$$\{F_a\}=\begin{Bmatrix} N_1 \\ V_1 \\ M_1 \\ N_2 \\ V_2 \\ M_2 \end{Bmatrix}=\begin{Bmatrix} K_{11} & 0 \\ 0 & K_{22} \end{Bmatrix}=\int p(s)\begin{Bmatrix} b_{u1}(s) \\ b_{v1}(s) \\ b_{\varphi 1}(s) \\ b_{u2}(s) \\ b_{v2}(s) \\ b_{\varphi 2}(s) \end{Bmatrix}ds \qquad \{F_b\}=\begin{Bmatrix} N_1 \\ V_1 \\ M_1 \\ N_2 \\ V_2 \\ M_2 \end{Bmatrix}=\begin{Bmatrix} K_{11} & 0 \\ 0 & K_{22} \end{Bmatrix}=\int q(s)\begin{Bmatrix} c_{u1}(s) \\ c_{v1}(s) \\ c_{\varphi 1}(s) \\ c_{u2}(s) \\ c_{v2}(s) \\ c_{\varphi 2}(s) \end{Bmatrix}ds \quad (1)$$

Where $\{b\}$ and $\{c\}$ are the matrixes of axial and vertical deformations due to subjected unit load and also $\{K\}$ is the nodal stiffness matrix. The definitions of $\{b\}$ and $\{c\}$ are shown in Figure 3. In order to obtain them, these structures have to be analyzed by applying unit load method.

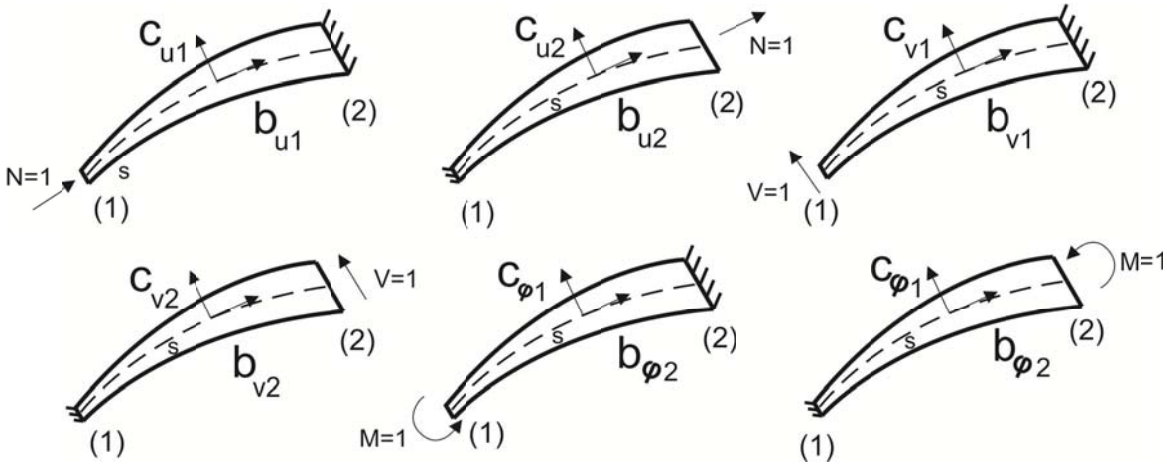


Figure 3: Definitions of $\{b\}$ and $\{c\}$

In accord with Figure 1 and 3, the necessary equations for obtaining {b} and {c} are presented in Table 1. Moreover, nodal stiffness matrixes are presented in Table 3.

$b(s)$	$c(s)$
$b_{u1}(s)=\int_s^1 \frac{m_1(t)M_{b1}(s,t)}{EI(t)}dt+\int_s^1 \frac{n_1(t)N_{b1}(s,t)}{EA(t)}dt$ $b_{v1}(s)=\int_s^1 \frac{m_2(t)M_{b1}(s,t)}{EI(t)}dt+\int_s^1 \frac{n_2(t)N_{b1}(s,t)}{EA(t)}dt$ $b_{\varphi 1}(s)=\int_s^1 \frac{m_3(t)M_{b1}(s,t)}{EI(t)}dt+\int_s^1 \frac{n_3(t)N_{b1}(s,t)}{EA(t)}dt$ $b_{u2}(s)=\int_0^s \frac{m_4(t)M_{b2}(s,t)}{EI(t)}dt+\int_s^1 \frac{n_4(t)N_{b2}(s,t)}{EA(t)}dt$ $b_{v2}(s)=\int_0^s \frac{m_5(t)M_{b2}(s,t)}{EI(t)}dt+\int_s^1 \frac{n_5(t)N_{b2}(s,t)}{EA(t)}dt$ $b_{\varphi 2}(s)=\int_0^s \frac{m_6(t)M_{b2}(s,t)}{EI(t)}dt+\int_s^1 \frac{n_{66}(t)N_{b2}(s,t)}{EA(t)}dt$	$C_{u1}(s)=\int_s^1 \frac{m_1(t)M_{c1}(s,t)}{EI(t)}dt+\int_s^1 \frac{n_1(t)N_{c1}(s,t)}{EA(t)}dt$ $C_{v1}(s)=\int_s^1 \frac{m_2(t)M_{c1}(s,t)}{EI(t)}dt+\int_s^1 \frac{n_2(t)N_{c1}(s,t)}{EA(t)}dt$ $C_{\varphi 1}(s)=\int_s^1 \frac{m_3(t)M_{c1}(s,t)}{EI(t)}dt+\int_s^1 \frac{n_3(t)N_{c1}(s,t)}{EA(t)}dt$ $C_{u2}(s)=\int_s^1 \frac{m_4(t)M_{c2}(s,t)}{EI(t)}dt+\int_s^1 \frac{n_4(t)N_{c2}(s,t)}{EA(t)}dt$ $C_{v2}(s)=\int_s^1 \frac{m_5(t)M_{c2}(s,t)}{EI(t)}dt+\int_s^1 \frac{n_2(t)N_{c2}(s,t)}{EA(t)}dt$ $C_{\varphi 2}(s)=\int_s^1 \frac{m_6(t)M_{c2}(s,t)}{EI(t)}dt+\int_s^1 \frac{n_6(t)N_{c2}(s,t)}{EA(t)}dt$
$M_{b1}(s,t)=sin\theta\,(s)\big(x(t)-x(s)\big)-cos\theta(s)(y(t)-y(s))$ $N_{b1}(s,t)=-cos\theta\,(s)cos\theta(t)-sin\theta(s)\sin\theta(t)$	$M_{b2}(s,t)=sin\theta\,(s)\big(x(s)-x(t)\big)-cos\theta(s)(y(s)-y(t))$ $N_{b2}(s,t)=cos\theta\,(s)cos\theta(t)+sin\theta(s)\sin\theta(t)$
$M_{c1}(s,t)=cos\theta\,(s)\big(x(t)-x(s)\big)+sin\theta(s)(y(t)-y(s))$ $N_{c1}(s,t)=sin\theta\,(s)cos\theta(t)-cos\theta(s)\sin\theta(t)$	$M_{c2}(s,t)=cos\theta\,(s)\big(x(s)-x(t)\big)+sin\theta(s)(y(s)-y(t))$ $N_{c2}(s,t)=-sin\theta\,(s)cos\theta(t)+cos\theta(s)\sin\theta(t)$
$m_1(t)=sin\theta_1\,(x(t)-x_1)-cos\theta_1(y(t)-y_1)$ $n_1(t)=-cos\theta_1\,(s)cos\theta(t)-sin\theta_1(s)\sin\theta(t)$	$m_2(t)=cos\theta_1\,(x(t)-x_1)+sin\theta_1(y(t)-y_1)$ $n_2(t)=sin\theta_1\,cos\theta(t)-cos\theta_1\sin\theta(t)$
$m_3(t)=-1$ $n_3(t)=0$	$m_4(t)=sin\theta_2\,\big(x_{2-}x(t)\big)-cos\theta_2(y_2-y(t))$ $n_4(t)=cos\theta_2\,cos\theta(t)+sin\theta_2\sin\theta(t)$
$m_5(t)=cos\theta_2\,\big(x_{2-}x(t)\big)-sin\theta_2(y_2-y(t))$ $n_5(t)=-sin\theta_2\,cos\theta(t)+cos\theta_2\sin\theta(t)$	$m_6(t)=1$ $n_6(t)=0$

Table 1: Equations regarding $\{b\}$ and $\{c\}$

Nodal Stiffness Matrix in Section 1	Nodal Stiffness Matrix in Section 2
$K_{11}=F_{11}^{-1}=\begin{bmatrix} f_{11}^{(1)} & f_{12}^{(1)} & f_{13}^{(1)} \\ f_{21}^{(1)} & f_{22}^{(1)} & f_{23}^{(1)} \\ f_{31}^{(1)} & f_{32}^{(1)} & f_{33}^{(1)} \end{bmatrix}^{-1}$	$K_{22}=F_{22}^{-1}=\begin{bmatrix} f_{11}^{(2)} & f_{12}^{(2)} & f_{13}^{(2)} \\ f_{21}^{(2)} & f_{22}^{(2)} & f_{23}^{(2)} \\ f_{31}^{(2)} & f_{32}^{(2)} & f_{33}^{(2)} \end{bmatrix}^{-1}$
$f_{ij}^{(1)}=\int_0^1 \frac{m_i(t)m_j(t)}{EI(t)}dt+\int_0^1 \frac{n_i(t)n_j(t)}{EA(t)}dt$	$f_{ij}^{(2)}=\int_0^1 \frac{m_{i+3}(t)m_{j+3}(t)}{EI(t)}dt+\int_0^1 \frac{n_{i+3}(t)n_{j+3}(t)}{EA(t)}dt$
m and n are defined in Table 1	

Table 2: Nodal Stiffness Matrixes

With respect to definition of external loads vector in finite element method, the new shape functions in non-prismatic curved beams are defined as Equation (2).

$$\{N_u\}=\begin{Bmatrix} N_{u1}^u \\ N_{v1}^u \\ N_{\varphi 1}^u \\ N_{u2}^u \\ N_{v2}^u \\ N_{\varphi 2}^u \end{Bmatrix}=\begin{Bmatrix} K_{11} & 0 \\ 0 & K_{22} \end{Bmatrix}=\begin{Bmatrix} b_{u1}(s) \\ b_{v1}(s) \\ b_{\varphi 1}(s) \\ b_{u2}(s) \\ b_{v2}(s) \\ b_{\varphi 2}(s) \end{Bmatrix} \qquad \{N^v\}=\begin{Bmatrix} N_{u1}^v \\ N_{v1}^v \\ N_{\varphi 1}^v \\ N_{u2}^v \\ N_{v2}^v \\ N_{\varphi 2}^v \end{Bmatrix}=\begin{Bmatrix} K_{11} & 0 \\ 0 & K_{22} \end{Bmatrix}=\begin{Bmatrix} c_{u1}(s) \\ c_{v1}(s) \\ c_{\varphi 1}(s) \\ c_{u2}(s) \\ c_{v2}(s) \\ c_{\varphi 2}(s) \end{Bmatrix} \tag{2}$$

Where u and v are displacement vectors.

3 SHAPE FUNCTIONS FOR DYNAMIC ANALYSIS

In a non-prismatic curved beam which is subjected to dynamic loads the equation of motion is assumed to be governed by

$$\frac{1}{R}\frac{\partial}{\partial s}\left(EI\left(\frac{\partial^2 v}{\partial s^2}-\frac{\partial\left(\frac{u}{R}\right)}{\partial s}\right)\right)-\frac{\partial}{\partial s}\left(EA\left(\frac{\partial u}{\partial s}+\frac{v}{R}\right)\right)+\rho A\frac{\partial^2 u}{\partial t^2}+ke_x u=p(x,t) \tag{3}$$

$$\frac{\partial^2}{\partial s^2}\left(EI\left(\frac{\partial^2 v}{\partial s^2}-\frac{\partial\left(\frac{u}{R}\right)}{\partial s}\right)\right)+\frac{1}{R}EA\left(\frac{\partial u}{\partial s}+\frac{v}{R}\right)+\rho A\frac{\partial^2 v}{\partial t^2}+ke_y v=q(x,t) \tag{4}$$

Where *s*= longitude of curvilinear, *u*= tangential displacement, *v*= vertical displacement, *EI* = flexural stiffness, *EA* = axial stiffness, *ke* = stiffness of elastic foundation, ρA = mass per unit length and *R*= radius of curvature. If the subjected dynamic load defines as a harmonic load, the deflection of structure can also be assumed as harmonic.

$$\frac{1}{R}\frac{d}{ds}\left(EI\left(\frac{d^2 v}{ds^2}-\frac{d\left(\frac{u}{R}\right)}{ds}\right)\right)-\frac{d}{ds}\left(EA\left(\frac{du}{ds}+\frac{v}{R}\right)\right)+\left(ke_x-\omega^2\rho A\right)u=p(s) \tag{5}$$

$$\frac{d^2}{ds^2}\left(EI\left(\frac{d^2 v}{ds^2}-\frac{d\left(\frac{u}{R}\right)}{\partial s}\right)\right)+\frac{1}{R}EA\left(\frac{du}{ds}+\frac{v}{R}\right)+\left(ke_y-\omega^2\rho A\right)v=q(s) \tag{6}$$

Where ω is the angular frequency of harmonic load.

Definitions of dynamic shape functions are similar to definition of static shape function as presented in the last section; the only difference is that in order to obtain the dynamic shape functions the equations of motion have to be solved. For this purpose in this study a numerical method called "Differential Transform Method" is employed. Differential transform of a function and differential inverse transform are as follow

$$\overline{Y}(k)=\frac{1}{k!}\left[\frac{d^k y(\xi)}{d\xi^k}\right]_{\xi=0} \quad \text{And} \quad y(\xi)=\sum_{k=0}^{N}\overline{Y}(k)\xi^k \tag{7}$$

Where $y(\xi)$ the original is function and $\overline{Y}(k)$ is the transformed function. In accord with Equation (7), it is readily proven that transformed functions complied with following basic mathematic operations

$$y(\xi)=u(\xi)\pm v(\xi) \quad \Rightarrow \quad \overline{Y}(k)=\overline{U}(k)\pm\overline{V}(k) \tag{8}$$

$$y(\xi)=C.u(\xi) \qquad \Rightarrow \qquad \overline{Y}(k)=C.\overline{U}(k) \tag{9}$$

$$y(\xi)=u(\xi).v(\xi) \qquad \Rightarrow \qquad \overline{Y}(k)=\sum_{r=0}^{k}\overline{U}(r)\overline{V}(k-r) \tag{10}$$

$$y(\xi)=\frac{d^{j}u}{d\xi^{j}} \qquad \Rightarrow \qquad \overline{Y}(k)=(k+1)(k+2)...(k+j)\overline{U}(k+j) \tag{11}$$

By applying the variable change $\varepsilon=\frac{x}{l}$, Equation (5) and (6) are rewritten as follow

$$\frac{1}{R}\frac{1}{L}\frac{d}{d\xi}\left(EI\left(\frac{1}{L^2}\frac{d^2v}{d\xi^2}-\frac{1}{L}\frac{d\left(\frac{u}{R}\right)}{d\xi}\right)\right)-\frac{1}{L}\frac{d}{d\xi}\left(EA\left(\frac{1}{L}\frac{du}{d\xi}+\frac{v}{R}\right)\right)+\left(ke_{\xi}-\omega^2\rho A\right)u=0 \tag{12}$$

$$\frac{1}{L^2}\frac{d^2}{d\xi^2}\left(EI\left(\frac{1}{L^2}\frac{d^2v}{d\xi^2}-\frac{1}{L}\frac{d\left(\frac{u}{R}\right)}{d\xi}\right)\right)+\frac{1}{R}EA\left(\frac{1}{L}\frac{du}{d\xi}+\frac{v}{R}\right)+\left(ke_{\xi}-\omega^2\rho A\right)v=0 \tag{13}$$

Applying differential transform to Equations (12) and (13) besides the theorems presented at Equations (8) to (11), the following recursive expressions are obtained

$$\sum_{r=0}^{k}\overline{\rho}(k-r)\overline{v}(r)-\frac{1}{L}(k+1)\overline{n}(k+1)+\sum_{r=0}^{k}k\overline{e}(k-r)\overline{U}(r)=\omega^2\sum_{r=0}^{k}\rho\overline{A}(k-r)\overline{U}(r) \tag{14}$$

$$\frac{1}{L}(k+1)(k+2)\overline{m}(k+2)+\sum_{r=0}^{k}\overline{\rho}(k-r)\overline{n}(r)+\sum_{r=0}^{k}k\overline{e}(k-r)\overline{V}(r)=\omega^2\sum_{r=0}^{k}\rho\overline{A}(k-r)\overline{V}(r) \tag{15}$$

Where$\overline{EI}$, $\overline{EA}$, $\overline{\rho A}$, $\overline{U}$ and $\overline{V}$ are the transformed functions of EI , EA , ρA , U and V and ρ is the reverse of radius of curvature (R). $\overline{m}$, $\overline{n}$ and $\overline{v}$ are the transformed functions of bending moment, axial force and shear force which are defined as follow

$$\overline{n}(k)=\sum_{r=0}^{k}E\overline{A}(k-r)\overline{\varepsilon}(r),\overline{\varepsilon}(r)=\frac{1}{L}(k+1)\overline{U}(k+1)+r=\sum_{r=0}^{k}\overline{\rho}(k-r)\overline{V}(r) \tag{16}$$

$$\overline{m}(k)=\sum_{r=0}^{k}E\overline{I}(k-r)\overline{\psi}(r),\overline{\psi}(r)=\frac{1}{L}(k+1)\varphi(k+1) \tag{17}$$

$$\varphi(k)=\frac{1}{L}(K+1)\overline{V}(K+1)-\frac{1}{L}\sum_{r=0}^{k}\overline{\rho}(k-r)\overline{U}(r) \tag{18}$$

$$\overline{v}(k)=\frac{1}{L}(K+1)\overline{m}(K+1) \tag{19}$$

Regarding the definitions of basic displacement functions and Figure 3, all boundary conditions are tabulated in Table 3.

c_{u1} , b_{u1}	c_{u2} , b_{u2}	c_{v1} , b_{v1}
$\sum_{k=0}^{N}\bar{U}(k)=0 \quad \bar{n}(0)=-1$ $\sum_{k=0}^{N}\bar{V}(k)=0 \quad \bar{v}(0)=0$ $\sum_{k=0}^{N}\bar{\varphi}(k)=0 \quad \bar{m}(0)=0$	$\sum_{k=0}^{N}\bar{n}(k)=1 \quad \bar{U}(0)=0$ $\sum_{k=0}^{N}\bar{v}(k)=0 \quad \bar{V}(0)=0$ $\sum_{k=0}^{N}\bar{m}(k)=1 \quad \bar{\varphi}(0)=0$	$\sum_{k=0}^{N}\bar{U}(k)=0 \quad \bar{n}(0)=-1$ $\sum_{k=0}^{N}\bar{V}(k)=0 \quad \bar{v}(0)=1$ $\sum_{k=0}^{N}\bar{\varphi}(k)=0 \quad \bar{m}(0)=0$
c_{v2} , b_{v2}	$c_{\varphi1}$, $b_{\varphi1}$	$c_{\varphi2}$, $b_{\varphi2}$
$\sum_{k=0}^{N}\bar{n}(k)=0 \quad \bar{U}(0)=0$ $\sum_{k=0}^{N}\bar{v}(k)=-1 \quad \bar{V}(0)=0$ $\sum_{k=0}^{N}\bar{m}(k)=1 \quad \bar{\varphi}(0)=0$	$\sum_{k=0}^{N}\bar{U}(k)=0 \quad \bar{n}(0)=0$ $\sum_{k=0}^{N}\bar{V}(k)=0 \quad \bar{v}(0)=0$ $\sum_{k=0}^{N}\bar{\varphi}(k)=0 \quad \bar{m}(0)=-1$	$\sum_{k=0}^{N}\bar{n}(k)=0 \quad \bar{U}(0)=0$ $\sum_{k=0}^{N}\bar{v}(k)=0 \quad \bar{V}(0)=0$ $\sum_{k=0}^{N}\bar{m}(k)=1 \quad \bar{\varphi}(0)=0$

Table 3: Boundary conditions in order to obtain $\{b\}$ and $\{c\}$

Once the first two terms of series $\bar{U}$ and first four terms of $\bar{V}$ derived, concerning mentioned boundary conditions, all terms of transformed functions of $\bar{U}$ and $\bar{V}$ are obtained by using the recursive Equations (14) and (15). Having $\{b\}$ and $\{c\}$ matrixes, nodal stiffness matrixes are calculated. With respect to section 2 of this paper, dynamic shape functions and stiffness matrixes are similarly obtained.

$$K_{11}=\begin{bmatrix} b_{u1}(0) & c_{u1}(0) & \frac{1}{L}\frac{dc_{u1}}{d\xi}\Big|_{\xi=0}-\frac{b_{u1}(0)}{R(0)} \\ b_{v1}(0) & c_{v1}(0) & \frac{1}{L}\frac{dc_{v1}}{d\xi}\Big|_{\xi=0}-\frac{b_{v1}(0)}{R(0)} \\ b_{\varphi1}(0) & c_{\varphi1}(0) & \frac{1}{L}\frac{dc_{\varphi1}}{d\xi}\Big|_{\xi=0}-\frac{b_{\varphi1}(0)}{R(0)} \end{bmatrix}^{-1}, K_{22}=\begin{bmatrix} b_{u2}(L) & c_{u2}(L) & \frac{1}{L}\frac{dc_{u2}}{d\xi}\Big|_{\xi=L}-\frac{b_{u1}(L)}{R(L)} \\ b_{v2}(L) & c_{v2}(L) & \frac{1}{L}\frac{dc_{v2}}{d\xi}\Big|_{\xi=L}-\frac{b_{v2}(L)}{R(L)} \\ b_{\varphi2}(L) & c_{\varphi2}(L) & \frac{1}{L}\frac{dc_{\varphi2}}{d\xi}\Big|_{\xi=L}-\frac{b_{\varphi2}(L)}{R(L)} \end{bmatrix}^{-1} \tag{20}$$

4 CANTILEVER AND ARCH ACTION

The most commonly accepted method of analyzing arch dams assumes the horizontal water load is divided between the arches and the cantilevers so that the calculated cantilever and arch deflections are equal at all conjugate points in all parts of structure. The cantilever elements are assumed to be fixed at foundation and the arch elements fixed at abutments. In this paper we used this theory and presented a new method for modeling the arch dams with dam-reservoir interaction. We model the arches as a non-homogeneous elastic foundation that prevents arch dam's cantilevers from free displacements. So we model the structure as a Non-prismatic cantilever curved beam resting on a continuous elastic foundation (Figure 4).

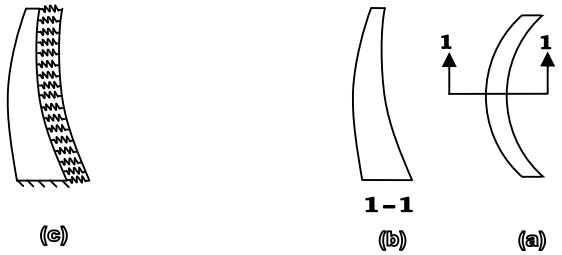


Figure 4: (a) Arch Element (b) Cantilever Element (c) Cantilever Beam Resting On an Elastic Foundation

5 NUMERICAL EXAMPLE

In order to verify the accuracy and competency of the presented method the double arch dam "Komarnica" in Yugoslavia with 195 m of height is chosen as a numerical example. Some of geometric properties of this dam are tabultaed in Table 4.

Radius (m)	Central Angle (degree)	Cord (m)	Height (m)
121	130	220	0
105	126	188	19.5
82	118	141	58.5
69	110	112	97.5
50	102	77	136.5
38	94	56	175.5
32	90	45	195

Table 4: Geometric Properties of Komarnica Dam

Considering the central cantilever of the structure, the thickness of this dam is assumed to be governed by

$$t(\xi) = -2.4\xi^2 - 17.7\xi + 29.3 \tag{21}$$

With regard the geometry of arches, a continuous elastic foundation is defined as

$$ke(\xi) = -4.71e10\xi^3 + 9.45e10\xi^2 - 6.07e10\xi + 1.26e10 \tag{22}$$

Now, with respect to section 4, the central arch of this structure can be modeled as non-prismatic cantilever curved beam which rests on a continuous elastic foundation (Figure 5).

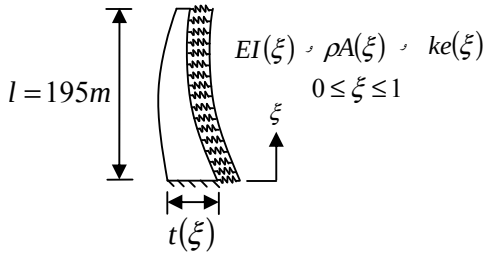


Figure 5: Modeling The Central Cantilever Of Komarnica Dam As a Curved Cantilever Resting On An Continuous Elastic Foundation

If the harmonic load $q(x,t)$ and material properties define as below, by obtaining $EI(\xi)$, $\rho A(\xi)$ and $ke(\xi)$ functions, the dynamic shape functions are obtained.

$$q(x,t) = q_0 \sin(\omega t)$$

$$p(x,t) = 0$$

$$\omega = 50 \qquad q_0 = 10^6 kg$$

$$\rho = 2400 \frac{kg}{m^3}$$

$$E_{static} = 2e9 \frac{kg}{m^2}$$

$$E_{dynamic} = 3.5e9 \frac{kg}{m^2} \tag{23}$$

By using mentioned dynamic shape functions the mass matrix, the stiffness matrix and the load vector are obtained. Finally, we analyzed the cantilever curved beam by using the Newmark method with coefficients $\beta = 0.25$ and $\gamma = 0.5$ and the time step $\Delta t = 0.01s$ with zero initial conditions. Maximum displacement of top of the structure wich calculated by applying this method and the comparison of it with normal beam elements are presented in Table 5 and Figure 6.

Case Number	Number of Ordinary Elements	Maximum Displacement of Top of the Structure (m)
1	5	0.0026952
2	10	0.0014896
3	20	0.0012011
4	50	0.0010523
5	100	0.0009597
6	Present Method (One Element)	0.0008982

Table 5: Maximum Displacement of Top of the Structure

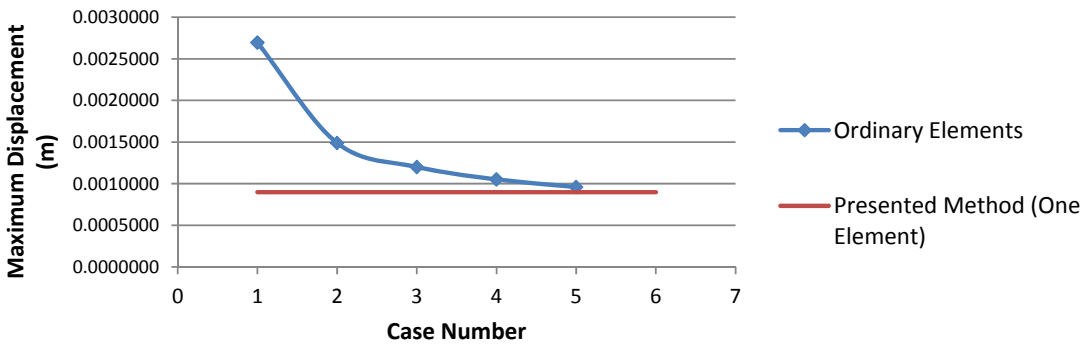


Figure 6: Convergence of the Maximum Displacement of Top of the Structure

6 CONCLUSIONS

- According to the numerical example the presented method has high accuracy and high performance for analyzing non-prismatic beams.
- The form of the defined static shape functions and the method that used for obtaining dynamic shape functions for non-prismatic curved beams, make this method capable of modeling any continues variation in geometric properties of the dams.
- Because the functions of thickness of the dam and stiffness of the elastic foundation are continues, this method is very practical for analyzing of arch dams.
- Concerning to the results of the numerical example highly acceptable results can be achieved by employing just one element.

REFERENCES

[1] Attarnejad ,Reza," On the Derivation of Geometric Stiffness and Consistent Mass Matrices for Non-prismatic Euler-Bernoulli Beam Elements", ECCOMAS 2000 , Barcelona , Spain, 2000.

[2] Attarnejad ,Reza,"Free Vibration Of Non-Prismatic Beams", EM2002 ,Columbia University, New York , NY,USA, 2002.

[3] Anil K. Chopra, 2012. Earthquake Analysis of Arch Dams: Factors to Be Considered. Journal of Structural Engineering, Vol. 137, No. 2, Pages 205-214.

[4] Xiangli, He and Tongchun, Li, 2010. Analysis of Seismic Response for Arch Dam Based on Gradual Enlargement Mesh Method. Earth and Space Conference 2010, Page 2625.

[5] Mei, C., 2008. Application of differential transformation technique to free vibration analysis of a centrifugally stiffened beam. Computers and Structures, 86, Pages 1280-1284.

[6] Mou, Y., Han, R.S.P and Shah, A.H, 1997. Exact Dynamic Matrix for Beams of Arbitrary Varying Cross Sections. International Journal of Numerical Methods in Engineering, Vol 40, Pages 233-50.

[7] Banerjee, J.R., 2000. Free vibration of centrifugally stiffened uniform and tapered beams using the dynamic stiffness method. Journal of Sound and Vibration, 233, Pages 857-875.

[8] Gunda, J.B. and R. Ganguli, 2008. New rational interpolation functions for finite element analysis of rotating beams. International Journal of Mechanical Sciences, 50, Pages 578-588.

[9] Paz, Mario, 1991. Structural dynamics: Theory and Computation. Van Nostrand Reinhold, New York.

COMPDYN 2013
4th ECCOMAS Thematic Conference on
Computational Methods in Structural Dynamics and Earthquake Engineering
M. Papadrakakis, V. Papadopoulos, V. Plevris (eds.)
Kos Island, Greece, 12–14 June 2013

CONTACT INTERFACE MODELING IN THE DYNAMIC RESPONSE OF RIGID BLOCKS SUBJECTED TO BASE EXCITATION

Oscar A. Ardila-Giraldo[1], Juan Carlos Reyes[2], and J. Paul Smith-Pardo[3]

[1] INGETEC SA
Carrera 6 Nº 30A-30, Bogotá-Colombia
e-mail: oardilag@hotmail.com

[2] Universidad de los Andes
Carrera 1 Nº 18A- 12, Bogotá-Colombia
jureyes@uniandes.edu.co

[3] Seattle University
901 12th Ave, Seattle, WA 98122, USA
smithjh@seattleu.edu

Keywords: Dynamics of Rigid Blocks, Earthquake Engineering Design.

Abstract. *A proper selection of the percentage of the live load that must be considered as inertia is critical to the seismic analysis and design of certain structures like pile-supported container yards, in which live loads are nearly permanent and exceed the total dead load. This selection is particularly relevant in the case of flexible structures, for which the containers are not likely to experience sufficient accelerations to slide or rock and thus behave as rigid attachments. For this case, there are no clear design guidelines available with regard to the portion of the live load that should be used in dynamic analyses. To shed some light on this problem, a series of tests on a 1:15 scale model subjected to arrays of ground motions is currently underway. Along with this experimental program, numerical simulation is being conducted to develop a simple yet robust finite element (FE) model that can capture not only sliding and rocking, but also inelastic collisions involved in the response of a rigid block to base excitation. The resulting model will later be used to estimate the seismic response of a platform-container system with dynamic characteristics similar to those of the laboratory test model. Thus, a comparison between test and analysis results can be established for FE model calibration purposes and sensitivity studies can ultimately be conducted to assess the effect of live load on the seismic response of pile-supported container yards. This paper mainly deals with one of the most important steps in the development of the FE model: the modeling of the platform-container contact interface. Results from preliminary analyses of rigid blocks subjected to base excitation and exhibiting different response modes (including sliding and rocking) are presented. The results are shown to be in agreement with literature test data.*

1 INTRODUCTION

In structures such as the pile-supported container yard schematically shown in Figure 1, live loads are nearly permanent and exceed the total dead load even by a factor of two or more. The contribution of containers to the inertial forces acting on the structure varies depending on how much they slide and rock during a ground motion. This is because the movement of the containers dissipates some of the energy imposed by the ground motion through friction and impact. Therefore, the seismic analysis and design of a pile-supported yard must carefully consider the portion of the live load that should be included as inertia, particularly in the case of flexible structures, for which the containers may not experience sufficient accelerations to slide or rock, and thus behave as rigid attachments. Unfortunately, no clear design guidelines are available with regard to the portion of the live load that should be used in the dynamic analyses of these types of structures [1, 2 ,3].

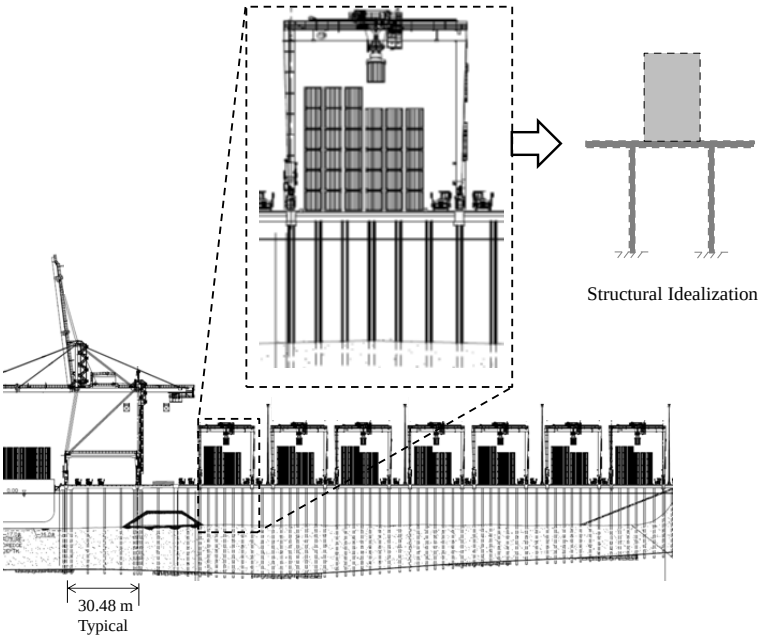


Figure 1: Pile-supported container yard and idealization.

The behavior of rigid bodies- like the containers in a terminal- is a complex problem of dynamics that has been studied extensively for over 50 years. The driving interest has been in the nuclear engineering industry and the need to determine the anchorage mechanisms for containers loaded with sensitive equipment or hazardous materials. The most influential formulation to describe the rocking motion of rigid bodies was introduced by Housner [4], who used basic principles to derive two piecewise equations of motion. Yim et al. [5] developed a numerical procedure to solve the nonlinear equations governing the rocking motion of rigid blocks on a rigid base subjected to horizontal and vertical ground motion. Shenton & Jones [6] proposed a general, two-dimensional formulation for the response of free-standing rigid bodies to base excitation. A series of criteria for initiation of slide, slide-rock and rock body modes from rest conditions for rigid boxes when subjected to horizontal ground pulses was developed by Shenton [7]; his analyses, which assume rigid foundation and Coulomb friction, show a transition of the mode of initiation of the response of the body from at-rest to sliding, rocking, or coupled sliding-rocking depending on the friction coefficient at the interface, the aspect ratio of the block and the magnitude of the horizontal ground acceleration as shown in

Figure 2. More recently, Peña et al. [8] conducted a comprehensive experimental investigation to study the rocking response of single rigid-block structures. They also developed two tools for the numerical simulation of the rocking motion observed in the tests: one analytical and one using the discrete element method (DEM).

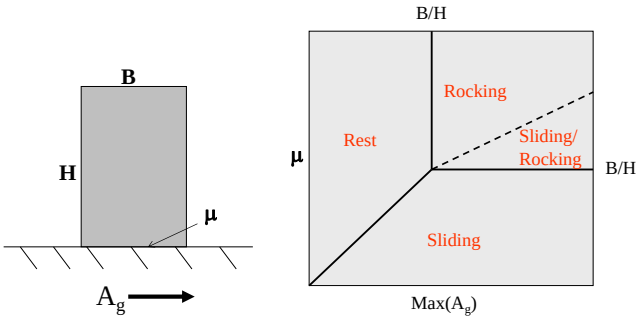


Figure 2: Mode initiation criteria for rigid blocks, after Shenton [7]

2 RESEARCH PROGRAM OVERVIEW AND SIGNIFICANCE

In order to shed some light on the determination of the portion of the live load to be considered as inertia in simple structure like the idealization depicted in Figure 1, a series of tests on a 1:15 scale model subjected to an array of ground motions is currently underway. The test structure, designed based on similitude requirements, consists of a platform and four steel columns as a representative portion of a pile-supported terminal. The model will be subjected to base excitation while supporting heavy rigid blocks of different aspect ratios which represent possible container stack configurations.

The experimental program is being supplemented with a simple finite element (FE) model that captures different phenomena involved in the response of a rigid block to base excitation. These phenomena include sliding and rocking of the block, as well as impact with the supporting structure. Other methodologies and formulations to address the different modes of response of rigid blocks to base excitation that are available, although robust, are often not simple for practical use in seismic design. The finite element method (FEM) is advantageous because it can be relatively easy to implement in design processes and also because of the increasing familiarity of structural engineers with the method and commercial FE software.

It is apparent that in order to capture appropriately the different phenomena of interest, the block-foundation contact interface must be carefully represented. This is the most important step in the model development and is the main topic of this paper.

3 FINITE ELEMENT (FE) MODEL

In this section, the main features of the FE model, developed using ANSYS release 13.0 (academic version), are described. Although the element types used in the model correspond to this program, the modeling concepts are applicable to other FE software.

3.1 Rigid block and foundation

The basic FE model developed consists of a rectangular block resting directly on a rectangular plate that simulates the foundation (Figure 3). If the base acceleration occurs in a direction parallel to one of the horizontal axes of symmetry of the block, and if perfectly symmetric response is assumed, the problem becomes two-dimensional (2-D) and the FE model can be simplified. Thus, both the block (with width B and height H) and the foundation plate (with width B_f and thickness H_f) are modeled using 2-D structural solid ANSYS element

type PLANE182 [9], which can be used either as a plane strain/stress element or an axisymmetric element. This element type is defined by four nodes, each having two translational degrees of freedom (DOF's), and has non-linear geometry capabilities (large strains/deflections). All the DOF's of the foundation plate are restrained to simulate a fixed base.

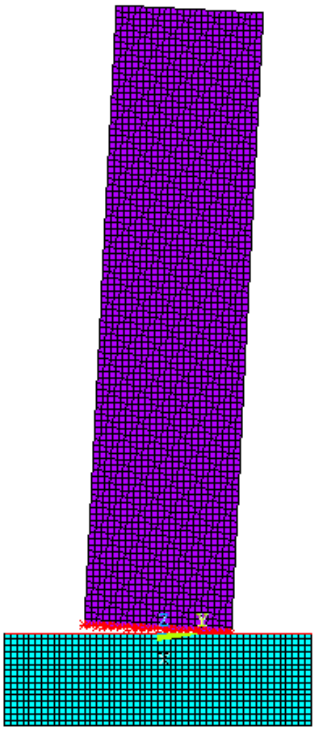


Figure 3: Finite element (FE) model of a rigid block resting on a rigid foundation

3.2 Block-foundation contact interface

To capture sliding and rocking of the block under base excitation, as well as impact with the foundation, the contact interface that exists between the block and the foundation plate is modeled via an ANSYS contact pair. This is defined by two surfaces designated as the contact and target surfaces, which can be initially in contact or are expected to make contact within the duration of the motion/response analyzed. Non-linear contact and target elements are used to model the two surfaces in the contact pair. These surfaces share a unique identifier and set of properties that allow ANSYS to detect any potential interpenetration and implement the contact algorithm selected by the user to guarantee geometric and kinematic compatibility.

The target surface is modeled using ANSYS element type TARGE169 [9], which is a 2-D target segment that can be paired with any of the 2-D contact elements available in the program. These target segments are used to overlay the top surfaces of the solid elements in the uppermost layer of the foundation plate mesh, thereby defining the target surface (Figure 4a). Forces and moments, as well as displacements and rotations can be imposed on the target elements.

The contact surface is generated by overlaying the bottom surfaces of the solid elements in the lowermost layer of the block mesh with contact elements (Figure 4b). The selection of this element type depends on the type of structural solid used in the model. There are two element types available in ANSYS that are compatible with PLANE182: CONTA171 and CONTA175 [9]. CONTA171 is a 2-D two-node surface-to-surface contact element used to represent contact and sliding between a 2-D target surface and a deformable surface.

CONTA175 is a 2-D/3-D node-to-surface contact element used to represent contact and sliding between two surfaces, a node and a surface, or a line and a surface.

For both contact elements described above, contact occurs when the element surface penetrates one of the segments (TARGE169) on the specified target surface. Interface friction and delamination can be modeled with both contact elements. Based on element geometry and using guidelines provided in Reference [10], CONTA171 is used in the FE model to analyze sliding-dominated problems, whereas CONTA175 is used to analyze rocking-dominated response. In both cases, a Coulomb friction model is used to capture friction and sliding at the contact interface.

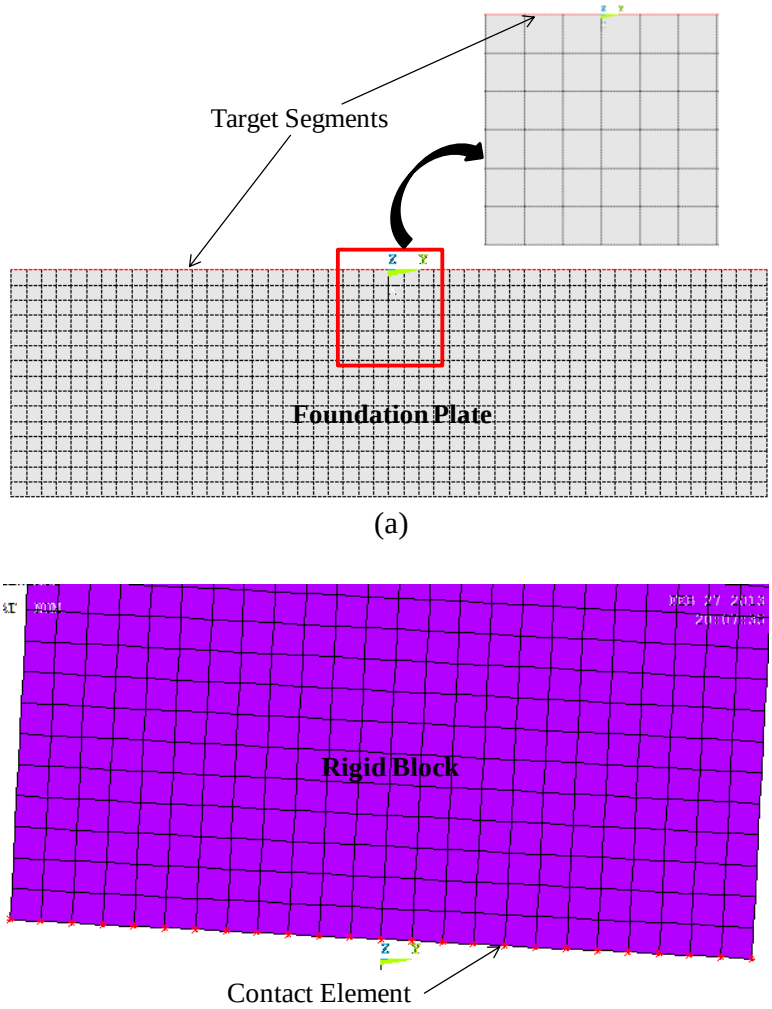


Figure 4: Modeling of block-foundation contact interface: (a) target surface and (b) contact surface

3.3 Material properties

Both the block and the foundation plate are modeled using linear-elastic material properties. Thus, only the Young's modulus (E), Poisson's ratio (ν), and mass density (ρ) need to be input. The contact elements use an isotropic Coulomb friction model [10], which assumes that sliding between two contacting surfaces begins at a threshold shear stress at the interface (τ) given by:

$$\tau = c + \mu p \tag{1}$$

where:

c = Cohesion at the contact interface
μ = Interface friction coefficient
p = Contact pressure

For the problem at hand, no cohesion is assumed to exist at the contact interface (c = 0 in Eq. (1)) and, therefore, the frictional shear stress is directly proportional to the contact pressure ($\tau = \mu p$). The friction coefficient μ is input as a material property for the contact elements, and it can depend on temperature, time, normal pressure, sliding distance, and sliding relative velocity. Based on the physics of the problem analyzed and for simplicity, μ is assumed to depend only on the relative velocity of the two surfaces in contact (V_{rel}). ANSYS provides an exponential decay friction model [10] to account for the variation of μ with V_{rel}, as indicated below:

$$\mu = \mu_d \left[1 + \left(\frac{\mu_s}{\mu_d} - 1 \right) \cdot e^{-DC \cdot V_{rel}} \right] \tag{2}$$

where:

μ_d = Dynamic friction coefficient
μ_s = Static friction coefficient
DC = Decay coefficient [time/length]

The purpose of Eq. (2) is to provide a smooth transition from a "sticking" condition ($V_{rel} = 0$ & $\mu = \mu_s$) to a sliding condition ($V_{rel} >> 0$ & $\mu = \mu_d$). The decay coefficient DC is obtained experimentally and, therefore, it is not always available. In this case, DC may be taken as zero, and Eq. (2) is rewritten to be $\mu = \mu_s$ for sticking and $\mu = \mu_d$ for sliding. Since typically $\mu_s > \mu_d$, there will be a sudden jump in the value of μ when the sliding condition is reached if no value of DC is specified. This discontinuity may lead to convergence difficulties and should be avoided.

In addition to the energy dissipation mechanism provided by friction, numerical viscous damping is provided to the FE model to account for other sources of energy dissipation such as the multiple impacts of the block with the foundation during rocking response.

3.4 Contact algorithm and impact modeling

The basic contact algorithm selected in ANSYS is the augmented Lagrangian method, which consists of an iterative series of Penalty methods [11]. The Penalty method uses normal and tangential springs to relate the two contacting surfaces, with the spring constants called the contact stiffnesses. Contact tractions (pressure and frictional stresses) at the interface are proportional to the contact stiffnesses, and they lead to values of penetration and slip (in the normal and tangential directions, respectively) that are lower than allowable values. This guarantees that the relative motion of the two surfaces and the deformation occurring at the interface are geometrically compatible.

In addition to the displacement constraints imposed by the basic contact algorithm on nodes at the interface, velocity constraints must also be imposed when modeling contact in a transient dynamic analysis. This is to guarantee that nodal velocities and accelerations are consistent with nodal displacements, thereby enforcing conservation of momentum at the contact interface.

3.5 Boundary conditions and loading

All the nodes of the foundation plate are restrained against translation. Vertical acceleration is applied to the block to simulate its self-weight, which is the only load that is considered in free rocking motion analysis. Horizontal acceleration is applied to the foundation plate to simulate an excitation at the base of the block resulting from either harmonic motion or an earthquake.

4 RELEVANT NUMERICAL SOLUTIONS AND EXPERIMENTAL RESULTS

4.1 Numerical solution of SDOF structure supporting a sliding block

Figure 5 shows the structural idealization of a linearly elastic single degree of freedom (SDOF) structure (platform) supporting a rigid block. The SDOF oscillator is characterized by a mass m_P, damping c, and a stiffness k; whereas the rigid block is characterized by a mass m_L and a constant static/kinematic friction coefficient μ at its contact interface with the structure.

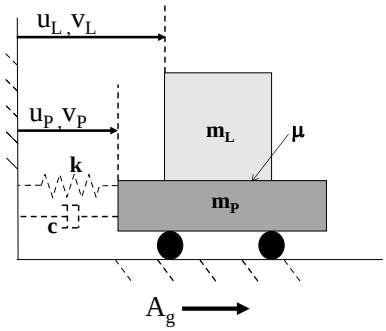


Figure 5: SDOF structure supporting a sliding rigid block

Provided that the rocking mode of the block is precluded, and letting u_P, u_L and v_P, v_L be the displacements and velocities of the SDOF oscillator and the block, respectively, the equations of equilibrium for the system can be written as (time derivatives are indicated with a dot directly above the variable):

$$\begin{aligned} m_L\left(\dot{v}_L + A_g\right) + f_x &= 0 \\ m_P\left(\dot{v}_L + A_g\right) + cv_P + ku_P - f_x &= 0 \end{aligned} \tag{3}$$

where A_g is ground acceleration, and f_x is friction force at the contact interface given by:

$$f_x = \begin{cases} -m_L\left(\dot{v}_P + A_g\right), & \dot{v}_P + A_g < \mu g \\ -\mu m_L g\,\mathrm{SIGN}\left(v_L - v_L\right), & \dot{v}_P + A_g < \mu g \end{cases} \tag{4}$$

Equations (3) and (4) were solved using a Runge-Kutta (R-K) numerical algorithm for a SDOF oscillator with the properties listed below:

$$\begin{aligned} \xi &= \frac{c}{2\sqrt{km_P}} = 0.05 \quad \text{(damping ratio)} \\ \alpha &= \frac{m_L}{m_P} = 2.0 \quad \text{(mass ratio)} \\ T_n &= 2\pi\sqrt{\frac{m_P}{k}} = 0.5\text{s} \quad \text{(natural period)} \end{aligned} \tag{5}$$

Excitation at the base consisted of a series of 30 far-fault ground motions corresponding to a seismic scenario with the characteristics indicated in Table 1. The calculated maximum displacements of the SDOF oscillator (platform) u_P are plotted in Figure 6 for all the ground motions analyzed. These results serve as a benchmark to the FE model in ANSYS for the sliding-only case (Section 5).

Parameter	Far-fault scenario
Magnitude	6.7±0.2
Distance	25±5 km (Joyner-Boore)
NEHRP Soil type	C and D
Highest usable period	4 sec
Number of records	30

Table 1: Selected seismic scenario used to test the sliding mode

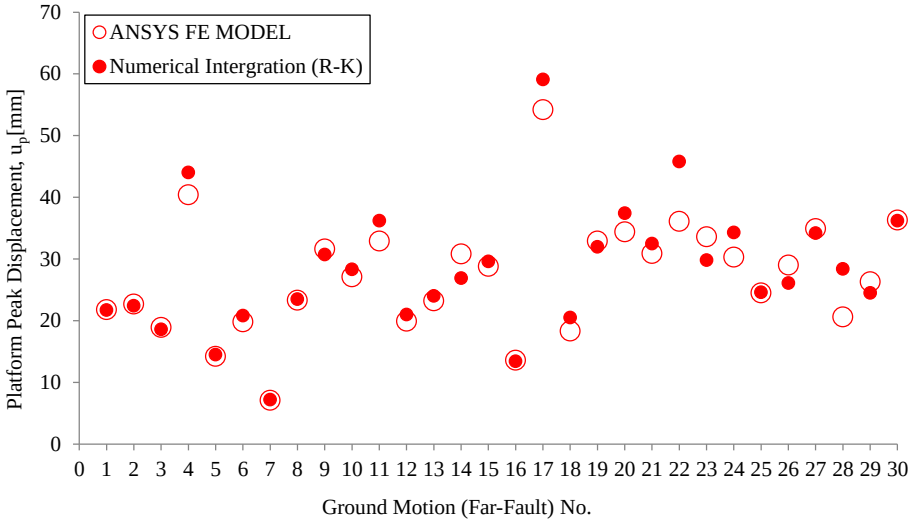


Figure 6: Platform displacements in SDOF structure supporting a sliding box

4.2 Experimental and Numerical Results on Rocking Motion of Rigid Blocks

Peña et al. [8] conducted a comprehensive experimental investigation to study the rocking response of single rigid-block structures. The investigation included 275 shaking table tests in total. In these tests, four blue granite stones with different geometric characteristics and supported by a foundation (bolted to the shaking table) made of the same material were subjected to free rocking, and harmonic and random base excitation. The stones had height-width ratios (H/B) ranging between 4 and 8, and a constant thickness-width ratio (t/B) of 3 to minimize 3-D effects. Light emission diodes (LED's) and high resolution cameras were used to measure displacements (and rotations) of the specimens and the shaking table. Similarly, accelerometers were used to measure corresponding accelerations. The main goal of the experimental program was to address the issues of repeatability of rocking motion response and its stability.

Two analysis tools were developed by Peña et al. [8] for the numerical simulation of the rocking motion observed in their experimental program. One tool is analytical and is referred to as the complex coupled rocking rotations (CCRR) method, while the other is numerical and uses the discrete element method (DEM). A new methodology was also proposed to find the parameters of the DEM model from the classical theory of rigid-block rocking motion

The harmonic/random base motion tests are the main portion of the experimental program mentioned above as they allow studying the dynamics of rigid blocks under rocking motion regime and earthquake excitation. However, the free rocking motion tests are essential for parameter identification and analytical model calibration. This consideration is also applicable to the FE model development described in this paper and, therefore, only free-rocking motion results reported by Peña et al. [8] are included here as an initial benchmark. Measured rocking angle histories for a block with a width of 0.25 m, height of 1.00 m, thickness of 0.75 m, total mass of 503 kg, and initial base rotation of 3° are presented in Figure 7. Comparison of these experimental results with the calibrated numerical and analytical formulation developed by the authors can be found in Peña et al. [8]

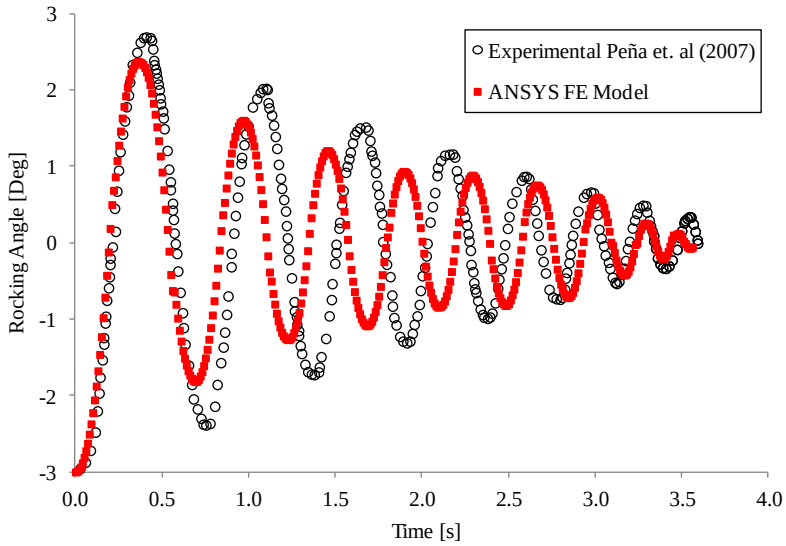


Figure 7: Response history of rigid block under free rocking, after Peña et al. [8]

5 RESULTS COMPARISON AND PRELIMINARY CALIBRATION OF THE FE MODEL

The basic FE model described in Section 3 was used to model the response to base excitation of an SDOF oscillator supporting a sliding rigid block as described in Section 4.1. To do so, the horizontal translation nodal restraints applied to the foundation plate (Section 3.5) were removed, and a horizontal spring element with stiffness k (determined from m_P and T_n) was attached to this plate to simulate the oscillator. The geometry of the rigid block was selected so that the target mass ratio (α = 2.0) was matched and the rocking initiation mode of response was precluded in compliance with the criteria presented by Shenton [7]. The maximum displacement u_P for each ground motion considered was calculated via finite element analysis (FEA) using the ANSYS model developed and it is included in Figure 6. The FEA results are found to be reasonably similar to those obtained with the numerical solution described in Section 4.1. The resulting mean ratio $u_{P_FEA}/u_{P_R\text{-}K}$ is 0.98, where u_{P_FEA} & $u_{P_R\text{-}K}$ are the peak displacements of the oscillator calculated via FEA and numerical integration using the Runge-Kutta method, respectively.

The FE model developed was also used to study the free rocking response of a rigid block with a height-to-width ratio (H/B) of 4 that was subjected to an initial base rotation of 3° as described in Section 4.2. The rocking angle history of the block was computed using the ANSYS model and it is included in Figure 7 for comparison purposes. The amplitudes of the rocking motion calculated with the model are within 25% of those measured in the tests described in Section 4.2. The period of the calculated response is consistently shorter than the

period measured in the experimental program. The discrepancies observed between the experimental and numerical (FEA) data can be attributed to an inaccurate representation in the FE model of the energy dissipation mechanisms available in the actual specimen/test. To capture these mechanisms more accurately and compute a rocking response closer to the test measurements, the viscous damping provided to the FE model (Section 3.3) through Rayleigh damping [12] must be calibrated. The classical Rayleigh damping model is summarized below:

$$[C] = \lambda[M] + \beta[K] \tag{6}$$

where:

$[C]$ = System damping matrix

λ = Mass-proportional Rayleigh damping coefficient

$[M]$ = System mass matrix

β = Stiffness-proportional Rayleigh damping coefficient

$[K]$ = System stiffness matrix

Assuming $\lambda = 0$ for simplicity, the damping provided to the FE model depends on stiffness only. To investigate the effect of damping on the rocking response of the rigid block being analyzed, different values of β were considered. The rocking angle histories of the block computed with the FE model and corresponding to different values of β are shown in Figure 8.

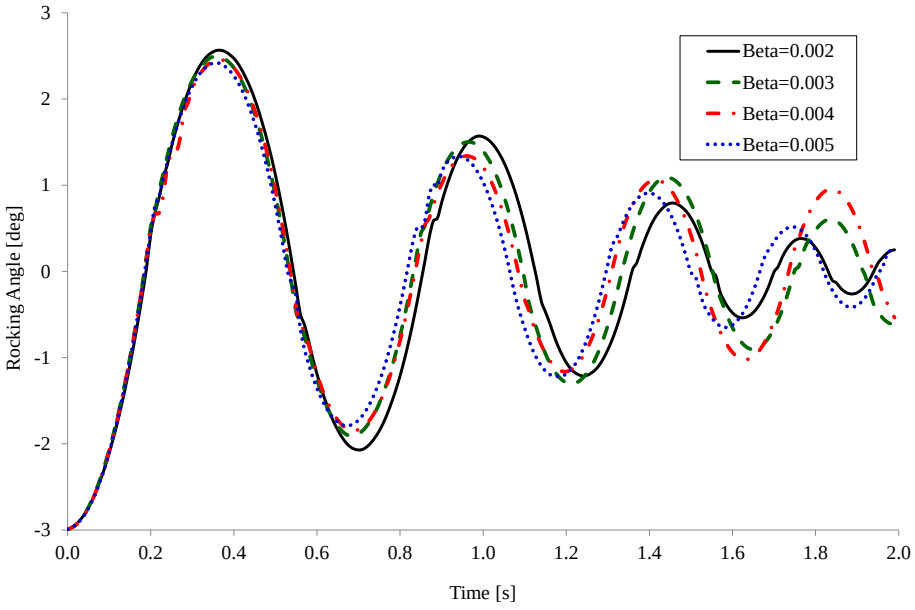


Figure 8: Effect of Rayleigh damping on computed free-rocking response of rigid block

6 APPLICABILITY OF THE FE MODEL TO SENSITIVITY STUDIES

Once the numerical model of the dynamic response of a rigid block under base excitation itself is found to be reasonably consistent with the results from experimental programs available in the literature, the FE analyses will proceed with modeling of the platform structure used

in the experimental program of this study. The results obtained in the laboratory will serve to further calibrate the numerical and finite element models and to conduct parametric studies aimed at the development of design recommendations on the portion of the live load that should be included as inertia in platform structures supporting rigid blocks. This will involve an iterative process in which an equivalent linear elastic structure, with the same lateral stiffness but with an attached rigid block of a portion of its actual mass, has an average lateral displacement that is equal to that of the actual structure supporting a sliding/rocking rigid block. It is anticipated that the proportion of the live load to be included in seismic analyses will be a function of dynamic properties of the structure, the aspect ratio of the supported rigid blocks, the maximum acceleration of the ground motion, and the friction coefficient at the interface between the rigid block and the platform. Intuition would suggest that the portion of the live load to be considered as inertia should increase with the fundamental period of the structure and also with the friction coefficient at the rigid block-platform interface.

7 CONCLUSIONS

This paper presents some of the preliminary steps taken in the development of a finite element model that can capture the sliding and rocking response of rigid blocks subjected to base excitation. For the case of a single-degree-of-freedom structure supporting sliding blocks, the FE model is found to estimate displacement demands of the platform within 2% on average of the values obtained through the numerical integration of the equation of motion of the system. For the case of free rocking, on the other hand, the FE model estimates the amplitude of the motion within 25% of the values measured in the experimental program conducted by Prieto et al.[8]. Further calibration of the model will be conducted in the near future using the results of an ongoing experimental program with a 1:15 test structure. The final FE model will serve to conduct parametric studies aimed at the development of design recommendations in regards to the portion of the live load that should be considered as inertia in structures supporting nearly permanent and heavy live loads.

REFERENCES

[1] ASCE/SEI 7-10, *Minimum design loads for buildings and other structures,* American Society of Civil Engineers, 2010.

[2] Port of Long Beach, *Wharf design criteria*, Version 3.0, 2012.

[3] American Association of State Highway Transportation Officials, *AASHTO LRFD Bridge design specifications and commentary, 6th Edition*, 2012.

[4] G. W. Housner, The behavior of inverted pendulum structures during earthquakes. *Bulletin of the Seismological Society of America*, **53**(2), 403-417, 1963.

[5] C.S. Yim, A. K. Chopra, J. Penzien, Rocking response of rigid blocks to earthquakes. *Earthquake Engineering & Structural Dynamics*, **8**, 565–587, 1980.

[6] H. W Shenton, N. P. Jones, Base excitation of rigid bodies. I: Formulation. *ASCE Journal of Engineering Mechanics*, **117**(10), 2286-2306, 1991.

[7] H. W Shenton, Criteria for initiation of slide, rock, and slide-rock rigid-body modes. *ASCE Journal of Engineering Mechanics*, **122**, 690-693, 1996.

[8] F. Peña, F. Prieto, P. B. Lourenço, A. Campos Costa, A., J. V. Lemos, On the dynamics of rocking motion of single rigid-block structures. *Earthquake Engineering & Structural Dynamics*, **36**, 2383–2399, 2007.

[9] ANSYS Mechanical APDL Element Reference, ANSYS Release 13.0, ANSYS Inc., 2010.

[10] ANSYS Contact Technology Guide, ANSYS Release 12.0, ANSYS Inc., 2009.

[11] ANSYS Mechanical APDL and Mechanical Applications Theory Reference, ANSYS Release 13.0, ANSYS Inc., 2010.

[12] E. L. Wilson, *Static and dynamic analysis of structures, 4th Edition*. Computers and Structures Inc., 2004.

COMPDYN 2013
4th ECCOMAS Thematic Conference on
Computational Methods in Structural Dynamics and Earthquake Engineering
M. Papadrakakis, V. Papadopoulos, V. Plevris (eds.)
Kos Island, Greece, 12–14 June 2013

NUMERICAL MODELLING OF PILES GROUP UNDER SEISMIC LOADING IN COHESIVE SOILS: INCLINATION EFFECT

F. Hage Chehade[1], M. Sadek[2], and D. Bachir[3]

[1] Lebanese University, IUT Saida, Modeling Center, Doctoral School of Science and Technology, Beirut, Lebanon

e-mail: fchehade@ul.edu.lb

[2] Laboratoire de Génie Civil et de Géo-Environnement, Université Lille I Sciences et Technologies, France

marwan.sadek@polytech'lille.fr

[3] Lebanese University, Modeling Center, Doctoral School of Science and Technology, Beirut, Lebanon

douaa_bachir@hotmail.com

Keywords: cohesive soil, inclination, interaction, modelling, non linear, piles group.

Abstract. *The system piles-foundation is widely used to ensure the stability of structures when subjected to seismic excitation. The analysis of the seismic response of soil-pile-structure systems constitutes a complex problem in earthquake engineering. Previous studies showed that the damage of piles in seismic area is mainly attributed to the kinematic interaction between piles and soils or (and) to the inertial interaction between the superstructure and the pile foundation which may cause foundation damages. In this paper we present a global numerical modeling of the pile-foundation-pile-cap-structure interaction using FLAC3D Software. The study is conducted by using measures recorded during real earthquakes. The influence of plasticity is investigated for cohesive soils where the soil behaviour is described using Mohr–Coulomb criterion. Moreover, the efficiency of inclined piles in seismic zones is commented, and a parametric study according to piles inclination is also performed. The analysis of the results could give the best piles group configuration in order to minimize the seismic effect on the structures.*

1 INTRODUCTION

Lebanon, which is of special topography of high and steep slopes, is exposed to a high seismic risk because it is crossed by one major and few secondary faults where someone have been discovered recently [1]. Due to demographical and social factors, new constructions in Lebanon are being settled in precarious sites which are often vulnerable to natural disasters. In order to minimize the effect of earthquakes on structures, there is a must of enhancing the foundations of old or new constructions in vulnerable areas.

In the past, several destructive earthquakes have been occurred in Lebanon (years 551, 1202, 1759, 1837 and 1956). Moreover, many earthquakes, of low magnitudes between three and five, have been registered in Lebanon during 2008. These events have increased the anxiety of Lebanese people because of the poor quality of the constructions and their behavior under moderate or severe earthquake events.

The system piles-foundation constitutes an appropriate way and it is commonly used to ensure the stability of constructions when subjected to seismic excitation. However, the analysis of the seismic response of soil-pile-structure systems is a complex problem in earthquake engineering. The phenomenon of soil-pile-interaction structure is complex as it involves many interactions such soil-pile, pile-pile, pile-cap and the whole soil-pile-cap-structure system. Due to the importance of this problem, several studies were conducted including experimental, analytical and numerical attempts to highlight the behavior of such interactions under seismic loading.

In addition to post-earthquake investigations, analytical and numerical analyses show that the damage of piles in seismic area is mainly attributed to the kinematic interaction between piles and soils and/or to the inertial interaction between the superstructure and the pile foundation which may lead to foundation damages, particularly at the pile-cap connection.

Full 3D nonlinear analyses including the soil, piles and the superstructure are still limited. Such studies ([2], [3], [4], [5] and [6]) were conducted in the linear domain to analyze the influence of micropiles inclination and boundaries conditions on the seismic behaviour of the soil-micropile structure system. In the other way, a full 3D finite element analysis was performed to investigate the seismic performance of inclined piles assuming a linear behaviour of the soil and the structure [7].

This paper includes a full 3D coupled modeling of the soil-pile-superstructure interaction under seismic loading considering the elastoplastic behaviour of the soil material. Analysis is performed using the FLAC3D (Itasca, 2005) program under real earthquake records (Kocaeli, 1999). The influence of plasticity is investigated for coherent soil where the soil behaviour is described using the simple and popular non-associated Mohr–Coulomb criterion largely used in engineering practice. The last part discusses the efficiency of inclined piles in seismic zones. Using inclined piles in seismic zones is generally not recommended by international codes, especially when piles are anchored in hard substrata. However, the analysis of the Loma Prieta earthquake ([8], [9] and [10]) showed that structures based on inclined piles were less affected or damaged than other structures.

2 NUMERICAL STUDY OF SOIL-PILE-STRUCTURE SYSTEM

A three-dimensional numerical modeling by finite differences using the software FLAC3D is used in this study to model the soil-pile-structure interaction problem. This part presents and discusses the details of the numerical modeling. We provide a better understanding of the interaction pile-soil-pile-cap-structure by adopting two types of seismic loading. The first type is harmonic and the second uses real recordings of the earthquake occurred in Turkey (Kocaeli, 1999).

For a given configuration of piles, the study was done in the case of coherent soil. The effect of soil behaviour on the system response was investigated by adopting respectively a linear and nonlinear behavior using the type elasto-plastic Mohr-Coulomb. Boundary condition used to simulate the infinite medium that surrounds the soil-pile models is discussed next.

2.1 Modeling description

Figure 1 shows a schematic representation of the numerical model, which contains a group of four piles of 1m of diameter and 10m of length, located in a 15m of a homogeneous soil. Piles are fixed in a cap of 1m thick with no contact with the ground, and supported a superstructure of column height H_{st} = 1m and a concentrated mass m_{st} = 100 tons placed on the top of the column and modeled by a single degree of freedom system. The spacing between piles is $S=3.75D_p$, where D_p is the diameter of the pile. The behaviour of the soil-pile-structure system is assumed to be elastic with Rayleigh damping. The fundamental frequency of the soil layer is equal to f_1 = 0.67 Hz. The rigidity (K_{st}) and the frequency of the superstructure (f_{st}), assumed fixed at its base, are calculated using the following expression:

$$K_{st} = \frac{3(E_{st} I_{st})}{H_{st}^3} \tag{1}$$

$$f_{st} = \frac{1}{2\pi}\sqrt{\frac{K_{st}}{m_{st}}} \tag{2}$$

Using equations (1) and (2), K_{st} = 86400 KN/m and f_{st} = 1.48 Hz.

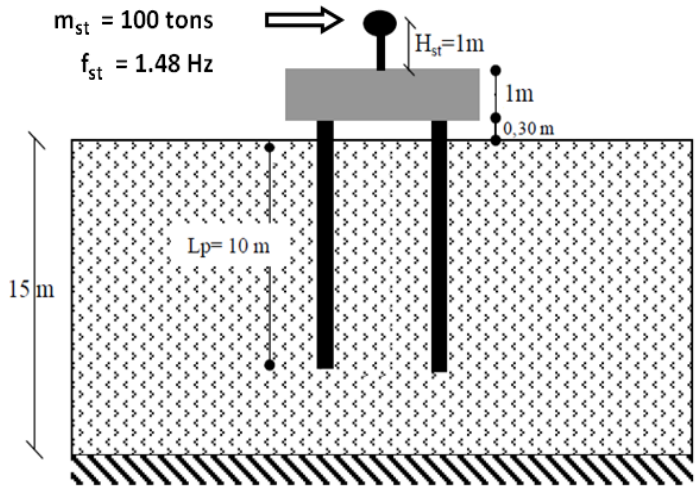


Figure 1: Modeling presentation.

2.2 Modeling mesh and boundary conditions

Figure 2 represent the mesh of the numerical model. Meshing was refined around piles and the area near the superstructure where the inertial forces induce high stresses. The basis of soil is assumed rigid. Transmitting boundary conditions are used to reduce wave reflections at model boundaries which are placed far enough from the structure with the use of finite elements and absorbing boundaries called "free field". The soil columns in the boundaries can be made to respond to the input motion, or for computational efficiency, free field displacements with time, computed separately, can be given as boundary conditions for the soil column nodes.

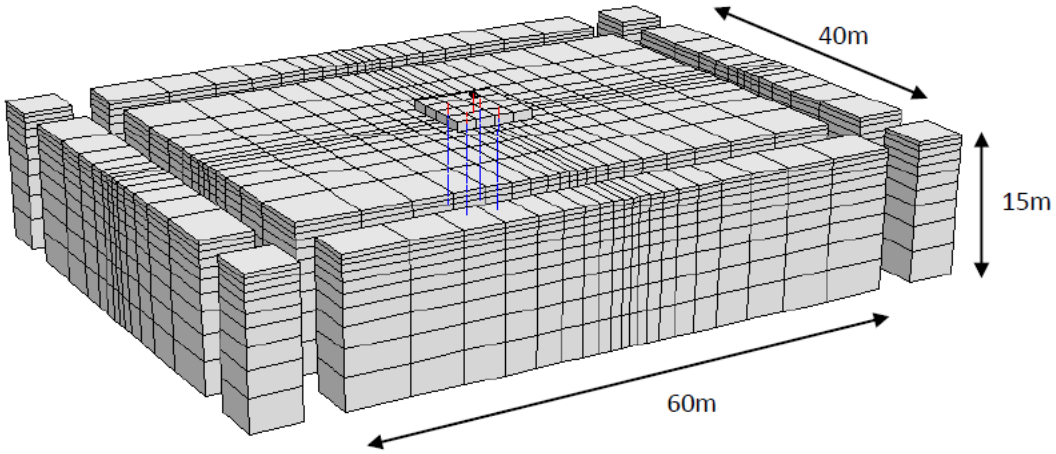


Figure 2: Modeling mesh and boundaries.

2.3 Mechanical properties of soil-pile-structure system

The soil and pile were modeled with elastic material with the properties given in Table 1. Rayleigh's damping was also incorporated in this study with 5% critical damping. The base was fixed while lateral boundaries were set as described in section 2.2.

Material	Density ρ (Kg/m^3)	Young's modulus E (MPa)	Poisson's ratio υ	Damping ratio ξ	Axial rigidity (MN)	Flexural rigidity ($MN.m^2$)
Soil	1700	8	0.45	5%		
Pile	2500	24000	0.30	2%	$E_p*A_p = 18850$	$E_p*I_p = 1178$
Structure	2500	24000	0.30	2%		

Table 1: Mechanical properties of soil-pile-structure system.

2.4 Seismic loading

In a seismic analysis, seismic load can be applied either as a displacement, acceleration, or velocity time history at the base of the model. In this paper, we provide a better understanding of the interaction pile-soil-pile-cap-structure by adopting two types of seismic loading. The first type is harmonic and the second uses real recordings of the earthquake occurred in Turkey (Kocaeli, 1999).

Initially, numerical simulations were performed with a harmonic load of 10 cycles, with a frequency equal to the fundamental frequency of the soil (floading = $f_{1,sol}$ = 0.67 Hz), and an acceleration amplitude of 0.2g (V_g = 0.46 m/s).

The real seismic loading chosen is registered in Kocaeli in Turkey 1999 (Station Ambarli; KOERI source). This loading is applied as a speed at the base of the soil mass. It marks a maximum speed of 40 cm/s and a maximum acceleration of 0.247g see Figure 3. It is found that the frequencies involved are lower than 3 Hz with a maximum peak corresponding to f=0.9 Hz, which is between the fundamental frequency of soil (f_1 = 0.67 Hz) and that of the structure (f_{st} = 1.48 Hz).

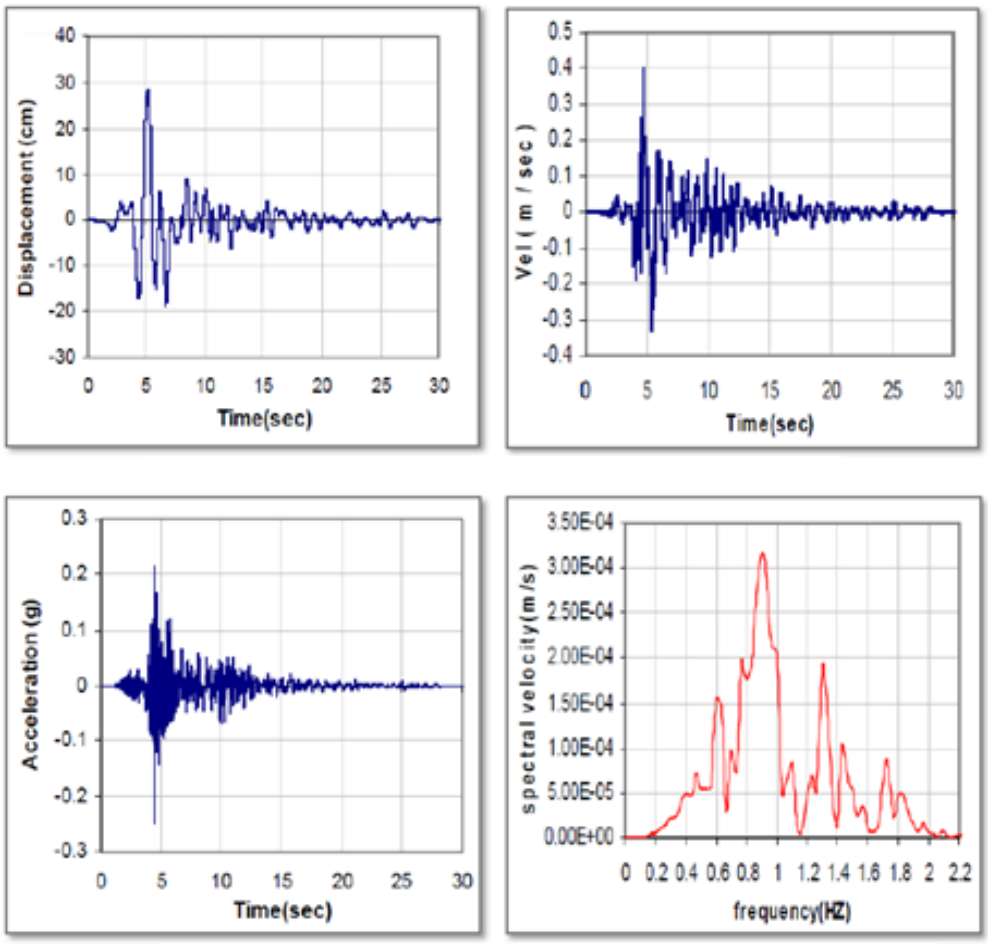


Figure 3: Real seismic loading -Turkey, Kocaeli.

3 DYNAMIC FORCES IN PILES

Figure 4 and table 2 shows the forces induced in the piles due to the real seismic loading of Kocaeli, of frequency f = 0.9 Hz. These forces are compared with forces induced in piles due to the harmonic load of frequency f = 0.67 Hz. Figure 4 shows a significant influence of the dominant frequency loading that can lead to significant efforts values exceeding the bearing capacity of piles and especially when this frequency equals to the natural frequency of the soil.

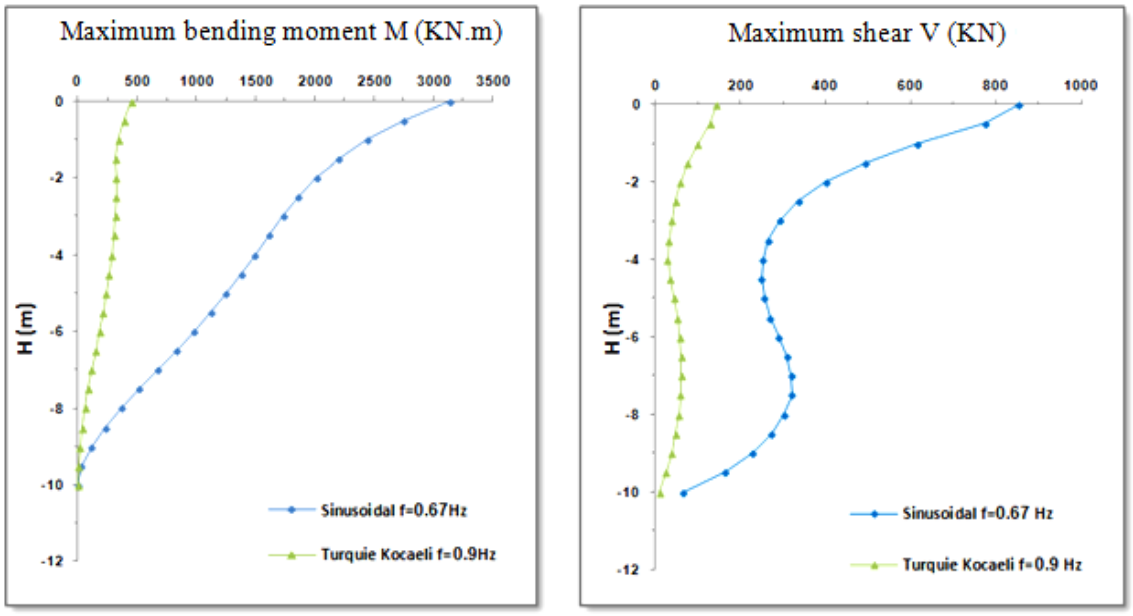


Figure 4: Maximum dynamic forces in piles.

Loading	Acc mass (m/s^2)	Acc cap (m/s^2)	Max shear force V (KN)	Max bending moment M (KN.m)
Sinusoidal	34.71	33.1	854.8	3137
Turkey, Koacaeli	7.36	5.4	145	453.8

Table 2: Response of piles for different types of loading.

4 SOIL PLASTICITY

Since the aim of this study is to understand the effect of nonlinearity on the behaviour of the soil-pile-structure system, in particular, the influence of soil plasticity on the system response, nonlinear soil models were used in the 3D finite element analyses. Numerical simulations are performed using real seismic loading (Turkey, Kocaeli 1999). The influence of plasticity is investigated for coherent soil where the soil behaviour is described using an elastic-perfectly plastic Mohr–Coulomb criterion.

4.1 Plastic calculation

The effect of plasticity for coherent soil on the seismic behaviour of the soil-pile-structure system is verified by a parametric study. To study the effect of plasticity cohesive soils on the seismic response of piles, calculations were performed with several values of cohesion (C = 20, C = 50, C = 100 kPa). The characteristics of the soil layer are given in Table 3. A slight Rayleigh damping is used for the soil to avoid the pseudo-resonance in small shear deformation. System behavior cap-structure is assumed to be elastic. The mesh is identical to that shown before.

ρ_s (Kg/m^3)	E_{0s} (MPa)	υ_s	K_0	ξ_s (%)	C (KPa)	ϕ (°)	ψ(°)
1700	8	0.3	0.5	5	2-50-100	0	0

Table 3: Mechanical properties of coherent soil.

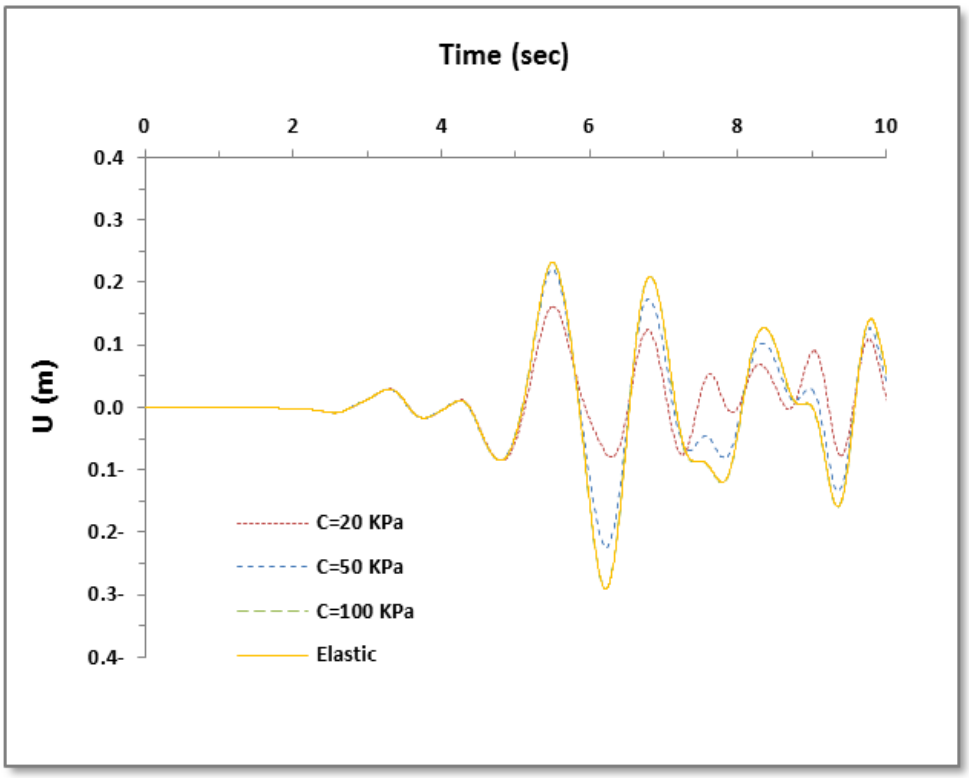


Figure 5: Amplification of the lateral displacement at the top of Superstructure in function of soil cohesion (Kocaeli, Turkey, Vg = 40 cm /s, f_{ch} = 0.9 Hz, A_g = 0.247g)

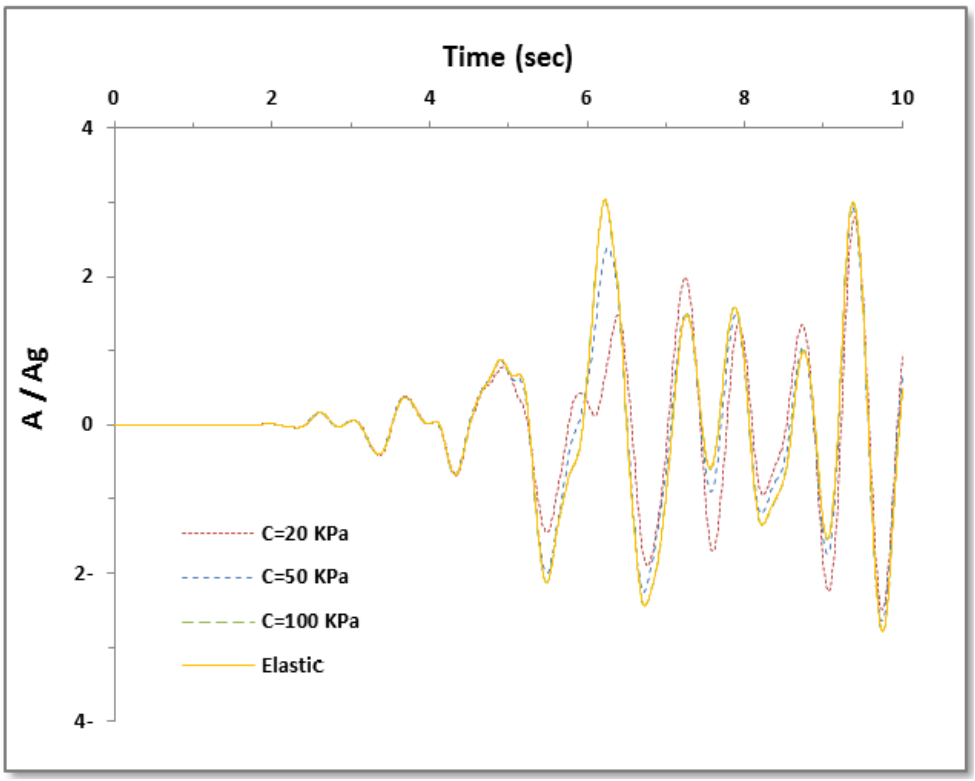
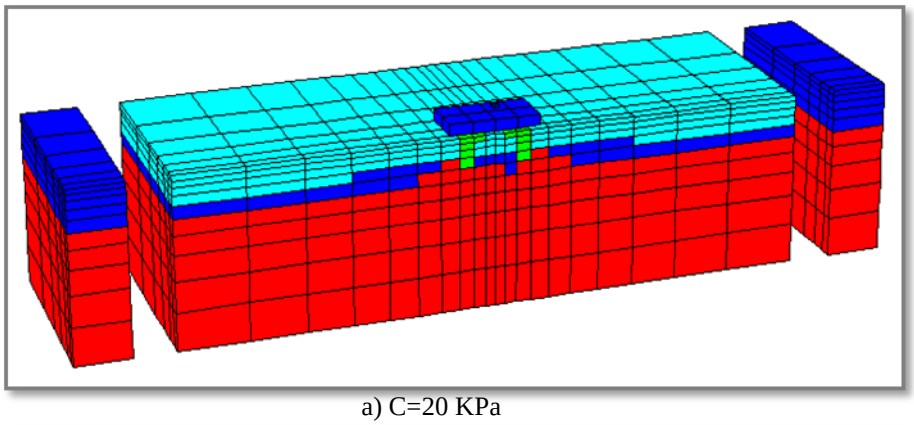


Figure 6: Amplification of the lateral acceleration at the top of Superstructure in function of soil cohesion (Registration of Turkey, Vg = 40 cm /s, f_{ch} = 0.9 Hz, A_g = 0.247g)

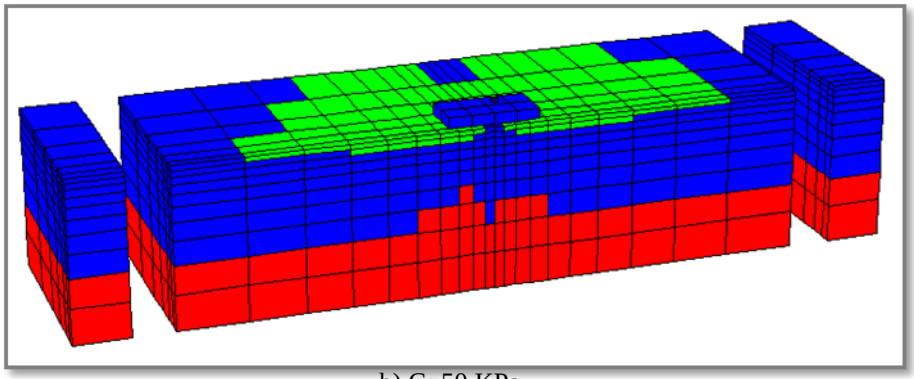
The Figures 5 and 6 illustrate a comparison between the elastic response and elasto-plastic. We observe that the two responses are identical at the beginning of loading until a time equal to 2.5 s. Beyond this time, the soil begins to plasticize and the two responses diverge in particular in the case of cohesion C = 20 kPa. The elasto-plastic response becomes weakened due to the damping induced by the plasticity of soil.

4.2 Extension of plasticity

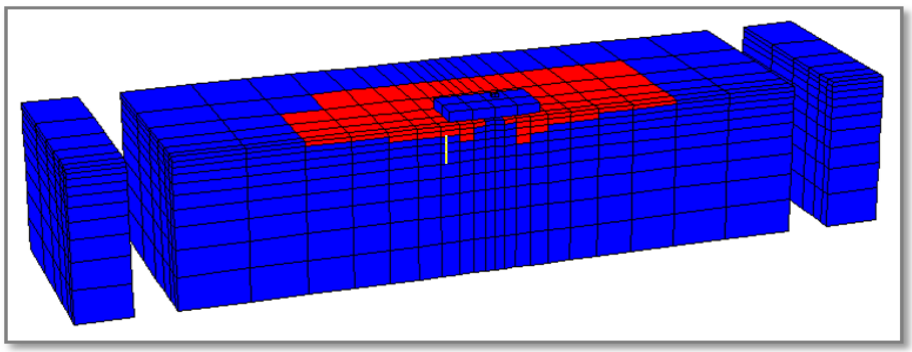
The extension of plasticity under seismic loading for the three values of cohesion is shown in Figure 7. The soil behavior is usually elastic with cohesion of 100 kPa (Figure 7-c). Decreasing cohesion, the plasticity spreads from the base and extends near the surface, (Figure 7-a). Note that, for a coherent soil, the plasticity criterion is exceeded at the base of the soil, which leads to a high energy dissipation and transmission of waves on the surface.



a) C=20 KPa



b) C=50 KPa



c) C=100 KPa

Figure 7: Extension of plasticity (C=20 KPa, C=50 KPa and C=100 KPa).

4.3 Comparison of Numerical Results in Elastic Zone and Elasto-plastic One

Figure 8 shows the internal stresses induced in piles. The variation of the maximum shear force at the top is related to the change of acceleration. For the bending moment, the results at the top are not significantly affected by the change of the angle of dilatancy. The results are illustrated in Table 4.

C (KPa)	Acc mass (m/s^2)	Acc cap (m/s^2)	Max shear force V (KN)	Max bending moment M (KN.m)
Elastic	7.360	5.777	145	453.8
20	6.783	3.232	144.1	292.3
50	7.113	4.574	156.5	421.2
100	7.322	5.6	168.9	455

Table 4: Influence of coherent soil plasticity on the dynamic forces in the piles.

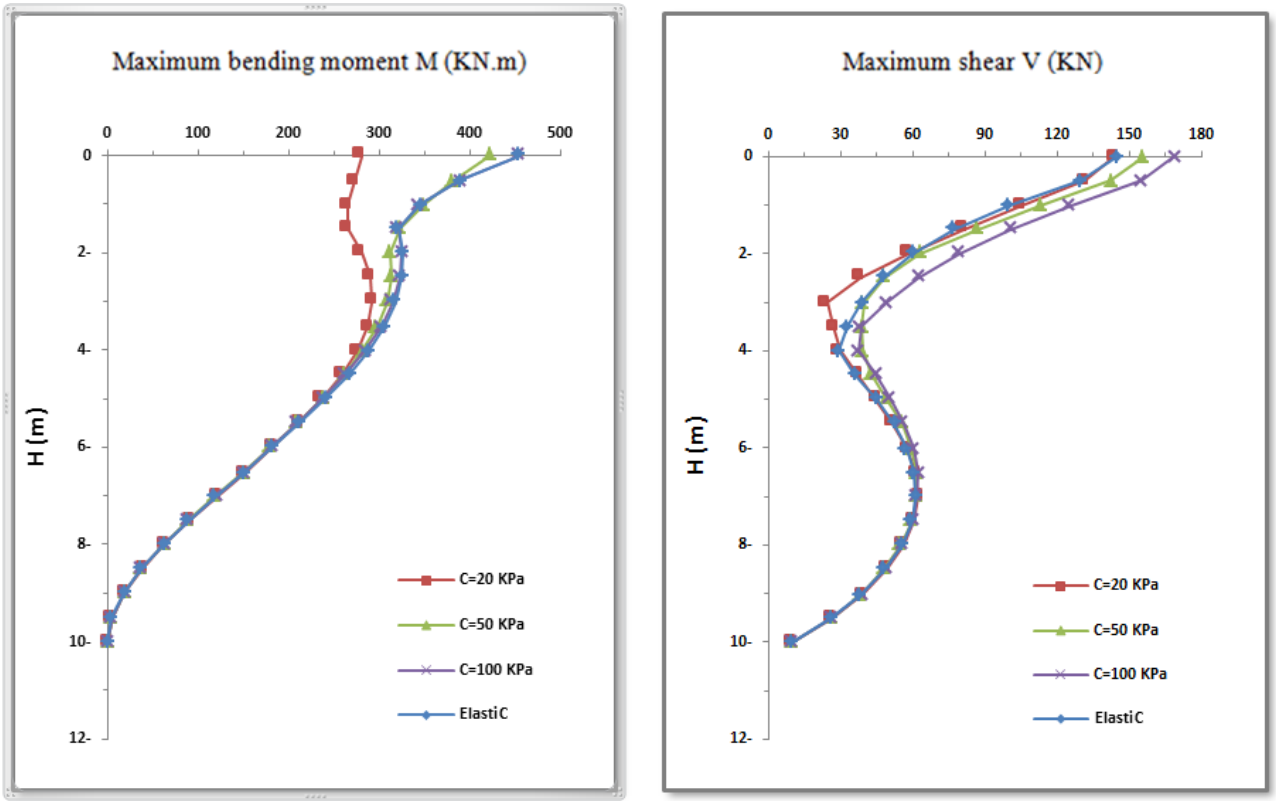
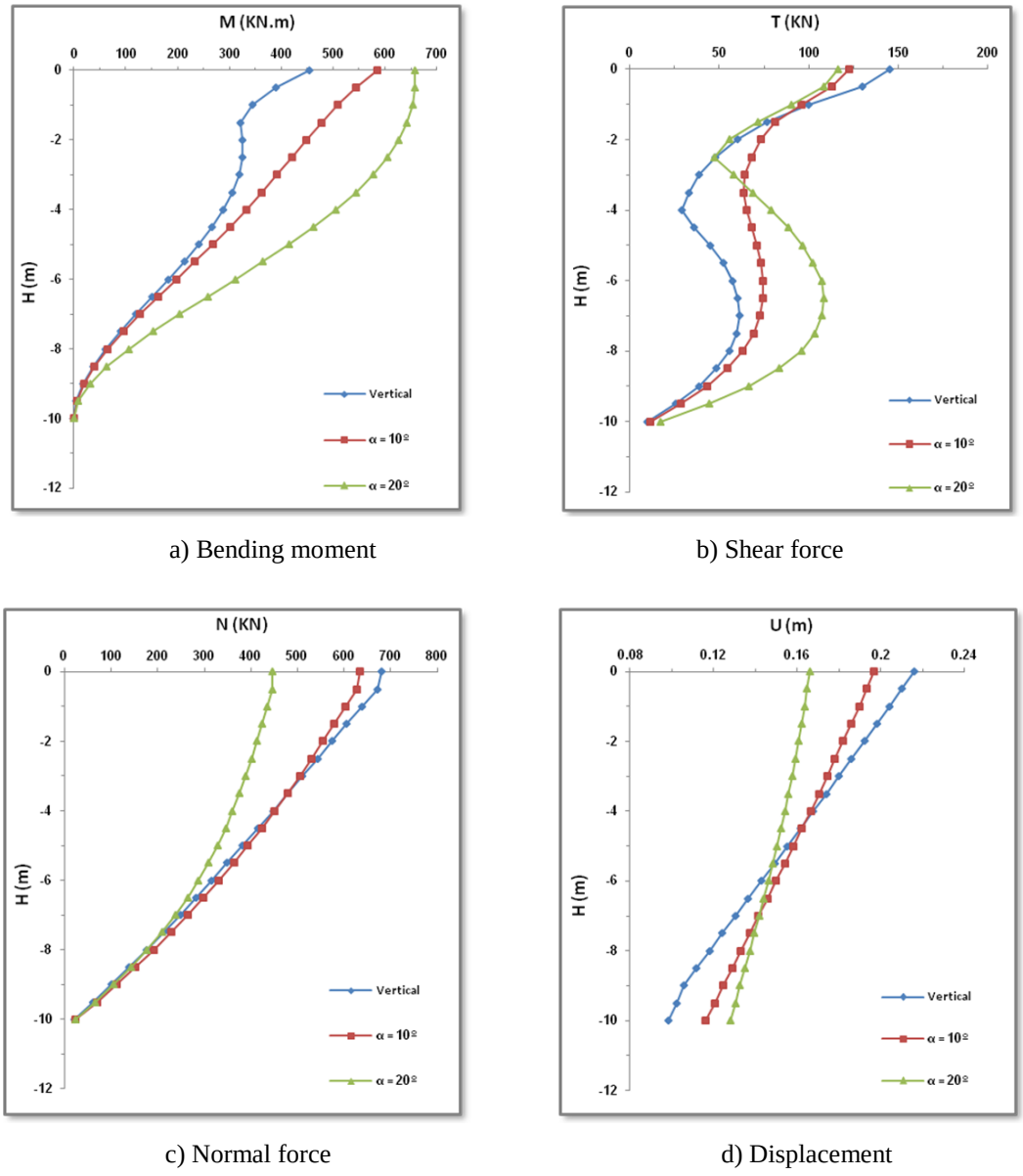


Figure 8: Influence of coherent soil plasticity on the dynamic forces in the piles (Kocaeli earthquake, Turkey 1999).

5 EFFECT OF INCLINATION

The model studied in this part is exactly the same presented above, except that the four piles are inclined outwardly by two angles $\alpha = 10^{o}$ and $\alpha = 20^{o}$. To properly analyze the influence of pile inclination on their seismic response, results of calculations are presented for the two values of inclination. For convenience, the normal force and the shear force are normalized by the maximum inertial force induced at the top of the superstructure. Meanwhile, the

bending moment is normalized by the maximum overturning moment induced by the inertial force at the base of the superstructure. The results are summarized in Fig. 9 and Table 5.



a) Bending moment

b) Shear force

c) Normal force

d) Displacement

Figure 9: Influence of inclination of piles on the seismic response of pile groups (Registration of Turkey, V_g = 40 cm/s, f = 0.9 Hz, A_g = 0.247g)

	α = 0º	α = 10º	α = 20º
Amplification at the head of cap	5.40	5.217	3.445
Amplification at the head of structure	7.36	6.526	3.580
Maximum bending moment M (KN.m)	453.8	584.6	657.6
Maximum shear force T (KN)	145	122.8	116.5
Maximum axial force N (KN)	681.1	633.4	446.8

Table 5: Influence of inclination on the seismic response of pile groups.

6 CONCLUSIONS

- The response of piles used as foundation elements is governed primarily by the inertial interaction which depends on the mass and frequency of the superstructure. The forces induced by this interaction are concentrated at the top of piles.
- The inertial forces of the superstructure induce significant efforts in the pile and contribute significantly to the damage of structures and their foundations under seismic forces. The forces induced by the inertial interaction depend substantially of the fundamental frequency of the superstructure and the soil, in comparison with the frequency of the load.
- For a cohesive soil, plasticity propagates from the base and extends to the surface. This leads to a high plasticity energy dissipation and transmission of waves on the surface. Contact with soil-pile head is assigned to a low value of cohesion. Taking into account that the plasticity reduces internal stresses in the piles.
- The inclination of piles leads to a reduction of the lateral amplification of the superstructure resulting from an increase in the rigidity of the system.
- The inclination of piles may be beneficial for the dynamic behavior of the superstructure. It depends on the interaction of the frequency of the load with the frequency of the soil-pile-structure.

REFERENCES

[1] C. Huijer, M. Harajli and S. Sadek, Upgrading the Seismic Hazard Of Lebanon In Light Of The Recent Discovery Of The Offshore Thrust Fault System. Lebanese Science Journal, Vol. **12**, No. 2, 2011.

[2] R. W. Boulanger, C. J. Curras, D. W. Wilson, A. A. Abghari, Seismic Soil-Pile-Structure Interaction Experiments and Analyses. Journal of Geotechnical and Geoenvironmental Eng., Vol 125, No. 9, 750-759, 1999.

[3] M. Sadek and I. Shahrour, Three Dimensional Finite Element Analysis of The Seismic Behaviour of Inclined Micropiles, Soil *Dynamics & Earthquake Engineering*, Elsevier, Vol. 24, pp 473-485, 2004.

[4] Y. Chung, Etude Numérique de l'interaction Sol-Pieu-Structure sous Chargement Sismique, Thèse de Doctorat, Université de Sciences et Technologie de Lille, 2000.

[5] N. Gerolymos, A. Giannakou, I. Anastasopoulos and G. Gazetas, Evidence of Beneficial Role of Inclined Piles: Observations And Summary of Numerical Analyses, Bulletin of Earthquake Engineering, **6(4):**705-722, 2008

[6] N. Gerolymos, S. Escoffier, G. Gazetas and J. Garnier, Numerical Modeling of Centrifuge Cyclic Lateral Pile Load experiments, *Earthquake Engineering and Engineering Vibration*, **Volume 8**: Issue 1, pp.61-76, 2009.

[7] J. P. Bardet, I. M. Idriss, O'Rourke, N. Adachi, M. Hamada, and K. Ishihara, North America-Japan Workshop on the Geotechnical Aspects of the Kobe, Loma 138 Prieta, and Northridge Earthquake, Report No. 98-36 to National Science Foundation,Air Force Office of Scientific Research, and Japanese Geotechnical Society. Osaka,Japan,1996.

[8] K. Tokimatsu, H. Arai and Y. Asaka, Deep Shear Structure and Earthquake Ground Motion. Characteristics in Sumiyoshi Area, Kobe City, Based on Microtremor Measurements, *J. Struct. Constr. Eng., AIJ*,491, 37-45, 1997

[9] G. Mylonakis, A. Nikolaou And G. Gazetas, Soil–Pile–Bridge Seismic Interaction: Kinematic and Inertial Effects. Part I: Soft Soil, *Earthquake Engineering & Structural Dynamics*, **26(3)**:337 - 359, 1998.

COMPDYN 2013
4th ECCOMAS Thematic Conference on
Computational Methods in Structural Dynamics and Earthquake Engineering
M. Papadrakakis, V. Papadopoulos, V. Plevris (eds.)
Kos Island, Greece, 12–14 June 2013

AN ANALYTICAL APPROACH FOR ASSESSMENT OF THE EFFECTS OF INFILL PANELS IN RC FRAMES

Siro Casolo[1], Francesco Porco[2], Giuseppina Uva[2]

[1] Dep. ABC, Politecnico di Milano
P.zza L. Da Vinci, 32, 20133, Milano (Italy)
siro.casolo@polimi.it

[2] DICATECh, Politecnico di Bari
address via Orabona, 4 - 70126 Bari (Italy)
f.porco@poliba.it, g.uva@poliba.it

Keywords: Existing Building, Seismic Assessment, Reinforced Concrete, Infilled Frame, Equivalent Strut, Meso-scale, RBSM model.

Abstract. *The use of macro-modeling approaches based on the concept of the equivalent strut for simulating infill panels presents a number of critical aspects, mainly related to the variability of the results from the parameters adopted (for example: width of the strut, non-linear constitutive law under cyclic actions, assignment of strut mechanical properties in multiple strut models). It should also be observed that it is particularly difficult to identify and calibrate the above mentioned quantities, even if the mechanical parameters of the masonry components (mortar and bricks) are known. It is thence highly desirable to define numerical procedures for aimed at this task, in order to reduce the variability of results due to the characteristics of the equivalent strut. In the present paper, the first results of a procedure aimed at the calibration of the macro-models of infill panels are presented. The adopted methodology directly considers the heterogeneity of materials and the texture effects at the micro-scale, exploiting a "Rigid Body and Spring Model"(RSBM), in which the masonry panel is described as a set of unitary cells constituted by rigid blocks and elasto-plastic springs. The non-linear cyclic law of the equivalent strut is then obtained by a simple numerical identification procedure. The approach has been validated on the basis of some reference experimental tests available in the technical literature, by comparing the experimental results and those obtained respectively by RBSM model and the strut model previously calibrated with the proposed procedure.*

1 INTRODUCTION

In RC framed buildings, infill panels are usually made by hollow masonry brickwork built within the frame mesh in contact with the surrounding structural RC elements (beams and columns), but without any reliable connecting device. For these reasons, in the common practice and technical standards [1,2], the infilled panels are considered as non-structural elements. It is commonly – but incorrectly – believed that neglecting the stiffness and strength contribution provided by infill walls is a conservative assumption, with regard to the structural safety. The observation of the damages caused by recent earthquakes on existing RC buildings has pointed out that the presence of infill panels modifies the behaviour of the frame under seismic loads. Furthermore, the effects induced can be very variable depending on the distribution of the infill panels and the interaction between panels and RC frames [3]. In some cases these aspects play a crucial role in the seismic assessment, and can void the complex procedures for the evaluation of the mechanical strength of the materials [4].

Actually, the increasing awareness of the crucial role played by infill is orienting the current research threads towards studies aimed at incorporating this aspect into the seismic vulnerability assessment of existing structures. In this sense, existing procedures like the N2 Method for the pushover analysis have been recently extended in order to account for the infill contribution [5].

Over the past years, the variability exhibited by the behaviour of infilled frames (in particular for buildings designed under vertical loads only) has strongly stimulated researchers to investigate the interaction between masonry panels and RC by means of experimental tests [6,7]. The results of these research studies have pointed out a great dispersion of the parameters which characterize the seismic response of the infilled frames. The main source of the scattering in the numerical results is, indeed, the high variability of the significant model parameters. Among these, the mechanical characteristics of the constituent materials (mortar and bricks) and of the overall masonry panel (intended as a continuous material) are crucial. But another fundamental aspect is represented by the model adopted for simulating the infills within the computational model of the building. In this context, there are several approaches, in the literature. The approaches based on the macro-modeling of the panel are surely the most popular. The composite panel is replaced by an equivalent beam element reacting only to compressive axial loads (strut), in which the material is an homogeneous continuum. The advantage of the approach is surely represented by a great reduction of the involved parameters – and thence of the computational burden (the only variables at stake are the geometrical and mechanical parameters of the equivalent strut: width b_W, stiffness, non-linear cyclic law). On the other side, it should be observed that the advantages related to the simplicity and versatility of the model are counterbalanced by the great uncertainty about the definition of these parameters, which actually varies in a wide range, making the results very disperse [8,9]. The availability of many different models further contributes to increase the uncertainty of the results: several numerical relationships have been recently proposed in order to calibrate the equivalent strut by considering the effects of the failure modes (which is very difficult to predict in the preliminary design phase) and of local effects (weakness at the ends of columns) [10].

Within this framework, the present study proposes a procedure aimed at calibrating the parameters of the equivalent strut on the basis of detailed meso-scale analyses of the infilled frame performed by a rigid elements approach. The basic idea is to define an automatic procedure in which, once the geometrical and mechanical parameters of the infilled frame are given as input data, the non-linear cyclic law of equivalent strut is provided as the output.

The procedure, is not intended to be used as an alternative to more refined models, but as a valid tool for obtaining reliable results within the framework of the equivalent strut method. In fact, it is of simple and rapid application, and able to reduce computational burden, especially when the global behaviour of a whole building has to be assessed. In the meso-scale model, the masonry panel is described as a periodical assembly of unitary cells constituted by rigid elements and elasto-plastic springs (RBSM) [11]. In the paper, after outlining the whole procedure and its theoretical basis, some preliminary results are presented, which are useful in order to validate the fundamental steps of the whole procedure. The current format of the procedure is actually a preview of a work which is presently in progress, and will involve the implementation of further refined analyses at the meso-scale level, as well as further validations performing laboratory tests with the use of modern technologies for stress and strain measurement [12,13].

2 STATE OF ART

As previously mentioned, many difficulties arise when trying to characterize the seismic response of infilled frames. These are due in part to the variability of the different parameters that govern the overall mechanical behaviour, in part to the problems encountered in the experimental testing, and also to the difficulties associated to the numerical modeling of masonry structures. The last aspect is particularly important, and will be briefly discussed in the following paragraph, with the aim of providing an overview of the available analytical models and modeling techniques. Two large categories are identified: finite element models (micro-modeling) and simplified or phenomenological models (macro-modeling).

2.1 Micro-modeling

Micro-models are aimed at simulating the non-linear nature of the masonry panel, taking into account the behavior of the individual constituents: brick and mortar. The analysis becomes quite complex, as a result of the kinematic induced by horizontal joints, that represent the weak point of the panel [14].

These approaches can be further subdivided into four categories, depending on the level of sophistication of the model adopted for the masonry components and, most of all, for the contact surfaces between the elements of the panel and between them and the structures of the boundary frame. The first group includes coarser methods, in which masonry is considered as a homogeneous material, and the effects induced by the presence of mortar joints are accounted at a global level, by introducing proper parameters. They are usefully applied to appraise the global structural behaviour without entering into the detail of the local tensional response of individual panels. The mechanical properties of the masonry are defined by a stress-strain law and a failure criterion (Von Mises, Drucker-Prager) is specifically assigned to the material [15]. The second group includes models in which masonry is considered as a two phase material, and both brick and mortar joints are modeled with continuous elements [16]. The contact surfaces between the elements are represented by a bed of springs (interface elements) in order to account for local debonding, sliding or detachment. This kind of models involve a large number of finite elements and parameters and thence require a heavy computational effort, which limits the applications to the analysis of small panels. The models belonging to the third group are in the mid between the previous ones, since they model the blocks with continuous elements and the mortar joints with springs, in which both the of elasto-plastic deformation of the mortar and the block-interface interaction is incorporated. The reference model, proposed by Page, provided only an elastic behaviour for the blocks [17].

Finally, the last group includes numerical models created as an extension of Page model. The distinguishing feature is the possibility of considering the post-elastic behavior of the blocks up to failure [18]. Actually, these approaches are not able to precisely identify the collapse mode, but allow to determine the failure condition thanks to the accurate reproduction of the stress (and hence the stiffness) associated to the generic node of the mesh. However, these methods often involve problems related to a strong mesh sensitivity, since many authors use triangular shape mesh. In this sense, Liaw and Kwan [19] have used three different types of element for studying the behavior of the infilled frame subject to monotonic loads. In particular, they used a one-dimensional element able to simulate the creep and debonding for the frame-infill contact surface, triangular planes elements (2 DoF nodes) for the panel, and a brittle material with an ideally linear elastic behaviour under tension. The distinguishing feature of the model is to consider an isotropic material before cracking, and an anisotropic material after cracking.

It should be noted that all the described models are characterized by a relevant computational burden, as the consequence of the micro-scale modeling of the mechanical behavior of heterogeneous materials (i.e., masonry infills). In continuous approaches, the effects due to the heterogeneity of the constituent materials is considered by means of homogenization procedures [20] aimed to the definition of an equivalent continuum to be used in the finite element analysis.

As an alternative to continuum models combined with homogenisation techniques, it is possible to adopt discrete models [21]. In the present work, indeed, this class of approaches is adopted, according to which the masonry panel (which is a heterogeneous periodic body) is macroscopically described as a "mechanism" composed by "periodic cells" connected by springs (RSBM, [11,22]).

Through this approach, it is possible to model the masonry panels at the "macro-scale" through a kinematic that take into account, in a simplified manner, also of the specific effects of masonry texture. These approach has have been fruitfully applied, in the last few years, for modeling the behaviour of masonry structures both in-plane and out-of-plane [23,24,25,26], allowing to perform the vulnerability assessment for whole masonry buildings [27,28,29,30].

2.2 Macro-modeling

In macro-modeling approaches, the simulation of the frame-infill interaction is based on the solution of simplified mechanical problems. Among them, it is worth mentioning the "equivalent strut" method [31,32]. It is based on the experimental observation that under horizontal actions, is the compressive stress substantially follows the diagonal path, and thence adopts one or more equivalent diagonal struts in order to simulate the infill masonry panel. This method is indeed one of the most used, thanks to easy and flexible application possibilities. On the other hand, it should be observed that the advantages related to the simplicity and versatility of the model are counterbalanced by the difficulties rising in the interpretation of the numerical results. Indeed, the most critical problem in the use of macro-models consists in the difficulty of correctly identifying the mechanical properties and the geometrical features of the equivalent diagonal struts, which haven’t a direct correspondence with the actual frame-panel system.

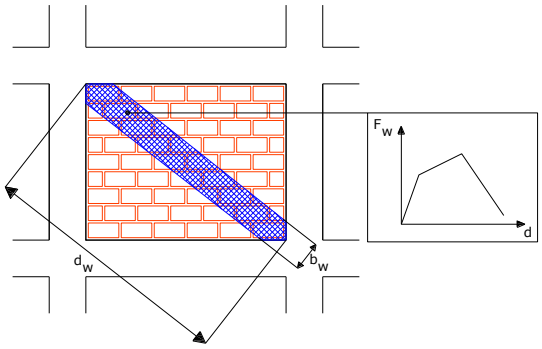


Figure 1: Modeling infilled frame using the "equivalent strut" method.

It must be underlined, however, that the opportunity of properly considering the role of infill panels in the structural seismic response, especially in the case of existing structures designed for vertical loads only [8,9] is, nowadays, widely acknowledged. Moreover the use of simplified models is a modern approach also for more complex problems [33].

The fundamental parameters of the methods are represented by the geometric features of the strut (length d_W, thickness t_W and width b_W), the stiffness λ, the hysteretic constitutive law F_W-d which governs the non linear cyclic behaviour of the panel (Figure 1).

Depending on the objectives of the analysis (whether the effect of the infills on the global behavior of the structure are to be appraised, or attention is focused on the local response of the structural elements), it could be necessary to adopt multi-strut systems to simulate the presence of the panel. This approach allows to evaluate the effects of shear induced by the panels on the ends of the reinforced concrete elements, highlight possible brittle behaviours [34]. There is an extensive literature in this field, that shows the interest of the scientific community for the topic, and but reveal also that there is a great variability of the results, depending on the formulation and application of the proposed procedures [10].

It's also important investigate the aspects relate to the hysteretic law that defines the equivalent strut response. Among the different proposals, examples can be found in which the law is expressed in terms of axial strain/stress [34], and formulations in which, regardless of the geometrical and mechanical characteristics of the infill, a predominant failure mode (which can consist in the crushing at the center or at the corners of the panel) is a-priori defined [35].

Anyway, the experimental evidence has pointed out that crushing represents only one of the possible failure modes of the infill panel. Thence, it should be first necessary to evaluate the ultimate load associated to each of the possible failure, and then to calculate the strength of the panel as the minimum of these loads [36].

Two other closely related factors that complicate the calibration of macro-models for simulating masonry infill panels are: *(i)* the large dispersion of the mechanical properties of the materials, that being intended for non structural elements, are usually scarcely qualified, *(ii)* the unreliability of the predictive methods available in this field.

The equivalent strut is a very effective and practical method but presents many drawbacks that may affect its reliability. For these reasons, this paper proposes a methodology based on a simplified analysis of the infill panels at the "meso-scale", that allows to calibrate the parameters that govern the method of the equivalent strut, in order to properly characterize the panel and reduce the differences observed with the experimental response.

3 RIGID BODY AND SPRING MODEL (RBSM)

The basic idea of the method (Figure 2) consists in describing the masonry (intended as a composite periodic material) as a mechanism composed of the unitary cells constituted by of rigid blocks and elasto-plastic springs (RBSM) [11] The elastic features of the springs are defined by means of a specific identification procedure with the objective of transferring the information about the main characteristics of the masonry texture from the "*meso-scale*" to "*macro-scale*" [37].

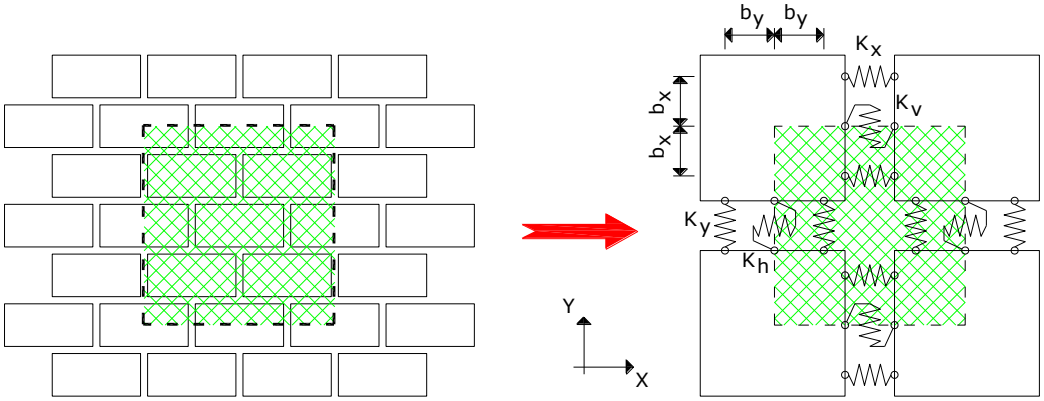


Figure 2: Scheme of a regular masonry texture and an example of the unit cell consists of four rigid blocks connected by elasto-plastic springs.

The connection between the rigid blocks occurs by means of two axial springs (indicated with K_x or K_y, depending on the direction) and a shear spring (K_h, K_v , depending on configuration) arranged along each of the common sides between the blocks at a distance equal, respectively, to b_x and b_y. The hysteretic behavior of the springs is obtained on the basis of the mechanical parameters of the constituents of the panel (mortar and blocks) and takes account of the mechanical degradation of mortar joints in the cycles of loading and unloading.

3.1 Discrete formulation of the kinematics

The masonry-like composite material is modelled as a plane solid body partitioned into m quadrilateral mass-elements Ω^i such that no vertex of one quadrilateral lies on the edge of another quadrilateral. Given a global reference frame $\{O, x, y\}$ the deformed configuration of the discrete model is described by the displacements and rotation $\{u_i\ v_i\ \psi_i\}$ of the local reference frames $\{o^i, \xi^i, \eta^i\}$ fixed in each element's barycentre o^i. These 3m variables are assembled into the vector of Lagrangian coordinates $\{u\}$ that is conjugated in virtual work with the corresponding vector of external loads $\{p\}$ (*see Figure 3*):

$$\{u\}^T = \{u_1, v_1, \psi_1, u_2, v_2, \psi_2, \dots\dots\dots, u_m, v_m, \psi_m\} \quad (1)$$

$$\{p\}^T = \{p_1, q_1, \mu_1, p_2, q_2, \mu_2, \dots\dots\dots, p_m, q_m, \mu_m\} \quad (2)$$

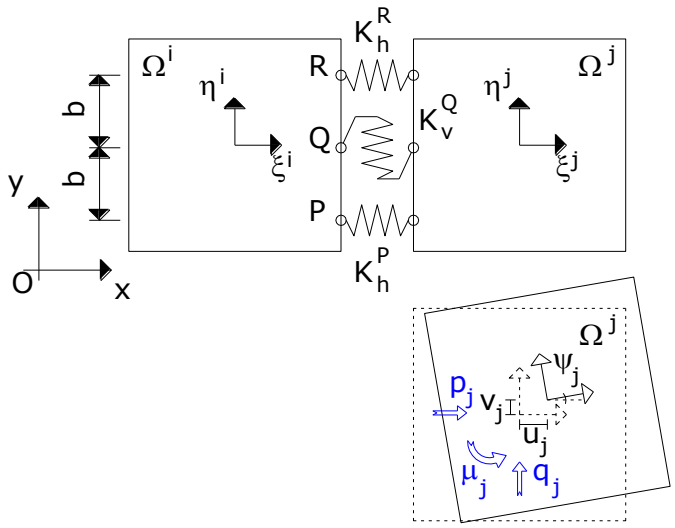


Figure 3: Kinematics of the j-th rigid body with the notation adopted [22].

The three points P, Q, and R, positioned on the sides of each rigid block, define the positions of the connection springs. These have the elastic force function of the deformation associated with the corresponding connection points. In detail, the average strain "shear" ε^Q is associated to the point Q, while the average axial deformations ε^P and ε^R are associated respectively to the points P and R. Under the assumption of small displacements, and denoting by r the number of sides of the connection between all the elements of the discrete model, the relationship between displacements and deformations can be expressed by defining the matrix *3r x 3m* $[B]$ as follows:

$$\{\varepsilon\} = [B]\{u\} \tag{3}$$

3.2 Elasto-plastic effects

A stress vector $\{\sigma\}$ is correspondingly assembled together with the diagonal matrices $[V]$ and $[D]$ which contain the reference volumes of the corresponding three-dimensional solid and the elastic stiffness of the springs:

$$\{\sigma\}^T = \{\sigma_1^P, \sigma_1^Q, \sigma_1^R, \sigma_2^P, \sigma_2^Q, \sigma_2^R, \dots\dots\dots, \sigma_r^P, \sigma_r^Q, \sigma_r^R\} \tag{4}$$

$$[V] = diag\{V_1^P, V_1^Q, V_1^R, V_2^P, V_2^Q, V_2^R, \dots\dots\dots, V_r^P, V_r^Q, V_r^R\} \tag{5}$$

$$[D] = diag\{k_1^P, k_1^Q, k_1^R, k_2^P, k_2^Q, k_2^R, \dots\dots\dots, k_r^P, k_r^Q, k_r^R\} \tag{6}$$

Consequently, given the constitutive laws of the springs, $\{\sigma\}=[D]\{\varepsilon\}$, and denoting with W_E and W_I respectively, the virtual work done by external loads and the internal virtual work done by the springs, the principle of virtual work is rewritten as follows:

$$\{\bar{u}\}^T\{p\} = W_E = W_I = \{\bar{\varepsilon}\}^T[V]\{\sigma\} = \{\bar{u}\}^T[B]^T[V][D][B]\{u\} \tag{7}$$

So for every arbitrary virtual displacement is valid the following expression:

$$\{p\} = [B]^T[V][D][B]\{u\} = [K]\{u\} \tag{8}$$

With $[K]$ generalized stiffness matrix of discrete system

3.3 Equation of motion and constitutive laws

In order to consider inertial effects, the mass of each element and the rotational inertia around its own local center of gravity are collected and assembled in the following diagonal matrix:

$$[M] = diag\{m_1, m_1, t_1, m_2, m_2, t_2, \dots \dots \dots, m_m, m_m, t_m, \} \tag{9}$$

Viscous damping is evaluated mainly on the first vibrational modes and is attributed through the definition of the damping matrix [C] assumed proportional to mass matrix. In the general case of material with non-linear constitutive law, the system of equations of motion of the discrete system, during a single time step, takes the following form [22]:

$$[M]\{\ddot{u}\} + [C]\{\dot{u}\} + \{f^*\} + [K^*]\{\Delta u\} = \{p\} \tag{10}$$

with $\{f^*\}$ the vector of generalized internal forces, and $[K^*]$ generalized tangent stiffness matrix. The system of equations of motion is integrated using the Newmark implicit method and iterating within individual steps according to the Newton-Raphson algorithm, until it reaches the desired degree of convergence. The stiffness of the springs and the distance between the connection points are assigned with the criterion to approximate the average strain energy in correspondence of the reference volume of each spring. Assigning to the shear springs different stiffnesses in horizontal and vertical direction, together with a calibration of the distances between the connections, it is possible to model the effects of some masonry texture (for example, stone blocks interlocking often present in the case of significant degradation of the masonry that significantly changes the resistance of the panel). The constitutive laws for elastic-plastic behaviour are assigned using a phenomenological approach [11], based on the results of cyclic tests available in the technical literature.

The next section illustrates the procedure for defining the characteristic points of the cyclic law F_W-d_W of the equivalent strut macro-scale level) on the basis of the afore mentioned meso-modeling of the masonry panel.

4 FROM THE MESO-SCALE TO THE MACRO-SCALE (EQUIVALENTI STRUT METHOD)

The aim of the research work is to use a meso-scale modeling to define the parameters of the equivalent strut through which infill panels are usually simulated. From an operational point of view, the sequence of operations that allow to link a meso-scale approach to a macro-modeling system can be summarized in the diagram shown in Figure 4.

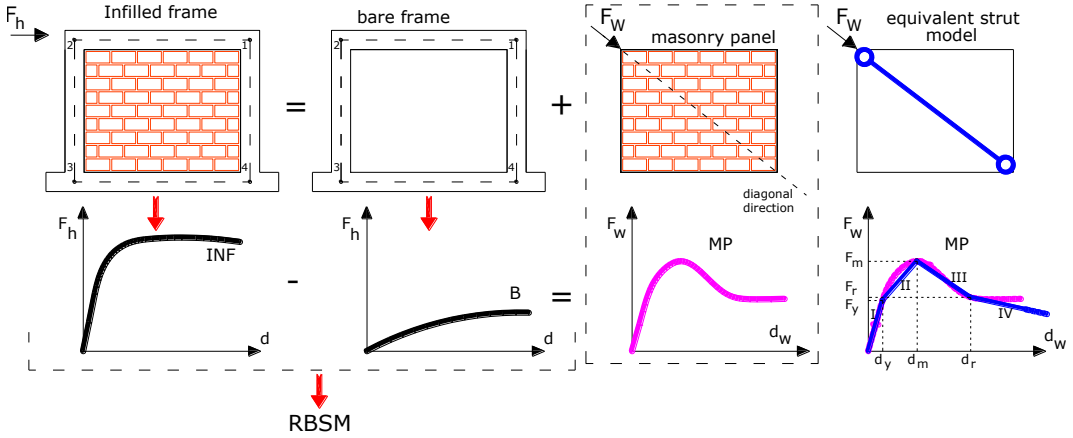


Figure 4: From meso-scale to the equivalent strut model

The procedure starts by evaluating the behaviour of the infilled frame using the RBSM approach. The parameters of blocks and springs, components of the periodic unit cell (*see Figure 2* and *§ 3*), are calibrated on mechanical parameters of bricks and mortar of the panel. The interactions between the unit cell and the elements of the frame are simulated by means of elasto-plastic springs, while the elements of the frame are modeled by means of rigid blocks having the mechanical characteristics of reinforced concrete.

A pushover analysis is then performed for the numerical model, obtaining the response curve, in which the total applied force F_h is plotted against the displacement d of the control node (which is chosen as the upper corner node). The F_h-d curve of the infilled frame (hereinafter indicated with the abbreviation INF) is intended as the "sum" of two contributions, respectively, due to the bare frame (B) and to the masonry panel (MP). The first contribution is always evaluated through RBSM approach, while the second is directly obtainable by eliminating the contribution of the bare frame (B) from the infilled frame configuration (INF).

By expressing the response of the masonry (MP) through the components directed along the diagonal of the panel, the non-linear law to be assigned to the equivalent strut F_W-d_W is defined once 3 characteristic points (in correspondence of significant stiffness variations) are identified. In detail, the associated points are, respectively: the yield strength, the maximum strength and the residual strength of the system, directly evaluated on the curve of the MP configuration.

This points single out a force-displacement law consisting of four branches: (I) initial elastic behavior of the panel, from zero up to the yield point; (II) formation of the strut in the panel (separation of infill from the frame), from yield strength point up to the maximum value; (III) force drop, due to exceeding the maximum threshold in terms of displacement. The last part (IV) corresponds to the final state of the panel after the collapse, with constant decrease of the resistance, which is necessary in order to improve the numerical stability of the analysis.

The width of the equivalent strut is evaluated assuming absence of degradation and uncracked conditions, deduced directly from the response of MP model. Therefore, considering the yield point, the width b_W is obtained by the following balance equation:

$$\frac{E \cdot t_W \cdot b_W}{d} = \frac{F_y}{d_y} \tag{11}$$

with E elastic modulus of the equivalent strut; F_y and D_y, respectively, force and displacement at yield.

5 BENCHMARK

5.1 Description of the structural scheme and of the experimental results

The proposed procedure has been validated on the basis of the results of experimental tests performed over a real scale infilled frame [38], which were specifically developed as part of a more general experimental study aimed to investigate the out of plane behaviour in relation to the damage level [39]. The geometry of the case study is shown in Figure 5, while the mechanical characteristics of the elements of the portal, of brick and mortar are collected in Table 1.

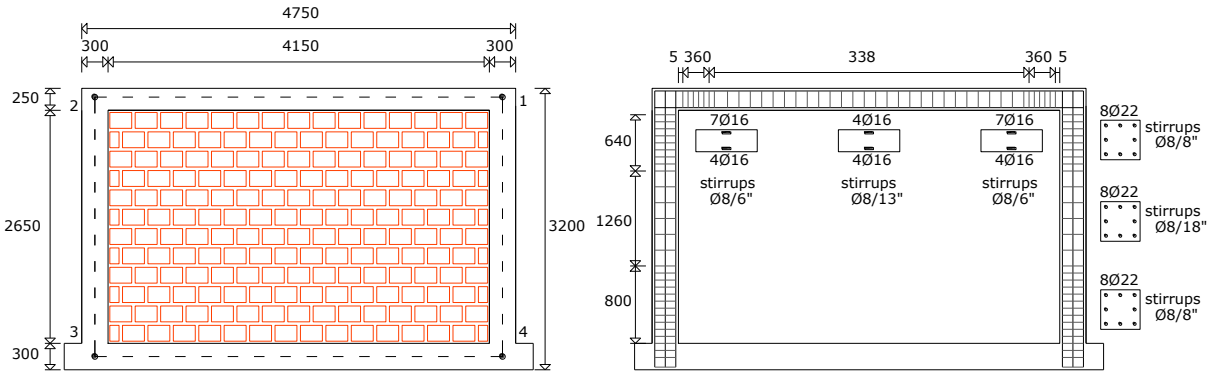


Figure 5: Infilled frame: geometry and amounts of reinforcing rebars

BRICK			
Nominal size	*Length*	250	*mm*
	Width	300	*mm*
	Height	190	*mm*
Unit weight		10.6	*kg*
Hole percentage		55	*%*
Compression strength parallel to hole *(UNI EN 772-1)*		13	*MPa*
Compression strength orthogonal to hole *(UNI EN 772-1)*		2.6	*MPa*
MORTAR - M10 [1]			
Compression strength		10	*MPa*
REINFORCED CONCRETE			
Average cylindrical compression strength $f_{cm,beam}$		34.54	*MPa*
Average cylindrical compression strength $f_{cm,column}$		29.32	*MPa*
MASONRY PANEL			
Vertical elasticity modulus		3238	*MPa*

Table 1: Mechanical and geometrical parameters of the components

The laboratory tests were carried out on several samples of infilled frames having the characteristics of Table 1, under a constant vertical load of *400 kN* in correspondence of the columns, in order to simulate the gravity loads at the ground floor of a building with 3 floors. The in-plane cyclic tests showed a non-linear behavior for a *0.1% -0.2%* value of the drift, in correspondence of the detachment between the columns and the infill. Between *0.2%* and *0.4*%, mortar joints' cracking occurs, with the rigid rotation of individual blocks, and the development of the damage is mainly concentrated at the center of the panel.

Afterwards, the cracking state increases, until reaches the maximum resistance of the panel in the range *0.8% -1.0%* of the drift. The load remains substantially constant after that a state of severe damage of the infill (indicative of the ultimate limit state of infill) is reached, due to crushing of the blocks in correspondence with a drift of *1.2%*.

By comparing the envelope curves of the in plane hysteresis cycles (Figure 6) in the two configurations: bare (B) and infilled (INF), a marked increase of shear at the base can be noticed, due to the strong contribution in resistance of the panel. At the range *0.8% -1.0%*, the maximum resistance of the infilled frame is more than *2.5* times the value found for the bare frame.

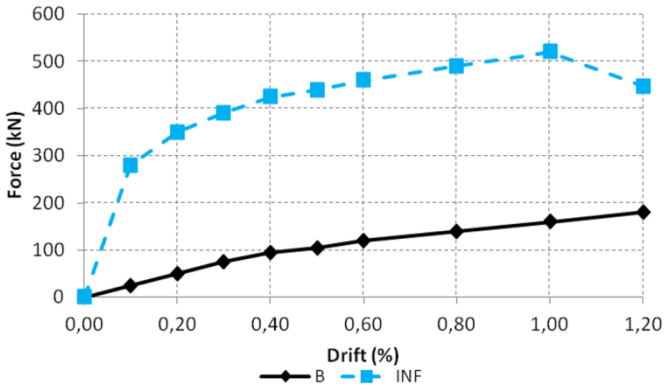


Figure 6: Envelope curves of the hysteresis cycle relative to the in plane test of the frame in the two configurations: bare (B) and infilled (INF).

5.2 From "*meso*" to *macro-modeling*

The infilled frame described in the previous section has been numerically implemented using the RBSM model (*see § 3*), in order to describe the structures at the "macro-scale" through a cinematic which allows to take into account, in a simplified way, also the effects of the masonry texture. The numerical analysis have shown a damage mechanics that reflects in large part the one shown by the reference experimental tests. In particular, Figure 7 shows the deformed configurations of the numerical model in correspondence of two drifts' values: *0.05%* (left) and *0.94%* (right). In particular, the two considered time instants identify the kinematic in correspondence of the first variation of stiffness of the system, and of collapse at a late stage.

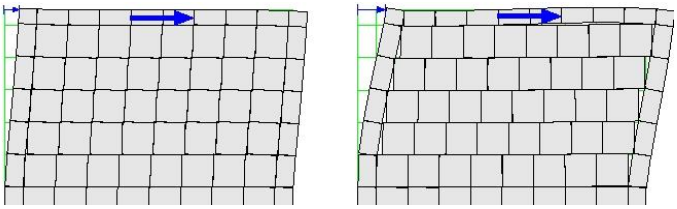


Figure 7: Kinematics of the infilled frame at 0.05% of drift (left) and at 0.94% of drift (right).

The incipient collapse condition, for the drift equal to *0.94%*, shows that the rotational component of the rigid blocks (present for low values of displacement) is predominant on the sliding mechanism along the horizontal joints, and as a result an evident detachment between frame and panel occurs.

For the aims of this paper, it is particularly interesting to express the response of the infilled frame as the trend of the F_h –D curve, where F_h is the horizontal resultant force and D is the horizontal drift. As described in *§ 4*, the response of the panel (MP) can be obtained, in a simplified way, by deducting from the behavior of the infilled frame (INF) the contribution of the bare frame (B). Figure 8 shows, respectively, the functions $F_h=F_h(Drift)$ for the configurations INF, B and MP_h (the letter *h* indicates the configuration associated with the kinematic mechanism in the horizontal direction).

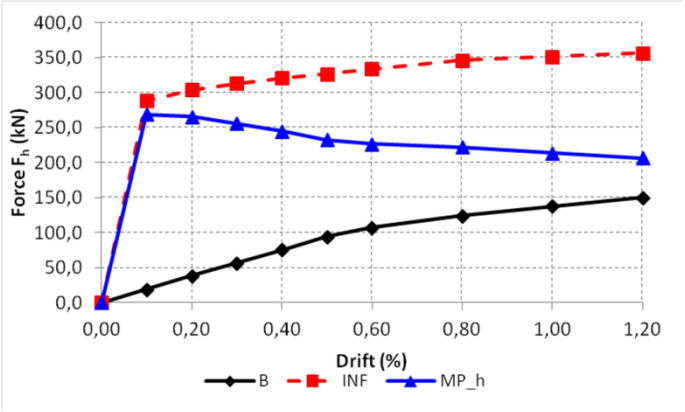


Figure 8: Force-drift curves obtained by RBSM modeling.

In accordance with the experimental results, the infill contribution is *2.4* times the strength of the bare frame. Obviously, the contribution of the panel (MP) (i.e., in the absence of the boundary frame) lays between the two configurations. For low drifts values, the response is very close to the infilled frame's one (INF), while at collapse is approaches the bare frame, demonstrating that the under conditions of non-cracked panel, the horizontal action is almost entirely absorbed by the masonry panel.

By representing the response of masonry (MP) with the diagonal components (F_W and d_W) along the diagonal direction of the panel, it is possible to build the non-linear law to be assigned to the equivalent strut. To this aim, 3 representative points should be identified (yield strength, maximum strength and minimum residual stress) corresponding to the main changes in the stiffness shown by the panel during development and propagation of damage. For the case under consideration, Figure 9 shows the adopted non-linear law of the equivalent strut in terms of F_W and d_W, compared with numerical response of the panel (MP).

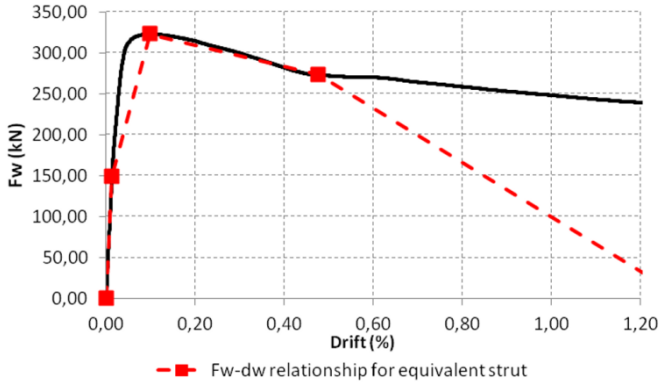


Figure 9: Graphic definition of the non-linear law of the equivalent strut.

Finally, once that the elastic response of the panel is obtained, by means of Eq. 11, it is possible to evaluate the width of the equivalent strut. In this case, b_W assumes a value of *1.92 m* which is to be understood as a measure of a geometric parameter derived by mechanical homogenization between panel (two-dimensional element) and strut (one-dimensional element).

5.3 Comparison between meso-scale, macro modeling and experimental tests

A further comparison has been performed in order to assess the quality of the results obtained by the macro-modeling calibrated on an meso-scale approach. To this purpose, the in-

filled frame has been implemented within a finite element solver [40]. The non-linear behavior of the frame has been evaluated by means of a "fibers" model, locating the non-linearity in the end sections of the structural elements by means of plastic hinges having a proper length. The constitutive laws assigned to the fibers are the Mander stress-strain law [41] for concrete, whereas an elastic perfectly plastic law with hardening has been assumed for steel. Both laws have been properly adapted on the basis of investigations carried on materials presented in [38]. As already mentioned, the non-linear law of the equivalent strut is obtained by deducting the dynamic behavior of the bare frame from that of the infilled frame, both evaluated with RBSM approach. Therefore, it is useful to compare the response of the bare frame obtained through the different modeling, meso-scale (RBSM) and macro-scale (by fiber model), with the experimental results (Figure 10).

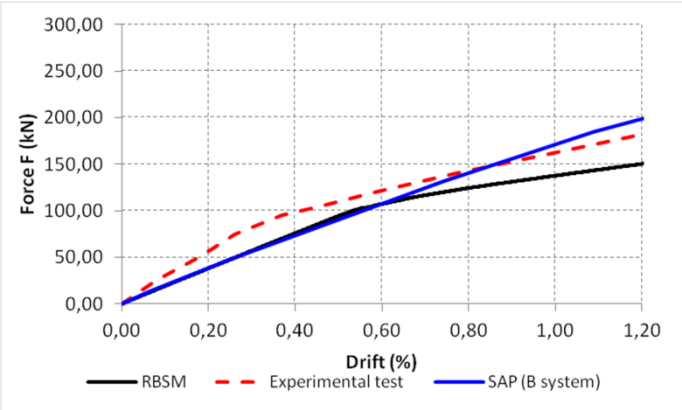


Figure 10: Bare frame (B): comparison of results..

Looking at the result, it is evident a good matching of the performance obtained by the different approaches considered. This is confirmed by evaluating the percentage errors E_r of horizontal force compared with the experimental results, reported in Table 2 in correspondence of significant *Drift* of the test (*0.2%*, *0.5%*, *1.0%* and *1.2%*)

drift *[%]*	Exp. test F_h *[kN]*	RBSM F_h *[kN]*	SAP (*B model*) F_h *[kN]*	RBSM E_r *[%]*	SAP (*B model*) E_r *[%]*
0.2	*56.0*	*40.7*	*47.8*	*27.2*	*14.7*
0.5	*111.0*	*88.4*	*95.2*	*20.4*	*14.2*
1.0	*165.4*	*140.9*	*159.1*	*14.8*	*4.1*
1.2	*181.7*	*154.3*	*179.8*	*15.1*	*1.0*

Table 2: Results provided by the different approaches for the bare configuration B: horizontal force and errors.

In Figure 11 and Table 3, similarly , the comparisons of the results for the infilled frame (INF) are compared.

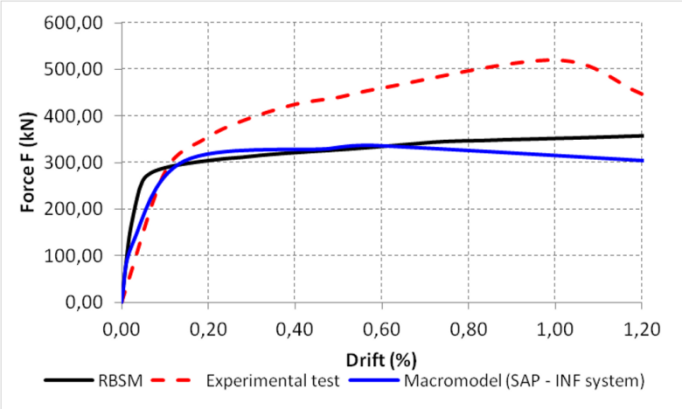


Figure 11. Infilled frame (INF): comparison of results

drift *[%]*	Exp. test F_h *[kN]*	RBSM F_h *[kN]*	Macro-model *(SAP - INFmodel)* F_h *[kN]*	RBSM E_r *[%]*	Macro-model *(SAP - INFmodel)* E_r *[%]*
0.2	*363.2*	*309.8*	*308.0*	*14.7*	*15.2*
0.5	*438.5*	*319.8*	*331.2*	*27.1*	*24.5*
1.0	*527.2*	*336.6*	*362.7*	*36.2*	*31.2*
1.2	*444.7*	*343.3*	*308.2*	*22.8*	*30.7*

Table 3: Results provided by the different approaches for the configuration INF: horizontal force and errors

6 FINAL REMARKS

The great interest of the scientific community about the issue of infilled frame modelling is testified by the presence of a vast literature produced. In the wide range of proposals developed over the past years, there is a relevant thread about the development of simplified models of a rapid application, such as the method of equivalent strut, which are clearly aimed at allowing the solution of real problems (analysis of whole, real buildings).

However, the method is basically a very simplified abstraction of the physical reality aimed at assessing the effects of the infill on the global response of the structure, but, also when are a specific mechanical characterization of masonry is available, the reliability of the numerical simulations is limited. It is very useful, therefore, to have a simple automatic procedure able to derive the parameters governing the definition of the equivalent strut, taking into account the interaction effects between the individual constituents (bricks and mortar) and the reinforce concrete frame.

To this end, this paper presents the preliminary results of an original procedure aimed at calibrating the constitutive non-linear law of the equivalent strut by a meso-scale modeling (RBSM model) of the infilled frame. An experimental analysis of the literature has allowed a first validation of the proposed procedure, which showed a substantial coherence with the experimental behavior.

The present study highlights, anyway, the need for further validation tests based on the direct availability of experimental analyses, and a refinement in the definition of the cyclic law of equivalent strut.

In the future, moreover, it is provided to perform dynamic analysis at the meso-scale, and the definition of an optimization process for deriving the mechanical parameters of the elasto-plastic springs starting from characteristics of the materials constituting the masonry texture.

AKCNOWLEDGEMENT

The research presented in this article was partially funded by the Department of Civil Protection, Project ReLUIS-DPC 2010-2013.

REFERENCES

[1] DM 14/01/2008. Norme Tecniche per le Costruzioni (NTC 2008) - *(in Italian)*. Gazzetta Ufficiale n.29. Roma; 2008.

[2] CEN. Eurocode 8: design of structures for earthquake resistance. Part 1: general rules, seismic actions and rules for buildings. Brussels; 2005.

[3] P. Negro, A. Colombo, Irregularities induced by non-structural masonry panels in framed buildings, *Engineering Structures* **19**,576-85, 1997.

[4] G. Uva, F. Porco, A. Fiore, M. Mezzina, Proposal of a methodology of in-situ concrete tests and improving the estimate of the compressive strength, *Construction and Building Materials*, **38**(1):72-83, 2013 - DOI: 10.1016/j.conbuildmat.2012.08.025.

[5] M. Dolšek, P. Fajfar, Simplified non-linear seismic analysis of infilled reinforced concrete frames. *Earthquake Engineering and Structural Dynamics*, **34**,49-66, 2005.

[6] H. Lee, S. Woo, Effect of masonry infill on seismic performance of a 3-storey rc frames with non-seismic detailing. *Earthquake engineering and structural dynamics*, **31**:353-378,2002.

[7] F. Colangelo, Pseudo-dynamic seismic response of reinforced concrete frames infilled with nonstructural brick masonry, *Earthquake engineering and structural dyna*mics, **34**(10):1219-1241, 2005.

[8] G. Uva, F. Porco, A. Fiore, Appraisal of masonry infill walls effect in the seismic response of RC framed buildings: a case study. *Engeneering Structures*, **34**(1),514–26, 2012.

[9] A. Fiore, F. Porco, D. Raffaele, G. Uva, About the influence of the infill panels over the collapse mechanisms actived under pushover analyses: two case studies. *Soil Dynamics and Earthquake Engineering*, **39**,11-22, 2012.

[10] G. Uva, F. Porco, D. Raffaele, A. Fiore, On the role of equivalent strut models in the seismic assessment of infilled RC buildings. *Engineering Structures*, **42**:83-94, 2012.

[11] S. Casolo, Macroscale modelling of microstructure damage evolution by a rigid body and spring model, *Journal of Mechanics of Materials and Structures*, 4:3, 551-570, 2009 - DOI: 10.2140/jomms.2009.4.551.

[12] Porco, F., Fiore, A., Porco, G., & Uva, G. (2013). Monitoring and safety for prestressed bridge girders by SOFO sensors. *Journal of Civil Structural Health Monitoring*, **3**(1),3-13, 2013.

[13] G. Uva, D. Raffaele, F. Porco, A. Fiore, G. Porco, Bridge monitoring by fiber optic deformation sensors: A case study, *Proceedings of the 6th International Conference on Bridge Maintenance, Safety and Management (IABMAS 2012)*, Como, Italy, 2012, ISBN 978-0-415-62124-3.

[14] F.J. Crisafulli, A.J. Carr, R. Park, Analytical modelling of infilled frame structures - a general review. *Bulletin of the New Zeland Society for Earthquake Engineering* **33**(1), 30-47, 2000.

[15] A.W. Page, Modelling the In-Plane Behaviour of Solid Masonry Under Static Loading. *Proceedings of the International Workshop on Unreinforced Hollow Clay Tile*, 2-5, 1995.

[16] S. Ali, A.W. Page, Finite Element Model for Masonry Subjected to Concentrated Loads. *Journal of Structural Engineering*, **114**(8), 1761–1784, 1998 - doi: 10.1061/(ASCE)0733 9445(1988)114:8(1761).

[17] A.W. Page, Finite element model for masonry. *Journal of the Structural Division*, 104(8), 1267-1285, 1978.

[18] A.B. Mehrabi, P.B. Shing, Finite element modelling of masonry-infilled rc frames. *Journal of Structural Engineering* (ASCE), 123(5), 604–613, 1995.

[19] T.C. Liauw, K.H. Kwan, Nonlinear behaviour of non-integral infilled frames, *Computers and Structures*, **18**, 551-560, 1984.

[20] G. Uva, G. Salerno, Towards a multiscale analysis of periodic masonry brickwork: A FEM algorithm with damage and friction, *International Journal of Solids and Structures*, **43**: 13, 3739-3769, 2006 DOI: 10.1016/j.ijsolstr.2005.10.004.

[21] J. V. Lemos, Discrete element modeling of masonry structures. *International Journal of Architectural Heritage: Conservation, Analysis, and Restoration*, **1**(2): 190–213, 2007.

[22] S. Casolo and F. Peña, Rigid element model for in-plane dynamics of masonry walls considering hysteretic behaviour and damage, *Earthquake Engineering and Structural Dynamics* **36**(8), 1029–1048, 2007 - **DOI:** 10.1002/eqe.670.

[23] S. Casolo, G. Milani, A simplified homogenization-discrete element model for the non-linear static analysis of masonry walls out-of-plane loaded, *Engineering Structures*, **32**:8, 2352-2366, 2010 - DOI: 10.1016/j.engstruct.2010.04.010

[24] S. Casolo, G. Milani, Simplified out-of-plane modelling of three-leaf masonry walls accounting for the material texture, *Construction and Building Materials*, **40**, 330-351, 2013- DOI: 10.1016/j.conbuildmat.2012.09.090

[25] S. Casolo, G. Uva, Out-of-plane seismic response of masonry façades some comparisons among full dynamic and pushover analysis, *Ingegneria Sismica*, ISSN: 03931420, **27**:3, 33-54, 2010.

[26] S. Casolo, G. Uva, Nonlinear analysis of out-of-plane masonry façades: Full dynamic versus pushover methods by rigid body and spring model, *Earthquake Engineering and Structural Dynamics*, 42: 499–521, 2013 - DOI: 10.1002/eqe.2224

[27] S. Casolo, C.A. Sanjust, Seismic investigation on the cathedral of Syracuse by finite elements and by a specific rigid body and spring model, *WIT Transactions on the Built Environment*, pp. 535, 2007 - DOI: 10.2495/STR070501

[28] S. Casolo, C.A. Sanjust, Seismic analysis and strengthening design of a masonry monument by a rigid body spring model: The "Maniace Castle" of Syracuse, *Engineering Structures*, **31:**7, 1447-1459, 2009 DOI: 10.1016/j.engstruct.2009.02.030

[29] Milani, G., Casolo, S., Naliato, A. & Tralli, A., "Seismic assessment of a medieval masonry tower in Northern Italy by limit, nonlinear static, and full dynamic analyses", International Journal of Architectural Heritage, vol. 6, no. 5, pp. 489-524. 2012 - DOI: 10.1080/15583058.2011.588987.

[30] S. Casolo, G. Milani, G. Uva, C. Alessandri, Comparative seismic vulnerability analysis on ten masonry towers in the coastal Po Valley in Italy, *Engineering Structures*, **49**, 465-490, 2013 – DOI: 10.1016/j.engstruct.2012.11.033.

[31] R.J. Mainstone, Supplementary note on the stiffness and strength of infilled frames. Current paper CP13/74. *Build. Res*. Establishment. London; 1974.

[32] B. Stafford Smith, Lateral Stiffness of infilled frames. *Journal of Structural Division, ASCE,* **6**:183-99, 1963.

[33] D. Raffaele, F. Porco, A. Fiore, G. Uva, Simplified Vulnerability Assessment of RC Circular Piers in Multi-Span-Simply-Supported Bridges. *Structure and Infrastructure Engineering*, 2013 - DOI:10.1080/15732479.2013.772642.

[34] F.J Crisafulli, *Seismic behaviour of reinforced concrete structures with masonry infills*, Ph.D. Thesis. Department of Civil Engineering, University of Canterbury; 1997.

[35] T.B. Panagiotakos, M.N. Fardis, Seismic response of infilled rc frames structures. *Proceedings of 11th World Conference on Earthquake Engineering*; Paper No.225, Acapulco, 1996.

[36] S.H. Bertoldi, L.D. Decanini, C. Gavarini, Telai tamponati soggetti ad azioni sismiche, un modello semplificato: confronto sperimentale e numeric (in Italian). *Atti del 6° Convegno Nazionale ANIDIS*, vol. 2, pp. 815-824, Perugia, 13-15 Ottobre 1993.

[37] S. Casolo, Macroscopic modelling of structured materials: relationship between orthotropic Cosserat continuum and rigid elements. *International Journal of Solids and Structures* **43**(3-4), 475–496, 2006 - DOI: 10.1016/j.ijsolstr.2005.03.037

[38] G. M Calvi, D. Bolognini, Seismic response of reinforced concrete frames infilled with masonry panels weakly reinforced, *Journal of Earthquake Engineering*, **5**, 153-185, 2001.

[39] F. Mosele, Risultati sperimentali sul comportamento sismico di elementi non strutturali (tamponature) in laterizio POROTON. http://www.poroton.it/user/articoli/n73/Ricerca-sulle-tamponature-esterne-antisismiche/Ricerca-sulle-tamponature-esterne-antisismiche.aspx, 2012.

[40] SAP2000. Advanced 14.2.2 Structural Analysis Program – Manual – (2010) Computer and Structures, Inc.

[41] J.B. Mander, M.J.N. Priestley, R. Park, Theoretical Stress-Strain Model for Confined Concrete. *Journal of Structural Engineering* ASCE, **114**(3):1804-1826, 1984.

COMPDYN 2013
4th ECCOMAS Thematic Conference on
Computational Methods in Structural Dynamics and Earthquake Engineering
M. Papadrakakis, V. Papadopoulos, V. Plevris (eds.)
Kos Island, Greece, 12–14 June 2013

A THREE DIMENSIONAL MULTISCALE FORMULATION FOR THE NONLINEAR DYNAMIC ANALYSIS OF MASONRY STRUCTURES

Savvas P. Triantafyllou[1], **Eleni N. Chatzi**[2]

Institute of Structural Engineering
ETH Zürich
Wolfgang-Pauli-Strasse 15
CH-8093 Zürich, Switzerland
e-mail: [1]triantafyllou.ibk.baug.ethz.ch, [2]chatzi.ibk.baug.ethz.ch

Keywords: Composites, Multiscale, Hysteretic, Masonry.

Abstract. *In this work, a three dimensional multiscale formulation is presented for the analysis of masonry structures based on the multiscale finite element formulation. The method is develloped within the framework of the Enhanced Multiscale Finite Element Method. Through this approach, two discretization schemes are considered, namely a fine mesh that accounts for the micro-structure and a coarse mesh that encapsulates the former. Through a numerically derived mapping, the fine scale information is propagated to the coarse mesh where the numerical solution of the governing equations is performed. Inelasticity is introduced at the fine mesh by considering a set of internal variables corresponding to the plastic deformation accumulatimg at the Gauss points of each fine-scale element. These additional quantities evolve according to properly defined smooth evolution equations. The proposed formalism results in a nonlinear dynamic analysis method where the micro-level state matrices need only be evaluated once at the beginning of the analysis procedure. The accuracy and computational efficiency of the proposed scheme is verified through an illustrative example.*

1 INTRODUCTION

Composite materials consist of two or more mechanically separable solid materials. As such, they in general exhibit a heterogeneous micro-structure whose specific morphology affects the mechanical behavior of the assembled structure [19]. Composites are therefore multiscale in nature, i.e. the scale of the constituents is of lower order than the scale of the resulting material. Furthermore, the resulting structure, that is an assemblage of composites, can be of an even larger scale than the scale of the constituents e.g. a textile strengthened masonry structure [14] or a bio-sensor consisting of several nano-wires [23]. Thus, the required modeling approach has to account for such a level of detailing that spreads through scales of significantly different magnitude. Throughout this paper, the term macroscopic (or coarse) scale corresponds to the structural level whereas the term microscopic (or fine) scale corresponds to the composite micro-structure properties such as the sizes, morphologies and distributions of heterogeneities that the material consists of.

Modeling of structures that consist of composites could be accomplished using the standard finite element method [35]. However, a finite element model mesh accounting for each micro-structural heterogeneity would require large amounts of computer memory and CPU time. Therefore, the finite element scheme is usually restricted to small scale numerical experiments of a representative volume element (RVE) [21, 28]. To properly capture the effect of micro-structural heterogeneities in the large scale, more refined methods have been developed. Instead of implementing the finite element method as is, upscaled or multiscale methods exist that account for such types of problems.

Multiscale methods can be separated in two groups, namely multiscale homogenization methods [24] and multiscale finite element methods (MsFEMs) [12]. Within the framework of the averaging theory for ordinary and partial differential equations, multiscale homogenization methods are based on the evaluation of an averaged strain and corresponding stress tensor over a predefined space domain denoted as Representative Volume (RVE). Amongst the various homogenization methods proposed [15], asymptotic homogenization has been proven to be very efficient both in terms of accuracy and required computational cost [7, 33]. However, homogenization methods rely on two basic assumptions, namely the full separation of the individual scales and the local periodicity of the RVEs. In practice, the heterogeneities within a composite are not periodic as in the case of fiber-reinforced matrices. In order to adapt to general heterogeneous materials, the size of the RVE must be sufficiently large to contain enough microscopic heterogeneous information [29, 16] which results in a considerable increase of the computational cost. Furthermore, in an elasto-plastic problem, periodicity on the RVEs also dictates periodicity on the damage induced which could result in erroneous results.

The multiscale finite element method, instead, relies on the numerical evaluation of a set of micro-scale basis functions that are used to map the micro-structure information onto the larger scale. These basis functions depend on the micro-structural geometry and constituent material properties. MsFEM was first introduced in [18] although a variant of the method was earlier introduced in the pioneering work of [5] for one-dimensional problems and later improved to account for higher order elements [4, 3]. Although MsFEMs have been extensively used in linear and nonlinear flow simulation analysis [12, 16] the method has not been implemented in structural mechanics problems. This is attributed to the inherent inability of the method to treat the bulk expansion/ contraction phenomena (i.e. Poissons effect). To overcome this problem, the enhanced multiscale finite element method (EMsFEM) has been proposed for the analysis of heterogeneous structures [34]. EMsFEM introduces additional coupling terms into the

fine-scale interpolation functions to consider the coupling effect among different directions in multi-dimensional vector problems. However, in a nonlinear analysis procedure, the numerical basis functions need to be evaluated at every incremental step due to the progressive failure of the constituents thus diminishing the computational advantage of the method. The problem is treated in [34] through the implementation of the the initial stiffness method [25] for the solution of the incremental governing equations. Nevertheless, this method is known to face serious convergence problems and usually requires a large number of iterations to achieve convergence [25]. The computational cost increases in a nonlinear dynamic analysis scheme, where a time integration scheme is also needed on top of the iterative procedure [17].

In this work, a modified multiscale finite element analysis procedure is presented for the nonlinear static and dynamic analysis of heterogeneous structures. In this, the evaluation of the micro-scale basis functions is accomplished within the hysteretic finite element framework [30]. Inelasticity is treated at the element level through properly defined evolution equations that control the evolution of the plastic part of the deformation component. Using the Principle of Virtual Work, the tangent stiffness matrix of the element is replaced by an elastic stiffness matrix and a hysteretic stiffness matrix that both remain constant throughout the analysis. A multiaxial smooth hysteretic model is implemented to control the evolution of the plastic strains. This model is derived on the basis of the Bouc-Wen model of hysteresis [8] and accounts for any kind of yield criterion and hardening law within the framework of classical plasticity [20]. Smooth hysteretic modelling has proven very efficient with respect to classical incremental plasticity in computationally intense problems such as nonlinear structural identi-fication [9] and stochastic dynamics [27, 32]. Furthermore, the proposed hysteretic scheme can be extended to account for cyclic damage induced phenomena such as stiffness degradation and strength deterioration [13].

2 HYSTERETIC MODELING

2.1 Multiaxial modelling of hysteresis

The material model implemented in this work is a generic rate-independent hysteretic model. This model accounts for any type of yield criterion and hardening law either isotropic, kinematic or combined. Both the case of linear and nonlinear kinematic hardening is considered.

The model is defined on the grounds of two rate equations. The first equation controls the evolution of the stress field with respect to the strain field and assumes the following form

$$\{\dot{\sigma}\} = [D]\left([I] - H_1 H_2 [R]\right)\{\dot{\varepsilon}\} \tag{1}$$

where $\{\sigma\}$ is the stress tensor, $[D]$ is the elastic constitutive matrix, $[I]$ is the identity matrix while $(\cdot)$ denotes differentiation with respect to time while H_1 and H_2 are smoothened Heaviside functions that will be defined later on. Matrix $[R]$ in equation (1) is a strain interaction matrix defined through the following relation

$$[R] = \{\alpha\}\left(-\{b\}^T \mathscr{G}\left(\{\eta\}, \Phi\right) + (\alpha)^T [D]\{\alpha\}\right)\{\alpha\}^T [D] \tag{2}$$

where $\{\alpha\} = \left(\partial\Phi/\partial\{\sigma\}\right)^T$, $\{b\} = \left(\partial\Phi/\partial\{\eta\}\right)^T$ and $\mathscr{G}\left(\{\eta\}, \Phi\right)$ is a hardening function corresponding to the kinematic hardening rule considered.

The second equation of the constitutive model used in this work defines the evolution of the back-stress with respect to the strain field and assumes the following form:

$$\{\dot{\eta}\} = H_1 H_2 \mathscr{G}\left(\{\eta\}, \Phi\right)\left[\tilde{R}\right]\{\dot{\varepsilon}\} \tag{3}$$

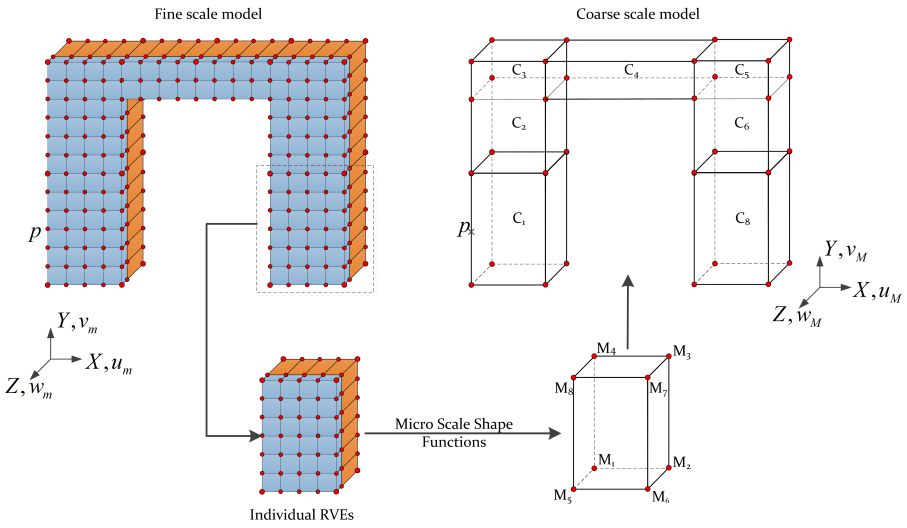


Figure 1: Multiscale Finite Element procedure

where $\left[\tilde{R}\right]$ is the corresponding hardening interaction matrix defined by the following relation

$$\left[\tilde{R}\right] = \left(-\{b\}^T \mathscr{G}\left(\{\eta\}, \Phi\right) + \{\alpha\}^T [D] \{\alpha\}\right)^{-1} \{\alpha\}^T [D] \tag{4}$$

The smoothed Heaviside functions H_1 and H_2introduced in relations (1) and (3) assume the following form, namely

$$H_1 = \left|\frac{\Phi\left(\{\sigma\}, \{\eta\}\right)}{\Phi_0}\right|^N, \quad N \geq 2 \tag{5}$$

and

$$H_2 = \beta + \gamma sgn\left(\{\varepsilon\}^T \{\dot{\sigma}\}\right) \tag{6}$$

where $\Phi = \Phi\left(\{\sigma\}, \{\eta\}\right)$ is a yield criterion, Φ_0 the yield limit,N a material parameter that determines the rate at which the yield criterion reaches its maximum value while β and γ are material parameters that control the stiffness at the moment of unloading.

3 THE MULTISCALE FINITE ELEMENT ANALYSIS METHOD

In this Section, the Enhanced Multiscale Finite Element Method (EMsFEM) is briefly discussed as a reference for subsequent derivations. A masonry frame is presented in Figure 1, consisting of two piers and a horizontal spandrel. An additional outer layer of reinforcement is also considered. The computational fine scale model consists of 8-node hex elements [35]. Instead of directly solving the fine scale computational model using the standard isoparametric finite element formulation, EMsFEM is based on a two-step approach. Grouping together clusters of micro-elements, a set of coarse elements is constructed. The nodes of the derived macro-elements are the macro-nodes of the coarse mesh. Accordingly, two displacement fields are defined, namely the micro-displacement field corresponding to the micro nodal displacements $\left\{ \begin{array}{ccc} u_m(x,y) & v_m(x,y) & w_m(x,y) \end{array} \right\}^T$ of the fine mesh and the macro-displacement field $\left\{ \begin{array}{ccc} u_M(x,y) & v_M(x,y) & w_M(x,y) \end{array} \right\}^T$ corresponding to the macro nodal displacements. Throughout this work, subscript m denotes a micro-measure while M is used to denote a macro-measure of the indexed quantity.

Next, a numerical mapping is constructed that maps the micro-displacement field within each RVE to the corresponding macro-displacements of the RVE macro-nodes. This numerical mapping assumes the following generic form:

$$\{d\}_m = \mathscr{M}\{d\}_M \tag{7}$$

where $\mathscr{M}$ is a mapping operator. EMsFEM is based on the assumption that the discrete micro-displacements within the coarse element are interpolated at the macro-nodes using the following scheme:

$$\begin{array}{l} u_m(x_j,y_j) = \sum_{i=1}^{n_{Macro}} N_{ijxx}u_{M_i} + \sum_{i=1}^{n_{Macro}} N_{ijxy}v_{M_i} + \sum_{i=1}^{n_{Macro}} N_{ijxz}w_{M_i} \\ v_m(x_j,y_j) = \sum_{i=1}^{n_{Macro}} N_{ijxy}u_{M_i} + \sum_{i=1}^{n_{Macro}} N_{ijyy}v_{M_i} + \sum_{i=1}^{n_{Macro}} N_{ijyz}w_{M_i} \quad j = 1...n_{micro} \\ w_m(x_j,y_j) = \sum_{i=1}^{n_{Macro}} N_{ijxz}u_{M_i} + \sum_{i=1}^{n_{Macro}} N_{ijyz}v_{M_i} + \sum_{i=1}^{n_{Macro}} N_{ijzz}w_{M_i} \end{array} \tag{8}$$

where u_m, v_m, w_m are the horizontal and vertical micro-displacement components, n_{Macro} is the number of macro-nodes of the coarse element, (x_j, y_j, z_j) are the local coordinates of the micro-nodes, u_{M_i}, v_{M_i}, w_M are the horizontal and vertical displacement components of the macro-nodes, N_{ixx}, N_{ixy}, N_{iyy}, N_{iyz}, N_{izz} are the micro-basis functions and n_{micro} is the number of micro-nodes within the coarse element.

In equation (8), N_{ijxx} stands for the displacement component of node j along the x axis induced by a unilateral displacement at the i node (also along the x axis). Likewise, N_{ijxy} stands for the displacement component of the i node, along the x axis induced by a unilateral displacement at node j and along the y axis. Contrary to MsFEM where the interpolation fields of the displacement components are considered uncoupled, the coupling terms N_{ixy}, N_{ixz}, N_{iyz} are introduced in EMsFEM. Thus, equation (8) results in a kinematical assumption consistent with the observation that a unit displacement in the boundary of a deformable body may induce displacements in both directions within the body.

From the interpolation field introduced in equation (8), the following relation can be established at the micro-elemental level

$$\{d\}_{m(i)} = [N]_{m(i)}\{d\}_M \tag{9}$$

where $\{d\}_{m(i)}$ is the nodal displacement vector of the i_{th} micro-element, $[N]_{m(i)}$ is a matrix containing the micro-basis shape functions evaluated at the nodes of the i_{th} micro-element while $\{d\}_M$ the vector of nodal displacements of the corresponding macro-nodes.

3.1 Numerical evaluation of micro-scale basis functions

The evaluation of the mapping operator $\mathscr{M}$ is performed numerically. Relation (8) successfully maps the micro-displacement field to the macro-displacement field if and only if the micro-shape functions adhere to the following property, namely, when the macro-displacement component is equal to unity at a macro-node, displacement is equal to zero at every other macro-node. The derivation of micro-basis functions with such properties can be accomplished by considering the following boundary value problem

$$\begin{array}{l} [K]_{RVE}\{d\}_m = \{\emptyset\} \\ \{d\}_S = \{\bar{d}\} \end{array} \tag{10}$$

where $[K]_{RVE}$ is the stiffness matrix of the RVE, $\{\emptyset\}$ is a vector containing zeros while $\{d\}_S$ is a vector containing the nodal degrees of freedom of the boundary S of the RVE and $\{\bar{d}\}$ is a

vector of prescribed displacements. The RVE stiffness matrix is formulated using the standard finite element method [8]. In this work, the solution of the boundary value problem established in equation (10) is performed using the Lagrange multiplier method [6].

The choice of the values of the prescribed boundary displacements is a key assumption of the EMsFEM and highly affects the accuracy of the derived multiscale scheme. Three different types of boundary conditions are established in the literature namely linear boundary conditions, periodic boundary conditions and oscillatory boundary conditions with oversampling. Further details on the procedure implemented for the derivation of the micro-basis functions can be found in [12].

4 THE PROPOSED NUMERICAL SCHEME

The evaluation of the micro-shape functions for each RVE is based on the solution of the equilibrium problem (10). Thus, the mapping depends on the material properties of the fine-scale model, e.g. for the case of the reinforced masonry RVE presented in Figure 1, the solution depends on the material properties of masonry and the composite matrix. Consequently, in a nonlinear analysis procedure, either static or dynamic, the evaluation of the micro to macro-mapping needs to be performed in every incremental step of the analysis procedure. To overcome this computational drawback, the hysteretic formulation of finite elements is implemented [30] in this work to account for the fine scale nonlinear material behaviour.

Considering the additive decomposition of the strain rate into a reversible elastic an an irreversible plastic part [22] within the micro-element, the following relation is established:

$$\left\{\dot{\varepsilon}\right\}_{m(i)} = \left\{\dot{\varepsilon}^{el}\right\}_{m(i)} + \left\{\dot{\varepsilon}^{pl}\right\}_{m(i)} \tag{11}$$

where $\left\{\varepsilon\right\}_{m(i)}$ is the tensor of total micro-strain within the i_{th} micro-element, $\left\{\varepsilon^{el}\right\}_{m(i)}$ is the tensor of the elastic strain, $\left\{\varepsilon^{pl}\right\}_{m(i)}$ is the tensor of the inelastic, irreversible strain while $(.)$ denotes differentiation with respect to time. The vectorial notation of the stress and strain tensors is used in this work. Using equation (11) the elastic Hooke's stress-strain law is cast into the following form

$$\left\{\dot{\sigma}\right\}_{m(i)} = \left[D\right]_{m(i)} \left\{\dot{\varepsilon}^{el}\right\}_{m(i)} = \left[D\right]_{m(i)} \left(\left\{\dot{\varepsilon}\right\}_{m(i)} - \left\{\dot{\varepsilon}^{pl}\right\}_{m(i)}\right) \tag{12}$$

where $\left\{\sigma\right\}$ is the stress tensor and $\left[D\right]_{m}$ is the elastic material constitutive matrix [11] of the micro-element. Comparing equations (1) and (12) the following expression for the evolution of the plastic strain component is readily derived:

$$\left\{\dot{\varepsilon}^{pl}\right\}_{m(i)} = H_1 H_2 \left[R\right]_{m(i)} \left\{\dot{\varepsilon}\right\}_{m(i)} \tag{13}$$

where the interaction matrix $\left[R\right]_{m(i)}$ is introduced in equation (2). The following rate form of the principle of virtual displacements is introduced [31] over the finite volume V_e of a single element:

$$\int_{V_e} \left\{\varepsilon\right\}_{m(i)}^{T} \left\{\dot{\sigma}\right\}_{m(i)} dV_e = \left\{d\right\}_{m(i)}^{T} \left\{\dot{f}\right\}_{m(i)} \tag{14}$$

where $\left\{d\right\}_{m(i)}$ is the vector of micro-nodal displacements introduced in relation (9) and $\left\{f\right\}_{m(i)}$ is the corresponding vector of nodal forces. For the sake of the presentation, only nodal loads are considered herein, however the evaluation of body loads and surface tractions can be derived

accordingly. Substituting equation (12) into the variational principle (14) the following relation is derived:

$$\int_{V_e} \{\varepsilon\}^T_{m(i)} [D]_{m(i)} \{\dot{\varepsilon}\}_{m(i)} dV_e - \int_{V_e} \{\varepsilon\}^T_{m(i)} [D]_{m(i)} \left\{\dot{\varepsilon}^{pl}\right\}_{m(i)} dV_e = \{d\}^T_{m(i)} \left\{\dot{f}\right\}_{m(i)} \quad (15)$$

Considering the standard isoparametric interpolation scheme [35] for the micro-displacement field $\{u\}_{m(i)}$

$$\{u\}_{m(i)} = [N]_{m(i)} \{d\}_{m(i)} \quad (16)$$

with the accompanying strain-displacement compatibility relation:

$$\{\varepsilon\}_{m(i)} = [B]_{m(i)} \{d\}_{m(i)} \quad (17)$$

where $[N]_{m(i)}$ is the matrix of shape functions for the 8-node solid element [35], and $[B]_{m(i)} = \partial [N]_{m(i)}$ is the corresponding strain-displacement matrix. Substituting equation (17) into equation (15) the following relation is derived:

$$\int_{V_e} [B]^T_{m(i)} [D]_{m(i)} [B]_{m(i)} dV_e \left\{\dot{d}\right\}_{m(i)} - \int_{V_e} [B]^T_{m(i)} [D]_{m(i)} \left\{\dot{\varepsilon}^{pl}\right\}_{m(i)} dV_e = \left\{\dot{f}\right\}_{m(i)} \quad (18)$$

Furthermore, introducing an interpolation scheme for the plastic part of the strain $\left\{\varepsilon^{pl}\right\}_{m(i)}$, namely:

$$\left\{\dot{\varepsilon}^{pl}\right\}_{m(i)} = [N]_{em(i)} \left\{\dot{\varepsilon}^{pl}_{cq}\right\}_{m(i)} \quad (19)$$

where $\left\{\varepsilon^{pl}_{cq}\right\}_{m(i)}$ is the vector of plastic stains retrieved at properly defined collocation points, the following relation is finally derived:

$$\left[k^{el}\right]_{m(i)} \left\{\dot{d}\right\}_{m(i)} - \left[k^{h}\right]_{m(i)} \left\{\dot{\varepsilon}^{pl}_{cq}\right\}_{m(i)} = \left\{\dot{P}\right\}_{m(i)} \quad (20)$$

where $\left[k^{el}\right]_{m(i)}$ is the elastic stiffness matrix of the micro-element

$$\left[k^{el}\right]_{m(i)} = \int_{V_e} [B]^T_{m(i)} [D]_{m(i)} [B]_{m(i)} dV_e \quad (21)$$

and $\left[k^{h}\right]_{m(i)}$ is the hysteretic matrix of the micro-element.

$$\left[k^{h}\right]_{m(i)} = \int_{V_e} [B]^T_{m(i)} [D]_{m(i)} [N]_{em(i)} dV_e \quad (22)$$

Both $\left[k^{el}\right]_{m(i)}$ and $\left[k^{h}\right]_{m(i)}$ are constant and inelasticity is controlled at the collocation points through the accompanying plastic strain evolution equations defined in equation (13).

Considering zero initial conditions for brevity, rates in equation (20) are dropped and the following relation is established

$$\left[k^{el}\right]_{m(i)} \{d\}_{m(i)} - \left[k^{h}\right]_{m(i)} \left\{\varepsilon^{pl}_{cq}\right\}_{(i)} = \{f\}_{m(i)} \quad (23)$$

Substituting equation (9) into equation (23) and pre-multiplying with $[N]^T_{m(i)}$ the following relation is derived:

$$\left[k^{el}\right]^M_{m(i)} \{d\}_M - \left[k^{h}\right]^M_{m(i)} \left\{\varepsilon^{pl}_{cq}\right\}_{(i)} = \{f\}^M_{m(i)} \quad (24)$$

where

$$\left[k^{el}\right]^{M}_{m(i)} = [N]^{T}_{m(i)} \left[k^{el}\right]_{m(i)} [N]_{m(i)} \tag{25}$$

is the elastic stiffness matrix of the i_{th} micro-element mapped onto the macro-element degrees of freedom while $\left[k^{h}\right]^{M}_{m(i)}$ is the hysteretic matrix of the i_{th} micro-element, evaluated by the following relation:

$$\left[k^{h}\right]^{M}_{m(i)} = [N]^{T}_{m(i)} \left[k^{h}\right]_{m(i)} \tag{26}$$

Finally, $\{P\}^{M}_{m(i)}$ in equation (24) is the equivalent nodal force vector of the micro-element mapped onto the macro-nodes of the coarse element.

$$\{f\}^{M}_{m(i)} = [N]^{T}_{m(i)} \{f\}_{m(i)} \tag{27}$$

Equation (24) is a multiscale equilibrium equation involving the displacement vector evaluated at the coarse-element nodes and the plastic part of the strain tensor evaluated at collocation points within the micro-scale element mesh.

4.1 Micro to Macro scale transition

Having established the micro-element equilibrium in terms of macro-displacement measures using the micro-basis mapping introduced in equation (9), a procedure is needed to formulate the global equilibrium equations in terms of the macro-quantities. Denoting with a subscript M the corresponding macro-measures over the volume V of the coarse element equation (14) is re-written as:

$$\int_{V_M} \{\varepsilon\}^{T}_{M} \{\dot{\sigma}\}_{M} \, dV_M = \{d\}^{T}_{M} \left\{\dot{f}\right\}_{M} \tag{28}$$

where $\{f\}_{M}$ is the vector of nodal loads imposed at the coarse element nodes. Equivalently to relation (20) the variation principle of equation (28) gives rise to the following equation:

$$\int_{V_M} \{\varepsilon\}^{T}_{M} \{\dot{\sigma}\}_{M} \, dV_M = [K]^{M}_{CR(j)} \left\{\dot{d}\right\}_{M} - \left[K^{h}\right]^{M}_{CR(j)} \left\{\dot{\varepsilon}^{pl}_{cq}\right\}_{M} \tag{29}$$

where $[K]^{M}_{CR(j)}$, $\left[K^{h}\right]^{M}_{CR(j)}$ are the equivalent stiffness matrix and the equivalent hysteretic matrix of the j_{th} coarse element respectively. These matrices need to be expressed in terms of micro-scale measures, to account for the micro-scale effect upon the macro-scale mesh. This is accomplished by demanding that the strain energy of the coarse element is additively decomposed into the contributions of each micro-element within the coarse-element. Thus, the following relation is established:

$$\int_{V} \{\varepsilon\}^{T}_{M} \{\sigma\}_{M} \, dV = \sum_{i=1}^{m_{el}} \int_{V_{mi}} \{\varepsilon\}^{T}_{mi} \{\sigma\}_{mi} \, dV_i \tag{30}$$

where $\{\varepsilon\}_{mi}$, $\{\sigma\}_{mi}$ are the micro-strain and micro-stress field defined over the volume V_{mi} of the i_{th} micro-element. Using relations and (14) (15), the following relation is established for the r.h.s of equation (30)

$$\sum_{i=1}^{m_{el}} \int_{V_{mi}} \{\varepsilon\}^{T}_{mi} \{\sigma\}_{mi} \, dV_i = \sum_{i=1}^{m_{el}} \left(\{d\}^{T}_{mi} \left[k^{el}\right]_{m(i)} \{d\}_{m(i)} - \{d\}^{T}_{mi} \left[k^{h}\right]_{m(i)} \left\{\varepsilon^{pl}_{cq}\right\}_{m(i)} \right) \tag{31}$$

Substituting relation (24) into relation (31), the following relation is derived

$$\sum_{i=1}^{m_{el}} \int_{V_{mi}} \{\varepsilon\}_{mi}^{T} \{\sigma\}_{mi} \, dV_i = \{d\}_M^T \sum_{i=1}^{m_{el}} \left([N]_{Mi}^T \left[k^{el}\right]_{m(i)} [N]_{Mi} \{d\}_M - [N]_{Mi}^T \left[k^h\right]_{m(i)} \left\{\varepsilon_{cq}^{pl}\right\}_{m(i)} \right) \tag{32}$$

Using equations (29) and (32), equation (30) assumes the following form:

$$[K]_{CR(j)}^M \{d\}_M - \left[K^h\right]_{CR(j)}^M \left\{\varepsilon^{pl}\right\}_{cq} = \sum_{i=1}^{m_{el}} \left[k^{el}\right]_{m(i)}^M \{d\}_M - \sum_{i=1}^{m_{el}} \left[k^h\right]_{m(i)}^M \left\{\varepsilon_{cq}^{pl}\right\}_{m(i)} \tag{33}$$

Relation (33) holds for every compatible vector of nodal displacements $\{d\}_M$ as long as:

$$[K]_{CR(j)}^M = \sum_{i=1}^{m_{el}} \left[k^{el}\right]_{m(i)}^M \tag{34}$$

and

$$\left[K^h\right]_{CR(j)}^M \left\{\varepsilon_{cq}^{pl}\right\} = \sum_{i=1}^{m_{el}} \left[k^h\right]_{m(i)}^M \left\{\varepsilon_{cq}^{pl}\right\}_{m(i)} \tag{35}$$

thus, the following multiscale equilibrium equation is derived for the coarse element:

$$[K]_{CR(j)}^M \{d\}_M = \{f\}_M - \{f_h\}_M \tag{36}$$

where $\{f_h\}_M$ is a nonlinear correction to the external force vector arising from the evolution of the plastic strains within the micro-structure

$$\{f_h\}_M = \sum_{i=1}^{m_{el}} \left[k^h\right]_{m(i)}^M \left\{\varepsilon_{cq}^{pl}\right\}_{m(i)} \tag{37}$$

while the plastic strain vectors $\left\{\varepsilon_{cq}^{pl}\right\}_{m(i)}$ are considered to evolve according to relation (13). Equations (36) and (37) are used to derive the equilibrium equation at the structural level.

4.2 Solution in the macro-scale

Considering the general case of a coarse mesh with $ndof_M$ free macro-degrees of freedom and using equation (36), the global equilibrium equations of the composite structure can be established in the coarse mesh. In the dynamic case the following equation is established:

$$[M] \left\{\ddot{U}\right\}_M + [C] \left\{\dot{U}\right\}_M + [K] \{U\}_M = \{F\}_M + \{F_h\}_M \tag{38}$$

where $[M]$, $[C]$, $[K]$ are the $(ndof_M \times ndof_M)$ macro-scale mass, viscous damping and stiffness matrix respectively. The mass matrix can be formulated following either the lamped or distributed mass approach while the viscous damping can be of either the classical or non-classical type [10]. The global stiffness matrix of the composite structure is formulated through the direct stiffness method by additively appending the contributions of the coarse elements equivalent matrices defined in equation (34). The $(ndof_M \times 1)$ vector $\{U\}_M$ consists of the nodal macro-displacements.

Equation (36) expresses the nodal equilibrium of the coarse element mesh. The coarse element equivalent stiffness matrices $[K]_{CR(j)}^M$ can be assembled through the direct stiffness

method to derive the stiffness matrix of the composite structure. The external load vector $\{F\}_M$ and the hysteretic load vector $\{F_h\}_M$ are assembled considering the equilibrium of the corresponding elemental contributions $\{f\}_M$ and $\{f_h\}_M$, defined in equations (28) and (37) respectively, at coarse nodal points.

Equations (38) are supplemented by the evolution equations of the micro-plastic strain components defined at the collocation points within the micro-elements. These equations can be established in the following form:

$$\left\{\dot{E}^{pl}_{cq}\right\}_m = [G]\left\{\dot{\varepsilon}_{cq}\right\}_m \tag{39}$$

where the vector

$$\left\{\dot{E}^{pl}_{cq}\right\}_m = \left\{ \begin{array}{cccc} \left\{\dot{\varepsilon}^{pl}_{cq}\right\}_{m(1)} & \left\{\dot{\varepsilon}^{pl}_{cq}\right\}_{m(2)} & \cdots & \left\{\dot{\varepsilon}^{pl}_{cq}\right\}_{m(m_{el})} \end{array} \right\}^T \tag{40}$$

holds the plastic strain components evaluated at the collocation points of its micro-element and

$$\left\{\dot{E}_{cq}\right\}_m = \left\{ \begin{array}{cccc} \left\{\dot{\varepsilon}_{cq}\right\}_{m(1)} & \left\{\dot{\varepsilon}_{cq}\right\}_{m(2)} & \cdots & \left\{\dot{\varepsilon}_{cq}\right\}_{m(m_{el})} \end{array} \right\}^T \tag{41}$$

Matrix $[G]$ in relation (39) is a band diagonal matrix that assumes the following form

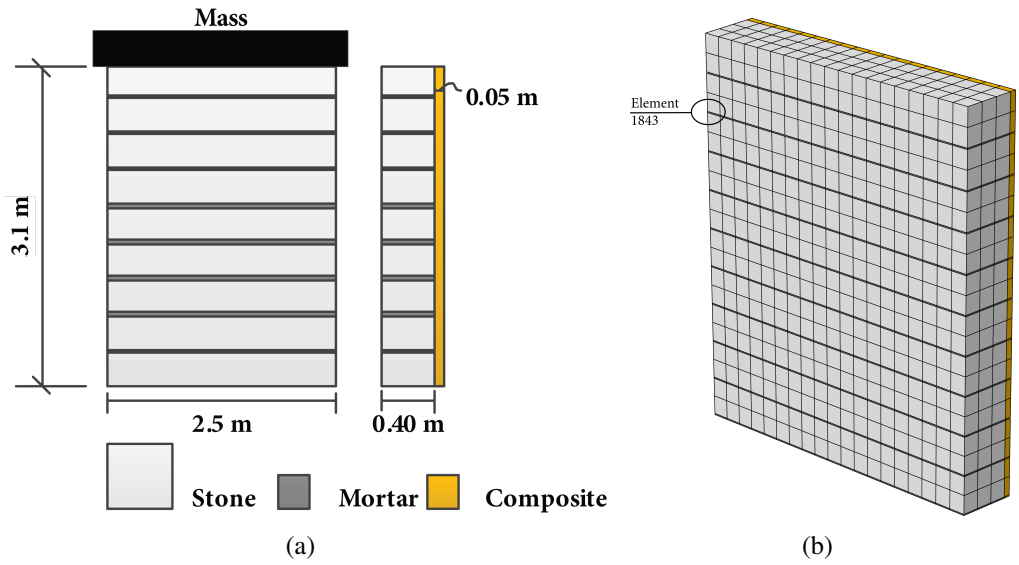
$$[G] = \left[\begin{array}{ccc} H_{1m(1)}H_{2m(1)}\left[R\right]_{m(1)} & & [0] \\ & H_{1m(2)}H_{2m(2)}\left[R\right]_{m(2)} & \\ [0] & & \ddots \\ & & H_{1m(m_{el})}H_{2m(m_{el})}\left[R\right]_{m(m_{el})} \end{array} \right] \tag{42}$$

Equations (39) are independent and thus can be solved in the micro-element level resulting in an implicitly parallel scheme. Relation (42) depends on the current micro-stress state within each micro-element. The corresponding stress tensors are evaluated from the current micro-strains, using equations (16) and (17).

5 EXAMPLE

In this example a benchmark problem is examined for the verification of the proposed method. The simplified masonry wall presented in Figure 2(a) is considered, consisting of stone blocks and bonding mortar. Furthermore, an outer layer of textile component reinforcement is considered. The stone and mortar material properties (Table 2) are derived from [26]. A J_2 plasticity model is assumed for the stone layer while a Mohr-Coulomb yield criterion is considered for the mortar [2]. For the purpose of this example, homogenized material properties are considered for the textile composite layer [14] whose behaviour is assumed to be elastic until failure. The corresponding anisotropic properties are presented in Table 1.

Two analysis models are considered, namely a fine meshed Finite Element model (FE) and a multiscale model. The FE model is analysed using the Abaqus commercial code [1]. The FEM model is meshed with 2280 hex elements(Figure 2(b)). The second model consists of a single coarse hex element, with the corresponding micro-structure being identical to the FE model. The micro-basis shape functions are evaluated considering periodic boundary conditions at the boundary surfaces of the coarse element. An average acceleration Newmark scheme is implemented for the solution of the governing equations of motion with a constant time step



(a) (b)

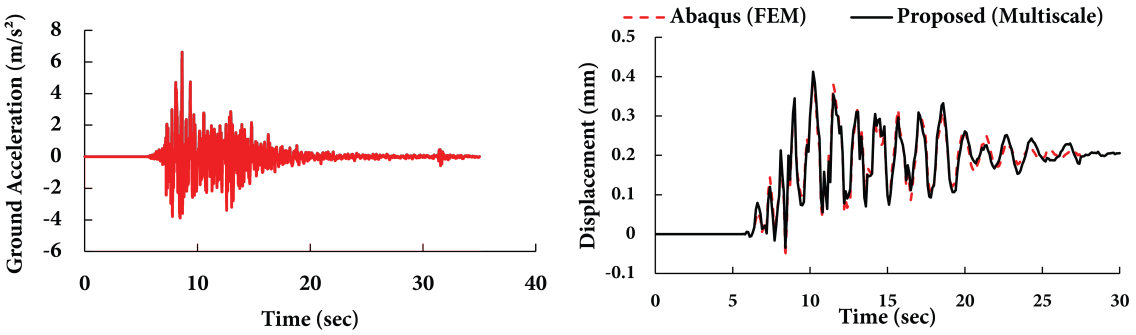
Figure 2: (a) Textile composite reinforced stone masonry wall (b) Fem hex-mesh

	Mortar	**Stone**
Young's modulus [MPa]	3494	20200
Poisson's ratio	0.11	0.2
Plasticity	Mohr-Coulomb	von-Mises
Friction angle [deg]	21.8	-
Cohesion [MPa]	0.1	-
Yield Stress [MPa]	-	69.2

Table 1: Masonry wall: Constituent Properties

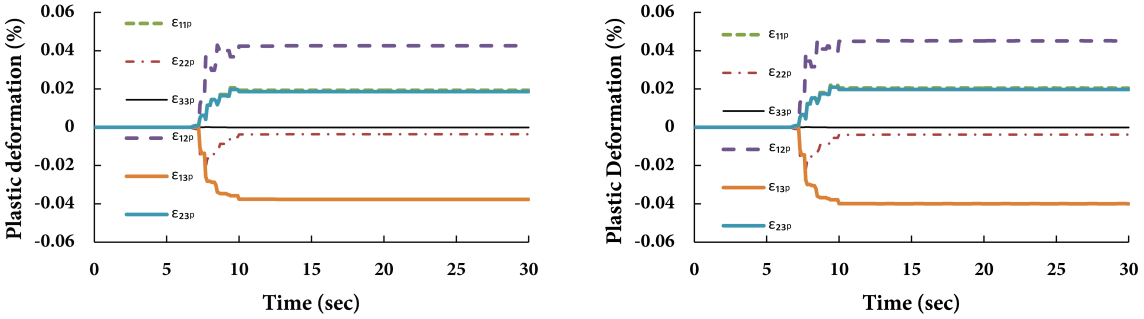
Young's modulus [MPa]	$E_{11} = 54000$	$E_{22} = 53200$	$E_{33} = 53200$
	$E_{12} = 53200$	$E_{23} = 54000$	$E_{23} = 54000$
Poisson's ratio	$\nu_{12} = 0.14$	$\nu_{23} = 0.2$	$\nu_{13} = 0.2$

Table 2: Textile Reinforcement Material Properties



(a) (b)

Figure 3: (a) V. A. Centro Valle ground acceleration record (L' Aquila, 2009) (b) Top layer horizontal displacement time history



(a) (b)

Figure 4: (a) FEM (b) Proposed Method

equal to $dt = 0.01sec$. Viscous damping is not taken into account in this example. Material nonlinearity in Abaqus is treated through a Full Newton scheme.

An additional mass of 400 KN is considered at the top of the wall. The structure is subjected to the L' Aquila ground motion record presented in Figure 3(a) with a peak acceleration equal to $a_{max} = 0.66g$ In Figure 3(a) the horizontal relative displacement time history at the top layer of the masonry is presented as derived from the two different analysis schemes.

The results obtained from the two different methodologies are in good agreement. The differences observed, especially in the low frequency oscillations near the end of the analysis, are attributed to the numerical assumptions governing the evaluation of the effective stiffness of the coarse element. The gradual shift of the horizontal displacement is a result of plastic deformation accumulating at the mortar joints. In Figure 4 the evolution of the plastic strain components evaluated at the mortar element -1843- (Figure 2(b)) are presented as derived from Abaqus (Figure 4(a)) and the proposed formulation (Figure 4(b))) respectively.

The evolution of the plastic strain components is practically identical in both methods. However, the values predicted in the multiscale model are slightly larger, in agreement with the displacement time-history presented in Figure 3(b).

6 CONCLUSIONS

In this work, a novel multiscale finite element formulation is presented for the nonlinear analysis of masonry structures. The method is based on the Enhanced Multiscale Finite Element Method and the hysteretic formulation of Finite Elements. A set of smoothly evolving inelastic quantities is considered in the fine scale that accounts for the plastic part of the deformation component. Implementing the EMsFEM micro to macro-mapping for the micro displacement components the motion equations of the structure are formulated in the macro-scale. The plastic deformation evolution equations are also transferred into the coarse scale governing equations. Thus, a multiscale formulation is derived where the state matrices, namely the coarse scale stiffness matrix and the fine scale hysteretic matrix are evaluated only once at the beginning of the analysis and remain constant throughout the solution process. The validity of the proposed method is verified through a benchmark test, simulating the dynamic response of a single wall element under earthquake load.

REFERENCES

[1] RI. Abaqus version 6.11 [Computer software]. Dassault Systmes Simulia, Providence.

[2] A. H. Akhaveissy. Limit state strength of unreinforced masonry structures. *Earthquake Spectra*, 29(1):1–31, 2013.

[3] I. Babuška and U. Banerjee. Stable generalized finite element method (sgfem). *Computer Methods in Applied Mechanics and Engineering*, 201204:91 – 111, 2012.

[4] I. Babuška, G. Caloz, and J. Osborn. Special finite element methods for a class of second order elliptic problems with rough coefficients. *SIAM Journal on Numerical Analysis*, 31(4):945–981, 1994.

[5] I. Babuška and J. E. Osborn. Generalized finite element methods: Their performance and their relation to mixed methods. *SIAM Journal on Numerical Analysis*, 20(3):pp. 510–536, 1983.

[6] T. Belytschko, Y. Y. Lu, and L. Gu. Element-free galerkin methods. *International Journal for Numerical Methods in Engineering*, 37(2):229–256, 1994.

[7] A. Bensoussan, J. L. Lions, and G. Papanicolaou. *Asymptotic Analysis for Periodic Structures*. North Holland, Amsterdam, 1978.

[8] R. Bouc. Forced vibration of mechanical systems with hysteresis. In *Proceedings of the Fourth Conference on Non-linear oscillation, Prague, Czechoslovakia*, 1967.

[9] Eleni N. Chatzi, Andrew W. Smyth, and Sami F. Masri. Experimental application of on-line parametric identification for nonlinear hysteretic systems with model uncertainty. *Structural Safety*, 32(5):326 – 337, 2010.

[10] A. Chopra. *Dynamics of Structures*. Prentice Hall, New York, 2006.

[11] E.P. J. Den Hartog. *Strength of Materials*. Dover, New York, 1999.

[12] Y. Efendiev and T. Y. Hou. *Multiscale Finite Element Methods*, volume 4 of *Surveys and Tutorials in the Applied Mathematical Sciences*. Springer, 2009.

[13] S. Erlicher and O. Bursi. Boucwen-type models with stiffness degradation: Thermodynamic analysis and applications. *Journal of Engineering Mechanics*, 134(10):843–855, 2008.

[14] C. Fuggini, E. Chatzi, and D. Zangani. Combining genetic algorithms with a meso-scale approach for system identification of a smart polymeric textile. *Computer-Aided Civil and Infrastructure Engineering*, 28(3):227–245, 2013.

[15] M. G. D. Geers, V. G. Kouznetsova, and W. A. M. Brekelmans. Multi-scale computational homogenization: Trends and challenges. *Journal of Computational and Applied Mathematics*, 234(7):2175–2182, 2010.

[16] Xinguang He and Li Ren. Finite volume multiscale finite element method for solving the groundwater flow problems in heterogeneous porous media. *Water Resources Research*, 41(10):n/a–n/a, 2005.

[17] Hans M. Hilber, Thomas J. R. Hughes, and Robert L. Taylor. Improved numerical dissipation for time integration algorithms in structural dynamics. *Earthquake Engineering & Structural Dynamics*, 5(3):283–292, 1977.

[18] Thomas Y. Hou and Xiao-Hui Wu. A multiscale finite element method for elliptic problems in composite materials and porous media. *Journal of Computational Physics*, 134(1):169 – 189, 1997.

[19] A.K. Kaw. *Mechanics of Composite Materials*. CRC Press, second edition, 1997.

[20] J. Lubliner. *Plasticity Theory*. Dover Publications, New York, 2008.

[21] M.R. Nedele and M.R. Wisnom. Finite element micromechanical modelling of a unidirectional composite subjected to axial shear loading. *Composites*, 25(4):263 – 272, 1994.

[22] S. Nemat-Naser. On finite deformation elasto-plasticity. *International Journal of Solids and Structures*, 18(10):857–872, 1982.

[23] Harold S. Park. A multiscale finite element method for the dynamic analysis of surface-dominated nanomaterials. *International Journal for Numerical Methods in Engineering*, 83(8-9):1237–1254, 2010.

[24] G. A. Pavliotis and A. M. Stuart. *Multiscale Methods, Averaging and Homogenization*. Texts in Applied Mathematics. Springer, Berlin, 2008.

[25] Graham Powell and Jeffrey Simons. Improved iteration strategy for nonlinear structures. *International Journal for Numerical Methods in Engineering*, 17(10):1455–1467, 1981.

[26] R. Senthivel and P.B. Loureno. Finite element modelling of deformation characteristics of historical stone masonry shear walls. *Engineering Structures*, 31(9):1930 – 1943, 2009.

[27] P. D. Spanos and I. A. Kougioumtzoglou. Harmonic wavelet-based statistical linearization of the bouc-wen hysteretic model. pages 2649–2656. Taylor and Francis Group, 2011.

[28] A. Taliercio. Macroscopic strength estimates for metal matrix composites embedding a ductile interphase. *International Journal of Solids and Structures*, 44(22-23):7213–7238, 2007.

[29] K. Terada, M. Hori, T. Kyoya, and N. Kikuchi. Simulation of the multi-scale convergence in computational homogenization approaches. *International Journal of Solids and Structures*, 37(16):2285–2311, 2000.

[30] S. P. Triantafyllou and V. K. Koumousis. A hysteretic quadrilateral plane stress element. 82(10-11):1675–1687, 2012.

[31] K Washizu. *Variational Methods in Elasticity and Plasticity*. Pergamon Press, Oxford, 1983.

[32] K. Worden and J. J. Hensman. Parameter estimation and model selection for a class of hysteretic systems using bayesian inference. *Mechanical Systems and Signal Processing*, 32:153–169, 2012.

[33] Q. Yu and J. Fish. Multiscale asymptotic homogenization for multiphysics problems with multiple spatial and temporal scales: A coupled thermo-viscoelastic example problem. *International Journal of Solids and Structures*, 39(26):6429–6452, 2002.

[34] H. W. Zhang, J. K. Wu, and J. Lv. A new multiscale computational method for elasto-plastic analysis of heterogeneous materials. *Computational Mechanics*, 49(2):149–169, 2012.

[35] O. C. Zienkiewicz, R. L. Taylor, and J.Z. Zhu. *The Finite Element Method: Its Basis and Fundamentals*. Elsevier, Amsterdam, 6 edition, 2005.

COMPDYN 2013
4th ECCOMAS Thematic Conference on
Computational Methods in Structural Dynamics and Earthquake Engineering
M. Papadrakakis, V. Papadopoulos, V. Plevris (eds.)
Kos Island, Greece, 12–14 June 2013

ALTERNATIVE INTEGRATORS AND PARALLEL COMPUTING FOR EFFICIENT NONLINEAR RESPONSE HISTORY ANALYSES

Khalid M. Mosalam[1], Xiao Liang[2], Selim Günay[3], Andreas Schellenberg[4]

University of California, Berkeley, USA
[1]mosalam@ce.berkeley.edu, [2]benliangxiao@berkeley.edu, [3]selimgunay@berkeley.edu
[4]andreas.schellenberg@gmail.com

Keywords: Convergence, Nonlinear Response History Analysis, Numerical Integration, Parallel Computing.

Abstract. *This paper is an attempt to address solutions to two common problems associated with nonlinear response history analysis* (*NRHA*). *The first is the convergence problems that occur at high levels of nonlinearity, while the second is the computational time which can be prohibitively excessive in certain cases. To overcome the first problem, suitability of the use of alternative integration methods in NRHA instead of the commonly used implicit Newmark integration is investigated. These alternative methods are Explicit Newmark and Operator-Splitting methods, which do not require iterations and convergence checks. NRHA conducted on highway overpass bridges with multiple-column bents showed that the Operator-Splitting method provides very close results to those from the Implicit Newmark method for some of the considered models even for high levels of nonlinearity. The Explicit Newmark method was not successful for the investigated bridge system because of the stability limits which were not feasible to satisfy. However, explicit methods, when applicable, can be useful since they eliminate the convergence problems and reduce the simulation time. Means to improve convergence are also investigated for the implicit Newmark integration method, especially when the use of alternative integration methods is not possible. To address the second problem, parallel and cloud computing resources are utilized together with the alternative time integration methods. Particularly, the parallel version of OpenSees* (*OpenSees MP*) *running on NEEShub, currently providing access to up to 4232 processors, is used where significant computing time savings are achieved.*

1 INTRODUCTION

In order to gain a better understanding of the behavior of structural components and systems, one of the most suitable methods is experimental testing. The experiments designed to investigate the structural behavior in question can provide remarkable insight. The response of a structure to earthquake excitation and the consequences of this response involve various uncertainties at different stages including the definition of hazard, structural response, damage, and the corresponding loss determination. Performance-based earthquake engineering (PBEE) approach aims to consider all these uncertainties in order to determine the most efficient decision about the seismic risk mitigation actions. In order to achieve this goal of the PBEE approach, considerable amount of structural simulations are required. Due to physical, economical, and time constraints, experimental testing is not feasible as the sole structural simulator in PBEE. Alternatively, analytical simulations, where the analytical models are calibrated using the results of the experimental tests, fit reasonably well within the PBEE framework. The most accurate analytical simulation method is nonlinear response history analyses (NRHA) where two problems usually exist and are of concern to the structural engineering community. First, convergence problems occur at high levels of nonlinearity. Second, the computational time of the simulations can be prohibitively excessive.

This paper is an attempt to address solutions to the previously mentioned two problems associated with NRHA. For this purpose, suitability of the use of alternative integration methods in NRHA instead of the commonly used implicit Newmark integration method is investigated. These alternative integrators are the Explicit Newmark and Operator-Splitting methods, which do not require iterations and convergence checks. Methods of convergence improvement are also investigated for the Implicit Newmark integrator. To reduce the simulation time, parallel and cloud computing resources are utilized in addition to the alternative time integration methods. Particularly, the parallel version of OpenSees (OpenSees MP) running on NEEShub is used, where significant computing time savings can be achieved. Applications of the above solutions to several bridge systems typically found in California under the effect of earthquake loading are also explored.

2 ALTERNATIVE INTEGRATION METHODS

The equations of motion of a multi-degree of freedom (MDOF) system under an external dynamic force excitation can be defined as follows:

$$\mathbf{m}\ddot{\mathbf{u}} + \mathbf{c}\dot{\mathbf{u}} + \mathbf{f} = \mathbf{p} \tag{1}$$

where $\mathbf{m}$ is the mass matrix and $\mathbf{c}$ is the damping matrix, and $\ddot{\mathbf{u}}$, $\dot{\mathbf{u}}$, $\mathbf{f}$, and $\mathbf{p}$ are the acceleration, velocity, restoring force and external force vectors, respectively. The restoring force can generally be defined as a function of displacement. Due to several factors, such as the random variation of the external force with time, e.g. due to earthquake shaking, and the nonlinear variation of the restoring force vector with displacement, closed form solution of Equation 1 is not possible [1]. Therefore, numerical integration methods are used for the sought solution.

Differences between direct integration methods are mainly introduced by the way they handle Equations 2-4, arranged as the Newmark difference equations for displacement and velocity and the discretized dynamic equilibrium equation, respectively.

$$\mathbf{u}_{i+1} = \mathbf{u}_i + \Delta t\,\dot{\mathbf{u}}_i + \frac{(\Delta t)^2}{2}\left[(1-2\beta)\ddot{\mathbf{u}}_i + 2\beta\,\ddot{\mathbf{u}}_{i+1}\right] \tag{2}$$

$$\dot{\mathbf{u}}_{i+1} = \dot{\mathbf{u}}_i + \Delta t\left[(1-\gamma)\ddot{\mathbf{u}}_i + \gamma\ddot{\mathbf{u}}_{i+1}\right] \tag{3}$$

$$\mathbf{m}\ddot{\mathbf{u}}_{i+1} + \mathbf{c}\dot{\mathbf{u}}_{i+1} + \mathbf{f}_{i+1} = \mathbf{p}_{i+1} \tag{4}$$

In the above equations, γ and β parameters define the variation of accelerations over a time step, Δt. For example, γ =1/2 and β =1/4 represent constant average acceleration over a time step, while γ =1/2 and β =1/6 define linear variation of acceleration during the time step.

The following sub-sections describe the alternative integration methods, namely the Explicit Newmark and Operator-Splitting integrators and the commonly utilized Implicit Newmark integration method, and their algorithms. This description starts from the basic three equations defined above and emphasizes departure points and differences between these methods.

2.1 Explicit Newmark Method

Explicit Newmark (EN) integration [2] is defined by setting $\beta = 0.0$. Accordingly, Equation 2 becomes

$$\mathbf{u}_{i+1} = \mathbf{u}_i + \Delta t\,\dot{\mathbf{u}}_i + \frac{(\Delta t)^2}{2}\ddot{\mathbf{u}}_i \tag{5}$$

Substituting Equations 3 and 5 in Equation 4, the linear system of equations defined by Equations 6 is obtained, which can be solved to determine the acceleration. Subsequently, Equation 3 is used to determine the velocity.

$$\begin{aligned} \mathbf{m}_{\mathbf{eff}}\ddot{\mathbf{u}}_{i+1} &= \mathbf{p}_{\text{eff}} \\ \mathbf{m}_{\mathbf{eff}} &= \mathbf{m} + \Delta t\,\gamma\,\mathbf{c} \\ \mathbf{p}_{\mathbf{eff}} &= \mathbf{p}_{i+1} - \mathbf{f}_{i+1} - \mathbf{c}\left[\dot{\mathbf{u}}_i + \Delta t(1-\gamma)\ddot{\mathbf{u}}_i\right] \end{aligned} \tag{6}$$

It is noted that setting $\beta = 0.0$ makes the method explicit. In this way, the implicit nature of Equation 2 is eliminated by removal of the $\ddot{\mathbf{u}}_{i+1}$ term. The algorithm for an integration time step of the EN method is summarized as follows:

1. Compute the displacement using Equation 5.
2. Obtain the restoring force, $\mathbf{f}$, corresponding to the computed displacement from the constitutive relationships of the defined materials and elements using a state determination method [3].
3. Calculate the acceleration by solving the linear system of equations defined by Equations 6.
4. Determine the velocity using Equation 3.
5. Increment *i* and proceed with the next integration step.

2.2 Operator-Splitting (OS) Method

Similar to the EN method, the OS method [4] eliminates the implicit nature of the equations of motion. However, instead of doing this elimination directly as in EN, OS uses a prediction and correction technique. The predicted displacement, $\tilde{\mathbf{u}}_{i+1}$, is obtained by neglecting the $\ddot{\mathbf{u}}_{i+1}$ term in the bracketed term of Equation 2, i.e.

$$\tilde{\mathbf{u}}_{i+1} = \mathbf{u}_i + \Delta t\, \dot{\mathbf{u}}_i + \frac{(\Delta t)^2}{2}\left[(1-2\beta)\,\ddot{\mathbf{u}}_i\right] \tag{7}$$

After the prediction of the displacement, the method is defined by setting the restoring force of the integration time step as the sum of the restoring force corresponding to the predicted displacement, $\tilde{\mathbf{f}}_{i+1}$, and the difference between the corrected and predicted displacements multiplied by the initial stiffness matrix, $\mathbf{k}_I$, i.e.

$$\mathbf{f}_{i+1} = \tilde{\mathbf{f}}_{i+1} + \mathbf{k}_I\left[\mathbf{u}_{i+1} - \tilde{\mathbf{u}}_{i+1}\right] \tag{8}$$

Subtracting Equation 7 from Equation 2 and substituting the result in Equation 8 gives

$$\mathbf{f}_{i+1} = \tilde{\mathbf{f}}_{i+1} + (\Delta t)^2 \beta\, \mathbf{k}_I\, \ddot{\mathbf{u}}_{i+1} \tag{9}$$

Substitution of Equations 3, 7 and 9 in Equation 4 leads to the linear system of equations defined by Equations 10, which can be solved to determine the acceleration.

$$\begin{aligned} \mathbf{m}_{\mathbf{eff}}\, \ddot{\mathbf{u}}_{i+1} &= \mathbf{p}_{\mathrm{eff}} \\ \mathbf{m}_{\mathbf{eff}} &= \mathbf{m} + \Delta t\, \gamma\, \mathbf{c} + (\Delta t)^2 \beta\, \mathbf{k}_I \\ \mathbf{p}_{\mathbf{eff}} &= \mathbf{p}_{i+1} - \tilde{\mathbf{f}}_{i+1} - \mathbf{c}\left[\dot{\mathbf{u}}_i + \Delta t(1-\gamma)\ddot{\mathbf{u}}_i\right] \end{aligned} \tag{10}$$

The method continues by the computation of the corrected displacement (Equation 11) and velocity (Equation 3).

$$\mathbf{u}_{i+1} = (\Delta t)^2 \beta\, \ddot{\mathbf{u}}_{i+1} + \tilde{\mathbf{u}}_{i+1} \tag{11}$$

The algorithm for an integration time step of the OS method can be summarized as follows:

1. Compute the predicted displacement using Equation 7.
2. Obtain the restoring force, $\tilde{\mathbf{f}}$, corresponding to the predicted displacement from the constitutive relationships of the defined materials and elements using a state determination method [3].
3. Determine the acceleration by solving the linear system of equations defined by Equations 10.
4. Calculate the corrected displacement using Equation 11.
5. Obtain the restoring force corresponding to the corrected displacement following similar procedure to that outlined in step 2 above.
6. Determine the velocity using Equation 3.
7. Increment *i* and proceed with the next integration step.

2.3 Implicit Newmark Method

The implicit nature of the equations of motion is eliminated in the EN and OS methods. In contrast to these methods, the Implicit Newmark (IN) integrator treats the equations of motion directly without altering its implicit nature. Rearranging the time-discrete equilibrium equations (Equation 4), one obtains,

$$\mathbf{p}_{i+1} - \mathbf{m}\ddot{\mathbf{u}}_{i+1} - \mathbf{c}\dot{\mathbf{u}}_{i+1} - \mathbf{f}_{i+1} = 0 \tag{12}$$

where $\mathbf{u}_{i+1}$ and $\dot{\mathbf{u}}_{i+1}$ are functions of $\ddot{\mathbf{u}}_{i+1}$ through Equations 2 and 3 and $\mathbf{f}_{i+1}$ is a function of $\mathbf{u}_{i+1}$. Therefore, Equation 12 represents a nonlinear system of equations in terms of $\ddot{\mathbf{u}}_{i+1}$ which can be solved using a nonlinear equation solver. The most common of these nonlinear equation solvers is the Newton-Raphson method, which seeks the root of a function by using Equation 13.

$$g'\left(x^k\right)\Delta x^k = -g\left(x^k\right) \tag{13}$$

where g and g' represent the function and its derivative, respectively, x is the root of the function, k is the iteration number and Δx^k is the difference between the value of x in the current and previous iterations. If the left-hand side of Equation 12 is considered as the function g in Equation 13, one can write the following in terms of the acceleration,

$$g'\left(\ddot{\mathbf{u}}_{i+1}^k\right)\Delta\ddot{\mathbf{u}}_{i+1}^k = -g\left(\ddot{\mathbf{u}}_{i+1}^k\right) \tag{14}$$

$$g\left(\ddot{\mathbf{u}}_{i+1}^k\right) = \mathbf{m}\ddot{\mathbf{u}}_{i+1}^k + \mathbf{c}\dot{\mathbf{u}}_{i+1}^k + \mathbf{f}_{i+1}^k - \mathbf{p}_{i+1} \tag{15}$$

$$g'\left(\ddot{\mathbf{u}}_{i+1}^k\right) = \mathbf{m} + \Delta t\,\gamma\,\mathbf{c} + \left(\Delta t\right)^2\,\beta\,\mathbf{k}_t \tag{16}$$

where, $\mathbf{k}_t$ is the tangential stiffness matrix corresponding to the displacement vector $\mathbf{u}_{i+1}^k$, which can be obtained as a result of a state determination method [3]. It is noted that derivation of Equation 16 from Equation 15 requires various steps as discussed in [5].

Substitution of Equations 15 and 16 in Equation 14 leads to the linear system of equations defined by Equations 17 in the same format as the alternative methods explained earlier.

$$\begin{aligned} \mathbf{m}_{\mathbf{eff}}\,\Delta\ddot{\mathbf{u}}_{i+1}^k &= \mathbf{p}_{\mathbf{eff}} \\ \mathbf{m}_{\mathbf{eff}} &= \mathbf{m} + \Delta t\,\gamma\,\mathbf{c} + \Delta t^2\beta\,\mathbf{k}_t \\ \mathbf{p}_{\mathbf{eff}} &= \mathbf{p}_{i+1} - \mathbf{m}\ddot{\mathbf{u}}_{i+1}^k - \mathbf{c}\dot{\mathbf{u}}_{i+1}^k - \mathbf{f}_{i+1}^k \end{aligned} \tag{17}$$

At this point, it is beneficial to state that all three methods discussed above reduce the nonlinear differential equation (equation of motion) to a system of linear algebraic equations. However, depending on the way each method treats the three basic equations (Equations 2-4), the resulting coefficient matrix (or the Jacobian matrix, referring to the derivative on the left-hand side of Equation 14), $\mathbf{m}_{\mathbf{eff}}$, and the effective load vector, $\mathbf{p}_{\mathbf{eff}}$ differ from one method to the other. Accordingly, these differences determine the adequacy and ease of application of each method as explained later.

After the determination of the acceleration increment for iteration k from Equations 17, the method continues by the calculation of the acceleration, velocity and displacement for iteration $k+1$ from Equations 18-20.

$$\ddot{\mathbf{u}}_{i+1}^{k+1} = \ddot{\mathbf{u}}_{i+1}^k + \Delta\ddot{\mathbf{u}}_{i+1}^k \tag{18}$$

$$\dot{\mathbf{u}}_{i+1}^{k+1} = \dot{\mathbf{u}}_i + \Delta t\left[\left(1-\gamma\right)\ddot{\mathbf{u}}_i + \gamma\,\ddot{\mathbf{u}}_{i+1}^{k+1}\right] \tag{19}$$

$$\mathbf{u}_{i+1}^{k+1} = \mathbf{u}_i + \Delta t\,\dot{\mathbf{u}}_i + \frac{\left(\Delta t\right)^2}{2}\left[\left(1-2\beta\right)\ddot{\mathbf{u}}_i + 2\beta\,\ddot{\mathbf{u}}_{i+1}^{k+1}\right] \tag{20}$$

An iterative method requires an initial guess for the sought value, i.e. for $\ddot{\mathbf{u}}_{i+1}^{k=1}$. For the Newton-Raphson method, acceleration of the previous iteration can be used as the initial

guess as defined in Equation 21. Subsequent substitution of this equation in Equations 2 and 3 leads to the corresponding velocity and displacement, i.e. $\dot{\mathbf{u}}_{i+1}^{k=1}$ and $\mathbf{u}_{i+1}^{k=1}$ vectors as follows,

$$\ddot{\mathbf{u}}_{i+1}^{k=1} = \ddot{\mathbf{u}}_i \tag{21}$$

$$\dot{\mathbf{u}}_{i+1}^{k=1} = \dot{\mathbf{u}}_i + \Delta t\, \ddot{\mathbf{u}}_i \tag{22}$$

$$\mathbf{u}_{i+1}^{k=1} = \mathbf{u}_i + \Delta t\, \dot{\mathbf{u}}_i + \frac{(\Delta t)^2}{2} \ddot{\mathbf{u}}_i \tag{23}$$

The algorithm for an integration time step of the IN method can be summarized as follows:

1. Determine the initial guess, $k = 1$, for acceleration from Equation 21 and the corresponding velocity and displacement from Equations 22 and 23, respectively.

For each iteration k=1: N where N is the total number of iterations:

2. Obtain the restoring force, $\mathbf{f}$, corresponding to the computed displacement from the constitutive relationships of the defined materials and elements using a state determination method [3].
3. Determine the acceleration increment by solving the linear system of equations defined by Equations 17.
4. Compute the acceleration, velocity and displacement using Equations 18-20.
5. Check convergence by comparing a calculated norm with a defined tolerance value. If the norm is smaller than the tolerance, set $N = k$, increment i and proceed to the next integration step; otherwise, increment k and go to step 2.

Regarding the above algorithm, three remarks can be stated as follows:

- This algorithm summarizes the IN method for the implicit formulation in terms of acceleration. It is also possible to have an implicit formulation in terms of displacement and the corresponding algorithm, which leads to fewer convergence issues than the acceleration based formulation [6]. However, the acceleration solution is presented herein to provide a similar format to the other two alternative methods to be able to indicate the differences of the methods using this same format.
- As can be observed from the algorithm above, presence of the convergence check requires at least two iterations. Therefore, unless a solution is separately coded for a linear case, a general nonlinear analysis software requires at least two iterations for the IN integration, even for the case of a linear problem.
- Different norms can be used for the mentioned convergence check in step 5 of the above algorithm. Examples of these norms are the acceleration increment and unbalanced force norms.

Among the three integration methods discussed above, the IN can be considered as the most accurate solution method for nonlinear problems since it seeks a solution to the implicit problem directly using commonly established nonlinear equation solving methods. In this sense, it can be considered as an accurate reference for other methods, whereas the described alternative methods can be considered as approximations. However, the reference IN method is subject to convergence problems (refer to step 5 of the above algorithm) due to the iterative nature of the method, while the approximate alternative methods are free from such convergence problems since they do not require any convergence checks. Therefore, the advantage

of such alternative methods can be considered in NRHA by employing these alternative methods whenever they are applicable with acceptable accuracy.

3 APPLICABILITY OF THE ALTERNATIVE INTEGRATION METHODS

3.1 General

The EN integration, providing a straightforward application and accordingly being computationally efficient, is unfortunately conditionally stable with the following stability limit,

$$\Delta t / T_n < \pi \tag{24}$$

where Δt is the integration time step and T_n is the period of the highest mode of vibration of the considered structure. The stability limit defined in Equation 24 prevents the use of the EN method for structures with massless degrees of freedom (DOF), since the presence of such DOF results in a singular mass matrix that yields zero-period modes. Accordingly, the EN method is not applicable to building and bridge structures which typically are modeled with massless rotational DOF, unless these DOF are condensed out. General purpose nonlinear analysis software such as OpenSees [7] or SAP2000 [8] do not perform such condensation since the architecture of the software is not designed to operate on specific structure types. However, it is within the future objectives of this study to implement a condensation algorithm in OpenSees to facilitate the use of the EN method for a wide range of typical structures.

The OS method is unconditionally stable as long as the tangential stiffness is smaller than the initial stiffness, i.e. for the case of softening (non-stiffening) nonlinearity. However, this condition does not restrict the use of the OS method for models with stiffening constitutive relationships. As demonstrated in the next section, the OS method can still provide accurate results for some stiffening models. Accordingly, the applicability of the OS method covers a broad range of nonlinear problems. It is to be noted that, the unconditional stability is a result of the choice of γ and β parameters as 1/2 and 1/4, respectively, following the recommendations in [9, 10].

The IN integration method is unconditionally stable for the parameter values $\gamma = 1/2$ and $\beta \geq 1/4$. Accordingly, the common use of the IN integration method assuming average acceleration, i.e. $\gamma = 1/2$ and $\beta = 1/4$, is unconditionally stable.

3.2 Investigation on Specific Bridge Structures

Applicability of the previously discussed integrators is investigated on two bridge structures in California, namely the La Veta Avenue Overcrossing, a bridge with two spans and a two-column bent and the Jack Tone Road Overcrossing, a bridge with two spans supported on a single-column bent. Peyman et al. [11] conducted extensive analytical simulations of these two bridges using OpenSees [7], on which the modeling assumptions adopted herein are based. For a detailed explanation of the employed modeling assumptions, please refer to the descriptions in [11, 12]. For completeness and convenience to the reader, the utilized modeling aspects are briefly summarized in the following two paragraphs.

Caltrans SDC [13] requires the superstructure of a bridge to be capacity protected and accordingly to remain elastic. Considering that the bridge is designed according to the code regulations, the bridge deck and the cap-beam that form the bridge superstructure are modeled as elastic beam-column elements with uncracked section properties as typical for prestressed concrete. The cap-beam was given arbitrarily high torsional and out-of-plane stiffness since the cap-beam and the deck were integrally constructed. The mass of the superstructure, in-

cluding the rotational mass, is distributed to the superstructure elements to accurately capture the dynamic response. To model the columns, nonlinear force-based beam-column elements are utilized with fiber-discretized sections considering 10 integration points. The boundary condition at each column base is considered as pin connection.

Regarding the abutment modeling, two approaches are considered: detailed modeling and simplified modeling. In both approaches, the longitudinal responses of the backfill and the expansion joint, the transverse responses of the shear keys, and the vertical responses of the bearing pads and the stemwall are considered explicitly. In the detailed modeling approach (Figure 1a), five nonlinear springs connected to gap elements in series are used to model the passive backfill response and the expansion joint. The strength and initial stiffness of the soil springs are determined according to Caltrans SDC [13]. The shear key response is modeled using a nonlinear spring with a tri-linear backbone curve. Vertical response of the bearing pads and the stemwall is modeled by two parallel springs that represent the stiffness of the bearing pads and the stemwall. In the simplified modeling approach, the number of nonlinear springs connected in series to the gap elements is reduced to two as shown in Figure 1b, and the shear key response is modeled using an elastic perfectly plastic backbone curve.

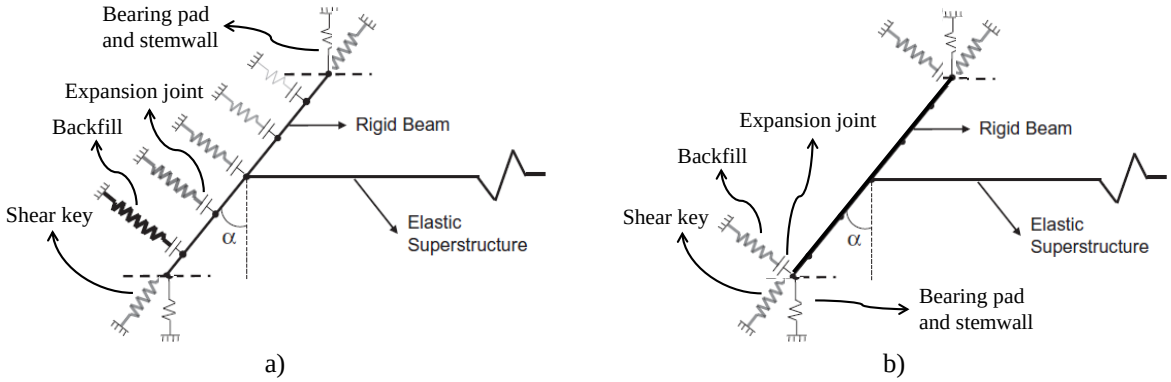


Figure 1: Springs and gap elements used to model various components of the abutment, a) detailed modeling, b) simplified modeling [11].

NRHA are conducted for both modeling approaches using the OS and IN methods for forty pulse-like three-component ground motions described in [11]. Considering the IN method as a reference, the accuracy of the OS method is investigated by comparing the obtained response quantities. Although analyses are conducted for all 40 ground motions, detailed results are presented herein for selected ground motions which result in the highest level of nonlinearity. The longitudinal direction displacement of a superstructure node (node105 in Figure 2) from the IN and OS methods applied to the La Veta Avenue Overcrossing model with simplified abutment modeling is plotted in Figures 3-6 together with moment-curvature plots (M_y-ϕ_y, plots) to reflect the corresponding level of nonlinearity. It is noted that M_y-ϕ_y plots are those obtained from the IN method.

In order to quantitatively compare the results of the OS and IN methods, two error measures are introduced as follows,

1. The error of maximum response defined as

$$Max_{error} = \left| \frac{Max_{IN} - Max_{OS}}{Max_{IN}} \right| \tag{25}$$

where Max_{IN} and Max_{OS} are the maximum absolute response provided by the IN and OS methods, respectively.

2. Root Mean Square Error, $RMSE$, defined as

$$RMSE = \frac{\sqrt{\sum_{i=1}^{n}\left(x_i^{OS} - x_i^{IN}\right)^2 \Big/ n}}{x_m^{IN}} \tag{26}$$

where n is the total number of time integration points, x_i^{OS} and x_i^{IN} are the response quantities at the i^{th} integration time step from the OS and IN methods, respectively, and x_m^{IN} is the median of the absolute of the response at all integration time steps from the IN method. Max_{error} and $RMSE$ for the longitudinal direction displacements of one node of the abutment (abut1000, not shown in Figure 2), one node of the column (node12), and one node of the superstructure (node105) are presented in Tables 1-4.

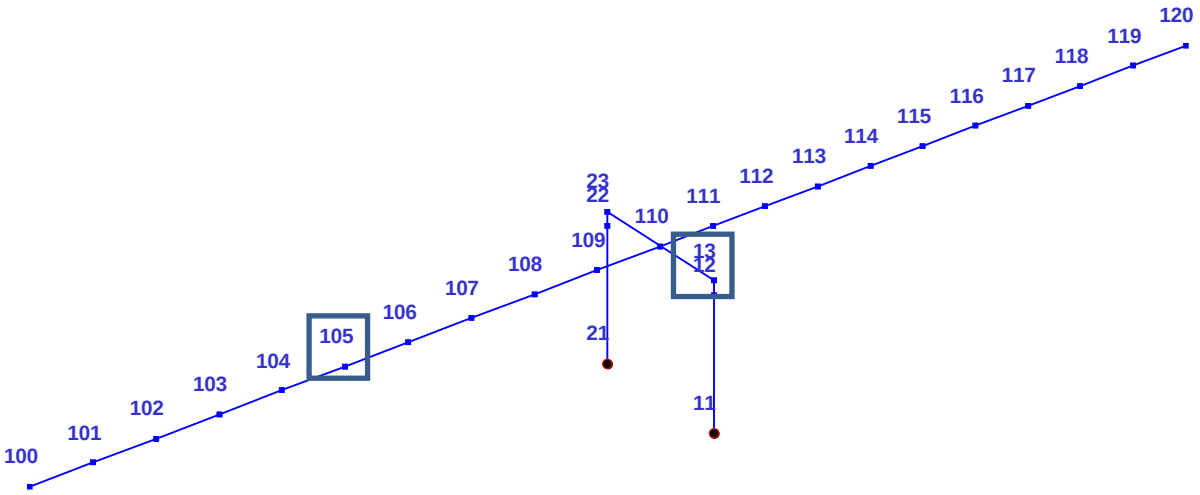
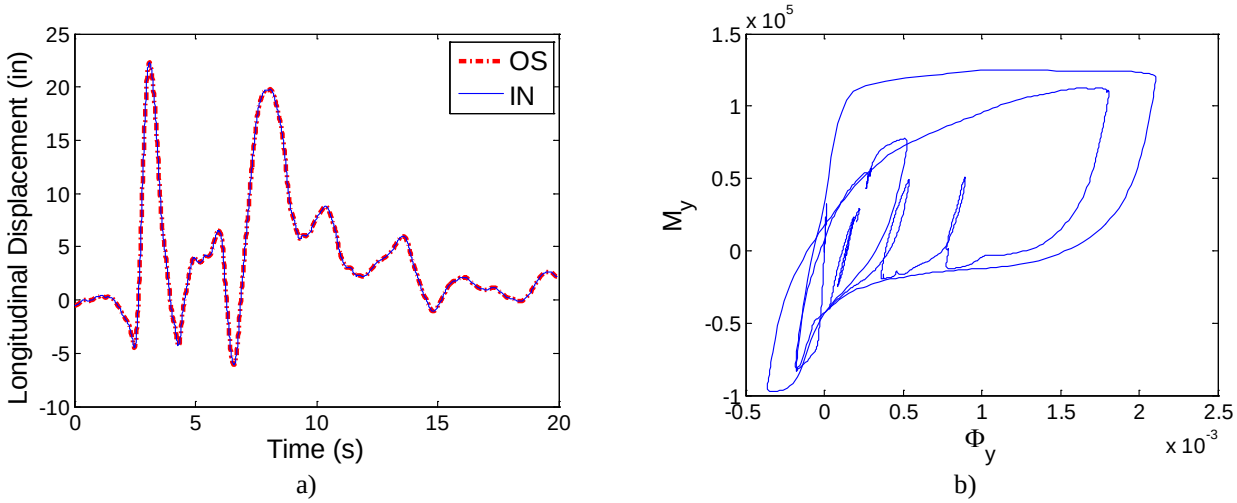
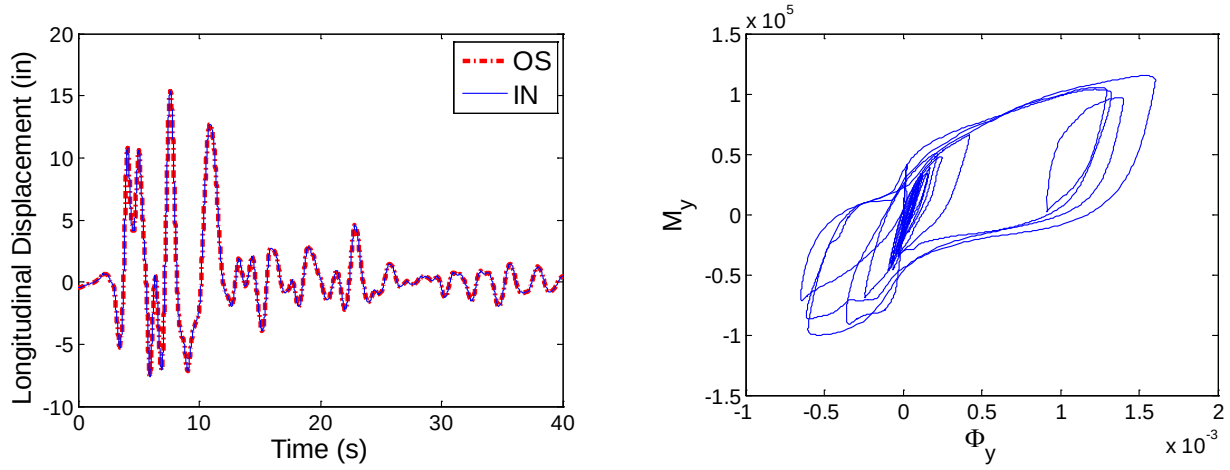


Figure 2: Superstructure and the column bent of the La Veta Avenue Overcrossing bridge model used in the NRHA with marked nodes for which the results are presented



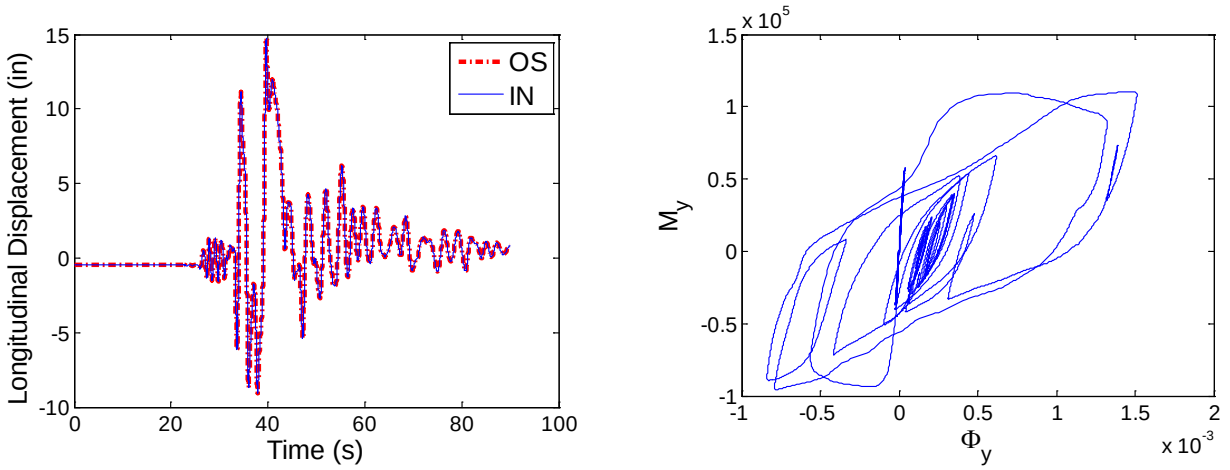
a) b)

Figure 3: Comparison of the IN and OS methods for the longitudinal displacement of node105 (a) and moment-curvature response (b) for GM18.



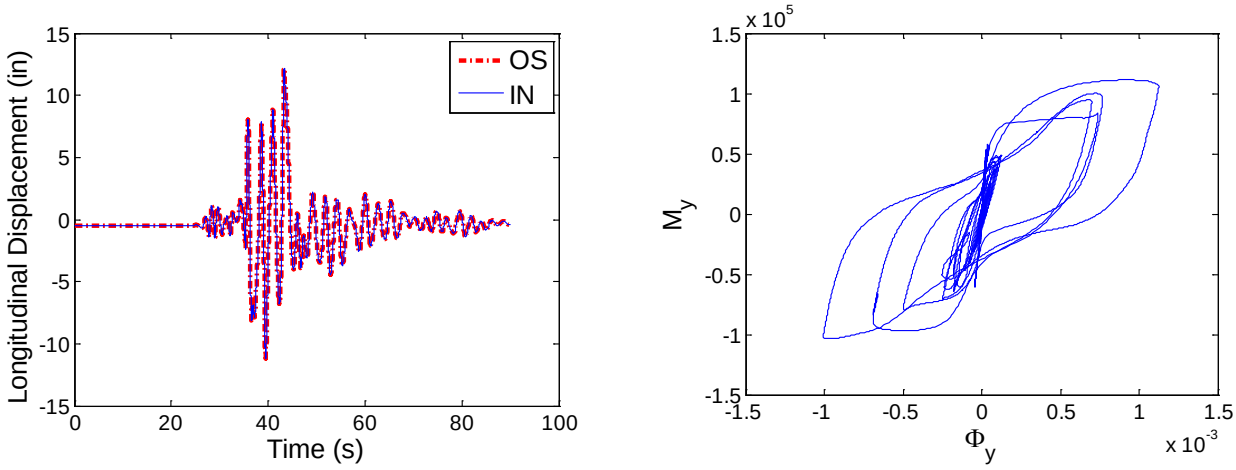
a) b)

Figure 4: Comparison of the IN and OS methods for the longitudinal displacement of node105 (a) and moment-curvature response (b) for GM19.



a) b)

Figure 5: Comparison of the IN and OS methods for the longitudinal displacement of node105 (a) and moment-curvature response (b) for GM28.



a) b)

Figure 6: Comparison of the IN and OS methods for the longitudinal displacement of node105 (a) and moment-curvature response (b) for GM31.

Table 1. Max_{error} for all DOF deformations of the node abut1000

DIR / GM	1	2	3	4	5	6
18	4.49×10^{-6}	2.02×10^{-4}	6.20×10^{-6}	4.48×10^{-5}	9.44×10^{-6}	6.87×10^{-4}
19	6.53×10^{-5}	1.34×10^{-5}	0.0	1.06×10^{-5}	0.0	9.07×10^{-5}
28	6.80×10^{-6}	9.93×10^{-6}	0.0	1.99×10^{-5}	3.75×10^{-6}	2.17×10^{-6}
31	8.19×10^{-6}	3.69×10^{-6}	6.16×10^{-6}	0.0	3.88×10^{-6}	3.16×10^{-5}

Table 2. *RMSE* for all DOF deformations of the node abut1000

DIR / GM	1	2	3	4	5	6
18	1.71×10^{-4}	4.06×10^{-4}	2.34×10^{-5}	3.42×10^{-4}	9.89×10^{-6}	2.53×10^{-3}
19	2.61×10^{-4}	4.16×10^{-4}	5.11×10^{-6}	1.36×10^{-4}	3.93×10^{-6}	1.36×10^{-3}
28	7.28×10^{-5}	8.41×10^{-6}	2.96×10^{-6}	6.92×10^{-6}	1.07×10^{-6}	4.48×10^{-4}
31	5.59×10^{-5}	3.60×10^{-5}	3.82×10^{-6}	2.04×10^{-5}	1.42×10^{-6}	2.97×10^{-3}

Table 3. Max_{error} and *RMSE* for longitudinal and transverse direction displacements of node12

DIR	1		2	
GM	Max_{error}	*RMSE*	Max_{error}	*RMSE*
18	5.87×10^{-6}	1.77×10^{-4}	6.18×10^{-5}	2.47×10^{-4}
19	6.06×10^{-5}	2.59×10^{-4}	2.26×10^{-6}	4.66×10^{-5}
28	1.12×10^{-5}	7.12×10^{-5}	1.02×10^{-5}	7.00×10^{-6}
31	8.57×10^{-6}	5.37×10^{-5}	7.37×10^{-6}	1.38×10^{-5}

Table 4. Max_{error} and *RMSE* for longitudinal and transverse direction displacements of node105

DIR	1		2	
GM	Max_{error}	*RMSE*	Max_{error}	*RMSE*
18	7.15×10^{-6}	1.84×10^{-4}	1.16×10^{-4}	1.96×10^{-4}
19	6.03×10^{-5}	2.47×10^{-4}	8.18×10^{-6}	2.00×10^{-4}
28	1.12×10^{-5}	7.25×10^{-5}	9.85×10^{-6}	7.80×10^{-6}
31	7.53×10^{-6}	5.01×10^{-5}	5.53×10^{-6}	1.24×10^{-5}

From the very good match of the responses for highly nonlinear cases in Figures 3-6 and very small values of the error measures in Tables 1-4, it can be concluded that the OS method is a good candidate to replace the IN method for NRHA of a structure such as the considered bridge with simplified abutment modeling. On the contrary, the OS method does not provide accurate results for the model with detailed abutment as shown in Figure 7, which compares the Max_{error} values from the simplified and detailed abutment modeling cases for all analyzed ground motions. The inaccuracy of the OS method for the detailed abutment modeling is attributed to the increased number of gap elements, which results in a considerable stiffening response and restricts the use of the OS method. Not shown here due to space limitations,

similar behavior is witnessed, i.e. very good match of results for simplified modeling and inaccurate results for the detailed modeling, for the Jack Tone Road Overcrossing model.

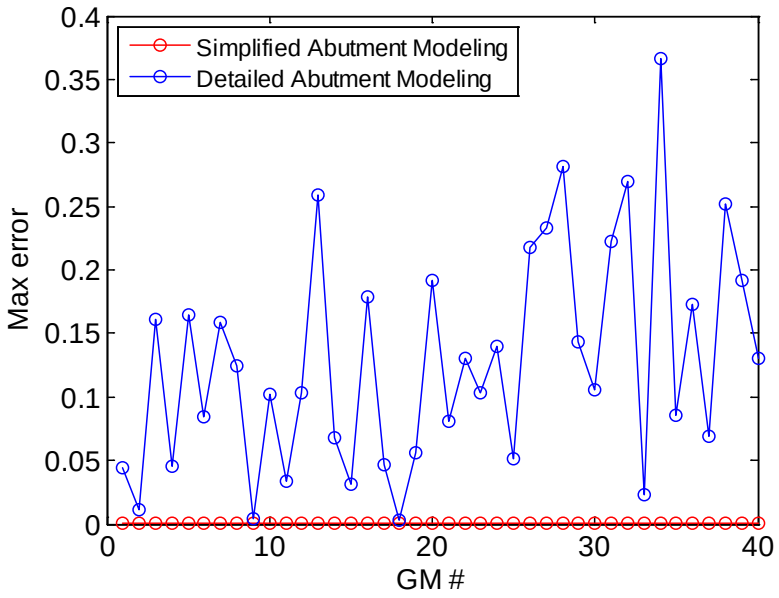


Figure 7: Max_{error} for the longitudinal direction displacement of node105 for the models with simplified and detailed abutment modeling.

Although rotational mass is utilized in some of the DOF, the EN method was not practically applicable for this bridge due to the existence of other DOF with zero mass and the corresponding zero-period modes. Therefore, the EN method was not pursued in these bridge analyses.

4 IMPROVING CONVERGENCE OF IMPLICIT NEWMARK INTEGRATION

As demonstrated in the previous section, the OS method is a suitable alternative to the IN method to avoid convergence problems. However, there exist some conditions where the OS method is not applicable, e.g. the case of significant stiffening response due to closing of the gap elements in the above mentioned bridge model. Moreover, aside from the chosen integration method, formulation of some of the elements, e.g. the force-based beam-column elements or the materials, e.g. Bouc-Wen type, in OpenSees [7] are iterative. Accordingly, the IN method may be the only option for NRHA of models containing such elements and materials if the convergence problems at the element and material levels cannot be eliminated while using the alternative integrators.

The following sub-sections investigate the effect of different parameters in improving the convergence properties of the IN method while preserving its accuracy for the OpenSees bridge models mentioned above. It is noted that this investigation is based on the displacement formulation of the method, which is observed to result in an improved convergence performance compared to the acceleration formulation. The considered parameters are categorized in four groups as follows:

1. Type and sequence of nonlinear equation solvers
2. Convergence test type
3. Convergence tolerance
4. Integration time step

4.1 Type and sequence of nonlinear equation solvers

In order to achieve convergence, OpenSees [7] allows trying various nonlinear solvers consecutively for an integration time step. Therefore, one of the potential items that can be considered to improve convergence is the type and sequence of the nonlinear equation solvers. This investigation is further divided into two sub-groups, namely, (a) determination of the most suitable initial solver and (b) sequence of other solvers after the initial one. In order to identify the most suitable initial solver, the following nonlinear solvers: Newton, KrylovNewton, Broyden–Fletcher–Goldfarb–Shanno (BFGS), Broyden, and Newton with Line Search (NLS) available in OpenSees [7] are tested for the Jack Tone Road Overcrossing with detailed abutment modeling. Based on the convergence situations from the simulations with several relatively strong ground motions (GM1, GM11, GM18, GM19, GM28, and GM31) with scale factors ranging from 1.0 to 2.0, NLS proves to be the most suitable initial solver. Table 5 shows the convergence condition for different scales of GM31, where it can be observed that all the simulations that used the NLS solver as the initial solver are completed, whereas the simulations with other initial solvers fail to converge for some of the scales.

Table 5. The convergence failure time [sec] of simulations for different initial nonlinear solvers under GM31

Scale Factor	Newton	KrylovNewton	Broyden	NLS	BFGS
1.0	Completed	21.820	Completed	Completed	Completed
1.1	35.645	21.820	35.660	Completed	35.820
1.2	35.650	21.820	Completed	Completed	41.010
1.3	35.655	6.115	35.655	Completed	Completed
1.4	Completed	6.115	35.260	Completed	28.985
1.5	Completed	6.115	78.505	Completed	Completed
1.6	Completed	6.115	Completed	Completed	42.600
1.7	Completed	6.115	Completed	Completed	36.155
1.8	35.710	6.115	Completed	Completed	37.270
1.9	Completed	6.115	35.265	Completed	35.915
2.0	35.730	6.115	52.540	Completed	24.675

Using the NLS as the initial solver, no difference was found when different subsequent orders of other solvers (Newton, Broyden, BFGS, and KrylovNewton) were investigated. It may be concluded that as long as a suitable initial solver is determined, the order of subsequent other solvers do not have significant impact on the convergence. It is beneficial to note that this finding may be specific to the investigated structure since this investigation is not repeated for other structures. However, it is still a useful conclusion because of two reasons. First, this finding sets the NLS to be a suitable initial solver as the first simulation trial of future nonlinear models. Second, it shows to the analyst the importance of proper selection of the initial solver compared to trying a variety of solver combinations afterwards.

4.2 Convergence test type

Similar to the previous sub-section, the Jack Tone Road Overcrossing with detailed abutment modeling is used in this sub-section. The following five convergence tests: Energy Increment, Norm Displacement Increment, Relative Norm Displacement Increment, Total Relative Displacement Increment, and Relative Energy Increment, are compared for the 4 ground motions (GM18, GM19, GM28, and GM31) with scale factors ranging from 1.0 to 2.0. The comparisons are based on counting the total number of iterations for each simulation, see

Table 6. It can be observed that the Energy Increment test leads to significantly less number of iterations compared to the other test types. It is to be noted that very small differences are obtained from the simulations with different convergence tests, as indicated by Max_{error} and $RMSE$ for the longitudinal direction displacements of one of the nodes of the abutment, i.e. abut100 (not shown in Figure 2) in Tables 7 and 8. Here, Max_{error} and $RMSE$ are calculated for the simulations with different convergence tests considering the simulations with the Energy Increment test as the reference.

It is beneficial to note that the same tolerance value of 1×10^{-8} is used for all the convergence tests, making the Energy Increment test to have the least amount of iterations. Multiplication of the displacement increment with the unbalanced force, both less than 1.0, results in a norm value smaller than the other norms. However, observing that the simulations with the less stringent Energy Increment leads to the same value of results with significantly less number of iterations compared to the other tests, it is concluded that the Energy Increment test is the most suitable convergence test for the analyzed model. Similar to the investigation in previous sub-section, this finding may be specific to the investigated model. However, for similar reasons as those mentioned above, it is still a useful conclusion by providing an initial trial suggestion for other models and simulations.

Table 6. Total number of iterations for simulations with different convergence tests under GM31

Scale Factor	EnergyIncr	NormDisIncr	RelativeNorm DisIncr	RelativeTotal NormDisIncr	Relative EnergyIncr
1.0	31227	48225	55821	55817	40949
1.1	31510	48514	56481	56472	41726
1.2	31671	48983	56656	56664	42324
1.3	32021	49340	56734	56733	42505
1.4	31979	49567	57093	57075	42605
1.5	32272	49844	57187	57187	42715
1.6	32580	50035	57023	57023	42522
1.7	32573	50074	57015	57011	42162
1.8	33077	50683	57291	57219	42077
1.9	33397	51537	57381	57372	42439
2.0	33780	Failed	61986	57876	42664

Table 7. Max_{error} due to different convergence tests for the longitudinal deformation of node abut100 for GM31

Scale Factor	NormDisIncr	RelativeNorm DisIncr	RelativeTotal NormDisIncr	Relative EnergyIncr
1.0	1.82×10^{-6}	1.82×10^{-6}	1.82×10^{-6}	1.82×10^{-6}
1.1	0.0	0.0	0.0	0.0
1.2	1.30×10^{-4}	0.0	0.0	0.0
1.3	8.67×10^{-6}	8.67×10^{-6}	8.67×10^{-6}	0.0
1.4	0.0	0.0	0.0	0.0
1.5	0.0	0.0	0.0	0.0
1.6	0.0	0.0	0.0	0.0
1.7	0.0	0.0	0.0	0.0
1.8	0.0	0.0	0.0	2.21×10^{-6}
1.9	0.0	0.0	0.0	0.0
2.0	Failed	1.91×10^{-4}	2.38×10^{-3}	2.70×10^{-6}

Table 8. *RMSE* due to different convergence tests for the longitudinal deformation of node abut100 for GM31

Scale Factor	NormDisIncr	RelativeNorm DisIncr	RelativeTotal NormDisIncr	Relative EnergyIncr
1.0	3.77×10^{-5}	3.77×10^{-5}	3.77×10^{-5}	3.80×10^{-5}
1.1	4.45×10^{-3}	4.83×10^{-3}	4.89×10^{-3}	4.78×10^{-3}
1.2	1.68×10^{-1}	1.55×10^{-2}	1.68×10^{-2}	1.53×10^{-2}
1.3	2.49×10^{-2}	2.29×10^{-2}	2.29×10^{-2}	1.90×10^{-2}
1.4	3.35×10^{-2}	3.07×10^{-2}	3.31×10^{-2}	3.26×10^{-2}
1.5	1.69×10^{-2}	1.69×10^{-2}	1.69×10^{-2}	2.20×10^{-2}
1.6	3.07×10^{-2}	3.07×10^{-2}	3.07×10^{-2}	5.50×10^{-3}
1.7	3.37×10^{-2}	3.30×10^{-2}	3.37×10^{-2}	6.14×10^{-2}
1.8	8.49×10^{-3}	8.49×10^{-3}	2.50×10^{-2}	4.01×10^{-4}
1.9	1.37×10^{-5}	1.37×10^{-5}	1.37×10^{-5}	1.53×10^{-5}
2.0	Failed	6.83×10^{-2}	9.54×10^{-2}	1.04×10^{-4}

4.3 Convergence tolerance

For the La Veta Avenue Overcrossing model with detailed abutment modeling, the effect of different tolerances of 1.0, 0.1, 10^{-3}, and 10^{-5} on the convergence and accuracy of the obtained results is investigated using Energy Increment test. Although analyses are conducted for all of the 40 ground motions, detailed results are presented herein for four selected ground motions (GM18, GM19, GM28, and GM31) and for the longitudinal direction deformation of one node of the abutment, abut100, and the longitudinal displacement of one node of the column, node12, for the simulations with different tolerances are presented in Tables 9-12. In the calculation of these error quantities, simulations with the tolerance of 10^{-8} are considered as the reference.

Table 9. Max_{error} due to convergence tolerance for the longitudinal deformation of node abut100

TOL / GM	1.0	0.1	10^{-3}	10^{-5}
18	6.78×10^{-2}	2.14×10^{-2}	6.0×10^{-4}	2.89×10^{-5}
19	6.00×10^{-4}	8.16×10^{-5}	0.0	3.14×10^{-6}
28	4.00×10^{-4}	1.79×10^{-5}	2.55×10^{-6}	2.55×10^{-6}
31	1.00×10^{-3}	2.14×10^{-5}	1.22×10^{-5}	3.05×10^{-6}

Table 10. *RMSE* due to convergence tolerance for the longitudinal deformation of node abut100

TOL / GM	1.0	0.1	10^{-3}	10^{-5}
18	1.13×10^{-1}	3.16×10^{-2}	1.00×10^{-3}	5.65×10^{-5}
19	2.90×10^{-3}	3.30×10^{-3}	7.70×10^{-5}	2.76×10^{-5}
28	8.00×10^{-4}	1.00×10^{-5}	5.61×10^{-6}	7.32×10^{-7}
31	1.00×10^{-3}	2.79×10^{-5}	1.01×10^{-5}	9.00×10^{-7}

Table 11. Max_{error} due to convergence tolerance for the longitudinal displacement of node12

TOL / GM	1.0	0.1	10^{-3}	10^{-5}
18	1.13×10^{-1}	3.16×10^{-2}	1.00×10^{-3}	5.65×10^{-5}
19	2.90×10^{-3}	3.30×10^{-3}	7.70×10^{-5}	2.76×10^{-5}
28	8.00×10^{-4}	1.00×10^{-5}	5.61×10^{-6}	7.32×10^{-7}
31	1.00×10^{-3}	2.79×10^{-5}	1.01×10^{-5}	9.00×10^{-7}

Table 12. *RMSE* due to convergence tolerance for the longitudinal displacement of node12

TOL / GM	1.0	0.1	10^{-3}	10^{-5}
18	3.40×10^{-2}	7.00×10^{-3}	2.00×10^{-4}	1.74×10^{-5}
19	2.35×10^{-1}	1.07×10^{-1}	3.90×10^{-3}	1.40×10^{-3}
28	1.46×10^{-2}	7.70×10^{-3}	1.40×10^{-3}	1.32×10^{-5}
31	1.90×10^{-2}	1.83×10^{-2}	1.17×10^{-2}	2.93×10^{-5}

Selected tolerances may have considerable effect on the nonlinear response. A large tolerance may result in a premature convergence and corresponding deviation from the true result. The small errors between the simulations with tolerances of 10^{-5} and 10^{-8} under the effect of the ground motions resulting in highly nonlinear response indicate that the increase of the tolerance can be used as a reasonable option to overcome convergence issues, while preserving accuracy. It is to be noted that the above tolerance values are used for all the integration time steps of a particular simulation. Considering that a common application is the increase of the convergence tolerance only at the integration time steps with convergence problems, the errors in the obtained results in such cases of selective adoption of tolerance values will be even less than the errors listed in Tables 9-12.

4.4 Integration time step

Use of a smaller integration time step during the simulation does not necessarily increase the convergence behavior as seen from Table 13, which compares the convergence condition for the simulations with different scales of GM31 using Newton-Raphson as the initial solver. However, based on the simulations conducted with the two bridges in this study, it is observed that reduction of the integration time step, only when needed, is useful to overcome the convergence problems. However, this requires attention to be paid to preventing the simulation from being completed before the duration of the external excitation, where the integration time step should be reset to its original value after completion of all of the reduced time steps that represent the original step size, e.g. using automatic adaptive time increments [14].

5 PARALLEL COMPUTING

Parallel computing is a form of computation in which many calculations are carried out simultaneously operating on the principle that large problems can often be divided into smaller ones, which are then solved concurrently [15]. The current state of structural and earthquake engineering profession is in need of high performance parallel computing for two reasons: (1) The considerable amount of structural simulations needed in PBEE as discussed

in the "Introduction" section; (2) To facilitate the use of computationally demanding detailed nonlinear three-dimensional finite element models, which is nowadays somewhat commonly used as an accurate NRHA approach in many important practical projects.

This paper is mainly focused on the first reason mentioned above, i.e. the execution of excessive amount of analytical simulations faster. OpenSees [7], which is utilized for the simulations of the studied bridge models, has two parallel versions: (1) OpenSees SP uses parallel processing for the state determination and equation solving stages, e.g. steps 2 and 3 in the algorithm of the EN method, of the numerical integration. It is very useful to shorten the simulation time of computationally expensive large models where minor changes are required in an input file to execute it in OpenSees SP [7]; (2) OpenSees MP is particularly useful for parametric analyses since different versions of a model can be executed simultaneously. The Tcl based interpreters of sequential OpenSees [7] allow conducting many simulations, e.g. consisting of different ground motions and diverse values of selected parameters, by using only a single input script. Minimal amount of changes are required to convert a sequential input script to the parallel version in OpenSees MP (Appendix A). Furthermore, OpenSees MP can handle the state determination and equation solving in a parallel manner. However, this requires more advanced commands.

OpenSees MP running on NEEShub [16], where a large number of processors is accessible, is utilized for the simulations discussed in this paper. The simulation duration was 536 seconds to run 40 ground motions using 8 processors of the NEES cluster in NEEShub, while the simulation took 1648 seconds (more than threefold increase) with a single processor on a local computer. The duration of the simulation is expected to be much shorter if all the 4232 processors available on NEEShub are allocated for the simulation.

Table 13. The convergence failure time [sec] of simulations for different integration time steps under GM31

Scale Factor	Δt = 0.01	Δt = 0.005	Δt = 0.0025	Δt = 0.001
1.0	Completed	Completed	Completed	Completed
1.1	35.6500	35.6450	35.6375	35.6360
1.2	35.6600	35.6500	35.6450	35.6430
1.3	35.6700	35.6550	35.6525	35.6510
1.4	Completed	Completed	Completed	Completed
1.5	Completed	Completed	Completed	Completed
1.6	Completed	Completed	Completed	Completed
1.7	Completed	Completed	Completed	Completed
1.8	35.7200	35.7100	35.7050	35.7040
1.9	Completed	Completed	41.7225	62.6450
2.0	35.7400	35.7300	36.3475	36.3460

6 CONCLUSIONS AND RECOMMENDATIONS

This paper addressed solutions to two problems associated with the nonlinear response history analyses (NRHA), namely convergence and execution time. For this purpose, suitability of the use of alternative integration methods in NRHA instead of the commonly used Implicit Newmark (IN) was investigated. In addition, methods were investigated to improve convergence of the IN method for the situations where alternative integrators are not applicable. In

order to avoid the excessive simulation durations, parallel processing tools are employed. Achieved conclusions are represented below in the form of recommendations to the analysts:

- The simulations conducted with the simplified abutment modeling of the investigated two bridges shows that the non-iterative Operator splitting (OS) method provides very close results to the IN method. However, OS method was not successful in producing the results of the IN method for the detailed abutment modeling cases. Accordingly, it can be concluded that OS method can serve as a suitable candidate for an alternative to the IN method in nonlinear models without significant stiffening nonlinearity.
- An analyst should be aware of the presence of the alternative methods such as Explicit Newmark (EN) and OS methods and should use these methods whenever they are applicable in order to avoid the convergence problems associated with the IN method. It is beneficial to verify the accuracy of these alternative methods by comparison with the IN method as demonstrated in this paper for highly nonlinear cases.
- Newton with Line Search is observed to be the most suitable initial nonlinear solver in terms of convergence. Accordingly, an analyst can start with this method as the initial solver in the first simulation trial of an analytical model.
- The sequence of the nonlinear solvers after the initial solver is observed to be insignificant. Accordingly, an analyst can pay more attention to the determination of the initial solver than the determination of the sequence of the subsequent solvers in NRHA.
- Simulations with Energy Increment lead to the same solution with significantly less number of iterations compared to other convergence tests. Accordingly, an analyst can consider the Energy Increment test in the first simulation trial of an analytical model.
- Simulations conducted with tolerances of 10^{-5} and 10^{-8} for all the integration time steps are observed to result in very similar response calculations. Accordingly, the increase of the convergence tolerance for the integration time steps with convergence problems is a valid option to achieve convergence improvement.
- Use of a smaller integration time step during the simulation does not necessarily increase the convergence behavior. However, reduction of the integration time step, only when needed, is useful to overcome the convergence problems, as long as the integration time step is reset to its original value after completion of the reduced time steps representing the original size of a time step, which is essential to prevent the simulation from being completed before the duration of the external excitation.
- The structural and earthquake engineering community is in need of the computation power offered by parallel computing. Analysts should be aware of the available parallel computing resources such as the parallel OpenSees, i.e. the SP and MP versions, in the NEEShub in order to make use of these resources whenever applicable.

ACKNOWLEDGEMENTS

This research was supported by Caltrans under Contract Number 65A0454 for the Project "Guidelines for Nonlinear Seismic Analysis of Ordinary Bridges: Version 2.0". Prof. Farzin Zareian, UC Irvine, is acknowledged for providing the OpenSees models of the analyzed bridges. The procedural guidance in Appendix A is generated from a combination of various documentation resources in the OpenSees website. OpenSees developer, Dr. Frank McKenna, is credited for the original documentation in the website.

REFERENCES

[1] A.K. Chopra, *Dynamics of Structures, Theory and Applications to Earthquake Engineering*. Pearson Prentice Hall, 3rd Edition, Upper Saddle River, NJ, 2006.

[2] N.M. Newmark, A method of computation for structural dynamics. *ASCE Journal of the Engineering Mechanics Division*, **85**(EM3), 67-94, 1959.

[3] E. Spacone, F.C. Filippou, and F.F. Taucer, Fibre beam-column model for non-linear analysis of R/C frame: Part I. Formulation, *Earthquake Engineering and Structural Dynamics*, **25**, 711-725, 1996.

[4] T.J.R. Hughes, K.S. Pister, R.L. Taylor, Implicit-explicit finite elements in nonlinear transient analysis. *Computer Methods in Applied Mechanics and Engineering* **17/18**, 159-182, 1979.

[5] S. Günay, A. Bakhaty. Hybrid Simulation: Integration Methods. *nees@berkeley 2012 Annual Hybrid Simulation Workshop.* Presentation available at http://nees.berkeley.edu/Events/201206a--workshop-hybridsim/Handouts/Integrationmethods_Gunay_Bakhaty.pdf

[6] A.H. Schellenberg, S.A. Mahin and G.L. Fenves, Advanced implementation of hybrid simulation. *PEER Technical Report 2009/104*, 2009.

[7] F. McKenna, G.L. Fenves, and F.C. Filippou, OpenSees, 2010 http://opensees.berkeley.edu.

[8] E. L. Wilson, and A. Habibullah, SAP2000-Structural analysis user's manual, *Computers and Structures, Inc.*, 1998.

[9] D. Combescure, P. Pegon, α-Operator splitting time integration technique for pseudo-dynamic testing error propagation analysis. *Soil Dynamics Earthquake Engineering*. **16**, 427–443, 1997.

[10] H.M. Hilbert, T.J.R. Hughes, and R.L. Taylor, Improved numerical dissipation for time integration algorithms in structural dynamics. *Earthquake Engineering Structural Dynamics*, **5**, 283-292, 1977.

[11] P Kaviani, F Zareian, E Taciroglu, Seismic behavior of reinforced concrete bridges with skew-angled seat-type abutments, *Engineering Structures*, **45**, 137–150, 2012.

[12] P. Kaviani, Performance-based seismic assessment of skewed bridges. *Ph.D Dissertation*. Irvine, California: University of California - Irvine; 2011.

[13] Caltrans SDC (ver. 1.6). Caltrans seismic design criteria version 1.6. California Department of Transportation, Sacramento; 2010.

[14] DIANA, User's Manual: Analysis Procedures Edited by: Frits C. de Witte and Wijtze Pieter Kikstra, *TNO DIANA*, 2005.

[15] A. Gottlieb, G.S. Almasi, Highly parallel computing. *Benjamin/Cummings.* Redwood City, California: ISBN 0-8053-0177-1, 1989.

[16] The George E. Brown Network for Earthquake Engineering Simulation (NEES), NEEShub: Cyberinfrastructure of the Network for Earthquake Engineering Simulation, 2013, http://nees.org.

[17] F. McKenna, M. H. Scott and G. L. Fenves, Nonlinear finite-element analysis software architecture using object composition, *ASCE Journal of Computing in Civil Engineering*, **24**, 95-107, 2010.

Appendix A: Procedural guidance on the use of OpenSees MP locally and on NEEShub

The application of parallel versions of structural analysis software is relatively new in structural and earthquake engineering [17]. Therefore, there is a need to provide procedural information on the use of such applications. This sub-section provides useful guidance on the use of OpenSees MP on a local computer and on NEEShub.

In order to execute the parallel version OpenSees MP on a local computer, the following three items are required: 1) A multi-core computer, 2) Installed MPICH2 binary (available for download from the following URL http://www.mcs.anl.gov/research/projects/mpich2) and 3) Installed OpenSees MP and TCL software. The installation of MPICH2 requires the following steps:

1. Check if the installation requires that windows SDK need to be installed on the computer.
2. Open an admin command prompt by right-clicking on the command prompt icon and selecting "run as administrator".
3. Run "msiexec /i mpich2-1.3.2p1-win-ia32.msi" from the admin command prompt to install MPICH2.
4. During the installation, select the option that installs MPICH2 for all users.
5. Run "wmpiconfig" and store username/password where the User account must also be an administrative one.
6. Add "C:\Program Files\MPICH2\bin" to the system path and reboot.
7. Check smpd using "smpd –status". It should return "smpd running on $hostname$".
8. To test the execution environment, go to the directory "$MPICHROOT\examples" and run "cpi.exe" using "mpiexec -n 4 cpi".
9. Make sure that the 32-bit version is installed, even on a 64-bit system, as OpenSees is released as a 32 bit version.

It is easy and straightforward to modify a tcl file for parallel computation. The example tcl file below loops over different ground motions, and it is modified from the sequential version by only adding six lines of code, as underlined in Figure A.1. Two of the commands in the tcl file for parallel runs are "getNP", which returns the number of processes in the computation and "getPID", which returns the unique process *id*, $0 \le id \le NP - 1$.

To run an application with *NP* processes, the following command is used on the command prompt "mpiexec -np numProcs? applicationName? inputFile?". Here, mpiexec is an MPICH2 or OpenMPI application, numProcs is the number of processors, *NP*, to be allocated on the local computer, applicationName is OpenSees MP, and inputFile is the name of the tcl script. An example of such a command is "mpiexec –np 4 OpenSeesMP main.tcl."

In order to be able to run OpenSees in NEEShub, the following steps are required:

1. Register in NEEShub using this URL http://nees.org/.
2. Launch the OpenSees Lab in Tools.
3. Download SynchroNEES, through which one can upload and download files and results. It is recommended to use SynchroNEES to upload files to "My NEEShub Files" and download results from "My Scratch Files", which allows uploading and downloading multiple files together.
4. Submit the job application. In order to submit the job application in this window, one has to perform the following sub-steps:
   a) Write the path of the previously uploaded file in the blank space of the "Main Script", e.g. "/home/neeshub/benliangxiao/data/sessions/41000L/main.tcl".
   b) Select the cluster from "Resource", where the available options are NEES (16 processors), Ranger (4096 processors), Steele (4232 processors), and Hansen (96 pro-

cessors). It should be noted that a support ticket needs to be submitted under “Support” at the top right portion of the screen under “Support” to get access to Ranger and Steele.

c) Choose the application, where the available options are OpenSeesSP and OpenSeesMP.
d) Select the number of processors.
e) Click on “Simulate” to start the analyses.

It is beneficial to note that:

- An email is sent to the user when the job is completed.
- A user can have 5 sessions running at once.
- The sessions stay alive until they are terminated by the user.
- Each user gets a new data directory with each session.
- Each user has default 1 GB storage, which is expandable to 10 GB.

5. After Simulation, all the results and related information can be obtained from a specific location in a user’s scratch folder.

```
set pid [getPID]
set np [getNP]
set recordsFileID [open "peerRecords.txt" r]
set count 0;
foreach gMotion [split [read $recordsFileID] \n] {
if {[expr $count % $np] == $pid} {
source model.tcl
source analysis.tcl
set ok [doGravity]
loadConst -time 0.0
set gMotionList [split $gMotion "/"]
set gMotionDir [lindex $gMotionList end-1]
set gMotionNameInclAT2 [lindex $gMotionList end]
set gMotionName [string range $gMotionNameInclAT2 0 end-4 ]
set Gaccel "PeerDatabase $gMotionDir $gMotionName -accel 384.4 -dT dT -nPts
nPts"
pattern UniformExcitation 2 1 -accel $Gaccel
recorder EnvelopeNode -file $gMotionDir$gMotionName.out -node 3 4 -dof 1 2 3
disp
doDynamic [expr $dT*$nPts] $dT
if {$ok == 0} {
puts "$gMotionDir $gMotionName OK"
} else {
puts "$gMotionDir $gMotionName FAILED"}
wipe}
incr count 1;}
```

Figure A.1. Example tcl file for looping over different ground motions as modified from the sequential version by adding the underlined lines

COMPDYN 2013
4th ECCOMAS Thematic Conference on
Computational Methods in Structural Dynamics and Earthquake Engineering
M. Papadrakakis, V. Papadopoulos, V. Plevris (eds.)
Kos Island, Greece, 12–14 June 2013

A COMPARATIVE STUDY BETWEEN ACCELERATION AND ENERGY-BASED SEISMIC DEMAND SPECTRA COMPUTED BY AN EXTENSIVE COMPUTER ALGORITHM ON A GRID COMPUTER (COMPDYN 2013)

A.A. Dindar[1]*, C. Yalcin[2], E. Yuksel[3], H. Ozkaynak[4], O. Buyukozturk[5]

[1]Istanbul Kultur University, Department of Civil Engineering
Bakırkoy, İstanbul, Turkey
adindar@iku.edu.tr

[2]Bogazici University, Department of Civil Engineering
Bebek, İstanbul, Turkey
cem_yalcin@yahoo.com

[3]Istanbul Technical University, Department of Civil Engineering
Maslak, İstanbul, Turkey
yukselerc@itu.edu.tr

[4]Beykent University, Department of Civil Engineering
Ayazağa, İstanbul, Turkey
hasanozkaynak@beykent.edu.tr

[5]Massachussets Institute of Technology, Department of Civil and Environmental Engineering
Cambridge, MA, USA
obuyuk@mit.edu

Keywords: Energy Spectra, Response Spectra, Inelastic Response, Constant Ductility, Grid Computing.

Abstract. *This study aims to define the Seismic Energy that is imparted into the structure. When compared the energy-based spectra with the acceleration response spectra that are used in various codes, the latter do not take the duration and the frequency contents of the ground motion records, while the energy-based spectra takes these features into account and also combines the ground excitation and the structural response in its formulation. Therefore, enormous computations are required in the construction of the energy-based spectra while covering all the related parameters of ground motion and also the structural properties. This requirement is overcome by developing an extensive computer algorithm that ran in grid computer system in a computer laboratory of Istanbul Kultur University Civil Engineering Department.*

1 INTRODUCTION

The parameters used in the seismic analysis and the design of the structures range from the properties of the structures and the ground motion characteristics those are included in the computations. Most of the current building codes consider the dynamic response analysis (RHA) of linear-elastic structures in determination of the seismic demand values in terms of structural responses such as velocity and displacement as a part of force-based approach. According to the computed response values, the structural members are designed [1, 2]. For the last two decades, the performance-based design methodologies have been part of the earthquake resistant design philosophy where the deformation of the members, such as plastic strain and rotations, has been explicitly included in the computations [3].

Even though the researchers develop new ideas and propose innovative methodologies in seismic analysis and design, a key fact, energy, has been either disregarded or implicitly included in the computations. The energy, as a concept, has a great potential in the definition of the seismic demand and also design of the structural members since it couples the deformation of an element and acting force [4].

This proceeding describes the energy concept in seismic analysis, explains an energy-based seismic demand computation procedure and compares this procedure with the current demand methods.

2 ENERGY CONCEPTY IN EARTHQUAKE ENGINEERING

The equation of the motion for a fixed based structure, represented by a Single Degree of Freedom System (SDOF), Fig. 1, contains the inertial, damping, kinetic and external forces acting on the system [5].

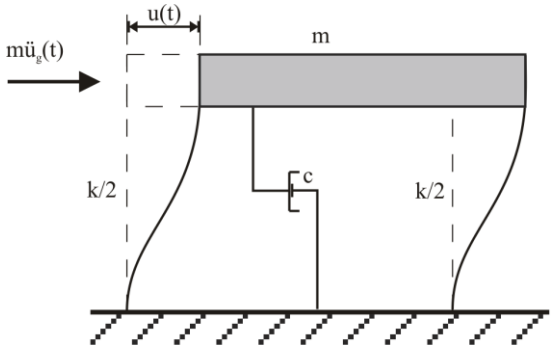


Figure 1: SDOF system.

The integration of this equation according to the relative displacement of the system, *u(t)*, under the ground motion results a new equation those are in energy units (1). The new equation governs the balance of the energy components found in the given SDOF system [5] and hence it is named as Energy Balance Equation (EBE).

$$\int m\ddot{u}(t)du + \int c\dot{u}(t)du + \int f_s du = -\int m\ddot{u}_g(t)du \tag{1}$$

The terms on the left hand side of EBE represent the energy components of the structure, namely, kinetic (E_K), damping (E_D) and absorbed (E_A) energies. The right-hand side of the equation represents the total input energy (E_I) that is imposed to the structure (2).

$$E_K + E_D + E_A = E_I \tag{2}$$

The input energy (E_I) in EBB represents the demand of the ground motion on the structure, Eq. 3.

$$E_I = -\int m\ddot{u}_g(t)du \tag{3}$$

The absorbed energy (E_A) in Eq. 2 is indeed contains the energy conserved by the elastic and inelastic deformations on the system. The inelastic deformations are actually the main parameter used in the performance-based seismic design in the next generation building codes. In this study the E_I will be taken into account and the comparison of the conventional demand values.

3 ALGORITHM AND COMPUTER ENVIRONMENT

3.1 Algorithm

The formulation given in Eq. 3 is computed after a dynamic time-history analysis is conducted on a linear SDOF system, Fig. 2. Therefore, the algorithm used in this study is developed in MATLAB® program [6]. The algorithm estimates the effective duration portion of the given earthquake record according to [7] and arrange the natural period of the system by changing the mass of the system so that the natural period is in the range of 0s and 3.0s. After the preparation phase in MATLAB®, the input parameters are sent to the time-history analysis program IDARC2D [8] that is ran within MATLAB command window. When IDARC2D completes the analysis, the MATLAB® scripts read the results of the response time-histories are then incorporates in the Eq. 3 to calculate the Input Energy (E_I) time-history values for the spectral analysis.

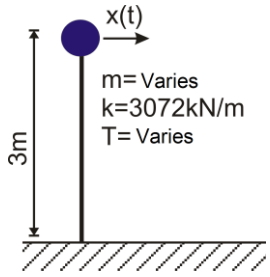


Figure 2: SDOF system.

The entire algorithm is developed in a way that it runs automatically, without any human intervention, for the given input variables such as ground motion, seismic intensity, a set of system mass, damping ratio and even different constitutive models. The further information is found in [9].

3.2 Computer Environment

The developed computer as a part of an extensive PhD thesis [4] has been conducted in a special grid computing system in Istanbul Kultur University (IKU) Department of Civil Engineering, Istanbul. The amount of the input variables considered in [4] requires enormous computer resource that is pretty challenging if a single personal computer is used. Therefore, 25 computers in the department's computer laboratory were integrated in a grid computing work frame which was again developed in MATLAB® program. The configuration of the each computer in the lab was Dell Precision T3500 Tower Computer Workstation with Windows XP operation system with Intel® Xeon® Processor X5570 2.93GHz and 4GB DDR3 RAM.

The computers were run during the no class periods, nights and weekends. The computers were programmed in a special grid system that divides the number of the large set of the ground motions into the small groups so that approximately 9 hours of spectral analysis computation between 7pm and 7am. In case the spectral computation is interrupted due to exceeding run time, the latest analysis level is kept in the memory to be continued in the following process time. The number of the time-history analysis conducted in the grid computer system was about 250,000 and it took in total 16 calendar days. At the end of every input parameter range completed, the algorithm compressed the results in zipped files and pushed to the data packages to a FTP server where the results were examined. Meanwhile, the algorithm sent the briefing emails to the researchers at the given process steps in order to keep them informed.

4 DEMAND SPECTRA FOR RESPONSE AND ENERGY VALUES

4.1 Response Spectra

For the linear elastic SDOF models with the changing natural period in a selected range, the dynamic time-history analyses result in the different responses (displacement, velocity and acceleration). The relation between the changing natural period and the response values are the basis of the spectral approach in the seismic design [10] and this is used in the force-displacement and performance-based design methodologies. Contrary to its wide use, the way of determination of the response spectrum inherently carries some major drawbacks. Since the absolute extreme response values are taken out from the dynamic time-history analyses, neither the entire ground motion duration nor the frequency content is taken into the extreme value computations which is extremely important from the view of accumulated damage propagation [11]. By this way, very important information on the destructiveness of the earthquake ground motion record is involuntarily lost in the estimation of the seismic demand values.

4.2 Energy Spectra

The input energy (E_I) in EBB, Eq. 3, and is influenced by the ground motion and structural characteristics concurrently. This fact increases the potential of the energy concept because the E_I term estimated in the integral is accumulated throughout the ground motion. By this way, the E_I covers the entire ground motion duration and its frequency content, Fig 3.

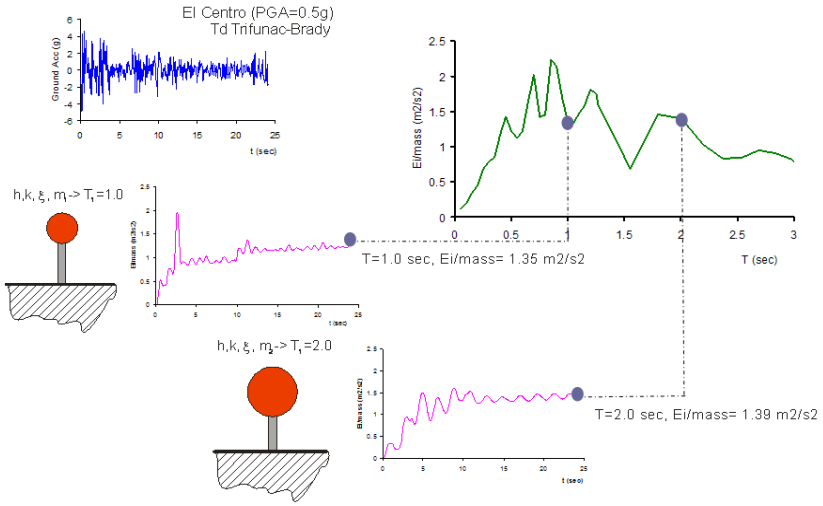


Figure 3: Energy Spectra.

Even if the interim values in the energy time history graph seem higher than the accumulated final value, Fig. 2, these interim values do also include the kinetic and elastic strain energies those diminish at the end of the motion record [12].

4.3 Comparison

The distinction between the conventional response and proposed energy demand spectra is apparent when two different earthquake records, given in Table 1, are examined [13].

Ground Motion Record	PGA (g)	Soil Condition (USGS)	T (sec)	T_d (sec)	Magnitude (Mw)	Focal Distance (km)
Chile Llolleo (3.Mar.1985) 10 component	0.71	A- Sandstone and volcanic soil	116	35.85	7.8	4.5
San Salvador (10.Sept.1986) 90 component	0.87	B- Shallow (stiff) soil	10	4.49	5.4	9.0

Table 1: Properties of the ground motions examined.

The duration, PGA values, Fig 4, and the frequency content, Fig. 5, of the both ground motions show that these records should have different effects on a structure. The darker portion of the ground motion record represent the effective duration according to [7].

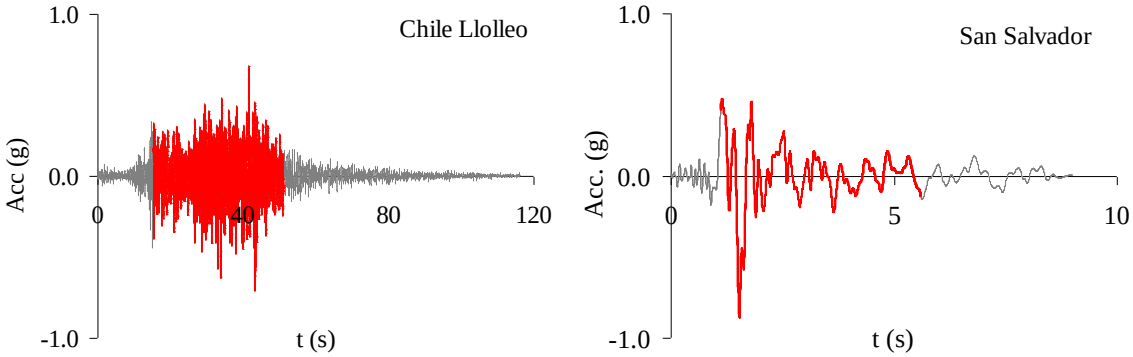


Figure 4: Duration of the two different earthquake motion records.

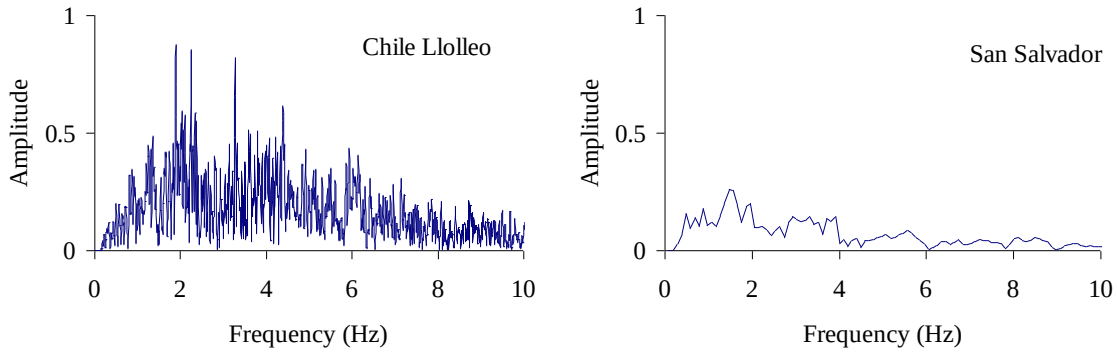


Figure 5: Frequency content of the two different earthquake motion records.

The drawback of the construction of the response spectra to the energy spectra is apparent when the both spectral values of the both earthquake motions are compared. Contrary to the distinction of the both earth records, the acceleration response values are almost identical throughout the entire natural period range, Fig 5a. However, the mass normalized Input Energy (E_I) spectrum significantly displays the gap between the energy spectra values that reflects the destructiveness of the earthquake records, Fig. 6b.

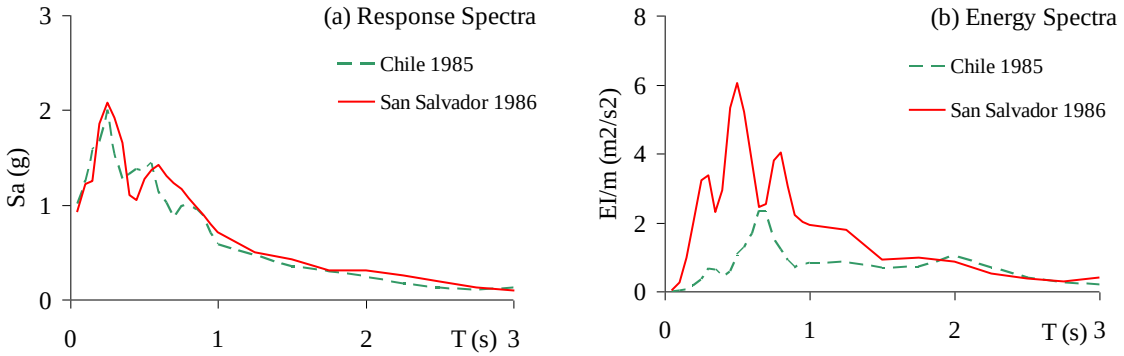


Figure 6: Response and Energy Spectra of the two different earthquake motion records.

5 CONCLUSIONS

The conventional response spectrum is widely used in the current building codes in order to determine the seismic demand on the structure. However, the construction of the response spectra inherently loses the valuable information in the ground motion records such as duration and the frequency content. The recently developed performance-based and also limit-state design approaches those are the preliminary examples of the next-generation seismic codes require the use of the ground motion data and also the structural properties comprehensively in the computations. Energy-based seismic demand analysis, explained in this study, and the design methodologies overcome the major drawback of the use conventional response spectrum by coupling the ground motion and structural properties. Hence, the energy-balance equation has the potential in giving a better-understanding in the destructiveness of the ground motion on the structures that is the key parameter in seismic design.

The computation resource in the construction of the dynamic time-history analysis and also determination of the energy demand spectral values were enormous in terms of the input parameters in the study. About 250,000 time-history analysis were conducted in an extensive PhD study. A well-developed computer algorithm with the use of grid computing system in the computer laboratory of an engineering department enabled the completion of the analyses in a very short time period. The success of the algorithm and the grid computing system proves that even if the next-generation design codes require extensive computations, the conditionally available computers in the engineering departments can be invaluable resources for the researches in the universities without going for investment of High Performance Computing (HPC) systems.

ACKNOWLEDGEMENT

The support of the Istanbul Kultur University Department of Civil Engineering in providing the computer laboratory to this study is gratefully acknowledged.

REFERENCES

[1] ACI 318, Building Code Requirements for Structural Concrete and Commentary, *American Concrete Institute*, 2005.

[2] Turkish Earthquake Code (TEC). Specification for Structures to be Built in Disaster Areas, *Ministry of Public Works and Settlement, Government of the Republic of Turkey*, Ankara, 2007.

[3] FEMA 273, Performance Based Seismic Engineering of Buildings, *Structural Engineers Assn. of California (SEAOC)*, 1997.

[4] A.A. Dindar, Energy-Based Earthquake Response Analysis and Design of Reinforced Concrete SDOF Columns, *Ph.D. Thesis*, Bogazici University, Istanbul, 2009.

[5] V.V., Bertero and C.M. Uang, Evaluation of seismic energy in structures, *Earthquake Engineering and Structural Dynamics*, **19**, **77-90**, 1990.

[6] MathWorks Inc., MATLAB R2010a. Natick, Massachusetts-USA, 2010.

[7] M.D. Trifunac, and A.G. Brady, A study of the duration of Strong Earthquake Ground Motion, *Bulletin of The seismic Society of America*, **65**, **581-626**, 1975.

[8] A. M Reinhorn, H. Roh, M. Sivaselvan, S. K. Kunnath, R. E. Valles, A. Madan, , C. Li, R. Lobo, and Y. J. Park, IDARC2D version 7.0: A Program for the Inelastic Damage Analysis of Buildings, Tech. Rep. MCEER-09-0006, *Multidisciplinary Center for Earthquake Engineering Research*, Buffalo, N.Y, 2009.

[9] A.A., Dindar, C. Yalçın, H. Özkaynak, E. Yüksel, and O. Büyüköztürk, The Use of Earthquake Energy Demand in Seismic Design of Structures, *submitted to Earthquake Spectra and under review*, 2012.

[10] A.K. Chopra, *Dynamics of Structures: Theory and Applications to Earthquake Engineering*, 3rd edition, Prentice Hall, Englewood Cliffs, NJ, 2006.

[11] A.K Gupta, Response Spectrum Method, *CRC Press Inc*, 1990.

[12] A.A. Dindar, C. Yalçın, H. Özkaynak, E. Yüksel and O. Büyüköztürk , Energy-Based Analysis and Design of RC members. *Advances in Civil Engineering (ACE2008)* Proceedings, **4**, **51-59**, Magosa, Turkish Republish of North Cyprus, 2008.

[13] V.V. Bertero and C.M. Uang, Implications of recorded earthquake ground motions on seismic design of building structures, *Research Report (UCB/EERC-88/13)*, University of California at Berkeley, USA, 1988.

COMPDYN 2013
4th ECCOMAS Thematic Conference on
Computational Methods in Structural Dynamics and Earthquake Engineering
M. Papadrakakis, V. Papadopoulos, V. Plevris (eds.)
Kos Island, Greece, 12–14 June 2013

NON-LINEAR DYNAMICS OF ELECTRICAL EQUIPMENT CABLES

Nicholas D. Oliveto[1] **and Mettupalayam V. Sivaselvan**[1]

[1] Department of Civil, Structural and Environmental Engineering, University at Buffalo, The State University of New York
212 Ketter Hall, Buffalo, New York 14260, USA
{noliveto, mvs}@buffalo.edu

Keywords: Cable Dynamics, Large Displacements, Large Rotations, Earthquake Excitation.

Abstract. *In power substations, electrical cables are commonly observed in configurations that cannot be explained by tension stress states only. Moreover, during extreme excitations such as earthquakes, they can be subjected to large displacements and rotations, as well as forces that can lead to failure of both the cables and the equipment to which they are connected. In this paper a three-dimensional geometrically exact beam model is presented and used to describe the static and dynamic behavior of electrical equipment cables. The model is implemented in MATLAB and applied to a flexible conductor recently tested at the SEESL laboratory at the University at Buffalo. Both static and dynamic numerical applications are performed. First the initial configuration of the tests is obtained by imposing the end displacements and rotations to a straight and unstrained cable. Then the cable is subjected to resonant harmonic out-of-plane and in-plane horizontal ground motions. Due to the high frequency components resulting from the axial response of the cable, and to the fact that the Newmark time-integration algorithm used herein generally fails to conserve energy, very small time steps are needed for the algorithm to converge. Although algorithms have been proposed in the literature, which introduce numerical damping to stabilize the computations, the introduction of real forms of damping in the model and the simulation of the dynamic experimental tests performed at the University at Buffalo are object of current work.*

1 INTRODUCTION

Cables are widely used in the power industry as essential components of the electrical transmission network. Although they are usually designed to mainly meet electrical standards rather than structural performance requirements, during earthquakes and other severe environmental hazards they are often subjected to large deformations and stresses that can result in failure of both the cables and the equipment to which they are connected. During extreme excitations the cables can undergo large displacements and rotations, and be subjected to three-dimensional states of stress. Besides tension, the cable can be subjected to shear, bending and torsion. Moreover it is common in electrical substations to observe cable configurations that cannot be explained by a state of stress of simple tension.

Dynamic interaction between cables and interconnected equipment has been studied, among others, by Der Kiureghian et al. [1] using a three-dimensional geometrically exact beam model originally proposed by Simo et al. [2,3,4]. Moreover, extensive experimental tests on flexible conductors provided by the Bonneville Power Authority have recently been conducted at the SEESL laboratory at the University at Buffalo in the form of pull-back tests, harmonic tests and shake table earthquake excitations [5].

In the present paper the theory developed by Simo and coworkers is exploited to set the stage for the simulation of the experimental tests carried out at the University at Buffalo on a Jefferson/TW AAC conductor. Of particular interest is the determination of the initial static configuration from which the dynamic tests on the cable are performed. The initial shape is obtained by imposing the end displacements and rotations to an initially straight and unstrained cable. The properties of the cable are taken so as to obtain a reasonably good match between the numerical and experimental configurations and frequencies.

The paper is organized as follows. In the first section the governing equations of the 3D geometrically exact beam model are presented, including kinematics, equilibrium and constitutive equations. The second section deals with the derivation of the weak form of the equilibrium equations. Its exact linearization and discretization in time and space then leads to the definition of a tangent operator and a system of equations solvable by means of an iterative scheme of the Newton type. The final section is concerned with static and dynamic numerical applications of an electrical cable. The results are compared where possible to those obtained from experimental tests performed at the University at Buffalo.

2 GOVERNING EQUATIONS

The purpose of this section is to describe the equations governing the motion of the three-dimensional geometrically exact beam model which will be used to model the cable.

2.1 Kinematics

Following Simo [2], the motion of the beam through time is uniquely defined by the position of the line of centroids $\mathbf{x_0}(S,t)$ and a rotation tensor $\mathbf{R}(S,t)$ specifying the orientation of a moving frame $\mathbf{t_I}(S,t)$ attached to the cross-section, relative to its initial position $\mathbf{E_I}$. The rotation tensor $\mathbf{R}(S,t)$ represents a rigid rotation of the cross-section such that

$$\mathbf{t_I}(S,t) = \mathbf{R}(S,t) \cdot \mathbf{E_I} \tag{1}$$

The derivatives of $\mathbf{R}(S,t)$ with respect to S and t represent the rates of change of $\mathbf{t_I}(S,t)$ and are defined by:

$$\frac{\partial \mathbf{R}(S,t)}{\partial S} = \hat{\boldsymbol{\omega}}(S,t) \cdot \mathbf{R}(S,t) = \mathbf{R}(S,t) \cdot \hat{\boldsymbol{\Omega}} \tag{2}$$

$$\frac{\partial \mathbf{R}(S,t)}{\partial t} = \hat{\mathbf{w}}(S,t)\cdot\mathbf{R}(S,t) = \mathbf{R}(S,t)\cdot\hat{\mathbf{W}} \tag{3}$$

where $\hat{\boldsymbol{\omega}}$ and $\hat{\mathbf{w}}$ are skew-symmetric tensors defining the spatial curvature and rotational velocity of a configuration, while $\hat{\boldsymbol{\Omega}}$ and $\hat{\mathbf{W}}$ are the corresponding material tensors.

2.2 Equilibrium equations

The spatial form of the linear and angular momentum equations is given by:

$$\begin{aligned} &\frac{\partial \mathbf{n}}{\partial S} + \bar{\mathbf{n}} = \rho A \ddot{\mathbf{x}}_0 \\ &\frac{\partial \mathbf{m}}{\partial S} + \frac{\partial \mathbf{x}_0}{\partial S}\times\mathbf{n} + \bar{\mathbf{m}} = \rho\mathbf{I}\cdot\dot{\mathbf{w}} + \mathbf{w}\times(\rho\mathbf{I}\cdot\mathbf{w}) \end{aligned} \tag{4}$$

In Eq. (4) $\mathbf{n}$ and $\mathbf{m}$ are the spatial force and moment resultants while $\bar{\mathbf{n}}$ and $\bar{\mathbf{m}}$ are the distributed applied forces and moments per unit length of the beam. Moreover, A and $\mathbf{I}$ are the area and spatial inertia tensor of the cross-section, ρ is the mass density and $\mathbf{w}$ is the spatial rotational velocity vector.

2.3 Constitutive equations

Large deformations but locally small strains are assumed so that forces and moments are linearly proportional to the corresponding strains and curvatures through a constant elasticity tensor **C.** The following expressions hold:

$$\mathbf{C} = \mathrm{diag}\left[GA_1, GA_2, EA, EI_1, EI_2, GJ_t\right] \tag{5}$$

$$\begin{bmatrix}\mathbf{N}\\ \mathbf{M}\end{bmatrix} = \mathbf{C}\begin{bmatrix}\boldsymbol{\Gamma}\\ \boldsymbol{\Omega}\end{bmatrix} \tag{6}$$

where $\mathbf{N} = \mathbf{R}^{\mathbf{T}}\cdot\mathbf{n}$ and $\mathbf{M} = \mathbf{R}^{\mathbf{T}}\cdot\mathbf{m}$ are the material force and moment resultants, while $\boldsymbol{\Gamma}$ and $\boldsymbol{\Omega}$ are the corresponding strains and curvatures defined as:

$$\begin{aligned} \boldsymbol{\Gamma} &= \mathbf{R}^{\mathbf{T}}\cdot\frac{\partial \mathbf{x}_0}{\partial S} - \mathbf{E}_3 \\ \boldsymbol{\Omega} &= \mathbf{R}^{\mathbf{T}}\cdot\boldsymbol{\omega} \end{aligned} \tag{7}$$

where $\boldsymbol{\omega}$ is the spatial curvature vector.

3 WEAK FORM OF THE EQUILIBRIUM EQUATIONS

Following Simo [3,4], the weak form of the equilibrium equations is obtained by multiplying the spatial balance equations (4) by an admissible variation $\boldsymbol{\eta} = (\mathbf{u}_0, \boldsymbol{\theta})$:

$$\begin{aligned} G(\mathbf{x},\boldsymbol{\eta}) = &\int_0^L \left[\left(\frac{\partial \mathbf{n}}{\partial S} + \bar{\mathbf{n}}\right)\cdot\mathbf{u}_0 + \left(\frac{\partial \mathbf{m}}{\partial S} + \frac{\partial \mathbf{x}_0}{\partial S}\times\mathbf{n} + \bar{\mathbf{m}}\right)\cdot\boldsymbol{\theta}\right] dS + \\ &-\int_0^L \left\{\rho A\ddot{\mathbf{x}}_0\cdot\mathbf{u}_0 + \left[\rho\mathbf{I}\cdot\dot{\mathbf{w}} + \mathbf{w}\times(\rho\mathbf{I}\cdot\mathbf{w})\right]\cdot\boldsymbol{\theta}\right\} dS = 0 \end{aligned} \tag{8}$$

If $\boldsymbol{\varphi}(S,t)=\left[\mathbf{x}_0(S,t),\mathbf{R}(S,t)\right]$ represents an arbitrary configuration, $\mathbf{u}_0$ can be interpreted as a superposed infinitesimal displacement on the line of centroids $\mathbf{x}_0$, and $\boldsymbol{\theta}$ as a superposed infinitesimal rotation onto the moving frame defined by $\mathbf{R}$. More precisely, $\boldsymbol{\theta}$ represents the axial vector of the skew-symmetric tensor $\hat{\boldsymbol{\theta}}$. It should be noted that by exponentiation of the incremental rotation tensor $\hat{\boldsymbol{\theta}}$ we are guaranteed to obtain an orthogonal tensor representing a finite rotation.

Integration by parts of the first integral of Eq. (8) leads to the following spatial version of the weak form of the equilibrium equations:

$$\begin{aligned} G(\boldsymbol{\varphi},\boldsymbol{\eta}) &= \int_0^L \left[\mathbf{n}\cdot\left[\frac{\partial \mathbf{u}_0}{\partial S}-\boldsymbol{\theta}\times\frac{\partial \mathbf{x}_0}{\partial S}\right]+\mathbf{m}\cdot\frac{\partial \boldsymbol{\theta}}{\partial S}\right]dS-\int_0^L\left(\bar{\mathbf{n}}\cdot\mathbf{u}_0+\bar{\mathbf{m}}\cdot\boldsymbol{\theta}\right)dS \\ &+\int_0^L\left\{\rho A\ddot{\mathbf{x}}_0\cdot\mathbf{u}_0+\left[\rho\mathbf{I}\cdot\dot{\mathbf{w}}+\mathbf{w}\times\left(\rho\mathbf{I}\cdot\mathbf{w}\right)\right]\cdot\boldsymbol{\theta}\right\}dS=0 \end{aligned} \tag{9}$$

The material version of the weak form can be easily obtained as:

$$\begin{aligned} G(\boldsymbol{\varphi},\boldsymbol{\eta}) &= \int_0^L \left[\mathbf{N}\cdot\mathbf{R}^{\mathrm{T}}\cdot\left[\frac{\partial \mathbf{u}_0}{\partial S}-\boldsymbol{\theta}\times\frac{\partial \mathbf{x}_0}{\partial S}\right]+\mathbf{M}\cdot\mathbf{R}^{\mathrm{T}}\cdot\frac{\partial \boldsymbol{\theta}}{\partial S}\right]dS-\int_0^L\left(\bar{\mathbf{n}}\cdot\mathbf{u}_0+\bar{\mathbf{m}}\cdot\boldsymbol{\theta}\right)dS \\ &+\int_0^L\left\{\rho A\ddot{\mathbf{x}}_0\cdot\mathbf{u}_0+\mathbf{R}\cdot\left[\rho\mathbf{J}\cdot\dot{\mathbf{W}}+\mathbf{W}\times\left(\rho\mathbf{J}\cdot\mathbf{W}\right)\right]\cdot\boldsymbol{\theta}\right\}dS=0 \end{aligned} \tag{10}$$

In Eq. (10) $\mathbf{J}=\mathbf{R}^{\mathrm{T}}\cdot\mathbf{I}\cdot\mathbf{R}$ is the material time-independent inertia tensor.

3.1 Time integration algorithm

Given the configuration $\boldsymbol{\varphi}_{\mathbf{n}}\left(\mathbf{x}_{0,\mathbf{n}},\mathbf{R}_{\mathbf{n}}\right)$ at time t_n, the problem of finding the configuration $\boldsymbol{\varphi}_{\mathbf{n+1}}\left(\mathbf{x}_{0,\mathbf{n+1}},\mathbf{R}_{\mathbf{n+1}}\right)$ at time t_{n+1} is dealt with as follows. As far as the translational part of the configuration is concerned the classical Newmark algorithm is used, whereas an extension of Newmark's algorithm to the orthogonal group SO(3) is considered for the rotational part of the configuration. The time integration algorithm proposed by Simo [4] is summarized below. For the translational part we have:

$$\mathbf{d}_{\mathbf{n+1}}=\mathbf{d}_{\mathbf{n}}+\mathbf{u}_{\mathbf{n}} \tag{11}$$

$$\mathbf{u}_{\mathbf{n}}=h\dot{\mathbf{d}}_{\mathbf{n}}+h^2\left[\left(\frac{1}{2}-\beta\right)\ddot{\mathbf{d}}_{\mathbf{n}}+\beta\ddot{\mathbf{d}}_{\mathbf{n+1}}\right] \tag{12}$$

$$\dot{\mathbf{d}}_{\mathbf{n+1}}=\dot{\mathbf{d}}_{\mathbf{n}}+h\left[(1-\gamma)\ddot{\mathbf{d}}_{\mathbf{n}}+\gamma\ddot{\mathbf{d}}_{\mathbf{n+1}}\right] \tag{13}$$

where we have introduced $\mathbf{d}=\mathbf{x}_0$ just to simplify the notation.

For the rotational part of the configuration the extension of Newmark's algorithm to SO(3) is given in material form by:

$$\mathbf{R}_{\mathbf{n+1}}=\mathbf{R}_{\mathbf{n}}\cdot\exp\left(\hat{\boldsymbol{\Theta}}_{\mathbf{n}}\right)=\exp\left(\hat{\boldsymbol{\theta}}_{\mathbf{n}}\right)\cdot\mathbf{R}_{\mathbf{n}} \tag{14}$$

$$\boldsymbol{\Theta}_{\mathbf{n}} = h\mathbf{W}_{\mathbf{n}} + h^2\left[\left(\frac{1}{2}-\beta\right)\dot{\mathbf{W}}_{\mathbf{n}} + \beta\dot{\mathbf{W}}_{\mathbf{n+1}}\right] \tag{15}$$

$$\mathbf{W}_{\mathbf{n+1}} = \mathbf{W}_{\mathbf{n}} + h\left[(1-\gamma)\dot{\mathbf{W}}_{\mathbf{n}} + \gamma\dot{\mathbf{W}}_{\mathbf{n+1}}\right] \tag{16}$$

In order to avoid singularities in the update of the rotation tensor, the exponentiation of the rotation tensor in the first of Eq. (14) is performed using a quaternion parameterization. The incremental material rotation vector $\boldsymbol{\Theta}_{\mathbf{n}}$ is then extracted by means of Spurrier's algorithm [3,6].

3.2 Linearization and space discretization of the weak form

The linear part of the material version of the weak form of the equilibrium equations (10) is given by:

$$L\left[G\left(\boldsymbol{\varphi}_{\mathbf{n+1}}, \boldsymbol{\eta}\right)\right] = G\left(\boldsymbol{\varphi}_{\mathbf{n+1}}, \boldsymbol{\eta}\right) + DG\left(\boldsymbol{\varphi}_{\mathbf{n+1}}, \boldsymbol{\eta}\right)\cdot\boldsymbol{\Delta}\mathbf{u} \tag{17}$$

In Eq. (17) $G\left(\boldsymbol{\varphi}_{\mathbf{n+1}}, \boldsymbol{\eta}\right)$ represents the unbalanced force at configuration $\left(\boldsymbol{\varphi}_{\mathbf{n+1}}, \boldsymbol{\eta}\right)$ while the term $DG\left(\boldsymbol{\varphi}_{\mathbf{n+1}}, \boldsymbol{\eta}\right)\cdot\boldsymbol{\Delta}\mathbf{u}$ leads to the definition of a tangent operator. As shown by Simo [3,4], space discretization of the linearized weak form yields the following system of equations:

$$\sum_{\mathrm{I,J=1}}^{\mathrm{N}}\left[\mathbf{P}_{\mathbf{I}}\left(\boldsymbol{\varphi}_{\mathbf{n+1}}\right) + \mathbf{K}_{\mathbf{IJ}}\left(\mathbf{R}_{\mathbf{n}}, \boldsymbol{\varphi}_{\mathbf{n+1}}\right)\boldsymbol{\Delta}\mathbf{u}_{\mathbf{J,n+1}}\right] = \mathbf{0} \tag{18}$$

where N is the number of discretization nodes, $\boldsymbol{\Delta}\mathbf{u}_{\mathbf{j,n+1}}$ represents the incremental displacement-rotation field and the tangent matrix $\mathbf{K}$ is given by the sum of the material stiffness matrix **S**, the geometric stiffness matrix **G** and the inertia matrix $\bar{\mathbf{M}}$, that is

$$\mathbf{K}_{\mathbf{IJ}} = \mathbf{S}_{\mathbf{IJ}} + \mathbf{G}_{\mathbf{IJ}} + \bar{\mathbf{M}}_{\mathbf{IJ}} \tag{19}$$

Expressions for the above matrices can be found in [3,4]. The system of equations (18) is solved by means of an iterative scheme of the Newton type. Details of the solution scheme, as well as of the linearization and discretization of the weak form can also be found in [3,4].

4 NUMERICAL APPLICATIONS

In this section the three-dimensional geometrically exact beam model is applied to describe the behavior of an electrical conductor tested at the University at Buffalo [5]. The cable considered is a Jefferson/TW AAC conductor made of 52 helically wrapped aluminum wires. All the numerical applications are performed using MATLAB.

4.1 Properties of the cable

The material properties used in the analyses are E=10x10^6 psi and $\nu = 0.33$, whereas the geometric properties of the cable are L=145 in, A=2.07 in^2, I_1=I_2=0.0068 in^4 and J_t=I_1+I_2. The weight of the cable is 0.188 lbs/in.

It is usually difficult to evaluate the effective moment of inertia of cables based on the geometry of the cross section only, as considerably different values can be obtained depending on whether the wires remain connected or can more or less slide with respect to one another during bending. The value taken herein was chosen to yield a good matching of the in-plane and out-of-plane fundamental frequencies measured during the experimental tests. Once the

static shape of the cable has been found numerically, its frequencies are estimated by linear eigenvalue analysis using the tangent stiffness matrix at the given configuration and an appropriate consistent mass matrix.

4.2 Cable form finding

The first application is concerned with determining the static configuration of the cable from which the dynamic tests were performed. This is obtained by imposing end displacements and rotations to an initially straight and unstrained cable. The conductor is discretized using 80 2-noded (linear) elements with 1-point Gaussian integration. The shape of the cable obtained by the numerical model is plotted in Figure 1 against the initial configuration measured prior to the dynamic experiments.

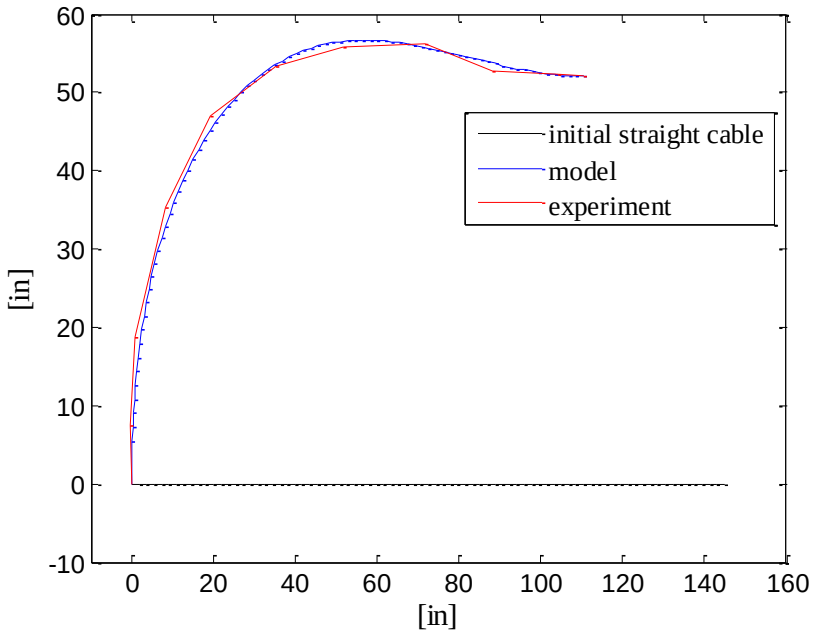


Figure 1: Numerical and experimental static configuration of the cable.

4.3 Response to harmonic ground motion

Starting from the configuration obtained in the previous section, the dynamic performance of the algorithm is tested by separately applying in-plane and out-of-plane horizontal harmonic displacements at the ends of the cable in the form:

$$u(t) = U \sin(2\pi ft) \tag{20}$$

where U and f are the amplitude and frequency of the applied motion.

4.4 Resonant responses

In the present applications displacement amplitudes of 1 inch are considered and the exciting frequencies are taken equal to the fundamental natural frequencies of the cable. These are 1.5 Hz for the out-of-plane motion and 4.15 Hz for the in-plane motion. The parameters used in the time integration scheme are $\beta = 0.25$ and $\gamma = 0.5$. A time step $\Delta t = 0.001$s is used for the out-of-plane excitation while $\Delta t = 0.0001$ s is used for the in-plane application. Small time steps are needed to avoid instability problems due to high frequency effects related to the

axial response of the cable. Moreover, it is known that the Newmark family of time-integration algorithms generally fails to conserve energy and can lead to unstable and inaccurate results. For this reason algorithms have been proposed in the literature, which introduce numerical damping to stabilize the computations [7,8]. In this paper we do not implement these algorithms but the introduction in the model of real forms of damping is object of current work.

For both the out-of-plane and the in-plane excitations, the first 10 seconds of motion are analyzed. 1-point Gaussian integration is used for the internal force vector and the material and geometric stiffness matrices, while 2-point Gaussian integration is used for the inertial force vector and the inertia matrix.

The components of the response of a reference point along the cable to the out-of-plane excitation are shown in Figure 2, along with the deformed shape of the cable at the time of maximum out-of plane horizontal displacement. The reference point is marked in Figure 2(d). It should be noted that the vertical displacements are of the same magnitude as the out-of-plane horizontal ones.

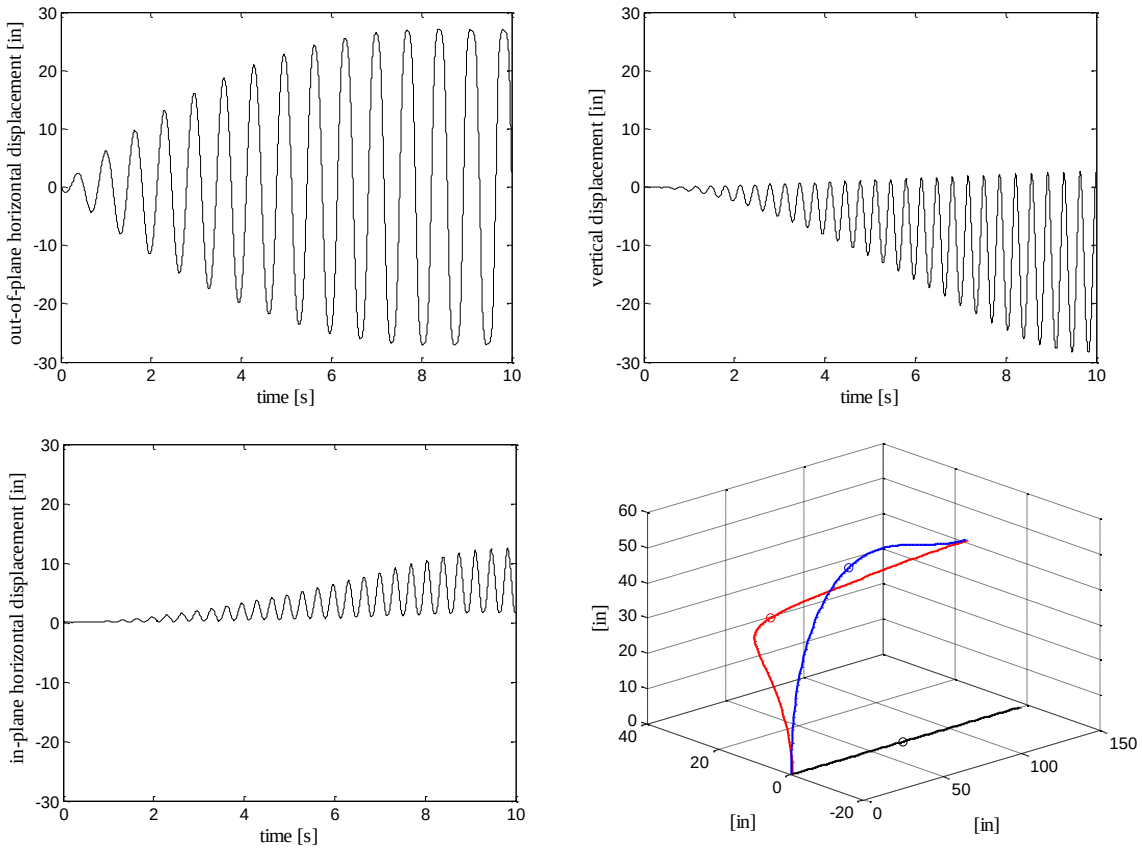


Figure 2: Numerical response of reference point to out-of-plane resonant excitation. (a) Out-of-plane horizontal displacement, (b) vertical displacement, (c) in-plane horizontal displacement, (d) deformed shape at maximum out-of-plane displacement.

The components of the response of the reference point due to the in-plane excitation are shown in Figure 3, along with the deformed shapes of the cable at the time of maximum vertical and horizontal displacements. It should be noted that in the case of in-plane horizontal excitation the cable undergoes no out-of-plane displacements.

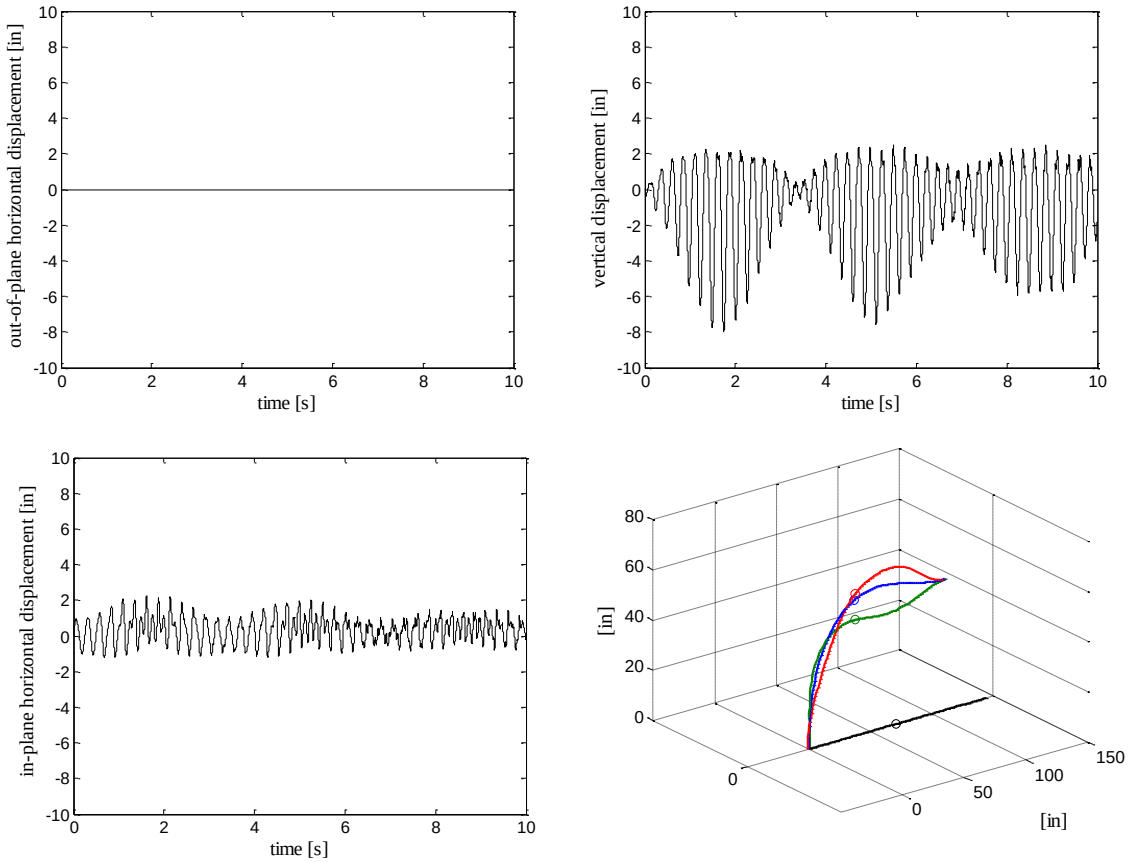


Figure 3: Numerical response of reference point to in-plane resonant excitation. (a) Out-of-plane horizontal displacement, (b) vertical displacement, (c) in-plane horizontal displacement, (d) deformed shape at maximum and minimum vertical displacements.

5 CONCLUSIONS

A three-dimensional geometrically exact beam model has been presented for the static and dynamic behavior of electrical equipment cables. The model has been implemented in MATLAB and applied to a flexible conductor tested at the SEESL lab at the University at Buffalo. The performance of the numerical algorithm has been evaluated through static and dynamic applications in the form of harmonic ground excitations. The results show that further investigation is needed to assess the accuracy and stability of the computations. The introduction of different forms of damping in the model and the simulation of the dynamic experimental tests performed at the University at Buffalo are object of current work.

REFERENCES

[1] K.J. Hong, A. Der Kiureghian, J.L. Sackman, Seismic Interaction in Cable-Connected Equipment Items. *Journal of Engineering Mechanics*, **127**(11), 1096-1105, 2001.

[2] J.C. Simo, A finite strain beam formulation. The three-dimensional dynamic problem. Part I. *Computer Methods in Applied Mechanics and Engineering*, **49**, 55-70, 1985.

[3] J.C. Simo, L. Vu-Quoc, A three-dimensional finite-strain rod model. Part II: Computational aspects. *Computer Methods in Applied Mechanics and Engineering*, **58**, 79-116, 1986.

[4] J.C. Simo, L. Vu-Quoc, On the dynamics in space of rods undergoing large motions - a geometrically exact approach. *Computer Methods in Applied Mechanics and Engineering*, **66**, 125-161, 1988.

[5] P. Chandran, Experimental and numerical studies on the seismic response of flexible conductors with vertical drops. *Master of Science Project Report*, University at Buffalo, NY, 2012.

[6] R.A. Spurrier, Comment on "singularity-free extraction of a quaternion from a direction-cosine matrix", *J. Spacecraft*, **15 (4)**, 255, 1978.

[7] J. C. Simo, N. Tarnow, K. K. Wong, (1992), Exact energy-momentum conserving algorithms and symplectic schemes for nonlinear dynamics. *Computer Methods in Applied Mechanics and Engineering*, **100 (1)**, 63-116, 1992.

[8] J. C. Simo, N. Tarnow, M. Doblare, Nonlinear dynamics of three-dimensional rods: Exact energy and momentum conserving algorithms. *International Journal of Numerical Methods in Engineering*, **38 (9)**, 1431-1473, 1995.

COMPDYN 2013
4th ECCOMAS Thematic Conference on
Computational Methods in Structural Dynamics and Earthquake Engineering
M. Papadrakakis, V. Papadopoulos, V. Plevris (eds.)
Kos Island, Greece, 12–14 June 2013

DISCRETE IMPEDANCE MATRIX FOR FLEXIBLE SURFACE FOUNDATIONS

Andreas Maravas[1], George Mylonakis[2] , and Dimitris L. Karabalis[2]

[1] Department of Civil Engineering, University of Patras
26504 Rio, Greece
anmaravs@upatras.gr

[2] Department of Civil Engineering, University of Patras
26504 Rio, Greece
mylo@upatras.gr, karabali@upatras.gr

Keywords:: Soil-Structure Interaction, Structural Dynamics, Flexible Foundations, Impedance Matrix

Abstract : *Knowledge on the subject of dynamic soil-structure interaction (SSI) has been derived mainly from studies on rigid foundations. The seismic response of structures resting on flexible foundations has received considerably less attention and the results of these efforts have not yet lead to established computational procedures of general acceptance, such as those developed for structures resting on rigid foundations (ATC-3, NEHRP-03, IBC, EC-8). In this paper, a rigorous computational procedure for the analysis of soil-flexible foundation–structure interaction is developed based on the finite element method. Thus, a full model of the soil-flexible foundation system is constructed and the discrete (in space), frequency dependent, impedance matrix of the system is obtained. To this end the special purpose finite element program ACS SASSI is utilized taking into consideration the infinite extent of the soil medium. A simplified, under certain conditions, frequency independent impedance matrix is also presented. The above impedance matrices are used in a straightforward manner for the dynamic/seismic analysis of structures resting on flexible mat foundations in frequency domain.*

1 INTRODUCTION

During the last decades the problem of dynamic soil-structure interaction (SSI), has received considerable attention. The main research effort has been focused on the dynamic behavior of rigid foundations and some of the produced publications have become standard references in the field, e.g. Richart *et al.* [1], Veletsos and his co-workers [2-4], Luco and his co-workers [5-10], Vaish and Chopra [11] and Wolf [12]. In comparison to this effort, the study of flexible foundations, particularly extensive mat foundations, has received limited attention, e.g. Refs [13-17]. In contrast to rigid foundations, the study of which is based on classic fundamental solutions for the half space, e.g. Refs [18,19], or discretization of the half space by either the FEM, e.g. Refs [20-22], or the BEM, e.g. Refs [23-25], the dynamic analysis of flexible foundations requires the discretization of both the half space and the foundation itself, a task usually accomplished with the help of the FEM for both domains, e.g. Ref. [26], or the BEM, e.g. Ref. [24], or a combination of FEM and BEM, e.g. Refs [14, 27, 28]. Comprehensive reviews of these matters can be found in various sources, e.g. Gazetas [29], Beskos [30], Karabalis [31], etc.

In this work, the main goal is the study of the dynamic response of extensive mat foundations resting on a homogeneous, isotropic, linear elastic half space. The FEM, in frequency and time domain, is used throughout this work. For the purposes of these analyses (a) the half space impedances are computed with the help of the computer code ACS SASSI [32] and subsequently are transformed to a non-dimensional form, and (b) the half space impedances are matched with the discretization of the mat foundation, within the platforms of the computer codes ACS SASSI [32] or ANSYS [33], and the dynamic analysis of the half space-foundation system is computed in frequency or time domain. Numerical results pertaining to half space impedances and dynamic analyses of flexible foundations, as well as comparisons with results from other published works are also presented in order to verify the accuracy and practical efficiency of the proposed methodologies.

2 PROBLEM STATEMENT AND ANALYSIS PROCEDURES

The problem under consideration consists of determining the dynamic response of linear flexible mat foundations resting on a homogeneous soil medium idealized as a linear elastic, isotropic half space. The FEM is used throughout this work and requires the discretization of both the half space and the finite foundation slab. The half-space is simulated with the help of the computer code ACS SASSI which, via the usage of transmitting boundaries, provides the means for efficient modeling of a semi-infinite medium. The superstructure, in this case the foundation slab, can also be modeled with ACS SASSI, thus providing for a total solution of the problem. However, the analysis of the entire soil-structure system can also be accomplished in two steps: (a) the impedances of a dense network of nodal points on the surface of the half space are computed by ACS SASSI, and stored in a non-dimensional form, and (b) the above impedances are imported to any standard general purpose FEM code, in this case ANSYS, where the solution of the soil-structure system can be solved for a variety of structural configurations and loading scenarios. Both approaches are used in this work and the obtained results are compared with results obtained in the literature.

2.1 Impedance of a half space

The soil simulation in the computer code ACS SASSI consists of two parts: (a) the original site model (“free field”) which is assumed to consist of horizontal soil layers overlying either a rigid base or an elastic half space boundary condition and (b) the boundary condition at the base of the “free field”. The material properties for the soil layer system are assumed to be

viscoelastic, i.e. complex modulus representation of the stiffness and damping properties of each soil layer. In the case of a half space simulation, the case of this work, the same material properties are used for both parts of the model and the elastic half space boundary condition is modeled using the variable depth method, where n extra layers are added to the base of the top soil layers.

The thickness of each soil layer depends on the minimum wavelength λ_{min} of the analysis and it should not exceed the value $\lambda_{min}/5$. The total depth of soil layers depends on the discretized surface dimensions, and for the purposes of this work is extended to at least ten times the dimension of the discretized free surface. The total depth H of the added layers (simulating the half space boundary condition under the "free field"), varies with frequency and is set to be equal to 1.5λ. The surface of the half space is discretized using three-dimensional quadrilateral thin shell elements. The nodes of the elements are the interaction points where the impedance values are calculated. The maximum distance between these nodes is set to be lower than $\lambda_{min}/8$.

The steps of the analysis are: (i) every surface interaction point is consecutively loaded with a unit harmonic load in the direction of a specific degree of freedom, (ii) the half-space flexibility complex matrix is calculated for all interaction points and (iii) the impedance matrix is computed by inverting the flexibility matrix.

Results of the above analysis are presented for a range of frequencies and half-space material properties. These results are normalized using the shear modulus of the half-space G_s. Impedance values are plotted as a function of dimensionless distance d_o, defined as

$$d_0 = \frac{d^2 G_s}{\sum F_{ext}} \tag{1}$$

where d is the distance from the loaded point and F_{ext} the external load. A characteristic set of impedance values for vertical and rocking oscillations, as a function of d_o and frequency f, are presented in Figure 1.

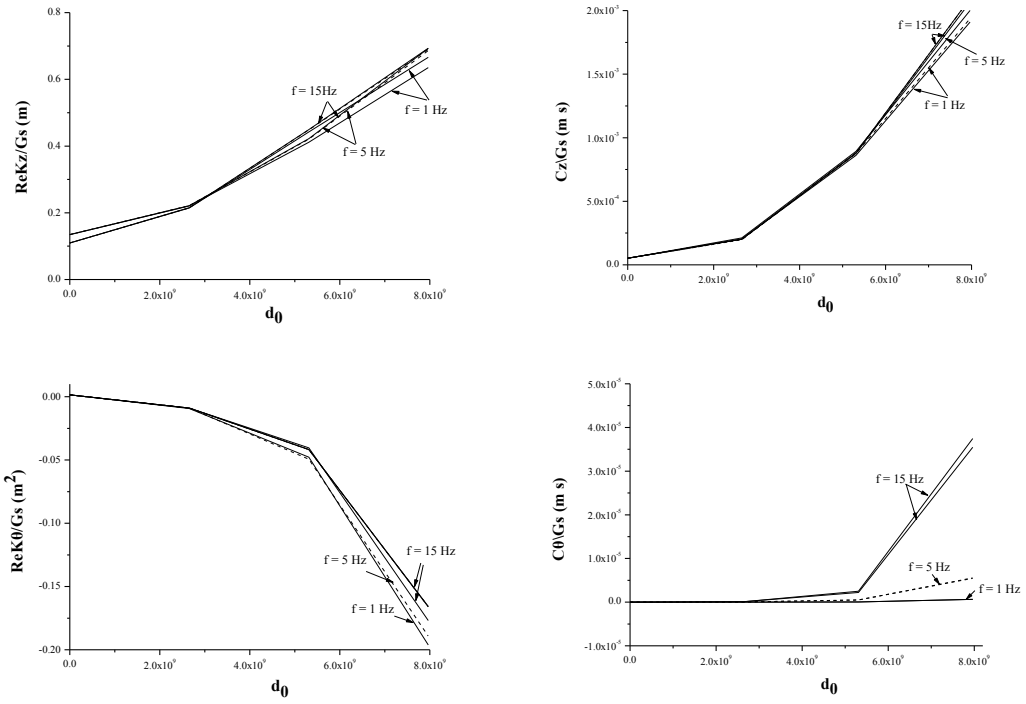


Figure 1. Half-space impedances for vertical and rocking oscillations as a function of dimensionless distance d_0 (ν_s= 0.30)

It is evident that impedance values depend on the spatial distance from the loading point, and they are practically independent of the frequency for a certain distance from the loading point. Moreover, the imaginary values (damping effects) increase substantially with increasing distance and, thus, the effect of the dynamic loading fades with distance. In general, imaginary values tend to be more sensitive to frequency variation, although this is observed at significant distances from the loading point.

2.2 Soil-Flexible Foundation Interaction

In this work, the dynamic response of a flexible foundation is computed using two distinct approaches. The first approach, used for comparison purposes, is based on a full soil-foundation model using the computer code ACS SASSI. To this end, the discretization of the half space described earlier, is supplemented with the finite model of a flexible slab resting on the surface of the half space, as shown in Figure 2. It is assumed that each nodal point of the discretized foundation medium coincides with an interaction point of the half space disretization. For the purposes of this work, a thin plate element is used for the foundation medium and separation (uplift) between the soil and the foundation is not allowed. The soil-foundation system can be loaded with a harmonic load at any nodal point and the frequency domain response (impedance) at any other nodal point can be computed following standard FEM procedures.

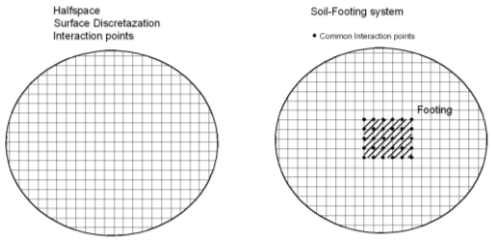


Figure 2. Soil-Foundation System. Surface Interaction Points

The second approach, of considerable practical importance, is based on the non-dimensional impedances of the previous section which can be used, in the context of any commercial FE code, in this case ANSYS, to simulate the half space medium. Thus, on top of these frequency dependent "springs" any structural model can be "built" and analyzed following, again, standard FEM procedures.

2.3 Presentation of Numerical Results

Solutions are presented for a series of harmonic excitations of the soil-foundation system. The main system parameters are the dimensionless stiffness ratio K and frequency α_o. The dimensionless stiffness ratio, expresses the relative stiffness between the soil and the foundation and is defined as [13]

$$K = \frac{\mathrm{E}_f t_f{}^3 (1-\nu_s)}{12(1-\nu_f^2) G_s B^3} \tag{2}$$

while the dimensionless frequency as

$$a_0 = \frac{\omega B}{Vs} \tag{3}$$

where E_f, ν_f, t_f and B are the elastic modulus, Poisson ratio, thickness and length of the footing, respectively, G_s, V_s and ν_s are the shear modulus, the shear wave velocity and Poisson ratio of the half-space and ω is the excitation frequency.

In addition, the dimensionless displacement Δ is defined as [13]

$$\Delta = \frac{uG_sB}{(1-\nu_s)\sum F_{ext}} \tag{4}$$

where u is the displacement due to dynamic loading F_{ext}.

In Figure 3 the values of computed impedances using ACS SASSI for various points of a flexible footing are plotted as a function of dimensionless frequency α_o, for vertical and rocking excitation. In this case only the center of the foundation is loaded. As expected impedance values differ from point to point due to foundation flexibility. It is also evident that the impedance values are more sensitive to spatial distance from the loading point, than to the excitation frequency.

In Figures 4 and 5 the dynamic response of a square, flexible foundation slab, is shown. The foundation is loaded with a harmonic concentrated vertical force at its center and the dimensionless vertical displacements, Δ, at 3 characteristic nodal points, i.e. center (loaded point), middle of side, and corner, are plotted versus the dimensionless frequency α_o. The foundation response shown in Figure 4 corresponds to a rather "soft" foundation (K=0.004) while the response shown in Figure 5 to a rather "stiff" foundation (K=0.06). For comparison purposes, the related results found in Refs [13,14] are also plotted in Figures 4 and 5, showing a good agreement between the various methods.

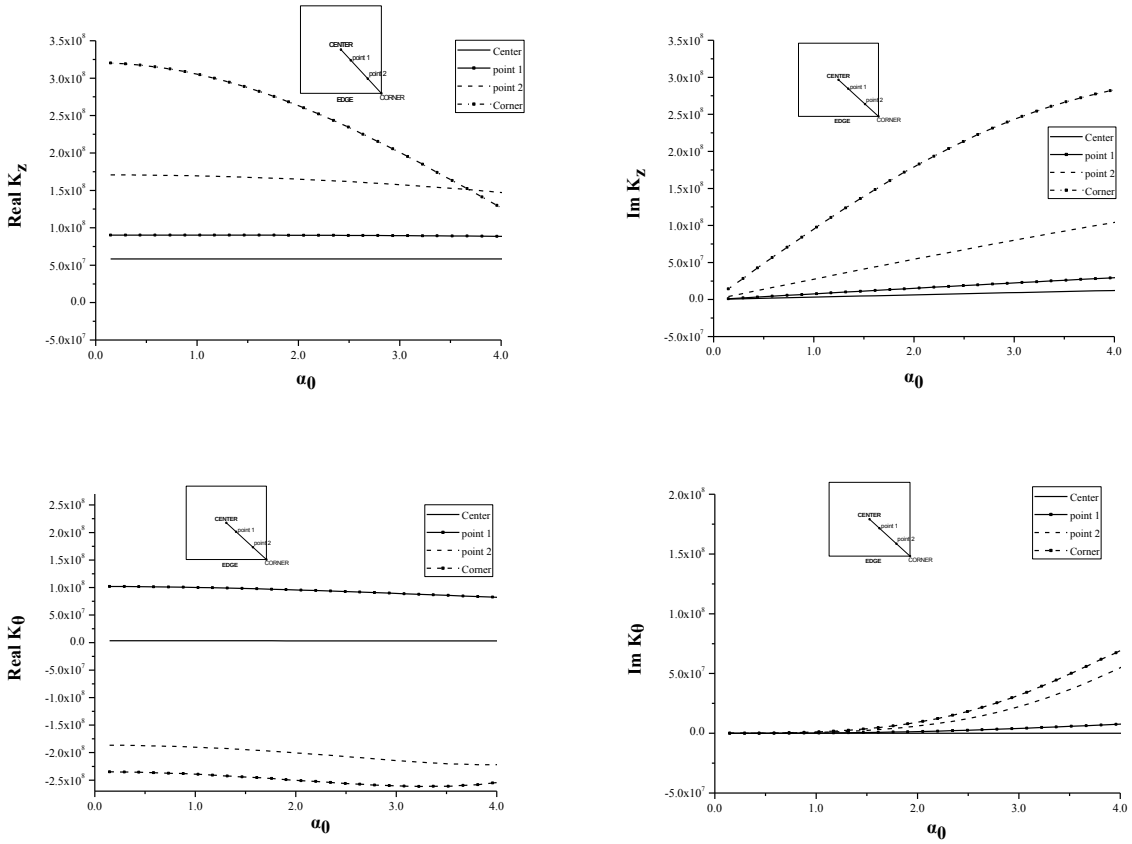


Figure 3: Real and Imaginary impedance values for vertical (K_z) and rocking (K_θ) oscillations as a function of frequency. (K = 0.004, ν_s = 0.45)

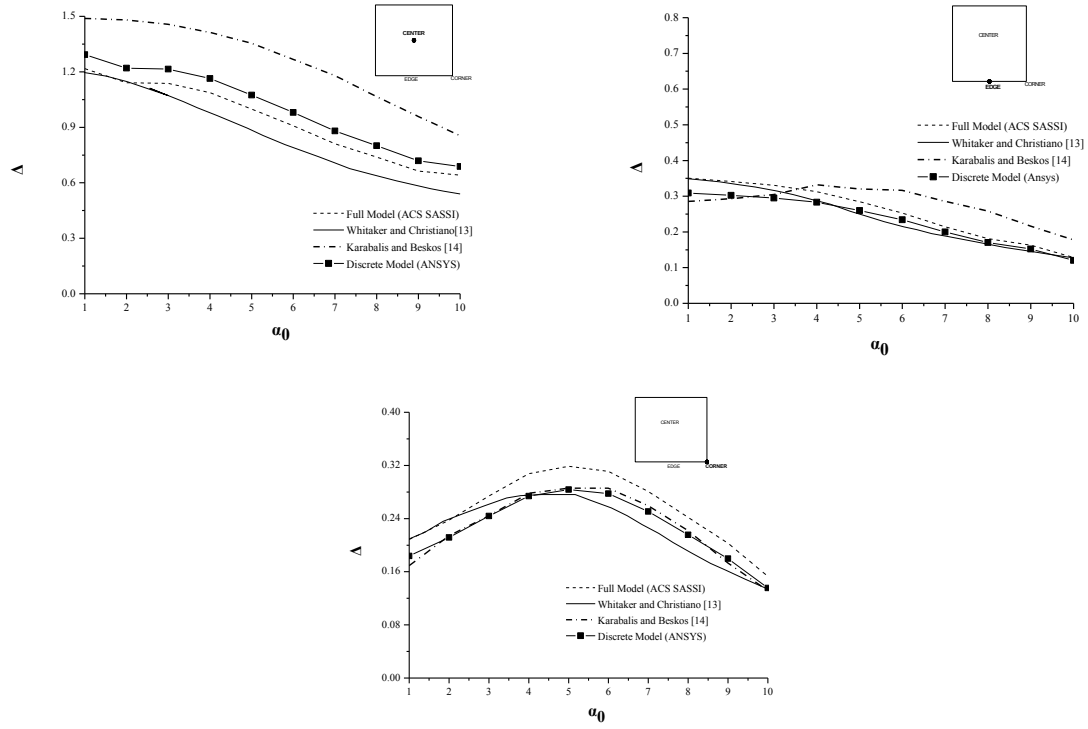


Figure 4: Flexible footing dynamic response versus frequency. (K = 0.004, ν_s = 0.45)

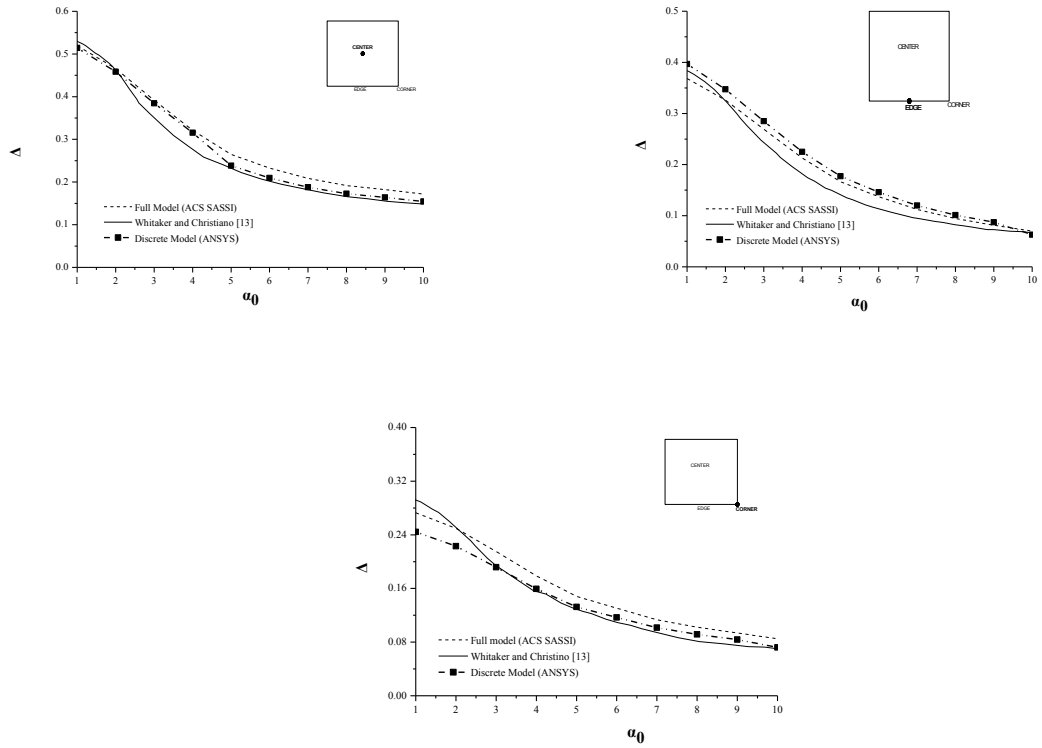


Figure 5: Flexible footing dynamic response versus frequency. (K = 0.06, ν_s = 0.45)

3 CONCLUSIONS

In this paper, a computational procedure for the analysis of soil-flexible foundation interaction is developed based on the finite element method. Impedance values for vertical and rocking oscillations of a half space are computed and used as the basis for the foundation-soil interaction problem. The discrete (in space), frequency dependent, impedance matrix of the soil-foundation system is also obtained. The main conclusions of this article are:

1) Impedance values of the half-space are practically frequency independent for relatively low excitation frequencies, at the neighborhood of the loaded point.
2) The proposed approaches are readily applicable to the analysis of flexible foundations and superstructures.
3) The proposed approaches are in good agreement with previous methodologies and easy to use.

4 REFERENCES

[1] F. E. Richart, R. D. Woods, and J. R. Hall, *Vibrations of soils and Foundations.* Prentice-Hall, 1970.

[2] A.S Veletsos, Y.T Wei, Lateral and rocking vibration of footings. *Proc. ASCE*, ***97***, *SM 9*, 1227-1248, 1971.

[3] A. S. Veletsos, B. Verbic, Vibration of viscoelastic foundations. *Earth. Engng. Struct. Dyn*., **2**, 87-102, 1973.

[4] A. S. Veletsos, *Dynamics of structure-foundation systems*. Structural and Geotechnical Mechanics (Englewood Cliffs, NJ: Prentice-Hall), P333–361, 1977.

[5] J. E. Luco, and R. A. Westmann, Dynamic response of circular footings. . *Proc. ASCE, 97,* ***EM 5***, 1381-1395, 1971.

[6] J. E. Luco, and R. A. Westmann, Dynamic response of a rigid footing bonded to an elastic half-space. *J. Appl. Mech.*, **39**, 527-534, 1972.

[7] H. L. Wong, J. E. Luco, Dynamic response of rigid foundations of arbitrary shape. *Earth. Engng. Struct. Dyn*., **4**, 579-587, 1976.

[8] H. L. Wong, J. E. Luco, Dynamic response of rectangular foundations to obliquely incident seismic waves. *Earth. Engng. Struct. Dyn*., **6**, 3-16, 1978.

[9] J. E. Luco, H. L. Wong, Response of structures to nonvertically incident seismic waves. *Bull. Seism. Soc. Amer.*, **72**, 275-302, 1982.

[10] J. E. Luco, Impedance functions for a rigid foundation on a layered medium.' *Nucl. Engng. Des*, ***31***, 204, 1974.

[11] A. K. Vaish, A. K. Chopra, Earthquake finite element analysis of structure-foundation systems. *Proc. ASCE,* ***100***, *EM 6*, 1101-1116, 1974.

[12] J. P. Wolf, *Dynamic soil-structure interaction.* Prentice-Hall, Englewood Cliffs, New Jersey. 1985.

[13] W.L. Whittaker, P. Christiano, Dynamic response of a plate on elastic half-space. *Journal of the Engineering Mechanics Division, Proceedings of the ASCE*, ***108***, *EM 1*, 133-154. 1982.

[14] D.L. Karabalis and D.E. Beskos, Dynamic Response of 3-D Flexible Surface Foundations by Time Domain Finite and Boundary Element Methods. *International Journal of Soil Dynamics and Earthquake Engineering*, **4**, 91-101, 1985.

[15] M. Iguchi, J. E. Luco, Dynamic response of flexible rectangular foundations on an elastic half-space. *Earthquake Engineering & Structural Dynamics*, **9 (3)**, 239-249, 1981.

[16] H. R. Riggs, G. Waas, Influence of foundation flexibility on soil-structure interaction. *Earthquake Engineering & Structural Dynamics*, **13 (5)**, 597-615. 1985.

[17] J. L Tassoulas, E. Kausel,. On the dynamic stiffness of circular ring footings on an elastic stratum. *International Journal for Numerical and Analytical Methods in Geomechanics*,**8 (5)**, 411-426. 1984.

[18] R. J. Aspel, *Dynamic Green's Functions for Layered Media and Applications to Boundary value problems*. Ph. D. Thesis, Univ. Of California, San Diego, Calif, 1979.

[19] L. R. Jonhson. Green's function for Lamb's Problem. *Geophysics Journal of Royal Astr. Society*, **37**, 99-131, 1974.

[20] G. Waas, *Linear Two-Dimensional Analysis of Soil Dynamics Problems in Semi-Infinite Layered Media*. Ph. D. Thesis, University of California, Berkeley, Calif., 1972.

[21] E. Kausel, J. L Tassoulas, Transmitting boundaries: a closed form comparison. *Bull. Seism. Soc. Amer.*, **71**, 143-159, 1982

[22] J. L Tassoulas, E. Kausel, and M. Roesset, Consistent boundaries for semi-infinite problems." *American Society of Mechanical Engineers, Applied Mechanics Division*, **AMD 46**, 149-166, 1981.

[23] D.L. Karabalis, D.E. Beskos, Dynamic Response of Rigid Surface Foundations by Time Domain Boundary Element Method. *Earthquake Engineering and Structural Dynamics*, **Vol. 12**, 73-93, 1984.

[24] S. Ahmad, P. K. Banerjee, Time-domain transient elastodynamic analysis of 3-d solids by BEM, *International Journal for Numerical Methods in Engineering*, **26**, 1709-1728, 1988.

[25] J. Dominguez, Dynamic Stiffness of rectangular foundations. *Dept. Of Civil Eng., M.I.T.*, Publ. No R78-20, 1978.

[26] J. A. Gutierrez, A. K. Chopra, A substructure method for earthquake analysis of structures including structure-soil interaction. *Earth. Engng. Struct. Dyn.*, **6**, 51-69, 1978

[27] A.P. Gaitanaros, D.L. Karabalis, Dynamic Analysis of 3-D Flexible Embedded Foundations by a Frequency Domain BEM-FEM. *Earthquake Engineering and Structural Dynamics*, **16**, 653-674, 1988.

[28] S.A. Savidis, T. Richter, Dynamic response of elastic plates on the surface of the half-space. *Int. J. Num. Anal. Meth. Geomech.*, **3**, 245-254, 1979.

[29] Gazetas, G., Analysis of machine foundation vibrations: State of the art. *International Journal of Soil Dynamics and Earthquake Engineering*, **2**, Issue 1, 2-42. 1983.

[30] D.E. Beskos, Applications of the boundary element in dynamic soil-structure interaction, *Developments in Dynamic Soil-Structure Interaction*, eds P. Gulkan and R.W. Clough, 61-90, Kluwer Academic Publishers, Dordrecht, 1993.

[31] D.L. Karabalis, Dynamic Soil-Structure Interaction by BEM, 351-374, in: C. A. Brebbia, Ed., *Boundary Elements X, Vol. 4: Geomechanics, Wave Propagation and Vibrations* , Computational Mechanics Publications, Southampton, 1988.

[32] ACS SASSI NQA, Version2.3.3, Revision 3, 2010

[33] ANSYS, Inc. Version 10.0, 2005

COMPDYN 2013
4th ECCOMAS Thematic Conference on
Computational Methods in Structural Dynamics and Earthquake Engineering
M. Papadrakakis, V. Papadopoulos, V. Plevris (eds.)
Kos Island, Greece, 12–14 June 2013

ENVELOPE PRINCIPLE IN MULTI-MODE PUSHOVER PROCEDURE FOR RC BUILDINGS

Ante Mihanović[1], Ivan Balić[1], Boris Trogrlić[1]
[1] University of Split, Faculty of Civil Engineering, Architecture and Geodesy
Matice hrvatske 15, 21000 Split, Croatia
boris.trogrlic@gradst.hr

Keywords: Multi-mode pushover, Target acceleration, Envelope, RC frames.

Abstract. *Pushover method is a practical procedure for comprehensive nonlinear analysis of structures subjected to seismic action. Application of this method, in accordance with the Eurocode 8 rules and due to engineering simplicity, favours application utilizing the first mode. Aim of research presented in this paper was to find the influence of multimodal combinations in assessing the bearing capacity of reinforced concrete (RC) frames and walls. This paper presents a procedure in which the most extreme state is defined by the lowest ground acceleration caused by a predetermined shape of an elastic spectrum. Extreme bearing value is obtained by the envelope principle. Mode shapes and period sizes are determined on a linear elastic model while the limit state of the load bearing system is evaluated in a nonlinear state of structures. Results of the analysis show that influences of higher modes are significantly bigger and that the safety/reliability, indicated by criteria for the target displacement, in accordance with Eurocode 8 (Annex B), is not achieved. Inclusion of higher modes, in some presented examples, decreases the limit ground acceleration by more than two times, which is significantly less favourable than the target displacement criteria.*

1 INTRODUCTION

A multi-mode pushover procedure for comprehensive nonlinear static analysis of structures subjected to seismic action is presented in paper. When combined with response spectrum of a single degree of freedom system it gives the assessment of bearing capacity and deformation of structures during earthquakes.

Pushover procedure is implemented in many international codes for design of structures, as well as recommended provisions of research institutions [1-3]. Development of procedure implemented in Eurocode 8 started three decades ago [4-6], while numerous improvements and applications [7, 8] are still current [9]. In practical application, pushover method based on linear or constant distribution of acceleration, is dominant. In numerous research papers, such as [10-16] influence of higher modes on the results of nonlinear static analysis applied through the pushover method were analysed with the conclusion of significant impact of higher modes.

This paper presents the approach of inclusion of higher modes through trial method in order to satisfy the envelope method. Method can be applied only on a specific elastic spectrum. In examples presented in this paper, spectrum type *1* and ground type *A* is chosen in accordance with the Eurocode 8.

Capacity curves are determined by pushover analysis, and then converted in ADRS (Acceleration-Displacement Response Spectrum) format according to previously selected spectrum for the first few modes. Input data for modal load vectors are determined based on linear elastic analysis.

Now, trial method can be applied by the trial principle as follows:

- Hypothetic acceleration is selected and joint to previously selected specific elastic spectrum.
- For each mode separately, based on capacity curve, corresponding level of spectral acceleration and spectral force must be determined taking into account target displacement according to Eurocode 8. Distribution of acceleration, i.e. shape of load vector, corresponds to the shape of the corresponding mode.
- Furthermore, general load vector must be formed as a load vector, according to some of possible combination of actual modes. As possible combinations, this paper analysed: linear combination (L) and square root of sum of square combination (SRSS).
- For thus formed total load vector on structure (starting load), bearing capacity of structures, i.e. computational limit load, is determined by nonlinear static analysis.

Solution is considered to be the one in which, within the limits of calculation accuracy, a computational limit load from ultimate limit state is equal to starting load from assumed ground acceleration. In couple selection attempts of various hypothetic acceleration and corresponding vectors, procedure leads to a solution quickly. Obtained solution gives us the *target acceleration*. It represents the lowest acceleration which, according to nonlinear static analysis and multi-mode analysis, leads to computation limit state.

Based on processed examples of linear and SRSS combinations it was logical to conclude that target acceleration must be lower than acceleration belonging to specific mode. That fact presents initial step in this trial method. Final solution has all the characteristics of an envelope principle.

2 TARGET ACCELERATION DETERMINATION

Procedure of target acceleration determination begins by determining structure's modes $\boldsymbol{\phi}_i$, corresponding periods T_i and modal masses m_{ei}, all based on linear elastic analysis. Load vector for each specific i-th mode $\boldsymbol{F}_i$ is determined by the intensity factor of total load p_i, as well as the product of diagonal mass matrix $\boldsymbol{M}$ and mode $\boldsymbol{\phi}_i$.

$$\boldsymbol{F}_i = p_i \, \boldsymbol{M} \, \phi_i \tag{1}$$

Capacity curves are calculated by material and geometric nonlinear numerical model [17] with monotonic increase of each load vector $\boldsymbol{F}_i$. This way, failure lateral forces in the base of model F_{fi} is obtained for each specific load vector.

In searching for target acceleration, each attempt starts with assumed value of target ground acceleration a_{gr}. For assumed a_{gr}, type of elastic spectrum (type *1* or type *2*), ground type (soil factor S) and damping correction factor (η=1 for ξ=5% viscous damping ratio), an ADRS curve is constructed. In that ADRS curve a capacity curve is embedded which is obtained for each specific load factor.

Spectral acceleration $a_{s,i}$ is obtained for each mode independently, in accordance with Eurocode 8 and Annex B, choosing that displacement on capacity curve at failure is 150% of target displacement, or

$$d_t = \frac{2}{3} d_u \tag{2}$$

Thereby, corresponding bilinear force-deformation diagram must be found, i.e. diagram where intersection of period T_i and related target displacement d_t exist on ADRS curve created for assumed ground acceleration. In other words, equality of obtained ground acceleration $a_{gr,i}$ in i-th attempt with assumed ground acceleration a_{gr} must be found, from which spectral acceleration $a_{s,i}$ will follow. Search procedure for corresponding bilinear force-deformation diagram is shown in Figure 1.

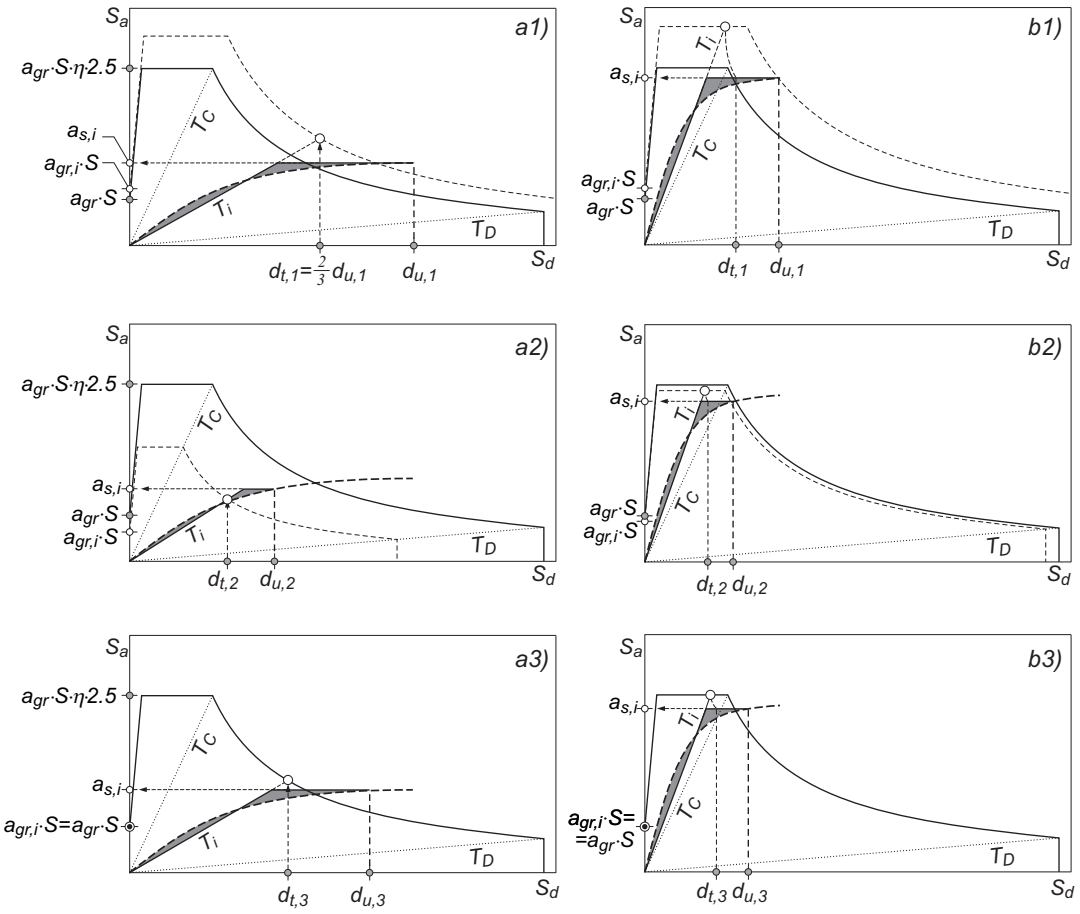


Figure 1: Spectral acceleration determination $a_{s,i}$: a1)-a3) for $T_i \geq T_C$; b1)-b3) for $T_i < T_C$.

In the case when the period is $T_i \geq T_C$, in Figures 1.a1) and 1.a2) chosen bilinear force-deformation diagrams are presented. In Figure 1.a1) chosen diagram gives bigger and on Figure 1.a2) lower ADRS curve ordinates than ADRS curve of assumed ground acceleration a_{gr}. In Figure 1.a3) chosen diagram for corresponding period T_i and related target displacement d_t gives intersection on ADRS curve, from which follows spectral acceleration $a_{s,i}$. Similar procedures have to be performed in case of $T_i < T_C$ when searching for intersection according to path defined by Eurocode 8 - Annex B.

After this is performed, for each vector, parameter δ should be defined, as a ratio between accordingly obtained spectral acceleration and assumed ground acceleration

$$\delta_i = \frac{a_{s,i}}{a_{gr}} = \delta_i\left(a_{gr}\right) \tag{3}$$

Hereafter, some modal combinations are defined. It is standard to use linear combination (L) and square root of sum of square combination (SRSS). Target acceleration result is obtained by applying successive attempts, varying assumed acceleration as initial data.

2.1 Target acceleration at linear combination of modes

Shape of the starting hypothetic vector of limit load $\boldsymbol{F}_L$ for linear combination is defined as

$$\sum F_i = \sum \pm\, m_{ei}\, \delta_i\, F_{fi} \tag{4}$$

where sign ± means more unfavourable influence on the characteristic section. Characteristic section, here presented on a specific example (RC frame), is a sum of bending moments at the bottom of the first floor. During the selection of the algebraic sign, group influence line for characteristic values can be used.

In numerical procedure, proposed loading is applied incrementally. As a result, associated computation limit loading is obtained, i.e. force in basis of model F_f.

Ratio between starting hypothetic vector F_L and computational limit load F_f shows the reality of the starting assumption. Only when aforementioned equality is obtained, within the limits of computational accuracy, required result is achieved; extreme, i.e. the lowest limit ground acceleration, named target acceleration $a_{gr,t}$.

2.2 Target acceleration according to SRSS modal combination

Square root of sum of square modal combination is a method which can be simplified, in case when the first mode is dominant, as a sum of the first member and half of other members. Half of participating loading of higher individual mode is approximately equal to total loading belonging to the spectrum with acceleration of $a_{gr}/2$ [18], so appropriate combination may be defined as

$$\sum F_i = \pm m_{e1}\, \delta_1\left(a_{gr}\right) F_{\underset{1}{f}} + \sum_{i=2}^{n} \pm\, m_{ei}\, \delta_i\left(a_{gr}/2\right) F_{fi} \tag{5}$$

Rest of the procedure is analogue to procedure described for linear combination.

3 EXAMPLE

Hereafter, example of 9-storey space reinforced concrete frame is analysed. Calculation is performed taking into account the following assumptions and limitations: (i) calculation of dynamic properties (ϕ_i, T_i, m_{ei}) is conducted on a linear model of RC frame with floor slabs

and with initial modulus of elasticity E_0; (ii) torsion effects are not included in the calculation; (iii) frames from both examples are symmetric around two axis.

3.1 Model description and calculation of loading vector

The 9-storey space RC frame, with dimensions shown in Figure 2a, is analysed. Dimensions and discretization of cross sections of beams are shown in Figures 2d and 2e, and dimensions and discretization of cross sections of columns are shown on Figure 2f. Properties of cross sections are assigned to frame according to Figure 2c. Distributed loading is assigned on beams according to Figure 2b, and concentrated forces are set in nodes on intersections of beams and columns. For computation of eigenvectors a concentrated mass is assigned (Figure 2b) and material modulus E=24.38 GPa, as initial elastic modulus of concrete. To calculate the capacity curve, numerical models of concrete and steel are used as shown in Figure 2g. Total weight of model is W=14903 kN, i.e. M=1519.2 tons.

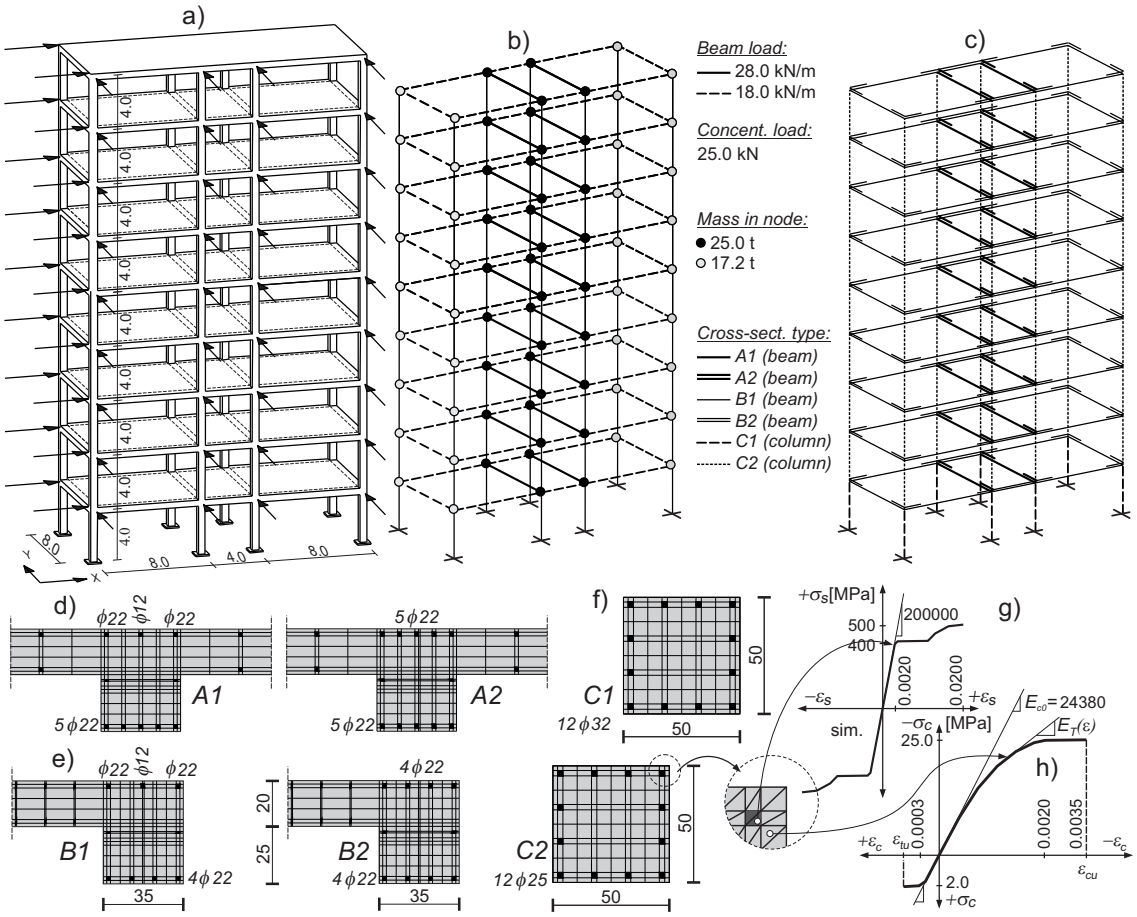


Figure 2: Example: a) Space frame; b) loading on beams and concentrated masses; c) labels of cross sections; d)-f) discretization of cross sections; g)-h) numerical model for steel and concrete.

By solving the linear dynamic analysis, eigenvectors are obtained $\boldsymbol{\phi}_i$, as well as periods T_i and modal masses m_{ei}, as shown in Table 1.

Load distribution and intensity of lateral forces are defined according to Equation 1. Thus defined shape of lateral loading vector is monotonically increased in nonlinear analysis, up to failure, i.e. achieving critical load factor. The sum of all horizontal forces gives failure force F_{fi} for the each eigen vector.

Vector	T_i [s]	m_{ei} [%]	m_{ei} [t]	F_{fi} [kN]
ϕ_1	2.298	79.87	1213.4	1330
ϕ_2	0.746	10.37	157.5	1530
ϕ_3	0.420	3.87	58.8	2035
ϕ_4	0.282	2.20	33.4	1770
ϕ_5	0.207	1.38	21.0	2490

Table 1: Properties of load vector for *x* direction.

Shape of the first vector in limit state and corresponding bearing capacity curve for *x* direction are shown on Figure 3.

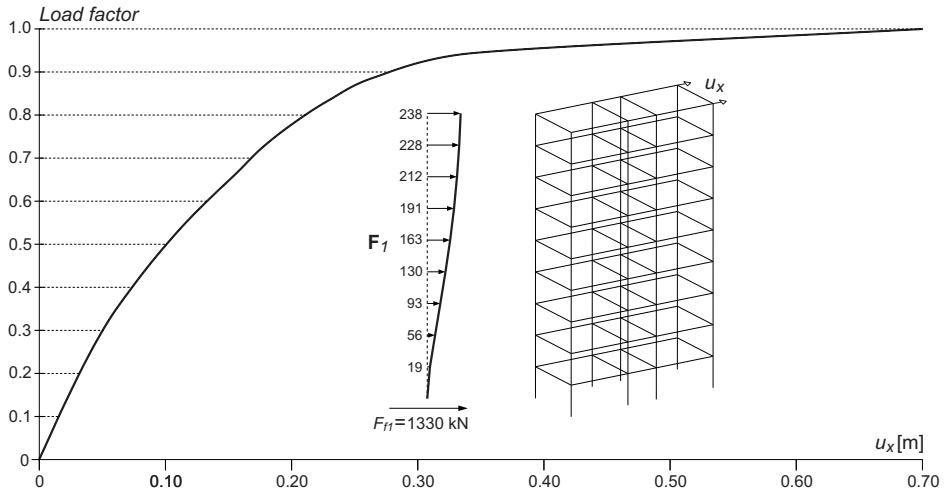


Figure 3: Capacity curve of vector ϕ_1 for *x* direction.

For the same direction *x*, conversion of capacity curve into ADRS format, determining the elasto-plastic equivalent, as well as limit (target) acceleration according to Eurocode 8 for the first mode, are all shown in Figure 4.

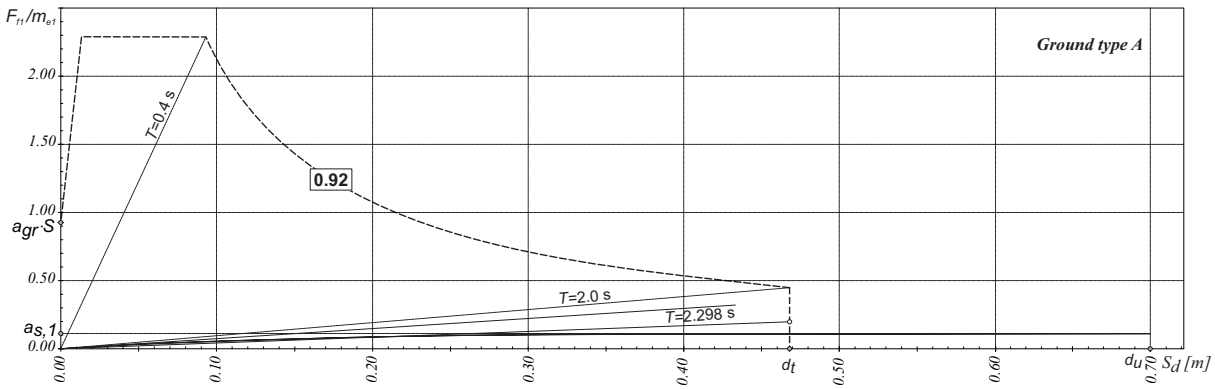


Figure 4: Computation of earthquake resistance for the first vector (F_1), for ground type *A*.

3.2 Determination of target acceleration for *x* direction

When searching for target acceleration, for assumed acceleration in the first step, assumed target acceleration obtained for the first vector is chosen, i.e. $a_{gr,1}$ = 0.92g. The same procedure is applied on other modes. Table 2 shows the procedure for trial method with result for minimal a_{gr} in case of target acceleration for linear combination. Obtained target acceleration has a value of $a_{gr,t}$ = 0.19g.

Figure 5 shows loading vector for all other participating modes, capacity curve as well as beginning of plastification and plastic hinge positions, for linear combination of modes. Early beginning of plastification is caused by loading in a way typical for pushover method, where gravity loading is set in the first phase, and in the second phase, horizontal loading is set. Hence, plastification begins immediately after start of the second phase - horizontal loading.

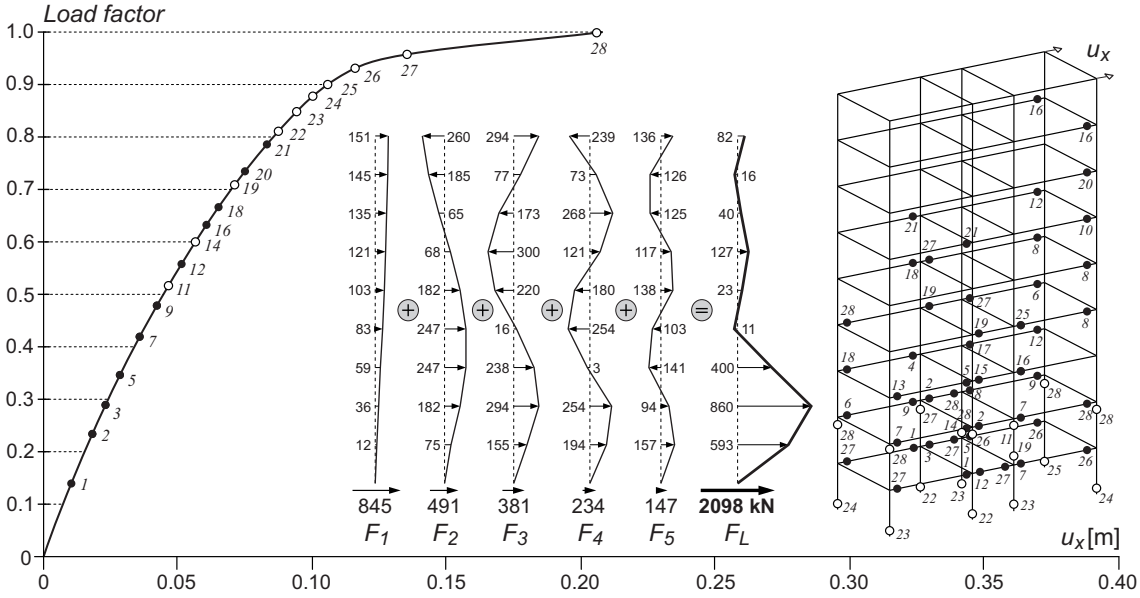


Figure 5: Capacity curve for linear combination of modes (*x* direction).

$a_{gr,i}$	$a_{s,1}$	F_1	$a_{s,2}$	F_2	$a_{s,3}$	F_3	$a_{s,4}$	F_4	$a_{s,5}$	F_5	ΣF_i	F_L	$F_L/\Sigma F_i$	δ_1	δ_2	δ_3	δ_4	δ_5
0.92	0.112	1330	0.923	1426	2.239	1292	2.700	886	3.161	651	5585	2681	0.48	0.121	1.003	2.434	2.935	3.436
0.50	0.107	1274	0.694	1072	1.428	824	1.749	574	1.858	383	4126	2476	0.60	0.214	1.388	2.856	3.498	3.716
0.20	0.073	869	0.448	692	0.689	398	0.750	246	0.750	155	2359	2123	0.90	0.365	2.240	3.445	3.750	3.750
0.19	0.071	845	0.318	491	0.660	381	0.713	234	0.713	147	2098	2098	**1.00**	0.374	1.674	3.474	3.753	3.753
0.18	0.068	809	0.307	474	0.623	359	0.675	221	0.675	139	2004	2164	1.08	0.378	1.706	3.461	3.750	3.750

Table 2: Target acceleration determination for linear combination (*x* direction).

Results for SRSS modal combination in *x* direction are shown in Table 3. Target acceleration is $a_{gr,t}$ = 0.25g. It is the minimal force in the base (1865 kN) does not correspond to target acceleration. Comparison of given target accelerations, gives the conclusion that linear combination is more unfavourable than SRSS combination because failure appears at lower target displacement.

$a_{gr,i}$	$a_{s,1}$	F_1	$a_{gr,i}/2$	$a_{s,2}$	F_2	$a_{s,3}$	F_3	$a_{s,4}$	F_4	$a_{s,5}$	F_5	ΣF_i	F_{SRSS}	$F_{SRSS}/\Sigma F_i$	δ_1	δ_2	δ_3	δ_4	δ_5
0.92	0.112	1330	0.46	0.651	1006	1.350	779	1.637	537	1.725	355	4010	2085	0.52	0.122	0.708	1.467	1.779	1.875
0.50	0.107	1274	0.25	0.391	604	0.845	488	0.938	308	0.938	193	2866	2064	0.72	0.214	0.782	1.690	1.876	1.876
0.30	0.093	1107	0.15	0.260	402	0.523	302	0.538	176	0.563	116	2103	2439	1.16	0.310	0.867	1.743	1.793	1.877
0.25	0.085	1011	0.125	0.225	348	0.442	255	0.469	154	0.469	97	1865	1865	**1.00**	0.340	0.900	1.768	1.876	1.876
0.20	0.073	869	0.10	0.182	281	0.354	204	0.375	123	0.375	77	1555	1368	0.88	0.365	0.910	1.770	1.875	1.875

Table 3: Target acceleration determination for SRSS combination (*x* direction).

Loading vector for each participating mode, capacity curve as well as beginning of plastification and plastic hinge positions, for SRSS combination of modes are shown in Figure 6.

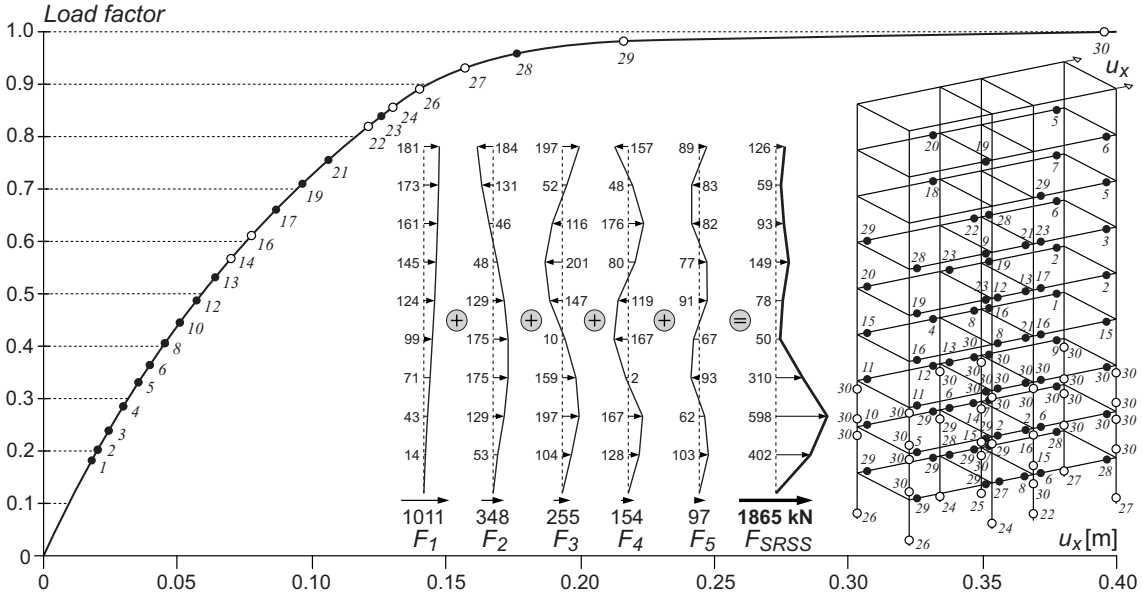


Figure 6: Capacity curve for SRSS combination (*x* direction).

3.3 Determination of target acceleration for *y* direction

Hereafter, results of analysis for *y* direction are presented. Properties of loading vector for each mode are shown in Table 4.

Vector	T_i [s]	m_{ei} [%]	m_{ei} [t]	F_{fi} [kN]
ϕ_1	2.715	78.91	1198.8	1410
ϕ_2	0.869	10.59	160.9	1735
ϕ_3	0.478	4.10	62.3	1965
ϕ_4	0.317	1.60	24.3	2340
ϕ_5	0.224	1.40	21.3	2435

Table 4: Properties of load vector for *y* direction.

Searching for target acceleration for linear combination in *y* direction is shown in Table 5. In searching for target acceleration, for assumed acceleration in the first step, assumed target acceleration obtained for the first vector is chosen, i.e. $a_{gr,1}$ = 1.05g. Obtained target acceleration has a value of $a_{gr,t}$=0.18g.

$a_{gr,i}$	$a_{s,1}$	F_1	$a_{s,2}$	F_2	$a_{s,3}$	F_3	$a_{s,4}$	F_4	$a_{s,5}$	F_5	ΣF_i	F_L	$F_L/\Sigma F_i$	δ_1	δ_2	δ_3	δ_4	δ_5
1.05	0.120	1410	0.917	1447	2.313	1413	3.900	928	3.606	754	5952	2619	0.44	0.114	0.873	2.203	3.714	3.434
0.40	0.097	1141	0.494	780	1.063	649	1.500	357	1.500	314	3240	2203	0.68	0.243	1.235	2.658	3.750	3.750
0.20	0.063	741	0.309	488	0.588	359	0.750	179	0.750	157	1923	1846	0.96	0.315	1.545	2.940	3.750	3.750
0.18	0.058	682	0.277	437	0.537	328	0.675	161	0.675	141	1749	1749	**1.00**	0.322	1.539	2.983	3.750	3.750
0.17	0.056	659	0.265	418	0.500	306	0.638	152	0.638	133	1667	1834	1.10	0.329	1.559	2.941	3.753	3.753

Table 5: Target acceleration determination for linear combination (*y* direction).

Loading vector for each participating mode, capacity curve for a linear combination as well as the sequence and place of the beginning of plastification and plastic hinge positions are shown in Figure 7.

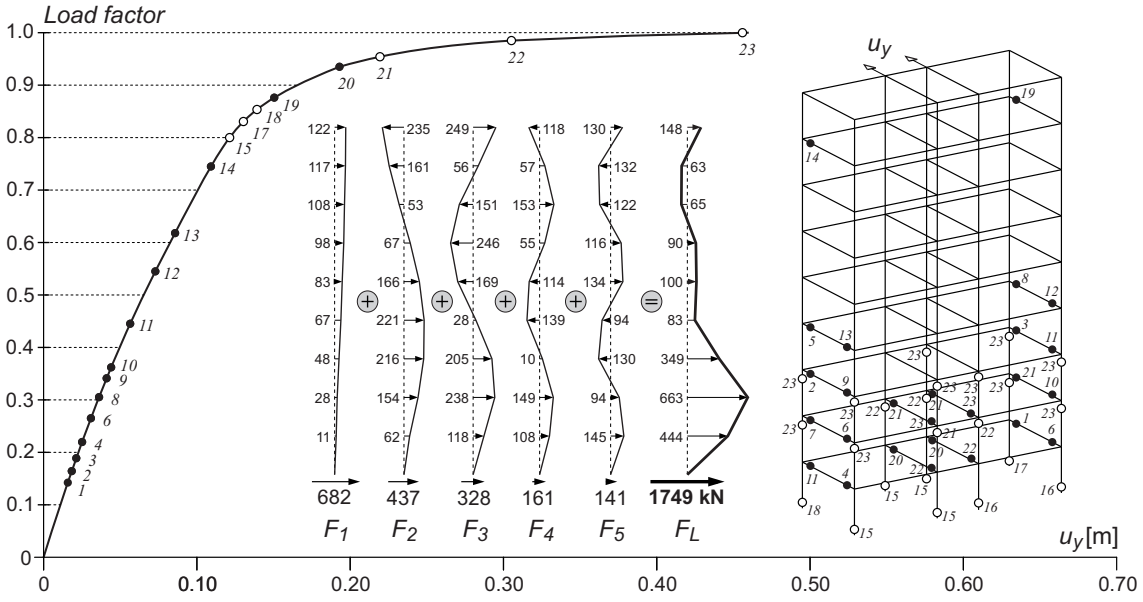


Figure 7: Capacity curve for linear combination (*y* direction).

Procedure of searching for target displacement in case of SRSS mode combination is shown in Table 6. Target acceleration is $a_{gr,t}$ = 0.245g. Linear combination has proven to be relevant *y* direction too, because the failure of structure appears at lower target acceleration ($a_{gr,t}$=0.18g) than target acceleration in case of SRSS mode combination ($a_{gr,t}$=0.245g).

$a_{gr,i}$	$a_{s,1}$	F_1	$a_{gr,i}/2$	$a_{s,2}$	F_2	$a_{s,3}$	F_3	$a_{s,4}$	F_4	$a_{s,5}$	F_5	ΣF_i	F_{SRSS}	$F_{SRSS}/\Sigma F_i$	δ_1	δ_2	δ_3	δ_4	δ_5
1.05	0.120	1410	0.525	0.610	963	1.300	794	1.968	468	1.879	393	4028	2175	0.54	0.114	0.581	1.238	1.874	1.790
0.40	0.097	1141	0.20	0.309	488	0.588	359	0.750	179	0.750	157	2323	1812	0.78	0.243	0.773	1.470	1.875	1.875
0.245	0.073	858	0.123	0.207	327	0.357	218	0.459	109	0.459	96	1608	1608	**1.00**	0.298	0.845	1.457	1.873	1.873
0.24	0.072	847	0.12	0.203	320	0.350	214	0.450	107	0.450	94	1582	1661	1.05	0.300	0.846	1.458	1.875	1.875
0.20	0.063	741	0.10	0.173	273	0.295	180	0.375	89	0.375	78	1362	1702	1.25	0.315	0.865	1.475	1.875	1.875

Table 6: Target acceleration determination for SRSS combination (*y* direction).

Loading vector for each participating mode, capacity curve as well as beginning of plastification and plastic hinge positions, for SRSS combination of modes is shown in Figure 8.

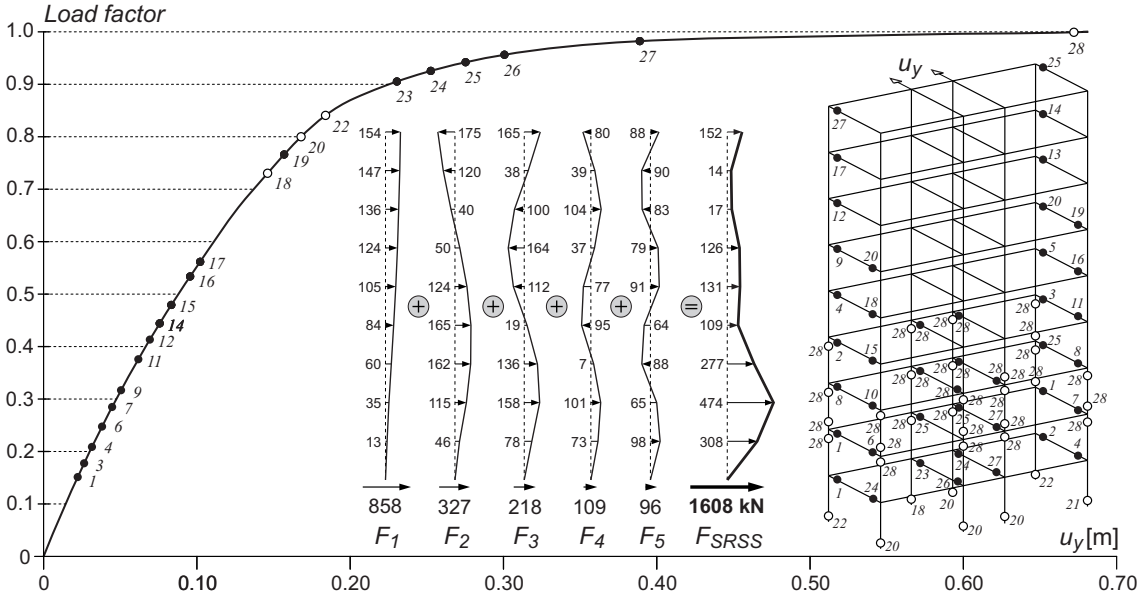


Figure 8: Capacity curve for SRSS combination (y direction).

4 APPEARANCE OF LINEAR (L) AND ROOT (SRSS) MODAL COMBINATION

The procedure that follows is intended to determine which of the specified combination of modes are likely to rally in the verification on the set of the following eight real earthquake accelerograms: Montenegro (Montenegro)-1979, Campano Lucano (Italy)-1980, Aigion (Greece)-1995, Olfus (Iceland)-2008, Calabria (Italy)-1978, Valnerina (Italy)-1979, Banja Luka (B&H)-1981 and Sicilia Orientale (Italy)-1990, all shown in Figure 9. Records of the earthquake accelerograms are taken from the European Strong-motion Database [19].

Verification of L and SRSS combination of modes on the linear and non-linear level of single degree of freedom system (SDOF) are taken as the obtained modes for observed 9-storey RC frames.

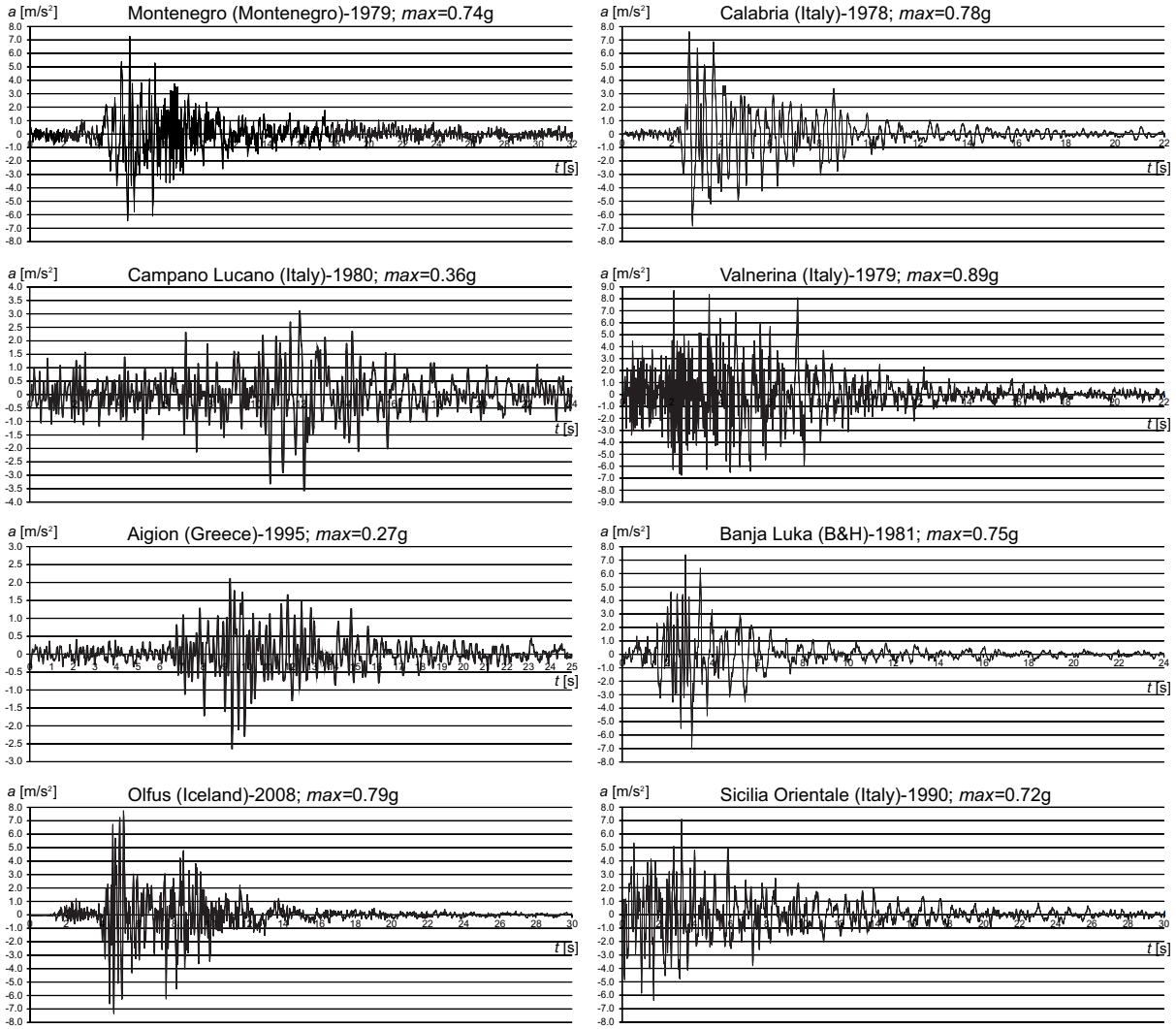


Figure 9: Eight real earthquake accelerograms.

Dynamic response of each SDOF is obtained by Newmark's average acceleration method. Numerical integration is written in computer program C++ according to the procedure described in [20].

4.1 Verification of L and SRSS combination of modes on the linear level

The 9-storey space RC frame from example in Figure 2 is analyzed. Shear forces in the cross section at the base of the calculation model (F_i) are calculated as a time function for each of the five eigen modes. Stiffness k of the linear SDOF is defined by the known period T_i and associated participating mass m_i corresponding to each own vector $\boldsymbol{\phi}_i$.

A relative measure of the force is introduced by which the greatest force of all modes ($|F_{max}|$) is equal to *1.00* and the others are relative to her.

Figure 10 shows a diagram of the shear forces in the cross section at the base of the calculation model (F_i) as a time function for all five eigen modes, for example of 9-storey RC frame loaded in the x direction by earthquake excitation Montenegro. It can be seen that in the relative scale of the force, the maximum amount of force of all five modes ($|F_{max}|$=689 kN) corresponds to a value *1.00*.

Maximum values of shear forces in the intersection at the base of the calculation model for all modes, which are shown in Tables 7 and 8, resulting from the action of eight real selected earthquake accelerogram records are obtained in an analogous way.

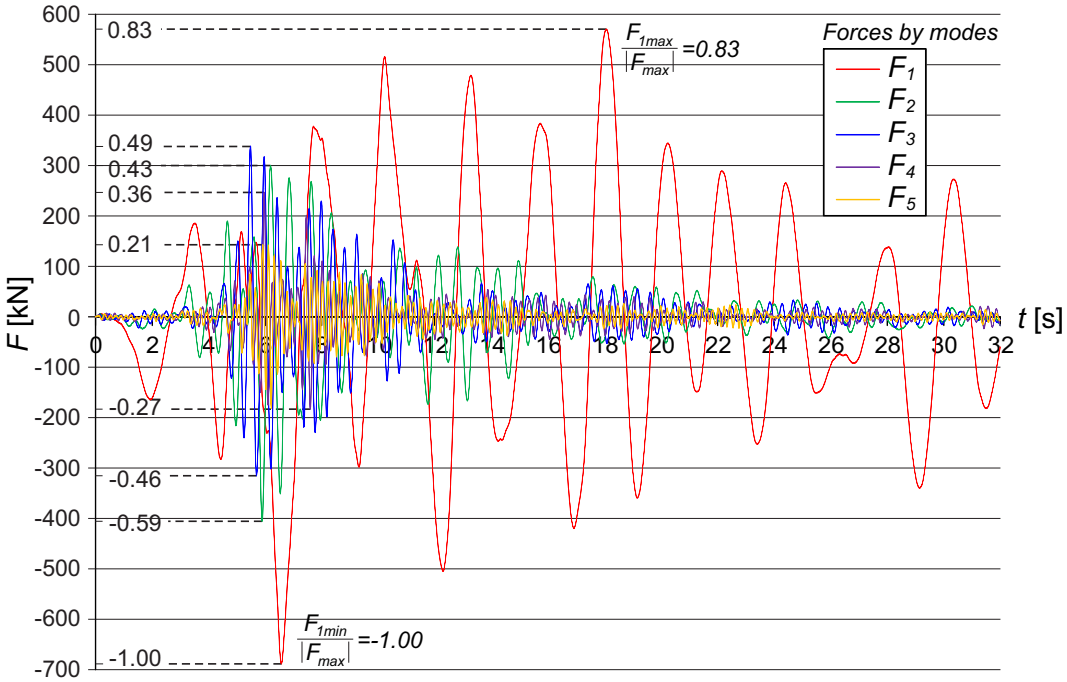


Figure 10: Shear forces in the cross section at the base of the calculation model of 9-storey RC frame for all five modes, as a time function of the earthquake excitation Montenegro for *x* direction.

Table 7 shows the results of analysis for the *x* and *y* directions, which presents the least favourable combination of simultaneous linear superposition of modes F_L as well as the least favourable combination of the square root of the sum of square of modes F_{SRSS}.

Montenegro **- 9-storey RC frame -** ***x*** **direction**						
F_{1max}	F_{2max}	F_{3max}	F_{4max}	F_{5max}	**for the same** ***t***	
0,83	0,43	0,49	0,36	0,21		
F_{1min}	F_{2min}	F_{3min}	F_{4min}	F_{5min}	F_L	-1,45
-1,00	-0,59	-0,46	-0,27	-0,26	F_{SRSS}	1,14

Campano Lucano **- 9-storey RC frame -** ***x*** **dir.**						
F_{1max}	F_{2max}	F_{3max}	F_{4max}	F_{5max}	**for the same** ***t***	
1,00	0,63	0,50	0,30	0,25		
F_{1min}	F_{2min}	F_{3min}	F_{4min}	F_{5min}	F_L	-1,36
-0,87	-0,47	-0,60	-0,25	-0,25	F_{SRSS}	1,14

Aigion **- 9-storey RC frame -** ***x*** **direction**						
F_{1max}	F_{2max}	F_{3max}	F_{4max}	F_{5max}	**for the same** ***t***	
0,90	0,52	0,51	0,84	0,40		
F_{1min}	F_{2min}	F_{3min}	F_{4min}	F_{5min}	F_L	-1,59
-1,00	-0,53	-0,59	-0,99	-0,35	F_{SRSS}	1,15

Olfus **- 9-storey RC frame -** ***x*** **direction**						
F_{1max}	F_{2max}	F_{3max}	F_{4max}	F_{5max}	**for the same** ***t***	
1,00	0,20	0,25	0,17	0,24		
F_{1min}	F_{2min}	F_{3min}	F_{4min}	F_{5min}	F_L	0,97
-0,92	-0,17	-0,22	-0,15	-0,21	F_{SRSS}	1,00

Calabria **- 9-storey RC frame -** ***x*** **direction**						
F_{1max}	F_{2max}	F_{3max}	F_{4max}	F_{5max}	**for the same** ***t***	
0,70	0,83	0,99	0,52	0,33		
F_{1min}	F_{2min}	F_{3min}	F_{4min}	F_{5min}	F_L	1,44
-0,67	-0,66	-1,00	-0,61	-0,36	F_{SRSS}	1,23

Valnerina **- 9-storey RC frame -** ***x*** **direction**						
F_{1max}	F_{2max}	F_{3max}	F_{4max}	F_{5max}	**for the same** ***t***	
0,83	0,65	0,37	0,27	0,15		
F_{1min}	F_{2min}	F_{3min}	F_{4min}	F_{5min}	F_L	1,35
-1,00	-0,72	-0,35	-0,28	-0,13	F_{SRSS}	1,09

Banja Luka **- 9-storey RC frame -** ***x*** **direction**						
F_{1max}	F_{2max}	F_{3max}	F_{4max}	F_{5max}	**for the same** ***t***	
0,75	1,00	0,31	0,20	0,17		
F_{1min}	F_{2min}	F_{3min}	F_{4min}	F_{5min}	F_L	-1,36
-0,53	-0,93	-0,37	-0,24	-0,19	F_{SRSS}	1,08

Sicilia Orientale **- 9-storey RC frame -** ***x*** **dir.**						
F_{1max}	F_{2max}	F_{3max}	F_{4max}	F_{5max}	**for the same** ***t***	
0,88	0,75	0,47	0,28	0,25		
F_{1min}	F_{2min}	F_{3min}	F_{4min}	F_{5min}	F_L	-1,54
-1,00	-0,86	-0,48	-0,25	-0,23	F_{SRSS}	1,21

Montenegro **- 9-storey RC frame -** ***y*** **direction**						
F_{1max}	F_{2max}	F_{3max}	F_{4max}	F_{5max}	**for the same** ***t***	
0,71	0,25	0,58	0,16	0,22		
F_{1min}	F_{2min}	F_{3min}	F_{4min}	F_{5min}	F_L	-1,06
-1,00	-0,39	-0,65	-0,14	-0,21	F_{SRSS}	1,00

Campano Lucano **- 9-storey RC frame -** ***y*** **dir.**						
F_{1max}	F_{2max}	F_{3max}	F_{4max}	F_{5max}	**for the same** ***t***	
0,90	1,00	0,58	0,18	0,23		
F_{1min}	F_{2min}	F_{3min}	F_{4min}	F_{5min}	F_L	1,72
-0,95	-0,80	-0,72	-0,25	-0,21	F_{SRSS}	1,11

Aigion **- 9-storey RC frame -** ***y*** **direction**						
F_{1max}	F_{2max}	F_{3max}	F_{4max}	F_{5max}	**for the same** ***t***	
0,97	0,32	0,39	0,45	0,27		
F_{1min}	F_{2min}	F_{3min}	F_{4min}	F_{5min}	F_L	-1,35
-1,00	-0,33	-0,40	-0,50	-0,25	F_{SRSS}	1,03

Olfus **- 9-storey RC frame -** ***y*** **direction**						
F_{1max}	F_{2max}	F_{3max}	F_{4max}	F_{5max}	**for the same** ***t***	
0,94	0,29	0,32	0,20	0,41		
F_{1min}	F_{2min}	F_{3min}	F_{4min}	F_{5min}	F_L	1,06
-1,00	-0,23	-0,33	-0,18	-0,34	F_{SRSS}	1,00

Calabria **- 9-storey RC frame -** ***y*** **direction**						
F_{1max}	F_{2max}	F_{3max}	F_{4max}	F_{5max}	**for the same** ***t***	
0,33	0,49	1,00	0,60	0,31		
F_{1min}	F_{2min}	F_{3min}	F_{4min}	F_{5min}	F_L	1,16
-0,25	-0,38	-0,93	-0,55	-0,28	F_{SRSS}	1,04

Valnerina **- 9-storey RC frame -** ***y*** **direction**						
F_{1max}	F_{2max}	F_{3max}	F_{4max}	F_{5max}	**for the same** ***t***	
0,96	0,64	0,35	0,21	0,15		
F_{1min}	F_{2min}	F_{3min}	F_{4min}	F_{5min}	F_L	1,46
-1,00	-0,50	-0,41	-0,21	-0,13	F_{SRSS}	1,18

Banja Luka **- 9-storey RC frame -** ***y*** **direction**						
F_{1max}	F_{2max}	F_{3max}	F_{4max}	F_{5max}	**for the same** ***t***	
0,79	1,00	0,76	0,29	0,29		
F_{1min}	F_{2min}	F_{3min}	F_{4min}	F_{5min}	F_L	-1,54
-0,50	-0,84	-0,73	-0,28	-0,30	F_{SRSS}	1,12

Sicilia Orientale **- 9-storey RC frame -** ***y*** **dir.**						
F_{1max}	F_{2max}	F_{3max}	F_{4max}	F_{5max}	**for the same** ***t***	
0,74	0,65	0,54	0,27	0,35		
F_{1min}	F_{2min}	F_{3min}	F_{4min}	F_{5min}	F_L	1,48
-1,00	-0,58	-0,61	-0,21	-0,33	F_{SRSS}	1,03

Table 7: Comparison of linear (L) and root (SRSS) combination of modes for 9-storey RC frame on linear level.

Presented results of dynamic response of linear system according to Table 7 shows that the linear combination of modes F_L is frequently unfavourable than the square root of sum of square combinations of modes F_{SRSS}.

4.2 Verification of L and SRSS combination of modes on the non-linear level

Non-linear levels is achieved so that each mode is treated as a nonlinear SDOF. Non-linear cyclic properties of SDOF are generated from the corresponding capacity curve as shown in Figure 11 and equation (6).

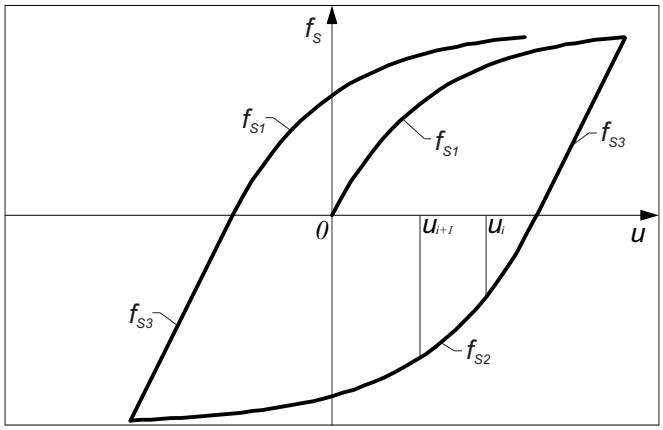


Figure 11: Cyclic capacity curve for the non-linear system.

Figure corresponding functions are defined in such a way to have the following analytical form:

$$f_{s1} = A\left(1 - e^{-\frac{u-B}{C}}\right) + D$$
$$f_{s2} = -A\left(1 - e^{\frac{u-B}{C}}\right) + D \tag{6}$$
$$f_{s3} = \frac{A}{C}(u - B) + D$$

The function f_{S1} corresponds to capacity curve for each mode. With it the coefficients A and C are defined in the expression (6). The function f_{S3} is linear and the slope of its corresponds to initial stiffness of SDOF. Coefficients B and D are calculated in each time step and by them translation of functions f_{S1} and f_{S2} to the axis u for the coefficient B and the axis f_S for the coefficient D are defined.

Table 8 shows the results of the analysis of non-linear SDOF for the x and y directions, which presents the least favourable combination of simultaneous linear superposition of modes F_L as well as the least favourable combination of the square root of the sum of square of modes F_{SRSS}.

Montenegro **- 9-storey RC frame - *x* direction**						
F_{1max}	F_{2max}	F_{3max}	F_{4max}	F_{5max}	**for the same *t***	
0,69	0,92	0,69	0,52	0,32		
F_{1min}	F_{2min}	F_{3min}	F_{4min}	F_{5min}	F_L	-2,02
-0,78	-1,00	-0,66	-0,60	-0,34	F_{SRSS}	1,31
Campano Lucano **- 9-storey RC frame - *x* dir.**						
F_{1max}	F_{2max}	F_{3max}	F_{4max}	F_{5max}	**for the same *t***	
0,73	0,95	0,67	0,33	0,27		
F_{1min}	F_{2min}	F_{3min}	F_{4min}	F_{5min}	F_L	-1,68
-0,68	-1,00	-0,65	-0,36	-0,29	F_{SRSS}	1,32
Aigion **- 9-storey RC frame - *x* direction**						
F_{1max}	F_{2max}	F_{3max}	F_{4max}	F_{5max}	**for the same *t***	
0,89	0,92	0,99	1,00	0,85		
F_{1min}	F_{2min}	F_{3min}	F_{4min}	F_{5min}	F_L	2,12
-0,98	-0,89	-0,99	-0,85	-0,93	F_{SRSS}	1,41
Olfus **- 9-storey RC frame - *x* direction**						
F_{1max}	F_{2max}	F_{3max}	F_{4max}	F_{5max}	**for the same *t***	
0,96	0,71	1,00	0,44	0,25		
F_{1min}	F_{2min}	F_{3min}	F_{4min}	F_{5min}	F_L	1,92
-0,97	-0,75	-0,90	-0,38	-0,26	F_{SRSS}	1,15
Calabria **- 9-storey RC frame - *x* direction**						
F_{1max}	F_{2max}	F_{3max}	F_{4max}	F_{5max}	**for the same *t***	
0,40	1,00	0,63	0,35	0,28		
F_{1min}	F_{2min}	F_{3min}	F_{4min}	F_{5min}	F_L	1,29
-0,42	-0,93	-0,56	-0,34	-0,26	F_{SRSS}	1,02
Valnerina **- 9-storey RC frame - *x* direction**						
F_{1max}	F_{2max}	F_{3max}	F_{4max}	F_{5max}	**for the same *t***	
0,79	0,78	0,59	0,44	0,39		
F_{1min}	F_{2min}	F_{3min}	F_{4min}	F_{5min}	F_L	-1,49
-1,00	-0,79	-0,56	-0,48	-0,37	F_{SRSS}	1,13
Banja Luka **- 9-storey RC frame - *x* direction**						
F_{1max}	F_{2max}	F_{3max}	F_{4max}	F_{5max}	**for the same *t***	
0,59	1,00	0,56	0,47	0,32		
F_{1min}	F_{2min}	F_{3min}	F_{4min}	F_{5min}	F_L	-2,04
-0,41	-1,00	-0,55	-0,58	-0,35	F_{SRSS}	1,08
Sicilia Orientale **- 9-storey RC frame - *x* dir.**						
F_{1max}	F_{2max}	F_{3max}	F_{4max}	F_{5max}	**for the same *t***	
0,75	0,90	1,00	0,42	0,25		
F_{1min}	F_{2min}	F_{3min}	F_{4min}	F_{5min}	F_L	2,34
-0,93	-0,93	-0,99	-0,39	-0,25	F_{SRSS}	1,37

Montenegro **- 9-storey RC frame - *y* direction**						
F_{1max}	F_{2max}	F_{3max}	F_{4max}	F_{5max}	**for the same *t***	
0,77	0,64	0,67	0,23	0,29		
F_{1min}	F_{2min}	F_{3min}	F_{4min}	F_{5min}	F_L	-1,49
-1,00	-0,60	-0,64	-0,24	-0,33	F_{SRSS}	1,13
Campano Lucano **- 9-storey RC frame - *y* dir.**						
F_{1max}	F_{2max}	F_{3max}	F_{4max}	F_{5max}	**for the same *t***	
0,93	0,90	0,71	0,15	0,33		
F_{1min}	F_{2min}	F_{3min}	F_{4min}	F_{5min}	F_L	-2,14
-1,00	-0,87	-0,68	-0,18	-0,36	F_{SRSS}	1,34
Aigion **- 9-storey RC frame - *y* direction**						
F_{1max}	F_{2max}	F_{3max}	F_{4max}	F_{5max}	**for the same *t***	
0,74	0,63	0,89	0,13	0,42		
F_{1min}	F_{2min}	F_{3min}	F_{4min}	F_{5min}	F_L	1,93
-0,75	-0,58	-1,00	-0,14	-0,47	F_{SRSS}	1,13
Olfus **- 9-storey RC frame - *y* direction**						
F_{1max}	F_{2max}	F_{3max}	F_{4max}	F_{5max}	**for the same *t***	
0,96	0,66	0,53	0,27	0,24		
F_{1min}	F_{2min}	F_{3min}	F_{4min}	F_{5min}	F_L	1,53
-1,00	-0,65	-0,57	-0,25	-0,25	F_{SRSS}	1,06
Calabria **- 9-storey RC frame - *y* direction**						
F_{1max}	F_{2max}	F_{3max}	F_{4max}	F_{5max}	**for the same *t***	
0,33	0,82	0,99	0,25	0,40		
F_{1min}	F_{2min}	F_{3min}	F_{4min}	F_{5min}	F_L	-1,58
-0,24	-0,89	-1,00	-0,20	-0,36	F_{SRSS}	1,35
Valnerina **- 9-storey RC frame - *y* direction**						
F_{1max}	F_{2max}	F_{3max}	F_{4max}	F_{5max}	**for the same *t***	
0,91	0,65	0,70	0,61	0,28		
F_{1min}	F_{2min}	F_{3min}	F_{4min}	F_{5min}	F_L	-2,31
-1,00	-0,71	-0,69	-0,59	-0,28	F_{SRSS}	1,33
Banja Luka **- 9-storey RC frame - *y* direction**						
F_{1max}	F_{2max}	F_{3max}	F_{4max}	F_{5max}	**for the same *t***	
0,44	0,90	0,47	0,25	0,41		
F_{1min}	F_{2min}	F_{3min}	F_{4min}	F_{5min}	F_L	1,40
-0,36	-1,00	-0,51	-0,29	-0,45	F_{SRSS}	1,08
Sicilia Orientale **- 9-storey RC frame - *y* dir.**						
F_{1max}	F_{2max}	F_{3max}	F_{4max}	F_{5max}	**for the same *t***	
0,69	1,00	0,68	0,28	0,30		
F_{1min}	F_{2min}	F_{3min}	F_{4min}	F_{5min}	F_L	-2,13
-0,87	-0,96	-0,63	-0,30	-0,26	F_{SRSS}	1,32

Table 8: Comparison of linear (L) and root (SRSS) combination of modes for 9-storey RC frame on non-linear level.

The presented results for the non-linear dynamic response of the system according to Table 8 shows that the linear combination of modes F_L in all cases is considerably unfavourable than the square root of sum of square combinations of modes F_{SRSS}.

5 CONCLUSIONS

This paper describes a procedure for determining the target acceleration, defined as the minimum ground acceleration that leads to ultimate limit state of construction using multi-modal pushover method, which represents the lowest earthquake resistance.

The procedure is based on the successive application of non-linear static analysis in multi-modal pushover method and successive trials in searching for targeted acceleration which has all the characteristics of an envelope principle.

Based on the results of presented examples, following conclusion is made:

- Influence of higher modes, especially the second and third mode is very significant.
- Target ground acceleration, respectively the lowest limit acceleration is not necessarily generated by the smallest lateral force in the base. Thereat minimal limit acceleration is lower than limit acceleration of each mode independently.
- Linear combination is more relevant because of lower target acceleration than the one obtained by SRSS combination of modes.
- The shape of general failure vector associated to the target acceleration differs significantly from the shape of the first vector loads and shape of loads with constant acceleration by height of structure contained in EN 1998.
- Appearance of linear combination (L) and square root of sum of square combination of modes (SRSS), tested for the actual series of real seismic records on the linear and nonlinear level confirms that the linear combination is more probable than combinations of square root of sum of square of modes.
- Multi-mode pushover method a priori assumes that in the real earthquake action all relevant modes are activated.
- Irrespective of the method of combining modes, the practical application of multimodal approach show that the safety/reliability of the observed RC frame are lower than that indicated by criteria for the target displacement, in accordance with Eurocode 8 (Annex B).
- Inclusion of higher modes, in presented examples, decreases the limit ground acceleration by more than two times, which is significantly less favourable than requirements for reserves in the capacity curve of 150% in relation to the target displacement of the peak of structure, i.e. target displacement criteria.

REFERENCES

[1] European Committee for Standardization (CEN): EN 1998-1. Eurocode 8: Design of Structures for earthquake resistance – Part 1: General rules, seismic actions and rules for buildings, Brussels, Belgium, 2004.

[2] ATC, Seismic evaluation and retrofit of concrete buildings, ATC-40 Report, *Applied Technology Council*, Redwood City, California, 1996.

[3] ATC, Improvement of nonlinear static seismic analysis procedures, FEMA 440 Report, *Applied Technology Council*, Redwood City, California, 2005.

[4] M. Saiidi, M.A. Sozen, Simple Nonlinear Seismic Analysis of R/C Structures, *Journal of the Structural Division*, **107**, 937-953, 1981.

[5] P. Fajfar, M. Fischinger, Non-linear seismic analysis of RC buildings: Implications of a case study, *European Earthquake Engineering*, **1**, 31-43, 1987.

[6] P. Fajfar, M. Fischinger, N2 – a method for non-linear seismic analysis of regular buildings, *Proc. 9th world conf. Earthquake eng.*, Tokyo, Kyoto, **5**, 111-116, 1988.

[7] P. Fajfar, P. Gašperšič, The N2 method for the seismic damage analysis for RC buildings, *Earthquake Engineering & Structural Dynamics*, **25**, 23–67, 1996.

[8] P. Fajfar, A Nonlinear Analysis Method for Performance Based Seismic Design, *Earthquake Spectra*, **16**, 573-592, 2000.

[9] N.D. Lagaros, M. Fragiadakis, Evaluation of ASCE-41, ATC-40 and N2 static pushover methods based on optimally designed buildings, *Soil Dynamics and Earthquake Engineering*, **31**, 77–90, 2011.

[10] A.K. Chopra, R.K. Goel, A modal pushover analysis procedures for estimating seismic demands for buildings, *Earthquake Engineering & Structural Dynamics*, **31**, 561–582, 2002.

[11] Y. Jiang, G. Li, D. Yang, A modified approach of energy balance concept based multimode pushover analysis to estimate seismic demands for buildings, *Engineering Structures*, **32**, 1272–1283, 2010.

[12] K.K. Sasaki, S.A. Freeman, T.F. Paret, Multi-mode pushover procedure (MMP) - a method to identify the effects of higher modes in a pushover analysis, *Proceedings of 6th U.S. National Conference on Earthquake Eng*ineering, Seattle (Washington), 1998.

[13] E. Kalkan, S.K. Kunnath, Assessment of current nonlinear static procedures for seismic evaluation of buildings, *Engineering Structures*, **29**, 305–316, 2007.

[14] A.K. Chopra, R.K. Goel, C. Chintanapakdee, Evaluation of a modified MPA procedure assuming higher modes as elastic to estimate seismic demands, *Earthquake Spectra*, **20**, 757-778, 2004.

[15] R.K. Goel, A.K. Chopra, Role of higher-"mode" pushover analyses in seismic analysis of buildings, *Earthquake Spectra*, **21**, 1027-1041, 2005.

[16] K. Shakeri, M. Mohebbi, Single-run modal pushover procedure based on the modal shear and moment in the stories, *Proceedings of 14th European Conference on Earthquake Eng*ineering, Ohrid, Republic of Macedonia, 6199-6207, 2010.

[17] B. Trogrlić, A. Mihanović, The comparative body model in material and geometric nonlinear analysis of space R/C frames, *Engineering Computations*, **25**, 155-171, 2008.

[18] B. Trogrlić, A. Mihanović, Ž. Nikolić, Modified Modal Pushover Analysis of RC Frames, *fib Symposium Prague 2011, Concrete engineering for excellence and efficiency, Proceedings*, Publisher: Czech Concrete Society (CBS) / Czech fib National Member Group, **2**, 95-98, 2011.

[19] http://www.isesd.hi.is, The European Strong-motion database, 04.04.2012.

[20] A.K. Chopra, *Dynamics of structures: Theory and Applications to Earthquake Engineering, University of California at Berkeley, Third Edition*, Prentice Hall, 2007.

COMPDYN 2013
4th ECCOMAS Thematic Conference on
Computational Methods in Structural Dynamics and Earthquake Engineering
M. Papadrakakis, V. Papadopoulos, V. Plevris (eds.)
Kos Island, Greece, 12–14 June 2013

EXPERIMENTAL STUDY AND NUMERICAL RESPONSE PREDICTION OF A STEEL MOMENT-FRAME WITH TAKING FATIGUE DAMAGE INTO ACCOUNT

Mohammad Saranik[1*], Louis Jézéquel[1] and David Lenoir[1]

[1]Laboratoire de Tribologie et Dynamique des Systèmes
École Centrale de Lyon, 36 Avenue Guy de Collongue, 69134 Écully Cedex, France
e-mail: mohammad.saranik@ec-lyon.fr

Keywords: Steel frame, bolted connections, LCF fatigue, damage, FDBH model, shaking-table test.

Abstract. *In this study, shaking-table test results of a steel moment-frame with end-plate bolted connections are presented. These experimental tests were carried out to understand the behavior of steel moment-frame structures subjected to dynamic and seismic loads. The purpose of these tests is also to study the changes in modal parameters due to the development of the elasto-plastic behavior and Low Cycle Fatigue LCF damage in bolted steel frame connections. The study presents a nonlinear numerical simulation of the steel moment-frame that was performed using a Fatigue Damage-Based Hysteretic FDBH model. The developed model is a degrading hysteretic model based on the LCF damage index. A comparison of the results obtained from numerical analysis and those of shaking table tests is presented. A reasonable agreement is observed, indicating a good simulation of the nonlinear behavior of the steel moment-frame by using the developed model.*

1 INTRODUCTION

In recent years, several attempts have been proposed in literature to take account of the stiffness degradation induced by the cumulative damage effects during Low Cycle Fatigue (LCF) deformations [1, 2, 3].

Ibarra *et al*. [1] presented the description, calibration and application of relatively simple hysteretic models. The modified models included most of the sources of deterioration. The hysteretic models included a post-capping softening branch, residual strength, and cyclic deterioration. The model could be employed to simulate the behavior of a bolted connection.

Lignos *et al*. [4] proposed a numerical model that was able to simulate complex deterioration phenomena and ultimately connection fractures due to LCF. The model was implemented in the open-source numerical simulation platform. The component model was calibrated against a large number of steel component tests that have been conducted over the past years around the world.

Saranik *et al*. [2, 5] developed a Fatigue Damage-Based Hysteretic (FDBH) model that allowed considering the stiffness degradation produced by the cumulative fatigue damage effects. The FDBH model was a hysteretic model based on LCF damage index. It can be applied to evaluate the performance of steel portal frames with bolted connections under dynamic loading.

Moreover, Saranik *et al*. [6] proposed an advanced approach to take into account the effects of nonlinear modes and frequencies by performing a nonlinear time history analysis. According to this approach, the nonlinear modes and frequencies were determined by an iterative procedure.

In this study, shaking-table test results of a steel moment-frame with end-plate bolted connections are presented. A steel portal frame was investigated under horizontal sinusoidal base excitations. These experimental tests were conducted to verify the validity of the FDBH model and to prove the efficacy of the nonlinear dynamic analysis techniques. The advanced approach proposed by Saranik *et al*. [2] was adopted to take into account the effects of nonlinear modes and frequencies by performing a nonlinear time history analysis. Consequently, this approach was used to evaluate the performance of steel frames under lateral loads applied by base excitation. A comparison of the results obtained from numerical analysis and those of shaking table tests is presented.

2 STIFFNESS DEGRADATION DUE TO FATIGUE DAMAGE

Several studies have indicated that bolted connections are vulnerable to the damage accumulation. Plastic hinges usually develop at beam-column connections [2, 3, 7]. The welds and the bolts can be largely affected by LCF which causes progressive and cumulative damage in the stiffness of bolted connections [3]. Korol *et al*. [7] found that the excessive yielding of the connection makes more prone to LCF and results in severe damage. Bolts can be loosen over time because of micro-macro slip in the bolt-nut and the assembled plates [8].

In recent years, different approaches have been developed on the use of a damage index to estimate the structural damage [1, 9]. They aim to clarify the different approach methodologies and to detail different proposed formulations. Several researchers have been performed in literature to take account of the stiffness degradation induced by the cumulative damage effects during LCF deformation [2, 3]. The experimental results, carried out by Tani *et al*. [3], showed that a damage variable D can be used to measure cumulative damage and provide a good estimate of the fatigue damage process, as well as to predict the fatigue life.

According to Tani *et al*. [3], a phenomenon of degradation in the stiffness of the bolted connection can be observed in the case of repeated loading. Tani *et al.* showed in a cyclic test the existence of the degradation phenomenon in the stiffness. They proposed to use the number of applied cycles n_i divided by the total number of cycles N_i, which corresponds to the fatigue damage according to Miner's rule [10], as damage parameters for the bolted connections. Then, Tani *et al.* constructed a model of connection stiffness degradation as a function of fatigue damage. Accordingly, the degradation of the connection stiffness k can be constructed on a normalized scale, as shown in Fig. 1, and an approximation model based on the mean curves of nine tests can then be written as:

$$\frac{k}{k_0} = f(D) \tag{1}$$

where k_0 is the initial connection stiffness for each fatigue test and $f(D)$ can be defined as:

$$f(D) = \begin{cases} 0.2exp(-3.5D) + 0.8 & for \;\; D < 0.9 \\ -2.4D + 3 & for \;\; 1 \geq D \geq 0.9 \end{cases} \tag{2}$$

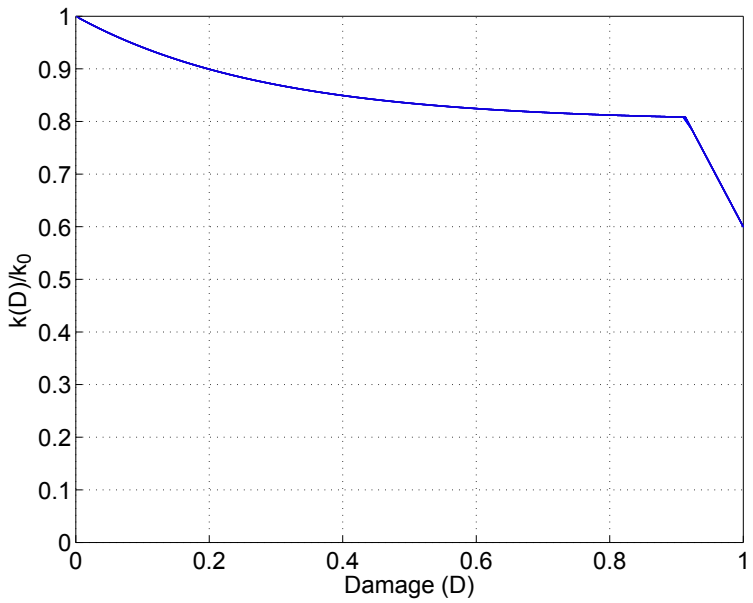


Figure 1: Degradation of connection stiffness as a function of the damage variable D.

The above results were used by Tani *et al*. [3] to performed fatigue analysis simulations with deterministic and random excitation.

Moreover, many experimental approaches confirm the presence of changes in modal parameters such as natural frequencies because of the damaged elements of the structure. The presence of damage or deterioration in a structure causes changes in the natural frequencies of the structure. Due to the fatigue damage in the bolted connection, the natural frequency can decrease [2, 3].

By using a standard Finite Element (FE) model, the evolution of the natural frequency can be evaluated based on the degradation of the connection stiffness as a function of fatigue damage on the basis of Miner's rule (*cf.* Eq. 2). Fig. 2 shows an example for the evolution of the

natural frequency with respect to the number of cycles for a bolted connection. The results were obtained from numerical simulation carried according the numerical method proposed by Tani *et al*. [3] to integrate the connection stiffness degradation due to fatigue loading.

These results are adopted by Saranik *et al*. [2] and incorporated into a simulation of a complex portal frame structure to determine the structure's lifetime, by assuming that fatigue damage occurs only at the beam−column connections. These proposed developments will be presented in the next sections.

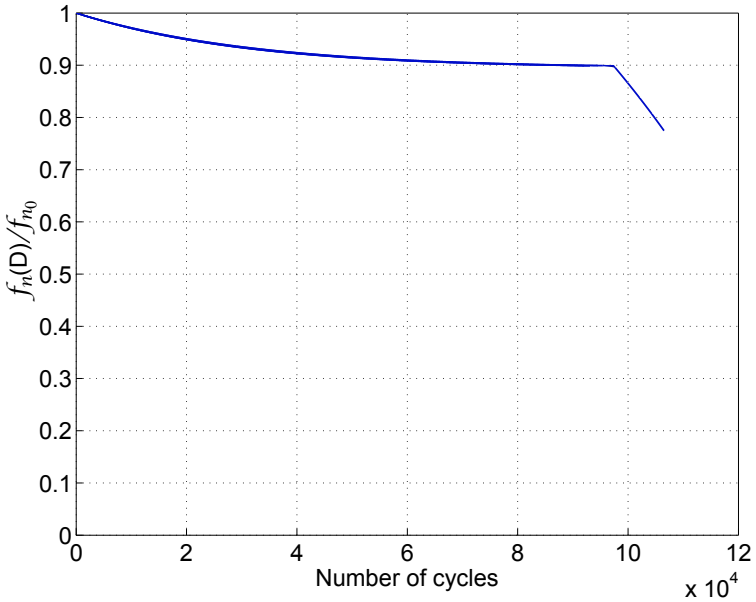


Figure 2: Evolution of the natural frequency as a function of number of cycles for a bolted connection.

3 DEVELOPED MODEL

Saranik *et al*. [2] modified Richard-Abbott model [11] to include the stiffness degradation of the connection produced by the cumulative phenomenon of LCF. The developed model is named Fatigue Damage-Based Hysteretic FDBH. This degrading hysteretic model is based on a LCF damage index D_n. In this model, the initial stiffness k_0 is modified with the factor $(1 - D_n)$ that takes account of the effect of cumulative fatigue (see Fig. 3).

In this way, the connection loses part of its stiffness in each cycle of excitation applied due to the cumulative phenomenon of LCF. The following equation presents FDBH model for the moment-rotation relationship:

$$M^* = M_a - \frac{(k_0.(1-D_n) - k_p).(\phi_a - \phi)}{\left(1 + \left|\frac{(k_0.(1-D_n)-k_p).(\phi_a-\phi)}{2M_0}\right|^{\gamma}\right)^{\frac{1}{\gamma}}} - k_p.(\phi_a - \phi) \tag{3}$$

where M^* is the degraded connection moment, ϕ is the relative rotation between the connecting elements, M_0 is the reference moment, and γ is the curve shape parameter. D_n is the fatigue damage index and k_p is the final plastic stiffness. (M_a, ϕ_a) is the load reversal point and (M_b, ϕ_b) is the next load reversal point as shown in Fig. 3. Saranik *et al* also proposed a value of the plastic stiffness k_p = 0 which can simplify the model.

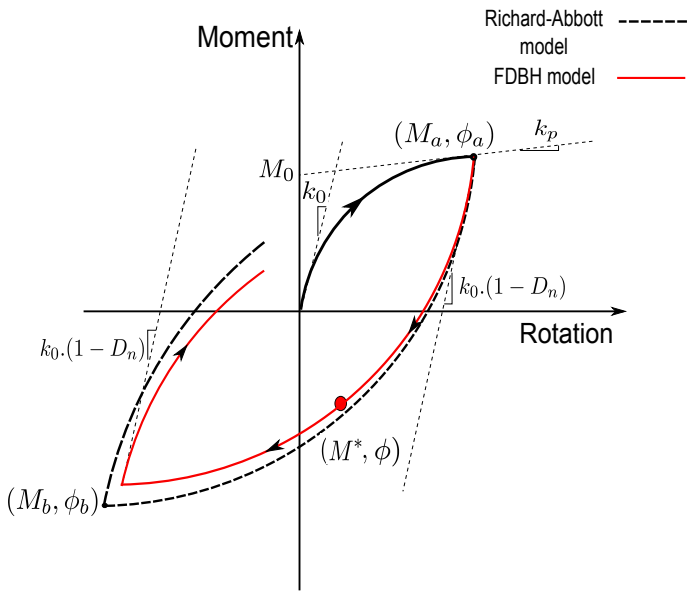


Figure 3: Fatigue Damage-Based Hysteretic model of bolted connection developed by Saranik *et al*. [2].

The tangent stiffness of the connection element can be written as:

$$k^* = \frac{(k_0.(1-D_n) - k_p)}{\left(1 + \left|\frac{(k_0.(1-D_n)-k_p).(\phi_a-\phi)}{2M_0}\right|^{\gamma}\right)^{\frac{\gamma+1}{\gamma}}} + k_p \tag{4}$$

where k^* is the degraded secant stiffness.

In this way, the secant stiffness in Eq. (4) can be modified and it is possible to combine the two indices by the equation:

$$D_p = 1 - \frac{k^*}{k_0} \tag{5}$$

where D_p is the plastic damage index. It can be observed that D_p depends on the tangent stiffness k^* of the connection and the LCF damage index D_n.

The FDBH model of Saranik *et al*. [2] uses recent concepts in the structural damage evaluation and it can allow taking account of the stiffness degradation produced by the cumulative fatigue damage effects. Thereby, the FDBH model is an efficient model to simulate inelastic response of structure under dynamic loading by combined damage indices.

To evaluate fatigue damage in structural components under arbitrary loading histories, Miner's rule is commonly employed [3, 10]. Though many models of damage have been proposed, Miner's rule is still widely used in the engineering field [3]. According to this rule, applying a cycle n_i times with a stress or strain amplitude which corresponds to a lifetime of N_i cycles is equivalent to consuming a portion n_i/N_i of the whole lifetime. This rule implies that rupture occurs when 100% of the lifetime is consumed. It also describes the phenomena of the cumulative linearity of fatigue damage if another application stress or strain is employed.

For simplicity, some global parameter such as plastic rotation can be used rather than strains or stress for applying Miner's rule [12]. In the case of connection subjected to many cycles of rotation, Miner's rule is expressed by the following equation:

$$D_n = \sum_i \frac{n_i}{N_i} \tag{6}$$

where n_i is the number of applied cycles for a given rotation level i and N_i is the number of cycles to failure for a rotation level i.

Moreover, to calculate the number of cycles to failure N, an analogous model based on the plastic connection rotation must be utilised therein. The information provided by the Rotation-Number of cycles curve is mainly applied by engineers for the prediction of the lifetime and resistance of structures under repeated loading. A useful method of describing the LCF life for a bolted connection is expressed in literature [2, 13]. Thus using the well known Manson-Coffin relationship [14], the plastic rotation may be related to the number of cycles to failure N by the following equation:

$$N = c.(\Delta\phi_p)^{-b} \tag{7}$$

where ϕ_p is the plastic rotation of the connection. c and b are the parameters of fatigue which depend on both the typology and the mechanical properties of the considered steel element. From experimental fatigue results performed by Saranik *et al*. [2], the fatigue parameters of Manson-Coffin are (c = 22 $\times$ 10^{-5}) and (b = 3). These parameters are used to analyse steel portal frames in this study. Manson-Coffin relation describes linearly this function between the applied rotation and the number of cycles to rupture on a double-logarithmic scale.

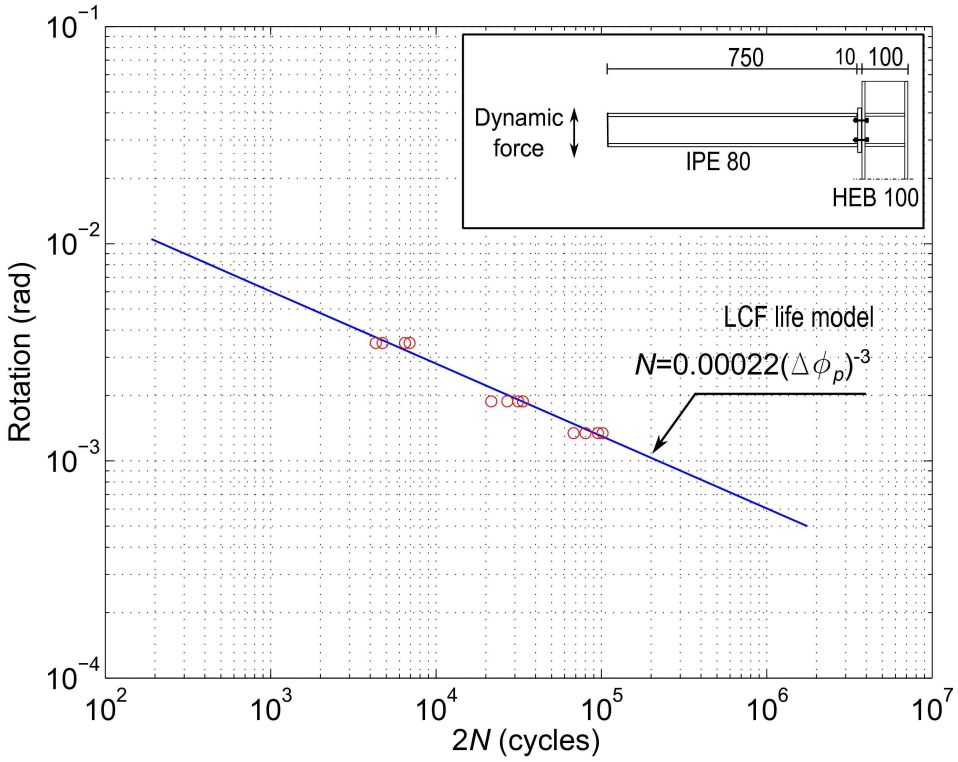


Figure 4: LCF life prediction model proposed by Saranik *et al*. [2].

4 TEST SPECIMENS AND EXPERIMENTAL PROCEDURES

A two story frame shown in Fig. 5(a) is used to carry out a series of shaking table tests. The test frame consists of elastic beam and column elements, joined together by bolted connections as shown in Fig. 5(b). The frame was constructed at the Structural Dynamics Laboratory of Ecole Centrale de Lyon.

The beam and column sections are chosen from Standard European Steel profiles IPE 80 and HEB 100, respectively. The nominal values of yield strength f_y and the ultimate values of tensile strength f_u of the I sections are respectively 260 MPa and 450 MPa. The steel members of the frame have a 210 GPa elasticity modulus.

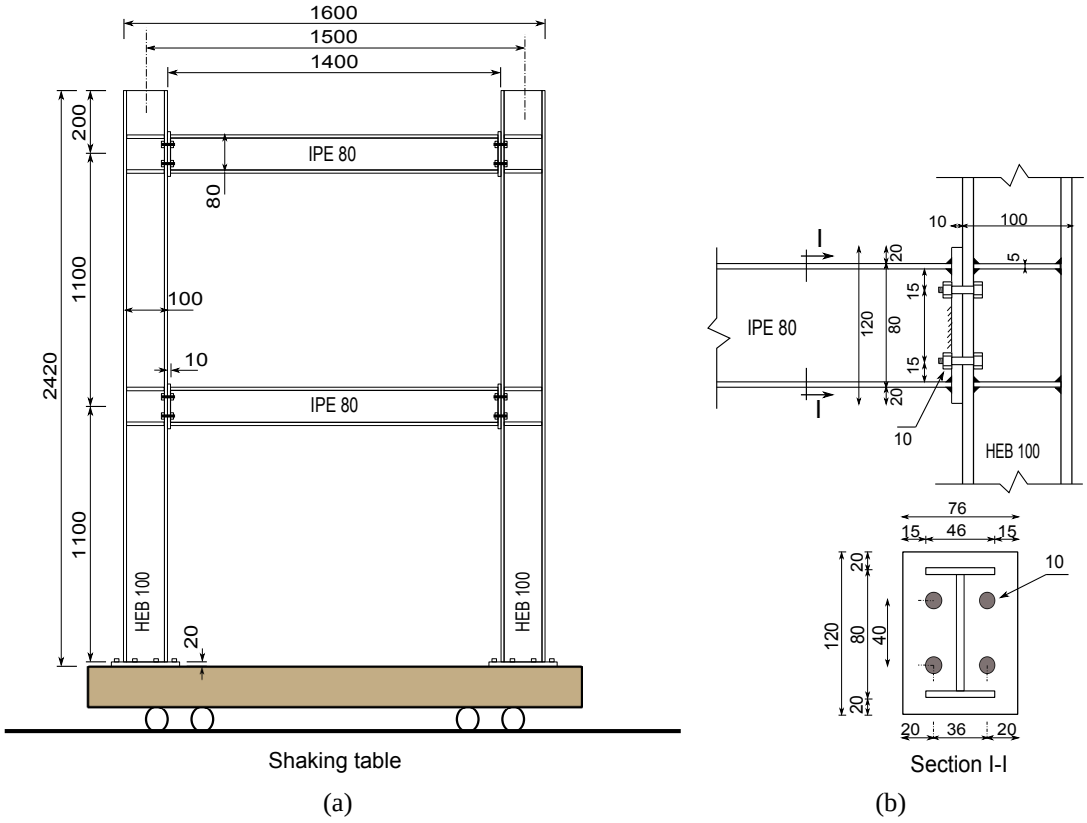
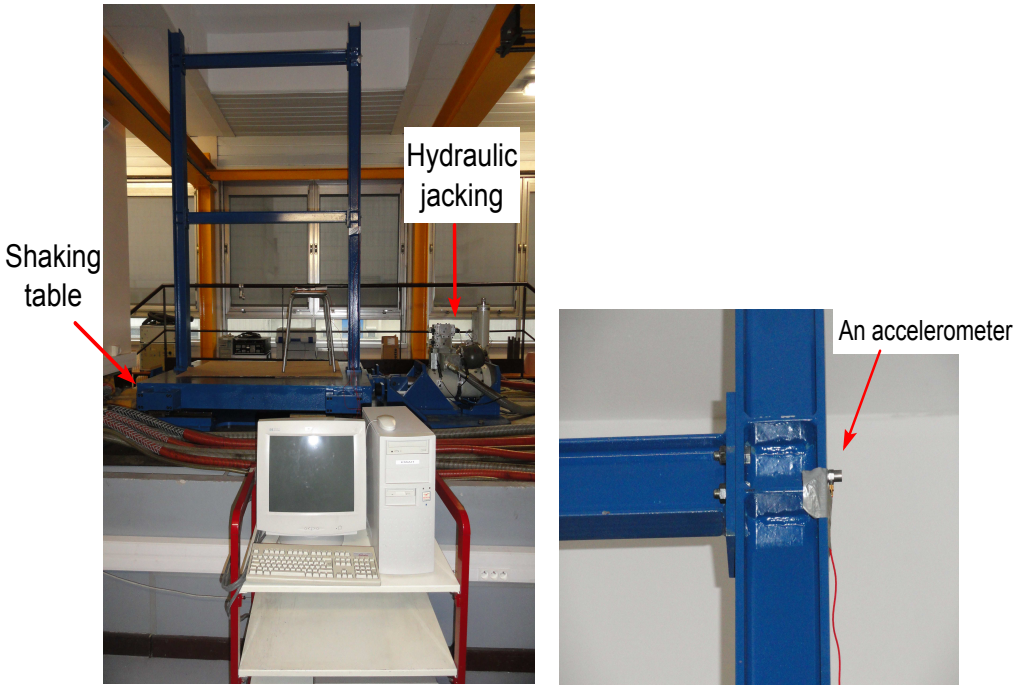


Figure 5: Steel portal frame test set-up details (in mm): (a) details of the portal frame; (b) details of the bolted connection.

Four standard bolts (M10-1.25 $\times$ 35 mm Grade 6.8 DIN 975 carbon steel) are employed for each connection of the beam. The general layout of the end plate is shown in Fig. 5(b), with thickness (10 mm) and dimensions (120 mm $\times$ 76 mm) of the plate detailed. The experimental setup, shown in Fig. 6(a), was used during shaking table tests. The shaking table, shown in Fig. 6(a), was derived by a hydraulic jacking system that has the capacity to apply various excitation frequencies between 0.1 and 30 Hz and various displacements between 0.1 mm and 30 mm. Before the formal shaking table tests were performed, a pre-test was conducted under sinusoidal loads to evaluate the capacity, the characteristic of the shaking table and the measuring equipment. The command displacement given in the computer and the real displacement of the shaking table were compared in each test.

A horizontal sinusoidal shaking at a frequency of 15 Hz was applied in this experiment. The amplitudes of the horizontal sinusoidal excitation were 3, 5, 6 and 10 mm. During each test, the data were acquired and saved using a data acquisition system.

The test assembly was instrumented with two accelerometers to measure the specimen's response. The accelerometers, with sensitivity 100 mV/g, were mounted on the beam using super glue and duct tape to collect the horizontal displacement responses of the first and second story (see Fig. 6(b)). The accelerometers were connected to a device for measuring the displacements



(a) (b)

Figure 6: Test arrangement: (a) the portal frame; (b) the tested bolted connection and an accelerometer.

and to a data acquisition system to record the measured data.

Moreover, a hammer-shock was utilized to determine the natural frequency of the frame. Two mini accelerometers PCB with 1.03 mV/(m/s^2) sensitivity were installed to record the signal impact. The accelerometers were placed successively to both stories, oriented in the horizontal direction.

A torque wrench was used to tighten the 4 bolts for each bolted connection to the same level for all tests and to ensure consistency in the boundary conditions. The bolts were tightened to the required tightening torque 39 N.m.

Each test was started with the assembly of the frame model. Before testing, the two columns were positioned and fastened to the shaking table by making use of twenty-four M10 high-strength bolts conforming to DIN 975. Thereafter, the two beams were assembled to the columns with bolted connections by using four M10 bolts for each connection. Column base connections were made as rigid as possible. The frame model was fixed in displacement and rotation at the base level, free to move at the first and second story. For all tests, the bolts of these connections were tightened, applying a torque wrench, to the required torque value. In this way, the tested frame could be placed in position in the shaking table as shown in Fig. 5(a).

During a shaking table test, a loosening phenomenon reduces the clamping force of the bolts due to repeated excitation. Subsequently the cyclic loading can cause sliding in the assembled elements, which can change the stress distribution and gradually produce fatigue damage. The frame model was tested until the ultimate connection failure occurred. Subsequently, the time at failure was recorded and the level of displacement was used for this test as well. These experimental results were compared with numerical results. After each shaking table test, the bolts of the four connections must be changed and tightened to the required torque value.

Before running shaking table tests, a hammer-shock test on the model was conducted to

determine the dynamic characteristics of the portal frame model such as natural frequencies. The hammer-shock test was also repeated before and after each shaking table test for detecting any changes in natural frequencies.

5 FINITE ELEMENT NUMERICAL SIMULATION

The damage in the structure could be identified as a change in FE stiffness matrices of the different beam elements of the structure. In this study, the FE model of the structure was a two-dimensional model developed by the Structural Dynamics Toolbox (SDT) under MATLAB 7.6 (R2008a) [2, 6]. The SDT, one of the widely used commercial FE analysis products that integrate OpenFEM as FE calculation source, was used to analyse the test frame.

The equation of motion for a damped structure with N degrees-of-freedom (dof) is given as follows:

$$\mathbf{M}\ddot{\mathbf{q}} + \bar{\mathbf{C}}\dot{\mathbf{q}} + \bar{\mathbf{K}}\mathbf{q} = \mathbf{F}(t) \tag{8}$$

where $\mathbf{M}$, $\bar{\mathbf{C}}$ and $\bar{\mathbf{K}}$ are respectively the mass, nonlinear damping and nonlinear stiffness matrix of the structure. $\mathbf{F}(t)$ is the applied forces vector and $\mathbf{q}$ is the relative response of system in normal coordinate. The stiffness matrix is nonlinear due to the nonlinearity of the beam-column connections and depends on the response of system and the nonlinear normal modes.

Rayleigh damping can be used to represent damping in the structure. It can be written as:

$$\bar{\mathbf{C}} = \alpha.\mathbf{M} + \beta.\bar{\mathbf{K}} \tag{9}$$

where α and β are the proportional damping factors and they are computed based on first two frequencies of the frame structure ω_1 and ω_2 as follows:

$$\alpha = \frac{2\xi\omega_1\omega_2}{\omega_1 + \omega_2}; \beta = \frac{2\xi}{\omega_1 + \omega_2} \tag{10}$$

where ξ is the damping ratio and a value of 3% is adopted for the frames analysed in the study.

The elements in the steel frame can be modeled as Euler-Bernoulli beams and each element beam or column is discretized into four finite elements. The matrix $\bar{\mathbf{K}}$ can be assembled by the stiffness matrices of each beam and column element in the system with the following equation:

$$\bar{\mathbf{K}} = \sum_{e=1}^{n_e} \bar{\mathbf{k}}_e \tag{11}$$

where n_e is the total number of elements in the system and members are generically identified by index e.

The nonlinear matrix for an element can be calculated using the correction matrix with the following equation [2, 15]:

$$\bar{\mathbf{k}}_e = \mathbf{k}_e \mathbf{Cr}_e \tag{12}$$

where $\mathbf{k}_e$ is the standard elastic stiffness matrix for the element. The correction matrix $\mathbf{Cr}_e$ is given as follows:

$$\mathbf{Cr}_e = \sum_q \sum_s c_{qs_e} : c_{qs_e} = f(D_{p_{e,l}}, D_{p_{e,r}}, L) \tag{13}$$

where $D_{p_{e,l}}$ and $D_{p_{e,r}}$ are the plastic damage indices of the connections (left l and right r, respectively) for the considered element. L is the length of this element. The plastic damages indices depend on LCF damage indices $D_{ne,l}$ and $D_{ne,r}$ for the considered element e.

According to Saranik *et al*. [2], eigenvalues and eigenvectors for a nonlinear system cannot be obtained by solving the standard eigenvalue problem. As the solution of a nonlinear system relies heavily on the amplitude of excitation, the frequencies and normal modes depend on the nonlinear modal amplitude. The introduction of the notion of nonlinear modes permits an extension of the method of linear modal synthesis to nonlinear cases in order to obtain the dynamical response of nonlinear multi-degree-of freedom systems.

The nonlinear normal modes and nonlinear frequencies can be calculated by an iterative procedure [2, 16]. In this paper, a procedure which is based on the method of equivalent linearisation was adopted. Considering the FE methods, the nonlinear modal problem can be written as following:

$$[\bar{\mathbf{K}}(\eta_{p_i}, \bar{\boldsymbol{\varphi}}_{p_i}(\eta_{p_i})) - \bar{\omega}^2_{p_i}(\eta_{p_i})\mathbf{M}]\bar{\boldsymbol{\varphi}}_{p_i}(\eta_{p_i}) = 0 \tag{14}$$

where η_{p_i}, $\bar{\omega}_{p_i}(\eta_{p_i})$ and $\bar{\boldsymbol{\varphi}}_{p_i}(\eta_{p_i})$ are respectively the structural response of the ith mode in modal coordinate, the nonlinear frequency and the nonlinear normal mode i.

For each time step of calculation, the stiffness and damping matrices of the system can be obtained that may transform the nonlinear system into an equivalent linear system. The frequencies and nonlinear normal modes can then be calculated using a standard solution of the eigenvalue problem given by Eq. (14). A set of N nonlinear modes and frequencies can be obtained according to their modal amplitudes. For this purpose, the response of nonlinear system in normal coordinate can be calculated efficiently by superposition of modal response as follows:

$$\mathbf{q}(t) = \bar{\boldsymbol{\varphi}}_p \boldsymbol{\eta}_p(t) \tag{15}$$

The response of system $\mathbf{q}(t)$ depends directly on the nonlinear modes matrix $\bar{\boldsymbol{\varphi}}_p$. This method is called nonlinear modal synthesis method.

6 NUMERICAL AND EXPERIMENTAL RESULTS

Experimental and numerical investigations were carried out on the two-story steel portal model for different base excitation displacements. This section presents the main observations obtained from the response of the test specimen during the sinusoidal displacement shaking. The shaking table tests were performed for four magnitudes of displacement excitations. The levels of displacements were 3, 5, 6 and 10 mm. The applied excitation frequency of all tests was fixed at 15 Hz. The results of the tests T3 and T4 will be discussed in detail in this section.

The simulated and measured story displacements along the height of the frame model are shown in Table 1.

Test	Δ Required (mm)	Δ Applied (mm)	Test duration (sec)	Time of measurement (t) (sec)	q_1 Exp (mm)	q_1 Num (mm)	q_2 Exp (mm)	q_2 Num (mm)	Failure modes
T3	5	2.32	300	10	2.8	2.3	5.9	5.5	Loosening of bolt-nut
				150	3.6	2.9	7.6	7	+
				260	11	9.6	25.5	24	Failure in bolts
T4	5	2.32	300	10	2.5	2.3	5.4	5.5	Loosening of bolt-nut
				150	3.4	2.9	7.4	7	+
				260	9	9.6	21.8	24	Failure in bolts

Table 1: Comparison of story displacements of the portal frame model.

In this table, q_1 and q_2 are the maximum relative story displacements of the frame. Furthermore, a comparison of maximum relative displacements between experimental and analytical results is shown in Table 1. The different failure modes resulting from these tests are also presented.

Under base excitation of $\pm$ 5 mm magnitude, the bolted connections were subjected to important damage after the tests T3 and T4. Based on the failure mechanism of bolted connection, the initial stiffness and the ultimate moment calculated are k_0 = 5.6 $\times$ 10^5 N.m/rad and M_u = 2.9 $\times$ 10^3 N.m, respectively. The stiffness values of connections were gradually degraded from an initial value k_0 to a finale value near to 0 as shown in Fig. 7. During tests T3 and T4, the location of the resonance point was observed at t = 260 sec. The displacements were amplified due to the damage of the connections at the 1st and the 2nd story. The damages occurred on the connections of both beams.

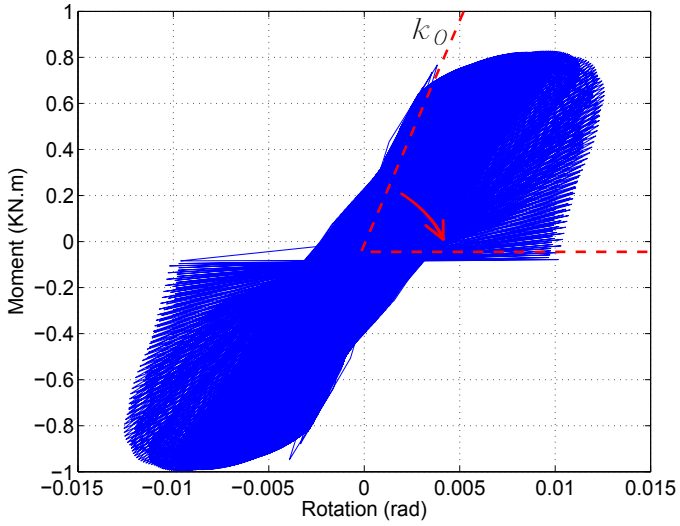


Figure 7: Numerical results corresponding to T3 and T4 : $M - \phi$ curve of the connection 1 at the first story.

Numerically from Fig. 8, the displacement responses of the frame increased gradually until the time t = 270 sec where the resonance may happen. Table 1 shows the comparison of the numerical and the experimental relative displacement responses under $\pm$ 5 mm required displacement excitation and at t = 10, 150 and 260 sec. Under this displacement, the numerical displacement responses q_1 and q_2 at the resonance point (t = 270 sec) were 9.6 and 24 mm, respectively. For test T3, the experimental displacement responses q_1 and q_2 were 11 and 25.5 mm. The results of the comparison between analytical and experimental responses indicated that the errors were 12.7% and 5.9%, respectively. Similarly, the displacement responses for test T4 were 9 and 21.8 mm at the resonance point, while the errors were 6.7% and 10%, respectively.

Fig. 9(a) and Fig. 9(b) display the LCF damage indices D_{n_1} and D_{n_2} and the plastic damage indices D_{p_1} and D_{p_2} for connections 1 and 2. The connection 1 was totally damaged at t = 275 sec after the resonance. At the same time, the index reached a value D_{n_2} = 66%. The plastic damage indices had the same values because the LCF damage was dominant. These results confirmed the experimental observation, because the damage in the 1st story was more than the 2nd story.

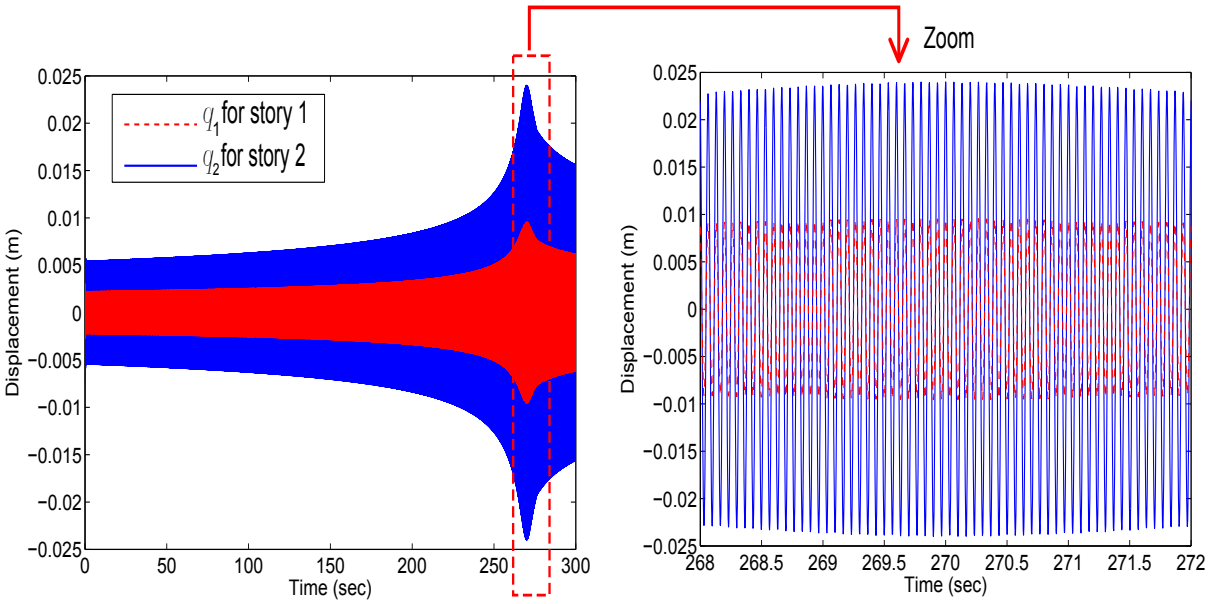
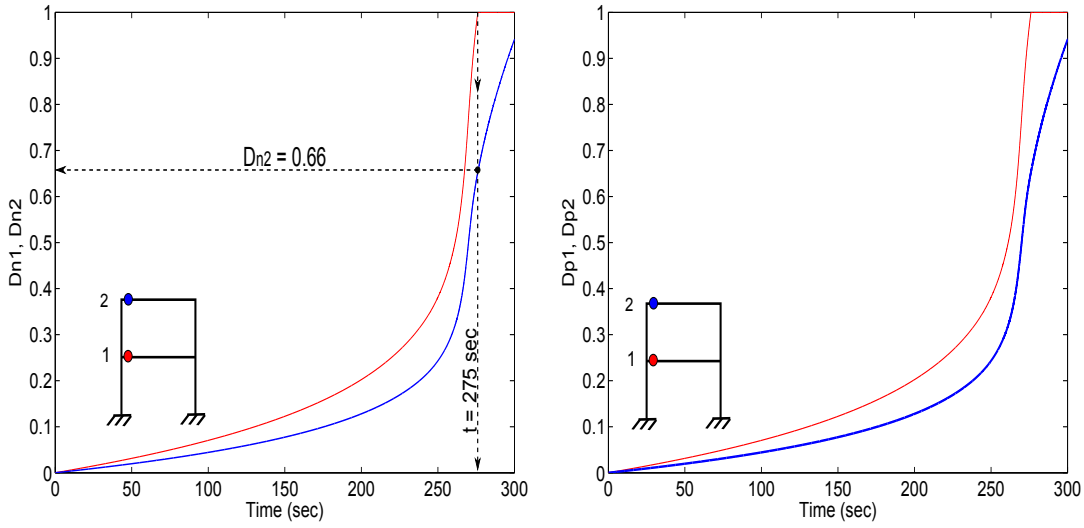


Figure 8: Numerical displacement responses q_1 and q_2 corresponding to tests T3 and T4.



(a) (b)

Figure 9: Numerical results corresponding to T3 and T4: (a) LCF damage indices of connections; (b) plastic damage indices of connections.

Moreover, the natural frequencies of the frame model were attained experimentally by hammer-shock tests and numerically by using the numerical simulation based on FE method instructed in MATLAB. Before the tests T3 and T4, the experimentally measured value of the first natural frequency f_{n1} was 18 Hz and the numerical value of f_{n1} was 18.5 Hz.

The loss of the first natural frequency was clearly observed in tests T3 and T4. According the numerical analyses, the natural frequency f_{n1} decreased gradually from initial value 18.5 Hz to a final value 12.55 Hz. Experimentally, the final value of f_{n1} was found to be 14 Hz in this case and by comparing with the numerical value, the error was 10.4%. Fig. 10, obtained

from numerical analysis, presents f_{n1} versus the time and it indicates the resonance point at t = 270 sec where f_{n1} can have a value of 15 Hz. After this point, the loss of frequency was accelerated.

Another comparison can be done by determining the value of f_{n1} from the numerical curve (see Fig. 10) at t = 260 sec which presents the resonance point experimentally located. It is possible to say that the frame was very close to the resonance point with f_{n1} = 15.6 Hz.

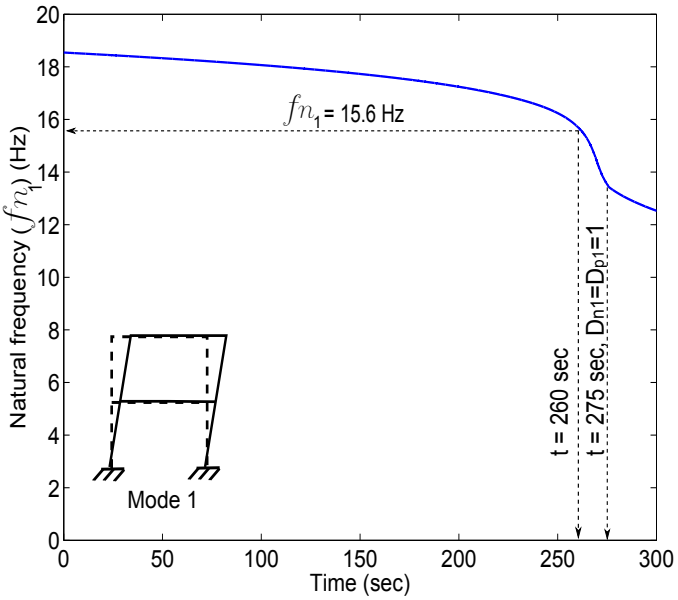


Figure 10: Numerical results corresponding to T3 and T4: frequency response $f_{n1}(t)$.

Figs. 11(a), (b), (c) and (d) display the failure modes of each bolted connection after test T3. A self-loosening and a backing-off of the nut were observed in connection bolts (see mark A). In addition, a failure by fatigue cracks due to repeated excitation was identified at a number of bolts. In these figures, arrows indicate the damaged bolts and it can be observed that the damage in bolts were much more severe in the first story.

Fig. 12 displays the measured frequency responses of the frame model after shaking table tests. The frequency responses indicated that the natural frequency values of a portal frame decrease as the damage increases. The amplitude (acceleration/force) increased in tests T3 to T5 because of the increase of damage and the same can be observed in test T6 (see Fig. 12). This proves that the modelling of damage due to LCF is important in order to predict the failure of a portal frame subjected to dynamic excitations.

From numerical and experimental results, the proposed FE method based on damage analyses can be employed to evaluate the damage in bolted connections and to estimate changes in dynamic properties. FBDH model integrated in FE method seems to provide reasonable estimates for the horizontal story displacements of the portal frame. This model can describe the accumulation of LCF damage and the damage induced by cyclic plasticity. Consequently, FDBH model can be used for nonlinear dynamic analysis of portal frame under long or short duration dynamic loading, for high or low amplitude of deformations. The model and the proposed approach can consider explicitly the main aspect of damage occurred in portal frames during dynamic excitation.

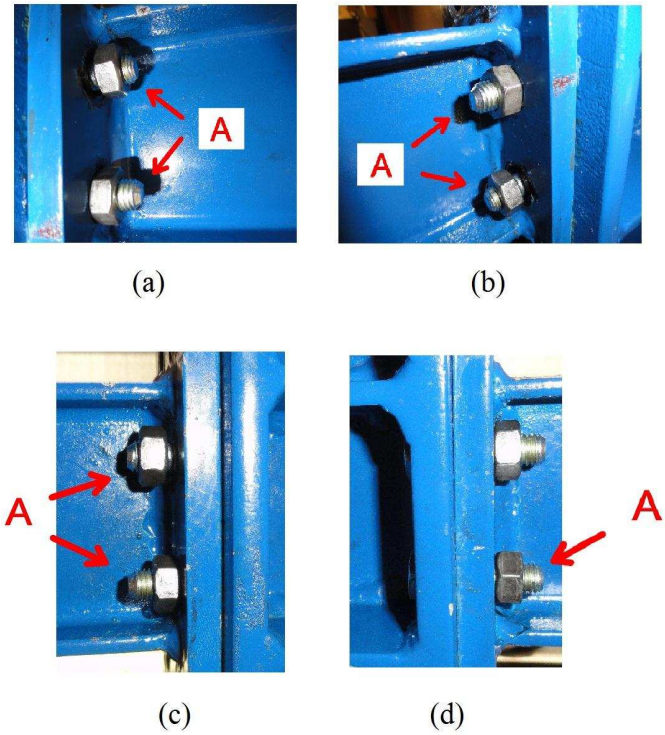


Figure 11: Damages in connections corresponding to T3 and T4: (a) connection 1 in the 1st story (side 1); (b) connection 1 (side 2); (c) connection 2 in the 2nd story (side 1); (d) connection 2 (side 2).

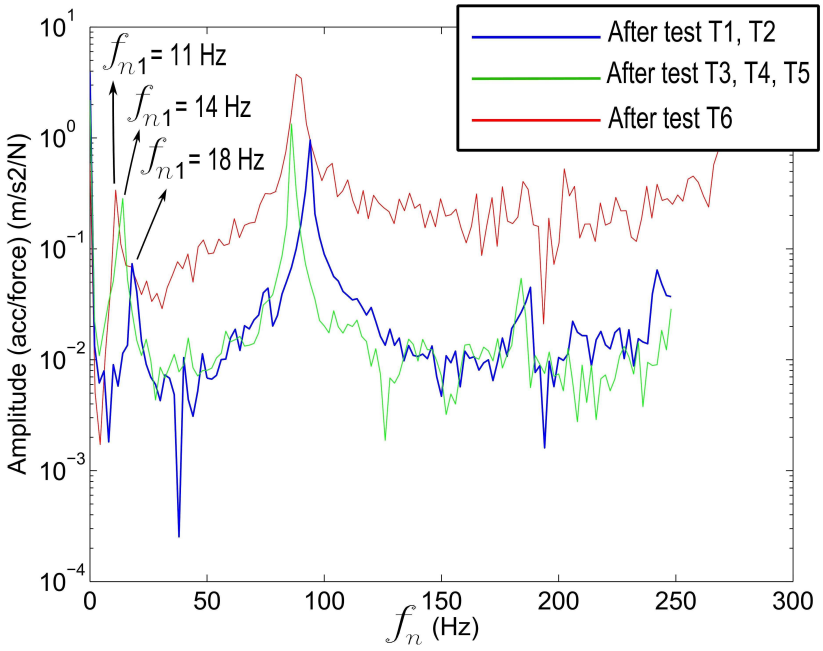


Figure 12: Comparison of experimental frequency responses.

7 CONCLUSIONS

In this study, a two story steel portal frame with bolted connections was investigated under horizontal sinusoidal base excitations. The results from shaking table tests were presented. The overall behavior of the structure was considered by comparing the numerical analysis and the experimental shaking table test results. The nonlinear numerical analyses of the frame were performed based on FDBH model. The study also proposed a contribution to the solution of nonlinear portal frame structures subjected to dynamic excitation by the method of nonlinear modal synthesis. This method involves a considerable simplification in the context of the analysis of nonlinear portal frame structures.

The results revealed a very good correlation between experimental and numerical displacement time history. The difference of the simulated response compared to the experimental results was attributed to the accuracy of measurements. Another reason for the observed differences is that there was uncertainty in bolted connection related to the variation in mechanical properties.

It is possible to recall that the LCF degradation of the initial stiffness of bolted connection was considered linear in the FDBH model using a factor (1-D_n). Therefore, an improvement could be made to improve the numerical results by adopting an experimental law.

REFERENCES

[1] L.F. Ibarra, R.A. Medina, and H. Krawinkler. Hysteretic models that incorporate strength and stiffness deterioration. *Earthquake Engineering and Structural Dynamics*, 34(12):1489 – 1511, 2005.

[2] M. Saranik, D. Lenoir, and L. Jézéquel. Shaking table test and numerical damage behaviour analysis of a steel portal frame with bolted connections. *Computers and Structures*, Volumes 112 - 113:Pages 327 341, December 2012.

[3] I. Tani, D. Lenoir, and L. Jézéquel. Effect of junction stiffness degradation due to fatigue damage of metallic structures. *Engineering Structures*, 27(11):1677 – 1688, 2005.

[4] D.G. Lignos, Y. Chung, T. Nagae, and M. Nakashima. Numerical and experimental evaluation of seismic capacity of high-rise steel buildings subjected to long duration earthquakes. *Computers and Structures*, 89(11-12):959 – 967, 2011.

[5] M. Saranik, D. Lenoir, and L. Jézéquel. Numerical and experimental analyses of damage behaviour of steel portal frame with bolted connections. VIbrations, SHocks and NOise VISHNO 2012 (Vibration, Choc and Bruit VCB 2012), Paris, France, July 3-5, 2012.

[6] M. Saranik, D. Lenoir, and L. Jézéquel. Nonlinear seismic analysis and fatigue-accumulated damage of steel frames with end-plate bolted connections. 3rd International Conference on Computational Methods in Structural Dynamics and Earthquake Engineering (COMPDYN 2011), Corfu, Greece, May 25-28, 2011. http://www.scopus.com.

[7] R.M. Korol, A. Ghobarah, and A. Osman. Extended end-plate connections under cyclic loading: Behaviour and design. *Journal of Constructional Steel Research*, 16(4):253 – 280, 1990.

[8] W. Chen and X. Deng. Structural damping caused by micro-slip along frictional interfaces. *International Journal of Mechanical Sciences*, 47(8):1191 – 1211, 2005.

[9] Wilfried B. Kraetzig and Yuri S. Petryna. On structural damage processes of storm- and earthquake-induced low-cycle fatigue. Conference on Computational Methods in Structural Dynamics and Earthquake Engineering; COMPDYN Rhodes, Greece, 22 - 24 June 2009.

[10] M.A. Miner. Cumulative damage in fatigue. *Journal of Applied Mechanics*, 12(Trans. ASME Vol. 67):A159 – A164, 1945.

[11] R.M. Richard and B.J. Abbott. Versatile elastic plastic stress strain formula. *ASCE Journal of the Engineering Mechanics Division*, 101(4):511 – 515, 1975.

[12] M. Saranik, D. Lenoir, and L. Jézéquel. Effects of low cycle fatigue damage in the end plate connection on steel frame seismic demands. 8th International Conference on Structural Dynamics (EURODYN 2011), Leuven, Belgium, July 4-6, 2011.

[13] John B. Mander, Stuart S. Chen, and Gokhan Pekcan. Low-cycle fatigue behavior of semi-rigid top-and-seat angle connections. *AISC Engineering Journal*, 31(3):111 – 124, 1994.

[14] P.P. Gillis. Manson-coffin fatigue. *Acta Metallurgica*, 14(12):1673 – 1676, 1966.

[15] R. Hasan, L. Xu, and D.E. Grierson. Push-over analysis for performance-based seismic design. *Computers and Structures*, 80(31):2483 – 2493, 2002.

[16] S. Setio, H.D. Setio, and L. Jézéquel. A method of non-linear modal identification from frequency response tests. *Journal of Sound and Vibration*, 158(3):497 – 515, 1992.

COMPDYN 2013
4th ECCOMAS Thematic Conference on
Computational Methods in Structural Dynamics and Earthquake Engineering
M. Papadrakakis, V. Papadopoulos, V. Plevris (eds.)
Kos Island, Greece, 12–14June 2013

NUMERICALMODELINGOFDYNAMICCOMPACTIONINDRY SAND USING DIFFERENT CONSTITUTIVE MODELS

M. Pourjenabi[1], E. Ghanbari[2], and A. Hamidi[3*]

[1]Kharazmi University
P.O.Box 15614, Tehran, Iran
m.pourjenabi@khu.ac.ir

[2]Kharazmi University
P.O.Box 15614, Tehran, Iran
std_ghanbari@khu.ac.ir

[3]Kharazmi University
P.O.Box 15614, Tehran, Iran
hamidi@khu.ac.ir

Keywords: Dynamic compaction, constitutive model, numerical modeling, cap plasticity, Mohr-Coulomb.

Abstract. *Dynamic compaction is a useful method of soil improvement for loose sands. In this method a tamper falls down from a specified height on the soil in order to reach the desired compaction depth. The method is invented and introduced by Louis Menard and applied at Nice airport in France. It has been developed and progressed afterward and has been used in several projects for land reclamation.*

Numerical modeling is a useful tool for simulation of dynamic phenomena in geotechnical engineering. Several researchers have worked on numerical simulation of dynamic compaction using different codes and implemented solutions for prediction of appropriate patterns of compaction. However, less attention has been paid to the effect of different constitutive models applied in numerical solution.

In present research, ABAQUS 6.10-1 software is used for two dimensional modeling of dynamic compaction operation in dry sand. The program is able to simulate process of dynamic compaction with high acquisition. Cap plasticity critical state model besides Mohr-Coulomb failure criterion are used in numerical simulation and the effect of these constitutive models are investigated on the peak particle velocity and peak ground acceleration besides the crater depth.

Results of comparison indicated that application of different constitutive models influences the numerical simulation of the phenomenon. Implementation of cap plasticity model results in better prediction of crater depth and variations of relative density in depth compared to the Mohr-Coulomb failure criterion.

1 INTRODUCTION

Dynamic compaction is a useful method for compacting granular soils which has first been introduced by Menard in 1975. This method is based on falling a tamper (weighting from 5 to 40 tons) from height of 15 to 30 meters on the loose sand that results in desirable compaction and increases the shear strength of base soil.

Many researchers have used numerical or physical modeling to study this phenomenon [1-8] and others have studied the results of dynamic compaction in the field [9-18]. In addition, analytical methods have been used for surveying different parameters of this method [19-22].

In numerical modeling process, it is very important to utilize a proper constitutive model for the soil in order to predict its behavior in a good manner. Unlike the behavior of soils in triaxial tests or failure of the soil under foundations, that the increase in axial stress has an important role in failure, increase in confining stress results in failure of soil during dynamic compaction.

Mohr-Coulomb criterion assumes that failure occurs when shear stress on any point in a material reaches a certain value that depends linearly on normal stress in the same plane [4].Unlike Drucker-Prager criterion, Mohr-coulomb criterion assumes that failure of typical geotechnical materials generally includes some small dependence on the intermediate principal stress. Mohr-Coulomb constitutive model has been used for simulating dynamic compaction in finite element code ABAQUS [4]. Cap-plasticity models have also been used by a number of researchers for simulation of dynamic compaction in granular materials [24-26].

In this paper, a two dimensional model in finite element code ABAQUS is used to survey the differences between cap-plasticity and Mohr-Coulomb constitutive models. Results are compared with an experimental centrifuge test [7].

2 CONSTITUTIVE MODELS USED IN THENUMERICAL ANALYSIS.

In present study, numerical analysis has been performed using two different constitutive models, i.e. Mohr-Coulomb and cap plasticity model.

2.1 Mohr-Coulomb model

Mohr-coulomb model is defined in τ-σ plane. In this model, shear strength increases with enhancement of normal stress on the failure plane:

$$\tau = c + \sigma \tan\phi \tag{1}$$

$\tau$is the shear stress, c is the cohesion of material, ϕ is the material friction angle andσ is the normal stress. Mohr-Coulomb failure criterion in Πplane is shown in Fig. 1.

According to this criterion, yield strength in compression is higher than that in extension. It shows the dependence of the behavior on the third invariant of the stress tensor. The criterion is expressed in terms of maximum and minimum principal stresses, and hence does not incorporate the effects of the intermediate principal stresses[27].

2.2 Cap plasticity model

The model predicts hardening behavior of soil and is useful for application in dynamic problems. Cap models particularly are used to predict the behavior of soils under impact loads [25, 28]. Also cap plasticity model with a linear shear yield surface has been used for modeling dynamic compaction process in granular soils [1]. In this study, similar cap plasticity model has been used. Figure 2 indicates yield criterion of the model in the first and second

stress invariants space, (J_1-$\sqrt{J_{2D}}$). The model has two different yield surfaces to consider soil hardening during shear and isotropic loading. First one is a linear shear yield surface based on Drucker-Prager yield criterion in Eq. 2 and is fixed. The second one is a moving cap that is defined by Eq. 3 and is used to express soil failure under isotropic effective stress.

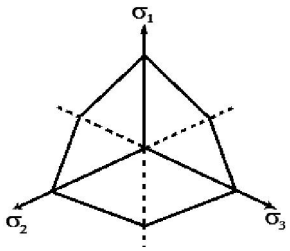


Figure 1:Mohr-Coulomb criterion in Πplane

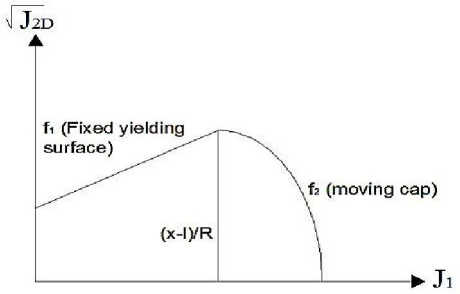


Figure2: Yield surface of the cap model in stress space.

$$\boldsymbol{f_1 = \sqrt{J_{2D}} - \alpha j_1 - \kappa = 0} \quad (2)$$

$$\boldsymbol{f_2 = (J_1 - 1)^2 + R^2 J_{2D} - (X - l)^2 = 0} \quad (3)$$

$$l = \frac{X - R.\kappa}{1 + \alpha.R} \quad (4)$$

α and κ are constants of Drucker-Prager failure criterion. X is the hardening parameter; R is the material parameter and l is the first invariant of stress tensor at the intersection point of the fixed yield surface and the moving cap. Cap is extended due to the soil hardening based on plastic volumetric strain in every step and is defined according to Eq.5.

$$X = -\frac{1}{D} Ln\left(1 - \frac{\varepsilon_v^p}{W}\right) + X_0 \quad (5)$$

Here, W and D are material parameters and X_0 is initial stresses due to gravity analysis.

3 NUMERICAL MODELING

Two dimensional axisymmetric model has been developed using ABAQUS as shown in Fig. 3. Compaction is performed using a 20 ton pounder falling from 20m height. Model height and width are 18m and 14m respectively. Also the number of impacts is considered 5 and 10 blows in the analysis. Features of pounder and soil parameters in two cases of Mohr-coulomb and cap plasticity models are shown in Tables 1 and 2 [7].

Interface elements have been used to define the contact between tamper and the ground surface. Friction coefficient is taken 0.5 for contact property. Total time for each impact is 60sec and minimum increment of time is 10^{-8}sec that is properly small for dynamic and specially impact problems. Large deformation condition is also considered in this model.

In the first step, gravity analysis is performed to exert initial stresses, also at the end of each step, void ratio is obtained by substituting volumetric strain in Eq.6.

$$e = e_0 - (1 + e_0)\varepsilon_v \tag{6}$$

Where e_0 is the initial void ratio and ε_v is volumetric plastic strain. Also e is void ratio at the end of each step. Soil density at the end of each step is calculated from Eq.7. Hence, by applying maximum and minimum void ratios in Eq. 8, relative density and its rate of increase can be determined.

$$\gamma = \frac{G_s \gamma_w}{1+e} \tag{7}$$

$$Dr = \frac{e_{max} - e}{e_{max} - e_{min}} \tag{8}$$

Here, e_{max} and e_{min} are 0.86 and 0.51, respectively. Also bulk modulus is reassigned through Eq.9 considering the role of change in relative density and mean effective stress in different soil layers. Applying bulk modulus in Eq.11, elasticity modulus is achieved in each step.

$$k = k_r P_a (\frac{\acute{p}}{P_a})^{0.5} \tag{9}$$

$$k_r = \beta \exp(\gamma . Dr) \tag{10}$$

$$E = 3(1 - 2\vartheta)K \tag{11}$$

Here,K is the bulk modulus, $\acute{p}$ is the mean effective stress, Dr is the relative density, P_a is atmospheric pressure, β and γ are 120 and 0.0134 respectively and ϑ is the poisson's ratio.

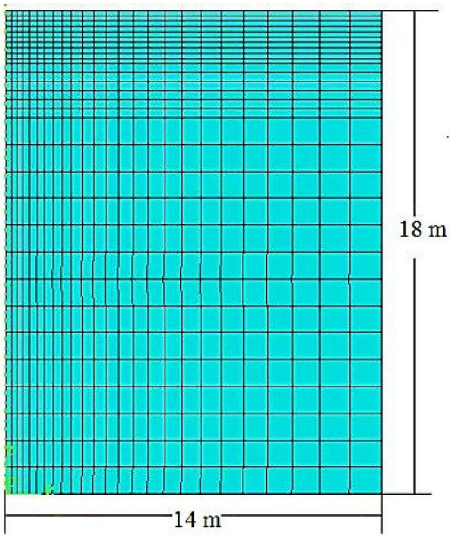


Figure 3:Dimensions and mesh of the model

Parameters	Value
Tamper weight	25 ton
Falling height	20 meter
Tamper cross section area	4.5 m^2
Elasticity modulus	90GPa
Poisson's ratio	0.2

Table 1: Tamper parameters

Parameters	Value
Internal friction angle	29.9 degree
Dilation angle	10 degree
Cohesion	0
Soil density	15.7 kN/m^3
Young modulus	25 MPa
Poisson's ratio	0.25
Damping constants(η_1, η_2)	0,0.01
R	4.33
W	0.4
D	18×10^{-5} (m^2/kN)

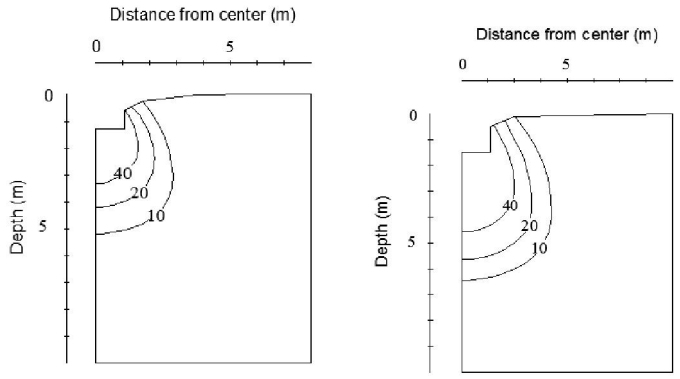
Table 2: Soil parameters

4 NUMERICAL MODELING RESULTS

Centrifuge tests have been used to simulate dynamic compaction process and the results have been represented in different conditions of impact [7]. Initial relative density of soil was 35%. Contours of increase in relative density in soil for 5 and 10 blows are represented in Figs.4-a and 4-b.As shown in Fig. 4-a, crater depth in 5blows, is about 1.2 meter. Also 40%, 20% and 10%increase in relative density induced in3.2, 4.2 and 5.2 meters depth respectively. Fig4-b represents similar contours for 10 blows. It can be observed that the crater depth in 10 blows is recorded as 1.5 meters and 40%, 20% and 10% increase in relative density induced in 4.55, 5.6 and 6.35meters depth respectively.

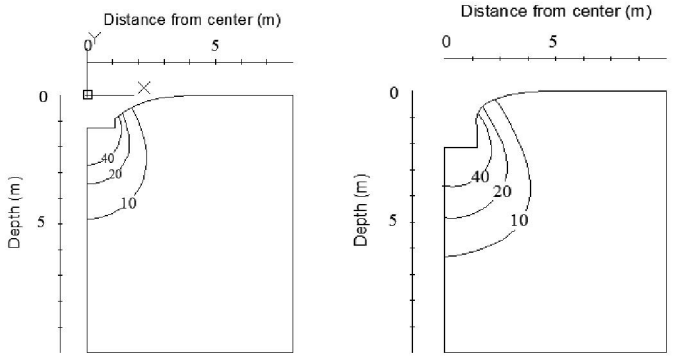
Figs 5-a and 5-b shows the results of numerical analysis using cap plasticity model for 5 and 10 blows respectively. Crater depth for 5blows is 1.27 meter and 40%, 20% and 10% increase in relative density occurred in 2.7, 3.45 and 4.8 meters depth. Based on Fig. 5-b, crater depth for 10blows is 2.12 meter sand 40%, 20% and 10% increase in relative density occurred in 3.6, 4.85 and 6.32 meters depth.

Figs.6-a and 6-b indicate the results of numerical analysis using Mohr-Coulomb failure criterion for 5 and 10blows respectively. Fig. 6-a shows the contours and crater depth for 5blows.It can be observed that cater depth is 0.275 meters and contours of 40%, 20% and 10% relative density are in 2.2, 3.11 and 3.67 meters depth. Based on Fig. 6-b, crater depth in 10blows is 0.377 meters and the depth associated to 40%, 20% and 10% increase in relative density are 3.2, 3.62 and 4 meters respectively.



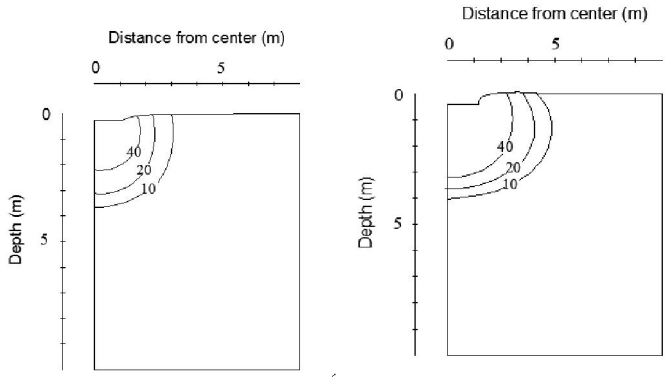
(a) (b)

Figure 4: Results of centrifuge test reported by Oshima and Takada [7] for (a) 5blows (b) 10blows



(a) (b)

Figure 5: Results of numerical analysis using cap plasticity model for (a) 5blows (b)10blows



(a) (b)

Figure6: Results of numerical analysis using Mohr-Coulomb model for (a) 5 blows (b) 10 blows

It is obvious from the figures that dynamic compaction process modeling using Mohr-Coulomb failure criterion results in lower crater depth and higher depth of relative density contours. It is due to the soil dilation after each impact which occurs using Mohr-Coulomb model which is not able to predict failure during compressive loading of confinement. On the contrary, modeling the soil behavior using cap plasticity model results is a higher crater depth and relative density contours which are more consistent with centrifuge model test results.

Figure 7 shows the variation of crater depth with time for two applied models. It is visible that crater depth in Mohr-Coulomb model is much lower than the other one. Also at the end of each impact there is an unusual increase in volume of the soil which has not occurred for cap plasticity model. As a result, Mohr-Coulomb failure criterion is not applicable for prediction of dynamic compaction in numerical analysis.

5 CONCLUSION

A two dimensional axisymmetric model was developed for simulation of dynamic compaction process using finite element code ABAQUS applying Mohr-Coulomb and cap plasticity models. Results are compared with a physical centrifuge mode and the following conclusions are made:

- Cap plasticity constitutive model is suitable for predicting dynamic compaction process because of its moving cap which enables the model to incorporate soil hardening during isotropic compression and confinement.
- Using Mohr-Coulomb failure criterion, the soil expands after each impact. The value of dilation angle affects this dilative behavior. As a result, this model results in lower volumetric strains and less crater depth besides more depth of relative density contours compared to the model tests. It can be concluded that Mohr-Coulomb criterion is not a suitable model for prediction of dynamic compaction process.

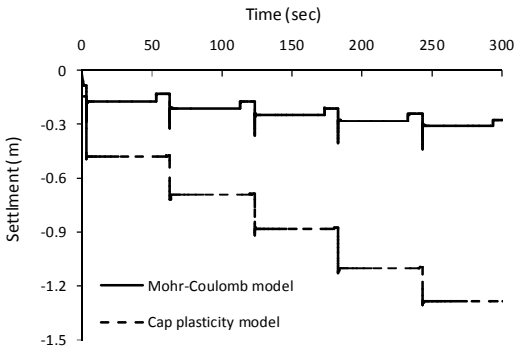


Figure 7: Variation of crater depth versus time for Mohr-Coulomb and cap plasticity models

6 REFERENCES

[1] A. Ghassemi, A. Pak, H. Shahir, Numerical study of the coupled hydro-mechanical effects in dynamic compaction of saturated granular soils. *Computers and Geotechnics*, **37**, 10–24, 2010.

[2] G. Jahangiri, A. Pak, A. Ghassemi, A novel numerical method for determination of print spacing in dynamic compaction operation of dry sand.*4th International Conference on Geotechnical Engineering and Soil Mechanics*, Tehran, Iran, 2010.

[3] M. Jia, J. Zhou, Investigation of mechanical response induced in dynamic compaction of sandy soils with PFC2D.*GeoShanghai International Conference*, Shanghai, China, 2010.

[4] J.L. Pan, A.R. Selby, Simulation of dynamic compaction of loose granular soils. *Advances in Engineering Software*, **33**, 631–640, 2002.

[5] W. Li, Q. Gu, L. Su, B. Yang, Finite element analysis of dynamic compaction in soft foundation. *Procedia Engineering*, **12**, 224–228, 2011.

[6] O.P. Minaev, Effective method for dynamic compaction of slightly cohesive saturated soils. *Soil Mechanics and Foundation Engineering*, **39**, 208-213, 2002.

[7] A. Oshima, N. Takada, Relation between compacted area and ram momentum by heavy tamping. *14th International Conference on Soil Mechanics and Foundation Engineering*, Hamburg, Germany, 1997.

[8] F. Jafarzadeh, Dynamic compaction method in physical model test. *Scientia Iranica*, **13**, 187-192, 2006.

[9] H. Arslan, G. Baykal, O. Ertas, Influence of tamper weight shape on dynamic compaction. *Ground Improvement*, **11**, 61–66, 2007.

[10] S.J. Feng, W.H. Shui, W.H. Gao, L.J. He, K. Tan, Field evaluation of dynamic compaction on granular deposits. *Performance of Constructed Facilities*, **25**, 241-249, 2010.

[11] L.J. Hua, Y.J. Bo, X. Hu, C. Wei, Dynamic compaction treatment technology research of red clay soil embankment in southern mountains. *Journal of Central South University of Technology*, **15**, 50−57, 2006.

[12] J.H. Hwang, T.Y. Tu, Ground vibration due to dynamic compaction. *Soil Dynamics and Earthquake Engineering*, **26**, 337–346, 2006.

[13] F. Kopf, I. Paulmich, D. Adam, Modelling and simulation of heavy tamping dynamic response of the ground.*14th Danube-European Conference on Geotechnical Engineering*, Bratislava, Slovak Republic, 2010.

[14] L. Menard, Y. Broise, Theoretical and practical aspects of dynamic consolidation. *Geotechnique*, **25**, 3-16, 1975.

[15] P.W. Mayne, J.S. Jones, Impact stresses during dynamic compaction. *Geotechnical Engineering*, **109**, 1342-1346, 1983.

[16] P.W. Mayne, J.S. Jones, J.C. Dumas, Ground response to dynamic compaction. *Geotechnical Engineering*, **110**, 757-774, 1984.

[17] K.M. Rollins, J. Kim, Dynamic compaction of collapsible soils based on U.S. case histories. *Geotechnical and Geoenvironmental Engineering*, **136**, 1178-1186, 2010.

[18] W.L. Zou, Z. Wang, Z.F. Yao, Effect of dynamic compaction on placement of high-road embankment. *Performance of Constructed Facilities*, **19**, 316-323, 2005.

[19] Y.K. Chow, D.M. Yong, K.Y. Yong, S.L. Lee, Monitoring of dynamic compaction by deceleration measurements. *Computers and Geotechnics*, **10**, 189-209, 1990.

[20] Y.K. Chow, D.M. Yong, K.Y. Yong, S.L. Lee, Dynamic compaction analysis. *Geotechnical Engineering*, **118**, 1141-1157, 1992.

[21] Y.K. Chow, D.M. Yong, K.Y. Yong, S.L. Lee, Dynamic compaction of loose granular soils: effect of print spacing. *Geotechnical Engineering*, **120**, 1115-1133, 1994.

[22] J.M. Roesset, E. Kausel, V. Cuellar, J.L. Monte, J. Valerio, Impact of weight falling onto the ground. *Geotechnical Engineering*, **120**, 1394-1412, 1994.

[23] R.G. Lukas, *Geotechnical engineering circular No. 1- Dynamic compaction*. FHWA-SA-95-037, 1995.

[24] A. Pak, H. Shahir, A. Ghasemi, Behavior of dry and saturated soils under impact load during dynamic compaction. *16th International Conference on Soil Mechanics and Geotechnical Engineering*, Osaka, Japan, 2005.

[25] Q. Gu, F.H. Lee, Ground response to dynamic compaction. *Geotechnique*,**52**, 481-93, 2002.

[26] H.S. Thilakasiri, M. Qunaratne, G. Mullins, P. Stinnette, C. Kuo, Implementation aid for dynamic replacement of organic soils with sand. *Geotechnical and Geoenvironmental Eng*ineering, **127**, 25-35, 2001.

[27] C.S. Desai, H.J., Siriwardane, *Constitutive laws for engineering materials, with emphasis on geologic materials.* Prentice Hall, 1984.

[28] C.J. Poran, J. Rodriguez, A finite element analysis of impact behavior of sand. *Soils and Foundations*,**32**, 68–80, 1992.

COMPDYN 2013
4th ECCOMAS Thematic Conference on
Computational Methods in Structural Dynamics and Earthquake Engineering
M. Papadrakakis, V. Papadopoulos, V. Plevris (eds.)
Kos Island, Greece, 12–14 June 2013

THE APPLICATION OF FEM/DEM METHOD IN ANALYSIS OF RC BEAM-COLUMN JOINTS

Željana Nikolić[1*], Nikolina Živaljić[1] and Hrvoje Smoljanović[1]

[1] Faculty of Civil Engineering, Architecture and Geodesy, University of Split
Matice hrvatske 15, 21000 Split
e-mail: zeljana.nikolic@gradst.hr; nikolina.zivaljic@gradst.hr; hrvoje.smoljanovic@gradst.hr

Keywords: Combined finite-discrete element method (FEM/DEM), Reinforced beam-column joint, Monotonic loading, Cyclic loading.

Abstract. *One of very interesting problem in civil engineering applications is reinforced concrete beam-column joints subjected to monotonic and cyclic load. Predicting of the behaviour of reinforced concrete beam-column joints under monotonic and cyclic loading imposes the need to develop numerical model which will be able to include effects of the behaviour of reinforced concrete structures due to dynamic action in linear elastic stage, crack initiation and propagation, energy dissipation mechanisms due to non linear effects, inertial effects due to motion, contact impact and finally to attain state of the rest that is a consequence of energy dissipation mechanisms in the system. It is possible to include all previously mentioned effects with the finite-discrete element method (FEM/DEM). In this paper, a robust numerical model of concrete reinforcement, which is based on approximation of the experimental curves for behaviour of the concrete and steel in crack, is aimed to predict the behaviour of reinforced concrete beam-column joints subjected to monotonic and cyclic load. Cracking of the structure is enabled by discrete model of cracks where the cyclic behaviour of concrete and steel was implemented. The development of the cracks is analyzed for mid and end RC beam-column joints.*

1 INTRODUCTION

For predicting the behaviour and collapse of reinforced concrete structures, the numerical model should be able to include effects of the behaviour of concrete structures due to dynamic action in linear elastic stage, crack initiation and propagation, energy dissipation mechanisms due to non linear effects, inertial effects due to motion, contact impact and finally to attain state of the rest that is a consequence of energy dissipation mechanisms in the system. It is possible to include all previously mentioned effects with the finite-discrete element method [1, 2].

There has been a number of fracture models proposed in the context of both discrete element methods and combined finite discrete element method. Some of the models are based on a global approach applied to each individual body, while others used a local smeared crack approach or local single-crack approach. In this work a model for plane crack initiation and crack propagation in concrete is used [3]. The model combines standard finite element formulation for the hardening part of the constitutive law with the single-crack model for the softening part of stress-strain curve. Finite elements are used to model behaviour of the material up to the ultimate tensile strength while a discrete crack model is used for modelling of the crack opening and separation along edges of finite elements.

In the model presented in this paper an embedded model of reinforcing bars [4, 5] is implemented in Y2D combined finite-discrete element code [6]. Cracking of the concrete is enabled by a combined single and smeared crack model. The concrete and reinforcing bars are analyzed separately, but they are connected by the relation between the size of the concrete crack and strain of the reinforcing bar [7]. Cyclic behaviour of the steel during the cyclic load is modelled with improved Kato's model [8].

In this paper the application of combined finite-discrete element method (FEM/DEM) in numerical analysis of reinforced beam-column joints is shown.

2 MODELLING OF THE REINFORCED CONCRETE STRUCTURE

In this work an embedded model of reinforcing bars is implemented in a combined finite-discrete element model based on Y2D-code. The concrete structure is discretized on triangular finite elements, while the reinforcing bars are modelled with linear one-dimensional elements which can be placed in arbitrary position inside the concrete finite elements. The model of the reinforced concrete structure with the embedded reinforcing bar is shown in Figure 1.

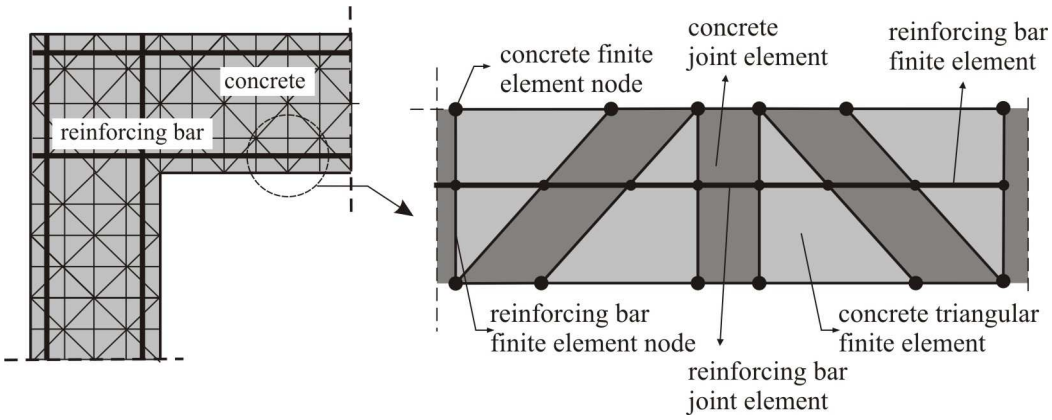


Figure 1: Discretization of reinforced concrete structure.

In the first step the reinforcement is modelled as bar (Figure 1). Intersection between the sides of concrete finite elements and reinforcing bars gives the reinforcement finite elements.

The structure behaves as continuum until opening of the crack. The deformation of the triangular element influence to the deformation of the reinforcing bars. When the crack in concrete appears, joint element in concrete as well as joint element in reinforcing bars is occurred. The concrete and reinforcing bars are analysed separately, but they are connected by the relationship between the size of the concrete crack and strain of the reinforcing bar.

2.1 Concrete model in joint element

In this work the concrete model is based on crack initiation and crack propagation of mode I and mode II loaded cracks [3]. The model is developed on the basis of experimental stress-strain curves for concrete in tension. The area under the stress-strain curve consists of two parts, first is the part used for modelling of the concrete behaviour up to the crack opening [3] while the second part represents strain softening after the tensile strength is exceeded [9]. The assumption of the discrete crack model is that the cracks coincide with the finite element edges. The total number of the nodes for each of the finite element meshes is doubled and the continuity between elements is realized through the penalty method [1]. Separation of the edges induces a bonding stress which is a function of the size separation δ [3].

No separation of the adjacent elements occurs before the tensile strength is reached, i.e. the edges of two adjacent elements are held together by normal and shear springs. Procedure of the separation of the elements and complete relationship for the normal and shear bonding stress are given in [3].

2.2 Steel material model in reinforcement joint element

In this work a model of the relationship between the concrete crack size and strain of the reinforcing bar developed by Shima [10] and Shin [7] is applied. The model is based on experimental strain-slip curves and represents well approximation of the behaviour of reinforcing bar with the expressed plastic strain caused by cyclic loading.

The steel strain-slip relation before the yielding of reinforcing bar is given by expressions:

$$s = \varepsilon_s (6 + 3500\varepsilon_s) \tag{1}$$

$$s = \left(\frac{S}{D}\right) \cdot K_{fc}, \quad K_{fc} = \left(\frac{f_c'}{20}\right)^{2/3} \tag{2}$$

where $s = s(\varepsilon_s)$ is normalized steel slip, D is bar diameter and f_c' is concrete strength.

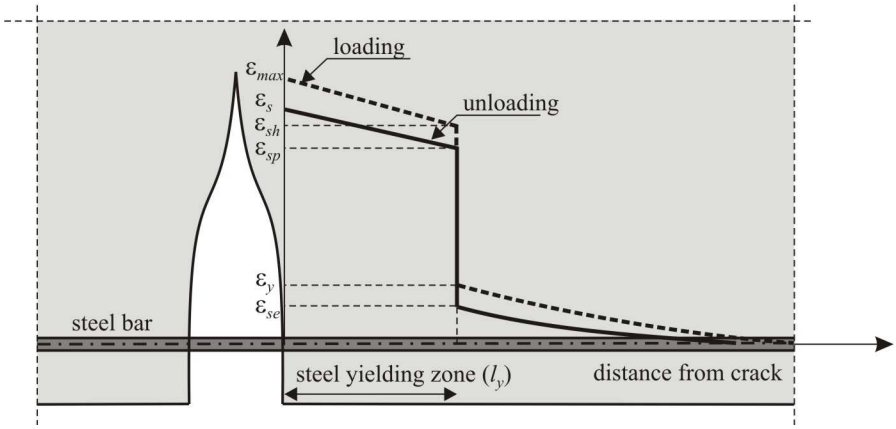


Figure 2: Strain distribution along the reinforcing bar in the post-yield range.

Normalized slip in the post-yield range is given by expression:

$$s = s_{pl} + s_e \tag{3}$$

where s_e is slip in the elastic region and s_{pl} is slip in the yield region. A strain distribution along the reinforcing bar in the post-yield region is shown in Figure 2, where ε_{se} is a strain at the yield boundary point on the elastic region and ε_{sp} is a strain at the yield boundary point on the yield region.

If the deformation of concrete is ignored, the steel slip can be determined by integration of the steel strain along the reinforcement axis. Normalized plastic steel slip in the yield region is given by an expression:

$$s_{pl} = \frac{(1+\beta)\varepsilon_s + \varepsilon_{sh} - \beta\varepsilon_{\max}}{\varepsilon_{\max} + \varepsilon_{sh}}(s_{\max} - s_y^*) \tag{4}$$

where $\beta = \sigma_{\max}/\sigma_y$ represents the gradient of the line shown in Figure 2, $\sigma_{\max}$ is the maximum stress in reinforcing bar under tensile loads, $s_{\max}$ is a function of $\varepsilon_{\max}$ and $s_y^* = \varepsilon_s(2+3500\varepsilon_s)$.

In the implemented model [11], calculation of shear force carried by the bar (Figure 3) is based on experimental curves [6] which describe curvature of the reinforcing bar in the vicinity of crack faces as function of deflection of the reinforcing bar at the interface t_s.

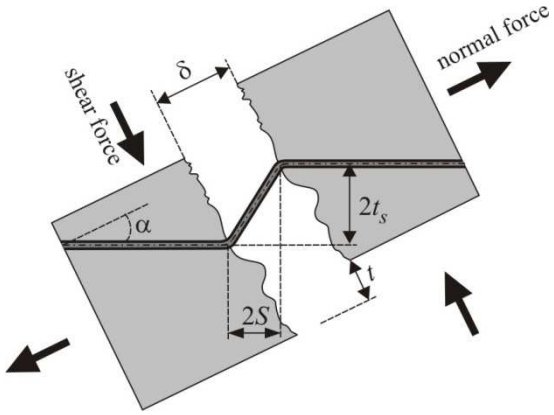


Figure 3: Discrete crack.

The effect of yield stress reduction due to the shear stress in the bar is taken into account by applying the Von Mises yield criterion and isotropic hardening rule as:

$$\sigma_y' = \sigma_y\sqrt{1-3\left(\tau_s/\sigma_y\right)^2} \tag{5}$$

where σ_y' is the reduced yield stress, τ_s is the shear stress of the reinforcing bar between the crack surfaces [11], which is obtained as:

$$\tau_s = \frac{V_s}{A_s} \tag{6}$$

where A_s is the cross-sectional area of the reinforcing bar.

The influence of adjacent cracks is approximately taken into account through a reduction factor α, which depends on crack distance l_{cr}. The steel slip s_{cr}, which considers the influence of adjacent cracks, is expressed for monotonic loading as:

$$s_{cr} = \alpha s \tag{7}$$

where s is non-dimensional slip defined by expression (14), while reduction factor α is given:

$$\alpha = 1 - e^{-(0.065 l_{cr}/D + 0.5)^3}, \quad \alpha \le 0.087 l_{cr} / D \tag{8}$$

In this work non-linear material model for steel is based on experimental stress-strain curve where cyclic behaviour of the steel during the cyclic load is modelled with improved Kato's model [6, 8].

3 EXAMPLES

The application of presented model for analysis of reinforced-concrete structures based on FEM/DEM method was performed in the numerical analysis of exterior and interior reinforced concrete beam-column joints.

3.1 Exterior RC beam-column joint

The application of presented numerical model is performed in the analysis of exterior RC beam-column joint subjected to monotonically increasing and cyclic load. The geometry characteristics of the RC beam-column joint are shown in Figure 4. Material characteristics are shown in Table 1.

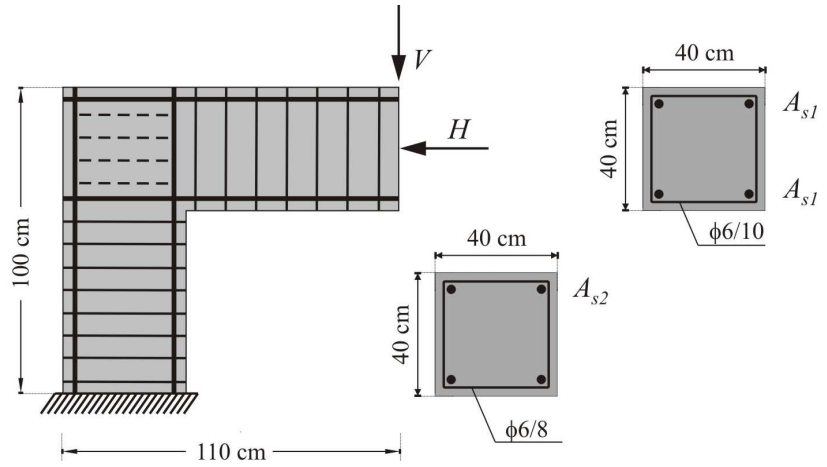


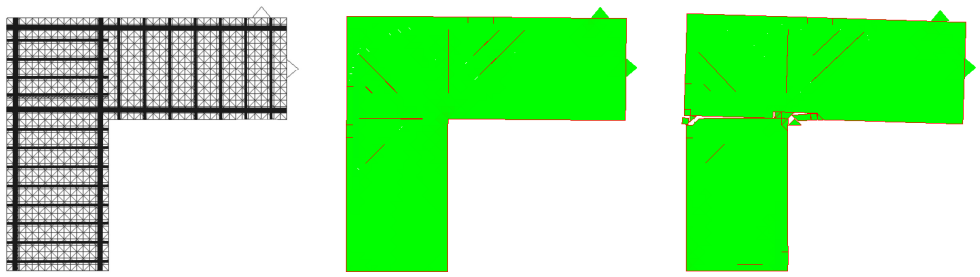
Figure 4: Geometry of exterior RC beam-column joint.

Concrete		Steel	
E_c (MPa)	29730	E_s (MPa)	210 000
ν	0.2	f_y (MPa)	400
f_t (MPa)	3.15	f_u (MPa)	500
f_c (MPa)	30.0	A_{s1} (m^2)	0.00026
G_f (N/m)	100	A_{s2} (m^2)	0.000452

Table 1: Material characteristics.

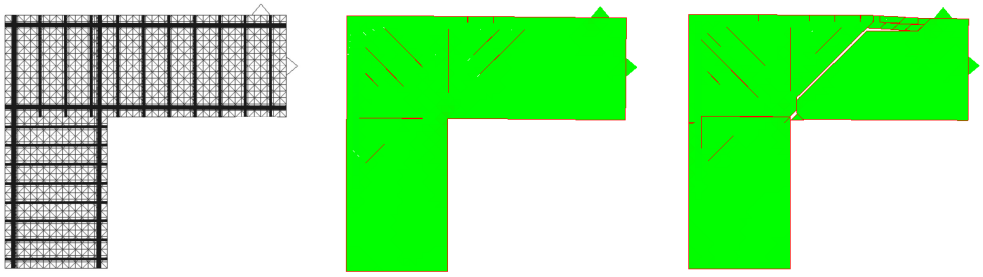
Exterior RC beam-column joint is reinforced in two different ways and subjected to monotonically increasing vertical and horizontal load with equal value. Initiation and propagation of the cracks in the RC beam-column and the ratio of vertical displacement at the collapse point v_c and vertical displacements at the moment when initial crack appears v_i for different reinforcement type were analyzed.

Failure patterns for two type of reinforcing are shown in figures 5 and 6.



(a) (b) (c)

Figure 5: Beam-column joint reinforced with horizontal stirrups (reinforcing type I): (a) discretization, failure patterns for: (b) V=H=254.8 kN, (c) after V=H=268.2 kN.



(a) (b) (c)

Figure 6: Beam-column joint reinforced with vertical stirrups (reinforcing type II): (a) discretization; failure patterns for: (b) V=H=265.3 kN, (c) after V=H=272.2 kN.

Figure 7 shows vertical load-displacement relation for two different types of reinforcing.

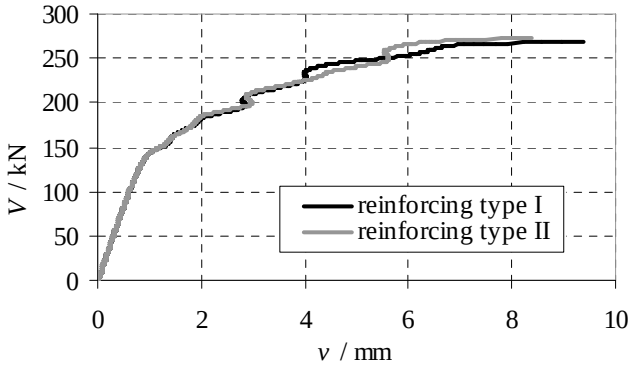


Figure 7: Vertical load - displacement relation.

The ratio of vertical displacement v_c at the collapse point and vertical displacements v_i at the moment when initial crack appears for different reinforcement type is shown in Table 2.

Reinforcing type	v_c / v_i
I	18.80
II	16.74

Table 2: Ratio v_c / v_i for each reinforcing type.

It can be seen that the larger vertical displacement was achieved for reinforcing type II. The greater capacity was achieved for reinforcing type II where the fracture is realized in the beam. Load capacity for beam-column joint reinforced with horizontal stirrups is 1.5% lower and dominant cracks occur at the top of the column.

Exterior RC beam-column joint, shown in Figure 4, is reinforced in two different ways and subjected to cyclic vertical and horizontal load (Figure 8). Initiation and propagation of the cracks in the RC beam-column and the ratio of vertical displacement at the moment of collapse v_c and vertical displacements v_i at the moment when initial crack appears for different reinforcement type were analyzed.

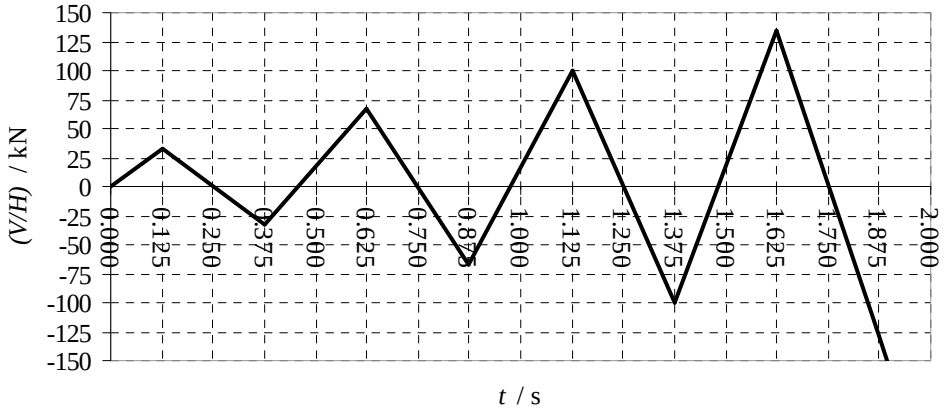
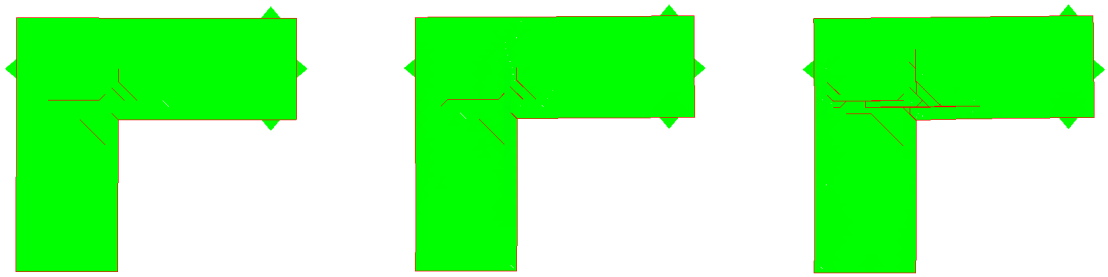


Figure 8: Load history.

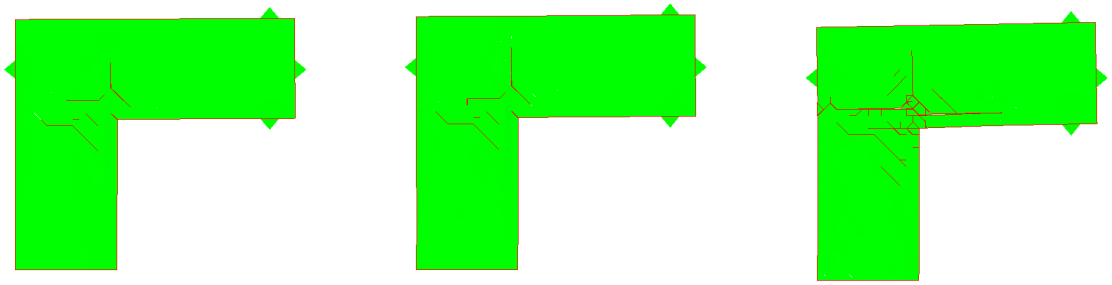
Failure patterns for two type of reinforcing are shown in figures 9 and 10.



(a) (b) (c)

Figure 9: Failure patterns for exterior beam-column joint reinforced with horizontal stirrups: (a) t=1.375s, (b) t=1.850s, (c) t=1.860s.

For exterior beam-column joint reinforced with horizontal stirrups, first crack occurs in the third cycle of loading for the force of 75.7 kN. At the time of the collapse vertical force was 116.5 kN with maximum vertical displacement v=10.77 mm.



(a) (b) (c)

Figure 10: Failure patterns for exterior beam-column joint reinforced with vertical stirrups: (a) t=1.375s, (b) t=1.850s, (c) t=1.870s.

For exterior beam-column joint reinforced with vertical stirrups, first crack also occurs in the third cycle of loading for the force of 75.7 kN. At the collapse point vertical force was 127.3 kN with maximum vertical displacement v =15.55 mm.

Figure 11 shows cyclic vertical load-displacement relation for two different types of reinforcing.

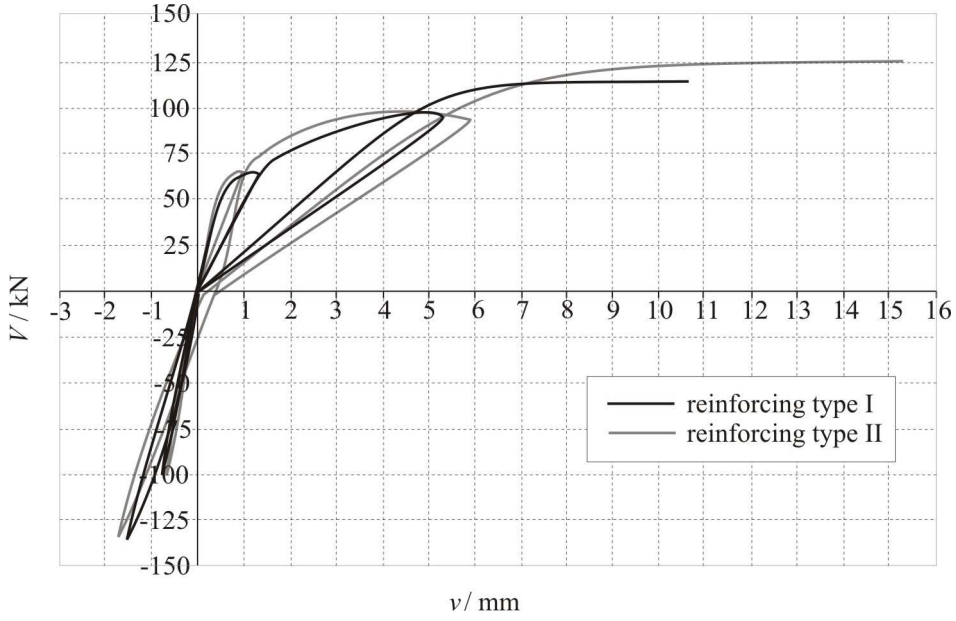


Figure 11: Vertical load - displacement relation.

The ratio of vertical displacement at the moment of collapse v_c and vertical displacement v_i at the moment when initial crack appears for different reinforcement type is shown in Table 3.

Reinforcing type	v_c / v_i
I	21.53
II	31.01

Table 3: Ratio of v_c / v_i for each reinforcing type.

It can be seen that larger vertical displacement and greater capacity was achieved for reinforcing type II. For the beam-column joint reinforced with horizontal stirrups (reinforcing type I) load capacity is 8.5% lower in regards to reinforcing type II.

3.2 Interior RC beam-column joint

The application of presented numerical model is performed in the analysis of interior RC beam-column joint subjected to monotonically increasing and cyclic load. The geometry characteristics of interior RC beam-column joint are shown in Figure 12. Material characteristics are shown in table 4.

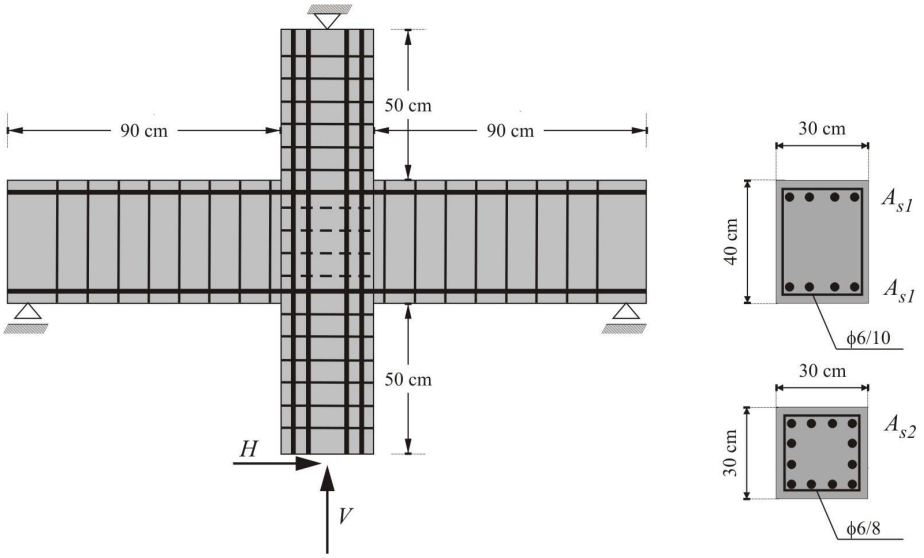


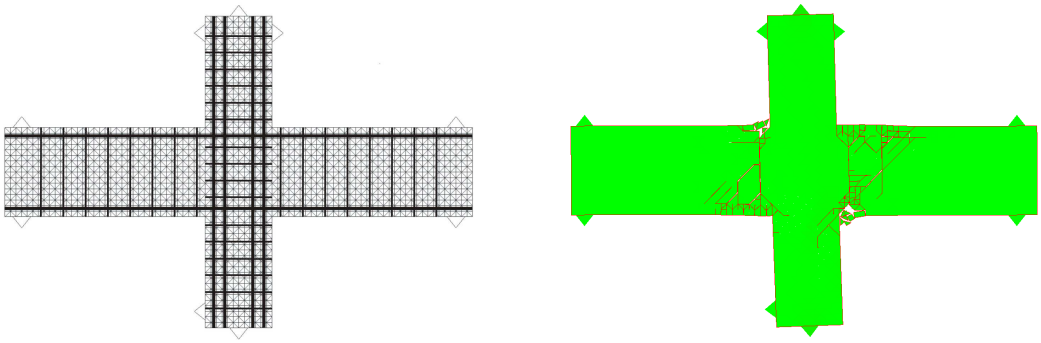
Figure 12: Geometry of interior RC beam-column joint.

Concrete		Steel	
E_c (MPa)	29730	E_s (MPa)	210 000
ν	0.2	f_y (MPa)	400
f_t (MPa)	3.15	f_u (MPa)	500
f_c (MPa)	30.0	A_{s1} (m^2)	0.000452
G_f (N/m)	100	A_{s2} (m^2)	0.001357

Table 4: Material characteristics.

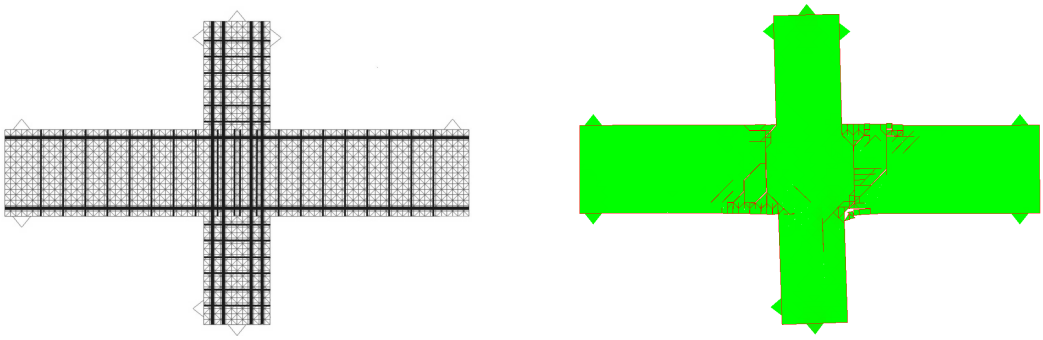
Interior RC beam-column joint is reinforced in three different ways and subjected to monotonically increasing horizontal load and constant vertical force V=700 kN. Initiation and propagation of the cracks in the interior RC beam-column and the ratio of horizontal displacement at the moment of collapse u_{Hc} and horizontal displacements at the moment when initial crack u_{Hi} appears for different reinforcement type were analyzed.

Failure patterns at the collapse point for three different types of reinforcing are shown in figures 13, 14 and 15.



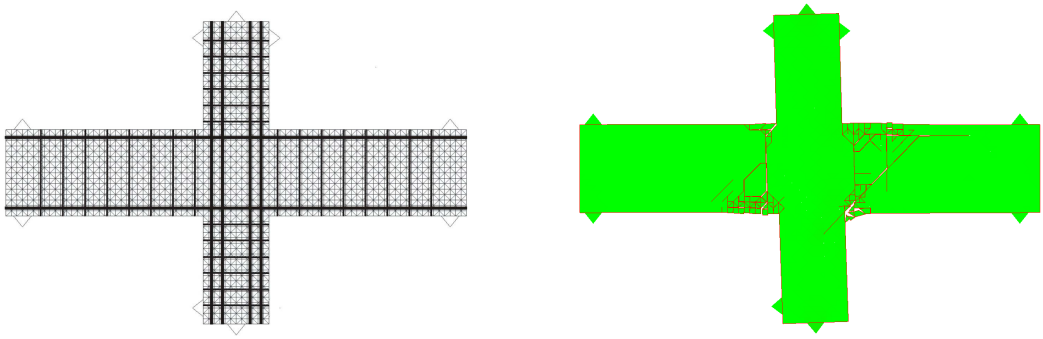
(a) (b)

Figure 13: Interior beam-column joint reinforced with horizontal stirrups: (a) discretization, (b) failure patterns for H=216.8 kN.



(a) (b)

Figure 14: Interior beam-column joint reinforced with vertical stirrups: (a) discretization, (b) failure patterns for H=215.13 kN.



(a) (h)

Figure 15: Interior beam-column joint without stirrups: (a) discretization, (b) failure patterns for H=216.4 kN.

Figure 16 shows horizontal load-displacement relation for three different types of reinforcing.

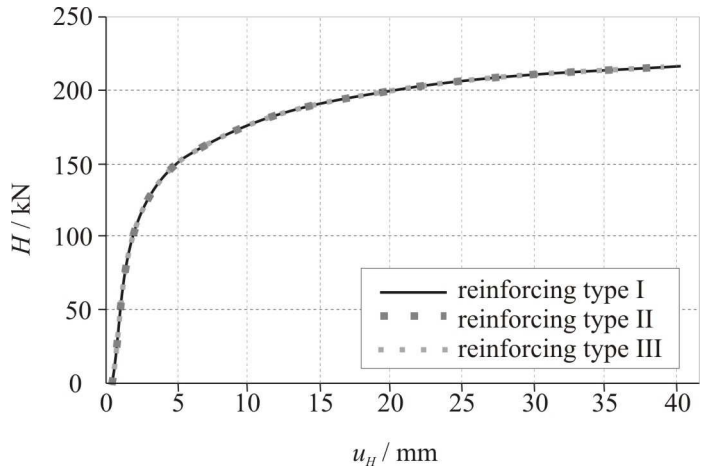


Figure 16: Horizontal load – displacement relation

The ratio of horizontal displacement at the moment of collapse u_{hc} and horizontal displacement at the moment when initial crack appears u_{Hi} for different reinforcement type are shown in Table 5.

Reinforcing type	u_{Hc} / u_{Hi}
I	42.10
II	39.94
III	41.10

Table 5: Ratio u_{Hc} / u_{Hi} for each reinforcing type.

It can be seen that the capacity for all three types of reinforcement is equal. The highest difference in capacity between these cases is 1.0% and the cracks propagated through the beam which is convenient to the structure.

Interior RC beam-column joint, shown in Figure 12, is reinforced in three different ways (Figures 13,14,15) and subjected to constant vertical force V=700 kN and cyclic horizontal load (Figure 17).

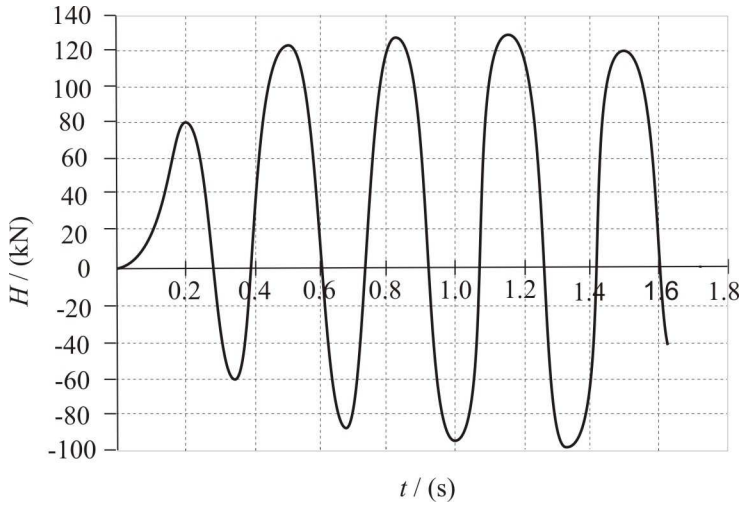
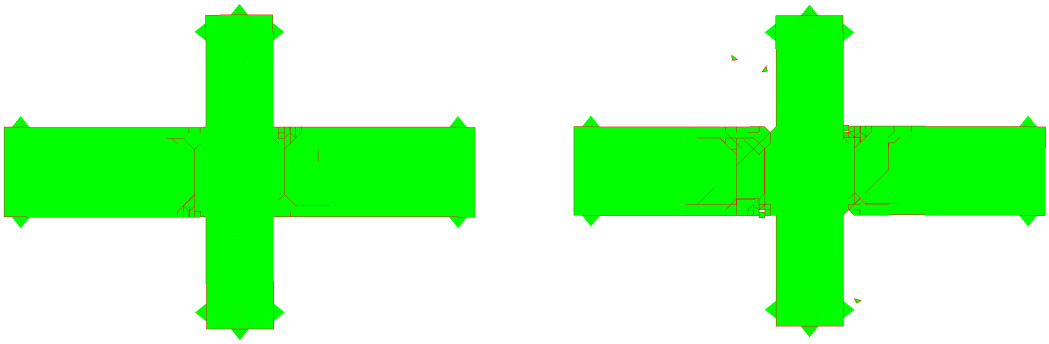


Figure 17: History load for interior beam-column joint.

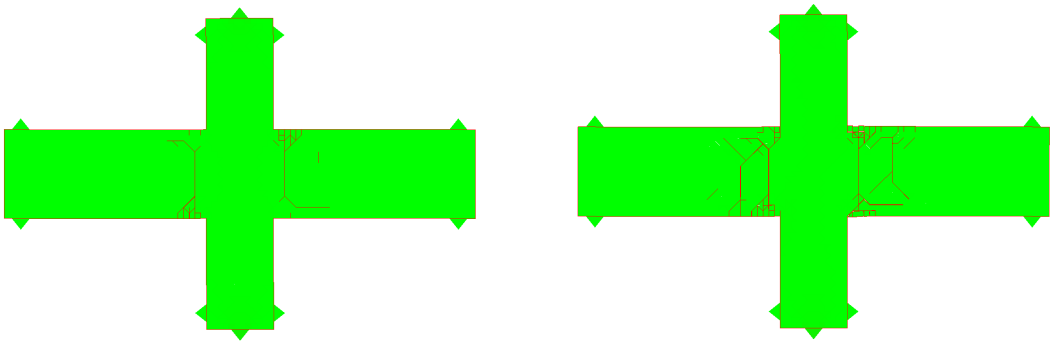
Initiation and propagation of the cracks in the interior RC beam-column and the ratio of the horizontal displacement at the collapse point u_{hc} and horizontal displacements at the moment when the initial crack appears u_{Hi} for different reinforcement types were analyzed.

Failure patterns for three type of reinforcing are shown in figures 18, 19 and 20.



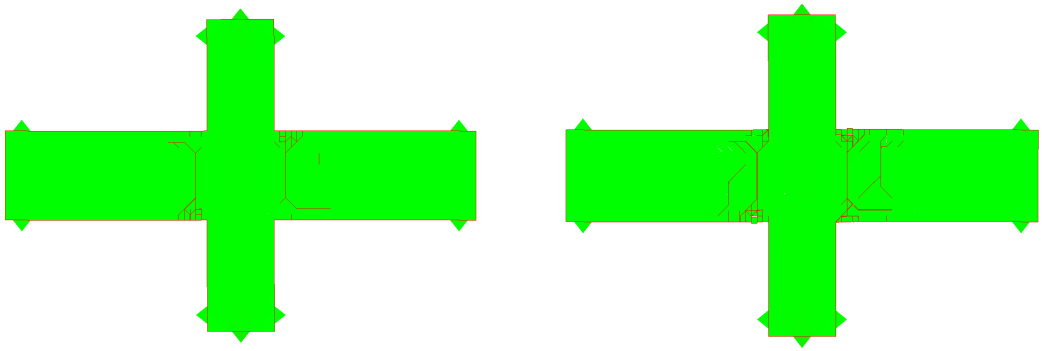
(a) (b)

Figure 18: Failure patterns for interior beam-column joint reinforced with horizontal stirrups: (a) t=1.083s, (b) t=1.61s.



(a) (b)

Figure 19: Failure patterns for interior beam-column joint reinforced with vertical stirrups: (a) t=1.083s, (b) t=1.61s.



(a) (b)

Figure 20: Failure patterns for interior beam-column joint without stirrups: (a) t =1.083s, (b) t =1.61s.

Figure 21 shows cyclic horizontal load-displacement relation for three different types of reinforcing. Very similar behaviour is achieved for all three types of reinforcing, as it is shown in figure 21.

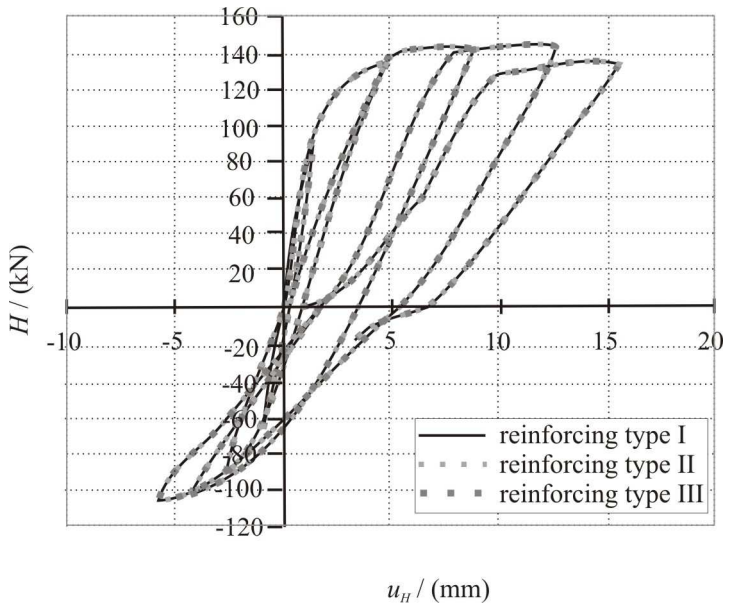


Figure 21: Horizontal load - displacement relation.

The ratio of the horizontal displacement u_{Hc} at the collapse point and horizontal displacement u_{Hi} at the moment when initial crack appears for different reinforcement type is shown in Table 6.

Reinforcing type	u_{Hc} / u_{Hi}
I	17.37
II	17.39
III	17.40

Table 6: Ratio u_{Hc} / u_{Hi} for each reinforcing type.

It can be seen that the highest degree of damage is achieved for the reinforcing type I, although load-displacement relation for all three types of reinforcing shows very similar behaviour. So it can be concluded that the influence of reinforcement is dominant in all cases.

4 CONCLUSIONS

- This paper presents the application of numerical model for reinforced concrete structures based on combined finite discrete element method in monotonic and cyclic loading of reinforced beam-column joints.
- The developed numerical model is based on embedded model of reinforcing bars, an approximation of the experimental curves for behaviour of the concrete and steel in crack and the interaction between the reinforcement and concrete which was taken into consideration by steel strain-slip relation. Cracking of the structure is enabled by discrete model of cracks where the cyclic behaviour of concrete and steel was implemented.
- RC beam-column joint is reinforced in three different ways: with the horizontal and vertical stirrups and without the stirrups. The analysis of exterior beam-column joint shows

larger bearing capacity for the reinforcing with vertical stirrups in joint. In interior beam-column joint almost identical load-displacement curve for all three types of reinforcing are obtained. The highest degree of damage is achieved for reinforcing with horizontal stirrups.

5 REFERENCES

[1] A. Munjiza, *The combined finite-discrete element method*, John Wiley & Sons, 2004.

[2] A. Munjiza, D.R.J. Owen, N. Bicanic, A combined finite-discrete element method in transient dynamics of fracturing solids. *Engineering Computations*, 12, 145-174, 1995.

[3] A. Munjiza, K.R.F. Andrews and J.K. White, Combined single and smeared crack model in combined finite-discrete element method. *Int. J. for Numerical Methods in Engineering*, 44, 41-57, 1999.

[4] N. Živaljić; Ž. Nikolić, A.Munjiza, A Combined Finite Discrete Element Model for Reinforced Concrete under Seismic Load. E. Onate, R. Owen, Đ. Perić, B. Suarez eds. COMPLAS XI, Barcelona, 2011.

[5] Ž. Nikolić and A. Mihanović, Non-linear finite element analysis of post-tensioned concrete structures, *Engineering Computations*, 14, 509-528, 1997.

[6] N. Živaljić, H. Smoljanović, Ž. Nikolić, A combined finite-discrete element model for RC structures under dynamic loading. *Engineering computations 2013* (accepted for publication).

[7] H. Shin, K. Maekawa, H. Okamura, Analytical approach of RC members subjected to reversed cyclic in plane loading. *Proceeding of JCI Colloquium on Ductility of Concrete Structures and its Evaluation*, 245-256, 1988.

[8] B. Kato, Mechanical properties of steel under load cycles idealizing seismic action. *Bulletin D'Information, AICAP-CEB symposium*, Rome, 131, 7-27, 1979.

[9] D.A. Hordijk, Tensile and tensile fatigue behaviour of concrete – experiments, modelling and analyses. *Heron*, 37, 3-79, 1992.

[10] H. Shima, L. Chou and H. Okamura, Micro and macro model for bond behaviour in RC, *Journal of the Faculty of Engineering*, The University of Tokyo, 39, 133-94, 1987.

[11] N. Živaljić, Finite-discrete element method for 2D seismic analysis of reinforced concrete structures, PhD thesis, University of Split, Croatia, 2012.

COMPDYN 2013
4th ECCOMAS Thematic Conference on
Computational Methods in Structural Dynamics and Earthquake Engineering
M. Papadrakakis, V. Papadopoulos, V. Plevris (eds.)
Kos Island, Greece, 12–14 June 2013

DYNAMICS OF MARINE STATIONARY PLATFORM UNDER ACTION OF HORIZONTAL SEISMIC LOADING

Alexey V.Shekhovtsov[1], Vyacheslav A.Shekhovtsov[1], Petr E.Tovstik[2] and Tatiana M.Tovstik [2]

[1]St.Perersburg Architecture Academy, Russia
address
e-mail: a.sheh-411@yandex.ru

[2] St.Perersburg State University, Russia
address
e-mail: peter.tovstik@mail.ru

Keywords: earthquake, horizontal seismic loading, marine stationary platform, deterministic and random motion, strength of piles

Abstract. *Dynamics of a fixed sea-based offshore platform under action of the horizontal seismic loading is investigated. The structure consists of a tube-like ferroconcrete rod, of an upper platform, and of a pile foundation. To describe the structure motion the beam-like model is used. Some deterministic and random models of the seismic loading are proposed. The depth of water is of the order 250 meters, the attached mass of water and its resistance is taken into account, the surface waves influence on the motion is not studied. The system of partial differential equation is reduced to the system with 3 degrees of freedom. The main attention is paid to the piles deformations and to their strength. Some numerical examples are studied.*

1 INTRODUCTION

Dynamics of a marine stationary platform under action of the horizontal seismic loading is investigated. The structure consists of a tube-like ferroconcrete rod. At its upper end the platform is attached. The similar structure is proposed in [1], where the foundation is modeled as a rigid body. Here a pile foundation is used to attach the rod with the ground. The depth of water is of the order 250 meters, the attached mass of water and its resistance is taken into account. Only the seismic loading is included at design in assumption, the surface gravity waves, the wind acting on the basic platform, the current, the ice loading, is not studied. The seismic loading is investigated also in [2], [3] but in this paper the more detailed analysis of foundation is proposed. The foundation stiffness is found as a result of the piles deformations. In contrast to [2], [3], where the concrete failure is assumed as the main reason of the structure destruction, here the strength of the entire structure is connected with the strength of piles. The deterministic and random models of seismic acceleration are used. Some numerical examples are studied.

2 MATHEMATICAL MODEL OF STRUCTURE

The structure consists of a tube-like iron-concrete rod *1* (see Fig. 1). At the upper end of rod a basis platform *2* is attached. A pile foundation *3* is used to attach the rod with the ground.

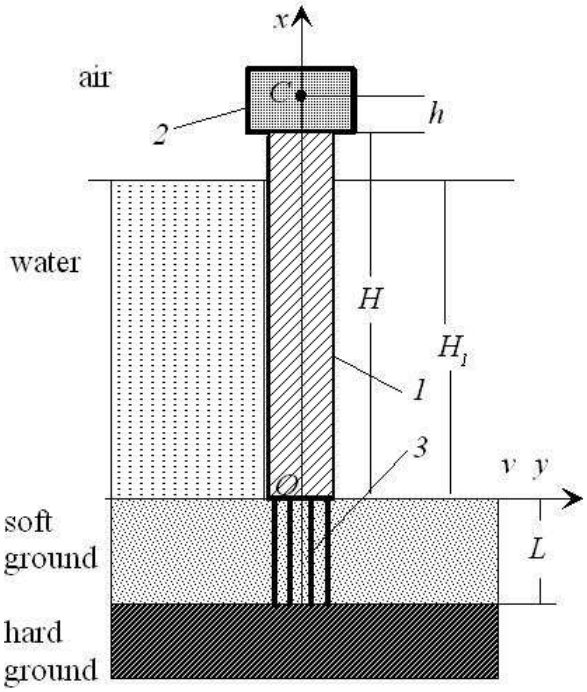


Fig. 1. The sketch of structure.

It is assumed that in limits of the foundation the ground acceleration does not depend on the space co-ordinates. The movable co-ordinate system, which moves with the given seismic acceleration $a(t)$ is accepted. To describe the rod bending a simple linear beam-like model is used

$$J\frac{\partial^4 v}{\partial x^4} + \frac{\partial}{\partial x}\left(P(x)\frac{\partial v}{\partial x}\right) + \rho(x)\left(\frac{\partial^2 v}{\partial t^2} + a\right) = f_v, \tag{1}$$

Here x $(0 \le x \le H)$ is the vertical coordinate; $v(x,t)$ is the horizontal deflection of the beam

axis, t is the time; J is the bending beam stiffness; $P(x) = P_0 + \rho_0(H - x)g$ is the axial compression, $P_0 = m_0 g$; $g = 9.81$ is the gravity acceleration, m_0 is the mass of the basic platform, ρ_0 is the beam mass density per unit length; $\rho(x) = \rho_0 + \rho_1(x)$ is the mass density with the attached mass of water,

$$\rho_1 = \pi R^2 \gamma_w g, \quad 0 \le x \le H_1; \quad \rho_1 = 0, \quad H_1 < x \le H, \tag{2}$$

R is the beam radius, γ_w is the water mass density, dimensions H and H_1 are shown in Fig. 1; f_v is the resistance of water proportional to the square of relative water velocity V,

$$f_v = -C_v \gamma_w R V|V|, \quad V = \frac{\partial v}{\partial t} + V_0, \quad V_0(t) = \int_0^t a(t)\,dt, \tag{3}$$

C_v is the resistance coefficient.

The boundary conditions at the upper end $x = H$ of the beam are the transversal and rotational motions of the basic platform which is studied as a rigid body with the mass m_0 and the central inertia moment J_0,

$$m_0\left(\frac{\partial^2 v_c}{\partial t^2} + a\right) = J\frac{\partial^2 \varphi_H}{\partial x^2} + P_0\varphi_H, \quad J_0\frac{\partial^2 \varphi_H}{\partial t^2} + m_0 h\left(\frac{\partial^2 v_c}{\partial t^2} + a\right) = -J\frac{\partial \varphi_H}{\partial x} + P_0 h\varphi_H, \tag{4}$$

where φ_H is the angle of axis inclination at $x = H$, and v_c is the horizontal deflection of the gravity center C (Fig. 1),

$$\varphi_H = \frac{\partial v_H}{\partial x}, \qquad v_c = v_H + h\varphi_H, \qquad v_H = v(H, t). \tag{5}$$

To formulate the boundary conditions at the lower end $x = 0$ we assume that the shear stress-resultant Q_0 and bending moment M_0, appearing at the contact of the beam with the pile foundation, are proportional to the lateral deflection v_0 and to the angle φ_0,

$$Q_0 = -J\frac{\partial^2 \varphi_0}{\partial x^2} - P(0)\varphi = c_{11}v_0 + c_{12}\varphi_0 = 0, \qquad M_0 = J\frac{\partial \varphi_0}{\partial x} = c_{12}v_0 + c_{22}\varphi_0 = 0. \tag{6}$$

The coefficients c_{ij} are to be found after examining the pile deformations.

3 THE BEAM STIFFNESS AND THE PILE DEFORMATIONS

The cross-section of the three layered ferroconcrete beam is shown in Fig. 2a (the steel layers are black and the concrete layers are spotted). The external radii of steel tubes are R and R_1 ($R_1 < R$), and the tube thicknesses are d and d_1. Between steel tubes there is a concrete layer ($R_1 \le r \le R - d$), containing N small steel tubes (in Fig. 2a $N = 8$), the polar co-ordinates r_k, θ_k of their centers are

$$r_k = R_0 = (R - d + R_1)/2, \quad \theta_k = \theta_0 + 2k\pi/N, \quad k = 1, 2, ..., N. \tag{7}$$

The radii and the thicknesses of these tubes are R_2 and d_2.

To calculate the beam bending stiffness J we accept the plane cross-section hypothesis [4] and take into account only the extension of material in the x direction. Then in linear approximation the stiffness J is

$$J = E_s \int\int_{S_s} y^2\,dS + E_c \int\int_{S_c} y^2\,dS,$$

where E_s and E_c are the elastic modules of steel and concrete, and S_s and S_c are the corresponding parts of cross-section occupied by steel and concrete. Calculations give

$$\begin{aligned} J = \ & \frac{\pi E_s}{4}\left(R^4-(R-d)^4+R_1^4-(R_1-d_1)^4\right)+\frac{\pi E_c}{4}\left((R-d)^4-R_1^4\right)+ \\ & \frac{N\pi R_0^2}{2}\left((E_s-E_c)R_2^2-E_s(R_2-d_2)^2\right)+\frac{N\pi}{4}\left((E_s-E_c)R_2^4-E_s(R_2-d_2)^4\right). \end{aligned} \tag{8}$$

The stiffness J does not depend on the angle θ_0 (see (7)).

For this cross-section the mass density ρ_0 is equal

$$\begin{aligned} \rho_0 = \ & \pi\gamma_s\left(R^2-(R-d)^2+R_1^2-(R_1-d_1)^2+N(R_2^2-(R_2-d_2)^2)\right)+ \\ & \pi\gamma_c\left((R-d)^2-R_1^2-NR_2^2\right), \end{aligned} \tag{9}$$

where γ_s and γ_c are the volume densities of steel and concrete.

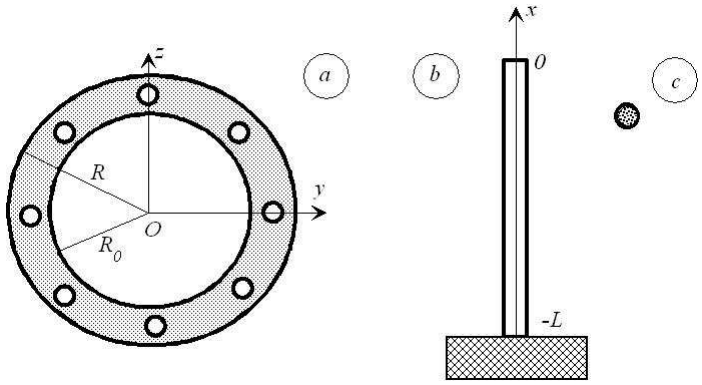


Fig. 2. (a) The cross-section of beam, (b) the pile, (c) the cross-section of pile.

For numerical calculations we take the following parameters given in SI. The dimensions of structure and radii of the tubes (see Fig. 2): $H_1 = 235$, $H = 250$, $R = 6$, $R_1 = 4.95$, $d = d_1 = 0.05$, $R_0 = 5.45$, $R_2 = 0.27$, $d_2 = 0.02$. The densities of water, steel, and concrete: $\gamma_w = 10^3$, $\gamma_s = 7.85 \cdot 10^3$, $\gamma_c = 2.2 \cdot 10^3$. The Young modules of steel and concrete: $E_s = 2.06 \cdot 10^{11}$, $E_c = 0.131E_s$. The parameters of body 2 (see Fig. 1): $h = 3$, $m_0 = 10^7$, $J_0 = 10^8$.

Then by using relations (8) and (9) for $N = 12$ we find $\rho_0 = 10^5$, $J = 1.1 \cdot 10^{13}$.

To find the coefficients c_{ij} in (6) it is necessary to study the piles deformations. The pile foundation is investigated in [5],[6],[7]. We use the simplest linear model in which the inertia of piles and their weight is neglected.

We assume that the pile deformations satisfy to the static boundary value problem

$$\begin{aligned} & J_p\frac{d^4v}{dx^4}+P_1\frac{d^2v}{dx^2}+k(x)v=0, \quad -L\le x\le 0, \\ & v(0)=v_0, \quad \left.\frac{dv}{dx}\right|_{x=0}=\varphi_0; \qquad v(-L)=\left.\frac{dv}{dx}\right|_{x=-L}=0, \end{aligned} \tag{10}$$

where L is the depth of the soft ground, J_p is the pile bending stiffness (see Fig. 2c),

$$J_p=\frac{\pi E_s}{4}\left(R_3^4-(R_3-d_3)^4\right)+\frac{\pi E_c}{4}(R_3-d_3)^4, \tag{11}$$

R_3 and d_3 are the radius of pile and its thickness; $P_1 = (P_0 + \rho_0 Hg)/N$ is the compressing force (we suppose that the force P_1 does not change during the studied time), $k(x)$ is the coefficient describing the lateral ground reaction. We accept that this coefficient linearly depends on x,

$$k(x) = -2R_3 c_g x > 0, \qquad 0.5 \cdot 10^6 \le c_g \le 10^7, \tag{12}$$

where c_g is the coefficient depending on the ground.

To find the numerical solution of the problem (10) we accept the following data: $L = 30$, $R_3 = 0.25$, $d_3 = 0.02$. Then for $N = 12$ we find $J_p = 2.386 \cdot 10^8$, $P_1 = 2.86 \cdot 10^7$, and solve the problem (10) for three values $c_g = 5 \cdot 10^5,\ 2 \cdot 10^6,\ 10^7$.

To formulate the boundary conditions (6) we seek dependence of the stress-resultant Q_p and stress couple M_p at $x = 0$ in the form

$$Q_p = b_{11} v_0 + b_{12} \varphi_0, \quad M_p = b_{12} v_0 + b_{22} \varphi_0. \tag{13}$$

After solution of the problem (10) we find coefficients b_{ij} for three given values of the ground stiffness coefficients c_g.

Table 1. Stiffness coefficients of pile.

c_g	b_{11}	b_{12}	b_{22}
$5 \cdot 10^5$	$0.555 \cdot 10^7$	$-2.004 \cdot 10^7$	$0.960 \cdot 10^8$
$2 \cdot 10^6$	$1.354 \cdot 10^7$	$-3.503 \cdot 10^7$	$1.319 \cdot 10^8$
10^7	$3.690 \cdot 10^7$	$-6.685 \cdot 10^7$	$1.852 \cdot 10^8$

The stretching pile density b_p is equal

$$b_p = \left(\pi E_s (R_3^2 - (R_3 - d_3)^2) + \pi E_c (R_3 - d_3)^2\right)/L, \tag{14}$$

and for the given parameters $h_p = 3.566 \cdot 10^8$.

Now we find the stiffness coefficients c_{ij} for the entire foundation with N piles,

$$c_{11} = N b_{11}, \quad c_{12} = N b_{12}, \quad c_{22} = N b_{22} + \frac{N}{2} R_0^2 b_p. \tag{15}$$

4 THE NATURAL FREQUENCIES AND MODES OF FREE VIBRATIONS

We seek the approximate solution of the boundary value problems (1), (4) and (6) as a partial sum of series of natural modes with the unknown coefficients $q_k(t)$ depending on time

$$v(x,t) = \sum_{k=1}^{K} V_k(x) q_k(t). \tag{16}$$

The natural modes may be found as a solution of the boundary value problem,

$$\begin{aligned}
&J\frac{d^4 V_k}{dx^4} + \frac{d}{dx}\left(P(x)\frac{dV_k}{dx}\right) - \omega_k^2 \rho(x) V_k = 0, && 0 \le x \le H,\\
&Q_k + c_{11} V_k + c_{12}\varphi_k = 0, \qquad -M_k + c_{12} V_k + c_{22}\varphi_k = 0, && x = 0,\\
&Q_k + m_0 \omega_k^2 V_{ck} = 0, \quad -M_k + \omega_k^2 (J_0 \varphi_k + m_0 h V_{ck}) + P h \varphi_k = 0, && x = H,
\end{aligned} \tag{17}$$

where

$$\varphi_k = \frac{dV_k}{dx}, \quad V_{ck} = V_k + h\varphi_k, \quad M_k = J\frac{d\varphi_k}{dx}, \quad Q_k = \frac{dM_k}{dx} + P\varphi_k. \tag{18}$$

Here V_{ck} is the horizontal deflection of the mass center C of the body 2 (see Fig. 1).

The eigen functions $V_k(x)$ satisfy to the orthogonality condition ($\omega_k \ne \omega_n$),

$$\int_0^H \rho(x) V_k(x) V_n(x) dx + \left(m_0 V_{ck} V_{cn} + J_0 \varphi_k \varphi_n\right)_{x=H} = 0. \tag{19}$$

5 THE APPROXIMATE SOLUTION

The single non-linear term in the equation (1) is the water resistance f_v. We delete it and introduce the linear resistance including the water resistance and the resistance in the beam and in the ground [8].

To deliver equations for the unknown functions $q_k(t)$ in (16) we multiply equation (1) by $V_k(x)$ and integrate the result in the limits $0 \le x \le H$. Then by using the condition (17) we get the equations,

$$\frac{d^2q_k}{dt^2} + \omega_k^2\left(\frac{\eta_k}{\omega}\frac{dq_k}{dt} + q_k\right) + \frac{f_k}{m_k}a(t) = 0, \quad k = 1, 2, , \ldots, K, \tag{20}$$

where

$$\begin{aligned} f_k &= \int_0^H \rho(x)V_k(x)dx + \left(m_0V_{ck} + J_0\frac{dV_k}{dx}\right)_{x=H}, \\ m_k &= \int_0^H \rho(x)V_k^2(x)dx + \left(m_0V_{ck}^2 + J_0\varphi_k^2\right)_{x=H}, \end{aligned} \tag{21}$$

and η_k is the dimensionless resistance coefficient (we take $\eta_k = 0.1$), ω is the typical frequency. The term with η_k is included in (20) formally to take the damping into account.

Therefore to solve equations (19) it is necessary to find the natural frequencies ω_k and parameters f_k and m_k by solving the problem (17). We nornalize the eigen functions $V_k(x)$ by condition $m_k = 1$. Then only parameter f_k which characterize the level of excitation of the k-th mode remains.

For three values c_g and for the given parameters of platform from system (17) three first natural frequencies ω_k are found. These frequencies and the corresponding values $V_(ck)$ and Δw_k are given in Table 2. Here $\Delta w_k = R_* f_k \varphi_k(0)$, (with $R_* = 5.7$) is the measure of the pile extension corresponding to k-th vibration mode.

Table 2. Parameters of the vibration modes.

c_g	k	ω_k	V_{ck}	Δw_k
$5 \cdot 10^5$	1	1.233	-0.000370	0.0162
	2	3.205	-0.000545	0.00465
	3	6.678	-0.000705	0.000697
$2 \cdot 10^6$	1	1.362	-0.000388	0.0142
	2	3.906	-0.000585	0.00294
	3	7.347	-0.000730	0.000501
10^7	1	1.429	-0.000401	0.0123
	2	4.489	-0.000614	0.00201
	3	8.675	-0.000776	0.000871

As it is seen from Table 2 the values Δw_k quickly decrease with the number k of the vibration mode. The ground stiffness c_g effect on the parameters ω_k, V_{ck}, and Δw_k not very essentially, and we will study later only the intermediate case $c_g = 2 \cdot 10^6$.

6 MODEL OF THE SEISMIC GROUND ACCELERATION

As in [2], [3] we take the test horizontal ground acceleration in the form

$$a(t) = At^2e^{-\alpha t}\,\sin(\alpha t + \theta). \tag{22}$$

The parameters in (22) satisfy to a restriction, which follows from the equality

$$\int_0^\infty a(t)dt = 0, \tag{23}$$

because in the opposite case the ground will move when the seismic impulse is finished. From (23) it follows that

$$\alpha(3\nu^2 - \alpha^2)\sin\theta + \nu(\nu^2 - 3\alpha^2)\cos\theta = 0. \tag{24}$$

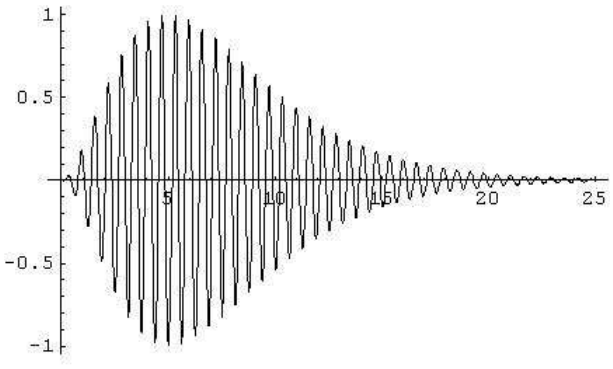


Fig. 3. The seismic impulse.

In Fig. 3 the seismic impulse with parameters $A = 0.295$, $\alpha = 0.4$, $\nu = 10$ is shown, and value θ is found from relation (24). For this impulse $\max_t\{a(t)\} = 1$.

We change impulse (22) by the following

$$a(t) = \tau^2 e^{2(1-\tau)}\sin(\nu t + \theta), \quad \tau = t/T; \quad \tan\theta = \frac{\alpha(3\nu^2 - \alpha^2)}{\nu(3\alpha^2 - \nu^2)}, \quad \alpha = \frac{2}{T}. \tag{25}$$

For impulse (25) $\max_\tau\{\tau^2 e^{2(1-\tau)}\} = 1$ at $\tau = 1$. Therefore, two parameters remain: the time T of amplitude growth, and the typical frequency, ν.

7 Numerical results. Discussion

We solve numerically equations (20) for $k = 1, 2, 3$, $c_g = 2 \cdot 10^6$ and for the various values T and ν, and find solution (16). The results are presented for the maximal ground acceleration $1\,m/c^2$. The problem is linear, and the results for the other acceleration levels may be obtaining by multiplying.

It occurs that the horizontal displacements of the upper body are less than $3 \cdot 10^{-5}\,m$, and details are not given here.

We analyze the strength of piles and find its maximal vertical displacements by relation

$$W = \max_t \left| \sum_{k=1}^{3} \Delta w_k q_k(t) \right|, \tag{26}$$

where Δw_k are given in Table 2, and $q_k(t)$ are the solutions of equations (16) with $f_k = m_k = 1$ and with the initial conditions $q(0) = dq(0)/dt = 0$.

The maximal vertical strains ε of piles are

$$\varepsilon = \frac{\Delta w}{L}. \tag{27}$$

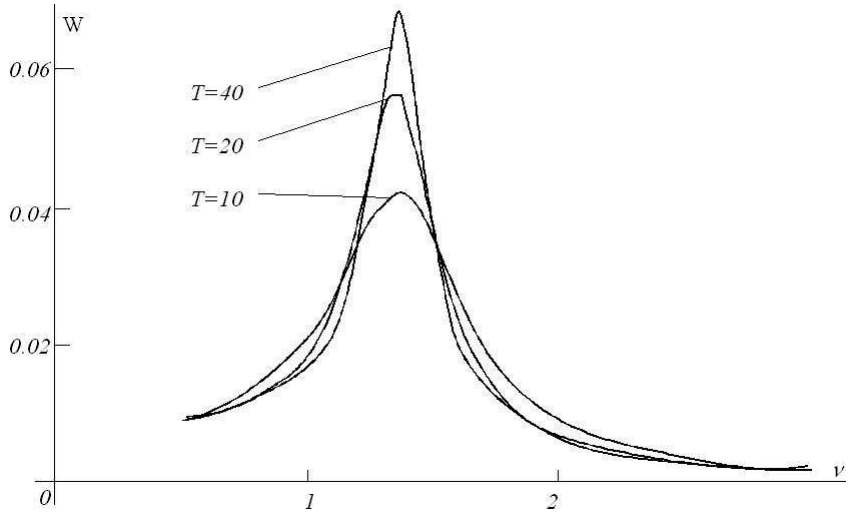


Fig. 4. The piles extension W.

The value ε is to be compared with the limiting values $\varepsilon_s = 0.00134$ and $\varepsilon_c = 1.16\varepsilon_s$ for a steel and a concrete respectively.

In Fig. 4 for three values $T = 10$, $T = 20$, and $T = 40$ dependences $W(\nu)$, $0.5 \le \nu \le 3$, are presented. It is seen the maximal value $W_* = \max_\nu\{W(\nu)\}$, is achieved at the first resonance $\nu \simeq \omega_1 = 1.362$. For example, for $T = 20$ the critical value A_* of the maximal seismic acceleration is

$$A_* = \frac{L\varepsilon_s}{W_*} = 0.7\,(m/c^2). \tag{28}$$

At the second resonance $\omega_2 = 3.906$ the value $\Delta w(\omega_2)$ is ten times smaller than W_*. The value Δw_* grows with T, and the limit,

$$\lim_{T\to\infty}\{W_*\} = \frac{\Delta w_1}{\eta\omega_1^2} = 0.0765, \tag{29}$$

what corresponds to the forced vibrations of system with one degree of freedom under the periodic excitation $\sin(\nu t)$. Indeed, for the system with one degree of freedom at $T \to \infty$ the maximal amplitude $W(\nu)$ is equal

$$W(\nu) = \frac{\Delta w_1}{\sqrt{(\omega_1^2 - \nu^2)^2 + \eta^2\nu^2\omega_1^2}} \tag{30}$$

and for $\nu = \omega_1$ we get relation (29).

8 Remark about the random seismic impulses

Methods of mechanical systems analysis under random excitation are described in [9], [10]. Random processes for earthquake simulation are described in [11]. Analysis of the structure shown in Fig. 1 under action of the random surface waves excitation is contained in [12], [13], [14].

The test seismic impulse (22) may give the upper estimation for the pile extension W because the resonance effect appears for the large T. It is interesting to compare the results of excitation (22) with the random excitation. In the exact statement the seismic acceleration may be studies as a non-stationary random process acting during the finite time $0 \le t \le T_0$. For simplicity we

assume that the seismic excitation is a random stationary process time with the given spectral density $S_a(\omega)$ acting during the infinite time. Then the motion of structure also will be a random stationary process.

To find approximately the spectral density $S_W(\omega)$ of the pile extension W we study the system (20) with one degree of freedom,

$$\frac{d^2W}{dt^2} + \eta\omega_1\frac{dW}{dt} + \omega_1^2 W + \Delta w_1 a(t) = 0, \tag{31}$$

with $\omega_1 = 1.362,\ \Delta w_1 = 0.0142$. Then [9], [10]

$$S_W(\omega) = \frac{(\Delta w_1)^2 S_a(\omega)}{(\omega^2 - \omega_1^2)^2 + \eta^2\omega_1^2\omega^2}. \tag{32}$$

To compare with the previous results we normalize the process $a(t)$ so that its dispersion,

$$D(a) = \int_{-\infty}^{\infty} S_a(\omega)\, d\omega = \frac{1}{2}, \tag{33}$$

because the average value of function $\sin^2(\omega t)$ is equal to 1/2. Here $D(z)$ is the dispersion of the process $z(t)$,

As a test spectral density $S_a(\omega)$ we take

$$S_a(\omega) = \frac{\eta_0\nu^3}{2\pi((\omega^2 - \nu^2)^2 + \eta_0^2\nu^2\omega^2)}. \tag{34}$$

Relation (34) satisfy to equality (32). Parameter ν is the typical frequency of excitation, and parameter η_0 describes the sharpness of curve. In Fig. 5 the curves $S_a(\omega)$ are shown for $\nu = 1$ and for two values of η_0.

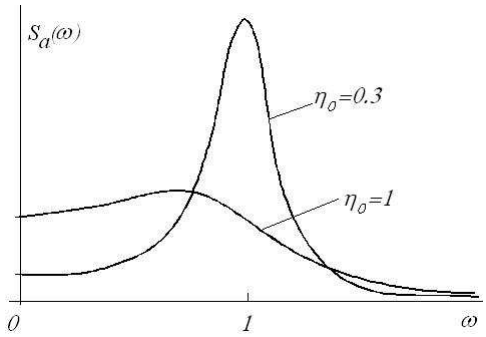


Fig. 5. The spectral density .

Function $S_a(\omega)$ is convenient to calculate the dispersion of the process W,

$$D(W) = \int_{-\infty}^{\infty} \frac{(\Delta w_1)^2\eta_0\nu^3\, d\omega}{\pi((\omega^2 - \omega_1^2)^2 + \eta^2\omega_1^2\omega^2)((\omega^2 - \nu^2)^2 + \eta_0^2\nu^2\omega^2)}. \tag{35}$$

After calculations we get

$$D(W) = \frac{(\Delta w_1)^2(\eta\omega_1^3 + \eta\eta_0\omega_1\nu(\eta\omega_1 + \eta_0\nu) + \eta_0\nu^3)}{2\eta\omega_1^3((\omega_1^2 - \nu^2)^2 + \eta\eta_0\omega_1\nu(\omega_1^2 + \nu^2) + (\eta^2 + \eta_0^2)\omega_1^2\nu^2)}. \tag{36}$$

The measure of the vibration amplitude is a root-mean-square σ_W,

$$\sigma_W = \sqrt{D(W)}. \tag{37}$$

Consider some partial cases. At $\eta_0 \to 0$ the frequencies ω are concentrated near ν (see Fig. 5), and relation (37) gives

$$\sigma_W(\nu) = \frac{\Delta w_1}{\sqrt{2}\sqrt{(\omega_1^2 - \nu^2)^2 + \eta^2\nu^2\omega_1^2}}. \tag{38}$$

This relation almost coincides with relation (30). Factor $\sqrt{2}$ marks a natural difference between a root-mean-square and an amplitude.

For $\omega_1 = \nu$ we obtain the simple relation

$$\sigma_W(\omega_1) = \frac{\Delta w_1}{\omega_1^2}\sqrt{\frac{1 + \eta\eta_0}{2\eta(\eta + \eta_0)}}. \tag{39}$$

To estimate the dependence $\sigma_W(\nu)$ on η_0 we compare the cases $\eta_0 = 0$ and $\eta_0 = 1$. The results are shown in Fig. 6.

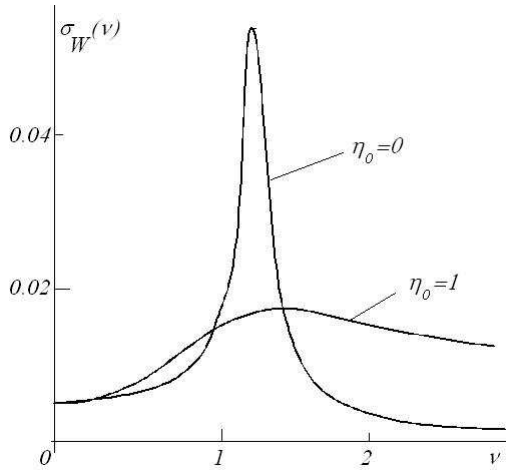


Fig. 6. The root-mean-square $\sigma_W(\nu)$ for $\eta_0 = 0$ and $\eta_0 = 1$.

It is seen in Fig. 6 that in the case $\eta_0 = 1$ the maximal amplitude is essentially smaller than for $\eta_0 = 0$.

9 CONCLUSIONS

Dynamics of a fixed sea-based offshore platform under action of horizontal seismic loading is studied. The main attention is paid to the strength of piles. The approximation with three degrees of freedom is used, but it occurs that only the first vibration mode is essential. Two test models for the ground acceleration are proposed. At the first of them the acceleration is presented as a function (Fig. 3) which allows to analyze the resonance effect. At the second model the seismic excitation is studied as a stationary random process. The presented results allow us to predict the possible behavior of structure under seismic loading

Acknowledgements

The paper is written with the financial support of Russian Foundation of Basic Researches, grants 12.01.92000.HHC-a, and 10-01.00244a.

REFERENCES

[1] V.A.Shekhovtsov. *Random nonlinear vibrations of the marine stationary platform*. St.Petersburg. 2004. 246 p. (in Russian)

[2] P.E.Tovstik, T.M.Tovstik, V.A.Shekhovtsov. *Dynamics of marine stationary platform under action of seismic loading.* III ECCOMAS Thematic Conference on Computational Methods in Structural Dynamics and Earthquake Engineering Corfu.Greece. 2011.

[3] P.E.Tovstik, T.M.Tovstik, V.A.Shekhovtsov. *Dynamics of marine stationary platform under action of seismic loading.* 39 Summer School-Conf. "Advanced Problems in Mechanics". St.Petersburg. 2011. pp. 492-501.

[4] S.P. Timoshenko, *Strength of materials*. Van Vistrand. New York. 1956.

[5] G.G.Boldyrev, M.V.Malyshev. *Mechanics of grounds. Bases and foundations*. Penza. 2009. (in Russian)

[6] *Design of hile foundations in liqueflable soils*. Imperial colledge press.

[7] A.N.Birbraer. *Design of structures at seismic-stability*. St.Petersburg. Nauka. 1998. 255 p. (in Russian)

[8] E.S.Sorokin. *To the theory of internal friction at vibrations of elastic systems*. Gosstroiizdat. Moscow. 1960. (in Russian)

[9] V.S.Pugachev. *Theory of random functions*. Moscow. Fizmatgiz. 1960. 884 p. (in Russian)

[10] Y.K.Lin. *Probabilic theory of structural dynamics*. McGraw-Hill. 1967.

[11] T.Hsu, M.C.Bernard. *A random process for earthquake simulation*. Engineering design and structural dynamics. Vol. 6. No 4. 1978.

[12] P.E.Tovstik, T.M.Tovstik, V.F.Shekhovtsov. *On the marine fixed offshore platform dynamics under random wave forces*. 33 Summer School-Conf. "Advanced Problems in Mechanics". St.Petersburg. 2005.

[13] P.E.Tovstik, T.M.Tovstik, V.F.Shekhovtsov. *On the marine fixed offshore platform dynamics under random wave forces*. Tagungsband. 7 Magdeburger Machinen- bau-Tage. 2005. 118-126.

[14] P.E.Tovstik, T.M.Tovstik, V.F.Shekhovtsov. *The Impact of the Shape of the Spectral Density of Random Wave Disturbance on the Vibrations of a Fixed Sea-Based Offshore Platform*. Vestnik St.Petersburg Univ. Mathematics. Vol. 45. No 2. 2012.

COMPDYN 2013
4th ECCOMAS Thematic Conference on
Computational Methods in Structural Dynamics and Earthquake Engineering
M. Papadrakakis, V. Papadopoulos, V. Plevris (eds.)
Kos Island, Greece, 12–14 June 2013

ECCENTRIC STEEL BUILDINGS DESIGNED FOR UNIFORM DUCTILITY DEMANDS UNDER EARTHQUAKE ACTIONS

Miltiadis T. Kyrkos[1] **and Stavros A. Anagnostopoulos**[2]

[1] PhD, Region of Attica, Greece
e-mail: mtkyrk@gmail.com

[2] Professor, Department of Civil Engineering
University of Patras, Greece
saa@upatras.gr

Keywords: Asymmetry, Torsion, Braces, Eccentricity, Non-linear Seismic Response, Plastic Hinge Model, Torsionally Stiff Buildings, Torsionally Flexible Buildings.

Abstract. *Research in the past few years has indicated that code designed eccentric buildings exhibit ductility demands under strong earthquake motions that are unevenly distributed throughout the structure. More specifically, it is found that elements at the so called "flexible" sides of the buildings exhibit substantially higher ductility demands than elements at the so called "stiff" sides. Such an uneven distribution indicates suboptimal material use and a potential for premature failure of certain members. In the present paper this problem is demonstrated for two L-shaped five story buildings, a torsionally stiff and a torsionally flexible. Subsequently a simple procedure is used to modify the original design that exhibits a substantially improved behavior in terms of ductility demand distribution. The results are quite promising and could be the basis for improving current codes.*

1 INTRODUCTION

One of the open research areas in earthquake resistant design of buildings is associated with torsion caused by strong earthquake excitations when the building is irregular or simply non-symmetric. Torsional motion during earthquakes can be caused due to a number of factors, some of which can be accounted for in design, while some others may be unknown at the time the structure is designed or may be difficult to quantify and be accounted for properly. Examples of such factors are accidental eccentricities due to mass and/or stiffness uncertainties and non coherent ground motion at the supports. Given also that buildings are designed to respond in the inelastic range under strong earthquakes, stiffness changes due to non symmetric yielding that current design and analysis methods cannot reliably predict, induce additional eccentricities and hence extra torsional motion.

Code provisions for designing eccentric buildings have been based mostly on elastic analyses of idealized multistory buildings or on inelastic analyses of highly simplified, one-story, inelastic models of the shear beam type with 3 degrees of freedom [4-10]. In the past decade, however, research on earthquake induced torsion started using more sophisticated, multi story, multi-degree of freedom inelastic models of the plastic hinge type [e.g. 11-18]. This research revealed that the widely used simplified, one story, 3 degree of freedom models used in most of the past studies, could lead to erroneous conclusions, unless model properties were very carefully selected to closely match key properties of the multistory building [18]. Hence code provisions based, in part at least, on such results might be questionable. Moreover, a number of controversies had been generated from such studies and a few publications were devoted to them [1-3,18].

The same studies of torsion with the detailed plastic hinge model also showed that the ductility demand differences between the two edges, “flexible” and “stiff”, were often very large, with the demands at the “flexible” edge being always substantially greater than the demands at the “stiff” edge of the building. This was initially found for concrete buildings, where both rotational ductility factors and damage indices were used as measures of inelastic deformations [13]. Subsequently the same behavior was confirmed for multi-story, eccentric, braced frame, steel buildings with rectangular layouts and a design modification was proposed to alleviate this problem [14-17].

In the present paper the aforementioned problem is demonstrated for two L-shaped, 5-story eccentric buildings, one planned and designed as torsionally stiff and the other as torsionally flexible. The results indicate the same problem for ductility demand distribution, as observed in the buildings with the rectangular layouts, and further that the same modification proposed before works well also for these two buildings.

2 BUILDINGS AND MOTIONS USED

The present investigation was carried out using two 5-story, steel, braced frame buildings, the first torsionally stiff and the second torsionally flexible. Both buildings are L shaped, and their typical layouts as well as typical frame elevations can be seen in Figures 1, 2 and 3. Note that each building is formed by 5 frames along the x axis, (FR-X01 to FR-X05) and 6 frames along the y axis (FR-Y01 to FR-Y06). In order to create a torsionally stiff and a torsionally flexible building just for the purpose of our work, braces were used to stiffen specific bays as shown in Figures 1 and 2, respectively. The stiffened bays in the second building (Fig. 2) were selected just to create a torsionally flexible variant of the first building. Both buildings have a typical story height of 3.00m and ground story height 4.00m.

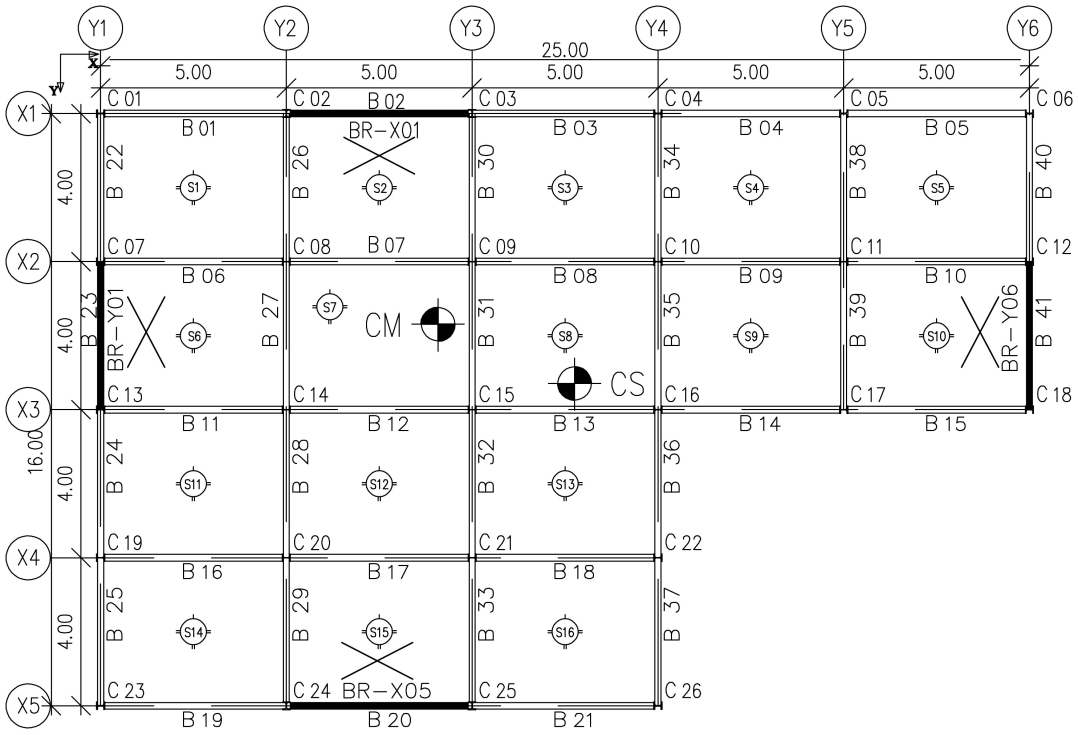


Figure 1: Typical layout of the 5-story torsionally stiff steel building.

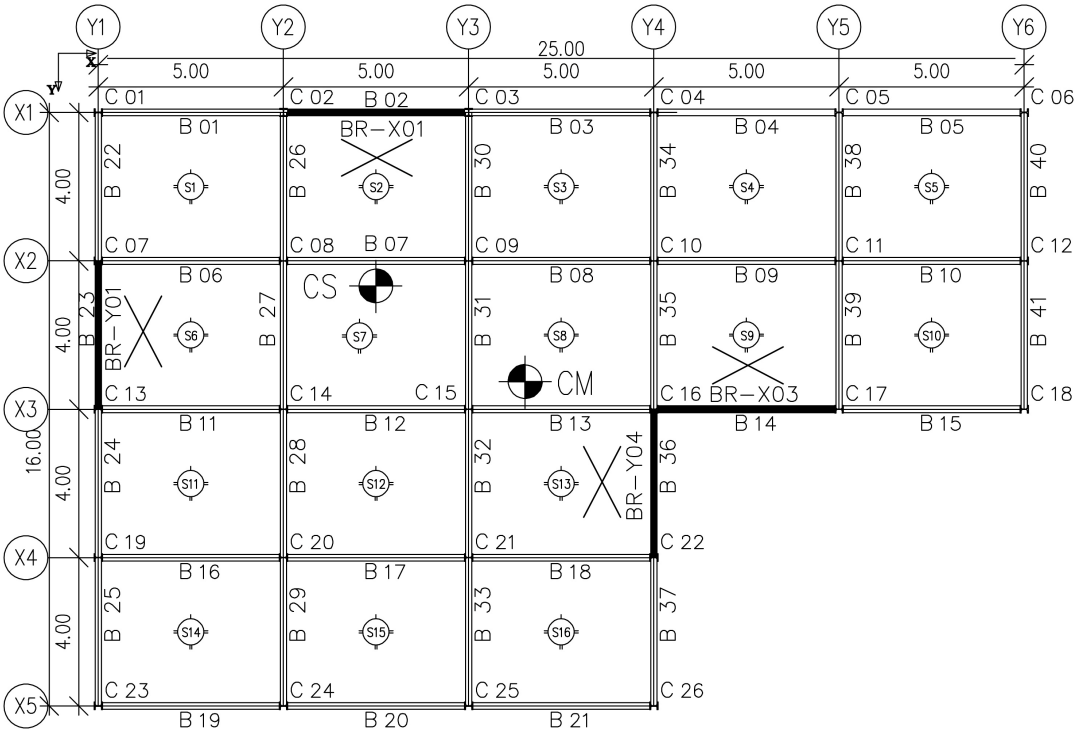


Figure 2: Typical layout of the 5-story torsionally flexible steel building.

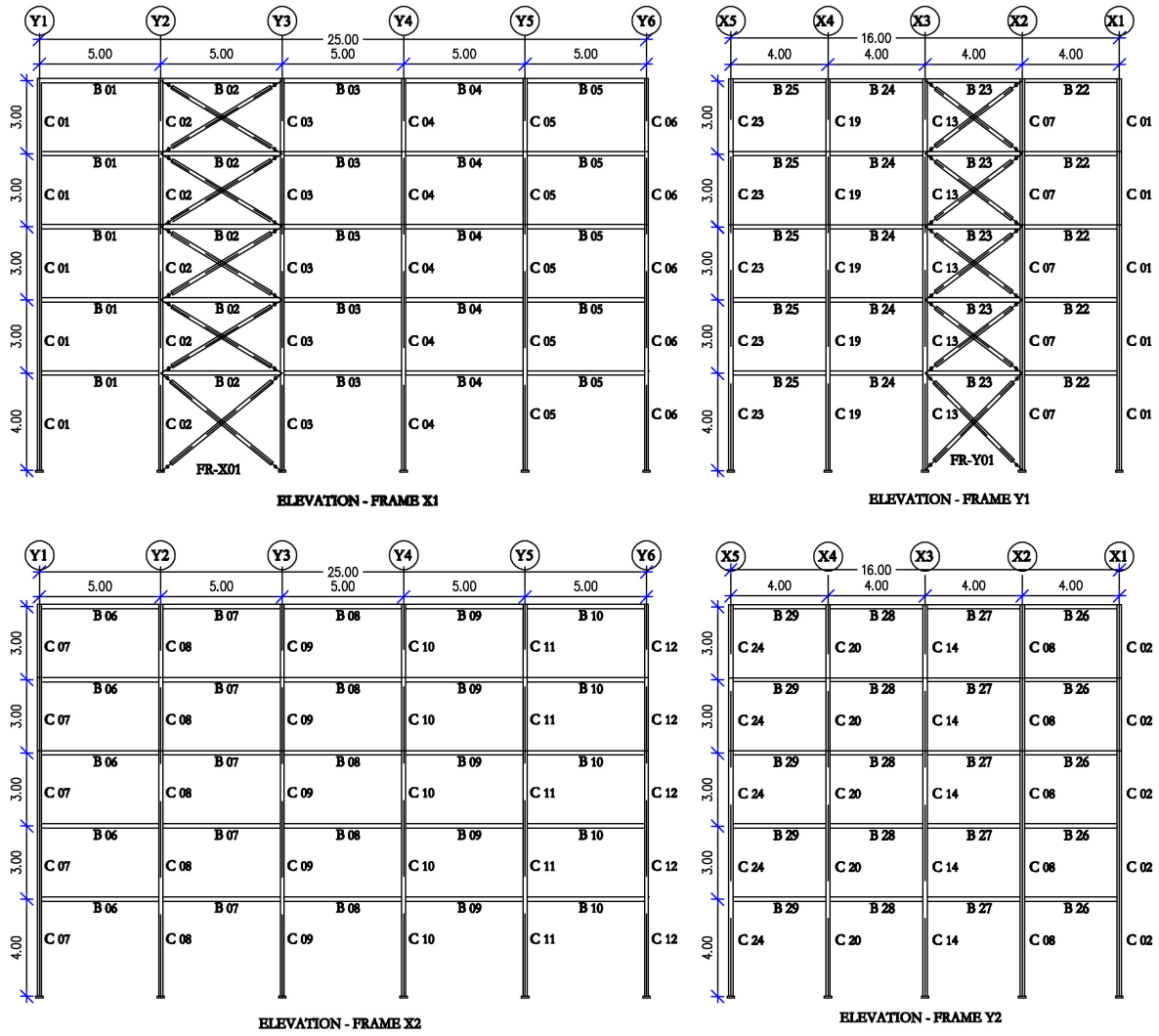


Figure 3: Elevations in X and Y directions of the 5-story torsionally stiff and flexible steel buildings.

Using appropriate distributions of the floor loads, e.g. through non-symmetric live load distribution, non-symmetric balconies (common causes of mass eccentricity in typical buildings, not shown in the given layout), non-symmetric joint masses were assigned at each floor, and mass eccentric floor plans, with $e_m \sim 0.15L$ in all five stories were generated.

The models used for both design and analyses are 3-D models with masses lumped at the joints and the floors acting as diaphragms. All buildings were designed as spatial frames for gravity and earthquake loads using the dynamic, response spectrum method, according to Eurocodes EC3 -steel structures- and EC8 -earthquake resistant design. The uneven mass distribution led to member forces and corresponding sections which created stiffness eccentricities and thus our buildings are both mass and stiffness eccentric. Earthquake actions were described by the design spectrum specified by the Greek Code for ground acceleration PGA=0.24g and soil category II.

As input for the nonlinear dynamic analyses, ten sets of two component semi-artificial motion pairs were used. They were generated from a group of five, two-component, real earthquake records, to closely match the code design spectrum (with a descending branch $1/T^{2/3}$), using a method based on trial and error and Fourier transform techniques [19]. Results were excellent, as may be seen in Figure 4 where the mean response spectrum of the ten semi-

artificial motions is compared with the target, code design spectrum. Each synthetic motion pair, derived from the two horizontal components of each historical record, was applied twice by mutually changing the components along the x and y system axes. Thus, each design case was analyzed for ten sets of 2-component motions and mean values of peak response indices were computed. In this manner, the effects of individual motions are smoothed and the conclusions become less dependent on specific motion characteristics.

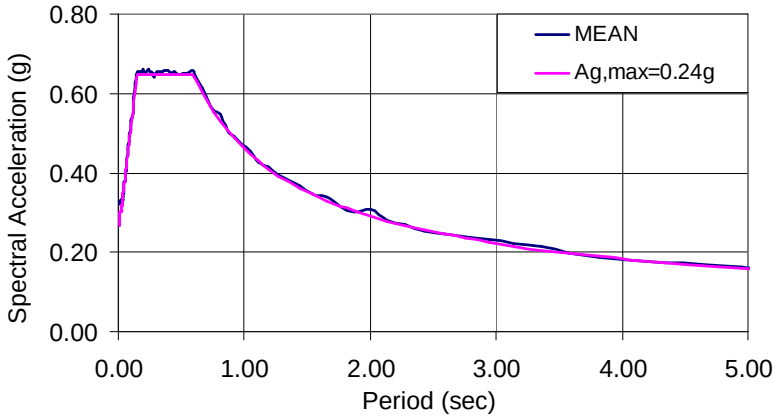


Figure 4: Design spectrum and mean spectrum of the ten semi-artificial motions.

The three lowest periods of the 5-story torsionally stiff building are T_x =0.82 sec, T_y =0.80 sec and T_θ=0.45 sec, while the mean natural eccentricities in each horizontal direction are ε_x=0.10 and ε_y=0.10. Notice that the first torsional period is lower than the two translational periods, as it is expected for a torsionally stiff building. The torsionally flexible building has a fundamental torsional mode with period T_θ=0.90 and two translational modes with periods T_x= T_y=0.82 sec, while its average natural eccentricities are ε_x=0.07 and ε_y=0.10. It is noted that in multistory buildings, the CR cannot be really defined, except under very restrictive conditions. Thus, an approximate CR was computed herein for reference purposes, on a floor by floor basis as follows :

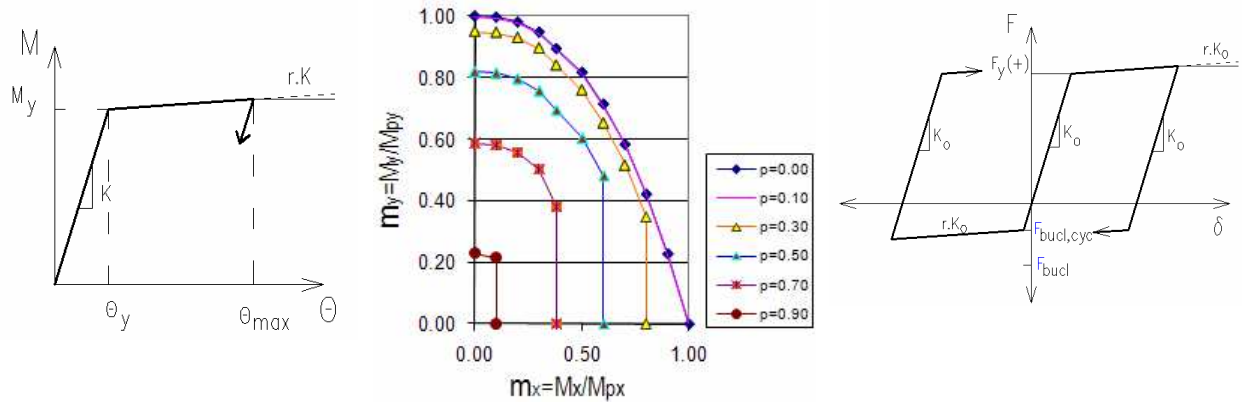
$$e_{sx} = \frac{\sum_{i=1}^{m} K_{f-iy}\, x_i}{\sum_{1}^{m} K_{f-iy}} \qquad e_{sy} = \frac{\sum_{i=1}^{n} K_{f-ix}\, y_i}{\sum_{1}^{n} K_{f-ix}} \tag{1}$$

$$K_{f-i} = \frac{24E}{h^2}\left[\frac{2}{\sum K_c} + \frac{1}{\sum K_{ba}} + \frac{1}{\sum K_{bb}}\right]^{-1} + \sum \frac{AE}{L}\cos^2\varphi \tag{2}$$

where: e_{sx}, e_{sy} are the x and y coordinates of the approximate stiffness center CR, K_{f-i} designates the approximate story stiffness of frame i, x and y the directions of the frame axis, m and n the number of frames along the y and x axes, respectively, E = modulus of elasticity, $K_c = I_c / h$, $K_b = I_b / \ell$, I_c, I_b = section moment of inertia of columns and beams, respectively, h = story height, ℓ = beam length, A= area of brace section, L=brace length and φ = angle of brace member and the horizontal plane. The second indices, a and b, in K_{ba} and K_{bb} designate the upper (above) and lower (below) floor beams of the frame in the considered story.

3 NON-LINEAR DYNAMIC ANALYSES

The non-linear analyses were carried out using the program RUAUMOKO [20]. Frame beams and columns were modelled with the well-known plastic hinge model, in which yielding at member ends is idealized with plastic hinges of finite length having bilinear moment-curvature relationship and strain hardening ratio equal to 0.05. A moment-axial force interaction diagram was also employed for columns, giving the yield moment as a function of the applicable axial force on the column section. Bracing members, yielding in tension and buckling in compression, were modelled with a non-symmetric bilinear force-axial deformation relationship (Figure 5).



(a) (b) (c)

Figure 5: (a) Nonlinear moment-rotation relations for beam-columns, (b) Column M-N interaction diagram and (c) nonlinear force deformation diagram for braces.

The basic measure used to assess the severity of inelastic response is the ductility factor of the various members. For bracing members the ductility factor is defined as:

$$\mu_u = 1 + \left(\frac{u_p}{u_y} \right) \tag{3}$$

where u_p is the maximum plastic member elongation and u_y the elongation at first yield.
For beams and beam-columns the rotational ductility factor has traditionally been defined as:

$$\mu_\theta = 1 + \left(\frac{\theta_p}{\theta_y} \right) \tag{4}$$

where θ_p is the maximum plastic hinge rotation at either end of a member (beam or column) and θ_y is a normalizing "yield" rotation, typically set equal to $\theta_y = M_y \ell / 6EI$. For columns, the yield moment M_y is usually taken to correspond to the yield moment under the action of gravity loads. In the present study, an alternative definition of the rotational ductility factor, based on the post yield plastic moment, has been used [21]

$$\mu = 1 + \left(\frac{\Delta M}{p \cdot M_y} \right) \tag{5}$$

where: $\Delta M = M_{max} - M_y$, M_y = yield bending moment and $p=0.05$, the strain hardening ratio.

In addition to the above measures, peak floor displacements and interstory drifts are used to assess the inelastic behavior of the buildings.

4 RESULTS FROM NON-LINEAR ANALYSES OF "AS DESIGNED" BUILDINGS.

Results from time history analyses of the two buildings are presented in terms of mean values of the peak response parameters over the ten pairs of applied motions. In the case of the beam ductility factors, the response parameter averaged over the ten pairs of motion is the maximum rotational ductility demand in any of the beams in the considered frame and floor. Following standard terminology based on static application of the lateral load in eccentric buildings, the edge where the displacement from rotation is added to the pure floor translation is called "flexible" edge, while the opposite edge, where the displacement due to rotation is subtracted from the translation is called "stiff" edge. Since the examined buildings have biaxial eccentricity, the edge distinction just mentioned applies to both the X and Y horizontal directions of the buildings. Thus, results are presented for each edge frame and each direction. In torsionally flexible buildings, however, it is not necessarily the "flexible" edge that experiences the largest translation but it could well be the "stiff" edge, depending on the relative values of the torsional and translational periods and on the input characteristics.

4.1. Five-story torsionally stiff building

The "flexible" and "stiff" edges of the five-story torsionally stiff buildings are presented in Figure 6. Displacement results and ductility demands for braces and beams of the "flexible" and "stiff" edges can be in Figures 7 and 8, respectively. Ductility demands are presented only for beams and brace members because the columns remained essentially elastic. Looking into Figure 7, we can see that displacements in the Y direction at the "flexible" edges of the torsionally stiff eccentric building are substantially greater than those at the "stiff" edges due to the induced earthquake rotations. The same is true for ductility demands of the braces and the beams (Figure 8).

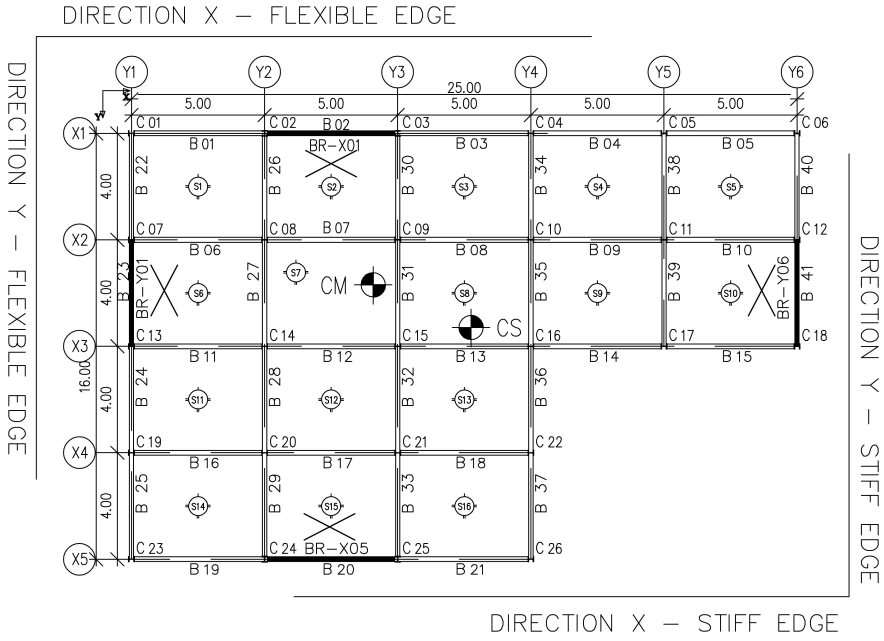


Figure 6: "Flexible" and "stiff" edges in torsionally stiff building.

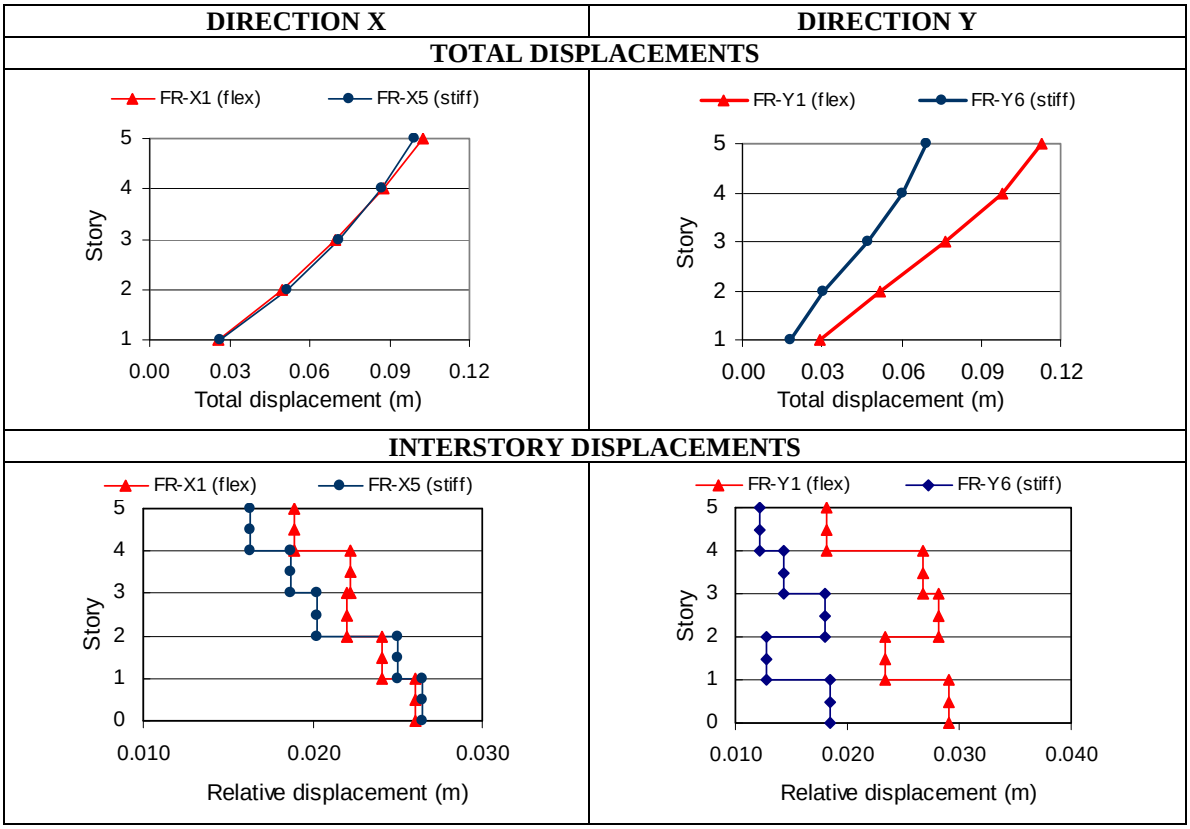


Figure 7: Total displacements and interstory drifts of 5-story torsionally stiff building (FR-X1 & FR-Y1: "flexible" edges, FR-X5 & FR-Y6: "stiff" edges).

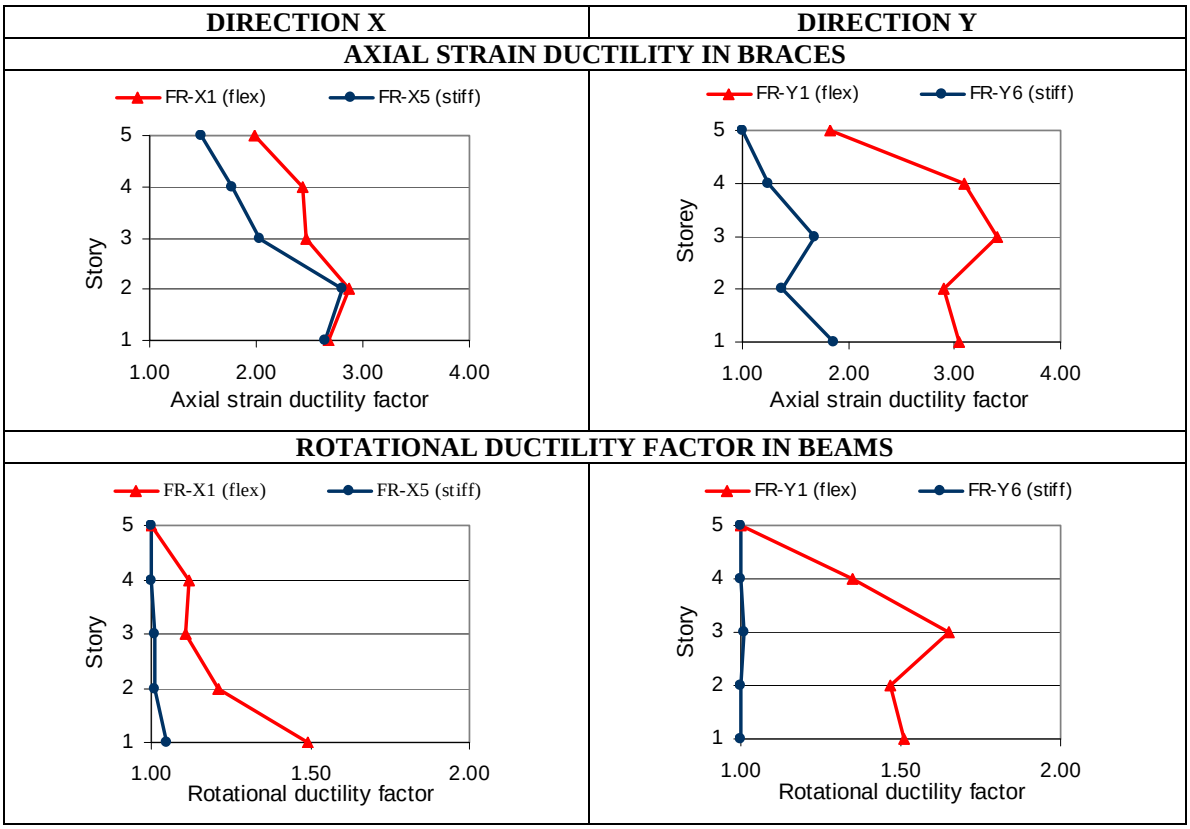


Figure 8: Member ductility demands of 5-story torsionally stiff building (FR-X1 & FR-Y1: "flexible" edges, FR-X5 & FR-Y6: "stiff" edges).

4.2. Five-story torsionally flexible building

The "flexible" and "stiff" edges of the five-story torsionally flexible buildings are presented in Figure 9. Displacement results for the torsionally flexible building are shown in Figure 10 and ductility demands in Figure 11. Compared to the results of the torsionally stiff building, quantitative differences aside, the behavior pattern is similar, with displacement and ductility demands being larger in the frames at the "flexible" edges or sides. It is further noticed that the differences in ductility demands in the braces here are much smaller than in the torsionally stiff building, since the braces in this case are placed near the core of the building.

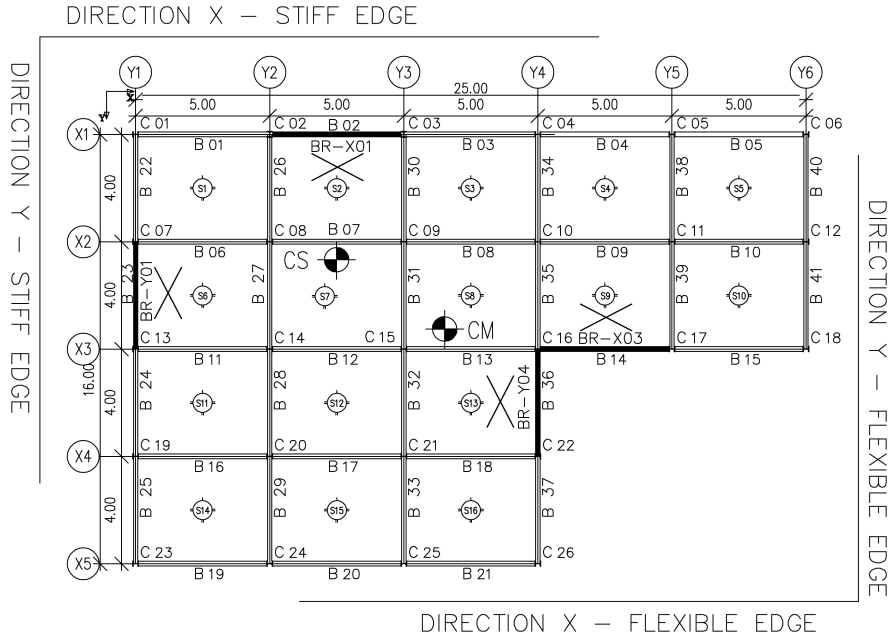


Figure 9: "Flexible" and "stiff" edges in torsionally flexible building.

5 MODIFICATION PROCEDURE

A structural design can be characterized as satisfactory when the limiting values of the controlling response parameters do not have wide variations within the groups of structural members to which they apply. In the opposite case, suboptimal use of material may be present as well as a potentially higher risk of failure in cases of unexpected overloads. Thus the observed substantial differences in ductility demands between the opposite edges of the examined buildings, point to the need for a design modification that would eliminate or reduce these differences. The modifications for the torsionally stiff building are the same as in Refs. [14,16]. A modified version of this modification will be applied to the torsionally flexible building [17].

5.1. Modification procedure and results for the torsionally stiff building.

The modification procedure for the torsionally stiff building aims at increasing the stiffness and strength of the bracing members at the "flexible" edges and reducing the same at the "stiff" edges without affecting the strength of the other structural elements (columns, beams). The first step for application of this modification is to obtain the top story displacements at the "flexible" and "stiff" edges of the building in both horizontal directions due to the earthquake loading considered and then compute the following factors in each horizontal direction:

$$f_{i,flex} = 2 \cdot \frac{u_{i,flex}}{(u_{i,flex} + u_{i,stiff})}$$
$$f_{i,stiff} = 2 \cdot \frac{u_{i,stiff}}{(u_{i,flex} + u_{i,stiff})} \quad (6)$$

where $u_{i,flex}$ is the top story displacement of the "flexible" edge in the i - direction and $u_{i,stiff}$ the top story displacement of the "stiff" edge also in the i - direction. These displacements are obtained by the dynamic response spectrum method for the seismic combinations considered. The factors are ratios of the top story displacements at the "flexible" and "stiff" edges in a given direction (x or y), to their mean values. The design modification that was subsequently applied was to multiply the axial areas of the bracing members in both the "stiff" and "flexible" edges by the corresponding factors in each direction. The values of these factors, for modifying frames in direction x, are 0.91 for the "stiff" edge and 1.09 for the "flexible" edge. Similarly the values for modifying frames in direction y are 0.80 for the "stiff" edge and 1.20 for the "flexible" edge. After this modification, each structure was checked again for full compliance with the applicable codes. The new, modified structures were again subjected to the same two component earthquake set and their responses were again computed as before.

Figures 12 and 13 show ductility demands for the torsionally stiff building for the initial and the modified designs. If we compare the results obtained from the modified design with that of the original design, we see a substantial improvement of response in all cases: the overall maximum ductility demand factor in each group is reduced and so are the differences between "flexible" and "stiff" edges, producing more uniform distribution of such demands.

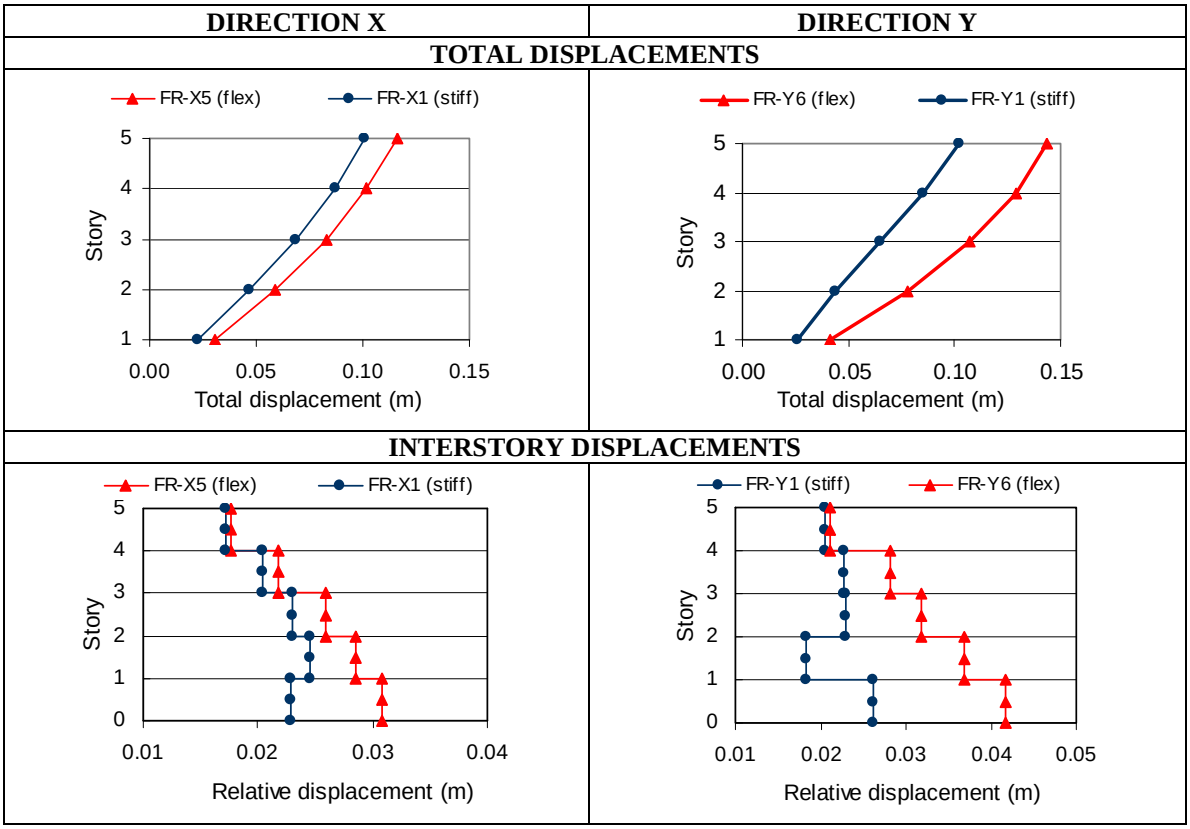


Figure 10: Total displacements and interstory drifts of 5-story torsionally flexible building (FR-X5 & FR-Y6: "flexible" edges, FR-X1& FR-Y1: "stiff" edges).

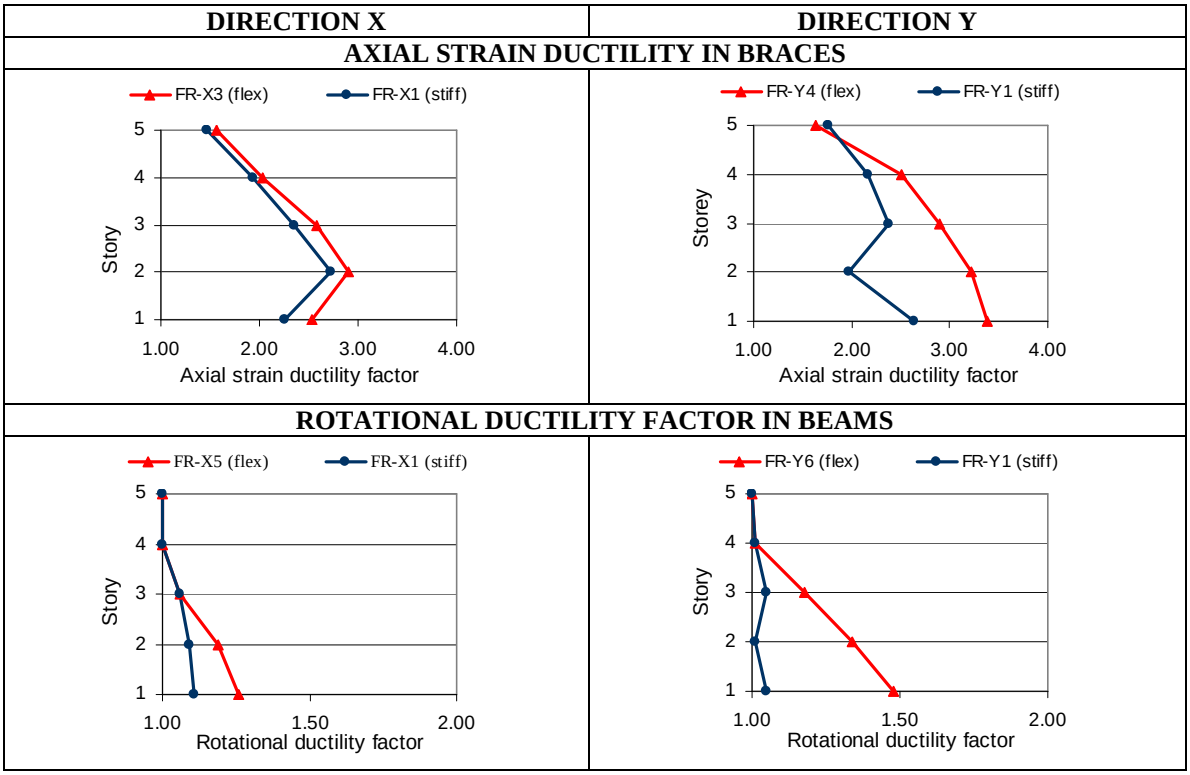


Figure 11: Member ductility demands of 5-story torsionally flexible building (FR-X5,X3 & FR-Y4,Y6: "flexible" sides, FR-X1 & FR-Y1: "stiff" sides).

5.2. Modification procedure and results for the torsionally flexible building

The modification procedure for the torsionally flexible building aim at increasing the stiffness and strength of the structural members (columns, beams and braces) at the "flexible" edges and reducing the stiffness and strength of the braces at the "stiff" edges without affecting the strength of the other structural elements (columns, beams). The ratios of the top story displacements $f_{i,flex}$ and $f_{i,stiff}$ (Eq. 6) are also used, but now the displacements are obtained by the equivalent static method for the seismic combinations considered. The design modification that was subsequently applied was to multiply the axial areas of the bracing members at both the "stiff" and "flexible" edges by the corresponding factors in each direction and to do the same for the beam and column sections, but **only** at the "flexible" edges. The cross sections of columns and beams of the "stiff" edges are not reduced, as their strength is controlled mainly by gravity loads. After this modification, each structure was checked again for full compliance with the applicable codes. This procedure gave modification factors of 0.88 and 0.79 for the braces in the stiff x and y sides, respectively and factors 1.12 and 1.21 for beams and columns in the "flexible" edges along the x and y directions, respectively. However, contrary to what happened in the torsionally stiff building, now the reduction in the brace sections at the stiff side proved excessive and these two factors were increased from 0.88 and 0.79 to 0.90 and 0.88, respectively, to satisfy all the code required checks. The new, modified structures were again subjected to the same two component motion earthquake set and their responses were again computed. Figures 14 and 15 show ductility demands for the torsionally flexible building for the initial and the modified designs. If we compare the results obtained from the initial and the modified designs, we see again some noticeable improvement of response: the overall maximum ductility demand factor in each group is reduced and so are the differences between "flexible" and "stiff" edges, producing more uniform distribution of such demands.

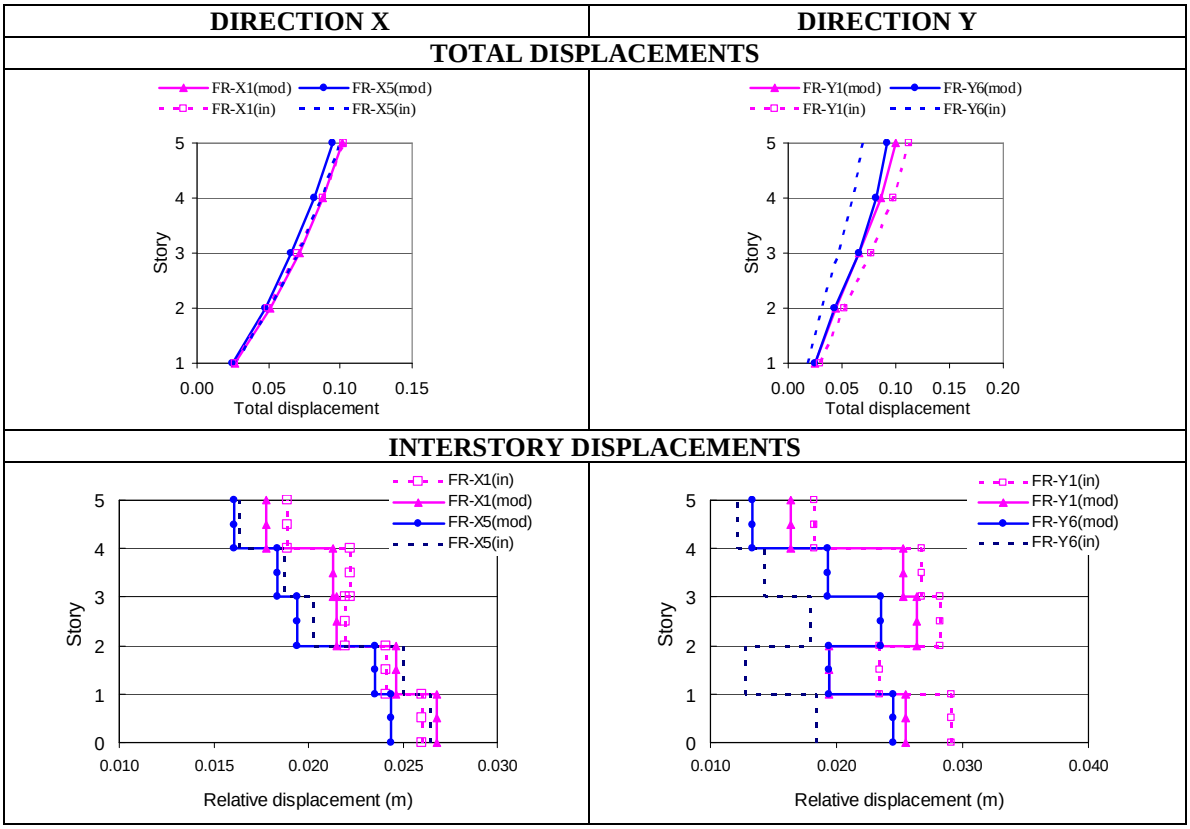


Figure 12: Comparison of total displacements and interstory drifts of 5-story torsionally stiff building, for the initial and modified design (FR-X1 & FR-Y1: “flexible” edges, FR-X5 & FR-Y6: “stiff” edges).

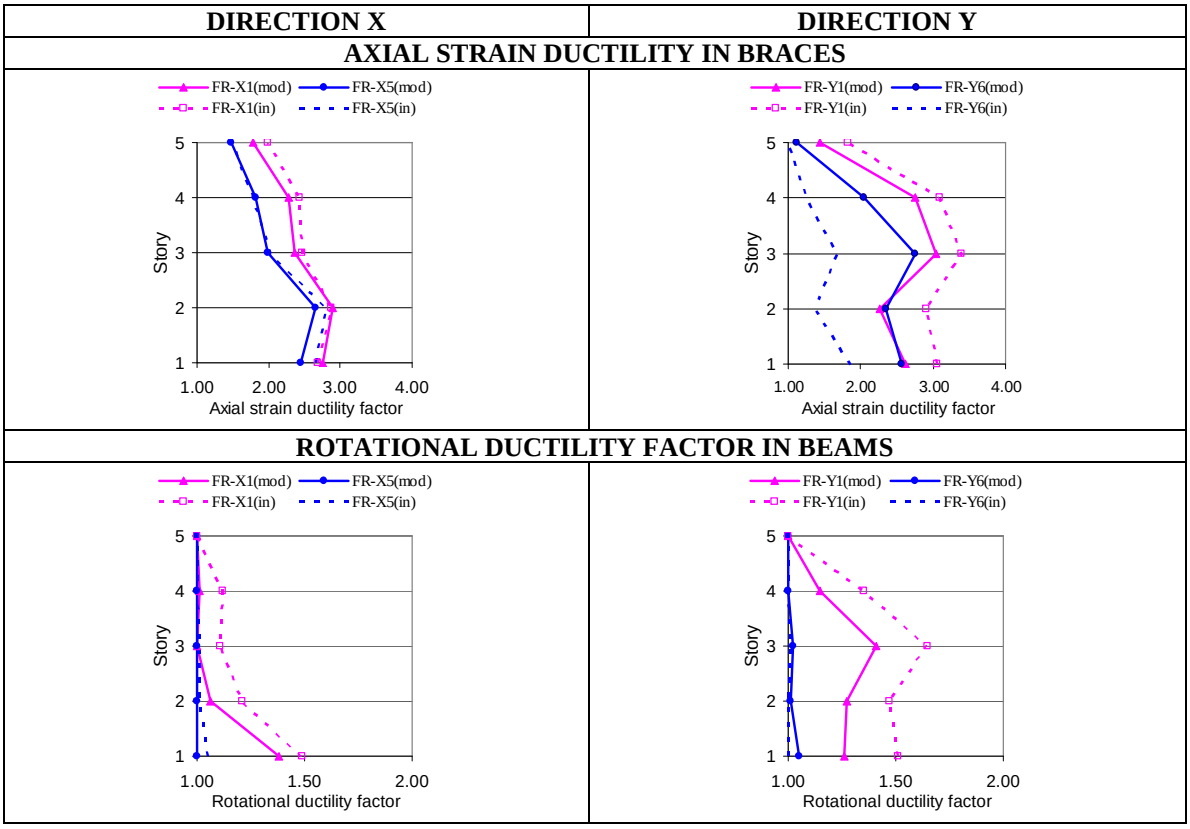


Figure 13: Comparison of ductility demands of 5-story torsionally stiff building, for the initial and modified design (FR-X1 & FR-Y1: “flexible” edges, FR-X5 & FR-Y6: “stiff” edges).

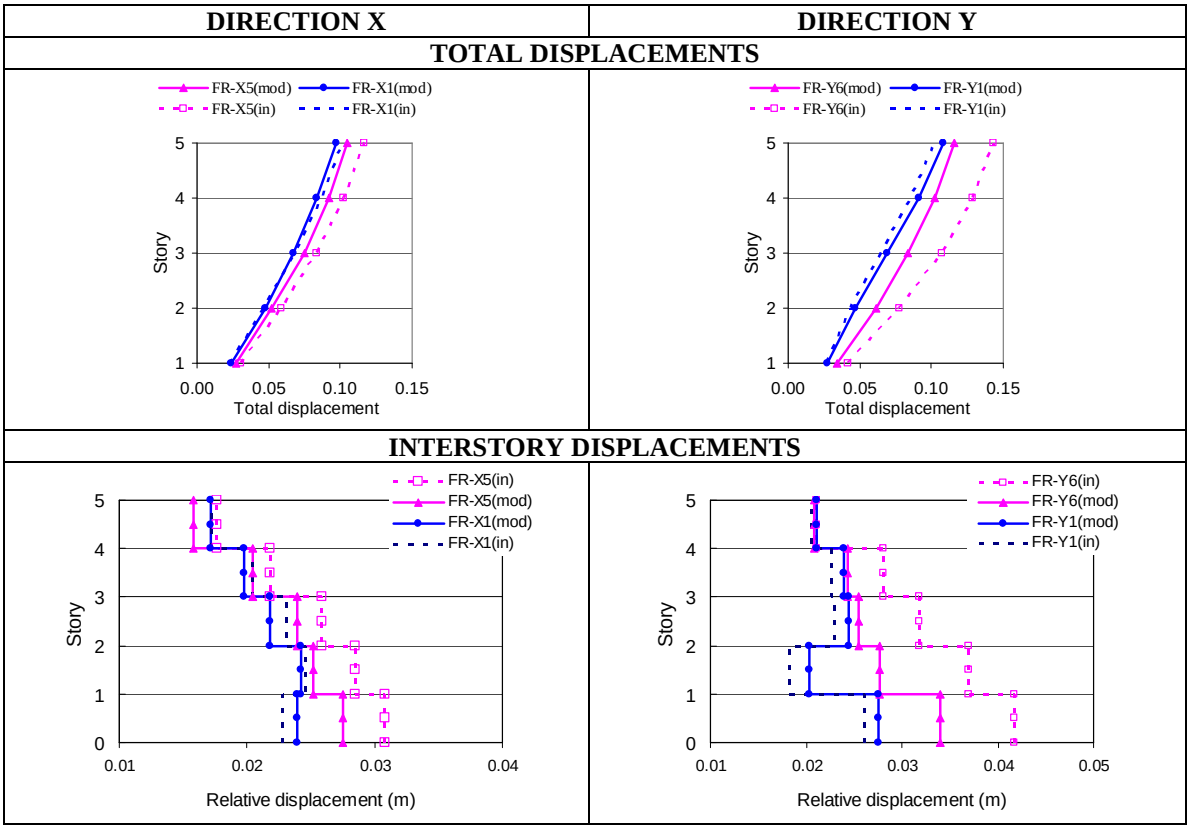


Figure 14: Comparison of total displacements and interstory drifts of 5-story torsionally flexible building, for the initial and modified design (FR-X5 & FR-Y6: "flexible" edges, FR-X1 & FR-Y1: "stiff" edges).

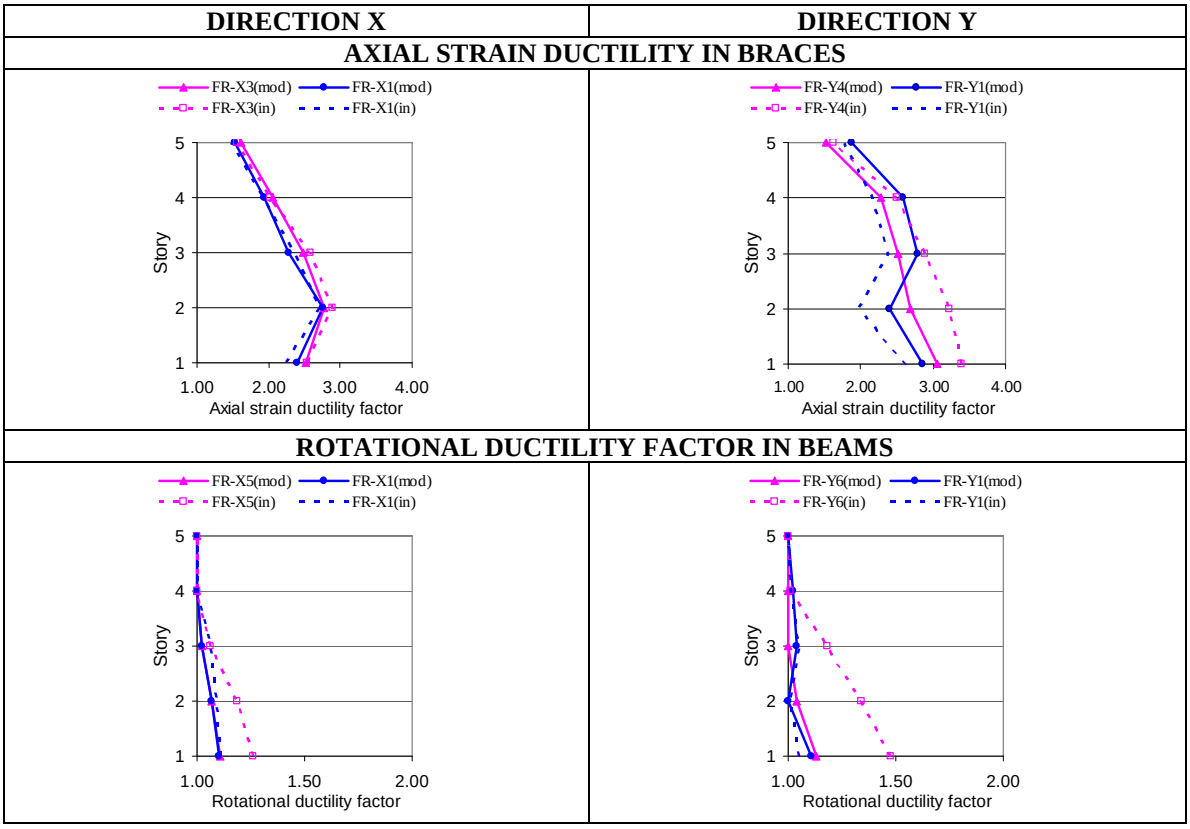


Figure 15: Comparison of ductility demands of 5-story torsionally flexible building, for the initial and modified design (FR-X3,X5 & FR-Y4,Y6: "flexible" sides, FR-X1 & FR-Y1: "stiff" sides).

6 COMMENTS ON THE PROPOSED MODIFICATION

To get more insight about the consequences of the proposed modification, the new stiffness centers of the modified buildings were computed using equations 1 and 2 and compared with those of the original designs. Results are presented in Table 1. We can see that the proposed modification brings the approximate stiffness center of each story closer to the mass center and thus the torsional motions are reduced. This reduction is obviously greater for the "flexible" edge and hence the reduction in the observed differences of ductility demands between "flexible" and "stiff" edges. We must note here that bringing the stiffness center as close as possible to the mass center, in other words trying to minimize the physical eccentricity, is a well known design objective in earthquake engineering as it minimizes torsional motion. The proposed modification is thus a "blind" way of achieving this without significant extra effort.

	MEAN NATURAL ECCENTRICITY			
	INITIAL DESIGN		MODIFIED DESIGN	
	ε_x	ε_y	ε_x	ε_y
5-st torsionally STIFF	0.10	0.10	0.04	0.03
5-st torsionally FLEXIBLE	0.07	0.10	0.03	0.06

Table 1: Mean natural eccentricities for the initial and modified designs of the 5-story buildings.

7 CONCLUSIONS

In the present paper the earthquake response of two irregular L shaped steel, braced frame buildings, one torsionally stiff and the other torsionally flexible, both designed in accordance with Eurocodes EC3 and EC8 was examined and similar, overall, results were obtained compared to earlier findings for eccentric rectangular, steel and reinforced concrete frame buildings. More specifically, it was found that under the action of two horizontal component earthquake loadings, compatible with the design spectra, ductility demands at the "flexible" edges were greater than ductility demands at the "stiff" edges. Subsequently, the original designs were modified using two slightly different procedures for each building and it was found that the response of the new designs was improved: ductility demands at the flexible edges generally decreased and the differences between the two sides diminished, so that a more uniform distribution of ductility demands was achieved.

On the basis of these findings, a code modification may appear desirable. However, additional studies covering other types of irregular buildings and a wider spectrum of parameters will be required, before any firm recommendation is put forward.

REFERENCES

[1] Rutenberg A. (1998). EAEE Task Group (TG)8: Behavior of irregular and complex structures – State of the art report : Seismic nonlinear response of code-designed asymmetric structures. *11th European Conference on Earthquake Engineering.*

[2] Rutenberg A. (2002). EAEE Task Group (TG)8: Behavior of irregular and complex structures – Asymmetric Structures- Progress since 1998. *12th European Conference on Earthquake Engineering.*

[3] De Stefano M. & Pintucchi (2008).A review of research on seismic behavior of irregular building structures since 2002. *Bulletin of Earthquake Engineering 6: 285-308*

[4] Chopra, A. K. & Goel, R. K. (1991). Evaluation of Torsional Provisions in Seismic Codes. *Journal of the Structural Division, (ASCE)* 117(12): 3762-3782

[5] De La Colina, J. (2003). Assessment of design recommendations for torsionally unbalanced multistory buildings. *Earthquake Spectra* 19 : No 1, 47-66

[6] Stathopoulos, K.G. & Anagnostopoulos, S. A. (2000). Inelastic Earthquake Response of Buildings subjected to Torsion. *12th World Conference on Earthquake Engineerin No.* 781, Auckland, New Zealand

[7] Stathopoulos, K.G. & Anagnostopoulos, S.A. (2003). Inelastic earthquake response of single-story asymmetric buildings : an assessment of simplified shear- beam models. *Earthquake Engineering and Structural Dynamics* 32: 1813-1831

[8] Chandler, A. M. & Duan, X. N. (1991). Evaluation of FactorsInfluencing the Inelastic Seismic Preformance of Torsionally Asymmetrical Buildings. *Earthquake Engineering and Structural Dynamics* 20:87-95

[9] Tso, W. K. & Zhu, T. J. (1992). Strength Distribution for Torsionally Unbalanced Structures. *10th World Conference on Earthquake Engineering* 7:3865-3868

[10] Humar, J. L. & Kumar, P. (2000). A new Look at the Torsion Design Provisions in Seismic Building Codes. *12th World Conference on Earthquake Engineering, No* 1707, Auckland, New Zealand

[11] Ghersi A., Marino E. & Rossi P. P. (2000). Inelastic response of multi-storey asymmetric buildings. *Proc 12th World Conference on earthquake Engineering, No 1716*

[12] Fajfar P, Marusic D, Perus I. Influence of ground motion intensity on the inelastic torsion response of asymmetric buildings. *The 13th World Conference on Earthquake Engineering*, Vancouver, Canada, 2004. *No.* 3496.

[13] Stathopoulos, K.G. & Anagnostopoulos, S.A. (2005). Inelastic torsion of multistory buildings under earthquake excitations. *Earthquake Engineering and Structural Dynamics* 34: 1449-1465

[14] Kyrkos M. T. & Anagnostopoulos S.A. (2010). Towards earthquake resistant design of steel buildings for uniform ductility demands, *Advances and trends in structural Engineering, Mechanics and Computation, Zingoni (Ed), SEMC 2010,* Capetown.

[15] Kyrkos M. T. & Anagnostopoulos S.A. (2011a). An assessment of code designed torsionally stiff asymmetric steel buildings under strong earthquake excitations. *Earthquakes and Structures, Vol.2* :109-126

[16] Kyrkos M. T. & Anagnostopoulos S.A. (2011b). Improved earthquake resistant design of torsionally stiff asymmetric steel buildings. *Earthquakes and Structures, Vol.2 :* 127-147

[17] Kyrkos M. T. (2011). Improved earthquake resistant design of eccentric steel buildings with diagonal braces, PhD Thesis, University of Patras, (in Greek).

[18] Anagnostopoulos S. A., Alexopoulou Ch. & Stathopoulos K. (2010). An answer to an important controversy and the need for caution when using simple models to predict inelastic earthquake response of buildings with torsion. *Earthquake Engineering and Structural Dynamics* 39: 521-540

[19] Karabalis, D.L. – Cokkinides, G.J. – Rizos, D.C. & Mulliken, J.S. (2000). Simulation of earthquake ground motions by a deterministic approach. *Advances in Engineering Software* 31 : 329-338

[20] Carr A.J. , (2005). Ruaumoko Manual. Volume 3. User manual for the 3-dimensional Version- Ruaumoko 3D.

[21] Anagnostopoulos, S.A. (1981) Inelastic Beams for Seismic Analyses of Structures. Journal of Structural Division, ASCE 107(7) : 1297-1311

COMPDYN 2013
4th ECCOMAS Thematic Conference on
Computational Methods in Structural Dynamics and Earthquake Engineering
M. Papadrakakis, V. Papadopoulos, V. Plevris (eds.)
Kos Island, Greece, 12–14 June 2013

INCLUSION OF GEOMETRIC NONLINEARITY IN CALCULATING SEISMIC BUILDING FRAMES

J.M. Martínez Valle[1], J.M. Martínez Jiménez [1], and P. Martínez Jiménez[2]

[1] Department of Mechanics
Leonardo Da Vinci Building. University of Córdoba, Spain
e-mail: jmvalle@uco.es, me1majij@uco.es

[2] Department of Applied Physics
Albert Einstein Building, University of Córdoba, Spain
e-mail: fa1majip@uco.es

Keywords: Seismic analysis, interstory drift sensitivity coefficient.

Abstract. *In calculating the seismic response of a building, the Spanish Instructions NCSE-02 and CTE, paragraph 3.7.7(also EUROCODE 8 paragraph 1.2 part 1-1), establish that if for all storeys the interstory drift sensitivity coefficient, ξ, satisfies:*

$$\xi = \frac{P \cdot d}{F \cdot h} \leq 0.1$$

then it will not be necessary to consider the effects of the 2nd order ($P-\Delta$ effects).
In this discussion we review this claim:

- *Because even for $\xi \leq 0.1$, increases of the bending moment at the ends of the columns due to the inclusion of second order effects can account for between 15% and 34% of its value for static service loads.*

- *Because most adverse effects are shown in the lower height buildings (up to 5 floors) which is precisely the range in which most of the housing stock of Spain is located.*

- *Also in paragraph 6 we delimit the coefficient for buildings of lesser height (up to 5 floors), proposing to lower it generally to $\xi \leq 0.06$.*

1 DESCRIPTION OF THE PROBLEM AND THE BUILDING USED AS AN EXAMPLE

The NCSE-02 [1] and CTE [2] Spanish Instructions are instructions that allow us to study dynamic effects in different structural elements. Spain is a country that has different provinces in which dynamic studies are important and mandatory. In this article, we analyze the interstory drift sensitivity coefficient, and consider whether or not the 2nd order effects are important in building structures to dynamic stresses.

This coefficient is defined in Eurocode 8 [3], but one of the conditions of whether or not to consider the effects of the 2nd order of coefficient, is formulated identically in Spanish Instructions NCSE 02 and the CTE.

The interstory drift sensitivity coefficient depends on the total gravity load at and above the story considered in the seismic design situation *P*, and the design interstory drift, evaluated as the difference of the average lateral displacements d_s at the top and bottom of the story under consideration *d*, which is directly proportional, and the total seismic story shear *F* and interstory height *h*, which is inversely proportional. To analyze the problem, we take a building type, as shown in Figure 1, and study the influence of 2nd order effects using the corresponding theoretical model we develop in the body of the article.

The example in Figure 1 is a regular rectangular concrete building of dimension 25 × 25 m with 25 columns arranged to give rise to 5 frames in each direction with lights of 5.50 m. For the analysis, we adopt the hypotheses that it might have 2, 4, 7, and 10 floors,the loadings considered are for medium duty use, and that the location of the building is in an average Spanish earthquake zone.

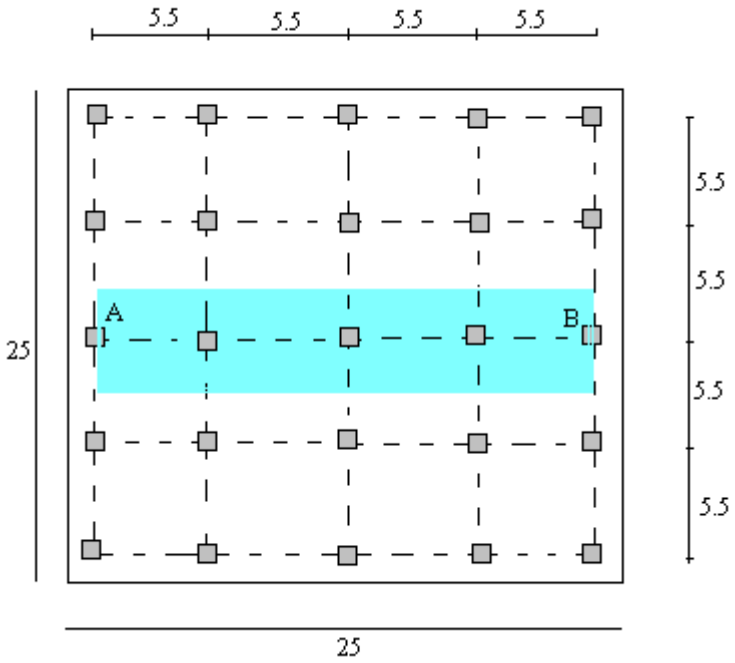


Figure 1:Rectangular Plant of 25 × 25 m with the situation of the columns.

The section of the beams of the floor is 0.30 × 0.40 m (Figure 2). The dead load is the corresponding estimated forged 0.28 m thick, flooring and ceiling. Overloading is the

appropriate use of public spaces with chairs and tables. The basic seismic acceleration is 0.102g and the coefficients of terrain features and contribution are C = 1.4 and K = 1.

With these dimensions, loads and frequently used materials (concrete HA-20 or 25 and reinforcement steels B-500) the obtained mechanical loading amounts of a permanent reinforcement are quite normal (e.g., 4–6 ϕ 16–20 for columns of 25 × 25 cm on two floors, or 10–12 ϕ 20 for columns, 40–45 × 40–45 cm in seven storys).

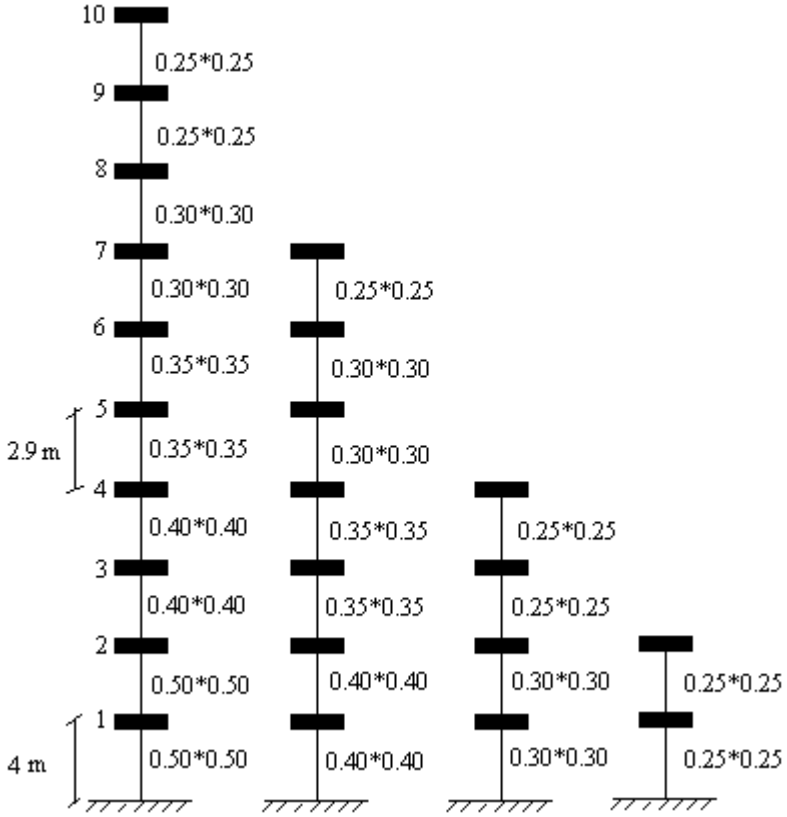


Figure 2: Simple Shear Model for the frame A-B
under the assumptions of 2, 4, 7, and 10 storys

2 GEOMETRIC STIFFNESS MATRIX OF FIRST ORDER OF BEAMS OF 2D FRAMES

In order to consider the 2nd order effects $(P-\Delta$ effects), we must know the stiffness matrix, including the axial force in local coordinates of a beam belonging to a planar structure of rigid nodes, connected rigidly at both ends. A very appropriate methodology for this deduction is based on the consideration of the equilibrium of the slice in the deformed geometry. Alternatively, we can consider nonlinear expressions of deformations of a beam in bending (valid for small deformations and moderate or large displacements) [4].In this paper, we choose the former for its better description of the problem.

Let us consider a beam whose initial neutral axis and deformed neutral axis initial imperfections are represented as in Fig.3a. As a consequence of geometric initial imperfections, the centerline of the beam is deflected by the amount $\hat{v}$ The transverse sections are rotated at an angle $\hat{\vartheta}$.

Consider a slice of this beam of length dx, unstressed axial, bending and shear, and its geometry deformed as in Fig.3b, where the slope of the centerline is given by the shift v along the axis relative to one side, and on the other is given by

$$OO_1 = \vartheta \cdot dx + \hat{\vartheta} \cdot dx = \frac{dv}{dx} \cdot dx + \hat{\vartheta} \cdot dx = dv + \hat{\vartheta} \cdot dx \quad . \tag{1}$$

We can express the sum $\hat{\vartheta} \cdot dx$ as a fraction loading α of the displacement v and consequently, we obtain

$$OO_1 = \vartheta \cdot dx + \hat{\vartheta} \cdot dx = \frac{dv}{dx} \cdot dx + \hat{\vartheta} \cdot dx = (1 + \alpha) \cdot dv \tag{2}$$

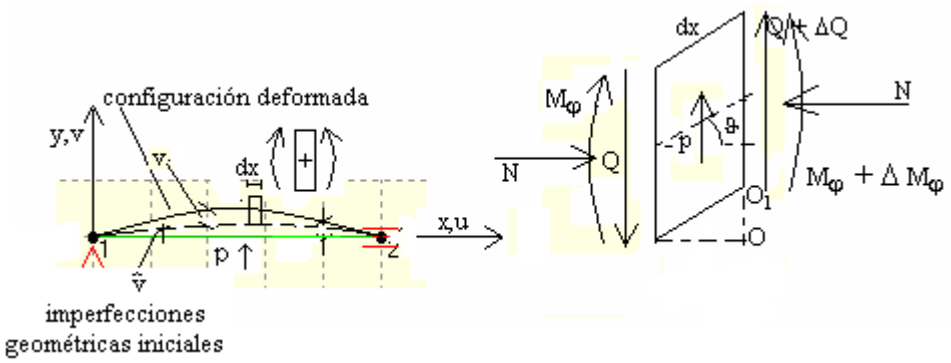


Figure 3a): Deformed configuration
b): Equilibrium of a slice of the beam in its deformed configuration.

If we use the bending theory of thin beams, where $M_\varphi = E \cdot I \, v''$ and establish the equilibrium of the slice into the deformed geometry, we obtain

$$\Sigma Fy = 0 \Rightarrow P \cdot dx - Q + Q + \Delta Q = 0 \tag{3}$$

$$\Sigma M = 0 \Rightarrow M_\varphi + \Delta M_\varphi - M_\phi + Q \cdot dx + N(1 + \alpha) \cdot dv = 0 \quad . \tag{4}$$

The coefficient α gives us an idea, as a percentage, of the level of imperfections on the deformed configuration. Solving for Q in the 2nd equation, and deriving and substituting in the 1st equation, we reach the following differential equation

$$P(x) = E \cdot I \frac{d^4 v}{dx^4} + (1 + \alpha) \cdot N \frac{d^2 v}{dx^2} \quad . \tag{5}$$

In studying free transverse oscillations P = 0, such that the equation reduces to

$$E \cdot I \frac{d^4 v}{dx^4} + (1 + \alpha) \cdot N \frac{d^2 v}{dx^2} = 0 \quad . \tag{6}$$

This is usually written as $\omega^2 = (1 + \alpha) \cdot N/(E \cdot I)$, as $\frac{d^4 v}{dx^4} + \omega^2 \frac{d^2 v}{dx^2}$, whose general solution is given by the following expression:

$$v = -\frac{A}{\omega^2} \cdot \cos(\omega \cdot x) - \frac{B}{\omega^2} \cdot \operatorname{sen}(\omega \cdot x) + C \cdot x + D \tag{7}$$

Integration constants A, B, C, and D are provided by our boundary conditions:

$$v_{x=0} = v_1 ; \quad v_{x=L} = v_2 ; \quad v'_{x=0} = \vartheta_1 \quad ; v'_{x=L} = \vartheta_2 \tag{8}$$

where v_i and ϑ_i, are respectively the deflection and rotation of the end i. If we particularize equation (7) on the values x = 0 and x = L, we obtain:

$$\begin{aligned} v_1 &= -\frac{A}{\omega^2} + D \\ v_2 &= -\frac{A}{\omega^2} \cdot \cos(\omega \cdot L) - \frac{B}{\omega^2} \cdot \operatorname{sen}(\omega \cdot L) + C \cdot L + D \\ \vartheta_1 &= -\frac{B}{\omega} + C \\ \vartheta_2 &= \frac{A}{\omega} \cdot \operatorname{sen}(\omega \cdot L) - \frac{B}{\omega} \cdot \cos(\omega \cdot L) + C \end{aligned} \tag{9}$$

which we can write in matrix form, as follows:

$$\begin{pmatrix} v_1 \\ \vartheta_1 \\ v_2 \\ \vartheta_2 \end{pmatrix} = \begin{pmatrix} -\frac{1}{\omega^2} & 0 & 0 & 1 \\ 0 & -\frac{1}{\omega} & 1 & 0 \\ -\frac{\cos(\omega \cdot L)}{\omega^2} & -\frac{\operatorname{sen}(\omega \cdot L)}{\omega^2} & L & 1 \\ \frac{\operatorname{sen}(\omega \cdot L)}{\omega} & -\frac{\cos(\omega \cdot L)}{\omega} & 1 & 0 \end{pmatrix} \cdot \begin{pmatrix} A \\ B \\ C \\ D \end{pmatrix} = \Im \cdot \begin{pmatrix} A \\ B \\ C \\ D \end{pmatrix} \tag{10}$$

If we suppose that the inverse matrix $\Im^{-1}$ is partitioned in the form

$$\Im^{-1} = \begin{pmatrix} \Im^{-1}_{11} & \Im^{-1}_{12} \\ \Im^{-1}_{21} & \Im^{-1}_{22} \end{pmatrix} \tag{11}$$

then, if we incorporate the horizontal displacements u_1 and u_2 from the beam ends, and we use the usual notation in the theory of structures in which displacements and rotations of the ends of the beam are expressed by

$$\begin{pmatrix} d^{e1x} \\ d^{e1y} \\ \vartheta^{e1} \\ d^{e2x} \\ d^{e2y} \\ \vartheta^{e2} \end{pmatrix} = \begin{pmatrix} u_1 \\ v_1 \\ \vartheta_1 \\ u_2 \\ v_2 \\ \vartheta_2 \end{pmatrix} \tag{12}$$

the equation of the deformed beam is:

$$v = -\frac{A}{\omega^2} \cdot \cos(\omega \cdot x) - \frac{B}{\omega^2} \cdot \operatorname{sen}(\omega \cdot x) + C \cdot x + D = \begin{pmatrix} -\frac{\cos(\omega \cdot x)}{\omega^2} & -\frac{\operatorname{sen}(\omega \cdot x)}{\omega^2} & x & 1 \end{pmatrix} \cdot \begin{pmatrix} A \\ B \\ C \\ D \end{pmatrix} =$$

$$= \left(\frac{-\cos(\omega \cdot x)}{\omega^2} \quad \frac{-\operatorname{sen}(\omega \cdot x)}{\omega^2} \quad x \quad 1 \right) \cdot \begin{pmatrix} \Omega & \Im^{-1}_{11} & \Omega & \Im^{-1}_{12} \\ \Omega & \Im^{-1}_{21} & \Omega & \Im^{-1}_{22} \end{pmatrix} \cdot \begin{pmatrix} d^{e1x} \\ d^{e1y} \\ \vartheta^{e1} \\ d^{e2x} \\ d^{e2y} \\ \vartheta^{e2} \end{pmatrix} \tag{13}$$

The matrix $\Im^{-1}$ is:

$$\Im^{-1} = \varsigma \cdot \begin{pmatrix} -\omega^2 \cdot (1-\cos(\omega \cdot L)) & \omega \cdot (\operatorname{sen}(\omega \cdot L) + \omega \cdot L \cdot \cos(\omega \cdot L)) & \omega^2 \cdot (1-\cos(\omega \cdot L)) & \omega \cdot (\operatorname{sen}(\omega \cdot L) - \omega \cdot L) \\ \omega^2 \cdot \operatorname{sen}(\omega \cdot L) & \omega \cdot (1+\cos(\omega \cdot L) + \omega \cdot L \cdot \operatorname{sen}(\omega \cdot L)) & -\omega^3 \operatorname{sen}(\omega \cdot L) & \omega^2 \cdot (1-\cos(\omega \cdot L)) \\ \omega \cdot \operatorname{sen}(\omega \cdot L) & 1-\cos(\omega \cdot L) & -\omega \cdot \operatorname{sen}(\omega \cdot L) & (1-\cos(\omega \cdot L)) \\ -1+\cos(\omega \cdot L) - \omega \cdot L \cdot \operatorname{sen}(\omega \cdot L) & -\operatorname{sen}(\omega \cdot L) + \omega \cdot L \cdot \cos(\omega \cdot L) & 1-\cos(\omega \cdot L) & \operatorname{sen}(\omega \cdot L) - \omega \cdot L \end{pmatrix}. \tag{14}$$

where ς is $\varsigma = \dfrac{1}{2 - 2 \cdot \cos(\omega L) - \omega L \cdot \operatorname{sen}(\omega L)}$

If the loads at the ends of the beam along the x-axis are designated by p^x, the matrix k_{viga} can be deduced from the bending moment expressions (M_φ), shear force (Q) and axial force (N) by

$$p^{e1x} = -p^{e2x} = \frac{E \cdot A}{L} \cdot (d^{e1x} - d^{e2x})$$

$$(Q)_{x=0} = -p^{e1y} = [-N \frac{dv}{dx} - E \cdot I \frac{d^3v}{dx^3}]_{x=0} = -N\vartheta_1 - E \cdot I \cdot (\frac{d^3v}{dx^3})_{x=0} = E \cdot I \cdot [-\omega^2 \cdot \vartheta_1 - (\frac{d^3v}{dx^3})_{x=0}] \tag{15}$$

$$(M_\varphi)_{x=0} = -M_1 = E \cdot I \cdot (v'')_{x=0}$$

$$(Q)_{x=L} = p^{e2y} = [-N \frac{dv}{dx} - E \cdot I \frac{d^3v}{dx^3}]_{x=L} = -N\vartheta_2 - E \cdot I \cdot (\frac{d^3v}{dx^3})_{x=L} = E \cdot I \cdot [-\omega^2 \cdot \vartheta_2 - (\frac{d^3v}{dx^3})_{x=L}]$$

$$(M_\varphi)_{x=0} = M_2 = E \cdot I \cdot (v'')_{x=L}$$

Substituting in the above equations the derivatives of the deflection v, calculated from equation (13), and particularizing at x equals zero or L, as appropriate, we obtain:

$$\begin{pmatrix} p^{e1x} \\ p^{e1y} \\ m^{e1} \\ p^{e2x} \\ p^{e2y} \\ m^{e2} \end{pmatrix} = \left\{ E \cdot I \cdot \begin{pmatrix} 0 & 0 & 0 & 0 \\ 0 & \omega & 0 & 0 \\ -1 & 0 & 0 & 0 \\ 0 & 0 & 0 & 0 \\ \omega \cdot \operatorname{sen}(\omega \cdot L) & -\omega \cdot \cos(\omega \cdot L) & 0 & 0 \\ \cos(\omega \cdot L) & \operatorname{sen}(\omega \cdot L) & 0 & 0 \end{pmatrix} \cdot \begin{pmatrix} \Omega & \Im^{-1}_{11} & \Omega & \Im^{-1}_{12} \\ \Omega & \Im^{-1}_{21} & \Omega & \Im^{-1}_{22} \end{pmatrix} + \right.$$

$$\left. + \begin{pmatrix} \frac{E \cdot A}{L} & 0 & 0 & -\frac{E \cdot A}{L} & 0 & 0 \\ 0 & 0 & \omega^2 \cdot E \cdot I & 0 & 0 & 0 \\ 0 & 0 & 0 & 0 & 0 & 0 \\ -\frac{E \cdot A}{L} & 0 & 0 & \frac{E \cdot A}{L} & 0 & 0 \\ 0 & 0 & 0 & 0 & 0 & -\omega^2 \cdot E \cdot I \\ 0 & 0 & 0 & 0 & 0 & 0 \end{pmatrix} \right\} \cdot \begin{pmatrix} d^{e1x} \\ d^{e1y} \\ \vartheta^{e1} \\ d^{e2x} \\ d^{e2y} \\ \vartheta^{e2} \end{pmatrix} \tag{16}$$

Replacing the four submatrices $\Im_{ij}^{-1}$ of order 2×2, in the above equation (13) and operating, we obtain the equation of beam loads movements, $p_{viga} = \bar{k}_{viga} d_{viga}$ in local coordinates:

$$\begin{pmatrix} {}_{p}e1x \\ {}_{p}e1y \\ {}_{m}e1 \\ {}_{p}e2x \\ {}_{p}e2y \\ {}_{m}e2 \end{pmatrix} = \bar{k}_{viga} \cdot \begin{pmatrix} {}_{d}e1x \\ {}_{d}e1y \\ {}_{\vartheta}e1 \\ {}_{d}e2x \\ {}_{d}e2y \\ {}_{\vartheta}e2 \end{pmatrix} \tag{17}$$

with $\bar{k}_{viga}$ equal to

$$\bar{k}_V = \begin{pmatrix} \frac{E\cdot A}{L} & 0 & 0 & -\frac{E\cdot A}{L} & 0 & 0 \\ 0 & \frac{\omega^3\cdot sen(\omega\cdot L)}{f(\omega)} & \frac{\omega^2\cdot(1-\cos(\omega\cdot L))}{f(\omega)} & 0 & -\frac{\omega^3\cdot sen(\omega\cdot L)}{f(\omega)} & \frac{\omega^2\cdot(1-\cos(\omega\cdot L))}{f(\omega)} \\ 0 & \frac{\omega^2\cdot(1-\cos(\omega\cdot L))}{f(\omega)} & \frac{\omega\cdot(sen(\omega\cdot L)-\omega\cdot L\cdot\cos(\omega\cdot L))}{f(\omega)} & 0 & -\frac{\omega^2\cdot(1-\cos(\omega\cdot L))}{f(\omega)} & \frac{\omega\cdot(\omega\cdot L-sen(\omega\cdot L))}{f(\omega)} \\ -\frac{E\cdot A}{L} & 0 & 0 & \frac{E\cdot A}{L} & 0 & 0 \\ 0 & -\frac{\omega^3\cdot sen(\omega\cdot L)}{f(\omega)} & -\frac{\omega^2\cdot(1-\cos(\omega\cdot L))}{f(\omega)} & 0 & \frac{\omega^3\cdot sen(\omega\cdot L)}{f(\omega)} & -\frac{\omega^2\cdot(1-\cos(\omega\cdot L))}{f(\omega)} \\ 0 & \frac{\omega^2\cdot(1-\cos(\omega\cdot L))}{f(\omega)} & \frac{\omega\cdot(\omega\cdot L-sen(\omega\cdot L))}{f(\omega)} & 0 & -\frac{\omega^2\cdot(1-\cos(\omega\cdot L))}{f(\omega)} & \frac{\omega\cdot(sen(\omega\cdot L)-\omega\cdot L\cdot\cos(\omega\cdot L))}{f(\omega)} \end{pmatrix} \tag{18}$$

or in a more compact form

$$p_{viga} = \bar{k}_{viga} \cdot d_{viga} \tag{19}$$

where $f(\omega) = \frac{2-2\cos(\omega\cdot L)-\omega\cdot L\cdot sen(\omega L)}{E\cdot I}$ and $\bar{k}_{viga}$ is the beam stiffness matrix in local coordinates, including the influence of the axial force N.Let us note that we have identified, for the differentiation of linear stiffness matrix k_{viga}, by the stroke located on k, and which depends, via ω, on the value of the axial force on the beams (N).

Apparently, the expression of the stiffness matrix of the beam expressed in equation (18) $\bar{k}_{viga}$, is quite different from the known k_{viga}, without the inclusion of the axial force. However, we can find a similar expression when we consider that

$$tg\frac{\omega\cdot L}{2} = \frac{1-\cos(\omega\cdot L)}{sen(\omega\cdot L)} \tag{20}$$

and if we call to

$$\Psi_1 = \frac{s\cdot(1+c)}{6} - \frac{N\cdot L^2}{12\cdot E\cdot I};\quad \Psi_2 = \frac{s\cdot(1+c)}{6};\quad \Psi_3 = \frac{s}{4};\quad \Psi_4 = \frac{s\cdot c}{2} \tag{21}$$

where c and s are adimensional functions, called *stability functions*

$$c = \frac{\omega\cdot L - sen(\omega\cdot L)}{sen(\omega\cdot L)-\omega\cdot L\cdot\cos(\omega\cdot L)};\qquad s = \frac{[1-\omega\cdot L\cdot cotg(\omega\cdot L)]\cdot\omega\cdot L/2}{tg\frac{\omega\cdot L}{2}-\frac{\omega\cdot L}{2}} \tag{22}$$

which were originally derived by Lundquist and Kroll [5], and later developed by Merchant [6] under different methodology and in another context (Figure 4). We prefer

the new original approach presented here[7], because we want to show the identity of procedures and goals achieved over time, even though at times the results appear to be different and have been obtained by using very different methodologies.

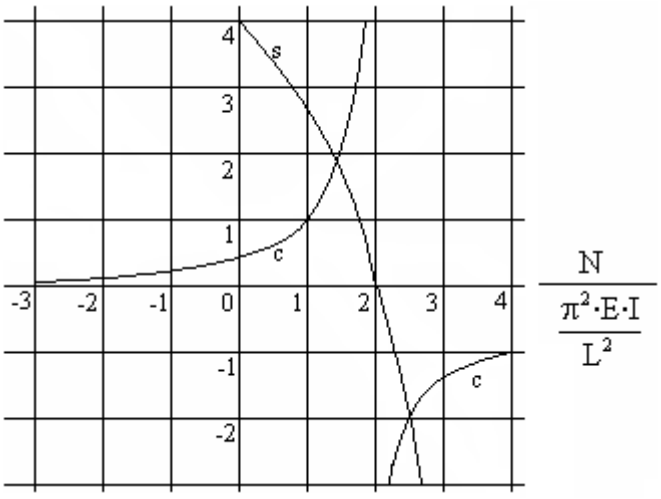


Figure 4: Stability Functions.

Operating conveniently we found that the matrix equation (16), for a beam rigidly connected at both ends and belonging to a 2D frame, is written as

$$\begin{aligned} p^{e1} &= \bar{k}^{11}\cdot d^{e1} + \bar{k}^{12}\cdot d^{e2} \\ p^{e2} &= \bar{k}^{21}\cdot d^{e1} + \bar{k}^{22}\cdot d^{e2} \end{aligned} \tag{23}$$

or in matrix form

$$\begin{pmatrix} p^{e1} \\ p^{e2} \end{pmatrix} = \begin{pmatrix} \bar{k}11 & \bar{k}12 \\ \bar{k}21 & \bar{k}22 \end{pmatrix} \cdot \begin{pmatrix} d^{e1} \\ d^{e2} \end{pmatrix} \tag{24}$$

being

$$\bar{k}^{11} = \begin{pmatrix} \frac{E\cdot A}{L} & 0 & 0 \\ 0 & \frac{12\cdot E\cdot I\cdot \Psi_1}{L^3} & \frac{6\cdot E\cdot I\cdot \Psi_2}{L^2} \\ 0 & \frac{6\cdot E\cdot I\cdot \Psi_2}{L^2} & \frac{4\cdot E\cdot I\cdot \Psi_3}{L} \end{pmatrix};\ \bar{k}^{12} = (\bar{k}^{21})^T = \begin{pmatrix} \frac{-E\cdot A}{L} & 0 & 0 \\ 0 & \frac{-12\cdot E\cdot I\cdot \Psi_1}{L^3} & \frac{6\cdot E\cdot I\cdot \Psi_2}{L^2} \\ 0 & \frac{-6\cdot E\cdot I\cdot \Psi_2}{L^2} & \frac{2\cdot E\cdot I\cdot \Psi_4}{L} \end{pmatrix}$$

$$\bar{k}^{22} = \begin{pmatrix} \frac{E\cdot A}{L} & 0 & 0 \\ 0 & \frac{12\cdot E\cdot I\cdot \Psi_1}{L^3} & \frac{-6\cdot E\cdot I\cdot \Psi_2}{L^2} \\ 0 & \frac{-6\cdot E\cdot I\cdot \Psi_2}{L^2} & \frac{4\cdot E\cdot I\cdot \Psi_3}{L} \end{pmatrix} \tag{25}$$

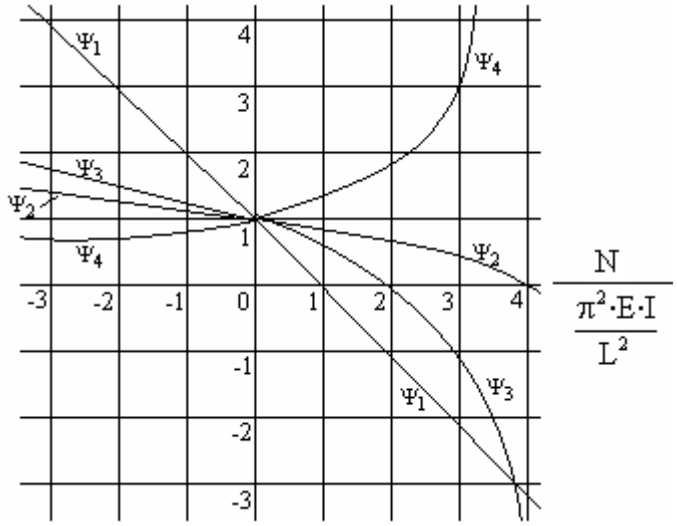


Figure 5.Stability Functions. Relation between axial force and Euler critical load.

Comparing these expressions with the known k_{ij}, it is clear that the functions Ψ are simply multiplier factors of the coefficients of the stiffness matrix of a beam without axial forces and can conveniently be expressed as functions of the relationship between axial force N and the Euler critical load $N_{cr} = \frac{\pi^2 \cdot E \cdot I}{L^2}$, as shown in Figure 5. Note that all Ψ are 1 for N = 0, so that $\bar{k}_{viga} = k_{viga}$ for N = 0.

3 GEOMETRIC STIFFNESS OF A COLUMN BELONGING TO SIMPLE SHEAR MODEL

If the beam is one of the groups of carriers of a frame modeled as a simple shear model, Figure 6, and we take the global axes of the figure

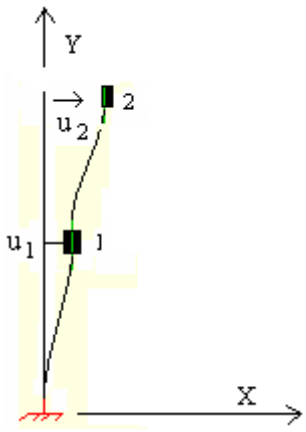


Figure 6: Simple Shear Model for a frame of 2 storys.

then equation (18) can be written as

$$\begin{pmatrix} p^{e1x} \\ p^{e1y} \\ m^{e1} \\ p^{e2x} \\ p^{e2y} \\ m^{e2} \end{pmatrix} = \begin{pmatrix} \frac{E\cdot A}{L} & 0 & 0 & -\frac{E\cdot A}{L} & 0 & 0 \\ 0 & \frac{\omega^3\,\mathrm{sen}(\omega\cdot L)}{f(\omega)} & \frac{\omega^2\cdot(1-\cos(\omega\cdot L))}{f(\omega)} & 0 & -\frac{\omega^3\,\mathrm{sen}(\omega\cdot L)}{f(\omega)} & \frac{\omega^2\cdot(1-\cos(\omega\cdot L))}{f(\omega)} \\ 0 & \frac{\omega^2\cdot(1-\cos(\omega\cdot L))}{f(\omega)} & \frac{\omega\cdot(\mathrm{sen}(\omega\cdot L)-\omega\cdot L\cdot\cos(\omega\cdot L))}{f(\omega)} & 0 & -\frac{\omega^2\cdot(1-\cos(\omega\cdot L))}{f(\omega)} & \frac{\omega\cdot(\omega\cdot L-\mathrm{sen}(\omega\cdot L))}{f(\omega)} \\ -\frac{E\cdot A}{L} & 0 & 0 & \frac{E\cdot A}{L} & 0 & 0 \\ 0 & -\frac{\omega^3\cdot\mathrm{sen}(\omega\cdot L)}{f(\omega)} & -\frac{\omega^2\cdot(1-\cos(\omega\cdot L))}{f(\omega)} & 0 & \frac{\omega^3\cdot\mathrm{sen}(\omega\cdot L)}{f(\omega)} & -\frac{\omega^2\cdot(1-\cos(\omega\cdot L))}{f(\omega)} \\ 0 & \frac{\omega^2\cdot(1-\cos(\omega\cdot L))}{f(\omega)} & \frac{\omega\cdot(\omega\cdot L-\mathrm{sen}(\omega\cdot L))}{f(\omega)} & 0 & -\frac{\omega^2\cdot(1-\cos(\omega\cdot L))}{f(\omega)} & \frac{\omega\cdot(\mathrm{sen}(\omega\cdot L)-\omega\cdot L\cdot\cos(\omega\cdot L))}{f(\omega)} \end{pmatrix} \cdot \begin{Bmatrix} d^{e1x}=0 \\ d^{e1y}=U^1 \\ \vartheta^1=0 \\ d^{e2x}=0 \\ d^{e2y}=U^2 \\ \vartheta^2=0 \end{Bmatrix} \quad (26)$$

Therefore, we obtain

$$p^{e1x}=p^{e2x}=0\ ;\ p^{e1y}=-p^{e2y}=-\frac{\omega^3\cdot\mathrm{sen}(\omega\cdot L)}{f(\omega)}\cdot\left(U^2-U^1\right)\ ;\ m^{e1y}=m^{e2y}=-\frac{\omega^2\cdot\left(1-\cos(\omega\cdot L)\right)}{f(\omega)}\cdot\left(U^2-U^1\right) \quad (27)$$

As for N=0, the functions $\frac{\omega^3\cdot\mathrm{sen}(\omega\cdot L)}{f(\omega)}$ y $\frac{\omega^2\cdot\left(1-\cos(\omega\cdot L)\right)}{f(\omega)}$ are preferred indeterminate, and we prefer to develop them using Taylor series and limiting the developments to the first two terms, we obtain

$$\begin{gathered} \frac{1}{f(\omega)}=\frac{E\cdot I}{2-2\cdot\cos(\omega\cdot L)-\omega\cdot L\cdot\mathrm{sen}(\omega\cdot L)}=\frac{12\cdot E\cdot I}{\omega^4\cdot L^4}\cdot\left(1+\frac{\omega^2\cdot L^2}{15}+\frac{67\omega^4\cdot L^4}{25200}+....\right) \\ \frac{\omega^3\cdot\mathrm{sen}(\omega\cdot L)}{f(\omega)}=\omega^3\left(\omega\cdot L-\frac{\omega^3\cdot L^3}{3!}+\frac{\omega^5\cdot L^5}{5!}+....\right)\cdot\frac{12\cdot E\cdot I}{\omega^4\cdot L^4}\left(1+\frac{\omega^2\cdot L^2}{15}+....\right)=\frac{12\cdot E\cdot I}{L^3}-\frac{36\cdot(1+\alpha)\cdot N}{30\cdot L} \\ \frac{\omega^2\cdot(1-\cos(\omega\cdot L))}{f(\omega)}=\omega^2\cdot\left(1-1+\frac{\omega^2\cdot L^2}{2!}-\frac{\omega^4\cdot L^4}{4!}+....\right)\cdot\frac{12\cdot E\cdot I}{\omega^4\cdot L^4}\left(1+\frac{\omega^2\cdot L^2}{15}+....\right)=\frac{6\cdot E\cdot I}{L^2}-\frac{(1+\alpha)\cdot N}{10} \end{gathered} \quad (28)$$

If we proceed similarly for all matrix elements, the second addends constitute the geometric stiffness matrix of the first order. If we increase the terms of the development, the third summands constitute the geometric stiffness matrix of second order and so on.

For the shear efforts at beam ends we have

$$p^{e1y}=-p^{e2y}=-\left(\frac{12\cdot E\cdot I}{L^3}-\frac{36\cdot(1+\alpha)\cdot N}{30\cdot L}\right)\cdot\left(U^2-U^1\right) \quad (29)$$

Thus, the stiffness of the column of the media set of a frame modeled as a simple shear model is

$$\bar{k}=\left(\sum\frac{12\cdot E\cdot I}{L^3}\right)-\frac{36\cdot(1+\alpha)\cdot N}{30\cdot L} \quad (30)$$

Where $\frac{12\cdot E\cdot I}{L^3}$ is the stiffness of each of the columns forming the group and N is the area weight condition of all floors above the considered column. As already discussed, α marks the level of initial imperfections, in percentage terms, relative to the deformed column.

To circumvent the approach that involves limiting the Taylor series expansion of ψ_1 to the first two terms, and also based on the representation of Figure 5, we can choose to use

a very approximate analytical expression for ψ_1. If we call $\beta = \frac{N}{\pi^2 \cdot E \cdot I / L^2}$ the function ψ_1 is given by $\psi_1 = -\beta + 1$, in which case the stiffness of the media set of columns of a frame modeled as a simple shear model is

$$\bar{k} = \sum_{i=1a\ n^o pilares} \frac{12 \cdot E \cdot I_i}{L_i^3} \cdot (1 - \beta_i) \tag{31}$$

Although the differences obtained by taking (30) or (31) are not significant, we have opted for the latter as being more accurate, even slightly, and is implemented in the program for use with equal ease.

4 RESULTS OF CALCULATING THE BUILDING TAKEN AS AN EXAMPLE

Case A) Two Story Type Building.

For the ratio of stiffnesses supposed in paragraph 1, the bending moments at the top of the column in the ground floor and at the end of the lintel for static loads are

$$M_\varphi^{pilar} \simeq \frac{q \cdot L^2}{40} = \frac{41 \cdot 5 \cdot 5^2}{40} = 31.2 \text{ kN} \cdot \text{m} \ ; \ M_\varphi^{d\,int\,el} \simeq \frac{q \cdot L^2}{25} = \frac{41 \cdot 5 \cdot 5^2}{25} = 50 \text{ kN} \cdot \text{m} \tag{32}$$

The Interstory Drift Sensitivity Coefficients and maximum deflections are

Interstory Drift Sensitivity Coefficient	
ξ1 = 0,0735	ξ2 = 0,0193
uMAX	
Without consideration to axial force	Coupling of bending moment and axial forces
U_1	$\overline{U_1}$
0,0335	0,0353
0,0405	0,0421

Table 1:Interstory Drift Sensitivity Coefficient for 2 Story Frame.

The stiffness k_p of the ground floor columns group is k_p = 7.0182 KN/m and the increases of shear force and bending moment, as a result of considering the coupling of axial bending, are

$$\Delta Q = \frac{12 \cdot E \cdot I}{L^3} \cdot (U_1 - \bar{U}_1) = \frac{7018.2 \cdot 10^3}{5} \cdot (0.0353 - 0.0335) = 2.53 \text{ kN} \tag{33}$$

$$\Delta M_\varphi = \frac{\Delta Q \cdot L}{2} = 5.05 \text{ kN} \cdot \text{m} \tag{34}$$

The latter increase in the bending moment on the column represents an increase of 16.2% from the value of the moment due to gravity loads, and an increase of 5% compared with the sum of the value of the moments due to static loads more dynamic loading. However, increases incurred as a result of considering a typical level of initial imperfections are not significant.

Case B) Four Story Type Building.

For the ratio of stiffnesses supposed in paragraph 2, the bending moments at the top of the column in the ground floor and at the end of the lintel for gravity loads are

$$M_{\varphi}^{pilar} \simeq \frac{q \cdot L^2}{40} = \frac{41 \cdot 5 \cdot 5^2}{40} = 31.2 \text{ kN} \cdot \text{m} \; ; \; M_{\varphi}^{dintel} \simeq \frac{q \cdot L^2}{20} = \frac{41 \cdot 5 \cdot 5^2}{20} = 62 \text{ kN} \cdot \text{m} \tag{35}$$

The Interstory Drift Sensitivity Coefficients and maximum deflections are:

Interstory Drift Sensitivity Coefficient	
ξ1 = 0,0709	ξ2 = 0,0279
ξ3 = 0,0386	ξ4 = 0,0193

uMAX	
Without consideration to axial force	Coupling of bending moment and axial forces
U_1	$\overline{U_1}$
0,0264	0,0282
0,0346	0,0364
0,0474	0,0493
0,0544	0,0562

Table2: Interstory Drift Sensitivity Coefficient for 4 Story Frame.

The stiffness k_p of the ground floor columns group is k_p = 14555 kN/m and the increases of shear force and bending moment, as a result of considering the coupling of axial bending, are

$$\Delta Q = \frac{12 \cdot E \cdot I}{L^3} \cdot \left(U_1 - \overline{U}_1 \right) = \frac{14555 \cdot 1}{5} \left(0.0282 - 0.0264 \right) = 5.24 \text{ kN} \tag{36}$$

$$\Delta M_{\varphi} = \frac{\Delta Q \cdot L}{2} = 10.48 \text{ kN} \cdot \text{m} \tag{37}$$

This latest increase of the bending moment on the column represents an increase of 33.59% from the value of the moment due to gravity loads, and an increase of 5.7% from the sum of the value of the moments due to gravity loads more dynamic loading. However, increases incurred as a result of considering a typical level of initial imperfections are not significant.

Case C) Seven Story Type Building.

For the ratio of stiffnesses supposed in paragraph 2, the bending moments at the top of the column in the ground floor and at the end of the lintel for gravity loads are

$$M_{\varphi}^{pilar} \simeq 1.15 \cdot \frac{q \cdot L^2}{35} = 1.15 \cdot \frac{41 \cdot 5 \cdot 5^2}{35} = 40.7 \text{ kN} \cdot \text{m} \; ; \; M_{\varphi}^{dintel} \simeq \frac{q \cdot L^2}{17.5} = \frac{41 \cdot 5 \cdot 5^2}{17.5} = 70.8 \text{ kN} \cdot \text{m} \tag{38}$$

The Interstory Drift Sensitivity Coefficients and maximum deflections are:

Interstory Drift Sensitivity Coefficient

ξ1 = 0,0392	ξ2 = 0,0302	ξ3 = 0,0251
ξ4 = 0,0193	ξ5 = 0.0279	ξ6 = 0.0386
	ξ7 = 0.0193	

uMAX

Without consideration to axial force	Coupling of bending moment and axial forces
U_1	$\overline{U_1}$
0,0126	0,0130
0.0201	0,0206
0,0266	0,0272
0,0370	0,0378
0.0454	0.0463
0.0588	0.0601
0.0668	0.0681

Table3: Interstory Drift Sensitivity Coefficient for 7 Story Frame.

The stiffness $k_p$of the ground floor columns group is k_p= 45999 kN/m and the increases in bending moment and shear forces, as a result of considering the coupling of axial deflection, are

$$\Delta Q = \frac{12 \cdot E \cdot I}{L^3} \cdot \left(U_1 - \bar{U}_1 \right) = \frac{45999}{5} \left(0.0130 - 0.0126 \right) = 3.68 \text{ kN} \tag{39}$$

$$\Delta M_{\varphi} = \frac{\Delta Q \cdot L}{2} = 7.36 \text{ kN} \cdot \text{m} \tag{40}$$

This latest increase of the bending moment on the column represents an increase of 18.08% over the value of the moment due to gravity loads, and an increase of 2.7% from the sum of the value of the moments due to static loads more dynamic loading. However, increases incurred as a result of considering a typical level of initial imperfections are not significant.

Case D) Ten Story Type building.

For the ratio of stiffnesses supposed in paragraph 2, the bending moments at the top of the column in ground floor and at the end of the lintel for gravity loads are

$$M_{\varphi}^{\text{pilar}} \simeq \frac{q \cdot L^2}{30} = \frac{41 \cdot 5 \cdot 5^2}{30} = 41.3 \text{ kN} \cdot \text{m} \; ; \; M_{\varphi}^{\text{d int el}} \simeq \frac{q \cdot L^2}{15} = \frac{41 \cdot 5 \cdot 5^2}{15} = 82.6 \text{ kN} \cdot \text{m} \tag{41}$$

The Interstory Drift Sensitivity Coefficients and maximum deflections are:

Interstory Drift Sensitivity Coefficient

ξ1 = 0,0230	ξ2 = 0,0109	ξ3 = 0,0236
ξ4 = 0,0206	ξ5 = 0,0302	ξ6 = 0,0251
ξ7 = 0,0372	ξ8 = 0,0279	ξ9 = 0,0386
	ξ10 = 0,0193	

uMAX

Without consideration to axial force	Coupling of bending moment and axial forces

U_1	$\overline{U_1}$
0,0066	0,0067
0,009	0,0091
0,0145	0,0146
0,0195	0,0196
0,027	0,0273
0,0335	0,0339
0,0438	0,0444
0,0522	0,053
0,0661	0,0673
0,0746	0,0759

Table 4.Interstory Drift Sensitivity Coefficient for 10 Story Frame.

The stiffness k_p of the ground floor columns group is k_p = 112150 KN/m and the increases in bending moment and shear forces, as a result of considering the coupling of axial deflection, are

$$\Delta Q = \frac{12 \cdot E \cdot I}{L^3} \left(U_1 - \bar{U}_1 \right) = \frac{112150}{5} \left(0.0067 - 0.0066 \right) = 2.24 \text{ kN} \tag{42}$$

$$\Delta M_\varphi = \frac{\Delta Q \cdot L}{2} = 4.49 \text{ kN} \cdot \text{m} \tag{43}$$

This latest increase of the bending moment on the column represents an increase of 10.87% from the value of the time due to gravity loads, and an increase in 1.35% from the sum of the value of the moments due to gravity loads more dynamic loading. However, increases incurred as a result of considering a typical level of initial imperfections are not significant.

5 DIMENSIONING INTERSTORY DRIFT SENSITIVITY COEFFICIENT

In the seismic calculation of a building, Spanish Instructions NCSE-02 and therefore, the CTE, establish in paragraph 3.7.7 that: “As long as the collapse of the head of the building does not exceed two per thousand of the height, it is not necessary to consider the 2nd order effects”.

On the other hand, it will not be necessary to consider the 2nd order effects, in line with that set by Eurocode Nº 8 (Paragraph1-2 Part 1-1), if for all storys the Interstory Drift Sensitivity Coefficient is less than 0.1.

As we can see, what is actually limiting the destabilizing moment is that the column is less than 10% of the stabilizing moment. Because the criterion of the 10% limit seems to be arbitrary, we propose to replace it with another limit that is more in line with the structural reality.

If we assume a square section column of side "b", for frequently used materials and for the dimensions set out in paragraph 1, the relationship between the critical load and the axial calculation is $\frac{N_{crit}}{N_{cálc}} \simeq 150 \cdot b^2$, so that we obtain $N_{calc} = 0.075 \cdot N_{crit}$ for b = 0.30m, and for b = 0.35m (corresponding to buildings of lesser heights) we have $N_{calc} = 0.055 \cdot N_{crit}$. Accordingly, we adopt

$$N_{calc} < 0.075 \cdot N_{crit} \tag{44}$$

Under this assumption,coefficient β, defined in paragraph 3, $\beta = \dfrac{N}{\pi^2 \cdot E \cdot I / L^2} = \dfrac{N_{calc}}{N_{crit}}$, gives

$$\beta \cdot N_{crit} = N_{calc} < 0.075 \cdot N_{crit} \tag{45}$$

Keeping the definition for the interstory drift sensitivity coefficient and by taking into account formula (27), we can write

$$\xi = \frac{N \cdot d}{F \cdot h} = \frac{N \cdot d}{\dfrac{12 \cdot E \cdot I}{L^3} \cdot \psi_1 \cdot d \cdot L} = \frac{\pi^2 \cdot \beta}{12 \cdot \psi_1} \tag{46}$$

From which we deduce $\beta = \dfrac{12 \cdot \psi_1 \xi}{\pi^2}$ and as $\psi_1 = -\beta + 1$,we obtain $1 - \psi_1 = \dfrac{12 \cdot \psi_1 \xi}{\pi^2}$. So,

$$\psi_1 = \frac{1}{1.216 \cdot \xi + 1} \tag{47}$$

By virtue of (45), it must be satisfiedthat $\beta < 0.075$, i.e.,$1 - \dfrac{1}{1.216 \cdot \xi + 1} < 0.075$. From which we deduce

$$\xi < 0.0667 \tag{48}$$

which is consistent with the results obtained in the practical cases A) and B) of paragraph 4.

6 CONCLUSIONS

In the seismic calculation of a building, Spanish Instructions NCSE-02 and thus, the CTE, establish in paragraph 3.7.7 that: “As long as the collapse of the head of the building does not exceed two per thousand of the height, it is not necessary to consider the effects of 2nd order”.

On the other hand, it will not be necessary to consider the 2nd order effects ($P-\Delta$ effects), in line with that set by Eurocode 8 (Paragraph1-2 Part 1-1), if for all storys the interstory drift sensitivity coefficient fulfills:

$$\xi = \frac{P \cdot d}{F \cdot h} \leq 0.1 \tag{49}$$

We show in this discussion, based on the current state of knowledge, it is not justified to ignore the 2nd order effects ($P-\Delta$ effects):

1)Because it is not justified that the spectral modal analysis be simplified, because a high-level program such as Matlab can very easily address a multimodal spectral analysis study for frames, the simple model of shear or associating the nodes of the structure of the inertial properties of the frame beams and performing a calculation of stiffness.

2)Because the inclusion of 2nd order effects (effects), does not add any conceptual effort nor complicate the calculation. Additionally, if we follow the line of

thought of Bazant [8] and truly think that the equilibrium, static or dynamic loading, occurs in the deformed geometry, it is logical that the calculation includes this.

3) Because we show that although the Interstory Drift Sensitivity Coefficient does not reach the value of 0.1, increases of the bending moment at the ends of the columns resulting from the refinement of the calculation including the second order effects, can account for between 15% and 34% of its value for static service loads.

4) Because most adverse effects are shown in lower height buildings (up to 5 floors), which is precisely the range in which most of the housing stock of Spain is located, to be in the highest limit allowed by the various planning regulations (PGOU).

5) As in section 5, we limited the Interstory Drift Sensitivity Coefficient to 0.0667 for buildings of lower height (up to 5 floors), so we propose that it is generally lowered to $\xi =\leq 0.06$

REFERENCES

[1] *Norma de Construcción Sismorresistente NCSE-02*.(2002).Parte General y Edificación. Ministerio de Fomento, España.

[2] *Código Técnico de la Edificación*. (2004). Ministerio de Fomento, España.

[3] European Committee for Standardization, *Eurocode 8. Design of Structures for Earthquake Resistance. Part 1: General Rules, Seismic Actions and Rules for Buildings*. Doc. EN 1998-1 2005.

[4] R.K. Livesley, *Matrix methods of Structural Analysis*. Pergamon Press, 1975.

[5] E.E. Lundquist and W.D. Kroll.*"Extended tables of stiffness and carry-over factor for structural members under axial load"*. Langley Field, VA.Langley Memorial Aeronautical Laboratory, 1944.

[6] W. Merchant, *The failure load of rigidly jointed frameworks as influenced by stability*, The Structural Engineer, 32,185-190, 1954.

[7] J.M. Martínez-Jiménez and J.M. Martínez-Valle,(2010). *Diseño y Calculo Elástico de los Sistemas Estructurales, p 886-902. Tomo II: Inestabilidad y pandeo de estructuras, líneas de influencia y cálculo dinámico*. Bellisco.

[8] Z.P. Bazant and L.Cedolin, *Stability of structures (Elastic, Inelastic, Fracture, and Damage Theories)*, 419-466, Oxford University Press, New York, USA, 1991.

COMPDYN 2013
4th ECCOMAS Thematic Conference on
Computational Methods in Structural Dynamics and Earthquake Engineering
M. Papadrakakis, V. Papadopoulos, V. Plevris (eds.)
Kos Island, Greece, 12–14 June 2013

ANALYSIS AND DESIGN OF STAIRCASES AGAINST SEISMIC LOADINGS

Ioannis A. Tegos[1], Vassilis P. Panoskaltsis[2] and Sevasti D. Tegou[3]

[1] Aristotle University of Thessaloniki
Department of Civil Engineering
e-mail: itegos@civil.auth.gr

[2] Demokritos University of Thrace
Department of Civil Engineering
e-mail: vpanoska@civil.duth.gr

[3] Aristotle University of Thessaloniki
Department of Civil Engineering
e-mail: stegou@civil.auth.gr

Keywords: Staircases, Space Structure, Multistory Building, Earthquake, Vertical Component of Earthquake, Finite Element Analysis.

In this work all types of staircases are studied with respect to: First, earthquake design requirements and second, their complex interactions with the multistory space frame in which they belong. In the first case the essential influence of the vertical component of the earthquake's acceleration on the structure's performance is examined. In the second case the staircases' behavior is studied, as well as the important role that they play as structural seismic connections, in the response and behavior of space structures. In particular, external staircases, which connect structurally independent multistory systems are studied. In addition, in this work, a multistory external staircase that connects buildings in an area of high seismicity is analyzed. Staircases that present special design challenges due to gravity and earthquake loadings are also investigated. These structures include staircases with a free landing as well as helical cases. This work, beyond its theoretical interest, may prove important to practicing engineers as well, since it contains (almost) all types of staircases.

1 INTRODUCTION

Staircases constitute a very important part of a structure, both architecturally and aesthetically, as well as structurally. They appear in different shapes and forms, each requiring its own method of analysis [1-2]. Regarding their structural configuration stairs usually fall in one of the following categories: a) Stairs with cantilever steps that are supported on a shear wall along the stair. b) Stairs whose steps are supported on a slab (Figure 1). In this case, the slab with its two landings constitutes one structure with one or three branches. c) Stairs whose steps are supported on two girders, like simply supported beams (Figure 2). d) Stairs with free standing landings, with branches perpendicular or parallel to each other (in plan view) (Figure 3). e) Helical stairs (Figure 4) which are supported on the slabs of the upper and lower floors, without intermediate supports.

The parts of buildings with staircases have an increased stiffness with respect to the rest of the building, because of the presence of shear walls supporting the staircases. It should be noted that in the areas of the buildings with staircases the elevators' pits also exist, whose reinforced concrete shear walls contribute to the stiffness of the structure. In the case of an earthquake stairs are crucial for the safe exit from the building. Stairs with cantilever steps (first group of staircases in the classification provided above) do not experience problems from earthquake action.

In the other cases, the earthquake's effect on the staircases may be detrimental to the structure's safety. For example, the relative displacement of the stair's ends which are on different floors, causes a considerable distress and must be taken into account in the design stage of the structure. Furthermore, the interaction between the staircases and the other parts of the three dimensional structure (space structure), i.e., the interaction with the beams, columns and shear walls, result to patterns of deformation that are not usually studied during the design process. For example, the increased strength and stiffness of a structure in the stairway region will influence the seismic torsional distress of the structure and may lead to shear failure of the staircase itself or of other elements of the structure.

It is noteworthy that in two recent earthquakes in New Zealand (Darfield, 2010 and Lyttleton, 2011) the staircases in at least four multistory buildings collapsed, while several others were damaged severely [2]. Because of the extensive damage of staircases both from reinforced concrete as well as metallic, the authorities revised the relevant codes regarding the design of new staircases as well as the evaluation of the response of the existing ones, under earthquake actions. The importance of the phenomenon of interaction of staircases and their buildings has made it a very active area of research in earthquake engineering. Recent research has shown that the presence of staircases has altered the mode shapes of the structure making, in several cases, the torsional mode shape the fundamental one of the structure [3]. Furthermore, in case of frame type of structures the columns and the beams which are close to the staircases are the most vulnerable part of the structure [4], while shear is the most prominent cause of failure in case of short columns that are formed in the staircases area [5].

In this work impressive architecturally staircases, which are usually avoided because of their complex structural behavior under vertical as well as seismic loading are studied. Structures of this type include the staircases with a free landing as well as the helical ones.

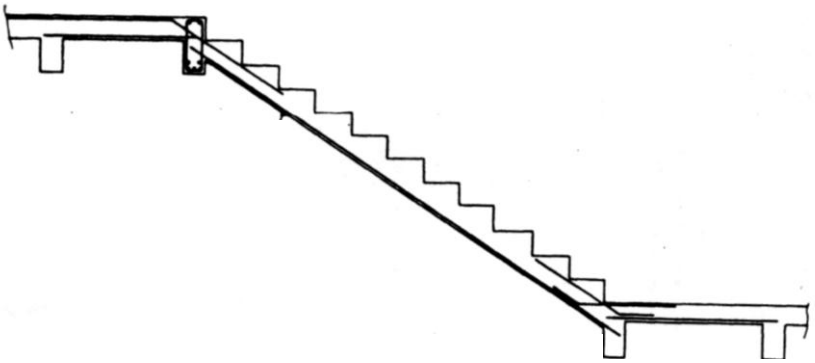


Figure 1: Typical stair whose stairs are supported on slabs.

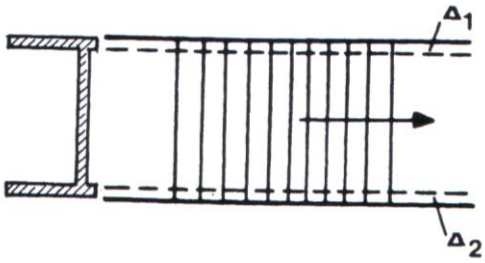


Figure 2: Stairs whose steps are supported on two girders.

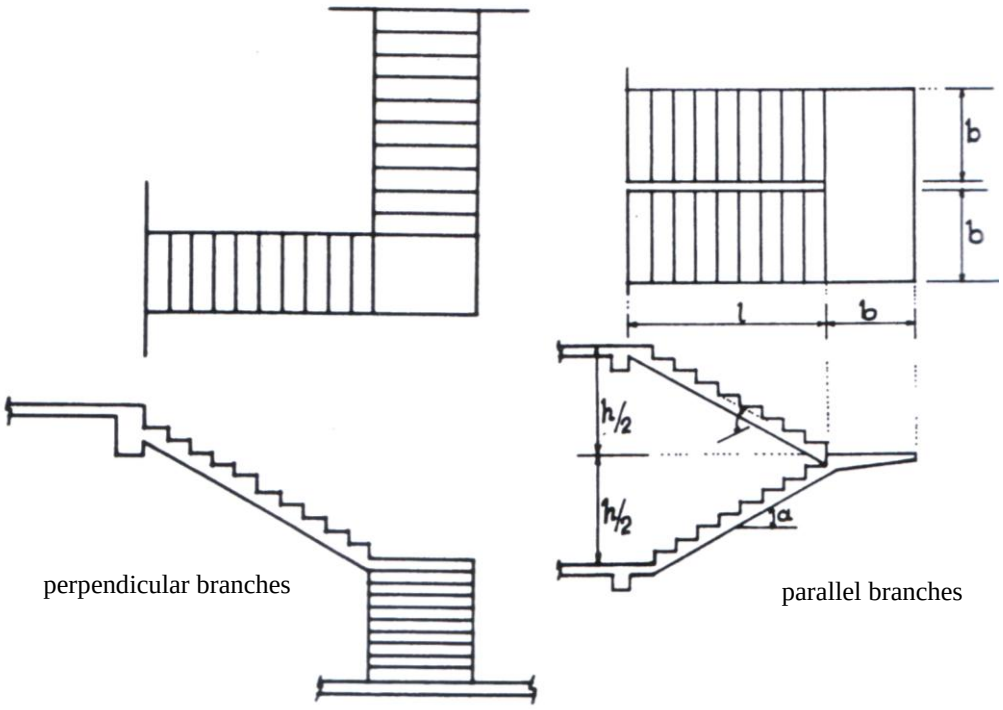


Figure 3: Stairs with free-standing landings.

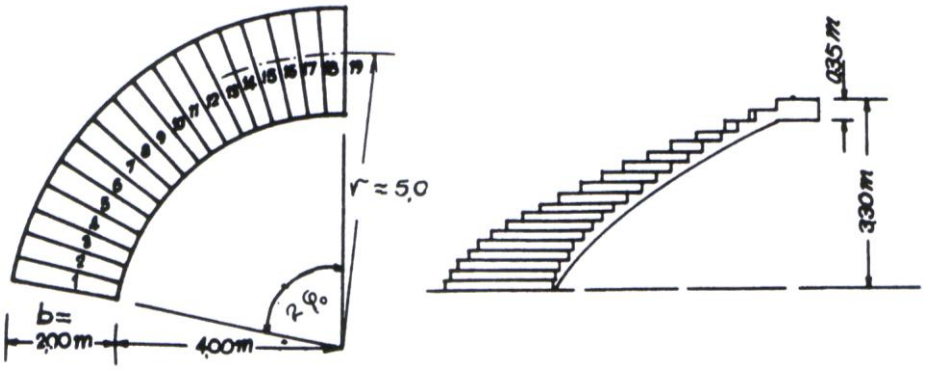


Figure 4: Typical helical stairs.

Furthermore, in this investigation the influence of the vertical component of the earthquake, which can sometimes prove to be crucial, as well as the role of staircases as seismic connections influencing to an important degree the behavior of the space (three dimensional) structure is also studied. External staircases connecting structurally, independent multistory buildings are also studied.

Finally, a multistory building with staircases whose steps are not fixed on the walls of the core is considered as the reference case. The response of this building under earthquake loading by taking the staircases into account as well as by ignoring them is compared, in order to obtain useful conclusions for the building's behavior.

2 INVESTIGATION ON THE INFLUENCE OF A STAIRCASE FORM TO THE RESPONSE OF A MULTISTORY BUILDING

2.1 Description of the structure studied

The structure studied in this work consists of a ground floor and eight floors. The height of each floor is h=3.0m, while the building's total height is H_{tot}=24m. The structure does not have a basement and its foundation consists of a slab on grade with depth equal to 1.0m. The allowable stress of the foundation soil was determined to be σ_{all}=260 kN/m^2. The building is in a seismicity zone II (α_g=0.24g, where g is the acceleration of gravity) and the foundation soil is of type B. The concrete that was used for the building's construction is of type C25/30, while the steel is B500C of high ductility.

In the building studied in this investigation there are no internal beams, resulting to large relative displacements between the slabs of the floors (drift). This configuration is chosen in order to study the effect of earthquakes on staircases under the worst possible conditions. There are shear walls in the staircase area as well as in the four corners of the building along the two main directions (Figures 5 to 9). The following five different types of staircases are studied: a) Staircase of figure Π. In this case the staircase has two branches with steps; each branch with its two landings may be considered as one structure (Figure 5). b) Staircase of figure Π with a free landing (Figure 6). c) Straight staircase with a free landing (Figure 7). d) Two staircases, one being a staircase of figure Π and the other a straight staircase with a free landing; this is a combination of cases (a) and (c) (Figure 8). e) A helical staircase (Figure 9).

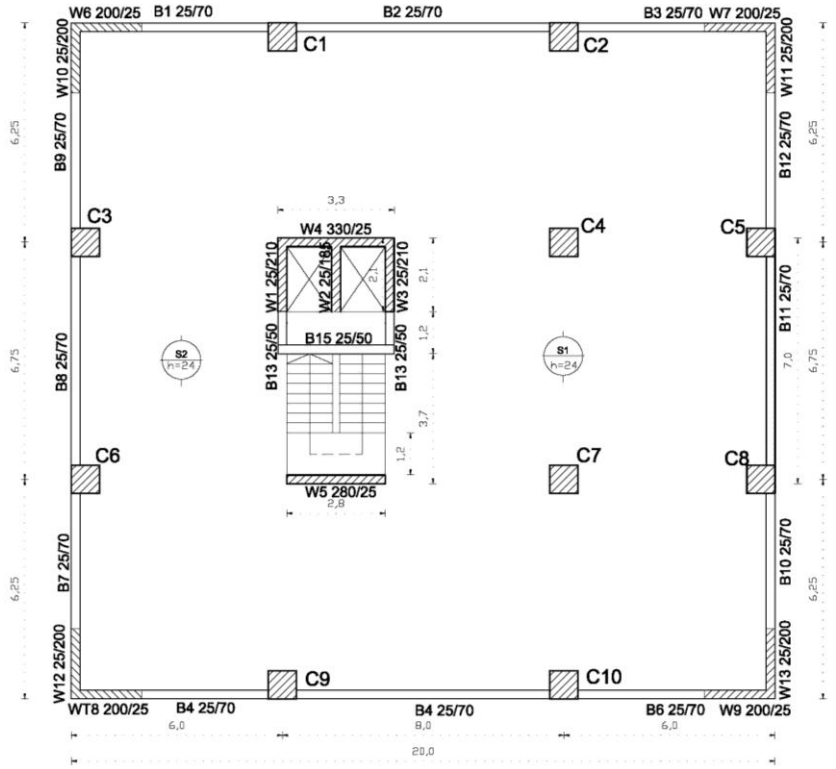


Figure 5: Plan view of a typical floor with staircase of figure Π (Type 1).

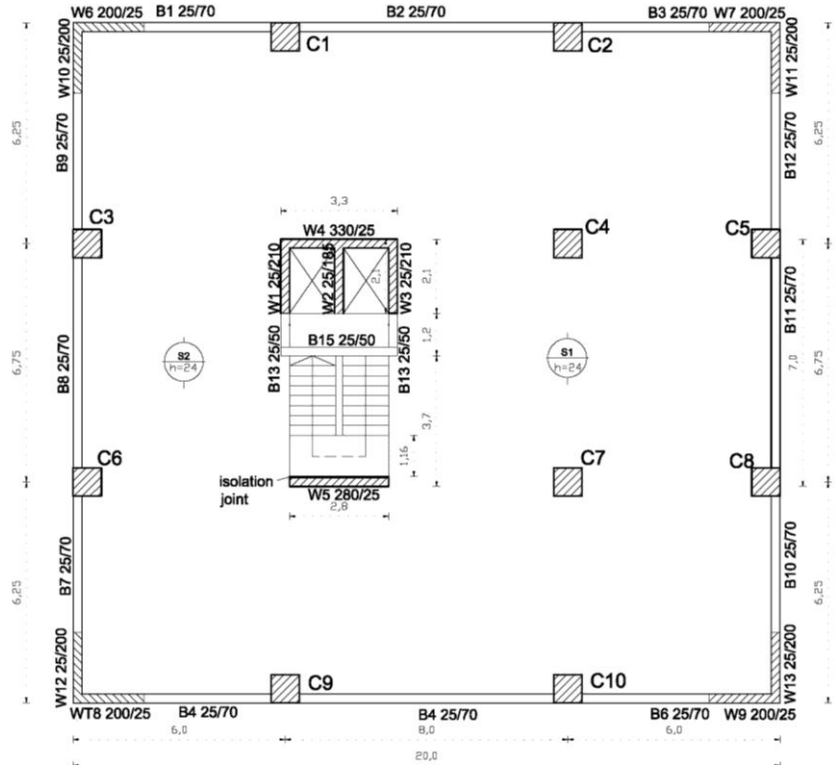


Figure 6: Plan view of a typical floor with staircase of figure Π with free landing (Type 2).

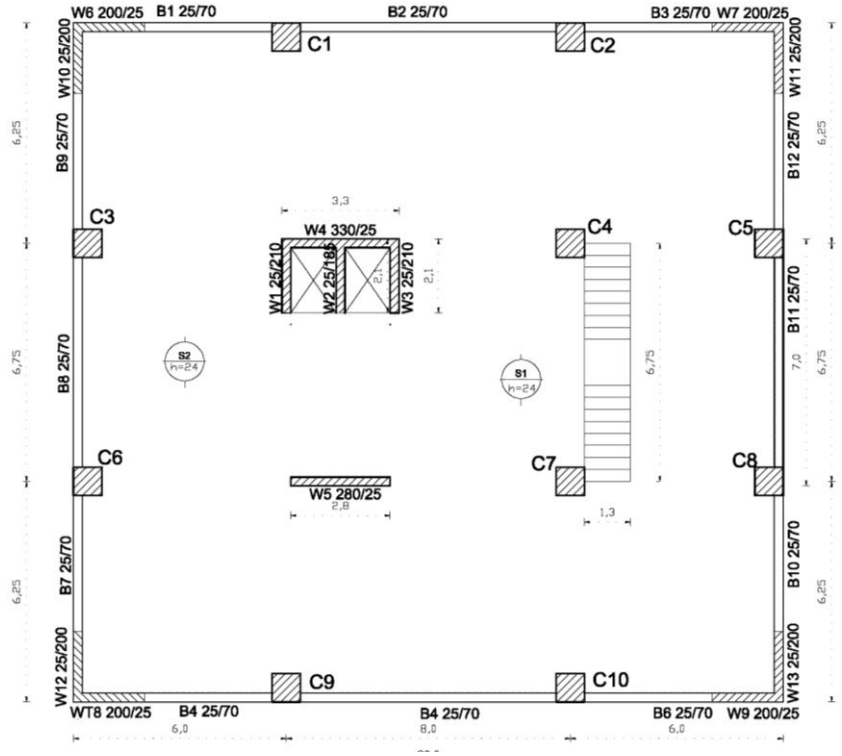


Figure 7: Plan view of a typical floor with straight staircase with free landing (Type 3).

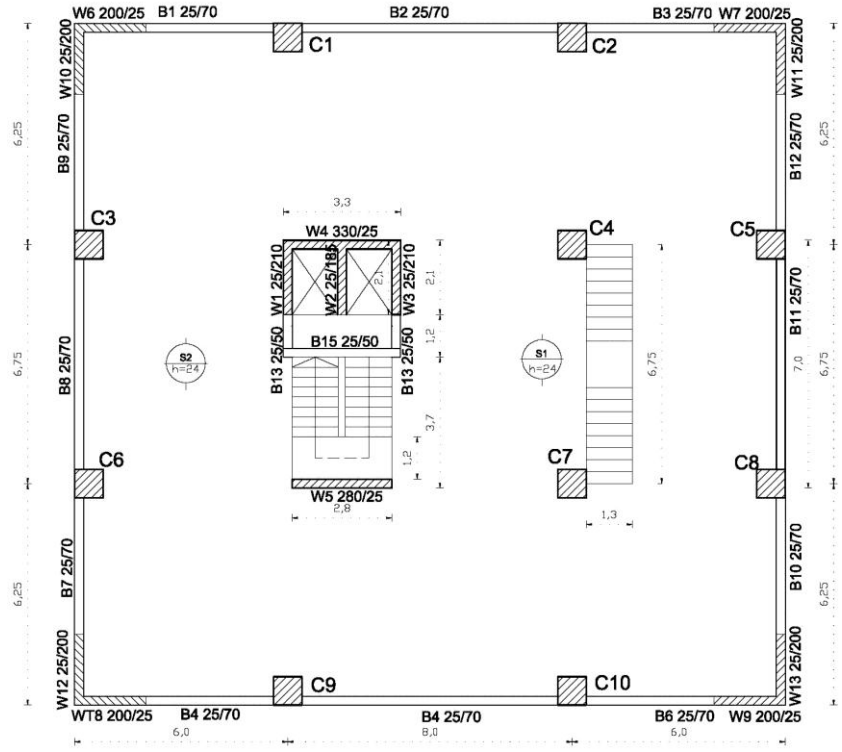


Figure 8: Plan view of a typical floor with two staircases (staircase of figure Π and straight staircase with free landing) (Type 4).

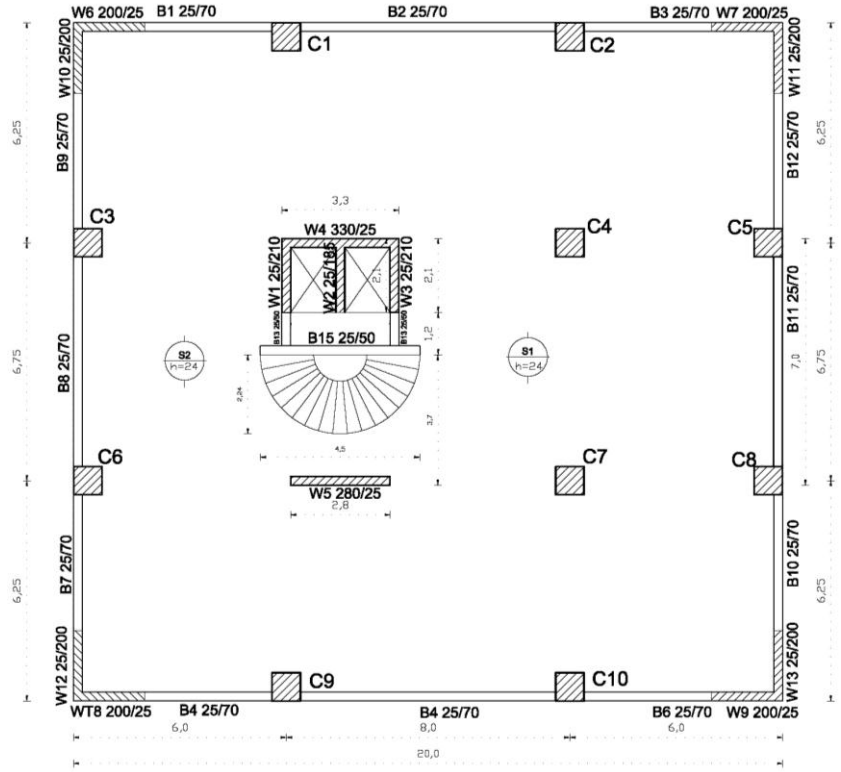


Figure 9: Plan view of a typical floor with helical staircase (Type 5).

2.2 Modeling and analysis of the structures considered

The modeling and the analysis of the structure was accomplished with the help of the finite element environment SAP2000 [6]. The three dimensional model of the structure that was formed is shown in Figure 10.

The slabs and the staircases were modeled with 3node or 4node shell elements with six degrees of freedom per node. With these elements the behavior of slabs and staircases can be modeled, either as 3D structures taking the bending into account or as 2D structures acting as membranes. In order to get more accurate results the mesh near the supports of the slabs and staircases, i.e., near the columns, as well as at the corners of shear walls and of the cores of the shear walls was refined. In Figure 11, details of modeling of staircases are shown. It should be mentioned that the modeling and analysis of the slabs of the structure (recall, that there are no internal beams) by using the method of the equivalent frames, described in the code would clearly lead to erroneous results, since in this case we don't have a regular distribution of vertical elements. Moreover, this method has several weaknesses and deficiencies regarding the decomposition of the vertical load along the directions x and y.

The core was modeled by equivalent columns at the centroids of the individual walls of the core, and by rigid beams at the floor levels. The rest of the structural elements (i.e., columns, individual shear walls and beams on the structure's perimeter) were modeled by one dimensional elements. The concrete's Young modulus was taken as E_{cm}=31 GPa, corresponding to the C25/30 type of concrete. The stiffnesses of the elements were reduced, according to the stage II assumption [7].

For the dynamic analysis of the structure (earthquake effect) the multi-modal response spectrum method was employed, according also to Eurocode 8 [8]. In the mass of each floor, the mass of half the upper and lower columns and shear walls are included. The total mass of each floor is considered to be lumped at its center of mass. The masses are calculated from the vertical loads $G+\psi_2 Q$, where G and Q are the representative values of permanent (dead) and live loads respectively and ψ_2 is the combination factor. This factor is taken equal to 0.3 for residence buildings, offices and stores, according to Eurocode 8 [8]. It should be noted that the permanent loading G and the live load Q act on the whole surface of the slab. The building's behavior factor is taken equal to 3.0.

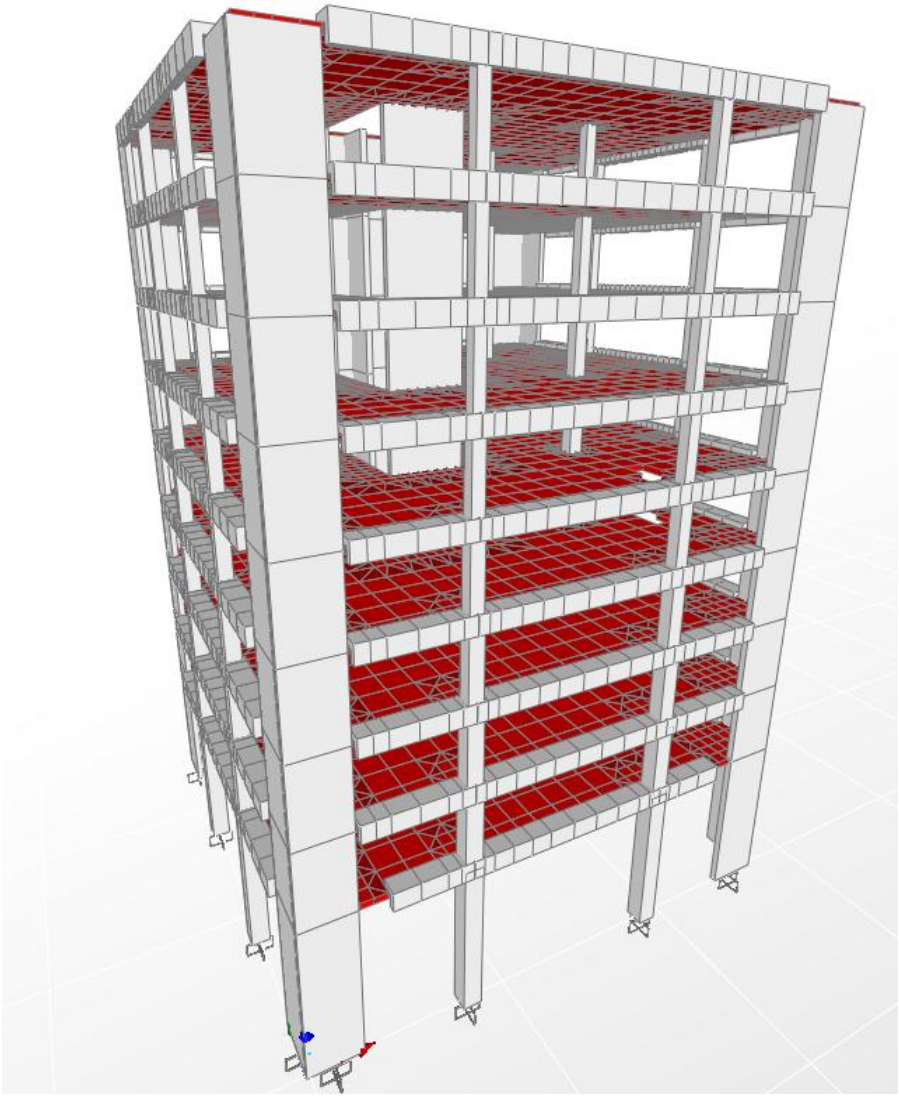
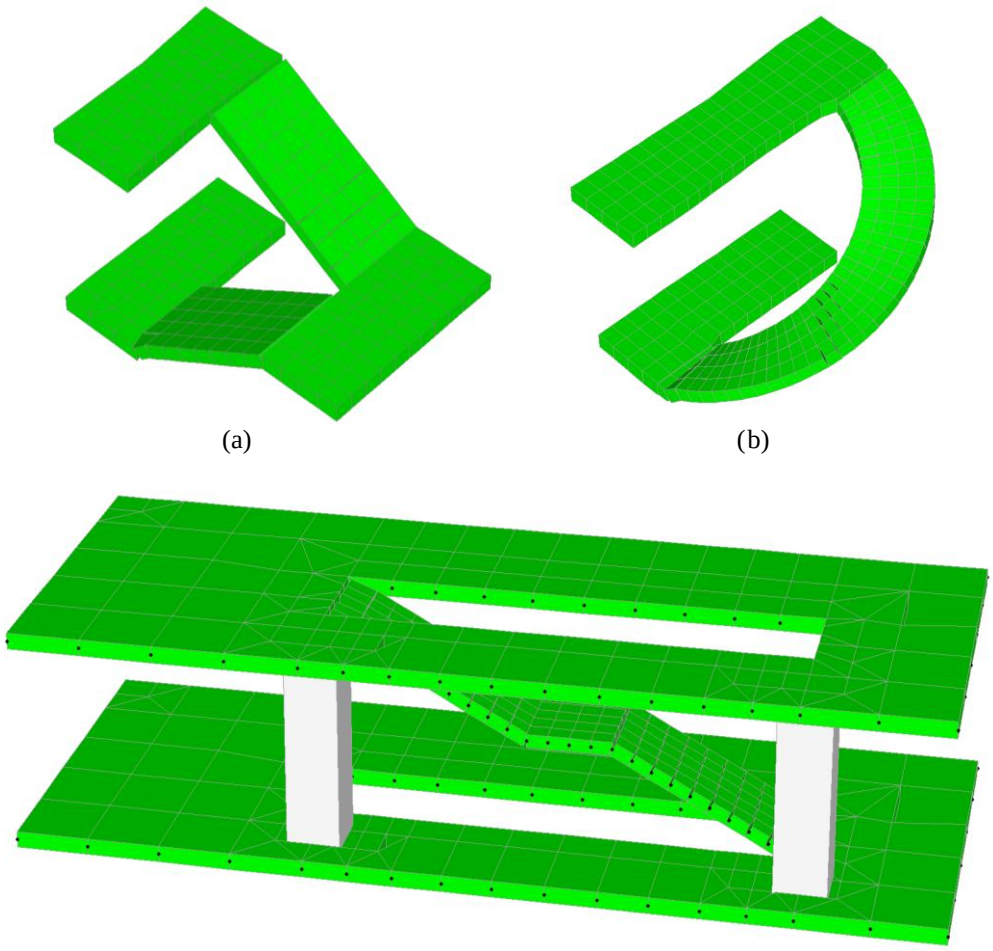


Figure 10: 3D model of the typical building studied in this investigation.



(a) (b)

(c)

Figure 11: Details of modeling of: (a) staircase of figure Π, (b) helical staircase and (c) crooked staircase with a free landing.

2.3 Results

For the dynamic analysis the multi-modal response spectrum method was employed. The structure was analyzed as a space frame, for six different cases. First, in the analysis any type of staircases was not included (Type 0 in Table 1). Next, the structure was analyzed five times, each time incorporating one of the five types of staircases referred to earlier in Section 2.1 (Types 1, 2, 3, 4 and 5 in Table 1). In Table 5 the results of the analysis for the two fundamental translational natural periods of vibration of the structure for the six different cases are reported. As is seen in the Table the inclusion of the staircase in the analysis reduces the structure's natural period of vibration in the transversal direction, for all types of staircases. The reduction is more prominent in case (d), in which two staircases exist in the building. The reduction in this case, results to the longitudinal modal shape becoming the first modal shape of vibration.

Moreover, the incorporation of staircases in the analysis results to a reduction of the relative displacements of the floors, under the action of the transversal design earthquake with acceleration a_g= 0.24g. The results are presented in Figure 12, in which it is seen that the reduction of the relative displacements is larger in higher floors. It is also seen that the reduction

is bigger in case (d), reaching the considerable amount of 22%. It was also found out that the influence of the staircases in the reduction of the relative displacements of the floors, under the action of a longitudinal earthquake is insignificant.

In Figures 13 to 17, the bending and torsional moments at three characteristic cross sections of the staircases connecting the last two stories of the structure are reported; in particular the moments at heights equal to 27.0m, 28.5m and 30.0m are reported. The failure effects because of the vertical combination of loads (1.35G + 1.50Q), as well as the earthquake combination of loads (G + 0.3Q ± E) were considered in the analysis. Regarding the earthquake action was considered each time the earthquake acting along one of the principal directions of the building (i.e., along x, y, z) in conjunction with the 30% of earthquake loading acting along the other two directions. It is seen from the analysis (Figures 13 to 17) that in most cases of staircases the moments resulting from seismic loadings are larger from those resulting from vertical loadings; therefore the seismic combination of loadings is crucial for the structure. Another of the findings is that the influence of the vertical component of the earthquake is crucial in staircases with a free landing (Type 2) as well in helical staircases (Type 5). Moreover, the resulting torsion, both from the earthquake loading as well as from vertical loads, are significant. In particular, in the helical staircase the combination of the vertical loads because of the combined action of bending, shear and torsion is the critical one, Figure 16.

Direction	Period					
	Without staircase	With staircase				
	Type 0	Type 1	Type 2	Type 3	Type 4	Type 5
X- long.	0.943	0.948	0.950	0.950	0.943	0.952
Y- trans.	1.065	0.969	1.046	1.011	0.891	1.050

Table 1: Natural Periods of vibration of the analyzed structures

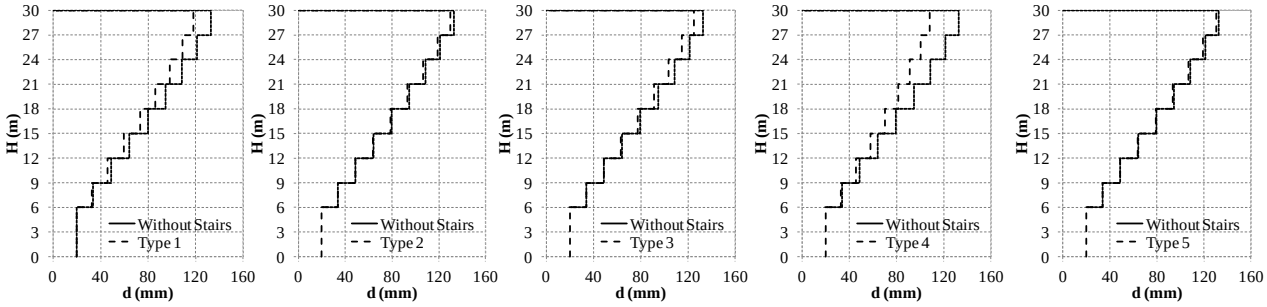


Figure 12: Relevant displacements between the floors' slabs due to the transverse design earthquake (ag=0.24g).

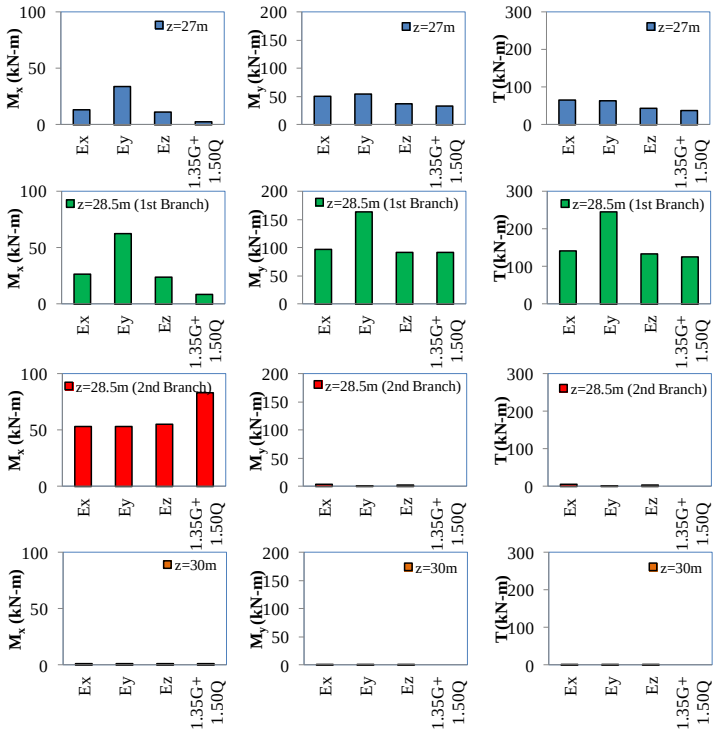


Figure 13: Bending moments (M_x and M_y) and torsional moments (T) at the ends of the branches of the staircase of figure Π (Type 1) of the upper floor due to X, Y and Z earthquake.

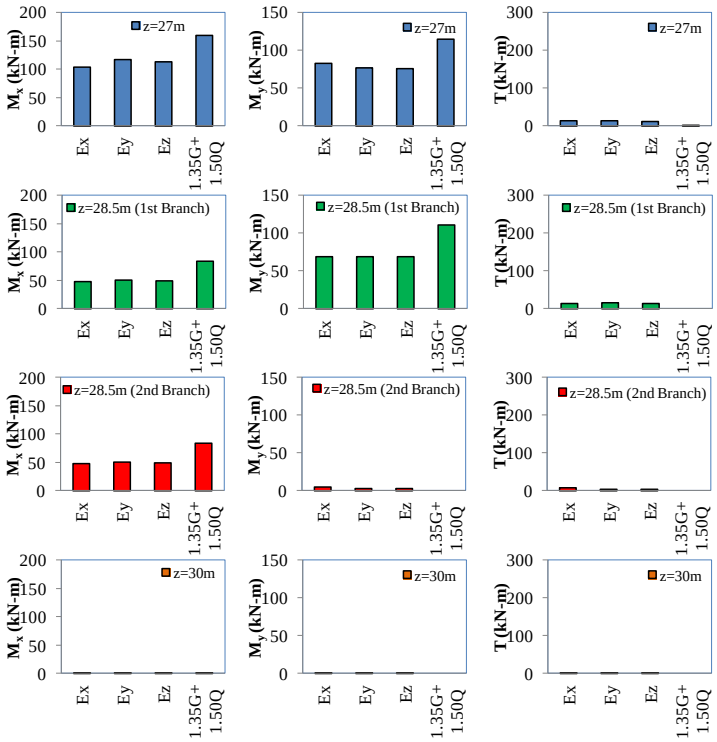


Figure 14: Bending moments (M_x and M_y) and torsional moments (T) at the ends of the branches of the staircase of figure Π with free landing (Type 2) of the upper floor due to X, Y and Z earthquake.

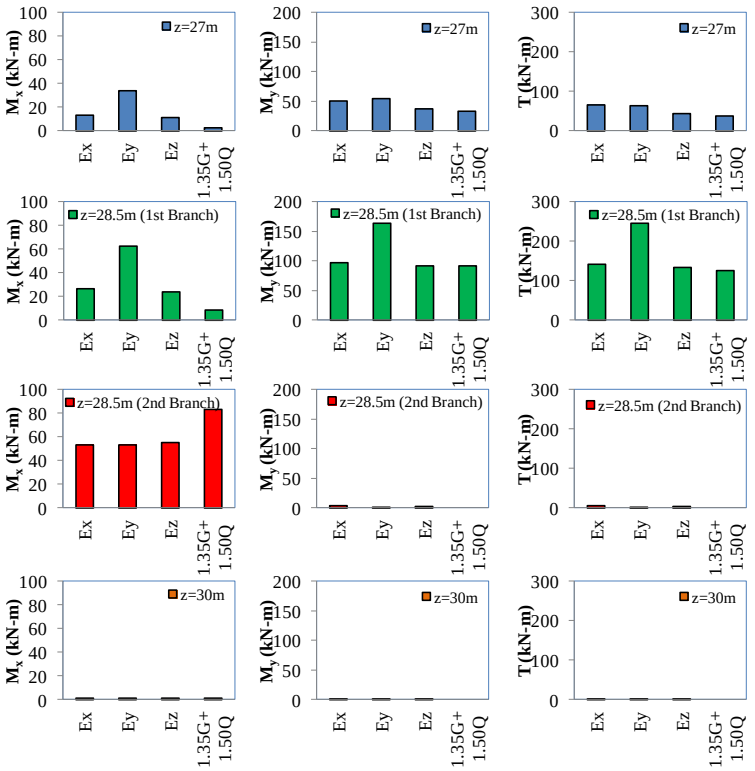


Figure 15: Bending moments (M_x and M_y) and torsional moments (T) at the ends of the branches of the straight staircase (Type 3) of the upper floor due to X, Y and Z earthquake.

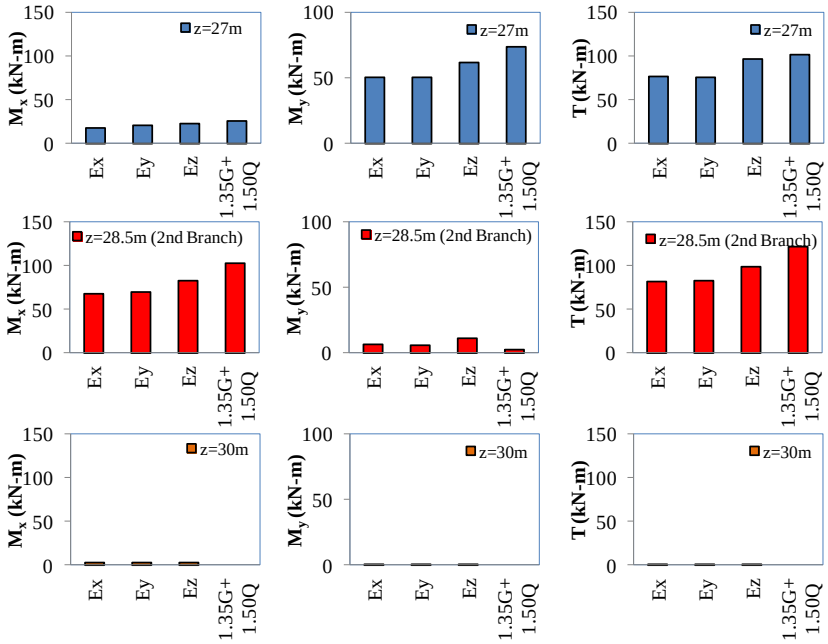


Figure 16: Bending moments (M_x and M_y) and torsional moments (T) at the ends of the branches of the helical staircase (Type 5) of the upper floor due to X, Y and Z earthquake.

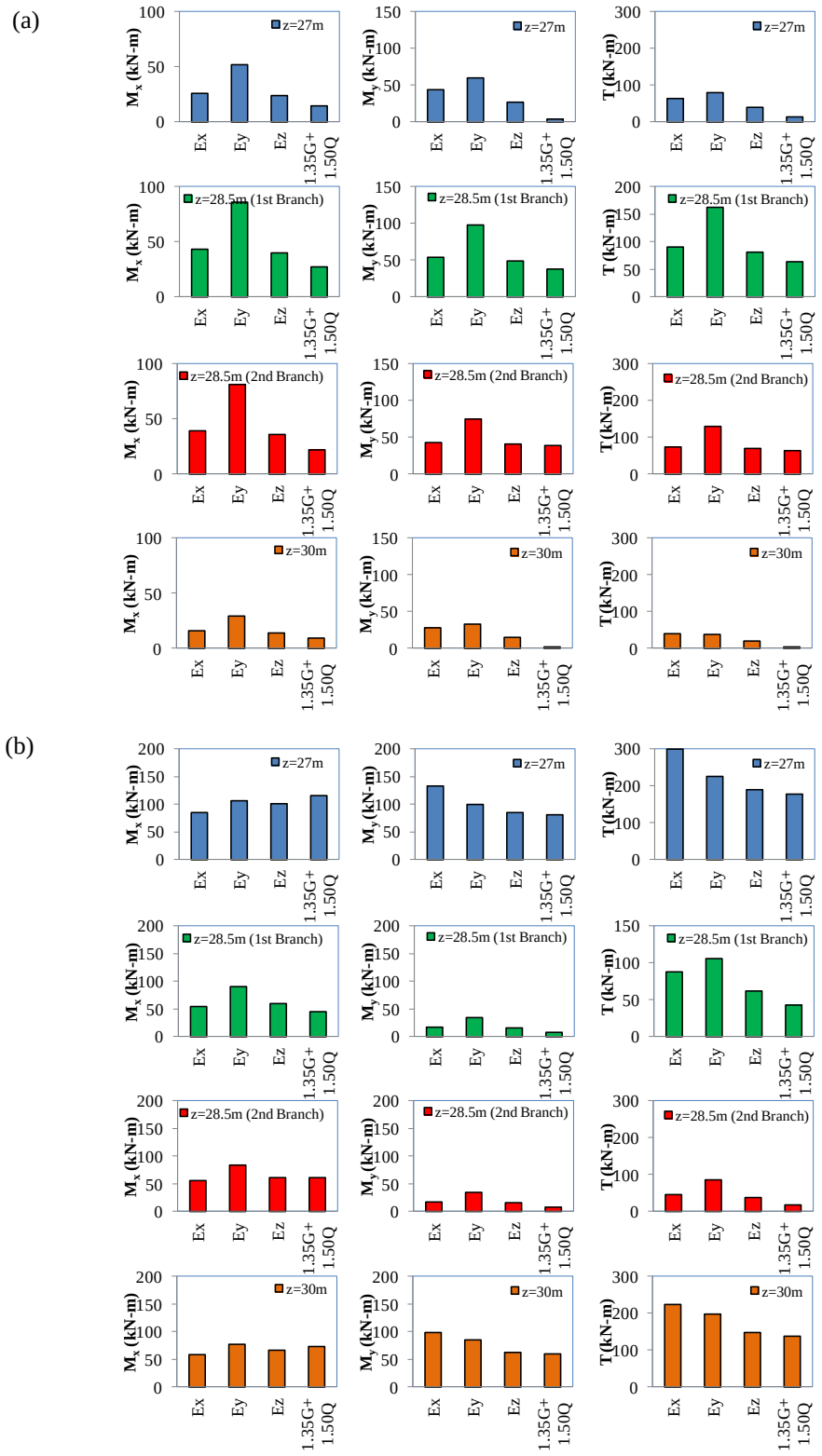


Figure 17: Bending moments (M_x and M_y) and torsional moments (T) at the ends of the branches of (a) the staircase of figure Π and (b) the straight staircase (Type 4) of the upper floor due to X, Y and Z earthquake.

3 INVESTIGATION OF AN EXTERNAL STAIRCASE CONNECTING MULTISTORY BUILDINGS

In this section an external staircase connecting two buildings that are otherwise structurally independent is studied. This is a problem with important applications as this is a case that is met frequently in practice. In Figure 18, the floor plans of the typical floors of the two buildings are shown. The whole structure under investigation consists of two independent buildings (I and II) above the ground floor. These buildings are connected with a central staircase, as shown in Figure 18. There are three basement (underground) levels extended in the whole area of the lot (i.e., common for the two buildings), used for parking purposes. Building I consists from a ground floor with height equal to 4.00m and eight stories, of height equal to 3.20m each. The total height of building I is equal to 29.60m. Building II consists from a ground floor with height equal to 4.00m and seven stories, of height equal to 3.20m each. The total height of building II is equal to 26.40m. It should be noted that there are inclined columns in the front view of both buildings, resulting to the gradual decrease of the area of the floors as we are moving up. There are separate elevators in each building.

The main staircase that connects the two buildings, provides access to the higher floors. The staircase's one end is connected rigidly to building I, while the other is supported via bearings to a short cantilever (of length 20cm). The short cantilever is fixed on building II (Figures 19 and 20). Between building II and the staircase's corridor there is a joint of width equal to 10cm.

The staircase is supported on the two buildings, without possessing any vertical structural elements. It should be noted that the bearings is an expensive solution, since they need to be replaced regularly and moreover they are considered to be expendable in the design for earthquake action. Finally, because of inherent uncertainties in calculating the seismic displacements, the distance between the face of the corridor and the face of the short cantilever (20cm) is critical in the highest floor of the staircase (i.e., in the 7^{th} floor with height equal to 26.40m), in which the displacements are crucial. In case in which the two buildings move in different directions under an earthquake action, the highest floor of the staircase may collapse; this may lead to a total collapse of the structure, because of the creation of consequent mechanisms. This is of course the worst case scenario, since the staircases must constitute the safest escape from a structure during an earthquake.

In this study, two alternative solutions, regarding the structural system of the staircase are proposed. In the first (Figures 21 and 22), two supporting columns (with a cross section of dimensions 90cm by 25cm) at the ends of the staircase are proposed. At the floor levels a beam (with a cross section of dimensions 120cm by 50cm) is constructed, on which the corridor-cantilever is supported. In addition, another beam is constructed (with a cross section of dimensions 220cm by 50cm), which has the same slope as the staircase, and on which the steps are fixed. With this solution enough stiffness is supplied by the columns in the direction x-x (i.e., the direction of the staircase). Therefore, and in order to prevent the transversal displacements it is proposed the introduction of seismic stoppers. These are four short cantilevers, of dimensions 30cm x 50cm with a height equal to 30cm, on both sides of the staircase, that are supported (with fixed supports) on the two buildings. With this scheme the central staircase becomes independent. Moreover, seismic joints between the staircase and the two buildings are added. The width of these joints is calculated from the seismic displacements of the two buildings and is equal to 15cm.

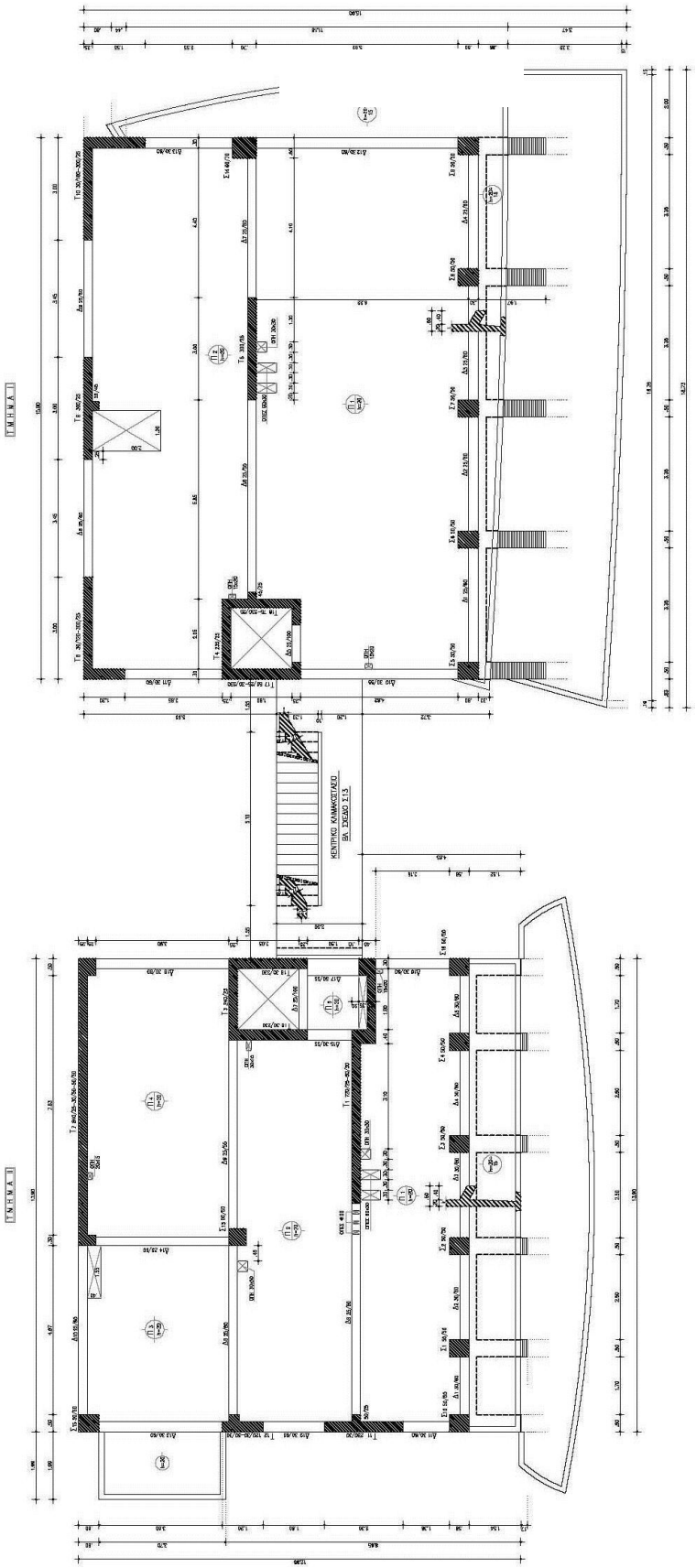


Figure 18: Plan view of the typical floors of the two buildings connected by external staircase.

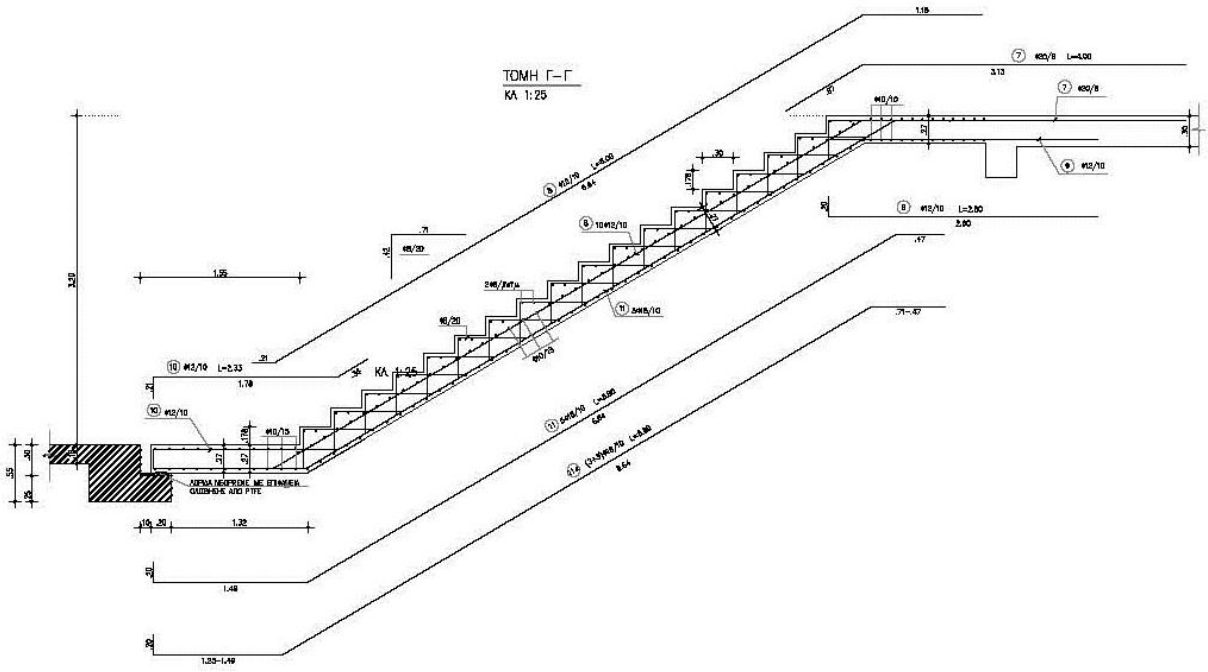


Figure 19: Section of the applied staircase.

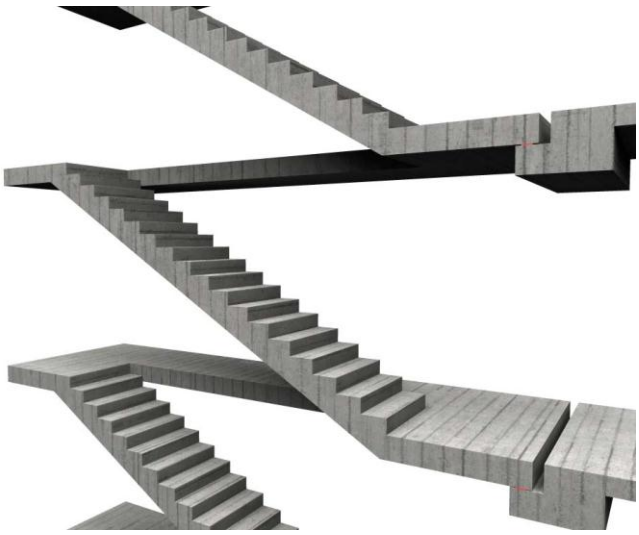


Figure 20: 3D view of the applied staircase.

In the second proposition, shown in Figures 23 and 24, one central column (with a cross section of dimensions 90cm by 25cm), on which the cantilever beams are supported is constructed. The corridor is supported on two horizontal beams, while the steps are supported on two inclined beams. It is noted that in this scheme the column is subjected to torsion, because of the transversal displacements of the staircase induced by the two buildings. The presence of four short cantilevers, of dimensions 30cm x 50cm with a height equal to 30cm, on both sides of the staircase, that are supported (with fixed supports) on the two buildings, prevents the torsional effects.

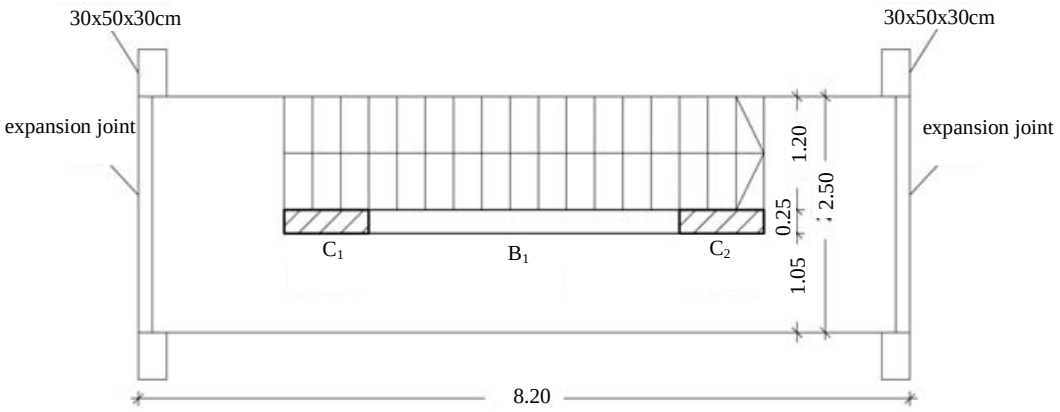
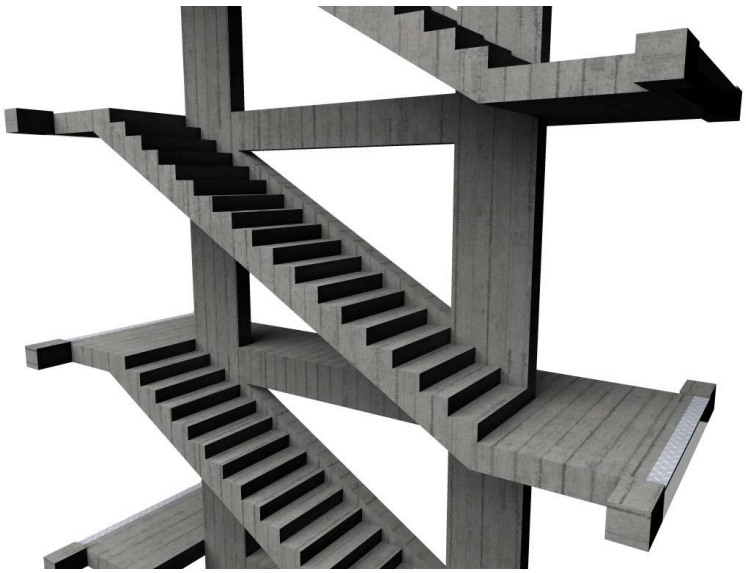


Figure 21: Plan view of the 1st alternative proposal.



(b)

Figure 22: 3D view of the 1st alternative proposal.

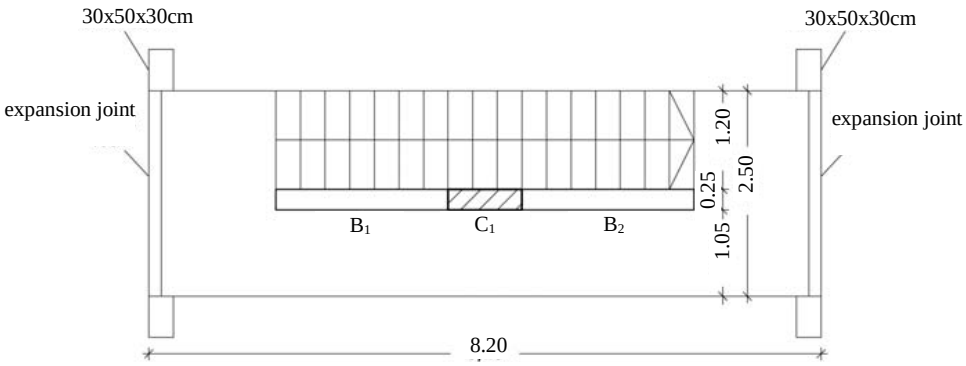


Figure 23: Plan view of the 2nd alternative proposal.

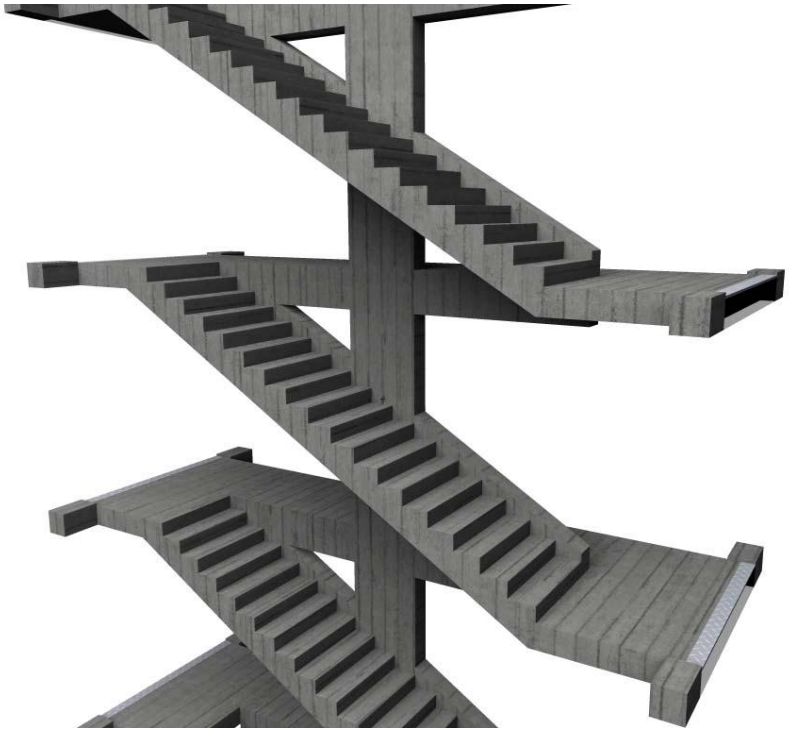


Figure 24: 3D view of the 2nd alternative proposal.

4 CONCLUSIONS

In this paper the response of several types of staircases under earthquake actions was exhaustively studied. For the purposes of the work the behavior of a multi-story building was investigated. In particular, the behavior and the response of the building in the presence, as well as in the absence of staircases was compared. The investigation –and the relevant results- concerned both the staircases, as well as the three dimensional (space) structure. The finite element method was employed in the modeling of the structures involved in the work. In addition, an external multi-story staircase, connecting two buildings in an area of high seismicity was studied. The main results of the work may be summarized as follows:

- The inclusion of staircases in the analysis of the three dimensional structure increases the stiffness of the structure in the transversal direction and reduces the relative displacement of the slabs of the floors. Also, the presence of staircases influences the dynamic response of the structure.
- The earthquake combination of loads is more crucial than the vertical combination of loads in most instances of staircases.
- The influence of the vertical component of the earthquake is crucial in staircases with a free landing as well as to the helical ones.
- In the occasion of an external staircase connecting multi-storey buildings, it was found that it is possible to make it independent from the buildings it connects. Furthermore, the use of seismic stoppers in the weak direction of the staircase has the beneficial result of reducing the conjugate seismic displacements.

ACKNOWLEDGMENTS

The authors of this study wish to express their gratitude to METE SYSM S.A. for the kind offer of the original study of the buildings connected by an external staircase.

REFERENCES

[1] P.I. Spyropoulos, *Reinforced Concrete Staircases, Static Calculations- Construction Details- Applications, Lecture Notes*. Aristotle University of Thessaloniki, Greece, 1983 (In Greek).

[2] D. Bull, *Stair and Access Ramps between Floors in Multi-storey Buildings, Technical paper prepared for the Canterbury Earthquakes.* Royal Commission, 2011.

[3] Q.W. Su, Finite Element Analysis of Staircase under Earthquake Action. *Advanced Materials Research*, **163**, 2964-2968, 2010.

[4] H. Dai and A. Qi, Analysis of performance of reinforced concrete frame structure with staircase based on ETABS. *Journal of Earthquake Engineering and Engineering Vibration*, **6**, 2009.

[5] E. Cosenza, G.M. Verderame, and A. Zambrano, Seismic performance of stairs in the existing reinforced concrete building. *14th World Conference on Earthquake Engineering*: Beijing, China, October 12-17, 2008.

[6] Computers and Structures Inc., *SAP 2000 Nonlinear Version 11.0.3, User's Reference Manual*. Berkeley, California, 2007.

[7] CEN [Comité Européen de Normalisation], *Eurocode 2: Design of concrete structures - Part 1-1: General rules and rules for buildings*, 2003.

[8] CEN [Comité Européen de Normalisation], *Eurocode 8: Design of structures for earthquake resistance, Part 1: General rules, seismic actions and rules for buildings*, 2003.

COMPDYN 2013
4th ECCOMAS Thematic Conference on
Computational Methods in Structural Dynamics and Earthquake Engineering
M. Papadrakakis, V. Papadopoulos, V. Plevris (eds.)
Kos Island, Greece, 12–14 June 2013

DYNAMIC EFFECT OF RAILWAY VEHICLE ON SEISMIC RESPONSE OF RAILWAY STRUCTURE

M. Tokunaga[1], S. Minoura and M. Sogabe[1]

[1]Railway Technical Research Institute
2-8-38, Hikari-cho, Kokubunji-shi
e-mail: {toku, minoura, sogabe}@rtri.or.jp

Keywords: Railway vehicle, Dynamic interaction, Seismic design, Train load, Earthquake.

Abstract. *The conventional seismic standard of Japan specifies that the seismic inertia force of trains is modeled as a uniformly-distributed load which has upper limit force of 30% of railway vehicle weight assuming that railway vehicles produce damping effects or do not always oscillate in the same phase as structures. However, the damping effect has not been specifically identified and the upper limit is unreliable because actual railway vehicles have a complicated vibration system. The object of this paper is to evaluate the dynamic effect of railway vehicles on seismic response of structures, and to develop a reasonable modeling method of railway vehicles in seismic design. As the result of numerical simulations, following conclusions were obtained: 1) The frequency response function of railway vehicles exceeds 1 without phase lag when the frequency is less than about 1Hz, whereas, that marks below 1 with phase lag when the frequency is more than about 1Hz. 2) The frequency response function of the railway vehicles exceeds 1 without phase lag in the range of less than 1Hz, whereas, that marks below 1 with phase lag in the range of higher than 1Hz. 3) The dynamic effect of vehicles affects the structure response under earthquake motions, and the effect depends on the characteristics of earthquakes, the degree of the plastic behavior of structures and the yield frequency. The structure response varies in the range of -50~20% at its maximum due to the dynamic effect. 4) An estimation method using the equivalent weight rate $\beta_{eq,V}$ was proposed in order to evaluate the dynamic effect of railway vehicles.*

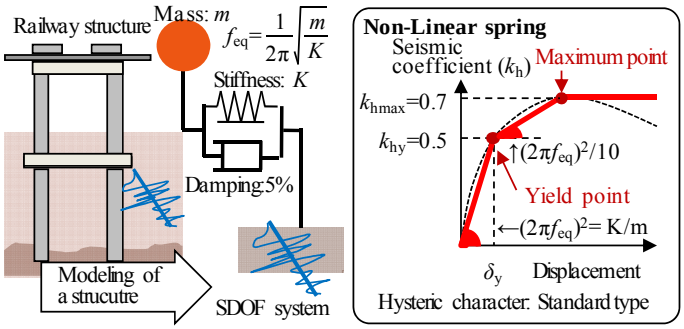


Figure 1: Dynamic model of structure

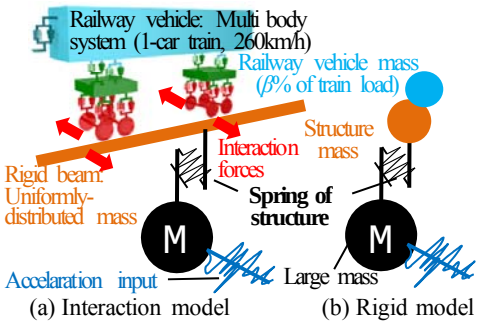


Figure 2: Modeling way of railway vehicles and interaction

1 INTRODUCTION

Lots of old railway steel bridges, which are of open floor type without concrete slabs, are light weight bridges of unit weight/length of 30 kN/m. Therefore, seismic response of these light bridges may be significantly affected by train behavior because the percentage of the train weight, which is assumed to be approximate 35 kN/m, to the entire bridge weight is high.

The Design Standards for Railway Structures and Commentary established by RTRI (Seismic Design)[1] specifies that the seismic inertia force of railway vehicle mas is modeled as a uniformly-distributed fixed load on the condition of riding capacity of 100% (70% for a freight car). The frequencies of trains determine the number of tracks where vehicle weight is loaded. The seismic inertia force has an upper limit value of 30% of the vehicle weight assuming that railway vehicles produce damping effects or do not always oscillate in the same phase as structures.

However, sufficient reasons why the upper limit of the inertia force is 30% of the vehicle weight in these methods have yet to be given, and no action on structures caused by the dynamic effect of vehicles during earthquake motions have been identified. Therefore, it is necessary to investigate more reasonable modeling methods for seismic actions of railway vehicles.

The object of this paper is to evaluate dynamic effects of railway vehicles on seismic response of structures, and to develop a reasonable modeling method of running railway vehicles in seismic design through the following investigations.

(1) To clarify the dynamic characteristics of railway vehicles
(2) To evaluate the dynamic characteristics of structures in consideration of the dynamic effect of railway vehicles
(3) To evaluate the dynamic effect of railway vehicles during earthquake motions
(4) To propose a reasonable railway vehicle modeling method in seismic design

2 ANALYSIS METHOD

A program called DIASTARSIII, which analyses dynamic interaction between vehicles and railway structures, was used in the numerical analysis [2].

2.1 Dynamic model of structure

Fig. 1 shows the dynamic model of structures. The dynamic behavior of railway structures can be often expressed by the single degree of freedom (SDOF). Therefore, structures were modelled as SDOF system with the tri-linear type skeleton curve and the standard type hysteric characters. For the skeleton curve, the yield seismic coefficient k_{hy}, the maximum seismic coefficient k_{hmax}, the yield frequency f_{eq}, and the structure unit weight/length w_s, were set as the parameters. The second gradient was fixed at 1/10 of the first gradient and the third gradi-

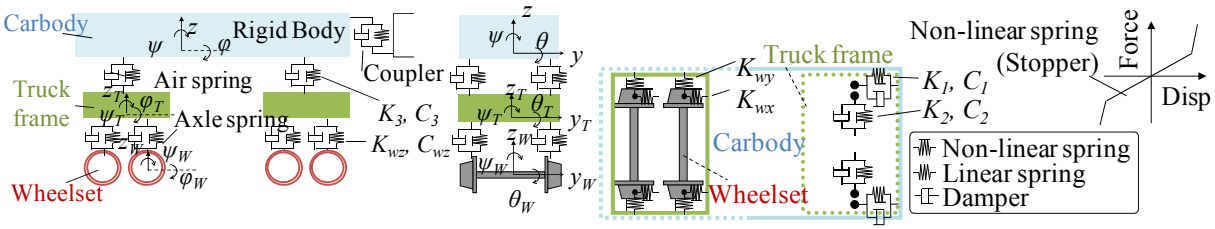
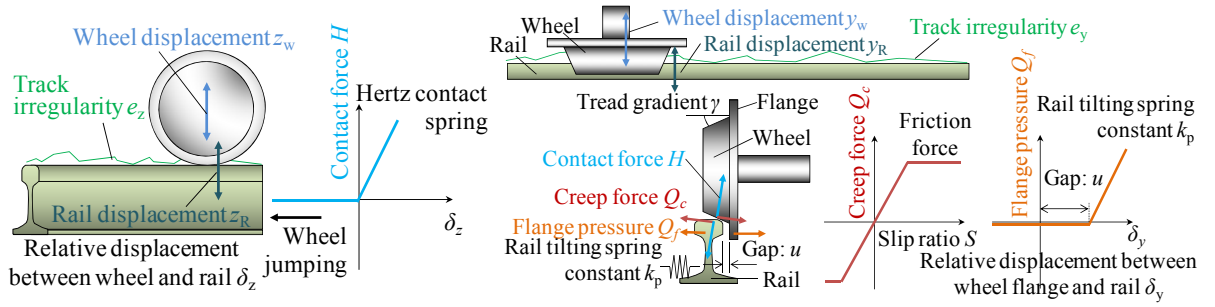


Figure 3: Dynamic model of railway vehicle of interaction



(a) Vertical direction (b) Horizontal direction

Figure 4: Interaction between wheel and rail of interaction model

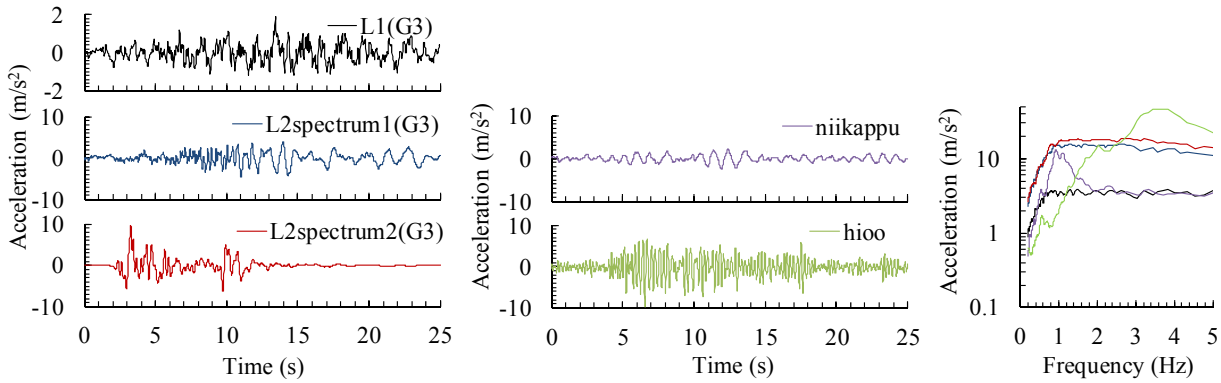
ent was fixed at infinitesimal. The yield frequency of structures f_{eq} was calculated on the basis of structure weight of 100% and train weight of 100%. The structure weight was fixed in consideration of 25m which is the same length as the railway vehicle. The unit weight ratio of structure to train α (= w_s/w_t) was set between 1~20. The unit weight w_t of the vehicle model used in this paper was set to 17kN/m. Old railway steel bridges, which are of open floor type without concrete slabs, are light weight structures of unit weight w_s of more or less 35 kN/m. Concrete RC structures used in Shinkansen lines are usually comparatively heavy weight structures of unit weight w_s of more or less 350kN/m. The value of k_{hmax} was obtained by adding 0.2 to k_{hy}.

2.2 Dynamic model of railway vehicles and interaction model between wheels and rails

Fig. 2 indicates conceptual diagrams of how to model railway vehicles and interaction between wheels and rails. An interaction model and a rigid model were established.

2.2.1 Interaction model

Fig. 3 shows the dynamic model of railway vehicles of the interaction. The railway vehicle model was created in the form of a rigid body, the elements of which was a body, 2 truck frames and 4 wheelsets with springs and dampers. Then, the vehicle has 31degrees of freedom. Actual vehicles have stoppers to control excessive relative displacement at each connection. In order to consider the stoppers, it was assumed that bi-linear springs were used for springs. Adequacy of these dynamic models has already been verified through vibration experiments using a vibration table and a full-scale vehicle model [3]. Tangible vehicle specifications were assumable in reference to a recent high-speed Shinkansen railway vehicle. The main input data of the mass are a vehicle length of 25m, a body mass of 312kN, a truck frame mass of 31kN, and a wheelset mass of 18kN for an empty vehicle. Therefore, the weight of the railway vehicle is 446kN and the unit weight/length of the vehicle is 17.8 kN/m. The main input data of springs and dampers are vertical and horizontal spring constants for the air-spring of 300kN/m and 180kN/m (half side of a truck), a damping constant for the air-spring of 50kN·s/m (half side of a truck), a damping constant for the lateral damper of 40kNs/m (a damper of a truck), 1200kN/m of the spring constant for the axle spring (half side of a wheelset) and the



(a) Design earthquake motions (b) Observed earthquake motions (c) Elastic acceleration response

Figure 5: Input earthquake motions

		3.1 Dynamic characteristics of railway vehicle	3.2 Dynamic characteristics of structure	3.3 Dynamic effect of railway vehicle during earthquake motion
Vehicle and interaction model		Interaction model	Interaction model Rigid model	Interaction model Rigid model
Structures	k_{hy}	-	0.3, 0.5, 0.7	0.3, 0.5, 0.7
	f_{eq}(Hz)	-	0.5, 1.0, 1.5, 2.0	0.1, 0.2, …, 3.0
	$\alpha(=w_s/w_t)$	-	1, 5, 10, 20	1
Input wave		Sinusoidal wave (0.01~5.0Hz, 50,200,400gal)	Sinusoidal wave (0.01~5.0Hz, 50,200,400gal)	L1 (G0 ~ 7), L2spectrum I (G0 ~ 7), L2spectrumII(G0 ~ 7) Tokachioki(observed in Niikappu), Tokachioki(observed in Hiroo)

k_{hy} is yield seismic coefficient; f_{eq} is yield frequency; w_s is structure unit weight/length; w_t is train unit weight/length

Table 1: Analysis cases

damping constant for the axle damper of 40 kNs/m (half side of a wheelset). In addition, gaps at each stopper were fixed at 20-30mm. Numerical simulations were conducted under the condition that 1-car train, which keeps running at 260km/h, interacts with structures without derailment and deviation. This condition was supposed to be severest for seismic response of structures.

Fig. 4 shows dynamic interactions between wheels and rails of the interaction model. Dynamic interaction forces between wheels and rails were calculated on the basis of vertical and horizontal relative displacement between them. The dynamic interaction force of vertical direction was modeled as the Hertz contact force and that of horizontal direction was modeled as the creep force and the flange pressure. The Hertz contact force is the vertical force which is a function of the vertical relative displacement δ_z between wheels and trails. The creep force is horizontal force due to the creep of the wheel moving forward by rolling on the rail. This creep force is saturated at the upper limit of friction force when the slipping ratio S of horizontal direction becomes large. The flange pressure is the horizontal force which is caused by the contact between the wheel flange and the rail. It was calculated with the rail tilting spring and the horizontal relative displacement between the wheel flange and the rail δ_y. These contact point and the contact angle were calculated on the basis of contact functions derived from the geometric configuration. Damping by the contact of wheels with rails was not considered.

2.2.2 Rigid model

As shown in Fig. 1**,** in the rigid model, railway vehicles and interactions between wheels and rails were modeled as one degree of freedom under the condition that the train weight of 100% was considered. In this model, the rigidity of the spring connecting a vehicle with a structure was sufficiently increased. This rigid model is a simple model commonly used in practical seismic design.

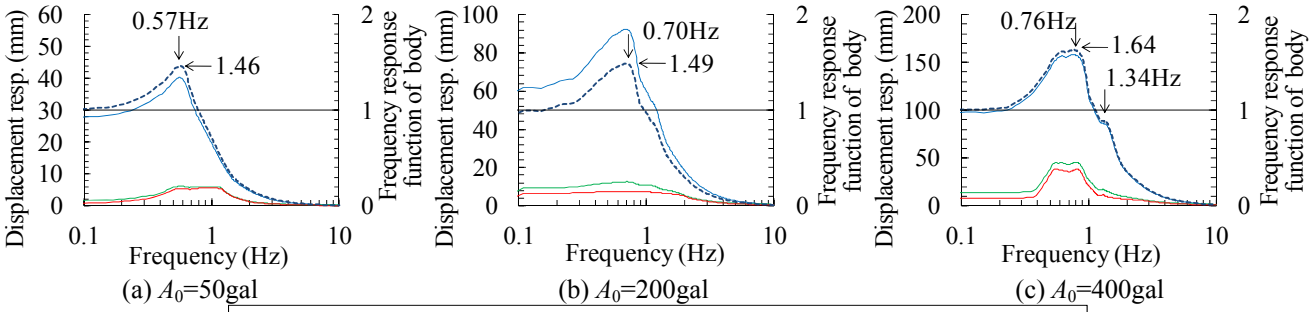


Figure 6: Frequency response function of railway vehicle

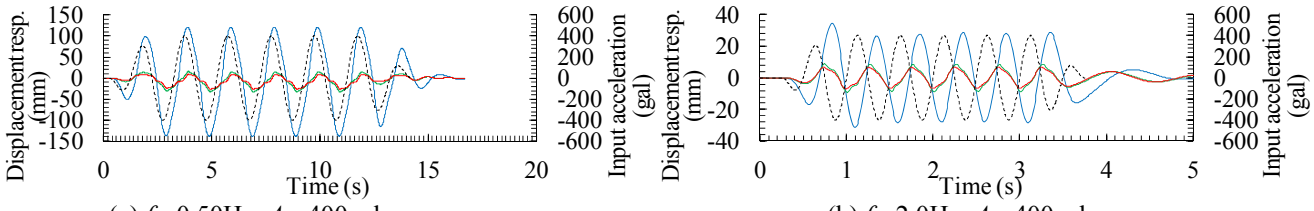


Figure 7: Time history of displacement response of railway vehicle in sinusoidal wave

2.3 Analysis cases

Table 1 indicates parameters and analysis cases in numerical analyses. This paper has 3 phases , to evaluate the dynamic characteristics of railway vehicles in **3.1**, to evaluate the dynamic characteristics of structures in **3.2** and to evaluate the dynamic effect of railway vehicles during earthquakes in **3.2**. Analytical parameter of vehicle and interaction model, structure and input wave was changed depending on each phase as shown in the Table. 24 design earthquake motions of L1, L2 spectrum I and L2 spectrum II for each of 8 ground classifications, G0 to 7 and two observed earthquake motions, at tokachioki(observed in Niikappu town or Hiroo town) , are used as shown in Fig. 5.

2.4 Numerical method

Equations of motion of vehicles and structures were solved in the modal coordinates for each time increment Δt by the *Newmark* time difference scheme. Iterative calculations were needed for each time increment until the unbalanced force becomes sufficiently small because the equations are nonlinear. The modal damping of 5% was considered for each eigenmode.

3 ANALYSIS RESULT

3.1 Dynamic characteristics of railway vehicle

The dynamic interaction analysis using sinusoidal waves was conducted to evaluate the frequency response function of railway vehicles.

The left axis of fig. 6 shows the maximum displacement response of the body, truck and wheelset in the cases where input acceleration is 50, 200 and 400gal, and the right axis of the figure shows the frequency response function of the vehicle body. The frequency response function is a ratio of the maximum displacement response of the body to the static displacement for which the displacement in the case where input acceleration frequency f_0 is 0.1Hz is substituted. The figure indicates that the predominant frequency of the body is 0.57Hz,

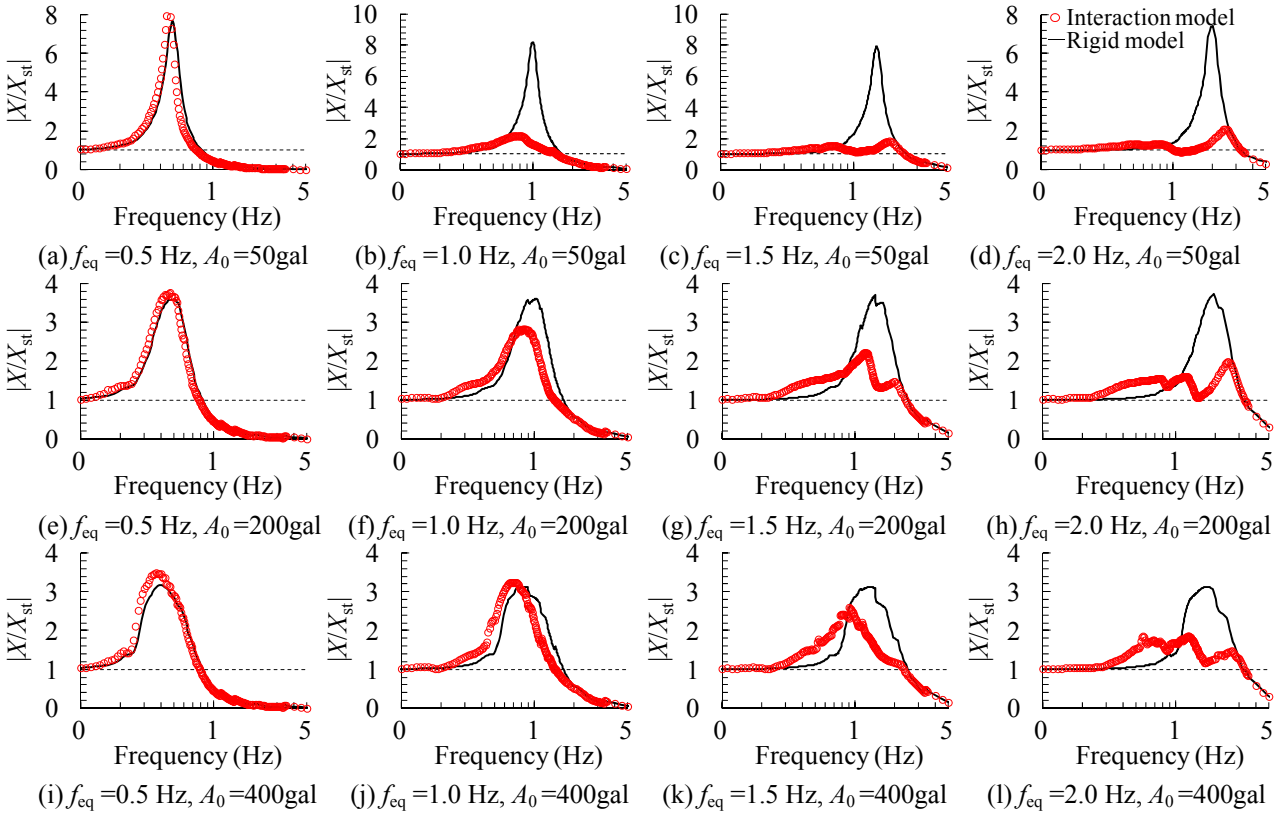


Figure 8: Frequency response function of structure (α=1, k_{hy}=0.5)

0.70Hz and 0.76Hz in the cases of 50, 200 and 400gal respectively. It means that the natural frequency of vehicle superficially rises with the increase of input acceleration. In addition, the value of the frequency response function also increases from 1.46 to 1.64 with the increase of input acceleration, which means that railway vehicles can resonate easily when the input acceleration becomes larger. This is because when the input acceleration becomes larger, the wheel flanges are constantly in contact with rails and vehicle stiffness increases due to the contact of the bolster spring to stoppers in horizontal and vertical directions. As shown in the figure, the maximum displacement response of the wheelset exceeds 5mm which is the gap between the wheel flange and the rail in most frequency in the case of 200 or 400gal.

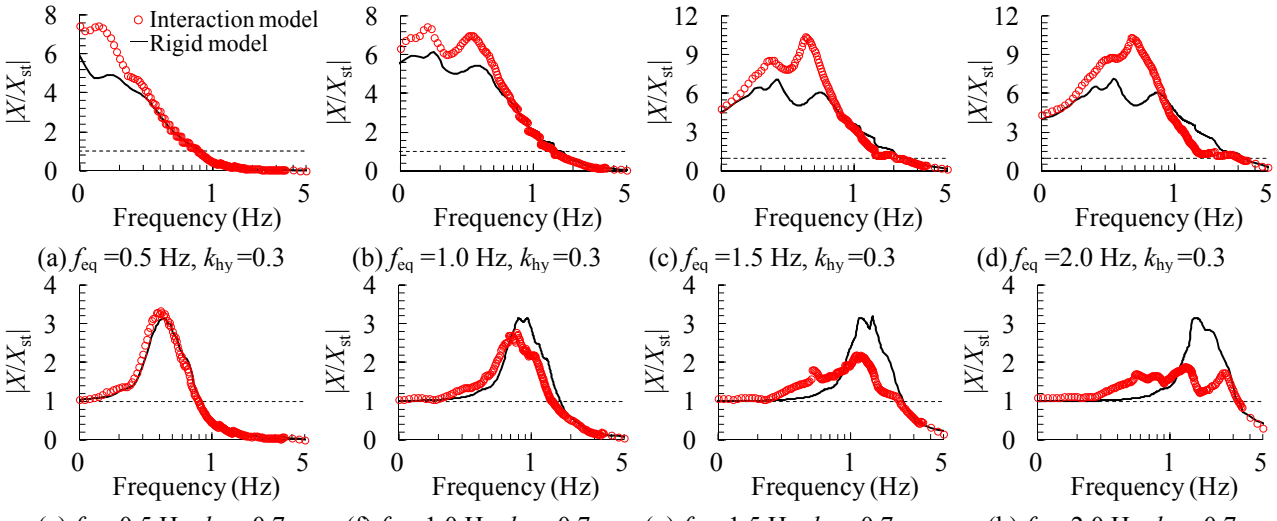
Fig. 7 depicts the representative time history of displacement of the body, truck and wheelset with input sinusoidal waves. The figure implies that each component of the vehicle vibrates in the same phase as the input wave in the case where input wave frequency f_0 is 0.5Hz. On the other hand, the phase lag can be observed in the case where f_0 is 2.0Hz

Therefore, it was found that the frequency response function of the railway vehicles exceeds 1 without phase lag in the range of less than 1Hz, whereas, that marks below 1 with phase lag in the range of higher than 1Hz.

3.2 Dynamic characteristics of structures in consideration of dynamic effect of railway vehicles

The dynamic interaction analysis using sinusoidal waves was conducted to evaluate the frequency response function of the structure.

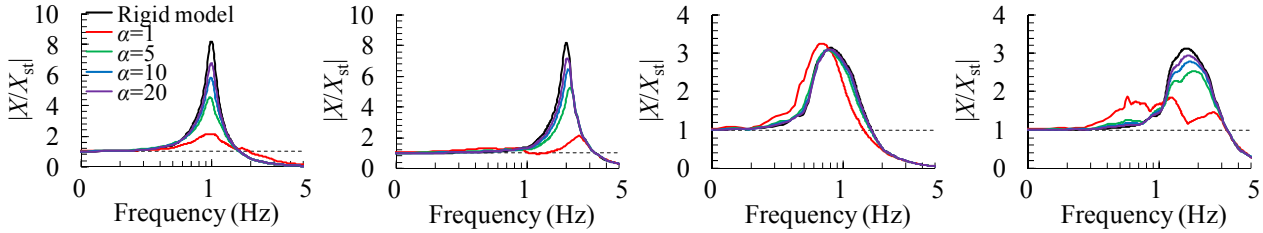
Fig. 8 shows the frequency response function of the structure $|X/X_{st}|$ of the interaction model and the rigid model when the unit weight ratio α is 1 and the yield seismic coefficient k_{hy} is 0.5. The function is a ratio of the maximum displacement response of the structure X to static displacement X_{st} which is gained by Eq. (1)



(a) f_{eq} =0.5 Hz, k_{hy} =0.3 (b) f_{eq} =1.0 Hz, k_{hy} =0.3 (c) f_{eq} =1.5 Hz, k_{hy} =0.3 (d) f_{eq} =2.0 Hz, k_{hy} =0.3

(e) f_{eq} =0.5 Hz, k_{hy} =0.7 (f) f_{eq} =1.0 Hz, k_{hy} =0.7 (g) f_{eq} =1.5 Hz, k_{hy} =0.7 (h) f_{eq} =2.0 Hz, k_{hy} =0.7

Figure 9: Effect of yield seismic coefficient k_{hy} on frequency response function of structure (α=1, A_0=400gal)



(a) f_{eq} =1.0 Hz, A_0 =50gal (b) f_{eq} =2.0 Hz, A_0 =50gal (c) f_{eq} =1.0 Hz, A_0 =400gal (d) f_{eq} =2.0 Hz, A_0 =400gal

Figure 10: Effect of unit weight ratio α on frequency response function of structure

$$X_{st} = \frac{k_h g}{(2\pi f_{eq})^2} \tag{1}$$

These figures indicate that, in the case of f_{eq} =0.5Hz, the frequency response function of the interaction model and that of the rigid model mostly agree with each other and that of the interaction model slightly exceeds that of the rigid model when the frequency is less than 0.5Hz as shown in Fig. 8(i). By contrast, when f_{eq} is more than 1.0Hz, a large difference can be observed between them, which imply dynamic effect of railway vehicles obviously appears. The dynamic effect increases the structure response when the frequency is less than about 1.0Hz, whereas the dynamic effect decreases it when the frequency is more than about 1.0Hz. In addition, the frequency response function of the structure of the interaction model becomes larger with the increase of input acceleration. This is because the amplification ratio of vehicle response becomes large with the increase of input acceleration. Therefore, the frequency response function of structures in consideration of the dynamic effect of railway vehicles varies depending on the degree of the railway vehicle response.

Fig. 9 shows the effect of the yield seismic coefficient k_{hy} on the frequency response function of structures in the case where the unit weight ratio α is 1 and input acceleration is 400gal. The figure, in the case of k_{hy}=0.3, shows that the frequency response function of the interaction model significantly exceeds that of the rigid model especially in a low-frequency, compared to the case of k_{hy}=0.5 as shown in Fig. 8(i)~(l). In addition, the reduction degree due to the dynamic effect which is found in the frequency from 1 to 2 Hz becomes lower. On the other hand, in the case where k_{hy} is 0.7 shown in Fig. 9(e)~(h), the plastic structure response becomes small and the frequency response function of the interaction model shows smaller value, which is the opposite trend to the case of k_{hy}=0.3. This is because structures of small k_{hy}

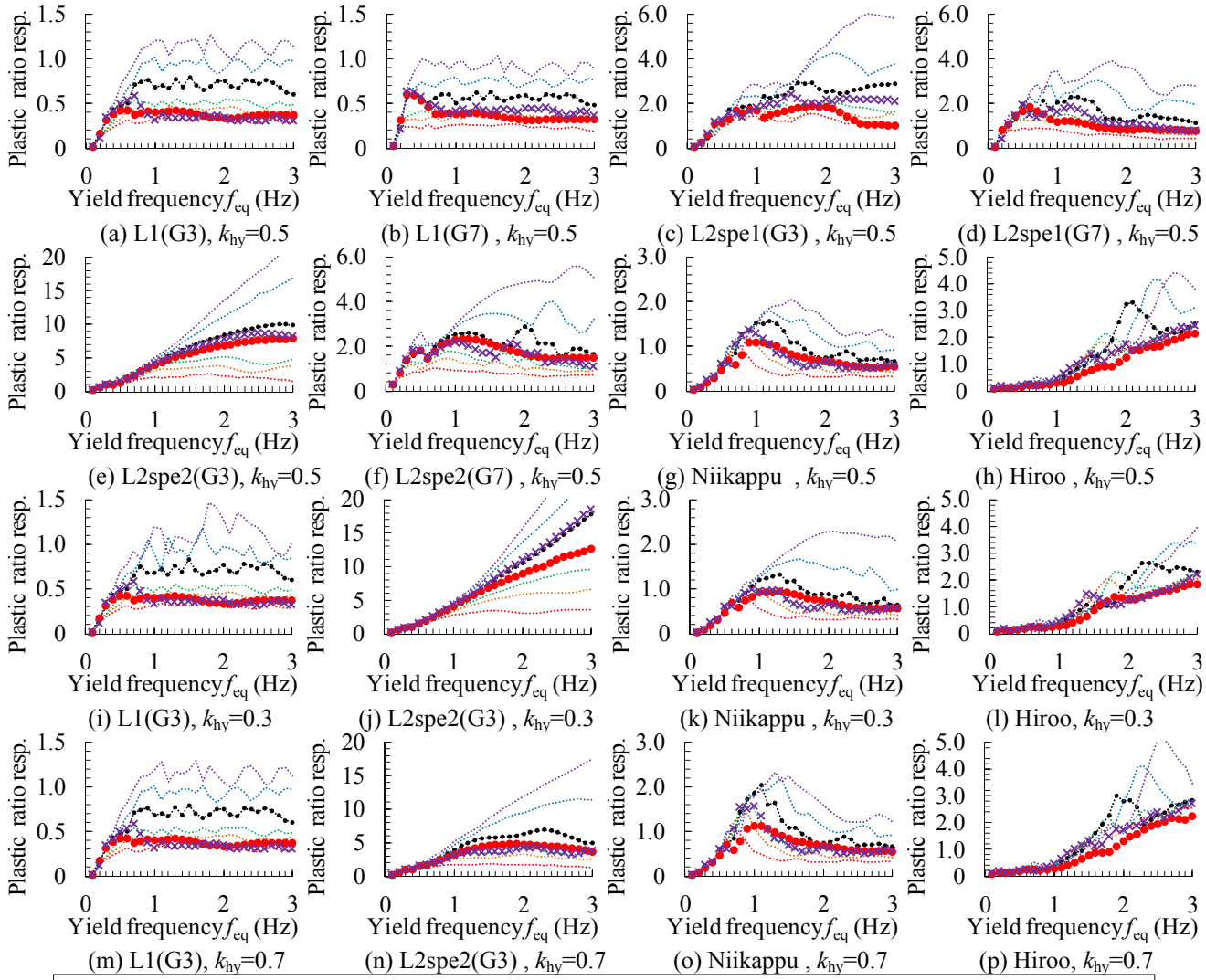


Figure 11: Dynamic effect of vehicle on structure under earthquake motion (α=1)

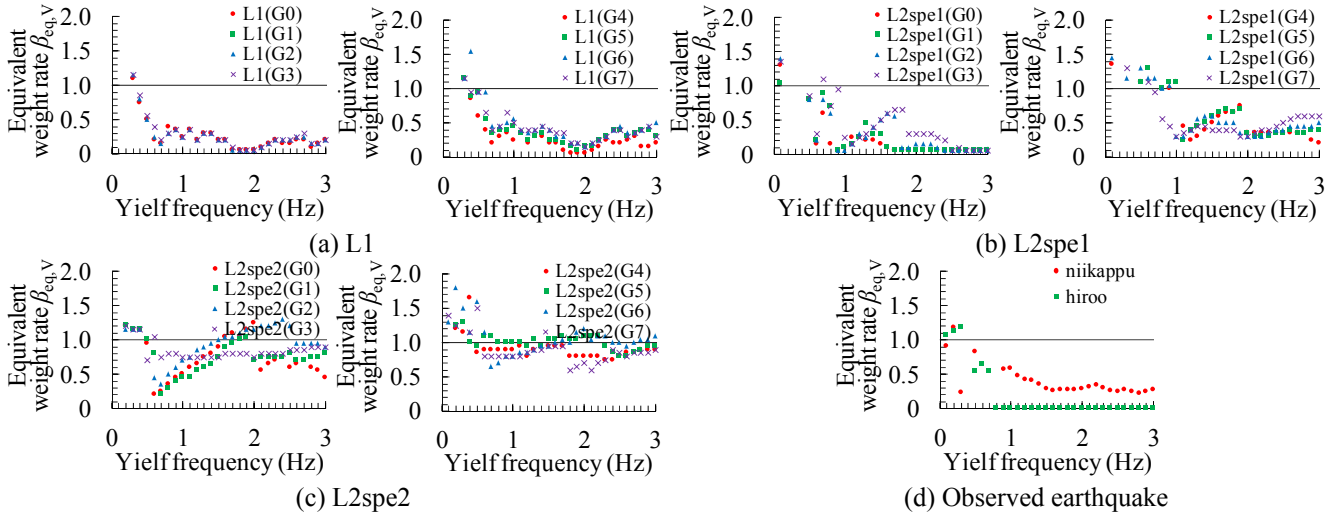
tend to respond plastically and the natural frequency of structures superficially decreases when the structure response is amplified.

Fig. 10 shows the effect of the unit weight ratio α on the frequency response function of structures in the case where f_{eq} is 1.0 or 2.0Hz and input acceleration is 50 or 400gal. The figure explains that the difference of functions between the interaction model and the rigid model becomes larger with the decrease of α, whereas the functions mostly matches and the dynamic effect of railway vehicles becomes small when α is larger than 10.

3.3 Dynamic effect of railway vehicles during earthquake motions

The dynamic interaction analysis using earthquake motions was carried out to evaluate the dynamic effect of vehicles on structures under earthquake motions.

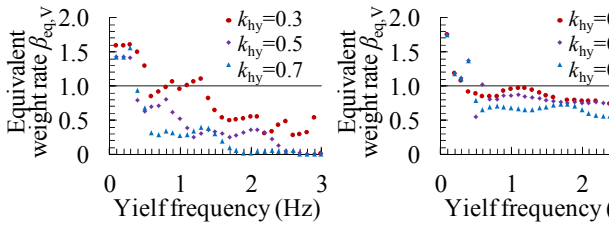
Fig. 11 shows the dynamic effect of vehicles on structures under earthquake motion by means of a comparison of plastic ratio response between the interaction model and the rigid model in the case where the unit weight ratio α is 1. The plastic ratio is a ratio of the maximum displacement to the yield displacement. Horizontal axis is the yield frequency f_{eq} calculated in consideration of 100% of vehicle weight. The f_{eq} of actual railway structures ranges approximately within 0.5~2.0Hz. As shown in these figures, in the cases where f_{eq} is less than 0.5Hz, the plastic ratio response of the interaction model mostly becomes equivalent to or ex-



(a) L1 (b) L2spe1

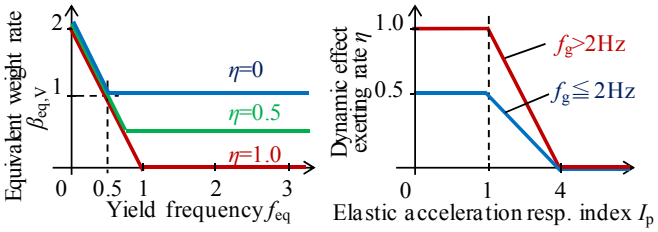
(c) L2spe2 (d) Observed earthquake

Figure 12: Equivalent weight rate to dynamic effect of railway vehicle $\beta_{eq,V}$ (α=1, k_{hy}=0.5)



(a) L2spe1(G3) (b) L2spe2(G3)

Figure 13: Effect of k_{hy} on $\beta_{eq,V}$



(a) Proposed method $\beta_{eq,V}$ (b) Proposed method η

Figure 14: Proposed method for estimating $\beta_{eq,V}$

ceeds that of the rigid model. On the other hand, in the cases where f_{eq} is more than 0.5Hz, that of the interaction model becomes smaller than that of the rigid model. The dynamic effect significantly appears especially in the case of small α. Furthermore, the dynamic effect is dependent on the earthquake, that is, it can be obviously seen when structures respond elastically due to small motions such as L1 earthquake, but it diminishes when structures respond plastically due to large motions such as L2 earthquake. In addition, there are characteristic cases in which the dynamic effect can be seen clearly even when the plastic ratio is comparatively large such as Niikappu earthquake or it becomes small even when the plastic ratio is comparatively small such as Hiroo earthquake. From these tendencies, the degree of the dynamic effect under earthquake motions depend on the difference of the frequency response function of the interaction model shown in Fig. 8 and the characteristics of input earthquake motions. For example, in the case of f_{eq}=0.5Hz shown in Fig. 8, there is little difference between the interaction model and the rigid model regardless of earthquake motions, because the frequency response function of both models matches. In the cases where f_{eq} is more than 0.5Hz, the response reduction effects exceed the enhancing effect because the frequency response function of the interaction model falls below that of the rigid model in a high frequency.

Therefore, the dynamic effect of vehicles affects the structure response under earthquake motions, and the effect depends on the characteristics of the earthquake, the degree of the plastic behavior of the structure and the yield frequency. The structure response varies in the range of -50~20% due to the dynamic effect of railway vehicles in the case of α=1.

3.4 Modeling of dynamic effect with equivalent vehicle weight rate $\beta_{eq,V}$

Fig. 12 shows the equivalent weight rate to dynamic effect of railway vehicles $\beta_{eq,V}$ in the cases where α=1 and k_{hy}=0.5. $\beta_{eq,V}$ is the value of β at which the plastic ratio response of the rigid model and that of the interaction model agree each other. It was calculated as a function of the characteristics of earthquake motions, f_{eq} and k_{hy}. As shown in Fig. 12(a)~(b), $\beta_{eq,V}$ marks less than 0.3 in the cases where f_{eq} is more than 1Hz under L1(G0~3) or L2spectrum2(G0~3) earthquakes and it marks more than 0.5, which is comparatively large value, in the cases where f_{eq} is more than 1Hz under L2spectrum2(G0~3) earthquakes. In the cases of earthquakes of G4~7 ground, $\beta_{eq,V}$ rises by 0.1~0.5 in comparison to the results of earthquakes of G0~3 ground because these earthquakes contain lots of low-frequency components which do not contribute to the response reduction effect. In most cases where f_{eq} is less than 0.5Hz, $\beta_{eq,V}$ exceeds 1 and the enhancing effect appears remarkably.

As shown in Fig. 12(c), $\beta_{eq,V}$ marks around 0 which is a small value under Hiroo earthquake because the earthquake contains lots of high-frequency components although the plastic ratio response of structures excessively exceed 1. On the contrary, $\beta_{eq,V}$ marks about 0.5 under Niikappu earthquake because the earthquake contains lots of low-frequency components although the plastic ratio response of structures is below 1.

Fig. 13 shows the effect of the yield seismic coefficient k_{hy} on the equivalent weight rate $\beta_{eq,V}$. As shown in the figure, $\beta_{eq,V}$ increases with decrease of k_{hy}, which explains that the dynamic effect doesn't tend to appear when k_{hy} is small.

Fig. 14 is the proposed method of estimating the equivalent weight rate $\beta_{eq,V}$. $\beta_{eq,V}$ was modeled on the basis of the result of Fig. 12~13; $\beta_{eq,V}$ varies from 0 to 2 depending on the characteristics of earthquake motions, f_{eq} and k_{hy}. It was calculated by Eq. (2) the function of which is f_{eq} and dynamic effect exerting rate η.

$$\beta_{eq,V} = \begin{cases} -2f_{eq} + 2 & (0.1 \le f_{eq} \le 0.5\eta + 0.5) \\ 1 - \eta & (0.5\eta + 0.5 \le f_{eq} \le 3) \end{cases} \tag{2}$$

The dynamic effect exerting rate η is defined as Eq. (3) which varies from 0 to 1 as a function of I_g depending on the ground natural frequency f_g and the elastic acceleration response index I_p.

$$\eta = \begin{cases} I_g & (0 \le I_p \le 1) \\ I_g(1.5 - 0.5I_p) & (1 \le I_p \le 4) \\ 0 & (4 \le I_p) \end{cases} \tag{3}$$

I_g is fixed at 1 when f_g is more than 2Hz and at 0.5 when f_g is less than 2Hz in order to express the frequency characteristics of earthquake motions containing lots of low-frequency components. I_g which expresses the degree of the plasticity of structures is calculated by a ratio of $A_r/k_{hy}g$. A_r is the elastic acceleration response in the case of f_{eq}.

Fig. 11 shows a comparison of plastic ratio response between the interaction model and the rigid model applying the proposed estimation method based on the equivalent weight rate $\beta_{eq,V}$. The figure shows that the estimation method is generally able to reproduce the response of the interaction model regardless of earthquake, including observed earthquake, motions, f_{eq} and k_{hy}. Thus, the validity of the proposed method is confirmed.

4 CONCLUSION

This paper aims to evaluate dynamic effects of railway vehicle on seismic response of structures, and to develop a reasonable modeling method of running railway vehicles in seismic design. As the result of numerical simulations, this paper concludes as follows.

- The frequency response function of the railway vehicles exceeds 1 without phase lag in the range of less than 1Hz, whereas, that marks below 1 with phase lag in the range of higher than 1Hz.
- The frequency response function of structures in consideration of the dynamic effect of railway vehicles varies depending on the degree of the railway vehicle response. The dynamic effect increases the structure response when the frequency is less than about 1Hz, whereas it decreases that when the frequency is more than about 1Hz.
- The dynamic effect of vehicles affect the structure response under earthquake motions, and the effect depends on the characteristics of the earthquake, the degree of the plastic behavior of structures and the yield frequency. The structure response varies in the range of -50~20% at its maximum due to the dynamic effect at a maximum.
- An estimation method using the equivalent weight rate $\beta_{eq,V}$ is proposed in order to evaluate the dynamic effect of railway vehicles.

REFERENCES

[1] Railway Technical Research Institute, *Design Standards for Railway Structures and Commentary (Seismic Design)*, Maruzen Co., Ltd, Tokyo, 2012 (in Japanese).

[2] Wakui, H., Matsumoto, N., and Tanabe, M., *A Study on Dynamic Interaction Analysis for Railway Vehicles and Structures - Mechanical model and practical analysis method -*, *Quarterly Report of RTRI*, *Vol.35*, *No.2*, 96-104, 1994.

[3] Miyamoto, T., Matsumoto, N., Sogabe, M., Shimomura, T., Nishiyama, Y. and Matsuo, M., *Full-scale Experiment on Dynamic Behavior of Railway Vehicle against Heavy Track Vibration*, *Journal of Environment and Engineering*, *Vol.2*, *No.2*, 419-428, 2007.

COMPDYN 2013
4th ECCOMAS Thematic Conference on
Computational Methods in Structural Dynamics and Earthquake Engineering
M. Papadrakakis, V. Papadopoulos, V. Plevris (eds.)
Kos Island, Greece, 12–14 June 2013

DYNAMIC COMPUTATION AND DESIGN OF A WORLD RECORD DEATH-RIDE

Vincent Denoël[1], **Thomas Canor**[2], **Johan Demanet**[3]

[1]Structural Engineering Division, University of Liege
1, Chemin des Chevreuils, B52/3, 4000 Liege, Belgium
e-mail: v.denoel@ulg.ac.be

[2] National Fund for Scientific Research, Structural Engineering Division, University of Liege
1, Chemin des Chevreuils, B52/3, 4000 Liege, Belgium
e-mail: t.canor@ulg.ac.be

[3] Regional Fire Brigade, GRIMP (Groupe de Reconnaissance et d'Intervention en Milieu Prilleux)
12, Rue des Bourgeois, 5000, Namur, Belgium

Keywords: Instructions, ECCOMAS Thematic Conference, Structural Dynamics, Earthquake Engineering, Proceedings.

Abstract. *A death-ride is a long cable tensioned between two dead ends. Its design should offer a comfortable and/or enjoyable journey to the riders, within the strength limits of the material. Actually, the tensioning operation is usually subtle as a too slack cable with a sagging area would not allow finish the race, while a too taut cable could produce excessive stresses in the cable. The paper presents the design methodology and the dynamic model that were used for the design of a world-record 1.2km long death-ride, with an only 10-mm diameter.*

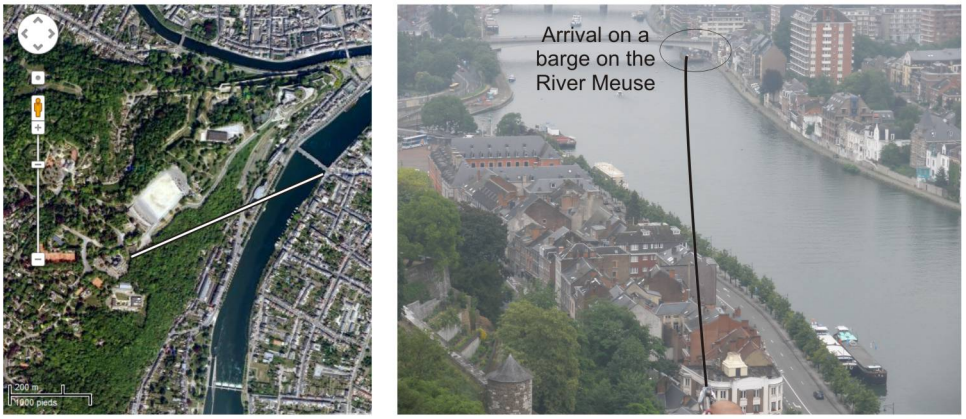


Figure 1: Location of the GrimpDay event, Namur-Jambes (Belgium) - June 2010.

1 Introduction

A death-ride is a long cable anchored between two dead ends, allowing the crossing of wide valleys. Besides mobility purposes, it also proves to be useful in rescue operations, or even sometimes simply for leisure.This paper reports the design of a world record death-ride, approx. 1200 m long in urban area. The cable was temporarily installed in June 2010 for an international competition organized by the special intervention group of the national fire brigade [13]. Figure 1 indicates the location of the event. In the heart of the city of Namur, Belgium, the cable planning was purposed to connect the citadel located on a hill to a barge in the river Meuse Δy =112 m below, and with a horizontal offset Δx =1163m.

From a serviceability viewpoint, a death-ride design should offer a safe, comfortable and also sometimes enjoyable journey to the riders, which is typically expressed in terms of maximum velocity. From a strength viewpoint, a death-ride should be designed in order to safely withstand the cable self-weight, wind forces, the rider's load and at last but not least, the initial tension in the cable.

The initial tension in the cable has to be tuned accurately. Indeed, in case of a loose cable, the rider may be stopped in the in-span sagging area, i.e. suspended above the river Meuse in this case. Conversely a too tight cable would generate large stresses but also a large velocity at the end of the ride, which could make it unsafe, for the rider has to be stopped. The design of a death-ride is a tradeoff between all these aspects.

There is a limitation in the acceptable length of a death-ride. Indeed, super long death-rides require large initial tension in order to maintain an acceptable deflection at mid-span [9, 8], and to limit the low-frequency oscillations resulting from wind buffeting [2, 11]. This large initial tension can only be withstood by the cable if it has a sufficient diameter, which in turn increases the distributed weight, reduces the natural frequencies and further necessitates the initial tension force to be increased. A peculiarity of the death-ride considered in this paper, which makes it thus remarkable in several aspects, is the limitation of the cable cross-section to an only 10-mm diameter, a constraint fixed in the very first stages of this project for compatibility reasons with some existing riding equipment.

Cables are usually modeled as structural elements without bending stiffness. The only way they can withstand external transverse forces is to find equilibrium in a largely displaced configuration [7]. While the model considered in this paper is limited to a planar representation

[4], some tridimensional models offer accurate modeling of the complex nonlinear vibrations of cable in both the vertical and the horizontal directions [7].

The zero bending stiffness assumption is actually defeated in the short zones near discontinuities such as clamped anchorages or concentrated forces. In this latter case, which is typically met as the rider travels along the cable, there exists a short zone on each side of the traveling force where the cable inclination varies rapidly. These short boundary layers [10] results in the relative inclination in the cable, between both sides of the force, as seen from a far-field viewpoint. Analytical methods are usually developed in order to avoid the difficult numerical modeling of these boundary layers [3, 5]; because this model is mainly devoted to be numerical, this feature is disregarded in this work. It is thus assumed that stresses resulting from this high-gradient bending is negligible with respect to tensile stresses.

The dynamic loading of structures under moving loads is extensively studied in [6]. In particular, the vibrations of a string subject to a moving force is a well-established theory. A major difference with the death-ride problem however, is that the traveling velocity of the rider is *a priori* unknown as it results from the interaction between the cable deflection and the rolling pulley. This aspect is further detailed in the next section.

2 The Death-Ride Model

2.1 The cable model

The cable is represented with a 2-D chain-like model composed of large displacement truss elements written with a corotational updated framework [14]. The cable is thus discretised as a set of n finite elements, each of them connecting two of the $n+1$ nodes of the model, see Fig. 2-a. In the initial configuration, nodes are uniformly distributed between two end points and are referenced with their position (x_i, y_i) in a fixed reference frame $(\mathbf{e}_x, \mathbf{e}_y)$. For simplicity in the notations, these coordinates are collected in a $(2n+2)\times 1$ vector $\mathbf{x}$ concatenating x- and y-positions, alternatively, for each of the $n+1$ nodes.

Elements are defined by two nodes and a uniaxial displacement field in the corotational frame. In the initial deformation, their description is complemented by an initial length and inclination given by

$$\ell_i = \left[\left(x_{i+1}-x_i\right)^2 + \left(y_{i+1}-y_i\right)^2 \right]^{1/2} \quad ; \quad \alpha_i = \arctan \frac{y_{i+1}-y_i}{x_{i+1}-x_i}. \tag{1}$$

The displacement field $\mathbf{u}\left(t\right)$ collecting the x- and y- components, in the reference frame, of the nodal displacements, provides the nodal coordinates $\mathbf{x}'\left(t\right)$ in the deformed configuration, see Fig. 2-b,

$$\mathbf{x}'\left(t\right) = \mathbf{x} + \mathbf{u}\left(t\right). \tag{2}$$

Nodal velocities and accelerations are readily obtained as the first and second time derivative of (2). The kinematics of each element are fully determined by the location of its two end nodes. Actually, the length and the inclination of each truss element in the deformed configuration,

$$\ell'_i = \left[\left(x'_{i+1}-x'_i\right)^2 + \left(y'_{i+1}-y'_i\right)^2 \right]^{1/2} \quad ; \quad \alpha'_i = \arctan \frac{y'_{i+1}-y'_i}{x'_{i+1}-x'_i} \tag{3}$$

allow estimation of the internal forces with

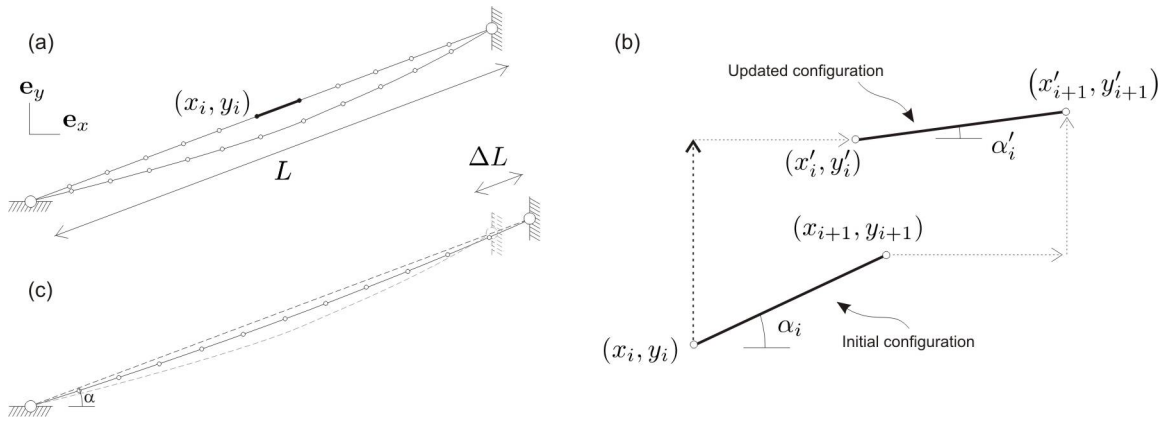


Figure 2: (a) Mesh of initial configuration and sketch of deformed configuration under self-weight, (b) Kinematics of a finite element, (c) Imposed displacement ΔL at the top node, in order to generate the initial tension in the cable.

$$\mathbf{f}_i(\mathbf{u}) = \mathbf{R}[\alpha'_i(\mathbf{u})] \begin{pmatrix} -1 \\ 0 \\ 1 \\ 0 \end{pmatrix} \frac{EA(\ell'_i - \ell_i)}{\ell_i} \tag{4}$$

where EA is the axial rigidity of the element, and $\mathbf{R}[\cdot]$ is a finite magnitude rotation matrix

$$\mathbf{R}[\varphi] = \begin{pmatrix} \mathbf{T} & \mathbf{Z} \\ \mathbf{Z} & \mathbf{T} \end{pmatrix}; \quad \mathbf{T} = \begin{pmatrix} \cos\varphi & -\sin\varphi \\ \sin\varphi & \cos\varphi \end{pmatrix}; \quad \mathbf{Z} = \begin{pmatrix} 0 & 0 \\ 0 & 0 \end{pmatrix}. \tag{5}$$

Localization and assembly of internal forces provide the resultant of internal forces $\mathbf{f}$,

$$\mathbf{f}[\mathbf{u}(t)] = \sum_{i=1}^{n} \mathbf{L}_i \mathbf{f}_i[\mathbf{u}(t)] \tag{6}$$

where $\mathbf{L}_i$ is a localization matrix, with size $(2n+2) \times 4$.

The equation of motion reads

$$\mathbf{M}\ddot{\mathbf{u}}(t) + \mathbf{C}\dot{\mathbf{u}}(t) + \mathbf{f}[\mathbf{u}(t)] = \mathbf{p}(t) + \mathbf{r}(t) \tag{7}$$

where $\mathbf{p}$ represents the external loads associated with the cable own weight and the traveling rider, $\mathbf{r}$ represents the reaction forces, while $\mathbf{M}$ represents the global mass matrix, written in this paper with a consistent approach [14], and $\mathbf{C}$ is a damping matrix constructed with a Rayleigh model, imposing a damping coefficient ξ in the first two modes. In the simulation of the structural dynamic response, this equation is integrated with an explicit formulation of Newmark's algorithm.

The response of the cable-rider system is determined in a two-step procedure.

First, the static deformed configuration of the cable under its own weight and initial tension is determined. This first step is achieved by imposing a displacement ΔL at the top node of the model, in the direction of the chord, see Fig. 2-c. The magnitude of this displacement is translated into a tension in the cable. In accordance with classical static theory of cable, the horizontal projection H of the internal force is used as a reference throughout this document. In more details, the static deflection of the cable $\mathbf{u}_s$ is obtained by solving (7) without the first

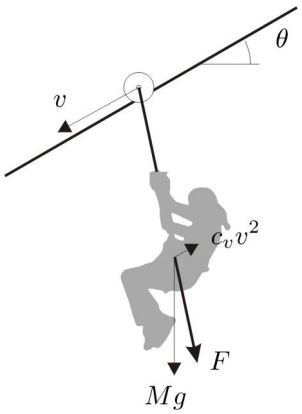


Figure 3: Free-body diagram of the rider (excl. inertial forces).

term —related to inertial forces—, and disregarding the first two and last two equations, as they correspond to unknown reactions. The horizontal force in the cable H is obtained in a post-processing operation, as the horizontal reaction at the base. Computation of the static deflection $\mathbf{u}_s$ as well as the horizontal force in the cable H is repeated for various top displacements ΔL, until the horizontal force maps the target force.

In a second step, the dynamic computation of the cable response is determined, with $\mathbf{u}_s$ as initial deformation field. A peculiarity of this problem consists in the determination of what is considered in (7) as external forces $\mathbf{p}$, i.e. those resulting from the coupled cable-rider system. Their expression is discussed in the following section. Apart from this term, the solution of (7) follows classical numerical integration methods.

2.2 Interaction with the rider

At the beginning of the computation, the rider leaves the top end of the cable with a zero velocity. Its position along the cable is represented by a supplementary degree-of-freedom s, considered as the curvilinear abscissa measured along the cable, from the upper end.

For compatibility reasons, the velocity vector of the pulley rolling on the cable is tangent to the cable supporting the rider, see Figure 3. Forces acting on the rider are its own weight $M\vec{g}$ and an aerodynamic force $c_v \left|v\right| \vec{v}$ whose intensity is proportional to the square velocity, as in Bernoulli equation. At the beginning of the ride, the velocity of the rider is rather high, which results in a significantly inclined reaction force F; on the opposite, as the rider slows down, its position naturally tends to be below the pulley.

Only the tangential component of the force F, i.e. in the direction of the cable, is considered to determine the motion of the rider,

$$F_\perp = Mg\sin\theta - c_v v^2. \tag{8}$$

Exactly as the motion of a wheel rolling on an inclined plane is determined by the component of the weight parallel to the inclined plane, the acceleration of the rider is determined by

$$a = g\sin\theta - \frac{c_v v^2}{M}. \tag{9}$$

In the numerical procedure, starting from the position s and velocity of the rider at the beginning of a time step, the position at the end of a time step is computed under the assumption that the

acceleration is constant along a time step

$$v_{t+\Delta t} = v_t + a\Delta t \quad ; \quad s_{t+\Delta t} = s_t + v_t\Delta t + \frac{a}{2}\Delta t^2 \tag{10}$$

2.3 Numerical Algorithm

The weakly coupled problem is thus solved in a staggered manner, with the algorithm represented by this pseudo-code.

```
initialize deformed configuration
loop on time
 1 update deformed configuration
 2 compute internal forces and tangent stiffness matrix
 3 compute the position and velocity of the rider ...
 at the end of the time step
 4 build vector of external forces p
 5 compute initial acceleration
 6 compute effective stiffness and load increment
 7 compute increment of displacement and velocity
end
```

Step 1 consists in the computation of the element lengths ℓ_i' and inclinations α_i' in the updated deformed configuration, see (3). In step 2, internal forces $\mathbf{f}_t$ are determined with (6) while the tangent stiffness $\mathbf{K}_t$ matrix is obtained by finite difference of internal forces. In step 3, the position and velocity of the rider at the end of the time step are determined by (10). Then the vector of external forces $\mathbf{p}_{t+\Delta t}$ is constructed as a sum of the self-weight forces and the force resulting from the rider. This latter component is mainly composed of zeros, except for the four degrees-of-freedom corresponding to the finite element on which the rider currently is. The magnitude of the force is determined in accordance with the free-body diagram of Fig. 3, and then is dispatched between the four degrees-of-freedom.

The following steps concern the determination of the structural response. In step 5, the acceleration at the beginning of the time step is determined, with

$$\ddot{\mathbf{u}}_t = \mathbf{M}^{-1}\left(\mathbf{p}_t + \mathbf{r}_t - \mathbf{C}\dot{\mathbf{u}}_t - \mathbf{f}_t\right) \tag{11}$$

Step 6 consists in determining the effective stiffness and increment of force

$$\tilde{\mathbf{K}} = \mathbf{K}_t + \frac{3}{\Delta t}\mathbf{C} + \frac{6}{\Delta t^2}\mathbf{M} \tag{12}$$

$$\Delta\mathbf{p} = (\mathbf{p}_{t+\Delta t} - \mathbf{p}_t) + \mathbf{M}\left(\frac{6}{\Delta t}\dot{\mathbf{u}}_t + 3\ddot{\mathbf{u}}_t\right) + \mathbf{C}\left(3\dot{\mathbf{u}}_t + \frac{\Delta t}{2}\ddot{\mathbf{u}}_t\right) \tag{13}$$

and finally, the increment of structural displacement and velocity are determined by

$$\Delta\mathbf{u} = \tilde{\mathbf{K}}^{-1}\Delta\mathbf{p} \tag{14}$$

$$\Delta\dot{\mathbf{u}} = \frac{3}{\Delta t}\Delta\mathbf{u} - 3\dot{\mathbf{u}}_t - \frac{\Delta t}{2}\ddot{\mathbf{u}}_t \tag{15}$$

so that the structural displacement and velocity at the end of the time step are given by adding these increments to the values at the beginning of the time step.

$\Delta x = 1163$ m		Vertical offset between both ends
$\Delta y = 112$ m		Horizontal offset between both ends
$\xi = 0.1\%$		Damping ratio
$\Omega = 77$ mm^2		Cable cross section
$E = 120$ GPa		Effective Young modulus
$\mu = 602$ g/m		Mass per unit length of the cable
$M_t = 120$ kg		Mass of the rider (plus equipment)
$c_w = 0.74$ N/(m/s)^2		Aerodynamic coefficient

Table 1: Numerical data of the problem.

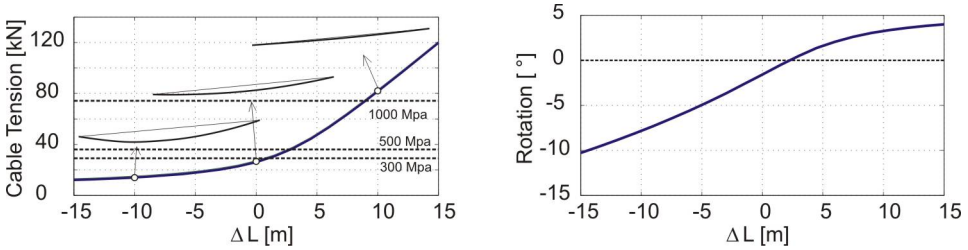


Figure 4: Intial tension vs shortening of the cable chord, and inclination of the lower anchorage.

3 Results

Table 1 summarizes the numerical values considered for the problem. The vertical and horizontal offsets Δx and Δy are determined from topological data. The damping coefficient ξ, set equal to 0.1% by comparison with former identification tests of similar cables, is used to construct the Rayleigh damping matrix. The cable cross section Ω and Young modulus E are obtained from the specification sheets of the cable. The traveling mass is assumed to be equal to $M_t = 120$ kg, which, according to the fire safety brigade, should correspond to a safe estimation of the body mass, plus equipment. The aerodynamic coefficient c_w is tuned in such a way that the results obtained with this model reproduce accurately the travel duration in a 550-m long death-ride which was formerly instrumented.

A number of 16 finite elements is considered throughout this paper. Figure 4 represents the results of the numerical tensioning operation. More precisely, the tension and the inclination at the bottom anchorage are represented in the cable as a function of the imposed kinematic chord extension ΔL. Figure 4-a indicates that the stress level in the cable, due to its own weight and initial tension, is rather large compared to the ultimate stress of the cable. For instance, stresses as large as 500 MPa correspond to a loose cable, while 1000 MPa at least are necessary to ensure a full stiffness. Figure 4-b is interesting in the sense that, as will be demonstrated clearly later, the inclination of the bottom end of the cable plays an important role in any preliminary design. In this respect, it is important to notice that, to a chord extension of $\Delta L \simeq 2.5m$, corresponds a more or less horizontal inclination of the static deflection of the cable, at the bottom anchorage. In order to allow for a safety margin with respect to the axial force under the riding operations, it is decided to limit the cable extension to $\Delta L = 4m$, so that the initial stress in the cable remains below 600 MPa in the static configuration.

The dynamic computation is performed with a constant time step $\Delta t = 0.02s$. In order to illustrate the influence of the initial tension in the cable, the dynamic analysis during the ride is performed for three different values of the initial tension in the cable $H = 21.7$kN ($\Delta L = -2m$), $H = 32.4$kN ($\Delta L = 2m$) and $H = 41.6$kN ($\Delta L = 4m$). The bottom rotation

		$\Delta L = -2m$	$\Delta L = 2m$	$\Delta L = 4m$
H	[kN]	21.7	32.4	41.6
φ_0	[ ]	-2.97	-0.16	-1.09
f_1	[Hz]	0.161	0.141	0.137
f_2	[Hz]	0.165	0.198	0.224
f_3	[Hz]	0.248	0.297	0.334

Table 2: Properties of the cable under different initial tensions.

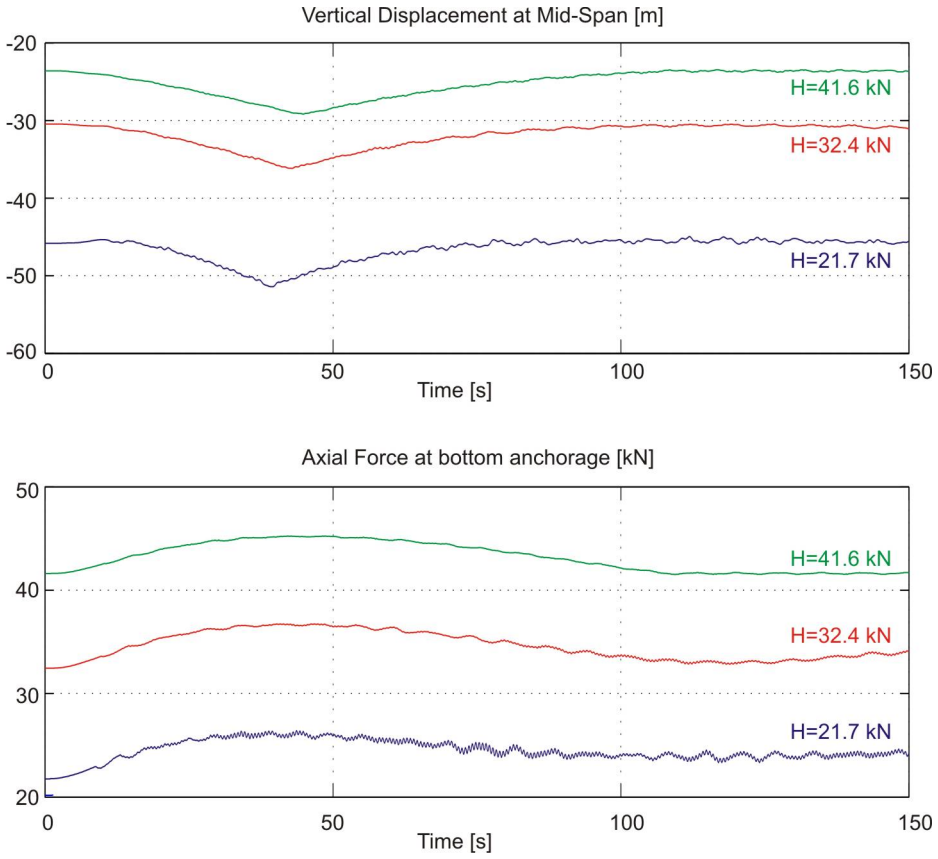


Figure 5: Vertical displacement at mid-span (from chord) and axial force at the bottom. Represented for various initial tension in the cable.

and the natural frequencies of the cable in these various configurations are provided in Table 2. If the former case, the first two eigen modes have close natural frequencies. This configuration is actually just above the crossover point, as the first mode shape exhibits two halfwaves, while the second one features only one.

Figure 5 represents the vertical displacement at mid-span as well as the axial force in the cable at the bottom anchorage. The static deflection of the loosest cable may reach 45m in the static case, plus an additional 10 meters in the dynamic case. For the first two cases ($H = 21.7kN$, $H = 32.4kN$), the cable is loosely taut, which results in (i) a more important increase of the tension force during the ride, (ii) a more flexible, and more oscillating cable. At the opposite, in the case with the highest axial force, the residual oscillations after the ride are damped out by the system.

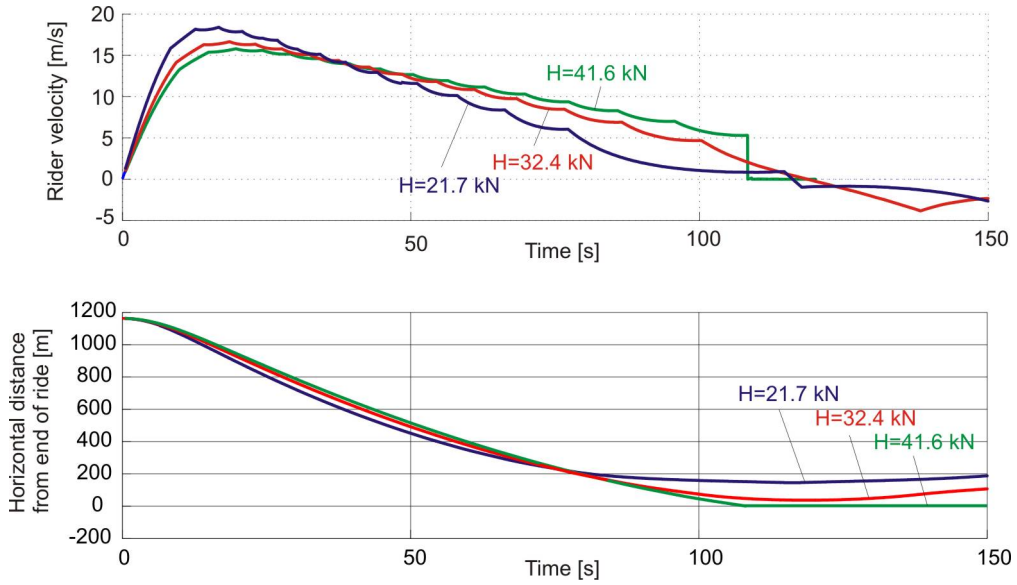


Figure 6: Velocity and vertical position of the rider for various initial tension in the cable.

Figure 6-a shows that the rider velocity computed with this simplistic model varies with some irregularities, in particular angular points, corresponding to discontinuities in the acceleration. This numerical inaccuracy results from the approximation of the smooth cable by a chain, i.e. a connection of articulated truss elements. At the beginning of the ride, the highest initial tension in the cable ($H = 41.6kN$) provides a smaller slope in the velocity history, i.e. a smaller acceleration than in the loose cable case. This is justified by the shape of the cable in the neighborhood of the origin, which is flatter for the cable with the highest initial tension. On the contrary, after the rider velocity has reached its maximum value which amounts to $15 - 20m/s$ in this particular case study, he/she travels faster when the cable is more tightened. Indeed, the smaller deceleration is attributable to the fact that the rider travels in a steeper zone of the cable.

Figure 6-b represents the horizontal distance between the rider and the lower anchorage. At first sight, there are few differences between the trajectories in the three considered cases, but in fact, they correspond to three significantly different solutions.

The slack cable ($H = 21.7$kN) has a steeper slope at the beginning, which causes the vertical position of the rider to decrease faster than for the other cases. As the ride goes on, the velocity decreases however rapidly and eventually the rider remains stuck in a sagging area above the River Meuse, more than 150m away from the end. This explains why the rider velocity becomes negative after approximately 115 seconds.

The second case, with the intermediate tension in the cable ($H = 32.4$kN) was actually considered to be optimum. Indeed, the ride ends after 120 seconds with a small rider velocity, which makes it easier to stop him/her, if necessary. Interestingly perhaps, this second case corresponds to a more or less horizontal cable slope at the lower anchorage.

The third case, with the largest initial tension in the cable ($H = 41.6$kN) was judged to be unsafe as the end velocity was still larger than 5 m/s at the end of the ride. Also, starting with an initial horizontal tension in the cable of 4.2 tons was judged to provide stresses in the cable during the dynamic loading that could be to close to the yield limit, with an acceptable safety margin though.

The plots in Figs 5-6 are the perfect tools to judge how large should the initial tension in the cable be. They contrast all aspects related to the decision making process: safety through the

determination of stresses, sensation through maximal velocity and initial acceleration, comfort through end velocity, feasibility through the horizontal distance from end. The optimal choice should also include considerations on the sensitivity to the rider's mass, i.e. how much these plots change under small or moderate perturbations of the rider's mass.

4 Conclusions

This case study on a world record death-ride was here reported with a set of thoughts and design criteria that were considered in the design of this remarkable structure, in particular regarding the proper selection of the initial tension in the cable. A simple numerical model of the problem was built as the connection of two basic features: a finite element model, constructed with 2-D large displacement truss elements in a corotational framework, and a simple staggered coupling model so as to determine the rider's position and velocity.

A parametric study on the initial tension revealed that there exists an optimal tuning of this tension that apparently provides simultaneously comfort, sensation and safety. This solution consists in selecting the initial tension in the cable in such a way that the static configuration of the cable before the ride presents a horizontal inclination at the lower anchorage. As simple as it is, this observation could most likely be extended to other death-rides.

REFERENCES

[1] Canor T., Denoël V., Vibration analysis of a cable with bending stiffness by a multiple scales approach, paper 292, SEMC 2013, Cape Town, South Africa 6 p. (2013).

[2] Carassale, L., Piccardo, G., Non-linear discrete models for the stochastic analysis of cables in turbulent wind, International Journal of Non-Linear Mechanics, 45 (3), 219-231, 2010.

[3] Denoël V., Detournay E., Multiple scales solution for a beam with a small bending stiffness, ASCE Journal of Engineering Mechanics, 2010. Vol. 136, 69-77, 2012.

[4] Denoël V., Detournay E., Eulerian formulation of constrained elastica, International Journal of Solids and Structures, 48 (3-4), 625-636, 2011.

[5] Denoël V., Canor T., Patching asymptotics solution for a beam with a small bending stiffness, Journal of Structural Engineering, ASCE, 139(2), 180–187, 2012. DOI: 10.1061/(asce)st.1943-541x.0000643.

[6] Fryba L., Vibration of Solids and Structures under Moving Loads, Thomas Telford, New York, 1999.

[7] Impollonia, N., Ricciardi, G., Saitta, F., Vibrations of inclined cables under skew wind, International Journal of Non-Linear Mechanics, 46 (7), 907-918, 2011.

[8] Irvine, H. M., Statics of suspended cables, Journal of the Engineering Mechanics Division-Asce, 101 (3), 187-205, 1975.

[9] Irvine H. M., Caughey T. K., The linear theory of free vibrations of a suspended cable, Proceedings of the Royal Society of London, Series A, 314, 299-315, 1974.

[10] Kevorkian J., Cole J. .D., Multiple Scale and Perturbation Methods, New York: Springer-Verlag, Inc, 1996.

[11] Rega, G., Nonlinear dynamics of suspended cables. Part I : Modeling and analysis; Part II : Deterministic phenomena, ASME Applied Mechanics Reviews, Vol. 57, 443-514, 2004.

[12] Stump, D. M. and van der Heijden, G. H. M., Matched asymptotic expansions for bent and twisted rods: applications for cable and pipeline laying, Journal of Engineering Mathematics, 38 (1), 13-31, 2000.

[13] www.grimpday.com

[14] Zienkievic O. C. , The finite element method in engineering, Pergamon Press, Oxford, 1982.

COMPDYN 2013
4th ECCOMAS Thematic Conference on
Computational Methods in Structural Dynamics and Earthquake Engineering
M. Papadrakakis, V. Papadopoulos, V. Plevris (eds.)
Kos Island, Greece, 12–14 June 2013

MODELLING A LARGE-SCALE UNIAXIAL SHAKING TABLE FACILITY

Paola Ceresa[1], **Franco Brezzi**[1] **and Gian Michele Calvi**[1]

[1] Istituto Universitario di Studi Superiori di Pavia (IUSS)
Piazza della Vittoria 15, 27100 Pavia (Italy)
paola.ceresa@iusspavia.it, franco.brezzi@iusspavia.it, gm.calvi@iusspavia.it

Keywords: Large-scale dynamic testing facility, nonlinear kinematics, high-order nonlinear differential equations, numerical solver, experimental data

Abstract. *Aim of this research is the development and the calibration of a mathematical model for simulating the response of a large-scale uniaxial shaking table facility. The system to be modelled is composed of several interacting components such as the shaking table, the specimen to be tested and the reaction mass. The latter could be isolated by air suspension springs and damped by heavy duly automotive shock absorbers or could rest directly on the supporting soil. The proposed model has been developed to take into account the stiffness and the damping due to suspension system/shock absorber system as well as the flexibility of the supporting soil.*

The main novelty of the proposed model is the nonlinear kinematics taken into account in the formulation of the equations of motion of the dynamic system. The rocking of the reaction mass is modelled and the nonlinear kinematics due to large rotations associated to an intended uniaxial motion of the shaking table is considered.

The nonlinear equations of motions are derived using the Lagrangian approach under the assumption of large displacements and large rotations.

The proposed mathematical model has been derived to be general and capable of predicting the response of any given uniaxial shaking table whose response could be strongly affected by the rocking of the reaction mass.

The derived system of nonlinear equations of motion has been applied for modelling the response of an existing large-scale dynamic testing facility – the shaking table of the Eucentre Laboratory. The obtained results seem very promising, useful for understanding the causes of the complex behaviour of the dynamic testing facility and instrumental for helping in future experimental campaigns.

1 INTRODUCTION

Large servo-hydraulic shaking table systems are essential tools in experimental earthquake engineering since they provide effective ways to subject structures to dynamic excitations similar to those induced by real earthquakes. Several shaking tables throughout Europe are being used to investigate the dynamic effects of earthquake on structures. The latter are usually characterised by more than one degree of freedom (3 and 6 DOFs are common), a payload of about 20-30 tonnes and limited performances in terms of payload, peak velocities, peak accelerations and stroke. With regards to the initiatives outside Europe, considerable funding and effort have been allotted over the past 40 years in the construction of continuously larger and powerful shaking table facilities [1]. Thus, the need for building large and powerful dynamic facilities capable of testing up to failure full-scale models has become clear.

In the search of improved earthquake simulation, increasing accuracy with which a shaking table can replicate a desired motion is of great interest. A comprehensive understanding of the dynamic characteristics of a shaking table is of fundamental importance for optimising its control algorithm and, eventually, assessing its limitations. Therefore, a mathematical model of the complete shaking table system is required for planning future experiments, optimising the system, understanding the causes of a complex behaviour and developing safety measurements.

The current study is devoted to a large-scale dynamic testing facility composed by the specimen (i.e., payload), shaking table, reaction mass, airbags, dampers and soil. In particular, the subject of the research is a large-scale and powerful shaking table designed for performing single-axis tests (1 DOF) whose behaviour could be affected by the rocking of the reaction mass. The effects of the support system (i.e. reaction mass, airbags, dampers and soil) interaction on the response of the shaking table are evaluated developing a deterministic model capable to take into account horizontal, vertical and rotational accelerations of the overall dynamic testing facility.

2 DERIVATION OF THE DETERMINISTIC MODEL

The behaviour of a large and powerful dynamic testing facility could be characterised and influenced by: i) large overturning moment due to the specimen located on the shaking table; ii) large lateral displacement of the shaking table as well as powerful performances in terms of both velocity and acceleration; iii) unbalanced configuration of the reaction mass; iv) deformability of the soil. All these factors could cause the presence of non-negligible nonlinear terms in the equations of motion describing the dynamic testing facility.

The model to be derived must be as general as possible and applicable to any given shaking table. The dynamics of the shaking table cannot be described by a single equation of motion related to its allowed longitudinal translation since the interactions between the specimen, shaking table, reaction mass, isolation and damping systems, foundation and soil have to be taken into account. The derived model has to be capable of simulating the behaviour of a shaking table that could be subjected to a possible large rotation since it moves in a rotating frame of reference which corresponds to the support system. Therefore, the motion of the shaking table has to be described by a set of equations written considering a reference system characterised by longitudinal and vertical translations and rotational degrees of freedom. The out-of-plane motion is not accounted for in this phase of the formulation. The Lagrange's approach for deriving the nonlinear equations of motions under the assumptions of large displacements is applied. In addition, the homogeneous matrix approach proposed by Legnani et al. [2, 3] is adopted since it allows to study kinematic and dynamic motions of rigid bodies in the form of a consistent method employing 4×4 matrices, following Lagrange's method. A

comprehensive description of the derivations of equations is given in [4]. However, a brief summary of the main assumptions and findings is given in the following sections in order to clearly catch the novelty of the proposed deterministic model and best exploit the potentials of the proposed model for studying complex dynamic problems as the validation examples discussed in Section 4.

Figure 1 shows the two main systems are modelled. The first (later named *system I*) is composed by the reaction mass, the isolators, the dampers and the soil. The second (*system II*) includes the shaking table and the payload to be tested. Three independent coordinates are introduced to describe the horizontal and vertical displacements and the rotation of the *system I* – Q_1, Q_2 and Q_3, respectively. The horizontal displacement between *system II* and *system I* is the fourth generalised coordinate – Q_4. It is assumed that the payload is perfectly restrained to the platform (of the shaking table) and it moves accordingly to the shaking table motion. Therefore, the relative vertical displacement Q_5 and the relative rotation Q_6 are disregarded and the rotation Q_3 becomes the rotation of both *system I* and *system II*. Hence, four differential equations are derived with respect to the coordinates Q_1, Q_2, Q_3 and Q_4. According to the homogeneous matrix approach [2, 3], the ingredients for writing the Lagrange's equation of motion are the position, velocity and acceleration matrices – **M**, **W** and **H**, respectively – which allow to handle both linear and angular terms at the same time. In addition, the pseudo-inertial matrix (**J**) which describes the mass distribution of a body has to be introduced. The relative motion between *system I* and *system II* is described using familiar concepts as the velocity composition theorem (or Rival's theorem) and Coriolis' theorem. Three frames of reference are considered during the derivation of the deterministic model: (X_1, Y_1, Z_1) is the absolute inertial frame of reference; (X_2, Y_2, Z_2) and (X_3, Y_3, Z_3) are embedded in the centres of gravity of *system I* and *system II*, respectively.

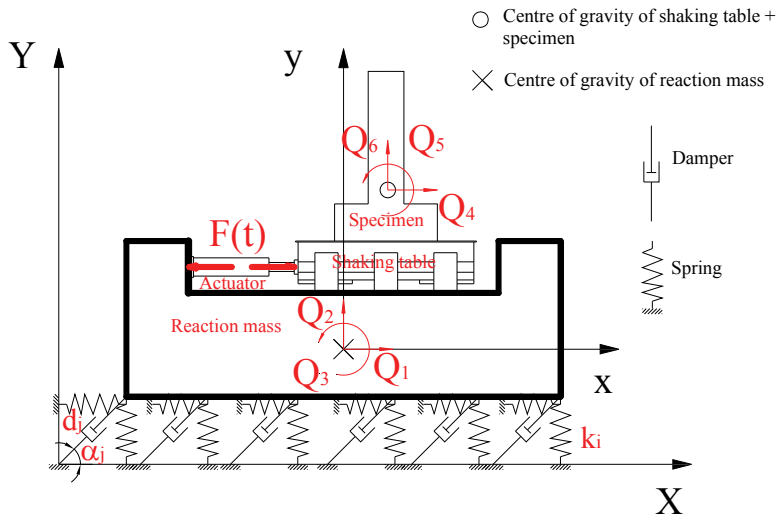


Figure 1: Dynamic testing facility to be modelled.

2.1 Kinetic energy of the overall dynamic system

The total kinetic energy (T) is the sum of the kinetic energies of *system I* and *system II*:

$$T_I = (1/2) \cdot Trace\left(\mathbf{W}_{12(1)}\, \mathbf{J}_{I(2)}\, \mathbf{W}_{12(1)}{}^T\right)$$
$$T_{II} = (1/2) \cdot Trace\left(\mathbf{W}_{13(1)}\, \mathbf{J}_{II(1)}\, \mathbf{W}_{13(1)}{}^T\right) \quad (1)$$

where $\mathbf{J}_{I(2)}$ is the pseudo-inertial matrix of *system I* in the reference frame (X_2, Y_2, Z_2), $\mathbf{J}_{II(1)}$ is the pseudo-inertial matrix of *system II* in the reference frame (X_1, Y_1, Z_1), $\mathbf{W}_{12(1)}$ and $\mathbf{W}_{13(1)}$ are the velocity matrices of *system I* and *system II*, respectively. The matrices that characterise the motion of *system I* are given in Eq. (2), where m_I is the mass of the system:

$$\mathbf{M}_{12(1)} = \begin{bmatrix} \cos Q_3 & -\sin Q_3 & 0 & Q_1 \\ \sin Q_3 & \cos Q_3 & 0 & Q_2 \\ 0 & 0 & 1 & 0 \\ 0 & 0 & 0 & 1 \end{bmatrix}, \quad \mathbf{W}_{12(1)} = \begin{bmatrix} 0 & -\dot{Q}_3 & 0 & \dot{Q}_1 \\ \dot{Q}_3 & 0 & 0 & \dot{Q}_2 \\ 0 & 0 & 0 & 0 \\ 0 & 0 & 0 & 0 \end{bmatrix}$$
$$\mathbf{J}_{I(2)} = \begin{bmatrix} I_{xx,I} & 0 & 0 & 0 \\ 0 & I_{yy,I} & 0 & 0 \\ 0 & 0 & I_{zz,I} & 0 \\ 0 & 0 & 0 & m_I \end{bmatrix} = \begin{bmatrix} \int x^2 dm_I & 0 & 0 & 0 \\ 0 & \int y^2 dm_I & 0 & 0 \\ 0 & 0 & \int z^2 dm_I & 0 \\ 0 & 0 & 0 & m_I \end{bmatrix} \tag{2}$$

The velocity matrix $\mathbf{W}_{13(1)}$ of the *system II* with respect to (X_1, Y_1, Z_1) is given by the sum of the drag component $\mathbf{W}_{12(1)}$ and the relative velocity $\mathbf{W}_{23(1)}$, according to the velocity composition theorem:

$$\mathbf{W}_{13(1)} = \mathbf{W}_{12(1)} + \mathbf{W}_{23(1)} = \mathbf{W}_{12(1)} + \mathbf{M}_{12(1)} \cdot \mathbf{W}_{23(2)} \cdot \mathbf{M}_{21(1)} \tag{3}$$

The position and velocity matrixes of the *system II* in the frame of reference (X_2, Y_2, Z_2) are equal to:

$$\mathbf{M}_{23(2)} = \begin{bmatrix} 1 & 0 & 0 & Q_4 \\ 0 & 1 & 0 & 0 \\ 0 & 0 & 1 & 0 \\ 0 & 0 & 0 & 1 \end{bmatrix}, \quad \mathbf{W}_{23(2)} = \begin{bmatrix} 0 & 0 & 0 & \dot{Q}_4 \\ 0 & 0 & 0 & 0 \\ 0 & 0 & 0 & 0 \\ 0 & 0 & 0 & 0 \end{bmatrix} \tag{4}$$

Using the general transformation law that works for pseudo-tensor of inertia [3], the mass distribution of the system II in (X_1, Y_1, Z_1) can be computed according to this expression:

$$\mathbf{J}_{II(1)} = \mathbf{M}_{12(1)}(\mathbf{M}_{23(2)}\mathbf{J}_{II(3)}\mathbf{M}_{23(2)}^T)\mathbf{M}_{12(1)}^T \tag{5}$$

where $\mathbf{J}_{II(3)}$ is the pseudo-matrix of inertia of *system II* when the frame of reference (X_3, Y_3, Z_3) is concerned.

$$\mathbf{J}_{II(3)} = \begin{bmatrix} I_{xx,II} & 0 & 0 & 0 \\ 0 & I_{yy,II} & 0 & 0 \\ 0 & 0 & I_{zz,II} & 0 \\ 0 & 0 & 0 & m_{II} \end{bmatrix} = \begin{bmatrix} \int x^2 dm_{II} & 0 & 0 & 0 \\ 0 & \int y^2 dm_{II} & 0 & 0 \\ 0 & 0 & \int z^2 dm_{II} & 0 \\ 0 & 0 & 0 & m_{II} \end{bmatrix} \tag{6}$$

The final expression of T is given by:

$$T = \begin{cases} 0.5m_I[\dot{Q}_1^2 + \dot{Q}_2^2] + (1/2)(I_{xx,I} + I_{yy,I})\dot{Q}_3^2 + \\ + 0.5m_{II}[\dot{Q}_1^2 + \dot{Q}_2^2 + \dot{Q}_4^2 + 2\dot{Q}_1\dot{Q}_4\cos Q_3 + 2\dot{Q}_2\dot{Q}_4\sin Q_3] + \\ 0.5\dot{Q}_3^2[(I_{xx,II} + I_{yy,II}) + m_{II}(Q_1^2 + Q_2^2 + Q_4^2 + 2Q_1Q_4\cos Q_3 + 2Q_2Q_4\sin Q_3)] + \\ + m_{II}\dot{Q}_3[Q_1\dot{Q}_2 - Q_2\dot{Q}_1 + (Q_1\dot{Q}_4 - Q_4\dot{Q}_1)\sin Q_3 + (-Q_2\dot{Q}_4 + Q_4\dot{Q}_2)\cos Q_3] \end{cases} \quad (7)$$

2.2 Potential energy of the overall dynamic system

The total potential energy V of the system is computed as the sum of the contributions due to gravity (Eq. 8), the *ns* springs k_i introduced to model the isolators and the stiffness of the soil (whose slopes could be general, different from each other and represented by the angle α_i) as shown in Eq. (9) and the translational spring k_4 representing the stiffness of the servo-hydraulic actuator, Eq. (10):

$$V_{Pi} = Trace\left(-\mathbf{H}_g \cdot \mathbf{J}_i\right) \text{ for i} = I,\ II \quad (8)$$

$$V_{i_springs} = 0.5\sum_{i=1}^{ns} k_i\bar{u}_i^2 = 0.5\sum_{i=1}^{ns} k_i \begin{Bmatrix} [(\cos Q_3 - 1)X_i - \sin Q_3 Y_i + Q_1](\cos\alpha_i) + \\ + [\sin Q_3 X_i + (\cos Q_3 - 1)Y_i + Q_2](\sin\alpha_i) \end{Bmatrix}^2 \quad (9)$$

$$V_{k4} = 0.5k_4(U_2 - U_1)^2 0.5k_4[Q_4 + \bar{x}Q_3\sin Q_3 - \bar{y}Q_3\cos Q_3]^2 \quad (10)$$

where $\mathbf{H}_g$ is the matrix of gravity acceleration (whose only non-null component is in the y-direction, g_y), $\bar{u}_i$ is the elongation or shortening of the k_i springs, X_i and Y_i are the coordinates of the *i-th* spring, U_1 and U_2 are the displacements of the two ends of the actuator computed in a rotated frame of reference. The total potential energy V is obtained as:

$$V = V_{PI} + V_{PII} + V_{i_springs} + V_{k4} \quad (11)$$

$$\begin{aligned} V = {} & g_y m_I Q_2 + g_y[m_{II}Q_4\sin Q_3 + m_{II}Q_2] + 0.5\sum_{i=1}^{ns} k_i\{[(\cos Q_3 - 1)X_i - \sin Q_3 \cdot Y_i + Q_1]\cdot \\ & \cdot(\cos\alpha_i) + [\sin Q_3 X_i + (\cos Q_3 - 1)Y_i + Q_2](\sin\alpha_i)\}^2 + 0.5k_4[Q_4 + \bar{x}Q_3\sin Q_3 - \bar{y}Q_3\cos Q_3]^2 \end{aligned} \quad (12)$$

2.3 Dissipation function of the overall dynamic system

The dissipation energy D can be introduced in the equations of motion assuming that it is a pseudo-potential energy and is given by the sum of the energy dissipated by the *nd* dampers characterised by a damping coefficients d_j (whose slopes could be general, different from each other and represented by the angle α_j) and the dissipation function related to the servo-hydraulic actuator (whose damping coefficient is name d_4):

$$D_{j_dampers} = 0.5\sum_{j=1}^{nd} d_j\bar{v}_j^2 = 0.5\sum_{j=1}^{nd} d_j[(-\dot{Q}_3 y_j + \dot{Q}_1)\cos\alpha_j + (\dot{Q}_3 x_j + \dot{Q}_2)\sin\alpha_j]^2 \quad (13)$$

$$D_{d4} = 0.5d_4(\dot{U}_2 - \dot{U}_1)^2 = 0.5d_4[\dot{Q}_4 + \bar{x}\dot{Q}_3(\sin Q_3 + Q_3\cos Q_3) - \bar{y}\dot{Q}_3(\cos Q_3 - Q_3\sin Q_3)]^2 \quad (14)$$

Therefore, the total dissipation function of the dynamic system is calculated as follows:

$$\begin{aligned} D = {} & 0.5\sum_{j=1}^{nd} d_j[(-\dot{Q}_3 y_j + \dot{Q}_1)\cos\alpha_j + (\dot{Q}_3 x_j + \dot{Q}_2)\sin\alpha_j]^2 + \\ & + 0.5d_4[\dot{Q}_4 + \bar{x}\dot{Q}_3(\sin Q_3 + Q_3\cos Q_3) - \bar{y}\dot{Q}_3(\cos Q_3 - Q_3\sin Q_3)]^2 \end{aligned} \quad (15)$$

2.4 Generalised forces applied to the overall dynamic system

The applied forces Q_i^* (i = 1, 4) are derived from the internal force given by the servo-hydraulic actuator; therefore, it is in the direction of the degree of freedom Q_4. This load could be defined as "follower load" since it is applied in a direction tangential to the centre line of the actuator following the motion of the entire system as it deforms. Being a follower load, the latter cannot be derived from a potential energy. Considering as input signal an external acceleration $\ddot{u}$, the Lagrangian force Q_4^* applied to *system II* is given by its mass times the applied acceleration. All the components related to the 4 DOFs are computed as:

$$Q_1^* = -|m_{II}\ddot{u}|\cos Q_3, \quad Q_2^* = |m_{II}\ddot{u}|\sin Q_3, \quad Q_3^* = -|m_{II}\ddot{u}|\cos Q_3 \cdot l, \quad Q_4^* = |m_{II}\ddot{u}| \quad (16)$$

where l is the distance between the load application line and the centre of mass of *system I*.

2.5 Derived nonlinear differential equations of motion

The equations of motion are derived as second-order Lagrange equations:

$$\frac{d}{dt}\left(\frac{\partial L}{\partial \dot{Q}_i}\right) - \left(\frac{\partial L}{\partial Q_i}\right) + \left(\frac{\partial D}{\partial \dot{Q}_i}\right) = Q_i^* \quad \text{for } i = 1, 4 \quad (17)$$

where L is computed as the difference between the total kinetic energy in Eq. (7) and the total potential energy in Eq. (12), D is given in Eq. (15) and the generalised forces in Eq. (16). Writing Eq. (17) with respect to the considered generalised coordinates, four nonlinear differential equations are obtained. For sake of brevity, the equations are not derived herein and the reader may refer to [4] where all the computations are shown and discussed in detail. It has to be pointed out that the strength of the Lagrange's approach is the possibility to directly account for the initial conditions, such as (if any) an initial rotation of the overall dynamic system. It is worth noting that the distribution and the location (Figure 1) of the k_i springs (i = 1, ns) and the dj dampers (j= 1, nd) are explicitly taken into account in the computations since this is one of the main features of the proposed dynamic model.

3 SOLUTION OF THE DEVELOPED DETERMINISTIC MODEL

As already stated in Section 1, one of the aims of this research effort is the formulation of a mathematical model capable of describing the behaviour of a large dynamic testing facility such as the uniaxial shaking table in Figure 1. The Laplace transforms cannot be applied to compute the solutions of the equations of motion since they are nonlinear. Solving these equations of motion accounting directly of the nonlinear contributions is the main feature of the proposed research. Therefore, numerical solution methods capable of solving nonlinear differential equations have been selected. In particular, the fourth order Runge-Kutta method (RK4) is employed because of its good efficiency well documented in literature. However, before solving the equations, preliminary verifications are performed and discussed in the two following sections. The first verification refers to the derivation of simplified models (i.e.,"linearised" models), which are well-known in literature. The second verification is related to the validation of the accuracy of the equations and numerical solver. The effects of both time step selection and initial conditions are presented.

3.1 Linearised simplified models

A proof of the accuracy of a developed model for describing very complex systems is the derivation of well-known and simple results. Therefore, some derived simplified models are presented.

a) System with three DOFs – Q_1, Q_2 and Q_4.

The set of equations describing this system is obtained from a linearization of Eq. (17) neglecting the strain energy V, the dissipation function D and the rotation of the system – $V = 0$, $D = 0$, $Q_3 = 0$ and $L = T$. The outcome of these assumptions leads to a system whose equations of motion with respect to the coordinates Q_1, Q_2 and Q_4 are given in Eq. (18). After substituting the third equation in the first one, the two expressions of Eq. (19) are derived. The latter represent the equations of motion of the *systems I* and *II* if they were totally free after the application of the horizontal forces F_{1x} and F_{2x}, acting in opposite directions. Each body develops an inertial force equal to the product of its own mass times its acceleration, in two opposite directions, respectively.

$$\begin{cases} (m_I + m_{II})\ddot{Q}_1 + m_{II}\ddot{Q}_4 = -F_{1x} + F_{2x} \\ (m_I + m_{II})\ddot{Q}_2 = -F_{1y} + F_{2y} \\ m_{II}\ddot{Q}_1 + m_{II}\ddot{Q}_4 = F_{2x} \end{cases} \tag{18}$$

$$\begin{cases} m_I\ddot{Q}_1 = -F_{1x} \\ m_{II}(\ddot{Q}_1 + \ddot{Q}_4) = F_{2x} \end{cases} \tag{19}$$

b) System with three DOFs – Q_1, Q_2 and Q_3.

Assuming that the coordinate Q_4 and the mass m_{II} can be neglected, the springs and the dashpots are lumped in the centre of gravity of *system I* and the rotation Q_3 is small (i.e., $Q_3 \approx 0$, $\sin Q_3 \approx Q_3$ and $\cos Q_3 \approx 1$), the following set of equations is obtained from Eq. (17):

$$\begin{cases} m_I\ddot{Q}_1 + c_{11}\dot{Q}_1 + c_{13}\dot{Q}_3 + k_{11}Q_1 + k_{13}Q_3 = F_{Q1} \\ m_I\ddot{Q}_2 + c_{22}\dot{Q}_2 + k_{22}Q_2 + g_y m_I = F_{Q2} \\ (I_{xx,I} + I_{yy,I})\ddot{Q}_3 + c_{33}\dot{Q}_3 + c_{31}\dot{Q}_1 + k_{33}Q_3 + k_{31}Q_1 = M_{Q3} \end{cases} \tag{20}$$

where the k_{ij} and c_{ij} coefficients represent the stiffness and the damping of the soils. The derived set of equations is similar to the one originally used in the design phase of an existing shaking table system [1]. The latter was developed for estimating acceleration, velocity and displacement of the reaction mass and studying the soil-structure dynamic interaction. From Eq. (20), it is possible to realise that the vertical motion Q_2 has no interaction with the horizontal and rotational coordinates, Q_1 and Q_3, respectively. This justified the choice of neglecting the vertical degree of freedom during the design phase of the shaking table presented in [1].

3.2 Accuracy of both derived equations and numerical solver

The verification of the accuracy of the derived equations is firstly carried out applying the mathematical procedure schematically depicted in Figure 2. Well-known solutions are imposed to the equations of motion and the forces satisfying the equilibrium are computed. The

latter become the external loads to be applied to the system of equations and the corresponding solutions are calculated. If the latter are similar, within some tolerance error, to the initially imposed solutions, this represents a proof that the equations of motion are accurate and that the numerical solver works properly. Several numerical examples have been studied and a very good agreement between the imposed and computed solutions was always found. In particular, the high quality of the results was due to the application of ad-hoc error tolerance properties: a relative error tolerance is applied to all the components of the solution vector, as well as the absolute error tolerance [6].

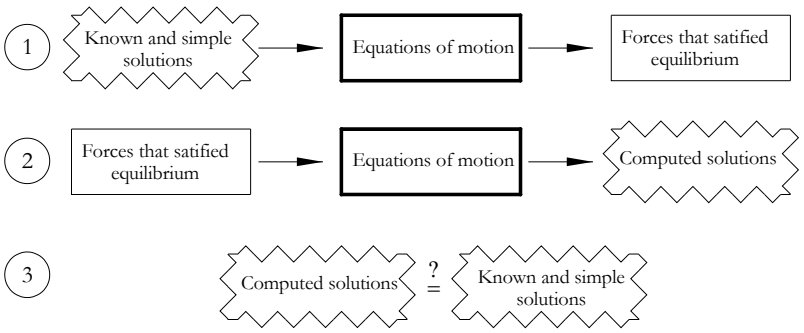


Figure 2: Steps for verifying the accuracy of the derived equations of motion.

Regardless of the integration technique used, the time step remains an important determinant of when to compute the solutions and when to compare the model to data. Fourth order Runge-Kutta integration has an error that is proportional to time step to the fifth power for an integration step and proportional to time step to the fourth power for the whole simulation.

Considering the configuration in Figure 3 with three DOF_s – Q_1, Q_3 and Q_4 – and lumped springs – k_1, k_3 and k_4 – whose nonlinear differential equations are derived from Eq. (17), some verifications of the accuracy of the solutions have been carried out investigating the influence of time step on the numerical solutions. Simple external loads, such as harmonic forces - $F_{Q1} = F_{Q1o}\cos(\omega t)$, $M_{Q3} = M_{Q3o}\cos(\omega t)$, $F_{Q4} = F_{Q4o}\cos(\omega t)$ - are applied to the system whose properties are summarised in the Table 1.

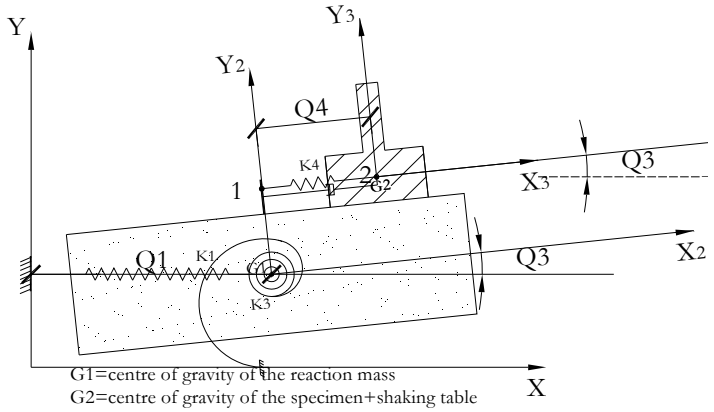


Figure 3: System with 3 generalised coordinates and lumped springs – Q_1, Q_3, Q_4 and k_1, k_3, k_4, respectively

The corresponding solutions are computed with Runge-Kutta methods using the time step as parameter. Figures 4-6 show the results obtained with a time interval Δt = 0.1, 0.001 and 0.00001 seconds, respectively. Unless the first set of solutions in Figure 4, the other two sets

of results show the same level of accuracy, even if the last one (Figure 6) is much more time consuming.

k_1 [N/m]	k_4 [N/m]	k_3 [N/rad]	m_I [kg]	m_{II} [kg]	$I_{zz,I}$ [tonnes m^2]	$I_{zz,II}$ [tonnes m^2]
5.E+3	2.E+3	10.E+3	500	5	5000	100

Table 1: Data of the numerical example for proving the effect of time step choice on the solutions of the system

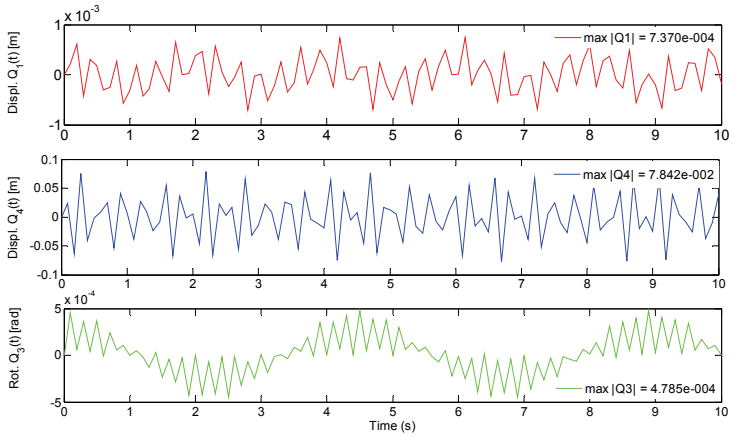


Figure 4: Numerical solutions of the system in Figure 3 for $\Delta t = 0.1$ s with Runge-Kutta (RK4) method

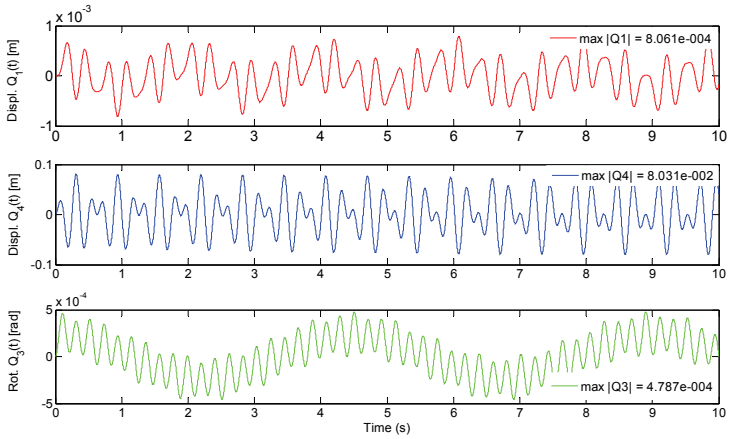


Figure 5: Numerical solutions of the system in Figure 3 for $\Delta t = 0.001$ s with Runge-Kutta (RK4) method

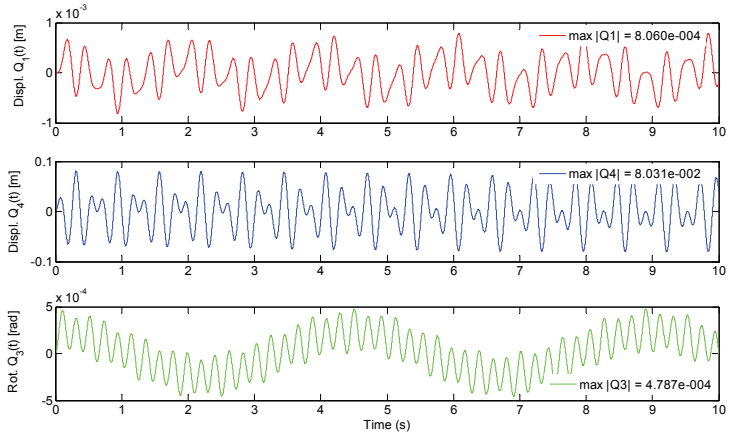


Figure 6: Numerical solutions of the system in Figure 3 for $\Delta t = 0.00001$ s with Runge-Kutta (RK4) method

As previously stated, one of the strengths of the Lagrange's approach is the possibility of taking into account the initial conditions. The influence of the initial conditions on the computed solutions is evaluated considering the system in Figure 3 subjected to an initial rotation Q_{3o} = -0.01 rad. The numerical responses due to the application of the harmonic forces F_{Q1}, M_{Q3} and F_{Q4} (previously defined) change in a non-negligible manner as it can be evaluated comparing the new time-histories plotted in Figure 7 with the ones in Figure 5. Since the damping has been neglected in this numerical case-of-study, the effect of the imposed initial rotation continues endlessly. This is only a simple example showing the interaction between the degrees of freedom and the influence of the initial rotation on the translational DOFs, Q_1 and Q_4. However, the damping is present in the real system and it makes the free vibration decay with time. One important outcome of this numerical case-of-study is that, if any initial rotation affects the overall dynamic system, its effect strongly influences the displacements, velocities and accelerations of the entire dynamic facility. Then, the transient effect disappears due to the effect of damping coefficients [5].

It can be stated that the contributions of the initial conditions (if any) should be accounted for during the experimental tests. One of the main advantages of the derived model is that the initial conditions can be directly considered and the computed responses could be used as predictions of the behaviour of the dynamic facility.

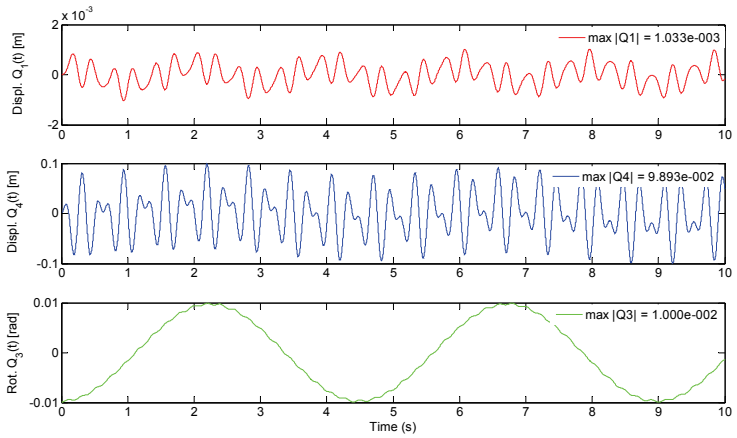


Figure 7: Numerical solutions of the system in Figure 3 for Δt = 0.001 s with Runge-Kutta (RK4) method and Q_{3o} = -0.01 rad

4 MODELLING THE RESPONSE OF AN EXISTING LARGE-SCALE DYNAMIC TESTING FACILITY

The developed model was formulated in a general manner. Therefore, it works or it could be validated considering any type of uniaxial shaking table system. In order to evaluate the accuracy of the equations of motion, numerical verifications should always be carried out, whenever feasible. The case-of-study for verifying the nonlinear differential equations is the large uniaxial shaking table built in the Laboratory of Eucentre (European Centre for Training and Research in Earthquake Engineering, www.eucentre.it), Pavia (Italy). The latter is chosen for its large dimensions and powerful performances in terms of stroke, velocity and accelerations applicable to the payload (Table 2). Furthermore, the system composed by the reaction mass, the shaking table and the specimen constitutes a non-equilibrated structure due to the eccentric position of both the platform and the specimen to be tested. The former is eccentric with respect to the centre of gravity of the reaction mass, the latter for its own configuration. Therefore, the system could suffer rotation and be characterised by a nonlinearity of the response. Moreover, it has been measured that the reaction mass suffered a rigid rotation proba-

bly due to the settlement of the system [7]. This rotation could be seen as an initial condition to be taken into account in predicting the response of such a complex dynamic testing facility.

Figure 8 shows the adopted solution for the system restraining the motion of the platform using hydrostatic bearings at each side and below the table in order to avoid transversal and vertical movements (all the details can be found in [1]).

The available data belong to the experimental campaign performed during the calibration phase of the dynamic facility [8] for the evaluation of the dynamic response of soil under the vibrations produced by the shaking table. Some of these data have been discussed in [4] in order to prove the rocking affecting the motion of the reaction mass. Additional comparisons are presented in the following sections.

Main properties	
Table size	5.6 m×7.0 m
Table mass	35 tonnes
Maximum specimen mass	60 tonnes
Controlled degree of freedom	X (longitudinal)
Peak displacement	± 500 mm
Peak velocity	± 1500 mm/s
Peak acceleration (bare table condition)	± 6.0 g
Maximum static force	2100 kN
Maximum dynamic force	1700 kN
Maximum overturning moment capacity	4000 kNm (1000 kN at 4 m from the top plate of the platform)
Maximum yaw moment	400 kNm
Operating frequency range	0-50 Hz

Table 2: Performance characteristics of the Eucentre shaking table [1]

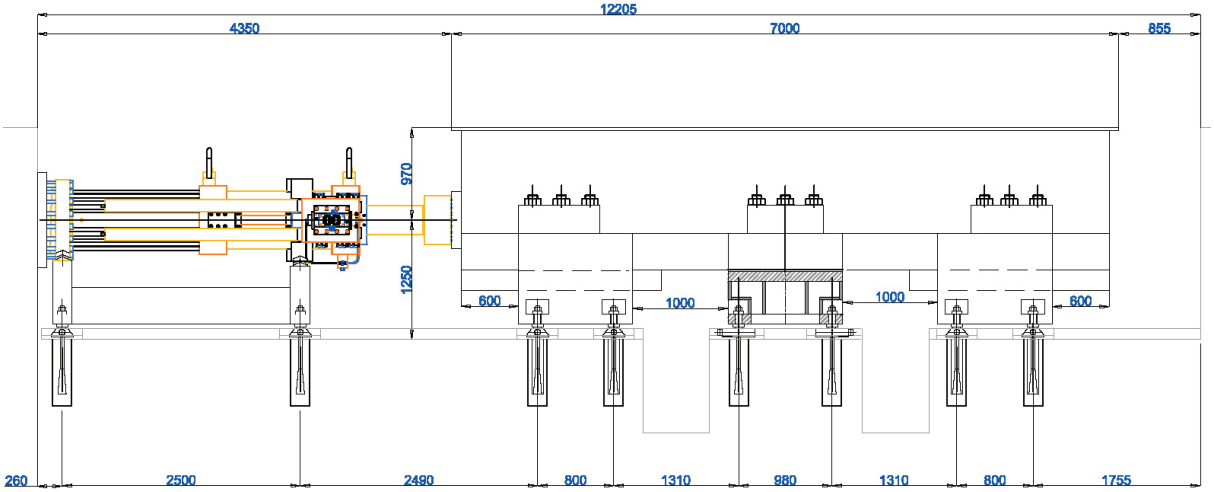


Figure 8: Longitudinal view of the final hydrostatic and mechanical configuration of the shaking table

4.1 First available experimental case-of-study

This test was characterised by the sudden stop while retracting the actuator and then consequent free vibration response. The objectives of the test were the analysis of the actual motion of the reaction mass and the fundamental frequency of the response under the excitation provided. Five servo-accelerometers were located over the reaction mass and one over a col-

umn of the laboratory (Figure 9). The test was performed at low-magnitude and excitation and bare-table condition. During this test, the rocking of the reaction mass was measured as shown in Figure 10. The observed response is complex and suggests that the distribution of the stiffness and damping coefficients of the soil is not uniform in the longitudinal direction, which is the direction of both the application of the force and the allowed motion of the dynamic testing facility.

The first application of the developed model attempts to reproduce the observed experimental results taking into account that the record of the excitation applied to the shaking table during the sudden stop while retracting the actuator is not available. Some assumptions were introduced for applying a reasonable forcing function and finding the solutions. A rectangular pulse was applied whose amplitude was related to the quantity of motion of the dynamic facility, i.e., the mass of the shaking table and its velocity. Some configurations of springs and dashpots were studied in order to optimise the simulation of the measured accelerations at both sides of the reaction mass, and in the horizontal and vertical directions. Due to the coupling of the degrees of freedom and the presence of nonlinear terms in the equations of motion (Section 2), the calibration procedure was not straightforward. The computed responses are plotted in Figure 11. The ratios between the maximum absolute amplitudes of accelerations are compared in Table 3. Taking into account the several unknowns of the case-study (i.e., the time-history, amplitude and duration of the applied force, and the right distribution of stiffness and damping coefficients of the soil), the obtained solutions are quite satisfactory and the rocking of the reaction mass is reproduced.

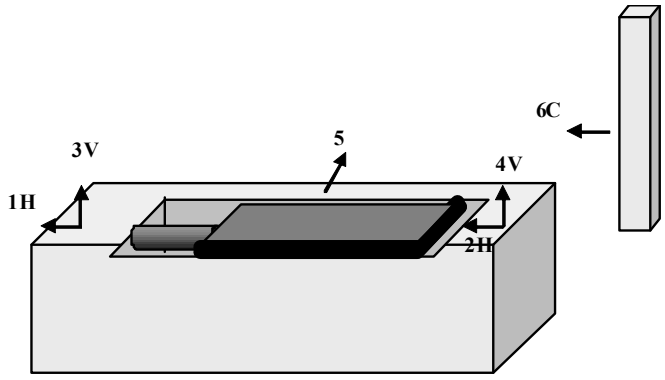


Figure 9: Location of the instrumentation for the first case-of-study

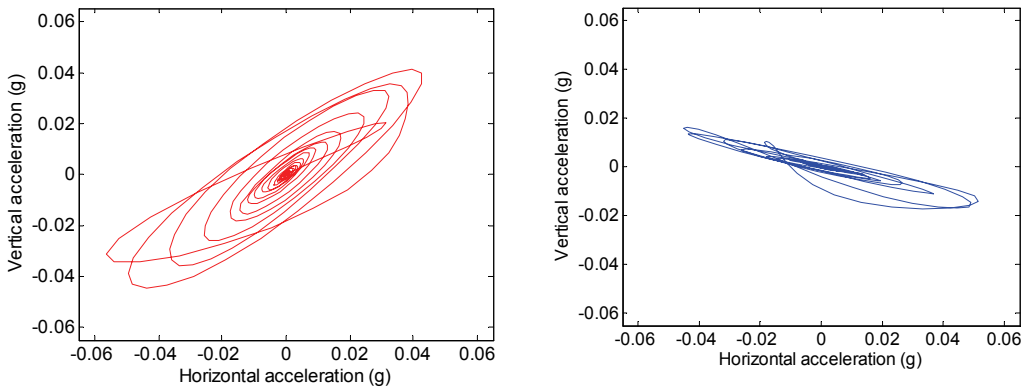


Figure 10: Compositions of the measured acceleration components at the two sides of the reaction mass – 1H vs 3V (at the actuator side) on the left, 2H vs 4V (at the opposite side) on the right

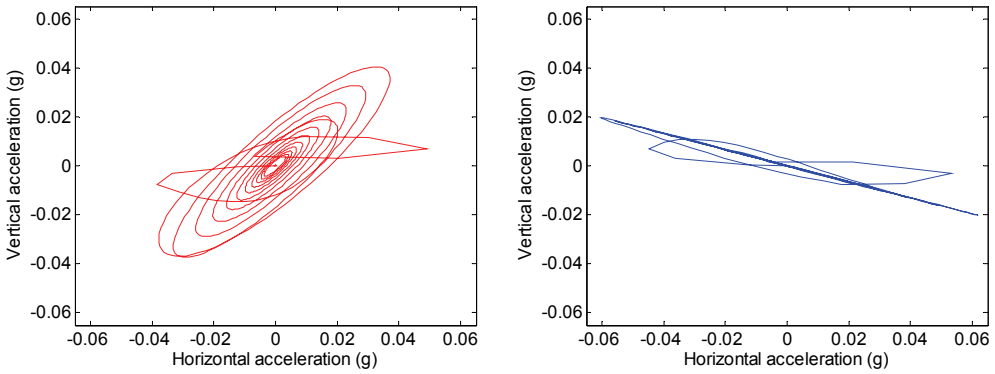


Figure 11: Compositions of the computed acceleration components at the two sides of the reaction mass – 1H vs 3V (at the actuator side) on the left, 2H vs 4V (at the opposite side) on the right

Measured accelerations	
1H/2H	1.091
3V/4V	2.576
1H/3V	1.263
2H/4V	2.984
Computed accelerations	
1H/2H	0.789
3V/4V	2.003
1H/3V	1.209
2H/4V	3.067

Table 3: Ratios between the maximum absolute amplitudes of accelerations of the first case-of-study

4.2 Second available experimental case-of-study

The input motion used during this test was the Coalinga record at 200 % magnitude. During this test a rigid payload of 60 tonnes composed by a layer of reinforced concrete cubic elements was located on the shaking table. The location of the instrumentation is shown in Figure 12: a geophone was located on the centre right hand side of the reaction mass plus eight servo-accelerometers located at the borders and edges of the reaction block. The available experimental data are the accelerations acquired by the servo-accelerometers (1V-8H in Figure 12). Figure 13 presents the time-histories of the vertical and horizontal components in three main locations of the reaction block. The label “down” refers to the signals measured at location C (Figure 12), “up-actuator” at the location B and “up-opposed” at location A. The figures show that there is a large discrepancy in the attenuation of the signals at the two sides of the reaction mass, reaching lower values at the side opposite to the actuator anchorage location – “up-actuator” vs “up-opposed”. Very different results are obtained even at the same side of the reaction block – “down” vs “up-actuator”. These measured response show that the behaviour of the Eucentre shaking table is complex.

The input signal applied during this test is not available. Therefore, the Coalinga record considered during the numerical simulation has been downloaded from the PEER strong motion database (http://peer.berkeley.edu/smcat) and then doubled. For this reason, the comparison between the measured and computed results is performed in terms of ratios between the peak response quantities. Table 4 compares the peak values of the numerical solutions versus

the measured ones. Notwithstanding with the unavailability of the real applied input signal, the obtained solutions are in good correlation with the measured peak responses. The amplitudes of the computed solutions strongly depend on the assigned distribution of the coefficients introduced for modelling the stiffness and the damping of the soil. The latter have to be deeply investigated.

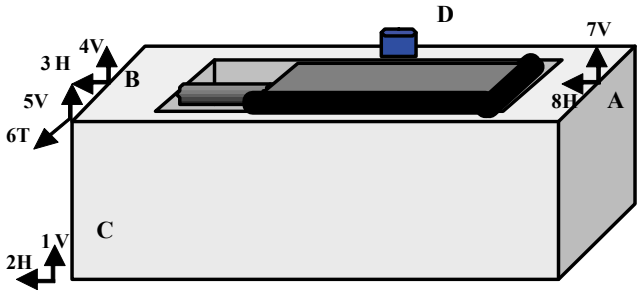


Figure 12: Location of the instrumentation for the second case-of-study

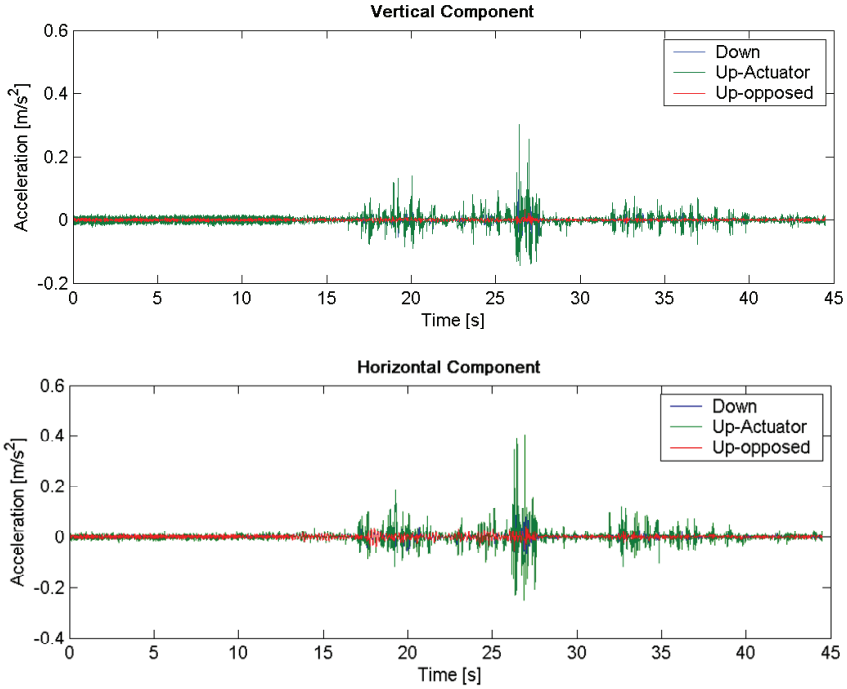


Figure 13: Vertical and horizontal accelerations recorded by the servo-accelerometers in 3 main locations on the reaction mass. With reference to Figure 12, label "Down" refers to location C, "Up-Actuator" to B, "Up-opposed" to A

Acceleration components	Peak values	Ratio Num./Exp.
Horizontal	Positive	0.95
	Negative	1.10
Vertical	Positive	1.18
	Negative	0.93

Table 4: Comparison of the peak accelerations of the second case-of-study: solutions of the proposed model vs acquired experimental responses (in Figure 13) at location B (shown in Figure 12)

5 CLOSURE

As stated by Crewe and Severn [9], for seismic testing the most used input is that of translation in one, or sometimes two or three directions, with rotations generally being small and unwanted. Following this statement, the proposed model has been formulated for simulating the performance of a shaking table whose longitudinal motion is produced by a servo-hydraulic actuator oriented in the horizontal direction. However, the nonlinear kinematics due to the possible rocking of the support system (i.e. reaction-mass/isolation-damping-systems/foundation-soil) are directly considered in the formulation since a large rotation associated with an intended uniaxial input could have a very strong influence on the response of the shaking table and the specimen. The novelty of the proposed research stays in the explicit consideration of the effects of nonlinear kinematics with the application of the motion composition rules (the velocity composition rule and Coriolis' theorem).

The model has been used to evaluate "a posteriori" if the performance of an existing shaking table could be affected by large rotations. The EUCENTRE shaking table has been considered. It is worth pointing out that the collected tests do not represent an exhaustive set of examples for validating the model and additional experimental data are required for calibrating the analytical model and characterising the motion of the dynamic facility. Notwithstanding the few available experimental data, the preliminary numerical validations seem very promising encouraging further developments and applications.

Further improvements of the results should be reached if rigorous optimisation methods will be implemented. One such is least-squares identification [10], in which a numerical optimisation routine selects the best combination of parameters so as to minimise the fit error.

ACKNOLEDGMENTS

The authors thank Mr. J. Londono Bustamante, Mr. F. Dacarro, Mr. R. Franzolin, Prof. A. Pavese and Dr. C. Strobbia for the assistance in retrieving experimental data related to the case-study considered in this research work. Many thanks are given to Dr. R. Pinho for his constant support throughout the progress of this research work.

REFERENCES

[1] G.M. Calvi, A. Pavese, P. Ceresa, F. Dacarro, C.G. Lai, C. Beltrami, *Design of a Large-Scale Dynamic and Pseudo-Dynamic Testing Facility*. IUSS Press, 2005.

[2] G. Legnani, P. Righettini, B. Zappa, F. Casolo, A Homogeneous Matrix approach to 3D Kinematics and Dynamics. Part 1: Theory. *Mechanics and Machine Theory*, **31(5)**, 573-587, 1996.

[3] G. Legnani, *Robotica Industriale*. (in Italian) Casa Ed. Ambrosiana 2003.

[4] P. Ceresa, F. Brezzi, G. M. Calvi, R. Pinho, Analytical modelling of a large dynamic testing facility. *Earthquake Engineering and Structural Dynamics*, **41**, 255-277, 2012.

[5] A. K. Chopra, *Dynamics of structures*. Second Edition, Prentice Hall, 2001.

[6] The MathWorks, Inc. Matlab, *The Language of Technical Computing*, 2002.

[7] DIET, *Misure delle variazioni di quota dei punti di controllo situati sul basamento della tavola vibrante (in Italian)*, Report of the Dipartimento di Ingegneria Edile e del Territorio, University of Pavia, 2007.

[8] J. Londono, *Dynamic response of soil under vibrations produced by the Eucentre shaking table*, Master Thesis (in preparation), ROSE School, Pavia, Italy.

[9] A.J. Crewe, R.T. Severn, The European Collaborative programme on evaluating the performance of shaking tables, *Philosophical Transactions of the Royal Society A: Mathematical, Physical & Engineering Sciences*, **359(1786)**, 1671-1696, 2001.

[10] G.F. Franklin, J.D. Powell, A. Emami-Naeini, *Feedback control of Dynamic Systems, Third Edition*, Addison-Welsey Publishing Company, 1994.

COMPDYN 2013
4th ECCOMAS Thematic Conference on
Computational Methods in Structural Dynamics and Earthquake Engineering
M. Papadrakakis, N.D.Lagaros, V. Plevris (eds.)
Kos Island, Greece, 12–14 June 2013

ON NUMERICAL MODELING OF DYNAMICS OF IRREVERSIBLE DEFORMING AND FRACTURE OF OIL-BEARING LAYER IN THE VICINITY OF A BOREHOLE

Alexey B. Kiselev*, Pavel P. Zacharov

Mechanics and Mathematics Faculty of Moscow M.V. Lomonosov State University
Leninskie Gory, 1, MSU, Main Bldg, Moscow 119992, Russia
e-mail: akis2006@yandex.ru jaquecostou@mail.ru

Keywords: Dynamics, Irreversible Deforming, Fracture, Oil-Bearing Layer.

Abstract. A paper dealing with numerical simulation in two-dimensional plane deformed state of dynamics for oil-gas saturated medium near borehole under sudden removal pressure on internal wall of the borehole. The layer is represented by the model of damageable thermoelastoplastic material with two parameters of damaging. The criterion of the beginning of new free surfaces within the material uses the principle of the critical value of specific dissipated energy. For explicitly construction of coasts of macroscopic infraction of material continuity we apply algorithm of decomposition Lagrangian mesh.

1 INTRODUCTION

In engineering practice widely used originating drilling artificial mining cavity circular cross-section having different diameters (holes, mine trunks, etc). Character of fracture of mining rock near hole depends from presence in rock structural nonhomogeneity different scales (pores, cracks). Present paper dealing with numerical simulation of dynamical deforming, micro- and macrofracture near borehole under sudden removal pressure on internal wall of the borehole.

Main used assumptions are: mass forces neglected; parameters of problem not depend of space coordinate which normal to plane of layer; assume that take place plane deformation of layer, problem solution in two-dimensional statement; layer modeling as damageable thermoelastoplastic medium; process of deforming is adiabatic.

Models of damageable deformable solids which describing so called continuum or dispersed fracture beginning from classical papers of L.M. Kachanov , Yu.N. Rabotnov and A.A. Il'yshin [1-3]. In [1, 2] for the first time was introduced one scalar damage parameter which describe accumulation of damages in material under creeping, and in [3] – tensor damaging degree for describing wide class of processes of irreversible and microfracture for different models of media. Use in following works of thermodynamical principals make possible construct many correct models of solids in which mechanical, thermal and processes of microfracture are correlated. This direction in mechanics takes very wide development and number of papers counts may hundreds. Therefore indicate only some new monographs [4-7] and review [8] which contained extensive bibliography.

Model of deformable damageable solid which used in present paper for describing dynamics of oil-gas layer based on works [9-13] which constructed with use thermomechanical approach and model of elastoplastic flow Prandtl-Rice type.

2 STATEMENT OF PROBLEM

Describing of deforming process produce in cylindrical coordinate system $Ozr\theta$, axis Oz coincide with axis of borehole (figure 1). Then any parameter depend on space coordinates r, θ and time t.

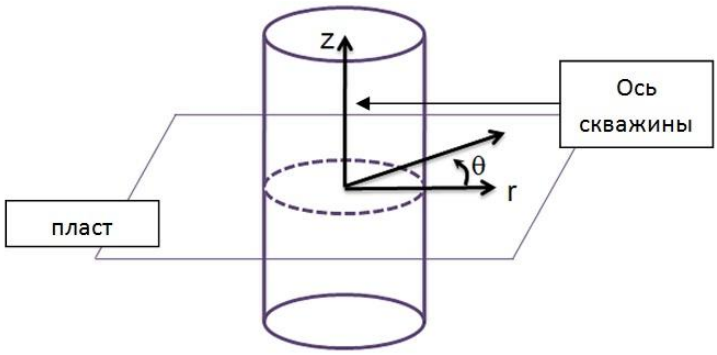


Figure 1: Cylindrical coordinate system connecting with borehole and layer.

Write equation of mass, momentum and internal energy:

$$\frac{\dot{\rho}}{\rho} = -\dot{\varepsilon}_r - \dot{\varepsilon}_\theta; \quad \rho\dot{v}_r = \frac{\partial\sigma_r}{\partial r} + \frac{1}{r}\frac{\partial\sigma_{r\theta}}{\partial\theta} + \frac{\sigma_r - \sigma_\theta}{r}, \quad \rho\dot{v}_\theta = \frac{\partial\sigma_{r\theta}}{\partial r} + \frac{1}{r}\frac{\partial\sigma_\theta}{\partial\theta} + 2\frac{\sigma_{r\theta}}{r}; \qquad (1)$$

$$\rho c_\sigma \dot{T} + \alpha_v \dot{\sigma} T = S_r \dot{\varepsilon}_r^p + S_\theta \dot{\varepsilon}_\theta^p + S_z \dot{\varepsilon}_z^p + 2S_{r\theta} \dot{\varepsilon}_{r\theta}^p + A\dot{\alpha}^2 + \Lambda \dot{\omega}^2$$

A last equation writing in form obtained in [9-13]. In (1) and further dote under symbol designate material derivation on time and introduce next notations: ρ - density; v_r, v_θ - components of velocity vector; $\sigma_r, \sigma_\theta, \sigma_z, \sigma_{r\theta}$ - components of stress tensor, which decompose on spherical and deviator parts: $\sigma_r = \sigma + S_r, \sigma_z = \sigma + S_z$, $\sigma_\theta = \sigma + S_\theta, \sigma_{r\theta} = S_{r\theta}$, $\sigma = (\sigma_r + \sigma_z + \sigma_\theta)/3$; $\dot{\varepsilon}_r$, $\dot{\varepsilon}_\theta$, $\dot{\varepsilon}_{r\theta}$ - components of velocity strain tensor; $\dot{\varepsilon}_r^p$, $\dot{\varepsilon}_\theta^p$, $\dot{\varepsilon}_z^p$, $\dot{\varepsilon}_{r\theta}^p$ - plastic components of velocity strain tensor; T - temperature; ω, α - scalar damage parameters of media ($0 \le \omega < 1$ – first invariant of symmetric damage tensor ω_{ij} $(\omega = \omega_{kk}/3)$ which interpreted as volume matter of micropores in material which filling liquid and/or gas; $0 \le \alpha < 1$– second invariant of deviator damage tensor ω_{ij} describing shear microfracture of material ($\alpha = \sqrt{(\omega_{ij} - \omega\delta_{ij})(\omega_{ij} - \omega\delta_{ij})}$); in no damage material $\omega = \alpha = 0$; c_σ - heat capacity under constant stresses; α_V - module of volume extension; Λ, A - media parameters which connecting thermal processes with processes of damage accumulation.

Velocity strain expressed from components of velocity vector:

$$\dot{\varepsilon}_r = \frac{\partial v_r}{\partial r}, \quad \dot{\varepsilon}_\theta = \frac{1}{r}\frac{\partial v_\theta}{\partial \theta} + \frac{v_r}{r}, \quad \dot{\varepsilon}_{r\theta} = \frac{1}{2}\left(\frac{\partial v_\theta}{\partial r} + \frac{1}{r}\frac{\partial v_r}{\partial \theta} - \frac{v_\theta}{r}\right) \tag{2}$$

and decomposed on elastic and plastic components:

$$\dot{\varepsilon}_r = \dot{\varepsilon}_r^e + \dot{\varepsilon}_r^p, \quad \dot{\varepsilon}_\theta = \dot{\varepsilon}_\theta^e + \dot{\varepsilon}_\theta^p, \quad \dot{\varepsilon}_{r\theta} = \dot{\varepsilon}_{r\theta}^e + \dot{\varepsilon}_{r\theta}^p, \quad \dot{\varepsilon}_z = \dot{\varepsilon}_z^e + \dot{\varepsilon}_z^p \equiv 0 \tag{3}$$

Plastic flow is incompressible: $\dot{\varepsilon}_r^p + \dot{\varepsilon}_\theta^p + \dot{\varepsilon}_z^p \equiv 0$.

System of constitutive equations coupled model of damageable thermoelastoplastic media have next form [9-13]:

$$\begin{cases} \dot{\sigma}' = K_0\left(\dot{\varepsilon}_r + \dot{\varepsilon}_\theta - \alpha_v \dot{T} - \dfrac{\Lambda}{3}\dot{\omega}\dfrac{\partial \dot{\omega}}{\partial \sigma}\right) \\ \left(S'_{ij}\right)^\nabla + \lambda S'_{ij} = 2\mu_0 \dot{e}_{ij} - 2A\dot{\alpha}\dfrac{\partial \dot{\alpha}}{\partial S_{ij}} \\ S'_{ij}S'_{ij} \le \dfrac{2}{3}Y_0^2(\sigma) \\ Y_0 = c_1\sigma + c_2 \end{cases} \tag{4}$$

Here symbol ∇ designate Jaumann derivative from components of deviator stress tensor on time: $\left(S'_{ij}\right)^\nabla = \dot{S}'_{ij} - S'_{ij}\Omega_{jk} - S'_{jk}\Omega_{ik}$; $\dot{e}_{ij}$ - deviator of velocity strain tensor; $\sigma' = \sigma/(1-\omega)$, $S'_{ij} = S_{ij}/(1-\omega)(1-\alpha)$; K_0 и μ_0 - volume module and shear module of no damageable media respectively; Ω_{ij} - rotation tensorтензор which components in considerate case are:

$$\Omega_r = \Omega_\theta = 0, \qquad \Omega_{r\theta} = -\Omega_{\theta r} = \frac{1}{2}\left(\frac{1}{r}\frac{\partial v_r}{\partial \theta} - \frac{v_\theta}{r} - \frac{\partial v_\theta}{\partial r}\right) \tag{5}$$

A last formula in (4) – low Mizes-Shleixer which connect yield limit under simple tension Y_0 and pressure in layer ($-\sigma$); c_1, c_2 – material constants.

System of equation (1) - (5) close kinetic equations for damage parameters ω and α:

$$\frac{\dot{\omega}}{\omega} = B(\frac{\sigma}{1-\omega} - \sigma_*)H(\frac{\sigma}{1-\omega} - \sigma_*) + \frac{\sigma-\sigma^+}{4\eta_0}H(\sigma-\sigma^+) + \frac{\sigma-\sigma^-}{4\eta_0}H(\sigma^+-\sigma),$$

$$\sigma^+ = -\frac{2}{3}Y_0\ln\omega - p_0\left(\frac{\omega_0}{\omega}\right)^\gamma, \quad \sigma^- = +\frac{2}{3}Y_0\ln\omega - p_0\left(\frac{\omega_0}{\omega}\right)^\gamma, \tag{6}$$

$$\dot{\alpha} = C\left(\frac{S_u}{(1-\omega)(1-\alpha)} - S_u^*\right)H\left(\frac{S_u}{(1-\omega)(1-\alpha)} - S_u^*\right)$$

Here η_0 - dynamic viscosity of no damage material; p_0 - initial pressure in pore ("mountainous" pressure); γ - index of media adiabatic which filling pore; ω_0 - initial porosity; $S_u = \sqrt{S_{ij}S_{ij}}$ - intensity of deviator stress tensor; S_u^*, σ_*, B, C - constants of material; $H(x)$ - Heviside function.

From equations (6) see that damage parameter ω depend with ball part of stress tensor σ and depending on which component in right part of first equation from (6) enclose parameter ω may increase or decrease. This parameter describes damage micropore type (so called viscous fracture). Parameter α depend from intensity of deviator stress tensor and describe shear fracture.

As criteria of beginning macrofracture of material (appearance new surfaces free from loading) used entropy criteria limit specific dissipation [9-15]:

$$D = \int_o^{t^*}\frac{1}{\rho}\left(S_{ij}\dot{\varepsilon}_{ij}^p + \Lambda\dot{\omega}^2 + A\dot{\alpha}^2\right)dt = D^* \tag{7}$$

Here t^* – time of beginning of fracture; D^* - limit specific dissipation (material constant); $d_M = S_{ij}\dot{\varepsilon}_{ij}^p$ - mechanical dissipation; $d_F = \mathrm{A}\dot{\alpha}^2 + \Lambda\dot{\omega}^2$ - dissipation of continuum fracture. Thermal dissipation $d_T = -\boldsymbol{q}\cdot grad\,T/T$ in (7) is absent because process consider as adiabatic ($\boldsymbol{q}$ – vector of heat flow).

Such model, but with one parameter of volume damage ω, used early for calculation problem of hydraulic fracture of oil layer ([14, 15]).

3 INITIONAL AND BOUNDARY CONDITIONS

In initial moment $t = 0$ layer is in rest condition: $v_r = v_\theta = 0$. In calculation for initial condition was take that $\rho = \rho(r,\theta) = \rho_0 = const$. It is necessary to set initial distribution of stresses $\sigma_r, \sigma_\theta, \sigma_z, \sigma_{r\theta}$ in layer, damage parameters ω and α as function of space coordinates r and θ.

As initial distribution of stresses in layer we used solution a next static linier-elastic problem. Consider infinite cylindrical body with circular cup; on infinite in two mutually orthogonal directions apply contractive stresses σ_1 and σ_2 corresponding so called "mountain pressure". In common case $\sigma_1 \neq \sigma_2$ that makes possible modeling nonhomogeneity stress condition of layer. On surface of circular cup applied contractive stress σ_3 which correspond

pressure into borehole (figure 2). This problem have solution in linear-elastic statement and in elastoplastic statement which well-known as Galin problem [17]. Some generalizations of Galin problem reduce in monograph [17] and in bibliography in this book.

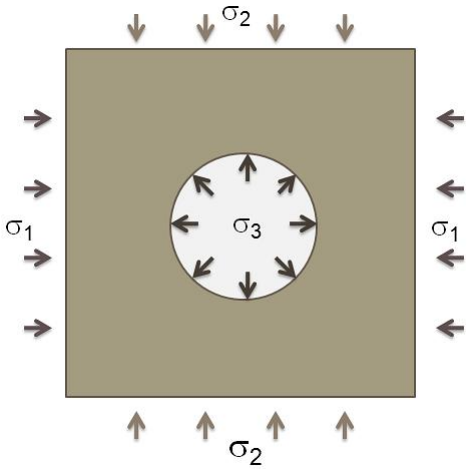


Figure 2: scheme of application of loading.

Solution in linear-elastic statement obtained as superposition of three solutions separately for stresses $\sigma_1, \sigma_2, \sigma_3$ and have next form [18]:

$$\begin{cases} \sigma_r = \dfrac{\sigma_1+\sigma_2}{2} + \dfrac{\sigma_1-\sigma_2}{2}\cos 2\theta + \dfrac{a^2}{r^2}\left(-\sigma_3 - \dfrac{\sigma_1+\sigma_2}{2} - 2(\sigma_1-\sigma_2)\cos 2\theta\right) + \\ + \dfrac{a^4}{r^4}\left(\dfrac{3}{2}(\sigma_1-\sigma_2)\cos 2\theta\right), \\ \sigma_\theta = \dfrac{\sigma_1+\sigma_2}{2} - \dfrac{\sigma_1-\sigma_2}{2}\cos 2\theta + \dfrac{a^2}{r^2}\left(\sigma_3 + \dfrac{\sigma_1+\sigma_2}{2}\right) + \dfrac{a^4}{r^4}\left(-\dfrac{3}{2}(\sigma_1-\sigma_2)\cos 2\theta\right), \\ \sigma_z = \nu(\sigma_r+\sigma_\theta), \\ \sigma_{r\theta} = -\dfrac{\sigma_1-\sigma_2}{2}\sin 2\theta - \dfrac{a^2}{r^2}\left(2(\sigma_1-\sigma_2)\sin 2\theta\right) + \dfrac{a^4}{r^4}\left(\dfrac{3}{2}(\sigma_1-\sigma_2)\sin 2\theta\right). \end{cases} \quad (8)$$

In moment $t = 0$ happen sharp fall pressure into borehole from value σ_3 to value $\Delta p > 0$. Therefore on borehole wall take place pressure $\sigma_3 + \Delta p$. Case then $\Delta p = -\sigma_3$ corresponded with condition on free surface.

4 CONSTRUCTION OF MACROFRACTURE DOMAINS

Considered problem solve numerically by method Wilkins type on Lagrange meshes [19, 20]. Modeling of macrofracture of layer realized by using method of decomposition Lagrange mesh [21-23]. As criteria of beginning of macrofracture we used entropy criteria of fracture (7): media lose continuity when specific dissipation D reach limit value D_*. In point in which realized criteria of fracture realize explicit construction of macrofracture banks (cracks). For this doing separation of nodes of calculated net on boundary meshes (figure 3) – internal nodes and corresponding them edges of meshes become boundary on which give condition of free surface, definite pressure or contact condition depending on situation. In detail this

algorithm presented in thesis [23]. Mark what earlier we used for explicit construction boundary of fracture in problem of hydraulic fracture of layer procedure of bifurcation Lagrange calculation nets [14, 15] which detailed described in [27].

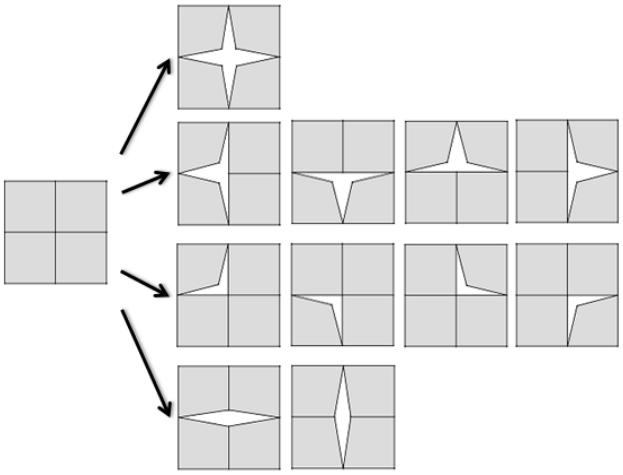


Figure 3: Alternative versions for “elemental” cracks for internal node.

Variant of decomposition defined from analysis of stress vector on adjacent for present note edge. Interaction of “elemental” cracks with already exist cracks to form fracture zones larger scale. In result of decomposition on new formed boundary edges set boundary conditions: condition of free boundary or contact conditions depending on situation.

Using in present paper algorithm for realization of boundary conditions on contact surfaces contained in correction of coordinates and velocities of boundary nodes of calculated meshes [24-26]. This algorithm is symmetric as under correction of coordinates interaction boundaries enter symmetric form.

5 RESULTS OF CALCULATIONS

Problem has two axis of symmetry therefore calculations conducted for one fourth of domain. On boundaries $\theta = 0$ and $\theta = \pi / 2$ under integration of momentum equations take into account contribution symmetric meshes so that be realized condition: $v_\theta = 0$. External boundary of calculated domain choose so remote that it is possible no take into account reflection waves from external boundary which extends from wall of borehole.

Calculations conducted in three different statements. *In first statement* under numerical calculation no realize explicit construction of fracture domains. *In second statement* fracture domains constructed explicit way, however it is not taking into account contact interaction on new free surfaces under decomposing of mesh. *In third variant* on free surfaces contact interaction take into account.

Under calculations used next values of parameters: $a = 0,5$ m, $\rho_0 = 2000$ kg/m^3; $K_0 = 14$ GPa; $\mu_0 = 8{,}4$ GPa; $c_1 = -0,09$; $c_2 = 0,04$ GPa; $S_u^* = 36$ GPa; $\eta_0 = 100$ Pa · c; $\Lambda = 1500$ Pa · c; $C = 8 \cdot 10^{-5}$ (Pa · c)$^{-1}$; $A = 1200$ Pa · c; $\gamma = 1,4$; $D_* = 334,4$ J/kg.

In lower represented calculations were take uniform distribution of initial volume damage (porosity) ω o material: $\omega_0 = \omega_0(r,\theta) = const = 0,05$. Initial pressure in pores p_0 in formula (6) - $p_0 = -\sigma|_{t=0}$ (under that $\sigma|_{t=0}$ defined from formula (8)).

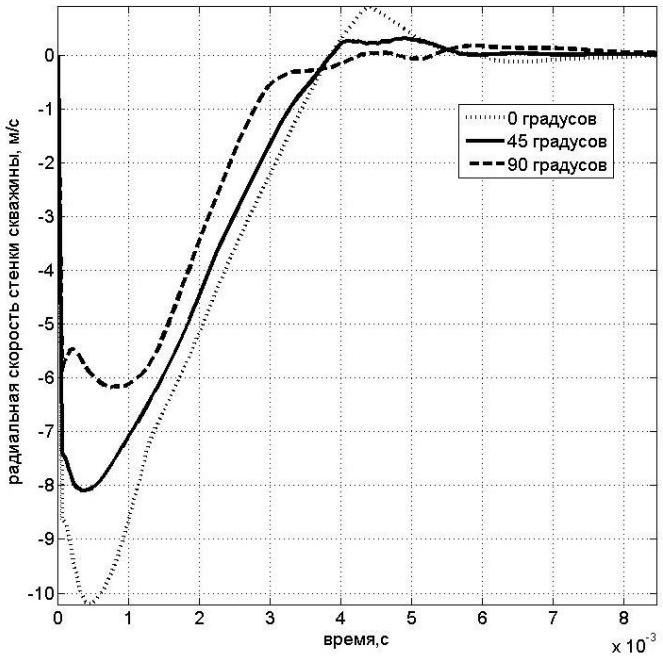


Figure 4: Dependence from time of radial velocity for different point of borehole wall (*first statement*).

Lower present results of calculations with initial distribution of stresses (8) for next case: $\sigma_1 = -65$ MPa, $\sigma_2 = -75$ MPa, $\sigma_3 = -75$ MPa; $\Delta p = |\sigma_3|$.

On figure 4 present dependence from time of radial velocity for points of borehole for different values of angle θ (*first statement*); difference caused thus that что $\sigma_1 \neq \sigma_2$.

As advancing wave unloading into layer perturbed domain in which media beginning motion to center $(v_r < 0)$ is increase. Later velocity of layer motion falls until zero.

After removal pressure into borehole wall of borehole turn to centre and media stretched in radial direction, radial stresses σ_r are growth remained negative (unloading wave propagation into layer). In ring direction media conversely contract and ring stresses σ_θ decrease (in absolute value they increase). Shear stresses for angles $\theta = 0$ and $\theta = \pi/2$ equal zero for all moments of time in view of symmetry of problem.

On figure 5 show distribution of specific dissipation in two sequential moments of time (*first statement*). Critical level D_* correspond white color. Obviously that fracture domain localized in zone which correspond to concentrate of biggest contractive stress (on vertical).

Thus from obtained results show that under modeling without explicit of fracture surfaces in layer its fracture take place directly near wall of borehole.

Fracture domain under realization of *second statement* quality changes her character. Now fracture realized as turnpike curvilinear crack (stretched comparatively restricted zones of fracture), which originated on wall of borehole and germinate into layer. On figure 6 show distributions of specific dissipation in three sequential moments of time on which it is possible to trace development of crack. Number of cracks, direction and velocity of their

growth depend on relation σ_1 / σ_2. For symmetric case ($\sigma_1 = \sigma_2$) zone of fracture is circle around borehole.

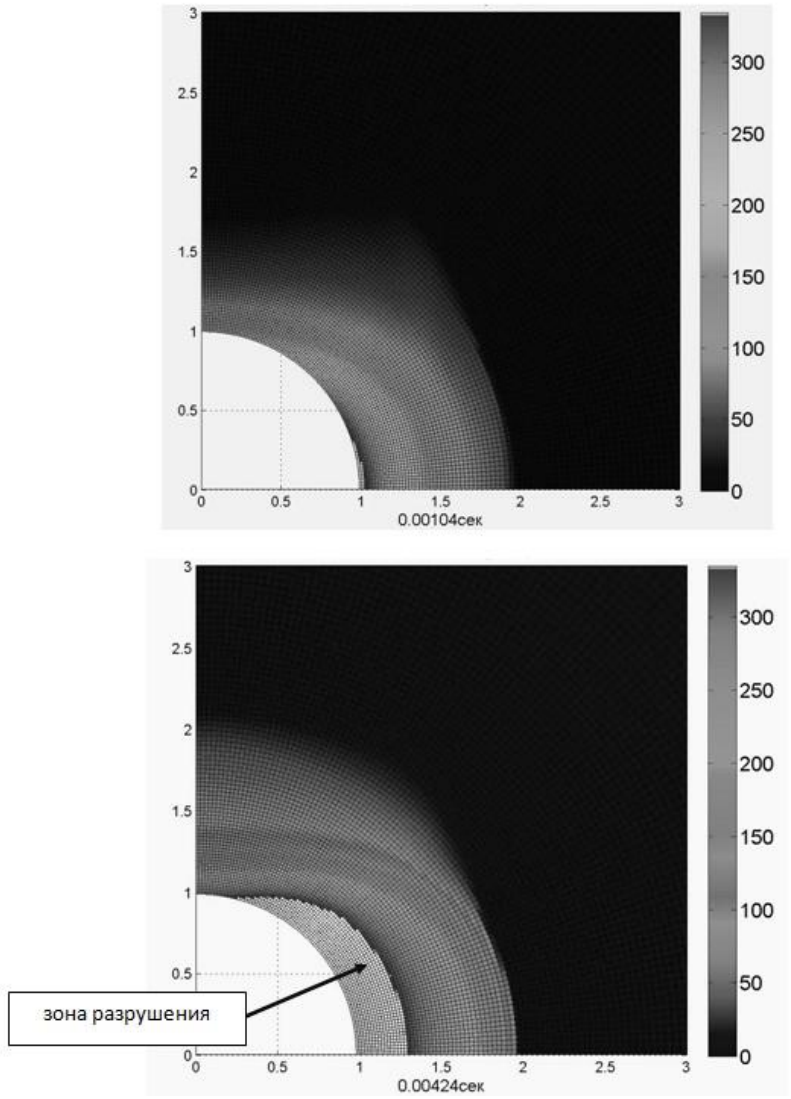


Figure 5: Distribution of specific dissipation D in sequential time moments (*first statement*).

Note that simple character of fracture with development of magisterial cracks, their rotation in processes of growth as on figure 6 observed and under modeling cracks of hydraulic fracture which formed in result of bury to layer liquid from borehole [14, 15]. In problem of hydraulic fracture cracks banks no closing and the more so no take place their constriction as presence liquid in cracks.

Graph of dependence of depth propagation of crack into layer from time for different relations σ_1 / σ_2 represent on figure 7 ($0,5 < \sigma_1 / \sigma_2 \le 1$). Obviously that ratio σ_1 / σ_2 less than 1 by that earlier crack appear and her depth of penetration more.

Modeling with taking account contact interaction of cracks banks (*third statement*) give qualitative another result then in case of separation of cracks banks without contact interaction (*second statement*). Fracture domain now not restricted lengthy zone but continuous domain which initial localized near borehole wall. Fracture domain represent on figure 8; here as

above white color corresponding critical value of dissipation D_*. Character of fracture having "fragmentation" character: into borehole fly fragments of layer (clusters of calculation Lagrangian particles which separated from layer in result of realized procedure of mesh decomposition) thus take place of bring down of borehole wall.

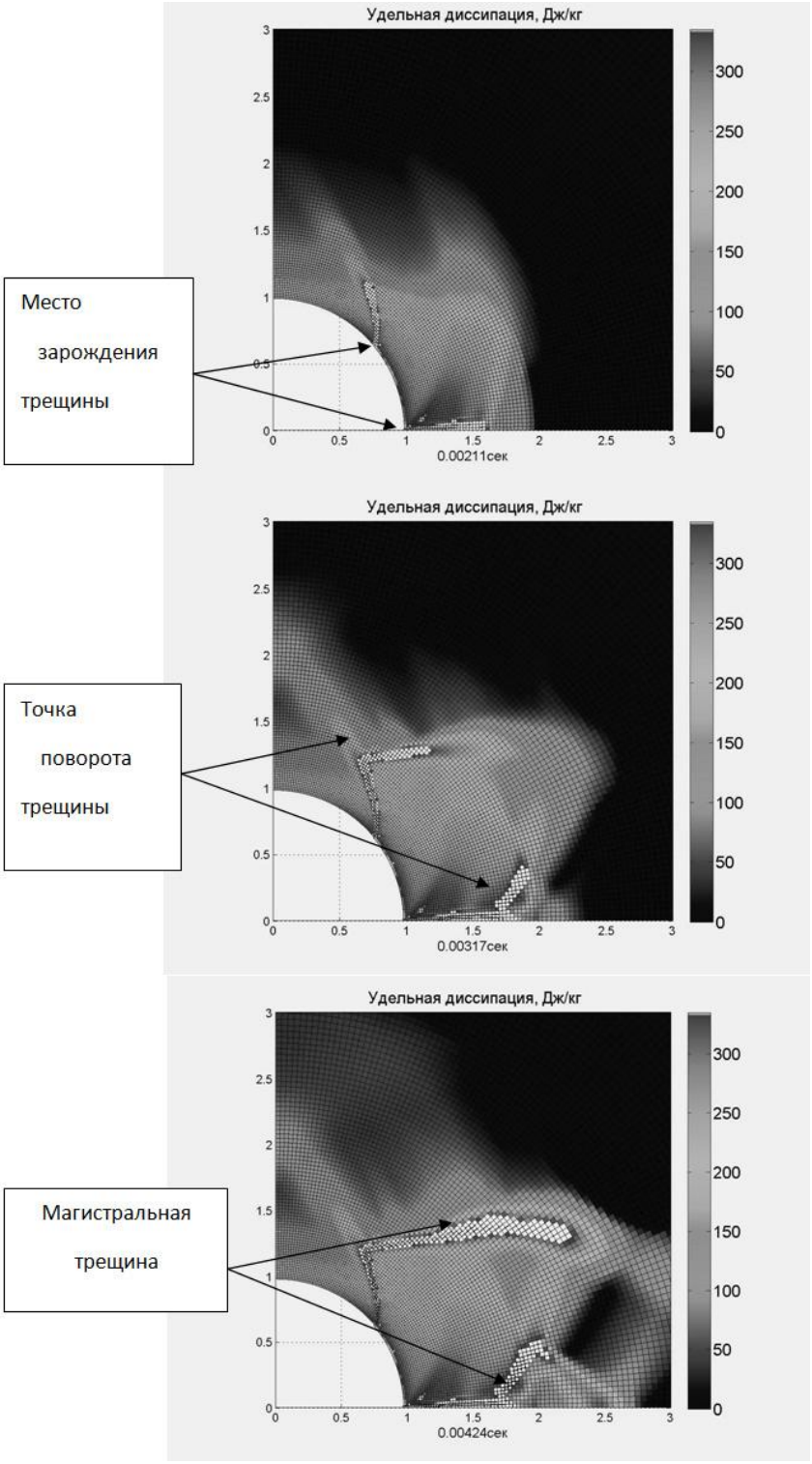


Figure 6: Forming of turnpike crack (*second statement*).

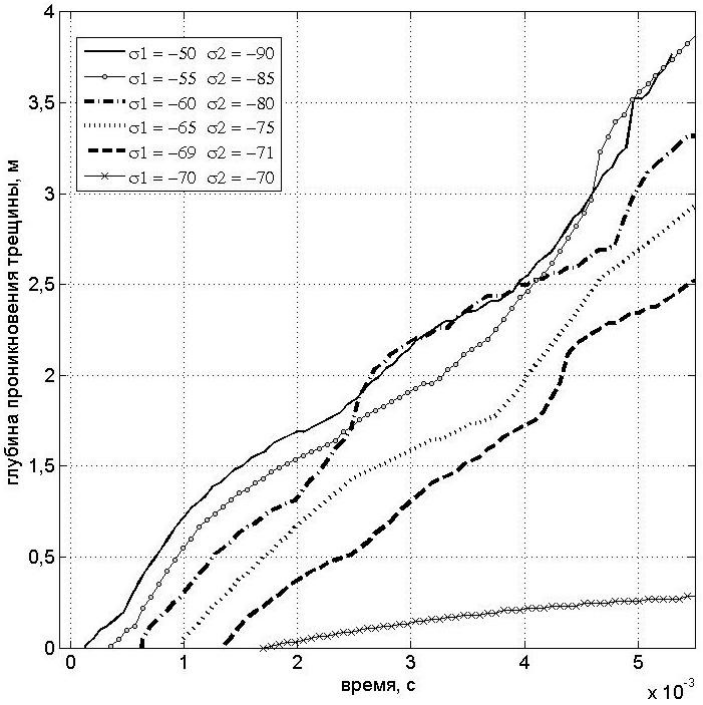


Figure 7: Dependence of depth of crack interaction in layer from time (*second statement*).

Shear damage α localize near borehole but on some distance from it. Volume damage ω too growth near borehole in domains of in intensive expansion of media originating as result its moving to center of borehole after harsh taking off pressure into borehole. Biggest contribution to dissipation D give mechanical dissipation $d_M = S_{ij}\dot{\varepsilon}_{ij}^p$. Dissipation of continuum volume fracture $d_F^\omega = \Lambda\dot{\omega}^2$ and shear fracture $d_F^\alpha = \mathrm{A}\dot{\alpha}^2$ types give noticeable contribution to full dissipation D only in fracture domains of layer (see formula (7)).

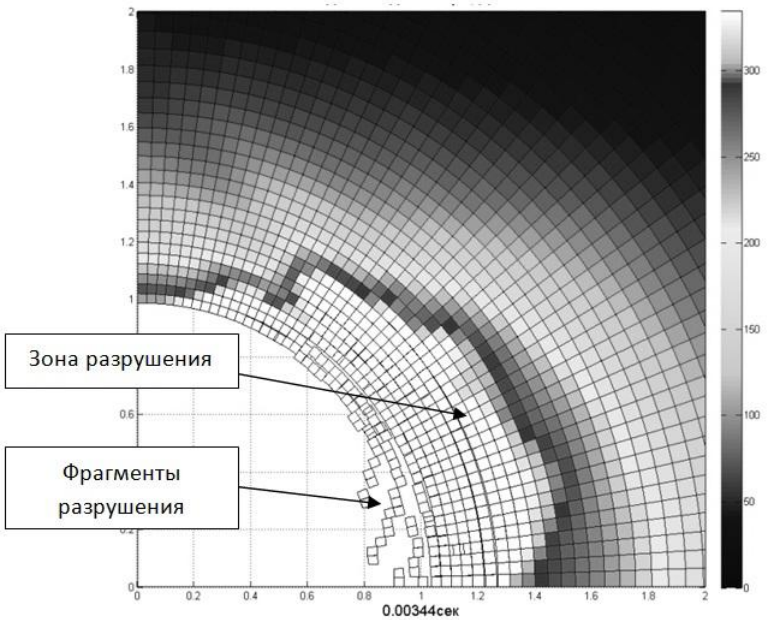


Figure 8: Dependence of specific dissipation (*third statement*).

6 CONCLUTIONS

Numerically investigated a problem of irreversible dynamic deforming and fracture of rock layer near borehole under sudden removal pressure in borehole. Solution was obtained in nonsymmetrical two-dimensional statement with taking into account both microfracture (volume and shear characters) as explicit structure of domains of macroftacture (curvilinear cracks which separated from layer).

Analyzed character and degree of fracture in layer depending on relation rock pressure far from borehole which acts on two orthogonal directions and from degree numerical realization of boundary conditions on banks of macrocracks.

Showed what simplification of algorithm calculation boundary conditions on crack banks reduced to principal different characters of layer fracture. Wherefore for obtain physically real results its need conduct numerical investigations under maximum fool realization boundary conditions on crack banks which formatted into layer.

REFERENCES

[1] L.M. Kachanov, About time of fracture under creeping. *Izv. AS of USSR. DTS. Mechanics and Machine-Building, 26-31, No. 8, 1958.*

[2] Yu.N. Rabotnov, Mechanism of long fracture, *Problems of Strength of Materials and Constructions.* Moscow, Publ. AS USSR, 5-7, 1959.

[3] A.A. Il'ushin, About one theory of long strength, *Izv. AS USSR. Mech. of Solids*, 21-35, No. 3, 1967.

[4] L.M. Kachanov, *Introduction to continuum mechanics*. Dordrecht, Boston: Nijhoff, 1986.

[5] B.I. Kondaurov, L.V. Nikitin, *Theoretical foundation of reology of geomaterials.* Moscow: Nauka, 1990.

[6] V.I. Astafiev, Yu.N. Radaev, L.V. Stepanova, *Nonlinear fracture mechanics*. Samara: Publ. Samara University, 2001.

[7] V.I. Kondaurov, V.E. Fortov, *Foundations of thermomechanics of condensed media.* Moscow: Publ. Moscow Inst. of Physics and Technology, 2002.

[8] V.N. Kukudganov, Coupled models of elastoplasticity and damage and their integration. *Izv. RAS. Mechanics of Solids,* 103-135, No. 6, 2006.

[9] A.B. Kiselev, M.V. Yumashev, Deforming and fracture under impact loading. Model of damageable thermoelastoplastic media. *Applied Mechanics and Technical Physics,* 116-123, No. 5, 1990.

[10] A.B. Kiselev, M.V. Yumashev, Mathematical model of deforming and fracture of solid fuel under impact loading. *Applied Mechanics and Technical Physics*, 126-134, No. 6, 1992.

[11] A.B. Kiselev, The model of thermoelastoplastic deformation and fracture of materials under multiaxial loading. *Fourth International Conference on Biaxial/Multiaxial Fatigue*, France, St. Germain en Laye, May 31 - June 3, 1994. Vol. 2, 183-186.

[12] A.B. Kiselev, Mathematical modeling of dynamical deforming and combined microfracture of damageable thermoelastoviscoplastic medium. *Studies in Applied*

Mechanics 45.Advanced Methods in Materials Processing Defects. Edited by M. Predeleanu and P. Gilormini. Amsterdam: Elsevier, 43-50, 1997.

[13] A.B. Kiselev, Mathematical modeling of dynamical deforming and combined fracture of thermoelastoviscoplastic medium. *Moscow University Mechanics Bulletin*, **53**, 32-40, No. 6, 1998.

[14] A.B. Kiselev, A.A. Lukyanov, M. Tiercelin, Numerical simulation of dynamic propagation of curvilinear cracks of hydraulic fracturing. *Moscow University Mechanics Bulletin*, **59**, 36-41, No. 1, 2004.

[15] A.B. Kiselev, A.A. Lukyanov, Numerical investigation of hydraulic fracture propagation. *Journal of Mechanical Behavior of Materials*, **19**, 297-305, No. 5, 2009.

[16] L.A. Galin, Plate elastoplastic problem. *Applied Mathematics and Mechanics*, **10**, 367-386, No. 3, 1946.

[17] L.A. Galin, *Elastoplastic problem*. Novosibirsk: Nauka, 1983.

[18] S.P. Timoshenko, J. Gudier, *Theory of elasticity, 2nd Edition.* M.: Nauka, 1975.

[19] M.L. Wilkins, Calculation of elastoplastic flow. *Methods in Computational Physics. Advances in Research and Applications. Volume 3. Fundamental Methods in Hydrodynamics.* New York and London: Academic Press, 1964, 212-263.

[20] M.L. Wilkins, *Computer simulation of dynamic phenomena.* Berlin: Heidelbery; New York: Springer-Verlag, 1999.

[21] M.M. Nemirovich-Danchenko, Model of gyperelastic brittle medium: application to calculation of deforming and fracture. *Physical Mesomechanics*, **1**, 107-114, No. 2, 1998.

[22] Y.M. Chen, M.L. Wilkins, Stress analysis of crack problems with a three-dimensional time-dependent computer program. *International Journal of Fracture*, **2**, 607-617, No. 4, 1976.

[23] Yu.P. Stefanov, Some peculiarities of numerical modeling of behavior of elastoplastic materials. *Physical Mesomechanics*, **8**, 129-142, No. 3, 2005.

[24] A.B. Kiselev, P.P. Zacharov, Mathematical modeling the irreversible dynamic processes of deformation and fracture of damageable media and constructions. R.M. Chugaliev eds. *X International Workshop "Supercomputing and Mathematical Modeling"*, Sarov: Russian Federal Nuclear Center – All Russian Research Institute of Experimental Physics, 202-207, 2011.

[25] A.B. Kiselev, P.P. Zacharov, O.V. Nekhaeva, Mathematically modeling the dynamic processes of irreversible deformation and failure of damageable media. Application to problems of geodynamics. *Vestnik of Lobachevsky State University of Nizhni Novgorod*, 459-461, No. 4, Part 2, 2011.

[26] P.P. Zacharov, *Numerical modeling of dynamics of deformation and fracture of oil-bearing layer: Thesis…candidate of physical-mathematical sciences.* Moscow: Mechanical and Mathematical Faculty of Moscow M.V. Lomonosov State University, 2011.

V.M. Fomin, A.I. Gulidov, A.B. Kiselev, et al, *High-speed interaction of bodies.* Novosibirsk: Sibirian Branch of RAS, 1999.

COMPDYN 2013
4th ECCOMAS Thematic Conference on
Computational Methods in Structural Dynamics and Earthquake Engineering
M. Papadrakakis, V. Papadopoulos, V. Plevris (eds.)
Kos Island, Greece, 12–14 June 2013

NONLOCAL MODAL ANALYSIS FOR NANOSCALE DYNAMICAL SYSTEMS

S Adhikari[1], D. Gilchrist[1], T. Murmu[2] and M. A. McCarthy[2]

[1]Civil & Computational Engineering Research Centre, Swansea University, Swansea, UK
[2]Department of Mechanical, Aeronautical and Biomedical Engineering, Irish Centre for Composites Research, Materials and Surface Science Institute, University of Limerick, Ireland

Keywords: Normal modes; nonlocal mechanics; finite element; nonlocal frequency.

Abstract. *This paper introduces the idea of nonlocal normal modes arising in the dynamic analysis of nanoscale structures. A nonlocal finite element approach is developed for the axial vibration of nanorods, bending vibration of nanobeams and transverse vibration of nanoplates. Explicit expressions of the element mass and stiffness matrices are derived in closed-form as functions of a length-scale parameter. In general the mass matrix can be expressed as a sum of the classical local mass matrix and a nonlocal part. The nonlocal part of the mass matrix is scale-dependent and vanishes for systems with larger length-scales. New analytical methods are developed to understand the dynamic behaviour of discrete nonlocal systems in the light of classical local systems. The conditions for the existence of classical normal modes for undamped and damped nonlocal systems are established. Closed-form approximate expressions of nonlocal natural frequencies, modes and frequency response functions are derived. Results derived in the paper are illustrated using examples of axial and bending vibration of nanotubes and transverse vibration of graphene sheets.*

1 Introduction

Nanoscale systems, such as those fabricated from simple and complex nanorods, nanobeams [1] and nanoplates have attracted keen interest among scientists and engineers. Examples of one-dimensional nanoscale objects include (nanorod and nanobeam) carbon nanotubes [2], zinc oxide (ZnO) nanowires and boron nitride (BN) nanotubes, while two-dimensional nanoscale objects include graphene sheets [3] and BN nanosheets [4]. These nanoscale entities or nanostructures are found to have exciting mechanical, chemical, electrical, optical and electronic properties. Nanostructures are being used in the field of nanoelectronics, nanodevices, nanosensors, nano-oscillators, nano-actuators, nanobearings, and micromechanical resonators, transporter of drugs, hydrogen storage, electrical batteries, solar cells, nanocomposites and nanooptomechanical systems (NOMS). Understanding the dynamics of nanostructures is crucial for the development of future generation applications in these areas.

Experiments at the nanoscale can be difficult as many parameters need to be taken care of. On the other hand, atomistic computation methods such as molecular dynamic (MD) simulations [5] are computationally prohibitive for nanostructures with large numbers of atoms. Thus continuum mechanics is an important tool for modelling, understanding and predicting physical behaviour of nanostructures. Although continuum models based on classical elasticity are able to predict the general behaviour of nanostructures, they lack the accountability of effects arising from the small-scale. At small-scale the theory and laws of classical elasticity may not hold. Consequently for accurate predictions, the employability of the classical continuum models have been questioned in the analysis of nanostructures and nanoscale systems. To address this, size-dependent continuum based methods [6–9] are getting in popularity in the modelling of small sized structures as they offer much faster solutions than molecular dynamic simulations for various nano engineering problems. Currently research efforts are undergoing to bring in the size-effects within the formulation by modifying the traditional classical mechanics. One popularly used size-dependant theory is the nonlocal elasticity theory pioneered by Eringen [10], and applied to nanotechnology by Peddieson et al [11]. The theory of nonlocal elasticity (nonlocal continuum mechanics) is being increasingly used for efficient analysis of nanostructures viz. nanorods [12, 13], nanobeams [14], nanoplates [15, 16] and carbon nanotubes [17, 18]. Nonlocal elasticity accounts for the small-scale effects at the atomistic level. At nanometer scales, size effects often become prominent. Both experimental and atomistic simulation results have shown a significant size-effect in the mechanical properties when the dimensions of these structures become small [19, 20]. In the nonlocal elasticity theory the small-scale effects are captured by assuming that the stress at a point as a function of the strains at all points in the domain. Nonlocal theory considers long-range inter-atomic interaction and yields results dependent on the size of a body [10]. Some of the drawbacks of the classical continuum theory could be efficiently avoided and size-dependent phenomena can be explained by the nonlocal elasticity theory. A good review on nonlocal elasticity and application to nanostructures can be found in [21]. Several researchers have used nonlocal theory for dynamic analysis of continuum systems such as nanorods, nanobeams and nanoplates. Nanorods have found application in energy harvesting, light emitting devices and microelectromechanical systems (MEMS). Using nonlocal elasticity, various work on mechanical behaviour of nanorods [12, 13, 22–24] were reported. Numerous works are seen in literature regarding analysis (mainly structural) of nanobeams using nonlocal elasticity [21] and coupled nanobeams [14].

From the brief literature review it is clear that significant research efforts have taken place in the analysis of nano structures modelled as a continuum. While the results have given sig-

nificant insights, the analysis is normally restricted to single-structure (e.g, a beam or a plate) with simple boundary conditions and no damping. In the future complex nanoscale structures will be used for next generation nano electro mechanical systems. Therefore, it is necessary to have the ability for design and analysis of damped built-up structures. The finite element approach for nanoscale structures can provide this generality. Work on nonlocal finite elements is in its infancy stage. Pisano et al. [25] reported a finite element procedure for nonlocal integral elasticity. Chang [26] studied the small scale effects on axial vibration of non-uniform and nonhomogeneous nanorods by using the theory of nonlocal elasticity and the finite element method. Narendar and Gopalakrishnan [27] used the concept of nonlocal elasticity and applied it for the development of a spectral finite element (SFE) for analysis of nanorods. Recently Adhikari et al. [28] reported the free and forced axial vibrations of damped nonlocal rods using dynamic nonlocal finite element analysis. Similar to the few works on nonlocal finite element analysis of nanorods, not many works were reported on the nonlocal finite element formulation of nanobeams (carbon nanotubes). Phadikar and Pradhan [29] have proposed basic finite element formulations for a nonlocal elastic EulerBernoulli beam using the Galerkin technique. Studies were carried out for bending, free vibration and buckling for nonlocal beam with four classical boundary conditions. Pradhan [30] updated the work of nonlocal finite element to Timoshenko beam theory and applied it to carbon nanotubes. With the finite element analysis bending, buckling and vibration for nonlocal beams with clampedclamped, hingedhinged, clampedhinged and clampedfree boundary conditions were illustrated. The basic nonlocal finite elements of undamped two-dimensional nanoplates (such as graphene sheets) were reported by Phadikar and Pradhan [29]. Recently, Ansari et al [31] developed nonlocal finite element model for vibration of embedded multi-layered graphene sheets. The proposed finite elements were based on the Mindlin-type equations of motion coupled together through the van der Waals interaction. Vibrational characteristics of multi-layered graphene sheets with different boundary conditions embedded in an elastic medium were considered.

The majority of the reported works on nonlocal finite element analysis consider free vibration studies where the effect of non-locality on the undamped eigensolutions has been studied. Damped nonlocal systems and forced vibration response analysis have received little attention. On the other hand, significant body of literature is available [32–34] on finite element analysis of local dynamical systems. It is necessary to extend the ideas of local modal analysis to nonlocal systems to gain qualitative as well as quantitative understanding. This way, the dynamic behaviour of general nonlocal discretised systems can be explained in the light of well known established theories of discrete local systems. The purpose of this paper is make essential contributions in this open area.

The paper is organised as follows. In section 2 we introduce the nonlocal finite element formulation for the axial vibration of rods and bending vibration of beams. Explicit expressions of element mass and stiffness matrices for the two systems are derived. Modal analysis of discrete nonlocal dynamical systems is discussed in section 3. The conditions for the existence of classical normal modes, approximations for nonlocal frequencies and modes are proposed. In section 4 dynamics of damped nonlocal systems and approximation to the frequency response function are discussed. Analytical results, including the approximations of the nonlocal natural frequencies and modes, are numerically illustrated for the two systems in section 5. In section 6 some conclusions are drawn based on the theoretical and numerical results obtained in the paper.

2 Finite element modelling of nonlocal dynamic systems

2.1 Axial vibration of nanorods

The equation of motion of axial vibration for a damped nonlocal rod can be expressed as

$$EA\frac{\partial^2 U(x,t)}{\partial x^2} + \widehat{c}_1\left(1-(e_0a)_1^2\frac{\partial^2}{\partial x^2}\right)\frac{\partial^3 U(x,t)}{\partial x^2\partial t} = \widehat{c}_2\left(1-(e_0a)_2^2\frac{\partial^2}{\partial x^2}\right)\frac{\partial U(x,t)}{\partial t} + \left(1-(e_0a)^2\frac{\partial^2}{\partial x^2}\right)\left\{m\frac{\partial^2 U(x,t)}{\partial t^2}+F(x,t)\right\} \quad (1)$$

In the above equation EA is the axial rigidity, m is mass per unit length, e_0a is the nonlocal parameter [10], $U(x,t)$ is the axial displacement, $F(x,t)$ is the applied force, x is the spatial variable and t is the time. The constant $\widehat{c}_1$ is the strain-rate-dependent viscous damping coefficient and $\widehat{c}_2$ is the velocity-dependent viscous damping coefficient. The parameters $(e_0a)_1$ and $(e_0a)_2$ are nonlocal parameters related to the two damping terms respectively. For simplicity the nonlocal effect in damping is ignored in this paper, that is, we consider $(e_0a)_1 = (e_0a)_2 = 0$. We consider an element of length ℓ_e with axial stiffness EA and mass per unit length m. An element of the axially vibrating rod is shown in Figure 1. This element has two degrees of

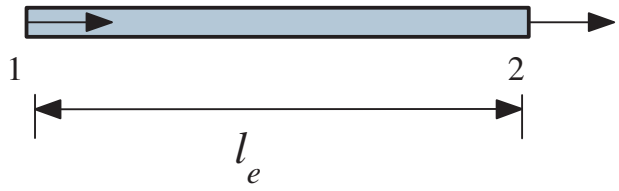


Figure 1: A nonlocal element for the axially vibrating rod with two nodes. It has two degrees of freedom and the displacement field within the element is expressed by linear shape functions.

freedom and there are two shape functions $N_1(x)$ and $N_2(x)$. The shape function matrix for the axial deformation [34] can be given by

$$\mathbf{N}(x) = [N_1(x), N_2(x)]^T = [1-x/\ell_e, x/\ell_e]^T \quad (2)$$

Using this the stiffness matrix can be obtained using the conventional variational formulation as

$$\mathbf{K}_e = EA\int_0^{\ell_e}\frac{d\mathbf{N}(x)}{dx}\frac{d\mathbf{N}^T(x)}{dx}\mathrm{d}x = \frac{EA}{\ell_e}\begin{bmatrix}1 & -1\\ -1 & 1\end{bmatrix} \quad (3)$$

The mass matrix for the nonlocal element can be obtained as

$$\mathbf{M}_e = m\int_0^{\ell_e}\mathbf{N}(x)\mathbf{N}^T(x)\mathrm{d}x + m(e_0a)^2\int_0^{\ell_e}\frac{d\mathbf{N}(x)}{dx}\frac{d\mathbf{N}^T(x)}{dx}\mathrm{d}x = \frac{m\ell_e}{6}\begin{bmatrix}2 & 1\\ 1 & 2\end{bmatrix} + \left(\frac{e_0a}{\ell_e}\right)^2 m\ell_e\begin{bmatrix}1 & -1\\ -1 & 1\end{bmatrix} \quad (4)$$

For the special case when the rod is local, the mass matrix derived above reduces to the classical mass matrix[34, 35] as $e_0a = 0$. Therefore for a nonlocal rod, the element stiffness matrix is identical to that of a classical local rod but the element mass has an additive term which is dependent on the nonlocal parameter.

2.2 Bending vibration of nanobeams

For the bending vibration of a nonlocal damped beam, the equation of motion can be expressed by

$$EI\frac{\partial^4 V(x,t)}{\partial x^4} + m\left(1-(e_0a)^2\frac{\partial^2}{\partial x^2}\right)\left\{\frac{\partial^2 V(x,t)}{\partial t^2}\right\} + \widehat{c}_1\left(1-(e_0a)_1^2\frac{\partial^2}{\partial x^2}\right)\frac{\partial^5 V(x,t)}{\partial x^4\partial t} + \widehat{c}_2\left(1-(e_0a)_2^2\frac{\partial^2}{\partial x^2}\right)\frac{\partial V(x,t)}{\partial t} = \left(1-(e_0a)^2\frac{\partial^2}{\partial x^2}\right)\{F(x,t)\} \tag{5}$$

In the above equation EI is the bending rigidity, m is mass per unit length, e_0a is the nonlocal parameter, $V(x,t)$ is the transverse displacement and $F(x,t)$ is the applied force. The constant $\widehat{c}_1$ is the strain-rate-dependent viscous damping coefficient and $\widehat{c}_2$ is the velocity-dependent viscous damping coefficient. The damping nonlocal parameters are assumed to be zero for simplicity. We consider an element of length ℓ_e with bending stiffness EI and mass per unit length m. An element of the beam is shown in Figure 2. This element has four degrees of freedom and

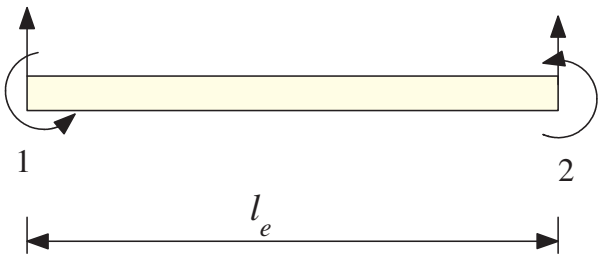


Figure 2: A nonlocal element for the bending vibration of a beam. It has two nodes and four degrees of freedom. The displacement field within the element is expressed by cubic shape functions.

there are four shape functions. The shape function matrix for the bending deformation [34] can be given by

$$\mathbf{N}(x) = [N_1(x), N_2(x), N_3(x), N_4(x)]^T \tag{6}$$

where

$$\begin{aligned} N_1(x) &= 1-3\frac{x^2}{\ell_e^2}+2\frac{x^3}{\ell_e^3}, & N_2(x) &= x-2\frac{x^2}{\ell_e}+\frac{x^3}{\ell_e^2}, \\ N_3(x) &= 3\frac{x^2}{\ell_e^2}-2\frac{x^3}{\ell_e^3}, & N_4(x) &= -\frac{x^2}{\ell_e}+\frac{x^3}{\ell_e^2} \end{aligned} \tag{7}$$

Using this, the stiffness matrix can be obtained using the conventional variational formulation [35] as

$$\mathbf{K}_e = EI\int_0^{\ell_e}\frac{d^2\mathbf{N}(x)}{dx^2}\frac{d^2\mathbf{N}^T(x)}{dx^2}\mathrm{d}x = \frac{EI}{\ell_e^3}\begin{bmatrix} 12 & 6\ell_e & -12 & 6\ell_e \\ 6\ell_e & 4\ell_e^2 & -6\ell_e & 2\ell_e^2 \\ -12 & -6\ell_e & 12 & -6\ell_e^2 \\ 6\ell_e & 2\ell_e^2 & -6\ell_e & 4\ell_e^2 \end{bmatrix} \tag{8}$$

The mass matrix for the nonlocal element can be obtained as

$$\begin{aligned}\mathbf{M}_e &= m\int_0^{\ell_e}\mathbf{N}(x)\mathbf{N}^T(x)\mathrm{d}x + m(e_0a)^2\int_0^{\ell_e}\frac{d\mathbf{N}(x)}{dx}\frac{d\mathbf{N}^T(x)}{dx}\mathrm{d}x \\ &= \frac{m\ell_e}{420}\begin{bmatrix}156 & 22\ell_e & 54 & -13\ell_e\\ 22\ell_e & 4\ell_e^2 & 13\ell_e & -3\ell_e^2\\ 54 & 13\ell_e & 156 & -22\ell_e\\ -13\ell_e & -3\ell_e^2 & -22\ell_e & 4\ell_e^2\end{bmatrix} + \left(\frac{e_0a}{\ell_e}\right)^2\frac{m\ell_e}{30}\begin{bmatrix}36 & 3\ell_e & -36 & 3\ell_e\\ 3\ell_e & 4\ell_e^2 & -3\ell_e & -\ell_e^2\\ -36 & -3\ell_e & 36 & -3\ell_e\\ 3\ell_e & -\ell_e^2 & -3\ell_e & 4\ell_e^2\end{bmatrix}\end{aligned} \tag{9}$$

For the special case when the beam is local, the mass matrix derived above reduces to the classical mass matrix [34, 35] as $e_0a = 0$.

Based on the discussions in this section for all the two systems considered here, in general the element mass matrix of a nonlocal dynamic system can be expressed as

$$\mathbf{M}_e = \mathbf{M}_{0_e} + \mathbf{M}_{\mu_e} \tag{10}$$

Here $\mathbf{M}_{0_e}$ is the element stiffness matrix corresponding to the underlying local system and $\mathbf{M}_{\mu_e}$ is the additional term arising due to the nonlocal effect.

3 Modal analysis of nonlocal dynamical systems

Using the finite element formulation, the stiffness matrix of the local and nonlocal system turns out to be identical to each other. The mass matrix of the nonlocal system is however different from its equivalent local counterpart. Assembling the element matrices and applying the boundary conditions, following the usual procedure of the finite element method [36] one obtains the global mass matrix as

$$\mathbf{M} = \mathbf{M}_0 + \mathbf{M}_\mu \tag{11}$$

In the above equation $\mathbf{M}_0$ is the usual global mass matrix arising in the conventional local system and $\mathbf{M}_\mu$ is matrix arising due to nonlocal nature of the systems. In general we can express this matrix by

$$\mathbf{M}_\mu = \left(\frac{e_0a}{L}\right)^2\widehat{\mathbf{M}}_\mu \tag{12}$$

where $\widehat{\mathbf{M}}_\mu$ is a nonnegative definite matrix. The matrix $\mathbf{M}_\mu$ is therefore, a scale-dependent matrix and its influence reduces if the length of the system L is large compared to the parameter e_0a. Majority of the current finite element software and other computational tools do not explicitly consider the nonlocal part of the mass matrix. For the design and analysis of future generation of nano electromechanical systems it is vitally important to consider the nonlocal influence. In this section we are interested in understanding the impact of the difference in the mass matrix on the dynamic characteristics of the system. In particular the following questions of fundamental interest have been addressed:

- Under what condition a nonlocal system possess classical local normal modes?
- How the vibration modes and frequencies of a nonlocal system can be understood in the light of the results from classical local systems?

By addressing these questions, it would be possible to extend conventional 'local' elasticity based finite element software to analyse nonlocal systems arising in the modelling of complex nanoscale built-up structures.

3.1 Conditions for classical normal modes

The equation of motion of a discretised nonlocal damped system with n degrees of freedom can be expressed as

$$\left[\mathbf{M}_0 + \mathbf{M}_\mu\right] \ddot{\mathbf{u}}(t) + \mathbf{C}\dot{\mathbf{u}}(t) + \mathbf{K}\mathbf{u}(t) = \mathbf{f}(t) \tag{13}$$

Here $\mathbf{u}(t) \in \mathbb{R}^n$ is the displacement vector, $\mathbf{f}(t) \in \mathbb{R}^n$ is the forcing vector, $\mathbf{K}, \mathbf{C} \in \mathbb{R}^{n\times n}$ are respectively the global stiffness and the viscous damping matrix. In general $\mathbf{M}_0$ and $\mathbf{M}_\mu$ are positive definite symmetric matrices, $\mathbf{C}$ and $\mathbf{K}$ are non-negative definite symmetric matrices. The equation of motion of corresponding local system is given by

$$\mathbf{M}_0\ddot{\mathbf{u}}_0(t) + \mathbf{C}\dot{\mathbf{u}}_0(t) + \mathbf{K}\mathbf{u}_0(t) = \mathbf{f}(t) \tag{14}$$

where $\mathbf{u}_0(t) \in \mathbb{R}^n$ is the local displacement vector. The natural frequencies ($\omega_j \in \mathbb{R}$) and the mode shapes ($\mathbf{x}_j \in \mathbb{R}^n$) of the corresponding undamped local system can be obtained by solving the matrix eigenvalue problem [32] as

$$\mathbf{K}\mathbf{x}_j = \omega_j^2 \mathbf{M}_0 \mathbf{x}_j, \quad \forall\, j = 1, 2, \ldots, n \tag{15}$$

The undamped local eigenvectors satisfy an orthogonality relationship over the local mass and stiffness matrices, that is

$$\mathbf{x}_k^T \mathbf{M}_0 \mathbf{x}_j = \delta_{kj} \tag{16}$$

$$\text{and} \quad \mathbf{x}_k^T \mathbf{K} \mathbf{x}_j = \omega_j^2 \delta_{kj}, \quad \forall\, k, j = 1, 2, \ldots, n \tag{17}$$

where δ_{kj} is the Kroneker delta function. We construct the local modal matrix

$$\mathbf{X} = [\mathbf{x}_1, \mathbf{x}_2, \ldots, \mathbf{x}_n] \in \mathbb{R}^n \tag{18}$$

The local modal matrix can be used to diagonalize the local system (14) provided the damping matrix $\mathbf{C}$ is simultaneously diagonalizable with $\mathbf{M}_0$ and $\mathbf{K}$. This condition, known as the proportional damping, originally introduced by Lord Rayleigh [37] in 1877, is still in wide use today. The mathematical condition for proportional damping can be obtained from the commutitative behaviour of the system matrices [38]. This can be expressed as

$$\mathbf{C}\mathbf{M}_0^{-1}\mathbf{K} = \mathbf{K}\mathbf{M}_0^{-1}\mathbf{C} \tag{19}$$

or equivalently $\mathbf{C} = \mathbf{M}_0 f(\mathbf{M}_0^{-1}\mathbf{K})$ as shown in [39].

Considering undamped nonlocal system and premultiplying the equation by $\mathbf{M}_0^{-1}$ we have

$$\left(\mathbf{I}_n + \mathbf{M}_0^{-1}\mathbf{M}_\mu\right) \ddot{\mathbf{u}}(t) + \left(\mathbf{M}_0^{-1}\mathbf{K}\right) \mathbf{u}(t) = \mathbf{M}_0^{-1}\mathbf{f}(t) \tag{20}$$

This system can be diagonalized by a similarity transformation which also diagonalise $\left(\mathbf{M}_0^{-1}\mathbf{K}\right)$ provided the matrices $\left(\mathbf{M}_0^{-1}\mathbf{M}_\mu\right)$ and $\left(\mathbf{M}_0^{-1}\mathbf{K}\right)$ commute. This implies that the condition for existence of classical local normal modes is

$$\left(\mathbf{M}_0^{-1}\mathbf{K}\right)\left(\mathbf{M}_0^{-1}\mathbf{M}_\mu\right) = \left(\mathbf{M}_0^{-1}\mathbf{M}_\mu\right)\left(\mathbf{M}_0^{-1}\mathbf{K}\right) \tag{21}$$

$$\text{or} \quad \mathbf{K}\mathbf{M}_0^{-1}\mathbf{M}_\mu = \mathbf{M}_\mu\mathbf{M}_0^{-1}\mathbf{K} \tag{22}$$

If the above condition is satisfied, then a nonlocal undamped system can be diagonalised by the classical local normal modes. However, it is also possible to have nonlocal normal modes which can diagonalize the nonlocal undamped system as discussed in the next subsection.

3.2 Nonlocal normal modes

Nonlocal normal modes can be obtained by the undamped nonlocal eigenvalue problem

$$\mathbf{K}\mathbf{u}_j = \lambda_j^2 \left[\mathbf{M}_0 + \mathbf{M}_\mu\right] \mathbf{u}_j, \quad \forall\, j = 1, 2, \ldots, n \tag{23}$$

Here λ_j and $\mathbf{u}_j$ are the nonlocal natural frequencies and nonlocal normal modes of the system. We can define a nonlocal modal matrix

$$\mathbf{U} = \left[\mathbf{u}_1, \mathbf{u}_2, \ldots, \mathbf{u}_n\right] \in \mathbb{R}^n \tag{24}$$

which will unconditionally diagonalize the nonlocal undamped system. It should be remembered that in general nonlocal normal modes and frequencies will be different from their local counterparts.

Under certain restrictive condition it may be possible to diagonalise the damped nonlocal system using classical normal modes. Premultiplying the equation of motion (13) by $\mathbf{M}_0^{-1}$, the required condition is that $\left(\mathbf{M}_0^{-1}\mathbf{M}_\mu\right)$, $\left(\mathbf{M}_0^{-1}\mathbf{C}\right)$ and $\left(\mathbf{M}_0^{-1}\mathbf{K}\right)$ must commute pairwise. This implies that in addition to the two conditions given by Eqs. (19) and (22), we also need a third condition

$$\mathbf{C}\mathbf{M}_0^{-1}\mathbf{M}_\mu = \mathbf{M}_\mu\mathbf{M}_0^{-1}\mathbf{C} \tag{25}$$

If we consider the diagonalization of the nonlocal system by the nonlocal modal matrix in (24), then the concept of proportional damping can be applied similar to that of the local system. One can obtain the required condition similar to Caughey's condition [38] as in Eq. (19) by replacing the mass matrix with $\mathbf{M}_0 + \mathbf{M}_\mu$. If this condition is satisfied, then the equation of motion can be diagonalised by the nonlocal normal modes and in general not by the classical normal modes.

3.3 Approximate nonlocal normal modes

Majority of the existing finite element software calculate the classical normal modes. However, it was shown that only under certain restrictive condition, the classical normal modes can be used to diagonalise the system. In general one need to use nonlocal normal modes to diagonalise the equation of motion (13), which is necessary for efficient dynamic analysis and physical understanding of the system. In this section we aim to express nonlocal normal modes in terms of classical normal modes. Since the classical normal modes are well understood, this approach will allow us to develop physical understanding of the nonlocal normal modes.

For distinct undamped eigenvalues (ω_l^2), local eigenvectors $\mathbf{x}_l$, $\forall\, l = 1, \ldots, n$, form a complete set of vectors. For this reason each nonlocal normal mode $\mathbf{u}_j$ can be expanded as a linear combination of $\mathbf{x}_l$. Thus, an expansion of the form

$$\mathbf{u}_j = \sum_{l=1}^{n} \alpha_l^{(j)} \mathbf{x}_l \tag{26}$$

may be considered. Without any loss of generality, we can assume that $\alpha_j^{(j)} = 1$ (normalization) which leaves us to determine $\alpha_l^{(j)}, \forall l \neq j$. Substituting the expansion of $\mathbf{u}_j$ into the eigenvalue equation (23), one obtains

$$\left[-\lambda_j^2 \left(\mathbf{M}_0 + \mathbf{M}_\mu\right) + \mathbf{K}\right] \sum_{l=1}^{n} \alpha_l^{(j)} \mathbf{x}_l = \mathbf{0} \tag{27}$$

For the case when $\alpha_l^{(j)}$ are approximate, the error involving the projection in Eq. (26) can be expressed as

$$\boldsymbol{\varepsilon}_j = \sum_{l=1}^{n} \left[-\lambda_j^2 \left(\mathbf{M}_0 + \mathbf{M}_\mu\right) + \mathbf{K}\right] \alpha_l^{(j)} \mathbf{x}_l \tag{28}$$

We use a Galerkin approach to minimise this error by viewing the expansion as a projection in the basis functions $\mathbf{x}_l \in \mathbb{R}^n, \forall l = 1, 2, \ldots n$. Therefore, making the error orthogonal to the basis functions one has

$$\boldsymbol{\varepsilon}_j \perp \mathbf{x}_l \quad \text{or} \quad \mathbf{x}_k^T \boldsymbol{\varepsilon}_j = 0 \quad \forall\ k = 1, 2, \ldots, n \tag{29}$$

Using the orthogonality property of the undamped local modes described by Eqs. (16) and (17) one obtains

$$\sum_{l=1}^{n} \left[-\lambda_j^2 \left(\delta_{kl} + M'_{\mu_{kl}}\right) + \omega_k^2 \delta_{kl}\right] \alpha_l^{(j)} = 0 \tag{30}$$

where $M'_{\mu_{kl}} = \mathbf{x}_k^T \mathbf{M}_\mu \mathbf{x}_l$ are the elements of the nonlocal part of the modal mass matrix. The j-th equation of this set obtained by setting $k = j$ and can be written as

$$-\lambda_j^2 \left(1 + M'_{\mu_{jj}}\right) + \omega_j^2 - \lambda_j^2 \sum_{l \neq j}^{n} \left(M'_{\mu_{jl}}\right) \alpha_l^{(j)} = 0 \tag{31}$$

Assuming the off-diagonal terms of the nonlocal part of the modal mass matrix are small and $\alpha_l^{(j)} \ll 1, \forall l \neq j$, approximate nonlocal frequencies can be obtained as

$$\lambda_j \approx \frac{\omega_j}{\sqrt{1 + M'_{\mu_{jj}}}} \tag{32}$$

This important equation gives an explicit closed-form expression relating nonlocal natural frequencies λ_j and local natural frequencies ω_j. If the length-scale parameter is large, then diagonal elements of the nonlocal part of the modal mass matrix becomes smaller and consequently the nonlocal frequencies approach the classical local frequencies. Equation (32) can also be viewed as a general correction to the local frequencies due to the nonlocal effect arising due to small length scale.

For the general case when $k \neq j$, from Eq. (30) we have

$$\left[-\lambda_j^2 \left(1 + M'_{\mu_{kk}}\right) + \omega_k^2\right] \alpha_k^{(j)} - \lambda_j^2 \sum_{l \neq k}^{n} \left(M'_{\mu_{kl}}\right) \alpha_l^{(j)} = 0 \tag{33}$$

Recalling that $\alpha_j^{(j)} = 1$, this equation can be expressed as

$$\left[-\lambda_j^2 \left(1 + M'_{\mu_{kk}}\right) + \omega_k^2\right] \alpha_k^{(j)} = \lambda_j^2 \left[M'_{\mu_{kj}} + \sum_{l \neq k \neq j}^{n} M'_{\mu_{kl}} \alpha_l^{(j)}\right] \tag{34}$$

Again assuming the off-diagonal terms of the nonlocal part of the modal mass matrix are small and $\alpha_l^{(j)} \ll 1, \forall l \neq j$, we can obtain

$$\alpha_k^{(j)} \approx \frac{\lambda_j^2 M'_{\mu_{kj}}}{-\lambda_j^2 \left(1 + M'_{\mu_{kk}}\right) + \omega_k^2} = \frac{\lambda_j^2}{\left(\lambda_k^2 - \lambda_j^2\right)} \frac{M'_{\mu_{kj}}}{\left(1 + M'_{\mu_{kk}}\right)} \tag{35}$$

Substituting this in the original expansion (26), the nonlocal normal modes can be expressed in terms of the classical normal modes as

$$\mathbf{u}_j \approx \mathbf{x}_j + \sum_{k \neq j}^{n} \frac{\lambda_j^2}{\left(\lambda_k^2 - \lambda_j^2\right)} \frac{M'_{\mu_{kj}}}{\left(1 + M'_{\mu_{kk}}\right)} \mathbf{x}_k \tag{36}$$

This equation explicitly relates nonlocal normal modes with the classical normal modes. From this expression, the following insights about the nonlocal normal modes can be deduced

- Each nonlocal mode can be viewed as a sum of two principal components. One of them is parallel to the corresponding local mode and the other is orthogonal to it as all $\mathbf{x}_k$ are orthogonal to $\mathbf{x}_j$ for $j \neq k$.
- Due to the term $\left(\lambda_k^2 - \lambda_j^2\right)$ in the denominator, for a given nonlocal mode, only few adjacent local modes contributes to the orthogonal component.
- For systems with well separated natural frequencies, the contribution of the orthogonal component becomes smaller compared to the parallel component.

Equations (32) and (36) completely defines the nonlocal natural frequencies and mode shapes in terms of the local natural frequencies and mode shapes. Accuracy of these expressions will be investigated through numerical examples in section 5. Dynamic response of nonlocal damped systems is considered next.

4 Dynamics of damped nonlocal systems

Forced response of damped nonlocal systems in the frequency domain is considered. Assuming all the initial conditions are zero and taking the Fourier transformation of the equation of motion (13) we have

$$\mathbf{D}(\mathrm{i}\omega)\bar{\mathbf{u}}(\mathrm{i}\omega) = \bar{\mathbf{f}}(\mathrm{i}\omega) \tag{37}$$

where the nonlocal dynamic stiffness matrix is given by

$$\mathbf{D}(\mathrm{i}\omega) = -\omega^2 \left[\mathbf{M}_0 + \mathbf{M}_\mu\right] + \mathrm{i}\omega\mathbf{C} + \mathbf{K} \tag{38}$$

In Eq. (37) $\bar{\mathbf{u}}(\mathrm{i}\omega)$ and $\bar{\mathbf{f}}(\mathrm{i}\omega)$ are respectively the Fourier transformations of the response and the forcing vectors. Using the local modal matrix (18), the dynamic stiffness matrix can be transformed to the modal coordinate as

$$\mathbf{D}'(\mathrm{i}\omega) = \mathbf{X}^T\mathbf{D}(\mathrm{i}\omega)\mathbf{X} = -\omega^2 \left[\mathbf{I} + \mathbf{M}'_\mu\right] + \mathrm{i}\omega\mathbf{C}' + \mathbf{\Omega}^2 \tag{39}$$

where $\mathbf{I}$ is a n-dimensional identity matrix, $\mathbf{\Omega}^2$ is a diagonal matrix containing the squared local natural frequencies and $(\bullet)'$ denotes that the quantity is in the modal coordinates. Unless all the conditions derived in subsection 3.2 are satisfied, in general $\mathbf{M}'_\mu$ and $\mathbf{C}'$ are not diagonal matrices. We separate the diagonal and off-diagonal terms of these matrices and rewrite Eq. (39) as

$$\mathbf{D}'(\mathrm{i}\omega) = \underbrace{-\omega^2 \left[\mathbf{I} + \overline{\mathbf{M}}'_\mu\right] + \mathrm{i}\omega\overline{\mathbf{C}}' + \mathbf{\Omega}^2}_{\text{diagonal}} + \underbrace{\left(-\omega^2\Delta\mathbf{M}'_\mu + \mathrm{i}\omega\Delta\mathbf{C}'\right)}_{\text{off-diagonal}} \tag{40}$$

$$= \overline{\mathbf{D}}'(\mathrm{i}\omega) + \Delta\mathbf{D}'(\mathrm{i}\omega) \tag{41}$$

From Eq. (37) the dynamic response of the system can be obtained as

$$\bar{\mathbf{u}}(\mathrm{i}\omega) = \mathbf{H}(\mathrm{i}\omega)\bar{\mathbf{f}}(\mathrm{i}\omega) = \left[\mathbf{X}\mathbf{D}'^{-1}(\mathrm{i}\omega)\mathbf{X}^T\right]\bar{\mathbf{f}}(\mathrm{i}\omega) \tag{42}$$

where the matrix $\mathbf{H}(\mathrm{i}\omega)$ is known as the transfer function matrix. From the expression of the modal dynamic stiffness matrix in Eq. (41) we have

$$\mathbf{D}'^{-1}(\mathrm{i}\omega) = \left[\overline{\mathbf{D}}'(\mathrm{i}\omega)\left(\mathbf{I} + \overline{\mathbf{D}}'^{-1}(\mathrm{i}\omega)\Delta\mathbf{D}'(\mathrm{i}\omega)\right)\right]^{-1} \tag{43}$$

$$\approx \overline{\mathbf{D}}'^{-1}(\mathrm{i}\omega) - \overline{\mathbf{D}}'^{-1}(\mathrm{i}\omega)\Delta\mathbf{D}'(\mathrm{i}\omega)\overline{\mathbf{D}}'^{-1}(\mathrm{i}\omega) \tag{44}$$

In the above equation the diagonal part $\overline{\mathbf{D}}'^{-1}(\mathrm{i}\omega)$ is expected to be the dominant term and its elements can be expressed as

$$\left\{\overline{\mathbf{D}}'^{-1}(\mathrm{i}\omega)\right\}_{jj} = \frac{1}{-\omega^2\left(1 + M'_{\mu_{jj}}\right) + 2\mathrm{i}\omega\omega_j\zeta_j + \omega_j^2} \tag{45}$$

In the above we defined the modal damping factors as

$$\left\{\overline{\mathbf{C}}'\right\}_{jj} = 2\omega_j\zeta_j \tag{46}$$

Substituting the approximate expression of $\mathbf{D}'^{-1}(\mathrm{i}\omega)$ from Eq. (44) into the expression of the transfer function matrix in Eq. (42) we have

$$\mathbf{H}(\mathrm{i}\omega) = \left[\mathbf{X}\mathbf{D}'^{-1}(\mathrm{i}\omega)\mathbf{X}^T\right] \approx \overline{\mathbf{H}}'(\mathrm{i}\omega) - \Delta\mathbf{H}'(\mathrm{i}\omega) \tag{47}$$

where

$$\overline{\mathbf{H}}'(\mathrm{i}\omega) = \mathbf{X}\overline{\mathbf{D}}'(\mathrm{i}\omega)\mathbf{X}^T = \sum_{k=1}^{n}\frac{\mathbf{x}_k\mathbf{x}_k^T}{-\omega^2\left(1 + M'_{\mu_{kk}}\right) + 2\mathrm{i}\omega\omega_k\zeta_k + \omega_k^2} \tag{48}$$

$$\text{and} \quad \Delta\mathbf{H}'(\mathrm{i}\omega) = \mathbf{X}\overline{\mathbf{D}}'^{-1}(\mathrm{i}\omega)\Delta\mathbf{D}'(\mathrm{i}\omega)\overline{\mathbf{D}}'^{-1}(\mathrm{i}\omega)\mathbf{X}^T \tag{49}$$

Considering that the matrix $\Delta\mathbf{D}'(\mathrm{i}\omega)$ has only off-diagonal terms, expanding the matrix multiplications a general term of the previous matrix can be expressed as

$$\Delta H'_{ij}(\mathrm{i}\omega) = \sum_{l=1}^{n}\sum_{k\neq l}^{n}\frac{x_{il}\Delta D'_{lk}(\mathrm{i}\omega)x_{jk}}{\left(-\omega^2(1 + M'_{\mu_{ll}}) + 2\mathrm{i}\omega\omega_l\zeta_l + \omega_l^2\right)\left(-\omega^2(1 + M'_{\mu_{kk}}) + 2\mathrm{i}\omega\omega_k\zeta_k + \omega_k^2\right)} \tag{50}$$

Equation (47) therefore completely defines the transfer function of the damped nonlocal system in terms of the classical normal modes. This can be useful in practice as all the quantities arise in this expression can be obtained from a conventional finite element software. One only needs the nonlocal part of the mass matrix as derived in section 2. Some notable features of the expression of the approximate transfer function matrix in Eq. (47) are

- For lightly damped systems, from Eq. (48) observe that the transfer function will have peaks around the nonlocal natural frequencies derived in the previous section. This justifies the consistency of the approximation used in the paper.

- The decomposition in Eq. (40) indicates that error in the transfer function depends on two components. They include the off-diagonal part of the of the modal nonlocal mass matrix $\Delta\mathbf{M}'_\mu$ and the off-diagonal part of the of the modal damping matrix $\Delta\mathbf{C}'$. While the error in in the damping term is present for non proportionally damped local systems, the error due to the nonlocal modal mass matrix in unique to the nonlocal system.

- For a proportionally damped system $\Delta\mathbf{C}' = \mathbf{O}$. For this case error in the transfer function only depends on $\Delta\mathbf{M}'_\mu$.

- In general, error in the transfer function is expected to be higher for higher frequencies as both $\Delta\mathbf{C}'$ and $\Delta\mathbf{M}'_\mu$ are weighted by frequency ω.

The expressions of the nonlocal natural frequencies (32), nonlocal normal modes (36) and the nonlocal transfer function matrix (47) allow us to understand the dynamic characteristic of a nonlocal system in a qualitative and quantitative manner in the light of equivalent local systems. Next we illustrate these new expressions by numerical examples of nanoscale structures.

5 Numerical examples

5.1 Axial vibration of a single-walled carbon nanotube

A single-walled carbon nanotube (SWCNT) is considered to examine the accuracy of the nonlocal finite element formulation and approximate expressions of the natural frequencies, normal modes and transfer functions. A zigzag (7, 0) SWCNT with Young's modulus $E = 6.85$ TPa, $L = 25$nm, density $\rho = 9.517 \times 10^3$ kg/m^3 and thickness t = 0.08nm is taken from [22]. The system considered here is shown in Figure 3. For a carbon nanotube with chirality (n_i, m_i),

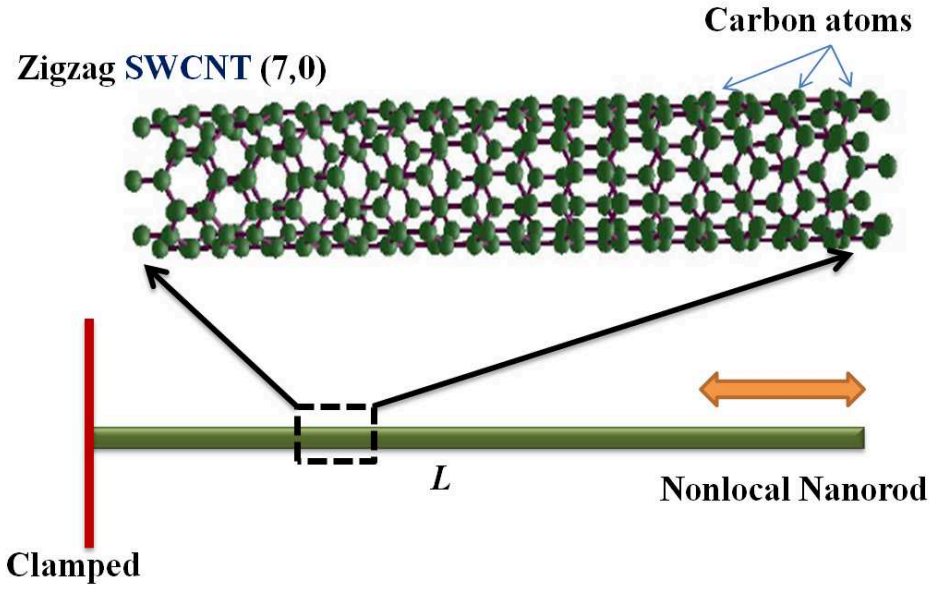


Figure 3: Axial vibration of a zigzag (7, 0) single-walled carbon nanotube (SWCNT) with clamped-free boundary condition.

the diameter can be given by

$$d_i = \frac{r}{\pi}\sqrt{n_i^2 + m_i^2 + n_i m_i} \tag{51}$$

where $r = 0.246$nm. The diameter of the SWCNT shown in Figure 3 is 0.55nm. A constant modal damping factor of 1% for all the modes is assumed. By comparing with MD simulation results [40, 41] it was observed that $e_0a = 1$ nm is the optimal value of the nonlocal parameter. In this study however we consider a range of values of e_0a within 0-2 nm to understand its role on the accuracy of the dynamic characteristics of the system.

We consider clamped-free boundary condition for the SWCNT. Undamped nonlocal natural frequencies can be obtained [12] as

$$\lambda_j = \sqrt{\frac{EA}{m}}\frac{\sigma_j}{\sqrt{1+\sigma_j^2(e_0a)^2}}, \quad \text{where} \quad \sigma_j = \frac{(2j-1)\pi}{2L}, \quad j = 1, 2, \cdots \tag{52}$$

EA is the axial rigidity and m is the mass per unit length of the SWCNT. For the finite element analysis the SWCNT is divided into 200 elements. The dimension of each of the system matrices become 200×200, that is $n = 200$. The global mass matrices $\mathbf{M}_0$ and $\mathbf{M}_\mu$ are obtained by assembling the element mass matrix given by (4). For this case it turns out (see element stiffness matrix in (3)) that the nonlocal part of the mass matrix is actually proportional to the stiffness matrix, that is $\mathbf{M}_\mu \propto \mathbf{K}$. Therefore, the condition for the existence of classical normal modes for the undamped system given by Eq. (22) is exactly satisfied in this case. This in turn implies that the error in the approximate expressions in subsection 3.2 should be zero as $M_{\mu_{kl}} = 0, \forall k \neq l$. We give numerical results to demonstrate that the theory for the existence of classical normal modes for nonlocal system derived in subsection 3.1 and the approximate expressions derived in subsection 3.2 are consistent.

In Figure 4, the natural frequencies obtained using the analytical expression (52) are compared with direct finite element simulation results. The frequency values are normalised with respect to the first local natural frequency ω_1. First 20 nonlocal natural frequencies are shown and four values of e_0a, namely 0.5, 1.0, 1.5 and 2.0nm have been used. In the same figure, natural frequencies obtained using the direct finite element method and the results obtained using the approximate expression (32) are also shown. It can be observed that the values obtains using three different approaches coincide for this problem. Natural frequencies corresponding to the underlying local system is shown in Figure 4. Local frequencies are qualitatively different from nonlocal frequencies as it increases linearly with the number of modes. Nonlocal frequencies on the other hand approaches to a constant value with increasing modes. This upper bound is known as the asymptotic frequency [28] and given by $\lambda_{\max} = \frac{1}{(e_0a)}\sqrt{\frac{EA}{m}}$. It is worth noting that the approximate expression of the natural frequency given by Eq. (32) is able to capture the asymptotic frequency for the axial vibration of SWCNT. Therefore, Eq. (32) can be used to understand both quantitative and qualitative behaviour of the natural frequencies of a nonlocal system.

In Figure 5 mode shapes corresponding to modes 2, 5, 6 and 9 are shown for four values of the nonlocal parameter. These mode numbers are selected for illustration only. The results obtained from the direct finite element is compared with the approximate expression given by Eq. (36). The mode shapes obtained by both approaches agree each other well.

Finally in Figure 6 the frequency response function of the tip of the SWCNT is shown for the four representative values of the nonlocal parameter. In the x-axis, excitation frequency normalised with respect to the first local frequency is considered. The frequency response is normalised by the static response δ_{st} (response when the excitation frequency is zero). The frequency response function of the underlying local model is also plotted to show the difference between the local and nonlocal responses. For the nonlocal system, the frequency response is

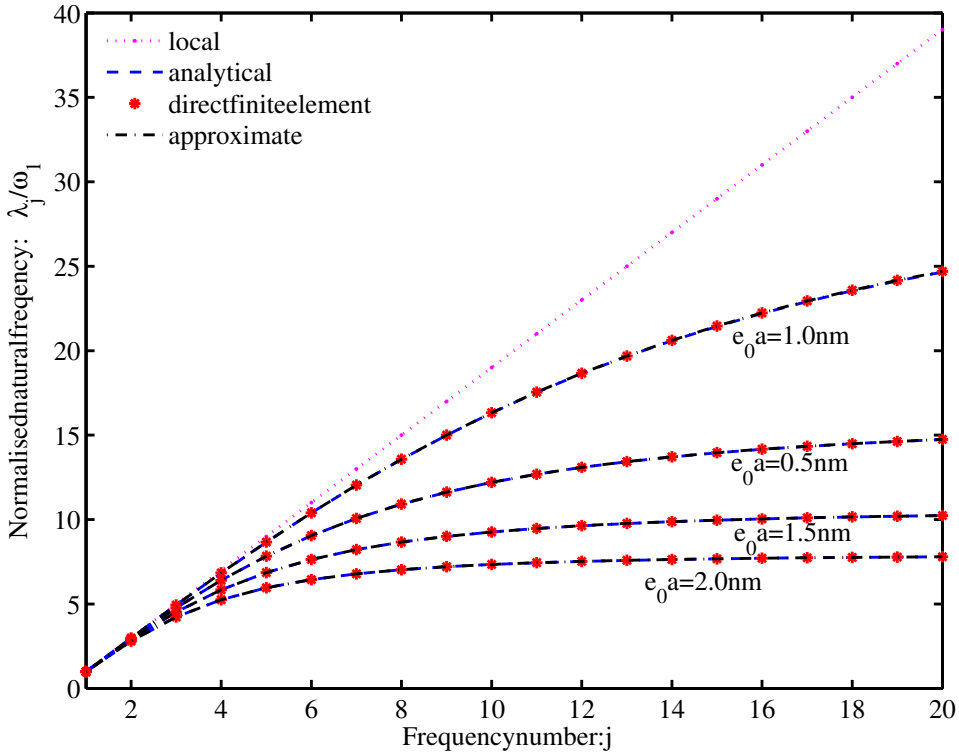


Figure 4: The variation of first 20 undamped natural frequencies for the axial vibration of SWCNT. Four representative values of e_0a (in nm) are considered.

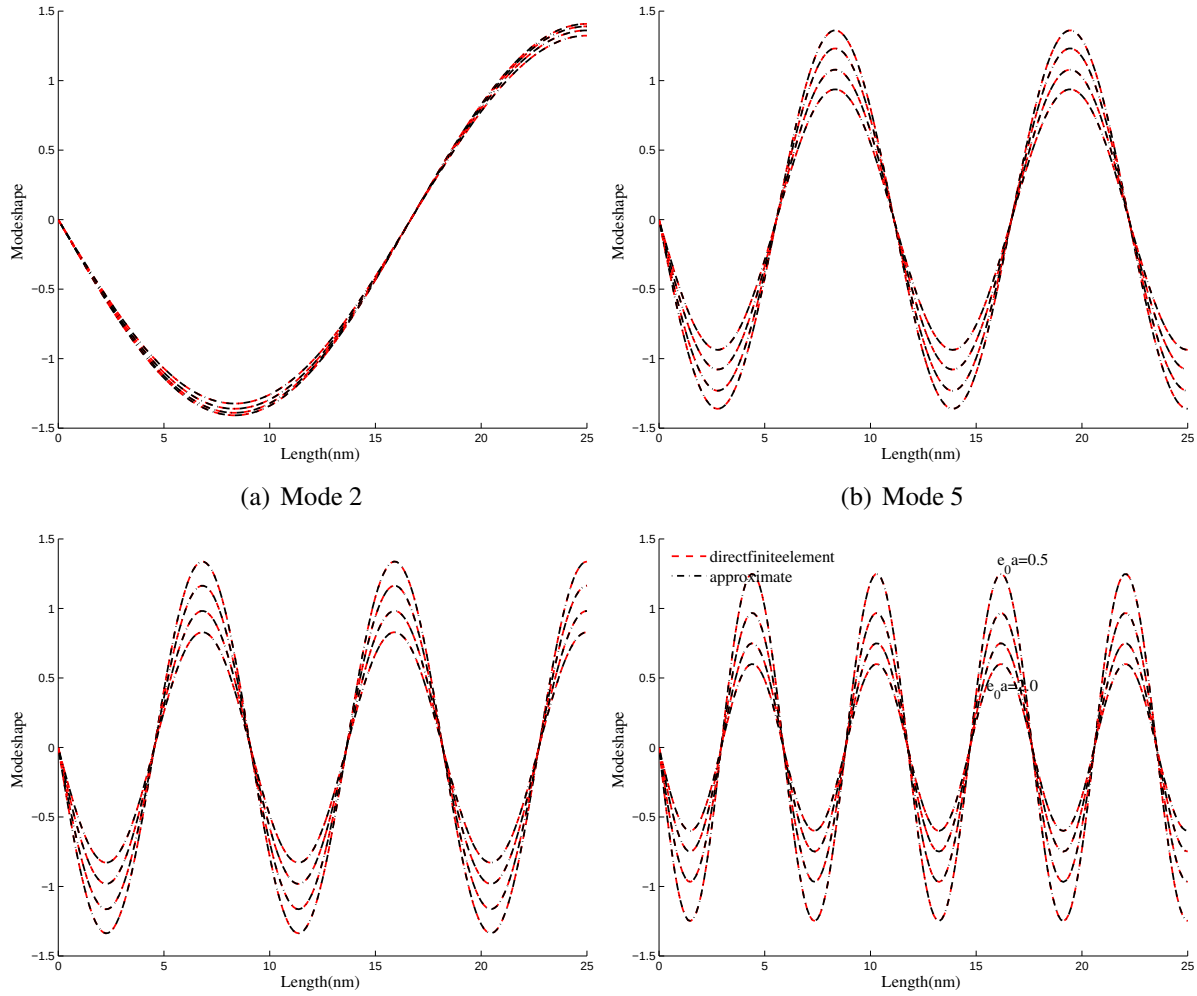
obtained by the direct finite element method and the approximation derived in section 4. As proportional damping model is assumed, the off-diagonal part of the modal damping matrix is a null matrix. For this case the approximate solution match exactly to the results obtained from the direct finite element method.

5.2 Bending vibration of a double-walled carbon nanotube

A double-walled carbon nanotube (DWCNT) is considered to examine the bending vibration characteristics. An armchair (5, 5), (8, 8) DWCNT with Young's modulus $E = 1.0$ TPa, $L = 30$ nm, density $\rho = 2.3 \times 10^3$ kg/m^3 and thickness t = 0.35 nm is considered as in [42]. The inner and the outer diameters of the DWCNT are respectively 0.68nm and 1.1nm. The system considered here is shown in Figure 7 . We consider pinned-pinned boundary condition for the DWCNT. Undamped nonlocal natural frequencies can be obtained [12] as

$$\lambda_j = \sqrt{\frac{EI}{m}} \frac{\beta_j^2}{\sqrt{1+\beta_j^2(e_0a)^2}} \quad \text{where} \quad \beta_j = j\pi/L, \quad j = 1, 2, \cdots \tag{53}$$

EI is the bending rigidity and m is the mass per unit length of the DWCNT. For the finite element analysis the DWCNT is divided into 100 elements. The dimension of each of the system matrices become 200×200, that is $n = 200$. The global mass matrices $\mathbf{M}_0$ and $\mathbf{M}_\mu$ are obtains by assembling the element mass matrix given by (9). Unlike the case of the axial vibration of rods, the nonlocal part of the mass matrix is not proportional to the stiffness matrix. Therefore, the condition for the existence of classical normal modes for the undamped system given by Eq. (22) is not satisfied for this case. This numerical study therefore quantifies the accuracy of the approximate expression proposed in the paper.



(a) Mode 2 (b) Mode 5

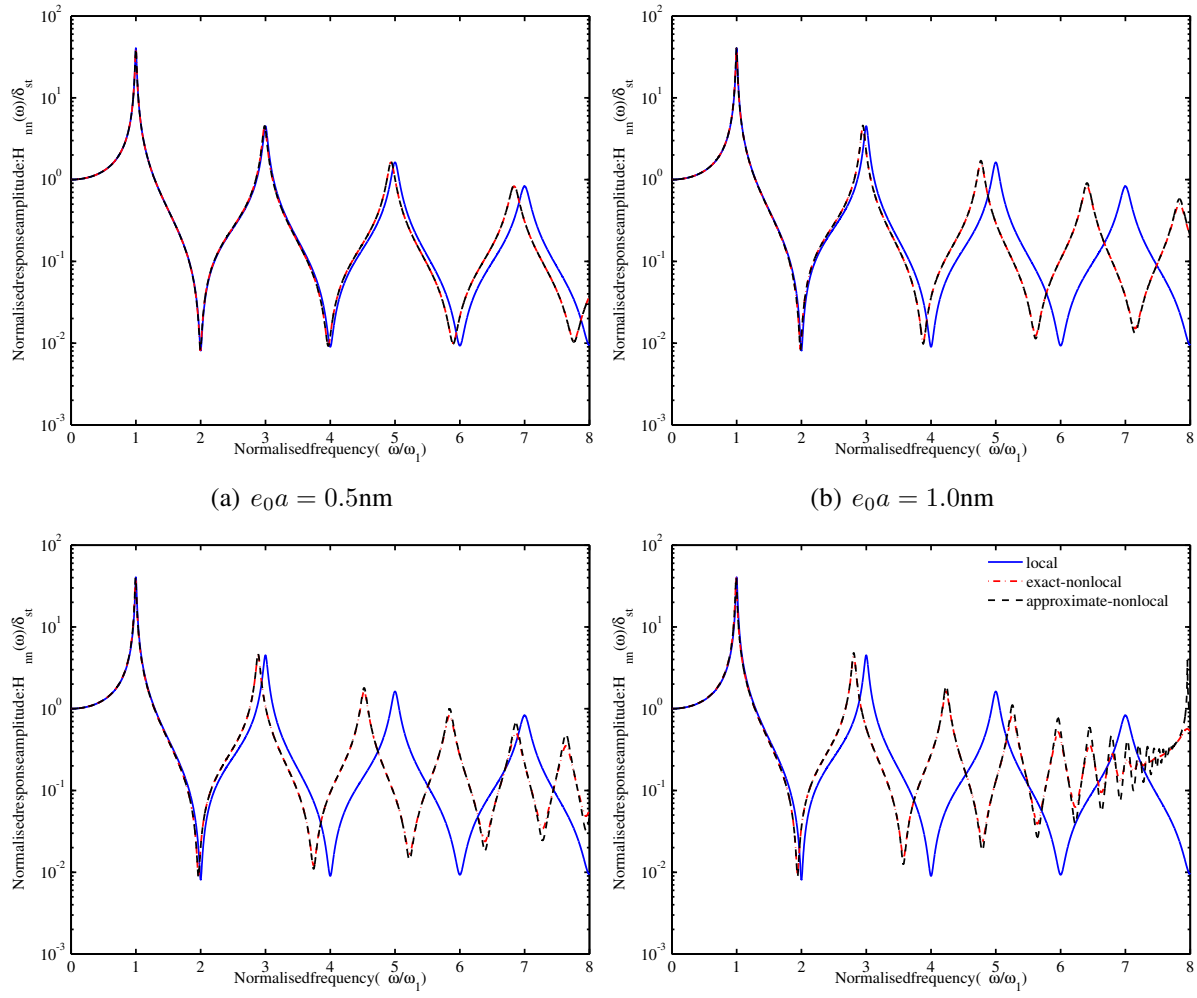
(c) Mode 6 (d) Mode 9

Figure 5: Four selected mode shapes for the axial vibration of SWCNT. Exact finite element results are compared with the approximate analysis based on local eigensolutions. In each subplot four different values of e_0a, namely 0.5, 1.0, 1.5 and 2.0nm have been used (see subplot d).

The natural frequencies obtained using the analytical expression (53) are compared with direct finite element simulation in Figure 8. The frequency values are normalised with respect to the first local natural frequency. First 20 nonlocal natural frequencies are shown for four distinct values of e_0a, namely 0.5, 1.0, 1.5 and 2.0nm. In the same figure, natural frequencies obtained using the direct finite element method and the results obtained using the approximate expression (32) are also shown. It can be observed that the values obtains using three different approaches almost coincide for this problem. Natural frequencies corresponding to the underlying local system is shown in Figure 8. Local frequencies are qualitatively different from nonlocal frequencies as it increases quadratically with the number of modes. Nonlocal frequencies on the other hand increases linearly with the number of modes. The approximate expression of the natural frequency given by Eq. (32) is able to capture this crucial qualitative difference.

In Figure 9 mode shapes corresponding to mode 2, 5, 6 and 9 are shown for four values of the nonlocal parameter. These mode numbers are selected for illustration only. The results obtained from the direct finite element is compared with the approximate expression given by Eq. (36). The mode shapes obtain by both approach agree to each other.

In Figure 10 the amplitude of the frequency response function $H_{ij}(\omega)$ for $i = 6, j = 8$ is



(a) $e_0a = 0.5$nm (b) $e_0a = 1.0$nm

(c) $e_0a = 1.5$nm (d) $e_0a = 2.0$nm

Figure 6: Amplitude of the normalised frequency response of the SWCNT at the tip for different values of e_0a. Exact finite element results are compared with the approximate analysis based on local eigensolutions.

shown for the four representative values of the nonlocal parameter. In the x-axis, excitation frequency normalised with respect to the first local frequency is considered. The frequency response is normalise by the static response d_{st}. The frequency response function of the underlying local model is also plotted to show the difference between the local and nonlocal response. For the nonlocal system, the frequency response is obtained by the direct finite element method and the approximation derived in section 4. As proportional damping model is assumed, the off-diagonal part of the modal damping matrix is a null matrix. For this case the approximate solution match closely to the results obtained from the direct finite element method. The dynamic response of the nonlocal system becomes very different from the corresponding local system for higher frequency values and higher values of the nonlocal parameter e_0a. The proposed approximate expression of the transfer function given in Eq. (47) can be used to understand this significant different behaviour for the bending vibration of DWCNT.

6 Conclusions

Nonlocal elasticity is a promising theory for the modelling of nanoscale dynamical systems such as carbon nantotubes. A finite element approach is proposed for dynamic analysis of

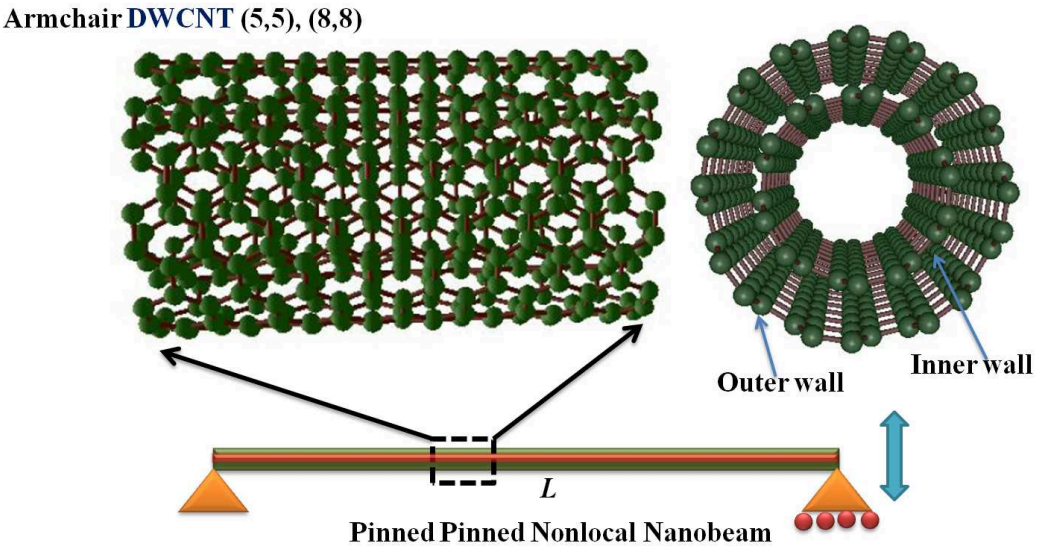


Figure 7: Bending vibration of an armchair (5, 5), (8, 8) double-walled carbon nanotube (DWCNT) with pinned-pinned boundary condition.

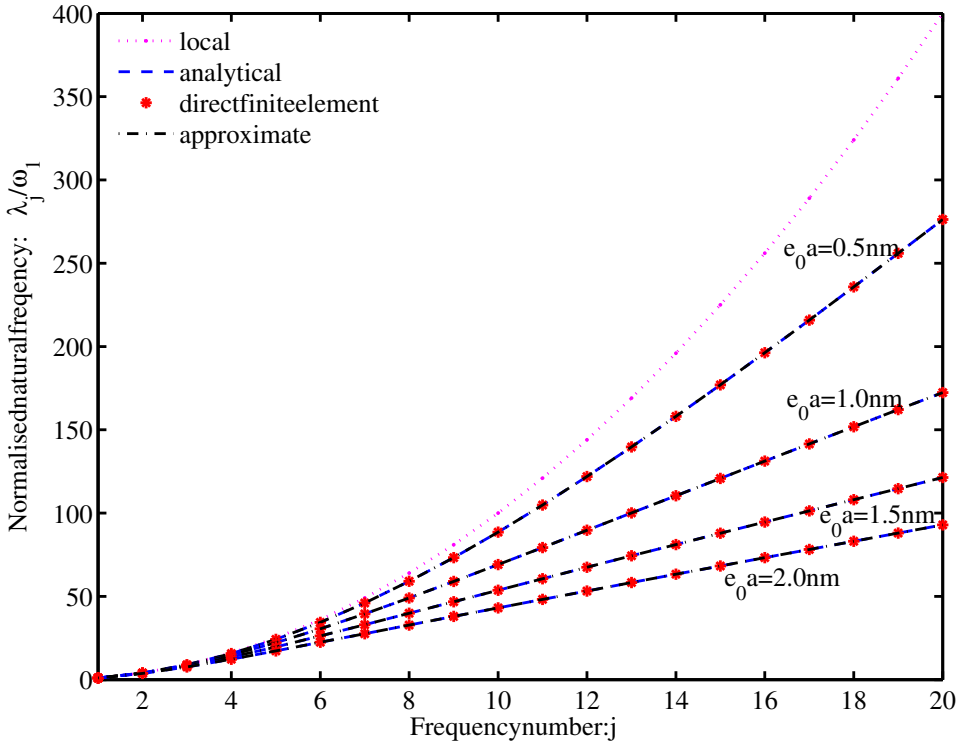
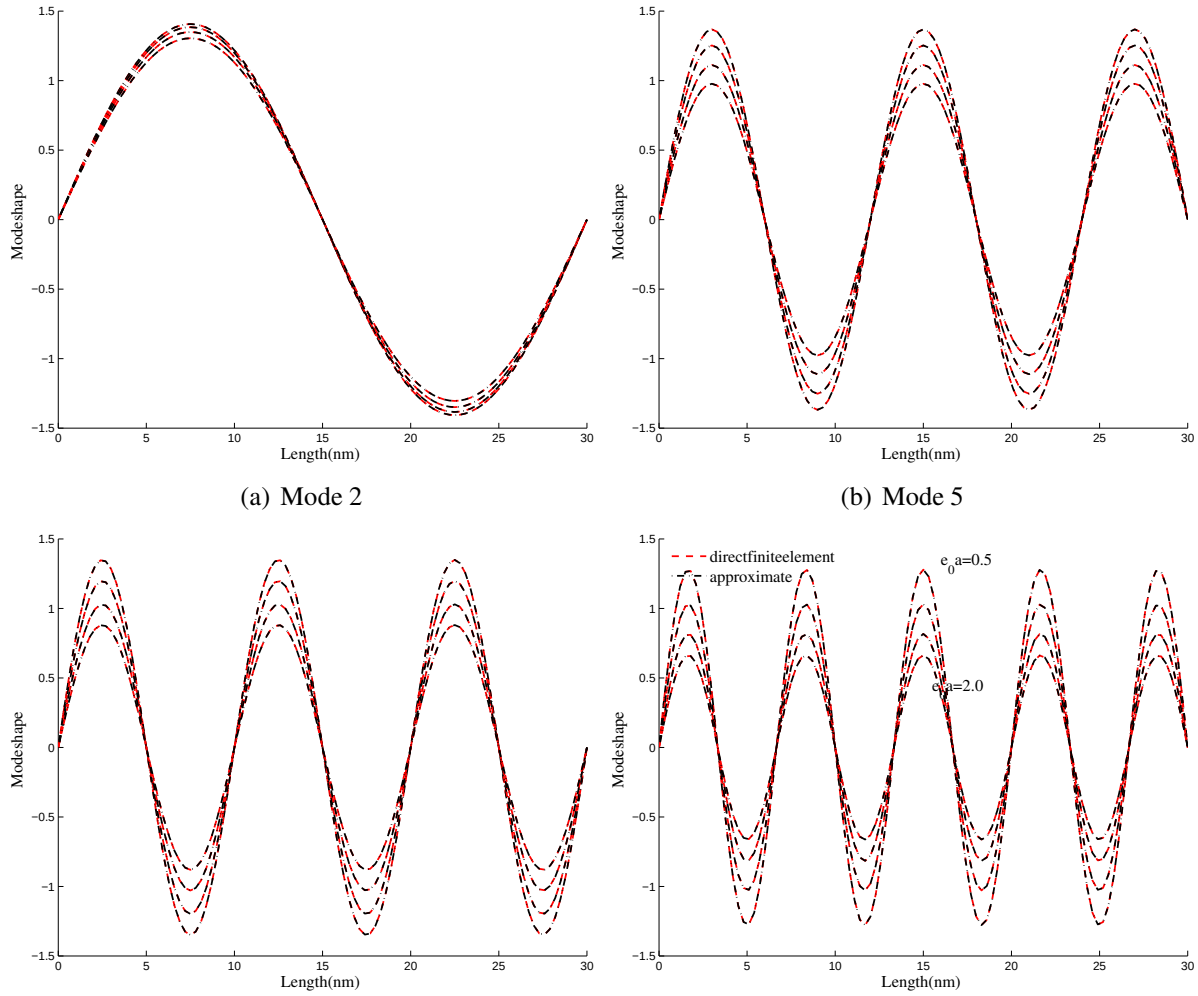


Figure 8: The variation of first 20 undamped natural frequencies for the bending vibration of DWCNT. Four representative values of $e_0 a$ (in nm) are considered.

general nonlocal structures. Explicit closed-form expressions of element mass and stiffness matrices of nanorods and nanobeams have been derived. The mass matrix can be decomposed into two parts, namely the classical local mass matrix $\mathbf{M}_0$ and a nonlocal part denoted by $\mathbf{M}_\mu$. The nonlocal part of the mass matrix is scale-dependent and vanishes for systems with large length-scale. New analytical approaches have been developed to understand the dynamic behaviour of general discrete nonlocal systems. Approximate expressions for nonlocal natural



(a) Mode 2 (b) Mode 5

(c) Mode 6 (d) Mode 9

Figure 9: Four selected mode shapes for the bending vibration of DWCNT. Exact finite element results are compared with the approximate analysis based on local eigensolutions. In each subplot four different values of e_0a, namely 0.5, 1.0, 1.5 and 2.0nm have been used (see subplot d).

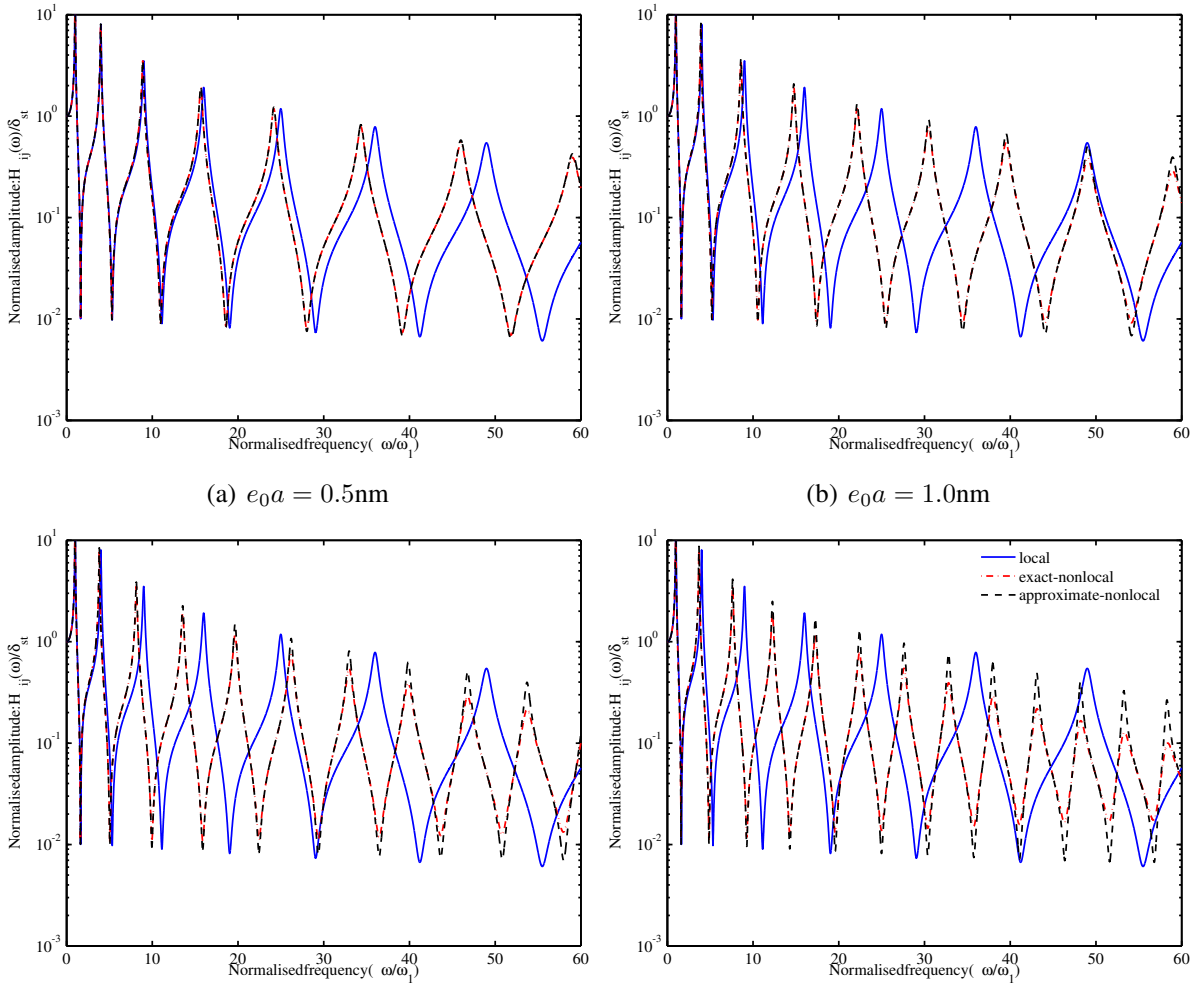
frequencies, mode shapes and frequency response functions have been derived. Major theoretical contributions made in this paper include the following results:

- An undamped nonlocal system will have classical normal modes provided the nonlocal part of the mass matrix satisfy the condition $\mathbf{K}\mathbf{M}_0^{-1}\mathbf{M}_\mu = \mathbf{M}_\mu\mathbf{M}_0^{-1}\mathbf{K}$ where $\mathbf{K}$ is the stiffness matrix.

- A viscously damped nonlocal system with damping matrix $\mathbf{C}$ will have classical normal modes provided $\mathbf{C}\mathbf{M}_0^{-1}\mathbf{K} = \mathbf{K}\mathbf{M}_0^{-1}\mathbf{C}$ and $\mathbf{C}\mathbf{M}_0^{-1}\mathbf{M}_\mu = \mathbf{M}_\mu\mathbf{M}_0^{-1}\mathbf{C}$ in addition to the previous condition.

- Natural frequency of a general nonlocal system can be expressed as $\lambda_j \approx \frac{\omega_j}{\sqrt{1+M'_{\mu_{jj}}}}, \forall j = 1, 2, \cdots$ where ω_j are the corresponding local frequencies and $M'_{\mu_{jj}}$ are the elements of nonlocal part of the mass matrix in the modal coordinate.

- Every nonlocal normal mode can be expressed as a sum of two principal components as



(a) $e_0a = 0.5$nm (b) $e_0a = 1.0$nm

(c) $e_0a = 1.5$nm (d) $e_0a = 2.0$nm

Figure 10: Amplitude of the normalised frequency response of the DWCNT $H_{ij}(\omega)$ for $i = 6, j = 8$ for different values of e_0a. Exact finite element results are compared with the approximate analysis based on local eigensolutions.

$\mathbf{u}_j \approx \mathbf{x}_j + (\sum_{k\neq j}^{n} \frac{\lambda_j^2}{(\lambda_k^2-\lambda_j^2)} \frac{M'_{\mu_{kj}}}{(1+M'_{\mu_{kk}})}\mathbf{x}_k), \forall j = 1, 2, \cdots$. One of them is parallel to the corresponding local mode $\mathbf{x}_j$ and the other is orthogonal to it.

The theoretical results obtained in the paper are applied to two representative problems, namely (a) axial vibration of a single-walled carbon nanotube, and (b) bending vibration of a double-walled carbon nanotube. These two systems are modelled by nonlocal rod, beam and plate respectively. Among these two systems, only the nonlocal rod model satisfy the condition of existence of classical normal modes. For the beam it was observed that the proposed approximate expressions of nonlocal natural frequencies, mode shapes and frequency response functions provide acceptable accuracy. The results obtained in the paper give physical insights into the dynamic behaviour of discrete nonlocal systems which can be understood in the light of well known dynamic behaviour of the underlying local systems.

Acknowledgments

SA acknowledges the support of Royal Society of London through the award of Wolfson Research Merit award. TM acknowledges the support from the Irish Research Council for

Science, Engineering & Technology (IRCSET).

References

[1] E. Wong, P. Sheehan, and C. Lieber, "Nanobeam mechanics: Elasticity, strength, and toughness of nanorods and nanotubes," *Science*, pp. 277–1971, 1997.

[2] S. Iijima and T. Ichihashi, "Single-shell carbon nanotubes of 1-nm diameter," *Nature*, pp. 363–603, 1993.

[3] J. Warner, F. Schaffel, M. Rummeli, and B. Buchner, "Examining the edges of multi-layer graphene sheets," *Chemistry of Materials*, pp. 21–2418, 2009.

[4] D. Pacile, J. Meyer, C. Girit, and A. Zettl, "The two-dimensional phase of boron nitride: Few-atomic-layer sheets and suspended membranes," *Applied Physics Letters*, p. 92, 2008.

[5] A. Brodka, J. Koloczek, and A. Burian, "Application of molecular dynamics simulations for structural studies of carbon nanotubes," *Journal of Nanoscience and Nanotechnology*, pp. 7–1505, 2007.

[6] B. Akgoz and O. Civalek, "Strain gradient elasticity and modified couple stress models for buckling analysis of axially loaded micro-scaled beams," *International Journal of Engineering Science*, vol. 49, no. 11, pp. 1268–1280, 2011.

[7] B. Akgoz and O. Civalek, "Free vibration analysis for single-layered graphene sheets in an elastic matrix via modified couple stress theory," *Materials & Design*, vol. 42, no. 164, 2012.

[8] E. Jomehzadeh, H. Noori, and A. Saidi, "The size-dependent vibration analysis of micro-plates based on a modified couple stress theory," *Physica E-Low-Dimensional Systems & Nanostructures*, vol. 43, no. 877, 2011.

[9] M. H. Kahrobaiyan, M. Asghari, M. Rahaeifard, and M. Ahmadian, "Investigation of the size-dependent dynamic characteristics of atomic force microscope microcantilevers based on the modified couple stress theory," *International Journal of Engineering Science*, vol. 48, no. 12, pp. 1985–1994, 2010.

[10] A. C. Eringen, "On differential-equations of nonlocal elasticity and solutions of screw dislocation and surface waves," *Journal of Applied Physics*, vol. 54, no. 9, pp. 4703–4710, 1983.

[11] J. Peddieson, G. Buchanan, and R. McNitt, "Application of nonlocal continuum models to nanotechnology," *International Journal of Engineering Science*, vol. 41, no. 305, 2003.

[12] M. Aydogdu, "Axial vibration of the nanorods with the nonlocal continuum rod model," *Physica E*, vol. 41, no. 5, pp. 861–864, 2009.

[13] M. Aydogdu, "Axial vibration analysis of nanorods (carbon nanotubes) embedded in an elastic medium using nonlocal elasticity," *Mechanics Research Communications*, vol. 43, no. 34, 2012.

[14] T. Murmu and S. Adhikari, "Nonlocal elasticity based vibration of initially pre-stressed coupled nanobeam systems," *European Journal of Mechanics - A/Solids*, vol. 34, no. 1, pp. 52–62, 2012.

[15] T. Aksencer and M. Aydogdu, "Levy type solution method for vibration and buckling of nanoplates using nonlocal elasticity theory," *Physica E-Low-Dimensional Systems & Nanostructures*, vol. 43, no. 954, 2011.

[16] H. Babaei and A. Shahidi, "Small-scale effects on the buckling of quadrilateral nanoplates based on nonlocal elasticity theory using the galerkin method," *Archive of Applied Mechanics*, vol. 81, no. 1051, 2011.

[17] R. Artan and A. Tepe, "Nonlocal effects in curved single-walled carbon nanotubes," *Mechanics of Advanced Materials and Structures*, vol. 18, no. 347, 2011.

[18] M. Aydogdu and S. Filiz, "Modeling carbon nanotube-based mass sensors using axial vibration and nonlocal elasticity," *Physica E-Low-Dimensional Systems & Nanostructures*, vol. 43, no. 1229, 2011.
[19] C. Kiang, M. Endo, P. Ajayan, G. Dresselhaus, and M. Dresselhaus, "Size effects in carbon nanotubes," *Physical Review Letters*, vol. 81, no. 1869, 1998.
[20] C. Tang, L. Meng, L. Sun, K. Zhang, and J. Zhong, "Molecular dynamics study of ripples in graphene nanoribbons on 6h-sic(0001): Temperature and size effects," *Journal of Applied Physics*, vol. 104, no. 1, 2008.
[21] B. Arash and Q. Wang, "A review on the application of nonlocal elastic models in modeling of carbon nanotubes and graphenes," *Computational Materials Science*, vol. 51, no. 303, 2012.
[22] T. Murmu and S. Adhikari, "Nonlocal vibration of carbon nanotubes with attached buckyballs at tip," *Mechanics Research Communications*, vol. 38, no. 1, pp. 62–67, 2011.
[23] T. Murmu and S. Adhikari, "Nonlocal effects in the longitudinal vibration of double-nanorod systems," *Physica E: Low-dimensional Systems and Nanostructures*, vol. 43, no. 1, pp. 415–422, 2010.
[24] S. Narendar and S. Gopalakrishnan, "Axial wave propagation in coupled nanorod system with nonlocal small scale effects," *Composites Part B-Engineering*, vol. 42, no. 2013, 2011.
[25] A. A. Pisano, A. Sofi, and P. Fuschi, "Nonlocal integral elasticity: 2d finite element based solutions," *International Journal of Solids and Structures*, vol. 46, no. 21, pp. 3836–3849, 2009.
[26] T. Chang, "Finite element analysis on vibration of nanorods with heterogeneous property and non-uniform cross section," *Advanced Science Letters*, vol. 13, no. 360, 2012.
[27] S. Narendar and S. Gopalakrishnan, "Spectral finite element formulation for nanorods via nonlocal continuum mechanics," *Journal of Applied Mechanics-Transactions of the Asme*, vol. 78, 2011.
[28] S. Adhikari, T. Murmu, and M. McCarthy, "Dynamic finite element analysis of axially vibrating nonlocal rods," *Finite Elements in Analysis and Design*, vol. 63, no. 1, pp. 42–50, 2013.
[29] J. K. Phadikar and S. C. Pradhan, "Variational formulation and finite element analysis for nonlocal elastic nanobeams and nanoplates," *Computational Materials Science*, vol. 49, no. 3, pp. 492–499, 2010.
[30] S. Pradhan, "Nonlocal finite element analysis and small scale effects of cnts with timoshenko beam theory," *Finite Elements in Analysis and Design*, vol. 50, no. 8, 2012.
[31] R. Ansari, R. Rajabiehfard, and B. Arash, "Nonlocal finite element model for vibrations of embedded multi-layered graphene sheets," *Computational Materials Science*, vol. 49, no. 831, 2010.
[32] L. Meirovitch, *Principles and Techniques of Vibrations*. New Jersey: Prentice-Hall International, Inc., 1997.
[33] M. Géradin and D. Rixen, *Mechanical Vibrations*. New York, NY: John Wiely & Sons, second ed., 1997. Translation of: Théorie des Vibrations.
[34] M. Petyt, *Introduction to Finite Element Vibration Analysis*. Cambridge, UK: Cambridge University Press, 1998.
[35] D. Dawe, *Matrix and Finite Element Displacement Analysis of Structures*. Oxford, UK: Oxford University Press, 1984.
[36] O. C. Zienkiewicz and R. L. Taylor, *The Finite Element Method*. London: McGraw-Hill, fourth ed., 1991.

[37] L. Rayleigh, *Theory of Sound (two volumes)*. New York: Dover Publications, 1945 reissue, second ed., 1877.

[38] T. K. Caughey and M. E. J. O'Kelly, "Classical normal modes in damped linear dynamic systems," *Transactions of ASME, Journal of Applied Mechanics*, vol. 32, pp. 583–588, September 1965.

[39] S. Adhikari, "Damping modelling using generalized proportional damping," *Journal of Sound and Vibration*, vol. 293, pp. 156–170, May 2006.

[40] R. Chowdhury, S. Adhikari, and F. Scarpa, "Vibrational analysis of zno nanotubes: A molecular mechanics approach," *Applied Physics A*, vol. 102, no. 2, pp. 301–308, 2011.

[41] R. Chowdhury, S. Adhikari, C. Y. Wang, and F. Scarpa, "A molecular mechanics approach for the vibration of single walled carbon nanotubes," *Computational Materials Science*, vol. 48, no. 4, pp. 730–735, 2010.

[42] T. Murmu, S. Adhikari, and M. McCarthy, "Vibration response of double-walled carbon nanotubes subjected to an externally applied longitudinal magnetic field: A nonlocal elasticity approach," *Journal of Sound and Vibration*, vol. 331, no. 23, pp. 5069–5086, 2012.

COMPDYN 2013
4th ECCOMAS Thematic Conference on
Computational Methods in Structural Dynamics and Earthquake Engineering
M. Papadrakakis, N.D.Lagaros, V. Plevris (eds.)
Kos Island, Greece, 12–14 June 2013

STABILITY OF EARTH RETENTION SYSTEM IN DRY COHESIONLESS SOIL UNDER STATIC AND SEISMIC CONDITION

S.S.Chowdhury[1], K. Deb[2], and A.Sengupta[2]
[1]Indian Institute of Technology, Kharagpur
Kharagpur – 721302, India
e-mail: chowdhurysubha@gmail.com
[2] Indian Institute of Technology, Kharagpur
Kharagpur – 721302, India
{K.Deb,A.Sengupta}kousik@civil.iitkgp.ernet.in, sengupta@civil.iitkgp.ernet.in

Keywords: Cohesionless, Earthquake, Shear Modulus, FLAC, Numerical modelling

Abstract. *The objective of this paper is to assess the stability of earth retention systems like supported excavation known as braced excavation (consisting of retaining wall and support members known as struts) under both static and seismic condition. A numerical analysis has been done considering the excavation in dry cohesionless soil with properties such as density, friction angle, dilatancy angle and Poisson's ratio as 2040 kg/m3, 35°, 0° and 0.3 respectively. The shear modulus of the soil depends on the mean effective stress below ground level. The bulk modulus also behaves similarly as shear modulus. The wall and the struts are modeled as beam elements. The soil structure interaction is modeled by introducing interface elements between wall and soil. It is concluded from the present study that there is a substantial increment in the values of maximum strut force, wall moment, wall deflection and the ground surface settlement under seismic condition as compared to static condition.*

1 INTRODUCTION

The construction of underground basement, pipeline network or transport system in congested urban area at a substantial depth below ground level is possible only when the earth can be excavated as a deep vertical cut. This vertical cut is supported on both sides by retaining wall (sheet pile wall or diaphragm wall) and support members (steel struts, wale, concrete slabs). The construction of braced excavation involves different stages such as installation of retaining wall, excavation of soil below strut level, installation of struts at the corresponding level. This sequence of soil excavation and strut installation continues till the final excavation level is reached. Thus, at different stages of the construction of the supported excavation, there will be different values of strut force, wall moment, wall deflection and the ground surface settlement. Out of all these values the maximum value of each of the above design parameters has been compared under both static and seismic conditions.

Numerical methods have been used for analysis of braced excavation under static condition ([1], [2], [3], [4], [5], [6]). The optimum values of the design parameters i.e. wall thickness, embedment depth of the wall, the stiffness of the struts and the depths of the struts below ground level have been obtained under static condition and a design guideline of braced excavation have been proposed under static condition [7]. However, very few studies have been done for analyzing the behavior of such type of excavation under seismic condition. Numerical analysis of embedded cantilever retaining walls in dry coarse-grained soil under seismic condition using Tolmezzo time acceleration history data has been analyzed in FLAC [8]. A number of studies has been done on other types of retaining walls such as gravity, cantilevered, anchored walls or mechanically stabilized earth retaining walls under seismic condition ([9], [10], [11], [12], [13], [14]).

In view of the previous works, an attempt has been made in the present study to assess the behavior of braced excavation under seismic condition. Based on the work [7], the depth of excavation (D_e), depth of embedment of the wall below the final excavation level (D_b), thickness of the wall (t_{wall}) and the stiffness of the struts are taken as 10m, 8m, 0.6m and $5x10^5$kN/m/m, respectively. The width of excavation is taken as 10m. Two levels of struts at 3m and 7m below ground level have been considered in the analysis. The effect of Tolmezzo earthquake which occurred in Italy is considered in the present study. The acceleration time history data has been taken from [8]. This history data is applied at the base of the model. The earthquake may occur at any stage of the braced excavation. So, in order to simúlate this uncertain condition, each stage of the excavation is analyzed under static condition and then under seismic condition.

2 NUMERICAL MODELLING

The numerical modeling, as shown in Figure 1, has been done using two dimensional plane strain finite difference code FLAC (Fast Lagrangian Analysis of Continua) [15]. In the seismic analysis, two diaphragm walls and the distance between the walls are taken as 10m. The horizontal boundary at the bottom of the model is located at a distance of 62m below the toe of the wall. The left and right vertical boundaries are located at 60m from the face of the diaphragm wall. The size of the zones are taken as square with 0.5m dimension. In the numerical model, the behavior of the soil under earthquake condition is described through a hysteretic model which updates the tangent shear modulus at each calculation step. The soil is assumed to behave as a linearly elastic-perfectly plastic material and fails according to Mohr-Coulomb criterion. The free-field conditions are applied along the vertical boundaries so that boundaries absorb outward propagating waves from the structure. Thus the lateral boundaries

of the main grid are connected with the free field grid by viscous dashpots [16]. The bottom boundary is fixed from movement both in the vertical as well as horizontal directions.

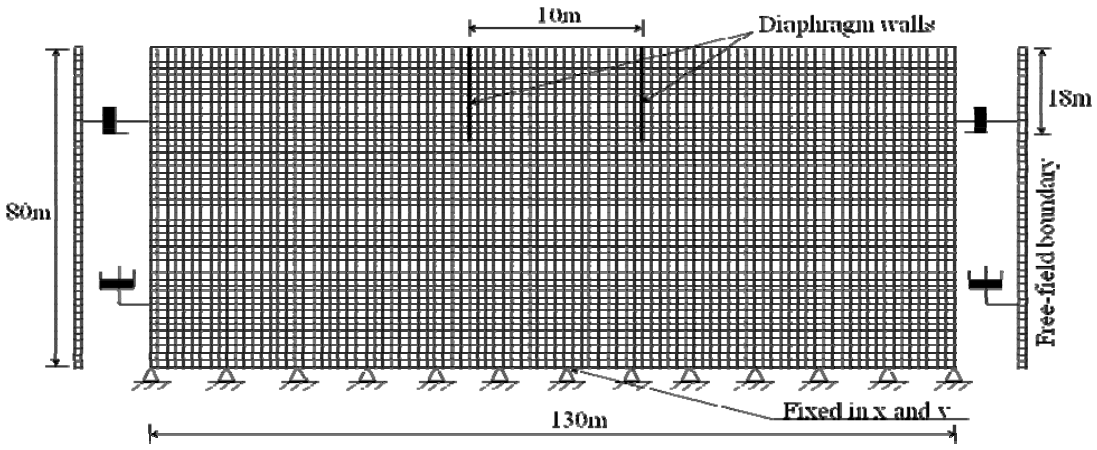


Figure 1: Numerical model in FLAC.

Earthquake may occur at any stage during the construction of braced excavation. Each stage of the excavation is analyzed simultaneously under static and seismic condition upto the final stage of excavation. The acceleration time history of Tolmezzo Earthquake as shown in Figure 3 has been applied at the nodes located along the base of the model.

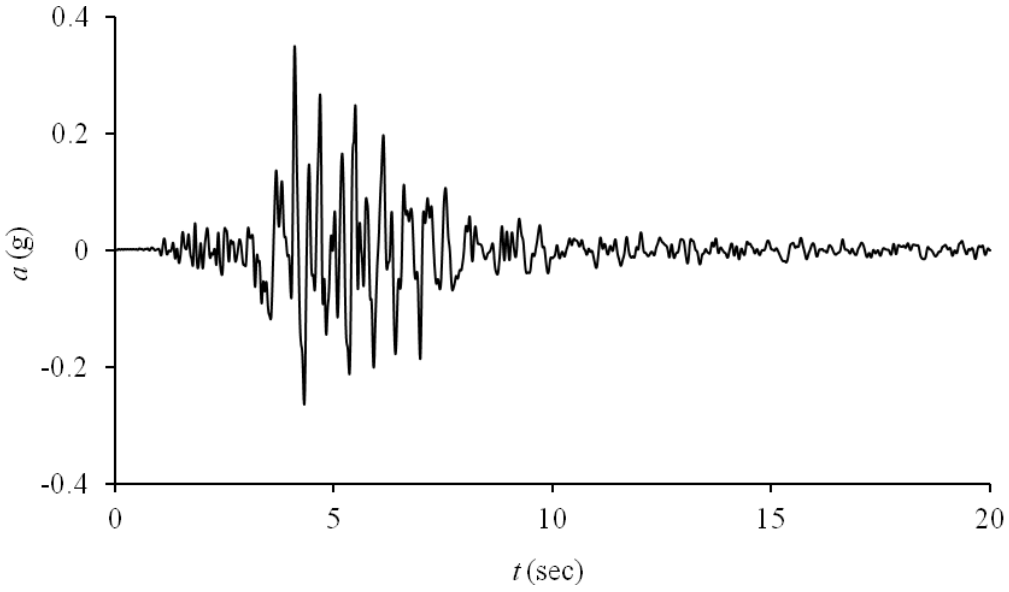


Figure 2: Input acceleration time history for Tolmezzo earthquake

As the dimension perpendicular to the plane of analysis is very large compared to other two dimensions, the problem is analyzed as a two-dimensional plane strain problem. The cross-sectional area (A_{wall}) and moment of inertia (I_{wall}) of the wall are given as input in the program. A typical cross-section of the excavation is shown in Figure 3.

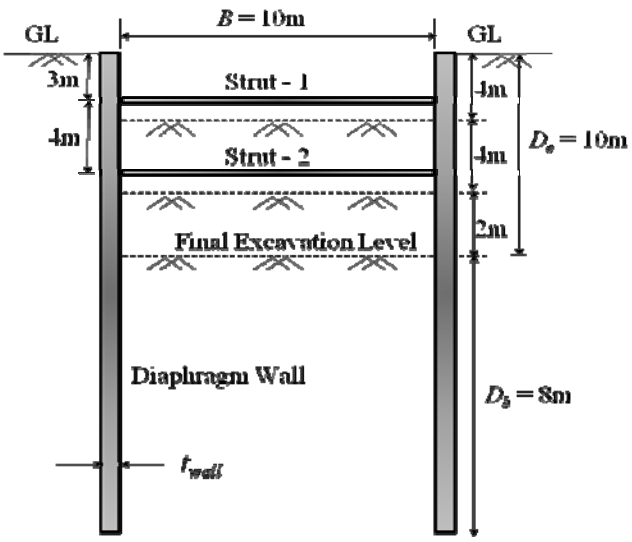


Figure 3: Cross-section of the braced excavation.

The soil properties namely, dry density, friction angle and initial shear modulus are taken from [8]. The coefficient of lateral earth pressure at rest (K_0) is taken as 0.426 (for ϕ equal to 35^o). A rigid rock layer has been considered at the bottom of the model, that is, at 62m below the bottom of the diaphragm walls. The wall friction angle (δ) and the Poisson's ratio (μ) of soil are taken as 20^o and 0.30 respectively. The small strain shear modulus (G_0) and mean effective stress (p') are related as [8]

$$\frac{G_0}{p_{ref}} = K_G \left(\frac{p'}{p_{ref}} \right)^{0.5} \tag{1}$$

where, p_{ref} is the reference pressure which is taken as 100 kPa, p' is the mean effective stress and K_G is the stiffness multiplier which is taken as 1000. The bulk modulus is calculated from shear modulus and Poisson's ratio. In the numerical modeling, the values of the shear modulus and bulk modulus has been given as input. The static analysis has been done considering the value of shear modulus as G_0. In the seismic analysis, the static simulation of each stage has been done with reduced value of small strain shear modulus, i.e. $0.3G_0$, because the model does not consider the reduction of soil stiffness with strain level [17]. The seismic stages are analyzed with shear modulus G_0.

3 RESULTS AND DISCUSSION

The values of the four design factors, i.e. strut force, wall moment, wall deflection and ground surface settlement as obtained from static and seismic are shown in Table 1.

Design factors	Static condition	Seismic condition
1st level Strut force (x10^3 kN/m)	1.2	2.8
2nd level Strut force (x10^3 kN/m)	1.1	3.9
Bending moment (x10^3 kN-m/m)	0.1	0.4
Wall deflection (mm)	3.2	55.2
Ground surface settlement (mm)	1.9	24.6

Table 1: Comparison of results obtained from static and seismic analysis

3.1 Effect on maximum strut force

The results between the maximum strut force obtained under static condition and seismic conditions are compared and shown in Table 1. From the above table, it is found that the maximum strut force at first and second levels under seismic conditions are around 2.3 and 3.5 times than that obtained under static condition.

3.2 Effect on maximum bending moment

The maximum bending moments developed in the wall during the two conditions are compared and it is found from Table 1 that the ratio of seismic moment to static moment comes out to be 4.

3.3 Effect on maximum wall deflection

The maximum deflections of the wall as obtained from static and seismic analysis are shown in Table 1. From the above table, it is found that the maximum wall deflection under seismic condition is 17.3 times than that obtained under static condition.

3.4 Effect on maximum ground surface settlement

The maximum ground surface settlement plays an important role in the stability analysis of the braced excavation and the adjacent structures. From the analysis, it is found that the maximum ground surface settlement during earthquake is 12.9 times the ground surface settlement obtained under static condition. Liquefaction of the soil during seismic event is not considered in the analysis.

4 CONCLUSION

From the present numerical analysis, it can be found that the values of maximum strut force, wall moment, wall deflection and the ground surface settlement are higher in seismic condition than that under static condition. The strut forces and the bending moment as obtained from the seismic analysis are (2 - 4) times higher than that obtained from static analysis. However, the effect of earthquake on the wall deflection and ground surface settlement are much higher and these are around (13 - 20) times than that obtained under static condition. Thus it can be concluded that there is significant influence of earthquake on wall deflection and ground surface settlement as compared to strut force and wall moment for this particular earthquake and the geometry of the problem selected.

5 ACKNOWLEDGEMENT

The financial support received from the Science and Engineering Research Board (SERB) of the Department of Science and Technology, Government of India, New Delhi is hereby gratefully acknowledged.

REFERENCES

[1] R.J. Finno, I.S. Harahap, Finite Element Analysis of HDR-4 excavation. *Journal of Geotechnical Engineering Division*, 117(10), 1590-1609, 1991.

[2] R.J. Finno, I.S. Harahap, P.J.M. Sabatini, Analysis of braced excavations with coupled finite element formulations. *Computers and Geotechnics*, 12(2), 91-114, 1991.

[3] R.A. Day, D.M. Potts, Modeling sheet pile retaining walls. *Computers and Geotechnics*, 15(3), 125-143, 1993.

[4] J.P. His, J.C. Small, Application of a fully coupled method to the analysis of an excavation. *Soils and Foundations*, 33(4), 36-48, 1993.

[5] S.K. Bose, N.N. Som, Parametric study of a braced cut by Finite Element method. *Computers and Geotechnics*, 22(2), 91-107, 1998.

[6] C.W.W. Ng, B. Simpson, M.L. Lings, D.F.T. Nash, Numerical analysis of a multi-propped retaining wall in stiff clay. *Canadian Geotechnical Journal*, 35, 115-130, 1998.

[7] S.S. Chowdhury, K.Deb, A.Sengupta, Estimation of design parameters for braced excavation: A numerical study. *International Journal of Geomechanics*, doi:10.1061/(ASCE)GM.1943-5622.0000207, 2012.

[8] L. Callisto, F.M. Soccodato, Seismic design of flexible cantilever retaining walls. *Journal of Geotechnical and Geoenvironmental Engineering*, 136(2), 344-354, 2010.

[9] S. Caltabiano, E. Cascone, M. Maugeri, Seismic stability of retaining walls with surcharge. *Soil Dynamics and Earthquake Engineering*, 20(8), 469-476, 2000.

[10] G. Gazetas, P.N. Psarropoulos, I. Anastasopoulos, N. Gerolymos, Seismic behavior of flexible retaining systems subjected to short-duration moderately strong excitation. *Soil Dynamics and Earthquake Engineering*, 24(7), 537-550, 2004.

[11] P.N. Psarropoulos, G. Klonaris, G. Gazetas, Seismic earth pressures on rigid and flexible retaining walls. *Soil Dynamics and Earthquake Engineering*, 25(10), 795-809, 2005.

[12] H.I. Ling, D. Leshchinsky, J.P. Wang, Y. Mohri, A. Rosen, Seismic response of geocell retaining walls: Experimental studies. *Journal of Geotechnical and Geoenvironmental Engineering*, 135(4), 515-524, 2009.

[13] J. Wartman, E.A. Rondinel-Oviedo, A. Rodriguez-Marek, Performance and analyses of Mechanically Stabilized earth walls in the Tecoman, Mexico Earthquake. *Journal of Performance of Constructed Facilities*, 20(3), 287-299, 2006.

[14] S.P.G. Madabhushi, X. Zeng, Simulating seismic response of cantilever retaining walls. *Journal of Geotechnical and Geoenvironmental Engineering*, 133(5), 539-549, 2007.

[15] FLAC (2005) User's guide (version 5.0) Itasca.

[16] J. Lysmer, R.L. Kuhlemeyer, Finite dynamic model for infinite media. *Journal of Engineering Mechanics*, 95, EM4, 859 – 877, 1969.

[17] S. Aversa, R.M.S. Maiorano, C. Tamagnini, Influence of damping and soil model on the computed seismic response of flexible retaining structures. *14th European Conference on Soil Mechanics and Geotechnical Engineering*, Madrid, 24 - 27 September, 2007.

8COMPDYN 2013
4th ECCOMAS Thematic Conference on
Computational Methods in Structural Dynamics and Earthquake Engineering
M. Papadrakakis, V. Papadopoulos, V. Plevris (eds.)
Kos Island, Greece, 12–14 June 2013

STABILITY ANALYSIS OF STEEP NAILED SLOPES IN SEISMIC CONDITIONS: NUMERICAL APPROACH

S. Sahoo[1], B. Manna[2], K. G. Sharma[3]

[1]Indian Institute of Technology Delhi
Research Scholar
Department of Civil Engineering
New Delhi - 110016, INDIA
s.sahoo.iitd@gmail.com

[2]Indian Institute of Technology Delhi
Assistant Professor
Department of Civil Engineering
New Delhi - 110016, INDIA
bmanna@civil.iitd.ac.in

[3]Indian Institute of Technology Delhi
Professor
Department of Civil Engineering
New Delhi - 110016, INDIA
kgsharma@civil.iitd.ac.in

Keywords: Steep slopes, soil nails, seismic performance, finite element modeling.

Abstract. *In this paper an attempt has been made to understand the seismic behavior and deformation characteristics of model steep nailed soil slopes by numerical studies. A two-dimensional plane-strain numerical model has been developed to simulate steep nailed slopes by finite element software, MIDAS GTS. The real time-history analyses are carried out to study the seismic response of nailed-soil slopes. The effect of various influencing parameters such as the nail inclinations and the slope angles on the seismic resistance and failure mechanism of the nailed slopes are studied in details. The numerical model developed has been used to examine the shaking table test results of steep nailed slopes [1]. The nailed soil slopes are modeled in FE analysis as per the geometry of shake table testing and the numerical analysis are carried out for different seismic excitations. The numerical results such as maximum lateral displacements at various heights of the facing are compared with the test results for various slopes angles, nail inclinations and peak amplitude of accelerations. The failure pattern of nailed soil slopes for different seismic conditions obtained from the numerical analysis are studied and compared with the experimental failure patterns. A reasonable agreement between the finite element analysis and shaking table test results are obtained.*

1 INTRODUCTION

The use of soil nailing method for the in-situ stabilization of existing slopes and excavations has now covered a wider part of the world. Soil nailing for improving the stability of slopes started in Versailles (France) for the first time in 1972 [2]. The fundamental concept of soil nailing method consists of placing of closely spaced passive inclusions in the ground to restrain the displacements and limit decompression of soils during and after excavation. A factor, which makes soil nailing technique more desirable than the other earth reinforcing techniques when performed on cuttings or excavations, is its easy and flexible top-down construction. Hence the soil-nailing method is a better in-situ reinforcement technique than others. It has also been proved in the literature [1], that the performance of nailed soil slopes is quite excellent than the gravity retaining structures under earthquake conditions. The literature survey on the nailed soil structures reveals that lots of work has been done on the design and construction methodologies, laboratory modeling and numerical modeling of nailed slopes and excavations under static load condition [3, 4, 5, 6, 7, 8, 9, 10]. Hong et al. [1] investigated the performance of nailed soil slopes under dynamic condition in the laboratory. Lou and Ye [11] and Sabahit et al. [12] studied theoretically the performance of such structures under seismic conditions. The failure or distress reported in the literature [13] due to Earthquakes showed how vulnerable these structures are to ground motions. Hence more research is required to properly understand the behavior of nailed soil structures under seismic conditions.

A series of laboratory shaking table tests were conducted on five model nailed soil slopes with various nail and slope arrangements [1]. In this paper, an attempt is made to back-analyze the three models out of the five models [1] for three input peak amplitude of accelerations (g) such as 0.474g, 0.598g and 0.818g which are summarized in table 1. The numerical models using finite element software, MIDAS GTS are developed to examine the effect of nail inclination and the slope angle on the seismic response of steep nailed soil slopes.

2 DETAILS OF THE NUMERICAL MODEL

Two-dimensional plain-strain model slopes with different slope angles and nail inclinations are developed using the same geometry as per the dimensions of the laboratory shaking table test [1]. The nails are modeled as one-dimensional linear elastic structures and the facing plate is modeled as two-dimensional plain-strain elastic structure. The dimensions of PMMA tubes (Nails) and PMMA plate (Facing) used in FE analysis are considered as per the reported literature [1]. The Mohr-Coulomb model is adopted for soil to simulate the elasto-plastic behavior of soil. The water table is assumed to be at great depth. The material parameters of soil, nail and facing plate are also considered same as those adopted for the shake table testing. The schematic diagram of geometry and generated mesh of the model no. 2 is shown in Figure 1.

Model No.	Slope angle (˚)	Nail length (m)	Nail inclination (˚)	Frequency amplification factor	Input peak amplitude of accelerations (g)
1	80	0.4	0	5.0	0.5952
2	80	0.4	30	5.0	0.8281
3	90	0.4	0	5.0	0.4784

Table 1. Summary of numerically developed model slope arrangements

In FE analysis, the meshing has been done using 8-noded quadrilateral elements. Since the meshing type chosen for soil elements and nail elements are quadratic and linear respectively, the connection between these two different type of elements are made by extracting the line (nail) elements and merging their nodes with the surrounding nodes of quadratic (soil) elements after dividing each linear element in to two. The interface elements are created around the nail elements by calculating the normal stiffness modulus, shear stiffness modulus, cohesion, internal friction angle and strength reduction factor from the material properties to provide the interface between soil and nail. Similarly interface elements are also created between the facing plate and the soil. In the FE analysis, the locations where the displacements are measured at various heights of the facing in the test [1] are marked by creating points on the facing as shown in Figure 1. The other two models are also developed similar to this model by adopting the same mesh type as well as same element size.

Then the boundary conditions have been provided. The Bottom soil boundary nodes are considered as fixed against displacement in both horizontal and vertical directions while at the side soil boundary nodes, displacement is restrained in horizontal direction and is allowed in vertical direction.

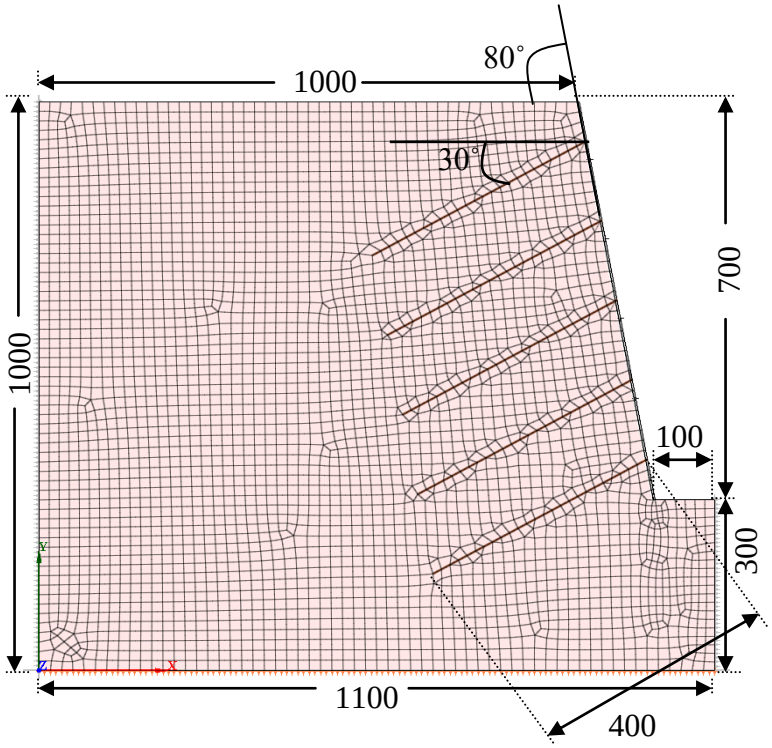


Figure 1. The mesh and boundary conditions used for the FE analysis for model 2. All dimensions are in millimeters.

All the three models developed using the finite element method with different slope and nail arrangements are analyzed with the respective input peak amplitude of accelerations (*g*) as per the shaking table test. The time history analyses are carried out on the developed FE model slopes using the inbuilt earthquake histories in the finite element software, MIDAS GTS. Figure 2 is a plot of the time history of the acceleration for all the three input peak amplitude of accelerations (*g*) with frequency amplification factor = 5.0 which are chosen for the finite element analysis. These data are used in finite element analysis to provide unidirectional (horizontal) seismic excitation which is similar to the laboratory shaking table test.

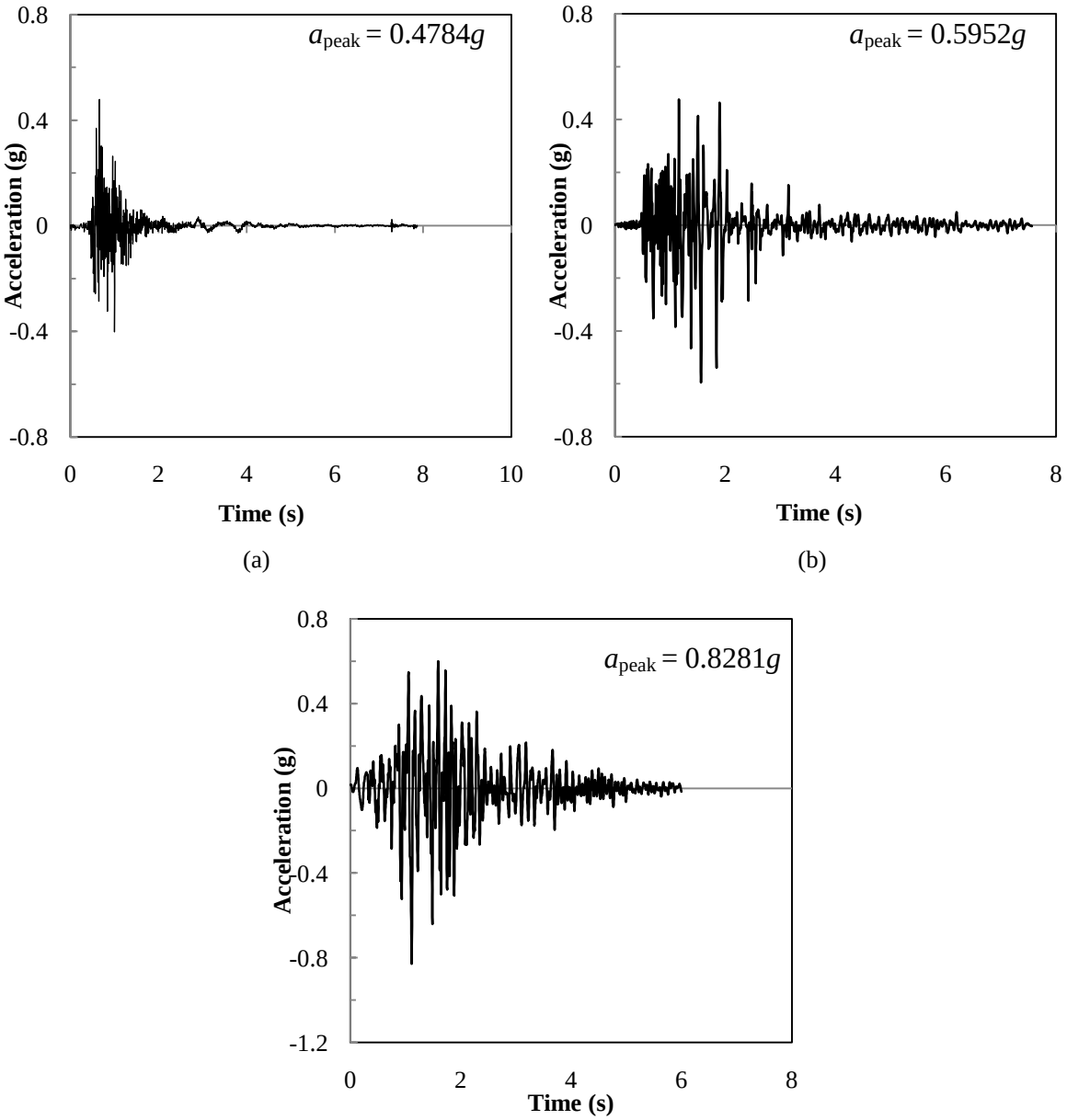


Figure 2. History of acceleration: (a) 1979, James RD. El Centro, Up ; (b) 1979, Bonds Corner El Centro, 310 Deg ; (c) T2-I-1 (1995, HYOUGOKEN South, NS)

In the numerical analysis, the peak amplitude of accelerations (g) are 0.4784g, 0.5952g, 0.8281g in place of 0.474g, 0.598g and 0.818g respectively and these values are adopted as per the available inbuilt earthquake histories. The input peak amplitude of accelerations (g) considered in shaking table test and the numerical analysis are nearly equal for the respective model slopes.

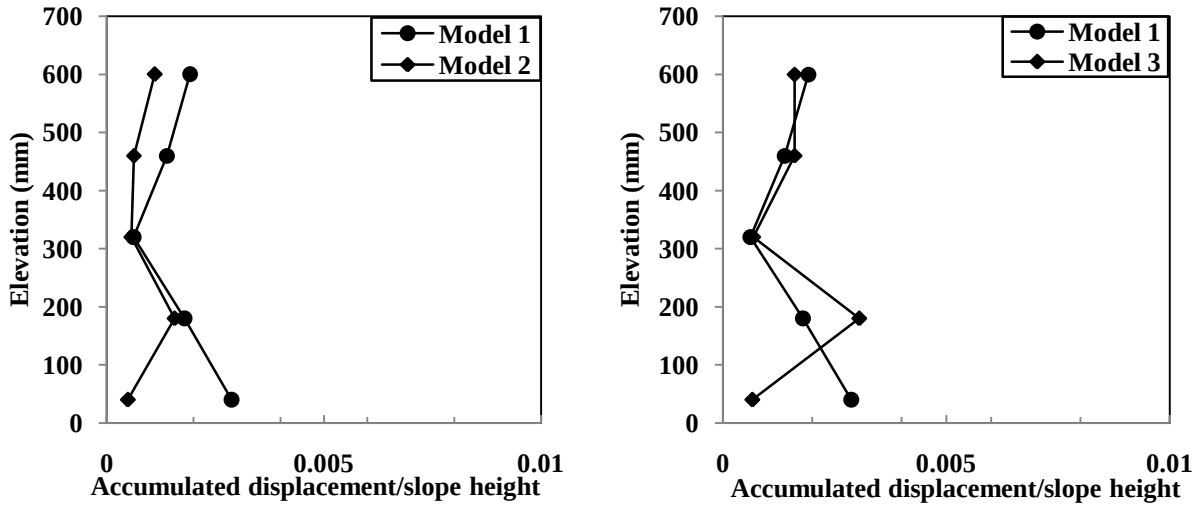
3 RESULTS AND DISCUSSIONS

The normalized accumulated displacements of the facing at the end of the seismic sequence is shown in Figure 3(a, b) for all the models with $a_{peak} = 0.5952g$.

3.1 Effect of nail inclination

The effect of nail inclination on the seismic response of slopes is studied for model 1 and model 2 having two different nail inclinations (0˚ and 30˚) keeping other parameters as constant and the variation of the response for various slope angles is shown in Figure 3. It can be seen from the plot that the outward movement of the toe of model 1 is greater than that of model 2 which shows translation of the entire slope mass in case of the slope with nail inclination of 0˚. The nature of movement of soil for the upper soil mass and the lower soil mass are just reverse of each other for model 1 as well as for model 2. For model 2, the upper soil mass exhibits greater outward movement than the lower soil mass which indicates the rocking of the slope with nail inclination of 30˚.

Hence it can be concluded from this plot that the translational movement is more predominant with a little rocking in case of the slope having nail inclination of 0˚. In case of the slope having nail inclination of 30˚, there is a combination of translational and rocking movement with lesser translational and rocking movement than model 1 (nail inclination of 0˚). The magnitude of facing displacement at all the measured points is also greater in case of horizontally placed nails than that of inclined nails. Therefore the inclined nail for steep slopes is better option than the horizontally placed nails.



(a) (b)

Figure 3. Normalized accumulated displacements of the facing at the end of the seismic sequence ($a_{peak} = 0.5952g$): (a) model 1 and model 2; (b) model 1 and model 3.

3.2 Effect of slope angle

The effect of slope angle on the seismic response of two model slopes such as model 1 and model 3 having slope angle of 80˚ and 90˚ respectively keeping other parameters same is shown in Figure 3(b). Though the upper part of the soil mass in both the cases follows the same pattern of movement, the translational movement is more predominant for model 1 than model 3. However, there is a combination of translation and rocking for model 3.

3.3 FE Analysis Vs Shake table test

The comparison of test results with the FEM results from the plot between the normalized accumulated displacements of the facing with the slope height at every measured location for all the three models is shown in Figure 4.

In the plot of Figure 4(a) for model 1, the pattern of facing movement at all the measured points except at the toe of the slope are similar in both the cases i.e., FE analysis and the shaking table test. The combination of translation and rocking movement are found in both the cases. The magnitude of facing displacement at all the measured points is found greater in case of shaking table test than the FE analysis.

It can be seen from Figure 4(b) for model 2, the pattern of facing movement at all the measured points are similar for both the test and analysis. The combination of translation and rocking movement are found in both the cases. The magnitude of facing displacement at all the measured points is found greater in case of shaking table test than the FE analysis for this model. The model also exhibits a greater horizontal displacement in the middle part of the facing than in other parts for both the cases and hence proved to have a significant tendency of outward convex displacement.

In the plot of Figure 4(c) for model 3, the movement pattern at the middle part of the facing is similar in case of shaking table test and numerical analysis. Similar to other models, the combination of translation and rocking movement are found. The magnitude of facing displacement at all the measured points except at the toe and crest points are greater in case of shaking table test than the FE analysis. This model exhibits a significant tendency of outward convex displacement for both the cases.

It has been shown in the results of finite element modeling [14, 15] that the seismic response of reinforced soil walls is a function of peak ground acceleration, peak velocity, duration of the ground motion, frequency content, distance from the source, and other factors. For the current numerical analysis, only one site characteristic (i.e., peak horizontal ground acceleration) has been considered. Hence the variation in the results of shake table test and the FE analysis may be due to the variation of acceleration history, earthquake duration and frequency of excitation considered in FE analysis and shake table testing.

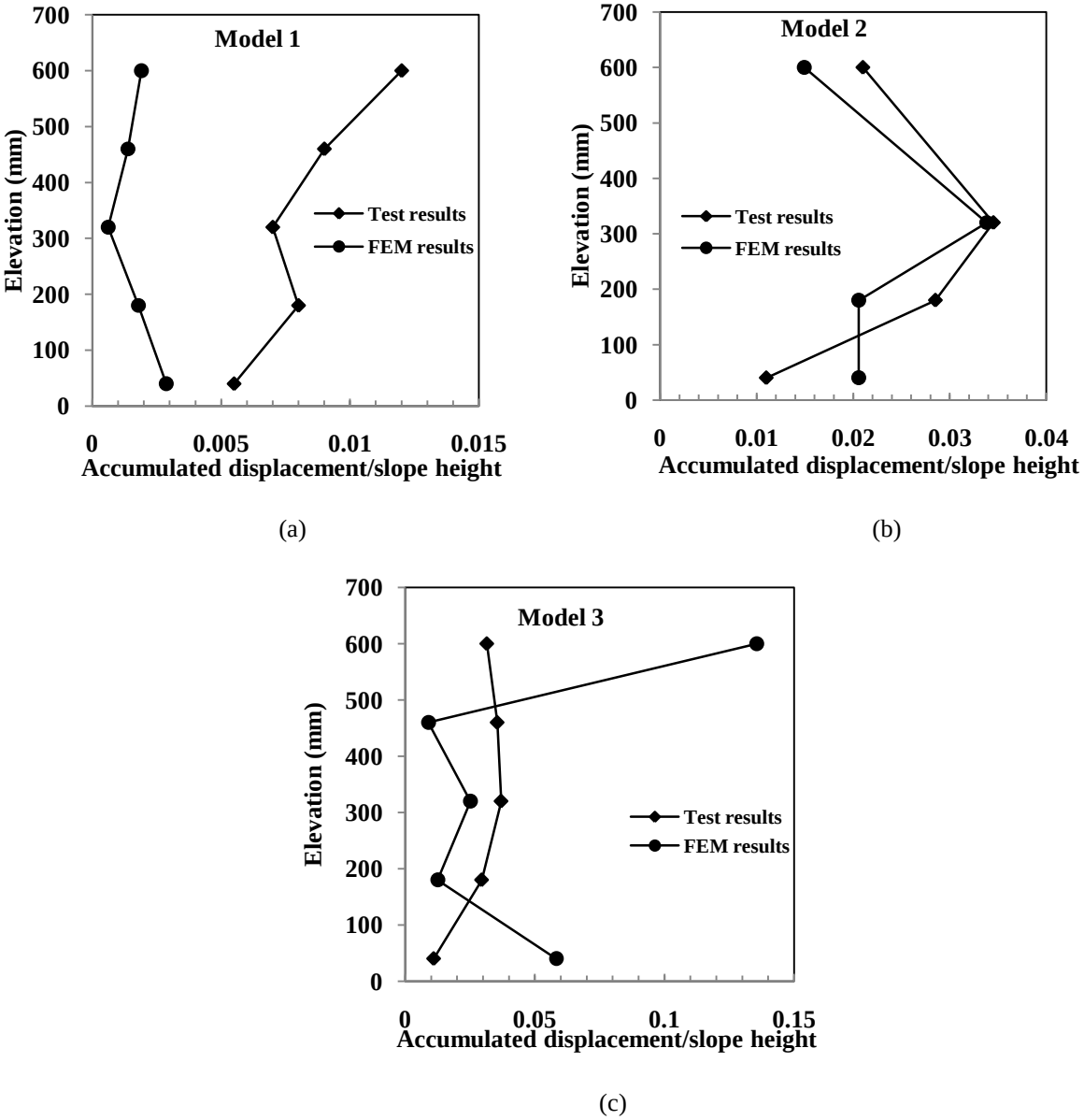
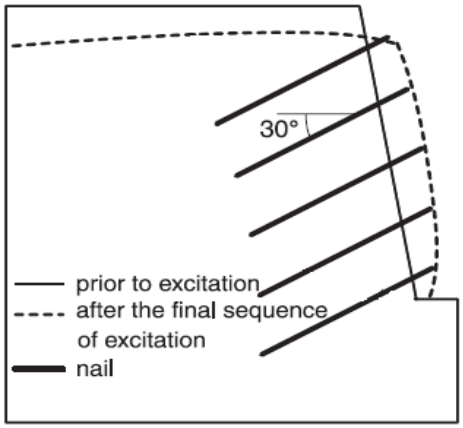
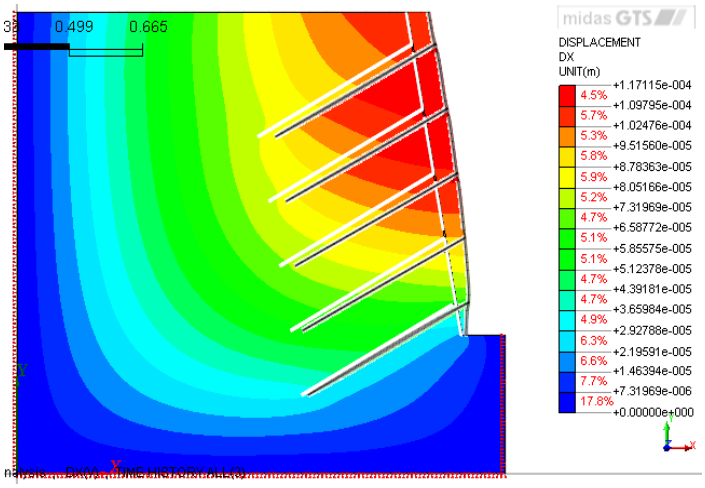


Figure 4. Normalized accumulated displacements of the facing at the end of each seismic sequence: (a) model 1; (b) model 2; (c) model 3.

The initial and final displacement diagram of model 2 at the end of the seismic sequence having $a_{peak} = 0.8281g$ has been depicted schematically in Figures 5(a) and (b) for shake table test and FE analysis respectively. The critical amplitude of acceleration for the model 2 at the end of a range of seismic sequences has already been found as $0.805g$ from the shaking table test. In the FE analysis, the peak amplitude of acceleration is considered as $a_{peak} = 0.8281g$ which is greater than the critical amplitude of acceleration ($0.805g$) obtained from the test. This may be the reason for higher deformation of the slope obtained in FE analysis.



(a)



(b)

Figure 5. Initial and final displacement diagram of model 2 at the end of the seismic sequence having a_{peak} = 0.8281g (a) Shake table test; (b) FE analysis.

4 CONCLUSIONS

The FE analysis has been conducted on the nailed soil slope models as per the geometry as well as the material parameters adopted in shaking table test [1]. The effect of angle of nails and the angle of slopes on the seismic resistance and failure mechanism of nailed soil slopes are analyzed by FE analysis corresponding to the three model slopes of the shaking table test. Some of the important conclusions drawn on the basis of the results obtained from the FE analysis and comparison with the shaking table test results are as follows:

- The effect of nail inclination on the seismic resistance of nailed soil slopes is very little though there is a substantial variation in the nature and magnitude of facing movement due to any particular earthquake loading. The magnitude of facing displacement is greater in case of horizontally placed nails than that of inclined nails. The translational movement is found more predominant in case of horizontally placed nails. The inclined nails exhibit a combination of translation and rocking and hence the inclined nails are better than the horizontally placed nails.

- The effect of slope angle on the seismic resistance of nailed soil slopes is quite significant as the magnitude of facing displacement is found high due under earthquake loading. The magnitude of facing displacement is greater in case of a slope having slope angle of 90˚ than the slope angle of 80˚. The translational movement is found more predominant in case of the 80˚ slope. A combination of translation and rocking is found for slope angle of 90˚.
- The deformation patterns in both the cases i.e., FE analysis and the shaking table test are found similar. The variation in magnitude of facing displacement at all the measured points as well as the movement pattern may be due to the chosen earthquake histories and their variation from the respective model tests.

REFERENCES

[1] Hong, Y.S., Chen, R.H., Wu, C. S., and Chen, J. R. (2005). "Shaking Table test and Stability Analysis of Steep Nailed Slopes." Can. Geotech. J., 42, 1264-1279.

[2] Dereck. Cornforth (2005). " Landslides in practice: investigation, analysis, remedial and preventive options in soils."

[3] Fan, C. C. and Jiun, H. L. (2008). "Numerical Study on the Optimum Layout of Soil–Nailed Slopes." Computers and Geotechnics, 35(4), 585-599.

[4] Chu, L. M. and Yin, J. H. (2005). "Comparison of Interface Shear Strength of Soil Nails Measured by both Direct Shear box and Pullout tests." J. Geotech. Geoenviron. Eng., 131(9), 1097-1107.

[5] Sheahan, T C. and Carlton, L. H. (2003). "Simplified Trial Wedge Method for Soil Nailed Wall Analysis." J. Geotech. Geoenviron. Eng., 129(2), 117-124.

[6] Li, J., Tham, L.G., Junaideen, S. M., Yue, Z. Q., and Lee, C. F. (2008). "Loose Fill Slope Stabilization with Soil Nails: Full-Scale Test." J. Geotech. Geoenviron. Eng., 134(3), 277-288.

[7] Yin, J. H. and Lok-Man, C. (2006). "A Laboratory Device to Test the Pull-Out Behavior of Soil Nails." Geotechnical Testing Journal, 28(5), 1-15.

[8] Plumelle, C., Schlosser, F., Delage, P., and Knochenmu, G. (1990). "French National Project on Soil Nailing : Clouterre." Design and Performance of Earth Retaining Structures, ASCE, Geotechnical Special Publication, 25, 660-675.

[9] Patra, C. R. and Basudhar, P. K. (2005). "Optimum design of Nailed Soil Slopes." Geotechnical and Geological Engineering, 23(3), 273-296.

[10] Yuan, J. X., Yang, Y., Tham, L. G., Kwong, P. K., and Tsui, T. (2003). "New Approach to Limit Equilibrium and Reliability Analysis of Soil Nailed Walls." Int. J. Geomechanics, 3(2), 145-151.

[11] Lou, G.C. and Ye, Z. L. (2008). "Risk Analysis of Soil-Nail Supporting Slope under the Earthquake Effect." Geotechnical Engineering for Disaster Mitigation and Rehabilitation, Proc. 2nd Int. Conf. GEDMAR08, Nanjing, China, pp. 887-891.

[12] Sabahit, N., Basudhar, P. K, .and Madhav, M. R. (1996). "Seismic Analysis of Nailed Soil Slopes." Proc. IS Kyushu Int. Symp. on Earth Reinforcement, Fukuoka.

[13] Bathurst, R.J. & Alfaro, M.C. 1996. Review of Seismic Design, Analysis, and Performance of Geosynthetic Reinforced Walls, Slopes, and Embankments. *Keynote Paper, IS-Kyushu '96.* 32 pp. Fukuoka, Japan.

[14] Cai, Z., and Bathurst, R.J. 1995. Seismic response analysis of geosynthetic reinforced soil segmental retaining walls by finite element method. Computers and Geotechnics, 17(4): 523–546.

[15] Segrestin, P., and Bastick, M.J. 1988. Seismic design of reinforced earth retaining walls - the contribution of finite element analysis. *In* Proceedings of the International Geotechnical Symposium on Theory and Practice of Earth Reinforcement, Fukuoka, Kyushu, Japan, October 1988. *Edited by* N. Miura, H. Ochiai, and T. Yamanouchi. A.A. Balkema, Rotterdam, the Netherlands. pp. 577–582.

COMPDYN 2013
4th ECCOMAS Thematic Conference on
Computational Methods in Structural Dynamics and Earthquake Engineering
M. Papadrakakis, V. Papadopoulos, V. Plevris (eds.)
Kos Island, Greece, 12–14 June 2013

STABILITY ANALYSIS OF A ROCK MASS IN SEISMIC CONDITIONS: CASE STUDY IN LEBANON

Mirvat A.Abdallah[1], Isam .Shahrour[2], and Fadi .Hage Chehade[3]

[1] Polytech'Lille University, Laboratory of Civil Engineering and geo-Environmental LGCgE, Lille, France
Lebanese University, Numerical center, PRASE, Doctoral School of Science and Technology, Beirut, Lebanon
mirvat.abdallah@hotmail.com

[2] Polytech'Lille University, Laboratory of Civil Engineering and geo-Environmental LGCgE, Lille, France
isam.shahrour@univ-lille1.fr

[3] Lebanese University, University Institute of Technology (Saida) & Modeling Center, Doctoral School of Science and Technology, Beirut, Lebanon
fchehade@ul.edu.lb

Keywords: Slope Stability, Rock mass, seismic loading, joints, Numerical modeling.

Abstract. *The objective of this work is to analyze the rock slopes stability under seismic conditions with a real Lebanese case study. High and steep slopes characterize the topography of Lebanon. Moreover, this country could be subjected to serious earthquakes because it contains one major fault and few secondary faults where some ones have been discovered recently. In Lebanon, slope areas become overcrowded because of the high population growth and migration of the population from urban zones. In this paper, we perform a numerical analysis using the UDEC code of the seismic response of fractured rock mass slope representing a real case in Lebanon. We use the seismic loading recorded during the Kocaeli earthquake (Turkey, 1999). The effect of different configurations of fracture networks is highlighted. In the absence of discontinuities, the rock mass is stable without the registration of permanent displacement in the upper part and it behaves as in the case of the rigid block. The presence of horizontal discontinuities leads to a permanent shift in the upper part of the rock, this shift tends to increase going towards the inside of the model; A small rocking motion induced in the solid by the seismic loading and could be neglected.*

1 INTRODUCTION

Lebanon is characterized by its high urbanized mountains and steep slopes. The major structures are Mount Lebanon and the Anti-Lebanon. In general, Lebanese mountains are formed by old rocks formations varying from sedimentary rocks to limestone, dolomite and volcanic ashes. Unfortunately, due to huge demographic expansion and land development even major steep slopes were populated. The absence of a public policy of controlled urbanization, new construction settles in precarious sites, often vulnerable to natural disasters especially in active seismic zone and in poor regions.

From geological point of view, Lebanon contains one major fault and few secondary faults where some ones have been discovered recently. Severe earthquakes could then lead to great human and material losses. In the past, several destructive earthquakes have been occurred in Lebanon for example in years 551, 1202, 1759, 1837 and 1956. Recently, many earthquakes, of low magnitudes between three and five, have been registered in Lebanon during 2008. These events have increased the anxiety of Lebanese people because of the poor quality of the constructions and their behavior under moderate or severe earthquake events. The efficient way to minimize seismic effects, material and human losses, still the prevention that could be deduced from a better comprehension of the behavior of slopes during and immediately after the seismic events. Given the high seismic risk, it seems necessary to conduct stability analysis of rock masses encountered in the Lebanese mountains.

Generally a discontinuous rock mass deforms preferentially by slipping on preexisting fractures. This movement may be accompanied by an extension of existing fractures and the creation of new fractures. Tracking and morphology of a fracture after brittle deformation are strongly influenced by the texture of the material, the nature of minerals and orientation of microscopic discontinuities with respect to the direction propagation of the fracture. The observation of a natural fracture in a granite sample showed that biotite, regardless of size, is systematically fractured and fracturing borrows their differences [3].

The effect of a filler material on the shear depends on the nature of the material, its thickness and the height of the asperities ([2], [5], [6] and [8]). In general, the shear strength of a joint decreases the thickness of the filler increases.

The seismic loading propagates in the ground by different types of waves. It induces deformations and stresses in the soil. In the presence of water, it may induce a variation of pore pressure, which leads to a variation of the effective stresses of contact and in some cases a reduction of the resistance of geo-materials. Crossing of fractured rock masses, seismic waves generally induce shear stresses at the discontinuity lines, which can cause slippage between the blocs and eventually instability of the rock mass. The vulnerability of a rock to seismic loading depends on many factors, including the magnitude of the seismic acceleration, the duration of the earthquake, the strength characteristics of the mass and dimensions [1].

The objectives of this work is to analyze the seismic response of fractured rock mass slope corresponding to a real case in Lebanon. We perform a numerical modeling by using the UDEC code. will be performed using the UDEC code. We present successively the numerical approach adopted in the UDEC, the case study (geometry, properties, loading ...) and the obtained results by taking different networks of fractures.

2 PRESENTATION OF NUMERICAL MODEL

The numerical method falls within the general classification of discontinuum analysis techniques. This approach can represent the geometry of joints and their behavior and to represent the large displacements as well as large deformations.

In this work, we utilized the software UDEC (Universal Distinct Element Code) developed by «ITASCA Consulting Group». The domain is represented by an assemblage of discrete blocks. The discontinuities are treated as boundary conditions between blocks; large displacements along discontinuities and rotations of blocks are allowed.

Blocks in UDEC can be either rigid or deformable. Deformable blocks are subdivided into a mesh of finite-difference elements, and each element responds according to a prescribed linear or nonlinear stress-strain law. The relative motion of blocs is governed by nonlinear force-displacement. UDEC is based on a "Lagrangian" calculation scheme that is well-suited to model the large transformations.

The dynamic analysis is represented numerically by a time-stepping algorithm in which the size of the time-step is limited by the assumption that velocities and accelerations are constant within the time-step. The time-step restriction applies to both contacts and blocks.

The calculations performed alternate between applications of a « force-displacement » law at all contacts and Newton's second law at all blocks. The « force-displacement » law is used to find contact forces from calculated displacements. Newton's second law gives the motion of blocks. Then, the application of the block material constitutive relations gives stresses within the elements and equivalent forces at nodes.

The mesh imposes a finite extension of the field. It is necessary to reduce reflections «artificial» of energy to the boundary of the model. A first solution is to remove significantly the limits of the model from the area of interest. This solution leads to make meshes large sizes, which results in a considerable increase in computation time and memory storage required for results. UDEC offers another alternative by applying, at the lateral boundaries, absorbing boundary conditions of type "Quiet Boundaries" or "Free-Field" (Itasca, 2000) [4]. Conditions such as "Quiet Boundaries" simulate free-field motion that would occur in a semi-infinite solid.

3 DESCRIPTION OF THE CASE STUDY

3-1 Site Description

The rock covered in this paper is located in Jezzine and which lies 40 km south of Beirut. Surrounded by mountain, pine forests, and at an average altitude of 950 m, this site is the main resort in southern Lebanon.

There is a lack of data about this site. They were collected from different sources, including field visits, consultation of Google Earth, an analysis of the geological map from CNRS-Lebanon (National Council for Scientific Research) and discussions with professionals who have worked on the site or on adjacent sites.

The site and the rock mass are shown in Figures 1-a and 1-b. The rock mass consists in a 16m high cliff. The fractures are visible on the mountains; especially we can observe the horizontal discontinuities.



Figure 1-a: Site of Jezzine in South Lebanon- view of the cliff



Figure 1-b: Site of Jezzine in South Lebanon- Surface view

3-2 Mechanical properties

The rock mass is formed of sandstone. The morphology of the slope has been strongly affected by erosion processes that have produced cavities and voids of a various sizes. The combined effects of this erosion, the washing out of sand and silt, and the presence of discontinuities leads to rock toppling and rock falls.

The mechanical properties of the rock were determined from the data available in the literature and discussions with professionals and researchers in Lebanon. This step was the main difficulty of this work because it has only few data. These parameters give an indication of the stability of the domain. A parametric study is carried out in order to investigate the effect of key parameters on stability.

The characteristics of the rock mass are summarized in Table 1: we have a soft rock with a Young's modulus of 6 GPa and a Poisson's ratio of 0.25.

Parameters		Sandstone
Deformation Modulus	E (GPa)	6
Unit weight	γ (KN/m^3)	24.7
Poisson's ratio	Γ	0.25

Table 1: Mechanical characteristics of the rock mass (Sandstone).

The mechanical parameters of discontinuities are summarized in Table 2. The normal stiffness is taken equal to the modulus of deformation of the rock. The tangential modulus is equal to half the normal module. The values attributed to the cohesion and of the friction angle are influenced by the filling and cementing of the joints. The tensile strength is neglected.

Parameters		
Normal Stiffness	Kn(MPa/m)	$6x10^3$
Shear Stiffness	Ks(MPa/m)	$3x10^3$
Cohesion	c (MPa)	0.02
Friction Angle	ϕ (°)	28
Tensile Strength	σ_t (MPa)	0

Table 2: Mechanical parameters of horizontal discontinuities.

Mechanical damping is used in the distinct element. The approach is conceptually similar to dynamic relaxation, proposed by Otter et al. [7]. The equations of motion are damped to reach a force equilibrium state as quickly as possible under the applied initial and boundary conditions. Damping is velocity-proportional (i.e., the magnitude of the damping force is proportional to the velocity of the blocks).

3-3 Seismic loading

Due to lacking of seismic records in the site, we have adopted for the seismic loading the data related to the Kocaeli earthquake occurred August 17, 1999 in Turkey. Figures 2-a and 2-b respectively give the variation of the horizontal component of the velocity and its spectrum. We note that the duration of the earthquake is about 30 s with a maximum speed of about 40 cm/s (reached after 5 seconds). The velocity spectrum shows that the loading frequency is mainly concentrated between 0 and 2Hz with a major peak at 0.9 Hz. The effect of the vertical component is neglected.

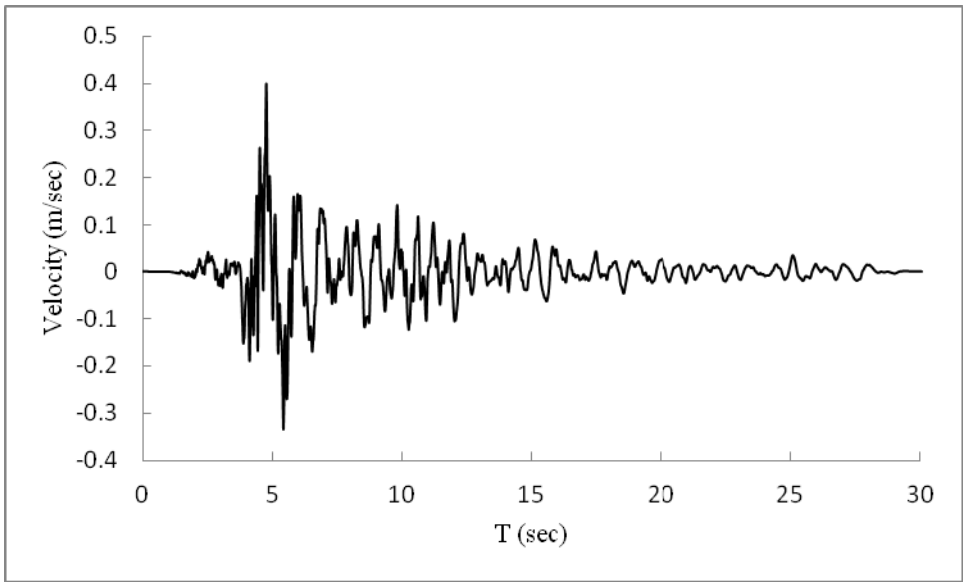


Figure 2-a: Horizontal component of seismic action (Kocaeli – 1999)

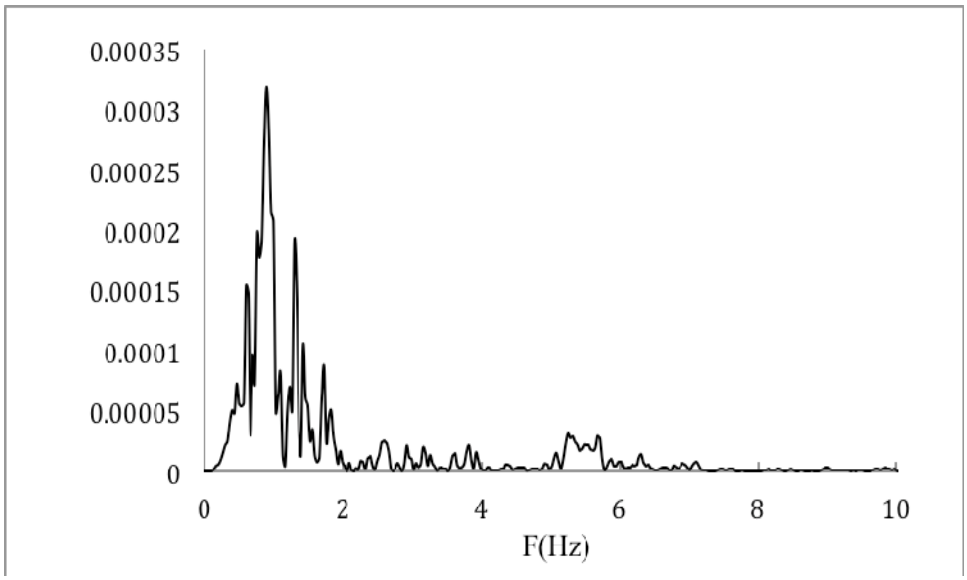


Figure 2-b: Power Spectrum of the horizontal components of the seismic action (Kocaeli-1999)

4 ANALYSIS OF THE SEISMIC BEHAVIOR OF THE ROCK MASS (WITHOUT DISCONTINUITIES)

In this section, we present an analysis of the seismic behavior of the rock mass without discontinuities. This step allows us to define the reference case used later for comparisons.

Figure 3 shows the area considered in the modeling with the horizontal discontinuities. Strong cohesion has been attributed to these discontinuities conditions to ensure perfect contact between the blocks. This figure also defines the position of the points (A, B, C, D, E and F) that will serve as reference points in our interpretation of the seismic response of the massif.

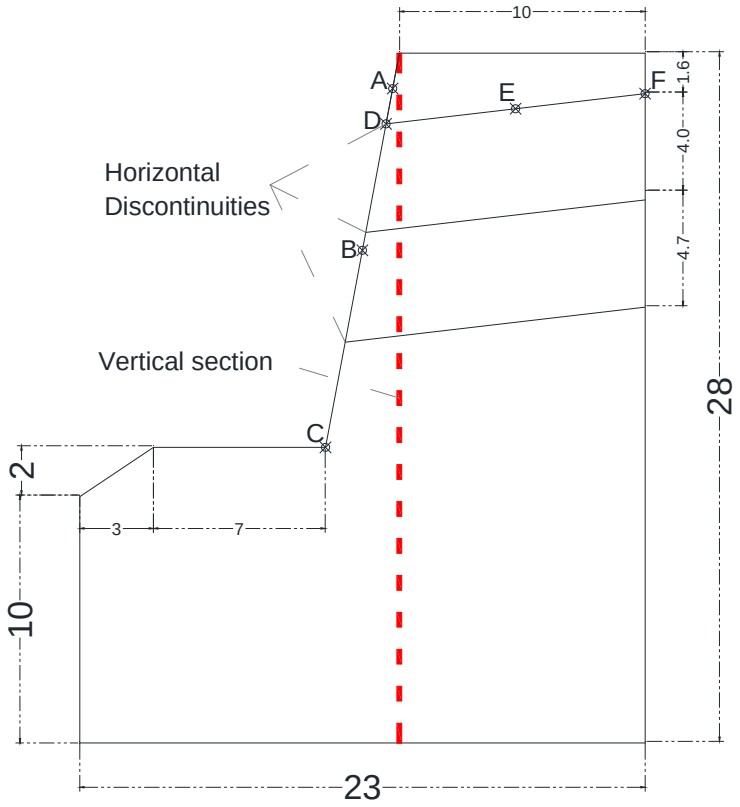


Figure 3: Domain considered in the modeling of the rock mass in jezzine

4-1 Initial state - static calculation

In a first step, a static calculation was performed to determine the initial constraints due to the weight of the mass. Figure 4 shows the displacements obtained. We note that these movements are directed downwards (settlement) resulting from the application of its own weight. These displacements are small (less than 1.5 mm), which indicates a good stability of the rock mass under its own weight.

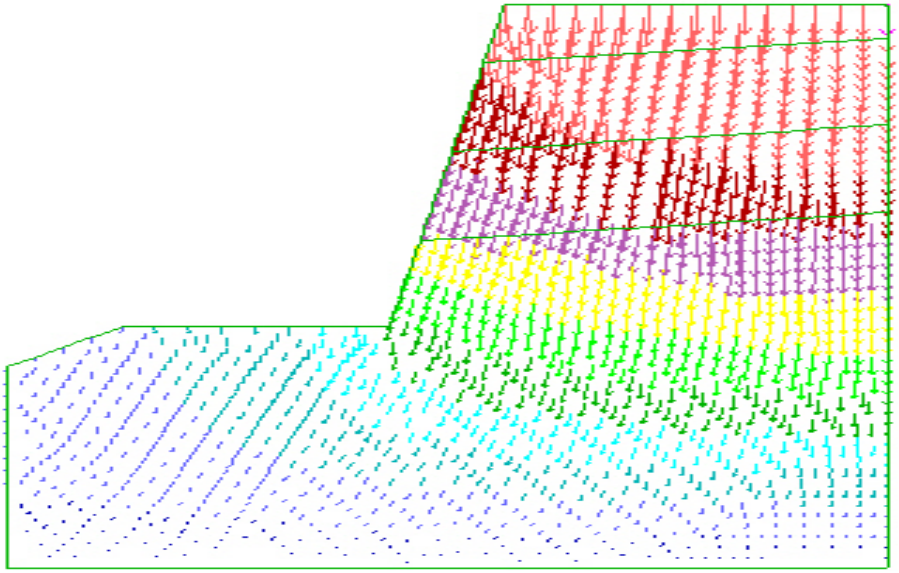


Figure 4: Initial displacement of the rock mass (due to own weight only)

4-2 Seismic Analysis

The calculation was carried out by applying the data of the Kocaeli earthquake (Figure 2-a) at the base of the rock. Boundary conditions of type "quiet boundary" imposed on the lateral boundaries of the domain.

Figure 5 shows the horizontal displacements at points A, B and C induced by seismic loading. We note that these movements have the same shape as the imposed loading (Figure 2-a). A maximum displacement of about 6 cm occurs when the seismic loading reaches its peak (at time t = 5 s). We note the following attenuation of lateral displacement to cancel at the end of seismic loading. We can conclude that there is no permanent displacement at the end of loading.

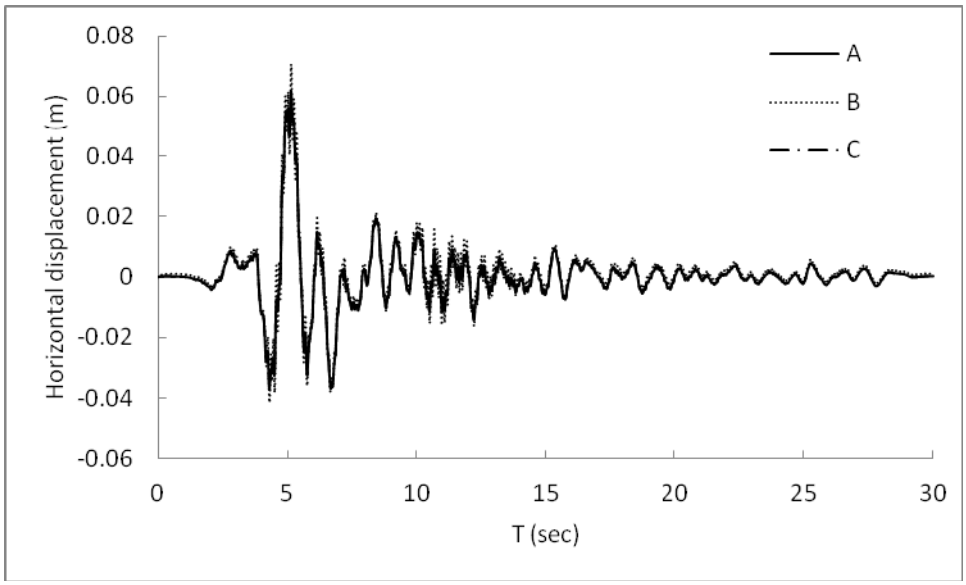


Figure 5: Horizontal displacement induced by seismic loading at three points of the rock mass (Rock mass without discontinuities)

Figure 6 shows the profile of the lateral displacement along a vertical section. There is a movement almost constant with depth, indicating that at the beginning of the loading mass undergoes a motion block with a lateral translation. A slight deformation appears at t = 5 s (peak load speed). Note the almost cancellation of lateral displacement at the end of loading (t = 25 s). In the absence of discontinuities, the rock behaves as in the case of a rigid block.

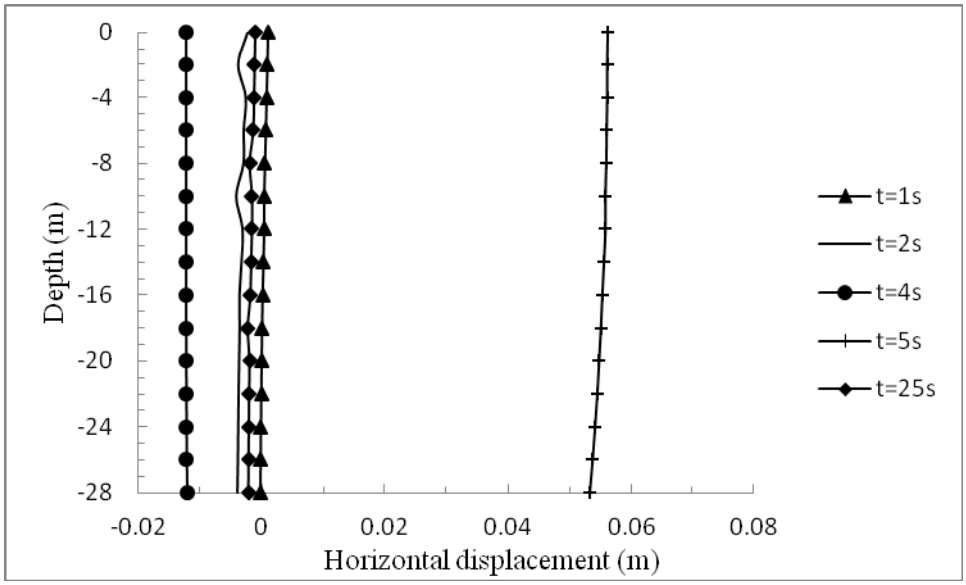


Figure 6: Lateral displacement along the vertical section of the rock mass (rock mass without discontinuities)

Figure 7 illustrates the variation of the lateral velocity at point A. This velocity reaches its maximum value at the same time of that of input loading (at time t = 5 s). By comparing the maximum value of the speed (1 m/s) with maximum speed imposed on the basis of the model (0.4 m/s), we obtain a dynamic amplification equal to 2.5.

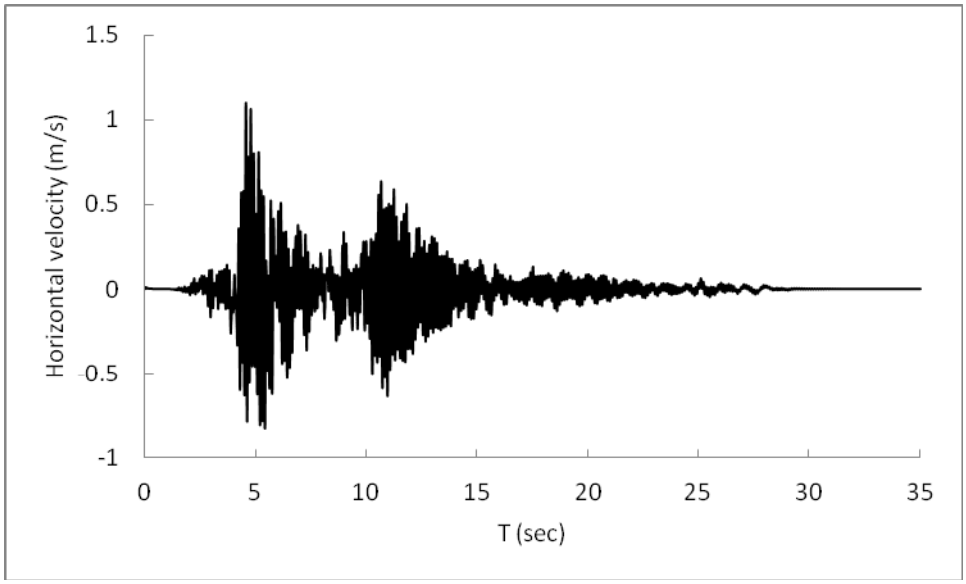


Figure 7: Variation of the velocity at point A of the rock mass (Rock mass without discontinuities)

5 ANALYSIS OF THE SEISMIC BEHAVIOR OF THE ROCK MASS - NETWORK OF HORIZONTAL FRACTURES

In this section, analyzes are performed considering the network of horizontal discontinuities (slight slope of 6.6 °). Three lines of discontinuities are considered in the calculation (Figure 3) with the mechanical properties given in Table 2.

5-1 Initial state - static calculation

A static calculation was performed to determine the initial constraints due to the weight of the mass. The displacement field obtained is close to that obtained in the previous case (Figure 4). Displacements obtained are small and rock mass is stable under the action of its own weight.

5-2 Seismic Analysis

Figure 8-a shows the induced horizontal displacements at points A, B and C of the cliff. At the beginning of loading, the displacements are identical in the three points. The maximum value of 6 cm is obtained 6cm at t = 5. Then, shapes are significantly different with a significant gap between the point C (at the foot of the cliff) and points A and B (at the top of the cliff). At the end of the load, there is a return from the point C to its initial position and a permanent displacement of 5 cm and at point B and 6 cm at point A. Such a trend shows that the seismic loading induced, in the presence of horizontal discontinuities, permanent sliding in the upper part of the rock.

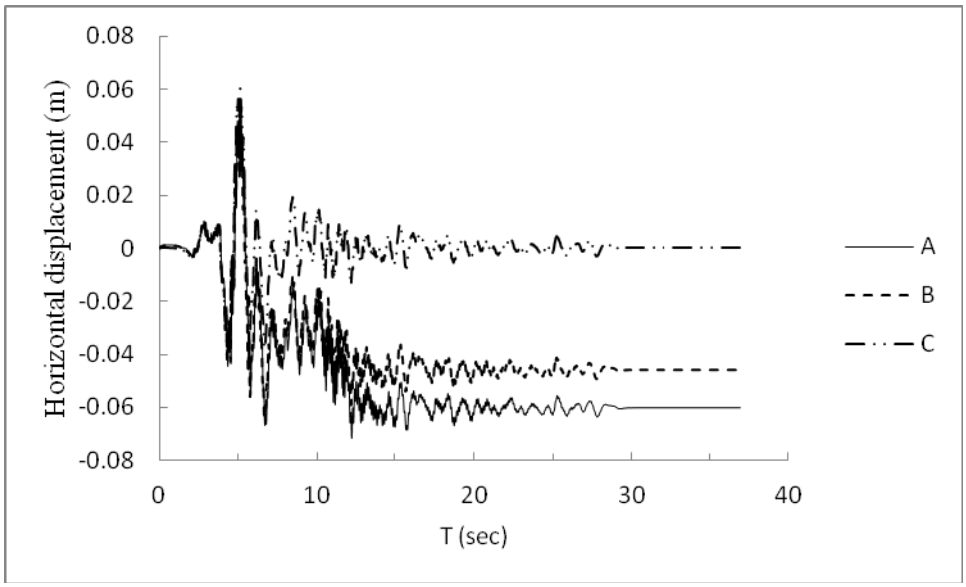


Figure 8-a: Lateral displacement induced in three points of the rock mass (Rock mass with horizontal discontinuities)

Figure 8-b shows the variation of horizontal displacement along the top discontinuity (DEF). We can note the presence of a permanent displacement along the discontinuity tends to increase when moving from point D to point F (inward massif, Figure 3).

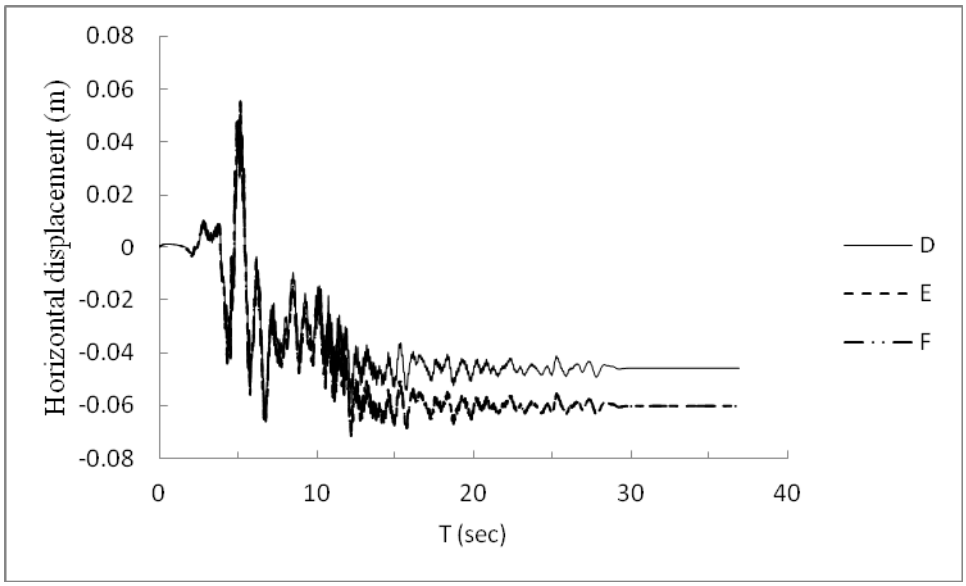


Figure 8-b: Lateral displacement induced at the top discontinuity (DEF) (Rock mass with horizontal discontinuities)

Figure 9 shows the profile of lateral displacement along the vertical section inside the area (Figure 3). At the beginning of loading (t = 2 s), there is a movement almost constant with depth, indicating a rigid block motion. At time t = 5 seconds, corresponding to the maximum loading, there is a shift of the upper part of the rock mass relative to the lower part. At the end of loading (t = 25 s), we note the return of the lower block to its original position (no lateral movement) and the presence of permanent sliding in the upper blocks.

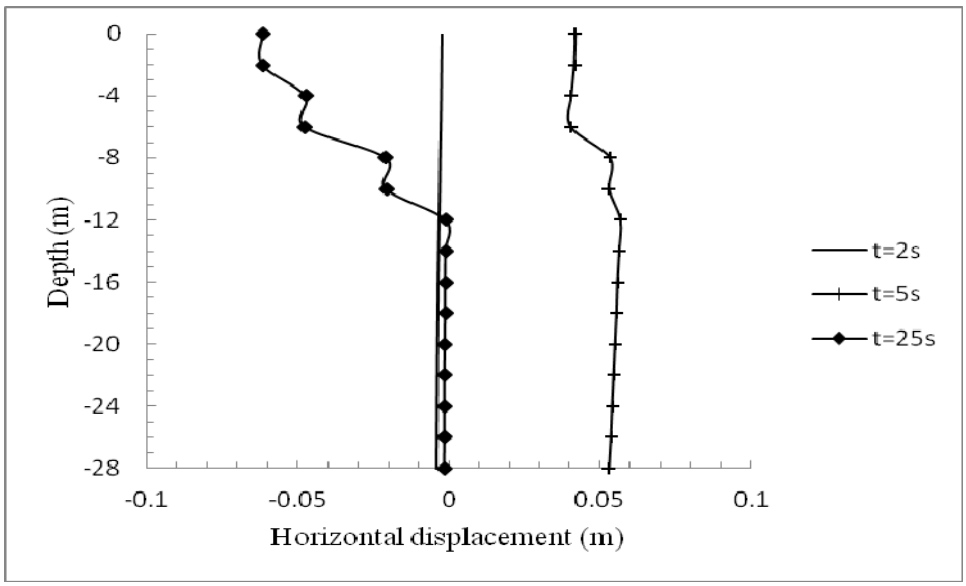


Figure 9: Lateral displacement along a vertical section (Rock mass with horizontal discontinuities)

Figure 10 shows the variation of the horizontal component of the velocity at point A. Note that this speed reaches its maximum (1 m/s) at the same moment of the maximum value of the applied load (t = 5s). As in the case without discontinuities, the amplification of the speed relative to the base is equal to 2.5.

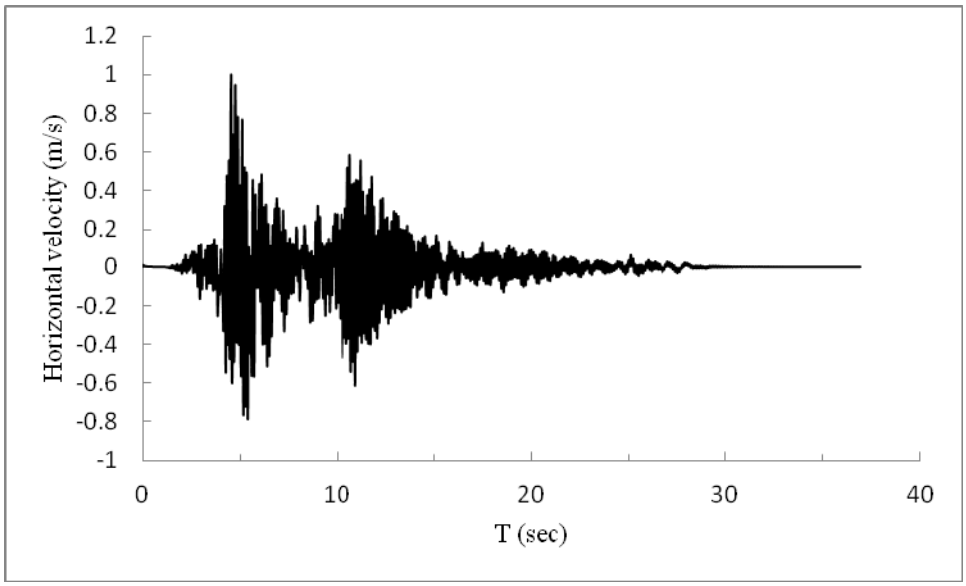


Figure 10: Variation of the horizontal component of the velocity at point A (Rock mass with horizontal discontinuities)

Figures 11-a and 11-b show the variations of normal and tangential components of the stress at point D. It may be noted that the normal stress is positive (compression), reaching its maximum value (1.2 MPa) at the moment when the seismic loading is maximum (t = 5 s). This constraint becomes almost zero beyond t = 15 s. Shear stress undergoes significant variations with the loading with a similar shape to that of the variation of the horizontal speed (Figure 10). Its maximum value is equal to 0.4 MPa. Figure 11-c shows the stress path in the plane defined by the axes normal stress and shear stress. The path obtained lies within the boundary surface:

$$|\tau| = c + \sigma_n tg(\varphi)$$

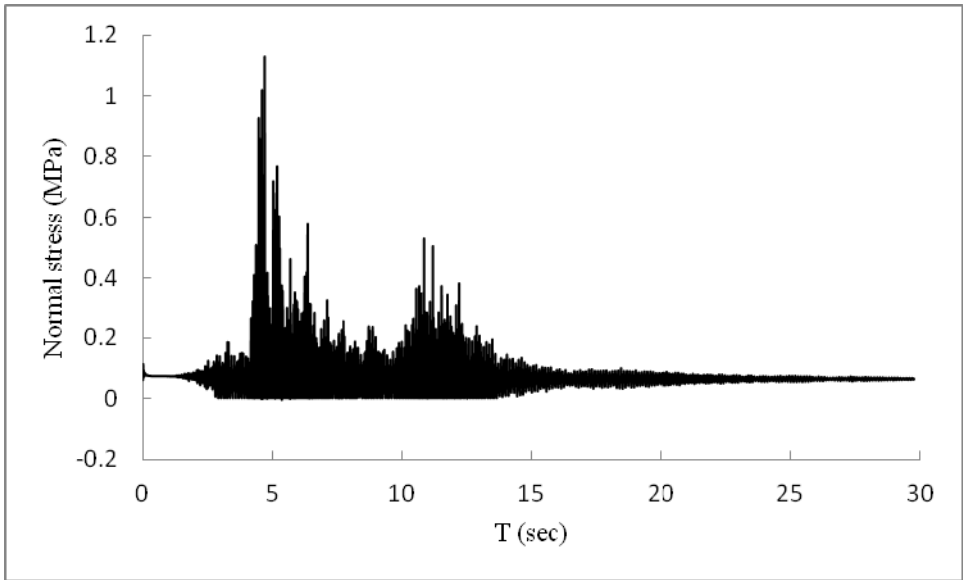


Figure 11-a: Variation of the normal stress in joint at point D (Rock mass with horizontal discontinuities)

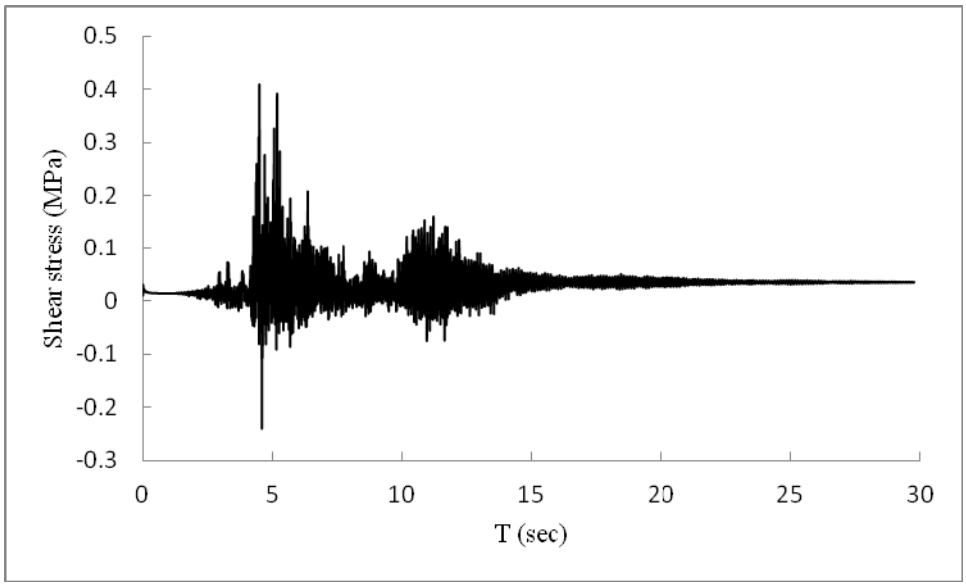


Figure 11-b: Variation of the shear stress in joint at point D (Rock mass with horizontal discontinuities)

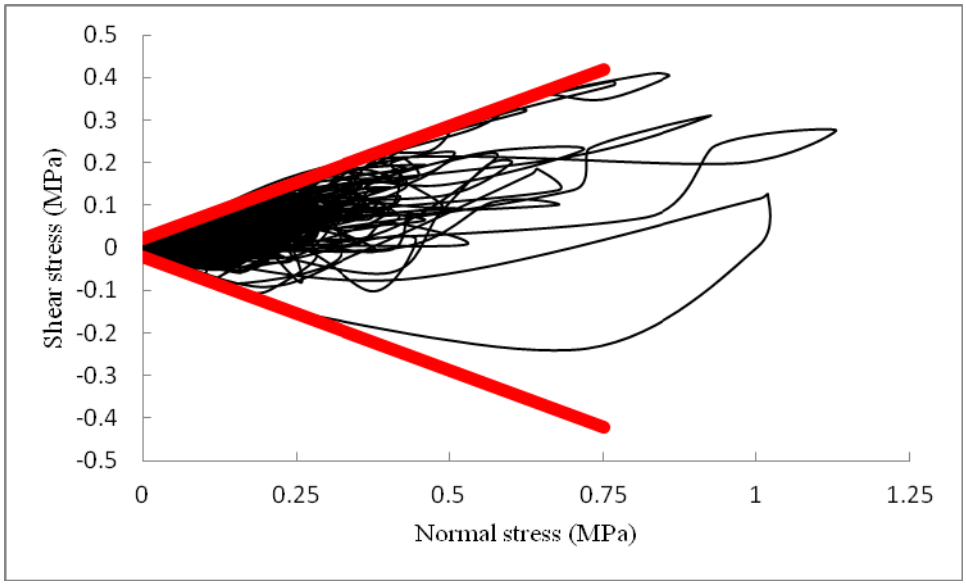


Figure 11-c: Path of stress in joint at point D (normal stress – shear stress) (Rock mass with horizontal discontinuities)

5-3 Parametric study

In this section, we present the influence of the strength joint (Friction angle and cohesion) on the seismic response of the massif:

Influence of joint strength

At first, we studied the influence of the angle of friction of the joint on the seismic response of the rock mass. The calculation was performed with a value of friction angle equal to zero.

Figures 12-a and 12-b show the variations of normal and tangential components of the stress at point D. We note that the variation of this stress has a similar shape to that obtained with a friction angle of 28° (Figure 11-a) but with an amplitude of about 50% greater. The

shear stress varies cyclically between -0.02 MPa and 0.02 MPa (i.e between – c and + c; c being cohesion) during the first 15 seconds of the load; then it decreases to finally cancel loading.

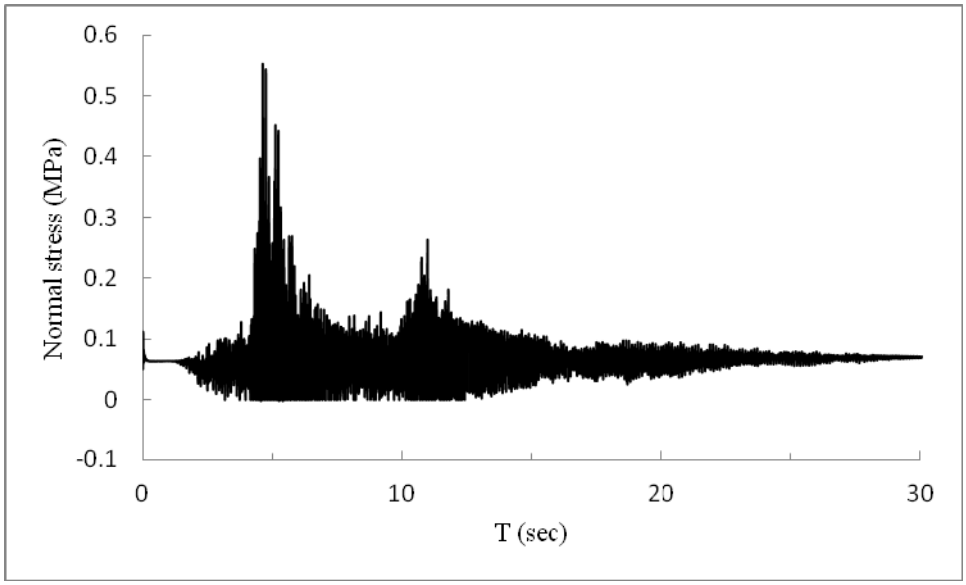


Figure 12-a: Variation of the normal stress at point D with an angle of friction in joint equal to zero(Rock mass with horizontal discontinuities)

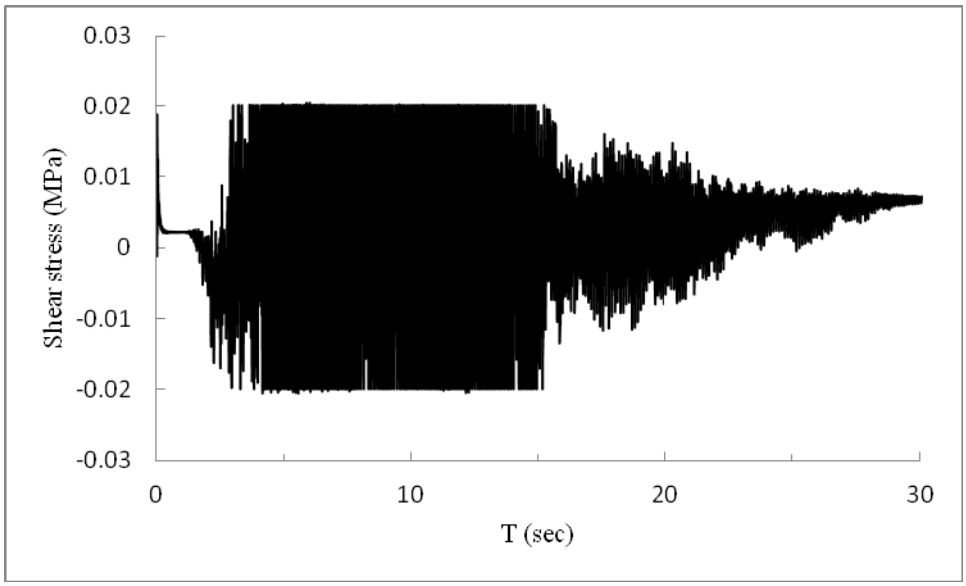


Figure 12-b: Variation of the shear stress at point D with an angle of friction in joint equal to zero (Rock mass with horizontal discontinuities)

Figure 13 shows the influence of the friction angle of the horizontal displacement along a vertical section (Figure 3). Note that this angle does not influence early answer (t = 2 s). Subsequently, we note that the disappearance of friction along the joints resulting in a significant increase in the displacement of the upper block. At the end of the load (t = 25 s), the reduction of the friction angle from 28° to 0° leads to an increase in the movement of the upper block from 6 cm to 21 cm.

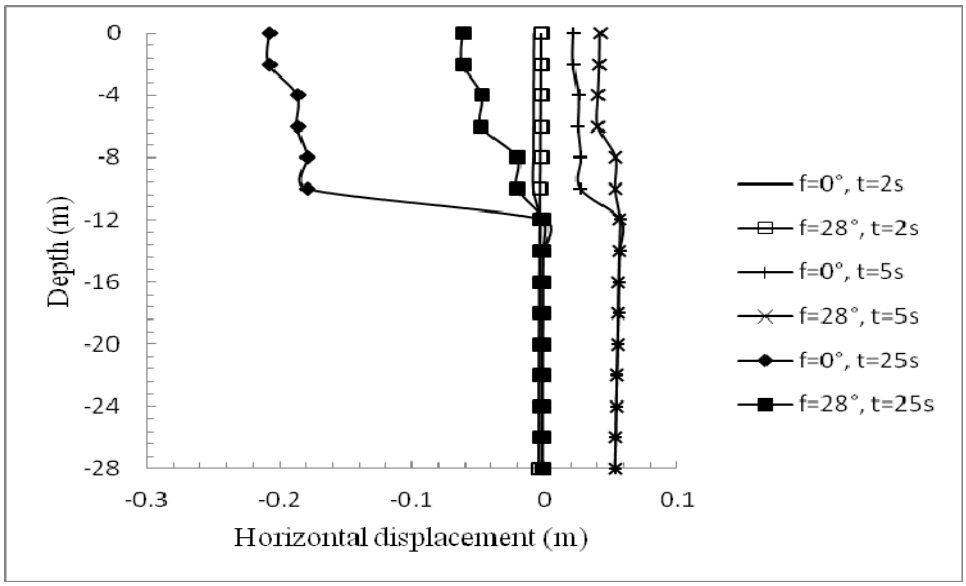


Figure 13: Effect of the friction angle on the horizontal displacement along a vertical section (Rock mass with horizontal discontinuities)

To investigate the influence of cohesion on the seismic response of the rock mass, calculations were made for a friction angle of zero, with two new values of cohesion c = 0.2 MPa and 2 MPa. Figure 14-a shows the influence of cohesion on the movement at point B. We note that the increase in cohesion results in a significant reduction of the horizontal displacement at this point with a return to its original position at the end of loading. This indicates that the discontinuity is in the elastic range when the cohesion is 0.2 MPa. Figure 14-b shows the influence of cohesion on the side profile of the movement in a vertical section. This figure confirms the result in Figure 14-a, we note that from a cohesion of 0.2 MPa, the blocks do not undergo any massive shift.

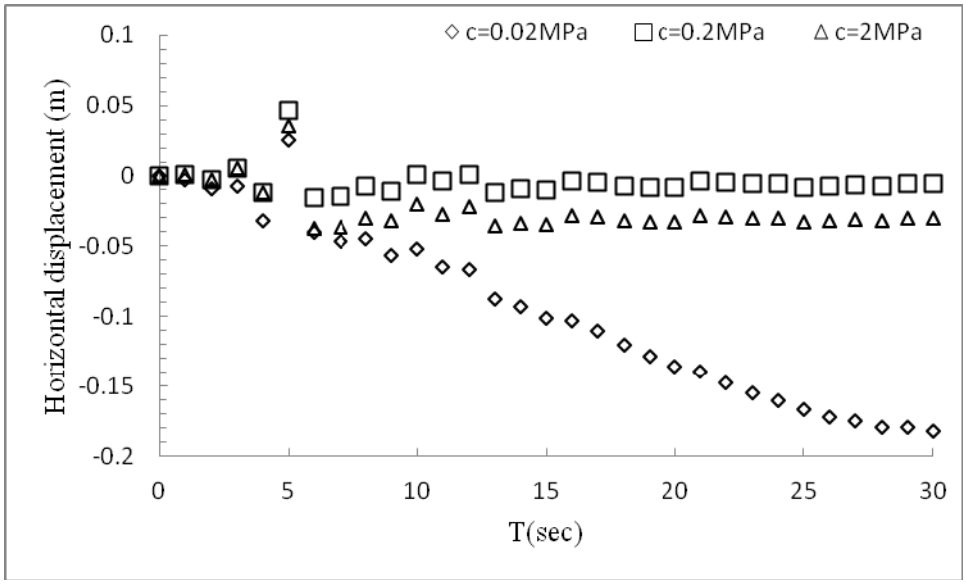


Figure 14- a: Effect of cohesion on the horizontal displacement at point B (φ= 0°; Rock mass with horizontal displacement)

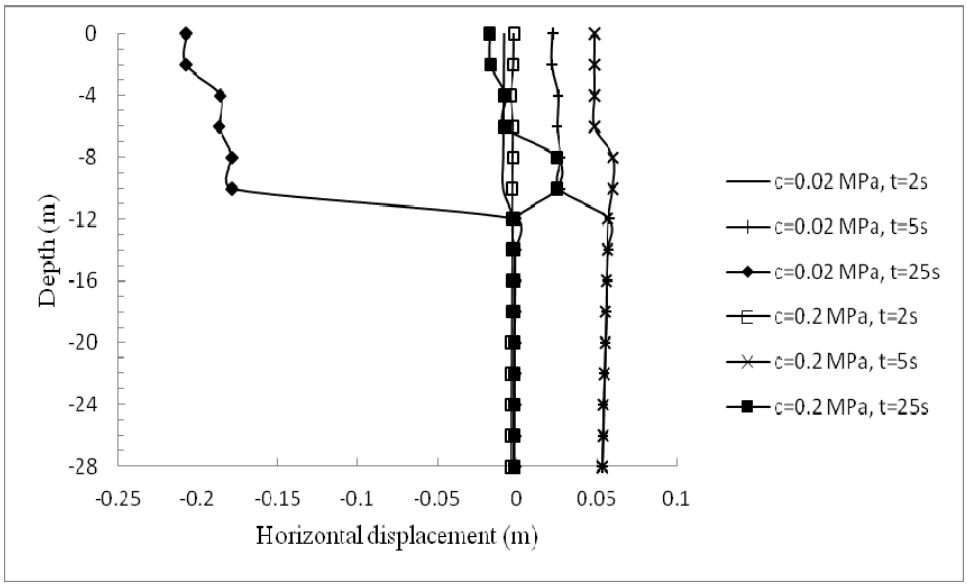


Figure 14-b: Effect of cohesion on the profile of the horizontal displacement along a vertical section (φ= 0°; Rock mass with horizontal discontinuities)

CONCLUSION

A fractured rock in an earthquake zone is exposed to hazard of instability with the possibility of slipping or (and) falling blocs. In such case, we can obtain significant damage that leads to important losses of properties and human lives. So, the analysis of this type of risk is therefore required for rock masses located in seismic zones.

This analysis is particularly important for Lebanon, a country that is predominantly composed of fractured rock and located in a seismic zone where a major earthquake could be expected in the coming years. The objective of this paper is to analyze types of cases encountered massive and study cases of vulnerability stabilization devices.

The behavior of fractured rock is mainly influenced by fractures (discontinuity surface) which are generally the potential locations of relative motions with slippage and separation. These massifs are generally vulnerable to seismic loads, including the lateral component of the load. This paper has been dedicated to the analysis and the numerical modeling of the behavior of rock joints. The approach of separate elements is the most appropriate because it allows good model surfaces of discontinuity and considers large displacements and large deformations.

The numerical modeling of a real case in Lebanon has lead to the following main conclusions :

- The rock mass is generally discontinuous, anisotropic, homogeneous and not elastic;
- The rock mass is stable under its own weight, initial state, in the absence of discontinuities and in the presence of horizontal discontinuities;
- Under seismic loading, and in the absence of discontinuities, we note that the rock is stable without permanent displacement in the upper part and it behaves as in the case of the rigid block;
- A dynamic amplification of the velocity of seismic loading applied to the base of the model;

- Under seismic loading and in the presence of horizontal discontinuities, there is a permanent shift in the upper part of the rock, this shift tends to increase going towards the inside of the model;
- A small rocking motion induced in the solid by the seismic loading and could be neglected;
- The stress path in the plane defined by the axes normal stress and shear stress obtained is well within the boundary surface:

$$|\tau| = c + \sigma_n tg(\varphi)$$

- The reduction of the friction along the joint results in a significant increase in the displacement of the upper block and leads to an increase in the movement of the upper block;
- The discontinuity is in the elastic range when increasing the value of the cohesion to 0.2 MPa and the blocs do not undergo any massive shift from this value.

REFERENCES

[1] L.W. Abramson, T. S. Lee., S. Sharma and G. M. Boyce. *Slope stability and stabilization methods*, John Wiley & Sons, Inc, 1996.

[2] N. Barton, R. Lien and J. Lunde, Engineering classification of rock Masses for the Design Support. *Rock Mechanics*, Vol **6**, pp. 189-236, 1974.

[3] S. Gentier, Morphologie et comportement hydromécanique d'une fracture naturelle dans le granite sous contrainte normale. Etude expérimentale et théorique. Thèse de l'Université d'Orléans. Spécialté Mécanique des Roches, 2 vol., 637 pages, 1986.

[4] ITASCA, UDEC user's guide. Ver. 3.1, Minnesota, 2000.

[5] B. Ladanyi and G. Rchambault, Shear strength and deformability of filled intended joints. In. Proc. Int. Sym. On Geotenics of Structurally Complex Formations, Vol. **1**, pages 317-326, Italian Geotech. Assoc., Capri, 1977.

[6] R. D. Lama, Influence of Clay fillings in shear behavior of joints. Int. Proc. 3rd Int. Conf. Tnt. Association of Engineering Geology, pages 27-34, Madrid, 1978.

[7] J. R. H. Otter, A. C. Cassell and R. E. Hobbs, Dynamic Relaxation," Proc. Inst. Civil Eng., **35**, 633-665, 1966.

[8] T. Papaliangas, S. R. Hencher, A. C. Lumsden A.C. and S. Manolopoulous, The effect of frictional fill thickness on the shear strength of rock discontinuities. *Int. J. Rock Mech. Min. Sci. & Geomech*. Abstr., vol. **30(2)**, pp. 81-91, 1993.

COMPDYN 2013
4th ECCOMAS Thematic Conference on
Computational Methods in Structural Dynamics and Earthquake Engineering
M. Papadrakakis, V. Papadopoulos, V. Plevris (eds.)
Kos Island, Greece, 12–14 June 2013

STATISTICAL EVALUATION OF THE SEISMIC SERVICEABILITY OF A BULLET TRAIN ALONG THE DEAD SEA FAULT

Shun Uchida[1] **and Assaf Klar**[2]

[1]Technion - Israel Institute of Technology
Technion City, Haifa 32000, Israel
e-mail: shun@icoeng.com

[2] Technion - Israel Institute of Technology
Technion City, Haifa 32000, Israel
e-mail: klar@technion.ac.il

Keywords: probabilistic seismic hazard analysis, nonlinear soil behavior, CAV, stochastic soil properties, differential displacement, Dead sea fault

Abstract. *The bullet train from Be'er-Sheva to Eilat in Israel is planned to be built in great vicinity to the Dead Sea Fault (DSF) and therefore susceptible to different seismic risks. Bullet trains are especially vulnerable to differential deformations and one of the engineering tasks associated with the train design is to evaluate the expected serviceability level with time.*

The paper presents statistical analyses conducted for the prediction of the anticipated deformation of the railway caused by multiple and single earthquake events as function of the exposure period. The analyses incorporate both a probabilistic seismic hazard analysis (PSHA) and statistical disaggregation to select controlling events, using local seismicity data.

The highlight of the analyses is its comprehensive approach to include four main features, from viewpoints of geotechnical engineering and earthquake engineering. Firstly, the soil constitutive model considers the effects of nonlinearity and plastic compaction due to cyclic loading. Plastic deformations during earthquakes are widely known phenomena and thus important to be taken into account for accurate deformation prediction. Secondly, the soil properties are distributed heterogeneously so that differential deformations can be evaluated, which are likely to occur in natural sediments. Thirdly, using an attenuation model, a potential cumulative absolute velocity (CAV) is evaluated at different return period based on Israeli local seismic zones and levels. Using statistical disaggregation, well representative earthquakes are selected and used for geomechanical analyses in order to predict deformation patterns. Forth, based on the results of 81 cases investigated, the fragility curves for the serviceability of the train are plotted. The resulting curves can be used as guideline to build the railway track for given exposure period of the structure and deformation tolerance.

1 INTRODUCTION

The high-speed train from Be'er-Sheva to Eilat in Israel is planned to be built in great vicinity to the Dead Sea Fault (DSF) and therefore susceptible to different seismic risks. High-speed trains are especially vulnerable to differential deformations and one of the engineering tasks associated with the railway design is to evaluate the expected serviceability level with time.

This paper presents statistical analysis for the prediction of the differential deformation of the railway track caused by single and multiple earthquake events. The highlight of the analysis is its comprehensive approach to incorporate advanced features from viewpoints of both earthquake engineering and geotechnical engineering. The former is the use of a probabilistic seismic hazard analysis (PSHA) [1], which integrates all possible earthquake ground motions (i.e. magnitudes, locations, and ground conditions). The latter is that the analysis also incorporates nonlinear soil behavior and heterogeneous soil properties in order to better represent true soil behavior.

2 MODELLING PROCEDURE

2.1 Model geometry

Fig. 1 shows the considered model geometry with the boundary conditions. In the analysis, it is assumed that a railway track is placed on top of an embankment, which has height of 10 meters, width of 15 meters and a sides slope of 25 degrees. Similar analysis should be repeated for other dimensions. Earthquake velocities are applied at the bottom of the base sediment and they are calibrated from the outcrop accelerations of several real earthquakes (discussed later). The lower boundary constitutes a transmitting boundary allowing any reflected waves to propagate downwards. The side boundaries are set such that they form periodic boundaries. The location of the considered site is in the middle range of the route of rail, at the middle of the Arava as shown later as the red circle in Fig. 5.

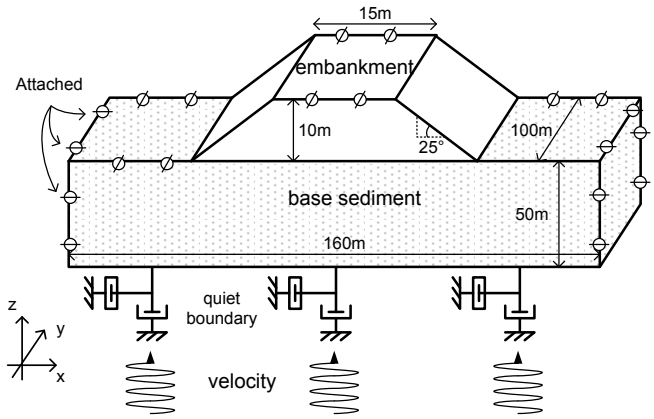


Figure 1: Model geometry and boundary conditions

2.2 Soil model

During earthquakes, the soil is subjected to cyclic loading. It is widely known that cyclic loading induces volumetric and deviatoric plastic deformation. Fig. 2 shows an idealized stress-

strain relation of a drained soil under cyclic loading. If the soil is a linear elastic material (i.e. no plastic deformation), the soil stresses and strains return to the original state at the end of loading cycle. However, in reality, the soil comprises grains which are rearranged due to shearing. The rearrangement of particles leads to both nonlinear plastic behavior in the deviatoric and volumetric spaces.

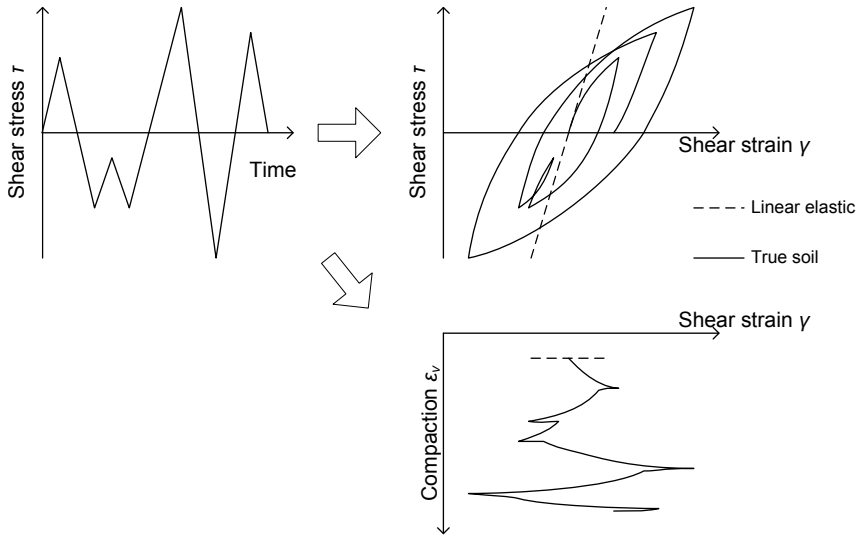


Figure 2: Idealised stress-strain and volumetric behaviour under cyclic loading

This plastic behavior is controlled by a nonlinear backbone curve that can be define using the degradation model suggested by [2],which is shown in Fig. 3a and given by:

$$\frac{G}{G_{max}} = \frac{1.014}{1 + \exp[-(\log\gamma - 1.249)/(-0.4792)]} \tag{1}$$

where G_{max} is the maximum shear stiffness (discussed in the next section) and γ is the shear strain. For the plastic compaction, the model by [3] is used, which is shown in Fig. 3b and given by:

$$\frac{\Delta\epsilon_v^p}{\gamma} = C_1 \exp\left[-\frac{0.4}{C_1}\frac{\epsilon_v^p}{\gamma}\right] \tag{2}$$

where ϵ_v^p is the plastic volumetric strain and C_1 is the soil parameter, which is related to density of soil (discussed in the next section).

It should be noted that when the soil is saturated with water, the reduction of pore space due to shear loading induces excess pore pressure and thus the effective stresses decrease (i.e. liquefaction if the effective stresses become zero). The reduction of effective stresses further decreases the soil stiffness. Thus, additional deformation is expected if the soil is saturated. While the current analysis does not consider this effect, the constructed model would be able to evaluate such conditions if required.

2.3 Stochastic soil properties

No differential deformation will develop (even longitudinally along a section of the railway track) when the soil is homogeneous in horizontal direction. This implies that, unless true

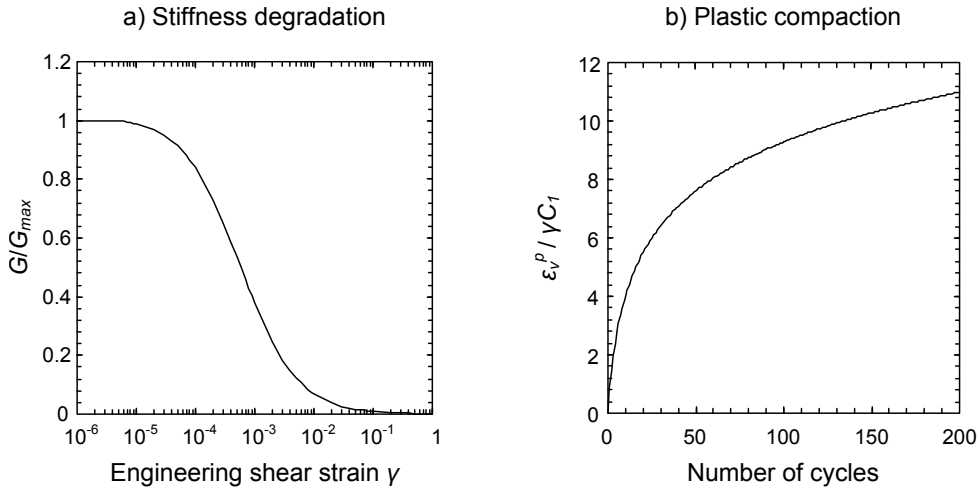


Figure 3: Models used for representation of grain rearrangement

variation of soil properties are considered, even a three-dimensional model will predict zero differential deformation (for the considered geometry). Natural sediments are heterogeneous and thus likely to cause differential deformation which may hinder serviceability of the railway track. The current analysis attempts to capture these important characteristics in a realistic manner by the following.

The current analysis adopts the normalized blow counts of Standard Penetration Test (SPT), $(N_1)_{60}$ ($= N\sqrt{p_a/\sigma'_z}$ [2], where p_a is atmospheric pressure), as an input and assumes that the values follow a normal Gaussian distribution. For the base soil, the distribution has the mean $(N_1)_{60}$ value of 20 ($\approx$ relative density of 70 %) with a coefficient of variation of 26 % (suggested by [4]). For the embankment, assuming thorough compaction is conducted, the mean $(N_1)_{60}$ value is set to be 35 ($\approx$ relative density of 89 %) with a coefficient of variation of 10 %.

In addition, in order to better represent natural soil properties, the distributed values are also spatially auto-correlated, that is, the values are correlated in relatively close locational positions (i.e. auto-correlation distance), rather than being completely random. A large auto-correlation distance implies that the soil property is highly correlated over a large spatial extent, resulting in a smooth variation within the soil profile. In this study, auto-correlation distance is set to be 10-20 m (based on work by [5]). Fig. 4 presents the distributions of the normalized SPT value in studied three cases, which are hereafter referred to as “Soil 1”, “Soil 2” and “Soil 3”.

The spatially distributed and auto-correlated $(N_1)_{60}$ are used to obtain the maximum shear stiffness G_{max} by [6]:

$$G_{max} = 21.7 \cdot p_a \cdot 20(N_1)_{60}^{1/3} \left(\frac{p'}{p_a}\right)^{0.5} \tag{3}$$

where p' is the mean effective stress. The plastic compaction model parameter C_1 is also obtained from $(N_1)_{60}$ by [3]:

$$C_1 = 8.7(N_1)_{60}^{-1.25} \tag{4}$$

A larger $(N_1)_{60}$ indicates that the soil is stiff and thus the maximum shear stiffness becomes large. As stiffer soil tends to induce less plastic strain, C_1 becomes smaller with increasing $(N_1)_{60}$. These values are used for the nonlinear soil model as described in Fig. 3.

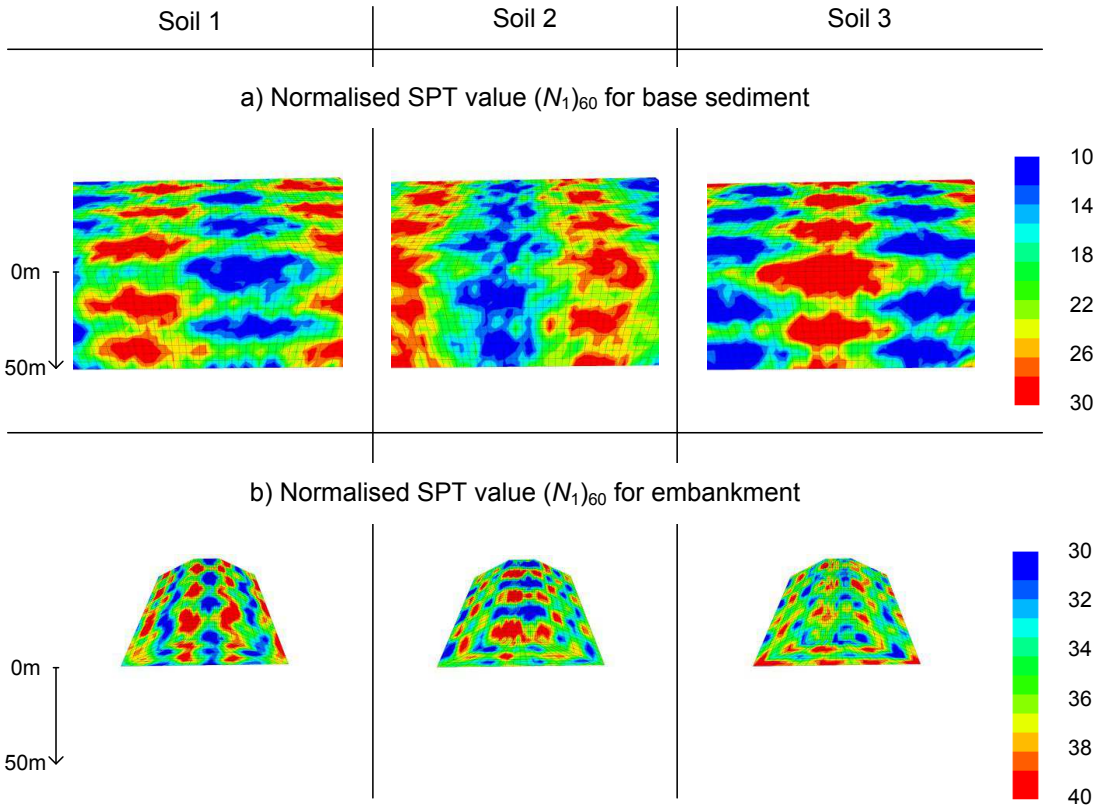


Figure 4: Distributions of normalised SPT value

3 PROCEDURE OF SELECTING EARTHQUAKES FOR TIME-DOMAIN ANALYSIS

This section describes the procedure of selecting input earthquake acceleration time histories for the analysis. This study takes an approach of probabilistic seismic hazard analysis incorporating:

- An attenuation model to evaluate cumulative absolute velocity (CAV) at a given return period based on the Israeli seismogenic zone;
- Disaggregation (or deaggregation) model to determine the dominant contributing factors (e.g. magnitude or location) to the estimated CAV;
- Scaling of real earthquake acceleration time history.

A Probabilistic Seismic Hazard Analysis (PSHA) is a probability-based framework capable of quantifying various ground-motion values (e.g. peak ground acceleration) at a considered site. It is known that ground-motion values vary with many uncertain factors such as location of the earthquake, fault type, variability of ground motion intensity, characteristics of ground and probability of occurrence of earthquake itself. Rather than ignoring the uncertainties present in earthquake-related problem, PSHA incorporates them into the calculation of potential ground motion intensities.

3.1 Potential cumulative absolute velocity based on its return period

Cumulative absolute velocity (CAV), defined as the integral of the absolute acceleration time series, has been used as an index to indicate the possible onset of structural damage and liquefaction of saturated soils. Although named the cumulative absolute velocity, CAV is not directly related to the ground motion velocity, rather, it originates from the fact that the integral over acceleration can be rewritten as summation of incremental (i.e., peak-to-valley and valley-to-peak) velocities. Thus, the value CAV is an indicator of cyclic loading. Since its introduction in 1988, a number of studies have shown that CAV is better predictor (also smaller standard deviation) than other energy related intensity measures such as Peak Ground Acceleration (PGA) of potential damage of soil and structures, which are prone to cyclic loading or fatigue failure [7, 8, 9, 10].

To obtain the exceedance value of CAV through PSHA analysis, one must consider all possible earthquake events (magnitude and distances) that may affect the site. In this work, the Israeli Catalogue of seismogenic zones by [11] is adopted. The solution, based on event occurrence following the Gutenberg-Richter with a limit on the maximum magnitude, may be obtained numerically by the following integral:

$$\lambda_{z^*}(x_0, y_0, z^*) = \sum_{i=1}^{NS} \sum_{k=NXS_i}^{NXE_i} \sum_{l=NYS_i}^{NYE_i} \sum_{j=1}^{NMW} \alpha_i P[z^*|m_j, r_{i,k,l}] f_{Mi,j} A_{i,k,l} \Delta m_i \tag{5}$$

$$m_j = M_{min,i} + (j - 0.5)\Delta m_i \tag{6}$$

$$r_{i,k,l} = \sqrt{(x_0 - (k - 0.5)\Delta x)^2 + (y_0 - (l - 0.5)\Delta y)^2} \tag{7}$$

$$f_{Mi,j} = \frac{\beta_i \exp[-\beta_i (j - 0.5)\Delta m_i]}{1 - \exp[-\beta_i (M_{max,i} - M_{min,i})]} \tag{8}$$

$$A_{i,k,l} = \frac{PIZ(i, (k - 0.5)\Delta x, (l - 0.5)\Delta y)}{NR_i} \tag{9}$$

$$\Delta m_i = \frac{M_{max,i} - M_{min,i}}{NMW} \tag{10}$$

where λ_{z^*} is the return period of the ground motion parameter of question z^* (CAV and PGA in this work), (x_0,y_0) are the coordinates for which this value z^* is evaluated, α_i, β_i, $M_{min,i}$, and $M_{max,i}$ are parameters of the Guttenberg-Richter (bounded by upper magnitude) model for the seismicity of the seismogenic zones of Israel (shown in Fig. 5 and given in Table 1), NS is the total number of seismogenic zones, NXS_i, NYS_i, NXE_i and NYE_i are the boundaries of indexes k and l for each seismogenic zone to form a rectangular in which the seismogenic zone is encompassed, NMW is the division of magnitude in the integration, $P[z^*|m_j, r_{i,k,l}]$ is the probability that the ground motion parameter at point (x_0, y_0) due to an event with magnitude m_j at distance $r_{i,k,l}$ will be larger than z^*, NR_i is the number rectangular element of size Δx times Δy found in seismogenic zone i and PIZ is a special function which gives one if the currently considered source (which is integrated for the all the area) is found in seismogenic zone i and zero otherwise. Note that in the solution we search for z^* that will give the required return period $R = 1/\lambda_{z^*}$.

A design return period R is the average interval of time between events leading to an equal or greater associated ground motion parameter. It may be used to define the exceedance probability P_e (i.e. probability that at least one event would occur) for a given exposure period t (or vice versa), using Poisson's model as:

$$P_e = 1 - \exp[-t/R] \tag{11}$$

Incorporating Campbell and Bozorgnia attenuation model [12] with its defined standard deviation into Eq. 5 (as part of $P[z^*|m_j, r_{i,k,l}]$) gives a solution for defining the CAV at the considered site in the Arava. It should be noted that the ground motion component used to define CAV in this study is the geometric mean of the two recorded horizontal components (often noted as $\mathrm{CAV_{gm}}$).

Fig. 6 shows the estimated CAV (and PGA for a comparison) with increasing return period at the considered site in the Arava. For example, at return period of 160 years, the expected CAV is 3.46 m/s. This implies that, at the Arava site, a chance of which CAV caused by earthquakes would exceed 3.46 m/s, at least once in 100 years, is 46 % (or 27 % in 50 years). The values given in Fig. 6 are calculated for a site with shear wave velocity v_s=180 m/s (classified as soil Type D by the Israeli standard, following ASCE-7-05 classification).

3.2 Disaggregation for a given CAV

In order to determine the dominating earthquake-related factors to the estimated CAV, all the combined data in the previous section for the attenuation model is now decomposed, a process known as disaggregation (or deaggregation). Through disaggregation process, the contribution of each earthquake to the considered ground motion (in this case CAV) can be known.

Fig. 7 shows the disaggregation for the CAV of 1.0, 3.5 and 8.9 m/s (a return period of 10, 160 and 2560 years, respectively). The notations M_m and R_m in the figure imply that the most dominant values of magnitude and distance (obtained as mean values), respectively, which contribute to the corresponding CAV. As can be seen, the concerned event at R = 10 years is dominated by earthquakes with relatively small magnitudes, while at R = 2560 years is controlled by earthquakes with high magnitudes. It appears that the distance to the source does not change with different return periods and the value is around 30 km. Together with the previous results shown in Fig. 6, it can be said that, at the Avara, there is 46 % chance that CAV

Table 1: Parameters of seismogenic zones

Zone name	α	β	M_{min}	M_{max}
W. Shiarnb	0.1546	2.21	4	6.0
Med1	0.3956	2.21	4	6.5
Beit Shean	0.0599	2.21	4	6.5
Jordan North	0.1044	2.21	4	5.5
Galil	0.0348	2.21	4	5.5
Roum	0.2887	2.21	4	7.5
Yamune	0.9144	2.21	4	7.75
Jordan V.	0.3729	2.21	4	7.5
Hula-Kineret	0.2526	2.21	4	7.5
Carmel	0.1199	2.21	4	6.5
Dead sea	0.2887	2.21	4	7.5
Central Israel	0.0232	2.21	4	5.5
Med2	0.2277	2.21	4	6.5
Med3	0.2158	2.21	4	6.5
Arava	0.3007	2.21	4	7.5
Suez	2.0425	2.46	4	7.0
Elat	0.1925	2.21	4	7.5
Aragonese	0.1925	2.21	4	7.5
Arnona	0.1925	2.21	4	7.5
Paran	0.0238	2.21	4	6.0
Barak	0.0371	2.21	4	5.5
Thamad	0.0642	2.21	4	6.0
Milhan	0.0162	2.21	4	5.5
Arif	0.0302	2.21	4	5.5
East Sinai	0.0333	2.21	4	6.0
Cyprus	2.7769	2.25	4	8.0
Palmira	0.1189	2.21	4	6.0

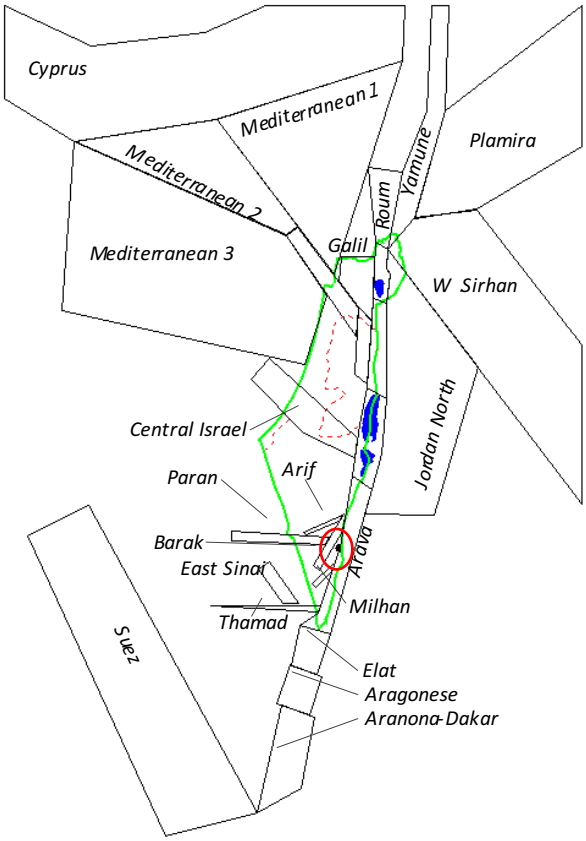


Figure 5: Seismogenic zones in Israel and adjacent areas

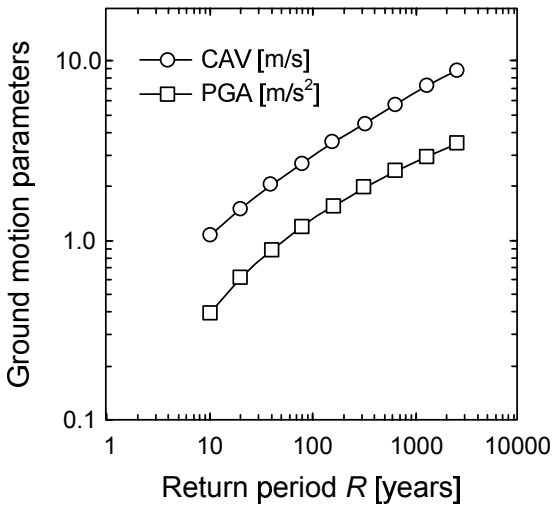


Figure 6: Expected CAV and PGA at a given return period for class D site

caused by earthquakes is likely to be 3.5 m/s (or greater) within 100 years and most likely will originate from earthquake distant by some 30 km.

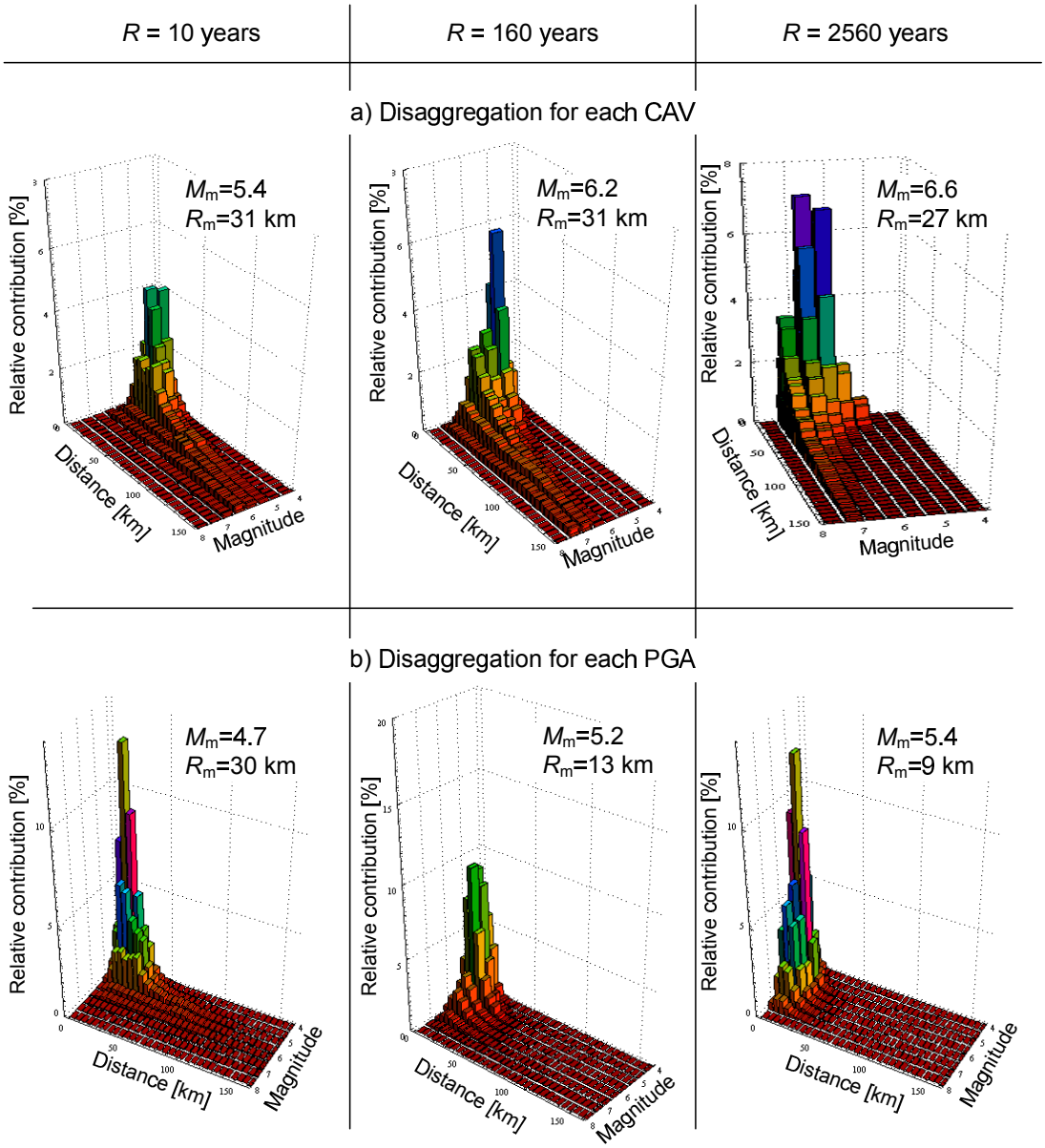


Figure 7: Disaggregation for the CAV and PGA

3.3 Selections of acceleration time history records

Considering the previous findings of most dominating magnitude and distance of earthquakes for a given CAV, a dataset of real earthquakes is constructed for time-domain analyses. Fig. 8 shows the acceleration time histories of selected earthquakes in this report. The information of the earthquake (e.g. event name, magnitude) is also shown in Fig. 8.

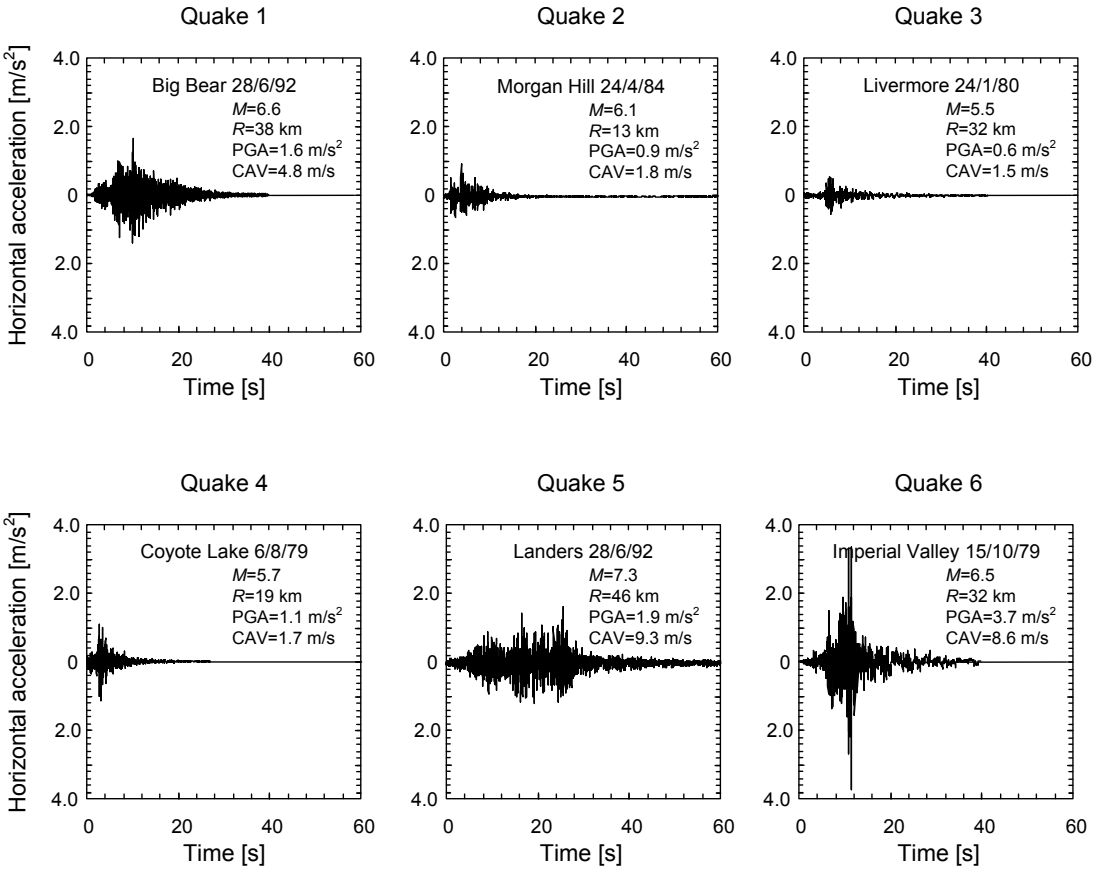


Figure 8: Selected earthquakes and their acceleration histories

Although it would be ideal that the selected earthquake induces the target CAVs, it is not often the case (it is, in fact, impossible to find an exact fit of characteristics). Thus, the selected earthquake is scaled (vertically) in order to shift the real CAVs into the target CAVs. By scaling the real CAV, the peak ground accelerations (PGA) of the earthquake is also scaled. While this paper does not study in detail the effect of PGA, the selected earthquakes are the ones that their scaled PGAs are also within the range of the target PGA. Table 2 lists the selected earthquakes, target CAV (which are also shown in Fig. 6) and corresponding scaled outcrop PGA.

It should be noted that the values of CAV and PGA shown in Table 2 are not exactly the same as the ones produced at the surface of the geomechanical analyses shown later, due to site effect regulations by the solution. This is because the soil is neither elastic nor homogeneous in the current work. In other words, if the soil was elastic, the exact input motion at the bedrock for the target surface CAVs could have been determined by deconvolution based on linear wave equations. Therefore, the analyses are conducted iteratively in order for the computed CAV values, in the free field surface, to fall within the considered range. It is found that the scaling for all conditions fall in the range of factors between 1/3 and 1.5.

Table 2: Parameters of seismogenic zones

Return Period R [years]		10	20	40	80	160	320	640	1280	2560
Target CAV [m/s]		1.04	1.47	2.00	2.65	3.45	4.44	5.63	7.06	8.72
Scaled outcrop PGA_{sc} [m/s^2]	Quake 1					1.20	1.55	1.97	2.47	3.05
	Quake 2	0.55	0.77	1.04	1.39	1.80				
	Quake 3	0.45	0.61	0.83	1.10	1.43				
	Quake 4	0.73	1.02	1.39	1.84					
	Quake 5						1.02	1.30	1.63	2.02
	Quake 6						1.93	2.46	3.08	3.80
Mean PGA_{sc} [m/s^2]		0.57	0.80	1.09	1.44	1.48	1.51	1.91	2.40	2.96
Target PGA [m/s^2]		0.39	0.60	0.87	1.18	1.53	1.94	2.38	2.87	3.39

As summarized in Table 2, for each return period, three different scaled earthquakes are applied to conduct geomechanical analyses. For example, for R = 10 years, Quake 2, Quake 3 and Quake 4 (all scaled to have CAVs to be approximately 1.04 m/s) are applied.

4 DEFORMATION PROFILES DUE TO EARTHQUAKES

Serviceability of the railway track would drop according to deformation of the embankment. Deflection of the embankment would also hinder serviceability. Thus, in this paper, the differential displacements (Δu_x, Δu_y, and Δu_z) are investigated (and later used for fragility curve). Displacements presented in this paper are obtained at the surface of the embankment. The analyses are conducted using a commercial finite difference programme $FLAC^{3D}$ [13] with dynamic option. The plastic soil models (cf. Fig. 3) and the spatially distributed and auto-correlated soil properties (cf. Fig. 4) are incorporated through Itasca's internal programming language.

4.1 Demonstration for CAV of 3.45 m/s (Return period of 160 years)

As the input acceleration histories are different in each direction, sediments and embankment are exposed to truly three-dimensional shaking movement, resulting in a complex behavior. Fig. 9 shows the displacement profile of embankment surface relative to the averaged surface displacement at the end of Quake 1 in the case of CAV $\approx$ 3.45 m/s for Soil 1, Soil 2 and Soil 3. The relative displacements are permanently induced due to cyclic loading and this contours can be an indicative of differential displacements. Due to the heterogeneity of soil properties, the displacements differ among Soil 1, Soil 2 and Soil 3 and even in the same soil they are not uniform. This induces a large relative displacement, which plays a key role for railway serviceability (discussed later). Since periodic boundaries are constructed for the model, the front and rear sides of the embankment produce the same displacements.

Fig. 10 shows the displacement profile relative to the averaged value under Quake 1, Quake 2 and Quake 3 within Soil 1 for CAV 3.45 m/s. Although all the quakes are scaled to have the same CAV and the heterogeneous soil properties are identical, each earthquake induces the embankment surface to behave differently from one to the others. Overall trends imply that the edge of the embankment slides downwards and the embankment surface settles relative to the ground surface.

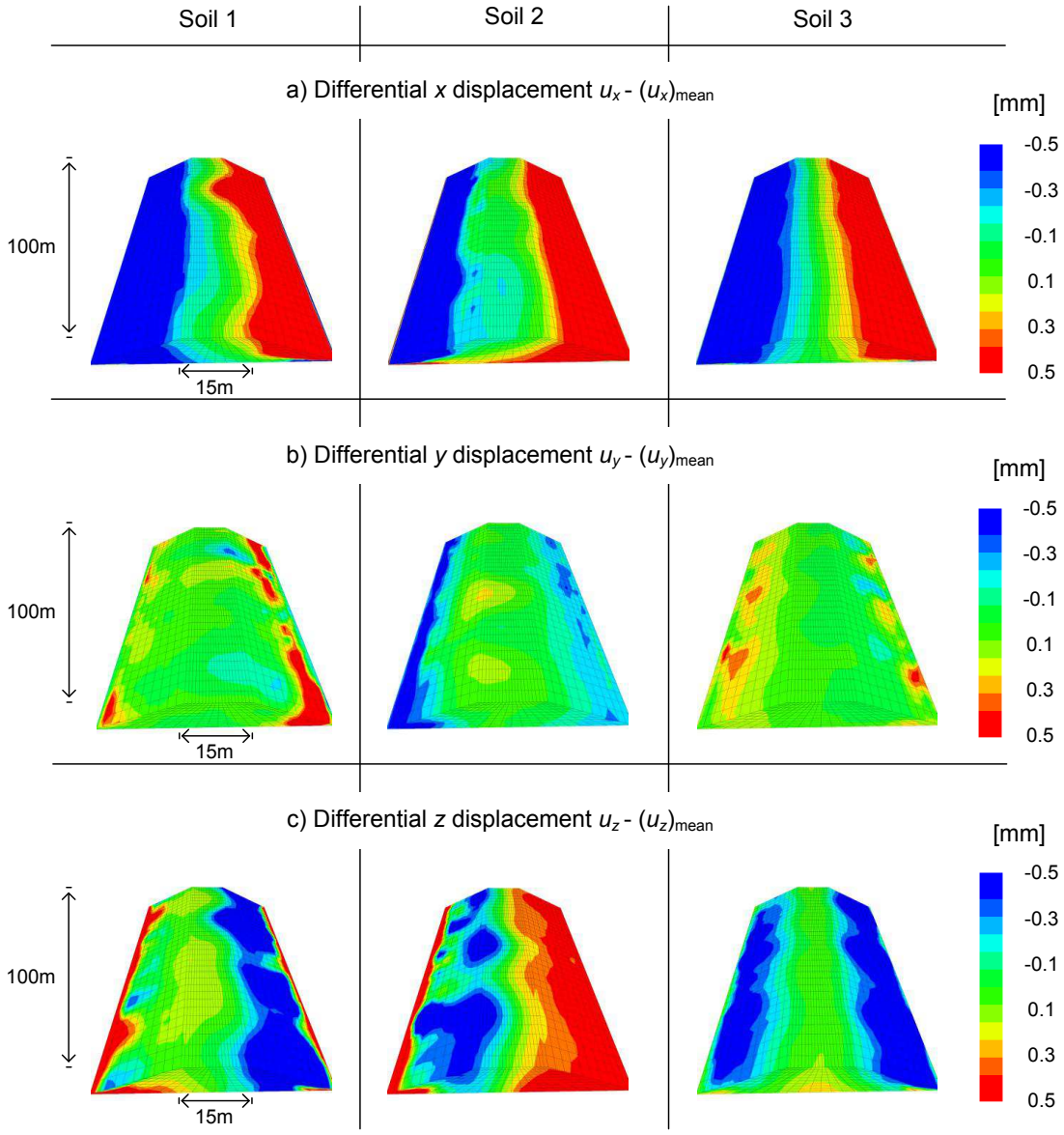


Figure 9: Displacement contours after Quake 1 for 3 soil patterns (CAV ≈ 3.45 m/s)

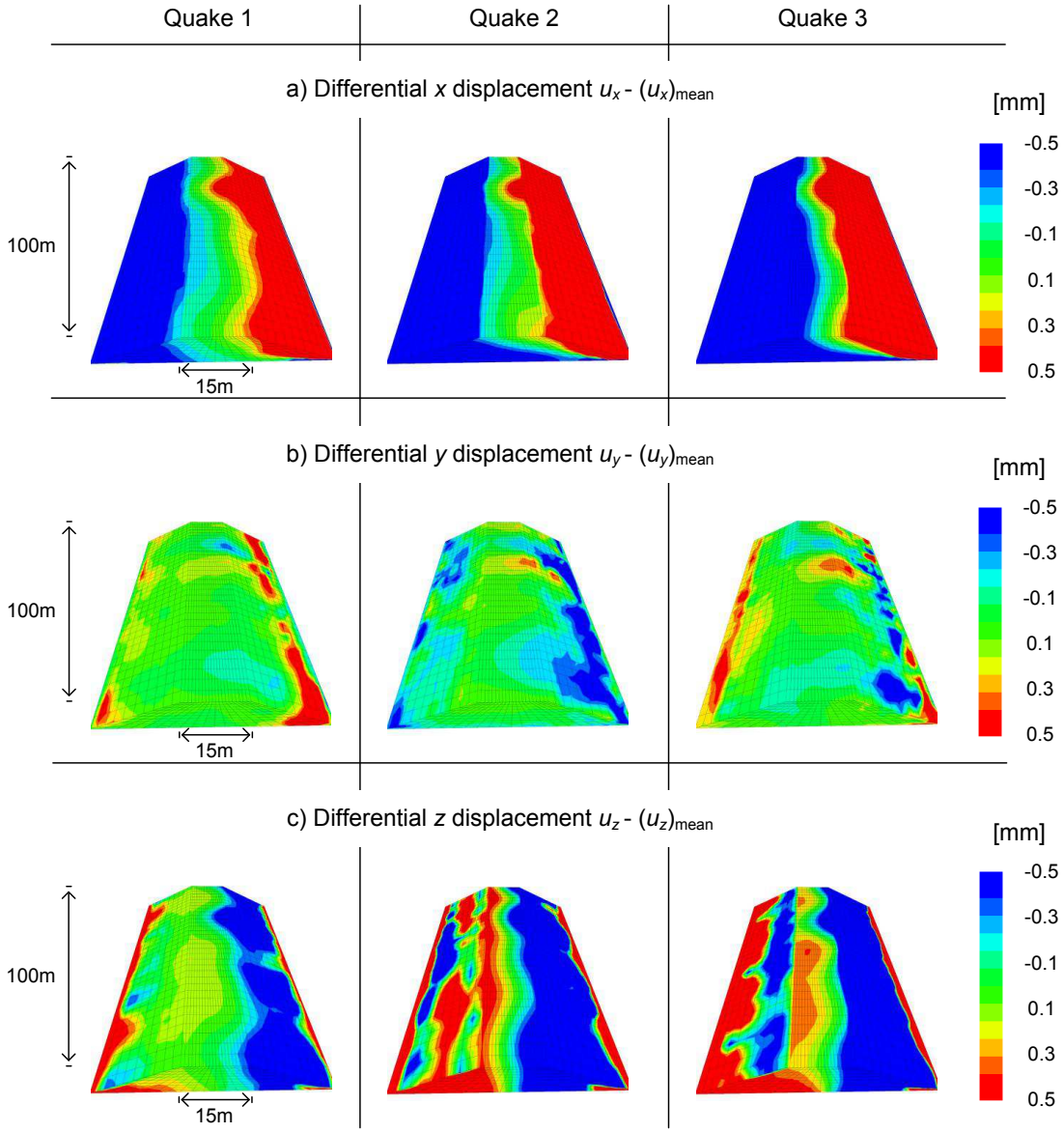


Figure 10: Displacement contours after 3 different earthquakes for Soil 1 (CAV ≈ 3.45 m/s)

4.2 CAVs of 1-10 m/s (Return periods of 10-3000 years)

The same analyses as the previous section are conducted for other 8 target CAVs, and in total 81 cases are considered (3 soil patterns times 3 earthquakes for 9 target CAVs). Fig. 11 presents the maximum differential permanent displacements with different CAVs. The maximum differential displacement is the maximum value of the induced relative displacements on the entire embankment surface. It is obvious that the displacements become larger when CAVs are larger. It may also be evident that at certain CAV levels the scatter becomes larger and the slope of the trend line changes. This trend relates to the onset of significant yielding of the embankment itself.

From the scattered data, deterministic relations of each differential displacement are obtained, which are also stated in Fig. 11 (denoted as the lines) with the standard deviation of each case (in natural logarithmic scale) is $s_{(\Delta u_x)_{max}}$=1.109, $s_{(\Delta u_y)_{max}}$=1.361 and $s_{(\Delta u_z)_{max}}$=1.049. As a result, the most likely induced permanent differential displacement of the embankment can be evaluated at a given CAV. For example, the maximum differential x displacement is approximately 15 mm when CAV = 5.6 m/s. This value is found in the same range of the estimated slope displacements by pseudostatistic analyses by [14] and [15] using corresponding PGA values found in Table 2. This finding supports the validity of the current analyses.

5 RAILWAY SERVICEABILITY CURVE

High-speed railway tracks require quality maintenance for track alignment retention, hence for safe train operation. High-speed railway tracks are especially vulnerable to differential deformations and evaluating deflections is a key engineering tasks associated with the train design. Table 3 lists examples of the serviceability standards for deflections of high-speed railway track.

Table 3: In service values for maximum railway deflections

Paulo Fonseca	German Regulation	IV International Congress	French Regulations
2.0 mm	1.5 mm	1.5 mm	1.5 mm

One may use the relation presented in the previous section (cf. Fig. 11) to evaluate the expected level of deformation using CAV in a deterministic manner. However, such evaluation would include significant uncertainty due to the scatter of the results. The framework of Probabilistic Seismic Hazard Analysis provides a consistent treatment of the problem by including the uncertainty implicitly in the calculation (and hence avoids the uncertainty). As a result, it enables to statistically evaluate the serviceability level of the railway track at the Arava.

A PSHA based formulations for such calculation can be written analytically as follows:

$$\lambda_{D^*} = \sum_{i=1}^{NS} \alpha_i \int\int\int P[D^*|CAV] \cdot f[CAV|m,r] \cdot f_{Mi}(m) \cdot f_{Ri}(r) dCAV dm dr \tag{12}$$

Or numerically as:

$$\lambda_{D^*} = \sum_{i=1}^{NS} \alpha_i \sum_{k=NXS_i}^{NXE_i} \sum_{l=NYS_i}^{NYE_i} \sum_{j=1}^{NMW} \int_{-\infty}^{\infty} P[D^*|\tau] \cdot f_{CAV}[m_j, r_{i,k,l}] d\tau f_{Mi,j} A_{i,k,l} \Delta m_i \tag{13}$$

$$P[D^*|CAV] = \frac{1}{\sqrt{2\pi}} \int_{\frac{\ln D^* - \ln D(CAV)}{s}}^{\infty} \exp[-\theta^2/2] d\theta \tag{14}$$

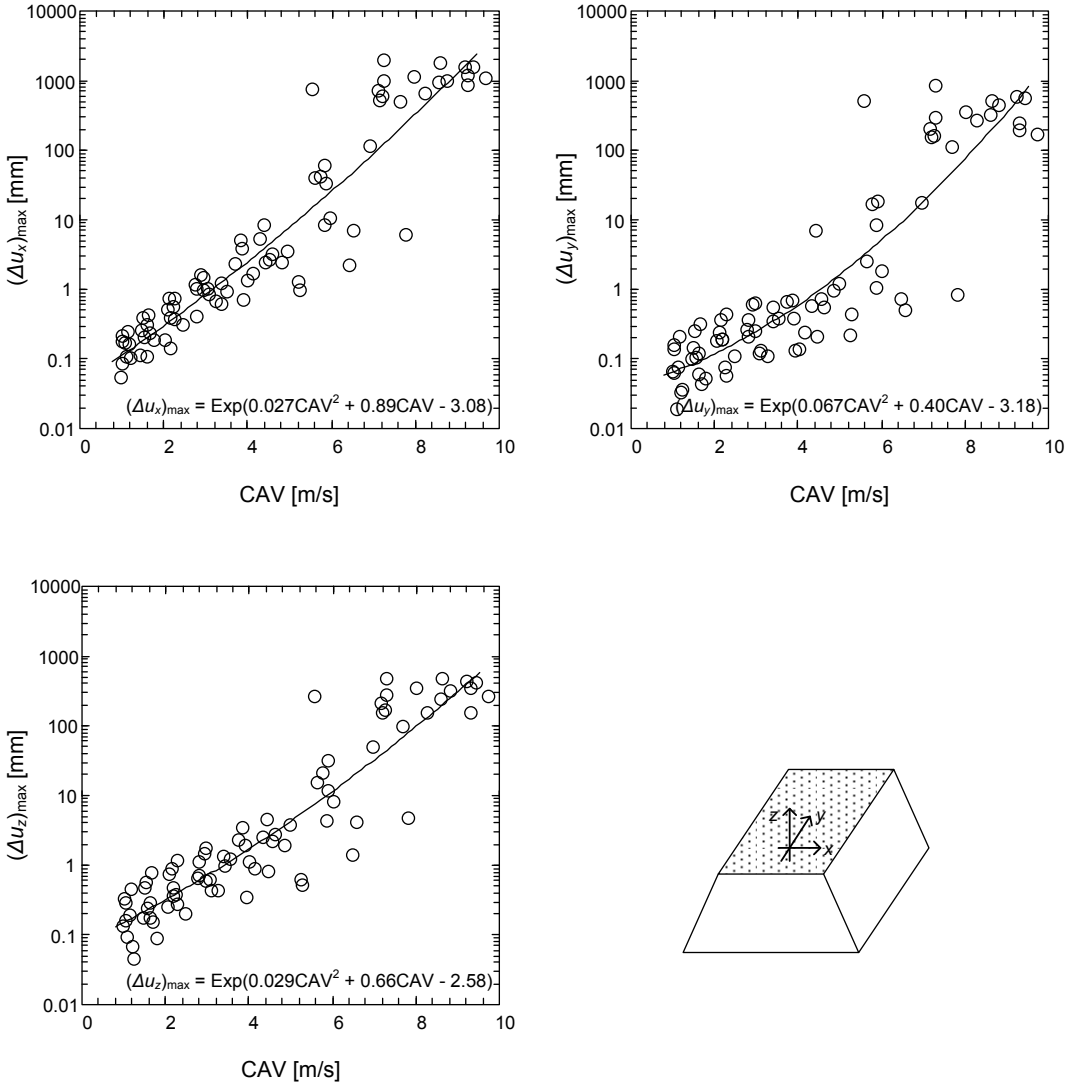


Figure 11: Maximum differential displacements with different CAVs (81 cases in total)

$$f_{CAV}[m_j, r_{i,k,l}] = \frac{1}{\sqrt{2\pi}} \exp\left[-\left(\frac{\tau - \ln CAV(m_j, r_{i,k,l})}{\sigma_{\ln CAV}}\right)^2 / 2\right] \quad (15)$$

where $\sigma_{\ln CAV}$ is the standard deviation of CAV as defined by [12] and s is the standard deviation of the natural logarithmic of the suggested curves for maximum differential displacements as given in the previous section. Essentially, the above equation is one order higher integration form of the conventional PSHA integral. Solving Eq. 13 results in the exceedance probability of D^* by a single event for a given exposure period t. In this work, it provides the answer to what the chance is in which a maximum differential displacement caused by a single earthquake would exceed the value D^* for a period of t.

Fig. 12 shows the solutions of Eq. 13 in each maximum differential displacement for exposure periods of 20, 40, 60, 80 and 100 years. The x axis is the maximum differential displacement and y axis is the exceedance probability. Thus, by drawing a straight vertical line to x axis, the intersection point to the curve represents its exceedance probability. For example, in the case of $(\Delta u_x)_{max}$, there is 8 % of chance that the differential displacement caused by a single earthquake would be greater than 2 mm within 20 years. The same line also states that the probability of exceeding the 2 mm value by a single earthquake event is 15 %, 21 %, 27 % and 33 % within periods of 40, 60, 80 and 100 years, respectively. Table 4 summarises the exceedance probability of the maximum differential displacement can be greater than 2 mm by a single event at Arava site.

Table 4: Exceedance probability of $(\Delta u)_{max}$ to be greater than 2 mm within exposure periods t

Exposure period t [years]	20	40	60	80	100
P[$(\Delta u_x)_{max} > 2$mm]	7.6 %	14.6 %	21.1 %	27.1 %	32.7 %
P[$(\Delta u_y)_{max} > 2$mm]	8.2 %	15.7 %	22.7 %	29.0 %	34.9 %
P[$(\Delta u_z)_{max} > 2$mm]	8.4 %	16.0 %	23.1 %	29.5 %	35.4 %

While an expected displacement induced by a single event has a great importance, it is also imperative to evaluate a cumulative displacement. For example, using Fig. 12, within 20 years of life cycle there is 88 % chance of the maximum differential x displacement to be greater than 0.25 mm, 51 % of greater than 0.5 mm and so on. Based on the Poisson's model (cf. Eq. 11), it is equivalent to the fact that, within 20 years, the event of 0.25 mm (or greater) deformation occurs on average 2.09 times, 0.5 mm deformation occurs on average 0.71 times and so on. If no regular alignment of railway is conducted, all these displacements may accumulate and eventually damage the railway to reach unserviceable state. Hence, by counting all possible events through statistical integration, the average rate of cumulative displacements are evaluated, which are: $(\Delta u_x)_{max}$ = 0.14 mm/year, $(\Delta u_y)_{max}$ = 0.13 mm/year and $(\Delta u_z)_{max}$ = 0.19 mm/year.

These annual values are, however, based on all the displacement values from return period of up to 4000 years and implicitly take account of extreme rare events. This implies that even though the event hardly occurs within the considered exposure period t (e.g. for R=4000 year event, 99.75 % chance of zero occurrence, 0.25 % chance of once, 0.0003 % chance of twice and so on within 100 years), the statistical integration still counts the value. In order to avoid this, the cumulative displacement is recalculated based on all possible combinations of events that comprise 95 % cumulative probability of occurring within the considered return period t (conducting the recalculation with 100 % leads to the same average value as stated above). This approach, in effect, drops out rare events within the considered exposure period t and thus the

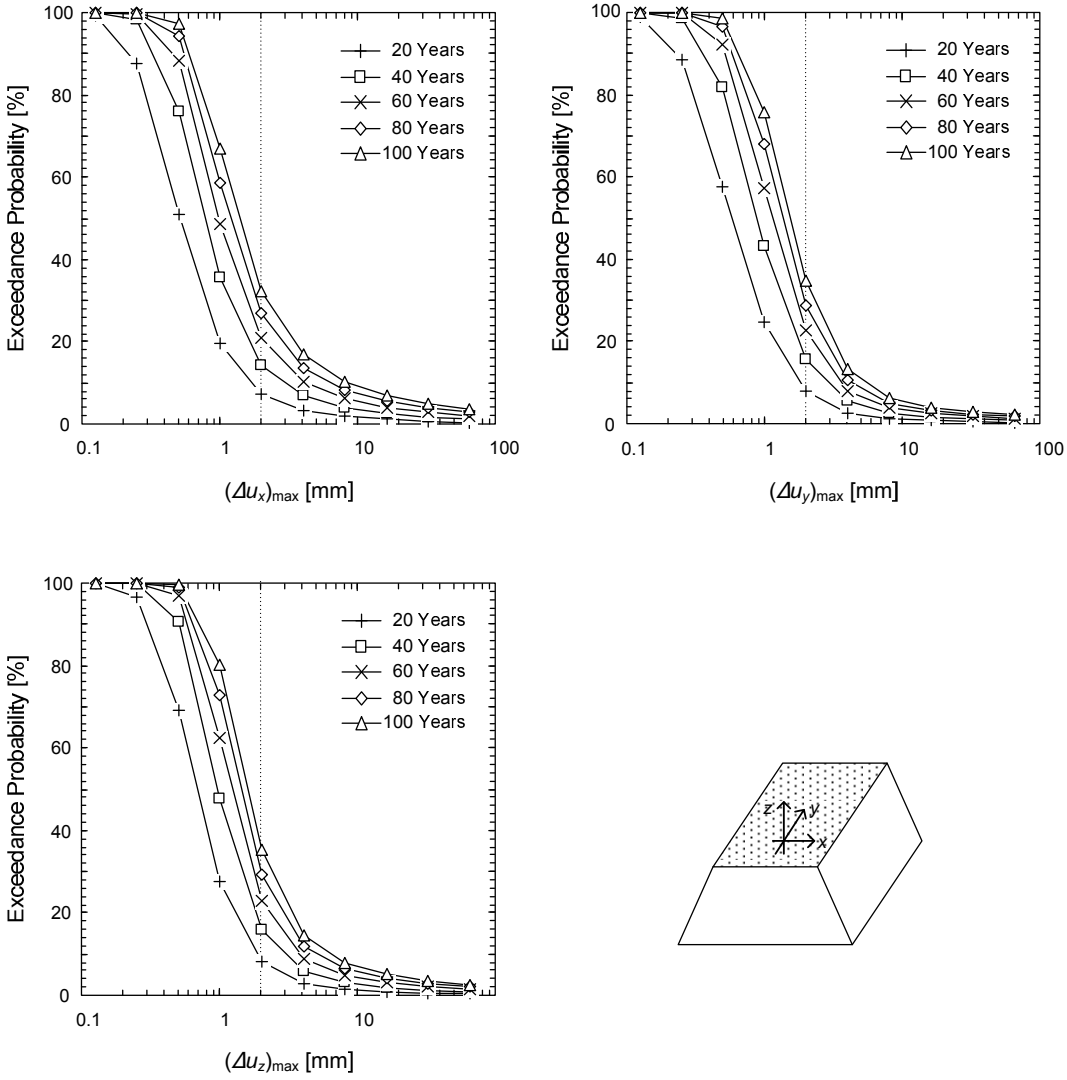


Figure 12: Exceedance probability of a maximum differential displacement

average rate becomes dependent on the considered exposure period. Assuming the exposure period of 100 years (i.e. a design life of the railway track is 100 years), the resulting values are summarised in Table. 5. It states that the limit of 2 mm deflection may be reached every 15 years, on average, throughout a life time of 100 years.

Table 5: Cumulative differential displacement for a design life of 100 years

	Annual rate	To reach 2 mm
$\Sigma(\Delta u_x)_{max}$	0.084 mm/year	23.9 years
$\Sigma(\Delta u_y)_{max}$	0.085 mm/year	23.5 years
$\Sigma(\Delta u_z)_{max}$	0.131 mm/year	15.3 years

6 CONCLUSIONS

This document presented a statistical analysis for the expected seismic induced differential deformation along the surface of the railway tracks of the Be'er-Sheval Eilat Train. The methodology was rather complex and involved integration of all possible earthquake events, together with nonlinear soil behaviour evaluation through advanced numerical and statistical analysis. It also included consideration of soil heterogeneity without which differential deformation would not be obtained from any numerical analysis.

The results presented in this document are relevant to a 10 metre heigh embankment over a natural soil Class-D site located in the middle section of the train route at the Arava. For the considered case, the statistical analysis indicated that there is a 35 % probability that the serviceability limit deflection value of 2 mm may be reached by a single event within the lifespan of 100 years. By considering the cumulative deformation for multiple events, it is estimated that this limit would be reached every 15 years, on average, in the next 100 years.

7 Acknowledgment

The presented analysis in the paper was conducted as part of seismic consulting for Netivey Israel - The Israeli National Round and Infrastructure Company. We wish to thank the engineers involved in the project for the discussion on the different issues of the problem. In specific, Eng. Dan Gronner of Gronner D.E.L. and Enggineers and Eng. Eliezer Shamir and Ronen Brown of Shamir-Posner-Brown Cons. Engineers LTD.

REFERENCES

[1] R. McGuire, Probabilistic seismic hazard analysis and design earthquakes: closing the loop, Bulletin of the Seismological Society of America 85 (5) (1995) 1275–1284.

[2] H. Seed, I. Idriss, Simplified procedure for evaluating soil liquefaction potential, Journal of Soil Mechanics & Foundations 97 (9) (1971) 1249–1273.

[3] P. Byrne, A cyclic shear-volume coupling and pore-pressure model for sand, in: Second International Conference on Recent Advances in Geotechnical Earthquake Engineering and Soil Dynamics, Missouri, 1991, pp. 47–55.

[4] M. E. Harr, Reliability-based Design in Civil Engineering, McGraw-Hill Inc., New York, 1987.

[5] H. El-Ramly, N. Morgenstern, D. Cruden, Probabilistic slope stability analysis for practice, Canadian Geotechnical Journal 39 (3) (2002) 665–683.

[6] H. B. Seed, R. T. Wong, I. M. Idriss, K. Tokimatsu, Moduli and Damping Factors for Dynamic Analyses of Cohesionless Soils, Journal of Geotechnical Engineering 112 (11) (1986) 1016–1032.

[7] M. Kostov, Site specific estimation of Cumulative Absolute Velocity, in: 18th International Conference on Structural Mechanics in Reactor Technology, Beijing, China, 2005, pp. 3041–3050.

[8] J. Klugel, L. Mualchin, G. Panza, A scenario-based procedure for seismic risk analysis, Engineering Geology 88 (2006) 1–22.

[9] S. Kramer, R. A. Mitchell, Ground motion intensity measures for liquefaction hazard evaluation, Earthquake Spectra 22 (2006) 413–438.

[10] L. Danciu, G.-A. Tselentis, Engineering Ground-Motion Parameters Attenuation Relationships for Greece, Bulletin of the Seismological Society of America 97 (1B) (2007) 162–183.

[11] G. Shamir, Y. Bartov, A. Sneh, L. Fleischer, V. Arad, M. Rosensaft, Preliminary seismic zonation in israel, Technical Report 550/95/01, Geophysical Institute of Israel (2001).

[12] K. Campbell, Y. Bozorgnia, A ground motion prediction equation for the horizontal component of cumulative absolute velocity (CAV) based on the PEER-NGA strong motion database, Earthquake Spectra 26 (3) (2010) 635–650.

[13] Itasca, FLAC3D 4.0 - User's Guide, Itasca Consulting Group Inc., Minneapolis, USA, 2009.

[14] N. N. Ambraseys, J. M. Menu, Earthquake-induced ground displacements, Earthquake Engineering & Structural Dynamics 16 (7) (1988) 985–1006.

[15] J. Bray, T. Travasarou, Simplified procedure for estimating earthquake-induced deviatoric slope displacements, Journal of Geotechnical and Geoenvironmental Engineering 133 (4) (2007) 381–392.

COMPDYN 2013
4th ECCOMAS Thematic Conference on
Computational Methods in Structural Dynamics and Earthquake Engineering
M. Papadrakakis, V. Papadopoulos, V. Plevris (eds.)
Kos Island, Greece, 12–14 June 2013

FUNDAMENTAL STUDY ON EVALUATING ROCK SLOPE STABILITY BY VIBRATION MEASUREMENTS USING REMOTE VIBRATION MEASURING SYSTEM

Shintaro Minoura[1], Fumiaki Uehan[1], and Hideki Saito[2]

[1]Railway Technical Research Institute
2-8-38 Hikari-cho, Kokubunji-shi, Tokyo 185-8540 Japan
e-mail: {minoura,uehan}@rtri.or.jp

[2] Oyo Corporation
43 Miyukigaoka, Tsukuba-shi, Ibaraki 305-0841Japan
e-mail: Saito-hideki@oyonet.oyo.co.jp

Keywords: rock slope stability, remote measurement, LDV, dominant frequency, safety factor

Abstract. *The purpose of this study is to clarify the relationship between the mechanical stability of rock brock and its vibration characteristics so as to propose a new method of rock stability evaluation by measuring the vibration of rocks using remote vibration measuring system. Preventing rockfall damages to railway caused by earthquake and other reasons is becoming important, and thus early detection methods for unstable rock blocks are necessary. Therefore, a new method of safe and efficient rock stability evaluation using remote vibration measurement system is needed. In this study, we executed model experiments using concrete blocks bound to the concrete base unit under different adhesion conditions using Laser Doppler Velocimeter (LDV). Through these experiments, quantitative relation between the mechanical stability and the dominant frequency of rock block vibration was clarified. In addition, we executed a numerical analysis using FEM and the relationship was confirmed by the analysis. From the results of the experiment and the analysis, we investigated the relationship between the overturn safety factor, which is defined as the ratio of overturning moment to the maximum resistance moment of the block, and the dominant frequency of the rock vibration, and proposed a new method of rock stability evaluation using this relationship. We also executed a numerical analysis of the relation between the mechanical stability and the dominant frequency of rock block vibration under the influence of seismic ground motion. From the results, we have evaluated the mechanical stability of the rock under the influence of earthquakes by calculating the safety factor.*

1 INTRODUCTION

In Japan, there are many railway lines running through the mountainous areas. On such lines, train accidents and suspending operation caused by falling rocks often have occurred. Currently in Japan, rockfall inspection is carried out mainly by the visual inspection. However, some rockfalls is caused by invisible crack propagation; so it is difficult to evaluate the stability of rock block only by the visual inspection. In order to prevent the falling rocks along the route and ensure the safety and reliability of railway transportation, safe and efficient methods for evaluating the risk of falling rocks quantitatively are required.

Recently, some techniques for evaluating stability of rock block by means of measuring its vibration characteristics such as predominant frequency have been developed[1]. However, these methods require rock vibration measurements by sensors attached to the rock and thus have a problem in the safety and efficiency of the evaluation work. In such circumstances, we introduced a method of evaluating the risk of falling rocks by measuring the vibrational characteristics of the rocks using "U-doppler"(Figure 2) which is a system developed by improving non-contact Laser Doppler Velocimeter (LDV)[2][3]. U-doppler is a long-distance non-contact vibration measuring system for the diagnosis of railway structures. U-doppler offers enhanced safety and efficiency for use in the field[4][5].

The purpose of this study is to clarify the relationship between the mechanical stability and vibration characteristics of rocks and propose a new method of rock stability evaluation by measuring the vibration of rocks using remote vibration measuring system.

In this study, we executed model experiments using concrete blocks bound to the concrete base unit under different adhesion conditions simulating the unstable rock. The dominant frequency of the concrete block vibration were measured using Laser Doppler Velocimeter (LDV) during the experiment. Through these experiments, we investigated the relationship between the mechanical stability of the concrete block and its dominant frequency using "overturn safety factor." Overturn safety factor is defined as the ratio of overturning moment to the maximum resistance moment of the block.

In addition, we executed a numerical analysis using FEM and the relation was confirmed by the analysis. Through the analysis, a similar relationship between the overturn safety factor and dominant frequency of rock block vibration was observed. We also executed a numerical analysis of the relation between the mechanical stability and the dominant frequency of rock block vibration under the influence of seismic ground motion. Based on the results, we have evaluated the mechanical stability of the rock under the influence of earthquakes by calculating the overturn safety factor.



Figure 1: Example of falling rock accident

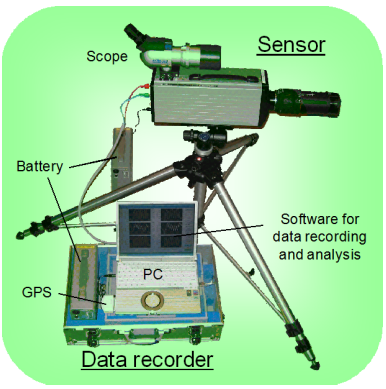


Figure 2: U-doppler

2 EXPERIMENT

In this section, we explain the model experiments executed using concrete blocks bound to the concrete base unit under different adhesion conditions simulating the unstable rock blocks. Through this experiment, dominant frequencies of concrete block were measured using LDV and the relationship between the mechanical stability and the dominant frequency of concrete blocks was clarified.

2.1 Experimental model

In this experiment, the relationship between the mechanical stability and the vibration characteristics of rocks was clarified using concrete block models which simulate the unstable rock. Figure 3 shows the state of experiments and Figure 4 shows the size of the whole model. From this subsection, the right-hand coordinate system shown in Figure 4 is used. The y-axis is defined as the direction of the back of the Figure 4.

The base unit and the block part are made of concrete and the bonding area of the block and the base unit is made of gypsum. In this experiment, we used 2 types of gypsum, ”Hi-stone” and ”Grade A gypsum”. These are product names of the gypsum manufacturer, *Yoshino Gypsum Co.,Ltd.* Table 1 shows the material properties used in this experiment.

In the experiment, three different sizes of concrete block were used. Table 2 shows the sizes of concrete blocks used in the experiment.



Figure 3: State of experiment

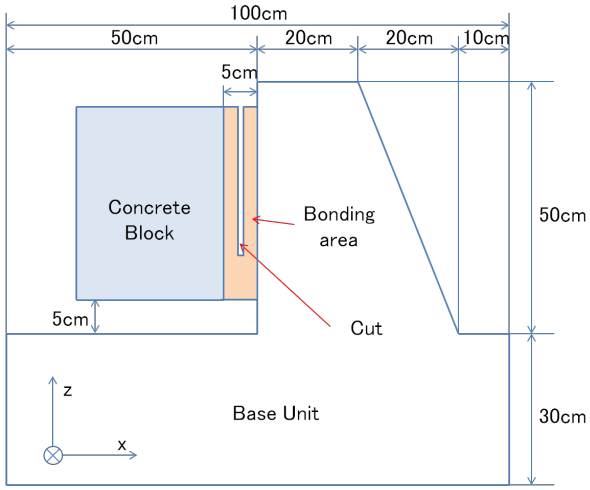
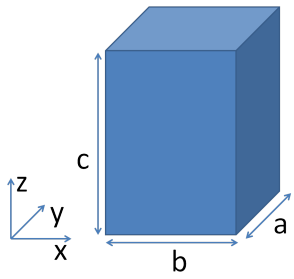


Figure 4: Size of experimental model

Material name	Concrete	Hi-stone	Grade A gypsum
Density(kg/m^3)	2100	1657	1538
Young’s modulus(MN/m^2)	22000	7800	2290
Poisson’s ratio	0.2	0.23	0.2
Tensile strength (MN/m^2)		2.91	0.849

Table 1: Material properties.



Block size	a(cm)	b(cm)	c(cm)	Mass(kg)
Large	20	30	40	57.6
Medium	15	22.5	30	24.3
Small	10	15	20	7.2

Table 2: Sizes of concrete blocks

2.2 Experiment method

In this experiment, the concrete block and the base unit were connected by gypsum part. We simulated the instability of the rock by making a cut in this gypsum part with a saw gradually and the bonding length of the concrete block and the base unit was adjusted. For each bonding length, the velocity of the concrete block was recorded with LDV until the concrete block fell. The velocity was recorded when vibrating the concrete base unit and the ground. The velocity of the concrete block by micro-tremors was also recorded. The dominant frequency was obtained by the Fourier transform of the recorded velocity waveform. This operation was repeated until the concrete block fell.

2.3 Result of the experiment

Figure 5 shows the relationship between the bonding length and the dominant frequency.

From Figure 5, the relationship between the bonding length and the dominant frequency could be approximated by a line. For gypsum with higher Young's modulus, gradient of the approximate line became greater. For the same type of gypsum, the gradient of the approximate line becomes smaller as the size of block is larger. For the same bonding length, the larger block has the smaller dominant frequency.

In the experiment, two types of destruction state were observed at the bonding area. One was observed on the extension of the cut made by a saw. For the other, crack extended horizontally from the tip of the cut made by the saw and the bonding area peeled off from the base unit. This

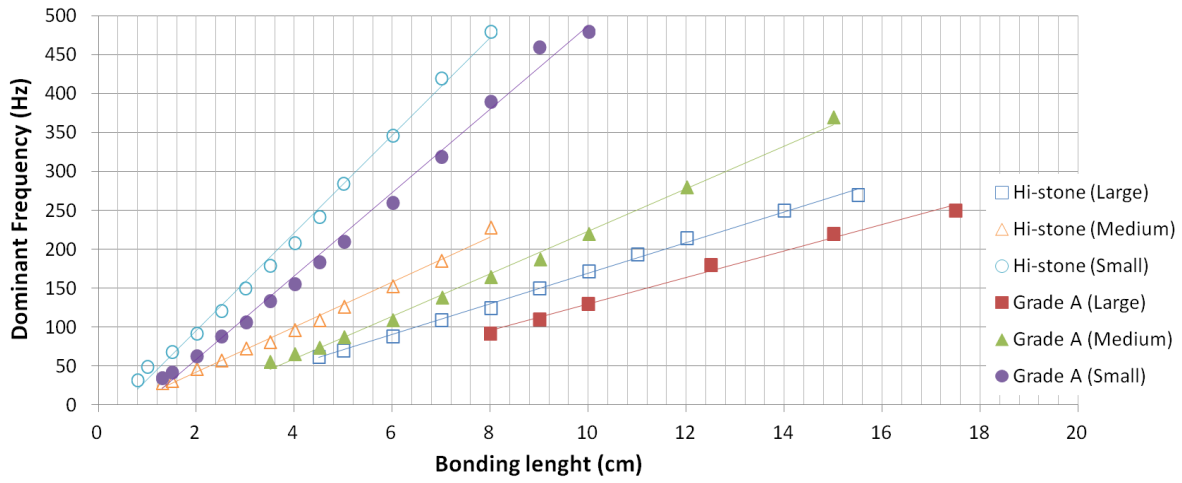
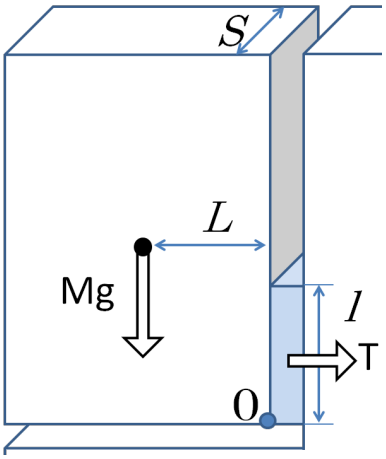


Figure 5: Relationship between the dominant frequency and the bonding length

type of destruction seems to occur only in model experiment.

In order to clarify the relationship between the dominant frequency and the stability of the concrete block, we introduced a parameter called ”overturn safety factor”. The overturn safety factor is defined as the ratio of overturning moment to the maximum resistance moment of the block. The lower-right corner of the block is considered as the rotation center of these moments. The gypsum is considered to be broken when a value of the overturn safety factor becomes less than 1. Figure 6 shows the idea of the overturn safety factor.



$$F = \frac{T}{(Mg \times L)/2} = \frac{(P \times l^2 \times S)/2}{(Mg \times L)/2}$$

F	:	Overturn safety factor
T	:	Total tensile strength
M	:	Mass of concrete block
g	:	Gravity
L	:	Distance to centroid of block
P	:	Tensile strength
l	:	Bonding length
S	:	Width of brock and bonding area
O	:	Center of rotation

Figure 6: Overturn safety factor

Before calculating the overturn safety factor, the tensile strength of each material was back-calculated for each block size on the assumption that the bonding area is destructed when the overturn safety factor is equal to 1. As the result, the back-calculated tensile strength is shown to be $1/2$ to $3/4$ of the tensile strength by laboratory tests. Therefore, when calculating the overturn safety factor, the $2/3$ of the tensile strength determined by the laboratory test is used. Figure 7 shows the summarized relationship between the dominant frequency and the overturn safety factor.

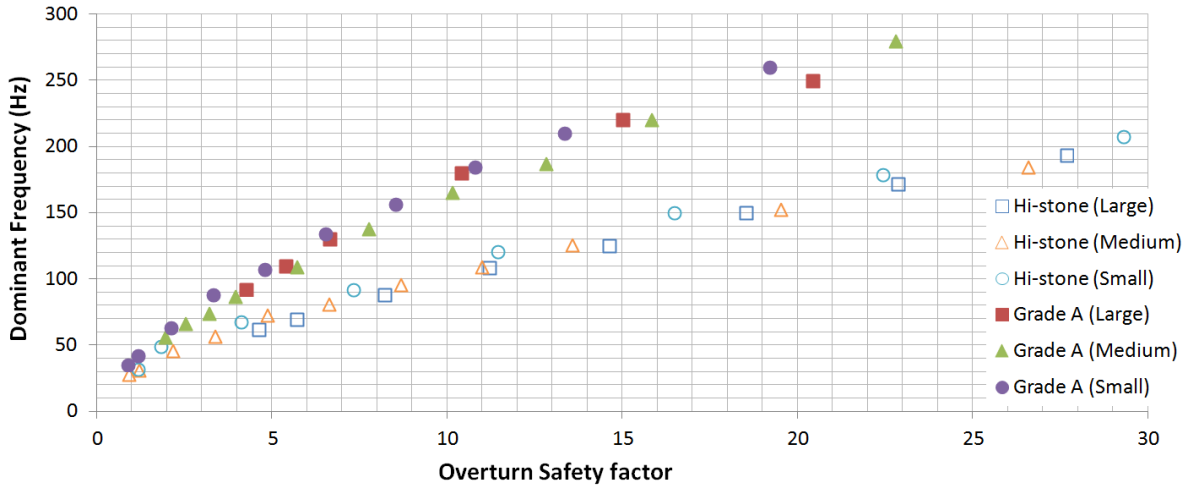


Figure 7: Relationship between the dominant frequency and overturn safety factor (Experiment)

From this figure, regardless of the size of the block, the relationship between the dominant frequency and overturn safety factor is able to be approximated by a single curve for each type of material. This indicates that if the tensile strength of the rock is known, the overturn safety factor can determined by measuring the dominant frequency of the rock.

3 NUMERICAL ANALYSIS

In this section, we explain the analysis using FEM executed corresponding to the experiment mentioned in the section 2. Two types of analyses were performed. The first analysis is eigenvalue analysis. The frequency of the first mode of vibration of blocks was calculated for each bonding length in this analysis. From this analysis, the relationship between the dominant frequency and the mechanical stability of the concrete block was discussed. The second analysis is dynamic analysis under seismic conditions. From this analysis, effects of ground motion on concrete block was evaluated. For both the analyses, structural analysis software "LS-DYNA" was used.

3.1 Analysis model

The analysis model was constructed with the objective to execute comparison between the analysis results and the results by the experiments. Figure 8 shows the model used in the analysis. In the experiment, the bonding length was adjusted by making a cut into gypsum with a saw. In the analysis, this was modeled as a gap with 2mm width. The base unit, concrete block, and bonding area were modeled as elastic bodies with hexahedral solid elements. For the bonding area, the two types of material, Hi-stone and Grade A gypsum, were also used. Material properties of concrete and gypsum used in the analysis were the same as those used in the experiment.

In the experiment, the base unit was long in the y-axis direction. However, compared with the concrete block, the vibration amplitude of the base unit was considered to be very small, and its dominant frequency is much higher. Furthermore, modeling the whole base unit significantly increases the number of elements. Therefore, the base unit was modeled only for the same length as the concrete block in the y-axis direction, and the bottom surface and the surface in the y-axis direction were fixed.

3.2 Eigenvalue analysis

The dominant frequency of the concrete block vibration for each bonding length was solved through the eigenvalue analysis. In the experiment, especially in shorter bonding length, on;y one clear peak had appeared in spectrum of the velocity of concrete block. Therefore, in the experiment, the dominant vibration of the block is mainly due to the first mode of vibration. The first mode of vibration is rotation around lower-right corner of the block. Figure 9 shows the first mode of concrete block vibration.

In the analysis, three different sizes of concrete block(large, medium, small) and two types of gypsum (Hi-stone and Grade A gypsum) were used. Sizes of concrete blocks used in the analysis were the same as those used in the experiment. For these 6 cases, eigenvalue for each bonding length was calculated.

The dominant frequencies of concrete blocks calculated in the analysis were compared with the dominant frequencies of concrete blocks obtained in the experiment. In Figure 10, relationships between the bonding length and dominant frequency obtained by the analysis are compared with those obtained by the experiment.

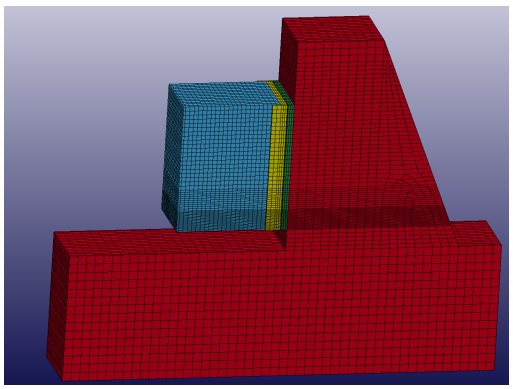


Figure 8: Analysis model

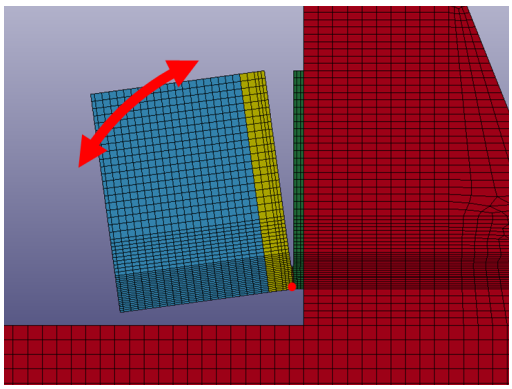
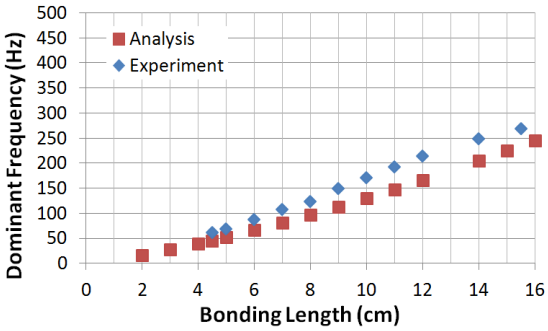
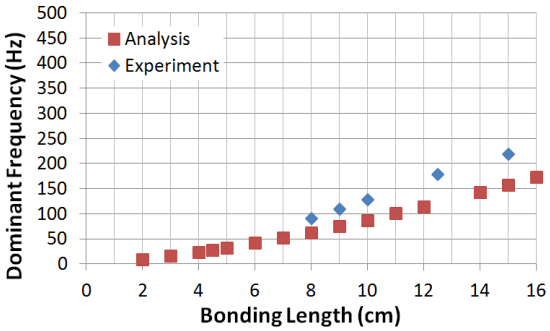


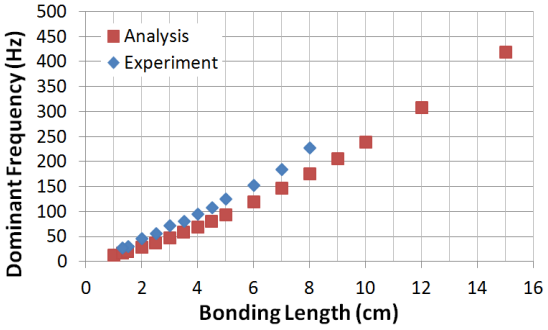
Figure 9: First mode of concrete block's vibration



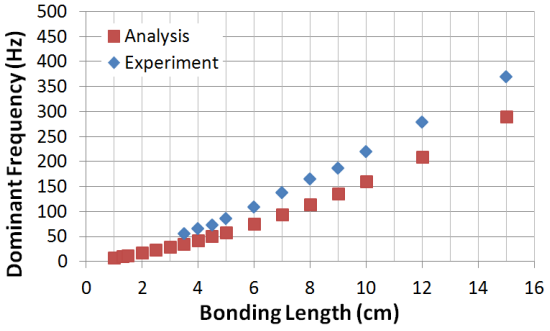
(a) Hi-stone (Large)



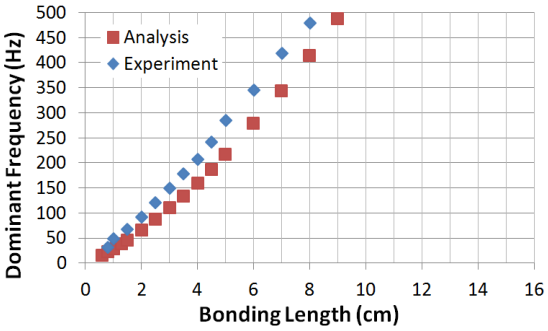
(b) Grade A gypsum (Large)



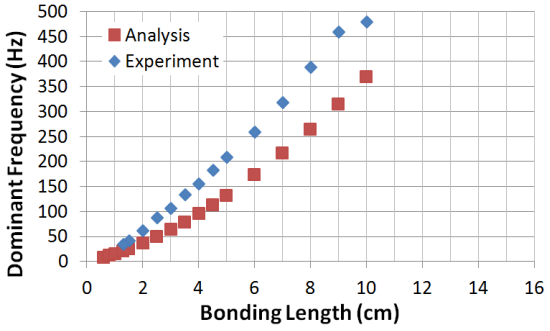
(c) Hi-stone (Medium)



(d) Grade A gypsum (Medium)



(e) Hi-stone (Small)



(d) Grade A gypsum (Small)

Figure 10: Comparison of relationships between the bonding length and dominant frequency

In Figure 10, dominant frequencies solved by the analysis show lower values than those obtained by the experiment in all cases. However, the tendency that the dominant frequency becomes lower as the bonding length becomes shorter which implies the increase of instability of concrete block is observed in both the experiment and the analysis. Similarly to the experiment, a larger block has a smaller dominant frequency for a given bonding length.

In the experiment, the relationship between bonding length and dominant frequency can be approximately linear. On the other hand, a quadratic function curve is in good agreement with the result of analysis. The dominant frequency was solved as the first mode of vibration in the analysis. However in the experiment, especially in the longer bonding length, the concrete block vibration might be influenced by other modes of vibrations; this might cause the different approximate curves for the analysis and for the experiment respectively.

The relationship between the dominant frequency and the overturn safety factor was summarized for the analysis in the same way as for the experiment. Figure 11 shows the relationship between the dominant frequency and overturn safety in analysis. When calculating the overturn safety factor, $2/3$ of the tensile strength of gypsum determined by the laboratory test was used as adhesive force.

Similar results were obtained from both the experiment and the analysis. The relationship between overturn safety factor and dominant frequency is able to be approximated by a single curve for each material regardless of the size of the block. From Figure 11, when the overturn safety factor is 1, the dominant frequency of Hi-stone is approximately 19Hz and dominant frequency of Grade A gypsum is approximately 23Hz by the analysis. On the other hand, from Figure 7, the dominant frequency of Hi-stone is approximately 30Hz and dominant frequency of Grade A gypsum is approximately 35Hz in by the experiment when the overturn safety factor is 1.

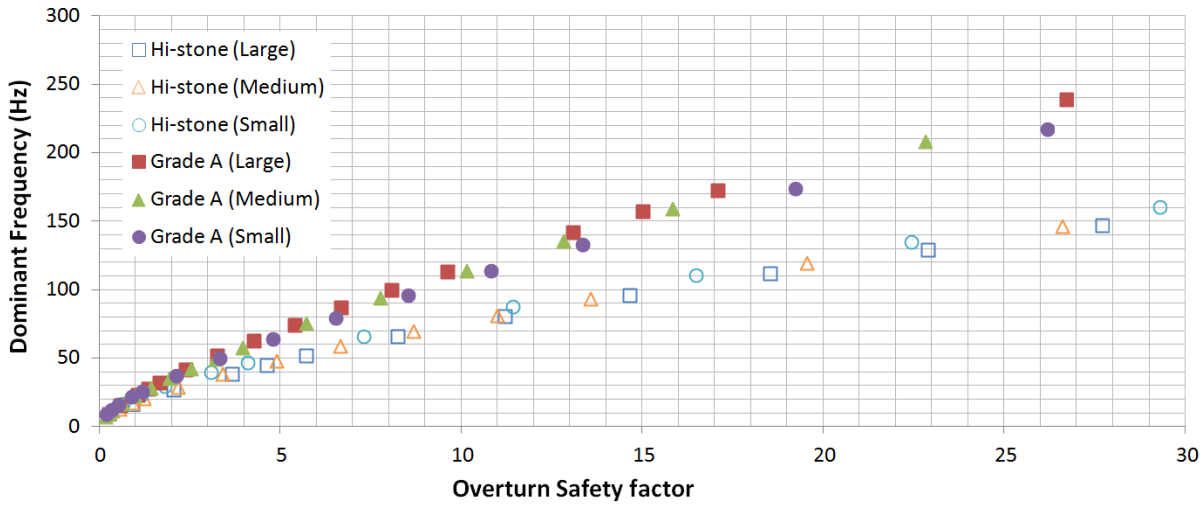


Figure 11: Relationship between dominant frequency and overturn safety factor (Numerical analysis)

3.3 Analysis under the influence of seismic ground motion

In this section, a numerical analysis under the influence of seismic ground motions was executed. The same analytical model as the one used in the subsection 3.2 was also used in the analysis.

In the seismic ground motion analysis, three types of ground motion were applied to the model. Figures 12 to 14 show the waveforms of ground motions applied in the analysis.

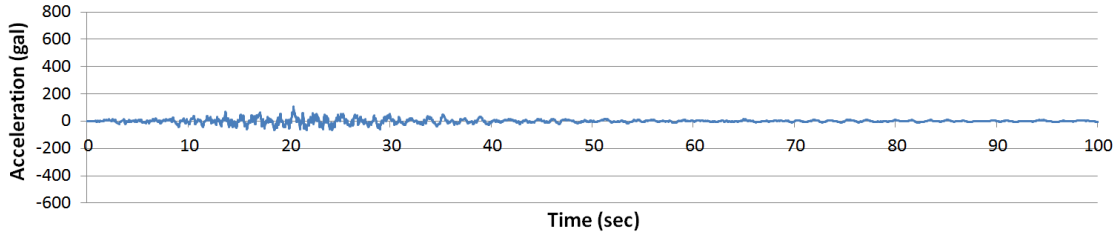


Figure 12: Ground motion No.1 (Level 1 earthquake ground motions)

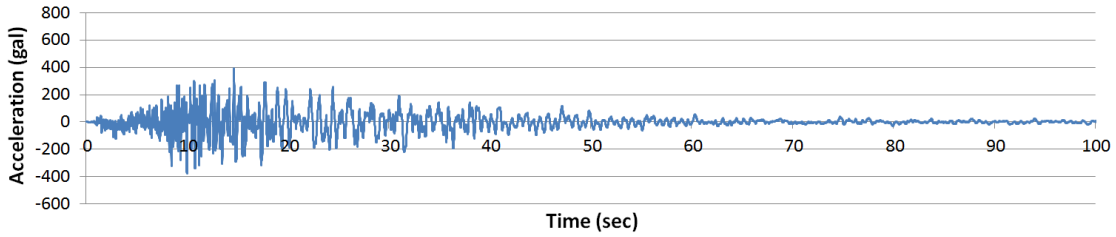


Figure 13: Ground motion No.2 (Level 2 earthquake ground motions by trench type earthquake)

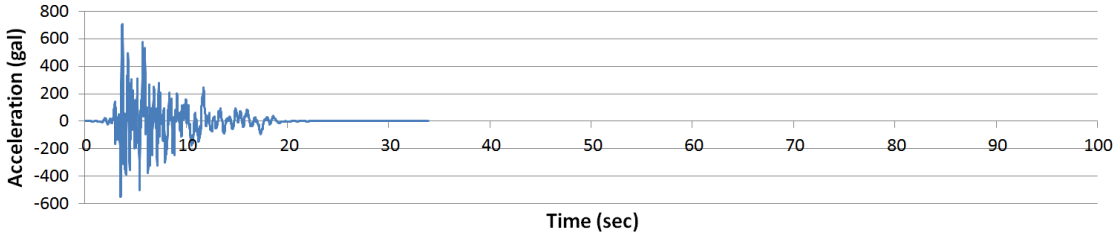


Figure 14: Ground motion No.3 (Level 2 earthquake ground motions by dislocation earthquake)

Waveform in Figure 12 is the waveform of ground motion No.1. This waveform is a type of Level 1 earthquake ground motion. Japanese seismic criterion defines Level 1 earthquake ground motion as an earthquake ground motion that is more likely to occur during the designed working life of facilities. Waveform in Figure 13 is the waveform of ground motion No.2. This waveform is a type of Level 2 earthquake ground motion caused by trench type earthquake. Japanese seismic criterion defines Level 2 earthquake ground motion as the largest earthquake ground motion that can occur the during designed working life of facilities. Waveform in Figure 14 is the waveform of ground motion No.3. This waveform is a type of Level 2 earthquake ground motion caused by dislocation earthquake.

In this analysis, effect on stability of concrete block under the ground motion was evaluated using the stress generated in the bonding area. It is thought that the destruction of the bonding area occurs when tensile force of the bonding area exceeds tensile strength. From the experiment, concrete blocks seemed to vibrate around the lower-right corner of the block. Therefore, it is considered that if the maximum x-axis stress of the bonding area reaches tensile strength, the bonding area destructs.

Before executing the ground motion analysis, the static analysis considering the dead load was executed. From this analysis, stress due to the concrete block's dead load in the bonding area was calculated. This analysis was executed for each bonding length using the implicit method.

From the result of the static analysis, the maximum stress of the bonding area in the analysis largely exceeded the tensile strength which was determined by the laboratory test even for the bonding length for which the bonding area was not destructed in the experiment. Due to this, we interpolate the relationship between the result of the static analysis and the overturn safety factor with piecewise linear functions. From this, the maximum x-axis stress of the bounding area when the overturn safety factor is equal to 1 was obtained. We considered this maximum stress as the criterion of whether bonding area destructs or not. If a maximum x-axis stress observed in the ground motion analysis exceeds this value, we regard the bonding area as destructed. Figure 15 shows the relationship between the maximum x-axis stress of the bonding area and the overturn safety factor.

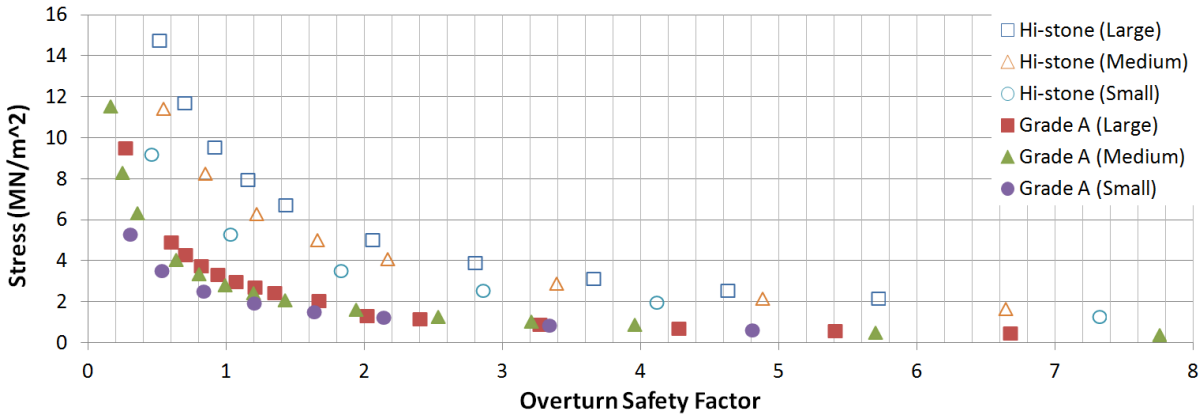


Figure 15: Relationship between the maximum x-axis stress of the bonding area and the overturn safety factor

For each block size and bonding length, the maximum x-axis stress generated in the bonding area was calculated under these three types of ground motion in the analysis. From the result of static analysis and ground motion analysis, the bonding length when bounding area destructs under the effect of each ground motion was obtained by piecewise linear interpolation of the result of the analysis. After that, the overturn safety factor corresponding to the bonding area destructs under each ground motion was calculated.

Table 3 and Table 4 show the boding length and overturn safety factor corresponding to destruction of the bonding area for each ground motion analysis. To clarify the effect of ground motions, we compared result of the ground motion analysis with the eigenvalue analysis. Figure 16 shows the relationship between the overturn safety factor and the dominant frequency with the results of the ground motion analysis shown in Table 3 and Table 4. The relationship between the results of eigenvalue analyses and overturn safety factor are also shown in Figure 16.

Form the result of the analysis, effect of the ground motion No.3 (Level 2 earthquake ground motion by dislocation earthquake) was the largest. For each material, the bonding area destructs at almost the same value of overturn safety factor regardless of the block size. For models whose bonding area is made of high stone, the bonding area is destructed even at the value of overturn safety factor of about 2.3 under the influence of ground motion No.3. Similarly, for models

Material	Block	Ground motion		
		No.1	No.2	No.3
Hi-stone	L	2.3cm	2.7cm	3.2cm
	M	1.5cm	1.7cm	2.1cm
	S	0.8cm	0.9cm	1.2cm
Grade A	L	4.1cm	4.8cm	5.2cm
	M	2.7cm	3.2cm	3.6cm
	S	1.5cm	1.7cm	2.0cm

Table 3: Bounding length

Material	Block	Ground motion		
		No.1	No.2	No.3
Hi-stone	L	1.17	1.70	2.28
	M	1.17	1.66	2.32
	S	1.22	1.73	2.44
Grade A	L	1.15	1.56	1.83
	M	1.16	1.61	2.06
	S	1.15	1.60	2.13

Table 4: Overturn safety factor

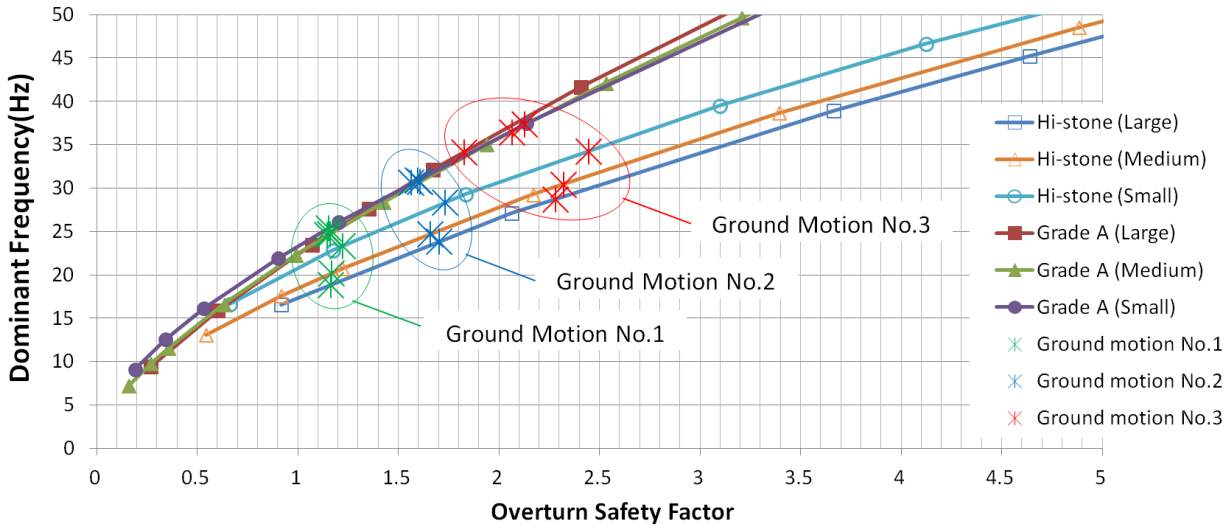


Figure 16: Effects of ground motion

whose bonding area is made of Grade A gypsum, the bonding area is destructed even at the value of overturn safety factor of about 2.0 under the influence of ground motion No.3

From these results, it is expected that if material property and overturn safety factor of a rock are known, it is possible to determine whether a rock collapses or not by a given earthquake. However, only 2 types of bonding area's material and 3 different sizes of blocks were used in this experiment and analysis. In the future, it is necessary to examine effects of bonding area's material and block size by testing more different types of materials and sizes of the blocks.

4 CONCLUSIONS

- The relationship between the dominant frequency and the overturn safety factor is able to be approximated by a single curve for each material regardless of the sizes of the blocks in the experiment. This indicates that the overturn safety factor can be determined by measuring the dominant frequency of the rock if the tensile strength of the rock is known.

- Similar relationships between the overturn safety factor and the dominant frequency are observed in the experiment and in the analysis. However, the dominant frequencies observed in the analysis are lower than those observed in the experiment. It is necessary to determine the cause of this difference by evaluating the adhesive strength more adequately and by introducing more appropriate modeling of bonding area.

- If the material property and the overturn safety factor of a rock are known, it is possible to determine whether a rock collapses or not by a given earthquake from the result of the ground motion analysis.
- A simple method was used to calculate the moment of resistance in calculating the overturn safety factor. Moreover, 2/3 of the tensile strength was used to calculate the overturn safety factor. It is necessary to determine the stress distribution or deformation of the bonding area and to introduce appropriate method in order to evaluate the tensile force and the rock stability in the future.
- In this study, only 2 types of bonding area's materials and 3 different sizes of blocks were used in the experiment and the analysis. In the future, it is necessary to examine effects of bonding area's material and block size by testing more different types of materials and sizes of the blocks.

ACKNOWLEDGEMENT

This study is financially supported by the Japanese government's Ministry of Land, Infrastructure, Transport and Tourism.

REFERENCES

[1] K. Ogata, H. Matsuyama, K. Amano, Evaluation of the rockfall potential utilizing the characteristics if vibration. *Journal of Japan society of Civil Engineers*, **VI-61,** 123-135, 2003. [In Japanese]

[2] O. Murata, F. Uehan, H. Saito, G. C. Ma, Fundamental Study on the Evaluation Method of Mechanical Stability of Rock Blocks by Remote Vibration Measurement. *RTRI report,* **Vol.25, No. 2**, 47-52, 2011. [In Japanese]

[3] F. Uehan, H. Saito, G. C. Ma, Fundamental Study on the Remote Vibration MeasuringSystem for Evaluating Rock Slope Stability. *The 15th World Conference on Earthquake Engineering (15 WCEE),* 2012.

[4] F. Uehan, O. Murata, H. Saito, Y. Ohtsuka, Fundamental study on the remote vibration measuring system for evaluating rock slope stability. *RTRI Report,* **Vol. 24, No. 4,** 5-10, 2010. [in Japanese]

[5] F. Uehan, Development of non-contact vibration measuring system for inspection of seismic damage to railway structures. *The 14th World Conference on Earthquake Engineering (14 WCEE),* 2008.

COMPDYN 2013
4th ECCOMAS Thematic Conference on
Computational Methods in Structural Dynamics and Earthquake Engineering
M. Papadrakakis, V. Papadopoulos, V. Plevris (eds.)
Kos Island, Greece, 12–14 June 2013

EFFECT OF COUPLING EXCESS PORE PRESSURE AND SOIL DEFORMATION ON THE NONLINEAR RESPONSE

Silvana Montoya-Noguera[1] **and Fernando Lopez-Caballero**[1]

[1]Ecole Centrale Paris
Grande Voie des Vignes, F-92295 Chtenay-Malabry
{silvana.montoya-noguera},
{fernando.lopez-caballero}@ecp.fr

Keywords: Earthquake engineering, Site response, Soil nonlinearity, Liquefaction.

Abstract. *The development of excess pore pressure (Δp_w) and consequent reduction in effective stress leads to the softening of a liquefiable soil deposit that can alter ground motions in terms of amplitude, frequency content, and duration. To assess these effects in a 1D medium to loose sand model, two analysis were made: (1) A BIOT hydraulic and mechanical computation of a saturated soil deposit and (2) a mechanical computation of a dry soil with equivalent behavior. The results regarding the profile of maximum accelerations and shear strains, the surface accelerations and their corresponding response spectra ratio are analyzed. The mean values of the normalized response spectra ratio between the wet and dry surface acceleration show a deamplification of high frequencies (i.e. $f > 1.0Hz$) and an amplification of low ones that tend to increase with the liquefaction zone size. Coupling of Δp_w and soil deformation is therefore of great importance to accurately model the ground motion response. On the contrary, while peak acceleration predictions could be conservative, the amplification on the low frequencies could be largely underestimated which would be highly prejudicial for tall buildings.*

1 INTRODUCTION

The performance of structures during earthquakes is strongly influenced by the soils that support them. Local site effects can influence structures performance in two primary ways: by imposing additional deformations on the structure through ground failure and by influencing the ground motions that excite the structure. The reliable and economical seismic design of structures requires that local site effects on the ground motions be accurately predicted.

Usually, equivalent-linear models like the one employed in SHAKE [1] program are used to quantify the effect of soil deposits on propagated ground motions. Moreover and in most cases, effects of local soil deposits are only included as an attenuation of the maximum acceleration at surface [2]. However, the behavior of liquefiable soils is dominated by pore pressure generation which is not included in these models. This paper studies numerically the effect of excess pore pressure (Δp_w) on the nonlinear response of liquefiable soils. For this purpose an elastoplastic multi-mechanism model, known as ECP model [3, 4], is used to represent the soil behavior. The soil deposit was subjected to 78 unscaled earthquake signals chosen from the Pacific Earthquake Engineering Research (PEER) Center database.

First of all, nonlinearity induced by both strong ground motion and liquefaction apparition was studied via a 1-D numerical modelling of a saturated sand deposit. Then and in order to solely quantify the effect of Δp_w on the nonlinear response of the sand deposit, two mechanically-equivalent models -one saturated and one completely dry - were analyzed. Three aspects of the motion response are evaluated: i) the maximum acceleration and shear strain profile, ii) the maximum surface acceleration and iii) the corresponding acceleration response spectra.

2 NUMERICAL MODEL

2.1 Model description

The studied site is composed principally of 20m of medium to loose sand with an average shear wave velocity ($V_{s,\,20}$) close to 200 m/s, corresponding to ground type C of Eurocode 8 [5]. As shown in figure 2a, the shear modulus of the soil increases with depth. The characteristic elastic site period (T_s) of the soil is calculated by a transfer function between the Fourier transforms of accelerations in the surface and at the bottom of the soil deposit, for a sample signal at very low amplitudes (e.g. $PHA \approx 1E-5g$) to ensure elastic soil behavior. The first amplification peak corresponds to the T_s and is approximated to 0.27s (see figure 2b). The saturated soil has a ground water table placed 1 meter below the surface and an impervious deformable bedrock is placed at the bottom of the column. The bedrock is assumed to follow an isotropic linear elastic behavior with a V_s equal to 551m/s.

2.2 Finite element mesh

As the soil is assumed to be horizontally homogeneous, 1D $u-p_w$ coupled finite element computations with plain-strain assumption were performed. The general purpose finite element code GEFDyn [6] was used . The saturated soil was modelled using quadrilateral isoparametric elements with eight nodes for both solid displacements and fluid pressures. The thickness of the elements is 0.5m, which is in agreement with the suggestions made by Foerster and Modaressi [7] to prevent numerical dispersion. An implicit Newmark numerical integration scheme is used in the dynamic analysis. The numerical parameters were calculated by the methodology of Kontoe et al. [8], by which γ and β are calculated from the spectral radius at infinity ρ_∞ to

achieve an "optimal high-frequency dissipation with minimal low-frequency impact". Furthermore, in order to quantify the numerical damping ξ related to these parameters a calibration procedure [9] was performed. Thus, a ρ_∞ equal to 0.8 is used, which corresponds to γ=0.611, β=0.301 and ξ equal to 1.64%.

Concerning boundary conditions and as the response of an infinite semi-space is modelled, equivalent boundaries have been imposed on the nodes of lateral boundaries (i.e. the normal stress on these boundaries remains constant and the displacements of nodes at the same depth in two opposite lateral boundaries are the same in all directions) [10]. For the bedrocks boundary condition, paraxial elements simulating deformable unbounded elastic bedrock have been used [11]. The vertically incident shear waves, defined at the outcropping bedrock, are introduced into the base of the model after deconvolution. Thus, the obtained movement at the bedrock is composed of the incident waves and the reflected signal.

2.3 Input earthquake motion

In order to define appropriate input motions to the non-linear dynamical analysis, a selection of recorded accelerograms are used. The adopted earthquake signals are proposed by Bradley et al. [12] and Sorrentino et al. [13]. Thus, 78 unscaled records were chosen from the Pacific Earthquake Engineering Research Center (PEER) database. The events range between 5.8 and 7.7 in magnitude and the recordings have site-to-source distance from 10 to 150km and dense-to-firm soil conditions (i.e. 30m averaged shear-wave velocity ($V_{s\,30}$) between 270 and 800m/s).

The statistics of some earthquake parameters calculated at outcropping conditions are shown in table 1. These intensity measures are peak horizontal acceleration (PHA), peak ground velocity (PGV), mean period (T_m), predominant period (T_p), period of equivalent harmonic wave ($T_{V/A}$), Arias intensity (I_a), significant duration ($t_{5\,95}$), root-mean-square intensity (I_{rms}), spectral intensity (SI) and specific energy density (SED). The coefficient of variation (CV) is above 50% for almost all parameters and it is above 100% for I_a. A higher variation in I_a is of great importance given that after the sensitivity analysis performed by Lopez-Caballero and Modaressi-Farahmand-Razavi [14], it was proved to be the most influential input variable on the liquefaction index ($Q_{H=10}$). Figure 1 shows the response spectra of all the input earthquake motions; accelerations were filtered to 15Hz and the spectral amplitude has a 5% structural damping. Similarly, a great variation is presented on the response spectra.

Table 1: Earthquake characteristics

Parameter	Range	Mean	CV [%]	Median
PHA [g]	0,05 - 0,91	0,25	65	0,18
PGV [cm/s]	4,82 - 69,95	23,44	62	21,08
T_m [s]	0,22 - 1,02	0,61	32	0,58
T_p [s]	0,08 - 1,38	0,4	66	0,35
T_{VA} [s]	0,21 - 2,43	0,53	64	0,45
I_a [m/s]	0,04 - 3,16	0,74	102	0,41
$t_{5\,95}$ [s]	2,92 - 62,13	15,84	76	11,7
I_{rms} $[m/s^2]$	0,07 - 0,88	0,29	63	0,23
SI [m]	0,21 - 2,55	0,85	59	0,77
SED $[cm^2/s]$	34,51 - 11646	1098,5	184	497,86

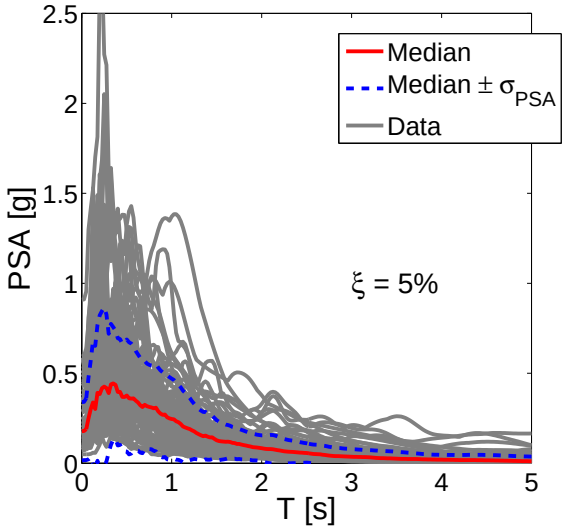


Figure 1: Response spectra of earthquake motions

2.4 Soil constitutive model

The soil behavior is simulated with the elastoplastic multimechanism model developed at Ecole Centrale Paris, ECP model also known as Hujeux model. This model can take into account the soil behavior in a large range of deformations. The model is written in terms of effective stresses. The model uses a Coulomb type failure criterion and the critical state concept. The evolution of hardening is based on the plastic strain (deviatoric and volumetric strains for the deviatoric mechanisms and only volumetric strain for the isotropic one). To take into account the cyclic behavior it uses a kinematical hardening which relies on the state variables at the last load reversal. The soil behavior is decomposed into pseudo-elastic, hysteretic and mobilized domains. Refer to Aubry et al. [3], Hujeux [4], Lopez-Caballero and Modaressi-Farahmand-Razavi [14] among others for a complete understanding of the ECP model. The soil parameters were determined with the procedure defined in Lopez-Caballero et al. [15] and are shown in table 2. The verification of these parameters and some laboratory test simulations can be found in Lopez-Caballero and Modaressi-Farahmand-Razavi [14].

3 EFFECT OF INDUCED PORE WATER PRESSURE

In order to solely quantify the effect of induced pore water pressure (Δp_w) on the nonlinear response of the sand deposit, two mechanically-equivalent models -one saturated and one completely dry - were analyzed. Firstly, to ensure that the only difference in these models behavior is due to pore water pressure generation, the shear modulus profile and transfer function are evaluated. The obtained maximum shear modulus profiles are shown in figure 2a for the elastic behavior and except for some differences at G_{max} at the bottom of the column, the initial behavior of both soils is identical. Therefore, it is proved that differences in the response will be due only to the effect of Δp_w on the wet column.

The spectral ratio, shown in figure 2b is the ratio between the Fourier transform of the motions at the ground surface and the bedrock. It characterizes the amplification produced by the soil deposits [9]. Both models present the same predominant frequencies (also called characteristic frequencies), although the dry column present lower amplifications.

Table 2: ECP model's parameters for the soil column

rho_s (kg/m^3)	2700
n $(\cdot)$	0.47
Elasticity	
K_{ref} (MPa)	628
G_{ref} (MPa)	290
n_e	0.5
p_{ref} (MPa)	1.0
Critical State and Plasticity	
ϕ'_{pp} $(^{\cdot})$	30
β	33
d	2.0
b	0.2
p_{co}(kPa)	81.80
Flow Rule and Isotropic Hardening	
$\psi'(^{\cdot})$	30
α_ψ	1.0
a_1	1.0E-4
a_2	2.0E-3
c_1	2.0E-3
c_2	1.0E-3
m	1.5
Threshold Domains	
γ^{ela}	5.0E-3
γ^{hys}	4.0E-2
γ^{mob}	8.0E-1
γ^{ela}_{iso}	1.0E-3

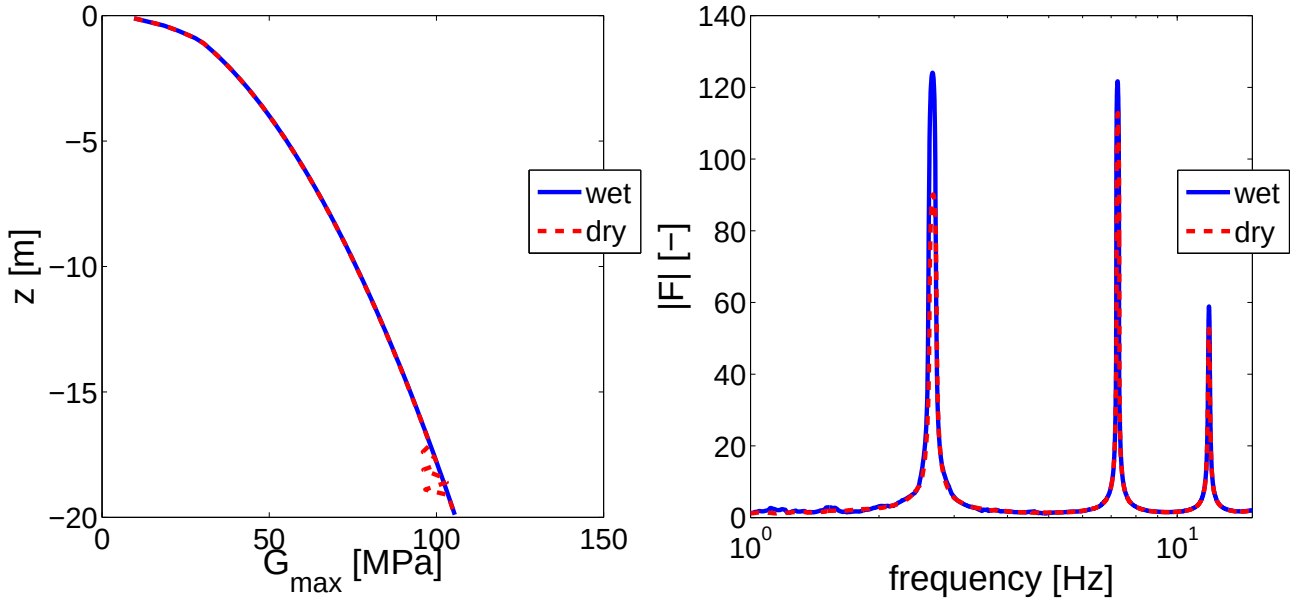
3.1 Peak surface acceleration

Regarding the relation between the peak horizontal acceleration at outcropping (PHA) and received at the surface (PGA), figure 3a shows an amplification of the signal for PHA less than 0.2g. As shown by others [16, 14, 17], in this case it appears that this value is a threshold for nonlinearity due to the ground motion. Above this threshold, the peak acceleration at surface is bigger for the dry column as the attenuation given by the liquefaction apparition is not present. Nonetheless, it appears some attenuation probably caused by the soil resistance degradation.

Figure 3b expresses the peak surface accelerations (PGA) of the dry column as a function of PGA of the wet column ranged by the Liquefaction Index (Q) for a selected depth H. This value is defined by Shinozuka and Ohtomo [18] as:

$$Q_H = \frac{1}{H}\int_0^H \frac{\Delta p_{w\,end}(z)}{\sigma'_{v0}(z)}\mathrm{d}z \tag{1}$$

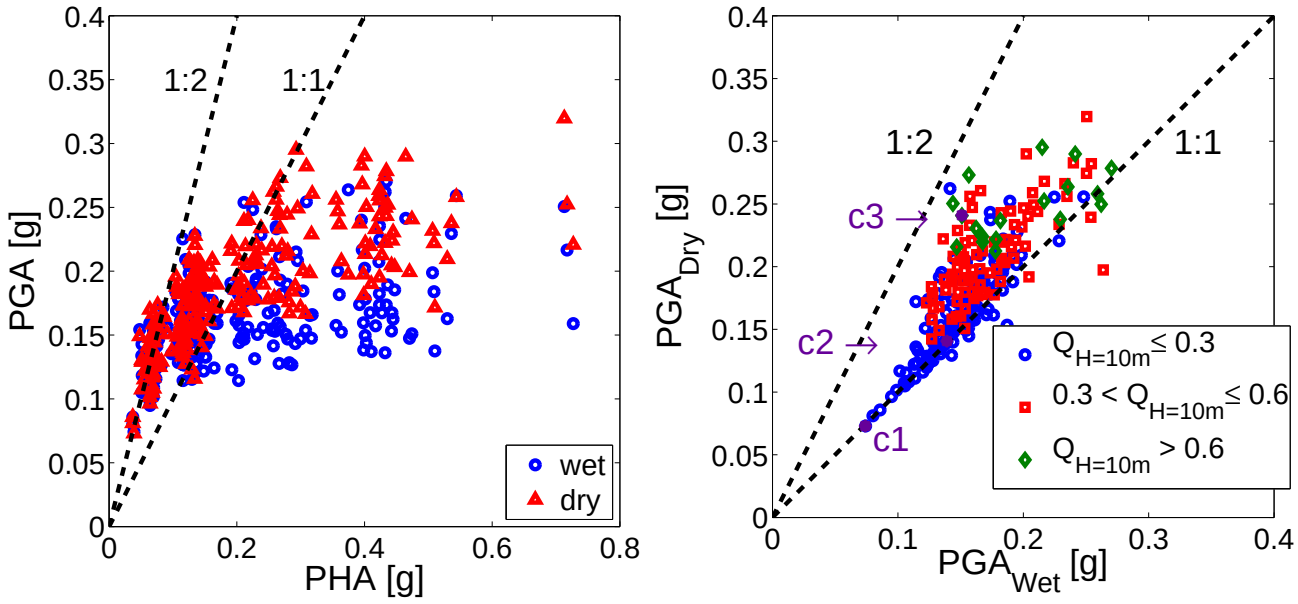
where $\Delta p_{w\,end}$ is the difference between the pore water pressure at the begging and at the end of the input motion at a certain depth z and σ'_{v0} is the initial effective vertical stress at the same depth. The Q value indicates the ratio of liquefaction initiation for a selected depth at the end of shaking. A value of 1.0 indicates conditions of initial liquefaction throughout the H meters column. As shown in the figure 3b, PGA values for the dry column can be twice as big as the



(a) (b)

Figure 2: Elastic behavior a) G_{max} profile and b) transfer function

ones of the wet column; moreover it appears to be a relationship between these differences and the liquefaction index Q.



(a) (b)

Figure 3: a) Peak ground acceleration at free field (PGA) as a function of peak horizontal acceleration at outcropping (PHA) and b) PGA of the dry and wet column grouped by Liquefaction index

3.2 Acceleration profile

For the purpose of analyzing the motion variation throughout the soil deposit, three cases were studied: c1) $PHA \simeq 0.05$g, c2) $PHA \simeq 0.15$g and c3) $PHA \simeq 0.5$g (shown in figure 3b). For the first case, both columns amplify the maximum acceleration by a factor of 2; for the second one, PGA is almost equal to PHA; and for the last case, the peak acceleration is greatly attenuated (i.e. $PGA \simeq 0.5PHA$). Moreover, the difference between dry and wet columns increases with cases. The time history profiles of the pore pressure ratio ($r_u(t) = \Delta p_w(t)/\sigma'_{v0}$) are shown in figure 4. The darkest blue color is $r_u = 0$ and the darkest red one is $r_u = 1.0$. Case 1 is not shown as r_u is less than 0.2 throughout the profile, while for the second case, starting at 7s, between 6 and 15m depth r_u values are greater than 0.5 and by 7m there is a concentrated totally liquefied zone (i.e. $r_u = 1.0$) from about 10s until the end of shaking. Case 3, however, presents two strong liquefied zones at around 2 to 5m and between 8 and 10m; the first one starting at 3s and the deeper one at 5s. Concerning the time history, it appears to be two clear drops of pore pressure at 5s and 8s, with others smaller ones in between. Finally, after 12s, pore pressure starts to gradually increase and spread through the soil deposit. It is interesting to note that while the same soil is tested, different motions liquefy different depths.

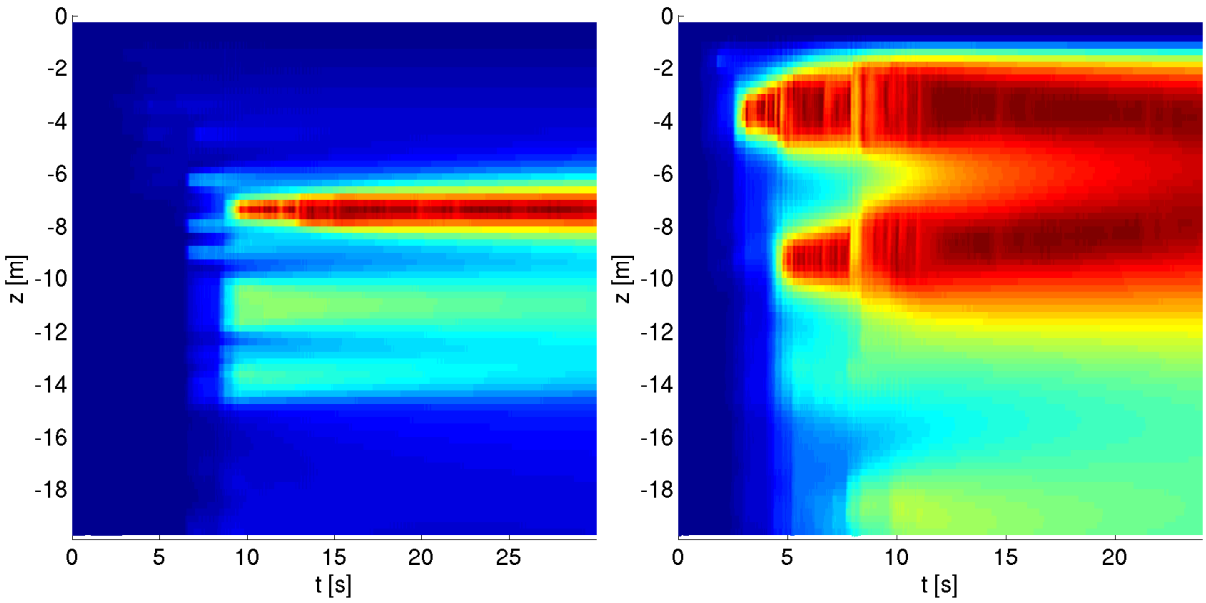


Figure 4: Time history of r_u profile a) c2 point and b) c3 point

In figure 5 the profiles of the pore pressure ratio r_u at the end of shaking, the maximum acceleration and the maximum absolute shear strain (γ) are shown for the three cases. In the first case, in figure 5a, it is clear that the peaks on the acceleration profile correspond to the peaks on shear strain at about 6 to 8m, whereas peaks on r_u are some meters above. As for the dry column, there are no relevant peaks neither on the acceleration nor the γ profile. Rather small differences on the PGA between the wet and dry column can be due to the low pore pressure ratio presented along the profile ($r_{u\,end} < 0.1$). As for the second case, in figure 5b, liquefaction initiated around 8m (i.e. $r_{u\,end} > 0.8$). The a_{max} profile presents almost the same peak with a maximum three times bigger than PHA value at 8m. The γ profile also presents it maximum

at the same depth, although other spikes are presented. By the other hand, the dry column presents some differences between the maximum on acceleration and on shear strain, which are presented some meters below. Finally, for the third case shown in figure 5c, liquefaction is presented from 3 to 10m, which as seen in figure 3a, gives to an attenuation of the PHA value in the wet column. In it, although the a_{max} profile is decreasing as it climbs up to the surface, four spikes can be distinguished at around 2, 5, 10 and 15m. These are also present at the $|\gamma_{max}|$ profile, with strains 6 times bigger than the average. Regarding the dry column, and like in the other cases, spikes in the a_{max} and $|\gamma_{max}|$ profiles are much smaller and are not related to those of the wet column. On the whole, shear strains are always smaller for the dry column, i.e. without the effect of coupled excess pore water pressure with deformation.

3.3 Acceleration response spectra

The influence of coupling excess pore water pressure to deformations is asset by calculating the response spectra of the surface acceleration from the wet and dry column. Because of the variation of the frequency content and by means of arriving to a general conclusion, the acceleration-time histories are divided into three cases which are then studied separately. The input motion accelerogram and the pore pressure ratio at the end of shaking evaluated at 10m depth in the wet model are shown in figure 6 for the three cases. As in the previous figure, the spikes on acceleration correspond to the rapid increase of r_u (e.g. at 8s in figure 6c. Two vertical lines show the t_5 and t_{95} values, defined as the time where 5 and 95% of Arias intensity is reached, which roughly coincides with the start and end of the r_u increase. These lines will be used to separate the different time windows.

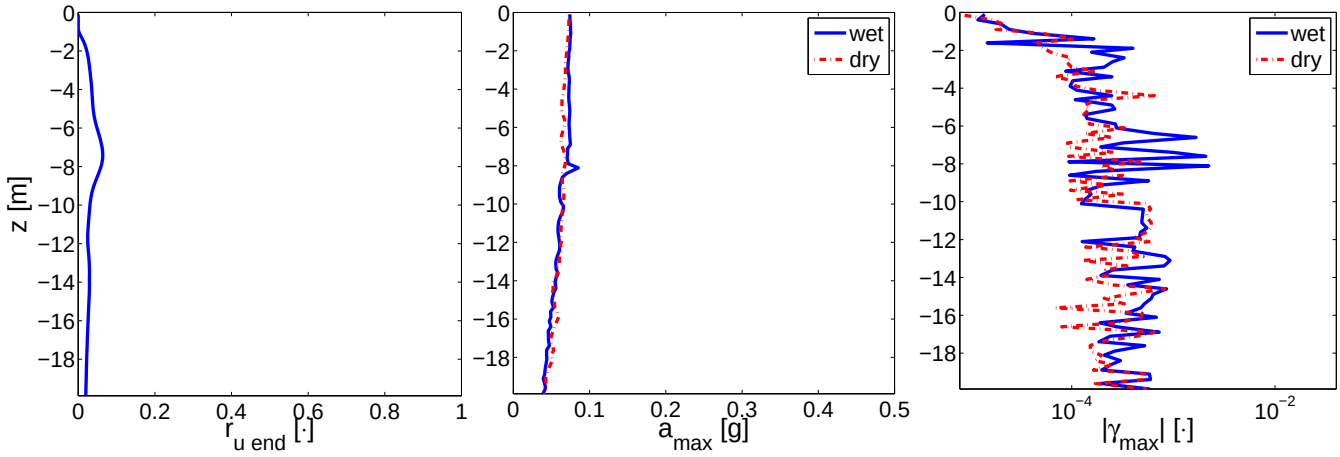
The response spectra at different time windows are plotted in figure 7 for the three cases and the three time windows. For the first case, $r_u(z = 10m) \leq 0.03$, the three time windows present near match between both columns which confirms that significant softening did not occur. While for the second and third cases, only for the first time window (i.e. prior to significant rise of pore pressure), responses of the wet and dry columns are similar. Afterwards and for short periods, the dry column produced a much higher peak whereas the coupling of excess pore pressure and its subsequent soil softening inhibits the transfer of the intense high-frequency peaks to the ground surface. For long periods, the wet column presents larger spectral values than the dry column. As the r_u value increases, i.e. in the third case (figure 7c), the difference between columns increases: for the wet column, amplification of long periods and for the dry one, amplification of short periods.

3.3.1 Normalized response spectral ratio

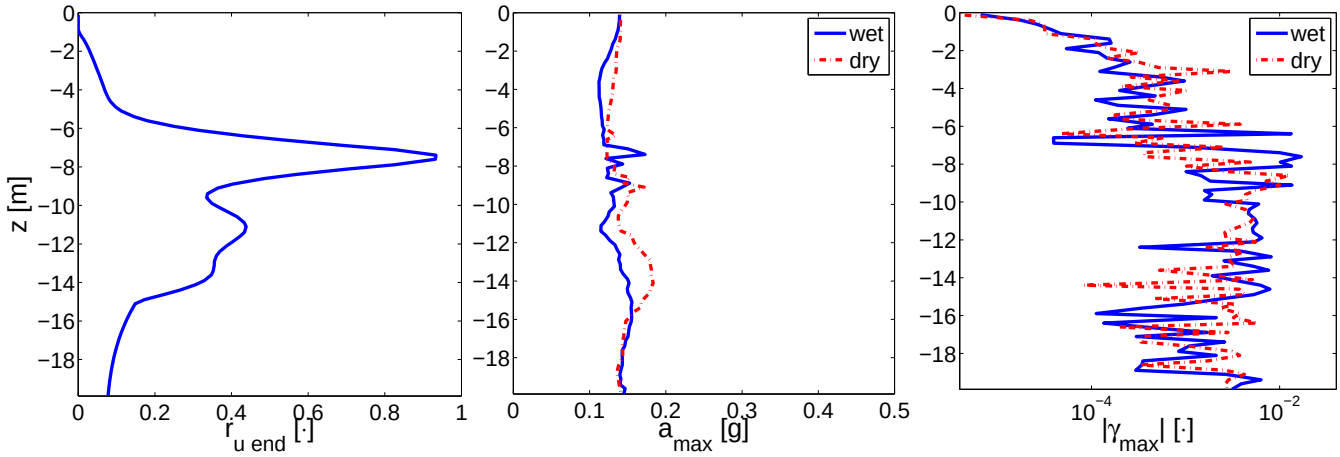
In order to assess the effect of the soil stiffening on the frequency content of the surface signal, Hartvigsen [19] proposed to characterize the effects of pore pressure with a response spectral ratio. Moreover, because the reduction in spectral acceleration showed for periods below about 1s is related to the differences between signals, the response has to be normalized. Therefore the normalized response spectral ratio (NRSR) is defined as:

$$NRSR(T) = \frac{PSA_{wet}(T)/PSA_{wet}(T=0)}{PSA_{dry}(T)/PSA_{dry}(T=0)} \tag{2}$$

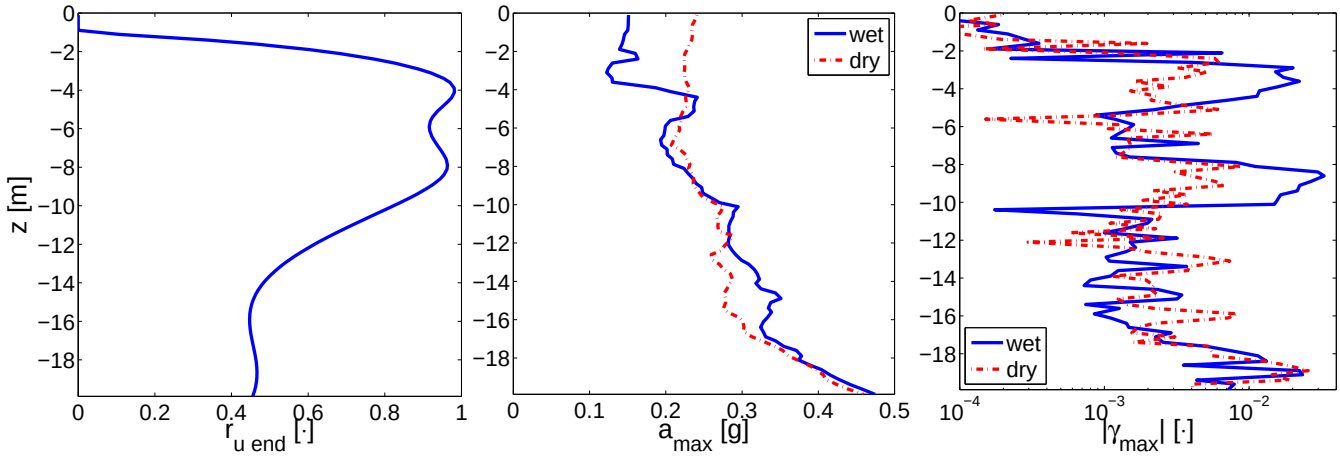
where $PSA_{wet}(T)/PSA_{wet}(T=0)$ correspond to the normalized response spectrum at surface when saturated and $PSA_{dry}(T)/PSA_{dry}(T=0)$ is the normalized response spectrum when dry. The responses were divided in three groups according to the $Q_{H=10m}$ value obtained when



(a) case 1



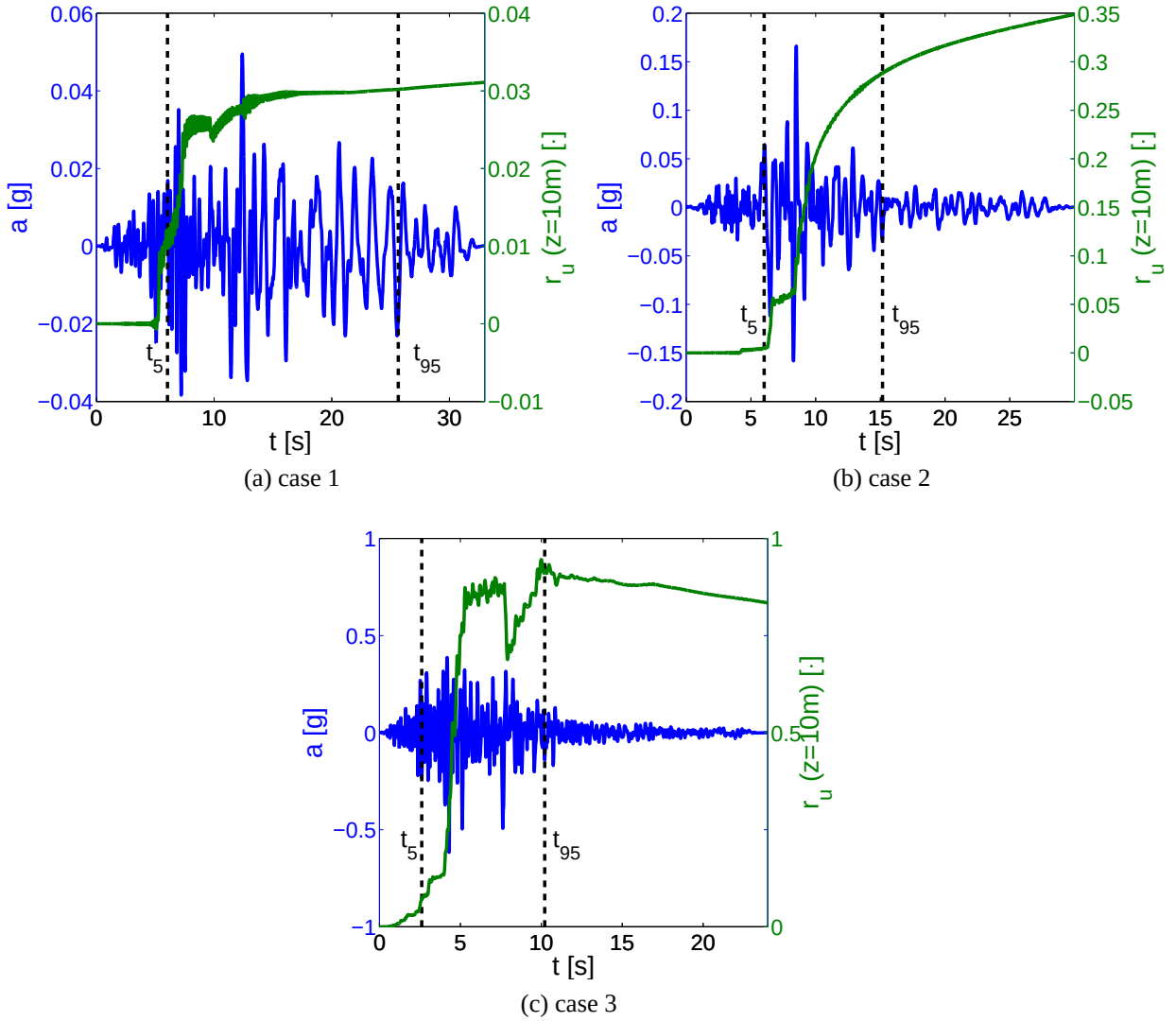
(b) case 2



(c) case 3

Figure 5: Maximum r_u, acceleration and γ profile

saturated, namely, $Q_{H=10m} \leq 0.3$, $0.3 < Q_{H=10m} \leq 0.6$ and $Q_{H=10m} > 0.6$. Figure 8 displays the mean NRSR curves obtained for each time window. It is interesting to note how as the liquefaction potential increases, the NRSR increases for the high periods (i.e. $T > 1.0s$). As a result, high period amplification in the more liquefied soils is not considered in models that



(a) case 1

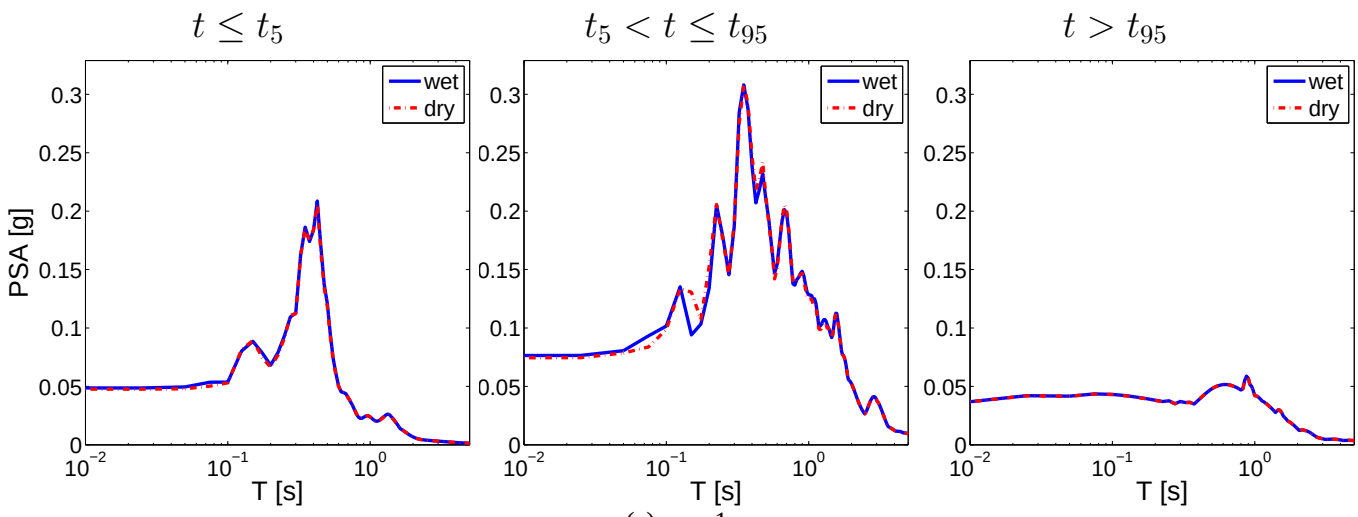
(b) case 2

(c) case 3

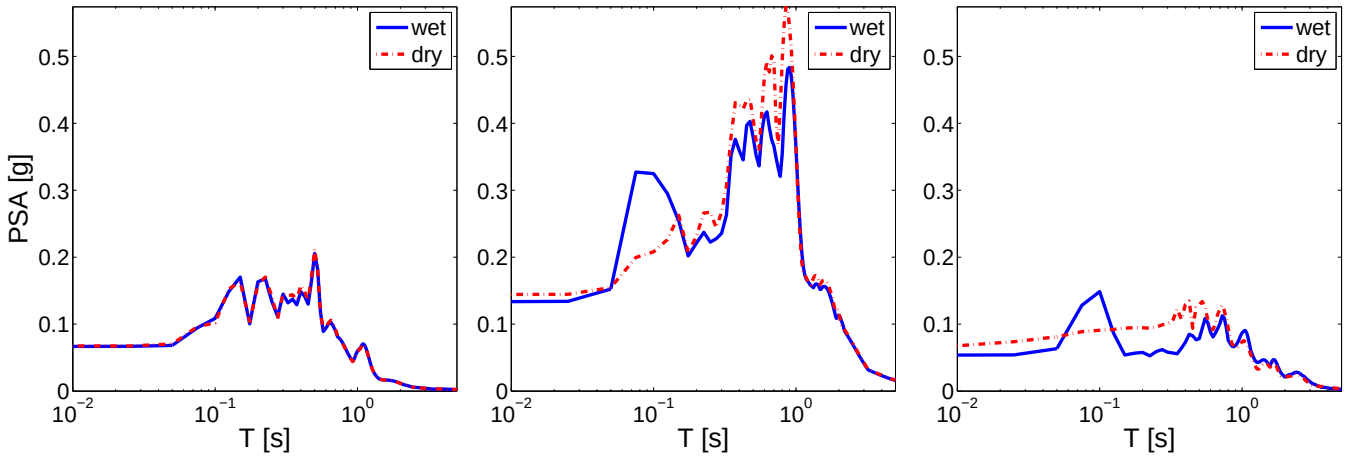
Figure 6: Time history of input acceleration and r_u at 10m depth (wet model)

lack of coupling pore pressure and responses of buildings with high predominant periods could be unconservative.

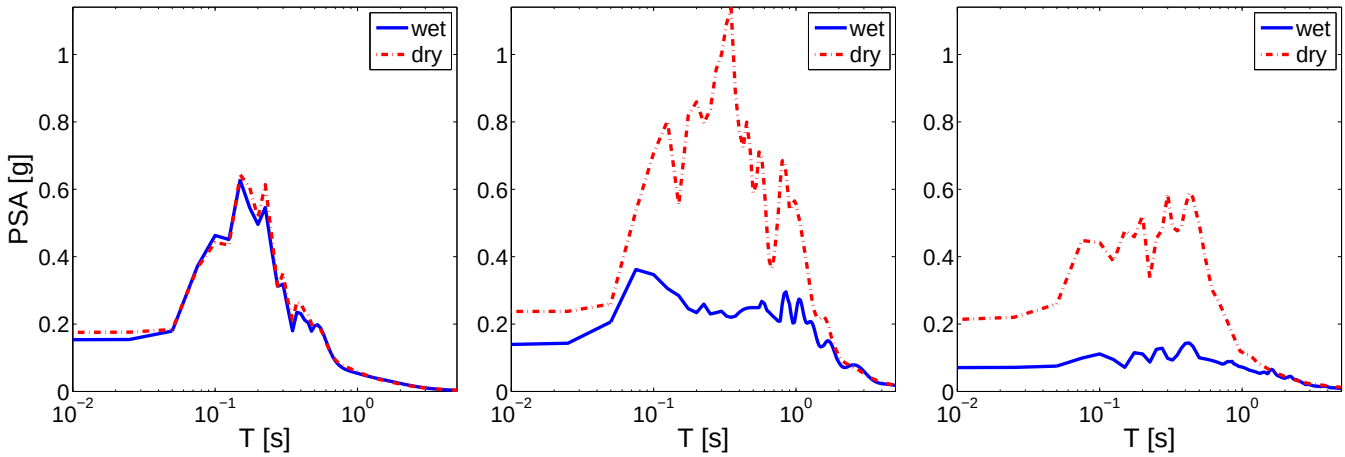
As an attempt to include the effects of pore pressure generation, several authors [19, 20] have proposed functions relating the amplification of the acceleration with the seismic hazard and the soil properties. However, given the great variability of the spectral ratio with period, it is unlikely to capture the detailed effects of Δp_w coupling on individual response spectra with an overall function. As an example the variation in figure 8b is shown in figures 9. The NRSR of all simulations are presented together with the mean and median values. Results are divided for each liquefaction index level. Due to the proper input motion variability, individual cases can be somewhat different of the general case (e.g. $Q_{H=10m} \leq 0.3$ in figure 9a); although, with a greater amount of simulations a relation could be given from a probabilistic framework. Nonetheless, for a complete analysis of important structures the use of a constitutive model with coupling excess pore pressure and soil deformation is required.



(a) case 1

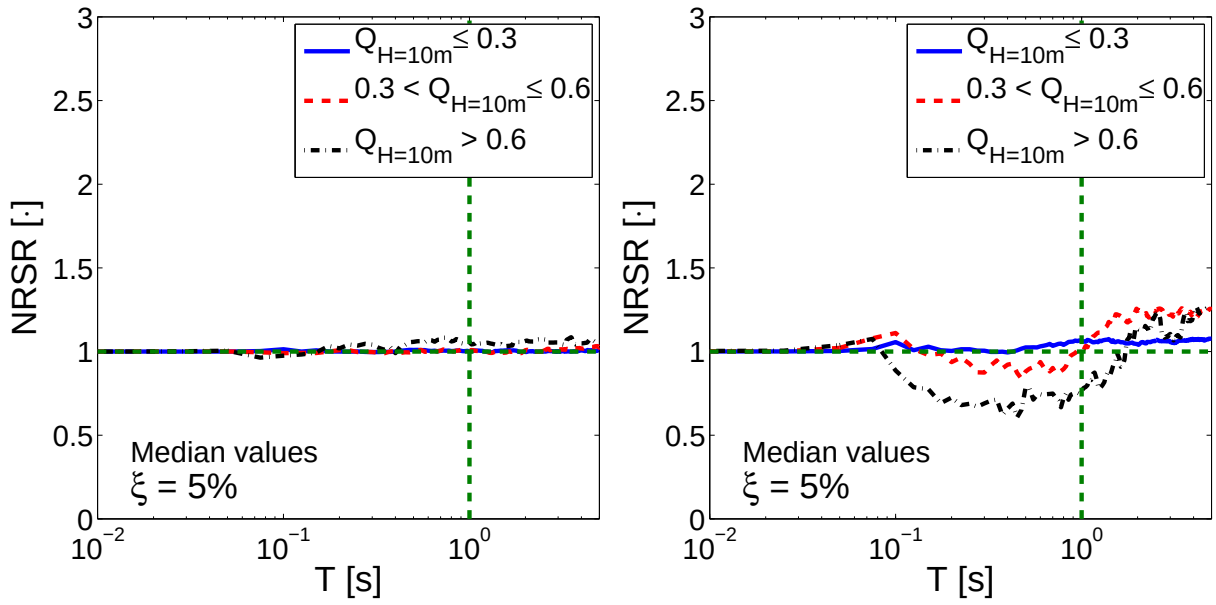


(b) case 2

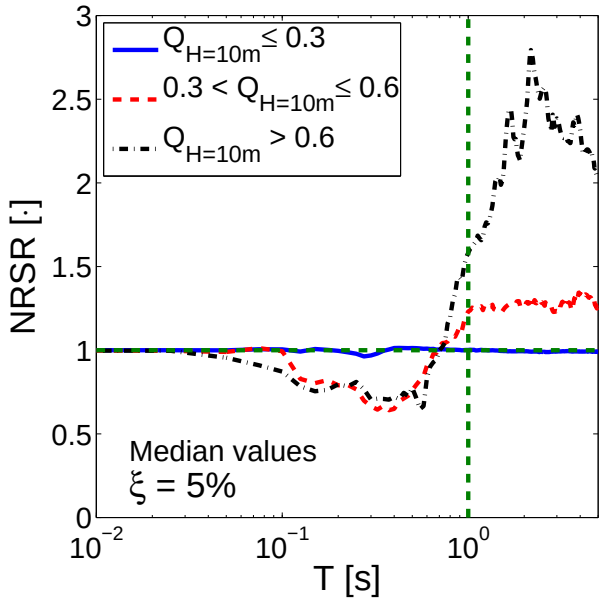


(c) case 3

Figure 7: Response spectra at different time windows

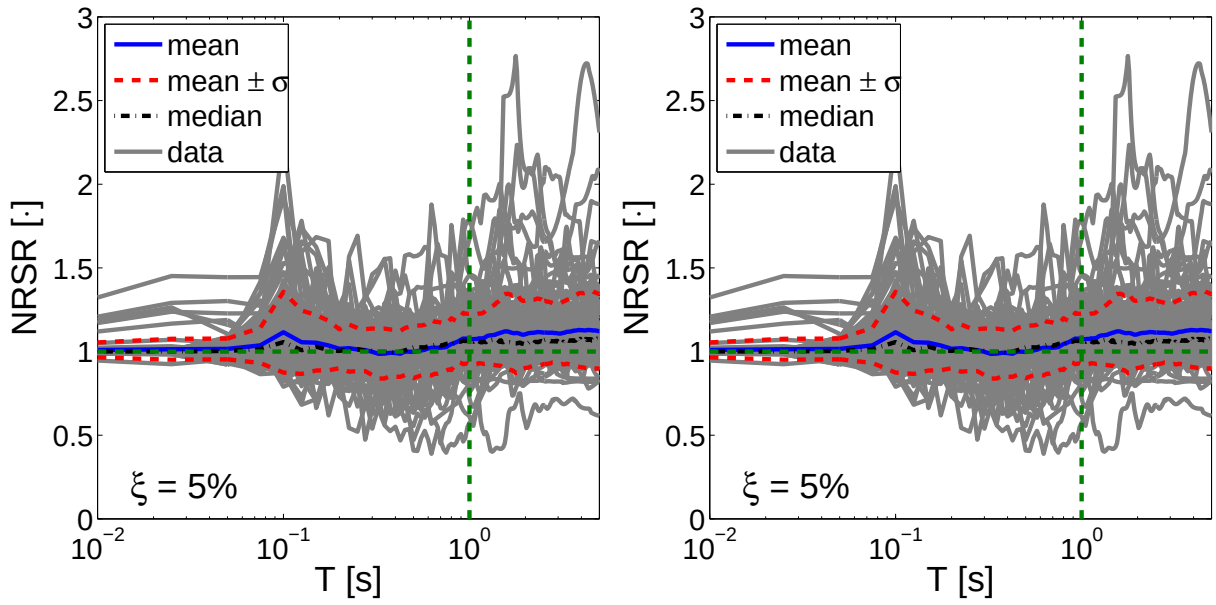


(a) $t \leq t_5$ (b) $t_5 < t \leq t_{95}$

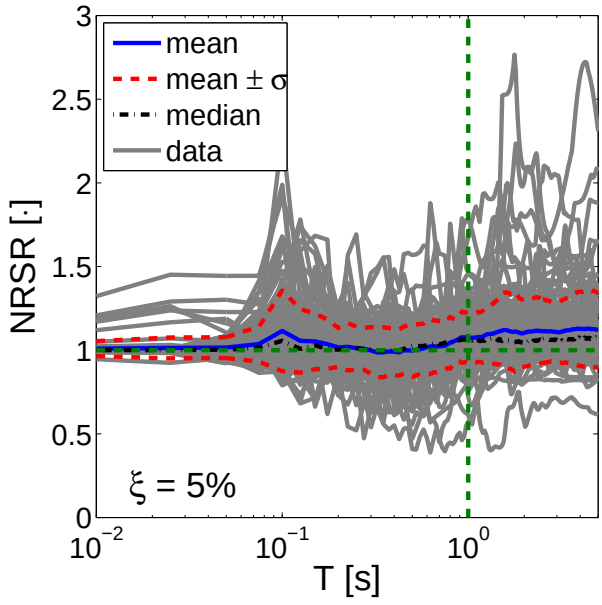


(c) $t > t_{95}$

Figure 8: Median Normalized Response Spectral Ratio NRSR values ranged by Q levels for each time window



(a) $t \leq t_5$ (b) $t_5 < t \leq t_{95}$



(c) $t > t_{95}$

Figure 9: Median Normalized Response Spectral Ratio NRSR values ranged by Q levels for each time window

4 CONCLUSIONS

A finite element analysis was used to investigate the effect of coupling excess pore pressure and soil deformation on the nonlinear response. A typically liquefiable soil profile of 20m has been used. Two mechanically equivalent models were subjected to 78 unscaled earthquake motions: one taking into account coupling (wet column) and one without (dry column). The main conclusions drawn from this study are as follows:

- The acceleration is amplified at surface for small input motions (i.e. $PHA \leq 0.2$g) in the dry as well as in the wet column. Nonetheless, deamplification for strong ground motions is more significant in the wet column and it increases with PHA. As a result, models that do not include coupling of excess pore pressure will predict bigger surface accelerations.

- It appears that the difference between maximum surface acceleration for the two columns is directly related to the Liquefaction Index ($Q_{H=10}$), hence as the liquefaction zone increases the need for a more complete model is required.

- Regarding the soil behavior throughout the profile, it can be concluded that spikes of acceleration are found at the same depth than spikes of shear strain and maximums on liquefaction ratio for the wet column; however, shear strains spikes on the dry column do not correspond to spikes in acceleration and thus other mechanisms are involved.

- Concerning the response spectra, it appears that the dry column overestimate the amplification of low periods while it underestimates it for high periods. This variation is more important in the time period after the 95% of Arias intensity as the soil has softened on the wet column. Moreover, this variation increases with the liquefaction zone.

- From a probabilistic point of view, the response spectra follows the same trend; although the variation between one event and another is significant. Therefore a generalization would be unlikely to capture the detailed effects of pore pressure coupling.

References

[1] P.B. Schnabel, J. Lysmer, and H.B. Seed. Shake: A computer program for earthquake response analysis of horizontally layered sites. Report no. eerc 72-12, Earthquake Engineering Research Center, 1972.

[2] T. L. Youd and S. K. Noble. Magnitude scaling factors. Technical report, National Center for Earthquake Engineering Research, State University of New York at Buffalo, 1997.

[3] D. Aubry, J.-C. Hujeux, F. Lassoudire, and Y. Meimon. A double memory model with multiple mechanisms for cyclic soil behaviour. *Int. Symp. Num. Mod. Geomech*, pages 3–13, 1982.

[4] J.-C. Hujeux. *Génie Parasismique: Une loi de comportement pour le chargement cyclique des sols*, pages 278–302. Presses ENPC, France, v. davidovici edition, 1985.

[5] CEN European Committee for Standardization. *Eurocode 8: Design of structures for earthquake resistance*, 1998-1 part 1: general rules, seismic actions and rules for buildings. EN, Brussels, Belgium, 2004.

[6] D. Aubry and A. Modaressi. Gefdyn - manuel scientifique. *Ecole Centrale Paris*, 2005.

[7] E. Foerster and H. Modaressi. A diagonal consistent mass matrix for earthquake site response simulations. *4th International Conference on Earthquake Geotechnical Engineering*, June 2007.

[8] S. Kontoe, L. Zdravkovic, and D. Potts. An assessment of time integration schemes for dynamic geotechnical problems. *Computers and geotechnics*, 35:253–264, 2008.

[9] E. Saez. *Dynamic non-linear soil structure interaction*. PhD thesis, Ecole Centrale Paris, 2009.

[10] F. Lopez-Caballero and A. Modaressi. Numerical analysis: Specification and validation of used numerical methods. Fp7-sme-2010-1-262161, PREMISERI project, Paris, France, 2011.

[11] H. Modaressi and I. Benzenati. Paraxial approximation for poroelastic media. *Soil Dynamics and Earthquake Engineering*, 13(2):117–129, 1994.

[12] B. Bradley, R. Dhakal, G. MacRae, and M. Cubrinovski. Prediction of spatially distributed seismic demands in specific structures: Ground motion and structural response. *Earthquake Engineering and Structural Dynamics*, 39(5):501–520, 2010.

[13] L. Sorrentino, S. Kunnath, G. Monti, and G. Scalora. Seismically induced one-sided rocking response of unreinforced masonry faades. *Engineering Structures*, 30(8):2140–2153, 2008.

[14] F. Lopez-Caballero and A. Modaressi-Farahmand-Razavi. Assessment of variability and uncertainties effects on the seimic response of a liquefiable soil profile. *Soil Dynamics and Earthquake Engineering*, 30:600–613, 2010.

[15] F. Lopez-Caballero, A. Modaressi-Farahmand-Razavi, and Hormoz Modaressi. Nonlinear numerical method for earthquake site response analysis i- elastoplastic cyclic model and parameter identification strategy. *Bulletin of Earthquake Engineering*, 5(3):303–323, 2007.

[16] G. T. Zorapapel and M. Vucetic. The effects of seismic pore water pressure on ground surface motion. *Earthquake Spectra*, 10(2):403437, 1994.

[17] L. Bonilla, C. Gelis, and J. Regnier. The challenge of nonlinear site response: field data observations and numerical simulations. *Seismic Motion*, august 2011.

[18] M. Shinozuka and K. Ohtomo. *Proceedings of the second US-Japan workshop in liquefaction, large ground deformation and their effects on lifelines*, technical report Spatial severity of liquefaction, page 193206. NCEER, 1989.

[19] A. Hartvigsen. Influence of pore pressures in liquefiable soils on elastic response spectra. Master's thesis, University of Washington, 2007.

[20] P. Bazzurro and C.A. Cornell. Nonlinear soil-site effects in probabilistic seismic-hazard analysis. *Bulletin of the Seismological*, 94(6):2110–2123, 2004.

COMPDYN 2013
4th ECCOMAS Thematic Conference on
Computational Methods in Structural Dynamics and Earthquake Engineering
M. Papadrakakis, V. Papadopoulos, V. Plevris (eds.)
Kos Island, Greece, 12–14 June 2013

ROLE OF SLIDING BLOCK ROTATION ON EARTHQUAKE-INDUCED PERMANENT DISPLACEMENT OF EARTH SLOPES

A. Lashgari[1], **Y. Jafarian**[2]

[1]Department of Civil Engineering, Semnan University
Semnan, Iran
a.lashgari@students.semnan.ac.ir

[2] Geotechnical Engineering Research Center, International Institute of Earthquake Engineering and Seismology
Tehran, Iran
yjafarianm@iiees.ac.ir

Keywords: Seismic Slope Stability, Permanent Displacement, Rigid block analysis, decoupled Analysis, Coupled Analysis, Rotation

Abstract. *Different methods are available for estimating earthquake-induced permanent deformation of earth slopes and embankments. Due to its simplicity, Newmarkian rigid block analogy has received considerable attention among the geotechnical practitioners and researchers. Since the conventional Newmarkian analogy has considered many limiting assumptions, conservative and unconservative estimate of sliding displacement would be possible. Thus, researchers have proposed many modifications to enhance the realistic features of this method. In reality, it is anticipated that the downward rotational (stabilizing) movement of the soil mass can significantly affect the yielding acceleration of the presumed slip surface. In this paper, the mentioned modification is numerically implemented to the conventional formulation of the Newmark approach for actual earthquake excitations. The results are presented for several conditions including the conventional rigid block, decoupled assumption of sliding and slope response, coupled consideration of sliding and slope response, and decoupled assumption with the effect of sliding block rotation. According to the results of this study, the period ratio (the ratio of natural period of slope to the mean period of input motion) and the length of slip surface can significantly vary the permanent displacement of sliding mass for these conditions.*

1 INTRODUCTION

Evaluation of earthquake-induced deformation of earth embankments and slopes is a matter of high importance for geotechnical engineers. Numerical and analytic methods could be used to calculate the permanent displacement of earth slopes . Since numerical methods with an appropriate constitutive model commonly need many soil parameters, engineers might be more interested to use analytic and semi-analytic methods. Among the analytic and semi-analytic methods, Newmark rigid block method [2], because of being simple, has the most applications. But in the initial form of this method, the effect of system response and rotation is not considered. Thereafter, the subsequent analyses considered the system response in the calculation of displacement through the coupled and decoupled procedures ([6]; [8]; [7]; [3]; [4]). Contrary to the decoupled assumption of system response and sliding, the dynamic response of the sliding mass and the permanent displacement are modeled together in the couple method so that the effect of plastic sliding displacement on the ground motions is taken into account [11]. Geometrically, downward movement of the sliding mass tries to stabilize the block; thereby increasing the yield acceleration. Such modification was initially proposed and formulated by Stamatopoulos [5] for the sliding block method and implemented within a decoupled analysis by Baziar et. al. [9].

The current study compares the permanent displacements which are obtained by the rigid-block, decoupled, coupled, and modified decoupled analyses. The latter analysis considers the effect of block rotation through the decoupled framework in the permanent displacement of earth slopes.

2 TYPES OF PERMANENT-DISPLACEMENT ANALYSIS

Several modifications of the initial Newmark's method were proposed to yield more accurate estimates of slope displacement by modeling the dynamic slope response more rigorously. Some of them together with the original sliding block method are summarized in the following sections.

2.1 Rigid-block analysis

The rigid-block model assumes that permanent deformation triggers once the earthquake-induced accelerations acting on a slide mass exceed the yield resistance on the slip surface. The sliding resistance is quantified by the seismic yield coefficient (k_y). Some limiting assumptions are including in this method for simplicity [11]:

1. The static and dynamic shearing resistances of the soil are taken to be the same ([2]; [12]).
2. The critical acceleration is not strain dependent and thus remains constant throughout the analysis ([2]; [13]; [12]; [14]).
3. The upslope resistance to sliding is taken to be infinitely large such that upslope displacement is prohibited ([2]; [12]; [14]).
4. The effects of dynamic pore pressure are neglected. This assumption generally is valid for compacted or overconsolidated clays and very dense or dry sands ([2]; [13]).
5. The effect rotation is not considered ([5]; [9]).

2.2 Decoupled analysis

This analysis, which was presented by Makdisi and Seed [13], is based on a rigid block but the dynamic response of the system is calculated to obtain the equivalent acceleration. The equivalent horizontal acceleration (HEA) is the time history of acceleration acting on the pre-

sumed sliding block. Therefore, instead the earthquake acceleration, the equivalent acceleration which contains the system response is applied to the block for displacement calculation. In this analysis rotation is not considered too rigid-block analysis.

2.3 Coupled analysis

The decoupled analysis does not consider the dynamic response of the slip, while this response is important. In a fully coupled analysis, the dynamic response of the sliding mass and the permanent displacement are modeled together so that the effect of plastic sliding displacement on the ground motions is taken into account [3]. In this analysis similar to two analysis previous rotation is not considered.

3 THE EFFECT OF BLOCK ROTATION

Stamatopoulos [5] considered dynamic motion of the Newmarkian sliding rigid block as a perfectly flexible chain sliding along planes with gradually gentler inclinations. This investigation has revealed that neglecting the downward-movement effect in the conventional sliding block analysis results in overconservative displacements. Downward-displacement effect would be significant in the case of smaller slippage lengths where downward-stabilizing-movement is predominant. For actual input ground motions, Stamatopoulos [5] concluded that downward-stabilizing effect would be insignificant when the ratio of yield acceleration to peak ground acceleration takes values greater than 0.2. As mentioned earlier, in spite of its advantage in considering the downward-motion effect, the model proposed by Stamatopoulos [5] does not take into account the effect of dynamic system response. It was found that the less is the length of sliding surface, the bigger gets the rotation effect and the created displacement gets smaller. Baziar et. al. [9] implemented the Stamatopoulos's model for decoupled analysis rather than the sliding block. They demonstrated how the rotation effect changes the permanent displacements obtained by the original decoupled solution.

4 THE ANALYSES

In this study, a computer code was written in time domain to capture the displacement time history using Rathje and Bray [3] equations for coupled and decoupled analysis. These equations were solved by using the time stepping method developed by Newmark [1] and also the central difference method. In the Newmark time step method, the coefficients β and γ can have different values. Figures 1 (a and b) shows the results obtained by coupled method for different values of β and γ. The earthquake motion of Pacoima Dam Downstream (PDD) station (horizontal component 175, T_m = 0.47 s) recorded from the 1994 Northridge earthquake, and Yerba Buena Island (YBI) motion (horizontal component 090, T_m =1) recorded from 1989 Loma Prieta earthquake were first scaled to MHA = 0.4g and used in the analyses. The curves were plotted in terms of the permanent displacements versus the period ratio; which stands for the ratio of system natural frequency and the mean period of input motion. This figure shows that the different values β and γ do not differ much if stability condition is provided. Stability condition for $\gamma = 0.5$ and $\beta = 1/6$ is $\Delta t \le 0.551 T_s$ and $\gamma = 0.5$ and $\beta = 0$ is $\Delta t \le \frac{T_s}{\pi}$ while for $\gamma = 0.5$ and $\beta = 0.25$ is always stable.

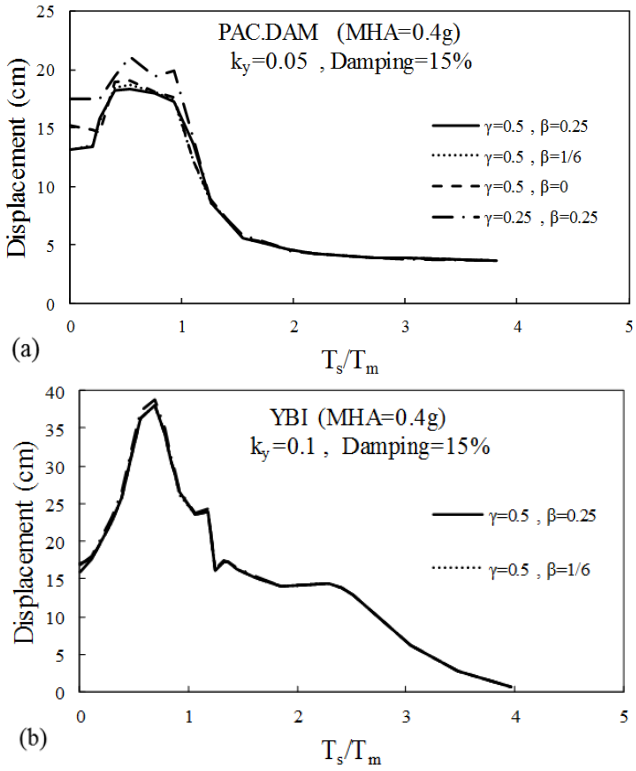


Figure 1. Results of coupled analysis using time stepping method with different values of β and γ for: (a); PAC.DAM k_y=0.05; (b) YBI, k_y=0.1.

As mentioned before, two numerical methods including the Newmark [1] time step and the central difference methods have been compared for coupled analysis, as shown in figure 2. The coupled analysis with these methods were carried out using the input motions of PAC.DAM with $k_y = 0.05$ and YBI with $k_y = 0.1$. The comparison shown in figures 2 (a and b) confirm that these methods yield similar results if stability condition is provided. Stability condition for finite difference method is $\Delta t \leq \frac{T_s}{\pi}$.

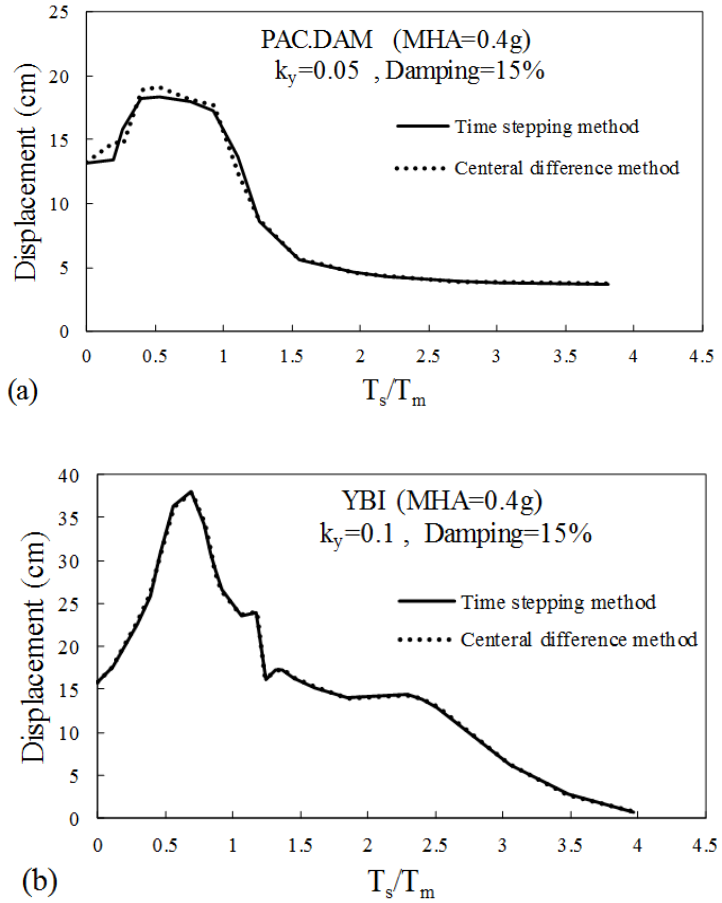


Figure 2. Comparison between the results of coupled analysis using time stepping and central difference methods for: (a); PAC.DAM k_y =0.05; (b) YBI, k_y =0.1.

Figure 3 compares the results of rigid block, decoupled, and coupled analyses for the yield acceleration of 0.05g subjected to YBI (see Figure 3a) and TAP (see Figure 3b) motion (horizontal component 051, T_m=0.99) recorded from 1999 Chi-Chi earthquake (scaled to MHA = 0.4g). This figure shows that the rigid block analysis is not conservative always. In low period ratios (T_s / T_m), the rigid block analysis, predicts unconservative displacement but it is conservative in large period ratios. As the figure illustrates, in low period ratios (T_s / T_m), the decoupled method compared with the coupled one, predicts the displacement more conservatively, but in larger period ratios, the coupled predicts larger displacements compared with the decoupled method. For systems with larger values of large fundamental periods, a decoupled analysis may predict smaller displacements than a fully coupled analysis [3]. Figure 3b, however, shows that the decoupled method obtains invariably conservative displacements for the whole range of period ratio.

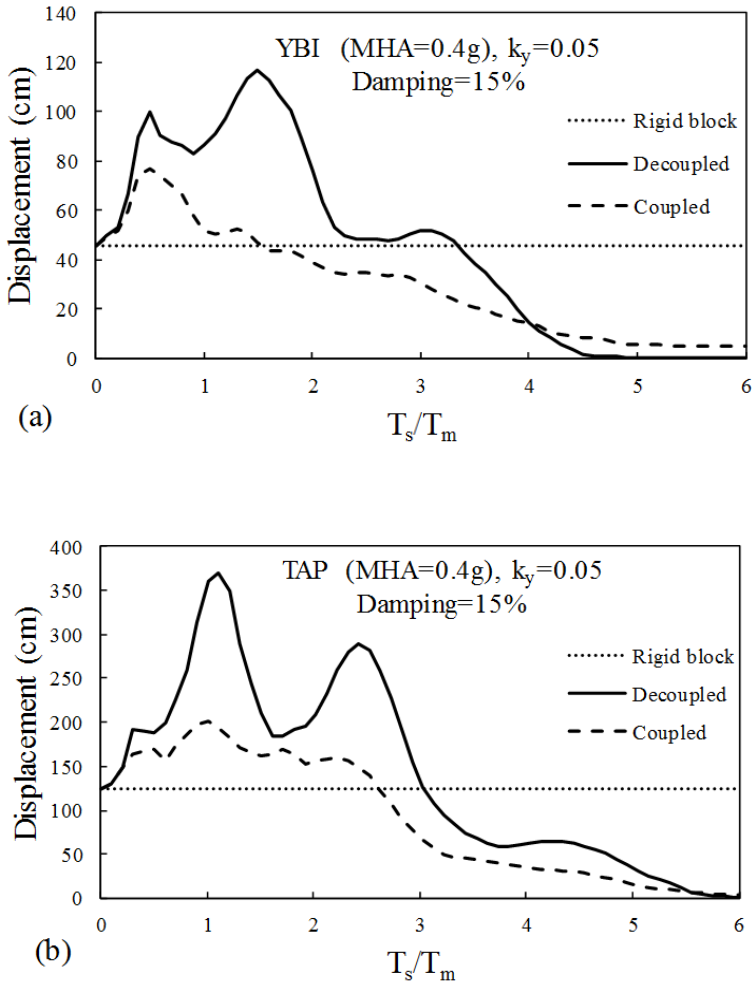


Figure 3. Permanent displacements obtained by coupled, decoupled, and rigid block analyses using time stepping and central difference method for: (a); PAC.DAM k_y =0.05; (b) YBI, k_y =0.1.

The coupled and decoupled permanent displacements shown in Figure 3 were calculated based on the formulations presented by Rathje and Bray [3] which ignore the effect of block rotation and the consequent increase in yielding acceleration. The formulations presented by Stamatopoulos [5] and Baziar et. al. [9] for the consideration of rotation in sliding block and decoupled analyses have been also coded in the current study using the time stepping method. There would be an opportunity to compare the permanent displacements obtained from the mentioned analyses and to evaluate the role of block rotation on the resultant displacements.

Figure 4 compares rigid block, modified rigid block, decoupled, modified decoupled, and coupled analyses using YBI and TAP records for two different sliding lengths and $k_y = 0.05g$. The results are presented in terms of permanent displacements versus the period ratio. As shown in the figure, modification for the rotation effect obtains smaller displacements in general. The decoupled approach obtains the most conservative displacement especially for the small period ratios and for the period ratios larger than 3 the original sliding block model obtains the greatest values. For the period ratios larger than 3, the decoupled and

coupled displacements are relatively close together. It is impossible to make a clear conclusion for the difference between the modified decoupled and coupled displacements. However, modification of the decoupled method for rotation declines the calculated displacements to the level of coupled displacements. As this figure indicates, difference between the calculated displacements is also dependent to the characteristics of input motion. Furthermore, as previously indicated, it is evident from this figure that downward-stabilizing effect is major in smaller slippage lengths.

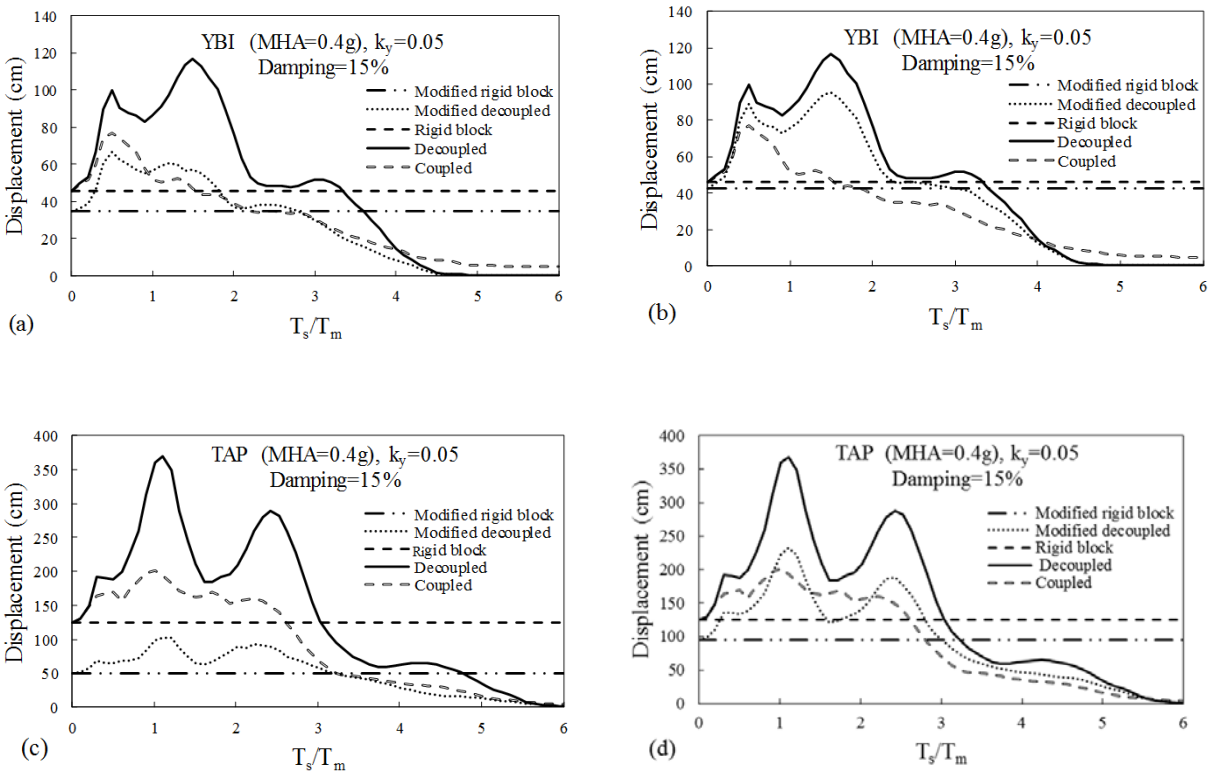


Figure 4. Comparison between the displacements of coupled, decoupled, sliding block, modified decoupled, and modified sliding block analyses versus period ratio for: (a) YBI, slippage length 10 m ; (b) YBI, slippage length 50 m; (c) TAP, slippage length 10 m; (d) TAP, slippage length 50 m.

The rotation of block, which is an inherent response of sliding block, plays an important role in the displacements obtained by rigid block and decoupled analyses. When sliding surface is shallower, lower contribution of sliding mass displacement is involved in calculating the whole dynamic response of slope body [6]. Based on the results shown in the present study, the mentioned modification for accumulated displacements is significant for smaller slippage lengths, i.e. shallow depths, for both rigid block and decoupled analysis.

5 CONCLUSION

Rigid block, decoupled, and coupled analyses were coded for estimating the earthquake-induced permanent displacement of earth slopes and embankments. To calculate the seismic response that utilized in the decoupled and coupled analysis the numerical time step methods

and the central difference method were used. The numerical methods do not differ much if stability condition is provided.

Similar to the previous studies, it was shown that the rigid block and decoupled analysis do not obtain conservative displacement in any condition and it depends on the period ratio and the characteristic of input motion. . The modified rigid block and decoupled analyses which account for the role of sliding lock rotation have been implemented for calculation of permanent deformation of earth slopes. The values of permanent displacement were calculated using the coupled, decoupled, sliding block, modified sliding block, and modified decoupled analyses. Comparison demonstrates that the decoupled approach obtains the most conservative displacement especially for the small period ratios and for the period ratios larger than 3 the original sliding block model obtains the greatest values. For the period ratios larger than 3, the decoupled and coupled displacements are relatively close together. Consideration of the rotation effect significantly reduces the resultant permanent displacement obtained by the decoupled method. This effect is more profound for the small slippage length. In fact for the earthquake-induced landslides with considerable slippage length the role of block rotation is negligible in the decoupled and sliding block analyses.

REFERENCES

[1] N.M. Newmark, A method for computation for structural dynamics. *ASCE Journal of the Engineering Mechanics Division* 85, 67–94, 1959.

[2] N.M. Newmark, Effects of earthquakes on dams and embankments. *Geotechnique* 15, 139–160, 1965.

[3] E.M. Rathje, J.D Bray, An examination of simplified earthquake–induced displacement procedures for earth structures. *Canadian Geotechnical Journal* 36(1), 72–87, 1999.

[4] E.M. Rathje, J.D Bray, Nonlinear coupled seismic sliding analysis of earth structures. *ASCE Journal of Geotechnical and Geoenvironmental Engineering* 126(11), 1002–1014, 2000.

[5] C.A. Stamatopoulos, Sliding system predicting large permanent co–seismic movements of slopes. *Earthquake Engineering Structural Dynamics* 25(10), 1075–1093, 1996.

[6] J.S. Lin, R.V. Whitman, Decoupling approximation to the evaluation of earthquake–induced plastic slip in earth dams. *Earthquake Engineering Structural Dynamics* 11, 667–678.1983.

[7] S.L. Kramer, M.W. Smith, Modified Newmark model for seismic displacements of compliant slopes. *ASCEJournal of Geotechnical and Geoenvironmental Engineering*123(7), 635–644, 1997.

[8] A.K. Chopra, L. Zhang, Earthquake–induced base sliding of concrete gravity dams. *ASCEJournal of Structural Engineering*117(12), 3698–3719, 1991.

[9] M.H. Baziar, H. Rezaeipour, Y. Jafarian, Decoupled solution for seismic permanent displacement of earth slopes using deformation-dependent yield acceleration. *Journal of Earthquake Engineering*16(1), 917-936, 2012.

[10] J.D. Bray, T. Travasarou, Simplified procedure for estimating earthquake-induced deviatoric slope displacements. *ASCEJournal of Geotechnical and Geoenvironmental Engineering*, 133(4), 381-392, 2007.

[11] R.W. Jibson, Methods for assessing the stability of slopes during earthquakes-A retrospective. *Engineering Geology*122, 43-50, 2010.

[12] C.J. Chang, W.F, Chen, J.T.P, Yao, Seismic displacements in slopes by limit analysis. *Journal of Geotechnical Engineering*110, 860-874, 1984.

[13] F.I. Makdisi, H.B, Seed, Simplified procedure for estimating dam and embankment earthquake-induced deformations. *ASCE Journal of the Geotechnical Engineering Division*104, 849–867, 1978.

[14] N.N. Ambraseys, J.M, Menu, Earthquake-induced ground displacements. *Earthquake Engineering and Structural Dynamics* 16, 985–1006, 1988.

COMPDYN 2013
4th ECCOMAS Thematic Conference on
Computational Methods in Structural Dynamics and Earthquake Engineering
M. Papadrakakis, V. Papadopoulos, V. Plevris (eds.)
Kos Island, Greece, 12–14 June 2013

FRAGILITY CURVES FOR ASSESSING THE SEISMIC VULNERABILITY OF GRAVITY QUAY WALLS

M. Miraei[1*], Y. Jafarian[2]

[1] Department of Civil Engineering, Semnan University
Semnan, Iran
m.miraie@students.semnan.ac.ir

[2] Geotechnical Engineering Research Center, International Institute of Earthquake Engineering and Seismology
Tehran, Iran
yjafarianm@iiees.ac.ir

Keywords: Fragility curves, Performance-based design, Gravity quay wall, Centrifuge tests, Uncertainty.

Abstract. *Ports and marine structures have an important role in global transportation and world economy. Seismic vulnerability of marine structures can be evaluated through the probabilistic approaches in order to account for the uncertainties involved the structural capacity and seismic demand of such projects. The purpose of this study is to develop fragility curves for gravity quay walls. Numerical analyses are preliminarily carried out to capture the seismic displacement response of such structures to earthquake excitations. The recorded displacements of a previously conducted physical model test are employed to validate performance of the numerical modeling. A fully nonlinear soil model is used in the seismic analyses. Numerous seismic analyses are then performed using actual earthquake motions with various characteristics such as peak ground acceleration and predominant period. The results of numerical simulations are then analyzed through the probabilistic procedure to derive fragility curves for the gravity quay walls. Various performance criteria including serviceable, repairable, and near collapse damages are consequently determined by the fragility curves. Finally, results of this study are compared with the performance criteria recommended by the available performance-based guidelines of the port structures*

1 INTRODUCTION

Earthquakes have caused lots of damages to quay walls in the world. Thus, the seismic response of such structures is so important. The most important damages to gravity quay walls have been reported during the Hyogoken Nanbo 1995 earthquake in Japan. Seismic damages to gravity quay walls are typically evaluated in terms of horizontal displacement, settlement, and tilting. The main reason of these damages might be liquefaction occurrence in the soils located beneath and back of the quay walls or existence of infirm foundation under the wall. Zeng and Steedman [1] examined the seismic response of a wall restrained by sheet pile and concluded that increase in excess pore pressure significantly lowers the stiffness of soil and increases wall deformation. Zeng [2] studied behaviour of gravity quay wall through a centrifuge model. Zeng and Madabhushi [3] performed an effective stress numerical simulation using a finite element program known as SWANDYNE in order to examine the seismic response of quay walls. They compared results of numerical modeling with the measured outputs of centrifuge model and found good agreement. Cooke [4] simulated response of centrifuge tests of quay walls via the numerical models in FLAC software. Ichii [5] evaluated seismic vulnerability of Kobe port based on effective stress analysis and presented fragility curves for various conditions such as soil resistance parameters like N_{SPT} and also different $\frac{W}{H}$ ratio. Dakoulas and Gazetas [6] examined response of gravity quay wall in Rokko Island in kobe port using effective stress seismic analysis through Pastor model (1990). Dakoulas and Gazetas [7] used the elasto-plastic constitutive model of Pastor-Zienkiewicz and performed effective stress analysis. They examined the displacement, excess pore pressure, and plastic strain in a gravity quay wall of Kobe port. They found that by increasing the density of the weak soil under and back of quay wall, displacement and excess pore pressure will decrease. Chiou et al [8] developed fragility curves for a marine structure (pile supported wharf) in Taiwan. Yang et al [9] carried out numerical modeling of pile supported wharf via nonlinear time-history analysis under two ground motions suite in western United States. They draw the fragility curve for the wharf in two states, with or without crane, and also evaluated the damage probability for the structure at 2%, 10%, 50% return periods during 50 years.

In this paper, numerical analyses have been done to study the seismic response of a quay wall which was previously modeled in centrifuge. The centrifuge experiment was conducted in Cambridge University during the VELACS project in 1992. After the preliminary calibration of the numerical model and reasonable agreement between the numerical and experimental outputs, for the quay wall were subjected to 17 actual input motions. Fragility curves were obtained through the process of numerical outputs in order to study the seismic vulnerability of such structures within a probabilistic framework.

2 THE CENTRIFUGE MODEL

The case study is VELACS model number 11 test that is a gravity quay wall in centrifuge experiment conducted by Zeng [1] in Cambridge University. The physical model configuration and location of the instruments including excess pore pressure transducers, accelerometers, and LVDTs for horizontal displacement at the crest of wall are seen in Figure 1. The input seismic signal in the centrifuge test is shown in Figure 2 with the peak acceleration of 0.234g. The system soil is saturated Nevada sand with 60% relative. Liquefaction was occurred during the shaking and it produced horizontal displacement, settlement, and tilting in this structure.

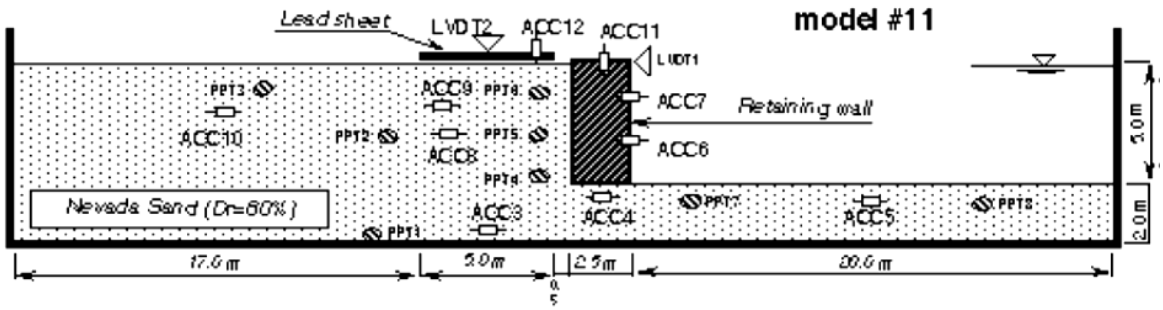


Figure 1. Configuration of the experimental model of the gravity quay wall.

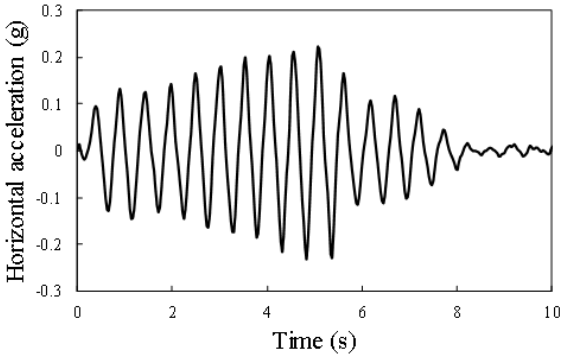


Figure 2. Time history of input acceleration for the centrifuge test at the base.

3 NUMERICAL ANALYSIS

In this study, the quay wall in VELACS model number 11 was modeled in FLAC 7 software which is a two dimensional finite difference program. The gravity block was made of aluminum alloy and so was considered as elastic material in modeling. A lead sheet with 0.1m thickness in prototype scale has been put on the soil surface as surcharge of the quay wall. The geometric features of the numerical model are shown in Figure 3. The properties of soil, caisson quay wall, and lead sheet are shown in Table 1. The friction angle between structure and soil is 17°. By the way, Finn model has been used to simulate liquefaction behavior while local damping was assumed 5%. Shear modules of the soil were estimated through the results of the resonant column tests conducted during the VELACS projects.

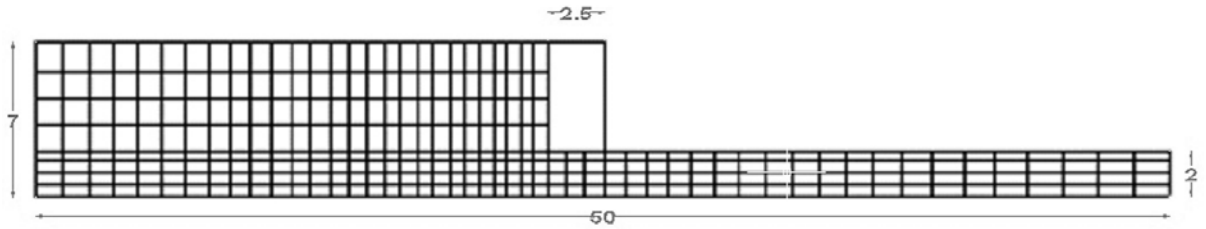


Figure 3. Numerical model mesh for the analysis

Material	Nevada Sand	Caisson Wall	Lead Sheet
Density (Kg/m^3)	1961	2700	11340
Shear modulus (KPa)	8.57E4	2.58E7	0.47E7
Poisson's ratio	0.4	0.334	0.431
Friction angle (°)	36	-	-

Table 1. Material parameters in this study

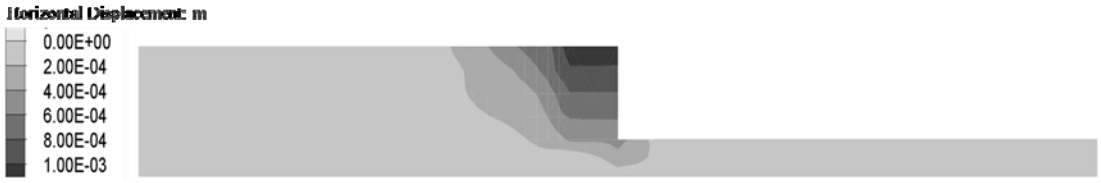


Figure 4. Contours of horizontal displacement of quay wall in static analysis

4 VERIFICATION OF PREDICTED AND MEASURED RESULT

Figure 4 shows contours of horizontal displacement of the system after the initial static equilibrium. This system was then subjected to the cyclic loading shown in Figure 2. The system response is attained via nonlinear time-history analysis and is compared with the centrifuge experiment outputs. Figures 5 (a and b) compares numerical and measured time histories of the horizontal displacement at the wall crest and the pore pressure buildup at PPT5 (see Figure 2). The maximum horizontal displacement at the top of the quay wall is predicted 0.25m via the numerical model, comparable with the measured value of 0.26m. Figure 6 also shows the time history of horizontal displacements on top of the wall which were predicted by the previous researchers. Figure 5 shows that the numerical model successfully predict the lateral deformation of quay wall while it fails to precisely predict the excess pore water pressure. For the current study, which deals with the displacement–based evaluation of seismic damage, the numerical model has sufficient preciseness for the subsequent numerical analyses.

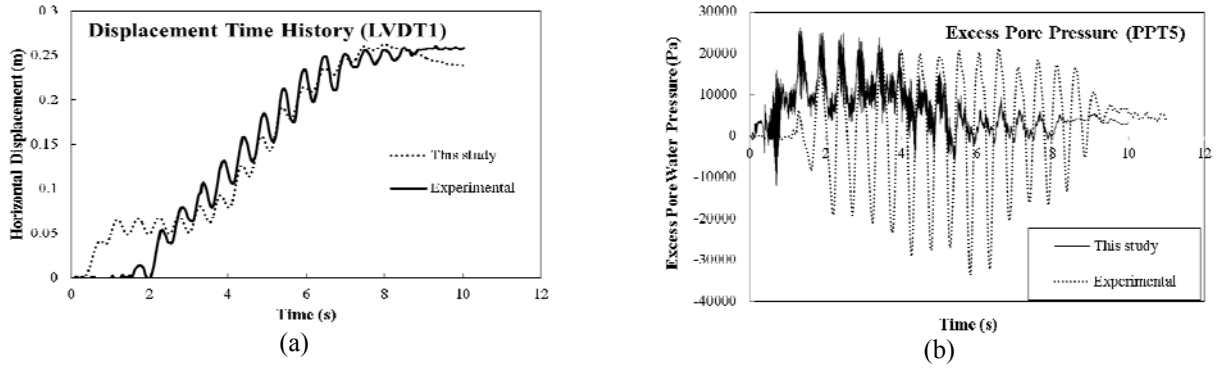


Figure 5. (a) Comparison of the numerical and experimental result in terms of the horizontal displacement on top of the wall (b) Comparison of numerical and experimental result in terms of the Excess pore pressure behind the wall

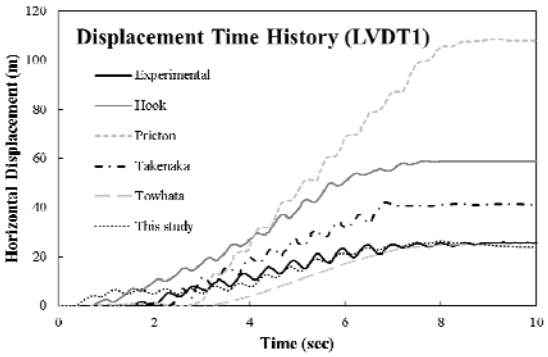


Figure 6. Comparison between the time history of horizontal displacement predicted by the previous researchers [12] with the prediction of the current study together with the experimental measurements

5 FRAGILITY CURVES

In the recent years many studies have been carried out for seismic behavior of a structural system. However, the performance improvement of a structural or geotechnical system is economically and scientifically critical

The seismic design of offshore structures might be better to quantify in probabilistic framework especially due to the existence of uncertainty in many cases. The probability of structural failure is a function of uncertainty in both structural capacity and earthquake demand. The capacity of a structure to withstand a load is a function of its geometry and material properties. Fragility curves can be used to evaluate the possibility of structural failures in large systems by considering the uncertainty in structural capacity and seismic demand

5.1 Ground motions

Fragility curves for seismic system is assessed based on numerical analysis in 17 input motions around the world as summarized in Table 2. These ground motions were recorded during 1971 to 1999 and some of which have occurred in the vicinity of offshore structures and caused lots of damages, such as Chi Chi earthquake in Taiwan port and Kobe earthquake in Kobe port. In the selection of these earthquakes it was tried to consider the important seismic parameters to be exist in a wide range. As can be seen in the histograms shown in Figure 7, seismic parameters such as PGA and PGV are reasonably distributed in the applicable range of these parameters. Similar strategy was considered for the other parameters such as T_p, T_m, I_a, and R_x. This type of selection for the input motions tries to reduce the possibility of considerable uncertainty in seismic demand. All of these input motions have been adopted from PEER (pacific earthquake engineering research center) strong motion database [12].

	Record	PGA(cm/s^2)	PGV(cm/s)	Magnitude
1	Anza 1980	0.131	5.1	4.9
2	Cape Mendocino 1992	0.229	7.1	7.1
3	Chi-Chi, Taiwan 1999	0.821	67	7.6
4	Chi-Chi, Taiwan 1999	0.311	34.2	7.6
5	Coyote Lake 1979	0.339	24.9	5.7
6	Duzce, Turkey 1999	0.348	60	7.1
7	Duzce, Turkey 1999	0.111	14.2	7.1
8	Erzincan, Turkey 1992	0.515	83.9	6.9
9	Imperial Valley 1979	0.775	45.9	6.5
10	Kobe 1995	0.616	120.7	6.9
11	Morgan Hill 1984	1.298	80.816	6.2
12	N. Palm Springs 1986	0.331	29.5	6
13	Northridge 1994	0.753	84.8	6.7
14	Northridge 1994	0.612	117.4	6.7
15	San Fernando 1971	0.268	25.9	6.6
16	San Fernando 1971	1.16	54.3	6.6
17	Tabas, Iran 1978	0.852	121.272	7.4

Table 2. Details of earthquake motions used in this study

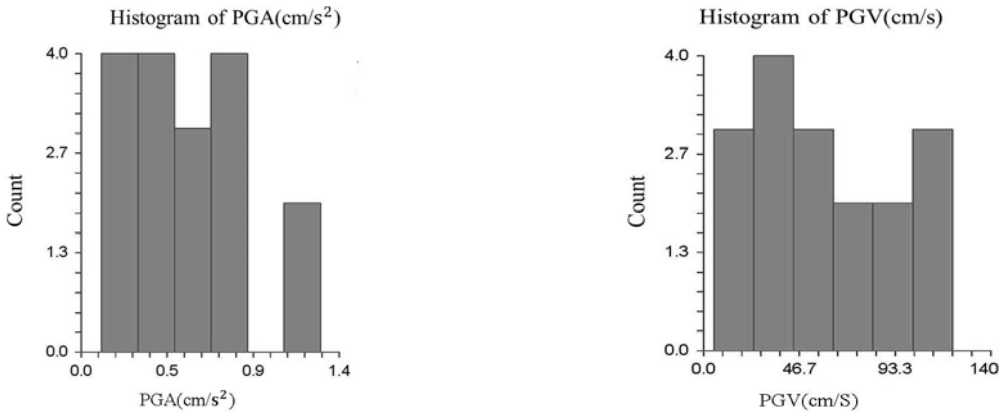


Figure 7. (a) Histogram of PGA for 17 record (b) Histogram of PGV for 17 record

5.2 Performance prediction

Performance-based design is a methodology born from the lessons learned from the previous earthquakes. In the conventional codes, seismic design is based on capacity to resist a design seismic force while structural performance is unknown when the capacity is exceeded. The International Navigation Association [10] proposed qualitative criteria for judging the degree of damage to a gravity quay wall based on the residual horizontal displacement at the top of the wall, as shown in Table 3. In this table, four damage states, I, II, III and IV, correspond to serviceable, repairable, near collapse, and collapse levels of a wharf structure, respectively. At the serviceable level, the structure should have minor or no structural damage and the structure should continue to function. At the repairable level, the structural damage is controllable and repairable. At the level of near collapse, the structural damage is extensive. At the level of collapse, the structural strength is completely lost. However, PIANC did not quantitatively provide the bound for each damage state. Damage states for every performance levels were defined based on PIANC guideline for fragility curves.

Level of damage	Degree I	Degree II	Degree III	Degree IV
Normalized residual horizontal displacement (d/H)	Less than 1.5%	1.5%-5%	5%-10%	Larger than 10%
Residual tilting towards the sea	Less than 3°	$3-5^{\circ}$	$5-8^{\circ}$	Larger than 8°

Table 3: Damage criteria for gravity quay wall by PIANC

5.3 System response

In this paper PGA is used as an intensity measure for analysis. For the fragility curves, all these input motions are scaled into 9 divisions from 0.1g to 0.9g based on PGA. In fact numerical analyses have been performed for more than numerous input motions. Responses obtained for each of the values can be assumed to be lognormally distributed with the probability density function (PDF) given by the following equation. λ and ζ are two parameters of the lognormal distribution of system responses which obtain from the mean (μ) and standard deviations (σ)values of the normal distribution of system response.

$$\lambda = \ln \mu - \frac{1}{2}\zeta^{2} \tag{1}$$

$$\zeta = \ln\left[1+\delta^{2}\right] \tag{2}$$

$$\delta = \frac{\sigma}{\mu} \tag{3}$$

5.4 Fragility analysis

To estimate the probability of a system failure during a seismic risk, a fragility function $P\left[EDP > LS \middle| IM\right]$ is used. This probability function shows the response of the selected engineering demand parameters (EDP) exceed the structural state (LS) for a specific intensity of seismic excitation. Engineering demand parameters value can be achieved by using a set of input motions during nonlinear time history analysis of gravity quay wall. The amount of probability based on PGA for lognormal distribution of system response is calculated according to Eq 4.

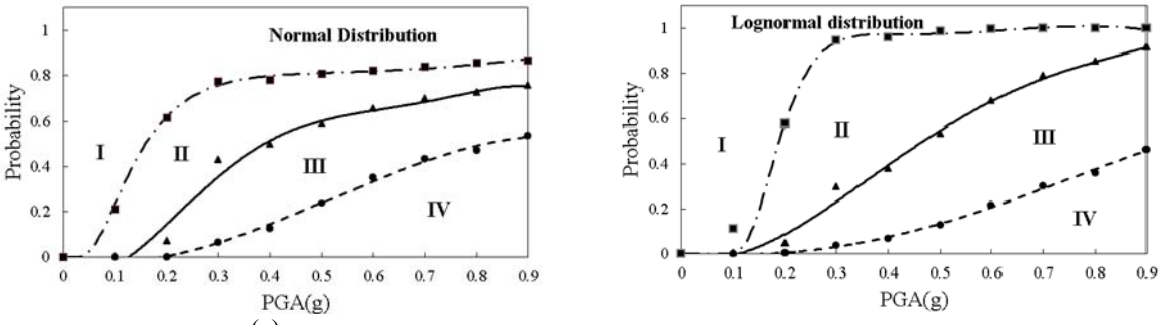
$$P\left[S > s \middle| PGA\right] = P\left[X > x_i \middle| PGA\right] = 1 - \phi\left[\frac{\ln(x_i) - \lambda}{\zeta}\right] \tag{4}$$

where $\phi(\circ)$ is the standard normal cumulative distribution function and x_i is the upper bound for x_i (i= I, II, III).

One can also obtain the probability for normal distribution of system responses based on PGA variation according to Eq 5.

$$P\left[S > s \middle| PGA\right] = P\left[X > x_i \middle| PGA\right] = 1 - \phi\left[\frac{x_i - \mu}{\sigma}\right] \tag{5}$$

Fragility curves of gravity quay wall in VELACS model number 11 is shown for two states of data by normal and lognormal distribution in Figure 8. Bounds of the damage states are selected based on the PIANC guideline. According to the statistical analyses of the results, it was found that the numerical results are more fit to the lognormal distribution. Therefore, fragility curves obtained from lognormal distribution is more appropriate. Figure 1(a) indicates that fragility curves achieved from normal distribution, probability of failure for PGA=0.5g in damage states I, II, III is 80%, 58.4%, 23.7% respectively. While Figure 1(b) indicates that fragility curves of system for lognormal distributions for PGA=0.5g in damage states I, II, III is 98.5%, 53.1%, 12.7% respectively.



(a) (b)

Figure 8: (a) fragility curve by normal distribution (b) fragility curve by lognormal distribution

6 CONCLUSION

In this paper Seismic risk assessment of a caisson gravity quay wall in centrifuge test is shown. Time-history analyses for this model were performed by nonlinear numerical methods. To evaluate the probability of the system, the seismic response of the system in terms of horizontal displacement at the top of the wall was evaluated. Fragility curves for the system was assessed based on the results of the numerical analyses by 17 input motions. Damage states for every performance levels defined based on PIANC guideline for fragility curves. According to the results and performance levels for three states including serviceable, repairable, and near collapse, the fragility curves for normal and lognormal data distributions have been presented. Since the distribution of results was more fit to lognormal distribution, the fragility curve of this distribution was found to be more reasonable. Damage probability for the performance levels of serviceable, repairable, and near collapse in PGA=0.5g have obtained 98.5%, 53.1%, 12.7%, respectively. When the peak ground acceleration increases to 0.9g, the probability of damages levels of serviceable, repairable, and near collapse increase to 99.9%, 91.2%, 46.4%, respectively.

REFERENCES

[1] X. Zeng, R.S. Steedman, *On the behavior of quay walls in earthquakes*, Geotechnique, 43(3), 417 -431 , 1993.

[2] X. Zeng, *Seismic response of gravity quay walls, I: Centrifuge modeling*, Journal of geotechnical and geoenvironmental engineering, 124, 406-417, 1998.

[3] X. Zeng, S. P. G. Madabhnshil, *Seismic response of gravity quay walls, I: Numerical modeling*, Journal of geotechnical and geoenvironmental engineering, 124, 418-427, 1998.

[4] G. Cooke, *Ground improvement for liquefaction mitigation at existing highway bridges*, Dissertation of Blacksburg, VA, July 13, 2000.

[5] K. Ichii, *Fragility curves for gravity-type quay walls based on effective stress analyses*, 13th World Conference on Earthquake Engineering, Vancouver, B.C, Canada, August 1-6, 2004.

[6] P. Dakoulas, G. Gazetas, *Seismic effective-stress analysis of caisson quay walls: application to kobe* , Journal of Soils and foundations 4, 133-147, 2005.

[7] P. Dakoulas and G. Gazetas, *Insight into seismic earth and water pressures against caisson quay walls*, Journal of Geotechnique, 58, 95–111, 2008.

[8] S.C. Jiunn, H.C. Chiou, H.I. Yang, I.H. Shang, *Developing fragility curves for a pile-supported wharf*, Soil Dynamic sand Earthquake Engineering, 31, 830–840, 2011

[9] S.W. Chuang, D. Reginald, J. Glenn, *Numerical Fragility Analysis of Vertical Pile-Supported Wharves in the Western United States*, Journal of Earthquake Engineering, 16, 579–594, 2012.

[10] A.A. Balkema Publishers, *Seismic design guidelines for port structures PIANC*, Swets & Zeitlinger B.Y. Lisse 2001.

[11] http://peer.berkeley.edu/smcat/search.html

[12] http://www.princeton.edu/~dynaflow/radu/soil/velacs/m11/index.html

COMPDYN 2013
4th ECCOMAS Thematic Conference on
Computational Methods in Structural Dynamics and Earthquake Engineering
M. Papadrakakis, V. Papadopoulos, V. Plevris (eds.)
Kos Island, Greece, 12–14 June 2013

SYSTEM IDENTIFICATION OF A 13-STORY REINFORCED CONCRETE BUILDING THROUGH AMBIENT AND FORCED VIBRATION

Sherif Beskhyroun[1*], Liam Wotherspoon[2], Quincy T. Ma[2]

[1] The University of Auckland, Faculty of Engineering,
Department of Civil and Environmental Engineering,
Private Bag 92019, Auckland, New Zealand,
s.beskhyroun@auckland.ac.nz

[2]The University of Auckland, Faculty of Engineering,
Department of Civil and Environmental Engineering,
Private Bag 92019, Auckland, New Zealand,
l.wotherspoon@auckland.ac.nz
q.ma@auckland.ac.nz

Keywords: Structural Dynamics, Earthquake Engineering, Modal Parameters.

Abstract. *This paper describes a unique research program that investigated the dynamic behavior of a full scale 13-story reinforced concrete building under forced vibration, ambient vibration and distal earthquake excitation. Modal parameters of the building were identified using the System Identification Toolbox (SIT) developed at the University of Auckland, New Zealand utilizing a range of methods in both the frequency and time domain. Initially, an eccentric mass shaker located on the upper floor of the building was used to excite the building while instrumented with eight accelerometers. Ambient vibrations were then recorded over a period of two weeks utilizing over 40 tri-axial accelerometers. During this period the building was also excited by a M6.5 earthquake roughly 350km away and high quality acceleration data was recorded. System identifications were carried out using test data from each excitation source, and comparisons were made between the results of each. Correlation of mode shapes was evaluated using the modal assurance criterion (MAC) and the variation in the natural frequency and damping values were statistically evaluated. Overall, consistent results were observed for modal parameters obtained from various methods. The influence of the excitation force characteristics on the performance of various system identification techniques was also investigated.*

1 INTRODUCTION

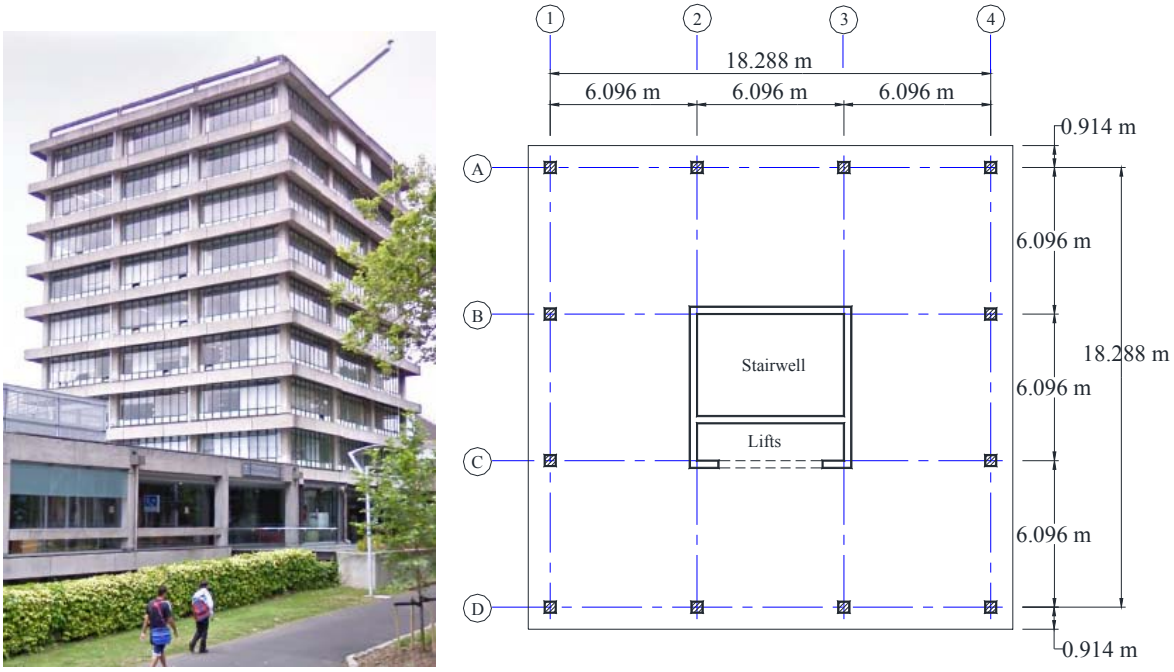
The identification of dynamic characteristics such as natural frequencies, mode shapes, and modal damping is a necessary and important task in the course of seismic design of civil engineering structures [1]. To accomplish this task, ambient vibration tests, forced vibration tests, free vibration tests, and earthquake response measurement can be carried out. Among these field tests, ambient vibration experiments are most common as they are economical, non-destructive, and fast and easy to implement. However, as the input excitation in ambient vibration tests is usually weak, these tests are not as effective in obtaining an accurate estimation of the higher modes data, and uncertainties remain as to whether the modal information applies in the higher strain ranges. Forced vibration tests overcome these issues by providing higher input forces. However, they are substantially more expensive, time consuming to conduct, and often require special permissions as there is an increased likelihood of damaging the structure. As ambient vibration testing is output driven, it is highly cost effective and is regarded as being harmless to the integrity of the structure [2, 3]. In ambient vibration measurements, the input force is unknown, thus output-only modal parameter identification techniques must be applied for modal analysis. Some researchers suggest that output-only analysis is superior with multiple-input data, and hence the distribution of the input forces across the structure will affect the quality of the identified modal parameters [4, 5]. Researchers also emphasize that for output-only analysis to be successful it is important to have sufficient quality data with good signal-to-noise ratio [6]. Another important issue that needs further investigation is whether output-only analysis can work well in both the time and frequency domains. This paper investigates some of these issues.

The successful implementation of large sensing networks is limited by the high cost of installing and maintaining the extensive lengths of wiring needed in a large civil structure to connect individual sensors to a central repository [7]. As a result of these high costs, micro-electro-mechanical system (MEMS) accelerometers became a potential economical alternative to conventional wired sensors. As these accelerometers generally have low power consumption, they can operate for an extended period of time powered only by a battery. Moreover, some battery operated MEMS accelerometers have the analogue-to-digital conversion and data recording capability built in, further simplifying the set up and permitting a higher number of points to be monitored than usual. In this research program, 49 tri-axial MEMS accelerometers were used to record ambient vibrations from a 13-storey concrete building over a two weeks period. During this period the building was also excited by a M6.5 earthquake roughly 350 km away and high quality acceleration data was recorded. System identification was carried out for each of the excitation sources, and comparisons made between the results of each. Correlation of mode shapes was evaluated using the modal assurance criterion (MAC) [8] and the variation in the natural frequency and damping values were evaluated.

2 TEST BUILDING

Forced and ambient vibration tests were performed on a 13-storey concrete office building in the University of Auckland (Figure 1 (a)). The tower block was built in 1964 and is structurally separate from the adjoining 3-4 storey buildings that were constructed in 2003. The height of the tower is 40.45 m and is serviced by two elevators and stairwells located at its centre. From level 5 onwards the building is essentially square with 18.288 m dimensions on either side (Figure 1 (b)). The building is supported by 12 reinforced concrete columns around its perimeter and pre-stressed shear walls at its core. The pre-stressed shear walls at the core provide the building with the majority of its lateral strength and stiffness [9], which are 305

mm thick throughout the entire structure. The thickness of all the floor slabs is 200 mm except on level 14 where the slab is 120 mm thick.



(a) (b)

Figure 1: (a) Engineering office building at the University of Auckland, (b) Plan view of levels 5 to 12.

3 DYNAMIC TESTS

3.1 Forced vibration testing

A forced vibration test was conducted on the building in 2002 using an eccentric mass shaker located on the top floor by Associate Professor John Butterworth and his Master student Jin Hee Lee [9]. Three different sets of mass, 10, 20 and 40 kg, were attached to the shaker and produced the excitations to the building with various force amplitudes. The building accelerations caused from the vibrations were measured through a network of eight wired accelerometers placed on the stairs landing of each floor and at the corners of the top floor in the building. The modal damping ratios were estimated using four different methods (half power bandwidth, logarithmic decrement, hybrid method and least squares exponential). Two types of forced vibration tests were conducted, frequency sweep and free vibration decay method. Using the frequency sweep method, four distinct modes of the structure were identified. The main conclusions drawn from the results of this testing were that damping is force amplitude-dependent, higher damping occurs in higher modes, and that damping is not purely viscous. These experimental results were then compared with the finite element model which showed good correlation (less than 10% discrepancy). The results from this forced vibration testing will be used later in this paper and compared with the modal properties derived using other excitation sources.

3.2 Ambient vibration testing

An ambient vibration test was conducted on the building in 2012 using large number of MEMS accelerometers. 49 MEMS tri-axial accelerometers were placed throughout the test building to measure ambient vibrations induced by wind, traffic and operational activities. 38 accelerometers were placed in the four corners of each floor, apart from level 3 and level 4

where only three corners were accessible. The remaining 11 accelerometers were positioned on the stairs running through the center of the building. Prior to setting up, the real time clock (RTC) of each accelerometer was synchronized to a common computer to ensure that each accelerometer had a common timestamp. The accelerometers were set to a sampling rate of 40 Hz, which was deemed appropriate for the measurement of the first four modes of the building based on simple calculations. At this sampling rate the accelerometers could be operated for a period of two weeks using a D-cell battery. During the recording period the building was also excited by a M6.5 earthquake roughly 350 km away and high quality acceleration data was recorded. Detailed information about the earthquake was obtained from the GeoNet website (http://www.geonet.org.nz). Three dynamic load cases were analyzed wind, operational use and the earthquake. To find the most desirable time intervals for wind loading recordings, 10-min interval wind speed data was generated for the test period using data from the National Institute of Water and Atmospheric Research (NIWA) (www.niwa.co.nz). The time periods with maximum wind speed were utilized to analyze the response of the building to wind loading. The peak operational use of the building was estimated as being around 4-5pm. During this period there is heavy use of the lifts as people head home. Additionally, the traffic on the nearby road is at its peak.

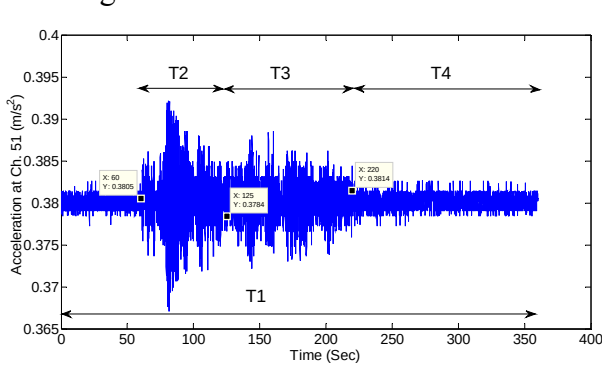
Spectrogram shows the frequency spectrum of the signal and how it changes over time. It returns the time-dependent Fourier transformation for a sequence and displays this information as a spectrogram. The spectrogram is, therefore, a view of the frequency content of the signal as a function of time. It is a useful tool to understand how different modes are excited over time and it can also be used to select the best time intervals for identifying particular modes. Figure 2 shows the acceleration response at level 12 of the building and the associated spectrogram from earthquake, wind and operational use excitation, respectively. Comparison of the spectrogram function from each loading type clearly indicates that the operational use excitation was the most efficient in exciting multiple modes.

4 MODAL PARAMETERS IDENTIFICATION

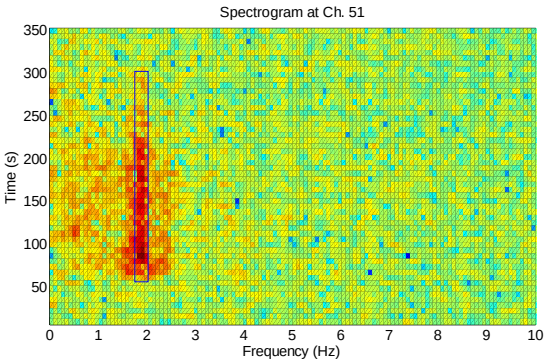
4.1 Time domain versus frequency domain identification techniques

Modal parameters of the building were identified using the System Identification Toolbox (SIT) program developed at the University of Auckland [10]. Three frequency domain based methods; peak picking (PP), frequency domain decomposition (FDD) [11], enhanced frequency domain decomposition (EFDD) [12] and one time domain based method; stochastic subspace identification (SSI) [13, 14] were utilized to estimate the modal parameters of the building. Two techniques were implemented to find stable poles in the SSI method. In both techniques the algorithm starts with a high system order, which is then reduced by two on each iteration until the final iteration was run with a system order of two. Stable poles identified in each of these iterations were compared by two techniques. In the first technique (SSI1), the stable poles identified around the singular values generated from the singular value decomposition of the power spectral density matrix [11] are compared. If two consecutive poles within a predefined offset of the singular value have change in frequencies, change in damping and a modal assurance criterion (MAC) within user defined values, both poles will be kept and averaged. If both poles do not meet these criteria the first pole is discarded and the second pole is compared to the subsequent one. This series of comparisons continue until all stable poles in the frequency range are found and averaged. The resulting mode shapes, natural frequencies and damping ratios are the combination of several stable poles and therefore provide a robust method of system identification. While the first technique (SS1) uses singular value decomposition of the power spectral density function (PSD) matrix to identify stable poles,

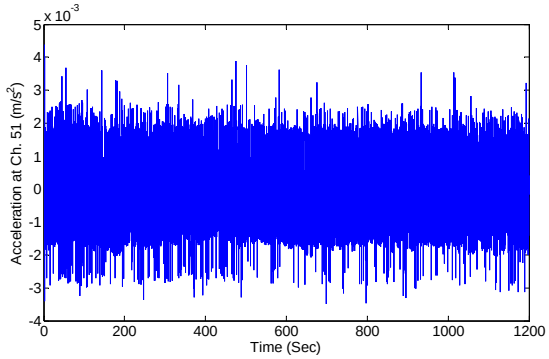
the second technique (SSI2) breaks up the entire frequency range tested into bands. Those bands with the most poles are considered to contain true modes and are then used to find stable modes. Stable poles are found within each band and averaged using the same procedures as in the previous SSI1 technique. Figure 3 shows the first four modes of the building as estimated by the PP method using 20 minutes of vibration data induced by operational activities in the building and nearby traffic. These figures clearly indicate that the high quality acceleration data captured by the accelerometers has resulted in a very clear identification of mode shapes. This is also true for the higher modes, despite the fact that ambient vibration tests are traditionally not as effective in obtaining an accurate estimation of the higher modes due to the low signal to noise ratio.



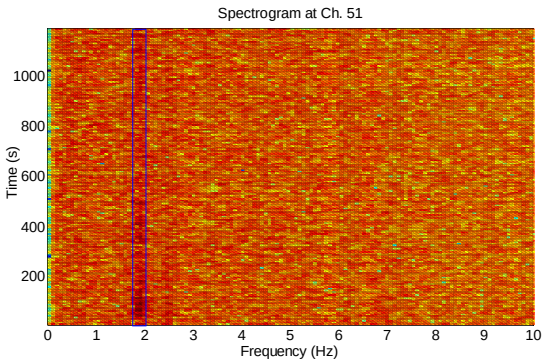
(a) Acceleration response from earthquake excitation



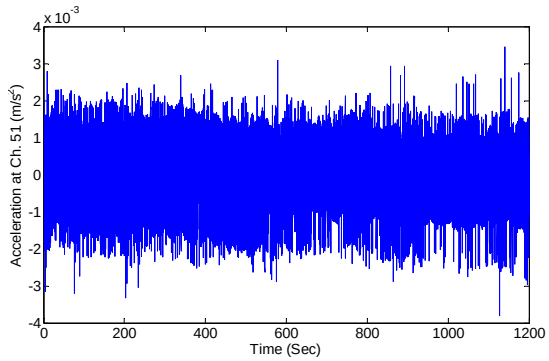
(b) Spectrogram from earthquake excitation



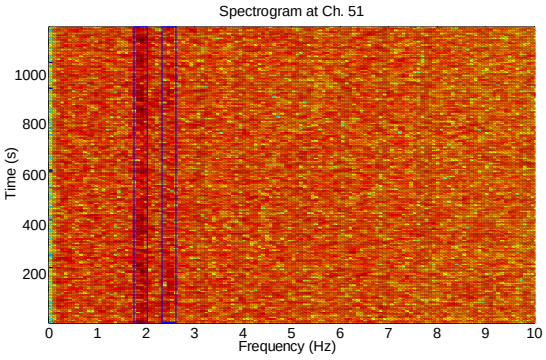
(c) Acceleration response from wind excitation



(d) Spectrogram from wind excitation

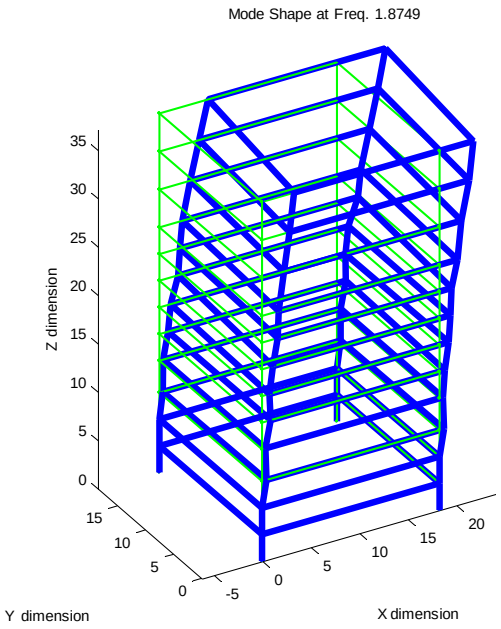


(e) Acceleration response from operational use excitation

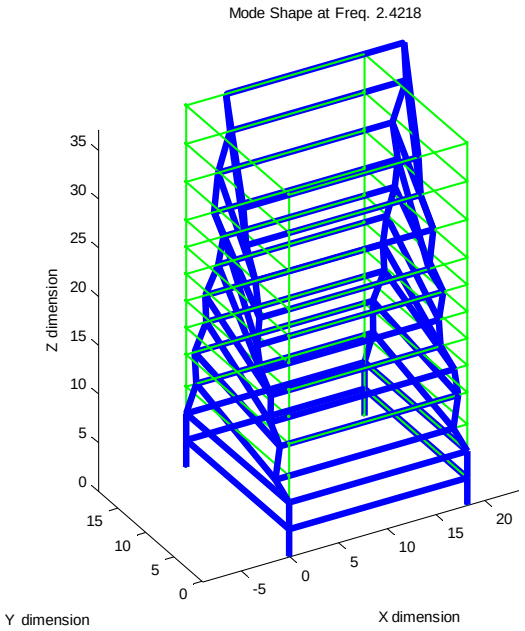


(f) Spectrogram from operational use excitation

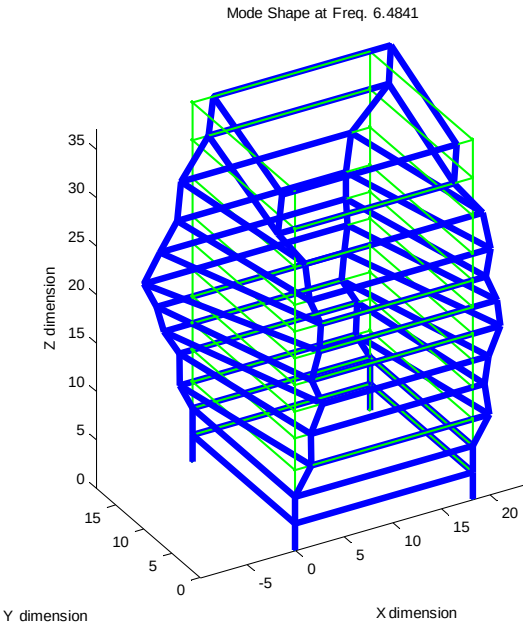
Figure 2: Acceleration response and the associated spectrogram from different excitation sources.



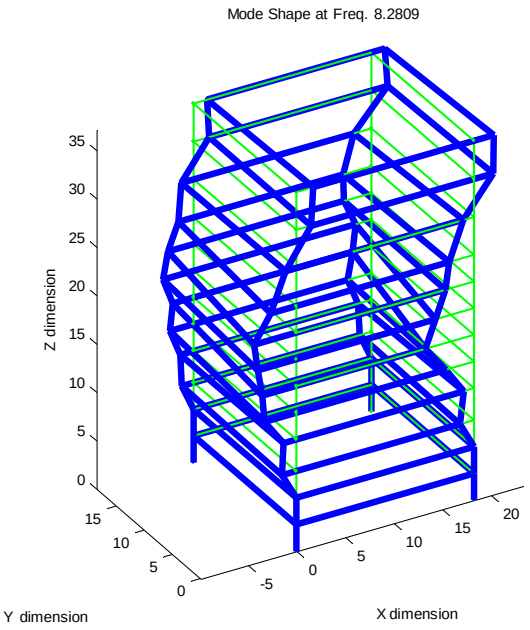
(a) First translational mode (NS)



(b) First torsional mode



(c) Second torsional mode



(d) Second translational mode (NS)

Figure 3: Mode shapes developed with operational use ambient vibration records.

The modal assurance criterion (MAC) is generally used as a measure of the correlation between two mode shapes. For the current study, the MAC value was used to compare mode shapes from various system identification methods. The MAC value corresponding to the i^{th} mode shapes, ϕ_{ij} and ϕ_{ij}*, is defined as [8]:

$$MAC_i = \frac{\left[\sum_{j=1}^{n} \phi_{ij} \phi_{ij}^{*}\right]^2}{\sum_{j=1}^{n} \phi_{ij}^2 \sum_{j=1}^{n} \phi_{ij}^{*2}} \quad (1)$$

where n is the number of elements in the mode shape vectors. A MAC value close to unity indicates perfect correlation between the two shapes and values close to zero indicate shapes that are orthogonal. Figure 4 shows MAC values for the second torsional mode identified by PP, FDD, EFDD, SSI1 and SSI2 methods. Each bar in the figure represents the MAC value when comparing a specific mode extracted from a pair of system identification methods. MAC values ranged from 0.80 to 1.00 for the first three modes (first translational, first torsional and second translational) which indicated a very high correlation between mode shapes identified by time domain and frequency domain identification techniques. A near perfect correlation was shown for the first bending mode and the first torsional mode. The perfect correlation of mode shapes identified by time domain and frequency domain based methods indicates that both techniques can be efficiently utilized with output-only data. The operational use data produced the most accurate mode shapes and can be attributed to the good distribution of input forces across the structure. The input force resembled a white noise signal and the drift in the accelerometers RTC was negligible shortly after the start of the test period.

Table 1 shows the natural frequencies of the first translational and first torsional modes of the building determined through PP, FDD, EFDD and SSI for the three different load cases. The natural frequencies determined using these techniques for the different load cases are very similar and the small variation (below 0.14 Hz) in these values can be attributed to mathematical errors or differing noise levels in the data. Table 2 summarizes the modal parameters determined for the building through forced vibration analysis [9]. The frequencies generated for the first two modes decrease in value as the force applied by the eccentric mass shaker is increased. The first translational mode frequency is between 1.88-1.91 Hz and the first torsional mode frequency is 2.45-2.48 Hz. All modal parameters from ambient and forced vibrations tests were very well correlated and only small differences were observed.

Table 1: Modal parameters developed from full scale ambient vibration testing.

Mode Shape	PP	FDD	EFDD	SSI1		SSI2	
	Freq. (Hz)	Freq. (Hz)	Freq. (Hz)	Freq. (Hz)	Damp. (%)	Freq. (Hz)	Damp. (%)
Wind							
1st Trans. (NS)	1.88	1.84	1.84	1.85	1.17	1.85	1.17
1st Torsional	2.34	2.42	2.42	2.45	1.41	2.45	1.4
Operational Use							
1st Trans. (NS)	1.88	1.88	1.88	1.87	1.95	1.87	1.95
1st Torsional	2.42	2.46	2.46	2.44	1.77	2.44	1.77
Earthquake							
1st Trans. (NS)	1.88	1.84	1.84	1.84	1.23	1.84	1.22
1st Torsional	2.27	2.31	2.31	2.41	1.62	2.41	1.62

Table 2: Modal parameters developed from full scale forced vibration test.

Mode Shape	Level of excitation					
	10kg		20kg		40kg	
	Freq. (Hz)	Damp. (%)	Freq. (Hz)	Damp. (%)	Freq. (Hz)	Damp. (%)
1st Trans. (NS)	1.91	1.525	1.90	1.556	1.88	1.707
1st Torsional	2.48	1.394	2.46	1.466	2.45	1.64

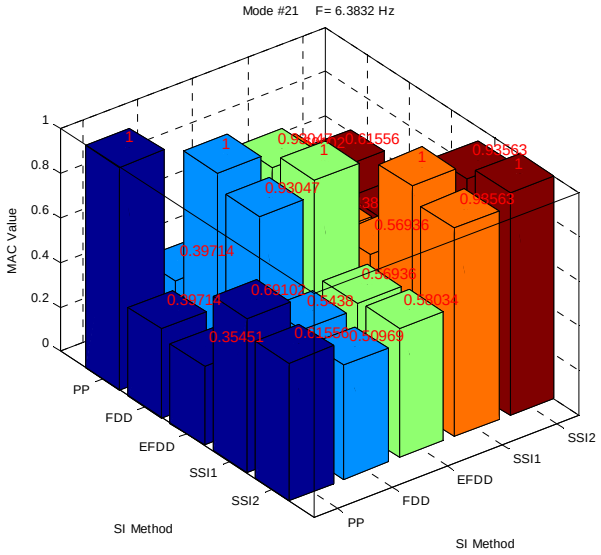
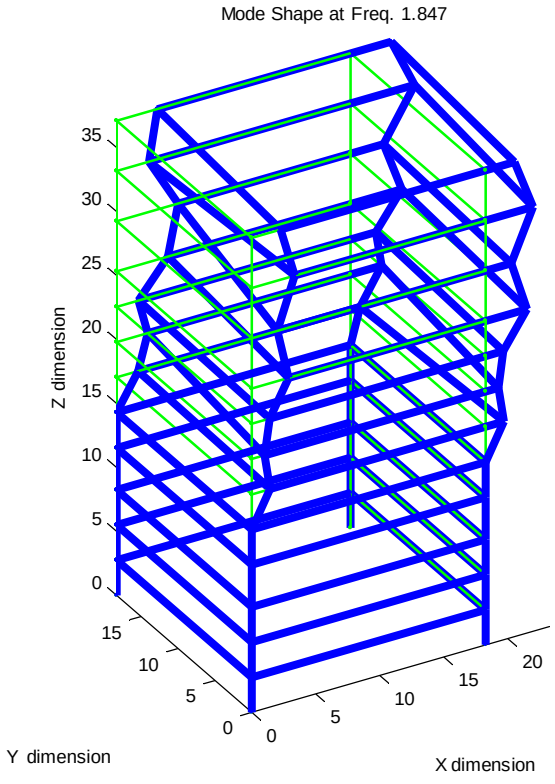


Figure 4: Comparison of the second torsional mode shape identified by different techniques using MAC.

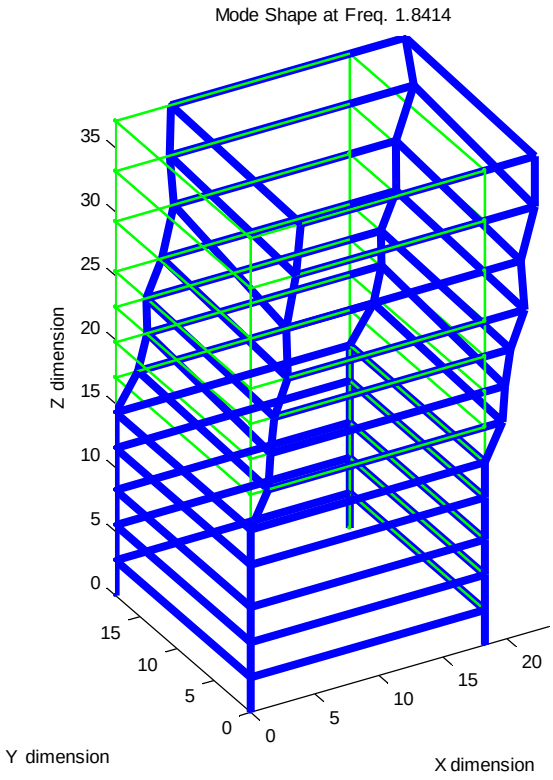
4.2 Modal parameters identification from non stationary vibration

In operational modal analysis and output-only modal identification it is assumed that the excitation is unknown and can be modelled by a Gaussian white noise. This assumption can be accepted with confidence in case of using ambient vibration data produced by wind, nearby traffic or operational use as the response is typically stationary and we can assume that the excitation signal is a Gaussian white noise. However, for the earthquake excitation this assumption is not valid especially in case of strong earthquakes.

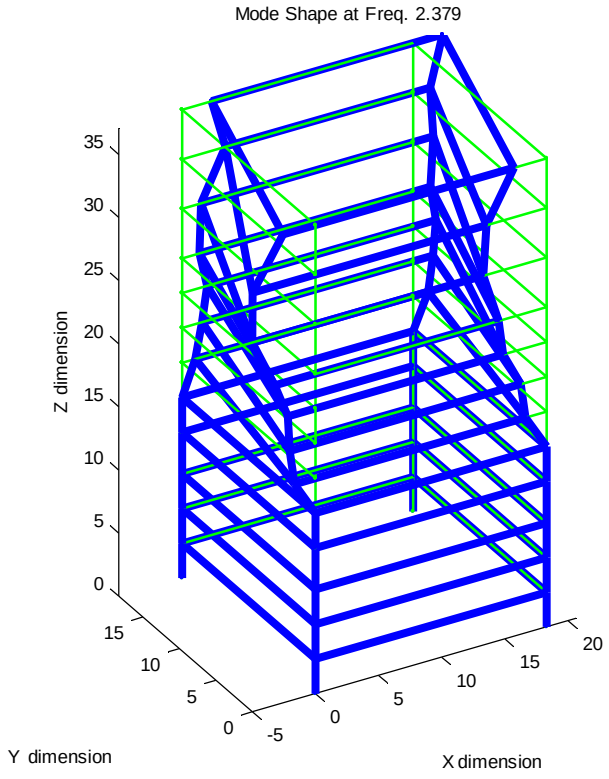
The test building was excited by a M6.5 earthquake roughly 350km away and high quality acceleration data was recorded especially at the top floors. It was therefore decided to divide the time history response to three sections as shown in Figure 2a to investigate the influence of using non stationary vibration on the identified modal parameters. As indicated in this figure, the second section T2 in the time interval between 60 and 125 seconds included the most non-stationary vibration while section T3 in the time interval between 125 and 220 seconds was considered the closest to the stationary signal. The first translational and the first torsional mode shapes identified by the SSI method using the time history response in sections T2 and T3 are shown in Figure 5 (a) through d, respectively. It is clearly shown in these figures that using the response data in the non-stationary interval resulted in a poor representation of all mode shapes despite the fact that the first translational mode was strongly excited during this interval as indicated in the spectrogram of the data (Figure 2b). Similar observations were found when frequency domain techniques were utilised to extract modal parameters.



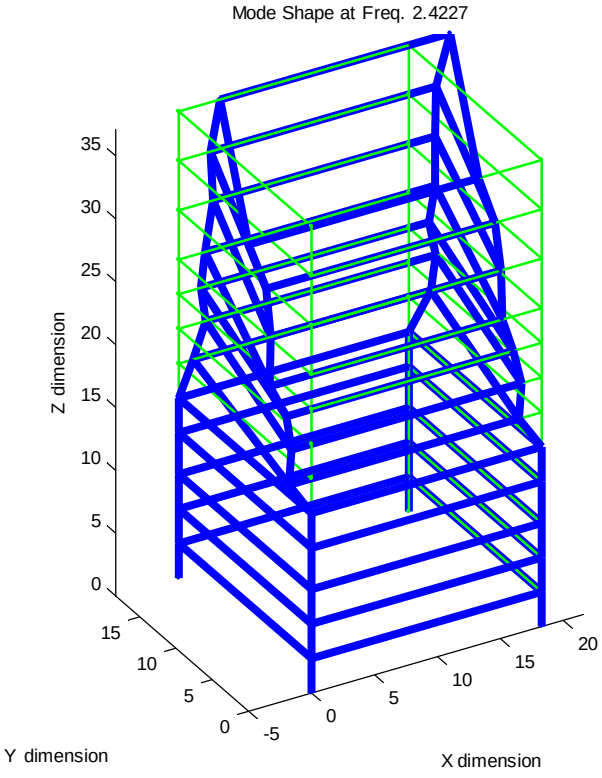
(a) First translational mode (NS) identified using non-stationary vibrations



(b) First translational mode (NS) identified using stationary vibrations



(c) First torsional mode (NS) identified using non-stationary vibration



(d) First torsional mode identified using stationary vibration

Figure 5: Comparison of the second torsional mode shape identified by different techniques using MAC.

5 CONCLUSIONS

A comparison between full scale forced and ambient vibration dynamic tests conducted on a 13-storey reinforced concrete building in the University of Auckland, New Zealand has been investigated in this paper. An eccentric mass shaker fixed at the top of the building was used to excite the structure and eight wired accelerometers captured the vibration response. A dense array of low cost MEMS accelerometers successfully recorded very small amplitudes of the building vibration under different forms of ambient excitation. Four system identification techniques, peak picking (PP), frequency domain decomposition (FDD), enhanced frequency domain decomposition (EFDD) and stochastic subspace identification (SSI) were implemented to extract modal parameters of the building. The recorded ambient data produced very accurate estimates of the modal parameters of the instrumented buildings including higher modes. Both time and frequency domain techniques provided very accurate estimates of modal parameters when used with output-only data. Strong correlation between modal parameters from the implemented methods was found. The modal parameters determined through ambient vibrations were comparable with the forced vibration analyses, providing substantial evidence that ambient vibration testing can be as effective as forced vibration testing in determining modal parameters for similar structures. It has been shown that the near stationary vibration data can produce accurate estimates of modal parameters. However, further study is required to estimate the level of non stationarity in the signal and facilitate the application of output only modal parameters identification techniques with non-stationary data.

ACKNOWLEDGEMENTS

The financial support of the New Zealand Earthquake Commission (EQC) is gratefully acknowledged. The authors would like to thank Annabelle Hale (Dean's assistant) for her help in the setting up of the accelerometers throughout the building. Special thanks to Bharat Popli and Morgan Wang, final year project students, for their assistance in instrumenting the building and preparing the recorded data.

REFERENCES

[1] Farrar C R, J. G. H. (1997) System identification from ambient vibration measurements on a bridge. *Journal of Sound and Vibration,* 205, 1−18.

[2] Endrun, B., Ohrnberger, M. & Savvaidis, A. 2010. On the repeatability and consistency of three-component ambient vibration array measurements. *Bulletin of Earthquake Engineering,* 8, 535-570.

[3] Çelebi, M. 2009. Comparison of recorded dynamic characteristics of structures and ground during strong and weak shaking. *Increasing Seismic Safety by Combining Engineering Technologies and Seismological Data*, 99-115.

[4] Au, S. K., Zhang, F. L. & To, P. 2012. Field observations on modal properties of two tall buildings under strong wind. *Journal of Wind Engineering and Industrial Aerodynamics,* 101, 12-23.

[5] Brownjohn, J. M. W. 2003. Ambient vibration studies for system identification of tall buildings. *Earthquake Engineering & Structural Dynamics,* 32, 71-95.

[6] Brincker, R., Ventura, C. E. & Andersen, P. 2003. Why output-only modal testing is a desirable tool for a wide range of practical applications. In *Proceedings of IMAC-21: A*

Conference on Structural Dynamics. Society for Experimental Mechanics. The Hyatt Orlando, Kissimmee, Florida. USA. s. 265-272.

[7] Çelebi, M. 2002. Seismic instrumentation of buildings (with emphasis on federal buildings). Menlo Park, CA, USA: United States Geological Survey.

[8] Ewins, D. J. 2000. *Modal testing: Theory, practice, and application*. Baldock: Research Studies Press.

[9] Lee, J. H. 2003. Assessment of modal damping from full scale structural testing. Master Thesis (ME--Civil and Resource Engineering)--University of Auckland, 2003.

[10] Beskhyroun, S. 2011. Graphical interface toolbox for modal analysis. In *Proceedings of the Ninth Pacific Conference on Earthquake Engineering*. Auckland, New Zealand.

[11] Brincker R., Z. L., & Andersen P. 2000. Modal identification from ambient responses using frequency domain decomposition. In *Proceedings of the 18th International Modal Analysis Conference (IMAC), USA.*

[12] Jacobsen N.-J., A. P. & Brincker R. 2007. Using EFDD as a robust technique to deterministic excitation in operational modal analysis. In *Proceedings of the 2nd International Operational Modal Analysis Conference (IOMAC), Copenhagen, Denmark.*

[13] Overschee, P. v. & Moor, B. L. R. d. 1996. *Subspace identification for linear systems: Theory, implementation, applications*. Boston ; London: Kluwer Academic.

[14] Katayama, T. 2005. *Subspace methods for modal parameters identification*.

[15] Çelebi, M., Bazzurro, P., Chiaraluce, L., Clemente, P., Decanini, L., DeSortis, A., Ellsworth, W., Gorini, A., Kalkan, E., Marcucci, S., Milana, G., Mollaioli, F., Olivieri, M., Paolucci, R., Rinaldis, D., Rovelli, A., Sabetta, F. & Stephens, C. 2010. Recorded motions of the 6 April 2009 MW 6.3 L'aquila, Italy. Earthquake and implications for building structural damage: Overview. *Earthquake Spectra,* 26, 651-684.

COMPDYN 2013
4th ECCOMAS Thematic Conference on
Computational Methods in Structural Dynamics and Earthquake Engineering
M. Papadrakakis, V. Papadopoulos, V. Plevris (Eds.)
Kos Island, Greece, 12–14 June 2013

DYNAMIC IDENTIFICATION AND EVALUATION OF THE SEISMIC SAFETY OF A MASONRY BELL TOWER IN THE SOUTH OF ITALY

Domenico Colapietro[1], Alessandra Fiore[2], Adriana Netti[2], Fabio Fatiguso[1], Giuseppe C. Marano[2], Mariella De Fino[4], Davide Cascella[3], Antonio Ancona[1]

[1] DICATECh, Technical University of Bari, Via Orabona 4, 70125 Bari, Italy
d.colapietro@poliba.it, f.fatiguso@poliba.it

[2] DICAR, Technical University of Bari, Via Orabona 4, 70125 Bari, Italy
a.netti@poliba.it, a.fiore@poliba.it, g.c.marano@gmail.com,

[4]B.Re.D. s.r.l., Polytechnic of Bari Spin – off, Via Orabona 4, 70125 Bari, Italy
m.defino@poliba.it

[3] WAVENG s.r.l., Innovative engineering solutions and consulting. Via Schuman 14, 70126 Bari, Italy
d.cascella@waveng.it

Keywords: bell tower, sensor networks, structural identification, model updating, non-linear dynamic analysis

Abstract. *Many countries, especially in southern Europe, are greatly exposed to seismic hazard, which is the cause of severe damage in historical buildings or even destruction in the case of strong earthquake ground motions. The recent experience of Italian seismic events (Umbria and Marche 1997, Puglia and Molise 2002, Abruzzo 2009, Emilia 2012) has highlighted the behavior, the damage and the intrinsic vulnerability of monumental buildings. Historical and monumental constructions are characterized by an inherent vulnerability to seismic action, due to the circumstance that most of them frequently lack basic seismic features and/or were never fitted with adequate provisions against earthquake actions. This entails the need to define urgent strategies for the protection of cultural heritage from seismic hazard. This paper deals with the structural monitoring and seismic assessment of a unique masonry tower in a Apulia region in southern Italy: the bell tower of "Santa Maria di San Luca" in the city of Valenzano. This monument was monitored by means of full-scale environmental vibration testing. Measured responses were then used for modal identification. The assessment procedure includes morphological and structural knowledge, full-scale ambient vibration testing, modal identification from ambient vibration responses, finite element modeling, dynamic-based identification of the model. A satisfactory improvement in modal parameters is so obtained, resulting in a close agreement between the modal properties observed in dynamic tests and those calculated from a numerical model. Nonlinear dynamic analysis allows to identify the potential collapse mechanisms and those dangerous structural weak points which may play a fundamental role in the seismic vulnerability of the towers.*

1 INTRODUCTION

Many countries, especially in the south of Europe, are heavily exposed to seismic risk, which is the cause of destruction or damage of the cultural heritage. The recent Italian experience of seismic events (Umbria and Marche 1997, Puglia and Molise 2002, Abruzzo 2009) has sanctioned considerable information about the behavior, the damage and the intrinsic vulnerability of monumental buildings. The historical buildings are usually characterized by an inherent vulnerability to seismic action, being the masonry, not very resistant to tensile strain, especially along the horizontal planes of the joints normally compressed [9, 10]. On the occasion of an earthquake, the horizontal action involved in fact might exceed the weak resistance of the material for the states of tangential stress and tension, causing injury to slide or detachment of the elements. In addition, the history of these artifacts, marked by different construction phases, accentuates that behavior for parts, which is in itself. The modifications and the addition extensions determine the presence of many facilities within the same building, whose behavior is strongly influenced by the action that strikes them [11, 12, 13, 14]. In the case of an earthquake, the inertial horizontal forces are capable of causing the loss of balance of these elements especially if they are slim or not properly connected to the rest of the building. This intrinsic vulnerability is extremely enhanced in some cases, by the lack of effectiveness assessment of some new construction techniques; solutions such as the remake of a reinforced concrete roof, the inclusion of too rigid curbs at the top of the walls, the use of armed seams as an alternative to traditional metal tie rods, have caused in many cases damages higher than those that the original structure would probably have presented. The safeguard of these historical and monumental buildings from earthquakes would preserve people from a serious hazard to their own safety, but also would protect unique art and architecture masterpieces from severe damage or even from destruction.

The definition of reliable models and methods for seismic risk assessment of historical constructions is thus a very interesting topic. The "knowledge", or better qualification of the traditional buildings, understood as the set of information in order to fully define the historical-material-constructive characters as well as the state of preservation and performance capabilities residual, assumes in this case a decisive role. For this way, a great number of studies in the literature are dedicated to destructive and non-destructive static and dynamic tests on masonry structures, to procedures for the identification of mechanical parameters as well as to calibration of reliable structural models [1, 3, 4]. The dynamic identification through input of environmental nature represents a valid alternative to appraise the characteristics of the materials and the conditions of the tie of the structure, with the purpose to define reliable numerical models, through the procedures of model updating [4, 8]. In particular, dynamic measurements may be very useful for the identification of mechanical properties and soil restraints and, consequently, for the calibration of advanced numerical finite element models. In other words, the knowledge of dynamic properties, together with non-destructive testing, is the starting point for an accurate estimation of the seismic safety of these structures [16, 20]. The main purpose of this article is to investigate the effect of the level of accuracy of the models adopted and the type of analysis performed for the evaluation of the seismic vulnerability of towers in historic masonry, also in relation to the indications of the Italian guidelines "Assessment and reduction of seismic risk of the cultural heritage" with reference to the Technical Code DM 14 2008-01" (DPCM 09 /02/2011). The study is carried out taking into consideration the bell tower of "Santa Maria di San Luca" in the city of Valenzano in Apulia region. In particular, the methodology defined to reach the goals aforementioned consisted of: 1) identifying the historical-material-constructive characters of the building; 2) defining a finite element model; 3) defining localization and direction of the measurement points from

modal analysis of the FEM model; 4) identifying mode shapes and frequencies, by environmental vibration measurements; 5) calibrating a refined numerical model; 6) seismic vulnerability analysis; 7) evaluating the need and effectiveness of earthquake recovery interventions.

2 PRELIMINARY INVESTIGATION

2.1 Structural and historic framework

The bell tower of "Santa Maria di San Luca" (Figure 1), in the city center of Valenzano in southern Italy, was built in 1774 beside of the seventeenth century church in the Franciscan convent.



Figure 1: Bell Tower of "Santa Maria di San Luca"

It has a square cross-section with a side of 6.25 m and rises up with a simple and massive tower structure characterized by a rusticated stone exterior just sketched. Its height is 46 m. Internally, in the bottom portion, it was divided into three parts (respectively to the shares of 0, 4.74 and 9.55 m), characterized by barrel vaults in hewn stone limestone**.** The top portion is divided into three compartments by floors with steel beams and brick tiles covered by concrete. The first block is a simple polyhedral volume with a few decorative episodes, which tend to be enriched with friezes; among them, the most significant one goes from the bottom to the top; the corners bend, digging; they extend out in a continuous movement. The simplicity of the initial part gives way to sophistication. The Romanesque style is overwhelmed by the baroque style. The second block is surmounted by a sandwiched crown by a frame bluish of majolica, windows appears the ogival arch. The third bin is composed of a cockpit to cusp, surmounted by a sphere with metal cross.

The tower is constituted by two different kinds of masonry typology: basement is in hewn stone with good weaving while an upper block is in square stone. It shows a fair state of conservation, even if some superficial cracks and damage patterns occur, due to exposure to at-

mospheric agents throughout the centuries. Even if the tower has no serious structural damage, the safeguard against potential seismic events future is of primary importance.

2.2 Non-destructive Diagnostic Investigation

In order to get more detailed information about the masonry typologies of the tower, a set of non destructive diagnostic technologies was applied to some representative walls. It is worth mention that such an investigation approach is paramount for historical structures, where the acquisition of missing data about materials and techniques by non invasive methods enables the comprehensive qualification of all the building elements - which might be very different due to construction characteristics and/or modifications over the time - as well as the preservation of their integrity and stability. Nevertheless, the selection of the most suitable diagnostic technologies should take into account all the data from the preliminary qualification of the building - through historical research, geometrical surveys, photographic documentation, mapping of materials and construction techniques, decay pattern surveys - in order to address the time and cost effective achievement of significant and reliable results [6,7,18,19].

Specifically, following the described methodology, the investigation concerned (Figure 2):

(i) high frequency radar scanning (IDS DAD 1ch Fastwave reading unit and IDS TRHF 2000 MHz antenna) of masonry surfaces at the ground and second floors up to the fourth floor, where the bells are located, in order to identify the stratigraphy from the reflection/attenuation of electromagnetic waves. For each investigated surface, two radargrams were acquired, at 1m and 1.5m from the corresponding floor.

(ii) semi-direct mode sonic testing (BOVIAR CMS reading unit, piezoelectric hammer up to 20 KHz, piezoelectric receiver 1,25MHz) of masonry corners on the second and fourth floors, belonging respectively to the bottom and the top portion of the tower, in order to assess the compactness from the travel time of mechanical waves. For each investigated corner, three measurement paths were acquired at 1m, 1.5m and 2m from the corresponding floor.

For all the investigated areas, the walls are 150cm thick.

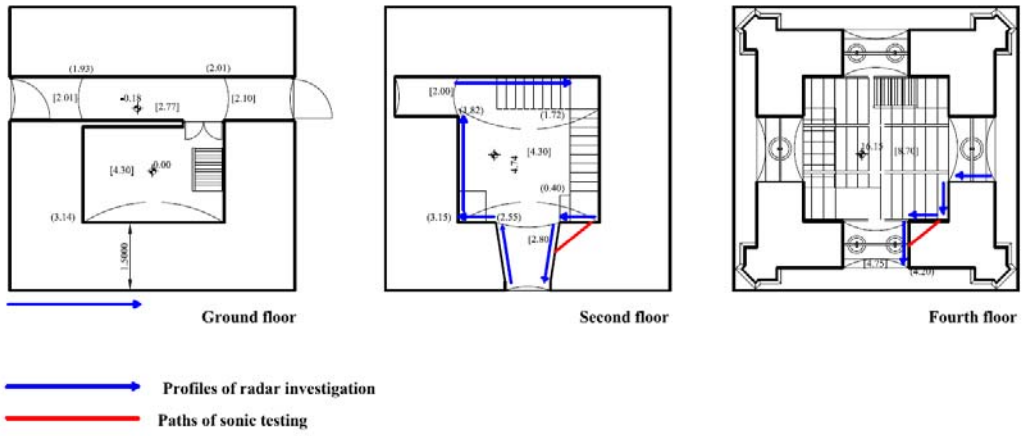


Figure 2. Scheme of diagnostic investigation

From the radargrams at the ground and first floors, it might be observed the presence of three main interfaces, which are all parallel to the external wall surface and respectively about 30cm, 120cm and 150cm deep. The third interface, corresponding to the internal wall surface, is generally about 155cm deep on the ground floor, where the walls are covered by plaster (Figure 3). Otherwise, at the fourth floor, the presence of six regular interfaces might be detected, with relative distance of about 25cm (Figure 4). In the former case, the walls are reasonably cavity masonries, composed of two outer hewn stone leaves and an inner nucleus,

made out of stone and mortar, which seems to be quite compact due to the slight reflection of the electromagnetic waves; whereas, in the latter case, the walls are probably solid, and, thus, composed of several squared stone leaves.

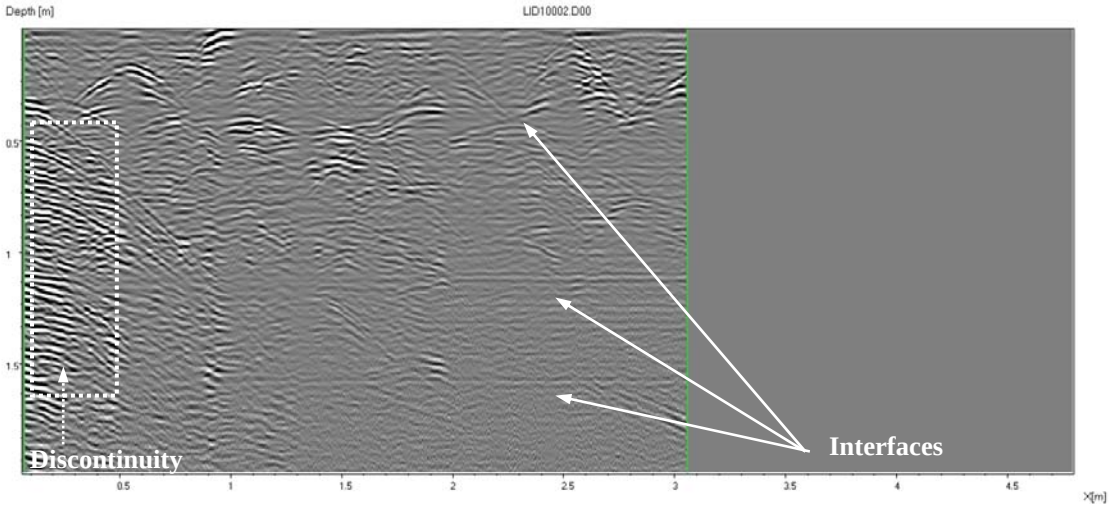


Figure 3. Radargram on an external surface at the ground floor

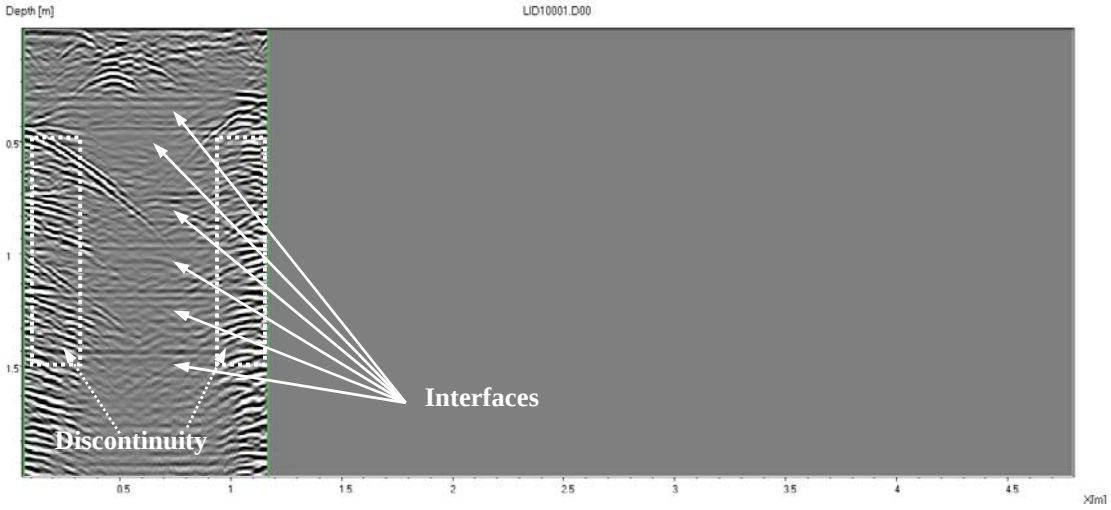


Figure 4. Radargram on an internal surface at the fourth floor

To support such a data interpretation, it should be observed that, at the fourth floor, although the masonry walls are still 150cm thick, the presence of wide and high openings could have made the realization of a cavity less feasible from the technical point of view and less convenient from the static point of view. The results from the radar scanning were confirmed by the semi-direct mode sonic testing (Table 1).

Identification	Range (m)	t_m (μs)	v_m (m/s)	σ_t	σ_v	$\Delta\sigma$ (%)
AB01	0,759	928,0	819,6	47,6	41,6	5,1
AB02	0,759	516,0	1475,0	32,2	86,7	5,9
AB03	0,759	472,8	1608,6	24,2	80,3	5,0
AJ01	0.707	305,6	2315,0	8,8	67,4	2,9
AJ02	0,707	480,0	1473,4	10,2	31,0	2,1
AJ03	0,707	336,8	2105,7	21,2	130,0	6,2

Table 1: Semi-direct mode sonic testing

The measurements, repeated six times on three paths for two elements, show an average velocity of 1300 m/s on the second floor (series AJ in Tab.1), where masonries are more heterogeneous due to the cavity, and 1964 m/s at the fourth floor (series AB in Tab.1).

2.3 Tests of dynamic monitoring

Ancient masonry buildings often have a high historical and monumental value and should be preserved. In this way, measurement of environmental vibrations, based on the natural noise and low frequency vibration from wind and traffic, may be carried out without direct excitation of the building. For this structure under investigation, experimental tests have been performed by applying Environmental Test Methods.

These methods, based on a careful choice of sensor positioning, have allowed obtaining correlations between natural frequencies and vibration modes of direct measurement.

The response of the structure in the time domain was assessed by using a combined network of high frequency force-balance accelerometers.

The instrumentation used for dynamic monitoring included a data acquisition system (THOR, www.waveng.it) based on force-balance accelerometers (EpiSensor ES-U2 Kinemetrics) (Figure 5). It is able to manage more distributed sensor networks with real-time acquisition and data processing for structural analyses.



Figure 5: Location of the vibration sensors

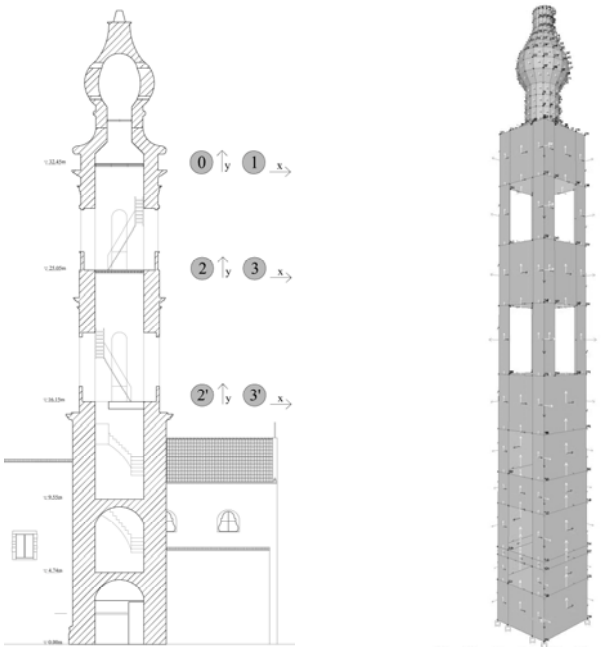


Figure 6: Bell tower finite element model

The tests were carried out by considering the action of the traffic and wind, acting on the bell tower in the months of October and December 2012. A preliminary three-dimensional solid element model was developed for selecting the location of the accelerometers during vibration testing. The construction of the model was undertaken using SAP2000© (version 14.2.4) and it is shown in Figure 6. Only structural elements were included in the model whereas non-structural elements are considered as extra masses. A relatively large number of finite elements (8-node brick element) have been used in the model so that a regular distribution of the masses could be obtained.

Although the geological characteristics of the soil were known, while conservation condition of the foundation was unknown, it was decided to model the interaction structure-foundation-ground by means of linear elastic springs. It was uncommonly modeled the interactions between the tower and the adjacent church by the insertion of elastic springs with elasticity coefficient mediated between the two masonry solutions in continuity.

The aim of the structural identification was the verification of the Young's modulus of the masonry in the upper and lower part of the tower, acquired by non-destructive tests so as to optimize consequently the degree of constraint provided by surrounding buildings. In particular, the range of the Young's modulus is 1500÷1980 MPa for the bottom body (masonry in hewn stone with good weaving) and 2400÷3200MPa (masonry in block squared stone) for the top body. The dynamic measurements were carried out inside a 0÷5 Hz frequency range which is selected on the basis of the first six natural frequencies of the tower obtained from the modal analysis. From the spectral analysis of the acquired signals, natural frequencies and the corresponding vibration modes were formed. Since the recorded signal, as well as the signal-to-noise ratio, is proved to be rather low, this was amplified and filtered through a 30 Hz low-pass filter. Data acquisition was driven by software, which allows the acquisition of signals with sampling rate of 1000 Hz, and the real time visualization of accelerograms and Fourier spectra. The identification was performed by using the techniques of modal extraction in the frequency domain (frequency domain decomposition - FDD). These techniques allow evaluating the natural frequencies and modal shapes of the tower. Fast Fourier Transform (FFT) was used to determine the frequency spectrum of the signal. The spectral analysis of the recorded signals gives the natural frequencies and the corresponding mode shapes (fig. 7-8).

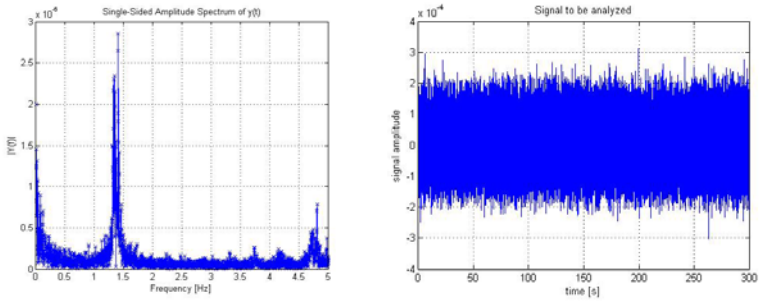


Figure 7: Fast Fourier transform and recorded signal. Accelerometer 0.

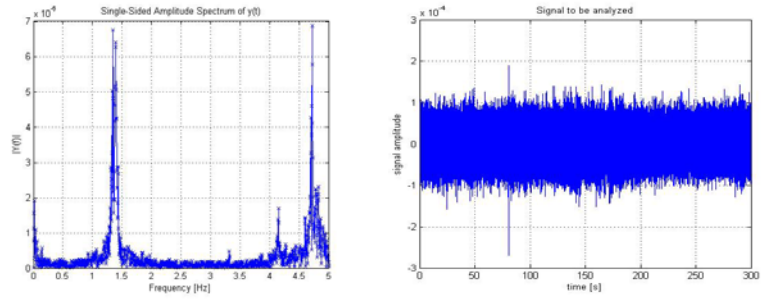


Figure 8: Fast Fourier transform and recorded signal. Accelerometer 1.

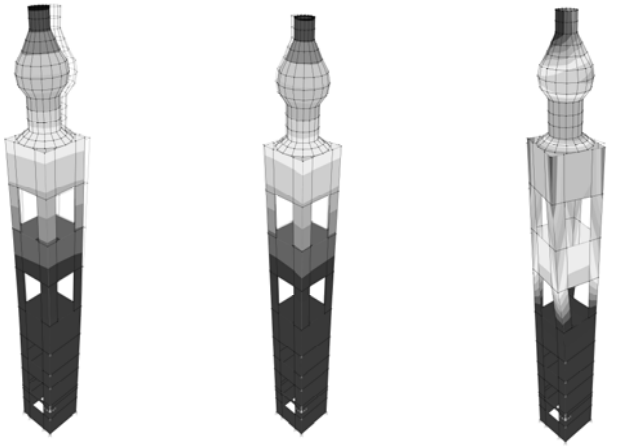
3 STRUCTURAL IDENTIFICATION PROCEDURE

The minimization of the error in frequencies, numerically determined, and those resulting from the measurements performed on site, is used to update the model of finite elements. As

expected the optimum value of Young's Modulus is related to the parameter chosen for calibration. In this case, mechanical parameters were defined minimizing the total frequency discrepancy (1), calculated with the following weighted mean:

$$D_f = \frac{\sum_{i=1}^{n} \left| \frac{f_{FEM,i} - f_{FDD,i}}{f_{FDD,i}} \right| * a_i}{\sum_{i=1}^{n} a_i} \quad (1)$$

where α_i is the i^{th} modal mass ratio and n is the number of the experimental mode shapes (figure 9).



1° Flexural 2° Flexural 1° Torsional

Figure 9. Vibration mode shapes - Bell tower of "Santa Maria di San Luca".

The minimum total discrepancy D_f =0.9239% is obtained for E_{bottom}=1935 MPa and E_{top}=3200 MPa for the upper levels. The mechanical parameters tuning the finite element model to accurately reflect the dynamic characteristics of the bell tower are reported in table 2.

Masonry	E (MPa)	υ	γ (KN/m^3)
Top	1935	0.15	22
Bottom	3200	0.15	21

Table 2: Optimized mechanical parameters.

The single comparison between the natural frequencies from dynamic identification and those from numerical modelling is reported in table 3.

Mode	f_{FDD} (Hz)	f_{FEM} (Hz)	$D_{fsingle}$ (%)
1°Flexural (x)	1.41367	1.41470	0.0739
2° Flexural (y)	1.39580	1.39830	0.1792
1° Torsional	4.79360	4.890	2.0110

Table 3: The correlation between the measured and calculated frequencies

A good correlation between measured and calculated frequencies was obtained, especially for the 1st flexural X ($D_{fsingle}$=0. 0739%) and the 2st flexural Y mode shape (Df_{single}= 0.17%).

4 SEISMIC VULNERABILITY ASSESSMENT

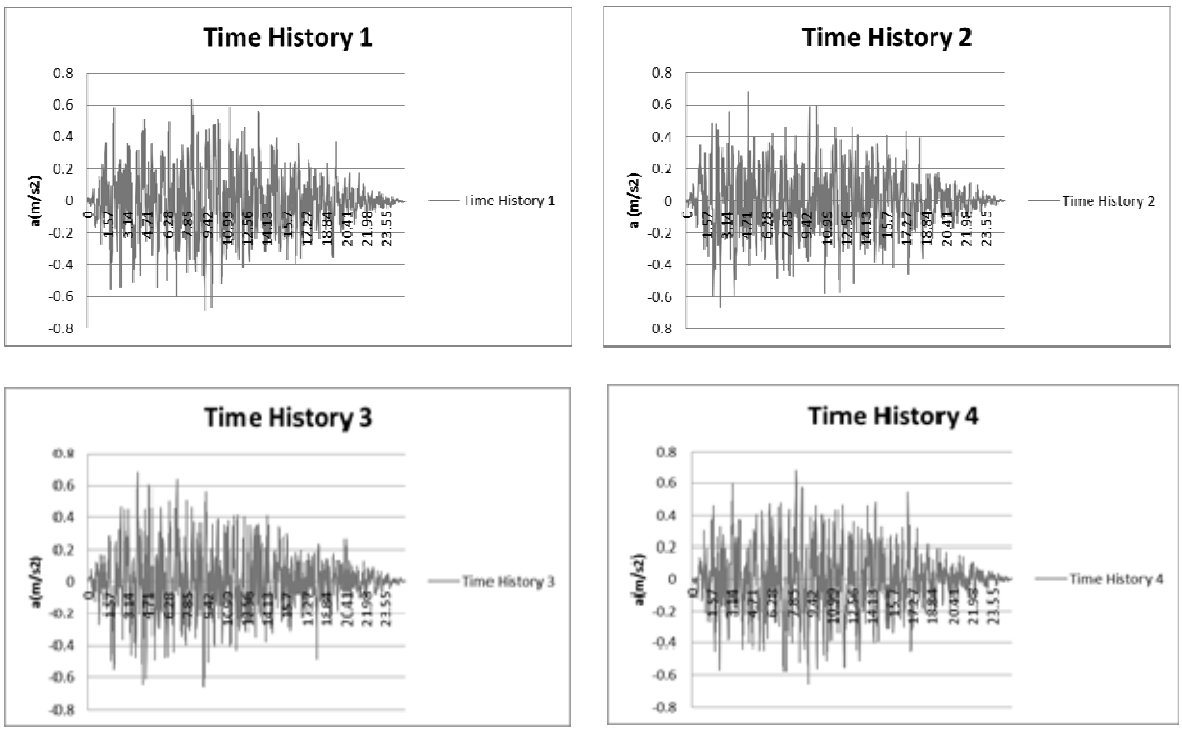
Different approaches have been developed to analyze the seismic behavior of buildings. The modeling strategies can be classified into micro-modeling or macro-modeling, based on the detail by which they represent structural elements, the computational effort and the information they provide about the behavior of a structure [15]. In this work a micro-modeling approach has been adopted. After being updated and refined on the basis of the modal force tuning, the model was implemented in COMSOL© multiphysic software (nonlinear structural materials module) for the seismic assessment. The compression behavior of the masonry was introduced through the model of Drucker Prager.

The parameters of cohesion c and friction ø were derived from the compression media strength, obtaining the values c = 0.48MPa and ø=13°. The tensile behavior was instead played through a smearing crack model, with a tensile strength of 0.1 MPa, constant cut-off criteria and linear softening up to a value of maximum deformation assumed equal to the 1 ‰.

In this way, the crack is simulated through a diffuse band of lesions and it is modeled through a modification of the materic properties.

The model was initially subjected to non-linear static analysis for gravity loads. After the pushover analysis, a series of non-linear dynamic analyses were carried out by applying at the base of the tower eight artificial earthquakes to safety life state.

They have been generated from the spectrum target, provided by the Italian legislation for the city of Valenzano, through the software REXEL (www. reluis.it), and suitably calibrated (Figure 10), defining specifications of the selection and combination.



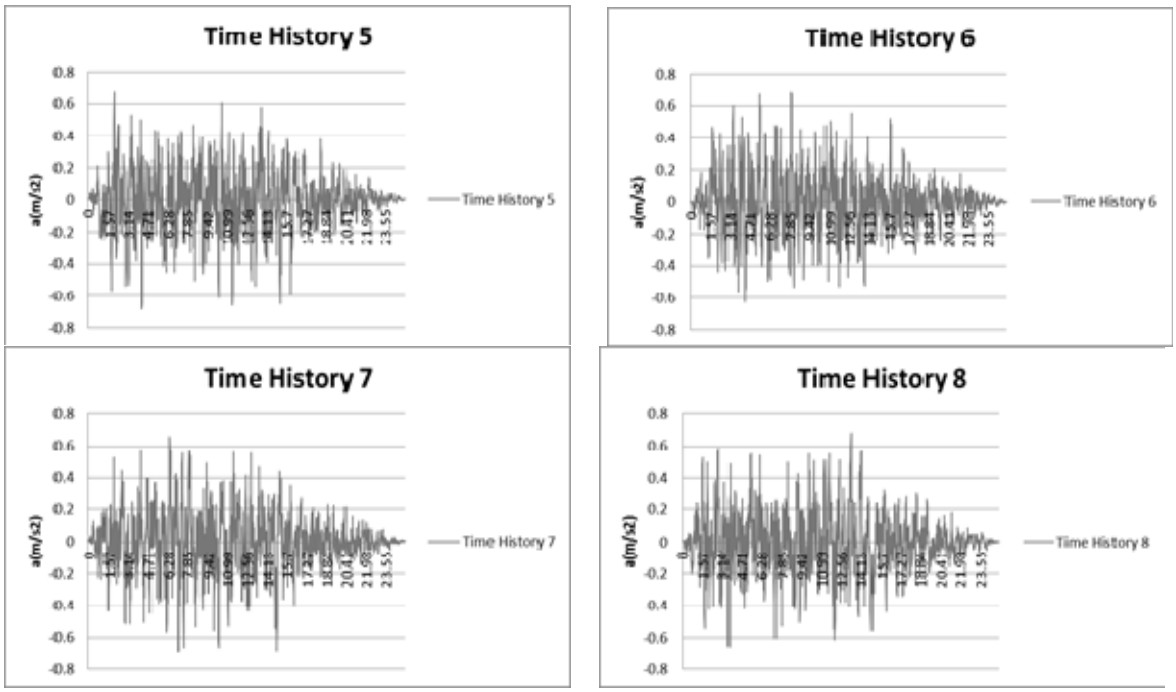


Figure 10. Artificial earthquakes for safety life state of the city of Valenzano

The analysis evidences that the tower is basically in elastic conditions, since the level of stresses is smaller than the strength in all parts of the tower. The structure is able to check all the collapse mechanisms with reference for the state limit adopted (Figure 11). This does not imply the need to define and implement appropriate interventions to enhance the ability of the seismic structure.

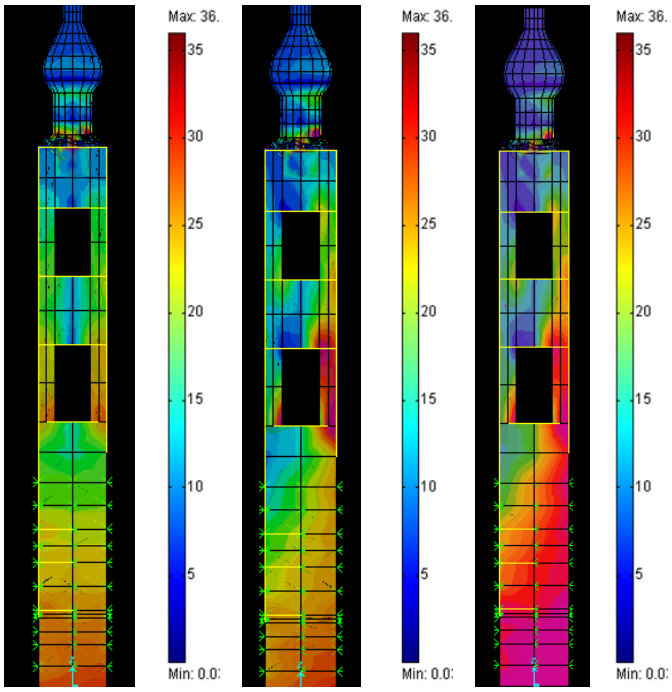


Figure 11. Vertical stresses [kg/cm^2] due to dead and seismic loads. PGA =0; PGA = 0,07g; PGA = 0.1105

This is the result of the correlation between non-destructive diagnostic and dynamic identification techniques. The set of information, suitable to fully define the historical-material-construction characters, in addition to sensitive non-linear dynamic analysis, allows a more reasonable result regarding the real vulnerability of the building. This ensures simultaneous safety and greater conservation of structure, favoring the criterion of minimum intervention, but also highlighting the cases in which it is appropriate to act more effectively.

As long as the seismic action increases its intensity, showing higher values of the safety life limit state, some cracks appear in the lower part of the upper block, mainly due to the "explosion" of some blocks for compression stress (figure 10).

When the compressive stress is greater than the yield strength of masonry, the cracks begin to open. As the amplification factor increases, the high compression stresses appear further in the lower block until the structure collapses.

The PGA for the structural collapse of the tower of “Santa Maria di San Luca” is lower than the reference peak ground acceleration at the Life Safety Limit State (PGALS=0.07g), and so the risk index is α_{LS}= PGAu/PGA_{SLS}=1.578.

5 CONCLUSIONS

The study has helped to define a practice for the evaluation of seismic vulnerability of historic buildings, which can ensure simultaneously safety and conservation, favoring the criterion of minimum intervention, thus avoiding unnecessary interventions, but also by highlighting the cases in which it is appropriate to act more efficiently.

It highlights the fundamental importance of correlation between the dynamic identification techniques and non-destructive diagnostic investigations in the evaluation of the seismic capacity of masonry structures.

Although this presupposes an integrated system of data acquisition and management of information and knowledge, however, it will be able to permeate the concept of structural safety of the historic buildings with all the aspects that are unlikely to be integrated within a mechanical model, even if it is refined.

In this way the intervention, that comes from it, is certainly appropriate, because it poses as not a distortion of the "logic" (formal and spatial-material) of the pre-existent, but in continuity with the "modal logic" (procedural) that it involves.

REFERENCES

[1] D. Abruzzese, L. Miccoli, Y. Jianli. Mechanical behavior of leaning masonry Huzhu Pagoda. *Journal of Cultural Heritage*, **10**, 480-486, 2009.

[2] D. Abruzzese, M. Ferraioli, L. Miccoli, A. Vari. Seismic improvement of masonry towers. *Proc. 8th International Seminar on structural masonry*. Istanbul, 395-403, 2008.

[3] A. Bayraktar, T. Türker, B. Sevım, AC. Altunisik, F. Yildirim. Modal Parameter Identification of Hagia Sophia Bell-Tower via Ambient Vibration Test. *Journal of Nondestructive Evaluation*, **28**, 37-47, 2009.

[4] S. Bennati, L. Nardini, W. Salvatore. Dynamic behavior of a medieval masonry bell tower. Part II: Measurement and modelling of the tower motion. *Journal of Structural Engineering. ASCE*, **131**, 1656-1664, 2005.

[5] K. Bernardeschi, C. Padovani, G. Pasquinelli. Numerical modelling of the structural behaviour of Buti’s bell tower. *Journal of Cultural Heritage*, **5**, 371- 378, 2004.

[6] L. Binda, A. Saisi, C. Tiraboschi, S. Valle, C. Colla M. Forde. Application of sonic and radar tests on the piers and walls of the Cathedral of Noto, *Construction and Building Materials*, **17**(8) 613–627, 2003.

[7] V. Bosiljkov, M. Uranjek, R. Žarnić, V. Bokan-Bosiljkov. An integrated diagnostic approach for the assessment of historic masonry structures, *Journal of Cultural Heritage*, **11**(3), 239-249, 2010.

[8] A. Carpinteri, S. Invernizzi, G. Lacidogna. In situ damage assessment and nonlinear modelling of a historical masonry tower, *Engineering Structures,* **27**, 387-395, 2005.

[9] D. D'Ayala. Seismic Vulnerability and Risk Assessment of Cultural Heritage Buildings in Istanbul, Turkey. *In: Proceedings of the 14th world conference on earthquake engineering*, Beijing, 2008.

[10] D. D'Ayala, E. Speranza. Definition of collapse mechanisms and seismic vulnerability of historic masonry buildings. *Earth Spectra* **19**(3): 479–509, 2003.

[11] A. De Sortis, E. Antonacci, F. Vestroni. Dynamic identification of a masonry building using forced vibration tests, *Engineering Structures*, **27**, 155-165, 2005.

[12] M. De Fino, G. De Tommasi, F. Fatiguso, Experimental studies to normalize the sonic test on masonry walls, *Proceedings of REHABEND 2009 "International workshop about rehabilitation and NDT*", 29-30 October 2009, Bilbao, Spain. ISBN 978-84-8873-404-4 2009.

[13] A. Fiore, P. Monaco, Earthquake-induced pounding between the main buildings of the "Quinto Orazio Flacco" school. *Earthquakes and Structures*, **1** (4), 371-390, 2010

[14] A. Fiore, P. Monaco, Analysis of the seismic vulnerability of the "Quinto Orazio Flacco" school [Analisi della vulnerabilità sismica del Liceo "Quinto Orazio Flacco"]. *Ingegneria Sismica*, **28**(1), 43-62, ISSN 0393-1420, 2011.

[15] A. Fiore, A. Netti, P. Monaco, The influence of masonry infill on the seismic behaviour of RC frame buildings. *Engineering Structures*, **44**, 133-145, 2012.

[16] S. Ivorra, FJ. Pallarés. Dynamic investigation on a masonry bell tower. *Engineering Structures*, **28**, 660-667, 2006.

[17] E. Júlio, C. Rebelo, D. Costa. Structural assessment of the tower of the University of Coimbra by modal identification. *Engineering Structures*, **30**, 3468-3477, 2008.

[18] C. Maierhofer, S. Leipold. Radar investigation of masonry structures, *NDT & E International*, **34**(2), 139-147, 2001.

[19] D.M. McCann, M.C. Forde. Review of NDT methods in the assessment of concrete and masonry structures, *NDT & E International*, **34**(2), 71-84, 2001.

[20] F. Peñaa, P.B. Lourenço, N. Mendes, D.V. Oliveira. Numerical models for the seismic assessment of an old masonry tower. *Engineering Structures*, **32**, 1466-1478, 2010.

COMPDYN 2013
4th ECCOMAS Thematic Conference on
Computational Methods in Structural Dynamics and Earthquake Engineering
M. Papadrakakis, V. Papadopoulos, V. Plevris (eds.)
Kos Island, Greece, 12–14 June 2013

IDENTIFICATION OF REINFORCED CONCRETE BEAM PARAMETERS USING INVERSE MODELING TECHNIQUE AND MEASURED DYNAMIC RESPONSES FOR STRUCTURE HEALTH MONITORING

J. Waeytens[1], V. le Corvec[2], P. Lévèque[1], D. Siegert[1] and F. Bourquin[1]

[1]Université Paris-Est, IFSTTAR
boulevard Newton, F-77747 Champs sur Marne, France
e-mail: {julien.waeytens,philippe.leveque,dominique.siegert,frederic.bourquin}@ifsttar.fr

[2] Numerical Engineering & Consulting Services
196, rue Houdan, F-F-92330 Sceaux, France
e-mail: veronique.lecorvec@necs.fr

Keywords: Inverse problem, optimal control, adjoint problem, structural dynamics.

Abstract. *Reinforced and prestressed concrete beams are widely employed in civil engineering structures, e.g. in simply supported spans using prestressed concrete beams (VIPP). To reduce the financial cost due to maintenance, structure damages have to be detected early. To achieve this purpose, one needs robust monitoring techniques.*
The paper deals with the determination of mechanical parameters, useful for Structure Health Monitoring, in a 2D beam using inverse modeling technique. The optimal control theory is employed. As an example, we aim to identify a reduction of the steel bar cross-section and a decrease of the concrete Young modulus in damaged area. In our strategy, the beam is instrumented with strain sensors, and a known dynamic load is applied. In the inverse technique, two space discretizations are considered: a fine dicretization (h) to solve the structural dynamic problem and a coarse discretization (H) for the beam parameter identification. To get the beam parameters, we minimize a classical data misfit functional using a gradient-like algorithm. A low-cost computation of the functional gradient is performed using the adjoint problem solution. The inverse problem is solved in a general way using engineer numerical tools: Python scripts and the free finite element software Code_Aster. First results show that a local reduction of the steel bar cross-sections and a local decrease of concrete Young modulus can be detected using this inverse technique.

1 INTRODUCTION

Prestressed and reinforced beams are widely employed in civil engineering structures. Between 1945 and 1965, 1000 prestressed concrete bridges were constructed, 550 were of the VIPP type (independent span viaducts with prestressed beams) [1]. Thus, the maintenance of such structures is a central issue. To reduce maintenance costs, the damaged beams in the structure have to be identified early. To achieve this purpose, the beams should be monitored and non-destructive control methods should be used. Inverse techniques using dynamic responses have been developed in [2] to identify the prestress force in a beam. A one-dimensional (1D) beam modelisation was considered. In the present article, we focus on inverse problems based on two-dimensional (2D) beam modelisation. As a matter of fact, by means of 2D modelisation, we can specify the 2D position of the sensors and we can precisely describe the geometry and the position of steel bars. Using dynamic strain responses, we are interested in identifying a local loss of steel bar cross-section and a local decrease of concrete Young modulus. For that, an inverse modeling technique based on the optimal control theory [3] is proposed. In the 2D elastodynamics direct problem, the dynamic loading is considered known. The inverse problem is solved in a general way using common engineering numerical tools: free finite element software Code_Aster [4], Python Numpy library and a Python mesh API provided by SALOME platform [5]. On a 2D concrete beam with a single steel bar, we show that a 25% local loss of the steel bar cross-section and a 25% local decrease of the concrete Young modulus can be detected with the proposed method.
The article is organized as follows: in Section 2, the inverse method is presented; in Section 3, details about the numerical implementation are given and in Section 4, the inverse method is illustrated on a 2D concrete beam with a steel bar.

2 METHODOLOGY TO IDENTIFY A REDUCTION OF THE STEEL BAR CROSS-SECTIONS AND A LOCAL DECREASE OF THE CONCRETE YOUNG MODULUS IN A 2D CONCRETE BEAM

We aim at identifying the steel bar cross-section $S_b(\underline{x})$ and the concrete Young modulus $E_c(\underline{x})$ in a 2D concrete beam from the knowledge of measured strain. Note that the dynamic loading applied to the concrete beam is considered known. To determine the beam mechanical parameters, an inverse modeling technique is employed. As usual in the optimal control theory, we seek the steel bar cross-section $S_b(\underline{x})$ and the concrete Young modulus $E_c(\underline{x})$ such that it minimizes a data misfit functional. The minimization process is performed in an iterative way using the steepest descent direction (gradient method). At each iteration, the main steps are the followings:

- solve the direct problem (elastodynamics equations forward in time) considering the beam parameters $S_b(\underline{x})$ and $E_c(\underline{x})$ of the previous iteration;
- solve the adjoint problem (elastodynamics equations backward in time);
- compute the functional gradient using the direct and the adjoint states;
- update the steel bar cross-section $S_b(\underline{x})$ and the concrete Young modulus $E_c(\underline{x})$.

2.1 Beam parameters to be determined

To reduce the number of beam parameters to be identified, $S_b(\underline{x})$ and $E_c(\underline{x})$ are sought under the form:

$$S_b(\underline{x}) = \sum_{j=1}^{n_b} \bar{S}_{bj} S_{b_{ud}}\, \phi_j^s(x),\ E_c(\underline{x}) = \sum_{j=1}^{n_c} \bar{E}_{cj} E_{c_{ud}}\, \phi_j^c(x) \tag{1}$$

where:

- $S_{b_{ud}}$ (resp. $E_{c_{ud}}$) corresponds to the undamaged cross-section of the steel (resp. the undamaged Young modulus of the concrete);
- $\bar{S}_{bj}$ (resp. $\bar{E}_{cj}$) represents the j^{th} normalized cross-section of the steel (resp. normalized Young modulus of the concrete) associated to the area Γ_j (resp. Ω_{c_j}), *i.e.* the area where $\phi_j^b(x)$ (resp. $\phi_j^c(x)$) is non-zero. $\bar{S}_{bj}$ and $\bar{E}_{cj}$ have to be determined using the inverse modeling technique;
- $\phi_j^b(x)$ and $\phi_j^c(x)$ are basis functions on a coarse grid mesh (H). They are *a priori* known. In practice, $\phi_j^b(x)$ (resp. $\phi_j^c(x)$) is a constant basis function equal to 1 in the area Γ_j (resp. in the subdomain Ω_{c_j}) and equal to 0 elsewhere.

2.2 Direct problem

In the present study, the shear work and the bending work in the steel bar are neglected. We also neglect the quantity of acceleration in rotation in the steel bar. We suppose that the steel bar and the concrete are perfectly adherent.
We seek the displacement field $\underline{u} \in \mathcal{U}_0 = \{\underline{u}^* \in H_1(\Omega) \backslash \underline{u}^* = \underline{0} \text{ on } \partial\Omega_i\}$ such that :

$$\begin{aligned} &\int_\Omega \rho_c \ddot{\underline{u}}.\underline{u}^* d\Omega + \int_\Gamma \rho_b S_b \ddot{\underline{u}}.\underline{u}^* d\Gamma + \int_\Omega \underline{\underline{\epsilon}}(\underline{u}) : \mathcal{K}_c \underline{\underline{\epsilon}}(\underline{u}^*) d\Omega + \int_\Gamma E_b S_b \frac{\partial u_x}{\partial x}\frac{\partial u_x^*}{\partial x} d\Gamma \\ &- \int_{\partial\Omega_f} \underline{F}_d.\underline{u}^* \partial\Omega = 0,\ \forall \underline{u}^* \in \mathcal{U}_0 \end{aligned} \tag{2}$$

The initial conditions are supposed to vanish.

2.3 Data misfit functional

We seek the normalized steel bar cross-section $\bar{S}_{bj}$ ($j \in \{1, .., n_b\}$) and the normalized concrete Young modulus $\bar{E}_{cj}$ ($j \in \{1, .., n_c\}$), minimizing the data misfit functional defined as:

$$\begin{aligned} J(\bar{S}_b, \bar{E}_c) = \frac{1}{2}\sum_{i=1}^{n_s} \int_0^T \left[\int_\Omega \epsilon_{xx}(x,t)\psi_i(\underline{x} - \underline{x}_i) d\Omega - (\epsilon_{xx}^{mes})_i(t)\right]^2 dt \quad &+\epsilon_1 \frac{\alpha_{n_1}}{2} \int_\Gamma \left[\frac{S_b(x)}{S_{b_{ud}}} - 1\right]^2 d\Gamma \\ &+\epsilon_2 \frac{\alpha_{n_2}}{2} \int_\Omega \left[\frac{E_c(x)}{E_{c_{ud}}} - 1\right]^2 d\Omega \end{aligned} \tag{3}$$

where:

- n_s is the number of strain sensors;

- $(\epsilon_{xx}^{mes})_i(t)$ is xx strain measured by sensor i located at $\underline{x}_i$;
- $\psi_i(\underline{x}-\underline{x}_i)$ is the spatial weight function associated to sensor i.

In (3), one has a classical quadratic data misfit term and regularization terms. ϵ_1 and ϵ_2 are normalized regularization parameters. α_{n_1} and α_{n_2} ensure the physical homogeneity of the terms in the functional J. Herein, we take:

$$\alpha_{n_1}=\frac{T}{L},\ \ \alpha_{n_2}=\frac{T}{L^2} \tag{4}$$

2.4 Adjoint problem, functional gradient and beam parameter update

To get the functional gradient at a low computational cost, we use the adjoint state. In this study, the adjoint problem corresponds to a backward elastodynamics problem (final conditions vanish).
We seek the displacement $\tilde{\underline{u}} \in \mathcal{U}_0=\{\underline{u}^* \in H_1(\Omega)\backslash \underline{u}^*=\underline{0} \text{ on } \partial\Omega_i\}$ satisfying:

$$\begin{aligned}&\int_\Omega \rho_c \ddot{\tilde{\underline{u}}}.\underline{u}^* d\Omega+\int_\Gamma \rho_b S_b \ddot{\tilde{\underline{u}}}.\underline{u}^* d\Gamma+\int_\Omega \underline{\underline{\epsilon}}(\tilde{\underline{u}}):\mathcal{K}_c\underline{\underline{\epsilon}}(\underline{u}^*)d\Omega+\int_\Gamma E_b S_b \frac{\partial \tilde{u}_x}{\partial x}\frac{\partial u_x^*}{\partial x}d\Gamma\\ &-\sum_{i=1}^{n_s}\int_\Omega\left[\int_\Omega \epsilon_{xx}(\underline{x},t)\psi(\underline{x}-\underline{x}_i)d\Omega-(\epsilon_{xx}^{mes})_i(t)\right]\psi_i(\underline{x}-\underline{x}_i)\frac{\partial u_x^*}{\partial x}d\Omega dt=0,\ \forall \underline{u}^*\in\mathcal{U}_0\end{aligned} \tag{5}$$

Note that this problem can be solved using classical finite element codes.

From the direct and the adjoint states, we obtain the gradient of the functional, as follows:

$$\begin{aligned}\frac{\partial J}{\partial \bar{S}_{bj}}=&-\int_0^T\int_\Gamma E_b S_{b_{ud}}\phi_j^b(x)\frac{\partial u_x}{\partial x}\frac{\partial \tilde{u}_x}{\partial x}d\Gamma dt-\int_0^T\int_\Gamma \rho_b S_{b_{ud}}\phi_j^b(x)\ddot{\underline{u}}.\tilde{\underline{u}}d\Gamma dt\\ &+\epsilon_1\alpha_{n_1}\int_\Gamma\left(\frac{S_b(x)}{S_{b_{ud}}}-1\right)\phi_j^b(x)d\Gamma\end{aligned} \tag{6}$$

$$\begin{aligned}\frac{\partial J}{\partial \bar{E}_{cj}}=&-\int_0^T\int_\Omega d\lambda_{DP}\phi_j^c(x)div(\underline{u})div(\tilde{\underline{u}})d\Omega dt-\int_0^T\int_\Omega 2d\mu_{DP}\phi_j^c(x)\underline{\underline{\epsilon}}(\underline{u}):\underline{\underline{\epsilon}}(\tilde{\underline{u}})d\Omega dt\\ &+\epsilon_2\alpha_{n_2}\int_\Omega\left(\frac{E_c(x)}{E_{c_{ud}}}-1\right)\phi_j^c(x)d\Omega\end{aligned} \tag{7}$$

where:

$$d\lambda_{DP}=\frac{E_{c_{ud}}\nu_c}{(1+\nu_c)(1-\nu_c)},\ d\mu_{DP}=\frac{E_{c_{ud}}}{2(1+\nu_c)} \tag{8}$$

Once we get the functional gradient, several solves of the direct problem are performed to determine the optimal descent step and we deduce the new set of beam parameters.

3 NUMERICAL IMPLEMENTATION

The inverse problem is solved in a general way using state of the art finite element softwares. A synthesis of the numerical steps is given in Figure 3. From a main Python script, we run the finite element software Code_Aster to solve the direct and adjoint problems, which are elastodynamics problems. We specify to Code_Aster Python supervisor to serialize, thanks to Python

pickle module, the fields useful for the gradient computation and to export the strain $(\epsilon_{xx}^{sim})_i$ computed at the sensor location $\underline{x}_i$. Note that the loading of the adjoint problem corresponds to a 'xx' internal stress $(\tilde{\sigma}_{0_{xx}})_i$ in the vicinity of the i^{th} sensor location. This loading (see (5)) is given by the data misfit δ:

$$(\tilde{\sigma}_{0_{xx}})_i(\underline{x},t) = \left[(\epsilon_{xx}^{sim})_i(t) - (\epsilon_{xx}^{mes})_i(t)\right] \psi_i(\underline{x}-\underline{x}_i),\ i \in \{1,..,n_s\} \tag{9}$$

In practice in Code_Aster, the spatial weight function $\psi_i(\underline{x}-\underline{x}_i)$ is constant in the patch of elements associated to the i^{th} sensor node. To compute the gradient of the data misfit functional according to the formulas (6,7), for the direct problem, one needs the acceleration $\underline{\ddot{u}}$ in the steel bar and the strain $\underline{\underline{\epsilon}}$ in the steel and the concrete parts. Concerning the adjoint problem, one needs the displacement $\underline{\tilde{u}}$ in the steel bar and the strain $\underline{\underline{\tilde{\epsilon}}}$ in the beam. Using these fields and mesh data, the gradient is computed from a python script. Then, to determine the optimal descent step, which minimizes the data misfit functional, several resolutions of the direct problem are performed using Code_Aster. Once the optimal descent step is obtained, we deduce the new set of beam parameters. The iterative process stops when the data misfit δ is about the sensor precision.

4 NUMERICAL EXAMPLE

4.1 Definition of the identification problem

A 2D concrete beam with a single horizontal steel bar is considered (see Figure 2). Plane strain is assumed. A dynamic load is applied to the top of the concrete beam, it is defined as:

$$\underline{F}_d(t) = \begin{cases} -F_{max} sin\left(\dfrac{2\pi}{T_c}t\right)\underline{y},\ t \in [0, T_c/2[\\ 0,\ t \in [T_c/2, T] \end{cases} \tag{10}$$

Numerical values: $F_{max} = 10^4 N/m^2,\ T_c = 2s,\ T = 5s.$

In this study, the steel bar is decomposed into 5 pieces ($n_b = 5$ in (1)). In each piece j, one has a constant steel bar cross-section S_{b_j}. Concerning the concrete zone, we only consider a loss of Young modulus in the concrete part named Ω_c which is under the steel bar. In the same way, the domain Ω_c is decomposed into 5 subdomains ($n_c = 5$ in (1)). In each concrete subdomain j, a constant Young modulus E_{c_j} is taken. We assume that the steel bar cross-section (resp. the concrete Young modulus) is known and undamaged in pieces 1 and 5 (resp. in subdomains 1 and 5): $S_{b_1} = S_{b_5} = S_{b_{ud}}$ (resp. $E_{c_1} = E_{c_5} = E_{c_{ud}}$). As a result, we aim at identifying by the inverse modeling technique the normalized steel bar cross-sections and the normalized concrete Young modulus $\bar{S}_{b2}, \bar{S}_{b3}, \bar{S}_{b4}, \bar{E}_{c2}, \bar{E}_{c3}, \bar{E}_{c4}$ defined as:

$$S_{b_j} = \bar{S}_{bj} S_{b_{ud}},\ \text{with } S_{b_{ud}} = 0,04; \quad E_{c_j} = \bar{E}_{cj} E_{c_{ud}},\ \text{with } E_{c_{ud}} = 40\ GPa \tag{11}$$

To avoid "inverse crime", we take as reference the numerical solution obtained with the finite element code Freefem++ [6] considering the loading (10) and the beam parameters:

$$\begin{cases} S_{b_1}^{ex} = S_{b_2}^{ex} = S_{b_4}^{ex} = S_{b_5}^{ex} = 0,04\ \& S_{b_3}^{ex} = 0,03 \\ E_{c_1}^{ex} = E_{c_2}^{ex} = E_{c_4}^{ex} = E_{c_5}^{ex} = 40\ GPa\ \& E_{c_3}^{ex} = 30\ GPa \end{cases} \tag{12}$$

To solve the elastodynamics problem, we take the inconditionally stable Newmark scheme ($\gamma = 1/2, \beta = 1/4$). In practice, the data outputs ϵ_{xx}^{mes} are measured. Nevertheless, herein, ϵ_{xx}^{mes} is

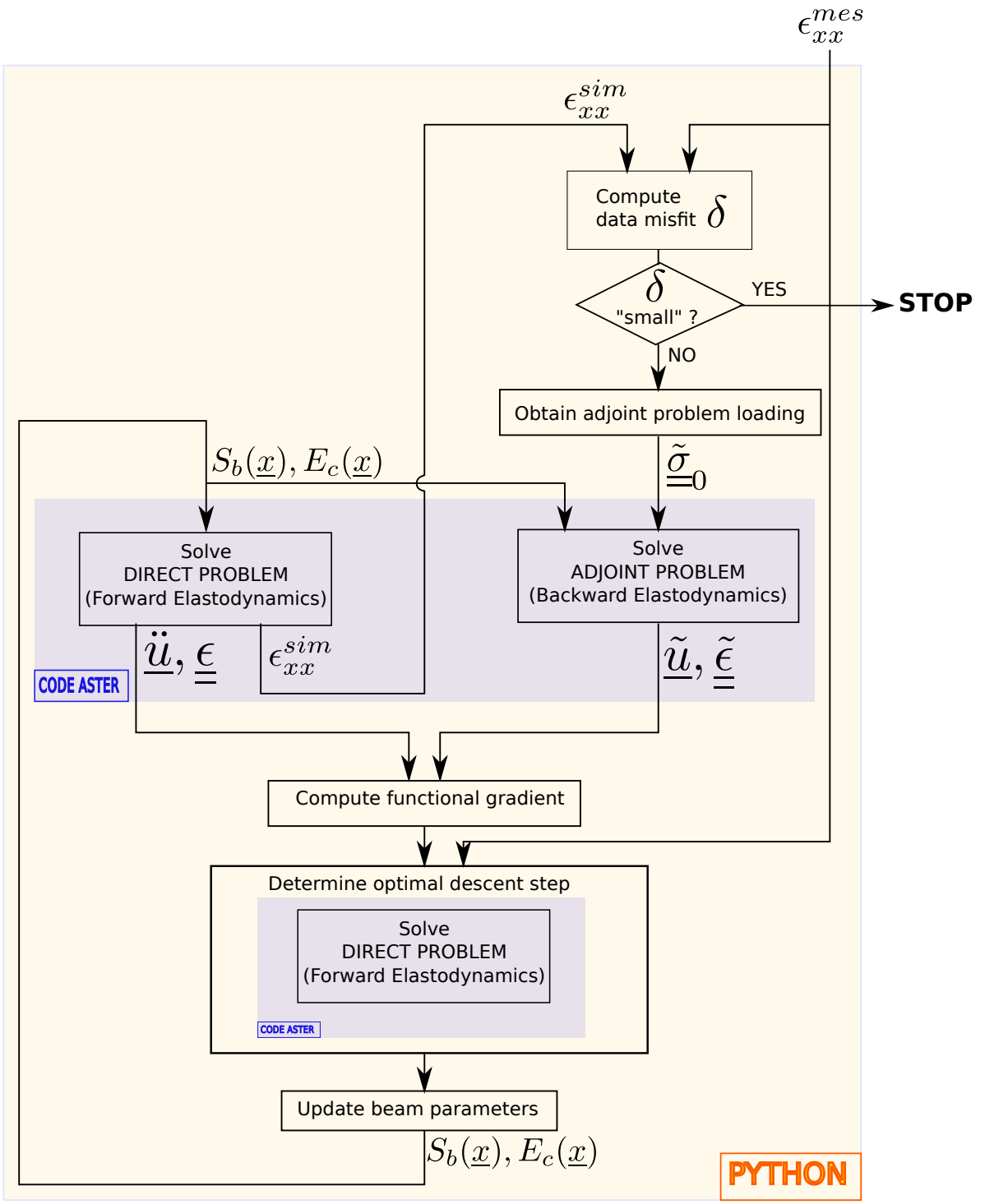


Figure 1: Methodology for beam parameter identification

deduced from the reference numerical solution. We consider 7 strain sensors in the concrete beam, there are located at:

$$S_1 : (3L/16, H/8); S_2 : (5L/16, H/8); S_3(7L/16, H/8); S_4(L/2, H/8); S_5(9L/16, H/8); \\ S_6 : (11L/16, H/8); S_7(13L/16, H/8). \tag{13}$$

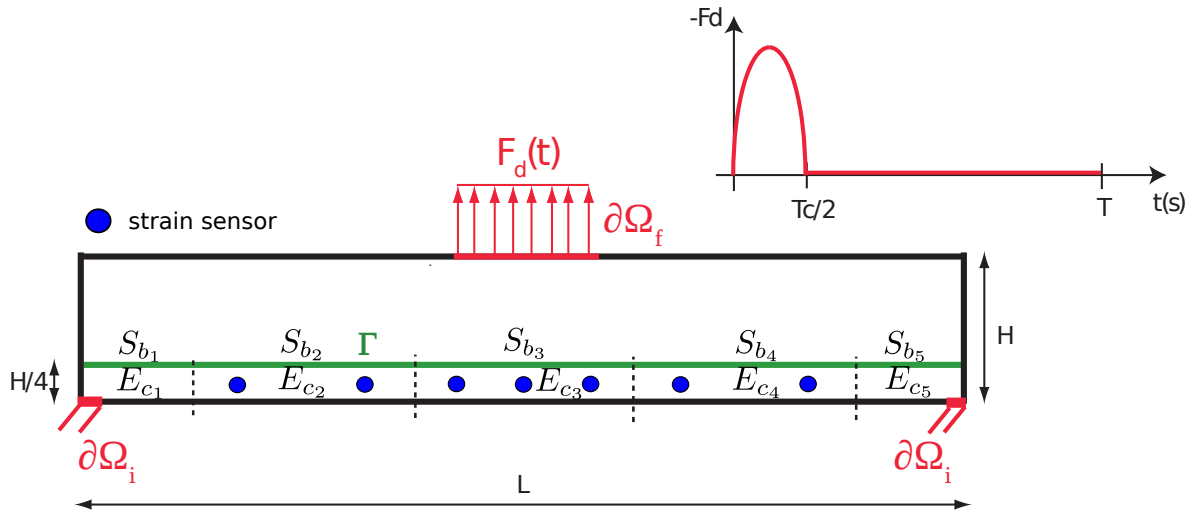


Figure 2: Concrete beam with a horizontal steel bar - Steel bar decomposed in 5 pieces. Each piece has a constant cross-section - Lower Concrete part decomposed in 5 subdomains. Each subdomain has a constant Young modulus - Beam instrumented with 7 strains sensors.

	k	δ_k	$e_k^{rel}(\%)$	S_{b_2}	S_{b_3}	S_{b_4}	$E_{c_2}(GPa)$	$E_{c_3}(GPa)$	$E_{c_4}(GPa)$
it 0	4	$2.9.10^{-7}$	10.3	0.040	0.040	0.040	40.0	40.0	40.0
it 1	2	$1.7.10^{-7}$	36.0	0.040	0.040	0.040	39.6	35.2	39.4
it 2	2	$1.6.10^{-7}$	33.7	0.040	0.039	0.040	40.0	34.1	39.4
it 3	2	$1.4.10^{-7}$	28.3	0.039	0.035	0.039	40.0	31.7	40.0
it 4	2	$1.4.10^{-7}$	28.0	0.040	0.035	0.039	40.0	31.5	40.0

Table 1: Steel bar cross-sections and Concrete Young modulus at each iteration of the inverse modeling technique

4.1.1 Solution of the inverse modeling technique

The results of the beam identification are given at each iteration of the inverse modeling technique in Table 1. At each iteration of the inverse technique, we evaluate the data misfit δ and its relative error e^{rel} defined by:

$$\begin{cases} \delta_i = \left(\int_0^T \left[(\epsilon_{xx}^{sim})_i(t) - (\epsilon_{xx}^{mes})_i(t) \right]^2 dt \right)^{1/2}, \ i \in \{1, .., n_s\} \\ e_i^{rel} = \dfrac{\delta_i}{\left(\int_0^T \left[((\epsilon_{xx}^{mes})_i(t) \right]^2 dt \right)^{1/2}}, \ i \in \{1, .., n_s\} \end{cases} \tag{14}$$

In Table 1, the value of the maximum data misfit and its associated relative error are given, k corresponds to the sensor number which has the highest data misfit.

We underline the fact that these results are obtained considering "small" regularization parameters ($\epsilon_1 = 10^{-16}, \epsilon_2 = 10^{-13}$). After the third iteration, we note that the data misfit reaches a plateau. It corresponds to the error between a numerical solution obtained with FreeFem++ and a numerical solution computed with Code_Aster. As a consequence, the inverse technique should be stopped at iteration 4. At iteration 4, one has a 28% error between the 'xx' strain

measured at sensor 2 and the reconstructed strain. This leads to a 5% error on the identification of the concrete Young modulus in subdomains 3 and to a 15% error on the identification of the steel bar cross-section in piece 3. We recall that the reference values of concrete Young modulus and steel bar cross-sections are given in (12).

5 CONCLUSIONS

To identify the beam parameters (steel bar cross-sections and concrete Young modulus), we proposed an inverse modeling technique based on 2D elastodynamics model and dynamic strain responses. On the 2D concrete beam with a single steel bar, we showed that a 25% local loss of the steel bar cross-section and a 25% local decrease of the concrete Young modulus could be detected. In forthcoming papers, real data outputs will be considered and more representative 2D beam models [7, 8] will be employed in the inverse technique.

6 ACKNOWLEDGMENTS

This research was supported by the region Ile de France. This work was conducted as part of the project "SIPRIS", which involves several partner: Advitam (leader), ASF (Highways of the South of France), CEDRAT, ESIEE Paris, NECS, NEWSTEO, SYROKKO and IFSTTAR.

REFERENCES

[1] J. Chatelain, R. Chaussin, B. Godart, B. Mahut, D. Poineau, P. C. Das, G. A. Paterson, B. Sadka, S. Shanmugan, D. B. Storrar, R. J. Woodward, *Post-tensioned concrete bridges*. Thomas Telford, 1999.

[2] Z.R. Lu, S. S. Law, Identification of prestress force from measured structural responses. *Mechanical Systems and Signal Processing*, **20**, 2186–2199, 2006.

[3] J.L. Lions, *Contrôle Optimal des Systèmes Gouvernés par des Equations aux Dérivées Partielles*. Dunod (Paris), 1961 (in french).

[4] Code_Aster, EDF R& D, Finite element code for structural analysis, GNU general public licence, *http://www.code-aster.org*.

[5] Salome, CEA/DEN, EDF R& D, OPEN CASCADE, Open Source Integration Platform for Numerical Simulation, *http://www.salome-platform.org*.

[6] O. Pironneau, F. Hecht, J. Morice, FreeFEM++, *http://www.freefem.org*.

[7] A. Castel, D. Coronelli, N. A. Vu, R. Francois, Structural response of Corroded, Unbonded Posttensioned Beams. *Structural Engineering*, **137**, 7, 761–771, 2011.

[8] A. A. Arab, S. S. Badie, M. T. Manzari, A methodological approach for finite element modeling of pretensioned concrete members at the release of pretensioning. *Engineering Structures*, **33**, 1918–1929, 2011.

COMPDYN 2013
4th ECCOMAS Thematic Conference on
Computational Methods in Structural Dynamics and Earthquake Engineering
M. Papadrakakis, V. Papadopoulos, V. Plevris (eds.)
Kos Island, Greece, 12–14 June 2013

IDENTIFYING THE DAMPING CONTRIBUTION OF BUILDING COMPONENTS BASED ON MEASURED TOP VIBRATION

Ronald L.J. van den Berg[1*], Raphaël D.J.M. Steenbergen[1],

[1] TNO Built Environment and geosciences, PO Box 49, NL 2600 AA Delft, The Netherlands
e-mail: rlj.vandenberg@tno.nl, raphael.steenbergen@tno.nl

Keywords: wind, dynamics, damping, tall buildings, comfort.

Abstract. *In this paper, a damping model for a high-rise building is introduced. This model is used to investigate the possibilities to identify the relative damping contribution of the internal material damping in building elements, energy loss at element interfaces and energy outflow at the interface with the ground. The building is modeled as an Euler-Bernoulli beam which is elastically supported at its base by a translational and rotation spring, including viscous damping elements. The beam has internal viscous material damping and is attached to a distributed viscous damper. Data obtained from conventional full scale measurements of the vibrations at the top of a high-rise building, is used to calibrate the model. Values of the model parameters which result in a best fit, are found from calculation of the least square error between the simulated and measured response. It is concluded that the conventional performed measurements don't provide enough data to uniquely determine the relative contribution of the different damping components. A new measurement method is needed in order to identify the relative contribution.*

1 INTRODUCTION

The design of Dutch high-rise buildings is dominated by the effect of dynamic wind loads. A minimum stiffness is required to keep the maximum occurring deflection during the lifetime of a building below the maximum allowable deformation. In most cases this aspect is leading in the design process. The dynamic wind load will also introduce vibrations of the building. Especially slender high-rise buildings are sensitive to these vibrations, because their natural frequencies (typically between 0.1-0.5 Hz) correspond with the low frequency region, in which the strongest wind gusts appear, causing a resonance effect. Vibrations with large accelerations can be noticeable for occupants. To avoid uncomfortable situations the maximum occurring accelerations should be lower than restrictions given in ISO6897 [1]. The application of high strength building materials and new building techniques, makes it possible to construct more slender and lighter high-rise buildings that satisfy the deflection criterion. However these high-rise buildings are more sensitive to the wind-induced vibrations and consequently the comfort criteria becomes more governing in the design. Dutch high-rise buildings are relatively slender in comparison with foreign buildings, because of the stern

legislation on daylight entrance. As a result of this comfort and legislation issues, the building height of Dutch residential buildings appears nowadays to be limited to about 160 m.

The dynamic response of a tall building depends on its mass, stiffness and damping properties. The maximum occurring acceleration depends to a large extend on the damping properties, while in contrast with the mass and stiffness, it is difficult to accurately estimate the damping because of its complex physical nature. The total energy dissipation in a building is a combination of the internal material damping in building elements, energy loss at element interfaces and energy outflow at the interface with the ground (soil structure interaction, see Figure 1). At this point the aerodynamic damping is neglected for tall buildings [2].

Structural designers, normally use the damping ratios that are based on measurement of actual building vibrations. The total damping of the primary vibration modes of a building are determined from measurement of the vibrations in *x*, *y* and torsion direction at the top floor, during strong winds. Damping ratios are indicated in the annex of Eurocode 1991-1-4 [3], 0.8% and 1.6% for steel and reinforced concrete structures respectively. However actual damping ratios of Dutch buildings deviate a lot from these values. Ratios up to 2-3% for steel structures and minimum values of 1.0% for reinforced concrete structures have been observed [4]. This illustrates the uncertainty around the used damping values.

Based on the observed damping behavior of reinforced concrete buildings, Jeary [5] explained the structural damping is caused by friction forces at interfaces between structural members and in microcracks inside the material. Based on this mechanism, an empirical formula with a low amplitude plateau, related to the frequency, is deduced. Also an increasing damping for increasing amplitude is deduced. Lagomarsino [6] performed statistical analyses on the damping ratios of 185 buildings to establish an empirical relation between the damping value in the low amplitude region and the natural frequency. Relations have been found for reinforced concrete, steel and mixed structures. It is also claimed that the internal material damping for steel structures is negligible in comparison with the damping at element interfaces. Furthermore some particular interesting results considering the amount of partition walls are indicated. Most recently Satake et. al. [7] studied the damping properties of 205 Japanese buildings and obtain an empirical formula based on Jeary's mechanism.

Despite these empirical formulae which are based on results for multiple buildings, their results show a lot of scatter because there is a large variety of buildings and relatively few buildings have been measured. The amplitude dependency makes it even more difficult to make a good comparison between different damping ratios.

By monitoring the vibrations of individual buildings over longer periods of time, in-depth investigations to the damping properties of buildings have been performed [8]. In the Chicago Full-Scale Monitoring Program [9], the dynamic response of 3 tall buildings has been monitored over a decade to study the amplitude dependency of the damping. Furthermore higher damping levels are observed at structural systems with a greater degree of frame action than cantilever action.

Up till now, researchers have tried to get a grip on the damping behavior of tall buildings, by studying the overall damping. Since this total damping is a result of many different energy dissipation mechanisms, it is particulary difficult to find a clear relation between this overall damping behavior and the building properties. Therefore it is proposed to focus on a method to identify the damping contribution of different building parts. In this way, their damping behavior with respect to the corresponding building part characteristics can be studied separately.

For this purpose, a dynamic building model is developed in which 4 viscous damping parameters represent the damping in different parts. First an explanation about the assumed mass, stiffness and damping properties in this model is given. The use of the model to identify

the relative damping contribution of building parts is illustrated by comparison of the dynamic behavior of this model with the response data of a real full-scale measurement.

2 BUILDING MODEL

2.1 Set-up of the model, equation of motion and boundary conditions

The dynamic behavior of a high-rise building is analyzed by considering its deflection due to an along-wind loading. Because most tall buildings are symmetrical, the deflection of the centre of rotation can be analyzed as a 2-dimensional problem. The deflection due to rotation can be neglected at this point. A model is developed (see Figure 1) in which a high-rise building is represented by an Euler-Bernoulli beam with distributed mass ρA, elastically supported at its base and subjected to an along-wind load $q(z,t)$.

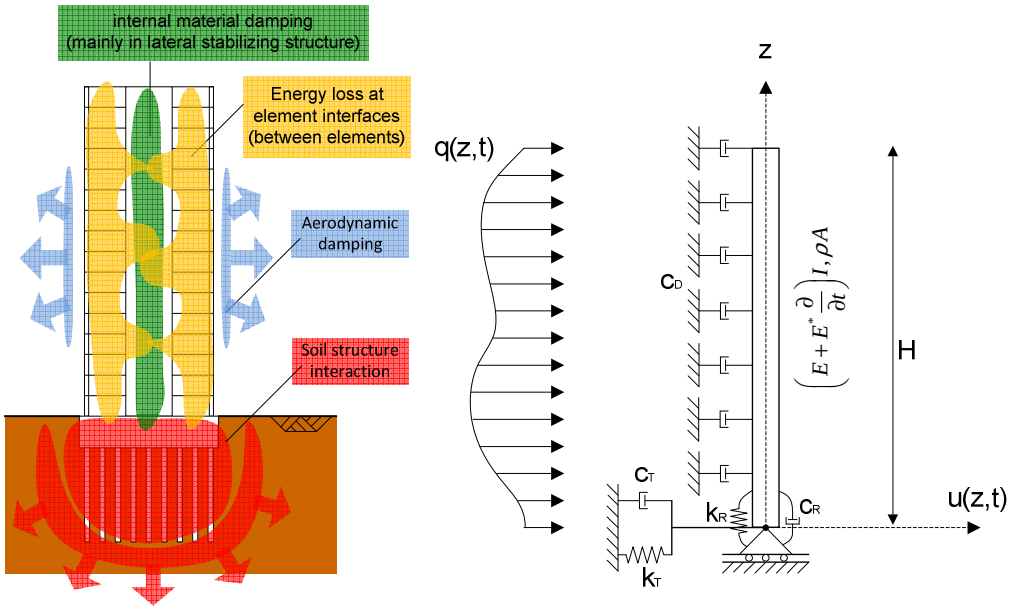


Figure 1 – Damping sources and dynamic model of a high-rise building

Since high-rise buildings are slender, the shear deformation is small in comparison with the bending deformation and can be neglected [10]. In addition the deformations are small compared to the building's dimensions. These two aspects justify the use of the Euler-Bernoulli beam to model the deformation of a high-rise building. The foundation of the building can rotate and translate under a horizontal load. The elastic rotation stiffness of the piles and soil is modeled with a rotational spring (k_R). The reaction of the soil against the translation of the underground structure in horizontal direction is represented by translational spring (k_T). Energy will be lost during loading and unloading of the soil. This damping due to soil-structure interaction is modeled by a translational (c_T) and rotational (c_R) viscous damper.

Internal material damping of a beam can be represented by a viscous damping model which is introduced by adding a time-dependent term to the modulus of elasticity.

$$E^* \frac{\partial}{\partial t} \tag{1}$$

In this way the stresses in the material are modeled according to the Kelvin-Voigt model. The non-structural elements of a building will move relative to each other, or relative to the main load bearing structure. Energy will be lost due to friction at the interfaces between these

elements. This energy loss has been modeled by the distributed dampers (c_D) across the whole length of the beam.

The transverse vibration of the beam is governed by a partial differential equation, the equation of motion (EM), in which *u(z,t)* is the transverse deflection of the beam at position *z* and time *t*.

$$\rho A\frac{\partial^2 u}{\partial t^2}+EI\frac{\partial^4 u}{\partial z^4}+E^*I\frac{\partial^5 u}{\partial t\partial z^4}+c_d\frac{\partial u}{\partial t}=q(z,t) \tag{2}$$

The boundary conditions (BCs) of the system at z=0 and z=H are

$$\left(E+E^*\frac{\partial}{\partial t}\right)I\left.\frac{\partial^2 u}{\partial z^2}\right|_{z=0}=k_R\left.\frac{\partial u}{\partial z}\right|_{z=0}+c_R\left.\frac{\partial^2 u}{\partial z\partial t}\right|_{z=0} \tag{3}$$

$$-\left(E+E^*\frac{\partial}{\partial t}\right)I\left.\frac{\partial^3 u}{\partial z^3}\right|_{z=0}=k_T u(0,t)+c_T\left.\frac{\partial u}{\partial t}\right|_{z=0} \tag{4}$$

$$\left(E+E^*\frac{\partial}{\partial t}\right)I\left.\frac{\partial^2 u}{\partial z^2}\right|_{z=H}=0 \tag{5}$$

$$\left(E+E^*\frac{\partial}{\partial t}\right)I\left.\frac{\partial^3 u}{\partial z^3}\right|_{z=H}=0 \tag{6}$$

2.2 Natural frequencies and mode shapes

For low modal damping ratios (ζ<0.10; as observed at the measured tall buildings), the natural frequency and mode shapes can be found by neglecting all damping mechanisms and solve the homogeneous EM.

$$\rho A\frac{\partial^2 u}{\partial t^2}+EI\frac{\partial^4 u}{\partial z^4}=0 \tag{7}$$

The BCs of the system at z=0 and z=H are:

$$EI\left.\frac{\partial^2 u}{\partial z^2}\right|_{z=0}=k_R\left.\frac{\partial u}{\partial z}\right|_{z=0} \tag{8}$$

$$-EI\left.\frac{\partial^3 u}{\partial z^3}\right|_{z=0}=k_T u(0,t) \tag{9}$$

$$EI\left.\frac{\partial^2 u}{\partial z^2}\right|_{z=H}=0 \tag{10}$$

$$EI\left.\frac{\partial^3 u}{\partial z^3}\right|_{z=H}=0 \tag{11}$$

The solution *u(z,t)* is assumed as the multiplication of an unknown coordinate related function, *U(z)* and an unknown time related function, $\psi(t)$.

$$u(z,t)=U(z)\Psi(t) \tag{12}$$

Using the method of separation of variables by inserting Eq. (12) in (7), the EM can be separated into the time and coordinate related differential equation.

$$\ddot{\Psi}+\omega_n^2\Psi=0 \tag{13}$$

$$U^{IV} - \beta^4 U = 0 \tag{14}$$

where

$$\beta^4 = \frac{\rho A \omega_n^{\,2}}{EI} \tag{15}$$

ω_n is the natural frequency. A dot denotes differentiation with respect to time t and roman numbers indicate differentiation with respect to position z. The time and coordinate related part are standard second and fourth order differential equations and their general solution can easily be derived.

$$\Psi(t) = A\sin(\omega_n \cdot t) + B\cos(\omega_n \cdot t) \tag{16}$$

$$U(z) = C_1\cosh(\beta \cdot z) + C_2\sinh(\beta \cdot z) + C_3\cos(\beta \cdot z) + C_4\sin(\beta \cdot z) \tag{17}$$

Constants A en B depend on the initial conditions and C_1-C_4 depend on the BCs. By substitution of the general solutions into the BCs, a set of 4 algebraic equations is obtained.

$$\underline{\underline{A}}\,\underline{C} = \underline{0} \tag{18}$$

$$EI\beta^2 \begin{bmatrix} 1 & -\frac{k_R}{EI\beta} & -1 & -\frac{k_R}{EI\beta} \\ k_T & \beta & k_T & -\beta \\ \cosh(\beta H) & \sinh(\beta H) & -\cos(\beta H) & -\sin(\beta H) \\ \beta\sinh(\beta H) & \beta\cosh(\beta H) & \beta\sin(\beta H) & -\beta\cos(\beta H) \end{bmatrix} \begin{bmatrix} C_1 \\ C_2 \\ C_3 \\ C_4 \end{bmatrix} = \begin{bmatrix} 0 \\ 0 \\ 0 \\ 0 \end{bmatrix} \tag{19}$$

Constants C_1-C_4 are found by solving this set of algebraic equations. To find the non-trivial solution of the set of equations, the determinant of A has to be equal to zero. The expression of the determinant is a function of ω_n. By setting this expression equal to zero, the frequency equation is obtained. This transcendental equation has infinite amount of solutions, which are the natural frequencies of the system. By substitution of the found natural frequencies in the set of equations, $C_{1,i}$-$C_{4,i}$ can be found for every natural frequency $\omega_{n,i}$. The natural frequencies are defined such that the determinant is zero, consequently the system is dependent. This means that the constants $C_{1,i}$-$C_{4,i}$ that need to be found depend on each other. In order to find the shapes of the modes, it is assumed that $C_{4,i}$=1. The total solution of the undamped free vibration is a summation over all modes. A_i and B_i depend on the initial conditions.

$$\begin{aligned} u(z,t) &= \sum_{i=1}^{\infty} U_i(z)\Psi_i(t) \\ U_i(z) &= C_{1,i}\cosh(\beta_i z) + C_{2,i}\sinh(\beta_i z) + C_{3,i}\cos(\beta_i z) + C_{4,i}\sin(\beta_i z) \\ \Psi_i(t) &= A_i\sin(\omega_{n,i} t) + B_i\cos(\omega_{n,i} t) \\ \beta_i^4 &= \frac{\rho A \omega_{n,i}^{\,2}}{EI} \end{aligned} \tag{20}$$

2.3 Calibation of the mass and stiffness to the measured natural frequency

On the 6th of December 2011, the accelerations at the top of a high-rise building in the centre of Rotterdam were monitored with 6 accelerometers. The accelerometers were placed as indicated in Figure 2. With the response-time data from these devices, it was possible to determine the vibrations in the three main directions of the building (x- and y-translation and

torsion). The data concerning the time-response in *x*-direction is used to illustrate the damping identification.

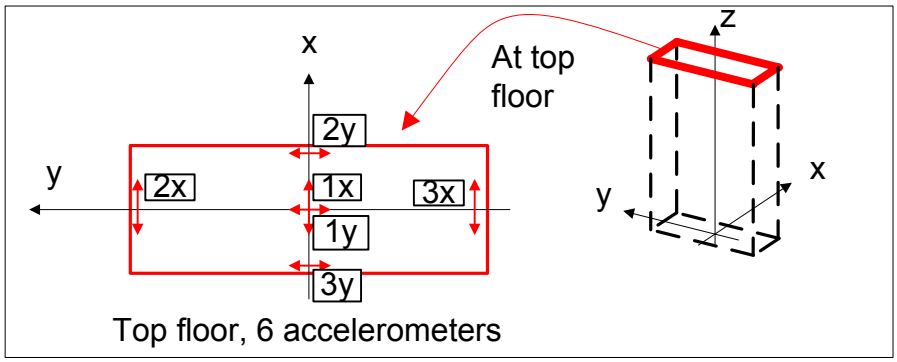


Figure 2 – monitoring of the accelerations with 6 accelerometers at the top of the building

Representative values of the model parameters concerning the mass, stiffness and height are derived from the design calculations of this building. By inserting these values in (19), the corresponding natural frequencies and mode shapes are found. The natural frequency of the first mode in the model is equal to $f_n=\omega_n/2\pi$ =3.39 /2π=0.230 Hz, however it doesn't correspond with the first natural frequency that is measured (f_n=0.536 Hz). Based on a sensitivity analysis and because of the conservative assumptions in the design process, a lower mass and higher stiffness have been assumed in order to calibrate the natural frequency of the model to the measurements [4]. Values of the calibrated mass, stiffness and mode shapes can be found in Table 1, Table 2 and Figure 3.

ρA [kg/m]	EI [Nm^2]	k_R [Nm/rad]	k_T [N/m]	H [m]
$2.30\cdot10^5$	$7.44\cdot10^{13}$	$4.42\cdot10^{12}$	$1.00\cdot10^{11}$	121.5

Table 1 – overview of calibrated mass and stiffness model parameters

Mode	ω [rad/s]	$C_{1,i}$	$C_{2,i}$	$C_{3,i}$	$C_{4,i}$
1	3.43	0.93	-0.57	-0.92	1
2	22.62	0.46	-0.48	-0.41	1

Table 2 –natural frequencies and corresponding mode shape constants for calibrated mass and stiffness

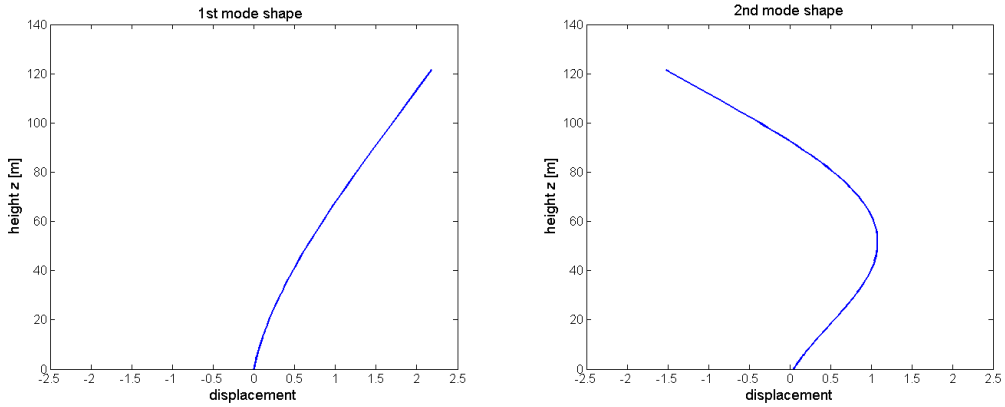


Figure 3 – Mode shapes of the first two translational bending modes

3 SIMULATED DYNAMIC RESPONSE

3.1 Wind loading conditions

No information about the local wind loading conditions were obtained during the monitoring of the response. Therefore theoretically based assumptions about the along-wind load are made to represent the statistical characteristics of the random wind load to which the building was subjected. The along-wind load at height z is split in a mean, $\overline{v}$ and fluctuating part $\tilde{v}$ [11].

$$p_w = \frac{1}{2}\rho_{air} v^2 = \frac{1}{2}\rho_{air}\left(\overline{v}+\tilde{v}\right)^2 = \frac{1}{2}\rho_{air}\left[\overline{v}^2 + 2\cdot\overline{v}\cdot\tilde{v} + \tilde{v}^2\right] \tag{21}$$

Since the fluctuating response was monitored around the mean deflection of the building, only the fluctuating wind load is modeled.

$$\tilde{q}(z,t) = B\cdot C_f \cdot \tilde{p}_w(z,t) = B\cdot C_f \cdot \rho_{air}\cdot\overline{v}(z)\cdot\tilde{v}(z,t) \tag{22}$$

The width B is constant over height. C_f is the shape factor which is inserted as an average of the local shape factors over the frontal area of the building. The term $\tilde{v}^2$ is neglected because it is relatively small. The mean wind velocity is described by a logarithmic wind profile depending on z. Gusts are the fluctuating part of the wind speed in time. A spectral description of the turbulence is a convenient tool to account for the energy contained in the sequence of gusts. The single sided variance spectrum of the fluctuating velocity (S_{vv}), shows how the energy of a sequence of gusts is distributed over the frequencies of the gusts. Because at a certain height there is a linear relation between the fluctuating wind velocity and wind load, the Fourier transform of the fluctuating wind load (S_q) and the single sided variance spectrum of the fluctuating wind load (S_{qq}) are equal to [11]:

$$S_q(z,\omega) = B\cdot C_f\cdot\rho_{air}\cdot\overline{v}_0\ln\left(\frac{z}{z_0}\right)\cdot S_v(z,\omega) \tag{23}$$

$$S_{qq}(z,\omega) = \left[B\cdot C_f\cdot\rho_{air}\cdot\overline{v}_0\ln\left(\frac{z}{z_0}\right)\right]^2 S_{vv}(z,\omega) \tag{24}$$

The shape of the wind spectrum (F_D) as given in the Eurocode [3] has been adopted for the wind velocity spectrum, the total variance (σ_v^2) is unknown. The shape of the spectrum is assumed to be constant over height with $z=z_s=0.6H$. Using the shape (F_D) of the spectrum, the following expression for the load spectrum is derived:

$$S_{qq}(z,\omega) = \left[B\cdot C_f\cdot\rho_{air}\cdot\overline{v}_0\ln\left(\frac{z}{z_0}\right)\right]^2\cdot\frac{\sigma_v^2}{\omega}F_D\left(z=0,6H;\ f=\frac{\omega}{2\pi}\right) \tag{25}$$

On a large surface, the peaks of the wind velocity at different places won't occur at exactly the same time. Thus the total wind load on a larger surface shows less variance. To take this effect into account, the spectrum has to be multiplied with the aerodynamic admittance $\chi(\omega)$.

$$S_{q_e q_e}(z,\omega) = \chi(\omega)^2\left[B\cdot C_f\cdot\rho_{air}\cdot\overline{v}_0\ln\left(\frac{z}{z_0}\right)\right]^2\cdot\frac{\sigma_v^2}{\omega}F_D\left(z=0,6H;\ f=\frac{\omega}{2\pi}\right) \tag{26}$$

In which (for R_b take H=B) [12]

$$\chi(\omega)^2 = R_h R_b \quad [-] \tag{27}$$

$$R_h = \frac{1}{\eta} - \frac{1-e^{-2\eta}}{2\eta^2} \tag{28}$$

$$\eta = \frac{4,6 \cdot \left(\frac{\omega}{2\pi}\right) \cdot H}{\overline{v}(z_s)} \tag{29}$$

The expression for the wind loading spectrum at different heights consists out of a constant part with unknown magnitude, a coordinate related part and a frequency dependent part.

$$S_{q_e q_e}(z,\omega) = C_w \cdot Q_z(z) \cdot Q_{\omega\omega}(\omega) \tag{30}$$

In which

$$\begin{aligned} C_w &= \left[B \cdot C_f \cdot \rho_{air} \cdot \overline{v}_0 \cdot \sigma_v \right]^2 \\ Q_z(z) &= \left[\ln\left(\frac{z}{z_0}\right) \right]^2 \\ Q_{\omega\omega}(\omega) &= \frac{\chi(\omega)^2 F_D\left(z = 0,6H;\ f = \frac{\omega}{2\pi}\right)}{\omega} \end{aligned} \tag{31}$$

3.2 The steady state response

The steady state response is determined from the EM and BCs as given in Eq. (2)-(6). Because the EM contains two terms related to damping (E^* and c_d) and the BCs contain damping terms (c_R and c_T), the equations can't be decoupled by making use of the modal analysis. Therefore the EM and BCs are transformed to the frequency domain by making use of the Fourier transformation:

$$\begin{aligned} &\int_{-\infty}^{\infty} \frac{\partial u(z,t)}{\partial t} \cdot e^{-i\omega t} dt = i\omega \int_{-\infty}^{\infty} u(z,t) \cdot e^{-i\omega t} dt = i\omega \cdot \tilde{U}_F(z,\omega) \\ &\int_{-\infty}^{\infty} \frac{\partial^2 u(z,t)}{\partial t^2} \cdot e^{-i\omega t} dt = i\omega \int_{-\infty}^{\infty} \frac{\partial u(z,t)}{\partial t} \cdot e^{-i\omega t} dt = -\omega^2 \int_{-\infty}^{\infty} u \cdot e^{-i\omega t} dt = -\omega^2 \cdot \tilde{U}_F(z,\omega) \\ &\textit{etc.} \end{aligned} \tag{32}$$

For every ω, the transformed EM is an ordinary differential equation with respect to z.

$$\tilde{U}_F(z,\omega)^{IV} - \beta_F{}^4 \tilde{U}_F(z,\omega) = \frac{\tilde{Q}_F(z,\omega)}{EI + i\omega E^* I} \tag{33}$$

In which

$$\begin{aligned} \beta_F{}^4 &= \frac{\rho A \omega^2 - i\omega c_d}{EI + i\omega E^* I} \\ \tilde{Q}_F(z,\omega) &= \int_{-\infty}^{\infty} q(z,t) \cdot e^{-i\omega t} dt \end{aligned} \tag{34}$$

The BCs, for z=0 become:

$$\left(EI + i\omega E^* I\right)\cdot \tilde{U}_F{}^{II} - k_R \cdot \tilde{U}_F{}^{I} - i\omega c_R \cdot \tilde{U}_F{}^{I} = 0 \tag{35}$$

$$\left(EI + i\omega E^* I\right)\cdot \tilde{U}_F{}^{III} + k_T \tilde{U}_F + i\omega c_T \tilde{U}_F = 0 \tag{36}$$

and for $z=H$:

$$\left(EI + i\omega E^* I\right)\cdot \tilde{U}_F{}^{II} = 0 \tag{37}$$

$$\left(EI + i\omega E^* I\right)\cdot \tilde{U}_F{}^{III} = 0 \tag{38}$$

Based on the derived wind loading spectrum (30), the Fourier transform of the load consist out of a multiplication of a constant, a logarithmic z-dependent function and a part depending on ω. To simplify calculations, the logarithmic function is fitted by an exponential functional.

$$\tilde{Q}_F(z,\omega) = \sqrt{C_w} Q_\omega(\omega) \ln\left(\frac{z}{z_0}\right) \rightarrow \sqrt{C_w} Q_\omega(\omega)\left(b_2 + b_1 \cdot e^{-z/c}\right) \tag{39}$$

The general solution of Eq. (33) to a load as in (39) $\left(\sqrt{C_w} = 1\right)$ is equal to:

$$\begin{aligned}
\tilde{U}_F(z,\omega) &= \tilde{C}_1 \cosh(\beta_F z) + \tilde{C}_2 \sinh(\beta_F z) + \tilde{C}_3 \cos(\beta_F z) + \tilde{C}_4 \sin(\beta_F z) \\
&\quad + C_0(\omega) + C_z(\omega) e^{-z/c} \\
C_0(\omega) &= \frac{-b_2 Q_\omega(\omega)}{\beta^4\left(EI + i\omega E^* I\right)} \\
C_z(\omega) &= \frac{b_1 Q_\omega(\omega)}{EI + i\omega E^* I} \frac{1}{\left[\left(-\frac{1}{c}\right)^4 - \beta^4\right]}
\end{aligned} \tag{40}$$

For every ω, the constants can be calculated from the 4 algebraic equations that can be found by substitution of the general solution into the BCs:

$$\left(EI + i\omega E^* I\right)\beta_F{}^2 \begin{bmatrix} 1 & -\frac{k_R + i\omega c_R}{\left(EI + i\omega E^* I\right)\beta_F} & -1 & -\frac{k_R + i\omega c_R}{\left(EI + i\omega E^* I\right)\beta_F} \\ \frac{k_T + i\omega c_T}{\left(EI + i\omega E^* I\right)\beta_F{}^2} & \beta_F & \frac{(k_T + i\omega c_T)}{\left(EI + i\omega E^* I\right)\beta_F{}^2} & -\beta_F \\ \cosh(\beta_F H) & \sinh(\beta_F H) & -\cos(\beta_F H) & -\sin(\beta_F H) \\ \beta \sinh(\beta_F H) & \beta \cosh(\beta_F H) & \beta \sin(\beta_F H) & -\beta \cos(\beta_F H) \end{bmatrix} \begin{bmatrix} \tilde{C}_1 \\ \tilde{C}_2 \\ \tilde{C}_3 \\ \tilde{C}_4 \end{bmatrix} = \begin{bmatrix} F_{0,1} \\ F_{0,2} \\ F_{0,3} \\ F_{0,4} \end{bmatrix} \tag{41}$$

In which

$$
\begin{aligned}
F_{0,1} &= -\left[\left(EI + i\omega E^* I\right)\cdot\left(-\frac{1}{c}\right)^2 + k_R \cdot \frac{-1}{c} + i\omega c_R \cdot \frac{-1}{c}\right] C_z(\omega) \\
F_{0,2} &= -\left[\left(EI + i\omega E^* I\right)\cdot\left(-\frac{1}{c}\right)^3 - k_T - i\omega c_T\right] C_z(\omega) - \left[k_T + i\omega c_T\right] C_0(\omega) \\
F_{0,3} &= -\left(EI + i\omega E^* I\right)\cdot\left(-\frac{1}{c}\right)^2 C_z(\omega) e^{-H/c} \\
F_{0,4} &= -\left(EI + i\omega E^* I\right)\cdot\left(-\frac{1}{c}\right)^3 C_z(\omega) e^{-H/c}
\end{aligned}
\tag{42}
$$

From (40)-(42) a linear relation between the load (Q_ω) and the response (U_F) can be observed. The velocity response is obtained by multiplication of the response with $i\omega$. The transfer function (see Figure 4) for the velocity at the top, H_{vTop} ,is the response to a unit load $Q_\omega(\omega)=1$.

$$H_{vTop}(\omega) = i\omega \cdot \tilde{U}_F\left(H, \omega, Q_\omega(\omega) = 1\right) \tag{43}$$

Because of the linear relation, in accordance with (23), (24) and (31), the single sided variance spectrum of the velocity at the top is equal to:

$$S_{vvTopP} = \left|H_{vTop}(\omega)\right|^2 C_w Q_{\omega\omega}(\omega) \tag{44}$$

In which

$$C_w Q_{\omega\omega}(\omega) = \left[B \cdot C_f \cdot \rho_{air} \cdot \bar{v}_0 \cdot \sigma_v\right]^2 \chi(\omega)^2 \frac{F_D\left(z = 0,6h;\, f = \dfrac{\omega}{2\pi}\right)}{\omega} \tag{45}$$

The right hand side of (44) doesn't contain the logarithmic distribution anymore because this is incorporated in the transfer function.

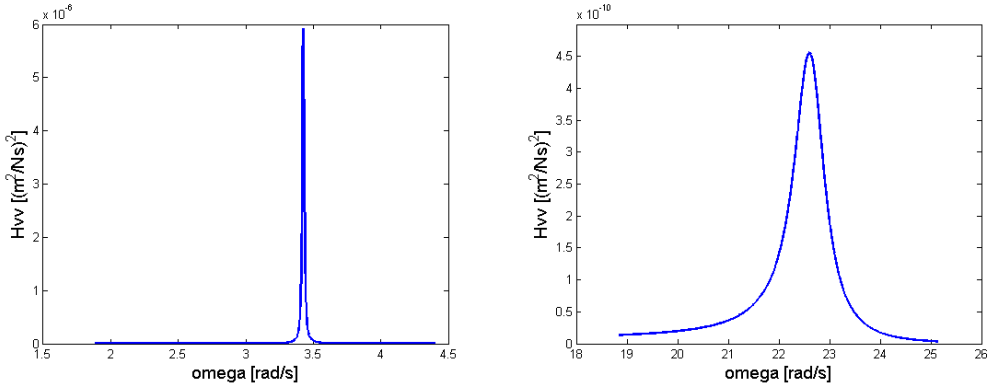


Figure 4 – Transfer function at the first and second natural frequency

4 CALIBRATION OF THE MODEL

4.1 Measured spectrum

The single sided variance spectrum of the time response signal in the main translation *x*-direction is obtained using Welch's method [13]. In this method, the measured signal is divided in multiple segments that partly overlap (50%). The spectrum of each segment is obtained

by using the Fast Fourier Transform (FFT). These spectra are averaged to find the spectrum of the complete time signal. Because of averaging, this method results in a smoother spectrum than by application of the FFT on the complete signal.

The response has been measured for 2 hours during a typical autumn storm (maximum 1-hour-average wind speed of 12 m/s and a maximum peak wind speed of 22 m/s) with a sampling frequency (f_s) of 50 Hz (360448 data points). Because averaging the signal with more segments will decrease the resolution of the spectrum, it has been decided to subdivide the signal in 10 segments, leading to a resolution of 0.0048 rad/s. From the definition of the single sided response spectrum [11], the area under the single sided variance spectrum is equal to the variance (σ_v^2). To check the statistical properties of the spectrum, the area has been compared to the standard deviation of the time signal (see Figure 5).

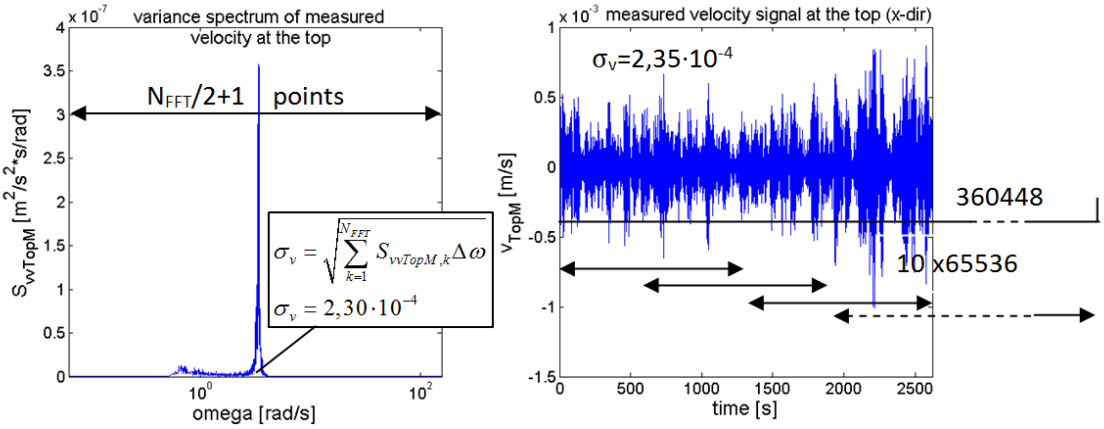


Figure 5 – Variance spectrum of the measured velocity and part of the measured time signal

4.2 Calibration method

In section 2.3 it is explained how the mass and stiffness parameters are calibrated to meet the measured natural frequency (f_n=0.536 Hz). Looking at (41)-(44), the simulated dynamic response depends on 5 unknown factors: a constant load factor C_w and 4 damping parameters, influencing the transfer function. Minimum, maximum and an initial guess values are derived for these parameters. These values (Table 3 and Table 4) are based on theoretical formula's concerning the wind velocity (σ_v, $\overline{v}_0$) and the expected modal damping ratio [14].

	c_D [Ns/m^2]	c_R [Nms/rad]	c_T [Ns/m]	E^*I [Nm^{2}s]
Initial estimate	$1.00\cdot10^4$	$1.00\cdot10^{10}$	$1.00\cdot10^{10}$	$1.00\cdot10^{10}$
minimum	$1.00\cdot10^2$	$1.00\cdot10^4$	$1.00\cdot10^4$	$1.00\cdot10^4$
maximum	$1.00\cdot10^6$	$1.00\cdot10^{15}$	$1.00\cdot10^{15}$	$1.00\cdot10^{15}$

Table 3 – Estimated damping values

	C_w [N^2/m^2]	σ_v [m/s]	C_f [-]	B [m]	ρ_{air} [kg/m^3]	$\overline{v}_0$ [m/s]
Initial estimate	$8.70\cdot10^5$	2.90	1.45	44.3	1.25	4.00
minimum	$2.60\cdot10^4$	1.45	1.00	44.3	1.25	2.00
maximum	$3.80\cdot10^7$	5.80	2.40	44.3	1.25	8.00

Table 4 – Estimated wind load values

The effect of the load is investigated in the case of minimum and maximum damping values according to Table 3. The linear relation between load and response is clearly visible in Figure 6 and Figure 7. For low damping, the absolute effect of the load on the response around the natural frequency is much larger than for frequencies around the quasi static peak (Figure 9). In case of maximum damping values, the effect is vice versa. The quasi static response is the response for a structure that only reacts statically, thus with transfer function at ω=0. The quasi static peak is the result of the peak in the wind spectrum which is visible in Figure 7.

The red line in Figure 8 shows a reasonable fit of the simulated spectrum with the measured spectrum. This fit is obtained by assuming minimum load and damping values and subsequently increasing c_D until it gives a resonance peak comparable to the measurement. As c_D increases, the peak decreases more than proportional and gets wider. The height of the quasi static response doesn't strongly depend on the damping parameters. The same behavior is observed for c_R and E^*I. For c_D=4,4·10^4 Ns/m^2, c_R=2,16·10^{11} Nms/rad and E^*I=2,03·10^{12} Nm^{2}s, a resonance peak comparable to the measurement is found. The influence of c_T is too small to reduce the peak of the resonance peak to match the measured spectrum. This is most probably caused by the large stiffness of k_T. The contribution of this damping term will be neglected and c_T is assumed to have its minimum value.

The question is which combination of load and damping parameters give the best fit with the measured spectrum. The load will mainly influence the height of the quasi static response, and it will also affect the height and width of the resonance peak. The damping parameters will mainly influence the shape of the resonance peak. Because of these three points, it is sufficient to execute a calibration procedure by comparison of the measured spectrum with the simulated spectrum over 6 small ranges of omega (see Figure 9). This reduces calculation time. Comparison over range 1 and 2 provide for proper calibration of the height for the quasi static response. Range 3 and 6 provide for proper calibration of the width of the spectrum, range 4 and 5 take the height of the resonance peak into account.

The response spectrum is simulated for many combinations of different values for C_w, c_D, c_R and E^*I, but c_T=1,0·10^4 Ns/m^2. For every simulation the square of the error between the simulated spectrum and the measured spectrum is calculated for the 6 ranges. The combination with the least square error is the best fitted combination.

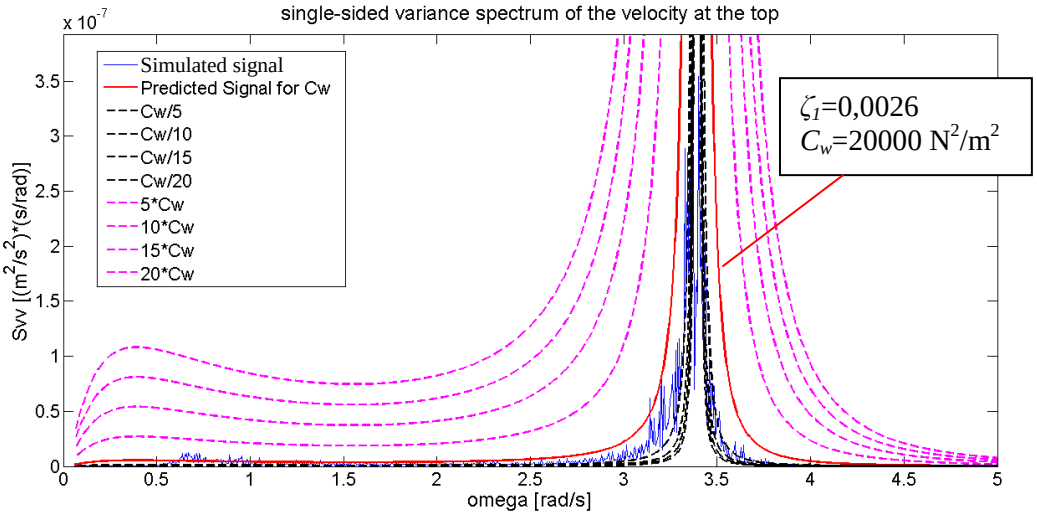


Figure 6 – the effect of load on the simulated response, minimum damping

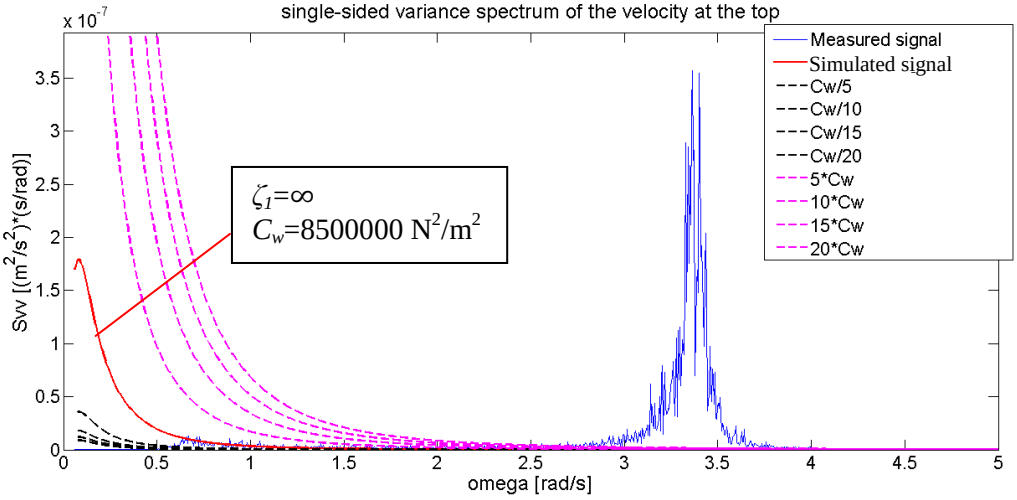


Figure 7 - the effect of the load on the simulated response, maximum damping

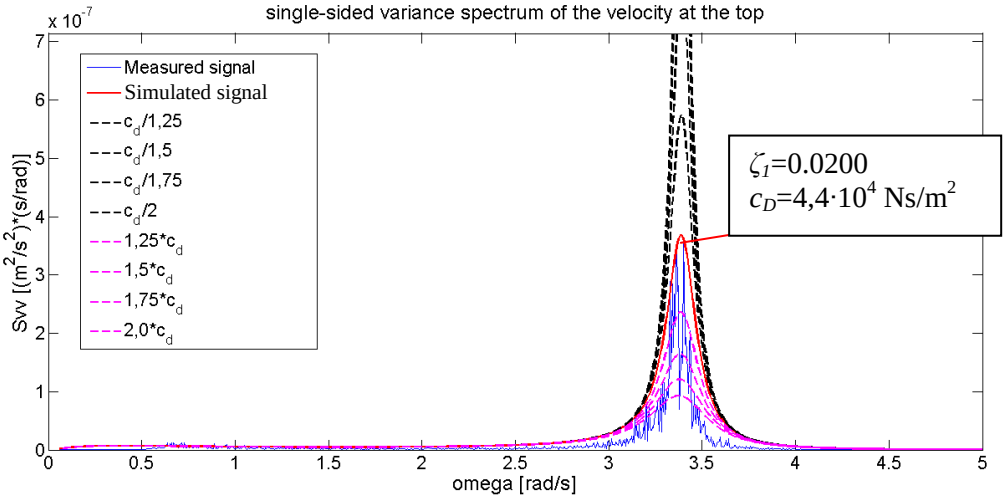


Figure 8 – influence of c_D for minimum C_w , c_R, c_T and E^*I

4.3 Results and conclusion

First the order magnitude is determined by considering the least square error of 3600 combinations of the values indicated in Table 5. An overview of the error, first natural frequency and modal damping ratio of the combinations can be found in Table 6.

	c_D [Ns/m^2]	c_R [Nms/rad]	c_T [Ns/m]	E^*I [Nm^{2}s]	C_w [N^2/m^2]
	$1.00\cdot10^2$	$1.00\cdot10^4$	$1.00\cdot10^4$	$1.00\cdot10^4$	$1.00\cdot10^4$
	$1.00\cdot10^3$	$1.00\cdot10^5$		$1.00\cdot10^5$	$1.00\cdot10^5$
	$1.00\cdot10^4$	$1.00\cdot10^6$		$1.00\cdot10^6$	$1.00\cdot10^6$
	$1.00\cdot10^5$	etc.		etc.	$1.00\cdot10^7$
	$1.00\cdot10^6$	$1.00\cdot10^{15}$		$1.00\cdot10^{15}$	$1.00\cdot10^8$
Number of values	5	12	1	12	5

Table 5 – values used to create combinations

	c_D [Ns/m^2]	c_R [Nms/rad]	c_T [Ns/m]	E^*I [Nm^{2}s]	C_w [N^2/m^2]	Error	ΔError [%]	$\omega_{n,1}$	ζ_1 [%]
1	$1.00\cdot10^{4}$	$1.00\cdot10^{10}$	$1.00\cdot10^{4}$	$1.00\cdot10^{12}$	$1.00\cdot10^{4}$	$1.43\cdot10^{-13}$	0.0	3.394	1.69
2	$1.00\cdot10^{4}$	$1.00\cdot10^{11}$	$1.00\cdot10^{4}$	$1.00\cdot10^{11}$	$1.00\cdot10^{4}$	$1.45\cdot10^{-13}$	1.2	3.394	1.58
3	$1.00\cdot10^{4}$	$1.00\cdot10^{9}$	$1.00\cdot10^{4}$	$1.00\cdot10^{12}$	$1.00\cdot10^{4}$	$1.46\cdot10^{-13}$	2.0	3.394	1.49
4	$1.00\cdot10^{4}$	$1.00\cdot10^{8}$	$1.00\cdot10^{4}$	$1.00\cdot10^{12}$	$1.00\cdot10^{4}$	$1.47\cdot10^{-13}$	3.0	3.394	1.50
5	$1.00\cdot10^{4}$	$1.00\cdot10^{4}$	$1.00\cdot10^{4}$	$1.00\cdot10^{12}$	$1.00\cdot10^{4}$	$1.47\cdot10^{-13}$	3.1	3.394	1.50
6	$1.00\cdot10^{4}$	$1.00\cdot10^{6}$	$1.00\cdot10^{4}$	$1.00\cdot10^{12}$	$1.00\cdot10^{4}$	$1.47\cdot10^{-13}$	3.1	3.394	1.50
7	$1.00\cdot10^{4}$	$1.00\cdot10^{5}$	$1.00\cdot10^{4}$	$1.00\cdot10^{12}$	$1.00\cdot10^{4}$	$1.47\cdot10^{-13}$	3.1	3.394	1.50
8	$1.00\cdot10^{4}$	$1.00\cdot10^{4}$	$1.00\cdot10^{4}$	$1.00\cdot10^{12}$	$1.00\cdot10^{4}$	$1.47\cdot10^{-13}$	3.1	3.394	1.50
9	$1.00\cdot10^{4}$	$1.00\cdot10^{11}$	$1.00\cdot10^{4}$	$1.00\cdot10^{10}$	$1.00\cdot10^{4}$	$1.58\cdot10^{-13}$	11	3.399	1.38
10	$1.00\cdot10^{4}$	$1.00\cdot10^{11}$	$1.00\cdot10^{4}$	$1.00\cdot10^{9}$	$1.00\cdot10^{4}$	$1.61\cdot10^{-13}$	13	3.399	1.39
11	$1.00\cdot10^{4}$	$1.00\cdot10^{11}$	$1.00\cdot10^{4}$	$1.00\cdot10^{8}$	$1.00\cdot10^{4}$	$1.62\cdot10^{-13}$	13	3.399	1.39
12	$1.00\cdot10^{4}$	$1.00\cdot10^{11}$	$1.00\cdot10^{4}$	$1.00\cdot10^{7}$	$1.00\cdot10^{4}$	$1.62\cdot10^{-13}$	13	3.399	1.39
13	$1.00\cdot10^{4}$	$1.00\cdot10^{11}$	$1.00\cdot10^{4}$	$1.00\cdot10^{6}$	$1.00\cdot10^{4}$	$1.62\cdot10^{-13}$	13	3.399	1.39
14	$1.00\cdot10^{4}$	$1.00\cdot10^{11}$	$1.00\cdot10^{4}$	$1.00\cdot10^{5}$	$1.00\cdot10^{4}$	$1.62\cdot10^{-13}$	13	3.399	1.39
15	$1.00\cdot10^{4}$	$1.00\cdot10^{11}$	$1.00\cdot10^{4}$	$1.00\cdot10^{4}$	$1.00\cdot10^{4}$	$1.62\cdot10^{-13}$	13	3.399	1.39
16	$1.00\cdot10^{2}$	$1.00\cdot10^{11}$	$1.00\cdot10^{4}$	$1.00\cdot10^{12}$	$1.00\cdot10^{4}$	$2.68\cdot10^{-13}$	88	3.394	2.02
17	$1.00\cdot10^{3}$	$1.00\cdot10^{11}$	$1.00\cdot10^{4}$	$1.00\cdot10^{12}$	$1.00\cdot10^{4}$	$2.84\cdot10^{-13}$	99	3.394	1.98

Table 6 – overview of combinations with the least error

When looking at the combinations with the lowest error it can be concluded that the load will have order of magnitude 10^4. The other combinations (1-17) with low error also show some interesting aspects because three ranges can be distinguished. In each range, one of the three relevant damping parameters (c_D, c_R and E^*I) can vary a lot without influencing the error significantly. Consider for example c_R for combination 1-8. The shape of the resonance peak is governed by the damping contribution of the other two damping sources (c_D and E^*I). The range in which c_R can vary freely, are values below the order of magnitude for the respective parameter (except for combination 2, where E^*I has a lower value, such that c_R can be higher). It can be concluded that the order of magnitude for the parameters that give the least error are:

c_D [Ns/m^2]	c_R [Nms/rad]	c_T [Ns/m]	E^*I [Nm^{2}s]	C_w [N^2/m^2]
$1.00\cdot10^{4}$	$1.00\cdot10^{11}$	-	$1.00\cdot10^{12}$	$1.00\cdot10^{4}$

Table 7 – order of magnitude for the parameters to obtain the best fit

In order to find an even better fit, the same procedure is repeated for values around the found order of magnitude for c_D, c_R, E^*I and C_w. For each parameter 19 values have been assumed, ranging from 10% to 190% of the found order of magnitude. For example considering c_D, these values are: $1\cdot10^3$, $2\cdot10^3$, $3\cdot10^3$, … $8\cdot10^4$, $9\cdot10^4$. Combinations with even smaller errors are found, an example of such fit can be found in Figure 9. However combinations with different damping values have comparable small errors. No unique solution is found and the relative contribution of c_D, c_R and E^*I can't be determined because the parameters influence the resonance peak in the same way. It can only be concluded that the damping parameters have a value between 10% and 190% of the values in Table 7. For the load parameters, C_w it is possible to give a more accurate estimation of the magnitude because the fits with the least square error all had a value of $1\cdot10^4$ or $2\cdot10^4$ N^2/m^2.

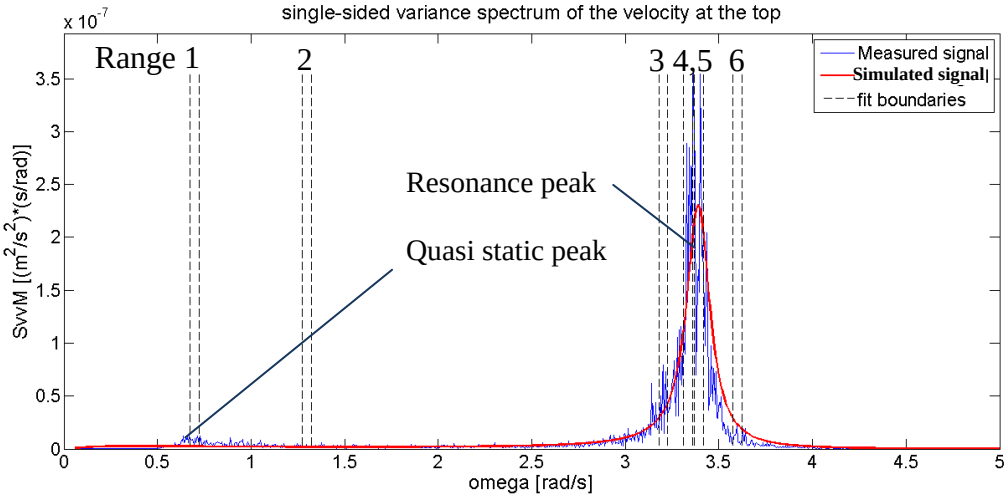


Figure 9 – simulated response for well fitted combination

5 CONCLUSION

In this paper a building model is introduced to investigate the possibilities on identifying the relative damping contribution of different building parts. This is done by a numerical calibration of the simulated response to the measured response (Figure 9). By making use of the design calculations and the measured dynamic response of the building, the mass and stiffness parameters of the building were calibrated by comparison of the simulated and actual natural frequency of the first mode. Since no information about the local wind loading conditions was available, the magnitude of the variance of the wind load at time of measurement was unknown. Theoretical assumptions made it possible to define the shape of the wind loading spectrum along the height of the building, which can be multiplied with an unknown wind loading factor C_w to obtain the wind loading spectrum. With the transfer function derived from the model, it was possible to simulate the response at the top of the building. The transfer function depends on the a priori unknown damping parameters: c_D, c_R, c_T and E^*I. The response spectrum is simulated for many combinations of different values for these parameters.

Best fit values for C_w, c_D, c_R, c_T and E^*I are found from the combination that resulted in the least square error between the simulated and measured response spectrum at the quasi static and resonance response. In conclusion it is possible to give a quite accurate estimation of the load factor C_w, the effect of c_T can be neglected, but it is not possible to identify the relative contribution of the other three damping parameters. The latter is caused by the fact the three parameters influence the shape of the resonance peak in the same manner. Many different combinations of values for these parameters lead to a fit with (almost) equal error. From this research it can be concluded that only the total damping of the first mode which has been identified from the measured response at the top only, is insufficient to determine the relative contribution of the four damping contributions as modeled.

6 FUTURE DEVELOPMENTS

Ongoing research focuses on the development of a physically more correct damping model together with an improvement/extension of the current measurement methods. This should result in a better identification of the effect of different damping mechanisms on the response spectrum and more data to be available for calibration. Eventually this should allow one to identify the damping contribution of the different building parts.

Current investigation explores the possibilities of a building model in which the main lateral stabilizing structural system (the core) and the non-stabilizing part (floors, beams etc.) are represented by an Euler-Bernoulli beam and a shear beam, coupled together. This model should allow us to better implement the damping mechanisms in, and the interaction between, these parts. Furthermore the usability and accuracy of implementation of theoretical formulae for the different damping mechanism is investigated. Another research topic is the implementation of other damping models than the viscous behavior. Literature indicates internal material damping is better described by a mathematical description based on frequency independent hysteresis damping. In addition, it is more realistic to implement friction elements to model the energy loss at the interfaces between elements [6; 14]. The characteristic effects of these different damping models on the simulated response should be investigated and compared to the actual response.

By measurement of the building response at different levels, it should be possible to identify the total damping of the second mode [15], this makes it possible to use two instead of one resonance peak to calibrate the model. It is investigated if this allows us to uniquely determine the values of the different damping parameters.

It is also planned to monitor the rotation at the building's base simultaneously with the lateral displacement to possible identify the contribution of the energy loss at the interface with the ground.

REFERENCES

[1] ISO6897: Guidelines for the evaluation of the response of occupants of fixed structures. (1986).

[2] Koten, H. van. (1977). CUR rapport 75, demping van bouwconstructies: TNO.

[3] NNI. (2005). NEN-EN 1991-1-4: general actions - wind actions. Delft.

[4] Berg, R.L.J. van den. (2012). *Investigation of damping in high-rise buildings: Identification and prediction in the serviceability limit state for wind-induced vibrations (MSc-thesis).* Faculty of Civil engineering and Geosciences, Delft.

[5] Jeary, A.P. (1986). Damping in tall buildings - a mechanism and a predictor. *Earthquake engineering and structural dynamics, 14*, 733-750.

[6] Lagomarsino, S. (1993). Forecast models for damping and vibration periods of buildings. *Journal of Wind Engineering and Industrial Aerodynamics, 48*, 221-239.

[7] Satake, N., Suda, K., Arakawa, T., Sasaki, A., & Tamura, Y. (2003). Damping evaluation using full-scale data of buildings in Japan. *Journal of structural engineering*, 470-477.

[8] Li, Q.S., & Wu, J.R. (2007). Time-frequency analysis of typhoon effects on a 79-storey tall building. *Journal of Wind Engineering and Industrial Aerodynamics, 95*, 1648-1666.

[9] Bashor, R., Bobby, S., Kijewski-Correa, T., & Kareem, A. (2012). Full-scale performance evaluation of tall buildings under wind. *Journal of Wind Engineering and Industrial Aerodynamics, 104-106*, 88-97.

[10] Simone, A. (2009). *An introduction to the analysis of slender structures, lecture notes CT4190*. Delft: Faculty of Civil Engineering and Geosciences.

[11] Vrouwenvelder, A.C.W.M. (2004). *Random Vibrations, Lecture notes CT5145*: Faculty of Civil Engineering and Geosciences.

[12] Oosterhout, G.P.C. van. (1996). *Thesis: Wind-induced dynamic behaviour of tall buildings.* TUDelft, Delft.

[13] Welch, P.D. (1967). The use of Fast Fourier Transform for the estimation of power spectra: a method based on time avergaging over short, modified periodograms. *IEEE Trans. Audio and electroacoust, AU-15*, 70-73.
[14] Lazan, B. (1968). *Damping of materials and members in structural mechanics*. London: Pergamon Press.
[15] Guo, Y.L., Kareem, A., Ni, Y.Q., & Liao, W.Y. (2012). Performance evaluation of Canton Tower under wunds based on full-scale data. *Journal of Wind Engineering and Industrial Aerodynamics, 104-106*, 116-128.

COMPDYN 2013
4th ECCOMAS Thematic Conference on
Computational Methods in Structural Dynamics and Earthquake Engineering
M. Papadrakakis, V. Papadopoulos, V. Plevris (eds.)
Kos Island, Greece, 12–14 June 2013

A MACRO-ELEMENT MODEL FOR THE NONLINEAR ANALYSIS OF MASONRY MEMBERS INCLUDING SECOND ORDER EFFECTS

A. Penna[1,2] and A. Galasco[1,2]

[1]Dept. of Civil Engineering and Architecture, University of Pavia
Via Ferrata 3, I-27100 Pavia, Italy
andrea.penna@unipv.it and alessandro.galasco@unipv.it

[2]European Centre for Training and Research in Earthquake Engineering
Via Ferrata 1, I-27100 Pavia, Italy

Keywords: Masonry, Second order effects, Nonlinear analysis, Rocking, Simulation.

Abstract. *The second order effects are often neglected in the evaluation of the global seismic response of masonry buildings. Pier in-plane response is often governed by shear failure modes, particularly in case of rather squat panels and relatively high compression. Shear failure is usually associated with a limited deformation capacity which makes acceptable an approach based on the undeformed geometry of the structure. In case of structural members with a prevailing bending behaviour, the displacement capacity can be significantly increased and second order effects may no longer be negligible. Indeed, experimental tests on panels with a marked rocking behaviour show a gradual reduction of lateral strength for increasing lateral displacements, also in the absence of significant toe-crushing effects. The 2-node macro-element model implemented in the TREMURI computer program concentrates in the two extremities the coupled axial and flexural behaviour allowing for a rigorous representation of flexural cracking and toe-crushing effects. The shear response is concentrated in the central body of the element and the interaction between shear and bending-rocking behaviours is allowed by two internal degrees of freedom. The kinematic formulation of the macro-element and in particular the presence of the additional internal degrees of freedom easily allowed the introduction of P-delta effects in the nonlinear element response. Numerical results obtained with the upgraded macro-element model showed a very good agreement with experimental results. The new feature implemented in the macro-element model makes its use in the equivalent frame modelling further reliable and opens new perspectives and applications in other fields such as the analysis of rigid or quasi-rigid block systems.*

1 INTRODUCTION

Second order effects are usually neglected when dealing with modeling of the in-plane behavior of masonry walls subjected to lateral forces, since their response is normally limited to relatively small lateral displacements and deformations. For this reason, the so-called P-Δ effects are usually considered to not significantly affect the response of masonry piers. This is normally an appropriate approximation for models aiming at representing the overall behavior of masonry buildings with reasonably stiff diaphragms well connected to perimeter walls, whose behavior is governed by the in-plane strength and stiffness of walls. Nevertheless, even in some in-plane cyclic shear-compression tests (e.g. [1]) it was shown that, in case of a clear bending-rocking response, masonry piers achieving in-plane drift ratios higher than 1% show some evidence of the influence of second order effects.

On the other hand, as presented in [2], modeling strategies for representing the out-of-plane response of masonry walls often refer to limit equilibrium analysis, incorporating P-Δ effects, but usually approximating as rigid bodies the masonry portions involved in the considered damage mode (e.g. [3],[4],[5],[6]). This is also in general the approach adopted by the Italian Building Code [7] for the seismic analysis of local failure modes in existing masonry buildings with sufficient masonry quality, for which in most cases it is possible to resort to the analysis of an equivalent system consisting of a kinematic chain of rigid bodies connected in predefined points by rotational or sliding hinges (e.g. [8]). Such as approach is then suitable for the analysis of simple local failure modes, although the rigid body hypothesis and the need for preliminarily identify the position of hinges and contact points constitute its major limitations. Moreover, the study of the dynamic response of these systems is not trivial and hence the evaluation of the expected structural performance (i.e. assessment of displacement demand) is usually carried out by means of very simplified approaches [3][7].

The macro-element technique for modeling the nonlinear response of masonry panels is particularly efficient and suitable for the analysis of the seismic behavior of complex walls and buildings. With the inclusion of second order effects, this modeling approach could be extremely powerful also for assessing the structural response of masonry systems prone to local and out-of-plane failure modes when subjected to static or dynamic loadings. Accounting for P-Δ effects would also slightly improve the ability of the models in assessing the wall in-plane behavior.

2 THE MACROELEMENT MODEL

The macro-element model originally proposed by Gambarotta and Lagomarsino [8] has been further refined in the representation of flexural-rocking and shear damage modes and it is capable of fairly simulating the experimental response of in-plane cyclic tests performed on masonry piers [9]. This model is currently included in the TREMURI analysis program [10].

Based on its kinematical structure including two additional internal degrees of freedom, this 2-node macro-element model allows to describe both the shear behaviour and the coupled axial-flexural one, as well as their mutual interaction. It includes a nonlinear shear model which is derived by the macroscopic integration of a nonlinear continuum model for masonry [11]. The non linear description of the coupled relation between flexural and axial degrees of freedom allows evaluating the cracking effects on rocking motion.

Figure 1 illustrates the basic idea of the macro-element formulation. The panel can be ideally subdivided into three parts: a central body where only shear deformation can occur and

two interfaces, where the external degrees of freedom are placed, which can have relative axial displacements and rotations with respect to those of the extremities of the central body.

The two interfaces can be considered as infinitely rigid in shear and with a negligible thickness. Their axial deformations are due to distributed system of zero-length springs.

These assumptions simplify the macro-element kinematics and compatibility relations allow obtaining a reduction of the actual degrees of freedom of the model. Since the central part is considered as a rigid body with only shear deformation capability, under small displacement hypotheses, the axial displacements and rotations of the ends can be considered equal to the centroid ones (w_e, φ_e), while the transversal displacements on the central body ends must be equal to the corresponding nodal displacements (u_i, u_j).

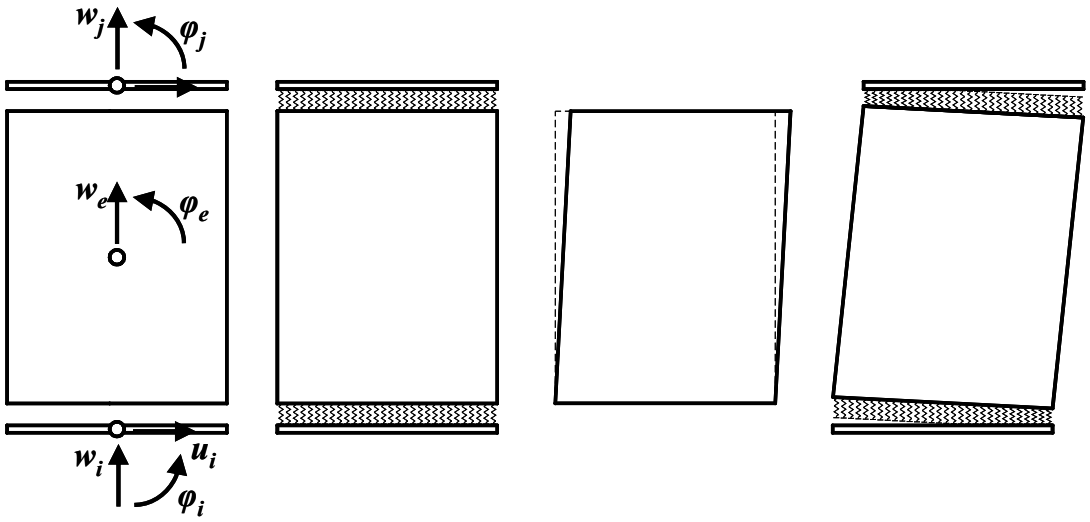


Figure 1: Kinematics of the macro-element (after [9])

Therefore the macro-element kinematics can be described by means of eight degrees of freedom, 6 nodal displacement components (u_i w_i, φ_i, u_j w_j, φ_j) and 2 internal components (w_e, φ_e).

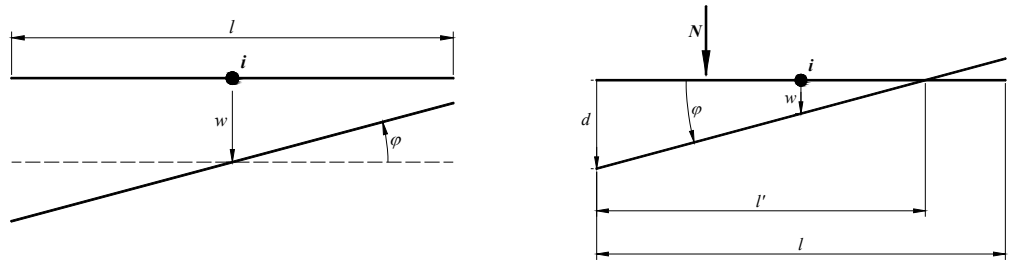
No distributed transversal actions are considered and so the internal shear force is constant along the element axis ($V_i = V_j = V$). The shear failure mode is considered to be macroscopically representative of both the shear failure modes, diagonal cracking and sliding on bed joints, with an equivalent approach.

A no tension model has been attributed to the zero-length springs at the interfaces, with a bilinear degrading constitutive model in compression. The axial and flexural behaviour of the two extremity joints is studied separately. The static and kinematic variables involved in joint model are the element forces N and M for the considered node and the relative displacement components w and φ (Figure 2a). The relations between such variables are directly derived from the constitutive model. If the whole cross section is compressed no cracking occurs and the problem is uncoupled, with linear relations linking N and M with w and φ respectively,

$$\begin{cases} N = kltw \\ M = \dfrac{k}{12} tl^3 \varphi \end{cases} \tag{1}$$

where l is the wall length, t is the wall thickness, $k = 2E/h$ is the spring axial stiffness for surface unit, with E compressive Young modulus of masonry and h wall height (in order to reproduce the axial stiffness of the panel), w is the relative axial displacement ($w = w_i - w_e$, at

node *i* and $w = w_e - w_j$ at φ is the relative rotation ($\varphi = \varphi_i - \varphi_e$, at node I and $\varphi = \varphi_e - \varphi_j$ at node *j*).



(a) (b)

Figure 2: Kinematic representation of node *i* interface in uncracked (a) and cracked (b) conditions

The cracking condition can be simply expressed in terms of kinematic variables (Figure 2b),

$$|\varphi| > \frac{2w}{l} \tag{2}$$

In cracked condition the axial force can be calculated as

$$N = -\frac{1}{2} ktl' d \,, \tag{3}$$

where *d* is the relative axial displacement at the compressed edge of the considered interface joint and *l'* is the compressed length of the cross section.

Under the small displacement hypothesis it is immediate to obtain

$$d = |\varphi| l' \,, \tag{4}$$

and therefore the expression of $|w|$

$$|w| = \left(l' - \frac{l}{2} \right) |\varphi| \,, \tag{5}$$

derived according to the similar triangles rule, can be inverted in order to obtain the length of the compressed part of the cross section, *l'*,

$$l' = \frac{w}{|\varphi|} + \frac{l}{2} = \frac{l|\varphi| + 2w}{2|\varphi|} \,, \tag{6}$$

Expression (6) can be substituted in (4) and (5) expressing the axial force as

$$N = -\frac{kt}{8|\varphi|} \left(l|\varphi| + 2w \right)^2 \,. \tag{7}$$

Imposing the rotational equilibrium around the mid point of the cross section the bending moment expression is then derived as

$$M = \frac{kt}{24} \frac{\left(l|\varphi| + w \right)}{\varphi|\varphi|} \left(l|\varphi| + 2w \right)^2 \,. \tag{8}$$

Equations (7) and (8) can be rewritten separating the elastic contribution and the corrections due to cracking.

It is evident that, in case of cracked cross section, axial force and bending moment are not uncoupled and therefore it is possible to obtain the relation between w and φ for a given axial force N,

$$w = \frac{|\varphi| l}{2} - \sqrt{\frac{-2|\varphi| N}{kt}}, \tag{9}$$

which is valid out of the uncracked range of φ values. Figure 3 shows the interaction between vertical displacement and rotation for different values of axial load.

Masonry compressive strength is usually high compared to the vertical stress due to static vertical loads. Nevertheless, from experimental tests it has been often observed that in-plane rocking mechanisms are characterized by toe crushing phenomena at the base of masonry piers, causing the limitation of the ultimate bending moment and some stiffness degradation in the further cycles. In order to include such effects into the nonlinear model, a phenomenological bilinear constitutive model with stiffness degradation has been assigned to the interface joint springs, as illustrated in [9]. These further contributions can be simply included in the nonlinear correction to N and M.

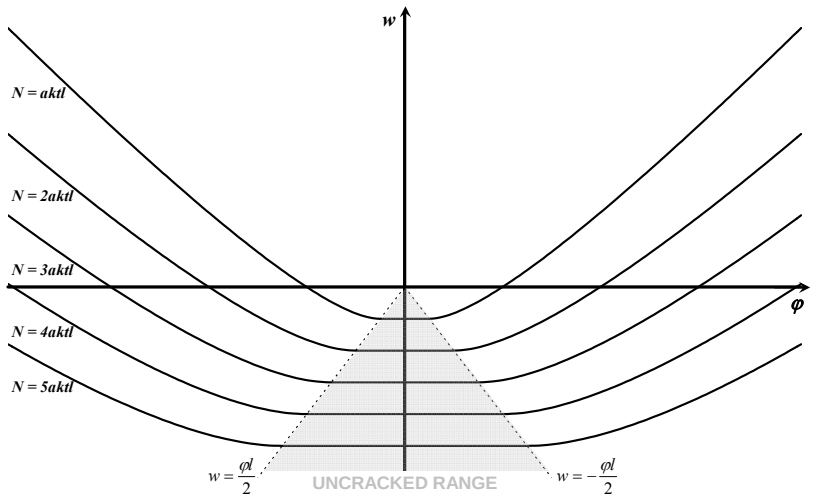


Figure 3: Interaction between w and φ for a sample wall subjected to different values of axial force (α is a constant, after [9]).

3 MACRO-ELEMENT MODEL INCLUDING SECOND ORDER EFFECTS

The constitutive model relations between the eight kinematic variables and the six nodal forces (N_i, V_i, M_i, N_i, V_j, M_j) have been derived. Internal equilibrium equations provide the forces acting on the additional degrees of freedom in the original configuration (without second order effects):

$$\begin{cases} N_e = N_j - N_i \\ M_e = M_j - M_i + Vh \end{cases}. \tag{10}$$

An easy way to include the second orders effect is to include the second order moment in the rotation equilibrium. The configuration is reported in Figure 4(b) and the relationship is given by

$$\begin{cases} N_e = N_j - N_i \\ M_e = M_j - M_i + Vh' + N_e \cdot (u_j - u_i) \end{cases} \quad (11)$$

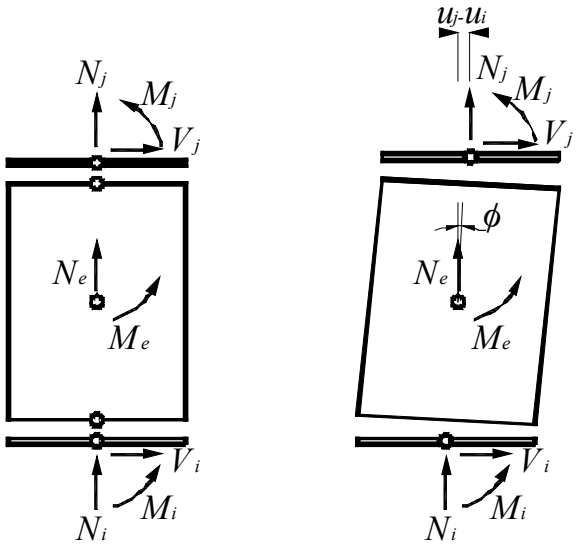


Figure 4: Equilibrium in first (a) and in second order approach (b).

Actually the arm *h'* of the moment induced by the shear force should be evaluated in the deformed shape considering both the variation in vertical displacement ($w_j - w_i$) and the rotation of the element ($h \cos \varphi$). However in a common masonry type the entity of the vertical displacement is little in comparison with the height of the element; similarly the cosine of the rotation is close to the unity so that a confusion between *h'* and *h* can be accepted.

To be consistent with the general nonlinear formulation, the second order moment can be treated as a non linear correction; according to the current notation its value is:

$$M_e^{II} = N_e \cdot (u_j - u_i) \quad (12)$$

In matrix form, subdividing the elastic and inelastic terms, the macro-element constitutive equations can then be written as

$$\begin{Bmatrix} N_i \\ V_i \\ M_i \\ N_j \\ V_j \\ M_j \\ N_e \\ M_e \end{Bmatrix} = \begin{bmatrix} klt & 0 & 0 & 0 & 0 & 0 & -klt & 0 \\ 0 & \frac{Glt}{h} & 0 & 0 & -\frac{Glt}{h} & 0 & 0 & -Glt \\ 0 & 0 & \frac{1}{12}ktl^3 & 0 & 0 & 0 & 0 & -\frac{1}{12}ktl^3 \\ 0 & 0 & 0 & klt & 0 & 0 & -klt & 0 \\ 0 & -\frac{Glt}{h} & 0 & 0 & \frac{Glt}{h} & 0 & 0 & Glt \\ 0 & 0 & 0 & 0 & 0 & \frac{1}{12}ktl^3 & 0 & -\frac{1}{12}ktl^3 \\ -klt & 0 & 0 & -klt & 0 & 0 & 2klt & 0 \\ 0 & -Glt & -\frac{1}{12}ktl^3 & 0 & Glt & -\frac{1}{12}ktl^3 & 0 & Glt + \frac{1}{6}ktl^3 \end{bmatrix} \begin{Bmatrix} w_i \\ u_i \\ \varphi_i \\ w_j \\ u_j \\ \varphi_j \\ w_e \\ \varphi_e \end{Bmatrix} - \begin{Bmatrix} N_i^* \\ V_i^* \\ M_i^* \\ N_j^* \\ V_j^* \\ M_j^* \\ 0 \\ M_e^{II} \end{Bmatrix}, \quad (13)$$

where the nonlinear correction terms identified by superscript «*» depend on cracking, toe-crushing and shear damage effects [2], while the one marked as «II» depends on the second order effects.

4 OVERTURNING BLOCK SOLUTION

The study of the overturning of a block assumed restrained only at the base (cantilever boundary conditions) represents a simple configuration to study the second order effects.

The macro-element describes a linear elastic solution up to the cracking condition according to the stiffness matrix and the boundary condition: the relationship between the horizontal top displacement u_j (here indicated only as u) and an horizontal associated forced F may be written as

$$u = \frac{Fh^3}{3EJ}, \tag{14}$$

under the hypothesis of negligible shear deformations (Euler beam solution).

At the base of the panel the equilibrium is granted by the restraint bending moment $M_i=Fh$. Usually in this phase the second order effects can be neglected. After cracking the bending moment has to satisfy the equilibrium with no tensile stress acting on the cross section (partialization). The presence of the axial vertical force N can grant a bending capacity by means of an eccentricity $e=M/N$, which, even neglecting the effect of masonry crushing (assuming an infinite compressive strength), is in any case limited to half the base of the panel.

For increasing lateral displacements (i.e. block rotations), overturning occurs and second order effects become more important contributing to the decrement of the capacity to withstand a lateral force. In Figure 5 the limit condition for which equilibrium is still possible under non-negative lateral forces is reported for the cases of only serf-weight (left) or concentrated mass at the top of the block (right). In both cases the ultimate equilibrium condition is reached when the centre of gravity of the block (or generally the application point of the vertical force) is aligned with the eccentric reaction force at the base (displacement $u=b$ for infinitely strong blocks), so that a further increase in the displacement causes an overturning of the system.

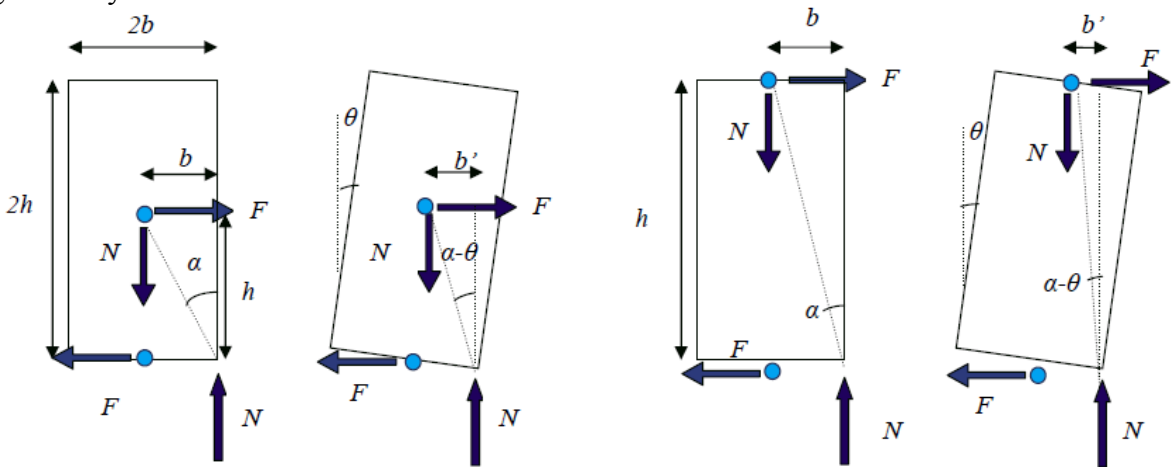


Figure 5: Limit equilibrium condition of a rigid block, subjected only to its self-weight (left) and a concentrated mass at the top (right).

With reference to the notation reported in Figure 5, the maximum lateral force that an infinitely rigid and strong block could withstand before activating overturning is given by

$$F_{\max} = \frac{Nb}{2h} \quad (15)$$

Considering the deformed configuration (block rotation), the increase of the horizontal displacement of the centre of gravity causes a reduction of the arm of the restoring moment. Assuming a rigid block and non-negative values of the angle α and θ (as reported in Figure 5) the horizontal force depends on the value of *b'* and *h'*. According to the previous consideration the value of *h* may be confused with *h'* so that only the arm of the restoring moment arm has to be evaluated:

$$F(\theta) = \frac{N \cdot b'}{2h} = \frac{N \cdot R \cdot \sin(\alpha - \theta)}{2h}, \quad (16)$$

with $R = \sqrt{b^2 + h^2}$.

For increasing values of rotation θ the lateral force decreases up to zero (for $\theta=\alpha$). In the Italian Code approach the linearization of this curve is allowed by means of the determination of $F_{\max}$ and overturning displacement [7].

4.1 Effect of elastic deformation

For non-rigid blocks, the elastic deformation is involved in the evolution of the later force capacity. As reported in Figure 6, first and second order approaches provide close results in the initial deformation phase, before cracking is reached and *u* and φ are coupled. Then the second order contribution is negative while the force due to the deformation of the interface springs increases for increasing values *u*. Hence, in the first order approach the force tends to the limit value of F_{max}, whist in the second order approach the force reaches a lower maximum value before decreasing and it is always smaller than the one of the rigid block solution (either linearized or not).

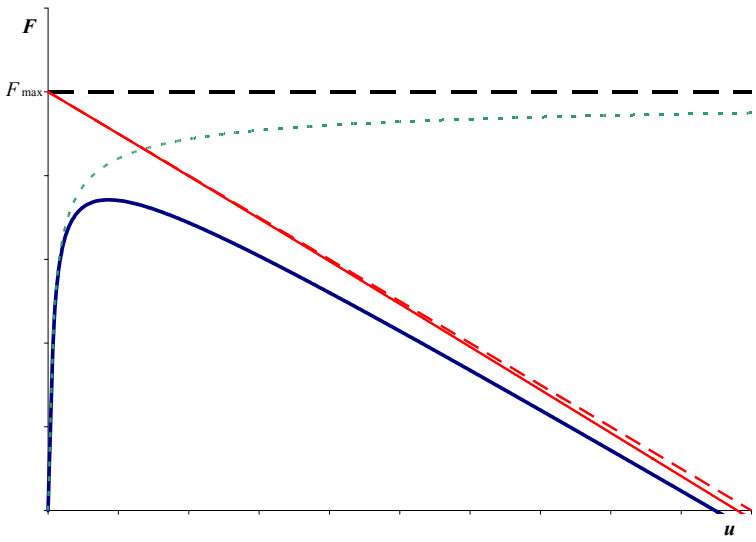


Figure 6: Comparison of force-displacement curves of a macro-element with (blue solid line) and without second order effects (green dotted line). The red curves are the rigid block solution (dashed line for the linearized solution)

In order to show the effect of the Young's modulus on the force-displacement curves, a simple numerical example is considered. It is based on a block 1.0 meter long, 2.0 meter high and 1.0 meter thick, subjected to a vertical compression of 0.5 MPa granted by a 500 kN force applied at the top (*b=0.50 m, h=2.00, t=1.00 m, N=500 kN*).

As evident fro Figure 7, for decreasing values of the Young's modulus E the value of the angle θ (assuming $\varphi \cong \theta$) corresponding to cracking condition increases, shifting the maximum value of F towards higher lateral displacements. On the other hand, the increased elastic deformation reduces the maximum value of lateral force as well as the ultimate displacement, so that decreasing E the curves are always below those of stiffer blocks.

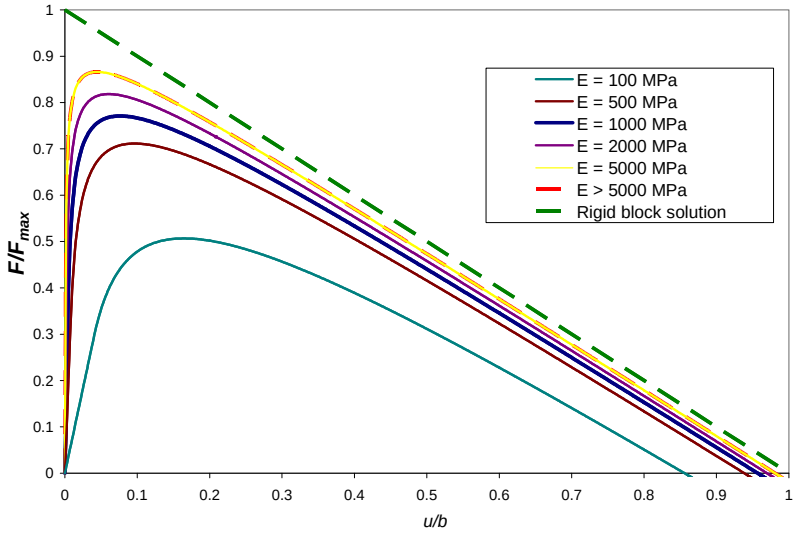


Figure 7: Force-displacement curve of a deformable macro-element for different values of the elastic modulus in compression.

4.2 Effect of limited compressive strength

The consideration of a non-infinite compression strength for the material, f_m, reduces both the value of $F_{\max}$ and the displacement corresponding to null lateral strength.

If the compressive stress is limited in its maximum value to be not greater than f_m, the maximum eccentricity of the axial force N is also limited. Assuming a complete plasticization of the compressed area of the cross section, the vertical translation equilibrium gives:

$$a = \frac{N}{2 \cdot f_m \cdot t}, \tag{17}$$

where a is the half-length of the compressed area of the cross section.

As f_m decreases, the length of the compressed area increases so that the maximum eccentricity of the axial force decreases, hence reducing the arm of the restoring moment. The reduced maximum value of F_{max} is given by

$$F'_{\max} = \frac{N(b-a)}{h} = F_{\max}\left(1 - \frac{N}{2 \cdot f_m \cdot b \cdot t}\right) \tag{18}$$

and the displacement corresponding to null lateral force decreases to

$$u'_0 = b - a = b\left(1 - \frac{N}{2 \cdot f_m \cdot b \cdot t}\right). \tag{19}$$

As shown in Figure 8, when a low value of f_m is considered, the resulting pushover curve has always lower strength than those obtained for higher values of compressive strength for corresponding displacements and it is limited by the corresponding linearized rigid body solution.

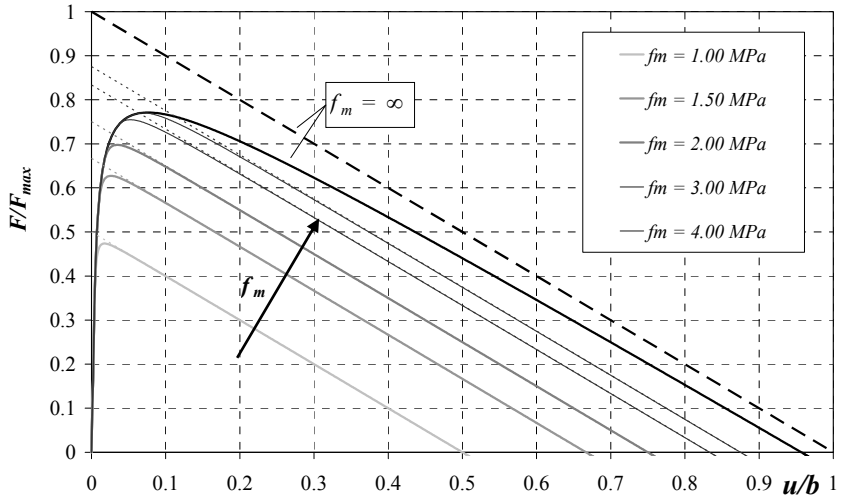


Figure 8: Comparison of force-displacement curves for a deformable macro-element obtained different values of f_m. The dashed lines correspond to the corresponding linearized rigid body solution.

5 SIMULATION OF AN IN-PLANE CYCLIC TEST ON A MASONRY WALL

The macro-element can easily reproduce the behaviour of a masonry panel during a static test (e.g. [12]); the second order correction can improve the simulation of slender panels where rocking effects involve larger displacements.

The test results reported in the following are from the testing campaign performed within the EC-FP6 ESECMaSE Project (www.esecmase.org) at the EUCENTRE Laboratory [1]. The considered specimen was a calcium-silicate masonry wall 175 mm thick, 2.5 m high and 1.25 m long, made with thin layer mortar bed- and head-joints. A vertical compression stress of 1.0 MPa was applied and several quasi-static displacement cycles were imposed to the top beam under double fixed boundary conditions.

Based on the experimental results, the macro-element parameters have been calibrated to reproduce the test results. The values are reported in the Table 1.

E [MPa]	G [MPa]	ρ [kg/m^3]	f_m [MPa]
18000	6000	1900	7.5

Table 1: Macro-element model parameters identified for the EsecMASE test CS05 [1][9]

Figure 9 shows the fair agreement between experimental and numerical results achieved considering the second order effects, which definitely improve the corresponding results from first order simulation in case of larger displacements.

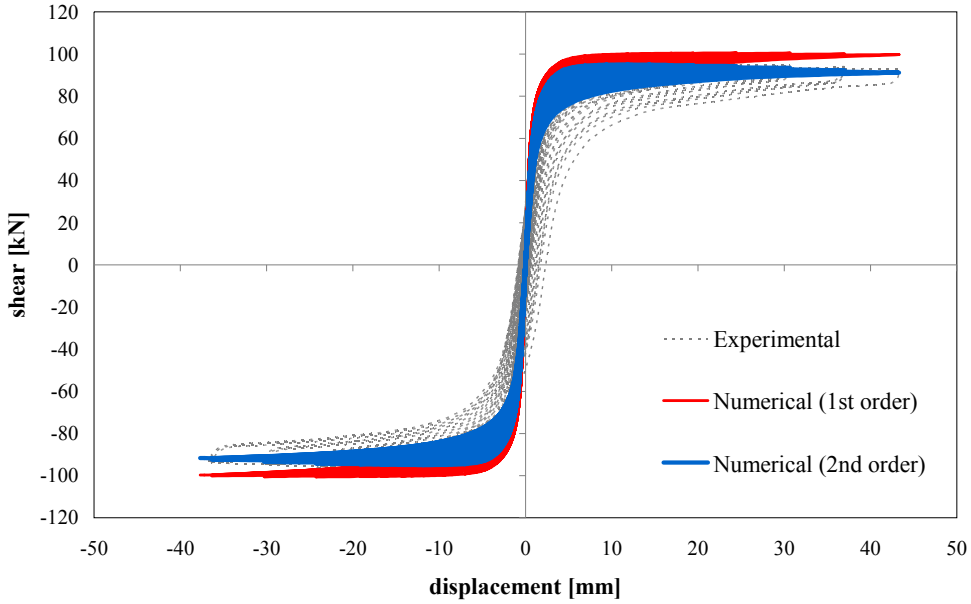


Figure 9. Comparison of the force-displacement curves obtained from in-plane cyclic test (grey dashed line) and numerical simulation with (blue) and without (red) second order effects.

6 DYNAMIC RESPONSE OF A RIGID BLOCK

The macro-element model was specifically developed to be used in dynamic simulation for seismic assessment of in-plane masonry walls [13]. The second order effect improvement can be useful to reproduce the behaviour under strong earthquake where great displacements are expected. In the following, the results obtained with the macro-element are compared to the classical theory of rocking of rigid blocks [14]. According to the Housner model [14] the free vibrations of a rigid block starting from an initial rotation around the bottom right corner (named *O*) can be expressed by the dynamic motion equation:

$$I_0 \frac{\partial^2 \vartheta}{\partial t^2} = -NR \sin(\alpha - \vartheta) \tag{20}$$

where I_0 is the moment of inertia around *O* and no energy dissipation is considered. According to the Housner's solution, assuming small angle both α and θ the equation becomes:

$$\begin{aligned} \theta'' - p^2 \vartheta &= -p^2 \alpha \\ p^2 &= NR / I_0 \end{aligned} \tag{21}$$

Assuming the initial condition $\theta = \theta_0$ *and* $\theta' = 0$ *for* $t = 0$ the analytical solution is expressed by

$$\theta = \alpha - (\alpha - \theta_0) \cosh pt \tag{22}$$

When the system falls back to the vertical position the rotation centre changes and the solution may be already working but the rotation verse of the two angle has to be inverted (a

symmetric solution around the point where θ=0). If the impact is assumed perfectly elastic no energy is dissipated due to the impact, the motion is periodic and its period is

$$T = \frac{4}{p}\cosh^{-1}\left(\frac{1}{1-\theta_0/\alpha}\right). \tag{23}$$

A very slender block, 0.2 m long, 0.1 m thick and 2.0 m high, with density equal to 1000 kg/m^3 (i.e. N = 392.4 N) is modelled using the macro-element with second order effects. According to the adopted notation b = 0.1 m, h = 1.0 m and α = 0.0997. The mass is equal to 40 kg and the moment of inertia is equal to 13.47 kg·m^2 around the centre of gravity and to 53.87 kg·m^2 around the bottom corner, respectively. The block is initially rotated imposing a horizontal translation of *0.02 m* to the center of mass, corresponding to a rotation $\theta_0 \approx 0.02$ rad, and then left oscillating in free vibrations.

As reported in Figure 10, the results are consistent with the analytical solution as shown and it can be noticed that the first order solution underestimates the period of vibration, while the second order solution provides results close to the ideal solution described by eqn. (22).

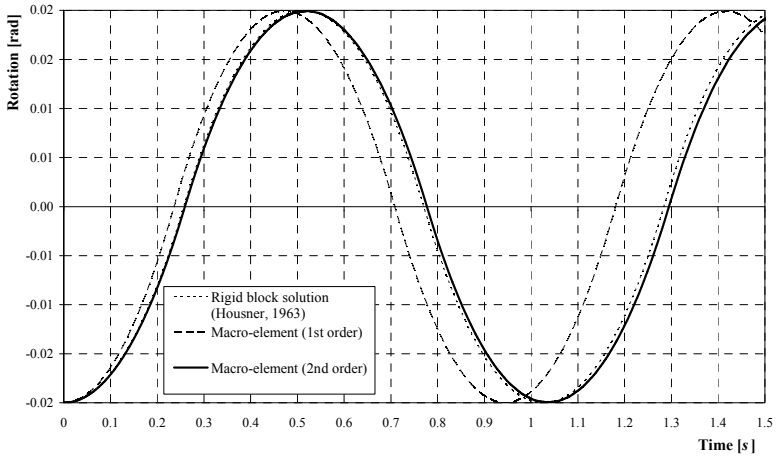


Figure 10: Rotation – time curves in analytical and numeric simulation.

In order to confirm the period prevision for different initial rotations, a comparison is reported in Figure 11. The left part of the figure show the rotation time-histories obtained for different values of relative initial rotation, while the right part of the figure illustrates the good matching between numerically obtained period values and the trend describe by eqn. (24)

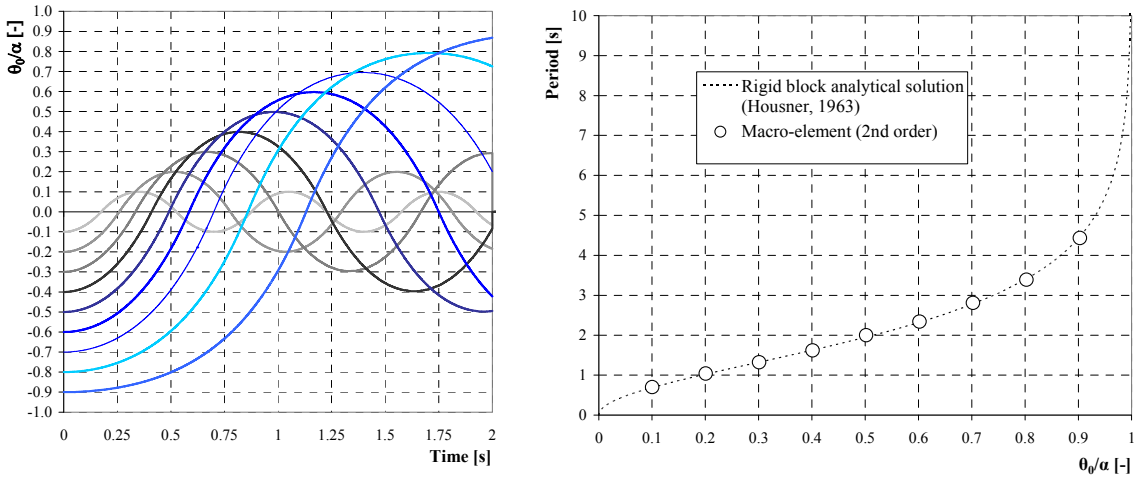


Figure 11: Left: free vibration curves of macro-elements with imposed initial rotation. Right: comparison of numerically derived vibration periods and analytical rigid block solution [14].

7 CONCLUSIONS

In this paper a modified two-dimensional macro-element model which accounts for second order effects in the analysis of blocks and/or masonry walls is presented.

The comparison of static and dynamic analysis results against experimental results and theoretical solutions confirmed that the upgraded model is able to capture the main aspects of the response of single blocks or masonry walls with rocking behaviour.

Future developments of the model will necessarily be oriented to include energy dissipation effects occurring in dynamic response.

The availability of this improved macro-element will be potentially useful for the study of out-of-plane and local failure modes occurring in masonry buildings during seismic events.

ACKNOWLEDGEMENTS

This work has been partially developed within the framework of the Eucentre Executive Project 2012-14 e3 “Seismic vulnerability of masonry buildings” and the Reluis Executive Project 2009-13 AT1-1-1 “Evaluation of the vulnerability of masonry buildings, historical centres, cultural heritage” both funded by the Italian Department of Civil Protection.

REFERENCES

[1] G. Magenes, P. Morandi, and A. Penna, In-plane cyclic tests of calcium silicate masonry walls, *Proceedings of the 14th Intl. Brick/Block Masonry Conference*, Sydney, Australia, 2008.

[2] G. Magenes, A. Penna A. Seismic design and assessment of masonry buildings in europe: recent research and code development issues, *Proceedings of the 9th Australasian Masonry Conference,* Queenstown, New Zealand, 2011.

[3] M.C. Griffith, G. Magenes, G. Melis, L. Picchi, Evaluation of out-of-plane stability of unreinforced masonry walls subjected to seismic excitation, *Journal of Earthquake Engineering*, Vol. 7, SI 1, 141-169, 2003.

[4] L. Sorrentino L., R. Masiani, M.C. Griffith, The vertical spanning strip wall as a coupled rocking rigid body assembly, *Structural Engineering and Mechanics*, 29 (4) , pp. 433-453, 2008.

[5] O. Al Shawa, G. de Felice, A. Mauro, L. Sorrentino, Out-of-plane seismic behaviour of rocking masonry walls, *Earthquake Engineering and Structural Dynamics*, 41 (5) , pp. 949-968, 2012.

[6] D. D'Ayala, Y. Shi, Modeling masonry historic buildings by multi-body dynamics, International Journal of Architectural Heritage 5 (4-5) , pp. 483-512, 2011.

[7] NTC08 Decreto Ministeriale 14 Gennaio 2008: "Norme tecniche per le costruzioni," Ministero delle Infrastrutture. S.O. n.30 alla G.U. del 4.2.2008, No. 29, 2008.

[8] L. Gambarotta and S. Lagomarsino, On the dynamic response of masonry panels, *Proc. of the National Conference "Masonry Mechanics Between Theory and Practice"*, Messina, Italy, 1996 (in Italian).

[9] A. Penna, S. Lagomarsino, A. Galasco, A nonlinear macro-element model for the seismic analysis of masonry buildings. *Earthquake Engineering and Structural Dynamics*, 2013 (in press).

[10] S. Lagomarsino, A. Penna, A. Galasco, S. Cattari, TREMURI program: an equivalent frame model for the nonlinear seismic analysis of masonry buildings. *Submitted to Engineering Structures*, 2013.

[11] L. Gambarotta, S. Lagomarsino, Damage models for the seismic response of brick masonry shear walls. Part II: the continuum model and its applications. *Earthquake Engng Struct. Dynamics* 1997; 26: 441-462.

[12] A.A. Costa, A. Penna, G. Magenes, Seismic performance of Autoclaved Aerated Concrete (AAC) masonry: from experimental testing of the in-plane capacity of walls to building response simulation, *Journal of Earthquake Engineering*, 15(1): 1-31, 2011.

[13] A. Penna, M. Rota, A. Mouyiannou, G. Magenes, Issues on the use of time-history analysis for the design and assessment of masonry structures, *Proc. 4th ECCOMAS Thematic Conference on Computational Methods in Structural Dynamics and Earthquake Engineering*, *COMPDYN 2013,* M. Papadrakakis, V. Papadopoulos, V. Plevris (eds.), Kos Island, Greece, 2013.

[14] G. W. Housner, The behaviour of inverted pendulum structures during earthquakes. *Bulletin of the Seismological Society of America*, Vol 53, No. 2, pp 403-417, 1963.

COMPDYN 2013
4th ECCOMAS Thematic Conference on
Computational Methods in Structural Dynamics and Earthquake Engineering
M. Papadrakakis, V. Papadopoulos, V. Plevris (eds.)
Kos Island, Greece, 12–14 June 2013

A 2-DOF MODEL FOR THE DYNAMIC ANALYSIS OF UNREINFORCED MASONRY WALLS IN OUT-OF-PLANE BENDING

R. Gabellieri[1], L. Landi[1], and P.P. Diotallevi[1]

[1] Department DICAM – University of Bologna
Viale Risorgimento, 2 – 40136 Bologna - Italy
e-mail: rocco.gabellieri@unibo.it, l.landi@unibo.it, pierpaolo.diotallevi@unibo.it

Keywords: Out-of-Plane Bending, Unreinforced Masonry, Dynamic Analysis, Flexible Diaphragms.

Abstract. *This paper investigates the dynamic behaviour of the external walls of unreinforced masonry historic buildings with flexible diaphragms subjected to out-of-plane bending. The influence of diaphragms flexibility on the displacement capacity and demand of walls in out-of-plane bending has been studied by means of dynamic analyses with a simplified two-degrees-of-freedom model (2DOF). The wall has been modelled as an assemblage of two rigid bodies connected by an intermediate hinge and restrained at the top by a spring: the damping has been modelled through the introduction of the coefficient of restitution. The equations of motion of the 2DOF system have been derived and integrated in the time domain. Dynamic analyses of a set of walls with Gaussian impulse and recorded ground motions have been performed in order to compare the response of the simply supported wall with the one of the wall with an elastic spring at the top.*

1 INTRODUCTION

The observation of the damages produced by earthquakes on historical unreinforced masonry buildings pointed out that out-of-plane collapses of the external walls are frequent and very dangerous even in terms of loss of human lives. Historical buildings are in fact characterized by weak connections between the different structural elements and tend therefore to exhibit local collapses before global ones. During earthquakes single parts separate from the rest of the building, often behaving as quite independent structural elements. The study of the behaviour of such mechanisms is then essential and has been undertaken by many authors in the recent years. Different approaches have been proposed, like static, kinematic or dynamic analyses, elasto-plastic, no-tension or rigid models but the experimental tests are still relatively few and have been concentrated on the simplest failure modes because of their simpler reproducibility and interpretation (parapet wall or simply supported wall).

Housner work [1] represented the basis of the dynamic studies on the wall as a single rigid block: other studies followed his hypotheses and delved into this topic, but only recently some analytical and experimental studies [2-8] highlighted the necessity of dynamic analysis in order to understand the real behaviour of walls in out-of-plane bending and to assess, without an over conservative approach, the vulnerability against earthquake action. They pointed out the fact that out-of-plane failures of walls are caused essentially by an excessive displacement demand rather than force or acceleration demand and that static methods, focused on the comparison between forces and resistance, cannot then catch some specific aspects related to the dynamic behaviour. Quite all the past works considered simplified hypotheses about the interaction of the wall with the rest of the building, assuming diaphragms as rigid and reducing therefore the complexity of the dynamic problem and the number of the degrees of freedom [9, 10]. The path of the seismic action from the ground to the out-of-plane walls implies a filtering effect of the shear walls and diaphragm response [11]: when the diaphragms cannot be considered as rigid, like in most historical buildings, the inputs to the out-of-plane walls at adjacent floors have different amplitude, phase and frequency content. In this case it is necessary to consider multiple-degrees-of-freedom instead of the usual single-degree model.

There are really few studies [12, 13] that take directly into account the influence of flexibility of diaphragms on the displacement capacity and demand. Extending some formulations proposed by other authors [2, 7, 12] a simplified 2DOF model has been developed to analyse the dynamic out-of-plane behaviour of a single wall with the hypothesis of flexible diaphragm [14]. The equations of motion of the wall have been derived and an algorithm for their numerical integration has been developed. The characteristics of the algorithm and the main results of its application are presented.

2 DESCRIPTION OF THE MODEL

A simplified 2DOF model has been developed to analyse the dynamic out-of-plane behaviour of a single wall, with an intermediate hinge and an elastic spring at the top. The wall, as shown in Fig. 1, is modelled as an assemblage of two rigid bodies, a lower and an upper part, each one free to rotate around the intermediate hinge. In Fig. 1 W_1 and W_2 are the weights of the lower and upper part of the wall, W_d is the overburden load from the diaphragm, K_d is the translational stiffness of the spring at the top, that simulates the in-plane stiffness of the upper diaphragm and is considered perfectly elastic, q_1 e q_2 are the rotations, respectively of the lower and the upper portion of the wall related to the vertical axis, that have been assumed as independent variables. The intermediate hinge has been assumed at the mid-height of the wall and the load W_d is supposed to be applied at the middle of the thickness, in order to reproduce

the hypotheses made by Doherty in his study on the simply supported wall [2] and to compare the results obtained by Doherty with the ones of the present study.

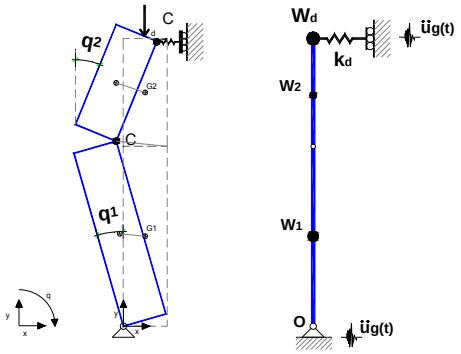


Figure 1: 2DOF model of the wall in out-of-plane bending.

3 EQUATIONS OF MOTION

The equations of motion of the 2DOF system have been derived by applying Lagrange equations, considering the kinetic energy due to the translation of the masses and to the rotation of the two parts of the wall around the respective centroids and the potential energy due to the translational spring at the top and to the contribution of the gravitational loads. The above mentioned quantities have been calculated with the assumption of small displacements.

3.1 Possible geometric configurations

The equations of motion are highly non linear because of the sudden change of the point of rotation at the base and at the intermediate hinge. There are four different conditions described by four corresponding sets of equations (see Fig. 2).

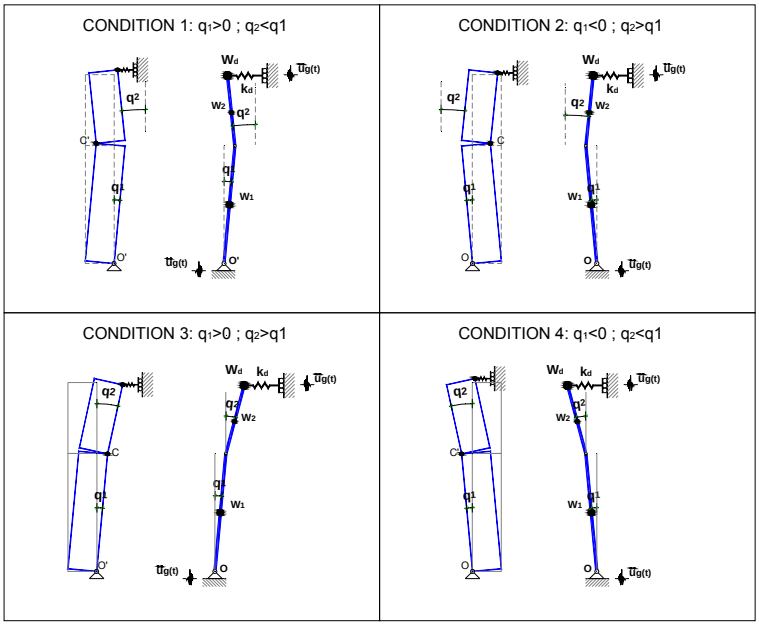


Figure 2: The four possible geometric configurations.

The passage from one condition to another is determined by an impact at the bottom or at the intermediate hinge associated with the change of the centre of rotation (see Fig. 3).

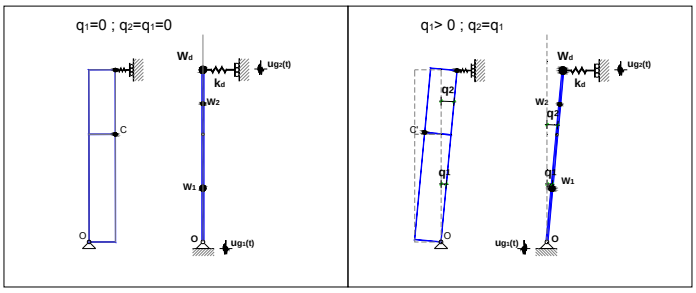


Figure 3: Impacts at the bottom hinge (left, q_1=0) and at the intermediate hinge (right, q_1= q_2).

Every time q_1 passes through the zero, there is an impact at the bottom and a change of the centre of rotation (O to O' or O' to O): similarly, every time $q_1 = q_2$, there is an impact at the intermediate hinge and a change of the centre of rotation (C to C' or C' to C).

3.2 Energy dissipation

Following the Housner model [1], the dissipation of energy is concentrated at every impact at the base of the wall and is modelled through the introduction of the coefficient of restitution, e_r <1, that relates the velocities after each impact to those immediately before, reproducing the loss of kinetic energy at each impact.

3.3 Equations of motion

Assuming h for the total height of the wall, g for the gravity acceleration, W_1=W_2, because of the position of the intermediate hinge at the mid-height of the wall, and the clockwise rotations as positive, the equations of motion are:

$$\begin{bmatrix} m_{11} & m_{12} \\ m_{21} & m_{22} \end{bmatrix} \cdot \begin{bmatrix} \ddot{q}_1 \\ \ddot{q}_2 \end{bmatrix} + \begin{bmatrix} k_{11} & k_{12} \\ k_{21} & k_{22} \end{bmatrix} \cdot \begin{bmatrix} q_1 \\ q_2 \end{bmatrix} = \begin{bmatrix} p'_{eff,1}(t) + A_i \\ p'_{eff,2}(t) + B_i \end{bmatrix} \tag{1}$$

The coefficients of the mass matrix are reported in Eq. (2):

$$\begin{cases} m_{11} = \left[\dfrac{W_1}{3} + \dfrac{W_d}{4} \right] \cdot \dfrac{h^2}{g} \\ m_{12} = m_{21} = \left[\dfrac{W_1}{8} + \dfrac{W_d}{4} \right] \cdot \dfrac{h^2}{g} \\ m_{22} = \left[\dfrac{W_1}{12} + \dfrac{W_d}{4} \right] \cdot \dfrac{h^2}{g} \end{cases} \tag{2}$$

The coefficients of the stiffness matrix are reported in Eq. (3):

$$\begin{cases} k_{11} = \left[\dfrac{K_d \cdot h^2}{4} - \dfrac{3}{4} \cdot W_1 \cdot h - W_d \cdot \dfrac{h}{2} \right] \\ k_{12} = k_{21} = \dfrac{K_d \cdot h^2}{4} \\ k_{22} = \left[\dfrac{K_d \cdot h^2}{4} - W_1 \cdot \dfrac{h}{4} - W_d \cdot \dfrac{h}{2} \right] \end{cases} \tag{3}$$

The terms $p_{eff,1}(t)$ and $p_{eff,2}(t)$ represent the contribution due to the ground acceleration. They are reported in Eq. (4):

$$\begin{cases} p'_{eff,1}(t) = -\ddot{u}_g \cdot \left[-3 \cdot W_1 - 2 \cdot W_d\right] \cdot \dfrac{h}{4 \cdot g} \\ p'_{eff,2}(t) = -\ddot{u}_g \cdot \left[-W_2 - 2 \cdot W_d\right] \cdot \dfrac{h}{4 \cdot g} \end{cases} \tag{4}$$

The terms A_i and B_i in Eq. (1) are different in the four conditions: they are expressed in Eqs. (5-8).

Condition 1 ($q_1>0$ and $q_2<q_1$):

$$\begin{cases} A_1 = -\dfrac{3 \cdot W_1}{2} \cdot b - W_d \cdot b \\ B_1 = \dfrac{W_1}{2} \cdot b + W_d \cdot \dfrac{b}{2} \end{cases} \tag{5}$$

Condition 2 ($q_1<0$ and $q_2>q_1$):

$$\begin{cases} A_1 = -\dfrac{3 \cdot W_1}{2} \cdot b - W_d \cdot b \\ B_1 = \dfrac{W_1}{2} \cdot b + W_d \cdot \dfrac{b}{2} \end{cases} \tag{6}$$

Condition 3 ($q_1>0$ and $q_2>q_1$):

$$\begin{cases} A_2 = +\dfrac{3 \cdot W_1}{2} \cdot b + W_d \cdot b \\ B_2 = -\dfrac{W_1}{2} \cdot b - W_d \cdot \dfrac{b}{2} \end{cases} \tag{7}$$

Condition 4 ($q_1<0$ and $q_2<q_1$):

$$\begin{cases} A_4 = +\dfrac{W_1}{2} \cdot b \\ B_4 = +\dfrac{W_1}{2} \cdot b + W_d \cdot \dfrac{b}{2} \end{cases} \tag{8}$$

4 NUMERICAL ALGORITHM

An algorithm for the numerical integration of the sets of the equations of motion in the time domain has been developed: a variable step size Runge-Kutta integration method of 4th-5th order, implemented in Matlab ODE-suite ODE45, has been used. A local error control has been performed at each step of the numerical integration: sufficiently small values of relative tolerance *RelTol* and absolute tolerance *AbsTol* have been assumed ($RelTol=10^{-5}$ and $AbsTol=10^{-10}$). The strong nonlinearity of the set of equations of motion is produced by the sudden change of the sign of the resisting moment of the weights W_1 and W_2 and of W_d about the effective centre of rotation at the bottom and intermediate hinges, corresponding to the sudden change of the position of the hinge at every impact.

$$M_{q_1} = \left[\frac{3}{4} \cdot W_1 \cdot h + W_d \cdot \frac{h}{2}\right] \cdot q_1 + A_i \tag{9}$$

$$M_{q_2} = \left[\frac{W_1}{4} \cdot h + W_d \cdot \frac{h}{2} \right] \cdot q_2 + B_i \tag{10}$$

Eq. (9) and Eq. (10) present the expression of M_{q1} and M_{q2}: M_{q1} is the resisting moment about the bottom hinge O or O' (depending on the actual condition) of the self weight W_1 of the lower part of the wall and of the weights W_2=W_1 and W_d transferred from the upper to the lower part of the wall at the intermediate hinge C or C'; M_{q2} is the resisting moment about the intermediate hinge C or C'(depending on the actual condition) of the weights W_2 and W_d. A_i and B_i are illustrated in Eq. (5), Eq. (6), Eq. (7) and Eq. (8) and represent the resisting moments M_{q1} and M_{q2} when the independent variables q_1 and q_2 are zero.

Fig. 4 shows the diagrams of M_{q1} in the 4 conditions (green and red continuous lines): the blue dotted line represents the diagram of M_{q1} in the hypothesis of rigid behaviour of the wall. Similarly to what proposed in Doherty studies [2], a finite stiffness instead of an infinite stiffness at q_1=0 is assumed, so that the two purple and yellow lines describe the transition from one condition to another at q_1=0. The algorithm follows then these lines instead of the blue ones of the rigid behaviour. The parameters -$D_{12,1}$, -$D_{34,1}$, $D_{34,1}$, $D_{12,1}$ are the values of q_1 at the intersections of the diagrams of M_{q1} in the 4 conditions with the line of finite stiffness. Transitions from condition 1 to 4 or from 4 to 1 and from 2 to 3 or from 3 to 2 take place when an impact at the intermediate hinge occurs (q_1=q_2) and are represented by the vertical black dotted lines.

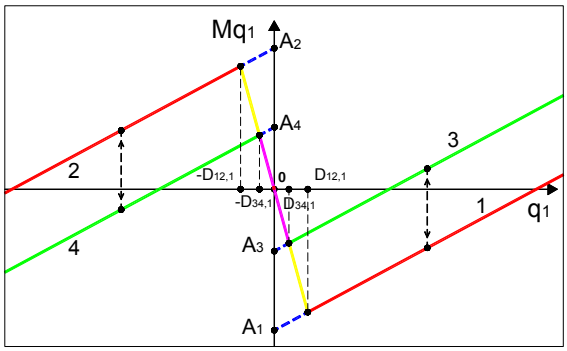


Figure 4: Resisting moment M_{q1} in the 4 conditions.

Fig. 5 shows the diagrams of M_{q2} in the 4 conditions (red continuous lines): the couples of conditions 1 and 4, 2 and 3 have the same diagram. Similarly to the diagram of Fig. 4 an initial finite stiffness is assumed (purple dotted line). The parameters -$D_{12,2}$, $D_{12,2}$ are the values of q_2 at the intersections of the diagrams of M_{q2} in the 4 conditions with the line of finite stiffness. Transitions from conditions 1 or 4 to conditions 2 or 3 or from conditions 2 or 3 to conditions 1 or 4, corresponding to an impact at the intermediate hinge (q_1=q_2), are represented by the vertical black dotted lines, while transitions at q_1=0 do not cause any jump in the diagram.

Defined the initial conditions $q_1(0)$, $q_2(0)$, $\dot{q}_1(0)$, $\dot{q}_2(0)$ the numerical algorithm integrates the equations of motion of the Eq. (1) until the first event: the algorithm can detect the events at the target values of q_1 and q_2: the integration stops when the variable q_1 assumes the values -$D_{12,1}$, -$D_{34,1}$, 0, $D_{34,1}$, $D_{12,1}$ or when the variable q_2 assumes the values -$D_{12,2}$, $D_{12,2}$ or when q_1= q_2. State variables identify the condition corresponding to each time step: the value of these variables at the event defines the condition before the event and allows the algorithm to decide which condition to assume afterwards and which line to follow in Fig. 2 and Fig. 3. Except for the impact for q_1=0, the values of the rotations q_1 and q_2 and the corresponding an-

gular velocities after every event are the same detected at the event. These are the new initial conditions of the differential equations that the algorithm assumes in order to integrate the appropriate equations, depending on the effective initial geometrical configuration of the wall. For q_1=0, the rotations after the impact are the same as the ones before the impact, while the angular velocities of the lower and upper part of the wall are reduced by the restitution coefficient e_r<1.

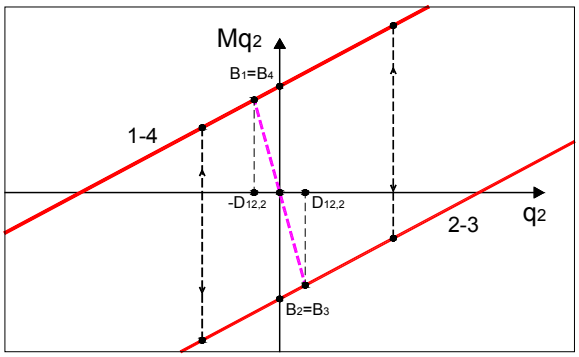


Figure 5: Resisting moment M_{q2} in the 4 conditions.

5 RESULTS OF THE ANALYSES

An algorithm for the integration of the equations of motion of the semi-rigid 1DOF model proposed by Doherty [2] has been implemented to validate the numerical strategy used in the present work and to compare Doherty's results to the ones obtained with the 2DOF model in the case of a very high value of stiffness of the top spring: in that case the top and bottom absolute displacements of the wall tend to be equal and in phase and the behaviour of the 2DOF model should coincide with the one of the simpler 1DOF model. The experimental and analytical results obtained by Doherty showed a good agreement with the 1DOF model developed in the present work. Dynamic analyses with Gaussian and recorded accelerogram inputs have been performed on a set of walls, varying the values of the stiffness K_d at the top and studying its influence on the displacement demand. A coefficient of restitution e_r=0.86 is used both for the 1DOF and for the 2DOF model.

5.1 Set of walls

A set of 3 walls with different characteristics, in terms of maximum resisting force and ultimate displacement in the hypothesis of rigid behaviour (see Table 1 and Fig. 6) has been considered. In Table 1 b is the thickness, h is the height, W is the self weight of the wall, Ψ is the ratio between W_d and W_1, R_{e1} is the rigid threshold resistance and Δ_u is the ultimate displacement, calculated following Doherty formulation [2, 3].

Wall	b [m]	h [m]	Ψ [-]	W [KN/m]	R_{e1} [KN/m]	Δ_u [m]	F_0/W [-]	Δ_u/b [-]
1	0,15	2,5	0	6,622	1,192	0,150	0,180	1,000
2	0,15	2,5	0,5	6,622	1,639	0,138	0,248	0,917
3	0,15	2,5	1	6,622	2,086	0,131	0,315	0,875

Table 1: Example of the construction of one table.

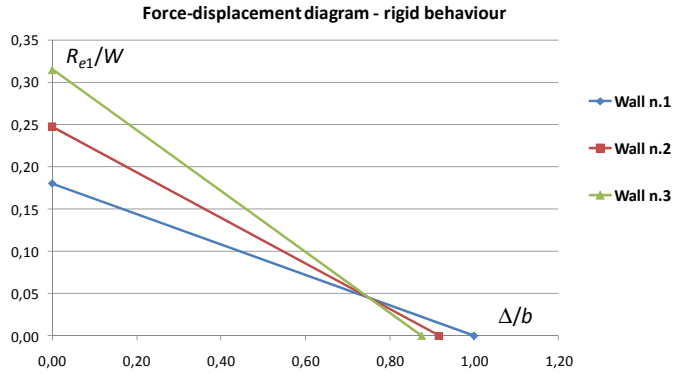


Figure 6: Adimensional force-displacement curves of the 3 walls.

5.2 Semi-rigid 1DOF model

The semi-rigid 1DOF model proposed by Doherty has been implemented. Fig. 7 shows the mid-height acceleration-displacement curve for the rigid (blue dotted line) and semi-rigid model (red line). In Fig. 7 Δ_u is the ultimate displacement, Δ_1 and Δ_2 are displacements related to material properties and to the state of degradation of the mortar joints at the pivot points. The values of Δ_1 and Δ_2 have been assumed in accordance with the proposed formulations of Sorrentino [7] and are expressed in Eq. (11) and Eq. (12).

$$\Delta_1 = 0.05 \cdot \Delta_u \tag{11}$$

$$\Delta_2 = 0.92 \cdot \Delta_1 + 0.21 \cdot \Delta_u \tag{12}$$

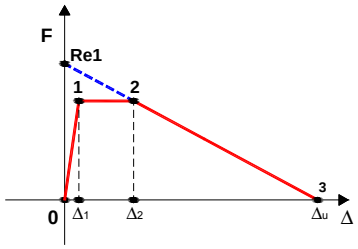


Figure 7: Simply supported wall (1DOF model): mid-height acceleration-displacement curve.

5.3 Gaussian inputs

Gaussian impulse inputs in terms of displacement with duration T_1=1 s and T_2=2 s and variable maximum amplitudes have been used to perform dynamic analyses on the set of walls. 4 different values of the stiffness K_d of the spring at the top in the 2DOF model have been considered (K_d= 1000 KN/m, 100 KN/m, 50 KN/m and 10 KN/m). Fig. 8 shows the displacement time-histories of wall n.1 for Gaussian input with amplitude D_p=40 mm and T_1=1 s for the 1DOF model and 2DOF model: increasing the value of K_d, the response of the 2DOF model tends to reproduce well the response of the 1DOF model, so that the top displacement s_2 becomes close to zero. Diminishing K_d the top displacement s_2 increases. The rotations q_1 and q_2, in opposition of phase in the 1DOF model, become more uncoupled and independent. The mid-height displacement s_1 increases passing from K_d=1000 KN/m to K_d=50 KN/m, but begins to decrease when K_d=10 KN/m. For that value of K_d the top displacement s_2 becomes larger than the mid-height displacement s_1 and s_2 and s_1 begin to be in phase.

Table 2 shows the maximum displacements s_1 and s_2 of walls n.1, 2 and 3 for Gaussian impulse inputs with duration T_1=1 s and different amplitudes. Fig. 9 shows the variation of the following quantities as a function of the spring stiffness for the wall n.1: the ratio between the

displacement s_1 obtained with the 2DOF model and the one derived with the 1DOF model, the ratio s_2/s_1 obtained with the 2DOF model.

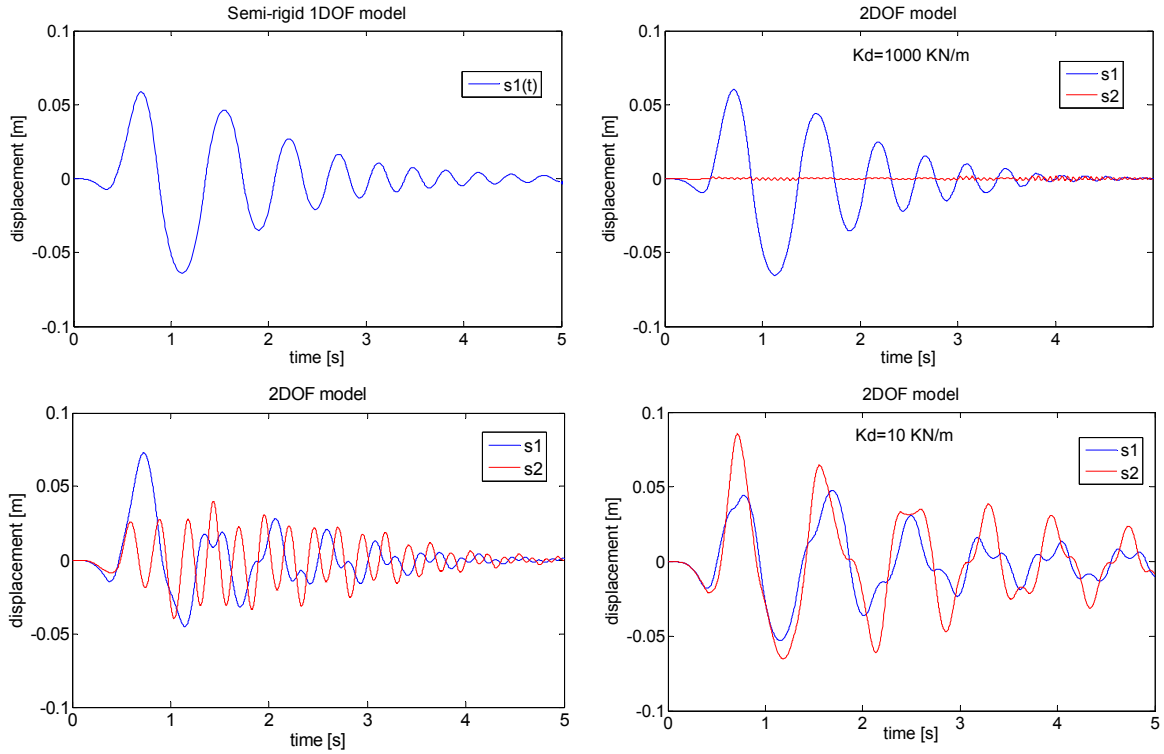


Figure 8: Wall n.1: displacement time-histories for 1DOF and 2DOF models with different values of K_d; s_1=mid-height displacement, s_2=top displacement; gaussian input with amplitude D_p=40 mm and duration T_1=1 s.

Wall	Impulse duration	Impulse amplitude	Maximum displacement $\|\Delta\|_{max}$								
			1DOF	2DOF							
				K_d=1000 KN/m		K_d=100 N/m		K_d=50 KN/m		K_d=10 N/m	
		[m]	s_1 [m]	s_1 [m]	s_2 [m]	s_1 [m]	s_2 [m]	s_1 [m]	s_2 [m]	s_1 [m]	s_2 [m]
1	T_1=1 s	0,040	0,064	0,066	0,002	0,069	0,021	0,073	0,040	0,053	0,085
2	T_1=1 s	0,040	0,040	0,613	0,003	0,093	0,036	0,058	0,047	0,033	0,073
3	T_1=1 s	0,050	0,033	0,068	0,008	0,056	0,056	0,034	0,063	0,030	0,053

Table 2: Gaussian input: maximum mid-height and top displacements s_1 and s_2; comparison between 1DOF and 2DOF results.

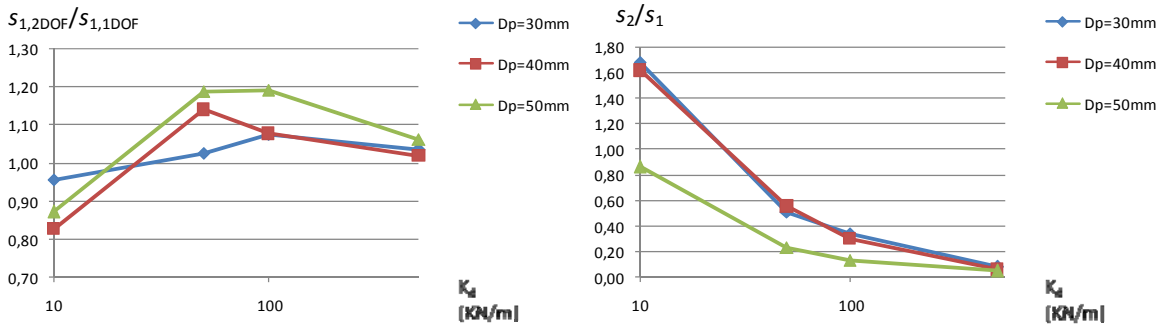


Figure 9: Wall n.1: ratio between the displacements s_1 obtained with the 2DOF model and the one derived with the 1DOF model, ratio s_2/s_1 obtained with the 2DOF model.

The trend described for wall n.1 in Fig. 8 is confirmed by the results shown in Table 2 and Fig. 9. Increasing the value of K_d the top displacement s_2 becomes close to zero, while the mid-height displacement s_1 increases until a specific value of K_d and then diminishes, so that s_2 becomes greater than s_1. With a significant overburden load (wall n.3) s_1 decreases while K_d gets smaller. The trend for Gaussian inputs with T_2=2 s is similar to the one with T_1=1 s.

5.4 Recorded ground motions

Six recorded ground motions have been assumed as input to perform dynamic analyses on the 3 walls. Table 3 describes the characteristics of the considered records. Fig. 10 shows the displacement time-histories of wall n.1 for El Centro record, scaled at 50% of PGA, for the 1DOF model and for the 2DOF model: for the value of K_d =500 KN/m, the response of the 2DOF model tends to reproduce the response of the 1DOF model, even better than for Gaussian inputs. Diminishing K_d the top displacement s_2 increases and has a significant magnification for K_d=50 KN/m, when it becomes quite 3 times the value for K_d=500 KN/m. For K_d=5 KN/m the top displacement s_2 becomes greater than the mid-height displacement s_1.

Event	Year	Station	Id.	Component	PGA
Imperial Valley	1940	El Centro	Elce	S00E	0.348 g
Friuli	1976	Tolmezzo	Tolm	270	0.315 g
Irpinia	1980	Sturno	Stur	270	0.358 g
Loma Prieta	1989	Capitola	Loma	000	0.529 g
Northridge	1994	Sylmar Hospital	Sylm	360	0.843 g
Kobe	1995	KJMA	Kjmh	000	0.821 g

Table 3: Recorded accelerograms used in the analyses.

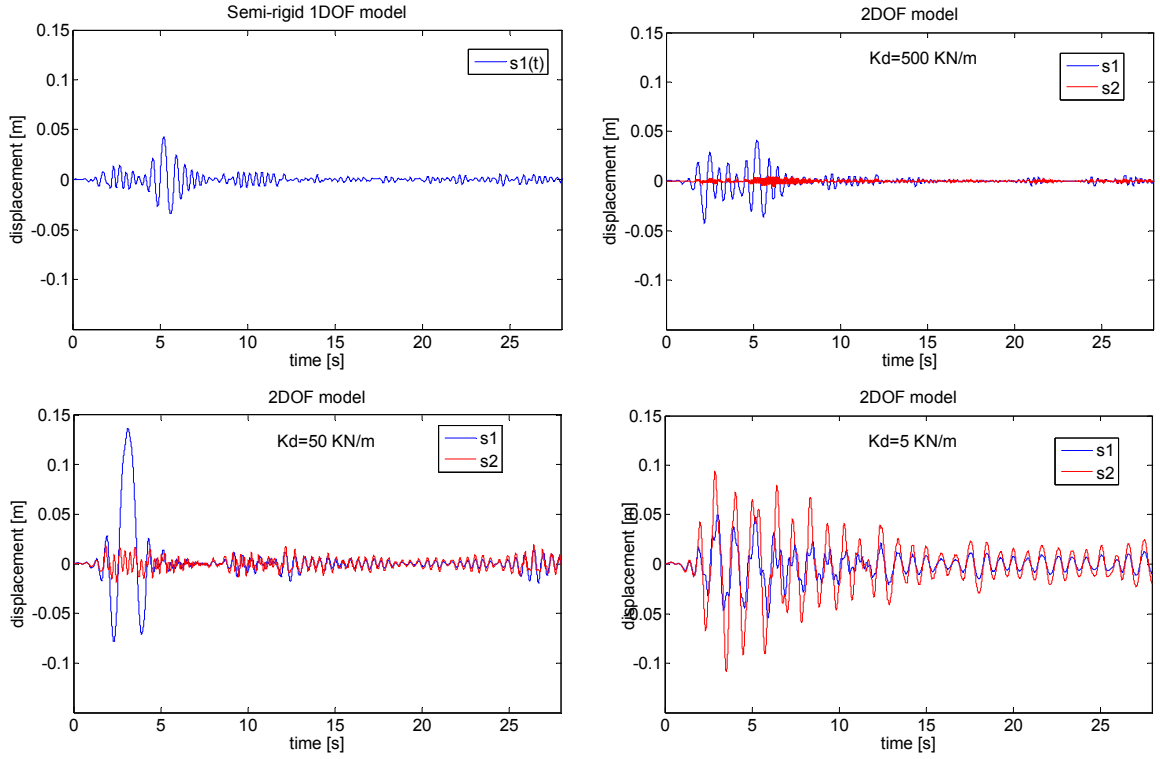


Figure 10: Wall n.1: displacement time-histories for 1DOF and 2DOF models with different values of K_d; s_1=mid-height displacement, s_2=top displacement; El Centro recorded ground motion scaled to 50% of PGA.

Wall 1		Maximum displacement $\|\Delta\|_{max}$						
		1DOF	2DOF					
Accelerogram	% PGA		K_d=500 KN/m		K_d=50 KN/m		K_d=5 KN/m	
		s_1 [m]	s_1 [m]	s_2 [m]	s_1 [m]	s_2 [m]	s_1 [m]	s_2 [m]
Elce	50	0,043	0,043	0,004	0,137	0,019	0,050	0,109
Tolm	100	0,094	0,094	0,004	0,114	0,036	0,048	0,095
Stur	80	0,053	0,048	0,005	0,035	0,023	0,082	0,074
Loma	50	0,031	0,034	0,004	0,039	0,026	0,056	0,078
Sylm	35	0,045	0,047	0,005	0,057	0,028	0,077	0,082
Kjmh	20	0,063	0,068	0,004	0,046	0,035	0,060	0,114

Table 4: Recorded ground motions: maximum mid-height and top displacements s_1 and s_2; comparison between 1DOF and 2DOF results.

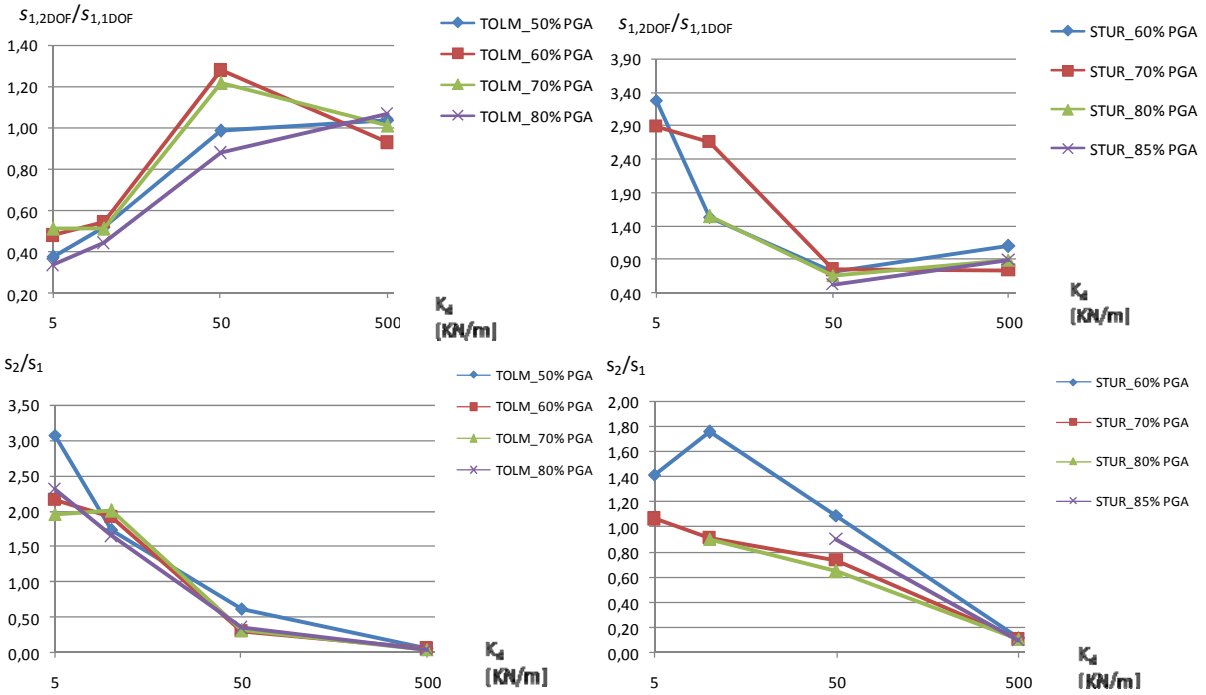


Figure 11: Wall n.1: ratio between the displacement s_1 obtained with the 2DOF model and the one derived with the 1DOF model (upper row), ratio s_2/s_1 obtained with the 2DOF model (lower row).

Table 4 shows the maximum displacements s_1 and s_2 of wall n.1 for recorded ground motions scaled at different percentage of PGA. Fig. 11 shows the variation of the same quantities illustrated in Fig. 9 as a function of the spring stiffness for two earthquake records.

The trend described in Fig. 10 is partially confirmed in Table 4 and Fig. 11, even if it is less regular for different ground motions. Increasing the value of K_d the top displacement s_2 becomes close to zero; the mid-height displacement s_1 does not follow a common trend for all the records. Anyway for very high values of K_d it tends to the value derived with the 1DOF model. With high values of K_d the collapse of the wall takes place because of excessive mid-height displacement demand as in the case of simply supported wall (1DOF). With small values of K_d, s_2 becomes greater than s_1 and collapse takes place for excessive top displacement demand, similarly to the parapet wall. Results obtained for wall n. 2 and n. 3 are similar to the ones obtained for wall n. 1.

5.5 Observations

An extension of the present study will be necessary to better investigate the influence of diaphragm flexibility on the out-of-plane behaviour of walls. It is anyway already possible to highlight that neglecting diaphragm flexibility can be either over conservative or can lead to a significant and dangerous underestimation of the displacement demand on the wall, depending on the characteristics of the input and of the wall. The flexibility of the diaphragms has in fact a strong influence on the displacement demand and appears to be an important parameter to be included in the dynamic analyses of out-of-plane behaviour of unreinforced masonry walls.

6 CONCLUSIONS

The present work is an attempt to extend some formulations and concepts proposed by other authors for the parapet wall and for the simply supported wall to the case of the out-of-plane bending of walls in buildings with flexible diaphragms. The results of dynamic analyses on a set of walls with Gaussian impulse or with recorded accelerogram inputs has been investigated: the stiffness of the diaphragm has a strong influence on the displacement demand of the walls, even if it seems that it is not possible to define a general rule to predict such demand without performing dynamic analyses. The hypotheses made in developing the model and the numerical algorithm need to be validated by experimental tests. Future developments could be the modelling of the inelastic behaviour of the spring at the top and the definition of a 3-degrees-of-freedom model that includes the in-plane walls.

REFERENCES

[1] G.W. Housner, The behavior of inverted pendulum structures during earthquakes. *Bulletin of the Seismological Society of America*, **53**, 403-417, 1963.

[2] K. Doherty, An investigation of the weak links in the seismic load path of unreinforced masonry buildings. PhD Thesis. Department of Civil and Environmental Engineering, The University of Adelaide, 2000.

[3] K. Doherty, M.C. Griffith, N.T.K. Lam, J. Wilson, Displacement-based seismic analysis for out-of-plane bending of unreinforced masonry walls. *Earthquake Engineering and Structural Dynamics*, **31**, 833-850, 2002.

[4] M.C. Griffith, G. Magenes, G. Melis, L. Picchi, Evaluation of out of plane stability of unreinforced masonry walls subjected to seismic excitation. *Journal of Earthquake Engineering*, **7**, 141-169, 2003.

[5] M.C. Griffith, N.T.K. Lam, J. Wilson, K. Doherty, Experimental investigation of Unreiforced Brick Masonry Walls in Flexure. *Journal of Structural Engineering ASCE*. **130**, 423-432, 2004.

[6] N.T.K. Lam, M.C. Griffith, J. Wilson, K. Doherty, Time-history analysis of URM walls in out-of-plane flexure. *Engineering Structures*, **25**, 743-754, 2003.

[7] L. Sorrentino, Dinamica di muri sollecitati fuori del piano come sistemi di corpi rigidi. PhD Thesis, University of Rome "La Sapienza", Italy, 2003.

[8] L. Sorrentino, R. Masiani, M.C. Griffith, The vertical spanning strip wall as a coupled rocking rigid body assembly, *Structural Engineering and Mechanics*, **29**, 433-453, 2008.

[9] A. Tena-Colunga, D.P. Abrams, Seismic behavior of structures with flexible diaphragms. *Journal of Structural Engineering ASCE.* 122(4), 439-445, 1996.

[10] S. Kim, D.W. White, Linear static analysis of low-rise buildings with flexible diaphragms using the structural separation method, *Engineering Structures*, **26**, 83–9, 2004.

[11] A. Menon, G. Magenes, Out-of-Plane Seismic Response of Unreinforced Masonry. Definition of Seismic Input. Research Report Rose 2008/04, Iuss Press, Pavia, 2008.

[12] C.C. Simsir, Influence of diaphragm flexibility on the out-of-plane dynamic response of unreinforced masonry walls. PhD Thesis, University of Illinois at Urbana Champagne, Illinois, USA, 2004.

[13] C.C. Simsir, M.A. Aschheim, D.P. Abrams, Out-of-plane dynamic response of unreinforced masonry bearing walls attached to flexible diaphragms. *13th World Conference on Earthquake Engineering*. Vancouver, Canada, 2004.

[14] R. Gabellieri, P.P. Diotallevi, L. Landi, Effect of Diaphragm Flexibility on the Dynamic Behaviour of Unreinforced Masonry Walls in Out-of-Plane Bending. *15th World Conference on Earthquake Engineering (15WCEE),* Lisbon, Portugal, September 24-28, 2012.

COMPDYN 2013
4th ECCOMAS Thematic Conference on
Computational Methods in Structural Dynamics and Earthquake Engineering
M. Papadrakakis, V. Papadopoulos, V. Plevris (eds.)
Kos Island, Greece, 12–14 June 2013

APPLCATION OF GENERALIZED PLASTICITY MODEL IN SQUARE CFT COLUMN ANALYSIS

Svetlana M. Kostic[1], Prof. Filip C. Filippou[2], and Prof. Biljana Deretic-Stojanovic[1]

[1] Faculty of Civil Engineering, University of Belgrade
Bulevar Kralja Aleksandra 73, Belgrade, Serbia
e-mail: {svetlana, biljads}@grf.bg.ac.rs

[2] Department of Civil and Env. Engineering, University of California
Berkeley, CA 94720-1710
filippou@ce.berkeley.edu

Keywords: CFT columns, Nonlinear Analysis, Beam-Column Element, Generalized Plasticity, Resultant Plasticity.

Abstract. *In the paper, an efficient three-dimensional concentrated plasticity nonlinear beam-column element is used for the simulation of the response of square CFT columns. The element adopts the concept of the generalized plasticity material model for the section resultant – element deformation relation and has plastic hinges located at the ends of the element and described with yield and limit surfaces. Determination of the adequate element parameters which are essential for a successful description of the CFT member behavior is discussed. Among these parameters, most important are the stiffness and yield surface parameters.*

1 INTRODUCTION

The use of composite concrete-filled steel tubes (CFT), see Figure 1, for the columns of frame structures is in increasing use due to advantages they offer over steel or reinforced concrete members: high stiffness and strength, increased ductility, delayed or prevented buckling, etc. Because of their highly nonlinear behavior, the adequate numerical model needs to address number of phenomena such as: nonlinear steel and concrete material behavior, buckling of steel tube and sleep at the steel-concrete interface.

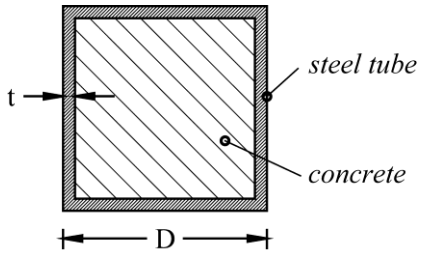


Figure 1: Square concrete filled tube (CFT).

To date, although a number of experimental studies have been performed on behavior of CFT columns [1], not many analytical models have been developed. Few researchers studied the ultimate strength of a composite cross-section under biaxial bending in presence of axial force [2, 3]. Besides continuum finite element models [4] which may be appropriate for detailed analysis of a part of a structure (e.g. joints), frame beam/column elements are still primarily used for the CFT member and composite frame analysis. Hajjar and Gourley [5, 6] developed a concentrated plasticity 3D finite element for the simulation of a CFT beam-column behavior. The plastic hinges at the element ends are described by a two-surface, bounding surface model in the stress-resultant P-M_y-M_z space. Iu, Bradford and Chen [3] developed a concentrated plasticity element with axial and rotational springs at element ends suitable for modeling composite beam-column members. It describes non-linear elastic-plastic with strain-hardening material behavior with gradual transition between elastic and plastic domain, under the interaction of axial force and two bending moments. More accurate, but also computationally more involving are distributed plasticity elements. Fiber-based distributed plasticity elements have proven to be successful in simulation of the hysteretic response of steel, concrete and composite structures [7-9]. For modeling of CFT columns, few proposals have been made [1, 8, 10]. They also account for geometrical nonlinearities and an interlayer sleep at the steel-concrete interface.

The purpose of this study is to show that the previously developed non-linear beam-column element [11] used for static and dynamic analysis of steel frames, with the proper choice of element parameters, can also be successfully used for modeling CFT column behavior. The element is of concentrated plasticity type and based on the principles of generalized plasticity material model [12]. It accounts for the interaction of the axial force and bending moments about the principal axes of the cross-section, gradual yielding of the cross section and the hardening behavior. With the implemented return mapping algorithm, it is computationally very efficient.

2 BASICS OF ELEMENT FORMULATION

More details about the element used in this study, named GP element, can be found in [11]. Here will be given only the basics of the element formulation. The element is of concentrated plasticity type and has two zero-length plastic hinges at element ends (Figure 2). It adopts

concept of the generalized plasticity material model [12] for the section resultant (forces) – element deformation relations. The plastic hinges are described by the yield function *f*, which encloses the elastic region, and the limit function *F*, which separates admissible from inadmissible stress-resultant states (see Figure 2). The basic forces of a three-dimensional frame element are **q**, and the corresponding deformations are denoted with **v** as shown in Figure 3 for the 3D case. Torsion is considered as elastic and uncoupled from the axial and flexural degrees of freedom and, thus, not shown in Figure 3.

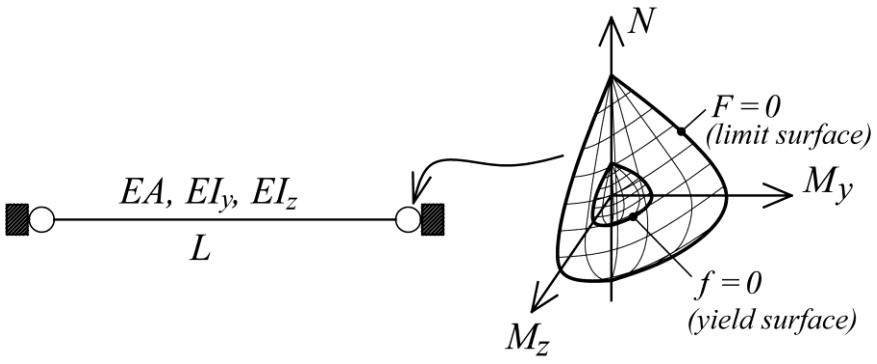


Figure 2: Element end plastic hinges with yield and limit surfaces.

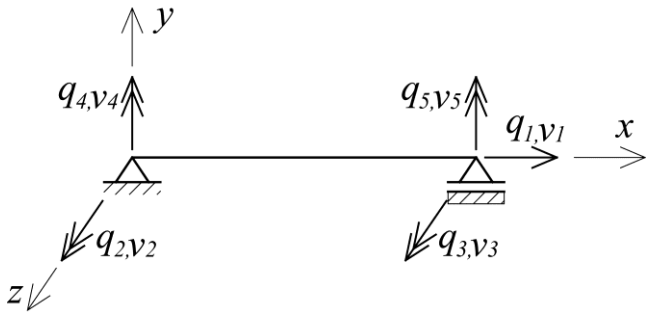


Figure 3: Basic element forces **q** and corresponding deformations **v**.

The basic element equations are:

1. The element deformations **v** are decomposed into the linear elastic, and the plastic contribution, i.e. $\mathbf{v}^{\mathbf{e}}$ and $\mathbf{v}^{\mathbf{p}}$:

$$\mathbf{v} = \mathbf{v}^{\mathbf{e}} + \mathbf{v}^{\mathbf{p}} \tag{1}$$

2. The relation between the basic element forces **q** and the elastic element deformations $\mathbf{v}^{\mathbf{e}}$ is assumed to be linear:

$$\mathbf{q} = \mathbf{k}_{\mathbf{e}}\mathbf{v}^{\mathbf{e}} = \mathbf{k}_{\mathbf{e}}\left(\mathbf{v} - \mathbf{v}^{\mathbf{p}}\right) \tag{2}$$

where $\mathbf{k}_{\mathbf{e}}$ is the elastic stiffness matrix.

3. The yield function *f* at each element end is assumed in the following form:

$$f(\mathbf{q}, \mathbf{a}, \alpha) = \Phi(\mathbf{q} - \mathbf{a}) - H_{iso}\alpha \tag{3}$$

A vector **a** describes the position of the center of the yield surface and its evolution determines the kinematic hardening mechanism. A variable α is a hardening variable which represents the isotropic hardening. More details about the adopted form of evolution laws for **a** and α can be found in [11]. H_{iso} is the non-dimensional isotropic hardening parameter.

4. The adopted limit function F has the following form (as proposed in the generalized plasticity models [12]):

$$F = h(f)\frac{d}{dt}(\Phi) - \lambda \tag{4}$$

$$h(f) = \frac{f}{\delta(\beta - f) + (H_{iso} + H_{kin})\beta} \tag{5}$$

H_{kin} is the non-dimensional kinematic hardening parameter, and δ and β are two positive non-dimensional constants. δ measures the rate of approaching the asymptotic behavior, and β is a measure of the distance between the yield function f and the asymptote, as shown in Figure 4. Parameter λ is the nonnegative consistency parameter.

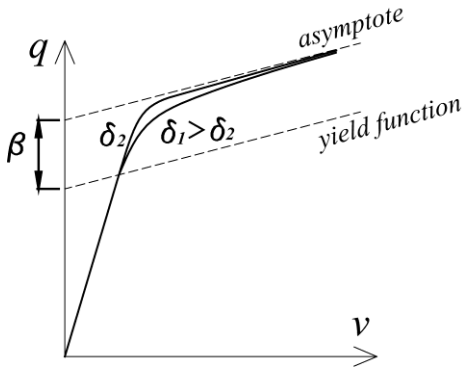


Figure 4: Meaning of parameters δ and β.

5. The flow rule is assumed as associative with the evolution relation:

$$\dot{\mathbf{v}}^{\mathbf{p}} = \lambda \frac{\partial f}{\partial \mathbf{q}} \tag{6}$$

As explained in [11], the proposed model, by applying the backward Euler algorithm, can be successfully transferred into a discrete problem that can be efficiently numerically solved by the two step elastic predictor – plastic corrector return mapping algorithm [13].

3 CHOICE OF ELEMENT PARAMETERS

The GP element was successfully applied for the analysis of steel beam/column and frame behavior. The aim of this study is to show that the element can also be successfully used for modeling the CFT column behavior, but with the proper choice of element parameters.

Considering behavior of CFT columns, the following assumptions are adopted. CFT sections are completely filled with concrete and without shear connectors at the steel concrete interface. The perfect bond between steel and concrete is assumed, without any sleep, which is an often assumption in analytical studies [2]. Viscous deformations of concrete, creep and shrinkage, have been neglected since it has been shown to have little influence on the CFT column behavior. Also, the flexural-torsional and the lateral-torsional buckling are neglected. Residual stresses present in the steel tube and the local buckling of the steel tube are taken into account indirectly, by the yield surface parameters [5].

The essential for a successful description of a CFT member behavior is the determination of the GP element parameters. The expressions and values adopted in this study for each of them are discussed in the following.

3.1 Stiffness of a CFT section

Since a CFT cross-section is made of two different materials, steel and concrete, stiffness of a composite section is determined as follows:

- The axial stiffness is taken as a summation of the axial stiffness of each part of a CFT section, i.e. $(EA)_{CFT} = E_s \cdot A_s + E_c \cdot A_c$, where E_s and E_c are moduli of elasticity of steel and concrete. A_s and A_c are areas of steel and concrete part of a composite section.
- The bending stiffness is taken as a summation of the bending stiffness of the steel part of a CFT section and the reduced stiffness of the concrete part of a composite section (due to the concrete cracking effects), i.e. $(EI)_{CFT} = E_s \cdot I_s + \beta \cdot E_c \cdot I_c$, where I_s and I_c are the moments of inertia of steel and concrete part of a composite section. To date, a number of proposals for the reduction coefficient β have been made [14]. However, the comparison made during this study has shown that a constant value of $\beta=0.6$ proposed by Eurocode 4 [15] ensures, for practical application, enough accurate results.
- The torsional stiffness is determined as the torsional stiffness of the steel part of a CFT section, i.e. $(GI_t)_{CFT} = G_s \cdot I_{t,s}$, where G_s is the shear modulus of steel, and $I_{t,s}$ is a torsion constant of the steel part of a CFT section. This approximation is acceptable in cases with small torsional effects.

3.2 Yield surface parameters for a CFT section

The yield surface equation in the N-M_z-M_y stress resultant space is adopted in the form proposed by Hajjar and Gourley [2] for analysis of a rectangular CFT section:

$$\begin{aligned} &f(p, m_z, m_y) = \\ &c_1 \cdot (m_y^2 + m_z^2) + c_2 \cdot p^2 + c_3 \cdot (m_y^2 \cdot p^2 + m_z^2 \cdot p^2) + c_4 \cdot m_y^2 \cdot m_z^2 - c \end{aligned} \tag{7}$$

Coefficients c_1, c_2, c_3 and c_4 are obtained by calibration with a fiber section and depend on the ratio between height and depth of steel section (D/t), and the ratio between the concrete compressive strength and the yield stress of steel (f_c'/f_y). The exact expressions for these coefficients can be found in [2]. The arguments p, m_z and m_y in the expression (7) are defined as:

$$p = \frac{P - \varphi \cdot P_0}{P_0}, \quad m_z = \frac{M_z}{M_{z0}}, \quad m_y = \frac{M_y}{M_{y0}} \tag{8}$$

where M_{z0} and M_{y0} are the bending moment ultimate strengths for the CFT section about the z and y axes, determined from the fully plastified section in the absence of axial force $(N=0)$, with the area of concrete in compression taken into account with full amount and the reduced area of concrete in tension, taken with the reduction factor 0.5. Concrete tension strength is taken as $f_t = 0.623\sqrt{f_c'}$ (in MPa) [2]. The value φ defines the eccentric position of the yield surface as Figure 5 shows and, here, it is taken as equal to

$$\varphi = \frac{0.5 \cdot (A_c \cdot f_c' - A_c \cdot f_t)}{P_0} \tag{9}$$

and P_0 is the axial compressive capacity of a CFT section. The parameter c in the expression (7) determines the size of the yield surface. Here, for monotonic loading, it is taken equal to the square of the radius of the initial loading surface proposed by Hajjar and Gourley [2]:

$$c = R_{LS,initial}{}^2 = \left(\frac{M_{yld}}{M_0} - 0.3 \cdot \frac{P_{c0}}{P_0} \right)^2 \tag{10}$$

In this expression, M_{yld} is the plastic moment capacity of a steel section; P_{c0} is the axial compressive capacity of the concrete part of a composite section, i.e. $P_{c0} = A_c \cdot f_c'$.

Under cyclic loading, the elastic zone decreases (the yield surface shrinks). Therefore, a better response of the GP model may be obtained if a lower value for the parameter c is adopted. The authors' recommendation is to use the following value under the cyclic loading conditions:

$$c = \left(\frac{R_{LS,initial} + R_{LS,final}}{2} \right)^2 \tag{11}$$

which has shown to be an adequate approximation. In the last expression, $R_{LS,final}=0.1$ is the final radius of the elastic zone proposed by Hajjar and Gourley [6]. The effect of this parameter c on a column response is demonstrated in one of the following examples.

The parameter β of the GP model is determined as the difference $\beta = (1.0 - c)$.

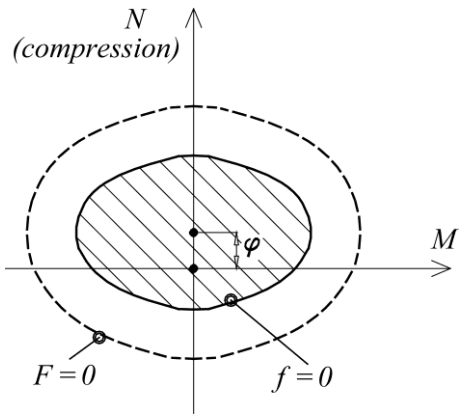


Figure 5: Eccentric position of yield surface (2D case).

3.3 Hardening parameters

The following two features are also important for the adequate simulation of a CFT column behavior.

- The Bauschinger effect is, principally, the result of the steel tube behavior [5]. It can be expressed by the kinematic hardening. In the GP element, it is specified through the H_{kin} parameter.
- Under the cyclic loading conditions, the strength of CFT columns decreases due to the concrete cracking and the local buckling of a steel tube [5]. As a consequence, the limit surface decreases. In the GP element, this effect is approximated with the isotropic hardening (softening) mechanism and a small negative value for the H_{iso} parameter.

4 NUMERICAL EXAMPLES

With the previously adopted element parameters, the capabilities of the GP element to simulate the behavior of composite CFT columns are verified through the following three examples. The response of the GP element is compared with the experimental results available in the literature. FEDEASLab, a Matlab toolbox for nonlinear static and dynamic analysis [16], is used for the simulation.

4.1 Simple beam tests

The first group of tests refers to the tests by Tomii and Sakino [17] on the simple beam exposed to constant axial compressive force and monotonically increasing end moments (Figure 6). Tests number II-2, II-3, II-5, II-6, IV-3 and IV-5 are performed. Details about the beam cross-section, loading and material parameters are given in Table 1. In these tests, steel hardening was about 1%, and in the GP model, it was counted with the kinematic hardening parameter $H_{kin}=0.006$. Results of the GP model are shown in Figure 7 with the full blue line. Experimental results, taken from [6], are presented with black dots.

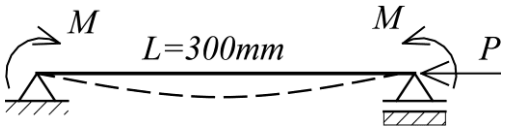


Figure 6: Simple beam and loading [17].

Test	Dimensions (mm)	fc' (MPa)	f_y (MPa)	P/P_0
II-2	100x100x2.27	25.9	339.0	0.18
II-3	100x100x2.20	25.9	339.0	0.26
II-5	100x100x2.22	25.9	289.0	0.48
II-6	100x100x2.22	25.9	289.0	0.57
IV-3	100x100x4.25	22.4	288.0	0.29
IV-5	100x100x4.25	23.8	285.0	0.48

Table 1: Details of CFT simple beam tests [17].

As can be seen from these results, there is a good correlation between the numerically obtained results with the GP model and experimental results considering the initial stiffness and also the limit value of bending moments for all levels of axial force.

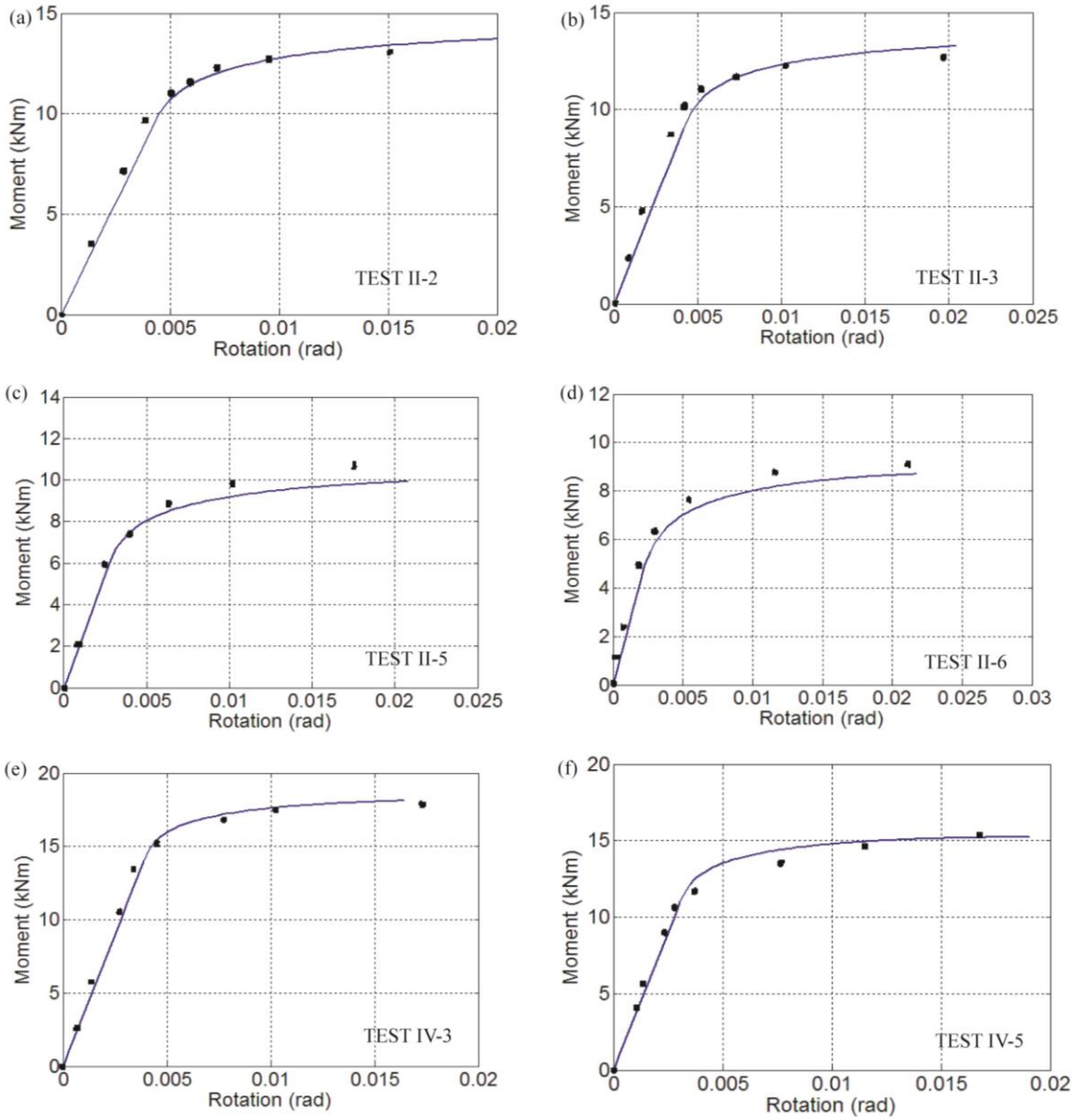


Figure 7: Comparison of experimental and numerical results of moment – rotation relation for Tomii and Sakino [17] tests number II-2, II-3, II-5, II-6, IV-3, IV-5 .

4.2 Beam-column joint

The next example is the 3D analysis of an interior beam-column joint experimentally studied by Kawaguchi and Morino [18]. The joint consists of a square CFT column and three wide flange steel beams, as shown in Figure 8. In this study, the test number I-15C20 is numerically simulated with the use of the GP element.

The joint is firstly loaded with the constant compressive force $P=0.15P_0$ acting on the top of the column, and with the constant axial force $W=21kN$ acting on the free ends of the beam in the *y-z* plane, to simulate gravity loading. The earthquake loading is simulated with the asymmetrical loading Q acting on the free ends of the beams in the *x-z* plane. The forces Q increase until reaching the following values for rotations R: *0.005*, *0.01*, *0.02* and *0.03*. For each value R, two full cycles are performed. The rotation R is determined from the displacements of points A and B, i.e. the vertical displacements D_1 and D_2 in Figure 9(a). The rotation R is then calculated from the expression:

$$R = \frac{D_1 + D_2}{L} \tag{12}$$

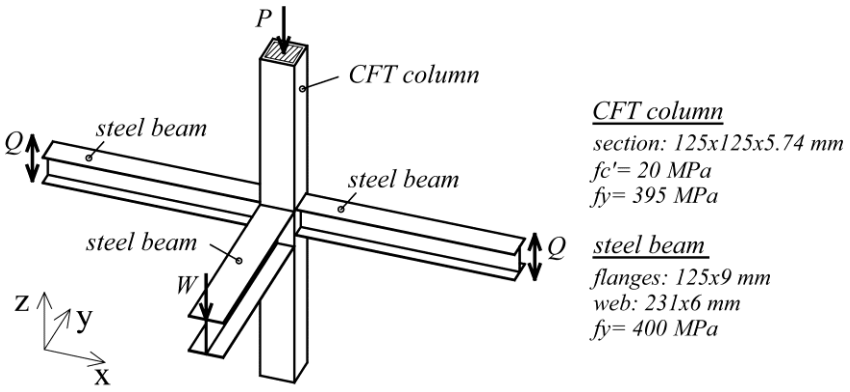


Figure 8: 3D model of interior frame joint and members data.

Figures 9(a) and 9(b) show the numerical model with boundary conditions and the used finite element mesh. It should be noted that, in the example, dimensions of the column and the beams are determined in a way that the joint capacity is governed by the capacity of the CFT column, while beams stay inside the elastic domain during the experiment. Therefore, modeling of beams is irrelevant and instead of the GP, simple linear-elastic elements could be used. In the test, steel tube hardening is 1%, and, in the GP model, it is counted with the kinematic hardening parameter $H_{kin}=0.06$. The slight shrinkage of the limit surface is approximated with the isotropic hardening parameter $H_{iso}=-0.05$.

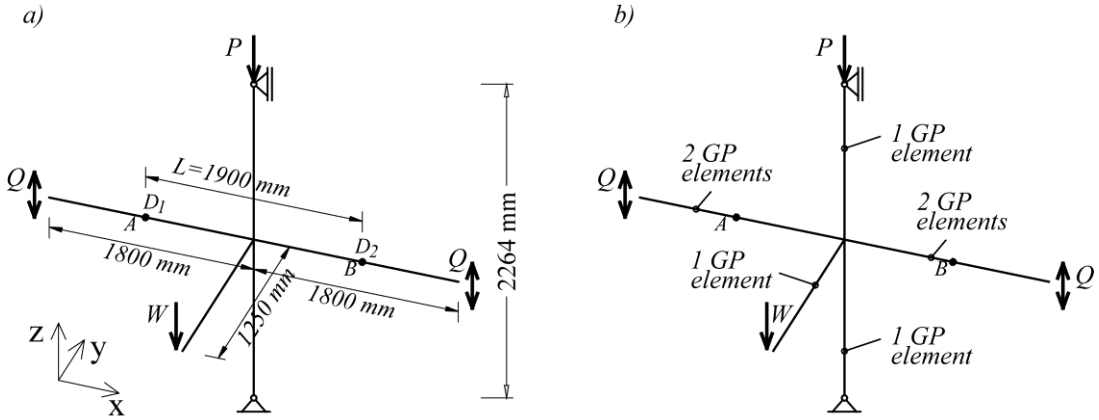


Figure 9: (a) Numerical model and dimensions; (b) Finite element mesh.

The comparison for the *Q*-*R* relation between the experimental results in Figure 10(a), taken from [18], and the numerical results in Figure 10(b) with the GP element and the parameter $c=(R_{LS,initial})^2$ suitable for monotonic loading, shows that the GP model represents well the whole hysteresis curve. The CFT column is exposed to the cyclic biaxial bending with the axial compressive force. As in the previous example, the initial stiffness and the ultimate strength are determined with a high precision. However, as mentioned before, since the elastic zone decreases under the cyclic loading conditions, as a consequence, the limit value for *Q* is approaching at a slower rate. Therefore, a better response of the GP model may be obtained with the proposed value for *c* (expression (11)) which is suitable for cyclic loading. Figure 11 shows results with this value *c*.

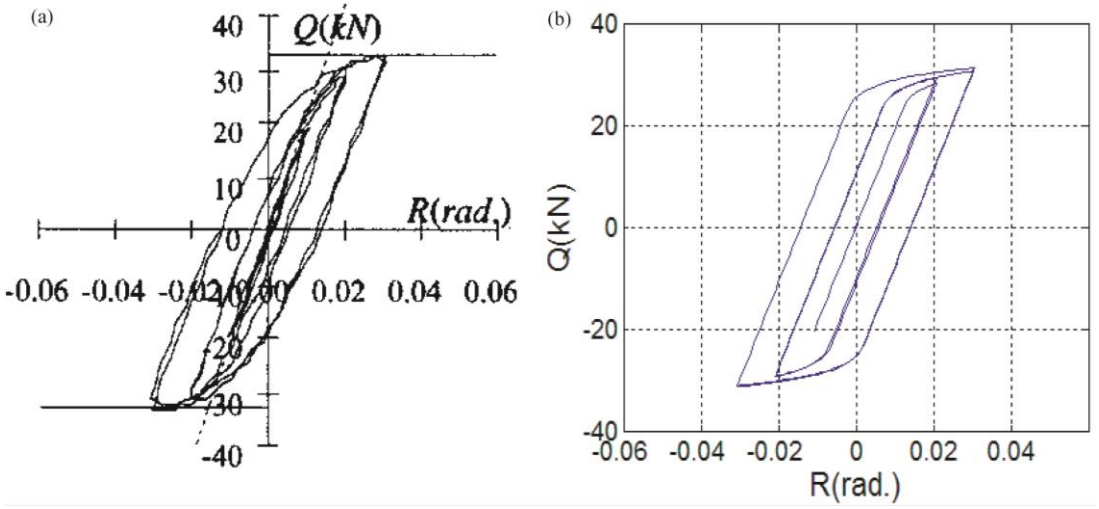


Figure 10: Q-R relation for Kawaguchi and Morino [18] beam-column joint: (a) experimental results; (b) numerical results with GP element and *c* determined from expression (10).

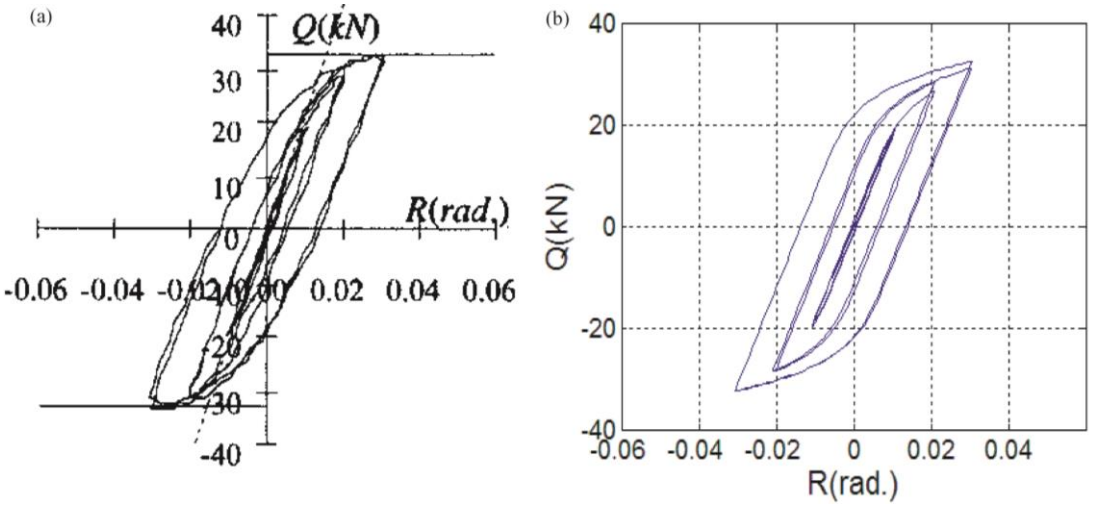


Figure 11: Q-R relation for Kawaguchi and Morino [18] beam-column joint: (a) experimental results; (b) numerical results with GP element and *c* determined from expression (11).

4.3 Portal frame

The last example is the portal frame in Figure 12, experimentally studied by Kawaguchi et al. [19]. The frame consists of two square CFT columns and a steel H-shaped beam. Gravity load is applied first and kept constant, while the frame is subjected to the cyclic lateral loading through the imposed lateral displacements. The loading history in Figure 13 shows the history of the column chord rotation angle R ($R=d/h$). The test number 21SCC30 is numerically simulated with the model with GP elements. In this test, the beam is designed to behave elastically until the end of the test, while the CFT columns yield. The nonlinear geometry under large displacements is accounted for with the corotational formulation [20]. The steel tube hardening is 1%, and the hardening parameters of the GP element are the same as in the previous example.

Figure 14 shows the results of the experiment, taken from [19], and the numerical simulation for the relation between the horizontal force H and the column chord rotation R. As can be seen, generally, the GP model represents well the experimental behavior. The ultimate

strength and the initial stiffness are determined quite accurately. The obtained hysteresis loop is less accurate because of faster (shallower) gradual stiffness reduction of the CFT column than in the GP model. This is also, somewhat, present in the previous example, in Figure 11. It is expected that better representation of this effect will be obtained if the damage mechanics parameters are included into the GP element formulation. However, despite of this fact, the results of the GP model are of acceptable accuracy in general.

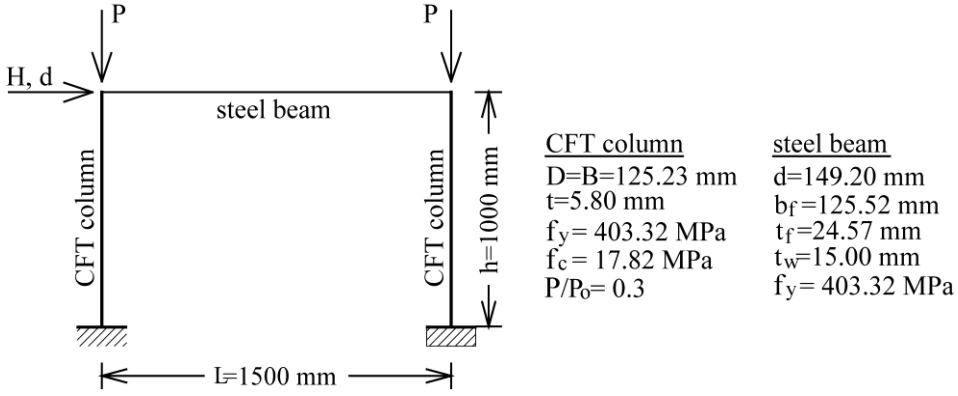


Figure 12: Portal frame [19].

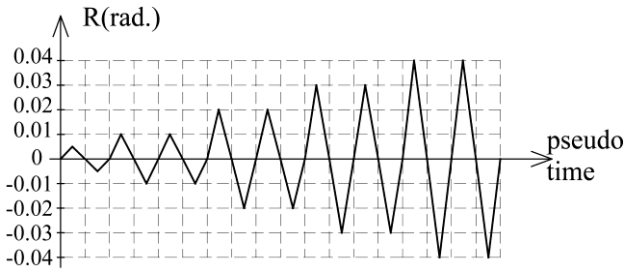


Figure 13: Column chord rotation loading history.

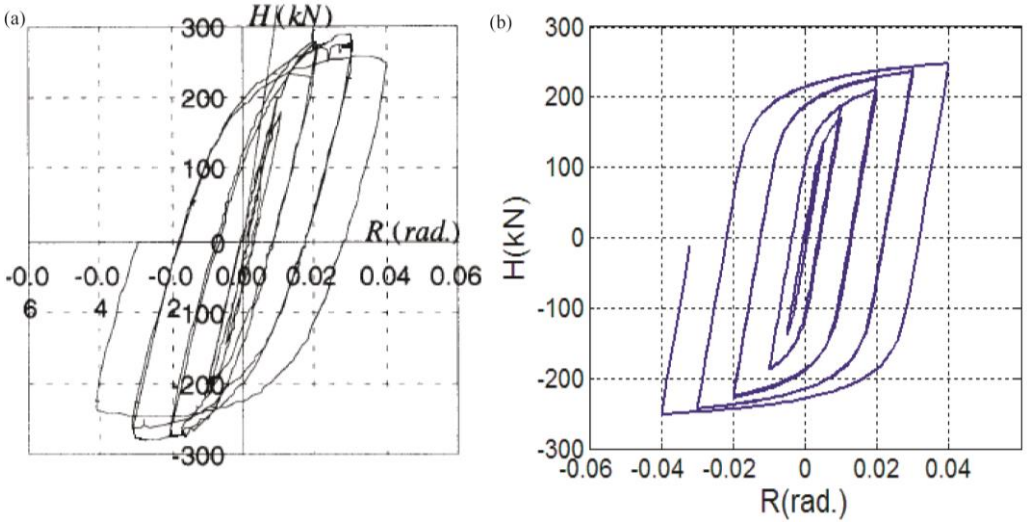


Figure 14: H-R relation for Kawaguchi et al. portal frame [19]: (a) experimental results; (b) numerical results with the GP element.

5 CONCLUSIONS

In the paper, the three-dimensional nonlinear beam-column element, named GP element, is used for the simulation of the response of square CFT columns under monotonic and cyclic loading conditions. The CFT column behaves highly nonlinearly due to number of different effects, i.e. nonlinear steel and concrete material behavior, buckling of steel tube, sleep at the steel-concrete interface, etc. The GP element is of concentrated plasticity type with plastic hinges at element ends and adopts the concept of the generalized plasticity material model for the section resultant – element deformation. It accounts for the interaction of the axial force and bending moments about the principal axes of the cross-section, gradual yielding of the cross section and the hardening behavior. In order to capture some of the most characteristic features of the CFT column behavior, determination of adequate element parameters is discussed in the paper: the loading and the limit surface, the element stiffness and the hardening parameters.

The capability of the GP element in simulation of the CFT column behavior is verified with the three examples where its response is compared with the experimental data. The results showed the high level of accuracy of the element response under monotonic loading conditions, and good accuracy under cyclic loading conditions. With the implemented return mapping algorithm and its high computational efficiency, it may be a good choice for practical applications.

ACKNOWLEDGE

The first author thanks the Ministry of Science of the Republic of Serbia for financial support under project TR 36046.

REFERENCES

[1] A. H. Varma, *et al.*, "Seismic behavior and modeling of high-strength composite concrete-filled steel tube (CFT) beam–columns," *Journal of Constructional Steel Research*, vol. 58, pp. 725-758, 2002.

[2] J. F. Hajjar and B. C. Gourley, "Representation of concrete-filled steel tube cross-section strength," *Journal of Structural Engineering*, vol. 122, p. 1327, 1996.

[3] C. K. Iu, *et al.*, "Second-order inelastic analysis of composite framed structures based on the refined plastic hinge method," *Engineering Structures*, vol. 31, pp. 799-813, 2009.

[4] H.-T. Hu, *et al.*, "Finite element analysis of CFT columns subjected to an axial compressive force and bending moment in combination," *Journal of Constructional Steel Research*, vol. 61, pp. 1692-1712, 2005.

[5] J. F. Hajjar and B. C. Gourley, "A cyclic nonlinear model for concrete-filled tubes. I: Formulation," *Journal of Structural Engineering*, vol. 123, p. 736, 1997.

[6] J. F. Hajjar and B. C. Gourley, "A cyclic nonlinear model for concrete-filled tubes. II: Verification," *Journal of Structural Engineering*, vol. 123, p. 745, 1997.

[7] E. Spacone, *et al.*, "Fiber Beam-Column Model for Nonlinear Analysis of RC Frames: II: Applications," *Earthquake Engineering and Structural Dynamics*, vol. 25, pp. 727-742, 1996.

[8] J. F. Hajjar, *et al.*, "A distributed plasticity model for cyclic analysis of concrete-filled steel tube beam-columns and composite frames," *Engineering Structures*, vol. 20, pp. 398-412, 1998.

[9] R. M. de Souza, "Force-Based Finite Element for Large Displacement Inelastic Analysis of Frames," Ph.D., Civil and Environmental Engineering, University of California, Berkeley, 2000.
[10] C. Tort and J. F. Hajjar, "Mixed Finite-Element Modeling of Rectangular Concrete-Filled Steel Tube Members and Frames under Static and Dynamic Loads," *Journal of Structural Engineering,* vol. 136, pp. 654-664, 2010.
[11] S. M. Kostic, *et al.*, "An Efficient Beam-Column Element for Inelastic 3D Frame Analysis," in *Computational Methods in Earthquake Engineering*. vol. 2, M. Papadrakakis, *et al.*, Eds., ed: Springer, 2013, p. to be published.
[12] J. Lubliner, *et al.*, "A New Model of Generalized Plasticity and Its Numerical Implementation," *International Journal of Solids and Structures,* vol. 30, pp. 3171-3184, 1993.
[13] J. C. Simo and T. J. Hughes, *Computational Inelasticity*. Secaucus, NJ, USA: Springer-Verlag New York, Incorporated, 1998.
[14] J. Moon, *et al.*, "Analytical modeling of bending of circular concrete-filled steel tubes," *Engineering Structures,* vol. 42, pp. 349-361, 2012.
[15] E. C. f. Standardization, "Design of Composite Steel and Concrete Structures - Part 1.1: General Rules and Rules for Buildings, Eurocode 4," ed. Brussels: European Comitee for Standardization, 2004.
[16] F. C. Filippou and M. Constantinides, "FEDEASLab Getting Started Guide and Simulation Examples," University of California, Berkeley, Technical Report2004.
[17] M. Tomii and K. Sakino, "Experimental Studies on the Ultimate Moment of Concrete Filled Square Steel Tubular Beam-Columns," *Trans. Arch. Inst. of Japan*, pp. 55-63, January 1979.
[18] J. Kawaguchi and S. Morino, "Experimental Study on Post-Local Buckling Behavior of CFT Beam-Columns Under Cyclic Loading, Elasto-Plastic Behavior of Square CFT Beam-Columns: Part 1," *J. Struct. Constr. Eng., Architectural Inctitute of Japan,* pp. 141-148, February 2001.
[19] J. Kawaguchi, *et al.*, "Structural Behavior and Characteristics of Concrete-Filled Tubular Frames," Faculty of Engineering, Mie University, Research report1997.
[20] M. A. Crisfield, *Non-linear finite element analysis of solids and structures*. West Sussex: John Wiley & Sons, 1991.

COMPDYN 2013
4th ECCOMAS Thematic Conference on
Computational Methods in Structural Dynamics and Earthquake Engineering
M. Papadrakakis, V. Papadopoulos, V. Plevris (eds.)
Kos Island, Greece, 12–14 June 2013

CONTROL OF THE EIGENSOLUTIONS OF A HARMONICALLY DRIVEN COMPLIANT STRUCTURE

Hugo J. Peters[1,2], Paolo Tiso[1], Johannes F.L. Goosen[1], and Fred van Keulen[1]

[1] Structural Optimization & Mechanics, Department of Precision and Microsystems Engineering,
Faculty of Mechanical, Maritime and Materials Engineering, Delft University of Technology
Mekelweg 2, 2628 CD Delft, The Netherlands
e-mail: {h.j.peters-1, p.tiso, j.f.l.goosen, a.vankeulen}@tudelft.nl

[2] DevLab, Development Laboratories
Den Dolech 2, Laplace 0.01, 5612 AZ Eindhoven, The Netherlands

Keywords: Compliant Structures, Eigensolutions, Systematic Control, Sensitivities, Local Structural Modifications

Abstract. *The motion amplitude of a harmonically driven compliant structure is maximized if the driving frequency equals one of the structural resonance frequencies. For practical use of resonating compliant structures control of the eigensolutions, i.e. eigenfrequencies and eigenmodes, is often required. In this work, a systematic way to control the eigensolutions of harmonically driven structures is presented while maintaining the advantages of a resonating structure. This control is realized using local structural modifications. Eigensolution sensitivities for these local structural modifications are used to indicate the locations for the most effective structural modifications, minimizing the required control power. This method uses the modal basis of the structure as the preferred basis. A simple harmonically driven compliant structure is used to show how local structural modifications are selected to obtain a desired change in the eigensolutions. The proposed method is found to be a convenient tool to determine effective local structural modifications to control the eigensolutions of resonating compliant structures. During the design phase it provides valuable insights in the possibilities and limitations of controlling specific eigensolutions.*

1 INTRODUCTION

The motion amplitude of a harmonically driven compliant structure is maximized if the driving frequency equals one of the structural resonance frequencies. Exciting a structure in its resonance frequency enables large output amplitudes at relatively low power consumption [1]. Typical examples of mechanical applications which use resonance to their advantage are ultrasonic and microlinear actuators [2, 3], resonant silicon sensors [4] and Micro-Electro-Mechanical Systems (MEMS) in general [5]. Ideally, the actuation power to excite a structure in its resonance frequency is determined by the dissipated energy, *e.g.* due to damping.

An example of intentional use of resonance within nature is found in insects. Insects use a resonating thorax structure to reduce the work to accelerate and decelerate their wings during flapping flight [6]. This limits the size of the flight muscles since the required actuation power is, ideally speaking, determined by the dissipated energy only, consisting of aerodynamic drag and damping. Nowadays, a number of Flapping Wing Micro Air Vehicle (FWMAV) designs mimics the resonating thorax structure of insects [7, 8]. These designs use the resonance of the structure to achieve large flapping amplitudes with low power consumption.

For practical use of resonating (compliant) structures control of the eigensolutions, *i.e.* eigenfrequencies and eigenmodes, is often required. For instance, flight control of a FWMAV design requires an asymmetric flapping motion, which implies a controlled change of the initially symmetric eigenmode. Controlling the eigensolutions of resonating FWMAV designs is particularly complicated by constraints on weight and power consumption. In literature, optimization methods are used to design vibrating structures that target desired eigensolutions [9, 10] and piezoelectric material is distributed over a structure to achieve a desired dynamic behavior [11]. However, systematic ways to control the eigensolutions of resonating structures during operation, while maintaining the advantages of a resonating structure, are not well established in literature.

The eigensolutions of a resonating structure are determined by its structural properties, *e.g.* mass, damping, stiffness and their spatial distribution. Local changes of these properties will result in changes of the eigensolutions. Local structural modifications, such as stiffness changes, can be obtained using actuators such as piezoelectric patches [12]. Besides being used as high frequency actuators, they may also alter the stiffness or change the stiffness indirectly by altering the shape of the structure. Additionally, they may be used as dampers.

The changes in eigensolutions due to local structural modifications can be estimated using sensitivity analysis. Although the calculation of the eigenfrequency sensitivity is straightforward, the eigenmode sensitivity is more involved. Fox and Kapoor [13] showed that the eigenmode sensitivity can be represented by a linear combination of the structural eigenmodes. Nelson [14] presented a method where only the eigenmode of interest was required to determine the eigenmode sensitivity. These methods have been extended to allow for eigensolution sensitivities of asymmetric non-conservative systems [15] and systems with repeated eigenfrequencies [16]. In our present work which is to find a systematic way to control the eigensolutions, conservative systems will be considered as a first step. Thus, damping is ignored for now. The eigenfrequencies are, besides the possible presence of rigid-body modes, assumed to be distinct. Moreover, a modal basis is used as a preferred basis, which allows for a more intuitive understanding and for maximum insight in the eigensolution control.

The well-known discretized eigenproblem for free vibrations and the eigenproblem sensitivities to structural modifications, using a modal basis, are presented in Section 2. The obtained expressions are interpreted to understand the consequences for systematic eigensolution control.

In Section 3, a method is presented to analyze the influence of local structural modifications on the eigenmode sensitivities. This method provides valuable insights in the possibilities and limitations of controlling specific eigensolutions. A simple 2D example of a compliant structure is used in Section 4 to demonstrate the usefulness of the method. In Section 5, conclusions and future research are presented.

2 EIGENSOLUTION SENSITIVITIES

This section starts with the well-known discretized eigenproblem for free vibrations and corresponding orthogonality relationships. Next, the forced harmonic response using mode superposition is summarized [17]. Subsequently, the sensitivity of the eigensolutions using the modal basis is shown for self containment [13]. Interpretations of the mathematical expressions are given to understand the consequences of this modal representation for systematic eigensolution control.

2.1 Eigenproblem formulation

The eigenfrequencies and corresponding eigenmodes of a conservative, N degrees of freedom system are determined by the general eigenproblem,

$$\left(\mathbf{K} - \omega_k^2 \mathbf{M}\right) \mathbf{v}_k = \mathbf{0} \quad \text{where} \quad k = 1 \dots N. \tag{1}$$

In Eq. (1), $\mathbf{M}$ and $\mathbf{K} \in \mathbb{R}^{N \times N}$ are the mass and stiffness matrix, respectively, ω_k^2 is the k^{th} eigenfrequency and $\mathbf{v}_k \in \mathbb{R}^N$ is the k^{th} eigenmode. The mass matrix, $\mathbf{M}$, is symmetric, positive definite and the stiffness matrix, $\mathbf{K}$, is symmetric, semi-positive definite. $\mathbf{M}$ and $\mathbf{K}$ both depend on the structural design parameters. The number of possible rigid-body modes is m and it is assumed that the remaining eigenvalues, ω_k^2, are distinct and ordered conform $\omega_k^2 < \omega_{k+1}^2$ where $k = m+1 \dots N$. Mass normalization of the eigenmodes is assumed such that the orthogonality relationships become,

$$\begin{aligned} \mathbf{v}_l^T \mathbf{M} \mathbf{v}_k &= \delta_{kl}, \\ \mathbf{v}_l^T \mathbf{K} \mathbf{v}_k &= \omega_k^2 \delta_{kl}, \end{aligned} \tag{2}$$

where $k, l = 1 \dots N$ and δ_{kl} represents the Kronecker delta.

2.2 Forced harmonic response

The transient response of a conservative, N degree of freedom system, submitted to a harmonic force with constant amplitude $\mathbf{s}$, is governed by equation,

$$\mathbf{M}\ddot{\mathbf{q}} + \mathbf{K}\mathbf{q} = \mathbf{s} \cos\left(\omega t\right), \tag{3}$$

where $\mathbf{q}$ represents the response and ω is the excitation frequency. The forced response is the part of the response, synchronous to the excitation,

$$\mathbf{q} = \mathbf{x} \cos\left(\omega t\right). \tag{4}$$

By substituting Eq. (4) into the equations of motion, Eq. (3), and by using an eigenmode series expansion, including the possible presence of m rigid-body modes, the forced response amplitude $\mathbf{x}$ is given by,

$$\mathbf{x} = \left\{ -\frac{1}{\omega^2} \sum_{i=1}^{m} \mathbf{v}_i \mathbf{v}_i^T + \sum_{s=m+1}^{N} \frac{\mathbf{v}_s \mathbf{v}_s^T}{\left(\omega_s^2 - \omega^2\right)} \right\} \mathbf{s}, \tag{5}$$

where eigenmode orthogonality is extensively used. This solution indicates, that the amplitude of the response $\mathbf{x}$ goes to infinity when the excitation frequency ω approaches an eigenfrequency, ω_s. Provided that the eigenmode $\mathbf{v}_s$ is not orthogonal to the constant amplitude $\mathbf{s}$, the harmonic oscillation of the structure is, in that case, determined by the shape of eigenmode $\mathbf{v}_s$. Controlling the response of a structure which is harmonically excited at a frequency close to a structural eigenfrequency ω_s is, thus, equivalent to controlling eigenmode $\mathbf{v}_s$.

2.3 Eigenproblem sensitivity

Suppose a number of design parameters, $\boldsymbol{\mu} \in \mathbb{R}^p$, where p represents the number of design parameters. The sensitivities of the rigid-body eigensolutions to a design parameter, μ_i, are zero in this study. The eigenfrequencies of the rigid-body modes remain zero and the rigid-body eigenmodes remain the same since the nodal position of the discretized elements is not influenced by the design parameters [18]. The sensitivity, or derivative, of Eq. (1) to a design parameter, μ_i, yields,

$$\left(\mathbf{K}' - \omega_k^2\mathbf{M}'\right)\mathbf{v}_k - \left(\omega_k^2\right)'\mathbf{M}\mathbf{v}_k + \left(\mathbf{K} - \omega_k^2\mathbf{M}\right)\mathbf{v}_k' = \mathbf{0}, \tag{6}$$

where $(..)' = {}^{\partial ..}/_{\partial \mu_i}$. Since the sensitivity of the rigid-body eigensolutions is zero, the subindex k excludes the rigid-body eigensolutions, *i.e.*, $k = m+1 \ldots N$ in the remainder of this work. Premultiplying Eq. (6) by eigenmode $\mathbf{v}_k$ and using Eq. (1) and Eq. (2), the eigenfrequency sensitivity is given by,

$$\left(\omega_k^2\right)' = \mathbf{v}_k^T\left(\mathbf{K}' - \omega_k^2\mathbf{M}'\right)\mathbf{v}_k, \tag{7}$$

which shows that the eigenfrequency sensitivity of the k^{th} eigenfrequency requires information of the k^{th} eigensolution only. Since the N structural eigenmodes form a complete and orthogonal basis, the eigenmode sensitivities, as present in Eq. (6), can be written as a linear combination of the structural eigenmodes,

$$\mathbf{v}_k' = \sum_{l=1}^{N} \alpha_{ki}^l \mathbf{v}_l, \tag{8}$$

where α_{ki}^l determines the contribution of each eigenmode $\mathbf{v}_l$ to the sensitivity of eigenmode $\mathbf{v}_k$ with respect to μ_i. Substitution of Eq. (8) into the sensitivity of the mass orthogonality relationship of Eq. (2) with respect to μ_i, yields,

$$\alpha_{ki}^l = -\frac{1}{2}\mathbf{v}_k^T\mathbf{M}'\mathbf{v}_k \quad \text{for} \quad l = k. \tag{9}$$

Premultiplying Eq. (6) by eigenmode $\mathbf{v}_n$, substituting Eq. (8) for $\mathbf{v}_k'$ and using the orthogonality relationships of Eq. (2) yields,

$$\alpha_{ki}^l = -\frac{\mathbf{v}_l^T\left(\mathbf{K}' - \omega_k^2\mathbf{M}'\right)\mathbf{v}_k}{\omega_l^2 - \omega_k^2} \quad \text{for} \quad l \neq k. \tag{10}$$

The coefficients α_{ki}^l, as given by Eqs. (9) and (10), arise from the definition of the eigenmode sensitivity as given by Eq. (8). This modal representation gives a convenient starting point for optimal eigensolution control since it uses the natural basis of the structure.

2.4 Consequences for systematic eigensolution control

To calculate the eigenfrequency sensitivity, Eq. (7), and the eigenmode sensitivity, Eq. (8) with Eqs. (9) and (10), only the sensitivity of the mass and stiffness matrix to a design variable μ_i needs to be determined. The sensitivity of the structural matrices is given by $\mathbf{M}'$ and $\mathbf{K}'$, respectively. In this work, changing a design variable μ_i implies a local structural modification. Thus, provided that the design variable, μ_i, influences the structural properties, the matrices $\mathbf{M}'$ and $\mathbf{K}'$ contain non-zero entries which correspond to the locations where the design variable is modified. Although the eigenfrequency sensitivity requires information on the eigensolution of interest only, the eigenmode sensitivity requires information on all N eigensolutions. Based on the expressions for the coefficients α_{ki}^{l} in Eqs. (9) and (10) it can be observed that:

- The magnitude of the numerator of Eq. (10) depends on the size and spatial location of the applied local structural modification. This dependency on the size and location is caused by the interplay between the segments of the eigenmodes $\mathbf{v}_k$ and $\mathbf{v}_l$ and the sensitivity of the structural matrices, $\mathbf{M}'$ and $\mathbf{K}'$, corresponding to the locations where the structural modifications are applied. The contribution of the eigenmodes $\mathbf{v}_k$ and $\mathbf{v}_l$ in the regions not affected by the structural modifications is irrelevant since the sensitivity of the structural matrices, $\mathbf{M}'$ and $\mathbf{K}'$, is zero corresponding to those locations.

- Since the eigenmodes are normalized using the mass matrix, Eq. (2), eigenmode $\mathbf{v}_k$ contributes to the sensitivity of eigenmode $\mathbf{v}_k$ if the sensitivity of the structural mass matrix, $\mathbf{M}'$, is non-zero, see Eq. (9). However, the actual shape change of eigenmode $\mathbf{v}_k$ will be determined by the contribution of the modes $\mathbf{v}_l$, where $l \neq k$.

- The term $\left(\mathbf{K}' - \omega_k^2 \mathbf{M}'\right) \mathbf{v}_k$ in Eq. (10) can be seen as a pseudo load which acts locally on the regions where the structural modifications are applied. Maximum gain is scored if the inner product between the pseudo load and the eigenmode $\mathbf{v}_l$ is maximized. For a specific l, this inner product can be maximized by adjusting the size and location of specific structural modifications.

- Due to the denominator in Eq. (10), $(\omega_l^2 - \omega_k^2)$, the contribution of eigenmode $\mathbf{v}_l$ to the sensitivity of eigenmode $\mathbf{v}_k'$, Eq. (8), is reduced if the corresponding eigenvalue ω_l deviate more from eigenvalue ω_k.

These observations will contribute to a better understanding and more insights into the control of a specific eigenmode using local structural modifications.

3 SYSTEMATIC EIGENSOLUTION CONTROL

This section shows how the eigenproblem sensitivity, as described with respect to a modal basis in Section 2.3, can be used to identify the most effective locations to apply structural modifications, to control a specific eigenmode. First, a projection is defined to indicate the effectiveness of a certain eigenmode change. Secondly, the consequences of this measure for the design and optimization of structural modifications with the aim of structural eigensolution control are investigated.

3.1 Measure effectiveness of eigenmode change

Our goal is to modify a certain vibration in a desired fashion. Prescribing the entire desired shape of the eigenmode of interest is rather complex and this level of detail is usually not

required. For controlling the eigenmode shape, spatial portions of the eigenmode shape are specified for which the desired dynamic response should be maximized or minimized and the remaining portion is left unspecified.

In former research on the design of vibrating structures that targets desired eigenmode shapes, unit loads are defined at specific spatial locations where modifications of the dynamic response are required [9, 11]. By projecting the eigenmode of interest onto these unit loads, a quantitative measure of the dynamic response was determined for each structural design. The value of this projection is used to determine the optimal structural design to achieve the desired eigenmode shape.

In this work, a unit projection vector $\mathbf{b} \in \mathbb{R}^N$ is defined, which has non-zero entries for the locations which correspond to the spatial locations where the desired dynamic response should be modified. A quantitative measure of the current dynamic response at the locations of interest is obtained by projection of the eigenmode of interest, $\mathbf{v}_k$, onto this projection vector, $\mathbf{b}$, while including the structural mass matrix, $\mathbf{M}$, as a weighting matrix. The structural mass matrix is included to simplify the intuitive understanding of the projection as shown in the remainder of this work. The projection is given by,

$$r_k = \mathbf{b}^T \mathbf{M} \mathbf{v}_k. \tag{11}$$

In this work, the projection value, r_k, can be changed using local structural modifications. Sec. 2.3 describes the change of eigenmode $\mathbf{v}_k$ due to structural modifications. Accordingly, the change of the projection of Eq. (11) is given by,

$$r'_k = \mathbf{b}^T \mathbf{M} \mathbf{v}'_k, \tag{12}$$

where the weighting matrix, the structural mass matrix $\mathbf{M}$, remains constant. The change of projection r'_k, Eq. (12), depends on the size and spatial location of the structural modifications. Depending on the desired dynamic response at the spatial locations of interest, the change of the projection value, Eq. (12), should be

- maximized if a specific control state requires that the dynamic response of eigenmode $\mathbf{v}_k$ is maximized at the locations of interest,
- minimized if a specific control state requires that the dynamic response of eigenmode $\mathbf{v}_k$ is minimized at the locations of interest.

The change of r'_k is maximized or minimized by determining the optimal location and dimension of structural modifications. Using the modal basis, the projection vector $\mathbf{b}$ can be written as,

$$\mathbf{b} = \sum_{m=1}^{N} \beta_m \mathbf{v}_m. \tag{13}$$

By combining Eq. (13) and the modal representation of the eigenmode sensitivity, Eq. (8), with the expressions for the coefficients α^l_{ki}, Eqs. (9) and (10), the change of the projection, Eq. (12), is rewritten to,

$$r'_k = \sum_{\substack{l=1 \\ l \neq k}}^{N} \frac{1}{\omega_k^2} \beta_l \frac{1}{1 - {}^{\omega_l^2}/_{\omega_k^2}} \left(\mathbf{v}_l^T \left[\mathbf{K}' - \omega_k^2 \mathbf{M}' \right] \mathbf{v}_k \right) - \frac{1}{2} \beta_k \mathbf{v}_k^T \mathbf{M}' \mathbf{v}_k, \tag{14}$$

where the mass orthogonality relationship of Eq. (2) is extensively used. The usefulness of Eq. (14) is investigated by examining each term.

This analysis shows that:

- the first term, $(1/\omega_k^2)$, depends on the eigensolution of interest. This term is, therefore, fixed and given in advance.
- the second term, (β_l), determines the modal contribution of each eigenmode $\mathbf{v}_l$ to the projection vector $\mathbf{b}$. The magnitude of this term depends on the alignment of eigenmode $\mathbf{v}_l$ with respect to the projection vector $\mathbf{b}$ resulting in zero if $\mathbf{v}_l$ is orthogonal to $\mathbf{b}$.
- the third term, $(1/(1-\omega_l^2/\omega_k^2))$, will drop rapidly if eigenfrequency ω_l starts to deviate from eigenfrequency ω_k. For a maximization of r'_k, contributions of eigensolutions for which ω_l deviates significantly from ω_k become marginally important.
- the fourth term, $\left(\mathbf{v}_l^T \left[\mathbf{K}' - \omega_k^2 \mathbf{M}'\right] \mathbf{v}_k\right)$, is a scalar that depends on the size and spatial location of the applied structural modifications. The magnitude of this term is determined by the interplay between the segments of the eigenmodes $\mathbf{v}_k$ and $\mathbf{v}_l$ and the sensitivity of the structural matrices, $\mathbf{M}'$ and $\mathbf{K}'$, corresponding to the locations where the structural modifications are applied. The magnitude of this scalar product can be maximized if eigenmode $\mathbf{v}_l$ is as much as possible aligned to the pseudo load, $(\left[\mathbf{K}' - \omega_k^2 \mathbf{M}'\right] \mathbf{v}_k)$, at the locations where the modifications are applied. However, if the second or third term of Eq. (14) are approximately zero for a specific l, a maximization of this term will not add much to the change of the projection, r'_k.
- the fifth term, $\left(\frac{1}{2}\beta_k \mathbf{v}_k^T \mathbf{M}' \mathbf{v}_k\right)$, originates from the normalization conditions, Eq.(2). Since there is only a contribution of eigenmode $\mathbf{v}_k$, this term is less interesting while considering the change of the response due to a shape change of eigenmode $\mathbf{v}_k$. However, this term is important to provide the exact magnitude of r'_k

The change of the projection, Eq. (14), together with the above described systematic breakdown, gives valuable insights in the systematic control of eigenmodes. Since the modal basis is used as a preferred basis, the influence of the individual eigensolutions becomes transparent.

3.2 Design and optimization of structural modifications

To control the eigensolution of interest of a resonating structure during operation, one would like to have a quick estimation and an understanding of the most effective spatial locations to apply structural modifications. The change of the proposed projection, r'_k, as introduced in Sec. 3.1, is found to be an effective measure to understand the possibilities and limitations of the potential achievable changes of the eigenmode of interest. Since the modal basis is used as the preferred basis in the entire formulation, an intuitive understanding of the eigenmode change due to local structural modifications is obtained.

The different terms of Eq. (14), as described in Sec. 3.1, show in an early phase the dominance of specific eigenmodes $\mathbf{v}_l$ to the change of the projection r'_k and, thus, to the change of eigenmode $\mathbf{v}_k$. The change of the projection, r'_k, is maximized if the local structural modifications are chosen in such a way that the fourth term of Eq. (14), $\left(\mathbf{v}_l^T \left[\mathbf{K}' - \omega_k^2 \mathbf{M}'\right] \mathbf{v}_k\right)$, is maximized for these specific, dominant eigenmodes, $\mathbf{v}_l$. The structural sensitivity matrices, $\mathbf{M}'$ and $\mathbf{K}'$, contain only non-zero entries corresponding to the location where the modifications are applied. The fourth term of Eq. (14) is therefore maximized for a specific l, if the eigenmodes $\mathbf{v}_k$ and $\mathbf{v}_l$ are well aligned at these spatial locations. This term results in zero if the segments of

eigenmode $\mathbf{v}_k$ are orthogonal to the eigenmode $\mathbf{v}_l$ at the locations where the modifications are applied.

At some point, optimization techniques can be used to find the optimal locations to apply local structural modifications for the control of a specific eigensolution more precisely. In that case, topology optimization techniques can be utilized to determine the locations where the actuator patches should be located. The presented projection r_k is attractive to use since the number of modes included in the analysis can be very limited. The eigenfrequency sensitivity, Eq. (7), depends also on the locations of the structural modifications. Thus, the shift of the eigenfrequency, due to the modifications, can be added to the optimization. This allows for a more comprehensive control of the eigensolutions.

4 NUMERICAL EXAMPLE

In this section, the method for the systematic control of eigensolutions, as described in Section 3, is applied to a simple 2D compliant structure. The numerical model of the compliant structure is discussed first, followed by the free vibration solutions of this structure. Thereafter, the projection, as introduced in Section 3, is used to demonstrate the usefulness of the proposed method for systematic eigensolution control.

4.1 Numerical model

Figure 1 shows the model of the 2D compliant structure used in this example. The model is composed using 2D beam elements which allow stretching and bending. Shear deformation is neglected by assuming slender elements. The global mass and stiffness matrix are composed by assembling consistent mass and stiffness element matrices for 2D beam elements [19]. The beam elements have a circular cross section with a diameter $d_e = 0.0035$ m. The ring of the structure has a diameter $d_r = 0.05$ m, and the length of the wing-type cantilevers $l_w = 0.05$ m, see Figure 1. The structure has a Young's modulus $E = 1.5$ GPa, and a density $\rho = 1175$ kg/m^3, which corresponds to the mechanical properties of plastic, *i.e.* polypropylene. The total mass of the structure is 4 g.

The 2D compliant structure of Figure 1 might be compared with a simplified FWMAV design. In that case, the ring of the structure represents the main body and the four cantilevers

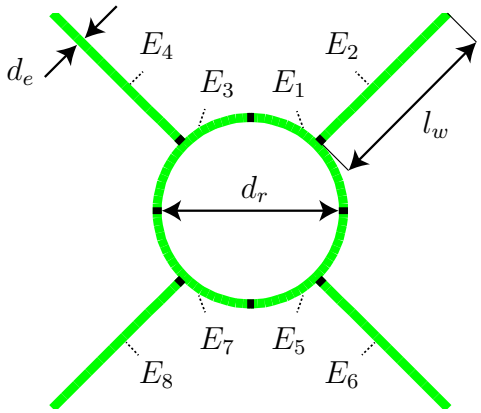
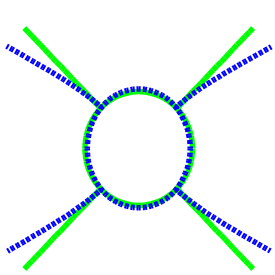


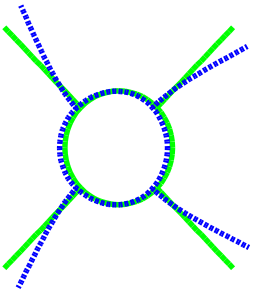
Figure 1: Compliant 2D model showing the circular beam diameter, d_e, the diameter of the ring, d_r, the length of the wing, l_w, and the eight different Young's moduli, E.

Young's modulus	[Gpa]
E_1	1.43
E_2	1.45
E_3	1.47
E_4	1.49
E_5	1.51
E_6	1.53
E_7	1.55
E_8	1.57

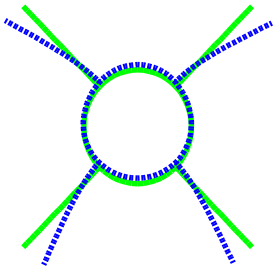
Table 1: The eight different Young's moduli required for asymmetry.



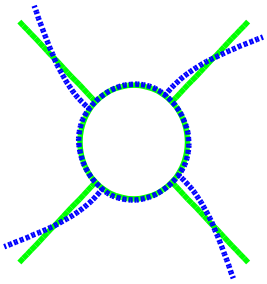
(a) The fourth eigenmode, eigenfrequency: 177.40 Hz.



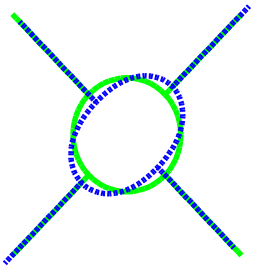
(b) The fifth eigenmode, eigenfrequency: 217.97 Hz.



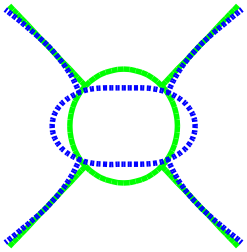
(c) The sixth eigenmode, eigenfrequency: 218.16 Hz.



(d) The seventh eigenmode, eigenfrequency: 384.05 Hz.



(e) The eighth eigenmode, eigenfrequency: 385.22 Hz.



(f) The nineth eigenmode, eigenfrequency: 767.58 Hz.

Figure 2: The first six eigensolutions with a non-zero eigenfrequency. In these figures, the green, solid structure represents the reference, static structure and the blue, dotted structure represents the eigenmode.

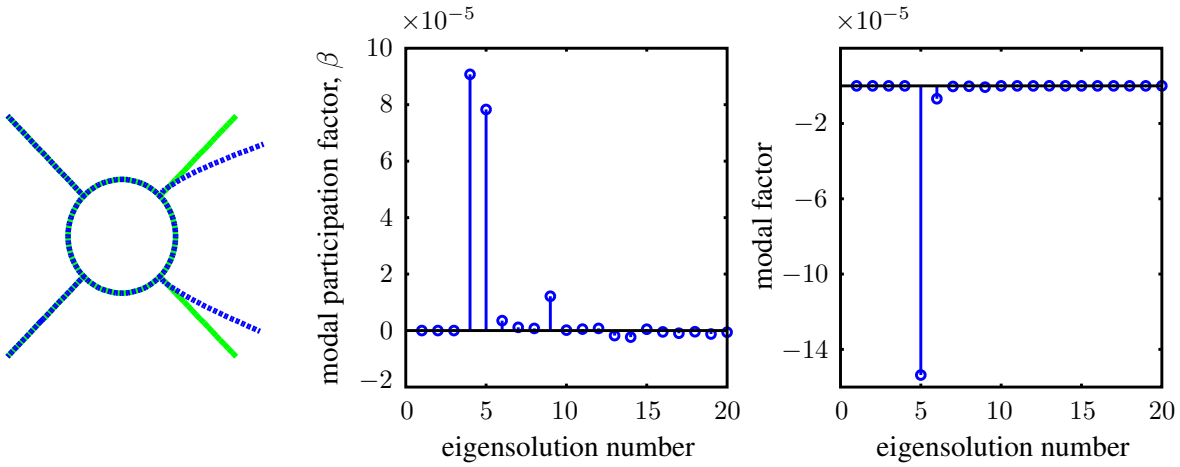
represent the wings. The geometrical model of Figure 1 is highly symmetric. This symmetry will result in free vibrations with repeated nonzero eigenfrequencies. To circumvent the particularities of repeated eigenfrequencies, the structure is divided in eight parts as shown in Figure 1. By slightly varying the Young's modulus of each of these parts, an asymmetric structure is obtained, see Table 1.

4.2 Eigensolutions

Since the 2D model as shown in Figure 1 is not constrained, the structure is floating. Therefore, the structure exhibit three orthogonal rigid-body eigensolutions, $i.e.$, translation in x- and y-direction and rotation about the z-axis. Figure 2 shows the first six eigensolutions with a non-zero eigenfrequency. Although the eigensolutions appear to have a high degree of symmetry, all eigenfrequencies are distinct due to the variations in Young's moduli, Table 1. Practically symmetric looking eigenmodes are called symmetric in the remainder of this work.

4.3 Amplification of the dynamic response in a specific region

An interesting oscillation is obtained if the structure of Figure 1 is harmonically excited with an excitation frequency close to the fourth eigenfrequency. Provided that the excitation is not orthogonal to the fourth eigenmode, the structure will vibrate according to the fourth eigenmode, (see Section 2.2). For FWMAV designs, this vibration mode is of particular interest since it corresponds to a symmetric flapping of the wings, required for hovering flight. The eigenfrequency associated to the flapping mode is somewhat to high for practical FWMAV.



(a) The unit projection vector, $\mathbf{b}$, in dotted blue.

(b) The modal participation factors, β, to the projection vector, $\mathbf{b}$.

(c) Modal factor showing the significant eigensolutions ($l \neq k$).

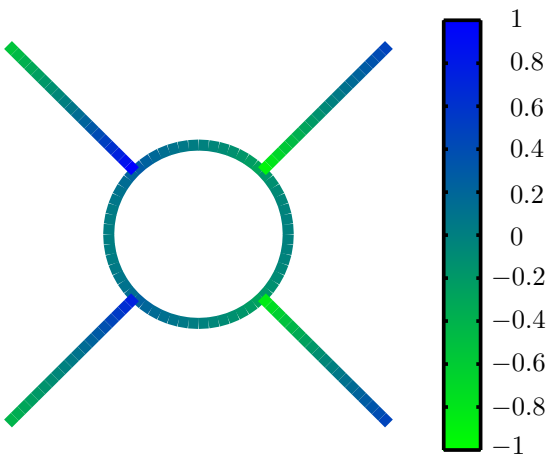
Figure 3: Consideration of dominant eigenmodes. (a) the unit projection vector, $\mathbf{b}$, represented by the dotted, blue line, (b) the modal participation factors of the projection vector, (c) and the multiplication factor between the modal participation factors and the eigenfrequency dependent factor for $l \neq k$.

However, the concept is nicely illustrated.

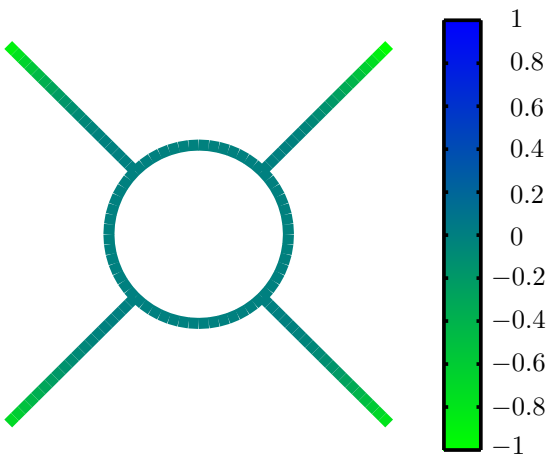
To study the locations at which structural modifications need to be applied to obtain an asymmetric flapping, a projection vector, $\mathbf{b}$, is defined. To modify the dynamic response of the wing-type cantilevers on the right side, $\mathbf{b}$ contains only non-zero entries on the right side, see Figure 3a. By maximizing or minimizing the change of the projection, r'_k, where $k = 4$, using structural modifications, the dynamic response of the wing-type cantilevers is modified.

In order to determine which eigenmodes $\mathbf{v}_l$ are most dominantly contributing to the change of the projection, r'_4 , the modal participation factors, β, (see Eq. (13)), are determined as a first step. Figure 3b shows that the the modal participation factor, β, is only significant for a very few eigenmodes, *i.e.* eigenmode 4, 5 and 9. For the eigensolutions $l \neq k$, where $k = 4$, the number of significant eigensolutions is even more convincingly reduced by multiplying the modal participation factor, β, with the eigenfrequency dependent factor, the third term in the change of the projection of Eq. (14), $\left({}^{1}/_{(1-\omega_l^2/\omega_k^2)}\right)$. Figure 3c shows the modal factors after this multiplication. The Figures 3b and 3c show clearly that eigensolutions 4, 5 and 6 (to a less degree) are most dominant in determining the change of the projection, r'_4.

Finally, to determine the total change of the projection, r'_4, the spatial location at which the local structural modifications are applied is required. Using these locations the sensitivity of the structural matrices, $\mathbf{M}'$ and $\mathbf{K}'$, to the design variable is determined. In this work, the circular beam diameter, d_e, is the design variable used which influences both the mass and stiffness matrix. Due to the high modal factor of eigensolution 5, (see Figure 3c), the magnitude of the fourth term of Eq. (14), $\left(\mathbf{v}_l^T \left[\mathbf{K}' - \omega_k^2 \mathbf{M}'\right] \mathbf{v}_k\right)$, for $l = 5$ will have a large influence on the final change of the response, r'_4. Figure 4a shows how the magnitude of this term depends on the location at which the circular beam diameter, d_e, is influenced. It is clearly shown, that the influence of a circular beam diameter change is highest at the root of the wing-tip cantilevers and around zero if the modification is applied at the central ring structure. The modal participation term of the fourth eigensolution, β_4, plays only a role in the fifth term of Eq. (14), $\left(\frac{1}{2}\beta_k \mathbf{v}_k^T \mathbf{M}' \mathbf{v}_k\right)$. Figure 4b shows how the magnitude of this term depends on the location at which the circular beam diameter is modified. Since this term depend on the fourth



(a) Location dependent, normalized measure of the term $\left(\mathbf{v}_l^T \left[\mathbf{K}' - \omega_k^2 \mathbf{M}'\right] \mathbf{v}_k\right)$ for $k = 4$ and $l = 5$.

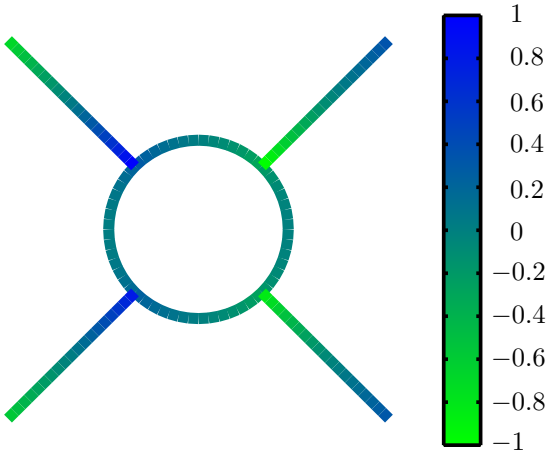


(b) Location dependent, normalized measure of the term $\left(\mathbf{v}_k^T \mathbf{M}' \mathbf{v}_k\right)$ for $k = 4$.

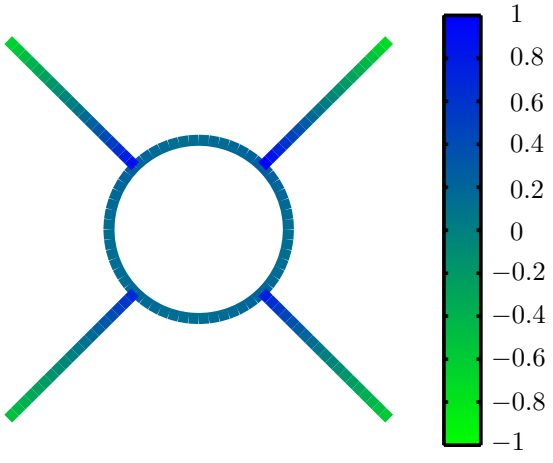
Figure 4: Location dependent, normalized plots of significant terms present in the change of the projection value. (a) shows the interplay between the eigenmodes $\mathbf{v}_4$ and $\mathbf{v}_5$ and the sensitivity of the structural matrices, (b) shows the interplay of eigenmode $\mathbf{v}_k$ and the sensitivity of the structural mass matrix.

eigensolution only, the shape of eigenmode $\mathbf{v}_4$, see Figure 2a, is clearly visible.

Based on Figure (4), the circular beam diameter should be modified at the root of the wing-type cantilevers to maximize the change of the projection, r_4'. Figure 5a shows the change of the projection r_4', as a function of the location where the circular beam diameter, d_e, is modified, while taking all N eigensolutions into account. Figure 5a confirms that the change of the projection is maximized if the circular beam diameter is modified at the root of the wing-type cantilevers. The dominance of eigensolutions 4 and 5 in the total change of the response is clearly visible while comparing Figure 4 with Figure 5a. This simple example shows, that the most effective spatial locations to apply structural modifications to maximize or minimize the change of the response, r_k', can be identified using by a very limited number of eigensolutions.



(a) Location dependent, normalized measure of the change of the total projection, r_4'.



(b) Location dependent, normalized measure of the change of the fourth eigenfrequency, ω_4^2.

Figure 5: Location dependent, normalized plots. (a) shows the change of the response, r_4' while taking all N eigensolutions into account, (b) shows the change of the fourth eigenfrequency depending on the location at which the circular beam diameter is modified.

A close look to the structural eigensolutions, (see Figure 2a), and the modal representation of the eigenmode sensitivity, (see Eq. (8)), shows already that a high contribution of the fifth eigenmode leads to a maximization of the change of the projection, r'_k. Detailed observation and knowledge of the eigensolution of interest and the neighboring eigensolutions will therefore provide insights into the possibilities and limitations of systematic eigensolution control.

Figure 5b shows how the change of the fourth eigenfrequency, ω_4^2, depends on the location at which the circular beam diameter d_e is modified. This figure can be used to limit the shift in eigenfrequency due to the applied modifications. Figure 5b shows, as an example, that the shift in eigenfrequency can be neglected by applying local structural modifications at the left wingroot and at the right wingtip. This means, while looking to Figure 5a, that the change of the response can be maximized while the eigenfrequency of the excited eigenmode is not varied.

5 CONCLUSIONS

In this work, a method is presented to increase the understanding of systematic eigensolution control via local modifications. The changes in the eigensolutions, due to local structural modifications, are determined using sensitivity analysis. The proposed method uses the modal basis of the structure as the preferred basis, which increases the insights into the possibilities and limitations during systematic eigensolution control. A projection is proposed to study the effectiveness of specific local structural modifications. With this projection, the initially present N-dimensional modal space is largely decreased towards a limited number of dominant eigensolutions. This leads to a more intuitive understanding of the eigensolution control. Subsequently, these most dominant eigensolutions can be used to obtain significant changes in the eigensolution of interest using minimal structural modifications.

Because of constraints on weight and power consumption, high effectiveness is of great interest in controlling the eigensolutions of resonating FWMAV designs. For active flight control, one often requires a controlled change of the initially symmetric flight mode towards an asymmetric flapping motion. In this work, a simple 2D model of a compliant structure is used to show the locations at which structural modifications should be applied to change a symmetric eigenmode into an asymmetric one. This simple study shows that a proper understanding of the neighboring eigensolutions contributes to the understanding of the required location of the structural modifications to obtain this asymmetry.

The proposed projection method will decrease computational costs for optimization methods, such as topology optimization. Optimization techniques might be used to determine the optimal size, number and spatial location of actuator more precisely. Since one is able to identify the most significant eigenmodes, the computation time will be decreased. The shift of the eigenfrequency, due to structural modifications, is easily taken into account such that constraints on the eigenfrequency shift can be incorporated.

Harmonically driven compliant structures, such as FWMAV designs, are generally non-conservative, due to aerodynamic damping. In future research, the systematic eigensolution control, using the modal basis, will be investigated for non-conservative systems. Subsequently, the potential of repeated eigenvalues for the rapid control of eigensolutions will be investigated. This is motivated by the reasoning, as presented in this work, that neighboring eigenmodes become more significant if their corresponding eigenfrequencies are closely spaced. Additionally, the presence of multiple control states will be investigated to allow for more advanced control of the eigensolution of interest.

REFERENCES

[1] S. Calmes, S. Schweizer, Ph. Renaud, Resonating Large Angle And Aow Consumption Micromachined Optical Scanner. M.E. Motamedi, R. Goring. eds. *Proc SPIE Int Soc Opt Eng, Conference of Miniaturized Systems with Micro-Optics and Micromechanics III*, San Jose, CA, January 26-27, **3276**, 96–102, 1998.

[2] P. Hagedorn, J. Wallaschek, Travelling wave ultrasonic motors, Part I: Working principle and mathematical modelling of the stator. *Journal of Sound and Vibration*, **155**(2), 31–46, 1992.

[3] K. Saitou, D.-A. Wang, S.J. Wou, Externally Resonated Linear Microvibromotor for Microassembly. *Journal of Microelectromechanical Systems*, **9**(3), 336–346, 2000.

[4] G. Stemme, Resonant silicon sensors. *Journal of Micromechanics and Microengineering*, **1**(2), 113–125, 1991.

[5] C.T.-C. Nguyen, Frequency-Selective MEMS for Miniaturized Low-Power Communication Devices. *IEEE Transactions on Microwave Theory and Techniques*, **47**(8), 1486–1503, 1999.

[6] C.H. Greenewalt, The Wings of Insects and Birds as Mechanical Oscillators. *Proceedings of the American Philosophical Society*, **104**(6), 605–611, 1960.

[7] R.J. Wood, The First Takeoff of a Biologically Inspired At-Scale Robotic Insect. *IEEE Transactions on Robotics*, **24**(2), 341–347, 2008.

[8] C.T. Bolsman, J.F.L. Goosen, F. van Keulen, Design Overview of a Resonant Wing Actuation Mechanism for Application in Flapping Wing MAVs. *International Journal of Micro Air Vehicles*, **1**(4), 263–272, 2009.

[9] Y. Maeda, S. Nishiwaki, K. Izui, M. Yoshimura, K. Matsui, K. Terada, Structural topology optimization of vibrating structures with specified eigenfrequencies and eigenmode shapes. *International Journal for Numerical Methods in Engineering*, **67**(5), 597–628, 2006.

[10] A. Takezawa, M. Kitamura, Sensitivity analysis and optimization of vibration modes in continuum systems. *Journal of Sound and Vibration*, **332**(6), 1553–1566, 2013.

[11] P.H. Nakasone, E.C.N. Silva, Dynamic Design of Piezoelectric Laminated Sensors and Actuators using Topology Optimization. *Journal of Intelligent Material Systems and Structures*, **21**(16), 1627–1652, 2010.

[12] E.F. Crawley, J. de Luis, Use of Piezoelectric Actuators as Elements of Intelligent Structures. *AIAA Journal*, **25**(10), 1373–1385, 1987.

[13] R.L. Fox, M.P. Kapoor, Rates of Change of Eigenvalues and Eigenvectors. *AIAA Journal*, **6**(12), 2426–2429, 1968.

[14] R.B. Nelson, Simplified Calculation of Eigenvector Derivatives. *AIAA Journal*, **14**(9), 1201–1205, 1976.

[15] S. Adhikari, M.I. Friswell, Eigenderivative analysis of asymmetric non-conservative systems. *International Journal for Numerical Methods in Engineering*, **51**(6), 709–733, 2001.

[16] I.U. Ojalvo, Efficient Computation of Modal Sensitivities for Systems with Repeated Frequencies. *AIAA Journal*, **26**(3), 361–366, 1988.

[17] M. Géradin, D. Rixen, *Mechanical Vibrations: Theory and Application to Structural Dynamics, 2nd Edition*. John Wiley & Sons, 1999.

[18] F. van Keulen, H. de Boer, Rigorous Improvement of Semi-Analytical Design Sensitivities by Exact Differentiation of Rigid Body Modes. *International Journal for Numerical Methods in Engineering*, **42**(1), 71–91, 1998.

[19] R.D. Cook, D.S. Malkus, M.E. Plesha, R.J. Witt, *Concepts and Applications of Finite Element Analysis, 4th Edition*. John Wiley & Sons, 2001.

COMPDYN 2013
4th ECCOMAS Thematic Conference on
Computational Methods in Structural Dynamics and Earthquake Engineering
M. Papadrakakis, V. Papadopoulos, V. Plevris (eds.)
Kos Island, Greece, 12–14 June 2013

DEVELOPMENT OF AN EFFICIENT UNSTRUCTURED FINITE VOLUME SOLVER FOR A NEW CONSERVATION LAW IN FAST STRUCTURAL DYNAMICS

M. Aguirre[1], A.J. Gil[1], J.Bonet[1] and C.H. Lee[1]

[1] Civil and Computational Engineering Centre, College of Engineering
Swansea University, Singleton Park, SA2 8PP, United Kingdom
e-mail: {m.aguirre,a.j.gil,j.bonet,c.h.lee}@swansea.ac.uk

Keywords: Instructions, ECCOMAS Thematic Conference, Structural Dynamics, Earthquake Engineering, Proceedings.

Abstract. *In this paper, the Jameson-Schmidt-Turkel scheme (JST) is implemented to solve a new mixed methodology in fast transient dynamics [1, 2]. The use of this numerical technique leads to a significant cost reduction compared to standard Finite Volume methods, which require the use of linear reconstruction and slope limiters to guarantee second order accuracy. Crucially, the JST algorithm is specially designed to be used in conjunction with unstructured meshes and is particularly suited for problems with discontinuities, since the artificial dissipation term appearing in the scheme includes an implicit shock capturing term. All of the above ingredients enable the efficient simulation of realistic large scale problems within the context of fast structural dynamics. In this paper, the JST scheme has been combined with a two-stage Total Variation Diminishing (TVD) Runge-Kutta time integrator. The capabilities of the resulting numerical technique, including the preservation of angular momentum and the excellent behaviour in bending dominated scenarios, are demonstrated for a series of benchmark problems. The solutions will be compared with solutions obtained using other methodologies, such cell centred upwind Finite Volume, Two Step Taylor Galerkin or Stream Upwind Petrov Galerkin (SUPG)[4][3][6][5]*

1 INTRODUCTION

Recently, a new Lagrangian mixed formulation [1] has been developed for the simulation of fast transient dynamics problems. This methodology is in the form of a system of first order conservation laws, where the linear momentum and the deformation gradient tensor are regarded as the two main conservation variables. The current paper presents a new implementation using the Jameson-Schmidt-Turkel (JST) scheme [3] widely know within the CFD community. The scheme uses a central differences approach, equivalent to a Galerkin Finite Element Discretisation with linear elements plus a blend of a non divided Laplacian and a biharmornic operator in order to add artificial diffusion. The attractiveness of this scheme relies mainly on computational cost aspects. First of all, it is a nodal based finite volume and therefore, the number of evaluations of the stress tensor (constitutive model) will be reduced drastically as compared to a cell centred scheme since the number of elements is from 5 to 7 times the number of nodes in a tetrahedral mesh. Secondly, the computational effort when computing the flux gradients is reduced to a half in a vertex centred mesh since the loops are performed on edges instead of faces. Furthermore, the combination of the artificial dissipation term and the shock capturing switch allows obtaining a second order monotonicity preserving algorithm without the use of linear reconstruction and slope limiters.

The work presented is the spatial discretisation of a set of governing equations (conservation of linear momentum and deformation gradient) by using the JST scheme. In order to adapt the scheme to the specificities of the problem, dissipation will only be added to the first equation, whereas the update of the deformation gradient will be left as a numerical gradient of the velocities with no additional dissipation. This will allow satisfying the compatibility conditions of the deformation mapping. Special care will be taken in the integration of the boundary fluxes, by the use of a weighted average of nodes at the boundary faces. The spatial discretisation will be combined with a two stages Total Variation Diminishing (TVD) Runge-Kutta time integrator in order to advance the solution in time. The displacements are integrated in time using a trapezoidal rule which, combined with a Lagrange multiplier minimisation procedure, ensure the conservation of angular momentum. An additional correction to the numerical dissipation of the linear momentum is as well added in order to ensure the conservation of that variable.

2 GOVERNING EQUATIONS

A mixed system of conservation laws was presented in [1] as

$$\begin{aligned} \frac{\partial \mathbf{p}}{\partial t} - \nabla_0 \cdot \mathbf{P} &= \rho_0 \mathbf{b} \\ \frac{\partial \mathbf{F}}{\partial t} - \nabla_0 \cdot (\mathbf{v} \otimes \mathbf{I}) &= \mathbf{0} \\ \frac{\partial E_T}{\partial t} - \nabla_0 \cdot \left(\mathbf{P}^T \mathbf{v}\right) &= 0 \end{aligned} \tag{1}$$

where $\mathbf{p} = \rho_0 \mathbf{v}$ is the linear momentum, ρ_0 is the material density, $\mathbf{v}$ is the velocity field, $\mathbf{b}$ is the body force per unit mass, $\mathbf{F}$ is the deformation gradient tensor, $\mathbf{P}$ is the first Piola-Kirchhoff stress tensor, E_T is the total energy per unit of undeformed volume, $\mathbf{I}$ is the identity tensor and ∇_0 describes the material gradient operator in undeformed space. The above system of equations can be rewritten in a more compact form, describing a first order hyperbolic system

as

$$\frac{\partial \mathbf{U}}{\partial t} + \frac{\partial \boldsymbol{F}_I}{\partial X_I} = \mathbf{S} \tag{2}$$

where

$$\mathbf{U} = \begin{pmatrix} p_1 \\ p_2 \\ p_3 \\ F_{11} \\ F_{12} \\ F_{13} \\ F_{21} \\ F_{22} \\ F_{23} \\ F_{31} \\ F_{32} \\ F_{33} \\ E_T \end{pmatrix}, \quad \boldsymbol{F}_I = \begin{pmatrix} -P_{1I}(\mathbf{F}) \\ -P_{2I}(\mathbf{F}) \\ -P_{3I}(\mathbf{F}) \\ -\delta_{I1} v_1 \\ -\delta_{I2} v_1 \\ -\delta_{I3} v_1 \\ -\delta_{I1} v_2 \\ -\delta_{I2} v_2 \\ -\delta_{I3} v_2 \\ -\delta_{I1} v_3 \\ -\delta_{I2} v_3 \\ -\delta_{I3} v_3 \\ -P_{iI} v_i \end{pmatrix}, \quad \mathbf{S} = \begin{pmatrix} \rho_0 b_1 \\ \rho_0 b_2 \\ \rho_0 b_3 \\ 0 \\ 0 \\ 0 \\ 0 \\ 0 \\ 0 \\ 0 \\ 0 \\ 0 \\ 0 \end{pmatrix}, \quad \forall I = 1, 2, 3 \tag{3}$$

Additionally, the conservation law (2) has to be supplemented with a constitutive model which satisfies the objectivity requirement as well as the relevant laws of thermodynamics.

3 SPACE DISCRETISATION

The JST is a vertex centred Finite Volume Method and, as such, requires the use of a dual mesh for the definition of control volumes. In this paper, the median dual approach for triangular meshes, as presented in [4] and [5], has been chosen. This approach constructs the dual mesh by connecting edge midpoints with element centroids in two dimensions (see Figure 1) and edge midpoints with face centroids and element centroids in three dimensions. Such a configuration ensures that only one node of the initial mesh exists in each control volume. For a given edge connecting nodes e and α an area vector is then defined as

$$\mathbf{C}^{e\alpha} = \sum_{k \in \Gamma_{e\alpha}} A_k \mathbf{N}_k \tag{4}$$

where $\Gamma_{e\alpha}$ is the set of facets belonging to edge $e\alpha$, A_k is the area of a given facet and $\mathbf{N}_k$ is the normal vector of the facet (see Figure 1).

On account of the definition of the dual mesh, the defined area vector satisfy $\mathbf{C}^{e\alpha} = -\mathbf{C}^{\alpha e}$. This area vector enables a substantial reduction in the computational cost when computing the boundary integral used in the Green Gauss divergence theorem (classical in FVM), since it saves an additional loop on facets. Consider a hyperbolic system of conservation laws generally written as

$$\frac{\partial \mathbf{U}}{\partial t} + \frac{\partial \boldsymbol{F}_I}{\partial X_I} = \mathbf{0} \tag{5}$$

where $\mathbf{U}$ is the vector of conserved variables and $\boldsymbol{F}_I$ the flux vector. This set of equations can be discretised in space by using the extended JST scheme (see [4] and [**?**]) to give, for a given

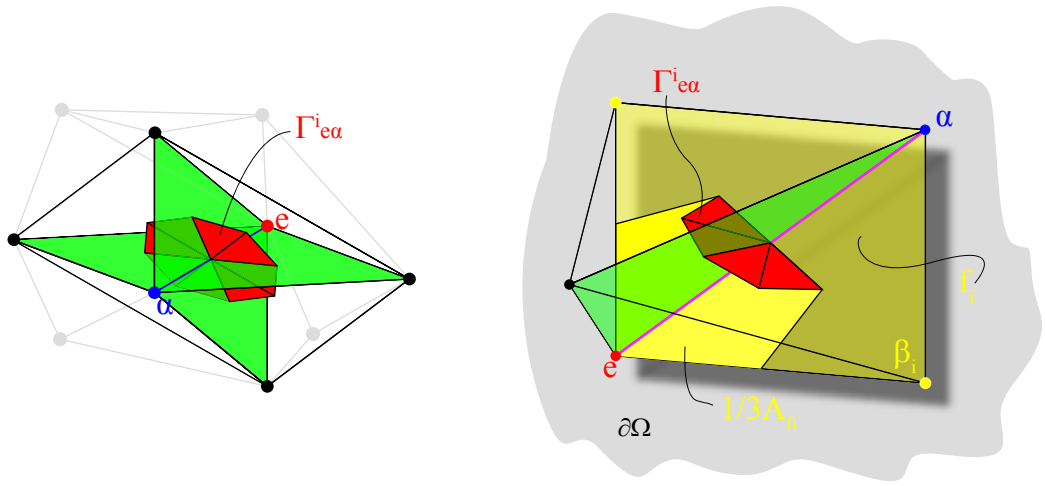


Figure 1: Set of facets related to an interior edge (left) and boundary edge (right) in three dimensions. The green surfaces correspond to the interior faces to which the edge belongs, whereas the dark yellow surfaces correspond to the boundary faces. The red surfaces are the set of interior facets $\Gamma_{e\alpha}$ corresponding to edge $e\alpha$. The bright yellow zone is the contributory area of the face $e\alpha\beta$ to node e.

node e,

$$\frac{d\mathbf{U}_e}{dt} = -\frac{1}{V_e}\left(\sum_{\alpha\in\Lambda_e}\frac{1}{2}(\boldsymbol{F}^e+\boldsymbol{F}^\alpha)\mathbf{C}^{e\alpha} + \sum_{\substack{\alpha\in\Lambda_e^B \\ \beta\in(\Lambda_e^B\bigcap\Lambda_\alpha^B)}}\frac{6\boldsymbol{F}^e+6\boldsymbol{F}^\alpha+6\boldsymbol{F}^\beta}{8}\mathbf{N}^{e\alpha\beta}A^{e\alpha\beta}\right)+\frac{1}{V_e}\mathbf{D}(\mathbf{U}_e) \tag{6}$$

where Λ_e is the set of nodes connected to node e by an edge, Λ_e^B is the set of nodes connected to node e by a boundary edge, $\boldsymbol{F}$ is a matrix gathering the flux vectors as $\boldsymbol{F}=(\boldsymbol{F}_1,\boldsymbol{F}_2,\boldsymbol{F}_3)$ and $\mathbf{D}(\mathbf{U}_e)$ is a dissipative operator. The first term of the equation is the actual Green Gauss evaluation of the cell boundary fluxes. The dissipative operator reads

$$\mathbf{D}(\mathbf{U}_e)=\sum_{\alpha\in\Lambda_e}\varepsilon_{e\alpha}^{(2)}\Psi_{e\alpha}\theta_{e\alpha}\left(\mathbf{U}_\alpha-\mathbf{U}_e\right)-\varepsilon_{e\alpha}^{(4)}\Psi_{e\alpha}\theta_{e\alpha}\left(\mathbf{L}(\mathbf{U}_\alpha)-\mathbf{L}(\mathbf{U}_e)\right) \tag{7}$$

where $\varepsilon_{e\alpha}^{(2)}$ and $\varepsilon_{e\alpha}^{(4)}$ are discontinuity switches which activate second or fourth order differences operators, $\Psi_{e\alpha}$ is the spectral radius and $\theta_{e\alpha}$ denote geometrical weights. The second order differences operator is defined as

$$\mathbf{L}(\mathbf{U}_e)=\sum_{\alpha\in\Lambda_e}\theta_{e\alpha}(\mathbf{U}_\alpha-\mathbf{U}_e) \tag{8}$$

The first term of the dissipative operator provides the second order differences operator and the second term the fourth order differences operator. The fourth order differences operator avoids the appearance of the odd-even decoupling of the solution (that would result from using averaged fluxes) whilst maintaining the second order accuracy of the scheme. The second order differences operator is introduced to smear out the solution in the vicinity of a shock whilst reducing the solution to first order locally.

4 TIME DISCRETISATION

The time discretisation is performed using a Total Variation Diminishing (TVD) Runge-Kutta time integrator as proposed by Shu and Osher [6]. For a set of equations discretised in space, but left continuous in time (method of lines) at a given node e,

$$\frac{d\mathbf{U}_e}{dt} = -\mathbf{R}_e(\mathbf{U}_e, t) \tag{9}$$

the method computes the solution at time step t^{n+1} from the solution at time step t^n as

$$\begin{aligned} \mathbf{U}_e^* &= \mathbf{U}_e^n - \Delta t \mathbf{R}_e(\mathbf{U}_e^n, t^n) \\ \mathbf{U}_e^{**} &= \mathbf{U}_e^* - \Delta t \mathbf{R}_e(\mathbf{U}_e^*, t^{n+1}) \\ \mathbf{U}_e^{n+1} &= \frac{1}{2}(\mathbf{U}_e^n + \mathbf{U}_e^{**}) \end{aligned} \tag{10}$$

In addition, the displacements are integrated in time using the trapezoidal rule, which combined with a Lagrange multiplier minimisation procedure, allows for the conservation of angular momentum.

5 NUMERICAL RESULTS

5.1 Punch test

A square flat plate of unite side length is constrained to move tangentially on the east, west and south sides, whereas it is free on the north side. The plate is subjected to an initial uniform velocity $v_{punch} = 100$ m/s on its right half side. The plate is composed of a NeoHookean rubber material with Young's modulus $E = 1.7 \times 10^7 Pa$, density $\rho_0 = 1.1 \times 10^3$ Kg/m^3 and Poissons ratio $\nu = 0.45$. The problem shows the performance of the method in nearly incompressible scenarios, with absence of volumetric locking and spurious modes (checker board) for the pressure. Figure 2 compares results obtained using Mean Dilatation technique and standard Finite Element Method (FEM) for the standard displacement based formulation and Cell Centred Finite Volume, Stream Upwind Petrov Galerkin (SUPG) and JST using the proposed formulation. It can be seen how the FEM solution suffers from volumetric locking, while the Mean Dilatation technique is capable of circumventing it. In addition, both solutions exhibit spurious oscillations in the pressure distribution. The methodologies based in the proposed conservation law formulation (equation (1)) alleviate both the volumetric locking and the appearance of the spurious pressure oscillations.

5.2 Spinning cube (3D)

A unit side cube free at its six faces is released with an initial angular velocity $\omega_0 = \frac{105}{\sqrt{3}}(1, 2, 3)^T$ rad/s. The cube is composed of a Neohookean nearly incompressible material with Young's modulus $E = 1.7 \times 10^7 Pa$, density $\rho_0 = 1.1 \times 10^3$ Kg/m^3 and Poissons ratio $\nu = 0.45$. Figure 3 shows the evolution in time of the deformed configuration and distribution of pressure. The algorithm is able to preserve the angular and linear momentum, as it is shown in Figure 4.

5.3 Column twist (3D)

This example is shown in order to show the robustness of the problem in highly nonlinear deformation scenarios. A column of rubber material is clamped on its bottom surface and free

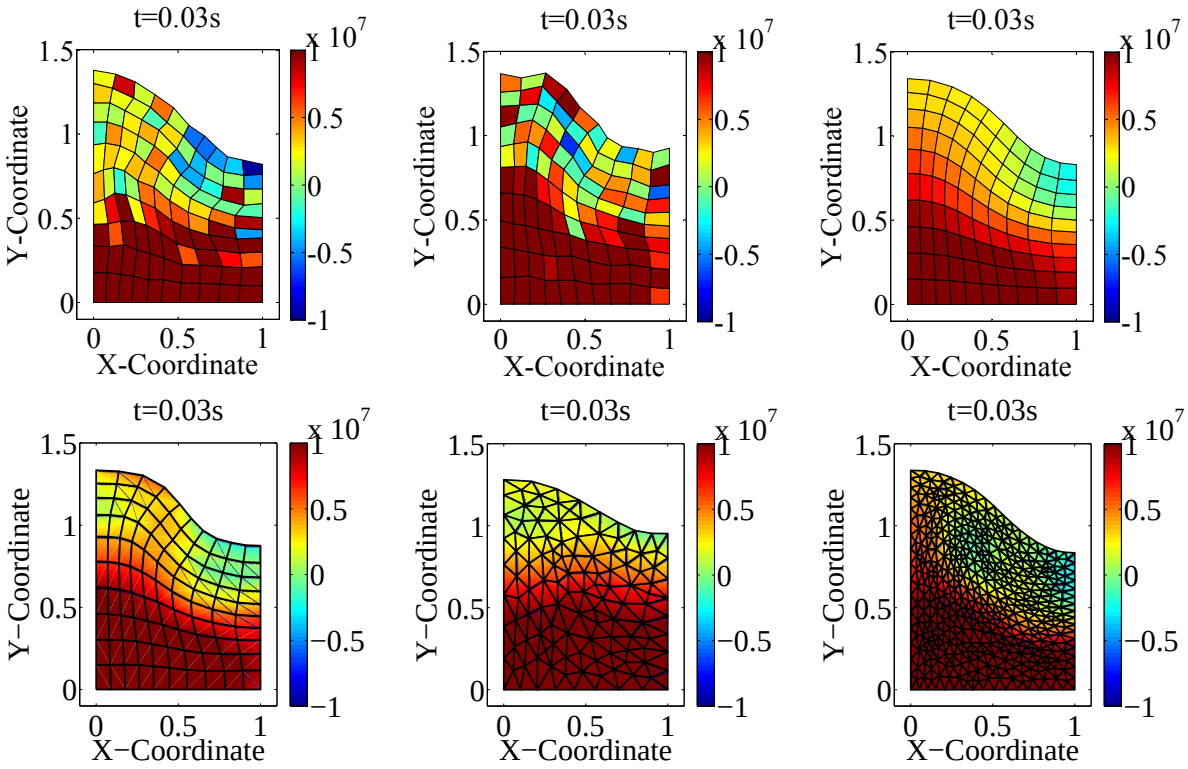


Figure 2: Numerical solution of the punch test case with an initial uniform velocity at the right hand side $v_{punch} = 100$ m/s. Material properties $E = 1.7 \times 10^7 Pa$, $\rho_0 = 1.1 \times 10^3 Kg/m^3$, $\nu = 0.45$ for a Neohookean material. The solution is shown at time $t = 0.03$s for different discretisations. From left to right and top to bottom: Mean dilatation technique, standard FEM, Cell Centred Finite Volume, SUPG and JST for the last two plots. The solution is obtained using a discretisation of 121 nodes for all the cases except for the last JST solution, where the number of nodes is doubled.

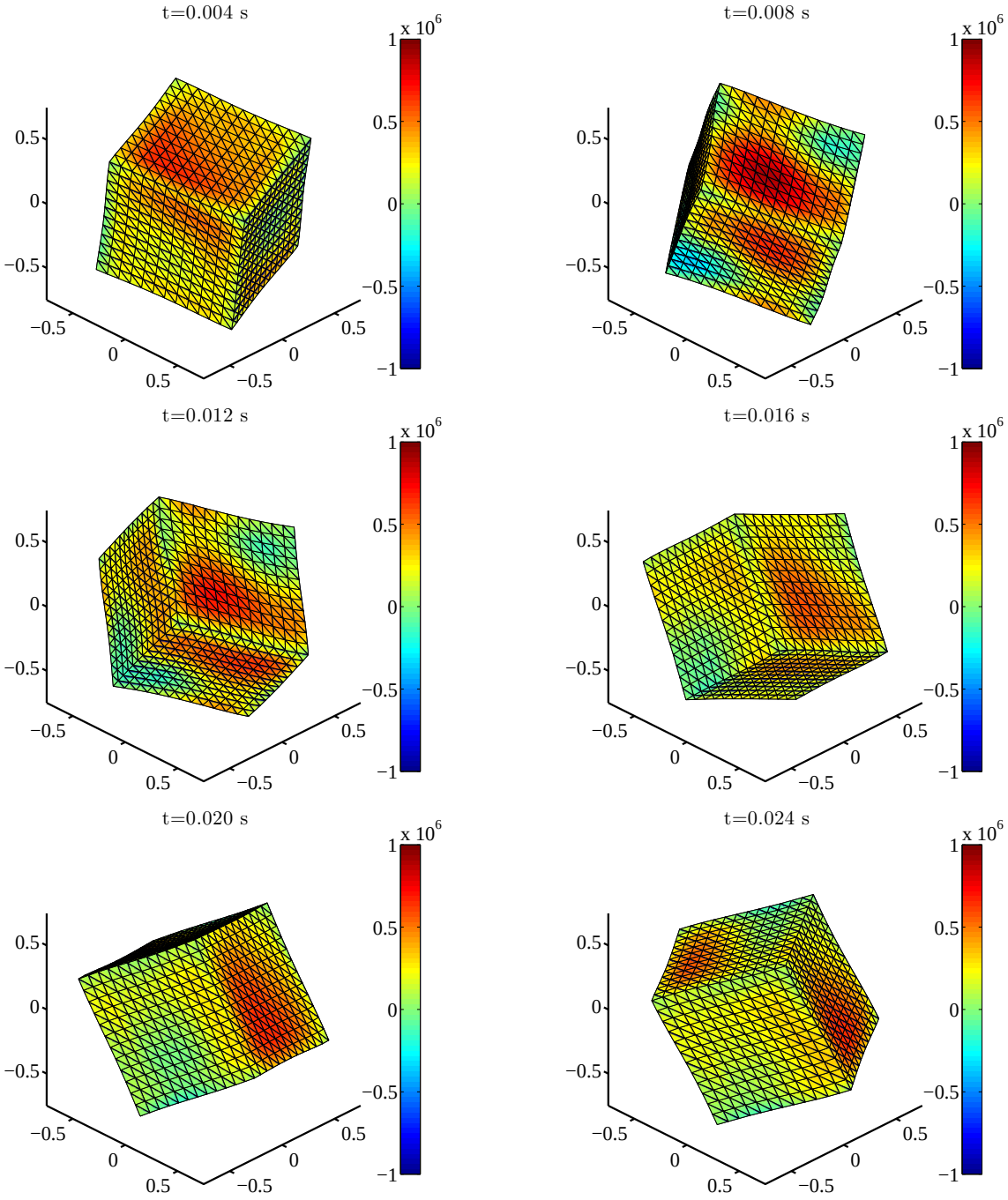


Figure 3: Spinning cube. Evolution in time of the pressure distribution in the deformed configuration. Initial angular velocity $\omega_0 = \frac{105}{\sqrt{3}}(1,2,3)^T$ rad/s. Neohookean nearly incompressible material with Young's modulus $E = 1.7 \times 10^7 Pa$, density $\rho_0 = 1.1 \times 10^3$ Kg/m^3 and Poissons ratio $\nu = 0.45$. JST spatial discretisation with $h = 1/12$ m, $\kappa^{(4)} = 1/128$ and $\alpha_{CFL} = 0.4$.

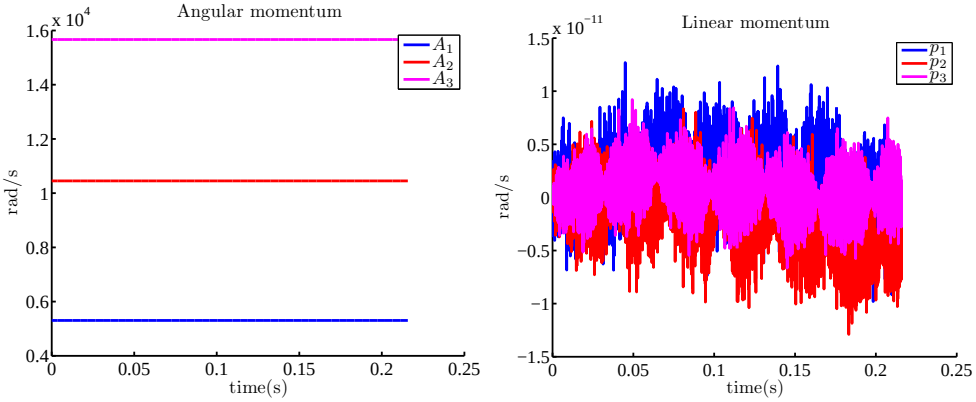


Figure 4: Spinning cube.(a) Conservation of angular momentum. (b) Conservation of linear momentum. Initial angular velocity $\omega_0 = \frac{105}{\sqrt{3}}(1,2,3)^T$ rad/s. Neohookean nearly incompressible material with Young's modulus $E = 1.7 \times 10^7 Pa$, density $\rho_0 = 1.1 \times 10^3$ Kg/m^3 and Poissons ratio $\nu = 0.45$. JST spatial discretisation with $h = 1/12$ m, $\kappa^{(4)} = 1/128$ and $\alpha_{CFL} = 0.4$.

on the rest. An initial angular velocity $\omega = (0,0,105)^T$ rad/s is imposed in the whole body except for its clamped bottom. The bar is then left oscillating in time. The problem is set by using a Neohookean nearly incompressible material with Young's modulus $E = 1.7 \times 10^7 Pa$, density $\rho_0 = 1.1 \times 10^3$ Kg/m^3 and Poissons ratio $\nu = 0.45$. Figure 5 shows the evolution in time of the problem. As it can be seen, the deformation of the column is well captured even as the solution advances in time. No numerical oscillations or instabilities are present.

6 CONCLUSIONS

The JST scheme has been implemented for a new mixed conservation law in fast transient dynamics for triangular and tetrahedral meshes. The implementation has been carried out with special care to numerical stability, fulfillment of compatibility conditions and treatment of boundary conditions. This results in an adapted JST scheme, where the numerical dissipation is only added to the first equation (conservation of linear momentum) and the boundary conditions are treated using an external loop on faces, where a weighted average of nodal values ensures accuracy and robustness of the solution. In addition, the numerical algorithm is modified to ensure preservation of linear and angular momentum. A set of numerical results has been presented both for two and three dimensions. These numerical results have proven second order convergence both for stresses and velocities. Furthermore, they circumvent the volumetric locking and spurious pressure modes as they appear in standard Finite Element (displacement based formulation) using linear elements for triangle and tetrahedra. The solutions compare well with other methodologies that discretise the proposed formulation, such as cell centred Finite Volume or Stream Upwind Petrov Galerkin. The proposed methodology allows for further research into more realistic real life problems. In fact, irreversible problems involving shocks can be easily implemented, due to the straightforward implementation of constitutive models and the built-in shock capturing term. Contact problems can as well be investigated by using Riemann-Solvers on the external faces.

REFERENCES

[1] C.H. Lee, A.J. Gil, J. Bonet *Development of a cell centred upwind finite volume algorithm for a new conservation law formulation in structural dynamics*, Computers and Structures

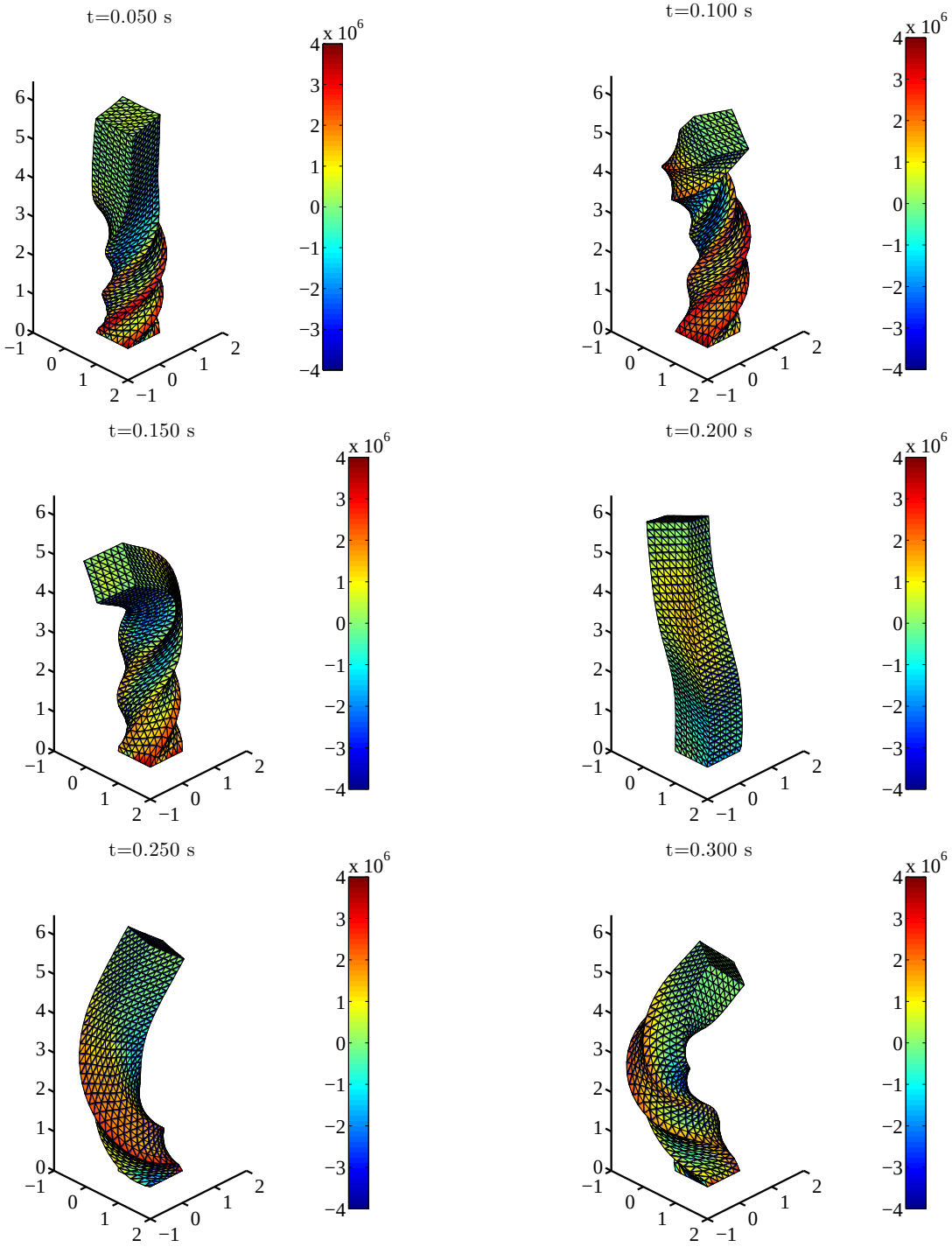


Figure 5: Twisting column. Evolution in time of the pressure distribution in the deformed configuration. Initial angular velocity $\omega_0 = \frac{105}{\sqrt{3}}(1,2,3)^T$ rad/s. Neohookean nearly incompressible material with Young's modulus $E = 1.7 \times 10^7 Pa$, density $\rho_0 = 1.1 \times 10^3$ Kg/m^3 and Poissons ratio $\nu = 0.45$. JST spatial discretisation with $h = 1/6$ m, $\kappa^{(4)} = 1/128$ and $\alpha_{CFL} = 0.4$.

(in press), 2012

[2] C.H. Lee, A.J. Gil, J. Bonet *Development of a New Stabilised Finite Element Methodology for the New Conservation Law Formulation in Lagrangian Fast Dynamics* Computers and Structures (under review)

[3] A. Jameson, W. Schmidt, Friedrichshafen, E. Turkel *Numerical solution of the euler equations by finite volume methods using runge-kutta time-stepping schemes* AIAA 5th Computational Fluid Dynamics Conference 1259, 1982

[4] J. Blazek *Computational fluid dynamics: principles and applications* 2nd Edition, Elsevier, 2005

[5] K. A. Sørensen, O. Hassan, K. Morgan, N. P. Weatherill *A multigrid accelerated hybrid unstructured mesh method for 3d compressible turbulent flow* Computational Mechanics 31 101114, 2003

[6] C.-W. Shu, S. Osher *Efficient implementation of essentially non-oscillatory shock-capturing schemes* Journal of Computational Physics 77 (2) 439 471, 1988

COMPDYN 2013
4th ECCOMAS Thematic Conference on
Computational Methods in Structural Dynamics and Earthquake Engineering
M. Papadrakakis, V. Papadopoulos, V. Plevris (eds.)
Kos Island, Greece, 12–14 June 2013

REDUCTION METHOD APPLIED TO VIBRATIONS OF VISCOELASTIC SANDWICH SHELLS

L.Duigou[1*], F.Boumediene[2], JM. Cadou[1], E.M. Daya[3]

[1] Laboratoire d'Ingénierie des Matériaux de Bretagne,
Université Européenne de Bretagne, Université de Bretagne Sud,
Rue de Saint Maudé, BP 92116,
56321 Lorient Cedex, France
{laetitia.duigou,jean-marc.cadou}@univ-ubs.fr

[2] Laboratoire de Mécanique Avancée,
Faculté de Génie Mécanique & Génie des Procédés, USTHB,
BP 32, El Alia, 16111 Bab Ezzouar,
Alger, Algeria
boumedienefaiza@yahoo.fr

[3]LEM3,
Ile du Saulcy 57045 Metz - cedex 01, France
daya@lpmm.sciences.univ-metz.fr

Keywords:. Frequency, damping, asymptotic numerical method, reduction

Abstract. *This work deals with the vibrations of sandwich visco-elastic structures. The central visco-elastic layer included between two metallic layers leads to solve a problem of complex and non-linear eigenvalues. Indeed the core material depends on the frequency. Several methods exist to solve this type of problem. But the dimension of matrices to be manipulated can become very large and generate substantial computational times. A reduction technique is proposed herein. It is applied and compared to the high order Newton method.*

INTRODUCTION

To reduce vibrations and noise, the industrialists propose damping sandwich structures, in which a visco-elastic layer is included between two layers of metal material such as aluminum, for instance. The analysis of free vibrations of these structures leads to solve a problem of complex and non-linear eigenvalues. The non-linearity is due to the frequency dependence of the visco-elastic central layer. A lot of models or methods have been developed to solve this non-linear problem. For example, Daya and Potier-Ferry [1] proposed a continuation method. From the linear eigenmode and using the perturbation technique, they determine the frequencies and loss-factors. Duigou and al. [2] developed two iterative methods based on homotopy technique, asymptotic numerical method and Padé approximants. One of them is a sort of high order Newton method. Other authors, like Damanpack and al. [3] or Banerjee and al. [4] used the dynamical stiffness method. Nevertheless, whatever the method used, the matrix sizes to be manipulated in a problem of non-linear vibrations can become quickly very large and generate substantial computational times. In order to reduce this cost, different methods exist like the condensation method proposed by Park and al. [5] or Lima and al. [6], the Lanczos's algorithm used by Chen [7].

In this work, we consider the high order Newton method proposed by Duigou and al [2]. This method is very efficient but it needs substantial computational time because of the matrix sizes to be inverted. That is why we propose to use a reduction method to decrease computational time.

1 PROBLEM OF VIBRATIONS

We consider a sandwich structure including a central layer made up of a visco-elastic material. The latter one generates a complex Young modulus. In order to determine the eigenvalues of this type of sandwich structures, the equation to be solved is written in the following discrete form :

$$\mathbf{R}(\omega, \mathbf{U}) = [\mathbf{K}(0) + E(\omega)\mathbf{K_v} - \omega^2\mathbf{M}][\mathbf{U}] = 0 \tag{1}$$

where **M** is the mass matrix, **K**(0) is the elastic stiffness matrix, E(ω) is the Young modulus depending on the pulsation ω and **U** represents the vector of generalized nodal displacements. The matrix K_υ does not depend on ω. Duigou [8] proposed a numerical method to solve the non-linear eigenvalue problem (1). This method is based on a homotopy technique and a perturbation method. The principle is the following one :

1- A starting point ($\mathbf{U_0}$, p_0) with (p = iω) is chosen and an incremental solution is introduced in the following way :

$$\begin{Bmatrix} \Delta U \\ \Delta p \end{Bmatrix} = \begin{Bmatrix} U - U_0 \\ p - p_0 \end{Bmatrix} \tag{2}$$

2- After inserting (2) into (1) and after several manipulations, the homotopy technique is applied. This one consists in introducing a parameter ε such as for $\varepsilon = 0$, the correction ($\Delta\mathbf{U}$, Δp) is equal to zero and for $\varepsilon = 1$, the exact non-linear problem (1) is solved.

For example, this modified problem can be defined by :

$$L.\Delta U+G.U_0\Delta p+2p_0\Delta pM\Delta U+\varepsilon(\Delta E(p)-E'(p_0)\Delta p)K_v.U_0 \\ +\Delta E(p)K_v.\Delta U+(\Delta p)^2M.U_0+(\Delta p)^2M.\Delta U+\varepsilon R_0=0 \quad (3)$$

with $L=K(0)+E(p_0)K_v+p_{0^2}M$ linear operator and $R_0=(K(0)+E(p_0)K_v+p_{0^2}M).U_0$, initial residue.

3- Finally, the perturbation technique is applied, that is to say, the increment ($\Delta\mathbf{U}$,Δp) is sought in the truncated series form depending on the perturbation parameter ε *:*

$$\Delta U=\sum_{i=1}^{N}\varepsilon^i U_i \quad et \quad \Delta p=\sum_{i=1}^{N}\varepsilon^i p_i \quad (4)$$

4- After inserting these series into the modified problem(3), a series of linear problems for each order is obtained and solved.

As the number of unknowns is greater than the number of equations, an equation to normalize the mode is introduced :

$$\Delta\mathbf{U}^t\,\mathbf{G}\,\mathbf{U_0}=0 \quad (5)$$

Then, the linear problems can be written at the ith truncature order, in the following matrix form :

$$\left[L_t\right]\begin{bmatrix}U_i\\p_i\end{bmatrix}=\begin{bmatrix}L & GU_0\\GU_0^t & 0\end{bmatrix}\begin{bmatrix}U_i\\p_i\end{bmatrix}=\begin{bmatrix}F_i^{nl}\\0\end{bmatrix} \quad (6)$$
$$avec \quad L=K(0)+E(p_0)K_v-p_0^2M$$

where $\mathbf{L_t}$ refers to the complex tangent operator and F^{nl}_i is a second member vector changing at each 'i' order but depending only on the variables calculated in previous orders and $(\,)^t$ indicates the transposed operator.

The characteristic parameters of this method are the truncature order of (N) series and a small tolerance parameter enabling to check if the method has converged towards the solution. This resolution technique, named high order Newton method gives good results compared to experimental results. The disadvantage of this method is computational time. Indeed, the problems to solve need triangulating large-size matrices. However, one must take into consideration that the high order Newton method needs one matrix triangulation only and the resolution of "N" linear systems (6) at each iteration for an initial solution ($\mathbf{U_0}$, p_0). In order to reduce computational times, the authors propose – in the reference [2] – to use real matrices instead of consistent complex matrices, corresponding to the $\mathbf{L_t}$ Operator. This method is faster but it diverges in some cases.

The objective of this work is to apply a reduction model to the high order Newton algorithm in order to reduce computational times while preserving the convergence properties of the algorithm.

2 REDUCTION METHOD

The reduction model is applied to the equation (1) : the displacement vector is projected on a small-sized base :

$$U=\Re\, u \quad (7)$$

where **u** is the reduced vector and $\Re$, the projection matrix. This matrix is built using the eigenvectors Φ of linear problems and the resulting vectors considering the visco-elastic part of the problem (1), that is to say, according to the reference [9] :

$$\Re = [\Phi \ , \Psi] \tag{8}$$

With the vectors Ψ , solutions of following linear problems :

$$\Psi = K(0)^{-1} K_v \Phi \tag{9}$$

Introducing the relation(7) in the equation(1) and left-multiplying by $\Re^T$, the equation (1) can be written in the reduced form :

$$\mathbf{r}(\omega,\mathbf{u})=[\mathbf{k}(0)+E(\omega)\mathbf{k_v}-\omega^2\mathbf{m}][\mathbf{u}]=0 \tag{10}$$

Where $\mathbf{m} = \mathfrak{R}^T \mathbf{M} \mathfrak{R}$, $\mathbf{k} = \mathfrak{R}^T \mathbf{K} \mathfrak{R}$, $\mathbf{k_v} = \mathfrak{R}^T \mathbf{K_v} \mathfrak{R}$

Then, this reduced equation is solved using the high order Newton method similarly to the real-size problem. A parameter of perturbation is introduced in equation (10) and the unknowns of the reduced problem are sought in the form of truncated series at "N" order, for example.

3 NUMERICAL EXAMPLES

To compare the high order Newton algorithms with or without reduction method, the finite element method is applied. The finite element used is the sandwich shell element with eight nodes and eight degrees of freedom (D.o.F.) developed by Duigou [8] and based on the element of Büchter and al. [9]. In the first part, the Young modulus of the beam is considered constant complex and in the second part, it is considered depending on the temperature. In order to check the convergence of results, a criterion based on the residue calculus is carried out at each step in the following way for the high order Newton method :

- without reduction : $RES = \dfrac{\|R(U,p)\|}{\|K(0).U\|} \leq \delta$
- with reduction : $RES = \dfrac{\|r(u,p)\|}{\|k(0).u\|} \leq \delta$

The tolerance, δ, has to be fixed for each method.

3.1 Example with a constant complex Young modulus

The considered example is a cantilever sandwich beam including a thin central visco-elastic layer and the Young modulus is constant and defined by:

$$E = E_0(1+i\eta c)$$

In this study, the parameter ηc is chosen equal to 1,5, representing quite high damping. The beam has the mechanical properties and the geometrical characteristics given in Table 1. This

one is discretized with 424 D.o.F., like in reference [2]. The used parameters by the high order Newton method are : a truncature order N=20, a tolerance equal to 1.10^{-7}. In order to apply the reduction method, 20 vectors are used. Then, the basis (8) is composed of 10 vectors Φ (from a linear vibration computation) and of 10 vectors Ψ solutions of the linear problem (9). The results obtained by the high order Newton method with – referred to as R-HONA) and without reduction – referred to as HONA – are given in Table 2 for the first two bending modes of the beam defined in Table 1.

Mechanical properties	Elastic layer – Aluminum	Visco-elastic layer
Young modulus	Ea = 6,9 1010 N/m2	E0 = 1794 103 N/m2
Poisson ratio	υa = 0,3	υp = 0,3
Density	ρa = 2766 kg/m3	ρp = 968,1 kg/m3
Thickness	ha = 1,524 mm	hp = 0,172 mm

Table 1. Mechanical and geometrical properties of Beam 1.

Mode		HONA [8]	R-HONA
64.32	Iteration	2	3
	Damped frequency	70.19647	70.19646
	Damping coefficient	0.228979	0.228978
	η_m / η_c	0.152653	0.152652
297.85	Iteration	2	3
	Damped frequency	310.4359	310.436
	Damping coefficient	0.295438	0.295435
	η_m / η_c	0.196959	0.196957

Table 2. First two bending modes of Beam 1. $E=E_0(1+i\,\eta_c)$= cst, η_c=1.5 and 20 vectors in the reduction base.

Table 2 shows that the reduction technique proposed enables to obtain the same values as the high order Newton method.

3.2 Example with a Young modulus depending on the temperature

A second cantilever sandwich beam with dimension (178*10 mm2) is considered. But this time, the Young modulus of the central visco-elastic layer is not constant. It is represented by the generalized Maxwell model :

$$E(\omega)=k_0+\eta_0 i\omega+\sum_{j=1}^{N_{max}}\frac{i\omega}{(\frac{i\omega}{k_j}+\frac{1}{\eta_j})} \tag{4}$$

The Maxwell number N_{max} is equal to 129. The other characteristics of the layer are shown in Table 3.

Here, for the finite element simulation, the temperature used is 20°C and the number of nodes used for discretization is equal to 53, that is to say, 424 D.o.F.. The parameters used by the high-order Newton algorithm with and without reduction method are the followings : a truncature order N=20, a tolerance parameter equal to 1.10^{-7} and 20 vectors in the projection basis. The first three bending modes are studied.

In the Table 4, we can note that the computational results carried out with the high order Newton with or without reduction diverge when the truncature order is equal to 20 in the series. That is why, in Table5, the computation of frequencies and dampings is carried out using a truncature order equal to 5. In this case, the two algorithms give good results.

Mechanical properties	Elastic layer – steel	Visco-elastic layer
Young modulus	$E_a = 2{,}1\ \ 10^{11}$ N/m^2	$E_p = 27{,}216\ \ 10^6$ N/m^2
Poisson ratio	$\upsilon_a = 0{,}3$	$\upsilon_p = 0{,}44$
Density	$\rho_a = 7800$ kg/m^3	$\rho_p = 1200$ kg/m^3
Thickness	$h_a = 0{,}6$ mm	$h_p = 0{,}045$ mm

Table 3. Properties of the beam 2.

Modes		HONA	R-HONA
29.96	Iteration	2	5
	Damped frequency	32.7725859	32.7725747
	Damping coefficient	0.033747927	0.033751093
	η_m / η_c	43.2200279	43.2240829
	RES	3.72228416E-11	1.14015107E-08
143.49	Iteration	3	4
	Damped frequency	197.870522	197.864831
	Damping coefficient	0.0981405456	0.0995990691
	η_m / η_c	125.68586	127.553749
	RES	2.53576098E-12	3.25600381E-09
349.78	Iteration	**Diverge**	**Diverge**

Table 4. First three bending modes of Beam 2. N=20.

Mode		HONA	R-HONA
29.99	Iteration	2	4
	Damped frequency	32.7842474	32.785868
	Damping coefficient	0.0335581189	0.0335753581
	η_m / η_c	42.9769478	42.9990273
143.75	Iteration	2	3
	Damped frequency	198.384908	198.635266
	Damping coefficient	0.0928710797	0.0931472569
	η_m / η_c	118.937401	119.291092
349.78	Iteration	3	4
	Damped frequency	548.090895	548.325729
	Damping coefficient	0.0922039246	0.117323568
	η_m / η_c	118.082993	150.253021

Table 5. First benfing modes of the beam 2. N=5.

4 CONCLUSION

These works deal with the vibrations of sandwich visco-elastic structures. The central layer leads to solve a non-linear eigenvalue problem. To do so, two techniques are compared herein : the high order Newton algorithms with and without reduction. Two examples of cantilever sandwich visco-elastic beams are studied. The first one has a constant complex Young modulus ($E= E_0(1+i\eta c)$) and the second one a Young modulus depending on frequency (Model of Maxwell for 20°C). In the two cases, the proposed methods give good results. Numerical tests of these works show that the use of a truncature order close to 5 leads to better convergence than a high order. Currently, numerical tests on more complex geometrical examples needing more final spatial discretization are being carried out in order to quantify computational time gains.

REFERENCES

[1] E.M. Daya, M. Potier-Ferry. A numerical method for nonlinear eigenvalue problems application to vibrations of viscoelastic structures. *Computers and Structures* **79**, 533-541, 2001.

[2] L. Duigou, E.M. Daya, M. Potier-Ferry. Iterative algorithms for non-linear eigenvalue problems. Application to vibrations of viscoelastic shells. *Comput. Methods Appl. Mech. Engrg.* **192**, 1323–1335, 2003.

[3] A.R. Damanpack, S.M.R. Khalili. High-order free vibration analysis of sandwich beams with a flexible core using dynamic stiffness method. *Composite Structures,* **94**, 1503–1514, 2012.

[4] X. Chen, H. L. Chen and X.L. Hu. Damping predication of sandwich structures by order-reduction-iteration approach, *Journal of Sound and Vibration* **222(5)**, 803-812, 1999.

[5] C. H. Park, D. J. Inman and M. J. Lam. Model reduction of viscoelastic finite element models, *Journal of Sound and Vibration* **219(4)** , 619-637, 1999.

[6] A.M.G. de Lima et al. Component mode synthesis combining robust enriched Ritz approach for viscoelastically damped structures. *Engineering Structures* **32**, 1479_1488, 2010.

[7] X. Chen, H. L. Chen and X.L. Hu. Damping predication of sandwich structures by order-reduction-iteration approach, *Journal of Sound and Vibration* **222(5)**, 803-812, 1999.

[8] L. Duigou. Modélisation numérique de l'amortissement passif des tôles sandwich comportant des couches viscoélastiques ou piézoélectriques. Thèse de Doctorat. Metz. 2002.

[9] N. Büchter, E. Ramm and D. Roehl. Three dimensional extension of non-linear shell formulation based on the enhanced assumed strain concept. *International Journal of Numerical Methods in Engineering*, **37**:2551-2568, 1994.

COMPDYN 2013
4th ECCOMAS Thematic Conference on
Computational Methods in Structural Dynamics and Earthquake Engineering
M. Papadrakakis, V. Papadopoulos, V. Plevris (Eds.)
Kos Island, Greece, 12–14 June 2013

EFFECT OF POUNDING ON THE SEISMIC RESPONSE OF TWO ADJACENT ASYMMETRIC BUILDINGS UNDER SINGLE UNI-DIRECTIONAL GROUND MOTION

Alessandra Fiore[1], Giuseppe C. Marano[1]

[1] DICAR, Technical University of Bari, Via Orabona 4, 70125 Bari, Italy
a.fiore@poliba.it, g.c.marano@gmail.com

Keywords: lateral-torsional pounding; two adjacent buildings; asymmetric buildings; non-linear behaviour; uni-directional seismic action; numerical analysis.

Abstract. *The aim of this paper is to present a detailed analytical study able to simulate the earthquake induced lateral-torsional pounding between two multi-storey adjacent buildings with different dynamic properties.*
Coupled lateral-torsional pounding between asymmetric structures has been investigated only in the last decades, but always with reference to impact between two single-storey structures, while most of the existing buildings are of course multi-storey. Moreover in many cases contact is modelled by linear impact elements, while contrarily pounding models utilizing the non-linear Hertz contact law appear to be more realistic, earthquake poundings being highly non-linear phenomena.
For this reason in the proposed model both a non-linear viscoelastic model to simulate impact and a non-linear behaviour of the storey shear forces and torques are considered, differently from many commercial codes which admit just one non-linearity. Torsional effects are taken into account by implementing all the possible impact scenarios, depending on the sign of the rotations of two adjacent floor-diaphragms. Moreover it is assumed that, at each storey-level, pounding occurs when a corner of one building impacts onto an arbitrary point of the other building. Just single uni-directional earthquake ground motion is incorporated in the analysis. As a consequence pounding-induced response is evaluated exclusively in the seismic direction, also due to the small values of rotations involved in the analysis.
The results show the significance of coupled lateral-torsional pounding responses on adjacent structures. Torsional vibrations of both structures are important components of the overall structural response and mainly influence the number of impacts.

1 INTRODUCTION

Pounding between adjacent buildings or between parts of the same building is one of the most frequent source of severe damage during earthquakes. This problem is particularly frequent in many cities located in seismically active regions, where, under the influence of socioeconomic factors and land usage requirements, building codes in the long run permitted contact between adjacent buildings. Moreover real structures are almost always irregular since perfect regularity is an idealization which rarely occurs. Focusing on plan irregularity, assessments of structural performances during past earthquakes demonstrate that this type of irregularity, which is due to asymmetric distributions of mass, stiffness and strength, significantly affect structural damage during earthquakes, since it results in floor torsional rotations in addition to floor translations [1-5].

Several researchers have studied seismic pounding problem. Nevertheless most of these studies focus only on translational pounding, often between two adjacent single or multi-storey symmetric buildings, neglecting torsional effects [6-16]. Among all the adopted approaches, pounding models utilizing the non-linear Hertz contact law appear to be more realistic, since earthquake poundings are highly non-linear phenomena [17-20]. On this topic, Jankowski [11] proposed a detailed investigation on pounding-involved response of two three-storey buildings with different dynamic properties, by adopting the Hertz contact law. Jankowski also showed the results of experimental studies in order to verify the validity of this impact law [21].

Coupled lateral-torsional pounding between asymmetric structures has been investigated only in the last decades, but always with reference to impact between two single-storey structures [22-25], while most of the existing buildings are of course multi-storey. Hao and Shen [23] employed the random vibration method to calculate the relative displacement of adjacent asymmetric single-storey structures. Gong and Hao [22] proposed a parametric study on coupled lateral-torsional pounding responses of adjacent symmetric and asymmetric single-storey structures, modelling contact by linear impact elements. Wang et al. [25] adopted the Hertz contact law to simulate lateral-torsional pounding between two single-storey towers, but in the analysis just few impact scenarios were taken into account.

In this framework a clear analytical model simulating lateral-torsional pounding, including all the most probable impact scenarios and easily usable for practical purposes, is not available in literature. The aim of the present study is to propose a reliable analytical model to simulate coupled lateral-torsional pounding between two adjacent multi-storey buildings, able to reproduce the highly nonlinear and complex pounding phenomenon. As explained in the following sections, a macro-model approach is adopted [26].

2 DYNAMIC EQUATION OF MOTION

The study herein presented is focused on earthquake-induced lateral-torsional pounding between two adjacent three-storey buildings. Without loss of generality, only ground excitation in the x-direction and eccentricity in the y-direction are considered, as shown in Fig. 1; CM and CS indicate mass center and stiffness center of each storey, while d is the initial separation gap. The motion of each building is described by 6 degrees of freedom: three translational displacements x_i along the x direction and three floor rotations θ_i.

An elastic-perfectly plastic approximation of storey shear forces and torques is enforced in the model. The dynamic equation of motion for such a structural model, including pounding between buildings at each floor level, can be written in matrix form as:

$$\boldsymbol{\Lambda}\cdot\ddot{\boldsymbol{\eta}}(t)+\boldsymbol{C}\cdot\dot{\boldsymbol{\eta}}(t)+\boldsymbol{\Gamma}^{S}(t)+\boldsymbol{\Gamma}\ (t)=-\boldsymbol{\Lambda}\cdot\ddot{\boldsymbol{\eta}}_{g}(t) \tag{1}$$

with:

$$\boldsymbol{\Lambda}=\begin{bmatrix} m_1 & 0 & 0 & 0 & 0 & 0 & 0 & 0 & 0 & 0 & 0 & 0 \\ 0 & m_2 & 0 & 0 & 0 & 0 & 0 & 0 & 0 & 0 & 0 & 0 \\ 0 & 0 & m_3 & 0 & 0 & 0 & 0 & 0 & 0 & 0 & 0 & 0 \\ 0 & 0 & 0 & I_1 & 0 & 0 & 0 & 0 & 0 & 0 & 0 & 0 \\ 0 & 0 & 0 & 0 & I_2 & 0 & 0 & 0 & 0 & 0 & 0 & 0 \\ 0 & 0 & 0 & 0 & 0 & I_3 & 0 & 0 & 0 & 0 & 0 & 0 \\ 0 & 0 & 0 & 0 & 0 & 0 & m_4 & 0 & 0 & 0 & 0 & 0 \\ 0 & 0 & 0 & 0 & 0 & 0 & 0 & m_5 & 0 & 0 & 0 & 0 \\ 0 & 0 & 0 & 0 & 0 & 0 & 0 & 0 & m_6 & 0 & 0 & 0 \\ 0 & 0 & 0 & 0 & 0 & 0 & 0 & 0 & 0 & I_4 & 0 & 0 \\ 0 & 0 & 0 & 0 & 0 & 0 & 0 & 0 & 0 & 0 & I_5 & 0 \\ 0 & 0 & 0 & 0 & 0 & 0 & 0 & 0 & 0 & 0 & 0 & I_6 \end{bmatrix}\quad \ddot{\boldsymbol{\eta}}(t)=\begin{bmatrix} \ddot{x}_1(t) \\ \ddot{x}_2(t) \\ \ddot{x}_3(t) \\ \ddot{\theta}_1(t) \\ \ddot{\theta}_2(t) \\ \ddot{\theta}_3(t) \\ \ddot{x}_4(t) \\ \ddot{x}_5(t) \\ \ddot{x}_6(t) \\ \ddot{\theta}_4(t) \\ \ddot{\theta}_5(t) \\ \ddot{\theta}_6(t) \end{bmatrix}\quad \dot{\boldsymbol{\eta}}(t)=\begin{bmatrix} \dot{x}_1(t) \\ \dot{x}_2(t) \\ \dot{x}_3(t) \\ \dot{\theta}_1(t) \\ \dot{\theta}_2(t) \\ \dot{\theta}_3(t) \\ \dot{x}_4(t) \\ \dot{x}_5(t) \\ \dot{x}_6(t) \\ \dot{\theta}_4(t) \\ \dot{\theta}_5(t) \\ \dot{\theta}_6(t) \end{bmatrix}\quad \ddot{\boldsymbol{\eta}}_{\boldsymbol{g}}(t)=\begin{bmatrix} \ddot{x}_g(t) \\ \ddot{x}_g(t) \\ \ddot{x}_g(t) \\ 0 \\ 0 \\ 0 \\ \ddot{x}_g(t) \\ \ddot{x}_g(t) \\ \ddot{x}_g(t) \\ 0 \\ 0 \\ 0 \end{bmatrix}\quad \boldsymbol{\Gamma}(t)=\begin{bmatrix} F_{x14}(t) \\ F_{x25}(t) \\ F_{x36}(t) \\ T_{\theta 14}(t) \\ T_{\theta 25}(t) \\ T_{\theta 36}(t) \\ -F_{x14}(t) \\ -F_{x25}(t) \\ -F_{x36}(t) \\ T_{\theta 41}(t) \\ T_{\theta 52}(t) \\ T_{\theta 63}(t) \end{bmatrix}$$

$$\boldsymbol{C}=\begin{bmatrix} c_{x1,2} & -c_{x2} & 0 & 0 & 0 & 0 & 0 & 0 & 0 & 0 & 0 & 0 \\ -c_{x2} & c_{x2,3} & -c_{x3} & 0 & 0 & 0 & 0 & 0 & 0 & 0 & 0 & 0 \\ 0 & -c_{x3} & c_{x3} & 0 & 0 & 0 & 0 & 0 & 0 & 0 & 0 & 0 \\ 0 & 0 & 0 & c_{\theta 1,2} & -c_{\theta 2} & 0 & 0 & 0 & 0 & 0 & 0 & 0 \\ 0 & 0 & 0 & -c_{\theta 2} & c_{\theta 2,3} & -c_{\theta 3} & 0 & 0 & 0 & 0 & 0 & 0 \\ 0 & 0 & 0 & 0 & -c_{\theta 3} & c_{\theta 3} & 0 & 0 & 0 & 0 & 0 & 0 \\ 0 & 0 & 0 & 0 & 0 & 0 & c_{x4,5} & -c_{x5} & 0 & 0 & 0 & 0 \\ 0 & 0 & 0 & 0 & 0 & 0 & -c_{x5} & c_{x5,6} & -c_{x6} & 0 & 0 & 0 \\ 0 & 0 & 0 & 0 & 0 & 0 & 0 & -c_{x6} & c_{x6} & 0 & 0 & 0 \\ 0 & 0 & 0 & 0 & 0 & 0 & 0 & 0 & 0 & c_{\theta 4,5} & -c_{\theta 5} & 0 \\ 0 & 0 & 0 & 0 & 0 & 0 & 0 & 0 & 0 & -c_{\theta 5} & c_{\theta 5,6} & -c_{\theta 6} \\ 0 & 0 & 0 & 0 & 0 & 0 & 0 & 0 & 0 & 0 & -c_{\theta 6} & c_{\theta 6} \end{bmatrix}\quad \boldsymbol{\Gamma}^{S}(t)=\begin{bmatrix} F_{x1}^{S}(t)-F_{x2}^{S}(t) \\ F_{x2}^{S}(t)-F_{x3}^{S}(t) \\ F_{x3}^{S}(t) \\ T_{\theta 1}^{S}(t)-T_{\theta 2}^{S}(t) \\ T_{\theta 2}^{S}(t)-T_{\theta 3}^{S}(t) \\ T_{\theta 3}^{S}(t) \\ F_{x4}^{S}(t)-F_{x5}^{S}(t) \\ F_{x5}^{S}(t)-F_{x6}^{S}(t) \\ F_{x6}^{S}(t) \\ T_{\theta 4}^{S}(t)-T_{\theta 5}^{S}(t) \\ T_{\theta 5}^{S}(t)-T_{\theta 6}^{S}(t) \\ T_{\theta 6}^{S}(t) \end{bmatrix}$$

where m_i and I_i (i=1,...,6) are the mass and the polar moment of inertia about a vertical axis through the CM of a single storey; $\ddot{x}_i$, $\dot{x}_i$, $\ddot{\theta}_i$, $\dot{\theta}_i$ (i=1,...,6) are the acceleration and velocity of a single storey in the longitudinal and torsional directions; $F_{xi}^{S}(t)$ (i=1,…,6) and $T_{\theta i}^{S}(t)$ (i=1,..,6) are the inelastic storey shear forces and torques; c_{xi} (i=1,…,6) and $c_{\theta i}$ (i=1,…,6) are the elastic damping coefficients, with $c_{xi,j}=c_{xi}+c_{xj}$ and $c_{\theta i,j}=c_{\theta i}+c_{\theta j}$; $F_{xij}(t)$ and $T_{\theta ij}(t)$ are the pounding forces and torques between storeys with masses m_i, m_j; $\ddot{x}_g(t)$ is the longitudinal acceleration component of the input ground motion. Since the proposed formulation concerns pounding between two adjacent buildings, it results $F_{xji}(t)=-F_{xij}(t)$ (i=1,...,3; j=4,...,6).

The storey shear forces $F_{xi}^{S}(t)$ and torques $T_{\theta i}^{S}(t)$, according to an elastic-perfectly plastic behaviour, are expressed for the elastic range by:

$$F_{xi}^{S}(t)=K_{xi}\left[x_i(t)-e_{yi}\theta_i(t)\right]\ (i=1,4);\ F_{xi}^{S}(t)=K_{xi}\left[\left(x_i(t)-e_{yi}\theta_i(t)\right)-\left(x_{i-1}(t)-e_{y(i-1)}\theta_{i-1}(t)\right)\right]\ (i=2,3,5,6); \tag{2}$$

$$T_{\theta i}^{S}(t)=\left(\sum_{j=1}^{n}k_{xj,i}\left(x'^{2}_{j,i}+y'^{2}_{j,i}\right)\right)\theta_i(t)-K_{xi}e_{yi}x_i(t)\quad(i=1,4);\tag{3}$$

$$T_{\theta i}^{S}(t)=\left[\sum_{j=1}^{n}k_{xj,i}\left(x'^{2}_{j,i}+y'^{2}_{j,i}\right)\right]\left[\theta_i(t)-\theta_{i-1}(t)\right]-K_{xi}\left[e_{yi}x_i(t)-e_{y(i-1)}x_{i-1}(t)\right]\quad(i=2,3,5,6);\tag{4}$$

and for the plastic range by:

$$F_{xi}^{S}(t)=F_{xi}^{Y}\qquad(i=1,...,6);\tag{5}$$

$$T_{\theta i}^{S}(t)=T_{\theta i}^{Y}\qquad(i=1,...,6);\tag{6}$$

where x_i and θ_i are the displacement in the x direction and the rotation of a single storey; $K_{xi}=\sum_{j=1}^{n}k_{xj,i}$ is the elastic structural stiffness in the x direction of storey i; $k_{xj,i}$ and n are respectively the j^{th}-column lateral stiffness and the number of columns of the concerned storey; $x'_{j,i}$, $y'_{j,i}$ are the co-ordinates of the j^{th} column with the origin at CM of the concerned storey; e_{yi} is the static eccentricity at storey i; F_{xi}^{Y} and $T_{\theta i}^{Y}$ are the storey lateral and torsional yield strengths. Figure 1 shows the positive signs of displacements and rotations.

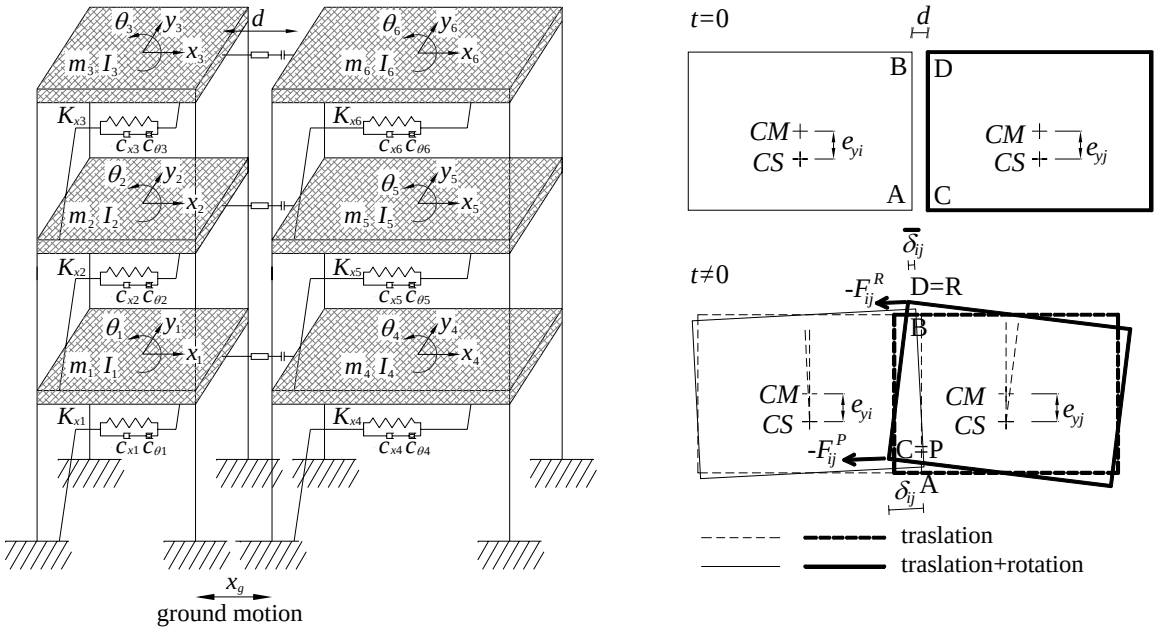


Figure 1: Analytical model.

2.1 Contact forces

In this formulation it is assumed that, at each storey-level, pounding occurs when a corner of one building impacts onto an arbitrary point of the other building. Actually if, at a generic time-step, the whole opposite edges AB and CD overlap due to floor rotation and translation, pounding forces are distributed along the entire contact segment. For the seek of simplicity, the resultant pounding forces are considered concentrated in correspondence of the impact point and of the second corner of the colliding edge. So the main pounding force $F_{ij}^{P}(t)$ is localized at the impact corner, while the pounding force at the second corner $F_{ij}^{R}(t)$ is different

from zero only when a full overlapping occurs (Fig. 1). Pounding-involved response is evaluated in the hypothesis of frictionless contact [25]. According to this assumption, the pounding force $F_{ij}^{P}(t)$ at each storey-level is always perpendicular to the edges AB or CD when they are impacted by a corner of the other building (Fig. 1). The same direction is assumed for the pounding force $F_{ij}^{R}(t)$. In the analysis pounding forces are simulated according to the non-linear viscoelastic model based on the Hertz's contact law [11, 17-20]; the force $F_{ij}^{P}(t)$ assumes the following form:

$$\begin{aligned} &F_{ij}^{P}(t)=0 \quad \text{for } \delta_{ij}(t)\le 0; \\ &F_{ij}^{P}(t)=\beta\delta_{ij}^{\frac{3}{2}}(t)+\bar{c}_{ij}(t)\dot{\delta}_{ij}(t) \quad \text{for } \delta_{ij}(t)>0;\ \dot{\delta}_{ij}(t)>0; \\ &F_{ij}^{P}(t)=\beta\delta_{ij}^{\frac{3}{2}}(t) \qquad\qquad \text{for } \delta_{ij}(t)>0;\ \dot{\delta}_{ij}(t)\le 0; \end{aligned} \tag{7}$$

with:

$$\bar{c}_{ij}(t)=2\xi\sqrt{\beta\sqrt{\delta_{ij}(t)}\frac{m_i m_j}{m_i+m_j}} \tag{8}$$

where $\delta_{ij}(t)$ is the penetration depth at the pounding point, β is the impact stiffness parameter simulating the local stiffness at the contact point, *d* is the initial separation gap and ξ denotes the impact-damping ratio. The term ξ is estimated using Jankowski's formula [19]:

$$\xi=\frac{9\sqrt{5}}{2}\frac{1-e^2}{e\left[e(9\pi-16)+16\right]} \tag{9}$$

where *e* is the coefficient of restitution accounting for the energy dissipation during impact.

The aliquot $F_{ij}^{R}(t)$ of pounding force can be obtained by Eqs. (7) replacing the quantity $\delta_{ij}(t)$ with the penetration depth $\bar{\delta}_{ij}(t)$ at the second corner of the impacting edge.

The resultant pounding force is given by:

$$F_{ij}(t)=F_{ij}^{P}(t)+F_{ij}^{R}(t). \tag{10}$$

The pounding torques can be expressed as:

$$\begin{aligned} T_{\theta ij}(t)=&-F_{xij}^{P}(t)\cdot\left(y_{Pij}(t)-y_{CMi}\right)+F_{yij}^{P}(t)\cdot\left(x_{Pij}(t)-x_{CMi}\right)+ \\ &F_{xij}^{R}(t)\cdot\left(y_{Rij}(t)-y_{CMi}\right)-F_{yij}^{R}(t)\cdot\left(x_{Rij}(t)-x_{CMi}\right) \\ &(i=1,2,3;\ j=4,5,6),\quad (i=4,5,6;\ j=1,2,3) \end{aligned} \tag{11}$$

where $F_{xij}^{P}(t)$, $F_{yij}^{P}(t)$ and $F_{xij}^{R}(t)$, $F_{yij}^{R}(t)$ are the *x*, *y* components of the pounding forces $F_{ij}^{P}(t)$ and $F_{ij}^{R}(t)$ respectively, while $x_{Pij}(t), y_{Pij}(t)$ $x_{Rij}(t), y_{Rij}(t)$ and x_{CMi}, y_{CMi} are the *x*, *y* coordinates of the pounding impact point *P*, of the second corner *R* and of the CM in the reference system chosen for the analysis. During the analysis the relative locations of the two buildings at each storey-level are checked at each time-step, to verify whether pounding occurs or not. In order to evaluate pounding forces and torques, it is necessary to identify all the possible pounding scenarios. Eight pounding scenarios are herein considered, depending on

the sign of rotations of two adjacent floor-diaphragms (Fig. 2). The scenarios so defined include also the cases in which one or both buildings do not rotate at the concerned level. On the basis of the above scenarios, the penetration depth $\delta_{ij}(t)$ at the pounding point, including also the torsional effect, can be evaluated by the following expression:

$$\delta_{ij}(t) = x_i(t) - x_j(t) + \delta_{ij,torq}(t) \tag{12}$$

where the term $\delta_{ij,torq}(t)$ denotes the overlapping aliquot of two adjacent storeys *i*, *j* due to torsional rotations; observing Fig. 2, it represents the distance between the impacting corner and the opposite edge of the other building and is calculated for each scenario with respect to the fixed reference system defined in Fig. 2 itself.

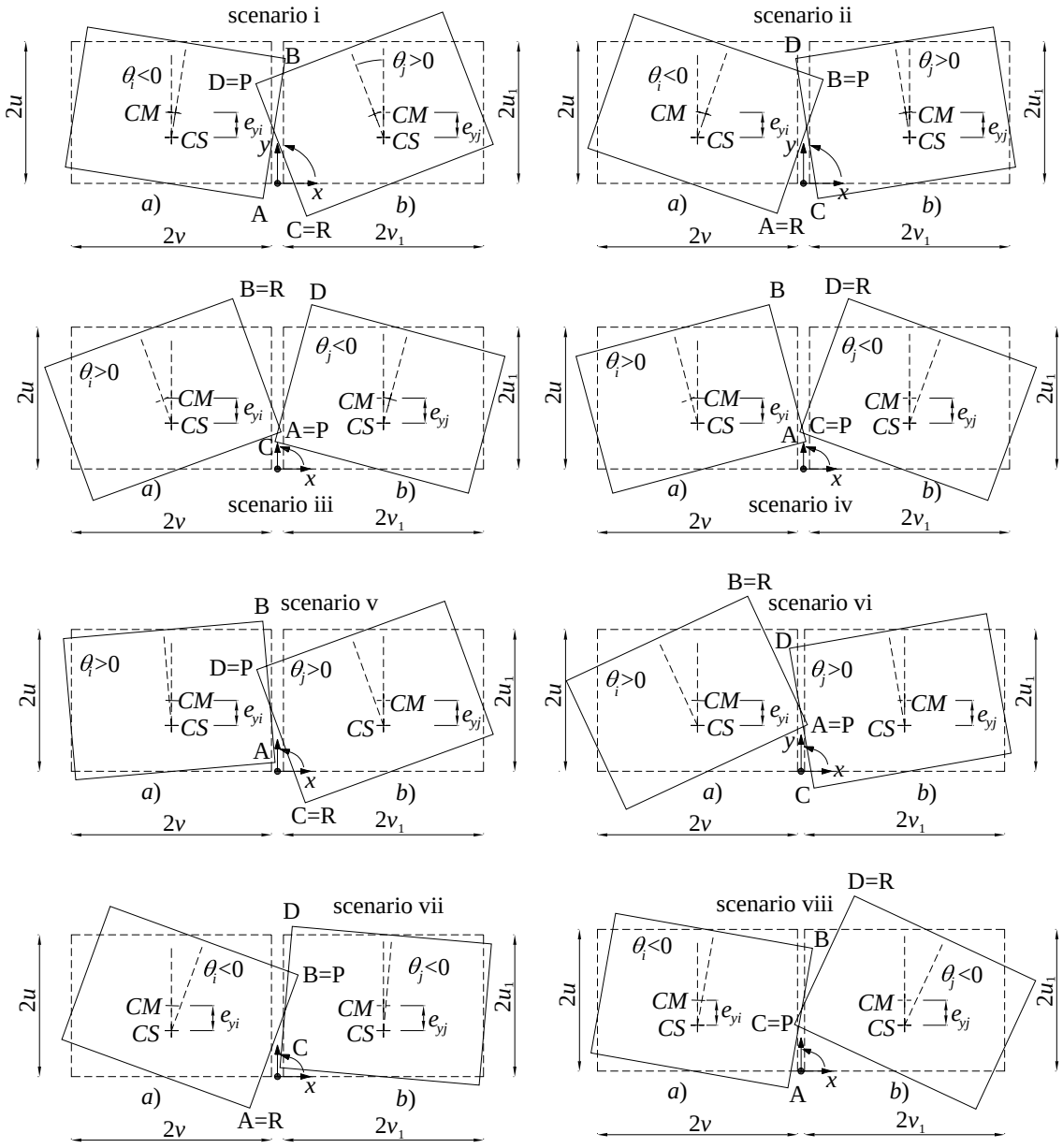


Figure 2: Impact scenarios.

3 RESPONSE ANALYSIS

The results of the numerical lateral-torsional pounding simulations are described with reference to two three-storey buildings having the following geometric and structural characteristics:

- left building:

  u=3 m, v=3 m, $e_{y1} = e_{y2} = e_{y3} = 2$ m,

  $m_1 = m_2 = m_3 = 2.85 \times 10^4$ kg,

  $I_1 = I_2 = I_3 = 5.079 \times 10^5$ kg·m^2,

  $K_{x1} = K_{x2} = K_{x3} = 3.44 \times 10^6$ N/m (ω_{lx}=11 rad/sec),

  $c_{x1} = c_{x2} = c_{x3} = 3.135 \times 10^4$ kg/s (ξ_{lx}=0.05),

  $c_{\theta 1} = c_{\theta 2} = c_{\theta 3} = 7.41 \times 10^5$ kg·m^2/s ($\xi_{l\theta}$=0.05, $\omega_{l\theta}$=14.6 rad/sec),

  $F_{x1}^Y = F_{x2}^Y = F_{x3}^Y = 1.2 \times 10^5$ N, $T_{\theta 1}^Y = T_{\theta 2}^Y = T_{\theta 3}^Y = 3.5 \times 10^5$ N·m.

- right building: u_1=2.5 m, v_1=2.5 m,

  $e_{y4} = e_{y5} = e_{y6} = 1.5$ m,

  $m_4 = m_5 = m_6 = 1.3 \times 10^6$ kg,

  $I_4 = I_5 = I_6 = 1.625 \times 10^7$ kg·m^2,

  $K_{x4} = K_{x5} = K_{x6} = 2.34 \times 10^9$ N/m (ω_{rx}=42.45 rad/sec),

  $c_{x4} = c_{x5} = c_{x6} = 5.518 \times 10^6$ kg/s (ξ_{rx}=0.05),

  $c_{\theta 4} = c_{\theta 5} = c_{\theta 6} = 8.5 \times 10^7$ kg·m^2/s ($\xi_{r\theta}$=0.05, $\omega_{r\theta}$=52.35 rad/sec),

  $F_{x4}^Y = F_{x5}^Y = F_{x6}^Y = 1.2 \times 10^7$ N, $T_{\theta 4}^Y = T_{\theta 5}^Y = T_{\theta 6}^Y = 4 \times 10^7$ N·m.

The above data concern two equal height structures with different dynamic properties. The initial separation gap d between buildings is set equal to 0.02 m. For the non-linear viscoelastic impact model's parameters, the following values are assumed: β=2.75x10^9 N/m$^{3/2}$, ξ=0.35 (e=0.66). As to the seismic input, the El Centro earthquake accelerogram has been incorporated in the analysis. In order to point out the torsional effects, the displacement time histories for the three storeys of both left and right building are shown in Fig. 3 with reference to the four corners A, B, C, D on the adjacent edges of the two structures (Fig. 2).

The pounding force and torque time histories are reported in Fig. 4.

Observing Figs. 3 and 4 it emerges that under the seismic action the response of the lighter and more flexible left building is significant, while the displacements of the heavier and stiffer right building are nearly negligible. Pounding force and torque reach their maximum values at the third storeys, while at the second and first storeys their values drop to about 80% and 50% respectively, but are anyway meaningful.

Figure 5 finally shows the displacement and pounding force time histories at the third level obtained neglecting the torsional effects, that is setting e_{yi}=0 (i=1,…,6). From Fig. 5 it is finally evident that plan eccentricity substantially changes the structural response, leading to an increasing of collisions and an overall reduction of peak displacements.

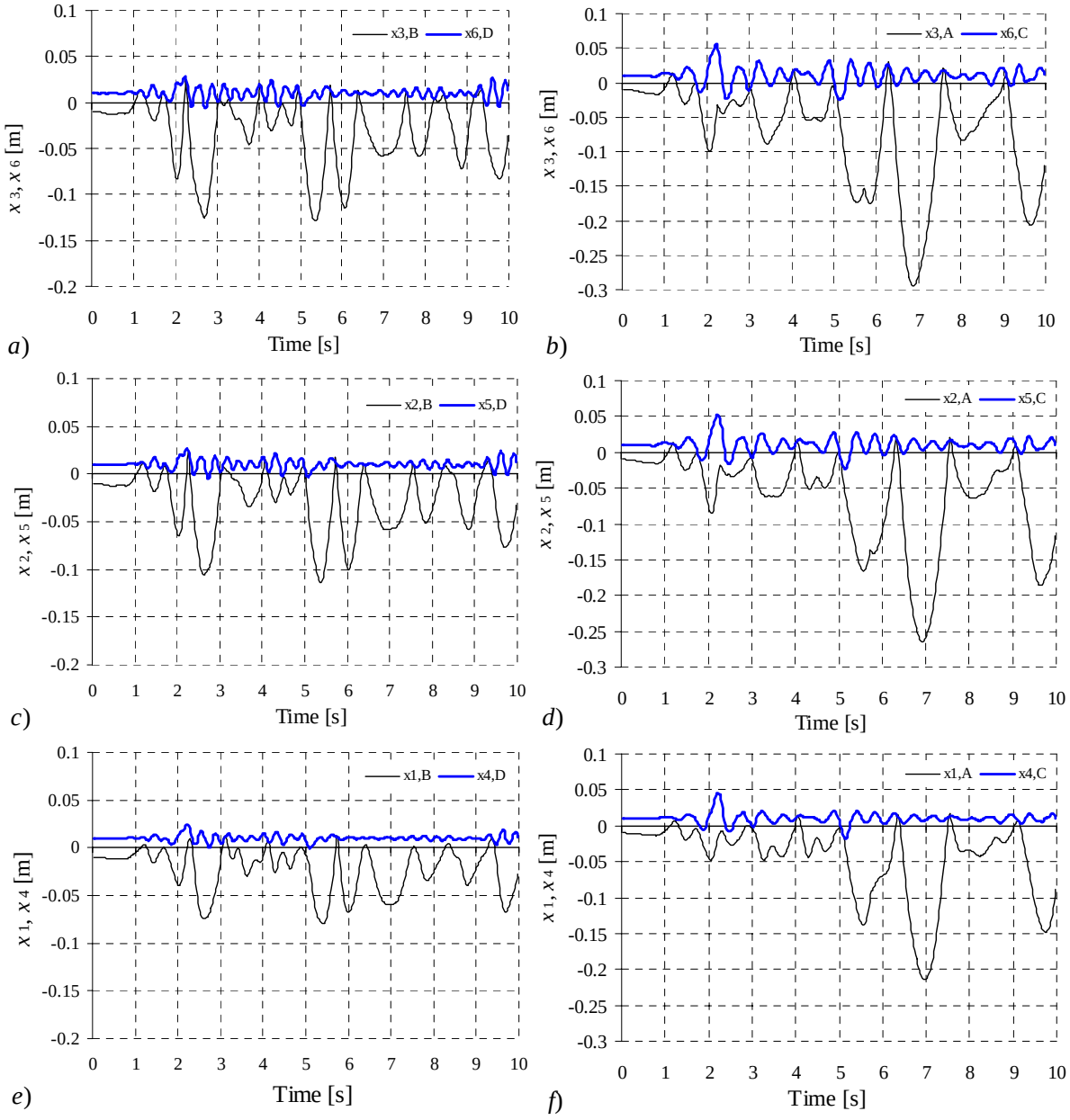


Figure 3: Displacement time histories of buildings at corners A, B, C, D, for each storey.

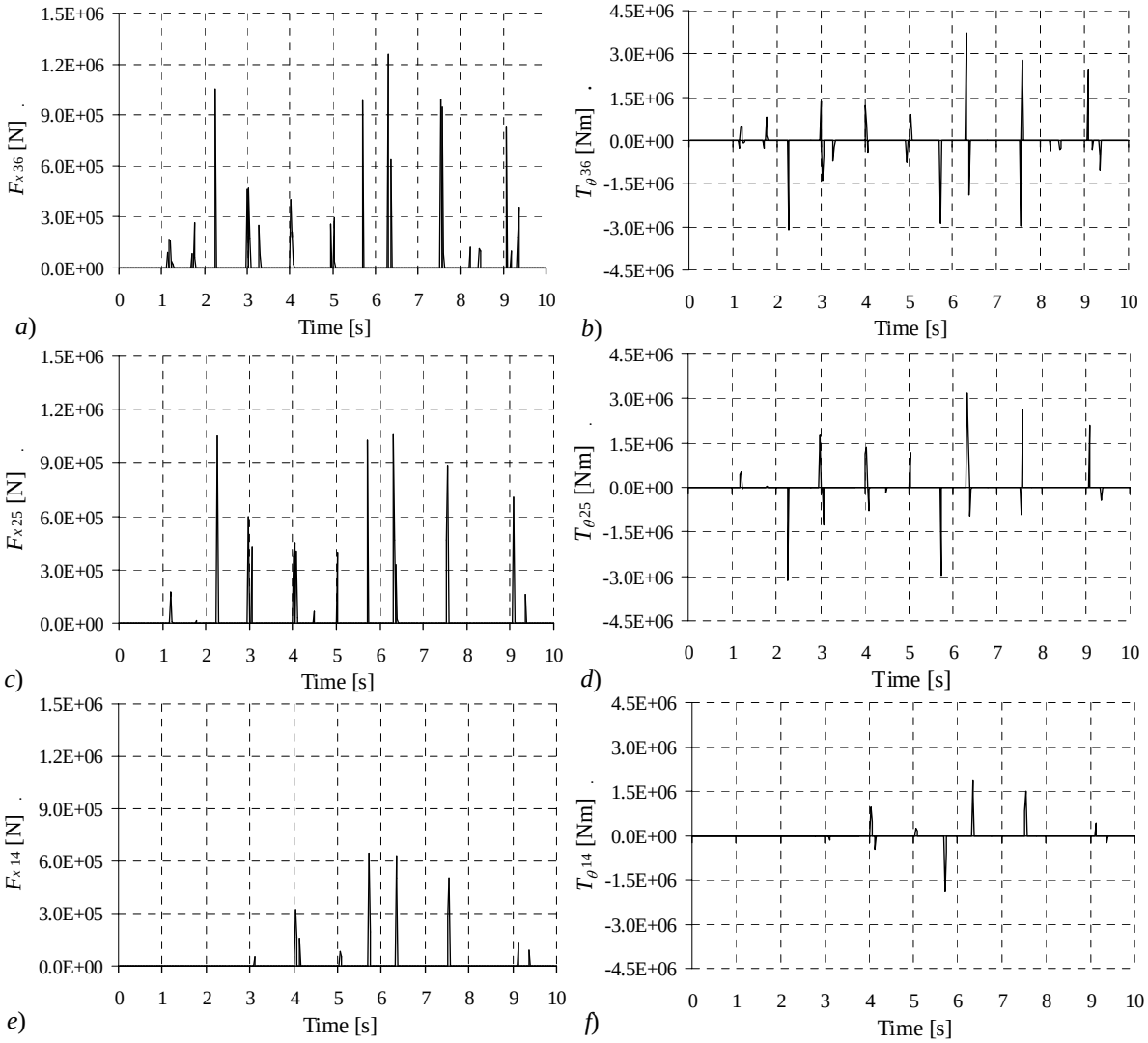


Figure 4: Pounding force and torque time histories of left building at each storey.

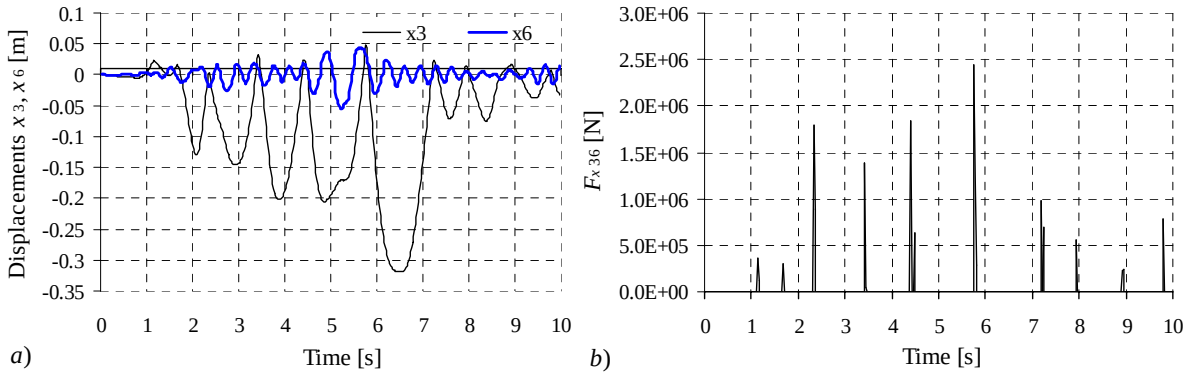


Figure 5: Displacement (a) and pounding force (b) time histories at the third storey neglecting torsional effects.

4 CONCLUSIONS

In this paper a theoretical and analytical lateral-torsional pounding-induced response analysis between two three-storey buildings under seismic action has been presented.

All the possible pounding scenarios have been implemented in the analysis, depending on the sign of rotations of two adjacent floor-diaphragms. Both a non-linear viscoelastic model to simulate impact and a non-linear behaviour of the storey shear forces and torques have been considered, differently from many commercial softwares which admit just one non-linearity. A single uni-directional seismic action, represented by El-Centro earthquake, has been incorporated in the analysis. Just response in the seismic direction has been calculated.

The results of the study show that torsional vibrations of both structures are important components of the overall structural response, affecting both the number of collisions and the entity of overall displacements. Results also indicate that pounding force and torque reach their maximum values at the third storeys, while at the first and second storeys their values drop to about 80% and 50%, but are anyway meaningful.

Finally the authors underline that in prospective the application of this specific formulation to the case of three or more buildings in series could furnish useful informations in order clarify the phenomenon of pounding between existing buildings, especially under the awareness that suitable mechanical models are not available in technical codes.

REFERENCES

[1] R.W. Clough and J. Penzien, *Dynamics of structures*, 2nd ed. New York: McGraw-Hill, 1993.

[2] H. Hao, Torsional response of building structures to spatial random ground excitations. *Engineering Structures*, **19** (2), 105-112, 1997.

[3] R. Hejal and A.K. Chopra, Earthquake analysis of a class of torsionally-coupled buildings. *Earthquake Engineering and Structural Dynamics*, **18**, 305-323, 1989.

[4] C.L. Kan and A.K. Chopra, Effects of torsional coupling on earthquake forces in buildings, Journal of the Structural Division. *Proceedings of the American Society of Civil Engineers*, 103 No. ST4, 1977.

[5] M.R. Maheri, A.M. Chandler and R.H. Bassett, Coupled lateral-torsional behaviour of frame structures under earthquake loading. *Earthquake Engineering and Structural Dynamics*, **20**, 61-85, 1991.

[6] S.A. Anagnostopoulos, K.V. Spiliopoulos, An investigation of earthquake induced pounding between adjacent buildings. *Earthquake Engineering and Structural Dynamics*, **21**, 289-302, 1992.

[7] S.A. Anagnostopoulos, Pounding of buildings in series during earthquakes. *Earthquake Engineering and Structural Dynamics*, **16**, 443-456, 1988.

[8] K.T. Chau and X.X. Wei, Pounding of structures modelled as nonlinear impacts of two oscillators. *Journal of Earthquake Engineering and Structural Dynamics*, **30**, 633-651, 2001.

[9] K.T. Chau, X.X. Wei, C. Guo and C.Y. Shen, Experimental and theoretical simulations of seismic pounding between adjacent structures. *Journal of Earthquake and Structural Dynamics*, **32**, 537-554, 2003.

[10] R.O. Davis, Pounding of buildings modelled by an impact oscillator. *Journal of Earthquake Engineering and Structural Dynamics*, **21**, 253-274, 1992.

[11] R. Jankowski, Earthquake-induced pounding between equal height buildings with substantially different dynamic properties. *Engineering Structures*, **30**, 2818–2829, 2008.

[12] R. Jankowski, Non-linear FEM analysis of earthquake-induced pounding between the main building and the stairway tower of the Olive View Hospital, *Engineering Structures*, **31**, 1851-1864, 2009.

[13] H.P. Mouzakis and M. Papadrakakis, Three dimensional nonlinear building pounding with friction during earthquakes. *Journal of Earthquake Engineering*, **8**(1), 107–132, 2004.

[14] M. Papadrakakis, C. Apostolopoulou, A. Zacharopoulos and S. Bitzarakis, Three-dimensional simulation of structural pounding during earthquakes. *Journal of Engineering Mechanics ASCE*, **122** (5), 423–431, 1996.

[15] A. Fiore, P. Monaco, Earthquake-induced pounding between the main buildings of the "Quinto Orazio Flacco" school, *Earthquakes and Structures*, **1** (4), 371-390, 2010

[16] A. Fiore, P. Monaco, Analysis of the seismic vulnerability of the "Quinto Orazio Flacco" school [Analisi della vulnerabilità sismica del Liceo "Quinto Orazio Flacco"], *Ingegneria Sismica*, **28**(1), 43-62, ISSN 0393-1420, 2011.

[17] K. Ye, L. Li, Impact analytical models for earthquake-induced pounding simulation, *Front. Archit. Civ. Eng. China*, **3**(2), 142-147, 2009.

[18] R. Jankowski, Non-linear viscoelastic modelling of earthquake induced structural pounding. *Earthquake Engineering and Structural Dynamics*, **34**(6), 595-611, 2005.

[19] R. Jankowski, Analytical expression between the impact damping ratio and the coefficient of restitution in the non-linear viscoelastic model of structural pounding. *Earthquake Engineering and Structural Dynamics*, **35**(4), 517-524, 2006.

[20] S. Muthukumar, R. DesRoches, A Hertz contact model with non-linear damping for pounding simulation. *Earthquake Engng. Struct. Dyn.*, **35**, 811-828, 2006.

[21] R. Jankowski, Experimental study on earthquake-induced pounding between structural elements made of different building materials, *Earthquake Engineering and Structural Dynamics*, **39**, 343-354, 2010.

[22] L. Gong and H. Hao, Analysis of Coupled Lateral-Torsional-Pounding Responses of One-Storey Asymmetric Adjacent Structures Subjected to Bi-Directional Ground Motions. Part I: Uniform Ground Motion Input. *Advances in Structural Engineering*, **8** (5), 463-479, 2005.

[23] H. Hao and J. Shen, Estimation of relative displacement of two adjacent asymmetric structures. *Earthquake Engineering and Structural Dynamics*, **30**, 81-96, 2001.

[24] E. Leibovich, A. Rutenberg and D.Z. Yankelevsky, On eccentric seismic pounding of symmetric buildings. *International Journal of Earthquake Engineering and Structural Dynamics*, **25**, 219-233, 1996.

[25] L.X. Wang, K.T. Chau and X.X. Wie, Numerical Simulations of Nonlinear Seismic Torsional Pounding Between Two Single-Story Structures, *Advances in Structural Engineering*, **12** (1), 87-101, 2009.

[26] A. Fiore, A. Netti, P. Monaco, The influence of masonry infill on the seismic behaviour of RC frame buildings, *Engineering Structures*, **44**, 133-145, 2012.

COMPDYN 2013
4th ECCOMAS Thematic Conference on
Computational Methods in Structural Dynamics and Earthquake Engineering
M. Papadrakakis, V. Papadopoulos, V. Plevris (eds.)
Kos Island, Greece, 12–14 June 2013

A NUMERICAL SCHEME FOR TIME-DOMAIN FE ANALYSIS OF VISCOELASTIC STRUCTURES WITH FRACTIONAL DERIVATIVE CONSTITUTIVE EQUATIONS

J.-F. Deü[1] **and D. Matignon**[2]

[1]Conservatoire National des Arts et Métiers (Cnam),
Structural Mechanics and Coupled Systems Laboratory,
2 rue Conté, F-75003 Paris, France
e-mail: jean-francois.deu@cnam.fr

[2]Université de Toulouse, ISAE,
10 avenue Edouard Belin, F-31055 Toulouse Cedex 4, France
e-mail: denis.matignon@isae.fr

Keywords: Fractional derivative, Diffusive representation, Viscoelasticity, Structural dynamics, Damping, Finite element method.

Abstract. *A numerical scheme is presented for time-domain simulations of structural dynamic problems with viscoelastic materials described by fractional derivative constitutive equations. The proposed approach combines a classical Newmark time-integration method used to solve second-order mechanical systems (obtained for example after finite element discretization), with a diffusive representation based on the transformation of the fractional operator into a system of linear differential equations. The focus is given on the general formulation of the problem, the algorithm implementation into a finite element framework, and the developpement of a closed-form solution for a fractionnally damped single degree-of-freedom equation.*

1 INTRODUCTION

The importance of fractional calculus for modeling viscoelastic material behavior has been recognized by the mechanical scientific community since the pioneering work of Bagley and Torvik [1]. The merits of using fractional differential operator lie in the fact that few parameters are needed to accurately describe the constitutive law of damping materials and the resulting model can be easily fitted to experimental data over a broad range of frequencies. The numerical approximation of such damped mechanical systems is today intensively studied with a special interest concerning the implementation of fractional constitutive equations within a time-domain finite element framework.

The resolution methods are classically either based on time discretization of the fractional dynamics (see e.g. [2, 3, 4]), or on diffusive representations (cf. [5, 6, 7]). For large scale systems, the first method proves memory consuming because it is necessary to store the whole displacement history of the system due to the non-local character of the fractional derivatives. The second method, based on diffusive realizations of fractional derivatives, is numerically more efficient because it has no hereditary behavior, thus avoiding the storage of the solution from all past time steps. In the second group of methods, a coupled Newmark-diffusive scheme has recently been proposed by the authors and analyzed through a single degree-of-freedom example [8].

In this contribution, we propose to extend our approach to more complex mechanical systems. The focus is given on the general formultation of the problem and the algorithm implementation compatible with the finite element method. The applications to damping prediction of complex structures containing viscoelastic materials will be presented at the conference.

2 FINITE ELEMENT VISCOELASTIC PROBLEM

We consider a structure composed of elastic and viscoelastic materials. The finite element discretization of such a problem leads to the following stiffness and mass matrices $\mathbf{K}_i$ and $\mathbf{M}_i$, associated to the volume of elastic ($i = 1$) and viscoelastic ($i = 2$) material:

$$\begin{aligned} \mathbf{K}_1 &= \mathop{\mathsf{A}}_{e=1}^{n_1^{\text{el}}} \int_{\Omega^e} \mathbf{B}^{\mathrm{T}}\mathbf{C}_1\mathbf{B}\mathrm{d}\Omega \qquad & \mathbf{M}_1 &= \mathop{\mathsf{A}}_{e=1}^{n_1^{\text{el}}} \int_{\Omega^e} \mathbf{N}^{\mathrm{T}}\rho_1\mathbf{N}\mathrm{d}\Omega \\ \mathbf{K}_2 &= \mathop{\mathsf{A}}_{e=1}^{n_2^{\text{el}}} \int_{\Omega^e} \mathbf{B}^{\mathrm{T}}\mathbf{C}_2\mathbf{B}\mathrm{d}\Omega \qquad & \mathbf{M}_2 &= \mathop{\mathsf{A}}_{e=1}^{n_2^{\text{el}}} \int_{\Omega^e} \mathbf{N}^{\mathrm{T}}\rho_2\mathbf{N}\mathrm{d}\Omega \end{aligned} \tag{1}$$

where A is the finite element assembly operator, n_i^{el} is the total number of finite elements meshing the volume i, $\mathbf{B}$ is the strain-displacement matrix, $\mathbf{N}$ is the shape function matrix, ρ_i and $\mathbf{C}_i$ are respectively the density and the material moduli matrix related to the volume i.

Assuming that the Poisson ratio of the viscoelastic material is constant, the stiffness matrix $\mathbf{K}_2$ in the frequency domain can be written as a constant stiffness matrix, calculated with unitary modulus $\mathbf{K}_2^0$, factor of the complex Young modulus $\hat{E}(\omega)$ of the viscoelastic material:

$$\mathbf{K}_2 = \hat{E}(\omega)\mathbf{K}_2^0 \tag{2}$$

In this work, the causal fractional Zener model is chosen to describe the frequency-dependent complex modulus:

$$\hat{E}(\omega) = \frac{E_0 + E_\infty(\mathrm{i}\omega\tau)^\alpha}{1 + (\mathrm{i}\omega\tau)^\alpha} = E_0 + \frac{(E_\infty - E_0)(\mathrm{i}\omega\tau)^\alpha}{1 + (\mathrm{i}\omega\tau)^\alpha} \tag{3}$$

where E_0 and E_∞ are respectively the relaxed ($E_0 = \hat{E}(\omega \to 0)$) and unrelaxed modulus ($E_\infty = \hat{E}(\omega \to \infty)$) satisfying $E_\infty > E_0$. The two other parameters are the fractional power α satisfying $0 < \alpha < 1$ and the relaxation time $\tau > 0$. This four-parameter fractional derivative model has been shown to be an effective tool to describe the weak frequency dependence of most viscoelastic materials [9, 10].

The semi-discrete equation of motion for the damped system can be expressed in the frequency domain as:

$$\left[\mathbf{K}_e + \mathrm{i}\omega\hat{h}(\omega)\mathbf{K}_v - \omega^2\mathbf{M}\right]\hat{\mathbf{u}} = \hat{\mathbf{f}} \tag{4}$$

where $\hat{\mathbf{u}}$ is the displacement response to an external harmonic excitation of amplitude $\hat{\mathbf{f}}$, $\mathbf{K}_v = (E_\infty - E_0)\mathbf{K}_2^0$ is a positive matrix, $\mathbf{K}_e = \mathbf{K}_1 + E_0\mathbf{K}_2^0$ and $\mathbf{M} = \mathbf{M}_1 + \mathbf{M}_2$ are definite positive matrices. In addition, according to the expression of the complex modulus in Eq. (3) and to the previuous notations, the function $\hat{h}(\omega)$ is given by:

$$\hat{h}(\omega) = \frac{\tau^\alpha}{(\mathrm{i}\omega)^{1-\alpha}[1 + (\mathrm{i}\omega\tau)^\alpha]}\,. \tag{5}$$

3 DIFFUSIVE FORMULATION

From the previous Eqs. (4) and (5), we obtain the following system of equations in time-domain:

$$\mathbf{M}\,\ddot{\mathbf{u}} + h(t) \star \mathbf{K}_v\,\dot{\mathbf{u}} + \mathbf{K}_e\,\mathbf{u} = \mathbf{f}(t) \tag{6}$$

where an over-dot indicates a time-derivative, the symbol $\star$ represents a convolution product, and the function $h(t)$, for $t > 0$, is given by:

$$h(t) = \int_0^\infty \mu(\xi)\, e^{-\xi\, t}\,\mathrm{d}\xi \tag{7}$$

with

$$\mu(\xi) := \frac{\sin(\alpha\pi)}{\pi}\frac{\tau^\alpha}{\xi^{1-\alpha}\left[1 + 2\,\cos(\alpha\pi)\,(\tau\xi)^\alpha + (\tau\xi)^{2\alpha}\right]}\,. \tag{8}$$

Following e.g. [5, 6, 11, 12], the function h is applied on the velocity field $\mathbf{v} := \dot{\mathbf{u}}$ as input, and will be realized equivalently by a standard diffusive representation of the form:

$$\partial_t\boldsymbol{\varphi}(\xi, t) = -\xi\,\boldsymbol{\varphi}(\xi, t) + \mathbf{v}(t),\ \boldsymbol{\varphi}(\xi, 0) = \mathbf{0}\,, \tag{9}$$

observed through the continuous superposition:

$$(h \star \mathbf{v})(t) = \int_0^\infty \mu(\xi)\,\boldsymbol{\varphi}(\xi, t)\,\mathrm{d}\xi\,. \tag{10}$$

It can be noted that Eq. (9) corresponds to a familly of first order differential equations indexed by ξ. The previous diffusive representation, which is *exact*, can be approximated by stable numerical schemes using standard *interpolation*, i.e.

$$\int_0^\infty \mu(\xi)\,\boldsymbol{\varphi}(\xi, t)\,\mathrm{d}\xi \approx \sum_{k=1}^{K} \mu_k\,\boldsymbol{\varphi}(\xi_k), \tag{11}$$

where K is the number of approximation nodes, ξ_k a sequence of angular frequencies in the frequency range of interest, and μ_k the corresponding *interpolated* or *optimized* weights. It is important to note that this finite-dimensional representation is only approximate and the quality of the approximation depends on the choice of these three parameters. More details on the optimization procedure of diffusive models have been presented first in [13], and fully detailed on a series of fractional systems in e.g. [14].

4 TIME-INTEGRATION SCHEME

Using the previous diffusive representation, a predictor-corrector algorithm based on the Newmark integration scheme is proposed for the computation of the dynamical system given by Eq. (6). This algorithm is detailed below:

1. Initialization
   $\mathbf{S} = \mathbf{M} + \beta\,\Delta t^2\,\mathbf{K}_e$
   $\mathbf{u}(0) = \mathbf{u}^0$, $\mathbf{v}(0) = \mathbf{v}^0$
   $\boldsymbol{\varphi}_k(0) = \mathbf{0}$ for $1 \leq k \leq K$
   $\mathbf{a}^0 = \mathbf{M}^{-1}(\mathbf{f}^0 - \mathbf{K}_e\,\mathbf{u}^0)$

2. Enter time step loop
   a) Prediction
   $\mathbf{u}_{\text{pr}}^{n+1} = \mathbf{u}^n + \Delta t\,\mathbf{v}^n + (0.5-\beta)\,\Delta t^2\,\mathbf{a}^n$
   $\mathbf{v}_{\text{pr}}^{n+1} = \mathbf{v}^n + (1-\gamma)\,\Delta t\,\mathbf{a}^n$

   b) Evaluation of $\boldsymbol{\varphi}_k^{n+1}$ for $1 \leq k \leq K$
   $$\boldsymbol{\varphi}_k^{n+1} = \exp(-\xi_k\,\Delta t)\,\boldsymbol{\varphi}_k^n + \frac{1-\exp(-\xi_k\,\Delta t)}{\xi_k}\,\mathbf{v}_{\text{pr}}^{n+1}$$
   c) Evaluation of $\mathbf{a}^{n+1}$
   $$\mathbf{a}^{n+1} = \mathbf{S}^{-1}(\mathbf{f}^{n+1} - \mathbf{K}_e\mathbf{u}_{\text{pr}}^{n+1} - \mathbf{K}_v\sum_{k=1}^{K}\mu_k\,\boldsymbol{\varphi}_k^{n+1})$$
   d) Correction
   $\mathbf{u}^{n+1} = \mathbf{u}_{\text{pr}}^{n+1} + \beta\,\Delta t^2\,\mathbf{a}^{n+1}$
   $\mathbf{v}^{n+1} = \mathbf{v}_{\text{pr}}^{n+1} + \gamma\,\Delta t\,\mathbf{a}^{n+1}$

3. Update time step and return to step 2

Some remarks can be made on this algorithm:

- In the Newmark algorithm we use $\beta = 1/4$ and $\gamma = 1/2$ corresponding to the *average acceleration method* which is unconditionally stable and second order accurate for *non-dissipative* linear systems;
- The prediction velocity vector $\mathbf{v}_{\text{pr}}$ is frozen as input of the diffusive sub-scheme b).
- Only the diffusive components $\boldsymbol{\varphi}_k^n$ for $1 \leq k \leq K$ at time step $n\Delta t$ are stored.

5 SINGLE DEGREE-OF-FREEDOM MODEL

We consider the single-degree-of-freedom dynamical model obtained from Eq. (4):

$$\left[K_e + \frac{(\mathrm{i}\omega\tau)^\alpha}{1+(\mathrm{i}\omega\tau)^\alpha}K_v - \omega^2 M\right]\,\hat{u} = \hat{f}\,, \tag{12}$$

In the Laplace domain, this equation writes:

$$[M\tau^\alpha s^{2+\alpha} + Ms^2 + (K_e+K_v)\tau^\alpha s^\alpha + K_e]\,U(s) = [1+\tau^\alpha s^\alpha]\,F(s)\,, \tag{13}$$

and a time-domain version is given by:

$$\left[M\tau^{\alpha}\,(D_t)^{2+\alpha} + M\,(D_t)^2 + (K_e + K_v)\tau^{\alpha}\,(D_t)^{\alpha} + K_e\right]\,u(t) = \left[1 + \tau^{\alpha}\,(D_t)^{\alpha}\right]\,f(t)\,. \quad (14)$$

where $(D_t)^{\beta}$ represents the time derivative of order β (integer or fractional).

In order to solve this equation analytically, let us introduce the following notations:

- $0 < \alpha = \frac{p}{q} < 1$, so $p < q$
- $\gamma = \frac{1}{q}$, so $\alpha = p\,\gamma$ and $1 = q\,\gamma$

With this notation at hand, we can rewrite the problem as:

$$[M\tau^{\alpha}\,(D_t^{\gamma})^{2q+p} + M\,(D_t^{\gamma})^{2q} + (K_e + K_v)\tau^{\alpha}\,(D_t^{\gamma})^{p} + K_e]\,u(t) = [1 + \tau^{\alpha}\,(D_t^{\gamma})^{p}]\,f(t)\,. \quad (15)$$

The trick consists in looking for a solution expressed by means of Mittag-Leffler functions (see [5]), which can also be expanded as fractional power series (by definition). This theoretical result legitimate the following Ansatz:

$$u(t) := \sum_{n=0}^{\infty} u_n\,\frac{t^{n\gamma}}{\Gamma(1+n\gamma)} \quad (16)$$

with initial conditions displacement $u(0) = u_0$ and velocity $v(0) = \dot{u}(0) = v_0$.

Reintroducing this Ansatz into equation (14) gives the following recursion on the coefficients:

$$M\tau^{\alpha}\,u_{n+2q+p} + M\,u_{n+2q} + (K_e + K_v)\tau^{\alpha}\,u_{n+p} + K_e\,u_n = 0\,, \quad \forall n \in \mathbb{N}\,, \quad (17)$$

which is easy to solve by induction, starting from known u_0 and $u_q = v_0$ and other low order coefficients equal to 0. This analytical solution will be helpful to test our numerical solutions.

6 CONLUSION AND PERSPECTIVES

We have proposed in this contribution a general approach for time-domain simulations of structural dynamic problems with viscoelastic materials described by fractional derivative constitutive equations. This approach combines a classical Newmark time-integration method with a diffusive representation used in fractional calculus. The proposed methodology is applicable to complex mechanical systems thanks to an appropriate finite element space discretization. We have also proposed in this paper a closed-form solution for a single degree-of-freedom system with fractional Zener model. This solution will be used to validate the numerical implementation of our algorithm. Fully 3D simulations will be presented at the conference and used to analyse the efficiency of our approach.

REFERENCES

[1] R. Bagley, P. Torvik, Fractional calculus – a different approach to the analysis of viscoelastically damped structures, AIAA Journal 5 (5) (1983) 741–748.

[2] J. Padovan, Computational algorithms for FE formulations involving fractional operators, Computational Mechanics 2 (1987) 271–287.

[3] A. Galucio, J.-F. Deü, R. Ohayon, Finite element formulation of viscoelastic sandwich beams using fractional derivative operators, Computational Mechanics 33 (4) (2004) 282–291.

[4] A. Galucio, J.-F. Deü, S. Mengué, F. Dubois, An adaptation of the Gear scheme for fractional derivatives, Computer Methods in Applied Mechanics and Engineering 1995 (44-47) (2006) 6073–6085.

[5] D. Matignon, Stability properties for generalized fractional differential systems, in: ESAIM: Proceedings, Vol. 5, 1998, pp. 145–158.

[6] D. Heleschewitz, Analyse et simulation de systèmes différentiels fractionnaires et pseudo-différentiels linéaires sous représentation diffusive, Ph.D. thesis, ENST (2000).

[7] H. Haddar, J.-R. Li, D. Matignon, Efficient solution of a wave equation with fractional order dissipative terms, Journal of Computational and Applied Mathematics, 234 (2010) 2003–2010.

[8] J.-F. Deü, D. Matignon, Simulation of fractionally damped mechanical systems by means of a Newmark-diffusive scheme, Computers and Mathematics with Applications, 59 (2010) 1745–1753.

[9] T. Pritz, Analysis of four-parameter fractional derivative model of real solid materials, Journal of Sound and Vibration 195 (1) (1996) 103–115.

[10] A. Lion, On the thermodynamics of fractional damping elements, Continuum Mechanics and Thermodynamics 9 (1997) 83–96.

[11] D. Matignon, C. Prieur, Asymptotic stability of linear conservative systems when coupled with diffusive systems, ESAIM: Control, Optimisation and Calculus of Variations 11 (3) (2005) 487–507.

[12] D. Matignon, An introduction to fractional calculus, in: Scaling, Fractals and Wavelets (Digital Signal and Image Processing Series), ISTE–Wiley, 2009, ch. 7, pp. 237–278.

[13] G. Garcia and J. Bernussou, Identification of the dynamics of a lead acid battery by a diffusive model, in: ESAIM: Proceedings, Vol. 5, 1998, pp. 87–98.

[14] T. Hélie, D. Matignon, Representations with poles and cuts for the time-domain simulation of fractional systems and irrational transfer functions, Signal Processing 86 (10) (2006) 2516–2528.

COMPDYN 2013
4th ECCOMAS Thematic Conference on
Computational Methods in Structural Dynamics and Earthquake Engineering
M. Papadrakakis, V. Papadopoulos, V. Plevris (eds.)
Kos Island, Greece, 12–14 June 2013

A NEW COROTATIONAL ELEMENT FOR NONLINEAR DYNAMIC ANALYSIS OF 3D BEAMS

Thanh-Nam Le [12], Jean-Marc Battini[2], and Mohammed Hjiaj[1]

[1]Université Européenne de Bretagne, INSA de Rennes - LGCGM/Structural Engineering Research Group
20 avenue des Buttes de Coësmes, CS 70839, 35708 Rennes Cedex 7, France
e-mail: Thanh-Nam.Le@insa-rennes.fr, mohammed.hjiaj@insa-rennes.fr

[2] KTH, Royal Institute of Technology - Department of Civil and Architectural Engineering, Division of Structural Engineering and Bridges
Brinellvägen 23, SE-10044 Stockholm, Sweden
e-mail: jean-marc.battini@byv.kth.se

Keywords: Corotational method, Nonlinear dynamics, 3D beam elements, Finite rotations.

Abstract. *The purpose of the paper is to present a corotational beam element for the nonlinear dynamic analysis of 3D flexible frames. The novelty of the formulation lies in the use of the corotational framework (i.e. the decomposition into rigid body motion and pure deformation) to derive not only the internal force vector and the tangent stiffness matrix but also the inertia force vector and the tangent dynamic matrix. As a consequence, cubic interpolations are adopted to formulate both inertia and internal local terms. In the derivation of the dynamic terms, an approximation for the local rotations is introduced and a concise expression for the global inertia force vector is obtained. To enhance the efficiency of the iterative procedure, an approximate expression of the tangent dynamic matrix is adopted. Several numerical examples are considered to assess the performance of the new formulation against the one suggested by Simo and Vu-Quoc [37]. It was observed that the proposed formulation proves to combine accuracy with efficiency. In particular, the present approach achieves the same level of accuracy as the formulation of Simo and Vu-Quoc but with a significantly smaller number of elements.*

1 Introduction

Flexible beams are used in many applications, for instance large deployable space structures, aircrafts and wind turbines propellers, offshore platforms. These structures undergo large displacements and finite rotations, but the strains remain small. Their nonlinear dynamic behavior is often simulated using geometrically nonlinear spatial beam elements. In the literature, several approaches have been used to develop such elements. A large number of them have been formulated in the total Lagrangian context [8, 9, 16, 20, 21, 23, 24, 28, 37, 42, 43, 44]. An other attractive way to develop effective nonlinear dynamic beam elements, which is adopted in the present work, is to use the corotational approach. Indeed, this framework has been adopted by several authors to develop efficient beam and shell elements for the nonlinear static and dynamic analysis of flexible structures. [1, 5, 7, 10, 11, 12, 14, 15, 18, 19, 22, 29, 31, 33, 38]. The main idea of the method is to decompose the motion of the element into rigid body and pure deformational parts. During the rigid body motion, a local coordinates system, attached to the element, moves and rotates with it. The deformational part is measured in this local system. The main interest of the approach is that different assumptions can be made to represent the local deformations, giving rise to different possibilities for the local element formulation.

For the geometrically and materially static nonlinear analysis of beam structures with corotational approach, several local formulations have been proposed by Battini and Pacoste [4], and Alsafadie et al. [2]. The results of a comparative study of 3D beam formulations, which can be found in [2], have shown that local beam elements based on cubic interpolations are more efficient and accurate than the ones which employ linear interpolations. However, in dynamics, one has to deal with the inertia terms which by nature are complicate to formulate. This is particularly true in the corotational formulation of Bernoulli-type beam elements. This difficulty has hampered the development of the corotational approach in nonlinear dynamics. To avoid the consistent derivation of the inertia terms, several routes have been considered.

For 2D dynamic analysis, quite a few authors [29, 31, 38] have adopted the constant lumped mass matrix without any attempt to check its accuracy. Iura and Atluri [22] suggested to simply switch to a Timoshenko beam model where the mass matrix is constant and therefore the inertial terms are simple to evaluate. Behdinan et al. [7] proposed a 2D corotational dynamic formulation where cubic interpolations have been used to describe the global displacements, which is not consistent with the idea of the corotational method as originally introduced by Nour-Omid and Rankin [30]. More recently, Le et al. [26] developed a consistent 2D corotational beam element for nonlinear dynamics. Cubic interpolations were used to describe the local displacements and to derive both inertia and internal terms. Numerical results demonstrated that the formulation is more efficient than the classic formulations (i.e. with the constant Timoshenko and the constant lumped mass matrices). For 3D dynamic analysis, Crisfield et al. [12] suggested to use a constant Timoshenko mass matrix along with local cubic interpolations to derive the internal force vector and the corresponding tangent stiffness matrix. As pointed out by Crisfield et al. [12], this combination is not consistent but it provides reasonable results when the number of elements is large enough. Hsiao et al. [19] presented a corotational formulation for the nonlinear analysis of 3D beams. However the corotational framework adopted in [19] is different from the classic one as proposed first by Nour-Omid and Rankin [30] and adopted in this paper.

The objective of this paper is to extend the consistent 2D corotational dynamic formulation presented in [26] to 3D beam structures. Hence, the corotational framework (i.e. the decomposition into rigid body motion and pure deformation) is used to derive not only the internal force vector and the tangent stiffness matrix but also the inertia force vector and the tangent dynamic matrix. The element has two nodes and is initially straight. The same cubic interpolations are adopted to formulate both inertia and internal local terms. In doing so, the complex expressions of the inertia terms are significantly simplified by adopting a proper approximation for the local rotations. To enhance the efficiency of the iterative procedure, the less significant term in the tangent dynamic matrix is ignored (see [27]).

Regarding the time-stepping scheme, the HHT α method (with $\alpha = -0.05$) is adopted in this work. This energy-dissipative method, which is implemented in several commercial FEM programs (Abaqus, Lusas) and was employed by many authors [9, 12, 24], limits the influence of high frequencies by introducing a numerical damping. The latter often avoids numerical instability, but also results in dissipation of the total energy.

Several numerical applications are presented with the objective to compare the performances of the new formulation against two other approaches. The first approach is similar to the one presented above, but linear local interpolations, instead of cubic ones, are used to derive only the dynamic terms. The purpose is to evaluate the influence of the choice of the local interpolations on the dynamic terms. The second approach is the classic total Lagrangian formulation proposed by Simo and Vu-Quoc [35, 36, 37].

The paper is organized as follows. Section 2 presents some aspects of the parametrization of finite rotations that are essentials for the subsequent developments. Section 3 is devoted to the corotational beam kinematics, whilst the local beam element formulation is introduced in Section 4. The internal force vector and the tangent stiffness matrix are briefly presented in Section 5. More details about the derivation can be found in [4]. Sections 6 focus on the derivation of the inertia terms. In Section 7, several examples are presented in order to assess the accuracy of the present dynamic formulation. Finally, conclusions are given in Section 8.

2 Parametrization of finite rotations

In this section, the relations required for the development of the present formulation are introduced. For a more complete description about the finite rotations, the reader is referred to textbooks and papers such as [3, 6, 13, 17, 25, 39, 40].

The coordinate of a vector $\mathbf{x}_o$ that is rotated into the position $\mathbf{x}$ (see Fig. 1) is given by the relation

$$\mathbf{x} = \mathbf{R}\,\mathbf{x}_o\,. \tag{1}$$

Due to its orthonormality, the rotation matrix $\mathbf{R}$ can be parameterized using only three independent parameters. One possibility is to use the rotational vector defined by

$$\boldsymbol{\theta} = \theta\,\mathbf{n}\,, \tag{2}$$

where $\mathbf{n}$ is a unit vector defining the axis of the rotation and $\theta = (\boldsymbol{\theta}^{\mathrm{T}}\boldsymbol{\theta})^{1/2}$ is the angle of the

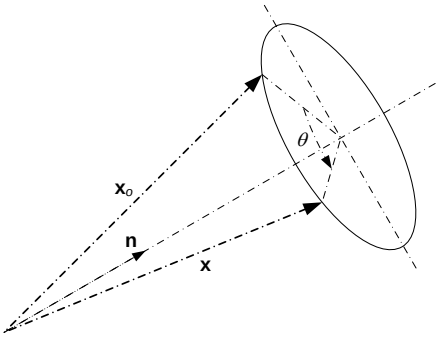


Figure 1: Finite rotation of a vector.

rotation.

The relation between the rotation matrix and the rotational vector is given by the Rodrigues' formula

$$\mathbf{R} = \mathbf{I} + \frac{\sin\theta}{\theta}\widetilde{\boldsymbol{\theta}} + \frac{1-\cos\theta}{\theta^2}\widetilde{\boldsymbol{\theta}}\widetilde{\boldsymbol{\theta}} = \exp(\widetilde{\boldsymbol{\theta}})\,, \tag{3}$$

where $\widetilde{\boldsymbol{\theta}}$ is the skew matrix associated with the vector $\boldsymbol{\theta}$, $\mathbf{I}$ is the 3×3 identity matrix.
The variation $\delta\mathbf{R}$ of the rotation matrix $\mathbf{R}$ is calculated according to

$$\delta\mathbf{R} = \widetilde{\delta\mathbf{w}}\mathbf{R}\,. \tag{4}$$

$\delta\mathbf{w}$, which is also denoted as spatial spin variables, is related to the variation of the rotational vector through

$$\delta\mathbf{w} = \mathbf{T}_s(\boldsymbol{\theta})\,\delta\boldsymbol{\theta}\,, \tag{5}$$

with

$$\mathbf{T}_s(\boldsymbol{\theta}) = \mathbf{I} + \frac{1-\cos\theta}{\theta^2}\widetilde{\boldsymbol{\theta}} + \frac{\theta-\sin\theta}{\theta^3}\widetilde{\boldsymbol{\theta}}\widetilde{\boldsymbol{\theta}}\,. \tag{6}$$

3 Beam kinematics

In this work, the corotational framework introduced by Nour-Omid and Rankin [30], and further developed by Pacoste and Eriksson [32] and Battini and Pacoste [4] is fully adopted.

The definition of the corotational two node beam element described in this section involves several coordinate systems, see Fig. 2. First a global reference system is defined by the triad of unit orthogonal vectors $\mathbf{e}_\alpha$ $(\alpha = 1,2,3)$. Next, a local system which continuously rotates and translates with the element is selected. The orthonormal basis vectors of the local system are denoted by $\mathbf{r}_\alpha$ $(\alpha = 1,2,3)$. In the initial (undeformed) configuration, the local system is defined by the orthonormal triad $\mathbf{e}^o_\alpha$. In addition, $\mathbf{t}^1_\alpha$ and $\mathbf{t}^2_\alpha$ $(\alpha = 1,2,3)$, denote two unit triads rigidly attached to nodes 1 and 2. The origin of the local system is taken at node 1 and thus the rigid translation is defined by $\mathbf{u}^g_1$, the translation at node 1. Here and in the sequel, superscript g

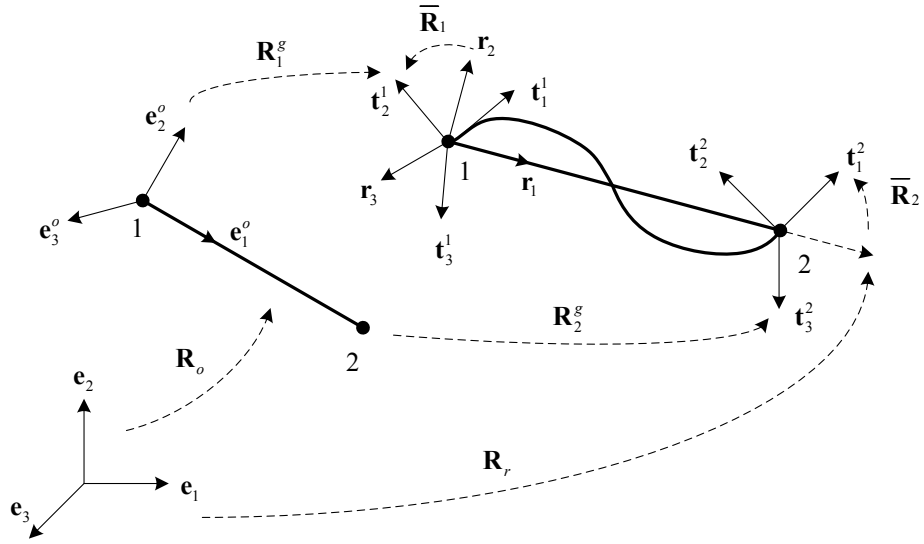


Figure 2: Beam kinematics and the coordinate systems.

indicates quantities expressed in the global reference system. The rigid rotation is such that the new orientation of the local reference system is defined by an orthogonal matrix $\mathbf{R}_r$, given by

$$\mathbf{R}_r = [\,\mathbf{r}_1\ \mathbf{r}_2\ \mathbf{r}_3\,]\,. \tag{7}$$

The first coordinate axis of the local system is defined by the line connecting nodes 1 and 2 of the element. Consequently, $\mathbf{r}_1$ is given by

$$\mathbf{r}_1 = \frac{\mathbf{x}_2^g + \mathbf{u}_2^g - \mathbf{x}_1^g - \mathbf{u}_1^g}{l_n}\,, \tag{8}$$

with $\mathbf{x}_i^g$ $(i = 1,2)$ denoting the nodal coordinates in the initial undeformed configuration and l_n denoting the current length of the beam, i.e.

$$l_n = \|\mathbf{x}_2^g + \mathbf{u}_2^g - \mathbf{x}_1^g - \mathbf{u}_1^g\|\,. \tag{9}$$

The remaining two axes are determined with the help of an auxiliary vector $\mathbf{p}$. In the initial configuration $\mathbf{p}$ is directed along the local $\mathbf{e}_2^o$ direction, whereas in the deformed configuration its orientation is obtained from

$$\mathbf{p} = \frac{1}{2}(\mathbf{p}_1 + \mathbf{p}_2)\,, \qquad \mathbf{p}_i = \mathbf{R}_i^g\,\mathbf{R}_o\,[0\ 1\ 0]^{\mathrm{T}} \qquad (i = 1,2)\,, \tag{10}$$

where $\mathbf{R}_1^g$ and $\mathbf{R}_2^g$ are the orthogonal matrices used to specify the orientation of the nodal triads $\mathbf{t}_\alpha^1$ and $\mathbf{t}_\alpha^2$ respectively, and $\mathbf{R}_o$ specifies the orientation of the local frame in the initial configuration, i.e. $\mathbf{R}_o = [\mathbf{e}_1^o\ \mathbf{e}_2^o\ \mathbf{e}_3^o]$. The unit vectors $\mathbf{r}_2$ and $\mathbf{r}_3$ are then computed by the following vector products

$$\mathbf{r}_3 = \frac{\mathbf{r}_1 \times \mathbf{p}}{\|\mathbf{r}_1 \times \mathbf{p}\|}, \qquad \mathbf{r}_2 = \mathbf{r}_3 \times \mathbf{r}_1\,, \tag{11}$$

resulting in the orthogonal matrix $\mathbf{R}_r$ (Eq. (7)) being completely determined.

The rigid motion previously described, is accompanied by local deformational displacements and rotations with respect to the local element axes. In this context, due to the particular choice of the local system, the local translations at node 1 are zero. Moreover, at node 2, the only non zero component is the translation along $\mathbf{r}_1$. This can easily be evaluated according to

$$\overline{u} = l_n - l_o\,, \tag{12}$$

with l_o denoting the length of the beam in the original undeformed configuration. Here and in the sequel, an overbar denotes a deformational kinematic quantity.

The global rotations at node i can be expressed in terms of the rigid rotation of the local axes, defined by $\mathbf{R}_r$, followed by a local rotation relative to these axes. The latter is defined by the orthogonal matrix $\overline{\mathbf{R}}_i$. Consequently, the orientation of the nodal triad $\mathbf{t}^i_\alpha$ can be obtained by means of the product $\mathbf{R}_r\,\overline{\mathbf{R}}_i$. On the other hand, (see Fig. 2) this orientation can also be obtained through the product $\mathbf{R}^g_i\,\mathbf{R}_o$, which gives

$$\overline{\mathbf{R}}_i = \mathbf{R}_r^{\mathrm{T}}\,\mathbf{R}^g_i\,\mathbf{R}_o \qquad (i=1,2)\,. \tag{13}$$

The local rotations are then evaluated from

$$\overline{\boldsymbol{\theta}}_i = \log\left(\overline{\mathbf{R}}_i\right) \qquad (i=1,2)\,. \tag{14}$$

Due to the choice of the local coordinate system, the local nodal displacement vector $\mathbf{d}_l$ has only seven components and is given by

$$\mathbf{d}_l = \left[\,\overline{u}\;\;\overline{\boldsymbol{\theta}}_1^{\mathrm{T}}\;\;\overline{\boldsymbol{\theta}}_2^{\mathrm{T}}\,\right]^{\mathrm{T}}. \tag{15}$$

The variation of the local nodal displacement vector is

$$\delta\mathbf{d}_l = \left[\,\delta\overline{u}\;\;\delta\overline{\boldsymbol{\theta}}_1^{\mathrm{T}}\;\;\delta\overline{\boldsymbol{\theta}}_2^{\mathrm{T}}\,\right]^{\mathrm{T}}, \tag{16}$$

and the global counterpart is given by

$$\delta\mathbf{d}_g = \left[\,\delta\mathbf{u}_1^{g\mathrm{T}}\;\;\delta\mathbf{w}_1^{g\mathrm{T}}\;\;\delta\mathbf{u}_2^{g\mathrm{T}}\;\;\delta\mathbf{w}_2^{g\mathrm{T}}\,\right]^{\mathrm{T}}, \tag{17}$$

with $\delta\mathbf{w}^g_i\;(i=1,2)$ denoting spatial spin variables defined by

$$\delta\mathbf{R}^g_i = \widetilde{\delta\mathbf{w}^g_i}\,\mathbf{R}^g_i\,. \tag{18}$$

For the rotational terms, the variation of Eq. (13) is needed

$$\delta\overline{\mathbf{R}}_i = \delta\mathbf{R}_r^{\mathrm{T}}\,\mathbf{R}^g_i\,\mathbf{R}_o + \mathbf{R}_r^{\mathrm{T}}\,\delta\mathbf{R}^g_i\,\mathbf{R}_o\,, \tag{19}$$

where $\delta\overline{\mathbf{R}}_i$ and $\delta\mathbf{R}_r$ are computed using Eq. (4), i.e.

$$\delta\overline{\mathbf{R}}_i = \widetilde{\delta\overline{\mathbf{w}}_i}\,\overline{\mathbf{R}}_i, \qquad \delta\mathbf{R}_r = \widetilde{\delta\mathbf{w}^g_r}\,\mathbf{R}_r\,. \tag{20}$$

$\delta\mathbf{R}_r^{\mathrm{T}}$ is calculated via the orthogonality condition $\mathbf{R}_r\,\mathbf{R}_r^{\mathrm{T}} = \mathbf{I}$. Taking variation of this relation and combining the outcome with Eq. (20) results in

$$\delta\mathbf{R}_r^{\mathrm{T}} = -\mathbf{R}_r^{\mathrm{T}}\,\widetilde{\delta\mathbf{w}^g_r}\,. \tag{21}$$

Using Eqs. (18), (20) and (21), Eq. (19) can be rewritten as

$$\widetilde{\delta\overline{\mathbf{w}}_i}\,\overline{\mathbf{R}}_i \;=\; (\widetilde{\delta\mathbf{w}_i^e} - \widetilde{\delta\mathbf{w}_r^e})\,\overline{\mathbf{R}}_i\,, \tag{22}$$

where use of Eq. (13) has been made along the fact that $\mathbf{R}_r$ transforms a vector and a tensor from global to local coordinates according to

$$\mathbf{x}^e = \mathbf{R}_r^{\mathrm{T}}\,\mathbf{x}^g, \qquad \widetilde{\mathbf{x}^e} = \mathbf{R}_r^{\mathrm{T}}\,\widetilde{\mathbf{x}^g}\,\mathbf{R}_r\,. \tag{23}$$

Thus, Eq. (22) gives

$$\delta\overline{\mathbf{w}}_i = \delta\mathbf{w}_i^e - \delta\mathbf{w}_r^e \qquad (i=1,2)\,. \tag{24}$$

Further, let

$$\delta\mathbf{d}_g^e = \mathbf{E}^{\mathrm{T}}\,\delta\mathbf{d}_g, \qquad \mathbf{E} = \begin{bmatrix} \mathbf{R}_r & \mathbf{0} & \mathbf{0} & \mathbf{0} \\ \mathbf{0} & \mathbf{R}_r & \mathbf{0} & \mathbf{0} \\ \mathbf{0} & \mathbf{0} & \mathbf{R}_r & \mathbf{0} \\ \mathbf{0} & \mathbf{0} & \mathbf{0} & \mathbf{R}_r \end{bmatrix}, \tag{25}$$

with $\mathbf{0}$ denoting the 3×3 zero matrix.
Eq. (24) can be rewritten as

$$\begin{bmatrix} \delta\overline{\mathbf{w}}_1 \\ \delta\overline{\mathbf{w}}_2 \end{bmatrix} = \left(\begin{bmatrix} \mathbf{0} & \mathbf{I} & \mathbf{0} & \mathbf{0} \\ \mathbf{0} & \mathbf{0} & \mathbf{0} & \mathbf{I} \end{bmatrix} - \begin{bmatrix} \mathbf{G}^{\mathrm{T}} \\ \mathbf{G}^{\mathrm{T}} \end{bmatrix} \right) \mathbf{E}^{\mathrm{T}}\,\delta\mathbf{d}_g = \mathbf{P}\mathbf{E}^{\mathrm{T}}\,\delta\mathbf{d}_g\,, \tag{26}$$

where the matrix $\mathbf{G}$ is defined by

$$\mathbf{G}^{\mathrm{T}} = \frac{\partial\mathbf{w}_r^e}{\partial\mathbf{d}_g^e}\,. \tag{27}$$

The expression of $\mathbf{G}$ is given by

$$\mathbf{G}^{\mathrm{T}} = \begin{bmatrix} 0 & 0 & \dfrac{\eta}{l_n} & \dfrac{\eta_{12}}{2} & -\dfrac{\eta_{11}}{2} & 0 & 0 & 0 & -\dfrac{\eta}{l_n} & \dfrac{\eta_{22}}{2} & -\dfrac{\eta_{21}}{2} & 0 \\ 0 & 0 & \dfrac{1}{l_n} & 0 & 0 & 0 & 0 & 0 & -\dfrac{1}{l_n} & 0 & 0 & 0 \\ 0 & -\dfrac{1}{l_n} & 0 & 0 & 0 & 0 & 0 & \dfrac{1}{l_n} & 0 & 0 & 0 & 0 \end{bmatrix}, \tag{28}$$

$$\eta = \frac{p_1}{p_2} \qquad \eta_{11} = \frac{p_{11}}{p_2}\,, \qquad \eta_{12} = \frac{p_{12}}{p_2} \qquad \eta_{21} = \frac{p_{21}}{p_2} \qquad \eta_{22} = \frac{p_{22}}{p_2}\,, \tag{29}$$

where (see Eq. (10)) p_j and p_{ij} are the components of the vectors $\mathbf{R}_r^{\mathrm{T}}\,\mathbf{p}$ and $\mathbf{R}_r^{\mathrm{T}}\,\mathbf{p}_i$, respectively.

4 Local beam kinematic description

In this section, the local beam kinematics, adopted to derive both inertia and internal terms, is presented. The local motion of a beam cross-section from the initial (i.e. rotated but still undeformed) configuration to the current configuration is defined by the translation of the cross-section centroid G and the rotation of the section (see Figs. 3 and 4).

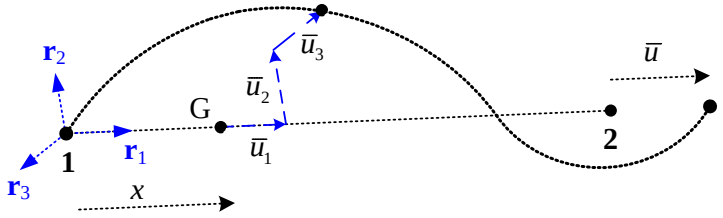


Figure 3: Local beam configuration - Translation.

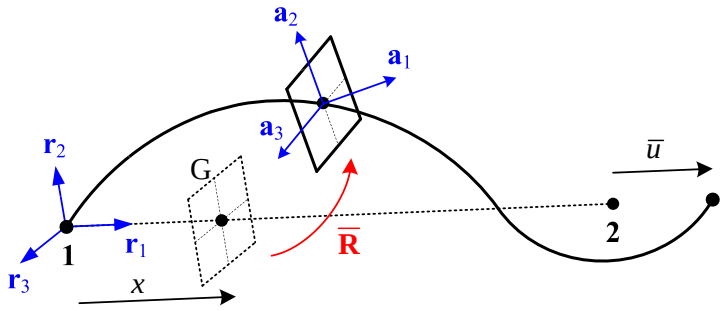


Figure 4: Local beam configuration - Rotation.

Let $[\,\bar{u}_1 \;\; \bar{u}_2 \;\; \bar{u}_3\,]^{\mathrm{T}}$ and $\bar{\boldsymbol{\theta}} = [\,\bar{\theta}_1 \;\; \bar{\theta}_2 \;\; \bar{\theta}_3\,]^{\mathrm{T}}$ denote the local displacement vector of G and the local rotation of the section, respectively. These quantities are interpolated from the local nodal values based on the Bernoulli hypothesis. Then, due to the particular choice of the local degrees of freedom, one has

$$\begin{bmatrix} \bar{u}_1 \\ \bar{u}_2 \\ \bar{u}_3 \\ \bar{\theta}_1 \\ \bar{\theta}_2 \\ \bar{\theta}_3 \end{bmatrix} = \begin{bmatrix} N_2 & 0 & 0 & 0 & 0 & 0 & 0 \\ 0 & 0 & 0 & N_3 & 0 & 0 & N_4 \\ 0 & 0 & -N_3 & 0 & 0 & -N_4 & 0 \\ 0 & N_1 & 0 & 0 & N_2 & 0 & 0 \\ 0 & 0 & N_5 & 0 & 0 & N_6 & 0 \\ 0 & 0 & 0 & N_5 & 0 & 0 & N_6 \end{bmatrix} \mathbf{d}_l\,, \tag{30}$$

where the local nodal displacement vector $\mathbf{d}_l$ is defined by Eq. (15).
The expressions of the interpolation functions are given by

$$N_1 = 1 - \frac{x}{l_o}\,, \qquad N_2 = \frac{x}{l_o}\,, \qquad N_3 = x\left(1 - \frac{x}{l_o}\right)^2\,,$$
$$N_4 = -\left(1 - \frac{x}{l_o}\right)\frac{x^2}{l_o}\,, \quad N_5 = \left(1 - \frac{3x}{l_o}\right)\left(1 - \frac{x}{l_o}\right)\,, \quad N_6 = \left(\frac{3x}{l_o} - 2\right)\frac{x}{l_o}\,.$$

Let $\mathbf{u}_l = [\,0 \;\; \bar{u}_2 \;\; \bar{u}_3\,]^{\mathrm{T}}$ denotes the local transverse displacement vector. This vector is calculated by

$$\mathbf{u}_l = \mathbf{P}_1 \begin{bmatrix} \bar{\boldsymbol{\theta}}_1 \\ \bar{\boldsymbol{\theta}}_2 \end{bmatrix}\,, \quad \mathbf{P}_1 = \begin{bmatrix} 0 & 0 & 0 & 0 & 0 & 0 \\ 0 & 0 & N_3 & 0 & 0 & N_4 \\ 0 & -N_3 & 0 & 0 & -N_4 & 0 \end{bmatrix}\,. \tag{31}$$

The local rotation of the cross-section is evaluated as follows

$$\overline{\boldsymbol{\theta}} = \mathbf{P}_2 \begin{bmatrix} \overline{\boldsymbol{\theta}}_1 \\ \overline{\boldsymbol{\theta}}_2 \end{bmatrix}, \quad \mathbf{P}_2 = \begin{bmatrix} N_1 & 0 & 0 & N_2 & 0 & 0 \\ 0 & N_5 & 0 & 0 & N_6 & 0 \\ 0 & 0 & N_5 & 0 & 0 & N_6 \end{bmatrix}. \tag{32}$$

In the present formulation, bending shear deformations are not considered. Such deformations can easily be introduced by modifying the Hermitian shape functions as suggested in the Interdependent Interpolation Element (IIE) formulation [34].

5 Internal force vector and tangent stiffness matrix

The purpose of this section is to present briefly the derivation of the inertial force vector and the tangent stiffness matrix. A complete description can be found in [4].
Using the local beam kinematics presented in Section 4 together with a shallow arch strain description, the local internal force vector $\mathbf{f}_l$ and the local tangent stiffness matrix $\mathbf{K}_l$ associated with $\delta\mathbf{d}_l$ (see Eq. (16)) are computed. The Maple codes for $\mathbf{f}_l$ and $\mathbf{K}_l$ are given in [4].
The global internal force vector $\mathbf{f}_{\mathrm{g}}$ and the global tangent stiffness matrix $\mathbf{K}_{\mathrm{g}}$ associated with $\delta\mathbf{d}_g$ (see Eq. (17)) are obtained through a change of variables based on the transformation matrix $\mathbf{B}$ defined by

$$\delta\mathbf{d}_l = \mathbf{B}\,\delta\mathbf{d}_g\,. \tag{33}$$

By equating the internal virtual work in both the global and local systems, the expression of the global internal force vector $\mathbf{f}_{\mathrm{g}}$ is obtained as

$$\mathbf{f}_{\mathrm{g}} = \mathbf{B}^{\mathrm{T}}\mathbf{f}_l\,. \tag{34}$$

By taking the variations of Eq. (34), the expression of the global tangent stiffness matrix $\mathbf{K}_{\mathrm{g}}$ is obtained

$$\mathbf{K}_{\mathrm{g}} = \mathbf{B}^{\mathrm{T}}\mathbf{K}_l\mathbf{B} + \left.\frac{\partial(\mathbf{B}^{\mathrm{T}}\mathbf{f}_l)}{\partial\mathbf{d}_g}\right|_{\mathbf{f}_l}. \tag{35}$$

The details regarding the final expressions of $\mathbf{f}_{\mathrm{g}}$ and $\mathbf{K}_{\mathrm{g}}$ are given in [4].

6 Inertia force vector and tangent dynamic matrix

This section is devoted to the derivation of the inertia force vector and the tangent dynamic matrix. The novelty of the approach presented here is that the same corotational kinematics description is adopted to formulate both inertia and internal terms, which ensures the consistency of the formulation. As already mentioned, the current 3D formulation is the extension of the 2D one proposed by the authors [26].

Using the cross-section centroid as the reference point, the variation of the kinetic energy can be expressed as (see [17])

$$\delta K = -\int_{l_o} \left\{ \delta\mathbf{u}^{\mathrm{T}} A_\rho \ddot{\mathbf{u}} + \delta\mathbf{w}^{\mathrm{T}} \left[\mathbf{I}_\rho \dot{\mathbf{w}} + \widetilde{\dot{\mathbf{w}}}\mathbf{I}_\rho \mathbf{w} \right] \right\} \mathrm{d}l\,, \tag{36}$$

where $\dot{\mathbf{u}}$, $\dot{\mathbf{w}}$ are the translational and angular velocity of the cross-section. Please note that in order to simplify the notations, in this section, the superscripts "g" which refer to global

quantities are dropped for $\mathbf{u}$, $\dot{\mathbf{w}}$ and their derivatives.
$\mathbf{I}_\rho$ is the spatial inertia dyadic tensor given by

$$\mathbf{I}_\rho = \mathbf{R}^g \mathbf{R}_o \mathbf{J}_\rho \left(\mathbf{R}^g \mathbf{R}_o\right)^{\mathrm{T}}, \tag{37}$$

in which $\mathbf{J}_\rho$ is the inertia dyadic of the cross-section in the initial configuration.
The inertia force vector is then derived from the following relation

$$\delta K = -\mathbf{f}_{\mathrm{k}}^{\mathrm{T}} \delta \mathbf{d}_g . \tag{38}$$

6.1 Translational displacement variables

The position of the cross-section centroid in the global coordinate system is given by (see Fig. 3)

$$\mathrm{OG} = \mathbf{x}_1^g + \mathbf{u}_1^g + (x + \overline{u}_1)\,\mathbf{r}_1 + \overline{u}_2 \mathbf{r}_2 + \overline{u}_3 \mathbf{r}_3 . \tag{39}$$

By using Eqs. (8), (12) and (30), one obtains

$$\mathrm{OG} = N_1 \mathbf{x}_1^g + N_2 \mathbf{x}_2^g + N_1 \mathbf{u}_1^g + N_2 \mathbf{u}_2^g + \mathbf{R}_r \mathbf{u}_l . \tag{40}$$

Then by taking the variation of the above equation, the following expression is obtained

$$\delta \mathrm{OG} = \delta \mathbf{u} = \mathbf{N}\,\delta \mathbf{d}_g + \mathbf{R}_r \delta \mathbf{u}_l + \delta \mathbf{R}_r \mathbf{u}_l , \tag{41}$$

with $\mathbf{N} = \begin{bmatrix} N_1\mathbf{I} & \mathbf{0} & N_2\mathbf{I} & \mathbf{0} \end{bmatrix}$.
One interesting property of $\mathbf{N}$ is that

$$\mathbf{N} = \mathbf{R}_r \mathbf{N} \mathbf{E}^{\mathrm{T}} . \tag{42}$$

The variation $\delta \mathbf{R}_r$ is calculated using Eqs. (20) and (23) as

$$\delta \mathbf{R}_r = \mathbf{R}_r \widetilde{\delta \mathbf{w}_r^e} . \tag{43}$$

From Eqs. (25) and (27), $\delta \mathbf{w}_r^e$ is obtained as

$$\delta \mathbf{w}_r^e = \mathbf{G}^{\mathrm{T}} \mathbf{E}^{\mathrm{T}} \delta \mathbf{d}_g . \tag{44}$$

By taking the differentiation of Eq. (31), one obtains

$$\delta \mathbf{u}_l = \mathbf{P}_1 \begin{bmatrix} \delta \overline{\boldsymbol{\theta}}_1 \\ \delta \overline{\boldsymbol{\theta}}_2 \end{bmatrix} . \tag{45}$$

In the corotational approach, the local rotations at the nodes $\overline{\boldsymbol{\theta}}_i$ $(i = 1,2)$, defined in Eq. (14), are small and the operator $\mathbf{T}_s(\overline{\boldsymbol{\theta}}_i)$ is close to the identity matrix. Consequently, see Eq. (5), the following approximation is adopted

$$\delta \overline{\mathbf{w}}_i \approx \delta \overline{\boldsymbol{\theta}}_i . \tag{46}$$

Then, using Eqs. (26) and (46), the expression in (45) becomes

$$\delta \mathbf{u}_l \approx \mathbf{P}_1 \begin{bmatrix} \delta \overline{\mathbf{w}}_1 \\ \delta \overline{\mathbf{w}}_2 \end{bmatrix} = \mathbf{P}_1 \mathbf{P} \mathbf{E}^{\mathrm{T}} \delta \mathbf{d}_g . \tag{47}$$

Inserting Eqs. (42) - (44) and (47) into Eq. (41), one obtains

$$\delta\mathbf{u} = \mathbf{R}_r \mathbf{H}_1 \mathbf{E}^{\mathrm{T}} \delta\mathbf{d}_g \,, \tag{48}$$

with

$$\mathbf{H}_1 = \mathbf{N} + \mathbf{P}_1 \mathbf{P} - \widetilde{\mathbf{u}}_l \mathbf{G}^{\mathrm{T}} \,. \tag{49}$$

Obviously, the translational velocity of the cross-section centroid is evaluated from

$$\dot{\mathbf{u}} = \mathbf{R}_r \mathbf{H}_1 \mathbf{E}^{\mathrm{T}} \dot{\mathbf{d}}_g \,. \tag{50}$$

By taking the time derivative of the above equation, the expression of the translational acceleration reads as follows

$$\ddot{\mathbf{u}} = \mathbf{R}_r \mathbf{H}_1 \mathbf{E}^{\mathrm{T}} \ddot{\mathbf{d}}_g + \mathbf{R}_r \mathbf{C}_1 \mathbf{E}^{\mathrm{T}} \dot{\mathbf{d}}_g = \mathbf{R}_r \ddot{\mathbf{u}}^e \,, \tag{51}$$

with

$$\mathbf{C}_1 = \widetilde{\dot{\mathbf{w}}_r^e} \mathbf{H}_1 + \dot{\mathbf{H}}_1 - \mathbf{H}_1 \mathbf{E}_t \,, \qquad \mathbf{E}_t = \begin{bmatrix} \widetilde{\dot{\mathbf{w}}_r^e} & \mathbf{0} & \mathbf{0} & \mathbf{0} \\ \mathbf{0} & \widetilde{\dot{\mathbf{w}}_r^e} & \mathbf{0} & \mathbf{0} \\ \mathbf{0} & \mathbf{0} & \widetilde{\dot{\mathbf{w}}_r^e} & \mathbf{0} \\ \mathbf{0} & \mathbf{0} & \mathbf{0} & \widetilde{\dot{\mathbf{w}}_r^e} \end{bmatrix} , \tag{52}$$

and $\dot{\mathbf{H}}_1$ given in Appendix A.

6.2 Finite rotation variables

Using Eqs. (23) and (24), the spatial spin variables, associated to the global rotation of a cross-section, are evaluated using

$$\delta\mathbf{w} = \mathbf{R}_r \delta\mathbf{w}^e = \mathbf{R}_r \left(\delta\mathbf{w}_r^e + \delta\overline{\mathbf{w}} \right) . \tag{53}$$

Combining Eq. (32) with the approximation defined in Eq. (46) and using Eq. (26), the local spatial spin variables are calculated as follows

$$\delta\overline{\mathbf{w}} = \mathbf{P}_2 \mathbf{P} \mathbf{E}^{\mathrm{T}} \delta\mathbf{d}_g \,. \tag{54}$$

Finally, by introducing Eqs. (44) and (54) into (53), the spatial spin variables are computed from the global nodal displacement vector by

$$\delta\mathbf{w} = \mathbf{R}_r \mathbf{H}_2 \mathbf{E}^{\mathrm{T}} \delta\mathbf{d}_g \,, \tag{55}$$

with

$$\mathbf{H}_2 = \mathbf{P}_2 \mathbf{P} + \mathbf{G}^{\mathrm{T}} \,. \tag{56}$$

The angular velocity is calculated with the following similar expression

$$\dot{\mathbf{w}} = \mathbf{R}_r \mathbf{H}_2 \mathbf{E}^{\mathrm{T}} \dot{\mathbf{d}}_g = \mathbf{R}_r \dot{\mathbf{w}}^e \,. \tag{57}$$

The angular acceleration is obtained by taking the time derivative of the angular velocity

$$\ddot{\mathbf{w}} = \mathbf{R}_r \mathbf{H}_2 \mathbf{E}^{\mathrm{T}} \ddot{\mathbf{d}}_g + \mathbf{R}_r \mathbf{C}_2 \mathbf{E}^{\mathrm{T}} \dot{\mathbf{d}}_g = \mathbf{R}_r \ddot{\mathbf{w}}^e \,, \tag{58}$$

with $\dot{\mathbf{H}}_2$ given in Appendix A and

$$\mathbf{C}_2 = \widetilde{\dot{\mathbf{w}}_r^e} \mathbf{H}_2 + \dot{\mathbf{H}}_2 - \mathbf{H}_2 \mathbf{E}_t \,. \tag{59}$$

6.3 Inertia force vector and tangent dynamic matrix

By inserting the expressions of $\delta\mathbf{u}$ and $\delta\mathbf{w}$ given in Eqs. (48) and (55) into Eq. (36), and using the local forms $\ddot{\mathbf{u}}^e$, $\dot{\mathbf{w}}^e$ and $\ddot{\mathbf{w}}^e$ (see Eqs. (51), (57) and (58)), the inertia force vector is obtained as

$$\mathbf{f}_{\mathrm{k}} = \mathbf{E}\left[\int_{l_o}\left\{\mathbf{H}_1^{\mathrm{T}} A_\rho \ddot{\mathbf{u}}^e + \mathbf{H}_2^{\mathrm{T}}\left[\mathbf{I}_\rho^e \ddot{\mathbf{w}}^e + \widetilde{\dot{\mathbf{w}}^e}\mathbf{I}_\rho^e \dot{\mathbf{w}}^e\right]\right\}\mathrm{d}l\right], \tag{60}$$

with (see Eq. (37))

$$\mathbf{I}_\rho^e = \mathbf{R}_r{}^{\mathrm{T}}\,\mathbf{I}_\rho\,\mathbf{R}_r = \overline{\mathbf{R}}\,\mathbf{J}_\rho\,\overline{\mathbf{R}}^{\mathrm{T}}. \tag{61}$$

$\overline{\mathbf{R}}$ is the rotation matrix associated with the local rotation of the section (see Fig. 4).
As shown in the above equation, the inertia force vector depends on $\mathbf{d}_g, \dot{\mathbf{d}}_g$ and $\ddot{\mathbf{d}}_g$. Hence, linearization of this force vector is evaluated as follows

$$\Delta\mathbf{f}_{\mathrm{k}} = \mathbf{M}\Delta\ddot{\mathbf{d}}_g + \mathbf{C}_{\mathrm{k}}\Delta\dot{\mathbf{d}}_g + \mathbf{K}_{\mathrm{k}}\Delta\mathbf{d}_g\,. \tag{62}$$

Some authors proposed to keep only the mass matrix $\mathbf{M}$, and to eliminate the gyroscopic $\mathbf{C}_{\mathrm{k}}$ and centrifugal $\mathbf{K}_{\mathrm{k}}$ dynamic matrices [9, 19]. However, in [27], extensive numerical studies have shown that it is better to keep also the gyroscopic matrix in order to enhance the computational efficiency. The same approach is used here. The centrifugal matrix, whose derivation is complicated and would give a large mathematical expression, is neglected. Therefore, the iterative scheme of the present formulation is implemented with the following approximative linearization

$$\Delta\mathbf{f}_{\mathrm{k}} \approx \mathbf{M}\Delta\ddot{\mathbf{d}}_g + \mathbf{C}_{\mathrm{k}}\Delta\dot{\mathbf{d}}_g\,. \tag{63}$$

The explicit expressions of the mass matrix $\mathbf{M}$ and of the gyroscopic matrix $\mathbf{C}_{\mathrm{k}}$ are given by

$$\mathbf{M} = \mathbf{E}\left\{\int_{l_o}\left(\mathbf{H}_1^{\mathrm{T}} A_\rho\,\mathbf{H}_1 + \mathbf{H}_2^{\mathrm{T}}\mathbf{I}_\rho^e\,\mathbf{H}_2\right)\mathrm{d}l\right\}\mathbf{E}^{\mathrm{T}} = \mathbf{E}\,\mathbf{M}^e\,\mathbf{E}^{\mathrm{T}}, \tag{64}$$

$$\begin{aligned}\mathbf{C}_{\mathrm{k}} =& \mathbf{E}\left\{\int_{l_o}\mathbf{H}_1^{\mathrm{T}} A_\rho\,(\mathbf{C}_1+\mathbf{C}_3)\,\mathrm{d}l + \int_{l_o}\mathbf{H}_2^{\mathrm{T}}\mathbf{I}_\rho^e\,(\mathbf{C}_2+\mathbf{C}_4)\,\mathrm{d}l\right.\\ &\left.+\int_{l_o}\mathbf{H}_2^{\mathrm{T}}\left(\widetilde{\dot{\mathbf{w}}^e}\mathbf{I}_\rho^e - \widetilde{\mathbf{I}_\rho^e\dot{\mathbf{w}}^e}\right)\mathbf{H}_2\mathrm{d}l\right\}\mathbf{E}^{\mathrm{T}} = \mathbf{E}\,\mathbf{C}_{\mathrm{k}}^e\,\mathbf{E}^{\mathrm{T}},\end{aligned} \tag{65}$$

with $\mathbf{C}_3$ and $\mathbf{C}_4$ given in Appendix B.

6.4 Numerical integration

The internal force vector $\mathbf{f}_{\mathrm{g}}$ and the tangent stiffness matrix $\mathbf{K}_{\mathrm{g}}$ are exactly evaluated without numerical integrations.

Concerning the dynamic terms, i.e. the inertia force vector $\mathbf{f}_{\mathrm{k}}$, the mass matrix $\mathbf{M}$ and the gyroscopic matrix $\mathbf{C}_{\mathrm{k}}$, two approaches have been implemented. The first one, referred to "cubic corotational approach", is the one presented in this section. Three Gauss points are used to integrate Eqs. (60), (64) and (65). The second approach, referred to "linear corotational approach", is obtained by assuming linear interpolations for all local quantities. This mean that the cubic interpolations N_5 and N_6 are replaced with N_1 and N_2 in Eq. (30), and that the local transverse

displacements $\overline{u}_2$ and $\overline{u}_3$ are zero (see Eq. (30)). For this linear approach, two Gauss points are used to calculate the inertia force vector and the tangent dynamic matrix. It can be observed that linear local interpolations imply $\mathbf{u}_l = \mathbf{0}_{3\times 1}$, which simplifies significantly the computations.

It should be noted that, in these two corotational approaches, all the quantities at the Gauss point are directly calculated from the nodal ones. Therefore, no extra storage is needed.

7 Numerical examples

The purpose of this section is to assess both the cubic and the linear corotational formulations. The first one employs cubic interpolation for all terms whereas the second uses cubic interpolation for the internal force vector and the corresponding stiffness matrix, the inertia terms being evaluated considering linear interpolation. The predictions of these formulations are compared against the total Lagrangian formulation proposed by Simo and Vu-Quoc [35, 36, 37]. In this formulation which employs spatial spin variables, the internal force vector and the tangent stiffness matrix are numerically integrated using one Gauss point whereas the inertia force vector and the dynamic tangent matrix are numerically integrated using two Gauss points. All the three formulations are implemented using Matlab. The same levels of optimisation in forming the element matrices and force vectors are carefully checked.

Several numerical applications are considered. For each application, the solutions given by the three dynamic formulations are compared against a reference solution. The latter is obtained by increasing the number of elements until the three dynamic formulations converge towards the same results.

The first numerical example has been proposed by Simo and Vu-Quoc [37]. This problem is very popular and has been considered by many authors as a test for nonlinear dynamic formulations involving large rotations. In this example, the reference solution is in a good agreement with the results found in the literature. For the second example, additional analyses with Abaqus are performed in order to assess the quality of the reference solutions. Two different beam elements are used. The first one is B31, which is based on the classical Timoshenko beam theory. The second one is B33, which is based on the classical Euler-Bernoulli beam theory. With refined meshes and refined time step sizes, these two elements converged towards the selected reference solutions. It can also be concluded that the shear effects are very small and can be neglected.

In their work, Simo and Vu-Quoc [37] employed the Newmark trapezoidal rule. When applied to nonlinear dynamics, this scheme can be unstable [10, 24, 41]. To avoid this problem, the HHT α method [13] with $\alpha = -0.05$ is employed in this work. This value of α, which is typically adopted in nonlinear dynamic analyses [9, 12, 24] and also used as default in Abaqus, gives a small numerical damping and limits the influence of high frequencies. However, a numerical damping gives also a dissipation of the total energy, which can affect long time analyses.

During the time period under consideration, the time step size remains constant. Except for the first example, where the time step size is taken as in the literature [20, 23, 24, 37, 44], the time step size is carefully selected. For that, the same example is run using $0.5\,\Delta t$. The time step is accepted if both runs provide the same results.

At the beginning of each time step, a predictor is used to initiate the iterative procedure. Several predictors are available in the literature and a comparative study of the performances of these predictors can be found in [27]. As shown in [27], the quality of the predictor has a significant influence on the convergence of the iterative procedure. In the present work, the predictor proposed by Crisfield [13] for the particular case of linear inertia force vector and further developed in the general case by the authors [27], is adopted. The idea of this predictor is to use the tangent operator at the time instant t_n to predict the values at the time instant t_{n+1}. This predictor is the most effective among the four ones compared in [27].

Damping is not considered and the following convergence criterion is adopted: the norm of the residual vector must be less than the prescribed tolerance $\varepsilon_f = 10^{-5}$.

7.1 Example 1: Right-angle cantilever beam

This classic example, introduced by Simo and Vu-Quoc [37], has often been used in order to validate various nonlinear dynamic formulations [19, 20, 24, 28]. A right-angle cantilever, depicted in Fig. 5, is subjected to an out-of-plane concentrated load applied at the elbow. Each member of the cantilever has a length $L = 10$. The material properties are $GA = EA = 10^6$, $GJ = EI = 10^3$. The mass per unit length of the beam and the inertia dyadic of the cross section in the initial configuration are $A_\rho = 1$ and $\mathbf{J}_\rho = \mathrm{diag}(20, 10, 10)$, respectively.
The load (see Fig. 6) acts only during $0 \leq t(s) \leq 2$ and thereafter the cantilever undergoes large-scale free vibrations. The applied force increases linearly until the value of 50 is reached at one second and decreases from there to zero within one further second. The resulting amplitude of vibration is of the same order of magnitude as the structure's dimensions. The reference solution has been obtained with a total of 20 beam elements (10 elements per member) whereas the predictions of the three aforementioned formulations have derived using only 4 elements (2 elements per member).
The time evolution of the out-of-plane displacement of node A is depicted in Fig. 7. The

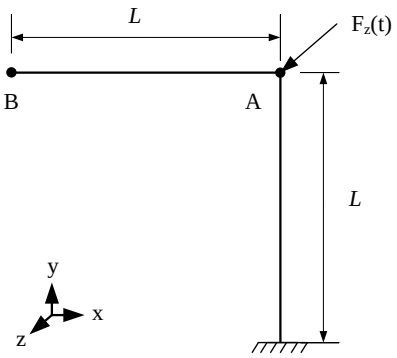


Figure 5: Right-angle cantilever beam : geometrical data.

computations are performed with $\Delta t = 0.25$ s. It can be noted that with only 4 beam elements, the cubic corotational approach gives almost the same results as the reference solution over the whole time domain. The results obtained with the linear corotational approach are very close to

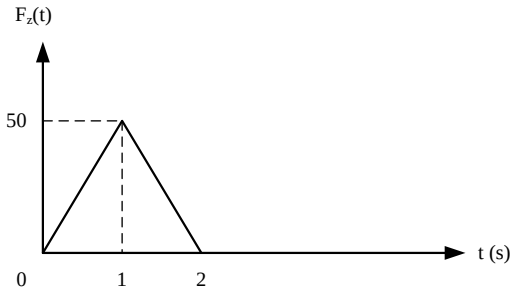


Figure 6: Right-angle cantilever beam - Loading history.

the reference solution with minor differences. However, the results obtained with the formulation of Simo and Vu-Quoc are far from the reference solution.

The time evolution of the out-of-plane displacement of node B, calculated with a total of 8

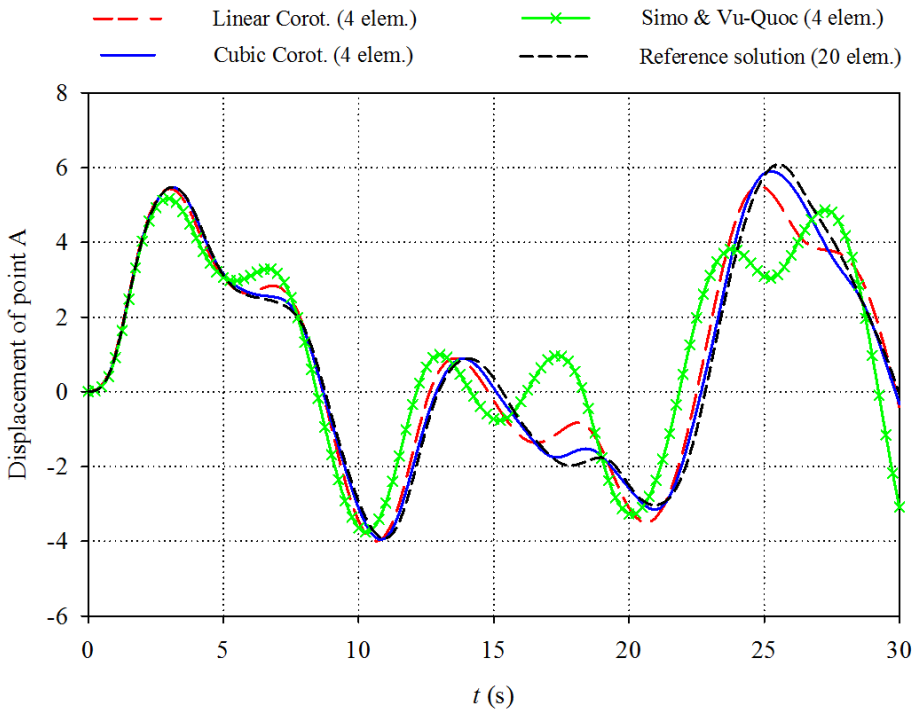


Figure 7: Right-angle cantilever beam - Time evolution of the out-of-plane displacement of point A.

beam elements (4 elements per member), is depicted in Fig. 8. It can be noted that the differences between the formulation of Simo and Vu-Quoc and the reference solution become smaller, but also that the cubic corotational formulation gives very accurate results.

In the current example, the energy blow-up can happen at approximately $t = 45$ s. This numerical instability has been reported by Jelenić and Crisfield [23, 24] and by Zupan et al. [44]. Therefore, to assess the stability of the HHT α method when combined with the new cubic formulation, this example is run for a time period of 150 s using a total of 20 beam elements

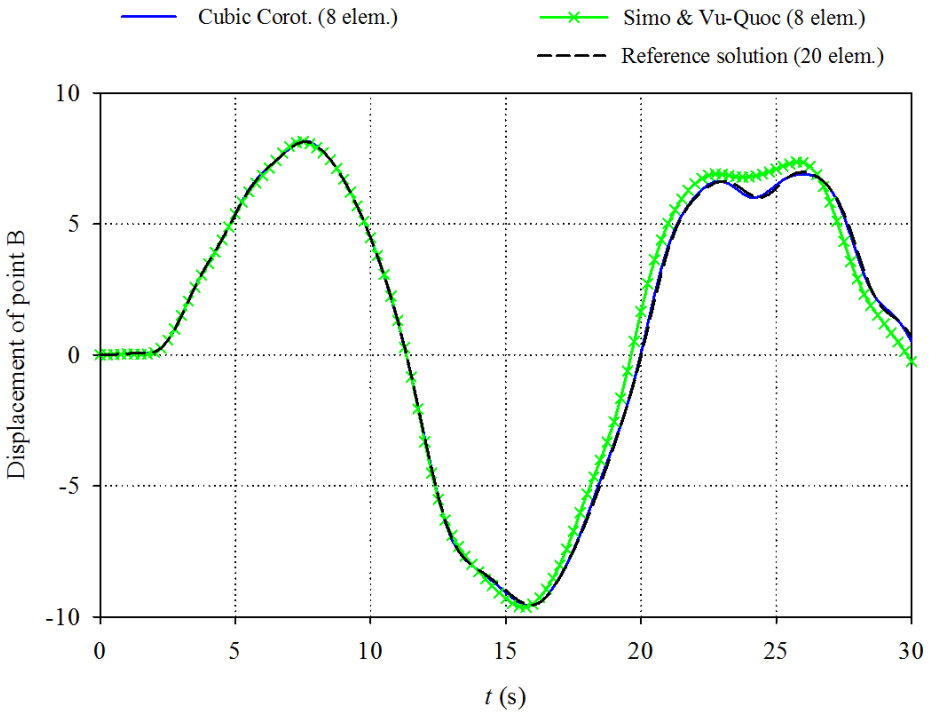


Figure 8: Right-angle cantilever beam - Time evolution of the out-of-plane displacement of point B.

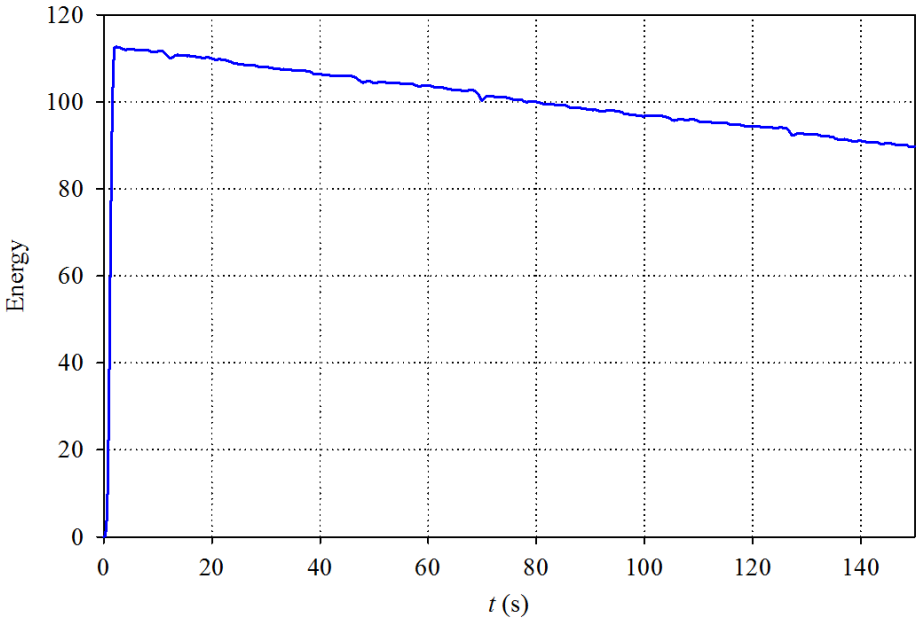


Figure 9: Right-angle cantilever beam - Time evolution of the total energy.

and a time step $\Delta t = 0.25$ s. The time evolution of the total energy is depicted in Fig. 9. The result indicates that the new formulation is stable during the time period under consideration. The dissipation of energy between $t = 2$ s and $t = 30$ s is about 3%.

The CPU time and the total number of iterations required for each formulation are presented

Table 1: Right-angle cantilever beam - CPU time (Total number of iterations).

Number of beam elements	Linear corot.	Cubic corot.	Simo & Vu-Quoc
4	3.66 (633)	5.31 (637)	4.59 (521)
20	19.84 (636)	25.61 (612)	22.90 (517)

in Tab. 1. With the same number of elements, the linear corotational approach is the fastest approach and the cubic corotational approach is the slowest one.

7.2 Example 2: Cantilever beam

The second example is a cantilever beam of length $L = 10$ m with uniform cross-section (see Fig. 10). The beam is clamped at one end and subjected to a sinusoidal out-of-plane force $F_z(t)$ and a bending moment $M_z(t)$ at the free end (see Fig. 11). The circular frequency of the force w is 50 rad/s. The bending moment increases linearly until the value of 3 is reached at 0.3 second and decreases from there to zero within a further 0.3 second. The cross-section width and depth are $e = 0.25$ m and $a = 0.3$ m, respectively. The elastic modulus of the beam E is 210 GPa and the Poisson's ratio ν is 0.3. The mass per unit volume is $\rho = 7850$ kg/m^3.
The time step size is chosen as $\Delta t = 5 \cdot 10^{-4}$ s.

The reference solution has been obtained with a total of 20 beam elements whereas only

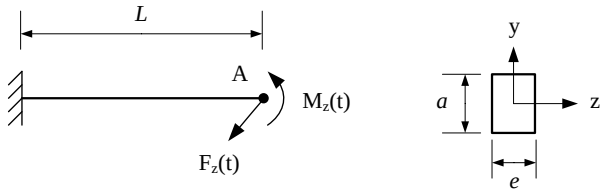


Figure 10: Cantilever beam : geometrical data.

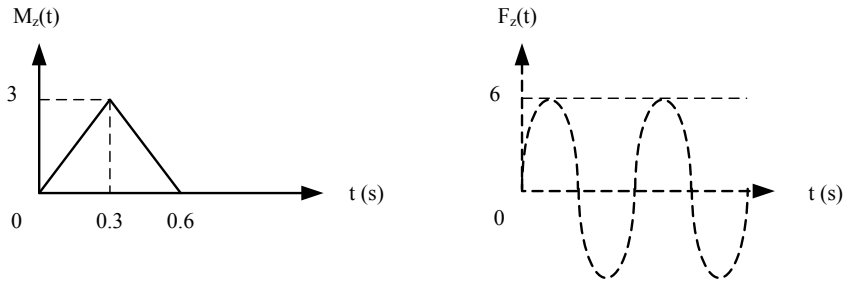


Figure 11: Cantilever beam - Loading history.

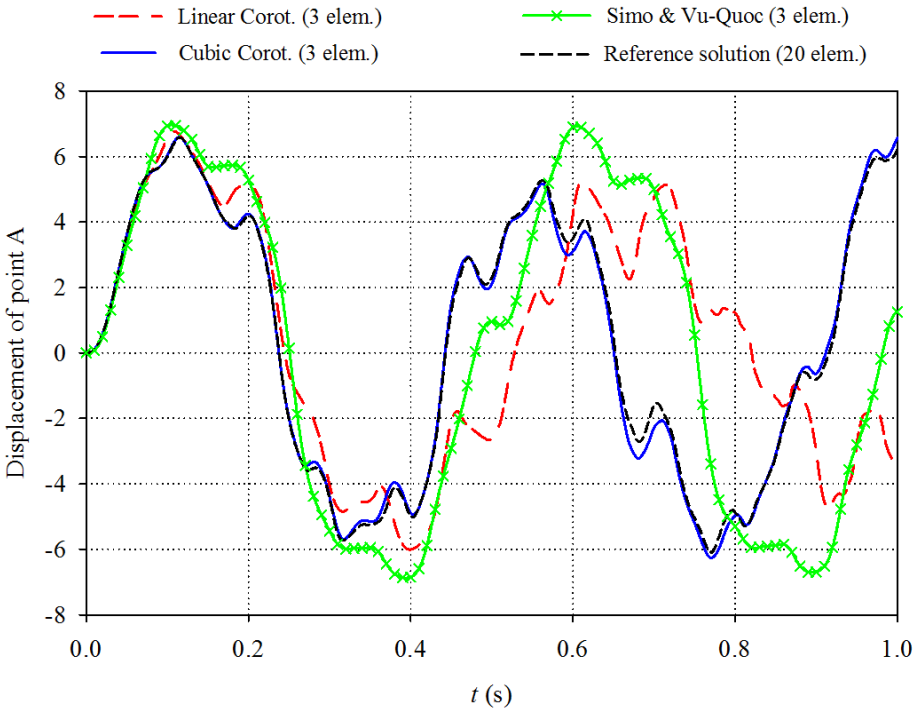


Figure 12: Cantilever beam - Time evolution of the out-of-plane displacement of point A.

Table 2: Cantilever beam - CPU time (Total number of iterations).

Number of beam elements	Linear corot.	Cubic corot.	Simo & Vu-Quoc
3	24.97 (5844)	34.22 (5829)	27.45 (4339)
20	164.86 (5346)	227.01 (5486)	220.94 (5394)

3 beam elements are used for the computations with the three formulations. The out-of-plane displacement of the free end A is depicted in Fig. 12.
It can be noted that the results obtained with the cubic corotational approach are very close to the reference solution. However, large discrepancies between the results obtained with the two other formulations and the reference solution can be observed. As for the first example, with the same number of elements, the linear corotational approach is the fastest formulation and the cubic corotational approach is the slowest one (see Tab. 2).

8 Conclusion

A new consistent 3D corotational beam element for nonlinear dynamics of flexible structures was presented. The novelty of the formulation is that the corotational framework (i.e. the decomposition into rigid body motion and pure deformation) was adopted to formulate not only the internal force vector and the tangent stiffness matrix, but also the inertia force vector and the tangent dynamic matrix. As consequence, the cubic interpolation functions were used to derive both the inertia and internal local terms. The inertia force vector and the tangent dynamic matrix were analytically formulated by introducing an approximation regarding the local rotations. To enhance the efficiency of the iterative procedure, an approximative tangent dynamic matrix was adopted.

Several numerical examples were considered to compare the new formulation with two other approaches. The first approach, called as "linear corotational approach", is derived from the new formulation by replacing cubic interpolations with linear ones. The second approach is the classic total Lagrangian proposed by Simo and Vu-Quoc [35, 36, 37]. Based on these examples, the following conclusions can be drawn:

- All formulations give the same results with fine meshes.
- With coarse meshes, Simo and Vu-Quoc's formulation and the linear corotational one give less accurate results compared to the cubic corotational approach which provides very accurate results. This demonstrated the importance of an accurate description of the deformations in the dynamic terms, which is not possible with linear interpolations (Simo and Vu-Quoc's formulation adopted linear interpolations for all the global variables).
- The linear corotational approach is faster than the cubic one. This was expected since several inertia terms disappear when local linear interpolations are adopted. Moreover, in the linear corotational approach, the inertia force vector and the tangent dynamic matrix are integrated using two Gauss points, whereas the dynamic terms of the cubic corotational one are integrated using three Gauss points.
- The cubic corotational approach is slightly slower (about 12%) and sometimes even faster than Simo and Vu-Quoc's one.

One can conclude that the new dynamic corotational formulation based on the local cubic interpolations is more efficient than the classic one proposed by Simo and Vu-Quoc. With the same number of elements, about the same computational time is required (this can differ a little from one example to another). However, with the present formulation, accurate results can be obtained with a smaller number of elements.

A Expressions of $\dot{\mathbf{H}}_1$ and $\dot{\mathbf{H}}_2$

The variation of Eq. (49) reads

$$\delta\mathbf{H}_1 = \mathbf{P}_1\,\delta\mathbf{P} - \widetilde{\delta\mathbf{u}_l}\,\mathbf{G}^{\mathrm{T}} - \widetilde{\mathbf{u}_l}\,\delta\mathbf{G}^{\mathrm{T}}, \tag{66}$$

where $\mathbf{u}_l$ are the local transverse displacements assumed to be small. Therefore, the last term in Eq. (66) is neglected.
By using the expressions of the matrices $\mathbf{P}_1$ and $\mathbf{P}$, and the variation of Eq. (9), it is straightforward to obtain

$$\delta\mathbf{H}_1 = \frac{N_7}{l_n^2}\,\mathbf{A}_1\,\mathbf{r}\,\delta\mathbf{d}_g - \widetilde{\delta\mathbf{u}_l}\,\mathbf{G}^{\mathrm{T}}, \tag{67}$$

with $N_7 = (N_3 + N_4)$, $\mathbf{r} = \begin{bmatrix} -\mathbf{r}_1^{\mathrm{T}} & \mathbf{0}_{[1\times3]} & \mathbf{r}_1^{\mathrm{T}} & \mathbf{0}_{[1\times3]} \end{bmatrix}$ and

$$\mathbf{A}_1 = \begin{bmatrix} 0 & 0 & 0 & 0 & 0 & 0 & 0 & 0 & 0 & 0 & 0 & 0 \\ 0 & -1 & 0 & 0 & 0 & 0 & 0 & 1 & 0 & 0 & 0 & 0 \\ 0 & 0 & -1 & 0 & 0 & 0 & 0 & 0 & 1 & 0 & 0 & 0 \end{bmatrix}.$$

Finally, one has

$$\dot{\mathbf{H}}_1 = \frac{N_7}{l_n^2}\mathbf{A}_1\,\mathbf{r}\,\dot{\mathbf{d}}_g - \widetilde{\dot{\mathbf{u}}}_l\,\mathbf{G}^{\mathrm{T}}. \tag{68}$$

By taking the variation of Eq.(56), and using the expressions of $\mathbf{P}_2$, $\mathbf{P}$ and $\mathbf{G}$, one obtains

$$\delta\mathbf{H}_2 = \frac{N_8}{l_n^2}\mathbf{A}_2\,\mathbf{r}\,\delta\mathbf{d}_g. \tag{69}$$

with $N_8 = N_5 + N_6 - 1$ and

$$\mathbf{A}_2 = \begin{bmatrix} 0 & 0 & 0 & 0 & 0 & 0 & 0 & 0 & 0 & 0 & 0 & 0 \\ 0 & 0 & 1 & 0 & 0 & 0 & 0 & 0 & -1 & 0 & 0 & 0 \\ 0 & -1 & 0 & 0 & 0 & 0 & 0 & 1 & 0 & 0 & 0 & 0 \end{bmatrix}.$$

Therefore, $\dot{\mathbf{H}}_2$ is computed as

$$\dot{\mathbf{H}}_2 = \frac{N_8}{l_n^2}\mathbf{A}_2\,\mathbf{r}\,\dot{\mathbf{d}}_g. \tag{70}$$

B Expressions of $\mathbf{C}_3$ and $\mathbf{C}_4$

$\mathbf{C}_3$ and $\mathbf{C}_4$ are calculated from the variations of $\mathbf{C}_1$ and $\mathbf{C}_2$ with respect to $\dot{\mathbf{d}}_g$

$$\mathbf{C}_3\,\mathbf{E}^{\mathrm{T}}\Delta\dot{\mathbf{d}}_g = \left(\frac{\partial\mathbf{C}_1}{\partial\dot{\mathbf{d}}_g}\Delta\dot{\mathbf{d}}_g\right)\mathbf{E}^{\mathrm{T}}\dot{\mathbf{d}}_g, \tag{71}$$

$$\mathbf{C}_4\,\mathbf{E}^{\mathrm{T}}\Delta\dot{\mathbf{d}}_g = \left(\frac{\partial\mathbf{C}_2}{\partial\dot{\mathbf{d}}_g}\Delta\dot{\mathbf{d}}_g\right)\mathbf{E}^{\mathrm{T}}\dot{\mathbf{d}}_g, \tag{72}$$

After some long but straightforward manipulations, the expressions of $\mathbf{C}_3$ and $\mathbf{C}_4$ are obtained as

$$\mathbf{C}_3 = -\widetilde{\mathbf{h}}_1\,\mathbf{G}^{\mathrm{T}} + \left(\frac{N_7}{l_n^2}\mathbf{A}_1\,\dot{\mathbf{d}}_g^e\,\mathbf{r}^e + \widetilde{\dot{\mathbf{w}}}_r^e\mathbf{P}_1\,\mathbf{P}\right) + \mathbf{H}_1\,\mathbf{F}_1\,\mathbf{G}^{\mathrm{T}}, \tag{73}$$

$$\mathbf{C}_4 = -\widetilde{\mathbf{h}}_2\,\mathbf{G}^{\mathrm{T}} + \frac{N_8}{l_n^2}\mathbf{A}_2\,\dot{\mathbf{d}}_g^e\,\mathbf{r}^e + \mathbf{H}_2\,\mathbf{F}_1\,\mathbf{G}^{\mathrm{T}}, \tag{74}$$

with

$$\mathbf{h}_i = \mathbf{H}_i\dot{\mathbf{d}}_g^e, \quad \mathbf{F}_1 = [\widetilde{\dot{\mathbf{u}}}_1^{e\,\mathrm{T}}\ \widetilde{\dot{\mathbf{w}}}_1^{e\,\mathrm{T}}\ \widetilde{\dot{\mathbf{u}}}_2^{e\,\mathrm{T}}\ \widetilde{\dot{\mathbf{w}}}_2^{e\,\mathrm{T}}]^{\mathrm{T}}, \tag{75}$$
$$\mathbf{r}^e = \mathbf{r}\,\mathbf{E} = \left[-[1\,0\,0]\ \mathbf{0}_{[1\times3]}\ [1\,0\,0]\ \mathbf{0}_{[1\times3]}\right].$$

REFERENCES

[1] R. Alsafadie, M. Hjiaj, J.-M. Battini, Corotational mixed finite element formulation for thin-walled beams with generic cross-section, *Comput. Methods Appl. Mech. Engrg.*, **199**, 3197-3212, 2010.

[2] R. Alsafadie, J.-M. Battini, M. Hjiaj, H. Somja, A comparative study of displacement and mixed-based corotational finite element formulations for elasto-plastic three-dimensional beam analysis, *Engerg. Computs.*, **28**, 7, 939-982, 2011.

[3] J. Argyris, An excursion into large rotations, *Comput. Methods Appl. Mech. Engrg.*, **32**, 85-155, 1982.

[4] J.-M. Battini, C. Pacoste, Co-rotational beam elements with warping effects in instability problems, *Comput. Methods Appl. Mech. Engrg.*, **191**, 1755-1789, 2002.

[5] J.-M. Battini, A modified corotational framework for triangular shell elements, *Comput. Methods Appl. Mech. Engrg.*, **196**, 1905-1914, 2007.

[6] J.-M. Battini, Large rotations and nodal moments in corotational elements, *CMES*, **33**, 1, 1-15, 2008.

[7] K. Behdinan, M.C Stylianou, B. Tabarrok, Co-rotational dynamic analysis of flexible beams, *Comput. Methods Appl. Mech. Engrg.*, **154**, 151-161, 1998.

[8] P. Betsch, P. Steinmann, Constrained dynamics of geometrically exact beams, *Comput. Mech.*, **31**, 49-59, 2003.

[9] A. Cardona, M. Geradin, A beam finite element non-linear theory with finite rotations, *Int. J. Num. Methods. Engrg.*, **26**, 2403-2438, 1988.

[10] M.A. Crisfield, J. Shi, An energy conserving co-rotational procedure for non-linear dynamics with finite elements, *Nonlinear Dynamics*, **9**, 37-52, 1996.

[11] M.A. Crisfield, G.F. Moita, A unified co-rotational framework for solids shells and beams, *Int. J. Solids Struct.*, **33**, 29692992, 1996.

[12] M.A. Crisfield, U. Galvanetto, G. Jelenić, Dynamics of 3-D co-rotational beams, *Comput. Mech.*, **20**, 507-519, 1997.

[13] M.A. Crisfield, *Non-Linear Finite Element Analysis of Solids and Structures, Volume 2: Advanced Topics*, Wiley, Chischester, 1997.

[14] H.A. Elkaranshawy and M.A. Dokainish, Corotational finite element analysis of planar flexible multibody systems, *Comput. Struct.*, **54**, No.5, 881-890, 1995.

[15] U. Galvanetto, M.A. Crisfield, An energy conserving co-rotational procedure for dynamics of planar beam structures, *Int. J. Num. Methods. Engrg.*, **39**, 2265-2282, 1996.

[16] M. Geradin, A. Cardona, Kinematics and dynamics of rigid and flexible mechanisms using finite elements and quaternion algebra, *Comput. Mech.*, **4**, 115-135, 1989.

[17] M. Geradin, A. Cardona, *Flexible multibody dynamics : A finite element approach*, 120-127. Wiley, Chischester, 2001.

[18] K.M. Hsiao, R.T. Yang, A co-rotational formulation for nonlinear dynamic analysis of curved Euler beam, *Comput. Struct.*, **54**, No.6, 1091-1097, 1995.

[19] K.M. Hsiao, J.Y. Lin, W.Y. Lin, A consistent co-rotational finite element formulation for geometrically nonlinear dynamics analysis of 3-D beams, *Comput. Methods Appl. Mech. Engrg.*, **169**, 1-18, 1999.

[20] A. Ibrahimbegović, M.A. Mikdad, Finite rotations in dynamics of beams and implicit time-stepping schemes, *Int. J. Num. Methods. Engrg.*, **41**, 781-814, 1998.

[21] M. Iura, S.N. Atluri, Dynamic analysis of finitely stretched and rotated three-dimensional space-curved beams, *Comput. Struct.*, **29**, 875-889, 1988.

[22] M. Iura, S.N. Atluri, Dynamic analysis of planar flexible beams with finite rotations by using inertial and rotating frames, *Comput. Struct.*, **55**, No.3, 453-462, 1995.

[23] G. Jelenić, M.A. Crisfield, Interpolation of rotational variables in nonlinear dynamics of 3D beams, *Int. J. Num. Methods. Engrg.*, **43**, 1193-1222, 1998.

[24] G. Jelenić, M.A. Crisfield, Geometrically exact 3D beam theory: implementation of a strain-invariant element for stactics and dynamics, *Comput. Methods Appl. Mech. Engrg.*, **171**, 141-171, 1999.

[25] S. Krenk, *Non-Linear Modeling And Analysis Of Solids And Structures*, 47-75, Cambridge University Press, New York, 2009.

[26] T.-N. Le, J.-M. Battini, M. Hjiaj, Efficient formulation for dynamics of corotational 2D beams, *Comput. Mech.*, **48**, No.2, 153-161, 2011.

[27] T.-N. Le, J.-M. Battini, M. Hjiaj, Dynamics of 3D beam elements in a corotational context: A comparative study of established and new formulations, *Finite Elem. Anal. Des.*, **61**, 97-111, 2012.

[28] J. Mäkinen, Total Lagrangian Reissner's geometrically exact beam element without singularities, *Int. J. Num. Methods. Engrg.*, **70**, 1009-1048, 2007.

[29] N. Masuda, T. Nishiwaki, M. Minaaawa, Nonlinear dynamic analysis of frame structures, *Comput. Struct.*, **27**, No.1, 103-110, 1987.

[30] B. Nour-Omid, C.C. Rankin, Finite rotation analysis and consistent linearization using projectors, *Comput. Methods Appl. Mech. Engrg.*, **93**, 353-384, 1991.

[31] C. Oran, A. Kassimali, Large deformations of framed structures under static and dynamic loads, *Comput. Struct.*, **6**, 539-547, 1976.

[32] C. Pacoste, A. Eriksson, Beam elements in instability problems, *Comput. Methods Appl. Mech. Engrg.*, **144**, 163-197, 1997.

[33] C. Pacoste, Co-rotational flat facet triangular elements for shell instability analysis, *Comput. Methods Appl. Mech. Engrg.*, **156**, 75110, 1998.

[34] J.N. Reddy, On locking-free shear deformable beam finite elements, *Comput. Methods Appl. Mech. Engrg.*, **149**, 113-132, 1997.

[35] J.C. Simo, A finite strain beam formulation. The three-dimensional dynamic problem. Part I, *Comput. Methods Appl. Mech. Engrg.*, **49**, 55-70, 1985.

[36] J.C. Simo, L. Vu-Quoc, A three-dimensional finite-strain rod model. Part II: computational aspects, *Comput. Methods Appl. Mech. Engrg.*, **58**, 79-116, 1986.

[37] J.C. Simo, L. Vu-Quoc, On the dynamics in space of rods undergoing large motions - A geometrically exact approach, *Comput. Methods Appl. Mech. Engrg.*, **66**, 125-161, 1988.

[38] Q. Xue, J.L Meek, Dynamic response and instability of frame structures, *Comput. Methods Appl. Mech. Engrg.*, **190**, 5233-5242, 2001.

[39] A. Ibrahimbegović, F. Frey, I. Kožar, Computational aspects of vector-like parameterization of three-dimensional finite rotations, *Int. J. Num. Methods. Engrg.*, **38**, 3653-3673, 1995.

[40] A. Ibrahimbegović, On the choice of finite rotation parameters, *Comput. Methods Appl. Mech. Engrg.*, **149**, 49-71, 1997.

[41] H. Weiss , Dynamics of geometrically nonlinear rods: II. Numerical methods and computational examples, *Nonlinear Dynamics*, **30**, 383-415, 2002.

[42] E.V. Lens, A. Cardona, A nonlinear beam element formulation in the framework of an energy preserving time integration scheme for constrained multibody systems dynamics, *Comput. Struct.* , **86**, 47-63, 2008.

[43] E. Zupan, M. Saje, D. Zupan, Quaternion-based dynamics of geometrically nonlinear spatial beams using the RungeKutta method, *Finite Elem. Anal. Des.*, **54**, 48-60, 2012.

[44] E. Zupan, M. Saje, D. Zupan, Dynamics of spatial beams in quaternion description based on the Newmark integration scheme, *Comput. Mech.*, **51**, 47-64, 2013.

COMPDYN 2013
4th ECCOMAS Thematic Conference on
Computational Methods in Structural Dynamics and Earthquake Engineering
M. Papadrakakis, V. Papadopoulos, V. Plevris (eds.)
Kos Island, Greece, 12–14 June 2013

RIGID BODY TIME INTEGRATION BY CONVECTED BASE VECTORS WITH IMPLICIT CONSTRAINTS

S. Krenk and M.B. Nielsen

Department of Mechanical Engineering
Technical University of Denmark
DK-2800 Kgs. Lyngby, Denmark
e-mail: sk@mek.dtu.dk, mbni@mek.dtu.dk

Keywords: Conservative Time Integration, Rigid Body Rotations, Implicit Constraints, Structural Dynamics.

Abstract. *A conservative time integration algorithm based on a convected set of orthonormal base vectors is presented. The equations of motion are derived from an extended Hamiltonian formulation, combining the components of the three base vectors with a set of orthonormality constraints. The particular form of the kinetic energy used in the present formulation is deliberately chosen to correspond to a rigid body rotation, and the orthonormality constraints are introduced via the equivalent Green strain components of the base vectors. The particular form of the extended inertia tensor used here implies a set of orthogonality relations between the base vector components and their conjugate momentum components. These orthogonality relations permit explicit elimination of the Lagrange multipliers associated with the constraints, leading to a projected form of the dynamic equation without explicit algebraic constraints. The differential equations of motion are recast into discrete form using a suitable combination of mean values and increments, which is identified by considering a finite increment of the Hamiltonian. Examples illustrate the accuracy and conservation properties of the algorithm.*

1 INTRODUCTION

Numerical time integration of the motion of rigid bodies has been subject to intensive studies. In [1] a new approach to time integration of rigid body motion was introduced in which energy and momentum conservation properties are obtained by judicious discretization in terms of mean values and increments. In contrast to earlier methods based on asymptotic properties, the conservative algorithms depend in an essential way on the parameter representation of the problem. A fully conservative algorithm in terms of quaternion parameters can be obtained when the normalization condition is carried through the integration process via a Lagrange multiplier [2]. It was demonstrated in [3] that the rigid body dynamics problem can be formulated in such a way that the increment of the constraint is embedded in the kinematic evolution equation, and the Lagrange multiplier can be eliminated, leading to the introduction of a projection operator on the force potential gradient. An alternative formulation of the rigid body motion in terms of a set of convected base vectors has been introduced in [4]. The use of the global components of the local base vectors as variables simplifies the formulation, but at the same time increases the problem size and changes the character of the problem by adding 6 Lagrange multipliers and introducing algebraic constraints.

In the present paper this problem is solved by extending the idea of 'implicit constraints' introduced in [3] to the formulation in terms of convected base vectors. The equations of motion are obtained from Hamilton's equations. It turns out, that when the kinetic energy is formulated via the angular velocity components under the assumption of a rigid body, the rigid body constraints are in fact contained in incremental form in the set of kinematic Hamilton equations. The generalized forces appear in the dynamic part of the Hamilton equations in the form of the gradient of the force potential. The special form of the inertial tensor in terms of the base vector components leads to a set of six orthogonality conditions between the base vector components and the corresponding momentum components. Elimination of the Lagrange multipliers by use of these orthogonality relations leads to a set of equations of motion, in which the effect of the constraints is represented via pre-multiplication of the full-component gradient by a projection matrix.

The modified Hamilton equations are discretized by appropriate mean values and increments to form an energy and momentum conserving time integration algorithm. The accuracy and conservation properties are illustrated by the 'flying brick' and the rotation of a Lagrangian top in a gravitational field.

2 CONVECTED BASE VECTOR REPRESENTATION

Let $\mathbf{x}$ denote the location of a rigid body in a fixed global frame of reference and let a local frame attached to the rigid body be described in terms of a set of orthonormal base vectors $\mathbf{q}_1, \mathbf{q}_2, \mathbf{q}_3$. For simplicity, the present formulation is developed for purely rotational motion where the origin of the local base coincides with the origin of the global frame, hence the global components $\mathbf{x}$ of a point inside the body with local coordinates $\mathbf{x}_0$ can be expressed as

$$\mathbf{x}(t) \;= \mathbf{Q}(t)\,\mathbf{x}_0\,, \tag{1}$$

where the deformation gradient tensor $\mathbf{Q}$ is defined as

$$\mathbf{Q} \;=\; [\,\mathbf{q}_1, \mathbf{q}_2, \mathbf{q}_3\,] \;=\; \frac{\partial \mathbf{x}}{\partial \mathbf{x}_0}. \tag{2}$$

The global components of the base vectors $\mathbf{q}_1, \mathbf{q}_2, \mathbf{q}_3$ constitute the independent variables of the present formulation. However, in order to represent a proper rigid body rotation the base vectors

must remain orthonormal at all time. This corresponds to vanishing of all Green strain components, which can be expressed by a set of constraint conditions on the deformation gradient tensor $\mathbf{Q}$ as

$$\mathbf{e} = \frac{1}{2}\begin{bmatrix} \mathbf{q}_1^T\mathbf{q}_1 - 1 \\ \mathbf{q}_2^T\mathbf{q}_2 - 1 \\ \mathbf{q}_3^T\mathbf{q}_3 - 1 \\ \mathbf{q}_2^T\mathbf{q}_3 + \mathbf{q}_3^T\mathbf{q}_2 \\ \mathbf{q}_3^T\mathbf{q}_1 + \mathbf{q}_1^T\mathbf{q}_3 \\ \mathbf{q}_1^T\mathbf{q}_2 + \mathbf{q}_2^T\mathbf{q}_1 \end{bmatrix} = \mathbf{0}. \tag{3}$$

In the present formulation the kinematic constraints appear via their time derivatives in the form

$$\dot{\mathbf{e}} = \mathbf{C}(\mathbf{q})\,\dot{\mathbf{q}} = \mathbf{C}(\dot{\mathbf{q}})\,\mathbf{q} = \mathbf{0}\,, \tag{4}$$

where the matrix $\mathbf{C}$ follows from differentiation of (3) with the 6×9 deformation gradient matrix

$$\mathbf{C}(\mathbf{q}) = \frac{\partial \mathbf{e}}{\partial \mathbf{q}} = \begin{bmatrix} \mathbf{q}_1^T & \mathbf{0} & \mathbf{0} \\ \mathbf{0} & \mathbf{q}_2^T & \mathbf{0} \\ \mathbf{0} & \mathbf{0} & \mathbf{q}_3^T \\ \mathbf{0} & \mathbf{q}_3^T & \mathbf{q}_2^T \\ \mathbf{q}_3^T & \mathbf{0} & \mathbf{q}_1^T \\ \mathbf{q}_2^T & \mathbf{q}_1^T & \mathbf{0} \end{bmatrix}. \tag{5}$$

.

The kinetic energy of a rigid body rotating with angular velocity $\boldsymbol{\omega}$ takes the following form when expressed in local components

$$T = \tfrac{1}{2}\boldsymbol{\omega}^T\mathbf{J}\,\boldsymbol{\omega}\,, \tag{6}$$

where $\mathbf{J}$ is the constant inertia tensor. The local components of the angular velocity in terms of the base vectors is obtained by projecting the derivatives $\dot{\mathbf{q}}_i$ on the base vectors $\mathbf{q}_j$. This can be arranged into the compact matrix form

$$\boldsymbol{\omega} = -\tfrac{1}{2}\mathbf{G}(\mathbf{q})\,\dot{\mathbf{q}}\,, \tag{7}$$

in terms of the 3×9 matrix

$$\mathbf{G}(\mathbf{q}) = \begin{bmatrix} \mathbf{0} & -\mathbf{q}_3^T & \mathbf{q}_2^T \\ \mathbf{q}_3^T & \mathbf{0} & -\mathbf{q}_1^T \\ -\mathbf{q}_2^T & \mathbf{q}_1^T & \mathbf{0} \end{bmatrix}. \tag{8}$$

This matrix $\mathbf{G}(\mathbf{q})$ has the same structure in terms of the base vectors $\mathbf{q}_1, \mathbf{q}_2, \mathbf{q}_3$ as the 3×3 skew-symmetric matrix associated with the standard vector product, and thus the matrix structure itself implies orthogonality with respect to $\mathbf{q}$ in the sense

$$\underset{3\times 9}{\mathbf{G}(\mathbf{q})}\,\mathbf{q} = \underset{3\times 1}{\mathbf{0}}\,. \tag{9}$$

Furthermore, it is an important property in the present formulation that $\mathbf{G}(\mathbf{q})$ satisfy the following relation with respect to the constraint matrix $\mathbf{C}(\mathbf{q})$ when the vectors $\mathbf{q}_j$ constitute an orthonormal base,

$$\underset{6\times 9}{\mathbf{C}(\mathbf{q})}\;\underset{9\times 3}{\mathbf{G}(\mathbf{q})^T} = \underset{6\times 3}{\mathbf{0}}\,. \tag{10}$$

Upon substitution of the expression for the angular velocity from (7) into (6), the kinetic energy takes the following bi-quadratic form

$$T \;=\; \tfrac{1}{8}\dot{\mathbf{q}}^T\mathbf{G}(\mathbf{q})^T\mathbf{J}\,\mathbf{G}(\mathbf{q})\,\dot{\mathbf{q}}\,, \tag{11}$$

when the base vectors $\mathbf{q}_j$ satisfy the constraint (3).

3 EQUATIONS OF RIGID BODY MOTION

The equations of motion for rigid body rotation are developed via the Hamilton's canonical equations leading to a set of first order differential equations for the generalized displacements, here represented as the base vector components $\mathbf{q}_j$, and their generalized momentum variables, see e.g. [5].

3.1 Hamilton's equations

The vector of generalized momentum components $\mathbf{p} = [\mathbf{p}_1^T, \mathbf{p}_2^T, \mathbf{p}_3^T]^T$ conjugate to the base vectors $\mathbf{q} = [\mathbf{q}_1^T, \mathbf{q}_2^T, \mathbf{q}_3^T]^T$ follows from time differentiation of the kinetic energy (11), as

$$\mathbf{p} \;=\; \frac{\partial T}{\partial \dot{\mathbf{q}}^T} \;=\; \tfrac{1}{4}\mathbf{G}(\mathbf{q})^T\mathbf{J}\,\mathbf{G}(\mathbf{q})\,\dot{\mathbf{q}}\,. \tag{12}$$

This gives the relation between the momentum $\mathbf{p}$ and the generalized velocity $\dot{\mathbf{q}}$. For a rigid body the base vectors $\mathbf{q}_j$ are orthonormal, and thus the relation (12) can be used to eliminate the velocity $\dot{\mathbf{q}}$ from the kinetic energy when pre-multiplicated with $\mathbf{J}^{-1}\mathbf{G}(\mathbf{q})$. Hereby the kinetic energy can be expressed in either of the forms

$$T(\mathbf{q},\mathbf{p}) \;=\; \tfrac{1}{2}\,\mathbf{p}^T\mathbf{G}(\mathbf{q})^T\mathbf{J}^{-1}\mathbf{G}(\mathbf{q})\,\mathbf{p} \;=\; \tfrac{1}{2}\mathbf{q}^T\mathbf{G}(\mathbf{p})^T\mathbf{J}^{-1}\mathbf{G}(\mathbf{p})\,\mathbf{q}\,, \tag{13}$$

where the latter expression is valid, since the structure of $\mathbf{G}$ ensures that simultaneous interchange of $\mathbf{q}$ and $\mathbf{p}$ in the factors appearing on each side of $\mathbf{J}$ does not change the value of the product.

The present formulation is based on an augmented form of the Hamiltonian where the sum of the kinetic energy $T(\mathbf{q},\mathbf{p})$ from (13) and the potential energy function $V(\mathbf{q})$ is supplemented by the homogeneous rigid body constraints (3), whereby

$$H(\mathbf{q},\mathbf{p}) \;=\; T(\mathbf{q},\mathbf{p}) \;+\; V(\mathbf{q}) \;-\; \mathbf{e}(\mathbf{q})^T\boldsymbol{\lambda}\,. \tag{14}$$

The constraints $\mathbf{e}(\mathbf{q}) = \mathbf{0}$ are initially introduced via a vector of Lagrange multipliers $\boldsymbol{\lambda}$. They are eliminated subsequently by a displacement-momentum orthogonality relation discussed in the following section.

The equations of motion follow from the augmented Hamiltonian (14) by differentiation, as

$$\dot{\mathbf{q}} \;=\; \frac{\partial H}{\partial \mathbf{p}^T} \;=\; \mathbf{G}(\mathbf{q})^T\mathbf{J}^{-1}\mathbf{G}(\mathbf{q})\,\mathbf{p}\,, \tag{15}$$

$$\dot{\mathbf{p}} \;=\; -\frac{\partial H}{\partial \mathbf{q}^T} \;=\; -\,\mathbf{G}(\mathbf{p})^T\mathbf{J}^{-1}\mathbf{G}(\mathbf{p})\,\mathbf{q} \;-\; \frac{\partial V}{\partial \mathbf{q}^T} \;+\; \mathbf{C}(\mathbf{q})^T\boldsymbol{\lambda}\,, \tag{16}$$

where the derivatives of the kinetic energy follow from (13), and the deformation gradient $\mathbf{C}(\mathbf{q})$ is given by (5).

3.2 Elimination of Lagrange multipliers

A basic feature of the present formulation is the elimination of the Lagrange multipliers by use of a set of orthogonality conditions between the generalized displacements $\mathbf{q}$ and the conjugate momentum vector $\mathbf{p}$. The orthogonality relations are obtained by pre-multiplication of the relation (12) defining $\mathbf{p}$ with $\mathbf{C}(\mathbf{q})$. When using the relation (10), valid for orthogonal base vectors, the following displacement-momentum relation is obtained,

$$\mathbf{C}(\mathbf{q})\,\mathbf{p} \;=\; \mathbf{0}\,. \tag{17}$$

In spite of the resemblance of this relation to the velocity relation (4), it is not a simple reformulation of the constraint derivative conditions.

The Lagrange multipliers are now eliminated by using the time derivative of the displacement-momentum orthogonality relations (17),

$$\mathbf{C}(\mathbf{p})\,\dot{\mathbf{q}} \;+\; \mathbf{C}(\mathbf{q})\,\dot{\mathbf{p}} \;=\; \mathbf{0}\,. \tag{18}$$

Substitution of the time derivatives from (15) and (16) into this equation leads to the following expression for the Lagrange multiplier vector

$$\boldsymbol{\lambda} \;=\; \big[\mathbf{C}(\mathbf{q})\,\mathbf{C}(\mathbf{q})^T\big]^{-1}\mathbf{C}(\mathbf{q})\frac{\partial V}{\partial \mathbf{q}^T}. \tag{19}$$

In particular, it is noticed that the Lagrange multipliers vanish in the absence of external loads, implying that the homogenous equations with the present form of the inertial matrix can be solved without explicit introduction of constraints. Substitution of the Lagrange multiplier vector (19) into the dynamic equation of motion (16) gives

$$\dot{\mathbf{p}} \;=\; -\,\mathbf{G}(\mathbf{p})^T\mathbf{J}^{-1}\mathbf{G}(\mathbf{p})\,\mathbf{q} \;-\; \Big(\mathbf{I} \;-\; \mathbf{C}(\mathbf{q})^T\big[\mathbf{C}(\mathbf{q})\,\mathbf{C}(\mathbf{q})^T\big]^{-1}\mathbf{C}(\mathbf{q})\Big)\frac{\partial V}{\partial \mathbf{q}^T}\,. \tag{20}$$

It is seen that the elimination of the Lagrange multipliers via the constraint derivative is equivalent to subtracting the projection of the external potential gradient on the deformation modes via $\mathbf{C}(\mathbf{q})$ from the unconstrained gradient, leaving only the components associated with the rotation modes. This is similar to the result in [3] when eliminating the single scalar normalization constraint from the four-component quaternion representation of rigid-body rotation.

4 STATE-SPACE TIME INTEGRATION

The basic idea of conservative time integration is to use an integrated form of the evolution equations. Hereby the discretized form of the equations of motion can be designed to yield the correct incremental change of energy and momentum over a finite time interval Δt from t_n to t_{n+1}. This is different from collocation based methods where the equations of motion are matched at discrete points in time. Similarly, when constraints are included in conservative methods via Lagrange multipliers, the role of the Lagrange multipliers is to ensure satisfaction of the integrated form of the constraints constraints over the current interval, and thus these are associated with interval rather than the end points. When a numerical time integration is initiated from a state that satisfies the constraints, the introduction of the corresponding incremental form of the constraints over the integration time intervals will lead to satisfaction of the constraints at the integration times.

A consistent discretization obeying conservation of energy and momentum can be derived by equating the finite increment of the Hamiltonian to zero, as

$$\Delta H(\mathbf{q},\mathbf{p}) \;=\; \Delta\mathbf{q}^T\frac{\partial H_*}{\partial \mathbf{q}^T} \;+\; \Delta\mathbf{p}^T\frac{\partial H_*}{\partial \mathbf{p}^T} = 0\,, \tag{21}$$

where the asterisk denotes the finite derivatives of H corresponding to the increments $\Delta\mathbf{q}^T$ and $\Delta\mathbf{p}^T$. The individual terms can be identified from (14). The kinetic energy is a biquadratic form in $\mathbf{q}$ and $\mathbf{p}$, hence the increment can be expressed as twice the product of one factor plus the increment of the other factor. The potential $V(\mathbf{q})$ is introduced via of its finite derivative $\partial V_*/\partial\mathbf{q}$, see e.g. [6], while the discrete form of the constraints follows from the increment of (3). This is a homogeneous quadratic form in $\mathbf{q}$ and can be represented by a combination of increments and mean values. The role of the Lagrange multipliers λ is to prevent violation of the internal constraints at the end of the interval when these are satisfied initially, hence these are introduced as effective mean values representing their role over the interval. Hereby the discretized equations of motion take the form

$$\Delta\mathbf{q} \;=\; \frac{\partial H_*}{\partial \mathbf{p}^T} \;=\; \Delta t\,\mathbf{G}(\bar{\mathbf{q}})^T\mathbf{J}^{-1}\overline{\mathbf{G}(\mathbf{q})\,\mathbf{p}}\,, \tag{22}$$

$$\Delta\mathbf{p} \;=\; -\frac{\partial H_*}{\partial \mathbf{q}^T} \;=\; -\,\Delta t\,\mathbf{G}(\bar{\mathbf{p}})^T\mathbf{J}^{-1}\overline{\mathbf{G}(\mathbf{p})\,\mathbf{q}} \;-\; \Delta t\left[\frac{\partial V_*}{\partial \mathbf{q}^T} \;-\; \mathbf{C}(\bar{\mathbf{q}})^T\boldsymbol{\lambda}\right], \tag{23}$$

These equations constitute a clear equivalent to the continuous evolution equations (15) and (16), when the respective gradients are introduced via their finite derivatives.

As in the continuous case it is advantageous to eliminate the explicit dependence of the Lagrange multiplier using the incremental form of the orthogonality relation between displacement and momentum (17),

$$\mathbf{C}(\bar{\mathbf{p}})\,\Delta\mathbf{q} \;+\; \mathbf{C}(\bar{\mathbf{q}})\,\Delta\mathbf{p} \;=\; \mathbf{0}\,. \tag{24}$$

Upon insertion of the increments from (22) and (23), solving for the Lagrange multiplier $\boldsymbol{\lambda}$ and back-substitution into (23), the dynamic equation take the form

$$\begin{aligned}\Delta\mathbf{p} \;=\; &-\;\Delta t\,\mathbf{G}(\bar{\mathbf{p}})^T\mathbf{J}^{-1}\overline{\mathbf{G}(\mathbf{p})\,\mathbf{q}} \;-\; \Delta t\left(\mathbf{I} \;-\; \mathbf{C}(\bar{\mathbf{q}})^T\big[\mathbf{C}(\bar{\mathbf{q}})\,\mathbf{C}(\bar{\mathbf{q}})^T\big]^{-1}\mathbf{C}(\bar{\mathbf{q}})\right)\frac{\partial V_*}{\partial \mathbf{q}^T}\\ &+\;\Delta t\,\mathbf{C}(\bar{\mathbf{q}})^T\boldsymbol{\lambda}_0\,.\end{aligned} \tag{25}$$

with

$$\boldsymbol{\lambda}_0 \;=\; \big[\mathbf{C}(\bar{\mathbf{q}})\,\mathbf{C}(\bar{\mathbf{q}})^T\big]^{-1}\Big[\mathbf{C}(\bar{\mathbf{q}})\mathbf{G}(\bar{\mathbf{p}})^T \;+\; \mathbf{C}(\bar{\mathbf{p}})\mathbf{G}(\bar{\mathbf{q}})^T\Big]\mathbf{J}^{-1}\overline{\mathbf{G}(\mathbf{p})\,\mathbf{q}}\,. \tag{26}$$

The dynamic equation (25) is the discrete analogue to (20). The term including $\boldsymbol{\lambda}_0$ is merely an artefact of the discretization. However, it must be included in order to ensure proper conservation of energy.

4.1 Integration algorithm

The equations of motion (22) and (25) are conveniently solved simultaneously by means of Newton-Raphson iterations where the elements of the residual vector $\mathbf{r} = [\mathbf{r}_q^T, \mathbf{r}_p^T]^T$ are defined as

$$\mathbf{r}_q \;=\; \Delta\mathbf{q} \;-\; \Delta t\,\mathbf{G}(\bar{\mathbf{q}})^T\mathbf{J}^{-1}\overline{\mathbf{G}(\mathbf{q})\mathbf{p}}\,, \tag{27a}$$

$$\mathbf{r}_p \;=\; \Delta\mathbf{p} \;+\; \Delta t\,\mathbf{G}(\bar{\mathbf{p}})^T\mathbf{J}^{-1}\overline{\mathbf{G}(\mathbf{p})\mathbf{q}} \;+\; \Delta t\left[\frac{\partial V_*}{\partial \mathbf{q}^T} \;+\; \left(\frac{\partial \boldsymbol{\Phi}_*}{\partial \mathbf{q}}\right)^T\boldsymbol{\lambda} - \mathbf{C}(\bar{\mathbf{q}})^T\boldsymbol{\lambda}\right]. \tag{27b}$$

Table 1: Conservative time integration algorithm.

1) Initial conditions:
   $\mathbf{u}_0^T = [\mathbf{q}_0^T, \mathbf{p}_0^T]$
2) Prediction step:
   $\mathbf{u} = \mathbf{u}_n$,
3) Residual calculation:
   $\mathbf{r} = \mathbf{r}(\mathbf{q}, \mathbf{p})$ from (27).
4) Update incremental rotation parameters:
   $\mathbf{K}_{ij} = \partial \mathbf{r}_i / \partial \mathbf{u}_j$,
   $\delta\mathbf{u} = -\mathbf{K}^{-1}\,\mathbf{r}$.
   $\mathbf{u} = \mathbf{u} + \delta\mathbf{u}$,
   If $\|\mathbf{r}\| > \varepsilon_{\mathbf{r}}$ repeat from 3).
5) Return to 2) for new time step, or stop.

The residual is reduced iteratively to zero by use of the linearized increment corresponding to changes in kinematics at t_{n+1}. This is performed in terms of $\delta\mathbf{u} = [\delta\mathbf{q}^T, \delta\mathbf{p}^T]^T$ via the equation

$$\mathbf{K}\,\delta\mathbf{u} \;=\; -\,\mathbf{r}\,, \tag{28}$$

where the elements of the tangential stiffness matrix $\mathbf{K}$ follow from partial differentiation as

$$\mathbf{K}_{ij} \;=\; \partial \mathbf{r}_i / \partial \mathbf{u}_j\,. \tag{29}$$

The implementation of the algorithm is illustrated in pseudo-code form in Table 1.

5 NUMERICAL EXAMPLES

The accuracy and conservation properties are illustrated by two simple examples, - a freely rotating brick and steady precession of a Lagrangian top in a gravitational field.

5.1 Free rotation of a rigid body

First the properties of the homogeneous form of the algorithm, i.e. with $V(\mathbf{q}) = 0$, are considered by application to free rotation of a rigid body. The moment of inertia tensor with

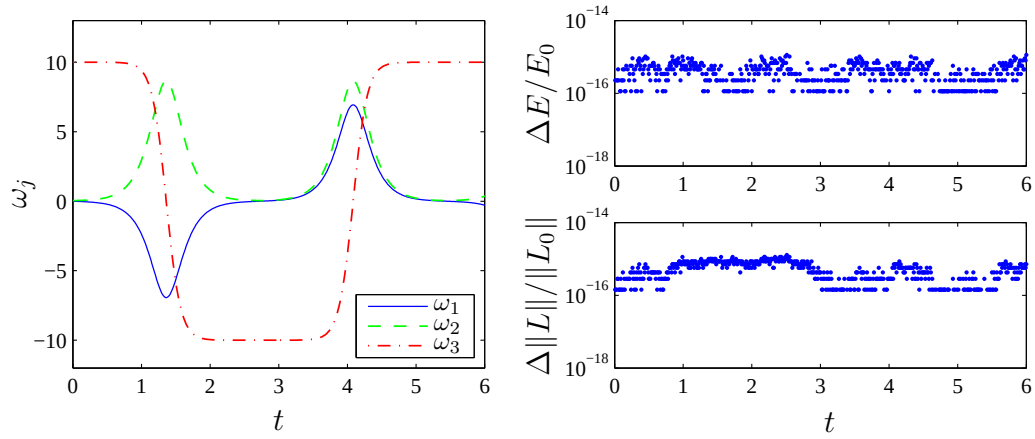


Figure 1: (a) Local angular velocity components, (b) Relative error on energy, (c) relative error on length of angular momentum vector.

respect to the center of mass is chosen as $\mathbf{J} = \text{diag}[13, 5, 10]$, which is equivalent to a box with side lengths $[1, 3, 2]$ and mass 12. The motion is initiated by the initial angular velocity $\boldsymbol{\omega}_0 = [0, 0.05, 10]^T$ leading to non-trivial rotation in which the body is reversed at regular intervals, see e.g. [3].

The unstable motion is illustrated in Fig 1(a) in terms of the local angular velocity where the sign change in ω_3 corresponds to the case where the box is turned upside down. The results are evaluated for the time step $\Delta t = 0.01$ and an iteration tolerance of $\varepsilon_{\mathbf{r}} = 10^{-8}$, which leads to conservation of the total mechanical energy E and the length of the local angular velocity vector $\|\mathbf{L}\|$ within a relative error of 10^{-15} as illustrated in Fig. 1(b) and 1(c).

5.2 Steady precession of top in gravitational field

This example considering a Lagrangian top in a gravitational field is used to illustrate the properties of the algorithm when $V(\mathbf{q}) \neq 0$. The special case of steady precession without nutation is considered. The top is represented as a cone as illustrated in Fig. 2(a) with height h and, max radius $r = h/2$ and mass $m = \rho\pi r^2/3$ with mass density is $\rho = 2700$. The center of mass is located at a distance $l = 3h/4$ from the tip, whereby the local moments of inertia become

$$J_1 = J_2 = \frac{3}{80} m\,(4r^2 + h^2) + ml^2\,, \qquad J_3 = \frac{3}{10} mr^2\,.$$

The top is located in a uniform gravitational field with acceleration $g = 9.81$. In order to exhibit steady precession without nutation the following relation must be satisfied for the nutation angle θ, the rate of precession $\dot{\varphi}$ and the spin velocity $\dot{\psi}$,

$$\dot{\psi} = \frac{mgl}{J_3\dot{\varphi}} + \frac{J_2 - J_3}{J_3}\,\dot{\varphi}\,\cos(\theta_0)\,,$$

see e.g. Goldstein [5]. The initial conditions correspond to the ones used in [2] and [3], $\dot{\varphi} = 10$ and $\theta_0 = \pi/3$.

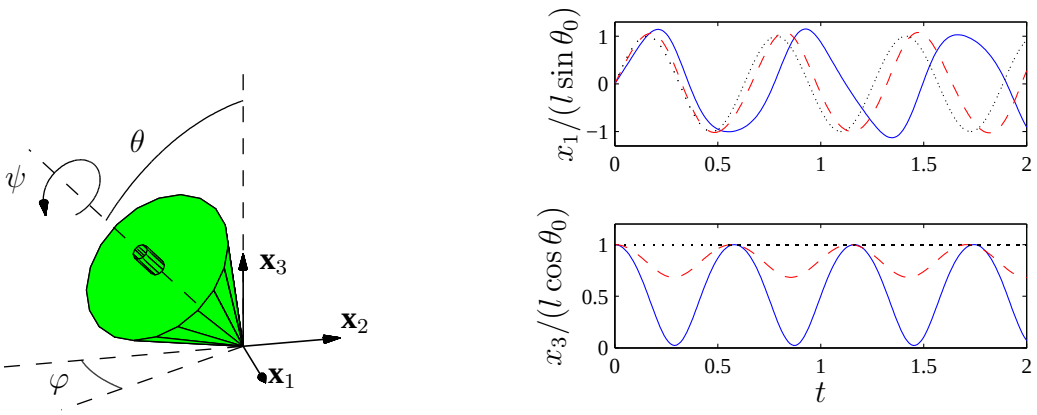


Figure 2: (a) Configuration of rotating top. (b) x_1-coordinate for center of mass. (c) x_3-coordinate for center of mass. $\Delta t = 0.01$ (—-), $\Delta t = 0.005$ (– –), Analytical ($\cdots$).

Simulations are performed for a time step of $\Delta t = 0.01$ and an iteration tolerance of $\varepsilon_{\mathbf{r}} = 10^{-8}$. For these parameters the conserved quantities, namely the mechanical energy and the vertical component of the angular momentum, are conserved within an accuracy of 10^{-9}. The x_1 and x_3-coordinates of the center of gravity are illustrated as the full line in Fig. 2(b) and 2(c). The results show a significant period error compared to the analytical solution (dotted

line), which leads to nutation since the criteria for steady precession is violated. This issue was discussed in [3]. However, when the time step of $\Delta t = 0.005$ is used, the error is decreased by a factor of four as illustrated by the dashed line in Fig. 2(b) and 2(c), thereby illustrating the second order convergence of the present algorithm.

6 CONCLUSIONS

A conservative algorithm for rigid body rotation has been developed using a convected set of 3×3 orthonormal base vector components as generalized displacements. The equations of motion are derived from an augmented Hamiltonian where rigid body constraints equivalent to vanishing of all Green strain components are included via 6 Lagrange multipliers. However, in the present formulation it is illustrated that these can be eliminated by use of a a set of orthogonality condition between the generalized displacements and their conjugate momentum vector, leaving only a projection of the external potential gradient. A consistent time discretization scheme satisfying the conservation laws of energy and momentum is identified by considering a finite increment of the Hamiltonian. Furthermore, it is illustrated that when Lagrange multipliers are included in a conservative method, they serve a role as the effective reaction forces needed to uphold the constraints over a finite time interval, and thus they should be considered as interval bounded quantities rather than associated with the end interval points.

REFERENCES

[1] J. C. Simo, K. K. Wong, Unconditionally stable algorithms for rigid body dynamics that exactly preserve energy and momentum. *International Journal for Numerical Methods in Engineering*, **31**, 19–52, 1991.

[2] P. Betsch, R. Siebert, Rigid body dynamics in terms of quaternions: Hamiltonian formulation and conserving numerical integration, *International Journal for Numerical Methods in Engineering*, **79**, 444–473, 2009.

[3] M.B. Nielsen, S. Krenk, Conservative integration of rigid body motion by quaternion parameters with implicit constraints. *International Journal for Numerical Methods in Engineering*, **92**, 734–752, 2012.

[4] P. Betsch, P. Steinmann, Constrained integration of rigid body dynamics. *Computer Methods in Applied Mechanics and Engineering*, **191**, 467–488, 2001.

[5] H. Goldstein, C. Poole, J. Safko, *Classical Mechanics*, 3rd ed. Addison Wesley: San Francisco, 2001.

[6] O. Gonzalez, Exact energy and momentum conserving algorithms for general models in nonlinear elasticity. *Computer Methods in Applied Mechanics and Engineering*, **190**, 1763–1783, 2000.

COMPDYN 2013
4th ECCOMAS Thematic Conference on
Computational Methods in Structural Dynamics and Earthquake Engineering
M. Papadrakakis, V. Papadopoulos, V. Plevris (eds.)
Kos Island, Greece, 12–14 June 2013

TRANSIENT RESPONSE OF FUNCTIONALLY GRADED BEAMS UNDER ARBITRARY DYNAMIC LOADING

Pedro D. Villamil[1], **Chuanzeng Zhang**[1], **Weiqiu Chen**[2]

[1]Chair of Structural Mechanics, University of Siegen
Paul-Bonatz-Str. 9-11, 57076 Siegen, Germany
e-mail: villamil@bauwesen.uni-siegen.de

[2] Institute of Applied Mechanics, Zhejiang University
Hangzhou 310027, PR China
e-mail: chenwq@zju.edu.cn

Keywords: Functionally Graded Beams, Structural Dynamics, Transient Analysis, Forced Vibrations

Abstract. *In this contribution, functionally graded beams (FGBs) with an arbitrary gradation of the material properties along the beam thickness are considered. Such FGBs are of special interest in civil and mechanical engineering to improve both the thermal and the mechanical behaviours of the beams.*
In order to simplify the coupled governing differential equations for the longitudinal and transversal vibration of FGBs based on the Euler-Bernoulli beam theory, the gradation of the material properties is described by means of simple functions. The free vibration solution (mode shapes and eigenfrequencies) has been derived analytically and can be applied to all boundary conditions of beams.
In this study, vibrations of FGBs due to periodic and non-periodic dynamic loadings are investigated. The dynamic response solution of the beams is derived analytically or numerically by means of the modal analysis with the eigenfrequencies from the free vibration analysis. Comparison is also made with the numerical results obtained by the Finite Element Method. The obtained solutions and their applications will be also discussed.

1 INTRODUCTION

For many applications in civil and mechanical engineering, classical beam elements can be replaced by novel and advanced structures like multi-layered composites or sandwich structures. They offer often better structural properties and can be optimized for different purposes according to the specific requirements. However, the transition between those layers made up of often very different materials is abrupt, and this may lead to delamination or cracks on the interfaces.

To avoid this problem, functionally graded materials (FGMs) can be employed, which possess a smooth property transition inside structural elements. They may consist of different materials which are mixed gradually with different ratios, or they consist of the same materials with varying properties like porosity, fiber content or fiber orientation, as the nature shows us in many cases (e.g. bamboo stem or human and animal bones).

For the engineering application, an appropriate theory is needed to correctly describe the static and dynamic behaviours of FGBs. In Ref. [2] closed-form solutions of the stress distributions, eigenfrequencies and eigenfunctions have been derived for FGBs based on Euler-Bernoulli and Timoshenko theory by means of a single differential equation of motion for the deflection. In Ref. [5] static Green's functions for functionally graded Euler-Bernoulli and Timoshenko beams are presented. In combination with Betti's theorem the Green's functions are applied to calculate internal forces and stress analysis of FGBs. Moreover, approximate eigenfunctions and eigenfrequencies are obtained using Fredholm's integral equation and the static Green's functions of FGBs.

However, these previous considerations did not take into account the coupling between the longitudinal and the transversal displacements and its effects on the eigenfrequencies and mode shapes of FGBs. This approximation is exact only for a symmetrical material gradation and not valid for general cases with an arbitrary material gradation.

In contrast to the work presented in [2], in Ref. [3] the coupling effects of the longitudinal and transverse displacements on the deformation and internal forces of FGBs have been investigated for different boundary conditions. In Ref. [4] free vibrations of Euler-Bernoulli-type FGBs have been considered. The eigenfrequencies and mode shapes of FGBs have been calculated for different boundary conditions by taking into account the coupling effects.

The objective of this paper is to extend the free vibration solution to FGBs subjected to periodic and non-periodic dynamic loadings. The eigenfrequencies and mode shapes obtained from the free vibration analysis are used to calculate the dynamic response of the beams by means of the modal analysis. The analytical results are also validated with the numerical results obtained by the Finite Element Method (FEM) and analyzed concerning their accuracy and their applications.

2 DIFFERENTIAL EQUATIONS OF FUNCTIONALLY GRADED BEAMS

We consider a functionally graded Euler-Bernoulli beam with an arbitrary material gradation in thickness direction as shown in Fig. 1. Since the geometrical principal axis does not correspond to the elastic principal axis for non-symmetric Young's modulus and density functions $E(z)$ and $\rho(z)$, there will be a coupling between the longitudinal and the transverse displacements. Most previous publications [1, 2] neglected this coupling in static and dynamic analysis of FGBs. The coupled partial differential equations (PDEs) describing the beam vibration are

given by

$$E_0\frac{\partial^2 u}{\partial x^2} - E_1\frac{\partial^3 w}{\partial x^3} - \rho_0\frac{\partial^2 u}{\partial t^2} + \rho_1\frac{\partial^3 w}{\partial x \partial t^2} = n\left(x,t\right), \tag{1}$$

and

$$E_2\frac{\partial^4 w}{\partial x^4} - E_1\frac{\partial^3 u}{\partial x^3} + \rho_0\frac{\partial^2 w}{\partial t^2} + \rho_1\frac{\partial^3 u}{\partial x \partial t^2} = q\left(x,t\right), \tag{2}$$

with the abbreviations $\rho_i = \int_A z^i \rho(z)\, dA$ and $E_i = \int_A z^i E(z)\, dA$.

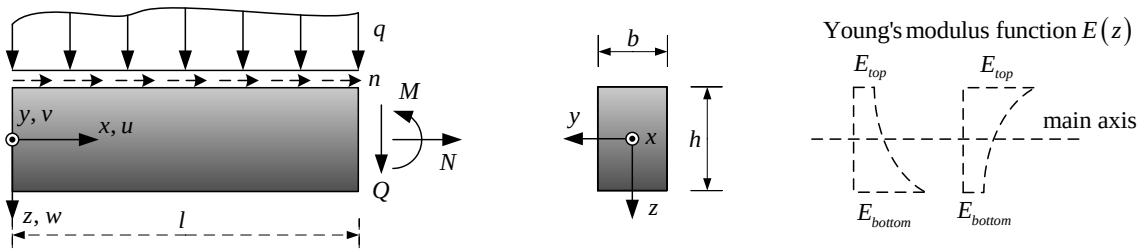


Figure 1: Functionally graded Euler-Bernoulli beam with non-symmetric material properties.

For the free vibration solution (homogeneous PDE), the time-dependent and time-independent components can be separated by using the ansatz

$$\begin{aligned} u(x,t) &= U(x)\cos\left(\omega t - \alpha\right), \\ w(x,t) &= W(x)\cos\left(\omega t - \alpha\right), \end{aligned} \tag{3}$$

with the assumption of the same eigenfrequency ω for both longitudinal and transverse vibrations. It leads to the ordinary differential equations

$$E_0\frac{d^2 U}{dx^2} - E_1\frac{d^3 W}{dx^3} = \omega^2\left(\rho_1\frac{dW}{dx} - \rho_0 U\right), \tag{4}$$

and

$$E_2\frac{d^4 W}{dx^4} - E_1\frac{d^3 U}{dx^3} = \omega^2\left(\rho_1\frac{dU}{dx} + \rho_0 W\right). \tag{5}$$

The solution of Eqs. (4) and (5) can be written as

$$\begin{aligned} W(x) = {} & C_1\sinh\left(\kappa_1 x\right) + C_2\cosh\left(\kappa_1 x\right) + C_3\sin\left(\kappa_2 x\right) + C_4\cos\left(\kappa_2 x\right) \\ & + \overline{\varepsilon} D_1\kappa_3\cos\left(\kappa_3 x\right) - \overline{\varepsilon} D_2\kappa_3\sin\left(\kappa_3 x\right) \end{aligned} \tag{6}$$

$$\begin{aligned} U(x) = {} & \overline{\gamma} C_1\kappa_1\cosh\left(\kappa_1 x\right) + \overline{\gamma} C_2\kappa_1\sinh\left(\kappa_1 x\right) + \overline{\delta} C_3\kappa_2\cos\left(\kappa_2 x\right) \\ & - \overline{\delta} C_4\kappa_2\sin\left(\kappa_2 x\right) + D_1\sin\left(\kappa_3 x\right) + D_2\cos\left(\kappa_3 x\right), \end{aligned} \tag{7}$$

with

$$\overline{\gamma} = \frac{E_1\kappa_1^2 + \omega^2\rho_1}{E_0\kappa_1^2 + \omega^2\rho_0}; \quad \overline{\delta} = \frac{E_1\kappa_2^2 + \omega^2\rho_1}{E_0\kappa_2^2 + \omega^2\rho_0}; \quad \overline{\varepsilon} = \frac{E_1\kappa_3^2 + \omega^2\rho_1}{E_2\kappa_3^4 - \omega^2\rho_0}. \tag{8}$$

The eigenvalues κ_1 and κ_2 define the transversal-dominated and κ_3 the longitudinal-dominated terms of the mode shapes $W(x)$ and $U(x)$.

3 MODAL ANALYSIS OF FUNCTIONALLY GRADED BEAMS

Once the homogeneous solution of Eqs. (4) and (5) is found, we can rewrite the transient response $w(x,t) = w_h(x,t) + w_p(x,t)$ and $u(x,t) = u_h(x,t) + u_p(x,t)$ as a series expansion of the mode shapes multiplied by a time-dependent term $T_k(t) + \bar{T}_k(t)$ as follows

$$w(x,t) = \sum_{k=1}^{\infty} W_k(x) \left(T_k(t) + \bar{T}_k(t)\right), \qquad u(x,t) = \sum_{k=1}^{\infty} U_k(x) \left(T_k(t) + \bar{T}_k(t)\right). \tag{9}$$

In analogy to homogeneous beams, the terms T_k and $\bar{T}_k$ describe the influence of the k^{th} mode shape on the global system response and must fulfill the homogeneous or inhomogeneous differential equations

$$\begin{aligned} \ddot{T}_k(t) + \omega_k^2 T_k(t) &= 0 \qquad \text{and} \\ \ddot{\bar{T}}_k(t) + \omega_k^2 \bar{T}_k(t) &= \frac{q(x,t)}{M_k}, \end{aligned} \tag{10}$$

respectively, with the k^{th} eigenfrequency $\omega_k = \sqrt{\dfrac{K_k}{M_k}}$ and the terms K_k (generalized stiffness) and M_k (generalized mass) given by

$$K_k = E_2 \int_0^l \left(W_k''(x)\right)^2 \, dx + E_0 \int_0^l \left(U_k'(x)\right)^2 \, dx - 2E_1 \int_0^l W_k''(x) U_k'(x) \, dx, \tag{11}$$

$$M_k = \rho_0 \int_0^l \left[W_k^2(x) + U_k^2(x)\right] dx - 2\rho_1 \int_0^l W_k'(x) U_k(x) \, dx. \tag{12}$$

The homogeneous solution with the initial values $w(x,0) = w_0$, $u(x,0) = u_0$, $\dot{w}(x,0) = \dot{w}_0$ and $\dot{u}(x,0) = \dot{u}_0$ can be written as

$$w_h(x,t) = \sum_{k=1}^{\infty} W_k(x) \left(G_{1,k} \cos \omega_k t + G_{2,k} \sin \omega_k t\right), \tag{13}$$

$$u_h(x,t) = \sum_{k=1}^{\infty} U_k(x) \left(G_{1,k} \cos \omega_k t + G_{2,k} \sin \omega_k t\right), \tag{14}$$

where the constants of integration can be determined by

$$G_{1,k} = \frac{\displaystyle\int_0^l \left[w_0 W_k(x) + u_0 U_k(x)\right] dx}{\displaystyle\int_0^l \left[W_k^2(x) + U_k^2(x)\right] \, dx}; \quad G_{2,k} = \frac{\displaystyle\int_0^l \left[\dot{w}_0 W_k(x) + \dot{u}_0 U_k(x)\right] dx}{\omega_k \displaystyle\int_0^l \left[W_k^2(x) + U_k^2(x)\right] \, dx}. \tag{15}$$

We can describe the transversal and longitudinal dynamic loading with a product ansatz as $q(x,t) = q^*(x) f(t)$ and $n(x,t) = n^*(x) g(t)$, and obtain for the particular solution of the transient response of the system

$$w_p(x,t) = \sum_{k=1}^{\infty} W_k(x) \frac{\omega_k}{K_k} \int_0^l W_k(\xi) q^*(\xi) \, d\xi \int_{-\infty}^{t} f(\tau) \sin\left[\omega_k (t-\tau)\right] \, d\tau, \tag{16}$$

$$u_p(x,t) = \sum_{k=1}^{\infty} U_k(x) \frac{\omega_k}{K_k} \int_0^l U_k(\xi) n^*(\xi) \, d\xi \int_{-\infty}^{t} g(\tau) \sin\left[\omega_k (t-\tau)\right] \, d\tau, \tag{17}$$

where the last term is a Duhamel's integral [6].

4 CANTILEVER FGB UNDER A VERTICAL LOAD AT THE FREE BEAM END

For the first example we consider a cantilever FGB with non-symmetric material gradation as shown in Figure 1 with the Young's modulus $E(z) = E_{bottom} + (E_{top} - E_{bottom}) \left(\frac{1}{2} - \frac{z}{h}\right)^2$ and the density distribution $\rho(z) = \rho_{bottom} + (\rho_{top} - \rho_{bottom}) \left(\frac{1}{2} - \frac{z}{h}\right)^2$, with the ratios $\frac{E_{bottom}}{E_{top}} = 0.2$ and $\frac{\rho_{bottom}}{\rho_{top}} = 0.2$. The longitudinal boundary conditions may be CC (constrained at both ends) or CF (constrained-free). The geometrical data and material properties as well as the first 10 eigenfrequencies are listed in Table 1. These eigenfrequencies are calculated with the present coupled beam theory (first two columns) and compared with the eigenfrequencies (last two columns) given by the uncoupled beam theory of Li [2]. For the CC boundary conditions, this example presents a difference of about $7.5\ \%$ for the first eigenfrequency and shows that the coupling between the longitudinal and the transversal beam vibrations should not be neglected.

Geometrical data
Length $l = 8.0\,[m]$
Height $h = 40\,[cm]$
Width $b = 20\,[cm]$
Material properties
$E_{top} = 20.000\,[N/mm^2]$
$\rho_{top} = 2.500\,[kg/m^3]$

k	$\omega_{k,CC}$	$\omega_{k,CF}$	$\omega_{k,CC}$ [2]	$\omega_{k,CF}$ [2]
1	17.986387	16.729478	16.729845	16.729845
2	107.43758	104.87972	104.84415	104.84415
3	296.17575	293.91101	293.56665	293.56665
4	576.91977	555.36037	575.27346	555.36037
5	942.38759	576.73058	950.96825	575.27346
6	1100.5816	955.15818	1110.7207	950.96825
7	1441.8223	1430.2464	1420.5819	1420.5819
8	1983.0178	1666.0811	1984.1185	1666.0811
9	2215.4974	2003.4353	2221.4415	1984.1185
10	2683.8256	2676.4925	2641.5779	2641.5779

Table 1: Material properties and first 10 eigenfrequencies $\omega_k\ [1/s]$ of the cantilever FGB

4.1 Harmonic loading $F(t) = F_0 \sin(\Omega t)$

The first considered case is a sinusoidal excitation. Figure 2 shows the vertical and horizontal displacements at the beam end for $F_0 = 50\ N$, $\Omega = 20\ s^{-1}$ and $0 \leq t \leq 4\ s$.
All FEM results have been obtained using 2D plain stress elements (PLANE82) in ANSYS 13.0 to model the functionally graded beam as a layered beam with 32 constant layers. In all cases $a)$, $b)$, $c)$ and $d)$, we find a very good agreement between the results of this study and the numerical results obtained with the FEM software. The results of Li [2] did not take into account the coupling between the longitudinal and transversal vibrationsand are therefore only valid for the vertical deflection if the beam is not constrained longitudinally. However, the model of Li [2] gives wrong results for the longitudinal displacements and the transversal vibration of longitudinally constrained beams, as shown in $a)$ and $b)$.

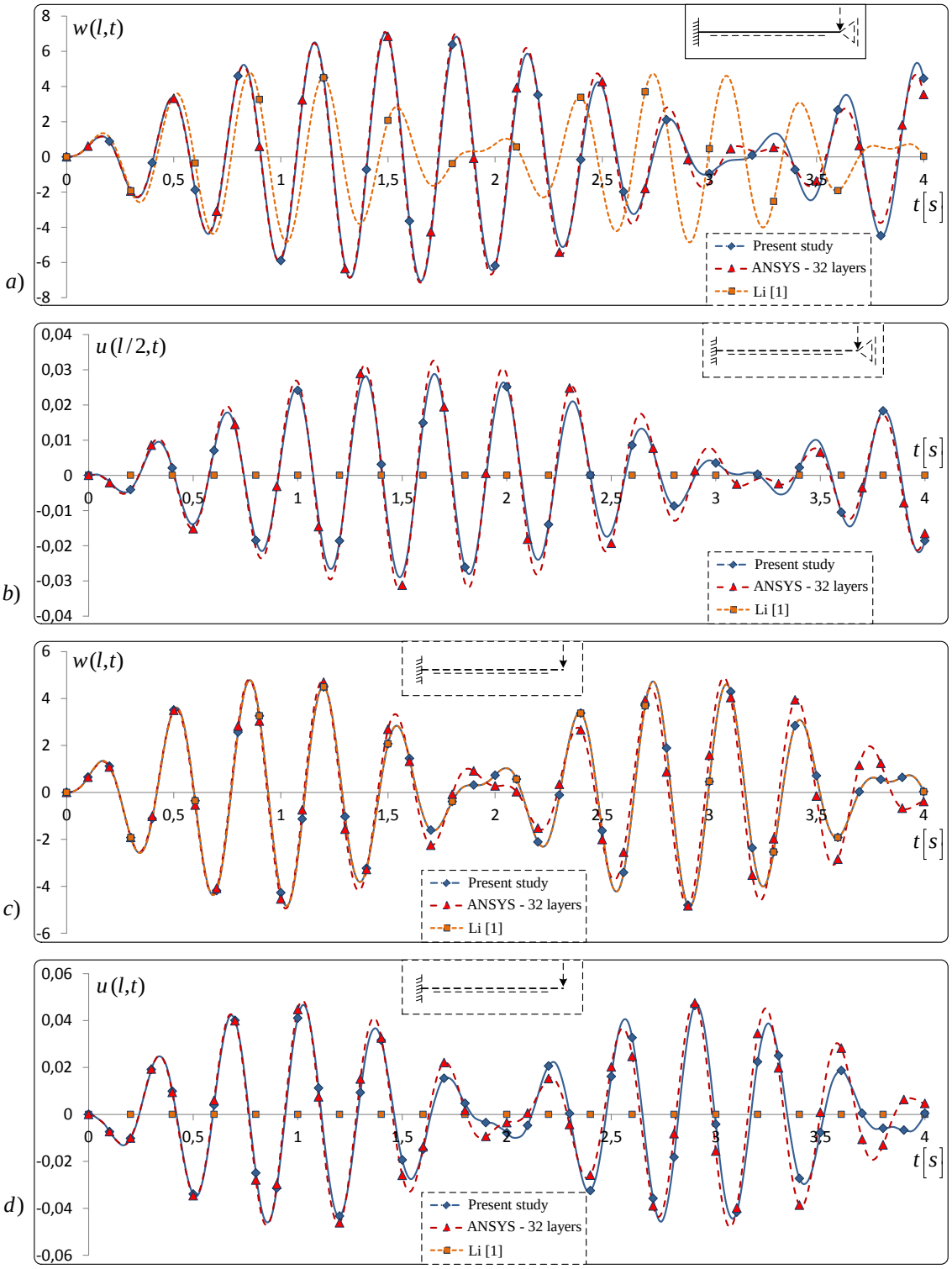


Figure 2: Displacements of the FGB for the first 4 s: $a)$ Vertical displacement at the beam end and $b)$ Horizontal displacement in the middle of the beam with CC boundary conditions, $c)$ Vertical and $d)$ Horizontal displacements at the beam end with CF boundary conditions.

4.2 Triangular impulse loading

The second loading for this example is a non-periodic triangular impulse loading which can be described by

$$F(t) = F_0 \left(1 - \frac{t}{t_0}\right), \tag{18}$$

with an impulse duration of $t_0 = 0.3\ s$ and the intensity $F_0 = 50\ N$. In Fig. 3, the vertical displacements of the beam due to this impulse loading are given. For the vertical vibration as shown in $a)$ and $b)$ we find again a good agreement between the results of this study and the numerical results. The time of calculation for $b)$ took $t_{calc} = 57.947\ s$ for the present study with MATLAB, and $t_{calc} = 257.667\ s$ for the FEM results performed with ANSYS. In $c)$ the vertical displacement of the beam for the time steps $t = 0.05\ s$, $t = 0.10\ s$, $t = 0.15\ s$, $t = 0.20\ s$, $t = 0.25\ s$ and $t = 0.30\ s$ is shown.

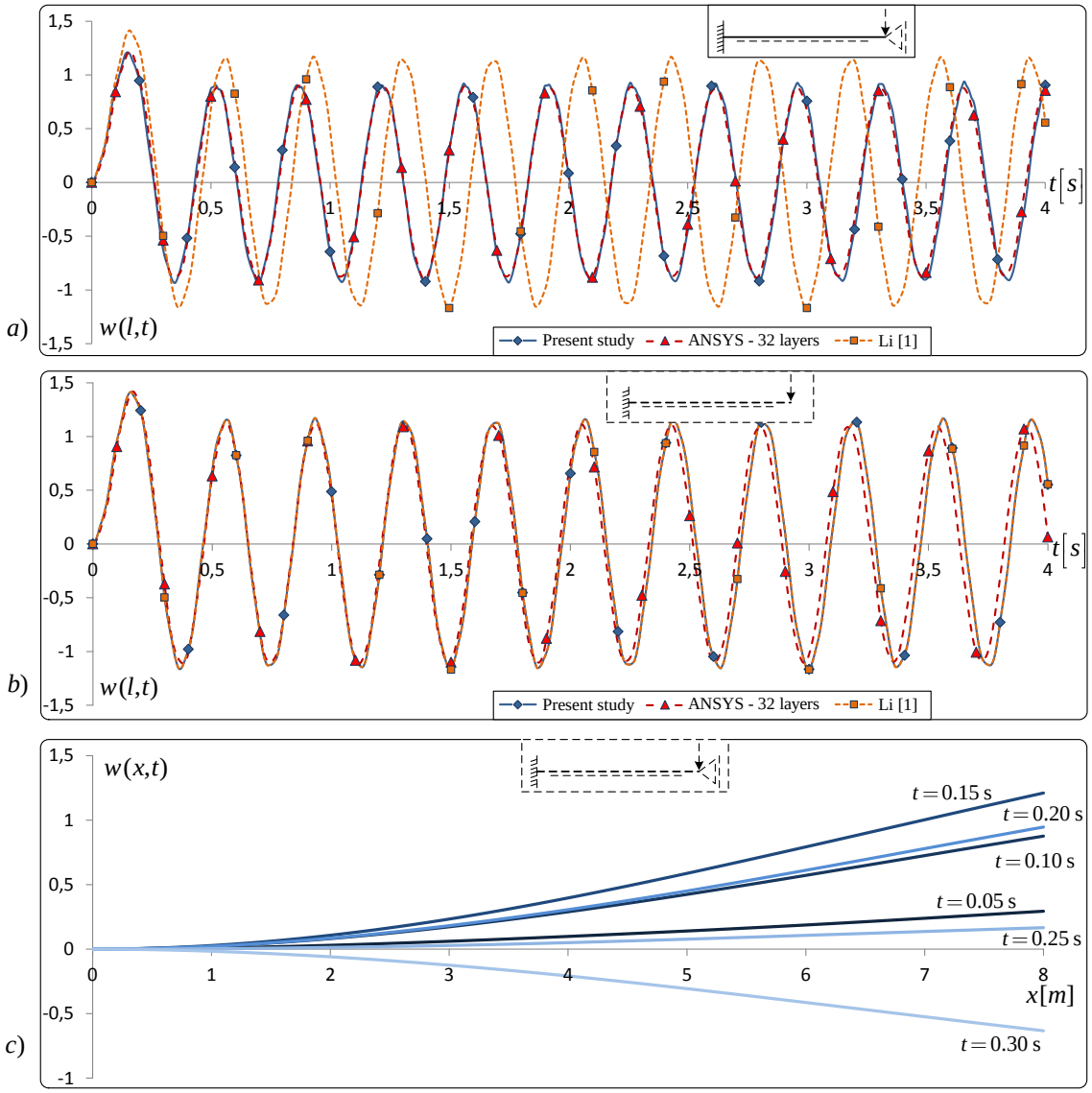


Figure 3: Vertical displacements of the FGB for the first $4\ s$: $a)$ With CC boundary conditions, $b)$ With CF boundary conditions, and $c)$ Beam deflection at 6 different time steps.

5 SIMPLY SUPPORTED FGB UNDER A UNIFORMLY DISTRIBUTED LOAD

As a second example we consider a simply supported beam with the same geometry and material properties as in Section 4. Its first 10 eigenfrequencies calculated with the coupled beam theory of the present study, and a comparison made with a FE analysis can be found in Table 2.

We apply a uniformly distributed loading $q(x,t) = q_0 \sin(\Omega t)$ with $q_0 = 50\ N/m$ on the FGB.

k	$\omega_{k,CC}$	$\omega_{k,CF}$	$\omega_{k,CC}$ FEM	$\omega_{k,CF}$ FEM
1	51.785111	46.949494	51.973881	46.751925
2	187.65204	187.62006	186.11423	186.08282
3	428.02624	296.17575	422.14209	413.74775
4	744.60570	576.91977	727.96985	559.31659
5	1094.3204	942.38759	1133.3610	741.41587
6	1180.6837	1100.5816	1139.7698	1139.7698
7	1715.5681	1441.8223	1635.5131	1600.3273
8	2141.2072	1983.0178	2117.8733	1704.5653
9	2381.3737	2215.4974	2332.5697	2180.5795
10	3015.1517	2683.8256	2788.6033	2748.5794

Table 2: First 10 eigenfrequencies $\omega_k\ [1/s]$ of the simply supported FGB.

Figure 4 presents the vertical displacements of the FGB for different excitation frequencies Ω. In the first case $a)$ with $\Omega = 50\ s^{-1}$, we have an excitation frequency near the first eigenfrequency, and the amplitudes are hence high. A comparison with the finite element analysis shows good agreements in the frequency of the vibration, but the maximal amplitude is about $16\ \%$ lower. The results given by Li [2] are invalid because they do not take into account the coupling between the longitudinal and the transversal vibrations. The other cases $b)$–$d)$ show the response of the system to the frequencies $\Omega = 100\ s^{-1}$, $\Omega = 150\ s^{-1}$ and $\Omega = 200\ s^{-1}$, respectively. Since the first eigenfrequency has the largest influence on the dynamic response of the system, and the excitation frequencies are far away from it, the vibration amplitudes are very low.

6 CONCLUSIONS

This paper deals with the transient response of functionally graded beams (FGBs) subjected to harmonic and non-periodic impulse loadings. The beams are supposed to be governed by the Euler-Bernoulli beam theory. The free vibration solution of the differential equations of motion has been derived analytically. With the obtained eigenfrequencies and mode shapes, this solution has been used to obtain the forced vibration solution by means of a modal analysis. For a cantilever and a simply supported beam, the eigenfrequencies as well as the forced vibration solution have been derived for different loading and boundary conditions. The present analytical solution has a good agreement with the numerical results obtained with the Finite Element Method.

The present study shows also that there is a significant difference between the present theory and the theory neglecting the coupling between the longitudinal and the transverse vibrations [2]. The most important differences can be found in the dynamic solution of FGBs which are constrained longitudinally at both ends. For future works the present coupled beam theory should be extended to two-dimensional functionally graded structures such as plates and shells.

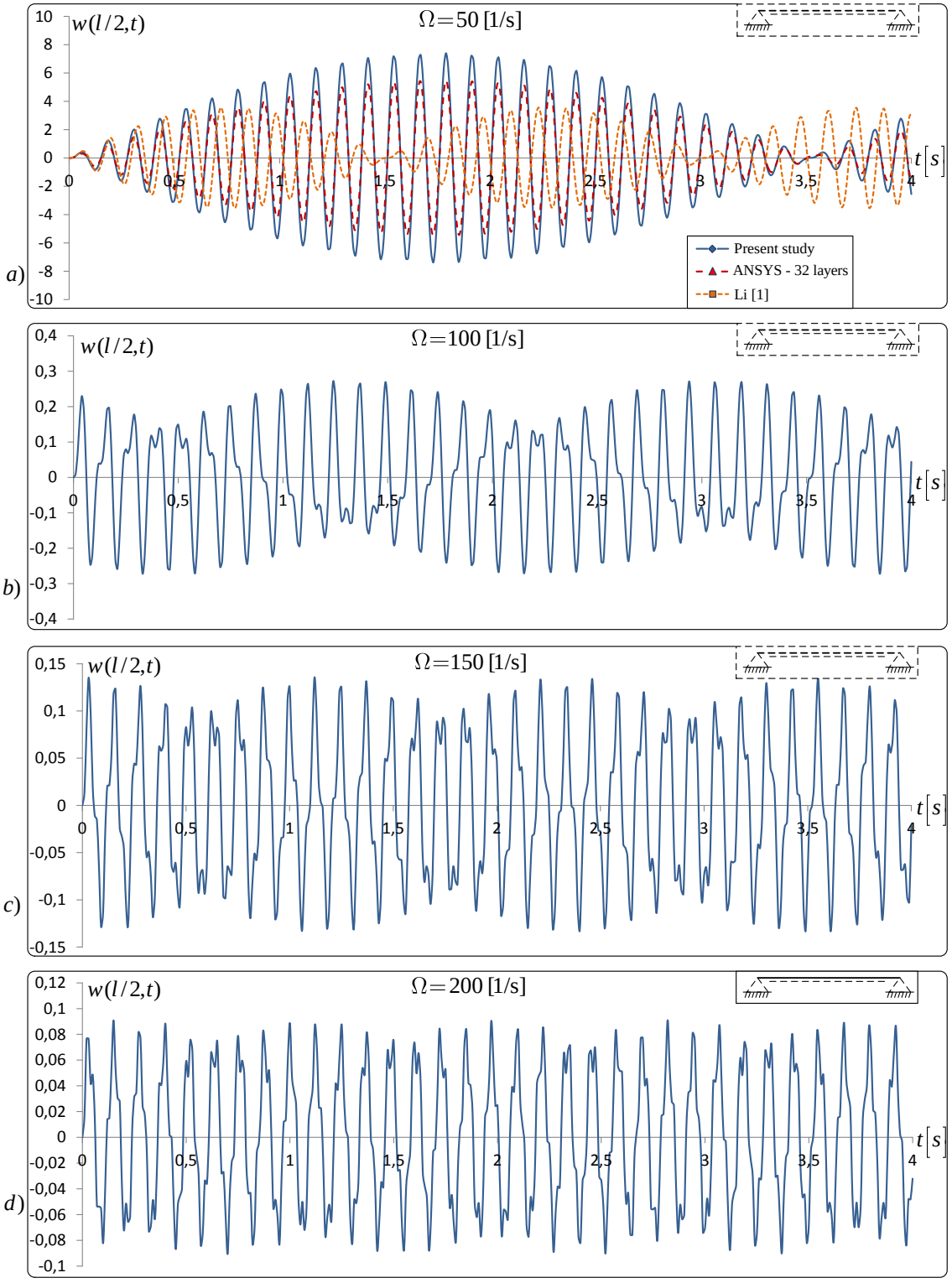


Figure 4: Vertical displacements of the simply supported FGB with CC boundary conditions for different excitation frequencies Ω.

REFERENCES

[1] B.V. Sankar, An elasticity solution for functionally graded beams. *Composites Science and Technology*, **61**, 689–696, 2001.

[2] X.F. Li, A unified approach for analyzing static and dynamic behaviors of functionally graded Timoshenko and Euler-Bernoulli beams. *Journal of Sound and Vibration*, **318**, 1210–1229, 2008.

[3] P.D. Villamil, Ch. Zhang, W.Q. Chen, Analysis of the coupling effects of the longitudinal and transverse displacements on the deformation and internal forces of functionally graded beams. *Proceedings in Applied Mathematics and Mechanics*, **12**, 217–218, 2012.

[4] P.D. Villamil, Ch. Zhang, Free vibrations of functionally graded beams (in German). R. Harte, J. Menkenhagen eds. *Forschungskolloquium Baustatik-Baupraxis*, pp. 125–129, Wesel, Germany, September 18-21, 2012.

[5] O. Carl, P.D. Villamil, Ch. Zhang, Stress and free vibration analysis of functionally graded beams using static Green's functions. *Proceedings in Applied Mathematics and Mechanics*, **11**, 199–200, 2011.

[6] R. Gasch, K. Knothe, R. Liebich, *Strukturdynamik, 2nd Edition*. Springer Vieweg, 2012.

COMPDYN 2013
4th ECCOMAS Thematic Conference on
Computational Methods in Structural Dynamics and Earthquake Engineering
M. Papadrakakis, V. Papadopoulos, V. Plevris (eds.)
Kos Island, Greece, 12–14 June 2013

FINITE ELEMENT FORMULATION FOR AN ARCH STRUCTURE FORMED BY USING BUILT-UP BEAMS ELEMENT

Eiji Nouchi[1], Mitsuharu Kurata[2] and Buntara S. Gan[3]

[1,2,3] Nihon University, College of Engineering
Department of Architecture

1-Nakagawara, Tokusada, Koriyama City, Fukushima, Japan 963-8642
[1]nouchi@arch.ce.nihon-u.ac.jp
[2]kurata@arch.ce.nihon-u.ac.jp
[3]buntara@arch.ce.nihon-u.ac.jp

Keywords: Built-up Beam, Formulation, Finite Element Analysis, Structural Analysis

Abstract. *In architecture of building history, the arch type of structures, especially made from timber elements, are aesthetically very attracting creation. Since the primitive era, human being has learned how to build the arch type of structures that have been used as roofs or beams for houses or bridges structures. They have learned from failures and experiences how to stack and connect pieces of timbers in order to assemble a large span arch type of structure.*

Present study reports the theoretical derivation and finite element formulation for an arch structure formed by using built-up beams elements.

Static experimental works were conducted to an arch structure formed by using built-up beams elements. The behavior of the arch structure formed by using built-up beams elements are evaluated numerically by means of the finite element method.

An analytical formulation is proposed to transform beam elements which can be commonly connected at both beam ends or can be intermittently built-up together as an element member. The formulation was derived based on the assumed stress distribution, shear deformation and expansion-contraction of the beam cross section within the context of linear elasticity theory.

1 INTRODUCTION

In architecture of building history, the arch type of structures, especially made from timber elements, are aesthetically very attracting creation. Since the primitive era, human being has learned how to build the arch type of structures that have been used as roofs or beams for houses or bridges structures. They have learned from failures and experiences how to stack and connect pieces of timbers in order to assemble a large span arch type of structure.

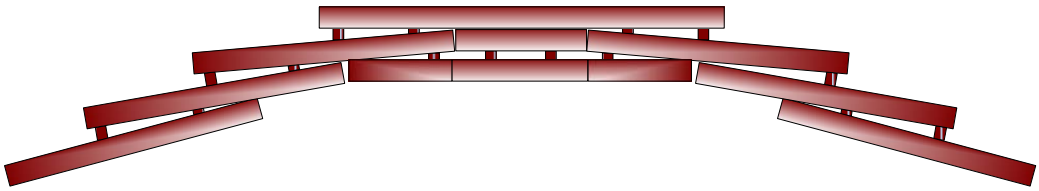


Figure 1: Illustration of a timber arch type structure.

Kawaguchi [1] reported a study on Japanese Traditional buildings which revealed that the builders had an excellent understanding of static mechanisms and structural behavior of the roofs; however their understanding were based on their long period experiences in building the structures. A hanging roof is considered rational and economical, because the pieces of timbers are only in tension, thus the strength requirement of timber is not need to be reduced to consider the buckling effects.

In structural design works, to analyze the deformations and strengths of each member of the roofs, the standard beam element combined with modified joint element for connection is usually adopted [2-4].

This paper is intended to derive a formulation in which each element of the timber is modeled by using four nodes with two displacement degree of freedoms at each node. The fundamental theory is based on the beam element formulation considering shear deformation [5].

2 BASIS FOR THEORETICAL FORMULATIONS

In this study, the standard four component of degree of freedoms which are used in the traditional two nodes beam element are converted into four arbitrary nodes lying within the beam element with two degree of freedoms attached at each node.

Based on the principle of virtual work displacement, the displacements of those four arbitrary nodes within the beam element are transformable to the beam end displacements is formulated. The present theory is applicable for analyzing an arch type structure built-up by four arbitrary nodes along the boundary of a beam element which is transformed from the standard beams element model.

3 PRINCIPLE OF VIRTUAL WORK

By applying virtual displacements, the virtual works experienced by a one dimensional elastic body lying on an *x*-*y* plane under the assumption $\sigma_y = \sigma_z = 0$ can be defined as

$$\int_V (\delta U \cdot X + \delta V \cdot Y) dV + \int_{S_\sigma} (\delta U \cdot X_\nu + \delta V \cdot Y_\nu) ds = \int_V (\delta \varepsilon_x \sigma_x + \delta \gamma_{xy} \tau_{xy}) dV \qquad (1)$$

where, δU and δV being the virtual displacements in the *x* and *y* directions, X and Y being the body forces applied in the *x* and *y* directions, X_ν and Y_ν being the surface tractions applied in the *x* and *y* directions, $\sigma_x = E\varepsilon_x$ and $\tau_{xy} = G\gamma_{xy}$ are the elastic properties of the beam following the linear Hooke's law.

By changing the integration boundaries to the length of the beam and both ends conditions, Eq. (1) can be expressed as

$$\begin{aligned}&\int_0^{\ell}\int_A \left(\delta U \cdot X + \delta V \cdot Y\right) dA dx + \int_{A_i} \left(\delta U \cdot X_\nu + \delta V \cdot Y_\nu\right) dA_i + \int_{A_j} \left(\delta U \cdot X_\nu + \delta V \cdot Y_\nu\right) dA_j \\ &= \int_0^{\ell}\int_A \left(\delta\{\boldsymbol{\varepsilon}\}[\mathbf{E}]\{\boldsymbol{\varepsilon}\}\right) dA dx\end{aligned} \tag{2}$$

where, $dV = dA\,dx$, dA_i is a small integration area at node $i(x=0)$, dA_j is a small integration area at node $j(x=\ell)$, ℓ is the length of the beam, with the strain and modulus properties defined as follow, $\{\varepsilon\} = \begin{Bmatrix}\varepsilon_x \\ \gamma_{xy}\end{Bmatrix}$, $[E] = \begin{bmatrix}E & 0 \\ 0 & G\end{bmatrix}$.

4 STRESS AND STRAIN RELATIONSHIP WITHIN A BEAM

The stress assumption of a beam can be given as

$$\sigma_y = \frac{E}{1-\nu^2}\left(\varepsilon_y + \nu\varepsilon_x\right) = 0 \tag{3}$$

,

with the strains in both directions can be obtained from

$$\varepsilon_y = \frac{\partial V}{\partial y} \text{ and } \varepsilon_x = -\frac{\partial U}{\partial x} \tag{4}$$

where, ν being the Poisson's ratio of the beam material.

The horizontal displacement of an arbitrary point can be expressed as

$$U = u + y\beta + \bar{f}_1(x,y) \tag{5}$$

where, $\varepsilon_y = \frac{\partial V}{\partial y} = -\nu\varepsilon_x = -\nu\frac{\partial U}{\partial x} = -\nu\left(\varepsilon + y\kappa + \frac{\partial \bar{f}_1(x,y)}{\partial x}\right)$, being $\varepsilon = \frac{du}{dx}$, $\kappa = \frac{d\beta}{dx}$.

It can be noted that the last term $\bar{f}_1(x,y)$ in the above equation is a function to incorporate the effect of shear deformation of the beam cross section.

The vertical displacement of an arbitrary point can be defined as

$$V = v - \nu\left(y\varepsilon + \frac{y^2}{2}\kappa + \int_0^y \frac{\partial \bar{f}_1(x,y)}{\partial x} dy\right) \tag{6}$$

where, $\frac{\tau_{xy}}{\tau_0} = \frac{QS}{b(y)I} \Big/ \frac{QS_0}{b(0)I} = \frac{b(0)S}{b(y)S_0} = \frac{G\gamma_{xy}}{G\gamma}$ being $\gamma_{xy} = \frac{\partial V}{\partial x} + \frac{\partial U}{\partial y} = \frac{b(0)S}{b(y)S_0}\gamma$. For a uniform width of beam cross section in which $b(y) = b(0) = b$, the term $b(0)/b(y)$ will vanish from the shear stress and strain equations.

By substituting Eq. (6), into the ε_y term, and integrating along the depth of the beam cross section, results in the following explicit equation considering shear deformation effect.

$$\frac{\partial \bar{f}_1(x,y)}{\partial y} = -\left(1 - \frac{b(0)S}{b(y)S_0}\right)\gamma + \nu\left(y\frac{d\varepsilon}{dx} + \frac{y^2}{2}\frac{d\kappa}{dx} + \int_0^y \frac{d^2\bar{f}_1(y)}{dx^2} dy\right) \tag{7}$$

with,

$$\bar{f}_1(y) \approx -\left(\int_0^y \left(1-\frac{S}{S_0}\right)dy\right)\gamma + \nu\left(\frac{y^2}{2}\frac{d\varepsilon}{dx}+\frac{y^3}{6}\frac{d\kappa}{dx}\right),$$

where,

$$\int_0^y \int_0^y \frac{d^2 \bar{f}_1(y)}{dx^2} dydy \approx 0 .$$

5 FORMULATION OF BEAM REPRESENTED BY FOUR ARBITRARY NODES

Figure 2 shows a standard two-node beam element with four arbitrary nodes (*k, l, m and n*) lying along the boundary of the beam element.

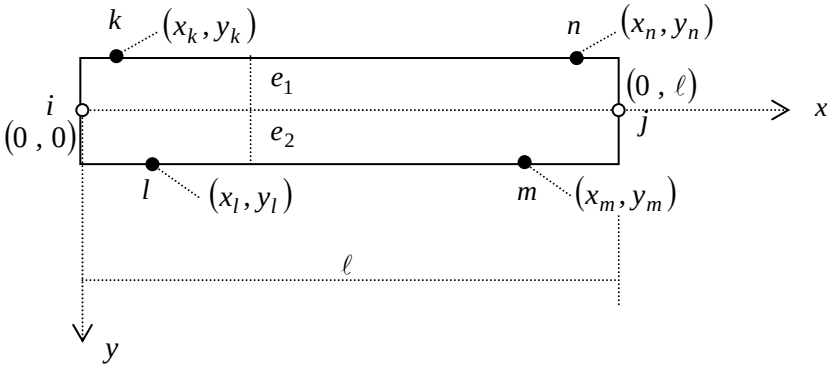


Figure 2: The schematic beam element with four arbitrary nodes.

5.1 General displacements functions

Displacements and rotations of an arbitrary node inside a beam element interpolated from both beam ends values can be expressed by using polynomial as follow

$$\begin{aligned}
u(x) &= \left(1-\frac{x}{\ell}\right)u_i + \frac{x}{\ell}u_j \\
v(x) &= v_i + \theta_i \cdot x + a \cdot x^2 + bx^3 \\
\theta(x) &= \frac{dv}{dx} = \theta_i + 2ax + 3bx^2 \\
\gamma(x) &= \beta + \theta = c + dx \\
\beta(x) &= -\theta + c + dx = -\theta_i - 2ax - 3bx^2 + c + dx
\end{aligned} \tag{8}$$

where, $u(x)$, $v(x)$, $\theta(x)$, $\gamma(x)$ and $\beta(x)$ are the horizontal displacement, vertical displacement, slope of the beam axis, shear rotation and beam cross section rotation, respectively, at a distance *x* along the beam axis.

By defining the boundary conditions of both ends values of the beam as

$$\begin{aligned}
&u_i = u(x=0),\ v_i = v(x=0),\ \theta_i = \theta(x=0),\ \beta_i = \beta(x=0) \\
&u_j = u(x=\ell),\ v_j = v(x=\ell),\ \theta_j = \theta(x=\ell),\ \beta_j = \beta(x=\ell)
\end{aligned} \tag{9}$$

and solving for all the parameters in Eq. (8), result in

$$
\begin{aligned}
a &= -\frac{1}{\ell}\left(2\theta_i + \theta_j + 3\frac{v_j - v_i}{\ell}\right) \\
b &= \frac{1}{\ell^2}\left(\theta_i + \theta_j + 2\frac{v_j - v_i}{\ell}\right) \\
c &= \beta_i + \theta_i \\
d &= \frac{1}{\ell}\left(\beta_j + \theta_j\right) - \frac{1}{\ell}\left(\beta_i + \theta_i\right)
\end{aligned}
\tag{10}
$$

Thus, an interpolation matrix between the arbitrary point displacement values and both ends values of the beam can be described as follow

$$
\begin{Bmatrix} u \\ v \\ \theta \\ \beta \end{Bmatrix} =
\begin{bmatrix}
1-\frac{x}{\ell} & 0 & 0 & 0 & \frac{x}{\ell} & 0 & 0 & 0 \\
0 & 1-\frac{3x^2}{\ell^2}+\frac{2x^3}{\ell^3} & x-\frac{2x^2}{\ell}+\frac{x^3}{\ell^2} & 0 & 0 & \frac{3x^2}{\ell^2}-\frac{2x^3}{\ell^3} & -\frac{x^2}{\ell}+\frac{x^3}{\ell^2} & 0 \\
0 & -\frac{6x}{\ell^2}+\frac{6x^2}{\ell^3} & 1-\frac{4x}{\ell}+\frac{3x^2}{\ell^2} & 0 & 0 & \frac{6x}{\ell^2}-\frac{6x^2}{\ell^3} & -\frac{2x}{\ell}+\frac{3x^2}{\ell^2} & 0 \\
0 & \frac{6x}{\ell^2}-\frac{6x^2}{\ell^3} & \frac{3x}{\ell}-\frac{3x^2}{\ell^2} & 1-\frac{x}{\ell} & 0 & -\frac{6x}{\ell^2}+\frac{6x^2}{\ell^3} & \frac{3x}{\ell}-\frac{3x^2}{\ell^2} & \frac{x}{\ell}
\end{bmatrix}
\begin{Bmatrix} u_i \\ v_i \\ \theta_i \\ \beta_i \\ u_j \\ v_j \\ \theta_j \\ \beta_j \end{Bmatrix}
\tag{11}
$$

or in a vector and matrix forms, Eq. (11) can be written as $\{\mathbf{u}\} = [\mathbf{x}]\begin{Bmatrix}\mathbf{u}_i \\ \mathbf{u}_j\end{Bmatrix}$.

5.2 Strains based on general displacement functions

Based on the general displacement functions derived in the previous section, the strains at any arbitrary location can be obtained from the following relationships.

$$
\frac{d\varepsilon}{dx} = \frac{d^2u}{dx^2} = 0 \ , \ \frac{d^2\kappa}{dx^2} = \frac{d^3\beta}{dx^3} = 0 \ , \ \frac{d^2\gamma}{dx^2} = 0 \tag{12}
$$

Where, κ being the curvature rate of the beam axis. By integrating Eq. (7) with respect to *y*, results in the following

$$
\bar{f}_1(x,y) = f_1(y)\gamma + \nu\frac{y^3}{6}\frac{d\kappa}{dx} \tag{13}
$$

where, $f_1(y) = -\left(\int_0^y\left(1-\frac{b(0)S}{b(y)S_0}\right)dy\right)$.

Substituting Eq. (13) into Eqs. (5) and (6), will give the following displacements,

$$
\begin{aligned}
U &= u + f_1(y)\theta + \left(y + f_1(y) + \nu\frac{y^3}{6}\frac{d^2}{dx^2}\right)\beta \\
V &= -\nu y\frac{du}{dx} + v - \nu\int_0^y f_1(y)dy\frac{d\theta}{dx} - \nu\left(\frac{y^2}{2} + \int_0^y f_1(y)dy\right)\frac{d\beta}{dx}
\end{aligned}
\tag{14}
$$

thus, the axial and shear strains can be obtained from the following

$$\varepsilon_x = \frac{du}{dx} + f_1(y)\frac{d\theta}{dx} + \left(y + f_1(y)\right)\frac{d\beta}{dx}$$
$$\gamma_{xy} = \left(1 + \frac{df_1}{dy}\right)\gamma = f_2(y)\left(\theta + \beta\right) \tag{15}$$

where, $f_2(y) = 1 + \dfrac{df_1}{dy}$.

5.3 Virtual Work Equations

Applying the virtual nodal displacements $\delta\{\mathbf{u}_q\}$ to Eq. (2), results in

$$\delta\{\mathbf{u}_q\}^T\{\mathbf{P}\} = \delta\{\mathbf{u}_q\}^T[\mathbf{K}]\{\mathbf{u}_q\} \tag{16}$$

and the following equilibrium equation can be obtained

$$\{\mathbf{P}\} = [\mathbf{K}]\{\mathbf{u}_q\} \tag{17}$$

where,

$\{\mathbf{u}_q\}^T = \{u \quad v \quad \theta \quad \beta\}^T$

$\{\mathbf{P}\} = \{\mathbf{q}\} + \{\mathbf{p}\}$

$\{\mathbf{q}\} = \int_0^\ell \int_A ([\mathbf{y}'][\mathbf{x}])^T \{\mathbf{X}\} dA dx$

$\{\mathbf{p}\} = \int_{A_i} ([\mathbf{y}'][\mathbf{x}(0)])^T \{\mathbf{X}_v\} dA_i + \int_{A_j} ([\mathbf{y}'][\mathbf{x}(\ell)])^T \{\mathbf{X}_v\} dA_j$

$[\mathbf{K}] = \int_0^\ell \int_A ([\mathbf{x}'][\mathbf{x}])^T ([\mathbf{E}][[\mathbf{x}'][\mathbf{x}]) dA dx$

$\{\mathbf{X}\} = \begin{Bmatrix} X \\ Y \end{Bmatrix}$

$\{\mathbf{X}_v\} = \begin{Bmatrix} X_v \\ Y_v \end{Bmatrix}$

$$[\mathbf{x}'] = \begin{bmatrix} \dfrac{d}{dx} & 0 & f_1(y)\dfrac{d}{dx} & \left(y + f_1(y)\right)\dfrac{d}{dx} \\ 0 & 0 & f_2(y) & f_2(y) \end{bmatrix}$$

$$[\mathbf{y}'] = \begin{bmatrix} 1 & 0 & f_1(y) & y + f_1(y) + \nu\dfrac{y^3}{6}\dfrac{d^2}{dx^2} \\ -\nu y\dfrac{d}{dx} & 1 & -\nu\displaystyle\int_0^y f_1(y)dy\dfrac{d}{dx} & -\nu\left(\dfrac{y^2}{2} + \displaystyle\int_0^y f_1(y)dy\right)\dfrac{d}{dx} \end{bmatrix}$$

6 TRANSFORMATION MATRIX FOR ARBITRARY 4 NODAL POINTS

The transformation matrix for arbitrary 4 nodal points in the beam can be obtained by substituting each point's coordinates $(x_k, y_k), (x_l, y_l), (x_m, y_m), (x_n, y_n)$ into the Eq. (14) by using Eqs. (8) and (10). The transformation matrix defined for the arbitrary 4 nodal points related with the beam ends nodal displacements can be given as follow,

$$\begin{Bmatrix} U(x_k,y_k) \\ V(x_k,y_k) \\ U(x_\ell,y_\ell) \\ V(x_\ell,y_\ell) \\ U(x_m,y_m) \\ V(x_m,y_m) \\ U(x_n,y_n) \\ V(x_n,y_n) \end{Bmatrix} = \begin{bmatrix} {}_kS_{11} & {}_kS_{12} & {}_kS_{13} & {}_kS_{14} & {}_kS_{15} & {}_kS_{16} & {}_kS_{17} & {}_kS_{18} \\ {}_kS_{21} & {}_kS_{22} & {}_kS_{23} & {}_kS_{24} & {}_kS_{25} & {}_kS_{26} & {}_kS_{27} & {}_kS_{28} \\ {}_\ell S_{11} & {}_\ell S_{12} & & & & & & \\ {}_\ell S_{21} & {}_\ell S_{22} & & & & & & \\ {}_mS_{11} & {}_mS_{12} & & & & & & \\ {}_mS_{21} & {}_mS_{22} & & & & & & \\ {}_nS_{11} & {}_nS_{12} & & & & & {}_nS_{17} & {}_nS_{18} \\ {}_nS_{21} & {}_nS_{22} & {}_nS_{23} & {}_nS_{24} & {}_nS_{25} & {}_nS_{26} & {}_nS_{17} & {}_nS_{28} \end{bmatrix} \cdot \begin{Bmatrix} u_i \\ v_i \\ \theta_i \\ \beta_i \\ u_j \\ v_j \\ \theta_j \\ \beta_j \end{Bmatrix} \tag{18}$$

rewritten into a matrix notation,

$$\{\mathbf{U}_q\} = [\mathbf{S}]\{\mathbf{u}_q\} \tag{19}$$

where,

$${}_kS_{11} = 1 - \frac{x_k}{\ell}$$

$${}_kS_{12} = y_k\left(\frac{6x_k}{\ell^2} - \frac{6{x_k}^2}{\ell^3}\right) - \nu\frac{2{y_k}^3}{\ell^3}$$

$${}_kS_{13} = f_1(y_k)\left(1 - \frac{x_k}{\ell}\right) + y_k\left(\frac{3x_k}{\ell} - \frac{3{x_k}^2}{\ell^2}\right) - \nu\frac{{y_k}^3}{\ell^2}$$

$${}_kS_{14} = \left(y_k + f_1(y_k)\right)\left(1 - \frac{x_k}{\ell}\right)$$

$${}_kS_{15} = \frac{x_k}{\ell}$$

$${}_kS_{16} = -y_k\left(\frac{6x_k}{\ell^2} - \frac{6{x_k}^2}{\ell^3}\right) + \nu\frac{2{y_k}^3}{\ell^3}$$

$${}_kS_{17} = f_1(y_k)\left(\frac{x_k}{\ell}\right) + y_k\left(\frac{3x_k}{\ell} - \frac{3{x_k}^2}{\ell^2}\right) - \nu\frac{{y_k}^3}{\ell^2}$$

$${}_kS_{18} = \left(y_k + f_1(y_k)\right)\frac{x_k}{\ell}$$

$$_kS_{21} = \nu\frac{y_k}{\ell}$$

$$_kS_{22} = \left(1-\frac{3x_k{}^2}{\ell^2}+\frac{2x_k{}^3}{\ell^3}\right)-\nu\frac{y_k{}^2}{2}\left(\frac{6}{\ell^2}-\frac{12x_k}{\ell^3}\right)$$

$$_kS_{23} = \left(x_k-2\frac{x_k{}^2}{\ell}+\frac{x_k{}^3}{\ell^2}\right)-\nu\frac{y_k{}^2}{2}\left(\frac{3}{\ell}-\frac{6x_k}{\ell^2}\right)+\nu\frac{1}{\ell}\int_0^{y_k} f_1(y)dy$$

$$_kS_{24} = \nu\frac{1}{\ell}\left(\frac{y_k{}^2}{2}+\int_0^{y_k} f_1(y)dy\right)$$

$$_kS_{25} = -\nu\frac{y_k}{\ell}$$

$$_kS_{26} = \left(\frac{3x_k{}^2}{\ell^2}-\frac{2x_k{}^3}{\ell^3}\right)+\nu\frac{y_k{}^2}{2}\left(\frac{6}{\ell^2}-\frac{12x_k}{\ell^3}\right)$$

$$_kS_{27} = \left(-\frac{x_k{}^2}{\ell}+\frac{x_k{}^3}{\ell^2}\right)-\nu\frac{y_k{}^2}{2}\left(\frac{3}{\ell}-\frac{6x_k}{\ell^2}\right)-\nu\frac{1}{\ell}\int_0^{y_k} f_1(y)dy$$

$$_kS_{28} = -\nu\frac{1}{\ell}\left(\frac{y_k{}^2}{2}+\int_0^{y_k} f_1(y)dy\right)$$

being the matrix coefficients for node *k* which fill the above two rows of the matrix $[\mathbf{S}]$. The other three nodes (*l*,*m*,*n*) construct similar matrix coefficients by replacing the coordinates (x_k, y_k) of node *k* with the other three nodes' coordinates $(x_l, y_l), (x_m, y_m), (x_n, y_n)$.

6.1 Equilibrium Equation

By substituting Eq. (19) into the virtual work equation of the beam in Eq. (16), the virtual work equation in terms of the arbitrary four node displacements can be given as

$$\delta\{\mathbf{U}_q\}^T\left([\mathbf{S}]^{-1}\right)^T\{\mathbf{P}\} = \delta\{\mathbf{U}_q\}^T\left([\mathbf{S}]^{-1}\right)^T[\mathbf{K}][\mathbf{S}]^{-1}\{\mathbf{U}_q\}, \tag{20}$$

and the static equilibrium equation for the arbitrary four nodal points in the beam element can be given as

$$\{\overline{\mathbf{P}}\} = [\overline{\mathbf{K}}]\{\mathbf{U}_q\} \tag{21}$$

where,

$\{\overline{\mathbf{P}}\} = \left([\mathbf{S}]^{-1}\right)^T\{\mathbf{P}\}$

$[\overline{\mathbf{K}}] = \left([\mathbf{S}]^{-1}\right)^T[\mathbf{K}]\left([\mathbf{S}]^{-1}\right)$.

7 CONCLUSIONS

- A finite element formulation for an arch structure formed by using built-up beams elements is derived.
- A transformation matrix was analytically derived which can be used to transform the degree of freedoms from the standard two nodes beam element to the arbitrary four nodes lying along the beam boundary.

- Based on the virtual works principle, the equilibrium equation for the developed element model can be obtained by using the transformation matrix with the standard two nodes beam element matrices.

REFERENCES

[1] M. Kawaguchi, Design problems of long span spatial structures. *Engineering Structures*, Vol. 13, 146-163. April 1991.

[2] R.H. Sangree, B.W. Schafer, Experimental and numerical analysis of a stop-splayed traditional timber scarf joint with key. *Construction and Building Materials*, Vol. 23, 376-385, 2009.

[3] E.M. Meghlat, M. Oudjene, H. A. Aider, J.L. Batoz, A new approach to model nailed and screwed timber joints using the finite element method. *Construction and Building Materials*, Vol. 41, 263-269, 2013.

[4] B.H. Xu, A. Bouchair, P. Racher, Analytical study and finite element modeling of timber connections with glued-in rods in bending. *Construction and Building Materials*, Vol. 34, 337-345, 2012.

[5] E. Nouchi, M. Kurata, B.S. Gan, K. Sugiyama, A consistent beam element formulation considering shear lag effect. IOP Conference Series : Materials Science and Engineering, Vol. 10, 012211, 2010.

COMPDYN 2013
4th ECCOMAS Thematic Conference on
Computational Methods in Structural Dynamics and Earthquake Engineering
M. Papadrakakis, N.D. Lagaros, V. Plevris (eds.)
Kos Island, Greece, 12–14 June 2013

OPTIMAL DESIGN OF VIBRATING RING-STIFFENED CYLINDRICAL SHELL

Sergei B. Filippov and Natalia V. Naumova

Saint Petersburg State University
address
e-mail: s_b_filippov@mail.ru

Keywords: Free vibrations, Stiffened cylindrical shell, Optimal design, Asymptotic methods.

Abstract. *Free vibrations of a thin elastic cylindrical shell stiffened by rings of rectangular cross-sections are considered. The parameters of the shell of the minimal weight, having a given fundamental frequency, are found. For the evaluating of the optimal parameters the asymptotic approach is used. The validation of the obtained asymptotic results are fulfilled by finite element analysis.*

1 INTRODUCTION

Ring-stiffened cylindrical shells are widely applied in engineering. Various analytical and numerical methods for analysis of stiffened shells have been developed. In [1] and [2] Fourier series for the solution of static and dynamic problems are used. In the early studies on vibrations and buckling of stiffened shells, the Rayleigh–Ritz method was applied. Nowadays this technique is still popular. For example, in [3] the Ritz method was used for buckling analysis of ring-stiffened cylindrical shells under general pressure loading. The study [4] has shown that the finite element method is quite suitable to analyze the vibration characteristics of ring-stiffened cylindrical shells under external pressure.

The approximate values of the natural frequencies for thin ring-stiffened shells may be obtained by solving eigenvalue problems for linear differential equations. The equations describing the vibration of thin shells contain the dimensionless shell thickness as a small parameter. Therefore, these boundary value problems lend themselves to be solved by asymptotic methods. By means of the asymptotic approach complex eigenvalue problems of the stiffened shells theory can be transformed into problems which have simple analytical solutions.

In [5] asymptotic approaches have been used for calculation of optimal parameters of ring-stiffened cylindrical shell with given mass, for which the fundamental vibration frequency have the largest value. In the presented paper some kind of an inverse problem is studied. We assume that the fundamental vibration frequency is given and seek optimal parameters corresponding to the ring-stiffened shell of the minimal mass.

To get simple approximate formulas for the lower frequencies a combination of asymptotic method is used. First we seek the solutions as a sum of slowly varying functions and edge effect integrals. Thus the initial singularly perturbed system of differential equations is reduced to an approximate system of the smaller order. Then the solution of the approximate eigenvalue problem is obtained by means of the homogenization procedure.

2 BASIC EQUATIONS

Consider the low-frequency free vibrations of a thin circular cylindrical shell stiffened by n_r identical rings at the parallels $s = s_j$, where s is the coordinate in the longitudinal directions, $j = 1, 2, \ldots n_r$ (see Figure 1).

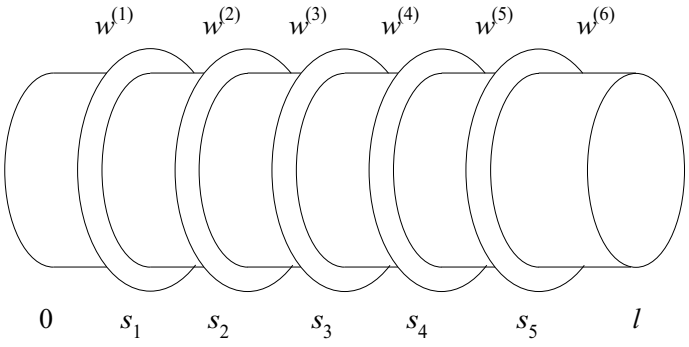


Figure 1: Ring-stiffened cylindrical shell.

If we take the radius R of the cylindrical shell as the characteristic size, then after the separation of variables the dimensionless equations describing vibrations of the shell may be written

as

$$\varepsilon^8 \Delta\Delta w^{(j)} - \frac{d^2\Phi^{(j)}}{ds^2} - \lambda w^{(j)} = 0, \qquad \Delta\Delta\Phi^{(j)} + \frac{d^2 w^{(j)}}{ds^2} = 0, \qquad j = 1, 2, \dots n, \quad n = n_r + 1, \tag{1}$$

where

$$\Delta w = \frac{d^2 w}{ds^2} - m^2 w, \quad \varepsilon^8 = \frac{h^2}{12\sigma}, \quad \sigma = 1 - \nu^2, \quad \lambda = \frac{\rho R^2 \omega^2}{E}, \tag{2}$$

m is the circumferential wave number, $w^{(j)}$ is the normal deflection, $\Phi^{(j)}$ is the force function, $\varepsilon > 0$ is a small parameter, h is the dimensionless shell thickness, ν is Poisson's ratio, ω is the frequency, ρ is the mass density, and E is Young's modulus. The solutions of equations (1) satisfy four boundary conditions on each shell edges $s = 0$ and $s = l$, where l is non-dimension shell length, and $8n_r$ continuity conditions on the parallels $s = s_j$, $j = 1, 2, \dots n_r$.

3 First approximation

It is shown in [5] that for sufficiently small ε the lowest eigenvalues, $\lambda \sim \varepsilon^4$, correspond to the eigenfunction with large circumferential wave number $m \sim \varepsilon^{-1}$. We represent the solutions of equations (1) as a sum of the slowly varying function and edge effect integrals. In the first approximation we get the following equations

$$\frac{d^4 w^{(j)}}{ds^4} - \alpha^4 w^{(j)} = 0, \quad \alpha^4 = m^4\lambda - \varepsilon^8 m^8, \quad j = 1, 2, \dots n. \tag{3}$$

The eigenvalue problem for equations (1) is singularly perturbed, because the equations (1) of order eight transform to differential equations (2) of order four. Therefore, solutions of equations (3) can not satisfy all boundary conditions of initial eigenvalue problem. The problem of extracting two boundary conditions for equations (3) out of four boundary conditions on the shell edges is discussed in detail in [6]. The boundary conditions for equations (3) in the case of freely supported shell edges have the form

$$w = \frac{d^2 w}{ds^2} = 0 \quad \text{for} \quad s = 0, \quad s = l. \tag{4}$$

If characteristic size of the ring cross sections $a \sim \varepsilon^3$, then the boundary conditions for equations (3) at the parallels $s = s_j$ are written as (see [5])

$$w^{(j)} = w^{(j+1)}, \quad \frac{dw^{(j)}}{ds} = \frac{dw^{(j+1)}}{ds}, \quad \frac{d^2 w^{(j)}}{ds^2} = \frac{d^2 w^{(j+1)}}{ds^2}, \quad \frac{d^3 w^{(j)}}{ds^3} - \frac{d^3 w^{(j+1)}}{ds^3} = -c w^{(j+1)}, \tag{5}$$

In case the centers of gravity of the ring cross sections lie on the shell neutral surface $c = m^8 I/h$, where I is the dimensionless moment of inertia of the ring cross-section with respect to the generatrix of the cylinder.

It follows from the second formula (3) that approximate value of frequency parameter is

$$\lambda_k(m) = \alpha_k^4/m^4 + \varepsilon^8 m^4, \tag{6}$$

where α_k is the eigenvalue of problem (3–5). The eigenvalue problem (3–5) also describe the flexural vibrations of a simply supported beam, stiffened by n_r identical springs of stiffness c at the points $s = s_j$.

4 Homogenization

In this section we consider the uniform arrangement $s_j = jl/n$ of the springs on a simply supported beam. If the number n_r of springs is large and the stiffness of each spring c is small, one can use the homogenization method [7] for the approximate evaluation of the eigenvalues α_k. Instead of the problem (3–5) we will solve the equivalent problem for the equation

$$\frac{d^4w}{ds^4} + cw\sum_{j=1}^{n-1}\delta(s-s_j) = \alpha^4 w \tag{7}$$

with the boundary conditions (4). Here $\delta(z)$ is Dirac's delta function. In the new variables $s = xl$ and $w = \hat{w}l$ equation (7) is

$$\frac{d^4\hat{w}}{ds^4} + \hat{c}n\hat{w}\sum_{j=1}^{n-1}\delta(\xi-j) = \kappa\hat{w}, \tag{8}$$

where $\hat{c} = cl^3$, $\kappa = (\alpha l)^4$, and $\xi = nx$. The boundary conditions (4) take the form

$$\hat{w} = \frac{d^2\hat{w}}{dx^2} = 0 \quad \text{for} \quad x = 0, \quad x = 1. \tag{9}$$

Assuming that $n \gg 1$ and $\hat{c}n \sim 1$, we write the solution of equation (8) as

$$\hat{w}(x,\xi) = w_0(x,\xi) + n^{-4}w_4(x,\xi) + \cdots, \quad \kappa = \kappa_0 + n^{-4}\kappa_4 + \cdots, \tag{10}$$

where $w_i(x,\xi) = w_i(x,\xi+1)$ and, consequently,

$$< \frac{\partial^k w_i}{\partial\xi^k} >= \int_\xi^{\xi+1}\frac{\partial^k w_i}{\partial\xi^k}d\xi = 0, \quad i = 0,4,\ldots, \quad k = 1,2,\ldots \tag{11}$$

The operator $< \cdot >$ is called the homogenization operator. The application of this operator to both part of an equation is called the homogenization of the equation.

If we substitute (10) into (8) and (9), then we obtain the equations

$$\frac{\partial^4 w_0}{\partial\xi^4} = 0, \quad \frac{\partial^4 w_4}{\partial\xi^4} + \frac{\partial^4 w_0}{\partial x^4} + \hat{c}n\sum_{i=1}^{n}\delta(\xi-i)w_0 = \kappa_0 w_0 \tag{12}$$

and the boundary conditions

$$w_0 = \frac{\partial^2 w_0}{\partial x^2} = 0, \quad w_4 = \frac{\partial^2 w_4}{\partial x^2} = 0 \quad \text{for} \quad x = 0, \quad x = 1 \tag{13}$$

as a result of equating the coefficients of n^4 and n^0. From the first of equations (12) and (11) it follows that

$$\frac{\partial^3 w_0}{\partial\xi^3} = v_3(x), \quad v_3(x) =< v_3(x) >=< \frac{\partial^3 w_0}{\partial\xi^3} >= 0.$$

A further integration followed by a homogenization gives

$$\frac{\partial^2 w_0}{\partial\xi^2} = v_2(x) = 0, \quad \frac{\partial w_0}{\partial\xi} = v_1(x) = 0, \quad w_0(x,\xi) = v_0(x).$$

After the homogenization of the second of equations (11) we get

$$\frac{d^4 v_0}{dx^4} + \hat{c} n v_0 = \kappa_0 v_0, \tag{14}$$

The first of the boundary conditions (13) takes the form

$$v_0 = \frac{d^2 v_0}{dx^2} = 0 \quad \text{for} \quad x = 0, \quad x = 1. \tag{15}$$

Eigenvalue problem (14), (15) describes the vibrations of a simply supported beam on an elastic base and has the solutions $v_{0k} = \sin(k\pi x)$,

$$\kappa_{0k} = (k\pi)^4 + \hat{c} n, \quad k = 1, 2, \ldots \tag{16}$$

In [8] it has been shown that although formula (16) is derived for $n \gg 1$ and $\hat{c} \sim 1/n \ll 1$, this formula provide good approximations for the exact values of κ_1 even for $n = 2$ (for one ring) and for a sufficiently large stiffness $\hat{c}$.

It follows from (16) that

$$\alpha_k^4 = \beta_k^4 + \eta(\varepsilon m)^8, \tag{17}$$

where

$$\beta_k = \frac{k\pi}{l}, \quad \eta = \frac{cn}{m^8 \varepsilon^8 l} = \frac{nI}{\varepsilon^8 h l}. \tag{18}$$

The dimensionless ring stiffness η is proportional to the ratio D_r/D, where $D_r = EIR^4$ is the bending stiffness of the ring and $D = Eh\varepsilon^8 R^3$ is the bending stiffness of the shell. Substituting (17) into (6) give the following approximate formula

$$\lambda_k(m) = \frac{\beta_k^4}{m^4} + (1 + \eta)\varepsilon^8 m^4. \tag{19}$$

To find the frequency parameters

$$\lambda_k^* = \min_m \lambda_k(m)$$

we calculate the partial derivative of the function $\lambda_k(m)$ m and set it equal to zero. The solution of the equation $\partial\lambda_k/\partial m = 0$ has the form

$$m = m_* = \frac{\sqrt{\beta_k}}{\varepsilon(1 + \eta)^{1/8}}.$$

The function $\lambda_k(m)$ attains its minimum,

$$\lambda_k^* = 2\varepsilon^4 \beta_k^2 \sqrt{1 + \eta} \tag{20}$$

for $m = m_*$. If m_* is an integer, then formula (20) gives the exact result. Replacing m_* by one of the integers closest to m_* we introduce an error whose absolute value is less than 1. Therefore, the relative error of formula (20) is small because $m_* \gg 1$.

It follows from (20) that

$$\lambda_k^*(\eta) = \lambda_k^*(0)\sqrt{1 + \eta}, \quad k = 1, 2, \ldots \tag{21}$$

where λ_k^* and $\lambda_k^*(0) = 2\varepsilon^4 \beta_k^2$ are the frequency parameters for ring-stiffened and non-stiffened cylindrical shells.

5 Effective stiffness

The lowest frequency parameter λ_1, corresponding to fundamental frequency ω_1, is the important characteristics of a shell. For a non-stiffened freely supported cylindrical shell the approximate value of λ_1 can be found from the formula

$$\lambda_1 \simeq \lambda_1^*(0) = 2\varepsilon^4\beta_1^2. \tag{22}$$

For the ring-stiffened shell with the uniform arrangement of rings the formula

$$\lambda_1^*(\eta) = \lambda_1^*(0)\sqrt{1+\eta}, \tag{23}$$

following from (21) gives the approximate value of $\lambda_1(\eta)$ only if the dimensionless ring stiffness η is not to large. The reason of it is that eigenvalue problem (3–5) in case $s_j = jl/n$ has solutions, which are independent of η. The minimal stiffness-independent eigenvalue $\alpha_n(0) = \pi n/l$ correspond to vibration mode $w = \sin(n\pi s/l)$ which satisfy equation (3) and boundary condition (4) and (5). The minimal stiffness-independent eigenvalue

$$\lambda_n^*(0) \simeq 2\varepsilon^4\beta_n^2 = n^2\lambda_1^*(0)$$

The root of equation $\lambda_1^*(\eta) = \lambda_n^*(0)$ is

$$\eta^* = n^4 - 1.$$

We call η^* effective stiffness. If $\eta \le \eta^*$ then $\lambda_1^*(\eta) \le \lambda_n^*(0)$ else $\lambda_1^*(\eta) > \lambda_n^*(0)$. Therefore for ring-stiffened shell

$$\lambda_1(\eta) \simeq \begin{cases} \lambda_1^*(0)\sqrt{1+\eta}), & 0 \le \eta \le \eta^*, \\ n^2\lambda_1^*(0), & \eta \ge \eta^*. \end{cases} \tag{24}$$

The asymptotic results, obtained from formula (24), are in good agreement with the numerical ones. In particular, for $n = 2$ numerical and asymptotic values of η^* are 14.6 and 15.

6 Optimal design of stiffened shells

We suppose that the fundamental vibration frequency of a ring-stiffened cylindrical shell is given and seek the optimal parameters, for which the mass of the stiffened shell, M_s, has the minimum value. We will compare M_s with the mass of the unstiffened shell, M_0, assuming that both shells have the identical fundamental frequencies, dimensionless length l, radius R and are made of the same materials of the density ρ.

Consider rings with rectangular cross-sections of dimensionless thickness a and width $b = ka$. In this case

$$M_0 = 2\pi R^3\rho l h_0, \quad M_s = 2\pi R^3\rho(lh + n_r a^2 k) \tag{25}$$

where h_0 and h are the dimensionless thicknesses of the unstiffened and the stiffened shells correspondingly.

If the parameters h_0, l, n_r and k are given then ratio M_s/M_0 depends only on a and $d = h/h_0$:

$$F(a,d) = \frac{M_s}{M_0} = d + Aa^2, \quad A = \frac{n_r k}{l h_0}. \tag{26}$$

The fundamental vibration frequency ω_0 of the unstiffened cylindrical shell of the thickness h_0 can be found by the approximate formula, following (2) and (22):

$$\omega_0^2 = \frac{E\lambda_1}{\rho R^2} = \frac{h_0 E\beta_1^2}{\sqrt{3\sigma}\rho R^2} \tag{27}$$

The approximate formula for the fundamental frequency ω_1 of the stiffened shell of the thickness h follows from (2) and (24):

$$\omega_1(\eta) = \frac{hE\beta_1^2}{\sqrt{3\sigma}\rho R^2} \begin{cases} \sqrt{1+\eta}), & \eta \le \eta^*, \\ n^2, & \eta \ge \eta^*. \end{cases} \tag{28}$$

For the ring with rectangular cross-sections of thickness a and width $b = ka$ the dimensionless moment of inertia of the ring cross-section is $I = ab^3/12$. Substituting I into second formula (18) we get

$$\eta = \frac{Ba^4}{d^3}, \quad B = \frac{\sigma n k^3}{h_0^3 l}. \tag{29}$$

We seek the minimum value of function $F(a,d)$ under the condition $\omega_0 = \omega_1$. Taking into account formulae (27–29) we can represent this condition in the form

$$d = d_* = 1/n^2 \quad \text{for} \quad \eta \ge \eta^*, \quad d^2(1+\eta) = 1 \quad \text{for} \quad \eta \le \eta^*. \tag{30}$$

In case $\eta = \eta_*$ it follows from condition (30) that

$$d = d_*, \quad a = a_* = (\eta_* d_*^3/B)^{1/4}, \quad F = F_* = d_* + Aa_*^2.$$

If $\eta \ge \eta_*$ then

$$d = d_*, \quad \eta = \frac{Ba^4}{d_*^3}, \quad \eta_* = \frac{Ba_*^4}{d_*^3}.$$

Since

$$a > a_*, \quad F(a,d) = d_* + Aa^2 > F_*$$

and F_* is the minimum of function F for $\eta \ge \eta_*$.

Assume that $\eta \le \eta_*$. Then

$$d \le 1, \quad a = \left(\frac{d-d^3}{B}\right)^{1/4}, \quad F(a,d) = f(d) = d + \gamma\sqrt{d-d^3}, \quad \eta = \frac{1}{d^2} - 1,$$

where $\gamma = A/\sqrt{B}$. Taking into account that $\eta_* = 1/d_*^2 - 1$ we obtain inequality $d \ge d_*$. Let us prove that the function $f(d)$ given in the interval $[d_*, 1]$ attains its minimum value at $d = d_*$.

The first and second derivatives of $f(d)$ are

$$f'(d) = 1 + \frac{\gamma(1-3d^2)}{2\sqrt{d-d^3}}, \quad f''(d) = -\gamma\left[\frac{(1-3d^2)^2}{4(d-d^3)^{3/2}} + \frac{3d}{\sqrt{d-d^3}}\right].$$

It follows from the inequality $n \ge 2$ that $d_* = 1/n^2 \le 1/4$ and $f'(d_*) > 0$. In view of

$$\lim_{d\to 1} f'(d) = -\infty$$

the function $f'(d)$ has the root $d = d_1$ in the interval $[d_*, 1]$. This root is unique because $f''(d) < 0$ and the function $f'(d)$ decreas for $d \in [d_*, 1]$. Hence the function $f(d)$ attains its maximum value at the point $d = d_1$ and

$$\min_{d\in[d_*,1]} f(d) = \min[f(d_*), 1].$$

because $f(1) = 1$. It is clear that one should choose the parameters of the stiffened shell so that the inequality

$$F(a_*, d_*) = f(d_*) = d_* + \gamma\sqrt{d_* - d_*^3} < 1$$

was satisfied. Otherwise the mass of the stiffened shell will be larger than the mass of the unstiffened one. If $f(d_*) < 1$ then the function $f(d)$ attains its minimum value at the point $d = d_*$. For all considered further examples the inequality $f(d_*) < 1$ holds.

Thus for all values of η

$$\min_{a,d} F(a, d) = F(a_*, d_*) = d_* + Aa_*^2,$$

where

$$d_* = \frac{1}{n^2}, \quad a_* = \left(\frac{\eta_* d_*^3}{B}\right)^{1/4} = \left(\frac{d_* - d_*^3}{B}\right)^{1/4} \tag{31}$$

are the optimal parameters.

The optimal value of the parameter η is η_*. Hence, the effective stiffness η_v^* is at the same time the optimal stiffness ensuring the minimal value of the ratio $F = M_s/M_0$.

7 NUMERICAL EXAMPLE

Consider the freely supported unstiffened shell of the thickness $h_0 = 0.01$ and the freely supported shell of the thickness h stiffened by $n_r = n - 1$ rings with square cross-sections for which $k = 1$. The masses of the stiffened and unstiffened shells are M_s and M_0 correspondingly. Both shells have the same length $l = 4$ and Poisson's ratio $\nu = 0.3$.

The values of the optimal parameters d_*, a_* and the ratio M_s/M_0 for various n_r are given in Table 1.

n_r	d_*	a_*	M_s/M_0
1	0,250	0.0268	0.268
2	0,111	0.0200	0.131
4	0,040	0.0137	0.059
6	0,020	0.0106	0.037
8	0,012	0.0088	0.028

Table 1: Optimal values of the parameters vs. n_r.

For the shells under consideration, the ratio M_s/M_0 decreases with the number of the rings, n_r. The mass of the optimal shell stiffened by eight rings is about 35 times less than the mass of the unstiffened shell which has the same fundamental vibration frequency as the stiffened shell. The ratio M_s/M_0, as a function of n_r and k is shown in Table 2.

The ratio M_s/M_0 decreases when k increases, but the suggested approximate approach is applicable only in the case $ka \ll 1$, since we use the beam model of the ring. For large values

	The ratio M_s/M_0.		
n_r	$k=1$	$k=3$	$k=5$
1	0.268	0.260	0.258
2	0.131	0.123	0.120
4	0.059	0.051	0.048
6	0.037	0.030	0.028
8	0.028	0.021	0.019

Table 2: The ratio M_s/M_0 vs. n_r and k.

of k, the ring is wide and it must be treated as an annular thin plate. From the other side if value of k is large the optimal thickness of the rings, a_*, is very small therefore this case is not interesting for applications.

For an estimation of accuracy of asymptotic results the FEM program package ANSYS was utilized. Geometric dimensions and material properties of the unstiffened shell are:

$$R = 0.2 \text{ m},\ l = 4,\ h_0 = 0.01,\ E = 206 \text{ GPa},\ \rho = 7860 \text{ kg/m}^3,\ \nu = 0.3.$$

According formula (27) the approximate value of the fundamental frequency of this shell is 249 Hz. The FEM program gives the fundamental frequency 283 Hz.

In case $n_r = 1$, $k = 3$ the optimal parameters of stiffened shell calculated by means of (31) are $d_* = 0.25$, $a_* = 0.0117$, and the ratio $M_s/M_0 = 0.26$. The approximate value of the fundamental frequency is 249 Hz.

The fundamental frequency of such stiffened shell computed by FEM is equal 264 Hz. The numerical analysis with use of the program package ANSYS has shown, that for $d = 0.292$, $a = 0.0117$ and $b = 6a$ the fundamental frequency of the stiffened shell, 283 Hz, coincides with frequency of the unstiffened shell. The ratio $M_s/M_0 = 0.312$ corresponding to these parameters on 17% is more than its asymptotic approximation, $M_s/M_0 = 0.26$.

8 CONCLUSIONS

The linear differential equations describing free vibrations of thin shells contain the dimensionless shell thickness as a small parameter. The asymptotic technique presented in this paper allows to obtain the simple approximate formulae for the lowest natural vibration frequencies of ring-stiffened shells. These formulae have been used for the evaluation of optimal parameters corresponding to the shell of the minimal weight, having a given fundamental frequency. The solution of the problem of the optimization is obtained in form of closed-form expressions (31). Calculations shows that the mass of the optimal stiffened shell can be about 35 times less than the mass of the unstiffened shell which has the same fundamental vibration frequency.

The numerical evaluation of the optimal parameters of the stiffened shells is time-consuming. Formulae (31) can be used to find first approximation of optimal shell design. Asymptotic results are in satisfactory agreement with the ones obtained by FEM.

REFERENCES

[1] J.T.S. Wang, Orthogonally stiffened cylindrical shells subjected to internal pressure, *AIAA Journal*, **3**, 455–461, 1970.

[2] B. Yang, and J. Zhou, Analysis of ring-stiffened cylindrical shells, *J. of Applied Mechanics*, **62**, 1005–1014, 1995.

[3] J. Tian, C.M. Wang, S. Swaddiwudhipohg, Elastic buckling analysis of ring-stiffened cylindrical shell under general pressure loading via the Ritz method, *Thin Walled Structures*, **35**, 1–24, 1999.

[4] C.T.F. Ross, P. Haynes, W.D. Richards, Vibration of ring-stiffened circular cylinders under external water pressure, *Computers & Structures*, **60**, 1013–1019, 1995.

[5] S.B. Filippov, Buckling, vibrations and optimal design of ring-stiffened thin cylindrical shells. *Advances in Mechanics of Solids. World Scientific Publishing Co Ltd.* 17–48, 2006.

[6] P.E. Tovstik, A. L. Smirnov. *Asymptotic methods in the buckling theory of elastic Shells*. World Scientific, Singapore, 2001.

[7] J. Awrejcewicz, I.V. Andrianov, L.I. Manevitch, *Asymptotic approaches in nonlinear dynamics*. Springer, Berlin, Heidelberg, 1998.

[8] S.B. Filippov, E. Haseganu, Low-frequency vibrations of a thin cylindrical shell joined with an annular thin plate. *Trans. of CSME* **27**, 169–178, 2003.

COMPDYN 2013
4th ECCOMAS Thematic Conference on
Computational Methods in Structural Dynamics and Earthquake Engineering
M. Papadrakakis, V. Papadopoulos, V. Plevris (eds.)
Kos Island, Greece, 12–14 June 2013

COMPUTATIONAL ASSESSMENT OF THE PROGRESSIVE COLLAPSE OF A FIVE STOREY STRUCTURE CONSIDERING TWO DIFFERENT BUILDING CODES

Cláudio E. M. Oliveira[1,2], Péter Z. Berke[2], Ricardo A. M. Silveira[1] and Thierry J. Massart[2]

[1] Federal University of Ouro Preto (UFOP)
Departamento of Civil Engineering –Graduate Program in Civil Engineering (PROPEC)
Campus Morro do Cruzeiro. Ouro Preto, MG. 35400-000. Brazil.
claudioernani@yahoo.com.br; ricardo@em.ufop.br

[2] Université Libre de Bruxelles (ULB)
Building Architecture and Town Planning (BATir) Department CP 194/2
Av. F. D. Roosevelt, 50, 1050, Brussels. Belgium.
pberke@batir.ulb.ac.be; thmassar@batir.ulb.ac.be

Keywords: Progressive Collapse, Structural Safety, Multiscale Analysis, Nonlinear Analysis, Eurocode, ABNT- NBR 6118.

Abstract. *The analysis and understanding of the progressive collapse of buildings plays significant role on the search for structural safety. The present work proposes the association of a corotational formulation, plasticity and a sectional degradation model for the analysis of reinforced concrete (RC) buildings designed in accordance to fib [1] and Eurocode [2] and also the Brazilian building code (ABNT - NBR 6118) [3]. The model makes use of a layered Euler/Bernoulli-based beam formulation and takes into account both nonlinear and dynamic aspects. The corotational formulation used for including geometrical nonlinearities is similar to the one proposed in [4]. The material nonlinearity is based on a one-dimensional elasto-viscoplastic model. A sudden column loss approach is considered, turning the formulation into a general one for dynamic analysis of planar RC frames. Also, by discretizing the transversal section into layers, it is possible to tackle the problem in a multiscale approach [5]. The chosen structures intentionally assume the minimum requirements for the design of multi-storey edifices that are proposed by fib [1] – Eurocode [2] and ABNT - NBR 6118 [3], being used to verify if these requirements are sufficient for enforcing structural safety and also to verify the major differences between those two building criteria concerning progressive collapse.*

1 INTRODUCTION

In the last few decades, progressive collapse (PC) has been addressed by many authors as a catastrophic nonlinear dynamic behavior of tall buildings which can lead to human and financial losses [6 - 9]. Its occurrence is connected to the redistribution of global loads after the loss of one or more key structural elements which, in turn, causes changes in the loading on the sectional level of these elements. Computational PC analysis not only tries to answer the question of whether a building will fail or not after such an initial structural damage, but may also allow the identification of parts of that building that could be reinforced or architectonically modified in order to prevent the occurrence of PC; thereby diminishes losses by keeping, as much as possible, the stability of the remaining structure. This is the reason why the identification of key elements and the quantification of the necessary structural robustness to prevent progressive collapse are subject to intensive research [10 - 12].

Considering that requirements of European and Brazilian codes for reinforced concrete structures are different, they would result for similar structures in different designs in terms of loads, sections, reinforcement schemes and, consequently, structural robustness. This work has the main purpose of comparing the PC structural response of a five storey building made of reinforced concrete, keeping the same architectural design but assuming the minimum requirements established by Eurocode [2] and ABNT - NBR 6118 [3], therefore leading to two structurally different planar frames with respect to element cross sections, reinforcement scheme and reinforcement ratio. The architectonic design of the analyzed building has been previously presented by Irribarren [5] and depicts a five-storey / eight-bay building (18x40 meters) made of reinforced concrete. The Eurocode based design was carried out using the Buildsoft commercial software, Diamonds [13]. The same building was also structurally designed on Cypecad, a software by Cype [14], in accordance with the Brazilian building code. More detailed information on these models is provided in the next section. This methodology is relevant since the obtained structures correspond to realistic designs, i.e. structures that could actually be built. The resulting designs are presented in Section 2.

The PC behavior of the above mentioned models is investigated in a multiscale approach [5], and takes into account nonlinear effects featured by the material behavior, i.e. strain rate dependent elastic-plastic behavior, under dynamic loading. Geometrically nonlinear effects (allowing for the representation of catenary effects) are here included in the multiscale framework and investigated by means of a corotational formulation [4]. The resulting numerical tool is presented in Section 3.

The obtained numerical results are compared in terms of damage extent correlated to the different structural designs. The results of the simulations and comparisons of structural designs obtained by the two different building codes are presented in Section 4 followed by the conclusions and perspectives of this work in Section 5.

2 STRUCTURAL DESIGN

This section is aimed at the description of the planar frame models used for the numerical PC analysis, with an emphasis on the loads and assumptions made during the process of structural design.

The architectural model comprises a 18 meter high office building composed of five floors. The ground floor is six meters high and each of the upper floors is three meters high. The 48 meters long facade is equally divided in eight bays and the unit depth of 6 meters. Progressive collapse is simulated by assuming the loss of the ground column located on the building's left side (Fig. 1).

Floor loads were distributed along the beams' length, in a way that the model could be analyzed as if it was a planar frame. Concrete slabs of 30 cm thickness were computed for the Eurocode based model and 13 cm thick slabs for the one based on the Brazilian building code. Live and dead loads are summarized in Tab. 1. The total load, shown in the same Table, assumes the combination of the total dead load value and 25% of the live loads, as recommended by GSA [10]. Self-weight load of beams and columns is calculated accordingly to the transversal section of the structural element, which is multiplied by the value of reinforced concrete weight density (24 kN/m^3). Analogous procedure is adopted for calculating the self-weight of the floors, i.e. multiplying transversal sectional area by the depth of the floor, and then by reinforced concrete density.

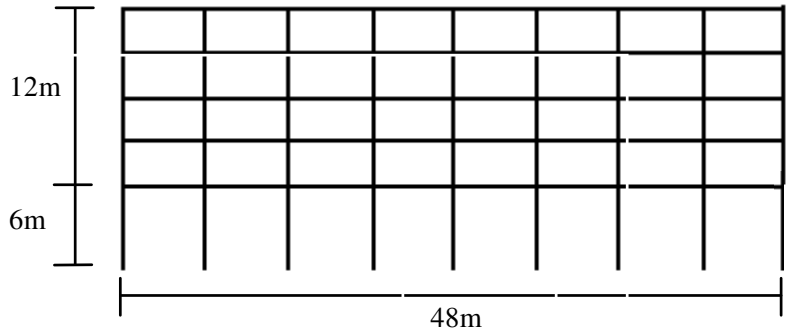


Figure 1: Architectural design [5].

	Eurocode based design			**ABNT - NBR 6118 based design**		
Loads (kN/m)	Dead	Live	Total	Dead	Live	Total
Floor Beams	43.2	18	47.7	18.7	12	21.7
Roof Beams	43.2	6	44.7	18.7	6	20.2

Table 1: Recommended beam loads.

As can be seen in Tab. 1, the value of the total loads obtained for the Brazilian reinforced concrete building code [3] is much smaller than the one obtained for Eurocode [2]. Due to this difference in the load levels, the structural analysis results in different sections of the columns and beams as well as their reinforcement schemes. In order to have a good agreement with guidelines applied in the practical construction, some requirements need to be defined before the structural designing process. These requirements are:

- all floor beams are the same, i.e. no difference regarding loads was considered from floor to floor;
- all columns are the same, i.e. although floor columns bear smaller loads, they have the same section and reinforcement scheme as ground columns;
- height and width of a structural element are constant along the length of that element;
- the concrete envelope (layer of concrete that covers steel bars) is of 5 cm and 2.5 cm for Eurocode and ABNT - NBR 6118 based designs, respectively;
- bottom reinforcements are continuous in both designs;
- both structural designs consider continuity of 2/3 of the top beam reinforcements (Fig. 2, Fig. 3) ;

Additionally, in the numerical simulations:

- Stirrups are considered during design, but not represented in input data for PC analysis.

Reinforcement schemes for both designs are shown on Figs. 2 and 3.

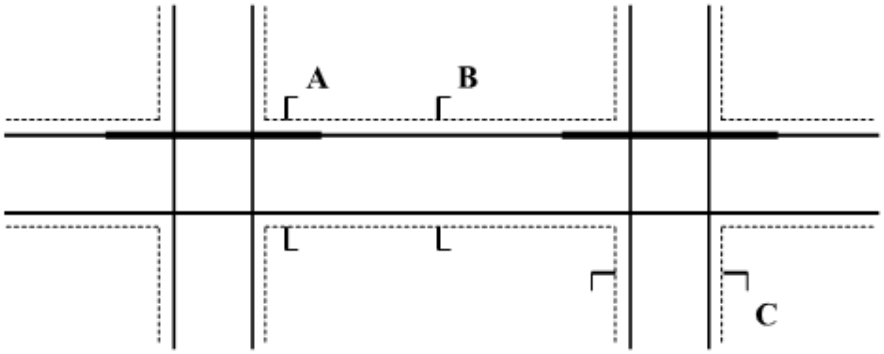


Figure 2: Reinforcement continuity [5].

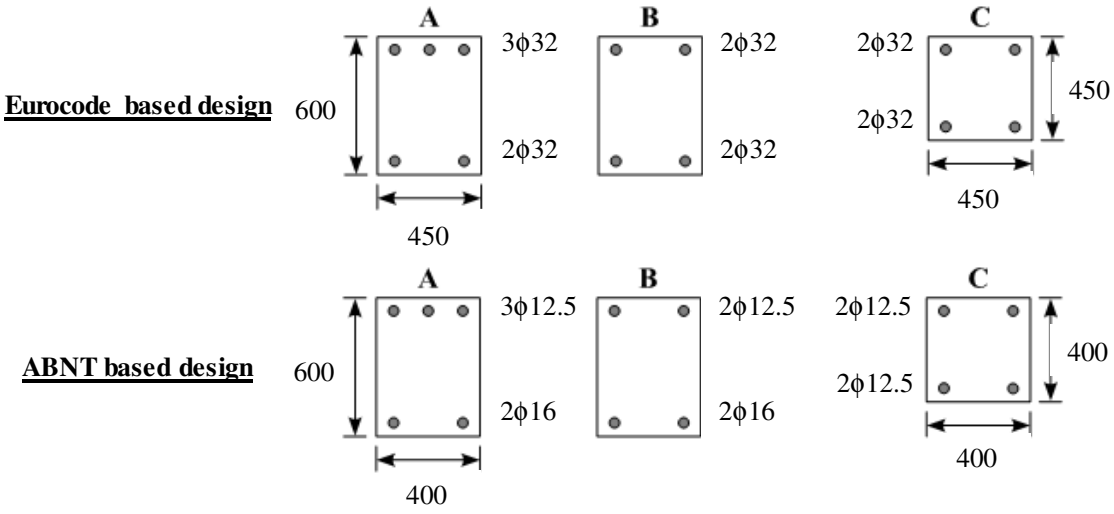


Figure 3: Reinforcement schemes (A, B and C correspond to the sections defined on Fig. 2).

3 FINITE ELEMENT FORMULATION: MULTILAYERED BEAM APPROACH, AND REPRESENTED NONLINEARITIES

The main contribution of this work from a computational point of view is the coupling of the multilayered computation of sectional stresses [5] and the geometrically nonlinear kinematics issued from a corotational Bernoulli beam formulation. This section summarizes the main ingredients of the numerical modeling tool. It presents aspects of the corotational formulation used for introducing nonlinear geometric effects in the multiscale numerical formulation, as well as the adopted material constitutive properties and the governing equations in dynamics.

3.1 Corotational beam kinematics

Geometrical nonlinear effects, as catenary actions, are the result of the interaction of both external and internal forces, and the *deformed shape of a structure*. Works as Batini *et al.* [15] and Souza *et al.* [16] have demonstrated the importance of considering these effects when analyzing composite structures. Dat and Hai [17] have also demonstrated that catenary effects may play an important role on mitigating PC. In this work, the beam's nonlinear kinematics represented by a corotational formulation allows the investigation of possible catenary effects developed in the studied problems.

A corotational formulation, as presented in Crisfield [4] and Batini [18], is a reinterpretation of the deformation of a beam element or, in the most general case, a tridimensional body. This reinterpretation consists in not using the same global reference system in which the structure is inserted for the calculation of strain and displacements of each element but to assume individual local reference systems for these elements instead (Fig. 4), decoupling rigid body rotation from deformation [18].

To implement the corotational formulation it is necessary to define the relation between the displacements in the global (structural) reference system, $\{q_e\}^T = \{u_1 \quad w_1 \quad \theta_1 \quad u_2 \quad w_2 \quad \theta_2\}$, and the ones in the local system, $\{\bar{q}_e\}^T = \{\bar{u} \quad \bar{\theta}_1 \quad \bar{\theta}_2\}$, as defined in Fig. 4. If l_f, l_i and α denote the deformed length, the initial length and the rigid body rotation of the element, respectively, the local kinematic variables are defined by:

$$\begin{bmatrix} \bar{u} \\ \bar{\theta}_1 \\ \bar{\theta}_2 \end{bmatrix} = \begin{bmatrix} l_f - l_i \\ \theta_1 - \alpha \\ \theta_2 - \alpha \end{bmatrix} = \begin{bmatrix} l_f - l_i \\ \theta_1 - \beta - \beta_0 \\ \theta_2 - \beta - \beta_0 \end{bmatrix} \tag{1}$$

where β represents the current angle between the element and the global reference system, and β_0 represents the original value of this angle in the undeformed configuration.

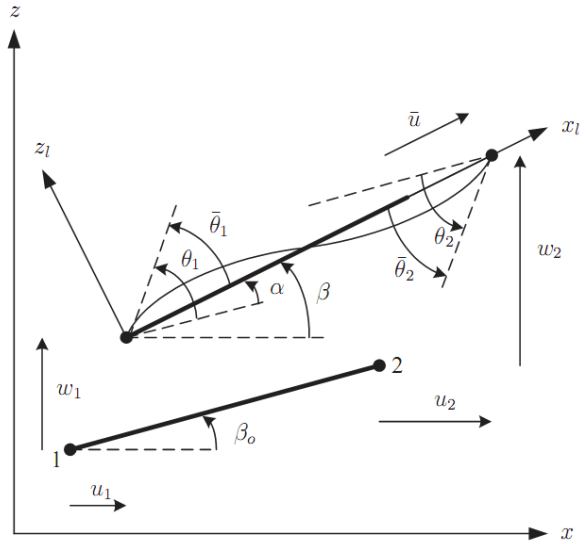


Figure 4: Corotational reference system and kinematic variables [18].

Horizontal displacements are interpolated by using a linear function, while a cubic one is used for vertical displacement of the beam element (Eq. 2). Consequently, axial strain and curvature are calculated through Eq. 3.

$$u = \frac{x}{L}\bar{u}$$
$$w = x\left(1-\frac{x}{L}\right)^2\bar{\theta}_1 + \frac{x^2}{L}\left(\frac{x}{L}-1\right)^2\bar{\theta}_2 \tag{2}$$

Technical information on how the internal force vector and the stiffness matrix of the finite element are derived can be found in [4] and [18].

3.2 Multilayer discretization of an Euler-Bernoulli beam

The formulation deals with a layer discretization of the transversal section for determining stresses in the section of an Euler-Bernoulli beam finite element. Internal forces are obtained from the integration of sectional stresses over three Gauss points along the length of the element.

The discretization of the transversal sections, defined at the Gauss points along the length of the beam, consists of the portioning of the reinforced concrete (composite) section into longitudinal layers (Fig. 5). Note that this produces a multilevel nature that links the dynamic equilibrium on the structural level to the sectional level.

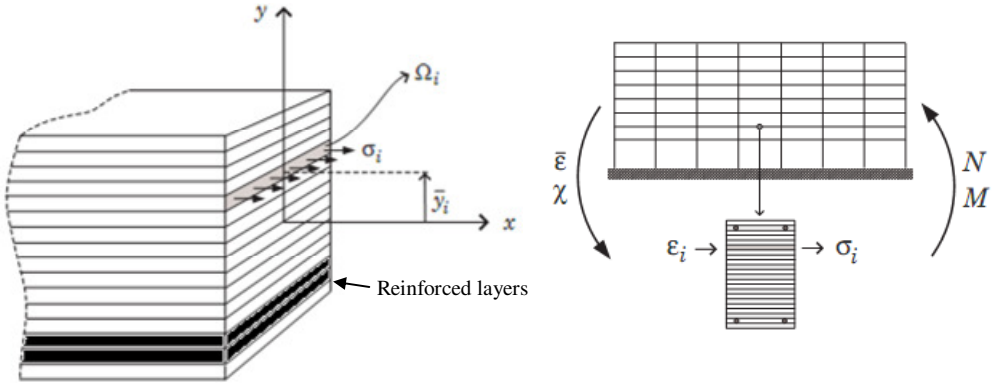


Figure 5: Multilayer discretization of a beam section and shceme of the multiscale framework [5].

The average axial strain and beam curvature computed at an integration point (Eq. 3) are used to obtain the layer total (axial) strain (Eq. 4).

$$\epsilon = \frac{\partial u}{\partial x} = \frac{\bar{u}}{L}$$
$$\chi = \frac{\partial^2 w}{\partial x^2} = \left(-\frac{4}{L}+\frac{6}{L^2}x\right)\bar{\theta}_1 + \left(-\frac{2}{L}+\frac{6}{L^2}x\right)\bar{\theta}_2 \tag{3}$$

$$\epsilon_i = \bar{\epsilon} - \bar{y}_i\chi \tag{4}$$

where,for each layer *i,* at an integration point $\bar{\epsilon}$ is the beam axial strain, $\bar{y}_i$ is the position of layer's center of mass in reference to the section's neutral axis, χ is the beam curvature and ϵ_i is the total strain.

Then, using the nonlinear constitutive relationships for concrete and steel, it is possible to determine the one-dimensional stress acting in each layer (σ_i). At each integration point, the section's generalized stresses are obtained using:

$$\begin{bmatrix} N \\ M \end{bmatrix} = \begin{bmatrix} \sum \sigma_i \Omega_i \\ -\sum \sigma_i \overline{y}_i \Omega_i \end{bmatrix} \tag{5}$$

where σ_i is the one-dimensional stress of layer *i,* Ω_i is the cross-sectional area of the layer and $\begin{bmatrix} N & M \end{bmatrix}^T$ is the vector of generalized stresses ($\sum^{gen}$).

Together with the generalized stresses, the matrix $[B]$ composed of the derivatives of the interpolation functions is used to obtain the internal force vector, as follows:

$$\left\{ f_e^{\text{int}} \right\}^T = \left\{ f_1^x \quad f_1^y \quad c_1 \quad f_2^x \quad f_2^y \quad c_2 \right\} = \int_{V_e} [B]^T \left\{ \sum^{gen} \right\} dV \tag{6}$$

One of the main advantages of this approach is that it makes possible the physical representation of the reinforcements within the cross-section. Another advantage is the inclusion of a gradual sectional degradation effect, consequence of progressive layer failure considering nonlinear constitutive relationships (see Sect. 3.3). Figure 6 exemplifies the stress pattern on the sectional level of an element. The use of a post processing tool allows the identification of the level of stress in each layer and the state of the layer (e.g. elastic/plastic/failed) by using different colors.

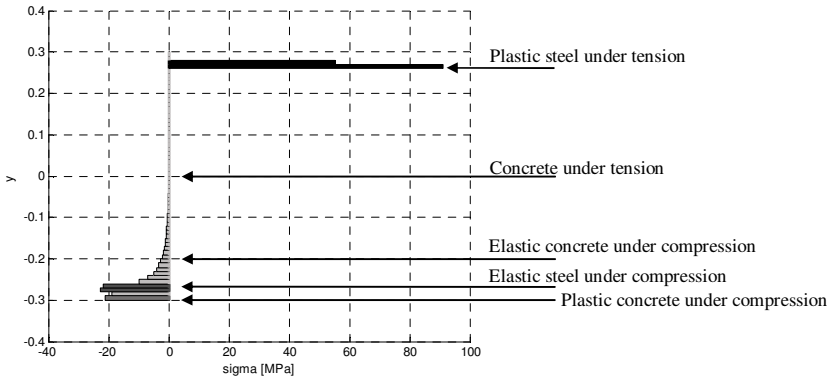


Figure 6: Example of layer stress and layer state plot for a given beam section.

3.3 Constitutive models for concrete and steel

According to Eurocode [2] and ABNT - NBR 6118 [3], class C30 concrete and S500 steel, and C20 concrete and CA50 steel were used for the structural designs, respectively. The constitutive model for these materials is described through a bilinear approximation of the stress-strain behavior as presented below.

a) Concrete

The modeling of concrete behavior was based on recommendations established by [2], [1] and [19], and is depicted on Fig.7. The following assumptions were made for defining this simplified model:

- although concrete develops moderate stresses when working under tension, any structural strength due to this kind of loading is not taken into account, i.e. once concrete is under tension it is considered to be fully cracked and stresses are neglected;
- strains and stresses are proportional during the elastic regime as recommended by [2], instead of the nonlinear curve proposed by [1] and [19]. Young's moduli were set as 32 GPa for C30 and 25 GPa for C20 concrete, respectively;
- for quasi-static loading conditions, the plastic regime is represented by a plateau on the level of 37.9 MPa for C30 concrete and 20 MPa for C20 concrete (Fig. 7);
- the maximum strain under compression in both types of concrete is defined as 0.35%, after which any increase in the strain level will immediately decrease the stress to zero and keeps it at this level in the subsequent loading steps. In this work, this assumption associated with the multilayer discretization allows the investigation of material degradation due to concrete failure (crushing).

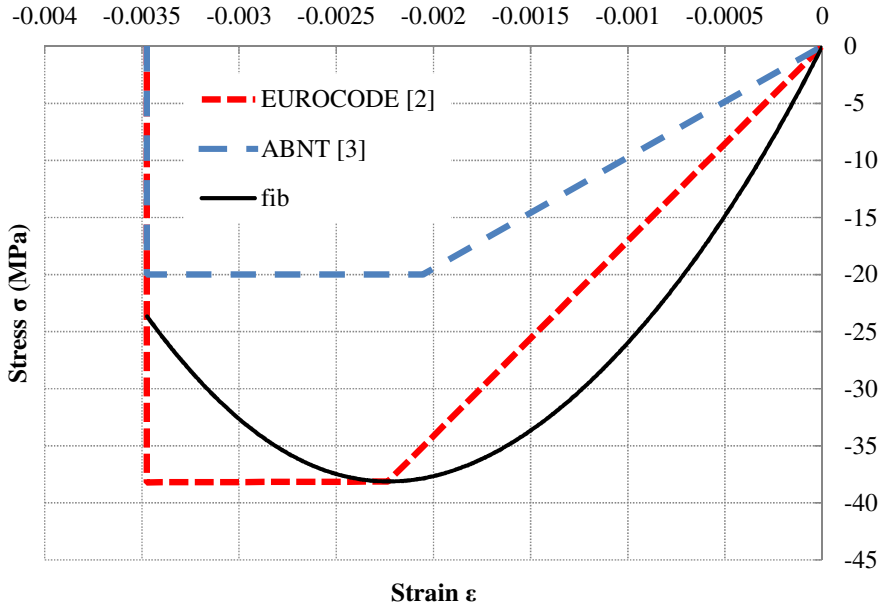


Figure 7: Constitutive model – concrete in compression for quasi-static loading.

b) Steel

According to [2] and [3], the bilinear curve on Fig. 8 represents the correlation between stress and strain for steel under quasi-static loading conditions. The following additional information can also be related to the constitutive behavior of S500 steel and CA50 steel:

- the steel behavior in tension is analogous to the one in compression;
- the steel Young's modulus in the elastic regime, yield stress and ultimate strain are equal to 200 GPa, 500 MPa and 4%;
- just as it was assumed for concrete, stresses in the layers vanish as the strain reaches values larger than 4%, representing steel fracture;
- the ratio between ultimate stress and yield stress is equal to 1.06 [5].

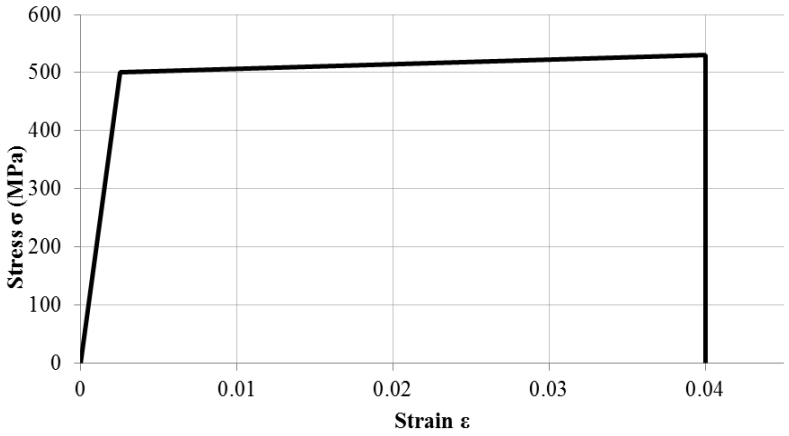


Figure 8: Constitutive model – steel for quasi-static loading

In order to account for the strength enhancement provided by the strain rate dependence of both steel and concrete material behavior [20 - 21], the constitutive models defined above are extended by a strain rate dependent material behavior. The Young's modulus of concrete is set as dependent on the strain rate [5].

To include the strain rate effects in the irreversible behaviour of concrete and steel, a Perzyna type of viscoplastic model is used [22], introducing viscous terms in the constitutive laws. The viscoplatic strain rate used in [5] and that was also used in the present work is a function of the overstress (f) value and is given as follows:

$$\dot{\epsilon}^{vp} = \frac{1}{\eta}\left\langle \frac{f}{\bar{\sigma}_0} \right\rangle^N \frac{df}{d\sigma} \tag{7}$$

where

$\dot{\epsilon}_{vp}$ = viscoplastic strain rate;

η = viscosity parameter, also dependent on the strain rate [5];

$f = (\sigma - \bar{\sigma})$, yield function that accounts for the overstress;

$N = 1$, viscosity parameter [5];

$\bar{\sigma}_0$ = initial one-dimensional yield stress;

σ = one-dimensional stress;

$\bar{\sigma}$ = current one-dimensional yield stress;

$\langle\ \rangle$ = MacAulay brackets;

3.4 Governing equations in dynamics

Equilibrium in dynamics is represented by the equation below, on which an implicit Newmark integration scheme is applied. Note that no artificial/numerical damping is introduced in the system of equations.

$$\left\{f^{\text{int}}(\{q\},\{\dot{q}\})\right\} + [M]\{\ddot{q}\} = \left\{f^{ext}\right\} \tag{8}$$

where $\left\{f^{\text{int}}\right\}$ represents the internal force vector, dependent on the displacement $\{q\}$ and displacements rates, $[M]$ represents the mass matrix and $\left\{f^{ext}\right\}$ is the external force vector.

Since the internal forces are strain rate dependent, their variation with respect to the displacements, i.e. the structural tangent operator, will also be dependent on those rates and include a viscous damping term (Eq. 9).

$$[K_T^*] = \frac{\partial\left\{f^{\text{int}}(\{q\},\{\dot{q}\})\right\}}{\partial\{q\}} = \left.\frac{\partial\left\{f^{\text{int}}(\{q\},\{\dot{q}\})\right\}}{\partial\{q\}}\right|_{\{\dot{q}\}=cte.} + \left.\frac{\partial\left\{f^{\text{int}}(\{q\},\{\dot{q}\})\right\}}{\partial\{\dot{q}\}}\right|_{\{q\}=cte.} \frac{\partial\{\dot{q}\}}{\partial\{q\}} \tag{9}$$

The second term of (Eq. 9) refers to the viscous damping matrix and introduces damping on the structural level *due to the strain rate dependent (viscoplastic) stress-strain relationships* assumed for the materials.

It is noteworthy that the mass matrix of the beam elements was calculated considering the undeformed shape of the structure and kept constant along the whole analysis in this work. Updating the mass matrix as a function of the displacements of the structure is part of future work [23].

4 ASSUMPTIONS CONCERNING THE NUMERICAL SIMULATION AND SIMULATION RESULTS

To prevent the influence of dynamic effects in the initial loading phase, the structure self-weight and service loads are applied in a large period of time, defined as 1000 s. The sudden removal of the column happens subsequently to this loading process. Column removal is modeled as the decrease of the reaction forces, equivalent to the presence of the column, applied at point E (Fig. 9) in a short period of time (0.01 s). The response of the structure is analyzed for a period of two seconds after column removal.

Each model was discretized into approximately 900 elements. Preliminary studies showed that a number between 40 and 60 layers was appropriate for discretizing the cross-sections of the structural elements, i.e. not too many that would make the analysis unaffordable or too few that would introduce significant errors in the obtained results. Thus, 40 layers were used for the discretization of the columns and 60 for the beams.

Besides the point of column removal (E), other reference points were defined for measuring displacements and stresses during the analysis. These points are shown in Fig. 9. The following nomenclature will be used in this section:

EUCO – Eurocode based model, analysed via corotational formulation;
BRCO – ABNT - NBR 6118 based model, analysed via corotational formulation.

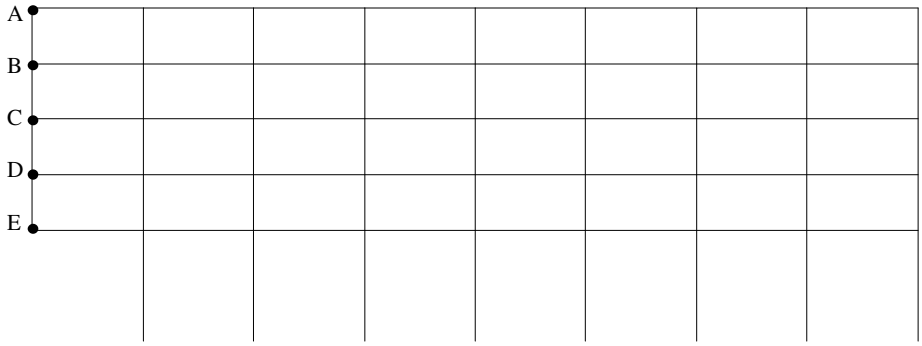


Figure 9: Reference points.

When comparing the final deformed configuration of the EUCO and BRCO models (Figs. 10 and 11), it is clear that the former presents smaller displacements. As shown in Tab. [2], the vertical displacements of BRCO on the reference points are approximately 2.15 times larger than the ones of EUCO. This difference can be associated to the larger sections of the structural elements, to the larger quantity of reinforcement, and to the different material behavior adopted for concrete in the two simulations (Fig. 7). However, it is important to highlight that *both structures were able to overcome the loss of the column and did not initiate the progressive collapse mechanism according to the simulation.*

An additional analysis, using a linear geometric formulation, resulted in displacements 2-3% smaller for both EUCO and BRCO cases. This is believed to be related to the corner position of the removed column that does not benefit from positive catenary effects. However, these effects may play a more important role if an internal column was removed, which can be verified in a future work.

	EUCO	**BRCO**	$V2/V1$
REF. Point	**V1**	**V2**	
A	-0.11700	-0.25007	2.14
B	-0.11924	-0.25523	2.14
C	-0.12134	-0.26021	2.14
D	-0.12349	-0.26525	2.15
E	-0.12645	-0.27208	2.15

Table 2: Vertical displacements at reference points.

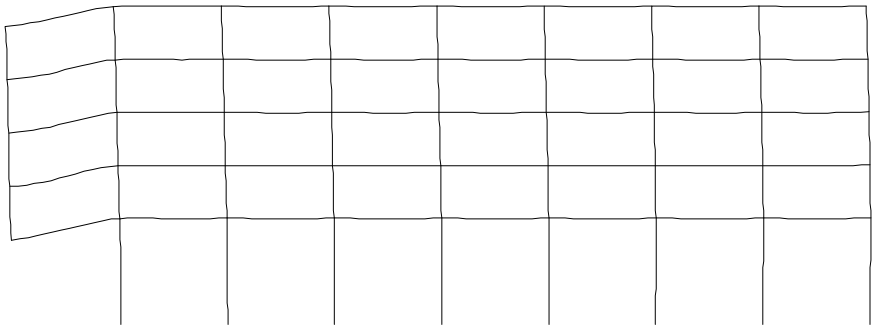


Figure 10: EUCO's deformed configuration (displacements multiplied by 10).

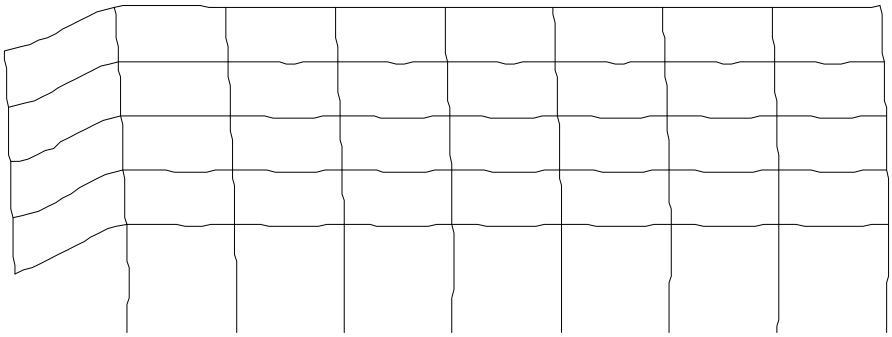


Figure 11: BRCO's deformed configuration (displacements multiplied by 10).

The variation of the vertical displacement of reference point E, after the removal of the column, is represented in Fig. 12 and indicates that although BRCO presents larger displacements, it stabilizes faster than EUCO. The mean displacement value is of approximately 12 cm for EUCO and 25 cm for BRCO. The oscillation observed for the beam's extremity introduces cyclic changes in the pattern of the loading of the structural elements, i.e. repeated reversal of bending moments.

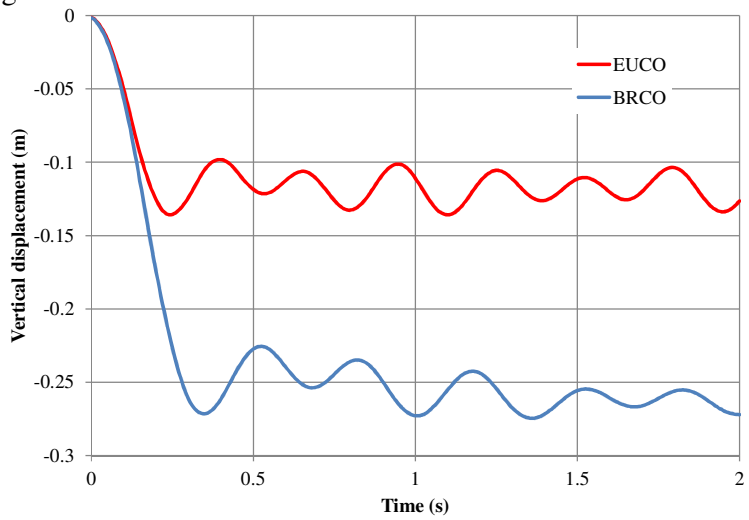


Figure 12: Time variation of vertical displacement at reference point E.

Figures (13) and (14) show that, in terms of plasticity distribution, the effects of the column removal spreads to the whole structure in the BRCO case. For the EUCO case, these effects can barely be identified on other beams than the ones above the removed column. The symbol (•) was used to represent sections in which steel has reached the plastic level and (∇) represents those in which concrete was crushed in less than 30% of the layers. Reinforcement bars did not fail in any of the models, consequently the structures withheld the column removal. It is important to point out that, for EUCO, only the floors immediately above the removed column were affected, which can diminish losses and make it easier to repair the remaining structure.

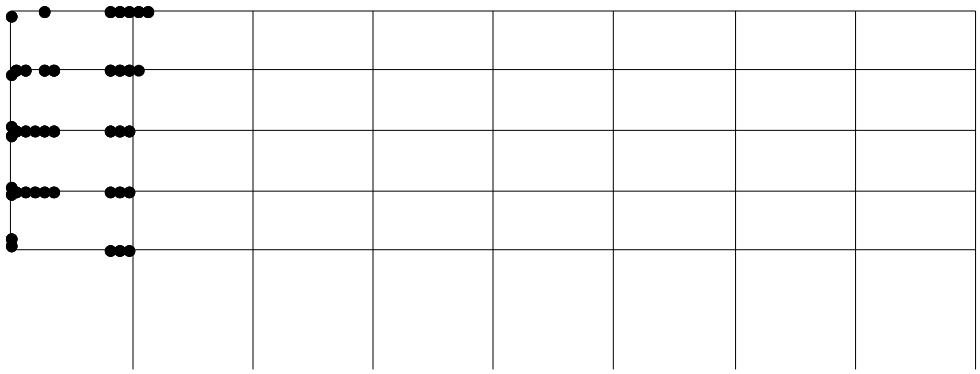


Figure 13: Plasticity distribution at the end of the analysis (EUCO, 2 s after column removal).

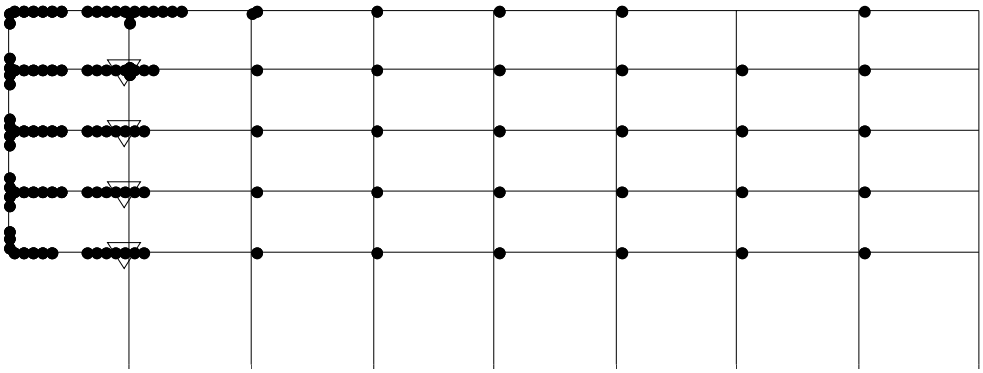


Figure 14: Plasticity distribution at the end of the analysis (BRCO, 2 s after column removal).

5 CONCLUDING REMARKS

This work presents a first attempt to combine dynamic effects, material and geometrical nonlinearities, and sectional degradation through a multilevel approach using a multilayer formulation for the numerical investigation of progressive collapse. Its main focus was to compare two structures, designed in accordance to the minimum requirements of two different building codes, from Europe and from Brazil. Details on the design and assumptions made during the design process were provided, as well as a summary of the applied numerical formulation and the material constitutive behavior.

The slenderer Brazilian structure presented larger displacements and the removal of the column affected the whole structure, in a distributed way. Although none of the structures triggered the progressive collapse mechanism, these results point to a better performance of the European design process, in which only the floors immediately above the removed column were affected.

Future research includes the updating of the structure mass matrix as a function of its deformation, the utilization of constitutive laws that couple plasticity and damage (elastic stiffness degradation), the use of a formulation including shear effects, and the refining of the structural input data, as for example, representing variations of the element's cross-sectional area along the its length.

ACKNOWLEDGMENTS

The authors would like to thank CAPES, CNPq, FAPEMIG, FNRS, Fundação Gorceix and PROPEC for the financial support, and Eng. Everton Batelo, for helping with the structural design of the ABNT - NBR 6118 based structure.

REFERENCES

[1] International Federation for Structural Concrete (fib), *Constitutive modelling of high strength/high performance concrete, State-of-art report*, fib Bulletin **42**, 2008.

[2] EN 1992-1-1, *Eurocode 2: Design of concrete structures - Part 1-1: General rules and rules for buildings*, December, 2004.

[3] ABNT - Associação Brasileira de Normas Técnicas, *NBR 6118: projeto de estruturas de concreto: procedimento*, Rio de Janeiro, 2003.

[4] Crisfield, M. A., *Non-Linear Finite Element Analysis of Solids and Structures, Vol. **I**.* John Wiley & Sons, 1997.

[5] Iribarren, B. S., Berke, P., Bouillard, Ph., Vantomme, J., Massart, T.J., Investigation of the influence of design and material parameters in the progressive collapse analysis of RC structures, *Engineering Structures*, Vol. **33**, 2805-2820, 2011.

[6] Marjanishvili, S., Agnew, E., Comparison of various procedures for progressive collapse analysis, *Journal of Performance of Constructed Facilities*, *Vol. **20***, 2006.

[7] TsaiM-H, Lin B-H., Investigation of progressive collapse resistance and inelastic response for an earthquake-resistant RC building subjected to column failure, *Engineering Structures*, Vol. **30**, 3619–28, 2008.

[8] Kim H-S, Kim J, An D-W., Development of integrated system for progressive collapse analysis of building structures considering dynamic effects, *Advances in Engineering Softwares*, Vol. **40**, 1–8, 2009.

[9] Kwasniewski, L., Nonlinear dynamic simulations of progressive collapse for a multistore building, *Engineering Structures*, Vol. **32**, 1223–35, 2010.

[10] United States General Services Administration (GSA), *Progressive collapse analysis and design guidelines for new federal office buildings and major modernization projects,* Washington DC, 2003.

[11] Izzuddin, B. A., Robustness by design – Simplified progressive collapse assessment of building structures, *Stahlbau*, Vol. **79**, 556–564, 2010.

[12] Khandelwal K., El-Tawil S., Pushdown resistance as a measure of robustness in progressive collapse analysis, *Engineering Structures*, Vol. **33**, 2653-2661, 2011.

[13] Buildsoft NV, *Diamonds 2010 r.01,* http://www.buildsoft.eu (Last access: 07/03/2013).

[14] Cype, Cypecad 2011, http://www.cype.pt/ (Last access: 07/03/2013).

[15] Battini, J-M., Nguyen, Q-H., Hjiaj, M., Non-linear finite element analysis of composite beams with interlayer slips, *Computer and Structures*, Vol. **87**, 904-912, 2009.

[16] Sousa Jr., J. B. M., Oliveira, C. E. M., Silva A. R., Displacement-based nonlinear finite element analysis of composite beam columns with partial interaction, *Journal of Constructional Steel Research*, Vol. **66**, 772 -779, 2010.

[17] Tan, K. H., & Pham, X. D., Membrane actions of RC slabs in mitigating progressive collapse of building structures. *Proceedings of the Design and Analysis of Protective Structures*, Singapore, 2010.

[18] Battini, J-M., *Corotational beam elements in instability problems*, Ph.D Thesis, Royal Institute of Tecnology, Department of Mechanics, Stockholm, Sweden.

[19] International Federation for Structural Concrete (fib), *Practitioners' guide to finite element modelling of reinforced concrete structures. State-of-art report*, fib Bulletin **45**, 2008.

[20] Malvar, L. J, Crawford, J. E., *Dynamic increase factors for concrete*, 28th DDESB seminar, Orlando, FL, USA, 1998.

[21] Bischoff, P. H, Perry, S. H., Compressive behaviour of concrete at high strain rates, *Materials and Structures*, Vol. **24**, 425–50, 1991.

[22] Heeres O. M., Suiker A. S. J., de Borst R., A comparison between the Perzyna visco-plasticmodel and the Consistency viscoplastic model, *European Journal of Mechanics A/Solids*, Vol. **21**, 1–12, 2002.

[23] Le, T-N, Battini, J-M, Hjiaj, M., Efficient formulation for dynamics of corotational 2D beams, *Computational Mechanics*, Vol. **48**, 153-161, 2011.

COMPDYN 2013
4th ECCOMAS Thematic Conference on
Computational Methods in Structural Dynamics and Earthquake Engineering
M. Papadrakakis, V. Papadopoulos, V. Plevris (eds.)
Kos Island, Greece, 12–14 June 2013

NONLINEAR STATIC ANALYSIS OF A PLAN IRREGULAR BUILDING ACCORDING TO EC8 PROVISIONS

Gennaro Magliulo[1], Giuseppe Maddaloni[2] and Edoardo Cosenza[1]

[1] Department of Structures for Engineering and Architecture, University of Napoli Federico II
Via Claudio 21, 80125 Naples, Italy
e-mail: {gmagliul, cosenza}@unina.it

[2] Department of Technology, University of Napoli Parthenope
Centro Direzionale, Isola C4, 80123 Naples, Italy
giuseppe.maddaloni@uniparthenope.it

Keywords: Nonlinear analysis, torsional effects, natural records, r/c frame building, plan irregular building.

Abstract. *The paper deals with the topic of nonlinear static and nonlinear dynamic analyses of multi-storey r/c frame buildings designed according to Eurocode provisions. In particular, the open problem of the extension of N2 method to plan irregular buildings, which makes up for the underestimation of the seismic demand on stiff side of the buildings, is focused. Three methods, which take into account the accidental eccentricity of the mass (due to its uncertainties in the location) are proposed. The main differences between the three nonlinear static analysis methods are: method n.1 combines the displacements of modal response spectrum analysis obtained by the 4 models (associate to 4 positions of the centre mass) by SRSS rule and, for each frame of the multi-storey r/c frame building, the maximum normalized displacement is assumed as reference; method n.2, works on 4 models and only at the end of the procedure combines the results by SRSS rule; method n.3 considers till the end of the procedure the double sign (+ and -) of pushovers. Nonlinear static analyses are carried out using both the "modal" and "uniform" force pattern. The "orthogonal effects", evaluated by SRSS rule, result to be negligible. The results, in terms of pushover curves, frame top displacements and interstory drifts, are compared with the ones obtained by nonlinear dynamic time-history analyses. The input adopted for nonlinear dynamic analysis (7 natural earthquakes) is selected in order to rigorously satisfy the EC8 provisions.*

1 INTRODUCTION

N2 method is one of the most spread methods for nonlinear static analysis: it is provided by EC8 [1] and other modern seismic codes. Since Fajfar [2] published it, its research group is working on its extension to plan irregular buildings, in order to make up for the underestimation of the seismic demand on the stiff side. They [3] proposed to combine the results obtained by pushover analysis of a 3D structural model with the results of a linear dynamic spectral analysis: the former results control the target displacements and the distribution of deformations along the height of the building, whereas the latter results define the torsional amplifications.

Such procedure, as proposed, does not consider that different models are to be computed due to different positions of centre of mass corresponding to different accidental eccentricities.

In the paper three different methods are proposed in order to apply the N2 method to a plan irregular building as formulated by Fajfar, taking into account the accidental eccentricity; such methods, characterised by different levels of accuracy, are described, applied to a three-storey r/c frame building and compared. It represents an enhanced version of the one proposed in Magliulo et al. [4]. The results are shown in terms of pushover curves, frame top displacements and interstory drifts.

Dynamic analyses are performed using a set of natural records fully satisfying EC8 provisions: average, standard deviation of results are considered.

The results reported herein, for sake of brevity, concern a single structure; however they are confirmed by analyses performed at the same seismic level on different buildings.

2 GEOMETRY OF THE BUILDING AND ELASTIC ANALYSIS

The geometry of the analysed three-storey r/c frame building is reported in Figure 1. The interstory height is equal to 3.20 m at all levels; at the first storey the columns section dimensions are 40 cm × 65 cm, while all the beams are 40 cm × 60 cm; at the second storey such dimensions are respectively 40 cm × 60 cm and 40 cm × 55 cm, at the third 40 cm × 55 cm and 40 cm × 50 cm. Column dimensions are kept larger than beam ones in order to take into account the capacity design. 2 m wide balconies are shown in Figure 1 as hatched areas.

Elastic analyses are performed by the computer program SAP2000 [5], according to Eurocode rules and considering a design spectrum soil B type 1 with a design ground acceleration a_g =0.35g. The design is performed according to the High Ductility Class rules, a behaviour factor equal to 2.4 is computed; such value takes into account that according to EC8 the building is "torsionally flexible" and irregular in elevation (the reduction of lateral stiffness from 1st to 2nd storey is larger than 40%).

Concrete characteristic cylinder strength equal to f_{ck}=30 N/mm^2 and steel characteristic yielding strength equal to f_{yk}=430 N/mm^2 are adopted.

3 NONLINEAR MODEL

Nonlinear analyses are performed by means of the computer program CANNY99 [6, 7]. Nonlinearity regards flexural rotations, while all the other deformations are assumed linear. Both beams and columns are characterised by lumped plasticity models; in the latter case for each section two independent nonlinear springs are assigned, one for each orthogonal direction. No axial force-bending moment interaction is considered at plastic hinge.

Bending moment springs are characterised by a tri-linear skeleton curve, defined by cracking and yielding moment and corresponding rotations; the post-yielding stiffness is assumed equal to zero. An elastic-perfectly plastic steel stress-strain diagram is considered, characterised by an yielding strength equal to 530 N/mm^2, computed as mean of tests on more than 200

steel bars performed at the laboratory of Department of Structures for Engineering and Architecture of the University of Naples Federico II.

The yielding and the ultimate rotations are evaluated as provided by EC8 [8] equations (A.10b) and (A.1) respectively, where the already cited average values are assigned to concrete maximum (fc=38 N/mm^2) and steel yielding (fy=530 N/mm^2) strength.

The hysteretic model is Takeda type; the pinching effect is also taken into account.

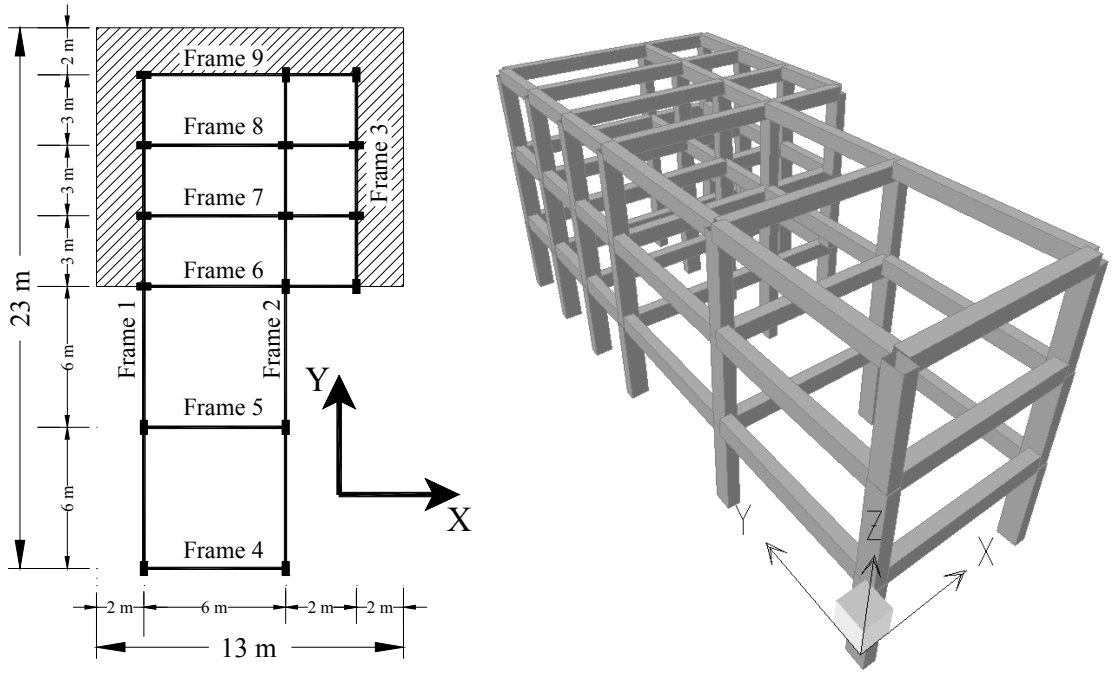


Figure 1: Geometry of the analysed building.

4 NONLINEAR STATIC ANALYSIS

Nonlinear static analyses (NLSA) are performed according to EC8, considering a force distribution proportional for each of the 2 orthogonal directions to the first modal shape in the relative direction by mass distribution ("modal" pattern). The first and the third modes of the building are translational and the square root of the ratio of torsional stiffness to lateral stiffness in each of the 2 orthogonal directions is smaller than the radius of gyration of floor mass in plan [1]; consequently the structure is torsionally flexible and the application of a specific procedure for the estimation of torsional effects is necessary.

Eight analyses, 2 opposite signs for 4 different positions of the centre of mass, are performed. In Figure 2, 2 of the 8 pushover curves in terms of adimensionalised top displacement vs base shear are shown. The bi-linear capacity curve is also presented along with capacity and demand points: "mech" indicates the mechanism of the structure, "ULS" (Ultimate Limit State) and "NC" (Near Collapse Limit State) the attainment in at least one hinge of the rotation value 3/4 Θu and Θu respectively and "t.ULS" the demand corresponding to the EC8 elastic design acceleration spectrum built considering soil type B and ag =0.35g; Θu is the total chord rotation capacity computed according to EC8 empirical formula (A.1) [8].

Figure 2 shows that in the examined case differences between NLSA performed on the same model and along the same direction but with opposite sign are negligible; this conclu-

sion justifies the possibility to consider only one NLSA between the two ones with opposite sign and, in particular, the one with the largest target displacement.

In order to evaluate the torsional effects three variants of the Fajfar's method are proposed and presented in the following; they consider different models characterised by different accidental eccentricities, indicating how to associate modal response spectrum analyses (MRSA) with nonlinear static ones.

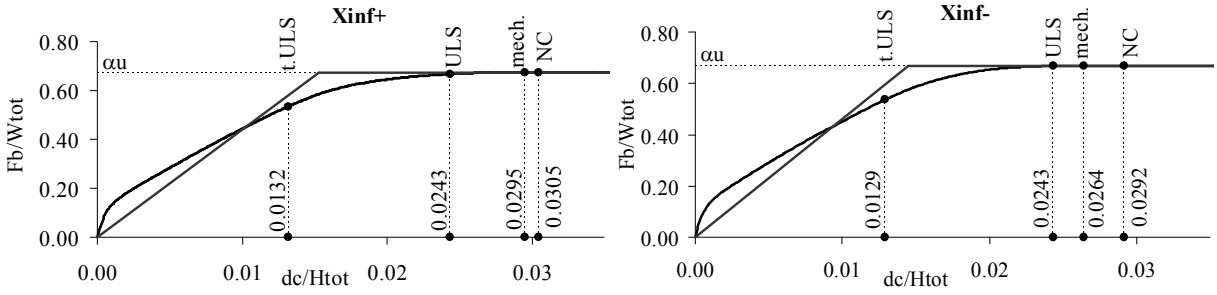


Figure 2: Capacity curves of 2 considered models given by a vertical force "modal" pattern.

4.1 Method n.1

Four modal response spectrum analyses are performed (called X_{inf}, X_{sup}, Y_{dx}, Y_{sx}, clearly depending on the direction of forces and on the position of centre of mass), one for each position of CM; obviously the load is applied along Y direction when CM is moved along X axis and, conversely, it is applied along X direction when CM is moved along Y axis;

The results (in particular top displacements of each frame and of centre of mass) obtained by each MRSA are combined by the SRSS rule:

$$\sqrt{u_{X\,\mathrm{sup}}^2 + u_{Ydx}^2}\ ;\ \sqrt{u_{X\,\mathrm{sup}}^2 + u_{Ysx}^2}\ ;\ \sqrt{u_{X\,\mathrm{inf}}^2 + u_{Ydx}^2}\ ;\ \sqrt{u_{X\,\mathrm{inf}}^2 + u_{Ysx}^2} \tag{1}$$

For each combination and for each frame the following normalized displacement is computed:

$$\eta_{\mathrm{MRSA,i}} = \frac{u_{\mathrm{MRSA,i}}}{u_{\mathrm{MRSA,CM}}} \tag{2}$$

where $u_{MRSA,i}$ is the "i" frame top displacement and $u_{MRSA,CM}$ is the CM top displacement; consequently, 4 $\eta_{MRSA,i}$ are computed for each frame and their maximum is assumed as the reference $\eta_{MRSA,i}$;

Eight nonlinear static analyses are performed, two signs (+ and -) for 4 models and for each model the NLSA with the maximum target displacement (t.ULS) is considered; consequently, 4 normalised displacements are obtained for each frame:

$$\eta_{\mathrm{NLSA,i}} = \frac{u_{\mathrm{NLSA,i}}}{u_{\mathrm{NLSA,CM}}} \tag{3}$$

where $u_{NLSA,i}$ is the "i" frame top displacement and $u_{NLSA,CM}$ is the CM top displacement;

For each frame 4 correction factors are computed:

$$\beta_i = \frac{\eta_{\mathrm{MRSA,i}}}{\eta_{\mathrm{NLSA,i}}} \tag{4}$$

where $\eta_{MRSA,i}$ is the reference one and 4 $\eta_{NLSA,i}$ (eq. 3) are considered;

The seismic demand related to frames on the stiff side of the structure is amplified multiplying all relevant quantities obtained by the 4 nonlinear static analyses by the corresponding correction factors;

The maximum value of demand parameters among the 4 ones given by nonlinear static analyses is considered and compared with the capacity one computed according to EC8 [8].

4.2 Method n.2

Four modal response spectrum analyses (called X_{inf}, X_{sup}, Y_{dx}, Y_{sx}) are performed, as at the 1st step of method n.1;

For each CM position and for each frame, the normalized displacement (eq. 2) is computed. Consequently, four $\eta_{MRSA,i}$ for each frame are obtained;

Eight nonlinear static analyses are performed, two signs (+ and -) for 4 models and for each model the NLSA with the maximum target displacement (t.ULS) is considered; consequently, 4 normalised displacements (eq. 3) are obtained for each frame, as at step 4 method n.1;

Four correction factors (eq. 4), corresponding to the 4 positions of centre of mass, are computed for each frame;

As at method n.1, the seismic demand related to frames on stiff side of the structure is amplified multiplying all relevant quantities obtained by the 4 nonlinear static analyses by the corresponding correction factors;

The results of the four amplified NLSA are combined according to the SRSS rule:

$$\sqrt{E_{X\,sup}^2 + E_{Ydx}^2}\ ;\ \sqrt{E_{X\,sup}^2 + E_{Ysx}^2}\ ;\ \sqrt{E_{X\,inf}^2 + E_{Ydx}^2}\ ;\ \sqrt{E_{X\,inf}^2 + E_{Ysx}^2} \tag{5}$$

where, as already said, “X” and “Y” indicate analysis direction, while “sup”, “inf”, “dx” and “sx” the centre of mass position;

The maximum value of demand parameters among the 4 ones given by SRSS combinations is considered and compared with the capacity one computed according to EC8 [8].

4.3 Method n.3

The first 2 steps are coincident with method n.2;

Eight nonlinear static analyses are performed, two signs (+ and -) for 4 models and, consequently, 8 normalised displacements (eq. 3) are obtained for each frame (as for methods n.1 and n.2 displacements at t.ULS are considered);

Eight correction factors (eq. 4), corresponding to 4 positions of centre of mass and both the signs (+ and -), for each frame are computed: to each $\eta_{MRSA,i}$ correspond 2 $\eta_{NLSA,i}$;

The seismic demand related to frames on stiff side of the structure is amplified multiplying all relevant quantities obtained by the 8 nonlinear static analyses by the corresponding correction factors;

The results of the 8 amplified NLSA are combined according to the SRSS rule:

$$\sqrt{E_{+X\,sup}^2 + E_{+Ydx}^2}\ ;\ \sqrt{E_{+X\,sup}^2 + E_{-Ydx}^2}\ ;\ \sqrt{E_{-X\,sup}^2 + E_{+Ydx}^2}\ ;\ \sqrt{E_{-X\,sup}^2 + E_{-Ydx}^2}\ ;\ \sqrt{E_{+X\,sup}^2 + E_{+Ysx}^2}\ ;$$
$$\sqrt{E_{+X\,sup}^2 + E_{-Ysx}^2}\ ;\ \sqrt{E_{-X\,sup}^2 + E_{+Ysx}^2}\ ;\ \sqrt{E_{-X\,sup}^2 + E_{-Ysx}^2}\ ;\ \sqrt{E_{+X\,inf}^2 + E_{+Ydx}^2}\ ;\ \sqrt{E_{+X\,inf}^2 + E_{-Ydx}^2}\ ;$$

$$\sqrt{E^2_{-Xinf} + E^2_{+Ydx}} \; ; \; \sqrt{E^2_{-Xinf} + E^2_{-Ydx}} \; ; \; \sqrt{E^2_{+Xinf} + E^2_{+Ysx}} \; ; \; \sqrt{E^2_{+Xinf} + E^2_{-Ysx}} \; ; \; \sqrt{E^2_{-Xinf} + E^2_{+Ysx}} \; ; \; \sqrt{E^2_{-Xinf} + E^2_{-Ysx}} \tag{6}$$

where, as already said, "X" and "Y" indicate analysis direction, "+" and "-" its sign and "sup", "inf", "dx" and "sx" the centre of mass position;

The maximum value of demand parameters among the 16 ones given by SRSS combinations is considered and compared with the capacity one computed according to EC8 [8].

Method n.3 provides results, which for sake of brevity are not shown, almost coincident with the ones provided by method n.2. This shows that, even when torsional effects are considered, the sign of pushover does not affect the results and, consequently, it is sufficiently accurate to consider the pushover with the maximum target displacement between the two pushovers with opposite sign.

4.4 Comments on SRSS combination rule

Table 1 shows the increment of frame top displacements due to the evaluation of orthogonal effects by the SRSS rule (eq. 5) of method n.2. In the 1st column the frames are listed, frames 1, 2 and 3 are parallel to Y axis as reported in Figure 1, while frames from 4 to 9 are parallel to X axis; the 2nd and the 3rd column show for the frames 4 to 9 and 1 to 3 respectively the top displacements resulting from (eq. 5), while the 4th and the 5th column present the corresponding displacements obtained by method n.2 before applying the combination (eq. 5); the 6th and the 7th column present the variation in percentage of the results.

It is evident that such variations are negligible; consequently the 6th step of method n.2, i.e. the application of combination (eq. 5), could be suppressed for computing such parameters.

	SRSS applied		SRSS NOT applied		Variation [%]	
Frame	u_x	u_y	u_x	u_y	u_x	u_y
	[m]	[m]	[m]	[m]	[-]	[-]
1	-	0.126	-	0.126	-	0.24
2	-	0.124	-	0.124	-	0.01
3	-	0.133	-	0.133	-	0.14
4	0.148	-	0.147	-	0.19	-
5	0.138	-	0.137	-	0.07	-
6	0.127	-	0.127	-	0.01	-
7	0.127	-	0.127	-	0	-
8	0.129	-	0.129	-	0.02	-
9	0.132	-	0.132	-	0.05	-

Table 1: Estimation of orthogonal effects evaluated by SRSS combination rule: frame top displacements computed according to method n.2.

5 STEP BY STEP NONLINEAR DYNAMIC ANALYSES

Both the horizontal components of a set of 7 earthquakes, i.e. 14 natural records, fully satisfying the EC8 provisions [9] are used for nonlinear dynamic analyses. According to the code, if the response is obtained from at least 7 nonlinear time histories analyses, as for the performed analyses, the average of response quantities should be used as the design value of the action effect E_d in relevant verifications.

Figure 3 shows the elastic spectrum of the 14 records used, along with the average spectrum (smooth thick line), the EC8 elastic design spectrum (black thick line) and the curve whose ordinates are equal to 90% of such spectrum ones (black thin line); SF indicates the value of factors used to scale the records for the purpose to matching code spectrum: only one record is scaled by a low SF equal to 1.08.

The matched code spectrum is the one used for the design of the building analysed, assigning q=1.

As for nonlinear static analyses, top centre of mass and frame displacements are considered. For each of the 4 models obtained moving the centre of mass, the average of the 7 maximum results obtained applying the 7 earthquakes is considered along with the average plus the standard deviation and the maximum of the 7 maximum results; the maximum effect on the 4 models is always considered.

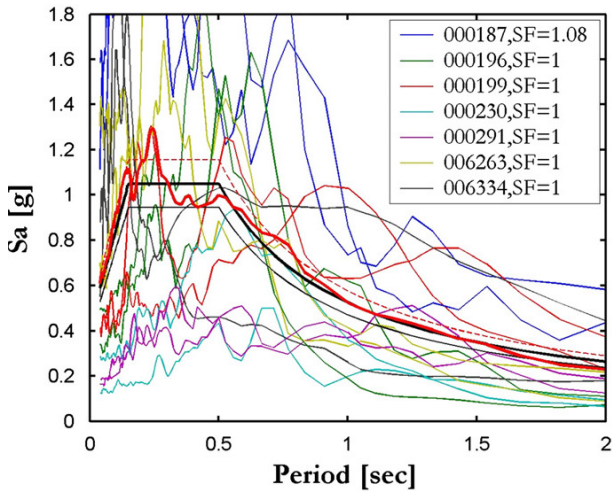


Figure 3: Spectra of records used for nonlinear analyses, their average and EC8 spectrum.

6 COMPARISONS BETWEEN THE ANALYSES RESULTS

In this chapter results of methods n.1 and n.2 are compared to the ones of nonlinear dynamic analyses (NLDA) in terms of displacements; as already written, such capacity at Ultimate Limite State is equal to 3/4 Θu.

In Figures 4 and 5 the following symbols are used: NLSA indicates results of nonlinear static analyses at "t.ULS" without considering torsional effects, i.e. the maximum of the 4 SRSS combinations (eq. 5), where the effects are not amplified by correction factors; NLSA(meth. n.1) and NLSA(meth. n.2) indicate the results of method n.1 and 2 respectively; NLDA(average) means that the average among the maximum results of the 7 nonlinear dynamic analyses is considered and the maximum among the 4 models is reported; as NLDA(av+SD) the average plus the standard deviation instead of the only average of the 7 results for each model is presented, while NLDA(maximum) means that the maximum among the maximum results of the 7 nonlinear dynamic analyses is taken and, as in the other 2 cases, the maximum of the 4 models is shown.

Figure 4 shows frame top displacements, absolute and normalized with respect to CM displacement, along X and Y direction.

It can be observed that NLSA(meth. n.1) gives displacements larger than NLSA and NLSA(meth. n.2), in particular for frames 4 and 5; this is due to the assumption of the maximum $\eta_{MRSA,i}$ in order to compute the four correction factors for each frame. This allows the NLSA(meth. n.1) displacements to better approximate the displacements of nonlinear dynam-

ic analysis when the standard deviation is also considered and, in particular, to estimate on safe side the displacements due to torsion. On the contrary, the positive aspects of NLSA(meth. n.2) are that the correction factor computed for a model coming from $\eta_{MRSA,i}$ and $\eta_{NLSA,i}$ computed for the same model and that the increment of displacements due to torsion effects is low, which is positive if the approximation of NLDA(average) absolute displacements is considered. Figure 4 also shows that NLSA methods provide displacements quite larger than NLDA(average) displacements and that, the standard deviation is not negligible with respect average results, as it can be observed by the difference between NLDA(average) and NLDA(av.+SD) displacements.

The comments reported above are confirmed by Figure 5, where interstory drifts are reported at corner 1 and 2 along X and Y direction respectively. The increment of the 2nd storey drifts, shown by all the analyses, is mainly due to the reduction of the 2nd storey stiffness with respect to the 1st storey one.

This demonstrates that the safety level associated to different analyses performed according to EC8 is correlated to their accuracy, i.e. the safety verification made by nonlinear static analysis is more conservative with respect to non-linear dynamic analysis, which is the most complicated [10].

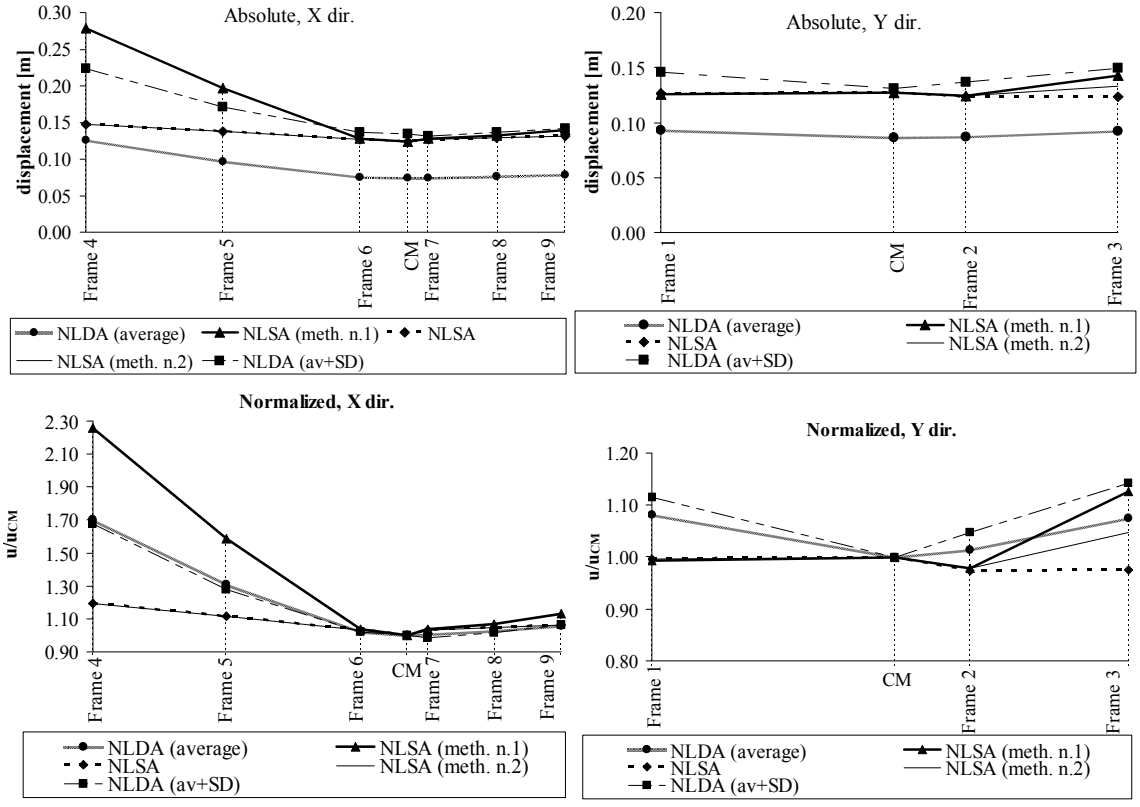


Figure 4: Absolute and normalized frame top displacements along X and Y direction.

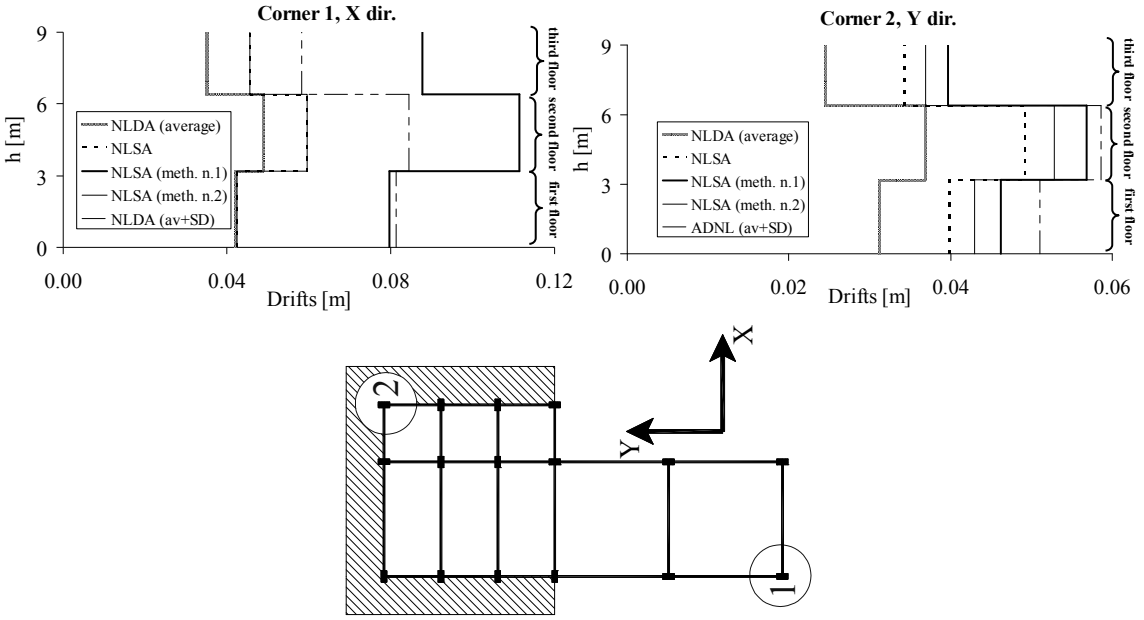


Figure 5: Drifts at corners 1 and 2 along X and Y direction.

7 CONCLUSIONS

In the paper the problem of extension of N2 method to plan irregular buildings, which makes up for the underestimate of seismic demand on stiff side, is discussed. Three methods, which take into account the accidental eccentricity (4 positions of centre of mass correspond to 4 models), are proposed, applied to a 3-storey, r/c frame plan irregular building and compared.

The main differences between the 3 nonlinear static analysis (NLSA) methods are: NLSA(meth. n.1) combines the displacements of modal response spectrum analysis obtained by the 4 models (associate to 4 eccentricities) by SRSS rule and, for each frame, the maximum normalized displacement is assumed as reference; NLSA(meth. n.2), works on 4 models and only at the end of the procedure combines the results by SRSS rule; NLSA(meth. n.3) considers till the end of the procedure the double sign (+ and -) of pushovers.

The results of NLSA(meth. n.3) are coincident with results of NLSA(meth. n.2), confirming that it is correct to consider the maximum target displacement given by the 2 pushovers performed on the same model in the same direction with different sign.

The influence of the orthogonal effects evaluated by the SRSS rule on the results of NLSA(meth. n.2) in terms of frame displacements is estimated and found negligible; this conclusion is confirmed by analyses performed on other buildings.

The input adopted for nonlinear dynamic analysis (7 natural earthquakes) is selected [9] in order to rigorously satisfy the EC8 provisions. 28 nonlinear dynamic analysis (7×4) are performed and the maximum effect of the 4 models is considered; for each model the average of 7 maximum results obtained from 7 earthquakes (NLDA(average)), the average plus standard deviation (NLDA(av+SD)) and the maximum of the 7 maximum results (NDLA(maximum)) are computed.

For some frames, NLSA(meth. n.1) gives displacements larger than NLSA(meth. n.2) , approximating better the displacements of nonlinear dynamic analysis when the standard deviation is also considered and estimating on safe side the displacements due to torsion. On the contrary, the positive aspects of NLSA(meth. n.2) are that the correction factor computed for a model comes from normalised displacements computed for the same model and that the in-

crement of displacements due to torsion effects is low, which is positive considering that NLDA(average) absolute displacements are smaller.

ACKNOWLEDGMENT

This research has been partially funded by Italian Department of Civil Protection in the frame of the national project ReLUIS 2010-2013

REFERENCES

[1] CEN. Eurocode 8: Design of structures for earthquake resistance – Part 1: General rules, seismic actions and rules for buildings. Final Draft, prEN 1998-1, Brussels: 2003.

[2] P. Fajfar, A nonlinear analysis method for performance-based seismic design. *Earthquake Spectra*, **16**, 573-592, 2000.

[3] P. Fajfar, D. Marusic, I. Perus, The N2 method for asymmetric buildings. *First European Conference on Earthquake Engineering and Seismology*. Geneva, Switzerland, 3-8 September 2006.

[4] G. Magliulo, G. Maddaloni, E. Cosenza, Extension of N2 method to plan irregular buildings considering accidental eccentricity. *Soil Dynamics and Earthquake Engineering*. **43**, 69-84, 2012.

[5] CSI Computer & Structures Inc. SAP2000. Linear and Nonlinear Static and Dynamic Analysis of Three-Dimensional Structures. Computer & Structures, Inc., Berkeley, California:2004.

[6] K.N. Li, CANNY99, Three-dimensional nonlinear dynamic structural analysis computer program package. Technical and Users' manual. Canny Consultants Pte Ltd, 1996.

[7] G. Magliulo, R. Ramasco, Seismic response of three-dimensional r/c multi-storey frame building under uni- and bi-directional input ground motion. *Earthquake Engineering and Structural Dynamics*, **36**, 1641-1657, 2007.

[8] CEN, Eurocode 8: Design of structures for earthquake resistance – Part 3: Assessment and retrofitting for buildings. Draft No 7, prEN 1998-3, Brussels, 2004.

[9] G. Maddaloni, G. Magliulo, E. Cosenza, Effect of the seismic input on non-linear response of R/C building structures. *Advances in Structural Engineering*, **15**, 1861-1877, 2012.

[10] G. Magliulo, G. Maddaloni, E. Cosenza, Comparison between non linear dynamic analysis performed according to EC8 and elastic and non linear static analyses. *Engineering Structures*, **29**, 2893-2900, 2007.

COMPDYN 2013
4th ECCOMAS Thematic Conference on
Computational Methods in Structural Dynamics and Earthquake Engineering
M. Papadrakakis, V. Papadopoulos, V. Plevris (eds.)
Kos Island, Greece, 12–14 June 2013

EXPERIMENTAL AND NUMERICAL ANALYSIS OF MR DAMPERS

Manuel T. Braz-César[1], **Rui C. Barros**[2]

[1] Polytechnic Institute of Bragança
Campus de Santa Aplónia – Apt. 134 – 5301-857 Bragança - Portugal
e-mail: brazcesar@ipb.pt

[2] Faculty of Engineering of the University of Porto
Rua Dr. Roberto Frias, s/n 4200-465 Porto - Portugal
rcb@fe.up.pt

Keywords: MR damper, Bouc-Wen model.

Abstract. *This paper provides a brief description of MR fluid technology and MR fluid based devices. Analytical and experimental investigations about MR dampers covering their rheological properties and hysteretic behavior will be carried out. In the first section an overview of the basic properties of the MR fluids and the fluid behavior under different flow regimes are presented. Then, a selection of numerical models to simulate MR dampers behavior will be presented based on the available literature. To obtain and analyze the hysteretic behavior of a MR damper, a commercial device was experimentally tested under several input excitations. Based on the experimental results an identification procedure was carried out to determine the necessary parameters to develop a numerical model. Finally, results from experimental investigations and numerical analyses are summarized and compared.*

1 INTRODUCTION

The so-called "smart materials" has received the attention of researchers and engineers due to their capability to create smart devices that can be easily controlled by a small external perturbation like temperature or a magnetic field. Some of the most promising smart devices are based on fluids with controllable properties like Electrorheological (ER) and Magnetorheological (MR) fluids. The performance of MR fluids is less sensitive to temperature because the magnetic polarization mechanism remains unchanged over the operating temperature range and MR fluids behaviour is not affected by impurities, which means that is insensitive to contamination, while ER fluids are highly sensitive to moisture or impurities as result of manufacture and usage process.

MR fluids are non-Newtonian and rheologically stable suspensions with a shear yield strength, which can be controlled by a magnetic field. These fluids react promptly to the application of an external magnetic field (in a few milliseconds) exhibiting a reversible and adjustable transition from a free-flowing state to a semi-solid state. Due to this property these materials exhibit a significant change in their rheological behavior (viscosity and plasticity).

The expression "apparent viscosity" is used because the carrier fluid viscosity does not change as the magnetic field intensity H is modified. The rheological behavior of MR fluids depends on the magnetic field strength H, however it is possible to define a pre and post yield areas as shown in Figure 1a. In the pre-yield region the MR fluid exhibits visco-elastic behavior and in the post-yield region it behaves like a viscous Newtonian fluid.

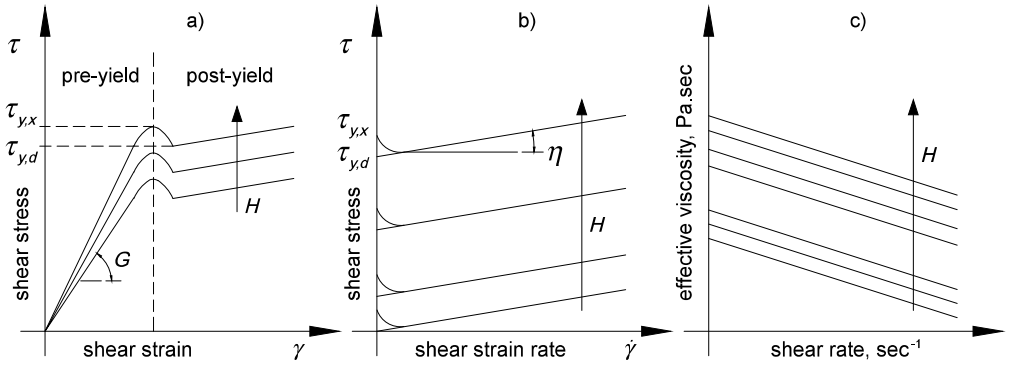


Figure 1: Constitutive behavior of a MR fluid: a) pre-yield and post-yield regions, b) non-Newtonian post-yield behavior and c) apparent viscosity.

In can be stated that the transition from pre-yield to the post-yield region occurs when the stress is greater than the yield shear stress. In this transition zone it is possible to identify the dynamic shear yield stress $\tau_{y,d}$ defined as the point of the zero-rate and the static shear yield stress $\tau_{y,s}$ defined as the shear stress necessary to initiate MR fluid flow [1, 2].

2 EXPERIMENTAL RESPONSE

The device employed in the testing, identification and modeling of the non-linear hysteretic response is the RD-1005-3 commercial prototype developed by the LORD Corporation.

An extensive experimental research was developed to evaluate and obtain the MR damper response data necessary to proceed with the identification procedure [3, 4]. The experimental tests were performed using a MTS universal testing machine load frame with a MTS load unit controller.

The LORD MR damper are usually commanded through a voltage-to-current controller unit designated as Wonder Box Device Controller and sold as a complementary product for MR devices. The device provides a closed-loop current control to compensate for changing electrical loads up to the limits of the power supply and can be used to investigate the control possibilities of the LORD MR technology since it can be operated as an interface device for PLC or computer control of the MR fluid devices. This controller was connected to a voltage power supply unit in order to feed the MR damper with a constant voltage converted to current supply through the Wonder Box.

The RD-1005-3 MR damper has a conventional cylindrical body configuration filled with 50 ml of MR fluid and comprising the piston, the magnetic circuit with a coil resistance of 5 Ω and the accumulator. The enclosing cylinder is 41.4 mm in diameter and the damper is 208 mm long in its extended position with ±2.5 cm stroke. The device can operate within a current range from 0.0 A up to 2.0 A with a recommended input value of 1.0 A for continuous operation and can deliver a peak force of 2224 N at a velocity of 51 mm/s with a continuous operating current level of 1.0 A. The MR damper can reach at least 90% of maximum level during a 0.0 amp to 1.0 amp step input in less than 25 milliseconds.

A series of sinusoidal displacement excitation tests were performed to measure the response under different loading conditions in order to obtain the hysteretic response of the MR damper. The MR damper was mounted into the MTS hydraulic actuation system and was then excited with a sinusoidal displacement. An extensive parametric study was carried out for several arrangements of amplitudes, frequencies and input current; these scenarios were studied in order to obtain the required experimental data to conveniently characterize the damper response [5, 6].

The selected parameters to develop the test program in order to determine the steady state characteristics of the damper for sinusoidal inputs comprise the set of frequencies, amplitudes and current supplies specified in Table 1. To refine the experimental response of the MR damper, the applied current ranges from 0.0A to a maximum of 1.0A in increments of 0.25A. The input current range was refined from 0.0A to 0.25A to conveniently characterize the current dependent MR damper response at low current input.

Parameter	Values
Frequencies (Hz)	(0.50, 1.00, 1.50, 2.00)
Amplitudes (mm)	(2.0, 4.0, 6.0, 8.0, 10.0)
Current supplies (A)	(0.00, 0.10, 0.20, 0.25, 0.50, 0.75, 1.00)

Table 1: Sinusoidal signal - Lord RD-1005-3 MR damper experimental analysis

The testing procedure was carried out with a fixed frequency and amplitude sinusoidal displacement for a specific current supply, repeating this process for every parameter combination. The experimental data of the parametric study for MR dampers are typically grouped according to the variability of the different parameters sets as frequency-dependent tests and amplitude-dependent tests.

The sinusoidal shaft displacement and the resulting force are measured though the MTS internal LVDT and a force transducer (load cell) with a sampling rate of 256Hz and logged for data analysis. The displacement and force transducers were calibrated previously to the experimental procedure to reduce measuring imprecisions. Based on the results it is possible to generate the force-displacement (f-d) and force-velocity (f-v) hysteresis cycles of the damper and therefore understand and investigate the device rheological behavior.

Figures 2 illustrate some of the experimental results obtained with the testing procedure. The plots were developed from the data records selecting an experimental response cycle for a steady state excitation.

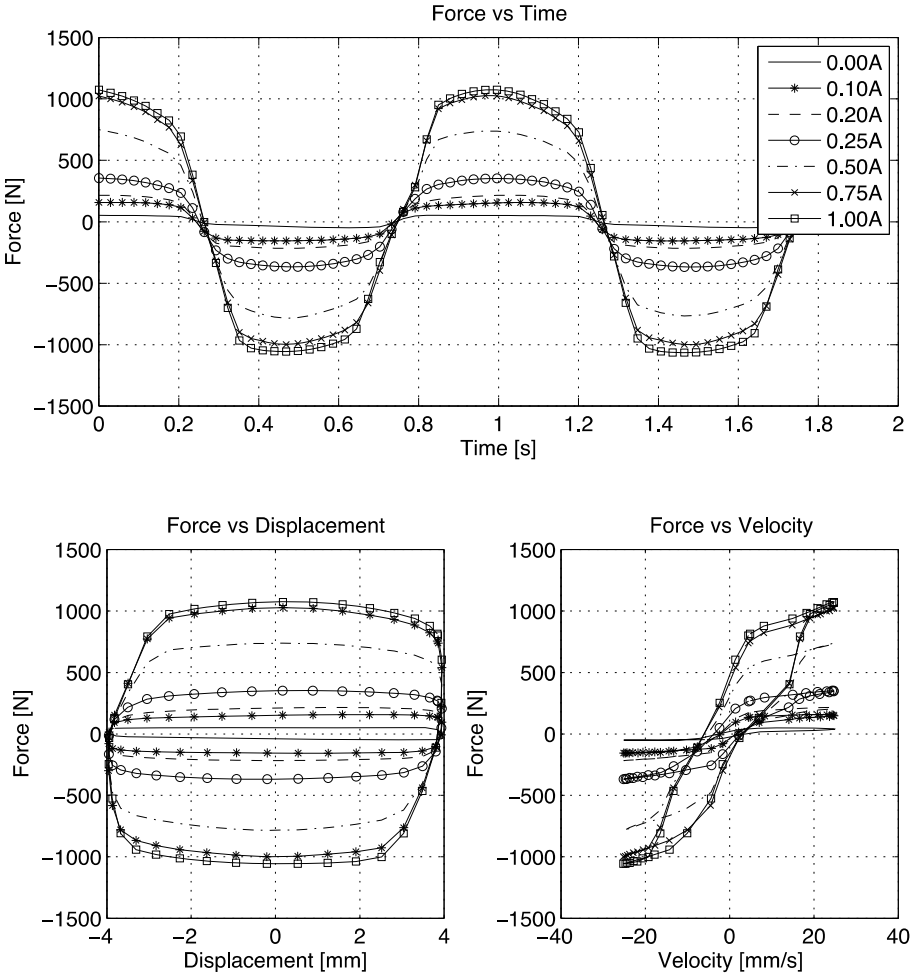


Figure 2: RD-1005-3 MR damper - Measured damping forces under a 1.00 Hz sinusoidal excitation with amplitude of 4.00 mm and variable input current.

3 NUMERICAL MODELS

MR dampers are semi-active devices whose damping characteristics can be modified in real time due to the capability to adjust the resistance to flow of a MR fluid within the damper through the application of a magnetic field. The particular properties of the MR fluid allow variations in the damping force that can be controlled by varying an applied current. Thus, the hysteretic behaviour of a MR damper is current dependent but also function of the amplitude of the excitation.

To predict the behaviour of MR dampers under certain magnetic fields or excitations, it is necessary to model the device with an appropriate approach. Hence a previous numerical simulation is needed to verify if the proposed properties are suitable for the system in which it is intended to apply the MR damper. Several numerical models are available to predict the response of MR dampers [7-11]. Table 2 presents a brief description of the available models for MR dampers.

Modelling technique	MR damper Models
Bingham models	- Original Bingham model - Modified Bingham model - Gamota and Filisko model - Updated Bingham model by Occhiuzzi *et al*. - Three-element model by Powell
Bi-viscous models	- Nonlinear bi-viscous model - Nonlinear hysteretic bi-viscous model - Nonlinear hysteretic arctangent model - Lumped parameter bi-viscous model
Visco-elastic-plastic models	- General visco-elastic-plastic models - Visco-elastic-plastic model by Li *et al*
Stiffness-viscosity-elasto-slide model	- Stiffness-viscosity-elasto-slide (SVES) model
Hydro-mechanical model	- Hydro-mechanical model
Maxwell models	- BingMax model by Makris *et al*. - Maxwell Nonlinear Slider model
Bouc-Wen models	- Simple Bouc-Wen model - Modified Bouc-Wen model - Bouc-Wen model for shear mode dampers - Bouc-Wen model for large-scale dampers - Current dependent Bouc-Wen model - Current-frequency-amplitude dependent Bouc-Wen - Non-symmetrical Bouc-Wen model
Dahl models	- Modified Dahl model - Viscous Dahl model
LuGre models	- Modified LuGre model by Jimenez and Alvarez - Modified LuGre model by Sakai et al
Hyperbolic tangent models	- Hyperbolic tangent model by Kwok *et al*
Sigmoid models	- Sigmoid model by Wang *et al* and Ma *et al*
Equivalent models	- Equivalent model by Oh and Onoda
Phase transition models	- Phase transition model

Table 2 - MR dampers Models classification

The main problem regarding the modeling of MR dampers is related with the significant non-linear response that these devices exhibit when subjected to an input excitation. Moreover, the hysteretic behavior observed is function of the amplitude and frequency of excitation but (due to their rheological nature and due to the semi-active controllable response) it is also current dependent, which considerably increases the difficulty level when a numerical model is developed.

To use the MR damper as a controllable semi-active device into a control system it is essential that the selected numerical model can capture its non-linear behavior in order to develop a feasible semi-active controller [3-6].

Since many mathematical models have been developed to describe such behavior and to take advantage of the MR properties of these devices in vibration control related problems, it is necessary to select and implement high-accuracy models capable to capture their non-linear hysteretic response. Among the modeling techniques, parametric models appear to be an easy and reliable approach to obtain a mathematical model of the physical MR damper.

Figure 3 illustrates the response of well-known Bingham, Bouc-Wen and Modified Bouc-Wen models [12-14], which are some of the most common models obtained by a deterministic approach.

The Bingham mechanical model consists of a Coulomb friction element placed in parallel with a viscous damper and comprises the identification of three parameters (Figure 3): the frictional force f_c, the viscous damping parameter c_0 and the force due to the presence of the accumulator f_0.

The simple Bouc-Wen model presents a highly effective model for hysteretic systems and has become one of the most common approaches to describe the hysteretic behavior of MR dampers. The force generated by the MR damper can be expressed by the combination of three elements (Figure 3): a dashpot defined by the damping coefficient c_0, a linear spring defined by the parameter k_0 and a Bouc-Wen component defined by the Bouc-Wen parameter α that represent the stiffness for the damping force component (yield stress of the MR fluid) associated with the evolutionary variable z that accounts for the history dependence of the response.

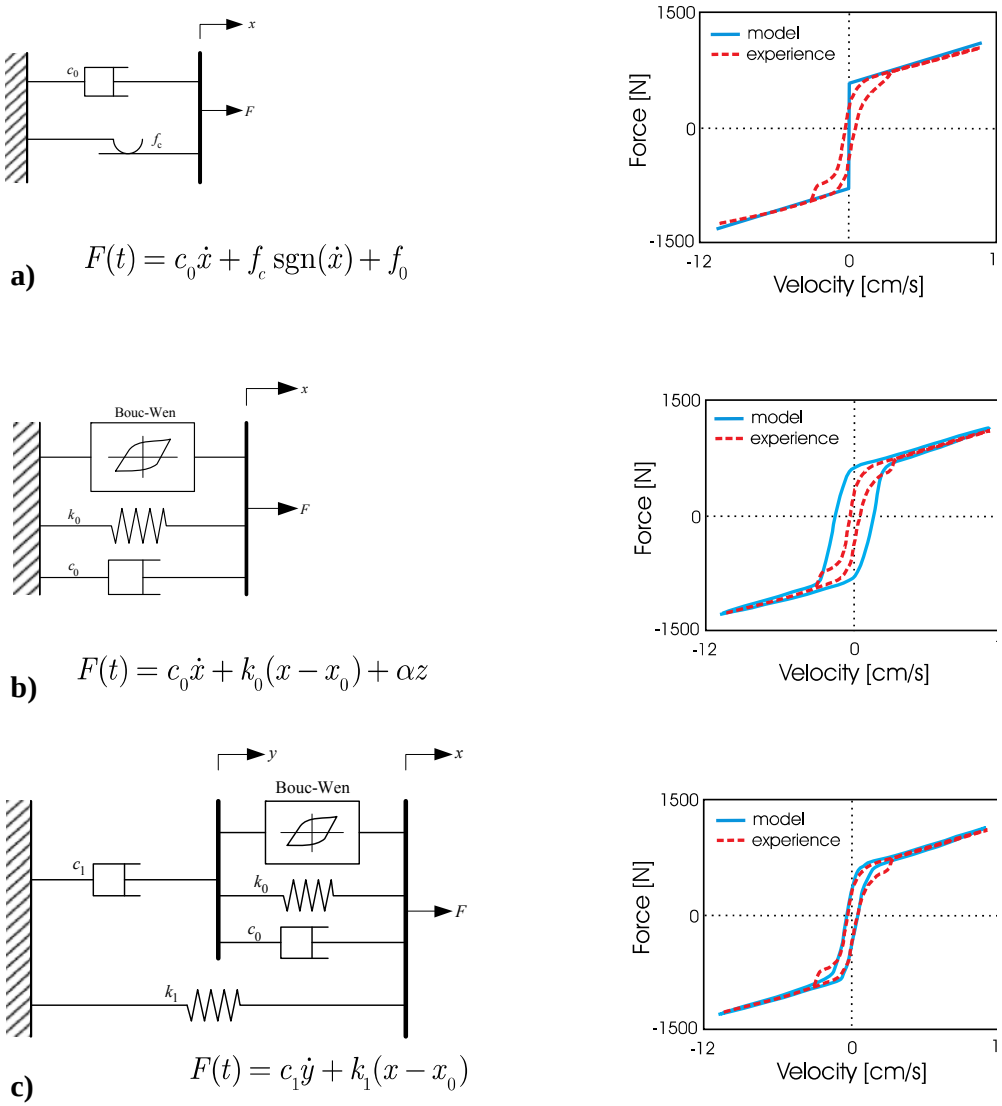


Figure 3: MR-fluid and MR-dampers models [12, 13]
a) Bingham model, b) Bouc-Wen model, c) Modified Bouc-Wen model

The non-linear hysteretic behavior of the device is controlled by the Bouc-Wen component that is related with the restoring force of a non-linear hysteretic system as proposed by [15]. According to the Bouc-Wen formulation, the restoring force of the nonlinear hysteretic system $Q(x,\dot{x})$ can be decomposed into two parts as

$$Q(x,\dot{x}) = g(x,\dot{x}) + z(x) \tag{1}$$

where $g(x,\dot{x})$ is a non-hysteretic component expressed by the displacement x and velocity $\dot{x}$, while $z(x)$ is a hysteretic component defined by the displacement and the evolutionary variable z given by

$$\begin{aligned} \dot{z} &= -\beta\left|\dot{x}\right| z^{n} - \gamma\dot{x}\left|z\right|^{n} + A\,\dot{x}, \qquad && n = 1,3,5,\ldots \\ \dot{z} &= -\beta\left|\dot{x}\right| z^{n-1} - \gamma\dot{x}\,z^{n} + A\,\dot{x}, \qquad && n = 2,4,6,\ldots \end{aligned} \tag{2}$$

These equations are implemented in the simple Bouc-Wen model with an equivalent formulation in which the evolutionary variable is written as

$$\dot{z}(t) = -\beta\left|\dot{x}(t)\right| z(t)\left|z(t)\right|^{n-1} - \gamma\dot{x}(t)\left|z(t)\right|^{n} + A\,\dot{x}(t) \tag{3}$$

The evolutionary variable equation depends on four parameters A, β, γ, and n that represent the linearity in the unloading region and the smoothness of the transition from the pre-yield to post-yield regions.

Parameters A, β and γ describe the shape and size of the hysteresis loop and the parameter n controls the smoothness of the transition from elastic to plastic response. To avoid numerical errors when $0< n <1$, the evolutionary variable equation can be rewritten in the following form

$$\dot{z}(t) = \dot{x}(t)\left\{ A - \left[\gamma + \beta\,\mathrm{sgn}(\dot{x}(t)\,\mathrm{sgn}(z(t))) \right] \left|z(t)\right|^{n} \right\} \tag{4}$$

that can be derived as

$$\frac{dz}{dx} = A - \left[\gamma + \beta\,\mathrm{sgn}(\dot{x}(t)\,\mathrm{sgn}(z(t))) \right] \left|z(t)\right|^{n} \tag{5}$$

and the ultimate value of z can be computed by setting $dz/dx = 0$ and is given by

$$z_{\max} = \left[\frac{A}{\beta + \gamma} \right]^{\frac{1}{n}} \tag{6}$$

It can be stated that setting the non-hysteretic component $g(x,\dot{x})=0$ the restoring force will become $Q(x,\dot{x})=z(x)$. Then, if $z=0$, $dQ/dx= dz/dx =A$, and hysteretic curves for different excitation and response levels will have the same slope when $Q=Q(z)$ and the loading and unloading path are identical [15]. Thus, the non-hysteretic term must be used to overcome inconsistencies between the numerical model and the experimental results. The force generated by the MR damper can be expressed by the four parameters (A, β, γ, and n) and a combination of the three parameters c_0, k_0 and α related with the physical components of the model.

The variable x_0 that appears in the Bouc-Wen model represent the initial displacement of the linear spring and is related with the force offset during the experimental tests. The evolutionary variable equation contains four parameters that have a strong effect on the hysteresis response curve.

A comprehensive analysis of the influence of the Bouc-Wen parameters on the hysteretic behavior of this model was addressed in some previous research programs [16-18]. According with the Bouc-Wen formulation, the shape of the hysteretic loop is defined by parameters A, β, γ and n. Parameters A, β and n are positive real numbers while γ can be a positive or negative real number. The following study will be carried out for a harmonic periodic excitation $x= x_0 \sin(w(t))$, where w= 1rad/s is the frequency and x_0 the amplitude of excitation.

The parameter A defines the scale and amplitude of the hysteresis loop and also controls the slope of the hysteresis loop at z=0 (the stiffness characteristic) as shown in Figure 4. In this plot, the parameters β and γ were kept constant (β= 0.5 and γ= -0.4) and parametric variation of A for a fixed value of n= 1.0 was carried out. Increasing the parameter A will generate a larger hysteresis loop that implies an increase in the energy dissipation.

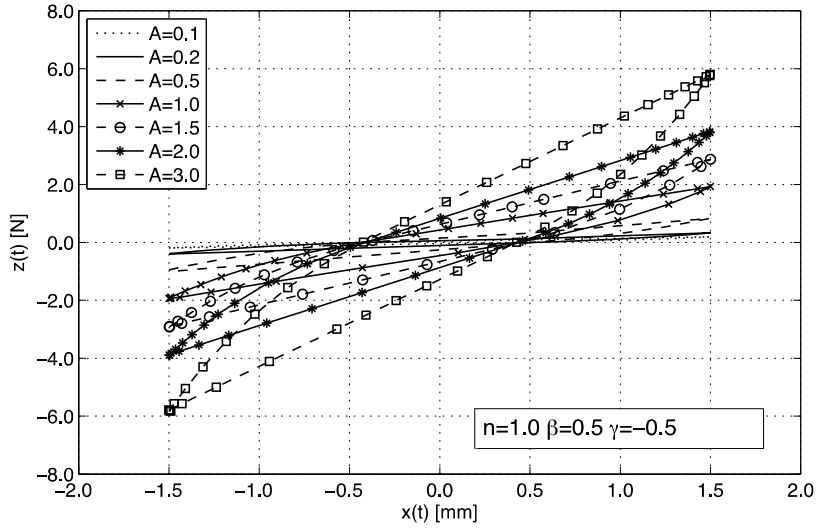


Figure 4: Influence of parameter A on the hysteretic behavior.

The parameter n is related with the smoothness of the transition from the linear to the non-linear region. The influence of this parameter in the hysteresis loop is shown in Figure 5.

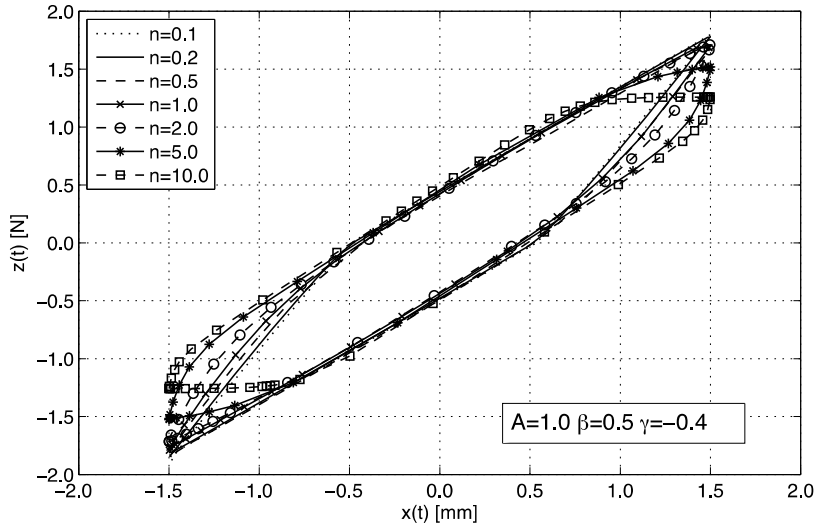


Figure 5: Influence of parameter n on the hysteretic behavior.

In this case, parameters β, γ and A are constant (β= 0.5, γ= -0.4 and A= 1.0) while the parameter n is changed. The parametric studies show that this power parameter n has a significant effect on the hysteresis loop when $1 < n < 2$ and practically no effect when $n > 2$.

The parameters β and γ are related with the shape of the hysteresis curve and different combinations of these parameters will describe several hysteretic loops with variations in the stiffness characteristics. The dependence of the hysteretic loops on the parameter β is shown in Figure 6 for A=1, γ=0.9 and n=1. Essentially, the parameter β controls the variation in the stiffness when the sign of the velocity variable changes. Hence, the response exhibits a linear hysteretic behavior when β=0, a hardening hysteretic behavior when β<0 and a softening hysteretic behavior when β>0.

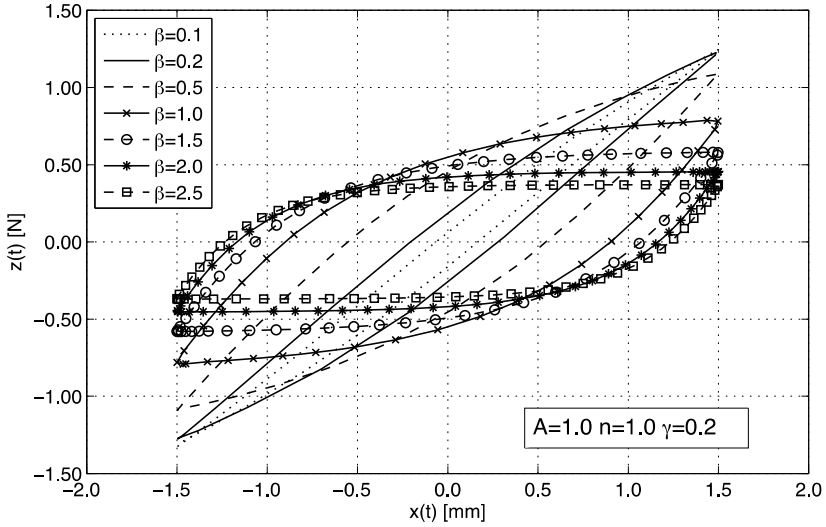


Figure 6: Influence of parameters β on force-displacement curves.

The parameter γ is related with the area and flatness of the hysteresis loop as displayed in Figure 7. Increasing the value of γ will produce a decrease in the loop inclination producing a flat hysteretic curve with a near horizontal branch.

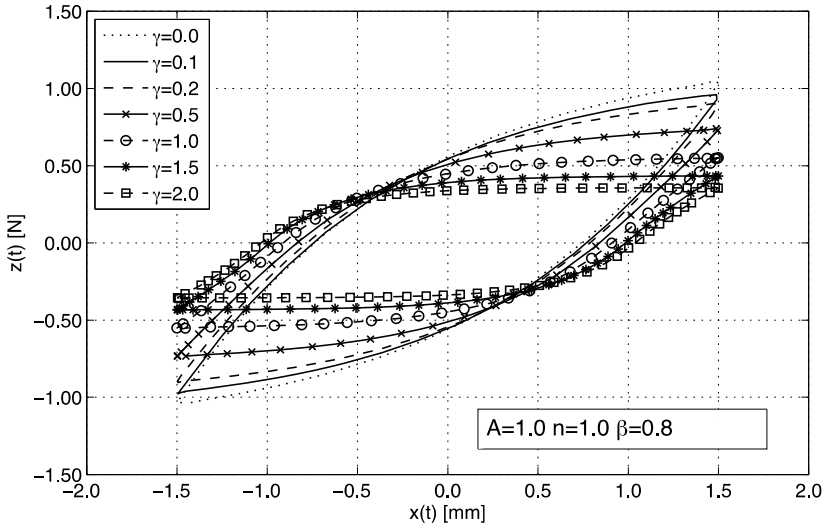
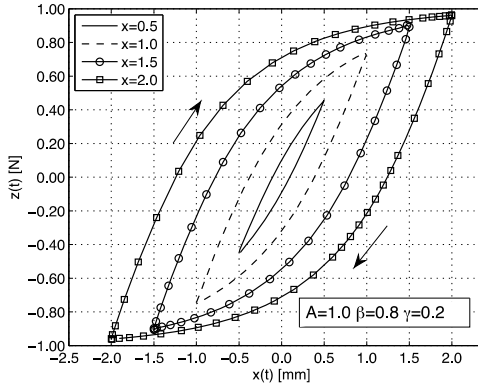
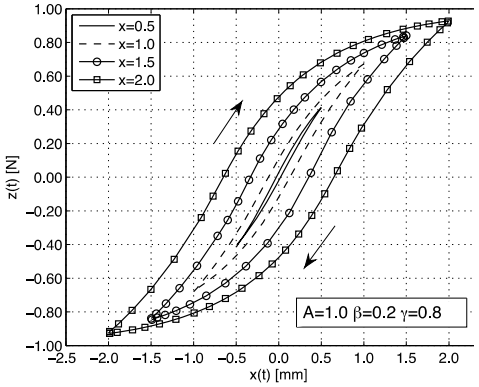


Figure 7: Influence of parameter γ on the hysteretic behavior.

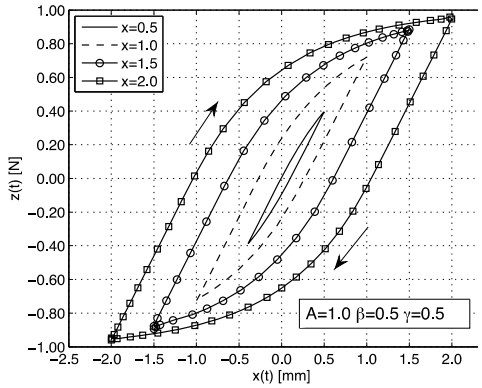
Also, when the parameter is bellow a certain value defined as γ_0 the area will increase. However, when γ is larger than γ_0, the hysteretic loop becomes almost horizontal and the area slightly decreases, i.e., the energy dissipated per cycle decreases. The parameters β and γ are related with the shape of the hysteresis curve and different combinations of these parameters will describe several hysteretic loops.



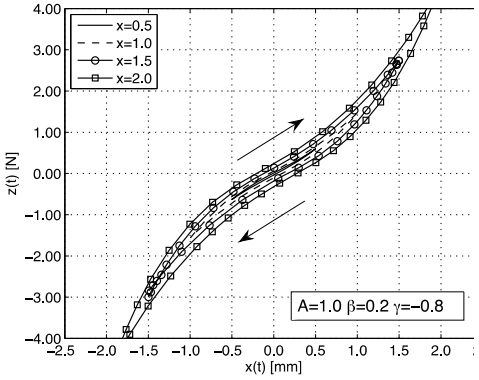
a) $(\beta+\gamma)>0$ and $(\beta-\gamma)>0$



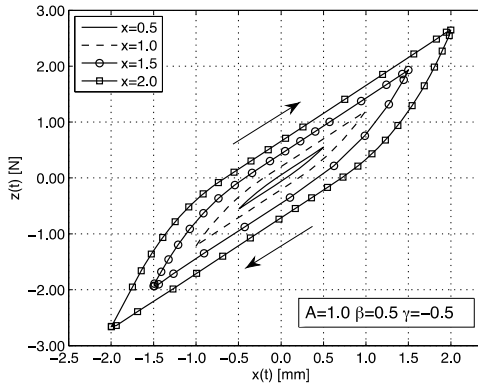
b) $(\beta+\gamma)>0$ and $(\beta-\gamma)<0$



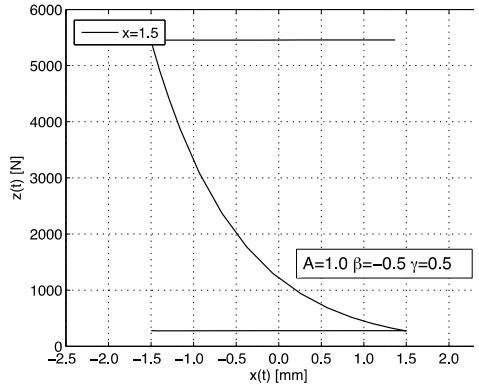
c) $(\beta+\gamma)>0$ and $(\beta-\gamma)=0$



d) $(\beta+\gamma)<0$ and $(\beta-\gamma)>0$



e) $(\beta+\gamma)=0$ and $(\beta-\gamma)>0$



f) Other $(\beta+\gamma)=0$ and $(\beta-\gamma)<0$

Figure 8: Hysteresis loops for several combinations of β and γ

Therefore, is important to study the relationship between these parameters to understand the influence of each combination in the hysteretic shape. The influence of the combination of these parameters in the hysteretic behavior can be studied investigating the slope dz/dx of the hysteresis curve under loading and unloading.

When the loop is loading, the model show a softening non-linear behavior that occurs due to the fact that the slope of the hysteresis curve for z>0 decreases with the increase of z when $(\beta+\gamma)>0$ displaying a softening effect. The model exhibits hardening non-linearity produced by the increase in the slope of the hysteresis curve for $z>0$ with the increase of z when $(\beta+\gamma)<0$. Finally, the slope during loading for $z>0$ is kept constant and the system behaves quasi-linearly when $(\beta+\gamma)=0$. On the other hand, when the loop is unloading, the slope of the hysteresis curve for z> 0 decreases with the decrease of z when $(\beta-\gamma)>0$, increases with the decrease of z when $(\beta-\gamma)<0$ and is kept constant when $(\beta-\gamma)=0$ [6]. Eight possible combinations of β and γ can be used, however, only five of these combinations define hysteresis curves (or cases) that have physical meaning.

A parametric study for each case and the corresponding hysteresis loops are displayed in Figure 8 [5, 6]. The parameters A and n were both kept constant at 1.0 and the arrow indicates the loading to unloading direction. In the first three cases is visible a softening non-linear behavior during loading as result of a decrease of the loop slope produced by an increase of z (for positive values of z) when $(\beta+\gamma)>0$. In the fourth case the system reveals a hardening non-linearity during loading as result of an increase of the loop slope produced by an increase of z (with $z>0$) when $(\beta+\gamma)<0$. In the fifth and final case with physical meaning, the slope during loading for $z>0$ remain constant and the system presents a quasi-linear behavior when $(\beta+\gamma)=0$.

As expected, when the curve is in the unloading path, the slope for $z>0$ decreases with the decrease of z when $(\beta-\gamma)>0$, increases with the decrease of z when $(\beta-\gamma)<0$ and remain constant when $(\beta-\gamma)=0$. The hysteretic curves in Figures 7a and 7c have a similar shape and amplitude, which suggest that different combinations of β and γ can produce the same hysteretic response. Thus the use of the two parameters can be redundant and the combination of β and γ can be replaced by a single parameter β. Figure 9 shows the hysteretic loops for two combinations of β and γ (β=0.8, γ=0.2 and β=γ=0.5) to demonstrate that different combinations of these parameters can generate the same hysteretic behavior.

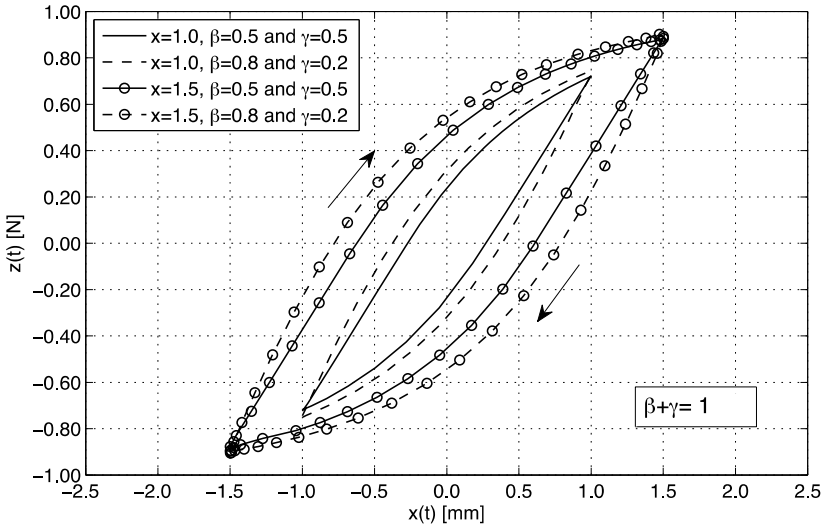


Figure 9: Hysteresis loops for two combinations of β and γ
Comb1 (β= 0.8, γ= 0.2) and Comb2 (β= 0.5, γ= 0.5).

In these combinations ($\beta+\gamma$)=1 and although a slight different in the hysteresis amplitude is present due to a larger value of β in the first combination, the hysteretic response in both cases is almost identical and adjusting the value of each parameter it is possible to obtain equivalent curves. Therefore it is possible to justify that $\beta+\gamma$ is constant.

The relevance of the softening or hardening effect is determined by the combination of these parameters. Observing the third hysteretic curve, the system exhibits softening hysteretic behavior since ($\beta+\gamma$)>0. Besides, in this case $\beta=\gamma$=0.5 and consequently the parameter γ can be neglected in the Bouc-Wen model leading to a simpler identification procedure.

Finally, a brief reference regarding the rest of the Bouc-Wen parameters (c_0, k_0 and α) will be made. These parameters are related with the three physical components of the model and they essentially affect the height of the global hysteretic loop and the slope and width of the hysteresis "tails", i.e., the shape of the extension branch of the hysteretic curve.

Essentially, the parameter α is a scale factor and the parameters c_0 and k_0 are related with the representation of a conventional damper behavior. Figure 13 shows the influence of the parameter α in the global hysteretic loop (since this parameter is a multiplier of the evolutionary variable z). In this case, the parameter α is increased from 10N to 60N with increments of 10N while the other parameters are kept constant (A= 20.0, $\beta=\gamma$= 5.0, n= 2.0 and c_0= k_0= 0.0).

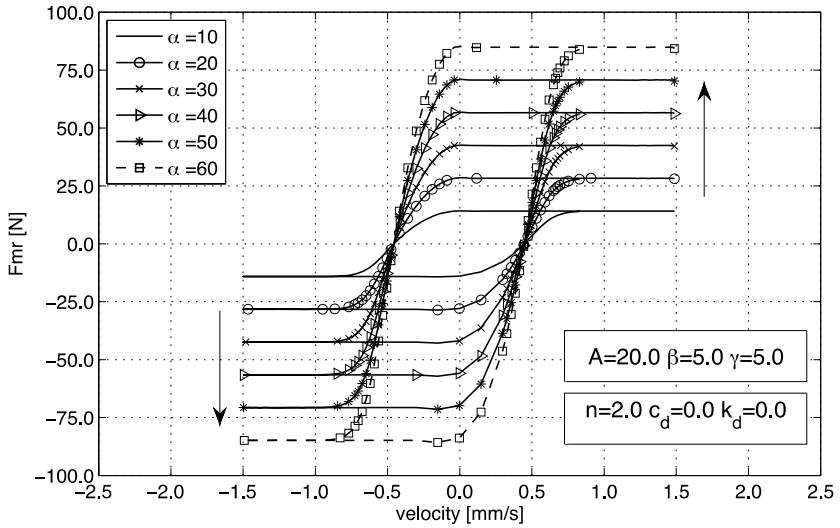


Figure 13: Influence of parameter α on force-velocity curves.

According with the resulting plot it is possible to verify that increasing the value of α will increase the height of the hysteresis loop. Thus, this parameter is responsible for the amplification of the vertical scale of the Bouc-Wen curve and can be seen as a scale factor of the hysteresis loop.

The parameter c_0 is a damping constant in the Bouc-Wen model that represents the post-yield relationship between the damper force and the velocity and generates an inclined line with a slope defined by the parameter value. This parameter essentially controls the slope of the hysteresis loop external branches. The effect of c_0 in the hysteresis loop is shown in Figure 14 for constant values of A= 20.0, $\beta=\gamma$= 5.0, n= 2.0, α= 30 and k_0= 0.0. Changing the parameter causes a variation of the hysteresis loop slope with particular incidence in the external branch of the loop. Then, increasing the damping coefficient causes a rising in slope of the hysteresis tails and large values of c_0 provides a steep inclination. Finally, the effect of the spring parameter k_0 in the hysteresis loop is studied.

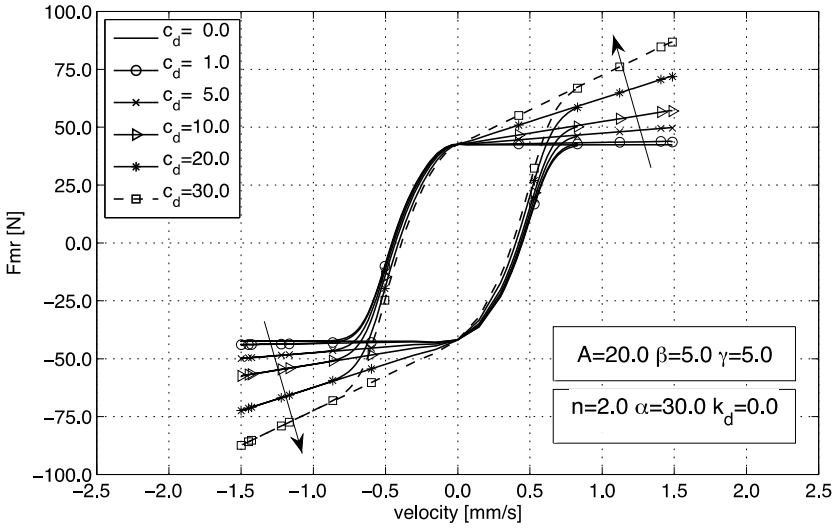


Figure 14: Influence of parameter c_0 on force-velocity curves.

This parameter represents a stiffness parameter that generates a horizontal ellipse and is responsible for widening the ellipse shape around zero velocity area.

Figure 15 represents the influence of this parameter in the global hysteresis shape when A= 20.0, β=γ= 5.0, n= 2.0, α= 30 and c_0= 10.0. When the coefficient k_0 is increased, the spring component of the Bouc-Wen model will become more significant producing an enlargement of the area enclosed in the hysteresis loop. Large values of k_0 will produce a significant widening effect on the post-yield hysteresis ends instead of the pre-yield region.

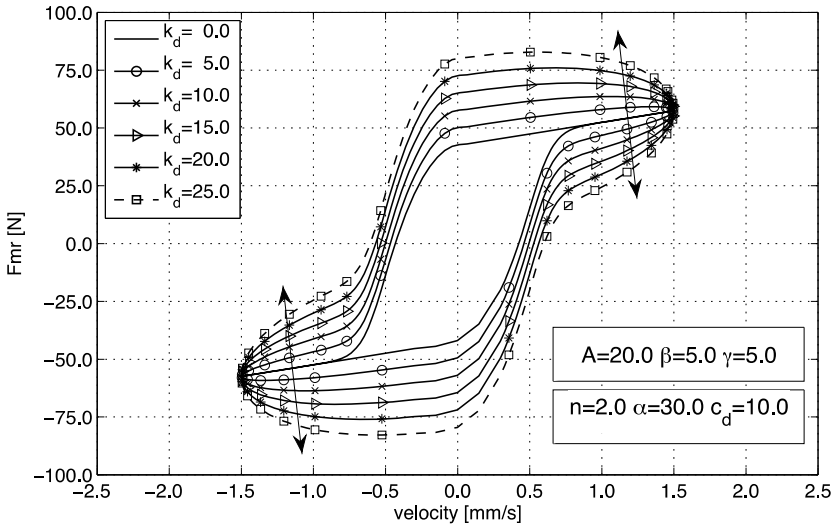


Figure 15: Influence of parameter k_0 on force-velocity curves.

The Modified Bouc-Wen model or Spencer model is a variation of the simple Bouc-Wen model presented previously. This model was developed to improve the nonlinear force-velocity hysteretic response of MR dampers since the simple Bouc-Wen model does not reflect the roll-off effect in the region where the acceleration and velocity have opposite signs and the magnitude of the velocities are small [2].

This model includes a simple Bouc-Wen block and two new mechanical components: a spring and a dashpot connected as shown in Figure 3. The spring represents the accumulator stiffness and is characterized by the model parameter k_1; while the dashpot, defined by the model parameter c_1, is included in the model to create the roll-off effect that is observed in the experimental data at low velocities.

The effect of the model parameter c_1 in the hysteretic loops is displayed in Figure 16. The numerical responses were made for a variable value of c_1 while the rest of the model parameters are kept with a constant value. This analysis shows that increasing the value of c_0 produces an increase in the hysteretic loop slope along with an increase in the hysteretic loop width. Moreover, the characteristic "S" shape of the hysteretic loop is visible for moderate or high values of c_1 (for the present constant model parameters). In this case, the typical hysteretic loop is achieved when the value of c1 is significantly higher than the value of c_0 (c_1>10c_0).

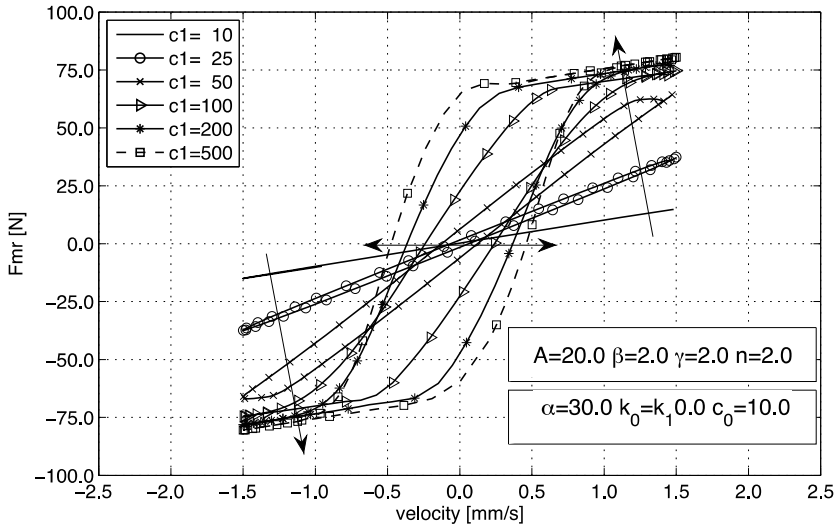


Figure 16: Influence of parameter c_1 on force-velocity curves

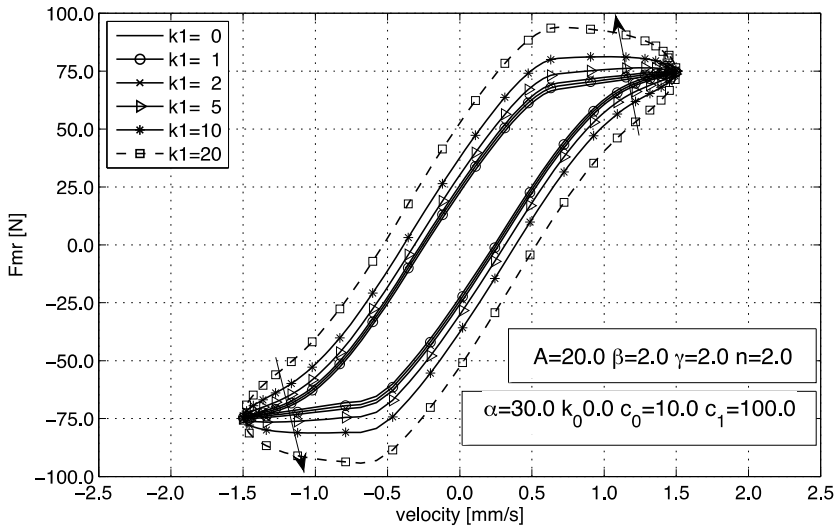


Figure 17: Influence of parameter k_1 on force-velocity curves

Although the overall effect of this parameter can be characterized by the curves plotted in Figure 16, is important to notice that the effect of this parameter is also dependent on the rest of the Bouc-Wen model parameters and different shapes can be obtained by changing the other parameters. The roll-off effect observed in the experimental data at low velocities can be adjusted varying this parameter in combination with the Bouc-Wen parameters.

Finally, the effect of the spring parameter k_1 is shown in Figure 17. This parameter has a similar effect as k_0, i.e., increasing the value of k_1 produces a widening of the hysteretic loop.

The experimental results obtained with these MR damper show that this widening effect is insignificant, which suggests that the contribution of the linear springs to the shape of the hysteretic loop is negligible compared to other model components.

4 PARAMETERS IDENTIFICATION

High-accuracy models usually comprise a large number of parameters that require a reliable parameter identification procedure to efficiently estimate the suitable model parameters and reduce large parameter identification errors.

The estimation of the model parameters can be established based on several numerical approaches such as least square methods, fuzzy methods, neural networks, genetic algorithm, etc. The least square method is a simple and standard approach to reduce the difference between an experimental value and the fitted value provided by a dynamic model, and the application of this method is mostly appropriate for models that have linear variations in the parameters.

However, the dynamic models for MR dampers are nonlinear in the parameters and a nonlinear approach should be considered to estimate model parameters. Nonlinear least squares regression generalizes and extends the linear least squares regression model to a much larger and more general class of functions, especially functions that cannot be linearized and is often used to identify the non-linear parameters of the numerical models of MR dampers. Therefore, the non-linear least square regression model will be used in the present study to estimate the model parameters for several numerical models.

There are several computational routines to solve nonlinear curve-fitting problems in the MATLAB Optimization Toolbox [19]. After defining the identification procedure it is necessary to select the main numerical models that will be considered to simulate the MR damper response. In this case, the Modified Bouc-Wen model will be used for the RD-1005-3 MR damper. The force generated by the MR damper is defined by the seven parameters of the Bouc-Wen block (A, β, γ, n, c_0, k_0 and $_{\alpha}$) and two new model parameters k_1 and c_1 related with the new mechanical components. Thus, the identification procedure involves nine model parameters (A, β, γ, α, c_0, k_0, k_1, c_1, and n), or ten if the force offset f_0 (or x_0) is considered as a variable, to be identified and the parameter vector is then defined as

$$\Theta = [\alpha, \beta, A, n, k_0, k_1, c_0, c_1, x_0] \tag{7}$$

The damper has a softening hysteretic effect with no signs of hardening (case I, II or III, i.e., $(\beta+\gamma) > 0$) and the parameters A, α, k_0 and c_0 are positive variables. The parameter c_0 should have a reduced value to avoid steep slopes and k_0 should be close to zero to reduce the widening effect. It was assumed that n=2 and the force offset, defined by $k_1(x-x_0)$ that represent the force due to the accumulator existence, has the same value of the Bingham and the simple Bouc-Wen model force offset (f_0 =40 N). The parameter c_1 is much higher than c_0 (a constrain $c_1 > 5c_0$ was imposed in this study) and the spring parameter k_1 has a small value due to the reduced widening effect observed in the experimental data. The different hysteretic loops of the numerical model were determined by a set of model parameters for each experimental excitation case.

Figure 18 shows the result that was obtained with the parameter identification procedure for the Modified Bouc-Wen model (1.50 Hz, 4 mm and 0.75 A).

This procedure was repeated for each set of experimental data and the values of the model parameters of the Modified Bouc-Wen model were determined for each dataset.

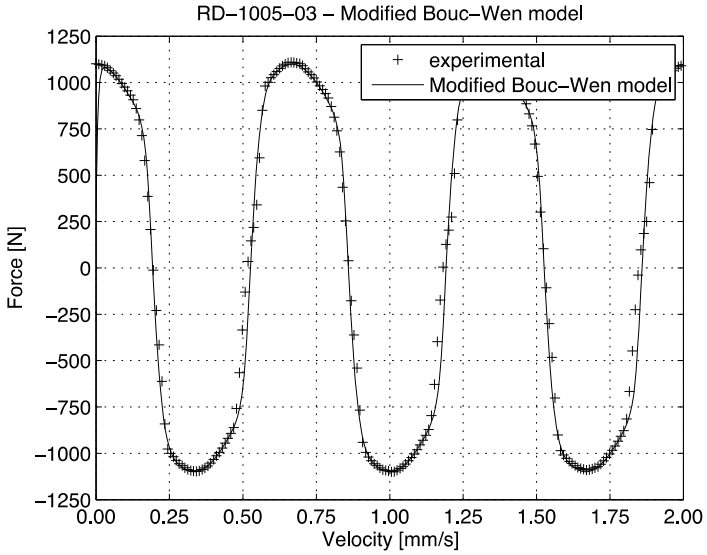


Figure 18: RD-1005-3 MR damper – Parameter identification of the Modified Bouc-Wen model (1.50 Hz, 4mm and 0.75A).

The average values of the current independent parameters of the Bouc-Wen model A=10.013, β=3.044 mm^{-2}, γ=0.103 mm^{-2} and k_0 =1.121 N/mm were found. The parameters α, c_0 and c_1 are described as functions of the input current by a polynomial curve fitting procedure as shown in Figures 19-21.

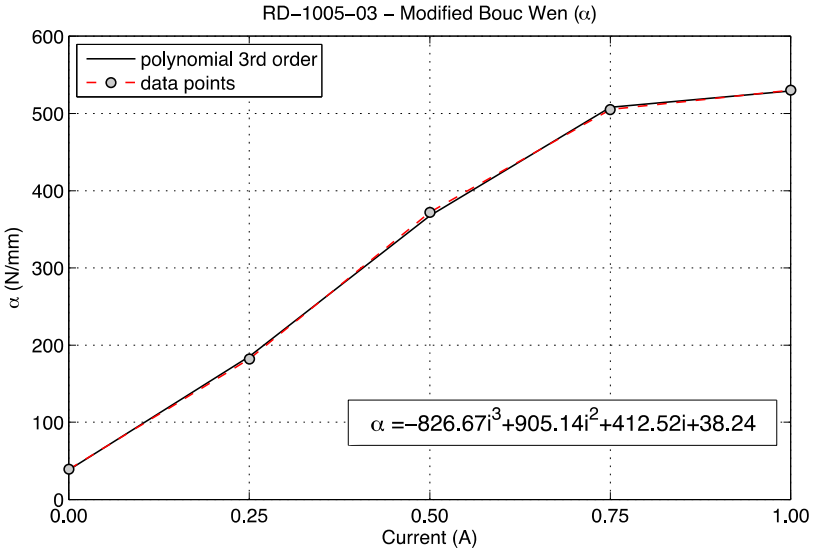


Figure 19: Curve fitting for $\alpha(I)$ of the Bouc-Wen model.

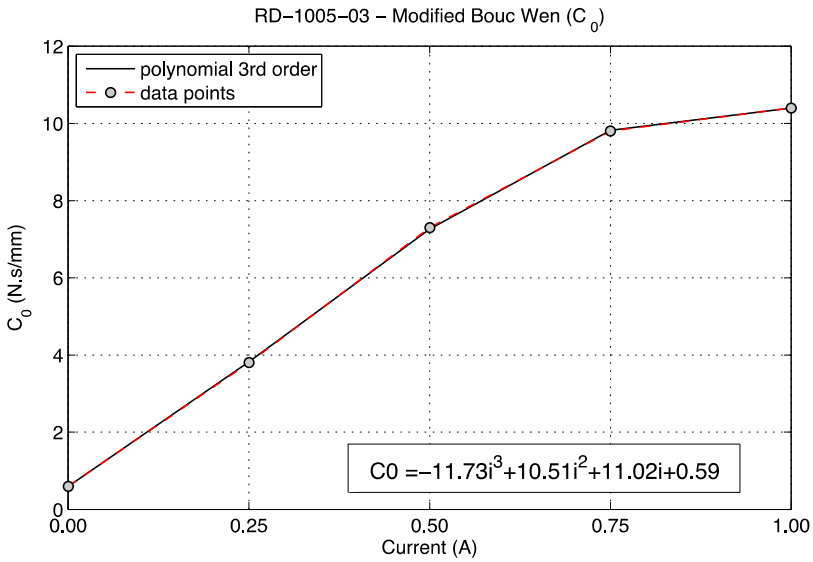


Figure 20: Curve fitting for $c_0(I)$ of the Bouc-Wen model.

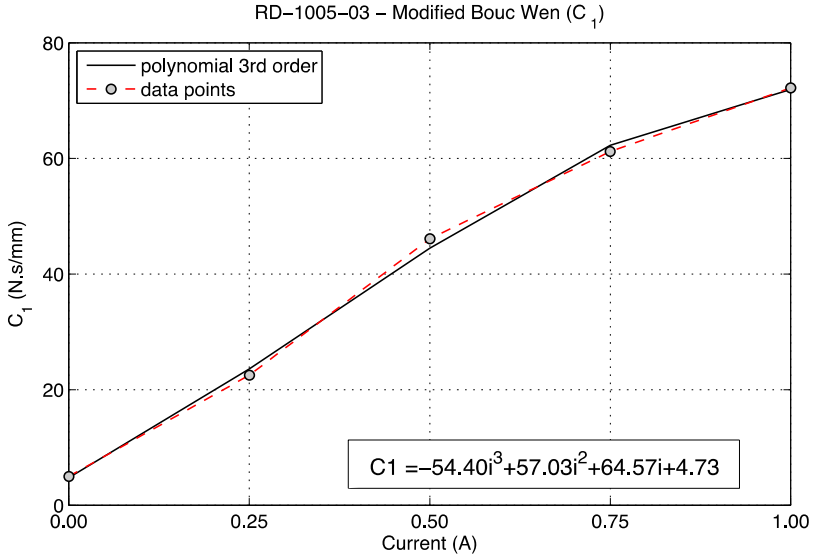


Figure 21: Curve fitting for $c_1(I)$ of the Bouc-Wen model.

According with the curve fitting procedure, the model parameters α, c_0 and c_1 can be described by

$$\alpha(I) = -826.67I^3 + 905.14I^2 + 412.52I + 38.24 \tag{8}$$

$$c_0(I) = -11.73I^3 + 10.51I^2 + 11.02I + 0.59 \tag{9}$$

$$c_1(I) = -54.40I^3 + 57.03I^2 + 64.57I + 4.73 \tag{10}$$

Results of experimental and numerical responses of the MR damper are presented in Figure 22 (1.5 Hz, 4 mm of amplitude and I=1.00 A). The results show that the Modified Bouc-Wen model is capable to characterize the MR damper hysteretic response.

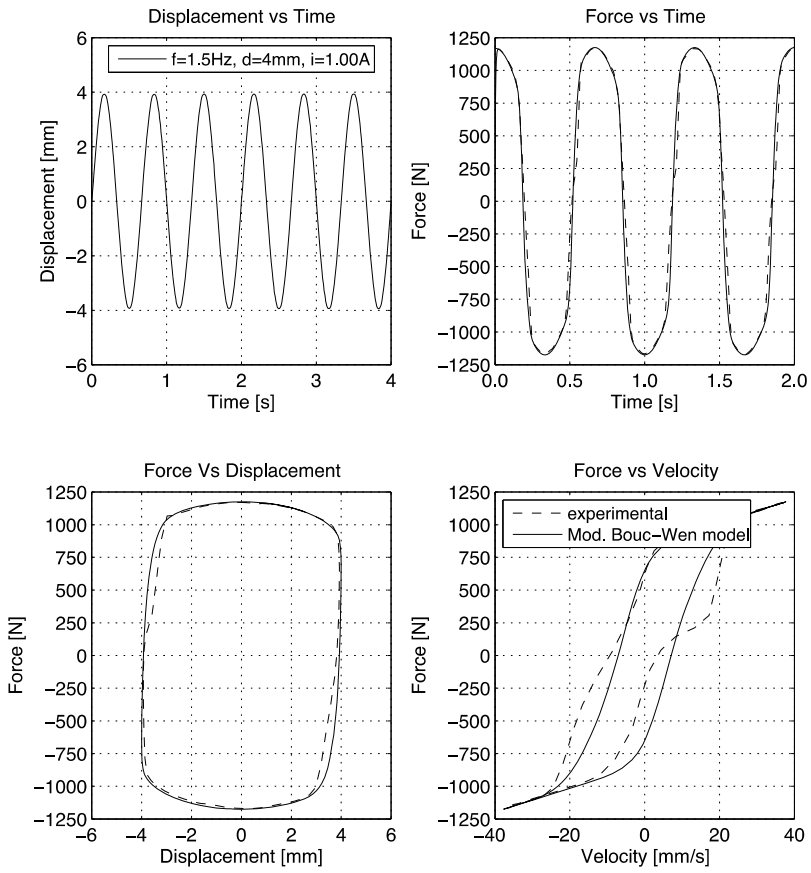


Figure 22: RD-1005-3 MR damper – Experimental vs. numerical response for the Bouc-Wen model

5 CONCLUSIONS

The present article addressed the non-linear hysteretic properties of MR dampers. An experimental testing procedure was carried out to characterize the response of a commercial MR damper and the experimental data were used to develop a numerical model. Some model parameters that must be initially found to construct a realistic numerical response. Thus, an identification routine was developed and the predicted response was compared with the experimental data. The results showed that the selected numerical model is capable to simulate the hysteretic behavior of the MR damper.

REFERENCES

[1] B. Sapiński, J. Filuś, *Analysis of parametric models of MR linear damper*, Journal of Theoretical and Applied Mechanics, 41-2, 215-240, 2003.

[2] J.M. Ginder, *Rheology Controlled by Magnetic Fields*. Encyclopedia of Applied Physics, 16, 487, 1996.

[3] M. Braz-Cesar, R. Barros, *Semi-Active Control of an Experimental Frame using MR Dampers: numerical results and experimental validation*, COMPDYN 2011 – 3rd International Conference on Computational Methods in Structural Dynamics & Earthquake Engineering, 2011.

[4] M. Cesar, R. Barros, *Semi-Active Vibration Control of a 3-DOF Scaled Frame with a Magneto-Rheological Damper*, CST2010 – The Tenth International Conference on Computational Structures Technology, 2010.

[5] M. Braz-César, R. Barros, *Semi-active Vibration Control of Buildings using MR Dampers: Numerical and Experimental Verification*, 14th ECEE – 14th European Conference on Earthquake Engineering, 2010.

[6] M. Braz-César, R. Barros, *Properties and Numerical Modeling of MR Dampers*, 15th ICEM - 15th International Conference on Experimental Mechanics, Porto, 2012.

[7] D.H. Wang, W.H. Liao, *Magnetorheological fluid dampers: a review of parametric modelling*, Smart Materials and Structures, 20, 023001, 2011.

[8] F. Gandhi, W. Bullough, *On The Phenomenological Modeling of Electrorheological and Magnetorheological Fluid Preyield Behavior*, Journal of Intelligent Material Systems and Structures, 16- 3, 237-248, 2005.

[9] F. Goncalves, J. Koo, M. Ahmadian, *A Review of The State of the Art in Magnetorheological Fluid Technologies – Part I: MR Fluid and MR Fluid Models*, The Shock and Vibration Digest, 38- 3, 203-219, 2006.

[10] S. Guo, S. Yang, C. Pan, *Dynamic Modeling of Magnetorheological Damper Behaviors*, JIMSS, 17-1, 3-14, 2006.

[11] M. Maślanka, B. Sapiński, *Experimental Study of Vibration Control of a Cable with an Attached MR Damper*, Journal of Theoretical and Applied Mechanics, 45-4, 893-917, 2007.

[12] B.F. Spencer Jr., S.J. Dyke, M.K. Sain, J.D. Carlson, *Phenomenological model of a magnetorheological damper*, Journal of Engineering Mechanics, 123, 230-238, 1997.

[13] M.T. Avraam, *MR-fluid brake design and its application to a portable muscular rehabilitation device*, PhD thesis, 2009.

[14] M. Kamath, H. Hurt, N. Wereley, *Analysis and Testing of Bingham Plastic Behavior in Semi-Active Electrorheological Fluid Dampers*, Smart Material & Structures, 5, 576–590, 1996.

[15] Y.K. Wen, *Method for random vibration of hysteretic systems*, Journal of the Engineering Mechanics Division, 102-2, 249-263, 1976.

[16] W. Schwanen, *Modelling and identification of the dynamic behavior of a wire rope spring*, Masters thesis, 2004.

[17] C.W. Wong, Y.Q. Ni, J.M. Ko, *Steady-State oscilliation of hystereric differential model. I: Response analysis*, Journal of engineering mechanics, 120, 2271-2298, 1994.

[18] F. Ikhouane, J. Rodellar, *Systems with hysteresis: Analysis, identification and control using the Bouc-Wen model*, John Wiley & Sons, 2007.

[19] The Mathworks, Inc. *Optimization Toolbox User's Guide*, USA, 2012.

COMPDYN 2013
4th ECCOMAS Thematic Conference on
Computational Methods in Structural Dynamics and Earthquake Engineering
M. Papadrakakis, V. Papadopoulos, V. Plevris (eds.)
Kos Island, Greece, 12–14 June 2013

EFFECTIVENESS AND ROBUSTNESS OF A SEMI-ACTIVE CONTROL STRATEGY BASED ON SEISMIC EARLY WARNING INFORMATION

Giuseppe Maddaloni and Nicola Caterino

Department of Technology, University of Napoli Parthenope,
Centro Direzionale, isola C4, 80123 Naples, Italy
{nicola.caterino, giuseppe.maddaloni}@uniparthenope.it

Keywords: Seismic early warning, semi-active control, earthquake forecasting, smart materials, dissipative devices.

Abstract. *A smart passive control strategy is herein investigated to protect seismically excited structures. It is based on the use of seismic early warning information to optimally calibrate variable dampers for an higher reduction of the structural response. In particular, the adoption of magnetorheological dampers calibrated according to the forecasted value of the seismic peak ground acceleration is proposed. Such variation of the devices' behavior is supposed to be commanded once few seconds before the earthquake actually arrives to strike the site and to be kept constant for the whole duration of the excitation.*

The effectiveness of such control technique is demonstrated with reference to a case-study structure consisting in a highway bridge located in Southern California. Several nonlinear time-history analyses using seismic registrations of natural events very different each other for magnitude, peak ground acceleration, and soil types have been performed. The results in terms of reduction in seismic demand are further compared with those other control techniques from literature, applied to the same structure, lead to.

The final part of the paper is dedicated to evaluate if and how possible errors related to the peak ground acceleration estimate may affect the efficacy of the proposed strategy in reducing structural response.

The control technique resulted to be promising for the ease of implementation for structures already served by a seismic early warning network, effectiveness, even compared with active control systems, and robustness.

1 INTRODUCTION

In the last decades, installation and use of seismic early warning systems (SEWS) to help communities in being more resilient regard earthquakes attacks are growing worldwide. Starting from the Japanese experience [1], this technology has been applied in Mexico [2], in Taiwan [3], and, more recently, also in Romania [4], Turkey [5], and Italy [6]. Many kinds of application of such innovative systems can be developed, all being based on a particular exploitation of early information to take decisions for protecting people and objects against severe earthquakes.

Recent studies [7-10] showed that a quite accurate estimate of the incoming earthquake intensity is nowadays possible in terms of ground motion peak indexes, i.e. the peak ground acceleration (PGA) and velocity (PGV). Such early information can be exploited to smartly control earthquake induced vibrations by optimally calibrating special, adjustable devices installed in the structure to be protected. Kanda et al. [11] firstly explored this kind application, proposing a structural control algorithm based on the estimate of the spectral characteristics of the arriving event. In the last decade authors of this paper made efforts to contribute to the development of such integrated seismic protection system [12-16], considering it really promising, especially for structures located in seismic zones already served by an early warning network. They promoted the passive smart use of variable dissipating devices. According to this idea, mechanical properties of adjustable dampers are set just before the arrive of a seismic event at the site, as a function of the estimate of an intensity measure of the incoming earthquake, as provided by a SEWS serving the area where the structure is located. This adjustment is supposed to happen only once, keeping unaltered the devices' behaviour for the whole duration of the seismic excitation. Energy dampers based on magnetorheological (MR) fluids are considered. They may reliably change their dissipative capacity by order of magnitudes through low intensity currents fed into the devices, with reaction times comfortably bounded to 10 milliseconds, including trigger and set up times [17-19]. Therefore they are suitable to adopt in control systems exploiting SEWS, even at sites where the early warning leading time is extremely short (less than 1 second).

This idea is herein applied to a case-study consisting in a two-span continuous pre-stressed concrete highway bridge located in California, USA (details about this structure can be found in [20]. Each span is 58.5 m long. Abutments are present at the ends of the bridge, whereas the central support is provided by a 31.4 m long pre-stressed beam which rests on two columns approximately 6.9 m high. The width of the deck is 12.95 m. The total mass of the bridge is about 4200 tons; the mass of the deck is about 3200 tons (Fig. 1).

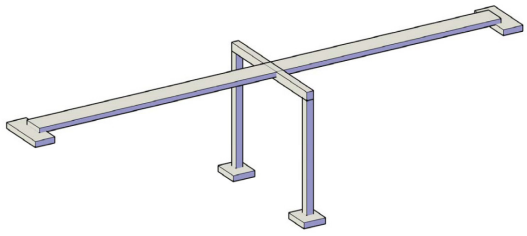


Figure 1: Schematic representation of the bridge.

The reference structure (hereafter referred to as "uncontrolled") corresponds to a non linear numerical model of the bridge including an isolation system made up of four lead rubber bearings (LRBs) at each deck-end and two LRBs at central support. At this regard note that the

bridge, for its configuration, can be considered irregular in plan. In this case, to evaluate the seismic behavior of the structure, nonlinear analysis is recommended and simpler methods could be conduct at false results [21].

The first six vibration periods results to 0.813 s (torsional shaped mode), 0.781 s (torsional/vertical), 0.645 s (vertical), 0.592 s (transverse), 0.565 s (vertical), 0.307 s (transverse). In the benchmark paper [20, 22, 23] three seismic upgrade alternatives are considered (passive, active, and semi-active, respectively) by introducing 16 devices between the deck and the abutments (nonlinear viscous dampers, hydraulic actuators, and magnetorheological – MR – dampers for the three control strategies, respectively). The performance of these techniques measured in terms of response reduction they lead to are herein compared with that of the proposed control strategy.

2 SMART PASSIVE VIBRATION CONTROL USING A SEWS

The use of MR dampers as smart passive devices is suggested herein to effectively control the case-study bridge under earthquake actions. The mechanical behaviour of such devices is considered to be adjusted once, shortly before the incoming earthquake, according to a forecasted intensity measure of the latter provided by a SEWS available at the site. Regarding the way to use SEWS information to calibrate the semi-active (SA) devices, the following procedure is proposed: (i) Modal analysis of the structure and foundation soil investigations are performed; (ii) once the SEWS provides an estimate of the PGA of an incoming earthquake, the elastic damped response spectrum according to the Eurocode 8 rules has to be defined; (iii) the spectral acceleration $S_a(T_1)$ is evaluated at the fundamental period of the bridge; (iv) this value is exploited to set the voltage u_c to be given to MR dampers within a given interval $0 \sim u_{c,max}$ (herein $u_{c,max}$ is assumed to be 10 V), according to a control algorithm $u_c(S_a)$ so as to obtain the higher reduction of the structural response during the seismic excitation.

It is worth noting that the effectiveness of the proposed strategy is strongly dependent on the ability of the control algorithm to drive MR dampers to be the optimal "passive" devices for the expected seismic action. A possible way to calibrate such control logic is presented in the following with reference to the case-study assumed. This procedure is based on the results of several nonlinear time-history analyses performed under natural accelerograms very different each other, testing a wide variety of configurations (i.e. values of feeding voltage) for the MR dampers, and measuring the achieved response reduction via the adoption of specific performance indexes.

2.1 Case-study structure: definition of the control algorithm to drive MR dampers

A total of sixteen natural earthquakes (Table 1) have been considered to calibrate the control logic needed to control the MR dampers' behavior for the case-study bridge as a function of the information (expected PGA) given by the SEWS about the incoming seismic event. The last six earthquakes as listed in Table 1 are those proposed in the benchmark paper [20, 22, 23]. The ten additional events have been chosen to cover a wider range of moment magnitudes (5.75 to 7.62), PGA values (0.151 to 1.157 g) and soil types (A to C, according to the Eurocode 8 [24] definition).

The effectiveness of the control strategies proposed for the bridge is herein measured through three performance indexes named J_i (i=1, 2, 3). They refer to the ratio of the values different response parameters assume in the controlled and in the uncontrolled conditions respectively (so that smaller values of J_i correspond to an higher reduction of the structural response). These indexes refer to the peak shear force at the base of the piers, the peak overturning moment in the same sections, and the peak mid-span displacement for the deck

respectively. Authors acknowledge that many other criteria could be adopted to compare alternative upgrade strategies for the bridge [20, 22, 23]. Nevertheless the adoption of multi-criteria decision procedure [25], mandatory to make a summary judgment when an high number of criteria is involved, is beyond the scope of this work.

N.	Earthquake	Country	Year	M_w	PGA EW / NS [g]	Soil type
1	Coyote Lake	California	1979	5.75	0.434 / 0.316	B
2	Friuli	Italy	1976	6.50	0.351 / 0.315	B
3	Northwest	China	1997	6.10	0.300 / 0.274	C
4	Irpinia	Italy	1980	6.90	0.358 / 0.251	B
5	Corinth	Greece	1981	6.60	0.240 / 0.296	C
6	San Salvador	El Salvador	1986	5.80	0.406 / 0.612	C
7	San Fernando	California	1971	6.61	0.324 / 0.268	B
8	Duzce	Turkey	1999	7.14	0.728 / 0.822	C
9	Taiwan	Taiwan	1986	7.30	0.242 / 0.160	C
10	Trinidad	Colorado	1980	7.20	0.156 / 0.151	A
11	Kobe	Japan	1995	6.90	0.503 / 0.509	C
12	Northridge	California	1994	6.69	0.472 / 0.838	B
13	Chi-Chi	Taiwan	1999	7.62	0.417 / 1.157	B
14	El Centro	California	1940	6.91	0.313 / 0.215	C
15	Izmit	Turkey	1999	7.60	0.728 / 0.822	B
16	North Palm S.	California	1986	6.10	0.612 / 0.492	C

Table 1: Main properties of the earthquakes assumed for the analyses.

Several nonlinear analyses of the bridge have been made, under each of the 16 selected earthquakes, each time feeding the MR devices with a different voltage value, keeping it constant for the overall duration of the motion. In particular, command voltage values u_c from 0 to 10 V with a step size of 25 mV have been assumed, for a total of 6416 analyses. For each of these, the following operations have been done:

a) the values of the performance indexes J_i (with i=1, 2, 3) have been recorded as measures of the structural response under a given earthquake and for a certain calibration of the variable control devices;

b) for each index and each earthquake, a diagram has been drawn showing the correlation between that index J_i and the value of command voltage u_c;

c) for each of these cases, the optimal value of voltage $u_{c,opt,i}$ (i.e. the one leads to the minimum value $J_{i,min}$ of J_i) has been found; then an interval of suggested voltage values $\Delta_{uc,opt,i}$ around $u_{c,opt,i}$ has been defined including all the u_c values corresponding to values of J_i less than $1.3J_{i,min}$ (i.e. assuming a tolerance of 30% in terms of structural performance) and also less than 1 (Fig. 2).

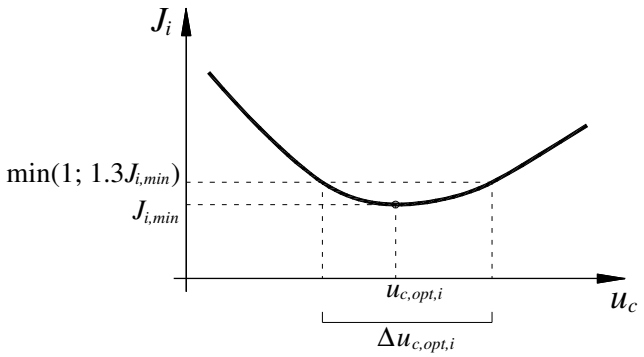


Figure 2: Definition of the optimal interval $\Delta_{uc,opt,i}$ of voltage for MR devices according to the i-th criterion.

Intervals $\Delta_{uc,opt,1}$, $\Delta_{uc,opt,2}$ and $\Delta_{uc,opt,3}$ in most cases resulted to be quite similar each other, obviously referred to the same seismic event. For the sake of brevity only intervals $\Delta_{uc,opt,2}$ (i.e. related to the index J_2, proportional to the peak base moment demand) are shown herein. Fig. 3 reports 16 vertical gray lines, each one having as abscissa the value $S_a(T_1)$ corresponding to one of the considered earthquakes, and as ordinates the interval $\Delta_{uc,opt,2}$ in which the command voltage for MR dampers should be chosen for a higher reduction of the structural response (measured by J_2) under the action of that seismic event. The black points represent the "best" value (namely $u_{c,opt,2}$) of the interval. In the paper, for each earthquake, the PGA value refers to the EW component (preliminarily chosen as the most significant for the present case).

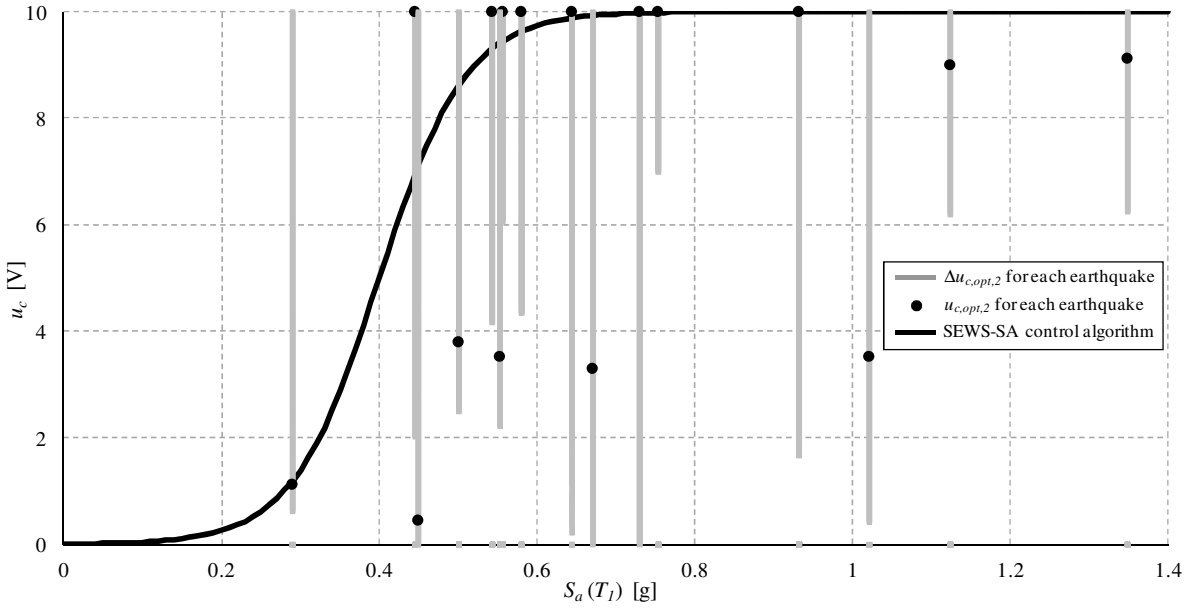


Figure 3: Values of $u_{c,opt,2}$ and of $\Delta_{uc,opt,2}$. Adopted control algorithm.

Starting from these results, a continuous control law $u_c[S_a(T_1)]$ able to give, for each value of $S_a(T_1)$, a voltage intensity u_c within the corresponding interval $\Delta_{uc,opt,2}$, as close as possible to the optimal value $u_{c,opt,2}$, has been investigated. The following relationship resulted to be a viable candidate, giving values of u_c tending to 0 V for small values of S_a, values tending to $u_{c,max}$=10 V for higher values of spectral acceleration:

$$u_c\left[S_a(T_1)\right] = \left[1 + tanh\left(\frac{S_a(T_1) - \alpha}{\beta}\right)\right] \cdot \frac{u_{c,max}}{2} \tag{1}$$

where α and β are two parameters (to be expressed in g – gravitational acceleration – as the spectral acceleration S_a) governing the shape of this monotonically increasing function. Values of α and β within the intervals 0.00~2.00 g and 0.01~0.50 g (with a step of 0.01 g) make the shape of the curve have a physical sense. The optimal value for α (0.40) and β (0.11) has been individuated among those allow the curve representing Eq. (1) to cross all the sixteen gray lines in Fig 3 as the one corresponding to the higher reduction of the structural response measured by J_1, J_2 and J_3. The resulting algorithm is herein proposed to semi-actively control the bridge by exploiting seismic early warning information (in the following this strategy will be referred to as SEWS-SA). It is graphically represented in Fig. 3 with a black line.

2.2 Effectiveness of the proposed control strategy

Table 2 shows the value of response parameters J_1, J_2 and J_3 the proposed strategy and the benchmark ones leaded to with reference to the 16 seismic inputs. Bold numbers indicate, for each earthquake, the best performance among those due to the different strategies. The same data are represented for an easier comparison in graphical form in Figs. 4 and 5.

These results demonstrate the effectiveness of the proposed strategy for earthquakes with different characteristics as magnitudes, PGA and soil types. In particular, the SEWS-SA technique turned out to give results in many cases better than the ones corresponding to the other strategies, in the remaining cases to comparable or slightly worse performances. Pie charts in Fig. 5 report the number of times (out of 16) each technique outperforms all others in terms of J_1, J_2 and J_3 separately. Information synthesized in this figure allow to conclude that the proposed strategy results to be more effective in a largest number of cases (34 out of 48 considering J_1, J_2 and J_3 together). This conclusion is furthermore emphasized by Table 3 that reports the mean values of J_1, J_2 and J_3 each control technique leads to with reference to the set of 16 seismic inputs. It shows how the proposed strategy on average gives a reduction of the peak base shear very close to the one corresponding to the other compared techniques, leading instead to significantly better results in terms of base moment and mid-span displacement.

Earthquake	J_1				J_2				J_3			
	SEWS-SA	Passive	Semi-Active	Active	SEWS-SA	Passive	Semi-Active	Active	SEWS-SA	Passive	Semi-Active	Active
1	**0.83**	0.83	0.93	0.94	**0.81**	0.82	0.93	0.94	0.74	**0.73**	0.81	0.82
2	0.81	**0.67**	0.74	0.73	**0.47**	0.58	0.72	0.73	**0.3**	0.59	0.74	0.72
3	**0.50**	0.61	0.82	0.84	**0.24**	0.53	0.72	0.74	**0.22**	0.60	0.79	0.80
4	0.87	**0.75**	0.86	0.95	**0.44**	0.62	0.87	0.96	**0.29**	0.61	0.88	0.97
5	0.92	**0.83**	0.83	0.86	**0.51**	0.62	0.82	0.85	**0.32**	0.62	0.83	0.85
6	**0.53**	0.77	0.94	0.93	**0.55**	0.81	0.98	0.98	**0.41**	0.61	0.75	0.75
7	0.87	0.77	**0.75**	0.76	**0.47**	0.52	0.70	0.74	**0.31**	0.55	0.75	0.76
8	0.96	**0.79**	0.91	0.92	**0.57**	0.89	0.98	0.99	**0.35**	0.59	0.73	0.76
9	0.92	0.98	0.96	**0.90**	**0.67**	0.70	0.69	0.80	**0.45**	0.53	0.67	0.78
10	0.90	0.94	0.76	**0.70**	**0.53**	0.55	0.65	0.70	0.51	**0.41**	0.66	0.70
11	1.06	0.86	0.81	**0.79**	**0.53**	0.54	0.69	0.71	**0.57**	0.62	0.69	0.71
12	**0.68**	0.78	0.9	0.91	**0.93**	0.96	0.98	0.98	**0.54**	0.70	0.86	0.88
13	**0.68**	0.76	0.85	0.88	**0.93**	0.97	0.98	0.98	**0.54**	0.71	0.78	0.81
14	0.68	**0.64**	0.80	0.79	**0.37**	0.57	0.72	0.76	**0.29**	0.65	0.79	0.78
15	0.97	**0.78**	0.91	0.93	**0.57**	0.88	0.98	0.99	**0.35**	0.59	0.73	0.76
16	1.67	1.26	**0.98**	0.98	0.86	**0.65**	0.78	0.78	**0.57**	0.64	0.82	0.83

Table 2: Comparison of the response reduction given by the four control strategies for the sixteen earthquakes considered

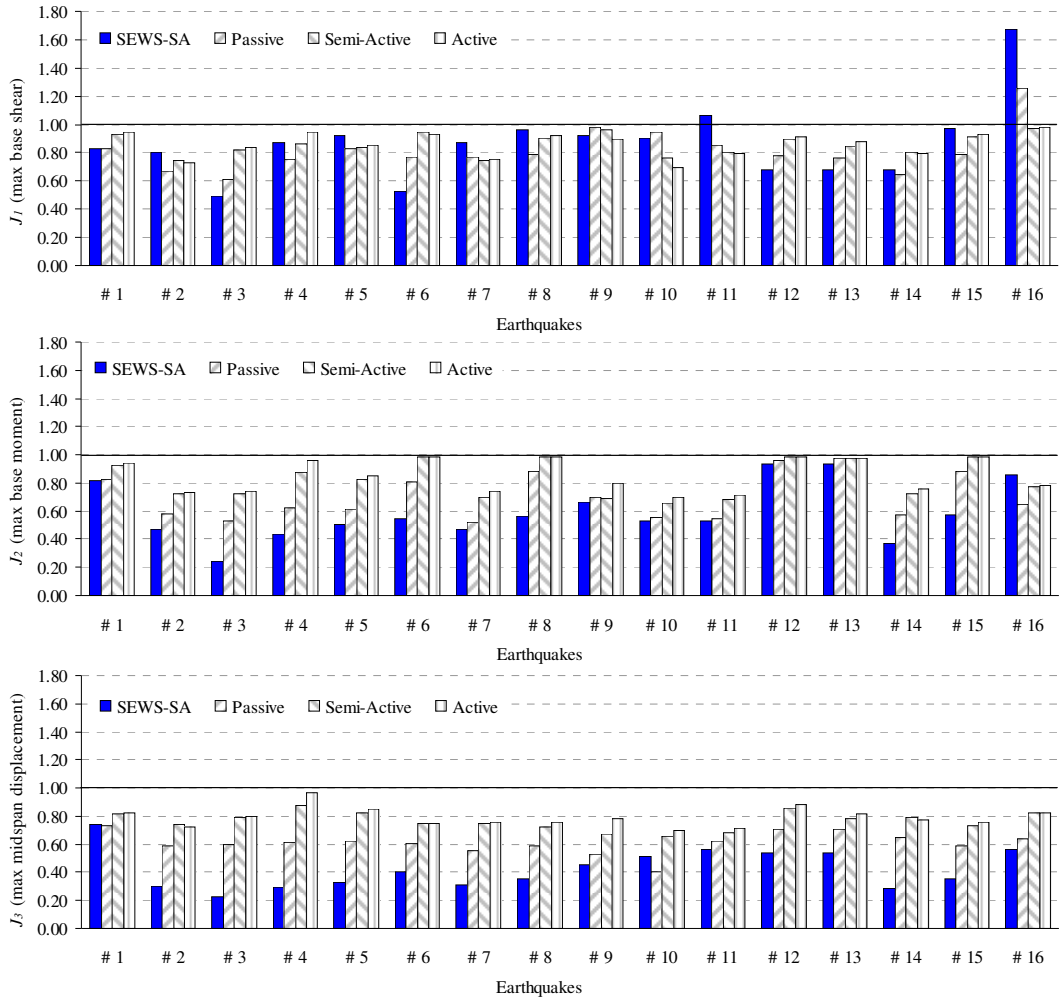


Figure 4: Comparison of the four control strategies in terms of J_1, J_2 and J_3, for each of the 16 earthquakes.

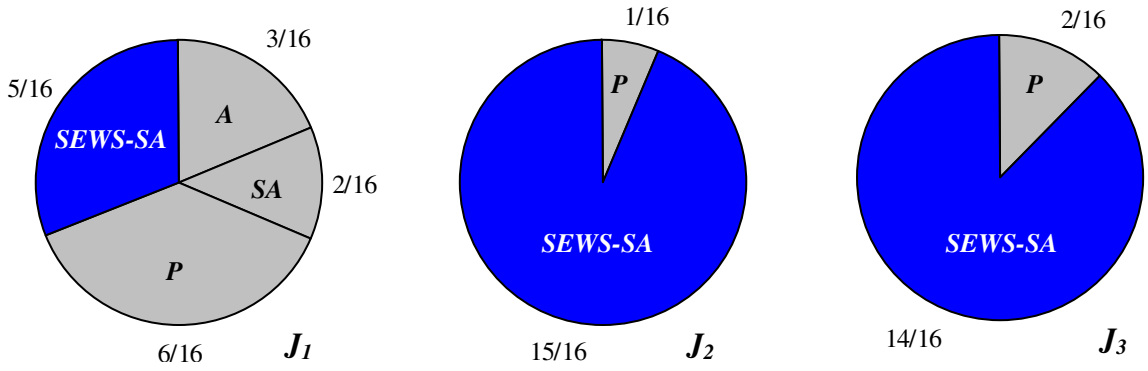


Figure 5: Number of times, out of the 16 cases, each strategy outperforms all others in terms of J_1, J_2 and J_3. "SEWS-SA": proposed strategy, "A": active, "SA": semi-active, "P": passive.

	SEWS--SA	Passive	Semi-Active	Active
mean J_1	0.87	0.81	0.86	0.86
mean J_2	0.59	0.70	0.83	0.85
mean J_3	0.42	0.61	0.77	0.79

Table 3: Mean values of performance indexes for the overall comparison of the four alternative control strategies

2.3 Robustness of the proposed control strategy. Role of SEWS uncertainties.

The sensitivity of the proposed SEWS-SA control algorithm (Eq. 1) to uncertainties in the estimate of PGA is analyzed as follows. The MR devices are calibrated as already explained in the previous sections but using a range of physical PGA values from a minimum of 0 g to a maximum of 2 g, considering that the PGA value estimated by SEWS (PGA_{SEWS}) can be even very different from the actual value (PGA_{ACTUAL}) due to a wrong estimation analysis.

As the PGA_{SEWS} value changes, MR are calibrated in a different manner according to the proposed control algorithm so as to modify the structural response even if the exciting earthquake (i.e. the real one) is the same. In this case, each of the performance indexes J_i can be intended as a function of the random variable PGA_{SEWS}. Fig. 6 shows the domain of values of J_1 for any given earthquake record when the algorithm driving the MR dampers is fed by a value of PGA_{SEWS} variable in the range 0~2 g, independently from the actual PGA value of that event. The circles indicate the values of index J_1 obtained from nonlinear analyses performed correctly setting the devices according to the proper estimate PGA_{ACTUAL}. For some earthquakes, J_1 appears to be very low sensitive to the value of PGA predicted (short lines). In other cases, its variation becomes more significant (longer lines). It is worth noting that in most cases the range of J_1 values due to the incorrect prediction of the PGA by the SEWS corresponds to a worst performance, but only in a very limited number of cases leads to values higher than 1. Finally, for each earthquake J_1 values corresponding to MR dampers turned off are also indicated in the same figure with a square, simulating black-out conditions. A fail-safe behavior of the proposed strategy can be easily drawn from the figure.

Similar results have been obtained with reference to J_2 and J_3 indexes, herein not reported for brevity.

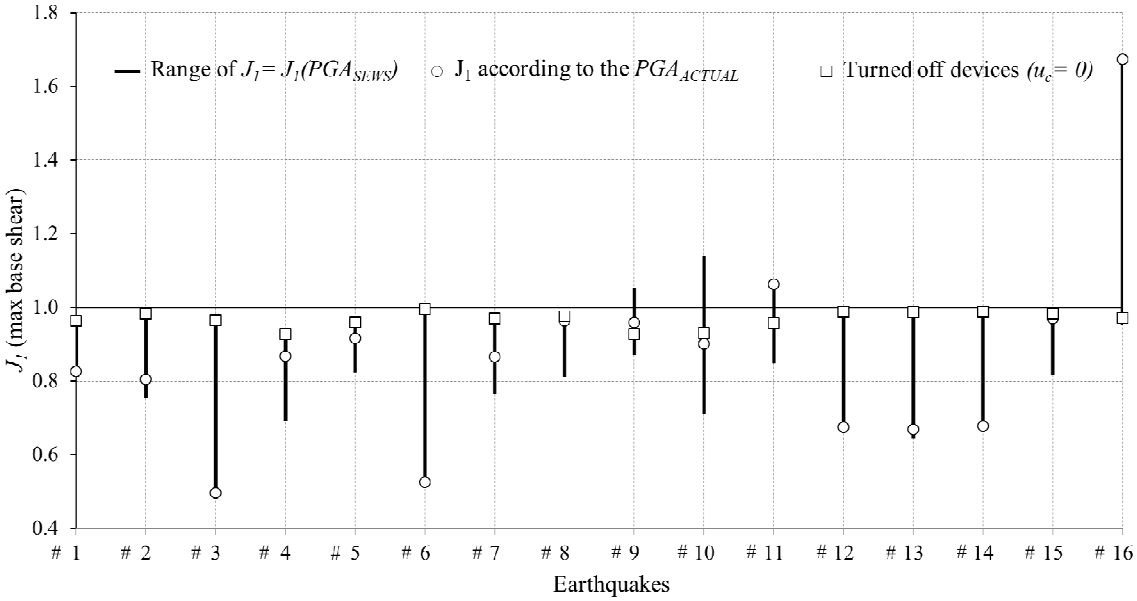


Figure 6. Seismic response of the bridge in terms of J_1 for PGA values given within 0~2g

To further assess the robustness of the proposed control strategy, the joint probability distribution of J_i (for i=1, 2, 3) has been evaluated starting from a given probability distribution for PGA. The latter has been assumed to be lognormal with a mean value equal to PGA_{ACTUAL} and coefficient of variation (CoV) equal to 0.45 (Fig. 7 shows the plot of the probability density function - PDF), according to the indications by Iervolino et al. [26].

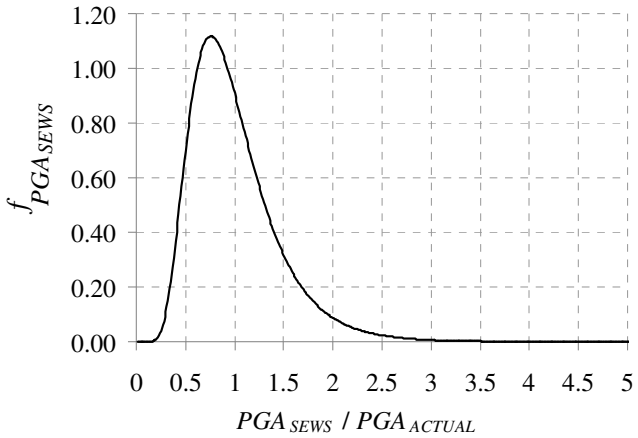


Figure 7. Lognormal PDF of PGA_{SEWS} with mean PGA_{ACTUAL} and CoV 0.45

For each earthquake and each performance index J_i the following steps have been performed: (i) the finite interval of PGA_{SEWS} values 0.01~2.00 g have been considered; this is sub-divided using a step size of 0.01 g; (ii) for each discrete value of PGA_{SEWS}, the probability mass value has been evaluated starting from the knowledge of the continuous PDF said above; in other words the transformation of the PDF into the PMF (probability mass function) of PGA_{SEWS} has been performed; (iii) for each discrete value of PGA_{SEWS}, the corresponding J_i value has been obtained; (iv) since the transformation $J_i=J_i(PGA_{SEWS})$ resulted to be not a one-to-one mapping, for a given j_i value of J_i let $PGA_{SEWS,k}$ (k=1, 2, …, m) represent the roots of the equation $J_i(PGA_{SEWS})=j_i$; then the probability of the event $J_i=j_i$ is obtained by adding the probability of PGA_{SEWS} at all the roots:

$$p_{Ji}(j_i) = \sum_{k=1}^{m} p_{PGA_{SEWS}}\left(PGA_{SEWS,k}\right) \tag{2}$$

This analysis has been performed with reference to J_1, J_2 and J_3, leading to similar results in terms of PMF shape and values. Outcomes for J_1 are shown in Fig. 8. The J_1 value corresponding to PGA_{ACTUAL} is individuated, within the range of values (i.e. vertical black lines), by a small white circle, as in Figure 10. Horizontal gray lines are the probability histograms of J_1. The following comments can be drawn:

- the $J_1(PGA_{ACTUAL})$ value resulted to be the most likely for the large majority of cases (15 out of 16 earthquakes), with a mass probability value ranging from 48% to 97% depending on the considered seismic action (earthquake #10 is the exception; for this, probability values resulted to be slightly scattered around the 10% value for each possible J_1 outcome);
- probability values for J_1 different from $J_1(PGA_{ACTUAL})$ generally are strongly reduced compared to the latter.

These results allow to confirm that unavoidable errors in the PGA estimates provided by the SEWS do not propagate to the seismic response. Conversely, the proposed strategy turns out to be able to damp these errors, resulting in a robust seismic behaviour of the protected structure.

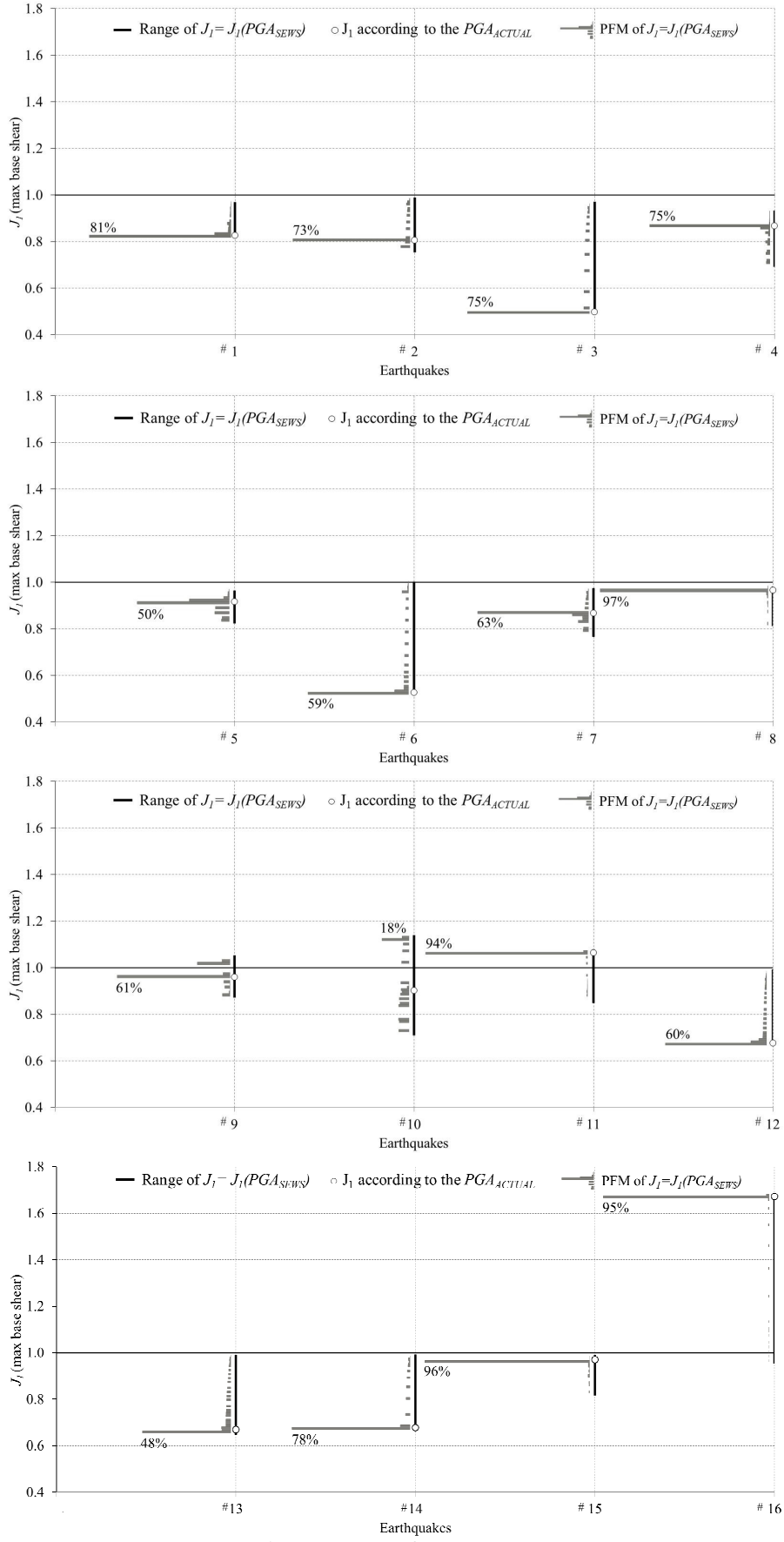


Figure 8. PMF of $J_1(PGA_{SEWS})$

3 CONCLUSIONS

A possible methodology for exploiting earthquake information derived by a seismic early warning system (SEWS) in the framework of semi-active control strategies by using magnetorheological (MR) dampers has been herein proposed. This system has a relatively simple, yet effective, objective. Starting from an existing SEWS, in addition to its standard feature of emitting a warning message, authors proposes to exploit the system so as to utilize it to optimize the structural response of a structure, without any additional sensor and by the adoption of passive, but smart (adjustable) damping devices.

The present paper describes the application of this innovative and integrated protection technique to a case-study highway bridge located in Southern California. The seismic response of the benchmark bridge is investigated by nonlinear time-history analyses under 16 real earthquake ground excitations covering a wide variety of magnitudes, PGA and soil types.

The research on seismic early warning is recently going in the direction so to make a SEWS capable to quickly give reliable estimate of many features of the incoming earthquake. Herein the prediction of the PGA value is assumed to be available. A fast forecast of the PGA at a given site starting from an estimate of typical intensity measures, like for instance the magnitude, actually seems to be quite a mature subject [7-10] compared to a reliable estimate of more sophisticated quantities like the frequency content and/or the spectral accelerations. Furthermore, the effect itself of these quantities on systems response is still largely debated [27].

Several trials and simulations have been performed to define the control algorithm, i.e. relationship useful to determine the optimal amount of voltage to be given to the dampers according to the spectral acceleration evaluated at the fundamental period of the structure, in turn defined starting from the forecasted PGA value.

The results demonstrate the effectiveness of the proposed strategy for earthquakes very different each other. In particular, the SEWS-SA technique turned out to give results sometimes better and sometimes comparable to other consolidated strategies at a fraction of the cost. Only in few cases the numerical analyses yielded slightly worse performances.

Possible errors on estimation of PGA provided by SEWS and their influence on the effectiveness of the proposed control system have been also discussed. The results obtained confirm that unavoidable errors in the PGA estimates provided by the SEWS do not propagate to the seismic response of the controlled structure. Conversely, the proposed strategy turns out to damp these errors, resulting in a robust seismic behaviour of the protected structure.

REFERENCES

[1] Y. Nakamura Y, Earthquake alarm system for Japan Railways. *Japanese Railway Engineering*, **8(4)**: 3-7, 1989

[2] J. Espinosa-Aranda, A. Jimenez, G. Ibarrola, F. Alcantar, A. Aguilar, M. Inostroza, S. Maldonado, Mexico City Seismic Alert System. *Seismological Research Letters*, **66(6)**, 42-53, 1995.

[3] Y.M. Wu, T.L. Teng, A virtual subnetwork approach to earthquake early warning. *Bulletin of the Seismological Society of America*. **92(5)**, 2008-2018, 2002.

[4] F. Wenzel, G. Marmureanu G, Earthquake Information Systems, in Pageoph Topical Issue, *Proc. Volume 22nd Int. Tsumani Symposium*, Chania, Greece, 2006.

[5] M. Erdik, Y. Fahjan, O. Özel, H. Alcik, A. Mert, M. Gul, Istanbul Earthquake Rapid Response and the Early Warning System. *Bulletin of Earthquake Engineering*. **1**, 157-163, 2003.

[6] G. Iannaccone, A. Zollo, L. Elia, V. Convertito, C. Satriano, C. Martino, G. Festa, M. Lancieri, A. Bobbio, T.A. Stabile, M. Vassallo, A. Emolo, A prototype system for earthquake early-warning and alert management in southern Italy. *Bulletin of Earthquake Engineering*, doi: 10.1007/s10518-009-9131-8, 2009.

[7] V. Convertito, I. Iervolino, A. Zollo, G. Manfredi, Prediction of response spectra via real time earthquake measurements. *Soil Dynamics and Earthquake Engineering*, **28**, 492-505, 2008.

[8] I. Iervolino, C. Galasso, G. Manfredi, Information-dependent lead-time maps for earthquake early warning in the Campania region. *Proc. 14th World Conference on Earthquake Engineering*, 2008.

[9] A. Zollo, G. Iannaccone, M. Lancieri, L. Cantore, V. Convertito, A. Emolo, G. Festa, F. Gallovic, M. Vassallo, C. Martino, C. Satriano, P. Gasparini, Earthquake early warning system in southern Italy: Methodologies and performance evaluation. *Geophysical research letters*, 2009.

[10] H.M. Brown, R.M. Allen, M. Hellweg, O. Khainovski, D. Neuhauser, A. Souf A, Development of the ElarmS methodology for earthquake early warning: Realtime application in California and offline testing in Japan. *Soil Dynamics and Earthquake Engineering*, **31**, 188-200, 2011.

[11] K. Kanda, T. Kobori, Y. Ikeda, H. Koshida, The development of a "Pre-arrival transmission system for earthquake information" applied to seismic response controlled structures. *1st World Conference on Structural Control*, TA-3, 23-32, 1994.

[12] A. Occhiuzzi, V.F. Grasso, G. Manfredi, Early warning systems from a structural control perspective. *3rd European Conference on Structural Control*, 2004.

[13] A. Occhiuzzi, I. Iervolino, G. Manfredi, Feedforward control algorithms for seismic early warning systems. *4th World Conference on Structural Control and Monitoring. 4WCSCM-266*, 2006.

[14] A. Occhiuzzi, N. Caterino, G. Maddaloni, Structural control strategies for seismic early warning systems. *14th World Conference on Earthquake Engineering*, 2008.

[15] G. Maddaloni, N. Caterino, A. Occhiuzzi, Semi-active control of the benchmark highway bridge based on seismic early warning systems. *Bulletin of Earthquake Engineering*, **9 (5)**, 1703-1715, 2011. doi:10.1007/s10518-011-9259-1

[16] G. Maddaloni, N. Caterino, G. Nestovito, A. Occhiuzzi, Use of seismic early warning information to calibrate variable dampers for structural control of a highway bridge: evaluation of the system robustness. *Bulletin of Earthquake Engineering*. (in press)

[17] A. Occhiuzzi, M. Spizzuoco, G. Serino, Experimental analysis of magnetorheological dampers for structural control. *Smart Materials and Structures*, **12(5)**,703-711, 2003.

[18] N. Caterino, M. Spizzuoco, A. Occhiuzzi, Understanding and modelling the physical behaviour of magnetorheological dampers for seismic structural control. *Smart Materials and Structuters*, **20** 065013, 2001. doi: 10.1088/0964-1726/20/6/065013.

[19] N. Caterino, M. Spizzuoco, A. Occhiuzzi, Promptness and dissipative capacity of MR dampers: experimental investigations. *Structural Control and Health Monitoring*, 2013 (in press).

[20] A. Agrawal, P. Tan, S. Nagarajaiah, J. Zhang, Benchmark structural control problem for a seismically excited highway bridge – Part I: Phase I Problem definition. *Structural Control and Health Monitoring*, **16**, 509-529, 2009.

[21] G. Magliulo, G. Maddaloni, E. Cosenza, Extension of N2 method to plan irregular buildings considering accidental eccentricity. *Soil Dynamics and Earthquake Engineering*, **43**, 69-84, 2012. doi: 10.1016/j.soildyn.2012.07.032

[22] P. Tan, A. Agrawal, Benchmark structural control problem for a seismically excited highway bridge— Part II: phase I sample control designs. *Structural Control and Health Monitoring*, **16**, 530–548, 2009.

[23] S. Nagarajaiah, S. Narasimhan, A. Agrawal, P. Tan, Benchmark structural control problem for a seismically excited highway bridge—Part III: phase II sample controller for the fully base-isolated case. *Structural Control and Health Monitoring*, **16**, 549–563, 2009.

[24] Eurocode 8, *Design of structures for earthquake resistance – Part 1: General rules, seismic actions and rules for buildings*. Brussels, 2003.

[25] N. Caterino, I. Iervolino, G. Manfredi, E. Cosenza, Multi-Criteria Decision Making for Seismic Retrofitting of RC Structure. *Journal of Earthquake Engineering*, **12**, 1-29, 2008. doi: 10.1080/13632460701572872

[26] I. Iervolino, M. Giorgio, C. Galasso, G. Manfredi, Uncertainty in early warning predictions of engineering ground motion parameters: what really matters? *Geophysical Research Letters*, **36** L00B06, 2009.

[27] G. Maddaloni, G. Magliulo, E. Cosenza, Effect of the seismic input on nonlinear response of r/c building structures. *Advances in Structural Engineering*, **15(10)**, 1861-1877, 2012. doi: 10.1260/1369-4332.15.10.1861.

COMPDYN 2013
4th ECCOMAS Thematic Conference on
Computational Methods in Structural Dynamics and Earthquake Engineering
M. Papadrakakis, V. Papadopoulos, V. Plevris (eds.)
Kos Island, Greece, 12–14 June 2013

REGIONAL-BASED CONTROL ALGORITHMS USING EARLY WARNING INFORMATION FOR SEISMIC PROTECTION OF A HIGHWAY BRIDGE

Giuseppe Maddaloni[1], Nicola Caterino[1], Gianluca Nestovito[1] and Antonio Occhiuzzi[1]

[1]Department of Technology, University of Napoli Parthenope, Centro Direzionale, isola C4, 80123 Naples, Italy
{giuseppe.maddaloni, nicola.caterino, gianluca.nestovito, antonio.occhiuzzi}@uniparthenope.it

Keywords: Early warning, semi-active control, benchmark highway bridge, magnetorheological dampers.

Abstract. *The possible exploitation of a seismic early warning system (SEWS) in the framework of semi-active (SA) structural control using magnetorheological (MR) dampers has been investigated by authors in the last years. The main idea consists in changing the MR damper behaviour according to the forecasted intensity (expressed in terms of peak ground acceleration, PGA) of an incoming earthquake provided by the SEWS to obtain the higher seismic demand reduction for the hosting structure. In other words, a "smart passive" use of MR dampers driven by a SEWS information has been promoted.*

The present paper focuses on the control algorithm needed to select the optimal voltage u_c to set the variable devices according to the PGA estimate. The authors found that the different characteristics of earthquakes that occur in different sites, as frequency content, duration and magnitude, could play a significant role in the definition of the best control algorithm. For this reason, these aspects are considered by generating regional-based control algorithms. Different u_c(PGA) logics have been built for three selected worldwide regions (Japan, California and Italy) on the basis of the results of several dynamic simulations performed using natural earthquakes recorded in each of these area.

The effectiveness of the proposed control algorithms has been checked with reference to a case-study: a prestressed concrete highway bridge.

1 INTRODUCTION

In the last decade the research for unconventional strategies for the seismic protection of structures has recorded remarkable progress. Most of the innovative approaches proposed aim to modify the dynamic response of the structures to reduce the vibrations induced by the earthquake [1]. In this field, the semi-active (SA) control is considered as the emerging technology for seismic protection [2].

In the same time, "geophysics science" has made important progress in the development of a system, usually called Seismic Early Warning System (SEWS), capable to predict, few seconds before, the arrival of an earthquake [3]. Generally speaking SEWS can be used to prevent devastating damages, by the knowledge, ahead of time, of some earthquake parameters. These measures can be used for different purposes, e.g. evacuation of buildings, shut-down of critical systems (nuclear and chemical reactors), stop of high-speed trains. Actually applications of SEWS are growing worldwide: first in Japan [4], more recently in California [5] and Italy [6].

The authors, in their recent studies, have tested an innovative technology capable to exploit a SEWS in the framework of semi-active control system [7, 8, 9] by the use of magnetorheological (MR) dampers. As known, the latter are able to achieve a wide range of physical behaviours using low-power electrical currents [10]. Authors are investigating a possible "smart passive" use of MR dampers with the aim of joining positive aspects of both semi-active (e.g. adaptability to seismic demand) and passive strategies (ease of implementation and use) and of overcoming the operational limits of the former (e.g. related to possible and unpredictable malfunctions of the control chain [11] and delays [12]). The strategy is proposed to effectively control a highway bridge proposed as a benchmark structural control problem by Agrawal et al. [13], Nagarajaiah et al. [14] and Tan et al. [15]. In order to set the optimal behaviour for MR dampers, appropriate algorithms have been evaluated.

Two alternative control algorithms (strategies) have been proposed in 2011 [7] to calibrate MR dampers (i.e. to select the optimal value of feeding voltage u_c). The first one is based on the estimate of the Peak Ground Acceleration (PGA) of the incoming earthquake, the second one (resulted to be more effective) on the forecasted elastic spectral acceleration (S_a) at the fundamental period of the structure (T_1). In that pioneering paper on the subject both strategies allowed a strong reduction of the structural response, even compared with the three control techniques considered in the benchmark paper. However, a fast forecast of the PGA at a given site starting from an estimate of typical intensity measures, like for instance the magnitude, seems to be quite a mature subject [5] compared to a reliable estimate of more sophisticated quantities like the frequency content and/or the spectral accelerations. Furthermore, the effect itself of these quantities on systems response is still largely debated [16].

In Maddaloni et al. [9] the Peak Ground Acceleration (PGA) value is considered as the unique seismic parameter available by the SEWS and a relationship u_c(PGA) is assumed to set the MR dampers. Several analyses have been performed to demonstrate the effectiveness of the innovative idea proposed.

In this paper, with the purpose to further increase the performance achieved, a regional-based control algorithms, i.e. different relationships u_c(PGA) for each one of three world regions selected (Italy, California and Japan) are presented. In this way the different characteristics of earthquakes that occur in different sites, as frequency content, duration and magnitude, can be considered.

The proposed strategy is investigated by several numerical simulations, considering a total of forty-five strong real earthquakes, fifteen for each region.

2 THE BENCHMARCK HIGHWAY BRIDGE

A brief description about technical characteristics of the benchmark bridge [13, 14, 15] is herein presented.

Located in Orange Country of Southern California, the bridge consists of a two-span continuous cast-in situ pre-stressed concrete. The total length of each span is 58.5 m long, while the long pre-stressed support beam is 31.4 m. This central support is linked to two columns 6.9 m high. The mass of the deck is about 3200 tons while the total mass of the bridge is 4200 tons (Fig. 1). The abutments are skewed at 33°, so the bridge can be considered irregular in plan. In this case, to evaluate the seismic behavior of the structure, nonlinear analysis is recommended and simpler methods could be conduct as false results [17].

The bridge deck is isolated using four non-seismic elastomeric pads at each abutment, while eight fluid dampers are installed between the end abutments and deck in order to reduce seismic response. However in evaluation model, lead rubber bearings are used to replace eight traditional non seismic elastomeric pads (Fig. 2). This configuration represents the uncontrolled structure used as comparison to establish the effectiveness of the control systems proposed. The first mode of the structure is torsional with a natural period T_1=0.813 s.



Figure 1. Two views of the benchmark highway bridge

In the benchmark paper three sample control strategies (passive, semi-active and active) including devices, control algorithms and sensors are designed and presented for comparison. The passive strategy is based on 16 nonlinear viscous dampers, placed between the deck and the abutments. The active strategy is based on 16 hydraulic actuators, placed as before. The semi-active strategy is based on 16 MR dampers modeled according to the Bouc–Wen hysteretic model.

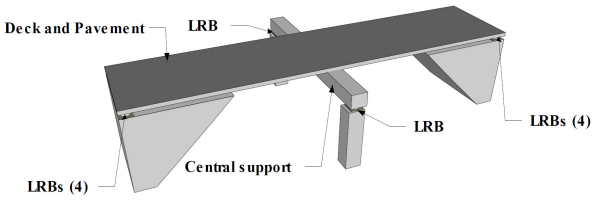


Figure 2. Uncontrolled configuration of the benchmark highway bridge

3 SEISMIC RECORDS FOR NONLINEAR ANALYSIS

As already cited, the present paper focuses on the control algorithm needed to select the optimal voltage u_c to set the variable devices according to the PGA estimate. The authors found that different characteristics of earthquakes occurring in several sites, as frequency content, duration and magnitude, could play a significant role in the definition of the best control algorithm. For this reason, three different worldwide regions are selected.

The considered regions are Italy, California and Japan. A total of forty-five strong real earthquakes, (fifteen for each region) all recorded on soil type B according the Eurocode 8 classification [18] are assumed as input for nonlinear analysis of the benchmark bridge. For the excitation of the longitudinal (EW) and transverse (NS) directions of the bridge, both

components are simultaneously used. The main characteristics of the earthquake ground motions are shown in Table 1, 2 and 3 for Italy, California and Japan regions respectively.

The seismic inputs have been downloaded from the Italian Acceleration Archive (ITACA) [19], the Pacific Earthquake Engineering Research Center (PEER) [20] and the National Research Institute for Earth Science and Disaster Prevention (NIED) [21].

For the evaluation of the seismic performance of the bridge all the earthquakes have been used at the full intensity. As visible, the fifty-five accelerograms, even if are all referred to the same soil type B, cover a wide range of magnitudes (from 4.70 to 7.30 at magnitude moment scale) and PGA (from 0.101 g to 2.080 g).

N.	Earthquake name	Date [dd-mm-yy]	M_w	PGA NS [g]	PGA EW [g]	Epicentral distance [km]
1	Ancona-Rocca	21-06-72	6.2	0.179	0.084	22.87
2	Aquila-V.Aterno	06-04-09	6.3	0.353	0.330	5.65
3	Aquila-V.Aterno	06-04-09	6.3	0.443	0.402	9.63
4	Aquila	06-04-09	6.3	0.657	0.545	8.87
5	Brienza	23-11-80	6.9	0.217	0.178	42.21
6	Conza-Piana	01-12-80	5.5	0.166	0.201	9.54
7	Forgaria	15-09-76	5.9	0.349	0.332	16.83
8	Forgaria	11-09-76	5.6	0.129	0.234	26.21
9	Forgaria Cornino	16-09-76	5.3	0.242	0.201	6.67
10	Gemona	11-09-76	5.1	0.190	0.155	9.39
11	Gemona	15-09-76	5.9	0.252	0.255	14.67
12	Gran Sasso	07-04-09	5.6	0.251	0.281	16.81
13	Irpinia	23-11-80	6.5	0.218	0.178	42.21
14	Mazara del Vallo	07-06-81	4.9	0.193	0.134	9.76
15	Valpassiria	17-07-01	4.8	0.170	0.062	18.66

Table 1. Proprieties of the fifteen selected Italian ground motions

N.	Earthquake name	Date [dd-mm-yy]	M_w	PGA NS [g]	PGA EW [g]	Epicentral distance [km]
1	Baja California	07-02-87	5.5	1.388	0.669	8.69
2	Cape Mendocino	25-04-92	7.0	0.228	0.183	36.28
3	Imperial Valley	15-10-79	6.5	0.195	0.109	59.54
4	Northen Calif.	07-06-75	5.2	0.179	0.115	30.54
5	Northridge	20-03-94	5.3	0.157	0.125	9.00
6	Northridge	17-01-94	6.7	0.178	0.162	19.19
7	Oroville	08-08-75	4.7	0.189	0.095	10.07
8	Oroville	08-08-75	4.7	0.209	0.140	8.60
9	Palm Springs	08-07-86	6.1	0.139	0.106	27.70
10	San Fernando	09-04-71	6.6	0.268	0.364	25.36
11	Sierramadre	28-06-91	5.6	0.113	0.091	19.95
12	Upland	28-02-90	5.6	0.233	0.223	12.19
13	Victoria	09-06-80	6.3	0.621	0.587	33.73
14	Whittier	04-10-87	5.3	0.188	0.156	6.59
15	Whittier	04-10-87	5.3	0.264	0.199	13.04

Table 2. Proprieties of the fifteen selected Californian ground motions

N.	Earthquake name	Date [dd-mm-yy]	M_w	PGA NS [g]	PGA EW [g]	Epicentral distance [km]
1	Fujieda	01-08-11	6.2	0.518	0.342	39.0
2	Inukai	19-10-96	6.4	1.423	1.683	144.0
3	Iwase	07-12-12	7.3	0.221	1.575	394.0
4	Kamitakara	27-02-11	5.5	0.666	0.800	12.0
5	Kasumigaura	12-10-12	5.0	0.101	0.095	33.0
6	Katsura	14-03-10	6.5	1.282	1.193	97.0
7	Motegi	07-12-12	7.3	1.348	1.625	384.0
8	Noheji	07-12-12	7.3	0.146	0.142	432.0
9	Oguti	25-03-07	6.9	0.388	0.417	106.0
10	Shirakawa	07-12-12	7.3	1.957	1.592	362.0
11	Takane	25-03-07	6.9	1.123	1.640	149.0
12	Tamayama	07-12-12	7.3	1.498	1.550	332.0
13	Taneichi	07-12-12	7.3	1.345	1.623	360.0
14	Uodu	25-03-07	6.9	1.424	1.409	79.0
15	Yatsuo	25-03-07	6.9	2.080	1.114	81.0

Table 3. Proprieties of the fifteen selected Japanese ground motions

4 COMPARISON PARAMETERS: EVALUATION CRITERIA

In the benchmark papers [13, 14, 15] sixteen evaluation criteria named J_i are suggested in order to evaluate the effectiveness of the different control strategies proposed by different authors in the worldwide competition. The criteria measure the reduction in peak response quantities of the benchmark highway bridge, evaluated by normalizing the response quantities by the corresponding ones for the uncontrolled reference bridge. Each criterion is organized so that a value less than 1 indicates a better performance of controlled systems compared to the reference uncontrolled one.

In this paper, only criteria J_1 and J_2 are considered as they are considered the most significant for the present case of an highway bridge. Applying multicriteria procedures to synthesize the whole set of indexes, even if possible [22], is beyond the scope of the present work. At the base of the piers, J_1 measures the peak base shear force in the controlled structure normalized by the corresponding base shear in the uncontrolled structure and J_2 measures the peak overturning moment in the controlled structure normalized by the corresponding moment in the uncontrolled structure.

5 CONTROL ALGORITHMS FOR SEMI-ACTIVE STRATEGY

The combination of semi-active control with seismic early warning system is introduced herein as additional control strategy of the bridge. It represents an enhanced version of the one proposed in Maddaloni et al. [9]. In this previous work, the use of MR dampers as smart passive devices is suggested to effectively control the bridge under the action of the 16 earthquakes that cover a wide variety of magnitudes, distances to fault and soil types. The mechanical behaviour of such devices is adjusted once, shortly before the incoming earthquake, according to the PGA provided by a SEWS. The results demonstrate that the control algorithm, i.e. the relationship u_c(PGA), results to be more effective in a largest number of cases.

With the purpose to further increase the performance achieved, in this paper is presented a regional-based control algorithms, i.e. a different relationship u_c(PGA) for each one of three world regions selected (Italy, California and Japan).

The way to use SEWS information to calibrate the MR devices, is hereinafter reported:

1) Modal analysis of the structure is preliminarily performed in order to know the fundamental period of vibration T_1 of the hosting structures;
2) Once the SEWS provide the expected PGA of an incoming earthquake, the elastic damped response spectrum according to the Eurocode 8 [18] rules is defined;
3) The spectral acceleration $S_a(T_1)$ evaluated at the fundamental period of the bridge is finally exploited to set the voltage u_c in the MR dampers according to a given control algorithm $u_c[S_a(\text{PGA})]$ (Fig. 3).

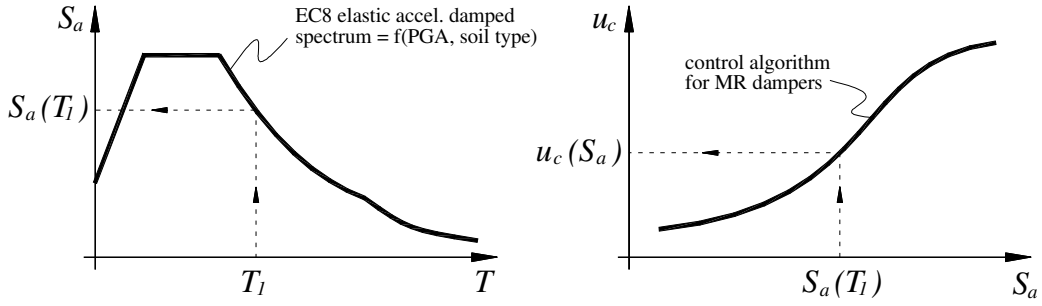


Figure 3. Procedure to calibrate MR dampers according to the expected PGA of the incoming earthquake

For each region, to find the best control algorithm $u_c[S_a(PGA)]$, several nonlinear analyses have been performed, each time feeding the MR devices with a different voltage value, starting from 0 V to 10 V and using a step of 0.01 V. Then for each analysis computed as above descript, the following steps are made:

a) The value of the performance indexes J_i (with i=1, 2) have been recorded;
b) For each index and each earthquake, a diagram showing the correlation between the index J_i and the value of command voltage u_c has been created;
c) For each of these cases, the optimal value of voltage $u_{c,opt,i}$ (i.e. the one leads the minimum value $J_{i,min}$ of J_i) has been found; then an interval of voltage values $\Delta u_{c,opt,i}$ around $u_{c,opt,i}$ has been defined including all the u_c values corresponding to J_i less than $1.3J_{i,min}$ (i.e. assuming a tolerance of 30% in terms of structural performance) and also more than 1 (Fig. 4).

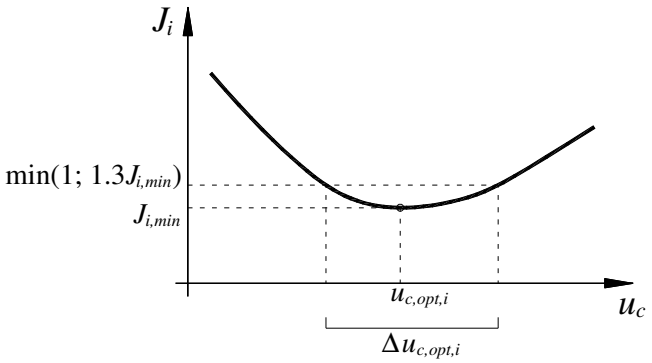


Figure 4. Definition of the optimal interval $\Delta u_{c,opt,i}$ of voltage for MR devices

For the same earthquake, the intervals $\Delta u_{c,opt,1}$ and $\Delta u_{c,opt,2}$ often result to be quite similar. For this reason and for brevity, herein only the interval $\Delta u_{c,opt,1}$ (i.e. related to the index J_1, proportional to the peak base shear force) is shown in Figs. 5, 6 and 7 as vertical gray lines. The lines having as abscissa the value $S_a(T_1)$ corresponding to one of the considered earthquakes, and as ordinates the interval $\Delta u_{c,opt,1}$. The black points represent the "best" values (namely $u_{c,opt,1}$) of the interval. The "x" are representative of the nonlinear analyses results when, for all the values of voltage u_c used to set the MR devices (from 0 V to 10 V), J_1 is larger than one (the x are located at minimum J_1 value).

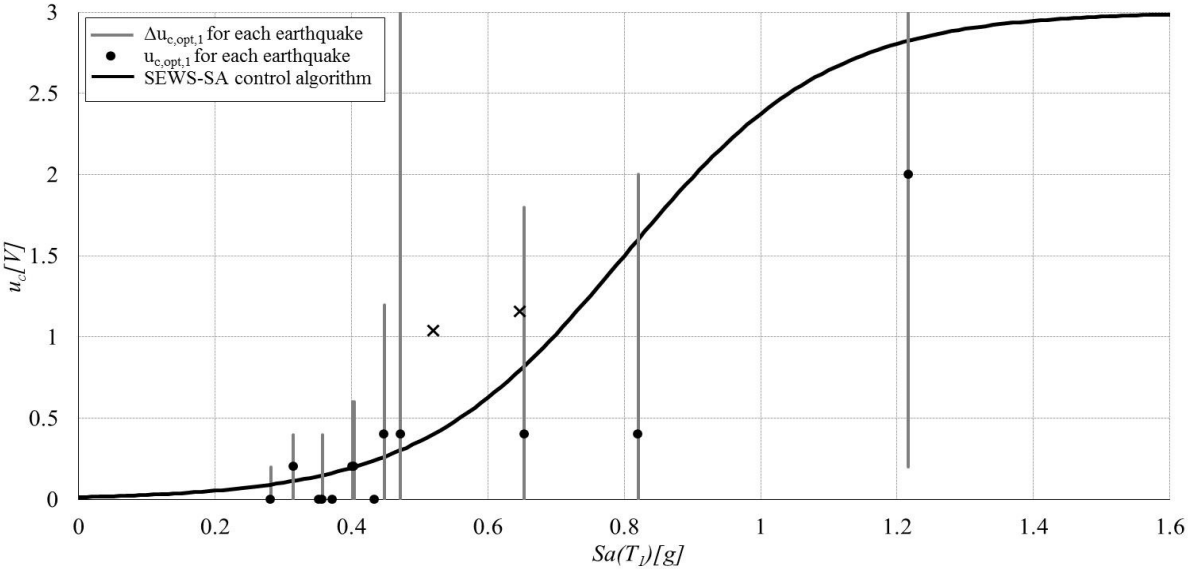


Figure 5. Values of $u_{c,opt,1}$ and of $\Delta u_{c,opt,1}$. Adopted control algorithm for Italian earthquakes.

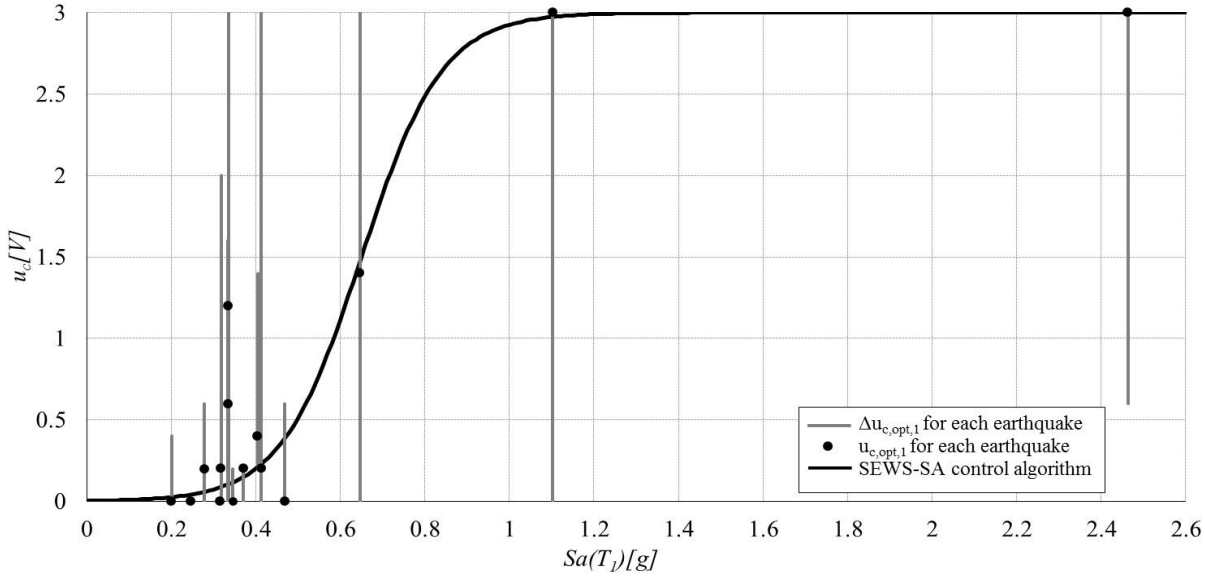


Figure 6. Values of $u_{c,opt,1}$ and of $\Delta u_{c,opt,1}$. Adopted control algorithm for Californian earthquakes.

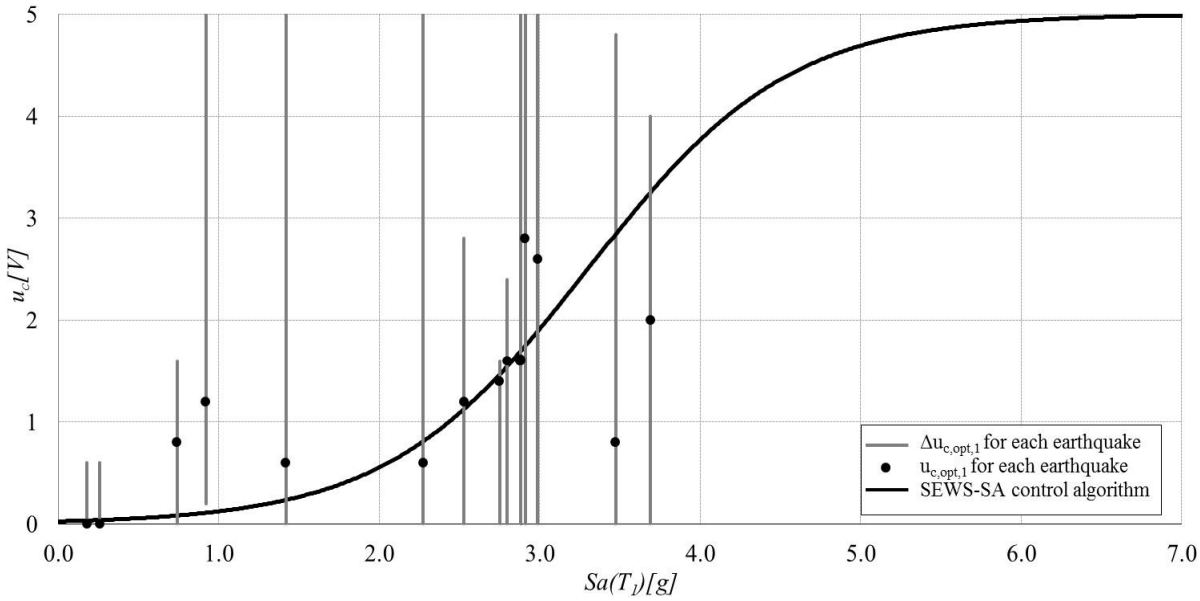


Figure 7. Values of $u_{c,opt,1}$ and of $\Delta u_{c,opt,1}$. Adopted control algorithm for Japanese earthquakes.

Starting from these results, three different control laws $u_c[S_a(T_1)]$ able to give, for each value of $S_a(T_1)$, a voltage intensity u_c as close as possible to the optimal value $u_{c,opt,1}$ or almost within the interval $\Delta u_{c,opt,1}$, have been founded (black line in Figs 5, 6 and 7).
The relationship is:

$$u_c\left[S_a\left(T_1\right)\right]=\left[1+tanh\left(\frac{S_a\left(T_1\right)-\alpha}{\beta}\right)\right]\cdot\frac{u_{c,max}}{2} \tag{1}$$

where α and β are two parameters (expressed in g, as the spectral acceleration S_a) governing the shape of the function, while $u_{c,max}$ represents the maximum voltage value.

The assumed values are:

- α =0.80, β =0.30, $u_{c,max}$=3 V for Italian region;
- α =0.65, β =0.19, $u_{c,max}$=3 V for Californian region;
- α =3.30, β =1.25, $u_{c,max}$=5 V for Japanese region.

As visible from the values of the assumed parameters, three completely different control algorithms have been funded. In the following, the proposed control strategy will be simply referred to as SEWS-SA.

Tables 4, 5 and 6 show the value of the bridge response parameters J_1 and J_2 obtained setting the MR devices by the three regional algorithms proposed. It is worth reminding that values of J_i greater than 1 correspond to performances of the controlled system worse that the uncontrolled ones.

The results are compared with that obtained using control strategies proposed in the benchmark and named passive, semi-active and active. Bold numbers indicate, for each earthquake, the best among the four strategies compared.

These results demonstrate the effectiveness of the proposed strategy for earthquakes with different characteristics as magnitudes and PGA. In particular, the SEWS-SA technique turned out to give results in many cases better than the one corresponding to the other strategies, in the remaining cases to comparable or slightly worse performances.

	J_1				J_2			
Earth.	*SEWS-SA*	*Passive*	*Semi-Active*	*Active*	*SEWS-SA*	*Passive*	*Semi-Active*	*Active*
#1	0.92	1.28	1.10	**0.88**	0.91	1.25	1.08	**0.86**
#2	**0.89**	0.94	0.81	0.89	0.73	**0.55**	0.81	0.89
#3	**0.72**	1.12	0.86	0.86	**0.49**	0.60	0.79	0.86
#4	**0.74**	0.81	0.81	0.83	**0.42**	0.63	0.81	0.83
#5	**0.87**	1.12	0.93	0.87	0.87	0.70	**0.70**	0.77
#6	**0.95**	1.31	1.08	0.97	0.92	1.03	0.85	**0.77**
#7	1.18	2.17	1.38	**1.14**	0.93	1.56	0.99	**0.83**
#8	1.09	2.05	1.20	**1.01**	0.99	1.31	0.79	**0.77**
#9	0.81	2.05	0.80	**0.74**	0.81	1.10	0.81	**0.75**
#10	1.16	1.09	1.03	**1.02**	1.13	1.17	1.00	**1.00**
#11	0.84	1.21	**0.77**	0.79	0.83	0.87	**0.77**	0.78
#12	1.05	0.88	1.08	**0.93**	0.93	0.95	0.95	**0.82**
#13	0.87	1.08	0.93	**0.87**	0.87	0.70	**0.70**	0.77
#14	**0.98**	1.12	1.00	0.98	**0.98**	1.25	1.00	0.98
#15	0.98	1.26	0.98	**0.92**	0.98	1.18	0.98	**0.92**

Table 4. Comparison of the four control strategies in terms of J_1 and J_2 for 15 Italian earthquakes

	J_1				J_2			
Earth.	SEWS-SA	Passive	Semi-Active	Active	SEWS-SA	Passive	Semi-Active	Active
#1	**0.72**	0.72	0.88	0.91	**0.69**	0.71	0.87	0.91
#2	0.81	0.91	**0.68**	0.76	0.81	0.93	**0.70**	0.75
#3	0.90	1.38	1.00	**0.89**	**0.89**	1.38	1.00	0.90
#4	0.88	0.95	**0.83**	0.90	0.88	0.96	**0.84**	0.90
#5	0.93	1.02	**0.83**	0.87	0.93	1.01	**0.83**	0.87
#6	**0.94**	1.13	0.96	1.03	1.05	**0.74**	0.87	0.90
#7	0.89	0.99	**0.87**	0.97	**0.92**	0.99	0.85	0.93
#8	1.00	1.13	1.15	**0.98**	1.00	1.15	1.20	**0.98**
#9	1.00	1.34	1.21	**0.84**	1.00	1.34	1.22	**0.84**
#10	0.80	0.77	**0.75**	0.76	0.75	**0.52**	0.70	0.74
#11	0.84	1.12	0.87	**0.82**	0.71	**0.55**	0.62	0.70
#12	0.81	0.87	0.76	**0.74**	0.80	0.85	0.75	**0.73**
#13	**0.81**	0.70	0.90	0.92	0.78	**0.68**	0.86	0.89
#14	0.89	0.96	0.87	**0.76**	0.89	0.96	0.87	**0.76**
#15	0.86	1.10	0.88	**0.78**	0.95	1.13	0.87	**0.90**

Table 5. Comparison of the four control strategies in terms of J_1 and J_2 for 15 Californian earthquakes

	J_1				J_2			
Earth.	SEWS-SA	Passive	Semi-Active	Active	SEWS-SA	Passive	Semi-Active	Active
#1	**0.77**	1.00	0.99	1.02	**0.64**	1.00	0.99	1.21
#2	**0.06**	1.00	1.00	1.00	**0.13**	1.00	1.00	1.00
#3	**0.90**	1.37	1.07	1.00	**0.90**	1.37	1.07	1.01
#4	**0.02**	1.00	1.00	1.02	**0.02**	1.00	1.04	1.00
#5	**0.72**	0.93	0.69	0.67	**0.72**	0.94	0.70	0.67
#6	**0.04**	1.00	1.00	1.00	**0.05**	0.99	1.00	1.00
#7	**0.04**	1.00	0.99	1.00	**0.05**	1.00	0.99	1.01
#8	**0.76**	0.93	0.76	0.71	**0.80**	0.93	0.75	0.72
#9	**0.94**	1.12	0.89	0.77	**0.95**	1.12	0.90	0.77
#10	**0.03**	1.00	0.99	1.01	**0.04**	1.00	1.00	1.01
#11	**0.06**	1.00	0.98	1.00	**0.09**	1.00	1.00	1.00
#12	**0.95**	1.00	0.96	0.95	**0.95**	1.00	0.96	0.95
#13	**0.85**	0.90	0.85	0.71	**0.85**	0.90	0.85	0.72
#14	**0.08**	0.99	0.99	1.00	**0.11**	0.99	1.00	1.00
#15	**0.97**	1.03	0.94	0.87	**0.81**	0.86	0.78	0.77

Table 6. Comparison of the four control strategies in terms of J_1 and J_2 for 15 Japanese earthquakes

Histograms in Figs. 8, 9 and 10 represent the SEWS-SA strategy in comparison with passive system. The latter is the more common and simple system present nowadays in the market and a victory against it, has been researched to validate the effectiveness of the strategy proposed.

The blue blocks indicate the number of times that SEWS-SA strategy reaches for J_1 and J_2 a value lower than the passive strategy. The gray-lines blocks indicate the number of times that the passive strategy reaches for J_1 and J_2 a value lower than the SEWS-SA strategy. For both technologies, the pointed block represents the number of times that is overpassed the limit equal to 1.00. As visible the proposed strategy, considering a combination of the semi-active control with seismic early warning system, results to be more effective in a largest number of cases.

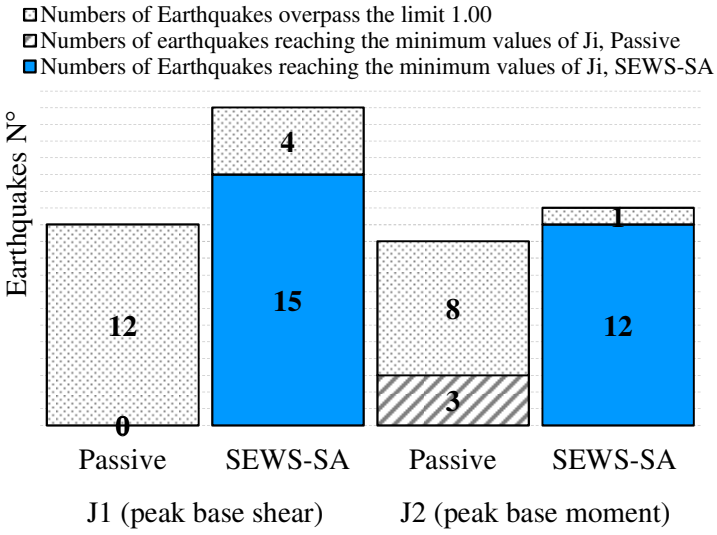


Figure 8. Comparison between Passive and SEWS-SA strategies in terms of J_1 and J_2 , Italy.

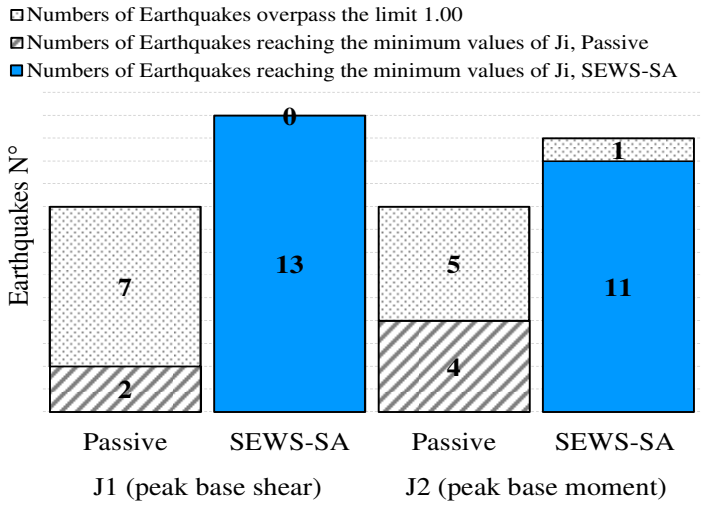


Figure 9. Comparison between Passive and SEWS-SA strategies in terms of J_1 and J_2 , California.

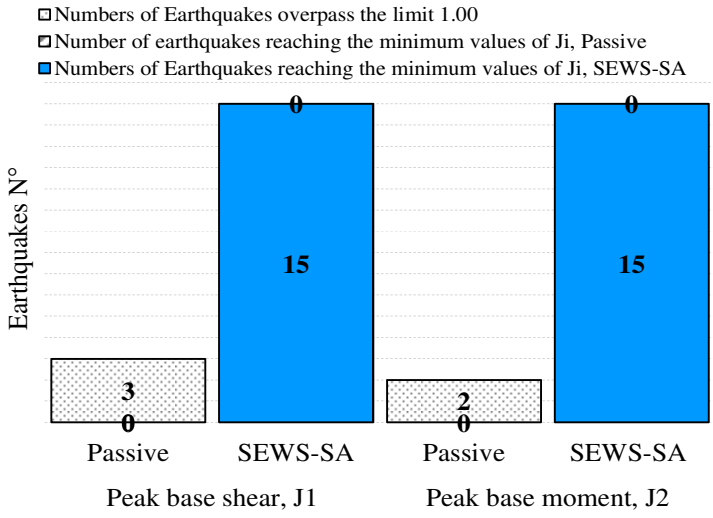


Figure 10. Comparison between Passive and SEWS-SA strategies in terms of J_1 and J_2 , Japan.

6 CONCLUSIONS

The present paper describes a methodology for exploiting earthquake information derived by a seismic early warning system (SEWS) in the framework of semi-active control strategies by using magnetorheological (MR) dampers. It represents an enhanced version of the one proposed in Maddaloni et al. [7, 9]. The main idea consists in changing the behaviour of MR dampers installed on the hosting structure, according to an anticipate estimate, provided by the SEWS, of the PGA of an incoming earthquake. The PGA value is adopted to build the elastic acceleration spectrum according to the Eurocode 8 rules [18]. Then, the spectral acceleration evaluated at the fundamental period of the structure is used to set the optimal voltage in the MR devices. The paper describes the application of this innovative and integrated protection technique to a case-study highway bridge located in Southern California. In this paper, is presented a regional-based control algorithms, i.e. a different relationship u_c(PGA) for each one of three world regions selected (Italy, California and Japan). The proposed strategy is investigated by several numerical simulations, considering a total of forty-five strong real earthquakes, fifteen for each region.

The results demonstrate that the effectiveness of the proposed idea enhances when an appropriate regional algorithm, i.e. a different relationship u_c(PGA) for each world regions selected (Italy, California and Japan), is considered. The SEWS-SA technique turned out to give results sometimes better and sometimes comparable to other consolidated strategies as a fraction of the cost. Only in few cases the numerical analyses yielded slightly worse performances.

REFERENCES

[1] L. Di Sarno, A.S. Elnashai, Innovative strategies for seismic retrofitting of steel and composite frames. *Journal of Progress in Structural Engineering and Materials*, **7**(3), 115-135, 2003.

[2] S.Y. Chu, T.T. Soong, A.M. Reinhorn, Active, hybrid, semi-Active structural control - a design and implementation handbook. *John Wiley and Sons*, ISBN-13 978-0-470-01352-6, 2005.

[3] K. Kanda, T. Kobori, Y. Ikeda, H. Koshida, The development of a "Pre-arrival transmission system for earthquake information" applied to seismic response controlled structures. *1st World Conference on Structural Control*, TA-3, 23-32, 1994.

[4] Y. Nakamura, Earthquake alarm system for Japan Railways. *Japanese Railway Engineering*, 8(4): 3-7, 1989.

[5] H.M. Brown, R.M. Allen, M. Hellweg, O. Khainovski, D. Neuhauser, A. Souf, Development of the ElarmS methodology for earthquake early warning: Realtime application in California and offline testing in Japan. *Soil Dynamics and Earthquake Engineering,* 31: 188-200, doi:10.1016/j.soildyn.2010.03.008, 2011.

[6] G. Iannaccone, A. Zollo, L. Elia, V. Convertito, C. Satriano, C. Martino, G. Festa, M. Lancieri, A. Bobbio, T.A. Stabile, M. Vassallo, A. Emolo, A prototype system for earthquake early-warning and alert management in southern Italy. *Bulletin of Earthquake Engineering*, doi: 10.1007/s10518-009-9131-8, 2009.

[7] G. Maddaloni, N. Caterino, A. Occhiuzzi, Semi-active control of the benchmark highway bridge based on seismic early warning systems. *Bulletin of Earthquake Engineering*, doi:10.1007/s10518-011-9259-1, 2011.

[8] G. Maddaloni, Use of a seismic early warning system to calibrate variable dampers for structural control of a highway bridge. *Proceedings of 5th International Conference on Structural Control-EACS*, Genoa, June 18–20, Italy, ISBN 978-88-95023-13-7, 2012.

[9] G. Maddaloni, N. Caterino, G. Nestovito, A. Occhiuzzi, Use of seismic early warning information to calibrate variable dampers for structural control of a highway bridge: evaluation of the system robustness. *Bulletin of Earthquake Engineering* (in press).

[10] N. Caterino, M. Spizzuoco, A. Occhiuzzi, Understanding and modelling the physical behaviour of magnetorheological dampers for seismic structural control. *Smart Materials and Structuters*, 20 065013. doi: 10.1088/0964-1726/20/6/065013, 2011.

[11] N. Caterino, M. Spizzuoco, A. Occhiuzzi A, Experimental comparison of control algorithms for systems based on SA MR dampers for seismic response reduction. *Smart Structures and Systems*. (in press)

[12] N. Caterino, M. Spizzuoco, A. Occhiuzzi, Promptness and dissipative capacity of MR dampers: experimental investigations. *Structural Control and Health Monitoring*, (in press).

[13] A. Agrawal, P. Tan, S. Nagarajaiah, J. Zhang, Benchmark structural control problem for a seismically excited highway bridge – Part I: Phase I Problem definition. *Structural Control and Health Monitoring*, 16: 509-529. doi: 10.1002/stc.301, 2009.

[14] S. Nagarajaiah, S. Narasimhan, A. Agrawal, P. Tan, Benchmark structural control problem for a seismically excited highway bridge—Part III: phase II sample controller for the fully base-isolated case. *Structural Control and Health Monitoring*, 16: 549–563. doi:10.1002/stc.293, 2009.

[15] P. Tan, A. Agrawal, Benchmark structural control problem for a seismically excited highway bridge— Part II: phase I sample control designs. *Structural Control and Health Monitoring*, 16: 530–548. doi: 10.1002/stc.300, 2009.

[16] G. Maddaloni, G. Magliulo, E. Cosenza, Effect of the seismic input on nonlinear response of r/c building structures. *Advances in Structural Engineering*, 15(10): 1861-1877, doi: 10.1260/1369-4332.15.10.1861, 2012.

[17] G. Magliulo, G. Maddaloni, E. Cosenza, Extension of N2 method to plan irregular buildings considering accidental eccentricity. *Soil Dynamics and Earthquake Engineering*, Volume 43, December 2012, Pages 69-84. ISSN: 02677261, DOI: 10.1016/j.soildyn.2012.07.032, 2012.

[18] Eurocode 8, Design of structures for earthquake resistance – Part 1: General rules, seismic actions and rules for buildings. Brussels, 2003.

[19] ITACA, Italian Acceleration Archive [http://itaca.mi.ingv.it]

[20] PEER, Pacific Earthquake Engineering Research Center [http://peer.berkeley.edu/smcat/]

[21] National Research Institute for Earth Science and Disaster Prevention (NIED); [http://www.k-net.bosai.go.jp/]

[22] N. Caterino, I. Iervolino, G. Manfredi, E. Cosenza, Multi-Criteria Decision Making for Seismic Retrofitting of RC Structure. *Journal of Earthquake Engineering* **12**: 1-29. doi: 10.1080/13632460701572872

COMPDYN 2013
4th ECCOMAS Thematic Conference on
Computational Methods in Structural Dynamics and Earthquake Engineering
M. Papadrakakis, V. Papadopoulos, V. Plevris (eds.)
Kos Island, Greece, 12–14 June 2013

SHAKING TABLE TESTS TO COMPARE SEMI-ACTIVE CONTROL ALGORITHMS FOR VARIABLE DAMPERS

N. Caterino[1], M. Spizzuoco[2] and A. Occhiuzzi[1],

[1] Department of Technology, University of Napoli Parthenope
Centro Direzionale, isola C4, 80123 Naples, Italy
{nicola.caterino, antonio.occhiuzzi}@uniparthenope.it

[2] Department of Structural Engineering, University of Napoli Federico II
Via Claudio 21, 80100 Naples, Italy
spizzuoc@unina.it

Keywords: shaking table tests, semi-active control, magnetorheological dampers, control algorithms, energy dissipation.

Abstract. *The authors present and discuss the main results of a experimental campaign performed on a near full-scale semi-actively controlled steel building, in the framework of a research program financed by the Italian Department of Civil Protection. Four control algorithms have been investigated through shaking table tests under seven different natural earthquakes. They belong to the family of control algorithms based on a sound physical sense, where semi-active devices are typically seen as smart damping devices for which the amount of dissipation can be quickly regulated: usually they require less measurements, which often are made in the close surroundings of the device; therefore, the computational effort is fairly moderate and, in principle, it could be sustained by small, battery-powered computing systems. After a literature review on semi-active control algorithms, the paper first summarizes the logic behind the ones adopted in the tests. Then a direct comparison among them is done on the basis of the results gained from the tests. Each of the control logics has been evaluated and compared each other in terms of effectiveness in the reduction of interstorey drifts and of amount of dissipated energy, leading to comments may be useful for the design of a semi-active control strategy based on the use of such kind of variable devices.*

1 INTRODUCTION

Dealing with semi-active (SA) structural control, where dissipative devices are usually adopted, the relative effectiveness of various control algorithms is highly questionable. In order to compare different logics, an experimental activity has been done in the framework of the JETPACS (Joint Experimental Testing on Passive and semi-Active Control Systems) Program financed by 2005-2008 ReLUIS Executive Project (sponsored by the Italian Department of Civil Protection). The SA controlled structural mock-up (Figure 1) is a near full scale 2-story steel frame, equipped with two SA bracing systems including two magnetorheological (MR) dampers designed and manufactured in Europe.

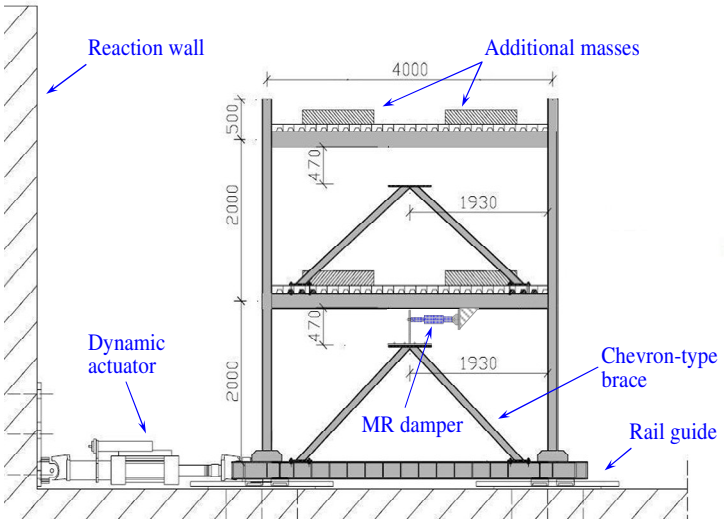


Figure 1: Experimental setup, with dimensions expressed in millimeters.

The tests have been performed by applying a set of earthquake records at the base of the structure, by utilizing a shaking table facility and four different control algorithms. All the considered control logics are "co-located", as they are able to change in real time the dynamical properties of the dampers according to the actual values of response quantities measured in the close surroundings of the dampers. They are much simpler to apply to real structures than control algorithms relying on a full state feedback. The first one (called "Energy") aims to maximize the amount of energy extracted by an SA damper and needs a flexible connection between the device and the floors among which the latter is installed. The second one ("Modulated Homogeneous Friction" - MHF) feeds the damper with a current proportionally to the last local maximum or minimum value of the 1st interstorey drift. The third control algorithm is referred to as "Sky Hook" since it aims to make the MR device mimics the behaviour of a damper constrained to the fixed space. The last investigated control logic ("Acceleration Reduction") aims to minimize the amount of absolute accelerations in the main structure, i.e. to minimize the energy transmission from the ground to the structure through the semi-active brace. Three of these algorithms are of bang-bang (i.e. ON-OFF) type and do not need any parameter to work. Their calibration consist only in setting the minimum (i_{min}) and maximum (i_{max}) values of current to be given to the damper in the OFF and ON condition, respectively. The other algorithm (MHF) belongs to the proportional type, feeding the damper with a current in the range [i_{min}, i_{max}] according to the instantaneous value of a specific response parameter. This logic is calibrated by setting the value of a gain constant, other than the i_{min} and i_{max} values.

The paper summarizes the logic behind the 4 adopted in the tests and shows the main experimental results they leaded to. A direct comparison among them is finally done in terms of effectiveness in the reduction of the structural response as well as in terms of capability to dissipate energy. The devices adopted for the tests were two full-scale prototype semi-active MR dampers manufactured by the German company Maurer Söhne, each being capable to react with a maximum force of about 30 kN with a stroke of ± 25 mm. The current in the dampers' circuit can be provided in the range 0÷3 A. Such dampers connected the base to the first floor of the frame through chevron type braces. Depending on the presence or not of stiffening plates above each brace, the link between each MR damper to the lower beam can be substantially rigid or flexible respectively (Figure 2). The electronic equipment used for the SA control of the devices is sketched in Figure 3 [1].

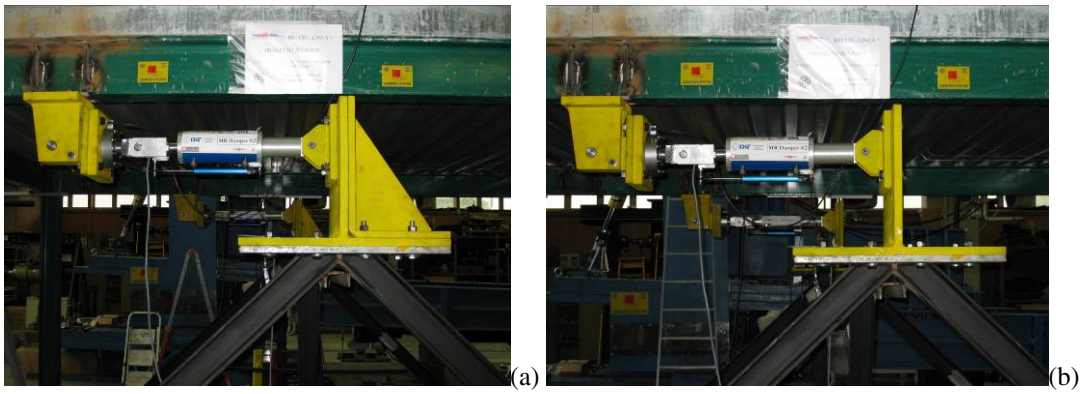

(a) (b)

Figure 2: Two setup configurations, with (a) or without (b) stiffening plates behind the device.

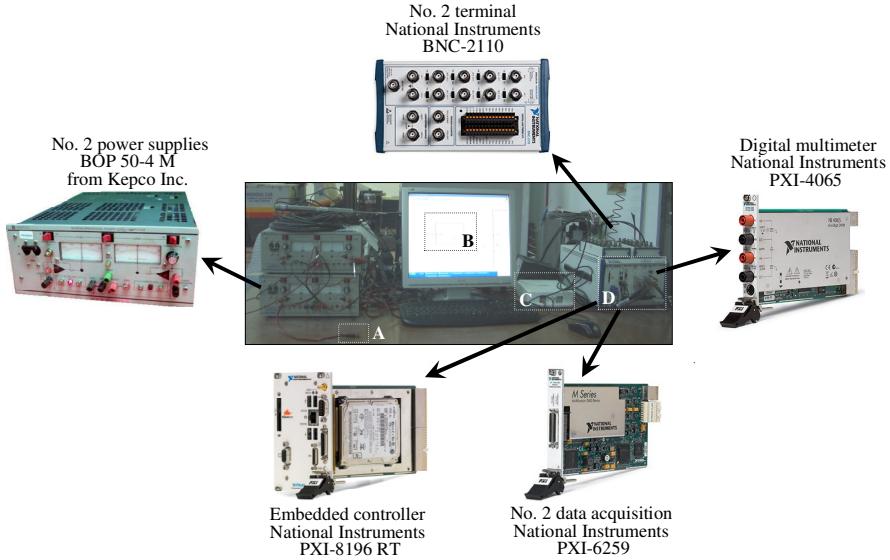


Figure 3: Main components of the electronic equipment adopted for the tests.

2 CONTROL ALGORITHMS ADOPTED FOR THE TESTS

The original formulation of the control algorithms has been modified to be used with SA MR dampers:

"Energy" algorithm: the 1st control algorithm aims to maximize the energy extracted by the SA damper from the structure [2]: when the force F_b acting on the semi-active brace and the velocity $\dot{x}_f$ of the point where the force is applied have the same sign, the power flows from

the main structure into the semi-active damper, and the current feeding the magnetic coils should be set to its maximum value i_{max}; when there is a power flowing from the SA brace into the hosting structure, the damper should be set at its minimum value of the current, namely 0, so as to reduce as much as possible the power transmission to the hosting structure. In practice:

$$\begin{aligned} &if \quad F_b(t)\cdot \dot{x}_f(t) > 0 \quad then\ i(t) = i_{max} \\ &if \quad F_b(t)\cdot \dot{x}_f(t) \le 0 \quad then\ i(t) = i_{min} = 0 \end{aligned} \tag{1}$$

"MHF" algorithm: the 2nd control algorithm ("Modulated Homogeneous Friction") was originally proposed by Inaudi [3], and modulates the current into the damper according to the actual response of the structure in terms of floor displacement. It is based on the definition of the "prior-to-peak" operator "*P*" related to the interstorey drift of the first floor $x_f - x_g$ (x_g is the ground displacement) and can be expressed as follows:

$$i(t) = g \cdot |P(t)| \tag{2}$$

where g is a gain constant, whose value has been assumed for each test such that the maximum intensity of current was given when the 1st interstorey drift ratio achieved the value of 0.005 (i.e. $x_f - x_g = 10$ mm).

"Sky Hook" algorithm: the 3rd control algorithm aims to make the semi-active damper behave like a sky hook damper, i.e. a damper constrained to the fixed space [4-6]. Sky hook dampers guarantee an overall response reduction at all frequencies and tend to cancel resonance. During a dynamic excitation of the device, a real damper can mimic a sky hook one if its constant c_{real} can vary so as the force $c_{real}\cdot\dot{x}_f(t)$ becomes equal to the one $c_{sky}\cdot[\dot{x}_f(t)+\dot{x}_g(t)]$ of a sky hook viscous damper. Therefore, the control algorithm has to be expressed as:

$$\begin{aligned} &if \quad \frac{\dot{x}_f(t)+\dot{x}_g(t)}{\dot{x}_f(t)} \le 0 \quad then\ i(t) = i_{min} = 0 \\ &if \quad \frac{\dot{x}_f(t)+\dot{x}_g(t)}{\dot{x}_f(t)} > 0 \quad then\ i(t) = i_{max} \end{aligned} \tag{3}$$

"Acceleration Reduction" algorithm: the 4th control logic aims to minimize the amount of absolute accelerations in the main structure and, therefore, tries to minimize the energy transmission from the ground motion to the structure through the semi-active brace [7]. By considering the global dynamic balance, reducing the sum of elastic and dissipative forces leads to the reduction of the inertial force, hence of the absolute acceleration of a given mass. The logic imposes to take the device switched on if the elastic and dissipative forces have opposite signs (i.e. they tends to balance one each other), according to the following relations:

$$\begin{aligned} &if \quad x_f(t)\cdot\left[\dot{x}_f(t)-\dot{x}_b(t)\right] > 0 \quad then\ i(t) = i_{min} = 0 \\ &if \quad x_f(t)\cdot\left[\dot{x}_f(t)-\dot{x}_b(t)\right] \le 0 \quad then\ i(t) = i_{max} \end{aligned} \tag{4}$$

3 DESCRIPTION OF THE TESTS

The mock-up steel structure has been dynamically tested commanding the actuator to move the frame in the longitudinal direction, according to seven different European natural records. They are characterized by a mean acceleration spectrum compatible with the elastic response spectrum of the Italian Seismic Code OPCM 3274 [8] and of the Eurocode 8 [9] for soil type B and seismic zone 1. Figure 4 shows the superposition of the corresponding elastic acceleration spectra and the elastic response spectrum defined by the cited building code according to the parameters defined above. Two records (named 187 and 535) have demonstrated to be

particularly damaging for the structure, even for the lowest intensity level (25%), so they are assumed as the main reference actions for the comparison of algorithms. The experimental activity consisted of 50 semi-active tests. Table 1 shows their characteristics. All the four control logics have been tested under the action of the heaviest earthquakes (187 and 535) allowing an effective comparison. The effectiveness of each control logic for a given earthquake at a certain input level has been also investigated repeating the same test with different values of imposed maximum intensity of current i_{max}. Table 1 also shows the type of connection of MR dampers to the chevron-type braces (flexible or rigid), depending on the algorithm. The control logic Energy requires a flexible connection (whose stiffness has been calibrated for this purpose) in order to work as described before, storing and dissipating energy in selected intervals of time, whereas the other control algorithms turned out to be more effective with a rigid link.

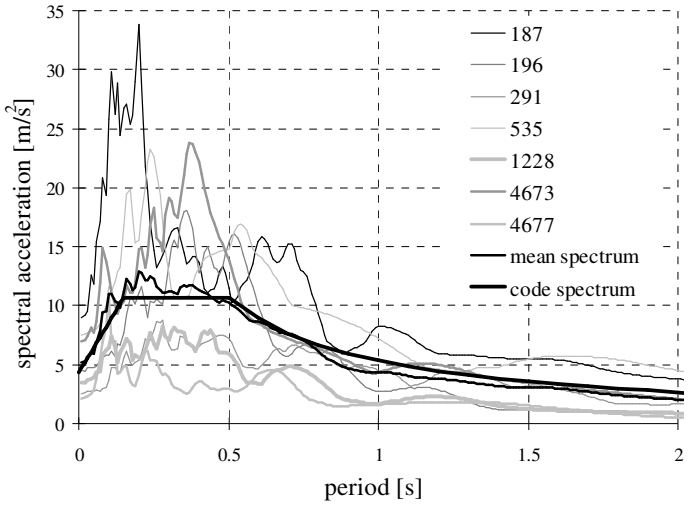


Figure 4: Elastic acceleration spectra (5% damping) of seismic inputs.

Earthquake signal	Input level [%]	Control algorithm	Maximum current [A]	Type of connection
187	50	Energy	1.0	Flexible
187	25, 50	MHF	1.5, 2.5	Rigid
187	25, 50	Sky Hook	1.0, 2.5	Rigid
187	25, 50	Acc. Red.	1.0, 2.0	Rigid
196	25, 50, 75	Energy	1.0, 2.5	Flexible
291	50, 100	Energy	1.0	Flexible
535	25, 50, 75	Energy	1.0, 1.5, 2.0, 2.5	Flexible
535	25	MHF	1.5, 2.5	Rigid
535	25	Sky Hook	1.0, 2.0	Rigid
535	25	Acc. Red.	1.0, 2.0	Rigid
1228	10, 25, 50, 75, 100	Energy	1.0, 2.5	Flexible
4673	50	Energy	1.0	Flexible
4677	50, 100	Energy	1.0	Flexible

Table 1: Experimental activity.

4 EXPERIMENTAL COMPARISON OF THE FOUR CONTROL ALGORITHMS

The control algorithms adopted for the above experimental activity are compared in the following in terms of capability to reduce the interstorey drifts as well as to dissipate energy. Finally they are compared according to six performance indexes accounting for different aspects related to the structural response (i.e. displacements, forces and energy demands). The most interesting results comes from tests performed using the 187 and 535 accelerograms scaled at 50% and 25%, respectively.

4.1 Comparison of the algorithms in terms of interstorey drifts' reduction

Each test has been analyzed in terms of floor horizontal displacements, leading to evaluate maximum interstorey drift values at the first and the second floor. Actually interstorey drifts are directly related to the structural and non-structural seismic demand to the frame [10]. For each algorithm, the current intensity corresponding to the greatest reduction of drifts has been selected. Figure 5 represents the corresponding peak interstorey drifts. The experimental data confirm that drift reduction achieved by SA control system, compared to the bare uncontrolled frame, can be close to 50%, consistently with the literature data based on numerical analyses. However, the response reduction provided by a SA control system can also be negligible, or even negative, depending on the occurrence of unavoidable misoperations [11] of the control algorithm as well as of delays in the control chain [12].

With reference to the 535-25% earthquake, Figure 6 reports, for 1 second time window corresponding to the most severe portion of the input motion, the superposition of 1st interstorey drifts for all the algorithms and the one relative to the uncontrolled structure. It allows a comparison of algorithms in terms of effectiveness, consistently with what already observed with reference to the peak values of the drift (Figure 5, right). Some remarks have to be given about the interstorey drift at the 2nd floor and the ability of control algorithms to manage it, also considering that neither measurements to be adopted in the control algorithms nor control forces existed at that floor. From Figure 5 one can observe that the 1-2 drift is often relatively large, sometimes overcoming the one corresponding to the uncontrolled structure. This can be explained as follows: *(i)* the presence of dampers only at the first floor of the building introduces an irregular distribution of damping over the height of the structure that affects the mode shapes; *(ii)* for the same reason the control system has little chances of actually control the drift at the second floor, that may strongly rise especially when the control forces excite, with their predominant frequencies, the second vibration mode of the structure.

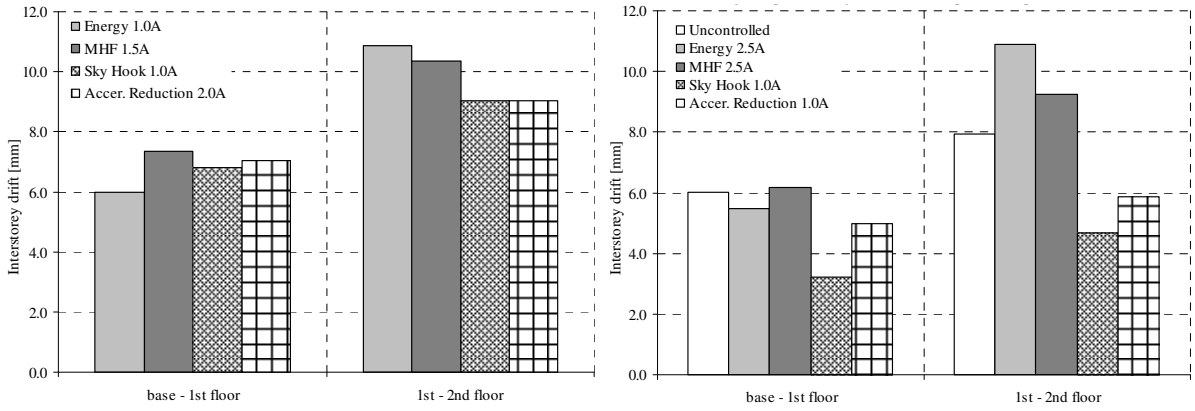


Figure 5: Comparison of algorithms in terms of peak interstorey drift demand: 187-50% (left), 535-25% (right) earthquakes.

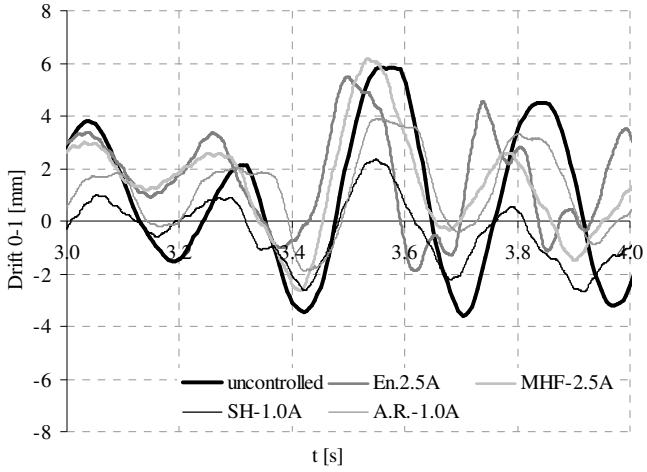


Figure 6: 1st interstorey drift response for a 1 second time window under the 535-25% earthquake: comparison of uncontrolled and SA controlled cases.

4.2 Comparison of the algorithms in terms of energy dissipation

The behaviour of the frame structure equipped with the semi-active bracing control systems has been analyzed also in terms of energy balance $E_{el}(t) + E_{kin}(t) + E_{diss}(t) = E_{inp}(t)$, where $E_{el}(t)$ is the elastic stored energy, $E_{kin}(t)$ is the absolute kinetic energy, $E_{inp}(t)$ is the seismic input energy, and $E_{diss}(t)$ is the dissipated energy. The instantaneous, final and maximum value of each one of the above energies have been computed in order to define, for each algorithm, the optimal value of the maximum current intensity i_{max}, i.e. the value corresponding to the minimum energy demand in the structure (the sum of elastic and kinetic energies is assumed as a measure of this demand). These values resulted to be coincident with those already found with reference to drifts and floor accelerations allowing to conclude that, for a given seismic input, the optimal calibration of each algorithm can be univocally defined. Table 2 reports for each test the maximum values of the input energy and of the sum of elastic and kinetic energies and describes the relative frequencies of occurrence of given threshold of energy, i.e., the percent occurrence of $E_{el} + E_{kin}$ values within given intervals of magnitude expressed in kJ.

The total input energy corresponding to a given earthquake resulted to be strongly dependent on the control algorithm adopted, allowing to highlight how the SA control via MR dampers is able to significantly modify the global dynamic properties of the structural system. In the two investigated cases, the Energy algorithm gives the largest amount of input energy, the Sky Hook logic the smallest one. This behaviour seems consistent with results in terms of drift and floor acceleration spectra shown in the previous section. As regard the sum of elastic and kinetic energies, the following comments can be drawn, for example, with reference to the 5 tests done with the 535-25% earthquake:

- the maximum value of $E_{el} + E_{kin}$ evaluated for each semi-active test again assumes the largest value for the Energy algorithm, even greater than the one corresponding to the uncontrolled case, highlighting a poor performance of the algorithm in this case; from this perspective the Sky Hook algorithm yielded the better performances;
- all the tested algorithms were able to bound most of the $E_{el} + E_{kin}$ values within the range 0.00-0.15 kJ, thus decreasing the number of strong cycles compared to the uncontrolled case; however, also in this case the Energy and Sky Hook algorithms corresponded to the worse and best response reduction respectively.

Control algorithm	max(E_{inp}) [kJ]	max(E_{el} + E_{kin}) [kJ]	Values of E_{el} + E_{kin} within intervals of magnitude [kJ]			
			0.00--0.05	0.05--0.10	0.10--0.15	0.15--0.80
Energy	1.01	0.79	87.6%	7.5%	1.1%	3.8%
MHF	0.93	0.38	87.4%	9.9%	0.7%	2.0%
Sky Hook	0.73	0.28	70.6%	26.3%	1.7%	1.4%
Accel. Reduct.	0.84	0.31	64.9%	29.7%	2.6%	2.8%
Uncontrolled	1.21	*0.41*	*53.5%*	*22.5%*	*13.8%*	*10.2%*

Table 2: Energy analysis referred to 5 tests done with earthquake 535-25%.

4.3 Synthetic comparison of the algorithms via performance indexes

The effectiveness of the four investigated control logics has been finally verified through six evaluation criteria related to the structural response and to the required performance of the control devices. They are defined as in Eq. (5). I_1 is related to the maximum peak interstorey drift ($max \mid d_{1,c} \mid$) of the 1st floor normalized by the corresponding value of the uncontrolled structure ($max \mid d_{unc,1} \mid$). I_2 is defined like I_1 but referred to the 2nd storey. I_3 is the ratio between the maximum value of the base shear and the one ($max \mid F_{b,unc} \mid$) registered during the uncontrolled test (m_i is the seismic mass of the i-th floor, $\ddot{x}_{tot,i}$ its absolute acceleration). I_4 is the maximum control force exhibited by the two MR devices normalized by the seismic weight W of the building (f_i is the force in the i-th device; i = 1, 2). I_5 is the maximum stroke Δ_i of the i-th control device normalized by the maximum 1st interstorey drift of the uncontrolled test. I_6 is the maximum value of the sum of elastic and kinetic energies normalized by the homologous value relative to the uncontrolled case.

They have been evaluated with reference to the 535-25% earthquake for which a larger amount of data is available for the comparisons. Figure 7 summarizes the results and allows a direct comparison of the algorithms. Almost for all the assumed criteria, the Energy algorithm leads to the worst performances, whereas Sky Hook to the best ones. Also the Acceleration Reduction algorithm determines a significant reduction of the structural response together with a fair behaviour of the control devices.

$$I_1 = \frac{\max_t \left| d_{c,1}(t) \right|}{\max_t \left| d_{unc,1}(t) \right|}, \quad I_2 = \frac{\max_t \left| d_{c,2}(t) \right|}{\max_t \left| d_{unc,2}(t) \right|}, \quad I_3 = \frac{\max_t \left| \sum_i m_i \ddot{x}_{tot,i}(t) \right|}{\max_t \left| F_{b,unc} \right|},$$

$$I_4 = \frac{\max_{t,i} \left| f_i(t) \right|}{W}, \quad I_5 = \frac{\max_{t,i} \left| \Delta_i(t) \right|}{\max_t \left| d_{unc,1}(t) \right|}, \quad I_6 = \frac{\max_t \left| E_{el}(t) + E_{kin}(t) \right|_c}{\max_t \left| E_{el}(t) + E_{kin}(t) \right|_{unc}} \tag{5}$$

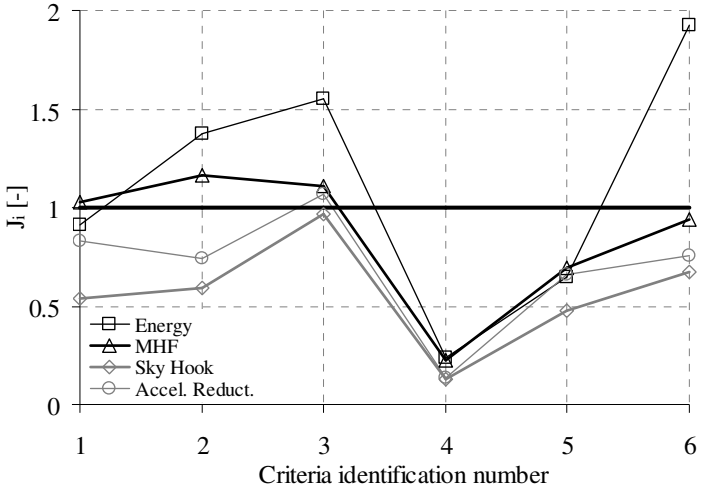


Figure 7: Performance indexes according to the 4 control algorithms (tests with 535-25% earthquake).

5 CONCLUSIONS

Four semi-active control algorithms have been investigated through shaking table tests on a near full-scale steel building, under seven different natural earthquakes. All the considered control logics are "co-located", as they are able to modify in real time the dynamical properties of the dampers according to the actual values of selected quantities representing the structural response in the close surroundings of the dampers. Three of these algorithms are of bang-bang type, while the forth algorithm belongs to the proportional type, feeding the damper with a current may range in a given interval according to the instantaneous value of a specific response parameter.

Although many control algorithms proposed in literature try to include the electric dynamics of the circuitry inside MR dampers, the matter can be satisfactorily addressed through an appropriate control hardware. In this way, the global reaction times of the SA damper can be bounded to 10 ms, leading to a negligible effect of the damper's internal dynamics.

In real applications, variations of the force provided by a MR damper are smooth also for control algorithms corresponding to sharp variations of the current inside the damper.

The experimental response reduction in terms of interstorey drift achieved by SA control system, compared to the uncontrolled frame, can be close to 50%.

Differently from passive control systems, reactive SA devices located only at few DOFs of a structure can increase the structural response at uncontrolled DOFs. This behaviour is dominated by the frequency content of the control action, rather than its discontinuous nature.

A SA control system can significantly modify the total input energy coming into a structure from a ground motion. Therefore, such an energy cannot be taken as a constant in evaluating the dissipation capabilities of a SA control system.

As possible future developments of the present work, the analysis of the floor response acceleration spectra [13] for each earthquake and each algorithm is programmed to explore how each algorithm modify the frequency content of the base accelerations throughout the height of the building. Finally a new experimental campaign on the same structures is programmed to assess the effectiveness of a "smart passive" control made by MR dampers and to compare it with the above SA strategies. In particular such tests will be performed calibrating the devices once before the test with a given intensity of current chosen according the intensity measures of the imposed strong motion [14-15].

REFERENCES

[1] N. Caterino, M. Spizzuoco, A. Occhiuzzi, Understanding and modelling the physical behaviour of magnetorheological dampers for seismic structural control. *Smart Materials and Structures*, **20** 065013 doi: 10.1088/0964-1726/20/6/065013, 2011.

[2] A. Occhiuzzi, M. Spizzuoco, Experimental analysis of a semi-actively controlled steel building. *Structural Engineering and Mechanics*, **19** (6), 721-747, 2005.

[3] J. A. Inaudi, Performance of variable-damping systems: theoretical analysis and simulation. *Structural Control for Civil and Infrastructure Engineering*, F. Casciati and G. Magonette (Eds), World Scientific, 301-16, 2000.

[4] M.J. Crosby, D.C. Karnopp, The active damper. *The Shock and Vibrations Bulletin*, **43**, Naval Research Laboratory,Washington DC, 1973.

[5] D.C. Karnopp, M.J. Crosby, R.A. Harwood, Vibration Control Using Semi-Active Force Generators. *ASME J. Eng. Ind.*, **96(2)**, 619–26, 1974.

[6] A. Preumont, *Vibration control of active structures,* Kluwer Academic Publishers, 2002.

[7] C.W. Stammers, T. Sireteanu, Control off building seismic response by means of three semi-active friction dampers. *Journal of Sound and Vibration*, **237(5)**, 745-59, 2000.

[8] OPCM 3274, President of the Council of Ministers (2003), "*Ordinance No. 3274 - First Elements Regarding the General Criteria for the Seismic Classification of the National Territory and Technical Standards for the Constructions in Seismic Zone*". (in Italian)

[9] Eurocode 8, UNI EN 1998-1 2005, "*Design of structures for earthquake resistance - Part 1: General rules, seismic actions and rules for buildings*".

[10] N. Caterino, E. Cosenza, B.M. Azmoodeh, Approximate Methods to Evaluate Storey Stiffness and Interstory Drift of RC Buildings in Seismic Area. *Structural Engineering and Mechanics*, 2013. (in press)

[11] N. Caterino, M. Spizzuoco, A. Occhiuzzi, Experimental comparison of control algorithms for systems based on SA MR dampers for seismic response reduction. *Smart Structures and Systems*, 2013. (in press)

[12] N. Caterino, M. Spizzuoco, A. Occhiuzzi, Promptness and dissipative capacity of MR dampers: experimental investigations. *Structural Control and Health Monitoring*, 2013. (in press)

[13] G. Maddaloni, K.P. Ryu, A.M. Reinhorn, Simulation of floor response spectra in shake table experiments. *Earthquake Engineering and Structural Dynamic*, **40(6)**, 2011. doi:10.1002/eqe.1035

[14] G. Maddaloni, N. Caterino, A. Occhiuzzi, Semi-active control of the benchmark highway bridge based on seismic early warning systems. *Bulletin of Earthquake Engineering*, doi:10.1007/s10518-011-9259-1, 2011.

[15] G. Maddaloni, N. Caterino, G. Nestovito, A. Occhiuzzi, Use of seismic early warning information to calibrate variable dampers for structural control of a highway bridge: evaluation of the system robustness. *Bulletin of Earthquake Engineering*, 2013. (in press).

COMPDYN 2013
4th ECCOMAS Thematic Conference on
Computational Methods in Structural Dynamics and Earthquake Engineering
M. Papadrakakis, V. Papadopoulos, V. Plevris (eds.)
Kos Island, Greece, 12–14 June 2013

RESPONSE TIME OF MR DAMPERS FOR SEISMIC SEMIACTIVE CONTROL: EXPERIMENTAL MEASURES AND POSSIBLE PREDICTION

N. Caterino[1] **and M. Spizzuoco**[2]

[1] Department of Technology, University of Napoli Parthenope, Centro Direzionale, isola C4, 80123 Naples, Italy
nicola.caterino@uniparthenope.it

[2] Department of Structural Engineering, University of Napoli Federico II, Via Claudio 21, 80100 Naples, Italy
spizzuoc@unina.it

Keywords: Semi-Active Control; Magnetorheological Dampers; Control Delays; Response time.

Abstract. *A wide experimental activity on two prototype magnetorheological (MR) semi-active (SA) dampers manufactured in Germany was conducted during an Italian research project, and it was partially devoted to investigate their promptness in the response. The experimental campaign has been performed on two properly designed setup configurations, by considering two different behaviours for the tested MR devices: a 'passive' behaviour (i.e., by keeping constant the feeding current during the entire test), or a 'semi-active' one, by driving them through an energy-based control algorithm. The experimental analysis of the devices' response time is presented in detail: it is shown how the control delays are strongly dependent on the effectiveness of the electric part of the control hardware, generally being less than 10 ms if special care is paid in designing the whole control chain. On the base of the experimental results, simple relationships are proposed to be assumed for the prediction of the amount of delay to be expected when a given change of current is going to be commanded, as well as the probability distributions of such delays calculated by fitting statistical available data. These distributions can be helpful for taking into account, in a refined model of a semi-actively controlled structure, the probability of occurrence of expected delays and/or to calibrate the compensation techniques included in some SA control algorithms, aiming at reducing the harmful effects these unavoidable delays may cause on the control effectiveness in terms of structural response reduction.*

1 INTRODUCTION

In the last decade, variable dampers have been widely considered in the framework of the seismic protection of structures, to implement semi-active (SA) control strategy of earthquake induced vibrations as well as smart passive ones [1, 2]. SA structural control via magnetorheological (MR) dampers is one of the most promising emerging technologies. The effectiveness of a SA strategy for vibration control strongly depends on the operation velocity. Unavoidable delays are involved in the control chain, even if a careful design of the system may strongly reduce their incidence. Few papers in literature show response time analyses of such devices [3-8], highlighting the need to further investigate this aspect, so crucial for the overall effectiveness of the above innovative control strategy. Data presented in some references numbered above seem to strongly disagree, setting the response time of MR dampers in a quite wide range: the apparent inconsistency is due to the different concepts of response times adopted by researchers. Herein a detailed analysis of the time response of a SA MR damper is presented, starting from the results of a wide experimental campaign conducted at the Laboratory of the University of Naples (Italy) Federico II on two full-scale (identical) prototype semi-active MR dampers provided by the German company Maurer Söhne [9].

2 TESTING APPARATUS

This section presents a comprehensive description of the testing set-up for the characterization of the prototype SA MR dampers. The total length of each device is 595 mm with a stroke of ± 25 mm, the external diameter is 100 mm, the mass is about 16 kg, and a maximum force of about 30 kN can be developed along its longitudinal axis (without rising of bending, shear and torsional moment in the piston rod). A patented magnetic circuit, composed by 3 coils in series, can generate the magnetic field in the device. The internal circuit of the damper has the following properties: a resistance of 3.34 Ω, a reactance of -1,27 Ω, an impedance (modulus) of 3,57 Ω and an inductance of 276 mH. The current i in the circuit is provided in the range 0~3 A by a specific power supply type BOP (Bipolar Power Supply) provided by Kepco Inc. (New York, USA), model 50-4M, maximum power output of 200 W, maximum input power of 450 W, power source-power sink capabilities in the range ± 50 V (voltage) and ± 4 A (current): it is commanded from a remote location through a voltage signal in the range 0~10V, with alternative operations as voltage driver or as current driver.

The MR dampers have been experimentally tested in two different configurations (Figure 1) of a self-balanced testing apparatus. The dynamic actuator utilized has a stroke of ±250 mm and can apply horizontal dynamic load up to 1,200 kN in tension and 440 kN in compression in the frequency range 0~5 Hz. Its external cylinder is firmly connected to a rigid steel plate through four steel bars with a diameter of 24 mm each. The MR device piston is connected to the moving part of the actuator through the interposition of a 100 kN load cell. In the first configuration, the main body of the damper is firmly linked to another rigid steel plate through four steel tubes with an external diameter of 114.3 mm and a thickness of 8 mm.

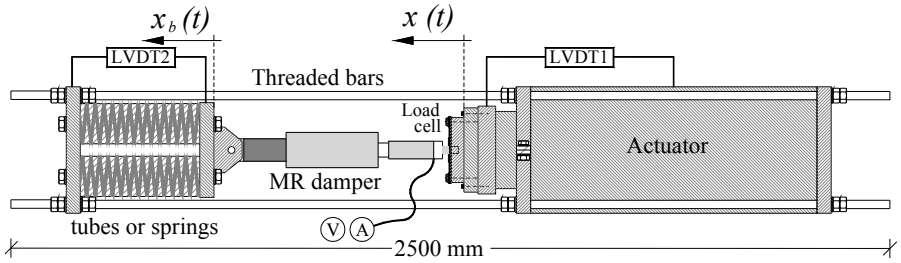


Figure 1: Schematic representation of the two experimental setups (with tubes and springs, respectively).

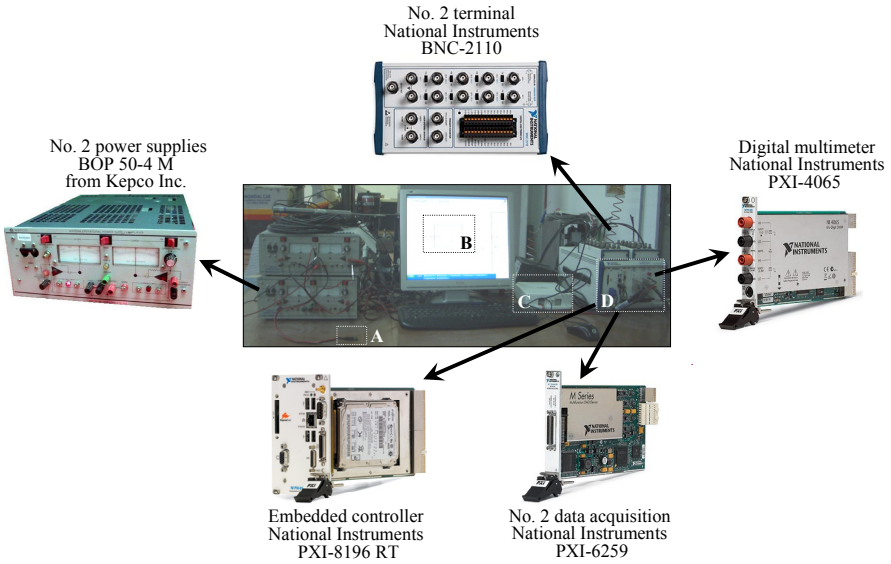


Figure 2: Main components of the electronic equipment adopted for the tests.

In the second configuration, the tubes are replaced by four elastic steel springs of stiffness 500 kN/m each, representing the elastic behaviour of an equivalent semi-active bracing system. An horizontal displacement transducer ("LVDT1" in Figure 1) was able to measure the displacement x of the actuator's piston for the displacement control of its motion. In the second set-up configuration, an additional horizontal displacement transducer ("LVDT2") with ±50 mm stroke was mounted to measure the extension or compression x_b of the springs, that is, to indirectly evaluate the relative displacement of the damper (x_b–x). The electronic equipment used for the tests is sketched in Figure 2.

3 EXPERIMENTAL ACTIVITY

Three groups of tests have been performed as listed in Table 1: they are labelled as 'PA' ('passive'), 'PR' ('promptness') and 'SA' ('semi-active'). Passive tests were addressed to investigate the dampers' behaviour when fed by a constant intensity of current. Tests of promptness were designed and implemented to measure time delays involved in the SA control chain. Finally, for the semi-active tests, an energy based control algorithm [10] was applied to instantaneously select the optimal value of feeding current. Table 1 specifies:

- Displacements law imposed at the ends of the device. Harmonic, with frequency f in the range 0.5~3.0 Hz and amplitude d = 10~20 mm, or constant velocity type, with velocity v (0.1~0.3 m/s), amplitude d (10~20 mm) and 2 seconds pauses before inverting the sign of the velocity.
- Setup configuration, with steel tubes or springs (Figure 1).
- Control scheme adopted to drive the MR damper's behaviour. In a voltage-driven scheme, the power supply provides a fixed voltage and the current slowly modifies until it reaches a value corresponding to the ratio voltage/resistance. In current-driven operations, the power supply provides a fast changing voltage spike so as to quickly modify the current inside the damper. Power supply having the capability of current-driven operation are referred to as 'power source – power sink'.
- Algorithm adopted for promptness tests. The change of damper's behaviour were commanded for each zero crossing of the displacement (x=0) or velocity ($\dot{x}$=0).

For the SA tests, the second above described setup configuration (with springs) has been adopted to simulate the semi-active operation of a dissipative bracing system installed on a

given structure. For these, the switch on of the damper has been commanded when the control force F and the relative velocity $\dot{x}$ between the damper's ends had the same sign ($F\dot{x} > 0$), the switch off in the contrary case ($F\dot{x} \leq 0$). The SA brace simulated by the assembly MR damper plus elastic elements (springs) is able to temporarily store inside the springs the energy associated with their displacement during the time intervals when the power flowing into the SA assembly is positive, then to release it during fast-dissipation processes, imposed when the power flowing becomes negative. During these tests, the power supply has been used according to a current-driven scheme. All these tests have been also analyzed from a dissipated energy point of view in [11].

Group	No. of tests	Displacement law	Setup configuration	Power supply driven by	On/Off when
PA-1	60	harmonic	with tubes	Current	-
PA-2	60	constant velocity	with tubes	Current	-
PA-3	60	harmonic	with springs	Current	-
PR-1	12	harmonic	with tubes	Current	$x = 0$
PR-2	12	harmonic	with tubes	Voltage	$x = 0$
PR-3	9	harmonic	with tubes	Current	$\dot{x} = 0$
PR-4	20	constant velocity	with tubes	Current	$x = 0$
PR-5	18	constant velocity	with springs	Current	$x = 0$
SA-1	9	harmonic	with springs	Current	$F \cdot \dot{x} > 0$

Table 1: Main features of the tests performed.

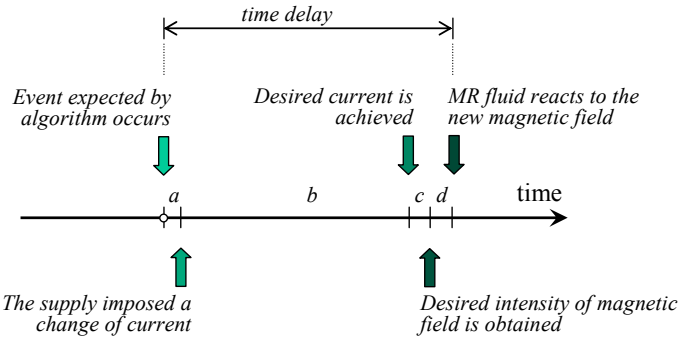


Figure 3: Schematic representation of time delays in a control chain involving MR dampers.

4 PROMPTNESS OF THE PROTOTYPE SA MR DEVICES

The effectiveness of a SA strategy for vibration control strongly depends on the operation velocity. Unavoidable delays are involved in the control chain, even if their incidence may strongly be reduced through a careful design of the overall control system. The time response of a SA MR damper, depends on (Figure 3): *a)* the time needed by the power supply to impose a change of the current; *b)* the time needed to achieve the desired value of the current, according to the corresponding inductance; *c)* the time needed to achieve the corresponding value of the magnetic field; *d)* the time needed by the fluid to react to the change in the magnetic field. Item *b* generally plays the most significant role in the promptness of MR dampers. The time needed to modify the current, in particular, is strongly dependent on operations of the power supply. Figure 4 demonstrates that the time interval needed for the current to achieve the commanded value in the voltage-driven scheme results to be one order of magnitude larger than the one needed into a current-driven approach: from two harmonic tests performed at 1.0 Hz, 10 mm amplitude and 2 A maximum current intensity, belonging to groups PR-1 and PR-2 respectively, a time interval including two off→on and one on→off phases are extracted. The time windows report displacement, MR voltage, MR current and command

signal as given by the power supply. Part (a) of such figure refers to the current-driven scheme, part (b) to the voltage-driven approach. With reference to Figure 4a, it can be observed that when V_{com} goes from 0 to 5 V, after about 1 ms the voltage sent by the power supply to the damper reaches a spike of about 50 V which lasts about 6 ms, i.e. the time needed by the current to increase from zero to desired value; after this time, the voltage generated by the power supply falls down to the steady-state value of about 8 V. Similarly, when V_{com} varies from 5 to 0 V, after about 1 ms the voltage generated by the power supply jumps to -50 V and is kept constant for about 4 ms, that is the time needed until the current goes from 2 A to 0 A; after that, the voltage provided by the power supply is kept at a constant value of 0 V. In the voltage-driven operations (Figure 4b) when V_{com} goes from 0 to 1.5 V, the voltage V given by the power supply to the damper instantaneously varies from 0 to approximately 8 V, whereas the current i slowly increases from 0 to 2 A, due to the electric inductance of the coils inside the damper, taking about 215 ms to reach 95% of the final value. Similarly, the time needed by the current in an on→off switch is somewhat longer than 220 ms. It is worth to note that in case of voltage-driven operation the requirement of the power supply is about 16 W, but it increases to approximately 100 W in case of current-driven operation. This larger requirement allows to reduce the electrical response time of a SA MR damper of more than a order of magnitude (215 to 5 ms).

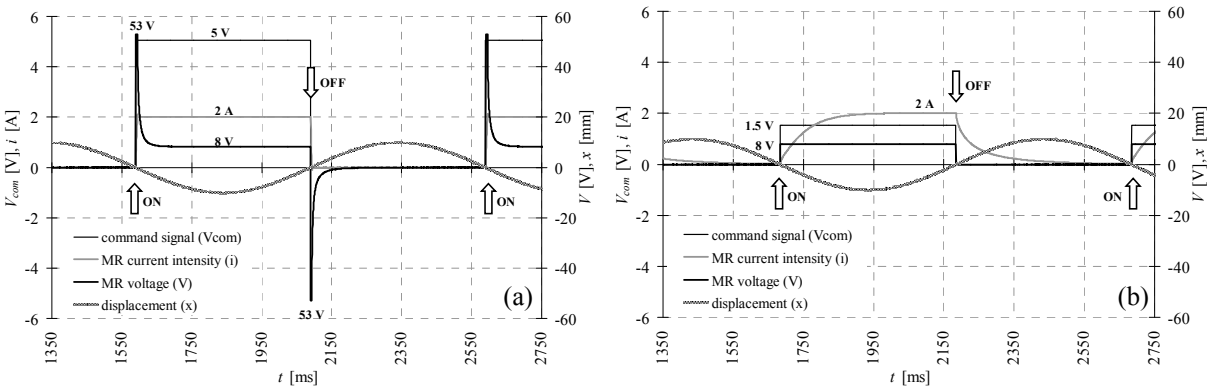


Figure 4: Some details of two tests of promptness. Current- (a) and voltage-driven (b) schemes.

Although the classification of the control delays described above (*a* to *d*) is based on a conceptual description, the testing apparatus was able to measure the response time of MR dampers as the sum $\tau = \tau_a + \tau_c + \tau_e + \tau_m$, where: *(i)* τ_a is the time delay of the control electronics (i.e. the time interval starting when the switching algorithm recognizes that a given condition has occurred and ending when the CPU issues a command signal to the power supply); *(ii)* τ_c is the time interval starting when the driving signal (in output from the algorithm) is issued to the power supply and ending when the current (in output from the power supply and in input to the device) begins to change; *(iii)* τ_e is the time delay of the electrical part of the damper, which is the time interval starting when the current (into the device) begins to change and ending when the current reaches the commanded nominal value within a ± 5% tolerance; *(iv)* τ_m is related to the mechanical part of the damper, representing the time interval between the instant when the current reaches its nominal value and the instant when the damper begins to react.

Figure 5 shows how the values of the electrical switch off delay measured during two types of harmonic tests (at 1.0 and 1.5 Hz, and 10 mm amplitude, groups PR-1 and PR-2) change according to the maximum value of feeding current i_{max} (1, 2 and 3 A).

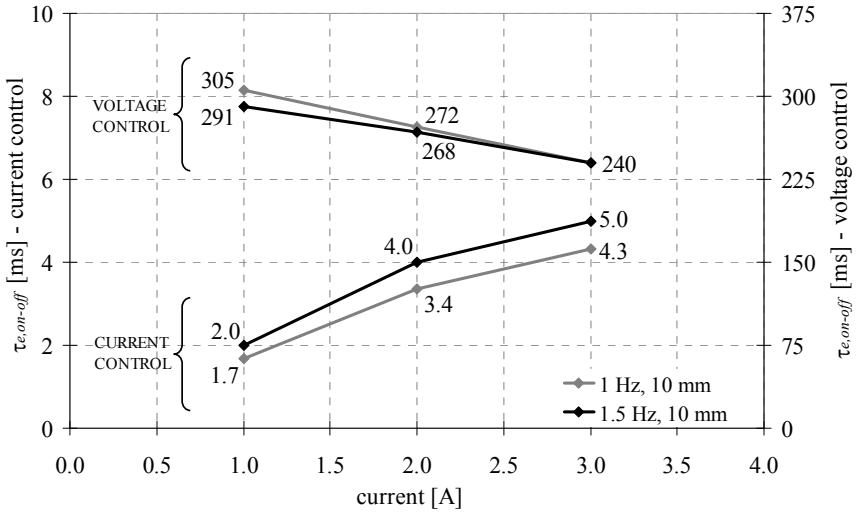


Figure 5: Amount of electrical switch off delay for harmonic displacement tests, as a function of the current.

Figure 6, which presents a time window of 200 ms extracted by three constant velocity tests of group PR-4 (at 0.2 m/s and 20 mm amplitude), shows 3 on→off (a) and 3 off→on phases (b), demonstrates that, when the current-driven approach was adopted, the time needed to the MR damper's force to get the final desired value resulted to be almost the same (about 30 ms) for each investigated maximum value of current intensity.

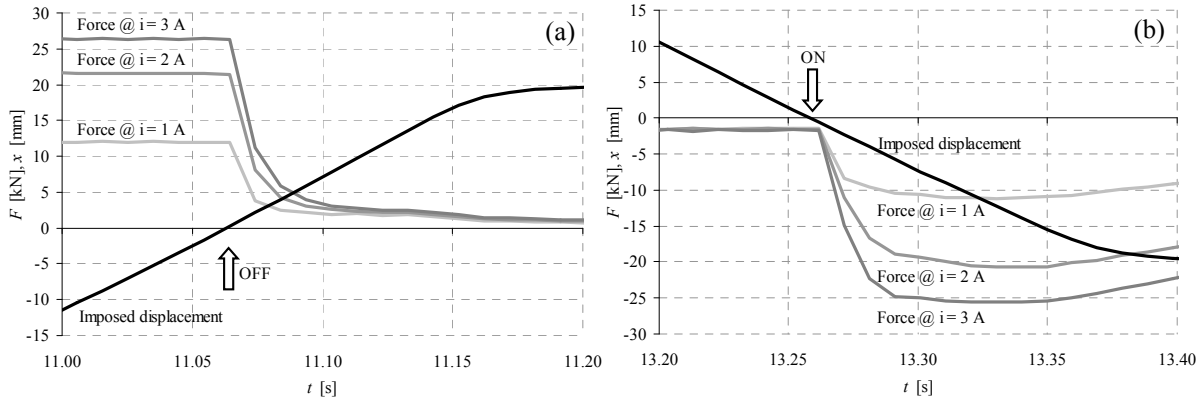


Figure 6: Constant velocity tests at 0.2 m/s, 20 mm. Decay (a) and rising (b) of the MR force when a switch off and a switch on are given respectively (current-driven approach).

The response times τ_a, τ_c, τ_e, τ_m have been measured at two on→off and two off→on phases for each of all performed tests. A total of 120 experimental values for each of them have been measured in the case of the current-driven scheme, 24 in that of the voltage-driven scheme. Time delays τ_a and τ_c turned out to assume a rather stable value equal to 0.4 ms for both the on→off and the off→on phases, resulting to be practically independent from the maximum commanded current. The mechanical response time τ_m, measured in both the switch off and switch on phases, resulted in an almost stable value, on average equal to 1 ms. Conversely, as expected, electrical delays τ_e resulted to be strongly dependent on the level of current intensity as well as on the adopted scheme (voltage- or current-driven) adopted to control MR damper's behavior. All the measured τ_e values are graphically reported in Figure 7, where those referred to a switch on are indicated by gray dots, those to a switch off by black dots. Parts (a) and (b) of such figure refer to the current-driven and voltage-driven approaches respectively. When the current-driven operations have been imposed, τ_e turned out to be in the

interval 2~6 ms for the on→off switches, 2~9 ms for the off→on phases. Results of the tests performed according to the voltage-driven scheme resulted to be included in the intervals 230~300 ms and 125~250 ms for cases of switch-on and switch off respectively. Regression lines and their equations (see Figure 7) may further help the reader in interpreting the trend of these data as a function of the current intensity. These equations can also be included in the numerical model of a semi-actively protected structures when control delays have to be explicitly accounted for.

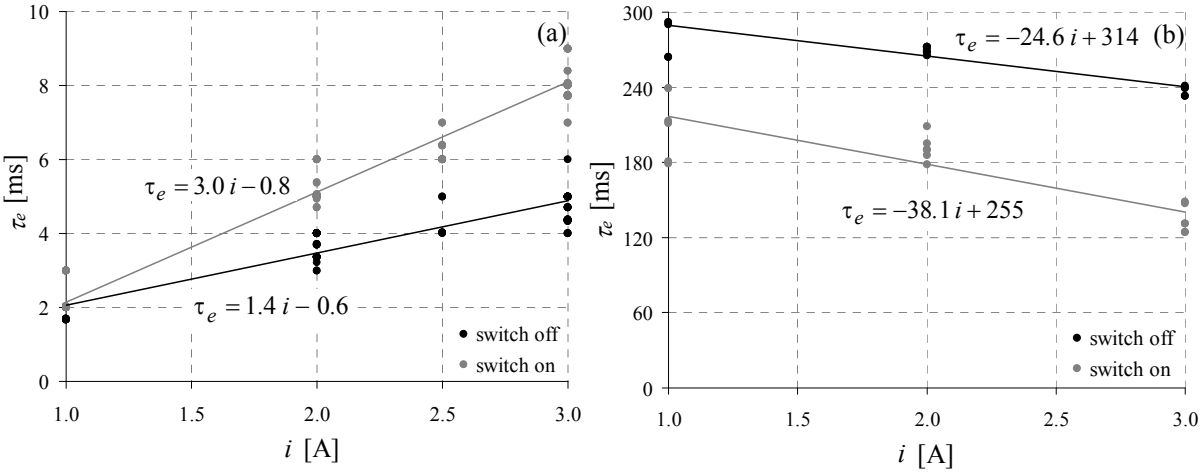


Figure 7: Summary of all the measured τ_e time delays: current-driven (a) and voltage-driven (b) approaches.

The experimental measures of τ_e at on→off switches ($\tau_{e,off}$) have been statistically analyzed by dividing each of them by the maximum feeding current i of the corresponding test, and by singling out 8 classes of values of the normalized delay $\tau_{e,off}/i$, from zero to 4.0 ms/A (each class has an amplitude of 0.5 ms/A). The relative frequency density has been calculated for each class as the ratio of the relative frequency over the amplitude of the class, being the relative frequency of a class the number of measures of $\tau_{e,off}/i$ belonging to it, normalized by the total number of measurements. The same operation has been done also with reference to the values of τ_e measured for off→on cases ($\tau_{e,on}$).

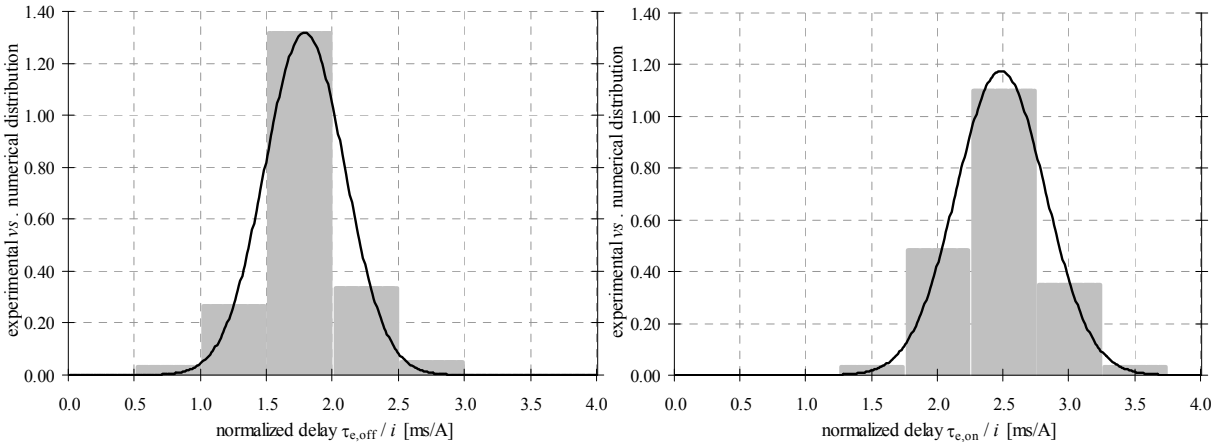


Figure 8: Statistical analysis of the values τ_e normalized by the current intensity. Fitting probability distributions.

The calculated densities correspond to the grey histograms of Figure 8, where the black curve fits the experimental data according to a Gaussian distribution function of variable x, measuring the electrical delay τ_e normalized by the current intensity, with mean μ (1.786

ms/A for $\tau_{e,off}$, 2.478 ms/A for $\tau_{e,on}$) and standard deviation σ (0.303 ms/A for $\tau_{e,off}$, 0.339 ms/A for $\tau_{e,on}$). These distributions can be helpful to predict the amount of delays associated to the SA control of a given structure equipped with the examined MR dampers, taking into account the probability they actually may occur during a seismic excitation.

5 CONCLUSIONS

The promptness of semi-active MR devices turned out to be almost exclusively dependent on the effectiveness of the electric part of the control hardware. Rheology and nature of MR fluids seem to play a negligible role on the response time of SA MR devices, while it is necessary a careful design of the electric part and of the power supply. The adoption of current-driven operations is practically mandatory. Provided that an adequate electric hardware be available and properly tuned, the experimental activity at the base of this paper demonstrated that the response time of a SA MR dampers can be comfortably bounded to 8~10 ms. In this case, the measured operating delay of such dampers is mainly associated to the time needed by the current to form the magnetic field in which the fluid is immersed and, in turn, to the design of the coils. In many practical applications, a time interval of 8~10 ms interval can be considered really short, and thus almost negligible, for example compared to typical periods of vibration of civil structures. The present paper proposes simple relationships useful to predict the amount of delay to be expected when a given change of current is going to be commanded, as well as it shows the probability distributions of such delays calculated by fitting statistical available data. The latters can be useful to be involved in the compensation schemes some SA control algorithms include, aiming at reducing the harmful effects of these unavoidable delays on the effectiveness of control systems.

A similar analysis is in progress with reference to data available from shaking table tests of a steel frame structure [12] equipped with the same two prototype devices herein discussed.

REFERENCES

[1] G. Maddaloni, N. Caterino, A. Occhiuzzi, Semi-active control of the benchmark highway bridge based on seismic early warning systems. *Bulletin of Earthquake Engineering*, **9 (5)**, 1703-1715, 2011. doi:10.1007/s10518-011-9259-1

[2] G. Maddaloni, N. Caterino, G. Nestovito, A. Occhiuzzi, Use of seismic early warning information to calibrate variable dampers for structural control of a highway bridge: evaluation of the system robustness. *Bulletin of Earthquake Engineering*. (in press)

[3] G. Yang, B.F. Spencer, J.D. Carlson, M.K. Sain, Large-scale MR fluid dampers: modeling and dynamic performance considerations. *Engineering Structures*, **24**, 309-323, 2002.

[4] A. Milecki, Investigation and control of magneto–rheological fluid dampers. *Intl. Jour. Mach. Tools & Manuf.*, **41**, 379-391, 2001.

[5] J.H. Koo, F.D. Goncalves, M. Ahmadian, A comprehensive analysis of the response time of MR dampers. *Smart Mater. Struct.*, **15**, 351–358, 2006

[6] A. Occhiuzzi, M. Spizzuoco, G. Serino, Experimental analysis of magnetorheological dampers for structural control. *Smart Materials and Structures*, **12**, 703-711, 2003.

[7] L. Yang, D.F. Fubin, A. Eriksson, Analysis of the optimal design strategy of a magnetorheological smart structure. *Smart Material and Structures*, **17**, 8 pp, 2008.

[8] X. Guan, P. Guo, J. Ou, Study of the response time of MR dampers. *2nd International Conference on Smart Materials and Nanotechnology in Engineering*, Proceedings of SPIE 7493, 2009.

[9] N. Caterino, M. Spizzuoco, A. Occhiuzzi, Understanding and modelling the physical behaviour of magnetorheological dampers for seismic structural control. *Smart Materials and Structures*, **20** 065013 doi: 10.1088/0964-1726/20/6/065013, 2011.

[10] A. Occhiuzzi, M. Spizzuoco, Experimental analysis of a semi-actively controlled steel building. *Structural Engineering and Mechanics*, **19** (6), 721-747, 2005.

[11] N. Caterino, M. Spizzuoco, A. Occhiuzzi, Promptness and dissipative capacity of MR dampers: experimental investigations. *Structural Control and Health Monitoring*, 2013 (in press).

[12] N. Caterino, M. Spizzuoco, A. Occhiuzzi A, Experimental comparison of control algorithms for systems based on SA MR dampers for seismic response reduction. *Smart Structures and Systems*. (in press)

COMPDYN 2013
4th ECCOMAS Thematic Conference on
Computational Methods in Structural Dynamics and Earthquake Engineering
M. Papadrakakis, V. Papadopoulos, V. Plevris (eds.)
Kos Island, Greece, 12–14 June 2013

VULNERABILITY ASSESSMENT OF RC BUILDINGS TO LANDSLIDE DISPLACEMENTS. APPLICATION TO CORNIGLIO CASE HISTORY, ITALY

Stavroula D. Fotopoulou[1], Alberto Callerio[2], Kyriazis D. Pitilakis[1]

[1] Aristotle University of Thessaloniki
Department of Civil Engineering, Thessaloniki, Greece
sfotopou@civil.auth.gr, kpitilak@civil.auth.gr

[2] Studio Geotecnico Italiano srl
Via Ripamonti 89, 20141 Milan, Italy
a.callerio@studiogeotecnico.it

Keywords: Landslide Vulnerability, RC Buildings, Corniglio Case History, Fragility Curves, Numerical Analysis.

Abstract. *The present study shows an application to a specific case history (the Corniglio village major landslide) of a recently proposed analytical method for the vulnerability assessment of RC buildings subjected to earthquake induced slow-moving slides [5]. In particular, the method is applied to a representative building which suffered considerable damage by the landslide movement [7]. The main goal is to verify the reliability and applicability of the proposed procedure and of the respective fragility curves through the comparison of the numerical prediction with the observed building damage. Two different approaches of increased complexity were followed for the fragility analysis of the building. At first, two sets of the already developed fragility curves derived from an extensive parametric analysis [6] are selected as the more representative of the Corniglio case history. Thus, the results obtained from their application are compared with the observed building damage, for the measured level of building displacement. The direct comparison carried out proved that the proposed fragility curves could in general capture the performance of the studied RC building when affected by a landslide induced displacement. Then, to enhance the effective implementation of the proposed methodological framework within a more general probabilistic risk assessment study, appropriate fragility curves were defined for a specific building in Corniglio village by means of a straightforward numerical computation. In particular, a two-step numerical approach which includes soil structure dynamic analysis and a structural pseudo-static calculation was followed to assess the expected building induced stress and damage [5]. As in the previous step, the obtained fragility curves were tested through their comparison with the observed building damage data, for a given level of landslide displacement.*

1 INTRODUCTION

Landslides constitute one of the most destructive natural hazards causing considerable damage and fatalities particularly in mountainous environments. Therefore, the estimation of the risk level associated with slope failures became a fundamental task in developing proper disaster management and mitigation policies.

One of the most important challenges in evaluating the landslide risk is represented by a comprehensive evaluation of vulnerability of the exposed elements. In the literature, everal different approaches to assess the vulnerability of the affected assets only in a qualitative manner or by using rather simplistic empirical or expect-judgment approaches were proposed [1, 2, 3]. This is principally due to the scarcity of quantitative damage data and the inherent uncertainties associated with them [4]. The heterogeneity of potentially vulnerable elements to similar landslide mechanisms, the type of landslide (e.g. rockfalls, debris flows, earth slides etc.) and their characteristics (e.g. size, shape, velocity, momentum), not forgetting the numerous categories of damages and their inherent dynamic nature, contributed to the insufficient and somewhat subjective treatment of the vulnerability to landslide induced movements.

Within the framework of SAFELAND European project (http://www.safeland-fp7.eu), Fotopoulou and Pitilakis [5] developed an analytical method to quantify the vulnerability of reinforced concrete buildings subjected to earthquake induced, slow-moving slides. There, vulnerability is described through the appropriate definition of fragility curves which provide the conditional probability to exceed a certain damage state under a landslide event of a given type and intensity. Several sets of fragility curves for RC low-rise, frame structures were proposed by the same authors [6] on the basis of an extensive numerical parametric analysis carried out on different slope geometry, soil conditions and distance of the building with respect to the slope's crest.

In this paper, stemming from a high-quality set of experimental and observational data in terms of landslide induced ground and building displacement, together with measured building damage, made available and post-processed for a population of buildings in the village of Corniglio in the North-Western Italian Appennines [7], an application of the recently published analytical methodology is presented [5]. More specifically, the aim of the research was twofold: (a) to explore the reliability of the fragility curves derived via extensive parametric investigation [6] through their comparison with the observed damage data for a representative RC frame building under the measured level of ground and building displacement, and (b) to enhance the applicability band of the proposed methodological framework [5] by comparison of appropriate fragility curves defined for the Corniglio case history by means of straightforward numerical computations with the observed building damage.

2 VULNERABILITY ASSESSMENT METHOD

The method proposed in [5] is applicable for the vulnerability assessment of a low-rise RC building located next to the crest of potentially unstable slopes. Usually, the affected structures are subjected to ground induced differential displacement which may cause structural distress and damage. The proposed method, basically based on numerical simulation and statistical analysis, is applied to earthquake induced landslides but in principle it can be easily modified to account for other triggering mechanisms (e.g. intense precipitation, erosion etc.). In terms of numerical computations, a two-step analysis is performed. In the first step, the deformation demand, i.e. total and/or differential displacements considering the actual weight and stiffness of the building and its foundation system due to the landslide displacement (hazard) is assessed, by means of non-linear finite difference dynamic analyses. In the second step, the building response to the statically imposed landslide differential displacement is estimated

by using a Finite Element code. Four damage limit states, which describe the exceedance of slight, moderate, extensive and complete structural damage of the building (respectively LS1, LS2, LS3, LS4), were defined in terms of threshold values of structural resistance by engineering judgment and pertinent literature investigation [8,9,10]. Different limit strains are adopted for "low" and "high" code designed structures. Then, vulnerability was assessed as log-normally distributed fragility functions, which describe the probability (P_i) of exceeding a limit state (LS_i) of the building, on a given slope, with respect to a given landslide intensity measure: the fragility parameters for each limit state are estimated as a function of peak ground acceleration (PGA) recorded on rock outcrop or the permanent ground displacement (PGD) at the slope area by correlating the structural response, in terms of strains, with the corresponding values assigned for each damage limit state.

In order to define a set (abacus) of fragility curves applicable to different RC building types, soil conditions and slope configurations, an extensive parametric investigation was performed on the basis of the proposed two-step numerical approach. A set of fragility curves to be used for several engineering applications is suggested, based on the parameters that have been proved to most significantly contribute to the structural vulnerability [6].

3 APPLICATION TO CORNIGLIO CASE HISTORY

3.1 Landslide movement and building damage data in Corniglio village

The Corniglio Village is located in the northern part of the Appennines, at an altitude of about 700 m a.s.l., between the towns of Parma and La Spezia (as shown in the map of Fig. 1). The morphology of the area of interest shows the characteristics features of an Appennine mountain site, with steep slopes alternating with narrow and deep valleys.

The time period of interest in the present study spans from September 1994 to December 1999, and was characterised by a nearly continuous landslide activity. During this period, the major re-activations of the landslide (the so-called "Lama", i.e. "blade", and nearby portions, see Fig. 1) were recognised to depend on two combined triggering factors:

- Intense rainfalls, particularly before the activation of Dec. 1995 and during November 1996;
- Weak and moderate earthquake ground motion, particularly on occasion of the Correggio Earthquake of October 1996, of magnitude M=5.4, at an epicentral distance of some 70 Km.

Through the entire period considered, the observed displacements reached tens of m on the main slide body, the so-called "Lama", while in the adjacent Corniglio Village (the main subject of the present research) the surface ground movements measured by the inclinometers reached typically 20 to 25 cm resulting to moderate/significant damage to the buildings located in the old centre of the village. In particular, the Corniglio Village was affected by two different slide movements: a deep rock block slide (along cross section A-A, see Fig.1) and a surface rotational landslide (cross section B-B). The geological profile of B-B cross section, on which this study is focused, is presented in Figure 2 [11]. Several re-activations of the landslides have affected Corniglio village damaging buildings, roads and other infrastructures. The landslide movements have been attributed mainly to a decrease of geomechanical parameters, caused by the weathering process due to intense precipitations and weak and moderate seismic activity.

A substantial set of instrumental observations has been gathered mainly from the Emilia Romagna Regional Administration in charge of the monitoring and surveillance activities, including the execution of inclinometer readings (monitoring ground movements in free field), geodetic levelling data on several buildings located within the village area and crack aperture

measurements in which damage revealed to be important. The inclinometers location, the position of the geodetic targets (and their ID's) and, for each building monitored, a letter from A to Z between brackets which indicates the crack meters installed, are depicted in Figure 3. The most damaged buildings are denoted by red filled polygons. The processing of the data set was conducted by Callerio et al. [7], focusing on establishing a correlation among ground displacement, building movements and damage induced during sliding so as to provide the basis for a probabilistically sound vulnerability assessment framework. The damage levels observed in Corniglio were defined in terms of ease of repair, based on the scale proposed by Standing et al. [12], identifying 3 damage levels: negligible to slight, slight to moderate and moderate to severe. The ease of repair was then related to the measure of cracks opening.

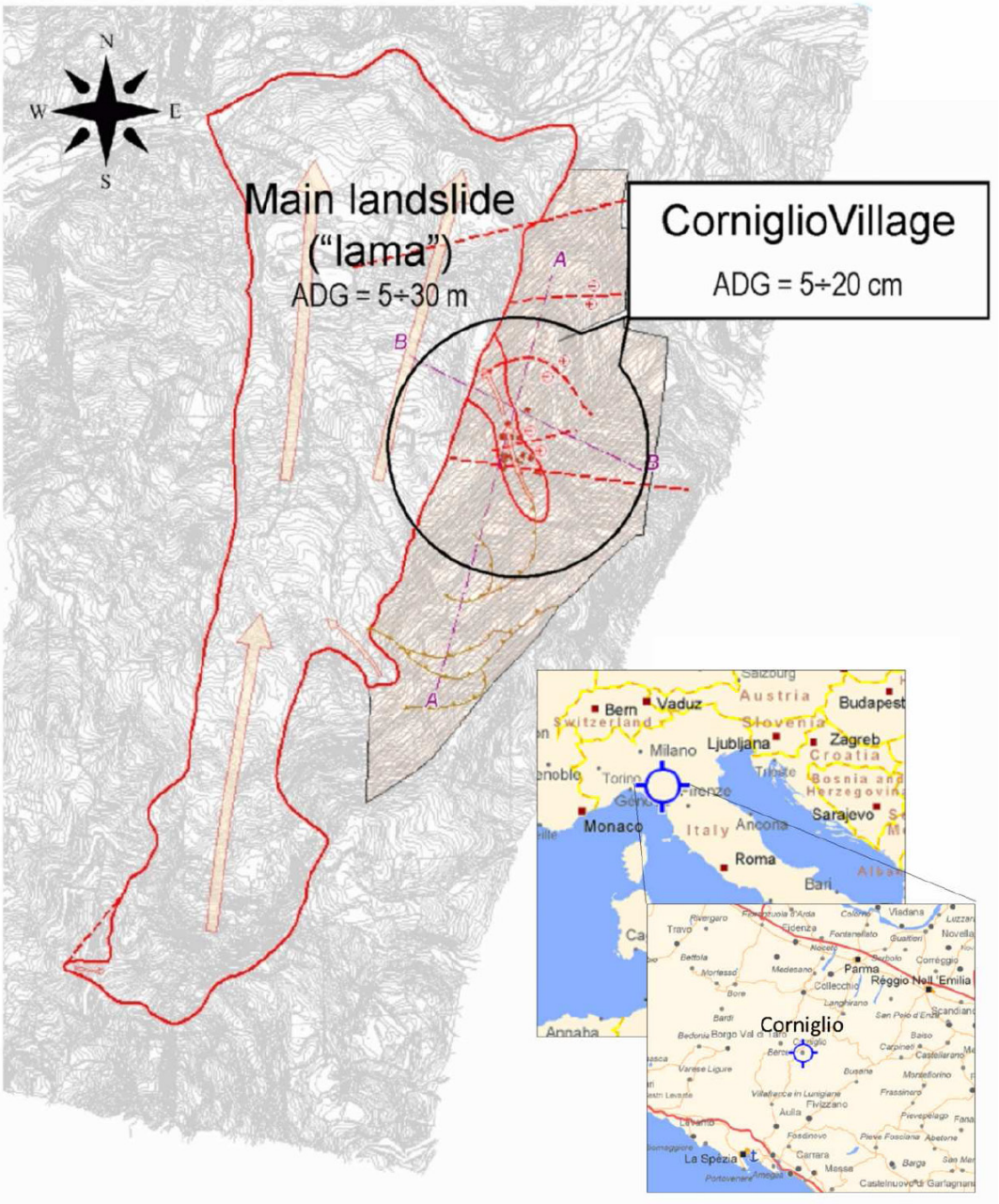


Figure 1: General plan of the area of Corniglio affected by the landslide phenomena during the years 1995-2000. The indicated displacements (ADG = Absolute Ground Displacement) are obtained by aerial photo interpretation ("Lama" area) and inclinometer readings (Village) [7].

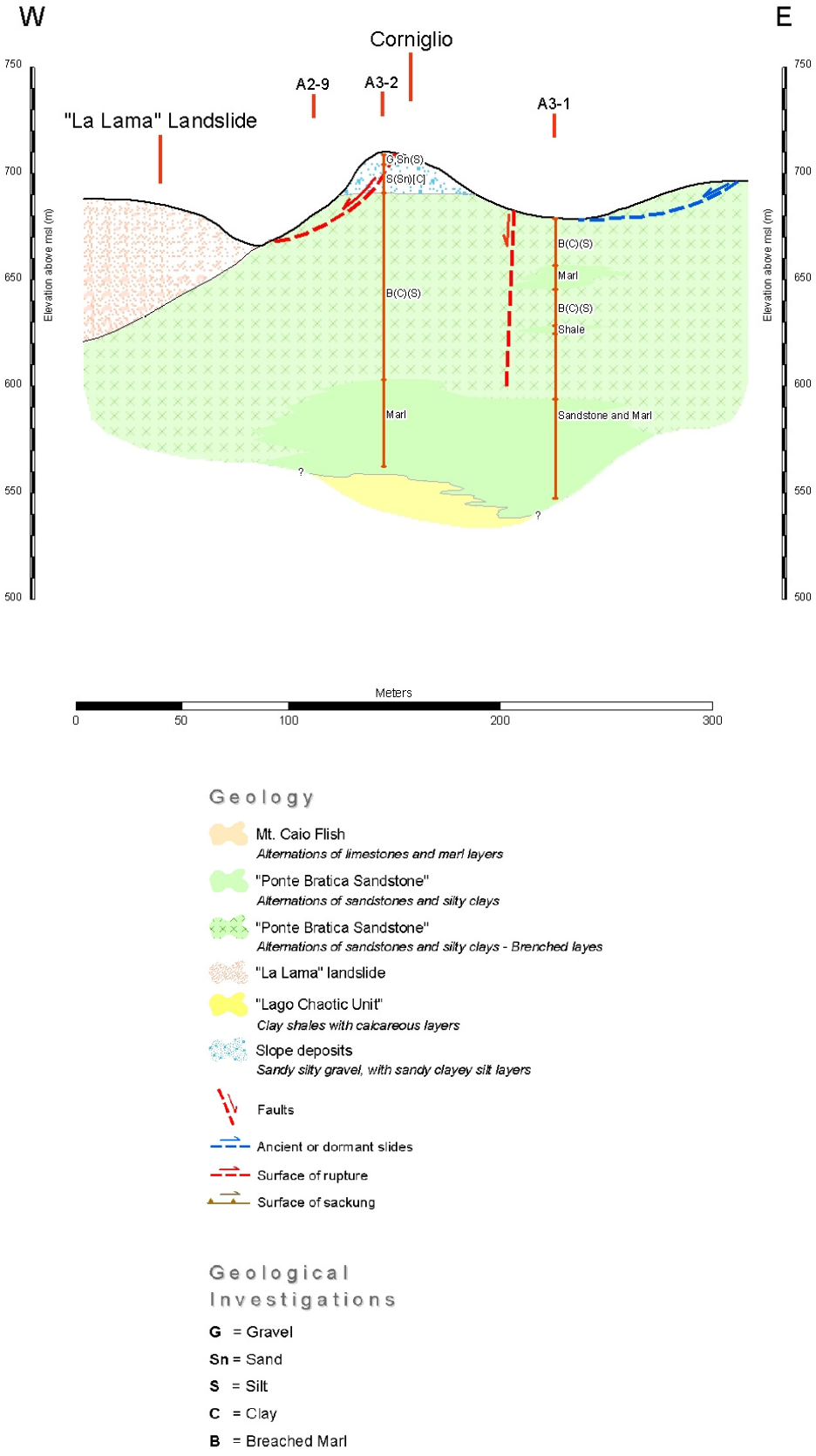


Figure 2: Soil profile along B-B cross section (see Fig. 1) [11].

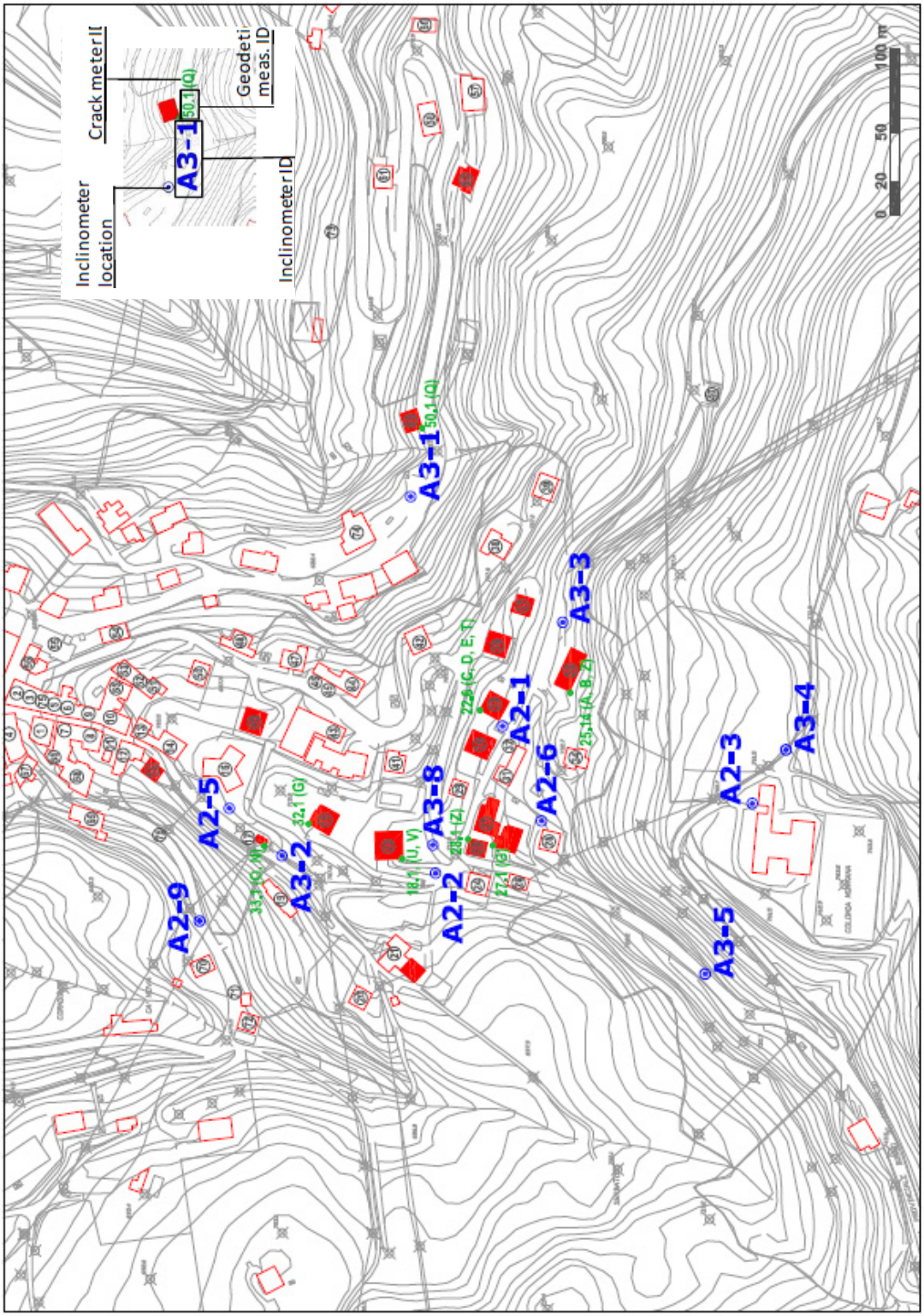


Figure 3: Location of inclinometers, geodetic and crack measurements on buildings. Buildings are denoted by red polygons, whereas the ones that suffered major damages due to the landslide movement are filled in red [7].

3.2 Comparison of the observed building damage with the damage predicted by the proposed and simulated fragility curves

The present study is focused on the fragility analysis of an electrical building (n. 17) due to its proximity to the inclinometer A3-2 (see Fig. 3), which is installed near the slope crown of the geotechnical profile B-B of the Corniglio case history (see Fig. 2). Building n. 17 can be considered a rather simple two-storey RC frame structure with masonry infill walls, which suffered considerable structural damage due to the continuous landslide activity. Figure 4a illustrates representative observed physical damage of the building, while Figure 4b shows the location on a map of the building and the nearby inclinometer A3-2. Despite the proximity of another building (n.18) to the inclinometer A3-2, an upper class mansion with well maintained masonry bearing wall structure with an heavy roof, this was not considered as appropriate for the herein fragility analysis, concentrated on RC buildings. Figure 5 displays the ground displacement measured by inclinometer A3-2, the building movement measured by geodetic leveling and the opening of each crack monitored on the structure [7]. The plot is over imposed on the damage scale in terms of cracks opening, to assess the expected damage state of the building. A rather linear relationship between the building movement and crack opening is detected.

As expected, the given data do not exactly fit those at the base of the calculation of fragility curves derived through numerical parametric analysis [6]. In particular, the studied slope configurations do not match very precisely to the given finite slope geometry and soil geotechnical properties of Corniglio case history (see Fig. 2, geotechnical profile B-B: average slope inclination≈ 37°, average height ≈43 m). Moreover, first-time failures were analyzed in Fotopoulou and Pitilakis [6] in the presence of a sliding surface allowed to be freely developed , as opposed to the Corniglio case study where the landslide movement is rather complex. Considering all the above, two different approaches of increased complexity for the fragility analysis of building n. 17 in Corniglio village are presented.

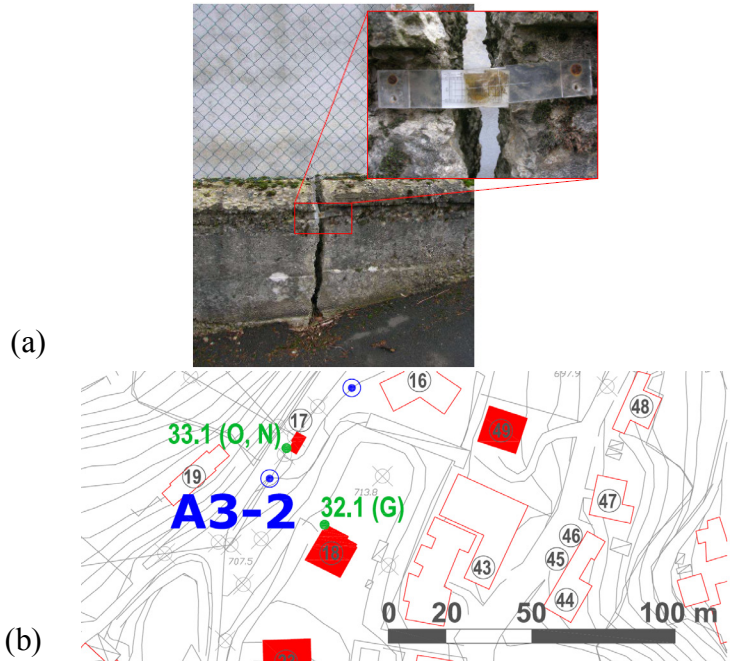


Figure 4: (a) Observed physical damage of building n. 17. (b) Closer view of the building under study and the nearby inclinometer A3-2 within the Corniglio area. The geodetic and crack monitored points on the building are also shown (in green) [7].

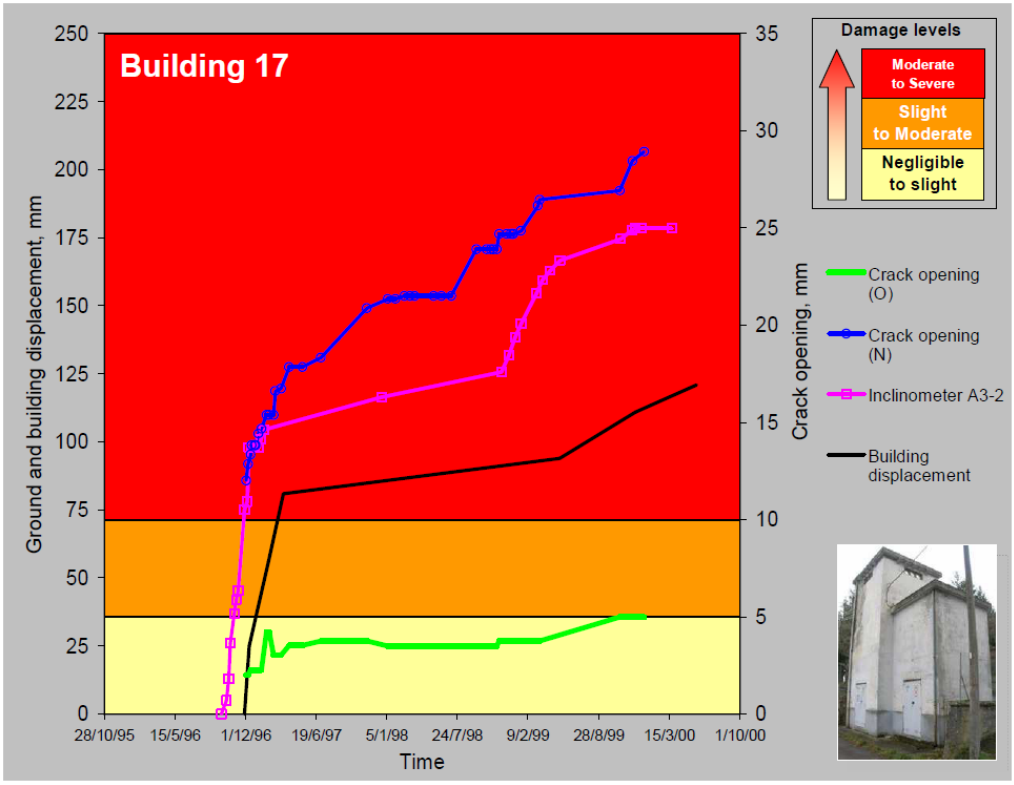


Figure 5: Correlation between absolute ground displacement (from nearby Inclinometer A3-2), building n. 17 displacement (from geodetic levelling) and crack opening (compared to the defined damage levels) as a function of time [7].

3.3 Reliability assessment of the proposed fragility curves

As a first step analysis, two sets of the already developed fragility curves [6] were selected, among those more representative for the Corniglio case history, to be compared with the observed building damage, for the measured level of building displacement (see Fig. 5). These curves have been developed for:

- slope height: 40 m,
- slope inclinations: 30° and 45° respectively
- sandy slope materials
- low code RC frame buildings with flexible foundations

A graph of the aforementioned developed curves is shown in Figure 6 for slope inclinations 30° and 45° respectively. It can be noted that the fragility curves are here presented as a function of the maximum permanent displacement at the foundation level to allow for a direct application to the data available, considering the site-specific nature of the problem under study. The derived lognormal median and dispersions of the fragility functions are given in Table 1. It is worth noting that the adoption of the steel and concrete strain as a damage index in this research [5] implies a structural damage (e.g. in terms of cracks) and a subsequent ductile failure of the building members. This is certainly the case for building n. 17 where extensive cracking was recorded (see Fig. 5).

The damages predicted by the curves are compared with that observed in building n. 17 for the measured level of displacement, i.e. 0.121 m. As shown in Figure 5, for this level of displacement, the building would be in *"moderate to severe"* damage level according to the damage states proposed in Callerio et al. [7].

The proposed curves predict *"slight to moderate" to "moderate to extensive"* damages that are in relatively good correlation with the corresponding assigned damage levels based on the field measurements and observations. As it can be easily seen in Figure 6, the expected damages when using the curves derived for 45° slope inclinations are more in line with the observed structural performance. In particular, the estimated probabilities of exceeding slight (LS_1) and moderate (LS_2) damage states are 1.0 and 0.4 respectively for the curves referring to the 45° inclined slope, whereas the corresponding probabilities are 0.84 and 0.08 respectively for the curves referring to the 30° inclined slope.

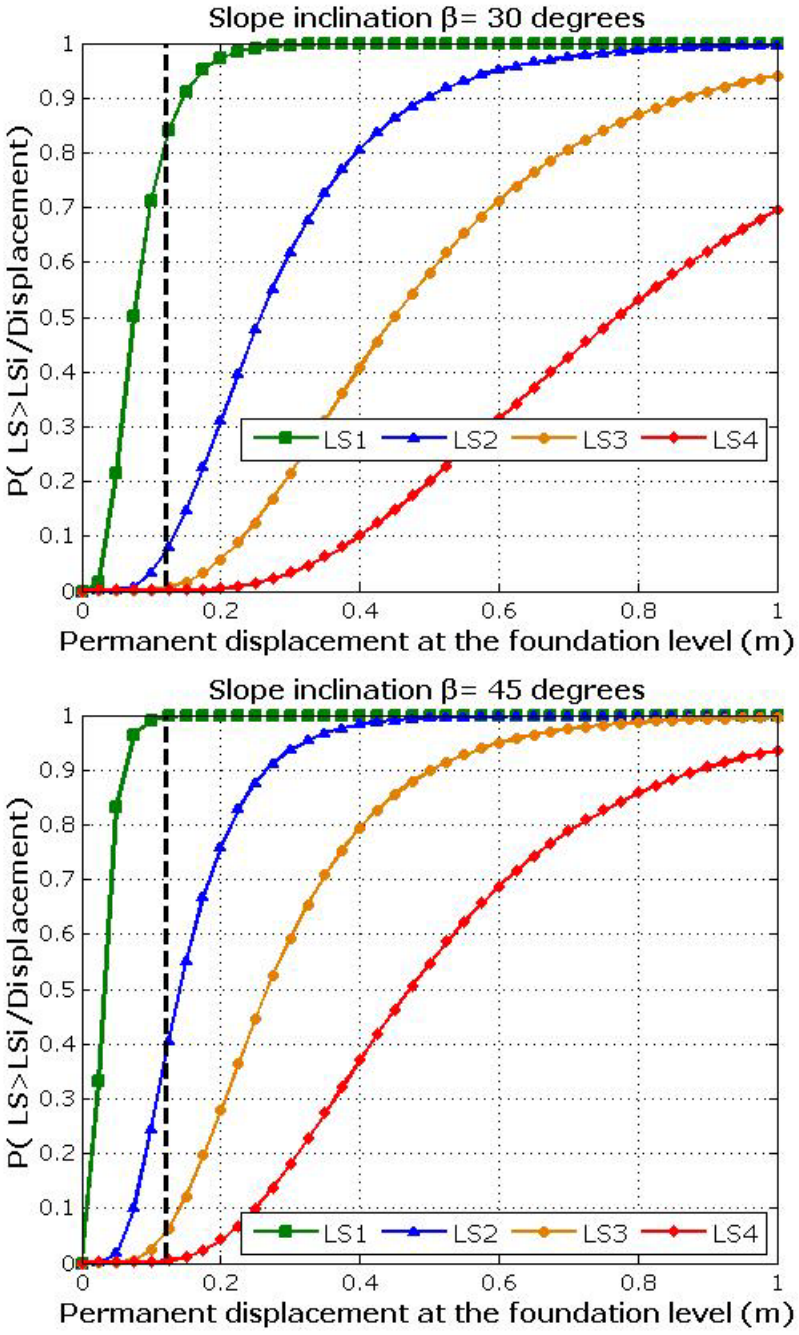


Figure 6: Representative fragility functions derived from the parametric analyses

Limit strain	Displacement at the foundation level (m)			
	Slope inclination angle $\beta=30^o$		Slope inclination angle $\beta=45^o$	
	Median	Dispersion β	Median	Dispersion β
Limit State 1	0.075	0.51	0.031	0.49
Limit State 2	0.257		0.141	
Limit State 3	0.450		0.267	
Limit State 4	0.770		0.472	

Table 1: Parameters of the lognormal distribution for representative fragility functions

3.4 Fragility curves for the Corniglio case history- Comparison with recorded damage data

Considering the relatively crude approximation that it may be achieved with the comparisons presented above a more sophisticated analysis resulting to the development of more appropriate fragility curves for the Corniglio case history based on the data provided (e.g. geotechnical profile B-B, inclinometer A3-2 records associated with building n.17 geodetic and crack measurements) was carried out. Fragility curves were derived from the study of the response of the slope to earthquake shaking, which in our case is the permanent cumulative ground displacement at the foundation level. This is a commonly used landslide intensity measure, which may sufficiently describe the destructive effect of a relatively slow-moving slide to a structure located within the landslide zone [13]. The final deformation demand for the building is given in terms of the corresponding differential displacement, which better describe the induced damage to the building. The ultimate goal of the analysis was to define more reliable correlations between the observed and simulated damage of the building for the measured displacement level so as to increase the reliability of the developed method [5].

The two-step numerical analysis as described in Fotopoulou and Pitilakis [5] was performed. Numerical codes FLAC2D 7.0 [14] and SEISMOSTRUCT [15] were used for the slope-foundation dynamic and structure's quasi-static analyses respectively.

Taking into account the various uncertainties related to the lack of a detailed geotechnical investigation, the simplified finite slope geometry shown in Figure 7 was adopted to describe the geotechnical profile B-B; the simplified model is characterized by three layers with different material properties (Soil 1, Soil 2, elastic bedrock) and a pre-existing sliding surface (Slide). The water table was assumed to lie at the base of the slope (-43m).

The soil materials overlaying the elastic bedrock were modelled through the adoption of an elasto-plastic constitutive law with a Mohr-Coulomb limit surface, coupled to an hysteretic damping scheme. In particular, FLAC 7.0 hysteretic damping formulation was implemented by selecting the "default" model to account for a nonlinear hysteretic soil behavior. The model fits the damping and shear modulus curves over a reasonable range of strains (e.g. up to 0.2-0.3%) which are expected to occur. In particular, the Seed and Idriss [16] sand-upper range curves were used for the slide material and the upper soil formation (Soil 1), whereas Sun et al. [17] clay-upper range curves were used for Soil 2. A small amount (e.g. 0.2%) of stiffness-proportional Rayleigh damping was also added to compensate for the low damping demonstrated by the program at small strains. In addition, for the elastic bedrock materials a constant 0.5% of Rayleigh-type damping was assigned. The geotechnical parameters of the soil formations for the assumed 2D cross-section are summarized in Table 2.

Free field boundary condition was applied along the vertical boundaries of the model, while a quiet (viscous) boundary was applied at the bottom in order to minimize the effect of artificially reflected waves [14]. The FLAC 2D grid and boundary conditions are schematically illustrated in Figure 8.

A single span, two storey, reinforced concrete building is assumed to be located at 10 m from the crest to approximately model building n. 17. No relative slip or separation between the structure and the underlying soil materials was allowed. The assumed bay length and storey height were 5 m and 3m respectively.

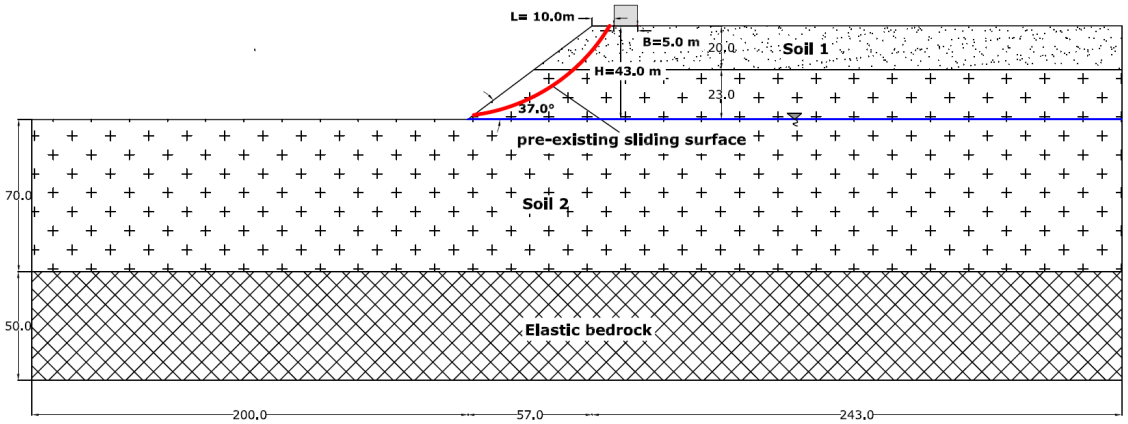


Figure 7: Slope configuration adopted for the geotechnical profile B-B

	Soil 1	Slide	Soil 2	Elastic bedrock
Soil thickness (m)	20	1.0-2.0	93	40
Density ρ (kg/m^3)	1800	1700	2000	2300
Young's modulus E (KPa)	2.93E+05	4.42E+04	1.30E+06	4.32E+06
Poisson's ratio v	0.3	0.3	0.3	0.3
Bulk modulus K (KPa)	2.44E+05	3.68E+04	1.08E+06	3.60E+06
Shear modulus G (KPa)	1.13E+05	1.70E+04	5.00E+05	1.66E+06
Cohesion (KPa)	10	8	50	-
Friction angle (degrees)	35	35	30	-
Shear wave velocity Vs (m/sec)	250	100	500	850
Max. allowed zone size (m)	2.5	1	5	8.5
Max. Allowed frequency	10	10	10	10

Table 2: Assumed soil properties for the geotechnical profile B-B

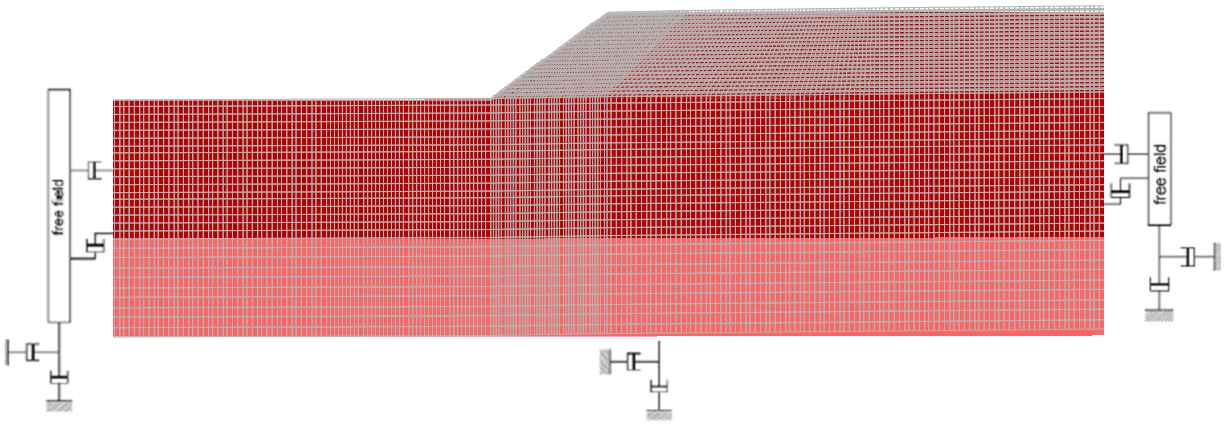


Figure 8: Simplified 2D FLAC dynamic model adopted for the geotechnical profile B-B

Earthquake Name	Country	Date	R (km)	M_W	Station Name	$V_{s,30}$ (m/s)	Database Code
Kalamata (Aftershock)	Greece	10/6/1987	17	5.36	Kyparrisia-Agriculture Bank	778	ESMD_126_H1
Ano Liosia	Greece	7/9/1999	17	6.04	Athens 4 (Kipseli District)	934	ESMD_335_H1
Kozani (Aftershock)	Greece	17/5/1995	16	5.3	Chromio-Community Building	623	ISESD_1210_H1
Friuli	Italy	6/5/1976	21.7	6.4	Tolmezzo-Diga Ambiesta	1030	ITACA_16_H1
Friuli (Aftershock)	Italy	15/9/1976	8.5	5.9	Tarcento	901	ITACA_116_H1
Umbria Marche (Aftershock)	Italy	14/10/1997	20	5.6	Norcia	681	ITACA_491_H2
App. Lucano	Italy	9/9/1998	6.6	5.6	Lauria Galdo	603	ITACA_613_H2
L Aquila Mainshock	Italy	6/4/2009	4.4	6.3	L Aquila - V. Aterno - Colle Grilli	685	ITACA_857_H2
San Fernando	USA	9/2/1971	20.04	6.61	Lake Hughes #12	602	NGA_71_H2
Coyote Lake	USA	6/8/1979	4.37	5.74	Gilroy Array #6	663	NGA_150_H2
Morgan Hill	USA	24/4/1984	36.34	6.19	Gilroy Array #6	663	NGA_459_H2
Loma Prieta	USA	18/10/1989	35.47	6.93	Gilroy Array #6	663	NGA_769_H1

Table 3: Ground motion records used in the numerical simulations derived from the SHARE database [17]

Prior to the dynamic simulations, a static analysis was carried out in order to establish the initial effective stress field throughout the model; a stationary ground flow analysis was also performed to assess the pore pressure distribution.

The seismic input applied along the base of the model consisted of a set of 13 real acceleration time histories from SHARE database ([18]; http://www.share-eu.org/), recorded during Italian, Greek and USA earthquakes on stiff soils, characterized by an average shear wave velocity in the upper 30 m, $V_{s,30}$, greater than 600 m/sec (Table 3). The 5%-damped acceleration response spectra of the selected records as well as the corresponding average and median spectra are shown in Figure 9.

To define the appropriate input motion to be applied at the base of the FLAC model, the selected time histories were first corrected with respect to baseline and filtered (band pass within 0.25 and 10 Hz) allowing for an accurate representation of wave transmission through the model by choosing a maximum propagated frequency of 10Hz by spacing the grid accordingly. Moreover, due to the compliant base used in the model, the appropriate input excitation corresponds to the upward propagating shear wave that is taken as one-half the target outcrop motion [19]. The selected input time histories were scaled to three levels of peak ground acceleration, namely PGA=0.1, 0.15, 0.2g in order to assess the building response for different ground differential displacement magnitudes, to study different damage states and construct the corresponding fragility curves. It is worth noting that that, due to the presence of a pre-existing sliding surface, the required amplitudes of the input excitations able to cause extensive slope and foundation deformations are generally lower the the corresponding amplitude considered in the case of first- time failures, as performed in Fotopoulou and Pitilakis [5].

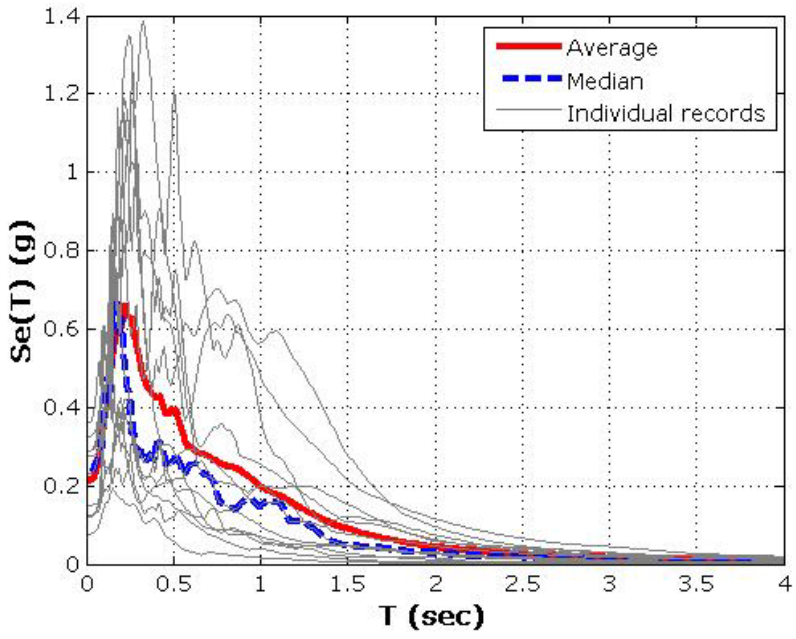


Figure 9: Linear 5%-damped acceleration response spectra of the records selected for numerical analyses. The average and median spectra are also shown.

Figures 10(a) and 10(b) depict the derived horizontal and vertical differential displacements time histories respectively at the closest edge of the assumed building from the slope's crest (i.e. 10 m), for input accelerograms scaled at 0.15 g. It is observed that the specific characteristics (frequency content and duration) of the seismic ground motions can significantly

affect the history and the amplitude of the computed differential displacement demand at the foundation level.

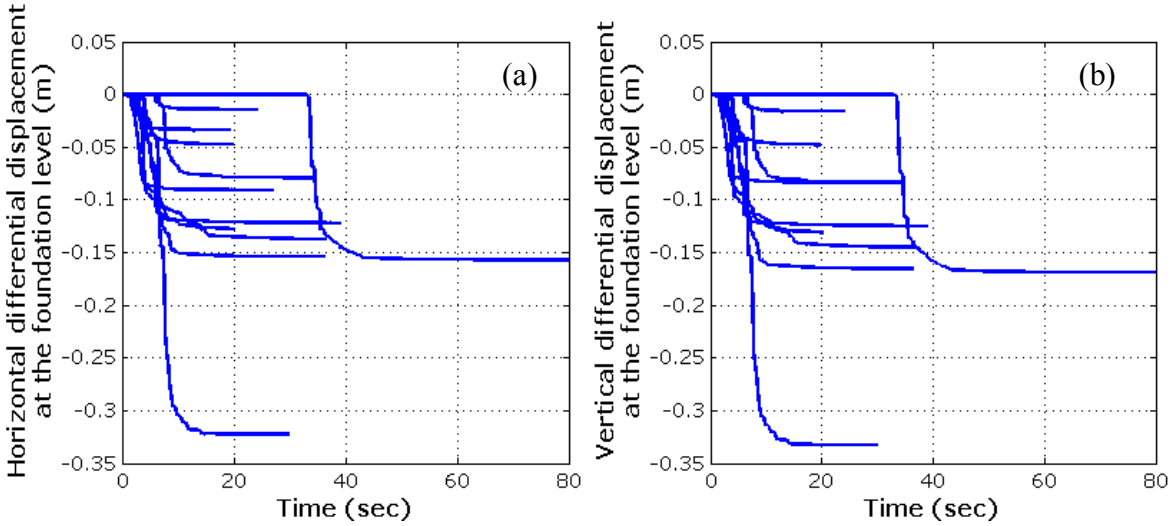


Figure 10: Differential horizontal (a) and vertical (b) ground displacements at the building's foundation level for input accelerograms scaled at 0.15 g.

Then, a non-linear quasi-static analysis was performed on the 1 bay-2 storey RC frame building model of Fig. 11 by means of the finite element code SEISMOSTRUCT [15]. More specifically, the derived differential displacement time histories extracted from FLAC dynamic analysis (see Fig. 10) were directly applied quasi-statically at one of the RC frame supports. The beneficial contribution of masonry infill walls to the building capacity was not considered in this study.

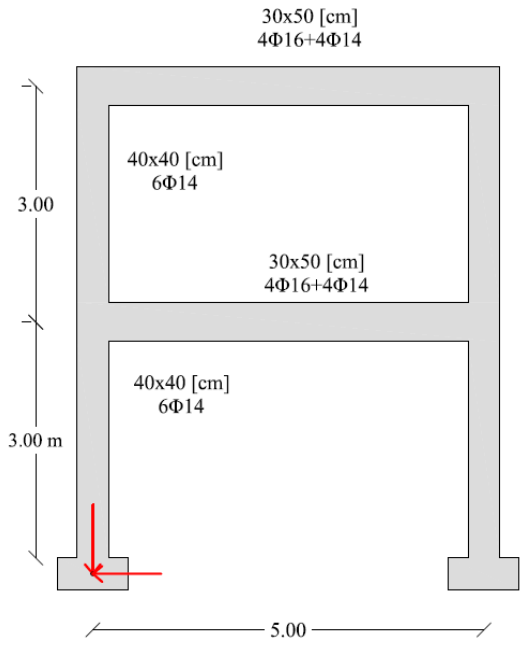


Figure 11: Schematic view of the studied building in Corniglio village and displacement loading pattern considered for the non-linear quasi-static analysis

Non-linear fiber-based material properties were assumed for the structural members of the RC frame building under investigation. More specifically, a uni-axial, nonlinear model considering a constant confining pressure throughout the entire stress-strain range was used for the concrete material [20] (parameters: f_c=20MPa, f_t=2.1MPa, strain at peak stress 0.002mm/mm, confinement factor =1 for unconfined and 1.2 for confined concrete, specific weight=24KN/m^3) and a uni-axial bilinear stress-strain model with kinematic strain hardening was used for the reinforcement (parameters: f_y=400MPa, E=200GPa, strain hardening parameter μ =0.005, specific weight=78KN/m^3).

Then, structural response data were statistically put in relation with the corresponding limit damage states and landslide intensity parameter in order to estimate structure's fragility curves. Figure 12 depicts a representative plot of damage evolution expressed in terms of maximum steel strain (damage index) as a function of the expected maximum permanent ground displacement at the foundation level for the low-rise, "low code" designed RC frame building. The figure also shows the limit steel strains needed to exceed yield and post-yield limit states for low-code RC buildings characterized by a low level of confinement, as defined in Fotopoulou and Pitilakis [5].

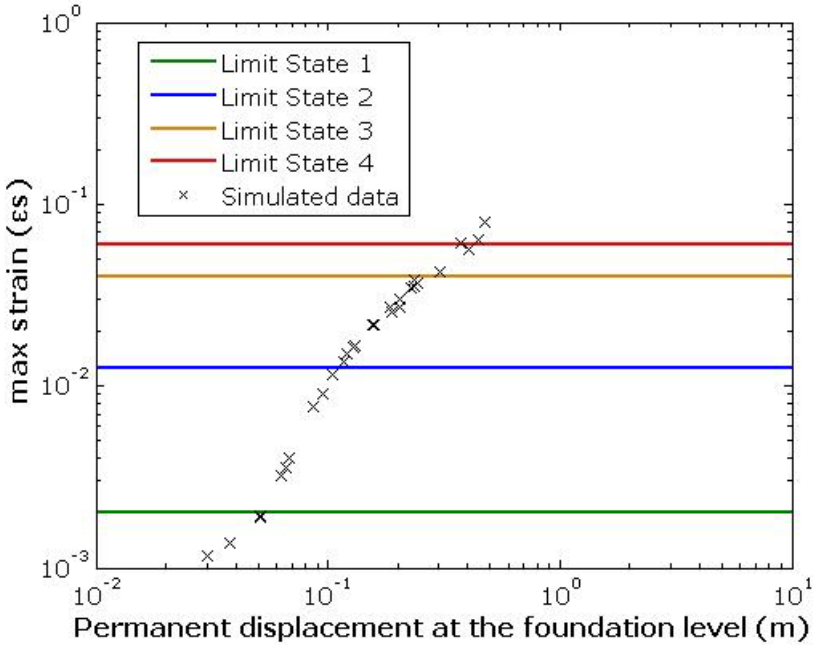


Figure 12: Maximum recorded steel strain as a function of permanent ground displacement at the foundation level for the studied building in Corniglio village

	Permanent displacement at the foundation level (m)	
	Median (m)	Dispersion β
Limit State 1	0.042	0.41
Limit State 2	0.093	
Limit State 3	0.168	
Limit State 4	0.315	

Table 4: Parameters of fragility functions for the studied building in Corniglio village

Finally, probabilistic fragility curves in terms of permanent displacement at the foundation level for building n. 17 in Corniglio village were derived with the aid of the Maximum likelihood Method (see [6] for details). Table 4 presents the lognormal parameters of the fragility functions, whilst Figure 13 depicts the corresponding plots. The simulated fragility curves predict that the building n. 17 studied herein is more likely to suffer *"moderate to extensive damage"*, for the measured level of displacement, i.e. 0.121 m. In particular, the estimated probabilities of exceeding moderate (LS2) and extensive damage (LS3) are 0.85 and 0.22 respectively. These observations are in fairly good agreement with the observed building damages (see Fig. 5), verifying in this specific case characterized by an extensive amount of observational data, the validity of the derived fragility curves, finally enforcing the robustness of the developed methodological framework [5].

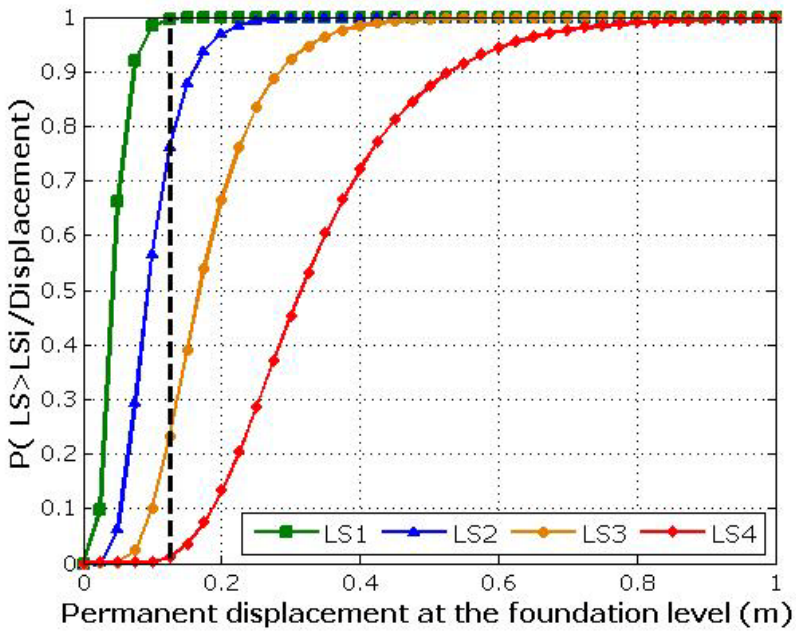


Figure 13: Fragility curves for the studied RC frame building in Corniglio village

4 CONCLUSIONS

The reliability and applicability of the developed methodology for assessing the vulnerability of low-rise RC buildings to earthquake induced landslide displacements has been assessed through its application to a representative RC building in Corniglio village-Italy. The studied building suffered moderate to extensive structural damage due to the landslide movement, well documented during and after the landslide event. The direct comparison of the observed damage with that predicted by the previously developed representative fragility functions proved that the suggested fragility curves could adequately capture the performance of the representative RC building which was affected by the slope co-seismic landslide differential displacement. In addition, to enhance the effective implementation of the proposed methodological framework within a probabilistic risk assessment study, more appropriate fragility curves were constructed for the studied building in Corniglio village based on straightforward numerical computations. The obtained fragility curves were compared to the observed build-

ing damage for the measured level of displacement. Although such a comparison revealed to be quite promising, a further validation of the proposed method on building damage data from past landslide events is certainly warranted to reinforce its reliability and accuracy in predicting damage levels for a certain exposure of the building and intensity of the landslide event.

REFERENCES

[1] F.C. Dai, C.F. Lee, Y.Y. Ngai, Landslide risk assessment and management: an overview, *Engineering Geology*, **64**(1), 65-87, 2002.

[2] J. Remondo, J. Bonachea, A. Cendrero, Quantitative landslide risk assessment and mapping on the basis of recent occurrences, *Geomorphology*, **94**, 496-507, 2008.

[3] J.L. Zêzere, R.A.C. Garcia, S.C. Oliveira, E. Reis, Probabilistic landslide risk analysis considering direct costs in the area north of Lisbon (Portugal), *Geomorphology*, **94**, 467–495, 2008.

[4] C.J. Van Westen, T.W.J. Van Asch, R. Soeters, Landslide hazard and risk zonation—why is it still so difficult?, *Bulletin of Engineering Geology and the Environment,* **65**, 167–184, 2006.

[5] S. Fotopoulou, K. Pitilakis, Vulnerability assessment of reinforced concrete buildings subjected to seismically triggered slow-moving earth slides, *Landslides,* 2012 (DOI: 10.1007/s10346-012-0345-5).

[6] S. Fotopoulou, K. Pitilakis, Fragility curves for reinforced concrete buildings to seismically triggered slow-moving slides. *Soil Dynamics and Earthquake Engineering*, 2013, http://dx.doi.org/10.1016/j.soildyn.2013.01.004

[7] A. Callerio, E. Faccioli, A. Kaynia, *Deliverable 121: Landslide risk assessment methods and applications (III) – Application to real active landslides – Phase II (68pp)*. LESSLOSS integrated project: Risk Mitigation for Earthquake and Landslides, Sub-Project 4 – Landslide risk scenarios and loss modelling, 2007.

[8] H. Crowley, R. Pinho, J.J. Bommer, A probabilistic displacement-based vulnerability assessment procedure for earthquake loss estimation, *Bulletin of Earthquake Engineering,* **2**(2),173-219, 2004.

[9] J.F. Bird, H. Crowley, R. Pinho, J.J. Bommer, Assessment of building response to liquefaction induced differential ground deformation, *Bul of the New Zealand Society for Earthquake Engineering,* 38(4), 215-234, 2005.

[10] C. Negulescu, E. Foerster, Parametric studies and quantitative assessment of the vulnerability of a RC frame building exposed to differential settlements, *Natural Hazards and Earth System Sciences,* **10**, 1781-1792, 2010.

[11] Lessloss, *The Corniglio landslide (Parma - Italy): Geological data*, Studio Geotecnico Italiano, 28 April, Milan, 2005.

[12] J.R. Standing, T.I. Addenbrooke, J.B. Burland, The assessment and building response to tunneling, risk of damage and structural monitoring, L.G.W. Verhoef ed., *Proc. of International Congress on Urban Heritage and Building Maintenance: Foundations*, Delft University of Technology, 1999.

[13] F. Leone, J.P. Aste, E. Leroi, *Vulnerability assessment of elements exposed to mass moving: working towards a better risk perception*. In K. Senneset (Ed.), Landslides, Balkema, Rotterdam. pp. 263-269, 1996.

[14] Itasca Consulting Group, Inc. *FLAC (Fast Lagrangian Analysis of Continua), ver. 7.0*, Itasca Consulting Group, Inc., Minneapolis, 2011.

[15] SeismoSoft, SeismoStruct, *A computer program for static and dynamic nonlinear analysis of framed structures*. Available from URL: www.seismosoft.com.

[16] H.B. Seed, I.M. Idriss, *Soil moduli and damping factors for dynamic response analyses*, Univ. of California, Berkeley, California, Report No. EERC 70-10, 1970.

[17] J.I. Sun, R. Golesorkhi, H.B. Seed, *Dynamic moduli and damping ratios for cohesive soils*, Earthquake Engineering Research Center, University of California, Berkeley, Report No. UCB/EERC-88/15, p. 42, 1988.

[18] E. Yenier, M.A. Sandikkaya, S. Akkar, *Report on the fundamental features of the extended strong motion databank prepared for the SHARE project (v1.0)*, 2010.

[19] L.H. Mejia, E.M. Dawson, Earthquake deconvolution for FLAC. *Proc. 4th International FLAC Symposium*, Madrid, Spain, 211-219, 2006.

[20] J.B. Mander, M.J.N. Priestley, R. Park, Theoretical stress-strain model for confined concrete, *Journal of Structural Engineering,* **114**(8), 1804-1826, 1988.

COMPDYN 2013
4th ECCOMAS Thematic Conference on
Computational Methods in Structural Dynamics and Earthquake Engineering
M. Papadrakakis, V. Papadopoulos, V. Plevris (eds.)
Kos Island, Greece, 12–14 June 2013

PERFORMANCE-BASED SEISMIC DESIGN OF A RETAINING WALL

Carlos Jurado Cabañes (Ph. D.)

Polytechnic University of Madrid
C/ Alfonso XII, 3 y 5, 28014 Madrid, Spain
e-mail: cjurado@ciccp.es

Keywords: Gravity wall, overturning, sliding, critical acceleration.

Abstract. *The design of containment walls suffering seismic loads traditionally has been realized with methods based on pseudoanalitic procedures such as Mononobe-Okabe's method, which it has led in certain occasions to insecure designs, that they have produced the ruin of many containment walls suffering the action of an earthquake. The recommendations gathered in Mononobe-Okabe's theory have been included in numerous Codes of Seismic Design. It is clear that a revision of these recommendations must be done. At present there is taking place an important review of the design methods of anti-seismic structures such as containment walls placed in an area of numerous earthquakes, by means of the introduction at the beginning of the decade of 1990 the Displacement Response Spectrum (DRS) and the Capacity Demand Diagram (CDD) that suppose an important change in the way of presenting the Elastic Response Spectrum (ERS). On the other hand in case of action of an earthquake, the dynamic characteristics of a soil have been referred traditionally to the speed of the shear waves that can be generated in a site, together with the characteristics of plasticity and damping of the soil. The Principle of the energy conservation explains why a shear upward propagating seismic wave can be amplified when travelling from a medium with high shear wave velocity (rock) to other medium with lower velocity (soil deposit), as it happened in the earthquake of Mexico of 1985. This amplification is a function of the speed gradient or of the contrast of impedances in the border of both types of mediums. A method is proposed in this paper for the design of containment walls in different soils, suffering to the action of an earthquake, based on the Performance-Based Seismic Design.*

1 INTRODUCTION

The calculation of the static and dynamics pressures of a soil against a wall, as well as the displacements of it under the action of an earthquake, can be realized by means of analytical pseudostatic, analytical dynamic methods or by means of numerical methods: finite differences, finite elements, etc.

For the first methods, different authors (Coulomb[2], Rankine[12], Newmark[7], Richards-Elms[13], Whitman-Liao[16], Prakash-Rafnsson-Wu[8], [9]) have developed approximations to the problem, consisting of analytical pseudostatic solutions, presenting in every case different limitations. Other authors (Wood[17], Scott[14], Veletsos and Younan[15]) have obtained analytical dynamic solutions based on the theory of the elastic waves.

For the numerical methods different commercial programs have been developed: SASSI[5], PLAXIS[1], FLAC/FLAC3D, etc.

The latter programs need normally a high time of preparation of input and an important consumption of computation. On the other hand few of them allow the integration of the dynamic equations in the time domain. Another limitation is the model behavior of the soil implemented in the program.

The analytical pseudostatic methods on the contrary, need a minor time of computer and have been implemented in the past for the calculation of walls submitted to static actions with satisfactory results.

For preliminary studies a program of computer have been developed by means of analytical pseudostatic methods for the calculation of the pressures and displacements of a gravity retaining wall, in static and dynamic conditions under the action of one earthquake. The situations of stability are verified to sliding and overturning, warning in case of failure, to increase the dimensions of the wall.

The analysis of a gravity wall submitted to the action of an earthquake by means of the calculation of the possible permanent displacement follows the line of the method of Performance Based Design.

2 PROGRAM MUROSIS

For the analysis of the behavior of a wall submitted to seismic actions, it have been developed the program MUROSIS based on pseudoanalític methods, for the calculation of static and seismic pressures on the back of the wall, as well as the permanent seismic displacement, in case the maximum acceleration of the earthquake overcomes the critical acceleration (Whitman-Liao[16], 1983).

The program calculates the total force and the moment at the base of the wall. The force in static conditions is calculated by Rankine's method or by Coulomb's method. The seismic force is calculated by Mononobe-Okabe's method, considering his action with agreement to Richards-Elms[13] of 0.66 H over the foot of the wall, being H the height of it.

Later it is calculated the maximum friction force that is opposed to the sliding and the stabilizing moment, obtaining finally the safety coefficients for sliding and overturning, in static and also in seismic conditions. In case the safety coefficient of sliding or overturning does not fulfill a prescribed valor the program warns to increase the dimensions of the wall.

3 STATIC ACTIVE FORCE ACCORDING TO COULOMB´S THEORY

The static pressure according to Coulomb´s theory on a wall of vertical back line has the expression:

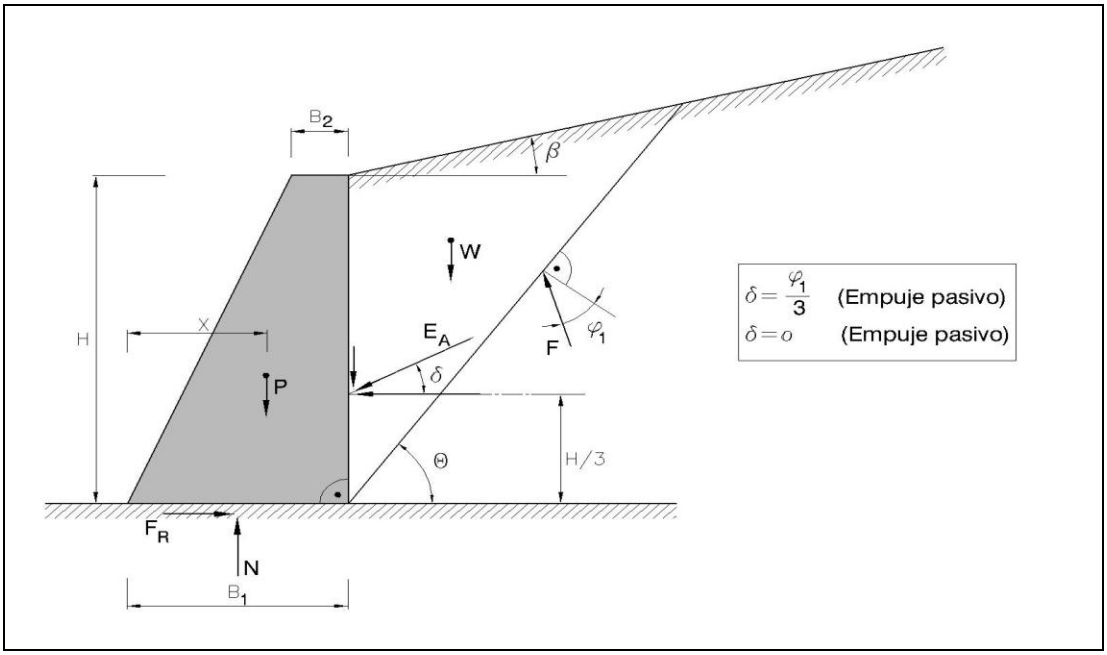


Figure 1. Static pressure against a wall according Coulomb´s theory

Active force:

$$E_A = \frac{1}{2}\gamma\, K_A\, H^2$$

$$K_A = \frac{\cos^2 \varphi_1}{\cos\left[1+\sqrt{\frac{sen(\varphi_1+\delta)\cdot sen(\varphi_1-\beta)}{\cos\delta\cdot\cos\beta}}\right]^2}$$

$$K_{Ah} = K_A \cos\delta \qquad K_{AV} = K_A\, sen\,\delta$$

$$E_{Ah} = \frac{1}{2}\gamma\, K_{Ah}\, H^2 \qquad E_{AV} = \frac{1}{2}\gamma\, K_{AV}\, H^2$$

$$F_e = F_R = \mu\, N = (P + E_{AV})\, tg\phi_2 \qquad F_d = E_{Ah}$$

$$M_e = P\cdot x + E_{AV}\cdot B_1 \qquad M_V = E_{Ah}\cdot\frac{H}{3}$$

The total active force according to Coulomb´s theory forms an angle δ with the normal to the wall (figure 1)

4 DYNAMIC ACTIVE FORCE ACCORDING MONONOBE-OKABE´S THEORY

With the conditions established in the program MUROSIS for a wall with vertical back line (i=0º), granular landfill (Mononobe-Okabe does not consider cohesion), friction angle of landfill - wall $\delta \neq 0$ and angle of inclination of the surface of the area ß $\neq 0$, the formulation used by the program calculates the active and passive pressures with the point of application defined by Prakash[13], Richards-Elms[13], Whitman-Liao[16].

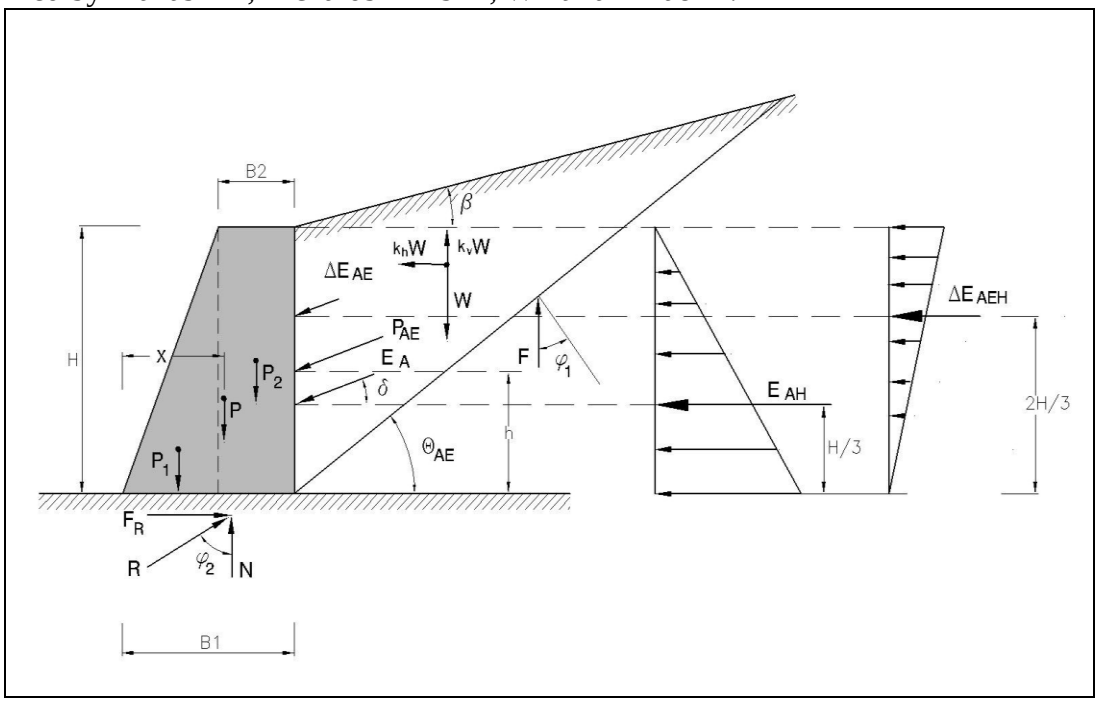


Figure 2. Dynamic pressure against a wall according Coulomb´s theory

Active force:

$$P_{AE} = \frac{1}{2}\gamma H^2 (1-k_v) \frac{\cos^2(\varphi-\psi)}{\cos\psi \ \cos^2 i \ \cos(\delta+\psi)\left[1+\sqrt{\frac{sen\,(\delta+\varphi)\,sen\,(\varphi-\beta-\psi)}{\cos(\delta+\psi)\cos\beta}}\right]^2}$$

$$\psi = arc\,tg\,\frac{k_h}{1-k_v} \qquad \varphi \geq \psi$$

$$K_{AE} = (1-k_V) \frac{\cos^2(\varphi-\psi)}{\cos\psi \ \cos^2 i \ \cos(\delta+\psi)\left[1+\sqrt{\frac{sen\,(\delta+\varphi)\,sen\,(\varphi-\beta-\psi)}{\cos(\delta+\psi)\cos\beta}}\right]^2}$$

Where $\boldsymbol{P_{AE} = E_A + \Delta E_{AE}}$, being E_A the active force according to Coulomb´s theory and ΔE_{AE} the active seismic force, with the value:

$$\Delta E_{AE} = \frac{1}{2}\gamma\, H^2 (K_{AE} - K_A)$$

Where $\boldsymbol{k_h}$ y $\boldsymbol{k_v}$ are the horizontal and vertical seismic coefficient accelerations relative to **g**, that is the horizontal and vertical pseudostatic accelerations are: $\boldsymbol{a_h = k_h\, g}$ y $\boldsymbol{a_v = k_v\, g}$.

The coefficient k_v can have positive or negative sign, if the vertical acceleration due to the earthquake is ascending or descending.

The total active force P_{AE} has his point of application at a height on the base of the wall of:

$$h = \frac{E_A \cdot \frac{H}{3} + \Delta E_{AE} \cdot \frac{2H}{3}}{P_{AE}}$$

Once calculated K_{AE}, it can be obtained:

$K_{AEH} = K_{AE} \cos \delta$ $\qquad$ $K_{AEV} = K_{AE}$ sen δ

$E_{AEH} = ½ \gamma K_{AEH} \cdot H^2$ $\qquad$ $E_{AEV} = ½ \gamma K_{AEV} \cdot H^2$

$F_e = F_R = \mu N = (P+E_{AV} \pm E_{AEV}) \cdot tg\varphi_2$ $\qquad$ $F_d = E_{AH} + \Delta E_{AEH}$

$M_e = P \cdot x + E_{AV} \cdot B_1 \pm E_{AEV} B_1$ $\qquad$ $M_V = E_{AH} \cdot \frac{H}{3} + \Delta E_{AEH} \cdot \frac{2H}{3}$

The safety coefficients with the action of earthquake are:

$$FSD = \frac{F_e}{F_d} \geq 1.1 \qquad \textit{and} \qquad FSV = \frac{M_e}{M_v} \geq 1.5$$

5 PERFORMANCE-BASED SEISMIC DESIGN OF A WALL

In a containment wall with the action of an earthquake, when the horizontal acceleration is lower than a critical or limit value $\mathbf{a_{crit}}$, the wall does not suffer movement.

But, when the acceleration of the soil equals the critical or limit acceleration, the wall is in situation of imminent sliding. In this instant the total active forces due to the static and seismic pressures equal the stabilizing force due to the friction between the wall and the soil at the base.

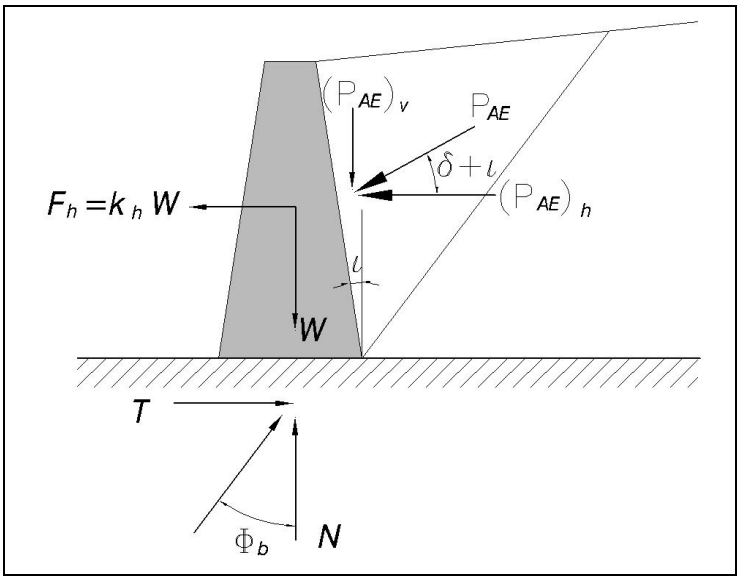


Figure 3 Seismic forces on the wall by MONONOBE-OKABE

Considering only horizontal acceleration and naming PAE the total static and seismic force calculated by Mononobe-Okabe´s method and by $(PAE)_h$ and $(PAE)_v$ the horizontal and vertical components of this, the horizontal and vertical balance of forces on the wall (figure 3.) direct to:

$$T = F_h + (P_{AE})_h$$

$$N = W + (P_{AE})_v$$

Substituting in these equations:

$$T = N\,tg\Phi_b; \qquad F_h = a_{crit}\frac{W}{g}; \qquad P_{AE\ h} = P_{AE}\cos\ \delta + \iota\ ; \qquad P_{AE\ v} = P_{AE}\ sen\ \ \delta + \iota$$

Where ι is the inclination of the back of the wall with the vertical one and δ is the friction angle between soil and wall, obtaining the value of the limit or critic acceleration that it puts in situation of imminent sliding the wall:

$$N\,tg\Phi_b = a_{crit}\frac{W}{g} + P_{AE}\cos(\delta + \iota)$$

$$N = W + P_{AE}\ sen(\delta + \iota)$$

Then:

$$W + P_{AE}\ sen(\delta + \iota)\ \ tg\Phi_b = a_{crit}\frac{W}{g} + P_{AE}\cos(\delta + \iota)$$

Wherefrom:

$$a_{crit} = \left(tg\Phi_b - \frac{P_{AE}\cos\ \delta + \iota\ - P_{AE}\ sen\ \ \delta + \iota\ \ tg\Phi_b}{W} \right) g$$

Being $\mathbf{\Phi_B}$ the friction angle between the base of the wall and the underlying soil. In this equation $\mathbf{P_{AE}}$'s value must be obtained with Mononobe-Okabe's method.

The solution of this equation must be solved by iterative form, since before to calculate PAE's value by Mononobe-Okabe's method is needed to know the value of $\mathbf{a_{crit}}$, and it is necessary to proceed by trial and error.

Richards y Elms[13] (1979) have calculated the permanent displacement of the wall when $a_{max} > a_{crit}$ obtaining the value:

$$D_{perm} = 0{,}087\ \frac{V_{max}^2 \cdot a_{max}^3}{a_{crit}^4}$$

Whitman y Liao[16] (1983) correcting Richards-Elms's simplifications have proposed the following expression for the permanent seismic displacement:

$$d_{perm} = \frac{37\,V_{max}^2}{a_{max}} \cdot e^{-9{,}4\left(\frac{a_{crit}}{a_{max}}\right)}$$

This value must not overcome the admissible limit for the permanent displacement of the wall. If this value is exceeded, it is necessary to increase the dimensions of the wall.

6 ORDER FOLLOWED BY THE PROPOSED PROGRAM

The order followed by the program is.

1. First it calculates the weight W of the wall
2. A previous value of $\mathbf{a_h = k_h \cdot g}$, will be supposed calculating for the value of $\mathbf{a_v = k_v \cdot g}$, the total active force by Mononobe-Okabe´s method.
3. For the value P_{AE} it calculates the critical or limit acceleration:

$$a_{crit} = \left(tg\Phi_b - \frac{P_{AE}\cos\ \delta + \iota\ - P_{AE}\ sen\ \ \delta + \iota\ \ tg\Phi_b}{W} \right) g$$

4. If the value of $\mathbf{a_{crit}}$ differs of $\mathbf{a_h = a_{max}}$ less than the one prearranged value (0,001), it calculates the permanent displacement by Whitman-Liao´s method according with the equation:

$$d_{perm} = \frac{37\, V_{max}^2}{a_{max}} \cdot e^{-9{,}4\left(\frac{a_{crit}}{a_{max}}\right)}$$

5. If the value of $\mathbf{a_{crit}}$ differs of $\mathbf{a_h = a_{max}}$ more than the one prearranged, new intermediate value $\mathbf{a_{max}}$ is used, following with the process, until $\mathbf{a_{crit}}$ and $\mathbf{a_{max}}$ fulfill this condition.
6. The value of d_{perm} finally calculated must be less than the prearranged limit value and in contrary the dimensions of the wall must be increased until the mentioned condition is fulfilled.

7 STUDIED CASES

It has been realized the seismic calculation of 16 cases of walls by means of the program named MUROSIS, using the next two types of walls:

1. Wall with 4,00 m of height
2. Wall with 6,00 m of height

In both cases the static pressures have been calculated by Coulomb´s theory. The dynamic pressures have been obtained by Mononobe-Okabe and the permanent seismic possible displacements by Whitman-Liao. All the exits have been verified manually and with the bibliography to check the kindness of the results. In all cases the surface of the embankment is horizontal $\beta = 0^o$ and the wall has the back vertical $\alpha = 90^o$. The thicknesses of the wall in the base and the on the top has been selected to the specific situations of every case.

The program verifies that the safety coefficients of sliding and overturning in seismic situation fulfill the following conditions:

$$FSD \geq 1.10 \qquad FSV \geq 1.50$$

The following situations have been studied for these two types of walls:

- **Wall with 4.00 m of height**

1. Without earthquake, without cohesion and without friction soil-wall
2. Without earthquake, without cohesion and with friction soil-wall
3. Without earthquake, with cohesion and without friction soil-wall
4. Without earthquake, with cohesion and with friction soil-wall

- **Wall with 6.00 m of height**

5. Without earthquake, without cohesion and without friction soil-wall
6. With earthquake, without cohesion and without friction soil-wall
7. With earthquake, with cohesion and without friction soil-wall
8. With earthquake, with cohesion and with friction soil-wall

The summary of obtained results in are included in the following tables:

Wall of 4.00 m

Wall	k_h (k_v = ½ k_h)	$c_1 = c_2$ (kPa)	δ (º)	B1 (m)	B2 (m)	k_{crit}	d_{perm} (mm)
1	0	0	0	1.80	1.30	0.120g	0
2	0	0	15	1.60	1.20	0.161g	0
3	0	10	0	1.50	1.20	0.083g	0
4	0	10	15	1.30	1.10	0.126g	0
5	0.10g	0	0	1.85	1.50	0.1497g	0.19
6	0.10g	0	15	1.80	1.50	0.202g	0
7	0.10g	10	0	1.60	1.30	0.1135g	1.84
8	0.10g	10	15	1.50	1.00	0.1435g	0.28

Table nº 1 Exit of results for wall of height H = 4.00 m

Muro de 6.00 m

Wall	k_h (k_v = ½ k_h)	$c_1 = c_2$ (kPa)	δ (º)	B1 (m)	B2 (m)	k_{crit}	d_{perm} (mm)
1	0	0	0	2.70	2,40	0.1439g	0
2	0	0	15	2.30	2,10	0.1712g	0
3	0	10	0	1.90	1,70	0.050g	0
4	0	10	15	1.80	1,50	0.104g	0
5	0.10g	0	0	2.80	2,50	0.163g	0
6	0.10g	0	15	2.70	2,50	0.212g	0
7	0.10g	10	0	2.20	1,90	0.0985g	4.72
8	0.10g	10	15	2.10	1,90	0.1575g	0

Table nº 2 Exit of results for wall of height H = 6.00 m

8 CONCLUSIONS

It has been analyzed 16 cases of walls of 4.00 m and 6.00 m of height for two values of the friction angle soil-wall and for two values of the cohesion of the landfill, one null and other different to zero.

The analysis of the permanent seismic displacement leads to the conclusion that walls that fulfill to stability in seismic situation can have unacceptable displacements, being advisable the determination of this value in the seismic design of a wall. This is the line followed nowadays for the "Performance Based Design"

9 REFERENCES

[1] Brinkgreve, R. B. J. *"Manual de Referencia de PLAXIS"* Delf, 2004.

[2] Coulomb, C. A. *"Essai sur une application des regles des maximis et minimis a quelques problemes de statique relatives a l'architecture"* Memoires de l'Academie Royale pres Divers Savants, Vol. 7, 1776.

[3] Fajfar P, Krawinker H. *"Seismic Design Methodologies for the next generation Codes*" . Ed. Balkema. 1977

[4] International Building Code (IBC 2006).

[5] Lysmer, John, Ostadan, Farhang, Tabataie, Manour, Tajirian, Frederick and Vahdani, Shahriar, "*SASSI 2000- A system for Analysis of Soil-Structure Interaction"*, 2000.

[6] Mononobe, N. and Matsuo H. *On the Determination of Earth Pressures during Earthquakes"* Proceedings 2nd World Engineering Conference, Vol. 9, paper nº 388, peg. 177-185, 1929.

[7] Newmark, N.M. *"Effects of earthquakes on dams and embankments"* Geotechnique, v. 15, n2, pag. 139-160, 1965.

[8] Prakash, S. and Wu, Y. *"Displacement of rigid walls during earthquakes".* Eleventh World Conference on Earthquake Engineering, 1996.

[9] Prakash, S. and Rafnsson, E. A. *"On Seismic Design Displacements of Rigid Retaining Walls"* Proceedings 3rd International Conference on Recent Advances on Geotechnical Earthquake Engineering and Soil Dynamics, Vol.3, pag. 1183-1192, St. Luis, Missouri, 1995.

[10] Prakash, S. and Basvanna, B. M. *"Earth Pressure Distribution Behind Retaining Walls During Earthquakes"* Proceedings Fourth World Conference on Earthquake Engineering, Chile, Vol. 3, pag. 133-148, 1969.

[11] Priestley MJN *"Performance Based Seismic Design*" New Zealand National Society for Earthquake Engineering. 2000.

[12] Rankine, W. *"On the Stability of loose Earth"* Philosophical Transactions of the Royal Society of London, Vol. 147, 1857.

[13] Richards, R. and Elms, D. G. *"Seismic Behavior of Gravity Retaining Walls"* Journal of Geotechnical Engineering Division, ASCE, Vol. 105, Nº GT4, pag. 449-464, 1979.

[14] Scott, R. F. "*Earthquake-Induced Earth Pressures on Retaining Walls"* Proceedinds 5th World Conference on Earthquake Engineering, Rome, Italy, pag. 1611-1620, 1973.

[15] Veletsos, A. S., Younan, A. H. and Bandyopadhyay *"Dynamic Response of Cantilever Retaining Walls"*. Department of Advanced Technology Brookhaven National Laboratory Associated Universities Inc. Upton, New York, October 1996.

[16] Whitman, R. V. and Samson Liao *"Seismic Design of Gravity Retaining Walls"*. Report to U. S. Army Engineer Waterways Experiment Station, Vicksburg, Mississippi, 1983.

[17] Wood, John H.. *"Earthquake Soil-Induced Soil Pressures on structures"* Ph. D. Thesis, California Institute of Technology, EERL, 73-05, Pasadena, California, 1973.

COMPDYN 2013
4th ECCOMAS Thematic Conference on
Computational Methods in Structural Dynamics and Earthquake Engineering
M. Papadrakakis, V. Papadopoulos, V. Plevris (eds.)
Kos Island, Greece, 12–14 June 2013
Paper # 1524

MECHANISM BASED ASSESSMENT OF DAMAGED BUILDING'S RESIDUAL CAPACITY

Maria Polese[1], Marco Marcolini[1], Andrea Prota[1] and Giulio Zuccaro[1]

[1] Department of Structures for Engineering and Architecture, University of Naples Federico II
via Claudio 21, 80125 Naples, Italy
e-mail: maria.polese@unina.it; marco.marcolini@unina.it; andrea.prota@unina.it; zuccaro@unina.it

Keywords: residual capacity, damaged building, capacity spectrum method, damage dependent vulnerability, post-earthquake assessment, collapse fragility curves.

Abstract. *Seismic behavior of damaged buildings may be expressed as a function of their REsidual Capacity (REC). The residual capacity REC_{Sa} is defined as the minimum spectral acceleration (at the period T_{eq} of the equivalent SDOF) corresponding to building collapse. When referring to peak ground acceleration a_g as damaging intensity parameter, REC_{ag} is defined as the minimum anchoring peak ground acceleration such as to determine building collapse. For a given spectral shape, REC_{ag} corresponds to REC_{Sa} scaled by the spectral amplification factor for T_{eq}. REC_{Sa} and REC_{ag}, generally indicated as REC, lower with increasing damage level in buildings; hence REC may be very useful in estimating the post-seismic building safety. In a recent work [1] it has been shown how it is possible to derive REC (REC_{Sa} and REC_{ag}) through Pushover Analyses (PA), where a suitable modification of plastic hinges for damaged elements is applied. The applicability of PA for damaged structures is verified in [2] by comparison of the PA results with those on nonlinear time-history analyses. On the other hand, it is unrealistic that in the aftermath of an earthquake, when the assessment of building safety has to be performed in an emergency situation, there would be time for the execution of detailed nonlinear analyses. Acknowledging the need for easier and faster evaluation tools, in [3] a simplified MEChanism based method (MEC) for evaluating the building REC was preliminary tested. The present work extends the comparison of the results (in terms of REC), that could be obtained by PA and MEC analyses, considering a number of Reinforced Concrete (RC) frames building typologies. Moreover, by adopting the MEC approach, the possible variation of REC as a function of seismic demand is investigated. The simplified method can be used to explore the possible ranges of REC variation for RC building classes considering the anticipated mechanism formation after an earthquake; in addition, it could be used in the post-seismic phase for estimating the REC of damaged buildings having undergone identifiable plastic mechanisms and for fast assessment of damage-dependent collapse fragility curves.*

1 INTRODUCTION

One of the most controversial problem in the aftermath of damaging earthquakes is the lack of agreed and transparent policies for acceptable levels of safety. With the purpose of facilitating the assessment process in the post-earthquake, it was evidenced the need of a method for measuring structural capacity for damaged buildings, to be compared with that related to the undamaged state [4]. In the ATC-43 project [5] the available instruments and methods for seismic analyses of damaged buildings were analyzed: by adopting pushover analysis as a nonlinear analysis tool, the behavior of damaged buildings may be simulated with suitable modification of plastic hinges for damaged elements. Taking into account the evaluation approach proposed in [5], and applied in [6, 7] for some steel buildings, the authors developed an assessment procedure that allows to express the seismic behavior of damaged RC buildings as a function of their REsidual Capacity (REC), that is a measure of seismic capacity, reduced due to damage [1]. As it will be explained in the paragraph 2.1, the REC may be evaluated via Pushover Analysis (PA) on a suitably modified lumped plasticity building model. On the other hand, acknowledging the need for easier and faster evaluation tools, in [3] a simplified method for evaluating the building REC was preliminary tested. This paper continues the study initiated in [3] extending the comparison of the results of pushover analyses with those of MEChanism based analyses (MEC) for a number of RC frames representative of existing building typologies in the Mediterranean area. In particular, paragraph 2.2 explains the main features of the MEC approach that is adopted, while section 3, after presentation of the studied RC frame buildings, compares the results of both type of analyses (PA and MEC) for the structures in their "intact" and "damaged" states. Next, in section 4 a possible application of MEC assessment for evaluation of variation of buildings residual capacity with increasing seismic demand (in terms of global ductility demand) is presented. As it will be shown (section 5) the proposed procedure may be applied for investigation of damage-dependent vulnerability and collapse fragility curves derivation for classes of buildings whose plastic mechanism is identified.

2 EVALUATION OF BUILDING'S RESIDUAL CAPACITY

The residual capacity REC is a parameter aimed at representing the building seismic capacity (up to collapse) in terms of a spectral quantity. In [1] REC_{Sa} is defined as the spectral acceleration (at period T_{eq} of the Single Degree Of Freedom SDOF system equivalent to the real structure) corresponding to suitably defined building collapse condition. Moreover, given the convenience of direct estimation of peak ground acceleration, a_g, as a damage-intensity parameter, the residual capacity is evaluated also in terms of a_g: given the spectral shape, REC_{ag} is the minimum anchoring peak ground acceleration such as to determine building collapse and corresponds to REC_{Sa} scaled by the spectral amplification factor for T_{eq}.

By way of example, with reference to an EC8 spectral shape and considering a system with $T_C<T_{eq}<T_D$, the following relation applies:

$$REC_{ag} = \frac{REC_{Sa}}{(S \cdot \eta \cdot 2.5)} \cdot \left(\frac{T_{eq}}{T_C} \right) \tag{1}$$

2.1 Pushover based approach

The flowchart in Figure 1, referring to framed structures, illustrates the basic steps needed in order to determine REC_{Sa} (or REC_{ag}) for the intact structure as well as considering different damaged states possibly caused by a main-shock. The method is briefly described next; for more detailed description the interested reader may refer to [1].

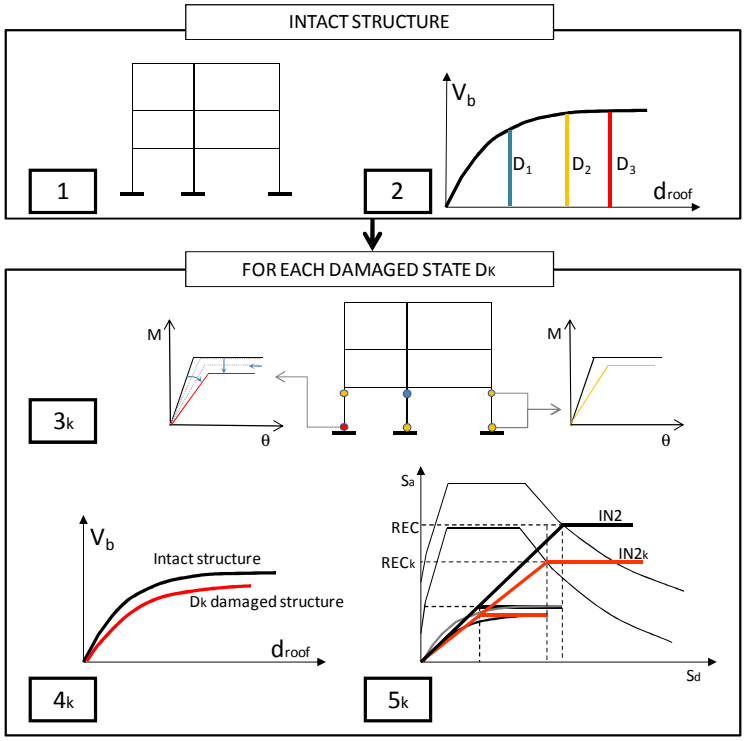


Figure 1: Flowchart illustrating the basic steps of the method for framed structures

In order to determine REC_{Sa} (or REC_{ag}) it is necessary to find the relationship between the seismic demand, expressed in terms of displacement, and the seismic intensity, that may be represented by the spectral acceleration $S_a(T_{eq})$ or by peak ground acceleration a_g. To this end, the incremental N2 method (IN2) [8] may be applied, that allows the construction, with reference to an equivalent SDOF obtained based on the Pushover Analysis (PA) of the building, of the curve approximately relating seismic demand to seismic intensity. In the simpler, but very common, case of applicability of the principle of equal displacement rule ($T_{eq} \geqslant T_c$) the IN2 curve is a straight line from the origin up to collapse point, the only point that needs to be determined and that corresponds to REC_{Sa}. It is easily verifiable that, in the hypothesis of the equal displacement rule, the REC_{Sa} may be simply calculated as the product of the base shear coefficient C_b and the displacement capacity in terms of ductility μ_{cap}:

$$REC_{Sa} = C_b \cdot \mu_{cap} \qquad \text{for } T_{eq} \geq T_c \tag{2}$$

Analogously, it can be verified that, for $T_{eq}<T_c$, the residual capacity may still be associated to C_b and μ_{cap}. Indeed, adopting the R-μ-T relation introduced in [9], and given that for a seismic intensity bringing the structure to collapse R equals the ratio REC_{Sa}/C_b:

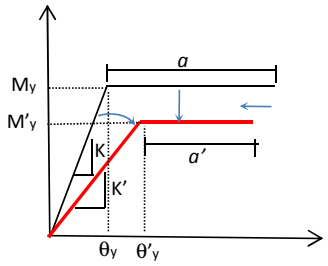
$$REC_{Sa} = C_b \cdot (\mu_{cap} - 1) \cdot \frac{T_{eq}}{T_c} + 1 \qquad \text{for } T_{eq}<T_c \tag{3}$$

When referring to the structure in its undamaged state the initial REC ($REC_{Sa,0}$ or $REC_{ag,0}$) is obtained. On the other hand, after a main-shock the structure may be damaged to a global damage state D_i and the structural elements in a RC frame may have been locally subjected to a ductility demand (also corresponding to local damage level). In this study, the near collapse damage state D_3 and the moderate damage state D_2 are defined based on the assumption that the most critical element controls the state of the structure; in particular, D_3 corresponds to the

first attainment of Collapse Prevention CP limit state for an element [10] and D_2 to the first attainment of 0.5 CP. For the limited damage state (D_1) it is assumed that it is attained at the Yield Displacement of the Idealized (YDI) pushover curve.

It is here noted that that the evaluation approach is very simplified, since brittle shear failures in columns or beams, that may be expected in existing under-designed buildings [11, 12], or brittle behavior of beam-columns joints [13], are not considered in this study. Further studies will have to address the influence of brittle failures on the safety loss of existing buildings.

In the hypothesis of studying the structural behavior via pushover analysis both the global damage state and the local ductility demand may be determined through the analysis. Then, the behavior of damaged buildings may be studied with nonlinear static analyses performed on a suitably modified structural model. In particular, considering the ductility demand in each of the structural elements caused by an hypothetical main-shock, the relative force-deformation or moment-rotation relationships may be modified through ductility dependent modification factors [14], see Figure 2, and pushover curves for the damaged structure may be derived [1]. Next, applying the same method used for determining $REC_{Sa,0}$ (and $REC_{ag,0}$) also the *REC* at damage state D_i ($REC_{Sa,i}$ or $REC_{ag,i}$) may be computed.



	stiffness	strength	Plastic rotation
intact	K	M_y	a
damaged	$K'=\lambda_K K$	$M_y'=\lambda_Q M_y$	$a'=a-a_d$

Figure 2: Modeling criteria for the damaged plastic hinges: the bilinear moment-rotation plastic hinge is modified with a suitable variation in the relative stiffness ($K'=\lambda_k K$), strength ($M_y'=\lambda_Q M_y$) and plastic rotation capacity ($a'= a-a_d = a-(\theta'_y - \theta_y)$ -RD = $a-(\theta_y(\lambda_Q/\lambda_k -1)$-RD), with λ stiffness or strength modification factors and residual drift (RD) of the element (for further details see [1, 13]).

2.2 Mechanism based approach

The assessment of the residual capacity *(REC)* of the structure via PA can be too computing expensive if a population of building is to be analyzed. Therefore, an approximate method, which allows to assess *REC* by simpler estimation of parameters (C_b, μ_{cap} and T_{eq}), is proposed. Indeed, by observing Eqs. (1), (2) and (3) it may be noted that, considering a system with $T_C<T_{eq}<T_D$, that is often the case for mid-rise existing RC buildings, REC_{Sa} depends on C_b and μ_{cap} of the equivalent system, while REC_{ag} varies proportionally to the product C_b μ_{cap} T_{eq}. These relationships apply either for the intact building either for the building in its generic damaged state, provided that in the latter case C_b, μ_{cap} and T_{eq} are computed accounting for the state of damage of the structural elements. Hence, estimation of these factors (C_b, μ_{cap} and T_{eq}) for different structural systems and mechanism types and for varying damage levels becomes crucial in the estimate of pre- and post-earthquake safety levels.

C_b, μ_{cap} and T_{eq} may be easily computed adopting a MEChanism based (MEC) procedure. In particular, the proposed steps of assessment for a given moment resisting frame in its "intact" state are:

1. Evaluation of probable plastic mechanism for the given frame

2. Calculation of base shear V_b and base shear coefficient C_b via simplified mechanism based formulations (see NOTATION section)
3. Calculation of yield and ultimate displacements, d^*_y and d^*_u for the equivalent SDOF system and evaluation of $\mu_{cap} = d^*_u / d^*_y$
4. Calculation of the equivalent period T_{eq}

In order to evaluate the probable mechanism that could be expected (local soft storey mechanism, involving mainly the columns at a single storey level, or a more global one, involving also the beams) a method that is based on the assessment of the sway potential index S_i [15, 16] and the sway-demand index SDi [17] may be applied.

In particular, the S_i is computed based on the relative strengths of beams and columns at each storey; in case of identification of a probable local mechanism type ($S_i \geq 0.85$), the assessment of the sole S_i index gives no indication at which floor the mechanism will occur. For this reason, the concept of a sway-demand index, SD_i, is introduced in [17], comparing the amount of the shear demand at each storey (i.e. storey shear demand vs base shear demand) to the relative storey shear strength (i.e. storey shear strength vs shear strength of the first storey). The higher the SD_i, the higher the likelihood of a column-sway forming at the ith storey.

Once the probable mechanism type is determined, the corresponding base shear V_b may evaluated by equilibrium relations, as suggested in [18]. For what concerns the external force distribution, two load paths are assumed, namely a linear distribution (identified as MO resembling the modal shape) and a uniform one (identified as MA resembling horizontal forces proportional to seismic masses). For example, Figure 3 depicts the system of external and internal forces that should satisfy equilibrium for two hypothesized mechanism types (kth storey sway local mechanism and global mechanism) and two distributions of horizontal forces (MO and MA).

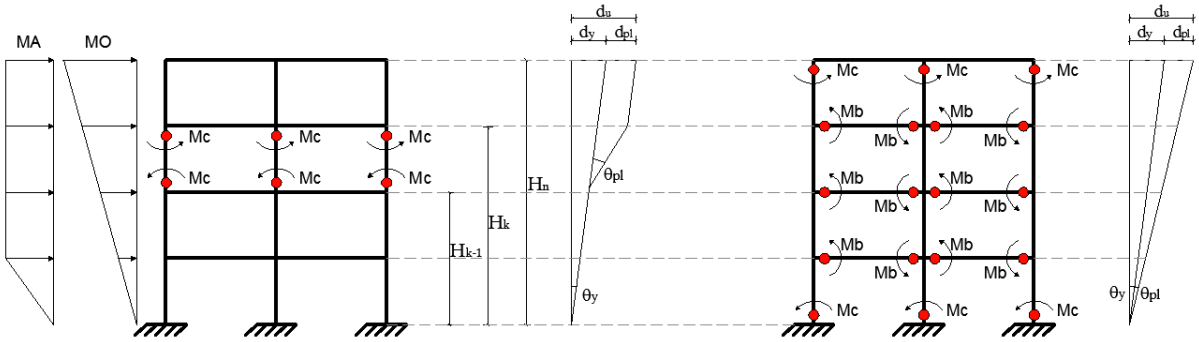


Figure 3: Example of collapse mechanism type and horizontal forces distribution. Left: local soft storey mechanism type; right: global mechanism type.

Accordingly the base shear corresponding to equilibrium of internal and external forces may be computed with Equation (4)-(5) for a local type mechanism with MO or MA horizontal forces distribution, while Eq. (6)-(7) may be adopted for a global type mechanism under MO or MA external forces distribution.

$$V_b = \frac{2 \cdot \sum M_C^k}{\sum_{i=k}^{n} H_i \cdot \left(H_k - H_{k-1}\right)} \sum_{i=1}^{n} H_i \tag{4}$$

$$V_b = \frac{2 \cdot \sum M_C^k}{\left(H_k - H_{k-1}\right)} \cdot \frac{n}{n-k+1} \tag{5}$$

$$V_b = \frac{\sum M_C^1 + \sum M_C^n + \sum_{i=2}^{n-1} \sum M_b}{\sum_{i=1}^{n} H_i^2} \cdot \sum_{i=1}^{n} H_i \tag{6}$$

$$V_b = \frac{\sum M_C^1 + \sum M_C^n + \sum_{i=2}^{n-1} \sum M_b}{\sum_{i=1}^{n} H_i} \cdot n \tag{7}$$

In the above equations $M_c^k (=M_{c,y}^k)$ represents the generic yielding moment at the base or top section of the k[th] floor columns (it is hypothesized that $M_{y,base}=M_{y,top}$ for the columns), ΣM_b $(=\Sigma M_{b,y})$ represents the sum of beam end yielding moments at a storey (selecting positive or negative ones depending on sway mechanism) and H_i is the i[th] storey height to foundation level. Once the base shear is calculated, the corresponding base shear coefficient C_b is easily determined.

For what concerns calculation of yield and ultimate displacements, a similar approach to the one proposed in [19] is adopted. In particular, the yield displacement d_y at the roof level of the MDOF system is calculated assuming a linear deformed shape within the elastic range (see Figure 3 and Eq. (8)), while the ultimate displacement at the same level is given by the sum of d_y plus the plastic contribution that is developed according to the hypothesized plastic mechanism (see Figure 3 left panel and Eq. (9) for the case of soft storey and Figure 3 right panel and Eq. (10) for the case of a global mechanism):

$$d_y = \vartheta_y \cdot H_n \tag{8}$$

$$d_u = d_y + \vartheta_{pl} \cdot (H_k - H_{k-1}) \tag{9}$$

$$d_u = d_y + \vartheta_{pl} \cdot H_n \tag{10}$$

Adopting a MEC approach it is very difficult to capture the roof displacements that may be determined via nonlinear static pushover analysis, where the mechanism is developed upon gradual loading of the structural system and the involved hinges have different local ductility demand. In order to minimize the scatter of yield and ultimate roof displacements that are obtained with the Equations (8)-(10) with the corresponding displacement values derived by the equivalent bi-linearization of the pushover curve, appropriate value for yield and plastic rotation θ_y and θ_{pl} should be chosen. In this study it is adopted a θ_y corresponding to the maximum yield rotation of the base columns in the (8), while θ_{pl} in the (9)-(10) is assumed as the minimum value of θ_u-θ_y among the hinges involved in the plastic mechanism, where θ_u is the rotation corresponding to Collapse Prevention CP limit state according to ACI 369R-11 [10] for the generic considered hinge.

Once the roof displacements of the MDOF system are known, the equivalent d^*_u and d^*_y for the SDOF and the relative ductility capacity are straightforwardly determined, as well as the equivalent period T_{eq} (see NOTATION section).

For what concern the study of the "damaged" structure it is hypothesized that the plastic mechanism is the same as the one that forms for the "intact" structure. Hence, the assessment of the behaviour of the damaged system comprises only the steps 2 to 4 of the previous list.

In particular, given the generic global roof displacement d_{roof} (e.g. due to an hypothetical mainshock), the corresponding demanded plastic rotation $\theta_{pl,d}$ and rotation demand θ are

straightforwardly determined by inversion of the (9) or (10) for local or global sway mechanisms, respectively:

$$\vartheta_{pl,d} = \vartheta - \vartheta_y = \frac{(d_{roof} - d_y)}{(H_k - H_{k-1})} \tag{11}$$

$$\vartheta_{pl,d} = \vartheta - \vartheta_y = \frac{(d_{roof} - d_y)}{H_n} \tag{12}$$

The knowledge of the rotation demand needed to attain d_{roof} with a plastic mechanism allows to determine the local ductility demand μ_j for the generic jth element involved:

$$\mu_j = \frac{\theta}{\theta_{y,j}} \tag{13}$$

where $\theta_{y,j}$ is the yield rotation for the jth element.

Then, adopting the formulation proposed in [14] based on local ductility demand μ_j, the plastic hinges of the elements involved in the plastic mechanism may be suitably modified, i.e. yield moment and stiffness are reduced as well as the plastic post-yield branch (see Figure 2). Once the plastic hinges are modified, the C_b for the damaged structure may be computed with the same methodology as described for the intact structure. For what concerns the ductility capacity and equivalent period it is here noted that the assessment of μ_{cap} and T_{eq} via MEC approach is strongly influenced by the evaluation of d^*_y (see NOTATION section); the latter parameter should be calculated based on Eq.(8) where the θ_y is modified due to damage in the plastic hinges. However, such a modification determines an unrealistic increase of the yield displacement of the equivalent SDOF, and consequently an abnormal decrease of the relative μ_{cap} and increase of T_{eq}. For this reason, when applying the MEC approach, it is proposed to calculate the d^*_y for a system having attained a generic damage state by multiplying the d^*_y calculated of the intact system by a correcting factor. Such factor is proportional to the mean ratio of the d^*_y calculated with PA for the damaged structure versus the d^*_y calculated with PA for the intact one. Accordingly, considering the d^*_y calculated with MEC applying the correction factor for the damaged state, the μ_{cap} and T_{eq} for the damaged structure can be coherently determined.

3 COMPARISON OF PUSHOVER AND MECHANISM BASED RESULTS

In this paper we want to extend the comparison between PA and MEC approach, initiated in [3] for a single case study, by considering a number of Reinforced Concrete (RC) frames building typologies. In particular, the comparison of the results of PA with those of the MEC analysis is performed confronting the parameters that may be retrieved by the equivalent bilinearization of equivalent SDOF capacity curve obtained with PA, i.e. C_b, μ_{cap}, T_{eq}, as well as REC_{Sa} (or REC_{ag}), with the homologous parameters that are computed as explained in § 2.2 with the MEC approach.

By way of example, Figure 4 (a) shows the pushover curves that are obtained for one of the studied moment resisting Reinforced Concrete Frames RCF (described in § 3.1) for the case of the intact building and building (D_0) that has attained a D_2 damaged state, together with the equivalent bi-linearization for both cases; analogously, Figure 4 (b) shows the bilinear curves that are obtained with MEC approach for the same structure in the same states (D_0 and D_2).

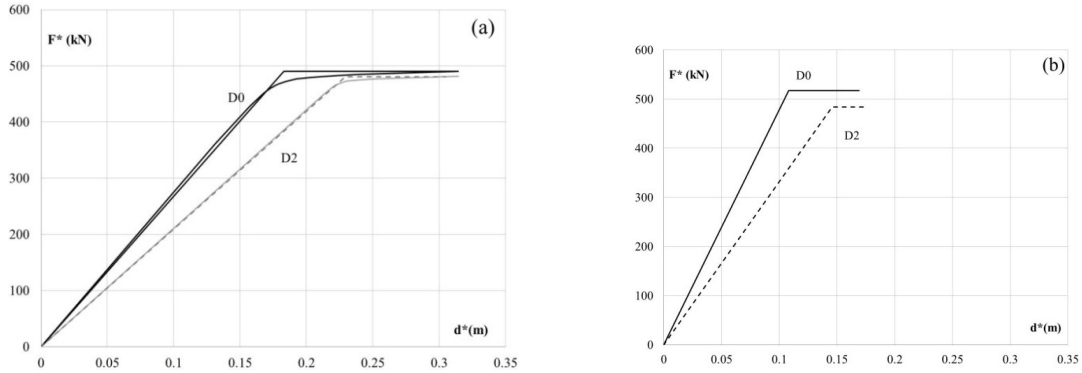


Figure 4: Pushover curve and bi-linearization for the 8_005_MA case, intact state D_0, and damaged state D_2 (a); bilinear curves obtained with the MEC approach for the 8_005_MA for intact state D_0, and damaged state D_2 (b)

3.1 Description of the RCF building models

The comparison of pushover with mechanism based analyses is performed considering nine Reinforced Concrete Frames RCF that are designed to be representative of Gravity Load Designed (GLD) buildings or buildings designed according to old Italian seismic standards in force at the beginning of age '60s [20], not applying principles of capacity design or proper reinforcement detailing and based on allowable stress method. In particular, the structural and mechanical characteristics of the frames belonging to 4, 6 or 8 storey buildings, are obtained with a simulated design approach as suggested in [21]. A common geometric planar configuration of a building having base dimensions 18mx10m, two bays in transversal direction and 4 bays in the longitudinal one, as well as 3 m inter-storey height (see Figure 5, referring to a 4 storey GLD building) is assumed. Then, the elements dimensions and reinforcement of the perimeter transversal frames (that are the ones chosen for PA-MEC comparison) are designed either for gravity loads either considering two different values of the seismic coefficient *C* 0.1, 0.05, i.e. in the first or second seismicity class according to [20]. Allowable stresses of σ_c=6 MPa for elements under pure axial load and 7.5 MPa for elements under combination of flexure and axial load are assumed, while the allowable stress for steel, that considering the design period is assumed to be a smooth type Aq50 [22], is σ_s=180 MPa [23]. The column area A_c is dimensioned based only on the axial load N and the concrete design stress σ_c where the axial load depends on the permanent and live loads on the area of influence of the generic column. The resulting columns dimensions for the perimeter frame are 30x30 (corner columns) and 40x30 (central column) at the base storey of the 4 storey GLD frame (see Figure 5). For the seismic design of the 4 storey building with C=0.1 and 0.05 the column section are equal to the gravitational load design. In 6 storeys and 8 storeys frames the columns size are proportionately greater up to the maximum size, for the 8 storey building designed with C0.1, of 45x35 for corner base columns and 55x35 for central ones. As a general rule, the column sections are gradually reduced in elevation, when possible according to design issues, to the minimum size 30x30.

The 4 storeys GLD beams have section 30x50 at all storeys; in the seismic design with C 0.1 and 0.05 beams section are 30x60 and 30x55, respectively for the first and second storeys. In 6 storeys and 8 storeys frames the beams size are proportionately greater up to the maximum size, for the 8 storey building designed with C 0.1, of 35x65 for first and second storeys.

The longitudinal bars percentage in the base columns vary from approximately 7.0‰ to 1.3%, consistently with low minima design requirements of old type codes. The lumped plasticity model for PA analysis is built considering bilinear flexural hinges, where yield and ultimate (at Collapse Prevention limit state, CP) moment and rotation are determined according

to ASCE-SEI/41[24], adopting a mean concrete strength of f_c=26.7 MPa and a steel yield stress of f_y=370 MPa.

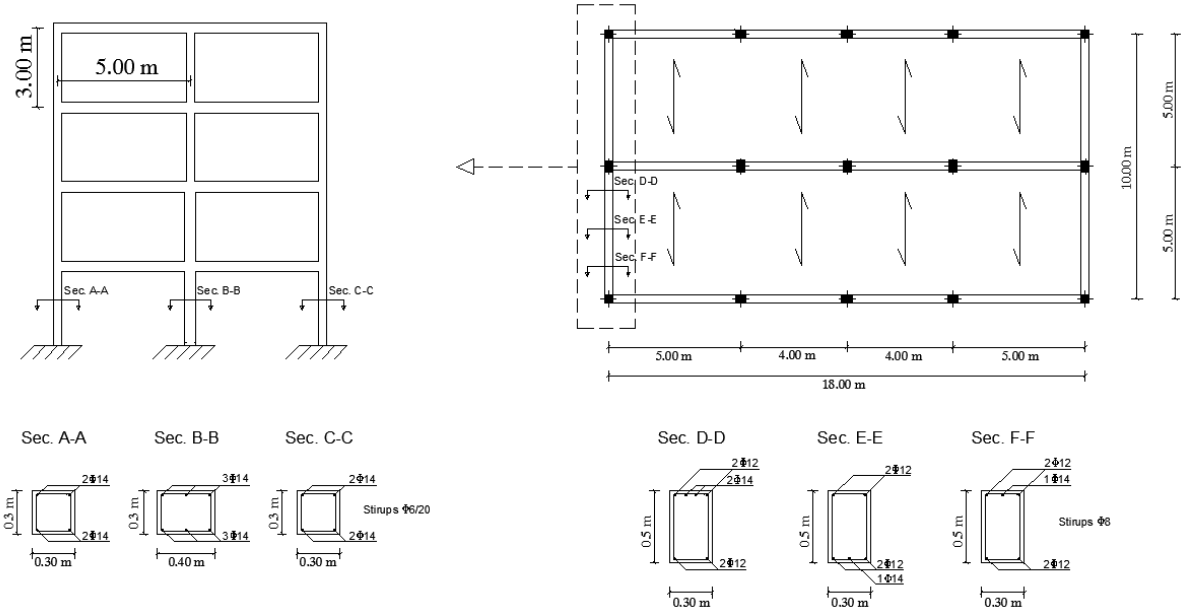


Figure 5: Building plan and elevation of perimeter frame for the 4 storey GLD building.

Each of the designed building have been analyzed with PA adopting two lateral load distributions, namely modal shape (MO) and constant shape (proportional to masses) MA. Hence, a total number of 18 PA analyses were performed. In the following, we identify the building and analysis type with notation N_D_FO where N, indicating the number of storeys, may be 4, 6 or 8, D indicating the design type, may be GLD, 01 or 005, and FO indicating the horizontal load path may be MO (for modal load) or MA (for constant load in elevation).

3.2 PA and MEC results and comparisons

Adopting the methodology described in § 2.1 and 2.2 the representative parameters C_b, μ_{cap} and T_{eq}, as well as REC_{Sa} and REC_{ag} are calculated for the 18 identified analyses cases with both the PA and MEC approaches and considering either the structures in their intact state (denoted as D_0) either structures that are supposed to have reached the D_2 damage state due to an hypothetical main-shock.

Table 1, referring to undamaged RCFs, and Table 2, referring to D_2 damaged RCFs, summarize the results for all the analyzed cases allowing for comparison of the PA and MEC approach. The subscripts m in Tables 1 and 2 indicate the results for the MEC analyses, while subscripts p the PA ones.

It is noted that, calculating the ratio of $d^*_{y,p}$ (D_2) versus $d^*_{y,p}$ (D_0) for all the considered cases, a mean value of 1.35 is obtained. Hence, as anticipated in § 2.2, the $\mu_{cap,m}$ (D_2) and $T_{eq,m}$ (D_2) are determined after suitable calculation of $d^*_{y,m}$ (D_2) (i.e. by increasing by 30% the $d^*_{y,m}$ (D_0)).

As a general comment, it is evidenced that adopting the sway index S_i and the sway demand index SD_i it was generally possible to identify the soft storey formation and the relative storey where the plastic deformations are concentrated for the MEC approach, finding good agreement with PA. On the other hand, when a soft storey is not evidenced (Si lower than 0.85), it was hypothesized the formation of a global mechanism developed over the whole

building height, involving also the beams of the RCF; this hypothesis is not always realistic according to PA results, where the global type mechanisms are generally developed only to a limited number of storeys, but it was chosen in order to remain at a more general level.

INTACT RCF (D_0)										
ID	T_{eq},m(s)	T_{eq},p(s)	μ_{cap},m	μ_{cap},p	C_b,m(g)	C_b,p(g)	REC_{Sa},m(g)	REC_{Sa},p(g)	REC_{ag},m(g)	REC_{ag},p(g)
4_01_MO	1.14	1.22	2.04	1.90	0.16	0.18	0.33	0.34	0.25	0.28
4_01_MA	1.37	1.40	1.92	1.80	0.15	0.15	0.29	0.27	0.26	0.25
4_005_MO	1.34	1.26	2.25	2.00	0.11	0.15	0.24	0.31	0.21	0.26
4_005_MA	1.38	1.45	2.03	1.85	0.13	0.13	0.27	0.25	0.25	0.24
4_G_MO	1.79	1.89	4.84	3.08	0.06	0.06	0.29	0.17	0.34	0.22
4_G_MA	2.04	2.15	4.84	2.81	0.06	0.05	0.28	0.15	0.39	0.23
6_01_MO	1.23	1.52	1.79	1.46	0.17	0.20	0.31	0.29	0.25	0.29
6_01_MA	1.37	1.78	1.69	1.45	0.19	0.19	0.32	0.27	0.29	0.32
6_005_MO	1.76	1.72	1.79	1.58	0.10	0.14	0.17	0.21	0.20	0.24
6_005_MA	1.61	2.00	1.65	1.77	0.15	0.13	0.25	0.24	0.26	0.32
6_G_MO	2.32	2.61	4.62	2.34	0.05	0.05	0.25	0.11	0.45	0.26
6_G_MA	2.72	2.98	4.62	2.45	0.05	0.04	0.24	0.11	0.59	0.32
8_01_MO	1.28	1.68	1.80	1.41	0.22	0.21	0.40	0.30	0.34	0.33
8_01_MA	1.36	1.97	1.60	1.52	0.20	0.19	0.31	0.29	0.28	0.39
8_005_MO	1.32	1.93	1.59	1.90	0.18	0.17	0.29	0.32	0.25	0.42
8_005_MA	1.67	2.23	1.56	1.72	0.16	0.15	0.24	0.25	0.27	0.42
8_G_MO	3.04	3.43	4.72	2.37	0.04	0.03	0.18	0.08	0.57	0.32
8_G_MA	3.63	4.01	4.72	2.24	0.04	0.03	0.18	0.07	0.78	0.40

Table 1: Representative parameters of the equivalent SDOF system for the structure in the intact (D_0) configuration and residual capacity in terms of spectral acceleration and anchoring (peak) ground acceleration; subscript p stays for results referring to PA, while subscript m refers to MEC.

DAMAGED RCF (D_2)										
ID	T_{eq},m(s)	T_{eq},p(s)	μ_{cap},m	μ_{cap},p	C_b,m(g)	C_b,p(g)	REC_{Sa},m(g)	REC_{Sa},p(g)	REC_{ag},m(g)	REC_{ag},p(g)
4_01_MO	1.36	1.49	1.36	1.31	0.15	0.17	0.21	0.22	0.19	0.22
4_01_MA	1.64	1.65	1.32	1.34	0.14	0.15	0.19	0.19	0.21	0.21
4_005_MO	1.61	1.55	1.45	1.36	0.10	0.15	0.14	0.20	0.15	0.21
4_005_MA	1.65	1.71	1.357	1.36	0.12	0.13	0.17	0.18	0.18	0.20
4_G_MO	2.20	2.42	2.27	1.95	0.05	0.05	0.12	0.10	0.19	0.20
4_G_MA	2.51	2.76	2.27	1.79	0.05	0.05	0.12	0.09	0.25	0.23
6_01_MO	1.46	1.69	1.28	1.19	0.17	0.19	0.21	0.23	0.21	0.26
6_01_MA	1.65	1.98	1.25	1.18	0.17	0.18	0.22	0.22	0.24	0.29
6_005_MO	2.11	1.95	1.28	1.26	0.09	0.13	0.11	0.16	0.17	0.21
6_005_MA	1.95	2.26	1.23	1.39	0.14	0.13	0.17	0.18	0.22	0.31
6_G_MO	2.83	3.18	2.15	1.56	0.05	0.05	0.11	0.07	0.28	0.25
6_G_MA	3.32	3.69	2.15	1.61	0.05	0.04	0.10	0.07	0.37	0.31
8_01_MO	1.53	1.88	1.28	1.15	0.15	0.21	0.19	0.24	0.19	0.30
8_01_MA	1.68	2.21	1.19	1.23	0.17	0.19	0.21	0.23	0.23	0.37
8_005_MO	1.58	2.25	1.21	1.34	0.17	0.17	0.21	0.22	0.22	0.38
8_005_MA	2.01	2.52	1.2	1.33	0.15	0.14	0.17	0.19	0.24	0.41
8_G_MO	3.78	4.21	2.31	1.50	0.03	0.03	0.08	0.05	0.38	0.29
8_G_MA	4.51	4.78	2.31	1.63	0.03	0.03	0.08	0.05	0.51	0.39

Table 2: Representative parameters of the equivalent SDOF system for the structure in the damaged (D_2) configuration and residual capacity in terms of spectral acceleration and anchoring (peak) ground acceleration; subscript p stays for results referring to PA, while subscript m refers to MEC.

Figures 6 to 8 show the comparison of PA and MEC for the single parameters.

In particular Figure 6 shows the comparison of PA and MEC in terms of C_b, for the intact structures (a) and D_2 damaged ones (b). As it may be observed, the parameter C_b can be satisfactorily represented with a MEC assessment for both the cases of intact D_2 damaged structures. The comparison of ductility capacity μ_{cap} is presented in Figure 7. Figure 7 (a), referring to intact structures, evidences that when the mechanism type is not adequately captured by MEC analysis the μ_{cap} may be considerably overestimated, while in case of good agreement of the hypothesized mechanism type the μ_{cap} are satisfactorily captured.

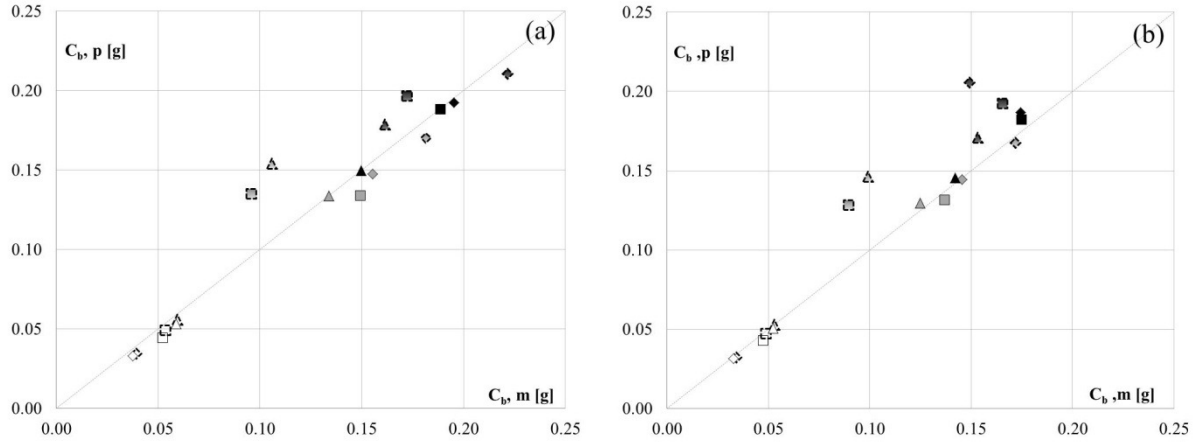


Figure 6: Comparison of C_b obtained with PA (denoted as $C_{b,p}$) with the one obtained with MEC approach (denoted as $C_{b,m}$) for intact structures (a) and structures that have reached D_2 damage state for an hypothetical main-shock (b)

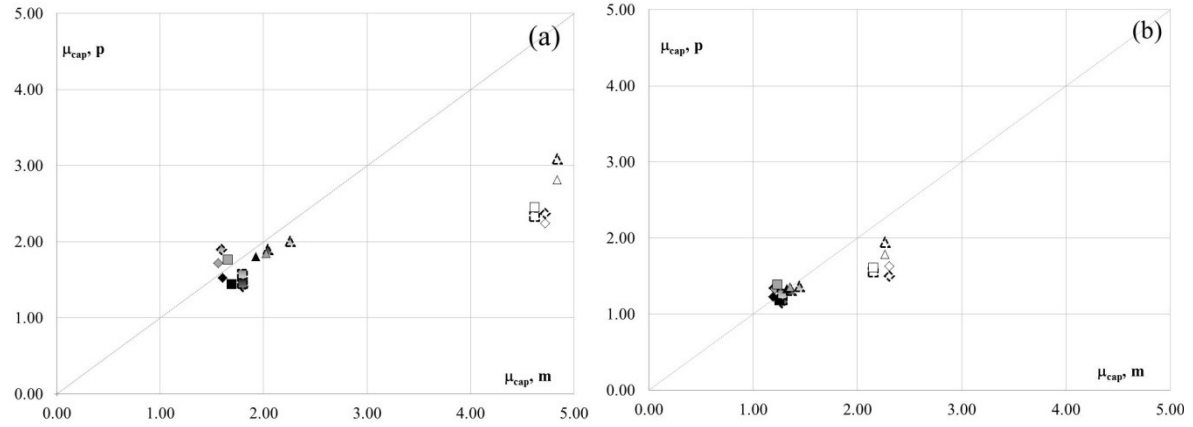


Figure 7: Comparison of μ_{cap} obtained with PA (denoted as $\mu_{cap,p}$) with the one obtained with MEC approach (denoted as $\mu_{cap,m}$) for intact structures (a) and structures that have reached D_2 damage state for an hypothetical main-shock (b)

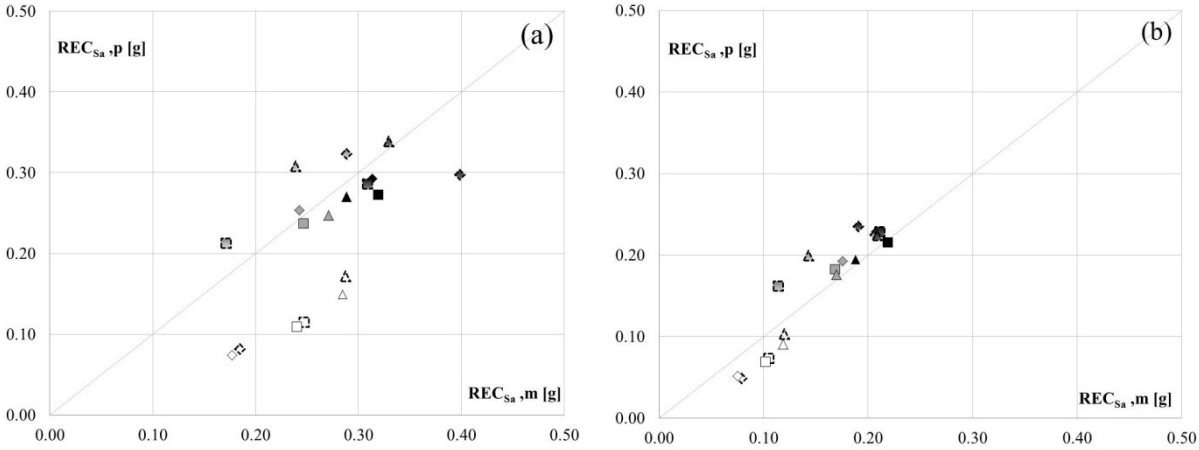


Figure 8: Comparison of REC_{Sa} obtained with PA (denoted as $REC_{Sa,p}$) with the one obtained with MEC approach (denoted as $REC_{Sa,m}$) for intact structures (a) and structures that have reached D_2 damage state for an hypothetical main-shock (b)

In fact, the white symbols in Figure 7 (a) represent the case of GLD buildings, where the global type mechanism that is hypothesized with MEC does not fully correspond to the mechanism that forms with PA. By multiplying the base shear coefficient C_b for the ductility capacity, the *REC* for the intact and damaged structures may be obtained, as explained in § 2.1.

Figure 8, representing the REC_{Sa} for the intact (Figure 8 (a)) and damaged structure (Figure 8 (b)), synthesizes those results evidencing the same discrepancies that were observed for μ_{cap}, as well as satisfactory agreement for the case of D_2 damaged structures.

4 REC VARIATION IN FUNCTION OF SEISMIC DEMAND

The comparison of the results of PA and MEC analyses shows that, when it is possible to realistically capture the plastic mechanism type that is forming in a RCF, the MEC allows to derive significant parameters with relatively small error and comparatively small computational effort. For this reason, MEC approach may be usefully adopted to investigate on the possible REC variation as a function of seismic demand. Indeed, once the bilinear representation of the equivalent SDOF capacity curve for the undamaged system is available, the seismic displacement demand, and ductility, may be determined by application of the Capacity Spectrum Method CSM [25]. Given the global ductility demand μ for the equivalent SDOF, it may be easily transformed in local ductility demand for the elements involved in the known plastic mechanism. By way of example, hypothesizing a first storey local mechanism with MEC approach, the elements rotation demand corresponding to the global ductility μ may be derived as:

$$\theta = \theta_y \cdot \left[1 + (\mu - 1) \frac{H_n}{H_1} \right] \tag{14}$$

On the other hand, if a global type mechanism, involving all storeys, is assumed, the rotation is simply μ times the yield rotation:

$$\theta = \theta_y \cdot H_n \tag{15}$$

In MEC approach, all the elements involved in the mechanism are subject to the same rotation; hence the element's ductility demand, depending on global μ, may be calculated based on Eq. (14) and (13) for a first storey mechanism or (15) and (13) for a global one. Given the local ductility demand μ_i for the generic plastic hinge, the relative M-θ relationship may be suitably modified to account for damage by introduction of the proper plastic hinges modification factors [14]. This way, apart from the REC_0 ($REC_{Sa,0}$ and/or $REC_{ag,0}$) that may be calculated for the structure in its initial undamaged state D_0, also the REC_μ ($REC_{Sa,\mu}$ and/or $REC_{ag,\mu}$) corresponding to given global ductility demand and the relative REC variation $REC_{ag,\mu}/REC_{ag,0}$, can be determined.

It has to be observed that the correction factor to be applied to $d^*_{y,m}$ of the damaged system, that with reference the studied structures was computed based on the ratio of $d^*_{y,p}$ (D_2) versus $d^*_{y,p}$ (D_0) for all the considered cases (see § 3.2), is significant for structures that have attained D_2 damage state; considering the analyzed structures, the latter corresponds to a mean ductility demand of 1.33. However, it may be expected that with increasing ductility demand for the structures, the ratio of $d^*_{y,p}$ (D_2) versus $d^*_{y,p}$ (D_0) shall increase. Accordingly, it is supposed that for the generic ductility demand:

$$\frac{d_{y,\mu}}{d_{y,0}} = \frac{1.35}{1.33} \cdot \mu \approx \mu \tag{16}$$

Hence, in the hypothesis that the variation of F^* with ductility demand may be neglected with respect to the variation of d^*_y, the ratio of $T_{eq,\mu}$ versus $T_{eq,0}$ corresponds to $\sqrt{\mu}$, and consequently Eq. (17) may be used to compute the ratio $REC_{ag,\mu}/REC_{ag,0}$:

$$\frac{REC_{ag,\mu}}{REC_{ag,0}} \approx \frac{REC_{Sa,\mu}}{REC_{Sa,0}} \cdot \sqrt{\mu} \tag{17}$$

An important information that may be inferred, once the REC variation is known, is the Performance Loss, *PL*, for each seismic demand. *PL*, that represents a measure of the loss of lateral capacity, is defined as:

$$PL = 1 - \frac{REC_{ag,\mu}}{REC_{ag,0}} \tag{18}$$

with $REC_{ag,\mu}$ residual capacity in terms of peak ground acceleration of the structure that has been subject to the global ductility demand μdue to main-shock and $REC_{ag,0}$ the residual capacity for the intact structure.

Considering the 9 RCF typologies and two types of hypothesized plastic mechanism, namely a soft storey at the first floor and a global one involving all storeys, the $REC_{ag,\mu}/REC_{ag,0}$ and the relative *PL* have been calculated up to a ductility demand of 4.

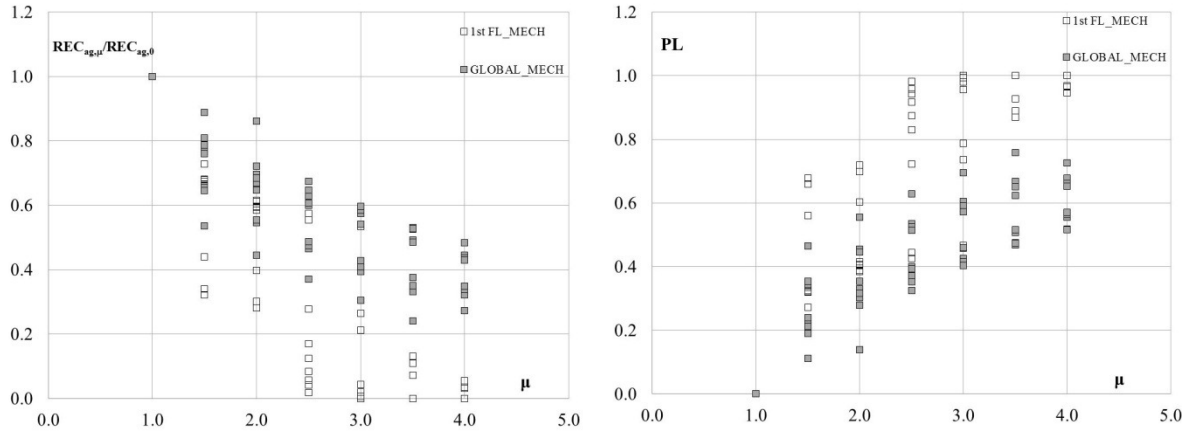


Figure9: $REC_{ag,\mu}/REC_{ag,0}$ variation for increasing global ductility demand for intact structure exhibiting local (first storey) or global plastic mechanism (left); Same variation for the PL (right)

Figure 9 shows the $REC_{ag,\mu}/REC_{ag,0}$ and *PL* variation with increasing ductility demand. As it can be noted, the *REC* ratio decreases more rapidly for structures exhibiting a local type mechanism with respect to those with a global one. Indeed, the local ductility demand for the elements involved in the mechanism, given the global μ, is higher in the former case and therefore a larger *REC* reduction is expected. Analogously, for local type mechanisms a larger *PL* with respect to global one is observed for each ductility demand. This trend confirms what was already noted in [1] for a detailed case study.

5 POSSIBLE APPLICATION IN THE CONTEXT OF DAMAGE DEPENDENT VULNERABILITY ASSESSMENT

As explained in [1], the REC_{ag} represents the peak ground acceleration corresponding to the 50% probability of attaining collapse damage state, hence it may be employed in a HAZUS like representation of collapse fragility curves:

$$P[col|a_g] = \Phi\left[\frac{1}{\beta}\cdot\ln\left(\frac{a_g}{\hat{a}_g}\right)\right] = \Phi\left[\frac{1}{\beta}\cdot\ln\left(\frac{a_g}{REC_{ag}}\right)\right] \tag{19}$$

where β represents a global value of dispersion, due to modeling uncertainties and inherent randomness associated to earthquake variability [1, 26]. Therefore, the knowledge of the *REC* variation due to a given ductility demand (see § 4) allows assessing the relative damage-dependent variation of collapse fragility curves (e.g. Figure 10) with a mechanical approach.

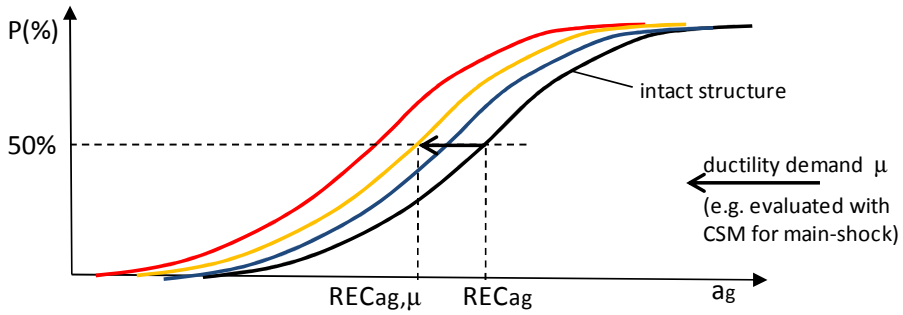


Figure 10: Example collapse fragility curves derived through Eq. (23) in function of REC_{ag}, and fragility curves variation depending on global ductility demand μ

The authors are aware that this simple collapse fragility representation, considering a collapse criterion defined assuming that only the most critical element controls the state of the structure, may be too restrictive for a realistic assessment of the ultimate load bearing capacities of existing RC frames. Indeed, some past studies [27, 28] point out the need for a proper calibration of mechanical based vulnerability assessment methodologies with empirical ones, that rely on observation of real damages from past earthquakes [29, 30, 31]. On the other hand, there is a lack of observational data allowing for empirical based derivation of damage-dependent fragility curves. Therefore, the proposed approach could be conveniently applied for assessment of damage (or ductility) dependent variation of fragility curves; the initial collapse fragility curves (referring to undamaged state) shall be preventively calibrated based on observational data.

6 CONCLUSIONS

This paper extends the comparison of PA and MEC analyses, initiated in [3], studying 9 RCF (4, 6 and 8 storey, 3 design typologies) under two different distributions of horizontal loads (linearly increasing with height MO, and proportional to storey masses MA); the parameters retrieved from 18 capacity curves obtained with PA are compared with those deriving from simplified MEC approach. Adopting the sway index *Si* and the sway demand index *SDi* it was generally possible to identify the soft storey formation and the relative storey where the plastic deformations are concentrated for the MEC approach, finding good agreement with PA. On the other hand, when a soft storey is not evidenced (Si lower than 0.85), it was hypothesized the formation of a global mechanism developed over the whole building height, involving also the beams of the RCF; this hypothesis is not always realistic according to PA results,

where the global type mechanisms are generally developed only to a limited number of storeys, but it was chosen in order to remain at a more general level. Accordingly, the MEC approach yields results that are closer to PA for the cases where a soft storey mechanism forms, while for more global type mechanisms a higher scatter is observed.

Despite the discrepancy of results of MEC and PA in case of global type mechanism, the MEC approach can be usefully adopted to assess the *REC* variation for structures that had sustained damaging main-shock and for which the plastic mechanism that has formed can be recognized. In fact, given the mechanism type, and having the possibility to derive the essential parameters C_b, μ_{cap} and T_{eq}, as well as REC_{Sa} and REC_{ag} by a simplified, MEC approach, the building relative Performance Loss may be easily determined, as it is shown in Section 4.

The REC variation is the starting point to build damage-dependent collapse fragility curves. Further study is required to calibrate initial collapse fragility curves with observational data from past earthquakes. Moreover, more studied building typologies should be considered, in order to investigate on possible ranges of variation of REC depending on building class.

Finally, the effect of brittle type mechanisms (e.g. joint failure, shear failure for beams and columns) should be properly considered in future studies.

7 ACKNOWLEDGEMENTS

This study was performed in the framework of EU CRISMA project. CRISMA is funded from the European Community's Seventh Framework Programme FP7/2007-2013 under grant agreement no. 284552.

NOTATION

$m^* = \sum m_i \cdot \Phi_i$	mass of the ESDOF system
$C_b = \frac{F_y^*}{m^* g}$	base shear coefficient
$T_{eq} = 2\pi\sqrt{\frac{m^* d_y^*}{F_y^*}}$	elastic period of the ESDOF
m_i	the seismic mass at the generic ith story
Φ	shape vector of the force distribution applied in pushover analysis (main vibration mode or linear distribution for the MO case, constant unit vector for the uniform load MA case)
$d^* = \frac{d_{roof}}{\Gamma}$	displacement for equivalent SDOF
$F^* = \frac{V_b}{\Gamma}$	force for equivalent SDOF
$\Gamma = \frac{\sum m_i \cdot \Phi_i}{\sum m_i \cdot \Phi_i^2}$	MDOF-ESDOF transformation factor

REFERENCES

[1] M. Polese, M. Di Ludovico, A. Prota, G. Manfredi, Damage-dependent vulnerability curves for existing buildings. *Earthquake Engineering and Structural Dynamics,* (in press), DOI: 10.1002/eqe.2249, 2012.

[2] M. Polese, M. Gaetani d'Aragona, A. Prota, G. Manfredi, Seismic behavior of damaged buildings: a comparison of static and dynamic nonlinear approach, *COMPDYN 2013, 4th ECCOMAS Thematic Conference on Computational Methods in Structural Dynamics and Earthquake Engineering*, paper #1134, Kos Island, Greece, June 12-14, 2013.

[3] M. Polese, M. Di Ludovico, A. Prota, G. Manfredi, Residual capacity of earthquake damaged buildings. *Proceedings of the 15th World conference on Earthquake Engineering,* paper # 1005, Lisboa, Portugal, September 24-28, 2012.

[4] W.T. Holmes , "Policies and standards for reoccupancy repair of earthquake-damaged buildings". *Earthquake Spectra*, **10 (3)**, 197-208, 1994.

[5] FEMA. "FEMA 306: Evaluation Of Earthquake Damaged Concrete And Masonry Wall Buildings – Basic procedures manual". *Federal Emergency Management Agency*, Washington D.C, 1998.

[6] P. Bazzurro, C.A. Cornell,, C. Menun,, M. Motahari,, Guidelines for seismic assessment of damaged buildings, *13th World Conference on Earthquake Engineering*. Paper No. 1708, Vancouver, B.C., Canada, 2004.

[7] J. Maffei, K. Telleen, D. Mohr,, W. Holmes, Test Applications of Advanced Seismic Assessment Guidelines, *PEER Report 2005/09*, Pacific Earthquake Engineering Research Center, University of California, Berkeley, 2006.

[8] M. Dolšek, P. Fajfar, IN2- A simple alternative for IDA. *13th World Conference on Earthquake Engineering*. Paper No.3353, Vancouver, B.C., Canada, 2004.

[9] T. Vidic, P. Fajfar, & M. Fischinger, Consistent inelastic design spectra: strength and displacement. *Earthquake Engineering and Structural Dynamics*, **23**, 507-521, 1994.

[10] ACI 369R-11. Guide for Seismic Rehabilitation of Existing Concrete Frame Buildings and Commentary. Reported by ACI committee 369, American Concrete Institute,ISBN: 978-0-87031-419-3, 2011.

[11] G.M. Verderame, M. Polese, E. Cosenza Vulnerability of existing R.C. buildings under gravity loads: A simplified approach for non sway structures, *Engineering Structures*, **31 (9)** 2141-2151, 2009.

[12] M. Polese, G.M. Verderame, G. Manfredi, Static vulnerability of existing R.C. buildings in Italy: a case study, *Structural Engineering and Mechanics,* Techno-Press, **39 (4)**, 599-620, 2011.

[13] C.A. Pagni, L.N. Lowes, Fragility Functions for Older Reinforced Concrete Beam-Column Joints, *Earthquake Spectra*, **22 (1)**, 215–238, 2006.

[14] M. Di Ludovico, M. Polese, M. Gaetani d'Aragona, A. Prota, G. Manfredi, A proposal for plastic hinges modification factors for damaged RC columns, *Engineering Structures*, **51**, 99-112, 2013.

[15] M.J.N. Priestley and G.M. Calvi Towards a capacity – Design assessment procedure for reinforced concrete frames, *Earthquake Spectra* **7(3)**, 413-437, 1991.

[16] M.J.N. Priestley, G.M. Calvi, M.J. Kowalsky, *Displacement-Based Seismic Design of Structures*, IUSS Press, Pavia, Italy, 2007.

[17] T. Sullivan, G.M Calvi, Consideration for the Seismic Assessment of Building Using the Direct Displacement-Based Assessment Approach, *Anidis,* Bari, 2011.

[18] E. Cosenza, G. Manfredi, M. Polese, G.M. Verderame, A multilevel approach to the capacity assessment of RC buildings. *Journal of Earthquake Engineering*, **9(1)**, 1-22, 2005.

[19] B. Borzi, R. Pinho, H. Crowley, Simplified pushover-based vulnerability analysis for large scale assessment of RC buildings. *Engineering Structures*, **30(3)**, 804-820, 2008.

[20] Regio Decreto Legge n. 2105 del 22/11/1937. Norme tecniche di edilizia con speciali prescrizioni per le località colpite dai terremoti. G.U. n. 298 del 27/12/1937. (in Italian)

[21] G.M. Verderame, M. Polese, C. Mariniello, G.M. Manfredi, A simulated design procedure for the assessment of seismic capacity of existing reinforced concrete buildings, *Advanced in engineering software*, **41**, 323-335, 2010.

[22] G.M. Verderame, A. Stella, E. Cosenza, Mechanical properties of reinforcing steel adopted in R.C. structures in the age '60 (in Italian), *Proceedings of the 10th National ANIDIS Conference: Seismic Engineering in Italy*, Potenza-Matera, Italy, 2001.

[23] Regio Decreto Legge n. 2229 del 16/11/1939. Norme per la esecuzione delle opere in conglomerate cementizio semplice od armato. G.U. n. 92 del 18/04/1940. (in Italian).

[24] ASCE-SEI 41–06. Seismic Rehabilitation of Existing Buildings, ASCE Standard, American Society of Civil Engineers, Reston, Virginia, 2007.

[25] P. Fajfar, Capacity spectrum method based on inelastic demand spectra. *Earthquake Engng Struct. Dyn*., **28**, 979–93, 1999.

[26] APPLIED TECHNOLOGY COUNCIL, FEMA P-58/ Pre-Release August 2012, Seismic Performance Assessment of Buildings Volume 1 – Methodology, 2012

[27] A. Goretti, F. Bramerini, G. Di Pasquale, M. Dolce et al., The italian contribution to the USGS PAGER project, *14th World Conference on Earthquake Engineering*. Beijing, China, 2008.

[28] S. Lagomarsino, S. Giovinazzi, Macroseismic and mechanical models for the vulnerability and damage assessment of current buildings, *Bulletin of Earthquake Engineering*, **4**,415–443, 2006.

[29] G. Zuccaro, V. Albanese, F. Cacace, C. Mercuri, F. Papa et al., Seismic Vulnerability Evaluations Within The Structural And Functional Survey Activities Of The COM Bases In Italy, *AIP Conf. Proc.*, paper ID 1020, 1665-1674, 2008; doi: http://dx.doi.org/10.1063/1.2963797.

[30] A.B. Liel, K.P. Lynch, Vulnerability of Reinforced-Concrete-Frame Buildings and Their Occupants in the 2009 L'Aquila, Italy, Earthquake, *Natural Hazards Review*, Feb, 11-23, 2012.

[31] T. Rossetto, A. Elnashai, Derivation of vulnerability functions for European-type RC structures based on observational data, *Engineering Structures*, **25**, 1241–1263, 2003.

COMPDYN 2013
4th ECCOMAS Thematic Conference on
Computational Methods in Structural Dynamics and Earthquake Engineering
M. Papadrakakis, V. Papadopoulos, V. Plevris (eds.)
Kos Island, Greece, 12–14 June 2013

IMPROVED PROCEDURE FOR DESIGN AND EVALUATION OF STRUCTURES: SINGLE-DEGREE-OF-FREEDOM BILINEAR SYSTEMS

B. Chikh[1], L. Moussa[2], Y. Mehani[1], A. Zerzour[2], H. Bechtoula[1] and A. Benyoucef[2]

[1]National Center for Applied Research in Earthquake Engineering, CGS
Rue Kaddour Rahim Prolongée , Hussein Dey, Alger
Cheikhpbsd@gmail.com

[2]High National School of Public Works, ENSTP
BP. 32, Garidi I, Vieux Kouba 16051, Algiers, Algeria

Keywords: Improved Procedure, Design, Evaluation, Bilinear System.

Abstract. *Current seismic codes require from the seismically designed structures to be capable to withstand inelastic deformations. Many studies dealt with the development of different inelastic spectra with the aim to simplify the evaluation of inelastic deformations and performance of structures. Recently, the concept of inelastic spectra has been adopted in the global scheme of the performance-based seismic design through capacity-spectrum methods. In this paper an improved procedure, applicable to evaluation and design of structures has been developed and illustrated by examples. This procedure uses inelastic spectra and gives peak responses consistent with those obtained when using the nonlinear time history analysis. The idea consists of solving the differential equation of motion for an increased horizontal displacement of the system. Also, is developed the modified Procedure A of ATC 40 for estimating the seismic deformation of SDOF systems.*

1 INTRODUCTION

Since the development of the Capacity-Spectrum Method (CSM) (Freeman et al. 1975) [1], many response spectra have been proposed to replace the conventional elastic spectra in order to achieve accurate evaluation of the inelastic response of structures.

Recently, Miranda (2000) [11] proposed procedures based on displacement modification factors in which the maximum inelastic displacement demand of multi-degree of freedom (MDOF) system is estimated by applying certain displacement modification factors to maximum deformation of equivalent SDOF system having the same lateral stiffness and damping coefficient as that of MDOF system. In another study, Miranda and Ruiz-Garcia (2002) evaluated six possible alternative methods to estimate the maximum inelastic deformations of SDOF systems [2]. The evaluated methods estimate the maximum inelastic deformation using functions of displacement ductility factor to compute equivalent periods and equivalent damping ratios (Rosenblueth and Herrera 1964, Gulkan and Sozen1974,Iwan1980,Kowalsky 1994), or to compute displacement modification factors (Newmark and Hall 1982, Miranda 2000) [11]. The study aimed at evaluating the accuracy of approximate methods for the preliminary design of structures. Later, Akkar and Miranda (2002) conducted a statistical evaluation of five of the above methods. The study showed that for periods longer than 1 second all methods produce relatively good results. In the short period region, equivalent linear methods proposed by Iwan and Guyader and the one proposed by Kowalsky tend to overestimate deformation demands [8]. The errors produced by any of the evaluated approximate methods can be relatively larger, particularly for lateral strength ratios larger than four.

The capacity-spectrum method gives an overall view of the inelastic behavior of structures subjected to ground motions. However, to be as more accurate as possible it requires a realistic capacity curve for the structure that is in accordance with its dynamic behavior when subjected to the design earthquake. Many refinements and corrections have been made to the pushover analysis to make it in accordance with the nonlinear time history analysis. For instance, the adaptive pushover analysis (A. S. Elnashai2001, among others) actually represents the best choice.

Based on the deficiencies in ATC-40 [1] procedures (Applied Technology Council 1996), Chopra and Goel (1999) proposed an improved Capacity-Demand-Diagram method that uses the constant-ductility design spectrum [3]. Their method has been evaluated using SDOF elastoplastic systems, and to retain the attraction of the graphical implementation of the ATC-40 procedures (A and B) Chopra and Goel developed an alternative graphical implementation of their improved method.

In this paper, we first present the development of the ductility demand response spectrum. Based on the inaccuracy of ATC-40 [1] procedures and the need to a graphical approach for the seismic design of structures, an improved procedure were proposed and investigated in this paper.

2 ATC-40 PROCEDURES

ATC-40 [1] specifies three different procedures of the Capacity Spectrum Method (CSM) to estimate the earthquake-induced deformation and finding the performance point, all based on the same principles, but differing in implementation. Procedures A and B are analytical and amenable to computer implementation, whereas procedure C is graphical and most suited for hand analysis. Designed to be the most direct application of the methodology, Procedure A is suggested to be the best of the three procedures [1]. The Capacity Spectrum Method (CSM) compares the capacity of a structure to resist lateral forces to the demands of earthquake response spectra in a graphical presentation that allows a visual evaluation of how the

structure will perform when subjected to earthquake ground motion. The method is easily understandable and generally consistent with other methods that take into account the nonlinear behavior of structures subjected to strong motion earthquake ground movements [5].

The procedure can be summarized by the following :

- Capacity curve: Estimate or calculate the capacity curve in terms of roof displacement *x*, and base shear, V_b (i.e. total lateral force at base).
- Dynamic characteristics: Estimate or calculate modal vibrational characteristics such as periods of vibration, mode shapes, modal participation factors, and effective modal mass ratios.
- Capacity Spectrum: Convert the V_b vs *x* capacity curve to a S_a vs S_d capacity spectrum by use of dynamic characteristics..
- Response Spectra: Obtain or calculate response spectra for several levels of damping, including the 5-percent damped spectrum.
- Graphical Solution: Plot capacity spectrum and family of damped response spectra on an ADRS format (i.e. S_a vs S_d coordinates with period T lines radiating from origin). The intersection of the capacity spectrum with the appropriately damped response spectrum represents the estimated demands of the earthquake on the structure.

3 IMPROVED PROCEDURE

A relatively simple method for determining the seismic demands of structures is presented. It combines the Pushover analysis of a single-degree-of-freedom (SDOF) bilinear model shown in figure (1), with a new inelastic response spectrum [2]. This spectrum formulated in the ductility demand – period format are applied. This feature represents the major difference with respect to the capacity spectrum method. Moreover, seismic demand can be obtained without iteration. The differences between the proposed method and the capacity spectrum method are discussed, and some examples are processed to check this difference.

3.1 Capacity curve

Using a Pushover analysis, a characteristic nonlinear force-displacement relationship of the SDOF bilinear system can be determined. The selection of an appropriate lateral load distribution is an important step within the Pushover analysis. Once you done Pushover analysis, the curve is characterized by some parameters. These features will be used for the construction of the demand diagram we will be see in the next step.

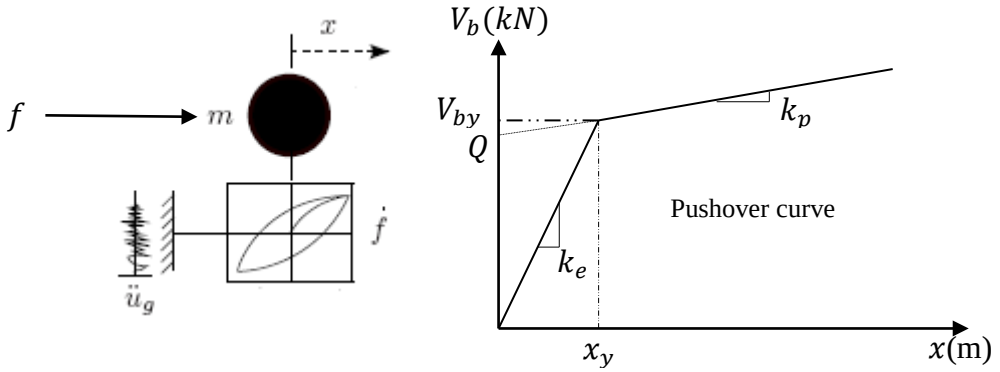


Figure 1: Capacity curve of a (SDOF) bilinear system .

3.2 Seismic demand

The seismic demand for the SDOF bilinear system can be determined by using the following procedure. Both the demand spectra and the capacity diagram are not plotted in the same graph.

3.2.1 Equation of motion in terms of ductility

Considering an inelastic single-degree of freedom system, its motion when subjected to an earthquake ground motion is governed by the following equation:

$$m\ddot{x} + c\dot{x} + f(x,\dot{x}) = -m\ddot{x}_g(t) \tag{1}$$

Where, m, c and f represent the mass, damping, and the resisting force of the system, respectively, $\ddot{u}_g(t)$ denotes the earthquake acceleration. The resisting force f is defined as the sum of a linear part and a hysteretic part:

$$f = k_p x + Qz \tag{2}$$

In the above, k_p is the postyield stiffness, Q is the yield strength, and z represents the dimensionless variable that characterizes the Bouc-Wen model of hysteresis [17], it is given by:

$$\dot{z} = \frac{\dot{x}}{x_y}\left[A - |z|^n\left(\gamma\,\mathrm{sgn}(\dot{x}z) + \beta\right)\right] \tag{3}$$

In the above equation, x_y is the yield displacement, $A, \eta, \gamma,$ and β are parameters that control the shape of the hysteresis loop. Material degrading is not considered in this study. However, to accommodate material degradation in the hysteresis model, the Baber-Noori (1985) version of the Bouc-Wen model may be used.

Substituting Eq. (2) into Eq. (1) and dividing by m yields :

$$\ddot{x} + 2\xi\omega\dot{x} + \frac{k_p}{m}x + \frac{Q}{m}z = -\ddot{u}_g(t) \tag{4}$$

Or simply:

$$\ddot{x} + 2\xi\omega\dot{x} + \alpha\omega^2 x + qgz = -\ddot{u}_g(t) \tag{5}$$

In which $\xi, \omega, \alpha,$ and q represent the damping ratio, circular frequency, post-to-preyield stiffness ratio, and the yield strength coefficient (defined as yield strength divided by the system weight $W : W = mg$, g stands for the gravity), respectively.

Equation 5 is solved for a single ground acceleration (see Fig. 2a) to obtain the deformation history $x(t)$ (Fig. 2b). Also shown is the yielding history through $z(t)$ (Fig. 2c) and the variation of the system force coefficient f/w with deformation (Fig. 2d).

Next, Eq. (5) is rewritten in terms of displacement ductility factor, μ. Substituting: $x = x_y\mu$, $\dot{x} = x_y\dot{\mu}$, and $x = x_y\ddot{\mu}$, in Eq. (5) and dividing by x_y gives [2]:

$$\ddot{\mu} + 2\xi\omega\dot{\mu} + \alpha\omega^2\mu + \frac{qgz}{x_y} = -\frac{1}{x_y}\ddot{u}_g(t) \tag{6}$$

By doing the same to the dimensionless variable z, Eq. (3) may be expressed in terms of $\dot{\mu}$ as:

$$\dot{z} = \dot{\mu}\left[A - |z|^n\left(\gamma\,\mathrm{sgn}(\dot{x}z) + \beta\right)\right] \tag{7}$$

The term $\frac{qg}{x_y}$ in Eq. (6) is rewritten as:

$$\frac{qg}{x_y} = \omega^2(1-\alpha) \tag{8}$$

Solving Eq. (8) for x_y yields:

$$x_y = \frac{qg}{\omega^2(1-\alpha)} \tag{9}$$

Substituting Eq. (8) and Eq. (9) into Eq. (6) gives [2]:

$$\ddot{\mu} + 2\xi\omega\dot{\mu} + \alpha\omega^2\mu + \omega^2(1-\alpha)z = -\frac{\omega^2(1-\alpha)}{qg}\ddot{u}_g(t) \tag{10}$$

We observe from Eq. (10) that for a given ground acceleration, $\mu(t)$ depends on ξ,ω,α, and q.

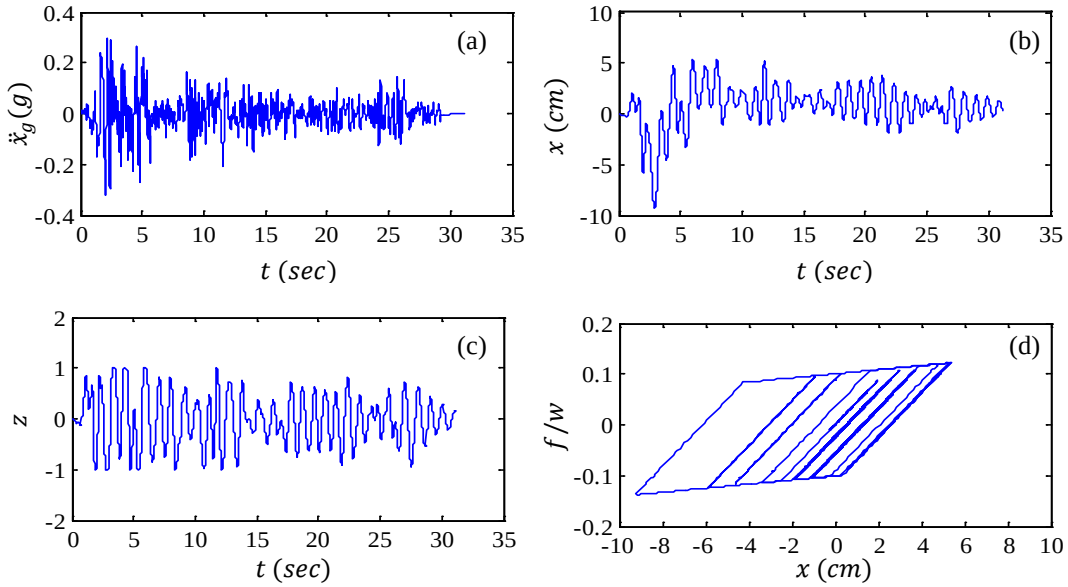


Figure 2 : (a) Strong component of El Centro 1940 ground motion, (b) system deformation, (c) yield function z(t), and (d) force-deformation relation. System parameters are $x_y = 2.5\ cm$, $T = 1.0\ sec$, $k_e = 17488.9\ N/cm$ and $\alpha = 10\%$.

3.2.2 System controlling parameters and normalization

To obtain meaningful system response to an ensemble of ground motions, the system yield strength coefficient has to be defined relative to the intensity of individual ground motions. Using the parameter η introduced by Mahin and Lin (1983) as [9]:

$$\eta = \frac{qg}{PGA} \tag{11}$$

where, PGA stands for the Peak Ground Acceleration. Incorporating η into Eq. (10) results:

$$\ddot{\mu} + 2\xi\omega\dot{\mu} + \alpha\omega^2\mu + \omega^2(1-\alpha)z = -\frac{\omega^2(1-\alpha)}{\eta}\overline{\ddot{u}_g}(t) \tag{12}$$

in which, $\overline{\ddot{u}_g}(t)$ represents the ground acceleration normalized with respect to the PGA:

$$\overline{\ddot{u}_g}(t) = \frac{\ddot{u}_g(t)}{PGA} \tag{13}$$

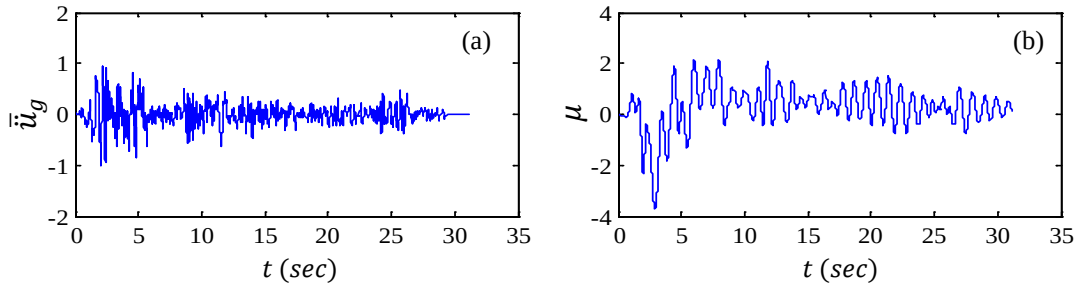


Figure 3: (a) Strong component of normalized ground acceleration of El Centro 1940 and (b) ductility demand μ for a system with $x_y = 2.5\ cm$, and $\eta = 0.25$.

Figure 3. demonstrates the normalized ground acceleration history of the strong component of El Centro 1940 and the resulting ductility demand, in contrast to Fig. 2 that presented their unnormalized counterparts.

The ground acceleration has been normalized such that its value varies from -1 to 1. Eq. (12) implies that for a given inelastic system, if α and η are fixed, the intensity of the ground motion has no effect on the peak normalized deformation, μ. This permits the construction of the ductility response spectrum for an ensemble of ground motions with common frequency content but variable intensity.

3.2.3 Constant $-\eta$ ductility response spectrum

The procedure to construct the ductility response spectrum for inelastic systems corresponding to specified levels of normalized yield strength η, is summarized in the following steps [2]

- Define the ground motion $\ddot{u}_g(t)$;
- Select and fix the damping ratio ξ and the post-to-preyield stiffness ratio α ($\alpha = 0$ for elastoplastic system) for which the spectrum is to be plotted;
- Specify a value for η;
- Select a value for elastic period T;
- Determine the ductility response $\mu(t)$ of the system with $T, \xi,$ and α equal to the values selected by solving Eq. (12) along with Eq. (7). From $\mu(t)$ determine the peak ductility factor μ;
- Repeat steps 4 and 5 for a range of T, resulting in the spectrum values for the η value specified in step 3;
- Repeat steps 3 to 6 for several values of η.

Given the excitation and the properties $T, \xi, \alpha,$ and η of an inelastic SDOF system, it is desired to determine the peak deformation, x_m. The yield displacement of the system is derived from Eq. (9) and Eq. (11) as follows:

$$x_y = \frac{\eta}{\omega^2(1-\alpha)} PGA \tag{14}$$

The value of the ductility factor is read from the spectrum developed by the above procedure and multiplied by x_y to obtain the peak deformation, x_m. The DDRS is constructed also for El Centro 1940 ground motion (N/S) component (PGA=0.32g, PGV=36.14 cm/sec, and PGD=21.34cm) and is shown in figure 4.

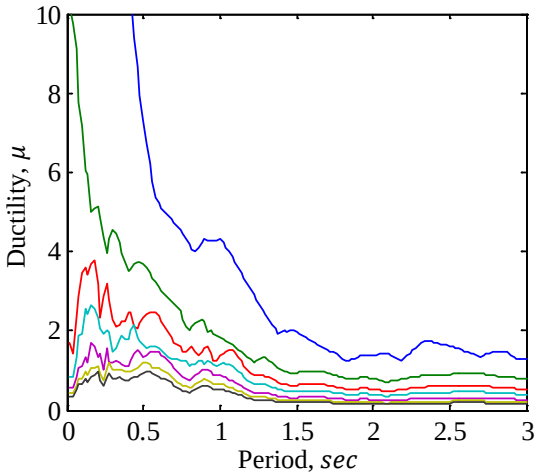


Figure 4: DDRS for inelastic system computed for El Centro 1940 (N/S) component (η = 0.25, 0.5, 0.75, 1, 1.5, 2, 2.5 from top line to bottom line).

4 APPLICATIONS

It is desired to analyze some examples subjected to the El Centro 1940 north-south component, each system has the properties shown in the table 1. Considered are two values of T: 0.5s in the acceleration sensitive spectral region and 1s in the velocity-sensitive region, and two levels of yield strength; ζ=5% for all systems.

system	$m(kg)$	$k_e(N/cm)$	$k_p(N/cm)$	$Q(N)$	$x_y(cm)$
1	1.86	293.72	14.68	290.19	1.04
2				435.29	1.56
3		90.65	4.53	290.23	3.37
4				435.77	5.06

Table 1 Characteristics of inelastic systems.

The results obtained from the nonlinear dynamic analysis (NL-THA) of the systems are summarized in table 2 with the parameter η, which has been calculated by the equation (11).

Systems Properties						(NL-THA)	
system	$T(s)$	$\alpha(\%)$	η	q	$x_y(cm)$	μ	$x_m(cm)$
1	0.5	5%	0.5	0.16	1.04	3.93	4.08
2			0.75	0.24	1.56	2.68	4.18
3	0.9	5%	0.5	0.16	3.37	2.28	7.68
4			0.75	0.24	5.06	1.79	9.05

Table 2 Properties of systems and their responses due to El Centro 1940.

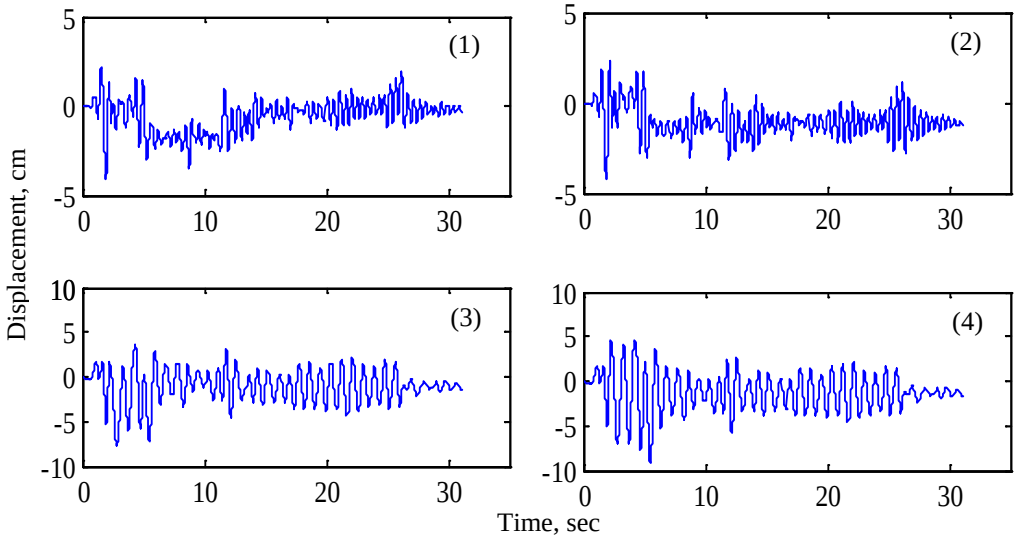


Figure 5: Dynamic nonlinear results of the four systems.

The CSM (Procedure A) is used to compute the earthquake-induced deformation of the four example systems listed in Table 1. Implementation details are presented next for selected systems and final results for all systems in table 3 and figure 6.

system	$D_p(cm)$	$A_p(g)$	μ	$\hat{\xi}(\%)$	Erreur (%)<5%
1	3.59	0.18	2.91	29.72	0.16
2	3.61	0.26	1.71	22.82	0.25
3	7.83	0.17	1.10	9.0	0.52
4	Divergence				

Table 3: Results from ATC-40 Procedure A analysis of four systems for El Centro (1940) ground motion.

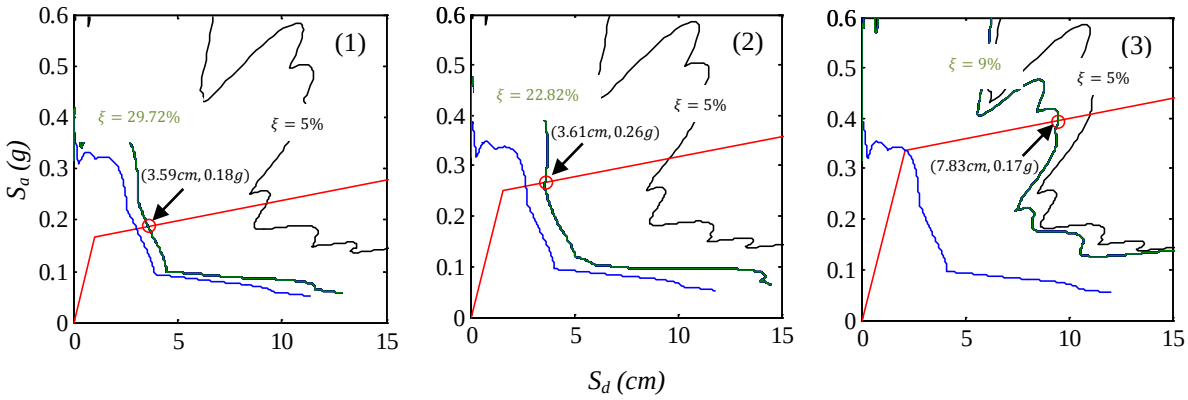


Figure 6: Application of ATC-40 Procedure A to System 1, 2 and 3 for elastic design spectrum - iterative procedure.

The period T and the properties α and η of an inelastic SDOF system are used to compute the ductility and the inelastic displacement of systems by the DDRS spectra. The results obtained from the DDRS of the systems are summarized in table 4.

System	Displacement (cm)			Errors (%)	
	ATC40	DDRS	NL-RHA	ATC40	DDRS
1	3.59	4.08	4.08	12.01	0.0
2	3.61	4.18	4.18	13.64	0.0
3	7.83	7.68	7.68	-02.01	0.0
4	-----	9.05	9.05	------	0.0

Table 4 Comparison of results obtained by DDRS and CSM.

It is clear from table 4 that the peak response of DDRS is equal to that obtained by the nonlinear dynamic (NL-THA) "exact" analysis. Therefore, the DDRS can be considered as an attractive tool since it leads to meaningful and accurate results.

5 CONCLUSION

An improved direct procedure for seismic demands of SDOF bilinear system has been developed and its accuracy was verified by examples, and a response spectrum, called DDRS, has been developed and its applicability was tested for the selected examples. This investigation led to the following conclusions:

- The efficiency of the DDRS is evident; the designer needs only to have the DDRS for the design earthquake (s) to determine peak response of any structure, namely, base displacement and base shear.
- This method is applicable to a variety of uses such as a rapid evaluation technique for a large inventory of buildings, a design verification procedure for new construction, an evaluation procedure for an existing structure to identify damage states.
- Based on this study the ATC-40 Procedure A did not converge for the fourth system analyzed. It converged in many cases but not to the exact deformation determined by nonlinear response history analysis of the inelastic system, nor to the value determined from the DDRS inelastic response spectrum.
- The ductility demand is given by the direct estimation where the ductility calculated from the DDRS diagram matches the value associated with the period of the system. This method gives the deformation value consistent with the selected DDRS inelastic response spectrum, while retaining the attraction of graphical implementation of the ATC-40 methods.

6 REFERENCES

[1] Applied Technology Council. 1996, "Seismic evaluation and retrofit of concrete buildings", *Report ATC 40*.

[2] Chikh B., Moussa L., eT Zerzour A, 2012. "Ductility and Inelastic Deformation Demands of Structures", Paper ID: *Structural Engineering and Mechanics* 17289C. Vol. 42, No. 5, June10, 2012. Techno Press P.O. Box 33, Yuseong-gu Daejeon 305-600 KOREA.

[3] Chopra, A. K. and Goel, R. K. (1999), "Capacity-demand-diagrams based on inelastic design spectrum", *Earthq. Spec*., 15(4), 637-656.

[4] 9-Fajfar, P. (1999), "Capacity spectrum method based on inelastic demand spectra", *Earthq. Eng. Struct. Dyn*., 28(9), 979-993.

[5] Freeman, S. A. Nicoletti, J. P. and Tyrell, J. V. (1975), “Evaluation of existing buildings for seismic risk-a case study of Puget Sound Naval Shipyard, Bremerton, Washington”, *Proceedings of 1st U.S. National Conference on Earthquake Engineering*, Earthquake Engineering Research Institute, Berkeley, 113-122.

[6] Gülkan, P. and Sözen, M. (1974), “Inelastic response of reinforced concrete structures to earthquake motions”, *ACI J*., 71(12), 604-610.

[7] Ibarra, L. F. (2003), "Global collapses of frame structures under seismic excitations", Ph.D. Thesis, *Department of Civil and Environmental Engineering, Stanford University*, Stanford, California.

[8] Iwan, W. D., (1980), “Estimating inelastic spectra from elastic spectra”, *Earthq.Eng. Struct.Dyn*., 8(4), 375-388.

[9] Mahin, S. A. Lin, J. (1983), "Construction of inelastic response spectra for single-degree-of-freedom systems. Computer program and applications", *Report No. UCB/EERC-83/17, University of California*, Berkeley.

[10] Miranda, E. (1992), "Nonlinear response spectra for earthquake resistant design", *Proceedings of the Tenth World Conference on Earthquake Engineering*, Balkema, Rotterdam, 5835-5840.

[11] Miranda, E. (2000), "Inelastic displacement ratios for structures on firm sites", J. *Struct. Eng*., 126(10), 1150-1159.

[12] Miranda, E. (2001), "Estimation of inelastic deformation demands of SDOF systems", J. *Struct. Eng*., 127(9), 1005-1012.

[13] Moussa. L, 2009 “Base Isolated Buildings Parametric Analysis and Design Guidlines”, Tesis in Civil Engineering, *Technical university of civil engineering, Bucharest*, September 2009.

[14] Nassar, A. and Krawinkler, H. (1991), “Seismic demands for SDOF and MDOF systems”, John A. *Blume Earthquake Engineering Center*, Report 95, Dept. of Civil Engineering, Stanford University.

[15] Newmark, N. M. and Hall, W. J. (1982), "Earthquake spectra and design", *Earthquake Engineering Research Institute*, Berkeley, California.

[16] Ruiz-Garcia, J. and Miranda, E. (2003), “Inelastic displacement ratios for evaluation of existing structures”, *Earthq.Eng. Struct.Dyn*., 32(8), 1237-1258.

[17] Wen, Y. K. (1976), "Method for random vibration of hysteretic systems", J. *Eng. Mech*., 102(2), 249-263.

COMPDYN 2013
4th ECCOMAS Thematic Conference on
Computational Methods in Structural Dynamics and Earthquake Engineering
M. Papadrakakis, V. Papadopoulos, V. Plevris (eds.)
Kos Island, Greece, 12–14 June 2013

EXPERIMENTAL RESEARCH OF SHEAR STRENGTH MODELS FOR REINFORCED CONCRETE MEMBERS

Despina V. Syntzirma[1] and Stavroula J. Pantazopoulou[2]

[1] Municipality of Pilea – Hortiatis, Public Works Dept.
55 Argonafton Str., Kalamaria, P.O. 55131, Greece
dsyntz@civil.duth.gr

[2] University of Cyprus, Dept. of Civil and Environmental Engineering
P.O. Box 20537, 1687 Nicosia, Cyprus
pantaz@ucy.ac.cy

Keywords: shear strength, tests, assessment, R.C. elements, Assessment Codes, Design Codes

Abstract. *The question of systematically calculating the shear strength of reinforced concrete (R.C.) elements in flexure-shear reversals with or without axial load has been central to the development of performance based design. The multitude of models in the international literature, some of which have been adopted by the Seismic Codes of Assessment or Design (such as ACI 318−2011, FEMA 273 and 356, ASCE/SEI 41–07, EC8−III (2005)) hints to the limited extent of the current level of understanding of this problem; the success of these models in reproducing strength values is very good when flexural failures dominate the response, but their performance, as measured by the amount of scatter between experiment and analysis, increasingly deteriorates when used to estimate shear capacity in shear driven modes of failure.*

The most important shear strength models [ACI 318−2011, FEMA 273 and 356, as modified by ASCE/SEI 41–07, EC8−III (2005)] are tested against two experimental databases comprising elements from the international literature. The first database consists of approximately 550 elements detailed according to the modern provisions whereas the second consists of 40 poorly detailed elements (inadequate transverse reinforcement with brittle details, inadequate lap splices in critical regions, low concrete and steel strengths etc.). Furthermore a parametric study was conducted with regards to the displacement ductility, the normalized axial load, the aspect ratio, the transverse reinforcement and other important design parameters.

The results are presented in the form of graphs, in order to highlight the deficiencies of each model whereas the scatter observed illustrates the need for additional investigation to improve the shear strength estimates.

1. INTRODUCTION

A primary objective of performance–based assessment and/or design is to dependably estimate the various strength indices that a R.C. member may sustain when subjected to seismic loads, namely the shear force required to develop the flexural capacity at the support, V_{flex}, the web shear strength, V_{shear}, the shear force that may be sustained when the anchorage of reinforcement or lap splice reaches its capacity, V_{lap}, and the shear force sustained when compression reinforcement buckles at the critical section, V_{buckl}. The most critical of these response mechanisms appears to be shear, as its occurrence prior to development of failure in other response mechanisms leads to brittle failure.

The issue of dependably estimating the shear strength of a R.C. element appears to be rather complicated as it presumes the full understanding of the several interacting behavior mechanisms under reversed cyclic loading whereas it is strongly affected by the imposed loading history, the dimensions of the element (e.g. the aspect ratio), the concrete strength, the longitudinal reinforcement ratio but mostly the ratio and the detailing of the transverse reinforcement. So far it has not been possible to theoretically describe the strength of the shear mechanism from first principles of mechanics without use of calibrated empirical constants. Therefore the shear strength estimates obtained from calibrated design expressions necessarily rely on the pool of experimental data used for correlation of the empirical expressions, but also on the preconceived notions of the individual researchers as to the role each variable has on the mechanics of shear.

In the present work the most widely used shear strength models, adopted by the modern Design and Assessment Seismic Codes (ACI 318−2011, FEMA 273 and FEMA 356, as modified by ASCE/SEI 41–07, Eurocode 8–2005) are compared. They are tested against two extensive experimental databases assembled from tests published in the literature international. The first database consists of approximately 550 elements detailed according to modern provisions whereas the second consists of 40 poorly detailed elements, referred to as 'old-type'. Particular emphasis is placed on these 'old type' elements as the inventory of R.C. structures that qualify under this classification is vast throughout the seismic regions of the world. A major shift in international seismic design codes occurred in the early 1980's introducing the modern form of detailing with closed stirrups and proper reinforcement anchorage as a required practice. Structures designed prior to that point conform to a variety of earlier standards, as these evolved through the years from the post world-war era to the 1980's. These structures are at the core of the "seismic assessment codes" such as ASCE–SEI 41 (2007) and EC8–III (2005); this concern has been motivated by the observed poor performance of these structures in strong earthquakes throughout the world from the 1990s till today [7, 8, 9].

Furthermore, a parametric study of the models describing the shear strength mechanism was conducted in order to study the parametric sensitivity against the most important design parameters such as the displacement ductility, the normalized axial load, the aspect ratio, the cross sectional area, the volumetric ratio of the transverse reinforcement, the normalized stirrup spacing, the ratio of the longitudinal reinforcement, the yield strength of the longitudinal and the transverse reinforcement and the concrete strength. The scope of this study was to check whether those models interpret consistently with basic mechanics, the influence of the design parameters on the behaviour of reinforced concrete members.

2. DESCRIPTION OF THE EXPERIMENTAL DATABASES

The first database the shear strength models are tested against consists of approximately 550 tests assembled from the international literature [10]. The elements are designed

according to modern provisions, hence this database will be referred to from here on as 'Modern type Database' or M.D. The tests it is assembled from are detailed with adequate transverse reinforcement, anchored inside the confined core with 135^0 hooks, lap splices are placed outside the critical region and the yield strength of the transverse and the longitudinal reinforcement is substantial. The Old type Database, referred to as O.D., consists of approximately 40 elements with poor and occasionally smooth longitudinal and transverse reinforcement, 90^0 stirrup hooks and lap splices with insufficient length located in the critical regions. Specimens of both databases were tested under cyclic lateral load reversals simulating earthquake effects with or without axial load. The most important database parameters are listed in Table 1.

Parameter	Modern type Database(M.D.)	Old type Database(O.D.)
$P/f_c'A_g$	0.0 to 0.85 (P=0 for 45% of the database)	0.0 to 0.60 (P=0 for 37% of the database)
L_s/h	0.8 to 10.0	2.0 to 6.0
r_c	0.5% to 6.0%	1.0 to 5.0% (lap-splices in the critical region: 60%)
$r_{s,vol}$	0.0% to 6.0% ($r_{s,vol}$= 0.0 for 10%)	0.2% to 1.5% (90^0 hooks for 55%)
s/D_{bl}	1.6 to 15.0	3.2 to 18.0
$k_{eff}\, r_s f_{yh}/f_c'$	0.0 to 0.7	0.002 to 0.150
$v_{fail}/\sqrt{f_c'}$	0.0 to 2.3 ($v_n/\sqrt{f_c'}$= 0.0 for 7%)	0.07 to 0.37
f_c' (MPa)	14.0 to 130.0	18.0 to 36.0
f_{sy} (MPa)	117.0 to 932.0	317.0 to 548.0
f_{yh} (MPa)	236.0 to 2050.0	210.0 to 481.0

$P/f_c'A_g$: normalized axial load, L_s/h: aspect ratio, r_c: ratio of the longitudinal Reinf., $r_{s,vol}$: volumetric ratio of transverse Reinf., s: stirrup spacing, D_{bl}: diameter of longitudinal Reinf., $k_{eff} r_s f_{yh}/f_c'$: effective normalized confining pressure provided by transverse Reinf. in the direction of lateral sway, $v_{fail}/\sqrt{f_c'}$: normalized applied shear stress, f_c': concrete strength, f_{sy}, f_{yh}: yield strength of the longitudinal and the transverse Reinf.

Table 1: Ranges of Database Parameters

3. SHEAR STRENGTH MODELS

In the following sections the shear strength models adopted by the Design Code ACI 318−2011 and the Assessment Codes FEMA 273 (1997) and FEMA 356 (2000), as modified by ASCE/SEI 41–07, and Eurocode 8 – III (2005) are considered. The analytical results from the implementation of each model on the two databases are graphically presented whereas an extra criterion was used concerning the ratio of the applied shear stress v_{fail} to the available shear capacity calculated according with the provisions of ACI 318 (2011), v_n^{ACI}. Based on recent tests it has become evident that shear strength of reinforced concrete degrades the faster with cyclic load, the higher the ratio of shear demand to shear supply. Wood and Sittipunt (1996) have proposed a limit of 60% as a cutoff point in identifying shear failures from other types of failures when processing the experimental literature on walls. Thus, a shear failure is likely to occur when $0.6v_n^{ACI}<v_{fail}$, even if the nominal check prescribed by the code holds, namely that $v_n^{ACI}<v_{fail}$. Furthermore the contribution of concrete V_c and of the axial load V_p to the total shear strength is graphically presented so as to highlight the influence of each mechanism.

3.1 Design Code ACI 318−2011

The shear strength model adopted by the American Design Code ACI 318−2011 is depicted by the following equations:

$$V_c = 0.17 \cdot \left(1 + \frac{P}{14A_g}\right) \cdot \sqrt{f_c'} \cdot b \cdot d \quad \text{and} \quad V_{s,ACI} = \frac{A_{tr} f_{yh} d}{s} \quad \text{(units in Nt, mm)} \tag{1}$$

where P is the axial load, A_g is the area of the cross section of the element, f_c' is the concrete strength, b is the width of the section and d is the effective cross section depth, A_{tr} is the area of the stirrups that may be crossed by a crack, f_{yh} is the yield strength of the stirrups and s is the stirrup spacing.

The analytical results of the model are presented in Fig. 1, graphs (a) and (b) for the M.D. and graphs (c) and (d) for the O.D. Note that the diagonal line drawn in each graph represents the equal value case (i.e., the case where test result equals the analytical prediction). The concrete contribution to shear strength V_c appears to be rather well estimated for elements failing in shear, whereas for the group where a flexural mode of failure is expected, values are overestimated. The results concerning the total shear strength for the shear-failing elements are in good agreement with the tests but significant scatter appears when the flexural elements are considered. Graphs (c) and (d) in Fig. 1 concerning the O.D. present similar trends, however it is noteworthy that the model adopted by ACI 318–2011 refers to design of R.C. elements and not to assessment and therefore does not take into consideration the imposed ductility level.

3.2 ASCE/SEI 41–2007

The above mentioned model is also used in FEMA Guidelines 273 (1997) and FEMA 356 (2000) and ASCE/SEI 41–07 under certain modifications that account for the concrete degradation under seismic loading using the reduction factor k:

$$V_c = k \cdot \left(\frac{0.5\sqrt{f_c'}}{L_s / d} \sqrt{1 + \frac{P}{0.5A_g\sqrt{f_c'}}}\right) \cdot 0.8A_g \quad \text{and} \quad V_s = k \cdot \frac{A_{tr} f_{yh} d}{s} \quad \text{(units in Nt, mm)} \tag{2}$$

where factor k equals to 1.0 for elements with ductility demand $m_D \leq 2.0$, $k = -0.1m_D + 1.2$ for elements with ductility demand $2.0 < m_D \leq 6.0$ and $k = 0.6$ for elements with higher ductility demands.

The analytical results are presented in Fig. 1, in graphs (e) and (f) for the M.D. and in graphs (g) and (h) for the O.D. There is sufficient accuracy in the concrete contribution to shear strength for both the group of the shear-controlled and the flexure-controlled elements. Yet the analytical results for the group of the flexure-controlled elements are overly optimistic when the total shear strength is under consideration. The analytical results for the O.D. seem to have very good correlation with the experimental data for both the flexure and the shear controlled elements.

3.3 Eurocode 8 – III (2005)

The shear strength model adopted by Eurocode 8 – III is presented in the following section. The cyclic shear resistance of a R.C. element V_R, decreases with the plastic part of ductility demand, expressed in terms of ductility factor of the transverse deflection of the shear span or of the chord rotation at member end: $m_{\Delta,pl} = m_\Delta - 1$. For this purpose $m_{\Delta,pl}$ may be calculated as the ratio of the plastic part of the chord rotation, q_{pl}, normalized to the chord rotation at yielding, q_y. The following expression is used for the shear strength, as controlled by the stirrups, accounting for the above reduction (with units Nt and mm):

$$V_R = \frac{1}{\gamma_{el}} \left\{ \begin{array}{c} \frac{h-c}{2L_s} min(P, 0.55 A_e f_c) + [1 - 0.05 min(5; \mu_{\Delta}^{pl})] \times \\ \times \left[0.16 max(0.5; 100\rho_{tot}) \cdot \left(1 - 0.16 min\left(5; \frac{L_s}{h} \right) \right) \sqrt{f_c} A_e + V_s \right] \end{array} \right\} \quad (3)$$

where g_{el} is a factor equal to 1.15 for primary seismic elements and 1.0 for secondary seismic elements (it is taken equal to 1.0 for the two databases), h is the depth of the cross-section (equal to the diameter D for circular sections), c is the compression zone depth, L_s is the shear span, P is the compressive axial load (positive, taken as being zero for tension), A_e is the cross-section area, taken as being equal to $b \cdot d$ for rectangular cross-sections (b is the width and d is the effective depth), or to $pD_c^2/4$ (where D_c is the diameter of the concrete core to the inside of the hoops) for circular sections.

The concrete compressive strength is f_c', r_{tot} is the total longitudinal reinforcement ratio and V_s is the contribution of transverse reinforcement to shear resistance, taken as being equal to:

$$V_s = \rho_{tr} b\, z\, f_{yh} \text{ for rectangular sections}, V_s = \frac{\pi}{2} \frac{A_{sp}}{s} f_{yh} (D - 2c_o) \text{ for circular sections} \quad (4)$$

where r_{tr} is the transverse reinforcement ratio, z is the length of the internal lever arm and f_{yh} is the yield stress of the transverse reinforcement, A_{sp} is the cross-sectional area of a circular stirrup, s is the centerline spacing of stirrups and c_o is the concrete cover.

If in a concrete column the shear span ratio L_s/h at the end sections where flexural moment is maximized is less or equal to 2.0, its shear strength, V_R, should not be taken greater than the value corresponding to failure by web crushing along the diagonal of the column after flexural yielding, $V_{R,max}$, which, under cyclic loading may be calculated from the expression (with units Nt and mm):

$$V_{n,max} = \frac{4/7 [1 - 0.02 min(5; \mu_{\Delta}^{pl})]}{\gamma_{el}} \left(1 + 1.35 \frac{P}{A_e f_c'} \right) [1 + 0.45(100\rho_{tot})] \sqrt{min(40; f_c')} b\, z \sin 2\theta \quad (5)$$

where q is the angle between the diagonal and the axis of the column ($\tan q = h/(2L_s)$).

The analytical results are shown in Figure 1, graphs (i) and (j) for the M.D. and graphs (k) and (*l*) for the O.D. The concrete contribution to shear strength is adequately estimated as compared to the experimental results both for the group of the shear-controlled elements and for the flexure-controlled group. The results of the total shear strength also appear to have rather sufficient accuracy when the shear-controlled elements are considered, yet the analytical results for the group of the flexure-controlled elements are overly optimistic. The analytical results for the O.D. also seem to have very good correlation with the experimental data.

4. PARAMETRIC INVESTIGATION OF THE SHEAR STRENGTH MODELS

A parametric study of the shear strength models was conducted in order to highlight the deficiencies of each model over the most important design parameters such as the displacement ductility, the normalized axial load, the aspect ratio, the cross sectional area, the volumetric ratio of the transverse reinforcement, the normalized stirrup spacing, the ratio of the longitudinal reinforcement, the yield strength of the longitudinal and the transverse

reinforcement and the concrete strength. The scope of this parametric investigation is to check whether the shear strength models interpret in a consistent manner the influence of the design parameters on the mechanical behaviour.

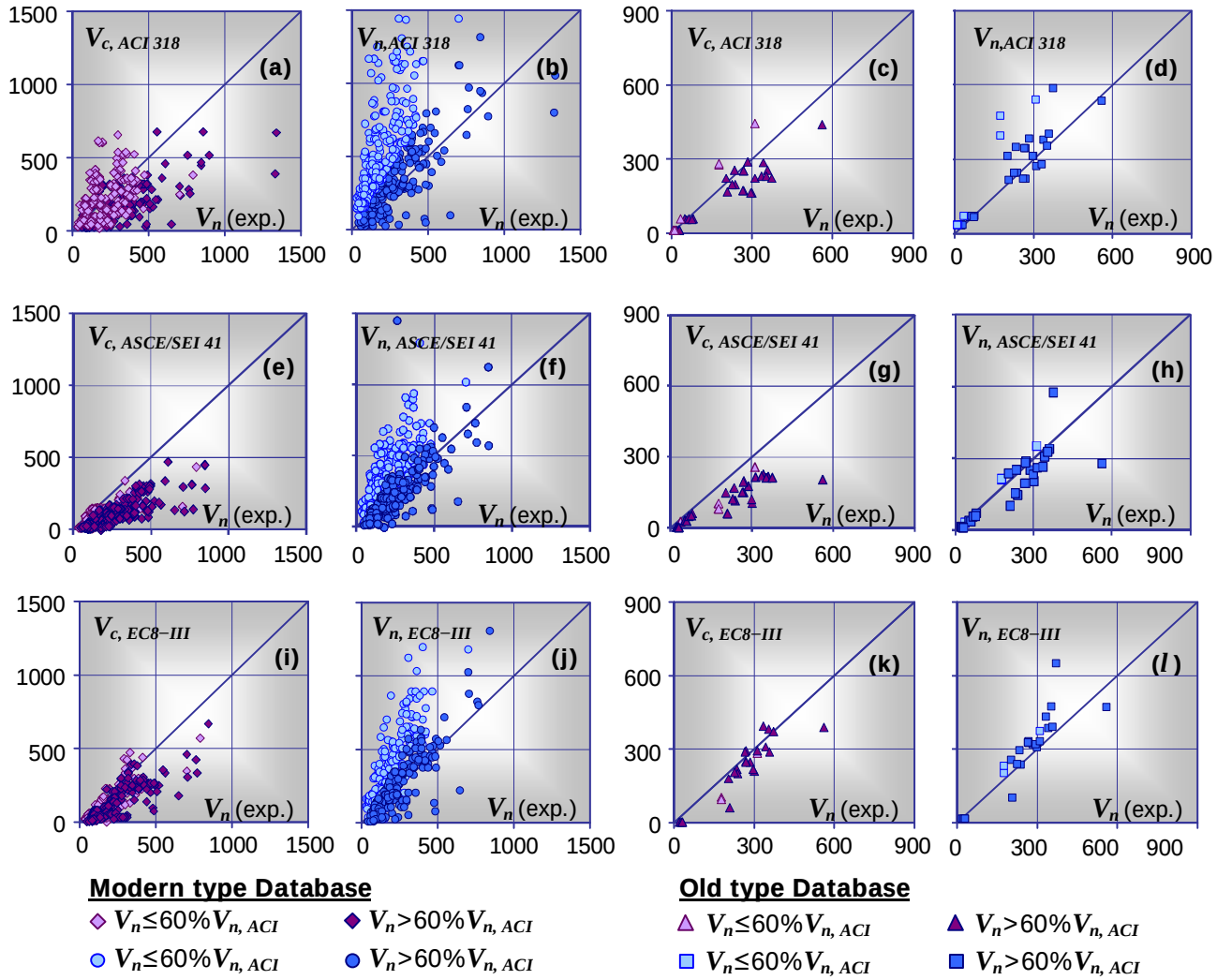


Figure 1 Implementation of the shear strength models upon the two experimental databases

As a reference point an element from Lynn et al. (1996) was used under the code name 3CLH18, with old type characteristics. The column had an aspect ratio of L_s/d=3.9 and a 457 mm square cross section and it was tested in double-curvature, by imposed lateral load reversals and a constant axial load equal to $P/(f_c'A_g)$=0.09, until loss of vertical load carrying capacity. The longitudinal reinforcement consisted of 8Ø32 bars evenly distributed around the perimeter of the cross–section, with yield strength f_{sy}=331 MPa and a clear cover of 50mm. The transverse reinforcement consisted of 9.5mm perimeter stirrups anchored with 90^0 bends and placed at a spacing of 457mm (≈d), having a yield strength f_{yh}=400MPa. The concrete strength was f_c'=25 MPa and the specimen failed in shear at a ductility level of m_D=1.6. The results of the parametric study are presented in Figures 2 and 3.

The estimated total shear strength V_n is plotted against the imposed ductility level m_D in the graph of Fig. 2a. Both the models adopted by ASCE/SEI 41–2007 and EC8–III (2005) show a mild descending curve when a case of moderate ductility demand is in question that is for m_D values greater than 3.0 or 4.0, whereas the ACI 318 model (2011) is insensitive to the

ductility demand as would be expected by a Design Code. The influence of the axial load is presented in graph 2b and seems to enhance the shear strength both for ACI 318 and ASCE/SEI 41 regardless of the imposed magnitude whereas the EC8−III correctly suggests a cutoff point for exceeding axial load values. The effect of the aspect ratio is shown in graph 2c and sets a strong influence both for the EC8−III and the ASCE/SEI 41 model though ACI 318 code is insensitive to any variation in this parameter. The influence that the size of the cross section may have upon the shear strength is explored in graph 2d. All the models have proportional results and are enhanced with the increase of the cross section area A_g. The shear strength is plotted in graph 2e against the volumetric ratio of the transverse reinforcement and all the shear models are enhanced with the increasing values of this ratio. Note that the reference point is also depicted in each graph with better correlation to EC8–III.

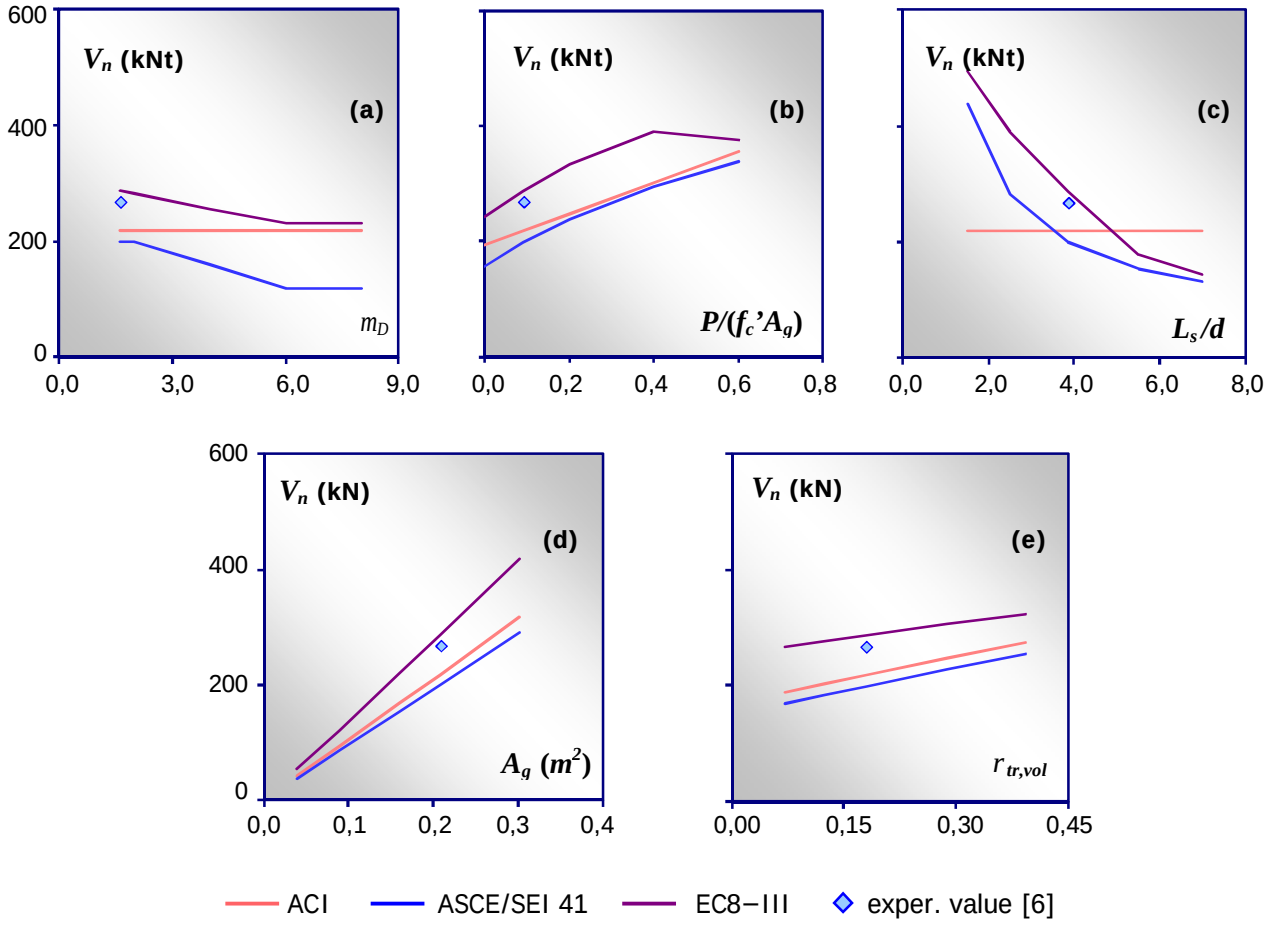


Figure 2 Parametric study of the shear strength models against the imposed ductility, the axial load, the aspect ratio, the cross section area and the transverse reinforcement

The next parameter tested is the ratio of the stirrup spacing normalized by the diameter of the longitudinal reinforcement, s/D_{bl}, a ratio that identifies the risk of reinforcement for compression buckling, as shown in graph 3a. The influence of this parameter is almost impalpable to all the shear strength values. The yield strength of the transverse reinforcement is under consideration in graph 3b showing the same ascending trend for all the shear strength models. Almost insensitive are the estimates provided by all the shear models when the yield strength of the longitudinal reinforcement is considered in graph 3c. The ratio of the total longitudinal reinforcement affects strongly the EC8−III shear model but almost does not affect any of the other models as plotted in graph 3d. Finally increasing the concrete strength

affects a proportional increase in the shear strength estimates obtained by all the models as shown in graph 3e.

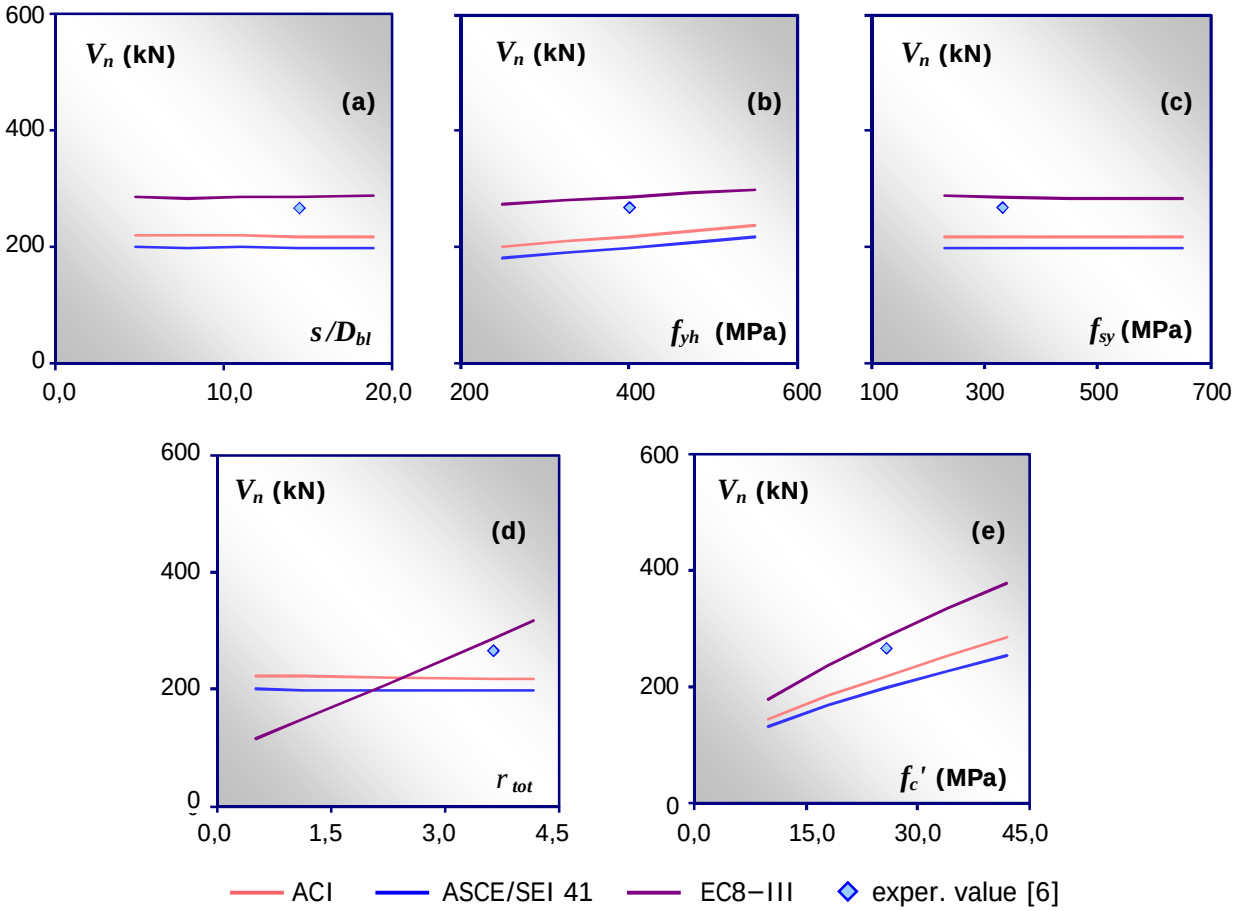


Figure 3 Parametric study of the shear strength models against the normalized stirrup spacing, the yield strength of the transverse and the longitudinal reinforcement, the ratio of the longitudinal reinforcement and the concrete strength.

5. CONCLUSIONS

The most important shear strength models adopted by current seismic Codes, namely the Design Code ACI 318−2011 and the Assessment Codes ASCE/SEI 41–07 and Eurocode 8 – III (2005), were presented and tested against two extensive experimental databases assembled with elements from the international literature. When the elements detailed according to modern provisions were considered, there was significant scatter and the correlation would deteriorate for the flexure-controlled tests. The results are similar for the old type elements (with insufficient longitudinal and transverse reinforcement, poor detailing, etc.) although the estimates according with EC8−III showed better correlation. Note that a criterion concerning the ratio of the applied shear stress to the available shear capacity was used in order to classify the available specimens in the two databases according to the anticipated type of failure, namely, shear-controlled and flexure-controlled failure.

A parametric study was also conducted with regards to various important design parameters such as the displacement ductility, the axial load, the transverse reinforcement, etc. and conclusions were drawn concerning the deficiencies of each model over those parameters; for this purpose the dimensions, the material properties and the details of an old-type specimen were used as a point of reference in the study. The scope of this study was to

check whether the shear strength models reproduce consistently the influence of the design parameters on the mechanical behaviour of the reference element.

Although the EC8−III model produced adequate results when the old type database was considered, the small number of tests discourages generalization of conclusions. Furthermore the equations the model were calibrated to match a great number of tests from the international literature therefore posing a remarkable bias on the observed good correlation. Thus the primary finding regarding the models describing the shear strength is that intense scatter persists today, underscoring the great uncertainty in the relevant expressions of assessment procedures.

REFERENCES

[1] ACI 318−08, "Building Code Requirements for Structural Concrete", *American Concrete Institut*e, chapter 11 "Shear and Torsion", (2008)

[2] ASCE/SEI 41 (2007), "Seismic Rehabilitation of Existing Buildings", *American Society of Civil Engineers*, Reston, VA

[3] Eurocode 8 (2005), "Design of structures for earthquake resistance − Part 3: Assessment and retrofitting of buildings", *European Committee for Standardisation*, Brussels, Annex A

[4] FEMA 273 (1997), "NEHRP Guidelines for the seismic rehabilitation of buildings", *Federal Emergency Management Agency,* Washington, D.C., chapter 6.4.4: "Shear and Torsion"

[5] FEMA 356 (2000), "Prestandard and commentary for the seismic rehabilitation of buildings", *Federal Emergency Management Agency,* Washington, D.C., chapter 6.4.4: "Shear and Torsion"

[6] Lynn A., Moehle J. Mahin S. and Holmes W. (1996), "Seismic Evaluation of Existing Reinforced Concrete Building Columns", *Earthquake Spectra*, Vol. 12, no. 4, November 1996, pp. 715−739

[7] Pantazopoulou S. J. and Syntzirma D. V. (2010), "Deformation capacity of lightly reinforced concrete members – Comparative evaluation", *Advances in Performance – Based Earthquake Engineering* (ACES workshop, Editor: M.N.Fardis), Series Geotechnical, Geological, and Earthquake Engineering, Vol. 13, Springer Publishers

[8] Syntzirma D. V., Pantazopoulou S. J. and Aschheim M. (2010), "Load history effects on deformation capacity of flexural members limited by bar buckling", *ASCE, Journal of Structural Engineering,* Vol. 136(1), pp. 1−11, January 2010

[9] Syntzirma D. V., Pantazopoulou S. J. (2006), "Deformation Capacity of R.C. Members with Brittle Details under Cyclic Loads", *ACI Special Publication,* Vol. 236, pp. 1−22, edited by ACI Committee 445 (Shear and Torsion)

[10] Syntzirma D., Pantazopoulou S. J. (2002), "Performance – Based Seismic Evaluation of R.C. Building Members", *12th European Conference on Earthquake Engineering*, London, September, Paper Ref.: 816

[11] Wood S. L, and Sittipunt C. (1996), "Cyclic Response of Reinforced Concrete Structural Walls", *Proceedings, Mete Sozen Symposium*, ACI SP−162: 399−430

COMPDYN 2013
4th ECCOMAS Thematic Conference on
Computational Methods in Structural Dynamics and Earthquake Engineering
M. Papadrakakis, V. Papadopoulos, V. Plevris (eds.)
Kos Island, Greece, 12–14 June 2013

LOCAL AND NON LOCAL APPROACHES FOR SIMULATING CFRP-REINFORCED CONCRETE SHEAR WALLS UNDER MONOTONIC LOADS

K. LE NGUYEN[1]*, M. BRUN[1], A. LIMAM[1], E. FERRIER[2], L.MICHEL[2]

[1]INSA-Lyon, Laboratoire de Génie Civil en Ingénierie Environnementale, Bât. Coulomb, 34 avenue des Arts, 69621, Villeurbanne, France; khuong.le-nguyen@insa-lyon.fr

[2] Université de Lyon 1, Laboratoire de Génie Civil en Ingénierie Environnementale, 82 bd Niels Bohr-69622 Villeurbanne, France

Keywords: Shear wall, Reinforcement with composite, Nonlinear pushover analysis.

Abstract. *In recent years, large efforts from the engineering and scientific communities have been underway for optimizing the behavior of reinforced concrete shear walls of buildings subjected to earthquake loading. The efficiency of shear walls to sustain the earthquake loads mainly depends on the aspect ratio H / L, where H and L are the height and the length of the wall, related to the moment-to-shear ratio M / VL, the vertical load P, and the percentages of vertical and horizontal reinforcements ρ_v and ρ_h. In this paper, two reinforced concrete walls have been experimentally and numerically investigated: the first one, corresponding to the squat wall, with an aspect ratio equal to 0.67, whose behavior is essentially controlled by shear, and the other one with an aspect ratio equal to 2.5, corresponding to the slender wall, whose behavior is governed by both shear and bending. The shear walls are designed for failing with inclined web cracking caused by diagonal tension. Different reinforcement strategies have been considered using CFRP materials. Finite element analyses have been carried out, adopting a plane stress approach with a local concrete model based on the smeared fixed crack approach. The reinforcement and the CFRP materials are provided by bar elements whose nodes are the same as the concrete elements (perfect bond assumption). The experimental and numerical results are compared in terms of the pushover curves (shear strength and ductility) and the cracking patterns.*

1 INTRODUCTION

Reinforced concrete shear walls represent one of the most widespread bracing systems for buildings. Post-earthquake observations surprisingly report good seismic behavior of structural wall buildings [1] while evaluation of existing buildings according to modern standards often concludes that they provide insufficient safety margins [2]. Although reinforced concrete walls are efficient to dissipate the seismic induced energy, they exhibit important damage. The main causes of damage are: occurrence of unpredictable high seismic activity, improper design and construction flaws. The RC wall response behavior depends to a great extent on its height to length ratio. The RC wall characterized by H/L ratio greater than 2 can be considered as slender or long wall, whereas the wall characterized by H/L ratio less than 2 is considered as short wall. Based on experimental works, some analytical models were developed to predict the inelastic strength of walls subjected to reverse cyclic loading and to calculate the natural frequencies of the walls (Mostofinejad D. *and al.* [3], Su and Jon [4], Greifenhagen [5]).

During an earthquake, the shear walls play a major role in resisting lateral loads for tall concrete buildings. They must be carefully designed to provide not only adequate strength, but also sufficient ductility to avoid brittle failure under strong lateral loads. In this context, there are many methods seeking to improve the bearing capacity and the coefficient of ductility with different materials. Current recommendations for the seismic retrofit of RC walls, provided in ASCE 41-06 [6], involve combinations of strengthening and/or ductility enhancement of the critical details by different methods such as the reduction of flexural strength, addition of confinement jackets at wall boundaries or the increase of the shear strength of the wall [7]. In the last decade, composite materials (carbon or glass fibers associated with polymeric matrices CFRP) applied to RC elements by bonding are proved to be effective for the protection and reinforcement of beams and columns. Recent research on reinforced concrete walls strengthened with FRP composites were conducted by Ferrier [8], Antoniades *et al.* [9,10], Demeter *et al.* [11], Dan [12] , El-Sokkary [13], showed the ability to restore the initial performance of the structural members by repairing and strengthening.

Beside experimental testing programs, a better understanding of the structural behavior of the RC wall buildings requires many parametric studies using relevant numerical models. The finite element approach can be employed to model the RC shear walls reinforced by FRP composites and stirrups [3]. In this paper, the finite element code Cast3M is used to model and interpret the behavior of two types of concrete walls reinforced by fiber carbon material. The nonlinear pushover analyses of the shear walls (without FRP and FRP-reinforced) also include the crack patterns and the failure modes.

2 EXPERIMENTAL DATABASE

2.1 Materials

In order to assess the concrete properties, 16x32 cylindrical specimens were cast and tested at 28 days. For the mix of slender walls, the average compressive strength is determined as 34.65 MPa ± 1 MPa. For the mix of short walls, the average compressive strength is 35.93 MPa ± 0MPa. The steels are consistent with the current standard with guaranteed yield strength equal to 500 MPa, the type of steel being S500B. The Freyssinet reinforcement was used. This reinforcement is called CFRP ® with 70% and 30% in each direction. Wicks are used as anchors into the footing of the walls.

Properties	Value
Average thickness	0.48 mm
Ultimate strength	1700 MPa
Module young	105000 MPa
Strength/1cm 1er direction	8.15 kN
Strength/1cm 2er direction	3.5 kN

Table 1: CFRP Material Properties

2.2 Specimen design

The test set-up is shown in the Figure 1. The specimen consists of three parts: the head beam through which the loads are transferred to the panel, the panel corresponding to the shear wall, and the footing at which the specimen is anchored. Uplift of the footing with respect to the laboratory floor is prevented by post-tensioned anchor rods. The test program included two series. The first one included two specimens of the slender type with labels VE1 (without CFRP) and VER1 (reinforced by CFRP). The second included two specimens of short type with labels VC1 (without CFRP) and VCR1 (reinforced by CFRP).

Specimen	l_w (m)	h_w (m)	T (m)	N (kN)
VE1	0.6	1.5	0.08	90
VER1	0.6	1.5	0.08	90
VC1	0.9	0.61	0.08	110
VCR1	0.9	0.61	0.08	110

Table 2: Geometric characteristics of specimens

The monotonic loading was applied by pushing the head beam with a hydraulic cylinder capacity of 500kN. In this case the lateral displacement was imposed at a speed of 0.01 mm/sec. Two post-tensioning bars were used to subject the specimens to axial loading. The bars were located at mid-length of the specimens on both sides of the panel. Before the static test, the bars were alternately post-tensioned in small increments up to the target force with the help of

a hydraulic jack. The vertical post-tensioning force could be maintained at a constant level during the test: 90kN for the slender wall and 110kN for the short wall.

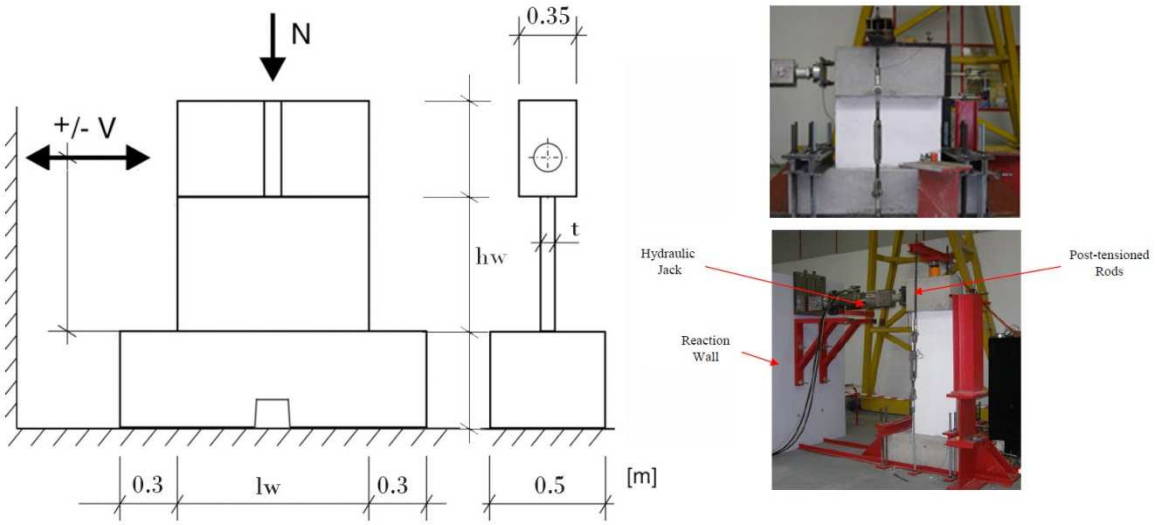


Figure 1: Set-up of the test

The reinforcement is composed of two sheets of wire mesh (Φ 4.5 mm spaced at 200 mm in both directions) and, at each end, of two bars of 6 mm diameter. Rebars of 12mm diameter were used for the reinforcement of the head beam and the footing (Figure 2 and Figure 3). In the case of reinforcement by CFRP, the CFRP 50mm wide bands were used. Three bands over the total height of the wall were applied on each side. The distance between vertical bands is equal to 225mm for the slender wall (VER1) and 230mm for the short wall (VCR1). Seven horizontal bands and four horizontal bands were put in place on each side of VER1 and VCR1, respectively (Figure 4).

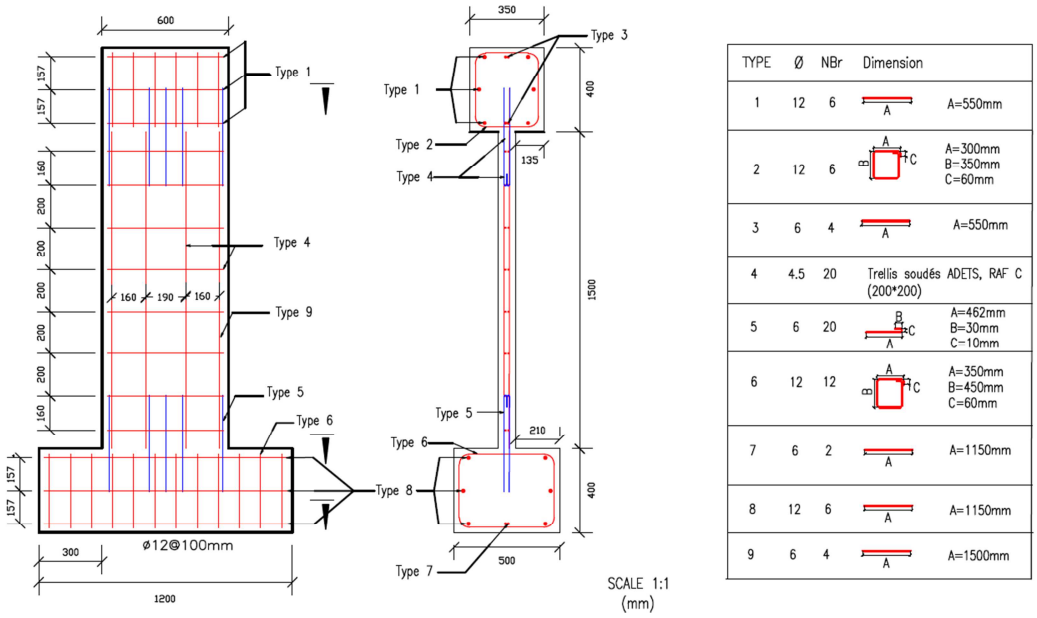
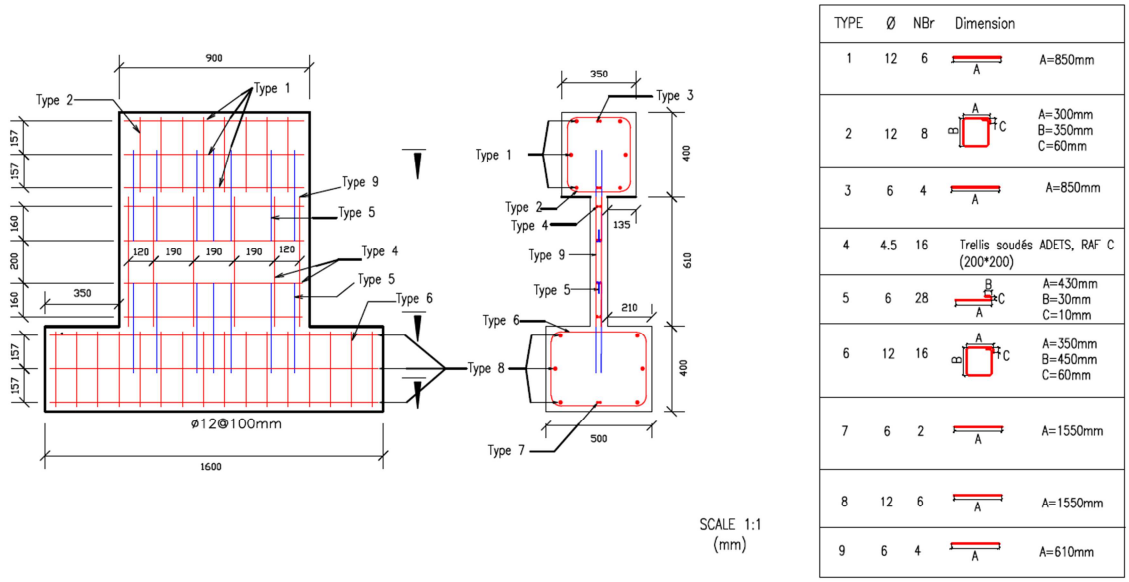


Figure 2: Reinforcement of the slender walls (VE1 and VER1)



TYPE	Ø	NBr	Dimension	
1	12	6	A	A=850mm
2	12	8	A, B, C	A=300mm B=350mm C=60mm
3	6	4	A	A=850mm
4	4.5	16	Trellis soudés (200*200)	ADETS, RAF C
5	6	28	A, B, C	A=430mm B=30mm C=10mm
6	12	16	A, B, C	A=350mm B=450mm C=60mm
7	6	2	A	A=1550mm
8	12	6	A	A=1550mm
9	6	4	A	A=610mm

Figure 3: Reinforcement of the short walls (VC1 and VCR1)

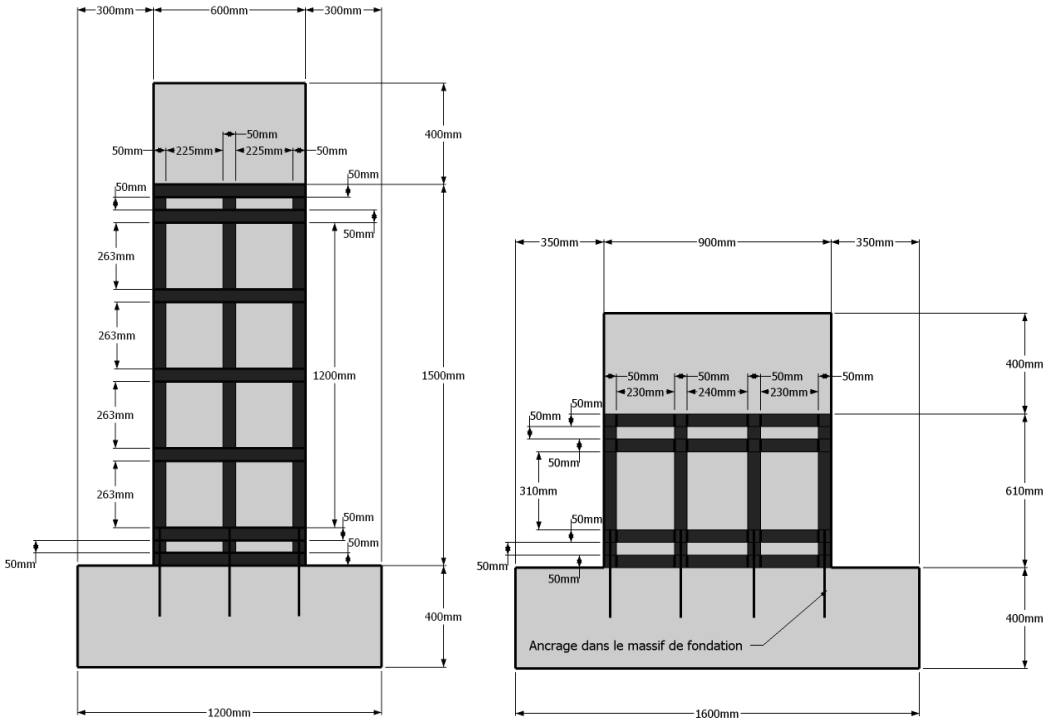


Figure 4: CFRP reinforcement design for VE and VC walls

3 CONSTITUTIVE MODELS FOR FINITE ELEMENT APPROACH

From a general point of view, the concrete is by far one of the most common quasi-brittle materials. It has an asymmetric behavior between tension and compression: weak in tension and ductile in compression, the concrete is a material whose main cause of damage is the cracking.

In the case of compressive cyclic loads, hysteretic phenomena appear as a signature of a sliding friction occurring between the lips of the cracks. All these mechanisms make the behavior of concrete complex to model. In order to evaluate safety margins of reinforced concrete buildings subjected to earthquakes, realistic nonlinear models are needed. With the rapid development of computer technology, considerable research has focused on developing more realistic concrete models for predicting the stress-strain behavior under various load time histories. Several concrete behavior models are implemented into the code Cast3M [14] of CEA. Two types of concrete model are explored: a classical smeared fixed crack approach developed in the LGCIE laboratory of INSA Lyon for cyclic loading and a coupled elasto-plastic damage model proposed by Richard *et al.* [15].

3.1 Smeared fixed crack model (INSA) for concrete

The concrete model INSA, developed at INSA Lyon, implemented into the code Cast3M [14] of CEA, is built in the framework of the theory of plasticity in plane stress. The model is defined by two distinctive behaviors depending whether the concrete is cracked or uncracked.

In its uncracked state, the model is based on the plasticity theory with an isotropic hardening and an associate flow rule. The cracked area is covered by the concept of distributed cracking considering the cracked material as a continuous medium. The crack detection surface in tension follows a Nadai criterion. In compression, load surfaces are of the same Nadai type. The evolution of the load surface to the ultimate load surface in compression follows a positive isotropic hardening. A softening regime occurs with a negative isotropic hardening when reaching the ultimate load surface in compression. The cracking surface in traction as well as the initial and ultimate load surfaces is depicted in the principal stress space in Figure 5.

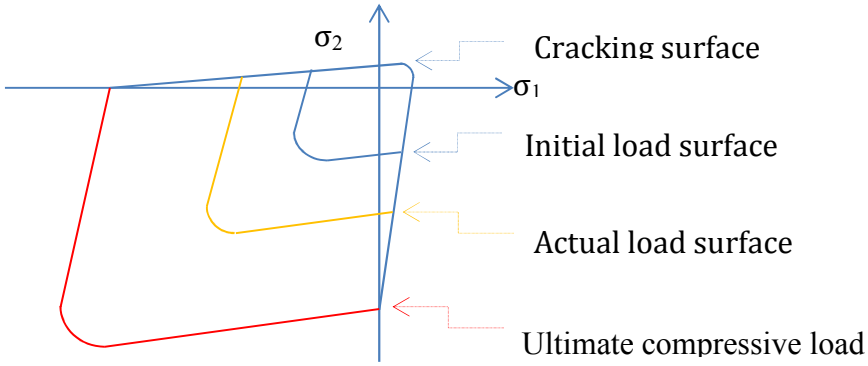


Figure 5: Load surfaces in compression and cracking surface for concrete material

The concrete model enters in its cracked state when the crack detection surface is reached in tension: a fictitious crack is considered perpendicularly to the principal stress direction and its orientation is kept as constant subsequently. A second crack can appear later but only at 90° with respect to the first one. The stress tensor in plane stress assumption is completed by the shear stress, elastically computed using a reduced shear modulus μG; μ parameter corresponds to the classical shear retention factor ($0 \leqslant \mu \leqslant 1$), depending on the crack opening strain for reproducing the loss of shear transfer capability at the crack level. The model's details are presented in [16].

3.2 Damage elasto-plastic (RICRAG) model for concrete

The model RICRAG proposed by Richard *et al.* [15] and available in the code Cast3M is a model for modeling quasi-brittle materials such as concrete in three dimensional. It is a con-

crete model based on isotropic damage mechanics in good agreement with experimental data up to failure; this agreement holds for monotonic loadings as well as for cyclic loadings. Residual strains and hysteretic loops due to friction between the cracks surfaces and elastic stiffness recovery have to be accurately taken into account. The main constitutive equations were formulated within the framework of the thermodynamics for irreversible processes in order to fulfill conservation and evolution principles. Firstly, a consistent state potential is introduced accounting for elasticity, damage, sliding between cracked surfaces and hardenings. Secondly, assuming the positive condition of the intrinsic dissipation rate, state equations can be deduced. Thirdly, complementary equations are introduced to handle the evolution of all the internal variables.

3.3 1D cyclic elasto-plastic model for steels and CFRP bands

The Menegotto-Pinto law [17] represents the behavior of the steels under cyclic loading. The monotonic curve of this law (Figure 6) is characterized by three phases: linear elastic defined by the Young's modulus E_a until the plastic strain σ_{sy},followed by a plateau stress of plastic deformation ε_{sy} at the beginning of the deformation hardening ε_{sh} , and finally a hardening curve until failure. Phases of the monotonic curve are given by:

$$\begin{aligned} &\sigma = E_a.\varepsilon && 0 < \varepsilon < \varepsilon_y \\ &\sigma = \sigma_{sy} && \varepsilon_y < \varepsilon < \varepsilon_{sh} \\ &\sigma = \sigma_{su} - \left(\sigma_{su} - \sigma_{sy}\right).\left(\frac{\varepsilon_{su} - \varepsilon}{\varepsilon_{su} - \varepsilon_{sh}}\right)^4 && \varepsilon \geq \varepsilon_{tm} \end{aligned} \quad (1)$$

where E_a is the elastic modulus of steel, σ_{su} is the ultimate stress and ε_{su} is the ultimate strain of the steel.

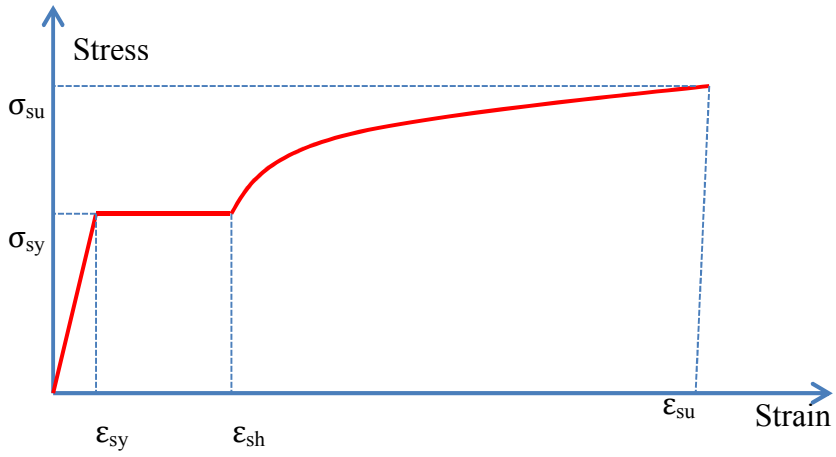


Figure 6: Menegotto-Pinto law under monotonic loading

This model is also used for modeling the CFRP materials.

4 PUSHOVER FINITE ELEMENT ANALYSIS

4.1 Meshes and material properties

The panel, the top beam and the footing were represented either by 2D elements with four nodes with bilinear shape function of displacements or by 3D cube elements with eight nodes.

Steels and CFRP were represented by uniaxial bars. The additional weights were taken into account by applying loads to the top beam as illustrated in Figure 7. The axial compressive load imposed is distributed over a length of 30cm to avoid problems of strain localization. The mesh size of the wall is chosen equal to 2.5cm to connect with steel elements close to the real reinforcement configuration. The adhesion between the steel and concrete materials is assumed to be perfect in this study.

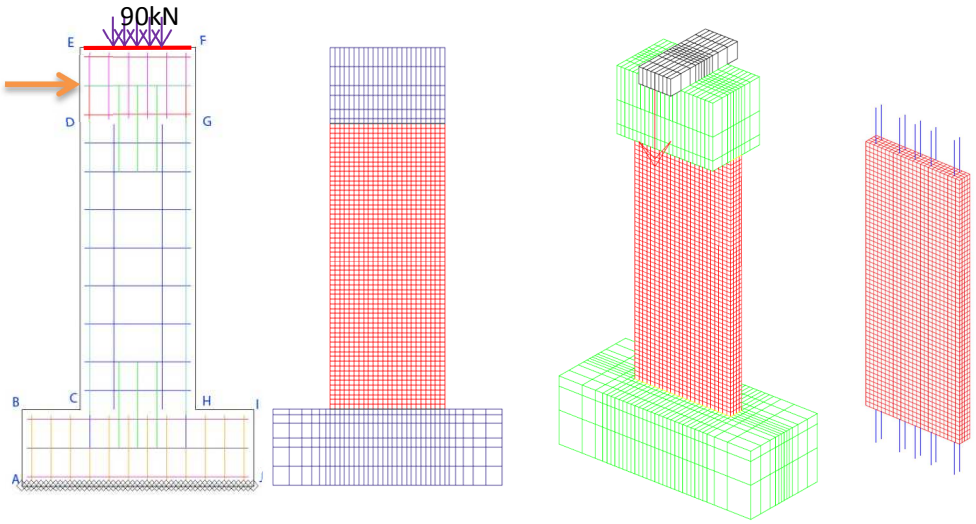


Figure 7: Mesh of the slender wall in 2D and 3D

The compressive loads of 90kN and 110kN are applied for the slender walls and the short walls, respectively. Displacement imposed load is put at the middle of the height of the top beam. The 3D model is shown in Figure 7. We added a rigid element for applying a distributed prior compressive load like in the experimental tests. (Figure 7 and Figure 8)

Table 3 resumes the numbers and the types of elements used in the pushover analyses.

	Approach	Material	Element type	Quantity	Load steps
Slender wall unreinforced by CFRP	2D	Concrete Steel	QUA4 SEG2	1800 864	800
	3D	Concrete Steel	CUB8 SEG2	7200 1728	800
Slender wall reinforced by CFRP	2D	Concrete Steel	QUA4 SEG2	1800 1100	800
	3D	Concrete Steel	CUB8 SEG2	7200 1968	800
Short wall unreinforced by CFRP	2D	Concrete Steel	QUA4 SEG2	4224 1242	700
	3D	Concrete Steel	CUB8 SEG2	18000 2484	700
Short wall reinforced by CFRP	2D	Concrete Steel	QUA4 SEG2	4224 2124	700
	3D	Concrete Steel	CUB8 SEG2	18000 4968	700

Table 3: Numerical approaches

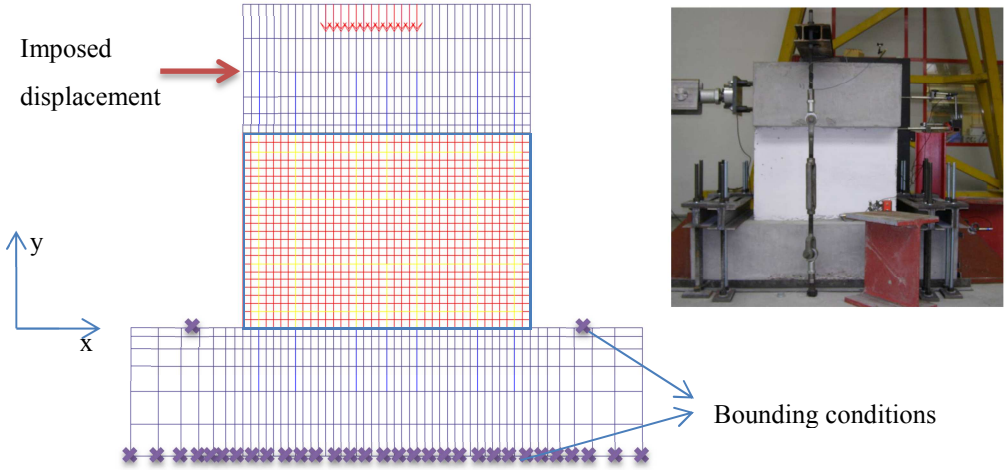


Figure 8: Mesh of the short wall

The parameters of the smeared fixed crack model and the damage elasto-plastic models are reported in Tables 4 and 5.

Symbol	Definition	Short wall	Slender wall
'E'	Young	11.E9 Pa	22.E9 Pa
'FT'	Ultimate stress in simple tension	1.5E6 Pa	1.5E6 Pa
'ALDI'	Brittleness in tension	1.E-2 J.m^3	2.E-2 J.m^3
'ALIN'	Brittleness in compression	5.E-04 J.m^3	10.E-04 J.m^3
'GAM1'	Hardening modulus 1	7.E8 Pa	7.E8 Pa
'A1'	Hardening modulus 2	7.E-07 Pa^{-1}	7.E-07 Pa^{-1}

Tableau 4: Numerical parameters of the model concrete INSA

Symbol	Definition	Short wall	Slender wall
'E'	Young modulus	11.E9 Pa	22.E9 Pa
'LCS'	Ultimate stress in simple compres-	29.E6 Pa	29.E6 Pa
'ALFB'	Stress ratio ultimate tensile	5.E-2	5.E-2
'EPUT'	Ultimate tensile strain	8.E-03	8.E-03
'EMAX'	Fracture strain in compression	1.51E2	1.51E2
'FTC'	Reduction of the shear modulus	5.E-02	5.E-02

Tableau 5: Numerical parameters of the model concrete RICRAG

In the experimental program, it has been observed that the CFRP does not achieve its ultimate strength due to debonding. A maximum strain measured in the CFRP has been assessed as equal to 4500µm/m. Consequently, we assume that the CFRP ultimate tensile strength is equal to 472.5MPa calculated by the formula:

$$\sigma_{rupt} = E_{TFC} \times \varepsilon_{\max} \tag{2}$$

where E_{CFRP} = 105000MPa and ε_{max} = 4500µm/m are identified in the experimental tests. So, we get: σ_{rupt} = 472.5MPa. This hypothesis is used for the short and slender walls.

	E (GPa)	σ_{sy}(MPa)	ε_{sy}	ε_{sh}	σ_{su}(MPa)	ε_{su}
Steel	210	500	2.38E-3	3.5E-3	550	0.05
CFRP	105	472.5	4.5E-3	6E-3	500	0.05

Tableau 6: Parameters of steel and CFRP

To solve the nonlinear equilibrium equations, a modified Newton-Raphson strategy has been adopted [16]. This method essentially uses the same algorithm as the Newton-Raphson process but replaces the tangent stiffness matrix by the initial stiffness matrix corresponding to the previous step of load step. Although the advantage of a quadratic rate of convergence of the Newton-Raphson iteration is lost if the exact tangent stiffness matric is not employed, some of the drawbacks of the classic Newton-Raphson algorithm (*i.e.* initially symmetric tangent stiffness matrix may become nonsysmmetric due to the concrete softening) are avoided. The complete monotonic load-displacement response of slender walls (VE1 and VER1) with this method is 800 load steps for 20mm of displacement. The complete monotonic load-displacement response of short walls (VC1 and VCR1) with this method is 700 load steps for 7mm of displacement. The criterion for convergence was set equal to 10^{-4} of the norm of the residue vector of the unbalanced loads.

4.2 Pushover simulations

For each wall, three pushover analyses were carried out: 2D analysis with the smeared fixed crack concrete model, 2D and 3D with the damage elasto-plastic model.

Slender wall unreinforced: Slender walls are mainly influenced by bending loads and encounter failure either by concrete crushing or yielding of the vertical reinforcement. In addition, it can be due to a combination of both previous mechanisms along with, in some cases, shear slipping of the wall relative to its foundation [18]. During the test on the shear wall VE1, three cracks appeared at a load of 15 kN and a lateral top displacement of 0.9 mm. Then, the yield of longitudinal bar reinforcement is noted at a load of 23.3 kN and a top displacement of 2.8 mm. Finally, the failure occurred due to buckling of the longitudinal bars and concrete spalling at a load and displacement of 25.2kN and 14.2mm, respectively. Figure 9 and Figure 10 show the load-displacement curves and a comparison between the observed mode failures of specimen VE1 in laboratory and the failure modes predicted by the three numerical approaches: 2D INSA concrete model, 2D and 3D RICRAG concrete model. The pushover curves displayed in Figure 9 are in a good agreement. From the failure mode point of view, we can observe that the four major cracks are predicted by the numerical simulation, matching well the experimental results. Each crack is composed of a horizontal crack from the end wall towards the interior of the wall, which is governed by bending, followed by an inclined crack propagating towards the footing, due to shear effects.

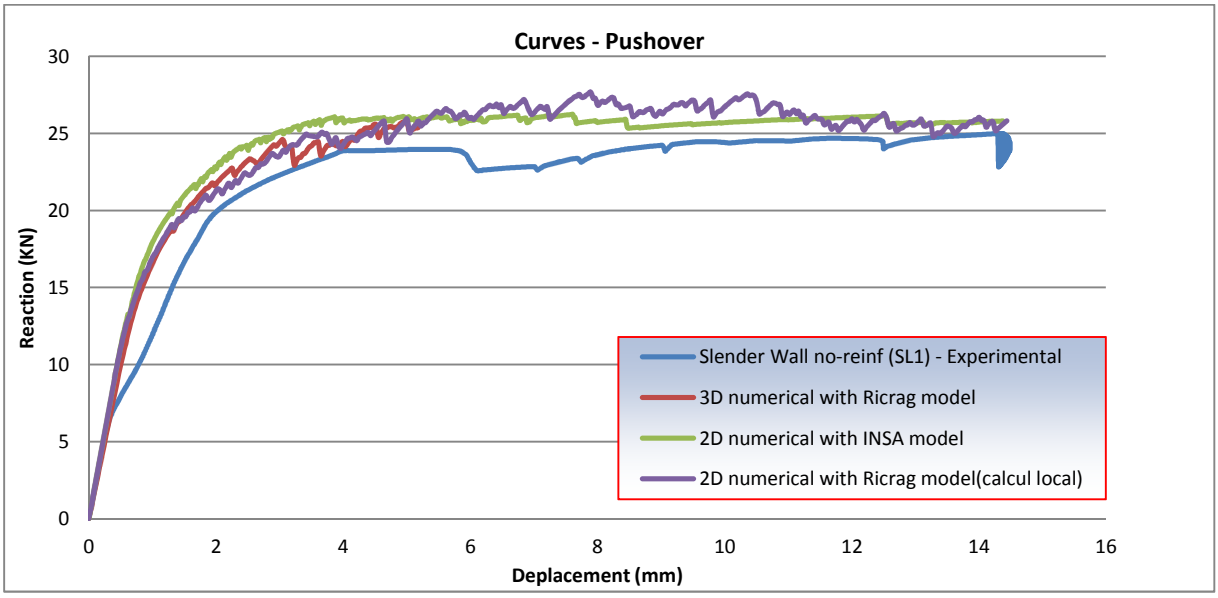


Figure 9: Pushover curves (force-displacement)-slender wall without reinforced

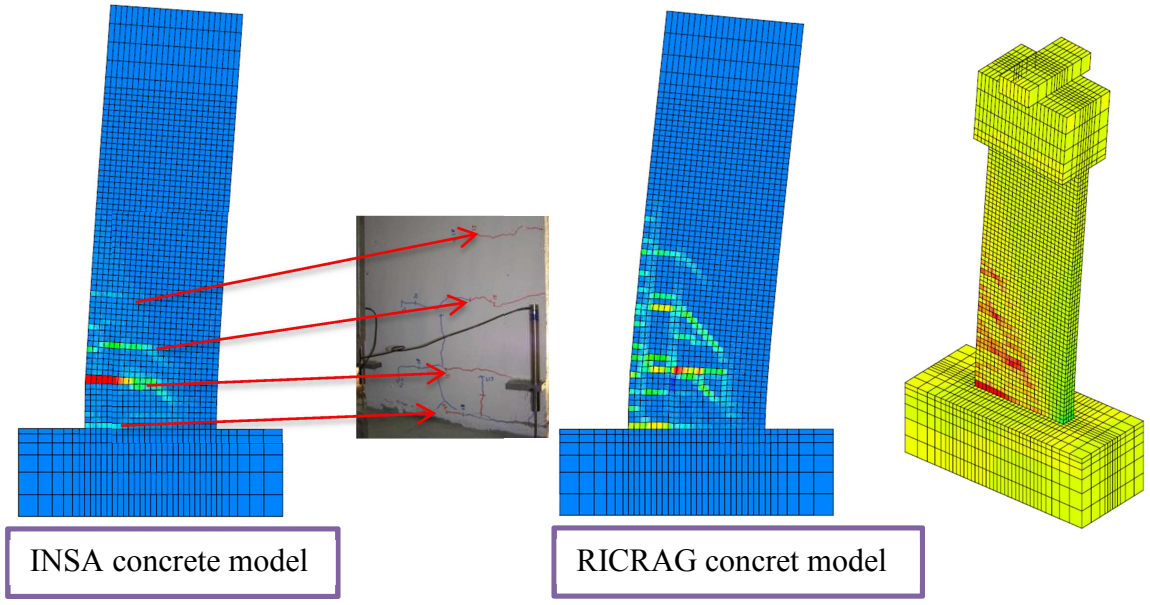


Figure 10: Failure mode – Slender wall unreinforced

Slender wall reinforced with CFRP bands: The mesh of the slender reinforced wall is similar to the one of the previous slender unreinforced wall. All steels and CFRP bands are modeled precisely (Figure 11). Each CFRP band was modeled by three truss-bars having a total section equal to 50x0.48 = 24mm^2. Each wall is reinforced at its footing over a vertical length equal to 250 mm using anchors composed of 26 CFRP threads. In addition, a tissue layer put on the vertical band is added to form a closed layer over the same length of 250 mm. Thus, the truss-bars of a total length of 500 mm were added into the numerical model. The total strength of these three truss-bars modeling a 50mm CFRP band is assessed as equal to 472.5kN.

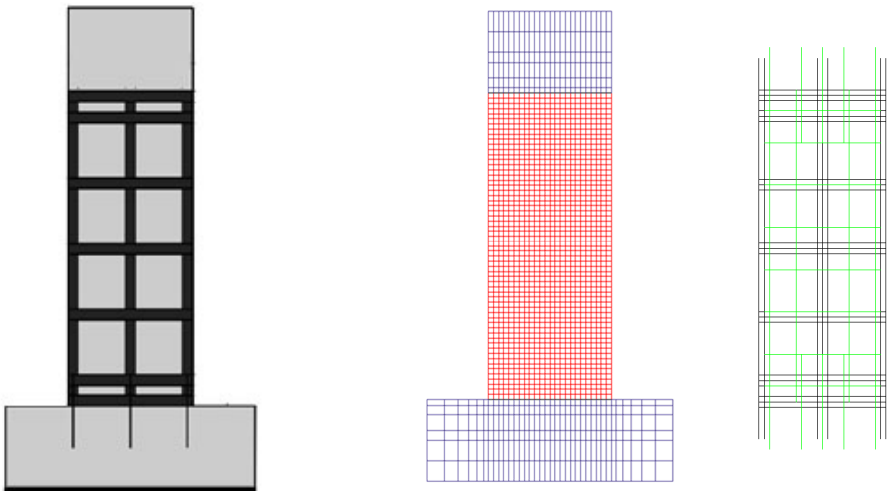


Figure 11: Mesh of the slender wall reinforced by CFRP

Pushover curves were presented in Figure 12, giving a comparison between the numerical results derived from 2D and 3D approaches and the test results. The strengthening with CFRP bands increases the load carrying capacity of the shear wall from 25 kN to 40 kN, that is approximately by 60%. The comparison of curves in Figure 9 and Figure 12 shows that the CFRP layers improves the overall structural behavior of the wall, including both loading capacity and ultimate displacement.

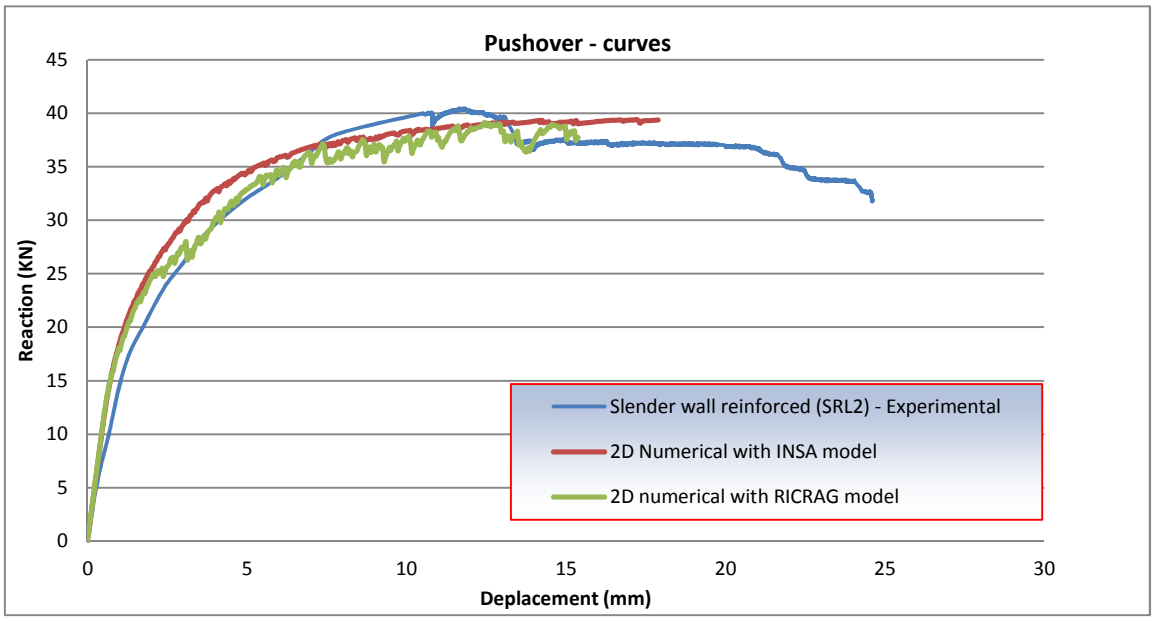


Figure 12: Pushover curves (force-displacement)-slender wall reinforced

The failure modes are displayed in Figure 13 at 20mm of displacement. The cracking patterns at the ultimate load experimentally observed and numerically predicted are compared in Figure 13. The strain localization area indicates the cracked area. It is observed that the numerical model is able to reproduce the cracking pattern along the height of the wall with a good accuracy.

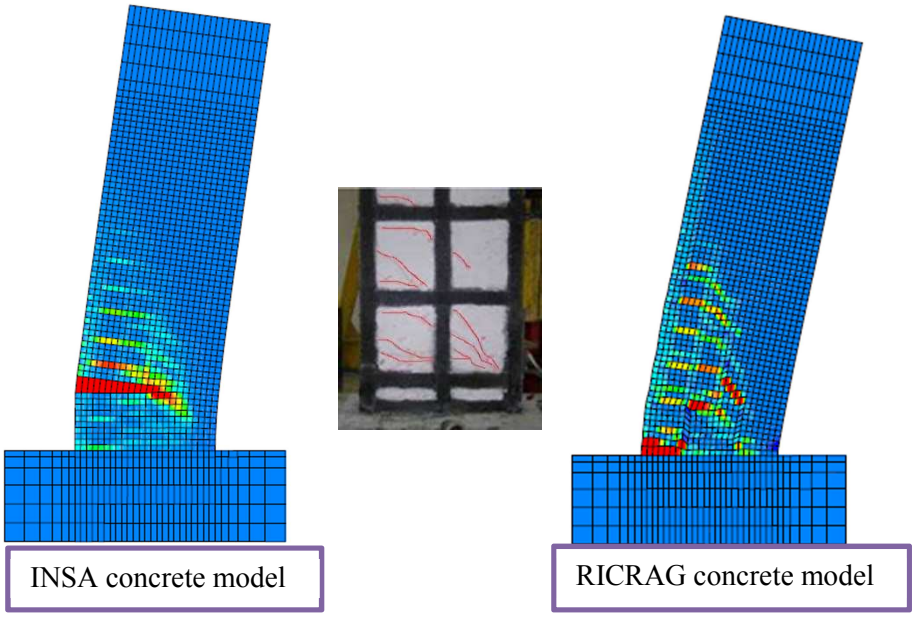


Figure 13: Failure mode – Slender wall reinforced

Short wall unreinforced: This wall constitutes a mixed case because it works in shear and bending. The shear stress cracking develops first in the horizontal direction over a length of 344 mm and then is inclined at an angle of 48° towards the opposite lower bottom corner. On the basis of observations during the experimental tests, we consider that there is a particular area of 35 cm length near the interface between the wall and the top beam. This area is modeled by the same type of concrete constitutive models (INSA or RICRAG concrete models) with a lower tensile stress so as to initiate the first cracking area as observed in the experimental tests. A linear elastic behavior is assumed for the footing.

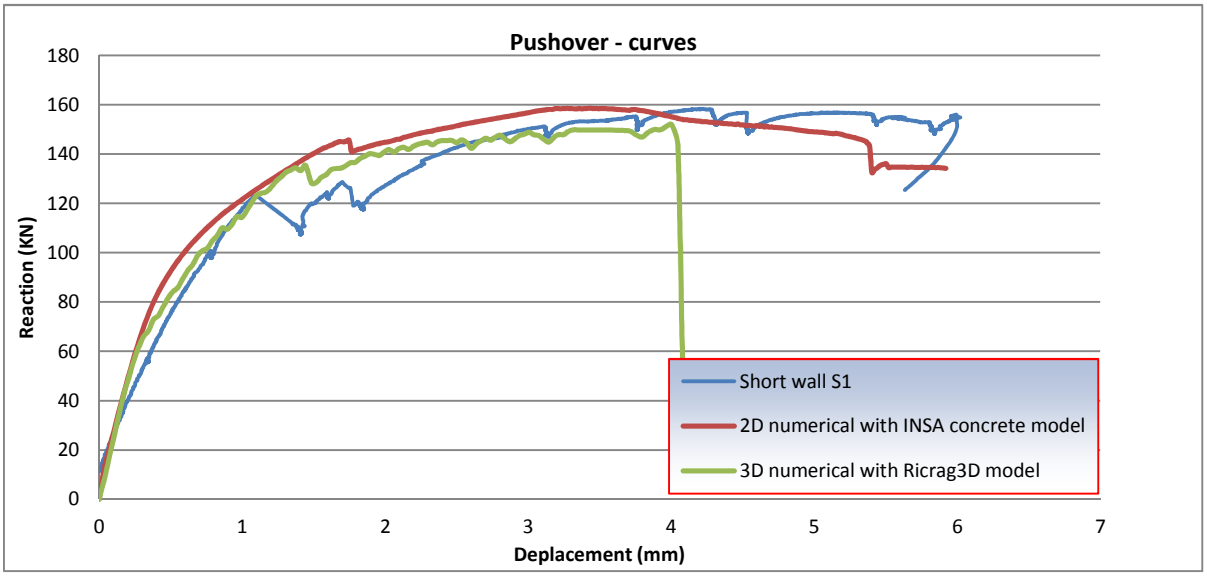


Figure 14: Pushover curves-short wall without reinforced

The results of numerical computations are compared with experimental results in Figure 14. The main failure mode displayed in Figure 15 is a diagonal crack, essentially due to the shear effects. This predicted failure mode is consistent with the experimental cracks observed during the tests and noted elsewhere by Greifenhagen [5] and [18].

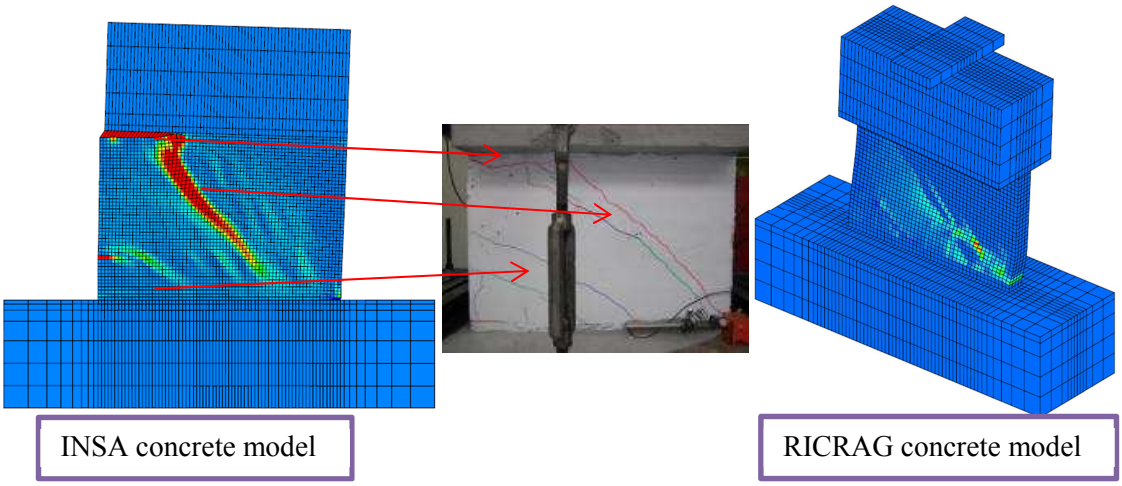


Figure 15: Failure mode of the short wall VC1

Short wall reinforced by CFRP bands: Similar to the modeling of slender wall reinforced by CFRP bands, the truss-bars of 500mm of length were introduced into the numerical model at the bottom of the short wall, with a strength taken as 472.5 kN.

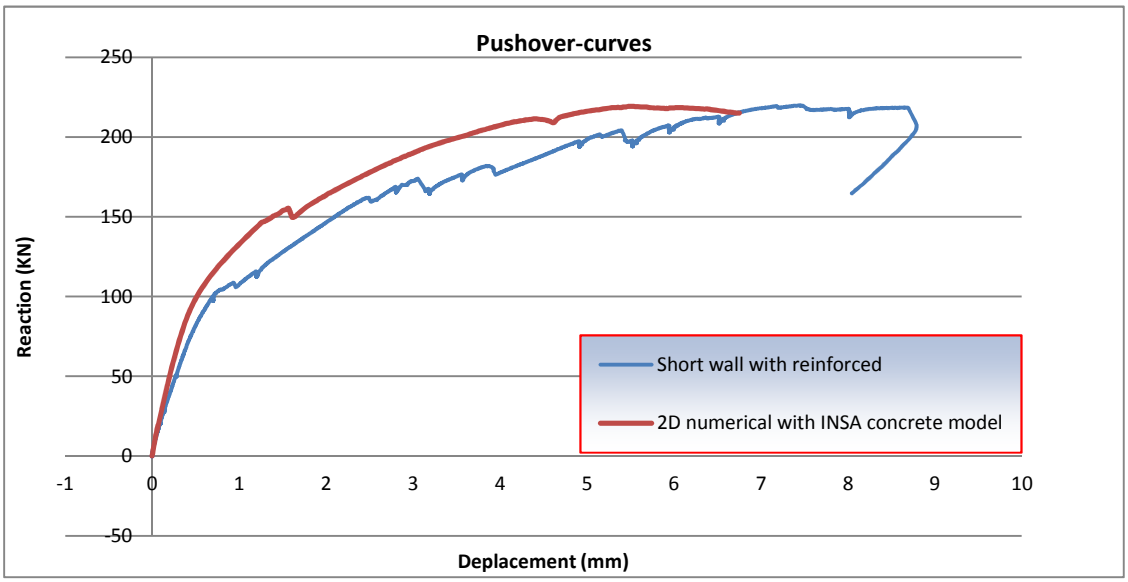


Figure 16: Pushover curves – short wall reinforced

The results in terms of pushover curves show that the model is able to reproduce the nonlinear behavior of the concrete shear wall composed of three phases: the elastic behavior, followed by the crack development and the steel reinforcement hardening. Small differences between the two curves noted in the post-yield region may be due to the imperfect bonding behavior between the concrete and steels, not taken into account in the numerical simulation. The shear strength of the short wall can be limited by both diagonal tension and concrete crushing. The overall deformation of the wall is limited by sliding, concrete crushing, and rupture of reinforcement.

.

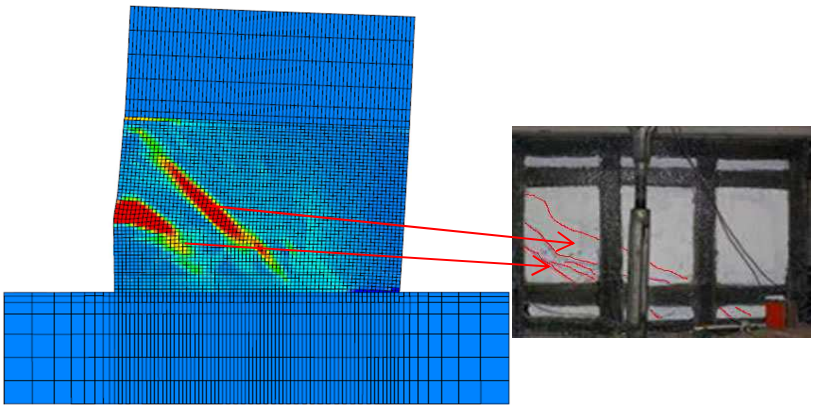


Figure 17: Failure mode of the short wall reinforced

The comparison of experimental and numerical failure modes presented in the Figure 17 exhibits clear similarities with inclined cracks appearing at the border of the wall and propagating towards the footing of the wall.

5 CONCLUSION

The numerical results reproduce the experimental behavior with sufficient accuracy. The numerical model requires a refined and realistic description of the geometry of the wall. Two different concrete models are employed based on either classical smeared fixed crack approach or damage elasto-plastic model. The numerical models are able to predict accurately the shear strength as well as the ultimate displacement and failure modes. It is shown that CFRP bands have to be introduced into the numerical model by considering only a third of his real strength due to the debonding of the bands observed during the experimental tests.

Since the proposed model is only based on limited experimental data, there is an obvious need for further experimental investigations. The present modeling focuses on the static-monotonic behavior of lightly reinforced concrete shear walls. Experimental investigations were made on small-scale test units. Improved modeling should include the static-cyclic behavior and the dynamic behavior. Another important aspect for further research is to study the behavior of the RC walls as a structural elements into a real building. In the present research, the walls were modeled as cantilevers. This assumption merits further investigations in existing building configurations.

REFERENCES

[1] Fintel M., Fintel M. « Performance of buildings with shear walls in earthquakes of the last thirty years ». *PCI journal*. Vol. 40, n°3, p. 62-80.

[2] Iervolino I., Maddaloni G., Cosenza E. « Eurocode 8 Compliant Real Record Sets for Seismic Analysis of Structures ». *Journal of Earthquake Engineering*. 2008. Vol. 12, n°1, p. 54-90.

[3] Mostofinejad D., Mohammadi Anaei M. « Effect of confining of boundary elements of slender RC shear wall by FRP composites and stirrups ». *Engineering Structures*, 2012. Vol. 41, p. 1-13.

[4] Su R. K. L., Wong S. M. « Seismic behaviour of slender reinforced concrete shear walls under high axial load ratio ». *Engineering Structures,* 2007. Vol. 29, n°8, p. 1957-1965.

[5] Greifenhagen C. *seismic behavior of lightly reinforced concrete squat shear walls*. [s.l.] : [s.n.], 2006.

[6] ASCE. *Seismic rehabilitation of existing buildings*. 2007.

[7] Jiang H., Kurama Y. C. « An analytical investigation on the seismic retrofit of older medium-rise reinforced concrete shear walls under lateral loads ». *Engineering Structures*, 2013. Vol. 46, p. 459-470.

[8] Ferrier E. *Mechanical behaviour of concrete wall under static loading*, 2011.

[9] Antoniades K. K., Salonikios T. N., Kappos A. J. « Evaluation of hysteretic response and strength of repaired R/C walls strengthened with FRPs ». *Engineering Structures*. 2007. Vol. 29, n°9, p. 2158-2171.

[10] Antoniades K. K., Salonikios T. N., Kappos A. J. « Tests on Seismically Damaged Reinforced Concrete Walls Repaired and Strengthened Using Fiber-Reinforced Polymers ». *Journal of Composites for Construction*, 2005. Vol. 9, n°3, p. 236-246.

[11] Demeter I. et al. « FRP composites for seismic retrofitting of RC wall panels with cut-out openings ». *Structures & Architecture,* 2010. p. 541-542.

[12] Dan D. « Experimental tests on seismically damaged composite steel concrete walls retrofitted with CFRP composites ». *Engineering Structures*, 2012. Vol. 45, p. 338-348.

[13] El-Sokkary H., El-Sokkary H. « Seismic Retrofit of Reinforced Concrete Shear Walls using Fibre Reinforced Polymer Composites », 2012.

[14] Le Fichoux E. *Présentation Et Utilisation De Cast3m*. CEA, 2011. 92 p.

[15] Richard B., Ragueneu F. « Isotropic continuum damage mechanics for concrete under cyclic loading, : stiffness recovery, inelastic strains and frictional sliding. » *Engineering Fracture Mechanics,* 2010.

[16] Ile N., Reynouard J. . « Nonlinear analysis of reinforced concrete shear wall under Earthquake loading ». *Journal of Earthquake Engineering*. 2000. p. 30.

[17] Menegotto M., Pinto P. *Method of analysis for cyclically loaded reinforced concrete plane frames including changes in geometry and non-elastic behaviour of elements under combined normal force and bending.* 1973.

[18] Greifenhagen C., Lestuzzi P. « Static cyclic tests on lightly reinforced concrete shear walls ». *Engineering Structures*, 2005. Vol. 27, n°11, p. 1703-1712.

COMPDYN 2013
4th ECCOMAS Thematic Conference on
Computational Methods in Structural Dynamics and Earthquake Engineering
M. Papadrakakis, V. Papadopoulos, V. Plevris (eds.)
Kos Island, Greece, 12–14 June 2013

AN INNOVATIVE PROPOSAL FOR THE IMPROVEMENT OF DURABILITY OF SLABS ON SOIL

Alexandros D. Bantias[1], Ioannis A. Tegos[2], Theodoros A. Chrysanidis[2], Asimina K. Athanatopoulou[2]

[1]Division of Structural Engineering, Department of Civil Engineering, School of Engineering, Aristotle University of Thessaloniki
54124, Thessaloniki, Greece
alexandrosbantias@hotmail.com

[2]Division of Structural Engineering, Department of Civil Engineering, School of Engineering, Aristotle University of Thessaloniki
54124, Thessaloniki, Greece
itegos@metesysm.gr, theodoros_gr@yahoo.com, minak@civil.auth.gr

Keywords: Ground slabs, restraints, durability, jointless, fatigue.

Abstract. *It is known that the slabs on soil constitute one of the most difficult types of structures despite their apparent simplicity. It is not accidental that there are still no regulations on their proper construction. As main cause of their failure, someone could mention the restraints expressed either as differential settlements or, mainly, as hindrance of contractions and expansions. For the confrontation of restraints, solution can be given by the joints (contraction joints, construction joints, isolation joints, etc.). Because of the big density of joints, the slabs are manufactured as non-reinforced or fiber reinforced with small percentages of steel fibers because of the unfavorable influence of big percentages in workability of fiber reinforced concrete. Also, at the joint locations, the suitable placement of dowels is required to guarantee the collaboration of neighboring segments. Another weak point is also the fatigue of concrete, which acts catalytic for the slabs in question. Joints, along with the absence of conventional reinforcements, constitute the Achilles' heel of these structures since they require maintenance, they are prone to local failures and for the slabs which are manufactured in the countryside, they constitute the entries of rain waters and of melted, via salt, ice. Failure of joints can happen also because of the phenomenon of pumping, which can lead to extensive cracking and detachment of segments of concrete from the surface of slab at the region of joint. In the present work, a solution is proposed with the following characteristics: (a) complete suppression of joints, (b) conventional reinforcement with meshes in the upper and lower fiber of the slab in order to confront and distribute cracking that is caused by hindrance of free contractions and expansions, (c) effective confrontation of problems of bulging. The proposal is in effect on one hand for industrial floorings and on the other hand for concrete pavings with large durability requirement.*

1 INTRODUCTION

The object of this document is to give a general survey of the design of ground supported slabs with the interposition of a suitable subbase. Despite the fact that the dimensioning of these slabs is seemingly easy, there are many unknown aspects that should be taken into consideration. Obviously, there is no correlation between ground slabs and those supported on beams. Another notable fact, indicative of our ignorance concerning this issue, is that there are no precise instructions referring to ground slabs. Furthermore, the multiple applications of ground slabs force engineers to research thoroughly the international bibliography for specific regulations concerning their construction and design.

The strains these slabs are subjected to are derived from point loads, uniformly distributed loads and restraints due to deformation hindrance. The causes of restraints are the expansions and contractions that concrete undergoes due to its drying, temperature changes, temperature difference between the top and bottom side of the slab and the differential settlements due to local subsoil deformation.

As in the case of conventional slabs, the main purpose is to calculate the thickness and reinforcement. Slab thickness is supposed to be determined by the flexural, shear and puncture loads. As far as the reinforcement is concerned, the ground slabs case is considerably different to the conventional slabs case. Traditionally, ground slabs in real life are weakly reinforced using grids on the top and bottom of slabs which operate as surface reinforcement rather than bearing. Today, these slabs are either unreinforced, therefore operating at stage I (uncracked concrete), or reinforced with steel fiber (steel per concrete ratio 25 – 30 kg/m^3). By using such low ratio, it is intended to accommodate two basic requirements: concrete workability and load bearing mechanism activation by the two sides of the slab. Steel fiber reinforcement imparts ductility to concrete, so bottom side failure activates the top side and that enables us to use the yield line theory. Certainly, steel fiber reinforcement does not affect considerably the flexural capacity of the slab, compared to the unreinforced concrete case.

Regarding the restraints, joints is the ‘remedy’ used for strain relief. Occasionally, in order to reduce the slab thickness, dowels are used to connect the adjacent parts of the slab which is divided in rectangular parts of size 5x5 m. However, it is no exaggeration to say that sometimes the ‘remedy’ proves to be worse than the disease that it is supposed to cure, more precisely, the profuse cracking of the slab. Currently, it is known that we are on the verge of releasing ourselves from the joints. Many large area buildings and long – span bridges are constructed jointless. According to the beliefs of the present article’s supervisor, who has a long experience in analyzing jointless solutions for bridges and buildings, it is time to apply this philosophy in ground slabs, since joints, as mentioned before, cause more troubles than restraints do.

The abolition of joints was on the table of discussion, the period when railways were constructed with expansion joints in every 30 m, due to intensive phenomena concerning thermal expansions and contractions. However, it was noticed that the rails displacements due to thermal changes were much lower than expected and as a result, joints were connected by welding. In today’s railways, welded connections are used and in that way deformations are confronted.

The study of the temperature changes’ influence on the length – deformation relationship of several elements and the abolition of joints in building and bridge construction, is addressed in many scientific papers. However, bridges outpace buildings in current bibliography.

Both the construction and the abolition of expansion and contraction joints in buildings include disadvantages which have to be taken into account during their design, operation and maintenance. More specifically, the existence of joints increases the construction cost and

their maintenance implies many difficulties. Moreover, the application of joints increases the possibility of moisture appearance and disrupts the building's uniformity (e.g. dual walls). In contrast, the abolition of joints intensifies strains due to restraints and as a result more reinforcement is required in areas where tensile forces are more likely to take place. For that reason, reinforcement is used on the top and bottom side of the slab. Additionally, in jointless constructions, it is essential that cracking control be performed, since constrained and imposed deformations due to restraints (temperature, creep, shrinkage, settlements) cause high stresses to indeterminate systems. In conclusion, a significant disadvantage of joints' abolition is the problematic application of precast methods, because of the difficulties arising in assembling and transporting precast members.

2 THE MAIN DISADVANTAGES OF CURRENT CONSTRUCTION METHODS

The seeming simplicity of dowels' application disorients us from their real behavior. For example, if dowels are not exactly perpendicular to the joint, they will hinder contraction of the slab, causing or contributing to cracking. Corrosion is another issue that impedes free movement of dowels in and out of the slab and can also cause spalling.

It is of outmost importance that doweled joints be able to open and close as concrete expands and contracts. For that reason, dowels should be slippery and smooth in order to slide in and out of the concrete without resistance. Smoothness alone does not guarantee free movement of the joints, so a bond – breaker is also needed at the dowel surface. In order to improve dowel performance, grease, mortar – tight sleeve or noncorrosive sleeve could be used.

Conventional round dowels must be parallel with each other and with the sides and surface of the slab. Dowels which are not aligned have to bend as the joint opens. This can generate immense tensile stresses in the concrete. As a result, cracking and reduction in load carrying capacity occur. Proper positioning of bars could be achieved by using prefabricated alignment cages but even with these, the problem persists. Fortunately misalignment is usually not obvious.

Whatever provision is made, several issues still come up. For example, if the top or bottom of the bar is heavily greased, one slab must deflect by an amount equal to the grease thickness before load is transferred to the adjacent slab. High stresses can occur long before the load is transferred. A similar problem may come up if there is any space between the bar and the sleeve. Additionally, if corrosion occurs on the bars and sleeves or mortar enters the sleeve, dowel movement will be hindered.

Even though dowels and tie – bars may be perfectly placed, movements perpendicular to the bars and parallel to the joints are restrained, causing notable stresses which lead to cracking or failure. However, these stresses were not included in the analysis and design of the slab.

Usually, large floor slabs or pavements are dealt with by using the long – strip method. More specifically, lanes are placed separately each day and the intervals are filled later. When placing the lanes, workers saw cut transverse contraction joints the same night or the next day. After one or two days, cracks occur below the saw cuts and thus the joints open. The main problem of this method takes place several days after the filling of the aforementioned intervals. The new concrete tries to contract but the bars in the longitudinal joints resist. Certainly, the new concrete has not developed its full strength and cannot withstand the tensile forces applied to it. Consequently, cracks are formed.

Another stress designers ignore, is the horizontal shear force occurring parallel to the joint at about the end of the bars. It is also essential to say that slabs, when put into service, can be already cracked or highly stressed. Especially at the intersection of transverse and longitudinal joints, stresses accumulate and thus cause corner cracking, as shown in figure 1 [1, 2].

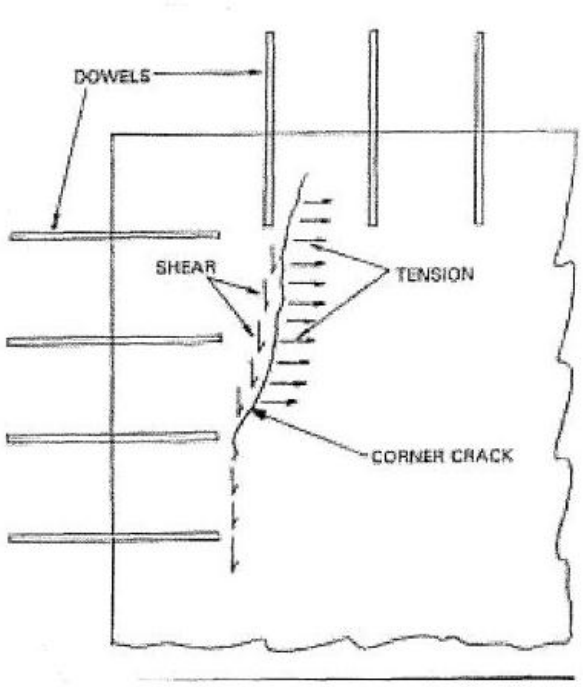


Figure 1: Cracking caused by bars at corner of slab.

3 DESCRIPTION OF A JOINTLESS SOLUTION

3.1 Floor loadings

The loads, slabs-on-ground are subjected to, fall into two categories: **Gravity loads** and **restraints**. The first category includes forklift and heavy wheeled vehicle traffic, block stacked pallet loads, racking loads, loads from bearing masonry or partition walls and loads from fixed machinery and equipment. The second category includes differential settlements, uniform temperature changes t_s, temperature difference between the top and bottom side of the slab Δt, concrete drying and concrete deformations.

Reliable load carrying capacity is of utmost importance in ground slabs design. Self-weights and service loads are determined by codes where point loads (derived from forklifts) are given. These point loads fall into 6 different categories. As far as the wheel loads and the dynamic amplification factor of machinery equipment are concerned, they have to be estimated with the help of the owner's contribution as well.

All the above apply both to the self-weight loads and service loads of racking systems, too. Attention should be paid to manufacturer's details. Furthermore, as for the racking systems, measures must be taken against their overturn caused by horizontal seismic load applied to the center of gravity of stored material. Regarding the racking systems and forklifts, it is critical for the stress calculation of ground slabs to consider their total load. Concerning the truck traffic loads, they have to be calculated with the help of the owner's contribution, likewise forklift loads.

Regarding indoor ground slabs, uniform temperature changes t_s equal to $\pm 25^{o}C$ according to EC-1 must be considered. Also, in order to estimate the deformations due to concrete drying, primarily in the incidence of large glass facades, it is possible even for indoor conditions that an equivalent temperature greater than $35^{o}C$ is required. In the case of indoor slabs, appli-

cation of temperature gradient is not required, provided that (i) the placement of the slab is accomplished after the construction of the roof and exterior walls, or (ii) the room is already heated.

For the sake of simplicity, live loads and restraints are calculated regarding a safety factor equal to γ_Q=1.5 and γ_Q=1 respectively. The application of ψ combination factors would give the illusion of computational accuracy but due to the multiple elements that influence the ground slab behavior, such an effort would be pointless. This fact characterizes as well the concrete modulus of elasticity estimation. For the design and construction of ground slabs, the modulus of elasticity of concrete is considered equal to E_c=30000 N/mm^2, which is quite accurate if it is referred to usual classes of concrete (C25/30, C30/37). The thermal expansion coefficient α_t for concrete and steel is assumed to be equal to $1.0 \cdot 10^{-5}$ K^{-1} according to EC-2. [3, 4, 5, 6, 7]

3.2 Restraints consequences

Uniform temperature changes: Friction between the slab and the soil generates compressive stresses at the bottom surface of the slab with increasing temperature and tensile stresses with decreasing temperature, as indicated in figure 2. Long span slabs exhibit greater sensitivity.

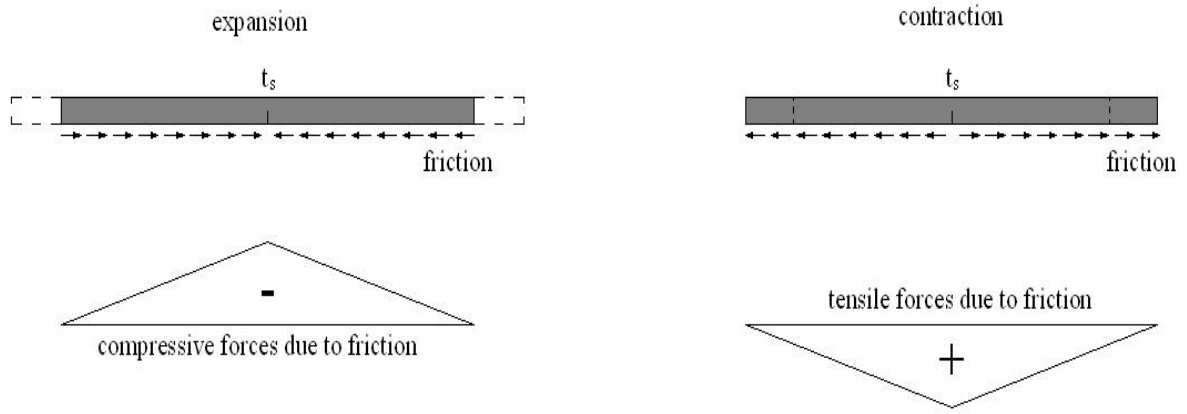


Figure 2: Forces developed at the slab with temperature changes.

A jointless slab lying on graded crushed aggregates, despite the presence of a slip membrane that hinders its movements, forms cracks under a temperature reduction of 20^{o}C.

$$\sigma_t = \alpha_t \cdot t_s \cdot E_{ct} = 1 \cdot 10^{-5} \cdot 20 \cdot \frac{30000}{2} = 3 \text{N/mm}^2 = f_{ctm} \quad (1)$$

E_{ct} = 0.5·E_c (E_{ct} = modulus of elasticity under tensile forces) and
f_{ctm} = 2.9 N/mm^2 for C30/37

Concrete flexural strength f_{ctm} is not sufficient to prevent cracking. It should be noted that expansion and contraction of concrete is an asymmetric phenomenon. More specifically, contraction due to concrete drying (from 0.02% to 0.04%, giving an equivalent temperature reduction from 20^{o}C to 40^{o}C) combined with contraction due to temperature reduction, results in a restraint load much greater than this of temperature increase. Moreover, if the EC-1 values ±25^{o}C for temperature changes are considered, it is apparent that the temperature in-

crease's influence is eliminated by the equivalent contraction due to drying, while the combination of the latter with the thermal contraction creates an equivalent contraction which corresponds to a 50°C to 60°C temperature reduction.

Uneven temperature changes: Temperature increase on the top surface of the slab accompanied by its delay in reaching the bottom surface, results in slab curling, as shown in figure 3.

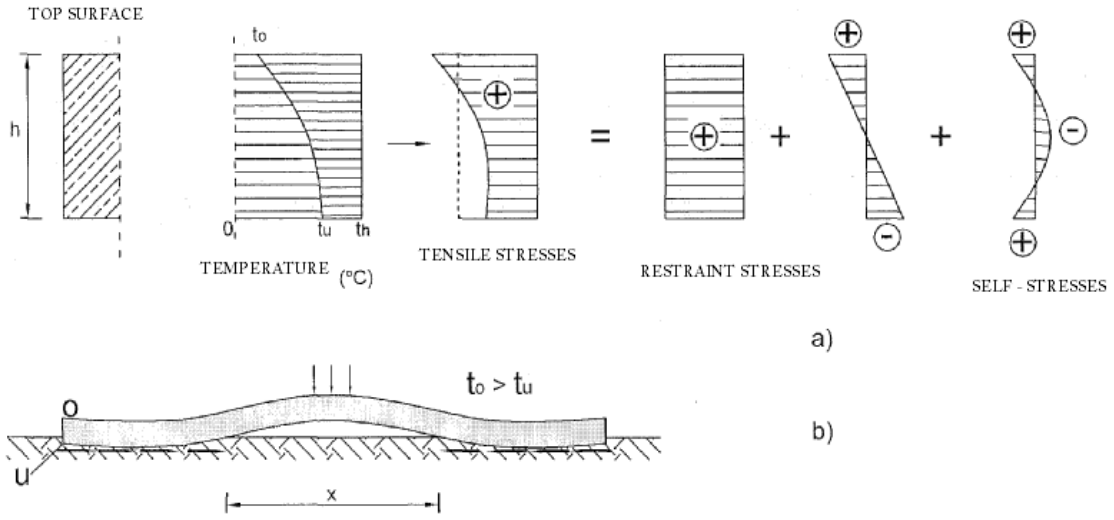


Figure 3: (a) Temperature distribution across the slab, (b) Slab curling.

In order to calculate the curling stresses in ground slabs, a temperature gradient Δt is initiated. Δt reaches a value of approximately 5°C at indoor slabs. This temperature difference between the top and bottom surface of the slab generates curling in its middle area. In response to this curling, self weight loads activate flexural stresses on the bottom side of the slab which are regarded as curling stresses. When the slab to be designed has theoretically infinite length, its shape of deformation is similar to this of a clamped slab on two or all four sides [3, 6].

4 DESCRIPTION OF THE JOINTLESS SOLUTION

4.1 Introductory elements

In order to design a ground slab, several requirements should be taken into consideration. Namely, the type of load applied (static loads, restraints), the desirable working life and soil conditions. Ground slabs require high quality concrete for the following reasons: (a) The high strength that characterizes high quality concrete, permits the reduction of slab thickness and that fact has beneficial effects on the elimination of the Δt restraint and on the better behavior regarding differential settlements, since the moment of inertia is drastically decreased and the modulus of elasticity remains more or less the same, (b) It is known that the impacts of contraction due to drying and creep weaken on high quality concretes, (c) By reducing slab thickness, self weight reduces as well and as a result, friction between the slab and the subbase lowers, (d) In the case that the slab is reinforced conventionally or with steel fibers, the controlled transition from uncracked to cracked phase (in terms of acceptable crack width) requires lower steel per concrete ratio, by virtue of concrete strength.

The issue of ground slabs reinforcement went through many phases before settling on steel fiber at low steel per concrete ratios (25 kg/m^3). The main purpose of this solution is to enhance concrete ductility rather than to increase its tensile strength, to which steel fiber rein-

forcement little has to offer. Additionally, it would be unwise to increase steel per concrete ratio, since concrete workability would be impaired and its placement time would be unprofitably elongated with few positive results on its strength. However, steel fiber reinforcement has two advantages. Firstly, the construction time is shortened and secondly, it does not influence the electromagnetic field that automated vehicles need to operate. In contrast, conventional reinforcement does affect the electromagnetic field and for that reason, is placed below the zone that concrete coverage requirements dictate. As a result, the static height of the reinforced slab shortens. [8]

4.2 Philosophy of recommended solution

After the analysis of the aforementioned factors, the description of this jointless solution for indoor ground slabs will be clearer. The basic points are given below.

Concerning the joints, only the isolation joints of vertical bearing elements are included in this solution, either being within the slab plan or on its perimeter. Around the perimeter of the slab, two construction methods could be applied:

In the first method, slab boundaries are not connected to the foundation walls which enclose the slab foundation (subbase and subgrade). In the second method, slab boundaries are monolithically connected to the foundation walls which partially impede the slab deformation towards the center of its plan. The restraint load, the upper edge of the foundation wall is subjected to, is not to be ignored, so measures should be taken to confront this problem. One of these measures could be the improvement of passive forces resulting from the subbase and subgrade (which constitute the slab foundation) resistance to the inward movement of the foundation wall. Another measure (that mostly helps the structural system to adapt to the problem rather than to solve it), is the expansion of the foundation wall footing in order to prevent high rotational movements. The thickness and reinforcement of the foundation wall in its base should be calculated regarding the aforementioned restraint load. The increase in passive forces of slab foundation could be achieved by impregnating the graded crushed aggregates with a cement mixture within a zone of 1 m width.

It is obvious that the method described in the beginning permits free movement of the slab with the exception of friction forces which oppose that movement. Friction forces are limited due to the low thickness, hence the low self weight of the slab, despite the increased value of the friction factor which varies from 1.5 to 1.8. In the second method, slab movement is impeded and friction forces are very low, provided that the deflection of the upper edge of the foundation wall is practically zero.

In the case of jointless slabs, their minimum thickness which is approximately 150 mm suffices to accommodate all requirements. The reason is that in jointed slabs, the maximum tensional stress when the load is applied to their perimeter is almost twice the value of the tensional stress when the load is applied to the middle area. The minimum thickness is estimated with regard to minimum concrete covers and the requirement of fitting two grid reinforcements inside the slab. Apart from the absence of joints, high quality concrete contributes significantly to the adequacy of load bearing capacity of slabs. Another reason leading to smaller slab thickness, is the minimization of reinforcement against restraints, which is expressed as a percentage of slab section area.

It is no exaggeration to say that the combination of high quality concrete, the absence of joints and the minimum slab thickness (15cm) ensures a reliable load bearing capacity to uncracked concrete and without the reinforcement's contribution. However, absence of joints implies restraint forces which provoke tensional and flexural stresses which will definitely result in cracking. This crack width could be limited by grid reinforcement which is calculated by the following formula:

$$A_s = k \cdot f_{ctm} \cdot \frac{A_{ct}}{\sigma_s} \quad (2)$$

A_{ct} = tension zone of uncracked concrete,

f_{ctm} = average tensile strength of concrete,

k = coefficient determined considering the stress condition of the structural element, for pure tension and rectangular section k values depend on the thickness of the structural element according to figure 4,

σ_s = reinforcement tension (cracked concrete), determined considering the selected diameter and the maximum tolerable crack width which is equal to 0.3 mm or 0.2 mm.

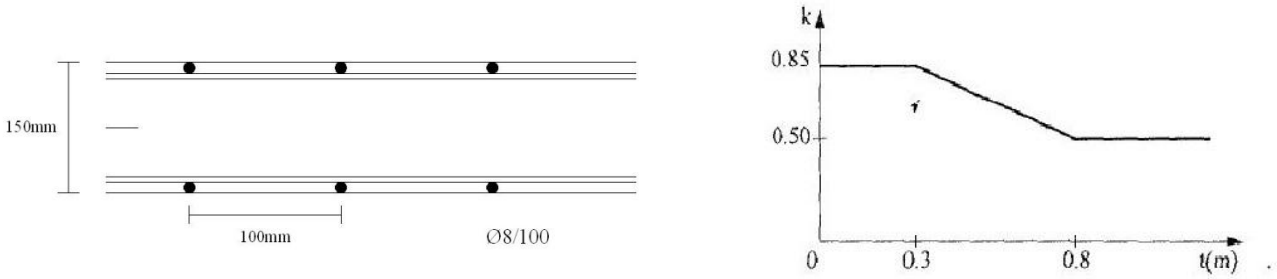


Figure 4: k coefficient values for pure tension.

Based on this formula, the reinforcement percentage in both directions equals to $\rho = 0.85 \cdot 2.9/350 = 0.007$.

Consequently, the per meter reinforcement area is $A_s = 0.007 \cdot 15 \cdot 100 = 10.6 \rightarrow 2Ø8/100mm$ (meaning that one bar is placed in the top and the other in the bottom of the slab).

Figure 5 shows the response of ground slab during winter, in terms of applied force vs. width of developed cracks. In the ground slab under tension, the stresses of the longitudinal reinforcement equilibrate the tensile stresses that are developed in the element.

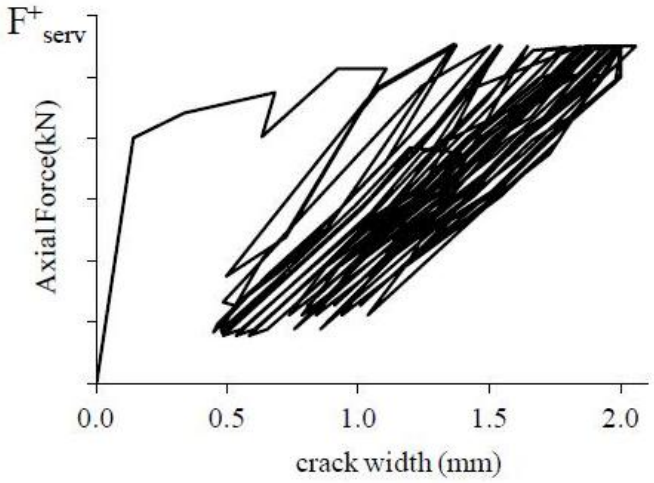


Figure 5: The response of slabs under changing tension.

Figure 6 presents the idealized behavior of a reinforced concrete tie. According to this figure, the contribution of the concrete may be considered to increase the stiffness of the tensile reinforcement (tension stiffening effect).

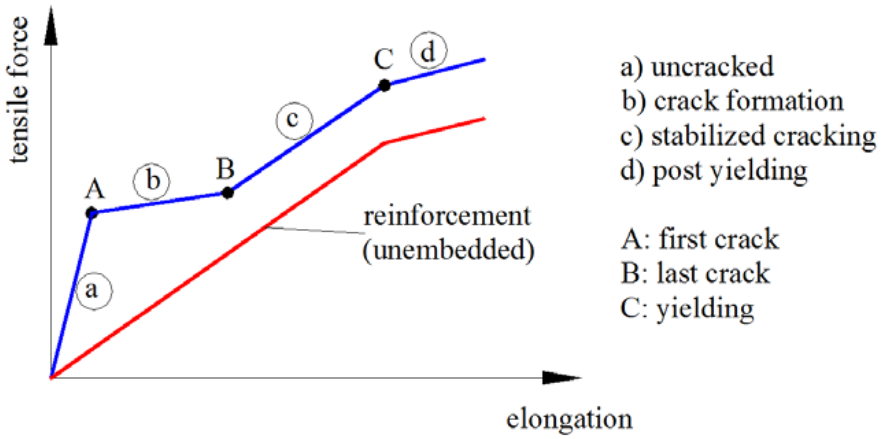


Figure 6: The idealized behavior of a concrete tie.

Figure 7(a) shows the distribution of strains after the appearance of the first crack, while figure 7(b) depicts the distribution of strains after the element has been fully cracked. In the areas between cracks, the tensile forces are transferred from steel to concrete by the friction (bonding) forces. Concrete contributes to reinforcement's axial stiffness increase. The aim is to reduce the width of the cracks induced and to keep them within acceptable limits according to the Eurocode 2-Part 1 (2004).

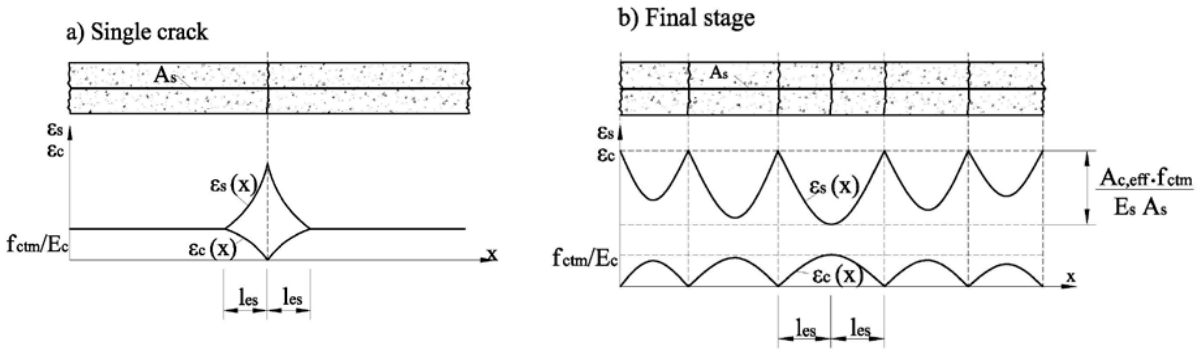


Figure 7: (a) The distribution of strains after the appearance of the first crack and (b) the distribution of strains after the element has been fully cracked.

The restraint load per meter, in the extreme scenario of immovable top edge of the foundation wall, is calculated as follows: $F_s = A_s \cdot \sigma_s = 10 \cdot 35 = 350$ kN. It is important to outline that the limited rigidity of the foundation wall contributes drastically in decreasing the restraints of the slab, since its movements are not totally hindered. The response of slabs subjected to restraints, is displayed in figure 8. According to figure 8, after the uncracked phase of the slab (until a strain of 0.015% which initiates cracking), the cracked phase follows during which reinforcement's tension remains almost stable up to a strain limit and eventually the restraint load does not increase. It is implied that due to the hindrance of slab contractions, its behavior resembles that of a reinforced concrete tie rod. In the case that the combination of temperature reduction and drying contraction (which is regarded as equivalent to a temperature reduction

of 30°C because of high quality concrete) is considered as the critical restraint load, then the total temperature reduction would be T=30+25=55°C, resulting in a strain of $\varepsilon=\alpha_t \cdot T=10^{-5} \cdot 55=0.00055$. According to figure 8, the strain value lies within the sawblade-like section of the diagram, meaning that the stresses of the slab reinforcement will not reach the maximum tolerable value of σ_s = 350 MPa. That being said, the crack width will be lower than the acceptable value. Moreover, the restraint load, which has been estimated equal to 350 kN, is actually smaller because of reinforcement stress reduction. Figure 8 displays the stress-strain diagrams of ties for several reinforcement percentages [9, 10].

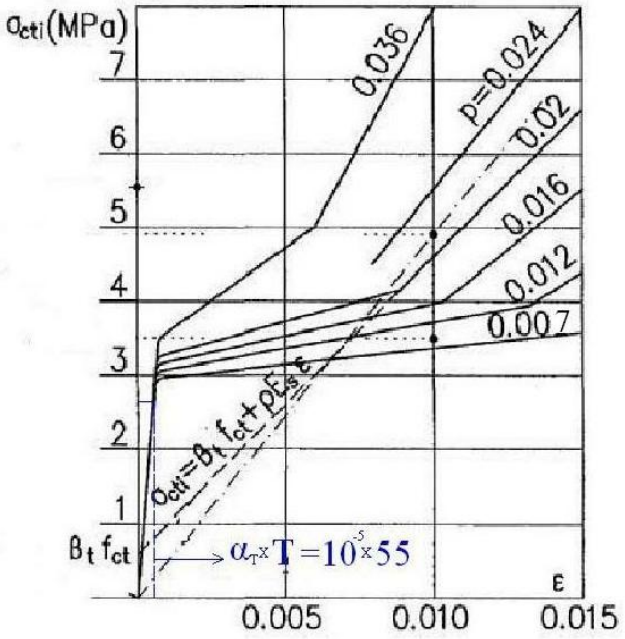


Figure 8: Stress-strain diagrams of ties for several reinforcement percentages.

Creep effect is an additional factor that increases significantly the movements at the top edge of the foundation wall. Creep introduces a lasting force which probably contributes to the most part of the foundation wall deflection. As mentioned before, this deflection permits the stress relief of the slab from restraints.

Fatigue is the Achilles' heel of unreinforced jointed slabs, whose durability becomes extremely low due to this fact. The recommended solution burdens the reinforcement with this problem, so slabs employing this solution hold a considerable advantage over fatigue.

The aforementioned curling issue and generally the elevational displacements of a slab, which does not have the relieving effects of joints, constitute a problem not to be ignored. However, in this particular instance, there are two favorable facts: The first is the small thickness of the slab and the second the favorable indoor conditions. Furthermore, reinforcement confronts the combination of stresses due to curling and those due to gravity loads effectively, in comparison with unreinforced slabs. Nevertheless, the present work recommends a mechanism which restrains the transverse displacements of the slab, at the intersection points of a rectangular grid whose size varies from 5x5m to 7x7m. It is essential to clarify that the slab plane is parallel to the grid plane. In the following paragraph, a typical restraining point is described.

Before the layers under the slab are compressed, a special "foundation-slab" measuring 1x1m area and 30cm thickness is concreted and slightly reinforced with a grid at its top sur-

face. To the center of the foundation-slabs, a plastic or stainless tube is clamped which extends almost up to the lower level of the slab. The diameter of the tube could be of the order of 10-15cm and its interior is partially filled with concrete, clamped to the foundation-slab via slim reinforcement bars. A 6/10-inch steel rope is embedded in the tube's concrete and its upper end is to be anchored in the slab. The installation of this mechanism is followed by the compression of the supporting layers of the slab and its concreting. The steel rope resistance to vertical displacements of the slab is assisted by the weight of the layers lying between the slab and the foundation-slab. Toward this end, the reason using steel rope instead of conventional reinforcement bar, is that the first can easily accommodate the displacements (due to expansions and contractions) parallel to the slab plane, in contradiction to the latter which no matter how slim or flexible is, cannot meet the requirements. Figure 9 displays this mechanism.

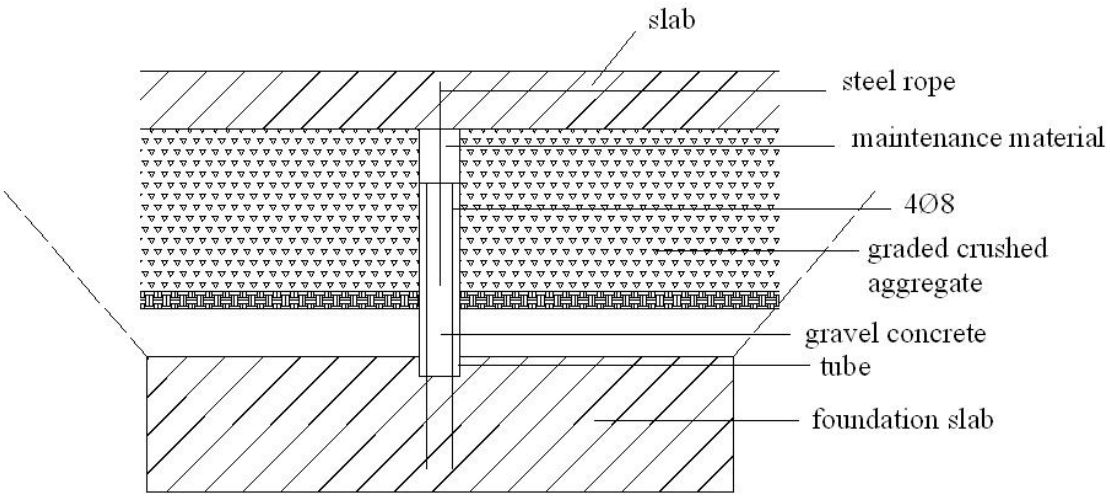


Figure 9: Curling prevention mechanism.

5 APPLICATION

The procedures described before were tested in one of the warehouses of the supermarket chain "MASOUTIS" located in Thessaloniki. The technique was applied to a part of the warehouse slab (15x120m area) which bears stored material loads and material handling equipment loads. The slab in question is located inside the warehouse and connects the top edge of the interior retaining wall with the top edge of the foundation wall of the elevated floor. This connection is intended to support the retaining wall which was designed as supported at both ends (the one end fixed, the other simply supported) and not as cantilever. After two years, no cracking has occurred in the slab which absolutely meets all serviceability demands. Figure 10 shows the method of application.

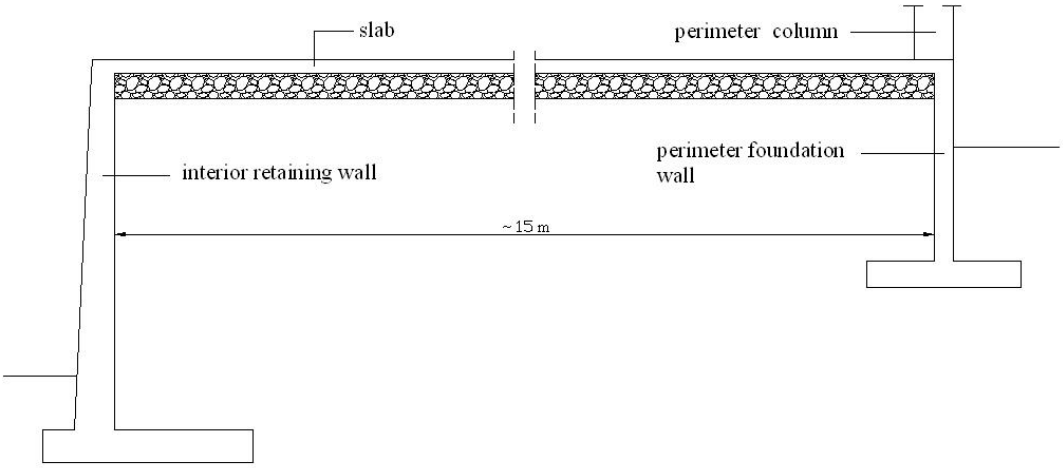


Figure 10: Jointless slab which connects the interior retaining wall with the perimeter foundation wall.

6 CONCLUSIONS

Recent years have shown that conditions for complete suppression of joints in large length and area constructions are now mature. Inspired by this fact, the authors of this paper present a solution for ground slabs that takes us one step forward concerning the monolithicity of these sensitive structures for which joints imply many problems. In the final part, six basic conclusions are described.

- The recommended solution constitutes a global approach to the problem, since it provides measures for all possible strains and especially those deriving from restraints.
- The recommended solution could be characterized as economical in terms of concrete consumption, as the slab thickness is significantly reduced.
- As for the construction time, the present proposition loses the edge due to the time consuming reinforcement placement, however it does not employ dowels and joints which also require time for their proper application.
- The present proposition prevails in terms of maintenance cost which is diminished.
- The recommended structure holds a considerable advantage against fatigue and lasts longer than the jointed one.
- A large-scale application, which could be considered as experimental confirmation, is proved successful after the lapse of two years.

REFERENCES

[1] E.K. Schrader, A solution to cracking and stresses caused by dowels and tie bars. *ACI Concrete International*, Vol. 13, Issue No. 7, 2001.

[2] ACI 360R-06, Design of slabs on ground.

[3] CEN (2003) Eurocode 1: Actions on structures - Part 1-5: General actions -Thermal actions, 2003.

[4] CEN (2004) Eurocode 2: Design of concrete structures - Part 1: General rules and rules for buildings.

[5] CEN (2004) Eurocode 2: Design of concrete structures - Part 2: Bridges.

[6] I.A. Tegos, N.C. Giannakas, Slabs on soil: the known-unknown concrete structural elements, *15th Greek Concrete Conference*, Alexandroupoli, Greece, October 18-20, 2006, pp 495-509.

[7] Concrete industrial ground floors - A guide to design and construction. Concrete Society Technical Report No. 34 Third Edition, 2003.

[8] S.A. Kolias, S.B. Tsoukantas, G.G. Kremmyda, T.D. Topintzis, Design of concrete ground floors, *16th Greek Concrete Conference*, Pafos, Cyprus, Greece, October 21-23, 2009.

[9] CEB-FIB (1991), Model Code 1990, Final Draft, CEB Bulletin No 204.

[10] I.A. Tegos, S.D. Tegou, V.P. Panoskaltsis, M.Tsitotas, Reduction in seismic actions of bridges by utilizing the sidewalks as restrainers, *15th World Conference on Earthquake Engineering* (15th WCEE 2012), Lisboa, Portugal, September 24-28, 2012.

COMPDYN 2013
4th ECCOMAS Thematic Conference on
Computational Methods in Structural Dynamics and Earthquake Engineering
M. Papadrakakis, V. Papadopoulos, V. Plevris (eds.)
Kos Island, Greece, 12–14 June 2013

NON-LINEAR SEISMIC ANALYSIS OF RC FRAMED BUILDING DESIGNED ACCORDING TO EC-8

Željana Nikolić[1*], **Mijo Nikolić**[1,2]

[1] University of Split, Faculty of Civil Engineering, Architecture and Geodesy
Matice hrvatske 15, 21000 Split, Croatia
e-mail: zeljana.nikolic@gradst.hr

[2] Ecole Normale Supérieure de Cachan, LMT-Cachan
61 Avenue du Président Wilson, 94235 Cachan, France
e-mail: nikolic@lmt.ens-cachan.fr

Keywords: Non-linear static analysis, Incremental dynamic analysis, Reinforced concrete frame building, Ductility classes.

Abstract. *One of the main aims of the design of earthquake resistant structures is to ensure that the design seismic action do not cause local or global collapse of the structure. Eurocode 8 includes prescriptions in order to guarantee ductile behaviour of the structure and its structural elements and adequate bearing capacity. Concrete buildings in high seismic area are classified in two ductility classes DCM (medium ductility) and DCH (high ductility) depending on their hysteretic dissipation capacity. To provide the appropriate amount of ductility, specific provisions for all structural elements shall be satisfied in each class. In this paper five-storey reinforced concrete frame building is studied using nonlinear static analysis and incremental dynamic analysis. The building was previously designed for DCM and DCH ductility class according to the prescriptions of EC-2 and EC-8, accepting the demands of the local ductility. The aim of this paper is the analysis of differences in the behaviour of the structure between these ductility classes. The mechanism of loosing the bearing capacity, collapse loads and behaviour factors obtained by non-linear static analysis and incremental dynamic analysis were analyzed and compared. A series of seven earthquakes taken from the European Strong-Motion Database, fully satisfying the EC-8 provisions, are used as input for incremental dynamic analysis. The results obtained by non-linear static analysis show higher yield ratio of base shear and building seismic weight for DCM in relation to DCH, while the target displacement and bearing capacity at the collapse is higher for DCH. Behaviour factors for both ductility classes obtained by incremental dynamic analysis and static non-linear analysis are larger than those demanded by EC-8.*

1 INTRODUCTION

Provisions of European norms EC-8 [1] are directed to design of structures which earthquake resistance is based on energy dissipation in provided critical zones. The design rules have to assure ductile behaviour of the structure and its structural elements and adequate bearing capacity.

Ductility class presents a level in which balance between the bearing capacity and capability of the energy deterioration is achieved. Ductility of the structures in linear analysis is based on reduced elastic spectrum of the ground acceleration. The reduction is performed by behaviour factor q which is equal for the whole group of the structures. This approach cannot give insight to the real behaviour of the structure and quantitative determination of the damage degree can be obtained only by non-linear analysis.

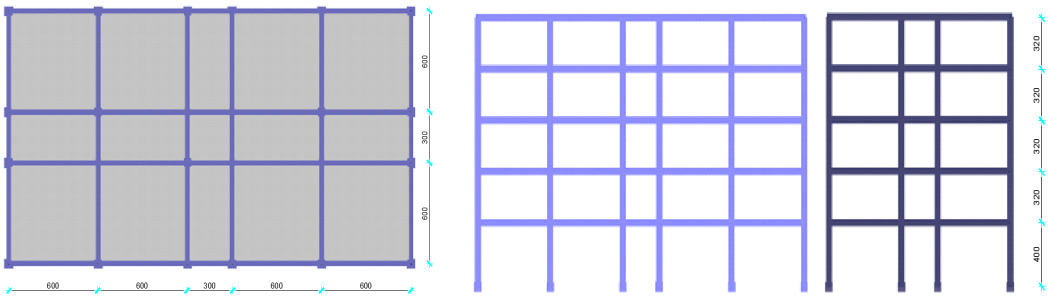
Concrete buildings in high seismic area are classified in two ductility classes, DCM (medium ductility) and DCH (high ductility), depending on their hysteretic dissipation capacity [1]. To provide the appropriate amount of ductility, specific provisions for all structural elements ought to be satisfied in each class.

In this paper five-storey reinforced concrete frame building is studied using nonlinear static analysis [2] and incremental dynamic analysis [3]. The building was previously designed for DCM and DCH ductility class according to the prescriptions of EC-2 and EC-8, accepting the demands of the local ductility. The aim of this paper is analysis of differences in the behaviour of the structure between these ductility classes. The mechanism of loosing the bearing capacity, collapse loads and behaviour factors obtained by non-linear static analysis and incremental dynamic analysis were analyzed and compared.

2 NON-LINEAR ANALYSIS OF RC FRAME BUILDING

2.1 Geometry of the building and modelling

Analyzed RC frame building (Figure 1) is a symmetrical five-storey building, regular in plan and elevation. The dimensions in plan are 27x15 m. The bottom storey height is equal to 4,0 m, while at the other levels it is equal to 3,2 m. The cross-section dimensions are 50x50 cm for all columns and 30x45 cm for all beams. The spans are 6 m and 3 m. The structure has reinforced plates with thickness equal to 16 cm. The concrete characteristic cubic strength is f_{ck}=30 N/mm^2 and steel characteristic yielding strength is f_{yk}=500 N/mm^2.



(a) plan (b) section

Figure 1: Geometry of the building.

The building loads are self-weight, additional dead load 2,8 kN/m^2 and imposed load 3,0 kN/m^2.

The building was designed according to EC-2 [4] and EC-8 [1] for ground type B, importance factor II (γ_I=1), type 1 response spectrum, damping ξ=5% and ductility classes DCM

and DCH. Design ground acceleration is a_g=0.3g. The behaviour factors equal to q=3,9 for DCM and q=5,85 for DCH are adopted.

The columns are reinforced by longitudinal bars 24ϕ16 and stirrups 4ϕ10/10 cm in critical region and stirrups ϕ8/20 cm out of critical region for DCH, while the beams have longitudinal bars 7ϕ16 in upper and lower section and stirrups ϕ8/15 cm. The additional horizontal bars ϕ10/5 cm are placed in beam-column joints to ensure ductility behaviour.

The columns are reinforced by 20ϕ18, stirrups 4ϕ10/10 cm in critical region and stirrups ϕ8/20 cm out of critical region for DCM. The beams are reinforced by longitudinal bars 7ϕ18 in upper and lower section and stirrups ϕ8/15 cm.

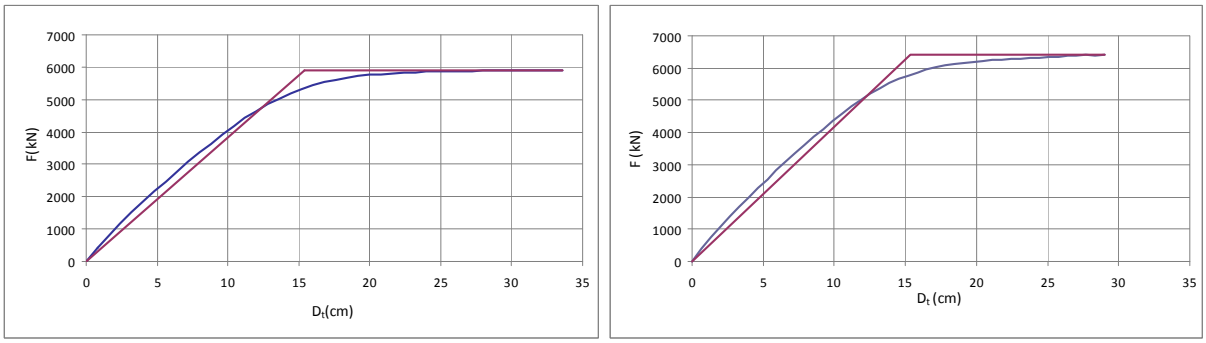
The non-linear static (pushover) analysis and incremental dynamic analysis are performed by computer program Seismosoft [5]. The behaviour of the reinforcing steel was modelled by bilinear model with kinematic hardening, while the concrete was modelled by Mander's non-linear model with possibility of including influence of stirrups.

The influence of the plate to flexural and torsional stiffness was taken by modelling the beams as T cross-section with effective width of 80 cm.

2.2 Non-linear static (pushover) analysis

Non-linear static (pushover) analysis according to EC-8 [1] was performed for presented RC frame building. Linear distribution of the lateral forces was taken. The mass matrix is diagonal with elements equal to storey masses (m_1=423 t i $m_{2,3,4,5}$=410 t). The equivalent mass m^* and transformation factor Γ have the values m^*=1274 t and Γ=1,36.

Pushover curves and their elasto-plastic idealizations for MDOF system and both ductility classes are shown in Figure 1.



(a) DCH (b) DCM

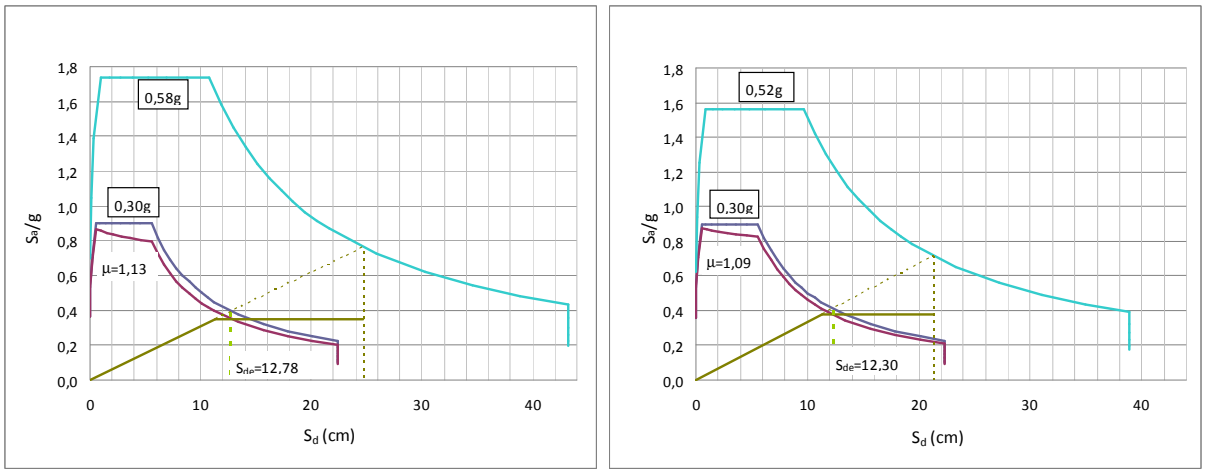
Figure 1. Pushover curves and their elasto-plastic idealization for MDOF system.

Table 1 shows characteristic values evaluated from the pushover curves for both ductility classes.

Figures 2a i 2b show elastic demand spectrum for ground acceleration a_g=0.3g, inelastic demand spectrum determined from the pushover analysis and elasto-plastic idealization of pushover curves for the equivalent SDOF system. Figures also show collapse curves which will be discuss hereafter.

Characteristic values	DCH	DCM
Yield strength (MDOF) F_y	5908 kN	6402 kN
Yield strength (SDOF) $F_y^* = F_y / \Gamma$	4343 kN	4706 kN
Yield displacement (SDOF) $D_y^* = D_y / \Gamma$	11,30 cm	11,32 cm
Elastic period (SDOF) $T^* = 2\pi\sqrt{m^* D_y^* / F_y^*}$	1,14 s	1,10 s
Acceleration on the yielding limit $S_{ay} = F_y^* / m^*$	0,348g	0,377g
Ductility factor $\mu = R_\mu = S_{ae}(T^*) / S_{ay}$	1,13	1,09
Displacemet demand (SDOF) D_t^*	12,78 cm	12,30 cm
Target displacement (MDOF) $D_t = D_t^* \Gamma$	17,4 cm	16,7 cm

Table 1: Characteristic values for ductility classes DCH and DCM.

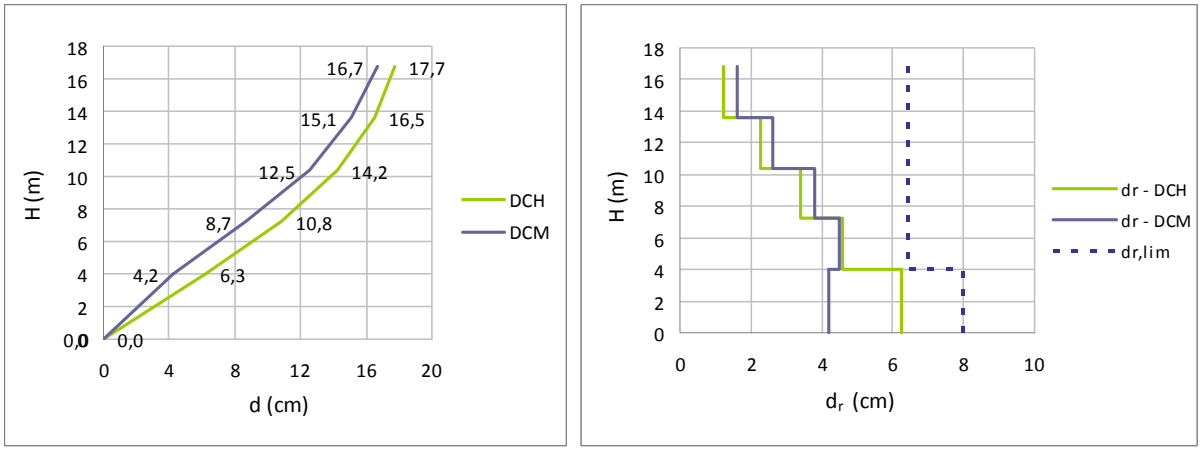


(a) DCH (b) DCM

Figure 2. Elastic demand spectrum, inelastic demand spectrum, elasto-plastic idealization of pushover curves and collapse curves for equivalent SDOF system.

Displacements of MDOF model and damage control

Displacements *d* and interstorey drifts d_r for target displacement are shown in Figure 3.



(a) (b)

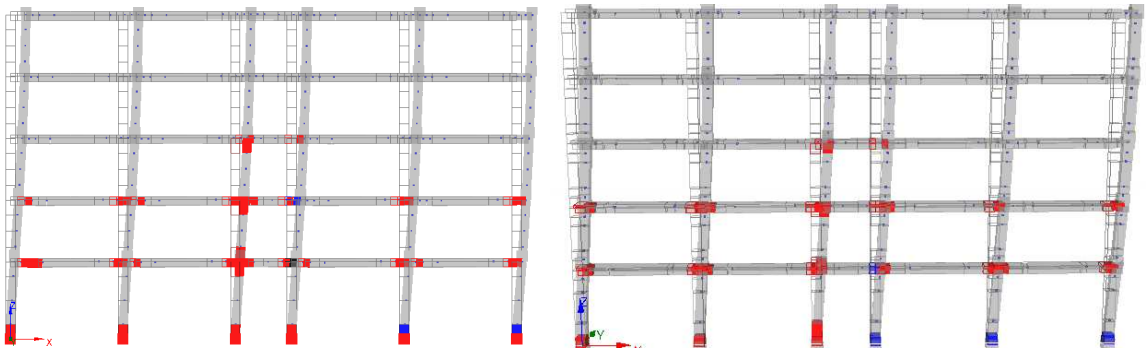
Figure 3. (a) Storey displacements *d*, (b) Interstorey drifts d_r.

Interstorey drifts d_r are compared with limited interstorey drifts $d_{r,lim}$ according to EC-8 [1] which, for the buildings having non-structural elements fixed in a way so as not to interfere with structural deformations, can be calculated as $d_r \nu \leq 0{,}010h$. The damage limitation requirement is satisfied (see Figure 3).

The response of the structure for target displacement is shown in Figure 4. The response is non-linear for both ductility classes. Reinforcement yielding (red colour in Figure 4) is achieved for deformation 0,25%, reinforcement failure (green) for deformation 6%, crushing of the concrete protective layer (blue) for deformation 0,35% and crushing of the concrete core (black) for deformation 0,8%.

The yielding of the reinforcing bars for DCM ductility class occurs in the beams critical regions of the first and second floors as well as in the columns lower critical regions of the first floor and in the columns of the second and third floors.

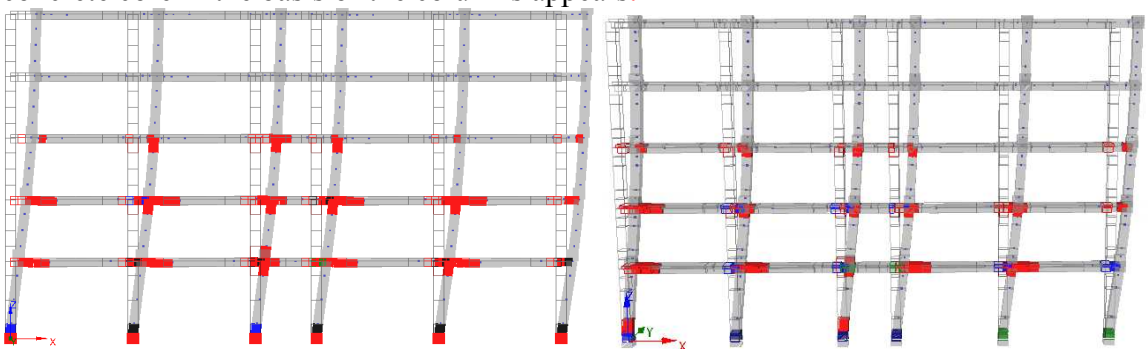
The behaviour of the structure for DCM ductility class is similar.



(a) DCH, D_t=17,4 cm (b) DCM, D_t=16,7 cm

Figure 4. Damage of the structure for target displacement D_t.

The damage of the building is also analyzed for 150%D_t. For DCH ductility class, several types of damages occur including the crushing of the concrete protective layer in the columns of the first floor, expanding of the plastic zones in the beams and further propagating of the plastification in the columns of the third floor. For DCM ductility class, the crushing of the concrete core in the basis of the columns appears.



(a) DCH, 150%D_t=26,1 cm (b) DCM, 150%D_t =25,1 cm

Figure 5. Damage of the structure for displacement 150%D_t.

Collapse of the structure

The collapse point of the structure can be obtained from idealized elasto-plastic curve on the basis of the ultimate displacement. In the analyzed example D_t is less from $3D_y$ for both ductility classes and collapse point is determined from the calculated ultimate displacement.

The intersection of the vertical axis placed in the point of ultimate displacement and radial line corresponding to the elastic part of the idealized elasto-plastic curve, gives the point of the collapse curve of the structure. Figure 2 shows graphical procedure for determining the structural collapse capacity. The same results can be also obtained analytically. The collapse point of the SDOF system corresponds to the acceleration value of 0,58g for DCH and 0,52g for DCM.

Behaviour factor

Non-linear static procedure based on pushover curves can be used for obtaining the values of the behaviour factor. The procedure is based on EC-8 which indicates that the ultimate displacement may not exceed the value $3D_y$. The behaviour factor depends on elastic force F_e, design force F_d and yield force F_y. In this example ultimate displacement is less than the value $3D_y$, so the value of the ultimate displacement is applied for obtaining the value of the behaviour factor.

The behaviour factor can be calculated from the pushover curve and it is presented as a product of two components [6]:

$$q = R_\mu R_S = \frac{F_e}{F_y}\frac{F_y}{F_d} = \frac{F_e}{F_d} \tag{1}$$

where R_μ and R_S are ductility reduction factor and overstrength factor respectively.

Table 2 shows a calculation of the behaviour factor for ductility classes DCH and DCM.

Characteristic values	DCH	DCM
S_{ae}	0,76g	0,71g
$V_e^* = S_{ae} m^* g$	9493 kN	8880 kN
F_d	2112 kN	2782 kN
$F_d^* = \frac{F_d}{\Gamma}$	1553 kN	2045 kN
F_y^*	4343 kN	4706 kN
$q = F_e / F_d$	6,11	4,34
q (EC-8)	5,85	3,90

Table 2: The calculation of the behaviour factor based on non-linear static (pushover) analysis.

2.3 Incremental dynamic analysis

In order to evaluate the dynamic response of the buildings, the incremental dynamic analysis (IDA) [3] was performed for seven accelerograms chosen from the European Strong-motion Database [7] for soil type B. The chosen accelerograms were scaled taking into account that maximum value of the acceleration ought to be a_gS, where a_g was design ground acceleration and S was the soil parameter according to EC-8 [1]. The acceleration spectra of the selected earthquakes for damping ξ=5%, their mean value and elastic spectrum for a_g=0,3g according to EC-8 are shown on Figure 6.

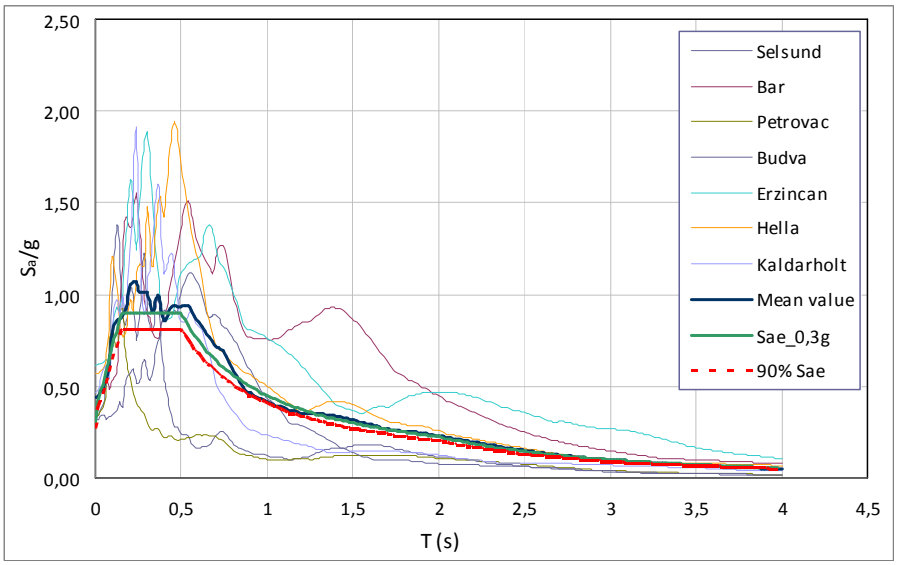
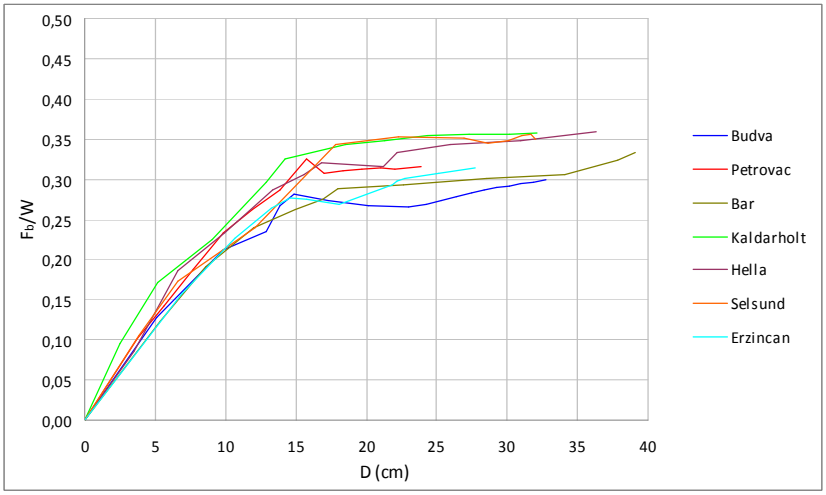
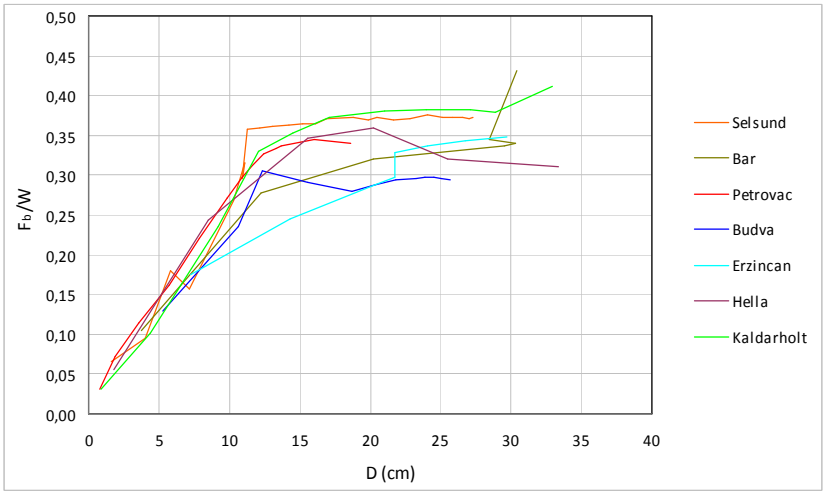


Figure 6: Spectra of the records used in incremental dynamic analysis, their mean value and EC-8 spectrum.



(a) DCH



(b) DCM

Figure 7: IDA curves.

The RC frame was analyzed by incremental dynamic analysis with gradual increasing of the acceleration spectrum ordinate to the collapse. Numerical instability is taken as indicator of the collapse. Figure 7 shows IDA response curves where the roof drift D between the top and base of the structure is presented on the x-axis, while the base shear force F_b/W is presented on the y-axis.

Incremental dynamic analysis is useful in assessing the collapse point of the structure and for obtaining the values of the behaviour factor q which is presented by following equation [6,8]:

$$q = \frac{a_{g(collapse)}}{a_{g(design\ yield)}} \tag{2}$$

where $a_{g(collapse)}$ and $a_{g(desing\ yield)}$ are the collapse and yield design peak ground acceleration respectively. The acceleration $a_{g(collapse)}$ is obtained from the IDA curves, while $a_{g(design\ yield)}$ is the yield acceleration assumed in the design.

Behaviour factor	q (DCH)	q (DCM)
Bar	6,49	5,60
Petrovac	6,33	4,49
Budva	5,84	4,10
Erzincan	6,11	4,58
Selsund	6,93	4,94
Hella	7,01	4,99
Kaldarhollt	6,96	5,35
Mean value obtained by IDA	6,53	4,86
Behaviour factor prescribed by EC-8	5,85	3,90

Table 3: Behaviour factors of the structure obtained by IDA.

The values of the behaviour factors for seven earthquakes and mean value of the computed factors are shown in Table 3. These values correspond to the dynamic response of the building subjected to the chosen accelelograms and are compared with the behaviour factors prescribed by EC-8. The mean value of the behaviour factor obtaining by IDA is higher than the behaviour factor according to EC-8.

3 CONCLUSIONS

- In this paper the behaviour of the five-storey reinforced concrete frame building, previously designed for DCM and DCH ductility class according to the prescriptions of EC-8, was studied using nonlinear static analysis and incremental dynamic analysis. The aim of the paper was analysis of the differences in the behaviour of the structure between these ductility classes, especially the mechanism of loosing the bearing capacity, displacements and storey drifts, collapse loads and behaviour factors.
- The longintudinal reinforcemet of the beams in critical region is 27% higher for ductility class DCM in comparison to DCH. The longintudinal reinforcemet of the columns is 6% higher for DCM. The additional horizontal bars ϕ10/5 cm are placed in beam-column joints.
- Non-linear static (pushover) analysis shows that the structural yielding for DCH arises for the lower value of the acceleration 0,348g in relation to DCM ductility class where it is 0,377g. The values of the target displacements for the structure are 17,4 cm for DCH

and 16,7 cm for DCM. These values for the equivalent SDOF are 12,78 cm and 12,30 cm for DCH and DCM respectively. The interstorey drifts for both ductility classes are less than the allowed value according to EC-8. They are significantly higher for DCH at the first storey, while they have similar values for both ductility classes for the other storeys. The value of the behaviour factors are 6,11 for DCH and 4,34 for DCM. The mechanisms of loosing the bearing capacity are very similar for the both classes. After the yielding of the reinforcement in the beam-column joint, the collapse for both ductility classes results due to the crushing of the concrete and reinforcement failure in the columns basis.

- The behaviour factors evaluated by incremental dynamic analysis as a mean value for seven accelerograms are 6,53 cm and 4,86 cm for DCH and DCM, respectively, and they are higher in relation to the values obtaining by non-linear static analysis.
- The bearing capacity of the frame for DCH is 12% higher in relation to DCM, although the acceleration corresponding to the yielding of the structure is less than for DCM.

REFERENCES

[1] CEN, Eurocode 8: *Design of structures for earthquake resistance – Part 1: General rules, seismic actions and rules for buildings. EN 1998-1*. Brussels, 2004.

[2] P. Fajfar, A non-linear analysis method for performance-based seismic design. *Earthquake Spectra*, **16**(3), 573-592, 2000.

[3] D. Vamvatsikos, C.A. Cornell, Incremental dynamic analysis. *Earthquake Engineering and Structural Dynamics*, **31**, 491-514, 2002.

[4] CEN, Eurocode 2: *Design of concrete structures – Part 1-1: General rules and rules for buildings, EN 1992-1-1*. Brussels, 2004.

[5] *SeismoStruct – A computer program for static and dynamic nonlinear analysis of framed structures*, http://www.seismosoft.com

[6] A.M. Mwafy, A.S. Elnashai, Calibration of force reduction factors of RC buildings. *Journal of Earthquake Engineering*, **6**(2), 239-273, 2002.

[7] European Strong-Motion Database, http://www.isesd.hi.is.

[8] A.H. Barbat, J.C. Vielma, S.Oller, Seismic safety of reinforced concrete framed buildings designed according to EC-2 and EC-8. *COMPDYN 2009, ECCOMAS Thematic Conf. on Comp. Meth. in Struct. Dynamic and Earth. Engineering*, Eds. M. Papadrakakis, N.D. Lagaros, M. Fragiadakis, Rodes, Greece, 2009.

COMPDYN 2013
4th ECCOMAS Thematic Conference on
Computational Methods in Structural Dynamics and Earthquake Engineering
M. Papadrakakis, V. Papadopoulos, V. Plevris (eds.)
Kos Island, Greece, 12–14 June 2013

ASSESSMENT OF THE RELIABILITY OF STRUCTURAL CONCRETES DURING EXECUTION PHASES

Francesco Porco[1], **Giuseppina Uva**[1]

[1] DICATECh, Politecnico di Bari
address via Orabona, 4 - 70126 Bari (Italy)
f.porco@poliba.it, g.uva@poliba.it

Keywords: Strategic Building, Monitoring Production, Concrete Laying, Concrete.

Abstract. *The quality control of concrete is basically an assessment of compressive strength from which also depends the durability of the material. In the case of important constructions, the control of design prescriptions is not always easy. In addition to the uncertainty factors related to the composition of the material, there are also factors relating to the construction phases. These problems are amplified if the production is on site. These reasons can often suggest to perform, destructive and non-destructive test after the completion of the structure, in order to obtain further information about in-place concrete strength. These investigations, if accompanied by appropriate evaluation procedures, allow to determine the degree of concrete compaction, that if unsatisfactory, makes the material more permeable, less durable and less mechanically efficient. This paper collects the numerical elaboration of resistances measured on cubes made during the concrete placing and on cores extracted after the completion of the structure, for the concrete used in the construction of the "Esaro" Dam facilities (Cosenza, Italy). In addition to the statistical treatment of the sample, aimed to assess the analytical congruence with the homogeneous classes provided in the design, the influence of compaction degree on in place strength value was qualitatively evaluate, with the aid of an analytical methodology.*

1 INTRODUCTION

In new structures, the quality control of concrete, and in particular of the compressive strength, is an essential step for the safety of the structure and its durability, and also plays an important role in the relations between the various professionals involved in the procedure. The operations to be performed in the quality inspections involve both the construction phases, (concrete casting), both a-posteriori “in situ" investigations, in order to verify that the material conforms to that required and specified in the project. This last point is very important in case of controversies about the concrete quality, especially in the case of new projects with strategic importance. However, despite the importance of the problem, both for the safety implications and for the relapses on the regular execution of the construction, concrete is actually one of the few products that is chosen and purchased in accordance with one feature - the compressive strength - that can’t be controlled at the time of purchase and use.

The technical rules [1,2,3] provide indications regarding the implementation of "acceptance tests" of homogeneous mixtures, which have to be controlled after 28 days from the concrete casting. These checks, based on the satisfying of analytical relationships on a statistical basis, are performed on specimens taken during concrete casting, which are properly moulded, compacted and cured in order to develop the so-called "*potential resistance*", that is the upper limit value that a given concrete is capable of developing. If the quality inspection (which is mandatory during the *supervision of works*) is positive, the concrete is “accepted”, i.e. it is considered compliant with the design and law requirements, and no additional verification is neede. In this case, from a strictly legal point of view, both the structural safety and contractual relations between manufacturer and constructor are fully satisfied. Leaving aside the non-compliance due to the negligence or poor check, a negative acceptance control is determined by an inadequate value of the concrete strength.
The factors that can induce a decay of the concrete strength in the acceptance control are related to:

- *Production process*: constituent materials (type of aggregates, cement, etc. ..), production technologies, methods and time of mixing;
- *Transport and installation*: duration and type of transport (in cases when the building site isn’t near the production plant); quantity of water added in the mixture; environmental temperature;
- *Preparation of concrete specimens*: temperature of curing (high values favour the hydration process and reduce resistance), moisture degree [4], executive procedures of the test.

As a consequence of the large number of parameters influencing the resistance value in the different realization phases, the building codes seem to neglect the aspects related to the durability and safety at the serviceability limit state. In fact, the rules, while provide specific requirements relating to the reference life in regard to seismic actions, don’t specify the procedures for guaranteeing that the performance requirements of the materials keep constant in time. The question is even more serious in the case of grand works, that not require a large quantity of concrete, but involve a long duration of the material production and execution phases. It should be noted, in fact, that even if the quality inspections are satisfied (i.e. the concrete supply is compliant with specific exposure conditions, consistency and resistance classes, prescriptions about maximum aggregate size and cement) it is not authomatically guaranteed that in the actual structure in-place will be the same as the prescribed one. There are two other operations involving concrete casting, whose performances are the responsibility of the builder and that can affect significantly the behaviour of the entire structure during the service life.

These are:

- Concrete *placing* (intended as the jet and compaction of in-place concrete) that induces a reduction of in situ strength compared to that of the specimens used in quality inspecttions [5]. In this sense, some of the proposals in the literature show how to quantify the effects of compaction on acquired resistance by in situ destructive tests [6];
- *Aging*. Temperature and time of aging significantly influence the final resistance of specimens. The routine control doesn't always provide consistent results for productions that continue for long periods of time.

In this paper, statistical processing of data collected during the realization phases of the works in support of the Esaro Dam (Calabria, Southern Italy) is presented. Numerical processing based on the resistance values collected by the tests carried out on samples taken during the executive phase, both by the Company and by the Building Supervisor (i.e. the person in charge of the control of materials on behalf of the client, hereinafter "BS"), allows to perform some remarks on the limits on the quality control of concrete for major works. These controls, by the heterogeneity of the mixtures and strength classes provided are made complex.

These operations, made during realization stages, may be useful if in the future the structural safety must be evaluated (typical is the case of existing buildings or infrastructure [7,8,9,10]. In such cases the features in time of concrete must be evaluated, especially for structures that do not have control or monitoring systems for the static capacity in time [11,12,13].

For a better understanding of the reflections produced by this note, a brief summary and critical framework of quality control in the standards are described. For this purpose in the next section there is an overview of the main indications contained in the Italian and European standards.

2 ITALIAN AND EUROPEAN RULES (REGULATORY FRAMEWORK)

2.1 Quality Inspections

As indicated by NTC2008[1], BS has the obligation to verify, during construction and concrete casting, at the end of 28 days from the execution, that the characteristic "*potential*" compressive strength of the concrete (hereinafter indicated with the abbreviation $R_{ck,pot}$) is higher than the characteristic resistance of project ($R_{ck,d}$):

$$R_{ck,pot} \geq R_{ck,d} \tag{1}$$

The characteristic "potential" value is defined as the experimental strength (determined by compression tests) of cubic specimens taken by PS during the control of the concrete supply.
The acceptance of the quantity of concrete is subsequent at the satisfaction of the inequations indicated, respectively, for the control of type A (*§11.1.5.1* - NTC2008[1]) or Type B (*§11.2.5.1* - NTC2008), by adopting the one or the other depending on the amount of homogeneous mixture employed in the realization of the work. For both types the smallest resistance (R_1) between all the specimens must firstly satisfy the following inequation:

$$R_1 \geq R_{ck,pot} - 3.5 \tag{2}$$

In particular, the control of type A, is based on a simplified verification (Eq. 3) and is adoptable only for structures with less than *1500* m^3 of homogeneous concrete, by taking a sample every *100* m^3 of casting and however a minimum of *3* samples (then *6* specimens, because one sample is equal to two specimens).

$$R_{ck,pot} \leq R_{cm,pot} - 3.5 \quad (3)$$

where $R_{cm,pot}$ is the average resistance of the samples (expressed in MPa).

If the amount of homogeneous mixture exceeds 1500 m^3, it is required to adopt control of type B, which is a purely statistical control, in which the correlation between the characteristic and average value is defined by the following equation:

$$R_{ck,pot} \leq R_{cm,pot} - 1.4 \cdot \sigma_{pot} \quad (4)$$

With σ_{pot} standard deviation of the resistance values evaluated on the cubes.

The number of samples to evaluate the mean value $R_{cm,pot}$ and the standard deviation σ_{pot} must be greater than or at least equal to *15* (*30* cubes). Furthermore, it should check that the coefficient of variation (CV) usually called *Relative Standard Deviation*, given by the ratio between standard deviation and average resistance, must not exceed the limit value of *0.3*. If CV exceeds the threshold value of *0.15*, BS must perform more accurate controls. Specifically, if CV is greater than *15%* is necessary to carry out the evaluation of the concrete strength by non-destructive in-situ tests (rebound-hammer or ultrasonic pulse velocity) and destructive tests (extraction of samples by core drilling).

As noted above, the rules state that the conglomerate is identified by its characteristic resistance (potential if verified by means of samples taken during casting), ie compression strength at below which is located only *5%* of all measurements.

However, in correspondence of the fractile of *5%* , the value of the multiplying factor of the standard deviation is equal to *1.64*, while for a value equal to *1.4* (indicated by the standard) the fractile is equal to *8%* [14]. This means that a positive acceptance of control implies that only *92%* of the values are greater than the characteristic value $R_{ck,pot}$. An important issue, always for type B controls, and thus for great quantities of conglomerate, is the possibility to perform accurate statistical analysis. The interpretation of the experimental results can be carried out by identifying the more appropriate law of the statistical approach (without necessarily to use the normal distribution as in the past).

In this case the minimum resistance of sampling (R_1) must be greater than the value corresponding to the lower fractile of *1%* ($R_{ck,pot\ -1\%}$).

$$R_1 \geq R_{ck,pot-1\%} \quad (5)$$

Therefore, the technical standard forces that *99%* of all the resistance of the sample is greater than the minimum resistance R_1.

2.2 Quality control of in-situ concrete strength

If the mechanical strength of the samples taken during the concrete casting doesn't satisfy Eq. 1, or in cases where there's doubt about the validity of the acceptance tests, BS or the *Static Tester* must carry out the assessment of the characteristic compressive strength of in situ concrete (also called "*structural*" strength $R_{ck,strutt}$) by executing experimental investigations based on core drilling and non-destructive tests.

The core drilling is the most commonly used destructive method. It is based on in the extraction of specimens of cylindrical shape. The specimens has *non-standard* size (ie having a *slenderness* λ - defined as ratio between height *H* and diameter *D* - equal to 1) if compression concrete strength value must be compared to the characteristic "cubic" strength of project or potential ($R_{ck,d}$ o $R_{ck,pot}$), while it has *standard* size (with λ equal to 2) when the comparison is in terms of the characteristic "cylindrical" resistance of project or potential ($f_{ck,d}$ o $f_{ck,pot}$).

For assessing of the *structural* strength (in situ), with reference to the cylindrical value $f_{ck,strutt}$ the indications contained in the main technical rules [15] provide two cases:

1. Evaluation of the average value in situ $f_{cm,strutt}$, when the number of cores is less than 15. In order to verify the conformity of the material in place, this value must be greater than *85%* of the average cylindrical value of design f_{cm}, according to the following relations:

$$f_{cm,strutt} \geq 0.85 \cdot \left(0.83 \cdot R_{ck,d} + 8\right) \tag{6}$$

2. Also evaluation of the characteristic value if the number of cores is greater than *15*. This kind of control is purely statistical and it is based on the correlation between characteristic and average value by the following equation:

$$f_{ck,strutt} = f_{cm,strutt} - 1.48 \cdot \sigma_{strutt} \tag{7}$$

where σ_{strutt} is the standard deviation of mechanical strengths of the cores. For this additional parameter, therefore, the acceptance control is to satisfy the following relation:

$$f_{ck,strutt} \geq 0.85 \cdot \left(0.83 \cdot R_{ck,d}\right) \tag{8}$$

With regard to the comparison between "structural" and "potential" strength, the NTC2008 *(§ 11.2.6*) clearly explain that the value $R_{cm,strutt}$ is generally less than the average value of the resistance $R_{cm,pot}$ of samples taken during concrete casting and preserved in optimal laboratory conditions (*20°C* e *φ>95%*).
At the end of the overview about acceptance tests, is reported below the casuistry on the possible responsabilities attributable to professionals when *Eqs. 6* and *8* are simultaneously satisfied and not satisfied:

1. *Eqs. 6 and 8 satisfied*: the strength of the in situ concrete is acceptable without further verification. It may, however, remain a possible dispute against the supplier if Eq. 1 is not verified.
2. *Eqs. 6 and 8 unsatisfied*: BS or the *static tester* can require the structural strengthening or even the whole demolition. In this case, the overall cost of such actions will be borne by the supplier if the concrete $R_{ck,strutt}$ is greater than *85%* of $R_{ck,pot}$ because the constructor has put in-situ a concrete lacking provided by the supply. If, however, the resistance characteristic of the structure is less than *85%*, the cost is borne also by the company because the concrete already poor, in a wrong way was casted.

2.3 Concrete laying

The care in concrete casting is an aspect that greatly affects the durability of the material, and as noted at the end of the previous paragraph, is one of the causes of legal challenges that arise during acceptance tests. In RC structures built with ordinary concrete (excluding the self-compacting concrete), the structural resistance R_{strutt} (average or characteristic value), that is determined on drilled cores, is less than the resistance measured on test specimens (cubic or cylindrical) taken during the casting phases. Thus, indicating, respectively, with $R_{C,pot}$ the mechanical strength of a cubic specimen, $f_{C,pot}$, the cylindrical strength of specimen (both taken by jets) and f_{core} the resistance of a sample extracted by a RC element of the structure by core drilling:

$$0.83R_{C,pot} = f_{C,pot} \geq f_{core} \tag{9}$$

The differences not only by the factors relating to the operations of drill are caused (such as the damage on the sample induced by core drilling), but especially to the incomplete compaction of the concrete than the highest obtained for samples taken during the cast.

The correlation between R_{CI} and f_{core} is strictly dependent on the care taken during the concrete casting. This care can be measured by the following parameter, called "*compaction degree*" g_c [5]:

$$g_c = \frac{m_V}{m_{VO}} \tag{10}$$

where m_{V0} is the density of the specimen and m_V is the density of the drilled core.

For an ordinary structural work, considering homogeneous classes of material, if the structural concrete has been compacted with the same care with which it has been the concrete of the specimen, the degree of compaction is unitary: $g_c=1$. The density m_V will, instead, less than m_{v0}, and consequently $g_c<1$, if the efficacy of the compaction of the core is lower than that of the specimen. By means of experimental tests on concretes having different consistency classes and resistances, the same author has evaluated the influence of g_c on the percentage decrease of the concrete mechanical strength ΔR_g inside the structure than the value of the corresponding specimen:

$$\Delta R_g = \frac{f_{C,pot} - f_{core}}{f_{C,pot}} \cong (1 - g_c)500 \tag{11}$$

It represents a linear relationship between ΔR_g and g_c valid in the range $0.90 < g_c < 1$ relative to concrete for structural uses.

The uniaxial compression test allows to derive the compression strength of the cylindrical core. The value is strongly dependent on various parameters associated with the test mode that make it substantially different from the effective resistance of the in situ concrete.
Guidelines on how to perform the test and the processing of the results obtained are the [16,17,18]. These documents take as reference the compressive strength measured on a "standard" core ($\lambda = 2$). It is possible, however, to take samples having *non-standard* size provided that, the value of the relative strength $f_{c,nst}$ is reported (by appropriate corrective coefficients) to a resistance associated with an equivalent sample of *standard* size:

$$f_{core} = F_{mc}F_d\left(F_{H/D}F_{dia}F_r f_{c,nst}\right) \tag{12}$$

$F_{H/D}$, F_{dia} and F_r are respectively the corrective coefficients which take account of the effects induced by the variability of λ, D and when the reinforcement bars are inside the core ("*internal*" or "*form*" factors). F_{mc} and F_d are correction factors to take account of, respectively, the storage conditions of the specimens before of the compression test and the damage induced by drilling core ("passive" factors).

The effects of these factors on the strength value and the different proposals to assess numerically the coefficients can be found in numerous research studies in the literature [19,20,21,22,23,24,25,26,27,28,29,30].

The numerical variability of the strength (f_{core}) is therefore intrinsic. It is to be intended as a sum of the variability of independent parameters relating to the execution method of the experimental test, the quality of the material, geometrical characteristics of the samples and the damage caused by the drilling core. With good approximation, the overall variability is between a minimum of *3.2%* [27] to a maximum of *6.0%* [31].

3 THE CASE STUDY

The Esaro dam is a strategic work made necessary by the growing problems of water supply of the entire territory of the Province of Cosenza. The completion of the dam (to date imminent) will allow an increase in water flow rate of *200* liters per second for the areas between the Tyrrhenian and Ionic coast of Cosenza. In this case, the generic name "dam"

means a collection of works which together with the main structure are fundamental to the enjoyment and the normal functioning of the entire structural system. At the present date, only the support works, necessary for the construction phase of the dam itself, have been completed. The construction of these works began in 2004 and ended in 2012.
These works can be collected in three large sub-categories (Table 1):

Sub-category	Volumes of Concrete *[mc]*	Number of specimens
Sedimentation-Basin	*27255*	*660*
Road	*4088*	*370*
Work for stability	*17118*	*430*
TOTAL	48461	1460

Table 1. Quantities of concrete in place and number of specimen taken during the operations of casting

In particular, within the category "sedimentation basin", the structure of water collection, the retaining structures, walls and boundary of basin are collected; In the "street" falls the entire road of the dam, which provides a bridge and a tunnel of connection; finally, under the category "works of stability", conglomerate volumes associated with "works restraint" (containment structures of the soil to protect the road subject to landslide risk as a result of the digging operations) and the related foundation are collected. The heterogeneity of the works has induced the use of mixtures very different not only for strength classes, but especially for exposure and consistency classes. The importance of the work and the long realization times, led us to adopt systematic control in building site of the mixtures used. To this end, the presence on site of the concrete mixing plant and of the testing laboratory has allowed to a systematic quality control of the material. Different strength classes for each category were used and Tab. 2 reports the number of cubes taken during the jets and crushed by the laboratory in building site and by the official one.

$R_{ck,d}$ *[MPa]*	In building site n. cubes	Official Laboratory n. cubes	Total n. cubes
22	*746*	*278*	*1024*
25	*16*	*42*	*58*
30	---	*312*	*312*
35	*34*	*24*	*58*
40	---	*8*	*8*
TOTAL		1460	

Table 2: Number of cubes taken during the execution stage for different strength classes

4 CONTROL DURING EXECUTION PHASE

The controls of the concrete used for the realization of works in support of the dam, can be divided into two groups:

- *Production controls*. These are based on statistical processing of values obtained by the samples of the various strength classes and by the control of the concrete curing;
- *Laying controls*. These are to assess the compaction degree by statistical approach, in according to specific relations of the literature on issue [5].

In the first group, the numerical processings have concerned samples constituted by cubes. The resistances correspond to values after 28 days by execution of the cast, while as regard to the second group, resistances after, respectively, 3, 7, 21 and 28 days were considered.

4.1 Production controls

On the basis of the volumes of concrete used for the construction of structures (quantity far greater than *1500 m^3*), the conformity of the material by assessing the acceptance check of type B was evaluated. In addition, for all the homogeneous classes analyzed statistical elaborations were carried out. The statistical approach allows to process the resistances at *28* days of cubes taken in-situ, in order to identify distribution laws alternatives to the normal one and evaluate main statistical parameters that are representative of every sampling. In particular, for samplings more numerous relating to a $R_{ck,d}$, equal, respectively, to *22*, *25*, *30* and *35 MPa*, significant statistical parameters (mean value μ, standard deviation σ, variance σ^2 and coefficient of variation, *CV* - Table 3) were identified and, furthermore, the normal and lognormal distribution laws were evaluated.

	Samplings			
$R_{ck,d}$ *[MPa]*	22	25	30	35
μ *[MPa]*	*27.71*	*31.24*	*37.09*	*40.21*
σ *[MPa]*	*2.14*	*2.20*	*2.50*	*1.47*
σ^2 *[MPa^2]*	*4.60*	*4.83*	*6.25*	*2.16*
CV *[%]*	*7.77*	*7.03*	*6.74*	*3.65*

Table 3. Main statistical parameters of samplings analyzed

It should be noted that the values of *CV* of each sampling are lower than the 15% threshold beyond which the Italian legislation requires more accurate tests (destructive and non-destructive test on samples extracted by structural elements).

The value of the "*potential*" characteristic strength of each sampling was evaluated by a lognormal distribution law, after a preliminary check in order to ascertain the good correspondence with the distribution of the relative frequencies. The Figure 1 shows the statistical distributions of the most numerous sampling (ie those associated with $R_{ck,d}$ equal to *22* and *30*) while Figure 2 shows the potential characteristic strength at the *5%* fractile of the cumulative lognormal distributions. Also this figure, in the spirit of statistical approach provided by the acceptance tests of type B, shows the value corresponding to the *1%* fractile $R_{ck,pot\ -1\%}$ as representative of the minimum strength of sample taking (ie. sampling).
For these samplings, the defined distribution laws approximate satisfactorily the experimental distribution, while it is interesting to note, that lognormal law, identified as an alternative to that normal, roughly follows the same normal distribution.

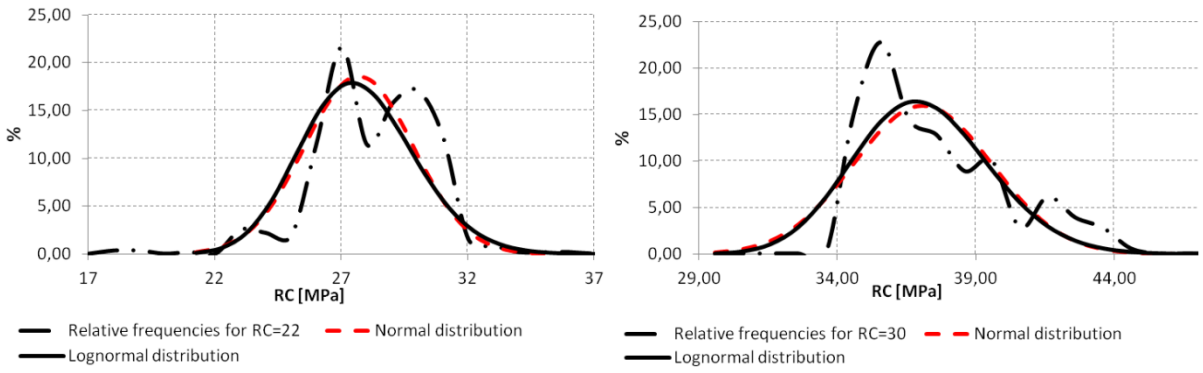


Figure 1: Relative frequencies, normal and lognormal distributions for analyzed samplings .

Instead the lognormal law, used in the calculation of the potential characteristic value $R_{ck,pot}$ (Figure 2) (as intersection with fractile of 5%), provides slightly lower values than those obtained by normal cumulative distribution (with the exception of the sampling associated with $R_{ck,d}$=22 MPa), but in any case values aren't higher than 5%.

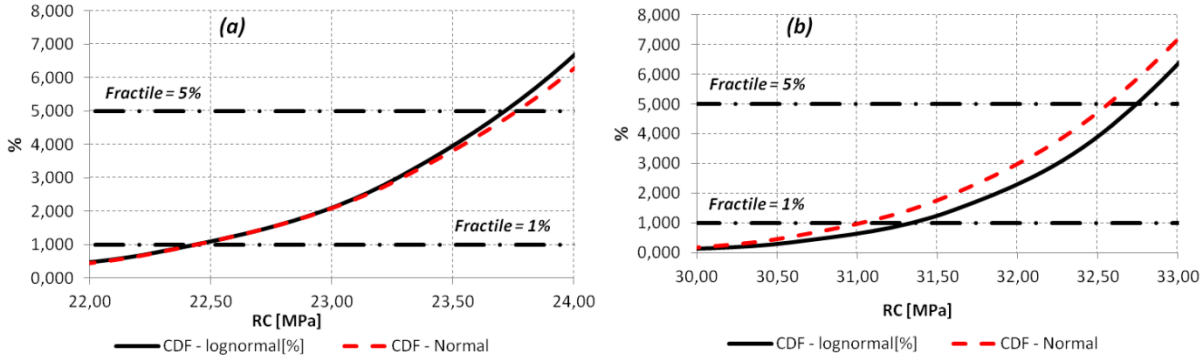


Figure 2. Acceptance control of type B: potential characteristic strength and lower threshold value for sampling associated with project resistance $R_{ck,d}$ equal to 22 (a) and 30 (b)

The values of the potential characteristic strength ($R_{ck,pot}$), those corresponding to 1% fractile ($R_{ck,pot\ -1\%}$) (as intersection of the lognormal law with fractile of 1%), the average resistances of sample taking ($R_{cm,pot}$) and the lower resistance of sampling (R_1) are reported in Table 4. It 's clear that for all samplings Eqs. 1, 4 and 5 are respected, although the latter applied improperly (ie not only every 3 samples but on the entire sampling), and furthermore, values exceed the lower threshold ($R_{ck,pot\ -1\%}$) required by statistical control.

Sampling	$R_{ck,pot}$ *[Mpa]* (fractile=5%)	$R_{ck,pot\ -1\%}$ *[MPa]* *(fractile =1%)*	$R_{cm,pot}$ *[Mpa]*	R1 *[MPa]*
$R_{ck,d}$=22 MPa	23.70 *Eq.1, OK!*	22.38	27.71 *Eq. 4,OK!*	22.41 *Eq. 5,OK!*
$R_{ck,d}$=30 MPa	32.58 *Eq. 1, OK!*	31.12	37.09 *Eq. 4, OK!*	33.64 *Eq. 5, OK!*

Table 4. Acceptance tests for the concretes of the case study

4.2 Laying controls

The laying control plays a predominant role in monitoring of conformity of the material. Indeed, it becomes important when is necessary to quantify, especially in the case of great infrastructure projects, the gap in strength between the *potential* material (corresponding to maximum compaction degree) and the *structural* material.

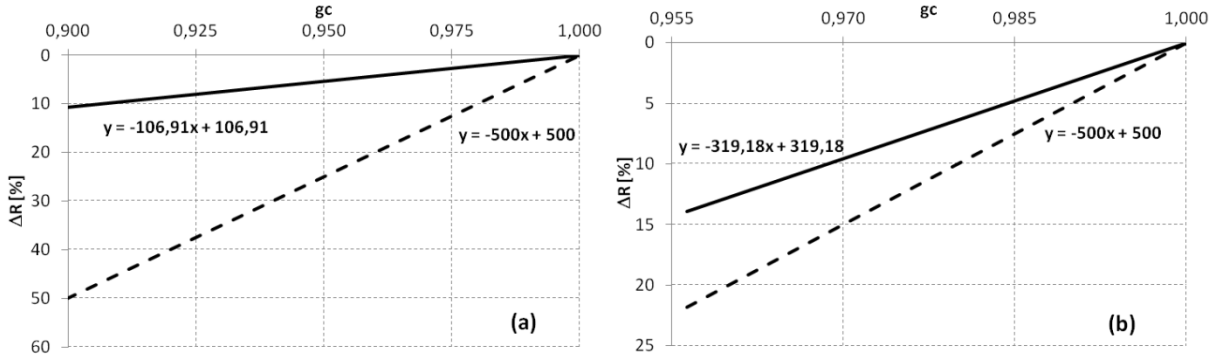


Figure 3. Comparison between percentage reductions of structural strength than the potential values and Collepardi's law [5], as a function of the compaction degree, for sampling associated, respectively, with $R_{ck,d}$=22 MPa (a) and $R_{ck,d}$=30 MPa (b).

The reduction of structural strength than that measured on samples taken during the concrete casting, for the samplings considered until now was evaluated as a function of the compaction degree g_c, according to the approach described in § 1.3. In particular, for each sample $\Delta R=\Delta R(g_c)$ law was identified by expressing it in a form similar to Eq. 11. The results shown in Figure 3 are particularly interesting.

The reductions ΔR for the sampling having strength class lower ($R_{ck,d}=22MPa$), are very small than the Collepardi's law (Fig. 3a). In addition, the reductions obtained are about *1/3* than the other sampling analyzed (relating to material having $R_{ck,d}=30MPa$ - Fig. 3b).
Therefore, graphs shows a good compaction of concrete having class equal to *22 MPa* (the reductions are approximately *1/5* of theoretical prevision) and the conservative trend of the Collepardi's law.

In the testing phase, several cores were extracted by core drilling, the reductions of strength as a function of the compaction degree were evaluated for cores relating to strength class $R_{ck,d}=22MPa$. The corresponding values were reported within the $\Delta R[\%]$-g_c format together with the distributions of ΔR for the whole sampling (respectively after 7 and 28 days of curing) and with theoretical trend proposed by Collepardi (Fig. 4).

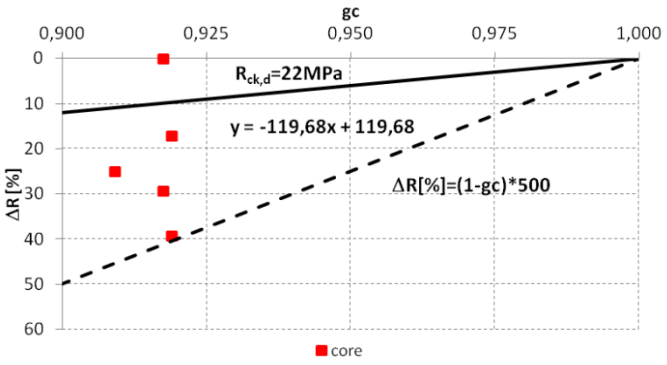


Figure 4. Comparison between percentage reductions of structural strength than the potential values and Collepardi's law [5], as a function of the compaction degree.

The reduction of resistance of the cores are between the performance of sampling and the theoretical one, this suggests that the strength values were influenced, not only by the concrete laying but also by other factors, as for example, those inherent execution of experimental test. In fact, it should be noted that the effect of damage on sample by core drilling was evaluated only by a coefficient based on experimental researches present in literature. Most likely, by reformulating this coefficient, the points obtained will be closer the trend of the theoretical strength reductions.

5 CONCLUSIONS

The current technical rules are based on an approach that aim to achieve a design conforms to the expected durability and the intended use of the structure. They provide, therefore, indications relating to the sizing of the structural elements and to the construction details in order to obtain structures able to mainly support seismic events. These on the effective characteristics of the ground type and geographic location of the structure are calibrated.

The need to preserve the structural safety in time, it isn't, however, extended to the materials commonly used. For this purpose, the rules provide a detailed control of the conformity of "potential" concrete strength, (ie the concrete strength measured on samples taken during the casting operations), compared to the design value. This control can be extended to the "structural" resistance. The assessment allows to resolve any disputes between some professional

figures involved in the construction process. In this context is evident that one of the possible causes of discrepancy is caused to poor laying of the concrete. This circumstance is amplified in major works, for the great concrete amount and the prolonged periods of execution.

This study, by data collected during the execution of some structure to support of a dam, provides some remarks on fundamental role of the laying of the concrete. The study highlights how the current rules are particularly restrictive. The statistical results together with specific numerical elaborations have led to consider appropriate the control, not only of the concrete strength, but also of the laying intended as a measure of the durability of the material in time.

It is therefore outlined by the description of the results collected, a systematic procedure based on the measurement of the compaction degree g_c for cubes in-situ packaged. The procedure allows to quantify the reductions of strength in percentage terms of the "structural" value (on site) than the corresponding "potential" value.

The convenience obtained by controlling the compaction degree in the construction phase is unquestionable. Specifically, it may allow a reduction of the drilling cores especially for relatively recent structure in favor of extensive non-destructive investigations. Any changes in concrete performance will be obtained by measurement of the rebound index or ultrasonic pulse velocity.

REFERENCES

[1] DM 14/01/2008. Norme Tecniche per le Costruzioni (NTC 2008). Gazzetta Ufficiale n.29. Roma, 2008.

[2] Circolare 2 febbraio 2009. n. 617 approvata dal Consiglio Superiore dei Lavori Pubblici. Istruzioni per l'applicazione delle "Nuove norme tecniche per le costruzioni" di cui al Decreto Ministeriale 14 gennaio 2008 – 2009.

[3] CEN. 2005. Eurocode 2: Design of concrete structures. Part 1-1: General rules and rules for buildings. European Committee for Standardization, Brussels, Belgium; 2005.

[4] L. Coppola, Controlli della resistenza a compressione del c.l.s. in opera in accordo alle nuove norme tecniche per le costruzioni. Contestazioni legali (In Italian). *L'edilizia*, **141**; 2005.

[5] M. Collepardi, *The new concrete*. Edizioni Tintoretto, Villarba, Italy, 2010.

[6] G. Uva, F. Porco, A. Fiore, M. Mezzina, Proposal of a methodology of in-situ concrete tests and improving the estimate of the compressive strength, *Construction and Building Materials* **38**(1),72-83, 2013.

[7] G. Uva, F. Porco, A. Fiore, Appraisal of masonry infill walls effect in the seismic response of RC framed buildings: a case study. *Engeneering Structures*, **34**(1):514–26, 2012.

[8] A. Fiore, F. Porco, D. Raffaele, G. Uva, About the influence of the infill panels over the collapse mechanisms actived under pushover analyses: two case studies. *Soil Dynamics and Earthquake Engineering*, **39**,11-22, 2012.

[9] G. Uva, F. Porco, D. Raffaele, A. Fiore, On the role of equivalent strut models in the seismic assessment of infilled RC buildings. *Engineering Structures*, **42**:83-94, 2012.

[10] D. Raffaele, F. Porco, A. Fiore, G. Uva, Simplified Vulnerability Assessment of RC Circular Piers in Multi-Span-Simply-Supported Bridges. *Structure and Infrastructure Engineering*, 2013 - DOI:10.1080/15732479.2013.772642.

[11] A. Fiore, M. Mezzina, F. Porco, D. Raffaele, G. Uva, Seismic safety assessment program of school building in Puglia (Italy): overview and case studies, Paper n. 3978 in *Proceedings of 15th World Conference on Earthquake Engineer*ing (WCEE 2012), Lisbon, Portugal, September 24-28, 2012.

[12] F. Porco, A. Fiore, G. Porco, G. Uva, Monitoring and safety for prestressed bridge girders by SOFO sensors, *Journal of Civil Structural Health Monitoring* **3**(1),3-18, 2013. DOI 10.1007/s13349-012-0029-9.

[13] G. Uva, D. Raffaele, F. Porco, A. Fiore, G. Porco, Bridge monitoring by fiber optic deformation sensors: a case study. In: Biondini, Frangopol (eds) Proceedings of the 6th international conference on bridge maintenance, safety and management, Como, Italy, 8–12 July 2012. Taylor & Francis Group, London - ISBN: 978-0-415-62124-3.

[14] V.A. Rossetti, A. Ferraro, Normativa e controllo di qualità del calcestruzzo: dalla produzione alla verifica in sito (In Italian). *In Concreto* **76**, 72-88, 2007.

[15] C.SS.LL.PP. Linee guida per la messa in opera del calcestruzzo strutturale e per la valutazione delle caratteristiche meccaniche del calcestruzzo indurito mediante prove non distruttive, Roma, 2008

[16] American Concrete Institute, Guide for Obtaining Cores and Interpreting Compressive Strenght Results. (ACI 214.4R-03), Detroit, Michigan, USA, 2003.

[17] ASTM Committee C-9, Standard test method for obtaining and testing drilled cores and sawed beams of concrete (ASTM C42-90). Annual Book of ASTM Standards. vol. 04.02. American Society for Testing and materials, Philadelphia, PA, USA, 1992

[18] British Standard n.1881. Part 120. Method for Determination of Compressive Strength of Concrete Cores, Londra, U. K., 1983.

[19] J.W. Murdock, C.E. Kesler, Effect of Length to Diameter Ratio of Specimen on the Apparent Compressive Strength of Concrete. *ASTM Bulletin* 68-73, 1957

[20] F.M. Bartlett, J.G. MacGregor, J.G., Effect of core diameter on concrete core strengths. *ACI Materials Journal* **91**(5), 460-470, 1994.

[21] R.C. Meininger, Effect of Core Diameter on Measured Concrete Strength. *Journal of Materials* **3**(2), 320-336, 1968.

[22] R.K. Lewis, Effect of Core Diameter on the Observed Strength of Concrete Cores. Commowealth Scientific and Industrial Research Organization Division of Building. *Research Report* **No. 50** Melbourne. Australia, 1976.

[23] R.H. Campbell, R.E. Tobin, Core and Cylinder strengths of natural and lightweight concrete. *ACI Journal. Proceedings* **64**(4), 190-195, 1967.

[24] Y.H Loo, C.W. Tan., C.T. Tam, Effects of embedded reinforcement on the measured strength of concrete cylinders. *Magazine of Concrete Research* **41**(146), 11-18, 1989.

[25] Federal Emergency Management Agency. 1997. NEHRP Commentary on the Guidelines for the Seismic Rehabilitation of Buildings. (FEMA 274). Washington D.C.

[26] D.L.Bloem, Concrete strength in structures. *ACI Journal. Proceedings* **65**(3), 176-187, 1968.

[27] R.C. Meininger, F.T. Wagner, K.W. Hall, Concrete core strength - the effect of length to diameter ratio. *Journal of Testing and Evaluation* **5**(3),147-153, 1977.

[28] F.M. Bartlett, J.G. MacGregor, J.G., Effect of core length to diameter ratio on concrete core strength. *ACI Materials Journal* **91**(4), 339-348, 1994.

[29] F.M. Bartlett, J.G. MacGregor, J.G., Effect of moisture condition on concrete core strengths. *ACI Materials Journal* **91**(3), 227-236, 1994.

[30] F.M. Bartlett, J.G. MacGregor, J.G., Variation of in-place concrete strength. *ACI Materials Journal* **96**(2), 261-70, 1999.

[31] Concrete Society. Concrete core testing for strength. C.S. *Technical Report* **N. 11**, Londra, U.K., 1987

COMPDYN 2013
4th ECCOMAS Thematic Conference on
Computational Methods in Structural Dynamics and Earthquake Engineering
M. Papadrakakis, V. Papadopoulos, V. Plevris (eds.)
Kos Island, Greece, 12–14 June 2013

COMPARATIVE EVALUATION OF DIFFERENT DAMAGE MEASURES FOR REINFORCED CONCRETE BUILDINGS CONSIDERING VARIABLE INCIDENT ANGLES

Konstantinos Morfidis[1], Konstantinos Kostinakis[2], and Christos Karakostas[3]

[1]Earthquake Planning and Protection Organization (EPPO-ITSAK)
5 Ag. Georgiou Str., 55535, Thessaloniki, Greece
e-mail: kmorfidis@itsak.gr

[2] Department of Civil Engineering, Aristotle University of Thessaloniki
Aristotle University campus, 54124, Thessaloniki, Greece
e-mail: kkostina@civil.auth.gr

[3]Earthquake Planning and Protection Organization (EPPO-ITSAK)
5 Ag. Georgiou Str., 55535, Thessaloniki, Greece
e-mail: christos@itsak.gr

Keywords: Reinforced Concrete Structures, Damage Index, Seismic analysis, Seismic excitation angles, Seismic Damage, Inelastic response.

Abstract. *One way of quantifying the extent of seismic damage induced to Reinforced Concrete (R/C) structures is the use of damage indices. Various damage indices have been introduced by many researchers incorporating different parameters for estimating structural damage. The aim of the present paper is the comparative evaluation of three of the most widely used damage indices for the R/C buildings taking into account the orientation of the strong motion. For the investigation of the present study three symmetric in plan R/C buildings are investigated: a low-rise building (3 stories), a medium-rise building (5 stories) and a high-rise building (8 stories). The three buildings are analysed by nonlinear time-history analysis using 20 bi-directional earthquake ground motions. The two horizontal accelerograms of each ground motion are applied along horizontal orthogonal axes forming 72 different angles with the structural axes. For each ground motion and incident angle, the local damage indices at every relevant cross section as well as the overall damage index of the building are computed using three different definitions of the damage index. The analyses results show that the numerical estimation of the seismic damage induced to R/C buildings depends on the damage index used to quantify the damage. Moreover, the overall damage state of the building is significantly affected by the incident angle of the ground motion.*

1 INTRODUCTION

The assessment of the level of the damages that is expected to come up in structural members of R/C buildings constitutes a very important piece of data in the process of planning scenarios of seismic risk of individual buildings as well as of a group of buildings. The procedures available nowadays are based on analytical methods, as well as in situ assessments of seismic vulnerability, or on a combination of both. One of the analytical methods available is based on use of suitable damage indices. Damage indices are analytical expressions of the damage level expected to appear in structural members and are generally defined in various ways in international literature. Their basic principle is the assessment of the damage level through its correlation with parameters that can be calculated analytically. Such parameters are ductility, strength, the reinforcement ratio, the hysteresis loop etc. Due to the fact that the inelastic response of structural elements that causes damages depends on a number of factors which cannot be easily taken into consideration simultaneously, several definitions of damage indices have been proposed. Among the various factors that affect the reliable analytical evaluation of damage indices, one should highlight the uncertainty introduced in the response of buildings by the seismic excitation angle. Research has shown (see e.g. [1, 2, 3, 4]) that in many cases the seismic excitation angle can radically alter the analysis results in terms of both the required reinforcement ratio of structural members (see e.g. [1, 4]) and of the damage level (see e.g. [2, 3]).

The objective of the present paper is the investigation of the level of the expected damages in R/C buildings by applying three different definitions of the damage index, i.e. the definitions of Park-Ang [5, 6], Bracci et al. [7] and Cosenza et al. [8]. The evaluation of these indices requires non-linear time-history analyses. The accelerograms demanded for these analyses were selected out of 20 different recordings, 10 of which correspond to near-fault strong motion records, while the rest correspond to far-fault records. This specific distinction was chosen since it is well-known that far-fault records have characteristics different from those of near-fault ones, resulting in a difference in the seismic response of buildings. With regard to the choice of the buildings, three R/C double symmetric buildings of low (3-storey), medium (5-storey) and high (8-storey) rise were selected. The rationale behind this choice was the investigation of the influence of the horizontal stiffness on the damage level in connection with the different characteristics of earthquakes. All selected buildings have a structural system which is a frame system along one direction and a wall-equivalent dual system along the other direction (which is perpendicular to the former), with walls that receive approximately 60% of the base shear of buildings in this specific direction. This choice was made in order to investigate the influence of the seismic excitation angle on buildings with horizontal stiffnesses that are considerably different along two perpendicular directions. The buildings were designed following the provisions of EN1992-1-1 [9], and EN1998-1 [10]. Then the buildings were analyzed by nonlinear time-history analysis for each one of the 20 earthquake records taking into account 72 different incident angles of the input motion. For each ground motion and incident angle the overall damage index of the three buildings was computed using the three aforementioned different definitions of damage indices.

The analyses results show that the use of Bracci et al. damage index leads to the largest values of the overall structural damage index of the buildings, whereas the use of Cosenza et al. damage index leads to the smallest values for the vast majority of the incident angles and earthquake records. Moreover, the most widely used Park and Ang damage index leads to the smallest influence of the excitation angle as well as of the number of stories.

2 DESCRIPTION OF THE PROCEDURE OF THE ANALYSIS

The procedure followed in order to achieve the goals of the present investigation consists of the following steps:

(a) Selection of the examined R/C buildings,
(b) Modeling of the elastic and inertia behavior,
(c) Design of the structural elements of the buildings,
(d) Modeling of the nonlinear behavior of the structural elements of the buildings,
(e) Selection of the seismic excitations used for the nonlinear analyses,
(f) Analysis of the buildings using the method of nonlinear time-history analysis for various angles of the seismic excitation,
(g) Calculation of damage indices for the structural elements, as well as for each building as a whole, with three different definitions of damage indices.

In the following, the details of the aforementioned steps are presented.

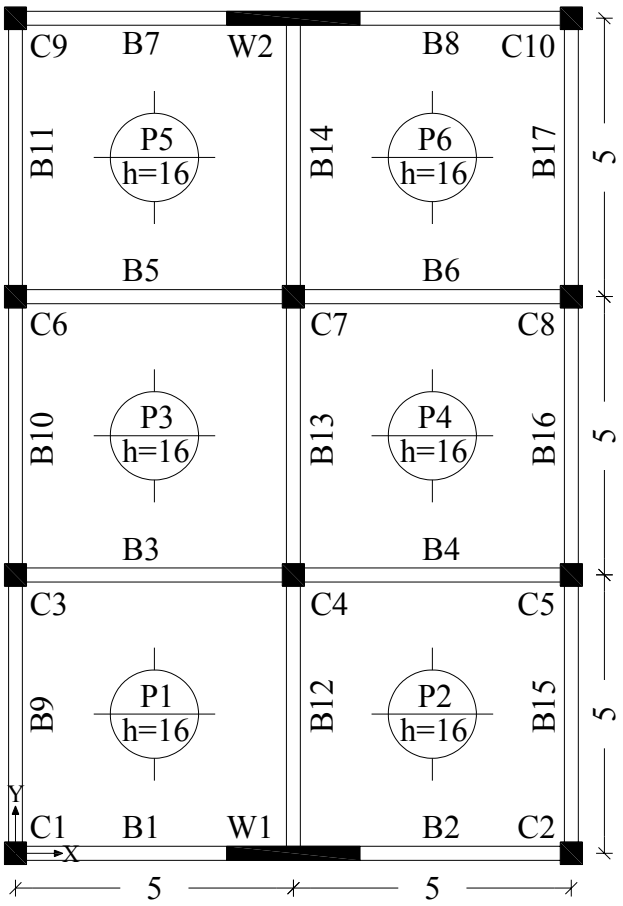
2.1 Description of the selected R/C buildings and assumptions of their elastic modeling

For the purposes of the investigation, three double symmetric R/C buildings, with design parameters as shown in Figure 1, were chosen. All three buildings have a structural system that consists of R/C frames in two orthogonal directions (axes X and Y). Along X-axis there are two R/C walls that receive approximately 60% of the base shear. According to the structural types described in EN1998-1 ([10], §5.2.2.1), all buildings belong to the type of frame systems along the Y-axis and to the type of wall-equivalent dual systems along X-axis. Therefore, their horizontal stiffness along the Y-axis is roughly equal to 65% of their horizontal stiffness along the X-axis. All buildings are regular in plan and elevation according to the criteria set by EN1998-1 ([10], §4.2.3.2, §4.2.3.3), and were designed as medium ductility class (DMC) buildings. Based on the above data, the process of calculating the upper limit value of the behavior factor q of EN1998-1 ([10], §5.2.2.2) led, in all three cases, to the values $maxq_x=3$ and $maxq_Y=3.9$. However, a unique value for the X and Y axes, equal to $q=min(maxq_X,maxq_Y)=3$, was taken in to account for the analysis and design.

In the modeling of the buildings, all basic recommendations of EN1998-1 [10] were taken into consideration, such as the diaphragmatic behavior of the plates, the rigid zones in the joint regions of beams/columns and beams/walls, and the values of flexural and shear stiffness corresponding to cracked R/C elements. All buildings were considered to be fully fixed to the ground.

2.2 Analysis and design of the buildings

The buildings were analyzed using the modal response spectrum analysis, as defined in EN1998-1 ([10], §4.3.3.3). The R/C structural elements were designed following the provisions of EN1992-1-1 [9] and EN1998-1 [10]. Consequently, a capacity design at frame joints was made only along Y-axis, where the buildings belong to the type of frame systems ([10], §4.4.2.3[5]). It should be noted that the choice of the dimensions of the structural element cross-sections as well as that of their reinforcement was made while bearing in mind the optimum exploitation of the structural materials (steel and concrete). Therefore, the capacity ratios (CRs) of all critical cross-sections due to bending and shear are close to 1.0 (the mean value of CRs ranges between 0.92-0.96). The professional program for R/C building analysis and design RAF [11] was employed in both the analysis and the design.



MATERIALS

Concrete:

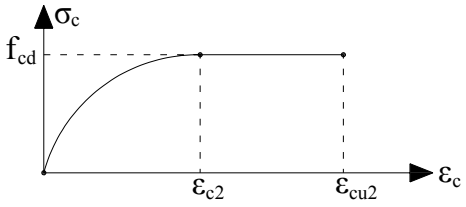
$E_c = 3.0 \cdot 10^7$ kN/m², v=0.2, w=25 kN/m³

Stress-Strain relation for design from EC2:

f_{ck} =20000 kN/m², f_{ctm}=2200 kN/m²

$f_{cd} = \alpha_{cc} f_{ck} / \gamma_c = 0.85 f_{ck} / 1.5 = 11333.3$ kN/m²

$\varepsilon_{c2} = 2.0‰$, $\varepsilon_{cu2} = 3.5‰$



Steel:

$E_s = 2.0 \cdot 10^8$ kN/m², v=0.2, w=78.5 kN/m³

Stress-Strain relation for design from EC2:

f_{yk} =500000 kN/m²

$f_{yd} = f_{yk} / \gamma_s = f_{yk} / 1.15 = 434783$ kN/m²

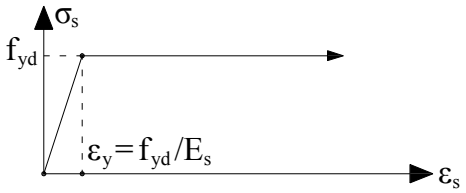


Plate loads: Permanent G=1.0kN/m², Variable Q=2.0kN/m²

Weight per unit of the masonry area: Perimetric beams 3.6kN/m², Internal beams 2.1kN/m²

Stories' heights: H_i=3.2m

Ductility class: Medium (DCM)

Design spectrum for elastic analysis: From paragraph 2.2.2.5 of EC8-1. Parameters:

Reference peak ground acceleration a_{gR}=0.24g
Importance class of buildings: II → γ_I=1.0
→ $a_g = \gamma_I a_{gR}$=0.24g

Ground type: C → S=1.15, T_B=0.2sec, T_C=0.6sec, T_D=2.5sec

Value of the behaviour factor q=3

Dimensions of the cross-sections of R/C members:

	3-Story Building (3SB)			5-Story Building (5SB)			8-Story Building (8SB)		
Storey	Beams	Columns	Walls	Beams	Columns	Walls	Beams	Columns	Walls
1st	25/45	35/35	115/25	25/55	40/40	150/25	25/55	45/45	160/25
2nd	25/45	35/35	115/25	25/55	40/40	150/25	25/55	45/45	160/25
3rd	20/45	30/30	115/25	25/50	35/35	150/25	25/55	40/40	160/25
4th	—	—	—	25/45	35/35	150/25	25/50	40/40	160/25
5th	—	—	—	20/45	30/30	150/25	25/50	35/35	160/25
6th	—	—	—	—	—	—	25/50	35/35	160/25
7th	—	—	—	—	—	—	25/45	30/30	160/25
8th	—	—	—	—	—	—	20/45	30/30	160/25

Figure 1: Design parameters of the investigated buildings

2.3 Selection of the seismic excitations used for the nonlinear time-history analyses

A suite of 20 pairs of horizontal bi-directional earthquake ground motions (10 far-fault and 10 near-fault records) obtained from the PEER [12] and the European [13] strong motion database was used as input ground motion for the analyses of the buildings investigated in the present study. The ground motions were recorded on Soil Type C according to EN1998-1. The characteristics of the input ground motions are shown in Tables 1 and 2 along with the correlation factor of the components. The correlation factor ρ is given [14] by Eq. 1:

$$\rho = \frac{\sigma_{xy}}{\left(\sigma_{xx} \bullet \sigma_{yy}\right)^{1/2}} \quad \text{with} \quad \sigma_{ij} = \frac{1}{s} \bullet \left(\int_0^s \alpha_i(t) \bullet \alpha_j(t) dt \right) \quad i = x, y \tag{1}$$

where $\alpha_x(t)$ and $\alpha_y(t)$ are the recorded ground accelerations along the two horizontal directions of the ground motion; σ_{xx}, σ_{yy} are quadratic intensities of $\alpha_x(t)$ and $\alpha_y(t)$ respectively; σ_{xy} is the corresponding cross-term; s is the duration of the motion.

It should be noted that, as ASCE 41-06 proposes [15], the uncorrelated horizontal components of ground motion have been used as seismic input in the present study. The accelerograms were scaled to Peak Ground Acceleration PGA = $a_g \cdot S$ = 0.276g, where a_g and S are the design ground acceleration and the soil factor respectively used for the elastic analysis of the buildings. Although it is known that PGA scaling does not correlate strongly with the expected damage levels, it was nevertheless applied herein for simplicity reasons, since in the present study the factor under investigation is, as already mentioned, the incident angle of the input motion. In Tables 1 and 2 the scale factors (SF) produced by the scaling procedure for each ground motion are presented. The SRSS of the 5%-damped spectra of the scaled accelerograms are depicted in Figures 2a and 2b.

No	Date	Earthquake name	Magnitude	Station name	Station number	Closest distance (Km)	Component (deg)	PGA (g)	Cor Factor (p)	SF
1	24/4/1984	Morgan Hill	6.2 (Ms)	Capitola	47125	38.1	042 132	0.099 0.142	0.26	2.40
2	1/10/1987	Whittier Narrows	6 (Ms)	LA - Hollywood Stor FF	24303	25.2	000 090	0.221 0.124	-0.09	1.67
3	17/1/1994	Northridge	6.7 (Ms)	Compton - Castlegate St	90078	49.6	000 270	0.088 0.136	-0.01	2.51
4	17/1/1994	Northridge	6.7 (Ms)	Downey - Birchdale	90079	40.7	090 180	0.165 0.171	0.24	1.90
5	17/1/1994	Northridge	6.7 (Ms)	LA - Saturn St	90091	30	020 110	0.474 0.439	-0.06	0.61
6	6/8/1979	Coyote Lake	5.7 (Ms)	Halls Valley	57191	31.2	150 240	0.039 0.050	0.15	6.90
7	2/5/1983	Coalinga	6.4 (Ms)	Parkfield - Cholame 5W	36227	47.3	270 360	0.147 0.131	-0.10	2.00
8	8/7/1986	N. Palm Springs	6 (Ms)	Indio - Coachella Canal	12026	45.7	000 090	0.053 0.050	0.09	5.52
9	13/6/1993	Mouzakaiika (Greece)	5.3 (Mw)	Lefkada-OTE Building	8	33	LONG TRAN	0.043 0.146	-0.39	3.21
10	15/4/1979	Montenegro	6.9 (Mw)	Stolac-PPD	2967	107	N-S W-E	0.034 0.042	0.02	6.99

Table 1: Far-fault ground motion records

No	Date	Earthquake name	Magnitude	Station name	Station number	Closest distance (Km)	Component (deg)	PGA (g)	Cor Factor (p)	SF
1	1/10/1987	Whittier Narrows	6 (Ms)	El Monte - Fairview Av	90066	9.8	000 270	0.120 0.228	0.23	1.49
2	20/9/1999	Chi-Chi, Taiwan	7.6 (Ms)	CHY	028	7.31	N W	0.821 0.653	-0.07	0.37
3	18/10/1989	Loma Prieta	6.9 (Ms)	Gilroy Array #3	47381	14.4	000 090	0.555 0.367	0.05	0.61
4	17/1/1994	Northridge	6.7 (Ms)	Simi Valley - Katherine Rd	90055	14.6	000 090	0.877 0.640	-0.02	0.36
5	1/10/1987	Whittier Narrows	6 (Ms)	LA - E Vernon Ave	90025	10.8	083 173	0.146 0.175	-0.09	1.67
6	1/10/1987	Whittier Narrows	6 (Ms)	LA - Fletcher Dr	90034	14.4	144 234	0.171 0.231	-0.04	1.45
7	11/9/1976	Friuli (Italy)	5.5 (Mw)	Buia	33	7	E-W N-S	0.105 0.230	0.04	1.64
8	24/2/1981	Aktion (Greece)	6.6 (Mw)	Korinthos-OTE Building	121	10	N30 N120	0.230 0.310	-0.28	1.03
9	26/9/1997	Umbria Marche (Italy)	6 (Mw)	Colfiorito	221	5	N-S W-E	0.199 0.223	-0.11	1.43
10	7/9/1999	Ano Liosia (Greece)	6 (Mw)	Athens-Neo Psihiko	1253	8	LONG TRANS	0.083 0.101	-0.05	3.00

Table 2: Near-fault ground motion records

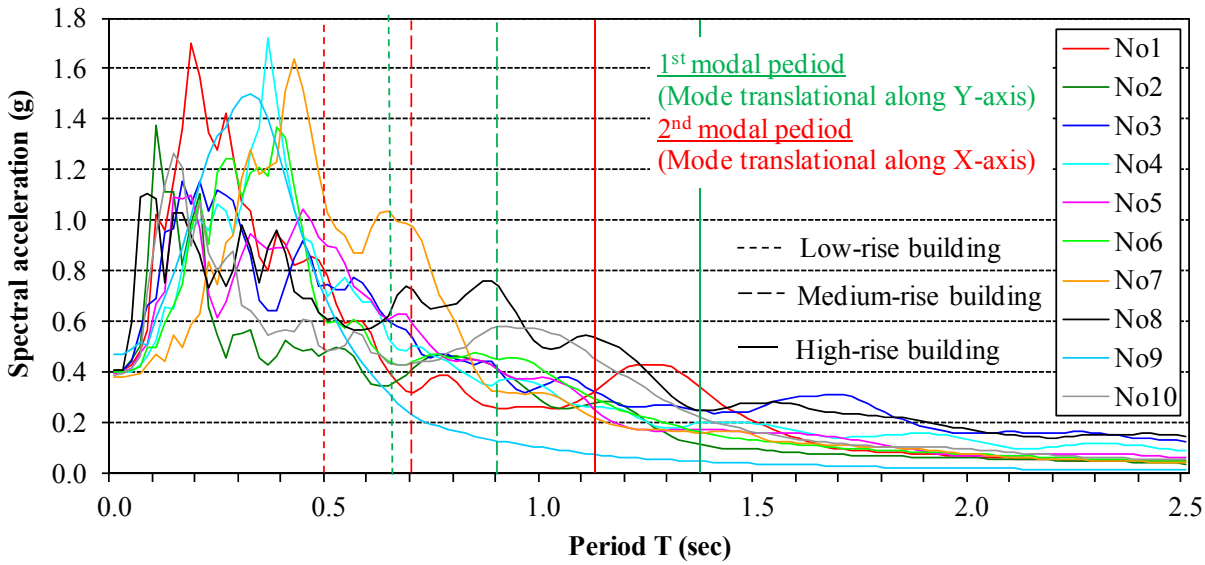


Figure 2a: SRSS of the 5%-damped spectra of the scaled accelerograms corresponding to far-fault records

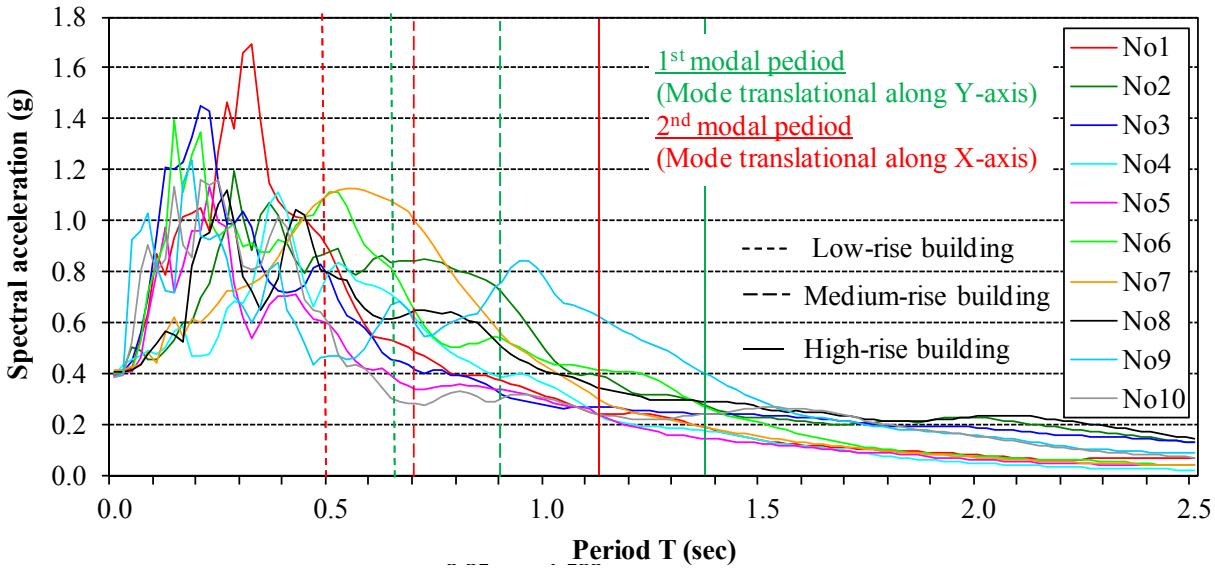


Figure 2b: SRSS of the 5%-damped spectra of the scaled accelerograms corresponding to near-fault records

2.4 Modeling of the nonlinear behavior and analysis of the buildings

Plastic hinges, which are located at the column and beam ends as well as at the base of the walls, were used to model the material inelasticity of the members by means of a Modified Takeda hysteresis model [16] (Figure 3(a)), where for the parameters α and β the values of 0.25 and 0 for the beams and 0.50 and 0 for the vertical frame elements were used [17]. It is important to notice that the effects of axial load-biaxial bending moments (P-M-M) interaction at column and wall hinges were taken into consideration by means of the P-M-M interaction diagram shown in Figure 3(b), which was implemented in the software used to conduct the analyses [18]. The plastic moments as well as the parameters needed to determine the P-M-M interaction diagram of the vertical elements' cross sections (Figure 3(b)) were calculated using appropriate software [19].

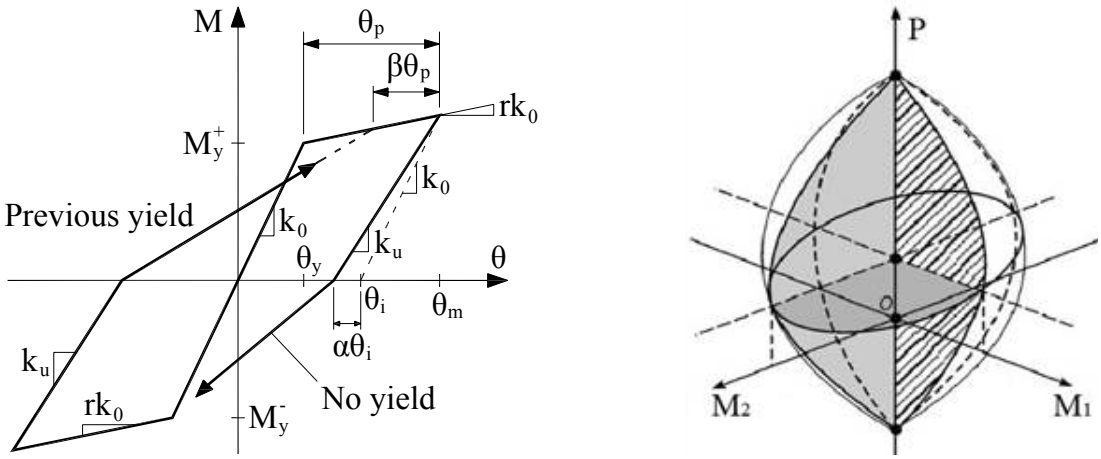


Figure 3: Moment (M) - Rotaion (θ) relationship (a) and P-M-M interaction diagram [18] (b)

The three buildings were then analyzed by Nonlinear Time-History Analysis (NTHA) for each one of the 20 earthquake ground motions. The analyses were performed with the aid of the computer program RUAUMOKO [18]. Furthermore, as the seismic incident angle with regard to structural axes is unknown, the two horizontal accelerograms of each ground motion

were applied along horizontal orthogonal axes forming with the structural axes consecutive angles of θ=0°, 5°, 10°, …, …, 355°. Thus for each building and each pair of accelerograms 72 different incident angles of the input motion were considered. As a consequence a total of 4,320 NTHA (3 buildings x 20 earthquake records x 72 incident angles) were conducted in the present study.

2.5 Calculation of damage indices

For each ground motion and incident angle, the local damage indices at every relevant cross section (columns' and beams' ends and at the bases of the walls) as well as the overall damage index of each one of the three buildings were computed. In particular, three different damage indices were considered: the Park and Ang damage index [5] modified by Kunnath et al. [6], the Bracci et al damage index [7] and the Cosenza, et al. damage index [8]. Note that the aforementioned local damage indices have been widely used for the inelastic assessment of structures [8, 20, 21, 22, 23].

More specifically, at a given cross section the local damage index (LDI) according to Park and Ang, Bracci et al. and Cosenza et al. is given by Eqs. 2, 3 and 4 respectively:

$$LDI^{\text{Park-Ang}} = \frac{\varphi_m - \varphi_y}{\varphi_u - \varphi_y} + \left(\frac{\beta}{M_y \bullet \varphi_u} \right) \bullet E_T \tag{2}$$

$$LDI^{\text{Bracci et al.}} = \frac{E_m}{E_u} \tag{3}$$

$$LDI^{\text{Cosenza et al.}} = \frac{\mu_m - 1}{\mu_u - 1} \tag{4}$$

where φ_m is the maximum curvature observed during the load history, φ_u is the ultimate curvature capacity, φ_y is the yield curvature, μ_m is the maximum ductility demand, μ_u is the maximum allowable value of the ductility, E_T is the dissipated hysteretic energy, E_m is the work done at maximum curvature, E_u is the work done at ultimate curvature, M_y is the yield moment of the cross section and β is a dimensionless constant determining the contribution of cyclic loading to damage, which is taken equal to 0.5 for the analyses conducted in the present study.

Moreover, the overall structural damage index (OSDI) of the building was computed as a weighted average of the local damage indices at the ends of each element. The dissipated energy was used as a weight factor (Eq. 4) [20, 24, 25]:

$$OSDI = \sum_{i=1}^{n} \left[LDI_i \bullet \left(E_{Ti} \Big/ \sum_{i=1}^{n} E_{Ti} \right) \right] \tag{5}$$

where LDI_i is the local damage index at cross section i determined by Eqs. 2, 3 or 4, E_{Ti} is the energy dissipated at cross section i and n is the number of cross sections at which the local damage is computed.

3 RESULTS OF THE ANALYTICAL INVESTIGATIONS

Figure 4 presents the variation of the OSDI with the incident angle under the No9 far-fault and No10 near-fault earthquake records (see Tables 1 and 2) for the three buildings investigated in the present study. We can see that the near-fault record leads to larger values of damage indices for the majority of incident angles than the corresponding values produced by the far-fault ground motion. This observation is more evident for the 3-story building.

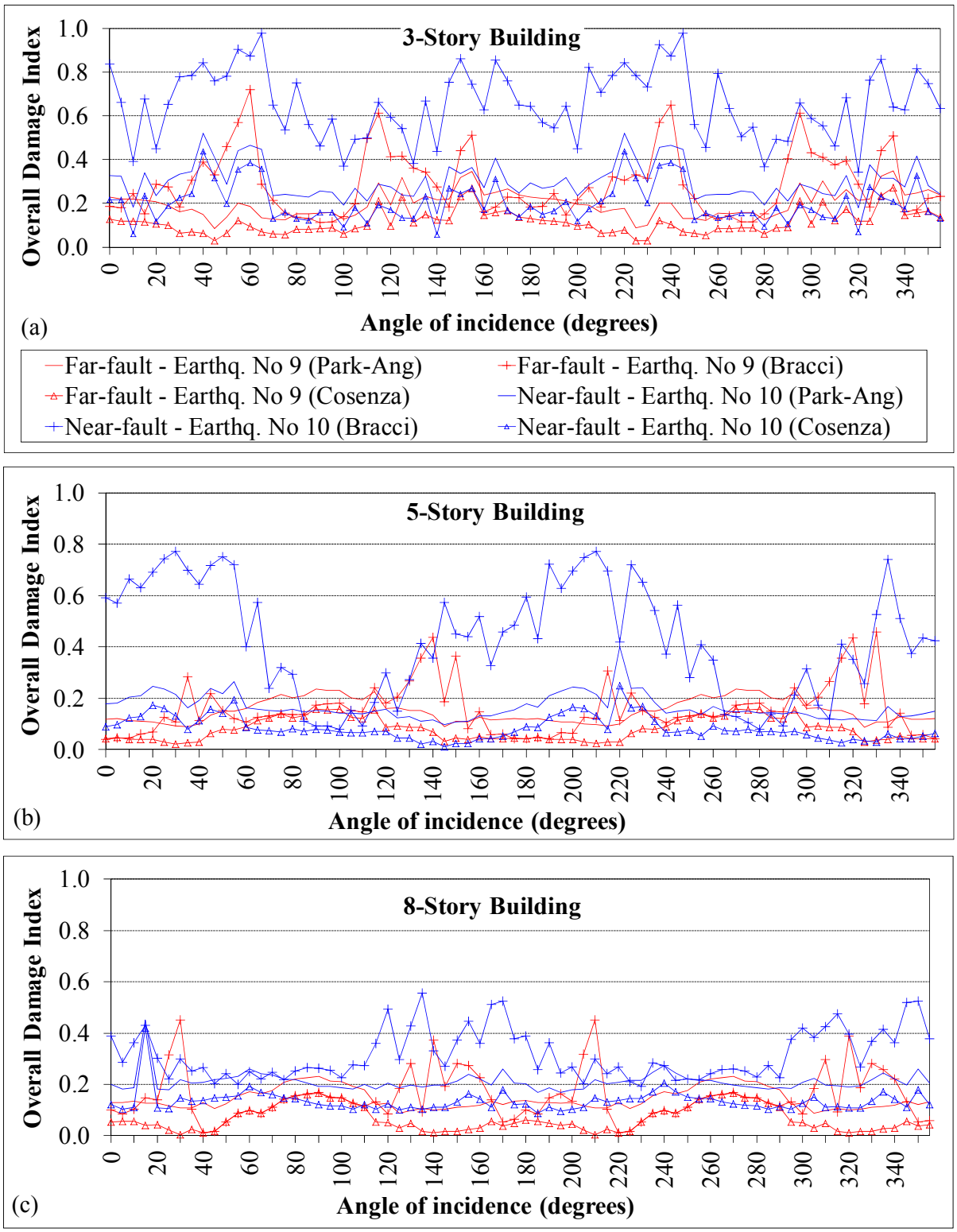


Figure 4: OSDI vs incident angle for earthquake records No9 (far-fault) and No10 (near-fault) for (a) the 3-story, (b) 5-story and (c) 8-story building

Concerning the 3-story building it is obvious from Figure 4a that the use of Bracci et al. damage index leads to the largest values of OSDI for the vast majority of incident angles, whereas the use of Cosenza et al. damage index leads to the smallest values. The same conclusion can be derived for the other two buildings under the near-fault earthquake record.

However, we observe that when the analyses are conducted using the far-fault ground motion there are certain angles of incidence for which Park and Ang gives larger values than the Bracci et al. damage index. See for example angles 0^o-15^o, 55^o-110^o and 235^o-290^o (Figures 4b and 4c). It must be mentioned that the difference between the values produced by the three different definitions of the local damage index strongly depends on the seismic record and its orientation. For example, note that the three damage indices produce similar values of OSDI for the 5-story building (Figure 4b) when the near-fault record No10 is applied with angle of incidence 85^o-100^o, whereas they lead to large differences when the orientation of the same earthquake record is 0^o-50^o.

Furthermore, we can see that the damage state of the building is affected by the excitation angle for all the buildings under investigation. See for example that the OSDI of the 5-story building under the far-fault seismic record No10 using the Bracci et al. damage index is equal to 0.77 and 0.08 for incident angles 30^o and 100^o respectively (Figure 4b).

In order to generalize behavior trends, for each ground motion the value of the OSDI for incident angle $\theta=0°$ ($OSDI_{,0}$) as well as the maximum value of OSDI (maxOSDI) over all incident angles are determined. Then, the average values of the above quantities due to all the seismic records are calculated. The results are illustrated in Figures 5 and 6 for the three buildings under investigation. It must be mentioned that the aforementioned values are determined separately for the far and near fault records as well as for the three different definitions of the local damage index investigated in the present study.

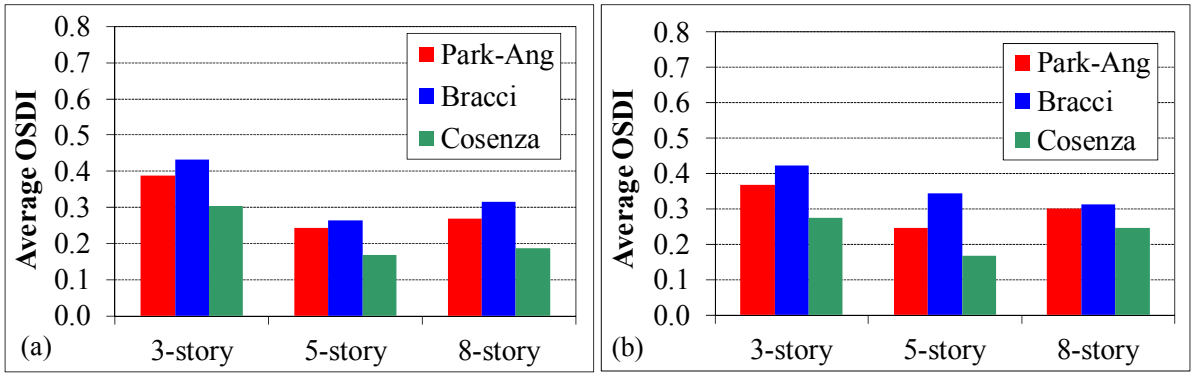


Figure 5: Average value of OSDI for incident angle $\theta=0°$ determined using the three different LDI for (a) far-fault and (b) near-fault earthquake records

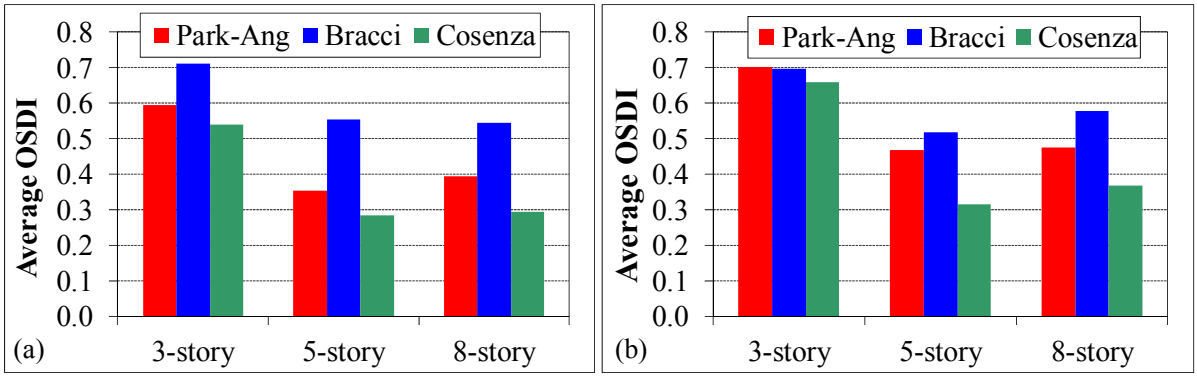


Figure 6: Average value of maxOSDI over all incident angles determined using the three different LDI for (a) far-fault and (b) near-fault earthquake records

Figures 5 and 6 clearly indicate that the use of Bracci et al. damage index leads to the largest values of OSDI, whereas the use of Cosenza et al. damage index leads to the smallest values. The above conclusion is obvious for both $OSDI_{,0}$ and maxOSDI. The difference between the three damage indices used in the present study depends on the number of stories and the type of the strong motion (far or near-fault), however no certain trend was observed. Note for example that the aforementioned difference is negligible for the maxOSDI of the 3-story building under the near-fault records, whereas it becomes much larger for the maxOSDI of the 5-story building under the far-fault records. This remark is very important, since different values of the OSDI imply different damage state of the structure. Furthermore, it is evident that the values of the three different OSDIs are larger for the 3-story building, something that can be attributed to the fact that, as can be seen in Figures 2a and 2b, the peaks of the most response spectra appear for values of period that is very close to the fundamental vibration period of the 3-story double symmetric structure. It is also interesting to notice that Figures 5 and 6 show no particular trend as far as the difference between the far and the near-fault records is concerned.

In order to better quantify the differences among the results produced for the 72 examined orientations of the ground motions, the maximum relative variation (MRV) of the OSDI for each seismic record is determined as:

$$\mathrm{MRV} = \left(\mathrm{maxOSDI}\right)/\left(\mathrm{minOSDI}\right) \tag{6}$$

where maxOSDI and minOSDI: maximum and minimum OSDI respectively over all seismic incident angles.

Then, the average and the maximum value of MRV for the 10 far-fault and the 10 near-fault records are computed. The results are presented in Figures 7 and 8.

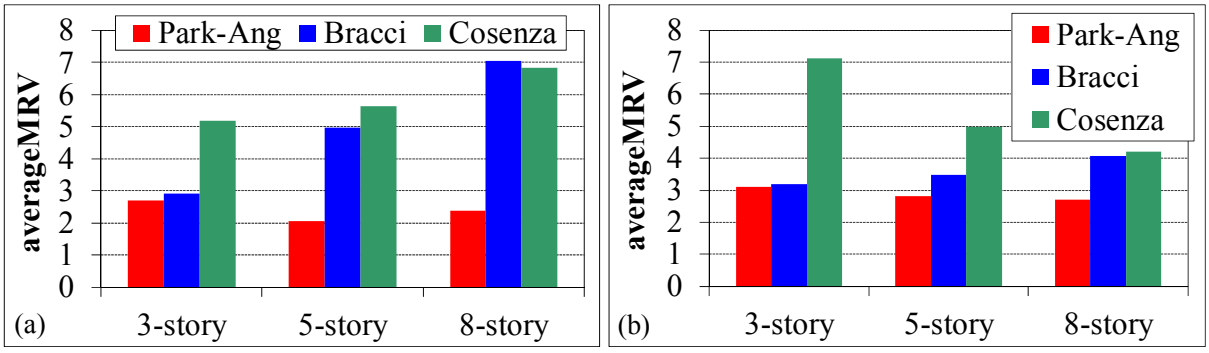


Figure 7: Average values of MRV for the OSDI determined using the three different LDI for (a) far-fault and (b) near-fault earthquake records

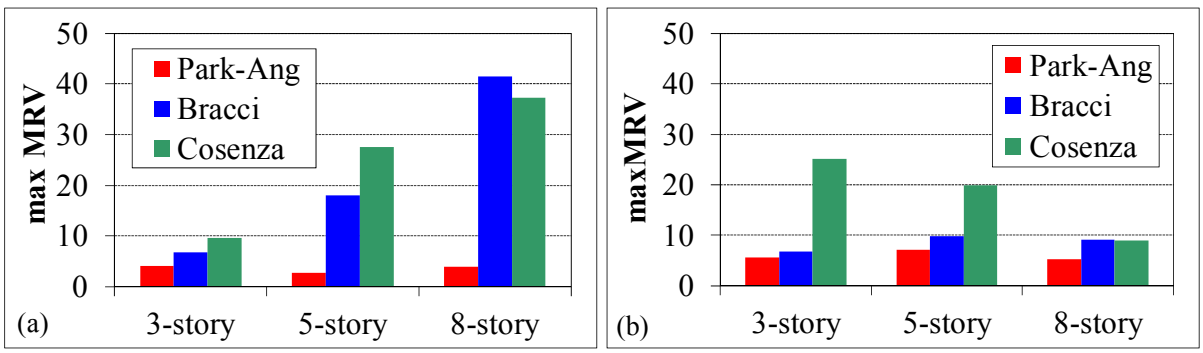


Figure 8: Maximum values of MRV for the OSDI determined using the three different LDI for (a) far-fault and (b) near-fault earthquake records

From Figures 7 and 8 it can be seen that the damage state of the building is strongly affected by the excitation angle for all the buildings under investigation. It is very interesting to notice that the average MRV can take the value of 7 (3-story building under near-fault records and 8-story building under far-fault records), whereas the maxMRV can take the value of 41 (8-story building under far-fault records).

The difference between the MRV determined using the three damage indices depends on the number of stories and the type of the strong motion (far or near-fault). The use of Cosenza et al. damage index leads to the largest values of MRV (with the exception of 8-story building), whereas the use of Park and Ang damage index leads to the smallest values. Moreover, concerning the far-fault records we can notice that the influence of the incident angle when the Bracci et al. and the Cosenza et al. damage indices are used becomes larger as the number of the stories increase. The opposite seems to happen for the Cosenza et al. damage index when the near-fault records are used. However, it is of great importance to notice that in most cases the most widely used Park and Ang damage index leads to the smallest influence of the number of stories

4 CONCLUSIONS

In the present research effort three damage indices for the R/C buildings are evaluated taking into account the incident angle of the strong motion. Three symmetric in plan R/C buildings are investigated: a low-rise (3 stories), a medium-rise (5 stories) and a high-rise (8 stories) one. The three buildings were analysed by nonlinear time-history analysis using 20 bi-directional earthquake ground motions, the horizontal accelerograms of each are applied along horizontal orthogonal axes forming 72 different angles with the structural axes. For each ground motion and incident angle, the local damage indices at every relevant cross section as well as the overall damage index of the building (OSDI) were computed using three different definitions of damage indices. The comparative assessment of the results leads to the following conclusions:

- The difference between the values of the three damage indices used in the present study varies depending on the number of stories, the earthquake ground motion and the incident angle.
- The use of Bracci et al. damage index leads to the largest values of OSDI, whereas the use of Cosenza et al. damage index leads to the smallest values for the vast majority of the incident angles and earthquake records.
- The damage state of the building strongly depends on the excitation angle. The influence of the incident angle depends on the damage index used, the number of stories and the strong motion.
- The most widely used Park and Ang damage index seems to be less influenced by the excitation angle as well as of the height of the building.

REFERENCES

[1] K.G. Kostinakis, A.M. Athanatopoulou, Avramidis, Orientation effects of horizontal seismic components on longitudinal reinforcement in R/C Frame elements, *Natural Hazards and Earth System Sciences*, **12**, 1-10, 2012.

[2] K.G. Kostinakis, A.M. Athanatopoulou, I.E. Avramidis, Evaluation of inelastic response of 3D single-story R/C frames under bi-directional excitation using different orientation schemes, *Bulletin of Earthquake Engineering*, DOI 10.1007/s10518-012-9392-5, 2012.

[3] I.-K.M. Fontara, K.G. Kostinakis, A.M. Athanatopoulou, Some issues related to the inelastic response of buildings under bi-directional excitation, *Proceedings of the 15th World Conference on Earthquake Engineering*, Paper No: 3715, Lisbon, Portugal, September 24-28, 2012.

[4] K. Morfidis, A.M. Athanatopoulou, I.E. Avramidis, Effects of seismic directivity within the framework of the lateral force procedure, *14th WCEE*, Beijing, China, October 12-17, 2008.

[5] Y.J. Park, A.H.-S. Ang, Mechanistic Seismic Damage Model for Reinforced-Concrete. *Journal of Structural Engineering-ASCE*, **111(4),** 722-739, 1985.

[6] S.K. Kunnath, A.M. Reinhor et al, IDARC Version 3: A program for the inelastic damage analysis of RC structures, *Technical Report NCEER-92-0022*. National Centre for Earthquake Engineering Research, State University of New York, Buffalo NY, 1992.

[7] J.M. Bracci, A.M. Reinhorn, J.B. Mander, S.K. Kunnath, Deterministic model for seismic damage evaluation of reinforced Concrete Structures, *Technical report NCEER-89-0033*, National Center for Earthquake Engineering Research, State University of New York at Buffalo, 1989.

[8] E. Cosenza, G. Manfredi, R. Ramasco, The use of damage functionals in earthquake engineering: A comparison between different methods, *Earthquake Engineering and Structural Dynamics*, **22**, 855-868, 1993.

[9] Eurocode 2: *Design of Concrete Structures, Part 1-1, General rules and rules for buildings*, European Committee for Standardization, Brussels, Belgium, 2004.

[10] Eurocode 8: *Design of structures for earthquake resistance - Part 1, General rules, seismic actions and rules for buildings*, European Committee for Standardization, Brussels, Belgium, 2003.

[11] RAF-Structural Analysis and Design Software v.3.3.2, TOL (Engineering Software House) Iraklion, Crete, Greece, 2012.

[12] Pacific Earthquake Engineering Research Centre (PEER), Strong Motion Database. http://peer.berkeley.edu/smcat/, 2003.

[13] The European Strong-Motion Database, http://www.isesd.hi.is/ESD Local/frameset.htm, 2003.

[14] J. Penzien, M. Watabe, Characteristics of 3-D earthquake ground motions, *Earthquake Eng. Struct. Dyn.*, **Vol. 3**, 365-373, 1975.

[15] ASCE 41/06, Seismic rehabilitation of existing buildings, American Society of Civil Engineers 2009.

[16] A. Otani, Inelastic Analysis of RC frame structures, *Journal of the Structural Division (ASCE)*, **100(7)**, 1433–1449, 1974.

[17] J.D. Pettings, M.J.N. Priestley, Dynamic Behaviour of Reinforced Concrete Frames Designed with Direct Displacement-Based Design, *Research Report No. ROSE-2005/02*, European School for Advanced Studies in Reduction of seismic Risk, 2005.

[18] A.J. Carr, Ruaumoko – a program for inelastic time-history analysis, Program manual. Department of Civil Engineering, University of Canterbury, New Zealand, 2004.

[19] Imbsen Software Systems, XTRACT: Version 3.0.5, Cross-sectional structural analysis of components, Sacramento, CA, 2006.

[20] J.V. Amiri, Q.Y. Ahmadi et al, Assessment of reinforced concrete buildings with shear wall based on Iranian Seismic Code (Third edition), *J Appl Sci*, **8(23)**, 4274-4283, 2008.

[21] K. Arjomandi, H. Estekanchi et al, Correlation Between Structural Performance Levels and Damage Indexes in Steel Frames Subjected to Earthquakes, *Scientia Iranica Transaction a-Civil Engineering*, **16(2)**, 147-155, 2009.

[22] E. Yüksel E., M. Sürmeli, Failure analysis of one-story precast structures for near-fault and far-fault strong ground motions, *Bull Earthquake Eng.*, **8**, 937-953, 2010.

[23] M.S. Williams, R.G. Sexsmith, Seismic Damage Indices for Concrete Structures: A State-of-the-Art Review, *Earthquake Spectra*, **11(2)**, 319-349, 1995.

[24] S.L. Dimova, P. Negro, Seismic assessment of an industrial frame structure designed according to Eurocodes. Part 2: Capacity and vulnerability, *Eng Struct*, **27(5)**, 724-735, 2005.

[25] A. Elenas, Correlation between seismic acceleration parameters and overall structural damage indices of buildings. *Soil Dyn Earthquake Eng*, **20(1-4)**, 93-100, 2000.

COMPDYN 2013
4th ECCOMAS Thematic Conference on
Computational Methods in Structural Dynamics and Earthquake Engineering
M. Papadrakakis, V. Papadopoulos, V. Plevris (eds.)
Kos Island, Greece, 12–14 June 2013

IMPACT OF SEISMIC CODES ON BUILDING PERFORMANCE IN THE CARIBBEAN

Laura M. Redmond[1], **Rebecca M. Stroecker**[1], **and Reginald DesRoches**[1]

[1] Georgia Institute of Technology
North Ave. Atlanta, GA 30332
laura.redmond@gatech.edu, rstroecker3@gatech.edu, reginald.desroches@ce.gatech.edu

Keywords: Seismic Design of Concrete, Seismic Vulnerability, Code Provisions, Equivalent Lateral Force Analysis, Time History Analysis

Abstract. *The 2010 Haiti earthquake was a strong reminder of the seismic hazard in the Caribbean and the fact that many buildings in the region are inadequately designed for earthquake loads. Although the Caribbean islands have very similar seismic and hurricane hazard, the design practices across the islands vary greatly. In some regions, building codes are specified and engineer's designs are checked by an authoritative body. In other regions, engineers can choose from among several different codes, and code compliance may not be enforced at all. Finally, there are some countries which do not specify design codes or hazard maps, and the prevailing belief is that designing for the region's large wind forces without considering earthquake design is adequate for the low to mid-rise structures typical of the region. The aim of this study is to determine the influence of different building code choices on the expected performance of mid-rise buildings in the Caribbean.*

The influence of code provisions on the design and performance of structures is characterized by conducting an analytical study of a single concrete moment resisting frame designed by each of the codes permitted in the Caribbean. A total of twelve different building designs were modeled in ETABS and each was subjected to the same suite of ground motions using records with similar period and amplitude characteristics to the present hazard maps from Trinidad. The physical differences between the designs with regard to member sizes and rebar sizes are discussed and the performance of each building as a result of the suite of ground motions is highlighted. The results suggest that all modern code provisions reviewed have similar capacities and seismic performance and if older seismic codes are used to obtain design forces, the design of typical low to mid rise structures in the Caribbean may be sufficient if seismic detailing from a modern concrete code is followed.

1 INTRODUCTION

Although the frequency of seismic activity in the Caribbean is low, the 2010 Haiti earthquake was a major tragedy that spurred new concern for the seismic vulnerability of infrastructure in the region. Although the Caribbean islands have very similar seismic and hurricane hazard, the vulnerability of infrastructure varies greatly. In some regions, building codes are specified and engineer's designs are checked by an authoritative body. In other regions, engineers can choose from among several different codes, and code compliance may not be enforced at all. Finally, there are some countries which do not specify design codes or hazard maps, and the prevailing belief is that designing for the region's large wind forces without considering earthquake forces, but including seismic detailing, is adequate for the low to mid rise structures typical of the region. This study seeks to compare the code provisions and determine the influence of these different choices on the performance of mid-rise buildings in the Caribbean. The influence of code provisions on the design and performance of structures is characterized by conducting an analytical study of a single concrete moment resisting frame designed by each of the codes permitted in the Caribbean.

2 PREVIOUS RESEARCH ON CODE PROVISIONS IN THE CARIBBEAN

Previous research efforts have been conducted by Myron Chin et al. [1] to review existing codes in the Caribbean and make recommendations for improvements of these codes. Additional work has been done by Tony Gibbs reviewing the wind maps in the Caribbean and return period basis [2]. These works have emphasized that the design forces in many of these codes may be inadequate for what is currently accepted as the level of seismic and wind hazard in the Caribbean. However, many of these codes also have more stringent deflection requirements and different resistance factors for material and behavior patterns complicates the ability to assess what impact lower values of design base shear or wind pressure have on a structures vulnerability. To the author's knowledge, a complete analytical study to determine the implications of the variations in code procedures on the final building design has not previously been conducted.

3 SCOPE AND DESIGN OF THE ANALYTICAL STUDY

The scope of this study is limited to the countries of Puerto Rico, Trinidad, Belize, Haiti, the Dominican Republic and Jamaica, selected based on the availability of information from those regions. Knowledge about the current design practices in the region was obtained from in-person interviews [3-19] and phone conversations [20] with design engineers and government officials, and information published by the various national standards associations, research institutions and building authorities [21-26].

In order to isolate the effect of code provisions on the seismic performance of structures in the Caribbean, a single set of wind and earthquake hazard data was used to design a structure by each of the codes used in the Caribbean. Trinidad was selected because it has very detailed seismic maps for PGA, 0.2 second period, and 1.0 second period ground motions at return periods of 2475 years, 975 years, and 95 years [26]. It also has a design peak 3-second gust speed defined by the Ministry of Works [16].

Within the Caribbean, the most common building design is a mid-rise (2-7story) concrete moment frame in-filled with masonry, which is lightly reinforced or unreinforced (Fig. 1). The concrete frame is used to resist lateral and part or all of the gravity loads, and the masonry walls are used to resist wind pressure, self weight, and in some cases, part of the gravity loads**.** The stiffness contribution of the masonry walls are typically ignored in engineering models and only their weight is considered. In this study, the concrete moment frame is de-

signed to resist all of the lateral and gravity forces and the masonry infill weight is accounted for with a heavy cladding load (500lb/ft).



Figure 1: Traditional infill construction in Belize.

The design of the masonry walls were not considered in this study for several reasons. Firstly, and most importantly, the masonry is not designed to resist seismic forces, and is unlikely to perform well in an earthquake. Secondly, the connections between the concrete moment frame and the masonry vary greatly, and the connection types discussed during our interviews may not comprise the entirety of masonry connections in the region. Finally, masonry codes were not able to be obtained from all the regions considered in this study.

3.1 Analytical Procedure

The final analytical study consists of a five-story concrete moment frame building modeled in ETABS. First, a baseline model was assembled and gravity loads were determined using ASCE 7-10, as these loads met or exceeded the gravity loading requirements of all the codes in this study. Gravity loads were kept constant for each subsequent model so that the influence of the seismic and wind codes could be isolated. Designs were based on a concrete strength of 4ksi and a reinforcement yield strength of 60ksi. The soil type was assumed to be equal to an IBC 2006 site class D and a damping ratio of 5% was assumed.

A new model for each of the codes was created using the same initial geometry and gravity loadings as the baseline model. Appropriate seismic and wind loadings were added to reflect the requirements of the equivalent lateral force procedures for the code provision being considered in that model. Each model went through multiple design iterations to satisfy both force requirements and drift limitations for the applicable building code. Drifts were obtained using the applicable displacement amplification factors provided in each code. The forces were output from ETABS and checked for p-delta effects, adequacy of member capacity, biaxial bending and drift requirements.

This resulted in one final building model for each code provision. Each model was then subjected to the same suite of ground motions in order to compare the seismic performance of each structure. A non-linear time history analysis was chosen because the results would best simulate performance in an actual earthquake, and subject the structure to both non-orthogonal and vertical earthquake loads, which are not included in several of the code design procedures. The IBC was used as a benchmark for seismic hazard as many of the Caribbean countries have adopted the IBC, and one can easily compare the buildings' performance to similar construction in the United States. The ground motions selected were scaled to the elastic design spectrum for IBC 2009, using the spectral acceleration maps from Trinidad. The un-factored spectral accelerations were S_s= 1.72g, and S_1=0.391g. The spectrum used to select

the ground motions was based on the elastic design spectrum for a site class D, for which the factored spectral accelerations were S_{DS}=1.15g, and S_{D1}=0.422g.

Ground motions were gathered from the PEER ground motion database, using a scaled search to the ASCE 7 design spectrum. Seven ground motions each containing two orthogonal and one vertical component were selected for the ground motion suite. The aim was to get a mix of ground motions that closely matched the design spectrum, particularly around the fundamental period of the structure (Fig. 2).

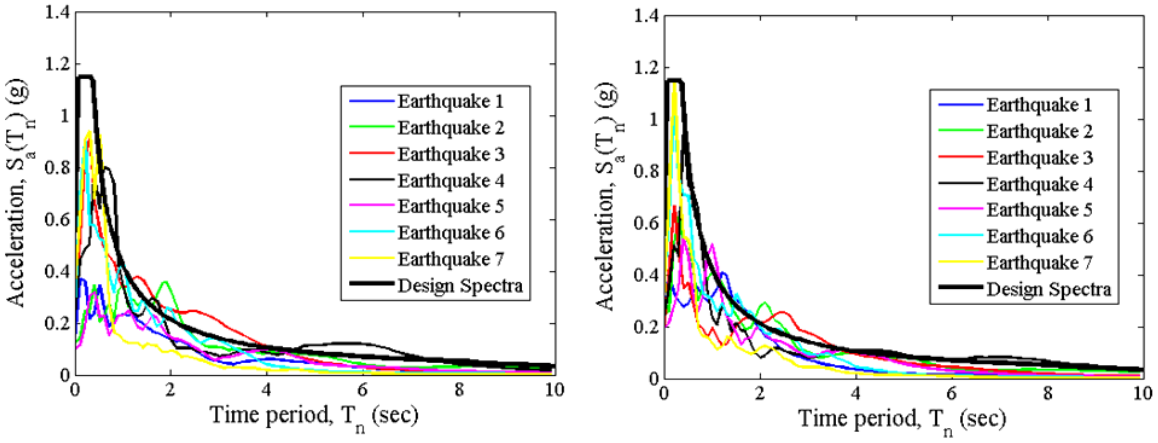


Figure 2: Ground motion suite for x (left) and y (right) directions plotted against the IBC elastic design spectrum.

After each model was subjected to this suite of ground motions, the physical differences between the designs with regard to member sizes and rebar sizes are discussed and the performance of each building as a result of the suite of ground motions is highlighted.

4 PARAMETERS USED IN SEISMIC AND WIND DESIGN

As the IBC was used as a benchmark for this study, the design level values for spectral acceleration and wind speed were based off the design level values for the IBC provisions in Trinidad. For codes based on different return periods, the equivalent ground acceleration for the new return period was calculated from the short period ground acceleration S_s. For wind codes which used the 1-hour average wind speed or 10 minute average wind speed for design, the 3-second gust speed from ASCE 7-10 was converted using the Derst curve. In cases where the return periods were not specified, the methodology for calculating the design spectral acceleration or seismic zone is briefly explained in the following section. Differences between the main design parameters can be found in Table 1.

4.1 Dominican Republic seismic code 2011

The structure was designed as a zone 1 except that the spectral acceleration values were taken as S_s =1.72 and S_1 =0.391 instead of 1.55 and 0.75, respectively. This was done to design each building to a consistent hazard level.

4.2 Dominican Republic seismic code 1979

This code provision contains a procedure based on the fundamental period of the building instead of a spectral map. The procedure was followed exactly, but design earthquake forces were amplified to reflect a slightly greater earthquake risk found in Trinidad. The 0.2s spectral acceleration for Trinidad is 1.72g, which is 11% greater acceleration than the current Do-

minican Republic code specifies (Ss= 1.55g). For the purposes of this study the design earthquake forces specified in the 1979 Dominican Republic Code were amplified by 11%.

4.3 Caribbean uniform building code (CUBiC)

The design forces were taken directly from the code using the tabulated values for Trinidad.

Code Provision	Initial Design Base Shear (kips)	Load Combinations for Seismic Actions	Drift Limits	Displacement Factor for Equivalent Inelastic Displacement	Resistance Factors for Concrete Design
IBC 2006 & 2009	651.2	1.2D +/- ($0.2S_{ds}$D) +/- E + 0.5L 0.9D +/- ($0.2*S_{ds}$D) +/- E **in this study:** 1.43D+E+0.5L 0.97D-E+0.5L 1.13D+E 0.67D-E	0.02	C_d/I **in this study:** 5.5	0.9 flexure 0.75 shear and torsion
UBC 1997	839.0	1.2D +/- ($0.5C_a$D) +/- E + 0.5L 0.9D +/- ($0.5C_a$D) +/- E **in this study:** 1.38D+E+0.5L 1.02D-E+0.5L 1.08D+E 0.72D-E	0.02	R **in this study:** 8.5	0.9 flexure 0.75 shear and torsion
DR 1979	504.6	0.75*(1.4D+1.7L+1.7*(1.1E)) 0.75*(1.4D+1.7*(1.1E)) 0.9D+1.43E	0.016	Cd **in this study:** 5.6	0.9 flexure 0.85 shear and torsion
DR 2011	958.6	1.2D +/- ($0.3S_{ds}$D) +/- E +0.5L 0.9D +/- ($0.3*S_{ds}$D) +/- E **in this study:** 1.544D+E+0.5L 0.856D-E+0.5L 1.244D-E 0.556D+E	0.016	Cd **in this study:** 4.75	0.9 flexure 0.75 shear and torsion
CUBiC	467.2	0.75*(1.4D+1.7L+1.7*(1.1E)) 0.75*(1.4D+1.7*(1.1E)) 0.9D+1.43E	0.005	1/K **in this study:** 1.25	0.9 flexure 0.85 shear and torsion
CNBC	633.3	1.0D+1.0E+0.5L	0.025	R_0R_d/I **in this study:** 6.8	factors based on material 0.65 concrete 0.85 reinforcement
Eurocode	1318.0	**no national annex for Caribbean countries, used recommended values** 1.0D +/- E +0.3L 1.0D +/-E	None req. for ULS	NA	1/1.5 concrete 1/1.15 reinforcement

Table 1: Values for design of analytical models.

4.4 Summary

The 1979 Dominican Republic Code and CUBiC are much lower than the base shear calculated by the IBC procedure. However, the drift limit for the 1979 Dominican Republic code is more stringent than the IBC and the displacement amplification factor C_d, is larger. CUBiC's displacement amplification factor is very low, but the drift requirements are also much lower than the IBC code, so it is difficult to determine the vulnerability of each structure based solely on the values of design forces.

5 COMPARISON OF MEMBER CAPACITY

The following section compares the final building models designed by the equivalent lateral force procedure for each of the code provisions. The design shear capacities of each building, found in Table 2 were calculated by summing the shear capacities at the base of all the columns at the foundation. It is interesting to note that the design shear capacity of the building designed by the 1979 Dominican Republic is actually greater than the IBC building, although the initial design forces were 22.5% less than the IBC design forces. The base shear capacity of the building designed by CUBiC is 19% less than the IBC capacity, which is nearly the same as the deficiency in initial base shear forces compared to the IBC design forces. Eurocode appears to be much more stringent than the other provisions, but for Ultimate Limit State design there are no drift requirements, so force-based design must be sufficient to ensure good seismic performance.

Code Name	**Base Shear Capacity (kips)**
CNBC	5612
Eurocode	15082
CUBiC	3504
DR 2011	12194
DR 1979	8607
UBC with BAPE	5064
UBC	5730
IBC with BAPE	4340
IBC	4340
Neglect EQ forces	3137

Table 2: Base shear capacity of each model.

The final section sizes and rebar details for the corner columns can be seen in Fig. 3. It is apparent that the section size of the columns when earthquake forces are not considered is significantly smaller than all of the other designs. It is interesting that all of the seismic code provisions resulted in comparable section sizes. However, the shear reinforcement spacing for the columns designed by the 1979 Dominican Republic code and CUBiC are much larger than present in any of the other columns. Large shear spacing may not provide enough confinement and may lead to poor performance of joint connections in seismic events. Additionally, large shear reinforcement spacing is the major reason for lower shear capacity in the CUBiC design compared to the IBC design. If shear reinforcement spacing were reduced to 4", as required by ACI 318-08, the shear capacity of the CUBiC design would increase from 3504 kips to 5252 kips.

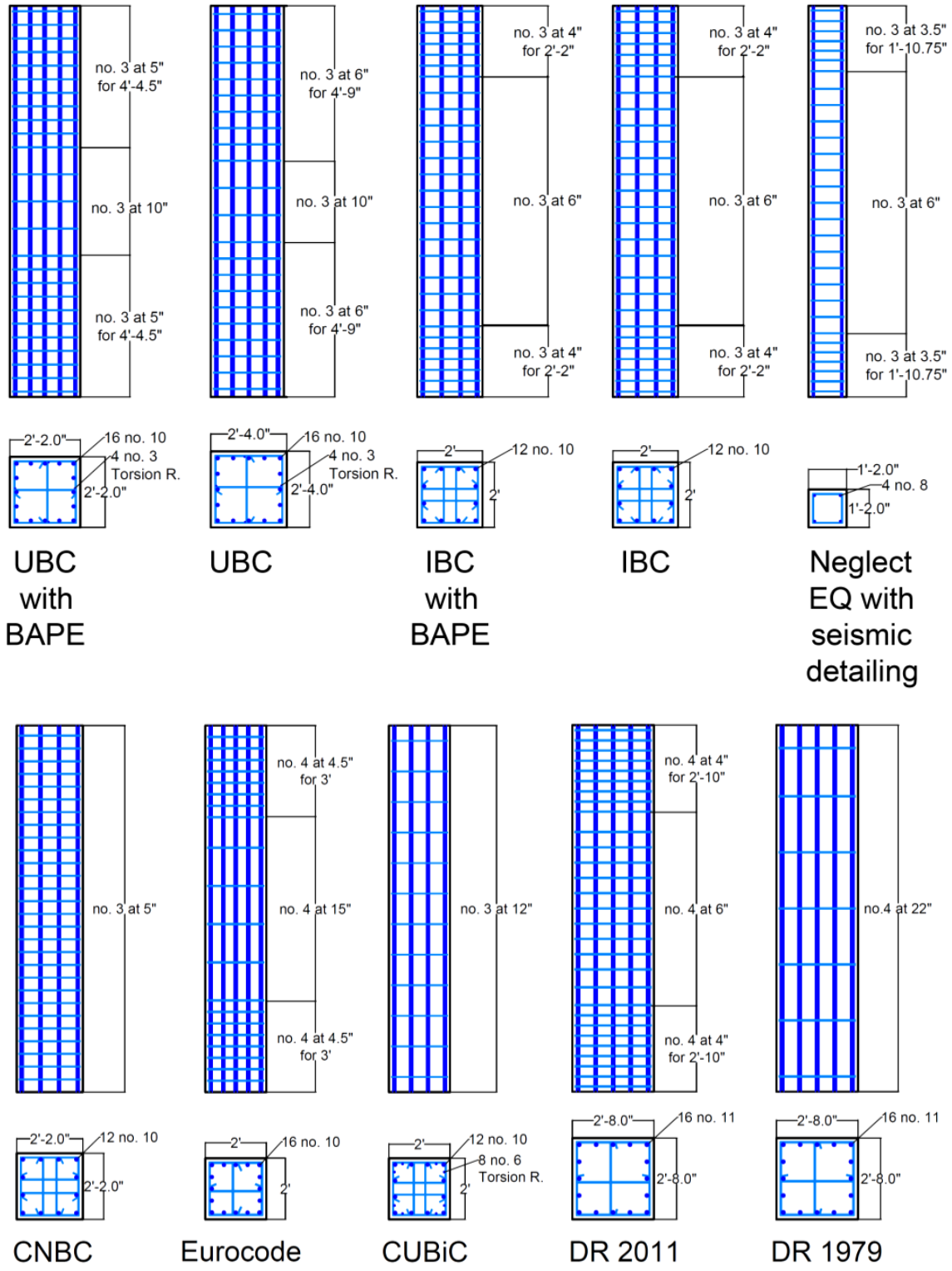


Figure 3: Reinforcement details for all models.

6 COMPARISON OF SEISMIC PERFORMANCE

All of the design buildings were subjected to a suite of ground motions representative of an IBC design-level earthquake. The maximum inter-story drifts for each structure are shown in

Fig. 4. The peak roof displacements for each structure are shown in Fig. 5. The average base shear demand to capacity ratio and the number cases in which base shear capacity was exceeded over the 28 non-linear time history loading combinations is shown in Fig. 6.

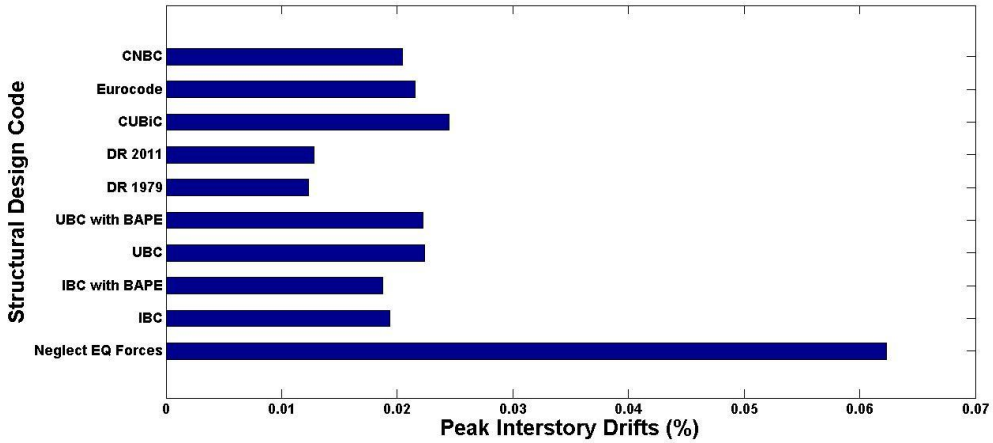


Figure 4: Maximum inter-story drifts.

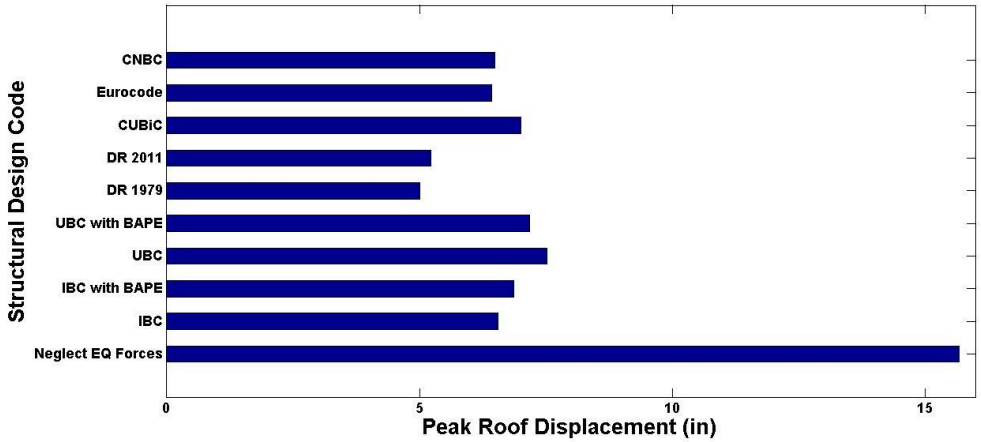
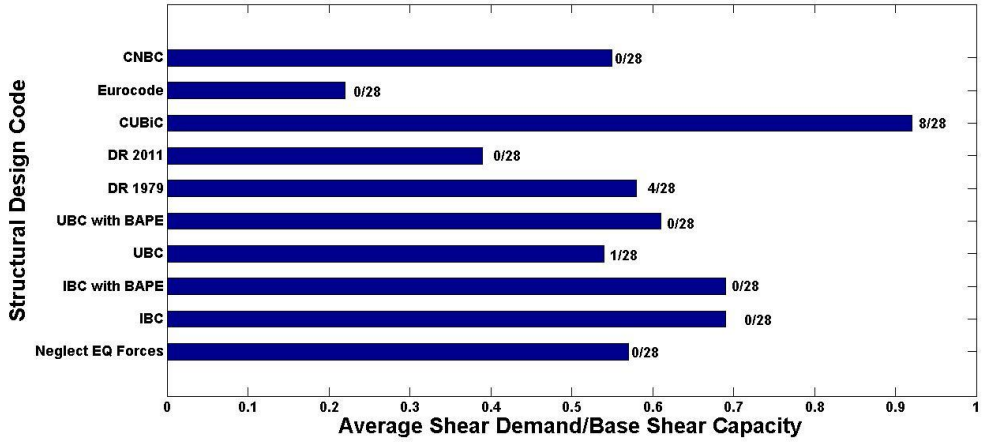


Figure 5: Maximum roof displacement.



2

Figure 6: Shear demand to capacity ratios and number of times base shear was exceeded.

Although all the structures have a demand to capacity ratio less than one, the structure designed by CUBiC has a ratio of 0.92. It is also important to note that the structures designed by 1979 Dominican Republic code and CUBiC experienced base shear forces which greatly exceeded their capacity at some instance within several the seismic events. The capacities of the structure designed by the 1979 Dominican Republic code and the structure designed by CUBiC can be greatly increased by following modern seismic detailing requirements. If the shear reinforcement spacing were reduced to 4" in the 1979 Dominican Republic code, the shear capacity would increase from 8607 kips to 15166 kips. The demand to capacity ratio with the additional detailing would be 0.33 and at no loading cases would have maximum shear demands which exceeded the base shear capacity. If shear reinforcement spacing were reduced to 4", as required by ACI 318-08, the shear capacity of the CUBiC design would increase from 3504 kips to 5252 kips. This would decrease the demand to capacity ratio to 0.61 and base shear capacity would only be exceeded in one out of twenty-eight time history loading combinations. Although the neglect earthquake procedure had sufficient base shear capacity, it also has excessive drifts (>6%) and roof displacements that are over double any other structure considered in this study.

7 CONCLUSION

In completing the study, the various building codes can be separated into three classes of structures. The first, which includes the design procedure neglecting earthquake forces but complying with seismic detailing, has significantly lower capacity than the IBC design and excessive drifts, but sufficient base shear capacity. The second class of structures, which includes the 1979 Dominican Republic code and the CUBiC, had comparable capacity when to the IBC design. However, these structures had large section sizes with less reinforcement and poor reinforcement detailing, which resulted in permissible levels of inter-story drift, but insufficient shear capacity. The third class of structures, which includes the CNBC, Eurocode, the 2011 Dominican Republic code, the UBC and the IBC, are both adequately designed and detailed.

It does not appear to matter significantly which design procedures are used to design buildings in the Caribbean, provided they are modern provisions. If older seismic codes are used to obtain design forces, the design of typical low to mid-rise structures in the Caribbean may be sufficient if seismic detailing from a modern concrete code is followed as the base shear capacity is significantly increased. However, even with the addition of modern seismic detailing, tall or irregular structures may still be poorly designed according to some of the seismic provisions due to the lack of irregularity checks, the use of only orthogonal seismic loadings and the failure to consider p-delta effects. It is difficult to determine if neglecting to design for earthquake forces and merely providing seismic details of the reinforcement is sufficient for good performance in a design-level earthquake, because the structure had adequate base shear capacity but excessive drifts.

ACKNOWLEDGEMENTS

This material is based upon work supported by the National Science Foundation Graduate Research Fellowship under grant no. 2011129510. Travel support to Trinidad, Belize, Jamaica, and Puerto Rico was provided by sources internal to Georgia Institute of Technology.

REFERENCES

[1] Chin, M., et al., Updating of Building codes of the Greater Caribbean. *Association of Caribbean States,* 2003. < http://www.acs-aec.org>

[2] Gibbs, T. Determination of Wind Loads used in Analysis. *Organization of American States,* 2000. <http://www.oas.org/pgdm/document/mhbdc/b1_text.pdf>

[3] Thurton, D., *Personal Interview*, Anthony Thurton and Associates Limited: Belize City, Belize. 2012.

[4] Waight, P., *Personal Interview*, Central Building Authority: Belize City, Belize. 2012.

[5] Young, C., *Personal Interview*, Young's Engineering Consultancy Limited: Belize City, Belize. 2012.

[6] Bras, R., *Personal Interview*, RBC Construction: San Juan, Puerto Rico. 2012.

[7] Mujca, A., *Personal Interview*, Levitt Homes Corp.: San Juan, Puerto Rico. 2012.

[8] Sosa Velasco, B. and C. Sosa, *Personal Interview*, Valcor Samcor: Gurabo, Puerto Rico. 2012.

[9] Vivoni, C., *Personal Interview*, Housing Promoters, Inc.: Saint Just., Puerto Rico. 2012.

[10] Azan, S., *Personal Interview*, P.J. Associates: Kingston, Jamaica. 2012.

[11] Chung, D., *Personal Interview*, FCS Consultants: Kingston, Jamaica. 2012.

[12] Clarke, D., *Personal Interview*, Kingston & St. Andrews Corp: Kingston, Jamaica. 2012.

[13] DaCosta, R. and J. Gordon, *Personal Interview*, Bureau of Standards, Engineering Division: Kingston, Jamaica. 2012.

[14] Hay, C., *Personal Interview*, NHL Engineering: Kingston, Jamaica. 2012.

[15] Miller, K., *Personal Interview*, Ministry of Local Government: Kingston, Jamaica. 2012.

[16] Fulchan, R., *Personal Interview*, Ministry of Works and Infrastructure Construction Division: Port of Spain, Trinidad. 2012.

[17] Khan, K., *Personal Interview*, Lee Young and Partners: Port of Spain, Trinidad. 2012.

[18] Latchman, J., Lynch, L., Robertson, R., & W. Salazar, *Personal Interview*, UWI Seismic Research Centre: Port of Spain, Trinidad. 2012.

[19] Trotter, N. and V. Ramlochan, *Personal Interview*, CEP Limited: Port of Spain, Trinidad. 2012.

[20] Fierro, E., *Phone Interview*, BFP Engineers Inc. (prev. work in the D.R.): Berkeley, CA. 2012.

[21] Professional College of Engineers and Land Surveyors (CIAPR). Puerto Rico. 2013. <https://www.cms.ciapr2.org>

[22] Sistema Integrado de Permisos. Puerto Rico. 2013. < https://www.sip.pr.gov>

[23] Central Building Authority (CBA). Belize. 2012. < http://cbabelize.com>

[24] Ministry of Works and Infrastructure. Trinidad and Tobago. 2011. <http://www.mowt.gov.tt>

[25] Kingston and St. Andrew Corporation. Jamaica. 2013. < http://www.ksac.gov.jm>

[26] The University of the West Indies Seismic Research Centre, Seismic Hazard Maps. 2012. < http://www.uwiseismic.com/Maps.aspx>

COMPDYN 2013
4th ECCOMAS Thematic Conference on
Computational Methods in Structural Dynamics and Earthquake Engineering
M. Papadrakakis, N.D.Lagaros, V. Plevris (eds.)
Kos Island, Greece, 12–14 June 2013

EFFECTS OF TORSION ON THE BEHAVIOUR OF NON-STRUCTURAL COMPONENTS MOUNTED ON IRREGULAR REINFORCED CONCRETE MULTI-STOREY BUILDINGS

A.B.B. Aldeka[1,†], **AHC. Chan**[2,‡], **and S. Dirar**[1,§]

[1] School of Civil Engineering, University of Birmingham
Edgbaston, Birmingham, B15 2TT, UK
[†] ABB037@bham.ac.uk
[§] s.m.o.h.dirar@bham.ac.uk

[2] School of Science, Information Technology and Engineering, University of Ballarat
Victoria, Australia, 3350 (formerly School of Civil Engineering, University of Birmingham)
[‡] achan@ballarat.edu.au

Keywords: Non-structural Components, Finite Element, Irregular RC Buildings, Torsion, Dynamic Analysis, Eurocode 8.

Abstract. *This paper considers the seismic responses of acceleration-sensitive non-structural components (NSCs) attached to irregular multi-storey reinforced concrete (RC) structures using Finite Element (FE) approach. The main objective of this study is to evaluate the behaviour of NSCs mounted on irregular RC buildings due to the effects of structural ductility and torsion which take place during earthquakes. Nonlinear dynamic analyses were used to evaluate the seismic behaviour of primary-secondary systems. The P-structures in this study include five irregular RC buildings which have the same asymmetric plan configuration, while having different number of stories, i.e., 5, 7, 10, 13, and 15-storeys. The P-structures were designed by the authors according to the full seismic provisions of Eurocode 8 (EC8). Distributed inelastic fibre elements are adopted to model the beams and columns of the P-structures. To simulate NSCs in P-structures, vertical cantilever beams fixed at their bases with masses on top are modelled with variety of lengths to adjust their natural frequencies to the natural frequencies of the P-structures. Full dynamic interaction is considered between the NSCs and P-structures during the analyses. A comparison is made between the numerical results and the EC8 formulation, and a general conclusion is drawn that the provisions of EC8 for design of NSCs are un-conservative in some cases.*

1 INTRODUCTION

The evaluation of seismic response of non-structural components (NSCs) attached to structures began over 40 years ago with a particular focus on equipment attached to regular 2D structures [1]. Various researchers presented state of the art reviews on NSCs [1-4]. Multi-storey structures with complicated geometries have become more widespread for many reasons but mainly because of modern architectural designs and materials. In such structures with asymmetries and irregularities, strong torsional effects induced by moderate and strong base motions are usually responsible for the damage of the structure and NSCs [5]. Realizing that the torsional behaviour of a primary structure (P-structure) could have an explicit effect that may increase the seismic response of NSCs attached to the P- structure, Yang and Huang [6, 7] proposed an analytical method with and without base isolation to evaluate the seismic behaviour of light equipment in such cases. Their approach was restricted to elastic primary-secondary systems with the eccentricity of floors in one direction only.

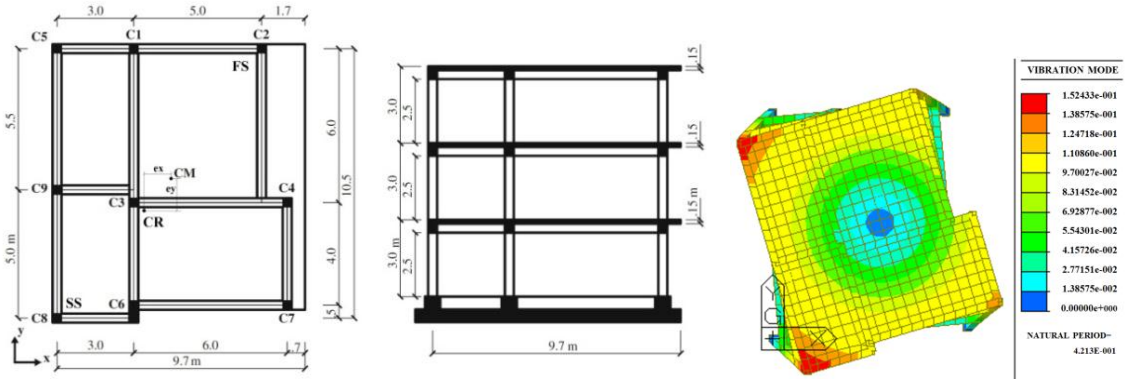
Analytical research studies were carried out by Agrawal and Datta [8-10]. They studied the response of a secondary element mounted over inelastic one-storey primary system (P-system) with torsional effect and subjected to base motion in one direction. Their model was 2-D model with the eccentricity of the P-system in one direction [8]. They also studied the dynamic response of a secondary element mounted on a torsionally inelastic P-system under base motions in two directions. Sets of coupled inelastic differential equations were used to evaluate the hysteretic force deformation behaviour of the inelastic P-system [9, 10]. Dynamic responses of acceleration-sensitive NSCs mounted on a multi-storey RC building with torsional effect were studied using a finite element (FE) approach by the present authors [11]. A single-bay three storey reinforced concrete (RC) frame was selected as the P-structure in order to investigate the behaviour of the NSCs under different eccentricities of the P-structure. Both acceleration and displacement responses of NSCs attached to the flexible side were investigated. In the majority of the above-mentioned studies, the NSCs were mounted over either a linear P-structure with eccentricity in one direction or an inelastic single-bay torsional building with eccentricity in both directions. Usually, the P-structures are too complicated in their dimensions and the use of composite materials in their elements for an analytical solution to be available; therefore, numerical analysis has to be employed.

The main objective of this paper is to evaluate the effects of structural ductility and torsion on the behaviour of NSCs mounted on irregular RC multi-storey buildings. Numerical results of NSCs attached to multi-storey buildings with different heights are presented and compared to the provisions of Eurocode 8 (EC8) [12] for the design of NSCs.

2 RC P-STRUCTURS CHARACTERISTICS AND MODELLING

In order to represent buildings in the range of low- and medium-rise, five irregular RC moment-resisting buildings having different number of storeys, i.e., 5, 7, 10, 13, and 15-storeys, are chosen to study the behaviour of NSCs. The plan configuration of a three-storey building, namely SPEAR building [13], was used as a reference plan for designing the multi-storey buildings in this study. The SPEAR building is asymmetric in the plan in the two horizontal directions, and characterized so as to have significant torsional behaviour as shown in Figures 1(a) [13] and 1(c) respectively. The multi-storey buildings in this study were designed by the authors according to the guidelines of the modern seismic provisions of EC8 [12] considering the Medium Ductility Class (DCM) rules. The buildings are labelled as “EC8 M#”; the term “EC8 M” refers to buildings designed as per EC8 and for Medium ductility. The symbol “#” is a number and indicates the number of stories (i.e., #=5, 7, 10, 13, and 15) respectively. All buildings were assumed to be constructed on ground soil type C. However,

the conclusions of this paper should apply to other soil types. A design peak-ground acceleration (a_g) of 0.25 g for moderate seismic zones is considered. Concrete Class C25/30 and steel reinforcement Class A, S400 were adopted in the design process of the five buildings. The characteristic values of loads are taken to be 2.7 and 2.0 kN/m^2 for permanent and variable actions respectively. The resulting members dimensions and the amount of longitudinal and shear steel reinforcements are shown in Table 1.



(a) (b) (c)

Figure 1: The SPEAR structure: (a) plan; (b) elevation [13]; and (c) torsional mode.

Building	Storey	Columns					Beams		
		C1,C2,C3,C4, C5,C7,C8,C9		C6		Shear Steel	Cross section	Long. steel	Shear steel
		Cross section	Long. steel	Cross section	Long. steel				
EC8 M5	1~2F	450x450	18Ø20	450x1000	20Ø20	Ø8 @120	350x500	9Ø16	Ø8 @90
	3~5F	400x400	14Ø20	400x850	20Ø20				
EC8 M7	1~2F	550x550	20Ø20	550x1000	22Ø20	Ø8 @110	350x500	10Ø16	Ø8 @90
	3~4F	500x500	20Ø20	500x1000	22Ø20				
	5~7F	450x450	18Ø20	450x850	20Ø20				
EC8 M10	1~2F	650x650	30Ø20	600x1000	30Ø20	Ø8 @110	350x500	13Ø16	Ø8 @90
	3~4F	600x600	30Ø20	550x1000	30Ø20				
	5~7F	550x550	28Ø20	550x1000	28Ø20				
	8~10F	500x500	22Ø20	500x850	22Ø20				
EC8 M13	1~2F	750x750	24Ø25	750x1000	26Ø25	Ø8 @90	400x600	17Ø16	Ø10 @110
	3~4F	650x650	24Ø25	650x1000	24Ø25				
	5~7F	650x650	24Ø25	650x1000	24Ø25				
	8~10F	600x600	20Ø25	600x1000	22Ø25				
	11~13F	500x500	24Ø20	500x850	26Ø20				
EC8 M15	1~2F	850x850	30Ø25	850x1000	32Ø25	Ø8 @90	450x650	13Ø20	Ø10 @100
	3~4F	750x750	30Ø25	750x1000	32Ø25				
	5~6F	700x700	30Ø25	700x1000	32Ø25				
	7~9F	650x650	28Ø25	650x1000	30Ø25				
	10~12F	600x600	24Ø25	600x1000	26Ø25				
	13~15F	500x500	18Ø25	500x850	20Ø25				

Table 1: Details of longitudinal and shear steel reinforcements of the buildings (all dimensions in mm).

The P-structures were modelled with a distributed inelastic fibre element using a FE computer code, MIDAS Ver. 3.1 [14], which leads to a very accurate description of the geometrical and mechanical properties of each element. Confined and unconfined concrete models proposed by Mander et al. [15] and the reinforcement model by Menegotto and Pinto [16] were used. Newmark method was used to integrate the equation of motion of the system

performing full Newton-Raphson iterations until convergence was achieved. Constant acceleration method was adopted with the Newmark time integration parameters, γ and β, equal to 0.5 and 0.25 respectively. Modal analyses were carried out for these buildings to estimate their natural fundamental periods as shown in Table 2.

		Building				
		EC8 M5	EC8 M7	EC8 M10	EC8 M13	EC8 M15
Period [s]	T1	0.66	0.84	1.17	1.29	1.39
	T2	0.64	0.83	1.15	1.26	1.31
	T3	0.51	0.66	0.92	1.02	1.12

Table 2: Fundamental periods of the buildings under consideration.

3 NON-STRUCTURAL COMPONENTS MODELLING

In the experimental studies reported in [17], in order to simulate the NSCs in the P-structures, single-degree-of-freedom (SDOF) mechanical oscillators were used and attached to the floors and adjusted to correspond to the natural frequencies of the P-structures. In this study, the NSCs were similarly modelled as vertical cantilever beams with variety of lengths and fixed at their bases with masses on the top. Each mass was modelled as a lump mass made of steel 152x152x51mm weighing about 9.2 kg. The arms of the cantilevers were modelled as circular sections, 40 mm in diameter, with varying lengths to match the frequencies of the P-structures. Full dynamic interaction was considered between the NSCs and P-structures during the analyses.

A damping ratio of 5% [18] was used for the P-structures. However, a damping ratio of 3% [19] and frequencies matching the first (transitional in x dir.) and third (torsional) fundamental periods of the P-structures, as well as rigid NSCs (Tc=0 s.), were adopted for the NSCs in the analyses.

4 THE EARTHQUAKE RECORDS

In this study, in order to evaluate the seismic responses of NSCs during the nonlinear dynamic analyses, a set of seven artificial base motion records were used. These artificial records were generated by using SIMQKE-I code [20]. This code generates a spectral density function from response spectrum (RS) data input and then obtains sinusoidal signals having random phase angles. Response spectrum type C–EC8 with a peak ground acceleration (PGA) of 0.25 g was used as input to generate seven accelerograms with duration of 30 s. Figure 2 displays the RS of the seven artificial records and their average, which match quite well with the elastic RS of EC8 for 5% damping.

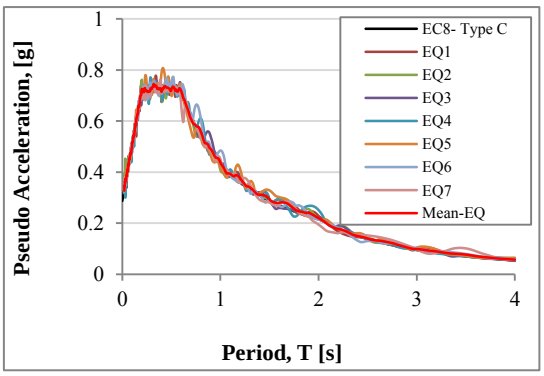


Figure 2: Artificial ground motions.

5 DYNAMIC RESPONSES OF NSCs

Eurocode 8 [12] (section 4.3.3.4.3) allows the use of the mean of the effects of seven or more base motion records on the structures, rather than the maximum effects, for analysis and design purposes. Hence, the results of this study are based on averages of seven ground motion inputs in the two horizontal directions. Dynamic analyses have been conducted to study the responses of NSCs attached to the floors of multi-storey buildings. Three periods of NSCs, T_C=0 s., T_C=T_1, and T_C=T_3 were considered in the analyses.

During earthquakes, in order to pick up the values of accelerations due to transitional modes only of P-structures, the values of accelerations at the centre of rigidity are recorded. Recorded values of accelerations at the flexible side of a building give accelerations due to lateral modes and any torsional modes [21]. Therefore, a relationship between these two recorded accelerations (i.e., records at centre of rigidity and flexible side of a building) gives the amplification in accelerations due to torsional modes only.

To evaluate the maximum response of NSCs attached to the P-structures, average values of peak component accelerations (PCA) and top floor rotations are calculated under the effect of base motions having a PGA that gives a value of structural ductility factor (μ) equal to 1.0. Therefore, a PGA value of 0.16 g was used as input for artificial ground motions so that the EC8 M5, EC8 M7, and EC8 M10 buildings attain their maximum elastic response (i.e., μ=1.0). A PGA value of 0.17 g was used for EC8 M13 and EC8 M15 buildings.

Figures 3(a) and 3(b) show respectively the average values of PCA_{xy} at the flexible sides (FS) and the corresponding values at centre of rigidity (CR), as well as the torsional amplification factors (F_T) for NSCs attached to the top floors of the buildings. The NSCs had periods equal to T1 and T3 of the P-structures. It can be seen form these Figures that the torsional amplification factor increases with the increase in total height of the buildings. This trend is affected by the top floor rotation patterns of the P-structures at μ equal to 1.0, as shown in Figure 4. It can be observed that the higher the value of top floor rotation, the higher the torsional amplification factor.

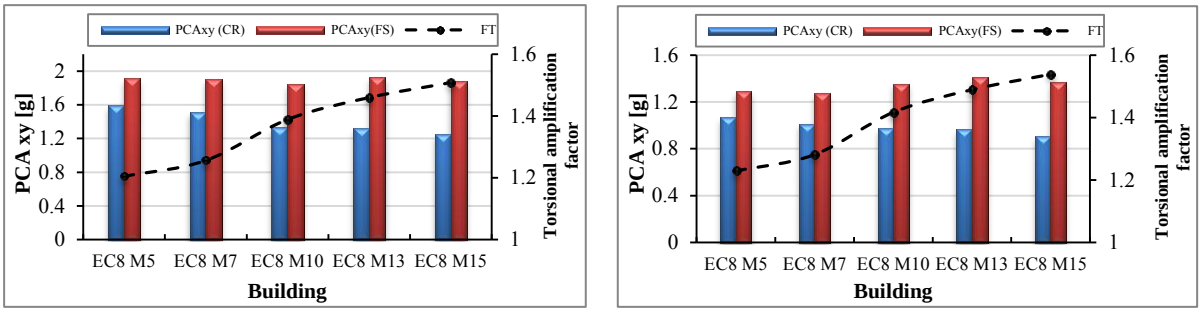


Figure 3: Average values of PCA_{xy} at flexible side and centre of rigidity of top floor of the buildings, and torsional amplification factors for NSCs having :(a) Tc=T1; and (b) Tc=T3.

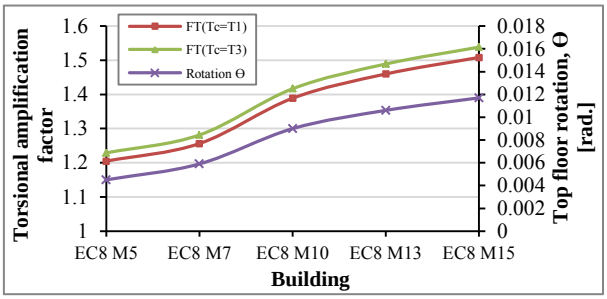


Figure 4: Torsional amplification factors of NSCs and top floor rotation values of the buildings at μ equal to 1.0.

Another trend that can be noticed in Figure 4 is that for a given building, the torsional amplification values are approximately equal for NSCs having periods equal to T1 and T3.

The results in Figures 5 to 7 illustrate the seismic response of NSCs attached along the heights of the buildings. These Figures compare the values of numerically-predicted acceleration amplification factors to the corresponding predictions of the current EC8 provisions (Eq. 4.25-EC8) for the design of NSCs. It can be seen from Figure 5 that the majority of acceleration amplification factors for rigid NSCs, T_C=0.0 s., attached along the heights of the buildings at centres of rigidity are within the range predicted by EC8. However, the acceleration amplification factors for NSCs attached to the flexible sides at the lower thirds of the buildings that have 10, 13, and 15-storey exceed the EC8 predictions. This result suggests that rigid NSCs should not be attached to such locations of the P-structures in order to avoid their failures.

For NSCs having periods equal to the first or third modes of P-structures, T_C=T1 or Tc=T3, the amplification values are higher than the corresponding values calculated using the EC8 provisions as shown in Figures 6 and 7 respectively. Figure 7 shows that, for NSCs having periods equal to the torsional modes of P-structures (T_C=T3), the acceleration amplification factors increase gradually from the lower to the higher floors. A similar trend can be observed for the floors rotation patterns of all the P-structures under consideration at μ equal to 1.0 as shown in Figure 8. This suggests that a correlation exists between the values of the NSCs amplification factors and the values of floor rotations. Further research is being carried out to investigate such a correlation.

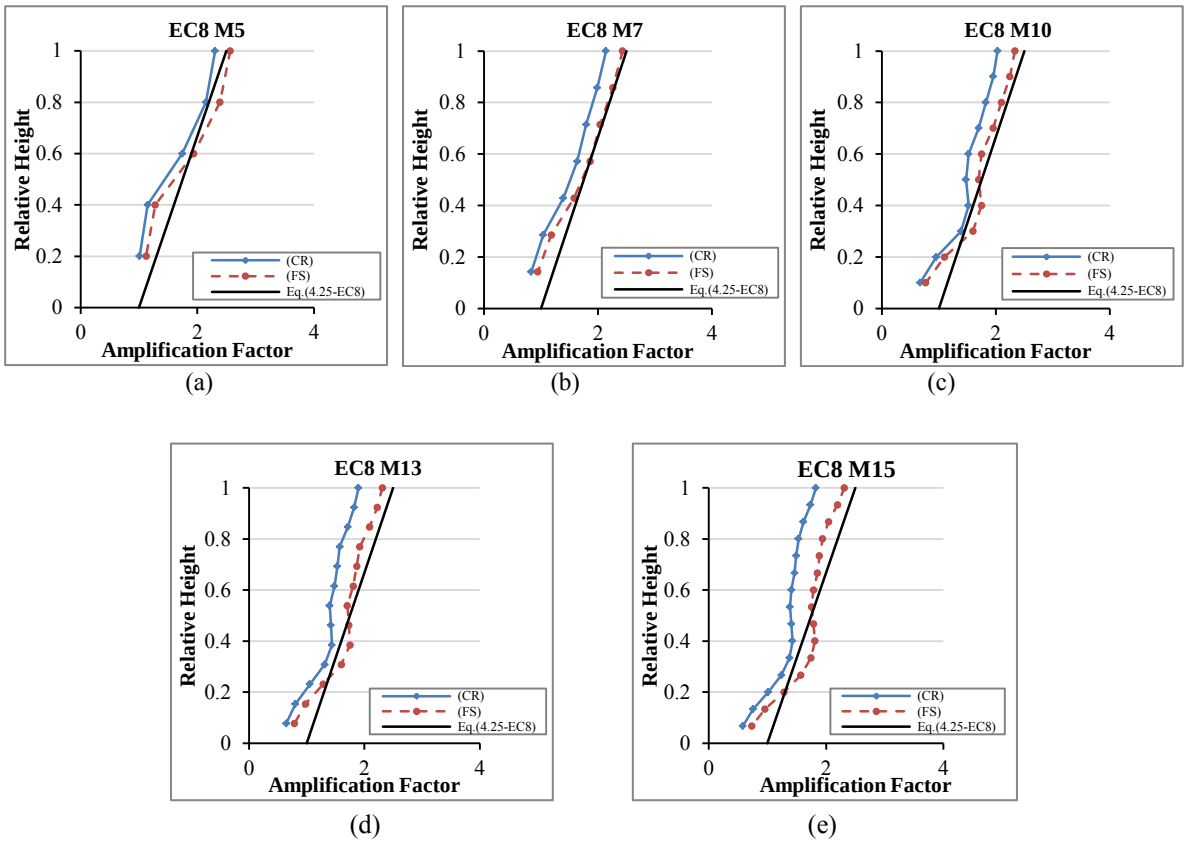


Figure 5: Comparison of the numerical results for acceleration amplification factors of NSCs with Tc=0 s to the corresponding values of EC8: (a) EC8 M5; (b) EC8 M7; (c) EC8 M10; (d) EC8 M13; and (e) EC8 M15.

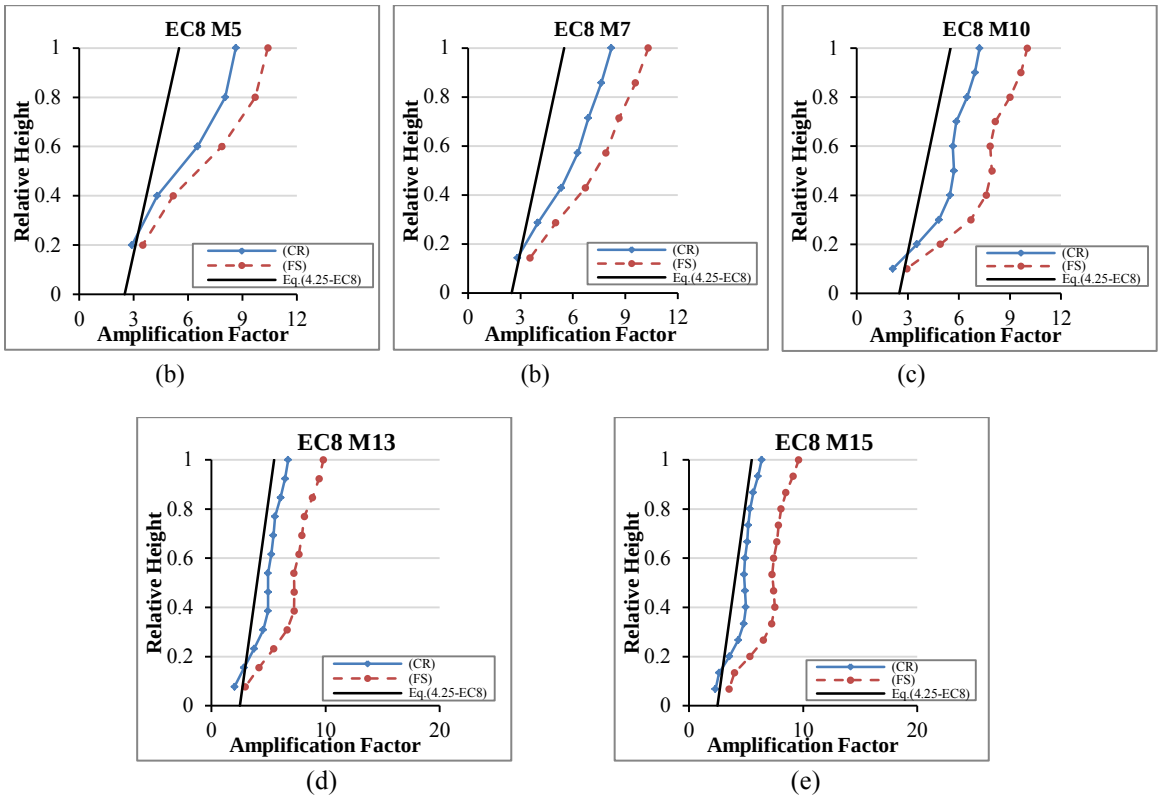


Figure 6: Comparison of the numerical results for acceleration amplification factors of NSCs with Tc=T_1 to the corresponding values of EC8: (a) EC8 M5; (b) EC8 M7; (c) EC8 M10; (d) EC8 M13; and (e) EC8 M15.

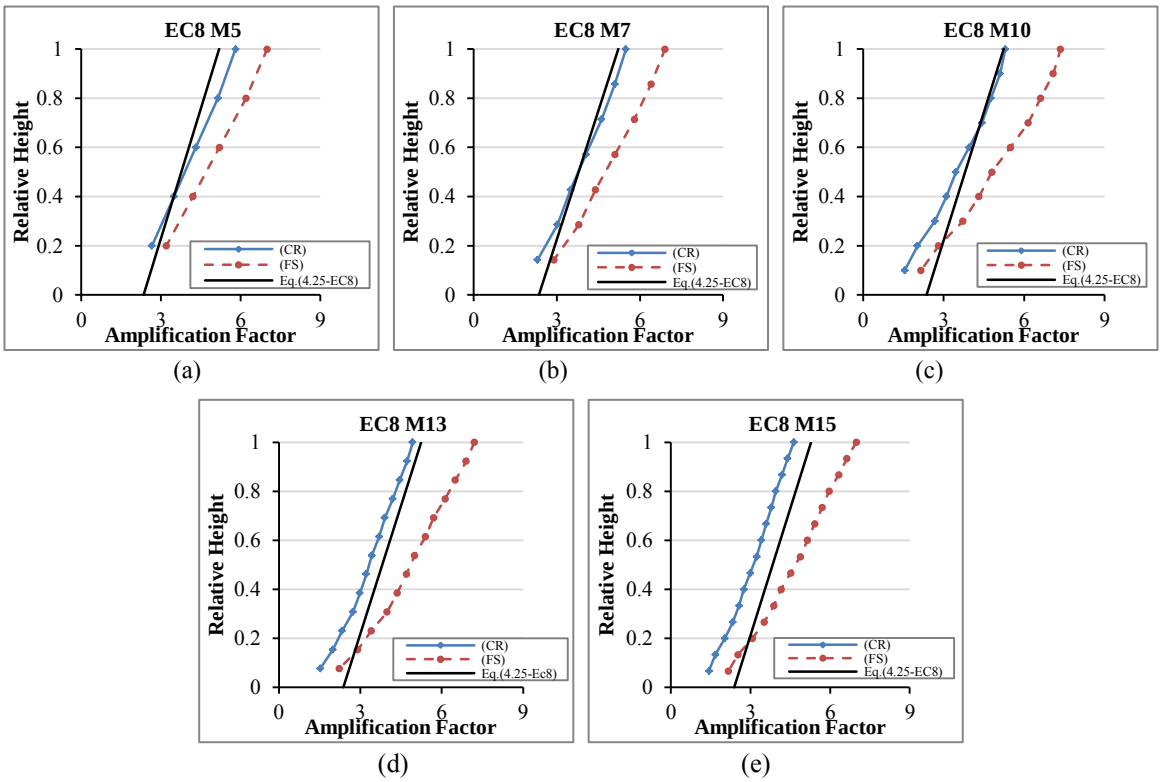


Figure 7: Comparison of the numerical results for acceleration amplification factors of NSCs with Tc=T_3 to the corresponding values of EC8: (a) EC8 M5; (b) EC8 M7; (c) EC8 M10; (d) EC8 M13; and (e) EC8 M15.

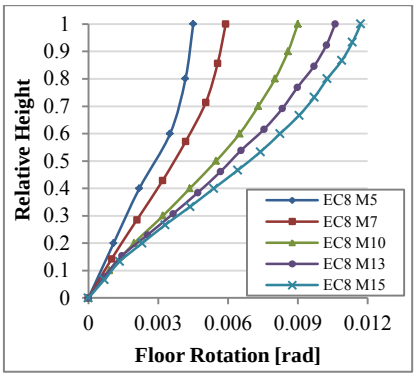


Figure 8. Average values of floor rotations of the buildings at μ equal to 1.0.

6 CONCLUSIONS AND RECOMMENDATIONS

Based on the results of the current study, the following conclusions can be drawn:

- The torsional amplification factors of NSCs increase with the increase in height of the buildings. This trend seems to be affected by the floor rotation patterns of the P-structures; the higher the value of top floor rotation, the higher the torsional amplification factor.
- For a given building, the torsional amplification values are approximately equal for NSCs having periods equal to T1 or T3 of the P-structures.
- The majority of amplification factors for rigid NSCs, T_C=0.0 s., attached along the heights of the buildings at centre of rigidity are within the range of the EC8 predictions. However, the values of amplification factors for NSCs attached to the flexible sides at the lower thirds of the buildings that have 10, 13, and 15-storeys exceed the EC8 predictions.
- For NSCs having periods equal to the first and third modes of P-structures, the NSCs amplification valuess are higher than the values calculated using the EC8 provisions.

According to the preceding numerical results and conclusions , the EC8 design provisions for NSCs need to be improved by taking into account the torsional effects of the P-structures.

REFERENCES

[1] Y.Q. Chen, T.T. Soong, Seismic Response of Secondary Systems, *Engineering Structures,* 10, 4:218-228, 1988.

[2] R. Villaverde, Seismic Design of Secondary Structures: State of the Art, *Journal of Structural Engineering-ASCE*, 123, 8:1011-1019, 1997.

[3] A. Filiatrault, C. Christopoulos, C. Stearns, Guidelines, Specifications, and Seismic Performance Characterization of Non-structural Building Components and Equipment. *Pacific Earthquake Engineering Research Centre, College of Engineering*, University of California, Berkeley, 102, 2002.

[4] A.S. Whittaker, T.T. Soong, An Overview of Nonstructural Components Research at Three U. S. Earthquake Engineering Research Centres, *Proceedings of ATC-29-2 Seminar on Seismic Design*, Performance, and Retrofit of Nonstructural Components in Critical Facilities, ATC-29-2 Report, Applied Technology Council, Redwood City, California, 271-280, 2003.

[5] A.M. Chandler, Building damage in Mexico City earthquake, *Nature*, 320, pp. 497-501, 1986.
[6] Y.B. Yang, W.H. Huang, Seismic Response of Light Equipment in Torsional Building, *Earthquake Engineering and Structural Dynamics,* 22:113-128, 1993.
[7] Y.B. Yang, W.H. Huang, Equipment-structure interaction considering the effect of torsion and base isolation, *Earthquake Engineering and Structural Dynamics,* 27:155-171, 1998.
[8] A.K. Agrawal, T.K. Datta, Behaviour of Secondary System Attached to a Torsionally Coupled Primary System, *Journal of European Earthquake Engineering,* 2:47-53, 1997.
[9] A.K. Agrawal, T.K. Datta, Seismic Response of a Secondary System Mounted on a Torsionally Coupled Non-linear Primary System, *Journal of Earthquake Engineering,* 2:339-356, 1998.
[10] A.K. Agrawal, T.K. Datta, Seismic Behaviour of a Secondary System on a Yielding Torsionally Coupled Primary System, *JSEE,* 2, 1:35-46, 1999.
[11] A.B. Aldeka, AHC. Chan, S. Dirar, Finite Element Modelling of Non-structural Components Mounted on a Torsionally Multi-storey Building, *Proceedings of the 20th UK conference of the Association for Computational Mechanics in Engineering (ACME2012)*, Manchester, United Kingdom, 67-70, 2012.
[12] EC8 Eurocode 8 EN 1998-1. Design of structures for earthquake resistance, 2004.
[13] P. Negro, E. Mola, J. Molina, and G. Magonette, Full-scale PSD testing of a torsionally unbalanced three-storey non-seismic RC Frame, *13th World conference on Earthquake Engineering*, Vancouver, Canada, No. 968, 2004.
[14] Midas Gen. Analysis Manual, version 3.1, 2012, http://www.MidasUser.com/.
[15] J.B. Mander, M.J.N. Priestley, R. Park, Theoretical stress-strain model for confined concrete, *Journal of Structural Engineering- ASCE,* 114, 8:1804-1826, 1988.
[16] M. Menegotto, P.E. Pinto, Method of analysis for cyclically loaded RC plane frames including changes in geometry and non-elastic behaviour of elements under combined normal force and bending. Symposium on the Resistance and Ultimate Deformability of Structures acted on by well defined loads, *International Association for Bridge and Structural Engineering*, Zurich, Switzerland, 15-22, 1973.
[17] J.L. Sackman, J.M. Kelly, Seismic analysis of internal equipment and components in structures, *Engineering Structure,* 1:179-190, 1979.
[18] M. Paz, International handbook of earthquake engineering: codes, programs, and examples, Springer, 1994.
[19] H. Graves, R. Morante, Recommendations for Revision of Seismic Damping Values in Regulatory Guide 1.61, 2006.
[20] SIMQKE User Manual. NISEE Software Library, University of California, Berkeley, USA, 1976.
[21] R.M. DiJulio, G.C. Hart, Torsional Response and Design of High-rise Buildings, *ULCA-ENG-7373,* Los Angeles, Calif. Univ. (L.A.) Sch. of Engineering & Appl. Sci. [Report], 1974.

COMPDYN 2013
4th ECCOMAS Thematic Conference on
Computational Methods in Structural Dynamics and Earthquake Engineering
M. Papadrakakis, V. Papadopoulos, V. Plevris (eds.)
Kos Island, Greece, 12–14 June 2013

RAPID EVALUATION OF NON-DUCTILE MULTISTOREY RC BUILDINGS

Georgia E. Thermou[1] **and Anastasia F. Palaiochorinou**[1]

[1] Aristotle University of Thessaloniki
Dept. of Civil Engineering, 54124, Thessaloniki, Greece
gthermou@civil.auth.gr; palaiochorinou@teeemail.gr

Keywords: Assessment, Gravity Load bearing buildings, Prioritizing of Failure Modes, Collapse, Reinforced Concrete.

Abstract. *The majority of existing building stock in southern Europe, as well as in other parts of the world, comprises non-ductile multistory reinforced concrete (RC) buildings designed for gravity loads only without any reinforcement detailing. The deficiencies of such structures lead to premature failure or collapse, posing a realistic threat to human life. Thus, assessment of their seismic vulnerability is deemed necessary, by examining in detail their response to various scenarios. Due to the large inventory of this type of buildings such an effort requires huge amounts of work, rendering the whole procedure unrealistic. For this purpose a rapid preliminary assessment methodology was proposed by Thermou and Pantazopoulou [1], Pardalopoulos et al. [2], which aims to single out those buildings that are at a greater risk for catastrophic collapse and in which further detailed assessment with the aid of advanced analytical tools is deemed necessary. The methodology is based on the stiffness index (used to determine the severity of seismic displacement demand) and the base-shear strength index (associated with typical column details representative of the state of practice from the era of the building's period of construction) criteria.*

Within the framework of current research, a database of ten representative multistory RC residential buildings that were built in the 1950's in Northern Greece (in the city of Thessaloniki) was created. This group of buildings was assessed by using the aforementioned rapid preliminary assessment methodology for various scenarios related to increasing peak ground acceleration (PGA) values. The characteristics of this prevalent construction type were recorded after extensive study of the design drawings of real structures of the era and are presented herein.

An eight-storey RC building was selected from the database for detailed implementation of the proposed rapid assessment methodology throughout its storeys. The validity of the preliminary assessment methodology was verified by conducting numerous detailed analyses. For this purpose, a three-dimensional finite element model was created and pushover analyses were carried out. The influence of the masonry infills was another parameter of study. The results verified the outcome of the rapid evaluation methodology and complied with the findings of the reconnaissance report.

1 INTRODUCTION

The design philosophy of buildings in earthquake prone areas has changed dramatically the last thirty years given the experience gained from major earthquake events which revealed the susceptibility of older construction units. It is a fact that the majority of multi-storey reinforced concrete (RC) buildings in southern Europe was designed according to older generation of codes where reinforcement detailing was at a primitive stage of knowledge. The deficiencies of such structures lead to premature failure or collapse, posing a realistic threat to human life. Recent earthquakes underlined the need for assessment of their seismic vulnerability. Considering the large inventory of this type of buildings analytical modeling requires huge amounts of work, rendering the whole procedure unrealistic. Therefore rapid and palatable tools for assessing the seismic vulnerability of the built environment need be developed. Within this context, a rapid preliminary assessment methodology was proposed by Thermou and Pantazopoulou [1], Pardalopoulos et al. [2], which aims to single out those buildings that are at a greater risk for catastrophic collapse and in which further detailed assessment with the aid of advanced analytical tools is deemed necessary.

One of the objectives of this paper is to shed light on the response of multistory RC residential buildings that were built in the 1950's in the city of Thessaloniki (Greece). Given that the first Greek Seismic Code was launched in 1959 and that RC walls were introduced in construction in the 1960's, multistory buildings of the '50's represent the cutting edge of the construction technology for gravity load designed frame buildings. A database of ten representative multistory RC residential buildings that were built in the 1950's in the city of Thessaloniki (in Northern Greece) was created. The characteristics of this prevalent construction type were recorded after extensive study of the design drawings of real structures of the era and are presented herein. Despite the fact that gravity load design principles were implemented, this type of building units survived the 1978 Thessaloniki earthquake (PGA=0.15g) with moderate or no damage at all.

The proposed preliminary assessment methodology was applied to one representative eight-storey RC building selected from the database. A common feature of this type of buildings is the change of column dimensions and longitudinal reinforcement from storey to storey. This implies that the methodology needs to be applied in each storey and that the critical storey cannot be defined a priori. The primary deficiencies of the building and the level of spectral acceleration that may be tolerated prior to failure were defined after implementation of the stiffness and strength criteria.

The validity of the rapid evaluation methodology was verified by conducting detailed pushover analyses. For this purpose, a finite element program was utilized where modeling required the determination of the nonlinear properties of each component in the structure, quantified by strength and deformation capacities. With parameters of study the existence or no of external infill walls throughout the structure, the type of the plastic hinges (automatic or user-defined hinges, shear hinges) a group of three-dimensional models was created and pushover analysis were carried out. The results verified the outcome of the rapid evaluation methodology and complied with the findings of the reconnaissance report.

2 CHARACTERISTICS OF THE GRAVITY LOAD DESIGNED RC BUILDINGS

A group of ten multistory representative RC residential buildings that were built in the 1950's in the city of Thessaloniki (Greece) comprises the database created for the needs of current research. A common feature of this type of building unit refers to the open first storey

for store or parking lot usage, known as *pilotis* (Fig.1), and the existence of penthouses introducing in-height irregularities of mass and stiffness distribution.

Given that the first Greek Seismic Code was launched in 1959, the gravity load design principles were followed in the 1950's buildings. The allowable stress design philosophy was implemented not allowing any control of the mode of failure and the corresponding deformation capacity of the individual members. Reinforcement detailing followed empirical rules of the era, rarely specified in official drawings. This was confirmed after studying the folders of numerous buildings of this era. One of the criteria followed for ending up to the ten representative buildings was the level of completeness of the folders. The information gathered and presented in the following two paragraphs refers to the material characteristics, construction detailing and geometrical configuration characteristics.



Figure 1: Typical multistory RC residential buildings with pilotis in Greece.

The materials used in the 1950's are characterized by low strength and lack of quality control. Concrete was constructed at site with the use of a concrete mixer machine and was carried by the workers. In case of steel, metallurgical testing was at a primitive stage and credentials were never questioned. Another parameter that influences greatly the quality of construction is supervision which was relatively lenient, thus rendering the experience of the workers a determinant factor for the quality of construction.

The concrete qualities used according to the Greek Royal Decree No.18.2/1954 [3] were the B120 and the B160 with a characteristic cylindrical strength equal to $f_{ck}\cong 8$ MPa and $f_{ck}\cong 10$ MPa. Smooth steel reinforcing bars were used of quality StI with a characteristic yield strength f_{yk}=220 MPa ([4]).

As far as construction practice is concerned, longitudinal reinforcement bars of 10 mm – 20 mm diameter and 6 mm – 8 mm diameter stirrups spaced at 200 mm – 600 mm were applied in both columns and beams. Stirrups in both columns' and beams' sections were anchored with 90° hooks in the ends (open stirrups). Lap splices were usually unconfined, whereas starter bars had random lengths. Joints were usually left without stirrups, for convenience of construction. Longitudinal reinforcement with hooks were used with arbitrary lengths not specified in the official drawings. Often in-plan column layout is not on grid leading to indirect supports (i.e. primary beam supporting secondary).

The buildings of the 1950's are characterized as frame buildings having usually up to three spans. The lack of a continuous vertical load path along the height of the buildings is a common feature of the buildings of that era. Symmetry in columns' layout along one or two axes in some cases is observed. Note that RC walls do not exist in the stuctures of the era

neither as an additional load bearing system nor in the stairwells or in the elevator shafts since their implementetaion was introduced in the early 1960's in Greece. Typical columns' cross section dimensions ranged between 300 mm – 600 mm decreasing in the upper floors. Their longitudinal reinforcement ratio ranged between 7‰ - 9‰ lower than the minimum reinforcement defined by the modern codes equal to 10‰ [6]. Referring to beams their typical cross section dimensions were 150 mm × 300 mm to 300 mm × 600 mm. Slab thickness ranged between 100 mm – 120 mm. The findings of real structures construction practice research are summarised in Table 1.

Construction practice characteristics	
Concrete quality	B120 ÷ B160 $^{(*)}$ (f_{ck}≅8-10 MPa)
Steel quality (longitudinal and transverse reinforcement)	Smooth StI (f_{yk}=220 MPa) $^{(**)}$
Typical columns' cross section dimensions	300 ÷ 600 mm
Typical diameters of columns' longitudinal reinforcement bars	Ø14 ÷ Ø20
Typical columns' transverse reinforcement	Ø6/250 ÷ 300 mm $^{(***)}$
Typical columns' longitudinal reinforcement ratio	7‰ ÷ 9‰ < 10‰
Typical beams' cross section dimensions	150×300 ÷ 300×600 mm
Typical diameters of beams' longitudinal reinforcement bars	Ø10 ÷ Ø18
Typical beams' transverse reinforcement	Ø6/200 ÷ 250 mm $^{(***)}$
Typical thickness of masonry infill walls	100 mm for internal 200 mm for external
Anchorage / lap splices construction practice	• Longitudinal reinforcement with hooks with arbitrary lengths. • Stirrups anchored with 90° hooks. • Unconfined lap splices.

$^{(*)}$ as per Greek Royal Decree No.18.2/1954 [3]. Later concrete quality B225 (f_{ck}≅14MPa) was introduced in construction, $^{(**)}$ as per DIN 1045 (1936) [4]. Later longitudinal reinforcement steel quality was differentiated to StIII (f_{yk}=400÷420MPa), $^{(***)}$ rarely diameter Ø8 was applied.

Table 1: Information of the typical construction practice followed in the early 1950's in Greece.

3 RAPID EVALUATION METHODOLOGY

Preliminary assessment of existing building stock targeted toward identification of the most vulnerable buildings must necessarily rely on a marginal collection of data that is readily available, such as the overall geometric details of the structure (number of floors, floor height, floor area, location and gross geometry of load carrying members in plan), on the implicit assumption that all reinforcing details are represented by the historical construction information for the period and region of construction of the building studied.

The rapid preliminary seismic vulnerability assessment methodology is based on the:

(a) Stiffness criterion, which is used to quantify interstorey drift demand and thus evaluate the severity of seismic displacement demand.

(b) Strength criterion, which is used to determine the weakest mechanism of resistance, likely to control the sequence of failure of the vertical elements of the structure.

3.1 Estimation of storey stiffness

The stiffness K_i of the i-th storey of a frame building that comprises columns (K_i^c) and masonry infill walls stiffnesses (K_i^{wm}) is given by [1]:

$$K_i = K_i^c + K_i^{wm} = \frac{A_f}{h_i}\left(D_c\rho_{c,i} + D_{wm}\rho_{wm,i}\right) = \frac{A_f}{h_i} D_c\rho_i^e \tag{1}$$

$$\text{with } D_c = E_c\left(\frac{h_{c,ave}}{h_i}\right)^2,\ D_{wm} = 0.10\frac{f_{bc}^{0.7} f_{mc}^{0.3}}{\mu_y^{wm}\theta_y^{wm}} \text{ and } \rho_i^e = \rho_{c,i}\left(1 + \frac{D_{wm}}{D_c}\frac{\rho_{wm,i}}{\rho_{c,i}}\right)$$

where A_f (m^2) is the i-th floor area, h_i (m) is the clear i-th storey height, $E_c=22\ (f_{ck}/10)^{1/3}$ (GPa) is the concrete modulus of elasticity [6], $h_{c,ave}$ (m) the average column cross section height, $\rho_{c,i}$ the dimensionless area ratio of columns at the i-th floor plan, $\rho_{wm,i}$ the dimensionless area ratio of masonry walls at the i-th floor plan, ρ_i^e is the equivalent dimensionless area ratio of vertical members at the i-th floor plan, f_{bc} (MPa) is the bricks compressive strength, f_{mc} (MPa) mortar compressive strength, μ_y^{wm} the drift ductility of masonry walls and θ_y^{wm} the drift of masonry walls at yield.

3.2 Interstorey Drift Spectra (IDS) for frame buildings

Interstorey Drift Spectra (IDS) was developed by Thermou et al. [5] as an efficient tool for the seismic upgrading of existing RC buildings. In this type of spectra, stiffness demand is related to the target response of the building. For the needs of assessment, stiffness demand is expressed as a function of the equivalent dimensionless area ratio of vertical members, whereas interstorey drift is considered a measure of the system's vulnerability and [1]. The methodology of derivation of the IDS for the i-th storey follows.

Type I elastic spectrum of Eurocode 8 [7] is used to define spectral displacement demand for a design region $0.15s < T < 2.00\ s$ for subsoil class B with S=1.20, β_0=2.50, T_B=0.15 s, T_C=0.50 s, q=1.00, as follows:

$$0.15 \le T \le 0.50:\ S_d(T) = 0.076\alpha_g T^2 \tag{2a}$$

$$0.50 < T \le 2.00:\ S_d(T) = 0.038\alpha_g T \tag{2b}$$

where a_g is the peak ground acceleration (pga), β_o is spectral acceleration amplification factor equal to 2.5, S is the soil parameter, and T_B, T_C are the period values that define the limits of the constant acceleration branch.

Period T of an n-storey building with constant distribution of storey stiffness and storey plan geometry along the height of the building is given by:

$$T = 2\pi/\omega = 2\left(2n+1\right)\sqrt{M_i/K_i} = 2\left(2n+1\right)\left(\frac{\gamma h_i}{D_c\rho_i^e}\right)^{0.5} \tag{3}$$

where n is the number of storeys, M_i is the storey mass, K_i is the storey stiffness (Eq. (1)), $\gamma(=M_i/A_f)$ is the mass per unit area of the floor, h_i is the i-th storey height, D_c is defined in Eq. (1) and ρ_i^e is the equivalent dimensionless area ratio of vertical members at the i-th floor plan.

The substitution of T in Eqs. (2) relates the spectral displacement demand with the equivalent dimensionless area ratio of vertical members at the i-th floor plan as follows:

$$0.15 \le T \le 0.50: \; S_d(T) = 0.304\alpha_g \left(2n+1\right)^2 \left(\frac{\gamma h_i}{D_c \rho_i^e}\right) \tag{4a}$$

$$0.50 < T \le 2.00: S_d(T) = 0.076\alpha_g \left(2n+1\right)\left(\frac{\gamma h_i}{D_c \rho_i^e}\right)^{0.5} \tag{4b}$$

where a_g is the peak ground acceleration (pga), n is the number of storeys, $\gamma(=M_i/h_i)$ is the mass per unit area of the floor, h_i is the i-th storey height, D_c is defined in Eq. (1) and ρ_i^e is the equivalent dimensionless area ratio of vertical members at the i-th floor plan.

For frame structures the deformed shape under lateral sway may be approximated by the response shape of a shear-type building:

$$\Phi(x) = \sin\left(\frac{\pi x}{2H_{tot}}\right) \tag{5}$$

where x is the storey height from the ground level and H_{tot} is the total building height (Fig. 2).

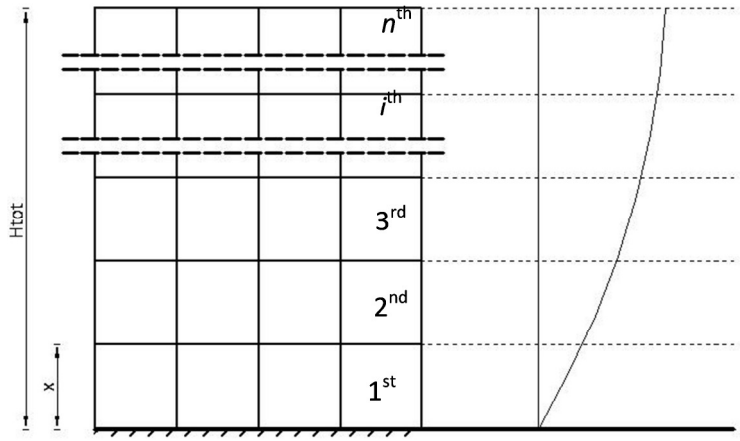


Figure 2: Lateral response shape for frame structures.

Interstorey drift of the i-th storey, Θ_i, is given by:

$$\Theta_i = S_d / h_i \Delta\Phi_i \tag{6}$$

where S_d is the spectral displacement, h_i is i-th storey height and $\Delta\Phi_i$ is the difference in the shape between successive floors.

By substituting Eqs. (4) into Eq. (6) and also by substituting the term D_c from Eq. 1, a design spectrum for the i-th interstorey drift demand under the design earthquake is extracted:

$$0.15 \le T \le 0.50: \; \Theta_i = 0.304\alpha_g \left(2n+1\right)^2 \frac{\gamma}{E_c}\left(\frac{h_i}{h_{c,ave}}\right)^2 \frac{\Delta\Phi_i}{\rho_i^e} \tag{7a}$$

$$0.50 < T \le 2.00: \; \Theta_i = 0.076\alpha_g \left(2n+1\right)\left(\frac{\gamma}{E_c}\right)^{0.5} \frac{h_i^{0.5}}{h_{c,ave}} \frac{\Delta\Phi_i}{\left(\rho_i^e\right)^{0.5}} \tag{7b}$$

3.3 Estimation of storey drift at failure, $\Theta_{fail,i}$

The comparison between the interstorey drift demand, Θ_i, and drift at failure, $\Theta_{fail,i}$, provides information relative to whether the building will fail or not. In case of inadequate shear resistance collapse could be prevented if $\Theta_i<\Theta_{fail,i}$. The interstorey drift at failure, $\Theta_{fail,i}$, is estimated by considering the average interstorey drift at failure of the vertical members, $\Theta_{fail,i}^{c}$, through coefficient λ_c that expresses the relative column stiffness ratio in the frame connections of the building [1]: $\Theta_{fail,i}=\Theta_{fail,i}^{c}/\lambda_c$. The average values of λ_c estimated for the 1950's building database ranged between 0.25 ÷ 0.50.

In order to determine $\Theta_{fail,i}^{c}$ the nominal drift at yield $\Theta_{y,nom,i}^{c}$ should be calculated first and then corrected by the strength index $r_{u,lim}$, i.e. $\Theta_{fail,i}^{c} = \Theta_{y,nom,i}^{c} \cdot r_{u,lim}$ [2]. Interstorey drift at column yielding may be estimated using the 'stick model' cantilever extending from the support to the point of inflection around the midheight of the column. Thus, $\Theta_{y,nom}^{c}=1/3\ \varphi_y L_s$, where $\varphi_y = 1.77\ \varepsilon_{sy}/h_c$ [8], ε_{sy} is the steel strain at yield, h_c is the height of the cross section and L_s is the shear span length equal to the half clear storey height.

Strength index $r_{u,lim}$ (= $min\ \{r_v;\ r_a;\ r_{lap};\ r_j;\ r_{pn}\}$ expresses the weakest shear mechanism of an individual column corresponding to the most common premature modes of failure (prior to the flexural one), i.e. shear failure, r_v, anchorage failure, r_a, failure at lap splices, r_{lap}, joint failure, r_j, and punching failure in cases of slabs without beams, r_{pn}. It is determined as the fraction between the base shear force at the occurrence of the controlling mode of failure of the column, $V_{u,lim}$, and the base shear corresponding to the onset of yielding of column reinforcement, $V_{y,flex}$; i.e. $r_{u,lim}=V_{u,lim}/V_{y,flex}$. The expressions for the various strength ratios are presented in Appendix A [2].

In case that beam yielding occurs prior to column failure, $r_{by}<r_{u,lim}$, then the shear force input to the column is limited by yielding of the adjacent beams. In case that interstorey drift demand is $\Theta_i<\Theta_{y,nom,i}^{b}/(1-\lambda_c)$, where $\Theta_{y,nom,i}^{b}$ is the average nominal drift at yielding of beams, then the structure may be assumed to be in the elastic (pre-yielding state). Otherwise, i.e. $\Theta_i>\Theta_{y,nom,i}^{b}/(1-\lambda_c)$, ductile plastic hinging in the beams may develop [2].

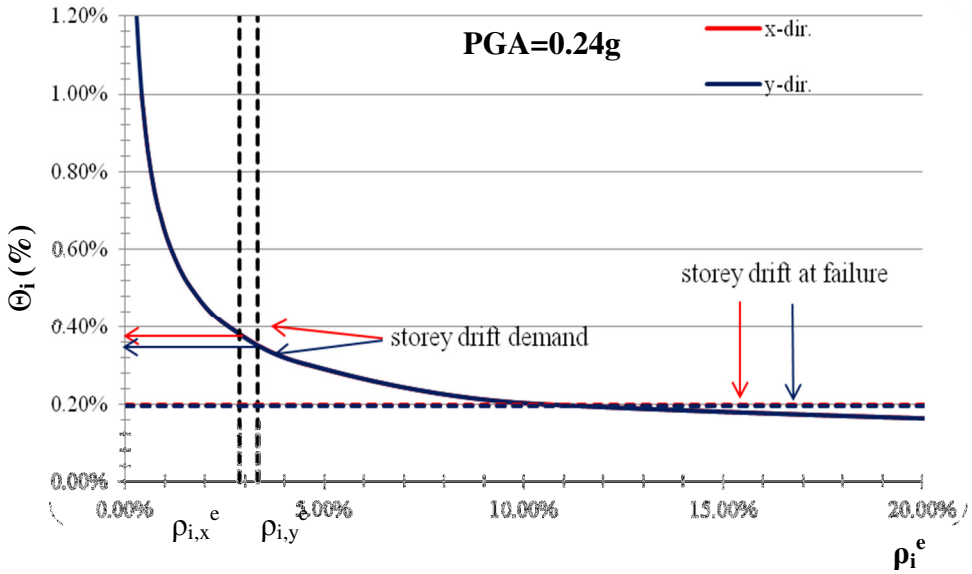


Figure 3: Vulnerability curve.

3.4 Assessment using the Interstorey Drift Spectra (IDS)

The use of the IDS as an efficient design tool for rapid preliminary assessment is illustrated in Fig. 3. First, the period of the building in each direction is estimated according to Eq. (3) and the IDS is plotted according to Eqs. (7) by selecting the adequate range of periods (in Fig. 3 the red curve corresponds to x direction, whereas the blue curve to y direction). The second step involves the estimation of the equivalent vertical members area ratio, ρ_i^e, for each direction of the building. This is depicted in the graph of Fig. 3 by the two vertical black dashed lines (the left dashed black line refers to direction x and the right one to direction y). The intersection of the dashed black line with the vulnerability curve determines the drift demand, Θ_i, per direction. This value is compared to the drift at failure of each direction, shown by the horizontal dashed lines in Fig. 3 (red colored line refers to x direction, whereas the blue colored line to y direction). As it is observed, the storey drift at failure is below the storey drift demand, $\Theta_i < \Theta_{fail,i}$, implying that failure is anticipated in both directions.

4 IMPLEMENTATION OF THE ASSESSMENT METHODOLOGY

4.1 Description of the building

The building studied is an 8-storey residential R.C. building with basement constructed in the center of the city of Thessaloniki (Greece) in 1951 with the first storey (ground floor) used as a commercial space (Fig. 4). The top floor is formed as a setback including two apartments and the end of the stairwell. The typical floor's area is 190.18 m^2, while the first floor's is 172.199 m^2 and the setback's is 160.58 m^2. The building is symmetric along y axis, thus information is provided only for the columns on the left handside. Note that columns C1, C2, C1', C2' (Fig.4) do not continue to the last floor. The building's total height from the ground level is 26.90 m, whereas the individual storey heights are 3.30 m for the 1st, 2nd and 3rd storey, 3.20 m for the 4th, 5th and 6th storey, and 3.00 m for the7th and 8th storey. The basement's height is 2.70 m. However, the columns at the perimeter of the building are captive with clear height 1.4 m (this is the height above the ground level).

It is highlighted that there are two skylights along the building height as well as a stairwell almost in the middle of the floor plan introducing a discontinuity in mass and stiffness distribution and consequently in stress distribution.

The materials considered were B120 concrete quality [3] (f_{ck}=10 MPa was taken in the application of the methodology) and smooth StI [4] for longitudinal and transverse reinforcement of the structural members (f_{yk}=220 MPa was taken). The slab thickness was 0.10 m constant at all floors.

Columns longitudinal reinforcement comprised smooth bars of 14 mm ÷ 20 mm diameter. The longitudinal reinforcement area ratio over the column section ranged between 6.5‰÷9‰ approximately. Column transverse reinforcement comprised rectangular stirrups of 6 mm diameter spaced at 170 mm ÷ 240 mm anchored with 90° hooks in the ends. Concerning longitudinal bars anchorage lengths and lap splices lengths the assumption of 1.00 m and 0.40 m, respectively, was made (consequent with the state of practice from the building's era of construction) lacking any official information. Details regarding column cross section dimensions and amount of longitudinal reinforcement are shown in Table B (Appendix B).

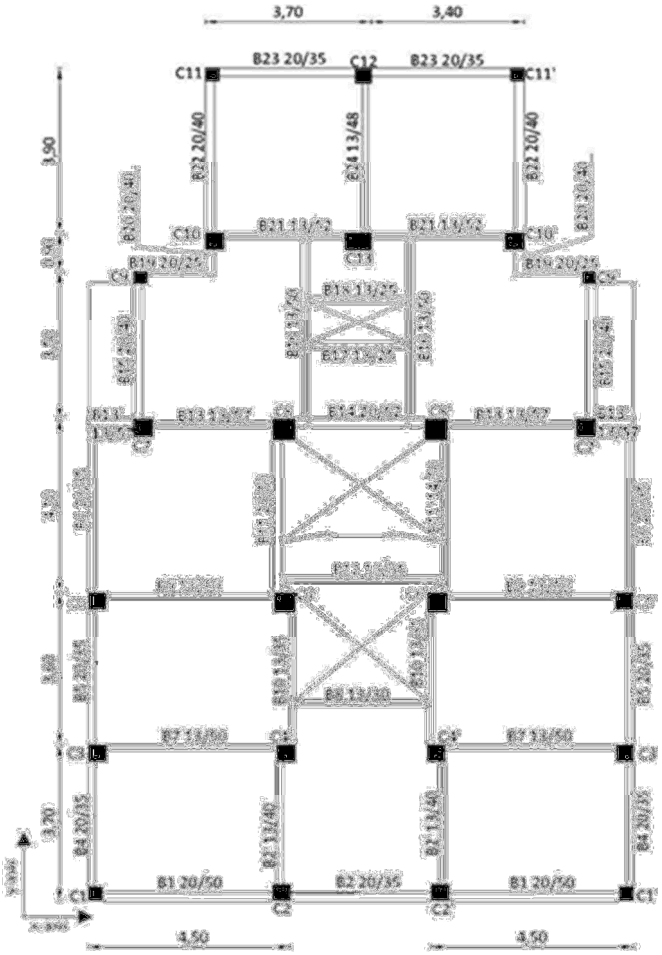


Figure 4: Typical floor plan configuration of the building.

Beams longitudinal reinforcement comprised smooth bars of diameter equal to 10 mm ÷ 18 mm. Note that in a few beams three different bar diameters are placed (e.g. 10 mm, 12 mm and 14 m). The longitudinal reinforcement area ratio ranged between 3.6‰ ÷ 17‰ approximately. Transverse reinforcement comprised rectangular stirrups of 6 mm diameter spaced at 150 mm anchored with 90° hooks in the ends.

Slab dead loads comprise self – weight (24.00 kN/m^3 was assumed as per the initial design of the building) and finishings load (0.60 kN/m^2); slab live load of 2.00 kN/m^2 was assumed. Beams were considered to carry their self - weight and the weight of the masonry infills. An average masonry wall height of 2.80 m was assumed. For external masonry infill walls a 0.20 m thickness was considered leading to 11.20 kN/m vertical dead load distributed onto the external beams. The internal beams are considered to carry the weight of the internal masonry walls of 0.10 m thickness, thus 5.60 kN/m uniform load was distributed on the internal beams. Balcony load was applied as uniform load on the external beams B15 (Fig. 4) giving an additional dead load of 3.40 kN/m and live load of 5.00 kN/m.

4.2 Application of the methodology

The average nominal drift at yield was estimated, $\Theta_{y,nom}^{c}$, and was reduced by the average strength index, $r_{u,lim}$, in order to estimate the average column drift at failure Θ_{fail}^{c} (see section 3.3). This procedure was repeated for each storey in both directions and the results are presented in Table 3 for both directions.

Direction	Parameters	1st	2nd	3rd	4th	5th	6th	7th	8th
x-x	$V_{u,lim}$ (kN)	45.14	30.97	33.76	28.16	20.93	14.30	9.88	8.40
	$V_{y,flex}$ (kN)	92.98	79.51	64.81	50.47	35.06	23.01	16.33	10.79
	$r_{u,lim}$	0.46	0.46	0.49	0.53	0.57	0.59	0.58	0.76
	$\Theta_{y,nom}{}^{c}$	0.24%	0.25%	0.26%	0.28%	0.30%	0.33%	0.32%	0.33%
	$\Theta_{fail}{}^{c}$	0.10%	0.11%	0.13%	0.14%	0.17%	0.20%	0.19%	0.24%
	r_{by}	0.20	0.23	0.29	0.39	0.57	0.86	1.27	1.89
	Failure*	X	X	X	X	X	√	√	√
y-y	V_{min} (kN)	38.34	33.28	28.74	23.45	17.46	12.00	8.46	7.32
	V_{flex} (kN)	89.41	77.33	62.97	47.87	33.21	22.06	16.33	10.79
	$r_{u,lim}$	0.40	0.41	0.43	0.46	0.50	0.52	0.50	0.66
	$\Theta_{y,nom}{}^{c}$	0.24%	0.25%	0.27%	0.28%	0.31%	0.34%	0.32%	0.33%
	$\Theta_{fail}{}^{c}$	0.09%	0.10%	0.11%	0.13%	0.15%	0.17%	0.16%	0.22%
	r_{by}	0.20	0.24	0.29	0.38	0.53	0.79	1.15	2.02
	Failure*	X	X	X	X	√	√	√	√

* *X corresponds to beam yielding ($r_{u,lim} > r_{by}$), √corresponds to column failure*

Table 2: Strength assessment results per storey.

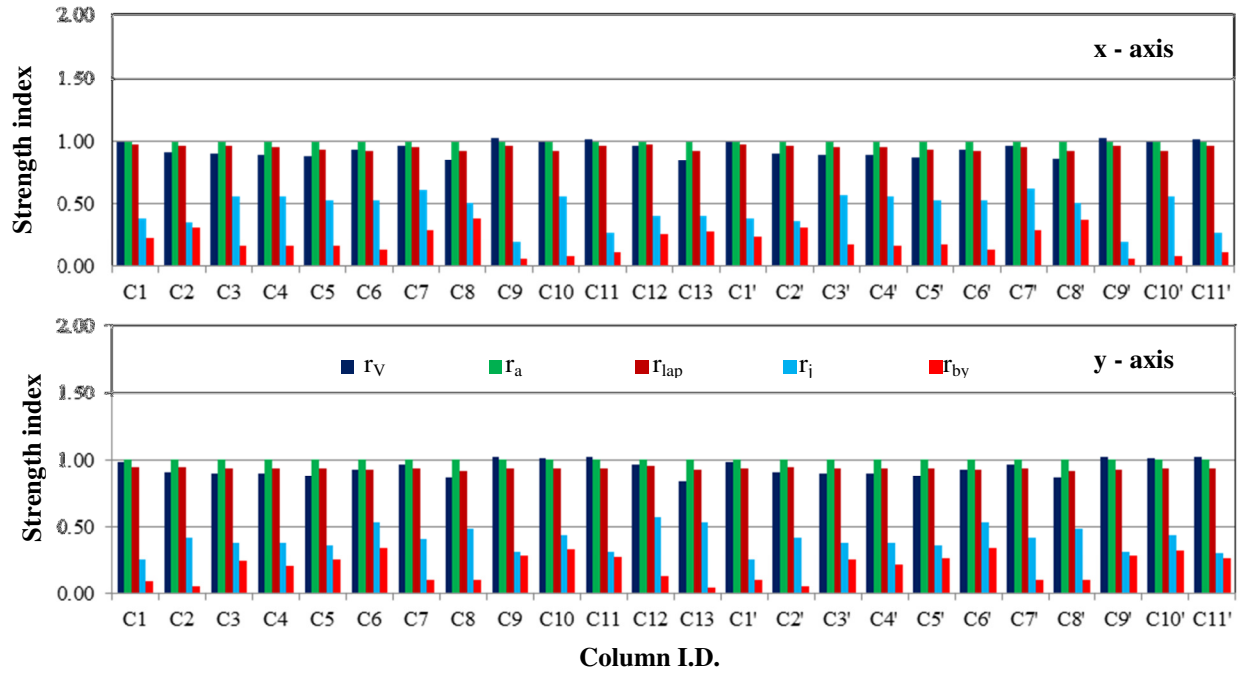


Figure 5: First storey column strength assessment along x – axis and y – axis.

The weakest column resistance mechanism as shown in the graphical representation of the various strength indices in Figs. 5, 6 and 7 for the first, fifth and sixth floor, respectively, is detected in the region of joints. Thus in most cases $r_{u,lim}$ is equal to r_j indicating the insufficient reinforcement detailing and confinement of joints. This mode of failure may be suppressed if the shear force input to the column is limited by yielding of the adjacent beams (i.e. $r_{u,lim} > r_{by}$). This is the case in the first till the fourth storey (Table 2). Column failure is expected in the rest of the storeys as shown by the tick marks in Table 2.

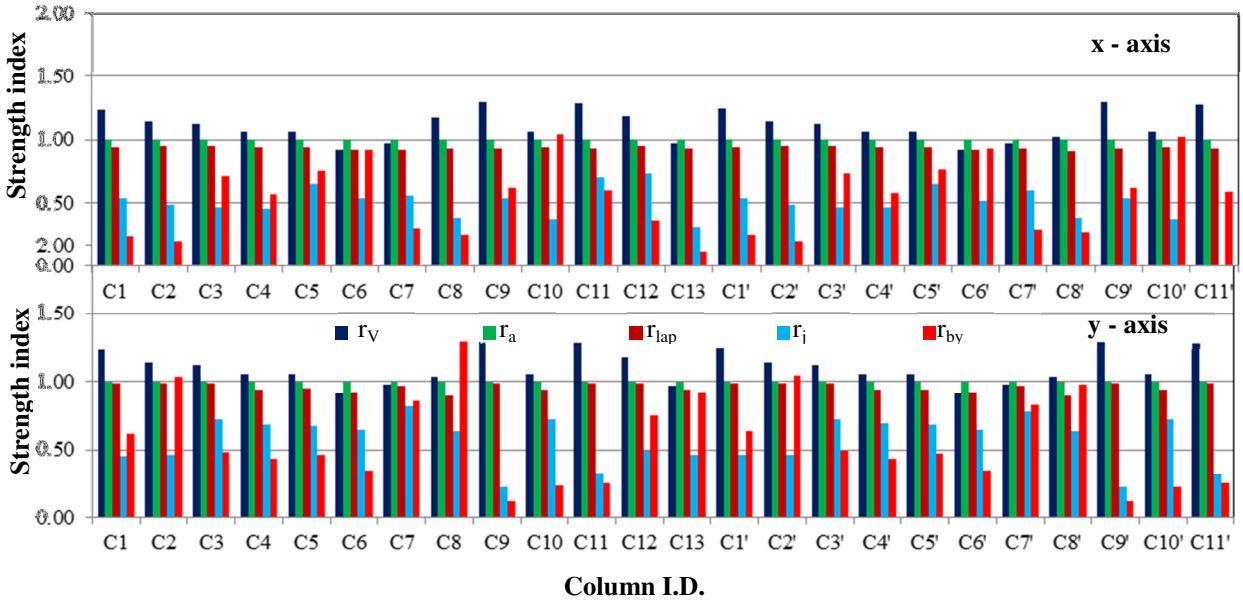


Figure 6: Fifth storey column strength assessment along x – axis and y – axis.

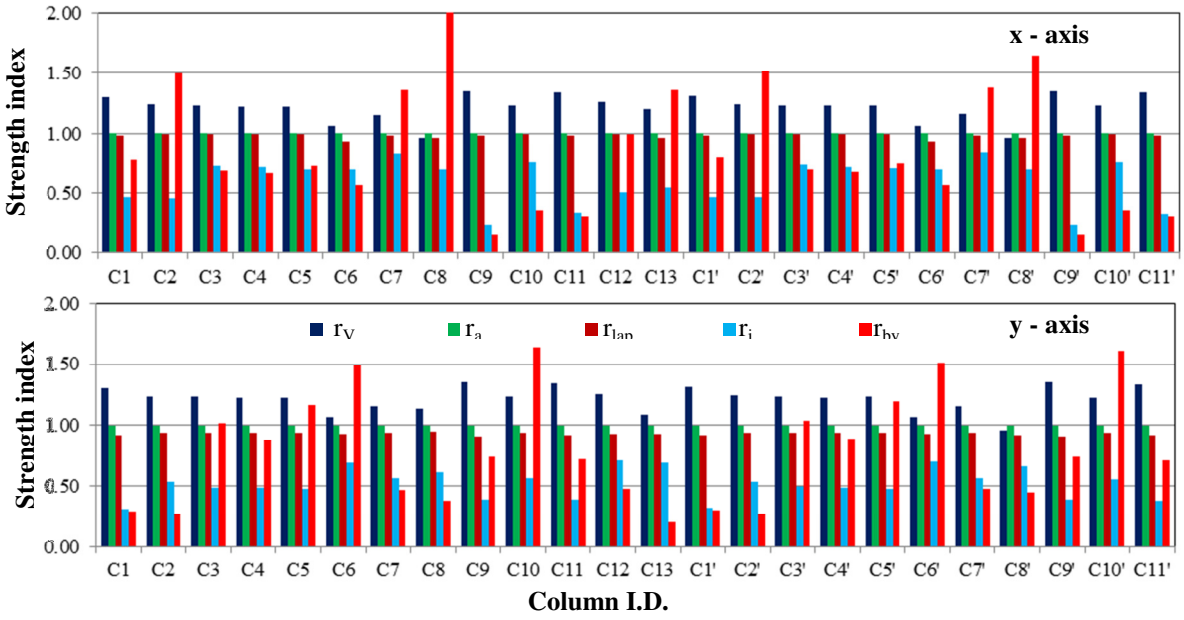


Figure 7: Sixth storey column strength assessment along x – axis and y – axis.

However, only the grey marked values in Table 3 are taken into consideration and used in assessment due to the fact that failure is not expected up to the 4th storey.

Stiffness assessment follows where the buildings's generalized mass and stiffness were estimated and the period in each direction was specified. After implementing the equation $M^* = \sum [N_{(G+0.30Q)} \cdot n/g \cdot \Delta\Phi_i^2]$, where $N_{(G+0.30Q)}$ is the total vertical load of the seismic load combination *(1.00G + 0.30Q)* at the base of all columns of every storey, n is the number of storeys, g = 9.81 m/s^2 is the gravity acceleration and $\Delta\Phi_i^2$ the difference in the response profile between successive storeys, the generalized mass results in M^* = *844.12 t*. The building's generalized stiffness was defined by $K^* = \sum K_i \cdot (\Phi_i - \Phi_{i-1})^2$, where $K_i = V_{min}/(2\theta_{fail}^c \cdot L_s)$

is stiffness at the initiation of failure of each column of the storey, *i*. Thus, $K_x^* = 21380.66$ *kN/m* and $K_y^* = 18220.75$ *kN/m* correspond to $T_x = 1.25$ *s* and $T_y = 1.35$ *s*, respectively. It is reminded that the lateral response shape adopted is that of the shear-type buildings (Eq. (5), Fig. 2).

Considering an average value of coefficient λ_c per storey Θ_{fail} is estimated as shown in Table 3.

Direction	Parameters	1st	2nd	3rd	4th	5th	6th	7th	8th
x-x	λ_c	0.36	0.40	0.45	0.52	0.61	0.69	0.71	0.70
	Θ_{fail}	0.28%	0.27%	0.27%	0.26%	0.27%	0.28%	0.26%	0.34%
y-y	λ_c	0.36	0.40	0.45	0.52	0.61	0.69	0.71	0.70
	Θ_{fail}	0.28%	0.27%	0.27%	0.26%	0.26%	0.26%	0.24%	0.32%

Table 3: Storey drifts at failure.

The column area ratio, $\rho_{c,i}$, and masonry walls area ratio, $\rho_{wm,i}$, are presented in Table 4. As it is observed $\rho_{c,i}$ is identical in both directions in all the storeys, whereas $\rho_{wm,i,y}$ in y direction is almost two and a half times higher than $\rho_{wm,i,x}$ in x direction. The equivalent area ratio of the vertical members in the floor plan ρ_i^e was also estimated (Table 4).

Area ratio (%)	1st	2nd	3rd	4th	5th	6th	7th	8th
$\rho_{c,i}$	2.08	1.87	1.70	1.43	1.15	0.92	0.82	0.85
$\rho_{wm,i,x}$	1.38	1.38	1.38	1.38	1.38	1.38	1.38	1.69
$\rho_{wm,i,y}$	3.63	3.67	3.67	3.67	3.67	3.67	3.67	4.32
$\rho_{i,x}^e$	2.48	2.32	2.20	1.98	1.83	1.77	1.67	1.89
$\rho_{i,y}^e$	3.20	3.11	3.07	2.97	3.05	3.27	3.07	3.50

Table 4: Vertical component's area ratios per direction and storey.

IDS were constructed for two levels of seismicity with PGA = 0.16g and PGA = 0.36g according to Eq. 7(b) (Fig. 8). The vulnerability curves have been plotted for the 1st, 5th and 6th storey. Since the response of the building (beam yielding occurs first) is the same up to the 4th storey, only the IDS of the 1st storey is shown in Fig. 8. In case of the 5th storey the response is differentiated for each direction as depicted in Fig. 8. From the 6th floor and upwards column failure is expected and the vulnerability curve corresponding to the 6th floor is considered representative (Fig. 8).

For the 1st storey and PGA=0.16g (Fig.8(a)) drift demand was estimated along x and y direction equal to Θ_1= 0.25% and 0.22%, respectively. No damage is expected since $\Theta_1 < \Theta_{fail}$ (Table 3). On the contrary, for PGA = 0.36 g (Fig.8(b)) drift demand was estimated along x and y direction equal to Θ_1= 0.56% and 0.51%, respectively. Column failure is anticipated since $\Theta_1 > \Theta_{fail}$. The same procedure was followed for the 5th and 6th storey, the results of which are presented in Tables 5 and 6.

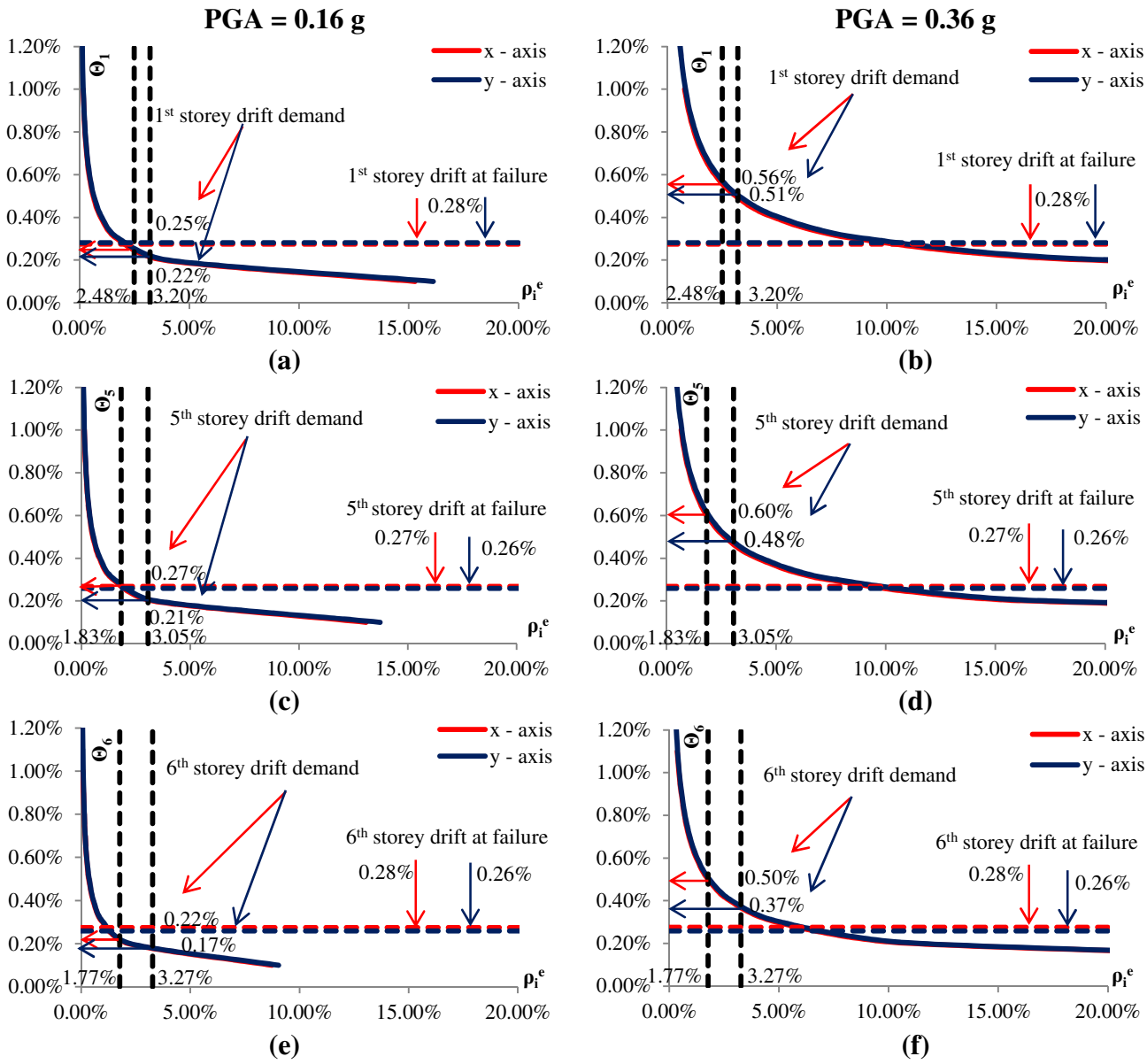


Figure 8: Vulnerability curves (a); (b) of the 1st storey for PGA=0.16g and PGA=0.36g, respectively; (c); (d) of the 5th storey for PGA=0.16g and PGA=0.36g, respectively; (e); (f) of the 6th storey for PGA=0.16g and PGA=0.36g, respectively (red and blue colored lines refer to direction x and y, respectively).

PGA	Dir.	Θ_5	Θ_5^c	Θ_5^b	Beam yielding	θ_{pl}^b	θ_{fail}^c	Column failure
0.16g	x	0.27%	0.17%	0.10%	×	-	0.17%	×
	y	0.21%	0.12%	0.09%	×	-	0.15%	×
0.36g	x	0.60%	0.38%	0.22%	√	0.05%	0.17%	√
	y	0.48%	0.28%	0.20%	×	-	0.15%	√

Table 5: Assessment results for the 5th storey of the building study (√: yes, ×: no).

PGA	Dir.	Θ_6	Θ_6^c	Θ_6^b	Beam yielding	θ_{pl}^b	θ_{fail}^c	Column failure
0.16g	x	0.22%	0.16%	0.06%	×	-	0.20%	×
	y	0.17%	0.11%	0.05%	×	-	0.17%	×
0.36g	x	0.50%	0.36%	0.14%	×	-	0.20%	√
	y	0.37%	0.25%	0.12%	×	-	0.17%	√

Table 6: Assessment results for the 6th storey of the building study (√: yes, ×: no).

5 VALIDITY OF THE RAPID EVALUATION METHODOLOGY THROUGH DETAILED ANALYSES

In order to verify the validity of the rapid evaluation methodology detailed analyses were performed including eigenvalue and pushover analyses. For this purpose a finite element program for static and dynamic analyses of structures SAP2000 Nonlinear Version 15 was used. Two groups of models were created (Fig.9): (i) Model A represents the bear structural system with the presence of external masonry infill walls of thickness t = 0.20 m and height equal to 1.40 m in order to model the captive (or short) column formation at the basement (free storey height is 1.30 m. The free lengths of the columns between successive spans may be characterized as captive columns) and (ii) Model B represents the masonry infilled frame building with external masonry infill walls of thickness t = 0.20 m along its height.

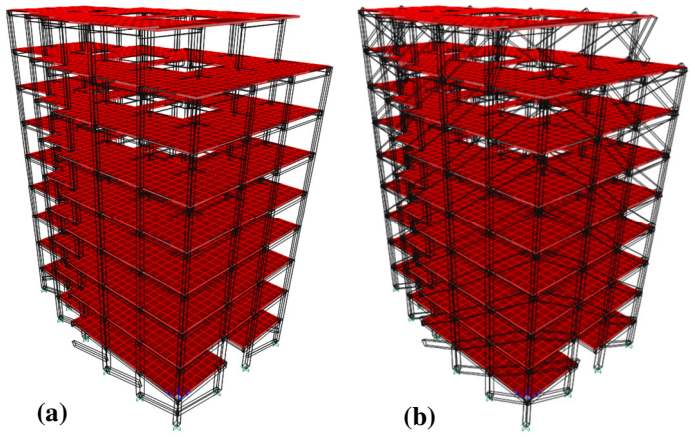


Figure 9: (a) Models A with no masonry infill walls but at the basement of the building; (b) Models B with masonry walls along the height of the building.

5.1 Modeling assumptions

A three-dimensional model of the structure was created in SAP2000 Version 15 where beams and columns were modeled as nonlinear frame elements, whereas shell elements were chosen to model slabs. Masonry infill walls were modeled as diagonal struts using linear frame elements rendering the assignment of their inelastic response more convenient.

Three different materials were defined. Material "Concrete" with mass per unit volume 24.00 kN/m^3, modulus of elasticity E_c=22 GPa [6] and compressive strength f_c =10 MPa [9]; material "Steel" with modulus of elasticity E_s=210 GPa, yield stress f_y=220 MPa and ultimate tensile stress f_u=330 MPa; material "Wall" with zero mass per unit volume (due to the fact that masonry vertical loads were distributed onto the subjacent beams and had already been assigned), modulus of elasticity E_w = 1.25 GPa were characterized.

The cross section dimensions along with the longitudinal and transverse reinforcement were assigned for both columns and beams (information regarding the columns' characteristics appear in Table B, Appendix B). Masonry infill walls were modeled as struts of rectangular cross section with t=0.20 m width by $0.15L_d$ depth [8] where $L_d=\sqrt{L_h^2+h_w^2}$ is the length of the diagonal strut calculated as the square root of the sum of the square of masonry wall horizontal length plus the square of its height. The loads applied were defined in section 4.1.

Elements (beams and columns) inelastic behavior was introduced by the assignment of moment – curvature plastic hinges at their ends. Two different cases were investigated: (i) the "default" plastic hinges whose properties were automatically defined by the program, and (ii) the "user defined" plastic hinges where moment – curvature diagrams were estimated separately for each element. In the case of the "default" plastic hinges interaction of compression N and biaxial flexure M2 and M3 was selected for columns since it represents more precisely their actual state of stress and uniaxial flexure M3 for beams. Note that the option "default" plastic hinges (defined automatically by the program) involves the automatic determination of the moment - curvature (M-phi) diagram for every cross section.

The properties of the "user defined" plastic hinges were estimated by first deriving the moment – curvature diagrams with the use of the sectional analysis program Response 2000 [10] considering interaction between compression N and uniaxial flexure M3 or M2 for columns. In case of beams only uniaxial flexure M3 was considered (Fig. 10). Bilinearization of the moment – curvature diagrams was done with the use of Bilin [11] (Fig. 10).

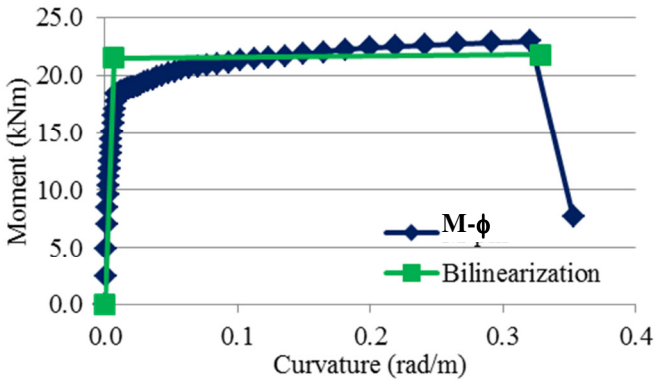


Figure 10: Example of moment – curvature diagram – Bilinearization of M-phi diagram by BILIN.

Plastic hinges were assigned at column and beam ends (Fig.11). The location of the plastic hinges is defined in Fig. 11. The plastic hinge at the column base was assigned at a distance from the joint equal to (h_f/2 + l_p/2), where h_f=0.10 m is the slab thickness and l_p =0.50h the

hinge length [12] (h the column section depth). Considering the top of the column, plastic hinge was assigned at a distance (h_i - h_{beam}^{ave} + $h_f/2$ - $l_p/2$) m from the joint, owing to the fact that column ends were defined in slabs middle plane. Plastic hinges at the left handside of beams were assigned at a distance ($h_c/2$ + $l_p/2$), where h_c is the column section depth and at the right handside at a distance (L_{beam} – $h_c/2$ - $l_p/2$), where L_{beam} the beam length.

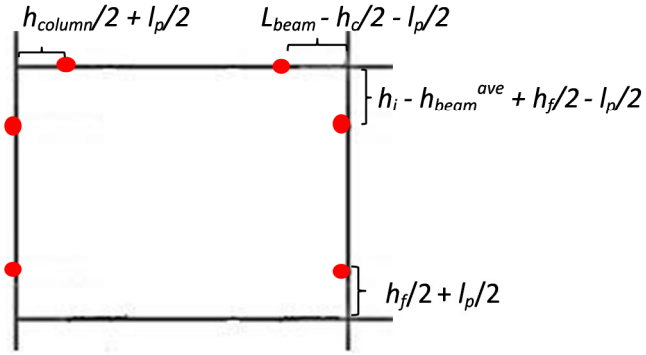


Figure 11: Plastic hinges locations.

Furthermore, the simultaneous existence of plastic and shear hinges was investigated since the model has to be capable of capturing the case of premature column failure, as it was observed in the upper storeys after applying the proposed rapid assessment methodology. Thus, shear hinges were introduced in order to depict this brittle mode of failure usually encountered in structures designed and constructed according to pre – modern code regulations. The value of shear force controlling the shear hinge development is the minimum of the values corresponding to each of the most common premature types of failure (Section 3.3, Appendix A). Shear hinges were assigned only to the column ends of those storeys were column failure prior to beam yielding is expected to occur according to the outcome of the rapid assessment methodology.

Model		Default hinges	User defined hinges	Shear hinges
A (bear frame building)	A.1.1.	√		
	A.1.2.	√		√
	A.2.1.		√	
	A.2.2.		√	√
B (masonry infilled frame building)	B.1.1.	√		
	B.1.2.	√		√
	B.2.1.		√	
	B.2.2.		√	√

Table 7: Definition of the various models examined.

Depending on the type of plastic hinges (automatic or user defined) and the existence or not of shear hinges, eight different analytical models result (Table 7). The identification code of each model follows the notation K.L.M. where K stands for Model A (with external masonry walls only in the lower half height of the basement) or Model B (external masonry infills throughout the building), L receives values “1” for default plastic hinges or “2” for user defined plastic hinges and M receives values “1” stands for M – ϕ plastic hinges whereas

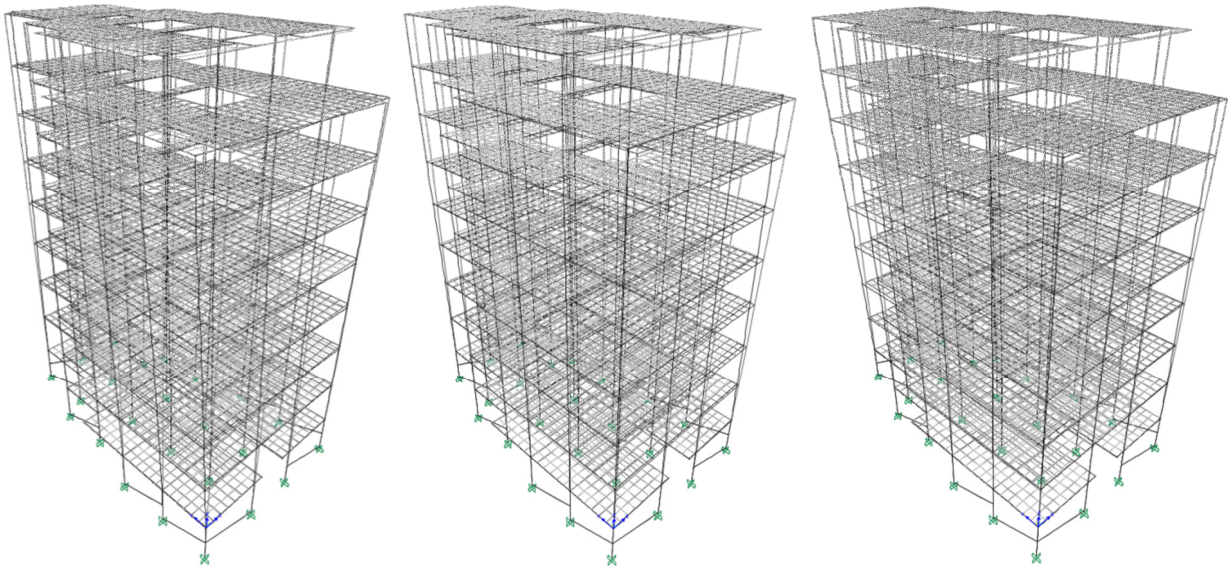
value "2" stands for both M – ϕ and shear hinges. Thus, the models studied are A.1.1, A.1.2, A.2.1, A.2.2, B.1.1, B.1.2, B.2.1 and B.2.2 (Table 7). For instance, model A.2.1 comprises basement external masonry walls and user defined plastic hinges M – ϕ. It should be reminded that eigenvalue and pushover analyses have been performed for all the above cases.

5.2 Eigenvalue analysis

Cracked sections were considered for columns and beams with a 50% reduction of their moment of inertia. In Figs. 12 and 13, the results of the eigenvalue analyses for the first three modes are presented. Information relative to the deformed shapes, the eigenperiods and the mass participation ratios appear.

Models A: The first mode shape for Models A is purely rotational; the second one purely translational towards the stronger axis of the structure (y – axis) while the third one is mixed (rotational/translational towards the weaker axis (x - axis)) (Fig. 12). The eigenperiod given in Fig. 12(c) refers to the x – translational component of the third mode.

Models B: For Models B the first mode shape is purely translational towards x - axis; the second one is purely translational towards y – axis ad the third one is purely rotational (Fig.13).

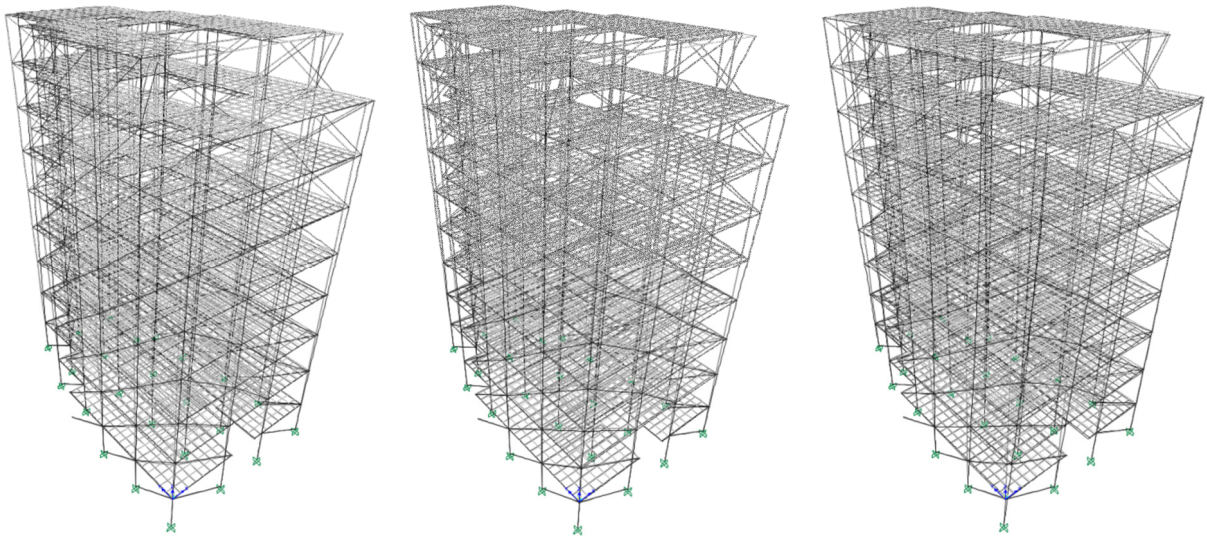


(a) T_1=1.99 s MPMR=1.0% **(b)** T_2=1.98 s MPMR=69.6% **(c)** T_3=1.85 s MPMR=57.6%

Figure 12: Deformed shape; eigenperiod and modal participating mass ratio (MPMR) from 3D eigenvalue analysis for Models A: (a) 1st mode; (b) 2nd mode; (c) 3rd mode.

Translational eigenperiod values of Models B are observed to be decreased in comparison to those of Models A as expected since masonry infill walls increase the structural system's stiffness. Furthermore, comparing eigenperiod values for Models B with those derived by the proposed assessment methodology (It is noted that the frame building responds with its fundamental modal shape) a good correlation is observed. It is reminded that eigenperiod values by the methodology application are T_x =1.25 s and T_y =1.35 s along the weaker and stronger axis of the structure, respectively. The difference recorded is +13% and -24% along x and y axis, respectively, which is considered acceptable given that the first translational mode

in Models B (Figs. 13(a)) is close to the fundamental shape considered in the assessment methodology.



(a) T_1=1.41 s MPMR=74.9% **(b)** T_2=1.03 s MPMR=74.3% **(c)** T_3=0.92 s MPMR=15.0%

Figure 13: Deformed shape; self - period and modal participating mass ratios (MPMR) from 3D eigenvalue analysis for Models B: (a) 1st mode; (b) 2nd mode; (c) 3rd mode.

5.3 Pushover analysis

The groups of Models A and B were subjected to pushover analyses separately for the two orthogonal directions x and y. Vertical gravity loads and lateral seismic loads were applied simultaneously on the structure. Three different lateral force distribution profiles along the height of the building for each model were investigated (Figs. 14, 15), the modal, the triangular and the uniform shape. In Figs. 14(a), (b) the modal lateral load profile is plotted for Models A along x and y axis, respectively. Similarly, the modal lateral load profile per direction is presented in Figs. 15(a), (b) for Models B. From the pushover analyses conducted, it was shown that response of the structure described by the base shear – roof displacement curve is slightly differentiated for the triangular and modal load pattern. However, uniform distribution led always to more favorable results. For this purpose, it was decided to be presented only the results from the application of the uniform and modal lateral load profile.

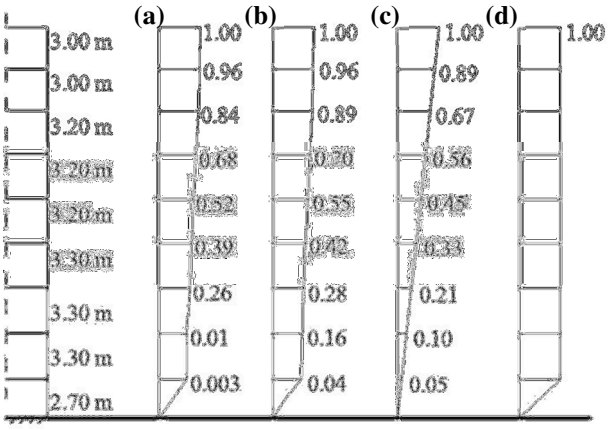


Figure 14: Lateral load profiles for Models a: (a) modal along x - axis; (b) modal along y - axis; (c) triangular (same for both directions); (d) uniform (same for both directions).

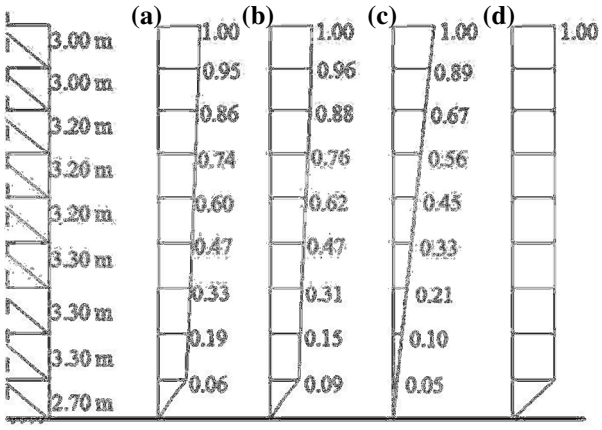


Figure 15: Lateral load profiles for Models B: (a) modal along x - axis; (b) modal along y - axis; (c) triangular (same for both directions); (d) uniform (same for both directions).

5.3.1. Comparison between the different modeling approaches

Model A.2.1. (masonry walls in the basement, user defined M-ϕ plastic hinges): In Fig.16 the pushover curves were plotted for x and y direction for the different load profiles (red colored lines refer to x – axis while blue colored lines refer to y - axis). The difference in the maximum base shear force as well as in the roof displacement between the two lateral load patterns is significant. The maximum base shear force value for uniform load distribution compared to that for the modal lateral force profile is 78% and 20% higher in x and y direction, respectively. As far as the maximum roof displacement attained again the values reached in the case of the uniform load distribution are higher compared to the modal shape load distribution (20% higher along x – axis (Fig.16(a)), and 24% higher in y-axis (Fig. 16(b))). The maximum drift reached at which failure occurs was 0.55% in both x and y directions for uniform load distribution whereas it was 0.45% in both directions for modal load distribution (allaxa th seira). The maximum peak ground acceleration that this model could sustain for the *G+0.3Q* load combination (average normalized axial load ratio v_{ave}=0.45, *W*=16791kN) was 10.3 % (=1729/16791 in the x direction and =1726/16791 in the y direction) of g for the uniform load pattern, whereas it was 5.8% (=973/16791) and 5.4% (=915/16791) of g, in the x and y directions, respectively, for the modal load pattern.

Model A.2.2 (masonry walls in the basement, user defined M-ϕ plastic hinges and shear hinges): The pushover curves derived for the orthogonal directions and the aforementioned load profiles are presented in Fig.17. Like the previous model (A.2.1.), the uniform load distribution results in higher values of maximum base shear force and roof displacement compared to the modal load pattern. Comparing the behavior of Model A.2.1 (without shear hinges, (Fig.16)) to that of Model A.2.2 (with shear hinges, (Fig.17)) it is evident that in the second case the structure failed at much lower levels of base shear. The maximum drift where brittle failure occurred is 0.17% and 0.16% in both x and y directions for the uniform and modal load distribution, respectively. In case that shear hinges were assigned, due to the premature failure of columns well before reaching their state of yielding, the whole building failed after the analysis had completed the first few loading steps. Since shear failure is a brittle mode of failure, the building's capacity to develop inelastic deformation after loss of its load bearing capacity is low. Thus, in pushover curves of this type of models no metelastic branch appears. The maximum peak ground acceleration that this model could sustain for the *G+0.3Q* load combination was 5.9 % (=992/16791) and 5.3% (=888/16791) of g along x and

y directions, respectively, for the uniform load pattern while it was only 3.5% (=583/16791) and 2.8% (=915/16791) of g in the x and y directions, respectively, for the modal load pattern.

From the above, it seems that the strength value assigned to the shear hinges, which corresponds to the weakest column resistance mechanism detected in the region of joints, leads to conservative results. The value of $\underline{r_j}$ is below 0.5 for the majority of the columns, implying that failure occurs when the shear strength reaches 50% of its flexural strength at yield.

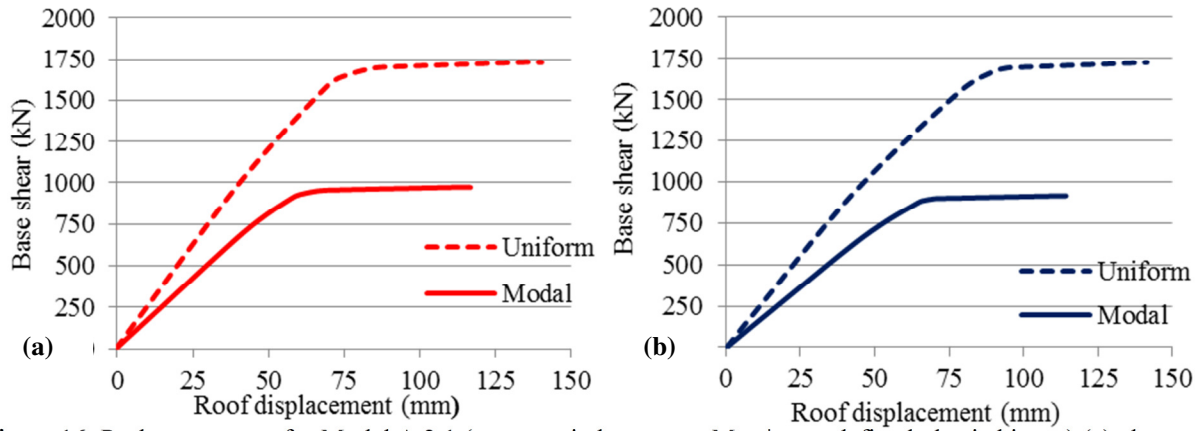


Figure 16: Pushover curves for Model A.2.1 (masonry in basement, M – ϕ user defined plastic hinges) (a) along x axis and (b) y axis.

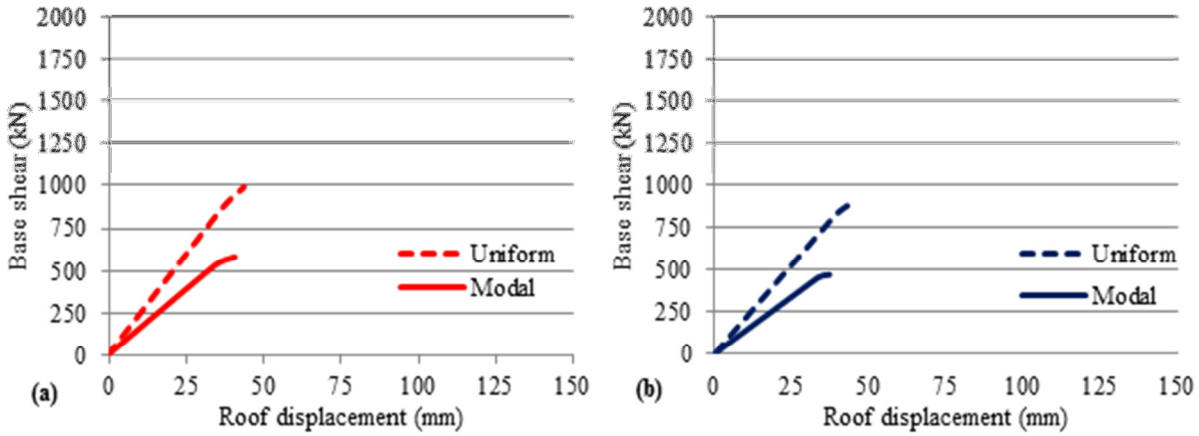


Figure 17: Pushover curves for Model A.2.2 (masonry in basement, M – ϕ user defined plastic hinges and user defined shear hinges) (a) along x axis and (b) y axis.

Model B.2.1. (external masonry infill walls throughout the building, user defined M-ϕ plastic hinges): As it is observed in Fig.18 roof displacement reached higher values along y direction compared to those in x direction due to the larger structural stiffness along y axis drift (the area ratio of masonry infill walls is higher along y – axis, Fig. 9(b)). The maximum drift in which failure occurred was 0.36% and 0.29% in x and y direction, respectively, for uniform load distribution. In case of modal distribution, the maximum drift at failure was 0.38 % and 0.36% in x and y directions, respectively. The maximum peak ground acceleration that this model could sustain for the *G+0.3Q* load combination was 16.8% (=2848/16791) and 20.2% (=3443/16971) of g, along x and y axis, respectively, for the uniform load pattern

whereas it was 13% (=2199/16791) and 18.1% (=3067/16791) of g, along x and y axis, re-respectively, for the modal lateral force profile. The addition of infill walls increased substan-substantially both stiffness and strength of the structural system rendering it capable of tolerating higher levels of peak ground acceleration. Failure of the masonry infill walls limited the deformation capacity of the structure.

Model B.2.2 (external masonry infill walls throughout the building, user defined M-ϕ plastic hinges and shear hinges): The maximum drifts at failure reached for Model B.2.2. were 0.37% and 0.28% along x and y direction for the uniform load pattern and 0.32 % and 0.36% in x and y direction for the modal load profile (Fig. 19). The maximum peak ground acceleration for the *G+0.3Q* load combination was 16.7% (=2833/16791) and 20.3% (=3453/16791) of g along x and y direction for the uniform load pattern. As far as the modal load shape is concerned, the maximum peak ground acceleration was 10.7% (=1814/16791) and 18.1% (=3071/16791) of g in the x and y direction, respectively. Comparing the response of B.2.1 (no shear hinges) and B.2.2. (with shear hinges), it seems that when masonry infills are modeled the assignment of shear hinges has almost no effect on the structural response.

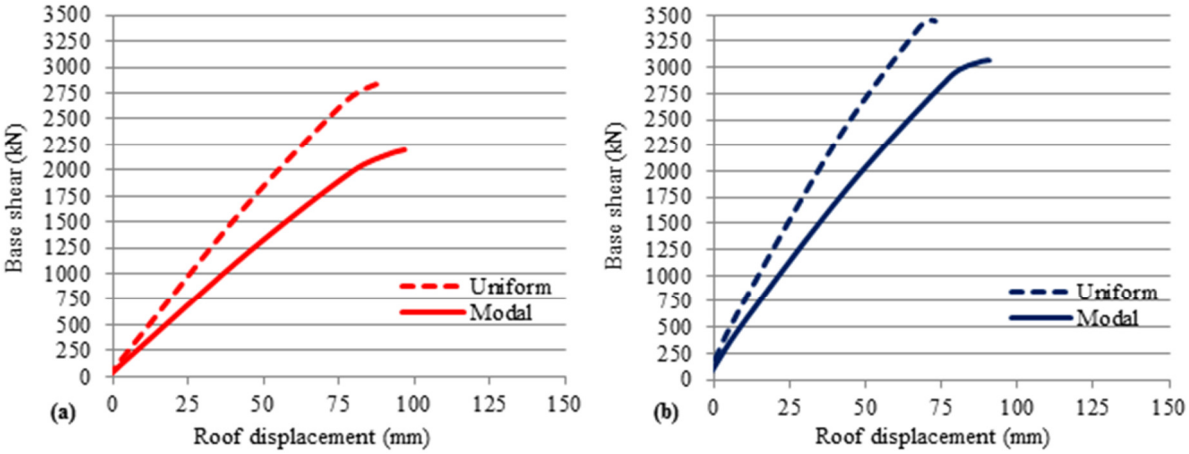


Figure 18: Pushover curves for Model B.2.1 (masonry along the building height, M – ϕ user defined plastic hinges) (a) along x axis and (b) y axis.

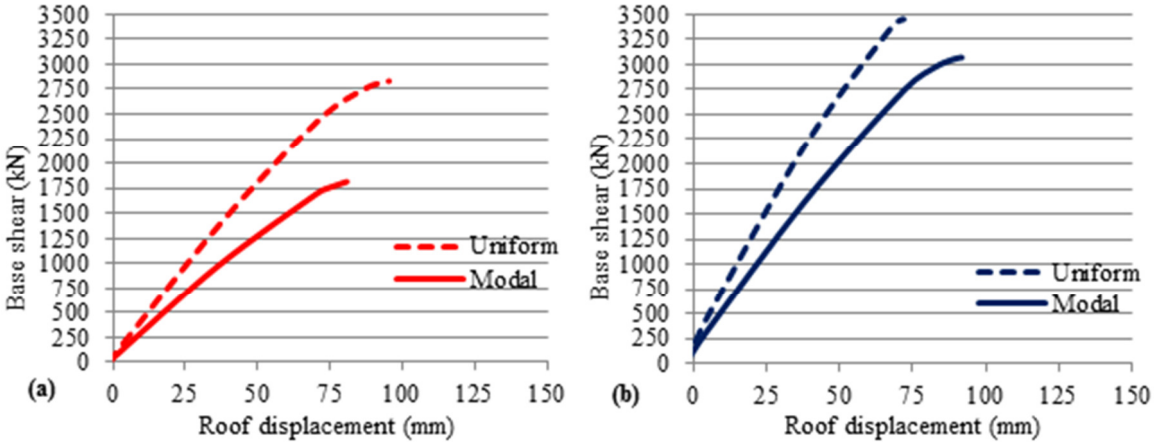


Figure 19: Pushover curves for Model B.2.2 (masonry along the building height, M – ϕ user defined plastic hinges and user defined shear hinges) (a) along x axis and (b) y axis.

5.3.2. Distribution of plastic hinge formation

As it has already been shown, in those models where shear hinges were considered (A.2.2, B.2.2.: user defined hinges and shear hinges), analysis was terminated at low levels of base shear. In order to shed light on the building state before and after failure, the distribution of plastic hinge formation is studied at two levels of drift corresponding to the end point of the elastic branch of the pushover curve (called hereafter "yielding drift") and to the ultimate value of roof displacement (called hereafter "ultimate"). In case of A.2.2., the sequence of plastic hinge formation is presented for drift levels 0.13% and 0.15% in x direction (Fig. 21) and for drift levels 0.12% and 0.14% in y direction (Fig. 22). The masonry infilled building, model B.2.2. is also considered and the drift levels for which the plastic hinge formation is presented are 0.26% and 0.30% in x direction (Fig. 23) and 0.27% and 0.31% in y direction (Fig. 24). The distribution of plastic hinge formation is shown for all the frames in both directions. The frame labeling is presented in Fig. 20.

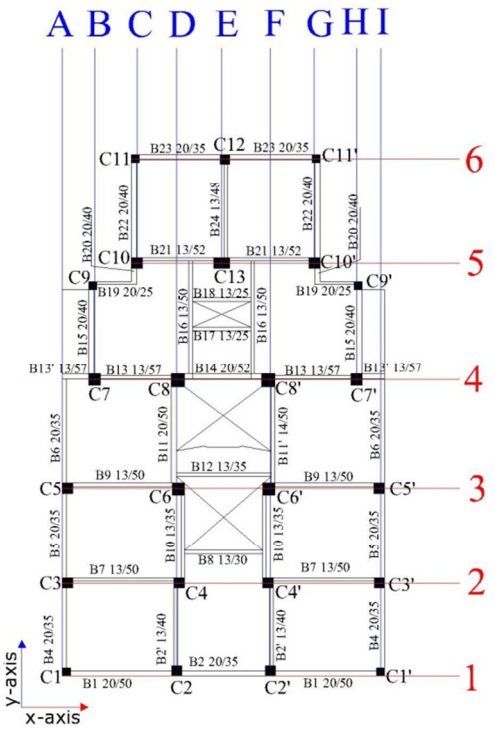


Figure 20: Frames definition.

Model A.2.2. (masonry walls in the basement, user defined M-ϕ plastic hinges and shear hinges):

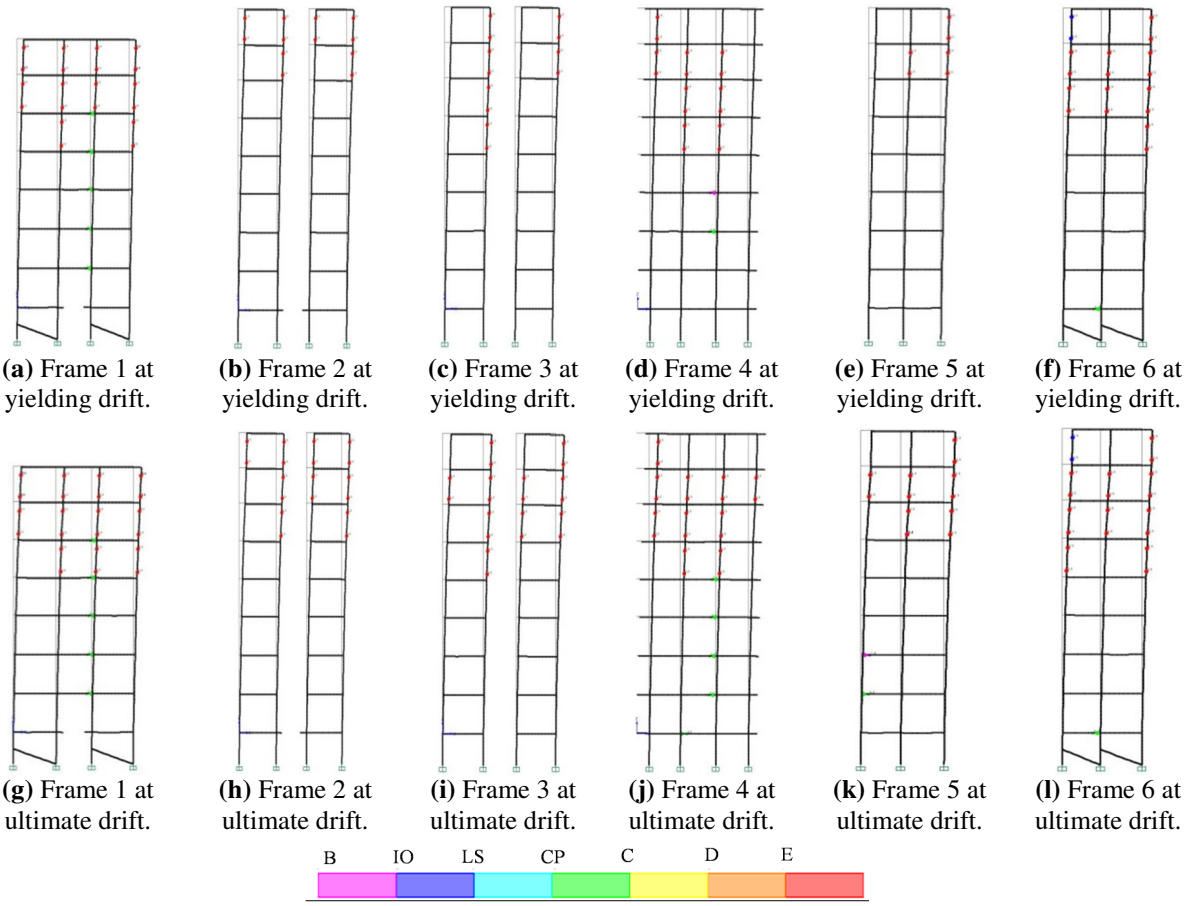
- Drift at "yielding" (0.13%) x direction: It is observed that at this level of drift, columns in the upper storeys (where shear hinges were assigned) lost their load bearing capacity and failled (red colored plastic hinges) (Fig. 21(a)-(f)). Plastic hinges developed in a few beam ends of the intermediate storeys in Frame 1 and 4 (Fig. 21(a); (d)).
- Drift at "yielding" (0.12%) y direction: Likewise x direction, premature shear failure occurred in most columns of the upper storeys. However, there are a few columns that reached deformations in the post-yield region (blue and turquoise colored plastic hinges) (Fig. 22(a)-(c)). Plastic hinges developed in a few beam ends in the external Frame A (Fig. 22(a)).
- Drift at "ultimate" (0.15%) x direction: Plastic hinges development propagated in a few beam ends of the intermediate and low storeys (Fig. 21(g); (j); (k)) without any alteration in the state of columns. It is observed that except for the upper storeys' columns, neither other columns nor beams yielded or failed.
- Drift at "ultimate" (0.14%) y direction: At this level of drift, shear failure progressed to columns of the upper storeys in Frames B; D and E (Fig. 22(g); (i) and (j)). Furthermore, beams of the intermediate storeys reached their yield state in Frame D (Fig. 22(i)).

Model B.2.2. (external masonry infill walls throughout the building, user defined M-ϕ plastic hinges and shear hinges):

- Drift at "yielding" (0.26%) x direction: It is observed that columns of the upper storeys failled owing to shear failure (the phenomenon was captured by the assignment of shear hinges). In addition, it is significant that two internal columns in Frame 4 (Fig.

23(d)) and one in Frame 5 (Fig. 23(e)) in an intermediate storey yielded. Plastic hinges developed in almost all beam ends of the first four storeys (Fig. 23(a)-(f)). No masonry walls' cracking was observed at this level of drift.

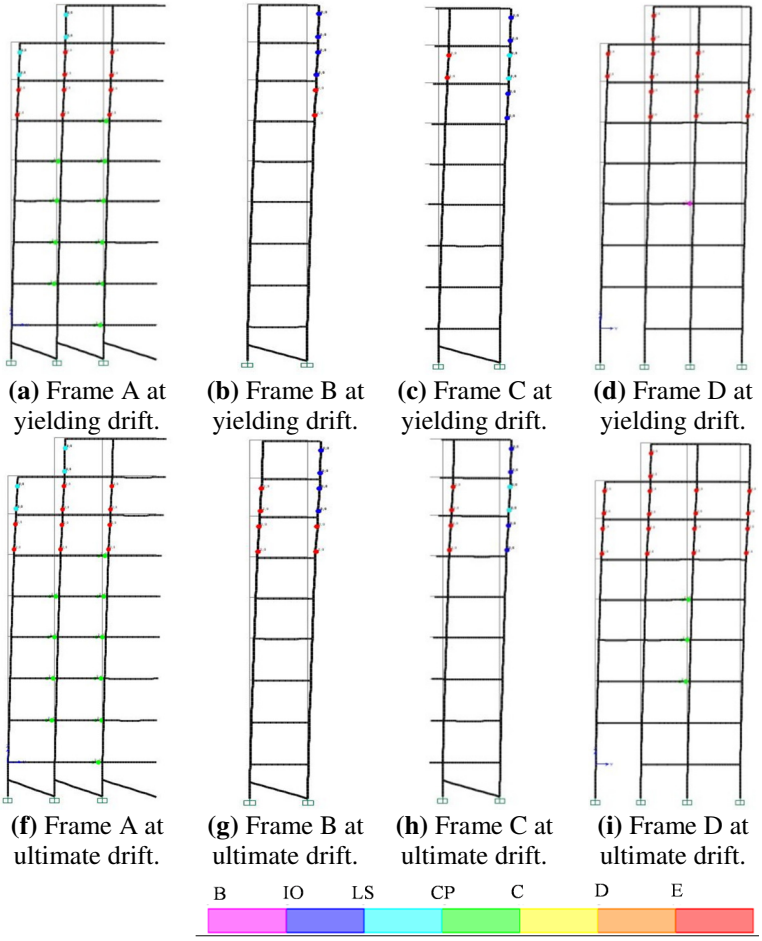
- Drift at "yielding" (0.27%) y direction: Also in this direction and at this level of drift column failure was dominant in the upper storeys. Significant deformation developed in almost all beam ends of the first four storeys (Frames A-E; Fig. 24(a)-(e)). At yielding drift the external masonry panels of the first two storeys cracked (Fig. 24(a)-(c)).
- Drift at "ultimate" (0.30%) x direction: Plastic hinges developped in all the internal columns of the first four storeys (Frames 4 and 5; Fig. 23(j); (k)). Beams' yielding occurred in the lower storeys in all frames. Masonry infill walls of an intermediate storey cracked. The presence of external infill walls prevented damage in the external columns. It is evident that masonry walls contributed to the stiffness of the structural system and in this case they behaved favorably concerning load bearing elements hierarchy of failure.
- Drift at "ultimate" (0.34%) y direction: At ultimate drift the internal columns in the intermediate storeys yielded (Fig. 24(h)-(j)). Concerning external columns their deformation was localized in the first storey. Plastic hinge development in beam ends was not differentiated compared to the "yielding" level of drift. Almost all masonry infill walls cracked. The building along direction y was subjected to higher values of base shear force compared to direction x. Therefore, external column deformation was not prevented in this direction since masonry panels cracked.



(a) Frame 1 at yielding drift. **(b)** Frame 2 at yielding drift. **(c)** Frame 3 at yielding drift. **(d)** Frame 4 at yielding drift. **(e)** Frame 5 at yielding drift. **(f)** Frame 6 at yielding drift.

(g) Frame 1 at ultimate drift. **(h)** Frame 2 at ultimate drift. **(i)** Frame 3 at ultimate drift. **(j)** Frame 4 at ultimate drift. **(k)** Frame 5 at ultimate drift. **(l)** Frame 6 at ultimate drift.

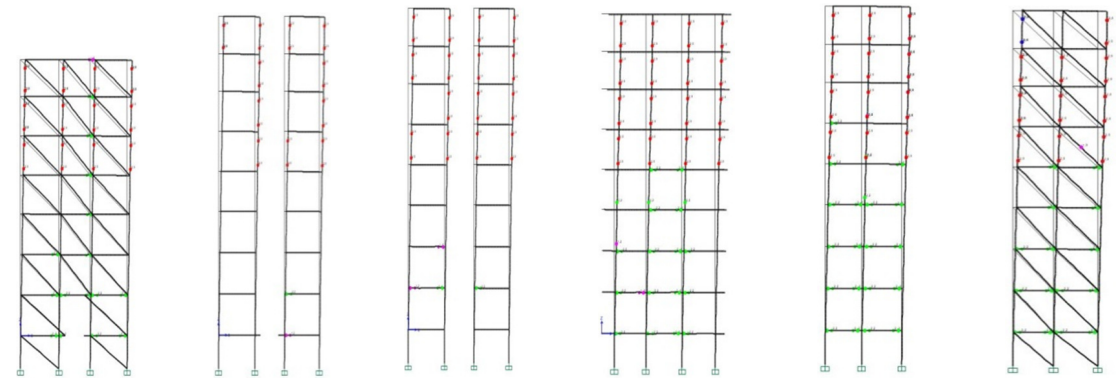
Figure 21: Distribution of plastic hinge formation in x – direction of Model A.2.2 at yielding and ultimate drift.



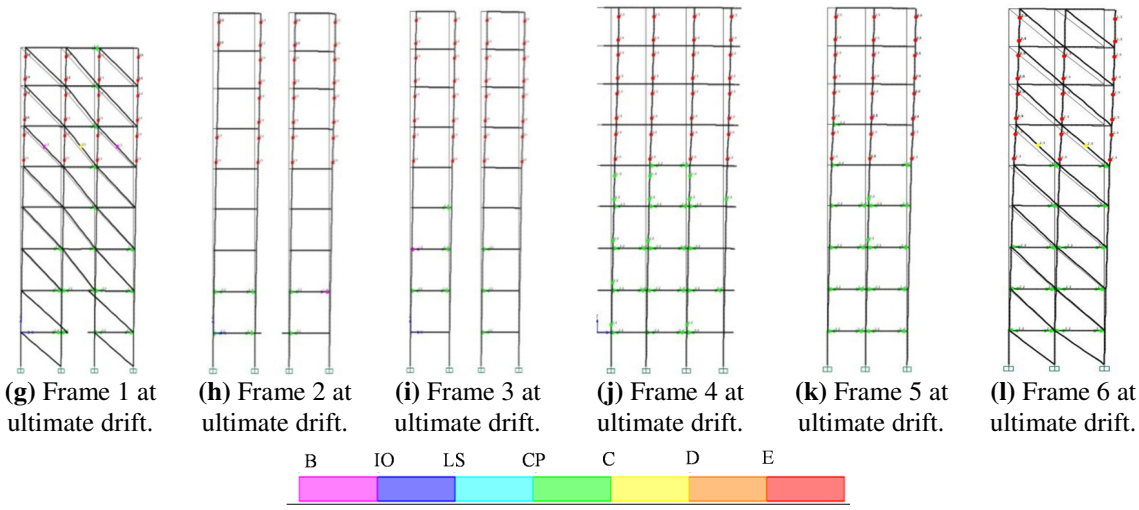
(a) Frame A at yielding drift. **(b)** Frame B at yielding drift. **(c)** Frame C at yielding drift. **(d)** Frame D at yielding drift. **(e)** Frame E at yielding drift.

(f) Frame A at ultimate drift. **(g)** Frame B at ultimate drift. **(h)** Frame C at ultimate drift. **(i)** Frame D at ultimate drift. **(j)** Frame E at ultimate drift.

Figure 22: Distribution of plastic hinge formation in y – direction of Model A.2.2 at yielding and ultimate drift.

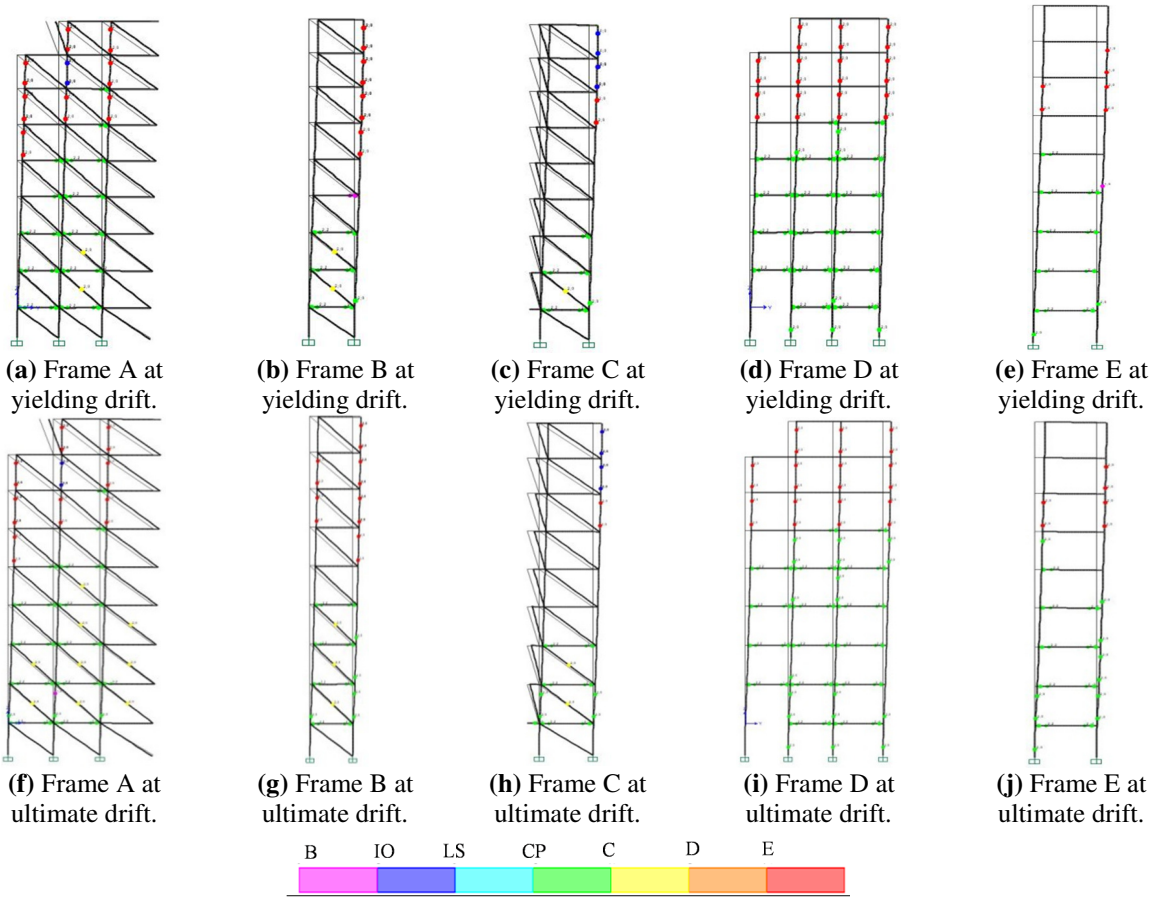


(a) Frame 1 at yielding drift. **(b)** Frame 2 at yielding drift. **(c)** Frame 3 at yielding drift. **(d)** Frame 4 at yielding drift. **(e)** Frame 5 at yielding drift. **(f)** Frame 6 at yielding drift.



(g) Frame 1 at ultimate drift. **(h)** Frame 2 at ultimate drift. **(i)** Frame 3 at ultimate drift. **(j)** Frame 4 at ultimate drift. **(k)** Frame 5 at ultimate drift. **(l)** Frame 6 at ultimate drift.

Figure 23: Distribution of plastic hinge formation in x – direction of Model B.2.2 at yielding and ultimate drift.



(a) Frame A at yielding drift. **(b)** Frame B at yielding drift. **(c)** Frame C at yielding drift. **(d)** Frame D at yielding drift. **(e)** Frame E at yielding drift.

(f) Frame A at ultimate drift. **(g)** Frame B at ultimate drift. **(h)** Frame C at ultimate drift. **(i)** Frame D at ultimate drift. **(j)** Frame E at ultimate drift.

Figure 24: Distribution of plastic hinge formation in y – direction of Model B.2.2 at yielding and ultimate drift.

6 CONCLUSIONS

A rapid evaluation methodology which renders preliminary assessment of the large inventory of non – ductile multistory RC buildings feasible was presented and implemented in the study conducted herein. Buildings following the pre-modern codes usually designed for gravity loads only without any reinforcement detailing are susceptible to future earthquake events. The proposed methodology requires information of the building's characteristics that are easily accessible, such as the building's geometry in plan and elevation, the number of storeys and their height as well as material properties and geometry and reinforcement of column and beam sections. In case that information relative to cross section detailing is not available, data could be extracted by the construction practice of the era of the building. The methodology establishes two criteria. The strength criterion highlights columns' weakest resistance mechanism under lateral load based on the most common premature modes of failure encountered in vertical load bearing elements with insufficient reinforcement detailing, i.e. shear, anchorage/lap splice, joint failure, the possibility of beam yielding prior to premature column failure is also taken into consideration. Stiffness criterion through the use of the Interstorey Drift Spectra (IDS) and given the estimated equivalent vertical members area ratio estimates the drift demand introduced by the excitation scenario. Assessment is conducted by comparing drift capacity to drift demand. The proposed methodology is recommended to be applied along the height of the building since the 1950's mutlistorey buildings are characterized by in height irregularities in mass and stiffness distribution. Observations made in the database of buildings of that era indicate significant reduction of the dimensions and reinforcement of columns at the upper storeys.

The proposed methodology was implemented in a multistory building constructed in the 1950's in the city of Thessaloniki, Greece. The building was subjected to two seismic scenarios for PGA=0.16g and 0.36g. The results obtained for PGA=0.16g demonstrate building's survival with no damage neither on beams nor on columns. For the second scenario (0.36g), beam yielding and damage localization is anticipated in the first 4 storeys, whereas premature column failure is expected from the 5^{th} to the last storey.

Validity of the proposed methodology was examined by conducting pushover analyses for two groups of models of the building under consideration. The two groups of analytical models are differentiated as per the existence or not of masonry infill walls. Modeling and analyses were performed using SAP2000 v15. Plastic hinges of two types were assigned to beams and columns. The "default" hinges were automatically defined by the program, whereas the user defined hinges properties were determined after sectional analysis. Furthermore, in some of the models shear hinges were also considered additional to the moment –curvature hinges in order to model the premature mode failure of columns.

The results of the rapid assessment methodology are in accordance with the results regarding the analytical model where masonry infill walls, user defined plastic hinges M- phi and shear hinges were considered. The methodology indicated column deficiencies and premature failure in the 3 upper storeys which was verified by the distribution of plastic hinge formation where damage localized in the columns of the 3 last storeys.

In conclusion, the proposed rapid assessment methodology provides a clear insight of the expected mode of failure of existing substandard buildings. The objective of the development of this preliminary assessment methodology is not to substitute detailed analyses but to be used as an efficient tool in order to single out the most deficient and seismic vulnerable that need to be examined further.

REFERENCES

[1] G.E. Thermou, S.J. Pantazopoulou, Assessment indices for the seismic vulnerability of existing RC buildings, Journal of Earthquake Engineering and Structural Dynamics, 40(3), 293-313, 2011.

[2] S.J. Pardalopoulos, G.E. Thermou, S.J. Pantazopoulou, Screening Criteria to Identify Brittle R.C. Structural Failures in Earthquakes, Bulletin of Earthquake Engineering, 11, 607-636, 2013.

[3] RD, Design regulation of reinforced concrete building works. *Royal Decree* (18.2/26.07.1954), Ministry of Public Works, Greece (in Greek), 1954.

[4] Deutsches Institut für Normung (DIN). Beton und Stahlbetonbau: Bemessung und Ausführung. DIN 1045, Berlin, 1936.

[5] Thermou GE, Pantazopoulou SJ, Elnashai AS. Design and assessment models and spectra for repaired reinforced concrete structures. *MAE Center Report*, CD release, 2009; 09–(01).

[6] Eurocode 2. Design of concrete structures—Part 1-1: General rules and rules for buildings. *EN1992-1-2005:E*, European Committee for Standardization (CEN), Brussels, 2004.

[7] Eurocode 8. Design of structures for earthquake resistance—Part 1: General rules, seismic actions and rules for buildings. *EN1998-1-2004:E*, European Committee for Standardization(CEN), Brussels, 2004.

[8] KANEPE, Interventions Code (of Greece). Earthquake Planning and Protection Organization (E.P.P.O.), 2012 (in Greek).

[9] Federation of Structural Concrete (fib). Seismic assessment and retrofit of reinforced concrete buildings. fib Bulletin 24 State-of-art report prepared by Task Group 7.1, 2003.

[10] Evan Bentz and Michael P. Collins, Response 2000, User manual, V. 1.1. September 2001.

[11] G. Panagopoulos, A.I. Kappos, Bilinear approximations of force-displacement curves, 16^{o} Concrete Conference, 21-23/10/2009, Pafos, Cyprus.

[12] Park R, Paulay T., Reinforced concrete structures. New York: John Wiley & Sons; 1975. 769 pages.

[13] ACI-ASCE Committee 352. Recommendations for Design of Beam-Column Connections in Monolithic Reinforced Concrete Structures, American Concrete Institute, Farmington Hills, MI, 2008.

APPENDIX A

The expressions for strength indices are presented below [2].

Shear strength ratio is defined as:

$$r_v = \frac{\nu \cdot \tan a \cdot b \cdot d \cdot f_c^{'} + A_{st} \cdot f_{st} \cdot \frac{d - \xi \cdot d}{s} \cdot \cot \theta_1}{\left[\rho_{\ell,tot} \cdot \frac{f_s}{f_c^{'}} \cdot (1 - 0.40 \cdot \xi) + \nu \cdot \left(\frac{h}{d} - 0.80 \cdot \xi \right) \right] \cdot \frac{b \cdot d^2 \cdot f_c^{'}}{h_{st}}} \Leftrightarrow$$

$$r_v = \frac{\nu \cdot \left(\frac{h}{d} - 0.80 \cdot \xi \right) + \frac{A_{st}}{b \cdot d} \cdot \frac{f_{st}}{f_c^{'}} \cdot \frac{h_{st}}{d} \cdot (1 - \xi) \cdot \cot \theta_1 \cdot \frac{d}{s}}{\rho_{\ell,tot} \cdot \frac{f_s}{f_c^{'}} \cdot (1 - 0.40 \cdot \xi) + \nu \cdot \left(\frac{h}{d} - 0.80 \cdot \xi \right)} \quad \text{(A1)}$$

Strength ratio for anchorage failure is defined as:

$$r_\alpha = \frac{\left[\rho_{\ell,tot} \cdot \frac{\min \left\{ \frac{4 \cdot L_b \cdot f_b}{D_b} + a_{hook} \cdot 50 \cdot f_b \ , \ f_y \right\}}{f_c^{'}} \cdot (1 - 0.40 \cdot \xi) + \nu \cdot \left(\frac{h}{d} - 0.80 \cdot \xi \right) \right] \cdot \frac{b \cdot d^2 \cdot f_c^{'}}{h_{st}}}{\left[\rho_{\ell,tot} \cdot \frac{f_y}{f_c^{'}} \cdot (1 - 0.40 \cdot \xi) + \nu \cdot \left(\frac{h}{d} - 0.80 \cdot \xi \right) \right] \cdot \frac{b \cdot d^2 \cdot f_c^{'}}{h_{st}}} \Leftrightarrow \quad \text{(A2)}$$

$$r_\alpha = \frac{\left[\rho_{\ell,tot} \cdot \frac{\min \left\{ 4 \cdot \psi \cdot f_b + a_{hook} \cdot 50 \cdot f_b \ , \ f_y \right\}}{f_c^{'}} \cdot (1 - 0.40 \cdot \xi) + \nu \cdot \left(\frac{h}{d} - 0.80 \cdot \xi \right) \right]}{\left[\rho_{\ell,tot} \cdot \frac{f_y}{f_c^{'}} \cdot (1 - 0.40 \cdot \xi) + \nu \cdot \left(\frac{h}{d} - 0.80 \cdot \xi \right) \right]}$$

Strength ratio for lap splices failure is defined as:

$$r_{lap} = \frac{\left[\begin{array}{c} \min \left\{ \left(\mu_{fr} \cdot L_b \left[\frac{A_{tr}}{s} \cdot f_{st} + a_b \cdot (b - N_b \cdot D_b) \cdot f_t \right] + a_{hook} \cdot 50 \cdot N_b \cdot A_b \cdot f_b \right) \ , \ N_b \cdot A_b \cdot f_y \right\} \cdot \\ \cdot d \cdot (1 - 0.40 \cdot \xi) + \nu \cdot b \cdot d^2 \cdot f_c \cdot (0.50 h / d - 0.40 \cdot \xi) \end{array} \right] \Big/ (h_{st}/2)}{\left[\rho_{\ell,tot} \cdot \frac{f_y}{f_c^{'}} \cdot (1 - 0.40 \cdot \xi) + \nu \cdot \left(\frac{h}{d} - 0.80 \cdot \xi \right) \right] \cdot \frac{b \cdot d^2 \cdot f_c^{'}}{h_{st}}} \Leftrightarrow$$

$$r_{lap} \cong \frac{\min \left\{ \left(2 \cdot \psi \cdot \mu_{fr} \cdot \frac{D_b}{d} \cdot \left[\frac{A_{tr}}{b \cdot s} \cdot \frac{f_{st}}{f_c^{'}} + a_b \cdot \frac{f_t}{f_c^{'}} \right] + a_{hook} \cdot 50 \cdot \rho_{\ell,tot} \cdot \frac{f_b}{f_c^{'}} \right) \ , \ \rho_{\ell,tot} \cdot \frac{f_y}{f_c^{'}} \right\} \cdot (1 - 0.40 \cdot \xi) + \nu \cdot \left(\frac{h}{d} - 0.80 \cdot \xi \right)}{\left[\rho_{\ell,tot} \cdot \frac{f_y}{f_c^{'}} \cdot (1 - 0.40 \cdot \xi) + \nu \cdot \left(\frac{h}{d} - 0.80 \cdot \xi \right) \right]}$$

(A3)

Strength ratio at joint failure is defined as:

$$r_j = \frac{\gamma_j \cdot f_{ct} \cdot \sqrt{1+\frac{v_j \cdot f_c^{'}}{f_{ct}}} \cdot b_j \cdot d \cdot d_{beam}/h_{st}}{\left[\rho_{\ell,tot} \cdot \frac{f_y}{f_c^{'}} \cdot (1-0.4 \cdot \xi) + v\left(\frac{h}{d} - 0.8 \cdot \xi\right)\right] \cdot \frac{b \cdot d^2 \cdot f_c^{'}}{h_{st}}} \Leftrightarrow$$

$$r_j = \frac{\gamma_j \cdot f_{ct} \cdot \sqrt{1+\frac{v_j \cdot f_c^{'}}{f_{ct}}} \cdot b_j \cdot d \cdot d_{beam}}{\left[\rho_{\ell,tot} \cdot \frac{f_y}{f_c^{'}} \cdot (1-0.4 \cdot \xi) + v\left(\frac{h}{d} - 0.8 \cdot \xi\right)\right] \cdot b \cdot d^2 \cdot f_c^{'}} \quad \text{(A4)}$$

Strength ratio for failure due to punching at slab – columns connections is defined as:

$$r_{pn} = \frac{\left[0.12 \cdot \min\left\{1+\sqrt{\frac{200}{d_{sl}}}\ ,\ 2\right\} \cdot \left(100\rho_{\ell,sl} \cdot f_c^{'}\right)^{1/3} \cdot d_{sl} \cdot 0.25 u_{crit} \cdot (h+4d_{sl})\right] / h_{st}}{\left[\rho_{\ell,tot} \cdot \frac{f_y}{f_c^{'}} \cdot (1-0.40 \cdot \xi) + v\left(\frac{h}{d} - 0.80 \cdot \xi\right)\right] \cdot \frac{b \cdot d^2 \cdot f_c^{'}}{h_{st}}} \Leftrightarrow$$

$$r_{pn} = \frac{\frac{0.12}{f_c^{'}} \cdot \min\left\{1+\sqrt{\frac{200}{d_{sl}}}\ ,\ 2\right\} \cdot \left(100\rho_{\ell,sl} \cdot f_c^{'}\right)^{1/3} \cdot \frac{d_{sl}}{d} \cdot \frac{0.25 u_{crit}}{b} \cdot \left(\frac{h}{d} + 4\frac{d_{sl}}{d}\right)}{\left[\rho_{\ell,tot} \cdot \frac{f_s}{f_c^{'}} \cdot (1-0.40 \cdot \xi) + v\left(\frac{h}{d} - 0.80 \cdot \xi\right)\right]} \quad \text{(A5)}$$

Column strength ratio at beam yielding is given by:

$$r_{by} = \frac{\left(M_{beam}^{+} + M_{beam}^{-}\right) / h_{st}}{\left[\rho_{\ell,tot} \cdot \frac{f_y}{f_c^{'}} \cdot (1-0.4 \cdot \xi) + v\left(\frac{h}{d} - 0.8 \cdot \xi\right)\right] \cdot \frac{b \cdot d^2 \cdot f_c^{'}}{h_{st}}} \Leftrightarrow$$

$$r_{by} = \frac{0.85 \cdot \rho_{beam}}{\left[\rho_{\ell,tot} \cdot \frac{f_y}{f_c^{'}} \cdot (1-0.4 \cdot \xi) + v\left(\frac{h}{d} - 0.8 \cdot \xi\right)\right]} \cdot \frac{b_{beam} \cdot d_{beam}^2}{b \cdot d^2} \cdot \frac{f_y^{beam}}{f_c^{'}} \quad \text{(A6)}$$

where $\rho_{l,tot}$ is the total longitudinal reinforcement ratio of the column; L_b is the lap/anchorage length expressed in multiples of the main bar diameter ($L_b=\psi \cdot D_b$); f_b was calculated according to Model Code 2010 (2010) ($f_b=2 \cdot f_{b,o}$ for ribbed bars, where $f_{b,o}= n_1 n_4 \cdot (f_c'/20)^{0.5}$, n_1=1.80 for ribbed bars, n_4=1.20 for f_y=400 MPa and =1.0 for f_y=500 MPa. The anchorage capacity of a smooth bar hook was taken equal with that of a ribbed bar, $=50 \cdot f_b A_b$); f_c' is the concrete compressive strength; $f_t=0.70 \cdot (0.30 \cdot (f_c)^{2/3})$ is the concrete tensile strength; D_b is the diameter of longitudinal reinforcing bars; f_y is the longitudinal reinforcement yield stress; f_{st} is the stirrup yield stress; ξ is the normalized depth of compression zone; v_j is the axial load ratio of the column above the joint, h is the column height; d is the column depth; b is the column width; h_{st} is the deformable length of the column (equal to free storey height or to the column length in the case of captive columns); μ_{fr} is the friction coefficient ($0.2 \leq \mu fr \leq 0.3$ for smooth bars, $1 \leq \mu_{fr} \leq 1.5$ for ribbed bars); a_b is a binary index (1 or 0) depending on whether ribbed or smooth reinforcement has been used (this variable regulates the contribution of the concrete cover); a_{hook} is a binary index (1 or 0) to account for hooked anchorages (a_{hook} =0 => no hooks); N_b is the number of tension bars; A_b is the area of a single tension bar; A_{tr} is the area of stirrup legs in a single stirrup pattern in direction normal to the splitting plane; s is the

stirrup spacing; γ_j equals to 1.60 for interior joints, 1.00 for exterior joints and 0.60 for corner joints (as per ACI-ASCE 352 [13]); b_j is the joint width; d_{beam} is the beam depth; $\rho_{j,horiz}$ is the area ratio of joint horizontal reinforcement (=total area of stirrup legs in the joint parallel to the plane of action, divided by $b_j \cdot d_{beam}$); $\rho_{l,sl}$ is the total slab reinforcement ratio, at the critical punching perimeter; d_{sl} is the slab depth; u_{crit} is the critical punching perimeter around the typical column in flat plate construction. Term ρ_{beam} in A(6) refers to the total longitudinal reinforcement ratio of the beam section adjacent to the column if an interior connection is considered; in exterior connections this variable assumes the value of the top or bottom beam reinforcement ratio (whichever is largest, since the numerator in the original form of A(6) is simplified to *abs* $\max\{M_{beam}^{+}; M_{beam}^{-}\}$.).

APPENDIX B:

Storey I.D. / Column I.D.		1st	2nd	3rd	4th	5th	6th	7th	8th
C1	b×h (m)	0.31×0.32	0.30×0.30	0.28×0.28	0.25×0.25	0.25×0.25	0.25×0.25	0.25×0.25	0.25×0.25
	Long.reinf.(mm)	4Ø16	4Ø16	4Ø14	4Ø14	4Ø14	4Ø14	4Ø14	4Ø14
C2	b×h (m)	0.39×0.39	0.37×0.37	0.35×0.35	0.32×0.32	0.27×0.27	0.25×0.25	0.25×0.25	0.25×0.25
	Long.reinf.(mm)	4Ø18	4Ø18	4Ø18	4Ø16	4Ø14	4Ø14	4Ø14	4Ø14
C3	b×h (m)	0.39×0.39	0.36×0.37	0.35×0.35	0.32×0.32	0.28×0.28	0.25×0.25	0.25×0.25	0.25×0.25
	Long.reinf. (mm)	4Ø18	4Ø18	4Ø18	4Ø16	4Ø14	4Ø14	4Ø14	4Ø14
C4	b×h (m)	0.39×0.40	0.37×0.37	0.35×0.36	0.32×0.33	0.29×0.29	0.25×0.25	0.25×0.25	0.25×0.25
	Long.reinf.(mm)	4Ø18	2Ø18+2Ø20	4Ø18	4Ø16	2Ø14+2Ø16	4Ø14	4Ø14	4Ø14
C5	b×h (m)	0.39×0.40	0.37×0.38	0.36×0.36	0.33×0.34	0.29×0.29	0.25×0.25	0.25×0.25	0.25×0.25
	Long.reinf.(mm)	2Ø18+2Ø20	2Ø18+2Ø20	4Ø18	4Ø16	2Ø14+2Ø16	4Ø14	4Ø14	4Ø14
C6	b×h (m)	0.46×0.46	0.43×0.44	0.41×0.42	0.38×0.38	0.34×0.34	0.29×0.29	0.25×0.25	0.25×0.25
	Long.reinf.(mm)	4Ø16+2Ø18	6Ø18	4Ø18+2Ø16	2Ø18+2Ø20	2Ø16+2Ø18	2Ø14+2Ø16	4Ø14	4Ø14
C7	b×h (m)	0.43×0.43	0.41×0.41	0.39×0.39	0.36×0.36	0.31×0.32	0.27×0.27	0.25×0.25	0.25×0.25
	Long.reinf.(mm)	6Ø16	4Ø16+2Ø18	6Ø16	4Ø18	4Ø16	4Ø14	4Ø14	4Ø14
C8	b×h (m)	0.50×0.50	0.48×0.48	0.46×0.46	0.42×0.42	0.37×0.38	0.32×0.32	0.25×0.25	0.25×0.25
	Long.reinf.(mm)	4Ø18+2Ø20	6Ø20	4Ø18+2Ø20	4Ø18+2Ø16	4Ø16+2Ø14	4Ø16	4Ø14	4Ø14
C9	b×h (m)	0.30×0.30	0.29×0.29	0.28×0.27	0.25×0.25	0.25×0.25	0.25×0.25	0.25×0.25	0.25×0.25
	Long.reinf.(mm)	4Ø16	2Ø14+2Ø16	4Ø14	4Ø14	4Ø14	4Ø14	4Ø14	4Ø14
C10	b×h (m)	0.40×0.42	0.38×0.38	0.36×0.37	0.34×0.34	0.29×0.29	0.25×0.25	0.25×0.25	0.25×0.25
	Long.reinf.(mm)	4Ø16+2Ø14	6Ø16	4Ø18	2Ø16+2Ø18	2Ø14+2Ø16	4Ø14	4Ø14	4Ø14
C11	b×h (m)	0.30×0.30	0.29×0.29	0.27×0.27	0.25×0.25	0.25×0.25	0.25×0.25	0.25×0.25	0.25×0.25
	Long.reinf.(mm)	4Ø16	2Ø14+2Ø16	4Ø14	4Ø14	4Ø14	4Ø14	4Ø14	4Ø14
C12	b×h (m)	0.36×0.36	0.34×0.34	0.32×0.32	0.29×0.30	0.26×0.26	0.25×0.25	0.25×0.25	0.25×0.25
	Long.reinf.(mm)	4Ø16	4Ø16	4Ø16	2Ø16+2Ø14	4Ø14	4Ø14	4Ø14	4Ø14
C13	b×h (m)	0.60×0.41	0.58×0.38	0.55×0.36	0.53×0.31	0.48×0.27	0.36×0.25	0.25×0.25	0.25×0.25
	Long.reinf.(mm)	4Ø18+2Ø20	4Ø18+2Ø20	6Ø18	6Ø16	4Ø18	4Ø16	4Ø14	4Ø14

Table B: Columns cross section dimensions and longitudinal reinforcement per storey of the building.

COMPDYN 2013
4th ECCOMAS Thematic Conference on
Computational Methods in Structural Dynamics and Earthquake Engineering
M. Papadrakakis, V. Papadopoulos, V. Plevris (eds.)
Kos Island, Greece, 12–14 June 2013

INFLUENCE OF LOW-CYCLE FATIGUE AND CORROSION PHENOMENA ON THE DUCTILE BEHAVIOUR OF STEEL REINFORCING BARS

A. Braconi[1], F. Braga[2], S. Caprili[3], R. Gigliotti[2], W. Salvatore[3]

[1] RIVA FIRE S.p.A
Viale Certosa 247, Milano (Italy)
e-mail: aurelio.braconi@rivagroup.com

[2] Dipartimento di Ingegneria Strutturale e Geotecnica, Università di Roma La Sapienza
Via Eudossiana 18, Roma (Italy)
e-mail: braga.franco@virgilio.it, rosario.gigliotti@uniroma1.it

[2] Dipartimento di Ingegneria Civile e Industriale, Università di Pisa
Largo L. Lazzarino 1, Pisa (Italy)
e-mail: silvia.caprili@ing.unipi.it, walter@ing.unipi.it

Keywords: Seismic demand, mechanical capacity, corrosion phenomena, Incremental Dynamic Analyses

Abstract. *Actual standards for constructions prescribe the realization of r.c. structures able to dissipate the energy stored during the earthquake through the development of global collapse mechanisms; the capacity design procedure is generally adopted, individuating specific "plastic hinges" in which the plasticization shall be located and using specific shear design actions opportunely over-dimensioned in order to avoid local brittle failures. The dissipative capacity of the structure is directly related to the rotational capacity of the elements in which plastic hinges are located and strictly depends on the geometrical and mechanical characteristics of the section itself and on the ductile capacity of steel reinforcing bars. The evaluation of the low-cycle fatigue behaviour of the rebars is obviously of relevant importance for the analysis of the structural behaviour of seismic r.c. buildings; two aspects shall be widely discussed, mainly related to the definition of the effective seismic demand on the rebars due to earthquakes and to the effective cyclic capacity of reinforcements. In the present work, developed inside the framework of a European research project called Rusteel (2009) the results coming from an accurate analysis of the seismic behaviour of r.c. structures is presented, evaluating, in particular, the effective level of strain and dissipated energy due to earthquake events on rebars. The mechanical characterization of the low-cycle fatigue behaviour of bars commonly used in r.c. buildings was also executed, leading to the comparison with the data coming from numerical analyses.*

1 INTRODUCTION

Reinforced concrete buildings in seismic areas are designed according to the capacity design (CD) approach, reference technique for anti-seismic constructions adopted by actual International standards [1, 2, 3]. Buildings shall be able to satisfy the deformation requirements due to increasing levels of seismic action without the exhibition of significant losses of strength and stiffness. Modern codes allow the development of significant plastic phenomena in specific structural elements during severe seismic excitations, causing the deterioration of the structural properties especially if deformations overpass the elastic limit. The failure of primary structural elements, as a consequence, can happen for strain levels lower than the ones corresponding to the collapse limit, condition generally known as "low-cycle fatigue" [4].

In the case of reinforced concrete (r.c.) buildings, in particular, the ability to dissipate the seismic energy stored during the earthquake is strictly connected to the development of global collapse mechanisms, and depends on an opportune location of plastic phenomena: plastic hinges, in the case of moment resisting frames (MRF), generally coincide with the ends of primary elements, following the scheme weak beams – strong columns. Elements shall present an adequate ductility level to prevent unexpected brittle failures and to globally dissipate seismic energy. Since the development of plastic hinges depends on the rotational capacity of primary structural elements [5], a deep knowledge of the cyclic response of the steel reinforcing bars in correspondence of plastic hinges is required to correctly understand the structural behaviour of r.c. buildings under seismic action.

Many works were presented in the current literature dealing with the evaluation of the effective seismic demand on different kinds of structures and sub-structures [4, 6, 7, 8, 9, 10, 11, 12] but in general, no information were provided about the effective ductility demand on steel reinforcing bars, in terms of both strain level and energy dissipation. In their work, Barrera et al. [13] presented the results of experimental tests executed on r.c. columns considering both vertical axial load and a monotonic increasing lateral force. Results were reported including the minimum and maximum strain levels on steel bars: nevertheless, also in this case, a detailed investigation of the cyclic behaviour of bars was not provided, with results limited to the monotonic condition.

Despite a large scientific literature about the cyclic structural behaviour of reinforced concrete buildings, few information are actually provided regarding the Low-Cycle Fatigue (LCF) performance of steel reinforcements, resulting in the absence of a specific procedure for the production control of the cyclic/seismic behaviour of steel bars to be used in modern buildings. Such problem is confirmed by the actual scenario of European standards for reinforcing steels, in which Mandate M115 *("Execution of standardisation work for harmonized standards on Reinforcing and prestressing steel for concrete")* of European Commission, in the framework of the revision of European standard EN10080:2005 [14], promoted the elaboration of a common protocol for the execution of LCF tests for the production control of steel reinforcing bars. Even if in some European Countries current standards for reinforcing steels include the LCF protocols (as, for example, Spanish code UNE 36065 EX:2000 [15] and Portuguese code LNEC E455-2008 [16]), such protocols are defined on the basis of empirical considerations, lacking any reliable background study. The lack of a codified procedure for LCF tests on steel bars is well evidenced in the current literature: Mander et al. [17], Brown and Kunnath [18], Crespi [19] executed LCF tests using levels of imposed deformation, testing frequencies and imposed number of cycles without any regard to the effective real earthquake demand.

Moreover, beside the problems already presented regarding the mechanical

characterization of the low-cycle fatigue/seismic behaviour of steel reinforcing bars, several works in the current literature [20] evidenced durability problems of TempCore bars in r.c. buildings located in aggressive environmental conditions (i.e. chloride exposition), with the decrease of their mechanical properties, both in terms of strength (yielding and tensile stress, R_e and R_m) and ductility (A_{gt}). In order to avoid such problems, Eurocode 2 [21] prescribes the adoption of an opportunely sized concrete cover in relation to the exposition class of the building and to the strength class of the concrete used in the design. Anyway, the knowledge of the mechanical behaviour of rebars after corrosion is necessary for the understanding of the monotonic and the cyclic/seismic behaviour of buildings and to evaluate the ability of the actually used reinforcing steels in sustaining the seismic ductile requirements also after corrosion attacks.

The present paper was developed in the framework of a European research project funded by the Research Fund for Coal and Steel (RFCS), Rusteel, *Effects of Corrosion on Low-Cycle Fatigue (Seismic) Behaviour of High Strength Steel Reinforcing Bars, 2009-2012* [22].

The main aim of the presented work consists in the evaluation of the seismic ductile demand (D) on steel reinforcing bars due to real earthquake events with respect to their effective ductile capacity (C), analyzed both in uncorroded and in corroded conditions.

In this way, the assessment of the structural behaviour of r.c. structures, representative of the actual scenario of European constructions, both at a global level and also considering the local hysteretic behaviour of steel reinforcing bars will allow the full knowledge of the structural response of selected buildings under natural seismic events of magnitude compatible with the one assumed during the design. Moreover, the ability of the actual European steel production usually adopted for new constructions to satisfy the ductile requirements imposed by earthquakes will be deeply investigated, taking into account the ability of corroded steel reinforcing bars, opportunely subjected to accelerated corrosion tests in salt spray chamber, to still satisfy the ductile requirements of seismic action, in terms of both deformation and energy dissipation.

2 THE ADOPTED METHODOLOGY

The main aim of the present work consists in the evaluation of the seismic ductility demand on steel reinforcing bars in r.c. structures and in the comparison of obtained results with the effective mechanical properties of bars, in terms of strain and dissipative capacity, both in uncorroded and corroded conditions.

In order to obtain the values of the effective levels of deformation and energy dissipation, Incremental Dynamic Analyses (IDA) shall be executed on non linear models of r.c. buildings representative of the actual scenario of European constructions.

Non linear bi-dimensional plane frame models of r.c. buildings characterized by different functional destinations (i.e. residential, commercial and office buildings), different plans and elevation dispositions (i.e. span length, interstorey height, number of spans), different ductility classes (High Ductility Class – HDC and Low Ductility Class – LDC) and designed following the prescriptions imposed by European and Italian standards (EN 1998-1:2005, D.M. 14/01/2008) for a peak ground acceleration (PGA) equal to 0.25g, were realized using OpenSees software [23].

The elaboration of the non linear models for the execution of IDAs required the individuation of a specific constitutive stress-strain law for steel reinforcements, allowing the correct evaluation of the levels of deformation and dissipated energy density due to earthquake events. Many works in the current literature [24, 25, 26], in fact, evidenced the inadequacy to consider full bond models for the representation of the hysteretic behaviour of r.c. components once that yielding is overpassed, due to significant relative slips between

steel and concrete, that cannot consequently be neglected.

The hardening slip model, based on the formulation by Braga et al. [25] and implemented to include hardening phenomena of steel reinforcements [27], was consequently developed and adopted for numerical simulations.

In order to maximize the seismic ductility demand on steel reinforcing bars and to reduce the time of analysis, specific accelerograms were selected from the European Strong Motion Database (ESMD), in relation to their PGA, number and the amplitude of cycles, to be used in the numerical IDA simulations. The maximization of the ductility demand on each designed building was developed through the adoption of an opportune procedure aiming to evaluate the Park and Ang (1989) damage index (DI_{PA}), taking into account the effects of seismic input in terms of both deformation (global displacement) and energy dissipation. The results of IDA simulations were then analyzed considering both the whole structure and the corresponding development of ductile and brittle mechanisms in relation to actual standards' prescriptions [1, 2], and the seismic/cyclic behaviour of steel reinforcing bars, in terms of stress, strain and dissipated energy (seismic demand, D).

For what concerns, on the other hand, the evaluation of the effective mechanical capacity (C) of steel reinforcing bars, experimental tensile and LCF tests were executed on a set of steel reinforcements representative of the actual European production, following a specific protocol elaborated inside the research project. Results of LCF tests were analyzed in terms of deformation and, in particular, energy dissipation in order to be comparable with the numerical data coming from IDAs.

Moreover, for taking into account the effects of corrosion phenomena on the mechanical behaviour of bars, accelerated corrosion tests in salt spray chamber were executed on a reduced set of specimens following a specific protocol elaborated inside Rusteel project; the corroded specimens were then subjected to both tensile and LCF tests, evaluating the modifications induced by corrosion on the mechanical behaviour of bars.

The comparison between demand (D) and capacity (C) allowed the assessment of the ability of actual European steel reinforcements' production to effectively satisfy the mechanical requirements induced by seismic events.

Figure 1 shows a schematic representation of the methodology adopted for the individuation of the effective ductile demand on reinforcements while Figure 2 presents the flowchart of the methodology adopted for the investigation of the capacity of bars.

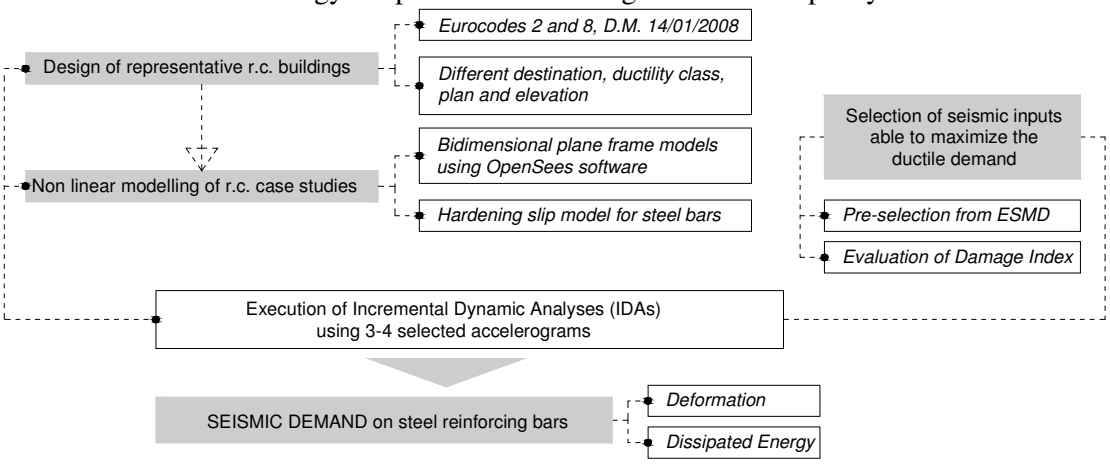


Figure 1: Flowchart for the definition of the effective seismic ductility demand on reinforcements.

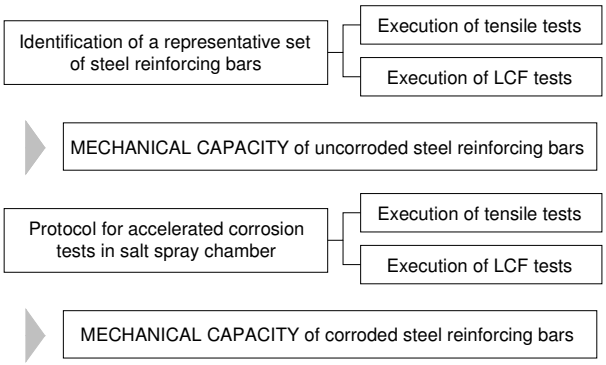


Figure 2: Flowchart for the definition of the effective seismic ductility capacity on reinforcements.

3 SELECTION AND DESIGN OF REPRESENTATIVE R.C. BUILDINGS

Reinforced concrete case-study buildings were designed following the prescriptions imposed by European and Italian standards for constructions [1, 2, 21]. Different distributions of structural elements, different functional destinations (commercial, residential and office buildings) and two different ductility classes (high ductility class – HDC and low ductility class – LDC) were considered.

Permanent gravitational loads were defined in relation to the typology of structural and not structural elements (storey slabs, roof, internal and external infills, equipments, etc…), while live loads were defined in relation to the functional destination selected and according to what specified by Eurocode, according to what presented in table 1.

The response spectrum adopted for the characterization of seismic action was defined in relation to Italian standard prescriptions [2], more restrictive than the one adopted by Eurocode 8: two different limit state, i.e. Life Safety limit state (LS), as regards strength, and Damage Limitation limit state (DL), as regards stiffness and displacements, were adopted, with corresponding return periods (T_R) respectively equal to 75 and 475 years respectively. Buildings were consequently designed using a peak ground acceleration (PGA) equal to 0.25g for LS and considering soil category B. For moment resisting frame (MRF) structures behaviour factors respectively equal to 3.90 and 5.85 for LDC and HDC were adopted [1, 2]. Steel grade B450C and concrete class C25/30 were used. Table 2 summarizes the main aspects assumed in the design phase.

Functional Destination	Ductility Class	Structural loads (kN/m^2)	Not structural loads (kN/m^2)	Q (kN/m^2)
Residential	HDC	3,35	2,80	2,00
Residential	LDC	3,35	2,80	2,00
Office	HDC	3,70	2,50	3,00
Commercial	HDC	4,00	2,35	5,00

Table 1: Loads adopted for the design of r.c. representative buildings.

Functional destination	PGA [g]	Ductility class	Steel grade	q factor
Residential building	0,25	HDC	B450C	5,85
Residential building	0,25	LDC	B450C	3,90
Commercial building	0,25	HDC	B450C	5,85
Office building	0,25	HDC	B450C	5,85

Table 2: Designed reinforced concrete case studies.

MRFs with span length of beams variable between 4.0 m and 7.0 m and storey height between 2.5 m and 5.0 m were adopted in relation to the functional destination of the buildings. Residential buildings in both HDC and LDC presented the same geometrical arrangement of structural elements, resulting in an area of 60,0x14,0 m^2 and a total height of 14,0 m (figure 3); commercial building in HDC was characterized by an area of 36,0x34,0 m^2 and a total height of 19,0 m (figure 4) and, finally, office building in HDC presented an area of 108,0x30,0 m^2 and a global height of 19,0 m (figure 5).

Tridimensional linear models were elaborated using SAP 2000 (v.14.1) software for the execution of linear modal analysis; in the linear models, mono-dimensional elements were used for both beams and columns, while for the slabs of the stairs two-dimensional plane "shell" elements were adopted to directly take into consideration the stiffening contribution of stairs and lift's rooms. The storey slabs were modeled introducing a rigid diaphragm in correspondence of each floor, since a concrete slab with reinforcement grid of 40 mm of thickness was adopted according to the design; columns were fixed at the base.

For taking into account the cracking phenomena of concrete at LS limit state, a reduction of the stiffness of primary structural elements (beams and columns) was adopted, according to what presented in the current standards and literature [1, 2, 5]: a reduction of stiffness equal to 50% was adopted for beam elements and a reduction of stiffness equal to 30% was adopted for column elements, characterized by a significant axial load, for all the designed buildings.

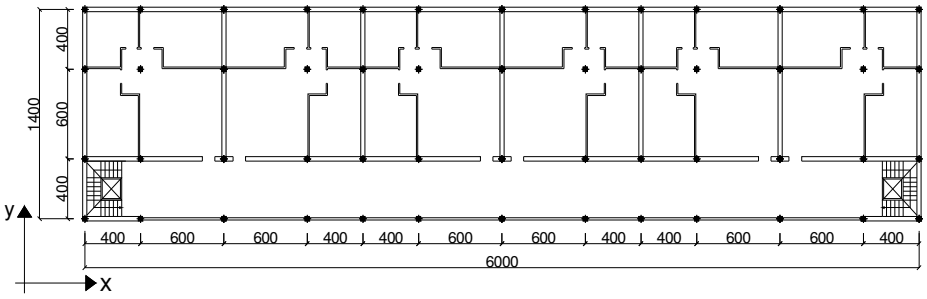


Figure 3: Geometrical scheme adopted for residential buildings.

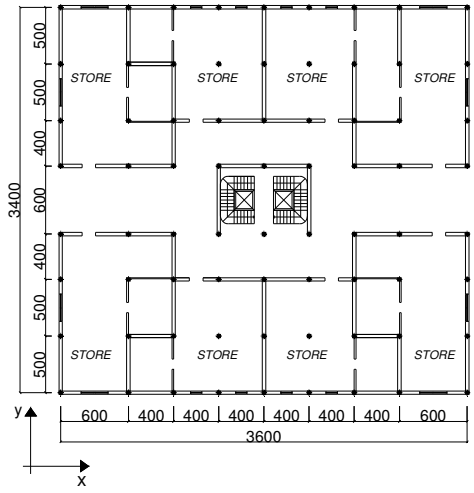


Figure 4: Geometrical scheme adopted for commercial building.

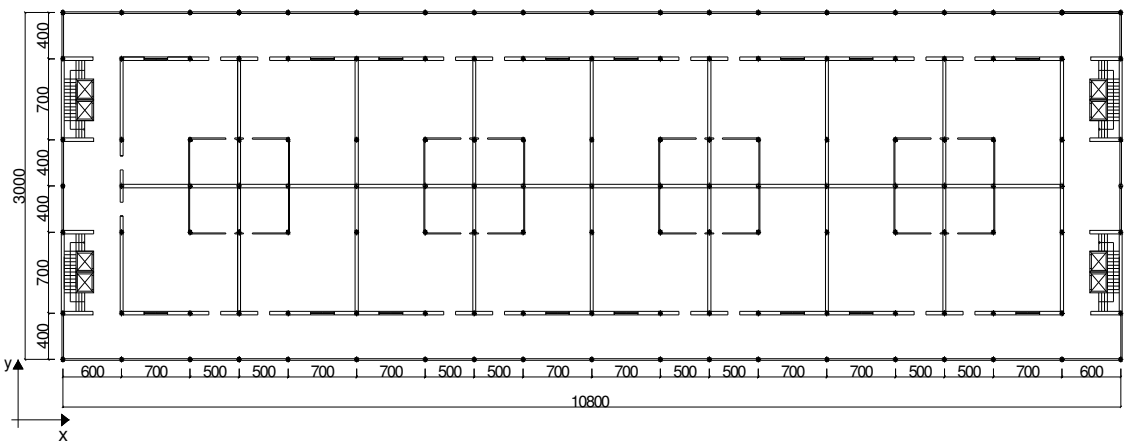


Figure 5: Geometrical scheme adopted for office building.

4 ELABORATION OF NON LINEAR MODELS OF R.C. BUILDINGS

Non linear bi-dimensional plane models were elaborated for each of the two main directions of designed buildings using OpenSees software (Mazzoni et al. 2007). The validation of the adoption of plane frame models instead of tri-dimensional ones was widely presented in Caprili [27] and Braconi et al. [28].

Beams and columns were modelled as "beam with hinge" (BWH) elements: each single element was divided into three different portions, two plastic hinges in correspondence of the two ends and an elastic central part (figure 6). The definition of the section in correspondence of the central part of the element required only the individuation of the transversal area (A) and of the elastic modulus of material (E_m); on the other hand, the sections in correspondence of the two ends of beams and columns were modeled as "fibre section" and an opportune plastic hinge length (L_p) was defined according to Panagiotakos and Fardis's formulation [29] for cyclic loading condition:

$$L_{pl,cy} = 0.12 \cdot L_s + 0.014 a_{sl} d_b f_y \tag{1}$$

Being L_s the shear span length, a_{sl} a coefficient for slip equal to 1 if there is slippage of the longitudinal bars from their anchorage beyond the section of maximum moment, or to 0 if there is not slip, d_b is the bar diameter and f_y the yielding strength. In the present work, the value of a_{sl} was assumed equal to zero, since the relative slip phenomena between bars and the surrounding concrete was directly taken into consideration in the adopted hardening slip model. Columns were fixed at the base and seismic masses, evaluated according to Eurocode 8 [1], were concentrated in correspondence of the top of the columns, where vertical loads were also applied. In order to reproduce the stiffening contribution of storey slabs, additional truss elements, opportunely sized, were introduced in the model between columns (figure 6).

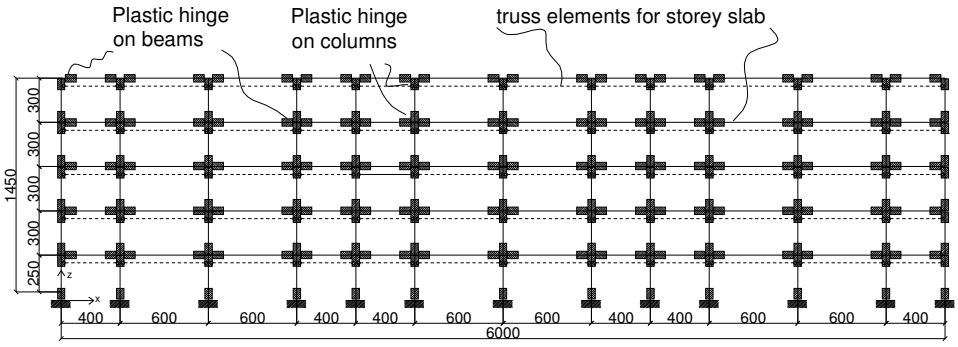


Figure 6: Simplified scheme of non linear model with beam with hinges elements (residential building).

For concrete material, the constitutive law proposed by Braga, Gigliotti and Laterza (BGL) [31] was used, able to directly represent the confinement contributions due to both longitudinal and transversal reinforcements.

For steel reinforcing bars, the "hardening slip model", widely presented in [27, 28], was adopted to represent the effects of relative slips between steel reinforcements and concrete. The hardening slip model was implemented in OpenSees using the trilinear hysteretic material [23], with the three characteristic points of the loading envelope opportunely determined in relation to the energy equivalence principle (figure 7), as well as already presented in [25].

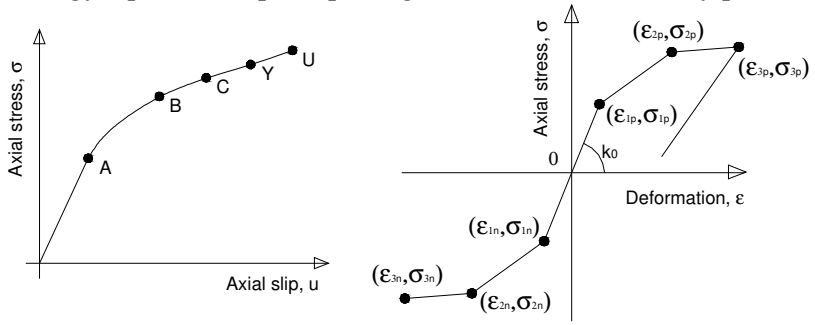


Figure 7: Shift from axial stress-slip model to axial stress-fictitious strain model for steel bars.

The following assumptions were made for the elaboration of the hardening slip model to use for steel reinforcing bars (figure 8):

- The constitutive stress-slip relationship was assumed elastic-plastic with hardening and the values adopted for yielding (f_y) and tensile strength (f_u) and for the elongation to maximum load (A_{gt}) were calibrated on the base of the mean values of the experimental tests' results on steel reinforcements B450C [29] and were respectively equal to 490 MPa, 600 MPa and 14.0%.
- The bond stress-slip relationship was assumed elastic-perfectly plastic (figure 8). The values provided by Model Code 90 [31] for ribbed bars were assumed; in order to consider the progressive deterioration and damaging of bond between steel and concrete due to cycling actions, the residual bond stress to use in the model (τ_d) was taken equal to the one prescribed for poor bond conditions in confined concrete (table 3). A linear approximation of the first branch between zero and the point with coordinates (u1, τ_d) was adopted (figure 8).

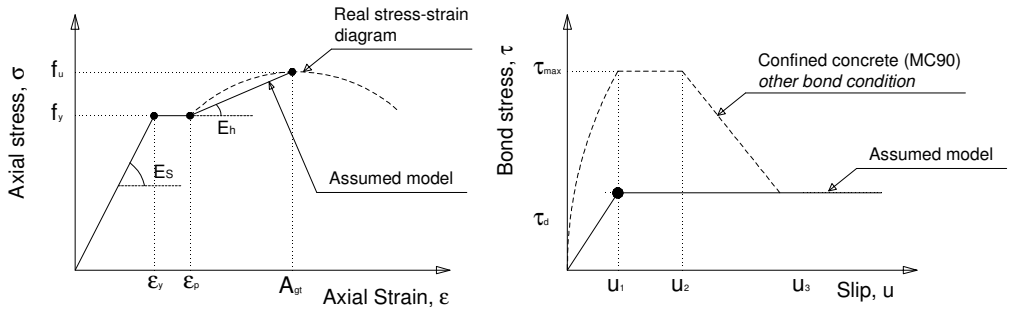


Figure 8: Assumed relationships for stress-strain constitutive law and for bond stress-slip law.

Confined concrete - All other bond condition			
Model Code 90 (CEB-FIP 1993)		Assumed values for modified slip model	
u_1 [mm]	1.0	u_b [mm]	0.4
u_2 [mm]	3.0	u_2 [mm]	-
u_3 [mm]	Clear rib spacing	u_3 [mm]	-
α	0.4	f_{ck} [MPa]	33
τ_{max} [MPa]	$1.25\sqrt{f_{ck}}$	τ_{max} [MPa]	7.18
τ_f [MPa]	$0.40\tau_{max}$	τ_f [MPa]	2.87

Table 3: Assumed values for the bond stress-slip relationship in modified slip model.

The axial stress-strain to be used in the numerical models was obtained according to what provided by D'Amato et al. [32]; a fictitious strain ε^* was individuated through the following equation:

$$\varepsilon^* = \frac{u_{L,tot}}{L_P} \tag{2}$$

in which the plastic hinge length L_p was defined according to Panagiotakos and Fardis [29]. Figures 9 represent the axial stress-slip and the axial stress-strain trilinear relationships obtained for different bar diameters, while table 4 summarizes the values adopted in the models.

Mechanical properties of material			Axial stress-slip relationships: coordinates of significant points								
f_y	490	MPa									
f_u	600	MPa	d	14	mm	d	16	mm	d	18	mm
ε_y	0.24	%	u_{p1}	0.400	mm	u_{p1}	0.400	mm	u_{p1}	0.400	mm
A_{gt}	12.50	%	σ_{p1}	318.56	MPa	σ_{p1}	297.80	MPa	σ_{p1}	280.77	MPa
E_s	206000	MPa	u_{p2}	0.743	mm	u_{p2}	0.839	mm	u_{p2}	0.936	mm
E_h	1047.00	MPa	σ_{p2}	517.30	MPa	σ_{p2}	517.44	MPa	σ_{p2}	517.59	MPa
τ_d	2.87	MPa	u_{p3}	11.475	mm	u_{p3}	13.104	mm	u_{p3}	14.734	mm
u_1	0.4	Mm	σ_{p3}	600.00	MPa	σ_{p3}	600.00	MPa	σ_{p3}	600.00	MPa

Table 4: Assumed values for the axial stress-slip model.

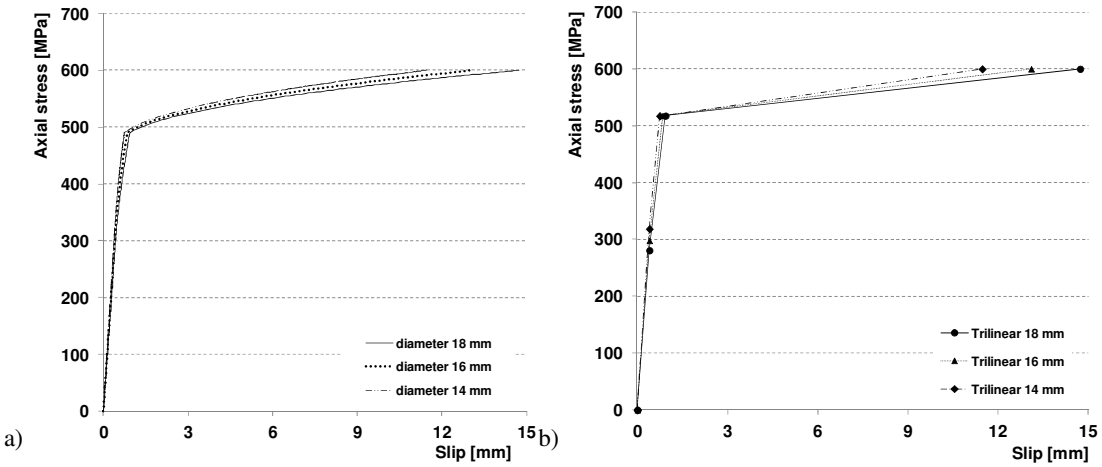


Figure 9: a) Axial stress-slip relationship and b) trilinear equivalent model.

5 GLOBAL ASSESSMENT OF CASE STUDIES

IDAs were executed on bi-dimensional frame models considering both the horizontal and the vertical components of accelerograms and PGA increment equal to 0.05g; the adopted time histories, selected from the European Strong Motion Database (EMSD) in order to maximize the seismic ductile requirements on buildings according to the procedure specified in Braconi et al. [33] are presented in table 5.

Building	Time histories			
Residential HDC	Montenegro x+z	Erzincan x+z	Campano Lucano x+z	Umbro Marchigiano x+z
Residential LDC	Montenegro x+z	Erzincan x+z	Campano Lucano x+z	Umbro Marchigiano x+z
Commercial	Montenegro y+z	Erzincan x+z	Campano Lucano y+z	Umbro Marchigiano x+z
Office	Montenegro y+z	Erzincan x+z	Campano Lucano y+z	Umbro Marchigiano x+z

Table 5: Adopted time histories for the IDAs.

The global structural assessments of designed buildings was executed following the prescriptions imposed by actual European and Italian standards [1, 2, 34]. The structural safety was checked at the member section level by comparing the demand, derived from numerical analyses, with its corresponding available capacity, evaluated in terms of strength or deformation respectively for brittle and ductile elements or mechanisms.

The ductile mechanisms were assessed evaluating the chord rotation demand and the corresponding capacity at the ends of each structural element (beams and columns); the brittle elements/mechanisms were assessed evaluating their strength capacity, in terms of static or cyclic shear resistance according to Eurocode 8.

The capacity of r.c. structural members at Damage Limitation limit state (DL) was expressed in terms of chord rotation at yielding θ_y, while the value of total chord rotation capacity (considering both the elastic and the inelastic parts) at ultimate (Near Collapse, NC) limit state were evaluated in agreement to what specified in the Annex A of Eurocode 8 [34]. For what concerns brittle elements/mechanisms, according to Eurocode 8 both the static and the cyclic shear capacity of elements were taken into account, since the effects of the inelastic response in the assessment of the shear capacity was necessarily taken into account decreasing the shear strength with the progressive increase of the cyclic inelastic deformations. The static

shear static strength was evaluated according to Eurocode 2 [21].

The cyclic shear resistance V_R was also evaluated at ultimate limit state (NC), according to the formula presented in the Annex A of Eurocode 8 (expression A.12 of [34]).

The results of numerical analyses on r.c. buildings designed in high ductility class (HDC) evidenced, in general, a good agreement with what imposed during the design, without the activation of shear mechanisms in beams and columns and the development of ductile ones for levels of PGA higher than the ones corresponding to the design one (0.25g). The reaching of the interstorey drift limit, equal to 4.0% according to [3], generally happened for PGA levels higher than 0.30g. Figures 10-12 represent the progressive activation of ductile mechanisms (chord rotation at yielding and ultimate) for increasing levels of seismic action for the three HDC buildings and for the most critical seismic event.

As visible, plastic hinges generally developed at the ends of beams of the first three levels and at the base of columns of the 1st floor, for increasing levels of seismic action: as an example, considering commercial building and Erzincan time history (figure 10), for PGA equal to 0.20g all the end sections of beams of 1st, 2nd and 3rd floors and the columns' base sections already reached chord rotation at yielding, while ultimate rotation was obtained for levels of seismic action generally higher than 0.35g. In any case, as visible from figures 10-12, beams and columns of the 5th floor were generally not involved in the development of ductile mechanisms for levels of seismic action lower than 0.50g. Similar considerations can be executed also for the other representative buildings analyzed.

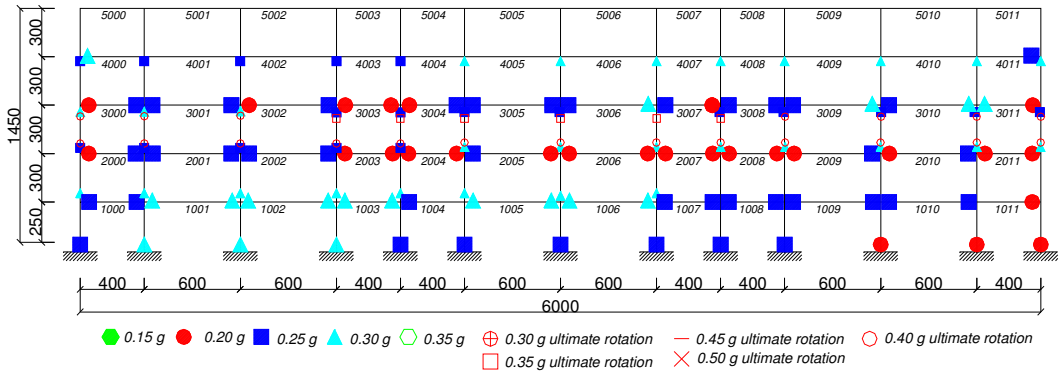


Figure 10: Structural behaviour of residential building in HDC for Erzincan earthquake.

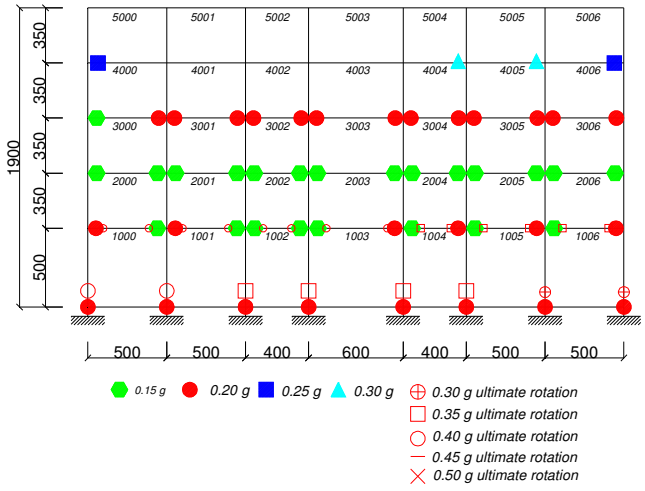


Figure 11: Structural behaviour of commercial building in HDC for Erzincan earthquake.

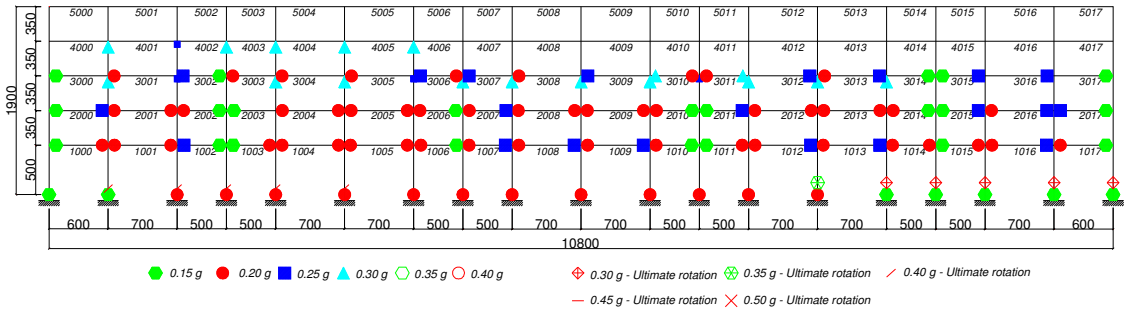


Figure 12: Structural behaviour of office building in HDC for Montenegro earthquake.

Looking at the structural behaviour of the residential building designed for LDC, some additional consideration shall be executed; as visible from figure 13, differently from what observed from buildings in HDC, some brittle mechanisms activated for levels of PGA between 0.25 and 0.30g, i.e. equal or slightly higher than the ones adopted in the design, in correspondence of the columns' base section of the 1st floor and, in some cases, at the ends of beams of the first storey. For what concerns, on the other hand, the ductile behaviour of structural elements, considerations similar to the ones presented for HDC buildings can be executed (figure 14), with first plastic hinges in correspondence of beams and columns of the first floors for PGA equal to 0.15g and the absence of ductile mechanisms at the 5th floor (beams and columns).

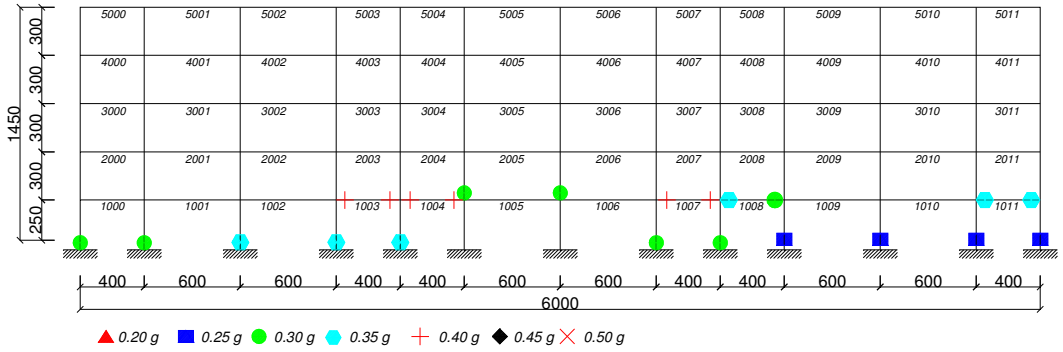


Figure 13: Structural behaviour of residential building in LDC for Erzincan earthquake: brittle mechanisms.

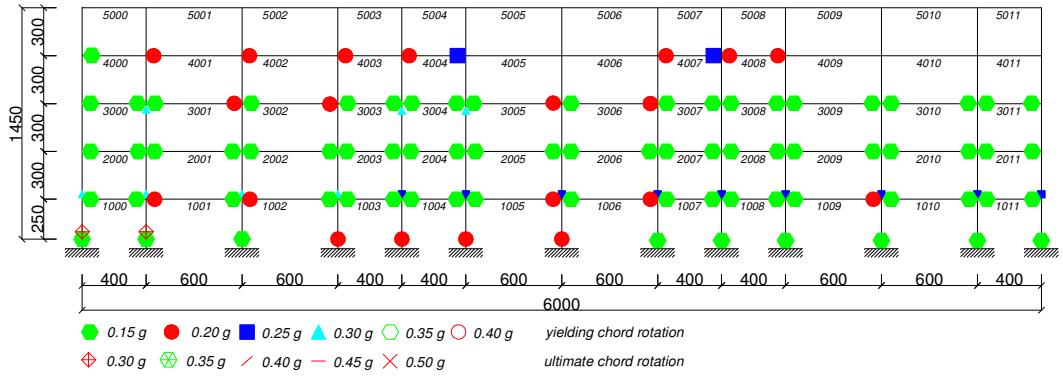


Figure 14: Structural behaviour of residential building in LDC for Campano Lucano earthquake: ductile mechanisms.

6 EVALUATION OF DUCTILITY DEMAND ON STEEL REINFORCING BARS

According to the formulation of the hardening slip model adopted for steel reinforcements, the results of IDAs on r.c. case studies are affected by the plastic hinge length: this means that while slips and stresses can be directly derived, further investigations are required for the effective strain levels on reinforcing bars. A simplified model of the bar was then elaborated and subjected to the stress histories coming from IDAs.

A zero-lenght element model [23] with Menegotto-Pinto law was used for the representation of the hysteretic behaviour of steel reinforcements, calibrating the parameters used for Steel02 material on the base of experimental LCF tests on steel reinforcing bars B450C presented in [27]. The calibration procedure was based on the first cycle tension-compression, since buckling generally happened after the first stress reversal and degradation phenomena were not taken into account.

Mean values of the mechanical properties (yielding strength R_e, tensile strength R_m, elongation to maximum load A_{gt}) of the corresponding steel grades, coming from the experimental mechanical tensile tests presented in [25], were adopted, while the hardening branch slope was defined according to Eqn. (8), in which ε_p represents the strain corresponding to the end of the yielding plateau (≅ 2.0%):

$$E_h = \frac{R_m - R_e}{A_{gt} - \varepsilon_p} \tag{8}$$

Finally, the parameters assumed for the Menegotto-Pinto law were the ones generally suggested by Mazzoni et al. [23]: $R0 = 0.20$, $cR1 = 0.925$, $cR2 = 0.15$.

6.1 Evaluation of the seismic ductility demand (D) on steel bars

A peak ground acceleration (PGA) equal to 0.25g, i.e. the design PGA for LS limit state according to the design codes used in the design [1, 2], was considered. In agreement to what already presented about the global structural behaviour of the buildings, steel reinforcing bars of 1st floor columns' base sections and of 1st and 2nd floors' beams were usually taken into consideration. The most significant results obtained are presented for each designed building.

Steel bars are individuated with an identification code (ID) providing the number of the element, according to the schematization adopted in figure 15, the section (i.e. s1 is the starting section and s6 the end section, figure 16) and the corresponding position of the bar (i.e. J or K, respectively on the top or on the bottom of the transversal plane section, figure 16).

Results are presented in terms of maximum and minimum deformation and stress and total density of dissipated energy, evaluated as presented by Apostolopoulos [20]:

$$W = \int \sigma \, d\varepsilon \tag{9}$$

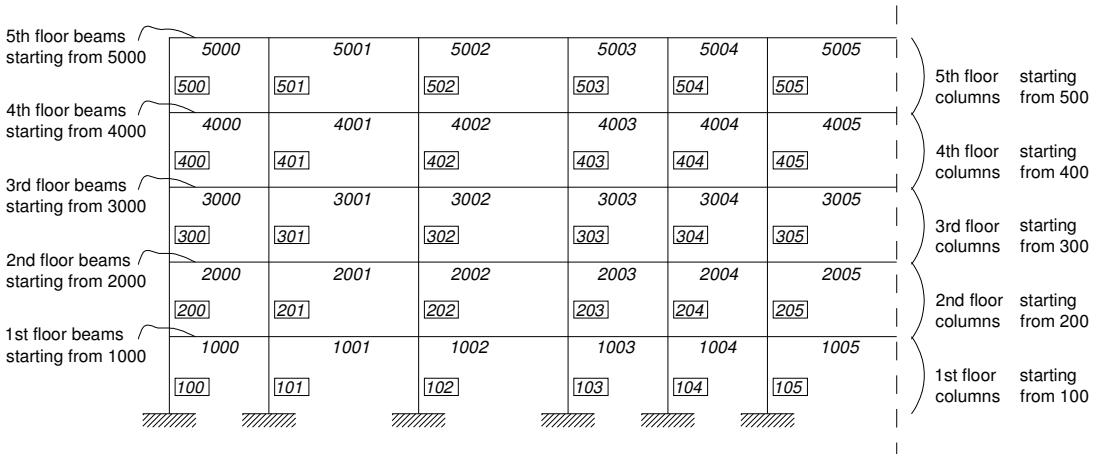


Figure 15: Schematization assumed for the identification of structural elements in the plane frames.

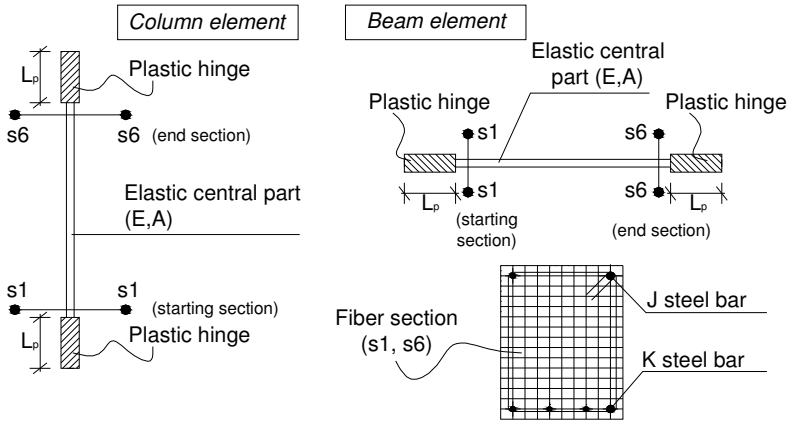
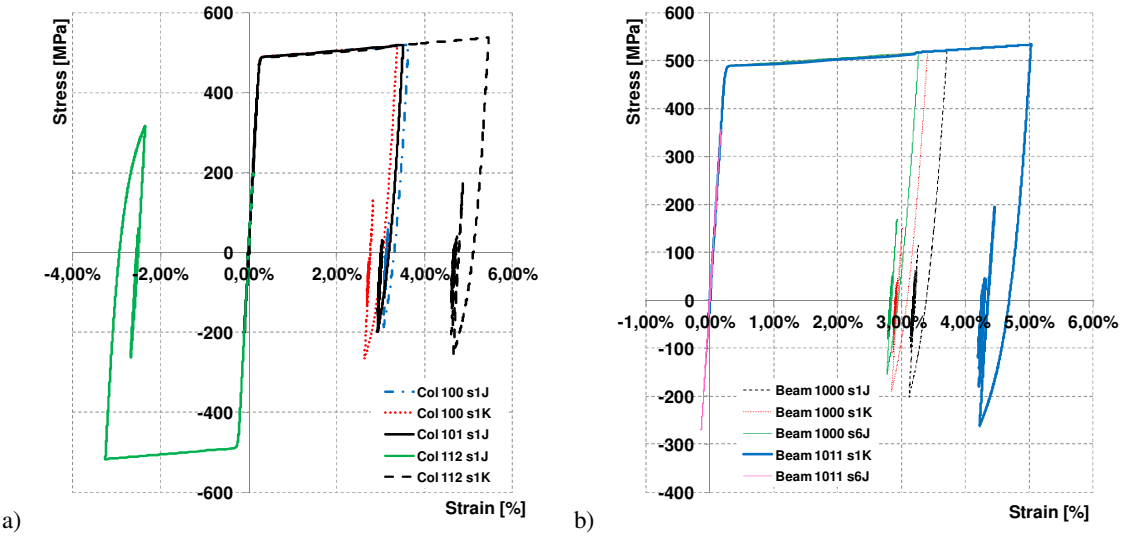


Figure 16: Schematization of section and steel fibre.

6.1.1 Residential building in HDC

The worst results in terms of maximum deformation level and dissipated energy were obtained considering Erzincan time history (figure 17); in the case of column n°112 (1st floor, external column) a maximum strain in tension equal to 5.45% was reached (steel bar S1K), while the minimum deformation in compression was equal to -3.26%. Despite the higher absolute values of strain, steel bars generally did not invert completely the sign of deformation, resulting in lower levels of dissipated energy (around 27 MPa). Similar considerations can be executed also for steel reinforcing bars in beam elements (table 7), in which the highest level of strain was equal to 5.03% (beam 1011, steel bar S6J) with dissipated energy density equal to 25 MPa.



a) b)

Figure 17: Residential building in HDC, Stress-strain histories on steel bars for Erzincan time history: a) columns 1st floor, b) beams 1st level.

Residential building in HDC – Erzincan time history - COLUMNS						
Element ID	PGA 0,25g	Max. def. [%]	Min. def. [%]	Max. Tens. [MPa]	Min. Tens. [MPa]	Energy [MPa]
100	s1 J	3,63%	-0,05%	521,13	-193,24	17,11
	s1 K	3,37%	-0,06%	518,74	-266,61	16,11
101	s1 J	3,51%	-0,10%	520,02	-200,33	16,49
	s1 K	2,76%	-0,05%	513,08	-242,09	12,79
112	s1 J	0,10%	-3,26%	316,36	-517,67	16,00
	s1 K	5,45%	-0,02%	537,79	-254,33	27,08

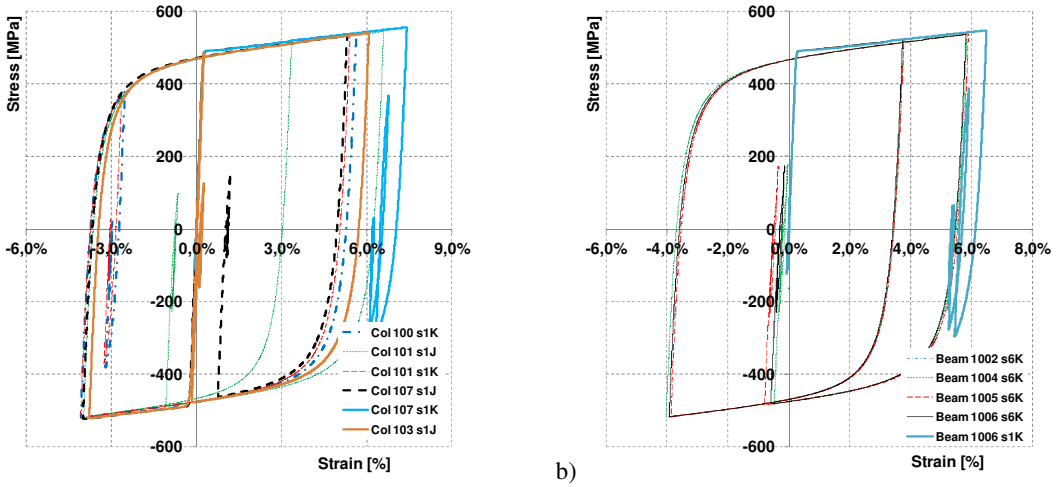
Table 6: Stress and strain values on steel reinforcing bars of columns (residential building in HDC).

Residential building in HDC – Erzincan time history - BEAMS						
Element ID	PGA 0,25g	max def [%]	min def [%]	max Tens [MPa]	min Tens [MPa]	Energy [MPa]
1000	s1 J	3,72%	-0,05%	521,88	-201,11	17,55
	s1 K	3,41%	-0,03%	519,09	-189,63	15,98
	s6 J	3,27%	-0,03%	517,81	-153,94	15,19
	s6 K	3,52%	-0,06%	520,09	-179,71	16,50
1011	s1 J	0,16%	-0,11%	334,62	-227,15	0,00
	s1 K	4,69%	-0,02%	530,84	-255,81	23,02
	s6 J	5,03%	-0,02%	533,96	-261,45	24,87
	s6 K	0,17%	-0,13%	357,39	-271,17	0,00

Table 7: Stress and strain values on steel reinforcing bars of beams (residential building in HDC).

6.1.2 Commercial building in HDC

The ID codes adopted for structural elements of commercial building in HDC followed the indications presented in figure 15. Also in this case, the worst results in terms of maximum deformation level and dissipated energy were obtained for Erzincan accelerogram (figure 18); in the case of column n°107 (1st floor, external column) a maximum strain in tension equal to 7.42% was reached (steel bar S1K), while the minimum deformation in compression was equal to -4.00% (steel bar S1J), with corresponding deformation in tension up to 5.08% and dissipated energy density equal to 74.4 MPa. The maximum values of dissipated energy density were obtained in correspondence of column n°101 (steel bar S1J, with 121.83 MPa, table 8) and of beam n°1002 (steel bar s6K, with 120.85 MPa, table 9), in which the internal forces were able to completely invert the sign of strain and to complete tension/compression cycles (figure 18).



a) b)

Figure 18: Stress-strain histories on steel bars for Erzincan time history: a) columns 1st floor, b) beams 1st level.

Commercial building in HDC – Erzincan time history - COLUMNS						
Element ID	PGA 0,25g	max def [%]	min def [%]	max Tens [MPa]	min Tens [MPa]	Energy [MPa]
101	s1 J	6,60%	-3,97%	544,05	-518,95	121,83
	s1 K	5,41%	-4,08%	537,39	-520,64	68,98
103	s1 J	6,08%	-3,78%	540,04	-522,47	84,11
	s1 K	5,81%	-3,81%	541,04	-518,07	71,37
107	s1 J	5,31%	-4,00%	532,49	-524,49	74,37
	s1 K	7,42%	-0,05%	555,80	-294,51	39,17

Table 8: Stress and strain values on steel reinforcing bars of columns (commercial building in HDC).

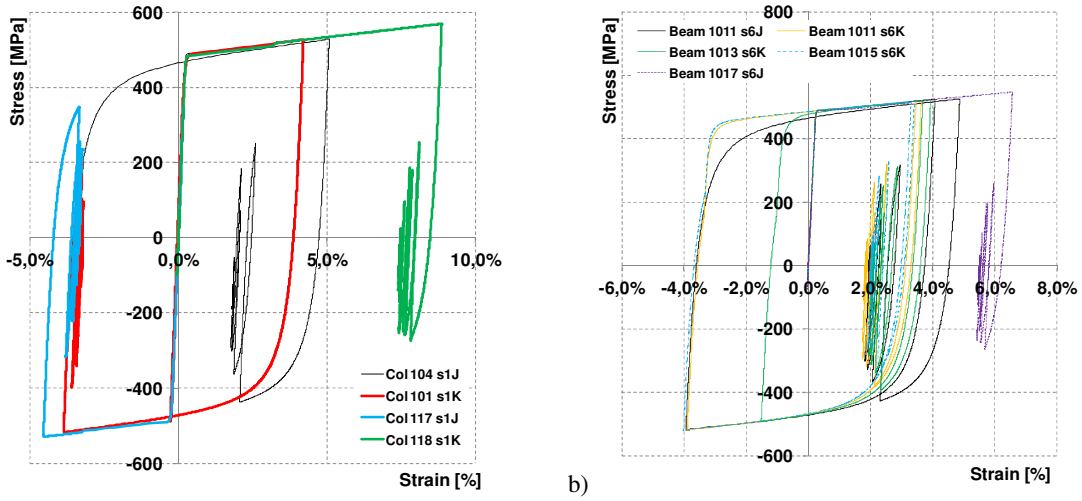
Commercial building in HDC – Erzincan time history - BEAMS						
Element ID	PGA 0,25g	max def [%]	min def [%]	max Tens [MPa]	min Tens [MPa]	Energy [MPa]
1002	s1 J	5,46%	-0,011%	534,89	-351,68	32,14
	s1 K	5,83%	-0,081%	541,30	-470,25	50,49
	s6 J	5,46%	-0,057%	537,91	-312,72	28,60
	s6 K	6,08%	-3,852%	538,78	-517,80	120,85
1004	s1 J	5,40%	-0,012%	533,46	-387,31	33,09
	s1 K	6,09%	-0,072%	543,68	-399,72	37,16
	s6 J	5,58%	-0,050%	539,00	-292,56	28,83

1006	s6 K	5,85%	-4,030%	536,59	-519,60	116,42
	s1 J	4,88%	-0,013%	530,86	-352,06	28,16
	s1 K	6,49%	-0,060%	547,34	-297,64	34,16
	s6 J	5,95%	-0,041%	542,38	-283,86	30,63
	s6 K	5,82%	-3,930%	536,23	-518,56	115,44

Table 9: Stress and strain values on steel reinforcing bars of beams (commercial building in HDC).

6.1.3 Office building in HDC

The ID codes adopted for structural elements of commercial building in HDC followed the indications presented in figure 15. The results in terms of maximum deformation level and dissipated energy obtained for Montenegro time history are presented in the figure 19; in the case of column n°118 (1st floor, external column) a maximum strain in tension equal to 8.82% was reached (steel bar S1K), while the minimum deformation in compression was equal to -4.54% (column n°117 steel bar S1J). The maximum value of dissipated energy density was obtained in correspondence of column n°104 (steel bar S1J) with 101.18 MPa (table 10) and maximum and minimum strain respectively equal to 5.08% and -3.86%, in which the internal forces were able to completely invert the sign of deformation and to complete tension/compression cycles (figure 19). Similar considerations and values were obtained also for beam elements (figure 19b, table 11)



a) b)

Figure 19: Stress-strain histories on bars for Montenegro time history: a) columns 1st floor, b) beams 1st level.

Office building in HDC – Montenegro time history - COLUMNS						
Element ID	PGA 0,25g	max def [%]	min def [%]	max Tens [MPa]	min Tens [MPa]	Energy [MPa]
104	s1 J	5,08%	-3,86%	528,63	-517,93	101,18
	s1 K	4,90%	-0,19%	532,70	-416,94	29,97
117	s1 J	0,17%	-4,54%	349,51	-529,48	24,14
	s1 K	7,92%	-0,09%	560,38	-274,88	41,38
118	s1 J	2,41%	-4,03%	502,49	-524,79	45,70
	s1 K	8,86%	-0,05%	569,05	-271,37	46,90

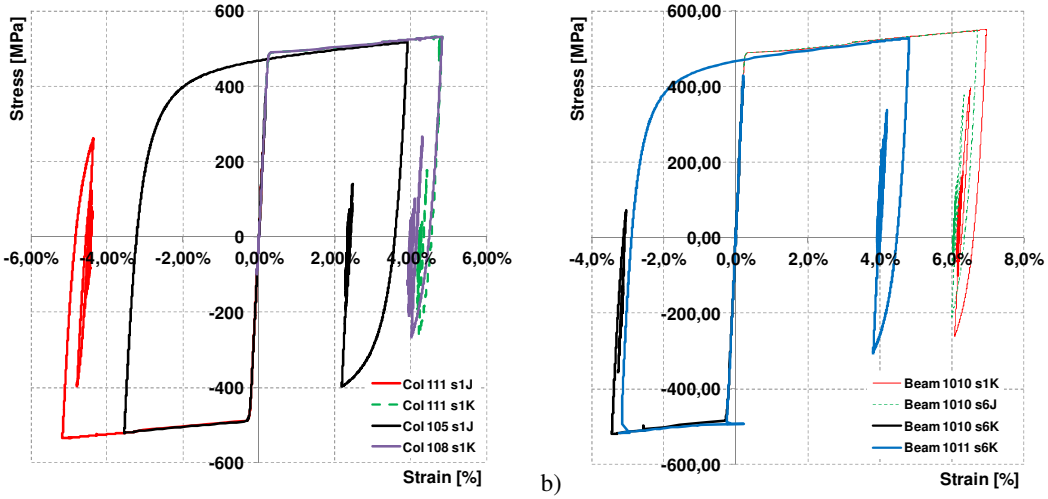
Table 10: Stress and strain values on steel reinforcing bars of columns (office building in HDC).

Office building in HDC – Montenegro time history - BEAMS						
Element ID	PGA 0,25g	max def [%]	min def [%]	max Tens [MPa]	min Tens [MPa]	Energy [MPa]
1011	s1 J	4,87%	-3,94%	526,63	-518,75	99,31
	s1 K	5,79%	-0,07%	540,86	-266,63	29,45
	s6 J	4,93%	-0,07%	532,98	-259,83	24,60
	s6 K	3,64%	-3,89%	520,78	-518,12	83,49
1015	s1 J	4,68%	-4,02%	524,76	-519,50	95,24
	s1 K	6,15%	-0,05%	544,21	-264,80	31,40
	s6 J	5,24%	-0,05%	535,82	-258,50	26,25
	s6 K	3,42%	-4,02%	518,95	-519,41	80,48
1017	s1 J	0,19%	-0,17%	388,01	-352,46	0,00
	s1 K	6,02%	-0,05%	543,02	-265,13	30,83
	s6 J	6,57%	-0,04%	548,02	-263,71	33,62
	s6 K	4,74%	-3,89%	525,28	-518,18	95,73

Table 11: Stress and strain values on steel reinforcing bars of beams (office building in HDC).

6.1.4 Residential building in LDC

Figure 15 shows the ID codes adopted for structural elements of residential buildings both in HDC and in LDC. The results in terms of maximum deformation level and dissipated energy obtained for Erzincan time history (figure 20); in the case of column n°111 (1st floor, external column) a maximum strain in tension equal to 4.84% was reached (steel bar S1K), while the minimum deformation in compression was equal to -5.18% (column n°111 steel bar S1J). The maximum value of dissipated energy density was obtained in correspondence of beam n°1011 (steel bar S6K) with 50.31 MPa (table 12) and maximum and minimum strain respectively equal to 4.82% and -3.24%, in which the internal forces were able to completely invert the sign of deformation and to complete tension/compression cycles (figure 20). The absolute maximum level of deformation, equal to 6.96%, was reached in correspondence of steel bar S1K in beam n°1010 (table 13).



a) b)

Figure 20: Stress-strain histories on bars for Erzincan time history: a) columns 1st floor, b) beams 1st level.

Residential building in LDC – Erzincan time history - COLUMNS						
Element ID	PGA 0,25g	max def [%]	min def [%]	max Tens [MPa]	min Tens [MPa]	Energy [MPa]
109	s1 J	0,15%	-5,06%	413,78	-534,25	30,66
	s1 K	4,08%	-0,04%	525,24	-263,35	19,65
105	s1 J	3,92%	-3,54%	518,41	-520,31	51,06
	s1 K	3,92%	-0,06%	523,80	-279,76	19,26
111	s1 J	0,13%	-5,18%	261,19	-535,26	25,88
	s1 K	4,84%	-0,04%	532,24	-262,58	23,65

Table 12: Stress and strain values on steel reinforcing bars of columns (residential building in LDC).

Residential building in LDC – Erzincan time history - BEAMS						
Element ID	PGA 0,25g	max def [%]	min def [%]	max Tens [MPa]	min Tens [MPa]	Energy [MPa]
1010	s1 J	0,14%	-0,15%	283,58	-312,18	0,00
	s1 K	6,96%	-0,04%	551,64	-260,57	35,53
	s6 J	6,71%	-0,03%	549,36	-210,40	33,68
	s6 K	0,20%	-3,44%	414,56	-519,36	15,71
1011	s1 J	3,63%	-0,16%	521,09	-321,58	16,95
	s1 K	5,63%	-0,03%	539,39	-280,50	27,91
	s6 J	5,44%	-0,02%	537,73	-271,56	26,20
	s6 K	4,82%	-3,24%	528,38	-517,50	50,31

Table 13: Stress and strain values on steel reinforcing bars of beams (residential building in LDC).

7 EVALUATION OF THE MECHANICAL CAPACITY OF STEEL BARS

7.1 Selection of the specimens

A representative set of steel reinforcing bars was selected inside the research project *Rusteel* in order to fully characterize the mechanical behaviour of the most significant steel grades actually used in Europe. All the most diffused mechanical production processes - TempCore (TEMP), Micro-Alloyed (MA), Stretched (STR) and Cold-Worked (CW) were considered, as well as different diameters (between 8 and 25 mm) and different producers (coming from France, Germany, Italy and Spain), in order to take into account the variability related to all the above mentioned aspects. Moreover, different steel grades (yielding strenght equal to 400, 450 or 500 MPa) and different ductility classes (A, B or C in relation to [21]) were selected. Table 14 presents the complete set of steel bars selected for experimental tests.

Steel Grade	Diameter	Steel Process	Ribs	Furniture	More information
B500A	8*,12*	CW	ribbed	Prod.1	
B500A	8*	CW	indented	Prod.2	
B500B	8*,16*,20*,25	TEMP	ribbed	Prod.1	Same cast for all diameters
	16*			Prod.2	From 3 different plants
B500B	8*,12	STR	ribbed	Prod.2	German plants
B400C	8*,16*,20*,25	TEMP	ribbed	Prod.2	Spanish plants
B400C	16*,20*,25	MA	ribbed	Prod.1	Same cast for all diameters
B450C	16*,20*,25	TEMP	ribbed	Prod.1	Same cast for all diameters
	16			Prod.2	From 3 different plants
B450C	8*,12*	STR	ribbed	Prod. 1+2	

Table 14: Selected steel grades for the mechanical characterization.

7.2 Execution of tensile and LCF tests on uncorroded specimens and results

Experimental tensile and low-cycle fatigue tests were executed on the bars presented in table 14; monotonic tensile tests were executed considering the prescriptions imposed by [35], while for the LCF tests an opportune protocol was elaborated inside Rusteel project, taking into consideration what provided by actual European standards [15, 16] and what presented in the current literature [19, 18].

The LCF protocol used for the experimental tests, briefly summarized in the table 15 for different diameters, prescribed the execution of symmetrical tension/compression cycles up to the failure of the bar with two different levels of imposed deformation, respectively equal to ±2.5% and ±4.0%, and two different free length of the specimens, respectively equal to 6ϕ and 8ϕ, corresponding to the minimum stirrups' spacing for buildings designed in HDC and LDC. The frequency to be used in the experimental tests was fixed equal to 2.0 Hz, but, according to what presented in Caprili [27], for high diameters (≥16mm) it was reduced to 0.5 Hz, since not significant differences in terms of dissipated energy were revealed.

Diameter ϕ [mm]	Frequency [Hz]	Free length L_0		Imposed strain ε [%]	Elongation Δl [mm]
20	0.05	6ϕ	120	± 2.5%	3.00
				± 4.0%	4.80
		8ϕ	160	± 2.5%	4.00
				± 4.0%	6.40
16	2.00	6ϕ	96	± 2.5%	2.40
				± 4.0%	3.84
		8ϕ	128	± 2.5%	3.20
				± 4.0%	5.12
12	2.00	6ϕ	72	± 2.5%	1.80
				± 4.0%	2.88
12	2.00	8ϕ	96	± 2.5%	2.40
				± 4.0%	3.84
8	2.00	6ϕ	48	± 2.5%	1.20
				± 4.0%	1.92
		8ϕ	64	± 2.5%	1.60
				± 4.0%	2.56

Table 15: Protocol for the execution of low-cycle fatigue tests on bars of different diameter.

Low-cycle fatigue tests results were analyzed in terms of maximum and minimum effective strain obtained (evaluated considering the contribution due to the machine deformability), maximum and minimum stress and density of dissipated energy, total and per cycle. In particular, in the present work the results obtained for steel reinforcing bars of diameter 16 mm, steel grade B450C and different producers are presented, in order to be compared with bars used in the design of representative r.c. buildings.

In the figures 21 and 22 the stress-strain diagrams obtained from bars B450C, diameter 16 mm, TempCore process are presented for the two different considered free lengths and imposed deformations. Moreover, figure 23 presents the trend of the dissipated energy density per cycle evaluated considering L_0=6ϕ and L_0=8ϕ. Table 17 presents the values of the effective maximum and minimum strain and stress on specimens and the total energy dissipated for all the considered specimens tested.

The behaviour of steel reinforcing bars of diameter 16 mm was more stable under lower level of imposed deformation, while for imposed strain equal to ±4.0%, despite higher values

of the dissipated energy density per cycle, the number of cycles up to failure rapidly decreased, showing, moreover, a more brittle behaviour in the case of free length equal to 8 diameters (figure 23). As an example, for $L_0=6\phi$ and imposed deformation equal to ±2.5%, steel bars B450C, diameter 16 (producer 1.1) were able to complete 19 cycles before failure without showing a significant decrease of the dissipative capacity per cycle; otherwise, considering a free length $L_0=8\phi$, the number of cycles before failure dropped to 9 with a sudden decrease of the dissipated energy per cycle. The total energy dissipated passed from 560 MPa to 260 MPa.

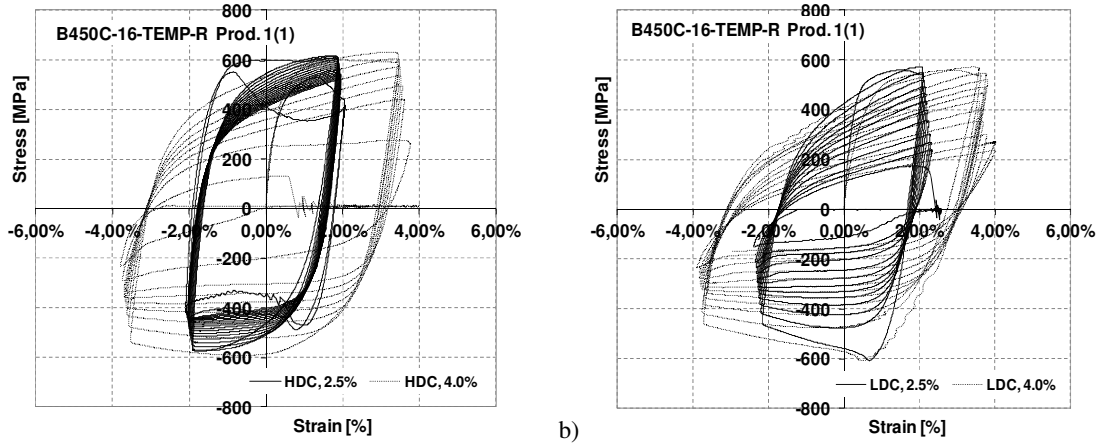


Figure 21: LCF tests on steel bars B450C-16-TEMP-R (Producer 1.1) for free length of the specimen equal to a) 6ϕ and b) 8ϕ and imposed deformation equal to ±2.5% and ±4.0%.

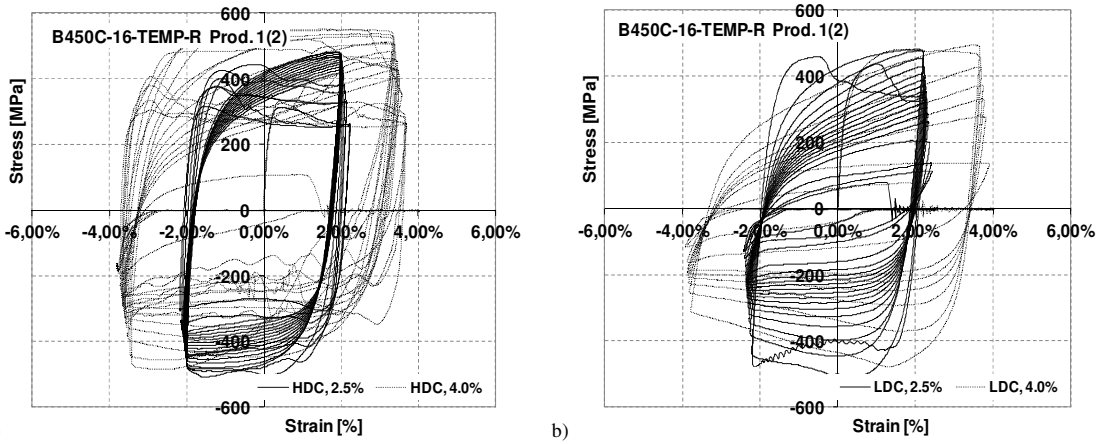


Figure 22: LCF tests on steel bars B450C-16-TEMP-R (Producer 1.2) for free length of the specimen equal to a) 6ϕ and b) 8ϕ and imposed deformation equal to ±2.5% and ±4.0%.

Specimen [-]	ϕ [mm]	L_0 [mm]	f [Hz]	Max ε [%]	Min ε [%]	Max σ [MPa]	Min σ [MPa]	Total dissipated energy [MPa]
B450C-16-TEMP-R Prod. 1(1)								
1	16	96	2	2,07%	-2,10%	616,66	-575,38	558,67
2	16	96	2	4,01%	-3,77%	631,22	-591,83	378,13
3	16	128	2	2,58%	-2,39%	572,16	-607,34	261,50
4	16	128	2	4,02%	-3,91%	613,85	-540,82	471,51
B450C-16-TEMP-R Prod. 1(2)								
1	16	96	2	2,23%	-2,18%	483,44	-508,73	516,86
2	16	96	2	4,01%	-3,80%	550,74	-483,86	726,01
3	16	128	2	2,51%	-2,43%	482,54	-508,39	353,75
4	16	128	2	4,01%	-3,93%	494,73	-477,06	230,29
B450C-16-TEMP-R Prod. 1.3								
1	16	96	2	2,19%	-2,10%	537,65	-557,82	532,15
2	16	96	2	4,03%	-3,76%	465,48	-515,36	550,99
3	16	128	2	2,51%	-2,37%	501,91	-550,97	291,96
4	16	128	2	4,50%	-3,92%	598,09	-491,88	380,03
B450C-16-TEMP-R Prod. 2								
1	16	96	2	2,51%	-2,26%	562,50	-560,12	477,75
2	16	96	2	2,51%	-2,41%	552,44	-555,05	329,95
3	16	128	2	4,10%	-3,81%	531,52	-502,24	316,67
4	16	128	2	4,11%	-3,92%	510,48	-471,70	224,46

Table 16: Maximum and minimum strain and deformation and total energy dissipated for B450C diameter 16 mm TempCore bars (producers 1.1, 1.2, 1.3 and 2).

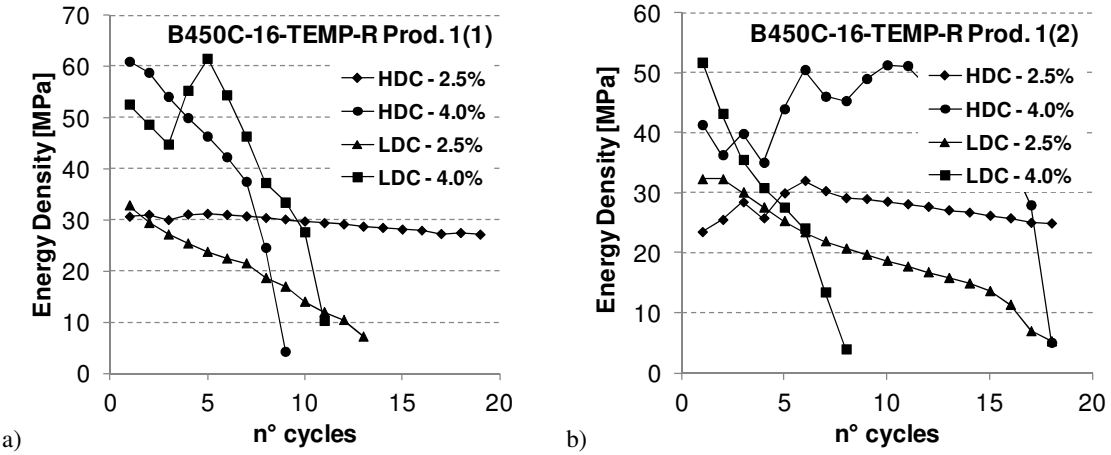


Figure 23: Dissipated energy density per cycle for bars B450C-16-TEMP: a) prod. 1.1, b) prod. 1.2.

All the LCF tests evidenced large buckling deformations of the specimens, independently from the test variables, i.e. type of bar and amplitude of the applied cycles. Buckling phenomena generally happened at the first cycle in compression, leading to values of the maximum strength at failure lower than the ones obtained from tensile tests. Moreover, the number of cycles up to failure generally decreased with the increase of the level of imposed deformation and of the free length of the specimen; as an example, for $L_0=6\phi$ and imposed strain equal to ±2.5% steel reinforcements were able to complete at least 18 cycles, independently from the diameter of the rebar and from the steel grade. The decrease of the

dissipated energy per cycle was, in general, quite uniform, even if some exceptions were individuated: as visible from figure 24, steel bars B450C (producer 2) exhibited a rapid decrease of dissipated energy after 15 cycles, differently from all the other considered specimens (different producer and plants).

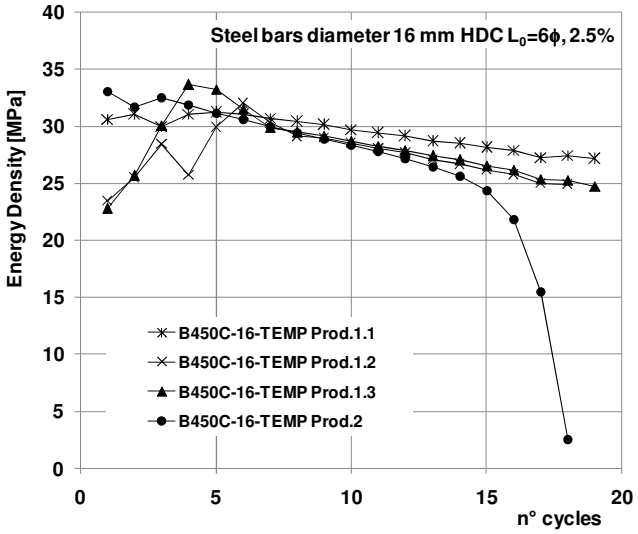


Figure 24: Dissipated energy per cycle for steel bars diameter 16 mm, $L_0 = 6\phi$ and ε equal to $\pm 2.5\%$.

7.3 Mechanical characterization of corroded steel bars

7.3.1 Elaboration of a protocol for accelerated corrosion tests

Recent studies in the current literature [20, 22] evidenced the progressive deterioration of the mechanical characteristics of steel reinforcing bars under aggressive environmental conditions. The effects of corrosion on the mechanical properties of bars were not usually taken into account since the presence of a correctly sized concrete cover, joined with ordinary external circumstances, is generally sufficient to guarantee the protection of reinforcing steel bars, providing a thin passive layer that covers the reinforcement avoiding the generation of rust. If the pH falls to values below 11 (in the case of degraded concrete the pH is close to 6.5), the passive layer starts to crack, becoming no more able to protect the spread of corrosion and leading to a decrease of the mechanical properties (strength and ductility) of bars. The effects of corrosion on steel reinforcing bars can be summarized in three main aspects:

- the reduction of the cross section of the bar (mass loss) with consequent decrease of the load carrying capacity, increasing with the duration of the exposure time;
- the cracking and spalling of concrete, leaving the reinforcements more exposed to buckling phenomena;
- the reduction of the ductility, expressed in terms of elongation to maximum load (A_{gt}).

In *Rusteel* project, a detailed investigation of the mechanical behaviour of corroded steel reinforcing bars was developed in order to individuate the effects of aggressive environmental conditions on both the tensile and the low-cycle fatigue mechanical properties.

A specific protocol for the execution of accelerated corrosion tests in salt-spray chamber was elaborated on the base of ISO 9227: the protocol foresees the execution of wet/dry cycles of 90 minutes (90 minutes dry, 90 minutes wet, resulting in 8 cycles/day) with a pH of the salt spray chamber between 5.5 and 6.2. Specimens of 500-600 mm length shall be opportunely prepared protecting them with a wax cover leaving free to corrode only a central part of about 20 mm (or the medium distance between subsequently ribs, Figure 25b-25c); the specimens

shall be positioned in salt spray chamber with a slope of 60° respect to the vertical walls of the chamber in order to prevent salt generation (figure 25a). After the end of the exposure period and before the execution of mechanical tests, steel corroded bars shall be maintained at a temperature lower than -5°, in order to kept inside the Hydrogen volatile part eventually developed during the salt-spray tests, that can lead to premature brittle failures of bars.

A reduced set of steel bars was selected to be subjected to corrosion for periods of 45 or 90 days of corrosion (table 17), and for the following execution of tensile and LCF tests. In the following, according to what already presented for uncorroded rebars, the results coming from steel reinforcements B450C, diameter 16 mm TempCore are presented.

ID	Quality	ϕ	Producer	Surface	Process	Salt-Spray chamber 45 days		Salt-Spray chamber 90 days	
-	-	-	-	-	-	N° Tensile tests	N° LCF tests	N° Tensile tests	N° LCF tests
1	B500B	16	2	Ribbed	TEMP	3	-	6	5*
2	B450C	16	2	Ribbed	TEMP	3	-	6	5*
3	B400C	16	2	Ribbed	TEMP	3	-	6	5*
4	B400C	16	1	Ribbed	MA	3	-	3*	5*
5	B500A	12	1	Ribbed	CW	3	-	3*	5*
6	B500B	25	1	Ribbed	TEMP	3	-	3*	5*
7	B500B	12	2	Ribbed	STR	-	-	3*	5*
8	B400C	25	1	Ribbed	MA	3	-	3*	5*
9	B450C	12	2	Ribbed	STR	-	-	3*	5*
10	B450C	25	1	Ribbed	TEMP	3	-	3*	5*

Table 17: Steel bars selected for salt-spray chamber tests and tests foreseen.

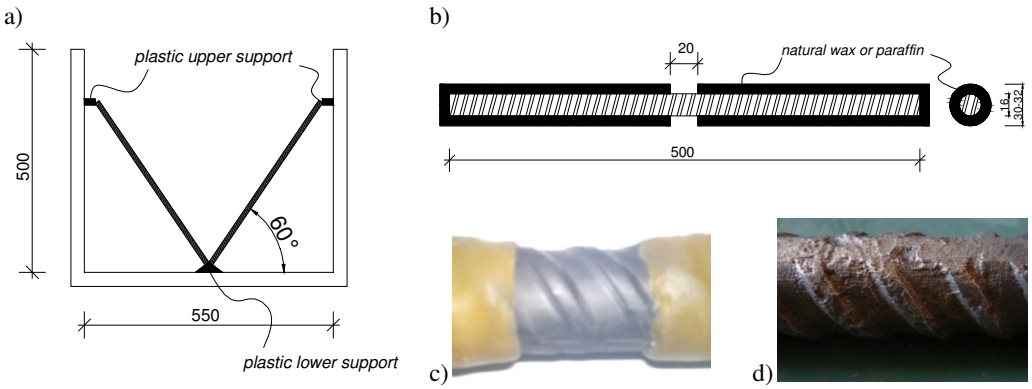


Figure 25: a) Disposition of bars in salt-spray chamber, b-c) protection of rebar with paraffin or wax, d) one specimen after 90 days in salt-spray chamber.

7.3.2 Results of tensile tests on corroded specimens

The results obtained from uncorroded and corroded specimens B450C diameter 16 mm (TempCore) after 45 and 90 days of exposure in salt spray chamber are presented and compared. Figure 26 shows the comparison between the stress-strain curves obtained from tensile tests on corroded and uncorroded specimens, while the values of yielding and tensile strength, A_{gt} and total elongation in corroded and uncorroded specimens are respectively presented in tables 18 and 19.

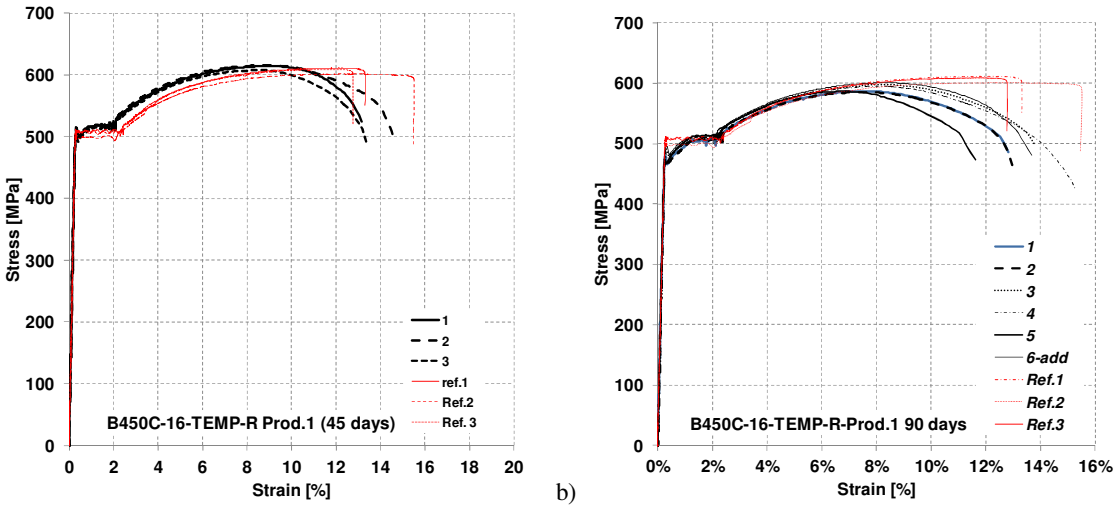


Figure 26: Stress-Strain diagrams for bars B450C-16-TEMP-R (prod. 1): a) 45 days of corrosion, b) 90 days.

Steel grade/diameter/ process/rib/producer	T_{corr} [days]	L_{corr} [mm]	ΔM [g]	$\Delta M/M_{uncorr}$ [%]	R_e [MPa]	R_m [MPa]	R_m/R_e [-]	A_{gt} [%]	A_5 [%]	Lab
B450C-16-TEMP-Prod.1-1	90	20,90	4,91	14,57	481,4	599,5	1,25	4,3	15,4	Lab. 1
B450C-16-TEMP-Prod.1-2	90	26,40	2,59	6,08	484,4	598,0	1,23	4,4	15,6	Lab. 1
B450C-16-TEMP-Prod.1-3	90	27,20	3,83	8,74	499,8	610,5	1,22	5,1	16,6	Lab. 1
B450C-16-TEMP-Prod.1-4	90	28,85	3,20	6,87	497,4	607,9	1,22	5,7	17,8	Lab. 1
B450C-16-TEMP-Prod.1-5	90	24,20	3,25	8,32	480,9	600,0	1,25	4,1	14,1	Lab. 1
B450C-16-TEMP-Prod.1-6	90	24,50	6,82	17,26	502,8	613,8	1,22	5,5	16,3	Lab. 1
B450C-16-TEMP-Prod.1-1	45	30,50	3,87	7,87	509,2	614,3	1,21	6,9	16,4	Lab. 1
B450C-16-TEMP-Prod.1-2	45	29,50	3,54	7,44	511,2	615,9	1,20	6,2	16,9	Lab. 1
B450C-16-TEMP-Prod.1-3	45	28,80	5,18	11,15	504,3	607,9	1,21	5,7	16,4	Lab. 1

Table 18: Experimental tensile tests on corroded specimens B450C TempCore, 16 mm (Prod. 1)

Steel grade/diameter/ process/rib/producer	Spec. [n°]	D [mm]	A [mm^2]	R_e [MPa]	R_m [MPa]	R_m/R_e [-]	A_{gt} [%]	A_5 [%]
B450C-16-TEMP-R Prod. 1	1	16,16	205,00	517,78	615,41	1,19	13,76	25,38
	2	16,18	205,71	507,42	610,42	1,20	14,96	25,13
	3	16,18	205,59	516,30	613,65	1,19	11,96	-

Table 19: Experimental tensile tests on uncorroded specimens B450C TempCore, 16 mm (Prod. 1)

As visible from table 18, results are presented in terms of mass loss, opportunely evaluated referring to the exposed length of the bar; the most significant results are the ones related to A_{gt}, that passed from a mean value of about 12% of uncorroded specimens, to values variable between 4.1% and 6.9% in relation to the exposure period (90 or 45 days). Deterioration of the mechanical characteristics in terms of yielding and tensile strength were also revealed, even if less significant.

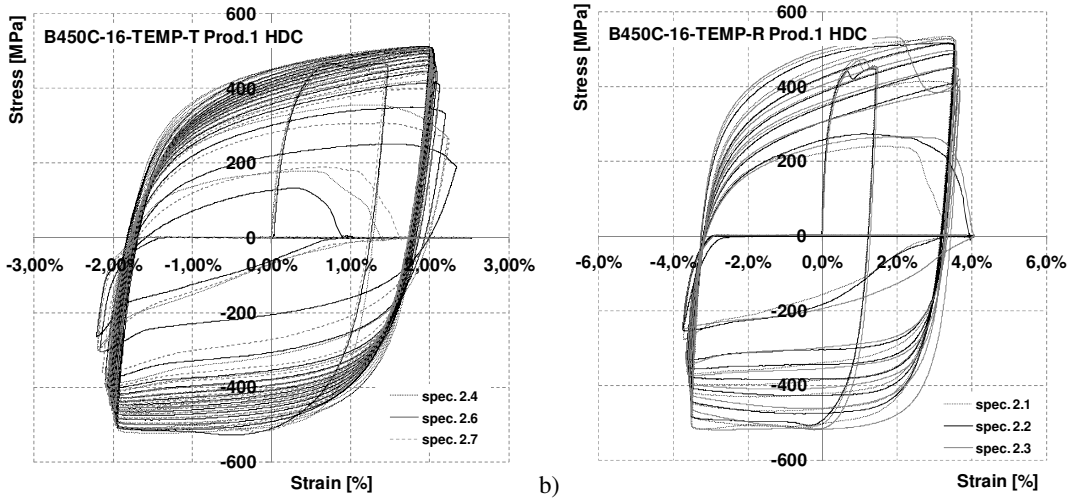
7.3.3 Results of LCF tests on corroded specimens

Results of low-cycle fatigue tests executed on corroded specimens B450C, diameter 16 mm, TempCore process following the protocol previously presented are reported in the Figures 27 and 28 in terms of stress strain curves. In general three different specimens were tested for each level of imposed deformation and free length of the specimens, in order to

obtained significant data also in relation to different mass loss.

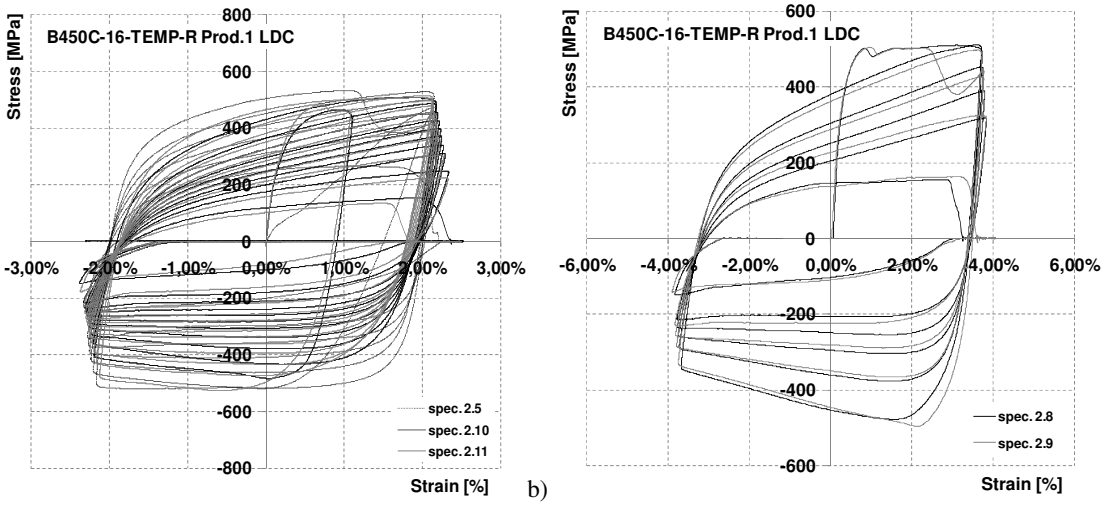
Moreover, table 20 shows the values of mass loss for each corroded specimen, the main testing specifications adopted and the total dissipated energy density obtained. In the figures 29 and 30 the dissipated energy per cycle is presented comparing the results obtained from corroded and uncorroded specimens, in all the different testing conditions considered. As visible, the behaviour of uncorroded specimens is more stable than the one associated to corroded bars: for example, in the case of $L_0=6\phi$ and ±2.5% of imposed strain, the total dissipated energy varied between 535 MPa (uncorroded specimen) and 370 MPa (corroded specimens), with a more sudden collapse in these last cases and number of cycles up to failure dropping from 19 to 15. Similar considerations can be executed also for $L_0=6\phi$ and ±4.0%, with total dissipated energy equal to 550 MPa for the uncorroded bars and around 300 MPa for corroded ones, with number of cycles up to failure dropping from 15 to 7.

Similar considerations can be executed also in the case of LDC ($L_0=8\phi$): for imposed strain equal to ±2.5% the total dissipated energy dropped from 290 MPa to 250 MPa (mean value), while for imposed strain equal to ±4.0% the difference was between 380 MPa and 250 MPa.



a) b)

Figure 27: Steel bars B450C-16-TEMP-R (prod. 1) after 90 days and $L_0=6\phi$, for : a) ε = ±2.5% and b) ε = ±4.0%.



a) b)

Figure 28: Steel bars B450C-16-TEMP-R (prod. 1) after 90 days and $L_0=8\phi$, for : a) ε = ±2.5% and b) ε = ±4.0%.

B450C-16 -TEMP Prod. 1 90 days (Laboratory 2)									
ID	M_{uncorr} [g]	L [mm]	M_{corr} [g]	L_{corr} [mm]	ΔM [g]	$\Delta M/M_{uncorr}$ [%]	L_0 [mm]	$\Delta\varepsilon$ [%]	Dissipated Energy [MPa]
2.4	808,42	501,00	805,96	19,90	2,46	7,66%	96	±2.5%	371,28
2.6	805,92	500,00	802,48	22,65	3,44	9,43%	96	±2.5%	370,80
2.7	810,25	501,00	808,04	18,60	2,21	7,33%	96	±2.5%	377,30
2.1	809,35	500,00	806,75	20,75	2,60	7,74%	96	±4.0%	307,28
2.2	810,34	501,00	806,89	22,40	3,45	9,53%	96	±4.0%	291,32
2.3	806,88	500,00	804,18	21,15	2,70	7,91%	96	±4.0%	306,62
2.5	810,50	500,00	807,69	21,20	2,81	8,18%	128	±2.5%	213,59
2.10	808,78	501,00	804,68	27,10	4,10	9,36%	128	±2.5%	215,10
2.11	808,11	501,00	804,58	23,83	3,53	9,18%	128	±2.5%	273,49
2.8	806,38	500,00	803,71	23,90	2,67	6,92%	128	±4.0%	206,68
2.9	809,54	501,00	807,39	20,55	2,15	6,49%	128	±4.0%	172,60

Table 20: Characteristic of corroded steel reinforcing bars B450C, 16 mm, TempCore and testing specifications.

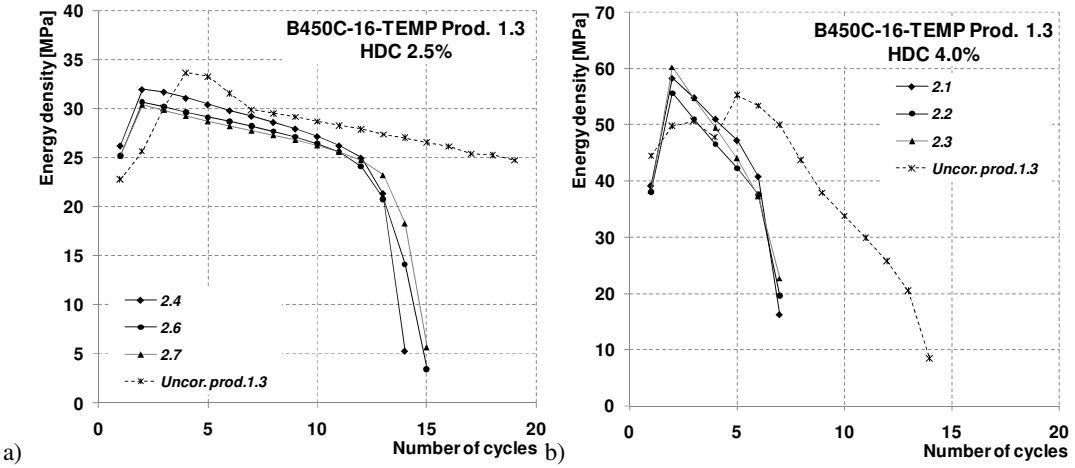


Figure 29: Comparison between corroded and uncorroded specimens B450C, diameter 16 mm (TempCore) in terms of dissipated energy per cycle: a) HDC and imposed deformation ±2.5% and b) HDC and ±4.0%.

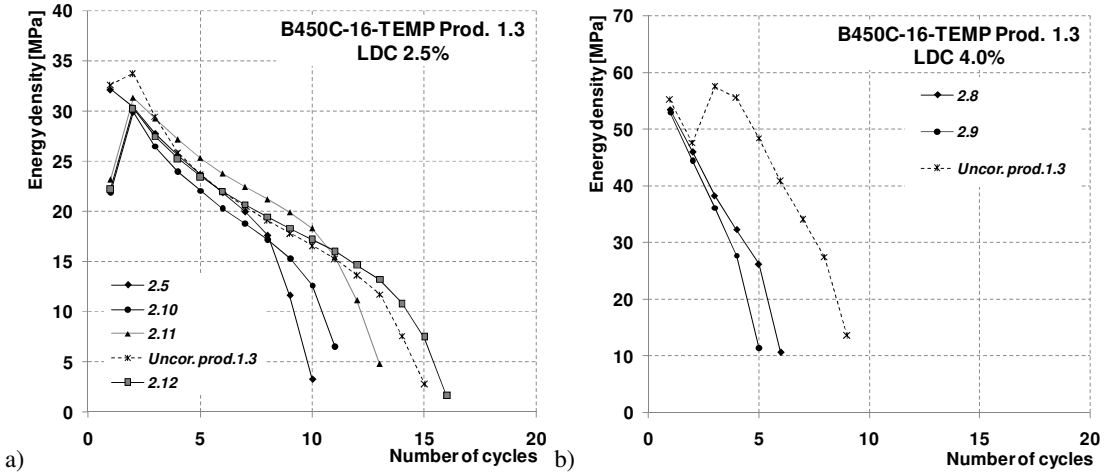


Figure 30: Comparison between corroded and uncorroded specimens B450C, diameter 16 mm (TempCore) in terms of dissipated energy per cycle: a) LDC and imposed deformation ±2.5% and b) LDC and ±4.0%.

8 CONCLUSIONS

In the present paper a specific procedure for the evaluation of the effective ductility demand on steel reinforcing bars in modern r.c. buildings was presented and applied to a set of significant case studies. Moreover, a detailed experimental test campaign was executed aiming at the complete mechanical characterization of the monotonic and cyclic behaviour of actual European steel reinforcing bars, both in uncorroded and in corroded conditions.

The effective levels of deformations induced by seismic events on bars were evaluated through the execution of Incremental Dynamic Analyses on a set of representative r.c. buildings opportunely designed according to the actual European and Italian prescriptions [1, 2], using the hardening slip model [27, 28] for steel reinforcing bars embedded in the concrete, able to include relative slips between steel bars and concrete and to fully characterize their cyclic behaviour.

IDAs were executed on the bi-dimensional fiber models of r.c. case studies opportunely elaborated using OpenSees software; specific natural time histories, selected to maximize the seismic requirements in terms of both energy dissipation and deformation, were used. The global seismic assessment of buildings, following the indications of actual design standards, evidenced a different behaviour between buildings designed in HDC or LDC, with the activation of brittle shear mechanisms in beams and columns of the 1st floor for levels of p.g.a. more or less equal to the one adopted in the design in the case of LDC. Moreover, despite what imposed during the design process according to the capacity design approach, the global assessment of the structures evidenced that beams and columns of the highest floors of the buildings (4th and 5th levels) were usually not directly involved in the global collapse mechanisms, since in general plastic hinges developed for very high values of the PGA (higher than 0.40-0.45g).

The investigation of the local ductile behaviour of steel reinforcing bars allowed, moreover, the individuation of the effective levels of deformation and energy dissipation due to real seismic action. The accurate analysis of numerical simulations' results evidenced two main general stress-strain conditions in steel reinforcing bars, in relation to both the level of axial deformation and the dissipated energy density. The first condition, well evidenced in the Figure 34, was typical of those elements, generally beams but in some cases also columns, in which the level of imposed deformation due to earthquakes was usually very high, around 8%, while the corresponding density of dissipated energy generally did not overpass 40-50 MPa, since the external axial load generally did not generate complete reversed cycles of tension/compression stresses and strains, with following very low values of deformation in compression (not higher than -1%). As an example, figure 31 shows the stress-strain curves obtained from steel reinforcing bars in column n°118 and in beam n°1017 (figure 15) in office building under, respectively, Erzincan and Montenegro time histories; the maximum level of strain in tension was equal to 8.86% and 6.57% and the corresponding dissipated energy was equal to 33.6 MPa and 46.9 MPa.

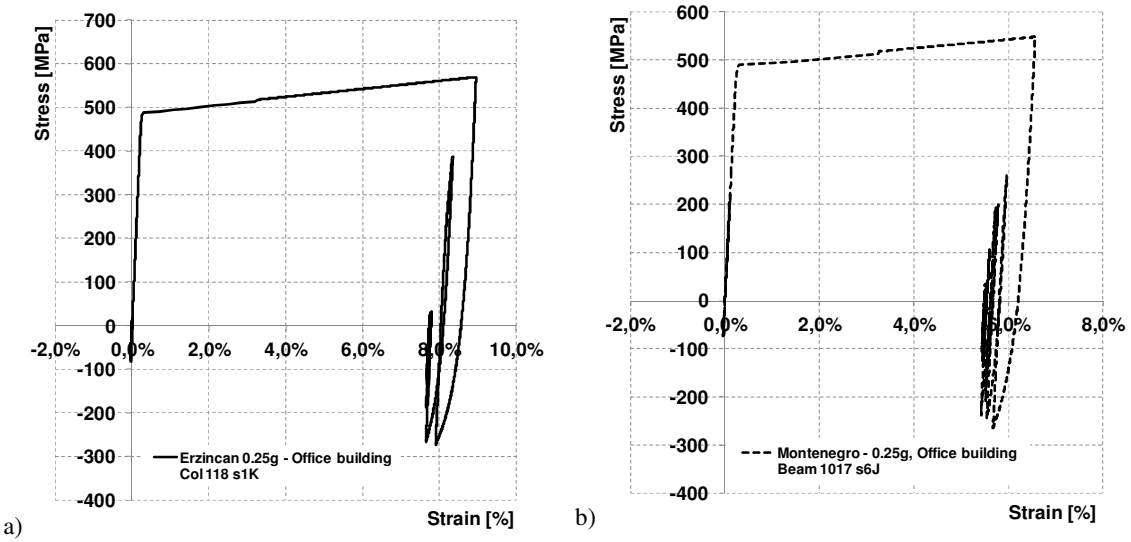


Figure 31: Stress-strain histories on bars characterized by mainly tension or compression.

The second condition, represented in the figure 32, at the opposite, was typical of those elements in which the seismic input was able to generate on steel reinforcing bars complete reversed tension/compression cycles; as a consequence, high absolute values of strain both in tension and in compression were reached (with mean values around 6% and -4%) and also the density of dissipated energy increased with respect to the other condition, with values up to 120 MPa. As an example, in the figure 32 the stress-strain curves obtained from steel reinforcing bars in columns n°101 and n°118 in office building under, respectively, Erzincan and Campano Lucano time histories; the maximum level of strain in tension was equal to 6.04% and 4.02% and the ones in compression were equal to -4.0%, while the corresponding dissipated energy generally varied between 90 and 120 MPa.

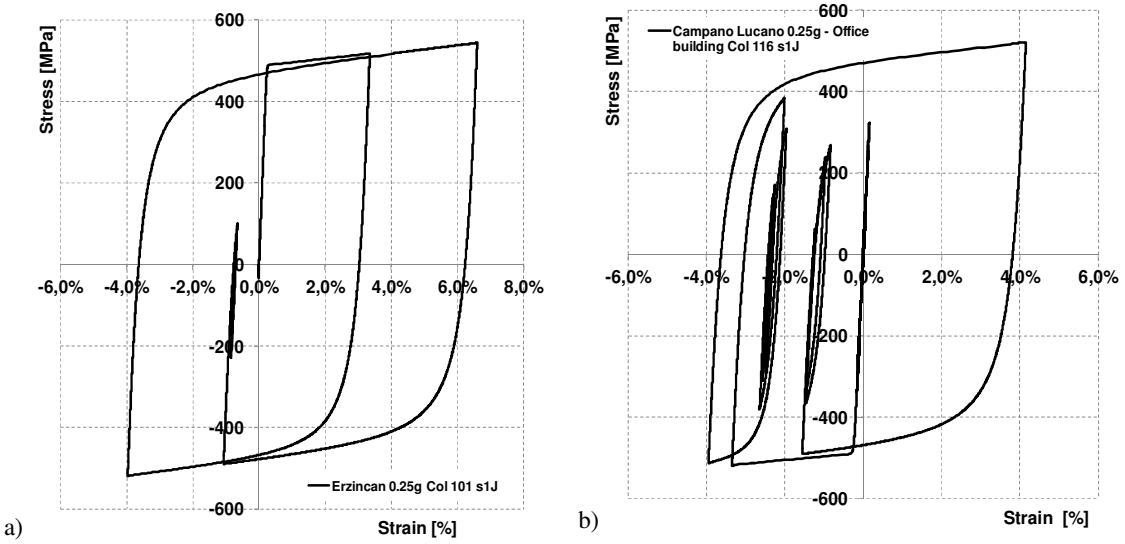


Figure 32: Stress-strain histories on bars subjected to complete reversed tension/compression cycles.

It's important to underline that, according to the numerical results obtained, natural time histories generated only one or two complete tension/compression cycles in steel reinforcing bars confirming, at the same time, the assumptions used for the calibration of the mechanical

model of the bar.

At the same time, for what concerns the evaluation of the mechanical capacity of steel reinforcing bars, experimental tensile and low-cycle fatigue tests were executed on a set of steel reinforcing bars representative of the actual European production. Tensile tests followed the prescriptions of EN 15630-1:2010 [35] while for LCF tests a new protocol was elaborated, taking into account what actually presented in literature and in the current standards (Spanish and Portuguese codes). Moreover, the effects of corrosion phenomena on the mechanical properties of steel reinforcing bars were evaluated: accelerated corrosion tests in salt spray chamber were executed on a reduced set of reinforcing steels considering two different exposure periods (45 and 90 days). Tensile and low-cycle fatigue were consequently executed on corroded specimens.

The results of tensile tests on corroded bars evidenced a strong reduction of the ductile capacity of steel bars, mainly in terms of A_{gt}, that for reinforcements B450C, diameter 16 mm (TempCore process) in some cases dropped from an initial mean value of 12% to values around 4-6%, for an average mass loss between 16 and 20%. Results similar to the ones obtained for B450C were individuated for all TempCore steel bars, while in general, Micro Alloyed steel showed a lower decrease of A_{gt} and higher reference values.

Looking at the low-cycle fatigue behaviour of corroded steel reinforcements, corroded steel reinforcing bars B450C diameter 16 mm evidenced a strong reduction of the total dissipated energy density with respect to the uncorroded condition, both considering a free length equal to six or eight diameters and for imposed deformation equal to ±2.5% or ±4.0%.

Despite the reduction of the dissipated energy density, comparing the results obtained from IDAs the maximum dissipated energy obtained in steel reinforcing bars of beams and columns of the designed r.c. buildings was equal to 121 MPa, and consequently also corroded rebars are able to satisfy the energy requirements due to seismic action. On the other hand, the worst problem consists in the strong reduction of the A_{gt}, reaching values lower than the maximum strain obtained from numerical simulations, in some cases around 8.0% (figure 33).

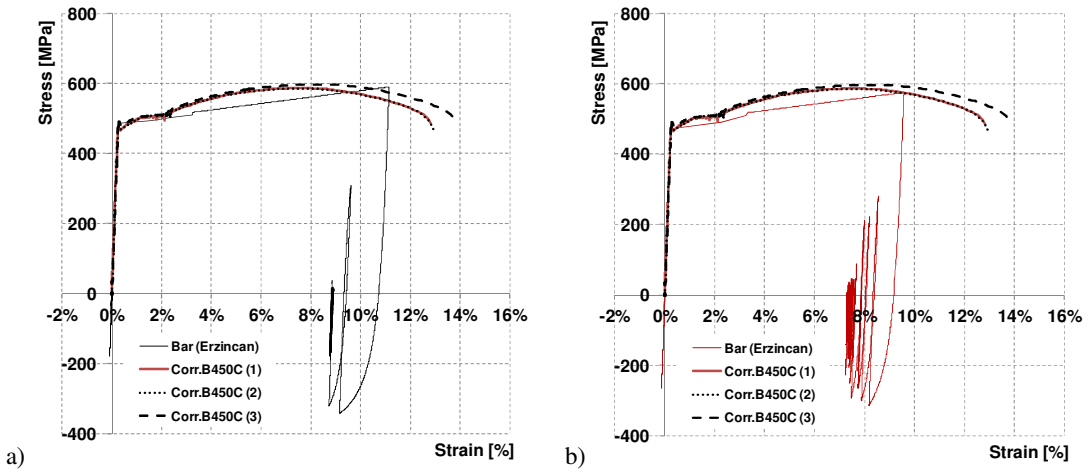


Figure 33: Comparison between the ductility demand imposed by Erzincan time history on a) 1st floor column's bar and b) beam's 1st floor bar and monotonic behaviour of corroded steel reinforcements (bar B450C, 16 mm).

As an example, the results of the Incremental Dynamic Analyses showed that the level of strain due to real seismic inputs in some cases reached maximum values around 8.8%, while usually, the 6-7% of deformation was overpassed. Moreover, in many cases, bars were subjected to a complete reversed tension/compression cycle with imposed strain equal, for example, to +6.30% - 4.25%. The behaviour of corroded bars (in this case steel grade B450C,

diameter 16 mm) is compared with the results of analysis for steel reinforcements in one column or in one beam of the first floor; the maximum strains imposed by seismic event were respectively equal to about 11% and 9%, while the average A_{gt} of corroded bars varied between 4.3% and 5.7% (manually measured values). Obviously, corroded bars also presented a residual deformation capacity, as presented in the figures 33, leading to values of the total elongation varying between 14% and 16%.

REFERENCES

[1] UNI EN 1998-1:2005, Eurocode 8 - Design of structures for earthquake resistance - Part 1: General rules, seismic actions and rules for buildings, 2005

[2] D. M. Infrastrutture Trasporti 14 gennaio 2008, Norme Tecniche per le Costruzioni NTC 2008.

[3] FEMA 356 (2000). Pre-standard and Commentary for the Seismic Rehabilitation of Buildings, Federal Emergency Management Agency, Washington DC.

[4] A. Teran-Gilmore, O. Jirsa, Energy demands for seismic design against low-cycle fatigue. *Earthquake engineering and structural dynamics,* **36**, 383-404, 2007.

[5] T. Paulay, M.J.N. Priestley, *Seismic design of reinforced concrete and masonry structures*, John Wiley and Sons, 1992.

[6] S.K. Kunnath, Q. Hu, Evaluation of cyclic demand in ductile RC structures. *13th World Conference on Earthquake Engineering*, Vancouver, Canada, August 1-6, 2004.

[7] G. Manfredi, M. Polese, E. Cosenza, Cumulative demand of the earthquake ground motions in the near source. *Earthquake engineering and structural dynamics*, **32**, 1853-1865, 2003.

[8] G. Manfredi, Evaluation of seismic energy demand. *Earthquake engineering and structural dynamics*, **30**, 485-499, 2001.

[9] S.K. Kunnath, Y.H. Chai, Cumulative damage-based inelastic cyclic demand spectrum. *Earthquake engineering and structural dynamics*, **33**, 499-520, 2004.

[10] S. Pampanin, G.M. Calvi, M. Moratti, Seismic behavior of R.C. beam-column joints designed for gravity loads. *12th European Conference on Earthquake Engineering*, London, UK, September 9-13, 2002.

[11] C. Fernandes, J. Melo, H. Rodrigues, A. Costa, H. Varum, A. Arede, Cyclic behaviour analysis of RC elements with plain reinforcing bars. *14th European Conference on Earthquake Engineering*, Ohrid, Macedonia 30 August – 03 September, 2010.

[12] G.M. Calvi, G. Magenes, S. Pampanin, Experimental test on a three storey r.c. frame designed for gravity only. *12th European Conference on Earthquake Engineering*, London, UK, September 9-13, 2002.

[13] A.C. Barrera, J.L. Bonet, M.L. Romero, P.F. Miguel, Experimental tests of slender reinforced concrete columns under combined axial load and lateral force. *Engineering Structures*, **33**(12), 3676–3689, 2011.

[14] EN 10080:2005, Steel for the reinforcement of concrete - Weldable reinforcing steel – General, European Committee for Standardization – CEN, 2005.

[15] UNE 36065 EX:2000, Norma Espanõla Experimental 2000 – Barras corrugadas de acero soldable con caracteristìcas especiales de ductilidad para armaduras de horigòn armado, 2000.

[16] LNEC E455-2008 – Varoes de aço A400 NR de ductilidade especial para armaduras de betão armado: caracteristìcas, ensaios e marcação, 2008.

[17] J.B. Mander, F.D. Panthaki, A. Kasalanati, Low-cycle fatigue behaviour of reinforcing steel. *Journal of Materials in Civil Engineering,* **6**(4), 453-468, 1994.

[18] J. Brown, SK. Kunnath, Low-Cycle Fatigue Failure of Reinforcing Steel Bars. *ACI Materials Journal*, **101**(6), 457-466, 2004.

[19] P. Crespi, Monotonic and cyclic behaviour of rebars in the plastic hinge of r.c. beams. PhD Thesis, 2002.

[20] C.A. Apostolopoulos, Mechanical behavior of corroded reinforcing steel bars S500s tempcore under low cycle fatigue. *Construction and Building Materials*, **21**, 1447–1456, 2006.

[21] UNI EN 1992-1-1:2005, Eurocode 2 (Annex C) - Design of concrete structures - Part 1-1: General rules and rules for buildings, 2005.

[22] C.A. Apostolopoulos, C. Ascanio, L. Bianco, A. Braconi, S. Caprili, G. Diamantogiannis, G. Ferreira Pimenta, M. Finetto, J. Moersch, W. Salvatore, Effects of corrosion on low-cycle fatigue (seismic) behaviour of high strength steel reinforcing bars. RFSR-CT-2009-00023 project. Final report, European Commission, Brussels, 2013.

[23] Mazzoni S, McKenna F, Scott MH, Fenves GL et al. (2007) OpenSees Command Language Manual, University of California, Berkley, USA.

[24] V. Ciampi, R. Eligenhausen, E.P. Popov, V.V. Bertero, Analytical Model tor Deformed Bar Bond under Generalized Excitations. Report EERC 82-23, Earthquake Engineering Research Center, University of California, Berkley, 1993.

[25] F. Braga, R. Gigliotti, M. Laterza, M. D'Amato, S. Kunnath, Modified Steel Bar Model Incorporating Bond-Slip for Seismic Assessment of Concrete Structures. *Journal of Structural Engineering*, **138**, 1342-1350, 2012.

[26] S. Hakuto, R. Park, H. Tanaka, Effect of deterioration of bond of beam bars passing through interior beam-column joints on flexural strenght and ductility. *ACI Structural Journal*, **96**(S94), 858-864, 1999.

[27] S. Caprili, Analysis of the low-cycle fatigue behaviour and corrosion phenomena on reinforcing bars of concrete structures in earthquake prone areas. PhD Thesis, University of Pisa, 2012.

[28] A. Braconi, F. Braga, S. Caprili, R. Gigliotti, W. Salvatore, Influence of low-cycle fatigue and corrosion phenomena on the structural behaviour of steel reinforcing bars. *15th World Conference on Earthquake Engineering*, Lisbon, Portugal, September 24-28, 2012.

[29] T.B. Panagiotakos, M.N. Fardis, Deformations of Reinforced Concrete Members at Yielding and Ultimate. *ACI Structural Journal*, **98**(2),135-148, 2001.

[30] F. Braga, R. Gigliotti, M. Laterza, Analytical Stress–Strain Relationship for Concrete Confined by Steel Stirrups and/or FRP Jackets. *Journal of Structural Engineering*, **132**, 1402-1416, 2006.

[31] CEB-FIP Model Code 1990 Design Code (1993), Comitè Euro-International du Beton.

[32] M. D'Amato, F. Braga, R. Gigliotti, M. Laterza, S. Kunnath, Validation of a Modified Steel Bar Model Incorporating Bond-Slip for Seismic Assessment of Concrete Structures. *Journal of Structural Engineering*, **138**, 1351-1360, 2012.

[33] A. Braconi, F. Braga, S. Caprili, R. Gigliotti, W. Salvatore, Seismic demand on steel reinforcing bars in reinforced concrete frame structures. Bulletin of Earthquake Engineering, under review, 2013.

[34] UNI EN 1998-3:2005, Eurocode 8 - Eurocode 8 - Design of structures for earthquake resistance - Part 3: Assessment and retrofitting of buildings, 2005.

[35] EN ISO 15630-1:2010, Steel for the reinforcement and prestressing of concrete - Test methods - Part 1: Reinforcing bars, wire rod and wire, 2010.

COMPDYN 2013
4th ECCOMAS Thematic Conference on
Computational Methods in Structural Dynamics and Earthquake Engineering
M. Papadrakakis, V. Papadopoulos, V. Plevris (eds.)
Kos Island, Greece, 12–14June 2013

STRUCTURAL ANALYSIS OF MULTISTORY BUILDING USING COUPLED BEM-STIFFNESS MATRIX

RAMIZ W. MOHAREB[1], YOUSSEF F. RASHED[1]*, MINA WAGDY[2], MOSTAFA E. MOBASHER[1,3]

1 Dept. of Structural Engineering, Cairo University, Giza, Egypt.

enramiz@yahoo.com, youssef@eng.cu.edu.eg

2 Dar Al-handasah consultant, department of structures, Dokki, Giza, Egypt.

mina.wagdy@dargroup.com

3 Civil Engineering Department, British University in Egypt, Sherouk, Egypt.

mostafa.mobasher@bue.edu.eg

Keywords: Boundary element method, multi-storey building, lateral analysis, matrix analysis.

Abstract. *This paper presents a structural analysis scheme for multistory buildings. In this analysis the boundary element method (BEM) is used to derive the stiffness. Such a matrix is coupled with the vertical skeletal elements using the traditional assembly procedures. Nodal displacements and end-forces are then computed, hence, post-processing is done for frame and floor elements. The results are compared against results of traditional finite element analysis.*

1 INTRODUCTION

Over the past decades, high-rise buildings became a part of the daily structural engineering practice. In high-rise buildings, the effects of lateral loads e.g seismic and wind loads are critical; they have to be considered in the structural analysis process.

Several methods were implemented to perform structural analysis of structures due to lateral loading. Initially, the simple structural geometry allowed simple manual calculations to provide a good enough solution [1]. The traditional Moment Distribution method and Matrix Analysis of structures were applied to regular framed structures. Many researches contributed to the techniques of modeling the irregular vertical elements (shear walls and cores). Some efforts presented analytical solutions via presenting a solution to partial differential equations [2]. Other solutions were based on numerical modeling of walls.

The increasing complexity of the geometries increased the difficulty of the implementation of manual calculations leading to a need for more flexible numerical techniques. Hence, the finite element method [3] started to present itself as a convenient solution for structural analysis problems. The flexibility of the finite element method allows the modeling of any floor shape, hence, get its stiffness matrix. A typical finite element model of a structure gets the stiffness of the floor as a two-dimensional element, either shell or plate, and assembles it with stiffness matrix of vertical elements modeled as one-dimensional element.

The finite element modeling of structures passed through many development stages. Works in [2-5] presented improved and more efficient modeling schemes to deal with tall structures containing coupled shear walls and cores. Improvements included reduction in computational effort and reduced numerical errors. Other models were concerned with the modeling of coupling beams as continuous connections; this is based on the high in-plane stiffness of horizontal floors. The impacts of the variations of the walls' cross-sections along the building's height were considered in [6-13].

In this paper a new scheme for the lateral analysis of structures is presented. The scheme is based on computerized matrix analysis of structures. The floor stiffness matrix is derived from a boundary element formulation; the floor stiffness matrix is condensed at the frame nodes. The stiffness matrices of columns are computed as one dimensional element. The stiffness matrices of complex wall shapes are computed as one dimensional element, however, the twisting behavior is included via adding warping degrees of freedom. The boundary element model of plates and the boundary element computation of warping functions for frames are reviewed. The computation of stiffness matrices and solution of equations is explained. Numerical examples are provided to illustrate the validity and efficiency of the proposed analysis scheme.

2 BEM APPLIED

This section reviews the boundary elements mathematical models that are utilized in the proposed analysis scheme. The first section, Section 2.1, reviews the boundary element analysis model for shear deformable plates. This model is the basis for the derivation of the plate stiffness matrix presented in Section 3. The second section,

Section 2.2, reviews the boundary element model implemented to calculate the warping functions and its derivatives for vertical supporting element cross sections. These values are required in the computation of the stiffness matrices of vertical elements presented in Section 4.

2.1 BEM for Plates

The problem of flat plates rested on column was studied by Rashed [14]. His work was done using the shear deformable thick plate theory. Columns or internal walls are modeled using internal supporting cells with the real geometry of the cross section. Three generalized forces are considered at each internal support: two bending moments in two directions as well as shear force in the vertical direction. These generalized forces are considered to vary constantly over the column cross-section.

The work presented herein uses the shear deformable plate bending theory according to Reissner's[15,16].In this section a review of this theory is outlined. Greek indices vary from 1 to 2 whereas; Roman indices vary from 1 to 3. The comma subscript is used to denote differentiation.

Consider a typical flat slab as in Figure 2.1, the boundary integral equation may be written as follows:

$$C_{ij}(\xi)u_j(\xi) + \int_{\Gamma(y)} T_{ij}(y,\xi)u_j(y)\,d\Gamma(y) = \int_{\Gamma(y)} U_{ij}(y,\xi)t_j(y)\,d\Gamma(y)$$
$$+ \sum_c \{ \int_{\Omega_c(c)} [U_{ik}(\xi,c) - \frac{\nu}{(1-\nu)\lambda^2} U_{i\alpha,\alpha}(\xi,c)\delta_{3k}]F_k(c)d\Omega_c(c)\} \quad (1)$$

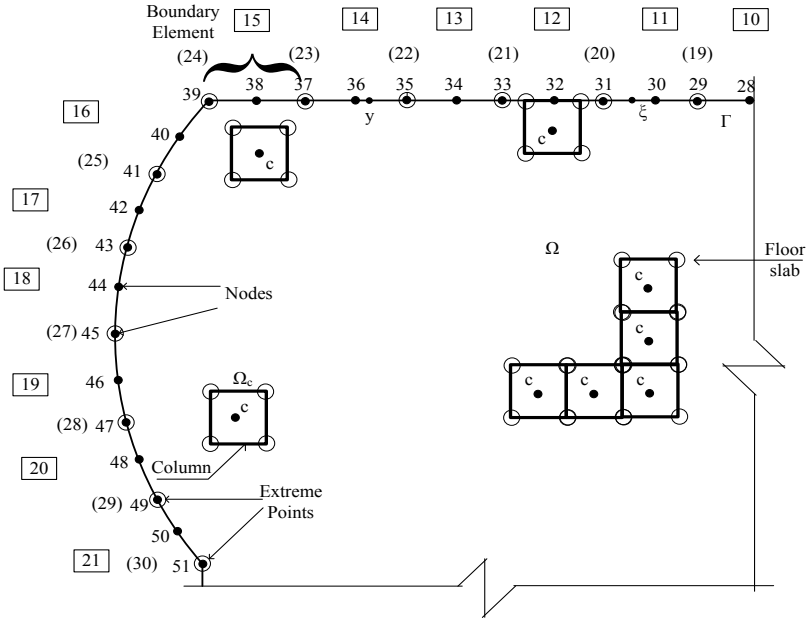


Figure 2.1: Geometry and boundary element discretization for a typical flat slab.

In which $U^*_{ij}(\xi, y)$ denotes a two-point kernel which represents the value of the generalized displacement in the j direction at a field point (y) due to a unit pulse (load) in

the *i* direction located at a source point ξ_k .The boundary traction fundamental solution $T_{ij}^{*}(\xi, y)$ .The column reactions are denoted by $F_k(c)$.

Equation (1) represents 3 equations in 6 unknowns. In order to solve the previous problem, a collocation scheme is carried out at each internal column center. This equation is as follows Rashed [14]:

$$u_i(c) + \int_{\Gamma} T_{ij}(c, y) u_j(\mathrm{y}) d\Gamma(\mathrm{y}) = \int_{\Gamma} U_{ij}(c, y) t_j(\mathrm{y}) d\Gamma(\mathrm{y})$$

$$+ \sum_{c} \left\{ \int_{\Omega_c(c)} [U_{ik}(\xi, c) - \frac{\nu}{(1-\nu)\lambda^2} U_{i\alpha,\alpha}(\xi, c)\delta_{3k}] F_k(c) d\Omega_c(c) \right\}$$

$$\times \left[\frac{-u_k(c) S_k(c)}{A(c)} \right] \qquad (2)$$

Where: c is a new source point located at each column center. This final equation provides additional three equations. Solving eq. (1) together with eq. (2), the values of the unknown boundary generalized tractions and displacement together with the column internal generalized displacement and tractions can be determined.

2.2 BEM for warping

In this section torsion analysis of sections is reviewed. Warping effects must be considered at designing core elements. Vlasov [17] was one of the leading developers of theory for warping torsion. The equations devised in [17] are used herein.
Consider an arbitrary cross-section twisted by moments Mt applied at its ends as shown in Figure 2-2. This torsion moment is considered constant over the length of the element. Saint venant torsion **Error! Reference source not found.**18] assumed, at any point A(x1, x2, x3), the displacements *u1* and *u 2*.

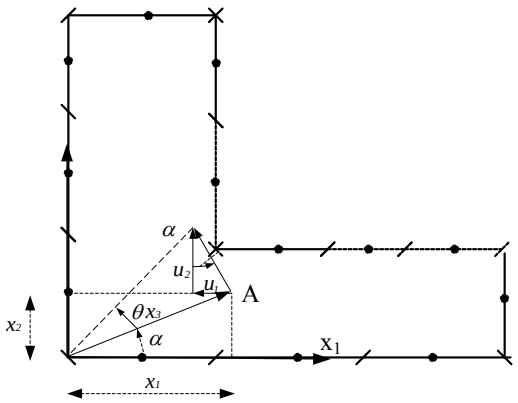


Figure 2-2 Displacement components in a cross-section of a twisted bar.

In order to obtain the boundary integral of the problem, any standard procedure such as suitable integral identity can be used. The final equation can take the form:

$$\phi(\xi) + \int_{\Gamma} \frac{\partial u^*}{\partial n_q} \phi(\mathrm{y}) d\Gamma = \int_{\Gamma} U^*(\xi, \mathrm{y}) \frac{\partial \phi}{\partial n} d\Gamma \tag{3}$$

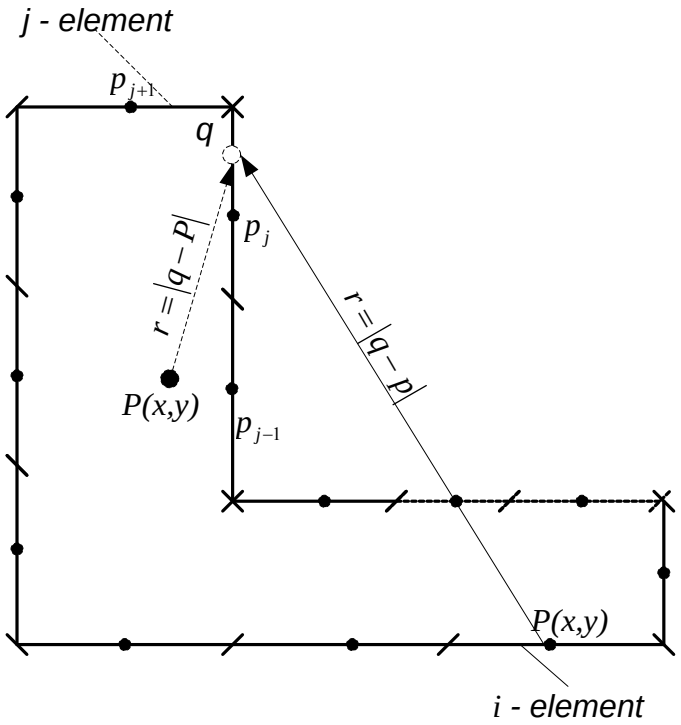


Figure 2-3 Nodal-point location and relative distances for constant element discretization.

The domain integral is transformed to the boundary integral form as follow:

$$\frac{1}{2}\phi(\xi) = -\int_{\Gamma} \left[U^*(\xi, \mathrm{y}) - u(\xi) \frac{\partial U^*(\xi, \mathrm{y})}{\partial n_q} \right] ds_q \tag{4}$$

The boundary Γ is discretized into N constant elements. The values of the boundary quantity ϕ and its normal derivative $\partial\phi/\partial n$ are assumed constant over each element and equal to their value at the mid-point of the element.

The discretized form of eq. (4) is expressed for a given point p, on Γ as

$$\frac{1}{2}\phi^i(\xi) = -\sum_{j=1}^{N} \int_{\Gamma} U^*(\xi, \mathrm{y}) \frac{\partial U^*(y)}{\partial n_q} ds_q + \sum_{j=1}^{N} \int_{\Gamma} u(y) \frac{\partial U^*(\xi, \mathrm{y})}{\partial n_q} ds_q \tag{5}$$

Where: Γ is the segment (straight line) on which the j-th node is located and over which integration is carried out.

Denoted the coefficients $\hat{H}_{ij}$ and G_{ij} are defined as:

$$\hat{H}_{ij} = \int_{\Gamma} \frac{\partial U^*(\xi, \mathrm{y})}{\partial n_q} ds \tag{6}$$

$$G_{ij} = \int_{\Gamma} U^*(\xi, \mathrm{y}) ds \tag{7}$$

Introducing the notation (6) and (7) into eq. (5), the discrete form of the solution becomes

$$\frac{1}{2}u^i + \sum_{j=1}^{N} \widehat{H}_{ij} u^j = \sum_{j=1}^{N} G_{ij} u_n^j \tag{8}$$

$$H_{ij} = \widehat{H}_{ij} - \frac{1}{2}\delta_{ij} \tag{9}$$

Eq. (2.78) may further be written as

$$\sum_{j=1}^{N} H_{ij} u^j = \sum_{j=1}^{N} G_{ij} u_n^j \tag{10}$$

The solution ϕ can be computed at any point y in the domain Ω by virtue of eq. (4). Applying the same discretization as in eq. (5), we arrive at the following expression:

$$u(y) = \sum_{j=1}^{N} \widehat{H}_{ij} u^j - \sum_{j=1}^{N} G_{ij} u_n^j \tag{11}$$

The coefficients G_{ij} and $\widehat{H}_{ij}$ are computed again from the integrals, but in this case the boundary point pi, is replaced in the expressions by the field point P in Ω.

3 PLATE STIFFNESS MATRIX

After discretizing the plate boundary to NE quadratic boundary elements, equation (1) could be re-written in a matrix form as follows:

$$[[A]_{3N\times 3N} \quad [A_2]_{3N\times 3N_c}] \begin{Bmatrix} \{u/t\}_{3N\times 1} \\ \{F\}_{3N_c\times 1} \end{Bmatrix} = \{RHS_b\}_{3N\times 1} \tag{12}$$

Combining equation (2)after discretization together with equation (1)gives:

$$\begin{bmatrix} [A]_{3N\times 3N} & [A_2]_{3N\times 3N_c} & [0]_{3N\times 3N_c} \\ [A_1]_{3N_c\times 3N} & [A_3]_{3N_c\times 3N_c} & [I]_{3N_c\times 3N_c} \end{bmatrix} \begin{Bmatrix} \{u/t\}_{3N\times 1} \\ \{F\}_{3N_c\times 1} \\ \{u_c\}_{3N_c\times 1} \end{Bmatrix} = \begin{Bmatrix} \{RHS_b\}_{3N\times 1} \\ \{RHS_c\}_{3N_c\times 1} \end{Bmatrix} \tag{13}$$

If the support elements are considered to have a free edge and no internal loading, considered equation (13) could be re-written as follows after placing the $\{u_c\}$vector on its right hand side:

$$\begin{bmatrix} [A]_{3N\times 3N} & [A_2]_{3N\times 3N_c} & [0]_{3N\times 3N_c} \\ [A_1]_{3N_c\times 3N} & [A_3]_{3N_c\times 3N_c} & [I]_{3N_c\times 3N_c} \end{bmatrix} \begin{Bmatrix} \{u\}_{3N\times 1} \\ \{F\}_{3N_c\times 1} \end{Bmatrix} = -\begin{Bmatrix} \{0\}_{3N\times 1} \\ \{u_c\}_{3N_c\times 1} \end{Bmatrix} \tag{14}$$

If different cases of loading are considered such that the number of load cases is chosen to be equal to 3Nc, hence equation (14) could be re-written as follows:

(15)

$$\begin{bmatrix} [A]_{3N\times 3N} & [A_2]_{3N\times 3N_c} & [0]_{3N\times 3N_c} \\ [A_1]_{3N_c\times 3N} & [A_3]_{3N_c\times 3N_c} & [I]_{3N_c\times 3N_c} \end{bmatrix} \begin{bmatrix} [u]_{3N\times 3N_c} \\ [F]_{3N_c\times 3N_c} \end{bmatrix} = -\begin{bmatrix} [0]_{3N\times 3N_c} \\ [u_c]_{3N_c\times 3N_c} \end{bmatrix}$$

In order to force the force matrix$[F]$to represent the slab stiffness matrix $[K]$corresponding to the previously degrees of freedom, $[u_c]$ should be set to the identity matrix$[I]$. Therefore equation (14) could be rewritten as follows:

$$\begin{bmatrix} [A]_{3N\times 3N} & [A_2]_{3N\times 3N_c} \\ [A_1]_{3N_c\times 3N} & [A_3]_{3N_c\times 3N_c} \end{bmatrix} \begin{bmatrix} [u]_{3N\times 3N_c} \\ [K]_{3N_c\times 3N_c} \end{bmatrix} = -\begin{bmatrix} [0]_{3N\times 3N_c} \\ [I]_{3N_c\times 3N_c} \end{bmatrix} \quad (15)$$

Rearranging equation (14) to give:

$$\begin{bmatrix} [u]_{3N\times 3N_c} \\ [K]_{3N_c\times 3N_c} \end{bmatrix} = -\begin{bmatrix} [A]_{3N\times 3N} & [A_2]_{3N\times 3N_c} \\ [A_1]_{3N_c\times 3N} & [A_3]_{3N_c\times 3N_c} \end{bmatrix}^{-1} \begin{bmatrix} [0]_{3N\times 3N_c} \\ [I]_{3N_c\times 3N_c} \end{bmatrix} \quad (16)$$

Equation (16) could be used to obtain the stiffness matrix of the slab panel at the corresponding degrees of freedom defined at column positions.

4 FRAME STIFFNESS MATRIX

he stiffness atri [c of vertical elements not including warping effects is defined by:

$$\left[\overline{\mathrm{K}}_{\mathrm{c}}\right]_{12\times 12} = \left[T_D\right]_{12\times 12}\left[R\right]_{12\times 12}\left[K_c^*\right]_{12\times 12}\left[R\right]_{12\times 12}^{T}\left[C_D\right]_{12\times 12}^{-1} \quad (17)$$

he stiffness atri [cw] of vertical elements including warping effects is defined by:

$$\left[\overline{\mathrm{K}}_{\mathrm{cw}}\right]_{14\times 14} = \left[T_{Dw}\right]_{14\times 14}\left[R_w\right]_{14\times 14}\left[K_{cw}^*\right]_{14\times 14}\left[R_w\right]_{14\times 14}^{T}\left[C_{Dw}\right]_{14\times 14}^{-1} \quad (18)$$

Where $\left[K_c^*\right]$is the local frame element stiffness matrix, [R] is the 3D transformation matrix,$\left[T_D\right]$and $\left[C_D\right]$are transformation matrices that change the position the degrees of the in-plane degrees of freedom to the plate master joint to apply the slab diaphragm effect[2 . he subscript “w” denotes a trices related to warping walls. The computation of warping functions and derivatives are based on [18].

5 NUMERICAL EXAMPLES

5.1 Example (1):Slab resting on three columns

The purpose of this example is to compute the lateral drift of a single story building by the proposed method, hence, a comparison is made between the present results to those of the finite element method. Three numerical models are considered, two are based on the finite element method (FEM) and the third one is based on the proposed method. A comparison is carried out for the computed drift of a twenty story building has a similar floor slab as that of the one-story building. A parametric study is carried out to study the effect of the real geometric properties of the connecting cross sectional area of the vertical supporting element to the slab. The slab has a thickness of 0.2 m, and dimensions of 4×4m. Column dimensions are 0.5×0.5m as shown in Figure 5-1. The slab material has a modulus of elasticity equal to 2210000 t/m2 and Poisson's ratio of 0.2.The columns modulus of elasticity is equal to 2210000 t/m2. A 10t is applied in the X direction at co-ordinates x=0, y=2 m at the level of the slab. The considered height of the story is 3m.

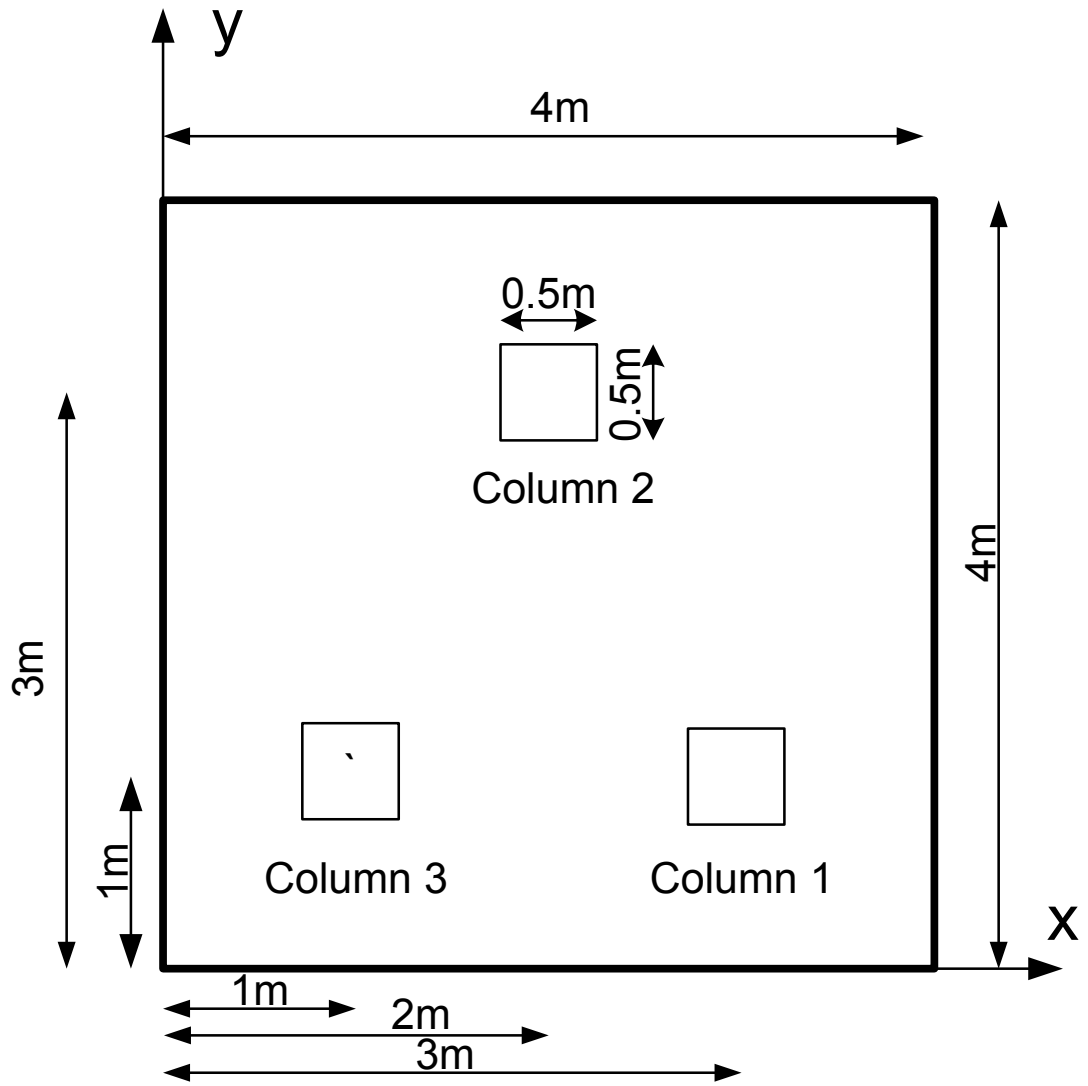


Figure 5-1: Dimensions considered for the slab in example (5.1).

The following numerical models are considered:
Model1: Considers the proposed method. The boundary element method is used to model slabs using continuous quadratic elements with element length of 1m as shown in Figure 5-2.
Model2: Considers columns as 3D solid finite elements with mesh of size 0.0625m. The slab is modeled using plate bending elements with a mesh size 0.0625m.A diaphragm constraint is enforced at the floor level as shown in Figure 5-3.
Model3: Considers columns as skeletal frame elements. The slab is modeled using the plate bending elements with a mesh size of 0.0625m. A diaphragm constraint at the floor level is enforced as shown in Figure 5-4.
It has to be noted that, in models 1 and 2 the Straus7 software [19] to carry out the finite element analysis.

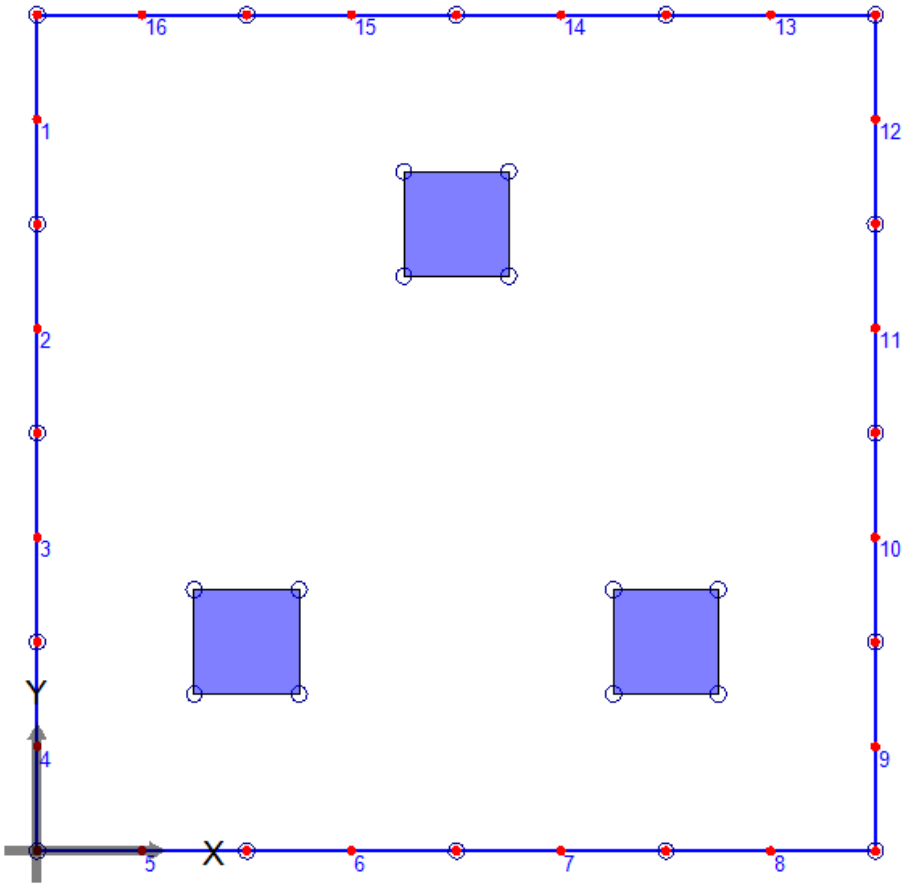


Figure 5-2: Boundary element model (model 1).

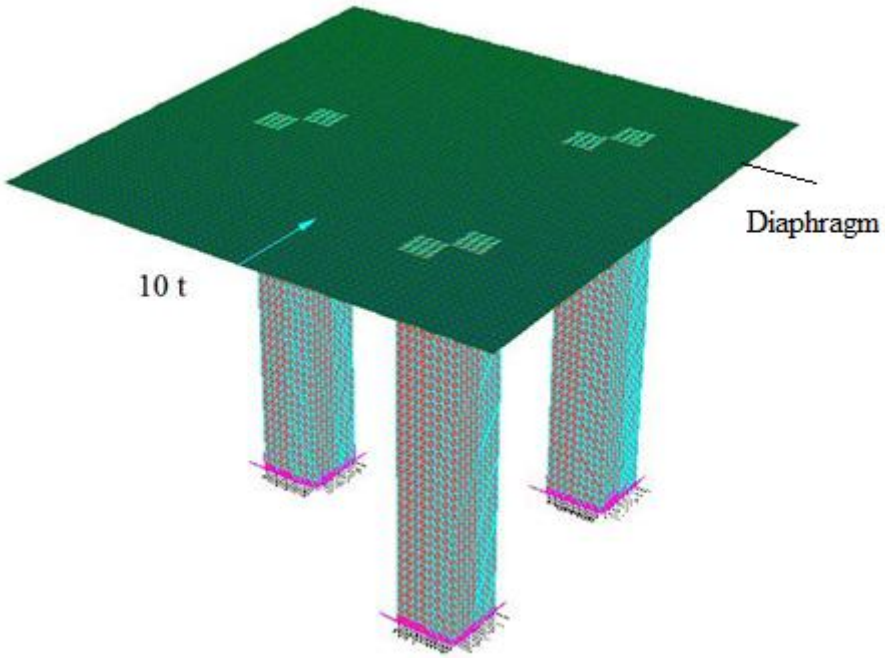


Figure 5-3: Solid element column model with slab plate bending finite element method (model 2).

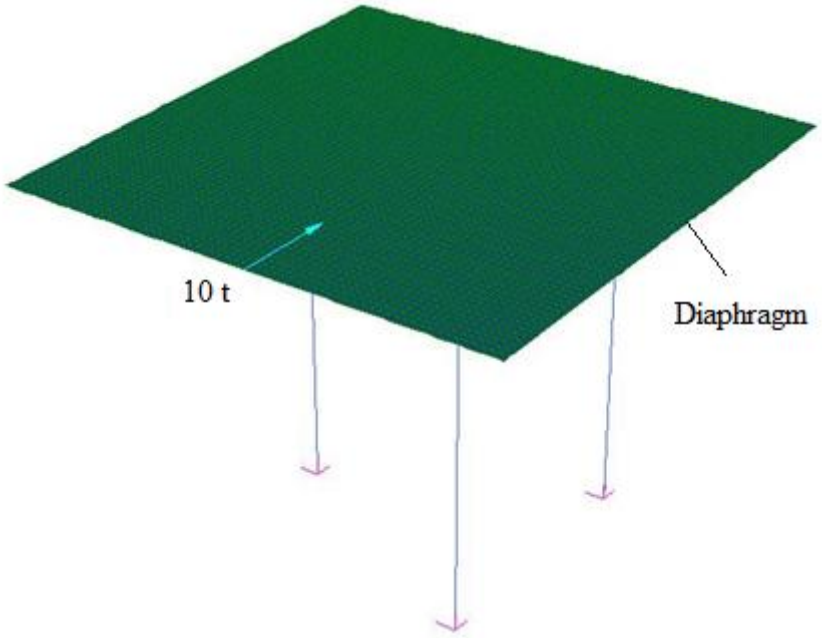


Figure 5-4: Frame element column model with slab plate bending finite element model (model 3).

Figure 5-5Figure 5- to Figure 5-7 demonstrate the bending moment a contour map and strips for the three models. In order to compare the results, Figure 5-8 demonstrates the same strip results for the three models together. It can be seen that the frame model (the common model that is used in practice of structural engineering) produces

peaking values for bending moments above support elements. If model 3 results are eliminated from 5-8, then Figure 5-9 is obtained. It is clear that the preset solution (model1) is as accurate as the (model2) in which columns are modeled as solid elements.

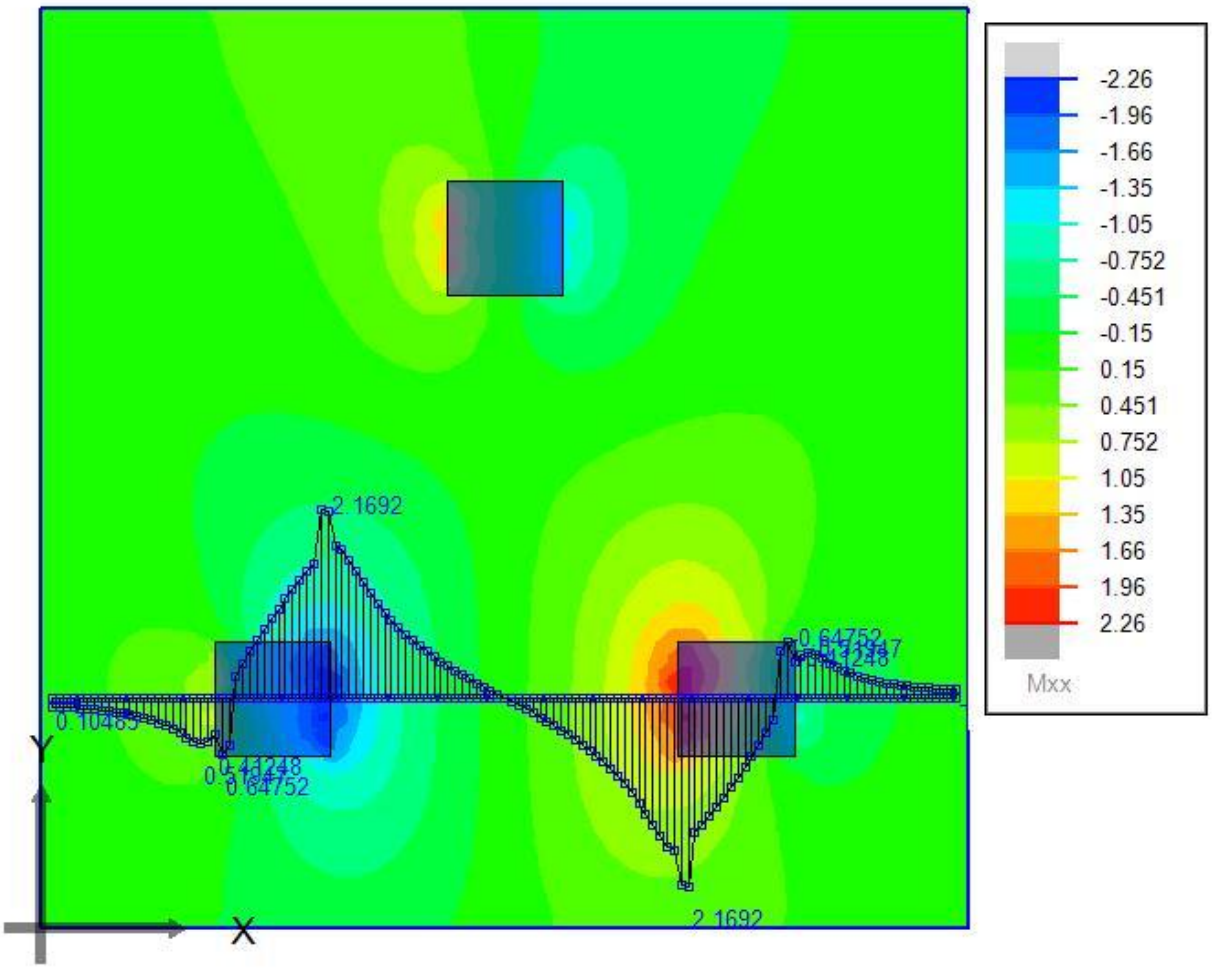


Figure 5-5: Bending moment Mxx contour in model 1.

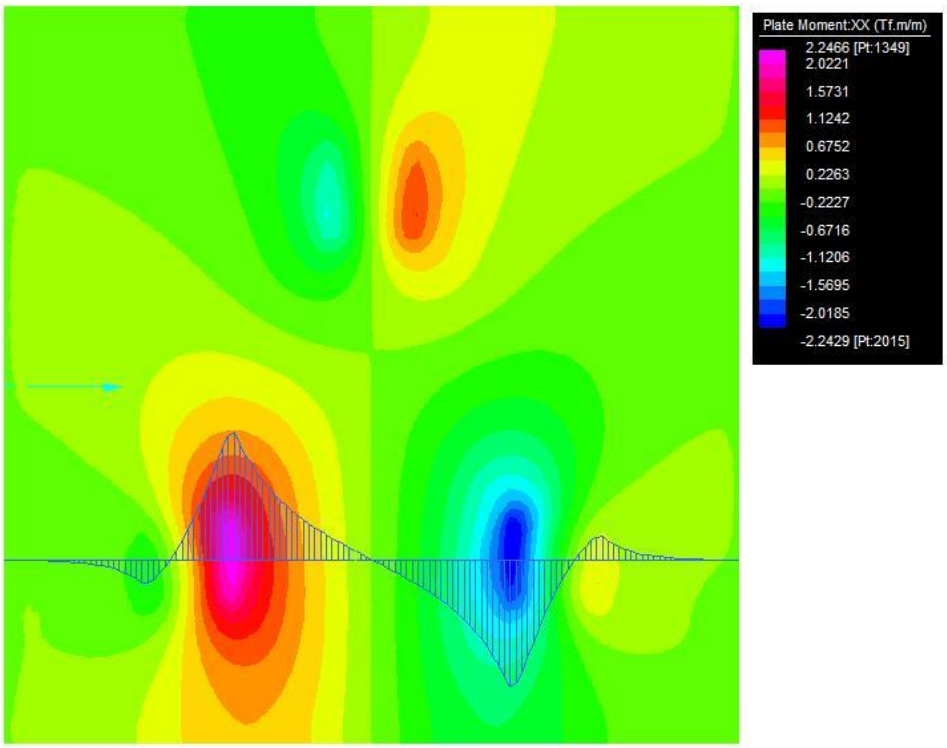


Figure 5-6: Bending moment Mxx contour map in the finite element model 2.

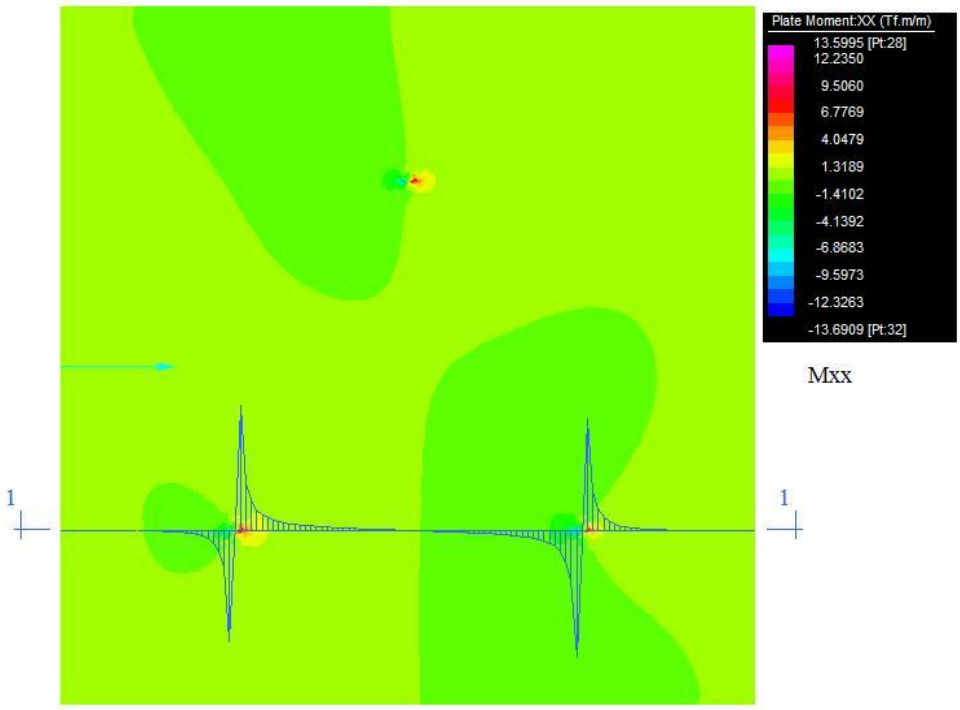


Figure 5-7: Bending moment Mxx contour map in the finite element model 3.

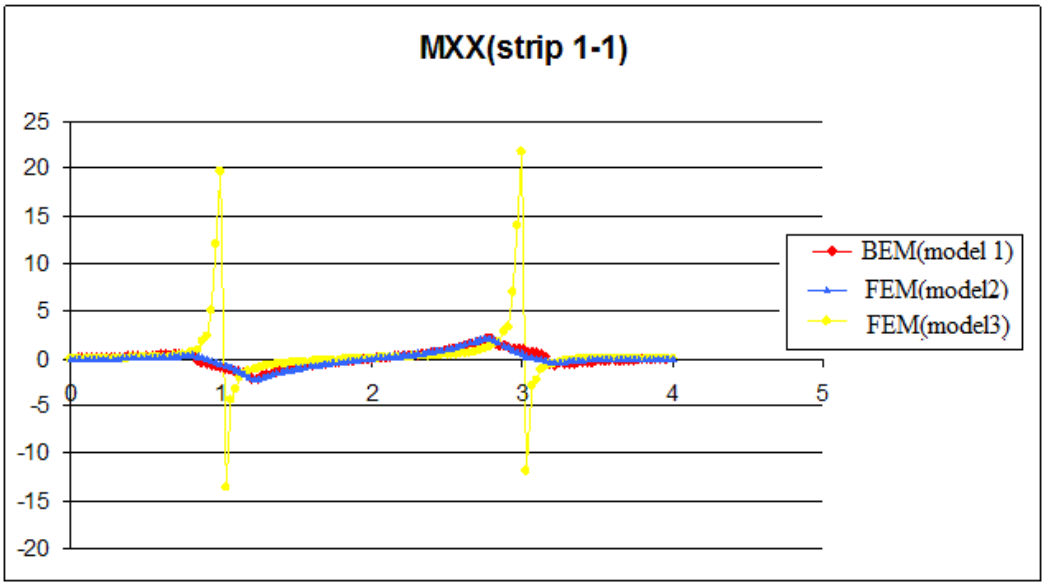


Figure 5-8: Comparison of bending moment Mxx for the considered three models.

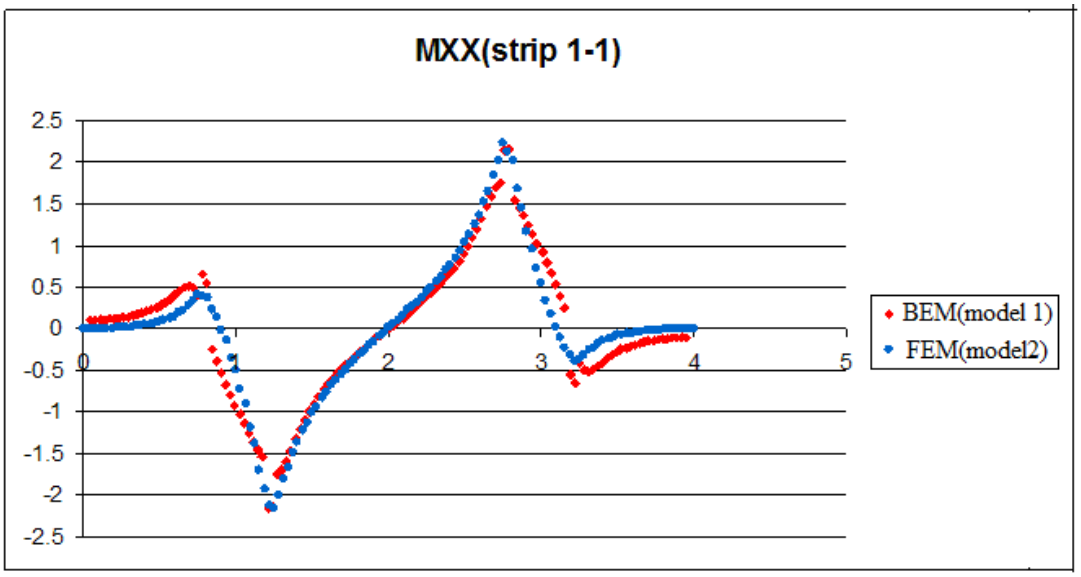


Figure 5-9: Comparison of bending moment Mxx for the considered two models.

In order to demonstrate the effect of consideration of real geometry of slab-column connection area, the following parametric study is carried out. The same example is re-considered but with 20 stories. The applied load is applied at the top floor only (floor no. 20). Two BEM models are considered, whereas the first model considered the actual connection area of columns and slab (0.5×0.5cm), whereas the second model considers the connections area between the slab and the column as a set to 10×10 cm with preserving the column stiffness properties a 0.5×0.5cm column. The drift results of the two models are demonstrated and compared to the FEM frame model (model3). It has to be noted that only the FEM model 3 is considered herein as

it is difficult to run a 20 story building with solid elements using the currently used personal computers. It can be seen from 5-10 to Figure 5-12 that both the FEM model3 and the present BEM of the 10×10cm connecting area give similar results. That means that the contact area between the slab and the column is effect in the total drift of the structural.

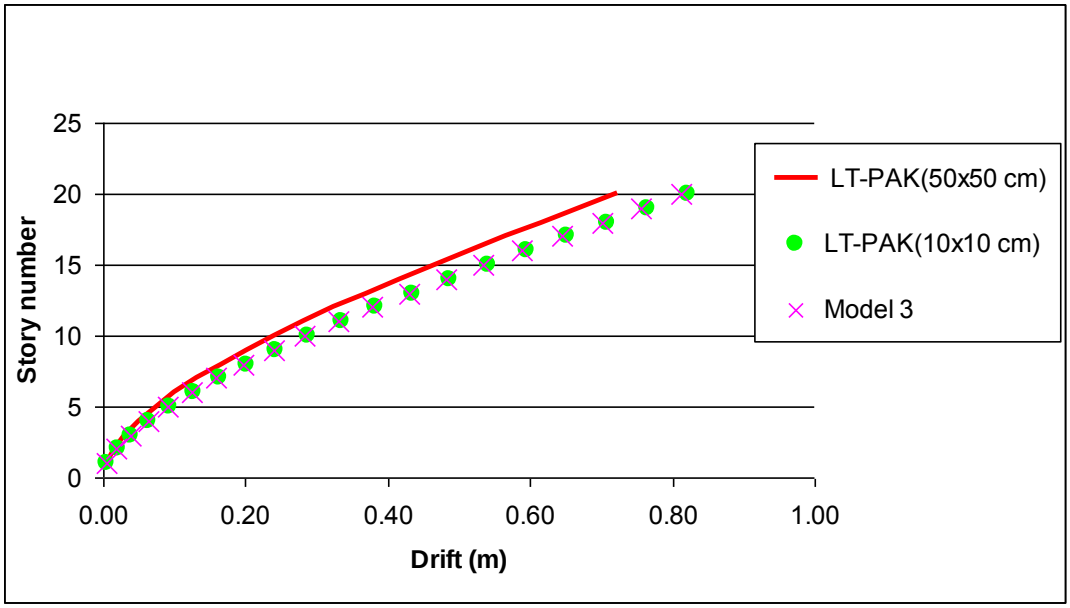


Figure 5-10 Drift in x axis.

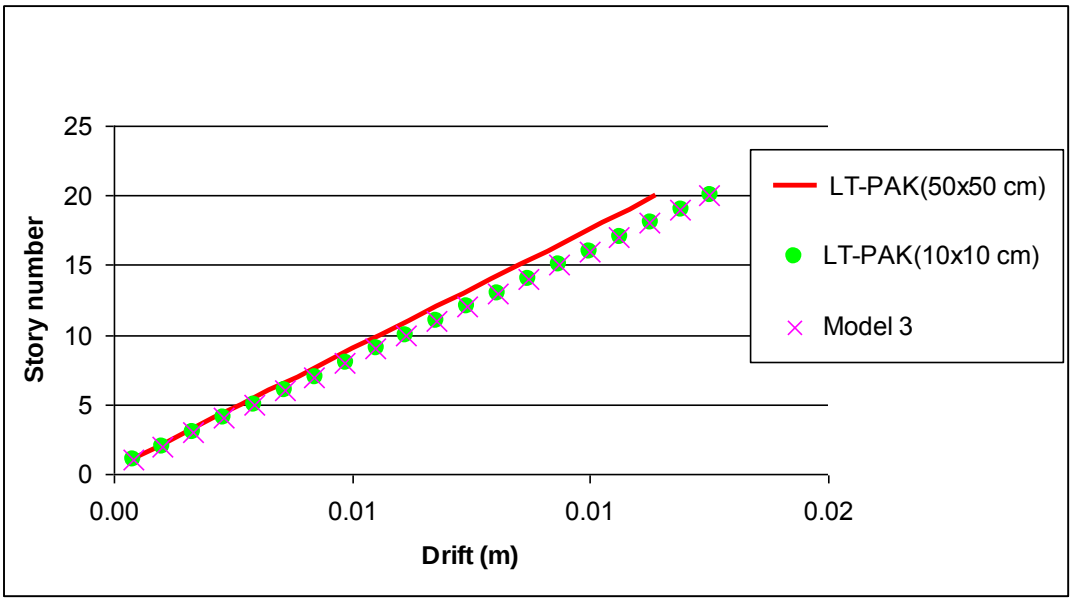


Figure 5-11 Drift in Y axes.

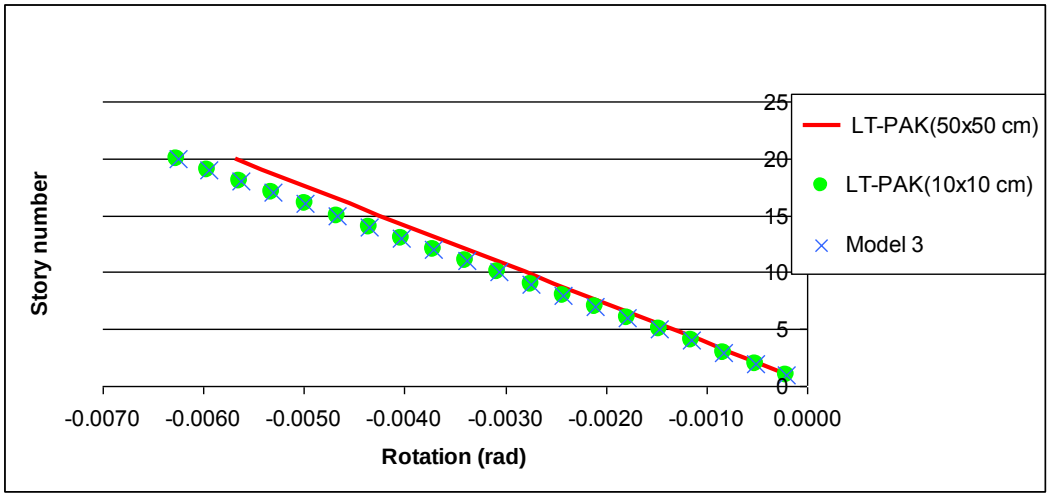


Figure 5-12 Rotation about Z axes.

5.2 Example (6): Practical Multi-Story Building

The purpose of this example is to demonstrate the capability of the present formulation to solve practical buildings. A 10 storey building is analyzed using the proposed method and the results are compared to those obtained from with the finite element method. The slab shown in Figure 5-13 is analyzed. It has a thickness of 0.23 m. Both the slab and vertical element materials have a modulus of elasticity equal to 2210000t/m2 and Poisson's ratio equal to 0.2. he height of each storey is 3.4m. A (1000 t) load is applied in the X-direction as show in 5-14 at all levels of the slabs. The boundary element mesh and associate discretization are shown in 5-15. The used finite element mesh is shown in 5-16, 5-17 with shell elements of size 0.5m. Columns are modeled using frame elements. A diaphragm constraint is applied at each floor level. The deflection of top slab as contour maps as shown in 5-18 and 5-19. Figures 20-26 demonstrate comparisons of deflections and lateral drifts.

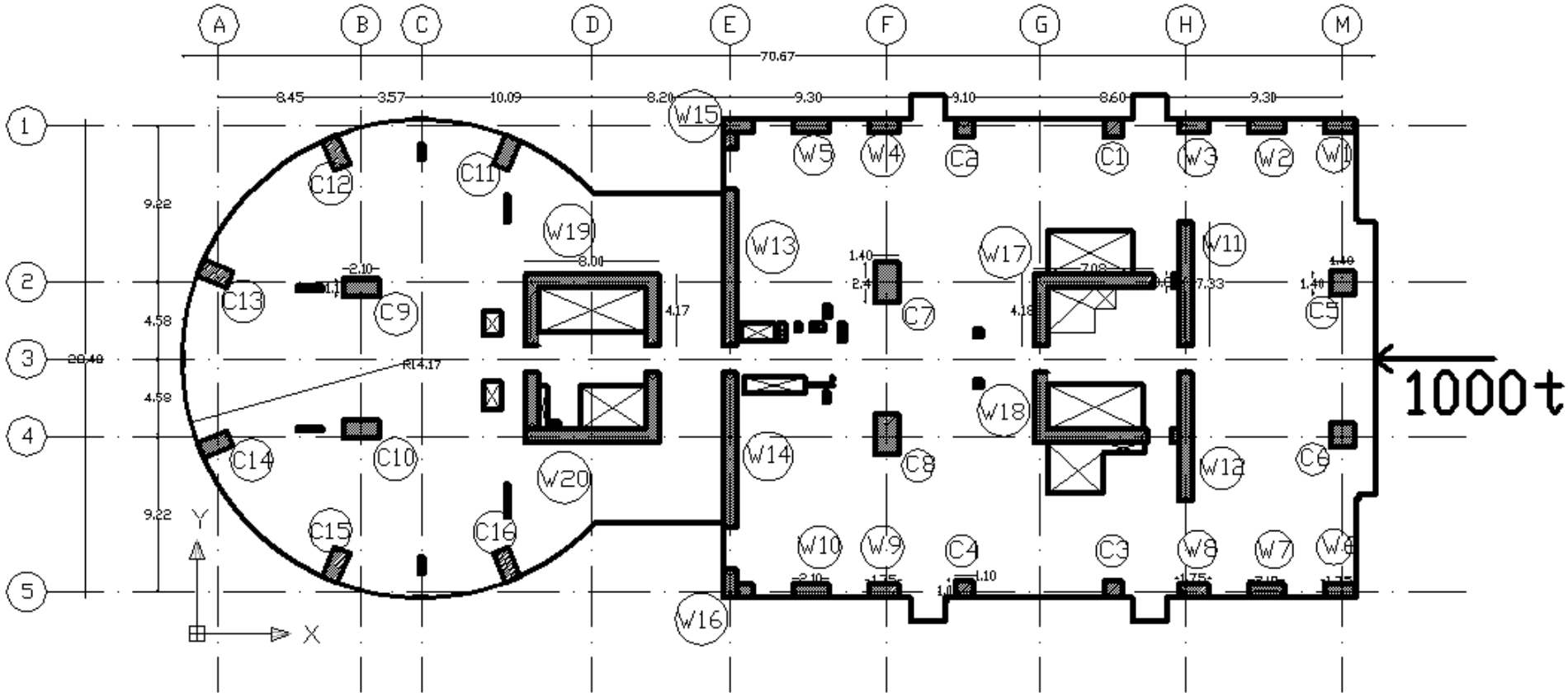


Figure 5-13: Dimensions of the Practical Building in example 5.2.

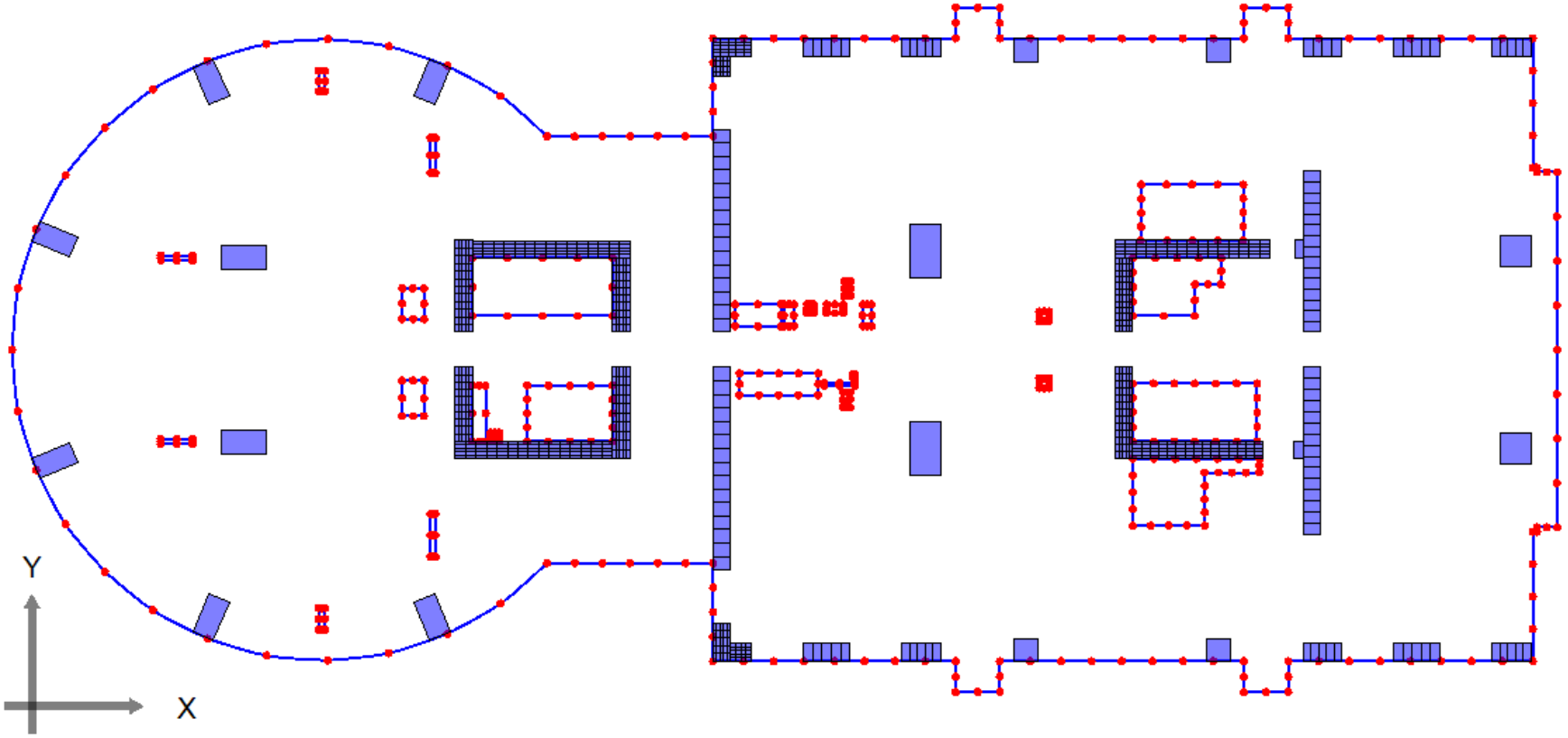


Figure 5-14: The used boundary element model in example 5.2.

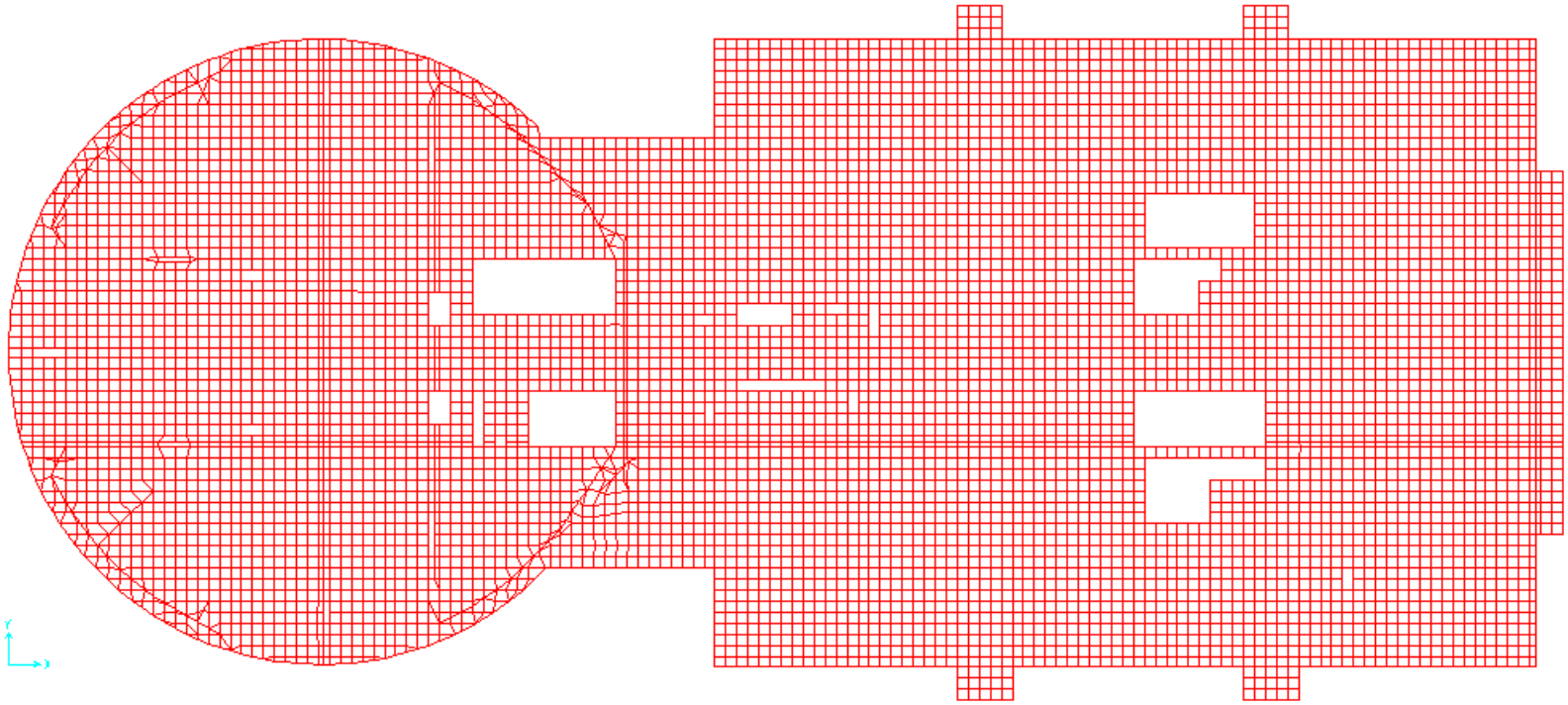


Figure 5-15: The finite element mesh used in example 5.2.

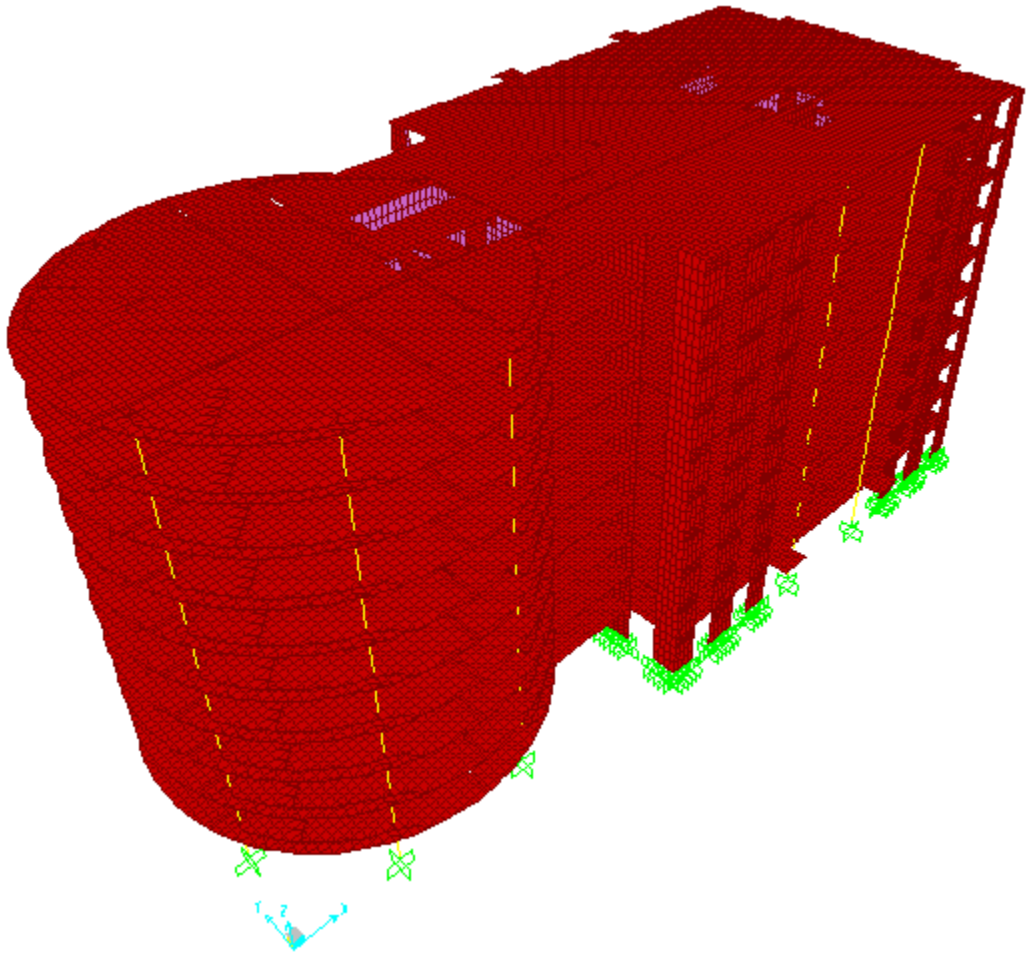


Figure 5-16: The multi-storey finite element model in example 5.2.

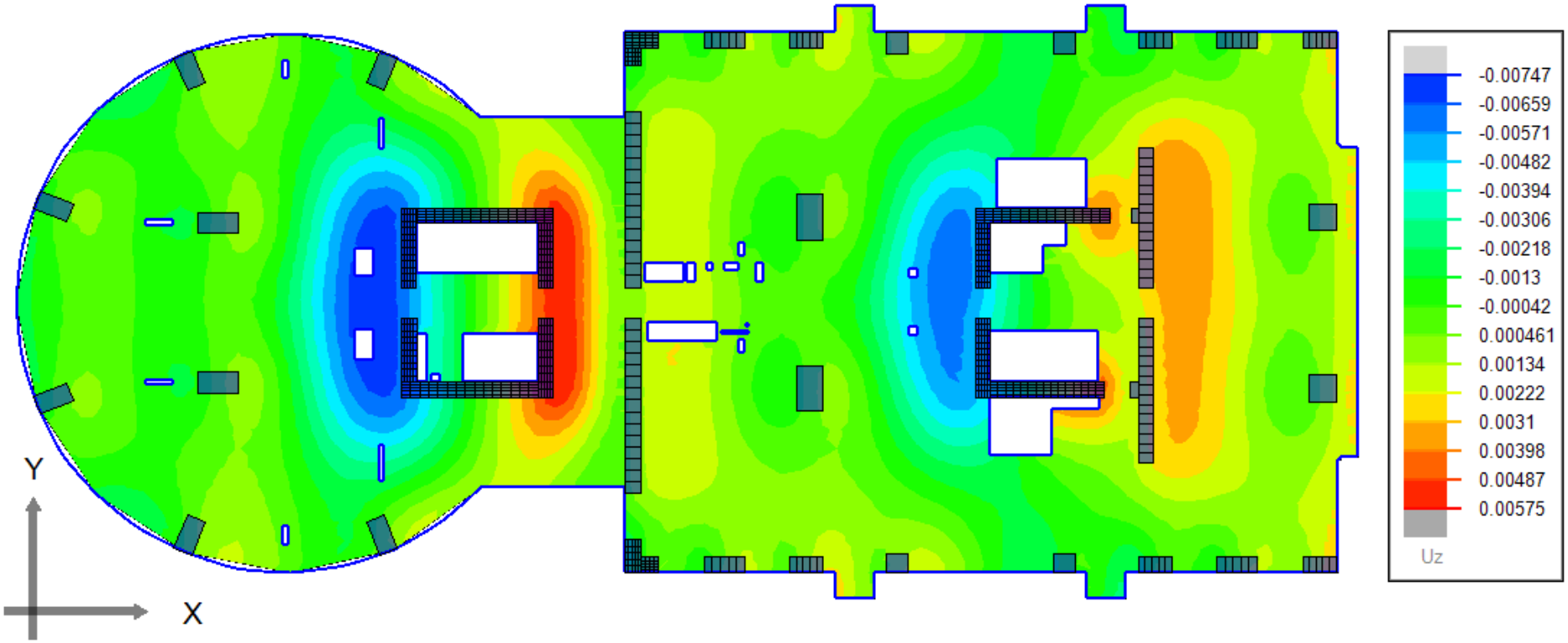


Figure 5-17 Slabs deflection UZ _BEM_Model (1).

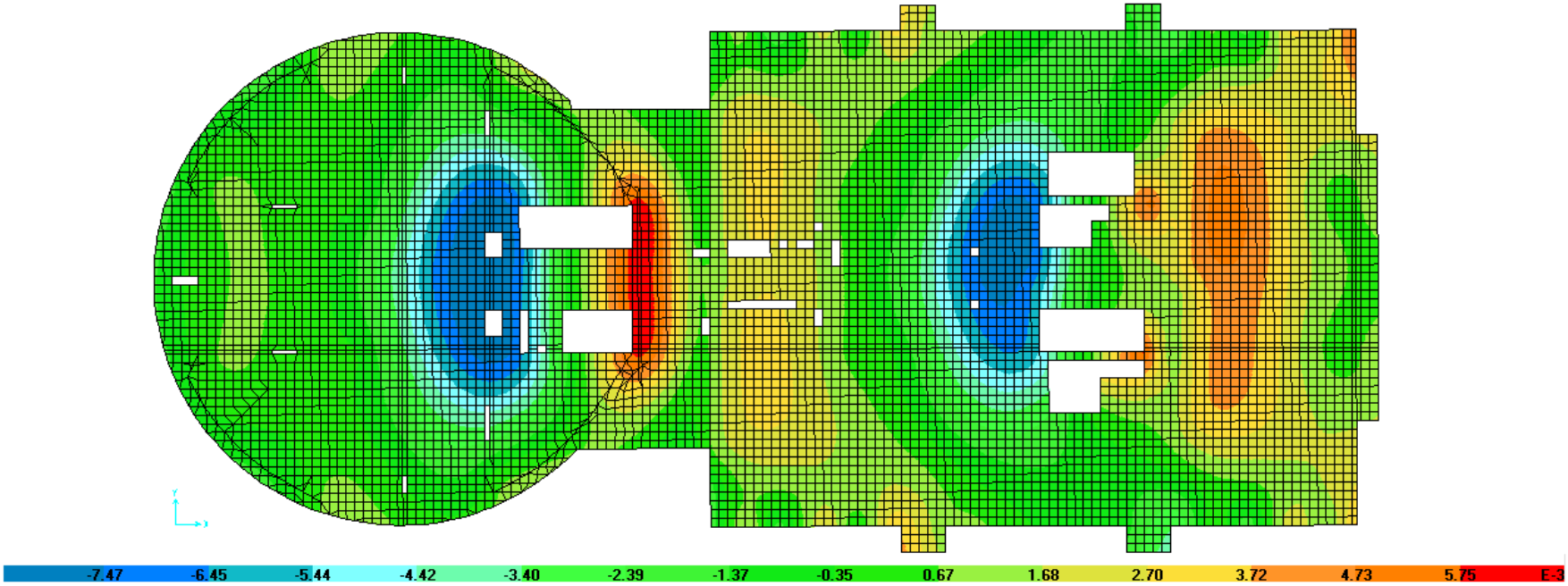


Figure 5-18: Slabs deflection UZ- FEM-Model (2).

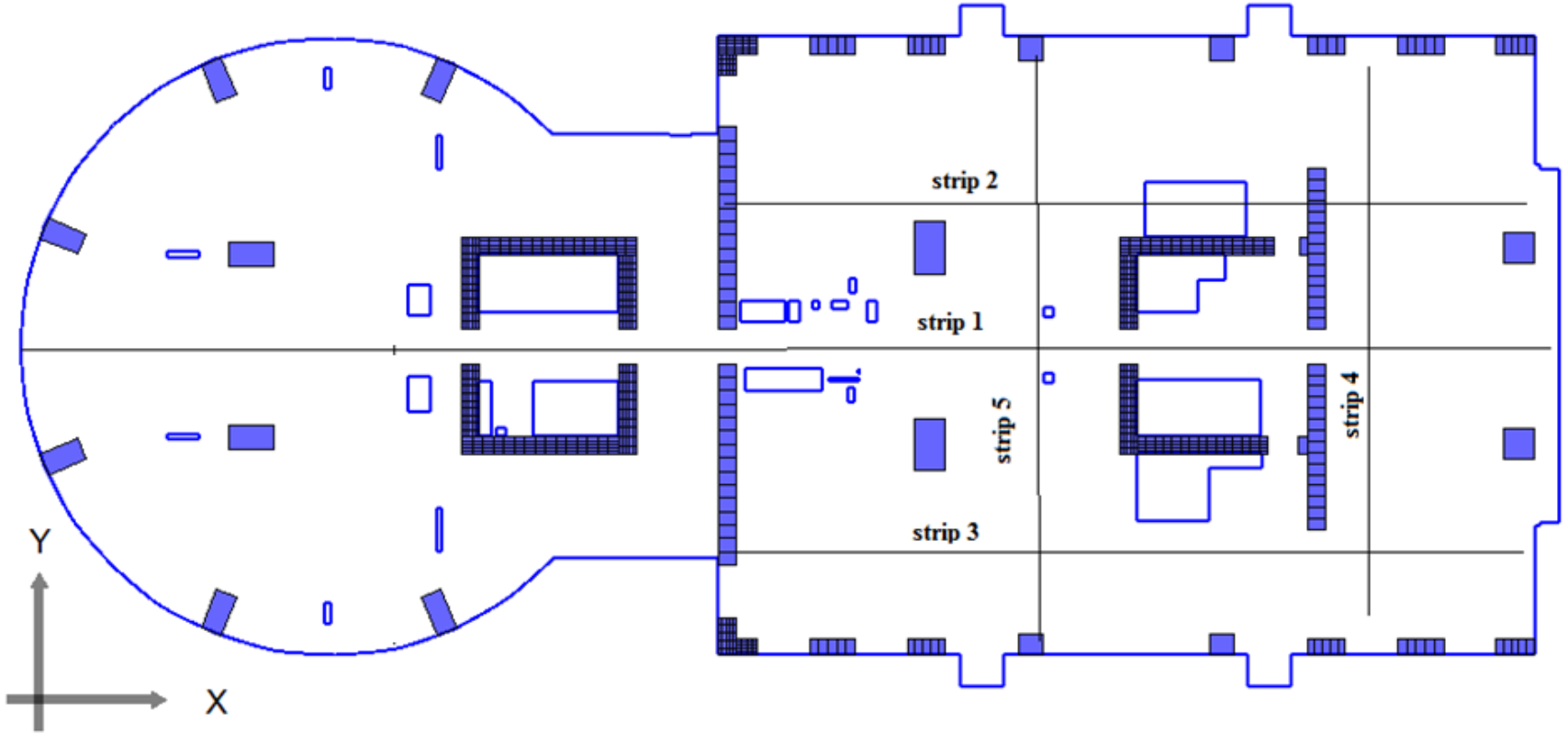


Figure 5-20: Strip guide

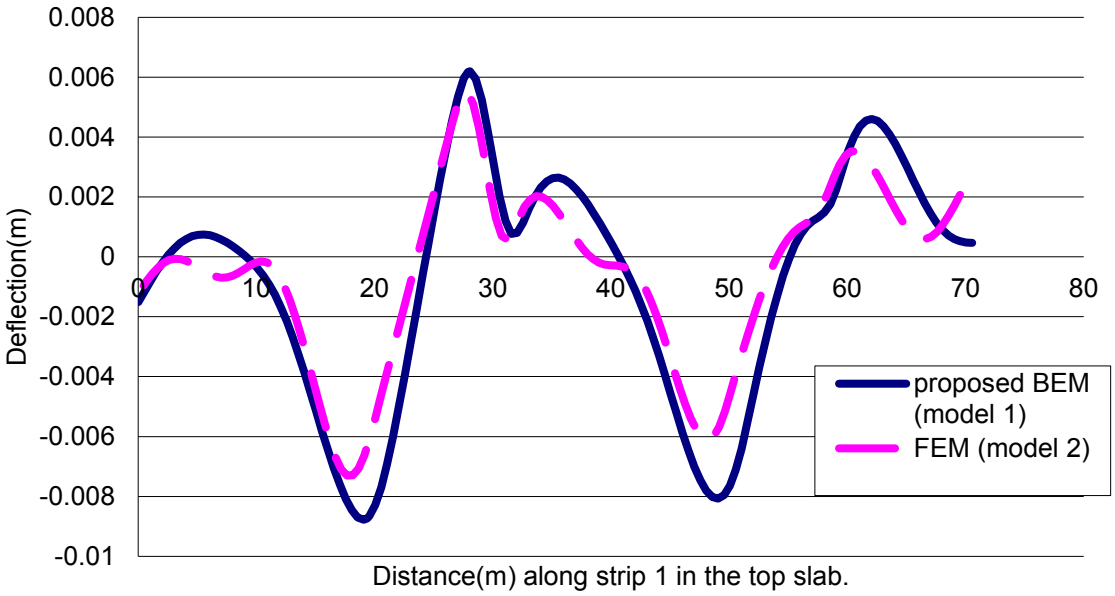


Figure 5-21: Comparison of deflection UZ diagram between two models strip 1.

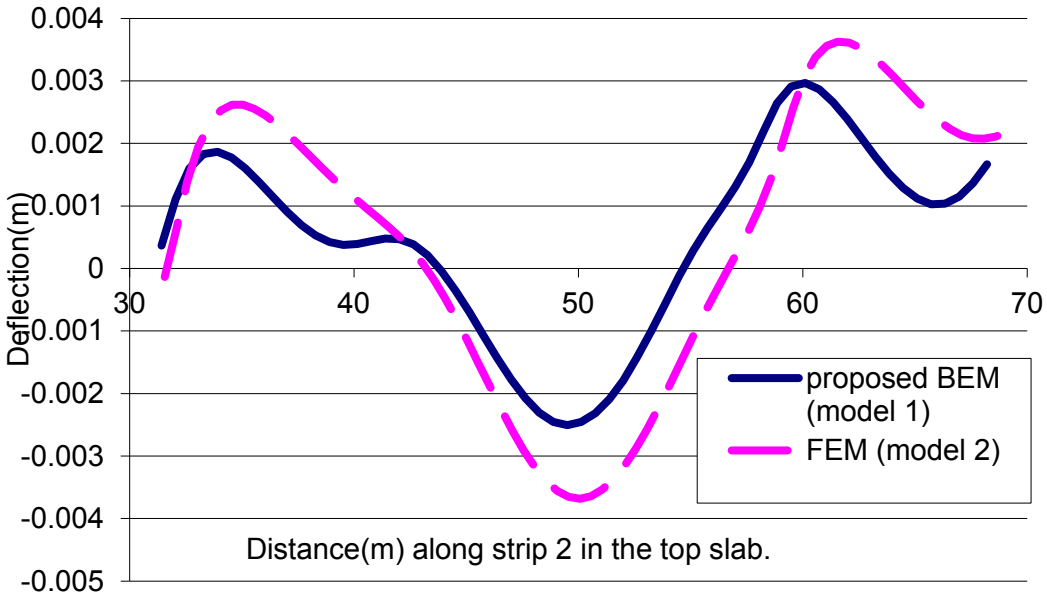


Figure 5-22 Comparison of deflection UZ diagram between two models strip 2.

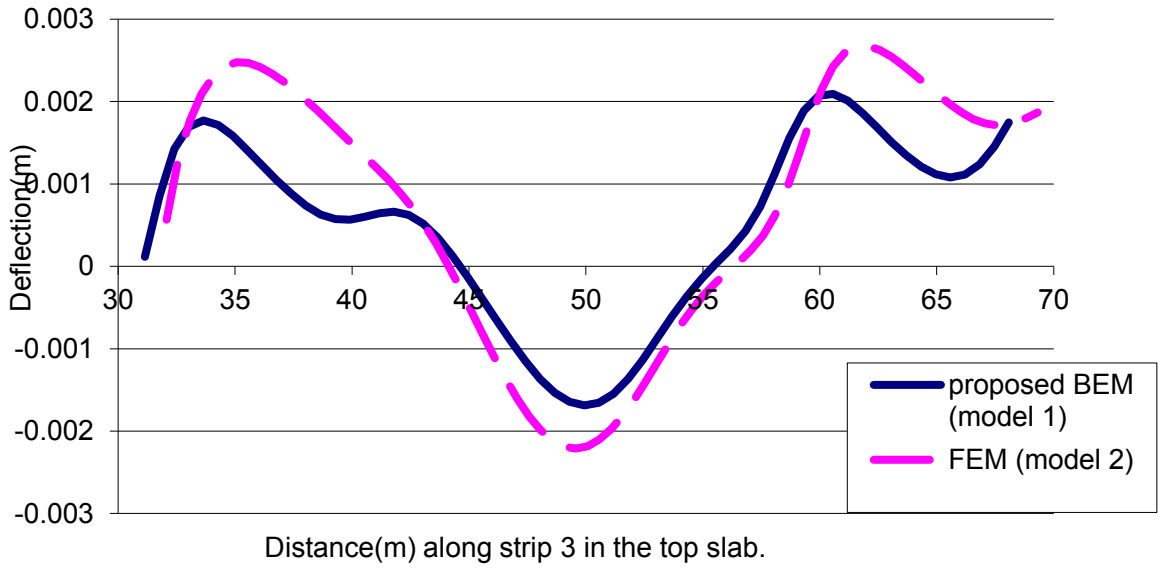


Figure 5-23 Comparison of deflection UZ diagram between two models strip 3.

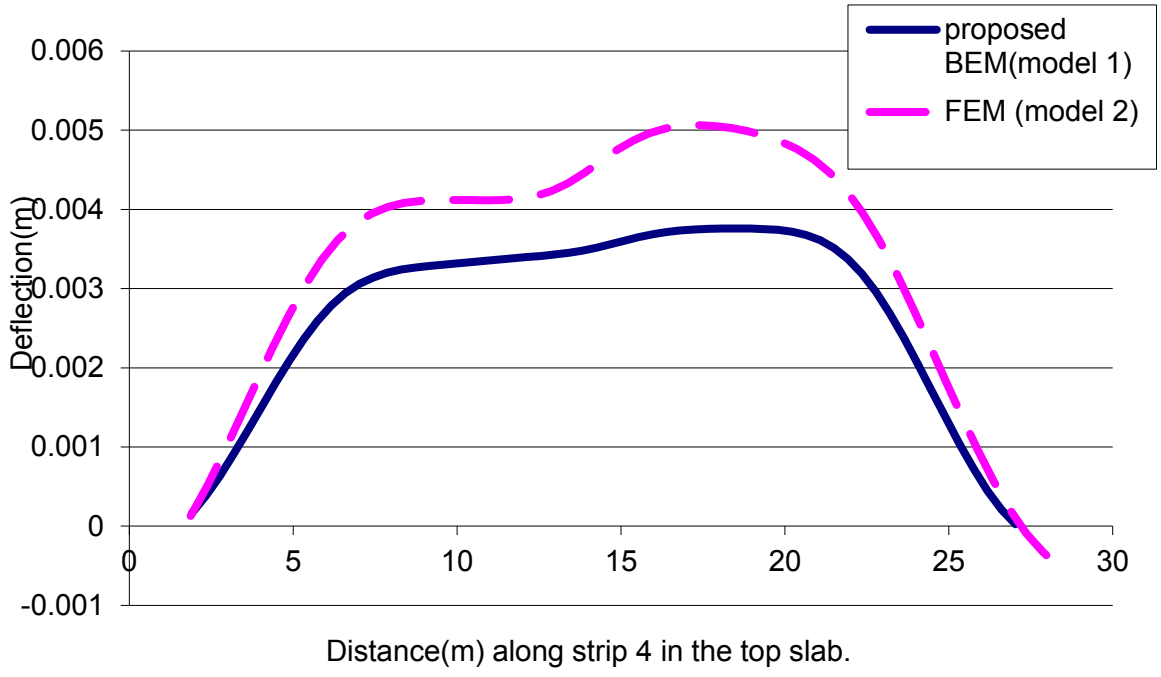


Figure 5-24 Comparison of deflection UZ diagram between two models strip 4.

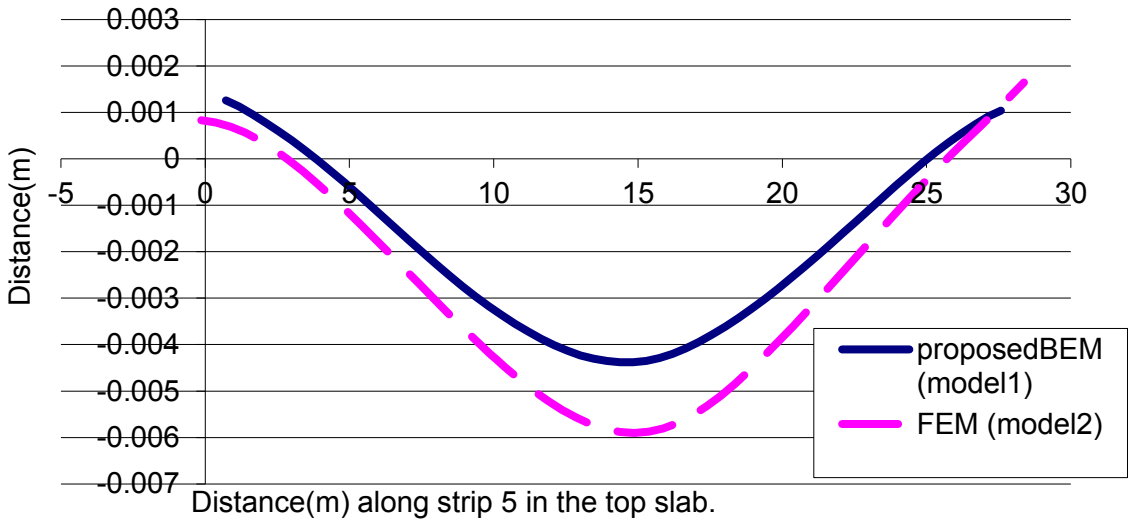


Figure 5-25 Comparison of deflection UZ diagram between two models strip 5.

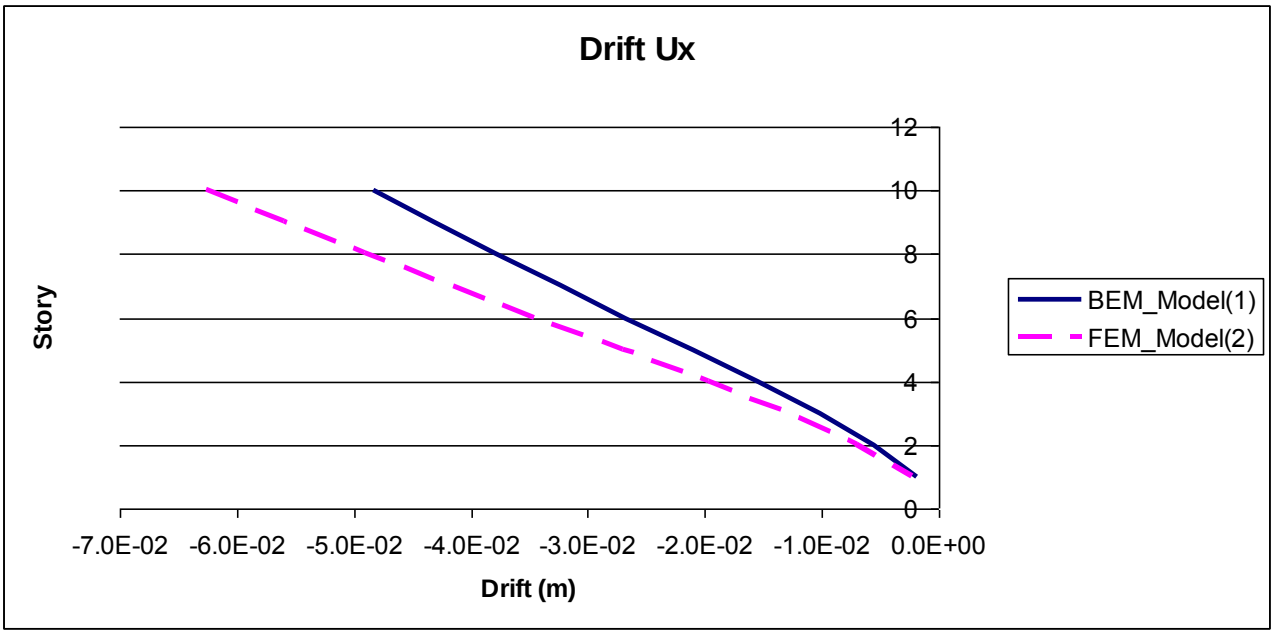


Figure 5-26: Comparison of lateral drifts in X direction.

6 CONCLUSIONS

This paper presents a new scheme for the lateral analysis of buildings using matrix analysis of structures. In the presented scheme, the stiffness matrices of vertical elements are computed; including the warping effects for large wall sections. The stiffness matrices of plate elements are computed using a boundary element formulation; the stiffness co-coefficients are condensed at vertical elements positions. The proposed scheme is applied to a couple of examples. The first one demonstrates the significance of the real geometry modeling presented by the

proposed boundary element modeling. The second demonstrates the applicability of the proposed scheme to practical applications.

ACKNOWLEDGMENT

The research reported here was supported by the European Union Project PIRSES-GA-2010-269222: Analysis and Design of Earthquake Resistant Structures (ADERS) of the FP7-PEOPLE-2010-IRSES, Marie Curie Actions. This support is gratefully acknowledged by the authors.

REFERENCES

[1] B., S. a ranath "Structural analysis and design of tall buildings," New York, McGraw-Hill, 1988.

[2] B. S. Smith and A. Coull, 'Tall Building Structures Analysis and Design, Tall' Buildings Structures-Analysis and Design, John Wiley & sons Publication.

[3] O.C., Zienkiewicz, 'The finite element method' McGraw Hill, 1977

[4] A. Ghali, A.M. Neville and .G . Brown 'structural analysis a unified classical and at ri approach 6th edition' by a ylor&francis Publication, Chapter 14 PP 417-428.

[5] H.C ,Chan, YK.,Cheung 1979. Analysis of shear wall using higher order finite elements. Building and Environment 14(3): 217–224.

[6] R., Rosman 'Statics of non-sy etric shear wall structures' Proceedings of the Institution of Civil Engineers 48–49(Suppl 12): 211–244, 1971.

[7] JK,Biswas WK. ,Tso 1974. 'Three-dimensional analysis of shear wall buildings to lateral load'. Journal of the Structural Division, Vol. 100, No. 5, 5,1974

[8] J ,Wdowicki, E, Wdowicka. 1993b. System of programs for analysis of three-dimensional shear wall structures. The Structural Design of Tall Buildings Vol. 2 ,1993.

[9 Jacek Wdowicki and Elz˙bieta Wdowicka Analysis of shear wall structures of variable cross section Structrl. Design Tall Spec. Build, 2012.

[10] A,Coull, RD , Puri. ‘Analysis of coupled shear walls of variable thickness’ Building Science , 1967

[11] A,Coull, RD , Puri. ‘Analysis of coupled shear walls of variable cross-section. Building Science, 1968.

[12] A. Pisanty, EE, Traum. ‘Si plifi ed analysis of coupled shear walls of variable cross-section’ Building Science, 1970

[13] O, Aksogan, HM, Arslan, BS, Choo.’Forced vibration analysis of stiffened coupled shear walls using continuous connection method’ Engineering Structures, 2003

[14] Y.F.Rashed, "Boundary element Modeling of flat plate floors under vertical loading", Int. J. Numer. Meth. Engng. Vol. 62:1606-1635,2005.

[15] E. Reissner, "On the theory of bending of elastic plates", Journal of Mathematics and Physics, Vol. 23, pp.184-191,1944.

[16]E.Reissner, "On bending of elastic plates", Quart. Applied Mathematics, Vol. 5, pp. 55-68,1947.

[17 Vlasov, Vasili Zakharovich , “ hin -walled elastic bea s “2. ed. rev. and augm. Tranl. From Russian,1906-1958.

[18] J. T. Katsikadelis ‘boundary ele e nts theory and applications’ by Elsevier science Ltd.2003.

[19] Sraus7 finite element analysis system –www.strand7.com.

COMPDYN 2013
4th ECCOMAS Thematic Conference on
Computational Methods in Structural Dynamics and Earthquake Engineering
M. Papadrakakis, V. Papadopoulos, V. Plevris (eds.)
Kos Island, Greece, 12–14 June 2013

NONLINEAR SEISMIC ANALYSIS OF INFILLED RC FRAMES WITH AN EQUIVALENT STRUT MODEL

L.Landi[1], **A.Tardini**[1], **P.P. Diotallevi**[1]

[1] Department DICAM – University of Bologna
Viale Risorgimento, 2 – 40136 Bologna - Italy
e-mail: l.landi@unibo.it, annalisa.tardini2@unibo.it, pierpaolo.diotallevi@unibo.it

Keywords: Infilled Frames; Equivalent Strut Model; Non Linear Dynamic Analysis

Abstract. *The objective of this paper was to simulate the seismic response of RC infilled frames. In order to evaluate the behaviour of these structures, it was fundamental to define an appropriate analytical model. Several models were proposed in literature for the masonry infills. In this study the equivalent strut model was considered. The study started from the model for monotonic loading proposed by Al-Chaar. This model was extended to the case of cyclic loading by calibrating the degradation of strength and stiffness, the residual strength and the loading and unloading branches. This calibration was performed by comparing the analytical results with the ones of available experimental tests on infilled frame. The model was then applied for investigating the seismic response of infilled RC frames: pushover and nonlinear dynamic analyses were carried out for obtaining the response in terms of base shear-top displacement and to assess the configuration of collapse.*

.

1 INTRODUCTION

The existing buildings, as for example the Italian ones, are characterized by numerous examples of RC frames with masonry infills. Various studies [1-8] showed how the presence of masonry infills may alter the overall behaviour of structures when subjected to seismic action. The presence of the masonry infills can produce positive or negative effects. In the first case it can increase the strength and the dissipative capacity of the structure, in the second case it can produce unexpected distributions of forces and consequent local phenomena of collapse. However, the most widespread and established practice of design does not consider the infills as structural elements, ignoring their strength and stiffness. For this reason, in the analytical models these elements are often neglected. This choice could be not proper especially in the evaluation of existing RC structures and in the subsequent choice and design of the retrofit strategy [10].

The aim of this study was to evaluate how the presence of infills could modify the structural response of the frames. To this purpose it was necessary to calibrate an analytical reliable model which could take into account the presence of the infills [3, 5]. The calibrated model was then used to perform several nonlinear dynamic and pushover analyses. The objective of these analyses was to determine the response in terms of base shear-top displacement and to investigate the configuration of collapse. In particular the lateral displacement profile at collapse and the plastic hinge distribution were examined. Finally a method was proposed for the prediction of the collapse mechanism and displacement profile in case of infilled frames. This method could be useful within the framework of the Dipslacement-Based approaches for the design or the assessment, where the possibility to predict the displacement profile plays a fundamental role [11, 12].

2 MODELS FOR THE INFILL PANELS

The first problem was to identify a reliable and simple model which could represent the masonry infill. Many difficulties were due to the intrinsic characteristics of masonry. As it is a non homogeneous and anisotropic material, it is difficult to find a generally valid constitutive law. Furthermore the masonry shows significant degradation of stiffness and strength under cyclic loading. In the seismic design it is necessary to take into account all these aspects but often the constitutive laws proposed in literature have a limited validity. Among the models proposed in literature, the most used is the equivalent strut model. In this model the infill is replaced by a single compression element (Fig. 1).

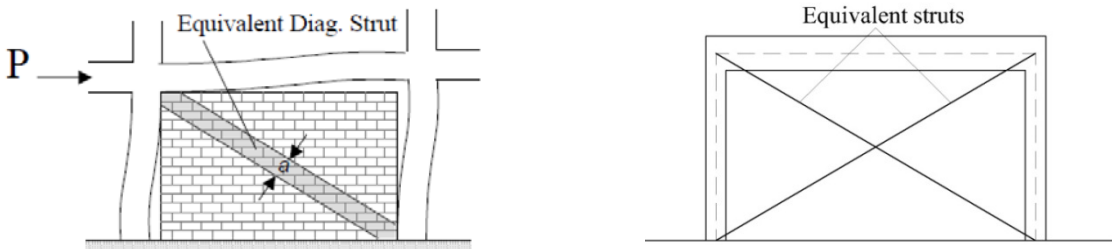


Figure 1: Equivalent diagonal struts.

The choice of the diagonal strut derived from the modes of failure of the infills. The diagonal, in fact, is the only portion of the panel that continues to sustain stresses also after the detachment. The characteristics of the strut (width, stiffness and strength) depend on the geometrical and mechanical properties of the masonry. The method used to calculate these

characteristics varies according to the author of the model. Models for monotonic or cyclic loads were proposed in literature. In the first case, the infill is replaced by a single strut with bilinear not degrading constitutive law. In the second case, instead, two struts are considered, so that each one responds to only one way of loading. In this last case the constitutive law takes into account the strength and stiffness deterioration due to loading and unloading cycles.

As models for monotonic loading it is possible to mention the ones proposed by Bertoldi et al. [1] and by Al-Chaar [3]. As models for cyclic loading it is possible to mention the ones proposed by Klingner and Bertero [4], by Cavaleri et al. [5, 9] and by Decanini et al. [6]. The calibration of the analytical model, which was carried out in this study, started from the models of Al-Chaar [3] for monotonic loading and of Cavaleri et al. [5] for cyclic loading.

2.1 Al-Chaar Model For Monotonic Loading

Al-Chaar used the dimensionless parameter λh in order to consider all the factors that determine how the infills affect the overall response of the frame; this parameter was introduced by Stefford-Smith [7] for the first time and is expressed as follows:

$$\lambda h = \sqrt[4]{\frac{E_m t sen(2\theta)}{4 E_c I_p h}}\ h_p \tag{1}$$

where E_c and E_m are the modulus of elasticity respectively of concrete and masonry, I_p is the moment of inertia of the column, t is the thickness of the infill, θ is the inclination angle of the diagonal strut, h is the infill height, h_p is the height between beams axis. Al-Chaar referred to the expression proposed by Mainstone [8] for determining the width w of the strut:

$$w = 0{,}175(\lambda h)^{0,4} \tag{2}$$

where D is the length of the strut. For masonry panels with openings it was introduced a reduction factor R_1 for the width w. This factor depends on the ratio between the size of the openings and that of the infill. Through experimental tests Al-Chaar noted that Eq. (2) lead to underestimate the actual stiffness of the infill. For this reason he suggested to use a modified modulus of elasticity for the masonry equal to $3E_m$. Finally, in order to determine the strength of the strut, he considered two modes of failure: compression and shear. The strength was set equal to the lesser of the compressive strength R_{cr} and the shear strength of the infill R_{shear}:

$$R_u = \min\left\{ R_{cr} = wt\sigma_{m0}; \frac{R_{shear}}{\cos\theta} = \frac{lt\tau_{m0}}{\cos\theta} \right\} \tag{3}$$

where σ_{m0} e τ_{m0} are respectively the compressive and the shear strength of masonry.

2.2 Cavaleri-Fossetti-Papia Model For Cyclic Loading

Concerning the model for the cyclic behaviour of the infill, these authors started from the model proposed by Klingner and Bertero [4], they observed some limits to the aforementioned model and proposed some changes in order to obtain a more general validity. With reference to the cyclic constitutive law in terms of axial force-deformation, the common features of the two models are:

- first linear elastic loading curve which continues until the panel reaches the total cracking
- strength envelope curve which accounts for the strength and stiffness degradation due to cracking; this curve considers also the residual strength of the infill after the cracking
- no tensile strength
- reloading branches with reduced stiffness compared to the elastic one

- unloading branches with slope equal to the linear elastic loading curve

In particular the modifications introduced by Cavaleri, et al. [5] are:

- double slope of the unloading branch before the restoring force vanishes
- new loading branch characterized by a zero value of the restoring force before the system begins to exhibit non zero stiffness
- envelope strength curve for the strut characterized by exponential degrading, according to the experimental results

The model suggested by Cavaleri, et al. [5] is shown in Fig. 2. The characteristics of the model are defined by a series of parameters, which depend on experimental results.

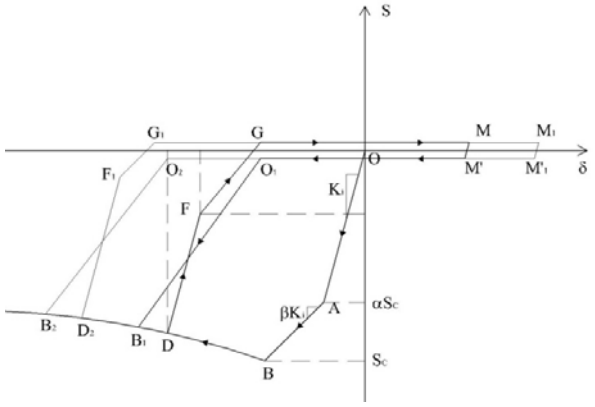


Figure 2: Cyclic behaviour of the strut according to the model proposed by Cavaleri et al. [5].

3 CALIBRATION OF THE ANALTYICAL MODEL

3.1 RC frame members

In this study a distributed plasticity model with fibre sections [13], implemented in OpenSees [14], was adopted. The elements of the RC frames were modelled by a single finite element for each beam or column. For each element 5 control sections were adopted. These sections were modelled through a fibre discretization characterized by a width of the single fibre equal to 1 cm. A bilinear stress-strain relationship with hardening ratio equal to 0.005 and Baushinger effect was assumed for the steel fibres. A constitutive law which includes the stiffness and strength degradation due to cyclic loading was considered for the concrete. Different types of behaviour were adopted for the cover concrete and the concrete core: in the first case the effect of confinement was neglected, in the second case it was included according to the model proposed by [15]. In order to validate the model two comparisons with experimental results were carried out (Fig. 3).

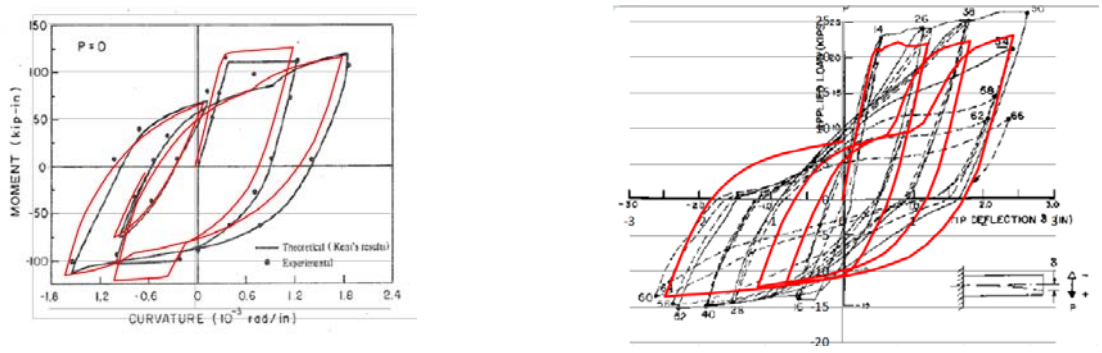


Figure 3: Analytical results (red line) compared to the experimental ones of Kent [16] (a) and Ma et al. [17] (b).

The first comparison regarded the moment-curvature response of a section and the test carried out by Kent [16]. The second comparison regarded the force-displacement response of a cantilever and the test carried out by Ma et al. [17].

In the modelling of all the tested frames an element was added at the top of the columns in order to account for possible shear failure in the column due to the interaction with infill. This is a zero length element with shear strength equal to the column one.

3.2 Infill

The infill was replaced by two struts. The width and strength were calculated according to the Al-Chaar model [3]. Once these characteristic were determined, the infill was modelled in OpenSees through a truss element that works only for axial stress. The stress-strain law of the strut was determined according to the axial force-displacement response derived from the Al-Chaar model (Fig. 4). In order to complete the modelling of the strut it was necessary to examine the cyclic behaviour. In particular it was necessary to define the parameter for determining the strength degradation and the loading and unloading cycles. The application of the model proposed by Cavaleri et al. [5] required the calibration of these parameters through comparisons with experimental results. The experimental tests considered were two: the first was conducted by the National Laboratory of Civil Engineering (LNEC) and it is available in Pires [18], the second was carried out by Colangelo [19].

3.3 Calibration of strength degradation

Initially it was necessary to determine the points which define the monotonic material behaviour assigned to the strut as shown in Fig. 4. In particular the problem was to identify as the constitutive law changes after yielding as a consequence of the strength degradation shown by the masonry. To this aim the slope of the second branch and the residual strength were varied in order to obtain a force-displacement response from the analytical model close to the envelope curve of experimental tests. The examined structures were subjected to a lateral force just in one way because only the force-displacement envelope curve was considered. Once the analyses were carried out, the constitutive law which provided the best agreement with experimental results was the one showed in Fig. 4. This law is characterized by a residual strength equal to the 25% of the ultimate strength and by a slope of the softening branch equal to 2% of the initial stiffness.

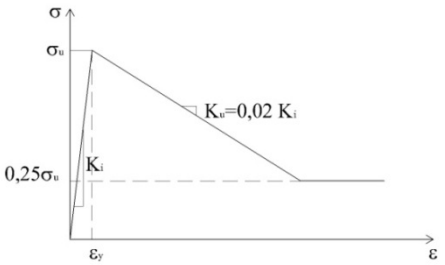


Figure 4: Constitutive law assigned to the strut.

3.4 Calibration of cyclic behaviour

The cyclic behaviour was analyzed using an hysteretic constitutive law implemented in OpenSees for the truss element. This law is characterized by three parameters related to the definition of the unloading and reloading branches: β, used to determine the degraded unloading stiffness; p_x, pinching factor used to reduce the deformation during reloading; p_y, pinching

factor used to reduce the axial force during reloading. These three parameters were calibrated in order to obtain a cyclic behaviour from the analytical model as close as possible to the one indicated by Cavaleri et al. [5]. The first examined aspect was the influence of the variation of the parameter β on the unloading branch of the strut (Fig. 5a). Cavaleri proposed a double slope of the unloading branch: the first slope equal to the elastic stiffness, the second slope lower than the first. With a value of β equal to 0.5 the constitutive law implemented in the software resulted similar to the one proposed in literature.

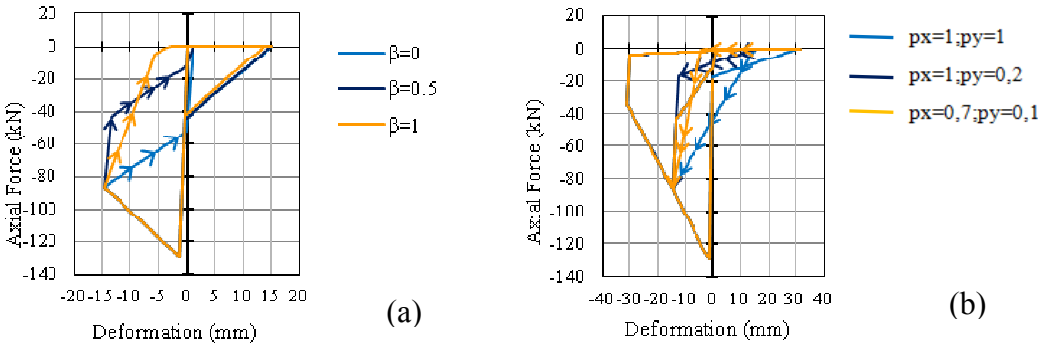


Figure 5. Strut response modified by the variation of the parameter β (a) of the parameters p_x and p_y (b)

Once β was defined, the subsequent examined aspect was the influence of the variation of the parameters p_x and p_y on the reloading branch (Fig. 5b). According to the model proposed by Cavaleri, the reloading branch should have a reduced stiffness compared to the initial one. This branch should point toward the maximum deformation which was reached at the previous cycle. Furthermore the authors identified a first reloading branch characterized by no strength but compressive strain different from zero (MO_1 in Fig. 2). With the values p_x=0.7 and p_y=0.1 the implemented constitutive law was similar to the one proposed in literature.

3.5 Comparisons between analytical and experimental results

Finally, the implemented hysteretic model was verified and improved through comparisons with experimental results (Fig. 6). Using the parameters previously defined (β=0.5, p_x=0.7, p_y=0.1), some little differences were observed between the numerical and experimental results. For this reason the model was updated in order to obtain a better correspondence between the two results: the new assumed parameters were β=0.8, p_x=0.8 and p_y=0.1.

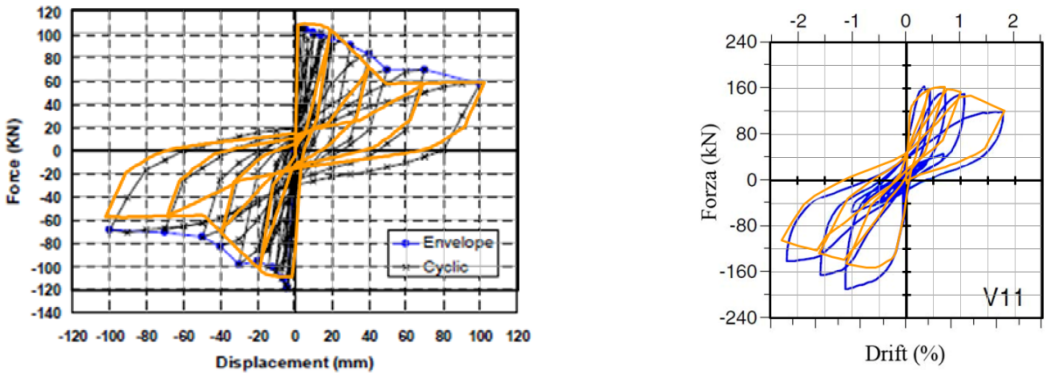


Figure 6: Numerical results for cyclic loading (orange curve) compared with experimental results (blue curve).

In Fig. 6 the numerical results obtained with these new values of the three parameters are compared with the experimental ones of Pires [18] and Colangelo [19]. From the figure it is possible to observe a good agreement between the numerical and experimental results.

4 EXAMINED CASES

Once the model was calibrated, several pushover and nonlinear dynamic analyses of existing frames were carried out in order to study the mechanisms of failure and the deformed configurations. The analyses were performed on bare and infilled RC frames in order to evaluate how the masonry panel could modify the collapse mechanism. The examined bare frame was a five storey and symmetrical structure which was designed only for gravity loads. The adopted dimensions of beams were: width equal to 300 mm and depth equal to 500 mm. The adopted dimensions of columns were variable and are indicated in Fig. 7a. The assumed mechanical properties of materials are: concrete cylinder strength f_{ck} equal to 25 MPa and steel yield strength f_{yk} equal to 430 MPa. With reference to beams and columns, the infilled frame was assumed identical to the bare one. Two types of masonry were examined: the infilled frame VAR has masonry characterized by compressive strength of 4.1 N/mm^2 and shear strength of 0.3 N/mm^2; the infilled frame UNIF has masonry characterized by compressive strength of 3.3 N/mm^2 and shear strength of 0.2 N/mm^2. Furthermore the infilled frame VAR has masonry panels with thickness variable between 24 cm and 15 cm; instead the infilled frame UNIF has all masonry panels with thickness of 15 cm. As shown in Fig. 7, three cases were examined for both infilled frames: totally infilled frame, totally infilled frame with square openings of 150 cm in all the panels, infilled frame without panels at the ground floor.

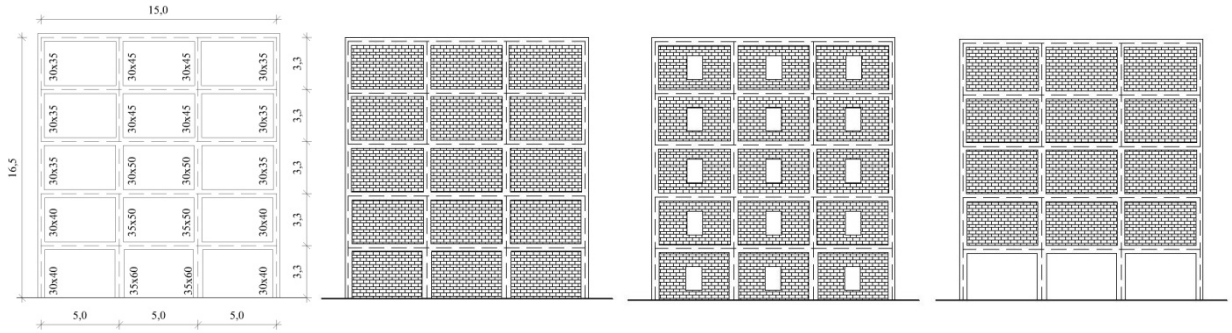


Figure 7: Representation of the examined frames: bare frame (a), totally infilled frame (b), totally infilled frame with openings (d) and infilled frame without panels at the ground floor (d).

5 PERFORMED ANALYSES

The objective of these analyses was to determine the response of the structures in terms of base shear-top displacement and to evaluate their displacement of collapse. At this displacement the configuration of collapse was examined by observing the distribution of plastic hinges and the displacement profile. The collapse, in this study, was defined according to three criteria [13]:

- achieving of the ultimate strain in confined concrete of columns
- achieving of the ultimate interstorey displacement
- achieving of the ultimate shear strength

The type of collapse “a” was associated to the first occurrence, in a confined concrete fibre, of the ultimate strain. The ultimate strain was determined using the relationship proposed by Mander et al. [15]. The second type of collapse was defined by the maximum interstorey

displacement which was determined for each floor. This displacement was determined using the ultimate drift multiplied by the storey height. The ultimate drift was calculated as the sum of the yield (θ_y) and the plastic (θ_{pl}) ones. The yield drift was calculated as a function of the geometry of the beam with the following expression proposed in literature [11]:

$$\theta_y = 0,5\varepsilon_y \frac{L_b}{h_b} \tag{4}$$

where L_b and h_b are beam length and section depth. The plastic drift θ_{pl} was determined from the ultimate ϕ_u and the yield ϕ_y curvatures and from the plastic hinge length l_p:

$$\theta_{pl} = l_p(\phi_u - \phi_y) \tag{5}$$

The yield drift of the examined frames resulted the same for all the storeys. Instead, the plastic drift was different for the external and the internal columns: for this reason the ultimate drift at each storey was assumed as the lower between the one of the external columns and the one of the internal columns. Once the ultimate drift was determined, the maximum displacement was calculated.

Pushover analyses were carried out using two set of forces: the first one with forces proportional to the first modal deformations and the second one with forces proportional to the masses. For each analysis, the displacements associated to the collapse conditions were identified. In correspondence of these displacements the plastic hinges were observed and the displacement profile was represented. This procedure allowed to find out which mechanism of collapse occurred. Subsequently incremental dynamic analyses were performed using three accelerograms (called here S1, S2, S3): each ground motion was scaled until the failure of the structure was reached. These three accelerograms are recorded ground motions characterized by an average displacement spectrum consistent with type 1 Eurocode 8 design spectrum. For each application of the accelerogram the maximum top displacement and the maximum base shear were obtained: in this way it was defined a point in the diagram top displacement-base shear. Once a point was determined for each dynamic analysis, we assessed which type of collapse occurred. At first we determined the intensity of the accelerogram which caused for the first time one of the defined collapse conditions. In correspondence of these values, the distribution of plastic hinges and the maximum displacement profile were evaluated. Furthermore each element of the frames was investigated in order to determine if it was collapsed according to one of the three conditions. The dynamic analyses were carried out only on the bare frame and on the totally infilled one.

6 RESULTS OF ANALYSES

Because of the large number of obtained results, only those related to the type of collapse "b" are illustrated in detail: in fact this type of collapse is the most significant as usually it is associated with a storey mechanism. We noted that the collapse "a" was reached for smaller displacements than the collapse "b" in all the conducted analyses, as it is shown in Fig. 10. The collapse "c", associated to the achieving of the ultimate shear strength, did never occur.

6.1 Pushover Analyses

The results of the pushover analyses are shown in Fig. 8. In general these results show that the contribution of the infill, in terms of base shear, was significant just for displacement lower than about 5 cm. For greater displacements the infills collapsed and their strength experienced a significant reduction. The collapse of the infilled frames always occurred at

displacements smaller than the ones of the bare frame. However, for a given distribution of forces, the mechanism of collapse of the infilled and of the bare frame always occurred at the same storey. Furthermore, the results relative to the infilled frame show that the presence of the openings did not modify substantially the response of the frame. The openings just reduced the lateral strength of the structure. The absence of infills at the ground floor produced, as expected, a collapse mechanism at the first storey.

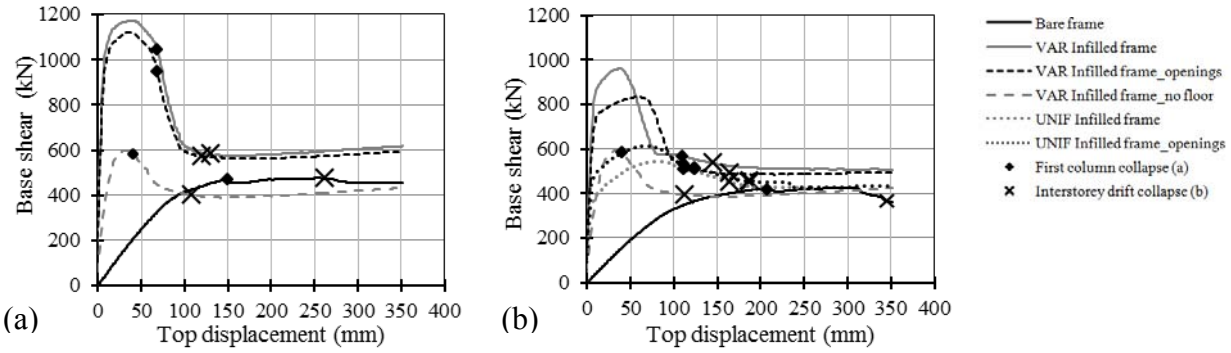


Figure 8: Pushover analyses: force proportional to masses (a), force proportional to the first mode (b).

At last we could note that the presence of the infill did not change the mechanism of collapse but affected the displacement profile: in fact, in the examined cases, the collapse occurred at the first or the third floor for both the bare and the infilled frame, while the displacement profile relative to the infilled frames was always characterized by lower values than the one of the bare frame (Fig. 9). This fact was related with the plastic hinges which, in the infilled frames, occurred only at the storey of collapse. With this distribution of hinges the collapse displacement was close to the ultimate displacement of the single storey, without taking advantage from the deformations of other the storeys.

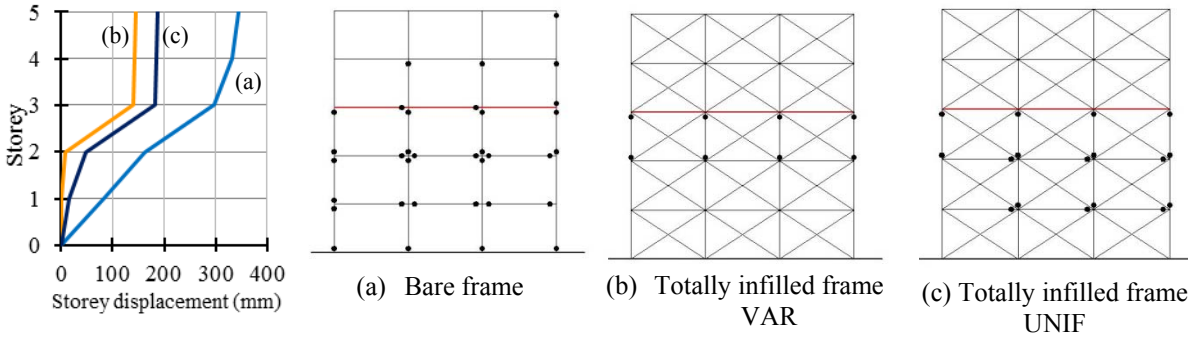


Figure 9: Displacement profile and distribution of plastic hinges at the collapse condition “b” (achievement of the ultimate interstorey drift) in the case of force proportional to the first mode.

6.2 Dynamic analyses

In the results obtained from dynamic analyses the infilled frames were characterized by a greater strength but a lower collapse displacement than the bare frames. This result is similar to the one obtained from the pushover analyses (Fig.10).

With reference to the location of the storey mechanism, a different result than the one from pushover analyses was obtained. In particular with the same accelerogram the collapse of the infilled and of the bare frames occurred at different storeys. Therefore we could not conclude that the collapse mechanism was not modified by the presence of infills. However the dynam-

ic analyses determined in the infilled frames a more spread distribution of plastic hinges at all the storeys than the pushover analyses. The displacement profile was affected by the displacements at all the storeys and not only by the one where collapse occurred. As a consequence of this distribution of plastic hinges the displacement profiles of the infilled frames resulted more similar to the one of the bare frame compared to the results of the pushover analyses. For example Fig. 11 shows the results relative to the application of the accelerogram S1.

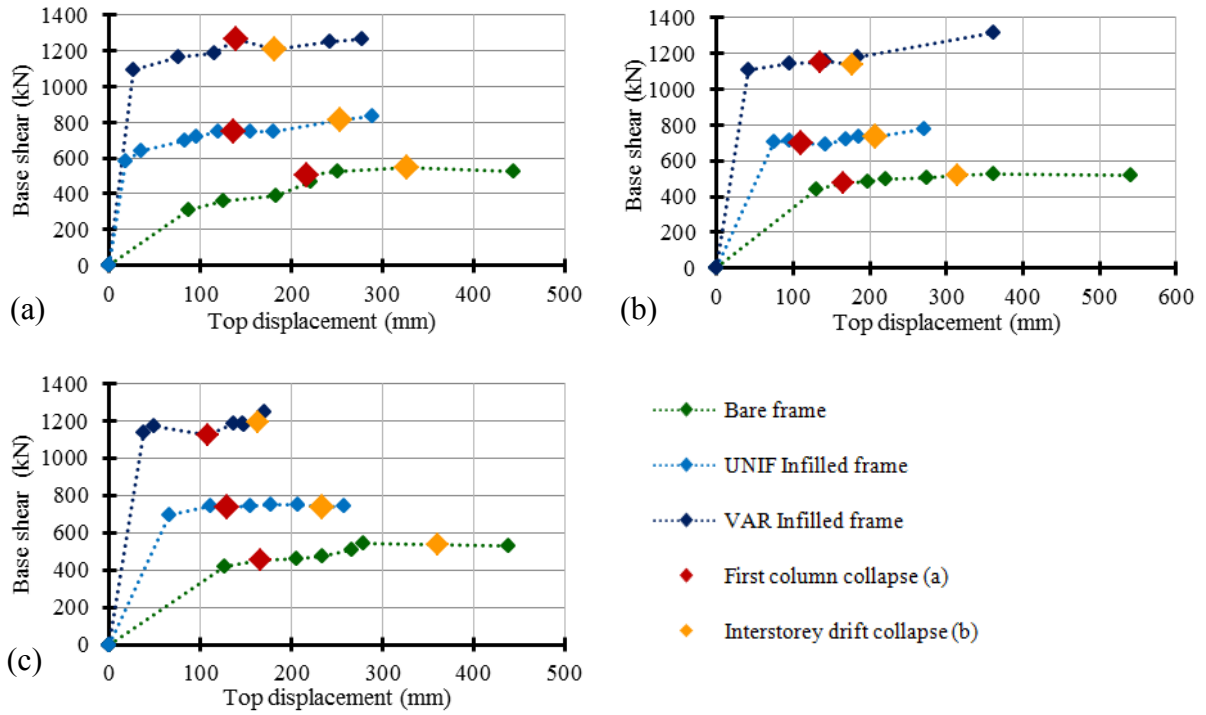


Figure 10: Top displacement-base shear curves from incremental dynamic analyses: S1 (a) S2 (b) S3 (c).

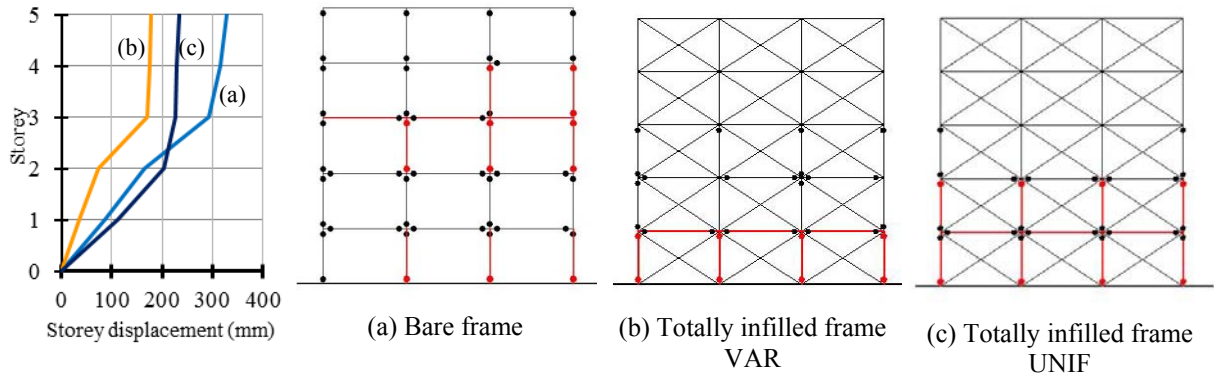


Figure 11: Displacement profiles and distribution of plastic hinges at collapse condition “b” for the record S1..

With the incremental dynamic analyses it was possible to evaluate the peak ground acceleration at the collapse. In Table 1 the values of peak ground acceleration are illustrated for the different examined cases. In particular the average of the values of the three accelerograms are shown. For all the cases the seismic input necessary to reach the collapse of the infilled frame resulted larger than the one required for the bare frame. It could be noted that the values relative to the infilled frame are about 70% higher than the ones relative to the bare frame at

collapse “a” and about 40% higher at collapse “b”. This result is related to the reduction of displacement demand in the infilled frames compared to the bare frame.

		Bare frame	Infilled frame VAR	Infilled frame UNIF
Collapse a	S1	0,408g	0,68g	0,612g
(ε_u)	S2	0.268g	0,54g	0,469g
	S3	0,26g	0,455g	0,52g
	$a_{average}$	0,312g	0,558g	0,534g
Collapse b	S1	0,544g	0,748g	0,952g
($\Delta_{u,inter}$)	S2	0,502g	0,67g	0,737g
	S3	0,585g	0.715g	0,78g
	$a_{average}$	0,544g	0,711g	0,823g

Table 1: Values of peak accelerations at collapse for each record and average values.

7 PREDICTION OF THE LIMITE-STATE DISPLACEMENT PROFILE

The Displacement Based procedure for the assessment of existing buildings, according to literature [11], requires the definition of the limite-state displacement profile at yielding and collapse. These displacement profiles could be determined in two ways, using a pushover analysis or using a simplified method based on the expected inelastic mechanism. According to the simplified approach, this study proposes a method in order to define the limite-state displacement profiles for infilled frames.

For the bare frame the limit-state displacement profile can be defined as literature proposes, adding yield displacement to the plastic displacement. The storey displacement at yield may be assumed to be linear along the height and can be determined using the Eq. (4). Assuming a column sway mechanism, at the floor in which collapse occurs the plastic displacement may be calculated as:

$$\Delta_P = \theta_P H_{0i} \tag{6}$$

where θ_P is the lower of the plastic rotation capacity of the column at base or at level i and H_{0i} is the height of level i. The limit-state displacement is thus obtained by adding yield displacement to the plastic displacement at the storey upper then the one in which collapse occurs; at the lower storeys the limit state displacement corresponds to the yield displacement.

For the infilled frames a new method is proposed. In particular the method is based on the definition of the values of yield displacements of the infilled frame as a fraction of the yield displacements of the corresponding bare frame and on the assumption that the collapse mechanism of the infilled frame is similar to the one of the bare frame. This method was then studied and applied for the considered frames. At first the displacement profile obtained from pushover analyses, for both bare and infilled frames, was observed. In particular the instant before the storey mechanism occurred was studied: at this time the displacement profile was assumed as the yield displacement. The displacement profile obtained from the pushover analyses are the ones represented with dot lines in Fig 12. In order to linearize the displacement profile, at each floor a ratio between the displacement of the infilled frame and the one of the bare frame was calculated. Then the mean of the values obtained for this ratios at each storey was applied to the displacement profile resulted from pushover analyses: for the infilled frame VAR a ratio equal to 0,18 was derived, while for the infilled frame UNIF a value equal to 0,44 was obtained. The linear displacement profile determined in this way was assumed as the yield displacement of the infilled frame (continuous lines in Figure 12).

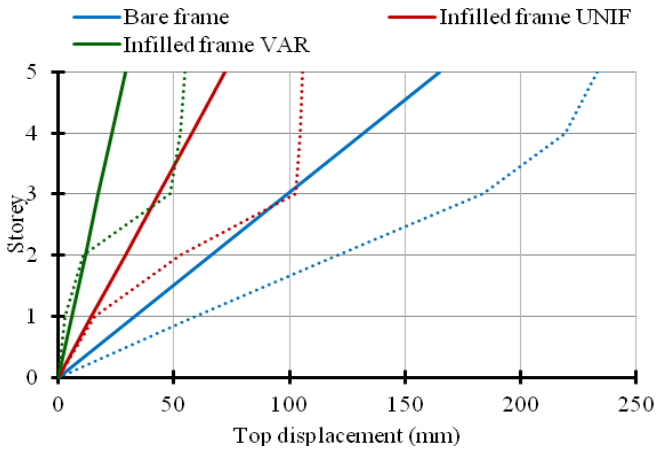


Figure 12: Yield displacement profile from pushover analyses (dot lines) and linearized (continuous lines).

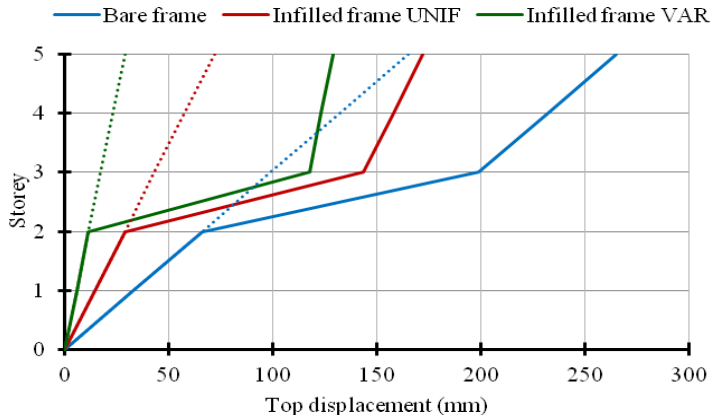


Figure 13: Limit state displacement profiles (continuous lines) compared to the yield ones (dot lines).

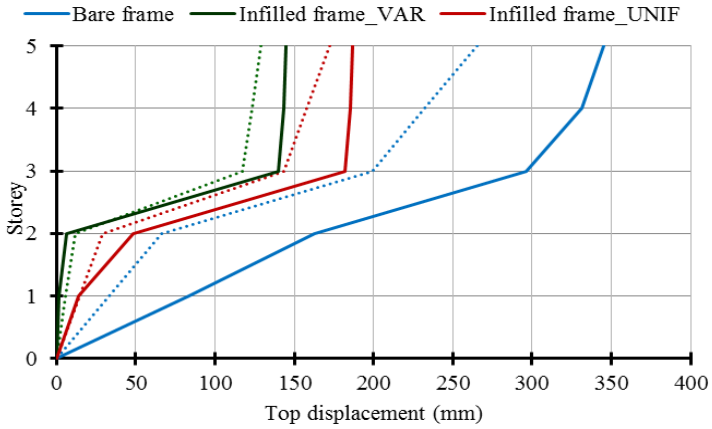


Figure 14: Limite-state displacement profile from pushover analyses (continuous lines) and from proposed procedure (dot lines).

As concern the limite-state displacement profile (Fig.13) the procedure used was the same of the bare frame, and the yield displacement was added to the plastic displacement at the storey upper than the one in which collapse occurred. In the examined cases the collapse occurred at the third floor for both the bare and infilled frames. In Fig. 14 the limit-state displacement profiles obtained from pushover analyses are compared with the ones obtained with the procedure proposed in this paper.

8 CONCLUSIONS

The analyses of the infilled frames revealed several difficulties which were especially due to the many variables related to the models of the masonry infills. In order to resolve these difficulties the comparison with experimental results was fundamental. This comparison allowed to calibrate a reliable and general model for the infills. This model is characterized by an equivalent strut with a constitutive law for cyclic loading. This model could be used also for further studies because it relies on an extensive investigation.

Once the model was calibrated, the study continued with a series of nonlinear analyses of infilled frames. The initial aim was to determine the response of structures in terms of base shear-top displacement and to evaluate the collapse displacement. At the collapse the distribution of plastic hinges and the displacement profile were analysed. In this way it was possible to determine which mechanism of collapse occurred. The obtained results show that the presence of the infill increase significantly the response in terms of strength and stiffness, while it reduced the deformation capacity. All the analyses showed a collapse of the infilled frame at displacements smaller than the ones of the bare frames. This result was related with the distribution of plastic hinges, which in the infilled frame were present only near the collapsed storey. Furthermore the larger stiffness and strength of the infilled structures caused a reduction of the displacement demand. For this reason the infilled frame was able to sustain larger peak ground accelerations than the bare frame.

Finally a simplified method was proposed for the prediction of the displacement profile of infilled frames at the yield and collapse conditions. The method, which could be used within Displacement-Based assessment procedures, was applied and verified for the examined cases.

REFERENCES

[1] S.H. Bertoldi, L.D. Decanini, C. Gavarini, Telai tamponati soggetti ad azioni sismiche. Un modello semplificato. Confronto sperimentale e numerico. *6th ANIDIS National Conference*, Perugia, Italy, 1993.

[2] Comite Euro-International Du Beton, RC frame under earthquake loading. State of the art report. Thomas Telford Publishing, London, 1996.

[3] G. Al-Chaar, Evaluating strength and stiffness of unreinforced masonry infill structures, US Army Corp of Engineers, Engineer Research and Development Center, 2002.

[4] R. Klingner, V. Bertero, Earthquake resistance of infilled frames. *Journal of the structural division,* 973-989, 1978.

[5] L. Cavaleri, M. Fossetti, M. Papia, Infilled frames: developments in the evalutaion of cyclic behaviour under lateral loads. *Structural Engineering and Mechanics,* **21***,* 469-494, 2005.

[6] L. Decanini, F. Mollaiolo, A. Mura, R. Saragoni, Seismic performance of masonry infilled R/C frame. *13th World Conference on Earthquake Engineering (13WCEE)*, Vancouver, Canada, 2004.

[7] B. Stefford-Smith, Behaviour of square infilled frames. *Journal of the Structural Division ASCE,* **91***,* 381-403, 1961.

[8] R. Mainstone, On the stiffness and strength of infilled frames. *Proceedings of the Institution of Civil Engineers,* 1971.

[9] L. Cavaleri, M. Fossetti, M. Papia, Infilled frames: developments in the evaluation of the stiffening effects of infill. *Structural Engineering and Mechanics,* **16***,* 675-693, 2003.

[10] L. Landi, O. Fabbri, P.P. Diotallevi, Simplified method for the assessment of the nonlinear seismic response of structures equipped with viscous dampers, *11th International Conference on Structural Safety & Reliability*, Columbia University, New York, June 16-20, 2013

[11] M.J.N. Priestley, G.M. Calvi, M.J. Kowalsky, *Displacement-Based Seismic Design of Structures,* IUSS Press, Pavia, 2007.

[12] A. Benedetti, L. Landi, D.G. Merenda, Rehabilitation of existing masonry structures with hysteretic dampers: a displacement based approach, *11th International Conference on Structural Safety & Reliability*, Columbia University, New York, June 16-20, 2013

[13] P.P. Diotallevi, L. Landi, Response of RC structures subjected to horizontal and vertical ground motions*. 8th U.S. National Conference on Earthquake Engineering,* San Francisco, California, USA, April 18-22, 2006.

[14] F. McKenna, G. Fenves, Open System for Earthquake Engineering Simulation. University of California, Berkley, 2005.

[15] J.B. Mander, M.J.N. Priestley, R. Park, Theoretical stress-strain model for confined concrete. *Journal of Structural Engineering, ASCE,* **114***,* 1804-1825, 1988.

[16] D. Kent, *Inelastic behaviour of reinforced concrete members with cyclic loading*, PhD Thesis, University of Canterbury, Christchurch, New Zealand, 1969.

[17] S. Ma, V. Bertero, E. Popov, Experimental and analytical studies on the hysteretic behaviour of reinforced concrete rectangular and T-Beams. EERC Report 76-02 Earthquake Engineering Research Center, University of California, Berkley, 1976.

[18] F. Pires, *Influencia das paredes de alvenaria no comportamento de estruturas reticuladas de betao armado sujeitas a accoes horizontais,* LNEC Lisbon, Portugal, 1990.

[19] F. Colangelo, Pseudo-dynamic seismic response of infilled RC frames designed for gravity load. *13th World Conference on Earthquake Engineering (13WCEE)*, Vancouver, Canada, 2004.

COMPDYN 2013
4th ECCOMAS Thematic Conference on
Computational Methods in Structural Dynamics and Earthquake Engineering
M. Papadrakakis, V. Papadopoulos, V. Plevris (eds.)
Kos Island, Greece, 12–14 June 2013

TRANSIENT FOKKER-PLANCK EQUATION WITH SPH METHOD APPLICATION IN SEISMIC DESIGN

T. Canor[1] **and V. Denoël**[2]

[1] National Fund for Scientific Research of Belgium
University of Liege, ArGEnCo Dept., Structural Engineering div.
Chemin des Chevreuils, 1 (bât B52/3)
e-mail: t.canor@ulg.ac.be

[2] University of Liege, ArGEnCo Dept., Structural Engineering div.
Chemin des Chevreuils, 1 (bât B52/3)
e-mail: v.denoel@ulg.ac.be

Keywords: Fokker-Planck equation, Smoothed Particle Hydrodynamics (SPH), Meshless method, Reliability problem

Abstract. *In reliability theory, the knowledge of the time evolution of the probability density function (pdf) of the response of a diffusive random system may be required. The time evolution of this pdf is described by the transient Fokker-Planck-Kolmogorov (FPK) equation. This equation models the conservation of probability in the system state space. The transient FPK equation is an interesting tool for the study of reduced models of structures in the context of transient random excitations such as earthquakes. In this case, the deterministic approach can be competitive compared with classical Monte Carlo simulations, especially for extreme value problems.*

This paper presents a flexible method for the resolution of transient FPK equation using a Lagrangian method inspired by the mesh-free method: Smoothed Particle Hydrodynamics (SPH) method.

Numerical implementation shows notable advantages of SPH method for solving FPK equation in an unbounded state-space compared with mesh-based method : (i) the conservation of total probability is explicitly written, (ii) no artefact is required in low density zones, (iii) the positivity of the pdf is ensured, (iv) the formalism offers straightforward extension to higher dimension systems, (v) the method is adapted for a large kind of initial conditions, even slightly dispersed distributions.

In the paper, the method is illustrated with a particular interest for reliability problems in seismic applications. Probabilities of failure are calculated for strongly nonlinear systems (nonlinear viscous forces, hysteretic behaviour) subjected to transient excitations, for reasonable computation times compared with stochastic simulations.

1 INTRODUCTION

In many engineering matters, systems are submitted to random excitations. Probabilistic theories aim at describing the time evolution of properties of a system by means of statistical characteristics such as probability density function ψ (pdf) or cumulants [1]. For a deterministic system driven by random loadings, governed by diffusive equations, the time evolution of the pdf is given by the transient Fokker-Planck-Kolmogorov (FPK) equation.

Generally, the time evolution of the random state vector $\mathbf{X}(t) \in \mathbb{R}^n$ is mathematically described by a stochastic differential equation [2],

$$d\mathbf{X} = \mathbf{f}dt + \mathbf{g}\,d\mathbf{B} \tag{1}$$

where $\mathbf{f}(t, \mathbf{X}(t)) : \mathbb{R}^+ \times \mathbb{R}^n \to \mathbb{R}^n$ is a nonlinear vector function, $\mathbf{g}(t, \mathbf{X}(t)) : \mathbb{R}^+ \times \mathbb{R}^n \to \mathbb{R}^{n\times m}$ a nonlinear matrix function and $\mathbf{W}(t) = d\mathbf{B}/dt$ a m-dimensional white noise vector. The FPK equation expresses the diffusion of probability density of $\mathbf{X}(t)$ and the conservation of the total probability. It takes the form of a second order partial differential equation [3]

$$\frac{\partial \psi}{\partial t} = -\sum_{i=1}^{n} \frac{\partial}{\partial x_i}\left(\tilde{f}_i \psi\right) + \sum_{i=1}^{n}\sum_{j=1}^{n} \frac{\partial^2}{\partial x_i \partial x_j}\left(D_{ij}\psi\right) \tag{2}$$

where $\psi(t, \mathbf{X}) : \mathbb{R}^+ \times \mathbb{R}^n \to [0, +\infty]$ is the joint-pdf of elements of $\mathbf{X}(t)$, with the initial state distribution $\psi_0(\mathbf{x})$, respecting the Kolmogorov axioms

$$\int_{\mathbb{R}^n} \psi d\mathbf{x} = 1 \qquad \text{and} \qquad \psi(\mathbf{x}, t) > 0, \forall \mathbf{x} \in \mathbb{R}^n. \tag{3}$$

and where $f_i(t, \mathbf{X}(t))$ are the drift coefficients and $D_{ij}(t, \mathbf{X}(t))$ the diffusion coefficients defined as $2D_{ij} = (\mathbf{g}\mathbf{g}^T)_{ij}$. For a dynamical system, the FPK equation models the transport of the probability density of the response $\mathbf{X}(t)$ across the state space of the system. A well-posed problem is obtained with additional far-field conditions (or vanishing condition) $\lim_{\|\mathbf{x}\|\to+\infty}(\psi f_i) = \lim_{\|\mathbf{x}\|\to+\infty}(\psi D_{ij}) = \lim_{\|\mathbf{x}\|\to+\infty}(\psi \partial_i D_{ij}) = 0$ at any time t, in an unbounded domain.

The common method to solve stochastic differential equations consists in simulating samples of the response of the system [4]. However, the rate of convergence decreases with the desired statistical order [5]. For years, many semi-analytical methods have been developed to avoid plethora of simulations (closure technique, statistical linearization or stochastic averaging), but they turn out to be too approximate or unstable in some applications. From this viewpoint, the resolution of FPK equation remains attractive for reduced systems, because a pdf contains all the statistical characteristics of a random vector and gives information about the tail distribution.

The exact explicit solution for transient FPK equation may be obtained in only few cases, in particular for linear systems driven by Gaussian excitation and some nonlinear Hamiltonian systems [3]. Nevertheless, for most of the nonlinear systems, such exact solutions cannot be calculated explicitly and the use of numerical methods is inevitable [6].

The first numerical technique used to solve FPK equation was the finite difference method [7]. In further attempts, the finite element (FE) method has also been used [8]. This method allows to solve the unsteady equation or immediately the stationary equation through an eigenvalue problem. Nevertheless, the finite element method encounters difficulties in modelling the far-field boundary conditions. To overcome this problem, Spencer [8] proposes to mesh a sufficiently large domain. In any case, the positivity of the pdf is not properly ensured: if elements

are too large or the meshed domain too small some spurious waves can propagate through the state space and spoil the quality of the solution. This FE method may thus fail in creating artificially and numerically the vanishing condition. Furthermore, the finite element method is tediously extended to multidimensional systems.

In the field of kinetic theory, the FPK equation presents a great interest for modelling complex fluid dynamics. Chauvière and Lozinski [9, 10] use a spectral discretization method. In this approach, some drawbacks similar to the FE method may be encountered as the dependence of the positivity with the refinement of the mesh and instability for high gradient in the pdf [10]. Ammar *et al.* [11, 12, 13] develop a method based on a separate representation of variables, which allows to decouple the numerical integration in each dimension of the system. In complex fluid theory, the FPK equation (1) is formulated for a random state vector $\mathbf{X}(t)$ defined on a bounded domain [14]. However, in mechanical or civil engineering [1], the occurrence of rare events is a major issue and the question of the tail distribution is not addressed. Furthermore, in a bounded domain, the stability and the efficiency of the method is not the same issue as it is in an unbounded state space.

The time dependence of systems modelled with Eq.(1) is explicitly considered in the time dependence of drift and diffusion coefficients. In the FE method, the matrices of the system must be computed at each time step and the modal reduction for transient problem is not possible anymore. And yet, the explicit time dependence of drift and diffusion coefficients is a basic problem in transient dynamics. For example, in earthquake engineering [15], the seismic excitation is usually modeled as a diffusive process modulated by a time window. Therefore, the FPK equation has explicit time-dependent coefficients.

In this work, a particle strategy is explored to deal with the FPK equation related to dynamical diffusive systems. The FPK equation is viewed as a convection-diffusion equation in a Lagrangian paradigm. The smoothed particle hydrodynamics (SPH) method, a meshfree particle method, is used for the resolution of FPK equation.

An efficient method for solving the transient FPK equation in an unbounded domain must be able (i) to adaptively cover all the state space from initial condition to steady-state, (ii) to ensure the vanishing condition in the far field (iii) to precisely capture important distortions of the pdf and (iv) to assuredly maintain the positivity of pdf. The SPH method, with the implementation details given next, fulfils all these requirements.

The SPH method, as other particle methods, has been widely used for the resolution of diffusion equations. This method was developed by Lucy in 1977 [16] and first applied to astrophysical problems. Thus far, the method has been applied to many problems of continuous and discontinuous dynamics as fluid flow problems [17], damage and fracture [18], impact computation [19] or heat conduction [20]. The main principles of the SPH method are widely developed in [21, 22, 23]. In the context of kinetic theory, Chaubal *et al.* [24] applies first SPH technique to the dynamics of liquid crystalline polymers on a closed domain. Particle strategies for solving the Fokker-Planck equation are commonly used in this theory [11, 25]. Inspired by these previous works, this paper proposes an application of the SPH formalism to solve the transient FPK equation related to diffusive random systems independently of their size. In this context, a new formulation of the conservation equation using the Lagrangian formalism is proposed and some considerations to deal with the vanishing condition are exposed.

In the following sections, the SPH method is briefly exposed, then the FPK equation is transformed into the SPH formalism. Finally, the developments are applied to some seismic engineering problems.

2 SMOOTHED PARTICLE HYDRODYNAMICS

The SPH method consists in transforming a set of PDE's into integral equations by the use of an interpolation function to numerically estimate scalar or vectorial fields (density, velocity, energy) at a point. Thus, the evaluation of an integral is transformed into a sum over some neighbouring particles. In this method, a grid is unnecessary, because interactions between neighbouring particles are modelled with interpolation functions.

2.1 Integral representation of a field

The concept of *integral representation* of a field $f(\mathbf{x})$ in SPH method uses the properties of the Dirac-delta function $\delta(\mathbf{x})$, i.e.

$$\int_{\mathbb{R}^n} f(\mathbf{x}')\delta\left(\mathbf{x}-\mathbf{x}'\right)d\mathbf{x}' = f(\mathbf{x}) \tag{4}$$

The function $\delta(\mathbf{x})$ cannot be numerically represented. Therefore, the Dirac delta function is replaced by a function $W(r,h)$, the *kernel function*, such that,

$$\lim_{h\to 0} W\left(|\mathbf{x}-\mathbf{x}'|,h\right) = \delta(\mathbf{x}-\mathbf{x}') \tag{5}$$

with h the *smoothing length*. The *kernel approximation* of $f(\mathbf{x})$ with the kernel function is

$$< f(\mathbf{x}) >= \int_{\mathbb{R}^n} f(\mathbf{x}')W(|\mathbf{x}-\mathbf{x}'|,h)d\mathbf{x}'\,. \tag{6}$$

According to the *Delta function property* (5), $< f(\mathbf{x}) >\to f(\mathbf{x})$ when $h\to 0$. Eq. (6), as a smoothed approximation of $f(\mathbf{x})$, is then discretized, for a number N_p of particles, as

$$< f(\mathbf{x}) >\approx \sum_{j=1}^{N_p} f(\mathbf{x}_j)W(|\mathbf{x}-\mathbf{x}_j|,h)\Delta V_j = \sum_{j=1}^{N_p}\frac{m_j}{\rho_j}f(\mathbf{x}_j)W(|\mathbf{x}-\mathbf{x}_j|,h) \tag{7}$$

where m_j, ρ_j and ΔV_j are respectively the mass, the density and the volume of a particle j, respectively. Eq. (7) is the *particle approximation* of the field $f(\mathbf{x})$, which can be particularized at a particle i,

$$< f(\mathbf{x}_i) >= \sum_{j=1}^{N_p} f(\mathbf{x}_j)W_{ij}\Delta V_j \tag{8}$$

with $W_{ij}=W(r_{ij},h_i)$ and r_{ij} the distance between $\mathbf{x}_i$ and $\mathbf{x}_j$. Eq. (8) highlights the difference between the particle value $f(\mathbf{x}_i)$ and the kernel approximation $< f(\mathbf{x}_i) >$. These values must not be confused [17], even if they can be sufficiently close if h is small enough.

2.2 Kernel function

In SPH method, a kernel function must [23] (i) be normalized to one, (ii) respect the Delta function property, (iii) be positively defined on a compact support, (iv) be monotonically decreasing, (v) be symmetric and (vi) smooth. In this work, the original Lucy kernel function is used. Introduced by Lucy in 1977 [16], this kernel is a polynomial function continuously derivable over its compact support, such that

$$W(R,h) = \alpha_d\left(1+3R\right)\left(1-R\right)^3\mathbb{I}(R\in[0,1]) \tag{9}$$

with $R = r/h$ and $\mathbb{I}(\mathcal{A})$ the indicator function of the subset $\mathcal{A}$. The parameter α_d depends on the dimension n of the state space. From (9), α_d is equal to $5/\pi h^2$, $105/16\pi h^3$ and $28/\pi^2 h^4$ in a two-,three- and four- dimensional state spaces, respectively.

3 SPH formulation of FPK equation

3.1 Lagrangian paradigm

In the context of fluid dynamics, an Eulerian description of motion can be imagined as the one given by a fixed observer looking at the evolution of fluid properties in a finite, fixed and undeformable volume. Contrarily, a Lagrangian description of motion can be viewed as the motion described by observers sitting on a moving particles. These views modify the interpretation of the equations of motion: in a Lagrangian formalism (in SPH), the integration points are moving according to trajectories depending on the modelled system.

The Eulerian formulation of a convection-diffusion phenomenon of a scalar field ϕ is transformed into a Lagrangian formulation by introducing the concept of *material derivative* D/Dt,

$$\frac{D\phi}{Dt} = \frac{\partial \phi}{\partial t} + \mathbf{v} \cdot (\nabla \phi) = \frac{\partial \phi}{\partial t} + \sum_{i=1}^{n} v_i \frac{\partial \phi}{\partial x_i} \tag{10}$$

where $\mathbf{v}$ is the medium velocity. The FPK equation (2) can also be recast into such a Lagrangian formalism, such as

$$\frac{\partial \psi}{\partial t} = -\sum_{i=1}^{n} \frac{\partial}{\partial x_i} \left(\psi \left(\tilde{f}_i - \sum_{j=1}^{n} \frac{\partial D_{ij}}{\partial x_j} - \frac{1}{\psi} \sum_{j=1}^{n} D_{ij} \frac{\partial \psi}{\partial x_j} \right) \right) = -\sum_{i=1}^{n} \frac{\partial}{\partial x_i} \left(v_i \psi \right) \tag{11}$$

where $v_i(\mathbf{X}, t)$ is the i-th component of $\mathbf{v}(\mathbf{X}, t)$ defined as

$$v_i = \tilde{f}_i - \sum_{j=1}^{n} \frac{\partial D_{ij}}{\partial x_j} - \frac{1}{\psi} \sum_{j=1}^{n} D_{ij} \frac{\partial \psi}{\partial x_j} \,. \tag{12}$$

The velocity $\mathbf{v}$, so-called *diffusion velocity* [26], has a term divided by ψ, but there is no hidden difficulties. Indeed, if ψ represents a density of probability, a particle cannot have a density equal to zero because it cannot have a mass equal to zero; nor it can occupy an infinite volume.

The conservation equation (11) is further developed to introduce the total derivative

$$\frac{\partial \psi}{\partial t} + \sum_{i=1}^{n} \frac{\partial}{\partial x_i} \left(v_i \psi \right) = \frac{D\psi}{Dt} + \sum_{i=1}^{n} \psi \frac{\partial v_i}{\partial x_i} = \frac{D\psi}{Dt} + \psi \nabla \cdot \mathbf{v} = 0 \,. \tag{13}$$

and the vectorial equation of transport across the state space simply reads

$$\frac{d\mathbf{X}}{dt} = \mathbf{v} \tag{14}$$

with $\mathbf{v}$ the velocity field defined in (12).

In this method, the steady-state regime must be interpreted from a Lagrangian perspective: the particle velocity is not null, but the particles keep on moving along $(n-1)$-dimensional isoprobability manifolds, as shown in [27].

3.2 Conservation equation

The *quantity of probability* μ_j carried by a particle j, (analogous to mass in fluid), is defined as the product of the particle volume ΔV_j and the particle density ψ_j. Taking into account (8), the particle approximation of ψ at particle i is

$$< \psi(\mathbf{x}_i) >= \sum_{j=1}^{N_p} \psi_j W_{ij} \Delta V_j = \sum_{j=1}^{N_p} \mu_j W_{ij} \tag{15}$$

where $\mu_j = \psi_j \Delta V_j$. In dedicated literature, Eq.(15) is mentioned as the *summation density* approach. The conservation of mass is explicitly formulated in the particle approximation, because the mass of each particle is invariant. From a computational point of view, there is no need to solve the conservation equation as a differential equation. At this stage, the positivity of the pdf is ensured, because each particle approximation is a sum of positive terms.

The initialization of masses is a key issue in the method. From the arbitrary initial distribution of particles in the state space, the reconstructed field is calculated where particles are initially located $< \psi(\mathbf{x}_j) >$. The masses μ_j and the initial particle values $\psi_{0,j}$ are related by $\mu_j = \psi_{0,j} \Delta V_{0,j}$, where $\Delta V_{0,j}$ is the initial volume associated with the j-th particle, which corresponds to a hypercubic subspace if the initial arrangement of particles is regular. After initialization, the particle masses are kept constant in time. Consequently, with this initialization technique, there is no equation to solve, neither for the initialization of masses, nor during the transient resolution.

3.3 Transport equation

According to (15), the probability density of a particle i depends on W_{ij} and therefore on particle positions at time t. To calculate the position of a particle i, Eq.(14) is integrated. A first-order forward Euler integration scheme is used

$$\mathbf{X}_i^{t+\Delta t} = \mathbf{X}_i^t + \mathbf{v}_i^t \Delta t \tag{16}$$

(the comparison with a leap-frog scheme is also shown in [27]). The velocity is discretized, according to the concept of integral approximation of a vector field. Equation (12) becomes

$$\mathbf{v}(\mathbf{X}) \;\; = \;\; \mathbf{f}(\mathbf{X}) - \mathbf{D} \frac{\nabla \psi(\mathbf{X})}{\psi(\mathbf{X})} \tag{17}$$

and the particle approximation of Eq.(17) is

$$\mathbf{v}_i^t = \mathbf{f}(\mathbf{X}_i^t) - \mathbf{D} \frac{< \nabla \psi(\mathbf{X}_i^t) >}{< \psi(\mathbf{X}_i^t) >} \tag{18}$$

where $< \psi(\mathbf{X}_i^t) >$ is calculated with Eq.(15) and $< \nabla \psi(\mathbf{X}_i^t) >$ calculated as

$$< \nabla \psi(\mathbf{X}_i^t) >= \sum_{j=1}^{N_p} \mu_j \nabla_i W_{ij} \, . \tag{19}$$

The Lagrangian formalism makes the method relatively independent with regard to the final solution. With SPH, particles move from the initial to the stationary distribution by themselves. Contrarily, in mesh-based method, the mesh must cover a large space to be able to represent every transient step of the solution.

3.4 Smoothing length

To adapt the smoothing length with particle position, different authors suggest relations to maintain the number of neighbouring particles constant. The simplest relation consists in keeping the product $(h_0 \sqrt[d]{\rho_0})_i$ for each particle constant in time, where d is the dimension of the considered space. The smoothing length is updated with the evolution of ρ_i, thus

$$h_i = h_{0,i} \left(\sqrt[d]{\frac{\rho_0}{\rho}} \right)_i . \tag{20}$$

Interaction between particles is a key problem in SPH method. Indeed, a particle i interacts only with particles contained in its compact support. Therefore, it is useless to check possible interaction if two particles are too far from each other. Specific literature widely covers this topic [22, 23].

3.5 Estimation of statistical moments

The SPH method and the integral representation of pdf also allow an approximation of statistical moments of the random state vector $\mathbf{X} = [X_1..., X_n]^{\mathbf{T}}$. Indeed, the particle approximation of statistical moments reads

$$< E[X_1^{\alpha_1}...X_n^{\alpha_n}] >= \int_{\mathbb{R}^n} x_1^{\alpha_1}...x_n^{\alpha_n} < \psi(\mathbf{x}) > d\mathbf{x} \tag{21}$$

where $E[\cdot]$ is the expectation operator and $\alpha_i \in \mathbb{N}$ for $i = 1..., n$. Therefore, if the masses are reasonably well calculated by the previous relations, Eq.(21) in an SPH formalism yields

$$< E[X_1^{\alpha_1}...X_n^{\alpha_n}] > \approx \sum_{i=1}^{N_p} \left(\prod_{k=1}^{n} (\mathbf{X}_i)_k^{\alpha_k} \right) < \psi_i > \Delta V_i. \tag{22}$$

In this approximation technique, particles are seen as integration points. The volume ΔV_i occupied by the i^{th} particle is also considered as the integration volume. This approximation means that the kernel approximation $< \psi_i >$ of the pdf is constant in the volume of the particle. This integration technique is similar to the rectangle integration method. The computation of statistical moments is posterior to the solution of the FPK equation.

The choice of ΔV_i as integration volumes is justified, if the reciprocity in the interaction between particles is imposed. The reciprocity exists, if W_{ij} is equal to W_{ji}, as demonstrated in [27]. Among available ways to have this property, the method adopted here consists in averaging the reciprocal kernel functions between two particles as

$$W_{ij} = W_{ji} = \frac{1}{2} \left(W(r_{ij}, h_i) + W(r_{ij}, h_j) \right) . \tag{23}$$

3.6 Probability of exceedance

The proposed SPH method also allows the computation of probability function depending on the pdf of the state vector $\mathbf{X}(t)$. The mathematical formulation of a structural reliability problem [15] consists in calculating the probability of exceedance P_f defined as the probability integral

$$P_f(t) = \int_{\Omega_f} \psi(t, \mathbf{x}) d\mathbf{x} \tag{24}$$

where $\Omega_f \in \mathbb{R}^n$ denotes the subspace where exceedance (or failure) occurs. In the presented SPH method, the calculation of such a probability may be estimated directly: at a given time, only the mass of particles contained in the domain Ω_f contributes to the probability of failure. Therefore, an estimation of the probability of failure $< P_f(t) >$ at a given time t is

$$< P_f(t) >= \sum_{j=1}^{N_p} \mu_j \mathbb{I}(\mathbf{X}_j(t) \in \Omega_f) \tag{25}$$

where $\mathbb{I}(\mathcal{A})$ is the indicator function of a subset $\mathcal{A}$.

4 Applications

The transient FPK equation finds a potential interest in seismic design. In this topic, reliability and probability of failure are usual questions. The estimation of a probability of exceedance is therefore required. In this section, the resolution of FPK equation with SPH method is applied to reduced models of structures submitted to seismic loadings. First, a two-dimensional system damped by a nonlinear fluid viscous devices is considered, and then a three-dimensional system system having a nonlinear hysteretic behaviour.

4.1 Probability of exceedance of a nonlinear SDOF oscillator

Fluid dampers installed on civil structures are commonly used as energy sinks for seismic protection. The structure is supposed to mainly respond in its first mode and a nonlinear viscous damper is considered to mitigate the vibrations due to an earthquake. The nonlinear behaviour of the damping device deeply influences the response of the structure [28]. The equation of motion for the modal coordinate q is

$$\ddot{q} + 2\xi\omega_0\dot{q} + \eta \text{sign}(\dot{q})|\dot{q}|^\alpha + \omega_0^2 q = aW \tag{26}$$

where ω_0 and ξ are the natural circular frequency and the damping ratio of the system, respectively. The nonlinear viscous force is characterized by the damper exponent α typically ranging from 0.2 to 1 [29] and η the damping coefficient (related to the generalized mass of the system). The excitation is modelled by a white noise $W(t)$ modulated by a time window $a(t)$ defined as

$$a(t) = \begin{cases} \left(\frac{t}{t_1}\right)^{n_1}, & t \leq t_1 \\ 1, & t_1 < t < t_2 \\ \exp\left(n_2\left(t_2 - t\right)\right) & t_2 \leq t \end{cases} . \tag{27}$$

Thus, the only non-zero element of the diffusion matrix is $D_{22}(t) = S_0 a^2$ with $E[W(t)W(t+\tau)] = 2S_0\delta(\tau)$. The approximation of the probability of exceedance P_f developed in Section 3.5 is illustrated in this example with an outcome space defined as $\Omega_{\mathcal{T}} = \{q \in \mathbb{R} : |q| > \mathcal{T} > 0\}$ with $\mathbf{x} = [q\ \dot{q}]^T$ the state vector of the system with $\mathcal{T}$ a threshold related to the ductility of the system.

The parameters have the numerical values: $\omega_0 = \pi$, $\xi = 1\%$, $\eta = 0.25$, $\alpha = 0.35$ and $S_0 = 0.2$. The time window is characterized by $n_1 = 1$, $t_1 = 2$, $n_2 = 2$ and $t_2 = 6$. The initial uncorrelated Gaussian distribution has standard deviations equal to 0.15 for q and 0.10 for $\dot{q}$ and mean values equal to zero. The number of particles is 1650 and the Courant number is 0.8. Initially, particles are regularly arranged in a rectangle with edge sizes of 1.2 and 0.8 in q and $\dot{q}$ directions, respectively.

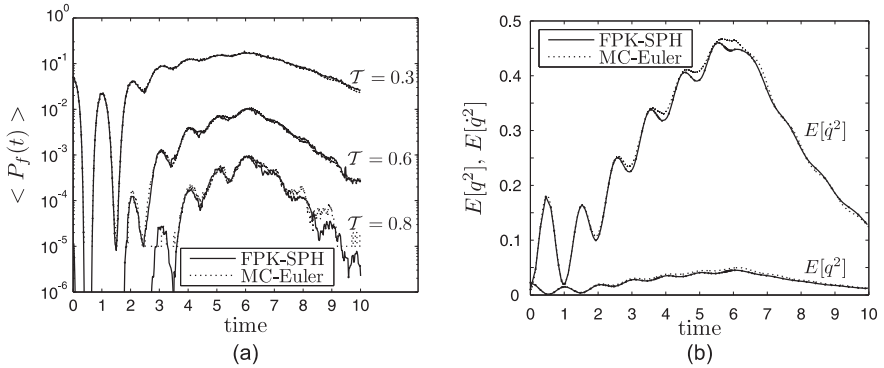


Figure 1: SDOF system with nonlinear viscous damper ($N_p = 1650$). The probability of exceedance P_f (a) for the system (26) is estimated for different thresholds $\mathcal{T}$. The results obtained by solving FPK with SPH are compared with Monte-Carlo (MC) simulations (10^5samples). The estimated second-order moments of q and $\dot{q}$ are compared with simulations (b) .

Figure 1-a shows $< P_f >$ for different thresholds $\mathcal{T}$ calculated with FPK equation and Eq.(25). These results are compared with Monte-Carlo simulations (10^5 samples and 2^{16} time steps). For the Monte-Carlo method, Eq.(26) is integrated with a forward Euler scheme [4]. This figure shows the good agreement between results obtained with both methods, especially for high probabilities of exceedance. As expected, the convergence of stochastic simulations for low probabilities (in the order of 10^{-4}) is not achieved. Because the response is not ergodic, a larger number of simulations is required to obtain accurate results. However, the computation of FPK equation has required about 11000 adaptive time steps and a single simulation has covered six orders of magnitude. Figure 1-b shows the estimation of the second-order moments of q and $\dot{q}$ estimated with Eq.(21) and highlights the ability of the method to capture the oscillations of the moments (and therefore in the system response). Some small differences with simulation results are observed, but the second-order moments of q and $\dot{q}$ are properly estimated, despite an order of magnitude of difference between them, because the pdf is more stretched in the $\dot{q}$ direction than in the q direction.

4.2 Probability of exceedance of a hysteretic oscillator

As another application, an SDOF system presenting a nonlinear elastoplastic behaviour and subjected to a transient seismic loading is considered. This example shows that the proposed method gives accurate information about the tail distribution through a reliability problem.

The equations of motion for a second-order structural system with hysteretic behavior are

$$\begin{cases} \ddot{q} + 2\xi\omega_0\dot{q} + \Phi = a^\star W \\ \Phi = \omega_0^2\left(\alpha q + (1-\alpha)z\right) \\ \dot{z} = \dot{q}\left(A - \left(\beta \text{sign}(\dot{q}z) + \gamma\right)|z|^n\right) \end{cases} \tag{28}$$

with q the dimensionless coordinate of the SDOF system, ξ the structural damping ratio and ω_0 the natural circular frequency. The excitation is a white noise $W(t)$ ($E[W(t)W(t+\tau)] = 2S_0\delta(\tau)$) modulated by a time window $a^\star(t)$, while $\Phi(q,z)$ is the elastoplastic restoring force. This force is a convex combination of a linear stiffness component and a hysteretic component depending on the hardening parameter α. The hysteretic behavior is controlled by the Bouc-Wen model characterized by the dimensionless variable z gathering the loading history and by the four parameters A, γ, β and n [30]. The outcome space is defined as $\Omega_\mathcal{T} = \{q \in \mathbb{R} : |q| > \mathcal{T} > 0\}$ for different values for the threshold $\mathcal{T}$.

In this example, the parameters of the system are chosen as $\omega_0 = \pi$, $\xi = 5\%$, $\alpha = 0.5$ and $S_0 = 1.0$ and those of the Bouc-Wen model are $A = 1$, $\gamma = 0.5$, $\beta = 0.5$, $n = 1$. This set of data provides a significantly nonlinear response. The time window is chosen as

$$a^\star(t) = f_{max} \frac{t}{t_{max}} \exp\left(1 - \frac{t}{t_{max}}\right) \tag{29}$$

with $t_{max} = 2$ and $f_{max} = 1$. The initial uncorrelated Gaussian distribution is slightly dispersed with standard deviations equal to 0.05 and means equal to zero for q, $\dot{q}$ and z. The number of particles is 9261 (=21^3) and the Courant number is 0.8. Initially, particles are regularly arranged in a cube with an edge size of 0.4, and thus with 21 particles along each dimension.

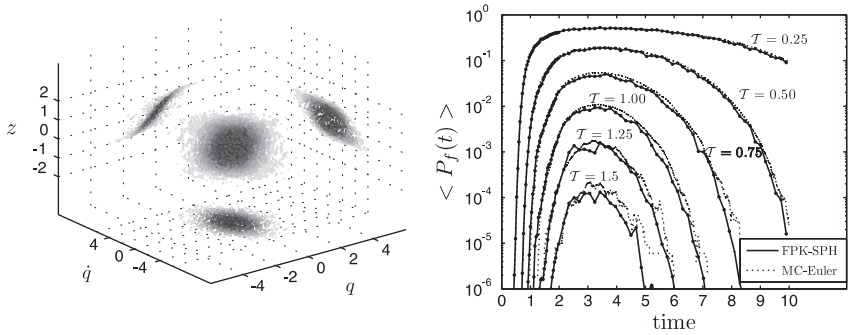


Figure 2: (a) Probability density function ψ of the elastoplastic oscillator calculated with 9261 particles at time $t = 3.6$ corresponding to the maximum variance. The darker the larger pdf, the lighter the lower pdf. Side and bottom views are projections on lateral faces; they illustrate the saturation effect on $z \in [-1; 1]$ although the solution space is $\mathbb{R}^3$. (b) Probability of exceedance P_f for system (28) estimated for different thresholds $\mathcal{T}$. Results obtained with SPH are compared with Monte-Carlo (MC) simulations ($5 \cdot 10^5$samples).

This example shows in a three-dimensional state space that information about the tail distribution is accurately obtained with a reasonable number of particles and a number of time steps limited to 35000. With only one run, the proposed method covers six orders of magnitude in the probability of exceedance, see Fig. 2-b, whilst the Monte Carlo simulation, presented here with $5 \cdot 10^5$ runs, poorly estimates probabilities lower than 10^{-5}. It would require approximately 10^8 runs to capture probabilities less than 10^{-5}.

Besides this apparent robustness regarding the adaptation of the particle field from initial to transient states, the SPH algorithm proves to be efficient in containing the particles in the authorized subspace of the response domain. Indeed, the history variable z in this model is known to be limited to $z \in [-A; A]$, as illustrated in Figure 2-a. Although no specific boundary condition is imposed, i.e. particles are thus free the move in the state space according to the governing equations, the SPH algorithm contains particles in the subspace limited by planes $z = \pm 1$, as shown by the S-shaped projection of the pdf in the (q, z) plane.

5 Conclusions

In this paper, a contribution in the topic of the resolution of FPK equation with SPH method has been exposed. Some results in two and three dimensions are shown to illustrate the relevance of the proposed developments and assumptions. To conclude, some advantages and limitations are objectively summarized.

The Lagrangian formalism makes the method robust to deal with a large range of initial conditions even very different from the steady-state distribution. Only an accurate representation of the initial condition (even slightly dispersed) must be worried about. Furthermore, the implemented SPH method ensures the positivity of the pdf.

Nevertheless, the method has also some limitations. For instance, the stationary distribution cannot be directly computed which makes it more suited to transient problems. In the context of extreme value problems, the SPH method is limited because particles are not necessary located in low density zones. From a computational point of view, for a large number of particles, the computation of the interaction can turn out to be time consuming and the recourse to advanced cell mapping or sorting algorithm could be mandatory.

Although being mainly exploratory, this work throws light on a new possible use of the SPH method. As presented in this paper, the method offers already the possibility to rapidly and easily extend the formalism to multidimensional spaces and to have an accurate representation of the transient regime of the FPK equation.

Acknowledgment

The authors would like to acknowledge the National Fund for Scientific Research of Belgium for its support.

REFERENCES

[1] Y.K. Lin and G.Q. Cai. *Probabilistic Structural Dynamics. Advanced Theory and Applications*. McGraw-Hill, New-York, 2nd edition, 2004.

[2] B. Oksendal. *Stochastic differential equations*. Springer-Verlag, 3rd edition, 1992.

[3] H. Risken. *The Fokker-Planck Equation. Methods of solution and applications*. Springer-Verlag, 2nd edition, 1996.

[4] D.P. Kroese, T. Taimre, and Z.I. Botev. *Handbook of Monte Carlo Methods*. Wiley series in probability and statistics, 2011.

[5] M. Grigoriu. *Stochastic Calculus. Applications in Science and Engineering*. Birkhauser, Boston, 1st edition, 2002.

[6] C. Soize. Steady-state solution of Fokker-Planck equation in high dimension. *Probabilistic Engineering Mechanics*, 3(4):196–206, 1988.

[7] J. S. Chang and G. Cooper. A practical difference scheme for Fokker-Planck equations. *Journal of Computational Physics*, 6:1–16, 1970.

[8] B.F. Spencer and L.A. Bergman. On the numerical solution of the Fokker-Planck equation for nonlinear stochastic systems. *Nonlinear Dynamics*, 4:357–372, 1993.

[9] A. Lozinski and C. Chauviière. A fast solver for Fokker-Planck equation applied to viscoelastic flows calculations: 2d fene model. *Journal of Computational Physics*, 189(2):607–625, 2003.

[10] C. Chauvière and A. Lozinski. Simulation of dilute polymer solutions using a Fokker-Planck equation. *Computers & Fluids*, 33(5-6):687–696, 2004.

[11] F. Chinesta, G. Chaidron, and A. Poitou. On the solution of Fokker-Planck equations in steady recirculating flows involving short fiber suspensions. *Journal of Non-Newtonian Fluid Mechanics*, 113(2-3):97–125, 2003.

[12] A. Ammar, B. Mokdad, F. Chinesta, and R. Keunings. A new family of solvers for some classes of multidimensional partial differential equations encountered in kinetic theory modeling of complex fluids. *Journal of Non-Newtonian Fluid Mechanics*, 139(3):153–176, 2006.

[13] A. Ammar, B. Mokdad, F. Chinesta, and R. Keunings. A new family of solvers for some classes of multidimensional partial differential equations encountered in kinetic theory modelling of complex fluids: Part II: Transient simulation using space-time separated representations. *Journal of Non-Newtonian Fluid Mechanics*, 144(2-3):98–121, 2007.

[14] L. Chupin. Fokker-Planck equation in bounded domain. *Annales de l'Institut Fourier*, 60(1), 2010.

[15] A. Der Kiureghian. Structural reliability methods for seismic safety assessment: a review. *Engineering Structures*, 18(6):412–424, 1996.

[16] L. B. Lucy. A numerical approach to the testing of the fission hypothesis. *Astronomical Journal*, 82:1013–1024, 1977.

[17] J. Feldman and J. Bonet. Dynamical refinement and boundary contact forces in SPH with applications in fluid flow problems. *International Journal for Numerical Methods in Engineering*, 72:295–324, 2007.

[18] T. Rabczuk and T. Belytschko. A three-dimensional large deformation meshfree method for arbitrary evolving cracks. *Computer Methods in Applied Mechanics and Engineering*, 196(29-30):2777–2799, 2007.

[19] G. R. Johnson, R. A. Stryk, and S. R. Beissel. SPH for high velocity impact computations. *Computer Methods in Applied Mechanics and Engineering*, 139(1-4):347–373, 1996.

[20] P.W. Cleary and J.J. Monaghan. Conduction modelling using Smoothed particle hydrodynamics. *Journal of Computational Physics*, 148:227–264, 1999.

[21] P. W. Randles and L. D. Libersky. Smoothed particle hydrodynamics: Some recent improvements and applications. *Computer Methods in Applied Mechanics and Engineering*, 139:375–408, 1996.

[22] J. J. Monaghan. Smoothed particle hydrodynamics. *Reports on Progress in Physics*, 68:1703–1759, 2005.

[23] G.R. Liu and M.B. Liu. *Smoothed Particle Hydrodynamics. A meshfree particle method.* World Scientific Publ., 2003.

[24] C.V. Chaubal, A. Srinivasan, O. Egecioglu, and L.G. van Leal. Smoothed particle hydrodynamics techniques for the solution of kinetic theory problems. *Journal of Non-Newtonian Fluid Mechanics*, 70:125–154, 1997.

[25] A. Ammar and F. Chinesta. *A Particle Strategy for Solving the Fokker-Planck Equation Modelling the Fiber Orientation Distribution in Steady Recirculating Flows Involving Short Fiber Suspensions - Meshfree Methods for Partial Differential Equations II*, volume 43 of *Lecture Notes in Computational Science and Engineering*, pages 1–15. Springer Berlin Heidelberg, 2005.

[26] G. Lacombe. Analyse d'une équation de vitesse de diffusion. *Comptes rendus de l'Académie des sciences, Math.*, 329:383–386, 1999.

[27] T. Canor and V. Denoël. Transient Fokker-Planck equation solved with smoothed particle hydrodynamics method. *Internation Journal of Numerical Methods in Engineering*, 2013. DOI : 10.1002/nme.4461.

[28] M. Di Paola, L. Mendola, and G. Navarra. Stochastic seismic analysis of structures with nonlinear viscous dampers. *Journal of Structural Engineering*, 133(10):1475–1478, 2007.

[29] G. Pekcan, J. B. Mander, and S. S. Chen. Fundamental considerations for the design of non-linear viscous dampers. *Earthquake Engineering and Structural Dynamics*, 28(11):1405–1425, 1999.

[30] M. Ismail, F. Ikhouane, and J. Rodellar. The hysteresis Bouc-Wen model, a Survey. *Archives of Computational Methods in Engineering*, 16(2):161–188, 2009.

COMPDYN 2013
4th ECCOMAS Thematic Conference on
Computational Methods in Structural Dynamics and Earthquake Engineering
M. Papadrakakis, V. Papadopoulos, V. Plevris (eds.)
Kos Island, Greece, 12–14 June 2013

IMPROVING THE SEISMIC PERFORMANCE OF EXISTING OLD PILOTIS TYPE BUILDINGS BY STRENGTHENING ONLY THE GROUND STORY

Themistocles A. Antonopoulos[1], **Stavros A. Anagnostopoulos**[2]

[1] Department of Civil Engineering, University of Patras
26500 Patras, Greece
e-mail: antonopoulos@upatras.gr

[2] Department of Civil Engineering, University of Patras
26500 Patras, Greece
saa@upatras.gr

Keywords: Reinforced concrete buildings, Open ground story, Inelastic earthquake response, Seismic evaluation, Seismic strengthening, Steel bracing.

Abstract. *The present paper deals with the problem of partial strengthening of old Reinforced Concrete (RC) buildings with open ground floors (pilotis). The strengthening is restricted to the ground level, so that the cost is kept to a minimum and the building remains in use during the intervention. Since strengthening of the ground story will typically transfer the problem to the story or stories above, it is necessary to determine the amount of required strengthening so that the net result will be an optimum, i.e. the maximum possible reduction of the building's vulnerability. In essence the intervention is aimed at increasing the overall seismic resistance for the said class of buildings by removing the "soft story" weakness. This limited intervention is not generally expected to bring the building up to the standards of seismic safety implied by the new codes. For dealing with this problem, plane RC frames corresponding to symmetric buildings, as well as non-symmetric buildings in plan, representative of the old building stock in Greece, are designed in accordance with the old codes (RC code and Code for earthquake resistant design). Subsequently they are subjected to a set of code compatible accelerograms and using nonlinear time history analyses conclusions are drawn regarding the effectiveness of ground story strengthening. Evaluation of their seismic performance is based on Part-3 of Eurocode 8 for assessment and retrofitting of buildings. It is shown that strengthening only the open ground story can effectively reduce the vulnerability of pilotis type buildings by removing the inherent weakness. For non-symmetric buildings, appropriate selection of the bracing location and size, can also improve building performance by reducing the ground story stiffness eccentricity and the consequent torsional response.*

1 INTRODUCTION

Existing multistory reinforced concrete (RC) buildings with brick infills and open ground stories (pilotis buildings) designed by the Old Greek Codes applicable till 1984, represent a structural type that has suffered most of the heavy damage and collapses during strong earthquake events in Greece in the past 30 years (e.g. in the Alcyonides 1981, Kalamata 1986, Aigion 1995 and Athens 1999 earthquakes) and worldwide (e.g. in the Mexico 1985 and Kocaeli-Izmit 1999 earthquakes). Earthquake response of such buildings is strongly dependant on the behavior of their open ground stories. Modern Earthquake Resistant Design Codes for new structures include special provisions for buildings with vertical irregularities and a weak ground story is one of them. As an example, Eurocode 8 [1] for earthquake resistant design of structures requires an increase in the resistance of the columns in the weak stories, by magnifying their internal forces due to seismic actions in order to prevent formation of a plastic side sway story mechanism.

The abrupt reduction in strength and stiffness due to the absence of infill walls in ground stories is a problem that unfortunately was not recognized by older Greek Codes. Combined with other code shortcomings and inadequate construction practices of the past, this major structural deficiency led to weaker than desired buildings, as numerically documented and witnessed by their performance in recent earthquakes [2, 3, 4]. A partial strengthening solution, i.e. a strengthening scheme restricted to the open ground story that effectively improves the seismic behavior of the building, is apparently a solution that minimizes the total cost, while allowing the building to remain operational during the intervention.

Seismic evaluation and upgrading of open ground story buildings has been examined by many researchers and various retrofitting alternatives have been proposed. Fakhouri and Igarashi [5] proposed an assembly of multiple-slider surface bearings set in parallel on the top of the first story columns as an isolation interface for the seismic retrofit of existing buildings with inadequate soft first stories. Briman and Ribakov [6] examined a new engineering solution for seismic isolation of soft first story buildings, by replacing existing weak columns with special seismic isolation columns and proposed a method for the design of buildings incorporating these devices. Pinarbasi et al. [7] presented results of a parametric study on a simplified five story model, showing that conventional base isolation can improve the overall seismic performance of existing buildings with soft first stories, being also effective in reducing the seismic demands on the most vulnerable, ground story level. Finally, the application of energy dissipation braces on the ground story bays of an existing six story building examined by Mezzi [8], showed significant improvement of the entire seismic response of the building.

Among these alternatives, conventional steel X-diagonal bracing, remains a common technique for seismic strengthening, which provides considerable increase in strength and stiffness of the building. This paper presents results of a study on partial strengthening of RC buildings with steel braces restricted to the open ground story. The following building sets were selected and designed according to the old Greek codes: (a) four plane frames with 3 bays each and with 2, 3, 5 and 8 stories (b) two, 5-story plane frames, with 2 and 4 bays, and (c) two eccentric buildings with 3 and 5 stories. These buildings are subsequently strengthened by means of suitable X-bracing in selected bays of the ground story, and their seismic performance, before and after strengthening, is evaluated according to the provisions of Eurocode 8 Part-3 for assessment and retrofitting of buildings, using nonlinear time history analyses for a set of code compatible artificial accelerograms. Finally, conclusions are drawn regarding the effectiveness and feasibility of the proposed partial retrofit solution.

2 BUILDING DESCRIPTIONS AND STRENGTHENING SOLUTIONS

The buildings analyzed herein represent multistory RC structures on "pilotis", having brick infill walls in all stories except the ground story. They are space frame structures with symmetric and non-symmetric (eccentric) in plan layouts. They were selected to represent typical Greek buildings on pilotis, constructed before 1984, year when the old codes were modified. Plane frames are used for the analyses of the symmetric buildings while three dimensional models are used to represent the non-symmetric ones. Figure 1 shows corresponding elevations of the six different plane frames considered in the study, indicating also the bays where steel braces are placed for strengthening. These frames correspond to orthogonal in plan buildings with geometrical (mass and stiffness) symmetry, in both principal directions. The masses and loads supported by each frame in the actual building are calculated considering a distance between adjacent (parallel) frames equal to 6m.

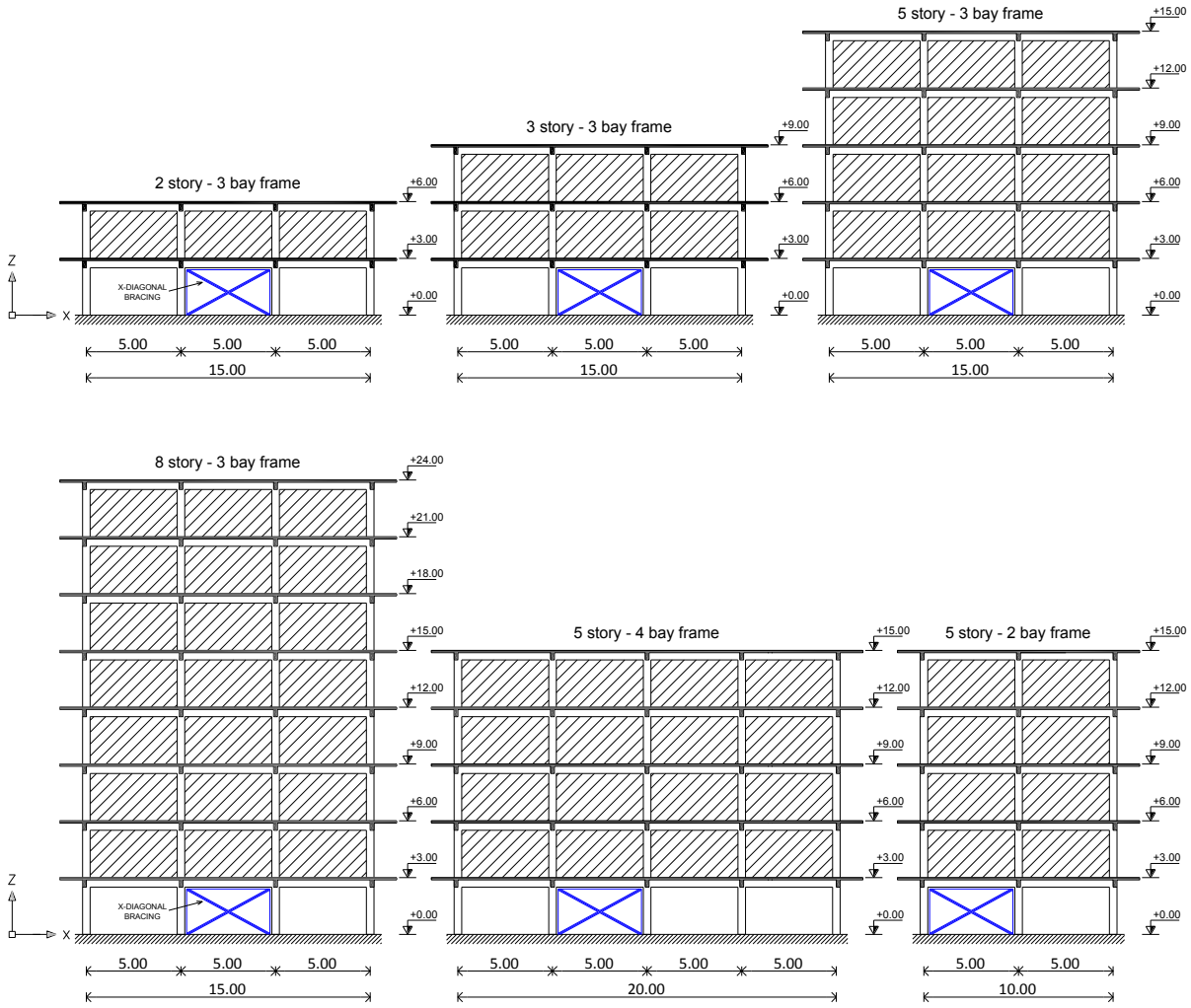


Figure 1: Typical elevations of the plane (2D) frames considered in the analyses.

Figure 2 shows the typical floor plan of both non-symmetric buildings (3 and 5 stories) and the elevations along x and y directions of the 5-story building. The elevator shaft, typical for similar old buildings, is located in the corner and causes bidirectional eccentricity with e_x=0.15 and e_y=0.19. These eccentricities are the projections on the x and y axes, respectively,

of the physical eccentricity, i.e. the distance between the centre of mass and an approximate center of stiffness, estimated for all floors according to Stathopoulos and Anagnostopoulos [9], and normalized by the corresponding maximum building dimensions along the x and y axes. The selected bays of the open ground story where steel braces are placed for strengthening are also shown in the figures.

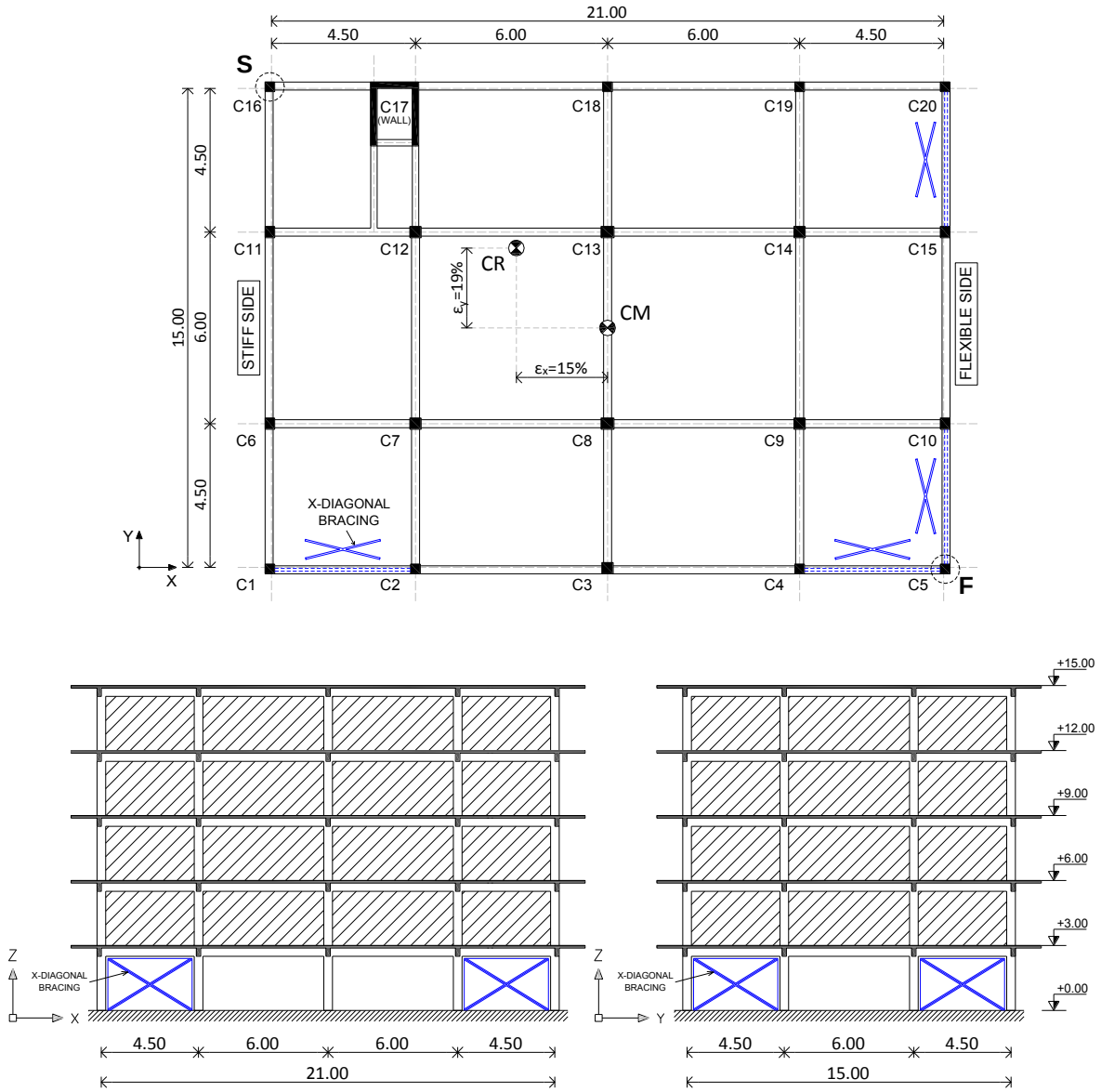


Figure 2: Typical layout of the non-symmetric 3 and 5 story buildings (top) and corresponding elevations along x and y directions of the 5-story building (bottom).

The original buildings have been designed in accordance with the old Greek Codes for reinforced concrete and for earthquake resistant design. A base shear coefficient equal to ε=0.04 was selected for seismic actions, corresponding to the lowest seismic zone (i.e. Zone I) and Soil Class A (rock) of the old 1959 Code, and thus, the design base shear of each building is equal to 4% of the total G+P (permanent plus live) gravity loads. Member dimensioning and corresponding design checks were done according to the allowable stress method of the old 1954 Reinforced Concrete Design Code for concrete quality/steel grade B160/St I, both typical construction materials during the sixties and seventies.

Following the common practice of that period, simplified models were used for the calculation of the internal forces and the dimensioning of the members. Simply supported continuous beams were assumed for the gravity loads, while the seismic forces of the columns and the shear walls were determined story by story, assuming no joint rotations (i.e. shear beam model).

Longitudinal steel reinforcement ratios for columns ranged between 0.8% and 1.1% of the gross section area, while transverse reinforcement consisted of smooth steel stirrups, 6mm in diameter, with open, 90° hooks, equally spaced at 20cm along the entire column length (non-seismically detailed transverse reinforcement). Longitudinal reinforcement of beams in all buildings was controlled mainly by gravity loads. For shear reinforcement in beams, 8 mm stirrups equally spaced at 15 and 25cm was provided in the beams of the frames and the eccentric buildings, respectively, according to the design.

Table 1 lists the section profiles of the steel braces used for the seismic strengthening of the buildings in the selected bays of their open ground stories.

Building	X – direction	Y – direction
2 story – 3 bay frame	CHS-133-4*	–
3 story – 3 bay frame	CHS-114.3-4.5	–
5 story – 3 bay frame	CHS-101.6-4.5	–
8 story – 3 bay frame	CHS-88.9-4	–
5 story – 2 bay frame	CHS-88.9-3.2	–
5 story – 4 bay frame	CHS-139.7-4	–
3 story eccentric building	CHS-114.3-5.6	CHS-114.3-3.6
5 story eccentric building	CHS-88.9-5	CHS-88.9-4
* Circular Hollow Section: 133mm diameter, 4mm thickness		

Table 1: Section profiles of the steel braces of the buildings.

The brace sections listed above were selected after a preliminary analysis with the objective not to overdesign (over-strengthen) the ground story, a case that would move the structural deficiency to the story above. Thus, the goal was to limit the interstory drift of the ground story to a level comparable to the interstory drift of the story above, and then compare the response of the original and the strengthened buildings for the selected earthquake actions. As illustrated in the subsequent sections, this goal was met and the buildings' performance was significantly improved.

3 NONLINEAR MODELING AND EARTHQUAKE INPUT

Seismic behavior of the buildings before and after strengthening was evaluated using nonlinear time history analyses, based on Part-3 of Eurocode 8 [10] for assessment and retrofitting of buildings. Seven pairs of artificial accelerograms were generated using the code by Halldorsson et al. [11]. The selected motions comply with the rules of EC8 [1] for time history representation of the seismic action, i.e. their 5% damped average response spectrum matches the target design spectrum of EAK [12] for seismic Zone I (PGA=0.16g) and Soil Class A (Rock), as illustrated in Figure 3.

The nonlinear dynamic analyses of the buildings were carried out using the computer program Ruaumoko 3D [13]. Beams, columns and the elevator shaft (wall) were modeled using prismatic frame elements, while brick infill walls and the steel braces were modeled using special spring elements. Effective stiffness of RC members was taken equal to the secant

stiffness at yield, based on mean material strengths (f_{cm}=12.8Mpa for B160 concrete, f_{ym}=253Mpa for St I grade longitudinal steel reinforcement and stirrups), according to EC8-Part 3 [10]. Nonlinearity at the two ends of RC members was idealized using one-component plastic hinge models, following the Takeda hysteresis rule with parameters a=0.3 and b=0.0 and a post yield strain hardening ratio equal to p=0.05. Axial force effects on the yield moments of column members were accounted for using appropriate N-M_y-M_z interaction diagrams, obtained from nonlinear fiber cross sectional analyses. Flexibility of joints was neglected but joint dimensions were taken into account through appropriate rigid offsets at member ends.

Each brick wall panel was modeled with two spring elements, one along each diagonal, with cyclic force-deformation relationships according to Crisafulli and Carr [14]. Based on data by Karantoni [15] for masonry bricks, the mean value of the compressive strength of the infills in the direction of the diagonal, was calculated equal to f_{wm}=2.3Mpa according to the provisions of the Greek Retrofitting Code [16] for masonry infills, and the corresponding strain was chosen equal to ε_w=0.0015. A constant width equal to 15% of the clear diagonal length was chosen for the infill struts with a thickness equal to 0.20m. The calculated strength of the infills, and thus the corresponding stiffness, was reduced to its half value for each panel of the plane frames, in order to account for any possible openings as well as for the influence on the global response of plane frames with no infills in the upper stories, parallel to those examined. Regarding the eccentric buildings, an approximate reduction equal to 60% of the initial strength of the infills was applied only in the panels where openings were considered, i.e. at selected bays in the perimeter of the buildings. For linear modal analysis, both struts are active, each assumed to work with half its stiffness. For nonlinear analysis, infill wall struts work only in compression and their axial stiffness is controlled by the hysteresis rule.

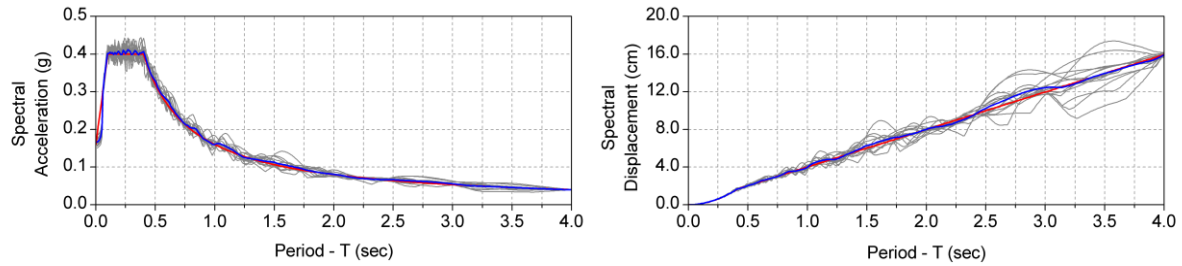


Figure 3: Mean response versus target design pseudo-acceleration (left) and displacement (right) spectra for the 14 synthetic accelerograms.

Diagonal steel cross-bracing members were also modeled with spring elements, following bilinear force deformation relationships. Brace tensile strength was calculated according to Eurocodes 3 and 8 [17, 1], while compressive strength was taken as a fraction of the buckling load (20%), according to the Greek Retrofitting Code [16]. Masses for the dynamic degrees of freedom were calculated from the quasi permanent static combination (G+0.3Q) and considered lumped at nodes. Rigid diaphragms were assumed at floor levels through appropriate nodal constraints. Rayleigh type viscous damping was used such that 5% modal damping was produced in the lowest two modes of the elastic models.

Fundamental periods of vibration and effective modal masses of the plane frames before and after strengthening are listed in Table 2. Looking at the effective modal masses of the original buildings, especially of those with fewer stories, we see that the presence of “pilotis” almost transforms the building to a single degree of freedom system, with nearly the total mass of the system vibrating in the fundamental mode.

Frame	Period T (sec)		Modal mass M^*_x (%)	
	original	braced	original	braced
2 story – 3 bay	0.609	0.268	99.6	87.0
3 story – 3 bay	0.653	0.366	98.6	84.4
5 story – 3 bay	0.772	0.604	93.5	82.4
8 story – 3 bay	1.053	0.965	86.4	80.8
5 story – 2 bay	0.770	0.615	92.9	82.4
5 story – 4 bay	0.766	0.606	93.4	82.9

Table 2: Modal data for the fundamental modes of the original and the braced frames.

Table 3 lists the modal data for the first three modes of the original and the braced eccentric buildings, along x and y directions. The potential for torsional response of these buildings is reflected in the effective modal mass ratios. The addition of steel braces at sides opposite to the stiff elevator shaft (see, Fig. 2 (top)) reduces the eccentricity and the resulting torsion, as can be inferred by comparing the effective modal mass ratios of the buildings before and after strengthening (original vs. braced).

Building	Mode	Period T (sec)		Modal mass M^*_x (%)		Modal mass M^*_y (%)	
		original	braced	original	braced	original	braced
3st – eccentric	1	0.664	0.461	33.0	8.0	31.0	76.0
	2	0.517	0.420	44.0	78.0	49.0	9.0
	3	0.418	0.336	17.0	1.0	13.0	2.0
5st – eccentric	1	0.829	0.709	32.0	2.0	38.0	80.0
	2	0.728	0.673	39.0	79.0	44.0	2.0
	3	0.592	0.542	16.0	2.0	4.0	0.0

Table 3: Modal data for the first 3 modes of the original and the braced eccentric buildings.

4 NONLINEAR ANALYSES RESULTS

Seismic performance of the buildings before and after strengthening (original vs. braced) was evaluated according to EC8-Part 3 [10]. Member verifications were carried out for all components (beams, columns and walls), both for flexure and shear. The design seismic action for which buildings were analyzed corresponds to the Limit State of Significant Damage. Each building was analyzed for the selected ground motions and peak response quantities were calculated through step by step post processing of large sets of time history analysis results. One accelerogram of each motion pair was used for the nonlinear dynamic analyses of each 2D frame, resulting in a total of 7 sets of results, while in the case of the 3D eccentric buildings, each motion pair was used twice by mutually interchanging the accelerograms in the x and y principal directions, resulting in a total number of 14 analyses and 14 sets of results. The results presented in the following pages are the mean values of the maxima from 7 (plane frames) or 14 (eccentric buildings) sets of analyses.

Key parameters for the seismic capacity assessment before and after strengthening are the mean values over all motions of the maxima of the following response quantities:

- Maximum displacements along building height (in absolute values).
- Interstory drifts (relative story displacements, in absolute values).

- Rotational ductility demands in beams and columns defined as

$$\mu_\theta = 1 + \frac{\theta_{pl}}{\theta_y} \tag{1}$$

where, θ_{pl} is the maximum plastic hinge rotation at either end of the members, and θ_y is the corresponding chord rotation at yield, calculated according to EC8-Part 3 [10]. Yield rotations θ_y for each member were assumed constant, and equal to those initially calculated under the action of the quasi permanent gravity loads for the determination of the effective stiffnesses of the members to be used in the mathematical models.

- Demand to capacity ratios (D/C) of the maximum hinge rotations to the instantaneous (due to variation of the axial loads) plastic rotation capacity of the members with smooth longitudinal bars, without detailing for earthquake resistance, based on mean material strengths, calculated according to EC8-Part 3 [10]. Strength and deformability modification due to lap-splicing of the column reinforcements at floor levels was ignored. In each analysis step, D/C ratios of the plastic rotations were calculated separately for each of the two principal axis of bending (y and z) at both member ends (i and j), as well as according to the following gross rule of instantaneous combination of the two plastic rotations along principal axes y and z at the cross section level

$$(D/C)_{\theta_{pl}} = \sqrt{\left(\frac{\theta_{pl,y}}{\theta_{um,EC8}^{pl,y}}\right)^2 + \left(\frac{\theta_{pl,z}}{\theta_{um,EC8}^{pl,z}}\right)^2} \tag{2}$$

In calculations of average values, plastic rotations and ductility factors were considered equal to zero and one, respectively, for members that remained elastic during the response.

- Demand to capacity ratios of the applied shear force, to the instantaneous cyclic shear resistance V_R. In this calculation, mean material strengths were additionally divided by the partial material factors, according to EC8-Part 3 [10]. The contribution of stirrups to the calculations of cyclic shear resistance was reduced to half its calculated value, due to open (non-seismically detailed) stirrups, see Biskinis et al. [18].

Peak story displacements and maximum interstory drifts of the original and the braced plane frame buildings are shown in Figures 4 to 9. Looking at the response of the original buildings (red dashed lines), a clear soft story behavior is apparent, because the largest portion of the total displacements is concentrated at the open ground story. In the 8-story frame the soft ground story drift is not as dominant as in the other frames, nevertheless it still remains the largest over all stories (Fig. 7).

Comparing the response of the buildings before and after strengthening, we observe a significant reduction of the ground story displacements, with relatively limited increase in the displacements of the stories above. It is worth to note that in some cases, in addition to significantly reducing the ground story displacements, the steel bracing reduces also the displacements of the first floor above, which may be attributed, to some extent, to the energy dissipated after braces yield in tension.

The results of the member checks are even better. This can be seen in Table 4 summarizing basic quantities for the overall seismic safety of the original and the braced buildings, i.e. maximum values of the shear D/C ratios of the ground and first story columns, maximum ductility demands, bending D/C ratios of the plastic hinge rotations of the ground story columns and D/C ratios of infill walls just above the ground story.

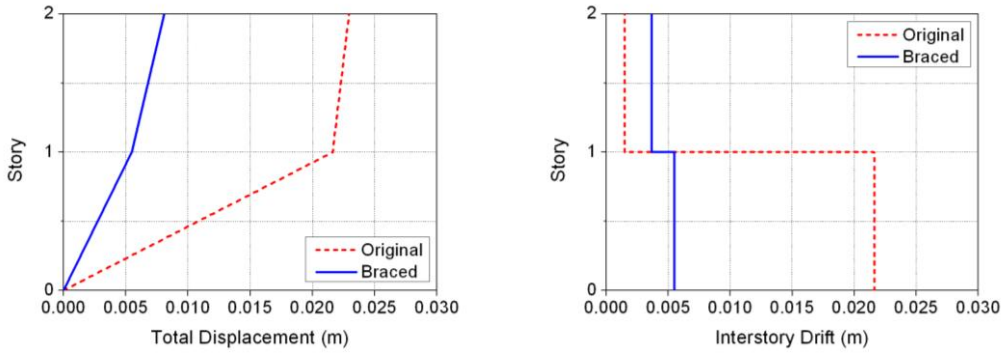


Figure 4: 2story-3bay frame, average values of maximum total displacements and maximum interstory drifts.

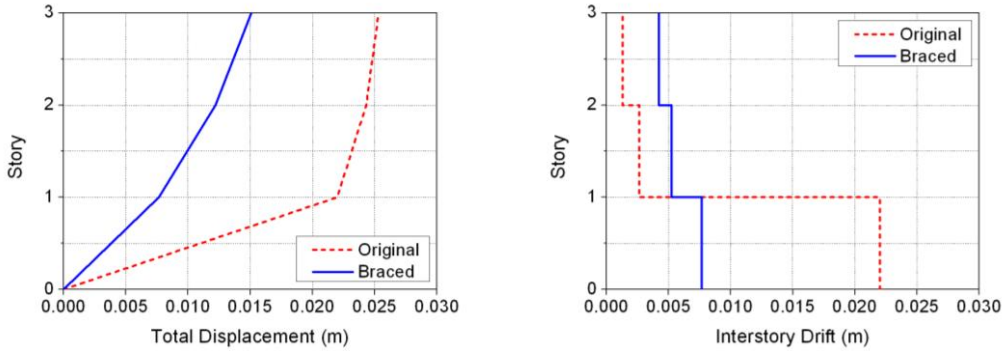


Figure 5: 3story-3bay frame, average values of maximum total displacements and maximum interstory drifts.

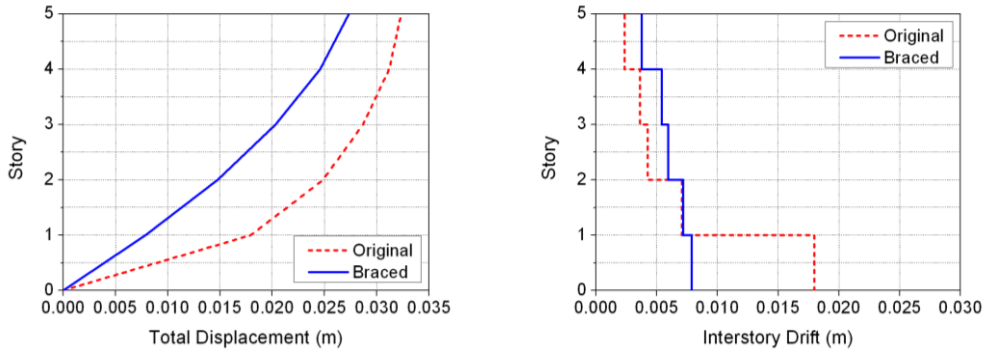


Figure 6: 5story-3bay frame, average values of maximum total displacements and maximum interstory drifts.

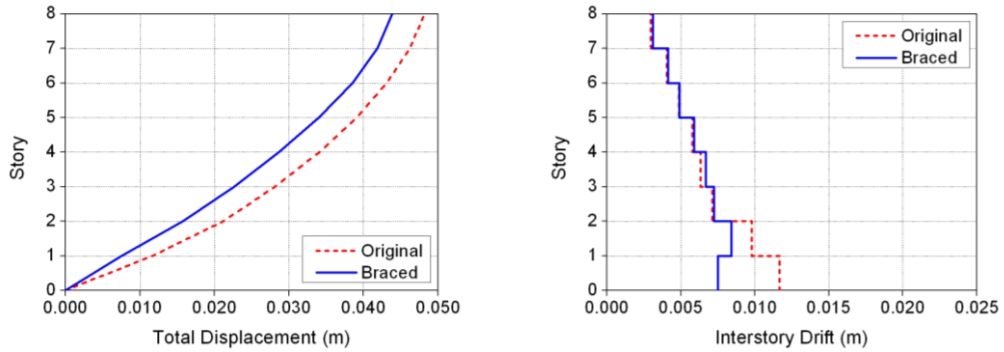


Figure 7: 8story-3bay frame, average values of maximum total displacements and maximum interstory drifts.

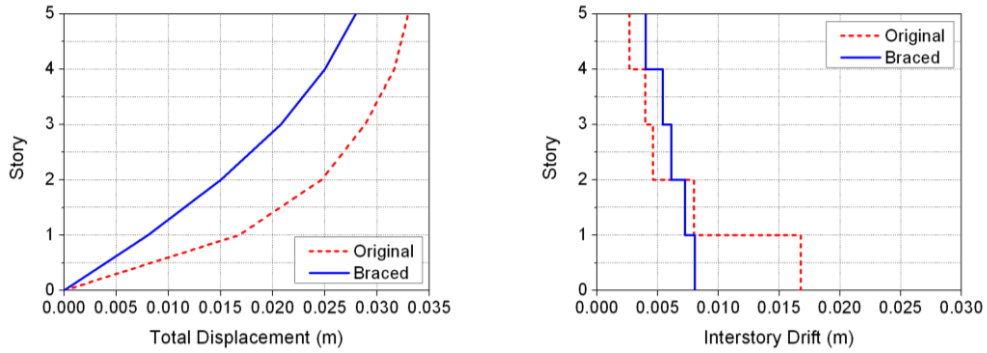


Figure 8: 5story-2bay frame, average values of maximum total displacements and maximum interstory drifts.

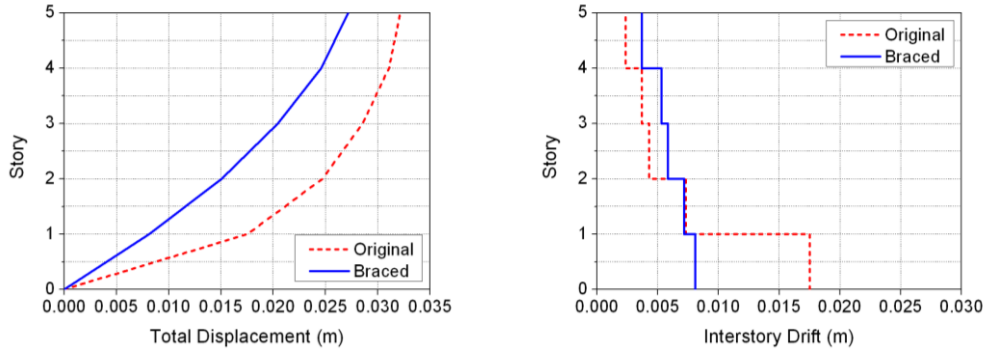


Figure 9: 5story-4bay frame, average values of maximum total displacements and maximum interstory drifts.

The substantial reduction of the ground story displacements resulted in lowering the corresponding maximum column shears, so that the several D/C ratios that exceeded 1.0 in the original buildings, indicative of high risk of failure, now were reduced to values below 1.0, as may be seen in Table 4. The expected increase of these ratios in the columns of the story just above the ground story is also shown in Table 4, but their values are still bellow 1.0.

Frame		D/C - V_R Pilotis Columns	D/C - V_R 1st Floor Columns	μ_θ Pilotis Columns	D/C - θ_{pl} Pilotis Columns	D/C ratio 1st Floor Infills
2 story – 3 bay	original	1.250	0.818	1.286	0.370	0.170
	braced	0.621	0.847	-*	-	0.406
3 story – 3 bay	original	1.272	0.628	1.343	0.459	0.301
	braced	0.689	0.716	-	-	0.579
5 story – 3 bay	original	1.334	0.570	1.242	0.410	0.737
	braced	0.734	0.697	-	-	0.783
8 story – 3 bay	original	0.995	0.632	1.010	0.012	1.078
	braced	0.715	0.676	-	-	0.944
5 story – 2 bay	original	1.328	0.630	1.192	0.238	0.806
	braced	0.806	0.707	-	-	0.793
5 story – 4 bay	original	1.323	0.579	1.198	0.360	0.762
	braced	0.743	0.691	-	-	0.787

*columns remained elastic during the response (no hinges were formed)

Table 4: Maximum member D/C ratios of the original and the strengthened frame buildings.

Regarding the masonry infills, which inevitably play their role on the global seismic response, their damage index (infills D/C ratio) was taken equal to the ratio of the maximum axial deformation to the deformation at maximum strength of each infill. Conventionally, values greater than 1.0 correspond to infills that have reached their maximum available strength and have started to degrade. After calculating this index for the two infills (springs) of each panel separately, average values among all infills in the story were calculated as global story infill damage indices.

Displacement results for the 3 and 5 story eccentric buildings are shown in Figures 10 and 11, respectively. They are given for the "stiff" and the "flexible" edges of the buildings at points "S" and "F", respectively (see, Fig. 2 (top)). Overall, the behavior in these cases is governed by torsional response, and any soft story effects are apparent on the "flexible" sides of the buildings, i.e. the sides forming a corner diagonally opposite the elevator shaft, where the displacements due to torsion are added to the translational displacements due to the earthquake lateral force. This is clearly seen in the response of the original 3-story eccentric building, while it is less evident in the case of the 5-story one. Contrary to the symmetric in plan buildings, where steel braces can be placed in any of the available bays provided that the symmetry in plan is maintained, in cases of eccentric open ground stories the strengthening scheme should aim not only at strengthening the soft story but also at reducing eccentricities and the subsequent torsional response. This is what happened in the case of the 3-story eccentric building where, after the addition of steel bracing, both of these negative response factors were minimized. On the other hand, in the case of the 5-story eccentric building, the beneficial effects of the ground story bracing are clear only where they are needed the most, i.e. in the ground story, while in the upper stories, where the original eccentricities have not been affected, a torsional response is still apparent.

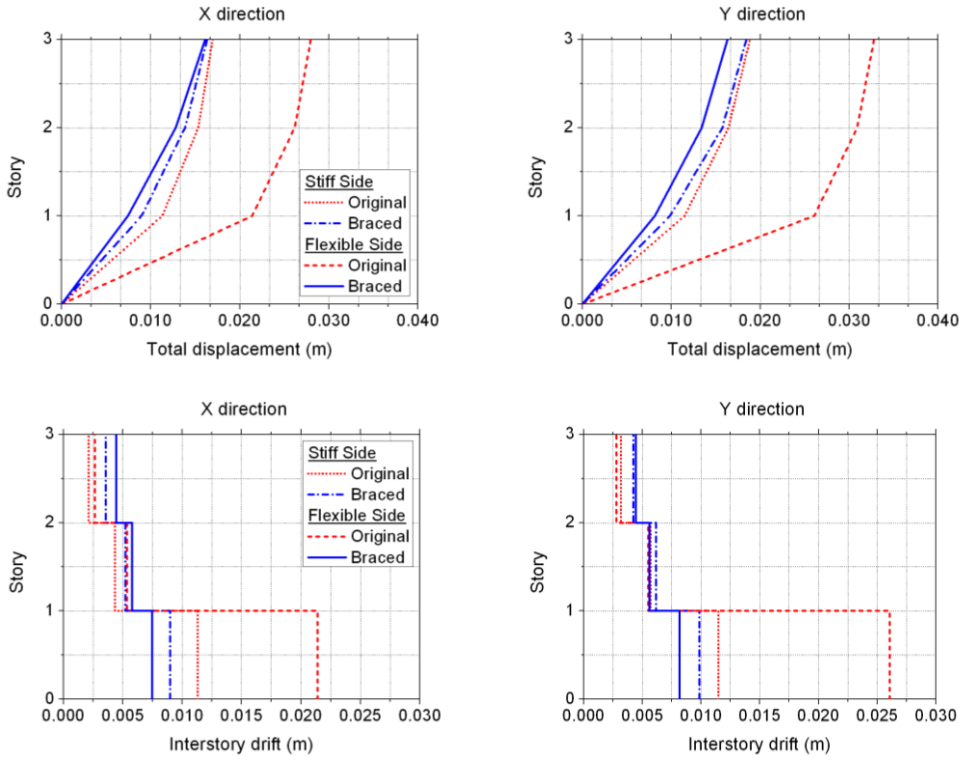


Figure 10: 3-story eccentric building, average values of maximum total displacements (top) and maximum interstory drifts (bottom) along X and Y direction.

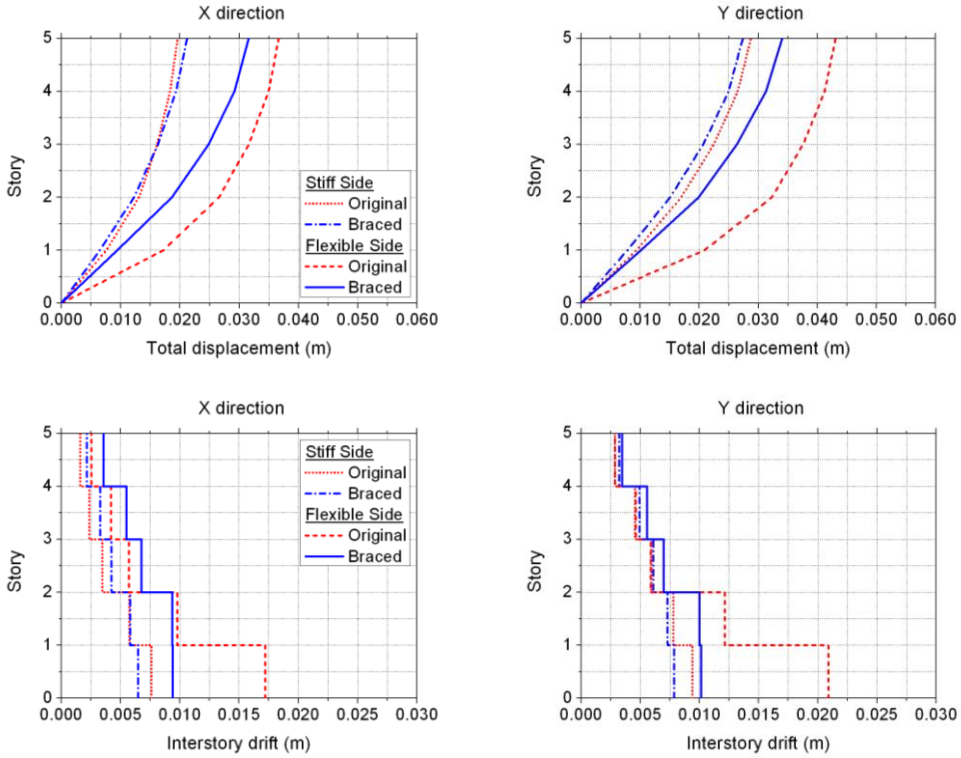


Figure 11: 5-story eccentric building, average values of maximum total displacements (top) and maximum interstory drifts (bottom) along X and Y direction.

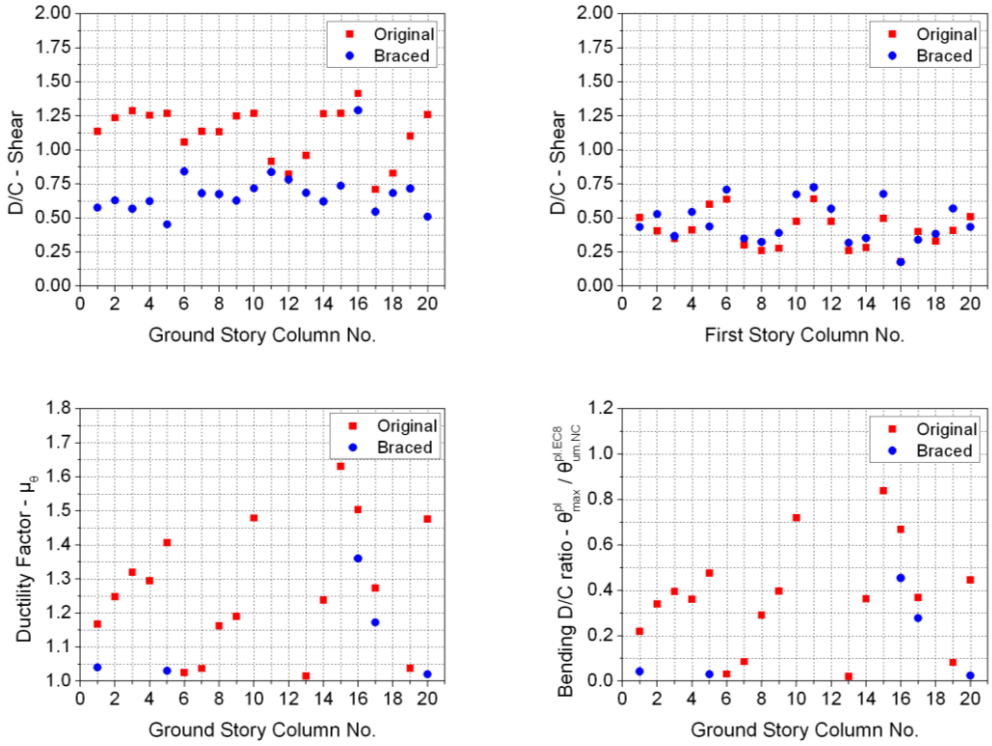


Figure 12: 3-story eccentric building, shear D/C ratios in ground story and first story columns (top), rotational ductility μ_θ and bending D/C ratios in ground story columns (bottom).

In order to have a better picture of the seismic performance of the eccentric buildings before and after strengthening, member checks are presented in a more detailed fashion, as illustrated in Figures 12 and 13. In addition D/C ratios for infill walls in all stories above the pilotis are shown in Figure 14. Looking at Figures 12 and 13, it is clear that steel bracing reduces significantly the potential for shear failures in the ground story columns. We note that even after the intervention, one column in the ground story of the eccentric buildings fails in shear and a few others suffer damage as the rotational ductility factors indicate (see, Fig. 12 and 13). Such cases should be dealt with local measures, e.g. using concrete jackets, because further strengthening of the ground story will create problems in the stories above.

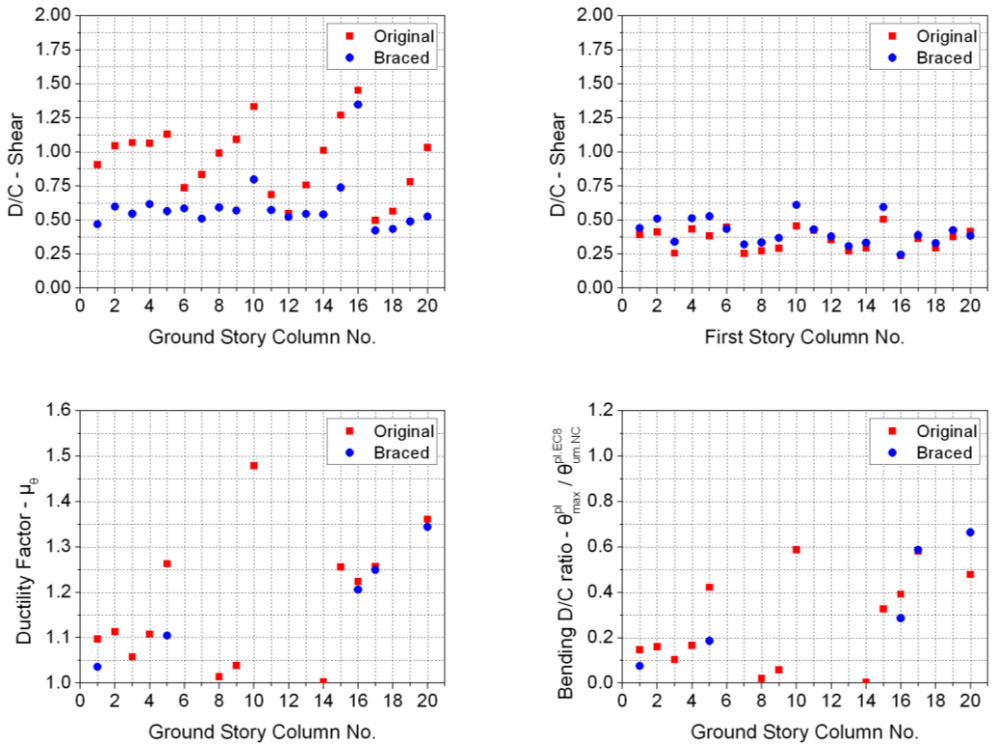


Figure 13: 5-story eccentric building, shear D/C ratios in ground story and first story columns (top), rotational ductility μ_θ and bending D/C ratios in ground story columns (bottom).

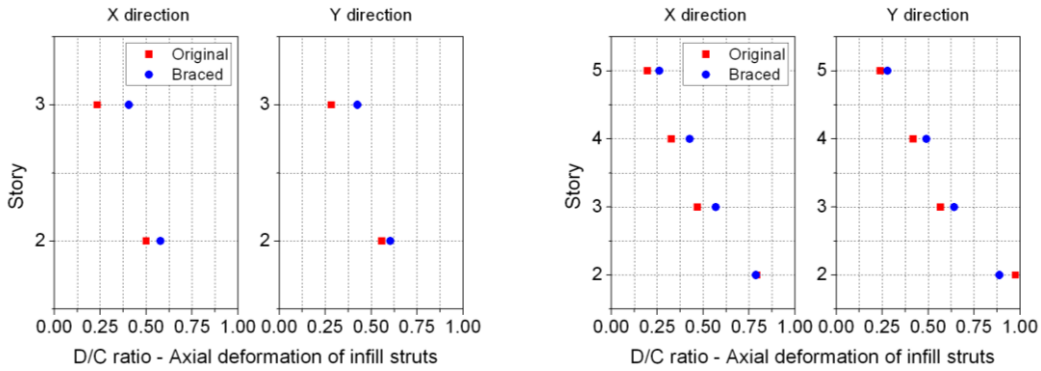


Figure 14: D/C ratios in infills of the 3-story (left) and 5-story eccentric building (right) along X and Y directions for all floors above the ground story.

For the evaluation of the steel braces maximum ductility factors in tension were computed for each brace and averaged over the number of analyses performed. The maximum over all the braces is the value listed in Table 5. As may be seen in the Table, the values of these ductility factors are relatively low, compared to the values expected in braced steel frames (in the case of the 2-story frame the braces remained elastic during the response).

Building	X – direction	Y – direction
2 story – 3 bay frame	0.783	–
3 story – 3 bay frame	1.119	–
5 story – 3 bay frame	1.127	–
8 story – 3 bay frame	1.106	–
5 story – 2 bay frame	1.150	–
5 story – 4 bay frame	1.160	–
3 story eccentric building	1.083	1.179
5 story eccentric building	1.377	1.506

Table 5: Average values of the maximum ductility factors of brace elements (tension only).

It is worth pointing out that the use of braces for seismic strengthening of RC structures is effective for global strengthening, provided that a reliable, well detailed and technically sound connection between the steel elements and the existing concrete buildings is ensured. Dimensioning of all the extra members (steel rims, anchors, headed studs, mortar joints e.t.c) required for the attachment of the steel bracing to the perimeter of each RC frame, is beyond the scope of this work.

5 CONCLUSIONS

The work reported herein looks into the problem of strengthening the most vulnerable class of existing RC buildings in Greece, namely buildings with an open ground story (pilotis), designed and built under old Greek codes and practices, and which have performed very poorly during strong earthquakes of the recent past. The present paper examined the feasibility of partial strengthening of such buildings, aiming at reducing their vulnerability due to weak first story and lowering it to a level comparable to that of regular buildings, i.e. having sufficient infill walls in the ground story. Based on inelastic dynamic earthquake response analyses of a set of plane frames, used to form symmetric buildings in plan, as well as two eccentric buildings, their vulnerability due to weak ground story was first confirmed. These buildings were subsequently strengthened with steel braces placed in appropriately selected bays of the ground story, and their performance was examined under the same earthquake action. In all cases the strengthened buildings showed significantly improved earthquake response, which met the initial objective of removing the ground story weakness without shifting the problem to higher stories. Note also that with the selected bracing locations in the case of non-symmetric buildings, it was possible to reduce the ground story eccentricity, and through that, the undesirable torsional-soft story response of the buildings. It is believed that partial strengthening by intervening only in the open ground story, as opposed to complete strengthening to comply with current standards for new buildings, is perhaps the only feasible way of intervention in the existing stock of the most vulnerable old buildings: first due to its low cost (that becomes even lower and hence affordable if split among the building several owners) and second because the building can remain functional during the intervention works.

REFERENCES

[1] EC8, Eurocode 8: Design of structures for earthquake resistance, Part 1: General rules, seismic actions and rules for buildings, European Standard EN 1998-1:2004. *Comite Europeen de Normalisation*, Brussels, 2004.

[2] T.A. Antonopoulos, S.A. Anagnostopoulos, F.N. Tsirlis, Evaluation of the seismic performance of old reinforced concrete buildings with an open ground storey, simple retrofitting solutions. *Proceedings of the 3rd Greek Conference on Earthquake Engineering and Engineering Seismology*, **2061**, Athens, Greece, 2008. (In Greek)

[3] T.A. Antonopoulos, S.A. Anagnostopoulos, Optimum partial strengthening for improved seismic performance of old reinforced concrete buildings with open ground story. *Advances in Performance-Based Earthquake Engineering, Geotechnical, Geological, and Earthquake Engineering, M.N. Fardis (ed.),* Springer, **13**, 395-404, 2010.

[4] C. Repapis, C. Zeris, E. Vintzileou, Evaluation of the seismic performance of existing RC buildings: II. A case study for regular and irregular buildings. *Journal of Earthquake Engineering*, **10**, 429-452, 2006.

[5] M.Y. Fakhouri, A. Igarashi, Multiple-slider surfaces bearing for seismic retrofitting of frame structures with soft first stories. *Earthquake Engineering and Structural Dynamics*, **42**, 145-161, 2013.

[6] V. Briman, Y. Ribakov, Using seismic isolation columns for retrofitting buildings with soft stories. *Structural Design of Tall and Special Buildings*, **18**, 507-523, 2009.

[7] S. Pinarbasi, D. Konstantinidis, J.M. Kelly, Seismic isolation for soft-story buildings. *10th World Conference on Seismic Isolation, Energy Dissipation and Active Vibrations Control of Structures*, Istanbul, Turkey, May 28-31, 2007.

[8] M. Mezzi, Enhancing the seismic performance of existing "Pilotis" configurations. *IABSE Symposium, Responding to Tomorrow's Challenges in Structural Engineering*, Budapest, Hungary, 2006.

[9] K.G. Stathopoulos, S.A. Anagnostopoulos, Inelastic torsion of multistory buildings under earthquake excitations. *Journal of Earthquake Engineering and Structural Dynamics*, **34**, 1449-1465, 2005.

[10] EC8-Part 3, Eurocode 8: Design of structures for earthquake resistance, Part 3: Assessment and retrofitting of buildings. European Standard EN 1998-3:2005. *Comite Europeen de Normalisation*. Brussels, 2005.

[11] B. Halldorsson, G. Dong, A.S. Papageorgiou, Earthquake Motion Input and its Dissemination Via the Internet. *Earthquake Engineering and Engineering Vibration*, **1**, 20-26, 2002.

[12] EAK, Greek Seismic Design Code – 2000. *Greek Organization for Seismic Planning and Protection (OASP), Greek Ministry for Environmental Planning and Public Works*, Athens, Greece, 2003. (In Greek): www.oasp.gr

[13] A.J. Carr, Ruaumoko Manual: Theory and User - Guide to Associated Programs. **1**, *University of Canterbury*, New Zealand, 2005.

[14] F. Crisafulli, A. Carr, Proposed macro-model for the analysis of infilled frame structures. *Bulletin of the New Zealand Society for Earthquake Engineering*, **40**, 69-77, 2007.

[15] F.V. Karantoni, A sampling research study of the fulfillment by Greek clay bricks of the EC6 specifications. *Tech. Chron. Sci. J. TCG, I,* **2**, 45-56, 1999.

[16] KAN.EPE., Greek Retrofitting Code. *Greek Organization for Seismic Planning and Protection (OASP), Greek Ministry for Environmental Planning and Public Works*. Athens, Greece, 2012. (In Greek): www.oasp.gr

[17] EC3, Eurocode 3: Design of steel structures, Part 1: General rules and rules for buildings. European Standard EN 1993-1:2005. *Comite Europeen de Normalisation*, Brussels, 2005.

[18] D.E. Biskinis, G.K. Roupakias, M.N. Fardis, Degradation of Shear Strength of Reinforced Concrete Members with Inelastic Cyclic Displacements. *ACI Structural Journal*, **101**, 773-783, 2004.

COMPDYN 2013
4th ECCOMAS Thematic Conference on
Computational Methods in Structural Dynamics and Earthquake Engineering
D. V. Achillopoulou, T. P. K. Tasiopoulos, A. I. Karabinis
Kos Island, Greece, 12–14 June 2013

STUDY OF THE BEHAVIOR OF RC COLUMNS STRENGTHENED WITH RC JACKETS CONTAINING DOWELS AND DIFFERENT CONFINEMENT RATIOS

D. V. Achillopoulou[1*], T. P. K. Tasiopoulos[1] & A. I. Karabinis[1]

[1]Democritus University of Thrace

Vas. Sofias 12, 67100, Xanthi, Greece

dimiachi@civil.duth.gr*

thomtasi@civil.duth.gr

karabin@civil.duth.gr

Keywords: *concrete jacket, interface, dowels, force transfer*

Abstract. *The current paper studies the force transfer mechanisms in retrofitted columns containing dowels crossing the interface of old and new concrete. It includes 10 specimens of square section (150x150x500mm) of 24,37 MPa nominal concrete strength with 4 longitudinal steel bars of 8mm diameter (500 MPa nominal strength) and different transverse reinforcement ratios (ω_c= 0,075, ω_c=0,15). All columns were subjected to initial axial compression up to maximum load. After repair with thixotropic high strength concrete, all columns were retrofitted with RC jacket of 80mm width of 31,8 MPa concrete strength, including 4 longitudinal bars of 8mm diameter (500 MPa nominal strength) and different confinement ratios(ω_{cj}= 0,035/0,071/0,142). The retrofitted columns contain dowel bars of either 10 or 14mm diameter that cross the interface. Two loading patterns were selected to test the strengthened columns, the behavior of which is investigated through P-δ, energy absorbed diagrams and the levels of ductility achieved. The results indicate that the initial damages affect the total behavior of the column and the capacity of the interface to shear mechanisms and to slip: a) the maximum bearing load of old column is decreased affecting at the same time the loading capacity of the jacketed element, b) suitable repair of initially damaged specimens increases the capacity of the jacketed column to transfer load through the interface.*

1 INTRODUCTION

Elements of high importance in reinforced concrete structures are columns due to their capacity in load-bearing. Columns can stand damages either due to overloading (gravity loads: changes in usage of the building, storey super induction, earthquakes, etc), due to construction damages (poor consolidation of concrete) or even due to exposure to environmental effects (corrosion, carbonation, etc). The need of repair of even strengthening of damaged columns is obvious in order to rehabilitate their capacity in loads and deformation [1], [2], [3], [4]. Nevertheless, structures designed with older seismic codes with luck of ductility need also retrofitting in order to upgrade their strength and capacity in deformation [6].

In recent decades extensive research has been conducted in repair and strengthening methods and the materials used for those purposes. Materials are usually of high strength in order to eliminate the loss in bearing capacity. After repair, when strengthening is decided several methods are applied such as: FRP wrapping (fibre reinforced polymer laminates, jacketing, etc.) or even reinforced concrete (RC) jacketing. All these methods have been proven efficient in enhancing the load capacity and the ductility of elements [7]. In all cases, the shear transfer mechanisms of the interface affect the transferring of loads and the effectiveness of the retrofit method, constituting its design crucial and of high interest [8], [9]. More specifically, in cases of strengthening with RC jacketing the main mechanisms that act are concrete-to-concrete cohesion and friction (aggregate interlock) and dowel action of the reinforcement the interface between old and new concrete (dowels, tack-welds, butt-welds, bend down bars etc.).

Researchers have studied the shear mechanisms apart or in combination, analytically or/and experimentally. The modern codes world-widely adopt results and semi-empirical relations considering the design of the jacket and the calculation of the shear mechanisms' components. Though, the initial damages of the column is ignored [10], the way of loading is not defined (directly- indirect loading of the jacket area) and finally parameters beyond the limits of design deformations are still vague. These parameters are investigated separately or in combination in this paper. In real structures columns are also subjected to horizontal forces (earthquake). In this paper only the parameters of shear transfer mechanisms examined. For those reasons the specimens were subjected to axial compression only. The experimental program held at the Reinforced Concrete Lab at Democritus University of Thrace (D.U.Th.). They contain different percentages of transverse reinforcement at core and jacket, providing different mean normal stress at the interface. The different treatment of the interface between old and new concrete such as the different kind of cohesion developed is tested (ex. due to coating with synthetic polymer sheets). In the current paper the factor of possible initial damage due to construction imperfections that is not referred and analysed extensively in the various codes that affects the efficiency of the repair is not examined.

2 SHEAR TRANSFER MECHANISMS

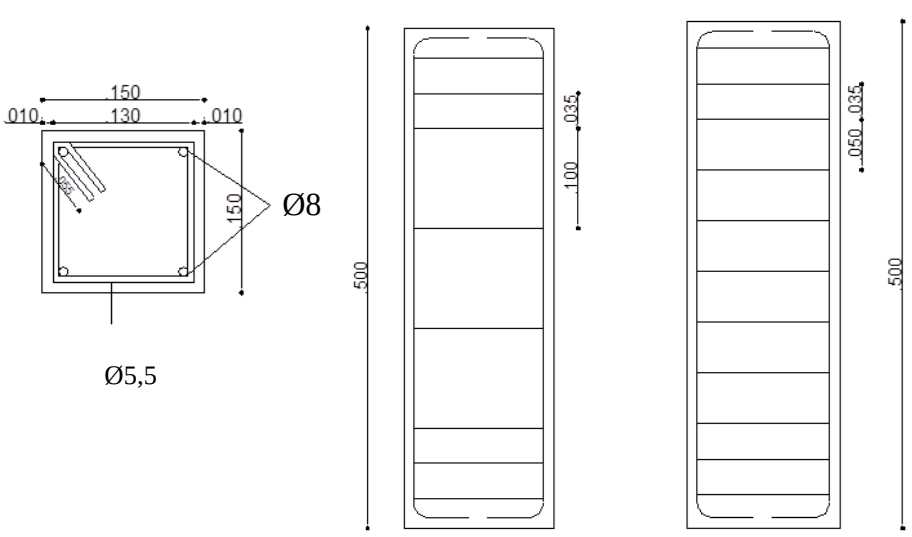
As already referred, the shear transfer mechanisms are concrete-to-concrete cohesion and friction (aggregate interlock) [11] and dowel action. The concrete-to-concrete cohesion depends strongly on the kind of the interface [12], [13], [14]. The treatment of the interface varies (smooth, rough, very rough, high pressure jetting, shotcrete etc.) providing different values of cohesion stress. The cohesion mechanism depends strongly on the tensile strength of the weakest of the two concretes in contact. As far as friction is concerned, it depends strongly on the friction coefficient between the two different concretes and the normal stress applied at the interface. Again, the kind of the interface provides different values of friction coefficient. The normal stress applied at the interface is the result of the clumping action of stirrups during loading due to the expansion of concrete. Dowel action refers to the reinforcement cross-

ing the interface keeping the two concretes in contact [15], [16], [17], [18]. It depends on the yield stress of the bar itself and of the angle forming with the interface (normal to etc.).

3 EXPERIMENTAL INVESTIGATION

3.1 Columns cores

The experimental investigation includes results of 10 columns of square section with 150 mm width and 500 mm height in scale 1:2 (typical column used in real structures) (Figure 1a). In the considered old columns (cores) concrete of 24,37MPa strength was used (24,4GPa modulus of Elasticity), commonly used in building structures in the last decades and 32mm maximum size of aggregate. Two columns were made of plain concrete (UR). The rest include four longitudinal steel bars of 8mm diameter (500MPa nominal strength), that is the minimum volumetric ratio defined by old and new codes (ρ=1%). One column contain closed stirrups spaced at 100mm (mechanical ratio of transverse reinforcement: ω_{wc}=0,075, 220MPa nominal strength, measured yield stress through tension tests f_y=250,76 MPa) and six with 50mm stirrup spacing (ω_{wc}=0,15), all adequately anchored (Figure 1b,c). The selection of the reinforcement was made according to the minimum percentage of longitudinal reinforcement (approximately 1%) and to low and medium transverse reinforcement ratios as practiced in structures with no high ductility requirements. Also, the diameters were selected in order to avoid any possible scale phenomena (Table 1).



a. Square section (mm) b. ω_{wc}=0,075 c. ω_{wc}=0,15

Figure 1. Section and transverse reinforcement of columns



a. Specimen B-$R_cR_jD_b$-7

Figure 2 View of specimens

Table 1. Details of Specimens

Specimen	Dowels	Longitudinal Reinforcement (Core/Jacket)	Transverse Reinforcement		Coating of Interface	Pre- Loading of Core
			Core ω_{wc}	Jacket ω_{wj}		
A-UR-2	-	-	-	-	-	YES (UR-2)
A-$R_cR_jD_b$-3	6Ø10	4Ø8/4Ø8	0,075 (Ø5,5/10)	0,4 (Ø5,5/10)	-	-
A-$R_cR_jD_b$-4	6Ø10	4Ø8/4Ø8	0,15 (Ø5,5/5)	0,92 (Ø5,5/5)	POLYMER	-
A-$R_cR_jD_b$-5	6Ø14	4Ø8/4Ø8	0,15 (Ø5,5/5)	0,92 (Ø5,5/5)	POLYMER	-
B-UR-3	-	-	-	-	-	-
B-URD_b-4	6Ø10	-	-	-	-	-
B-$R_cR_jD_b$-1	6Ø14	4Ø8/4Ø8	0,15 (Ø5,5/5)	0,035 (Ø5,5/10)	POLYMER	-
B-$R_cR_jD_b$-2	6Ø10	4Ø8/4Ø8	0,075 (Ø5,5/10)	0,035 (Ø5,5/10)	POLYMER	-
B-$R_cR_jD_b$-6	6Ø10	4Ø8/4Ø8	0,15 (Ø5,5/5)	0,71 (Ø5,5/5)	-	YES (Rc-6)
B-$R_cR_jD_b$-7	6Ø10	4Ø8/4Ø8	0,15 (Ø5,5/5)	0,035 (Ø5,5/10)	-	YES (Rc-7)
B-$R_cR_jD_b$-8	6Ø10	4Ø8/4Ø8	0,15 (Ø5,5/5)	0,142 (Ø5,5/10)	-	YES (Rc-8)
Note:			**Note:**			
A: Load Pattern A, **B: Load Pattern B** **D_b: dowels**			**UR: unreinforced core** **UR_j: unreinforced jacket** **R_c: reinforced core** **R_j: reinforced jacket**			

3.2 Pre-Loading

Four columns (Figure 2) were pre-loaded monotonically up to maximum bearing load (A-UR2, B-RcrjDb-6, B-RcRjDb-7, B-RcRjDb-8). The pre-loading procedure held in order to simulate any possible minor damages of design gravity loads happening at structures before strengthening is decided. The specimens were tested in a compression machine with a capacity of 3000 KN under axial monotonic loading (Figure 3). The stress strain curves are shown in Figure 4.



Figure 3 Experimental Setup

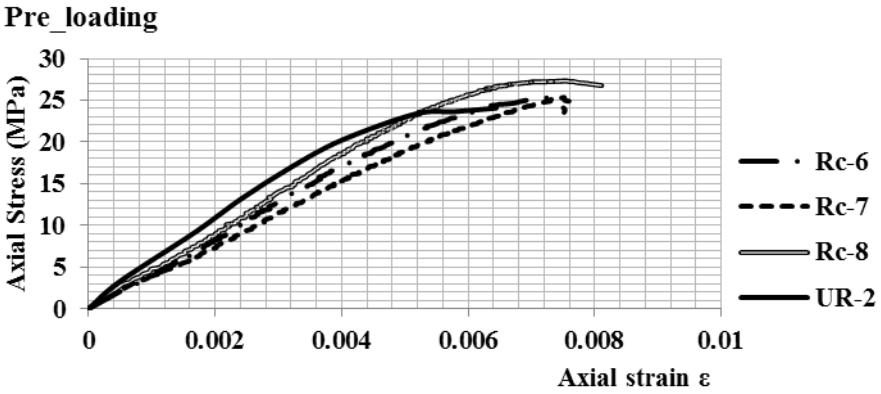


Figure 4 Axial stress vs axial strain diagram of pre-loading

3.3 Retrofit

All ten columns were strengthened with RC jacket of 80 mm thickness (total dimension of width: 310 mm) of high strength concrete (nominal compression strength: f_c=31,52 MPa, modulus of Elasticity: E_c=31,6 GPa, maximum aggregate: d_{AGR}=8 mm).

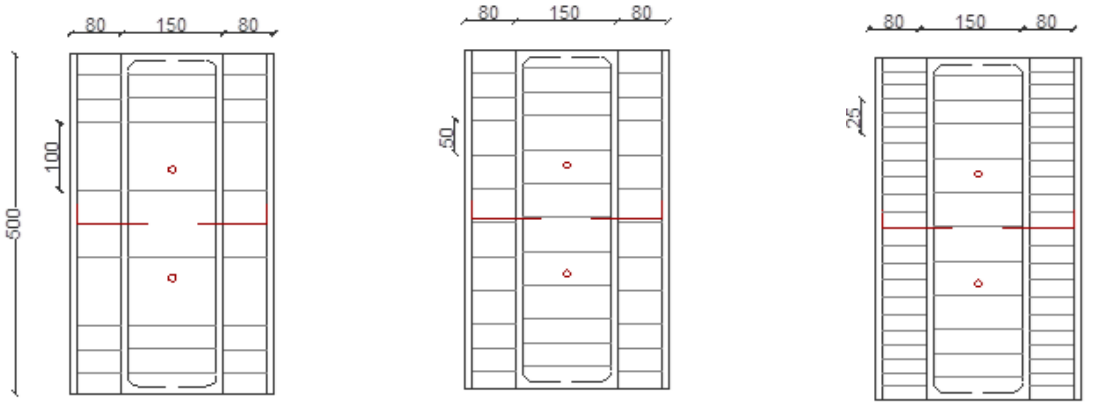
In six columns six dowels of 10 mm diameter (500 MPa nominal strength) were placed (A-$R_cR_jD_b$-4, B-URD_b-4, B-$R_cR_jD_b$-2, B-$R_cR_jD_b$-6, B-$R_cR_jD_b$-7, B-$R_cR_jD_b$-8) (Figure 5 a) with injected cementitious grout of very small particle size and thixotropic consistency (steady expansion grout), (Sika Ancorfix3) to connect core and jacket. In two columns the dowel diameter was 14mm (A-$R_cR_jD_b$-5, B-$R_cR_jD_b$-1). Dowels were designed according to the minimum percentage of reinforcement normal to the interface per area given by codes. EN 1998 part 3-GRC defines as minimum ratio ρ=1,2‰ but were placed ρ=1,6‰. Five columns were coated with resin of two-component without solvents (Sikadur-32N, LP), so as to achieve adequate adhesion between old and new concrete. Four columns were coated with synthetic polymer sheets so as to minimize the friction forces at the interface (Figure 5 b). Finally, two columns contain no bars, both core and jacket is made of plain concrete.



a. Specimen (core) with dowels (B-$R_cR_jD_b$-6)

b. Specimen coated with synthetic polymer sheet (B-$R_cR_jD_b$-2)

Figure 5 Preparation of specimens before jacketing



a. w_c=0,075 - w_j=0,035 b. w_c=0,15 - w_j=0,071 c. w_c=0,15 - w_j=0,142

Figure 6 Transverse reinforcement of core and jacket

The jackets included 4 longitudinal bars of 8 mm diameter and closed stirrups spaced at 25 mm (ω_{wj}=1,86: mechanical percentage of stirrups, normalised at the confined area of the jacket only), 50 mm (ω_{wj}=0,92) and 100 mm (ω_{wj}=0,40), again of 220 MPa nominal yield stress (measured yield stress through tension tests f_y=250,76 MPa). The top and bottom of each specimen contain more stirrups in order to secure that in these regions no damage will take place during test (Figure 6). Table 1 resumes all specimens' characteristics. The jacketed specimens were subjected to axial compression only according to two different Load Patterns (Figure 7):

Table 1. Details of Specimens

Specimen	Dowels	Longitudinal Reinforcement (Core/Jacket)	Transverse Reinforcement		Coating of Interface	Pre- Loading of Core
			Core ω_{wc}	Jacket ω_{wj}		
A-UR-2	-	-	-	-	-	YES (UR-2)
A-$R_cR_jD_b$-3	6Ø10	4Ø8/4Ø8	0,075 (Ø5,5/10)	0,4 (Ø5,5/10)	-	-
A-$R_cR_jD_b$-4	6Ø10	4Ø8/4Ø8	0,15 (Ø5,5/5)	0,92 (Ø5,5/5)	POLYMER	-
A-$R_cR_jD_b$-5	6Ø14	4Ø8/4Ø8	0,15 (Ø5,5/5)	0,92 (Ø5,5/5)	POLYMER	-
B-UR-3	-	-	-	-	-	-
B-URD_b-4	6Ø10	-	-	-	-	-
B-$R_cR_jD_b$-1	6Ø14	4Ø8/4Ø8	0,15 (Ø5,5/5)	0,035 (Ø5,5/10)	POLYMER	-
B-$R_cR_jD_b$-2	6Ø10	4Ø8/4Ø8	0,075 (Ø5,5/10)	0,035 (Ø5,5/10)	POLYMER	-
B-$R_cR_jD_b$-6	6Ø10	4Ø8/4Ø8	0,15 (Ø5,5/5)	0,71 (Ø5,5/5)	-	YES (Rc-6)
B-$R_cR_jD_b$-7	6Ø10	4Ø8/4Ø8	0,15 (Ø5,5/5)	0,035 (Ø5,5/10)	-	YES (Rc-7)
B-$R_cR_jD_b$-8	6Ø10	4Ø8/4Ø8	0,15 (Ø5,5/5)	0,142 (Ø5,5/10)	-	YES (Rc-8)
Note:			**Note:**			
A: Load Pattern A, B: Load Pattern B D_b: dowels			**UR: unreinforced core UR_j: unreinforced jacket R_c: reinforced core R_j: reinforced jacket**			

- Load Pattern A (LPA): Direct loading of old column (core) and support of jacket section only. The purpose is the investigation of load transfer from core (old concrete) to jacket (new concrete) depending on the resistance mechanisms of the interface (cohesion, aggregate interlock, dowels, anchors).

• Load Pattern B (LPB): Direct loading of core with the entire retrofitted element supported. That case simulates the function of a retrofitted column of a real structure where the growth of the axial load takes place through the old column (core).Even if the jacket crosses the beam- column joint, due to the different time of casting; the concrete of the jacket presents shrinkage phenomena. As a result there is a region of the old column not fully jacketed.

Briefly, the current experimental program considers the following parameters: a. kind of connection of core and jacket: cohesion, epoxy glue, dowels and anchors, b. percentage of transverse reinforcement (stirrups) of core and jacket, c. type of loading- Load Patterns, d. damages of the core (construction or overloading). In the current paper the construction damages are not examined.

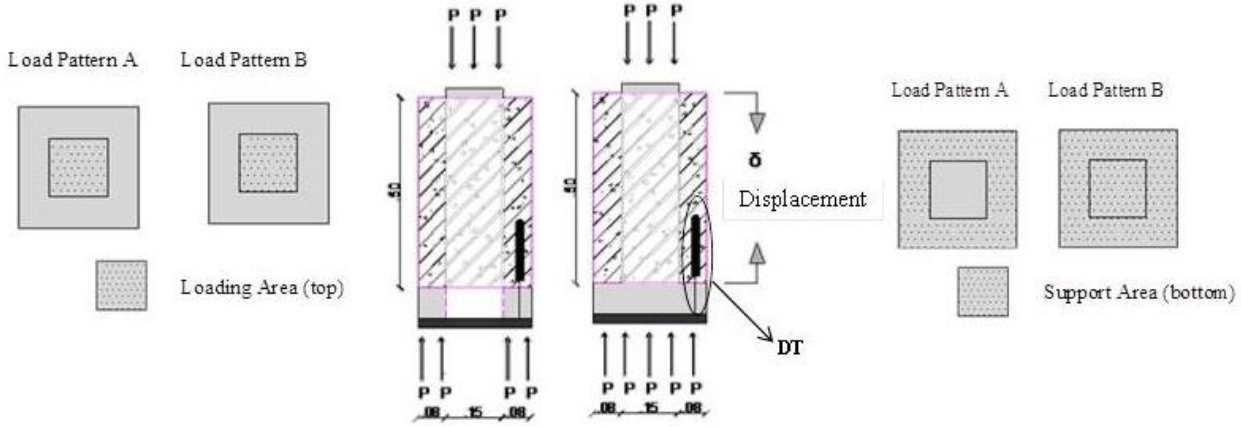


Figure 7 Shape of Load Patterns

4 EXPERIMENTAL RESULTS

4.2 Load Pattern Results

Table 2 shows the results of the specimens tested in the specific Load Pattern. Also the envelopes of the results of the cyclic test are shown in Figure 8 to 13. It is noted that columns were tested in high levels of axial displacements that are not feasible to the real structures in order to investigate the load transfer mechanisms. Table 2, though, includes the measured quantities: δ_{peak} is the displacement that corresponds to the maximum load (P_{max} also included), δ_u is the displacement corresponding to the ultimate load (δ_u>25mm, P_u=20%Pmax), E_n is the total absorbed energy normalized to the volume of the core and μ are the deformation ductility achieved. All deformations are the relative displacements of the two loading plates at the top and bottom of the specimens as shown in Figure 7. It is assumed that all deformations equal with the slip of the interface between core and jacket.

In Load Pattern B which simulates a retrofitted column in real structures, (Figure 7) specimen with no reinforcement at all (B-UR-3) presents higher load than an unreinforced column with dowels crossing the interface (B-URD_b-4). Specimen only with dowels crossing the interface (B-URD_b-4) proves that their presence affects the maximum load in small levels but increases the resistance of the interface to slip. The strong difference between those specimens is the actual mechanism of failure. The unreinforced column works only with tensile strength of the weakest concrete. The presence of dowels, on the other hand, creates damaged regions around the dowel bar that augment throughout the loading and the make the failure easier to expand. The influence of dowels is shown in Figure 9.

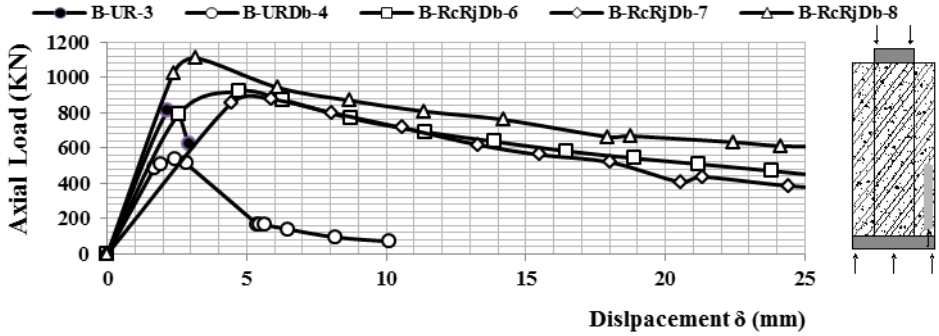


Figure 8 Displacements versus Axial Load for Load Pattern B (Envelopes)

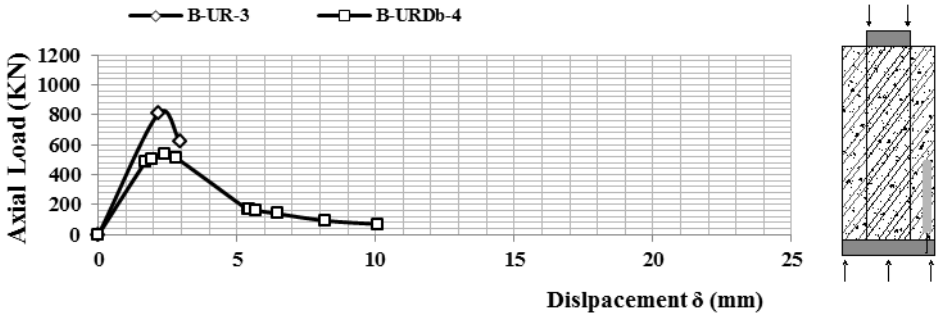


Figure 9 Cohesion and dowel contribution to the shear transfer mechanisms

The influence of the diameter of dowels is again examined by the columns covered with polymer sheets. Dowels of larger diameter (B-$R_cR_jD_b$-1, 6Ø14) presented 28% higher maximum load at 96% lower values of slip than smaller diameters (B-$R_cR_jD_b$-2, 6Ø10) (Figure 10).

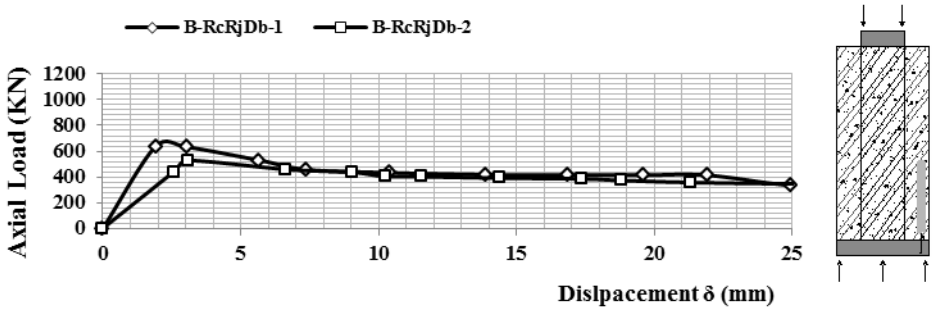


Figure 10 Dowel action

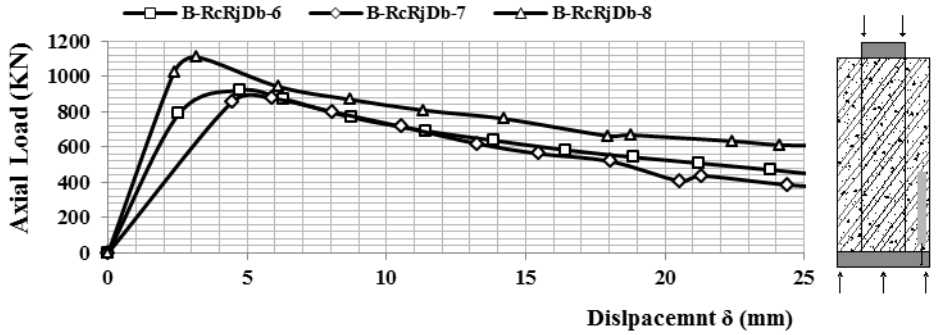


Figure 11 Confinement effect of the jacketed area

The mechanical percentages of stirrups in the jacket area affect the maximum bearing load, as shown in Figure 11. Specimen with dense stirrups (B-$R_cR_jD_b$-8) presented the highest axial load capacity up to 19,7%, proving the activation of the confinement mechanisms of jacket.

All above are also confirmed by the energy absorbed diagram (Figure 12). The activation of confinement is also obvious specimen with the high percentage of stirrups absorbed the most energy (B-$R_cR_jD_b$-8: ω_{wj}=0,142). Finally, again, the energy of the dowel action or cohesion alone or even in combination (B-UR-3, B- URD_b-4, B-$R_cR_jD_b$-1, B-$R_cR_jD_b$-2,) range in lower values.

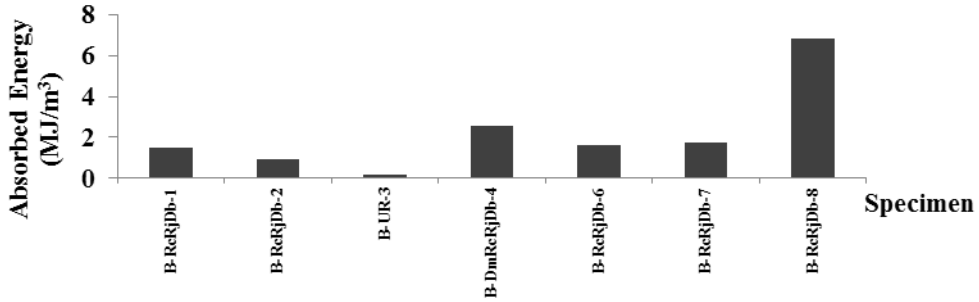


Figure 12 Energy Absorbed Diagram for Load Pattern B

In both Load Patterns the pre-loading effect is proven to be of minor importance to the final behavior of the retrofitted element. Pre-loaded specimens were not affected in terms of maximum bearing load.

It is important to note that the values of the bearing load of Load Pattern A are similar to those of Load Pattern B. This means, that in Load Pattern B the forces are totally transferred to the jacket area.

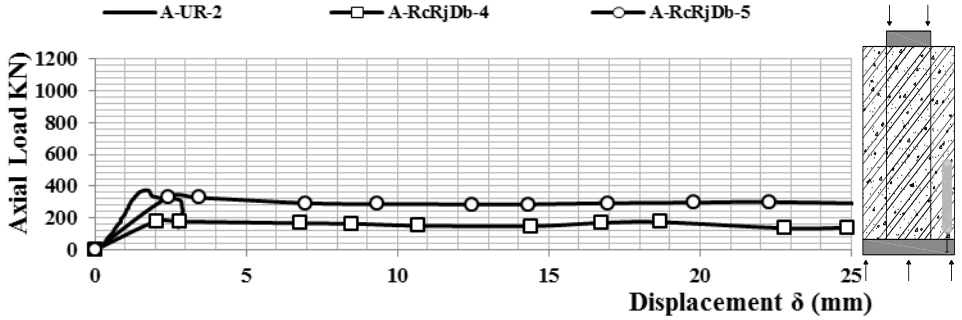


Figure 12 Displacements versus Axial Load for Load Pattern A (Envelopes)

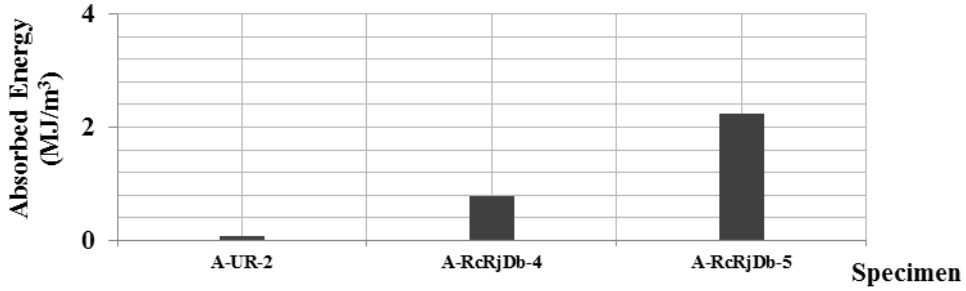


Figure 13 Energy Absorbed Diagram for Load Pattern A

Table 2. Experimental Results

Specimens	Cores					Jackets					
	δ_u (mm)	δ_{peak} (mm)	P_u (KN)	P_{peak} (KN)	E_n (MJ/m^3)	δ_u (mm)	δ_{peak} (mm)	P_u (KN)	P_{peak} (KN)	μ_δ	E_n (MJ/m^3)
A-UR-2	-	-	-	-	-	2.86	1.63	303.11	375.10	2	0.08
A-RcRjDb-4	-	-	-	-	-	66.86	2.03	54.74	181.60	33	0.77
A-RcRjDb-5	-	-	-	-	-	90.95	2.42	246.36	329.74	38	2.24
B-UR-3	-	-	-	-	-	5.02	2.17	169.11	810.31	2	1.51
B-RcRjDb-1	-	-	-	-	-	45.01	1.92	318.30	638.83	23	0.93
B-RcRjDb-2	-	-	-	-	-	27.73	3.09	352.40	526.72	9	0.19
B-DmRcRjDb-4	-	-	-	-	-	53.17	6.52	268.24	1062.00	8	2.56
B-RcRjDb-6	-	-	-	-	-	43.38	4.73	160.53	922.34	9	1.62
B-RcRjDb-7	-	-	-	-	-	46.54	5.87	176.04	876.39	8	1.75
B-RcRjDb-8	4.85	3.60	532.13	612.00	0.12	145.94	3.17	443.85	1110.78	46	6.83

5 CONCLUSIONS

The present study focuses on the shear mechanisms that contribute to the behaviour of a retrofitted element strengthened with RC jacket. The different Load Patterns demonstrate the variable activation of the transverse reinforcement of the jacket and the dowel action. These factors contribute to maximum bearing load as well as to the resistance of the interface to slip. What is more, in both Load Patterns the load is transferred to the jacket in the same way. Initial damages up to design loads do not affect the ability of the element to act as monolithic even when repair is not applied.

REFERENCES

[1] Ersoy, Ugur, Tankut, A.Tugru, Suleiman, Ramadan , *Behavior of jacketed columns*, Structural Journal, 1993

[2] Kaliyaperumal, G., Sengupta, A.K., *Seismic retrofit of columns in buildings for flexure using concrete jacket* , ISET Journal of Earthquake Technology, 2009

[3] Rodriguez, M., Park, R., *Seismic load tests on reinforced concrete columns strengthened by jacketing*, Structural Journal, 1994

[4] J. J. Guerrero, B. Gomez and O. M .Gonzalez, *Jacketing of reinforced concrete members*, Eleventh world conference on earthquake engineering, 1996

[5] Júlio, E.N.B.S., Branco, F.A.B., *Reinforced concrete jacketing - Interface influence on cyclic loading response*, Structural Journal, 2008

[6] Bousias, S.N., Biskinis, D., Fardis, M.N., *Spathis, A.-L., Strength, stiffness, and cyclic deformation capacity of concrete jacketed members*, Structural Journal, 2007

[7] R.N.F. Carmo, H. Costa, T. Simões, C. Lourenço, D. Andrade., *Influence of both concrete strength and transverse confinement on bending behavior of reinforced LWAC beams*, Engineering structures, 2013

[8] Anna Halicka, *Influence new-to-old concrete interface qualities on the behaviour of support zones of composite concrete beams*, Constructions and building materials, 2011

[9] Shin, H.-C. , Wan, Z., *Interfacial properties between new and old concretes*, Second international conference on sustainable construction materials and technologies, 2010

[10] Dimitra V. Achillopoulou, Theodoros C. Rousakis, Athanasios I. Karabinis, *Force transfer between existing concrete columns with reinforced concrete jackets subjected to axial loading*, 15th WCEE, Lisboa 2012.

[11] Nasersaeed, H., *Evaluation of behavior and seismic retrofitting of RC structures by concrete jacket*, Asian journal of applied sciences, 2011

[12] J. C. Walraven, Aggregate Interlock and Dowel Action under Monotonic and Cyclic Loading, Delft University Press, 1988-06-14.

[13] Dong-Uk Choi, James O. Jirsa, David W. Fowler , *Shear Transfer across Interface between New and Existing Concretes Using Large Powder-Driven Nails*, ACI Structural Journal, March-April 1999

[14] Elizabeth Vintzileou, Vassiliki Palieraki, *Shear Transfer along Interfaces in Repaired/Strengthened RC Elements subjected to Cyclic Actions*, 2007

[15] Tanaka, Y., Murakoshi, J., *Reexamination of dowel behavior of steel bars embedded in concrete*, Structural Journal, 2011

[16] S. Dei Poli, M. Di Prisco, P. G. Gambarova, *Shear Response, Deformations, and Subgrate Stiffness of a Dowel Bar Embedded in Concrete*, ACI Journal, November- December 1992

[17] E. N. Vintzileou, T.P.Tassios , *Behavior of Dowels under Cyclic Deformations* , ACI Structural Journal, 1/7/87

[18] Park, H.-G., Hwang, H.-J., Lee, C.-H., Park, C.-H., Lee, C.-N., *Cyclic loading test for concrete-filled U-shaped steel beam-RC column connections*, Engineering structures, 2012

[19]

COMPDYN 2013
4th ECCOMAS Thematic Conference on
Computational Methods in Structural Dynamics and Earthquake Engineering
D. V. Achillopoulou, T. A. Pardalakis, A. I. Karabinis
Kos Island, Greece, 12–14 June 2013

INVESTIGATION OF FORCE TRANSFER MECHANISMS IN RETROFITTED RC COLUMNS WITH RC JACKETS CONTAINING WELDED BARS SUBJECTED TO AXIAL COMPRESSION

D. V. Achillopoulou[1*], T. A. Pardalakis[1] & A. I. Karabinis[1]

[1]Democritus University of Thrace

Vas. Sofias 12, 67100, Xanthi, Greece

dimiachi@civil.duth.gr*

theopard@civil.duth.gr

karabin@civil.duth.gr

Keywords: concrete jacket, interface, bend down welded steel bars, force transfer

Abstract. *In the current research program the force transfer mechanisms are investigated in retrofitted columns containing bend down welded steel bars. It includes 6 specimens of square section (150x150x500mm) of 24,37 MPa nominal concrete strength with 4 longitudinal steel bars of 8mm diameter (500 MPa nominal strength) and different transverse reinforcement ratios (ω_c= 0,075, ω_c=0,15). All columns were subjected to initial axial compression up to maximum load. After repair with thixotropic high strength concrete, all columns were retrofitted with RC jacket of 80mm width of 31,8 MPa concrete strength, including 4 longitudinal bars of 8mm diameter (500 MPa nominal strength) and different confinement ratios (ω_{cj}= 0,035/0,071/0,142) . The jacket's longitudinal bars are welded to the ones of the core using steel bars of either 8 or 10mm diameter. To test the strengthened columns a loading pattern is selected in order to simulate the real structures, even though the experimental set up includes only axial loads (moments and horizontal loads are not examined). The behavior of specimens is investigated through P-δ, σ-ε, energy absorbed diagrams and the levels of ductility achieved. The results indicate that the initial damages affect the total behavior of the column and the capacity of the interface to shear mechanisms and to slip: a) welded bars of higher diameter present early phenomena of buckling and as a result the retrofitted columns can bear lower maximum load, b) the presence of dowel action increases the capacity of the jacketed column to transfer load through the interface.*

1 INTRODUCTION

The ability of columns to transfer loads and bear horizontal loads makes them crucial elements for design. In reinforced concrete structures, columns can stand damages either due to overloading (gravity loads: changes in usage of the building, storey super induction, earthquakes, etc), due to construction damages (poor consolidation of concrete) or even due to exposure to environmental effects (corrosion, carbonation, etc). In order to rehabilitate their capacity in loads and deformation repair or even strengthening is inevitable. What is more, in structures designed without ductility (older generation codes) need also retrofitting in order to upgrade their strength and capacity in deformation.

In recent decades extensive research has been conducted in repair and strengthening methods [1], [2], [3]. High strength materials are commonly used in order to upgrade the bearing capacity [4]. After repair, in cases of strengthening several methods are used such as: FRP wrapping (fibre reinforced polymer laminates, jacketing, etc.) or even reinforced concrete (RC) jacketing. All these methods have been proven efficient in enhancing the load capacity and the ductility of elements [5], [6], [7]. The key to the strengthening design is proven to be the interface capacity in transferring loads and in terms of deformation [8], [9], [10]. More specifically, in cases of strengthening with RC jacketing the main mechanisms that act in shear transfer are concrete-to-concrete cohesion and friction (aggregate interlock) and dowel action of the reinforcement the interface between old and new concrete (dowels, tack-welds, butt-welds, bend down bars etc.).

All these mechanisms have been studied apart or in combination, analytically or/and experimentally. Modern codes of all scientific communities adopt results and semi-empirical relations considering the design of the jacket and the calculation of the shear mechanisms' components. The initial damages of the column are ignored, the type of loading is not defined (directly- indirect loading of the jacket area) and finally the state beyond the limits of design deformations is still vague. These parameters are investigated separately or in combination in this paper. In real structures columns are also subjected to bending and horizontal forces (earthquake). In this paper only the parameters of shear transfer mechanisms examined. For those reasons the specimens were subjected to axial compression only. The experimental program held at the Reinforced Concrete Lab at Democritus University of Thrace (D.U.Th.). They contain different percentages of transverse reinforcement at core and jacket, providing different mean normal stress at the interface. In the current paper the factor of possible initial damage due to construction imperfections [11] that is not referred and analyzed extensively in the various codes that affects the efficiency of the repair is not examined.

2 TRANSFER MECHANISMS

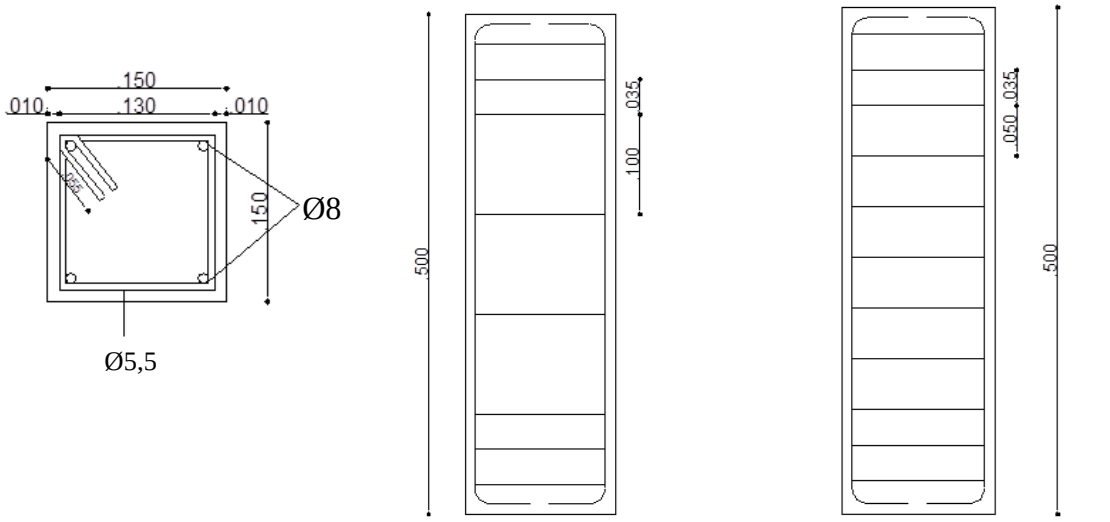
As already discussed, the shear transfer mechanisms are concrete-to-concrete cohesion and friction (aggregate interlock) [12] and dowel action. The concrete-to-concrete cohesion depends strongly on the kind of the interface. The treatment of the interface varies (smooth, rough, very rough, high pressure jetting, shotcrete etc.) resulting in different values of cohesion stress. The cohesion mechanism depends strongly on the tensile strength of the weakest concrete of the interface. Friction coefficient between the two different concretes and the normal stress applied at the interface affect the friction values [13]. Again, the kind and the treatment of the interface provide different values of friction coefficient. The normal stress applied is the result of the clumping action of stirrups during loading due to the expansion of concrete. Dowel action refers to the reinforcement crossing the interface keeping the two concretes in contact. It depends on the yield stress of the bar itself and of the angle forming with the interface (vertical, etc.). Instead of dowels, welding the longitudinal bars of both old and

new column with bend down bars crossing the interface has been common use during the last years [14].

3 EXPERIMENTAL INVESTIGATION

3.1 Old Columns

The experimental investigation includes results of 10 columns of square section with 150 mm width and 500 mm height in scale 1:2 (typical column used in real structures) (Fig.1a). In the considered old columns (cores) concrete of 24,37MPa strength was used (24,4GPa modulus of Elasticity), commonly used in building structures in the last decades and 32mm maximum size of aggregate. Columns include four longitudinal steel bars of 8mm diameter (500MPa nominal strength), which is the minimum volumetric ratio defined by old and new codes (ρ=1%). Half columns contain closed stirrups spaced at 100mm (mechanical ratio of transverse reinforcement: ω_c=0,075, 220MPa nominal strength, measured yield stress through tension tests f_y=250,76 MPa) and the rest three with 50mm stirrup spacing (ω_c=0,15), all adequately anchored (Fig.1b,c). The selection of the reinforcement was made according to the minimum percentage of longitudinal reinforcement (approximately 1%) and to low and medium transverse reinforcement ratios as practiced in structures with no high ductility requirements. Also, the diameters were selected in order to avoid any possible scale phenomena.



a. Square section (mm) b. ω_{wc}=0,075 (mm) c. ω_{wc}=0,15 (mm)

Figure 1. Section and transverse reinforcement of columns

3.2 Pre-Loading Effect

The pre-loading procedure held in order to simulate any possible minor damages of design loads happening at structures before strengthening is decided. The specimens were tested in a compression machine with a capacity of 3000 KN under axial monotonic or repeated loading (pseudo-seismic loading) of cycles of 5‰ axial strain (Figure 2). Two columns were preloaded up to maximum bearing load (Rc-9, Rc-10). The stress strain curves are shown in Figure 3.



Figure 2 Experimental Setup

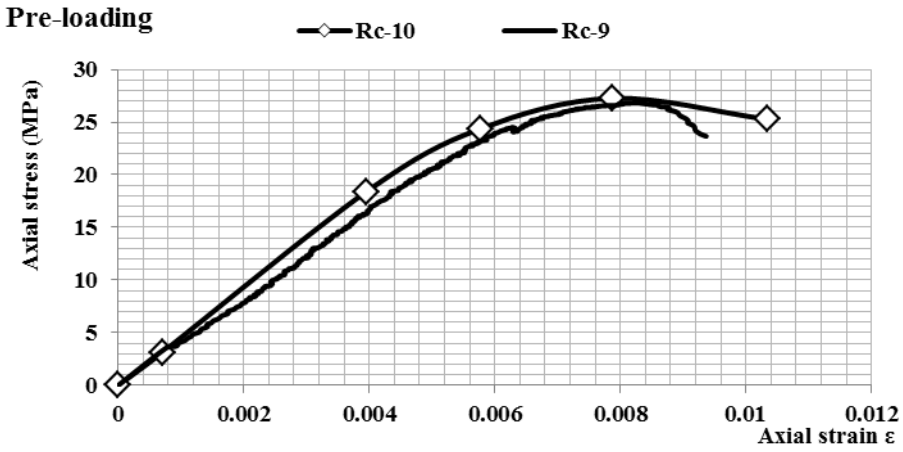


Figure 3: Axial stress vs axial strain diagram of pre-loading.

3.3 Repair and Retrofit Procedure

All six columns were strengthened with RC jacket of 80 mm thickness (total dimension of width: 310 mm) of high strength concrete (nominal compression strength: f_c=31,52 MPa, modulus of Elasticity: E_c=31,6 GPa, maximum aggregate: d_{AGR}=8 mm).

In two columns four (4) welded bend-down bars of diameter 8 mm (500 MPa nominal strength) were placed (Fig. 4) to connect core and jacket. The rest four columns contained welded bend-down bars of 10mm diameter.

The jackets included 4 longitudinal bars of 8 mm diameter and closed stirrups spaced at 50 mm (ω_{wj}=0,071: mechanical percentage of stirrups, normalized at the confined area of the jacket only) and 100 mm (ω_{wj}=0,035), again of 220 MPa nominal yield stress (measured yield stress through tension tests f_y=250,76 MPa). The top and bottom of each specimen contain more stirrups in order to secure that in these regions no damage will take place during test (Fig. 4 a, b). Table 1 resumes all specimens' characteristics.



a. ω_{wj}=0,071 b. ω_{wj}=0,035

Figure 4 Preparation of specimens before jacketing:
Transverse reinforcement of jackets and bend down bars.

Table 1. Details of Specimens

Specimen	Dowels	Bend down bars	Longitudinal Reinforcement (Core/Jacket)	Transverse Reinforcement		Pre- Loading of Core
				Core ω_{wc}	Jacket ω_{wj}	
B-$R_cR_jD_w$ -9	-	4Ø8	4Ø8/4Ø8	0,15 (Ø5,5/50)	0,035 (Ø5,5/100)	Repeated (Rc-9)
B-$R_cR_jD_w$-10	-	4Ø10	4Ø8/4Ø8	0,075 (Ø5,5/100)	0,035 (Ø5,5/100)	-
B-$R_cR_jD_w$-11	-	4Ø10	4Ø8/4Ø8	0,15 (Ø5,5/50)	0,071 (Ø5,5/50)	-
B-$R_cR_jD_w$-12	-	4Ø10	4Ø8/4Ø8	0,075 (Ø5,5/100)	0,035 (Ø5,5/100)	YES (Rc-6)
B-$R_cR_jD_w$-13	-	4Ø8	4Ø8/4Ø8	0,15 (Ø5,5/50)	0,035 (Ø5,5/100)	YES (Rc-7)
B-$R_cR_jD_bD_w$-14	6Ø10	4Ø10	4Ø8/4Ø8	0,15 (Ø5,5/50)	0,071 (Ø5,5/50)	YES (Rc-8)

Note:

A: Load Pattern A,
B: Load Pattern B
D_b: dowels
D_w: bend down bars (welded)

UR: unreinforced core
UR_j: unreinforced jacket
R_c: reinforced core
R_j: reinforced jacket

The jacketed specimens were subjected to axial compression only according to Load Pattern B (Fig.5):

Load Pattern B (LPB): describes the direct loading of core with the entire retrofitted element supported. That case simulates the function of a retrofitted column of a real structure where the growth of the axial load takes place through the old column (core). Even if the jacket crosses the beam- column joint, due to the different time of casting, the concrete of the jacket presents shrinkage phenomena. As a result there is a region of the old column not fully jacketed.

Briefly, the current experimental program considers the following parameters: a. kind of connection of core and jacket: cohesion, epoxy glue, dowels and anchors, b. percentage of transverse reinforcement (stirrups) of core and jacket, c. type of loading- Load Patterns, d.

damages of the core (construction or overloading). In the current paper construction damages are excluded.

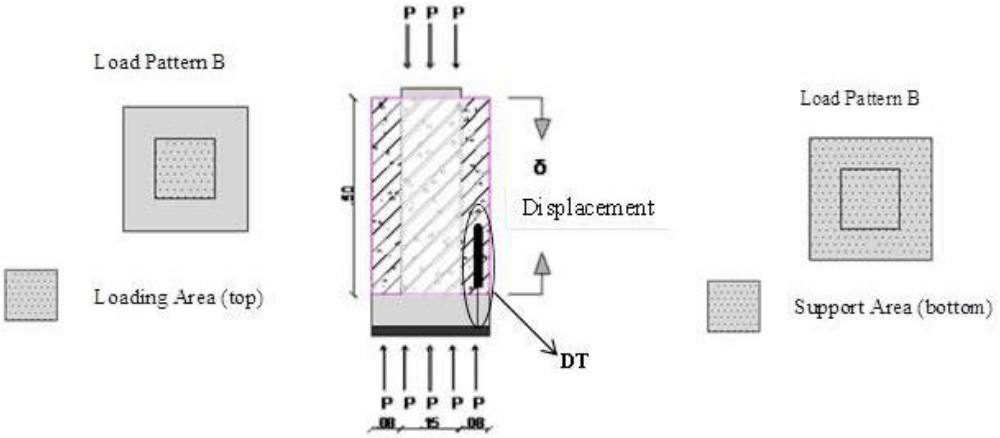


Figure 5 Shape of Load Patterns

4 RETROFITTED COLUMNS' EXPERIMENTAL RESULTS

Table 2 shows the results of each Load Pattern and the specimens tested respectively. Also the envelopes of the results of the cyclic test are shown in Figure 6 to 13. It is noted that the columns were tested in high levels of axial displacements that are not feasible to the real structures in order to investigate the load transfer mechanisms and the remaining strength. Table 2, though, includes the measured quantities: δ_{peak} is the displacement that corresponds to the maximum load (P_{max} also included), δ_u is the displacement corresponding to the ultimate load (δ_u>25mm, P_u=20%Pmax), E_n is the total absorbed energy normalized to the volume of the core and μ_δ are the deformation ductility achieved at the jackets' loading. All deformations are the relative displacements of the two loading plates at the top and bottom of the specimens as shown in Figure 5.

Table 2. Experimental Results

Specimens	Cores					Jackets					
	δ_u (mm)	δ_{peak} (mm)	P_u (KN)	P_{peak} (KN)	E_n (MJ/m^3)	δ_u (mm)	δ_{peak} (mm)	P_u (KN)	P_{peak} (KN)	μ_δ	E_n (MJ/m^3)
B-RcRjDw-9	4.65	4.25	537.08	599.18	0.10	87.98	1.58	207.95	1127.72	56	2.96
B-RcRjDw-10	-	-	-	-	-	121.76	2.09	236.00	793.21	58	3.66
B-RcRjDw-11	-	-	-	-	-	54.14	2.48	235.50	1055.75	22	2.26
B-RcRjDw-12	-	-	-	-	-	48.20	2.15	271.54	1016.86	22	1.70
B-RcRjDw-13	-	-	-	-	-	108.84	2.63	537.65	1158.68	41	3.44
B-RcRjDbDw-14	4.82	3.59	568	613.4	0.18	131.56	2.41	126.54	1053.48	55	5.34

The envelopes of all tested specimens are shown in figure 6. The preloading procedure doesn't seem to affect the total behaviour of the retrofitted element in terms of maximum bearing load and of deformation (Figure 7). Slightly, after the maximum bearing load, the preloaded specimen (B-$R_cR_jD_w$-9) presents lower load (15%) at the same values of displacement.

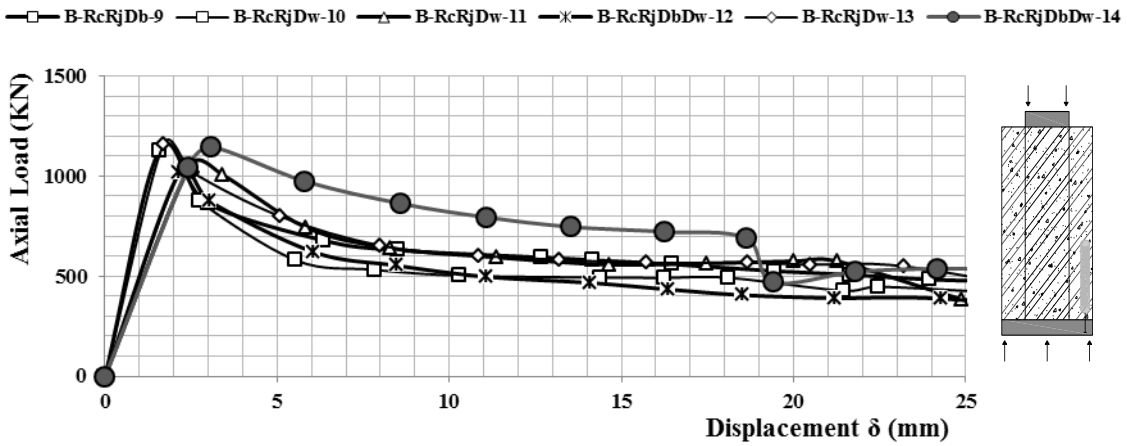


Figure 6 Displacements versus Axial Load for Load Pattern B (Envelopes)

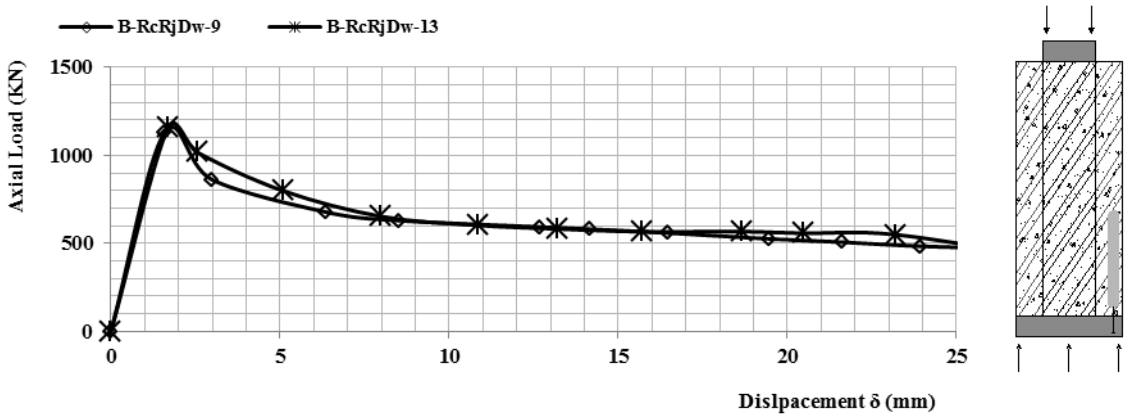


Figure 7 Pre-loading effect on total behaviour of column (Envelopes)

What is more, the contribution of confinement is examined (Figure 8). Specimen with dense stirrups is capable of bearing higher load than the one with lower percentage of transverse reinforcement. In fact, with twice the percentage of stirrups (B-$R_cR_jD_w$-11) 25% higher load is achieved at the same values of displacement. It is concluded that the load is transferred at the jacketed area energising the confinement mechanisms.

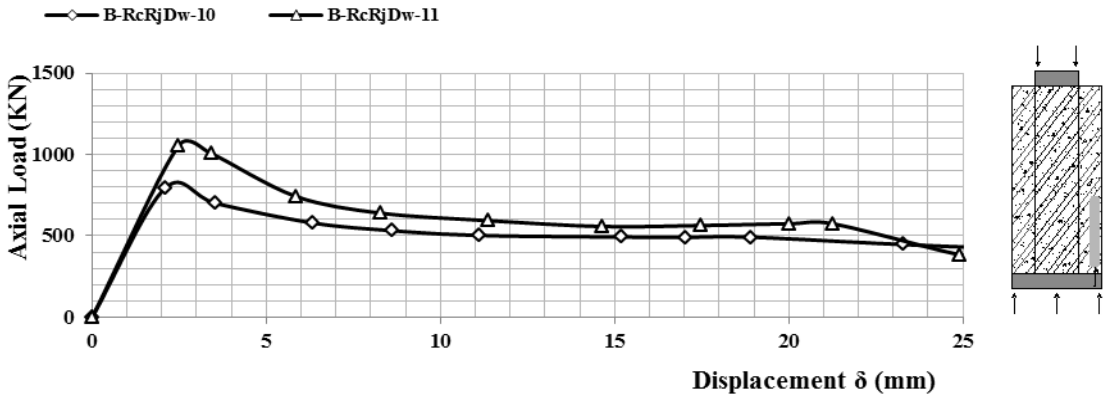


Figure 8 Confinement effect at the behaviour of the retrofitted element (Envelopes)

An important remark is that columns containing welded bars of diameter higher than that of the longitudinal bar (B-$R_cR_jD_w$-10) can bear lower maximum load in higher values of slip (Figure 9). The welded bars absorb and transfer the load at the jacketed area and provoke lateral stress at the longitudinal bar. As shown in figure 10 the failure of specimen with 4Ø10 welds crossing the interface is provoked by the buckling of the longitudinal bars of the jacketed area. On the other hand (Figure 11) the buckling of longitudinal reinforcement of a column with the same diameter in welds and longitudinal bars is in lower levels.

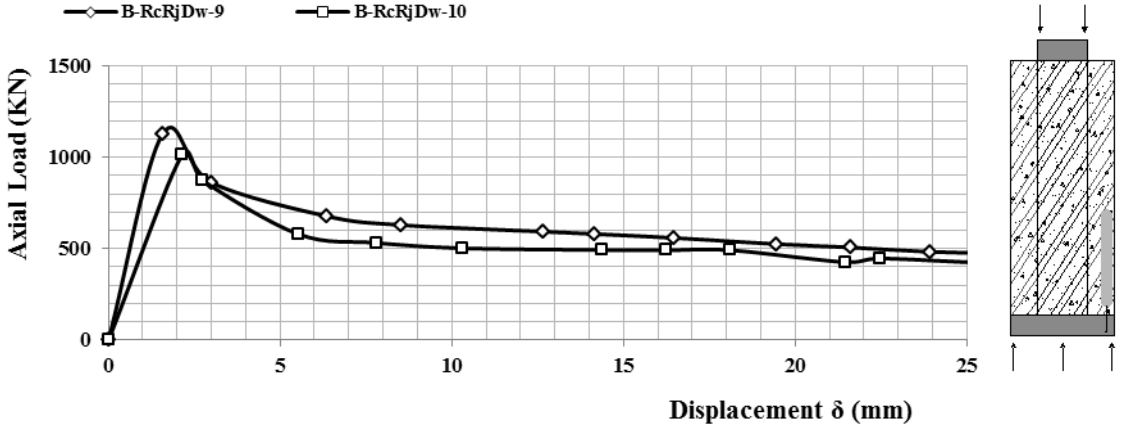


Figure 9 Welds' diameter effect on the jacketed columns performance (Envelopes)

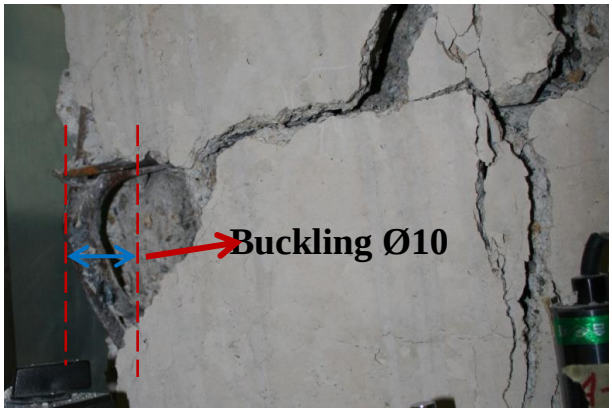


Figure 10 Buckling of the longitudinal bar_ welds 4Ø10

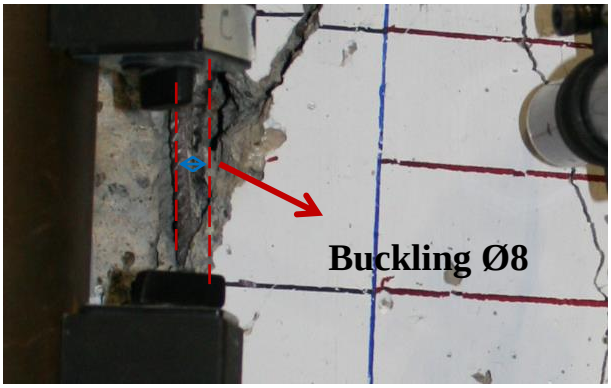


Figure 11 Buckling of the longitudinal bar_ welds 4Ø8

Additionally, the column containing both welds and dowels (B-$R_cR_jD_bD_w$-14) presents higher load than the one without dowels (B-$R_cR_jD_w$-11). Both initial branches coincide fully but the descending ones differ: it remains 24% higher at all the deformation spectra (Figure 12). Even though the regions near the dowel bars pass to a plastic behaviour due to the local damage been done through loading, the column continues to bear more load. In higher values of slip (over 3mm- almost 6‰) the dowel action stops and the bar continues to act in tension.

All above are also depicted at the energy absorbed diagram (Figure 13). The column with welds and dowels (B-$R_cR_jD_bD_w$-14) absorbs up to 68% higher energy of all. Again, specimens containing smaller welds (B-$R_cR_jD_w$-9, B-$R_cR_jD_w$-13) present higher energy than the ones with larger welds.

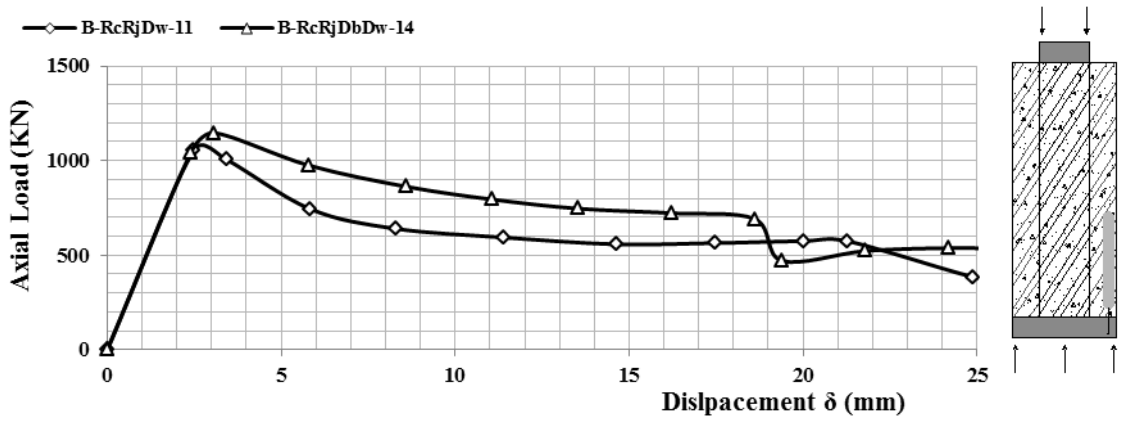


Figure 12 Dowel contribution on the behaviour of the retrofitted column containing welded bars (Envelopes)

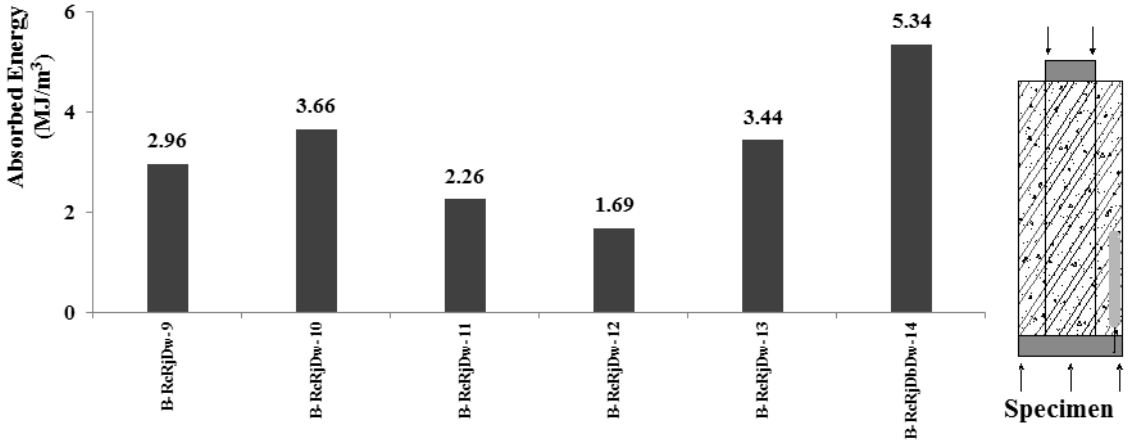


Figure 13 Total absorbed energy (MJ/m^3)

In terms of ductility (Table 2), even though the columns were subjected to high values of deformation that does not happen in real structures, specimen with small diameter of welded bars (B-$R_cR_jD_w$-10) presented up to 62% higher ductility of deformation. It is remarkable that specimen with both dowels and welds (B-$R_cR_jD_bD_w$-14) presents 6% lower ductility than the one without dowels (B-$R_cR_jD_w$-10). The plastic regions created around the dowel bar affect the ability of the interface to slip.

5 CONCLUSIONS

The present study focuses on the capacity of welded bend down bars-placed at the interface of old and new concrete in retrofitted RC columns with RC jackets- to the final bearing load. Due to initial overloading damages the loading capacity is decreased but the deformation ability is affected (pre-loading effect). The welded bars are proven to transfer the loads from old to new concrete since the confinement mechanisms are activated rising the maximum bearing load. Though, large diameters of welds connected to smaller diameters of longitudinal reinforcement bars lead to early phenomena of buckling. Buckling results in lower maximum loads and decreased stiffness. Finally, the dowel presence results in plastic regions around the dowel bars that do not reduce the capacity of the interface to transfer loads, but on the other hand result in higher percentages of bearing loads.

REFERENCES

[1] Rodriguez M., Park R, Seismic load tests on reinforced concrete columns strengthened by jacketing, Structural Journal, 91, 150-159, 1994.

[2] Júlio, E.N.B.S., Branco, F.A.B., Reinforced concrete jacketing - Interface influence on cyclic loading response, ACI Structural Journal, Title no. 105-S45, 2008.

[3] Konstantinos G. Vandoros, Stephanos E. Dritsos, Concrete jacket construction detail effectiveness when strengthening RC columns, Construction and Building Materials, 22, 264-276, 2008.

[4] Simon Austin, Peter Robins, Youguang Pan, Shear bond testing of concrete repairs, Cement and Concrete Research, 29, 1067–1076, 1999

[5] Hamidreza Nasersaeed, Evaluation of behavior and seismic retrofitting of RC structures by Concrete Jacket, Asian Journal of Applied Sciences, 4, 211-228, 2011.

[6] Shin, H.-C. , Wan, Z, Interfacial properties between new and old concretes, 2nd International Conference on Sustainable Materials and Technologies, Ancona, Italy, June 28-30, 2010.

[7] Anna Halicka, Influence new-to-old concrete interface qualities on the behaviour of support zones of composite concrete beams, Construction and Building Materials, 25, 4072-4078, 2011.

[8] Jean Louis Granju, Interface Between an Old Concrete and a Bonded Overlay: Debonding Mechanism, Interface Science, 12, 381-388, 2004.

[9] Ersoy Ugur, Tankut, A.Tugru, Suleiman Ramadan, Behavior of jacketed columns, Structural Journal, 90, 288-293, 1993.

[10] Andreas P. Lampropoulos, Ourania T. Tsioulou and Stephanos E. Dritsos, Monolithic Coefficient Values for Design when Seismically Strengthening RC Columns with Jackets, Journal of Earthquake Engineering, 16, 1023-1042, 2012.

[11] Dimitra V. Achillopoulou, Theodoros C. Rousakis, Athanasios I. Karabinis, Force transfer between existing concrete columns with reinforced concrete jackets subjected to axial loading, 15th WCEE, Lisboa 2012.

[12] J. C. Walraven, Aggregate Interlock and Dowel Action under Monotonic and Cyclic Loading, Delft University Press, 1988-06-14.

[13] R.N.F. Carmo, H. Costa, T. Simões, C. Lourenço, D. Andrade, Influence of both concrete strength and transverse confinement on bending behavior of reinforced LWAC beams, Engineering Structures, 48, 329-341, 2013.

[14] Avoid martensite when welding rebar, Firth, Mark, Williams, William M.

COMPDYN 2013
4th ECCOMAS Thematic Conference on
Computational Methods in Structural Dynamics and Earthquake Engineering
M. Papadrakakis, V. Papadopoulos, V. Plevris (eds.)
Kos Island, Greece, 12–14 June 2013

DYNAMICAL CHARACTERIZATION OF TYPICAL MEXICAN COLONIAL CHURCHES

Fernando Peña, Julio Manzano and Laura Robles

Instituto de Ingeniería, Universidad Nacional Autónoma de México
Edificio 2 – 401, Circuito Escolar, Ciudad Universitaria, Mexico city, Mexico
e-mail: fpem@pumas.iingen.unam.mx, JManzanoO@ii.unam.mx, MRoblesA@ii.unam.mx

Keywords: Dynamical Characterization, Colonial Churches, Historical Masonry, Seismic Vulnerability, Seismic Safety.

Abstract. *The dynamical characterization of ancient masonry churches built in the colonial era in Mexico by means of a case study is presented. The seismic assessment of old masonry churches is not an easy task, mainly due to the fact that the churches are large structures with complex geometries and built with materials with highly nonlinear behavior. These constructions vary in architectural styles, but mostly follow some basic typologies. The simplest one is the small parochial church which can be found in every village and town in Mexico.*

The dynamical characterization was performed by means of a study case of a typical church of the center of Mexico. The aim of the characterization is to develop a methodology to study the seismic vulnerability of this type of constructions. The study is based on complementary analysis approach. Thus, three steps were performed: a)preliminary studies, which must include historical information, materials and geometry description and survey of the structure, monitoring, non–destructive tests, etc; b) calibration and validation of numerical models, based on the results obtained from the previous step; and c) the dynamical characterization. This approach allows to overcome the complexity of the study of the seismic behavior of ancient masonry structures; by combining the results of different type of models and analysis.

The paper is based on a case study but also provides a very relevant discussion on an issue that has received insufficient attention: the seismic analysis of masonry structures without a box behavior. From the results obtained, it was identified that roof system cannot be considered as rigid diaphragm. The dynamical characterization shows that the belfry and the roof (dome and vaults) are the most critical elements. The church is very rigid, since the lateral wall drifts are so low. Thus out-of-plane and shear behavior in walls are not critical behaviors.

1 INTRODUCTION

The dynamical characterization of structures is in general a useful tool for the evaluation of seismic safety. The churches built in the colonial era in Mexico vary in size and architectural styles. However, churches of a particular zone follow some basic typologies (both architectural and structural), which depend mainly on the seismic zone where they were built [1, 2]. Thus, by case studies is possible to extrapolate the results to other similar churches.

The dynamical characterization should be based on theoretical (structural analysis) and experimental bases (NDT). But, in the first place, it must respect the integrity and the artistic and architectural values of the building. In this way, the methodology used must follow the ISCARSAH principles [3, 4]. Therefore, a specific methodology for historic buildings in each country must be developed. Thus, the study of particular cases will allow the development of a methodology for the Mexican case.

The aim of the paper is the dynamical characterization of typical colonial churches, through a case study. The study was limited only to the study of the Saint Bartholomew the Apostle church. This church was chosen for its historical and architectural significance within the area of study.

The methodology followed is based on a stepped strategy named complementary analyses approach [5]. This strategy helps to overcome the difficulties inherent to the analysis of historic structures, through a series of levels or steps:

- **Step 1. Preliminary studies**. At this step, the preliminary studies of the selected temple was performed. The information collected must include: an historical study and the geometrical, architectural and structural surveys.

- **Step 2. Studies for the calibration and validation of the structural models**. An ambient vibration test was performed in order to obtained the dynamical characteristics of the temple. It is necessary to have a preliminary numerical model in order to design and perform correctly this test. With the numerical model, it is possible to identify critical areas of the structure, as well as to define the correct position of the equipment used in the experimental tests. Also, at this step was calibrated and validated the numerical models with the results of the ambient vibration test.

- **Step 3. Dynamical characterization**. With the numerical models calibrated and validated, the dynamical characterization of the temple was carried out. This includes the identification of the mechanical characteristics of the materials and the seismic behavior. As well as the identification of critical elements as appendices or weak elements.

2 STEP 1. PRELIMINARY STUDIES

In this step, all information available for further studies is collected. Which must include, among others: historical information, materials and geometry description, architectural and structural survey, preliminary studies, etc. Historical information is very important, because it allows to understand the structural behavior of the building along the time. It is also necessary to have a good description of the temple; since in general, geometry of historic buildings is quite complex. So often there is not a clear difference between structural and architectural elements.

The architectural and structural survey of the temple is one of the most important information that must be collected. With this information, it is possible to carry out preliminary numerical models. These models were developed based on the geometric information obtained from surveys and nominal properties of the materials found in the literature.



Figure 1: Actual view of the church

2.1 Historical study

The St. Bartholomew the Apostle church is located at the north of Mexico city. In the colonial era, it was common to establish Indian towns around religious centers, in order to make easier the evangelization. In this way, the village of St. Barth was founded, which soon became an important town. The date of construction of the church is not known, but there are some administrative records from 1649 [6]. This means that its construction should be between the late 16^{th} and early 17^{th} century. The church was founded by the Franciscan order and has a modest and simple architecture without great decorations, according to the canons of the Franciscan Order [7].

The church has been struck by several seismic events of medium and high intensity. Due to this, the temple has been repaired and modified along the time. Unfortunately, there are not detailed historical records about these changes. However, by means of a photo record of the 20^{th} century [8] was possible to identify some important changes.

For example, Figures 1 and 2a show the façade actually and at the middle of the 40's. Comparing both figures is possible to observe significant changes in the façade. The right side window was expanded. The frontispiece is different, although it tried to preserve the original style. The buttress on the right side of the main door is new. Figure 2b seems to be from the 50's of the past century. Compared with Figure 2a, it is possible to see that the frontispiece is the same but without the pinnacles. The right side door and the buttress of the façade were already built but with a different architectural style.

It is reported that in the second half of 1960, the temple had several damages. The main façade was on risk to collapse. Several structural and architectural elements partially collapsed. The frontispiece collapsed. Due to these collapses, the temple was reinforced and restructured. Vaults were rebuilt with concrete and reinforced with concrete ribs. Several walls were reinforced, the belfry and the chapel and chorus slabs were rebuilt with concrete. The frontispiece and the portal were totally reconstructed with reinforced concrete elements.

2.2 Architectural and structural survey

The church has a Latin–cross floor plan, oriented in direction East–West. The main nave has a length of 31.5 m and a width of 7 m. While the transverse nave is 14 x 8 m^2. In the first

a)  b) 

Figure 2: View of the Façade [8] in the past century, decade of: a) 40's; b) 50's

bay there is an intermediate floor for the chorus. The roof is constituted by a barrel vaulting system with a thickness of 20 cm. A hemispherical dome is placed over the transept bay and it is supported by the drum. The average height of the walls is 6 m, while the height of the vaults, from the ground, is 8.75 m. The total height of dome is 13.95 m. The church has a bell tower of 13.75 m high. In plan, the tower has a rectangular section of 3.5 x 4.2 m^2. The thick of the walls varies from 0.85 to 1 m. Trapezoidal buttresses are placed along the longitudinal walls of the nave and in the apse.

The main material of construction is a heterogeneous masonry constituted by stones agglutinated by lime–sand mortar. Frequently, broken clay bricks or lightweight volcanic stones were added to the masonry. This heterogeneous masonry constitutes a kind of concrete whose composition varies according to the structural element; it is lighter than normal stone masonry, and has a tensile strength bigger than brick masonry, due mainly to the absence of weak planes constituted by the mortar layers. Walls are made by stone masonry, while vaults and the dome were rebuilt with concrete.

2.3 Numerical model

Based on the information collected, a finite element model was performed (see Fig. 3). Rectangular solid elements of eight nodes were used. The model has 22,509 elements, 96,066 degrees of freedom and 33,650 nodes.

Three types of materials were considered. Walls, columns, buttresses, tower base and arcs are of irregular stone masonry. The belfry was considered of masonry, but different from the walls. Since it presents some concrete and steel reinforcements. Finally, the vaults, the frontispiece, ribs and dome were considered of reinforced concrete. Table 1 shows the mechanical properties used in the model, which were obtained from the literature [9].

Table 2 shows the frequencies and percentages of modal mass for the first five modes. The structure is very rigid, as the first frequency is 3.66 Hz. The first two modes correspond to the vibration modes of the tower, which is the most flexible part of the church (Fig. 4a). The third mode is the first mode in the transverse direction with a frequency of 5.05 Hz (Fig. 4b). The fourth and sixth modes correspond to torsional mode of the tower, while the fifth mode is the first mode in longitudinal direction. It should be noted that all modes have a torsional component, and there is no one mode with a pure form.

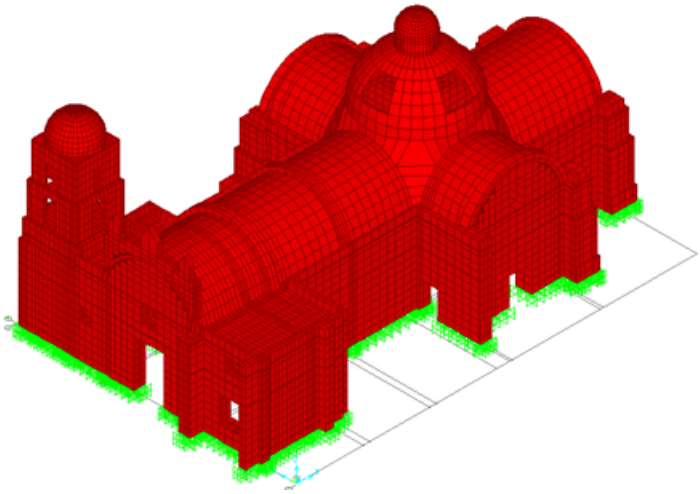


Figure 3: Finite element model of the church

Material	Compressive strength (MPa)	Tensile strength (MPa)	Elastic modulus (MPa)	Density (kg/m^3)
Wall masonry	1.5	0.12	0.60	1600
Belfry masonry	3.0	0.24	0.25	1800
Concrete	20	2.10	21.7	2400

Table 1: Mechanical properties of the materials [9].

3 STUDIES FOR THE MODEL CALIBRATION AND VALIDATION

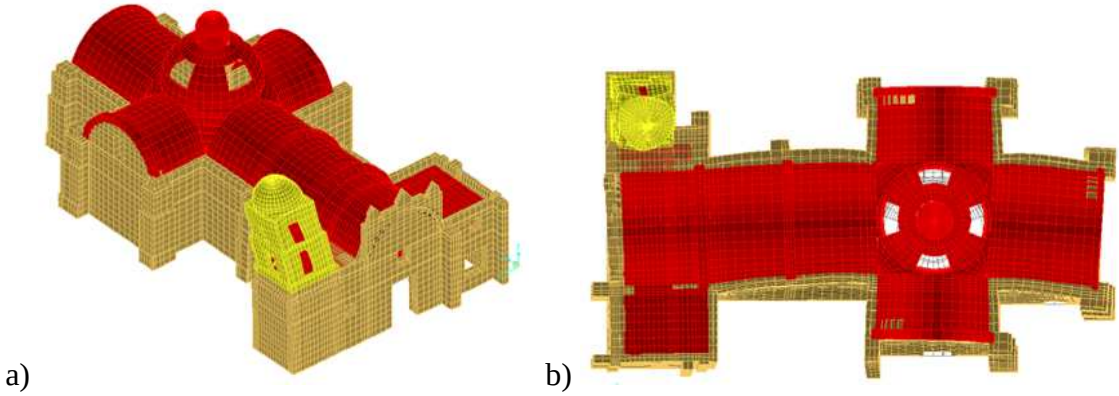
The aim of the ambient vibration tests is to define the dynamic properties of the church, which include vibration frequencies, mode shapes and damping coefficients. These tests may also be used to assess the degree of connection between the various structural elements of the church. With the results of the test, the numerical models were calibrated. In this way, the mechanical properties of the materials were obtained by calibrating the frequencies and mode shapes of the analytical model with the ambient vibration test.

3.1 Ambient vibration test

Based on the results of the finite element model and field survey, the points where the accelerometers should be placed for ambient vibration test were defined. Figure 5 shows schematically the points selected for the installation of the accelerometers. The signals obtained from the tests were processed and interpreted by using an spectral analysis program. For each test, the average power spectra and the corresponding spectral ratios, phase angles and coherence between signal pairs were obtained. For these analyses, each record was processed in sections of 40.96 s, considering a 50% of overlap between two consecutive segments and a Hanning window weighting type. The analysis of the spectra allowed to obtain several frequencies. Table 3 shows the significant frequencies of the tower, while Tables 4 to 6 shows the significant frequencies of the body of the church.

Mode	Frequency (Hz)	Percentage Longitudinal	of modal Transverse	mass (%) Vertical
1	3.66	2.2	1.9	0.0
2	3.71	1.3	3.7	0.0
3	5.05	0.1	55	0.0
4	6.41	1.8	5.7	0.0
5	6.66	62	0.0	0.0
6	7.05	0.8	2.5	0.1
7	7.17	0.2	1.0	0.0
8	7.27	4.8	0.1	0.0
9	8.07	0.0	0.6	0.5
10	8.46	1.1	0.8	0.7

Table 2: Dynamical properties.



a) b)

Figure 4: Shape modes: a) first mode; b) third mode

3.2 Calibration of the numerical model

The numerical model performed in the previous step considered the properties of the materials found in the literature. In order to have a more reliability model, it was calibrated with the ambient vibration tests. In this particular case, the mechanical properties of the materials were the variables to be calibrated. Thus, four variables were calibrated. Three elasticity modules corresponding to each materials (Table 1). The last variable was the mass density of the masonry of the belfry, since it has a concrete reinforcement. Table 7 shows the base values, limited values and the optimized values. Obviously, the base values correspond to the values used in the preliminary model (Table 1).

The variables were optimized by using five frequencies. The first two corresponding to the tower and the frequency corresponding to the first mode in transverse, longitudinal and vertical

Mode	Longitudinal	Transverse	Vertical
1	3.15	3.47	7.9–8.0
2	7.7–7.9	8.5–8.8	——

Table 3: Measured frequencies of the tower (Hz).

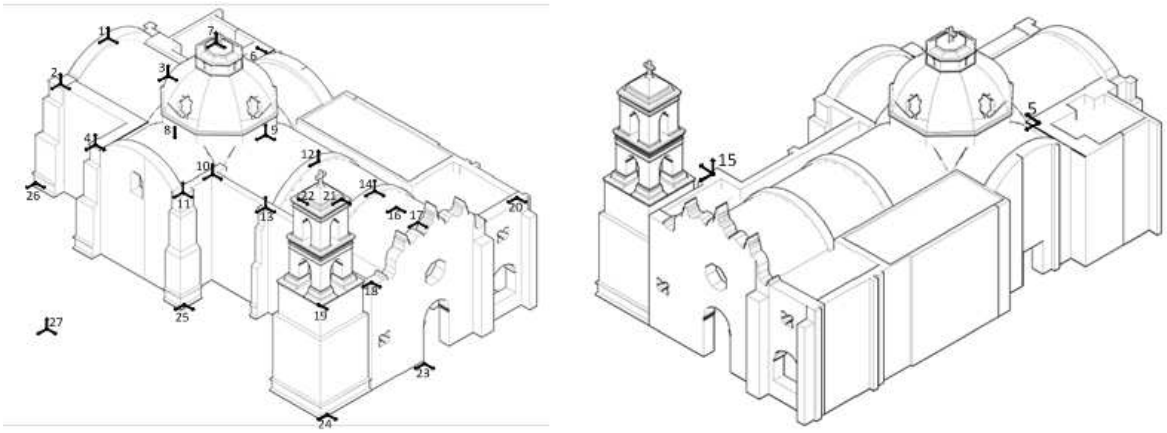


Figure 5: Localization of the measurement points

Mode	Nave	Façade	Cupola
1	5.6–6.3	——	——
2	8.0–10.3	——	8.2–8.7
3	12.0–15.0	13.5–15.5	——

Table 4: Measured frequencies of the church, longitudinal direction (Hz).

direction. Table 8 compares the calculated frequencies with the calibrated numerical model with the values measured in the ambient vibration tests. It is noted that errors are acceptable, which are below 10%.

4 DYNAMIC CHARACTERIZATION

4.1 Own weight analysis

The total weight of the structure is equal to 15,175 kN, being the average axial stress in the foundation equal to 0.13 MPa. Figure 6a shows the map of vertical axial stresses due to its own weight, while Figure 6b shows the deformed model.

4.2 Modal description

Table 9 shows the dynamical properties of the calibrated model. It is noted that the mode shapes are virtually the same of the original model, only mode 5 was exchanged with mode 6.

Mode	Apse	Nave	Cupola	Façade
1	——	3.47	——	——
2	——	4.3–4.8	4.5–4.8	——
3	5.7–7.3	5.7–7.3	5.7–7.3	——
4	6.1–7.1	6.1–7.1	——	——
5	——	——	8.3–9.3	——
6	——	——	10.9–12.7	14.8–15.7

Table 5: Measured frequencies of the church, transversal direction (Hz).

Mode	Nave vaults	Cupola
1	8.1–8.2	——
2	——	18.0–19.0

Table 6: Measured frequencies of the church, vertical direction (Hz).

Material	Variable	Base	Up Limit	Down Limit	Optimized
Masonry	Elasticity modulus (GPa)	0.60	1.00	0.40	0.40
Belfry masonry	Elasticity modulus (GPa)	0.25	9.81	0.20	0.25
Belfry masonry	Mass density (t/m^3)	1.80	2.20	1.60	1.60
Concrete	Elasticity modulus (GPa)	21.72	25.70	16.82	16.82

Table 7: Values used in the optimization of the variables.

This means that the mode 6 is now the first longitudinal mode, while the mode 5 is a torsional mode of the tower. Likewise, it is observed that the vault can not be considered as an infinitely rigid diaphragm. Since the motion of the plant is not uniform as it can be observed in Figure 7.

4.3 Modal spectral analysis

A modal spectral analysis was performed considering the design spectrum proposed by the Mexican building code [10]. The church was founded in rock soil, zone I in accordance with the building code. As the structure is considered as type A (historical structure), the stresses must be multiplied by the factor 1.5. Thus, the spectrum will have a maximum ground acceleration equal to 0.6 m/s^2, while the acceleration of the plateau is equal to 2.4 m/s^2. Since the beginning of the plateau starts in the period equal to 0.2 s, only the first two modes (corresponding to the vibration of the tower) fall in the plateau, whereas the other modes lie in the ascending branch. The seismic factor Q is equal to one, since the masonry is considered as non ductile material. This means that the design spectrum was not reduced.

Figures 8 shows the deformed shape with the map of vertical axial stresses, when the earthquake is applied in the transverse and longitudinal direction respectively. It is noted that the analyses consider the combination of the earthquake in the two directions (100% for one direction plus 30% in the other). It is observed that regardless of the direction of the earthquake, the deformed shape obtained is similar in both cases. The tower has a torsional behavior, which is concentrated in the upper body of the belfry. Likewise, the dome has a slight vertical movement, which produce a stress concentration at the base of the drum.

The vertical axial stresses are also concentrated in the pillars of the belfry and at the base of

Mode	Direction	Calculated frequency	Measured frequency	Error (%)
1	1^{st} Tower	3.17	3.15	0.56
2	2^{nd} Tower	3.21	3.47	8.23
3	1^{st} Transversal	5.02	4.55	9.39
6	1^{st} Longitudinal	6.62	5.95	10.18
9	1^{st} Vertical	7.81	8.15	4.31

Table 8: Frequencies used in the calibration (Hz).

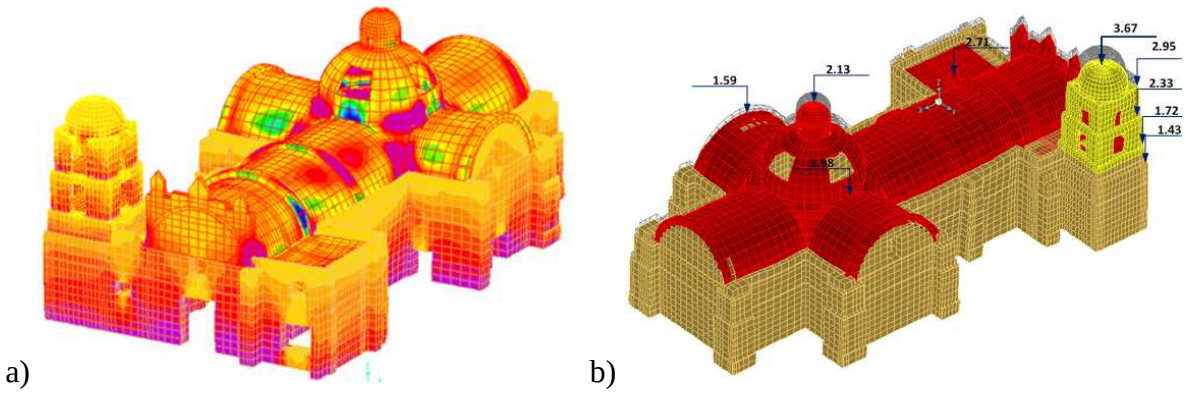


Figure 6: Own weight analysis: a) map of vertical axial stresses; b) deformed shape (displacements in mm)

Mode	Frequency (Hz)	Percentage Longitudinal	of modal Transverse	mass (%) Vertical
1	3.17	2.2	1.7	0.0
2	3.21	1.3	3.9	0.0
3	5.02	0.0	77.8	0.3
4	6.35	0.1	6.2	0.0
5	6.42	10.2	1.0	0.0
6	6.62	78.5	0.1	0.0
7	7.13	0.0	4.5	2.0
8	7.41	4.7	0.2	3.9
9	7.81	0.1	0.3	29.5
10	8.51	0.8	2.4	32.8

Table 9: Dynamical properties of the calibrated model.

walls and buttresses. A slight vertical stress concentration can be observed in the base of the ribs, which indicates that they are working due to vertical vibration of the vaults. Furthermore, the shear is concentrated in the body of the pillars of the belfry, in the drum and the ribs. It is interesting that the walls do not show important shear stresses. This is because the church has virtually no lateral or longitudinal distortions. Since the motion is concentrated in the tower and roof (dome and vaults). These results show a seismic behavior similar to those found in historical records: the critical elements of this church are the bell tower and the roof.

5 CONCLUSIONS

- The dynamical characterization of colonial Mexican churches was performed by means of a case study.
- Ambient vibration test was performed in order to calibrate and validate a finite element model of the church.
- This study follows a stepped strategy in order to overcome the difficulties in the study of historical structures.
- The roof system cannot be considered as rigid diaphragm.

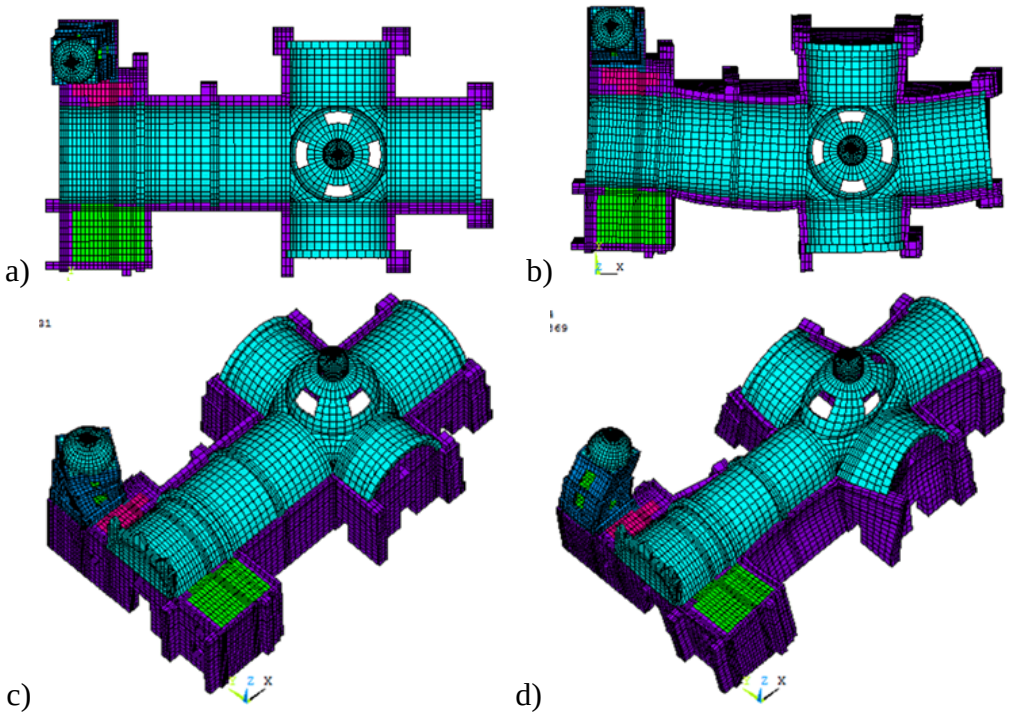


Figure 7: Shape modes: a) first mode; b) third mode; c) fifth mode; d) eight mode

- The dynamical characterization shows that the belfry and the roof (dome and vaults) are the most critical elements.
- The church is very rigid, since the lateral wall drifts are so low. Thus out-of-plane and shear behavior in walls are not a critical behaviors.

6 ACKNOWLEDGMENTS

The financial support of the Instituto de Ingeniería, UNAM, by means of the project 1651 ***Dynamical characterization of colonial churches*** is acknowledge.

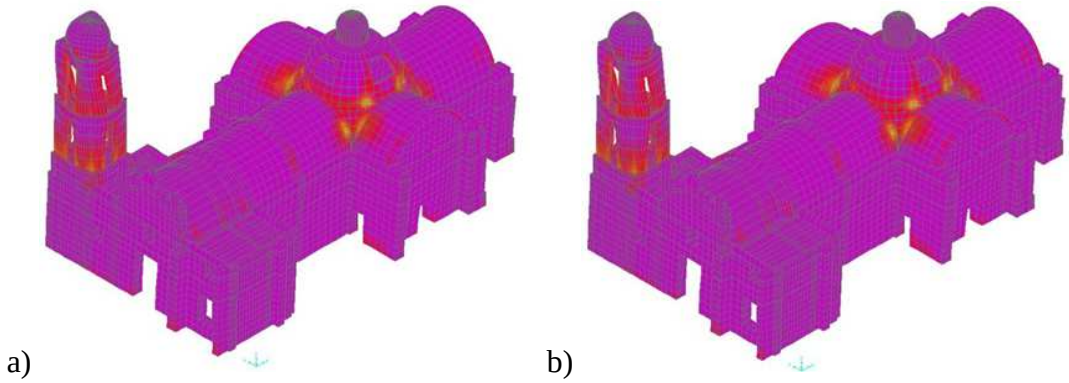


Figure 8: Deformed shape and map of vertical axial stresses: a) 100% in lateral direction plus 30% in the longitudinal; b) 30% in lateral direction plus 100% in the longitudinal

REFERENCES

[1] R. Meli, F. Peña, On elastic models for evaluation of the seismic vulnerability of masonry churches. Lourenço, Roca and Modena eds. *Proceeding of Structural Analysis of Historical Constructions (SAHC2004)*, Padova, Italia, 1121–1131, 2004.

[2] F. Peña, J.M. Meza, Seismic assessment of bell towers of Mexican colonial churches. Lourenço, Roca and Modena eds. *Proceeding of Structural Analysis of Historical Constructions (SAHC2010)*, China, 585–590, 2010.

[3] ICOMOS, *International Charter for the Conservation and Restoration of Monuments and Sites (The Venice Charter)*. ICOMOS, 1964. Available at http://www.icomos.org

[4] ICOMOS, *Principles for the Analysis, Conservation and Structural Restoration of Architectural Heritage*. ICOMOS, 2003. Available at http://www.icomos.org

[5] F. Peña, P.B. Lourenço, N. Mendes, D.V. Oliveira, Numerical models for the seismic assessment of an old masonry tower. *Engineering Structures*, **32**, 1466–1478, 2010.

[6] R. Lopez, L. Cordoba, *Parroquia de San Bartolomé Apóstol. El corazón de Naucalpan*. Arquidiócesis de Tlanlneplantla, Mexico, 2011.

[7] C. Astorga, J.L. Rodriguez, *Historia de la Arquitectura en México:época virreinal*. Editorial UNAM, Mexico, 2009.

[8] INAH, *Fototeca Constantino Reyes–Valerio*. Coordinación Nacional de Monumentos Históricos, CONACULTA, INAH, Mexico, 2012.

[9] R. Meli, *Ingeniería estructural de los edificios históricos*. Fundación ICA, Mexico, 1998.

[10] NTC, *Normas Técnicas Complementarias para Diseño por Sismo*. Reglamento de Construcciones para el Distrito Federal, Mexico, 2004.

COMPDYN 2013
4th ECCOMAS Thematic Conference on
Computational Methods in Structural Dynamics and Earthquake Engineering
M. Papadrakakis, V. Papadopoulos, V. Plevris (eds.)
Kos Island, Greece, 12–14 June 2013

BRIDGES WITH SIMPLY SUPPORTED DECKS: A SIMPLIIFIED VULNERABILITY ASSESSMENT

Domenico Raffaele[1], **Mauro Mezzina**[1] **and Antonio Tosto**[1]

[1] DICATECh, Politecnico di Bari
address via Orabona, 4 - 70126 Bari (Italy)
d.raffaele@poliba.it

Keywords: Bridges, Reinforced Concrete, Seismic Vulnerability, Circular pier.

Abstract. *The paper proposes a simplified procedure for the seismic vulnerability analysis of bridges with simply supported decks and single solid circular piers. The proposed method can be applied to the structural typology for which the seismic response of the whole bridge depends from the critical pier. For an assigned limit state, the procedure determines a general form of the capacity curve that is approximately calculated for equivalent system (SDoF) of the critical pier as a function of 3 parameters (elastic stiffness, displacement at yielding, displacement at collapse). Starting from the behaviour under combined axial and flexural stress, the method taking then into account the different possible collapse modes (shear failure; lap splice failure of the longitudinal bars; buckling) and the geometric non linearity.*
A N2-like procedure is then applied in order to identify the "Capacity Return Period", which represents the performance level, to be compared with the design spectrum. A significant numerical example is presented in which the traditional FEM solution is compared with the proposed simplified procedure. The basic idea of the procedure is that, by only knowing few information usually contained in the regional archives (general geometry, sections, year of construction) it will be possible to assess the infrastructures of a vast territory, providing priority lists in terms of capacity level and cost of retrofitting.

1 INTRODUCTION

In seismic prone areas, the seismic risk assessment of strategic buildings and infrastructures is a crucial question. A particularly relevant category is represented by bridges, to which a great attention has been devoted in the last few years, in order to perform the vulnerability inventory at the regional scale and possibly obtain priority lists and preliminary indications for the retrofitting interventions. To this aim, many research studies have been devoted to the definition of "damage indexes" or "indexes of criticality" [1,2]. The safety assessment of existing bridges is based on the appraisal of the dissipative capacity of the structure and its actual available ductility by means of suitable non linear methods of analysis. A very effective method, if applicable, is the pushover analysis (PO). The theoretical foundation of this procedure, which uses static structural analysis for appraising the non linear behaviour under seismic loads, is dated back to more than thirty years ago [3]. Since then, the method has been extensively developed, so that today many variants exist, which are characterized by a greater accuracy, but also by greater complexity [4,5]. Therefore, it should be noticed than most of these studies are aimed at the analysis of buildings and in some cases propose very detailed procedure, including, for example, the modeling of elements usually considered as "secondary" [6,7,8], while specific procedures for the assessment of existing bridges are relatively few [9,10]. In fact, there are several recent studies, but also if for the purposes of structural safety, relate to different fields of civil engineering, as for example that the structural monitoring [11,12] In the field of the existing bridges, research has been mostly oriented at the development of the multi-modal and adaptive extensions of PO methods, which are very interesting, but unfortunately are computationally very expensive. In the last few years, an increasing attention has been devoted to simplified PO procedures in which the capacity curve of RC structures is calculated only by defining the position of some characteristic points, and without performing any analysis of thrust [13,14]. In these approaches, the non-linear properties of the structure are modelled by introducing equivalent systems - usually a single degree of freedom system – which corresponds to the original structure in terms of vibration period, energy dissipation and displacement capacity [15]. The fundamental objective is to assess the seismic vulnerability of building by relying only on poor data that can be easily retrieved even by a limited preliminary investigation, without the need to perform a detailed protocol of investigation aimed at the complete geometric and mechanical characterization of the structure.

The research study presented in the paper is referred to this theoretical framework, and proposes a simplified procedure to define the capacity curve of existing bridges, expressed by Moment-displacement relationship M-δ, taking into account the different failure modes that can possibly affect the structural ductility. The capacity curve is defined starting from the Moment-Curvature response (M-χ) of the base section for an equivalent SDoF system. Strength and ductility (in terms of displacement) are then properly modified in order to account for a possible early collapse triggered by one of the following collapse mechanisms: i. inadequate overlapping length of the longitudinal bars; ii. buckling of the longitudinal bars, iii. shear. The ultimate shape of the capacity curve is finally determined by evaluating the further loss of strength related to the II order effects induced by geometric nonlinearity. The research study has been developed for the analysis of vulnerability of RC girder bridges with simply supported deck and single-column piers with solid circular section, which were very popular in Italy in the 70's. Anyway, the methodology can be easily extended to the case of piers having different types of section. In the paper, after outlining the sequential steps of the procedure, a numerical validation is presented on a representative example, comparing the proposed simplified response under combined axial stress and bending (which is the basis of the entire procedure) with a more refined non linear FEM pushover analysis.

2 REFERENCE FRAMEWORK OF THE PROCEDURE

For bridges with simply supported decks and single-columns piers it is possible to define simplified approaches for the structural vulnerability assessment as an alternative to more accurate methods [15]. In this type of bridges, in fact, the deck is not significantly involved in the seismic response and thence the global behaviour of the structure under seismic loads is determined by the supporting structures (piers). In particular, the vulnerability of the deck is strongly dependent on the behaviour of the "critical" pier, which is defined as the pier characterized by the lowest value of the *Seismic Vulnerability Coefficient* $CVS=\delta^{C}_{SL}/\delta^{D}_{SL}$ (where δ^{C}_{SL}, δ^{D}_{SL} respectively are the displacement "Capacity" and "Demand" of the structure for the Limit State assumed for the assessment), both in the transversal and in the longitudinal direction. It should be remarked that if the retrofitting interventions programmed provide a substantial modification of the static scheme (for example a solidarization of the deck, or its complete replacement with a continuous deck), the afore-mentioned assumptions for the simplified vulnerability analysis cannot be applied.

In order to evaluate the deformation capacity of the structure beyond the elastic limit, it is fundamental to determine the *capacity curve* of the structure, which is usually obtained by the application of non-linear static procedures (PO). In view of vulnerability analyses at a regional scale, involving a large number of structures, the availability of simplified and rapid approaches to be used as an alternative to the full non linear procedures, is particularly useful. In a simplified approach, the capacity curve expressed in terms of the Force-displacement relationship F-δ (or equivalently, the Moment-displacement relationship M-δ), can be represented by a bi-linear function (Figure 1), that is completely known once the two points A and B are identified.

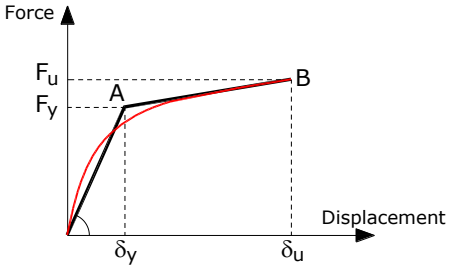


Figure 1: The simplified bi-linear representation of the F-□ relationship

The pair of coordinates $A(F_y - \delta_y)$ and $B(F_u - \delta_u)$ characterizes the structure, respectively, at the elastic limit state and at the ultimate limit state [15]. The reference model is an equivalent Single degree of Freedom system (SDoF, Figure 2 - right). In the transversal direction to the axis of the bridge ("*T*"), each pier behaves as a simple oscillator.

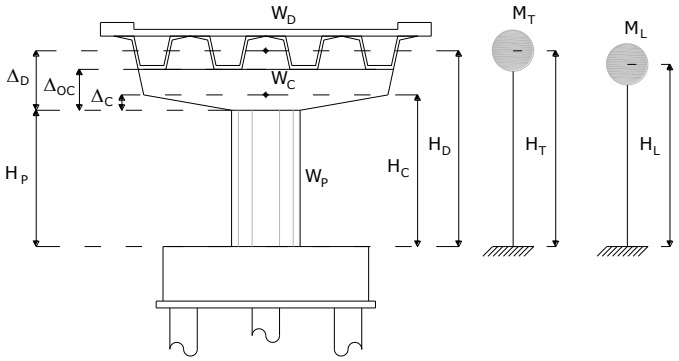


Figure 2: The equivalent SDoF schematization.

In the longitudinal direction ("*L*"), in the presence of seismic bearings (the so called "fixed" pier), the pier can also be model by a SDoF scheme, in which the mass is given by the reactions of the supported decks.
Thence, there are two distinct simplified models: one in the transversal direction, having a mass M_T and height H_T, another in the longitudinal direction, having a mass M_L and height H_L (Fig. 2). Depending on the direction of the analysis, the centers of application of the masses have different heights. The masses of the two models can be calculated by means of the following expressions:

$$M_T = \frac{W_T}{g} = \frac{n_T \cdot W_D + W_C + W_P}{g} \; ; \; M_L = \frac{W_L}{g} = \frac{n_L \cdot W_D + W_C + W_P}{g} \tag{1}$$

where W_D, W_C, W_P respectively are the weight of the deck, of the pulvino and of the pier; g is the gravitational acceleration; n_T and n_L are the number of spans loading the pier in the transversal and longitudinal direction, as a function of the constraint type. The height of the centers of the masses M_T and M_L, measured from the base section of the pier, are given by:

$$H_T = \frac{0.3 \cdot W_P \cdot 0.85 \cdot H_P + W_C \cdot H_C + W_D \cdot H_D}{W_T};$$
$$H_L = \frac{0.3 \cdot W_P \cdot 0.85 \cdot H_P + W_C \cdot H_C + W_D \cdot (H_D + \Delta_{OC})}{W_T} \tag{2}$$

where: H_P, H_C, H_D are the heights of the pier, of the pulvino and of the deck (see Figure 2); Δ_{OC} is the overall height of the pulvino-bearing device (measured from the top section of the pier). In order to simplify the procedure and reduce the parameters involved, in the proposed procedure the interaction between the super-structure and the foundation structures is neglected, and the piers are supposed to be fully clamped at the base.

3 COLLAPSE MODES

In existing bridges, which are mostly characterized by an unsatisfactory level of the technical design (mainly because the reference building codes are very obsolete), piers often reveal a number of critical states such as: poor confinement at the base; inadequate amount of longitudinal reinforcements (sometimes a brittle behaviour of the section is engaged). A number of experimental studies carried out in this field [16], and in particular concerning single-column piers with circular section, have shown that the crisis can be triggered by different mechanisms, according to the value of the significant structural parameters (height of the pier, diameter of the pier's section, amount of longitudinal and transversal reinforcements, …). The variation of even one of these parameters can change the actual type of failure mechanism, and it is nearly impossible to predict which of these occurs at the limit state, and thence it is difficult to evaluate the capacity curve (points A and *B* in Figure 1). Thus, it becomes important to quantify with a good approximation the effects induced by each possible collapse mechanism, in order to determine the variations on the response of the pier in terms of strength (force or moment) and deformation capacity (displacement or ductility). Different failure modes are taken into account and for each of them, a procedure for properly correcting the capacity curve, as obtained by the basic analysis of the critical section (base section) under bending and normal stress, is defined. The analysis is performed with reference to the base section, because the non linear zone is assumed to be located here (fully clamped constraint), in the tract of length L_P (usually referred to as "length of the plastic hinge"). The collapse modes included in the procedure are:

a) Failure under c*ombined axial stress and bending*, in the presence of effective confinement, $\chi=\chi_U$ (*§ 3.1*);
b) *Lap-splice failure of longitudinal bars* (*§ 3.2*);
c) *Buckling of longitudinal bars* (*§ 3.3*);
d) *Shear* (*§ 3.4*).

Whenever the failure under combined axial stress and bending is anticipated by one of the mechanisms listed at the points *b), c)* e *d),* and the final capacity curve is correspondingly modified.

3.1 Failure under combined axial stress and bending

As previously remarked, in the simplified model of Figure 2, the capacity curve M-δ is defined starting from the moment-curvature relationship (M-χ) of the critical section, which is located at the base of the pier, within the tract of length L_P. The first simplification assumed in the proposed procedure consists in the transformation of the M-χ relationship calculated at the level of the section (red line in Figure 3), in an elastic-perfectly plastic law (M_y=M_u) (black dotted line). In order to identify the characteristic points of the moment-curvature curve of the critical section, that is to say the curvatures χ_y and χ_u and the ultimate moment M_u, the following geometrical and mechanical parameter should be first determined: i. longitudinal reinforcement area (A_s); ii. confinement level, expressed as the geometric volumetric percentage of the transverse reinforcement (ρ_s); iii. compressive strength of concrete (f_c); iv. yield strength of the steel f_y; v. compressive normal stress acting on the *N-th* pier. The values f_c and f_y are to intended as average values of the results provided by experimental in-situ tests, or derived by existing information, divided by the "*Partial Safety Factor*" (PSF) corresponding to the "Knowledge level" (KL) attained [17].

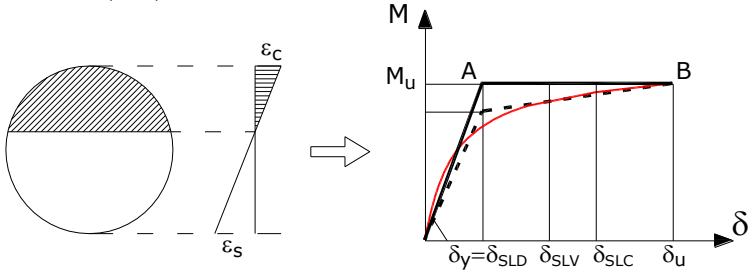


Figure 3: From M-χ relationship (of the critical section) to capacity curve of the SDoF oscillator.

For circular sections, when the M-χ law can be expressed by means of a bilinear relationship, Priestley [18] proposes a numerical expression in which the curvature at yielding (χ_y) is independent from the above mentioned parameters, and is only a function of the strain at yielding of the steel (ε_{sy}) and of the diameter D of the pier section. Consequently, the capacity at yielding in terms of chord rotation (θ_y) can be obtained by a purely elastic analysis under bending that, in the specific case, corresponds to a perfectly elastic behaviour of the pier up until the yielding moment M_y is attained:

$$\chi_y = \frac{2.25}{D}\cdot\varepsilon_{sy} \implies \theta_y = \frac{\delta_y}{L_V} = \chi_y \cdot \frac{L_V}{3} \tag{3}$$

where δ_y is the displacement of the top section and L_V is the shear length (= M/F).
The capacity at collapse can be expressed instead by the relationship proposed by Panagiotakos [17,19], in which a quote of plastic rotation at the critical base section is added to the yielding rotation:

$$\theta_u = \frac{\delta_u}{L_V} = \chi_y \cdot \frac{L_V}{3} + (\chi_u - \chi_y) \cdot L_P \cdot \left(1 - \frac{0.5 \cdot L_P}{L_V}\right) \quad (4)$$

The only unknown term in Eq. 4 is the ultimate curvature χ_u, which can be derived by assuming a strain distribution associated to the collapse of the section, involving the failure of the concrete in compression and the yielding of the steel under tension. Although this approach, based on the evaluation of chord rotations, is quite simple and easy, there is the problem of defining the length of the plastic hinge (L_P), which is not so immediate, since it strongly depends on the constitutive laws of the materials, the load type, the geometry of the transversal section, the shear stress. Several formulations can be found in the literature, [20,21] that can be all equivalently used within the proposed methodology. In the numerical application presented in Section 5 the relationship contained in Eurocode 2 has been adopted [22]:

$$L_P = 0.1 \cdot L_V + 0.17 \cdot h + 0.24 \cdot \frac{d_{bL} \cdot f_y}{\sqrt{f_c}} \quad (5)$$

where d_{bL} is the diameter of the longitudinal bars.

The displacement capacities δ_{SLD}, δ_{SLV} and δ_{SLC} corresponding, respectively, to the Damage Limit State (SLD) and the Ultimate Limit State (which are respectively represented by the Limit State of Life Safety - SLV and Near Collapse - SLC), according to the indications of the Italian Seismic Code [23], can be evaluated as $\delta_{SLD} = \delta_y$, $\delta_{SLV} = 3/4\delta_{SLC}$ and $\delta_{SLC} = \delta_u/\gamma_{el}$, with $\gamma_{el} = 1.5$ for primary structural elements and $\gamma_{el} = 1.0$ for secondary structural elements (Figure 3). For the calculation of the ultimate moment, a numerical formulation in a closed form is proposed (Eq. 6), depending on the following parameters: i. ν = axial force normalised to $A_c \cdot f_{cd}$; ii. ω = mechanical ratio of tension longitudinal reinforcement; iii. ρ_s; iv. f_c; v. f_y. The range of variation considered for the above mentioned quantities are: $0.1 < \nu < 0.6$; $0.05 < \omega < 0.6$; $0.0000475 < \rho_s < 0.000285$; $15\text{MPa} < f_c < 45\text{MPa}$; $300\text{MPa} < f_y < 405\text{MPa}$.

$$M_U = (a\nu^2 + b\nu + c) \cdot (d\omega^2 + e\omega + f) \cdot (g\rho_s + h) \cdot (if_c + l) \cdot (mf_y + n) \quad (6)$$

where a, b, c, d, e, and f are the numerical constants of the II order regression, whereas g, h, i, l, m, and n are the numerical constants of the linear regression.

3.2 Lap-splice failure of longitudinal bars

An effective model for appraising the flexural strength of the pier in the presence of longitudinal bars joined by overlapping, which is also supported by several experimental results, has been proposed by Priestley et al. [24]. In the presence of confinement, when lap-splice failure occurs ($\rho_s < \rho_h$), the model introduces a degradation of the flexural strength (ΔM) given by the difference of the ultimate Moment M_u corresponding to an optimum level of confinement ρ_h (see Eq. 7) and a reduced moment M^* (this is obtained by interpolation between a minimum value M_0, corresponding to $\rho_s = 0$ and M_u):

$$\rho_h = 1.4 \cdot \frac{\pi \cdot d_b^2}{4 \cdot p \cdot L_s} \cdot \frac{f_{yk}}{f_{sh}}; \ \rho_s \neq 0 \implies M^* = M_0 + \frac{\rho_s}{\rho_h} \cdot (M_u - M_0) \quad (7)$$

L_S is the length of overlapping of the bars, f_{yk} is the characteristic resistance of the steel, f_{sh} is the maximum tension applied by the transversal reinforcements (which is assumed to be equal to *200 MPa*). By applying the above described model, within the proposed procedure, in the presence of lap-splice failure, the capacity curve derived in *§ 3.1* is reduced by a quantity equal to ΔM (Figure 4).

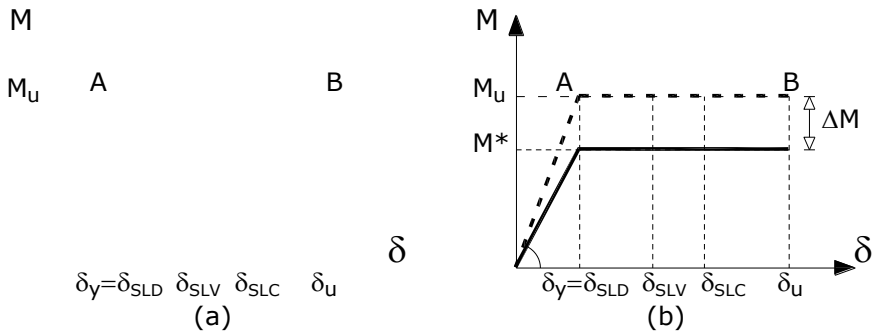


Figure 4: Modification of the flexural capacity curve according to the possible lap-splice failure.

3.3 Failure of buckling of longitudinal rebars

The effects due to the possible buckling of longitudinal bars are evaluated by using the empirical model proposed by Berry & Eberhard [25]. The model is based on the assumption that the instability involves only a reduction of the hysteresis loops and a decrease of the displacement capacity of the structural element. Starting by this assumption, the authors proposed a numerical relationship for the assessment of the ultimate displacement in the presence of instability, δ_{bb}, which was calibrated on the basis of a hundreds of tests.

$$\delta_{bb} = 0.0325 \cdot L_V \cdot \left(1 + 150 \cdot \rho_s \frac{f_y}{f_c} \cdot \frac{d_{bl}}{D}\right)\left(1 - \frac{N}{A_c \cdot f_c}\right)\left(1 + 0.1 \cdot \frac{L_V}{D}\right) \tag{8}$$

In the proposed procedure, the effects of the buckling are taken into account by reducing the displacement capacity of the SDoF system, after checking the value of δ_{bb} against the available displacement corresponding to the different limit states assumed in the verification, i.e. LS and NC (see Figure 5).

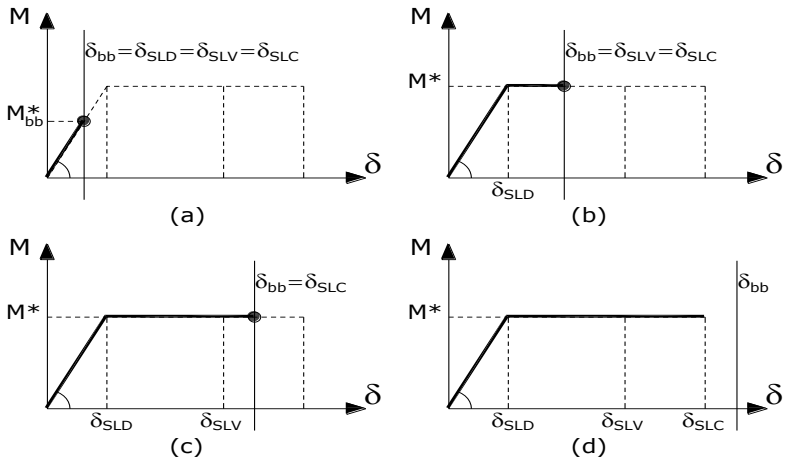


Figure 5: Modification of the capacity curve in order to account for the buckling of longitudinal bars.

3.4 Shear collapse

An effective model of the shear mechanism for circular sections, that provides a good feedback with experimental results, was proposed by Priestley et al. [26]. In the model, the shear strength V_U of the RC elements under combined axial stress and bending is defined as the sum of three contributions: i. V_N = horizontal component of the axial force N acting on the concrete strut; ii. V_{ST} = contribution of the transversal reinforcement; iii. V_C = contribution related to the aggregate interlocking effect. The shear collapse determines a significant reduc-

tion of the deformation capacity, and therefore of the displacement ductility of the structural element. On the basis of these observations, it can be concluded that there are four possible configurations that can be represented in the M-δ plane, as summarized in Figure 6, showing the reduction of the displacements at the different limit states. The blue line corresponds to the reduced capacity curve, whereas the curve of the shear resistance is plotted in red.

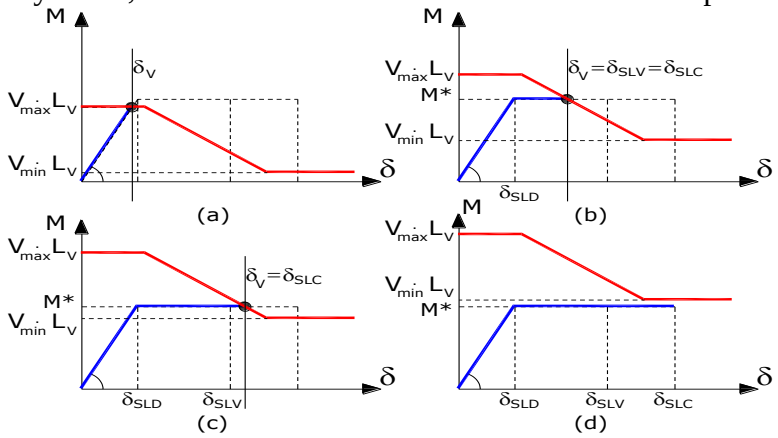


Figure 6: The modification of the flexural capacity curve in the presence of a shear failure of the pier.

3.5 Appraisal of II order effects

By referring to the SDoF system, II order effects can be considered as equivalent to a reduction of the resistance of the critical section. Once the capacity curve of the pier has been derived by following the procedure outlined *§ 3* (by applying the necessary modifications), it is finally possible to evaluate the reduction of the strength capacity M_U induced by II order effects as a function of the displacement δ: $\Delta M_{SL}^{II} = N^*\delta_{SL}$ (δ_{SL} is the displacement associated to the specific limit state).

The ductility $\mu_{SL}= \delta_U/\delta_Y$ varies from a minimum value of 1 (for the damage limit state SLD) to a maximum value corresponding to the limit state of near collapse (SLC).

4 SYNOPSIS OF THE PROCEDURE

The whole procedure is summarized in Table 1, starting from the definition of the initial capacity curve and indicating the sequential steps in which the capacity of the section is "corrected" by considering the possible additional collapse modes.

Step / §	Collapse Mode/Effects	Modification
0: *§2-3.1*	Combined normal stress and bending	Linearization of the M-χ curve
1: *§3.2*	Lap-splice failure of long. bars.	Reduction of the resistance by $\Delta M=M_u-M^*$
2: *§3.3*	Buckling of long. bars	Comparison between δ_{SL} and δ_{bb} and correspondent reduction of the available displacement capacity
3: *§3.4*	Shear	Comparison between δ_{SL} and δ_V and correspondent reduction of the available displacement capacity
4: *§3.5*	Geometric non linearity	Reduction of the resistance by $\Delta M_{SL}^{II} = N^*\delta_{SL}$

Table 1: Synopsis of the proposed procedure.

5 STEP "0": NUMERICAL APPLICATION

As already remarked in *§ 2* and *§ 3.1*, the entire proposed procedure is based on a simplified sectional analysis consisting in the linearization of the *M-δ* curve (determination of the two characteristic points corresponding to the yielding and collapse - step "0" in Table 2). Considering the importance of the first step for the subsequent development of the procedure, a preliminary numerical validation of the sectional analysis has been performed. The response of a circular section subjected to bending has been determined according to the procedure described in *§ 3.1* and then compared with the results of a FEM pushover analysis (based on fiber model) performed by using software SAP2000 V14.2.2 [27]. The pier has been modelled by means of 12 beam elements, discretizing the cross section into 52 fibers. With regard to the constitutive aspects, law of for the concrete, the relationship shown in Fig. 6.1, proposed by Mander, Priestley e Park [28] has been adopted, whereas for the steel an elastic-plastic law with hardening has been used. It should be noted that in the case of existing structures, the strength of materials must be evaluated by specific experimental surveys and numerical processing [29,30]. In Tab. 6.1 the geometric and mechanical parameters of the pier analyzed are summarized (symbols are the same used in previous sections).

Materials		**Geometry [m]**		**Self weight**		**Reinforcement**	
f_c *[MPa]*	20	H_f	6	W_I *[t]*	800	ϕ_{bl} *[cm]*	2.6
f_s *[MPa]*	450	Δ_P	0.8	W_P *[t]*	140	ϕ_{st} *[cm]*	1.0
γ_c *[kg/mc]*	2500	Δ_I	3.2	n_T	1.5	ω	0.137
ε_{sy}	0.002	Δ_{OP}	1.7	n_L	2	ρ_s	0.0035
ε_{su}	0.038	D	2			**Stress**	
ε_{cu}	0.013	c	0.05			ν	0.157

Table 2: The characteristic parameters of the pier analyzed for the numerical validation

The pushover analysis under a load distribution proportional to the first vibration mode has been performed, and in Figure 7 the resulting capacity curves, representing the structural response of the pier under combined normal stress and bending are reported. In particular, the curve obtained with the FEM analysis by the solver SAP (dashed blue line) has been transformed into the equivalent bilinear curve (solid blue line), by assuming that the elastic branch ended up with the yielding of the first longitudinal bar and that the peak resistance was 85% of the maximum moment. The criterion adopted is coherent with the principle of the energy equivalence between the areas under the two curves.

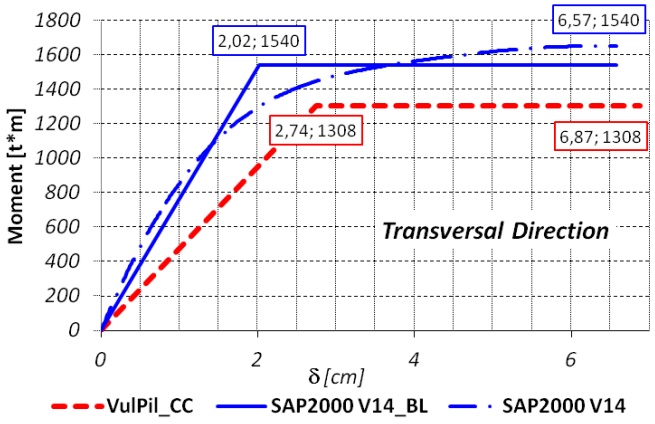


Figure 7: Capacity curves and constitutive law of concrete

From a simple graphic comparison, it can be clearly seen that the approximate procedure that will be thereafter referred to as "VulPil_CC" is very close to the numerical solution provided by the FE model. A more detailed comparison is presented in Table 3, in terms of ultimate moment M_U, ultimate displacement δ_U δ and *PGA* (*Peak Ground Acceleration*) corresponding to the Near Collapse limit state. It can be seen that the differences are always below 7% and can therefore be considered fully satisfactory for a validation of the foundation of the proposed simplified procedure.

	M_U		**δ_U**		**PGA_SLC**	
	*[t*m]*	*Δ [%]*	*[cm]*	*Δ [%]*		*Δ [%]*
VulPil_CC	*1308.15*	*- 15.07*	*6.87*	*+ 4.62*	*0.454g*	*- 3.40*
SAP V14_BL	*1540.20*	*/*	*6.57*	*/*	*0.470g*	

Table 3: Proposed simplified procedure VS numerical FEM analysis: comparative table of the results

6 CONCLUSIONS

In the last few years, the need to develop effective and manageable procedures for performing the vulnerability inventory of strategic infrastructures at a regional scale, and obtaining priority lists for the intervention, has become increasingly urgent. In this paper, a simplified procedure (which resorts to poor data that can be easily obtained) aimed at the seismic vulnerability assessment of girder bridges with simply supported decks and single-circular RC piers is proposed. The main approximation of the procedure consists in the evaluation of the *M-δ* relationship for the critical pier under combined normal stress and bending. Thence, after describing the theoretical formulation of the whole procedure, which includes the modification of the capacity curves in order to account for possible additional collapse modes, a comparative numerical analysis between the main approximation proposed and a non-linear FEM analysis (based on a traditional fiber model) has been carried out. The differences found are negligible, especially considering that the input data of the simplified procedure are very few.

AKCNOWLEDGEMENT

The research presented in this article was partially funded by the Department of Civil Protection, Project ReLUIS-DPC 2010-2013

REFERENCES

[1] Wen-I Liao, Ching-Hsiung Loh, Preliminary study on the fragility curves for highway bridges in Taiwan. *Journal of the Chinese Institute of Engineers*, **27**(3),367-375, 2004.

[2] D. Raffaele, F. Porco, A. Fiore, G. Uva, Simplified Vulnerability Assessment of RC Circular Piers in Multi-Span-Simply-Supported Bridges. *Structure and Infrastructure Engineering*, 2013 - DOI:10.1080/15732479.2013.772642.

[3] P. Fajfar, M. Fischinger, N2 - A method for non-linear seismic analysis of regular buildings. *Proceedings of the 9th World Conference and Earthquake Engineering*, Tokyo-Kyoto, Japan, 1988.

[4] S. Antoniou, R. Pinho, Development and verification of a displacement-based adaptive pushover procedure. *Journal of Earthquake Engineering*, **8**(5),643-661,1996.

[5] P. Fajfar, P. Gaspersic, The N2 method for seismic damage analysis of RC buildings. *Earthquake Engineering and Structural Dynamics*. **25**(1**)**,31– 46, 1996.

[6] G. Uva, F. Porco, A. Fiore, Appraisal of masonry infill walls effect in the seismic response of RC framed buildings: a case study. *Engeneering Structures*, **34**(1):514–26, 2012.

[7] A. Fiore, F. Porco, D. Raffaele, G. Uva, About the influence of the infill panels over the collapse mechanisms actived under pushover analyses: two case studies. *Soil Dynamics and Earthquake Engineering*, **39**,11-22, 2012.

[8] G. Uva, F. Porco, D. Raffaele, A. Fiore, On the role of equivalent strut models in the seismic assessment of infilled RC buildings. *Engineering Structures*, **42**:83-94, 2012.

[9] T. Isakovic, M. Fischinger, Higher modes in simplified inelastic seismic analysis of single column bent viaducts. *Earthquake Engineering and Structural Dynamics*. **35**(1),95-114, 2006.

[10] A.J. Kappos, T.S. Paraskeva, A.G. Sextos, Extension of modal pushover analysis to seismic assessment of bridges. *Earthquake Engineering and Structural Dynamics*, **35**(10),1269–1293, 2006.

[11] Porco, F., Fiore, A., Porco, G., & Uva, G. (2013). Monitoring and safety for prestressed bridge girders by SOFO sensors. *Journal of Civil Structural Health Monitoring*, **3**(1),3-13, 2013.

[12] G. Uva, D. Raffaele, F. Porco, A. Fiore, G. Porco, Bridge monitoring by fiber optic deformation sensors: A case study, *Proceedings of the 6th International Conference on Bridge Maintenance, Safety and Management (IABMAS 2012)*, Como, Italy, 2012, ISBN 978-0-415-62124-3

[13] B. Borzi, R. Pinho, H. Crowley, Simplified Pushover-Based Vulnerability Analysis for Large Scale Assessment of RC Buildings. *Engineering Structures*. **30**(3),804-820, 2007.

[14] H. Crowley, R. Pinho, J.J. Bommer, A probabilistic displacement-based vulnerability assessment procedure for earthquake loss estimation. *Bulletin of Earthquake Engineering*. **2:2**,173-219, 2004.

[15] P.E. Pinto, P. Franchin, A. Lupoi, *Valutazione e consolidamento sismico dei ponti esistenti - [In Italian]*. IUSS Press, Pavia, Italy, 2009.

[16] G.M. Calvi, A. Pavese, A. Rasulo, D. Bolognini, Experimental and numerical studies on the seismic response of R.C. hollow bridge piers, *Bulletin of Earthquake Engineering*, **3**(3),267-297, 2005.

[17] CEN. Eurocode 8: Design of structures for earthquake resistance. Part 3: Strengthening and repair of buildings. Brussels, Belgium, 2005.

[18] M.J.N. Priestley, Myths and Fallacies in Earthquake Engineering, Revisited, IUSS Press, Pavia, Italy, 2003.

[19] T. Panagiotakos, M.N. Fardis, Deformation of R.C. members at yielding and ultimate. *ACI Structural Journal*. **98**(2),135-148, 2001.

[20] M.J.N Priestley, R. Park, Strength and Ductility of Concrete Bridge Columns Under Seismic Loading. *ACI Structural Journal*, **84**(1),259-281, 1987.

[21] Fardis, M.N.. LESSLOSS – Risk mitigation for earthquakes and landslides. *Guidelines for displacement-based design of buildings and bridges, Report n°5/2007*, IUSS Press, Pavia, Italy, 2007.

[22] CEN. Eurocode 2: Design of concrete structures, Part 1-1: General rules and rules for buildings. Brussels, Belgium, 2005.

[23] D.M. LL. PP. 14/01/2008, Norme Tecniche per le Costruzioni (NTC 2008) - [In Italian]. Gazzetta Ufficiale n.29. Roma, Italy; 2008.

[24] M.J.N. Priestley, F. Seible, G.M. Calvi, Seismic design and retrofit of bridges, John Wiley and Sons, 1996.

[25] M.P. Berry, M.O. Eberhard, Practical Performance Model for Bar Buckling. *ASCE Journal of Structural Engineering*, **131**(7),1060-1070, 2005.

[26] M.J.N. Priestley, M.J. Kowalsky, N. Vu, C. Mc Daniel, Comparison of recent shear strength provisions for circular bridge columns. *Proceedings of the 5th Caltrans seismic workshop*. Sacramento, 1998.

[27] Computer and Structures INC. SAP2000 Advanced 14.2.2, Static and Dynamic Finite Element Analysis of Structures; 2010.

[28] J.B. Mander, M.J.N. Priestley, R. Park, Theoretical stress–strain model for confined concrete. *ASCE Journal and Structural Engineering*. **114**(8),1804–26, 1988.

[29] G. Uva, F. Porco, A. Fiore, M. Mezzina, Proposal of a methodology for assessing the reliability of in situ concrete tests and improving the estimate of the compressive strength. *Construction and Building Materials*, **38**(1), 72–83, 2012.

[30] M. Mezzina, F. Palmisano, D. Raffaele, Designing simply supported R.C. bridge decks subjected to in-plane actions: Strut-and-Tie model approach", *Journal of Earthquake Engineering*, **16**:4, 496-514, 2012 - DOI: 10.1080/13632469.2011.653866D

COMPDYN 2013
4th ECCOMAS Thematic Conference on
Computational Methods in Structural Dynamics and Earthquake Engineering
M. Papadrakakis, N.D.Lagaros, V. Plevris (eds.)
Kos Island, Greece, 12–14 June 2013

Effect of Spatially Variable Ground Motions on the Seismic Fragility of Box Girder Continuous Bridges

H.A. Elhowary[1], O. Ramadan[2], S.S.F. Mehanny[3]

[1]Bridge Design Engineer, Dar Al-Handasah, Giza, Egypt
Ph.D. Graduate student, Cairo University, Egypt
Hesham.Ayman2010@gmail.com

[2]Professor of Structural Engineering, Faculty of Engineering, Cairo University, Giza, Egypt
omoramadan@yahoo.ca

[3]Professor of Structural Engineering, Faculty of Engineering, Cairo University, Giza, Egypt
sameh.mehanny@stanfordalumni.org

Keywords: Spatially variable ground motions, Seismic Fragility, Box Girder Continuous bridges

Abstract. *Seismic design of bridges is usually performed assuming that all bridge supports experience the same ground motion (i.e. uniform input). However, strong-motion recorders of special seismograph arrays already demonstrated that significant spatial variation do exist in seismic ground motions [1]. The spatial variation of seismic ground motions is due to various sources including the loss of coherency, which results from random reflections and refractions as the waves travel through the soil, and the wave-passage effect.*

The present paper illustrates the impact of ground motion spatial variability on the seismic performance of continuous box girder bridges in both bridge orthogonal directions (longitudinal and transverse). For illustration purposes, a nine-span bridge with a total length of 430m is adopted. Non-linear time history analyses are carried out using OPENSEES software [2]. The wave passage effects are examined individually using a set of real records originally extracted from the PEER (Pacific Earthquake Engineering Center) Strong Motion Database using different apparent wave propagation velocities. Then, the loss of coherency effect is investigated using a set of artificially simulated seismic ground motions using the SIM software developed by Ramadan and Novak [3& 4] considering different degrees of loss in coherency and various ground motion frequency contents.

Results of the non-linear time history analyses performed in an incremental dynamic analysis context are hence manipulated through a probabilistic analysis framework to generate fragility curves associated with various performance levels for the case study bridge. Fragility curves giving the conditional probability of exceeding various performance levels are then integrated with generated hazard curves defining the expected seismic hazard in Egypt. The outcome of this integration process results in values of mean annual frequency of exceeding pre-defined performance levels.

1 INTRODUCTION

In the current seismic-resistant design of structures, the seismic ground motion excitations at their supports are assumed to be identical (i.e. uniform excitation for a given structure). However, for extended lifeline systems, the implementation of identical motions at the supports of these extended structures can yield un-conservative structural responses. Therefore, spatially variable seismic ground motions should be considered in their seismic response analysis and design. Since the 1960s, the effects of seismic ground motion spatial variation on lifeline structures have been studied. The results indicate that the type of response (conservative or un-conservative) induced by the spatially variable motions compared to that of identical ones depends strongly on the spatial variation models used in the analysis, and a realistic characterization of seismic ground motion spatial variation is highly desired. It is hence further realized that spatially variable seismic ground motions reflect the true motions at the supports of a given bridge [5].

The present paper studies the effect of spatially variable ground motions on the seismic response of continuous concrete highway bridges. Finite element models of a case study bridge are hence created for the non-linear incremental dynamic time history analyses. Linear models are developed for design purposes using SAP2000, while nonlinear analyses are carried out using OPENSEES (Open System for Earthquake Engineering and Simulation). After designing the case study bridge, displacement controlled non-linear pushover analyses are carried out using OPENSEES software. Displacement controlled non-linear pushover analyses in both bridge orthogonal directions are performed prior to the non-linear time history analyses in order to quantify the resistance of the bridge to the lateral deformation and to gauge the mode of deformation. Pushover analyses are carried out by applying gravity loads to the bridge deck and then applying incremental displacement at the deck level up to values corresponding to various performance levels until reaching collapse. Drift values/limits associated with various performance levels are hence identified.

The spatial variation in seismic ground motions has three main sources summarized as follows: firstly is the wave passage effect resulting from the difference in the arrival time of the seismic waves at different locations within the structure; secondly is the incoherence effect resulting from the differences in the manner and the method of the superposition of seismic waves due to the arrival from an extended source and scattered irregularities and in-homogeneities along the path and at the site; and finally is the "Local" site effects due to the differences in the local soil conditions at each support which may alter the frequency content and amplitude of the bedrock motions.

While studying the wave passage effects the parametric analyses are carried out using five actual time history records with different apparent propagation velocities (100m/sec, 200m/sec, 400m/sec and v=Infinity which is equivalent to the uniform excitation scenario) of the seismic waves. The five records pertain to the large database of records gathered in Medina (2002) [6] and are originally extracted from the PEER (Pacific Earthquake Engineering Center) strong motion database (PEER Strong Motion Catalog). The ground motions represented by the records are characteristic of the non-near-fault motions recorded in California.

On the other hand, when studying the loss of coherency effects on the seismic performance of the case study bridge, various sets of artificially simulated ground motions have been adopted. These sets of the seismic ground motions are generated using the SIM software developed by Ramadan and Novak [3&4] considering various levels of loss in coherency (c/v=0.0001, 0.001, 0.002) in addition to c/v=zero representing the fully coherent seismic waves. In addition to the different loss of coherency degrees, three response spectra representing various soil types are examined.

Performed fragility analyses consider various types of uncertainties: demand uncertainty ($\beta_{D|Sa}$), capacity uncertainty (β_{CL}), and modeling uncertainty (β_M). Different levels of uncertainties in both capacity and modeling are examined and the influence of such uncertainties on altering the results is also presented. Modeling of uncertainties is performed as per Taylor (2007) [7].

2 DESCRIPTION OF THE CASE STUDY BRIDGE

The selected case study bridge is a 9-span bridge with a total length of 430m (40+7×50+40) as shown in figure 1. The two central piers are monolithic with the deck while their adjacent piers (one pier at each side of the monolithic piers) are equipped with fixed pot bearings. In addition, guided bearings allowing translation of the deck in the longitudinal direction are adopted at all other piers and at abutments in order to release all thermal effects away from the central restrained part.

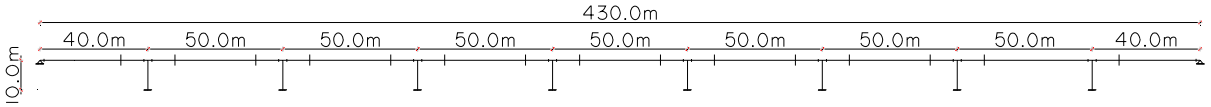


Figure 1: Layout and span arrangement of the case study bridge

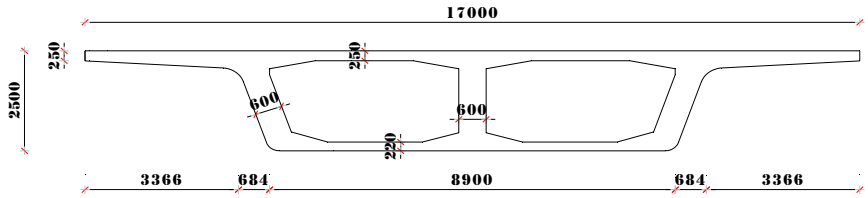


Figure 2: Typical section for the case study bridge (Dimensions in mm)

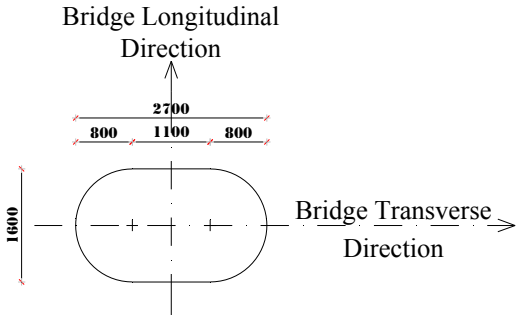


Figure 3: Typical pier section (Dimensions in mm)

The bridge deck is a post-tensioned double vent box section with a typical section as shown in figure 2. It has a constant depth of 2.5m (Span/Depth=20) and total width of 17.0m while the bridge piers are reinforced concrete piers with typical dimensions of 1.6m x 2.7m and a constant height of 10m as shown in figures 1 and 3.

The case study bridge is designed to sustain gravity loads according to [8] (ECP 201-2008 - Egyptian code for determination of loads and forces in the structural and civil works). Gravity loads include dead and super-imposed dead loads in addition to the highway live loads and pedestrian live loads. Seismic design loads are also in accordance with (ECP 201-2008) based on zone 5A. In this seismic zone, bridges shall be designed to withstand expected seismic loads resulting from a peak ground acceleration of 0.25g. This value of 0.25g as a peak ground acceleration represents nearly the highest seismic hazard in Egypt, while it corresponds to a medium seismic hazard in California USA. The seismic design is performed by the multi-modal response spectrum method as per clause 9.5 and Table 9-2 of ECP 201-2008 [8].

Type (1) response spectrum for Soil type B is adopted for the bridge seismic design. Type (1) spectrum is used for all regions in Egypt except coastal regions on the Mediterranean Sea (within 40 km alongside the coastline). In addition to the above stated seismic design criteria, the response modification factor (force reduction factor) "R" is taken equal to 5. This value corresponds to the use of reinforced concrete piers with sufficient ductility and relevant reinforcement details enabling the formation of a plastic hinge mechanism as per Table 9-3 of ECP 201-2008.

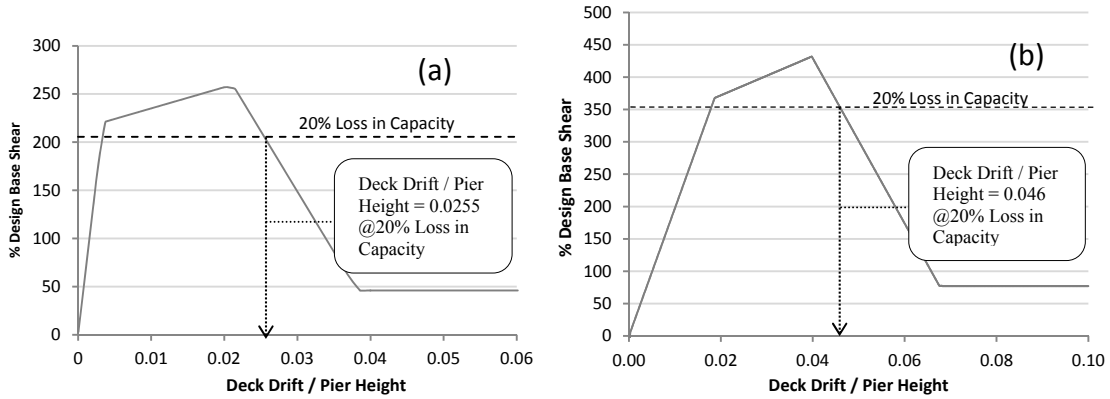
3 PUSHOVER ANALYSES AND MONITORED DAMAGE INDICES

3.1 Pushover analyses for the case study bridge in longitudinal and transverse directions

Displacement-controlled pushover analyses are conducted herein on the OPENSEES baseline models for the case study bridge. Pushover analysis consists of first applying the distributed gravity load to the bridge and then applying incremental displacements at the deck level until reaching a given target displacement. The main advantage of carrying the pushover analysis as widely presented in the literature is to determine the lateral load capacity of the bridge by plotting the relation between the base shear and the deck drift; or by plotting the percentage of the design base shear versus the deck drift of the bridge. This percentage, when above 100%, simply defines the so-called static over-strength of the bridge as-designed. The relation between the percentages of design base shear and the deck drift for the bridge in both directions is given below in figures 4a and 4b.

Referring to figures 4a and 4b, the collapse limit state for the case study bridge performing non-linear pushover analysis in the longitudinal direction is captured at a deck drift ratio of 2.55% (δ_θ =2.55 %). This collapse is assumed at 20% loss in the piers section capacity. Such result is in close agreement with previous research work in the literature as presented in table 2. On the other hand, performing the non-linear pushover analysis in the transverse direction results in different deck drift values corresponding to the same damage limit states monitored for the longitudinal direction. For instance, the collapse limit state in the transverse direction is captured at a deck drift ratio equal to 4.60% (δ_θ =4.60 %). This difference is due to the following

main factors affecting the transverse direction relative to the longitudinal direction: firstly, the end conditions for the pier in the longitudinal direction are different from those in the transverse direction. Secondly, the inertia and the section moment capacity/strength of the piers in the transverse direction are larger than those in the longitudinal direction (usually 5 to 10 folds in the majority of bridges). Moreover, the number of piers resisting the transverse seismic loads is larger than the number of piers resisting the longitudinal loads due to the adopted bearings articulation. In other words, it is common practice to adopt larger number of bearings guided (i.e., allowing translation) in the longitudinal direction to minimize the thermal effects; to the contrary all these bearings are restrained in the transverse direction. Finally is the deformed shape of the bridge deck under the effect of the horizontal monotonic loads (or under seismic loads) in the transverse direction which totally differs from that in the longitudinal direction due to the absence of the framing action that exists in the longitudinal direction.



Figures 4: Deck drift ratios versus % of design base shear for the bridge longitudinal direction (figure a) and the transverse direction (figure b)

Due to all above mentioned factors, higher values for deck drift capacity in the transverse direction relative to these in the longitudinal direction are observed for the same damage limit states.

Table 1: Summary of the pushover analysis results for the case study bridge

Loading Direction	**Capacity as % Design Base Shear (Static Over-strength x 100)**	**Deck Drift/ Pier Height @ 20% loss in capacity**	**$R_{eff.}$**
Longitudinal	257	0.0255	2.20
Transverse	430	0.0460	3.70

Table 1 also presents another format of the over-strength values ($R_{effective}$) that is calculated according to [9] as follows:

$$R_{effective} = \frac{S_a(T_1)\,|_{\text{Elastic code response spectrum (R=1)}}}{S_{ay}} \qquad (1)$$

Where, S_{ay} is the yield spectral acceleration and may be computed as $F_y/(W/g)$. F_y is the yield base shear (i.e., the base shear at the end of the first linear part of the "base shear-deck drift" curve).

3.2 Monitored damage indices

For a given S_a (T1) for a specific bridge the time history inelastic analyses are carried out as outlined in sections 4 and 5 and different potential damage indices (or, damage measures) are monitored. The different damage indices monitored herein are as follows:

A- Maximum deck drift which is a pre-defined value corresponding to a certain performance level or even to collapse level. The deck drift value at a certain excitation level in the longitudinal direction is only one value for the whole deck as the deck is acting as a rigid diaphragm in the longitudinal direction. However, under transverse direction excitation the deck drift referred to herein is corresponding to the maximum drift value occurring in the deck. Table 2 presents the different deck drift limits in accordance with the corresponding values extracted from the pushover analyses presented in section 3.1.

Table 2: Deck drift damage limit states as previously defined in SEAOC [10] for the longitudinal and transverse directions

Damage Scale Definition (Limit States)	**Damage description**	**Deck Drift (δ_θ %)**	
		Longitudinal Direction	**Transverse Direction**
Fully Operational	Negligible	**<0.2**	**<0.5**
Operational	Minor local yielding at some piers may occur. No observable fractures. Minor buckling or observable permanent distortion of the bridge members.	**0.2 to 0.5**	**0.5 to 1.0**
Life safety	Hinges form. Local buckling of some elements. Severe joint distortion. Isolated connection failures. A few elements may experience fracture.	**0.5 to 1.5**	**1.0 to 3.5**
Near Collapse	Extensive distortion for the structure components and pier panels. Many fractures in connections.	**1.5 to 2.5**	**3.5 to 5.0**
Complete Collapse	-	**> 2.5**	**> 5.0**

It is worth reporting that complete collapse has been captured in the present research at deck drift ratios very close to values shown in table 2 gathered from the literature [10]. Collapse is defined herein at 20% loss in the base shear capacity as previously proposed in the literature.

B- Maximum pier rotation (considered a direct measure of both global and local damage of the bridge) at a certain performance level. Performance levels can be directly correlated to the piers rotation values as follows: (a) yield performance level, (b) post yield performance level which corresponds to the isotropic hardening rotation of the piers and (c) ultimate rotation which corresponds to the collapse level where the rotation of the pier section is uncontrolled.

C- Shear failure in the bridge piers.

D- Unseating of the deck at the piers where the deck is supported by guided sliding bearings.

E- Excessive deck compressive or tensile stresses which may result in the failure of the deck pre-stressing system.

Note that due to space limitations only results considering the deck drift damage index are presented herein. However, other damage indices are investigated and presented in [11], but they are found to be non-controlling from design/performance perspective when compared to the deck drift.

4 WAVE PASSAGE EFFECT ON CASE STUDY BRIDGE

Wave passage effect results from the difference in the arrival times of seismic waves at different locations along the bridge. The influences of the wave-passage effect on the responses of bridges have been investigated by several researchers. However, most of these studies focus on the elastic behavior of the structure with very few of those studies dealing with the nonlinear responses of bridges. Monti et al. [12] studied the nonlinear responses of symmetric bridges with symmetric boundary conditions. They have found that the travelling wave effect on the response results essentially in a reduction of the dynamic part due to the incomplete synchronization of the excitation for the range of apparent velocities in excess of 500 m/s. Tzanetos et al. [13] studied the wave-passage effect on the inelastic responses of symmetric bridges with symmetric or asymmetric boundary conditions. They concluded that special consideration should be given to bridges with asymmetric boundary conditions since they may respond in higher modes more readily than symmetric structures and the demands are likely to increase on those bridges. However, their studies adopted simplified structural models.

In this research work, a study of the inelastic seismic responses of the case study bridge is carried out in both longitudinal and transverse directions using the OPENSEES software. Parametric analyses using five different time history records with different propagation velocities of the seismic waves are conducted to assess the wave-passage effect on the response of the bridge. The response of the bridge to asynchronous input motions at different pier bases consists of two components [14]: a dynamic component induced by the inertia forces and a so-called pseudo-static component, due to the difference between the adjacent support displacements. It is observed that the propagation velocity of seismic waves has a significant effect on the response of the bridge. When the travelling apparent wave velocity is lower than 150 ~ 250m/s, the response is dominated by the pseudo-static component. As the travelling wave velocity increases, the pseudo-static component is considerably reduced and the dynamic component increases rapidly. When the travelling wave velocity is higher than 150~250m/s, the response is dominated by the dynamic component, Wang et al. [15].

4.1 Ground motions selected for the wave passage effect analyses

A bin of 5 ground motions is selected for the present time history analysis in the context of the fragility/vulnerability seismic assessment of case study bridges presented in this research work. The 5 records pertain to the large database of records gathered in Medina [6] and are originally extracted from PEER Strong Motion Catalog. The ground motions represented by the records are characteristic of non-near-

fault motions recorded in California; details of the adopted 5 records are presented in table 3.

Table 3: Summary of the earthquake records used in wave passage effect analyses

Record ID	Event	Year	Mw	Station	R (km)	Mechanism	f_{HP} (Hz)	PGA (g)	PGV (cm/s)	PGD (cm)	Duration Length (sec)
IV79dlt	Imperial Valley	1979	6.5	Delta	43.6	strike-slip	0.05	0.24	26.0	12.10	99.90
CO83c05	Coalinga	1983	6.4	Parkfield-Cholame 5W	47.3	reverse-oblique	0.20	0.13	10.0	1.30	40.00
IV79cc4	Imperial Valley	1979	6.5	Coachella Canal #4	49.3	strike-slip	0.20	0.13	15.6	3.00	28.50
IV79cmp	Imperial Valley	1979	6.5	Compuertas	32.6	strike-slip	0.20	0.19	13.9	2.90	36.00
WN87bir	Whittier Narrows	1987	6	Downey-Birchdale	56.8	reverse	0.15	0.30	37.8	5.00	28.60

where,

M_w = Earthquake Magnitude,
R = Fault rupture distance,
F_{HP} = High-pass frequency,
and $f_{HP} \leq 0.2$

4.2 Results of the wave passage effect analyses in bridge longitudinal and transverse directions

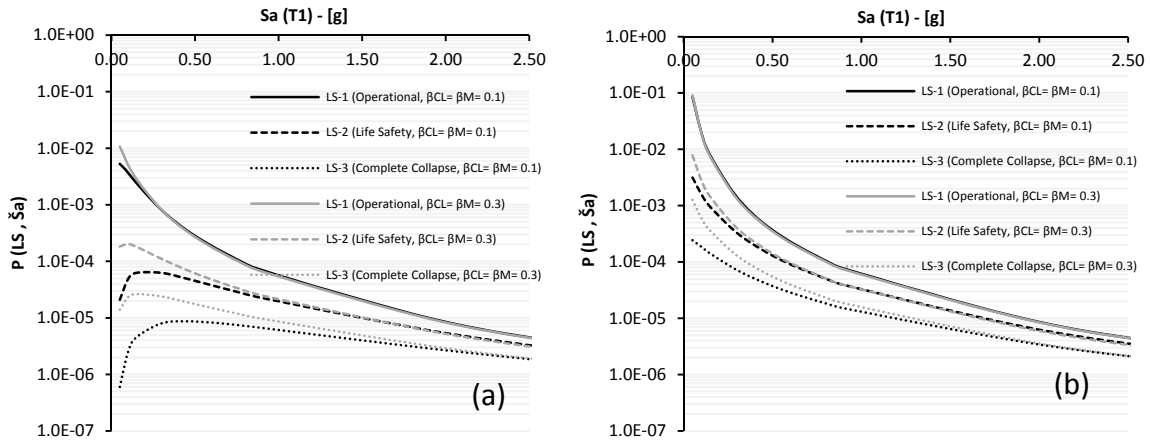


Figure 5: Joint probability curves of exceeding various performance levels versus S_a levels at different levels of uncertainty in capacity and modeling in the bridge longitudinal direction at v =100m/sec (figure a) and v =Infinity (figure b) (Log-scale)

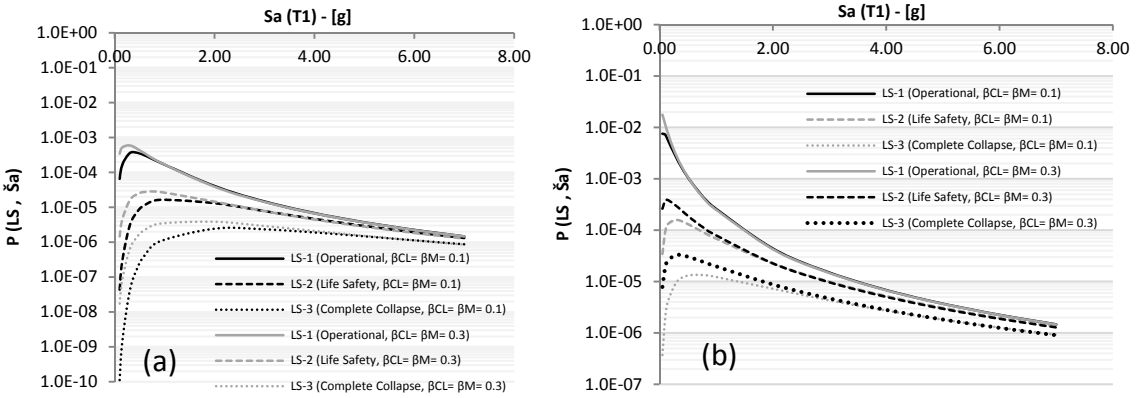


Figure 6: Joint probability curves of exceeding various performance levels versus S_a levels at different levels of uncertainty in capacity and modeling in the bridge transverse direction at v =100m/sec (figure a) and v =Infinity (figure b) (Log-scale)

Figures 5 and 6 represent samples of the joint probability curves of exceeding various performance levels versus S_a levels considering different levels of uncertainties in demand, capacity and modeling.

The "joint" probability equals the probability of exceeding a certain limit state (conditional probability) integrated over the whole expected hazard (shown in figure 7) during the life time of the structure. For detailed information refer to El-Howary (2014) [11]. Referring to the sample figures 5 and 6, one could notice that considering the uncertainties in demand, modeling and capacity may alter the results and adversely affect (i.e., underestimate) the capacity of the structure by a considerable amount. In other words, considering uncertainties may increase the probability of reaching pre-defined performance levels or reaching collapse.

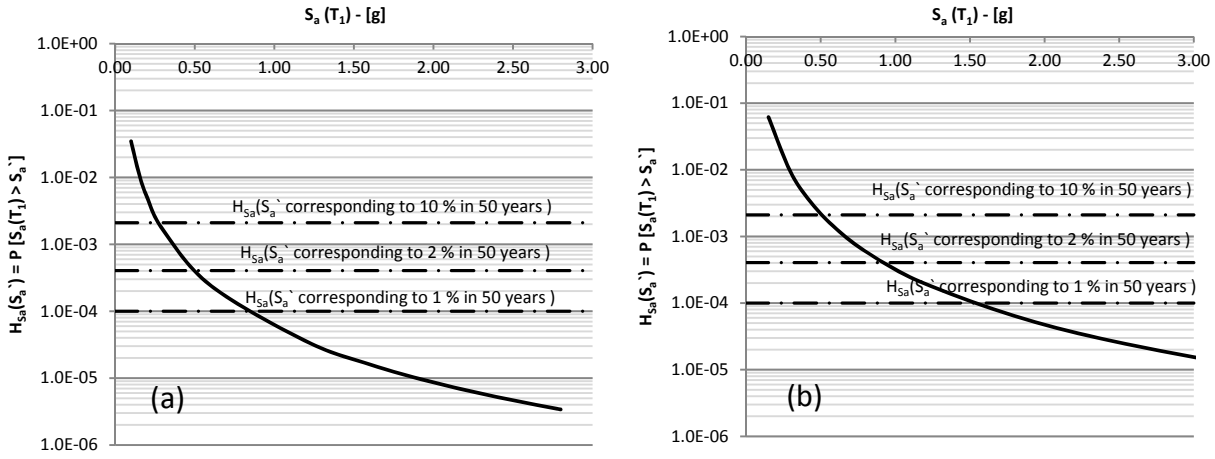


Figure 7: Annual hazard curves for case study bridge (5 % Damping – Soil class B) in the longitudinal direction (figure a) and in the Transverse direction (figure b) - El-Howary (2014) [11]

The hazard curves shown in figure 7 are generated following the same approach as in previous research work which adopts similar hazard curves in the probabilistic seismic assessment of RC moment frame buildings in Egypt [16].

The mean annual frequency of exceeding the target performance levels at different selected levels of uncertainties is illustrated in table 4. Reported results in table 4 are given for some apparent wave propagation velocities investigated in the present research.

Table 4: Mean Annual Frequency of exceeding various performance levels for the case study bridge in longitudinal and transverse directions

Limit State*	Apparent Wave propagation Velocity (m/sec)	λ (MAF of exceeding target performance levels)					
		Longitudinal Direction			Transverse Direction		
		$\beta_{CL}=\beta_M=0.1$	$\beta_{CL}=\beta_M=0.2$	$\beta_{CL}=\beta_M=0.3$	$\beta_{CL}=\beta_M=0.1$	$\beta_{CL}=\beta_M=0.2$	$\beta_{CL}=\beta_M=0.3$
LS-1	100	1.29E-02	1.57E-02	2.01E-02	1.80E-03	2.16E-03	2.93E-03
	200	6.66E-02	7.11E-02	7.71E-02	2.51E-02	3.05E-02	4.04E-02
	400	9.41E-02	9.74E-02	1.02E-01	2.58E-02	3.16E-02	4.22E-02
	∞	1.15E-01	1.17E-01	1.20E-01	2.37E-02	2.94E-02	3.97E-02
LS -2	100	3.43E-04	4.95E-04	8.63E-04	8.85E-05	1.14E-04	1.67E-04
	200	2.39E-03	3.50E-03	5.70E-03	9.64E-04	1.28E-03	2.00E-03
	400	4.31E-03	6.08E-03	9.37E-03	8.99E-04	1.21E-03	1.94E-03
	∞	6.37E-03	8.73E-03	1.29E-02	7.65E-04	1.05E-03	1.72E-03
LS -3	100	5.26E-05	7.89E-05	1.49E-04	1.28E-05	1.61E-05	2.39E-05
	200	2.77E-04	4.75E-04	9.89E-04	1.03E-04	1.42E-04	2.35E-04
	400	4.98E-04	8.56E-04	1.73E-03	8.96E-05	1.26E-04	2.15E-04
	∞	7.58E-04	1.28E-03	2.51E-03	7.18E-05	1.03E-04	1.80E-04

* LS-1=Operational Limit state, LS-2=Life safety and LS-3=Complete Collapse (Refer to table 2 for limit states description)

As shown in table 4, the total probabilities of attaining various performance levels in the longitudinal direction decrease with the decrease in the apparent wave propagation velocity. In other words, considering the uniform excitation scenario increases the probability of attaining various performance levels (including collapse) when compared to other adopted wave propagation velocities scenarios. On the other side, the transverse direction analysis is resulting in a different behavior when adopting different wave propagation velocities. The total probabilities of attaining a performance level or reaching collapse at apparent velocity=200m/sec are the largest (λ for reaching collapse $1.03\text{x}10^{-4}$ at v=200m/sec while $\lambda=7.18\text{x}10^{-5}$ at v=infinity). One could instead express the same information by reporting $1/\lambda$ which gives the return period for exceeding certain performance level (Return period for reaching collapse at v=200m/sec is $1/1.03\text{x}10^{-4} \approx 9700$ years and is $1/7.18\text{x}10^{-5} \approx 14000$ years at uniform excitation scenario). This means that considering the wave passage effect in the bridge transverse direction in this case results in increasing the probability of collapse (or of reaching certain performance level) by a factor of 1.5 relative to the uniform excitation scenario which may be considered a significant jump.

5 SPATIALLY VARIABLE SEISMIC GROUND MOTIONS

The current section is dedicated to study the effect of spatial variability of induced ground motions on the seismic performance and vulnerability of the case study continuous bridge. As will be mentioned later, various parameters affecting the severity of the spatial variability in the seismic ground motions are investigated in the current research work.

5.1 Adopted model for spatial variability in the ground motions

Spatial variability can be described in terms of the cross-power spectral density function between two stations [3] which is given by:

$$S_r(r,\omega) = S_l(\omega)\,.\,R(r,\omega)\,.\exp(i.\omega.\frac{r_v}{v}) \qquad (2)$$

Where,
$S_r(r,\omega)$: Cross-spectrum of a stationary homogenous random ground motions between any two stations
ω: Circular vibration frequency
$S_l(\omega)$: Local in-variant auto-spectrum function; the adopted auto-spectrum function is the modified Kanai-Tajimi spectrum with S_o = 0.01 m^2/sec^3as per Clough and Penzien (1975) [14]. Other parameters which describe the two filters of this spectrum model are listed in table 5.
R(r,ω): Frequency-dependent coherency function, assumed in the form given in Equation 3.
r_v: Separation distance between the two concerned stations projected into the dominant travelling wave direction
v: Apparent travelling wave velocity

It is useful to introduce the following non-dimensional function called coherency function. The shown coherency function in Equation 3 is the adopted one in our model (refer to [11] for all relevant specific details and definitions):

$$R(r,\omega) = \gamma_{ij}(\omega) = \frac{S_{ij}(\omega)}{\sqrt{S_{ii}(\grave{u}).S_{jj}(\grave{u})}} = \exp(-c(\frac{\grave{u}r}{v})) \qquad (3)$$

Where,
c: Loss of coherency parameter
c/v: Ratio between the loss of coherency parameter and the apparent velocity. This ratio usually ranges from 0.0033 to zero. It is basically the inverse of v/c ratio (also referred to by v/α in the literature) ranging from 300m/sec to ∞ [17].

Table 5: Soil filter parameters adopted in the artificially simulated ground motions (refer to [3, 4 & 11] for definitions of all parameters)

Spectrum Type	Soil Type	ω_g (rad/sec)	ζ_g	ω_f (rad/sec)	ζ_f
Type "1"	Soft	2π	0.4	0.2π	0.4
Type "2"	Medium	5π	0.6	0.5π	0.6
Type "3"	Firm	10π	0.8	π	0.8

A simple approach to introduce non-stationary characteristics to the generated stationary motions is through their multiplication by an intensity modulating (envelope) function I(t), commonly referred to as amplitude modulating function. A large number of such intensity modulating functions has been introduced since the 1960's. The adopted function in the current research work is the piecewise-continuous function given by Equation 4 [18]:

$$I(t) = \begin{cases} I_o \left(\frac{t}{t_1}\right)^2 & t \leq t_1 \\ I_o & t_1 \geq t \geq t_2 \\ I_o e^{-b(t-t_2)} & t \geq t_2 \end{cases} \quad (4)$$

5.2 Results under spatially variable ground motions

Results of the non-linear analyses considering the spatial variability in the seismic ground motions are presented in tables 6 and 7 in addition to figures 8 and 9. The total probabilities of attaining various performance levels in both bridge directions (longitudinal and transverse) are presented.

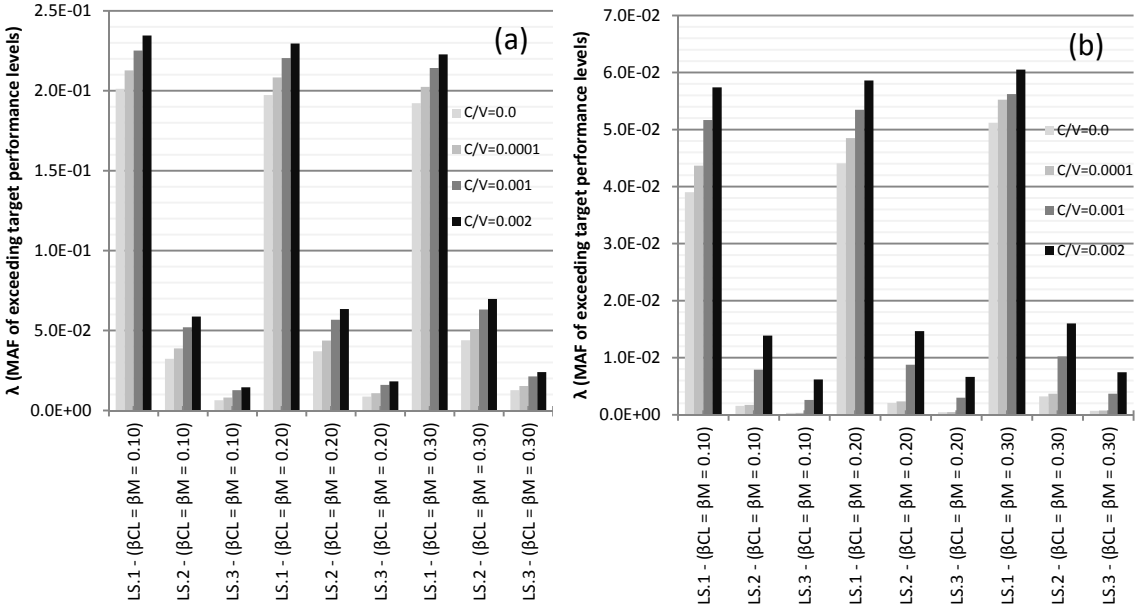


Figure 8: Total probability curves of exceeding various performance levels at different levels of uncertainty in the bridge longitudinal direction for response spectrum type-1 (figure a) and response spectrum type-3 (figure b)

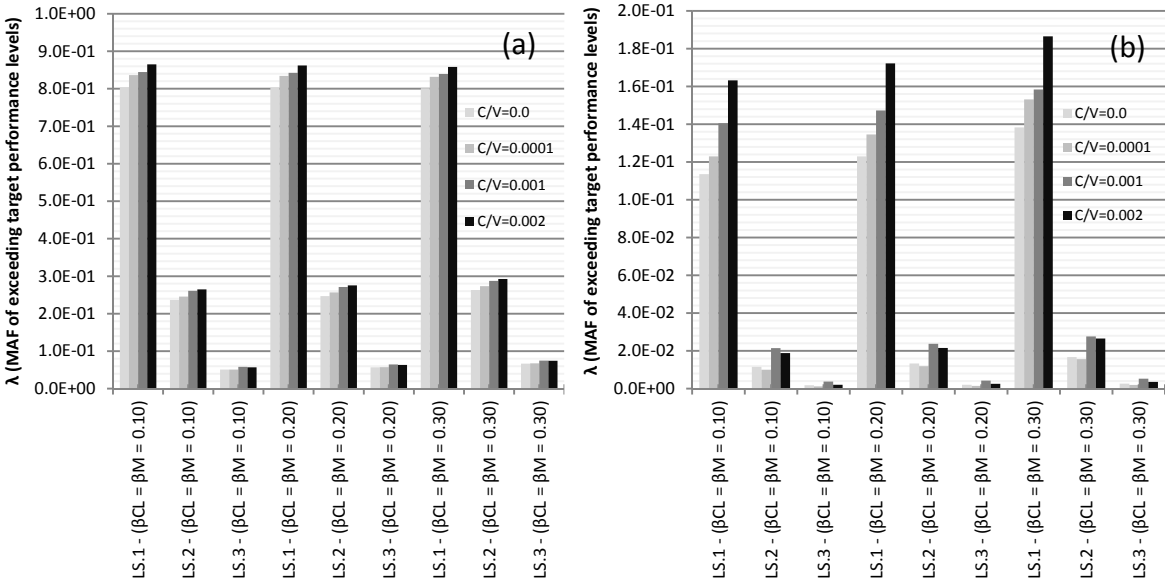


Figure 9: Total probability curves of exceeding various performance levels at different levels of uncertainty in the bridge transverse direction for response spectrum type-1 (figure a) and response spectrum type-3 (figure b)

Table 6: Mean Annual Frequency of exceeding various performance levels for the case study bridge in the longitudinal direction for response spectrum type-1and type-3

Limit State*	c/v	λ (MAF of exceeding target performance levels)					
		Response spectrum type-1			Response spectrum type-3		
		$\beta_{CL}=\beta_M=0.1$	$\beta_{CL}=\beta_M=0.2$	$\beta_{CL}=\beta_M=0.3$	$\beta_{CL}=\beta_M=0.1$	$\beta_{CL}=\beta_M=0.2$	$\beta_{CL}=\beta_M=0.3$
LS-1	0.0000	2.01E-01	1.97E-01	1.92E-01	3.90E-02	4.41E-02	5.12E-02
	0.0001	2.13E-01	2.08E-01	2.02E-01	4.37E-02	4.85E-02	5.52E-02
	0.0010	2.25E-01	2.20E-01	2.14E-01	5.17E-02	5.35E-02	5.62E-02
	0.0020	2.35E-01	2.30E-01	2.23E-01	5.74E-02	5.86E-02	6.05E-02
LS -2	0.0000	3.23E-02	3.70E-02	4.39E-02	1.56E-03	2.07E-03	3.22E-03
	0.0001	3.88E-02	4.38E-02	5.07E-02	1.74E-03	2.35E-03	3.69E-03
	0.0010	5.21E-02	5.67E-02	6.31E-02	7.90E-03	8.76E-03	1.02E-02
	0.0020	5.87E-02	6.34E-02	6.98E-02	1.39E-02	1.47E-02	1.60E-02
LS -3	0.0000	6.37E-03	8.67E-03	1.27E-02	3.32E-04	4.36E-04	6.93E-04
	0.0001	8.06E-03	1.08E-02	1.53E-02	3.35E-04	4.57E-04	7.60E-04
	0.0010	1.27E-02	1.60E-02	2.12E-02	2.60E-03	2.99E-03	3.70E-03
	0.0020	1.45E-02	1.82E-02	2.40E-02	6.18E-03	6.65E-03	7.45E-03

* LS-1=Operational Limit state, LS-2=Life safety and LS-3=Complete Collapse (Refer to table 2 for limit states description)

Table 7: Mean Annual Frequency of exceeding various performance levels for the case study bridge in the transverse direction for response spectrum type-1and type-3

Limit State*	c/v	λ (MAF of exceeding target performance levels)					
		Response spectrum type-1			Response spectrum type-3		
		$\beta_{CL}=\beta_M=0.1$	$\beta_{CL}=\beta_M=0.2$	$\beta_{CL}=\beta_M=0.3$	$\beta_{CL}=\beta_M=0.1$	$\beta_{CL}=\beta_M=0.2$	$\beta_{CL}=\beta_M=0.3$
LS-1	0.0000	8.03E-01	8.02E-01	8.01E-01	1.09E-01	1.18E-01	1.33E-01
	0.0001	8.36E-01	8.34E-01	8.32E-01	1.19E-01	1.30E-01	1.48E-01
	0.0010	8.44E-01	8.42E-01	8.39E-01	1.37E-01	1.44E-01	1.55E-01
	0.0020	8.65E-01	8.62E-01	8.58E-01	1.61E-01	1.69E-01	1.83E-01
LS -2	0.0000	2.37E-01	2.47E-01	2.63E-01	1.15E-02	1.31E-02	1.63E-02
	0.0001	2.46E-01	2.57E-01	2.74E-01	9.96E-03	1.18E-02	1.53E-02
	0.0010	2.61E-01	2.71E-01	2.87E-01	2.13E-02	2.35E-02	2.73E-02
	0.0020	2.65E-01	2.76E-01	2.92E-01	1.88E-02	2.15E-02	2.63E-02
LS -3	0.0000	5.09E-02	5.68E-02	6.66E-02	1.82E-03	2.09E-03	2.65E-03
	0.0001	5.11E-02	5.72E-02	6.76E-02	1.27E-03	1.52E-03	2.03E-03
	0.0010	5.81E-02	6.45E-02	7.50E-02	3.81E-03	4.33E-03	5.31E-03
	0.0020	5.70E-02	6.35E-02	7.45E-02	2.11E-03	2.62E-03	3.62E-03

* LS-1=Operational Limit state, LS-2=Life safety and LS-3=Complete Collapse (Refer to table 2 for limit states description)

As shown in figures 8 and 9 in addition to tables 6 and 7, the total probabilities of attaining various performance levels in both bridge directions (longitudinal and transverse) increase due to spatial variability of ground motions for the different loss of coherency degrees. This means that when the degree of the loss of coherency increases the probability of attaining various performance levels including collapse limit state increases accordingly. Moreover, considering the uncertainties in demand, capacity and in modeling results also in increasing the probability of attaining various performance levels including collapse. For example, the total probability of attaining a performance level (or even reaching collapse) at c/v = 0.002 is the largest (λ for reaching collapse is $1.45\text{x}10^{-2}$ at c/v=0.002 while $\lambda=6.37\text{x}10^{-3}$ at c/v=0.0 in the longitudinal direction for $\beta_{CL}=\beta_M=0.1$). This means that accounting for the spatial variability of the ground motions generally results in increasing the total probability of reaching collapse for this specific example to 2.3 times its value for the uniform excitation scenario. Similar results are obtained in the bridge transverse direction as shown clearly in figure 9. Also, considering the uncertainties in demand, capacity and modeling alters the results and increases the total probability of attaining a certain performance level by a factor of 1.3 on average.

Finally, considering the response spectrum type 1 (soft soil) results in a significant increase in the total probability of attaining a performance level (or reaching collapse) relative to other harder soil types. For example, λ associated with reaching collapse limit state equals $1.45\text{x}10^{-2}$ for response spectrum type 1 (soft soil) while λ equals $6.18\text{x}10^{-3}$ for response spectrum type 3 (firm soil) at c/v=0.002 in the longitu-

dinal direction at $\beta_{CL}=\beta_M=0.1$, which means that the probability of collapse in soft soil may be 2.4 times that in case of firm soil.

6 CONCLUSIONS

A few conclusions that could be drawn from the presented research are:

1- Considering uncertainties in the demand, capacity and modeling may significantly affect the vulnerability analyses results as it could occasionally underestimate the mean annual frequency of reaching collapse if such uncertainties are inaccurately assumed. For instance, an underestimation in the order of about 60% in the mean annual frequency of reaching collapse is reported herein for the case of a travelling apparent wave velocity, v=400m/sec, in the transverse direction of the case study bridge if uncertainties in capacity, β_{CL}, and modeling, β_M, are inaccurately considered as 0.1 instead of 0.3 in the vulnerability analysis.

2- The bridge transverse direction is more sensitive to the difference in the arrival time of the seismic records at different supports than the longitudinal direction due to the bridge relatively smaller out-of-plane stiffness compared to its longitudinal direction in which the deck acts as a rigid diaphragm.

3- The wave passage effect depends on the frequency content of the adopted seismic record. As the frequency content in the seismic record increases, the effect of the difference in the wave's arrival time accordingly increases.

4- Considering the spatial variability in the seismic ground motions results in increasing the total probability of attaining a performance level or reaching collapse relative to the uniform excitation scenario. Besides, increasing the degree of loss in coherency between the induced ground motions increases the probability of attaining a performance level or reaching collapse accordingly.

5- The soft soil profiles result in increasing the bridge sensitivity and vulnerability to the spatial variability in the seismic ground motions compared to firm soil types.

ACKNOWLEDGEMENT

The research reported here was supported by the European Union Project PIRSES-GA-2010-269222: Analysis and Design of Earthquake Resistant Structures (ADERS) of the FP7-PEOPLE-2010-IRSES, Marie Curie Actions. This support is gratefully acknowledged by the authors.

REFERENCES

[1] Abrahamson, N.A., Schneider, J.F. and Stepp, J.C. (1991). "Empirical spatial coherency functions for application to soil-structure interaction analyses". Earthquake Spectra, Vol.7 (2) pp. 1-27.

[2] Open System for Earthquake Engineering Simulation (Opensees) (2009). Pacific Earthquake Engineering Research Centre, University of California, Berkeley, http://opensees.berkeley.edu/.

[3] Ramadan, O.M.O. and Novak, M. (1994). "Simulation of multi-dimensional, anisotropic ground motions," J. engrg. mech., ASCE, Vol. 120, No 8, pp 1773-1785.

[4] Ramadan, O.M.O. and Novak, M. (1993). "On the simulation of spatially incoherent random ground motions," J. engrg. mech., ASCE, Vol. 119, No. 5, pp 997-1016.

[5] Liao, S. (2006) "Physical Characterization of Seismic Ground Motion Spatial Variation and Conditional Simulation for Performance-Based Design" Ph.D. thesis, Drexel University.

[6] Medina, R. (2002) "Seismic Demands for non-deteriorating frame structures and their dependence on ground motions". Ph.D. thesis, Stanford University.

[7] Taylor, E. (2007)." The Development of Fragility Relationships for Controlled Structures". Master of Science thesis, Washington University.

[8] ECP 201 (2008) "Egyptian Code of Practice no. 201 for Determination of Loads and Forces for the Structural and Civil Works", Research Centre for Housing and Construction, Ministry of Housing, Utilities and Urban Planning, Cairo, Egypt. Final Draft 2009.

[9] Haselton, C.B. (2006),"Assessing Seismic Collapse Safety of Modern Reinforced Concrete Moment Frame Buildings". Ph.D. thesis, Stanford University.

[10] Seismic design manual (2000), Structural Engineering Association of California.

[11] Elhowary, H.A. (2014) "A Probabilistic framework for assessing seismic performance of concrete bridges subjected to spatial variable seismic ground motions" (2014). Ph.D. thesis, Cairo University, to be published.

[12] Monti, G., Nuti, C, and Pinto, P.E. (1996). "Nonlinear Response of Bridges UnderMultisupport Excitation."Journal of Structural Engineering, ASCE, Vol. 122 (No. 10).

[13] Tzanetos, N., Elnashai, A.S., Hamdan, F, Antoniou, S. (1998). "Inelastic Dynamic Response of RC Bridges to Non-Synchronous Earthquakes Input Motion" ESEE Research Report No.98-6, Civil Engineering Department, Imperial College, London, UK.

[14] Clough, R.W., and Penzien, J. (1993). Dynamics of structures, 2nd Ed., McGraw-Hill, New York.

[15] Wang, J., Athol, C., Nigel, C., and Peter, M. (2004). "Inelastic Responses of Long Bridges to Asynchronous Seismic Inputs", 13th World Conference on Earthquake Engineering.

[16] Elhowary, H.A. and Mehanny, S.S.F. (2011), "Seismic Vulnerability Evaluation of RC Moment Frame Buildings in Moderate Seismic Zones," Earthquake Engineering and Structural Dynamics, Vol. 40, Issue 2, pp. 215-235.

[17] Zerva, A. (2009) Spatial Variation of Seismic Ground Motions: Modelling and Engineering Applications (Advances in Engineering Series). Ed. Haym Beranoya. CRC Press, Taylor & Francis Group, FL.

[18] Zerva, A. (1992). "Seismic ground motion simulations from a class of spatial variability models." Earthquake Engineering and Structural Dynamics, 21, 351–361.

COMPDYN 2013
4th ECCOMAS Thematic Conference on
Computational Methods in Structural Dynamics and Earthquake Engineering
M. Papadrakakis, V. Papadopoulos, V. Plevris (eds.)
Kos Island, Greece, 12–14 June 2013

AN ANALYTICAL TECHNIQUE FOR THE SEISMIC RESPONSE ASSESSMENT OF SLENDER BRIDGE PIERS

E. Tubaldi[1], L. Tassotti[2], A. Dall'Asta[1], L. Dezi[2]

[1] School of Architecture and Design (SAD), University of Camerino
Viale della Rimembranza, 63100, Ascoli Piceno (AP), Italy
e-mail: etubaldi@gmail.com, andrea.dallasta@unicam.it

[2] Department of Civil Engineering, Construction and Architecture (DICEA), Polytechnic University of Marche, Via Brecce Bianche, 60131 Ancona (AN), Italy
e-mail: tassottiluca@gmail.com, l.dezi@univpm.it

Keywords: Axial load effects, Analytical model, Vibration, Earthquake Engineering.

Abstract. *This work proposes an analytical technique for the analysis of the effects of axial loads on the dynamic behaviour and seismic response of tall and slender bridge piers. The pier is modeled as a linear elastic Euler-Bernoulli cantilever beam with uniformly distributed mass, representing the pier mass, and a tip mass at the free end, representing the deck mass. The beam is subjected to the reaction due to deck loads, and to the pier self weight.*

The seismic problem is described by a linear partial differential equation of seismic motion with variable coefficients. This equation is decoupled by using the exact vibration modes which are obtained by applying the Frobenius method. By this way, the seismic response can be evaluated in terms of superposition of modal contributions.

The proposed formulation is applied to the seismic analysis of a realistic slender bridge pier. The results of the study permit to shed light on the effect of axial load on the various vibration modes that contribute to the seismic response and to evaluate the suitability of amplification factors commonly used by seismic codes to account for axial load effects.

1 INTRODUCTION

A large number of bridges over mountain areas and deep valleys are built on tall piers. Because of the rugged topography of these areas, the height of bridge piers could even reach 200 m. The seismic assessment and design of slender piers usually differs from that of short piers because of the influence of axial load effects on the dynamic behaviour.

It is well known that axial load effects induce in general a reduction of the transverse bending stiffness and this may have different consequences on the transverse structural response depending on the type of loading experienced by the system. In the case of static loadings, the axial load effects usually increase the response beyond the values obtained by first order analysis. On the other hand, in the case of dynamic loadings such as earthquake-induced loadings, the interaction between axial loads and transverse displacements induces changes in the system dynamic properties and elastic periods elongation [1, 2], which in turn may result on either a decrease or an increase of displacements and internal action demands.

In bridge engineering-design practice, the axial-load effects are usually taken into account in a simplified manner by introducing an amplification factor for the piers seismic moments [3] evaluated via first-order analysis. Many studies in past years have been devoted to the calibration of expressions for the amplification factor [1, 4-9], on the basis of simple single-degree-of-freedom (SDOF) models. These models often consisted in a rigid inverted pendulum with an elasto-plastic rotational restraint at the base, and a tip mass at the free end with a concentrated weight force. Recent works [10, 11] extended the application of the amplification factor method also to the direct displacement based design of bridge piers. Other alternative methods were defined to account for axial load effects in a simplified way, without recourse to the amplification factor. In this context, the method proposed in [12] introduced the concepts of effective height and yield point spectra for the design of piers behaving as SDOF system.

The main limitation of the SDOF model employed in these studies is that it is adequate to represent only short bridge piers, for which the inertia is concentrated at the top whereas the distributed pier mass and the relevant variation of axial loads can be neglected. Slender piers, as those considered in this study, are on the contrary characterized by significant distributed masses and the analysis of their dynamic behavior should also consider higher modes effects [13]. Only few studies analyzed the axial-load effects on slender piers by employing refined multi-degree-of- freedom (MDOF) models. In this context are the work of [14] and [15], analyzing the evolution of plastic hinges formation in tall piers, and the works of [16] and [17], focusing more on the nonlinear modeling of the problem.

In this paper, an analytical continuous model is specifically developed to analyze the dynamic and seismic response of slender bridge piers by including axial load effects and higher mode effects as induced by masses distributed along the pier length. The model consists of a linear-elastic Euler-Bernoulli cantilever beam with a concentrated mass at the pier top and a uniform distributed mass, prestressed by a linearly varying axial load representing the deck loads and the pier self weight. The choice of employing a continuous model instead of a discrete model is motivated by the fact that the former permits to derive an exact solution of the dynamic and seismic problem, by making explicit the characteristic parameters that control the behaviour of the system. This is also convenient for performing parametric studies and for developing and validating more efficient and accurate numerical methods. It is noteworthy that the model considered in this paper is linear elastic. Although bridge piers can be designed to yield in order to dissipate the seismic energy [3], the high flexibility of slender piers is such that the displacement demand imposed by the seismic excitation is very unlikely to induce

inelastic deformations. Therefore, the linear elastic model appears adequate for slender piers under moderate seismic excitations.

In this paper, the equation of perturbed motion in the neighborhood of the axially loaded configuration of the pier is derived by applying the D'Alembert principle. The seismic response is expressed in terms of superposition of the contributions from the exact vibration modes of the system. In order to decouple the equation of motion, the exact orthogonality conditions for the vibration modes are derived. It is noted that the eigenvalue problem that needs to be solved to determine the vibration modes of the systems involves a differential equation with variable coefficients. The solution of this problem is obtained by extending previous formulations and results for similar problems [2, 18-21], in particular by application of the Frobenius method [19].

The proposed formulation and analysis technique are applied to a case study consisting of slender RC piers belonging to a three-span bridge. The followed approach, based on exact mode superposition, permits to evaluate the effect of axial loads separately on each mode contributing to the seismic response.

2 ANALYTICAL MODEL AND FORMULATION

The slender pier is modeled (Fig. 1) as an Euler-Bernoulli cantilever beam with stiffness $b(x)$, mass per unit length $m(x)$, and with a tip mass M at the top. In the reference configuration, the beam is subjected to a concentrated compression force, P, at the free end, and to a distributed compressive load, $m(x)g$, corresponding to the pier self weight, producing an internal compressive action $N(x)$ expressed as (positive if compressive):

$$N(x) = P + \int_x^H m(\xi)\, g\, d\xi \tag{1}$$

The concentrated mass and force at the pier top represent the contribution respectively to loads and inertia of the portion of the deck sustained by the pier. In general, P may differ from Mg.

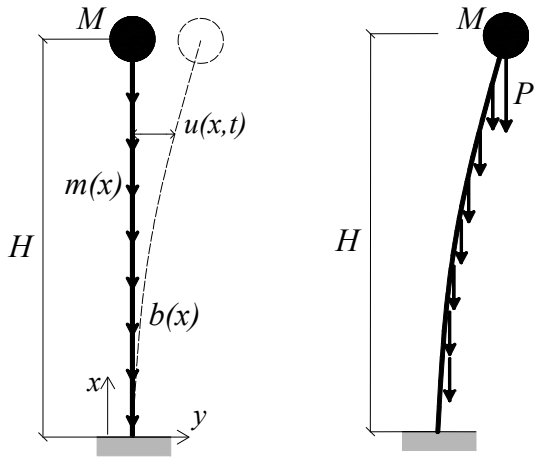


Fig. 1. a) Geometry of the problem and pier model, b) deformed pier configuration.

Let $V = \{v(x) \in L^2[\Omega] : v(0) = v'(0) = 0\}$ be the space of transverse displacement functions defined along the spatial interval $\Omega = [0, H]$ and satisfying the kinematic (essential)

boundary conditions, and $u(x,t) \in U \subseteq C^2\left(V;[t_0,t_1]\right)$ be the motion (Fig. 1), defined in the time interval considered $[t_0,t_1]$. The known functions $b(x)$, $N(x)$, $m(x)$ are continuous, bounded and positive. The differential dynamic problem can be derived from the D'Alembert principle. This variational principle states that the external virtual work $\delta W_E(u,\eta)$ resulting from external and inertia forces acting through every virtual displacement $\eta \in V$ consistent with the geometric restrains, is equal to the internal virtual work $\delta W_I(u,\eta)$ resulting from the stresses acting through the corresponding virtual strains. The dynamic problem describing the infinitesimal perturbed motion in the neighborhood of the axially-loaded reference configuration has the following expression [22]:

$$\begin{aligned}&\int_0^H b(x)u''(x,t)\eta''(x)dx - N(x)u'(x,t)\eta'(x) + m(x)\ddot{u}(x,t)\eta(x)dx + M\ddot{u}(H,t)\eta(H)dx = \\ &= -\left[\int_0^H m(x)\eta(x)dx + M\eta(H)\right]\ddot{u}_g(t) \qquad \forall \eta \in V; \forall t \in [t_0,t_1]\end{aligned} \tag{2}$$

where $\ddot{u}_g(t)$ denotes the ground motion input. The problem is completed by assigning the initial conditions $u(x,t_0) = \dot{u}(x,t_0) = 0$. Eqn. (2) can be formally rewritten as:

$$K(u,\eta) - N(u,\eta) + M(\ddot{u},\eta) = -\ddot{u}_g M^*(\eta) \qquad \forall \eta \in V; \forall t \in [t_0,t_1] \tag{3}$$

where K, N, M are bilinear symmetric forms mapping functions defined in the spatial interval V into real numbers, and $M^*: V \to \mathbb{R}$ is a linear form. They are defined as follows:

$$\begin{aligned}K(u,\eta) &= \int_0^H b(x)u''(x,t)\eta''(x)dx \\ N(u,\eta) &= \int_0^H N(x)u'(x,t)\eta'(x)dx \\ M(\ddot{u},\eta) &= \int_0^H m(x)\ddot{u}(x,t)\eta(x)dx + M\ddot{u}(H,t)\eta(H) \\ M^*(\eta) &= \int_0^H m(x)\eta(x)dx + M\eta(H)\end{aligned} \tag{4}$$

The strong form of the seismic problem can be derived through integration by parts of the terms K, N, M in Eqn. (2). The following partial differential equation of motion and the relevant boundary conditions is obtained:

$$\begin{aligned}&\left[b(x)u''(x,t)\right]'' + \left[N(x)u'(x,t)\right]' + m(x)\ddot{u}(x,t) = -m(x)\ddot{u}_g(t) \\ &u(0,t) = u'(0,t) = b(H)u''(H,t) = 0 \\ &b(H)u'''(H,t) + Pu'(H,t) - M\ddot{u}(H,t) = M\ddot{u}_g(t) \\ &u(x,t_0) = \dot{u}(x,t_0) = 0\end{aligned} \tag{5}$$

3 EIGENVALUE PROBLEM

The free vibrations of the system can be studied by analyzing the homogeneous problem ($\ddot{u}_g = 0$). As usual, the problem is solved by separation of variables technique. The motion $u(x,t)$ is expressed in terms of the product of a spatial function $\psi(x) \in V$ and of a time-dependent function $Z(t) = Z_0 e^{i\omega t}$ as follows:

$$u(x,t) = \psi(x) Z(t) \tag{6}$$

After substituting Eqn.(6) into Eqn.(5) for $\ddot{u}_g = 0$, the following boundary-value problem is obtained:

$$\begin{aligned} &\left[b(x)\psi''(x)\right]'' + \left[N(x)\psi'(x)\right]' - m(x)\omega^2\psi(x) = 0 \\ &\psi(0) = \psi'(0) = \psi''(H) = 0 \\ &b(H)\psi'''(H) + P\psi'(H) + \omega^2 M\psi(H) = 0 \end{aligned} \tag{7}$$

It is noteworthy that Eqn.(7) is satisfied by an infinite set of eigenvalues, ω_s, and of eigenvectors, $\psi_s(x)$, for $s = 1, 2, \ldots, N$.

3.1 Generalized orthogonality conditions for vibration modes

The orthogonality conditions, useful to decouple the equation of motion, can be obtained from the weak form corresponding to Eqn. (3) and written for the generic s-th vibration mode:

$$K(\psi_s,\eta) - N(\psi_s,\eta) - \omega_s^2 M(\psi_s,\eta) = 0 \qquad \forall \eta \in V \tag{8}$$

Substituting η by ψ_m in Eqn. (8) written for mode $s = l$, and substituting η by ψ_l in Eqn. (8) written for mode $s = m$, one has:

$$K(\psi_l,\psi_m) - N(\psi_l,\psi_m) - \omega_l^2 M(\psi_l,\psi_m) = 0 \tag{9}$$

$$K(\psi_m,\psi_l) - N(\psi_m,\psi_l) - \omega_m^2 M(\psi_m,\psi_l) = 0 \tag{10}$$

After subtracting Eqn. (10) from Eqn. (9), by virtue of the symmetry of the forms K, M, N, one obtains the first generalized orthogonality condition:

$$\left(\omega_m^2 - \omega_l^2\right) M(\psi_l,\psi_m) = 0 \tag{11}$$

Since $\omega_l \neq \omega_m$, Eqn.(11) also reads as:

$$M(\psi_l,\psi_m) = M\psi_l(H)\psi_m(H) + \int_0^H m(x)\psi_l(x)\psi_m(x)\,dx = 0 \tag{12}$$

Upon substitution of Eqn. (12) into Eqn. (9), the second orthogonality condition is obtained:

$$K(\psi_l,\psi_m) - N(\psi_l,\psi_m) = \int_0^H b(x)\psi_l''(x)\psi_m''(x)\,dx - \int_0^H N(x)\psi_l'(x)\psi_m'(x)\,dx = 0 \tag{13}$$

It is noteworthy that a closed-form analytical expression of the circular frequency for the *s*-th vibration mode can be derived from Eqn. (8) for $\eta = \psi_s$ and reads as follows:

$$\omega_s^{\,2} = \frac{K\left(\psi_s,\psi_s\right) - N\left(\psi_s,\psi_s\right)}{M\left(\psi_s,\psi_s\right)} = \frac{\bar{k}_s}{\bar{m}_s} \tag{14}$$

where $\bar{k}_s$ and $\bar{m}_s$ are the generalized stiffness and mass of the *s*-th mode.

3.2 Eigenvalue problem solution

The boundary-value problem corresponding to Eqn.(5) contains a differential equation with variable coefficients. A closed-form solution for this problem can be obtained through the Frobenius method by expressing the eigenvectors in terms of power series [19]. Appendix A reports the application of the Frobenius method to the specific problem analyzed, in the case of uniform distributed mass and stiffness through the pier length. It is noteworthy that the proposed solution can be regarded as "exact" only for an infinite series expansion and that for practical purposes the series is truncated at some order.

4 SEISMIC RESPONSE BY MODE SUPERPOSITION METHOD

In this study, the exact mode superposition method is employed to obtain a solution of the seismic problem corresponding to the assessment of the system response under the earthquake input. The advantage of this method over other analysis method is that it permits to represent the motion as the sum of the contributions of the exact vibration modes of the system. This allows to evaluate separately the contribution of each vibration mode to the response parameters of interest, and also to evaluate the effect of axial loads on the modal responses.

The motion is expressed as the following summation series:

$$u\left(x,t\right) = \sum_{s=1}^{\infty} \psi_s\left(x\right) q_s\left(t\right) \tag{15}$$

where $\psi_s\left(x\right) \in V$ is the *s*-th mode shape, and $q_s\left(t\right) : \left[t_0, t_1\right] \to \mathbb{R}$ is the corresponding generalized coordinate.

Substituting Eqn. (15) into Eqn. (3), one obtains:

$$\sum_{s=0}^{\infty} \ddot{q}_s\left(t\right) M\left(\psi_s,\eta\right) + q_s\left(t\right)\left[K\left(\psi_s,\eta\right) - N\left(\psi_s,\eta\right)\right] = -\ddot{u}_g\left(t\right) M^*\left(\eta\right) \qquad \forall \eta \in V \tag{16}$$

Substituting in the both sides of Eqn. (16) η by the *m*-th eigenfunction $\psi_m\left(x\right)$ one obtains:

$$\sum_{l=0}^{\infty} \ddot{q}_s\left(t\right) M\left(\psi_s,\psi_m\right) + q_s\left(t\right)\left[K\left(\psi_s,\psi_m\right) - N\left(\psi_s,\psi_m\right)\right] = -\ddot{u}_g\left(t\right) M^*\left(\psi_m\right) \qquad \forall \psi_m \in V \tag{17}$$

This is evidently a diagonal problem, by virtue of the two previously derived orthogonality conditions. The *s*-th decoupled equation reads as follows:

$$\ddot{q}_s\left(t\right) + \omega_s^2 q_s\left(t\right) = -\rho_s \ddot{u}_g\left(t\right) \tag{18}$$

where ω_s^2 is the circular frequency of Eqn. (14) and ρ_s denotes the *s*-th mode participation factor, expressed as:

$$\rho_s = \frac{M^*(\psi_s)}{M(\psi_s,\psi_s)} \tag{19}$$

Eqn.(18) represents the equation of motion of a generalized SDOF system with circular vibration frequency ω_s, subjected to the seismic input $\rho_s \ddot{u}_g(t)$. A viscous damping source is added a posteriori to this system, thus resulting in the following equation:

$$\ddot{q}_s(t) + 2\xi_s\omega_s\dot{q}_s(t) + \omega_s^2 q_s(t) = -\rho_s\ddot{u}_g(t) \tag{20}$$

where ξ_s denotes the *s*-th mode damping factor. The values of ξ_s for the various vibration modes can be calibrated based on experimental observations [13].

By applying the mode superposition method, Eqn.(15) can be expressed as follows:

$$u(x,t) = \sum_{s=1}^{\infty} \rho_s \psi_s(x) D_s(t) \tag{21}$$

where $D_s(t)$ denotes the response of an oscillator with natural frequency ω_s subjected to the seismic input $\ddot{u}_g(t)$ and homogeneous initial conditions

$$D_s(t) = \frac{1}{\omega_{ds}} \int_0^t \ddot{u}_g(\tau) e^{-\xi_s\omega_s(t-\tau)} \sin\left[\omega_{ds}(t-\tau)\right] d\tau \tag{22}$$

Having evaluated the displacement response history, the histories of the bending moment and of the shear along the beam can be obtained as follows:

$$M(x,t) = -b(x)u''(x,t) = -b(x)\sum_{s=1}^{\infty} \rho_s \cdot \psi_s''(x) \cdot D_s(t) \tag{23}$$

$$V(x,t) = \left[-b(x)u''(x,t)\right]' - N(x)u'(x,t) = -\sum_{s=1}^{\infty}\left\{\left[b(x)\psi_s''(x)\right]' + N(x)\psi_s'(x)\right\}\rho_s \cdot D_s(t) \tag{24}$$

5 SEISMIC RESPONSE OF A CONTINUOUS BRIDGE WITH SLENDER PIERS

5.1 Case study

In this section, the application of the proposed analysis technique is illustrated by considering the case study of a realistic bridge slender pier subjected to earthquake excitation. The pier belong to a three-span bridge [24] consisting of a steel-concrete composite deck (with span length of 60 m+80 m+60 m) and of two identical RC piers. These piers, of height H = 40 m, have a circular hollow transverse section with external diameter of 4.0 m and internal diameter of 3.2 m. The pier head has a rectangular transverse section with dimensions 4.0 m x 8.0 m, and is 1.5 m high. The longitudinal rebars reinforcement ratio is 1.5%. Class C30/37 concrete is used for concrete and S500 steel is used for the longitudinal rebars [25].

The pier effective stiffness accounting for concrete cracking is $b(x) = EI = 7.3086 \cdot 10^7$ kNm^2, the pier distributed mass is $m(x) = \bar{m} = 11.53$ ton/m, whereas the mass concentrated at the top and describing the deck and pier head inertia is M = 2145 ton. The axial force along the pier is a linear function of the form $N(x) = P + \bar{m}g(H-x)$, where P is the weight of the

deck acting at the top of the pier equal to 15470 kN. The value of the buckling load of a cantilever beam with the same flexural stiffness of the pier is $P_{cr} = \pi^2 EI/4H^2 = 1.27 \cdot 10^8$ kN, corresponding to a ratio $P/P_{cr} = 0.18$.

The seismic action is defined by the EC8 type I soil type B (soil factor S = 1.20) spectrum [3], for an importance factor $\gamma_I = 1$ and a peak ground acceleration PGA = 0.30g. The bridge has been designed for limited ductile behaviour, because the piers are very flexible and there is no need for dissipative behaviour or seismic isolation.

The analytical model and analysis technique proposed in this study are used to investigate the response of one of the two equal piers under a seismic input acting along the longitudinal direction.

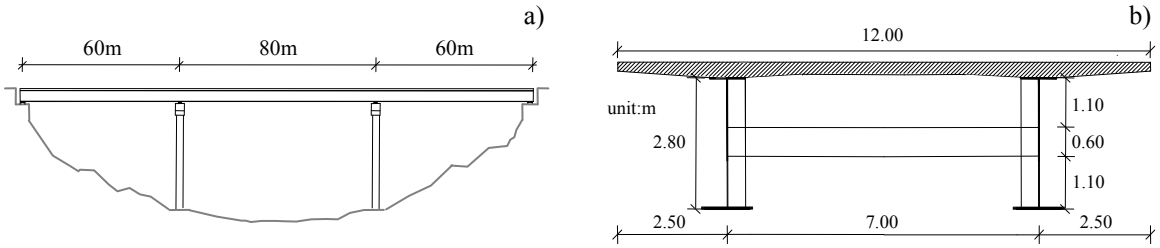


Fig. 2. Bridge geometry: a) longitudinal profile, b) transverse deck cross-section.

5.2 Modal analysis

The eigenvalue problem is solved by applying the Frobenius method as described in Appendix A. The first 6 vibration periods and modes of the system have been evaluated by truncating the series expansion of the modal shapes after 100 terms. It is noteworthy that the number of terms required to obtain accurate estimates of the vibration periods increases with increasing mode order. In fact, while the estimate of the fundamental vibration periods exhibits negligible variations for increasing number of terms beyond 5, to estimate accurately the sixth vibration periods 100 terms are needed.

The first three longitudinal vibration periods of the pier in the longitudinal direction disregarding axial load effects are 5.03s, 0.26s, and 0.08s, in agreement with the values reported in [24] and based on a bridge refined finite element model. Table 1 reports the modal vibration periods and participation factors obtained by accounting for axial load effects and by disregarding axial load effects (i.e., for $N(x) = 0$).

	Without axial load effects		With axial load effects	
Mode	T_i [s]	M_i [%]	T_i [s]	M_i [%]
1	5.0328	91.4915	5.4023	91.4620
2	0.2512	4.9658	0.2532	4.5479
3	0.0781	1.2494	0.0784	1.4117
4	0.0375	0.7667	0.0376	0.6769
5	0.0220	0.3454	0.0220	0.3975
6	0.0144	0.2966	0.0144	0.2592

Table 1. Modal analysis results accounting for and disregarding the second-order effects.

It is observed that only the first mode vibration period is significantly affected by the axial load effects. An opposite trend can be observed for the mass participating factors where variations increase for higher order modes.

Fig. 3 reports the first two modal shapes obtained accounting for and disregarding the effect of axial loads. The modal shapes are normalized with respect to the norm $\|\psi_l\|_2 = \left(\int_0^H \psi_l(x)^2 \, dx \right)^{1/2}$. With reference to the first mode, the influence of axial load increases for increasing derivative order. In fact, the displacement shape is practically the same as that obtained by neglecting axial load effects, whereas the second order (proportional to the bending moment) and particularly the third order derivative (related to the shear) are significantly affected by axial load effects. The influence of axial load effects on the second and higher vibration modes and relevant derivatives is practically negligible.

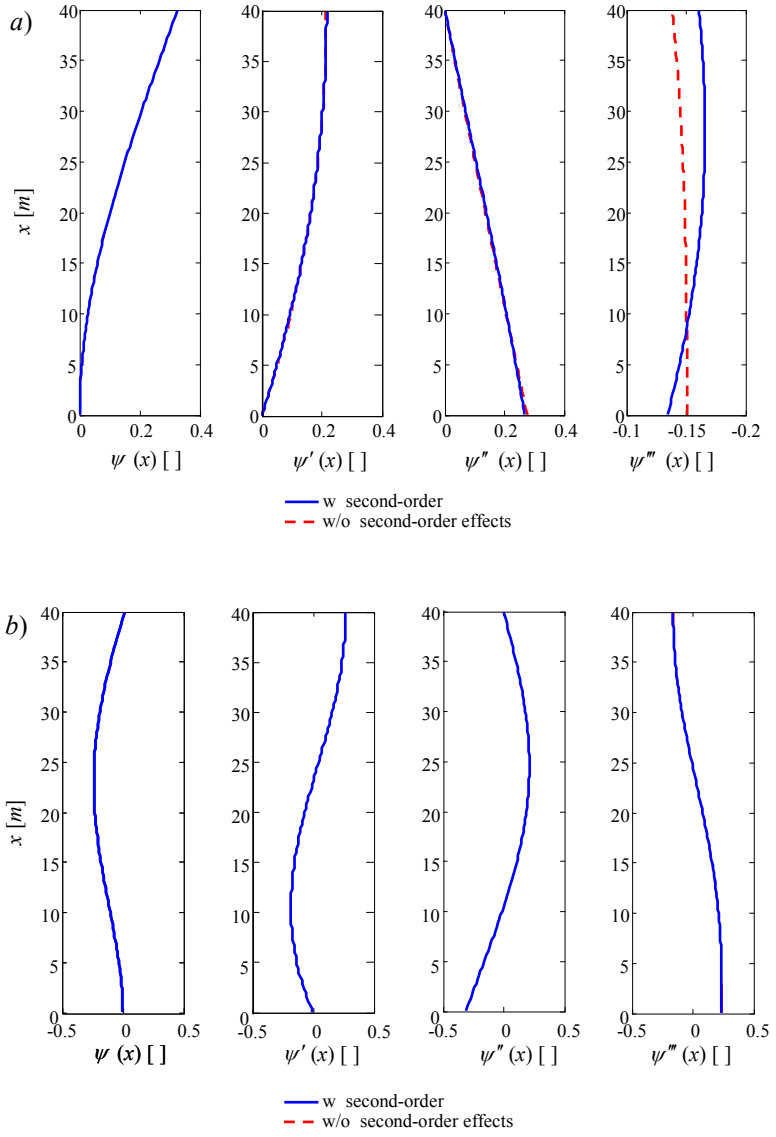


Fig. 3. Comparison of modal shapes and derivatives obtained by accounting for and by disregarding second-order effects : a) mode 1, b) mode 2.

5.3 Seismic response

In order to evaluate the influence of axial load on the seismic response of the bridge, the pier model has been subjected to a set of 7 real ground motion records [26] compatible to the

EC8 pseudo-acceleration response spectrum [3]. Fig. 4a reports the acceleration response spectrum of the real records, the mean spectrum, and the code spectrum, whereas Fig. 4b reports the displacement response spectrum of the records, and the mean spectrum.

The seismic displacement response to the ground motion record denoted as 000232 ya is reported in Fig. 5, where the time histories of the pier top displacement obtained by accounting for and by disregarding axial load effects are compared. In this figure, the period elongation due to axial load effects can be observed, together with a reduction of the displacement demand of about 15% with respect to the case disregarding axial load effects. This can be explained by noting that the displacement response is dominated by the fundamental vibration mode, and by observing in Fig. 4b that the fundamental period elongation due to axial loads corresponds to a reduction of the spectral displacement ordinates.

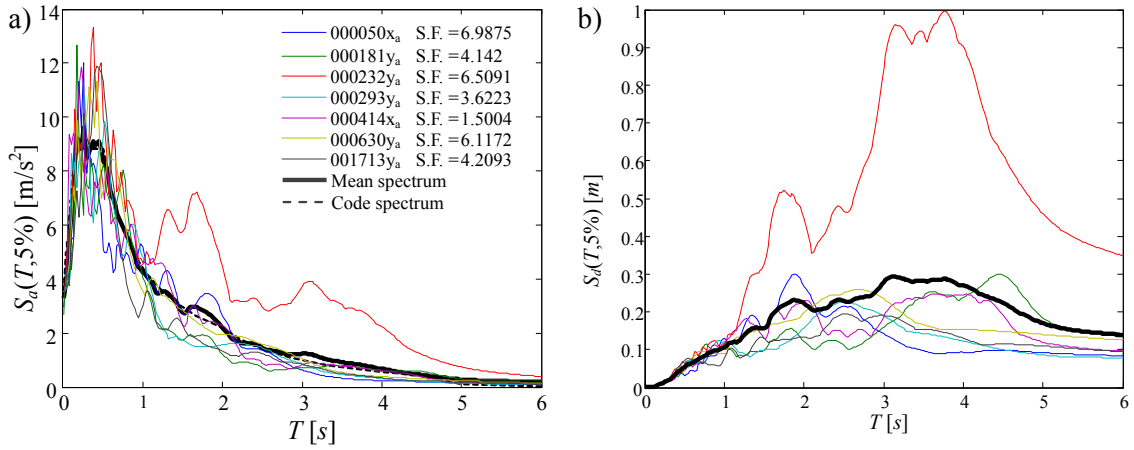


Fig. 4. Acceleration (a) and displacement (b) response spectra of spectrum-compatible natural records.

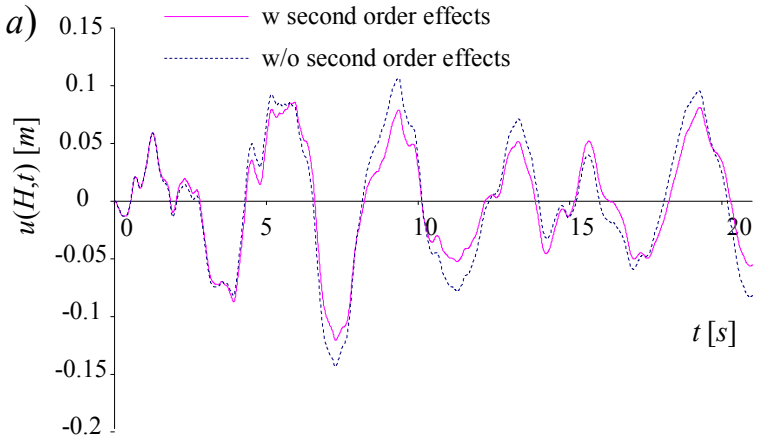


Fig. 5. Time history of pier top displacement under record 000232 ya: comparison of estimate obtained by accounting for and by disregarding axial load effects.

Fig. 6a shows the seismic response envelopes obtained for record 000232ya. The cumulative contributions of the first 6 modes, that account for axial load effects, are plotted separately. It is observed that while the displacement demand is dominated by the first mode contribution only, the shear demand is affected significantly by the higher modes. Also the moment demand at the pier top is slightly influenced by higher modes. However, this effect is not significant for design/assessment purposes, since the moment is highest at the base.

Fig. 6b compares the response envelopes obtained by accounting for and by disregarding axial loads. The increase of vibration period due to axial load effects results in a reduction of the displacement and internal action demands for the pier. The shear demand reduction is less significant than the reduction of the other response parameters. This can be explained by recalling the strong influence of higher vibration modes on the shear demand for this system, and the almost negligible influence of axial load effects on modes of order higher than one.

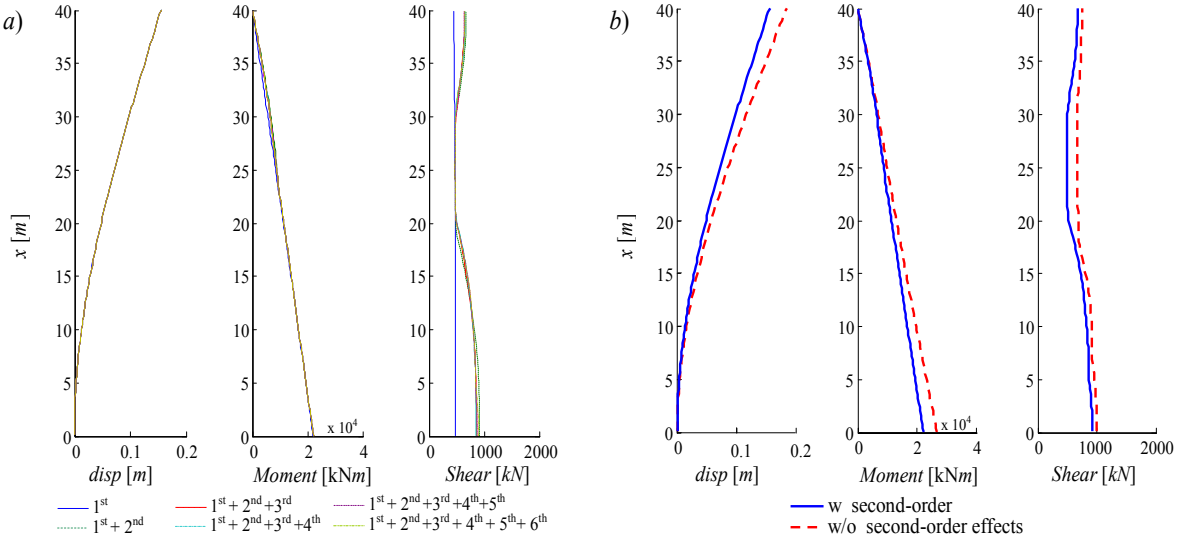


Fig. 6. Seismic response under record 000232 ya: a) Contribution of the first 6 modes to the average seismic response envelopes in terms of displacements, bending moments and shear, b) comparison between the response evaluated by accounting for and disregarding axial load effects.

Fig. 7a shows the average of the peak absolute responses (in terms of displacements, bending moments and shear) evaluated by considering the seven different ground motion records and by accounting for axial load effects. The contribution of the first 6 modes are plotted separately for the response parameters considered. Fig. 7b compares the average response envelopes obtained by accounting for and by disregarding axial load effects.

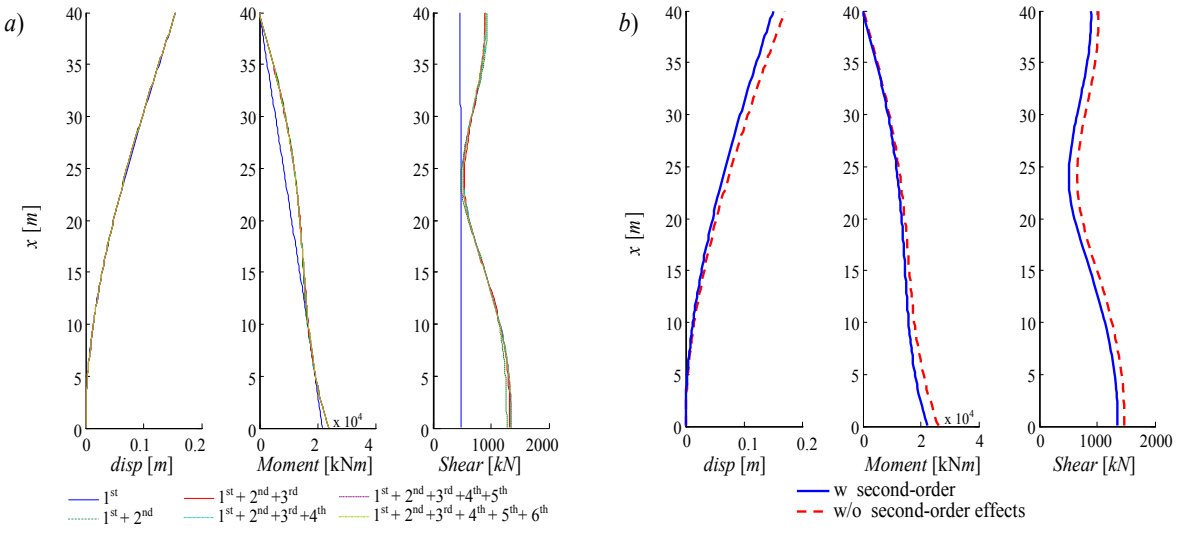


Fig. 7. a) Contribution of the first 6 modes to the average seismic response envelopes in terms of displacements, bending moments and shear, b) comparison between the response evaluated by accounting for and disregarding axial load effects.

In Fig. 7a, one notes that the displacement demand is dominated by the first mode contribution whereas higher vibration modes contribute more significantly to the shear and bending moment demand. In particular, the first two modes contribute significantly to the bending moments and the first three modes to the shear. Although the bending moment shape is not linear as it would be observed in the case of absence of distributed masses and axial loads, its maximum value is reached at the base section, and is significantly smaller than the yield moment. This confirms that the assumption of linear elastic behaviour for such a slender pier is correct, despite the high level of seismicity of the site. The shear diagram shape also significantly deviates from the constant shape that would correspond to a pier with no distributed mass, thus demonstrating the significant influence of higher vibration modes.

In Fig. 7b, it is observed that the axial load effects reduce in general the average response in terms of displacements, moments and shear of about 10%. This result is a consequence of the reduction of the first mode spectral ordinates in terms of both displacements and accelerations (Fig. 4). The observed behaviour contradicts the prescriptions of current seismic design code which use amplification factors for the bending moment demand. In fact, according to EC8-2 [3], the value of the base section bending moment demand evaluated by first order analysis, i.e., by neglecting the axial load effect (M_{Ed}), should be amplified by a factor of 1.1. On the contrary, the results of this study show that it should be reduced by a factor of 0.946.

6 CONCLUSIONS

In this paper, an analytical technique is presented for investigating the effects of axial loads on the dynamic behaviour and seismic response of slender bridge piers. The technique is based on a continuous model of the pier, which is described by a linear elastic Euler-Bernoulli cantilever beam with uniformly distributed mass, representing the pier mass, and a tip mass at the free end, representing the deck. A concentrated load, acting at the pier top, simulates the pier reaction to deck loads, whereas a distributed axial load simulates the pier self weight. The linearly varying axial load leads to a linear partial differential equation of motion with variable coefficients. This equation is decoupled by using the exact vibration modes of the system, obtained by applying the Frobenius method, and the orthogonality conditions between the modes derived in this study. By this way, the effect of axial loads on the response parameter of interest (i.e., the displacement, the bending moment, and the shear demand along the pier) can be evaluated separately on each vibration mode.

A realistic slender bridge pier is considered as case study to validate the proposed analysis technique and illustrate its capabilities. First, a free-vibration analysis is performed to evaluate the influence of axial load on the pier dynamic behavior. It is observed that axial load effects induce an elongation of the vibration period of the first mode, whereas the higher order modes are less sensitive to these effects. While the displacement shape of the first mode is slightly affected by axial loads, the third order spatial derivative, related to the shear, changes significantly in presence of axial load, and the second order derivative, proportional to the bending moments, changes only moderately. Moreover, the displacement shapes and relevant derivatives of higher modes obtained by accounting for and by disregarding axial load effects are practically indistinguishable.

Successively, the average seismic response to a set of seven compatible natural records in terms of displacement, bending moments and shear envelopes is evaluated and the following conclusions are drawn.

1. The main effect of axial load is to increase the first mode vibration period. The vibration periods, shapes and relevant derivatives of modes of order higher than one are practically not affected by axial loads.

2. Higher modes notably influence the demand of internal actions and their distribution along the beam.

3. The variation of dynamic properties of the bridge piers due to axial loads may provide significant reduction of the demand in terms of displacements, bending moments, and shear, as observed in this application. By contrast, according to current seismic codes prescriptions, the bending moment seismic demand evaluated by first order analysis should always be amplified to account for axial load effects.

REFERENCES

[1] D. Bernal, Amplification factors for inelastic dynamic p–Δ effects in earthquake analysis. *Earthquake Engineering & Structural Dynamics*, **15**(5), 635–651, 1987.

[2] L. N. Virgin, R. H. Plaut, Effect of axial load on forced vibrations of beams. *Journal of Sound and Vibration*, **222**, 395–405, 1993.

[3] European Committee for Standardization (ECS), *Eurocode 8 - Design of structures for earthquake resistance*, Brussels , 2005.

[4] E. Rosenblueth, Slenderness effects in buildings. *Journal Structural Division*, **91**(1), 229 – 252, 1965.

[5] T. Paulay, A consideration of p - delta effects in ductile reinforced concrete frames. *Bulletin of the New Zealand National Society for Earthquake Engineering*, **11**(3), 151–160, 1978.

[6] T. Pauley, M. J. N. Priestley, *Seismic Design of reinforced concrete and masonry buildings*. John Wiley & Sons INC, 1992.

[7] S. Mahin, R. Boroschek, *Influence of geometric nonlinearities on the seismic response and design of bridge structures*. Background report to California Department of Transportation, 1991.

[8] R. C. Fenwick, B. J. Davidson, e B. T. Chung, P - delta actions in seismic resistant structures. *Bulletin of the New Zealand National Society for Earthquake Engineering*, **25(**1), 56–69, 1992.

[9] G. A. MacRae, P-Δ effect on single-degree-of-freedom structures in earthquakes. *Earthquake Spectra*, **10**(3), 539–568, 1994.

[10] M. J. N. Priestley, G. M. Calvi, e M. J. Kowalsky, *Displacement-based seismic design of structures*. IUSS Press, 2007.

[11] B. Wei, Y. Xu, e J. Li, Treatment of P-Δ Effects in Displacement-Based Seismic Design for SDOF Systems. *Journal of Bridge Engineering*, **17**(3), 509–518, 2012.

[12] M. Aschheim, E. H. Montes, The representation of P- Δ effects using Yield Point Spectra. *Engineering Structures*, **25**, 1387–1396, 2003.

[13] K. Chopra, *Dynamics of structures: Theory and Applications to Earthquake Engineering*. Prentice - Hall Inc., 1995.

[14] Z. Guan, J. LI, Y. XU, H. LU, Higher-order mode effects on the seismic performance of tall piers. Frontiers of Architecture and Civil Engineering in China, **5**(4), 496–502, 2011.

[15] R. Ceravolo, G.V. Demarie, L. Giordano, G. Mancini, D. Sabia, Problems in applying code-specified capacity design procedures to seismic design of tall piers. *Engineering Structures*, **31**(8), 1811–1821, 2009.

[16] R. P. Dhakal K. Maekawa, Analytical Prediction of Collapse of RC Piers Induced by Geometrical Nonlinearity. *The First International Conference on Structural Stability and Dynamics*, Taipei, Taiwan, 2000.

[17] H.-G. Kwak, J.-K. Kim, Effect of slender RC columns under seismic load. *Engineering Structures*, **29**(11), 3121–3133, 2007.

[18] A. Bokaian, Natural frequencies of beams under compressive axial loads. *Journal of Sound and Vibration*, **126(**1), 49–65, 1988.

[19] S. Naguleswaran, Transverse vibration of an uniform Euler–Bernoulli beam under linearly varying axial force. *Journal of Sound and Vibration*, **275**(1-2), 47–57, 2004.

[20] I. Elishakoff, *EIGENVALUES OF INHOMOGENEOUS STRUCTURES Unusual Closed-Form Solutions*. CRC PRESS, 2005.

[21] S. S. Rao, *Vibration of Continuous Systems*. Wiley, New York, 2007.

[22] A. Dall'Asta, G. Leoni, Vibrations of beams prestressed by internal frictionless cables. *Journal of Sound and Vibration*, **222**(1), 1–18.

[23] E. Tubaldi, A. Dall'Asta. Transverse free vibrations of continuous bridges with abutment restraint. *Earthquake Engineering & Structural Dynamics*, **41**(9), 1319–1340, 2012.

[24] Y. Bouassida, E. Bouchon, B. Kolias et al., Bridge Design to Eurocodes Worked examples. A. Athanasopoulou, M. Poljansek, A. Pinto, G. Tsionis, S. Denton eds. *Workshop "Bridge Design to Eurocodes"*, Vienna, Austria, October 4-6, 2010.

[25] European Committee for Standardization (ECS), *Eurocode 2 - Design of concrete structures*, Brussels , 2004.

[26] Iervolino, C. Galasso, E. Cosenza, REXEL: computer aided record selection for code-based seismic structural analysis. *Bulletin of Earthquake Engineering*, **8**(2), 339–362, 2009.

APPENDIX A: EIGENVALUE PROBLEM SOLUTION BY THE FROBENIUS METHOD

The eigenvalue problem is solved for the case with uniform distributed mass and stiffness along the spatial variable. Substituting $b(x)$ by *EI* and *m(x)* by $\bar{m}$ into Eqn. (7) the strong form of the seismic problem can be conveniently rewritten as

$$\begin{cases} \psi^{iv}(x) + g\psi''(x) - h\left[x\psi'(x)\right]' + \Omega^4\psi(x) = 0 \\ \psi(0) = \psi'(0) = \psi''(H) = 0 \\ EI\psi'''(H) + P\psi'(H) + \omega^2 M\psi(H) = 0 \end{cases} \tag{A1}$$

where $g = \left(\frac{P}{EI} + \frac{\bar{m}gH}{EI}\right)$, $h = \frac{\bar{m}g}{EI}$, and $\Omega^4 = -\frac{\bar{m}}{EI}\omega^2$.

The Frobenius method seeks the solution to Eqn.(A1) in the form

$$\psi(x,c)=\sum_{n=0}^{n=\infty}a_{n+1}(c)\,x^{c+n} \tag{A2}$$

in which the coefficients a_{n+1} are functions of the undetermined exponent *c*.

By differentiating Eqn. (A2), and substituting into Eqn.(A1), one has

$$\begin{aligned}&\sum_{n=0}^{n=\infty}a_{n+1}(c)(c+n)(c+n-1)(c+n-2)(c+n-3)x^{c+n-4}+\\&ga_{n+1}(c)(c+n)(c+n-1)x^{c+n-2}-ha_{n+1}(c)(c+n)^2x^{c+n-1}+\Omega^4a_{n+1}(c)x^{c+n}=0\end{aligned} \tag{A3}$$

From Eqn. (A3) one obtains an indicial equation for *c* and a set of equations for the coefficients a_{n+1} as shown below.

Without loss of generality, the lead coefficient a_1 is assumed equal to 1. The allowable values for *c* are the roots of the indicial equation, obtained by setting the lowest power of *x* in Eqn.(A3) (i.e., *c*-4) equal to zero

$$a_1(c)c(c-1)(c-2)(c-3)=0 \tag{A4}$$

Based on Eqn. (A4), Eqn. (A3) is rewritten as

$$\begin{aligned}&\sum_{n=0}^{n=\infty}a_{n+2}(c)(c+n+1)(c+n)(c+n-1)(c+n-2)x^{c+n-3}+\\&ga_{n+1}(c)(c+n)(c+n-1)x^{c+n-2}-ha_{n+1}(c)(c+n)^2x^{c+n-1}+\Omega^4a_{n+1}(c)x^{c+n}=0\end{aligned} \tag{A5}$$

The summations indices of the four terms of the sum are then shifted to obtain a common power of x equal to $(c+n-3)$.

$$\begin{aligned}&\sum_{n=0}^{n=\infty}a_{n+2}(c)(c+n+1)(c+n)(c+n-1)(c+n-2)x^{c+n-3}+\sum_{n=3}^{n=\infty}\Omega^4a_{n-2}(c)x^{c+n-3}+\\&\sum_{n=1}^{n=\infty}ga_n(c)(c+n-1)(c+n-2)x^{c+n-3}+\sum_{n=2}^{n=\infty}-ha_{n-1}(c)(c+n-2)^2x^{c+n-3}=0\end{aligned} \tag{A6}$$

From Eqn. (A6) to be zero, each power of *x* must vanish and, thus:

$$\begin{aligned}&a_{n+2}(c)(c+n+1)(c+n)(c+n-1)(c+n-2)+ga_n(c)(c+n-1)(c+n-2)\\&-ha_{n-1}(c)(c+n-2)^2+\Omega^4a_{n-2}(c)=0\end{aligned} \tag{A7}$$

for all the allowed *n*. This gives the following recurrence relationship:

$$a_{n+2}(c)=-\frac{ga_n(c)(c+n-1)(c+n-2)-ha_{n-1}(c)(c+n-2)^2+\Omega^4a_{n-2}(c)}{(c+n+1)(c+n)(c+n-1)(c+n-2)} \tag{A8}$$

subject to $a_k(c)=0$ for $k\le 0$.

For *c*= 0,1,2,3 and *n*=0,1,2, Eqn.(A8) gives:

$$
\begin{aligned}
&a_2(0)=a_2(1)=a_2(2)=a_2(3)=0;\\
&a_3(0)=-\frac{g}{2}, a_3(1)=-\frac{g}{6}, a_3(2)=-\frac{g}{12}, a_3(3)=-\frac{g}{20}\\
&a_4(0)=0, a_4(1)=\frac{h}{24}, a_4(2)=\frac{h}{30}, a_4(3)=\frac{h}{40}
\end{aligned}
\tag{A9}
$$

The four power series solutions that satisfy Eqn.(A1), each corresponding to a root of Eqn.(A4), are:

$$
\begin{aligned}
&\psi(x,0)=\psi_0(x)=\sum_{n=0}^{n=\infty} a_{n+1}(0)\,x^n\\
&\psi(x,1)=\psi_1(x)=\sum_{n=0}^{n=\infty} a_{n+1}(1)\,x^{n+1}\\
&\psi(x,2)=\psi_2(x)=\sum_{n=0}^{n=\infty} a_{n+1}(2)\,x^{n+2}\\
&\psi(x,3)=\psi_3(x)=\sum_{n=0}^{n=\infty} a_{n+1}(3)\,x^{n+3}
\end{aligned}
\tag{A10}
$$

The general modal shape $\psi(x)$ is obtained by combination of these four power series linearly independent:

$$
\psi(x)=C_0\psi_0(x)+C_1\psi_1(x)+C_2\psi_2(x)+C_3\psi_3(x) \tag{A11}
$$

Substituting Eqn. (A11) into the boundary conditions at the clamped end one obtains $C_0=C_1=0$ whereas the boundary conditions at the free end give:

$$
\begin{cases}
C_2\psi_2''(H)+C_3\psi_3''(H)=0\\
C_2\left[EI\psi_2'''(H)+P\psi_2'(H)+\omega^2M\psi_2(H)\right]+\\
C_3\left[EI\psi_3'''(H)+P\psi_3'(H)+\omega^2M\psi_3(H)\right]=0
\end{cases}
\tag{A12}
$$

Eqn. (A12) corresponds to a homogeneous system of two equations in the unknown C_2 and C_3. In order to obtain a non-trivial solution, the determinant of the coefficient matrix must to be equal to zero, thus yielding the following transcendental equation in the eigenvalue λ:

$$
\begin{aligned}
&\psi_2''(H)\left(EI\psi_3'''(H)+P\psi_3'(H)+\omega^2M\psi_3(H)\right)-\\
&-\psi_3''(H)\left(EI\psi_2'''(H)+P\psi_2'(H)+\omega^2M\psi_2(H)\right)=0
\end{aligned}
\tag{A13}
$$

This equation yields an infinite set of eigenvalues. The corresponding eigenvectors are obtained from Eqn.(A12), for which $C_3=-C_2\psi_2''(H)/\psi_3''(H)$, and their expression is:

$$
\psi(x)=C_2\left[\psi_2(x)-\frac{\psi_2''(H)}{\psi_3''(H)}\psi_3(x)\right] \tag{A14}
$$

COMPDYN 2013
4th ECCOMAS Thematic Conference on
Computational Methods in Structural Dynamics and Earthquake Engineering
M. Papadrakakis, N.D. Lagaros, V. Plevris (eds.)
Kos Island, Greece, 12–14 June 2013

A COMPARATIVE STUDY OF SEISMIC FRAGILITY ESTIMATES USING DIFFERENT NUMERICAL METHODS

Tushar K. Mandal[1], **Nikil N. Pujari**[2], **and Sidhhartha Ghosh**[3]

Department of Civil Engineering
Indian Institute of Technology Bombay
Mumbai 400076, India
e-mail: [1]tusharm78@gmail.com, [2]pujarinikil@gmail.com, [3]sghosh@civil.iitb.ac.in

Keywords: Seismic Fragility, Incremental Dynamic Analysis, Nuclear Power Plant, Primary Containment, Probabilistic Safety Assessment.

Abstract. *Seismic fragility estimations constitute the primary part of the probabilistic seismic safety assessment of important structures, such as nuclear containments, dams, important bridges, etc. The seismic fragility of a structure is expressed through a family of 'fragility' curves, which plot the conditional probabilities of failure against varying intensities of the seismic hazard. The failure probability of the structure can be defined for multiple limit states. Over the last three decades, various numerical techniques have been developed to estimate the seismic fragility of structures. Among these, three prominent methods selected for the present study are the ones proposed by Kennedy et al. [1], Shinozuka et al. [3] and Ellingwood et al. [4]. These methods vary in terms of the numerical analysis of analytical data in estimating the seismic fragility of a structure. The present work applies these three different fragility analysis techniques to the seismic fragility estimation of a nuclear containment structure and compares the results obtained from the three different methods. The inner containment structure of an Indian PHWR is used for this case study. The results obtained show that the method proposed by Shinozuka et al. provides the most accurate fragility estimations; however, it is also the most computation intensive. The conventional method proposed by Kennedy et al. provides the least accurate results and needs to use an updated uncertainty database.*

1 INTRODUCTION

The seismic fragility estimation forms the core of probabilistic safety assessment of structures. Specifically for important structures, such as nuclear power plants or large dams failure of which is likely to result into a great amount of loss of human lives, the need for seismic fragility evaluations (and re-evaluations) is considered to be the foremost in their design or qualification. In the light of the recent seismic events (for example, the 2011 Great East-Japan Tsunami and Earthquake), there has been a greater awareness about the potential hazards related to nuclear power plants (NPP) during a high-seismic event. These events have led to the reassessment of existing methods for structural safety analysis of NPP, which is the primary motivation for the work presented here.

The seismic fragility of a structure is typically expressed through 'fragility curves'. A fragility curve plots the fragility (or, the conditional probability of failure for a given level of hazard intensity) of the structure against varying intensities of the seismic hazard. The failure probability of the structure can be defined for various types of limit states depending on how the structural failure is defined. For a selected type, a fragility plot sometimes includes multiple fragility curves corresponding to different limit states or performance levels. The seismic fragility of a NPP can be defined both at component levels and at the system level.

The pioneering works in the area of seismic fragility analysis of nuclear structures were initiated in the late 1970s and continued till the mid-1980s [1, 2]. The methodologies proposed during this period relied on sound probabilistic analyses and quite significantly on engineering judgement. However, these methods suffered due to the lack of rigorous seismic structural analysis tools, necessary computational power and available earthquake damage data. Over the last decade, seismic structural analysis have changed significantly through the use of intensive seismic structural analysis methods (such as the nonlinear response-history analysis), complexity in structural/finite element modelling techniques using damage-based nonlinear material models, probabilistic models based on real data, and the enhanced computing powers of today's computers. In this paper, we look at two different methods of seismic fragility of structures, which use detailed computation to arrive at the final fragility curves. Shinouzuka et al. [3] focussed on the statistical analysis of fragility data for bridges and Ellingwood et al. [4] focussed on the fragility analysis of building structures using incremental dynamic analysis. The primary objective of this paper is to perform a comparison of these two methods of fragility analysis, along with the 'conventional' method mentioned earlier [2], through the test case of the seismic fragility analysis of the primary containment dome of a typical Indian PHWR.

2 THREE METHODS OF SEISMIC FRAGILITY ANALYSIS

2.1 Conventional method

The work by Kennedy et al. [1] was the first to present a detailed methodology for the estimation of the median ground acceleration capacity and associated uncertainties for the estimation of fragility curves of an existing NPP. Later, a detailed procedure for the estimation of fragility curves based on the selection of components, identification of failure modes and evaluation of uncertainties using factors of safety was given by Kennedy and Ravindra [2]. The fragility of a structure in this method is estimated using a lognormal model:

$$F_r = \Phi\left[\frac{\ln(x/m_a) + \beta_U \Phi^{-1}(Q)}{\beta_R}\right] \tag{1}$$

where, $\Phi(.)$ is the standard normal CDF operator, x is the seismic intensity (typically, PGA) at which the fragility is evaluated, m_a is the median ground acceleration capacity, β_R and β_U respectively measure the randomness (aleatory) and uncertainty (epistemic) associated with the estimation of the ground acceleration capacity, and Q is the non-exceedance probability level. The ground acceleration capacity (a) is expressed in terms of its median capacity (m_a) and associated uncertainties:

$$\begin{aligned} a &= m_a \epsilon_R \epsilon_U \\ &= a_{\text{DBE}} \bar{F} \epsilon_R \epsilon_U \\ &= a_{\text{DBE}} (F_S F_\mu F_R) \epsilon_R \epsilon_U \end{aligned} \tag{2}$$

where ϵ_R and ϵ_U follow lognormal distributions with a median equal to one and lognormal standard deviations β_R and β_U, respectively. a_{DBE} is the intensity of the design basis earthquake, $\bar{F}$ is the median factor of safety, which is composed of three different factors of safety. Details of these factors of safety and the associated uncertainties were discussed in depth in a recent paper by Pisharady and Basu [5]. As mentioned earlier, due to the lack of necessary tools and data, the quantification of these uncertainties depended significantly on engineering judgement. Although this method originally used response spectrum based linear elastic analyses, Pisharady and Basu [5] showed that modern analysis techniques, such as the nonlinear static pushover analysis can easily be incorporated in this framework. The two-parameter lognormal model of Equation 1, in its various forms, has now been widely accepted for seismic fragility analysis of structures. The two other fragility methods discussed in this paper also conform to this.

2.2 Maximum likelihood method

The method proposed by Shinouzuka et al. [3] uses a maximum likelihood estimation method to determine the parameters m_a and β_R to evaluate fragilities as a function of the intensity measure x:

$$F_r = \Phi \left[\frac{\ln(x/m_a)}{\beta_R} \right] \tag{3}$$

The likelihood function takes the form of a Bernoulli distribution:

$$L = \prod_{i=1}^{N} [F_r(x_i)]^{p_i} [1 - F_r(x_i)]^{q_i} \tag{4}$$

where $F_r(x_i)$ represents the fragility at PGA = x_i based on a specific limit state, and is calculated using Equation 3. N represents the number of sample response points at the selected PGA. p is 1 or 0 depending on whether the limit state is exceeded or not, respectively, and $q = 1 - p$. This method can incorporate data from random samples of earthquake response, either observed or obtained through analysis. The two parameters m_a and β_R are evaluated by maximizing the likelihood function:

$$\frac{d \ln L}{dm_a} = \frac{d \ln L}{d\beta_R} = 0 \tag{5}$$

These values are substituted in Equation 3 to obtain the final fragility curve.

2.3 Method based on IDA and regression

Incremental dynamic analysis (IDA) [6], which have been used very commonly in the last 10 years in probabilistic seismic demand analysis, was used by Ellingwood et al. [4] for the

fragility evaluation of steel and concrete building frames. Using multi-IDA response data for a set of acceleration records, they generated sample responses for a scaled intensity measure, which was the first-mode pseudo spectral acceleration (S_a). The variation in the response quantity (maximum interstorey drift ratio, $\theta_{\max}$) at any given intensity was then modelled with a lognormal distribution. The response was expressed as an exponential function of the intensity adopting a regression approach:

$$\theta_{\max} = c(S_a)^d \epsilon \tag{6}$$

where, c and d are regression parameters and ϵ quantifies the dispersion in the estimation of the response parameter. ϵ follows a lognormal distribution with a median equal to one and lognormal standard deviation β_R. Finally, fragility values are calculated using a displacement-based approach, where the failure is defined by the exceedance of the limit state response θ_{LS}:

$$F_r = \Phi\left[\frac{\ln\{c(S_a)^d/\theta_{\text{LS}}\}}{\beta_R}\right] \tag{7}$$

3 STUDY MODEL

The primary containment (PC) structure of a 700 MWe Indian pressurised heavy water reactor (PHWR) is considered for a comparison of the three selected methods of fragility analysis. It consists of a prestressed concrete cylindrical wall capped by a segmental prestressed concrete dome through a massive ring beam. The containment shell is supported on a circular raft. The PC structure is idealised using a 2D 'stick model' with lumped masses connected by 2D beam-column elements [7]. A simple illustration of the containment structure along with its stick idealisation is shown in Figure 1.

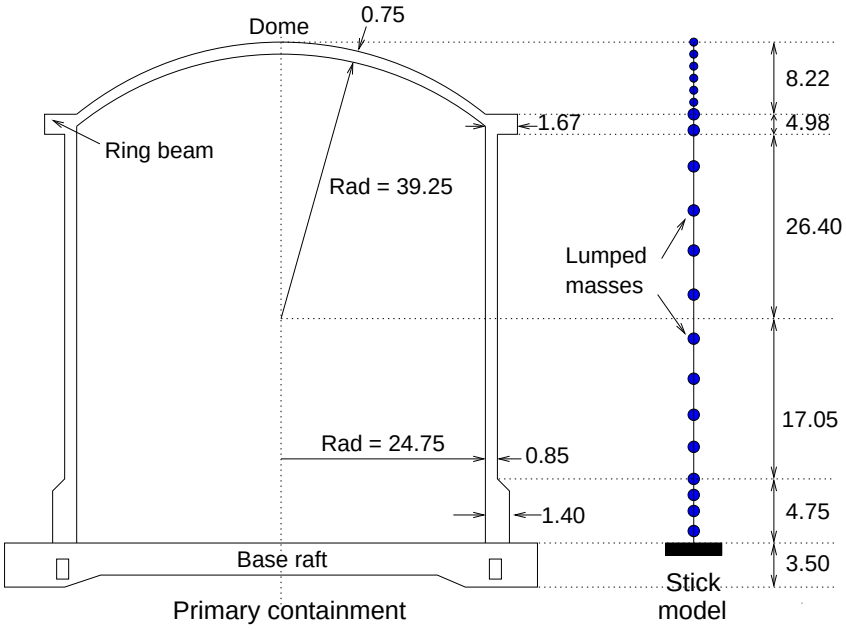


Figure 1: Schematic of the primary containment structure and its stick model (dimensions in m).

The containment structure responds to horizontal base excitation like a cantilever beam with an annular cross-section. This cantilever is modelled using the *nonlinearBeamColumn* element in the OpenSees platform [8]. This element is a force-based element and it considers the spread

of plasticity along the length of the member and five integration points are considered along the length of an element for this purpose. The cross-section is modelled with a *FiberSection*, where concrete is modelled as an annular patch of the *concrete02* material and reinforcing steel as a circular layer of *steel01* material. A damaged plasticity model (for both compression and tension behaviour) is considered for concrete, while the steel has a elastic-1% strain hardening plasticity behaviour. The shear deformation behaviour is modelled using the *sectionAggregator* approach. For simplicity, an elastic-perfectly plastic (EPP) type of shear force-deformation model is considered. This model requires two parameters: slope of the elastic curve and yield strength of the material. The slope of this curve is GA_s, where, G is the shear modulus of concrete and A_s is the shear area of the particular annular section. The yield shear strength of each section is calculated as per ACI-318 [9]. Further details of the 2D stick model can be found in the dissertation by Mandal [10].

4 FRAGILITY ANALYSIS

Seismic fragility analysis of the study structure is carried out using the 'Conventional', 'Likelihood' and 'Regression' methods discussed in Section 2. For the 'Conventional' method, a nonlinear static pushover analysis is conducted to obtain the response of the structure. Using the method suggested by Pisharady and Basu [5], the 50 percentile fragility curve is obtained based on the results of this pushover analysis. The median ground acceleration capacity is based on the Collapse Prevention (CP) limit state for maximum interstorey drift ratio defined in FEMA-356 [11]: $\theta_{\text{LS}} = 0.75\%$. The associated uncertainties are obtained from the tables compiled in their paper.

For the 'Likelihood' and 'Regression' methods, sample responses are generated using a multi-IDA study. The multi-IDA involves nonlinear response-history analysis (NLRHA) subjected to scaled intensities of 25 recorded accelerations. For this, intra-plate records suitable for the NPP site (in peninsular India) are selected, details of which are provided in Table 1. PGA is selected as the intensity measure (IM) and $\theta_{\max}$ as the damage measure (DM) in this IDA study. The IDA plots for the 25 records are shown in Figure 2. This plot also contains the pushover curve in PGA vs. $\theta_{\max}$ format which is used in the 'Conventional' fragility analysis. The vertical line labelled 'LS' represents the limit state of performance mentioned earlier. The probability of exceedance of this limit state is calculated at every intensity level to get the direct IDA-based fragility values. For the 'Likelihood' method, where the NLRHA-based responses are considered as random samples, this exceedance gives the p (and q) values for different intensity levels. The 'Likelihood' fragilities are obtained using Equation 3 after solving for m_a and β_R for maximizing the likelihood function. For the 'Regression' method, the multi-IDA data is modelled with a lognormal distribution at each intensity level and the median value is expressed as a function of PGA. c and d are obtained from the nonlinear regression and β_R from the lognormal distributions. The final fragility curve is obtained using Equation 7, while replacing S_a with PGA. It should be noted that for both of these methods, only the randomness due to the variation in possible earthquakes is included and the (epistemic) uncertainties are ignored, based on the consideration that the primary source of uncertainty in this case is the inherent randomness in earthquakes [12].

5 COMPARISON OF RESULTS

The fragility curves obtained using the three selected methods are presented in Figure 3. This figure also shows the discrete fragility data points obtained directly from the multi-IDA

Record	Event	Station	Component	R (km)	PGA (g)
GM-1	Bhuj, 2001	Ahmedabad	Radial	239.00	0.106
GM-2	Bhuj, 2001	Ahmedabad	Transverse	239.0	0.080
GM-3	Koyna, 1967	Koyna Dam	Radial	35.30	0.474
GM-4	Saguenay, 1988	St.-Ferreol	Radial	117.23	0.121
GM-5	Saguenay, 1988	St.-Ferreol	Transverse	117.23	0.097
GM-6	Saguenay, 1988	Quebec	Radial	149.40	0.051
GM-7	Saguenay, 1988	Quebec	Transverse	149.40	0.051
GM-8	Saguenay, 1988	Tadoussac	Radial	163.03	0.027
GM-9	Saguenay, 1988	Tadoussac	Transverse	163.03	0.002
GM-10	Saguenay, 1988	Baie-St-Paul	Radial	106.34	0.125
GM-11	Saguenay, 1988	Baie-St-Paul	Transverse	106.34	0.174
GM-12	Saguenay, 1988	La Malbaie	Radial	125.70	0.124
GM-13	Saguenay, 1988	La Malbaie	Transverse	125.70	0.060
GM-14	Saguenay, 1988	St.-Pascal	Radial	167.00	0.046
GM-15	Saguenay, 1988	St.-Pascal	Transverse	167.00	0.056
GM-16	Saguenay, 1988	Riviere-Ouelle	Radial	150.20	0.040
GM-17	Saguenay, 1988	Riviere-Ouelle	Transverse	150.20	0.057
GM-18	Saguenay, 1988	Ste.-Lucie-de-Beauregard	Radial	136.36	0.014
GM-19	Saguenay, 1988	Ste.-Lucie-de-Beauregard	Transverse	136.36	0.023
GM-20	Saguenay, 1988	Chicoutimi-Nord	Radial	45.69	0.107
GM-21	Saguenay, 1988	Chicoutimi-Nord	Transverse	45.69	0.131
GM-22	Saguenay, 1988	St-Andre-du-Lac-St-Jean	Radial	92.96	0.156
GM-23	Saguenay, 1988	St-Andre-du-Lac-St-Jean	Transverse	92.96	0.091
GM-24	Saguenay, 1988	Les Eboulements	Radial	114.31	0.125
GM-25	Saguenay, 1988	Les Eboulements	Transverse	114.31	0.102

Table 1: Details of the ground motion records considered.

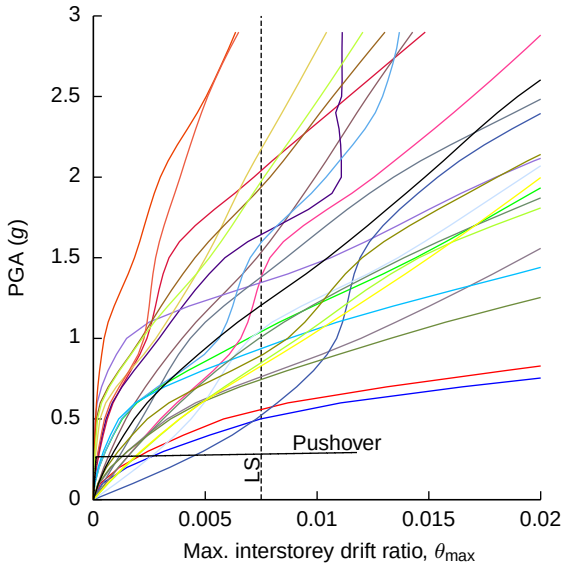


Figure 2: IDA plots for 25 acceleration records, along with the normalised pushover curve.

response at each PGA level. For the two methods using responses from the multi-IDA, these data points are treated as representing the 'actual' fragility values. The 'Conventional' fragility curve is very 'steep' compared to the others. It attains the 100% fragility by PGA = 1.5g. The

very high slope of the curve indicates to relatively smaller uncertainties (small β_R). Although the other two methods consider uncertainties only in the earthquake's randomness, that amounts to a greater uncertainty compared to the 'Conventional" fragility analysis.

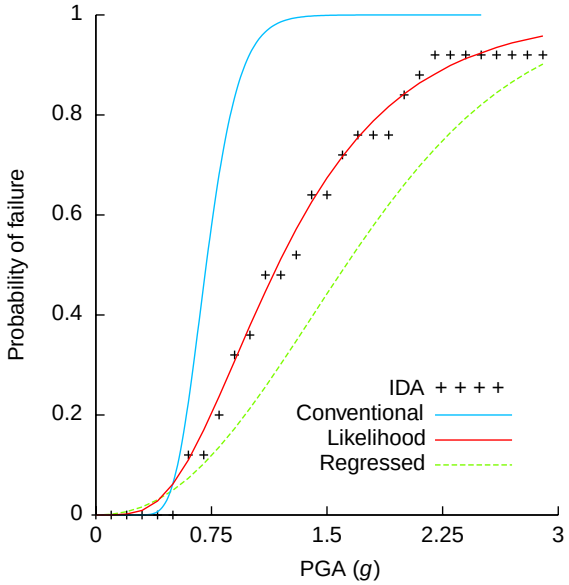


Figure 3: Fragility curves obtained using different methods.

A quick look at the 'Likelihood' and 'Regression' curves shows that the former is a better approximation of the discrete IDA-based fragility data points. This is because of the levels of approximations involved in the 'Regression' method, whereas the maximum likelihood based method is a more direct approach at the idealisation. However, there remains a need for a quantitative comparison of fragility estimates based on these two methods with respect to the IDA-based fragility data. The comparison is performed using three quantities: sum squared error (SSE) averaged over the total number of intensity levels (E), coefficient of determination (R^2), and Pearson's product-moment correlation coefficient (ρ_P). This comparison is summarised in Table 2. All of the three measures show very clearly that the 'Likelihood' method provides more accurate results than the 'Regression' method.

	Likelihood	Regression
E	0.827×10^{-3}	0.0194
R^2	0.995	0.948
ρ_P	0.997	0.974

Table 2: Accuracy/error in IDA-based fragility curves.

6 CONCLUSIONS

A comparison of three selected methods of fragility analysis is performed in this paper through the case study of the seismic fragility analysis of a primary containment structure of a typical Indian NPP. The methods are selected based on their popularity, and differences in the basic approach focussed primarily on how data and computational tools are used. Of the

three methods selected here, the 'Conventional' method gives very different results as compared to the other two. Although this method is easy to use, the database of uncertainty quantification used in this method does not seem realistic and it needs to be updated/calibrated based on thorough probabilistic and seismic structural analysis.

The 'Likelihood' and the 'Regression' methods are computation intensive because sample earthquake responses need to be generated through a large set of NLRHA. However, looking at the level of accuracy these methods can achieve and the computational prowess available with today's engineers (at least for important structures, such as NPP), these are definitely recommended over the 'Conventional' method. Between these two methods, the 'Likelihood' fragility analysis proves to be the more accurate one, but the user needs to note that solving Equation 5 is quite computation heavy. The fragility analyses performed here are based on several important assumptions (such as, no epistemic uncertainty, no soil-structure interaction, etc.); however, we do not expect the conclusions to change when more rigourous analyses are performed incorporating all reasonable sources of uncertainty.

References

[1] R. P. Kennedy, C. A. Cornell, R. D. Campbell, S. Kaplan, and H. F. Perla. Probabilistic seismic safety study of an existing nuclear power plant. *Nuclear Engineering and Design*, **59**(2):315–338, 1980.

[2] R. P. Kennedy and M. K. Ravindra. Seismic fragilities for nuclear power plant risk studies. *Nuclear Engineeiring and Design*, **79**(1):47–68, 1984.

[3] M. Shinouzuka, M. Q. Feng, J. Lee, and T. Naganuma. Statistical analysis of fragility curves. *Journal of Engineering Mechanics, ASCE*, **126**(12):1224–1231, 2000.

[4] B. R. Ellingwood, O. C. Celik, and K. Kinali. Fragility assessment of building structural systems in Mid-America. *Earthquake Engineering and Structural Dynamics*, **36** (13):1935–1952, 2007.

[5] A. S. Pisharady and P. C. Basu. Methods to derive seismic fragility of NPP components: A summary. *Nuclear Engineering and Design*, **240**(11):3878–3887, 2010.

[6] D. Vamvatsikos and A. Cornell. Incremental dynamic analysis. *Earthquake Engineering and Structural Dynamics*, **31**(3):491–514, 2002.

[7] G. R. Reddy, H. S. Kushwaha, S. C. Mahajan, S. P. Kelkar, and G. V. Karandikar. Development of 3-D beam model for seismic analysis of 500 MWe reactor building. Technical Report BARC/1996/I/004, Bhabha Atomic Research Centre, Mumbai, India, 1996.

[8] S. Mazzoni, F. McKenna, and G. L. Fenves. *Opensees Command Language Manual*. The Regents of the University of California, Berkeley, USA, 2006.

[9] ACI-318. *Standard Code Requirements for Reinforced Concrete and Commentary (ACI318-M05)*. American Concrete Institute, Detroit, USA, 2005.

[10] T. K. Mandal. Seismic fragility analysis of a primary containment structure using IDA. Master's thesis, Department of Civil Engineering, Indian Institute of Technology Bombay, Mumbai, India, 2012.

[11] FEMA-356. *Prestandard and Commentary for the Seismic Rehabilitation of Buildings*. Federal Emergency Management Agency, Washington, USA, 2000.

[12] N. Shome. *Probabilistic seismic demand analysis of nonlinear structures*. PhD thesis, Department of Civil and Environmental Engineering, Standford University, Palo Alto, USA, 1999.

COMPDYN 2013
4th ECCOMAS Thematic Conference on
Computational Methods in Structural Dynamics and Earthquake Engineering
M. Papadrakakis, V. Papadopoulos, V. Plevris (eds.)
Kos Island, Greece, 12–14 June 2013

EVALUATION OF THE EFFECT OF MODELING UNCERTAINTIES ON THE SEISMIC RESPONSE OF EXISTING MASONRY BUILDINGS

M. Rota[1], S. Bracchi[2], A. Penna[1,3] and G. Magenes[1,3]

[1] European Centre for Training and Research in Earthquake Engineering
via Ferrata, 1 I-27100 Pavia, Italy
maria.rota@eucentre.it

[2] ROSE Programme, UME School, IUSS Pavia
via Ferrata, 1 I-27100 Pavia, Italy
stefano.bracchi@umeschool.it

[3] University of Pavia, Department of Civil Engineering and Architecture
via Ferrata, 3 I-27100 Pavia, Italy
{andrea.penna, guido.magenes}@unipv.it

Keywords: modeling uncertainty, masonry buildings, seismic assessment, pushover analysis, equivalent-frame modeling.

Abstract. *An accurate seismic assessment of existing masonry buildings requires consideration of the sources of uncertainty and their effect on the seismic response. Among them, uncertainties related with modeling assumptions are definitely non-negligible. They include the choice of the modeling approach (continuum finite elements, equivalent frame, etc…), the analysis type (static/dynamic, linear/nonlinear) and the different options followed in defining the model. This work provides a quantitative evaluation, in probabilistic terms, of the effect of modeling uncertainties on the seismic response, in terms of the peak ground acceleration corresponding to the attainment of predefined limit states. Nonlinear static analysis was used, considered as the reference method to be adopted for the seismic assessment of existing buildings. The equivalent-frame macro-element approach was selected, being a satisfactory compromise between computational effort and accuracy in the results. Different possible choices regarding definition of the geometry of the equivalent frame, distribution of loads among the piers, distribution of loads on the floor systems, modeling of masonry spandrels, degree of coupling between orthogonal walls, definition of the cracked stiffness of structural elements, were considered. To quantify their effect on the response, a logic tree approach was followed, assigning a value of probability to each choice and hence obtaining the distribution of the acceleration corresponding to the selected limit states. This procedure was applied to a prototype building, for which a quantitative measure, in probabilistic terms, of the dispersion in the results due to the considered modeling uncertainties was evaluated.*

1 INTRODUCTION

Masonry structures constitute an important part of the existing building stock in many world countries, both for residential use and to host economical activities and very important social functions. The majority of these buildings was not conceived to survive earthquakes and it hence needs a seismic safety assessment, as demonstrated by the recent Italian seismic events in the Abruzzi region and in Emilia. It is hence particularly important that the seismic assessment methodology is accurate, leads to more reliable results as knowledge on the structure (and hence cost) increases and allows to correctly take into account all the uncertainties involved in the process.

The evaluation of the seismic safety of existing buildings is currently carried out with conventional methods, like those adopted in the most advanced codes, in which knowledge and uncertainties are accounted for in an all-in way. In particular, the approach included in Eurocodes [1] and in the Italian building code [2] simply accounts for knowledge by defining three discrete levels of knowledge and associating to each of them a value of confidence factor, to be applied as a reduction of material strengths.

Previous literature works have demonstrated that this methodology provides in many cases inconsistent results, both for the case of reinforced concrete [3] and masonry [4] buildings. Also, this approach does not take into account all the other sources of uncertainty, such as for example those related with the selected modeling strategy and options, the adoption of deterministic thresholds identifying the ultimate element drifts, the epistemic uncertainty in the definition of the seismic action.

A previous work [5] proposed a probabilistic methodology for quantifying the effects of these sources of uncertainty on the results of nonlinear static analyses, based on the definition of coefficients (called variability factors), which are calibrated based on a logic tree approach. However, in that work, only a preliminary estimate of the effects of different modeling assumptions was reported, taking into account only some of the possible hypotheses related with the equivalent-frame macro-element modeling of masonry buildings.

Still keeping the same methodological approach proposed in [5], this paper presents a more accurate evaluation of the effects of such modeling uncertainties, trying to consider all the possible analysis options, although only concentrating on nonlinear static analysis and on the equivalent-frame macro-element modeling strategy. The choice of considering only nonlinear static analysis derives from the consideration that this analysis method can be currently considered as the best-established approach for the seismic assessment of masonry buildings. Indeed, although nonlinear dynamic analyses are universally considered the most accurate analysis technique, their application in the engineering practice is still quite rare (e.g. [6]), also due to the high computational effort and to objective difficulties related for example with the definition of seismic input in terms of appropriate acceleration time histories (e.g. [7], [8]) and the identification of appropriate damage limit states (e.g. [9]).

The proposed methodology is applied to a case study building, which is described in the following section and corresponds to one of the buildings considered in [5] to allow comparison of the results obtained.

2 CASE STUDY BUILDING AND MODELING APPROACH

The proposed methodology was applied to a three-story building, with an approximately square plan configuration (Figure 1). This building, which is one of the structures (building H) considered in [5] for a preliminary estimate of the effect of modeling uncertainty, is realized with “roughly dressed stone masonry with good bonding”, according to the predefined ma-

sonry typologies reported in Table C8.A.2.1 of the Commentary to the Italian code [10]. Mechanical parameters were hence assumed equal to the central values of the intervals reported in [10], neglecting their spatial variability within structural elements. No confidence factor was applied, assuming a perfect knowledge on material properties (level of knowledge at least equal to 3). This building has rigid diaphragms and its construction details are such to guarantee a global type of response with no premature activation of local (out-of-plane) failure mechanisms. To reach this scope, simple construction details are sufficient, as demonstrated for example in [11] and [12].

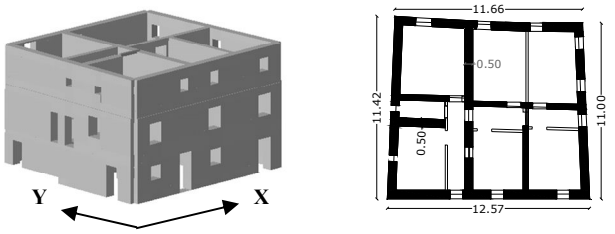


Figure 1: 3D model view and plan view of the considered case study building.

As mentioned in the introduction, the choice of the software used for carrying out all the analyses can strongly affect the results obtained. In this work, a single software has been selected, without hence taking into consideration the effect on the results of the adoption of different analysis programs and modeling approaches. The selected software, called Tremuri, is based on the macro-element approach and allows execution of nonlinear static and nonlinear dynamic analyses of entire masonry buildings, by means of an equivalent-frame idealization of the structure. Details about this program and its algorithm can be found elsewhere (e.g. [13], [14]).

3 CONSIDERED MODELING OPTIONS

As already discussed, in this work only nonlinear analyses were performed and a single equivalent frame macro-element model was adopted. Under these hypotheses, the main modeling uncertainties, i.e. the different options that the engineer has to select when modeling the building, can be identified as being related with:

- Definition of the geometry of the equivalent frame, i.e. identification of masonry piers, definition of rigid and deformable portions
- Definition of cracked versus initial stiffness
- Modeling of masonry spandrels
- Distribution of loads on the horizontal diaphragms
- Distribution of vertical loads among the different masonry piers
- Degree of coupling between orthogonal walls

Another possible source of uncertainty is related with the capacity models used and, in particular, with the criterion used to evaluate the shear strength. Among the different criteria available in the literature, only the diagonal shear cracking failure criterion (proposed by Turnsek and Cacovic [15]) was adopted, as suggested in [10]. Additional uncertainty may be related with the definition of the effective length of tie beams, but this was not taken into consideration as the selected stone masonry building prototype (which is actually a real building) does not have any tie beam. The adopted software does not model the out-of-plane wall stiffness. Consideration of this additional stiffness could add an additional uncertainty to the results.

Each of the considered modeling options corresponds to one of the branches of the logic tree and hence its influence was evaluated separately.

In a previous paper [5], a preliminary estimate of the variability factor due to modeling uncertainties was carried out by considering only some of these sources of uncertainty, i.e. identification of masonry piers, distribution of loads on the floor systems, modeling of masonry spandrels and definition of cracked versus initial stiffness. This paper aims at providing a more precise quantification of the effects of modeling uncertainties, by considering all the elements listed above.

3.1 Definition of the height of masonry piers

Regarding the definition of the effective height of the piers, *h'*, three different criteria were considered, each one with the same probability of being selected. According to the first criterion (Figure 2 (a)), the pier height coincides with the minimum clear height between the adjacent openings. The second criterion (Figure 2 (b)) assumes a maximum 30° inclination of the cracks starting from the opening corners and consistently provides an increased height for the external piers. This was also the initial hypothesis used by Dolce [16] for the definition of the equivalent height of models based on the story mechanism. The third criterion (Figure 2 (c)), default criterion of the automatic mesh generator included in the 3muri program [14], provides an effective height equal to the average height of the adjacent openings (story height in case of external openings).

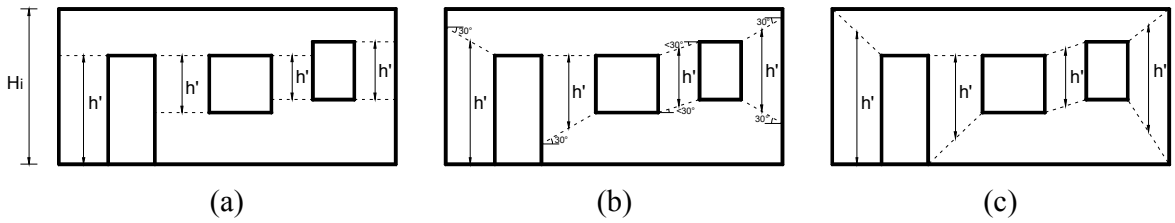


Figure 2: Effective pier height, *h'*, evaluated assuming three different discretization criteria: (a) minimum clear height, (b) effective height assuming a maximum inclination of cracks, and (c) average height of adjacent openings (after [5]).

3.2 Definition of cracked versus initial stiffness

A typical way of accounting for cracked material properties consists in reducing the values of the elastic moduli *E* and *G*, as also suggested in [10], which reports uncracked values of the elastic moduli *E* and *G* for different masonry typologies and suggests to appropriately reduce them to account for cracked conditions in the structure.

In this work, three values of the ratio of cracked versus initial (uncracked) stiffness were assumed, corresponding to 100%, 75% and 50%, with assigned probabilities equal to 45%, 10% and 45%, respectively. The first option may appear in contrast with the indications of [10], but it was considered reasonable for those cases in which the engineer believes the values reported in the table are already low if compared with the results of experimental tests. 50% is a reduction coefficient which is often adopted in the engineering practice and it also constitutes the default of several analysis programs . Finally, the value of 75% is the most consistent with experimental results (e.g. [17], [18], [19]) and therefore it is probably, in many cases, the most appropriate choice. This value was given a low probability, as it is believed that only a small percentage of engineers would resort to experimental results for the evaluation of this reduction coefficient.

3.3 Modeling of masonry spandrels

The degree of coupling exerted by masonry spandrels can strongly affect the buildings' structural response (e.g. [20], [21]). In this study, two extreme options were considered, which correspond to those most commonly adopted by structural analysis programs for the seismic assessment of masonry buildings. The two options were assumed to be equally probable.

In the first case, spandrels are modeled as deformable beams belonging to the equivalent frame and their lateral strength is determined either based on the compression forces deriving from the analysis (reliable only for walls not connected to rigid diaphragms) or on the strength of the tension resisting elements. The latter applies when tie rods or tie beams are present in parallel to the spandrels. In the second option, spandrels are modeled as axially rigid trusses simply coupling the horizontal displacements of the piers (cantilever model).

3.4 Distribution of loads on the floor systems

Two possible alternatives (with the same probability) were considered for the distribution of loads on floors and roofs, assuming these diaphragms are one-way floor systems. According to the first option, 100% of the load is acting on the walls crossing the direction of spanning of the floors, whilst in the second option this percentage is reduced to 75%, assuming that also walls parallel to the direction of spanning carry part of the loads acting on the floor (approximated as 25% of the total load).

3.5 Distribution of vertical loads among the different masonry piers

As well known, the lateral strength of masonry piers is strongly dependent on the applied vertical force which governs both shear and flexural strength criteria and hence the expected failure mode. Tributary floor areas can be defined in order to calculate the vertical load applied from the floor system to each pier. Different levels of refinement can be adopted in calculating the in-plane eccentricity of the vertical load acting on each masonry pier. The different assumptions can lead to different pushover analysis results in terms of both base shear and displacement capacity.

The following three criteria for calculating the longitudinal eccentricity of the vertical force transmitted by floors to walls have been considered, with an equal probability of being chosen:

a) the vertical load is concentrated at the center middle of each pier (left part of Figure 3) with no in-plane eccentricity;
b) the vertical load is applied in the point corresponding to the resulting vertical force transmitted by the floor elements pertaining to the tributary area (maximum longitudinal eccentricity);
c) the floor area is subdivided into strips (or equivalent joists) parallel to the spanning direction. Each strip is considered to distribute half of the vertical load corresponding to its area to the two intersecting walls (loading points corresponding to the strip ends). In case the strip directly loads a masonry pier, the load both contributes to the applied vertical force and bending moment based on the eccentricity of the loading point with respect to the pier center. The strip loads applied to beams or spandrels are instead reported to the beam/spandrel ends with an inverse proportionality with the distances between the loading point and the beam ends. The sum of all strip contributions at the beam-pier edge is then reported as a vertical load contribution to the pier center plus a bending moment obtained multiplying the load by half of the pier length. As a result of this more general approach, which was in-

cluded in the 3muri program also to account for any floor spanning direction [14], the load eccentricity is reduced with respect to criterion b).

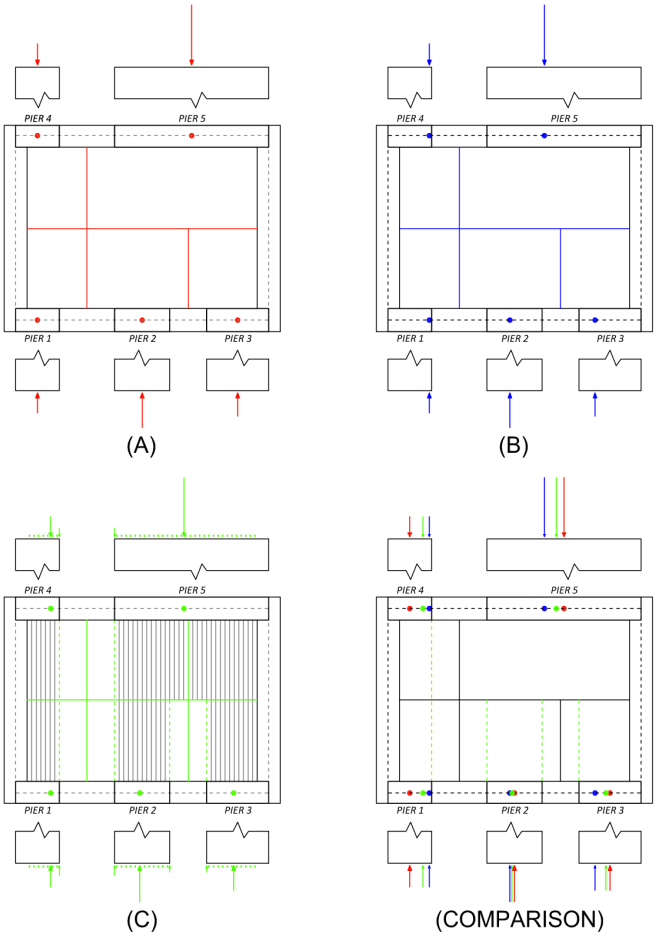


Figure 3: Three criteria considered for the evaluation of longitudinal eccentricity of vertical loads on masonry piers: (a) load centered on masonry piers, (b) eccentric load, and (c) strip model included in 3Muri.

3.6 Degree of coupling between orthogonal walls

For what concerns the degree of coupling between orthogonal walls, two criteria have been considered. According to the first one, the two orthogonal walls are connected by an infinitely stiff element providing a kinematic restraint. In this way the beam has a flange effect. This is the default's option of the Tremuri computer program and it was given a probability of 75% as it is considered to be the most correct modeling approach. Another alternative was also considered (with a probability of 25%), according to which the two orthogonal walls are connected by a link element, which means that there is no flexural and shear coupling between the walls.

4 ANALYSIS PROCEDURE

Two different force distributions (e.g. mass proportional and first mode distribution) were used in nonlinear static analyses, as indicated by several codes (e.g. [1] and [2]) to account for the dynamic response in the different phases of damage evolution. These force distributions were applied along two orthogonal directions (both positive and negative), considering the presence of the accidental eccentricities introduced by the codes (e.g. [22] and [2]) to account

for uncertainties in the location of masses. Since the building has rigid floors, the choice of the control node is not very critical and one of the nodes belonging to the top level was selected.

Three limit states were considered, i.e. the two required by the Italian building code and indicated as life safety (ULS) and damage limitation (DLS) limit states, and the operational (OLS) limit state, which however is not explicitly required by the code for the building under study. The seismic input was defined by means of the elastic horizontal acceleration response spectrum of Type 1 proposed by EC8-1 [22] for rigid soil conditions (ground type A). The values of the ultimate shear and flexural drift at the element level were set equal to the values indicated in the Italian code, i.e. 0.4% and 0.6% respectively. As discussed in [5] these values are also affected by some uncertainty, which should be considered by defining an appropriate probability distribution. However, the purpose of this work is simply to evaluate modeling uncertainties and therefore all other sources of uncertainty are neglected.

The logic tree approach was used to evaluate the influence of modeling uncertainties, as discussed in the following section. Structural capacity was calculated according to the N2 method [23].

4.1 Definition of the logic tree and statistical treatment of the results

Similarly to what done in [4] and [5], the assessment of the structure was simulated by taking into account the effect on the assessment results of the possible choices related to modeling uncertainties. The different options were schematized in the form of a logic tree (reported in Figure 4), with each branch of the tree having a different probability of being chosen and each leaf corresponding to the results of the analysis carried out with the assumptions corresponding to the path followed within the tree. The definition of the probabilities associated with the different choices within the logic tree is subjective and it was based on the relative likelihood of each choice, determined based on engineering judgment, as discussed in the previous sections for each considered option.

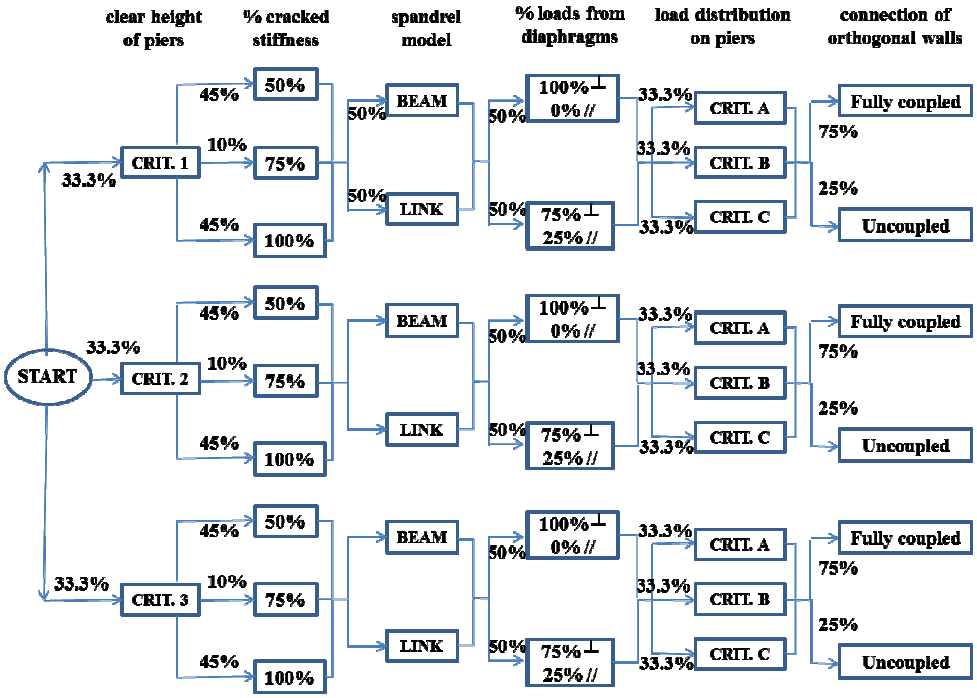


Figure 4. Logic tree followed for the definition of the effects of modeling uncertainties – the percentage values associated with the different braches indicate their probability of being selected.

Each analysis hence provided a value of the acceleration corresponding to the achievement of a given limit state and an associated probability obtained as the product of all the probabilities of the different branches followed. A histogram of values was then constructed and the corresponding cumulative distribution was fitted by a lognormal distribution, with parameters determined using the Levenberg e Marquardt ([24], [25]) nonlinear regression algorithm. As previously mentioned, three different limit states were considered and they were all defined according to the indications of [2] and [10]). The acceleration corresponding to the attainment of the life safety limit state (indicated as ultimate limit state, ULS) was obtained by applying the N2 method [23] reported in Annex F of [22] and in [2]. As specified in [10], for the case of nonlinear static analysis, the ULS is identified as the displacement corresponding to a 20% strength deterioration with respect to the maximum strength. To identify this point, the force-displacement curve obtained from the analysis is converted into the curve of an equivalent single degree of freedom system, which is then approximated by a bilinear curve. This last step was carried out according to the indications of [2]. With reference again to nonlinear static analysis, the damage limitation state (DLS) is identified as the minimum between the displacement corresponding to the maximum base shear and that for which the relative displacement of two adjacent stories exceeds $0.003h$, where h is the inter-story height [10]. The operational limit state (OLS) is instead identified as the displacement for which the relative displacement of two adjacent stories exceeds 2/3 of the value corresponding to DLS. An additional condition was also considered, imposing the displacement corresponding to OLS to be not larger than that corresponding to DLS. With these values of displacement it was then possible to derive the displacement of the equivalent single-degree-of-freedom system and then the acceleration corresponding to the attainment of these limit states.

From the probability distribution of the accelerations corresponding to the attainment of each damage state, the variability factor for that damage state was calculated as the ratio of the value corresponding to the 5th percentile to the mean value of acceleration, i.e.:

$$\alpha = \frac{a_{g,5\%}}{a_{g,mean}} \tag{1}$$

This variability factor is a measure of the dispersion of the acceleration values with respect to the mean value of the distribution and hence of the variability in the results caused by the considered modeling uncertainties.

5 RESULTS

This section summarizes the results obtained from the analyses of the considered building prototype and presents some comparisons with the results of the preliminary estimate of the effects of modeling uncertainties presented in [5].

Figure 5 shows the pushover curves obtained from analyses in the two perpendicular directions indicated in Figure 1 as X and Y. Each curve reported in the plot corresponds to the analysis providing the minimum value of the acceleration corresponding to the attainment of the ultimate limit state and derives from one of the branches of the logic tree (i.e. it corresponds to one set of modeling options), for a total of 216 curves. The dispersion of these pushover curves is significant in both directions.

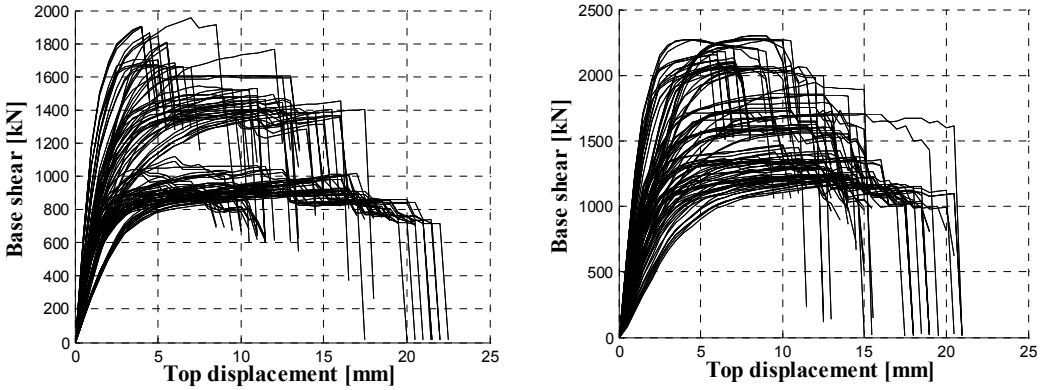


Figure 5. pushover curves corresponding to the minimum $a_{g,ULS}$ in direction X (left) and Y (right).

Figure 6 shows instead the cumulative distribution of the values of acceleration corresponding to the attainment of the ultimate limit state in the two directions and their lognormal approximations, whilst Figure 7 shows the lognormal approximations obtained for the three considered limit states.

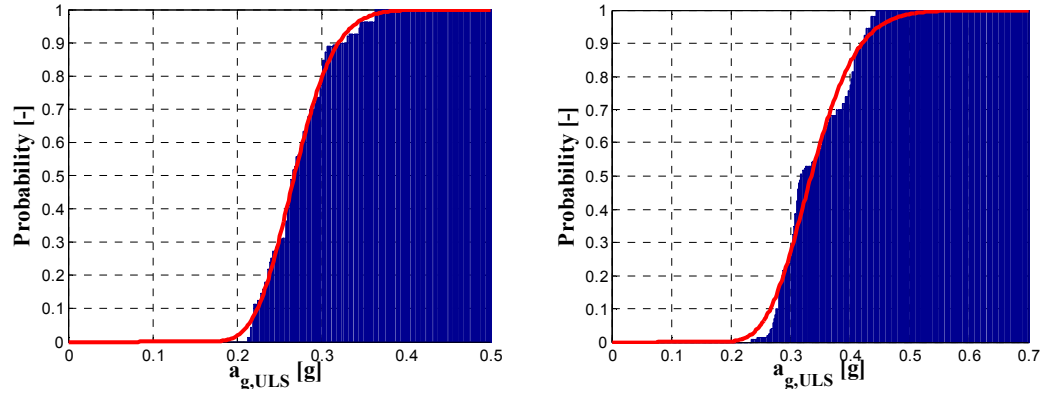


Figure 6. Cumulative distribution and lognormal approximation of the values of $a_{g,ULS}$ in direction X (left) and Y (right).

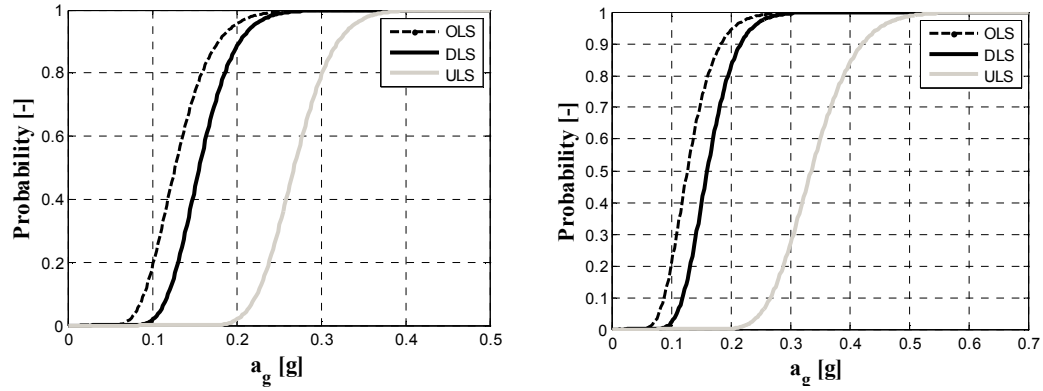


Figure 7. Lognormal approximation of the cumulative distribution of the acceleration capacity for the three considered limit states in the X (left) and Y (right) directions.

Comparison with the results of the preliminary study, whose assumptions are discussed in [5], shows that in the case presented in this paper the dispersion in pushover curves is more significant, as could be expected since additional sources of uncertainty have been included. Nevertheless, a comparison of the parameters characterizing the lognormal approximation curves reported in Figure 6 with those obtained in the preliminary study shows that they are not significantly different, as reported in Table 1. In particular, in both directions, the lognormal standard deviation (representing variability in the results) is higher than in the preliminary estimate for the OLS and DLS, whilst it is lower for the ULS. This may be due to the limitation on the maximum allowable spectrum reduction factor imposed by the Italian code ($q^* \leq 3$), which governs the ultimate displacement capacity of the structure, hence reducing the dispersion in the analysis results.

Limit state	This study				Preliminary evaluation			
	Direction X		Direction Y		Direction X		Direction Y	
	μ	σ	μ	Σ	μ	σ	μ	σ
OLS	-2.064	0.266	-2.064	0.288	-1.935	0.249	-1.905	0.263
DLS	-1.860	0.210	-1.830	0.234	-1.756	0.198	-1.702	0.219
ULS	-1.317	0.140	-1.093	0.179	-1.206	0.155	-1.000	0.193

Table 1: Comparison of the parameters of the normal distributions associated with the lognormal approximations obtained in this study and from the preliminary evaluation of modeling uncertainties reported in [5].

The variability factors were calculated based on the distribution of the acceleration corresponding to the attainment of the different limit states. For each limit state, two values of α_{mod} were calculated, one for each direction. Table 2 shows a comparison between the values of the variability factors obtained in this study and those obtained in the preliminary evaluation carried out with the assumptions discussed in [5]. It can be noted that, in both directions, the variability factor accounting for modeling uncertainties obtained in this study are lower than in the preliminary evaluation for the OLS and DLS, whilst the opposite occurs for the ultimate limit state. This indicates that, as expected, consideration of additional sources of modeling uncertainty tends to increase the dispersion in the results for the damage limit states, hence leading to lower values of the variability factors. The opposite occurs for the ultimate limit state, for the same reason discussed above regarding the lognormal parameters.

Limit state	This study		Preliminary evaluation	
	Direction X	Direction Y	Direction X	Direction Y
OLS	0.6237	0.5971	0.6435	0.6265
DLS	0.6929	0.6626	0.7078	0.6816
ULS	0.7871	0.7335	0.7653	0.7148

Table 2: Values of α_{mod} obtained for the three limit states considered in this study and in the preliminary evaluation whose hypotheses are discussed in [5].

6 CONCLUSIONS

This paper presented the results of a quantitative estimate of the effects of modeling uncertainties on the seismic response of a stone masonry building, evaluated by means of nonlinear static analyses with an equivalent frame macro-element approach. The effect of the different modeling choices on the seismic response, represented by the peak ground acceleration corre-

sponding to the attainment of predefined limit states, is considered by means of a logic tree approach, in which each option corresponds to a branch of the tree, with a given probability of being selected.

From the probability distribution of the values of acceleration obtained from the analyses, values of the so-called variability factor were obtained. This factor, defined as the ratio between the value corresponding to the 5th percentile of the distribution and the mean value, provides a quantitative measure of the dispersion in the analysis results due to consideration of the different modeling options.

The study concentrated on nonlinear static analysis, as it is considered the best-established method currently adopted in Italy for the seismic assessment of existing masonry buildings. Moreover, only the equivalent-frame macro-element modeling strategy has been adopted.

The results obtained for a case study building seem to indicate that the effect on the seismic response of masonry buildings of the uncertainty in modeling options is definitely non-negligible. Nevertheless, the methodology presented in this paper needs to be applied to other prototype buildings, such as for example those presented in [5], in order to derive more general indications on the quantitative estimate of the variability factor accounting for modeling uncertainty. This factor could then be adopted in the probabilistic approach proposed in [5], which allows carrying out the seismic assessment of masonry buildings considering the different sources of uncertainty involved in the problem and overcoming some of the main limitations of the current code approach adopted in Italy and in Europe.

ACKNOWLEDGEMENTS

This work was carried out within the framework of the 2012-14 EUCENTRE Executive Project e1.b “Seismic assessment of masonry buildings accounting for the knowledge level and the different sources of uncertainty” funded by the Italian Department of Civil Protection. The valuable help of Mr. Marco Tondelli is gratefully acknowledged.

REFERENCES

[1] EN 1998-3. Eurocode 8: Design of structures for earthquake resistance - Part 3: Assessment and retrofitting of buildings. CEN, Bruxelles, 2005.

[2] NTC08 Decreto Ministeriale 14 Gennaio 2008: “Norme tecniche per le costruzioni,” Ministero delle Infrastrutture. S.O. n.30 alla G.U. del 4.2.2008, No. 29, 2008.

[3] P. Franchin, P.E. Pinto, P. Rajeev, Confidence factor? *Journal of Earthquake Engineering*, **14**(7), 989-1007, 2010.

[4] M. Tondelli, M. Rota, A. Penna, G. Magenes, Evaluation of uncertainties in the seismic assessment of existing masonry buildings. *Journal of Earthquake Engineering*, **16**(S1), 36-64, 2012.

[5] M. Rota, A. Penna, G. Magenes, A framework for the seismic assessment of existing masonry buildings accounting for different sources of uncertainty. *Submitted to Earthquake Engineering and Structural Dynamics*, 2013.

[6] A. Penna, M. Rota, A. Mouyiannou, G. Magenes, Issues on the use of time-history analysis for the design and assessment of masonry structures. *4th International Confer-*

ence on Computational Methods in Structural Dynamics and Earthquake Engineering (COMPDYN), Kos Island, Greece, 2013.

[7] M. Corigliano, C.G. Lai, M. Rota, C.L. Strobbia, ASCONA: Automated Selection of COmpatible Natural Accelerograms. *Earthquake Spectra*, **28**(3), 965-987, 2012.

[8] M. Rota, E. Zuccolo, L. Taverna, M. Corigliano, C.G. Lai, A. Penna, Mesozonation of the Italian territory for the definition of real spectrum-compatible accelerograms. *Bulletin of Earthquake Engineering*, **10**(5), 1357-1375, 2012.

[9] A. Mouyiannou, M. Rota, A. Penna, G. Magenes, Identification of suitable limit states from nonlinear dynamic analyses of masonry structures. *Submitted to Journal of Earthquake Engineering*, 2013.

[10] MIT Ministry of Infrastructures and Transportation Circ. C.S.Ll.Pp. No. 617 of 2/2/2009 "Istruzioni per l'applicazione delle nuove norme tecniche per le costruzioni di cui al Decreto Ministeriale 14 Gennaio 2008," Consiglio superiore dei lavori pubblici. S.O. n.27 alla G.U. del 26.02.2009, No. 47, 2009.

[11] G. Magenes, A. Penna, I. Senaldi, M. Rota, A. Galasco, Shaking table test of a strengthened full scale stone masonry building with flexible diaphragms. *Submitted to International Journal of Architectural Heritage*, 2013.

[12] I. Senaldi, G. Magenes, A. Penna, A. Galasco, M. Rota, The effect of stiffened floor and roof diaphragms on the experimental seismic response of a full scale unreinforced stone masonry building. *Submitted to Journal of Earthquake Engineering*, 2013.

[13] A. Penna, S. Lagomarsino, A. Galasco, A nonlinear macro-element model for the seismic analysis of masonry buildings. S*ubmitted to Earthquake Engineering and Structural Dynamics*, 2013.

[14] S. Lagomarsino, A. Penna, A. Galasco, S. Cattari, TREMURI program: an equivalent frame model for the nonlinear seismic analysis of masonry buildings. *Submitted to Engineering Structures*, 2013.

[15] V. Turnsek, F. Cacovic, Some experimental results on the strength of brick masonry walls. *2nd International Brick Masonry Conference*, Stoke on Trent, 1971.

[16] M. Dolce, Schematizzazione e modellazione per azioni nel piano delle pareti, *L'Industria delle Costruzioni*, 44-57, 1991 (in Italian).

[17] G. Magenes, P. Morandi, A. Penna, In-plane cyclic tests of calcium silicate masonry walls. *14th International Brick Block Masonry Conference*, Sydney, Australia, 2008.

[18] A.A. Costa, A. Penna, G. Magenes, Seismic performance of autoclaved aerated concrete (AAC) masonry: from experimental testing of the in-plane capacity of walls to building response simulation. *Journal of Earthquake Engineering* **15**(1), 1-31, 2011.

[19] M. Mandirola, A. Penna, M. Rota, G. Magenes, Experimental assessment of the shear response of autoclaved aerated concrete (AAC) masonry with flat truss bed-joint reinforcement. *15th International Brick Block Masonry Conference*, Florianopolis, Brazil, 2012.

[20] M. Tomazevic, Earthquake-resistant design of masonry buildings, *Imperial College Press, Series on innovation in structures and constructions*, 1999.

[21] G. Magenes, A. Della Fontana, Simplified non-linear seismic analysis of masonry buildings. *Proc. British Masonry Society* **8**, 190-195, 1998.

[22] EN 1998-1 Eurocode 8: Design of structures for earthquake resistance - Part 1: General rules, seismic actions and rules for buildings. CEN, Bruxelles, 2004.

[23] P. Fajfar, A nonlinear analysis method for performance-based seismic design. *Earthquake Spectra*, **16**(3), 573–592, 2000.

[24] K. Levenberg, A method for the solution of certain non-linear problems in least squares. *Quarterly of Applied Mathematics*, **2**(2), 164–168, 1944.

[25] D.W. Marquardt, An algorithm for the least-squares estimation of nonlinear parameters. *SIAM Journal of Applied Mathematics*, **11**(2), 431–441, 1963.

COMPDYN 2013
4th ECCOMAS Thematic Conference on
Computational Methods in Structural Dynamics and Earthquake Engineering
M. Papadrakakis, V. Papadopoulos, V. Plevris (eds.)
Kos Island, Greece, 12–14 June 2013

TIME-DEPENDENT VULNERABILITY ASSESSMENT OF RC BUILDINGS CONSIDERING SSI AND AGING EFFECTS

Sotiria T. Karapetrou[1], Argyro M. Filippa[1], Stavroula D. Fotopoulou[1] & Kyriazis D. Pitilakis[1]

[1] Aristotle University of Thessaloniki
address
e-mail: {gkarapet,afilippa,sfotopou,kpitilak}@civil.auth.gr

Keywords: Time-dependent seismic vulnerability, RC buildings, Soil-structure interaction, Direct method, Sub-structuring method, Aging effects.

Abstract. *The present study aims at the assessment of the seismic vulnerability of reinforced concrete (RC) buildings taking into account the soil –structure –interaction (SSI) and the aging effects due to reinforcement corrosion. Two-dimensional non-linear dynamic analyses are performed to assess the seismic performance of initial (t=0 years) and 50 years old RC frame structures. Soil-structure interaction is modeled by applying the two most commonly used approaches, i.e. the substructure and the direct method, to allow for direct comparison. Chloride induced corrosion is taken into account based on probabilistic modeling of corrosion initiation time and corrosion rate. The time-dependent fragility functions are derived for predefined damage states at different time periods in terms of outcrop peak ground acceleration. The results indicate an increase of seismic vulnerability over time due to aging effects (corrosion). An overall increase in structure's fragility is also observed when considering the soil deformability and SSI. Moreover, the comparison between the two methods of SSI modeling (sub-structuring and direct) indicates the conservativeness of the sub-structuring over the direct method with the former predicting higher vulnerability compared to the later.*

1 INTRODUCTION

The seismic vulnerability of structures is commonly expressed through fragility functions, which provide the probability of exceeding prescribed levels of damage for a wide range of ground motion intensities. The assessment of the structure's seismic fragility represents a major step towards the seismic loss estimation and risk management. The soil conditions, which affect the foundation compliance, as well as the soil structure interaction, have not received much attention within the framework of structural vulnerability assessment. Although some fragility curves are available for different soil conditions taking into account the local site effects ([1]), in general, the influence of SSI effects on the seismic performance of RC structures are assumed to be beneficial and thus they are usually ignored. Nevertheless, it has been recently shown ([2], [3]) that soil deformability as well as foundation compliance may modify the structural response and fragility leading to either beneficial or unfavorable effects depending on the dynamic properties of the soil and the structure as well as the characteristics (frequency content, amplitude, significant duration) of the input motion.

In common practice it is also implicitly assumed that the structures are optimally maintained during their lifetime neglecting any deterioration mechanism which may adversely affect their structural performance. On this basis, the impact of progressive deterioration of the material properties caused by aggressive environmental attack is not accounted for. Corrosion of RC members is considered as a primary source of structural deterioration, usually associated to carbonation process and chloride penetration, leading to the variation of the mechanical properties of steel and concrete over time. Consequently, both the safety and the serviceability of RC structures may be affected under the action of seismic (or even static) loading, compromising the ability of the structures to withstand the loads they are designed for. The severe uncertainties involved in corrosion phenomena pointed out the need for a probabilistic approach to predict degradation phenomena [4]. Recognizing the importance of this issue, researchers have introduced several probabilistic models into the time-variant vulnerability assessment of corroded bridges and RC frame buildings (e.g. [5], [6], [7]).

Based on the above considerations, the aim of this study is the development of time-dependent fragility curves taking into account the SSI and aging effects. To demonstrate the methodology for the time-dependent vulnerability assessment, two reference RC moment resisting frames are selected as case studies. In total, eight structural models are analyzed based on the initial reference buildings considering (or not) the effect of SSI and aging. Soil structure interaction is studied by applying the two most commonly used methods, i.e. the sub-structuring (uncoupled) and the direct (coupled) methods, to allow for direct comparison. The direct method is based on a one-step approach where the entire soil–foundation–structure system is analyzed in a single step by a finite element model. In the substructure method, on the other hand, the SSI phenomenon is divided in two sub-domains that are finally coupled through the concept of the foundation dynamic impedance functions. The consideration of aging is achieved by including probabilistic models of chloride induced corrosion deterioration of the RC elements within the vulnerability assessment framework. Fragility curves are finally developed for the initial (t=0 years) and the corroded buildings (t=50 years) for predefined damage states based on the statistical exploitation of the results of two-dimensional nonlinear dynamic analyses of the given structures. The derived curves are compared to gain insight into the effect of SSI and reinforcement corrosion highlighting the importance of their incorporation in the vulnerability analysis (Figure 1).

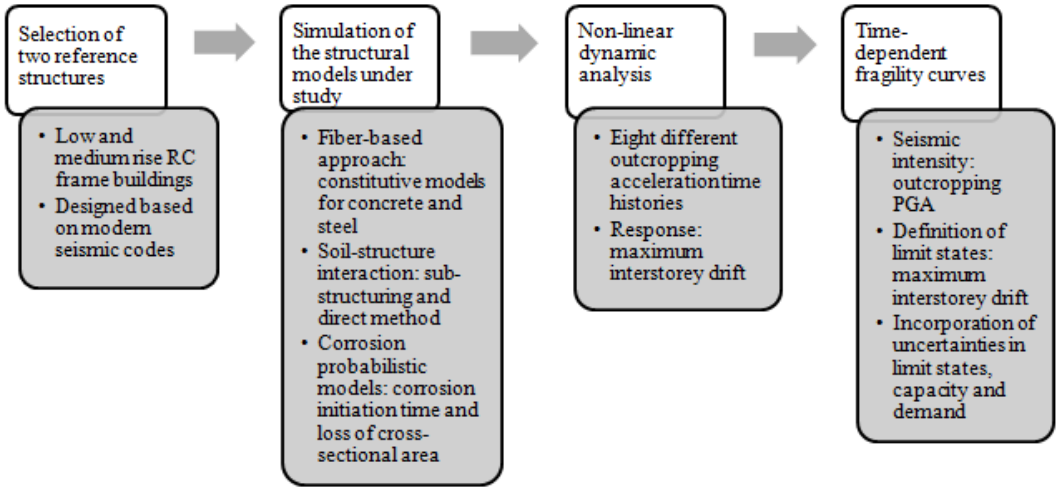


Figure1. Methodological framework adopted in this study.

2 METHODOLOGY

2.1 Description of structural models

Two reference moment resisting frames (MRFs), designed on the basis of modern seismic codes are selected for the present study. The first one [8] is a two storey – one bay frame model that is considered representative of low – rise buildings designed by the Greek seismic code [9]. The second one is a four storey frame model with three bays [10] that is considered to be representative of mid – rise buildings designed based on the modern seismic code of Portugal (Figure 2). Table 1 represents some of the main characteristics of the reference models such as the fundamental period and the strength of concrete and steel. The main analytical modeling of the structures is conducted using the Open System for Earthquake Engineering Simulation (OpenSees) software [11], an object-oriented open source software framework for finite element analysis developed by PEER. In addition, the finite element code Seismostruct [12] is used to enhance the reliability of the analysis and to permit correlations on the seismic structural response and fragility.

The OpenSees platform is designed around an object-oriented architecture facilitating the use of existing features and the development of new components, making it particularly attractive for the modeling of complex structural or geotechnical systems subjected to static or dynamic loading. An extensive library of material models and non-linear elements are provided, supporting also a wide range of solution procedures and computation models. Inelastic force-based formulations are employed for the simulation of the nonlinear beam-column frame elements considering four Gauss-Lobatto[13] integration points along each member's length. The applied formulations allow both geometric and material nonlinearities to be captured. Distributed material plasticity along the element length is considered based on the fiber approach to represent the cross-sectional behavior [14]. Each fiber is associated with a uniaxial stress-strain relationship and the sectional stress-strain state of the beam-column elements is obtained through the integration of the nonlinear uniaxial stress-strain response of the individual fibers in which the section is subdivided. The fiber section has a general geometric configuration formed by sub-regions including the concrete patches of simple regular quadrilateral shapes and the reinforcement layers. Concrete and steel fiber behaviors may be modeled and defined in the direction of each member length representing the flexural component in the fiber based analysis. Modified Kent and Park model [15] is used to define

the behavior of the concrete fibers, yet different material parameters are adopted for the confined (core) and the unconfined (cover) concrete.

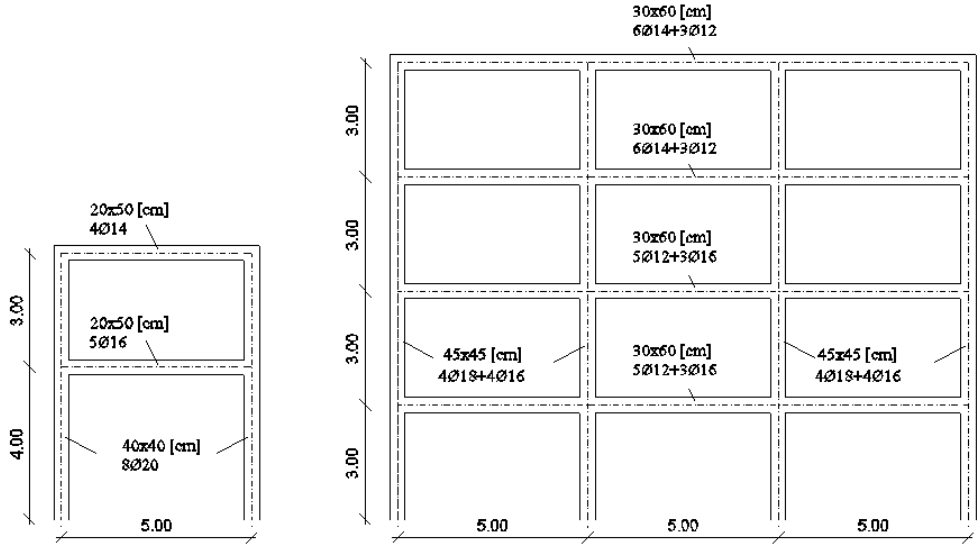


Figure 2. Reference MRF models used for time – dependent vulnerability assessment

RC building		Sections [cm]	Mass [t/m]	Fundamental period T[sec]	f_c [MPa]	f_y [MPa]
Low-rise	Column	40x40	0.41	0.3936	20	500
	Beam 1st - 2nd floor	20x50	3.15			
Mid-rise	Column	45x45	0.51	0.5018	28	460
	Beam 1st - 2nd - 3rd floor	30x60	4.77			
	Beam 4rth floor	30x60	3.41			

Table 1. Characteristics of the studied buildings

The uniaxial 'Concrete01' material is used to construct a uniaxial Kent-Scott-Park concrete material object with degraded linear unloading/reloading stiffness according to the work of Karsan-Jirsa [16] with zero tensile strength. The steel reinforcement is modeled using the uniaxial 'Steel01' material to represent a uniaxial bilinear steel material object with kinematic hardening with no isotropic hardening described by a nonlinear evolution equation (Figure 3).

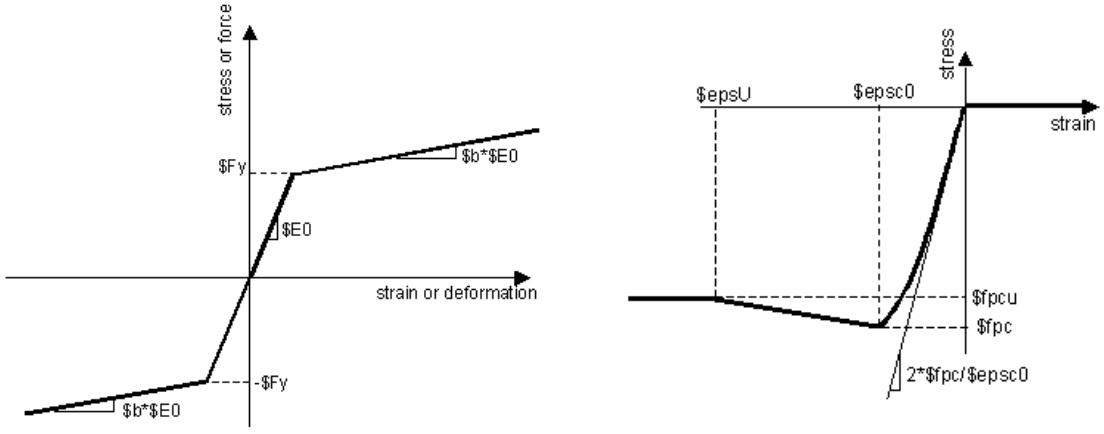


Figure 3. 'Steel 01' (left) and 'Concrete01' (right) material properties (Mazzoni et al. 2009)

2.2 Soil-structure interaction modeling

For the reference structural models fixed base conditions are considered assuming that they are founded on rigid rock (see fig. 4 (a)). For the SSI models, two different approaches are applied, namely the direct (see fig. 4 (b)) and the substructure method (see figs. 4 (c) and (d)). The applied modelling approaches are summarized in Figure 4. A representative soil profile with an average low strain velocity $V_{so,ave}$ taken equal to 300m/sec is used for the SSI simulations as illustrated in Figure 5.

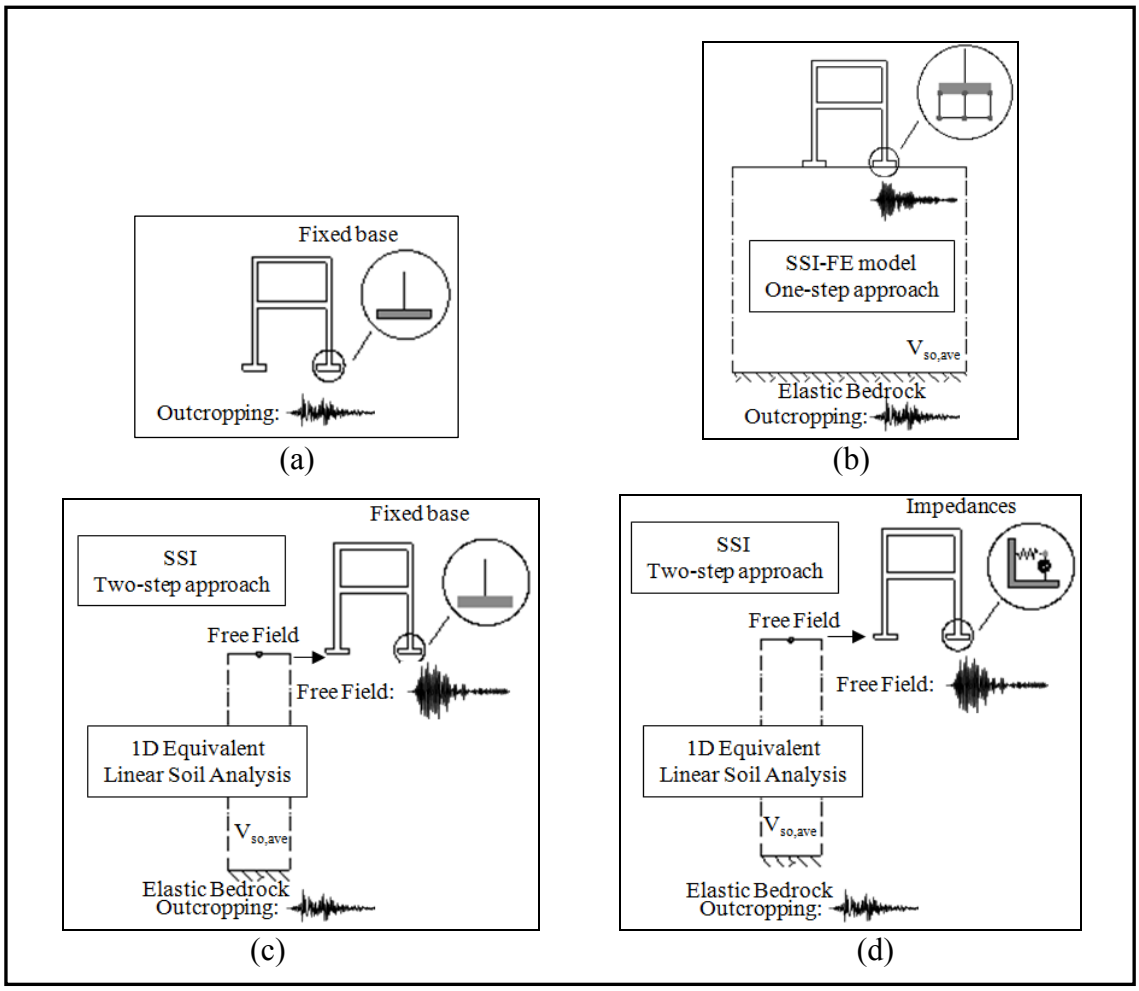


Figure 5. Schematic view of the applied approaches

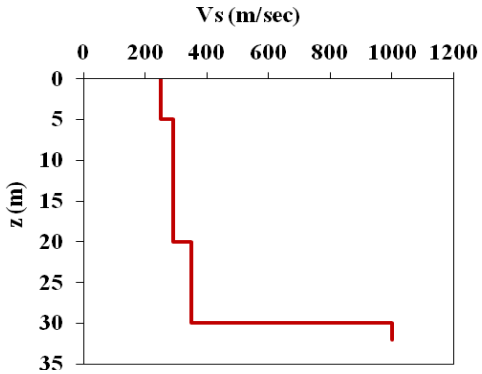


Figure 4. Properties of considered soil profile

2.2.1 Two-step analysis

In the two-step approach the coupling of the two sub models (soil and structure) is achieved by introducing appropriate impedance functions (e.g. rotational/translational springs and dashpots) into the base of the structural models. For the outcropping seismic motion, one – dimensional equivalent linear analyses for the given soil profile (corresponding to shear wave velocity V_{so}=300m/sec) (see fig. 4) are performed using Cyberquake [17] to obtain the free field motion which is subsequently imposed as input motion at the base of the structures. The consideration of an elastic half space (elastic bedrock Vs=1000m/sec), which is assumed 30m beneath the ground surface, allows applying directly the outcropping rock motion at the base of the soil model [18]. The shear modulus reduction and damping curves proposed by Darandeli [19] are used to model the strain depended soil nonlinearity. Following the equivalent linear soil formulation, the effective shear strain amplitude of the surface layer ($\gamma_{eff}=0.65\cdot\gamma_{max}$) is used for the calculation of the new compatible shear modulus and material damping ratio values. Subsequently, based on the new dynamic soil properties, coupling impedances proposed by Mylonakis et al. [20] for surface foundation on homogeneous halfspace are estimated. The dimensions of the footings are 1.7m x 1.7m and 2.0m x 2.0m for the low and medium rise structures respectively according to modern seismic code standards. The non-linear dynamic analyses of the considered structures are then conducted using the FE code Seismostruct [12] (see [3] for details).

2.2.2 One-step analysis

A general schematic view of the considered soil-structure model used for the one step approach is illustrated in Figure 6. OpenSees is used for the finite element modeling of the soil-structure system. The soil is modeled in two-dimensions with two degrees-of-freedom using the plane strain formulation of the quad element. To account for the finite rigidity of the underlying half-space, a Lysmer-Kuhlemeyer [21] dashpot is incorporated at the base of the soil profile. The soil profile is excited at the base by a horizontal force time history which is proportional to the known velocity time history of the ground motion ([22], [23]). The soil profile model adopted in this study has a total length of 120m and width of 30m and includes approximately 3600 four-node quadrilateral elements. The geometry of the mesh is based upon the concept of resolving the propagation of the shear waves at or below a particular frequency by ensuring that an adequate number of elements fit within the wavelength of the chosen shear wave. This ensures that the mesh is refined enough such that the desired aspects of the propagating waves are well captured in the analysis. Considering that the maximum frequency of interest is 10Hz and adopting a relatively dense discretization, quad elements with dimensions 1.0m x 1.0m are implemented. Even though soil material nonlinearity can be incorporated in the direct approach, in this study elastic soil layers are considered that are calibrated in terms of modulus of elasticity and Rayleigh damping, based on the response of the 1D equivalent linear soil analyses conducted in CyberQuake for the sub-structure method, to allow for direct comparison of the two SSI modeling approaches. The elastic bedrock (Vs=1000 m/sec) lies at 30 m beneath the ground surface. The Lysmer-Kuhlemeyer [21] dashpot is defined based on the viscous uniaxial material model and the zeroLength element formulation used to connect the two previously defined dashpot nodes. The connection of the soil and the structure is achieved by applying common nodes and appropriate constrains (to ensure equal displacement) for both the soil and structure's footings that are modeled as rigid beam-column elements.

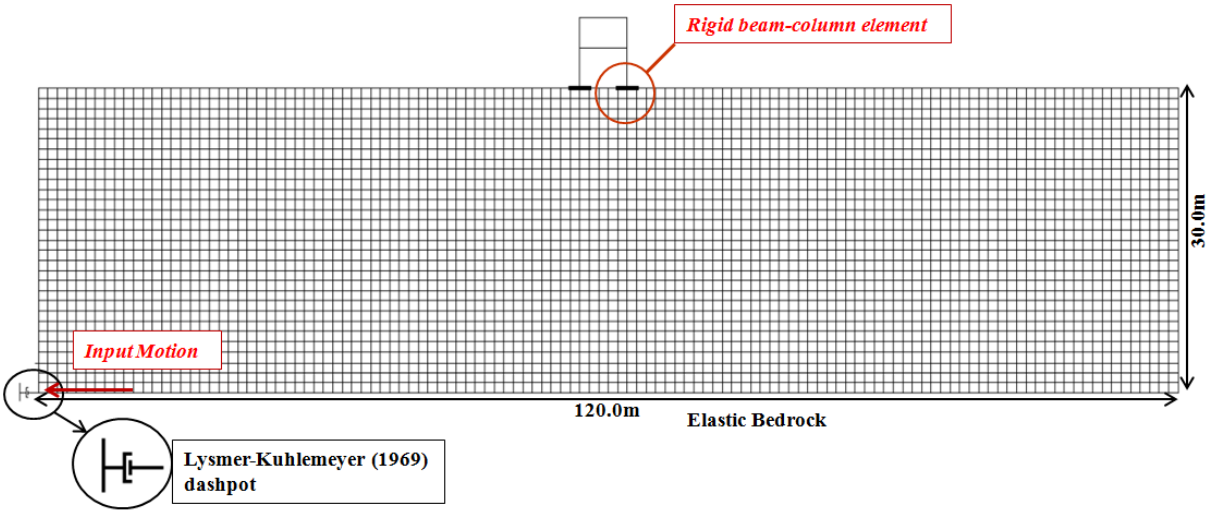


Figure 6. OpenSees 2D soil-structure model

2.3 Corrosion modeling

Several models have been proposed to quantify structural degradation due to corrosion that may be applied within the vulnerability analysis framework. A summary of these models can be found in DuraCrete [24]. In this study corrosion of reinforcing steel due to the ingress of chloride ions from the concrete surface to the steel bars is investigated. The probabilistic model proposed by FIB- CEB Task Group 5.6 [25] is adopted herein to determine the corrosion initiation time due to chloride ingress:

$$T_{ini} = \left(\frac{\alpha^2}{4 \cdot k_e \cdot k_t \cdot D_{RCM,0} \cdot (t_0)^n} \cdot \left(erf^{-1}\left(1 - \frac{C_{crit}}{C_s}\right)\right)^{-2} \right)^{\left(\frac{1}{1-n}\right)} \quad (1)$$

where T_{ini}=corrosion initiation time (years), α =cover Depth (mm) $C_{crit.}$=critical chloride content (wt % cement); C_s = the equilibrium chloride concentration at the concrete surface (wt % cement); t_0= reference point of time (years); $D_{RCM,0}$=Chloride migration Coefficient (m^2/s); k_e=environmental function; k_t=regression parameter; *erf*=Gaussian error function and n=aging exponent.

Once the protective passive film around the reinforcement dissolves due to continued chloride ingress, corrosion initiates and the time dependent loss of reinforcement cross-sectional area can be expressed as (e.g. [5]):

$$A(t) = \begin{cases} n \cdot D_i^2 \cdot \dfrac{\pi}{4} & \text{for } t \le T_{ini} \\ \max\left[n \cdot \left(D \cdot (t)\right)^2 \cdot \dfrac{\pi}{4},\ 0 \right] & \text{for } t \ge T_{ini} \end{cases} \quad (2)$$

where n=number of reinforcement bars; D_i=initial diameter of steel reinforcement; t=elapsed time in years and D(t)=reinforcement diameter at the end of ($t - T_{ini}$) years, which can be defined as:

$$D(t) = D_i - i_{corr} \cdot \kappa \cdot (t - T_{ini}) \quad (3)$$

where i_{corr}=rate of corrosion (mA/cm^2); κ =corrosion penetration (μm/year) (κ =11, 6μm/year uniform corrosion penetration for generalized corrosion).
The statistical quantification of the model parameters involved within the calculation of the chloride induced corrosion initiation time adopted for the present study is given in Table 2 based on FIB- CEB Task Group 5.6 (2006) prescriptions and the available literature (e.g. [26], [27], [5]). The chloride exposure condition considered is a relatively aggressive atmospheric exposure environment (e.g. k_e=0.67, [6]) corresponding to an adverse chloride induced deterioration scenario (w/c=0.6, high corrosion level). A lognormal distribution for the corrosion initiation time with a mean value of 2.96 years and standard deviation of 2.16 years is estimated based on crude Monte Carlo simulation that is found to be a good fit to the simulated data for the corrosion initiation time (Figure 7).

Parameter	Mean	COV	Distribution
Cover Depth (mm) α	25	0.20	Lognormal
Environmental transfer variable k_e	0.67	0.10	Normal
Chloride migration Coefficient ($D_{RCM,0}$) (m^2/s)	2.5E-11	0.10	Normal
Aging exponent n	0.3	cov=0.05, a=0.0, b=1.0	Beta
Critical Chloride Concentration (C_{cr}) wt % cement	0.6	cov=0.05, a=0.2, b=2.0	Beta
Surface Chloride Concentration (C_s) wt % cement	1.539	0.10	Normal
Rate of Corrosion (i_{corr}) mA/cm^2	10	0.20	Normal

Table 2. Statistical characteristics of the parameters affecting the chloride induced corrosion deterioration of RC elements adopted in the present study

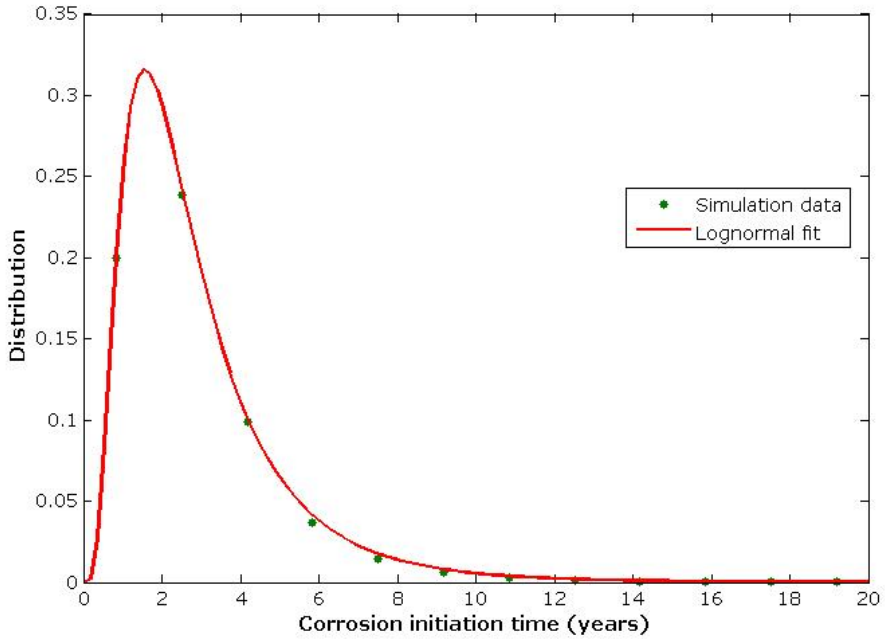


Figure 7. Lognormal distribution of chloride corrosion initiation time T_{ini} (mean = 2.96 years, Standard Deviation = 2.16 years.

Table 3 presents the loss of reinforcement area due to corrosion within the elapsed time ($t-T_{ini}$). It is assumed that the loss of steel area is uniformly distributed along the reinforced concrete members whereas neither the degradation of steel material properties nor the cover concrete strength reduction are taken into account.

RC Building	Element	Reinforcement (t=0 years)	Reinforcement area		Loss of Reinforcement area at t=50 years
			Ao (t=0years) (mm^2)	A(t=50years) (mm^2)	A(t)/Ao
Low-rise	Column	8Φ20	2513.20	1340.00	0.53
	1st floor beam	5Φ16	1005.31	447.65	0.45
	2nd floor beam	4Φ14	615.75	238.72	0.39
Mid-rise	Column	4Φ18	1017.88	502.78	0.49
		4Φ16	804.25	358.14	0.45
	1st and 2nd floor beams	2Φ10	157.08	37.99	0.24
		5Φ12	565.49	180.59	0.32
		3Φ16	603.19	268.62	0.45
	3rd and 4th floor beams	6Φ10	471.24	113.86	0.24
		3Φ12	339.29	108.22	0.32

Table 3. Reinforcement area in different points in time (t= 0 and 50 years) for the low and mid-rise RC buildings

3 NONLINEAR TIME-HISTORY ANALYSES

In order to study the SSI and aging effects on the behavior of the reinforced concrete frames under dynamic loading, 2-dimensional nonlinear time-history analyses are performed to determine the inelastic seismic response of the un-corroded (t=0 years) and corroded (t=50 years) structures to a series of earthquake records of varying intensity. Eight different ground motion records are selected as input excitation for the analyses performed in the present study. They are all referring to outcrop conditions recorded at sites classified as rock or stiff soil according to EC8 (Table 4). In Figure 8 the normalized elastic response spectra of the records is illustrated in comparison to the proposed elastic design spectrum of EC8 [28] for soil type A (rock). Each ground motion is progressively scaled to three different levels of peak ground acceleration PGA (0.1, 0.3 and 0.5g) to capture the variability in seismic demand prediction and the effect of different characteristics of earthquake ground motion (amplitude, frequency content, duration) on the structural dynamic response in relation to the dynamic properties of soil and structure.

Various parameters are investigated such as the top-floor acceleration and displacement histories, the peak ground acceleration PGA and the spectral acceleration $S_a(T)$ (at fundamental period of the structure) at the base and top of the models and the transfer functions with respect to the frequency content of the input motion. The output response parameter used in this study as a damage index in the seismic fragility analysis is the maximum inter-storey drift ratio (ISD_{max}%).

Earthquake	Record station	Mw	R (km)	PGA (g)
Valnerina, Italy 1979	Cascia	5.9	5.0	0.15
Friuli, Italy 1976	San Rocco	5.9	15.0	0.11
Parnitha, Athens 1999	Kypseli	6.0	10.0	0.12
Montenegro 1979	Hercegnovi Novi	6.9	60.0	0.26
Northridge, California 1994	Pacoima Dam	6.7	19.3	0.42
Palm Springs, California 1986	Whitewater Trout Farm	6.2	7.3	0.52
Campano Lucano, Italy 1980	Sturno	7.2	32.0	0.32
Umbria, Italy 1998	Cubbio-Piene	4.8	10.0	0.24

Table 4. List of outcropping records used for the dynamic analysis

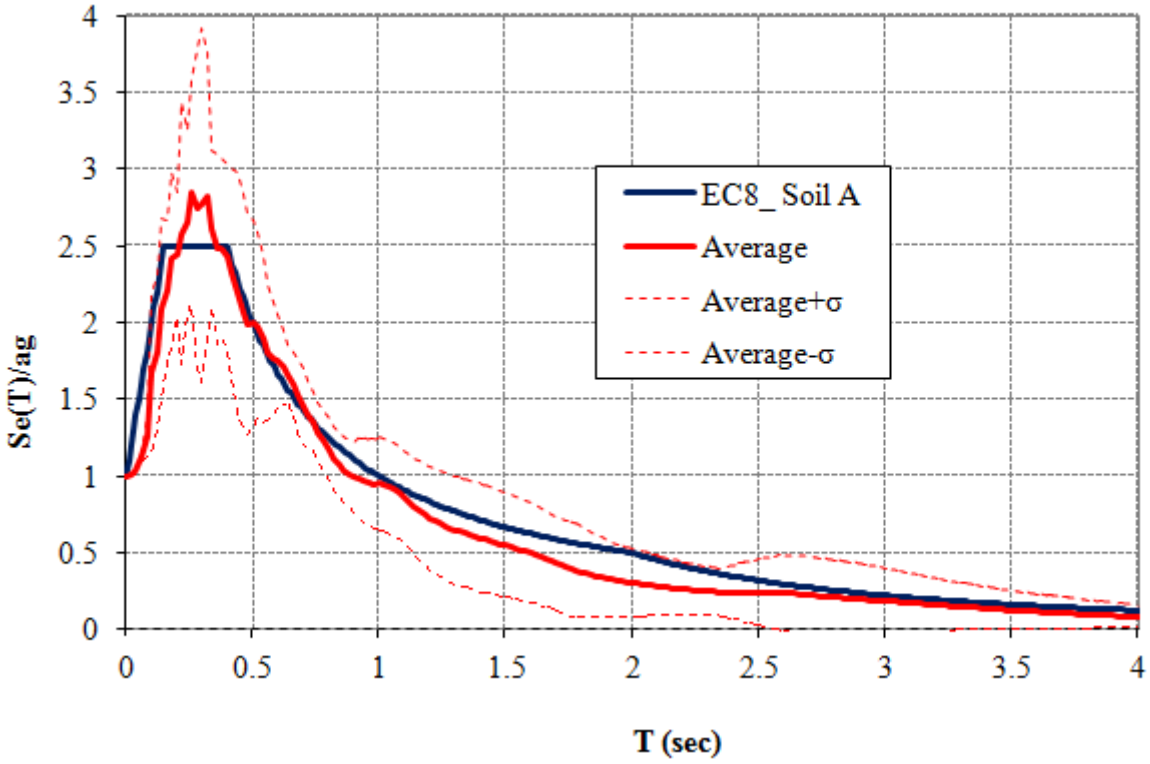


Figure 8. Normalized average elastic response spectrum of the input motions in comparison with the corresponding elastic design spectrum for soil type A (rock) according to EC8

4 TIME-DEPENDENT FRAGILITY CURVES

Fragility curves represent graphical relationships yielding the probability of exceeding a certain level of damage under an excitation of certain intensity. The selection of well-defined and realistic damage states is a key parameter in the development of seismic fragility curves. The selection in the present study of the maximum inter-storey drift ratio (ISD_{max}%) as a global measure of damage is made because it is a comprehensive and easily calibrated indicator and as that it has been widely used in similar studies. Four damage states (slight, moderate, extensive, complete) are defined based on the drift limits proposed by Ghobarah [39]. Under the reasonable assumption that the corroded structures (t=50 years) present limited ductility compared to their initial non-corroded state (t=0 years), different drift limits are adopted for each time scenario. On this basis, the limit values corresponding to ductile

moment resisting frames (MRFs) are assigned to the non-corroded structures whereas for the corroded ones the drifts corresponding to the non-ductile MRFs are adopted (Table 5).

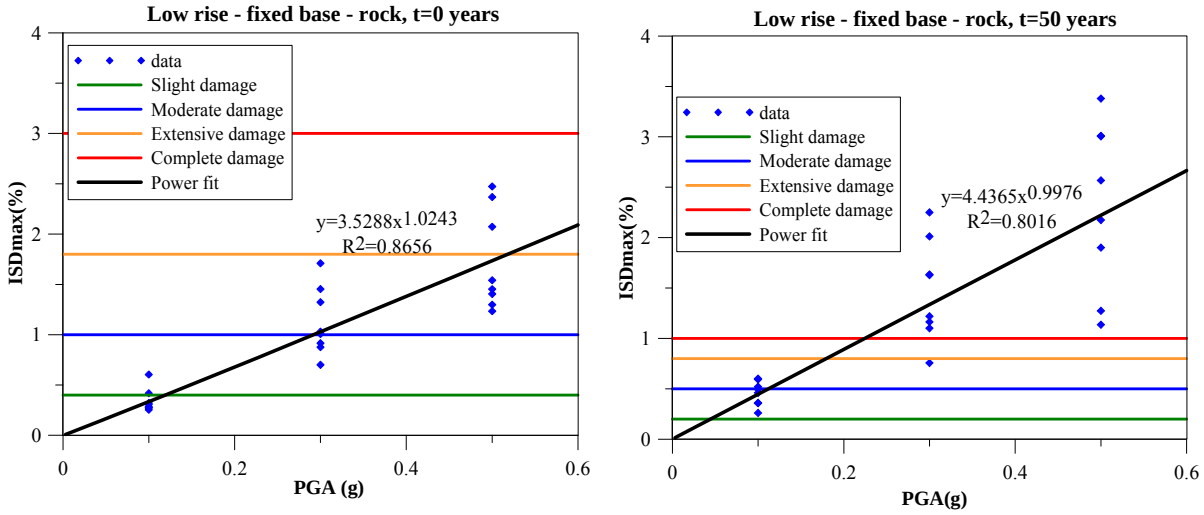
State of damage	Ductile MRF	Nonductile MRF
Slight/Light damage	0.4	0.2
Moderate damage	1.0	0.5
Extensive damage	1.8	0.8
Complete	3.0	1.0

Table 5. Damage states for Ductile and nonductile MRFs used in this study (after [30])

The time dependent fragility functions of the buildings can be mathematically expressed as two-parameter time-variant lognormal distributions:

$$P\left[DS / IM\right] = \Phi\left(\frac{In\left(IM\right) - In\left(\overline{IM}\left(t\right)\right)}{\beta\left(t\right)}\right) \tag{3}$$

where, Φ is the standard normal cumulative distribution function, IM is the intensity measure of the earthquake expressed in terms of PGA (in units of *g)* at the ground surface, $\overline{IM}\left(t\right)$ and β(t) are the median values (in units of *g)* and logarithmic standard deviations of the building fragilities at different points in time along its service life and *DS* is the damage state. The median values of PGA corresponding to the prescribed damage limit states are determined based on a regression analysis of the nonlinear dynamic analyses results (PGA (g) and ISD_{max}(%)) for each structural model and time scenario (t=0 and 50 years). In Figure 9 representative PGA - ISD_{max}% relationships are illustrated for the low rise structure considering fixed and flexible (SSI effect for $V_{so,ave}$ =300m/s) foundation conditions for the initial (t=0 years) and corroded (t=50 years) scenario.



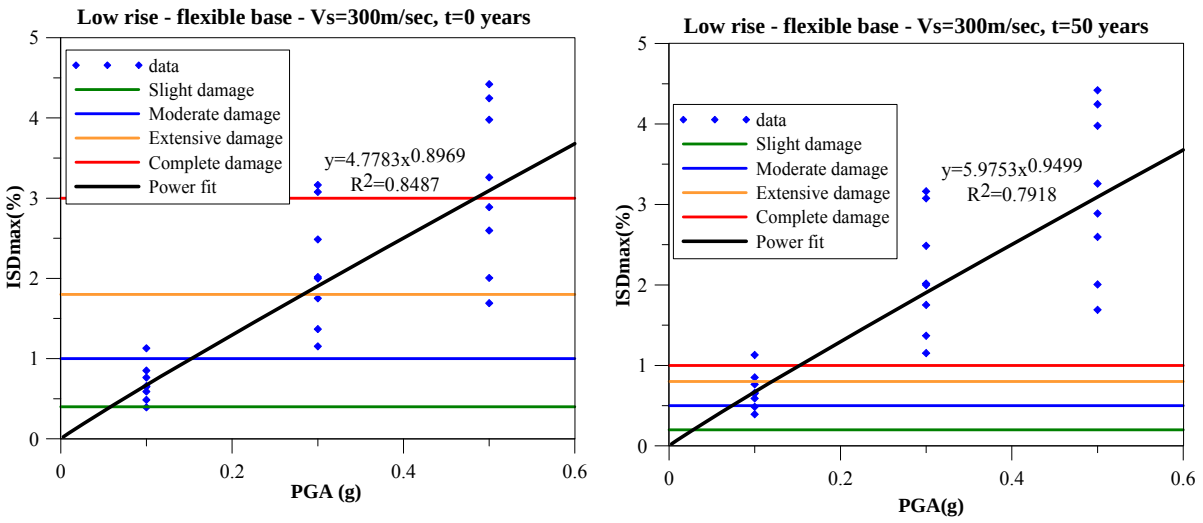


Figure 9. PGA-ISD_{max}(%) relationships for the low rise structures considering fixed and compliant condition for the initial and corroded scenario.

The various uncertainties are taken into account through the log-standard deviation parameter β(t), which describes the total dispersion related to each fragility curve. Three primary sources of uncertainty contribute to the total variability for any given damage state (NIBS, 2004), namely the variability associated with the definition of the limit state value, the capacity of each structural type and the seismic demand. The uncertainty in the definition of limit states is assumed to be equal to 0.4 while the variability of the capacity is assumed to be 0.25 (NIBS, 2004). The third source of uncertainty associated with the demand, is taken into consideration by calculating the variability in the results of the numerical simulations. Under the assumption that these three variability components are statistically independent, the total variability is expressed as the root of the sum of the squares of the component dispersions.

5 RESULTS AND DISCUSSION

In Figures 10 and 11, the derived fragility curves for the fixed and the flexible base (compliant foundation) structures are compared. For the fragility curve set referring to the flexible base models, in both aforementioned figures, soil structure interaction is taken into account based on the one-step direct method (modeling approach b in Figure 4). Regarding the reference fixed base structures, foundation on rigid rock is assumed in Figure 10 by directly imposing the outcropping input motion whereas a modified input excitation due to the considered soil profile is taken into account in Figure 11 (modeling approach a and c in Figure 4 respectively). It is seen that the consideration of soil-foundation compliance and SSI effects may significantly increase the structure's fragility in relation to the fixed-base case. Moreover the increase in vulnerability appears to be higher for the sub-structure in comparison to the direct method of SSI simulation (Figure 12). On the contrary, studying soil-structure interaction effects may result to a slight decrease in vulnerability compared to the fixed-base models, when for the later ones the modified input motion due to the underlying soil profile is considered. This decrease seems to be more pronounced in the case of the one-step approach of SSI modeling (Figure 13). These remarks may be attributed to the fact that in the two-step approach the effect of radiation damping as a result of soil nonlinearity is generally neglected in contrast to the direct one-step method where both hysteretic and radiation damping are taking place simultaneously. Modeling uncertainties associated with the

two different codes used for the uncoupled and coupled SSI analysis (Seismostruct and Opensees respectively) may have also contributed to the observed differences in seismic fragility. Similar trends are expected to occur for both low and mid-rise structural configurations. Overall, it should be noted that the consideration of SSI and site effects may either increase or decrease the expected structural damage depending on the type of the structure, ints foundation system and its fundamental period in relation to the dynamic input motion and the soil dynamic properties.

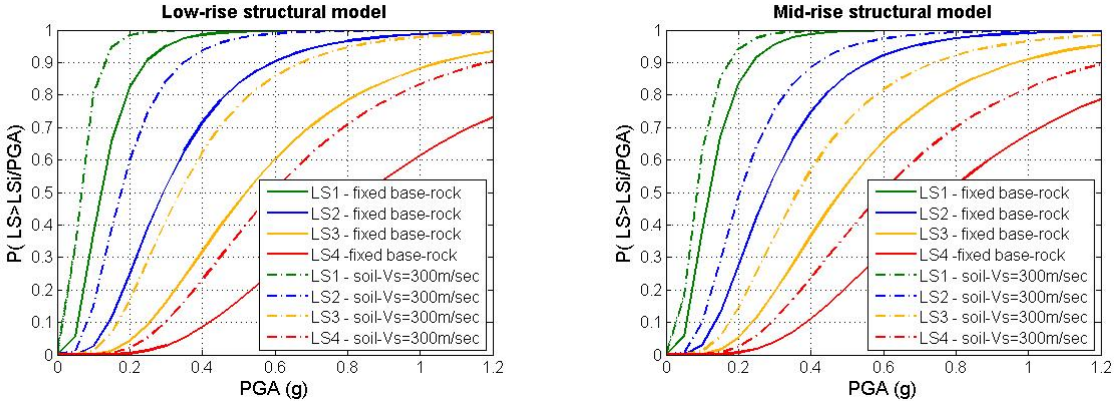


Figure 10. Comparison of fragility curves for the low rise (left) and mid-rise (right) structures considering fixed and compliant (Vs=300m/sec) foundation condition for the initial (t=0years) scenario.

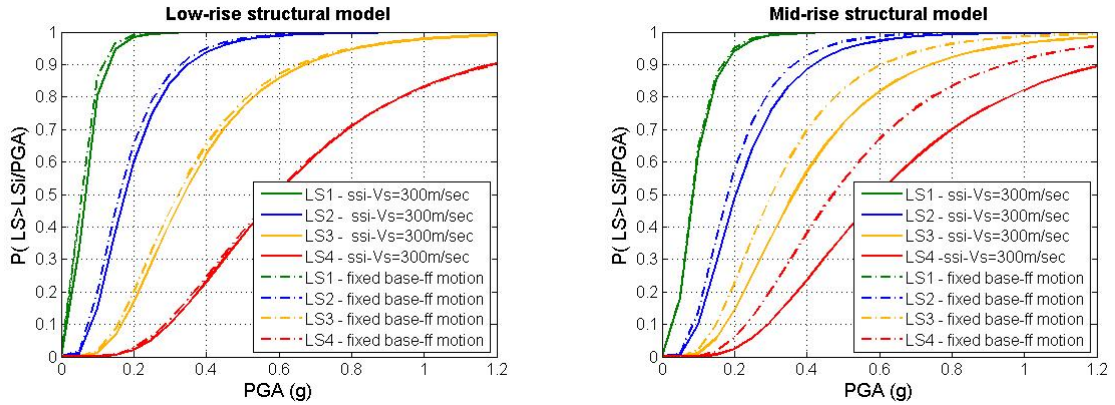


Figure 11. Comparison of fragility curves for the low rise (left) and mid-rise (right) structures considering fixed foundation with free field input motion and flexible foundation and soil structure interaction effects for the initial (t=0years) scenario.

Furthermore Figure 14 illustrates the derived sets of fragility curves for the different building configurations for the initial non-degraded state, compared to the corresponding curves when considering corroded structural members. As expected, for both low and mid-rise building typology, the fragility curves for the corroded structures display a great shift to lower acceleration values for the same earthquake scenario indicating a significant increase due to aging. The large differences observed between the curves for un-corroded and corroded frame buildings could be attributed to the most adverse deterioration scenario adopted herein to better illustrate the phenomenon. It is also attributed to the different damage state thresholds adopted for the initial and corroded structure, which again may be considered as an extreme case (see Table 5). Table 6 presents the corresponding median and beta values of each damage state for all the building configurations and time scenarios analyzed.

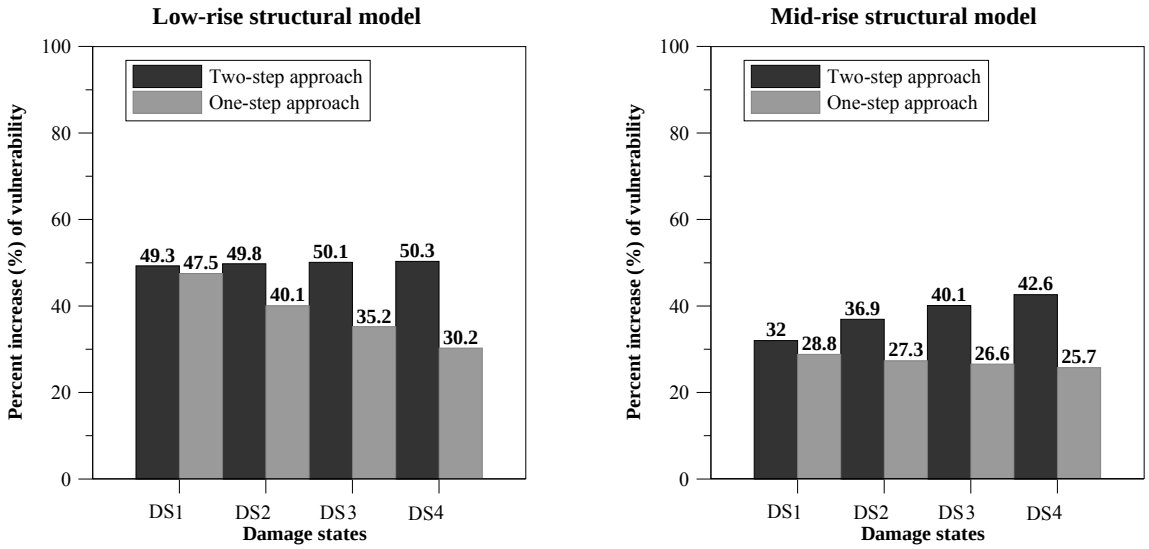


Figure 12. Comparison of the percent increase in vulnerability for the low rise (left) and mid-rise (right) with flexible foundation structures for the sub-structure (two-step) and the direct (one-step) method of SSI modeling in relation to the fixed base models.

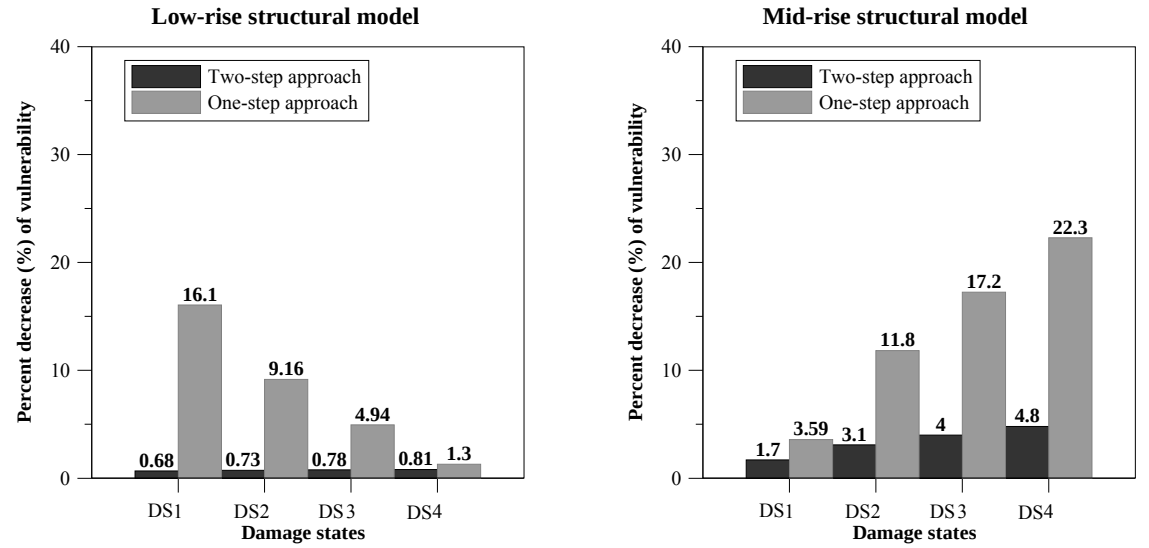
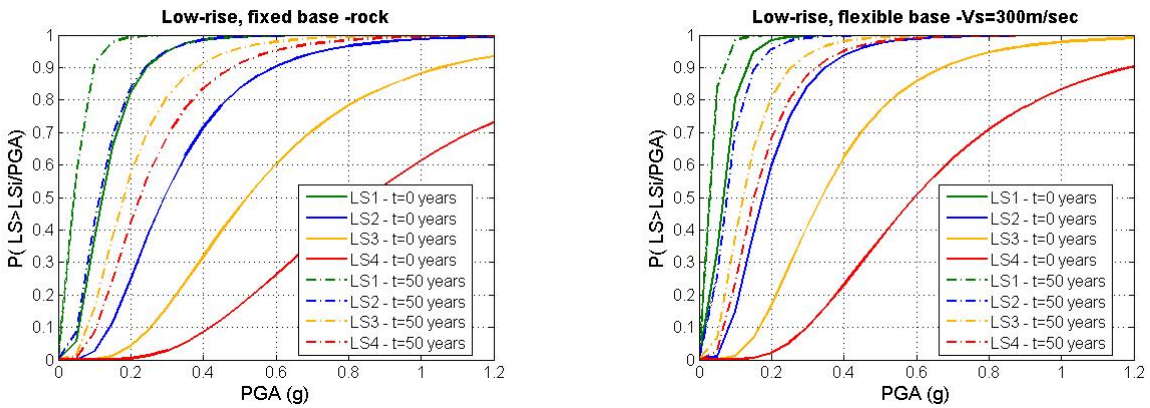


Figure 13. Comparison of the percent decrease in vulnerability for the low rise (left) and mid-rise (right) with flexible foundation structures for the sub-structure (two-step) and the direct (one-step) method of SSI modeling in relation to the fixed base models with free field input motion.



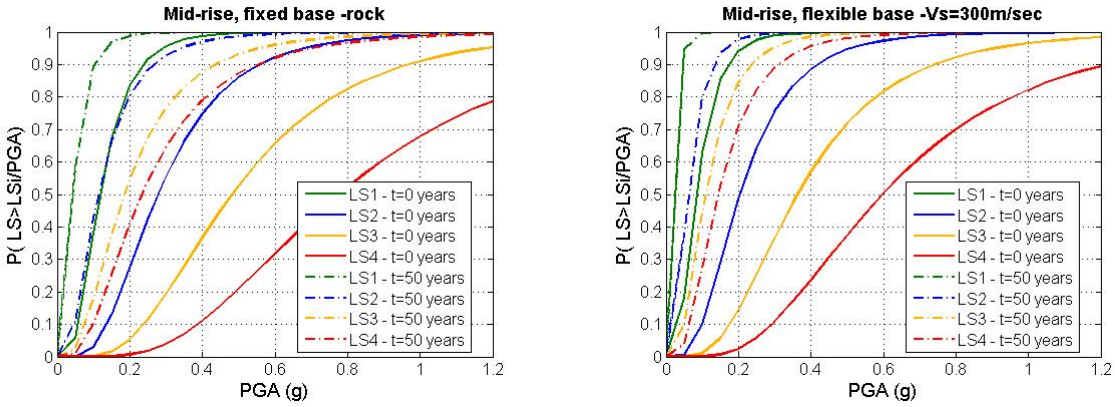


Figure 14. Fragility curves for the low rise (left) and mid-rise (right) structures considering fixed and compliant (Vs=300m/sec) foundation conditions for the initial (t=0 years) and the corroded (t=50 years) scenario)

RC building	Foundation conditions	Time scenario (years)	Median PGA (g)				Dispersion
			Slight	Moderate	Extensive	Complete	
Low-rise	Fixed base - rock	t=0	0.12	0.29	0.52	0.85	0.551
		t=50	0.05	0.11	0.18	0.23	0.588
	Flexible base V_{so}=300 m/s	t=0	0.06	0.18	0.34	0.6	0.538
		t=50	0.03	0.07	0.12	0.15	0.585
Mid-rise	Fixed base - rock	t=0	0.12	0.28	0.48	0.78	0.544
		t=50	0.04	0.11	0.19	0.23	0.668
	Flexible base V_{so}=300 m/s	t=0	0.08	0.2	0.36	0.6	0.557
		t=50	0.02	0.06	0.11	0.14	0.599

Table 6. Parameters of fragility functions

6 CONCLUSIONS

The seismic vulnerability of RC frame buildings has been assessed taking into account foundation compliance and SSI effects as well as the corrosion of the RC structural members. Two low and mid-rise bare frame structures were analyzed using 2D nonlinear dynamic computations. Time-dependent probabilistic fragility functions have been derived for predefined damage states for two time periods (t=0, 50 years) in terms of outcropping peak ground acceleration. The results indicate an overall increase in the structure's vulnerability when soil deformability and foundation compliance are taken into account. However, this should not be regarded as a general trend as the seismic structural vulnerability may decrease or increase depending on the characteristics of the buildings, the input motion and the soil properties. Furthermore when the modified input motion due to the underlying soil profile is used for the anlysis of the fixed base models, a slight decrease in structure's fragility is observed when soil-structure interaction is taken into account. The comparison of the two SSI modeling techniques indicates that the uncoupled two-step approach (substructure method) leads to higher vulnerability levels, certainly due to uncertainties related, among others, to the evaluation of the foundation impedances. A significant increase in the seismic fragility of the structures is observed over time due to the consideration of aging effects (corrosion). This important increase is due to the voluntary selection of the "worst cas scenario" for the damage

states and the corrosion process. In order to increase the robustness of the conclusions presented herein, further research is needed in the definition of limit states for corroded structures based on adequate analytical, experimental and empirical data and in the incorporation of the fully probabilistic corrosion models within the dynamic analysis. In summary, the results presented in this paper prove that the seismic fragility curves used so far for RC buildings considering fixed base conditions and assuming no aging effects, may, under certain circumstances, underestimate the real vulnerability of the structures.

AKCNOWLEDGEMENT

Most of the work reported in this paper was carried out in the framework of the ongoing REAKT (http://www.reaktproject.eu/) project, funded by the European Commission, FP7-282862.

REFERENCES

[1] National Institute of Building Sciences, *Direct physical damage – General building stock,* HAZUS-MH Technical manual, Chapter 5, Federal Emergency Management Agency, Washington, D.C.

[2] E. Saez, Effect of the inelastic dynamic soil-structure interaction on the seismic vulnerability assessment, *Structural Safety,* **33**, 51-63, 2011.

[3] S.D. Fotopoulou, S.T. Karapetrou, K.D. Pitilakis, Seismic vulnerability of RC buildings considering SSI and aging effects, *15WCEE International Conference*, Lisboa, 2012.

[4] DuraCrete, *Probabilistic performance based on durability design of concrete structures: Statistical quantification of the variables in the limit state functions,* Report No.: **BE 95-1347**, 62-63, 2000.

[5] J. Ghosh, J.E. Padgett, Aging considerations in the development of time-dependent seismic fragility curves, *Journal of Structural Engineering,* **136:12**, 1497-1511. 2010.

[6] D.E. Choe, P. Gardoni, D. Rosowsky, Fragility increment functions for deteriorating reinforced concrete bridge columns, *Journal of Engineering Mechanics,* **136:8**, 969-978, 2010.

[7] H. Yalciner, S. Sensoy, O. Eren, Time-dependent seismic performance assessment of a single-degree-of-freedom frame subject to corrosion, *Engineering Failure Analysis,* **19**, 109-122, 2012.

[8] F. Gelagoti, *Metaplastic Response and Collapse of frame-foundation systems, and the concept of rocking isolation*, Ph.D. Dissertation, National technical University of Athens, 2010.

[9] EAK2000, *Greek Seismic Code, Organization of Seismic Planning and Protection*, 2000.

[10] A. Abo El Ezz, *Deformation and strength based assessment of seismic failure mechanisms for existing RC frame buildings*, Master Dissertation, Rose School, Pavia, 2008.

[11] S. Mazzoni, F. McKenna, M.H. Scott, G.L. Fenves, *Open System for Earthquake Engineering Simulation User Command-Language Manual,* Pacific Earthquake Engineering Research Center, Berkeley, California, 2009.

[12] SeismoSoft, SeismoStruct, A computer program for static and dynamic nonlinear analysis of framed structures, (online): Available from URL: www.seismosoft.com , 2011.

[13] A. Neuenhofer and F.C. Filippou, Evaluation of nonlinear frame finite-element models, Journal of Structural Engineering, 123:7, 958-966, July, 1997

[14] E. Spacone, F.C. Filippou, F.F Taucer, Fibre beam-column element for nonlinear analysis of R/C frames, Part I: Formulation, *Earthquake Engineering and Structural Dynamics*, **25**, 711-725, 1996.

[15] D.C. Kent, R. Park, Flexural members with confined concrete, *Journal of the Structural Division*, Proc. Of the American Society of Civil Engineers, **97(ST7)**, 1969-1990, 1971.

[16] I. Karsan, J. Jirsa, Behavior of concrete under compressive loadings, *ASCE J. of the Structural Division*, **95**, 2543-2563, December, 1969.

[17] BRGM (French Geological Survey) Software Cyberquake, version 1.1, User's quide, 1998.

[18] A.O.L. Kwok, J.P. Stewart, Y.M. Hashash, N. Matasovic, R. Pyke, Z. Wang, Z. Yang, Use of exact solutions of wave propagation problems to guide implementation of nonlinear seismic ground response analysis procedures, Journal *of Geotechnical Engineering*, **133:11**, 1385-1398, 2007.

[19] M. Darendeli, *Development of a new family of normalized modulus reduction and material damping curves*, Ph.D. Dissertation, Univ. of Texas, 2001.

[20] G. Mylonakis, S. Nikolaou, G. Gazetas, Footings under seismic loading: Analysis and design issues with emphasis on bridge foundations, *Soil Dynamics and Earthquake Engineering,* **26**, 824-853, 2006.

[21] J. Lysmer, R.L. Kuhlemeyer, Finite dynamic model for infinite media, *J. Eng. Mech.*, **95**, 859-877, 1969.

[22] W.B. Joyner, A.T.F. Chen, Calculation of nonlinear ground response in earthquakes, *Bulletin of the Seismological Society of America*, 65:5, 1315-1336, October, 1975.

[23] J. Lysmer, *Analytical procedures in soil dynamics*, University of California at Berkeley, Earthquake Engineering Research Center, Richmond, **Report No. UCB/EERC-78/29**, CA, 1978.

[24] DuraCrete, Modeling of Degradation, BRITE-EURAM-Project BE95-1347/R4-5, 1998.

[25] CEB-FIB Task Group 5.6, Model for Service Life Design, fédération internationale du béton (fib), 2006.

[26] D.E. Choe, P. Gardoni, D. Rosowsky, T. Haukaas, Seismic fragility estimates for reinforced concrete bridges subject to corrosion, *Structural Safety* **31**, 275-283, 2009.

[27] M. Stewart, Spatial variability of pitting corrosion and its influence on structural fragility and reliability of RC beams in flexure, *Structural Safety*, **26**, 453-470, 2004.

[28] CEN-European Committee for Standarization prENV 1998-1 – Eurocode 8: design of structures for earthquake resistance. Part 1: deneral rules, seismic actions and rules for buildings, Draft No.4, Brussels, Belgium, 2003.

[29] A. Ghobarah, On drift limits associated with different damage levels, *International Workshop on Performance-Based Seismic Design*, Department of Civil Engineering, McMaster University, Ontario, Canada, June 28-July1, 2004.

COMPDYN 2013
4th ECCOMAS Thematic Conference on
Computational Methods in Structural Dynamics and Earthquake Engineering
M. Papadrakakis, V. Papadopoulos, V. Plevris (eds.)
Kos Island, Greece, 12–14 June 2013

INSTRUCTIONS OVERVIEW ON THE REGIONAL SCALE ANALYSIS OF SCHOOL BUILDINGS IN PUGLIA (ITALY)

Domenico Raffaele[1], **Mauro Mezzina**[1] **and Antonio Tosto**[1]

[1] DICATECh, Politecnico di Bari
address via Orabona, 4 - 70126 Bari (Italy)
d.raffaele@poliba.it

Keywords: Vulnerability Assessment, School Building, Existing Buildings, Safety Levels.

Abstract. *Thanks to a specific fund provided by AdP-Puglia, a research study has been developed by the Department DIAC of Politecnico di Bari, drawing up a volume of "Guidelines for the seismic assessment of strategic RC and masonry buildings" addressed to the professionals in charge with the assessment procedures.*
In the present paper shows the results of the seismic vulnerability assessment carried out on same school buildings located in the Province of Foggia (Italy). The analysis following the protocol of investigation and verification contained in the Guidelines were carried out. The paper shows, through the simple statistical representation as the whole sample analyzed can be identified by some features related to a typology sample. The statistical representation of the data collected from the seismic assessment shows that the buildings analyzed are all referable at predominant typology having common characteristics to all buildings. The materials, age and structural regularity are just some of the parameters taken into account, and these show the degradation prevailing of the building heritage of the territory well as the deficiency in regard to seismic actions. In particular, the seismic vulnerability has been quantified by a specific vulnerability coefficient (SVC). The value taken on the coefficient allows to identify the most critical areas of the territory and consequently to draw up priority scales in the preparing of projects and in the choice of seismic retrofitting interventions.

1 INTRODUCTION

The observation of post-earthquake damages after recent seismic events has confirmed the need of systematically assessing the safety levels of existing buildings, which are mostly characterized by an unsatisfactory level of the technical design (mainly because the reference building codes are very obsolete) [1,2]. These considerations lead, for strategic structures such as bridges [3], to develop techniques for the seismic assessment of existing construction and to install monitoring systems for the new ones [4,5]. Recently, the Italian laws [6,7] have stated that the public administrations have the obligation to perform the vulnerability assessment of the strategic buildings of their properties. This circumstance has determined, in the last years, a great attention of the technicians towards the procedures for the seismic safety assessment of existing structures, especially considering the necessity of updating their know-how with regard to the new developments of the scientific and regulatory framework. In this context, Politecnico di Bari and AdB Puglia have stipulated an agreement for the definition of *Guidelines for the safety assessment of RC and masonry public buildings* [8] and for the execution of the seismic vulnerability assessment of school buildings in the Province of Foggia. The guidelines are addressed to the professionals who are appointed for the assessment, with the objective of providing proper methodological and operational indications, with reference to the current Italian and European regulations [7,9,10,11]. The procedures outlined in the guidelines are designed in order to provide results consistent with current legal regulations, so that all the operations related to the preliminary knowledge and to the assessment can be used also in the subsequent phase of definition and execution of the retrofitting intervention.

In the present paper, a statistical elaboration of the first set of results provided by the assessment program is presented, which concerned a limited number of school buildings located in the Province of Foggia. The data processing was made on the base of the summary data sheets compiled by the technicians in charge with the assessment, in which all the relevant design data and the results of the calculations were summarized (Fig. 1).

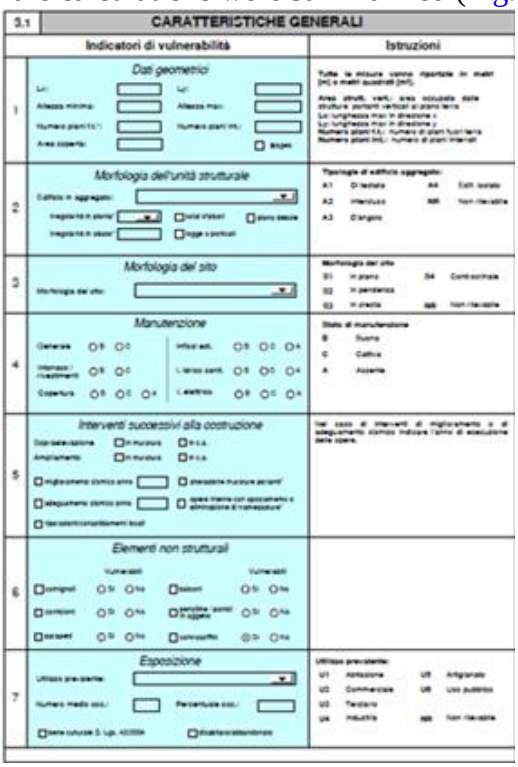


Figure 1. Extract from the summary data sheet form compiled by the technicians.

All data have been statistically processed in order to identify a paradigmatic typology which could represent, in the average, the characters and quality of the school buildings on the analyzed territory. In particular, the "average" features have been determined by using the percentage distribution of some significant parameters related to the geometrical, structural and seismic aspects. Moreover, a seismic vulnerability parameter *SVC* has been calculated for each school building. Such parameter is useful in order to establish a priority rating in the planning of the seismic retrofitting interventions and funding allotment.

2 CONTENTS OF GUIDELINES

The *Guidelines* include 4 Sections and 2 Annexes. In particular, in the 1st Section the general methodological aspects regarding all the structural systems are discussed, and the procedural protocol is outlined, specifying all the necessary steps, from the retrieving of existing data and information to the preparation of technical drawings and technical reports to be delivered. Sections 2-4 are specifically devoted to the safety assessment of existing buildings and in particular, Section 3 deals with existing RC buildings, whereas Section 4 deals with existing masonry buildings (which are not comprised in the present analyses), providing detailed indications about the determination of the confidence factor, the various methods of analysis and verification, as well as procedures for estimating the seismic vulnerability parameter *SVC* depending on the method of analysis used. The synopsis of the protocol provided by the Guidelines is shown in Fig. 2.

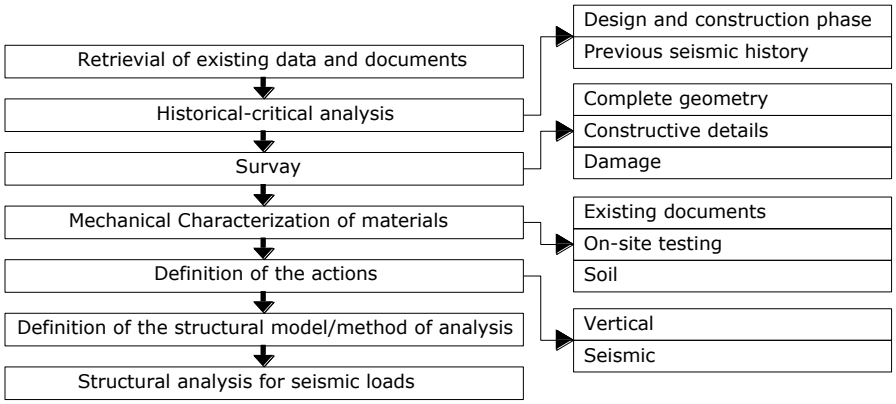


Figure 2. Synopsis of the protocol for the preliminary investigations and the safety assessment.

In the figure, the difference between the assessment performed in the presence of vertical loads and the assessment related to seismic loads is clearly highlighted. In fact, in the case of a negative result of the assessment, the choices that the technician has to do will be different depending on the type of load.

In the case of vertical loads, there are the following possibilities:

1. determining whether the use of the construction can continue without intervention;
2. indicate whether the use should be changed (downgrade, change of destination and/or imposition of restrictions and/or caution in using);
3. indicate whether it is necessary to increase or restore the carrying capacity.

In the presence of seismic loads, instead, it will be necessary:

1. to verify that the safety level is adequate to the present Italian Seismic Code;
2. to evaluate the seismic vulnerability coefficient (*SVC*), which will measure, on a homogeneous basis, the seismic safety level.

The vulnerability coefficient is aimed at providing an evaluation tool that is useful in order to establish the most appropriate intervention strategy and, at the same time, to identify, at the

regional scale, a priority ranking for the mid and long-term mitigation programs and the related allocation of funding.

At the end of the different steps of the procedural protocol, the representative results obtained after the safety assessment for each school building have been summarized in a specific "*summary data sheet"*(Fig. 1). In the present paper, a preliminary analysis of the investigation is presented, on the basis of a statistical elaboration of the data sheet regarding a first set of buildings.

3 VULNERABILITY SEISMIC RISK ASSESSMENT

3.1 General remarks

A structural vulnerability analysis involves the assessment of the consistency of the existing building stock in a given area both from a qualitative and quantitative point of view, specifically appraising the propension of the constructions to be damaged by the earthquake. First of all, a methodology for the seismic assessment on territorial scale should thence specify how to carry out the inventory of the buildings, establish the level of detail and develop suitable models to correlate the ground motion's severity with the possible economic and physical damage. Finally, the buildings shall be classified according to a priority list.

In the past twenty years, two different approaches for the seismic vulnerability assessment have been developed, generally known as *Level I* and *Level II* approach. The *Level I* methods recognize a number of typological classes within the building stock, and for each of them define the vulnerability class (usually A, B and C). For a vulnerability class, the relationship between the seismic input and the damage suffered by the structure is provided by probability matrices - DPM (Damage Probability Matrix). Clearly, this type of approach does not provide an assessment of the individual building, but can sort the analyzed building within a homogeneous typological set by its vulnerability index. The *Level I* methods are based on the data collected by the compilation of specific seismic vulnerability sheets, which contain typological and constructive records about the single building. The different records are scored on the basis of pre-defined scales and combined in order to define a *Vulnerability Index* $I_V=I_V(PGA)$, which is a function of the maximum peak ground acceleration on a rigid soil [12]. More recently, "multi-level" approaches are used, which provide different levels of deepening, with a progressive increase of the amount and detail of the information, and accuracy of the results obtained [13,14]. An example is given by HAZUS methodology, which represents very well the current standard adopted for seismic risk analyses. HAZUS methodology is based on the comparison between the "seismic demand", expressed in terms of the Adimensional Displacement Response Spectrum (ADRS), and the "structural capacity", expressed by an equivalent force-displacement curve obtained from an incremental non linear analysis. These approaches, which are usually called "semi-quantitative", are organized into multiple levels of analysis: they start from the regional scale up and finally arrive to the scale of the individual building, and are used to establish the seismic vulnerability of the constructions. Their application is conditioned by the great amount of basic data and by the relevant computational effort that is required for the assessment at the scale of the building. If the methodology is to be applied to a large urban area, it is then appropriate to single out a set of typological models that will represent a plurality of buildings, and it is appropriate, also to adopt some simplifications in the approach..

The methodology outlined in the Guidelines belongs to the class of semi-quantitative approaches, and operates on two levels, providing the indications for the safety assessment of the building and quantifying the vulnerability level, according to the local seismic hazard and to the considered limit state.

3.2 The Seismic Vulnerability Coefficient (SVC)

As previously remarked, for the generic building the *Guidelines* provide the calculation of the coefficient *SVC*, defined as the ratio between the seismic action corresponding to the attainment of the *limit structural capacity* and the *seismic demand*, both evaluated in correspondence of the Limit State of Life Safety (LS) and expressed in terms of Peak Ground Acceleration (PGA):

$$SVC = \frac{PGA_C^{LS}}{PGA_D^{LS}} \quad (1)$$

Because of the variability of the spectrum with the period T_r, Eq. 1 becomes quite complex. In a first approximation, it is possible to neglect this variability and to assume a constant acceleration spectrum corresponding to the return period used in the analysis (in the case of school buildings, and for the LS, it is: T_R= 712 years). Based on these assumptions:

- in a linear analysis, the coefficient SVC coincides with the ratio between the capacity of the first structural element which collapses under an increasing seismic action, and the effect produced, on the element itself, by the design seismic action (associated with T_R);
- in a non linear analysis, the coefficient SVC is the ratio between the displacement capacity and the seismic displacement demand, in correspondence of the LS ultimate state.

For RC buildings, the capacity expressed in the acceleration format ($PGA_C{}^{LS}$) is the PGA associated to the specific demand spectrum (i.e. with a non-unitary behaviour factor) which induces one of the following effects on a structural element:

1. attainment of shear collapse;
2. attainment of the failure in a beam-column node;
3. attainment of the ultimate chord rotation;
4. attainment of the limit capacity in the foundation.

4 ANALYSIS OF THE SAMPLE

The analysis presented concerns a first sample of school buildings located in the Province of Foggia, where the assessment procedures and the related gathering of data is currently still in progress. At the end of the research work, the sample will consist of about 20 school buildings, while presently the statistical evaluation regards a sample consisting of 9 school buildings. The areas covered by the investigation, within the territory of the Province of Foggia (Italy), are shown in Fig. 3: the red dots indicate the location of the school buildings included at present in the analysis, whereas the blue dots indicate the buildings still under evaluation. The seismicity of the investigated area (in Fig. 4 the current PGA for return period T_R=475 years), expressed in terms of "maximum horizontal acceleration at the site - a_g", is comprised between *0.173g* and *0.253g*. Even if the coverage of the sample is still incomplete, the preliminary elaborations, which are summarized in the following sections, offer some interesting points for reflection.

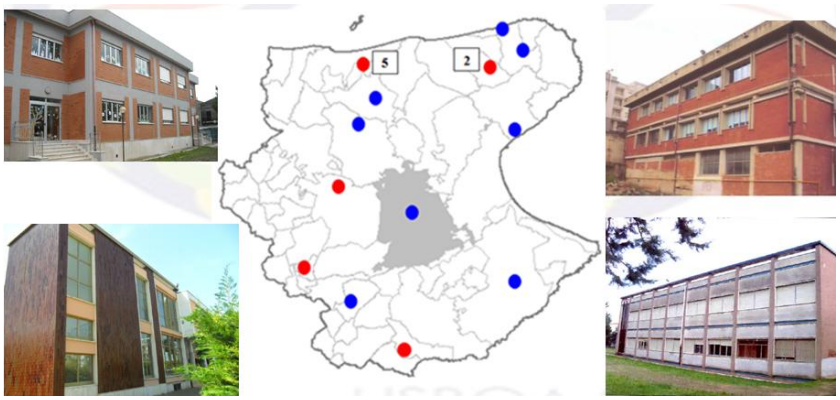


Figure 3. The area covered by the seismic risk analysis in the Province of Foggia (Italy)

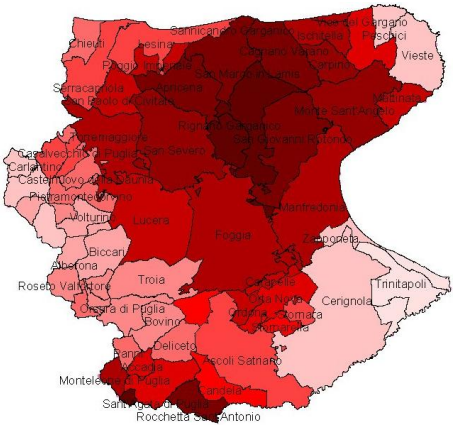


Figure 4. Current PGA for T_R=475 years

4.1 The age of the sampled buildings

For an existing building, the age is important information, since it reflects the state of the knowledge at the time of the construction. Therefore, the classification of the buildings included in the sample is based, first of all, on the knowledge of the evolution of the Italian building codes in the twentieth century, taking into account also the progressive modification of the seismic zonation in the Italian territory. The Italian rules concerning RC buildings can be divided into two groups called respectively *first* and *second generation* [15]. The regulations belonging to the *first generation* range from 1925 to 1939, and among them the main reference is represented by the Regio Decreto no. 2229 of 16/11/1939 [16], which has ruled the standard for the design and the execution of RC structures for about thirty years. The *first generation* ends with the issuing of the law 05/11/1971 n. 1086 that, for the first time, introduced the mandatory notification of any structural construction to the competent territorial offices. All the building codes issued until today belong to the *second generation*. In 1972, the law D.M. 30/05/1972 [17] introduced several innovations, including the concept of "*characteristic strength*", which paved the way for the probabilistic approach to the structural safety. The 1980 is a particularly significant year, since the semi-probabilistic limit state design method was introduced in Italy, and a vast operation of seismic zoning of the territory was completed. Furthermore, it is worth noting that only after 1980 the linear methods for the seismic analysis (equivalent static analysis and modal analysis), already introduced in the 70's, found a widespread application, also thanks to the new seismic classification of the territory. According to the evolution of the codes depicted in this short overview, two reference dates have been singled out for the classification of the buildings: 1972 and 1980. In Fig. 5, it is re-

ported a pie chart showing the percentage distribution of the buildings with respect to the construction period. Actually, all the school buildings constructed after 1980 (green portion) are comprised within the range 1980-1983, and can then be reasonably considered very close to those of the class 1972-1980 with regard to the adopted construction practices. After this simplification, it can be assumed that more than 75% of the sample is referred to the regulatory and constructive practice of the '70s.

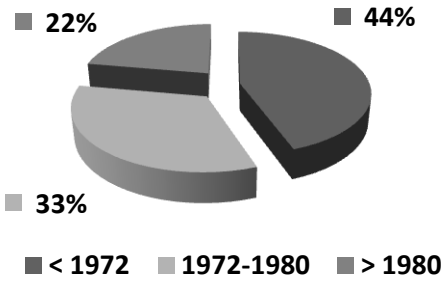


Figure 5. Period of construction

4.2 Number of storeys and structural regularity

For the Level II vulnerability assessment, i.e. the assessment at the scale of the building, it is necessary to preliminarily determine the parameters which characterize the geometric and structural configuration of the building. Two particularly significant parameters are the number of storeys and the regularity in plan and in elevation. The first one is related to the deformation capacity required to the structure, whereas the second one has important implications on the choice of the methods of analysis. The infilled frames have a important role because the plan and height position affect the structural regularity. Furthermore, when there are infills in the numerical modeling, the response of the structure varies and it depend on approach used to simulate the panels [18,19,20] The influence of the geometric configuration on the structural response of the building is worldwide recognized in all the national building codes. In particular, Eurocode 8 [10] provides a detailed indication of the simplification that can be adopted in the numerical modelling and of the methods that can be adopted in the presence of the structural regularity. With regard to the non-linear static analysis (pushover), when the geometrical configuration is irregular (in plan and/or elevation), it is mandatory to adopt a spatial model, and to apply a lateral force distribution along one direction (*EC8 - §4.3.3.4.2.1(2) and (3)*)

The Italian Standards, instead, doesn't allow the use of the pushover analysis if less than *75%* of the total participant mass is activated by the principal modal shape. In Fig. 6, the percentage distribution of the number of storeys (on the left) and structural regularity (on the right) are shown for the sample. It can be noticed that the generic building has been classified as irregular either if the plan or the elevation were irregular.

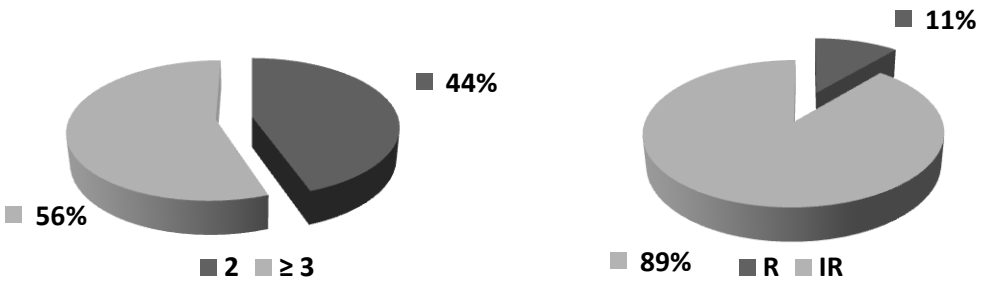


Figure 6. Percentage distribution of the number of storeys (left) and structural regularity (right).

The graphs show that the typological characters of the buildings in the analyzed territory have a high degree of homogeneity, that is the necessary basis for the application of "semi-quantitative" methods aimed at identifying the representative typological class of a local context (see § 3.1). Indeed, for almost 90% of the sample, the geometric configuration is irregular ("IR"), mainly in plan, with a number of storeys that is generally equal to 2-3 (i.e. 1-2 levels in which seismic masses are concentrated).

4.3 The quality of materials

Some remarks about the quality of in place concrete will be now presented, by analysing the data obtained by the experimental on site investigations performed over the buildings. In fact, it was found that the concrete was typically affected by the greatest dispersions, and thence it plays the major role in the vulnerability assessment. With regard to the steel, in the buildings dated back to the 70's reinforcement bars are of non-corrugated type, with values of the admissible tensile strength comprised between *140* and *200 MPa.* It is worth mentioning that in those years the possibility of using high adherence bars had just been introduced, but their widespread use only began in the 80's. The resistances obtained from tensile and bending tests performed on specimens extracted from the structural elements were in line with the original design specifications.

The considerations about the quality of in-place concrete in the sampled school buildings are based on the average strength indicated by the technicians in charge in the technical reports, and therefore are taken "as they are", without discussing the specific problems about the procedures adopted for the numerical elaboration of the experimental results and for the correlation with non destructive tests, as well as for the identification of the homogeneous classes of concrete. In fact several researches [21,22] show that the strength value obtained by the on-site tests depends on a lot of factors (compaction degree, decay of materials, damage, ...). However, this issues aren't the core of the present work that it only wants to provide an overview on the regional scale analysis of the school buildings of Foggia.

The percentage distribution of the compressive strength of concrete for the sampled buildings has been calculated by referring to the minimum characteristic value (R_{ck}) provided by the reference code of the time [17], which is R_{ck} *= 15 MPa.* In the analyses, it was accounted for the deviation that is typically found between the strength of in-place concrete and that measured on cast specimens during the concrete placement, that is related to the different curing conditions. In particular, the Italian Building Code *NTC* - § 11.2.6, reports verbatim: "*the average value of the in-place strength (which is defined as the structural resistance) is generally lower than the average values provided by strength test results from standard-cured cast specimens (which is defined as the potential resistance)*", and that "*an acceptable average value of the structural strength should be not lower than 85% of the design value.*". The diagram presented in Fig. 7 illustrates the comparison between the average strength (f_m) provided by the tests, both with the design value f_{cm} = medium cylindrical compressive strength (red line) evaluated according to the following relationship:

$$f_{cm} = 0.83R_{ck} + 8 \quad (2)$$

The values reported in the figure have been normalized by f_{cm}.

In the study, the evaluation of the medium values of the compressive strength has been made by assuming as a reference the minimum acceptable value provided by the building code "D.M. 30/05/1972" (according to the preliminary analysis presented in § 4.1, this is the reference law for more than *75%* of the buildings of the sample), which is equal to R_{ck}*=15MPa*. By this assumption, derive the following reference value: f_{cm}*=20.5 MPa*. The approach is similar to that proposed some years before by the American Standards ACI 228

[23], which provide the acceptance criteria for the compressive strength of concrete based on core testing. By denoting with f_{core} the strength obtained from cores, and with $f_{c,st}$ the standard strength deriving from normalized cast specimens, the concrete can be accepted if: $f_{c,mean} > 0{,}85f_{c,st}$ and $f_{c,min} > 0{,}75f_{c,st}$.

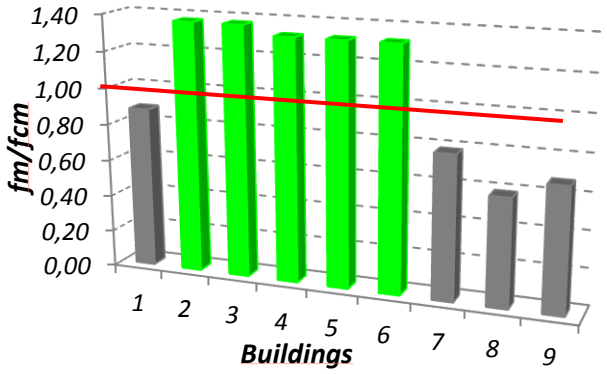


Figure 7. Strength of in-place concrete for the sample compared with the medium value of the design strength f_{cm}= 20.5MPa (in the normalized scale).

In the elaboration of this first sample the heterogeneity of the results is evident, and mainly a basic division into two main groups can be made: a group for which the concrete strength is well above the required minimum, and a group for which the values are instead significantly below the minimum.

4.4 Seismic vulnerability assessment of the samples: SVC

From the seismic assessment of the individual buildings, the values of the coefficient SVC defined in § 3.2 have been extrapolated. In Fig. 8 it is shown the graphical representation of the percentage distribution of the school buildings that have, respectively, a SVC coefficient comprised in the intervals: *SVC < 0.5*; *0.5 < SVC < 1*; *SVC > 1*. This diagram allows having an immediate idea of the seismic "efficiency" of the analyzed buildings. The definition of the aforementioned reference intervals for SVC is a simplified method aimed at providing a qualitative but effective representation of the seismic vulnerability, which actually corresponds to three coarse vulnerability levels: "*severe*", "*light*", "*absent*"

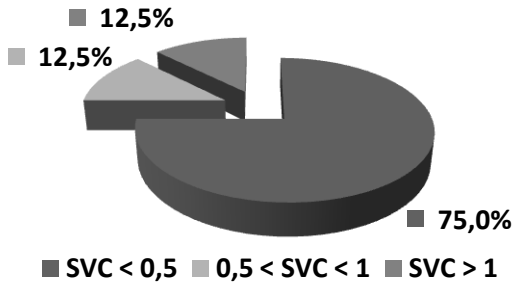


Figure 8. Percentage distribution of the seismic vulnerability of the school buildings expressed as a function of the coefficient SVC.

By the analysis of the results, it is quite evident that the presence of a severe seismic vulnerability for the samples is mainly related to the inadequacy of the technical standards used as reference in the period of construction, above all with regard to the prescriptions about the seismic design. In fact, the only group of buildings for which the seismic vulnerability is absent are those dated back after 1980 (which only represent 12.5% of the sample).

5 CONCLUSIONS

In the present paper, a statistical elaboration of the first set of results provided by the seismic assessment of a number of school buildings located in the Province of Foggia (Italy) is presented. Even if the sample is still quite small (9 case studies have been presently completed on a total number of 20 school buildings included in the research program) the elaboration of the preliminary data, with regard to some significant parameters (period of construction, number of storeys, structural regularity), in the form of percentage distribution charts, provided some interesting elements of analysis. In particular, it was possible to identify a paradigmatic typology representing, in the average, the characters and quality of the school buildings on the analyzed territory. The features of this model building are: irregular geometric configuration; low rise; adequate safety level only under vertical loads. The comparative analysis between the average strength of in-place concrete (provided by destructive and non-destructive tests, f_m) and the reference value (medium cylindrical design strength f_{cm}), points out that the differentials are particularly relevant, with samples characterized by very low values and others showing very good values. In particular, for some buildings the strength of in-place concrete is even 40% lower than the required standard. With regard to the seismic vulnerability, it was appraised by means of a specific coefficient *SVC*, which highlighted that as many as 75% of the buildings have a very low *SVC* (<50% than the minimum threshold).

AKCNOWLEDGEMENT

This research work was developed under a general agreement between the Department Diac (Politecnico di Bari) the Basin Authority of Regione Puglia (AdB Puglia): "*Development of methodologies for the assessment and the mitigation of seismic risk in the Province of Foggia (Italy), with regard to residential and strategic buildings".*

REFERENCES

[1] L.D. Decanini, A. De Sortis, A. Goretti, L. Liberatore, F. Mollaioli, L. Bazzurro, Performance of reinforced concrete buildings during the 2002 Molise, Italy. *Earthquake Spectra* **20** (S1),S221–S255, 2004.

[2] T. Rossetto, N. Peiris, Observations of damage due to the Kashmir earthquake of October 8, 2005 and study of current seismic provisions for buildings in Pakistan. *Bulletin of Earthquake Engineering* **7**(3),681–699, 2009.

[3] D. Raffaele, F. Porco, A. Fiore, G. Uva, Simplified Vulnerability Assessment of RC Circular Piers in Multi-Span-Simply-Supported Bridges. *Structure and Infrastructure Engineering*, 2013 - DOI:10.1080/15732479.2013.772642.

[4] G. Uva, D. Raffaele, F. Porco, A. Fiore, G. Porco, Bridge monitoring by fiber optic deformation sensors: a case study. In: Biondini, Frangopol (eds) Proceedings of the 6th international conference on bridge maintenance, safety and management, Como, Italy, 8–12 July 2012. Taylor & Francis Group, London - ISBN: 978-0-415-62124-3.

[5] F. Porco, A. Fiore, G. Porco, G. Uva, Monitoring and safety for prestressed bridge girders by SOFO sensors, *Journal of Civil Structural Health Monitoring* **3**(1),3-18, 2013. DOI 10.1007/s13349-012-0029-9.

[6] O.P.C.M. n. 3274. Primi elementi in materia di criteri generali per la classificazione sismica del territorio nazionale e di normative tecniche per le costruzioni in zona sismica, G.U. 8 maggio 2003. Roma, Italy, 2003.

[7] D.M. LL. PP. 14/01/08. Norme Tecniche per le Costruzioni (NTC 2008) - *(In Italian)*, G.U. n. 29 del 4 febbraio 2008, Supplemento Ordinario n. 30. Roma, Italy.

[8] A. Fiore, M. Mezzina, F. Porco, D. Raffaele, G. Uva, Seismic safety assessment program of school building in Puglia (Italy): overview and case studies, Paper n. 3978 in *Proceedings of 15thWorld Conference on Earthquake Enginee*ring (WCEE 2012), Lisbon, Portugal, September 24-28, 2012.

[9] Circolare 2 febbraio 2009. n. 617 approvata dal Consiglio Superiore dei Lavori Pubblici. Istruzioni per l'applicazione delle "Nuove norme tecniche per le costruzioni" di cui al Decreto Ministeriale 14 gennaio 2008 – 2009.

[10] CEN. Eurocode 8: Design of structures for earthquake resistance. Part 3: Strengthening and repair of buildings. Brussels, Belgium, 2005.

[11] CEN. Eurocode 2: Design of concrete structures, Part 1-1: General rules and rules for buildings. Brussels, Belgium, 2005.

[12] D. Benedetti, V. Petrini, On seismic vulnerability of masonry buildings: proposal of an evaluation procedure. *L'Industria delle Costruzioni* **18**,66-78, 1984.

[13] Federal Emergency Management Agency, HAZUS. Earthquake Loss Estimation Methodology, Washington, D.C., 1999.

[14] E. Faccioli, V. Pessina, *The Catania Project: earthquake damage scenarios for a high risk area in the Mediterranean*, CNR-GNDT Roma, Italy, 1999.

[15] A. Sollazzo, C. Sgobbo, *Le norme ufficiali italiane sul cemento armato e il loro sviluppo durante il XX secolo (in Italian)*. In: Sicurezza e conservazione delle prime costruzioni in calcestruzzo armato, a cura di Mezzina, M., Uva G., Greco, R. CittàStudi Edizioni, Torino, Italy, 2011.

[16] R.D. 16/12/1939 n. 2229. Norme per la esecuzione delle opere in conglomerato cementizio semplice ed armato. *(in Italian)*, Roma, Italy, 1999.

[17] D.M. LL. PP. 30/5/1972. Norme tecniche alle quali devono uniformarsi le costruzioni in conglomerato cementizio, normale e precompresso, ed a struttura metallica *(in Italian)*. G.U. n. 190 del 22/7/1972.Roma, Italy.

[18] G. Uva, F. Porco, A. Fiore, Appraisal of masonry infill walls effect in the seismic response of RC framed buildings: a case study. *Engeneering Structures*, **34**(1):514–26, 2012.

[19] A. Fiore, F. Porco, D. Raffaele, G. Uva, About the influence of the infill panels over the collapse mechanisms actived under pushover analyses: two case studies. *Soil Dynamics and Earthquake Engineering*, **39**,11-22, 2012.

[20] G. Uva, F. Porco, D. Raffaele, A. Fiore, On the role of equivalent strut models in the seismic assessment of infilled RC buildings. *Engineering Structures*, **42**:83-94, 2012.

[21] G. Uva, F. Porco, A. Fiore, M. Mezzina, Proposal of a methodology of in-situ concrete tests and improving the estimate of the compressive strength, *Construction and Building Materials*, **38**(1):72-83, 2013 - DOI: 10.1016/j.conbuildmat.2012.08.025.

[22] F.M. Bartlett, J.G. MacGregor, Variation of in-place concrete strength, *ACI Materials Journal*, **96**(2):261-70, 1999.

[23] American Concrete Institute. Nondestructive Test Methods for Evaluation of Concrete in Structures, ACI 228. 2R-98, Detroit, Michigan, USA, 1998.

COMPDYN 2013
4th ECCOMAS Thematic Conference on
Computational Methods in Structural Dynamics and Earthquake Engineering
M. Papadrakakis, V. Papadopoulos, V. Plevris (eds.)
Kos Island, Greece, 12–14 June 2013

AN ANALYSIS OF METHODS FOR DERIVING MAGNITUDES OF HISTORIC EARTHQUAKES THAT ARE BASED ON PHYSICAL PRINCIPLES

Christopher S. Belsham

Office for Nuclear Regulation
Redgrave Court, Merton Road, Bootle, Merseyside, L20 7HS, United Kingdom
c_belsham@o2.co.uk

Key words: Macroseismic Intensity; Stable Continental Regions; Historical seismicity; Stochastic Method; spectral ground acceleration; attenuation quality factor.

Abstract. *A large proportion of the land mass of the world is classified as Stable Continental Regions, these are generally regions where the seismic activity is low. Consequently there is little instrumentally recorded strong-motion data available from which to build robust models for seismic hazard evaluation for these regions. Recourse is therefore made to using spatial events as a surrogate for temporal events, on the assumption that the regions selected spatially have similar tectonic characteristics. Even this approach requires the addition to the database of historic events, these are events that have been recorded pre-instrumentally using macroseismic intensity records as the basis. This leads to a key objective of the analysis of historic seismic data is the determination of a relationship between an events macroseismic intensity records and its magnitude through regression analysis of a large set of known data.*

An important part of regression analysis for this type of data is the development of a functional form that matches the nature of the data and models the physical processes that gives rise to it. The equations which are considered and compared in this paper are those of Frankel, Johnston, Ambraseys, Murphy and O'Brien and Kövesligethy. In addition, to explain how these equations relate to the physical process, Frankel's equation is compared with the equation from Boore's Stochastic Method.

The paper then compares, in detail, the magnitude-intensity relationships developed by Johnston and Ambraseys, the interest focusing on the different regression techniques used. This is followed by an exploration of the merits of each approach with the analysis using Johnston's global dataset of Stable Continental Region events. The discussion between these models provides the basis for the development of a typical value for the attenuation quality factor Q for Stable Continental Regions in the frequency range 1 to 5 Hz. Together the findings in this paper provide the opportunity for developing ground motion prediction equations from a mixed macroseismic and instrumented approach. It also provides a means to further improve the knowledge of macroseismic data and notes potential uncertainties in the values of the derived magnitudes.

1 INTRODUCTION

The advantage of being able to enlarge the earthquake database in regions of low seismic activity using historic earthquakes has been understood for several decades and a number of major studies have been carried out to derive the magnitudes for historic earthquakes. Two studies in particular stand out because they consider large regions using geological rather than political boundaries to define the scope of the data considered. In addition they are developed from underlying physical principles and therefore satisfy the conclusions in NERIES [1]. The first of these studies was carried out by Ambraseys [2] and considered the Intraplate region of North Western Europe (NWE). The second study was by Johnston [3] which considered data collected from regions worldwide that satisfied the criteria that defined them as Stable Continental Regions (SCR). The term SCR was introduced in Johnston [4], prior to which tectonic regions were classified as either interplate or intraplate. Johnston identified nine SCRs; Africa, East Antarctica, North America, South America, Europe, Asia, India, China, Australia. NWE forms a subset of the European Stable Continental Region. The remaining regions of the world are termed Non Stable Continental Regions (NSCR).

Johnston and Ambraseys used different types of regression analysis and functional forms but the underlying principle is the same. The method relies on selecting a range of earthquakes for which there are both instrumented and macroseismic intensity data available thus giving both the magnitude and the isoseismals. Then a regression analysis is performed to determine the values of the coefficients in the functional equation or a set of functional equations. The functional equations with assigned values for the coefficients, derived from the regression, relate the magnitude of an event to the macroseismic intensity data. The equation(s) can then be used to find the magnitudes for those cases where macroseismic intensity records are the only data available.

The Johnston [3] study recognised that in order to construct a large database for SCRs it is necessary to extend the spatial region to compensate for the lack of temporal data in a particular region. This required that a global view be adopted and involves an underlying assumption that all SCRs are fundamentally the same. In contrast the Ambraseys [2] dataset is for the much smaller region of NWE. On the basis that the larger of the two dataset is Johnston's, it has been selected for use in exploring the methodologies developed by Johnston and Ambraseys and to compare the two approaches. An important measure of the robustness of these types of methods is how well they recreate the input dataset; this test is applied to both methods.

The database presented in Johnston [3] has multiple entries for many of the events. For this study, the entry that contains the highest number of isoseismal radii are selected. The resulting dataset used in this study is given in Appendix A.

Validation of complex models such as those considered in this study is very difficult. It might at first appear that testing with an independent event would be a strong test; however, because the regressions have a large uncertainty such a test is in fact only weak. In cases such as this it is preferable to rely on how well the methodologies match the physical process and the quality of the data used. The physical process is considered to be adequately represented by the equation presented in the Stochastic Method, Boore [5].

2 METHODS USED TO DERIVE EVENT MAGNITUDES FROM INTENSITIES

Many equations have been developed for the study of macroseismic intensity; in this paper those by Frankel [6] as used by Johnston [3], Ambraseys [2], Murphy and O'Brien [7] and Kövesligethy [8] are considered. The study of these equations and their parameters shows

there is a close relationship between them and it is also shown that they are closely related to the source to site model that forms the basis of the Stochastic Method, Boore [5].

A notable difference between the approach of Johnston and Ambraseys is that the parameters *m* and *n* are free to vary with intensity in Johnston's method but are constrained to a single value in Ambraseys method. This is particularly important for the determination of the value of *Q*. Johnston recognised the significance of the spectral response frequency but did not have sufficient information to refine the values beyond blocks of 3Hz and 5Hz. Belsham [9] determined the frequencies that are characteristic of each intensity level through dynamic analysis of the intensity indicators. Those values are used in this paper to assign specific response frequencies to each intensity level between II and VIII. With this new information an alternative study of *Q* is possible.

In this article the terms macroseismic intensity is used interchangeably with intensity and both Roman and Arabic numerals are used to define intensity levels. MSK and MMI scales are used interchangeably based on the comparison in Murphy and O'Brien [7].

3 JOHNSTON'S APPROACH

Johnston bases his analysis on an equation developed by Frankel [6], which has the form shown by equation (1)

$$A = A_0 r^{-n} e^{-mr} \tag{1}$$

where *n* is a geometric spreading factor and *m* is a coefficient of attenuation. Starting by taking the log of equation (1) results in equation (2)

$$\log A = \log A_0 - n \log r - 0.435mr + c \tag{2}$$

where *c* is a constant. For a given isoseismal, with an equivalent circular felt area *S*, the radius is $r = (S/\pi)^{½}$ and as log *A* is a constant for each felt area equation (2) therefore reduces to equation (3)

$$\log A_0 = 0.5n \log\left(S/\pi\right) - 0.435m\sqrt{S/\pi} + c \tag{3}$$

To finish relating the moment magnitude M_w to the felt area *S*, the Fourier amplitude A_0 needs to be found in terms of M_w. From the seismic moment M_0 Boore [5] derives the relationship shown in equation (4)

$$\log A_0 = \frac{1}{3} \log M_0 + C \tag{4}$$

Frankel then uses equation (5) from Hanks and Kanamori [10]

$$\log M_0 = 1.5M_w + 16.0 \tag{5}$$

and substitutes it into equation (4) to give equation (6)

$$\log A_0 = 0.5M_w + C \tag{6}$$

then substituting equation (6) into equation (3) produces equation (7)

$$M_w = n \log\left(S/\pi\right) + 0.87m\sqrt{S/\pi} + c \tag{7}$$

where *n* and *m* are factors to be determined from the regression analysis of the data. As the Johnston [3] data values differ from those used by Frankel [6], A new analysis of Johnston's

data has been carried out. Using intensity level II shows that the example in Frankel [6] is compatible with the data from Johnston [3] with the revised results shown in Figure 1. A visual comparison with figure 1 in Frankel's paper indicates that any changes are very small.

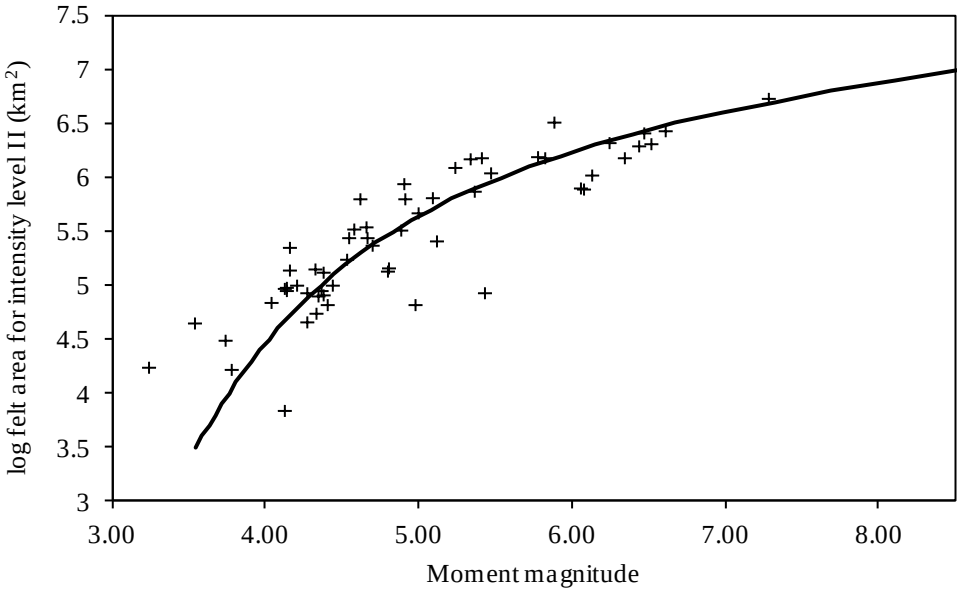


Figure 1 Plot showing that Frankel's functional form is compatible with Johnston's revised data

4 AMBRASEY'S APPROACH

The equation developed by Ambraseys [2] uses the equation for energy decay from a point source which is given by equation (8)

$$E = \frac{E_S}{4\pi r^n} \exp(-mr) \tag{8}$$

where E is the energy density at a distance r from the point source and n and m represent the same parameters as in equation (1) and E_S is the source energy given by equation (9)

$$\log(E_S) = \varphi + \theta M_S \tag{9}$$

where φ and θ are constants and M_S is the surface wave magnitude. According to Ambraseys [2] the constants are approximately $\varphi = 12.0$ and $\theta = 1.50$. Referring to equation (1), equation (8) is its equivalent in terms of energy. Using equations (8) and (9) in conjunction with other equations Ambraseys [2] derived equation (10)

$$M_S = c_1 I + c_2 \log r + c_3 r + c_0 \tag{10}$$

where $c_2 = n/\theta$ and $c_3 = 0.43m/\theta$, which for a typical value for $\theta = 1.5$ gives $c_2 = 0.67n$ and $c_3 = 0.29m$. The regression analysis determines the coefficients c from which the values for m and n can be found.

Murphy and O'Brien [7] found that the peak ground acceleration a in terms of intensity I is given by equation (11)

$$\log a = b_1 I + b_0 \tag{11}$$

where b_0 and b_1 are constants depending on the region. For the global case, with a in units of m/s^2 they are 0.25 and -1.75 respectively. Substituting equation (11) into equation (10) and gathering b_0 into c_0 and adjusting c_1 results in equation (12)

$$M_S = c_1 \log a + c_2 \log r + c_3 r + c_0 \tag{12}$$

In equation (12) log a is constant and for a given felt area can be combined into c_0. Then setting $c_2 = n$, $c_3 = 0.87m$ and $c_0 = C$ gives equation (7) and shows that Frankel's approach is the same basic formulation as that of Ambraseys.

As shown by Ambraseys [2] equation (12) can be developed from an equation formulated by Kovesligethy [8], which is equation (13)

$$I = a_1 \log(E) + a_0 \tag{13}$$

where E is the energy and the a's are constants to be determined from the data, it therefore follows that equation (1) is related to equation (13). In passing, the similarity between equations (11) and (13) is noted.

5 COMPARISON OF FRANKEL'S MODEL WITH THE POINT SOURCE MODEL

This section will show that equation (1) used by Frankel [6] is equivalent to a source model approach where the Fourier amplitude spectra is found from a source term multiplied by a path term. Boore [5], [11] has developed the point source model into the Stochastic Method, to the point where it is generally accepted as a robust analysis approach. The principle equation has the form shown in equation (14)

$$A(f,r) = A_0 Z(r) D(f,r) S(f) \tag{14}$$

where A_0 is the Fourier Amplitude of the seismic source at depth, $Z(r)$ is the dispersion term or spreading function, $D(f,r)$ is the attenuation term and $S(f)$ is the site response term, the combined terms giving the Fourier Amplitude $A(f,r)$ at the surface for frequency f at epicentral distance r. The source model therefore derives the Fourier acceleration at the rupture and then determines what the Fourier acceleration is at the surface at a given distance from the source taking into account the attenuation and spreading with distance.

In Frankel's model the site term is not present. Frankel's model therefore consists of a Fourier acceleration A_0 at the source below the epicentre, a dispersion term for the distance r from the source, which for the far-field considered by Frankel is given by r^{-n} and an attenuation term $\exp(-(\pi f/Q\beta)r)$, where f is the frequency, Q is the quality factor and β is the shear wave velocity in the basement rock. Frankel equates $\pi f/Q\beta$ to m. It is therefore seen that Frankel's equation (1) is a form of point source model, which from Boore [11] has the form shown in equation (15)

$$a = \frac{VR_\theta F M_0}{4\pi\rho\beta^3} \frac{(2\pi f)^2}{1+(f/f_0)^2} Z(r) \exp\left(-\frac{\pi f}{\beta Q} r\right) \tag{15}$$

here A_0 is given by equation (16), which is the first two terms in equation (15)

$$A_0 = \frac{VR_\theta F M_0}{4\pi\rho\beta^3} \frac{(2\pi f)^2}{1+(f/f_0)^2} \tag{16}$$

where M_0 is the seismic moment, ρ is the density of the basement rock, V is the component factor normally $1/\sqrt{2}$, R_θ is the source radiation factor with a typical value of 0.55 and F is the surface reflection factor, f_0 is the corner frequency and f is the frequency at which a is

required. The geometrical spreading term $Z(r)$ equates to r^{-n} in Frankel's equation and the last term, the attenuation, is the same in both cases. This shows the equivalence of Frankel's approach and the point source model.

6 COMPARISON OF REGRESSION METHODS USED TO DERIVE EARTHQUAKE MAGNITUDES FROM MACROSEISMIC INTENSITIES

Studies to derive earthquake magnitudes from macroseismic intensities from historic events are a major undertaking and as a consequence there are not a large number of such studies; of those that have been carried out, two stand out. These are the studies discussed above, namely, Ambraseys [2] and Johnston [3]. Although the fundamental philosophy is the same in each of these studies, the details are different. It is important for future studies in this subject to understand the differences between the two approaches and if possible draw a conclusion as to which approach gives the more representative results. This later requirement introduces the need to find a means of measuring the results of the analyses.

6.1 The data

The database used in this study is tabulated in Appendix A and is presented graphically in figures 2 and 3. It has been divided into two graphs because of the density of the data and by plotting every other intensity level in each figure it provides improved clarity.

During the processing of the regression analysis it was found that using just Table A.1. data resulted in a poor fit for intensity level VI data and an extremely poor fit for intensity level VII and VIII data. A first step in improving the regression was to include the data from Table A.2. in Appendix A. This made improvements to those intensity levels but the shape of

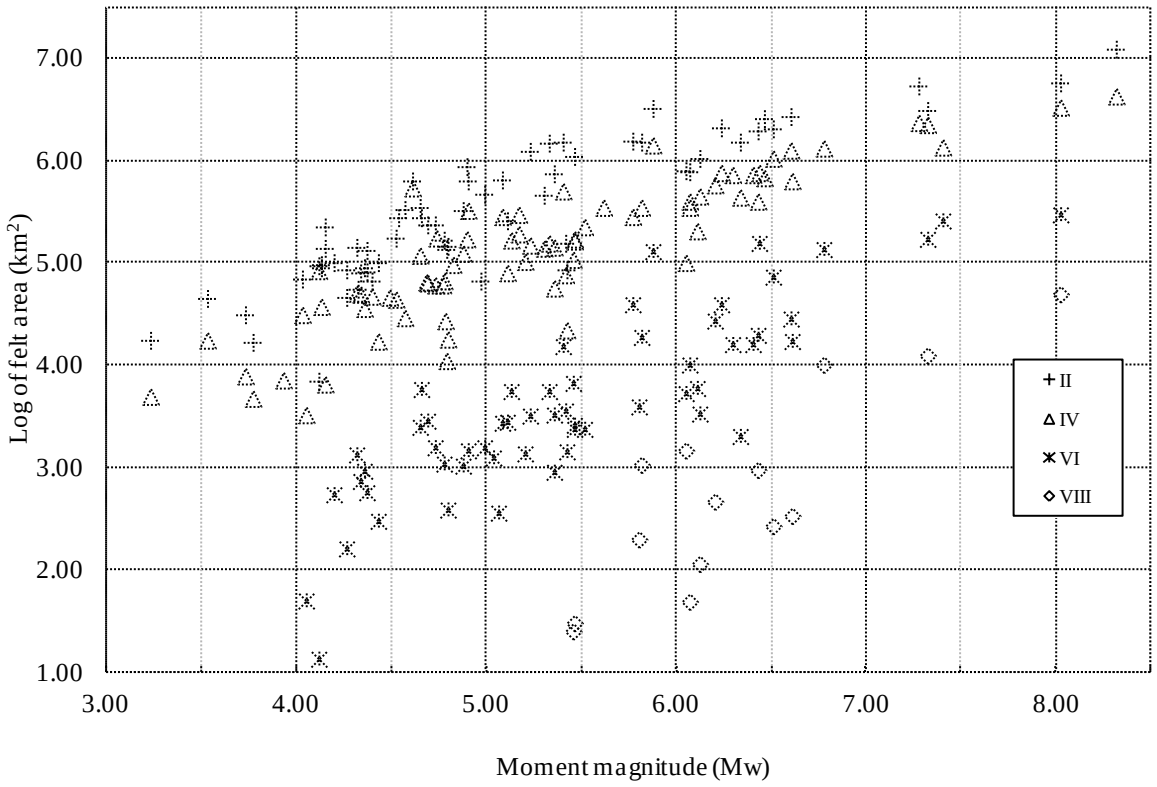


Figure 2. Data points from the database in Appendix A for intensity levels II, IV, VI and VIII

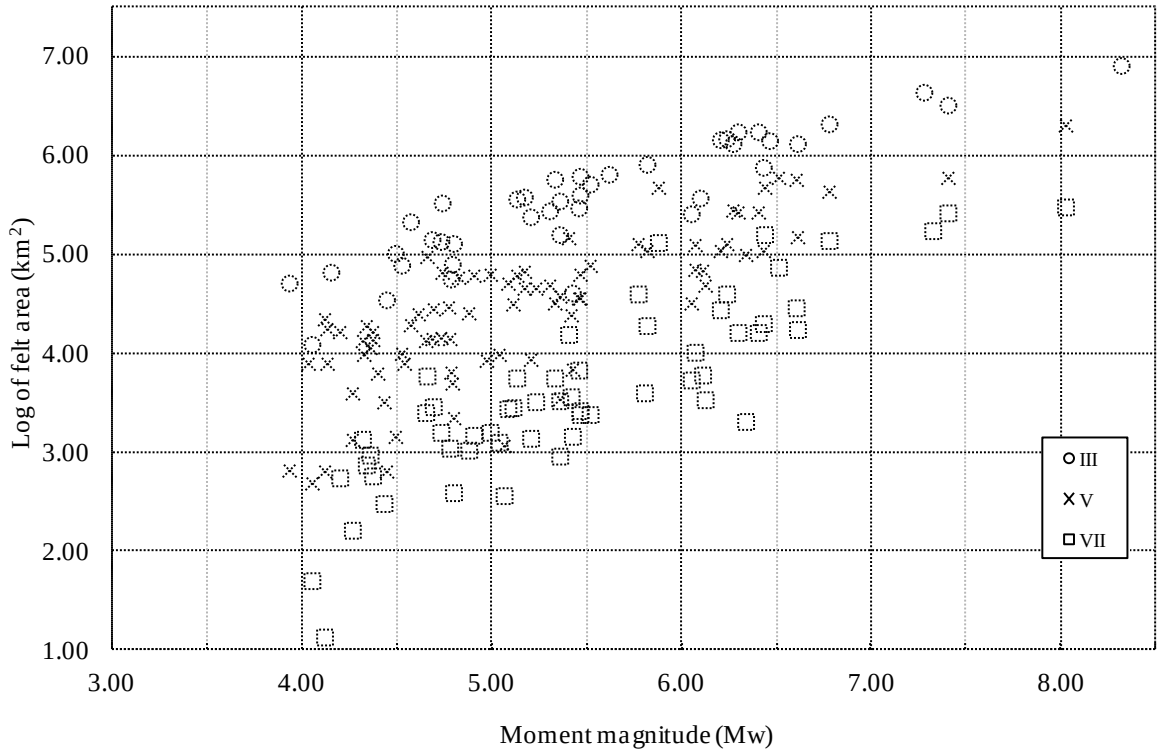


Figure 3. Data points from the database in Appendix A for intensity levels III, V, VII

the intensity level VI curve remained at variance with the other intensity curves. Investigation of the database for intensity VI using trial adjustments revealed that the entry from the Bihar, India 1934 event was constraining the regression curve. Inspection of the data entry showed it to have a large associated uncertainty and examination of the plot of the isoseismal included in Johnston [3] showed an elongated shape. Further evidence for this is found in [12] where Kriging has been used to determine the isoseismals, which is shown in figure 4(j) in that paper. Although the isoseismal radii are not given in the report, simple scaling from the plot gives r_{VI} of 0.3e6. This shows that the intensity level VI area A_{VI} can be significantly reduced from 1.2e6 to 0.3e6, giving $\log(A_{VI}) = 5.48$. This then requires that the intensity level VII area A_{VII} is also reduced from 0.316e6 to 0.1e6, giving $\log(A_{VI}) = 5.00$. Including these revised isoseismal area reductions in the regression analysis results in values for the attenuation quality factor Q which are consistent with the other intensity levels. These reduced values have therefore been assessed as being the more appropriate.

6.2 Johnston's method – individual regression of each intensity level

Johnston [3] based his analysis on equation (7). In this section the key elements of Johnston's approach are set down and then applied to the Johnston dataset, which consists of worldwide SCR events covering moment magnitudes 3.2 to 7.25. In his part II paper Johnston [3] notes that he chose not to follow Ambraseys' approach but instead uses equation (7) for each individual intensity level in the form shown by equation (17)

$$M_{0i} = 10^{k_0 + k_1 \log(S_i) + k_2 \sqrt{S_i}} \tag{17}$$

Where M_{0i} is the seismic moment and S_i is the felt area for the contributing intensity level i with k_0, k_1 and k_2 coefficients whose values are given in Table 1.

Intensity level i	k_1	k_2	k_0
2	0.959	0.00126	17.31
3	1.020	0.00139	17.59
4	0.971	0.00194	18.10
5	0.788	0.00260	19.83
6	1.032	0.00176	20.23
7	0.559	0.00328	23.22
8	0.440	0.00586	24.05

Table 1. Coefficients in Johnston's equations from Johnston [3]

Alternatively equation (17) can be written in the form shown in equation (18) which is the same as equation (7)

$$M_w^i = n\log\left(S/\pi\right) + 0.87m\sqrt{S/\pi} + c \tag{18}$$

where n, m and c are constants for intensity level i to be determined from a regression analysis for each intensity level and are related to the coefficients with k_0, k_1 and k_2 by the equations (19), (20), (21) and (22).

$$c = 0.667k_0 + 0.497n - 10.7 \tag{19}$$

$$n = 0.667k_1 \tag{20}$$

$$m = 1.361k_2 \tag{21}$$

$$m = \left(\pi/3.5\right)\left(f/Q\right) = 0.898\left(f/Q\right) \tag{22}$$

where f is frequency and Q is a regional attenuation quality factor that relates to the decay of the shear wave amplitude.

The results of the regression analysis using the functional form of equation (18), for each macroseismic intensity level are shown in Table 2. Equations (19), (20), (21) and (22) provide a way of converting the values in Table 1 into those given in Table 3 for n', m' and c' so that they can be compared directly with the values in Table 2.

Intensity level	n	m	c
2	0.3254	0.0028	2.4986
3	0.5646	0.0023	1.9096
4	0.6464	0.0028	1.7109
5	0.3934	0.0047	3.1691
6	0.6690	0.0035	3.2245
7	0.3882	0.0068	4.6988
8	0.2503	0.0148	5.4749

Table 2. Coefficients in equation (18) from regressions

The curves for each macroseismic intensity level II to VIII is shown plotted in Figure 4. The equations are plotted in alternative form to that presented in Johnston's paper to aid

comparison with the results from Ambraseys analyses which are presented in Section 6.2. The curves are plotted with the log of the felt area against the moment magnitude. To derive the moment magnitude for an event where *n* isoseismals are known Johnston simply derives the average value from the moment magnitudes of all the contributing intensity levels as shown in equation (23)

$$M_W = \frac{1}{n}\sum_{i=1}^{n} M_W^i \tag{23}$$

where *i* only includes cases where there are felt areas. M_w represents the best estimate of the moment magnitude of the event.

Figure 5 shows the results of processing Johnston's data through equations (18) and (23), the figure compares the magnitude values in the original data with the magnitude produced by the same data processed through the equations. If the equations produced ideal results then the plotted points would all lie on the diagonal solid line which is a line with slope 1.0 which passes through the origin, however clearly they do not. The dashed line shows the results of a

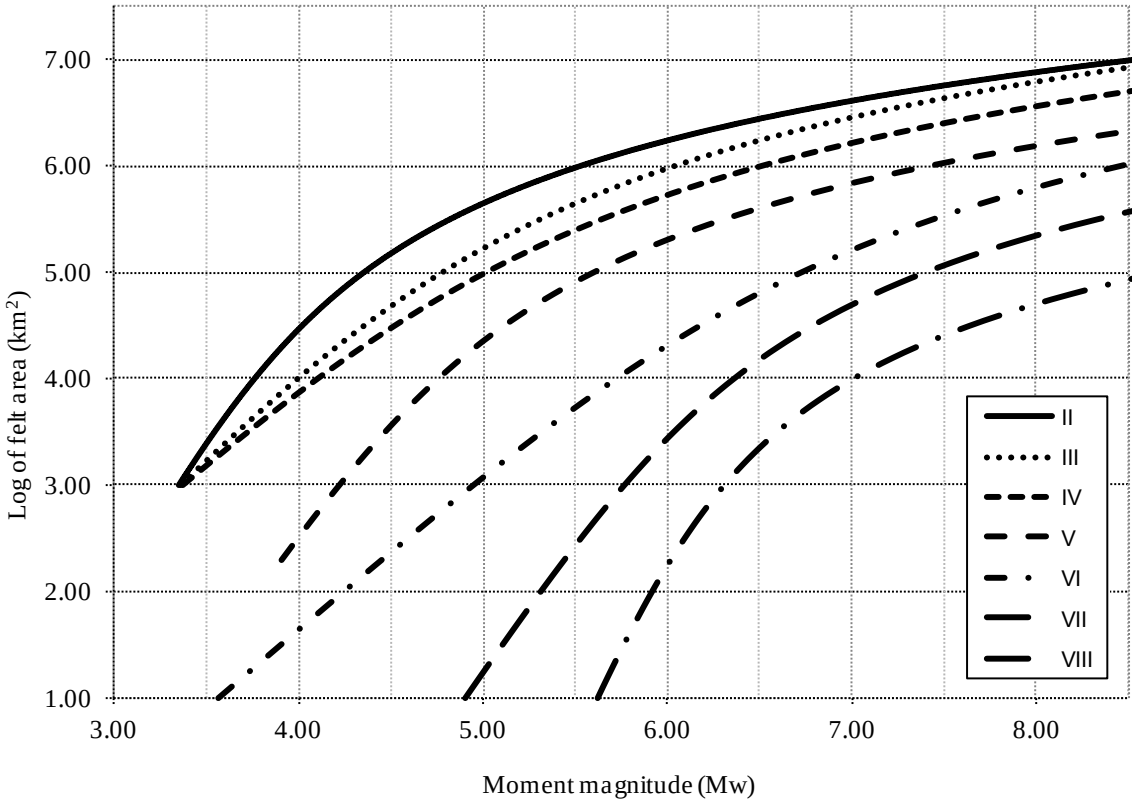


Figure 4. Analysis of Johnston's Moment Magnitude data using equation (18)

linear regression performed on the data and its position relative to the dotted line is an indicator of how well the equations reproduce the original data. It can be seen that the equations over estimate the moment magnitudes less than 6.0 and under estimate those greater than 6.0. The distance between the regression line and the diagonal line gives a measure of the

Intensity level	*n'*	*m'*	*c'*
2	0.64	0.0017	1.164
3	0.68	0.0019	1.370
4	0.65	0.0026	1.700
5	0.53	0.0035	2.790
6	0.69	0.0024	3.136
7	0.37	0.0045	4.972
8	0.29	0.0079	5.486

Table 3. Coefficients converted from Table 1
to an equivalent form to those in Table 2

accuracy of the equations at a given moment magnitude. The equation for the regression line is given by equation (24)

$$M = 0.997 + 0.823m \tag{24}$$

where M is the derived M_w and m is the original M_w from the dataset.

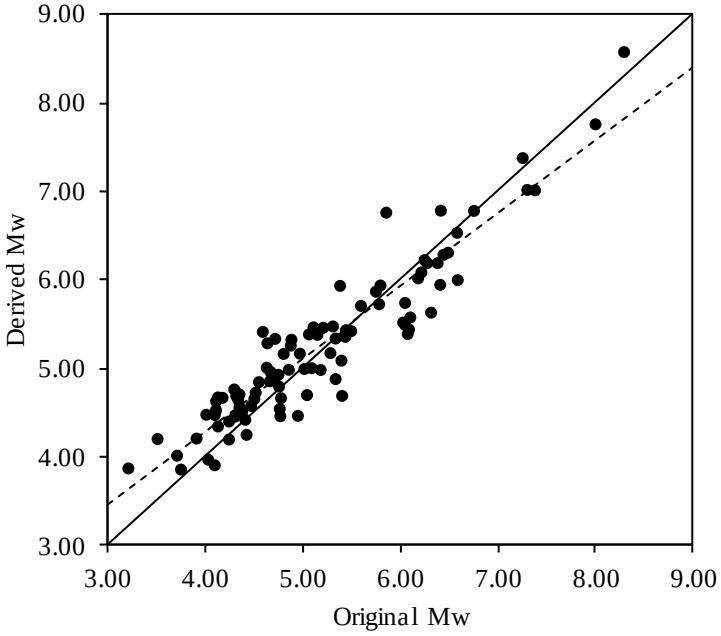


Figure 5. Plot showing the scatter in the results from the Johnston based data through equations (18) and (23). Dashed line is the regression equation which is compared with the solid line which represents a perfect reproduction by the equations (18) and (23)

6.3 Ambraseys method – simultaneous regression across all intensity levels

In a similar manner to the previous section, Johnston's dataset is analysed using the approach in Ambraseys [2]. Ambraseys studied NWE, which is part of the European SCR and considered events with surface wave magnitudes of 4.0 to 5.8.

Ambraseys adopted a regression method that simultaneously considers all intensity levels and then derives the magnitude by averaging the contribution from each intensity level. Ambraseys equation from the regression on NWE data is given by equation (25)

$$M_S = -1.10 + 0.62I + 0.0013D + 1.62\log(D) \tag{25}$$

where M_s is the surface wave magnitude I is the intensity level of the isoseismal with effective radii of felt areas D. To find the magnitude for an event with more than one isoseismal equation (25) is generalised to give the average value for the sum of the isoseismals which results in equation (26)

$$M_S = -1.10 + 0.62\, j^{-1}\sum_{i}^{j} I_i + 0.0013\, j^{-1}\sum_{i}^{j} D_i + 1.62\, j^{-1}\sum_{i}^{j} \log(D_i) \tag{26}$$

here j is the number of isoseismals available for an event and I_i is the numeric values of the macroseismic intensity levels and D_i is the radii of felt area of isoseismal i.

Applying Ambraseys method to Johnston's data using a method of minimisation of the least squares which incorporates a Levenberg-Marquardt non-linear convergence routine results in equation (27) which is in terms of moment magnitude

$$M_w = -0.796 + 0.58I + 3.462.10^{-7} D + 0.746\log(D) \tag{27}$$

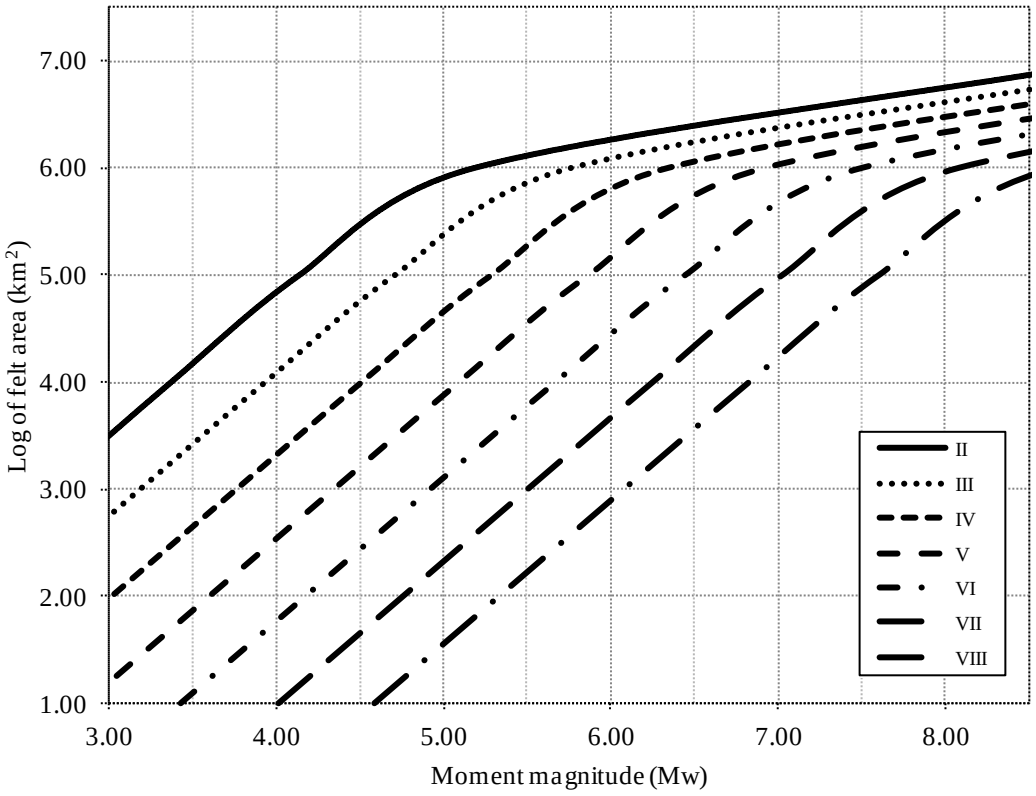


Figure 6. Analysis of Johnston's Moment Magnitude data using Ambraseys' approach of simultaneous regression over all intensity levels using equation (28)

It can be seen that the first two terms in equation (27) become a combined constant for each specific intensity level but that the third and four terms do not, unlike the terms in equation (18). Figure 6 shows a plot of equation (27).

Introducing the averaging process over the number of isoseismals available produces equation (28)

$$M_w = -0.796 + 0.58\, j^{-1} \sum_i^j I_i + 3.462 \times 10^{-7}\, j^{-1} \sum_i^j D_i + 0.76\, j^{-1} \sum_i^j \log\left(D_i\right) \qquad (28)$$

in the same way as for equation (26).

Figure 7 shows the results of processing Johnston's data through equations (27) and (28) the figure compares the magnitude values in the original data with the magnitude produced by the same data processed through the equations. As in Section 6.1 if the equations produced ideal results then they would all line on the diagonal dotted line however as in the case of Johnston's method they do not. Consistent with Section 6.1, the dashed line shows the results of a linear regression performed on the data and its position relative to the solid line is an indicator of how well the equations reproduce the original data. It can be seen that the equations over estimate the moment magnitudes that are less than 5.3 and under estimates those greater than 5.3. The equation for the regression line is given by equation (29)

$$M = 1.252 + 0.776m \qquad (29)$$

where M is the derived Mw and m is the original Mw from the dataset. Comparing this with equation (18) it can be seen that the Ambraseys method does not reproduce the results as well as Johnston's method.

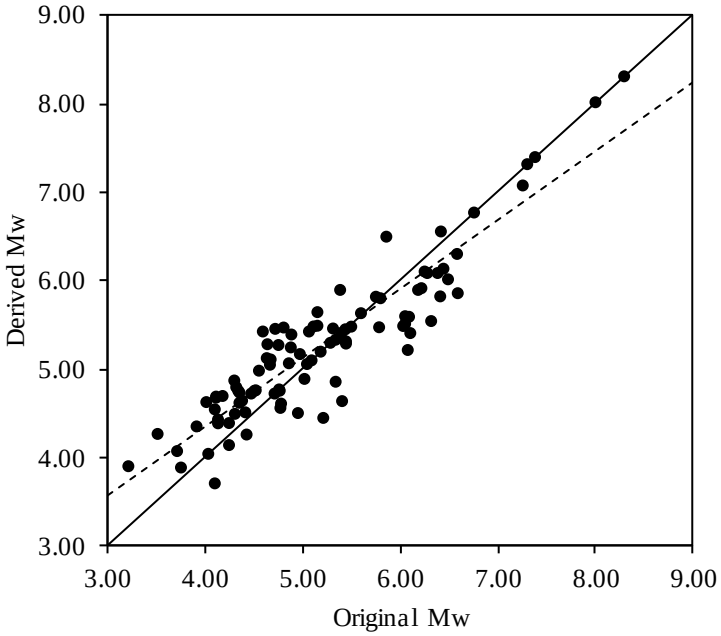


Figure 7. Plot showing the scatter in the results from Ambraseys regression on the Johnston based data through equations (28). Dashed line is the regression equation which is compared with the solid line which represents a perfect reproduction by equations (28)

7 THE ATTENUATION FUNCTION

The analysis by Frankel [6] only considered macroseismic intensity level II in the context of the felt area; it is however possible to apply the same form of analysis to other macroseismic intensity levels and that extension is described in this section and is similar to the approach used by Johnston [3].

Murphy and O'Brien's equation (11) correlates the peak ground acceleration a with macroseismic intensity I and shows that increases in peak ground acceleration are correlated

with increasing intensity. As that study was based on the peak ground acceleration, it made the implicit assumption that each of the macroseismic intensity levels is associated with a zero period amplitude (zpa), in other words, the intensity indicators behave as rigid bodies. Inspection of the intensity indicators in the MMI scale used by Murphy and O'Brien clearly show that they are all dynamic systems of one form or another that vibrate and have natural frequencies that are much lower than the frequency of 33 Hz, which is commonly taken to be the typical natural frequency for systems that effectively behave as rigid bodies under seismic input motions. This suggests that macroseismic intensities are functions of their natural or characteristic frequencies and that the correlation should therefore be with the spectral ground acceleration rather than the peak ground acceleration.

The idea that intensities are more closely related to the spectral ground acceleration as opposed to the peak ground acceleration was considered in detail by Brazee [13] with a further study being undertaken by O'Brien [14] although neither study could arrive at specific values. Based on Frankel [6], Johnston [3] used these studies as guides and took intensities II

Intensity (MMI)	Mean Frequency (Hz)	Prime intensity indicator
2	1.0	people at rest on upper floors of houses
3	1.1	Hanging objects
4	1.5	Cars rocking
5	1.8	Small objects move or turn
6	2.5	Everyone feels movement
7	4.0	Car drivers feel shaking
8	5.0	Even heavy furniture moves and partly overturns

Table 4. The characteristic frequency range associated with intensity levels II to VIII

to VI as having a response frequency of 3 Hz as they are associated with the response of the human body. Although in Frankel [6], the frequency finally used for the felt area, intensity II, is 4.2 Hz on the assumption that the corner frequency is the relevant frequency. It was noted in [9], that the magnitude of the Fourier acceleration for intensity II agrees with that determined by Frankel [6] but the frequency at which it occurs is much lower than that determined by Frankel. This is because Frankel assumed that intensity level II would correspond to the acceleration plateau, which is defined by the corner frequency, whereas the approach used here uses intensities that are spread across a range of frequencies between 1.0 to 5.0 Hz.

Intensity level	0.66(f/Q)	f	Q
2	0.00126	3	1571
3	0.00139	3	1424
4	0.00194	3	1020
5	0.00260	3	761
6	0.00176	3	1125
7	0.00328	5	1006
8	0.00586	5	563

Table 5. The values for *Q* for SCR taken from the results in Johnston [3]

For intensities VII to VIII Johnston noted that they are associated with the response of structures and used a response frequency of 5 Hz based on the paper by Nuttli and Herrmann [15]. In their paper Nuttli and Herrmann do not actually make such a statement but note that peak acceleration usually occurs at approximately 5 Hz. Johnston notes that some structures could have natural frequencies that may be higher or lower than 5 Hz, depending on their stiffness. The subject of the frequencies of intensity indicators has been explored by Belsham [9] using the dynamic characteristics of selected intensity indicators for levels II to VIII. The studies revealed that, within this range of intensities, the natural frequency of the indicators increase with increasing level of intensity and this has enabled a refinement of Johnston's analysis of *Q*, the results from [9] are summarised in Table 4.

Intensity level	0.898(f/Q)	f	Q
2	0.0028	1.0	320
3	0.0023	1.1	430
4	0.0028	1.5	481
5	0.0047	1.8	346
6	0.0035	2.5	606
7	0.0068	4.0	528
8	0.0148	5.0	303

Table 6. The values for *Q* for SCRs from the results from this study

Johnston [3] calculates the values for *Q* from the second term in equation (18), which reduces to 0.66(*f*/*Q*) and equates this term to the coefficient that results from the regression analysis for each intensity level. The results are reproduced in Table 5 where the effect of the assumptions made on the frequencies that correspond to the intensity levels become clear.

The analysis is repeated in this study using the frequencies from Table 4 in conjunction with the coefficients in Table 2, which correspond to the revised analysis in this study. The results are given in Table 6 where it can be seen the value of *Q* is fairly constant at an average of 430 across the frequency range 1 to 5 Hz.

8 DISCUSSION

In this article the use of macroseismic intensity to determine the moment magnitudes of earthquakes is discussed in terms of the datasets and the statistical methods used to analyse the data. The relationship between the underlying equations is explored and is extended to show that the point source model provides a theoretical physical basis for the functional forms of the statistically derived equations.

The dataset used in this study is a condensed version of the SCR data given in Johnston [3]. The data has been used in the analyses of both Johnston's approach and the approach in Ambraseys [2] using functional forms of the equations from each method configured to provide a common output presentation format that allows a direct comparison.

The equations of Johnston and Ambraseys have been assessed for their ability to derive consistent values for the magnitudes of earthquakes from the isoseismal felt areas by comparing the calculated data against the original magnitude data for each event in the dataset. This process revealed that both Johnston's method and Ambraseys method overestimate low magnitude events and underestimate the higher magnitude events which

introduces uncertainty in the derived magnitudes. The consistency of these processes can be improved and the uncertainty reduced by introducing weighing functions.

The functional forms of the equations underlying the statistical methods used by Johnston's and Ambraseys to derive the magnitudes from the macroseismic data are found to differ by the Murphy and O'Brien [7] simple two parameter equation, equation (11). This should inform in developing future analysis of isoseismal data.

The results from applying the modified Johnston's equations have been used in conjunction with macroseismic intensity characteristic frequencies derived in Belsham [9], to refine Johnston's model in terms of determining the shear wave attenuation quality factor *Q*.

An important consideration when comparing the methods of Johnston and Ambraseys is that Johnston's method allows for independent coefficients for each intensity level whilst the Ambraseys approach constrains the coefficient to one representative value. As discussed above, this study has highlighted the significance of the attenuation function and that the quality factor should be a constant, at least for SCRs. In the Ambraseys' approach the attenuation term is almost negligible due to the very small value for c_3. In addition, this study has shown that Johnston's approach aligns with theoretical source models. These are strong reasons for giving preference to Johnston's methodology.

9 CONCLUSIONS

For regions with low seismic activity, which in most cases are SCRs, the determination of the magnitudes of historical events is an important consideration. Approaches have been developed by both Johnston and Ambraseys, and others, to derive historic magnitudes using events for which both instrumented magnitudes and macroseismic data is available. The approaches of Johnston [3] and Ambraseys [2] differ in their methodology, both in terms of the functional form used to model the attenuation and the method used for the regression analysis. This study has shown that the approach used by Johnston gives the closer estimate of the magnitude of a historical event for the general SCR.

Johnston used a functional form of attenuation equation developed by Frankel [6], whereas Ambraseys developed a functional form of attenuation equation based on the Köveslighethy equation. As these equations are representing the same physical process they should be closely related and this study has shown that to be the case. Additionally, they are also shown to be forms of a point source model. The similarity between the equation from Murphy and O'Brien and the Köveslighethy equation is also noted.

Based on Frankel [6], Johnston associated a response frequency of 3.0 Hz with macroseismic intensities II to VI and 5.0 Hz for macroseismic intensities V to VIII. Through dynamic analysis of key intensity indicators Belsham [9] has determined characteristic frequencies associated with each macroseismic intensity level these have been used in this study as a refinement in Johnston's approach. The inclusion of those frequencies points towards an almost constant quality factor across the frequency range 1 to 5 Hz. This suggests that the quality factor for shear waves in SCRs is only weakly frequency dependent.

The findings from this study should help improve the determination of the moment magnitude of historic events when using an events collected intensity records. In addition, the explanation of the interrelationships between various approaches for determining the seismic moment and the determination of key seismic parameters should also help in improving the calibration of seismic source models for both instrumented and historic events. This is possible by relating the accelerations at the surface of a homogenous half-space to an intensity level through the relationship between Johnston's method and point source theory such as used in the Stochastic Method.

REFERENCES

[1] Report: Macroseismic estimation of earthquake parameters, *NEtwork of Research Infrastructures for European Seismology*, 2007.

[2] Ambraseys N. N., (1985), Intensity-attenuation and Magnitude-Intensity relationships for Northwest European Earthquakes, Earthquake Engineering and Structural Dynamics, 13, pp. 733 - 778.

[3] Johnston A. C., (1996), Seismic moment assessment of earthquakes in stable continental regions – II Historical Seismicity, Geophys. J. Int. 124, pp. 381 - 414.

[4] Johnston A. C., (1989), The Seismicity of 'Stable Continental Interiors', Earthquakes at North Atlantic Passive Margins: Neotectonics and Postglacial Rebound, pp. 299 - 327, Kluwer Academic Publishers.

[5] Boore D. M., (1983), Stochastic simulation of high-frequency ground motions based on seismological models of the radiated spectra, Bulletin of the Seismological Society of America, 73, pp. 1865 - 1894.

[6] Frankel A., (1994), Implications of Felt Area-Magnitude Relations for Earthquake Scaling and the Average Frequency of Perceptible Ground Motion, Bulletin of the Seismological Society of America, 84, 2, pp. 462 - 465.

[7] Murphy J. R. and O'Brien L. J., (1977), The correlation of peak ground acceleration amplitude with seismic intensity and other physical parameters, Bulletin of the Seismological Society of America, 67, pp. 877 – 915.

[8] Köveslighethy R. von, (1907), Seismicher Starkegrad und intensitat der Beben, Gerlands Beitr.z. Geophysik, 1907, vol. 8, pp. 363 – 366.

[9] Belsham C. S., (2008), The Dynamic Response of Seismic Intensity Indicators, Proceedings of the Ninth International Conference on Computational Structures Technology, Athens, Greece.

[10] Hanks and Kanamori (1979), A Moment Magnitude Scale, J. Geophys. Res. 84, pp. 2348 – 2350.

[11] Boore D. M., (2003), Simulation of Ground Motion Using the Stochastic Method, Pure and Applied Geophysics 160: pp. 635 - 676.

[12] Ambrasesys N. N. and Douglas J., (2004), Magnitude calibration of north Indian earthquakes, Geophys. J. Int., 159, pp. 165 - 206.

[13] Brazee R. J., (1979), Reevaluation of the Modified Mercalli Intensity Scale for Earthquakes using Distance as Determinant, Bulletin of the Seismological Society of America, 69, p. 911.

[14] O'Brien L. J., (1980), The correlation of response spectral amplitudes with seismic intensity, NUREG/CR-1259, R6, RA; United States Nuclear Regulatory Commission; Division of Reactor Safety Research. Washington, DC.

[15] Nuttli, O.W. & Herrmann, R.B., (1984), Ground motion of Mississippi Valley earthquakes, J. tech. Topics civ. Eng., 110, pp.54 - 69.

APPENDIX A

Ref	log M_0	M_W	r_{II}	r_{III}	r_{IV}	r_V	r_{VI}	r_{VII}	r_{VIII}
NA-25-0301	25.70	6.47	6.42	6.15	5.84	5.16	4.81	4.01	3.27
NA-29-0812	23.35	4.90	5.95		5.24	3.94	3.08	3.20	
NA-29-1118	26.92	7.28	6.74	6.64	6.38	5.94	5.43		
NA-35-1101	25.36	6.24	6.33	6.17	5.89	5.11	4.60	2.88	
NA-39-1019	24.00	5.33	6.18	5.76	5.20	4.51	3.75		
NA-40-1220	24.20	5.47	5.62	5.79	5.24	4.56	3.85	2.61	
NA-44-0905	24.73	5.82	6.06	5.91	5.55	5.04	4.32	3.76	3.03
NA-62-0202	22.40	4.27	4.94			3.60	2.21		
NA-63-0303	23.04	4.69	5.38		4.81	4.45	3.71		
NA-65-1021	22.98	4.65	5.55		5.08	4.13	3.60		
NA-66-0101	22.40	4.27	4.67			3.13			
NA-67-0604	22.49	4.33	4.75			3.99			
NA-67-0613	22.18	4.12	3.85			2.81			
NA-68-1109	24.11	5.41	6.19		5.71	5.17	4.45	3.71	
NA-69-0101	22.56	4.37	4.92			4.14			
NA-69-1120	22.86	4.57	5.53	5.53	4.47	4.29			
NA-70-1117	22.20	4.13	4.99			4.25			
NA-72-0915	22.23	4.15	5.36						
NA-73-0615	22.79	4.53	5.25	4.89	4.65	4.00			
NA-73-1130	22.18	4.12	4.98		4.93	4.35	1.13		
NA-74-0215	22.60	4.40	4.83		4.68	3.80			
NA-75-0613	21.66	3.77	4.23		3.68				
NA-75-0709	22.51	4.34	4.91		4.70	4.28	2.87		
NA-75-0712	22.23	4.15	5.15	4.82	3.82				
NA-76-0325	22.99	4.66	5.45			4.98	3.77		
NA-78-0218	21.90	3.93		4.71	3.86	2.82			
NA-78-0616	22.81	4.54	5.45			3.90			
NA-79-0819	23.18	4.79		4.75	4.44	3.81			
NA-80-0727	23.63	5.09	5.82		5.46	4.71	4.06	2.60	
NA-82-0109a	24.28	5.52		5.71	5.36	4.89	3.38		
NA-82-0109b	23.19	4.79	5.14	4.90	4.05	3.70			
NA-82-0111	23.67	5.11	5.42		4.91	4.50	3.45		
NA-82-0119	22.56	4.37	5.13			4.22	2.76		
NA-82-0121	22.67	4.45		4.54		2.81			
NA-82-0331	22.20	4.13	4.96		4.58	3.90			
NA-82-0402	21.60	3.73	4.50		3.90				
NA-82-0616	22.05	4.03	4.85		4.50	3.90			
NA-82-0713	20.85	3.23	4.25		3.70				
NA-82-0813	21.30	3.53	4.66		4.25				
NA-83-1007	23.36	4.91	5.81		5.52	4.79	3.42		
NA-84-0908	23.46	4.97	4.83			3.93			
NA-86-0131	23.32	4.88	5.52		5.10	4.41	3.02		
NA-86-0712	22.65	4.43	5.01		4.24	3.51	2.48		
NA-87-0610	23.49	4.99	5.68			4.80	3.20		

Ref	log M_0	M_W	r_{II}	r_{III}	r_{IV}	r_V	r_{VI}	r_{VII}	r_{VIII}
NA-88-1125	24.82	5.88	6.52		6.16	5.68	5.12		
NA-89-1225b	25.11	6.07	5.90		5.55	4.85			
NA-90-0926	22.48	4.32	5.16		4.71	4.13	3.13		
NA-90-1019	22.92	4.61	5.81		5.74	4.40			
NA-91-0504	22.54	4.36	4.96		4.56	4.06	2.97		
NA-94-0116	22.08	4.05		4.09	3.52	2.69	1.70		
AF-39-0622	25.77	6.51	6.32		6.03	5.78	4.87	2.80	2.43
AF-45-0912	25.15	6.10		5.57					
AF-55-0912	25.66	6.44			5.89	5.68	5.20	4.92	
AF-69-0929	25.65	6.43	6.30	5.88	5.61	5.04	4.30	3.37	2.98
AF-83-1222	25.41	6.27		6.12		5.45			
AU-66-0503	22.74	4.49		5.01	4.67	3.16			
AU-68-1014	25.92	6.61		6.12	5.81	5.18	4.24	3.09	2.53
AU-73-0309	23.76	5.17			5.48	4.66			
AU-79-0602	25.19	6.13	6.03		5.66	4.69	3.53	2.41	2.06
AU-82-1121	23.03	4.69		5.15	4.82	4.15			
AU-88-0122a	25.45	6.30		6.24	5.87	5.43	4.21	3.74	
AU-88-0122b	25.61	6.41		6.24	5.87	5.43	4.21	3.74	
AU-88-0122c	25.91	6.61	6.44		6.11	5.76	4.46		
CH-62-0318	25.11	6.07			5.61	5.10	4.11	2.85	1.69
CH-69-0725	24.71	5.81					3.60	3.03	2.30
CH-69-1217	23.24	4.83			4.99	4.77			
CH-69-1220	23.16	4.77			4.79	4.47			
CH-74-0422	24.04	5.36		5.20	4.76	3.54	2.96	1.97	
CH-79-0709	24.20	5.47		5.60	5.22	4.80	3.38	2.60	1.48
CH-84-0512	25.17	6.11			5.32	4.84	3.78		
CH-87-0802	23.56	5.04				3.99	3.10	1.82	
EU-78-0903	23.70	5.13		5.56	5.23	4.79	3.75	3.11	
EU-83-1108	23.20	4.80	5.17	5.11	4.26	3.35	2.59	1.96	
EU-86-0205	23.11	4.74		5.52	5.25	4.82			
EU-88-0808	24.43	5.62		5.81	5.55				
EU-89-0123	23.76	5.17		5.58	5.29	4.83			
EU-92-0413	24.04	5.36	5.88	5.54	5.16	4.58	3.82	2.81	
IN-56-0721	25.08	6.05	5.91	5.41	5.01	4.51	3.73	3.55	3.17
IN-67-1210	25.51	6.34	6.19		5.65	5.00	3.31	2.79	
IN-69-0413	24.66	5.77	6.20		5.46	5.11	4.60		
IN-70-0323	24.14	5.43	4.94	4.61	4.35	3.84	2.95	2.04	
IN-93-0929	25.31	6.21		6.16	5.77	5.04	4.44	3.17	2.67
SA-80-1120	23.85	5.23	6.10		5.18	4.66	3.51	3.12	

Table A.1. Table is a condensed version of that given in Johnston [3] which details the events in global SCR which have information on both instrumentally measured magnitudes and isoseismals data

Notes for Table A.1.:
Ref is the same as given in Johnston [3]. Log M_0 is the logarithm to the base 10 of the seismic moment measured instrumentally. M_W is the moment magnitude. r_i are the isoseismals radii where *i* is the intensity level
In the refs column the prefixes are: NA – North America, AF – Africa, AU – Australia, CH – China, EU – Europe, IN – India, SA - South America

Ref	log M_0	M_W	r_{II}	r_{III}	r_{IV}	r_V	r_{VI}	r_{VII}	r_{VIII}
CH-18-0213	26.99	7.33	6.50		6.36		5.24	4.66	4.10
AU-41-0429	26.17	6.78		6.32	6.13	5.64	5.14	4.54	4.01
CH-79-0521	23.6	5.07				3.07	2.56	1.81	
EU-84-0719	23.81	5.21		5.38	5.02	3.94	3.14		
AU-87-1222	23.17	4.78	5.23		4.83	4.15	3.04		
AU-89-0528	24.13	5.42	5.20		4.89	4.39	3.56	2.81	
AU-89-1227	24.19	5.46		5.47	5.04	4.56	3.83	2.18	1.40
EU-90-0402	23.10	4.73	5.38	5.13	4.79	4.16	3.20		
AU-92-0930	23.96	5.31	5.67	5.44	5.15	4.69			
IN-34-0115	28.04	8.03	6.77		6.53	6.31	5.40*	5.00*	4.70*
SA-77-1123	27.11	7.41		6.51	6.14	5.78	5.42		
AU-77-0819	28.48	8.32	7.10	6.91	6.64				

Table A.2. Table is a condensed version of that given in Johnston [3] which details the events occurring outside of SCR but for which there are isoseismals in the SCR, which have information on instrumentally measured magnitudes

Notes for Table A.2.:
Ref is the same as given in Johnston [3]. Log M_0 is the logarithm to the base 10 of the seismic moment measured instrumentally. M_W is the moment magnitude. r_i are the isoseismals radii where *i* is the intensity level
In the refs column the prefixes are: AU – Australia, CH – China, EU – Europe, IN – India, SA - South America
Entries marked with an * have the following average values in [3] - 6.08, 5.5, 5.03.

COMPDYN 2013
4th ECCOMAS Thematic Conference on
Computational Methods in Structural Dynamics and Earthquake Engineering
M. Papadrakakis, V. Papadopoulos, V. Plevris (eds.)
Kos Island, Greece, 12–14 June 2013

CONDITIONS FOR MEASURING SEISMIC SHOCKS AND THEIR ANALYSIS AND RESPONSE ON BUILDINGS AND INDUSTRIAL STRUCTURES

Stanislav Ziaran[1], Milos Musil[1] and Michal Cekan[1]

[1]Faculty of Mechanical Engineering, Slovak University of Technology in Bratislava, Nam. slobody 17, 81231 Bratislava, Slovakia
e-mail: stanislav.ziaran@stuba.sk, milos.musil@stuba.sk, michal.cekan@stuba.sk

Keywords: Seismic shock, FFT analysis, buildings, industrial structure, integrity, resonance

Abstract. *The goal of this contribution is to define the conditions and basic principles for measuring seismic loads generated by seismic shocks, process and analyze the measured response of seismic* (*low frequency mechanical vibration*) *on buildings and industrial structures and to develop a methodology for measuring on a specific structure. The conditions and basic principles for measuring can be applied for different kinds of seismic sources of excitation such as: explosions, wind, random excitation from local transportation, periodic excitation from large rotating and/or machines with reciprocating motion, metal forming processes such as forging, shearing and stamping, chemical reactions, construction and earth moving work, earthquakes and other strong deterministic and random energy sources caused by human activities. All of which negatively affect the integrity of buildings and industrial structures as well as the environment of those who live or work in such conditions. In evaluating the effects of such seismic shocks* (*vibration*) *on buildings and industrial structures, the response of these structures and the possible negative impact on them is performed. The contribution includes the appropriate analytical methods where the frequency, duration of, and amplitude is definable as well as the processing and verification of methodology and preparation of measurements, optimal location of measuring points, how to attach the sensors, the measurement equipments used, measured variables and procedure are also given. For the detection of a seismic shock resulting from an explosion the FFT analysis and modal analysis, in the frequency domain, is used and the signal was acquired and evaluated also in the time domain. In the conclusions the measured results of a seismic shock caused by blasting in a nearby quarry and its effect on a nearby structure* (*house*) *is evaluated. The response on the house, including the natural frequency and possible fatigue damage is also assessed.*

1 INTRODUCTION

The response of buildings and industrial structures on seismic excitation depends on the type of excitation, because there are differences between earthquakes and mechanical vibrations (further just vibration) and/or shock (dynamic loading) resulting from human activities which effect the conditions of the measured data. Sources of earthquakes are dimensionally large and much deeper than most vibration sources caused by human activity. Earthquakes cause damage over large distances, are characterized by a much larger flow of seismic energy, duration and different types of seismic wave propagation. Therefore, for the same evaluating parameter, for example, the peak value of the measured objects element velocity, the effects on buildings and industrial structures vary. In this respect, seismic measurements are affected by the source of the shock (vibration) and thus its frequency, duration and amplitude, where the low frequency vibration caused by an earthquake, wind, explosions [1], aerodynamic impact, machines installed in buildings or industrial structures and/or in the vicinity of these structures [2, 3, 4], technological processes such as forging, shearing and forming [5], chemical processes [6], transportation, construction activity and other sources of unwanted seismic excitation, must be considered. The effects of seismic events on buildings and industrial structures can by evaluated analytically. In such an analysis the resonant frequency of the basic construction and its parts must be considered, for example, for buildings it is the resonance of the walls, floors and windows. Also of importance is the modal damping characteristics of the structure and its parts, type of construction, its state and material properties including its nonlinearity of the amplitude at response of the monitored construction and finally the spectral properties of the construction such as the mode shapes but also the spectral of the seismic excitation. In such an evaluation of the procedure, source of seismic excitation, transfer path and transfer function, exposition of the construction and its response must also be taken into consideration.

2 MEASUREMENT CONDITIONS IN THE SEISMIC EXPOSITION OF THE STRUCTURES

In assessing the effects of seismic shock and/or low frequency vibration on buildings and industrial structures, rules dictate that the following be performed before measurement:

- technical assessment of the monitored construction, documentation of its important structural nodes, mainly its foundation, characteristic dimensions, finishing method and construction material, study of available documentation and defining procedures for the solution of the problem;
- analysis of the structures current state and its documentation;
- implementing the plan for experimental testing corresponding to the source of the seismic action, transfer path and position of the monitored structure *in situ* with respect to the source of the dynamic loading;
- evaluation of the terrain in the path of the seismic wave, mainly in terms of the transverse relief in the direction of the seismic wave propagation (For example, over a plane, in a valley, over hills) where deflection, interference or dispersion of the energy of the seismic wave can occur;
- determination of the measurement areas in the building and/or the industrial structure in terms of the location of the explosion (see fig. 1);

- measurement of seismic shock (vibration) and its transfer from the source of the natural areas to the object being measured, including the FFT analysis and time domain;
- measurement and vibration analysis of secondary vibration (background analysis) and its evaluation;
- evaluation of the effects of the seismic shock on the measured structure, for example, in terms of standards ISO 4866 [8], scientific literature [9. 10, 11] and current experience of the evaluators.

2.1 Quantification of the Seismic Excitation Source

Seismic loading (vibration, shocks) can be classified as deterministic or random loading. For example, a seismic shock generated by an explosion, which is the case in this paper for analysis, is considered to be between deterministic and non-periodic dynamic loading.

The duration of the dynamic excitation force is an important parameter and the response of such loading can considered continuous or transient. The type of response is given by the relationship between the time constant with the response of the structure and force action. The time constant of the resonance response for resonance (indicated by index r), τ_r , in seconds, is given by [8]:

$$\tau_r = \frac{1}{2\pi\xi_r f_r} \tag{1}$$

where ξ_r represents the damping effects and depends on the type of excitation (linear or nonlinear);
f_r is the resonant frequency.

In this way two scenarios can be defined (regardless whether the excitation is deterministic or random), and that is:

- continuous, if the structure is acted on by a continuous force effect for more than $5\tau_r$, the vibration is considered to be continuous. For example, a series of blasts with a high number of individual explosions;
- transient, if the action of force is shorter than $5\tau_r$, the response is considered to be transient. For example, one explosion or a series of blasts with a small number of individual explosions.

Demolition work, when a series of blast is used, can be considered as a transient or continuous case that is dependent on the length of the resonance response. In the given case, the response generated by one explosion can be considered as transient.

The frequency interval (range) of vibration, which is the case in this contribution, depends on the distribution of the spectra in the frequency range of excitation and from the mechanical response of the structure. This emphasizes the limits of the spectra's contents as one of the most important properties of input vibration (shock). In the interest of simplification, the frequency range is taken to be from 0.1 Hz to 500 Hz, which covers the response for a wide variability in buildings and industrial structures and their structural elements excited by natural sources (winds and earthquakes) and human activities (construction work, mechanical and chemical industries, demolition work, transportation of heavy vehicles, etc…), in the

excitation of internal mechanical equipment, measurement of higher frequencies may be required [2].

More so, damage to buildings and industrial structures caused by human activity occur in the frequency range from 1 Hz to 150 Hz. Natural sources, such as earthquakes, typically have intensive energy, which has damaging effects at lower frequencies (from 0.1 Hz to 30 Hz). Excitations caused by wind have significant energy in the frequency range of 0.1 Hz to 2 Hz. Apart from these realities, for the given situation (nearby explosion) the frequency range of measurement is defined up to 200 Hz.

The level of vibration velocity, in the range which is of interest, depends on the frequency and the value of their velocity is from a few millimeters per second to as much as a few hundred millimeters per second. For more detailed information regarding vibration velocity – strength of vibration, see [7].

2.2 Quantification of Buildings and Industrial Structures

The reaction of building and industrial structures (and their components) on seismic excitation depends on the frequency characteristic (on the natural frequency, and natural modes of vibration and modal damping), as well as the contents of the excitation spectra. Practice dictates that the cumulative effects are taken into consideration, especially for high levels of response and long exposition time, where fatigue damage is possible [2, 5].

The basic natural frequencies of a structure or its parts impact their response. Therefore it is necessary to know the methods in evaluating vibration, which are used in the assessment of structures. It can consist of the spectral analysis with low level response on the surrounding excitations or the use of exciters [8, 9].

Experimental studies [9] have shown a range of basic frequencies from 4 Hz to 15 Hz for transverse vibration (shear loading) on low structures (from 3 m to 12 m high). The damping properties are typically dependent on the amplitude. The building in this paper belongs to this category of structures, therefore it is expected to obtain the natural frequencies in this range (fig. 1).



Figure 1: Measured object (left); location of explosion 1250 m away from the object (right)

Vibrations propagating through the ground can have a wavelength from a few meters to a few hundred meters. The response of short wavelength vibrations is complex and the foundation of buildings or industrial structures can act as a filter. Smaller structures, such as homes and cottages, typically have foundations that are dimensionally smaller than the basic

wavelength of all seismic sources except for sources with the highest frequencies [8], which have an effect on the dynamic loading of the structures.

Evaluating the interaction effects of the floor is sometimes done while vibration induced by human activity. Evaluation conditions are defined such as: the velocity of the transverse wavelength (shear effects on the structure) or dynamic module of elasticity from an appropriate volume of earth. Foundations on poor ground can cause the foundation to sink or loose stability. The risk of such effects is a function of the granular size of earth, its homogeneity, compaction, moisture level, internal stress state, as well as the peak value of multidirectional acceleration and duration of the grounds excitation. Especially sensitive ground are free, loose, sand with high water content, which for extreme cases can become quicksand [3, 4]. The transverse relief of the terrain should also be taken into consideration, since it transmits the seismic waves. In flat terrain the area dispersion of seismic energy occurs. For valleys this dispersion is minimal, and the size of the propagating seismic energy rebounds off of steep slopes in the valley and is affected by wave interference.

The measured object is built on rigid ground, which simplifies the measurement since a single sensor can be used to measure the horizontal direction of the transmitted vibration. On the other hand, the object is located in a narrow valley, where the dispersion of seismic energy is minimized from the source of the dynamic excitation generated by human activities such as a blast in a quarry.

3 METHODOLOGY OF THE EXPERIMENT

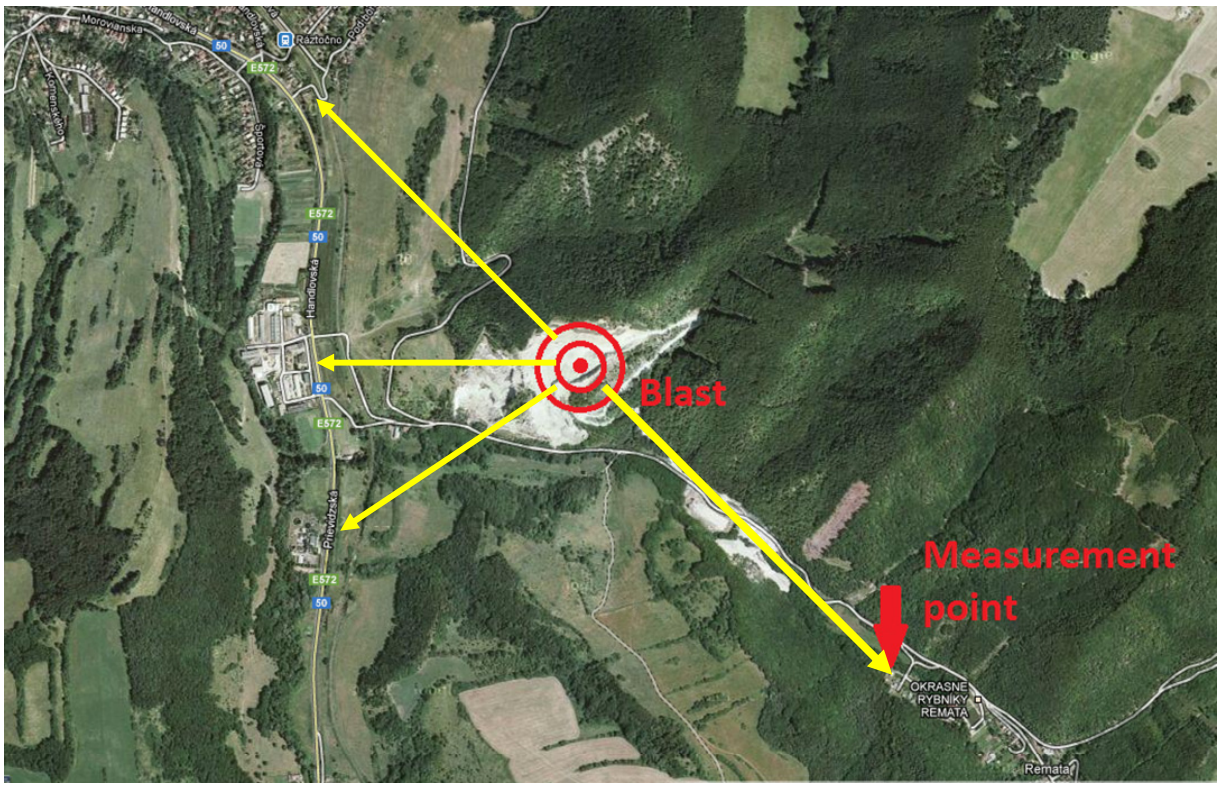
The goal of the experimental tests is to determine the effects of seismic shocks (mechanical impulse, random or periodic vibration) and the possible damage to buildings and/or industrial structures, systems they may cause and the effects on human beings in the area of these objects with respect to their comfort and disturbance [12, 13, 16]. In order to realize such a test it is needed to:

- determine the location of the monitored structure with respect to the source of the seismic shock, if it is known (fig. 2 top);
- appropriately select three (or in some cases two) measurement areas, one in the horizontal plane and two perpendicular to each other in the vertical plane on ground floors. In the case that the object is placed at a known location to the source of the seismic shock, two measurement areas are sufficient, where the measurement in the horizontal direction coincides closely to the direction of the Rayleigh surface wave ray (fig. 2 bottom);
- measurement of the seismic shock (source of the dynamic load on the structure) including FFT analysis, during the exposition of the structure [7, 14];
- measurement and analysis of secondary vibrations (background) and their assessment;
- evaluate the source of the generated seismic shock (vibration) with respect to the important value, which can affect the measurements of the structure.

3.1 Measurement Locations

The structure measured is a three story house (see fig. 1), for which the first floor is built into a slope and used as a garage and basement. The location of the house with respect to the source of the explosion (seismic shock) is shown in fig. 2 top. The lower part in fig. 2 shows the floor plan of the house, measuring locations for the vertical and horizontal measurement

directions, and location of the source (approximately 1250 m away). The plan also shows the direction of progression of the Rayleigh wave ray,



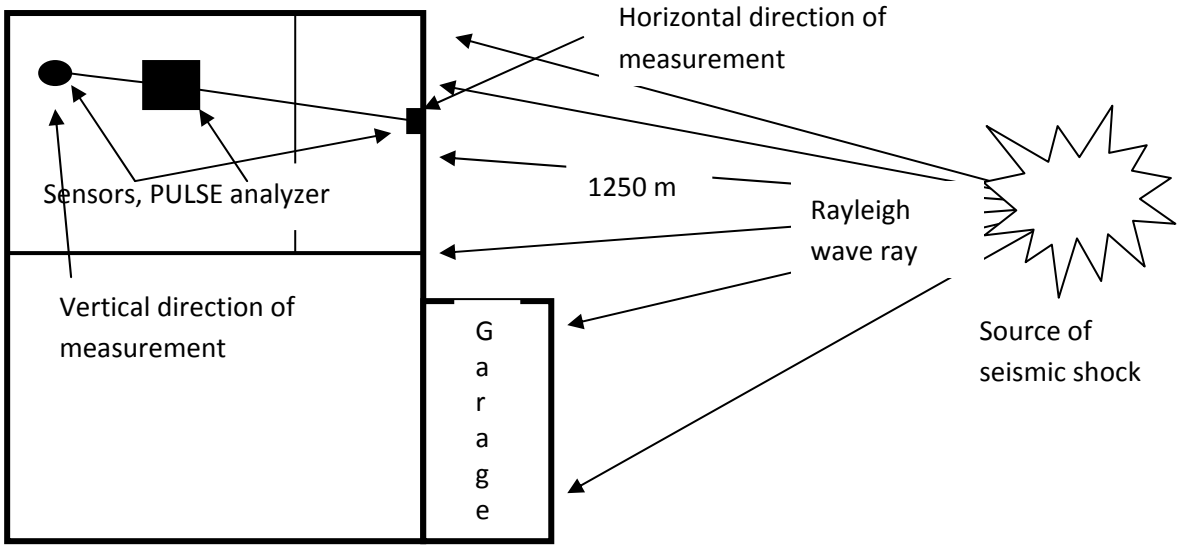


Figure 2: Source of the explosion with respect to the measured object (above), measurement points within the measured object (below)

3.2 Measurement Equipment

To measurement of the seismic shock (vibration) the PULSE Analyzer, Dyn-X, FFT, MI 3560-B-X10 made by Bruel & Kjaer (fig. 3) was used. This analyzer represents an open system, which allows for new possibilities, more information and reliability in the

measurement process, analysis, and evaluation. Part of this system is the piezoelectric accelerometer, microphone, display and memory module (laptop PC).



Figure 3: PULSE analyzer system with accessories

An appropriate aid in the measurement of kinematic parameters of seismic shocks (vibration) is a solid steel cylinder, which is used in the measurement of vertical vibrations in horizontal structural elements (fig. 4 left). This aid has three adjustable tips, which allow for the correct selection of sensor position even on an uneven base. For the measurement of kinematic parameters in the horizontal direction (vertical structural elements) various aids which rigidly attach to vertical (and perpendicular) load bearing walls (fig. 4 right). In the case that the location of the seismic event is known, horizontal measurements can be taken by only one sensor positioned such that its sensitive axis is positioned towards the seismic source. If the source is unknown, it is advised to use a tri-axial vibration sensor.

Sensor mounting on structural elements of the building must coincide with the ISO 5348 standard with respect to accelerometers [14]. The goal is to ensure that the sensor correctly reproduces the motion of the structural element or foundation without interfering with the response, thus the upper areas of the foundation were selected as a suitable element (fig. 4 right). It should be taken into consideration that any aid used in measuring kinematic parameters of seismic events in the horizontal direction are considered to be non acceptable.



Figure 4: Measuring position and sensor placement for vertical vibrations (left); measuring position and sensor placement for horizontal vibrations (right)

3.3 Measured Parameters and Procedures

The measurement device and its technical parameters must be calibrated before measuring any seismic event. Proper calibration and setup is very important in measuring short non-repeating seismic events. Other than the frequency range, for the type of signal, it is also very important to select the appropriate type of averaging as well and number of averages per unit time as well as a suitable time window [15]. Definition of the measured parameter, such as the vibration velocity (strength of vibration) and other performance parameters must be done. For short non-repeatable seismic events caused by human activity (blasting in a quarry) it is indispensable to setup the time interval of the measurement such that the signal is measured before the event occurs (background signal), during the seismic event, and after the seismic event (background signal).the time interval of the seismic signal is the basis for determining the strength of the vibration, since this energy parameter is used to evaluate the effect of the seismic event on the structure. For example, basic parameters for vibration induced by blasting can be seen in tab. 1. Before and after the measurement of non-repeatable seismic events it is beneficial to measure any secondary vibrations from external and/or internal sources of dynamic loading.

Force induced by vibration	Frequency range Hz	Amplitude range μm	Segment velocity range mm/s	Segment acceleration range m/s^2	Time characteristic	Measured variable
Vibration from blasting, propagated through ground	1 - 300	100 - 2500	0,2 - 500	0,02 - 50	T	pvth

Key
C = continuous; T = transient; pvth = particle velocity time history
NOTES:
1. – The ranges are extreme but indicate values which can be identified from experience and which can be measured (see note 3). The extreme range in amplitude, deviations and frequency are not used to derive the segment velocity and acceleration.
2. – The frequencies reflect the response of the building and structural segments with respect to individual types of excitation. Its character is only for orientation.
3. – Vibration values in the given ranges can be the cause of disturbance. No standard exists, which cover all building changes, state and duration of exposition, but many national codes connect boundary visual effects of peak value segment velocity of the building foundation for more than a few mm/s. significant possibility of damage is related to the peak value segment velocity, whose value reaches a few hundred mm/s. The level of vibration below human feeling (ISO 2631-2 [14]) should be considered in cases of sensitive industrial work procedures.

Table 1: Basic parameters for blasting [8]

Throughout the measurements other variables are recorded that are essential to the frequency analysis, identification of measurement location and their corresponding frequency spectra, such as possible unique effects during measurements (random impacts and shocks caused by human activities in the surrounding areas). Such unique events, which can impact the correctness of the results, are an essential part of seismic measurements. By means of FFT analysis, the natural frequency of the measured building is determined.

Overall, six auto spectrum are recorded from the defined measurement locations by means of contact vibration sensors (accelerometers), and coincidentally, the time history can be saved in memory for both measurement locations. Two auto spectrum and time history represent the blast itself and the remaining secondary dynamic loading (background).

4 EVALUATION OF SEISMIC SHOCKS AND DISCUSSION

Seismic shocks are beneficial to evaluate with respect to the frequency distribution of the signal, which allows for the determination of the structures mode shapes as well as time

history, which records the maximum amplitude of vibration velocity and is used also in the further laboratory processing of the signal.

The environment of the measured object was seismically quite which means that there were no other sources of dynamic loading, such as from transportation, industry or other human activities. The measured object is located in a quite valley of mountains, which the frequency analysis of the background proves (no secondary vibrations from external sources was measured).

4.1 Frequency Analysis of Seismic Shocks

The frequency analysis of secondary vibration (background) from either measurement locations clearly confirms that no significant source of dynamic loading existed internally or externally (fig. 5). Significant vibration amplitudes at higher frequencies are caused by human activities, who were dwelling within the home (owner, child, operators) but had little effect on the results. From the frequency analysis of the background and seismic excitation, it is possible to state that the structure is sensitive to internal vertical excitation (fig. 5 right), while the horizontal excitation is sensitive to the seismic event.

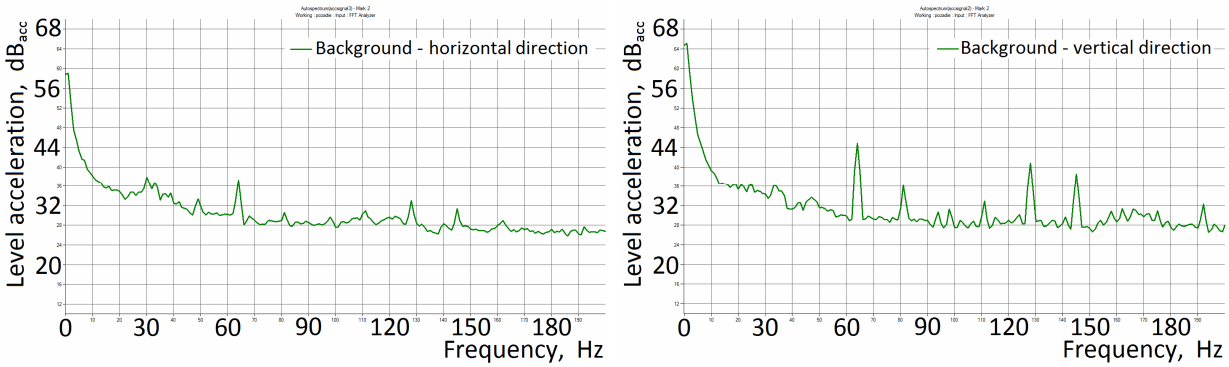


Figure 5: Frequency spectrum of the background in the horizontal direction (left) and vertical direction (right)

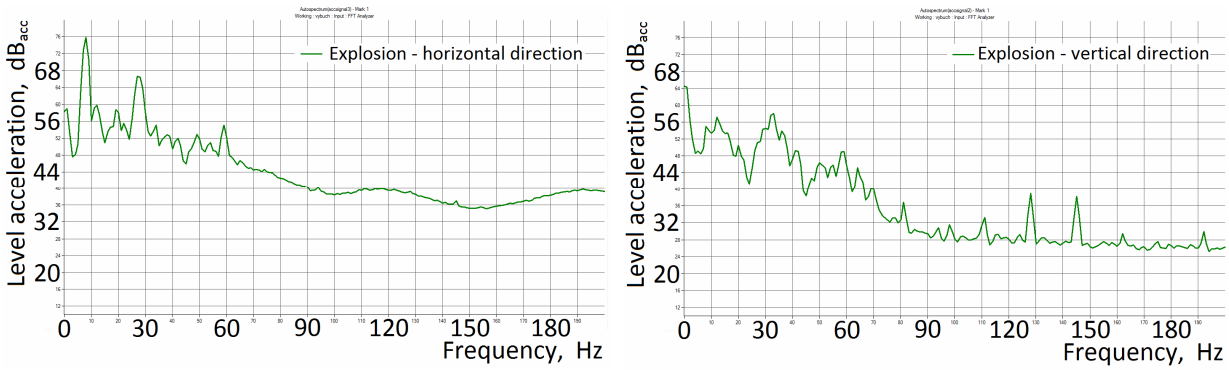


Figure 6: Frequency spectrum of a seismic shock in the horizontal direction (left) and vertical direction (right)

By means of the FFT analysis the levels of seismic acceleration (explosive) are determined in the measured locations. Due to the short duration of the seismic shock the highest possible averaging is used in order for the amplitudes of vibration, at the monitored frequencies, reached the correct value as closely as possible. The results of the FFT analysis of the seismic shock are given in fig. 6. The dominant amplitude of vibration is at 8 Hz in the horizontal direction, that is the direction of the seismic wave propagation. This frequency represents the natural frequency of the monitored structure (house). Therefore, according to relation (1) for the estimation of damping the duration of the dynamic excitation can be determined. On the

other hand, with known response duration the modal damping properties of the structure can be determined. At this frequency, vibration amplitudes are significantly lower in the vertical direction which corresponds with the shear stress excitation (greatest in the horizontal direction). In general, the amplitudes of the structures vertical vibration are significantly lower. Comparing the right sides of fig. 5 and 6 the amplitude and frequency correlation can be seen, which documents the activities of a household appliance (possibly the refrigerator).

Comparison of the frequency spectra of the seismic shock and secondary vibrations (background) can be seen in fig. 7. In this comparison a noticeable increase in dynamic loading during the seismic event can be observed at lower frequencies. However this increase is not so significant as to negatively impact the structure of the building. This fact is solidified by the subjective feeling of the investigator and operator who were not able to feel the shock in the building. Graphs of the frequency analysis in units of vibration velocity are also shown In fig. 7, which can be a measure of seismic threat to buildings and industrial structures. It is important to remark that the time interval of the frequency analysis was one minute and so the energetic averaging coincides to this.

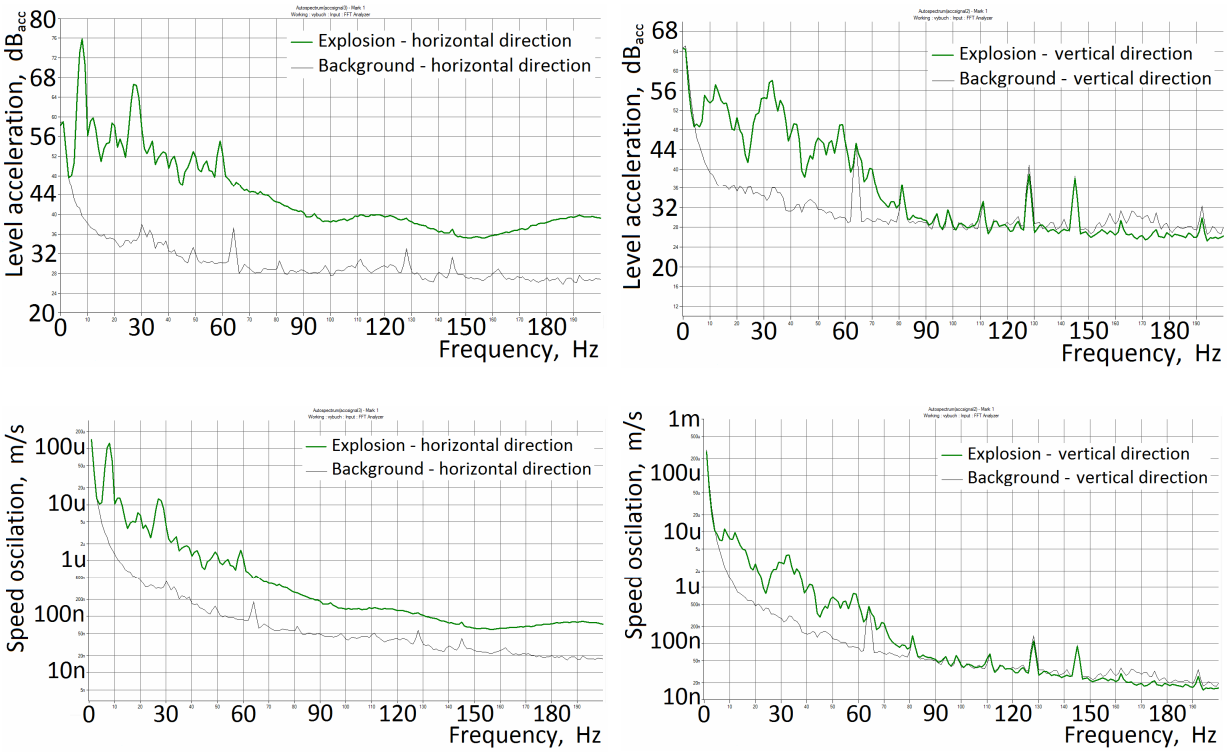


Figure 7: Comparison of the frequency spectra for an explosive shock and background in the horizontal direction (left) and vertical direction (right|)

4.2 Time Character of an Explosive Shock (blast)

With the frequency analysis, the time character of secondary dynamic loading in the monitored building was also measured with the time character of the seismic shock. The recorded time character serves further analysis of the dynamic loading in the structure. The time character of the seismic shock for both directions is seen in fig. 8. From the time character, it is possible to accurately determine the peak value of the building segments velocity where the sensor is placed. From fig. 8 (top) it is possible to state that the peak value in the vertical direction is not significant when compared to the peak value in the horizontal direction. The maximum segment acceleration of the building reached a value of 1.6 m/s^2,

which gives a peak value of velocity of v = 31.84 mm/s. From fig. 8 it is possible to calculate the peak-to-peak value [10], whose velocity was 15.92 mm/s.

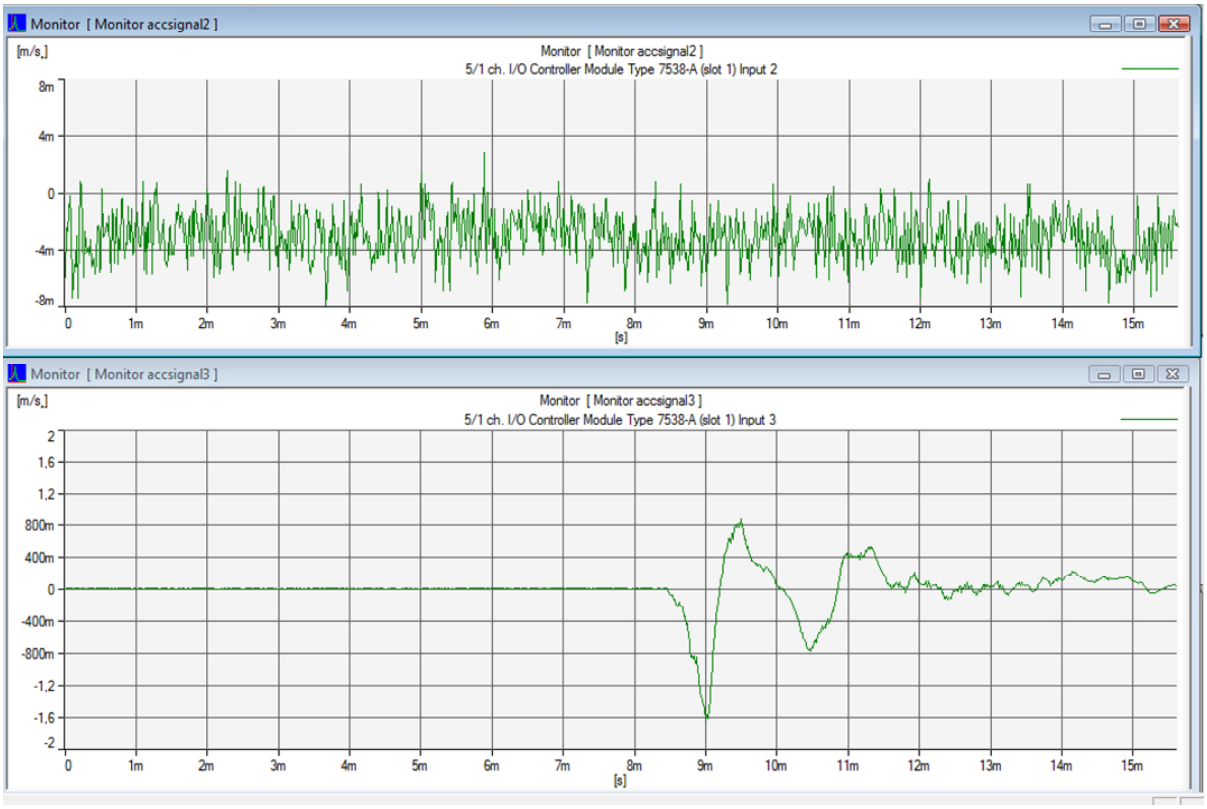


Figure 8: Time history of an explosive shock and background in the horizontal direction (bottom) and vertical direction (top)

4.3 Evaluating the Effects of a Seismic Shock on the Given Building

In terms of the standard ISO 4866, the monitored building can be categorized as a modern structure using relatively hard materials, which are connected in all directions and is relatively light with low damping factor. This category consists of the skeletal structure of the building as well as type of materials and load bearing. Buildings can be single level or multi leveled. All roofed types are included. This category contains older types of housing who's construction has been made with modern materials, constraints and damping.

ISO 4866 states that the foundation of the monitored building is categorized by A [8], which consist of these types of foundations: bound concrete rebar or steel piles and rigid concrete rebar footing and floor, on which the structure can be organized into the following types of ground: stones or hard rock, brittle rock, cemented or compacted sand, horizontally seated earth.

The type of analysis is obvious, if it is identified to which category the structure belongs in [8]. The variables, for this type of dynamic loading, are characterize as deterministic, and thus it is enough to use a simple analysis (effective value, peak value, peak-to-peak value, mean quadratic value).

Greater changes in cyclic stress cause a high risk of fatigue damage. In the given case, fatigue damage is not a factor because, for low levels of vibration which the analyzed source

generated, it would require 10^{10} load cycles (blasts) [1]. Fatigue damage can be considered with high levels of response over a longer exposition duration.

A significant possibility of damage is related to the peak value of the structures segment velocity, whose value reaches a few hundred millimeters per second. In the given case, this value is significantly lower and the peak value of the velocity of the load bearing wall at the foundation reaches about 32 mm/s, which is almost at the beginning of the monitored range (see tab. 1 [8]) the value of peak-to-peak value is even smaller equal to only 16 mm/s. These values are not so great as to negatively affect the monitored building. This fact is confirmed by the subjective feeling of the investigator and operator which were present at the place if measurement during the seismic event.

5 CONCLUSION

In the measurement of seismic shocks (vibrations) it is very important, in the evaluation of seismic event on building and industrial structures, to correctly place the accelerometers. Each placement can cause significant deviation from the actual kinematic parameters of excited vibration. In determining the place of measurement it is important to respect also the height of the structure since vibrations tend to increase higher up in the structure. For the given object (house) the measurement point for the horizontal direction were chosen directly below the top of the buildings foundation on the main load bearing wall, which corresponded to the level of terrain outside, and was oriented perpendicular to the direction of high energy wave (toward the source). The sensor must always be mounted on load bearing elements of the structure or at least as close as possible. Measurement of vertical vibrations was performed near the load bearing wall, since this place better represents the structural integrity of the building than in the middle of the floor. The sensor was placed on a free standing steel cylinder placed horizontally on the floor. In no way should horizontal vibrations be measured in this way, doing such can result in more than 40 % error [7, 15].

The International standard in [8] evaluates the level of damage in buildings by different categories. One of these categories is cosmetic damage, which is characterized by thin hairline cracks on the surface of a wall without finish (stucco), growth of existing cracks in drywall or on the surface of an unfinished wall (without stucco). Such damage, or any other form of damage, was not observed during the measurements.

Acknowledgments

This contribution was made possible by the project “Improving the safety of nuclear installations in seismic events” (ITMS project code: 26220220171), on the basis of support from the operational program for research and development financed by the European fund for regional development.

REFERENCES

[1] S. Ziaran, M. Musil, Action of seismic shocks on civil and industrial structures Part 1: General principles. Journal Physical Environmental Factors, 2nd year, p. 93-100, October 2012.

[2] S.Žiaran, Research report V a K, *Analysis of sources of mechanical vibration in water pumps*, Bratislava 1992.

[3] S. Žiaran, Research report for woodworkers production center, *Dynamic analysis of a single frame sawmill and the transfer of vibro-acoustic energy to its surroundings*, Bratislava 2002.

[4] S. Žiaran, Research report for the woodworkers production center, *Dynamic analysis of a sawmill and recommendations for lowering the transfer of vibration to the surrounding areas*, Bratislava 2003.

[5] S. Žiaran, Research report for PSL, *Analysis of dynamic loading on industrial structures and foundations of machines DPR20, DPR26 and press LE 250 with recommendations for their vibro-isolation*, Považská Bystrica, Bratislava 2005.

[6] S. Žiaran, Research report for NCHZ, *Dynamic assessment of vibration for reactor R11*, Bratislava 2001.

[7] S. Žiaran, *Vibration and acoustics. Reducing vibration and noise in industry*, Monograph, Published. STU Bratislava 2006.

[8] ISO 4866:2012 *Mechanical vibration and shock. Vibration of buildings. Guidelines for the measurement of vibration and evaluation of their effects on buildings*.

[9] K Medearis, *Development of rational damage criteria for low rise structures subject to blasting vibrations*. K. M. Assoc. Report, 1976.

[10] D.E. Siskind, M.S. Stagg, J.W. Kopp, C.H. Dowding, Report of Investigations No. RI. 8507, *Structure response and damage produced by ground vibration from surface mine blasting,* United States Bureau of Mines, 1980.

[11] Building Research Establishment (UK), *Cracking in buildings*. Digest No. 5, 1966 (reprinted 1975).

[12] S. Žiaran, M. Musil, *Factors affecting internal air conditioning in building during seismic events*, 23rd conference on internal building climate, Contributions, High Tatras 2012, p. 47-52.

[13] ISO 2631-2:2003, Evaluation of human exposition to vibrations on the body. Part 2: continuous and shock induced vibration in buildings (from 1 Hz to 80 Hz)

[14] ISO 5348:1987, Mechanical vibration and shocks. Mechanical mounting of accelerometers.

[15] S. Žiaran, *Technical diagnostics*. Scientific monograph. In press, STU Bratislava 2013

[16] L. Soltes, M. Cekan, B. Hucko, Biomechanical model for seat comfort in automobiles. In Biomechanics 2012: *International conference of the Polish Society of Biomechanics*. Contributions, Bialystok, Poland, 2012, p. 265-266.

COMPDYN 2013
4th ECCOMAS Thematic Conference on
Computational Methods in Structural Dynamics and Earthquake Engineering
M. Papadrakakis, V. Papadopoulos, V. Plevris (eds.)
Kos Island, Greece, 12–14 June 2013

QUANTIFICATION OF RESIDUAL AXIAL CAPACITY OF BEAM-COLUMN JOINTS IN EXISTING CONCRETE BUILDINGS UNDER SEISMIC LOAD REVERSALS

Wael M. Hassan[1] **and Jack P. Moehle**[2]

[1] American University in Cairo
New Cairo, Egypt
waelhassan@aucegypt.edu

[2] University of California, Berkeley
Berkeley, CA, USA
moehle@berkeley.edu

Keywords: Beam-Column Joint, Axial Capacity, Seismic, Concrete, Existing Buildings.

Abstract. *Earthquake reconnaissance has reported the substantial damage that can result from inadequate beam-column joints in earthquake shaking. In some cases, failure of older-type corner joints appears to have led to building collapse. Insignificant research attention has been focused on beam-column joints of older construction that may be seismically vulnerable. Concrete buildings constructed prior to developing details for ductility in the 1970s normally lack joint transverse reinforcement (unconfined joints). The available literature concerning the performance of such joints is relatively limited, but concerns about their seismic axial failure exist. The main goal of this study is to quantify the axial collapse vulnerability of shear-damaged unconfined exterior and corner beam-column joints under cyclic load reversals. The quantification of the residual axial capacity of these joints is performed incorporating the test results of four full-scale three dimensional corner beam-column joint sub-assemblages, along with few other tests available in the literature to develop analytical models for joint axial capacity. Two axial capacity models designed for unconfined joints were developed. The proposed models correlated with previous test results. Within the practical range of beam-column joint dimensions, the axial failure appears unlikely. However, this result is obtained based on a small dataset. More tests are needed to verify the developed models and to investigate the axial failure likelihood for joint dimensions not included in the presented models.*

1 INTRODUCTION

Very few unconfined joint tests are available with confirmed axial failure. Unfortunately during laboratory joint tests, a common practice has been to terminate the test after dropping to 80% of lateral load resistance without testing the axial capacity of the joint. However, many post-earthquake reconnaissance studies report building damage or collapse that might be attributed to exterior and corner beam-column joint failures. No interior joint axial failures have been identified. An important aspect of the assessment of an existing building is to assess drift capacity after the onset of shear failure until reaching axial failure. Shear failure of joints and columns in older buildings can occur at relatively low drifts. Whether the axial failure of a shear damaged joint will precede the axial failure of a shear damaged column leading to a progressive collapse is not certain. The axial capacity of shear damaged columns and joints should be input as limit states in building simulation models, such as the macro model presented in Hassan and Moehle [9], to realistically represent the ignition of progressive collapse. From an economic viewpoint, if a joint can reliably support gravity load after its lateral strength degradation begins, it may be possible to achieve considerable savings by considering this particular joint as a secondary component.

2 MODES AND MECHANISMS OF JOINT AXIAL FAILURE

Different approaches were used to decide the point of joint axial failure during previous joint tests. Since most tests were performed under constant axial load, a common sign of joint axial failure was a significant drop in axial load even without full disintegration of the joint. This approach could be sometimes misleading since the axial load may decrease for several reasons including axial stiffness degradation because of cracking, or hydraulic pressure drop for a mechanical reason. A better indicative sign of axial failure is the axial shortening below a threshold limit. Axial failure in most of the joints tested in Hassan [7] seemed indicated for an axial joint strain of about 0.005 to 0.006. The third approach of confirming axial failure is the total collapse of the specimen by dynamic instability due to reaching joint axial capacity.

Different modes of joint axial failure were observed during previous tests and following past earthquakes. Figure 1 shows joint damage interpreted as axial failure during past earthquakes and joint tests. For the past earthquake axial failures, whether the joint axial failure occurred first, triggering partial or total collapse, or the joint axial failure was a consequence of column axial failure is unknown.

Figure 2 displays the axial failure modes of specimens U-J-1, U-J-2, U-BJ-1 and B-J-1 of Hassan [7]. In specimen U-J-1, the starting gravity load ratio was 0.21. The axial load ratio at peak joint shear strength was 0.31 while that at axial failure was 0.20. The drift ratio capacity at axial failure was relatively high (9.68%). The joint core was severely damaged prior to reaching axial failure. During axial failure, a sliding failure on the diagonal shear failure plane occurred. As can be seen in Fig. 2, the failure mode of the column longitudinal reinforcement is a “side-sway” mode rather than a “buckling” mode.

Figure 2.c shows the failure mode of specimen U-J-2 whose axial load ratio at peak joint shear strength was 0.44 while that at axial failure was 0.41. The drift capacity at axial failure was 3.06%, with a maximum drift ratio 3.42% before axial failure. A buckling failure mode of column reinforcing bars is obvious. A sliding failure on the diagonal shear failure surface was observed following removal of damaged concrete debris, although it was less apparent than that in specimen U-J-1. Similar axial failure modes to that of specimen U-J-2 were observed in specimens B-J-1 and U-BJ-1.

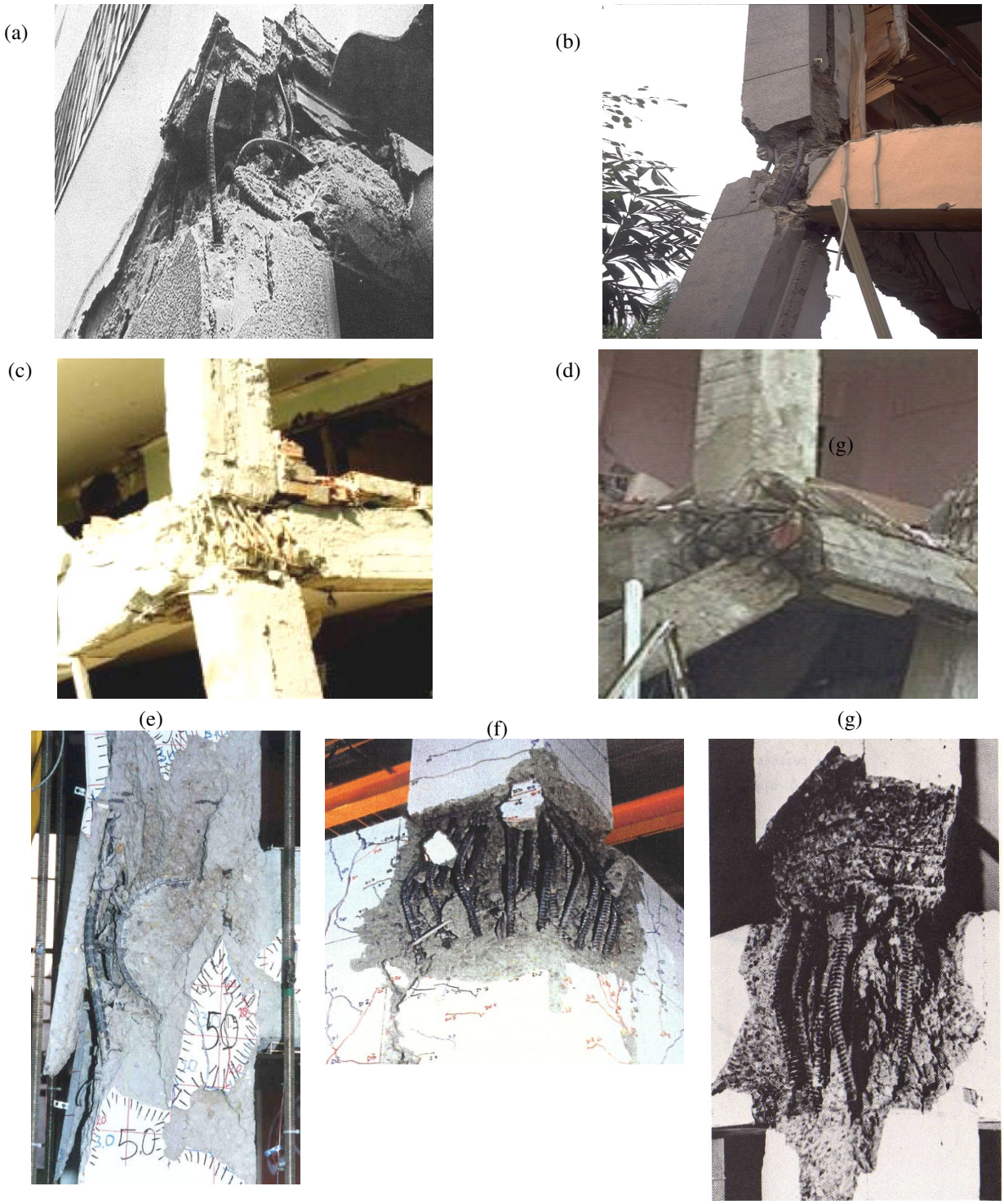


Figure 1 Joint axial failure during past earthquakes and laboratory tests: Caracas, Venezuela earthquake, Pagni [14], (b) Taiwan Chi-Chi 1999 earthquake, NISEE [13], (c) Izmit, Turkey earthquake of 1999, Engindeniz [4], (d) Izmit, Turkey earthquake of 1999, NISEE [13], (e) Exterior joint test, Pantelides et al. [15], (f) Corner joint test, Priestley and Hart [17], (g) Corner simulated joint test, Uzumeri [19]

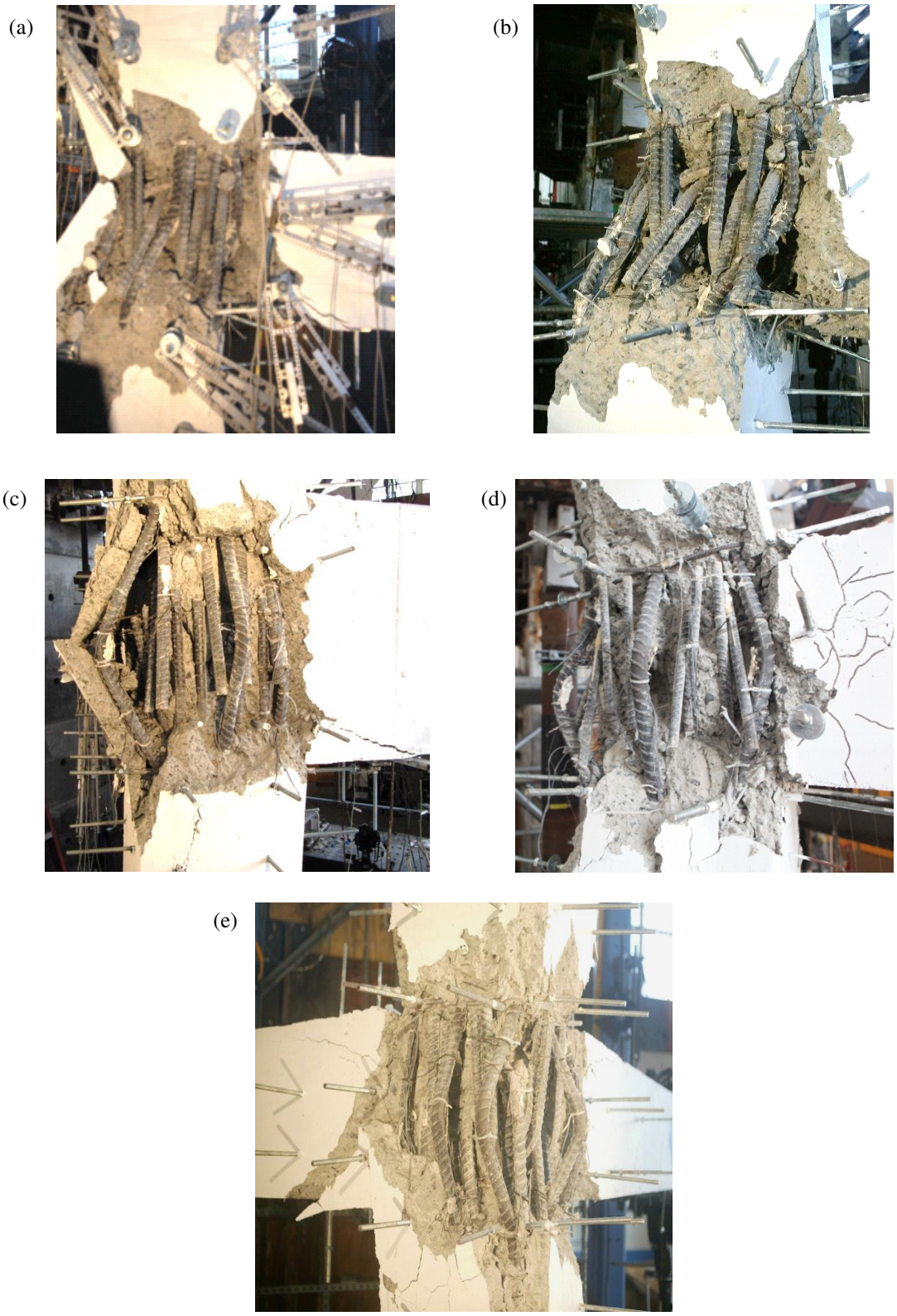


Figure 2 (a), (b) Column bar "side-sway" axial failure mode in specimen U-J-1, (c) Bar buckling axial failure mode in specimen U-J-2, (d) specimen U-BJ-1, and (e) specimen B-J-1, Hassan [7]

The different failure modes observed for the different test specimens are believed to be due to the different levels of axial loads in the tests. The "sliding" axial failure on the previously damaged shear failure plane in the joint suggests that the classical shear friction theory can be used to explain the failure mechanism. Elwood and Moehle [3] presented a derivation for an axial capacity model for shear-damaged columns based on the interaction between shear-friction surface and axial capacity of column longitudinal reinforcement.

As described in Elwood and Moehle [3], axial failure of a shear-damaged column can occur by sliding along an inclined crack plane, with resistance provided by transverse reinforcement clamping the crack and longitudinal reinforcement supporting axial force directly. Axial failure of a joint may be viewed similarly. After developing joint shear failure, the axial load will be supported by shear friction on the diagonal shear failure plane and the axial capacity of column reinforcing bars. Whether these two mechanisms work concurrently is dependent on the location of column bar within the joint. The share of each column bar of the axial load at the joint region might not be equal. However, for simplification purpose, it will be generally assumed that all column bars will share equally a small portion of axial load in the shear-damaged joint.

3 OBSERVED AXIAL CAPACITY OF BEAM-COLUMN JOINTS

As mentioned earlier, few previous joint tests were continued until reaching axial failure. For exterior unconfined joint tests, four such test specimens were reported by Pantelides et al. [14]. In this group of tests called Unit 3, Unit 4, Unit 5, and Unit 6, axial failure was identified by a drop in the constant axial load applied to the column. Priestley and Hart [16] report axial failure of an unconfined corner joint. Axial failure of this corner joint, denoted "As built", was identified by crushing of joint core along with buckling of column bars in the joint and eventually loss of axial carrying capacity. In addition, one corner simulated joint, SP5, with a pre-cracked transverse stub experienced axial failure in tests performed by Uzumeri [19]. All four unconfined corner joints tested in Hassan [7] (denoted NEES Joints) experienced axial failure as described in a previous section.

Figure 3 plots the relationship between axial failure load and the maximum drift reached prior to axial failure for the ten joints mentioned above. In addition, a database of 37 previous exterior and corner joint tests in which axial failure was not reached also is included. The axial load ratio and drift ratio for this database reflect the test termination values. This database includes joints tested by Wong [20], Park [16], Hwang et al. [11], Karayannis et al. [12], Clyde et al. [2], Uzumeri [19], Tsonos [18], Hanson and Conner [5] and [6] and Antonopoulos and Triantafillou [1]. The size of axial failure joints database is relatively small compared to that of non-axial failure joints. However, several useful observations can be made from this plot:

1. It appears that exterior and corner joints may be susceptible to axial failure under very large drifts or under high axial loads.
2. A general trend of a decreased axial failure drift capacity is associated with higher axial loads except for joint U-BJ-1, which will be discussed later.
3. Excluding joint U-BJ-1, an inverse proportionality between axial failure load and drift ratio can be observed.
4. The proportionality between axial failure load and drift ratio for the NEES J-Failure joints is offset from that between previous joint tests with axial failure. J-Failure mode is defined as the joint shear failure without beam or column yielding. Some differences exist between NEES J-Failure joints and other tests. The NEES tests include a

slab whereas others did not, and relatively fewer cycles were included than were included for some of the other tests.

5. Based on previous joint tests that did not experience axial failure, an axial failure safe zone can be drawn as shown in Fig. 3. Inclined line A defines a fairly clear demarcation between tests with and without axial failure. Line B is more tenuous, as it extends to high axial load levels for which few tests are available. The inclined line A can be algebraically expressed as

$$\left(\frac{\Delta}{L}\right) \leq \frac{1}{9} - \frac{P}{2.72 f_c' A_g}$$

6. One test shown in Fig. 3 is the first unconfined joint test reported by Hanson and Conner (Specimen V) [5]. In this test, an unrealistically constant high axial load ratio of 0.95 was used. In spite of the substantial axial load, the specimen was able to survive 5.2% drift without axial failure. The somewhat peculiar combination of high axial load and high drift ratio could not be explained.
7. Specimen U-BJ-1 also stands apart from the trend of the other data. The reason for this is that the drift ratio is not the best marker of joint deformation capacity in this specimen, since most of the drift was contributed by significant beam yielding before shear failure (BJ-Failure mode), with joint axial failure delayed until very late stages of loading. Specimen 7 tested by Hanson and Conner [5] showed similar behavior. It was loaded under 0.50 constant axial load ratio and experienced a BJ-shear failure mode, with a substantial yielding and deformation of the beam. Under this high axial load, the specimen was able to survive a 5.1% drift ratio without axial failure. This result is also off the trend shown in Fig. 3 and suggests a much more relaxed axial failure drift capacity for specimens failing in shear by BJ failure mode under very high axial load. It is then likely that joints with BJ-Failure mode under high axial load ratio (more than 0.30) will survive drift ratios much larger than their J-Failure counterparts.
8. It is surprising that joint SP5, with 0.51 axial load ratio, experienced a BJ-Failure mode at 1.6% drift and axial failure at 3.5% drift only, unlike specimens U-BJ-1 and Specimen 7 mentioned above. This might be attributed to the arbitrary loading history used by Uzumeri [19] that decided number of cycles and displacement amplitudes during the test based on the observed behavior.

Figures 4 and 5 compare drifts at shear failure and drifts at axial failure for joints sustaining axial failures. The vertical axis plots the axial load at axial failure. Joints with higher axial load tended to sustain axial failure sooner after shear failure than did joints with lower axial loads, although the trend is not strong and there are exceptional cases. Specimen U-BJ-1 is one of the exceptions, for the reason explained earlier. It is highly informative to observe that a minimum μ_f of 2 seems a lower bound for drift ratio at axial failure to that at shear failure.

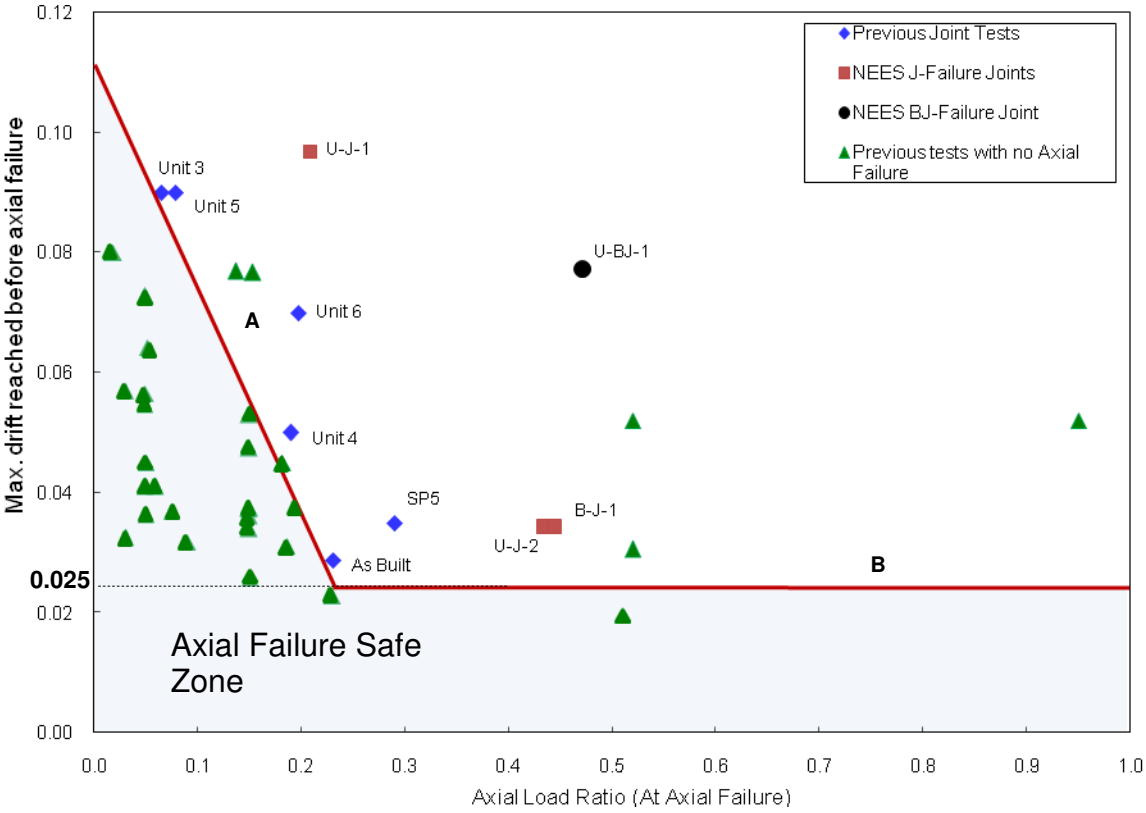


Figure 3 Axial load-drift ratio relationship at axial failure (or test termination) for exterior and corner joints

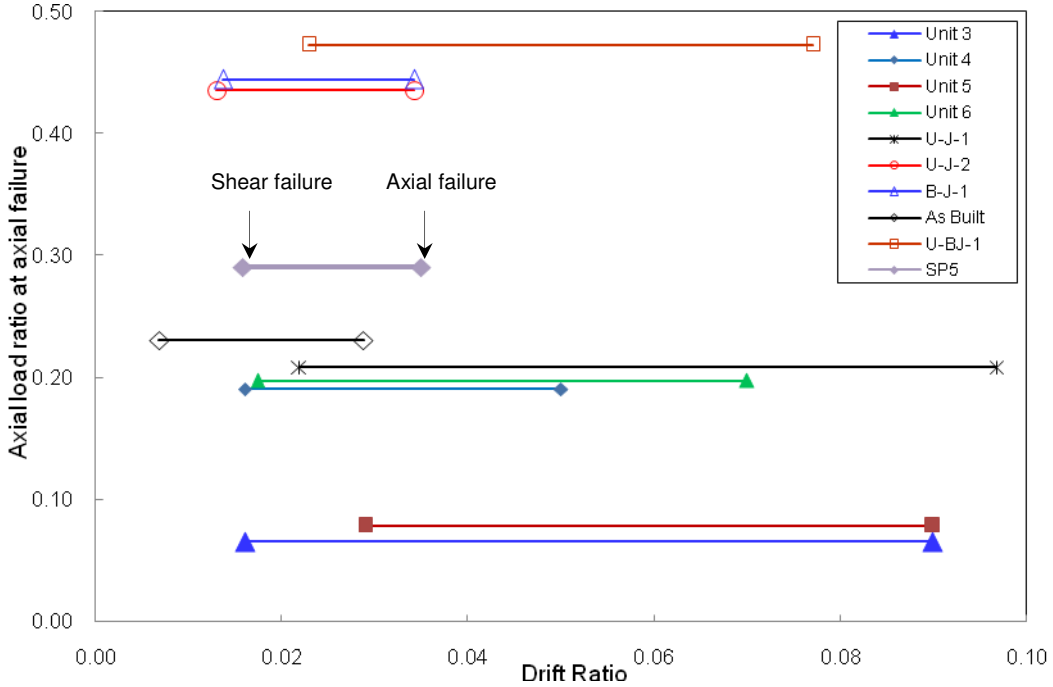


Figure 4 Relation between axial load at axial failure and drift ratio

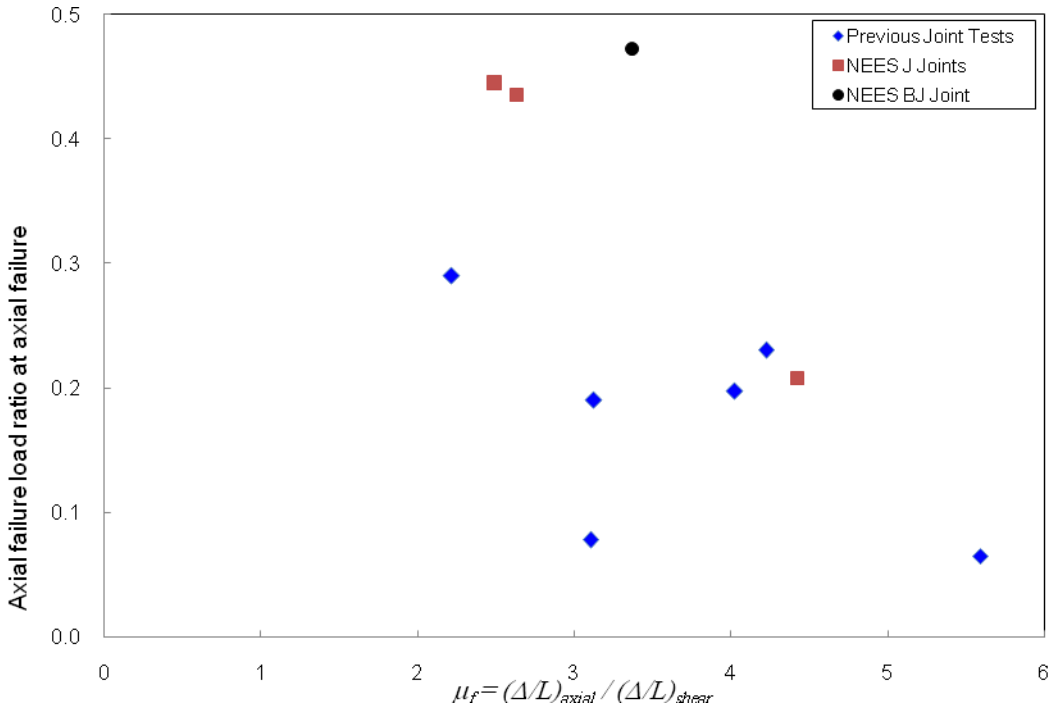


Figure 5 Relation between axial load at axial failure and drift at shear failure and at axial failure.

4 PROPOSED AXIAL CAPACITY MODELS FOR UNCONFINED JOINTS

4.1 Background

Based on Elwood and Moehle [3] axial capacity model for columns, an analogous model for application to unconfined joints is proposed. The model is based on observation of axial failure modes. The model assumes that the primary failure mechanism is along a shear friction surface of the previously shear-damaged joint, with column longitudinal reinforcement acting in axial load providing a secondary mechanism triggered after shear-friction failure on the shear failure plane. This section presents two axial capacity models for unconfined beam-column joints. These models are intended to be used with joints experiencing J-shear failure mode with any axial load level and BJ-failure mode with axial load ratio below 0.3. As discussed in a previous section, the axial failure of a BJ shear failure controlled joint under high axial load is not likely until very large drifts.

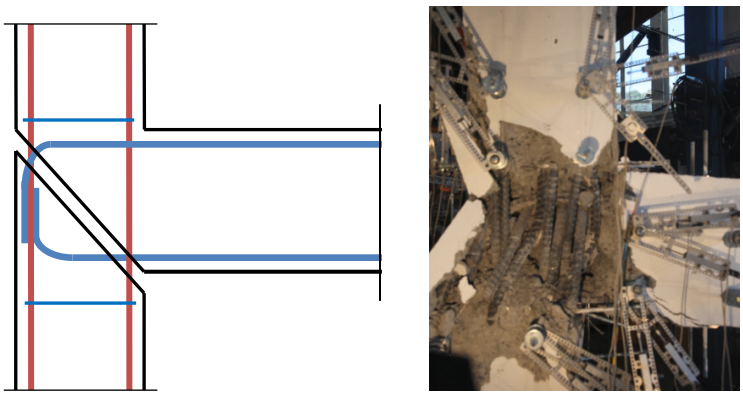


Figure 6 Development of shear-friction model for joint axial capacity based on experimental observation, (a) Proposed sliding mechanism, (b) Observed damage after axial failure, specimen U-J-1

4.2 Model 1: Analytical Shear-Friction Capacity Model

After joint shear failure along the major diagonal crack corresponding to the inclination of the main diagonal concrete joint strut, shear resistance starts to degrade. In many cases, however, the axial load at peak displacement does not immediately drop as discussed Hassan and Moehle [8]. Substantial axial load from the upper column must be transferred across the joint shear failure surface. Experimental observation of joint axial failure suggests transferring this axial load by shear-friction across the shear failure plane. Several shear-friction models are available; however, the classical shear-friction model adopted by ACI 318-08 and used by Elwood and Moehle [3] for shear-critical columns is used here.

Figure 7 shows the free body diagram of the upper block of the beam-column joint sub assemblage after shear failure. The critical crack angle θ can be calculated using the strut-and-tie model developed in Hassan, et al. [10] for joint shear strength. The axial failure is evident to take place during the downward loading of beam. Some simplifying assumptions are made next.

V_b and V_j are the beam shear force and joint shear force at join shear failure, respectively. Since the beam shear force $V_{b,a}$ and joint shear force $V_{j,a}$ at axial failure are not always insignificant like the case of columns (Elwood and Moehle [3]), they cannot be neglected in formulating the equilibrium equations. The dowel action provided by the longitudinal column and beam reinforcement will be implicitly included in the shear friction resistance $V_{sf;}$ hence they will not appear in the equilibrium equations. The total axial capacity of column reinforcement bars is denoted ΣP_s. The beam longitudinal reinforcement will act as shear-friction reinforcement holding the lower concrete block (the column) from separation. At the axial failure, the force in both top and bottom longitudinal beam bars will be tensile within the joint regardless the sense of the force within beam span.

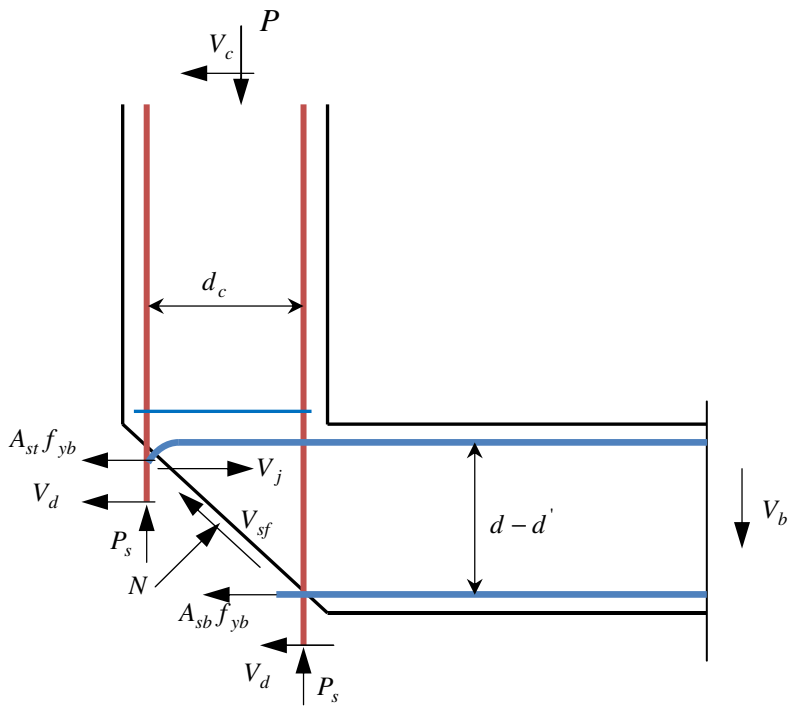


Figure 7 Free body diagram for beam-column joint at the onset of axial failure

The top beam longitudinal reinforcement appears to be less efficient in resisting shear friction since it experiences bond failure at earlier stage. More importantly, the portion of the

top beam bars holding the lower concrete block is usually the hook tail which is very poorly embedded and bonded to concrete at late stages of loading because of cover spalling or detachment. Accordingly, the resistance of top beam bars will not be included in the equilibrium equations. Based on the abovementioned simplifying assumptions, the equilibrium equations in the horizontal and vertical directions can be respectively written as:

$$N\sin\theta + V_j = V_{sf}\cos\theta + A_{sb}f_{yb} + \Sigma V_d \tag{1}$$

$$P + V_b = N\cos\theta + V_{sf}\sin\theta + \Sigma P_s \tag{2}$$

The proposed model assumes that joint axial capacity is primarily dependent on shear-friction mechanism. Column longitudinal axial capacity is considered secondary to shear-friction mechanism, which is triggered only after shear-friction failure. The calculation of axial capacity of column bars presented in Hassan [7] shows that this capacity is relatively small. Even if a portion of axial load is supported by column bars immediately before axial failure, suggesting a concurrent collective mechanism, this portion is insignificant as suggested by Elwood and Moehle [3]. Accordingly, this quantity will not be included in the model. Only the final model equations are presented herein for brevity. The model derivation is thoroughly presented in Hassan [7]. The model relates the axial load P to the drift capacity at axial failure $(\Delta/L)_{axial}$. It can also be used reversely to find the axial load capacity for a given drift ratio. More test data regarding axial failure of exterior and corner beam column joints is needed to refine and validate the expressions for lateral load capacity at axial failure.

$$\left(\frac{\Delta}{L}\right)_{axial} = 0.031\left\{\frac{(P+V_{b,a})\tan\theta + (V_{j,a} - A_{sb}f_{yb})}{(P+V_{b,a}) - (V_{j,a} - A_{sb}f_{yb})\tan\theta}\right\}^{-0.25} \tag{3}$$

$$\left(\frac{\Delta}{L}\right)_{axial} = 0.031\left\{\frac{(P+\chi\chi_a V_j)\tan\theta + (\chi_a V_j - A_{sb}f_{yb})}{(P+\chi\chi_a V_j) - (\chi_a V_j - A_{sb}f_{yb})\tan\theta}\right\}^{-0.25} \tag{4}$$

$$V_{j,a} = \left(1.1\frac{P}{f_c' A_j} - 0.03\right).V_j = \chi_a V_j \tag{5}$$

$$V_{b,a} = \left(1.1\frac{P}{f_c' A_j} - 0.03\right).V_b = \chi_a V_b \tag{6}$$

$$V_b = \frac{1}{\dfrac{L - h_c/2}{jd_b} - \dfrac{L}{H}} = \chi V_j \tag{7}$$

where: L is half the beam span, H is floor height, h_c is column depth, j=0.9, and d_b is the effective beam depth.

4.3 Empirical Shear-Friction Capacity Model

The above theoretically based shear-friction model is plausible if enough knowledge on the residual joint shear capacity at axial failure can be confirmed. It also contains two

empirical components, namely the estimation of effective shear-friction coefficient and the residual shear capacity at axial failure. The model is delivered finally in a rather lengthy expression. These factors motivated investigating the possibility of the presence of a trend between drift ratio and the axial failure load normalized by the influential parameters of the shear-friction phenomenon. The goal of this attempt was to develop a simpler empirical expression for quick estimation of drift capacity at axial failure eliminating the need for residual joint shear strength at axial failure. To achieve this goal, a simple expression based on the linear trend observed in Hassan [7] for NEES joints and for previous joint tests (with no slab and more cycles per drift level) that experienced axial failure can be formed as:

For NEES joints:

$$\left(\frac{\Delta}{L}\right)_{axial} = 0.15 - 0.27\left(\frac{P}{f_c^{'} A_j}\right) \tag{8.a}$$

For previous joint tests:

$$\left(\frac{\Delta}{L}\right)_{axial} = 0.11 - 0.28\left(\frac{P}{f_c^{'} A_j}\right) \tag{8.b}$$

Equation 8 is a generic empirical relation that can be used for preliminary purposes unless more test data is available to confirm it.

Another empirical expression can be developed based on shear friction influence parameters. Figure 8 shows the relationship between drift ratio at axial failure and the axial failure load normalized by beam bottom reinforcement strength (acting as shear friction reinforcement) and the critical angle of inclination of the crack, a key parameter in beam-column joint shear and axial capacity. The figure suggests an inverse proportionality reflected by a power based relationship that can be fitted directly relating drift ratio and normalized axial load as:

$$\left(\frac{\Delta}{L}\right)_{Axial} = 0.057\left(\frac{P.\tan\theta}{A_{sb} f_{yb}}\right)^{-0.5} \tag{9}$$

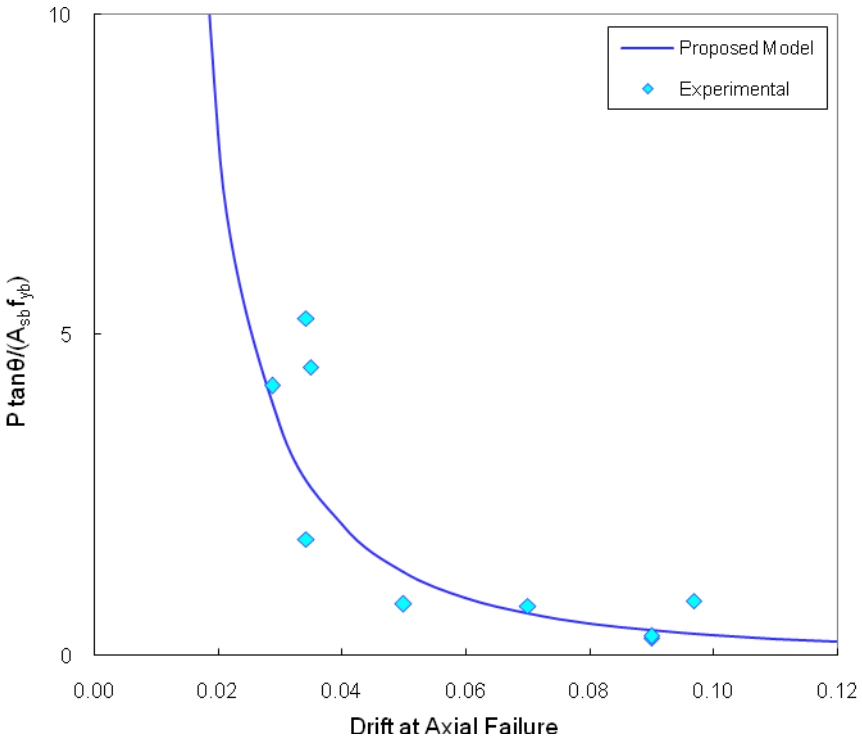


Figure 8 Proposed empirical model (Eq. 9) for drift capacity at axial failure

It was worthy also investigating the influence of other important parameters such as the concrete strength, joint effective area and column longitudinal reinforcement strength. These factors are common in axial capacity studies of columns. The results of this investigation presented in Hassan [7] suggested weak sensitivity of the axial failure model to these parameters.

This above discussion suggests the appropriateness of the empirical expression (Eq. 9) for quick estimation of drift capacity at joint axial failure. It is important to notice that this expression is based on a rather small joint axial failure database. Thus, more joint axial failure tests are needed to further verify this relation. In addition, it is worth mentioning that this expression is suitable for J-Failure joints with any axial load ratio, BJ-Failure joints with small axial load ratio, and BJ-Failure with high axial load ratio when the flexural capacity of the beam is close to the direct J-Failure strut-and-tie model capacity. The case of high axial load on a joint in a subassembly where the beam flexural capacity is much smaller than the direct J-failure capacity is excluded from the application of this model for reasons mentioned earlier.

5 PROPOSED MODELS EVALUATION

Figure 9 presents the correlation of the experimental drift capacity at axial failure to the calculated one using the shear-friction model for axial capacity (Eq. 3). The average test to model drift ratio is 1.00 and the COV is 0.27. It is also worth mentioning that residual shear capacity at axial failure is based on the NEES joint results; which led to the drift for other tests loaded with greater number of displacement cycles to be overestimated by the model.

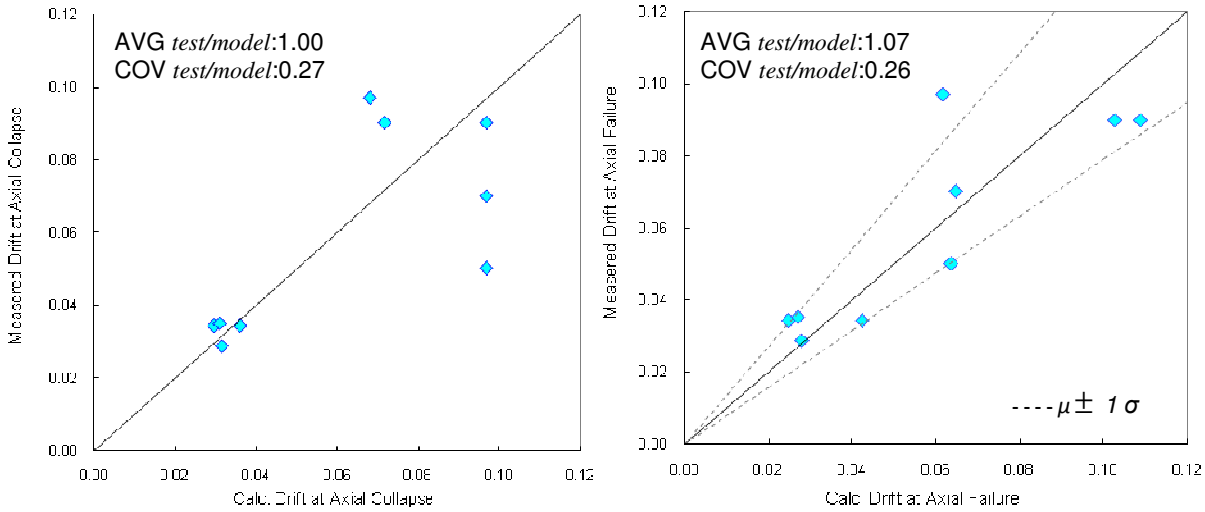


Figure 9 Correlation of the proposed axial capacity models to test results

The empirical axial capacity model proposed by Eq. 9 is evaluated against test results in Fig. 9. The ratio of test-to-model drift capacity was mean of 1.07 and COV of 0.26. Note that the calculated drift for specimen U-J-1 is underestimated by about 43%. During the U-J-1 test, the axial load dropped accidently after onset of shear failure. It is plausible that the drift ratio would have been decreased had the axial load remained high.

6 CONCLUSIONS

- An inverse proportionality between axial load and maximum drift reached before axial failure is evident for joints failing in the J-Failure mode. Joints with very high axial loads (perhaps larger than $0.45f_c'A_j$) experiencing BJ-Failure mode may benefit from higher axial load, such that they do not follow the aforementioned inverse relation.
- Although not isolated as an independent variable in this study, joints undergoing more rigorous loading history (for example, more cycles) generally had smaller drift at axial failure.
- The main resisting mechanism that supports axial loads in a shear damaged joints is believed to be shear friction on the previously damaged shear failure plane. The buckling capacity of column reinforcement is believed to be a secondary mechanism to shear friction mechanism, which is triggered upon shear friction failure.
- Unlike some cases of column axial failure, joint axial failure does not immediately follow joint shear failure. The ratio of drift at axial failure to drift at shear failure ranged from 2.5 to 3.3 for high axial loads, and from 3 to 5.5 for low axial load.
- An "axial failure safe zone" was identified based on the current and previous tests with and without axial failure. Joint axial failure was not observed for drift ratio demand below 2.5% - 3%. For drift ratios higher than 2.5% - 3%, axial failure was observed especially with increasing drift, axial load, or both.
- Joint axial capacity models were proposed based on the shear friction concept. The models correlated well with available data, but the data set was relatively small, such that additional model calibration is warranted.

ACKNOWLEDGEMENT

Financial assistance provided by U.S. National Science Foundation (NSF) award #0618804 through George E. Brown Jr. Network for Earthquake Engineering Simulation (NEES) and the Egyptian Department of Education award #2005292 through Building National Research Center is greatly appreciated.

REFERENCES

[1] Antonopoulos, C.P., and Triantafillou, T.C., Experimental Investigation of FRP Strengthened RC Beam-Column Joints, *ACSE Journal of Composites for Construction,* V.7, No. 1, pp 39-49, 2003.

[2] Clyde, C., Pantelides C. and Reaveley L., Performance-Based Evaluation of Exterior Reinforced Concrete Building Joints for Seismic Excitation. *PEER Report 2000-5, Pacific Earthquake Engineering Research Center (PEER)*, University of California, Berkeley, CA, July 2000.

[3] Elwood, K.J., and Moehle, J.P., Shake Table Tests and Analytical Studies on the Gravity Load Collapse of Reinforced Concrete Frames. *PEER Report 2003-01*, *Pacific Earthquake Engineering Research Center (PEER),* University of California, Berkeley, 2003.

[4] Engindeniz, M., Repair and Strengthening of Pre-1970 Reinforced Concrete Corner Beam-Column Joints Using CFRP Composites, *PhD Thesis, Civil and Environmental Engineering Department, Georgia Institute of Technology*, August 2008.

[5] Hanson N. W., and Connor, H. W., Seismic Resistance of Reinforced Concrete Beam Column Joints. *Journal of the Structural Division, Proceedings of the American Society of Civil Engineers*, Vol. 93, No. ST5, pp. 533-560, October 1967.

[6] Hanson N. W., and Connor, H. W., Tests of Reinforced Concrete Beam-Column Joints under Simulated Seismic Loading. *Research and Development Bulletin RD 012*, Portland Cement Association, 1972.

[7] Hassan, W. M., Analytical and Experimental Investigation of Seismic Vulnerability of Beam-Column Joints without Transverse Reinforcement in Concrete Buildings. *PhD Dissertation, University of California, Berkeley*, May 2011.

[8] Hassan, W. M. and Moehle, J. P., Experimental Assessment of Seismic Vulnerability of Corner Beam-Column Joints in Older Concrete Buildings. *Proceedings of the 15th World Conference of Earthquake Engineering*, Lisbon, Portugal, September, 2012.

[9] Hassan, W. M. and Moehle, J. P., A Cyclic Nonlinear Macro Model for Numerical Simulation of Beam-Column Joints in Existing Concrete Buildings. *Proceedings of the 15th World Conference of Earthquake Engineering*, Lisbon, Portugal, September, 2012.

[10] Hassan, W. M., Park, S., Lopez, R.R., Mosalam, K. M., and Moehle, J. P., Seismic Response of Older-Type Reinforced Concrete Corner Joints*, Proceedings of the 9th U.S. National and 10th Canadian Conference on Earthquake Engineering*, Toronto, Ontario, Canada, July 25-29, 2010.

[11] Hwang, S.J., Lee, H.J., Liao, T.F., Wang, K.C., and Tsai, H.H., Role of Hoops on Shear Strength of Reinforced Concrete Beam-Column Joints. *ACI Structural Journal*, V. 102, No. 3, pp. 445-453, 2005.

[12] Karayannis, C.G., Chalioris, C.E., and Sirkelis, G.M., Local Retrofit of Exterior RC Beam-Column Joints Using Thin RC Jackets: An Experimental Study. *Earthquake Engineering and Structural Dynamics*, V. 37, pp. 727-746, 2008.

[13] National Information Service for Earthquake Engineering (NISEE), *Pacific Earthquake Engineering Center*, University of California, Berkeley, 2010.

[14] Pagni, C.A., Modeling of Structural Damage of Older Reinforced Concrete Components. *M.Sc. Thesis, University of Washington*, 2003

[15] Pantelides, C., Hansen, J. and Reaveley, L., Assessment of Reinforced Concrete Building Exterior Joints With Substandard Details. *Technical Report PEER 2002-18, Pacific Earthquake Engineering Research Center (PEER)*, University of California, Berkeley, CA, May 2002.

[16] Park, S., Experimental and Analytical Studies on Old Reinforced Concrete Buildings with Seismically Vulnerable Beam-Column Joints. *PhD Dissertation, University of California, Berkeley*, December 2010.

[17] Priestley, M.J.N. and Hart, G., Royal Palm Resort, Guam, Seismic Behavior of As-Built and As-Designed Corner Joints. *SEQAD Consulting Engineers*, Solana Beach, CA, 1994.

[18] Tsonos, A. G., Effectiveness of CFRP-Jackets and RC-Jackets in Post-Earthquake and Pre-Earthquake Retrofitting of Beam–Column Sub-assemblages, *Engineering Structures,* Vol.30, pp. 777-793, 2008.

[19] Uzumeri, S. M., Strength and Ductility of Cast-in-Place Beam Column Joints. *Reinforced Concrete Structures in Seismic Zones, SP-53, Hawkins, N. M., ed., American Concrete Institute*, Detroit, Michigan, pp. 293-350, 1977.

[20] Wong, H.F., Shear Strength and Seismic Performance of Non-Seismically Designed Reinforced Concrete Beam-Column Joints. *PhD Dissertation, Department of Civil Engineering, The Hong Kong University of Science and Technology,* August 2005.

COMPDYN 2013
4th ECCOMAS Thematic Conference on
Computational Methods in Structural Dynamics and Earthquake Engineering
M. Papadrakakis, N. D. Lagaros, V. Plevris (eds.)
Kos Island, Greece, 12–14 June 2013

ROCKING AND SLIDING OF UNANCHORED BODIES SUBJECTED TO SEISMIC LOAD ACCORDING TO CONVENTIONAL AND NUCLEAR RULES

H. Schau[1] and M. Johannes[2*]

TÜV SÜD Energietechnik GmbH Baden-Württemberg
Dudenstraße 28, 68167 Mannheim, Germany

[1]Henry.Schau@tuev-sued.de
[2]Michael.Johannes@tuev-sued.de

Keywords: Dynamics, Rigid Body, Rocking, Overturning, Seismic Loads, Rules, Impact.

Abstract. *In nuclear and nonnuclear facilities unanchored components like storage casks for spent fuel may cause unacceptable damage in case of an earthquake. It must be proven that the unanchored body will not tip over and/or slide impermissible distances. Rocking and sliding are highly nonlinear phenomena which cannot be completely described analytically. Therefore, the rocking and sliding motion of a rigid body under various conditions will be analysed analytically and numerically by numerical integration of the equations of motion and by using the Finite Element Method (implicit time integration). It is shown that a finite element program with an implicit time integration method can solve the impact problem. By using the Finite Element Method it is possible to investigate the influence of the properties of the base, the contact conditions and slightly deviations from the ideal geometry on the motion of the body and especially on the coefficient of restitution. Additionally, the influence of occasionally used anti-slip pads below the rocking body is investigated. In practice most unanchored bodies are not slender and therefore this paper studies a compact body with an aspect ratio of 2. One focal topic is the discussion of the coefficient of restitution. It is shown that more realistic finite element models, which take into account the above mentioned influences, lead to higher coefficients than those derived analytically from simplified models. The agreement between results from finite element analyses and the numerical integration of the equations of motion is very good if the coefficients of restitution are based on best estimate values from finite element analyses. The dynamic investigations consider an excitation by sine, triangle or rectangle vibrations and time histories from earthquake ground accelerations. It is remarkable, that in the some cases of the amplitudes will increase significantly over time until overturning. The criteria and methods given in European (German) and US standards with regard to overturning and impermissible sliding are presented. The safety margins against overturning and impermissible sliding will be discussed.*

1 INTRODUCTION

In nuclear power plants but also chemical plants unanchored components can cause unacceptable damage in the case of an earthquake (but also of a blast wave or a plane crash). This applies also if the components such as e.g. storage casks are designed for the loads from overturning or hitting. To avoid damage it must be demonstrated that under these loads no overturning or impermissible slipping of unanchored components occurs. Therefore, in this paper the behaviour of unanchored components excited by earthquakes will be analysed. In principle it is the dynamic of a rigid, elastic or plastic body on a rigid, elastic or plastic foundation. The mechanical problem for a rigid body looks simple at the first sight, but becomes difficult due to the impacts. In literature the question of rocking or tilting oscillations of a rigid body has been found to be of great interest, so that there are a large number of publications on the subject. In this context the fundamental works [1] to [7] and further studies [8] to [22] should be mentioned. Based on these works, the dynamics of unanchored bodies, especially for the rocking and sliding of a rigid body under various conditions, will be analysed analytically and numerically by numerical integration of the equations of motion and using the Finite Element Method. Especially the influence of the supporting flexibilities, the material properties of the base, the contact conditions, slight deviations from the ideal geometry and the kind of excitation on the motion of the body will be investigated. In contrast to most other studies more compact bodies are considered. The suitability of an implicit Finite Element Method for such studies will be investigated. Additionally, it is shown, how rocking and sliding are treated in the nuclear and non-nuclear rules.

2 THEORY OF ROCKING AND SLIDING MOTION

A rigid body (block) in a plane subjected to an earthquake excitation can perform the following kinds of motions: Rest, rotation (rocking), sliding, sliding rotation, translation and rotation jump [2]. A plane model to describe the rotation or rocking motion of a rigid body (on a rigid base) is shown in Figure 1, where CG denotes the centre of gravity of the body. The symbols are explained in Table 1.

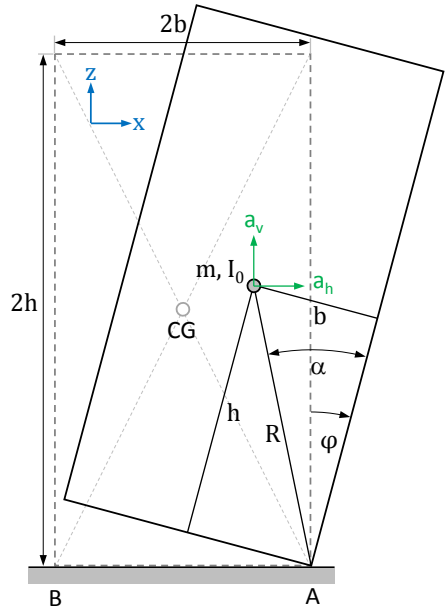


Figure 1: Plane model of a rigid body

Symbol	Parameter
2h	height
2b	width
$R = \sqrt{b^2 + h^2}$	length of the half diagonal
φ	angle of rotation
m	mass
I_0	moment of inertia about CG
$I = I_0 + mR^2$	moment of inertia about A/B
α	critical angle of rotation
$b/h = \tan\alpha$	aspect ratio
g	acceleration of earth gravity
$a_h(t)$	horizontal seismic acceleration
$a_v(t) + g$	vertical seismic acceleration
$p = \sqrt{mgR/I}$	frequency parameter
r	coefficient of restitution
E	modulus of elasticity

Table 1: Important characteristics and parameters

Assuming that the coefficient of friction is large enough, so that there is no sliding, the dynamic equilibrium conditions for the moments about the points A and B give the following equations of motion for the rigid body, which are also known from the literature [1] to [5]:

$$\begin{aligned} \ddot{\varphi} - p^2 \left\{ \frac{a_v(t)}{g} \sin(\alpha - \varphi) + \frac{a_h(t)}{g} \cos(\alpha - \varphi) \right\} = 0, \ \varphi > 0 \qquad \text{(Point A)} \\ \ddot{\varphi} + p^2 \left\{ \frac{a_v(t)}{g} \sin(\alpha + \varphi) - \frac{a_h(t)}{g} \cos(\alpha + \varphi) \right\} = 0, \ \varphi < 0 \qquad \text{(Point B)} \end{aligned} \tag{1}$$

Or as a single equation:

$$\ddot{\varphi} - p^2 \left\{ \operatorname{sgn}(\varphi) \frac{a_v(t)}{g} \sin(\alpha - |\varphi|) + \frac{a_h(t)}{g} \cos(\alpha - |\varphi|) \right\} = 0 \tag{2}$$

The term $\operatorname{sgn}(\varphi)$ denotes the signum-function:

$$\operatorname{sgn}(\varphi) = \begin{cases} -1 & \varphi < 0 \\ 0 \quad \text{for} & \varphi = 0 \\ 1 & \varphi > 0 \end{cases}$$

For a homogeneous rectangular block

$$I_0 = \frac{m}{3}(b^2 + h^2) \quad \text{and} \quad p^2 = \frac{3}{4}\frac{g}{R}.$$

When the condition

$$|a_h(t)| \leq |a_v(t)| \tan \alpha \tag{3}$$

is satisfied, rocking motion is not initiated and the body remains at rest. For $\varphi > \alpha$ the body will overturn if there is no restoring moment from the horizontal earthquake acceleration. In the case of pure rocking the Equations (1) or (2) give the motion before and after the impact. These equations are coupled by the angular velocities immediately before and after the impact. Housner [1] has derived a model to calculate the angular velocity of the rigid body after the impact and the energy dissipation during the impact. The model uses the following assumptions:

- The body and the base are rigid.
- There is no bouncing or complete lifting off of the body.
- The impact is a point impact (point contact).
- The time interval of the impact is very short.
- The body remains at the same position during the impact time.

Under these assumptions the principle of conservation of angular momentum immediately before and after the impact gives the following equation for the rigid body:

$$I\dot{\varphi}_{(+)} = I\dot{\varphi}_{(-)} - 2mbR\dot{\varphi}_{(-)} \sin \alpha \tag{4}$$

($\dot{\varphi}_{(-)}$ - angular velocity before the impact, $\dot{\varphi}_{(+)}$ - angular velocity after the impact)

From this follows the simple relation:

$$\frac{\dot{\varphi}_{(+)}}{\dot{\varphi}_{(-)}} = r = 1 - \frac{2mR^2}{I}\sin^2\alpha \quad \text{or for a rectangular block} \quad \frac{\dot{\varphi}_{(+)}}{\dot{\varphi}_{(-)}} = 1 - \frac{3}{2}\sin^2\alpha \qquad (5)$$

The value r denotes the coefficient of restitution in literature. Combining the Equations (1) or (2) and Equation (5) it is possible to solve the problem piecewise numerically. For the ratio of the kinetic energy before W_k^- and after the impact W_k^+ follows using (5):

$$\frac{W_k^+}{W_k^-} = \frac{\frac{1}{2}I\dot{\varphi}_{(+)}^2}{\frac{1}{2}I\dot{\varphi}_{(-)}^2} = r^2 = \left[1 - \frac{2mR^2}{I}\sin^2\alpha\right]^2 \qquad (6)$$

Since $r < 1$ the impacts have to be inelastic. During the impact kinetic energy is dissipated mainly by energy radiation into the foundation. Other possible mechanisms for dissipation are plasticity and friction. Equation (5) gives the maximum value for the coefficient of restitution for which a rigid body will undergo rocking motion. For $\alpha = \arcsin\sqrt{2/3} \approx 54.74°$ and therefore $b/h = \sqrt{2}$ the body stays in rest after the first impact. It is noted that the value of r according to the Equation (5) and consequently the energy dissipation according to (6) depends only on the geometry and mass distribution of the body. Since this also applies to the equations of motion the rocking of a rigid body (on a rigid base) is completely determined by the geometry and the accelerations. For a (homogeneous) rectangular block the height h and the width b are the important geometrical parameters.

For the case of a free rocking motion after an initial angular displacement φ_0 of the rigid body follows from (1):

$$\ddot{\varphi} \pm p^2 \sin(\alpha \mp \varphi) = 0 \qquad \text{(signs like in Equations (1))} \qquad (7)$$

For the angular velocity after the nth impact a simple consideration of the potential and kinetic energy gives the following equation:

$$\dot{\varphi}_n = r\dot{\varphi}_{n-1} \quad \text{with} \quad \dot{\varphi}_0^2 = \frac{2mgR}{I}\{\cos(\alpha - \varphi_0) - \cos\alpha\} \quad \text{and} \quad n = 1, 2, \ldots \qquad (8)$$

The kinetic energy W_k^n after the nth impact has the value:

$$W_k^n = \frac{1}{2}I\dot{\varphi}_0^2\, r^{2n} \qquad (\dot{\varphi}_0 \text{ from the Equation (8)}) \qquad (9)$$

For small angles $(\alpha - \varphi) \ll 1$ (slender bodies) it is possible to linearize the Equations (7) by using the well-known approximations $\sin(\alpha - \varphi) \approx \alpha - \varphi$ and $\cos(\alpha - \varphi) \approx 1$ and to solve the obtained equation analytically:

$$\ddot{\varphi} \mp p^2\varphi = \mp p^2\alpha \qquad \text{with the solution} \qquad \varphi(t) = \alpha \mp (\alpha \mp \varphi_0)\cosh(pt). \qquad (10)$$

The angle φ_0 denotes the initial angular displacement (or initial rotation). This solution can be used to calculate the time period T (the time for the first rocking cycle) as a function of the initial angle φ_0:

$$T = \frac{4}{p}\cosh^{-1}\frac{1}{1-\frac{\varphi_0}{\alpha}} \tag{11}$$

Equation (11) can be used for an estimation of the natural frequencies of a rocking body.

The Equations (1) or (2) determine together with Equation (5) under the stated assumptions completely the rocking motion of a rigid body. For a rocking motion to take place after the impact, a significant part of the kinetic energy of the body (minimum of 51 % for a rectangular block with $h/b = 2$) has to be dissipated into the foundation during the impact. In other cases the body will perform complicated kinds of motion like bouncing or jumping. Further attempts to understand the impact and the motion after the impact are given in [9], [10], [16] and [21]. The Equations (1) or (2) were derived under the assumption that rocking and sliding motions do not occur at the same time. The equations of motion for a simultaneous occurrence of rocking and sliding motion are given in [2], [10], [19] and [22].

3 NUMERICAL ANALYSES

3.1 Analysis methods

The numerical solution of the Equations (1) or (7) is done by using the (explicit) classical fourth-order Runge-Kutta method with a maximum time step of 0.001 s and an additional method for the accurate determination of the contact time. For every new time step the contact condition $\varphi_n \cdot \varphi_{n+1} \leq 0$ (φ_n - rotation of the current step, φ_{n+1} - rotation of the new step) is checked. In the case of contact, the time interval will decrease until the specified accuracy of the angle φ is reached. Because the Runge-Kutta method also provides the velocity for every time step, the velocity immediately before the impact $\dot{\varphi}_{(-)}$ is given. The procedure is restarted with the initial conditions for the angular displacement $\varphi(t_c) = 0$ and the angular velocity $\dot{\varphi}_{(+)}$ immediately after the impact according to Equation (5), where the time t_c denotes the contact time. For solving Equations (7) the velocity after the impact can be calculated by Equation (8) as well. A comparison of the numerically and analytically determined velocities shows an excellent agreement. For the case of no initial displacement, Equation (3) is used to test if the rocking motion can be initiated. The numerical solutions of Equations (1) or (7) will be mostly used as a reference (quoted as theoretical curve) for the further finite element analyses.

In most publications the authors developed (analytical) mechanical models to describe the motion of the rigid body and used numerical methods for the solution. There are only few works [23] to [26] on this issue using finite element (FE) analyses. FE analyses allow the consideration of elastic or plastic properties of the material, especially of the base. Additionally, the influence of geometrical parameters and their variations from the ideal geometry can be studied. By using infinite elements for the base it is also possible to take the radiation of energy in the foundation into account. Of particular interest is the influence of these parameters on the coefficient of restitution, which can be simply calculated from the ratio of the kinetic energies of two successive maxima. The FE analyses use the implicit code of the program Abaqus [27]. It is also of interest to determine if an implicit finite element program can be used to solve such problems. Because the impacts have the main influence on the further movement in most analyses, the excitation was done by an initial angular displacement $\varphi_0 < \alpha$. After preliminary calculations a maximum time increment of 0.001 s and automatic time stepping will be used for all calculations from now on.

3.2 Analyses for initial displacements

The first FE analyses were done with the discrete and abstract FE model in Figure 2 using rigid R2D2 elements for the geometry of the body and SPRING1 (a spring between a node and ground) or DASHPOT1 (a dashpot between a node and ground) elements for the base. The value c denotes the spring stiffness and k the damping constant. With a high stiffness and no damping this FE model is very similar to the analytical model. The results for a rectangular block with an aspect ratio of 2 and a nearly rigid base with stiffness $c = 2 \cdot 10^{16}$ N/m and without damping are shown in Figure 3 and 4. In addition, the curves resulting from Equation (7) for the best estimate coefficient of restitution $r = 0.69$ are given in the figures. The time history of the kinetic energy normalized to the maximum in Figure 3 shows as a result of the FE analyses that the block is bouncing and jumping multiple times during the impact. However, the theoretical curve from Equation (7) can be considered as a global approximation of the time history obtained by the FE analysis. In spite of the multiple bouncing and jumping during the impacts, the differences between the theoretical and the FE curves for the relative angular displacements φ/α are relatively small.

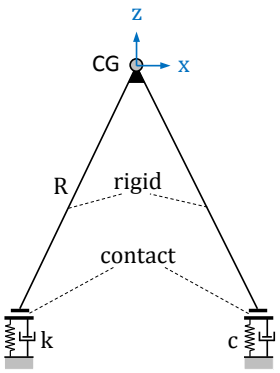


Figure 2: Rigid FE model with spring and damper

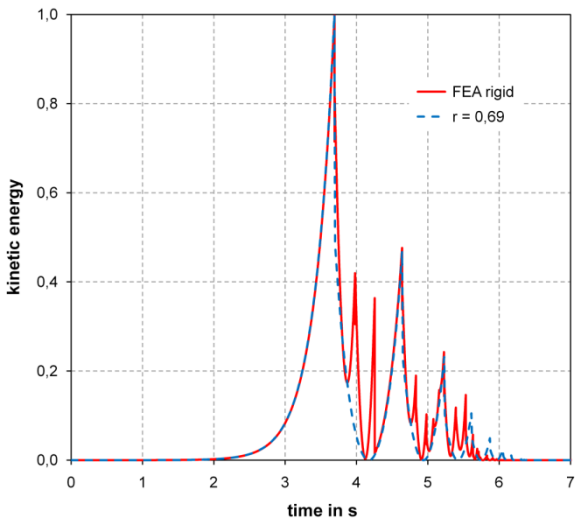


Figure 3: Time histories of the kinetic energy for the model with a rigid body on a nearly rigid base

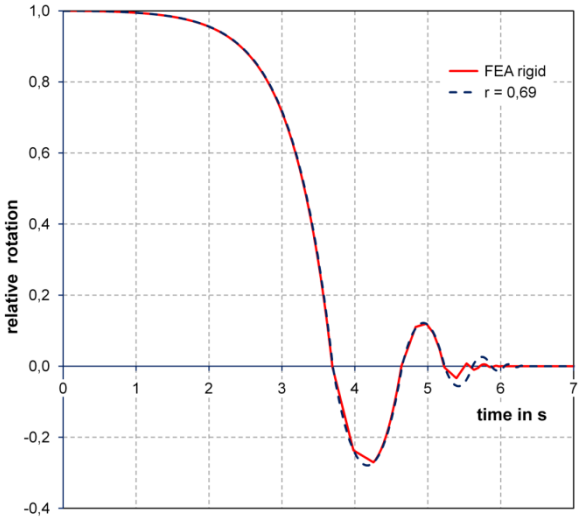


Figure 4: Time histories of the relative rotation for the model with a rigid body on a nearly rigid base

A basic problem of the previously used rigid model is that the rigid base does not dissipate energy during the impact. Therefore, additional analyses were done with the same model but using a smaller stiffness $c = 2 \cdot 10^{10}$ N/m and a damping value $k = 1{,}4 \cdot 10^{8}$ kg/s. The dimensions of the rectangular block are 2 m x 2 m x 4 m (width/depth/height), the mass is 124.8 t (similarly to a storage cask). The results obtained for a rigid block with an h/b-ratio of 2 are presented in the Figures 5 and 6. There is no bouncing or jumping with these values for the parameters c and k. Other combinations of c (especially large c) and k often produce bouncing and/or jumping. The comparison between the curves of the FE analysis and those from Equation (7) show a very good agreement. The curves resulting from Equation (7) for the best estimate coefficient of restitution $r = 0.7$ are also given in the figures. The coefficient of restitution of 0.7 is identical with the value from Equation (5) but decreases slightly from 0.7 to 0.69. A problem is the determination of the real stiffness and damping of the ground.

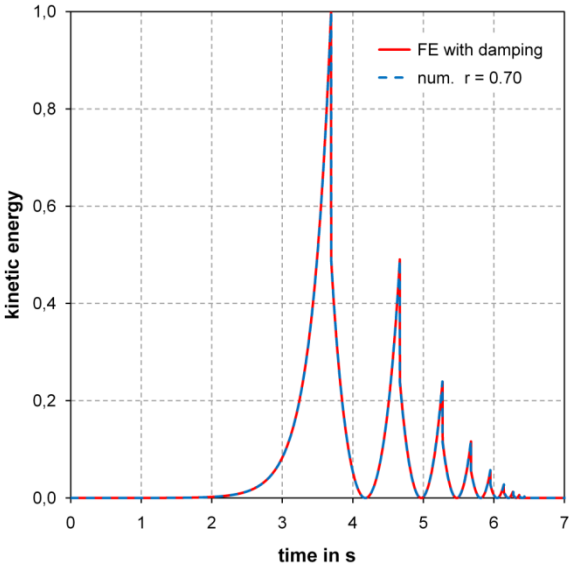


Figure 5: Time histories of the kinetic energy for the FE model with spring and damper

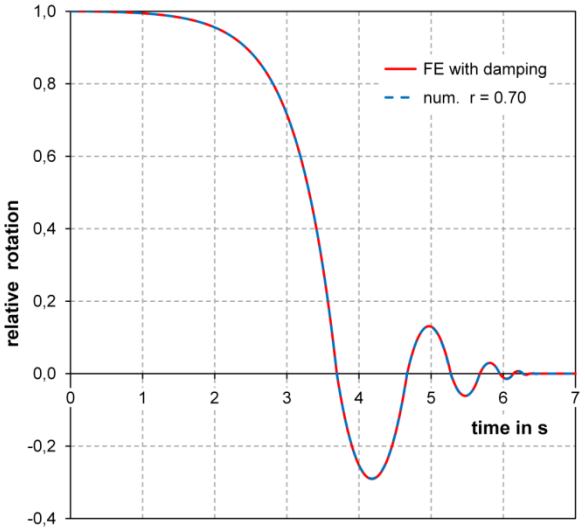


Figure 6: Time histories of the relative rotation for the FE model with spring and damper

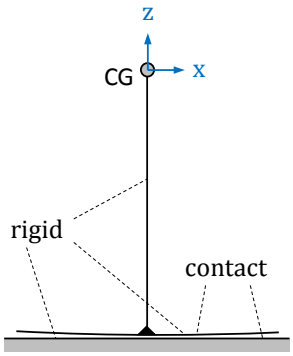


Figure 7: Rigid model with a curved contact line

In the analytical but also in the FE model in Figure 2 the rotation point changes immediately (or in a very short time) and discontinuously from one corner point to the other. To simulate a continuous transition of the rotation centre from corner to corner, the model in Figure 7 with a curved contact line is investigated. The curvature may be considered as a very small deviation from the ideal straight line geometry. Figures 8 and 9 show the time histories of the normalized kinetic energy and the relative angular displacement for a block with an aspect ratio of 2 for three different radii. With the radii used, the deviations between the two bottom corner points of the block and the ideal geometry of the rectangular block are only 0.1 mm, 0.5 mm und 1.0 mm, respectively.

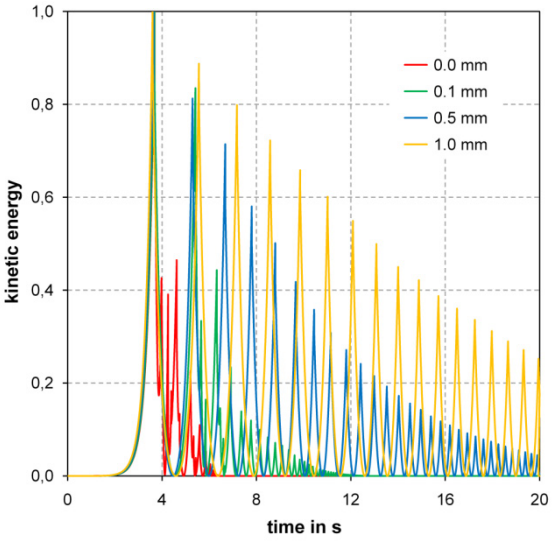


Figure 8: Time histories of the kinetic energy for the model with a curved bottom and b/h = 2

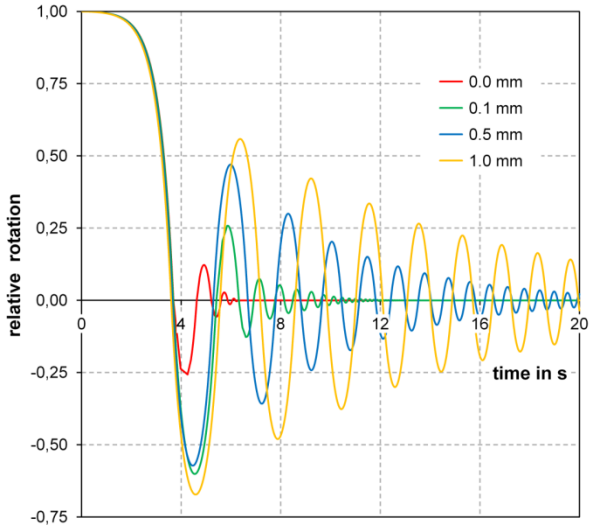


Figure 9: Time histories of the relative rotation for the model with a curved bottom and b/h = 2

Despite the very small deviation from the ideal geometry (in respect to the width of the block of 2 m only 0.05 ‰ to 0.5 ‰), the differences between the curves are very large. In all cases with the exception of the reference (0.0 mm) the coefficients of restitution are significantly greater than the value from Equation (5) and reach a maximum value of about 0.95. It is remarkable, that for a deviation of only 0.1 mm the coefficient for the first impact is already 0.9. Although the considered deviations are idealized, the obtained results show that very small geometrical deviations produce significantly larger coefficients of restitution and therefore different curves.

The previous models are not classical FE models because they use rigid bodies and have no real stiffness. Therefore, in the next step, the plane FE model in Figure 10 with CPS4 and CINPS4 elements (plane stress elements) is considered. The block is rigid by using the 'rigid body'-constraints in the FE model. In the regions of the contact points the mesh is refined. For the base one row of the infinite elements CINSP4 is used. These elements do not reflect elastic waves on the boundaries of the model. Without the thereby resulting radiation of energy into the foundation, the impact will excite elastic base vibrations, which especially without additional damping influence the impact. For comparison with the other models the first calculations were performed with a relative stiff base (modulus of elasticity E = 1000 GPa, density 7800 kg/m³). Figures 11 and 12 show the results obtained for a block with h/b = 2 and a mass of 124.8 t (similar to a typical storage cask). During the first impact a slight bouncing and jumping occurs. There is a very good agreement between the theoretical (numerical integration of Equations (1)) and the FE results, if a coefficient of restitution of 0.75 is used instead of the theoretical value 0.7 according to Equation (5).

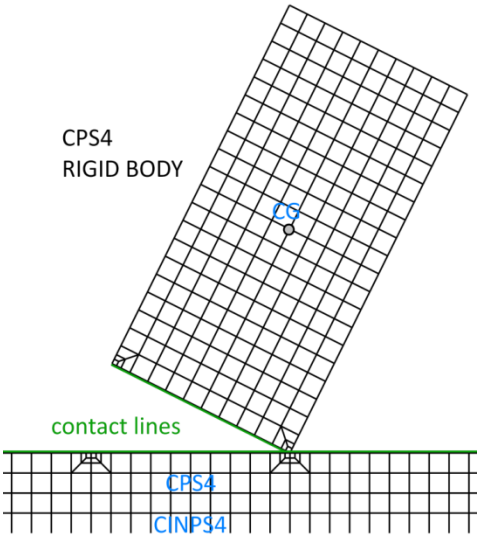


Figure 10: Plane FE model using a rigid body, CPS4 and CINSP4 elements

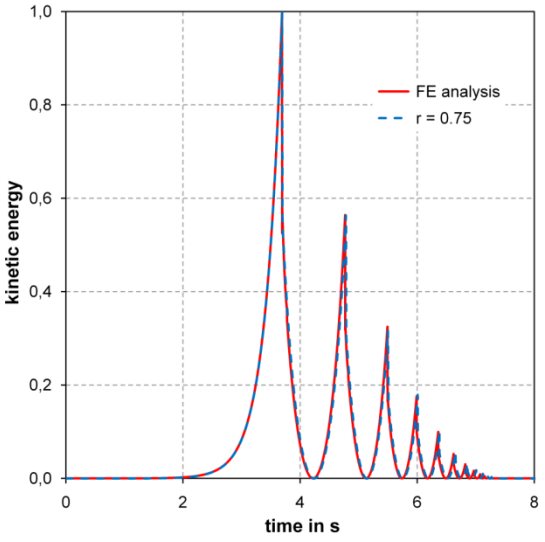


Figure 11: Time histories of the kinetic energy for the plane FE model with a very stiff base

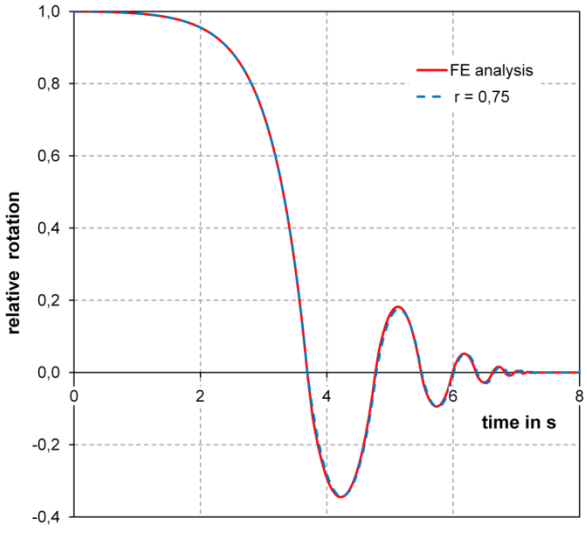


Figure 12: Time histories of the relative rotation for the plane FE model with a very stiff base

The previously used model has been modified with respect to the contact conditions and a smaller stiffness of the base (E = 200 GPa). In the case of point contact the contact occurs on the two corners. The case of the line contact is shown in Figure 10. In the last case the corners (edges) are slightly bevelled (0.5 mm on a length of 25 mm). The results are presented in Figures 13 und 14. As expected, the contact conditions have a significant influence on the coefficient of restitution and the time histories. The coefficients have the maximum values 0.72, 0.76 und 0.82 for the three respective contact conditions. The theoretical value is 0.7.

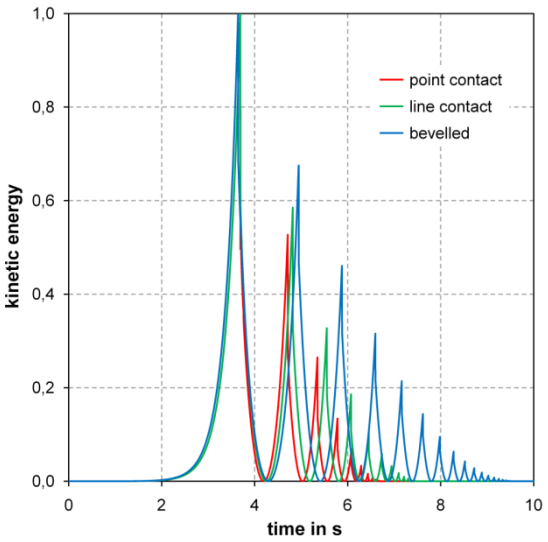


Figure 13: Time histories of the kinetic energy for the plane model with different contact conditions

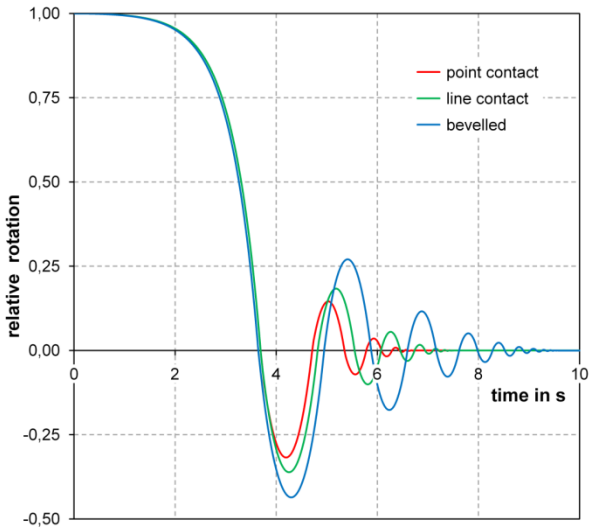


Figure 14: Time histories of the relative rotation for the plane model with different contact conditions

To study the influence of the plasticity, additional calculations were done using an ideal elastic-plastic material for the base. The materials have a modulus of elasticity of 200 GPa and a yield stress of 200 MPa (similar to austenitic steel, block mass 124.8 t), as well as a modulus of 35 GPa and a yield stress of 50 MPa (similar to concrete, mass 35.2 t). The results and the theoretical curves for the best estimate coefficients r are shown in Figures 15 and 16.

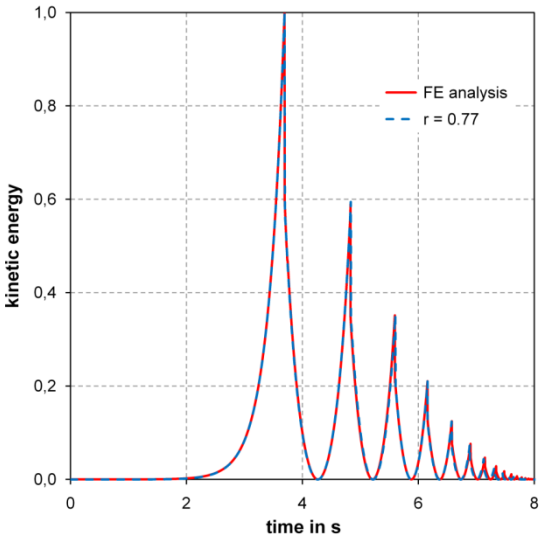


Figure 15: Time histories of the kinetic energy for a model with an elastic-plastic material like steel

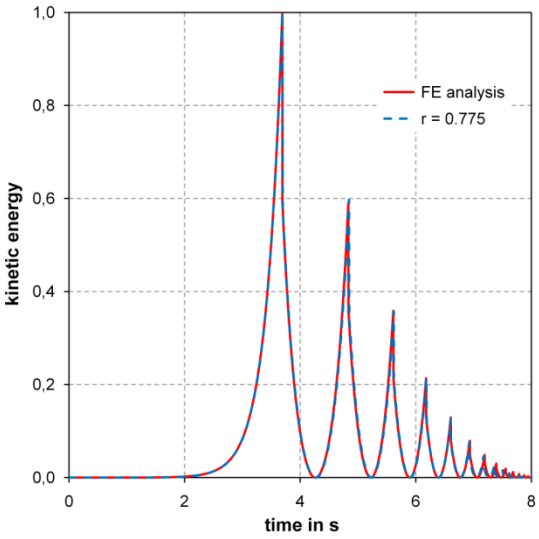


Figure 16: Time histories of the kinetic energy for a model with an elastic-plastic material like concrete

There is a very good agreement between the theoretical and the FE results in both figures if the coefficients of restitution stated in the figures are used instead of the theoretical value 0.7. The differences between the two best estimate coefficients in the figures 0.77 and 0.775 are very small, but again significantly larger than the theoretical value. In the range below 10 % of the maximum kinetic energy and therefore for small amplitudes, the agreement between the two curves becomes lower, which may indicate a dependence of the coefficient on the amplitude. Because of the small values of the kinetic energy this question cannot be resolved completely.

In many cases anti-slip pads are used to prevent sliding. To investigate the effect of such a pad on the motion, the model is modified by a 1 cm thick mat between the body and the base. The material of the pad is assumed to be elastic with a modulus of 50 MPa (density 1200 kg/m³, Poisson ratio 0.49). There is no bouncing and jumping, but because of the low horizontal stiffness a horizontal oscillation of the rotation point occurs at large deflections in addition to the rocking motion. The results are shown in Figures 17 and 18. The coefficient of restitution reaches values around 0.9 and varies in some cases from impact to impact. The initial impact is done after 3.05 s, in difference to the approximate 3.69 s for all other models. The curves in Figure 17 und 18 can no longer be described using Equation (1) or (2).

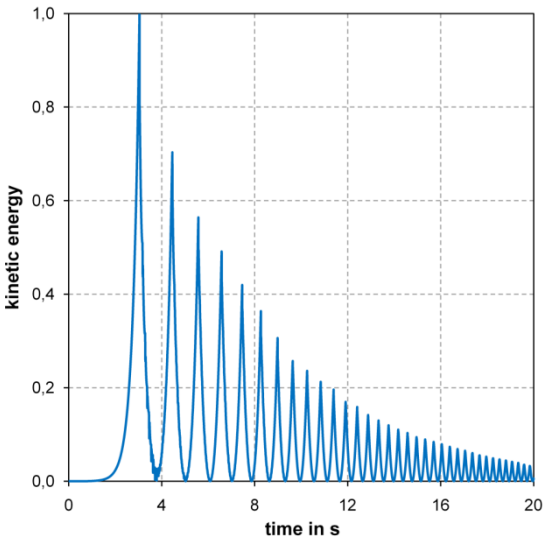


Figure 17: Time history of the kinetic energy for a rigid block with an anti-slip pad

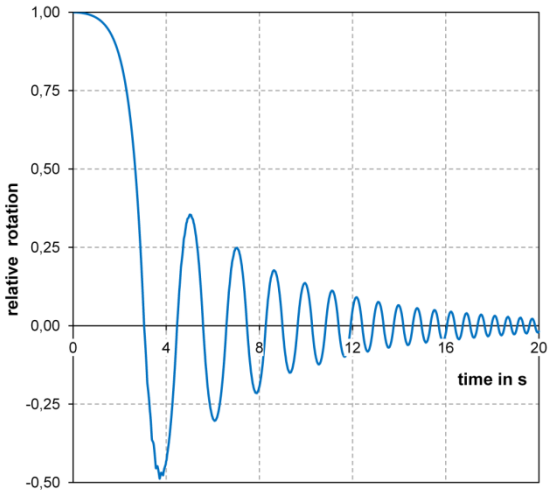


Figure 18: Time history of the relative rotation for a rigid block with an anti-slip pad

Additional FE analyses with 3D models give similar results and dependencies, so there is no reason for an additional presentation of these results. These models will be used for future studies under multiaxial excitation.

3.3 Analyses with dynamic excitations

The dynamic response of the body does not only depend on the geometric parameters and the coefficient of restitution but also on the type and strength of the excitation. Therefore, the excitation is further investigated. Because the previous studies have shown a very good agreement between the numerical solutions of Equation (1) with the best estimate coefficient of restitution (calculated by FE analyses) and FE analyses, most calculations are performed by using the numerical integration of the equations of motion.

In the first case, the block is excited by sine, triangle or rectangle vibrations with an ampli-

tude of 1 g (about 9.81 m/s²) and a frequency of 1 Hz. The results obtained for the block with h/b = 2 using a coefficient of restitution of 0.7 and 0.85 are shown in Figures 19 and 20. As expected, the largest displacements are caused by rectangle vibrations. The maximum rotation is usually found during the first four impacts. It is remarkable, that in the case of an excitation with rectangle vibrations and using the conservative coefficient of restitution of 0.8, the amplitudes will increase significantly over time until overturning. For a verification of the results, some FE analyses with the model in Figure 10 with h/b = 2 (mass 124.6 t) on an elastic base (E = 200 GPa, density 7800 kg/m³) have been performed. The curves in Figure 21 confirm the previous statements about the very good agreement between theoretical and FE results. Figure 22 illustrates the dependency of the maximum rotation at an excitation using sine or rectangle vibrations. For a assumed sine oscillation of the block the dependency of the maximum amplitude φ_{max} on the frequency f is given by the relation $\varphi_{max} \sim 1/f^2$. The dependency in Figure 22 corresponds to a power slightly over 2.

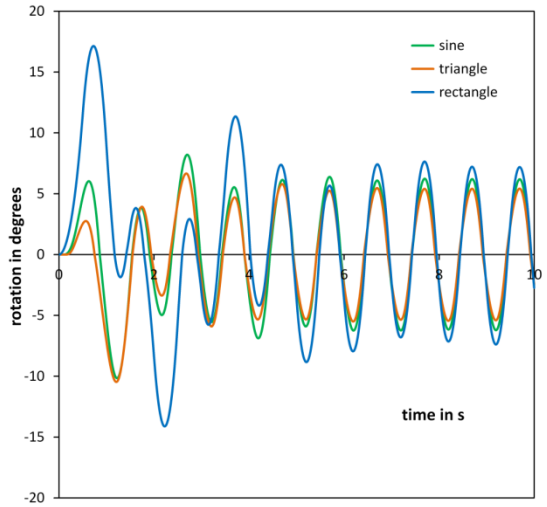


Figure 19: Time history of the rotations for different excitations with r = 0.7 and a frequency of 1 Hz

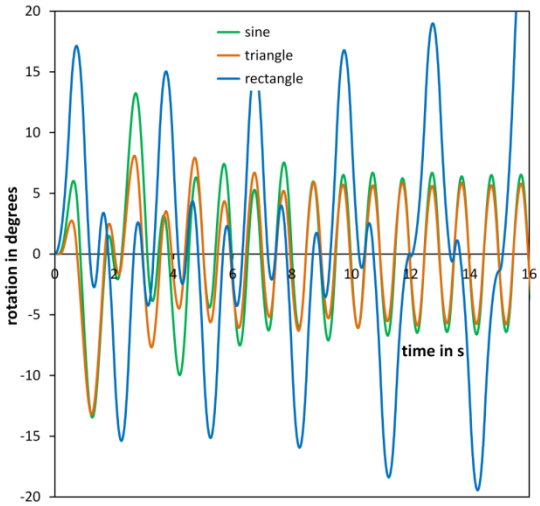


Figure 20: Time history of the rotations for different excitations with r = 0.85 and a frequency of 1 Hz

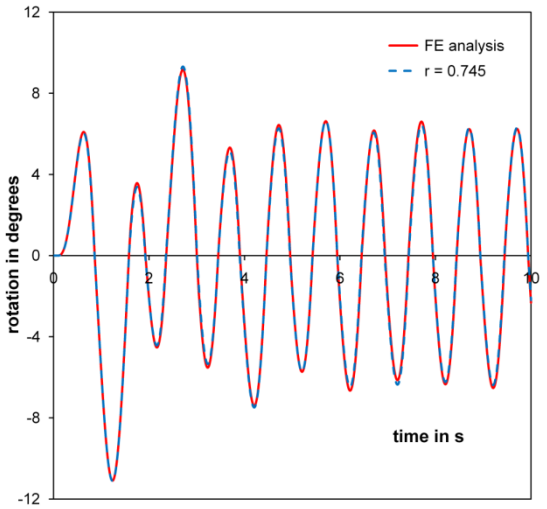


Figure 21: Time history of the rotations for an excitation with a sine vibration 1 Hz

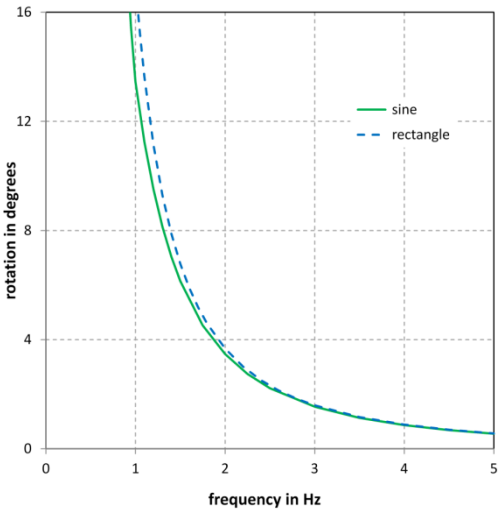


Figure 22: Maximum angular displacements for different excitations with r = 0.85

Additionally, calculations are done with time histories using earthquake ground accelera-

tions from the European strong-motion database. As examples two time histories of earthquake ground accelerations are shown in Figures 23 and 25. Both time histories are normalized to peak ground accelerations (PGA) at 1 g. The calculations use the previously described method for the numerical integration of the equations of motion. The resulting motions of a rigid block with h/b = 2 using the conservative coefficient of restitution of 0.8 are presented in Figure 24 and 26. The maximum rotations are about 0.5° and 1.7°. Further calculations for other additional time histories cause an even greater variation in the results.

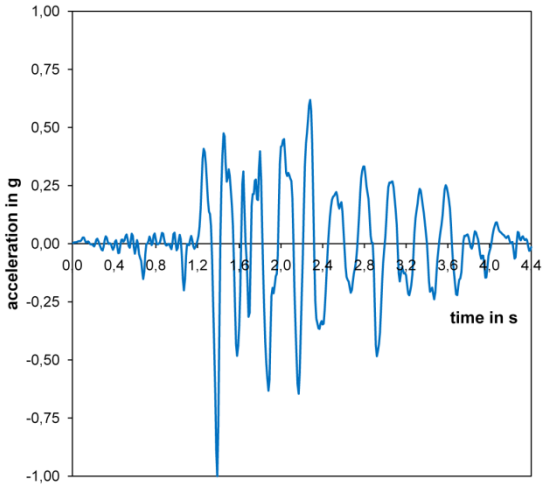


Figure 23: Time history of the acceleration for the Albstadt earthquake (Germany, 16.01.1978)

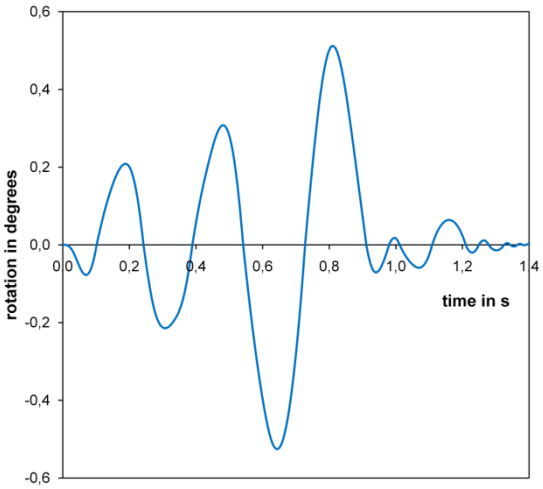


Figure 24: : Time history of the rotations for the Albstadt earthquake with r = 0.8

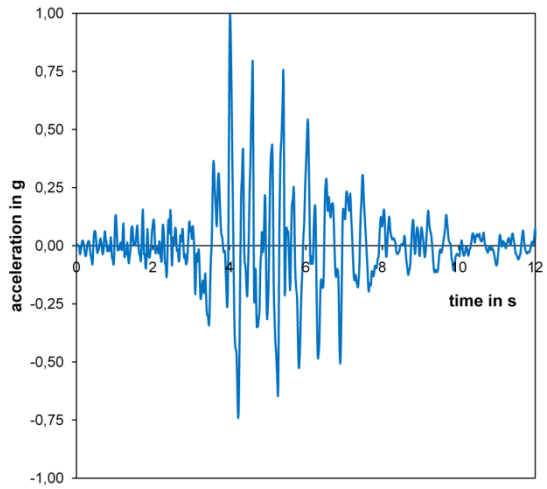


Figure 25: Time history of the acceleration for the Friuli earthquake (Italia, 06.05.1976)

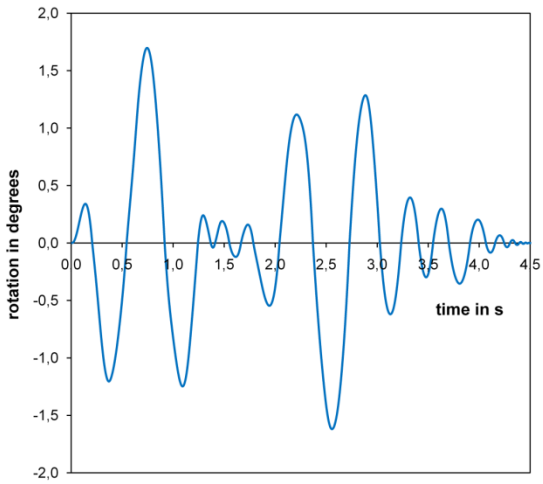


Figure 26: : Time history of the rotations for the Friuli earthquake with r = 0.8

Because the previous studies investigate only pure rocking motions, now the transition between rocking and sliding motion will be shortly considered. For the FE analyses the model in Figure 10 (h/b = 2, mass 124.6 t, E = 200 GPa, density 7800 kg/m³) is used. The results for coefficients of friction μ between 0.1 und 1.0 show that for μ = 0.6 the block performs a (nearly) pure rocking motion. For μ = 0.55 it is a combined rocking and sliding motion with an amplitude of about 68 mm. For μ = 0.5 the amplitude of sliding amounts to about 300 mm. For μ = 0.45 the block performs a pure sliding motion with an amplitude of about 390 mm. The motion is very sensitive to small changes of the geometry of the base.

4 CONVENTIONAL AND NUCLEAR RULES

The European standards EN 1990 [33] and EN 1998 [34] and the US standard ASCE 7-10 [30] give design criteria for rocking and sliding of structures in non-nuclear facilities. For nuclear facilities the US standard ASCE/SEI 43-05 [29] and the German KTA 2201.1 [35] and KTA 2201.4 [36] provide guidance for analysis of rocking and sliding.

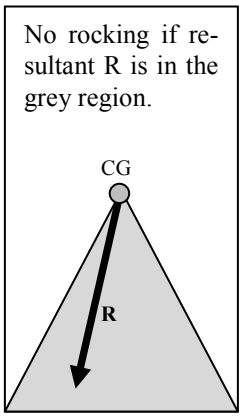


Figure 27: Static evaluation of rocking stability

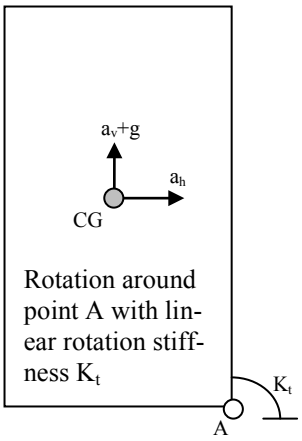


Figure 28: Model of ASCE/SEI 43-05, Appendix A.2 for the determination of the rocking angle φ_{max}

The easiest way to show that a body will not tip over is to show that the resultant force due to gravity and the seismic accelerations is within the grey area of Figure 27. This criterion prevents rocking. It is used by all the standards mentioned above except the standard ASCE/SEI 43-05. In order to see how large the safety factors are, Table 2 shows how the dead load component is determined for the different standards. The value of the vertical seismic acceleration is also given.

Code	ASCE/SEI 7-10	EN 1990 and EN 1998	KTA 2201.1 and 2201.4
Factor for dead load	0.9	1.0	0.95
Upward seismic load	Two-thirds of the horizontal seismic acceleration	30 % of the vertical seismic acceleration (permitted to be neglected if the vertical PGA is less than 0.25 g)	30 % of the vertical seismic acceleration, which can be assumed to be two-thirds of the horizontal seismic acceleration

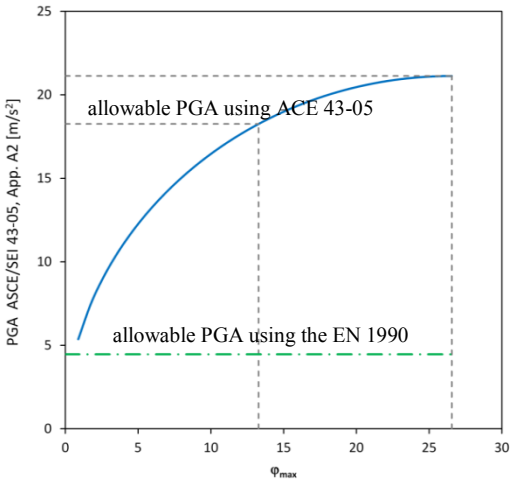
Table 2: Static evaluation of rocking stability of a rigid body

Standard ASCE/SEI 43-05 gives an approximate method for the determination of the best estimate rocking angle φ_{max} for given spectral accelerations. How these formulas were derived is mentioned in Appendix B.2 of the standard. The main idea is to reduce the nonlinear system to a linear system, where the body rotates around its corner and is restraint by a linear torsion spring (see Figure 28). The spring's torsion coefficient K_t is determined in such a way that at the maximum rocking angle φ_{max} the energy of the spring equals the potential energy of the φ_{max} inclined body. With these assumptions, the governing equation is that of the well-known single degree of freedom system:

$$I\ddot{\varphi} + 2D\sqrt{K_t I}\dot{\varphi} + K\varphi = m\{a_h h + (a_v + g)b\} \tag{12}$$

with $$K_t = \frac{2mgh}{\varphi_{max}^2}\left\{\cos\varphi_{max} + \frac{b}{h}\sin\varphi_{max} - 1\right\} \quad (13)$$

As defined in Table 1, $(a_v + g)$ denotes the vertical seismic acceleration. With this model it is possible to use given design spectra of an earthquake for the determination of φ_{max}. The rotation due to the vertical and horizontal earthquake acceleration is combined by the square root of the sum of the squares (SRSS). The damping factor of the spectrum is based on the coefficient of restitution. The equivalent viscous damping is derived in such a way, that the energy loss per cycle of the free oscillating linear system of Figure 28 equals that of the system in Figure 1 and Equation (5). For a homogeneous rectangular block with h/b = 2 the damping factor D is 11.3 %. The rotations are best estimate values and the maximum rocking angle has to be multiplied by a safety factor of 2.0. Because the real system is simplified by this method, the question arises, if this method is sufficiently proven for all types of bodies.



Parameters
Rigid body
2h = 4 m
2b = 2 m
Instability angle α = 26.6 °
Elastic Spectrum type 1 acc. to EN 1998
Ground type A = Rock
Vertical seismic acceleration equals 2/3 horizontal acceleration

Figure 29: Allowable peak ground acceleration and effect of the safety factor = 2.0 of ASCE 43-05

Figure 29 shows the allowable peak ground acceleration (PGA) according to ASCE/SEI 43-05 using a spectrum which is given in EN 1998. For the given geometry the safety factor of 2.0 applied to the deformation results in a much smaller safety factor regarding the allowable PGA. The allowable PGA according to the ASCE/SEI 43-05 is 4.1 times higher than that derived from a static evaluation according to Table 2 using the Eurocode procedure.

Comparison of ASCE 43-05 Appendix A Results with NUREG/CR-6865 Time History Results

μ = 0.80, RG 1.60, All Soil Profiles
Critical Angle = 29.2 degrees

PGA	Median Peak Cask Rotation (Degrees)	
	NUREG/CR-6865 Median	ASCE 43-05 App. A, 10% Damping
0.25	0.1	0
0.40	1.2	0.8
0.50	3.7	1.4
0.60	9.1	2.1
0.80	37.9	4.4
1.00	114.0	7.9

Table 3: Comparison of ASCE 43-05 with time history analyses (μ - coefficient of friction, from [23])

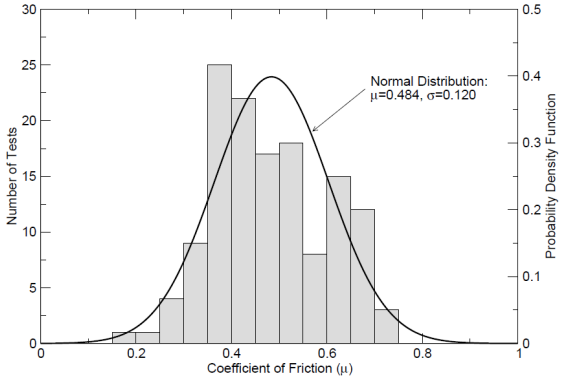


Figure 30: Histogram of steel/concrete coefficient of friction test results (published in [23])

The U.S. Nuclear Regulatory Commission (NRC) published a presentation [23] where Table 3 is shown. It summarizes the results of different time history analyses using the FE code Abaqus explicit and compares it to ASCE/SEI 43-05 results. The rocking body is a cylindrical cask. ASCE/SEI 43-05 predicts much smaller angles φ_{max}. A cylindrical body may roll around its edge, which leads to less energy dissipation.

According to [37] a new revision of the standard ASCE 4-98 is planned to provide guidance for analysis of rocking and sliding of unanchored bodies subjected to seismic load based on ASCE/SEI 43-05. Up to now it has not been published.

All mentioned codes above except ASCE/SEI 43-05 prevent sliding by checking that the horizontal force divided by the resultant vertical force is less than the existing friction coefficient. The ASCE/SEI 43-05 in Appendix A.1 provides a procedure for computing a best estimate sliding distance. This procedure needs the spectrum and the coefficient of sliding at the 95 % exceedance level as input data. The procedure is stated as conservative and the result shall be increased by a safety factor of 2.0. The safety factor 3.0 is necessary for best estimate sliding distances derived from time history analyses (mean value of at least five time histories). Figure 30 shows test results of the steel/concrete coefficient of friction.

5 SUMMARY

The rocking motion of unanchored bodies under seismic excitation was investigated by numerical integration of the equations of motion and with the Finite Element Method. For numerical integration the classical fourth-order Runge-Kutta method and for the finite element analyses the programs Abaqus (implicit code) were used.

An important part of the investigations is the calculation of the coefficient of restitution with FE analyses. The results obtained from calculations for a rectangular block with an aspect ratio of 2 for models with geometric variations, different contact conditions and different properties of the base result in the following conclusions for the case of an initial angular displacement:

- Rigid FE models without additional damping are not suitable because they produce an unrealistic bouncing and jumping. For 2D or 3D FE models the usage of infinite elements is recommended.

- In most cases the agreement between results from FE analyses and the numerical integration of the equations of motion is very good, if the coefficients of restitution are based on best estimate values from FE analyses.

- All variations from the ideal geometry and contact conditions cause larger coefficients of restitution in comparison to the theoretical value 0.7 of the Housner model. The consideration of plasticity gives higher values as in the elastic case. The maximum values for the coefficients are about 0.9. It is recommended to use a value of at least 0.8 for theoretical calculations.

- Some investigations show a dependence of the coefficients of restitution on the amplitude.

- Anti-slip mats lead to greater coefficients of restitution and shorter rocking periods. The usage can only be recommended if the body is compact and overturning not a problem.

The dynamic investigations consider an excitation by sine, triangle or rectangle vibrations and time histories from earthquake ground accelerations. The calculations for a rectangular block with an aspect ratio of 2 result in the following conclusions:

- The agreement between results from FE analyses and the numerical integration of the equations of motion is very good if the coefficients of restitution are based on the FE analyses.

- Because of the possible dependence of the coefficients of restitution on the amplitude additional calculations with 2D or 3D FE models are recommended. In the case of a horizontal and vertical excitation 2D models provide a good accuracy.

- Calculations for coefficients of friction between 0.1 und 1.0 show, that for values below 0.45 the block performs a pure sliding motion. For 0.5 to 0.55 it is a combined rocking and sliding motion. The motion is very sensitive to small changes of the geometry of the base or the body.

- Because of the large variations of the results the investigation of a large number of time histories is recommended.

Additionally, it will be noted that implicit FE programs are suitable to study the rocking and sliding problem.

All investigated codes prevent rocking by the requirement that the overturning moment at the base is less than the resisting moment due to dead load minus the vertical seismic acceleration. Sliding is prevented by checking that the required coefficient of friction is smaller than the existing one. From the mechanical point of view the mentioned rocking proof of the codes is correct and needs no assumptions. It is a lower bond value. The standard ASCE/SEI 43-05 provides a procedure for the determination of a best estimate rocking angle due to seismic accelerations beyond the lower bond value. By linearizing the highly nonlinear phenomenon it is possible to use design spectra. There are no restrictions with regard to the type of body. The question if the procedure of ASCE/SEI 43-05 is sufficiently conservative for all geometries of rigid bodies cannot be answered. Based on our own investigations and those of the U.S. Nuclear Regulatory Commission there are doubts.

REFERENCES

[1] G.W. Housner, The behavior of inverted pendulum structures during earthquakes. *Bulletin of the Seismological Society of America*, **53**, 403-417, 1963.

[2] Y. Ishiyama, Motions of rigid bodies and criteria for overturning by earthquake excitations. *Earthquake Engineering & Structural Dynamics*, **10**, 635-650, 1982.

[3] M. Aslam, W.G. Godden, D.T. Scalise, Rocking and overturning response of rigid bodies to earthquake motions. LBL-7539, Lawrence Berkeley Laboratory, November 1978.

[4] C.S. Yim, A.K. Chopra and J. Penzien, Rocking response of rigid blocks to earthquakes. *Earthquake Engineering & Structural Dynamics*, **8**, 565-587, 1980.

[5] A.S. Koh, P.-T.D. Spanos, Seismically induced rocking of rigid structures. *Proceedings of Eighth World Conference on Earthquake Engineering*, San Francisco, CA, Vol. IV, 251-258, 1984.

[6] W.K. Tso, C.M. Wong, Steady state rocking response of rigid blocks part 1: Analysis. *Earthquake Engineering & Structural Dynamics*, **18**, 89-106, 1989.

[7] C.M. Wong, W.K. Tso, Steady state rocking response of rigid blocks part 2: Experiment. *Earthquake Engineering & Structural Dynamics*, **18**, 107-120, 1989.

[8] S.J. Hogan, On the dynamics of a rigid block, tethered at one corner, under harmonic forcing. *Proceedings of the Royal Society, Series A*, **439**, 35-45, 1992.

[9] H.W. Shenton III, N.P. Jones, Effect of friction and restitution on rocking response. *Earthquake Engineering, Tenth World Conference*, Balkema, Rotterdam, 1933-1938, 1992.

[10] P.R. Lipscombe, S. Pellegrino, Free rocking of prismatic blocks. *Journal of Engineering Mechanics*, **119**, 1387-1410, 1993.

[11] N. Makris, Y. Roussos, Rocking response and overturning of equipment under horizontal pulse-type motions. *Report PEER-1998/05*, Pacific Earthquake Engineering Research Center, College of Engineering, University of California, Berkeley, 1998.

[12] N. Makris, J. Zhang, Rocking response and overturning of anchored equipment under seismic excitations. *PEER Report 1999/06*, Pacific Earthquake Engineering Research Center, University of California, Berkeley, 1999.

[13] Andreaus, On the rocking-uplifting motion of a rigid block in free and forced motion: influence of sliding and bouncing. *Acta Mechanica*, **138**, 219-241, 1999.

[14] F. Prieto, P.B. Lourenand C.S. Oliveira, Impulsive Dirac-delta forces in the rocking motion. *Earthquake Engineering & Structural Dynamics*, **33**, 839–857, 2004.

[15] M. Apostolou, G. Gazetas, E. Garini, Seismic response of slender rigid structures with foundation uplifting. *Soil Dynamics and Earthquake Engineering*, **27**, 642-654, 2007.

[16] C. Yilmaz, M. Gharib and Y. Hurmuzlu, Solving frictionless rocking block problem with multiple impacts. *Proceedings of the Royal Society, Series A*, **465**, 3323-3339, 2009.

[17] D. Konstantinidis, N. Makris, Experimental and analytical studies on the response of freestanding laboratory equipment to earthquake shaking. *PEER Report 2005/07*, Pacific Earthquake Engineering Research Center, University of California, Berkeley, 2005.

[18] F. Pena, F. Prieto, P.B. Lourenc, A. Campos Costa and J.V. Lemos, On the dynamics of rocking motion of single rigid block structures. *Earthquake Engineering & Structural Dynamics*, **36**, 2383-2399, 2007.

[19] A.N. Kounadis, On the overturning instability of a rectangular rigid block under ground excitation. *The Open Mechanics Journal*, **4**, 43-57, 2010.

[20] H. Zhang, B. Brogliato, Multiple impacts with friction in the rocking block. *Nosmooth contact and impact laws in mechanics (Euromech 2011)*, Grenoble, France, July 6-8, 2011.

[21] H. Zhang, B. Brogliato, The planar rocking-block: analysis of kinematic restitution laws, and a new rigid-body impact model with friction. *Institut National de Recherche en Informatique et en Automatique*, Grenoble - Rhône-Alpes, No. 7580, 2011.

[22] M.-Y. Jeong, I.-Y. Yang, Characterization on the rocking vibration of rigid blocks under horizontal harmonic excitations. *International Journal of Precision Engineering and Manufacturing*, 13, 229-236, 2012.

[23] NUREG/CR-6865. Parametric evaluation of seismic behavior of freestanding spent fuel dry cask storage systems. Sandia National Laboratories, U.S. Nuclear Regulatory Commission, 2005.

[24] Q.T. Ma, J.W. Butterworth and B.J. Davidson, Modelling rocking structures using standard finite elements. *NZSEE Conference*, Wairakei Resort, Taupo, New Zealand, 2005.

[25] S. Lamarche, F. Voldoire, H. Ben Dhia and C. Zammali, Validation of contact-impact approaches for FEM software. *EURODYN 2005*, September 4-7, Paris, France, 2005.

[26] R. Kourkoulis, P. Kokkali, Parametric dimensional analysis on rocking of 1-dof systems. *4th Japan-Greece Workshop on Seismic Design of Foundations and Innovations in Seismic Protection*, September 2-9, Kobe, Japan, 2011.

[27] Abaqus, Version 6.11, SIMULIA (ABAQUS Inc., Providence, USA).

[28] M. Demosthenous, G.C. Manos, Dynamic response of rigid bodies subjected to horizontal base motions. *Earthquake Engineering, Tenth World Conference*, Balkema, Rotterdam, 2817-2821, 1992.

[29] ASCE/SEI 43-05, Seismic design criteria for structures, systems, and components in nuclear facilities. *American Society of Civil Engineers*, Reston, Virginia, USA, 2005.

[30] ASCE/SEI 7-10. Minimum design loads for buildings and other structures. *American Society of Civil Engineers*, Reston, Virginia, USA, 2010.

[31] ANSI/AISC N690-12, Specification for safety-related steel structures for nuclear facilities. *American Institute of Steel Construction*, Chicago, Illinois, USA, 2012.

[32] S.R. Jensen, O. Gurbuz, Sliding and rocking of unanchored components and structures: Chapter 7.6 ASCE 4 Revision 2. *2011 Structures Congress*, Las Vegas, Nevada, April 14-16, 2011.

[33] EN 1990:2002 (A1:2005, A1:2005/AC:2010 D), Eurocode - Basis of structural design, European Standard. *European Committee for Standardization*, Brusseles, Belgium, 2010.

[34] EN 1998-1:2004 (AC:2009 D), Eurocode 8: Design of structures for earthquake re-

sistance - Part 1: General rules, seismic actions and rules for buildings, European Standard. *European Committee for Standardization*, Brusseles, Belgium, 2009.

[35] KTA 2201.1 (2011-11), Design of Nuclear Power Plants against Seismic Events; Part 1: Principles. *German Nuclear Safety Standards Commission (KTA)*, Germany, 2011.

[36] KTA 2201.4 (2012-11), Design of Nuclear Power Plants against Seismic Events; Part 4: Components. *German Nuclear Safety Standards Commission (KTA)*, Germany, 2012.

[37] G. S. Bjorkman, Methodologies Acceptable to the Staff for Performing Seismic Stability Analyses of a Stack-up Configuration within a 10 CFR Part 50 Facility. *U.S. NRC Spent Fuel Storage and Transportation Division*, November 1, 2011.

COMPDYN 2013
4th ECCOMAS Thematic Conference on
Computational Methods in Structural Dynamics and Earthquake Engineering
M. Papadrakakis, V. Papadopoulos, V. Plevris (eds.)
Kos Island, Greece, 12–14 June 2013

EFFECTS OF "REINFORCED" INFILLED FRAMES ON EXISTING RC BUILDINGS

Andrea Fiore[1], **Giuseppina Uva**[2]

[1] DICATECh, Politecnico di Bari
address via Orabona, 4 - 70126 Bari (Italy)
andrea.fiore@poliba.it, g.uva@poliba.it

Keywords: Masonry Panel, Infilled Frames; Seismic Assessment; Nonlinear Static Analysis; Equivalent Strut Models, Existing Building.

Abstract. *This paper presents some considerations about the role of strengthening interventions involving the solidarization of the infill panels to the RC frame on the seismic retrofitting of existing buildings. Within this context, an appraisal of the actual resulting displacement capacity and of possible alteration induced on the global collapse mechanism and on is provided. Nowadays, it is well-established that infill panels contribute in increasing the overall in-plane resistance to horizontal actions within a variable range of the displacement intervals before they start to degrade. Anyway, in most cases there is also an effect of significant alteration of the overall seismic behaviour and collapse mode, which should be properly taken into account.*
With reference to a real case study concerning a school building (which was part of a wide vulnerability assessment investigation performed in the Province of Foggia, Italy), an appraisal of the effect of strengthening interventions is here discussed. In particular, the seismic analysis by non linear static procedure has been performed both on the reinforced configuration and on the original structure and critically discussed.

1 INTRODUCTION

The seismic vulnerability of existing buildings is surely a direct consequence of the deterioration of materials and poor constructive details, but, most of all, is related to the theoretical and technical reference framework according to which the structural design has been performed. This is especially true when speaking of seismic design concepts, that have made substantial progress in the last decades, whereas the structures designed and constructed according to old standards and legislations have revealed to have an inadequate seismic performance. In addition, for existing structures, when there aren't specific structural monitoring systems, it becomes very difficult to evaluate the performance of the materials in time [1,2].

Recent earthquakes in Italy and all over the world have clearly highlighted that the seismic response of existing RC framed buildings are strongly influenced by the presence of infill panels, which significantly contribute to the global strength and, consequently, to the formation of the collapse mechanism. Another important effect is related to the regularity of the structural geometric configuration, both in plan and elevation, which might be significantly altered by the presence of very stiff and irregular infill walls, triggering unexpected storey mechanisms and/or torsion effects. The additional problem related to mechanisms that directly involve infill panels is that they may be brittle, to an extent more or less noticeable depending on the specific mechanical properties and stiffness and of the numerical model adopted [3,4].

In current design practice of RC framed structures, the contribution in terms of stiffness and strength of non-structural elements like infill walls is not included in the numerical model. Such an approach is actually contained in the present Building Codes [5,6], in which it is suggested that infill panels, under in-plane horizontal actions, should be considered as completely disconnected by the surrounding frame.

Instead, the awareness of the role of infill panels in the structural seismic response is maturing in the scientific community, and also in the professional field, with regard to the possibility of improving the seismic behaviour of existing buildings. Dolsek and Fajfar [7,8], for example, have proposed the extension of the "N2 Method" (which is actually included in many building codes as the reference method for the non linear static analysis) to infilled RC frames. An example in which the contribution of infill walls has been exploited in seismic strengthening and repair interventions is provided by the case of L'Aquila Earthquake (April, 2009): special attention has been paid to the connection of masonry panels to the surrounding frame. Here, local interventions have been applied to non-confined nodes and infill panels, in order to mitigate the risk of brittle mechanisms (shear failure of column-beam nodes or beam/column end sections under the shear actions transmitted by the infill panel; shear failure). The adopted techniques mainly consisted in the implementation of effective connections between the panel and the surrounding RC elements along the top and lateral edges (Figure 1a), or in the application of plaster reinforced with a regular steel wire mesh (Figure 1b).

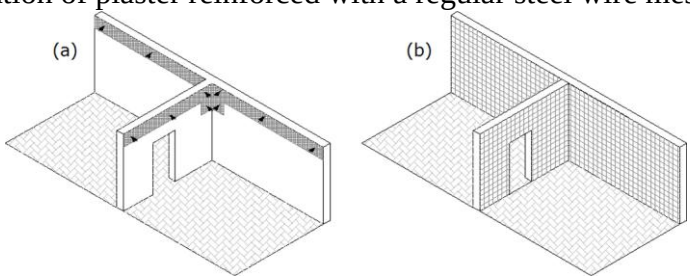


Figure 1: Scheme of the perimetric connection of infill panels to the surrounding RC frame: application of a steel wire mesh and tassels (a); reinforced plaster (b).

The above mentioned techniques allow to achieve three objectives: preventing the out-of-plane overturning of the panels; improving the in-plane stiffness and strength; reducing undesired local effects at the columns' end sections. Thanks to the connections, in fact, it is possible to distribute the actions flowing through the infill panel along the top edge, whereas the shear stress concentration that usually affects the columns' ends is significantly reduced, if not canceled at all. Under this new stress distribution, however, the collapse mechanisms attained by the whole structure can be modified even significantly.

In conclusion, it is evident that the contribution of infill panels – especially if they can be defined as "strong" (i.e., they are characterized by high stiffness/strength values for a sufficient wide displacement range) – can be crucial in the response to medium-high earthquakes. In this context, clearly, the specific numerical approach used to model the infill-frame system under the horizontal actions becomes a fundamental element. For example, macro-models based on the use of the equivalent strut for simulating the presence of infill panels are affected by a strong sensitivity to a number of parameters: number of struts; width b_w of the equivalent strut; constitutive law of the panel [9].

In the present paper, with reference to a real case study concerning a school building located in Southern Italy (more precisely, in the City of Cerignola, Province of Foggia, Puglia), the effect of reinforcement interventions on infill panels is investigated. An extensive comparison of the response of different structural configurations analyzed by non linear static procedure is presented. Besides the bare frame, two possible cases have been considered: RC frame with non-reinforced and with reinforced infill panels (respectively, this corresponds to a "strong" and to a "weak" infill behaviour [3,4].

The objective is to investigate in detail the behaviour of the framed building in the case in which the infill panels (that are usually considered – and modelled – as non-structural elements having no interaction with the surrounding frame) are solidarized with the frame, becoming a part of the primary structural system, with a particular reference to the modifications induced on the global collapse mechanisms and displacement capacity of the building.

2 NON LINEAR MODELING OF INFILL PANELS: A SHORT STATE OF THE ART

With regard to the frame-infill system, many models have been proposed in the literature, and can be divided into two classes. The first class includes models based on a macro-modelling approach that will be later discussed. The second is based on the detailed modelling of both RC and infill masonry panels by means of proper discretization techniques and non linear constitutive law of the materials [10,11,12].

The equivalent diagonal strut method [13,14] is based on the observation that, within a masonry panel, the compressive stress substantially follows the diagonal path, and thence adopts one or more equivalent diagonal struts in order to simulate the infill masonry panel. This method belongs to the class of macro-element models, and is indeed the most used, thanks to easy and flexible application possibilities. On the other hand, it should be observed that the advantages related to the simplicity and versatility of the model are counterbalanced by the difficulties rising in the interpretation of the numerical results. Indeed, the most critical problem in the use of macro-models consists in the difficulty of correctly identifying the mechanical properties and the geometrical features of the equivalent diagonal struts, which haven't a direct correspondence with the actual frame-panel system (for example, the case of the panel with an opening). A promising approach could be that of exploiting the results coming from a detailed but effective computational modelling [15,16,17,18] for interpreting and calibrating strut-like macro-models and the parameters.

The fundamental parameters of the methods are represented by the geometric features of the strut (length d_W, thickness t_W and width b_W), the stiffness λ, the hysteretic constitutive law F_W-d which governs the non linear cyclic behaviour of the panel (Figure 2).

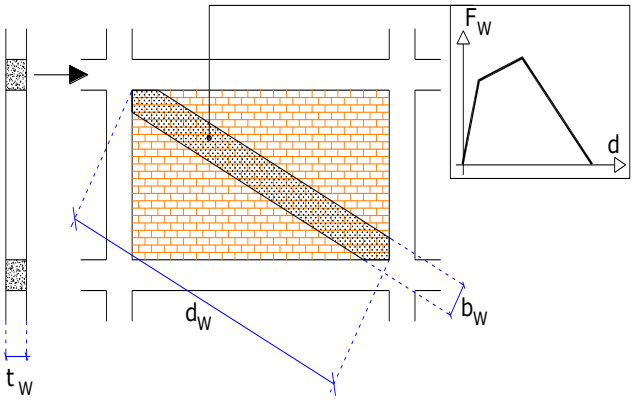


Figure 2: The equivalent diagonal strut model.

In the most recent approaches, the width b_W of the equivalent strut is expressed in terms of the ratio b_W/d_W. A well-acknowledged method is the one proposed by Bertoldi et al. (1993)[19].

$$\frac{b_W}{d_W} = \frac{K_1}{\lambda H} + K_2 \tag{1}$$

Where the parameters K_1 and K_2 are expressed as a function of λh (h= distance between the axis line of the top and bottom beam of the frame). The λ factor defines the relative stiffness between the infill panel and the surrounding frame, and can be calculated according to different expressions proposed by different authors [20]. The most used expression for λ, anyway, is the one defined by Stafford Smith & Carter [14], which was actually the basis for all the successive research studies.

$$\lambda = \sqrt[4]{\frac{E_{W\theta} t_W \sin 2\theta}{4 E_c I_C H_W}} \tag{2}$$

where E_C is the elastic modulus of the concrete, I_C is the moment of inertia of the columns surrounding the panel, $E_{W\theta}$ is the elastic modulus of the masonry, calculated as a function of the slope angle θ of the diagonal strut to the horizontal.

With regard to the hysteretic law F_W-d which describes the cyclical behaviour of the strut under axial loads, several models can be found in the literature, which are derived from the phenomenological observation of experimental tests in which scale models are dynamically brought to collapse. Among the different proposals, examples can be found in which the law is expressed in terms of axial strain/stress [21] and formulations in which, regardless of the geometrical and mechanical characteristics of the infill, a predominant failure mode (which can consist in the crushing at the center or at the corners of the panel) is a-priori defined [22].

The model proposed by Bertodi et al. (1993)[19], which is adopted in the present research work, considers four different types of failure mechanisms, and to each of them associates an ultimate stress value σ_w, which is constant along the diagonal strut:

$$F_W = (\sigma_W)_{min} t_W b_W \cos\theta \tag{4}$$

- Crushing at the center of the panel:

$$\sigma_{W1} = \frac{1{,}16 f_{Wv} \tan\theta}{K_1 + K_2 \lambda H} \tag{5}$$

- Crushing at the corners f the panel:

$$\sigma_{W2} = \frac{1{,}12 f_{Wv} \sin\theta \cos\theta}{K_1(\lambda H)^{-0{,}12} + K_2(\lambda H)^{0{,}88}} \tag{6}$$

- Sliding on the mortar bed joints:

$$\sigma_{W3} = \frac{(1{,}2 \sin\theta + 0{,}45 \cos\theta) f_{Wu} + 0{,}3\sigma_v}{\frac{K_1}{\lambda H} + K_2} \tag{7}$$

- Diagonal tension:

$$\sigma_{W4} = \frac{0{,}6 f_{Ws} + 0{,}3\sigma_v}{\frac{K_1}{\lambda H} + K_2} \tag{8}$$

in which f_{Wv} , f_{Wu} and f_{Ws} are, respectively, the compressive strength of the masonry in the vertical direction; the shear strength for sliding of mortar joints in the absence of compression (cohesion) and the shear resistance to diagonal cracking; σ_v is the value of the axial stress for gravity loads (it is zero in the case of panels that have no load-bearing function).
According to this model, the Force-displacement law (Figure 3) is defined once two parameters are known: K_m and F_m. Which are, respectively, the stiffness and the peak strength of the equivalent strut.

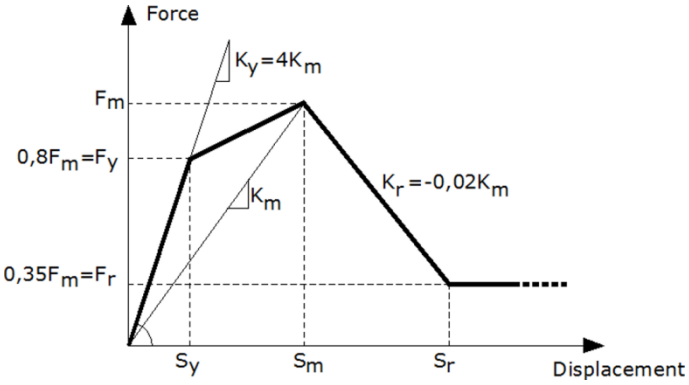


Figure 3: The Force-displacement law proposed by Bertoldi et al. [19]

3 THE CASE STUDY

3.1 Vulnerability analysis of school buildings in the Province of Foggia

The case study proposed in this paper is one of the 20 school buildings (80% of which has a RC framed structure) included in a specific regional research program aimed at the seismic safety assessment of a sample of school buildings in the Province of Foggia. This was part of a wider research Project was funded by *Regione Puglia* (Fund CIPE 20/2004) and managed by the *Autorità di Bacino della Puglia* (Basin Authority of Puglia) in cooperation with a number of Public Institutions (Department *Dicatech* of the University "*Politecnico di Bari*", Municipality of Foggia, Administration of the Province of Foggia) targeted at the multi-hazard risk assessment of current building stock, critical bridge infrastructures [23].

The vulnerability assessment of the school buildings has provided information about the actual safety level, both with regard to the vertical and the seismic loads, and moreover, has allowed to collect a precious database which includes not only information about the geometry, the history, the materials, …of the buildings, but also detailed data about the structural

performance parametrs (such as the displacement capacity, strength, …). The pie chart in Figure 4 shows the percentage distribution of some constructive and typological features of the analyzed sample (age of construction, number of storey, irregularity), from which a representative "reference building type" can be deduced: age of construction before 1980; presence of strong in-plane irregularity; low rise building (number of storeys<4). An indicative value of the seismic vulnerability (CVS),

defined as the ratio between the seismic action corresponding to the attainment of the limit structural capacity and the seismic demand, both evaluated in correspondence of the Limit State of Life Safety (LS). The chart, in which it can be seen that the CVS values are mostly below the unit, highlights the strong seismic vulnerability of the school buildings located in the area.

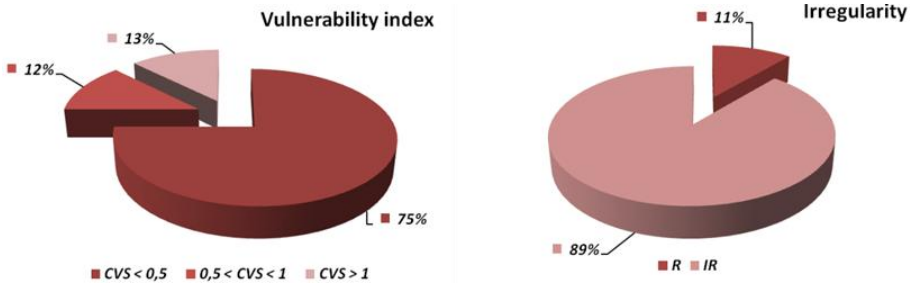


Figure 4: Distribution of some significant parameters for the analyzed sample

The seismicity of the investigated area, expressed in terms of "maximum horizontal acceleration at the site - a_g", is comprised between *0.173g* and *0.253g*. On the basis of the Italian scale, thence, the seismic hazard of the region, can be classified as low-medium.

3.2 Description of the case study and investigation about the quality of in-place materials

The school building chosen as case study is located in the city of Cerignola (Province of Foggia, Puglia, Italy). It is apart from other constructions, with two storeys (ground floor and first floor) containing the classrooms and the related facilities and flat, non accessible roof. According to the available documents, the building was constructed in the years '68-'70. According to the technical regulations of that period, and being the considered area classified at that time as not seismic prone, the structural design was simply based on the verification of the safety level with regards to vertical loads, whereas no specific design and calculation criterion for the seismic actions was considered. The building has an extension of about *356* m^2 in plan, and a height of about *8.5 m*. The structural system is provided by a RC frame, with mixed slabs (cast-in place concrete and hollow tile bricks) having a thickness of *20 cm* at the intermediate levels, and *43 cm* at the roof. There are no significant irregularities in elevation (protrusion, recesses, stiffness/mass variations) which may affect the vertical regularity. The beams of the first level have a rectangular section (*30 cm x 50 cm*; *30cm x 60 cm*); those of the second level have sections of dimensions *30 cm x 50 cm* and *40cm x 50 cm* (frame #X2). In the transverse direction, there are connecting slab beams *30 cm* wide. There are three types of column sections: *30 cm x 50 cm, 40 cm x 40 cm, 45 cm x 45 cm*, that remain constant for all their height.

On the basis of retrieved data and in-situ inspections, the reinforcements' arrangement for the structural elements has been derived. In Figure 5, the longitudinal reinforcement for the main structural elements is shown. The transversal reinforcement is the same for all the elements ($\phi 6$ stirrups, uniformly spaced every *20 cm*).

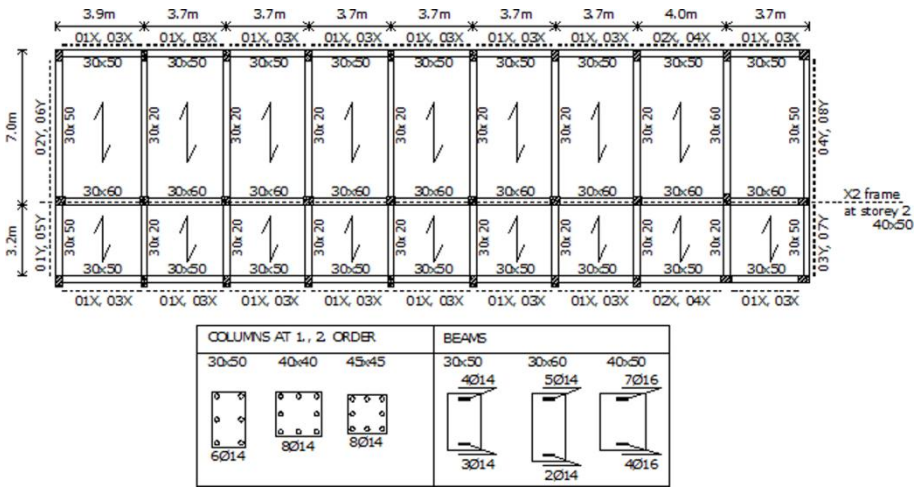


Figure 5: The case study: structural plan of the ground floor and scheme of the longitudinal reinforcement in the main structural elements.

After completing the general geometrical survey and the direct inspections aimed at investigating the geometrical features of the hidden structural elements, a detailed experimental program was planned, including on site non-destructive testing and laboratory tests on the specimens pulled put from the structural elements, in order to evaluate the mechanical properties of materials and achieve a "*Knowledge Level 2*" [5,6].

Destructive (drilled cores) and non-destructive tests (rebound hammer and ultrasonic pulse velocity test) have been performed on the most significant structural elements (with regard to the stress level under both vertical and seismic actions). The data acquired by non destructive methods have been used in order to support and integrate the estimate of in-place concrete strength provided by the compressive tests on drilled cores. In the literature, several methods and procedures have been proposed for the correlation of significant data (for example, the compaction degree) in order to obtain reliable estimates of the compressive strength and assess the possible presence of different homogeneous classes of concrete [24]. In the present case, the numerical processing has involved the use of rebound hammer index, ultrasonic pulse velocity and compressive core strength. A good homogeneity of the material has been found, allowing to define a single homogeneous concrete class, characterized by a compressive strength equal to *22 MPa*. Tensile tests over the steel bars extracted have provided a reference strength value of *301 MPa*.

With regard to the infill walls, the endoscopic investigation has revealed that the infill consists of a cavity wall (the external layer is made of solid bricks *12 cm* thick, the internal one is made of hollow bricks 8 cm thick). It is actually very similar to the infill panels used in the research work Bertoldi et al. (1993) [19] and, in the absence of specific on site tests, the mechanical parameters provided in this reference have been adopted, which are collected in Table 1.

f_{Wv} *[MPa]*	f_{Wu} *[MPa]*	f_{Ws} *[MPa]*	E_{Wh} *[MPa]*	E_{Wv} *[MPa]*	G *[MPa]*	W *[MPa]*
1.5	0.25	0.31	991	1873	1089	6.87

Table 1. Mechanical parameters adopted for the infill wall

3.3 Numerical modeling

The numerical modelling was carried out by using a finite element approach, implementing proper spatial models of the building's structure within the solver "SAP2000" [25]. In particular, 9 three-dimensional models of the building have been initially considered: one for the analysis of the bare frame; four for the analysis of the structure in the actual configuration (unreinforced infill panels); four for the analysis of the structure with the infill panels reinforced according to the techniques described in the introduction and shown in Figure 1. The case of the infilled frame has involved the definition of four different numerical models depending on the direction of the analysis (directions +X and +Y; -X and -Y). The presence of the infill panels has been considered only in the frames parallel to the direction of the analysis, in order to overcome possible problems of convergence in the numerical solver. Actually, the results found in the + X and + Y directions are very similar to those of the dual directions -X and-Y, and therefore are not presented in the paper. Henceforward, all the discussion will concern three structural models (regardless of the direction of analysis), that will be indicated, respectively, by the letters "B" (bare frame), "IS" (initial infilled structure); "R-IS " (reinforced infilled structure). In the "IS" and "R-IS " cases, the infill panels have been modeled by means of equivalent diagonal struts arranged along one of the two diagonal of the panel, in order to react to compression according to the direction of the pushover analysis (as an example, in Figure 6, the three-dimensional model of the structure used for the analysis in the + X direction is shown).

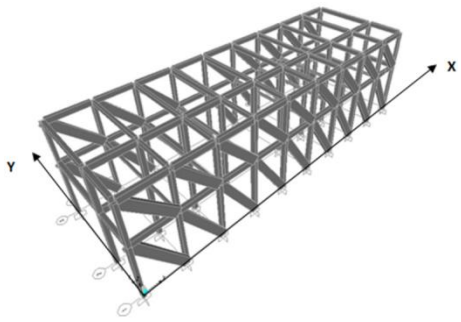


Figure 6: The 3D frame model with the single equivalent struts in +X

With regard to the constitutive laws for the materials, and on the basis of the results of in-situ tests, the following choices have been made: stress-strain law for confined concrete proposed by Mander et al. (1984) [26]; elastic – hardening diagram for the steel. The non linear behaviour of columns and beams was described according to a lumped plasticity approach. According to this, the post-elastic behaviour is modelled by introducing plastic hinges, in which all non linearity is localized at the ends of the elastic beams representing the structural elements.

In order to appraise the alteration of the structural behaviour in the presence of the reinforced infill panels, the increased mechanical parameters of the infill have been assumed according to the indications provided by the Italian Building Code [4], depending on the kind of intervention that is applied. In this case, the reinforcement technique is that of the reinforced plaster, and the code suggests the application of a correction factor of 1.3 to the original parameters of the masonry.

It should be mentioned that the interventions based on the use of tassels or of a steel welded mesh involve an alteration of the collapse mechanism of the panel and, consequently, a substantial modification of the overall failure mode of the frame-infill system. In fact, in both kind of interventions, the behaviour of the infill wall becomes similar to that of a reinforced panel, which is usually not affected by local collapse mechanisms (especially at the corners).

In this sense, the tests performed by Calvi & Bolognini (2001)[27] on unreinforced and reinforced panels (the reinforcement consisted in the insertion of vertical steel bars in the vertical holes of the bricks) are particularly relevant. It was shown that the failure mechanism, in the two cases, can be very different according to the drift value. For reinforced panels, the failure was characterized by the crushing, with a concentration of the damage in the central part of the panel, whereas the contact surfaces with the frame presented a very limited cracking. These results confirm that the approach proposed by Bertoldi et al. does not fully reproduce the actual behaviour in the case of a reinforced panel.

In order to obtain a more realistic representation of the structural behaviour, a calibration of the hysteretic law F_W-d has been performed for each of the strut, on the basis of the maximum force (*see* ***Eq. (4)***) corresponding to the crushing at the center of the panel.
In Figure 7 respectively for the reinforced structure (R-IS model) and the unreinforced structure (IS model), the hysteretic curves obtained for the 4 struts for the pushover analysis in the X direction are shown.

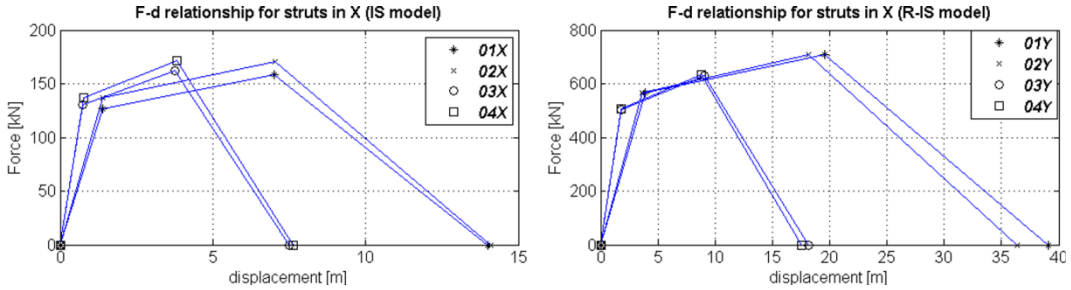


Figure 7. the force–displacement relationship of the diagonal struts (under compression) for IS and R-IS models in the X direction.

According to this assumption, the behaviour of the strut correspond to a “strong “ infill, for which the beginning of the plastic phase starts for very large strength values (approximately 4 times higher than in the case of unreinforced panels). Overall, the global behaviour of the structure is comparable to that of a mixed masonry-RC structure, in which the masonry walls are true primary elements side by side with RC columns and beams

4 RESULTS

The performance capacity has been calculated by non linear pushover analysis at the Limit States of Damage (SLD), Life Safety (SLV) and Near Collapse (SLC), for the three models (B, IS, R-IS). As the lateral distributions of incremental loads, the first fundamental mode was assumed as a shape vector (no significant difference between the cases of bare or infilled structure was found for the shape).

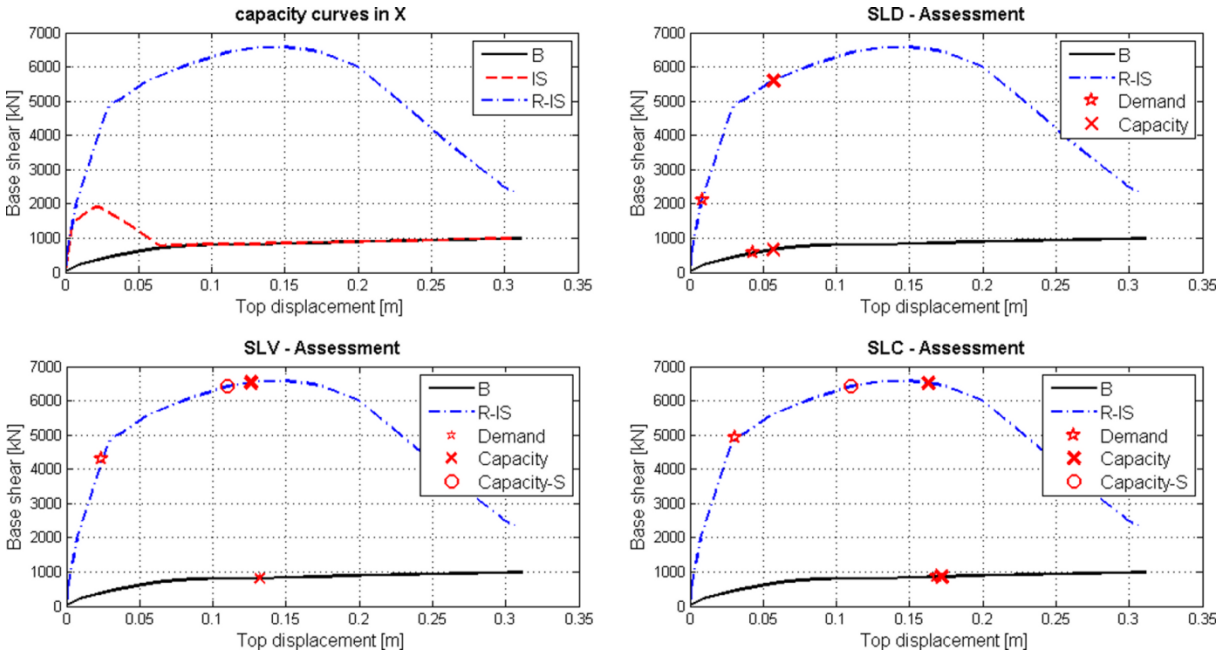


Figure 8: Pushover analyses in the X direction: comparison between the capacity curves for the three models B, IS, R-IS and graphic performance assessment at the different limit states.

As previously mentioned, the presence of the infill increases of stiffness and strength of the structure. This is confirmed by the curves shown in Figure 8, which shows the results of the pushover analyses in the X direction (where there are more infill panels). The ratio between the maximum shear force, V_b^{IS}/V_b^{B} and $V_b^{R\text{-}IS}/V_b^{B}$, is respectively equal to 1.65 and 5.72. In the figures, the seismic demand and the actual structural capacity at the different limit states are also indicated. It should be precised that it has been assumed that the limit structural capacity is attained in correspondence with the collapse of the first primary vertical element. The determination of the seismic demand has been performed according to the N2 Method **[28]** (original version implemented in EC8) both for the infilled frame and the bare structure. As already pointed out, the overall structural response can be assimilated to that of a frame-wall system, in which the walls assume a primary behaviour under horizontal actions. Two capacity points have been thence indicated on the curves relative to the R-IS model: collapse of the first primary element (point "X"); collapse of the first infill panel (point "O"). The results graphically shown in Figure 8 are also summarized in Table 2, where the explicit quantification of the safety level, expressed as the ratio between the capacity C and the seismic demand D.

Pushover in X direction	SLD		SLV		SLC	
	B	R-IS	B	R-IS	B	R-IS
D *[m]*	0.043	0.009	0.132	0.024	0.169	0.031
C *[m]*	0.057	0.057	0.132	0.126	0.172	0.163
Cs *[m]*	-	0.057	-	0.110	-	0.110
SC	1.32	6.33	1.00	4.58	1.01	3.54

Table 2. Seismic demand and structural capacity at the different limit states for the pushover analyses in the X direction for the models B and R-IS.

The reinforcement intervention increases the structural ductility with respect to the bare frame: in particular, the increments at the different limit states are equal to $4.79\mu_{SLD}^{B}$, $4.58\mu_{SLV}^{B}$ and $3.50\mu_{SLC}^{B}$ in the X direction.

5 CONCLUSIONS

A case study concerning a RC school building dated back to the '70's, and located in a low-medium seismic zone is presented. The results obtained can be summarized as follows:

- The solidarization of the infill panel to the RC frame allows allows to stiffen the structure and to obtain optimum performance capacity for earthquakes of low intensity. The advantages are similar to those provided by frame-wall systems (relevant strength and stiffness increase for small displacement values of the control node). In contrast, the high base shear can drive an excessive stress concentration on the foundation structures and on horizontal structures, which should be therefore properly verified and possibly reinforced.
- The disconnection of the panels from the frame requires that the bare frame is able to resist by itself to high intensity earthquakes, since the infill contribution, in this case, is not effective. This means that most of the columns of the frame shall be properly retrofitted (e.g., by incrementing the resisting section). Moreover, it should be mentioned that the cost of this solution is often very high.

AKCNOWLEDGEMENT

The research presented in this article was partially funded by the Department of Civil Protection, Project ReLUIS-DPC 2010-2013.

REFERENCES

[1] G. Uva, D. Raffaele, F. Porco, A. Fiore, G. Porco, Bridge monitoring by fiber optic deformation sensors: a case study. In: Biondini, Frangopol (eds) Proceedings of the 6th international conference on bridge maintenance, safety and management, Como, Italy, 8–12 July 2012. Taylor & Francis Group, London - ISBN: 978-0-415-62124-3.

[2] F. Porco, A. Fiore, G. Porco, G. Uva, Monitoring and safety for prestressed bridge girders by SOFO sensors, *Journal of Civil Structural Health Monitoring* **3**(1),3-18, 2013. DOI 10.1007/s13349-012-0029-9.

[3] G. Uva, F. Porco, A. Fiore, Appraisal of masonry infill walls effect in the seismic response of RC framed buildings: a case study. *Engeneering Structures*, **34**(1),514–26, 2012.

[4] A. Fiore, F. Porco, D. Raffaele, G. Uva, About the influence of the infill panels over the collapse mechanisms actived under pushover analyses: two case studies. *Soil Dynamics and Earthquake Engineering*, **39**,11-22, 2012.

[5] DM 14/01/2008. Norme Tecniche per le Costruzioni (NTC 2008) - *(in Italian)*. Gazzetta Ufficiale n.29. Roma; 2008.

[6] CEN. Eurocode 8: design of structures for earthquake resistance. Part 1: general rules, seismic actions and rules for buildings. Brussels; 2005.

[7] M. Dolšek, P. Fajfar, Simplified non-linear seismic analysis of infilled reinforced concrete frames. *Earthquake Engineering and Structural Dynamics*, **34**,49-66, 2005.

[8] M. Dolšek, P. Fajfar, The effect of masonry infills on the seismic response of a four storey reinforced concrete frame – a deterministic assessment, *Engineering Structures*, **30**(7),1991-2001, 2008.

[9] G. Uva, F. Porco, D. Raffaele, A. Fiore, On the role of equivalent strut models in the seismic assessment of infilled RC buildings. *Engineering Structures*, **42**:83-94, 2012.

[10] G. Uva, G. Salerno, Towards a multiscale analysis of periodic masonry brickwork: A FEM algorithm with damage and friction, *International Journal of Solids and Structures*, **43**: 13, 3739-3769, 2006 DOI: 10.1016/j.ijsolstr.2005.10.004

[11] S. Casolo, G. Uva, Out-of-plane seismic response of masonry façades some comparisons among full dynamic and pushover analysis, *Ingegneria Sismica*, ISSN: 03931420, **27**:3, 33-54, 2010.

[12] S. Casolo, G. Milani, G. Uva, C. Alessandri, Comparative seismic vulnerability analysis on ten masonry towers in the coastal Po Valley in Italy, *Engineering Structures*, **49**, 465-490, 2013 – DOI: 10.1016/j.engstruct.2012.11.033.

[13] R.J. Mainstone, Supplementary note on the stiffness and strength of infilled frames. Current paper CP13/74. *Build. Res*. Establishment. London; 1974.

[14] B. Stafford Smith, C. Carter, A method of analysis for infilled frames. Proceedings of the Institution of the Civil Engineers **44**,31-48, 1969.

[15] S. Casolo, G. Milani, A simplified homogenization-discrete element model for the non-linear static analysis of masonry walls out-of-plane loaded, *Engineering Structures*, **32**:8, 2352-2366, 2010 - DOI: 10.1016/j.engstruct.2010.04.010.

[16] S. Casolo, Macroscale modelling of microstructure damage evolution by a rigid body and spring model, *Journal of Mechanics of Materials and Structures*, 4:3, 551-570, 2009 - DOI: 10.2140/jomms.2009.4.551.

[17] S. Casolo, C.A. Sanjust, Seismic analysis and strengthening design of a masonry monument by a rigid body spring model: The "Maniace Castle" of Syracuse, *Engineering Structures*, **31:**7, 1447-1459, 2009 DOI: 10.1016/j.engstruct.2009.02.030.

[18] S. Casolo, G. Uva, Nonlinear analysis of out-of-plane masonry façades: Full dynamic versus pushover methods by rigid body and spring model, *Earthquake Engineering and Structural Dynamics*, 42: 499–521, 2013 - DOI: 10.1002/eqe.2224.

[19] S.H. Bertoldi, L.D. Decanini, C. Gavarini, Telai tamponati soggetti ad azioni sismiche, un modello semplificato: confronto sperimentale e numeric (in Italian). *Atti del 6° Convegno Nazionale ANIDIS*, vol. 2, pp. 815-824, Perugia, 13-15 Ottobre 1993.

[20] A.B. Mehrabi, Experimental evaluation of masonry-infilled RC frames. *Journal of Structural Engineering*, **122**(3):228-237, 1996.

[21] F.J Crisafulli, *Seismic behaviour of reinforced concrete structures with masonry infills*, Ph.D. Thesis. Department of Civil Engineering, University of Canterbury; 1997.

[22] T.B. Panagiotakos, M.N. Fardis, Seismic response of infilled rc frames structures. *Proceedings of 11th World Conference on Earthquake Engineering*; Paper No.225, Acapulco, 1996.

[23] D. Raffaele, F. Porco, A. Fiore, G. Uva, Simplified Vulnerability Assessment of RC Circular Piers in Multi-Span-Simply-Supported Bridges. *Structure and Infrastructure Engineering*, 2013 - DOI:10.1080/15732479.2013.772642.

[24] G. Uva, F. Porco, A. Fiore, M. Mezzina, Proposal of a methodology of in-situ concrete tests and improving the estimate of the compressive strength, *Construction and Building Materials* **38**(1),72-83, 2013.

[25] SAP2000. Advanced 14.2.2 Structural Analysis Program – Manual – (2010) Computer and Structures, Inc.

[26] J.B. Mander, M.J.N. Priestley, R. Park, Theoretical Stress-Strain Model for Confined Concrete. *Journal of Structural Engineering*. ASCE, **114**(3),1804-1826, 1984.

[27] G.M. Calvi, D. Bolognini, Seismic response of reinforced concrete frames infilled with masonry panels weakly reinforced, *Journal of Earthquake Engineering*, **5**, 153-185, 2001.

[28] P. Fajfar, P. Gaspersic, The N2 method for the seismic damage analysis of RC buildings. *Earthquake Engineering and Structural Dynamics* **25**(1):23-67, 1996.

COMPDYN 2013
4th ECCOMAS Thematic Conference on
Computational Methods in Structural Dynamics and Earthquake Engineering
M. Papadrakakis, N.D. Lagaros, V. Plevris (eds.)
Kos Island, Greece, 12–14 June 2013

SEISMIC FRAGILITY ANALYSIS OF A NUCLEAR PRIMARY CONTAINMENT STRUCTURE

Sayantani Lala[1], Siddhartha Ghosh[2], and Nikil N. Pujari[3]

Department of Civil Engineering
Indian Institute of Technology Bombay
Mumbai 400076, India
e-mail: [1]sayantani.lala@gmail.com, [2]sghosh@civil.iitb.ac.in, [3]pujarinikil@gmail.com

Keywords: Seismic Fragility, Concrete Damage Plasticity, Nuclear Power Plant, Primary Containment, Tensile Cracking.

Abstract. *A seismic fragility curve is an important tool in the probabilistic performance assessment of a structure when subjected to earthquake loads. The seismic fragility of a structure can be defined as the probability of exceeding certain limit state(s) of performance, given a specific level of seismic hazard. The current study deals with the seismic fragility estimation of a nuclear primary containment structure of a typical PHWR in India. The focus of this work is to estimate the seismic fragility of this structure considering a failure defined in terms of tensile cracking of the damaged concrete which leads to leakage. The structure is modelled using 3D layered shell elements with detailed damaged plasticity model for concrete. Seismic responses in terms of equivalent plastic tensile strain are studied for a set of earthquake records at different intensity levels through a series of nonlinear response-history analyses. Using regression, the ground acceleration capacity of the structure are obtained for each record. The seismic fragility curve of the structure is derived using a lognormal model using the sample capacity data. This seismic fragility curve is compared to the conventional fragility curve based on an interstorey drift ratio based failure. The results show that tensile cracking based fragilities are more severe to the drift based fragilities.*

1 INTRODUCTION TO SEISMIC FRAGILITY ANALYSIS

Seismic fragility is the probability that a geotechnical, structural or a non-structural system violates at least one limit state when subjected to a seismic event of a specified intensity. It is the conditional probability of failure of the system given a specific intensity of the seismic hazard. The necessity of conducting seismic fragility assessments for important structures – such as nuclear power plants, large dams and bridges – is acknowledged in the engineering community worldwide. The objective of seismic probabilistic safety assessments (PSA) for nuclear power plants (NPP) is to examine the existence of vulnerabilities against postulated earthquake hazards [1]. Seismic fragility analysis of a NPP is conducted both at its component levels and at the system level. The pioneering work on the development of a systematic methodology for seismic fragility analysis of a nuclear power plant and its components was conducted by Kennedy et al. [2]. This method was modified later to a more systematic approach by Kennedy and Ravindra [3]. They obtained the fragility of a structure, using a lognormal model, as

$$F_r = \Phi\left[\frac{\ln(x/m_a) + \beta_U \Phi^{-1}(Q)}{\beta_R}\right] \tag{1}$$

$\Phi(.)$ is the standard normal CDF operator; x is the seismic intensity (typically, PGA) at which the fragility is evaluated, m_a is the median ground acceleration capacity, β_R and β_U respectively measure the randomness (aleatory) and uncertainty (epistemic) associated with the estimation of ground acceleration capacity, and Q is the non-exceedance probability level. The ground acceleration capacity (a) is expressed in terms of its median capacity (m_a) and associated uncertainties:

$$\begin{aligned} a &= m_a \epsilon_R \epsilon_U \\ &= a_{\text{DBE}} \bar{F} \epsilon_R \epsilon_U \\ &= a_{\text{DBE}} (F_S F_\mu F_R) \epsilon_R \epsilon_U \end{aligned} \tag{2}$$

where ϵ_R and ϵ_U follow lognormal distributions with a median equal to one and lognormal and standard deviations β_R and β_U, respectively. a_{DBE} is the intensity of the design basis earthquake, $\bar{F}$ is the median factor of safety, which is composed of three different factors of safety. The details of these factors of safety and the associated uncertainties were discussed in depth in a recent paper by Pisharady and Basu [4]. Due to the lack of necessary tools and data, the quantification of these uncertainties depended significantly on engineering judgement. Although this method originally used response spectrum based linear elastic analyses, Pisharady and Basu [4] showed that modern analysis techniques, such as the nonlinear static pushover analysis can easily be incorporated in this framework. The two-parameter lognormal model of Equation 1, in its various forms, has now been widely accepted for seismic fragility analysis of structures. For example, Ellingwood et al. [5] used this model for fragility analysis of building structures in the following form:

$$F_r = \Phi\left[\frac{\ln\{c(S_a)^d/\theta_{\text{LS}}\}}{\beta_R}\right] \tag{3}$$

where, the failure was defined by the maximum interstorey drift ratio ($\theta_{\max}$) exceeding its limiting value θ_{LS}. The median value of $\theta_{\max}$ was expressed as a continuous function of the intensity measure S_a, using nonlinear regression:

$$m_\theta = c(S_a)^d \tag{4}$$

where, c and d were regression parameters and S_a was the pseudo-spectral acceleration corresponding to the fundamental mode of vibration of the structure. The regression was based on the earthquake response data from a series of nonlinear response-history analysis (NLRHA).

2 OBJECTIVE

Conforming to these basic formats of seismic fragility estimation, the work presented here shifts focus to the performance limit state that is used to define the failure of a structure. Initial research works in this area defined performance in terms of force capacities or ground acceleration capacities. Later, seismic structural engineering moved into performance-based seismic design and performance-based seismic evaluation, where structural 'failure' is defined by multiple performance limits described by displacement-based limits. For example FEMA-356 [6] defined performance limits for building structures in terms of maximum interstorey drift ratio values. This damage measure is able to represent both the structural and non-structural damages in a seismic event more efficiently than any force-based demand parameter. Although drift-based limit states have been suggested for containment structures in NPP, this demand/response parameter is not a good indicator of the associated risks.

The primary containment structure is the last barrier to radioactive leakage, and is therefore considered to be the most important civil/structural engineering component in a NPP. From this understanding, the limit state of failure is defined here by the possibility of any leakage through the inner/primary containment. Such leakages can only take place if the seismic event leaves a through crack in the concrete shell. Assuming that tensile cracking in concrete takes place much earlier compared to crushing under compression, the limit state of failure in this work is defined by a positive equivalent plastic tensile strain ($\tilde{\varepsilon}_t^{pl} > 0$) in concrete, anywhere in the containment structure.

3 MODELLING OF TENSILE CRACKING IN CONCRETE

Available literature shows a variety of concrete material modelling approaches that can incorporate the inelastic behaviour of concrete, including tensile cracking. Since the study structure is analysed using the general purpose finite element package Abaqus [7], the discussion here is limited to the concrete inelastic material modelling options available with this software. These are

1. Brittle cracking model (Section 19.6.2 of [7]),
2. Concrete smeared cracking (Section 19.6.1 of [7]), and
3. Concrete damaged plasticity (Section 19.6.3 of [7]).

Although the brittle cracking model is assumed to be good for modelling tensile cracking, it suffers from the fact that concrete under compression is always assumed to behave as a linear elastic material. The smeared cracking approach is based on damaged elasticity concepts. This model does not track individual cracks but distributes/'smears' the overall effect of these cracks. The cracking effect is incorporated by specifying a reduction in the shear modulus as a function of the opening strain across the crack. A reduced shear modulus for closed cracks can also be specified. However, its application should be limited to cases where concrete is subjected to essentially monotonic straining at low confining pressure.

The concrete damaged plasticity model combines isotropic damaged elasticity in the elastic domain with isotropic tensile and compressive plasticity to represent the inelastic behaviour

of concrete. It can be used for cyclic and dynamic loading conditions, such as earthquake excitations. This modelling approach is selected for fragility estimations in this work. Two hardening variables, equivalent plastic tensile strain ($\tilde{\varepsilon}_t^{pl}$) and equivalent plastic compressive strain ($\tilde{\varepsilon}_c^{pl}$) control the change in the yield surface. $\tilde{\varepsilon}_t^{pl}$ also represents the existence of a crack in concrete because it is the residual or plastic equivalent strain. Figure 1 shows this quantity for the uniaxial stress-strain plot for the damaged plasticity concrete model. E_0 is the linear elastic undamaged modulus in tension and ε_t^{el} is the recoverable or elastic tensile strain. Following Lubliner et al. [8], it is assumed that cracking initiates at points where the equivalent plastic tensile strain is greater than zero.

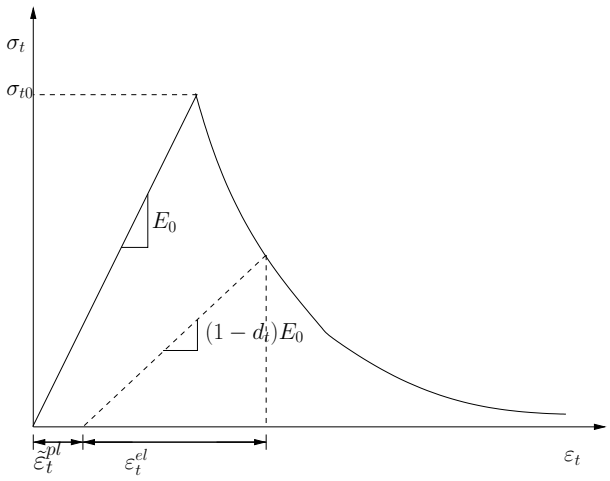


Figure 1: Concrete damaged plasticity under uniaxial tension.

4 STUDY STRUCTURE AND ITS FINITE ELEMENT ANALYSIS

The primary/inner containment (PC/IC) structure of the 700 MWe Indian PHWR is considered for this case study. The PC is a prestressed concrete cylindrical wall capped by a segmental prestressed concrete dome through a massive ring beam (Figure 2). At the bottom of the PC there is a base raft. The cylindrical wall has two rectangular access holes, and the dome has two circular steam generator openings. The containment wall is thickened near the base raft, near the ring beam and around the openings.

This structure is modelled in Abaqus [7] using 3D linear shell elements, S4R (and some S3R). The cross-section is defined as a layered shell, so that reinforcement layers can be modelled suitably along the thickness of the containment. Prestressing effects are not included based on the simplifying assumption, that prestressing effects will be nullified by the presence of internal pressure (and also prestress loss over time). The containment is assumed to be fixed at the base. The meshing of the study structure, with 10503 layered shell elements and 10515 nodes, is also shown in Figure 2. The uniaxial compression and tension behaviours of concrete are modelled using damaged plasticity and the Drucker-Prager flow rule following the work by Jankowiak and Lodygowski [9], after normalising the behaviour to M45 grade concrete as per IS:456 [10]. The Fe500 grade reinforcements are modelled to have elastic-curvilinear plastic behaviour as per IS:456.

This structural model is subjected to uni-directional horizontal ground acceleration time-histories and nonlinear response-history analyses (NLRHA) are performed. For running these

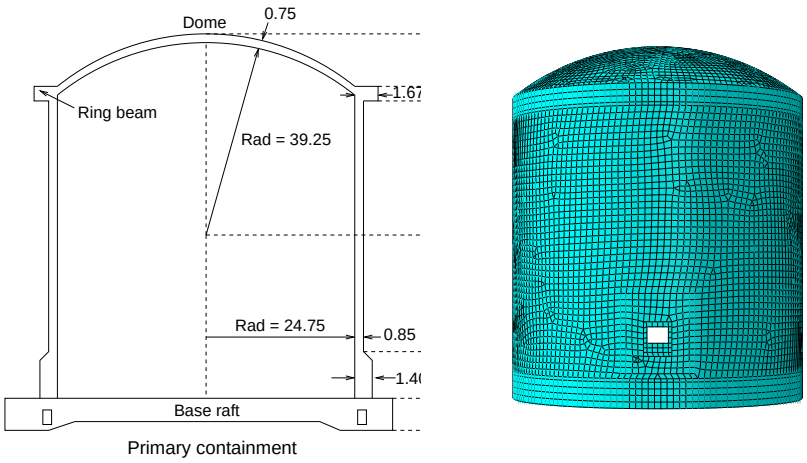


Figure 2: Schematic of the structure and its finite element model.

NLRHA, the implicit dynamic mode is used in Abaqus to ensure greater accuracy of results. From the output data, $\tilde{\varepsilon}_t^{pl}$ is recorded over all the shell elements.

5 FRAGILITY ANALYSIS OF THE CONTAINMENT STRUCTURE

The containment is assumed to be located in the peninsular India, and 13 recorded ground motions are selected from similar seismo-geological sources for the NLRHA. For each record, NLRHA are conducted at increasing intensity levels – similar to an incremental dynamic analysis (IDA) approach – and $\tilde{\varepsilon}_t^{pl}$ values are noted. Since, each NLRHA is a significantly computation intensive effort, instead of performing this at a large number of intensity scale factors, we try to narrow down to the intensity scale factor that indicates the upcrossing $\tilde{\varepsilon}_t^{pl} > 0$. This needs six-eight trials for each earthquake record. However, for most of these ground motion records, intensity measures (in terms of the peak ground acceleration or PGA) are identified corresponding to very low positive values of $\tilde{\varepsilon}_t^{pl}$ (of the order 10^{-6}). Figure 3 shows the $\tilde{\varepsilon}_t^{pl}$ contours ('PEEQT' in Abaqus), for the whole containment, as well as a magnified view around the rectangular hole where the cracking takes place.

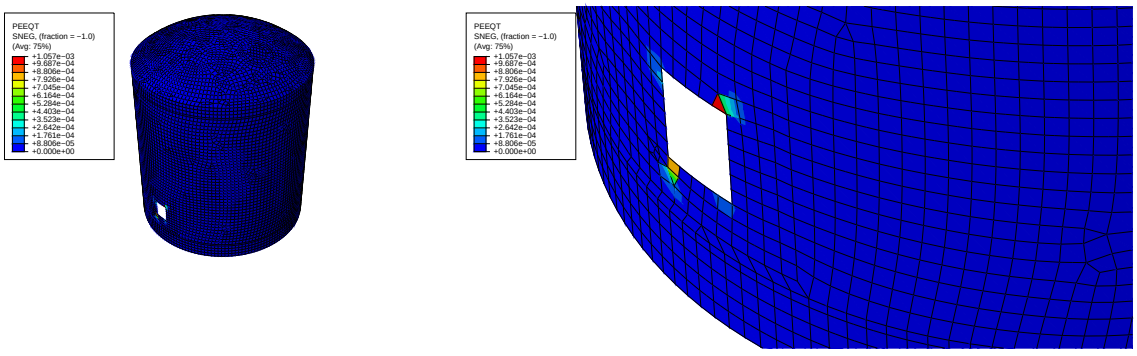


Figure 3: $\tilde{\varepsilon}_t^{pl}$ contours for a sample earthquake record at a selected intensity level.

To find the lowest PGA level at which $\tilde{\varepsilon}_t^{pl}$ has a positive value, all data points for an earthquake in a PGA vs. $\tilde{\varepsilon}_t^{pl}$ plot are fitted with an approximating curve. For each earthquake, results from only those NLRHA can be used that give a positive equivalent plastic tensile strain. The

regression curves are selected in the following the general form

$$\tilde{\varepsilon}_t^{pl} = Ax^2 + Bx + C \tag{5}$$

at a PGA of x. A, B and C are regression coefficients. This form is selected so that $\tilde{\varepsilon}_t^{pl}$ is a monotonically increasing function of the intensity level x. Although IDA curves with displacement-based damage parameters sometimes show rebounds, it is safer to make the simplistic assumption that equivalent plastic tensile strain values do not decrease with increasing seismic intensity levels. Values of the regression coefficients are provided in Table 1 and the fitted PGA level vs. $\tilde{\varepsilon}_t^{pl}$ curves are shown in Figure 4. The intercept of these curves at $\tilde{\varepsilon}_t^{pl} = 0$ gives the ground acceleration capacity of the structure for each of these records. These limiting PGA values are also provided in Table 1.

Record	A	B	C	PGA at $\tilde{\varepsilon}_t^{pl} = 0$ (g)
GM-12	0.08469	-0.02465	0.001729	0.1732
GM-13	0.1398	-0.07274	0.009387	0.2833
GM-14	1.245	-0.2218	0.009807	0.09666
GM-15	-0.006588	0.001804	0	0
GM-16	0.1219	-0.02798	0.001602	0.1202
GM-17	0.005737	-0.001112	0.4000	0.1938
GM-18	1.742	-1.158	0.1923	0.3415
GM-19	1.655	-0.4375	0.02886	0.1379
GM-20	18.88	-2.845	0.1068	0.07981
GM-21	0.00191	-0.0002237	-9.536×10^{-6}	0.1503
GM-22	-0.014	0.004044	0	0
GM-23	0.01783	-0.00367	0.0001883	0.1085
GM-24	0.01407	-0.002843	0	0.2021

Table 1: Regression coefficients for the selected records.

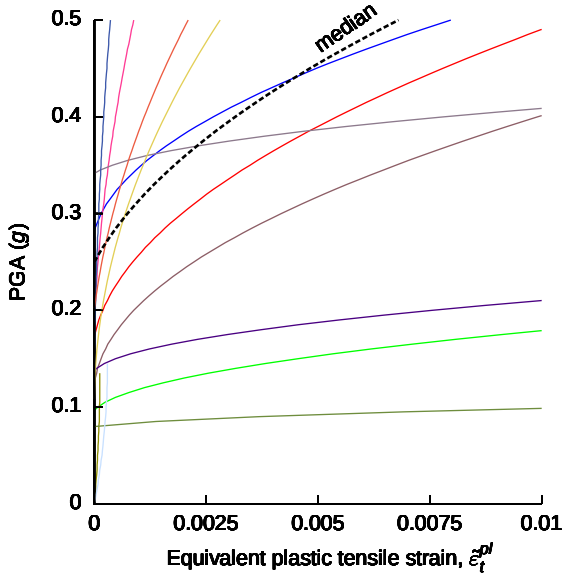


Figure 4: Regressed intensity vs. damage curves for selected records.

The variation in ground acceleration capacities (as listed in Table 1) is modelled using a two-parameter lognormal distribution, with median $m_a = 0.1732g$ and lognormal standard deviation $\beta_R = 0.4461g$. A Kolmogorov-Smironov goodness-of-fit test gives a $D^n_{\max}$ value of 0.1010, which is well within the limiting D^n_α values for all acceptable significance levels. These m_a and β_R vales are used to obtain the fragility curve based on tensile cracking, using Equation 1. The epistemic uncertainties are neglected in this fragility estimation in comparison with the (aleatory) randomness in the earthquakes. The fragility curve based on tensile cracking is plotted in Figure 5. For a comparison, the fragilities are also obtained considering a maximum interstorey drift ratio based failure. For this, the 'immediate occupancy' (IO) limit state defined in FEMA-356 is considered: $\theta_{\text{LS}} = 0.004$ [6]. This fragility estimation is based on the method used by Pisharady and Basu [4] using the results of a nonlinear static pushover analysis. This fragility curve is also presented in Figure 5.

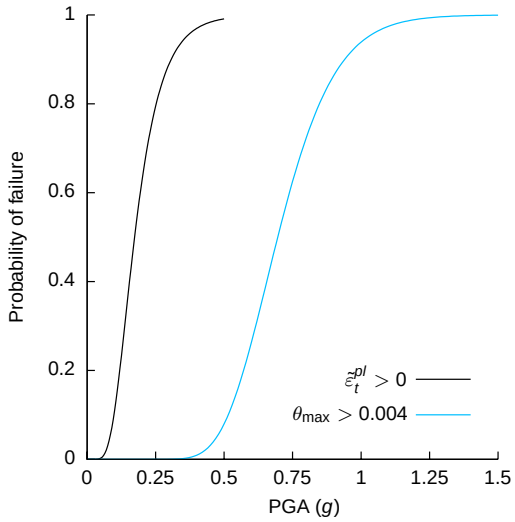


Figure 5: Fragility curves based on tensile cracking and drift based failure.

6 CONCLUDING REMARKS

This paper presents a preliminary attempt in obtaining fragility estimates for the primary containment structure of a NPP in terms of the possibility of leakage through the damaged concrete due to seismic events. The first results show that tensile cracking based fragilities are much higher compared to drift ratio based fragilities, even when the drift limit is defined at the immediate occupancy performance level. It points to the fact that crack/leakage-based performance levels should be considered for this type of structures.

The primary challenge in this task has been in the amount of computation involved in non-linear response-history analysis while adopting a reasonably accurate damage model for the containment. This has lead to several simplifying assumptions, which should be avoided. For example, the number of ground motion records may be considered to be less than adequate, and so are the number of data points with positive $\tilde{\varepsilon}_t^{pl}$ values for each earthquake. Similarly, the validity of the assumption that prestressing effects have not been present needs to be checked. This work needs to be verified again after these issues are properly addressed using better data and probabilistic analysis tools.

References

[1] M. Hari Prasad, P. N. Dubey, G. R. Reddy, R. K. Saraf, and Ghosh A. K. Seismic PSA of Nuclear Power Plants: A case study. Technical Report BARC/2006/E/015, Bhabha Atomic Research Centre, Mumbai, India, 2006.

[2] R. P. Kennedy, C. A. Cornell, R. D. Campbell, S. Kaplan, and H. F. Perla. Probabilistic seismic safety study of an existing nuclear power plant. *Nuclear Engineering and Design*, **59**(2):315–338, 1980.

[3] R. P. Kennedy and M. K. Ravindra. Seismic fragilities for nuclear power plant risk studies. *Nuclear Engineeiring and Design*, **79**(1):47–68, 1984.

[4] A. S. Pisharady and P. C. Basu. Methods to derive seismic fragility of NPP components: A summary. *Nuclear Engineering and Design*, **240**(11):3878–3887, 2010.

[5] B. R. Ellingwood, O. C. Celik, and K. Kinali. Fragility assessment of building structural systems in Mid-America. *Earthquake Engineering and Structural Dynamics*, **36** (13):1935–1952, 2007.

[6] FEMA-356. *Prestandard and Commentary for the Seismic Rehabilitation of Buildings*. Federal Emergency Management Agency, Washington, USA, 2000.

[7] Simulia. *Abaqus FEA User's Manual, Version 6.9*. Vélizy-Villacoublay, France, 2009.

[8] J. Lubliner, J. Oliver, S. Oller, and E Oñate. A plastic-damage model for concrete. *International Journal of Solids and Structures*, **25**(3):299–329, 1989.

[9] T. Jankowiak and T. Lodygowski. Identification of parameters of concrete damage plasticity constitutive model. *Foundations of Civil and Environmental Engineering*, **6**:53–69, 2005.

[10] Bureau of Indian Standards. *IS:456 Indian Standard for Plain and Reinforced Concrete – Code of Practice*. New Delhi, India, 2000.

COMPDYN 2013
4th ECCOMAS Thematic Conference on
Computational Methods in Structural Dynamics and Earthquake Engineering
M. Papadrakakis, N.D.Lagaros, V. Plevris (eds.)
Kos Island, Greece, 12–14 June 2013

SIMULATION OF STRUCTURAL POUNDING WITH THE SEARS IMPACT MODEL

Sushil Khatiwada[1], Nawawi Chouw[2], and Tam Larkin[2]

[1] The University of Auckland
Private Bag 92019
Auckland 1142, New Zealand
e-mail: skha178@aucklanduni.ac.nz

[2] The University of Auckland
n.chouw@auckland.ac.nz
t.larkin@auckland.ac.nz

Keywords: Adjacent structures, Building pounding, Distributed mass impact, Sears model.

Abstract. *Seismic pounding affects some buildings and bridge spans with insufficient expansion joints. During pounding, structures exert repeated hammer- like blows on adjacent structures or structural elements which causes a range of effects from minor cosmetic spalling to major structural damage in buildings while bridge spans may be unseated.*
Several methods have been proposed for numerical simulations of pounding. The most common method is the contact element model, where a link is introduced between the pounding masses to allow simulation of the contact force. Unfortunately, most of these models have been developed based on the collision of spheres, idealized as concentrated masses, while the pounding structures have distributed masses. These models also suffer from uncertainties regarding the stiffness of the links and the duration of contact as well as the amount of energy lost during contact. Some studies have also proposed a pounding model as an impact between two bars whose response is governed by stress wave propagation. These models can predict the energy loss during impact and the duration of impact but have a major drawback that the strain in the bars rises instantaneously to a finite value, which results in an infinite acceleration. Similarly, they can predict a negative value of the coefficient of restitution which makes no sense from a physical stand-point.
This paper proposes a quasi-empirical impact mechanism for simulation of structural pounding. The model includes the effects of both the contact surface properties and the cross-sectional properties of the bars. The pounding force is calculated from the deformation and stiffness at the contact location, but the duration of contact and the development of the local deformation is a function many factors for which a parametric analysis is presented. Finally, an example of a building pounding analysis with the proposed model is provided.

1 INTRODUCTION

Building pounding has been observed in many urban earthquakes. The most publicized occurrence was in Mexico City in 1985, where pounding was identified as the cause of 15% of all collapsed buildings [1]. Recently, many instances of pounding were observed during the 2011 Christchurch earthquake [2]. Pounding is defined as the collision between structures or parts of structures, for instance, between bridge decks, due to the at-rest separation being insufficient to accommodate the relative seismic displacement. The relative displacement is due to the out-of-phase motion between affected structures or structural elements. Such motion can be caused by the differing dynamic properties of the structures, foundation flexibility effects, or the spatial variability of ground motion in bridge piers [3].

Pounding has long been identified as a recurring hazard. Several solution methods and models have been produced to simulate pounding analytically. All these models rely on time history analysis of the structures. In all models, the structures are assumed to vibrate independently of each other, until the relative closing motion is less than a predefined gap. When the gap closes, and the structures come into contact, the methods differ in the treatment of the impact. Some of the early studies on pounding treated the impact with the laws of stereomechanics [4]. The loss of mechanical energy is incorporated by a predetermined coefficient of restitution, *e*, which is defined as the ratio of relative separation velocity to relative approach velocity of the colliding masses. The post-impact velocities of the masses can be calculated once the masses and initial velocities are known.

A major drawback of stereomechanics is the need to interrupt the time history analysis at every contact to update the velocities of the masses, which necessitates renewed calculation of all the coefficients used in the considered time window. This method is generally not included in commercial finite element software. Thus, the 'impact element method' was developed where an elastic or viscoelastic link is introduced with an accompanying gap at possible contact locations (Figure 1). The link is activated when there is contact, and deactivated at separation. The impact force is a function of the stiffness and damping of the impact element. The damping of the impact element is calculated so that the post-impact velocity is same as that calculated from stereomechanics. The inclusion and exclusion of the impact element's properties in the damping and stiffness matrices in time history analysis is supported by most of the commercial finite element software, so this method is more common than the stereomechanical method.

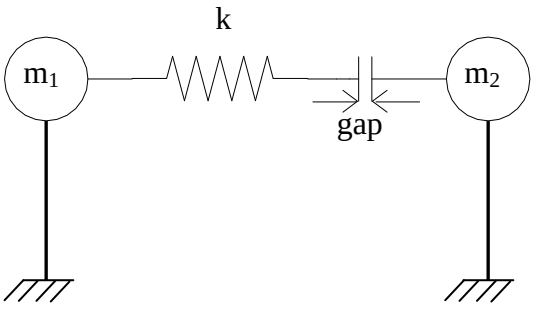


Figure 1: Lumped mass model with impact element.

The previous two methods idealize the building slabs or bridge decks that collide as point masses i.e. the whole bodies undergo a velocity change simultaneously. In reality, the structural members have sufficient length to introduce a finite time-lag for the stress waves to travel from impact locations to the other ends of the members. Malhotra [5] demonstrated the effects of the propagation of stress waves on the pounding of bridge decks. It was shown that

for the decks of identical material and cross sectional properties, the resulting coefficient of restitution was given by the ratio of the length of the shorter deck to the longer deck. Thus, even for an elastic contact, there was apparent energy loss due to unequal length of the decks. While the contact duration is a function of colliding masses and contact stiffness in the impact element method, it only depends on the material properties and length of the bodies in stress wave methods.

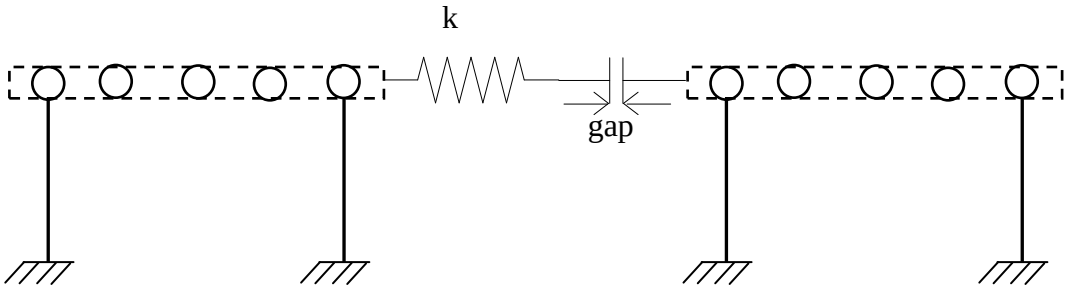


Figure 2: Distributed mass model of impact.

Malhotra [5] proposed that the coefficient of restitution may be determined from the ratio of lengths and a method similar to stereomechanics to analyze the pounding of bridges. Watanabe and Kawashima [6] proved that finite element software can be employed to simulate the stress wave propagation in colliding bridge decks. The impacting members were discretized as shown in Figure 2. The authors proposed that the stiffness of the link should be equal to the stiffness of the adjoining segments for the best agreement with wave theory. Cole *et al*. [7] extended the model to the analysis of building pounding. The authors derived a coefficient of restitution for colliding members with different material and geometrical properties by considering the first modes of axial vibration of building slabs. It was shown that finite element discretization of colliding building slabs produced similar results.

The methods based on wave theory of impact also have some significant drawbacks. For instance, both Malhotra [5] and Cole *et al.* [7] predict a constant duration of contact for two given bodies, but experiments have shown that the duration depends upon the relative impact velocity [8]. The impact force from distributed mass simulations showed significant positive and negative variation about the value predicted by wave theory [6, 7]. Another concern is the abrupt changes in velocity resulting in a nearly instantaneous imposition of strain, which can be construed as nearly infinite acceleration at the contact location. Finally, the relationships derived from wave theory for the general cases of contact have been found to result in a negative coefficient of restitution which is at variance with the laws of physics [7].

Thus building pounding has been modeled either as the impact of lumped masses, where only the local surface geometries are instrumental in the analysis; or as wave propagation effects in longitudinal bars which are defined by the cross-sectional properties of the diaphragm. Experiments have shown that the impact force of two bars depends on a combination of the local and cross-sectional properties [9]. Wagstaff [8] showed that the point mass contact can better predict the impact of short bars with rounded ends, while wave theory was found to be more effective for contact forces of longer bars. None of the models that have been proposed for the simulation of pounding can combine the effect of both these situations.

A composite contact model was first proposed by Sears [10] in which the contact force is determined by Hertz theory but the state of the distant portions of the bars is given by wave theory. The current article proposes the adaptation of the Sears impact model for structural

pounding simulations. A parametric study of the behavior of the model is presented. Finally, a simulation of pounding between a pair of one story buildings is shown.

2 THEORY OF THE SEARS IMPACT MODEL

The theory has been adapted from Goldsmith [9] and is discussed with respect to the contact of two circular bars with rounded ends, as shown in Figure 3. Sears proposed that there is a zone of compression adjacent to the contact surface which extends to the vertical plane containing point P1 on the left bar and to the vertical plane containing point P2 on the right bar. The impact force is generated by the compression of this zone. As the contact occurs, stress waves propagate away from the location of contact in both bars. As the stress waves reach a section, its velocity undergoes a more gradual change depending on the magnitude of the force, while the distant sections keep moving with the initial velocities. Initially the force is insufficient to stop the compression, so the compression keeps increasing. After a certain time, the stresses in the compression zone are high enough to cause a gradual release of stress at the contact zone and eventually separation.

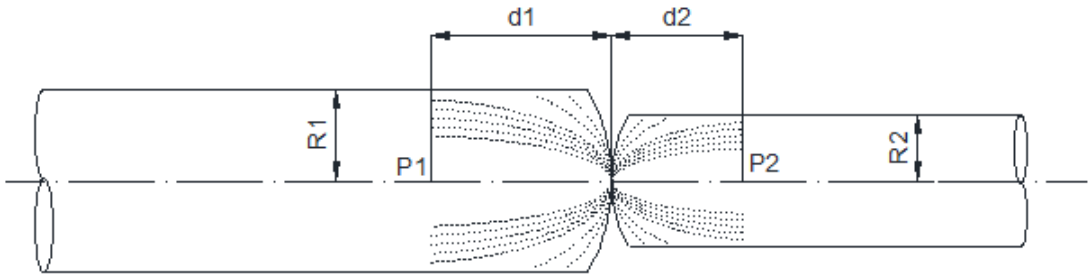


Figure 3: Collision of two circular bars with rounded ends.

If the two bars are moving with velocities v_1 and v_2, where subscript 1 refers to the left bar and 2 refers to the right bar, the compression δ at any time t before the stress wave reaches points P_i is given by,

$$\delta = v_1 t - v_2 t \tag{1}$$

Because of the deformation, a force F develops at the contact location given by

$$F = k\,\delta^{3/2} \tag{2}$$

where k is the stiffness of contact. For the spherical contact surfaces, according to the Hertz contact law,

$$k = \frac{4}{3\pi(h_1 + h_2)}\left(\frac{r_1 r_2}{r_1 + r_2}\right)^{1/2} \tag{3}$$

where, r_1 and r_2 are the radii of the rounded ends,

h_1 and h_2 are given by,

$$h_i = \frac{1-\mu_i^2}{\pi E_i} \tag{4}$$

where μ_i and E_i are the Poisson's ratio and Young's modulus of the i^{th} bar.

Sears [10] proposed the length of the deformation zone as,

$$d_i = R_i \left[\sqrt{\frac{3}{2}} + \frac{1}{\sqrt{6}} (1+\mu)(3-2\mu) \right] \tag{5}$$

where R_i is the radius of the ith bar.

The stress wave reaches point P_i at $t = d_i/c_i$ where $c_{i\ is}$ the compression wave propagation velocity in i^{th} bar given by $c_i = \sqrt{E_i / \rho_i}$ where ρ_i is the density of the ith bar. The expression for compressive deformation becomes

$$\delta = v_1 t - v_2 t - \frac{1}{\rho_1 A_1 c_1} \int_0^t F_{\left\langle t - \frac{d_1}{c_1} \right\rangle} dt - \frac{1}{\rho_2 A_2 c_2} \int_0^t F_{\left\langle t - \frac{d_2}{c_2} \right\rangle} dt \tag{6}$$

where A_1 and A_2 are the cross-sectional areas of the bars and the force F becomes zero when the expression within the conical brackets is zero.

The stress waves will travel to the far end of the bars and undergo reflection. When the reflected waves reach points P_i, Equation 6 becomes

$$\delta = v_1 t - v_2 t - \frac{1}{\rho_1 A_1 c_1} \int_0^t \left[F_{\left\langle t - \frac{d_1}{c_1} \right\rangle} + F_{\left\langle t - \frac{d_1 + l_1}{c_1} \right\rangle} \right] dt - \frac{1}{\rho_2 A_2 c_2} \int_0^t \left[F_{\left\langle t - \frac{d2}{c2} \right\rangle} + F_{\left\langle t - \frac{d_2 + l_2}{c_2} \right\rangle} \right] dt \tag{7}$$

where l_i is the length of the ith bar outside the compression zone.

If separation does not occur, the waves will reach the contact end and once again be reflected, leading to a new term being added to the right hand side of Equation 7. For each successive reflection from either end in either bar, a new expression is similarly added. The expression for deformation can be generalized as,

$$\begin{aligned} \delta = v_1 t - v_2 t &- \frac{1}{\rho_1 A_1 c_1} \int_0^t \left[F_{\left\langle t - \frac{d_1}{c_1} \right\rangle} + F_{\left\langle t - \frac{d_1 + l_1}{c_1} \right\rangle} + F_{\left\langle t - \frac{d_1 + 2l_1}{c_1} \right\rangle} + F_{\left\langle t - \frac{2d_1 + 2l_1}{c_1} \right\rangle} + \ldots \right] dt \\ &- \frac{1}{\rho_2 A_2 c_2} \int_0^t \left[F_{\left\langle t - \frac{d2}{c2} \right\rangle} + F_{\left\langle t - \frac{d_2 + 2l_2}{c_2} \right\rangle} + F_{\left\langle t - \frac{d_2 + 2l_2}{c2} \right\rangle} + F_{\left\langle t - \frac{2d_2 + 2l_2}{c_2} \right\rangle} + \ldots \right] dt \end{aligned} \tag{8}$$

The reflective terms will be added to Equation 8 until δ becomes zero or negative. When this occurs, the two bars separate and the contact force vanishes. Equation 8 can be solved for incremental time steps to find the resultant impact force time history.

3 PARAMETRIC INVESTIGATIONS OF THE SEARS MODEL

The impact force from the Sears model is affected by a multitude of parameters whose effects are not readily apparent. Hence, a parametric investigation of a simple impact of two circular rods is presented here. A circular steel rod of diameter 0.1 m is assumed to strike another rod of the same diameter at a relative impact velocity of 1 m/s. The impacted end of the first bar has a rounded end of diameter 0.1 m, while the impacted end of the second bar is flat. The simulations are carried out with a time step of 1 microsecond except in the case of

very stiff contact elements which required a time step of 0.1 microseconds. The length of the bars is first varied to best reflect the effect of that parameter. A discussion of the effects of other parameters follows.

3.1 Effect of length of bars

Changes in bar lengths produced surprising changes in the force time history (Figure 4). It readily becomes apparent that for a given cross-sectional area, there is an upper limit for the maximum impact force, no matter what the lengths of the participating bars. For bars with identical cross-sectional and material properties, the limit is same as that obtained in wave theory [5, 7], i.e. $0.5\rho Ac(v_1\text{-}v_2)$. For shorter bars, this maximum force may never be attained. For longer bars, after a relatively short rise time, the force remains at the maximum for a large part of contact time, followed by a steep attenuation to zero.

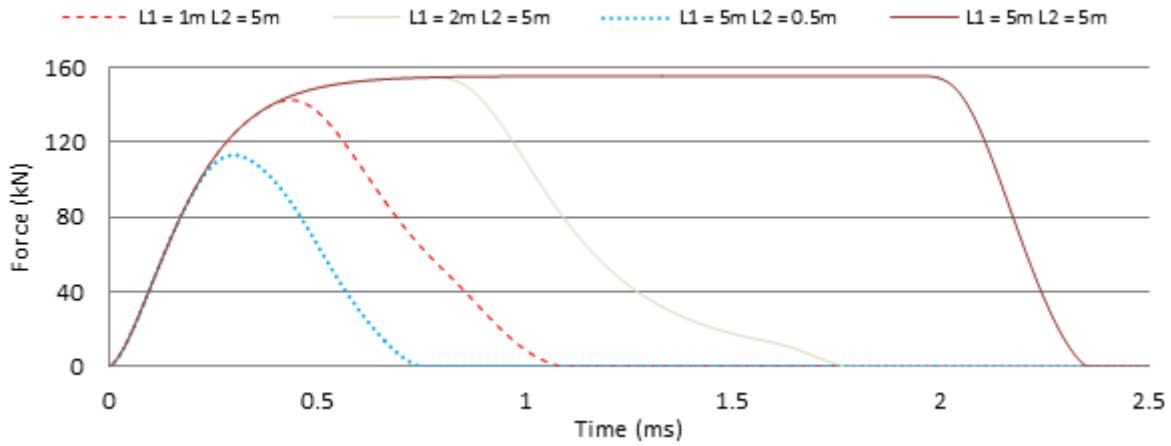


Figure 4: Impact force for different bar lengths.

Figure 5 shows the force time histories produced by Sears, Hertz and wave propagation models. The force from Hertz's model is based on Equation 2 while the force from wave theory, according to Cole *et al*. [7] equals $0.5\rho Ac(v_1\text{-}v_2)$ over a duration obtained by dividing twice the length of the short bar by the compression wave velocity in the bars. The results prove that the Sears model for impact force is governed by the mechanics at the point of contact for short bars and distributed mass effects for longer bars.

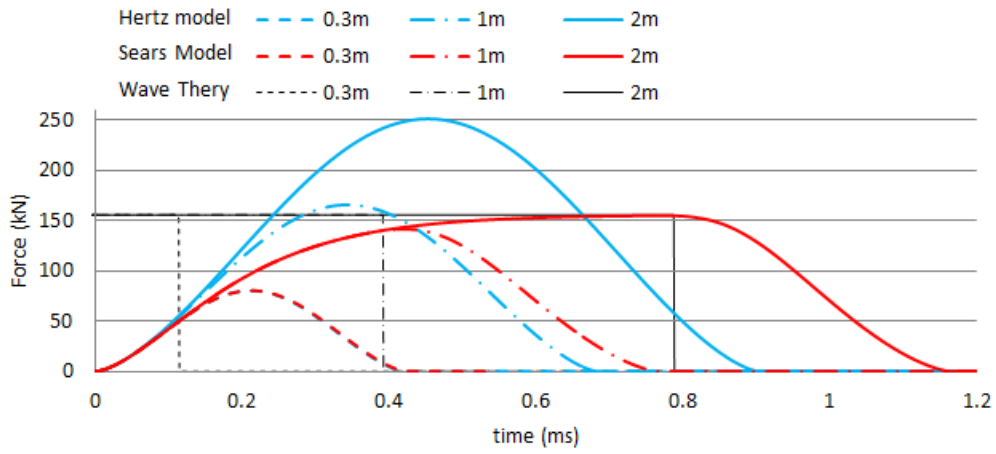


Figure 5: Impact force from various models for bars of equal length and cross section.

The final velocities of the bars were calculated by equating the impulse of the impact force with the change in momentum of the bars. The calculated effective coefficients of restitution are shown in Figure 6. In Hertz contact, the coefficient of restitution has to be predetermined, while in the wave theory it is equal to the ratio of the lengths of the short bar to the long bar. Thus, when at the contact location no energy loss is assumed in these computations, the Hertz model would give a coefficient of restitution as 1. It was seen that while the Sears model was also affected by the ratio of the lengths, it depended equally upon the length of the shorter bars. For very short bars, the coefficient approached unity but for longer bars, it became similar to wave theory. When both the bars are very long, the results become indistinguishable with those from wave propagation theory.

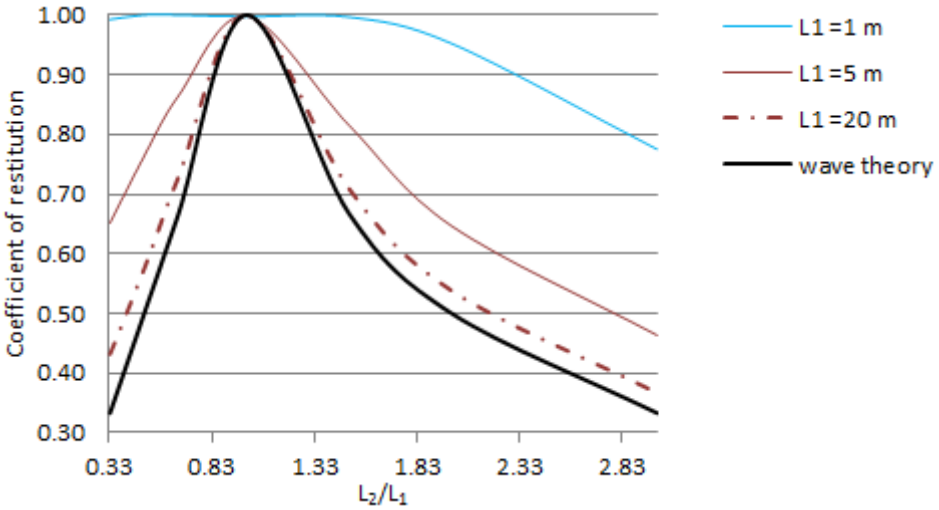


Figure 6: Coefficient of restitution for impact of unequal bars.

3.2 Effect of relative impact velocity

An increase in the relative impact velocity between bars of unequal length resulted in the duration of contact decreasing and *vice versa* (Figure 7). The decrease in contact duration was accompanied by a decrease in coefficient of restitution, see Figure 7. Thus, for higher impact velocities, more energy was trapped in the internal vibration of the bars. The impact of short bars was affected more than that of the longer bars. Thus, an increase in the relative impact velocity shifts the impact behavior more towards wave theory.

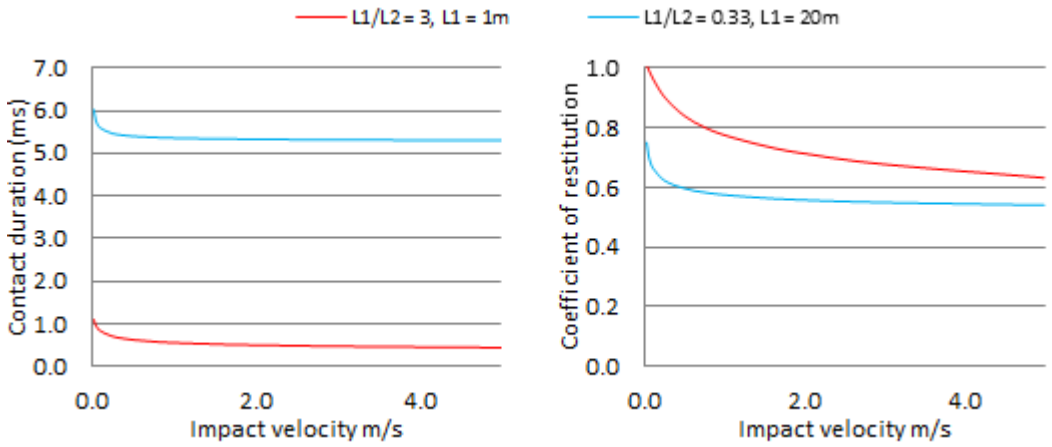


Figure 7: Variation of (a) contact duration, and (b) coefficient of restitution with relative impact velocity

3.3 Effect of mass

This section describes the outcome of analyses using the Sears model and varying the contributing mass. The participating mass could be increased in two ways, by putting a superimposed mass on the bars or by increasing the cross-sectional area. For simplicity, the superimposed mass was assumed to be uniformly distributed over the length of the bars. It was observed that the behavior was same for both these cases. The duration of contact and coefficient of restitution both increased with increasing mass. Thus, the contact behavior is shifted toward that of a lumped mass model by an increase in mass. The effective coefficient of restitution was always positive, even where the mass and length ratio produced negative values in methods from wave theory [7].

3.4 Effect of contact stiffness

The contact stiffness was varied by changing the diameter of the spherical cap. It was observed that the contact duration as well as coefficient of restitution decreased with increasing stiffness (larger dome diameter). Both as a ratio, and in seconds, the decrease in contact duration was significantly more for shorter bar collisions than for longer bars. With sufficiently high contact stiffness, all of the impacts generated a force almost identical to the wave theory, while the softer contact skewed the behavior towards a lumped mass collision.

3.5 Effect of the length of compression zone

The effect of the variation in the length of the compression zone d_i was investigated because it is based on assumptions [10]. The length d_i was varied from a hundredth of the calculated value to ten times as much. Surprisingly the results showed that the contact force was not very sensitive to d_i. The maximum variation observed was 4% when a hundredth of the default value was employed. Thus, despite the considerable effort expended to calculate d_i in the original derivation of theory, the behavior of the model is very little affected by this factor.

3.6 Effect of material properties

Figure 8 shows the effect of material variation. First the participating steel bars were replaced by M20 concrete of the same dimensions. It was observed that, due to the reduction in stiffness and mass, the contacts force is softer and the duration is longer. A uniformly distributed mass was placed on the concrete bars to allow comparison of the results for concrete and steel bars of equal mass. It can be seen that, the increased mass shifted the contact proper-

ties toward lumped mass impact, and a maximum limiting force is never reached. The effective coefficient of restitution did not change for the change in materials, but did change significantly with additional mass.

From the results presented, it is obvious that the Sears model is capable of simulating both lumped mass and distributed mass impacts, as well as the intermediate transition zone. The buildings undergoing pounding can be of different shapes, sizes, material or utility with differing supports. When modeled as a lumped mass contact, the effective coefficient of restitution can vary widely from the predetermined coefficient. Similarly, application of wave theory may significantly underestimate the effective coefficient of restitution for low velocity or heavy mass contacts.

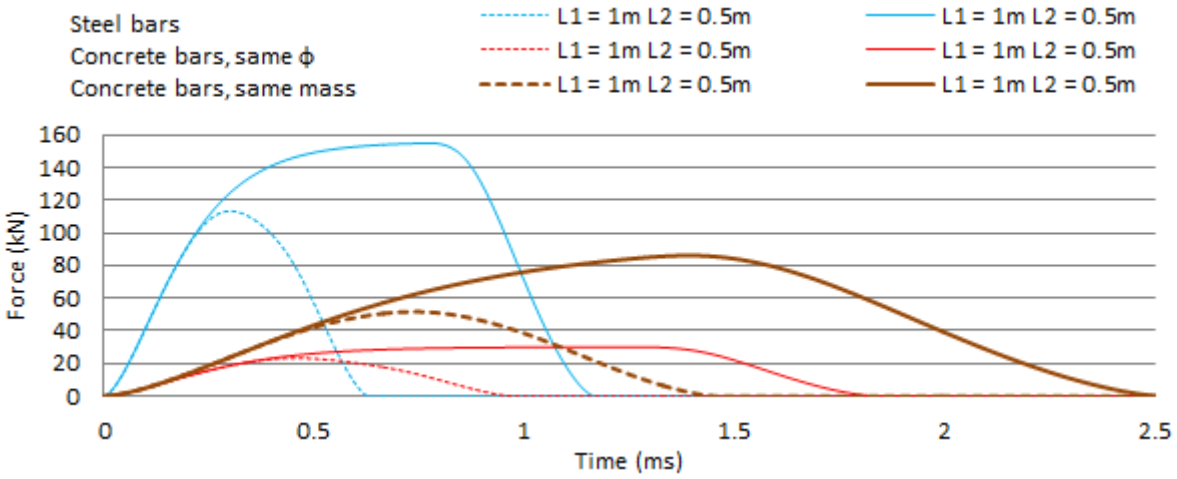


Figure 8: Effect of material properties on the impact force

4 BUILDING POUNDING SIMULATION

The implementation of the proposed model in building pounding simulation is complex. It is not possible to pre-calculate the coefficient of restitution as suggested by Malhotra [5], since the coefficient does not remain constant. Creation of an equivalent lump mass model, as suggested by Cole *et al.* [7] is also not advisable as the contact duration cannot be predetermined.

An integral part of the formulation presented here is the Hertz theory for the stiffness of spheres in contact (Equation 2 and subsequently Equations 3 and 4). The Hertz theory has certain assumptions which are only valid for curved surfaces, and it cannot be applied for contact of plane surfaces [9]. Since most of the structural pounding problems involve contact between two flat surfaces, the current authors postulate that the linear force-deformation relationship (Equation 10) is more suitable.

$$F = k_L \, \delta; \qquad \delta > 0 \tag{10}$$

where k_L is the linear stiffness of the collision element and δ is the longitudinal deformation of the contact zone.

Contact stiffness k_L is calculated as $[EA/(L/n)]$ when $n = d/L$ is the ratio of the length of the deformation zone to the length of the whole bar. The contact element stiffness k_L cannot be determined currently with any degree of certainty. It was found that the stiffness calculated assuming the total length of the slab or beam as a single element tended to produce a very soft contact which results in the contact force not reaching the limiting force, F_{max}. If only a part of the bars was assumed to participate in the development of impact force, the contact dura-

tion became shorter and the limiting force was achieved. Figure 9 shows the effect of increasing value of *n* for contact between two concrete slabs of dimension 10 m x 8 m x 0.15m, with impact velocity 1 m/s. Stiffness k_L is calculated as [EA/(L/n)] where n is the number of discrete elements. It was observed that the rise time of the force, and total contact time decreased as *n* was increased. Large scale experiments to measure the effective contact zone of diaphragms will need to be carried out to forecast the contact stiffness with certainty. For the analysis presented here, the zone of axial deformation of slab is assumed to be a tenth of the length of the stiffer slab.

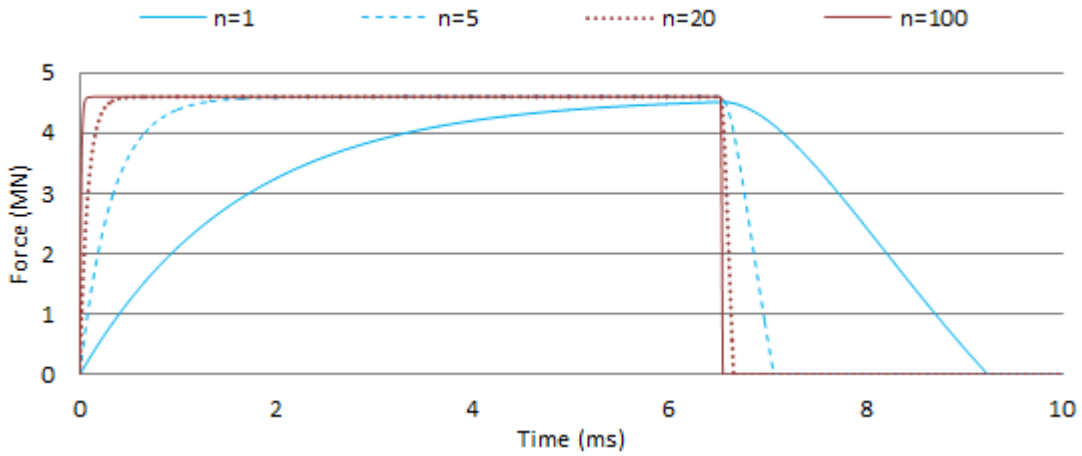


Figure 9: Variation in impact force with the increasing ratio of total length to the length of compression zone

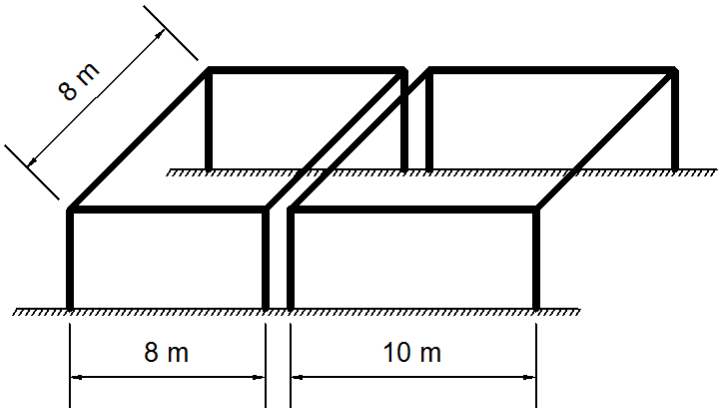


Figure 10: One-story buildings for pounding simulation.

Properties	Left Building	Right Building
Floor height	4 m	4 m
Slab thickness	0.15 m	0.15 m
Building stiffness	1.16 x 10^7 N/m	7.11 x 10^6 N/m
Seismic mass	36,000 kg	45,000 kg
Natural period	0.35 s	0.5 s

Table 1: Properties of the buildings subjected to pounding.

The buildings shown in Figure 10 were subjected to eight seconds of El Centro ground motion (Figure 11). Table 1 shows the relevant properties of the buildings. The seismic weight of

the building was assumed to be uniformly distributed over the whole area of the roof. The at-rest separation was 1 mm. The contact stiffness was calculated to be 15 GN/m. The roofs were modeled as single uniaxial members for the calculation of impact force, while the buildings were idealized as single degree of freedom structures for time history analysis. The displacement responses of the building with and without pounding are presented in Figure 12.

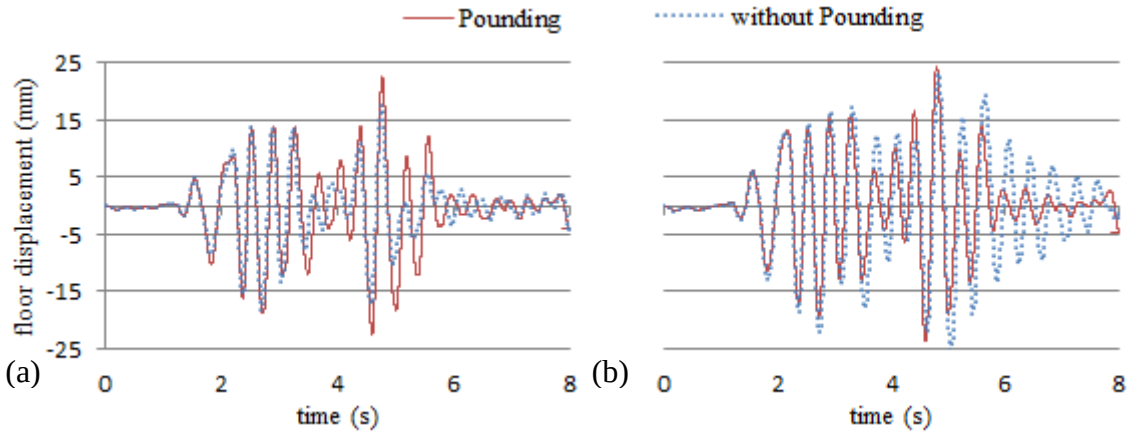


Figure 12: displacement time histories with and without pounding (a) left building and (b) right building.

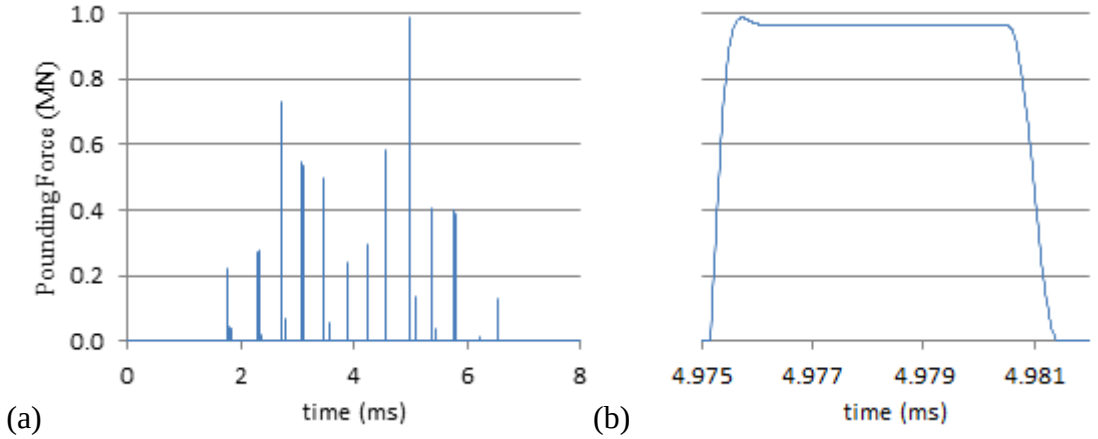


Figure 13: (a) Pounding forces throughout the simulation and (b) Pounding force during thirteenth impact.

Figure 13a shows the pounding forces generated throughout the simulation. Nineteen contacts occurred in total. The time history of force during the strongest impact is presented in figure 13b. The contact force resembled that from wave theory due to the stiff contact element. When the deformation zone was assumed to be longer, the contact softened, and the impact force shifted toward Hertzian contact for which the results are not shown here.

5 CONCLUSIONS

- A method that can incorporate the behavior of distributed mass as well as lumped mass models is proposed for building pounding. The impact force has a finite rise time, as opposed to the instantaneous peak force in wave theory. While the force time-history has a flat plateau after it reaches a maximum value which is dependent on the density and Young's modulus of elasticity of the material as well as the cross sectional area and velocity of the bodies. This plateau can only occur in a lumped mass model if there is plastic deformation at the contact location.

- A parametric study of the model was presented. It was observed that the contact could behave more like that of point masses or distributed masses depending on the values of the parameters involved. An increase in impact velocity shortened the contact duration and produced impact forces similar to that in wave theory. An increase in masses of the bodies shifted the contact behavior toward lumped mass impact. Wave propagation was the predominant mode when the bodies were longer while the contact of shorter bodies was governed by lumped mass effects. Finally, if the bars of softer material (concrete) were loaded with the same mass, the lumped mass behavior becomes more significant.
- The effective coefficient of restitution was found to be dependent upon the length ratio of the bars as in wave theory. For elastic contact of two bars of equal lengths the coefficient of restitution was always one, but for unequal lengths it was governed by almost all the parameters studied. The coefficient of restitution approached unity for short bars while for longer bars it approached the ratio of the length of the shorter bar to that of longer bar. Thus, lumped mass models can significantly over-estimate the effective coefficient of restitution while models based on wave theory can underestimate it equally severely.
- The Sears model was derived for impact of curved ends. A modification is proposed for building pounding analysis, where a linear force deformation equation is adopted instead of the Hertz model to calculate the impact force at the contact location. This requires the length of the deformation zone to be determined. The effect of this length is also presented. Unfortunately, the current state of the art is insufficient to predict this with any certainty.
- Finally, a procedure for the implementation of the Sears model in the simulation of building pounding is outlined. The contact zone was assumed to be a tenth of the length of the stiffer slab, and the results from a sample analysis are presented. It was observed that the simulated forces were similar to the wave propagation model, but contained definite rise and fall durations. The oscillations observed in the force time history from previous published studies on distributed mass modeling were absent.
- In summary, the Sears model is recommended for implementation in building pounding analysis as it can combine into one methodology two currently used models as well as rectify some weaknesses in both. Large scale testing of the impact between slabs is also recommended to determine the force development at the contact zone.

ACKNOWLEDGEMENTS:

The first author is deeply indebted to The University of Auckland for the grant of the University of Auckland International Doctoral Scholarship.

REFERENCES

[1] E. Rosenblueth, R. Meli, The 1985 earthquake: causes and effects in Mexico City. *Concrete International*, **8**, 23-34, 1986.

[2] Chouw, N., Hao, H. (2012). Pounding damage to structures in the 2011 Christchurch earthquake. *International Journal of Protective Structures*, 3**(**2), 123-139.

[3] B, Li, K. Bi, N. Chouw, J.W. Butterworth, H. Hao, Experimental investigation of spatially varying effect of ground motions on bridge pounding. *Earthquake Engineering and Structural Dynamics*, **41**, 1959-1976, 2012.

[4] C.J. Athanassiadou, G.G. Penelis, A.J. Kappos, Seismic response of adjacent buildings with similar or different dynamic characteristics. *Earthquake Spectra*, **10**, 293-317, 1994.

[5] P.K. Malhotra, Dynamics of seismic pounding at expansion joints of concrete bridges. *ASCE Journal of Engineering Mechanics*, **124**, 794–802, 1998.

[6] G. Watanabe, K. Kawashima, Numerical simulation of pounding of bridge decks. *Thirteenth World Conference on Earthquake Engineering*, Vancouver, B.C. Canada, August 1-6, 2004.

[7] G.L. Cole, R.P. Dhakal, A.J. Carr, D.K. Bull, The effect of diaphragm wave propagation on the analysis of pounding structures. *4th ECCOMAS Thematic Conference on Computational Methods in Structural Dynamics and Earthquake Engineering (COMPDYN 2009)*, Rhodes, Greece, June 22-24, 2009.

[8] J.E.P. Wagstaff, Experiments on the Duration of Impacts, Mainly of Bars with Rounded Ends, in Elucidationof the Elastic Theory. *Proceedings of the Royal Society of London. Series A, Containing Papers of aMathematical and Physical Character*, **105**, 544-570, 1924.

[9] W. Goldsmith. *Impact: the theory and physical behaviour of colliding solids, Dover ed*. Dover, 2001.

[10] J.E. Sears, On longitudinal impact of metal rods II. *Transactions of the Cambridge Physical society*, **21**, 49-106, 1912.

COMPDYN 2013
4th ECCOMAS Thematic Conference on
Computational Methods in Structural Dynamics and Earthquake Engineering
M. Papadrakakis, V. Papadopoulos, V. Plevris (eds.)
Kos Island, Greece, 12–14 June 2013

FREE VIBRATIONS OF A CYLINDRICAL SHELL MADE OF AN ANISOTROPIC MATERIAL

Petr E.Tovstik [1] **and Tatiana P.Tovstik** [2]

[1]St.Perersburg State University, Russia
address
e-mail: peter.tovstik@mail.ru

[2] Institute of Problems of Mechanical Engineering RAS, Russia
address
e-mail: tovstik_t@mail.ru

Keywords: material with general anisotropy, cylindrical shell, free vibrations

Abstract. *Two-dimensional model of shell made of an anisotropic material described by 21 elastic moduli is delivered. It is shown that, in the general case (in contrary to isotropic or orthotropic materials), both the Kirchhoff-Love and the Timoshenko-Reissner hypotheses result in 2D models, which are inconsistent in the major terms with respect to the small thickness parameter equal to the ratio between the thickness of shell and the wavelength. For this aim the generalized Timoshenko-Reissner hypothesis is proposed. The asymptotic analysis of the obtained 2D shell model is used to investigate the cylindrical shell free vibrations. The main types of the vibration modes are described and they are compared with the modes of the isotropic shell. The membrane modes are investigated. The system of Donnell type is delivered. This system is used to investigate free vibrations of a circular cylindrical shell. The example of material with the general anisotropy is given.*

1 INTRODUCTION

Numerous investigations including monographs [1–6] are devoted to derivation of two-dimensional (2D) models of plates and shells from three-dimensional (3D) equations of the theory of elasticity. The presence of anisotropy of material introduces the additional difficulties. The 2D models for isotropic and transversely isotropic materials [2–8] have been investigated in detail. The general anisotropy described by 21 elastic moduli have not been sufficiently investigated [9]. The problem of anisotropic beam in the case of the general anisotropy is considered in [10], and the 3D stress state is studied in [11]. It is shown that, in the general case (in contrast to isotropic or orthotropic materials), both the Kirchhoff–Love (KL) and Timoshenko–Reissner (TR) hypotheses lead to 2D models, which are incorrect in the principal terms with respect to the small thickness parameter. The generalized TR hypothesis is used in [10,11] for deriving the 2D model.

The hypotheses accepted in [10,11] should be defined more accurately because some boundary conditions at the upper and lower planes of the plate are not satisfied. More accurate hypotheses, free from this imperfection, are introduced in [12] for a beam and these hypotheses are used for a shell in the present paper. This definition is essential in the case of comparatively small elastic moduli in the transversal directions and also in construction of a boundary layer. As is well known (see [1,2,8]) in the TR model the effective transverse shear moduli kG contains the correcting factor k which depends on the studied problem (here $k = 5/6$). The hypotheses [10,11] lead to $k = 1$.

Under the assumption that the transverse elastic moduli are of the same order as the tangential ones the asymptotic analysis and simplification of the obtained system are made. Our aim is to deliver the system with a minimal exactness however such that the principal terms with respect to the small thickness parameter are correct. We assume that the external load acting on the shell varies slowly. Then (see [7,8]) the stress-strain state (SSS) of the shell consists of three parts: the main membrane state with the small variability, the edge effect with the intermediate variability which is standard in the KL model, and the boundary layer with the large variability which appears only in the TR model. The wave length in the boundary layer is of the order of shell thickness h and the corresponding SSS quickly decreases away from the edges. The boundary layer SSS is poorly described by 2D models and it is necessary to use 3D equations [6]. One of the aims of the presented simplification is to exclude the boundary layer from the consideration. In this case the differential order of the system decreases from 10 to 8, and the number of boundary conditions decreases from 5 to 4.

The asymptotic analysis of the obtained 2D shell model is used to investigate the cylindrical shell free vibrations. The main types of the vibration modes are described and they are compared with the modes of the isotropic shell. The membrane modes are investigated. The system of Donnell type is delivered, and this system is used to investigate the low-frequency free vibrations of a circular cylindrical shell. The example of material with the general anisotropy is given.

2 THE MAIN ASSUMPTIONS AND ELASTICITY RELATIONS

Consider a thin circular cylindrical shell of radius R and of the constant thickness h. We introduce curvilinear co-ordinates $x_1 = Rs,\ x_2 = R\theta$ in the midsurface coinciding with the longitudinal and circumferential directions. The third co-ordinate $x_3 = z$ ($|z| \le h/2$) coincides with the midsurface normal (Fig. 1). The Lame coefficients of the shell body are $H_1 = R,\ H_2 = R + z,\ H_3 = 1$. We neglect h/R compared with 1, and put $H_2 \simeq R$.

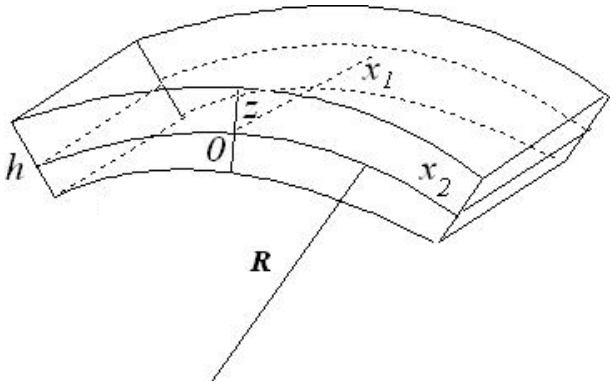


Figure 1: The shell.

Consider a material with the general anisotropy containing 21 elastic moduli. To describe elasticity relations it is more convenient to use matrix designations instead of the tensor of 4th rank. Let us introduce strains ε_{ij} in cylindrical co-ordinate system as

$$\begin{aligned} &\varepsilon_{11}=\frac{\partial u_1}{\partial x_1}, && \varepsilon_{12}=\frac{\partial u_1}{\partial x_2}+\frac{\partial u_2}{\partial x_1}, && \varepsilon_{13}=\frac{\partial u_1}{\partial z}+\frac{\partial w}{\partial x_1},\\ &\varepsilon_{22}=\frac{\partial u_2}{\partial x_2}+\frac{w}{R}, && \varepsilon_{23}=\frac{\partial u_2}{\partial z}+\frac{\partial w}{\partial x_2}-\frac{u_2}{R}, && \varepsilon_{33}=\frac{\partial w}{\partial z}. \end{aligned} \tag{1}$$

Writing the relations between the stresses σ_{ij} and the strains ε_{ij} in the shell body we divide them into groups of tangential $\boldsymbol{\sigma}_t,\ \boldsymbol{\varepsilon}_t$ and the non-tangential $\boldsymbol{\sigma}_n,\ \boldsymbol{\varepsilon}_n$ stresses and strains,

$$\begin{aligned} &\boldsymbol{\sigma}_t=(\sigma_{11},\,\sigma_{12},\,\sigma_{22})^T, && \boldsymbol{\sigma}_n=(\sigma_{13},\,\sigma_{23},\,\sigma_{33})^T,\\ &\boldsymbol{\varepsilon}_t=(\varepsilon_{11},\,\varepsilon_{12},\,\varepsilon_{22})^T, && \boldsymbol{\varepsilon}_n=(\varepsilon_{13},\,\varepsilon_{23},\,\varepsilon_{33})^T; \end{aligned} \tag{2}$$

the superscript ^{T} designates the transposition. Then the relations between stresses and strains are written in the matrix form

$$\boldsymbol{\sigma}_t=\mathbf{A}\cdot\boldsymbol{\varepsilon}_t+\mathbf{B}\cdot\boldsymbol{\varepsilon}_n,\quad \boldsymbol{\sigma}_n=\mathbf{B}^T\cdot\boldsymbol{\varepsilon}_t+\mathbf{C}\cdot\boldsymbol{\varepsilon}_n, \tag{3}$$

where $\mathbf{A}=\{A_{ij}\},\ \mathbf{B}=\{B_{ij}\},\ \mathbf{C}=\{C_{ij}\}$ are the elastic-moduli matrices, the matrices $\mathbf{A}$ and $\mathbf{C}$ being symmetric. Relations (3) contain 21 elastic moduli. It is assumed that the matrix

$$\begin{pmatrix} \mathbf{A} & \mathbf{B} \\ \mathbf{B}^T & \mathbf{C} \end{pmatrix}$$

of the 6th order is positively determined.

Assume that the face surfaces $z=\pm h/2$ are free

$$\sigma_{13}=\sigma_{23}=\sigma_{33}=0,\quad z=\pm h/2. \tag{4}$$

As in the KL and the TR models we accept that the normal stresses can be neglected $\sigma_{33}\equiv 0$, and that the normal deflection w does not depend on z. Using the relation $\sigma_{33}=0$ we exclude the strain ε_{33} from the relations (2). Then they become

$$\boldsymbol{\sigma}_t=\mathbf{A}^*\cdot\boldsymbol{\varepsilon}_t+\mathbf{B}^*\cdot\boldsymbol{\varepsilon}_n^*,\quad \boldsymbol{\sigma}_n^*=\mathbf{B}^{*T}\cdot\boldsymbol{\varepsilon}_t+\mathbf{C}^*\cdot\boldsymbol{\varepsilon}_n^*, \tag{5}$$

where in contrast to (2) $\boldsymbol{\sigma}_n^* = (\sigma_{13},\, \sigma_{23})^T$, $\boldsymbol{\varepsilon}_n^* = (\varepsilon_{13},\, \varepsilon_{23})^T$. The elements of matrices $\mathbf{A}^*(3\times 3)$, $\mathbf{B}^*(3\times 2)$, $\mathbf{C}^*(2\times 2)$ are as follows

$$A_{ij}^* = A_{ij} - \frac{B_{i3}B_{j3}}{C_{33}}, \quad B_{ij}^* = B_{ij} - \frac{B_{i3}C_{j3}}{C_{33}}, \quad C_{ij}^* = C_{ij} - \frac{C_{i3}C_{j3}}{C_{33}}. \tag{6}$$

3 THE GENERALIZED TIMOSHENKO–REISSNER MODEL

In order to obtain the 2D shell model one should accept some assumptions about the distribution of the transversal shear strains $\varepsilon_{i3},\ i=1,2$ in the normal direction. According to the KL model the relation $\varepsilon_{i3}=0$ is accepted. According to the TR model the relation $\varepsilon_{i3}=\gamma_i$ or the more exact relation $\varepsilon_{i3}=\gamma_i(1-4z^2/h^2)$ is accepted. In the case of the latter relation for the orthotropic material the boundary conditions (4) are satisfied.

Both the KL and the TR hypotheses in the case of the general anisotropy do not lead to correct principal terms with respect to the small thickness parameter (see [10,11]). Therefore as in [12] we accept

$$\varepsilon_{i3} = \gamma_i + \delta_i z + P_2^0(z)\beta_i, \quad i=1,2, \quad P_2^0(z) = z^2/h^2 - 1/12, \tag{7}$$

where the functions $\gamma_i, \delta_i, \beta_i$ do not depend on z. The functions γ_i are the average shear angles, and the functions δ_i, β_i will be chosen to satisfy the conditions (4).

Equating expressions (1) and (7) for ε_{13} and ε_{23}, we find the tangential displacements

$$u_i(z) = u_i^0 + \varphi_i z + P_2(z)\delta_i + P_3(z)\beta_i, \quad P_2 = \frac{z^2}{2} - \frac{h^2}{24}, \quad P_3 = \frac{z^3}{3h^2} - \frac{z}{12}, \tag{8}$$

where u_i^0 are the average displacements and $\varphi_1 = \gamma_1 - \partial w/\partial x_i,\ \varphi_2 = \gamma_2 + u_2/R - \partial w/\partial x_2$ are the average angles of the normal fibers rotation.

The strains $\varepsilon_{ij},\ i,j=1,2$ are

$$\begin{aligned} &\boldsymbol{\varepsilon}_t = (\varepsilon_{11},\varepsilon_{12},\varepsilon_{22})^T = \boldsymbol{\varepsilon}_t^0 + z\mathbf{K}(\boldsymbol{\varphi}) + P_2(z)\mathbf{K}(\boldsymbol{\delta}) + P_3(z)\mathbf{K}(\boldsymbol{\beta}),\\ &\mathbf{K}(\boldsymbol{\xi}) \equiv \left(\frac{\partial \xi_1}{\partial x_1},\, \frac{\partial \xi_1}{\partial x_2} + \frac{\partial \xi_2}{\partial x_1},\, \frac{\partial \xi_2}{\partial x_2}\right)^T, \qquad \boldsymbol{\varepsilon}_t^0 = \mathbf{K}(\boldsymbol{u}^0) + \left(0,0,\frac{w}{R}\right)^T. \end{aligned} \tag{9}$$

Here $\boldsymbol{\varepsilon}_t^0$ are the tangential strains of the midsurface. The operator $\mathbf{K}(\cdot)$ will be applied to the 2D vectors $\boldsymbol{\gamma} = (\gamma_1,\gamma_2)^T$, $\boldsymbol{\varphi} = (\varphi_1,\varphi_2)^T$, $\boldsymbol{\delta} = (\delta_1,\delta_2)^T$, $\boldsymbol{\beta} = (\beta_1,\beta_2)^T$. According to relations (7) and (9) the boundary conditions (4) are satisfied if

$$\mathbf{B}^{*T}\cdot\mathbf{K}(\boldsymbol{\varphi}) + \mathbf{C}^*\cdot\boldsymbol{\delta} = 0, \qquad \mathbf{B}^{*T}\cdot\left(\boldsymbol{\varepsilon}_t^0 + h^2\mathbf{K}(\boldsymbol{\delta})/12\right) + \mathbf{C}^*\cdot(\boldsymbol{\gamma} + \boldsymbol{\beta}/6) = 0.$$

Omitting the small term $h^2\mathbf{K}(\boldsymbol{\delta})/12$ we find

$$\boldsymbol{\delta} = -(\mathbf{C}^*)^{-1}\cdot\mathbf{B}^{*T}\cdot\mathbf{K}(\boldsymbol{\varphi}), \quad \boldsymbol{\beta} = -6\left(\boldsymbol{\gamma} + (\mathbf{C}^*)^{-1}\cdot\mathbf{B}^{*T}\cdot\boldsymbol{\varepsilon}_t^0\right). \tag{10}$$

Then we re-write the expressions (7) and (9) for the strains in the form

$$\begin{aligned} &\boldsymbol{\varepsilon}_n^* = \boldsymbol{\gamma} - z(\mathbf{C}^*)^{-1}\cdot\mathbf{B}^{*T}\cdot\mathbf{K}(\boldsymbol{\varphi}) - 6P_2^0(z)\left(\boldsymbol{\gamma} + (\mathbf{C}^*)^{-1}\cdot\mathbf{B}^{*T}\cdot\boldsymbol{\varepsilon}_t^0\right),\\ &\boldsymbol{\varepsilon}_t = \boldsymbol{\varepsilon}_t^0 + z\mathbf{K}(\boldsymbol{\varphi}) - P_2(z)\mathbf{K}\left((\mathbf{C}^*)^{-1}\cdot\mathbf{B}^{*T}\cdot\mathbf{K}(\boldsymbol{\varphi})\right) - 6P_3(z)\mathbf{K}\left(\boldsymbol{\gamma} + (\mathbf{C}^*)^{-1}\cdot\mathbf{B}^{*T}\cdot\boldsymbol{\varepsilon}_t^0\right). \end{aligned} \tag{11}$$

Using strains (11) we calculate stresses $\boldsymbol{\sigma}_t$ and $\boldsymbol{\sigma}_n^*$ by relations (5). The stress-resultants T_{ij}, Q_i and the stress-couples M_{ij} are to be found over integration in the thickness direction

$$\{T_{ij}, Q_i\} = \int_{-h/2}^{h/2} \{\sigma_{ij}, \sigma_{i3}\}\, dz, \quad \{M_{ij}\} = \int_{-h/2}^{h/2} \{\sigma_{ij}\}\, z dz, \quad i,j = 1,2. \tag{12}$$

In the case when the elastic moduli **A**, **B**, **C** do not depend on z relations (12) can be re-written as

$$\begin{aligned} &\mathbf{T} = h\left(\mathbf{A}^* \cdot \boldsymbol{\varepsilon}_t^0 + \mathbf{B}^* \cdot \boldsymbol{\gamma}\right), && \mathbf{T} = (T_{11}, T_{12}, T_{22})^T, \\ &\mathbf{Q} = h\left(\mathbf{B}^{*T} \cdot \boldsymbol{\varepsilon}_t^0 + \mathbf{C}^* \cdot \boldsymbol{\gamma}\right), && \mathbf{Q} = (Q_1, Q_2)^T, \\ &\mathbf{M} = J\left(\mathbf{A}^{**} \cdot \mathbf{K}(\boldsymbol{\varphi}) + \mathbf{A}^* \cdot \mathbf{K}(\boldsymbol{\gamma} + (\mathbf{C}^*)^{-1} \cdot \mathbf{B}^{*T} \cdot \boldsymbol{\varepsilon}_t^0)/5\right), && \mathbf{M} = (M_{11}, M_{12}, M_{22})^T, \end{aligned} \tag{13}$$

where

$$J = \frac{h^3}{12}, \quad \boldsymbol{\gamma} = \boldsymbol{\varphi} + \nabla w, \quad \nabla = \left(\frac{\partial}{\partial x_1}, \frac{\partial}{\partial x_2}\right)^T,$$

$$\mathbf{A}^{**} = \mathbf{A}^* - \mathbf{B}^* \cdot \mathbf{C}^{*-1} \cdot \mathbf{B}^{*T} = \mathbf{A} - \mathbf{B} \cdot \mathbf{C}^{-1} \cdot \mathbf{B}^T. \tag{14}$$

Therefore the 2D stress-resultants and the stress-couples are expressed as functions of the main unknown variables, namely of the deflections of a midsurface u_1^0, u_2^0, w and of the average angles of the normal fibers rotation φ_1, φ_2. Further we omit the index ^{0} at u_i^0.

4 THE 2D EQUATIONS AND BOUNDARY CONDITIONS

The 2D equations are exactly the same as those in the KL and the TR models. The difference lies in the elasticity relations (13).

$$\begin{aligned} &\frac{\partial T_{11}}{\partial x_1} + \frac{\partial T_{12}}{\partial x_2} + \rho h \omega^2 u_1 = 0, && \frac{\partial T_{12}}{\partial x_1} + \frac{\partial T_{22}}{\partial x_2} + \frac{Q_2}{R} + \rho h \omega^2 u_2 = 0, \\ &\frac{\partial Q_1}{\partial x_1} + \frac{\partial Q_2}{\partial x_2} - \frac{T_{22}}{R} + \rho h \omega^2 w = 0, \\ &\frac{\partial M_{11}}{\partial x_1} + \frac{\partial M_{12}}{\partial x_2} - Q_1 + \rho J \omega^2 \varphi_1 = 0, && \frac{\partial M_{12}}{\partial x_1} + \frac{\partial M_{22}}{\partial x_2} - Q_2 + \rho J \omega^2 \varphi_2 = 0. \end{aligned} \tag{15}$$

System (15) is used for the investigation of free vibrations. It is obtained after the separation of variables of type $w(x_1, x_2, t) = w(x_1, x_2) e^{i\omega t}$, where t is the time, ω is the natural frequency.

System (15) is of the 10th order. The simplest boundary conditions at the egdes $x_1 = 0$ and $x_1 = L_0$ are

$$\begin{aligned} &u_1 = 0 \quad &or \quad &T_1 = 0, \\ &u_2 = 0 \quad &or \quad &T_{12} = 0, \\ &w = 0 \quad &or \quad &Q_1 = 0, \\ &\varphi_1 = 0 \quad &or \quad &M_1 = 0, \\ &\varphi_2 = 0 \quad &or \quad &M_{12} = 0, \end{aligned} \tag{16}$$

where from the each line of table (16) is to be taken only one condition. The shell edge element in TR model has 5 degrees of freedom with the generalized co-ordinates $u_1, u_2, w, \varphi_1, \varphi_2$. The left side of conditions (16) corresponds to the clamped co-ordinate and the right side corresponds to the free coordinate. For clamped edge

$$u_1 = u_2 = w = \varphi_1 = \varphi_2 = 0 \tag{17}$$

and for free edge

$$T_{11} = T_{12} = Q_1 = M_{11} = M_{12} = 0. \tag{18}$$

Rewrite system (15) in the dimensionless form. For this aim we put

$$h_*=\frac{h}{R}, \quad \Lambda=\frac{\rho h^2\omega^2}{E}, \quad \{u_i, w\}=h\{\hat{u}_i, \hat{w}\}, \quad \{T_{ij}, Q_i\}=Eh\{\hat{T}_{ij}, \hat{Q}_i\}, \quad M_{ij}=ERh\hat{M}_{ij},$$

where h_* is the main small parameter equal to the relative shell thickness, Λ is the unknown frequency parameter, E is the typical value of elastic moduli in (3). After omitting superscript $\hat{}$ we get

$$\begin{aligned}
&\frac{\partial T_{11}}{\partial s} + \frac{\partial T_{12}}{\partial \theta} + \Lambda u_1 = 0, && \frac{\partial T_{12}}{\partial s} + \frac{\partial T_{22}}{\partial \theta} + Q_2 + \Lambda u_2 = 0,\\
&\frac{\partial Q_1}{\partial s} + \frac{\partial Q_2}{\partial \theta} - T_{22} + \Lambda w = 0, &&\\
&\frac{\partial M_{11}}{\partial s} + \frac{\partial M_{12}}{\partial \theta} - Q_1 + \frac{h_*^2}{12}\Lambda\varphi_1 = 0, && \frac{\partial M_{12}}{\partial s} + \frac{\partial M_{22}}{\partial \theta} - Q_2 + \frac{h_*^2}{12}\Lambda\varphi_2 = 0
\end{aligned} \tag{19}$$

with

$$\begin{aligned}
&\mathbf{T} = \mathbf{A}^* \cdot \boldsymbol{\varepsilon}_t^0 + \mathbf{B}^* \cdot \boldsymbol{\gamma}, \quad \mathbf{Q} = \mathbf{B}^{*T} \cdot \boldsymbol{\varepsilon}_t^0 + \mathbf{C}^* \cdot \boldsymbol{\gamma},\\
&\mathbf{M} = \frac{h_*^2}{12}\left(\mathbf{A}^{**} \cdot \mathbf{K}(\boldsymbol{\varphi}) + \frac{\mathbf{A}^*}{5} \cdot \mathbf{K}\left((\mathbf{C}^*)^{-1} \cdot \mathbf{Q}\right)\right),
\end{aligned} \tag{20}$$

where the elastic moduli are related to E.

The 2D potential energy density

$$\Pi_2 = \frac{1}{2}\left(\mathbf{T}^T \cdot \boldsymbol{\varepsilon}_t^0 + \mathbf{Q}^T \cdot \boldsymbol{\gamma} + \mathbf{M}^T \cdot \mathbf{K}(\boldsymbol{\varphi})\right)$$

corresponds to the system (19).

5 EXAMPLE OF A MATERIAL WITH GENERAL ANISOTROPY

As in [10], we study the shell of the anisotropic material whose parameters are obtained by the averaging of the isotropic material (matrix) reinforced by the system of small extensible fibers. The angle between the axis z of the fiber is equal to β, and the angle between the axis x_1 and the plane containing axis z and fiber is equal to α (Fig. 2).

If the stiffness of fibers is mach larger than the stiffness of matrix, then the potential energy density Π for this anisotropic material may be accepted in the form

$$\begin{aligned}
\Pi = &\frac{1-b}{2}\left(\lambda(\varepsilon_{11}+\varepsilon_{22}+\varepsilon_{33})^2 + 2\mu\left(\varepsilon_{11}^2+\varepsilon_{22}^2+\varepsilon_{33}^2\right) + \mu\left(\varepsilon_{12}^2+\varepsilon_{13}^2+\varepsilon_{23}^2\right)\right) +\\
&+\frac{1}{2}bE_f(\varepsilon_{11}a_1^2 + \varepsilon_{22}a_2^2 + \varepsilon_{33}a_3^2 + \varepsilon_{12}a_1a_2 + \varepsilon_{13}a_1a_3 + \varepsilon_{23}a_2a_3)^2,
\end{aligned} \tag{21}$$

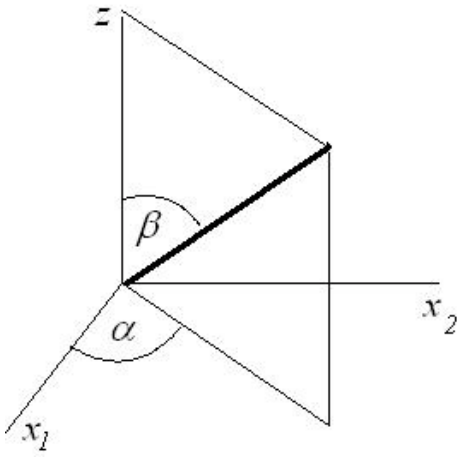


Figure 2: The direction of fibers.

with $a_1 = \cos\alpha \sin\beta,\ a_2 = \sin\alpha \sin\beta,\ a_3 = \cos\beta$, where $\lambda = E\nu/[(1+\nu)(1-2\nu)]$ and $\mu = E/[2(1+\nu)]$ are the Lame coefficients of the matrix, E_f is the Young modulus for fibers, and b is the part of volume occupied by fibers.

We assume that the stresses σ_{ij} are obtained from the relation

$$\sigma_{ij} = \frac{\partial \Pi}{\partial \varepsilon_{ij}}$$

and calculate the elements of matrices $\mathbf{A}$, $\mathbf{B}$, $\mathbf{C}$

$$\begin{array}{lll}
A_{11} = E_1 + E_4 a_1^4, & A_{12} = E_4 a_1^3 a_2, & A_{13} = E_2 + E_4 a_1^2 a_2^2, \\
A_{22} = E_3 + E_4 a_1^2 a_2^2, & A_{23} = E_4 a_1 a_2^3, & A_{33} = E_1 + E_4 a_2^4, \\
B_{11} = E_4 a_1^3 a_3, & B_{12} = E_4 a_1^2 a_2 a_3, & B_{13} = E_2 + E_4 a_1^2 a_3^2, \\
B_{21} = E_4 a_1^2 a_2 a_3, & B_{22} = E_4 a_1 a_2^2 a_3, & B_{23} = E_4 a_1 a_2 a_3^2, \\
B_{31} = E_4 a_1 a_2^2 a_3, & B_{32} = E_4 a_2^3 a_3, & B_{33} = E_2 + E_4 a_2^2 a_3^2, \\
C_{11} = E_3 + E_4 a_1^2 a_3^2, & C_{12} = E_4 a_1 a_2 a_3^2, & C_{13} = E_4 a_1 a_3^3, \\
C_{22} = E_3 + E_4 a_2^2 a_3^2, & C_{23} = E_4 a_2 a_3^3, & C_{33} = E_1 + E_4 a_3^4,
\end{array} \tag{22}$$

where

$$E_1 = \frac{E(1-b)(1-\nu)}{(1+\nu)(1-2\nu)}, \quad E_2 = \frac{\nu E_1}{1-\nu}, \quad E_3 = \frac{E(1-b)}{2(1+\nu)}, \quad E_4 = bE_f. \tag{23}$$

In the next sections we study some examples and take the following values of parameters in (22), (23)

$$b = 0.05,\ \nu = 0.3,\ E_f = 20\,E,\ \alpha = \pi/6,\ \beta = \pi/4.$$

The matrices $\mathbf{A}$, $\mathbf{B}$, $\mathbf{C}$ are not used directly, and we take the numerical values of matrices

$\mathbf{A}^*$, $\mathbf{B}^*$, $\mathbf{C}^*$, $\mathbf{A}^{**}$ (see (6),(14))

$$\frac{\mathbf{A}^*}{E}=\begin{pmatrix}1.0656 & 0.0291 & 0.3012\\ 0.0291 & 0.4146 & -0.0162\\ 0.3012 & -0.0162 & 1.0506\end{pmatrix},\qquad \frac{\mathbf{B}^*}{E}=\begin{pmatrix}0.0582 & 0.0336\\ 0.0784 & 0.0453\\ -0.0323 & -0.0187\end{pmatrix},$$
$$\frac{\mathbf{A}^{**}}{E}=\begin{pmatrix}1.0577 & 0.0185 & 0.3056\\ 0.0185 & 0.3903 & -0.0103\\ 0.2056 & -0.0103 & 1.0482\end{pmatrix},\qquad \frac{\mathbf{C}^*}{E}=\begin{pmatrix}0.5222 & 0.0906\\ 0.0906 & 0.4177\end{pmatrix}. \tag{24}$$

The material with moduli (22) is the general anisotropic material, but if the direction of one of the axes x_1, x_2, z coincides with the direction of fibers, then this material becomes transversely isotropic one.

6 THE GENERAL SOLUTION AND ASYMPTOTIC ANALYSIS PRINCIPLES

Investigate system (19), (20) with boundary conditions (16) at the assumptions that all elastic moduli are constant and they are of the same asymptotic orders

$$\{A_{ij},\, B_{ij},\, C_{ij}\}\sim E. \tag{25}$$

The opposite case when the transversal (C_{ij}) and mixed (B_{ij}) elastic moduli are much smaller than the tangential ones (A_{ij}) requires the additional investigations. For anisotropic beams this case is studied in [7, 12]. Also we assume that the length of wave in the tangential direction is much larger than the shell thickness.

These assumptions (for small h_*) lead to the following simplifications of system (19), (20): the inertia terms $h_*^2\Lambda\varphi_i/12$ in the last two equations may be omitted, and the expression for $\mathbf{M}$ (instead of (20)) may be taken in the more simple form

$$\mathbf{M}=\frac{h_*^2}{12}\mathbf{A}^{**}\cdot\mathbf{K}(\boldsymbol{\varphi}). \tag{26}$$

To solve system (19), (20) we fulfill the separation of variables

$$Z(s,\theta)=Z(s)e^{in\theta},\quad n=0,1,2,\ldots,\quad i=\sqrt{-1}, \tag{27}$$

where n is the number of waves in the circular direction and $Z=(u_1,u_2,w,\ldots)$ is the any unknown function in this system. Then the system becomes one-dimensional and its general solution is

$$Z(s)=\sum_{k=0}^{10}C_kZ_ke^{\lambda_k s}, \tag{28}$$

where C_k are arbitrary constants, Z_k are definite constants, and λ_k are the roots of of the system (19) characteristic equation of 10th order. As usually the frequency equation

$$\Delta_{10}(\Lambda)=0 \tag{29}$$

has the form of a determinant of the linear homogeneous system of 10th order obtained after substitution of the solution (28) into the boundary condition (16). This way is complex enough as for the qualitative investigation so for the numerical solution. That is why the asymptotic analysis at $h_*<<1$ is used.

Introduce the indexes of variability [14] to describe the asymptotic properties of the stress-strain states (SSS). The partial indexes of variability t_1 and t_2 are introduced by relations

$$\frac{\partial Z}{\partial s} \sim h_*^{-t_1} Z; \quad \frac{\partial Z}{\partial \theta} \sim h_*^{-t_2} Z, \quad or \quad n \sim h_*^{-t_2}, \tag{30}$$

where Z is any unknown function.

We refer to $t = \max(t_1, t_2)$ as to the common index of variability.

We study the following main SSS:

1) the membrane state with

$$\mathbf{T} \neq \mathbf{0}, \quad \{\mathbf{M}, \mathbf{Q}\} = \mathbf{0}, \quad t = 0, \quad \Lambda \sim 1, \tag{31}$$

2) the bending state with

$$\mathbf{T} = \mathbf{0}, \quad \{\mathbf{M}, \mathbf{Q}\} \neq \mathbf{0}, \quad t = 0, \quad \Lambda \sim h_*^2, \tag{32}$$

3) the mixed state of Donnell's type [2] with

$$\{\mathbf{T}, \mathbf{M}, \mathbf{Q}\} \neq \mathbf{0}, \quad \mathbf{T} \sim \mathbf{M}\, h_*^{-1}, \quad t > 0, \tag{33}$$

4) the semi-momentless state [15] as a partial case of Donnell's type with

$$t_1 = 0, \quad t_2 = 1/4, \quad \Lambda \sim h_*, \tag{34}$$

5) the edge effect state [14,15] as a partial case of Donnell's type with

$$t_1 = 1/2, \quad t_2 < 1/2, \tag{35}$$

6) the boundary layer state with

$$t_1 = 1. \tag{36}$$

These SSS are the same as for the isotropic shell, the difference lies in the concrete equations and it is discussed in the next sections. The approximate value of Λ may be found from the states 1–4, and sometimes from the state 5, the states 5 and 6 are used to satisfy all boundary conditions only.

7 THE MEMBRANE SOLUTION

For the membrane solution the essential simplification of system (19), (20) is possible. Due to $\mathbf{Q} = \mathbf{0}$ we find from two first relations (20)

$$\boldsymbol{\gamma} = -\mathbf{C}^{*-1} \cdot \mathbf{B}^{*T} \cdot \boldsymbol{\varepsilon}_t^0, \quad \mathbf{T} = \mathbf{A}^{**} \cdot \boldsymbol{\varepsilon}_t^0, \quad \boldsymbol{\varepsilon}_t^0 = (u_1', u_2' + in\, u_1, in\, u_2 + u_3)^T, \quad (\,)' = \frac{d(\,)}{ds}, \tag{37}$$

and first three equations (19) are

$$T_{11}' + inT_{12} + \Lambda u_1 = 0, \quad T_{12}' + inT_{22} + \Lambda u_2 = 0, \quad -T_{22} + \Lambda w = 0. \tag{38}$$

System (38) of 4th order contains only unknown functions u_1, u_2, w. Let us study the clamped boundary conditions (17) at the both edges $s = 0$ and $s = l = L_0/R$. Solving system (38) we satisfy only conditions $u_1 = u_2 = 0$ and as a result we find the approximate values

of membrane natural frequencies and the corresponding vibration modes. The rest boundary conditions $w = \varphi_1 = \varphi_2 = 0$ may be satisfied by adding to the membrane mode the edge effect and the boundary layer to the membrane mode. As a result the membrane natural frequencies are defined more precisely. To fulfill this definition it is necessary to know the relative orders of all unknown functions

$$\{u_i, w, \gamma_i, \varphi_i, T_{ij}\} \sim 1, \quad \{M_{ij}, Q_i\} \sim h_*^2. \tag{39}$$

As an example we study the simplest case $n = 0$ and find only the approximate membrane frequencies for the elastic moduli (24) and for the shell length $l = 3$. For isotropic shell the problem divides to the longitudinal and to the torsion vibrations, and here these problems are joined. The characteristic equation has the form

$$a_0(\Lambda)\lambda^4 + a_2(\Lambda)\lambda^2 + a_4(\Lambda) = 0, \qquad a_0 = L - \omega_*^2, \quad \omega_* = 0.973. \tag{40}$$

Calculations show that the set of the dimensionless frequencies $\omega = \sqrt{\Lambda}$ is the following $0.42,\ 0.56,\ 0.70,\ 0.83,\ 0.92,\ 0.955,\ 0.963,\ 0.966,\ 0,968,\ 0.9690,\ 0.9692,\ 0.9699,\ 0.9704,$ $0.9706, \ldots,\ 1.04,\ 1.15,\ 1.20,\ 1.29, \ldots$. This set has the point of accumulation $\omega_* = 0.973$ because two roots of equation (40) go to infinity at $\omega \to \omega_*$. For the isotropic shell the presence of the point of accumulation in the spectrum of axisymmetric vibrations of cylindrical and spherical shells is well known [14,16,17]. As for the isotropic shell here in the neighborhood of the point $\omega = \omega_*$ the membrane approximation is incorrect because assumptions (31) and (40) are not fulfilled.

8 THE BENDING STATE

The pure bending state is described by relations (32). The very low frequencies correspond to this state. This state exists only if there exists the non-zero solution of equations $\boldsymbol{\varepsilon}_t^0 = \mathbf{0}$ (the so called pure bending of surface). This state is possible if the shell edges are free or weakly supported [14,18].

Let us study the cylindrical shell with free edges and write more detailed estimates than (3.2)

$$t = 0, \quad \{u_i, w\} \sim 1, \quad \{\varepsilon_{ij}, \gamma_i, M_{ij}, Q_i, \Lambda\} \sim h_*^2. \tag{41}$$

There exist the solution $w = \cos(n\theta),\ u_1 = 0,\ u_2 = -\sin(n\theta)/n$, which satisfies equations $\boldsymbol{\varepsilon}_t^0 = \mathbf{0}$. For these functions the second and the third equations (19) accept the form

$$\frac{\partial T_{22}}{\partial \theta} + Q_2 + \Lambda u_2 = 0, \quad \frac{\partial Q_2}{\partial \theta} - T_{22} + \Lambda w = 0, \qquad Q_2 = -\frac{h_*^2 A_{33}^{**}}{12} n(n^2-1)\sin(n\theta)$$

Excluding T_{22} from these equations we obtain

$$\Lambda = \frac{h_*^2 A_{33}^{**}}{12}\frac{(n^2-1)^2}{n^2+1}, \quad n = 2, 3, \ldots. \tag{42}$$

For $n = 0$ and $n = 1$ the shell moves as a rigid body, and $\Lambda = 0$. Relation (42) describes vibrations of inextensible ring [18], the influence of anisotropy is contained in elastic modulus A_{33}^{**}.

9 THE APPROXIMATION OF THE DONNELL TYPE

For this approximation the value $t = 1/2$ of index of variability is typical. In the general case for $w \sim 1$ the orders of the rest unknown functions are

$$\{u_i, Q_i\} \sim h_*^{1/2}, \quad \{\gamma_i, \varepsilon_{ij}^0, T_{ij}\} \sim 1, \quad \varphi_i \sim h_*^{-1/2}, \quad M_{ij} \sim h_*. \tag{43}$$

Admitting the error of the order $h_*^{1/2}$ we obtain (as in (37)) from relations (20)

$$\boldsymbol{\gamma} = -(\mathbf{C}^*)^{-1} \cdot \mathbf{B}^{*T} \cdot \boldsymbol{\varepsilon}_t^0, \qquad \mathbf{T} = h\mathbf{A}^{**} \cdot \boldsymbol{\varepsilon}_t^0, \tag{44}$$

and system (19) may be rewritten in the form

$$\frac{\partial T_{11}}{\partial s} + \frac{\partial T_{12}}{\partial \theta} = 0, \quad \frac{\partial T_{12}}{\partial s} + \frac{\partial T_{22}}{\partial \theta} = 0, \quad \frac{\partial^2 M_{11}}{\partial s^2} + 2\frac{\partial^2 M_{12}}{\partial s\, \partial \theta} + \frac{\partial^2 M_{22}}{\partial \theta^2} + T_{22} - \Lambda w = 0. \tag{45}$$

In system (45) the shear angles γ_i and shear stress-resultants are excluded, the comparatively small tangential inertia is neglected. Let us put this system in the Donnell form [2] containing two unknown functions which are the normal deflection w and the stress function Φ with

$$T_{11} = \frac{\partial^2 \Phi}{\partial \theta^2}, \quad T_{12} = -\frac{\partial^2 \Phi}{\partial s \partial \theta}, \quad T_{22} = \frac{\partial^2 \Phi}{\partial s^2}. \tag{46}$$

The first and the second equations (45) are satisfied. We accept approximately

$$K(\varphi) = -\left(\frac{\partial^2 w}{\partial s^2}, \frac{\partial^2 w}{\partial s\, \partial \theta}, \frac{\partial^2 w}{\partial \theta^2}\right). \tag{47}$$

Then excluding u_1^0 and u_2^0 from the relation $\boldsymbol{\varepsilon}_t^0 = (h\mathbf{A}^{**})^{-1} \cdot \mathbf{T}$ we obtain the system

$$L_4\left(\frac{\partial}{\partial s}, \frac{\partial}{\partial \theta}\right)\Phi - \frac{\partial^2 w}{\partial s^2} = 0, \quad \frac{h_*^2}{12} N_4\left(\frac{\partial}{\partial s}, \frac{\partial}{\partial \theta}\right) w + \frac{\partial^2 \Phi}{\partial s^2} - \Lambda\, w = 0, \tag{48}$$

where the differential operators of 4th order are

$$\begin{aligned} &L_4(p,q) = a_{11}q^4 - 2a_{12}pq^3 + (a_{22}+2a_{13})p^2q^2 - 2a_{23}p^3q + a_{33}p^4, \quad \{a_{ij}\} = (\mathbf{A}^{**})^{-1}, \\ &N_4(p,q) = A_{11}^{**}p^4 + 4A_{12}^{**}p^3q + 2(2A_{22}^{**} + A_{13}^{**})p^2q^2 + 4A_{23}^{**}pq^3 + A_{33}^{**}q^4. \end{aligned} \tag{49}$$

For the material described in Section 5 the elements of matrix $(\mathbf{A}^{**})^{-1}$ are

$$(\mathbf{A}^{**})^{-1} = \{a_{ij}\} = \begin{pmatrix} 1.0438 & -0.0583 & -0.3370 \\ -0.0583 & 2.5662 & 0.0466 \\ -0.3370 & 0.0466 & 1.1639 \end{pmatrix}. \tag{50}$$

System (48) is convenient for analytical and numerical investigations. With accuracy of the order h_*^t system (48) may be used also for the index of variability $0 < t < 1/2$.

If we neglect the summand $\partial^2\Phi/\partial s^2$ then the second equation (48) describes the transversal vibrations of an anisotropic plate [11].

The system (19) is of the 10th order, and the orders of system (48) is equal to 8. In order to formulate correctly the boundary conditions for system (48) it is necessary to construct the boundary layer solution.

10 THE SEMI-MOMENTLESS STATE

For this state according of (34) index of variability t_2 in circular direction is larger than index t_1 in longitudinal direction, and as a result $|M_{22}| >> |M_{11}|$ and moment M_{11} may be neglected. That is why this state is named as a "semi-momentless" one [15]. Excluding the cases with free or weakly supported edges the minimal natural frequency have the semi-momentless mode [15].

If the estimates (34) are fulfilled then system (48) may be essentially simplified. In zero approximation (with the error of order $h_*^{1/4}$) we put approximately

$$L_4\left(\frac{\partial}{\partial s},\frac{\partial}{\partial\theta}\right)\Phi = a_{11}\frac{\partial^4\Phi}{\partial\theta^4}, \qquad N_4\left(\frac{\partial}{\partial s},\frac{\partial}{\partial\theta}\right)w = A_{33}^{**}\frac{\partial^4 w}{\partial\theta^4}, \tag{51}$$

and system (48) accepts the form

$$a_{11}\frac{\partial^4\Phi}{\partial\theta^4} - \frac{\partial^2 w}{\partial s^2} = 0, \quad \frac{h_*^2 A_{33}^{**}}{12}\frac{\partial^4 w}{\partial\theta^4} + \frac{\partial^2\Phi}{\partial s^2} - \Lambda\, w = 0. \tag{52}$$

We seek solution of this system in the form

$$w(s,\theta) = w(s)\cos(n\theta), \quad \Phi(s,\theta) = \Phi(s)\cos(n\theta), \quad n = O(h_*^{-1/4}), \tag{53}$$

and excluding $\Phi(s)$ from system (52) reduce it to the ordinary problem of the beam vibrations

$$\frac{d^4 w}{\partial s^4} - p^4 w = 0, \quad p^4 = n^4 a_{11}(\Lambda - n^4\mu^8 A_{33}^{**}), \quad \mu^8 = \frac{h_*^2}{12}. \tag{54}$$

For the given p and n the frequency parameter is equal to

$$\Lambda = n^4\mu^8 A_{33}^{**} + \frac{p^4}{n^4 a_{11}} \tag{55}$$

and find the minimal value $\Lambda_* = \min\Lambda$ and the corresponding value n_* of number of waves in the circular direction are

$$\Lambda_* = 2\mu^4 p^2\left(\frac{A_{33}^{**}}{a_{11}}\right)^{1/2}, \qquad n_* = \frac{1}{\mu}\left(\frac{p^4}{a_{11}A_{33}^{**}}\right)^{1/8}. \tag{56}$$

Integer n close to n_* is to be taken to find $\min\Lambda$ from (55).

The order of equation (54) allows us to satisfy only two (main) boundary conditions at the each shell edge. For the isotropic shell the way of choosing main boundary condition is discussed in [13,18]. If both edges are clamped ($w = dw/ds = 0$) then $p = 4.73/l$.

For the material described in section 5 with $l = 3,\ R/h = 250$ the dimensionless natural frequencies $\omega = \sqrt{\Lambda}$ close to the minimal one are ($n_* = 6.82$)

$$\begin{array}{lcccccc} n = & 5 & 6 & 6.82 & 7 & 8 & 9 \\ \omega = & 0.1013 & 0.0788 & 0.0740 & 0.0742 & 0.0814 & 0.0959 \end{array} \tag{57}$$

The approximate results (53), (55)–(57) may be made more precise by solving two problems. At first the approximation (51) leads not only to the quantitative error of the order μ, but also contains the qualitative error. If in zero approximation the vibration modes (53) are elongated in the longitudinal direction then the more exact system (48) leads to the slightly inclined modes (Fig. 3).

At second it is necessary to satisfy not only two main boundary conditions, but 5 conditions (17). Two of the additional conditions may be satisfied by the edge effect solutions and the rest one may be satisfied by the boundary layer.

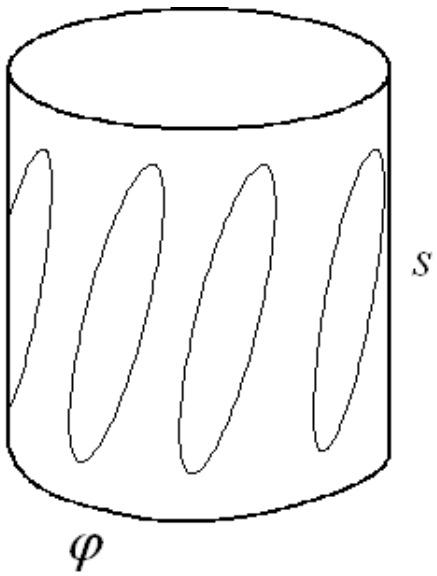


Figure 3: The vibration mode.

11 THE EDGE EFFECT

If $t_1 > t_2$ then the main terms of operators L_4 and N_4 are

$$L_4\left(\frac{\partial}{\partial s},\,\frac{\partial}{\partial \theta}\right)\Phi = a_{33}\frac{\partial^4\Phi}{\partial s^4}, \qquad N_4\left(\frac{\partial}{\partial s},\,\frac{\partial}{\partial \theta}\right)w = A_{11}^{**}\frac{\partial^4 w}{\partial s^4}, \tag{58}$$

and system (48) leads to the edge effect equation

$$\frac{\partial^4 w}{\partial s^4} + p_e^4 w = 0, \quad p_e^4 = \frac{12}{h_*^2 a_{33} A_{11}^{**}}(1 - \Lambda a_{33}). \tag{59}$$

If $\Lambda < 1/a_{33}$ then due to $|p_e| >> 1$ equation (59) has two solutions $w = C(\theta)e^{\pm p_e x}$ quickly decreasing away from the shell edges. For $\Lambda > 1/a_{33}$ two solutions of equation (59) oscillate, the edge effect degenerates, and the equation (59) gives the natural frequencies with $t = 1/2$.

12 THE BOUNDARY LAYER

As in the TR model for the boundary layer the index of variability $t = 1$. Assuming that $w \sim 1$ we find the following asymptotical orders of the remaining unknown variables

$$u_i \sim 1, \quad \{\gamma_i,\, \varphi_i,\, \varepsilon_{ij}^0\} \sim h_*^{-1}, \quad \{T_{ij}, Q_i\} \sim h_*^{-1}, \quad \{M_{ij}\} \sim h_*^{-2}, \quad i,j = 1,2. \tag{60}$$

According to these estimates the boundary layer in zero approximation can be found from the system

$$\frac{\partial T_{i1}}{\partial y_1} + \frac{\partial T_{i2}}{\partial y_2} = 0, \quad \frac{\partial M_{i1}}{\partial y_1} + \frac{\partial M_{i2}}{\partial y_2} + Q_i = 0, \quad i = 1,2, \qquad \frac{\partial Q_1}{\partial y_1} + \frac{\partial Q_2}{\partial y_2} = 0, \tag{61}$$

where in the 2D elasticity relations (44) in contrast to (9) $\boldsymbol{\varepsilon}_t^0 = \mathbf{K}(\boldsymbol{u}^0)$.

To construct the boundary layer near the edge $x_1 = x_1^0$ we suppose that one of the indexes of variability $t_1 = 1$, and the other index of variability $t_2 < t_1$ (for example, $t_2 = 1/2$ if the boundary layer is constructed to formulate the boundary conditions for system (32)).

We seek the boundary layer in the form

$$Z(x_1, x_2) = e^{py_1/h_*} Z^b(x_2), \quad p = p(x_2), \quad y_1 = A_1(x_2)x_1, \tag{62}$$

where Z is any unknown function, and the co-ordinate x_2 is a parameter. Then in zero approximation system (61) yields

$$T_{11} = 0, \quad T_{12} = 0, \quad Q_1 = 0, \quad M_{11} = 0, \quad M_{12} + Q_2 = 0. \tag{63}$$

System (63) is a linear system with respect to $u_1^b, u_2^b, w^b, \gamma_1^b, \gamma_2^b$ with the coefficients depending on p and the elements of matrices $\mathbf{A}$, $\mathbf{B}$, $\mathbf{C}$. The determinant of this system has the form $\Delta(p) = p^8(ap^2 - b)$. Its non-zero roots $p = \pm\sqrt{b/a}$ correspond to the boundary layer. Notice that the boundary layer in zero approximation does not depend on the curvatures k_1, k_2, and therefore the boundary layer for a shell is same as for a plate.

To illustrate the influence of the boundary layer on the boundary conditions we study the clamped edge $x_1 = x_1^0$ and write the boundary conditions in the form

$$u_i^m + Cu_i^b = 0, \quad \varphi_i^m + C\varphi_i^b = 0, \quad i = 1, 2, \qquad w^m + Cw^b = 0, \tag{64}$$

where index ^{m} corresponds to the solution of system (32) (which we call the main solution), and the constant C is to be chosen to exclude the boundary layer. It follows from estimates (30) and (31) that $C \sim h^{1/2}$. Then $|Cw^b| \ll |w^m|$ and the orders of summands in the rest equations (64) are equal to each other. Then (for example) $C = -\varphi_2^m/\varphi_2^b$, and four boundary conditions for system (51) are

$$u_i^m + C\varphi_2^m = 0, \ i = 1, 2, \quad w^m = 0, \quad \varphi_1^m + C\varphi_2^m = 0. \tag{65}$$

The values Z^b are very unwieldy functions of the elements of matrices $\mathbf{A}$, $\mathbf{B}$, $\mathbf{C}$ and for this reason are not given here.

The previously discussed states 1–5 are described by the 2D model with the error which goes to zero at $h_* \to 0$. According to the estimate of the 2D shell theory [13,20]

$$\Delta \sim \max\{h_*, h_*^{2-2t}\}, \tag{66}$$

where t is the index of variability of studied SSS, the error Δ of the boundary layer, obtained from 2D model, is $\Delta \sim 1$. The boundary layer may be found only from the 3D equations. To construct the full 3D solution it is necessary to execute the asymptotic matching of the boundary layer and of the interior solution. This problem is out of frames of the presented paper. Our aim is to find the correct interior SSS. The governing system (19) contains the (inexact) boundary layer, and in its simplifications 1-5 the boundary layer is excluded. The problem is to formulate 4 boundary conditions at the shell edges by excluding the boundary layer. Remind that the well known condition $Q_1 + \partial M_{12}/\partial x_2 = 0$ in the KL theory my be delivered from the TR theory by excluding the boundary layer.

13 CONCLUSIONS

By using the cinematic hypothesis (7) the 2D model of thin elastic shell made of an anisotropic material described by 21 elastic moduli is delivered. The obtained system is comparatively new and insufficiently studies. Here we are restricted with the asymptotic analysis of the case when all elastic moduli in the elasticity relations (3) are of the identical orders. It would be interesting

to investigate the case when the moduli in the transversal directions are much smaller than in the tangential directions. It would be interesting to study the various boundary conditions and solve the problem of excluding from them the boundary layer, and as a result to reduce the system of 10th order to the system of 8th order. Also it would be interesting to study the buckling problems for this anisotropic material and to compare the results with the case of the isotropic material.

Acknowledgements. The paper is written with the financial support of Russian Foundation of Basic Researches, grants 12.01.92000.HHC-a, and 10-01.00244a.

REFERENCES

[1] S.P. Timoshenko, *Strength of materials*. Van Vistrand, New York, 1956.

[2] L.H. Donnell, *Beams, Plates and Shells*. McGraw Hill, 1976.

[3] S.A. Ambartsumjan, *General theory of anisotropic shells*. Nauka, Moscow, 1974.

[4] W. Pietraszkiewicz, *Finite Rotations and Lagrangian Description in the Nonlinear Theory of Shells*. Polish Scientific Publishers, Warszawa, Poznan, 1979.

[5] V.A. Rodionova, B.F. Titaev, K.F. Chernykh, *Applied theory of anisotropic plates and shells*. St.Petersburg Univ. Press, 1996.

[6] L.A. Agalovjan, *Asymptotic theory of anisotropic plates and shells*. Nauka, Moscow, 1997.

[7] P.E. Tovstik, *On the asymptotic character of approximate models of beams, plates and shells*. Vestnik St.Petersburg Univ. Mathematics. Allerton Press. N 3, 49–54, 2007.

[8] P.E. Tovstik, T.P. Tovstik, *On the 2D models of plates and shells including the shear*. ZAMM. **87**. No 2. 160–171, 2007.

[9] V.A. Shachnev, *Bending equation for a quasianisotropic plate*. Mechanics of Solids. Vol. 45, Issue 5, 712–723, 2010.

[10] P.E. Tovstik, T.P. Tovstik, *Two-dimensional models of plates made of an anisotropic material. In "Computer methods in mechanics of continuous media"*. Issue 3. St. Petersburg Univ. Press, 4–16, 2008.

[11] P.E. Tovstik, *Two-dimensional models of plates made of an anisotropic material*. Doklady Physics. Vol. 54. No 4, 205–209, 2009.

[12] P.E. Tovstik, T.P. Tovstik, *One-dimensional models of a beam made of an anisotropic material with oblique anisotropy*. Mechanics of Solids. Vol. 46, Issue 6, 888–897, 2011.

[13] A.L. Goldenweizer, V.B. Lidsky, P.E. Tovstik, *Free vibrations of thin elastic shells*. Nauka, Moscow, 1979.

[14] A.L. Goldenweizer, *Theory of Elastic Thin Shells*. Nauka, Moscow, 1976.

[15] V.V. Novozhilov, *Theory of Thin Shells*. Leningrad, Sudpromgiz, 1962.

[16] V.V. Bolotin, *On the density of natural frequencies of thin shells of revolution*. Appl. math. mech. Vol. 27(2), 362–364, 1963.

[17] P.E. Tovstik, *On the density of natural frequencies of thin elastic shells*. Appl. math. mech. Vol. 36(2), 290–300, 1972.

[18] P.E. Tovstik, A.L. Smirnov, *Asymptotic methods in the buckling theory of thin shells*. World scientific. Singapore, New Jersey, London, Hong Kong, 2002.

[19] S.P. Timoshenko, *Vibration Problems in Engineering*. D. Van Norstrand Co. INC. Toronto, New York, London, 1955.

[20] W.T. Koiter, *On the nonlinear theory of thin elastic shells*. Proc. Koninkl.Nederl. Acad. Westenchap. Vol. 69, pp. 1-56, 1966.

COMPDYN 2013
4th ECCOMAS Thematic Conference on
Computational Methods in Structural Dynamics and Earthquake Engineering
M. Papadrakakis, N.D.Lagaros, V. Plevris (eds.)
Kos Island, Greece, 12–14 June 2013

AN EFFICIENT NUMERICAL APPROACH FOR THE PARAMETRIC INVESTIGATION OF THE EFFECTS OF POUNDING ON THE 3D DYNAMIC RESPONSE OF BUILDINGS DURING EARTHQUAKES

Panayiotis C. Polycarpou[1] and Petros Komodromos[2]

Department of Civil and Environmental Engineering, University of Cyprus
75 Kallipoleos Str., P.O. Box 20537, 1678 Nicosia, Cyprus

[1]ppanikos@ucy.ac.cy, [2]komodromos@ucy.ac.cy

Keywords: Pounding, three-dimensions, torsional effects, earthquake, impacts, adjacent buildings.

Abstract. *This paper presents a new methodology that is used to numerically simulate buildings in three-dimensions, which are subjected to pounding during strong earthquakes. The structures are modeled as 3D MDOF dynamic systems, while an innovative, simple and efficient approach is used to model impacts, taking into account the geometry at the vicinity of impact and without the use of any contact elements that require the "a priori" determination of the impact location. A simple example of two adjacent buildings that are subjected to pounding is also presented, along with some parametric investigation of the effects of certain factors on the 3D dynamic response of the buildings during pounding incidences.*

1 INTRODUCTION

The problem of structural pounding of adjacent buildings during strong earthquakes has shown great interest in the last decades, since significant numbers of pounding occurrences have been recorded during past seismic events worldwide [1-4]. An example of such pounding incident is shown in Figure 1 as has been identified by the EERI/PEER reconnaissance team after the L'Aquila Earthquake, which hit Central Italy on April 2009 [5]. Several numerical studies have been performed in order to investigate the effects of earthquake induced pounding of buildings, with the majority of researchers simulating the problem in two dimensions (2D) [6-8]. The results from the various 2D parametric studies have demonstrated the detrimental effects of pounding on the dynamic response of multistory buildings and showed the importance of this problem regarding the safety and functionality of these structures. Studies have also revealed the consequences of structural pounding on the dynamic response of seismically isolated buildings, which exhibit quite different dynamic characteristics from fixed-supported buildings [9-11]. Actually in the case of seismically isolated buildings the problem of the amplification of the response due to pounding is considered to be more serious since it is more likely to have more demanding performance requirements and higher expectations than for conventionally fixed-supported buildings. However, as mentioned above, the great majority of past numerical studies involved only 2D simulations of buildings, especially in the case of seismically isolated buildings, while almost no parametric investigation of pounding effect has been conducted using three-dimensional (3D) simulations.



Figure 1: Damage of a four-story conventional building due to pounding with its adjacent two-story building, during the L'Aquila earthquake in Italy, in April 2009 [5].

Although some basic effects of pounding on the dynamic response of buildings can be identified using 2D simulations, other factors that are directly related to the spatial movement of the structures are excluded due to this simplification. Specifically, the fact of using both orthogonal seismic components of the excitation in the case of 3D simulations has a significant effect on the overall response of the building, compared to the corresponding unidirectional excitation in the 2D models. In addition, in 2D simulations involving structural pounding, the impacts are considered to be central, without any friction developed in the tangential direction. In a real case of pounding between adjacent buildings, friction phenomena

occur during an impact, which in the case of a 3D analysis may significantly affect the torsional vibration of the buildings. Furthermore, any eccentricities, irregularities or asymmetries in plan, which may excite the torsional vibration of a building and increase the possibility of impacts during earthquakes, are essential parameters that can be considered only through a 3D analysis. The aim of the current research work is to present an efficient methodology that enables the parametric investigation of the effects of such factors on the 3D response of both conventional & seismically isolated buildings, utilizing a software application that has been specifically developed for this cause, using modern Object-Oriented Programming (OOP).

2 MODELING OF STRUCTURES

The proposed methodology considers buildings as three-dimensional multi-degree-of-freedom (MDOF) systems with shear-type behavior for their stories in the horizontal direction. The slab at each floor level is represented by a rigid diaphragm that is mathematically simulated as a convex polygon, while the masses are considered to be lumped at the floor levels, having three dynamic degrees of freedom (DOFs), i.e. two translational, parallel to the horizontal global axes, and one rotational along the vertical axis (Figure 2). Therefore, considering ground excitations only in the horizontal directions, which is the most important in the current case, no displacement occurs in the vertical direction, since the translational dynamic DOF of the structure refer only to horizontal planes. Accordingly, it is assumed that the impact forces occur only in horizontal planes.

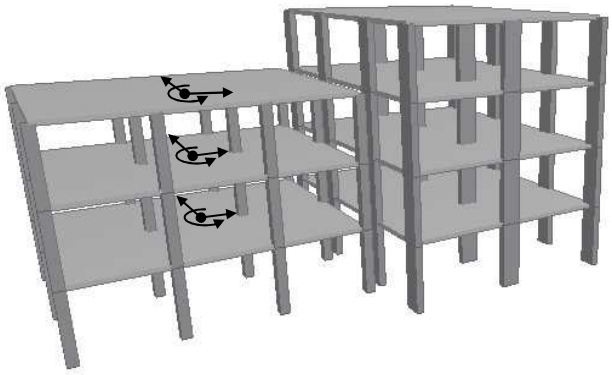


Figure 2: Three-dimensional modeling of adjacent buildings.

Both linear elastic and non-linear inelastic behavior can be considered for the columns of the simulated buildings, while, in the case of seismically isolated buildings, a bilinear inelastic behavior is used for the seismic isolation system. In the case of a linear elastic system, the $3N \times 3N$ global stiffness matrix is composed based on the 3×3 stiffness matrices of the N floors of the building, which are, in turn, composed by superposing the 3×3 stiffness matrices of the floor's columns. The corresponding $3N \times 3N$ damping matrix of the system is computed using the Rayleigh method, based on providing two damping ratios ζ_i and ζ_j for two eigenfrequencies of the system ω_i and ω_j [12]. All matrices are transposed to global coordinates.

The equations of motion of the system can be expressed in matrix form as follows:

$$\bar{M} \cdot \underline{\ddot{U}}(t) + \bar{C} \cdot \underline{\dot{U}}(t) + \bar{K} \cdot \underline{U}(t) + \bar{F}_{imp} = -\bar{M} \cdot \left[\bar{I}_L \cdot \ddot{u}_g^L(t) + \bar{I}_T \cdot \ddot{u}_g^T(t) \right] \quad (1)$$

where $\underline{U}(t)$ is the vector of displacements in global coordinates at time *t*, $\overline{F}_{imp}$ is the vector of the computed impact forces, acting on each DOF, $\overline{I}_L$ and $\overline{I}_T$ are the influence vectors coupling the DOFs of the structure to the two ground motion components $\ddot{u}_g^L(t)$ and $\ddot{u}_g^T(t)$ in the longitudinal and transverse directions, respectively. In particular, the influence vectors for the two horizontal components are provided by the following expressions:

$$\begin{matrix} \overline{I}_L = I_X \cdot \cos\theta + I_Y \cdot \sin\theta \\ \overline{I}_T = -I_X \cdot \sin\theta + I_Y \cdot \cos\theta \end{matrix} \text{, where } I_X = \begin{bmatrix} 1 & 0 & 0 \end{bmatrix}^T \text{ and } I_Y = \begin{bmatrix} 0 & 1 & 0 \end{bmatrix}^T \quad (2)$$

θ is the excitation angle in respect to the system's principle axes.

The differential equations are directly integrated using the Central Difference Method (CDM), computing the displacements at time $t+\Delta t$. At each time-step of the analysis the algorithm performs a check for detecting potential impacts, based on the deformed position of each floor diaphragm in space. For this reason the time-step size, Δt, is selected to be small enough (usually in the range of *1* to 2×10^{-5} sec) to ensure the stability and maximize the accuracy of the method. When an impact is detected, the resulting impact forces are computed according to the impact model and the methodology that is presented in the next section.

3 EXISTING KNOWLEDGE ON IMPACT MODELLING

The numerical modeling of impact and the estimation of the impact forces acting on the colliding bodies is an essential topic, not only for the cases of structural poundings, but also for other research purposes involving numerical simulation of contact and impact problems. In most cases, impacts involve local plastic deformations, friction, thermal, acoustic and other complex phenomena that render their detailed modeling very difficult, if not impossible. However, in the case of structural poundings, a simple impact model that can be used to estimate with sufficient accuracy the impact forces acting on the colliding structures is only needed. Usually, in numerically simulated dynamic systems, such as multistory buildings under earthquake excitations, structural impact is considered using force-based methods, also known as "penalty" methods. These methods allow relatively small interpenetration between the colliding structures, which can be justified by the local deformability at the point of impact. The interpenetration depth is used along with an impact-stiffness coefficient, representing an impact spring, to calculate the impact forces that act on the colliding structures, pushing them apart.

In 2D simulations involving structural pounding, the impacts are considered to be central, i.e. without frictional forces developed in the tangential direction. However, as mentioned above, in a real case of poundings between adjacent buildings, frictional phenomena occur during an impact, which may significantly affect the torsional response of the simulated buildings. Therefore, in the case of simulating impacts in 3D, a quite different approach should be followed, since during the overlapping of the two colliding bodies an area is formed instead of an indentation depth. In addition, the frictional forces in the tangential direction of the contact surface, which are omitted in the case of 2D analyses, must also be taken into account. Therefore, in the frame of the proposed methodology, an effective and efficient approach for modeling 3D impacts needs to be developed and implemented in the specially developed software application to simulate structural pounding.

In general, very limited numerical studies in the literature have considered pounding of fixed-supported structures in three dimensions (3D), mainly due to the involved complexities. A summary of the conducting research on 3D impact modeling, considering the advantageous 'penalty' method is presented in the following paragraphs.

Fujino et al [13] have presented a 3D impact model that they have used in simulations of earthquake induced pounding of bridges' segments [14] and which is quite similar to that used by Goyal et al [15] who simulated the contact between distinct rigid bodies. In particular, Fujino et al considered the case of a point of the impacting body hitting against the target surface. The impact model is constituted by an impact spring in the direction of impact and two dashpots in the normal and tangential directions of the target surface. The direction of impact is defined by two nodes, which are the contactor node and the initial point of impact, respectively. The impact force, which is calculated, based on the spring's stiffness and the interpenetration depth (distance between the two nodes) is analyzed in normal and tangential components to the target surface, with the tangential force representing the friction following the Coulomb's friction law.

Following a similar approach, Guo et al [16] have examined, both experimentally and analytically the problem of earthquake induced pounding in bridges, considering also the case of point-to-surface pounding, which was represented in the simulations by using a modified contact-friction element. In particular, based on the rotation and displacements of the centre of masses of each of the colliding rigid bodies, the point of impact is located when overlapping occurs and the impact force, which is composed by the normal and tangential (frictional) force components, is calculated as a function of the relative displacements in the normal and tangential directions. The impact parameters (stiffness and damping) used in the performed analyses were defined through experiments.

A similar methodology has been followed by Wei et al [17] to represent the case of a single mass tower, pounding against a rigid barrier under sinusoidal excitations. However in that case, no tangential or frictional forces were taken into account. The same practice of omitting the tangential contact forces was followed by Gong and Hao [18] when they parametrically examined the lateral-torsional-pounding responses of two single-storey systems due to an earthquake excitation.

4 PROPOSED IMPACT MODEL

As described in previous paragraphs, the majority of the force-based impact models calculate the impact force as a function of the interpenetration depth between the colliding bodies. However, this approach has a significant drawback in the case of 3D impact modeling. Specifically, this approach assumes that the calculated impact force depends only on the indentation and not the geometry at the contact region. This would be true if the later was taken into account for the calculation of impact stiffness at each time-step based on the deformed position of the colliding structures, but at least for the presented studies that was not the case. Therefore, based on this observation, it is crucial and more appropriate to take into account the area of the overlapping region instead of the interpenetration depth in the calculation of the impact force, since it is widely accepted that the impact stiffness depends on the geometry at the contact region [19].

Figure 3 describes schematically how the proposed impact model works. In particular, when two polygons, representing the buildings' slabs, come in contact they form an overlapping region which in the most of the cases is either a triangle (Case A) or a quadrilateral (Case B). The algorithm uses the geometry of the overlapping region at each time-step in order to determine: (i) the location of the action point of the impact forces, (ii) the direction of the impact forces and (iii) the magnitude of the impact forces.

4.1 Location of the action point of the impact force

As will be shown later in this paper, the location of the action point of the impact forces is a very important issue in the case of simulating poundings of buildings in 3D. While in the case of 1D impact models the location of the resultant force vector clearly is at the point of contact, in the case where contact conditions exist over a finite surface area on both bodies, the exact point where the contact force should be applied is not so obvious. For the specific problem of modeling impact between rigid diaphragms, the contact forces in the normal and tangential directions are assumed to act on the centroid of the overlapping region, and applied at the corresponding position of the bodies in contact.

4.2 Direction of the impact forces (contact plane)

For the proposed impact model, it is also necessary to determine the normal and tangential contact directions in order to be able to properly apply the corresponding normal and tangential impact forces as well as the Coulomb's Law of Friction. Taking into account the assumptions of the current problem and specifically the considered case of colliding diaphragms (rigid plates) of constant thickness the contact plane is actually a line. So, the contact plane is assumed to pass through the centroid *C* of the overlapping region and to be parallel to the line that is determined by the two nodes *P1* and *P2* of intersection between the boundaries of the two colliding bodies (Figure 3). The methodology that is used defines a normal and a tangential direction in such a way to assure that no directional jump occurs, between two sequential time-steps of the analysis. Specifically, the contact plane smoothly changes direction, while the overlapping contact area changes from triangular to quadrilateral and vice-versa.

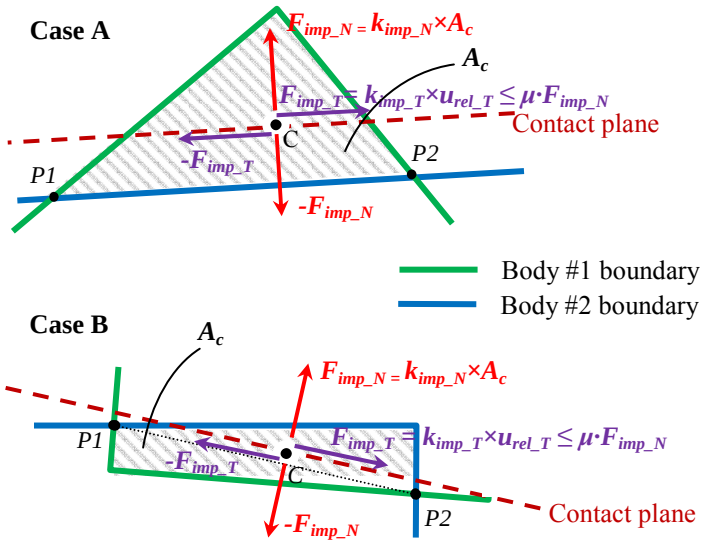


Figure 3: Schematic representation of the proposed impact model

4.3 Calculation of the impact forces

As mentioned in previous, in the proposed impact model the stiffness of the impact spring is used along with the area (A_c) of the overlapping region to calculate the elastic impact force. Since the impact response differs between the normal and tangential directions, two different equations are needed to calculate the normal and tangential elastic impact forces, respectively, at each iteration time step:

$$^{(t+\Delta t)}F_{imp,N} = {}^{(t)}A_c \cdot k_{imp,N} \tag{3}$$

$$^{(t+\Delta t)}F_{imp,T} = {}^{(t)}F_{imp,T} + {}^{(t)}u_{rel,T} \cdot k_{imp,T} \tag{4}$$

The indices N and T in the above equations indicate the normal and the tangential directions, respectively, as indicated in Figure 2. $k_{imp,N}$ (in kN/m^2) and $k_{imp,T}$ (in kN/m) are the impact stiffness coefficients in the normal and tangential directions, respectively. A_c is the area of the contact region and $u_{rel,T}$ is the relative displacement along the tangential direction. The time instance $(t+\Delta t)$ represents the current time-step, since the Central Difference integration method is used, while (t) represents the previous time-step.

The Coulomb friction law is used to limit the tangential impact force below a certain magnitude taking into account the magnitude of the normal impact force and the static and kinetic friction coefficients of the contact surface:

$$\begin{aligned} &\text{If } \left|{}^{(t+\Delta t)}F_{imp,T}\right| \le \left|{}^{(t+\Delta t)}F_{imp,N} \cdot \mu_s\right| \quad \rightarrow \quad \text{use Equation (4)} \\ &\text{If } \left|{}^{(t+\Delta t)}F_{imp,T}\right| > \left|{}^{(t+\Delta t)}F_{imp,N} \cdot \mu_s\right| \quad \rightarrow \quad {}^{(t+\Delta t)}F_{imp,T} = {}^{(t+\Delta t)}F_{imp,N} \cdot \mu_k \end{aligned} \tag{5}$$

where μ_s and μ_k are the static and kinetic friction coefficients, which are applied in the 'stick' and 'slide' mode of contact, respectively.

As in the case of 1D impact models, a viscous dashpot can be used, in parallel with the impact spring to represent the dissipation of energy during impact (e.g. thermal and acoustic energy) and along with the relative velocity of the bodies in contact can provide the damping impact force. However, for simplicity, in the frames of the current paper only the elastic impact forces are considered in the performed simulations, saving the details for the description of the corresponding viscoelastic impact model and the methods of determining the damping coefficients for future publications.

4.4 Impact stiffness coefficients

The estimation of the impact parameters, i.e. the impact stiffness and impact damping coefficients is a common difficulty when using forced-based impact models and it is often considered one of the major disadvantages of this method. Nevertheless, several numerical studies in 2D showed that in the case of simulating the problem of earthquake induced pounding of adjacent buildings, the values of the impact parameters slightly affect the overall structural response, besides of the acceleration at the impacting floor [9]. In the frames of the current study, a simple approximation is followed in order to determine a reasonable value for the impact stiffness and impact damping in both normal and tangential directions of the contact plane.

As it is well known the impact stiffness value depends mainly on the material characteristics of the colliding structures and the geometry at the vicinity of contact. If we assume that the contact geometry is taken into account with the use of the area of the overlapping region instead of the indentation depth, then the impact stiffness should be directly related to the moduli of elasticity of the colliding bodies. Based on fundamental theories of contact mechanics [19, 20], it is assumed that the normal impact stiffness value can be approximated as follows:

$$k_{imp,N} = \left[\frac{1-\nu_1^2}{E_{Dyn,1}} + \frac{1-\nu_2^2}{E_{Dyn,2}}\right]^{-1} \tag{6}$$

where $$E_{Dyn,i} = 5.82 \cdot \left(E_{St,i}\right)^{0.63}, \text{ in } GPa \quad (7)$$

is the dynamic elastic modulus for normal strength concrete as has been determined through relevant experiments [21], expressed in terms of the static elastic modulus E_{st} and v_i is the Poisson's ratio for the material of body i. In a similar manner, the tangential impact stiffness is approximated using the shear moduli of the materials of the colliding bodies:

$$k_{imp,T} = \left[\frac{2-\nu_1}{G_{Dyn,2}} + \frac{1-\nu_2}{G_{Dyn,2}}\right]^{-1} \quad (8)$$

where $$G_{i,Dyn} = \frac{E_{i,Dyn}}{2\left(1+\nu_i\right)} \quad (9)$$

The above methodology of predicting the impact stiffness coefficients is based on the assumption that the materials of the colliding bodies maintain an elastic behavior during impacts. However, during pounding the colliding structures, especially in the case of concrete structures, experience local damage, exhibiting highly non-elastic behavior at the vicinity of impact. Therefore, the impact stiffness is not actually constant but gradually decreases during impact due to the local plastic damage of the structures. Probably, it would be more appropriate to use a smaller equivalent impact stiffness value in order to take into account this local inelastic behavior of concrete. Having all that in mind, during this research study we will examine the effect of the magnitude of the impact stiffness value in order to evaluate how important is to predict a representative value for this parameter. The same approach has been followed in the case of studying the effects of pounding in 2D and was found that the specific parameter determines the magnitude of the impact force and affects mainly the acceleration response at the pounding floors.

5 DEVELOPED SOFTWARE

Considering the specific needs and demands of this numerical problem, as well as the limited flexibility and efficiency of the available general-purpose commercial software applications, the primary aim of the current research has been the development of a suitable software application in order to implement the presented methodology. In particular, the specially developed software application enables the effective and efficient performance of 3D numerical simulations and parametric analyses of both fixed-supported and seismically isolated buildings with contact detection capabilities, which allow the automatic consideration of structural poundings. Modern object-oriented design and programming approaches are utilized and the Java programming language and relevant technologies are employed in the development of the software application, taking into account the significant advantages that these technologies offer.

A significant advantage of the specially developed software is that it provides the desired flexibility, maintainability and extensibility in order to fulfill the needs of the proposed, while also facilitating extensions to accomplish future research plans. Moreover, a robust Graphical User Interface (GUI) with various capabilities has been designed and implemented, using the Java Swing API, to facilitate the effective performance of simulations and parametric analyses (Figure 4). The developed software allows the input data to be either imported from input files or specified using the GUI, while the computed results can be exported in output files or used to generate and store plots and animations in vector formats.

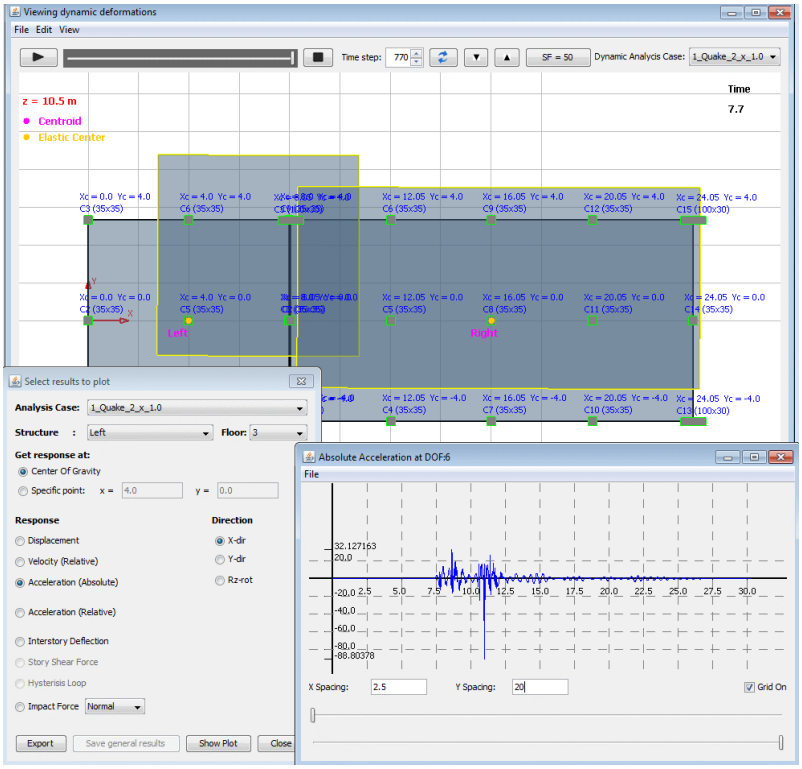


Figure 4. Typical view of Graphical User Interface of the developed software application

6 EXAMPLE APPLICATION

In order to demonstrate the capabilities of the methodology and the developed software application, as well as some of the basic effects of pounding on the 3D response of buildings, a representative example of colliding adjacent buildings is presented. In particular, two regular and symmetric reinforced concrete buildings of three and four stories, respectively, were selected for this example. Although the methodology supports the simulation of more complicate structures with irregularities both in plan and height, the selection of the particular buildings has been made in order to more easily identify the effects of the various parameters on the response during pounding.

The side view and the typical floor-plans of the simulated adjacent buildings are illustrated in Figure 5. All the columns sections have dimensions 35×35 *cm* except from the corner columns of the right 3-story building C1, C3, C13 and C15 which have dimensions 100×30 cm. The elastic modulus of concrete has been taken equal to 21 *GPa* with a Poisson's ratio equal to 0.2. A uniformly distributed mass of 1000 kg/m^2 has been considered for all floors that resulted to a 64 *tons* concentrated floor mass for the left building and a 128 *tons* floor mass for the right building. A constant viscous damping ratio of 0.05 was considered for all modes for both buildings. The two horizontal components of the real seismic recording at the 0KJMA station during the 1995 Kobe earthquake were selected as excitation. The seismic gap d was taken to be equal to 5 *cm*. The normal impact stiffness was calculated using Eq. (6) and was found to be to be $k_{imp,N} = 2.06\times10^7$ kN/m^2, while the corresponding tangential impact stiffness $k_{imp,T} = 4.59\times10^6$ kN/m. The static and kinetic friction coefficients were taken to be μ_s = 0.8 and μ_k =0.6, respectively.

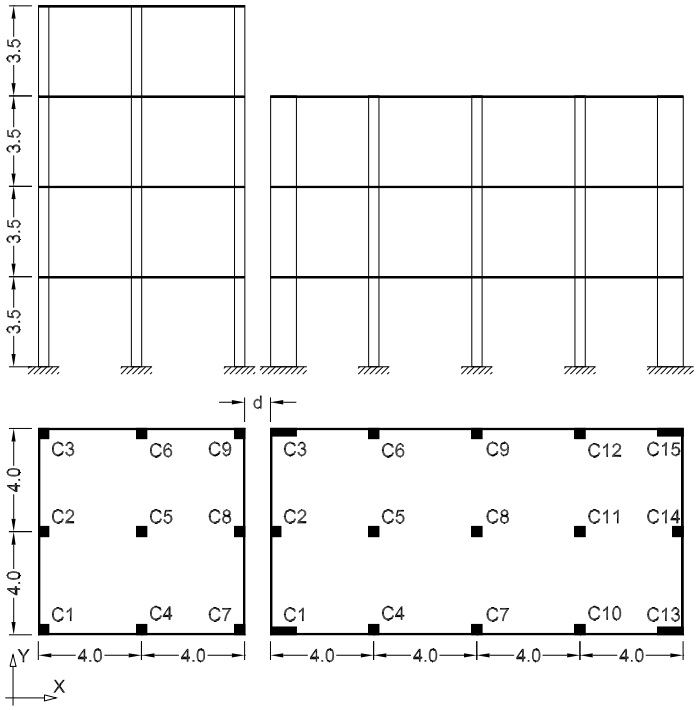


Figure 5. The side views and floor plans of the buildings considered in the presented example.

6.1 Effect of mass eccentricity

One of the parameters that can be examined through 3D simulations, in contrast to the case of modeling buildings as frames in 2D, is the accidental eccentricity of the floor mass. Many seismic codes demand the consideration of an accidental mass eccentricity when performing dynamic analysis of buildings. For example, Eurocode 8 suggests an eccentricity of the concentrated floor mass from its nominal location equal to 5% of the floor-dimension perpendicular to the direction of the seismic action. In order to examine the effects of this parameter on the response of the two above buildings during pounding, we simulated the structures using only the one of the two horizontal components of the Kobe seismic record (PGA=0.821g) and considering three cases regarding the position of the center of mass, with the possibility of pounding and two more cases without the consideration of any impacts. In particular, the following cases were considered:

- Case 1: the center of mass coincides with the floor's center of gravity for both buildings.
- Case 2: an eccentricity of 0.4 *m* is considered only for the left building.
- Case 3: both buildings have a 0.4 *m* eccentricity along Y axis but in opposite directions.
- Case 4: same as Case 1, but d = ∞ (no pounding).
- Case 5: same as Case 2, but d = ∞ (no pounding).

The horizontal interstory deflections at the corner-column C9 of the left building are compared for each case. The results, which are presented in the plots of Figure 6, indicate that by omitting the accidental mass eccentricity, following probably a 2D analysis (represented here by Case 1) leads to smaller deflections in the X-direction, while the deflections in the Y-direction and the torsion due to eccentricity are obviously omitted. In addition, it is observed that the deflections of the column in X-direction are reduced due to pounding for the first three stories, which are below the last impacting floor (3rd), but the corresponding deflection

at the top floor is significantly increased due to impact with the adjacent 3-story building. Finally, the deflections in Y-direction and the torsion of the column are substantially increased due to pounding in the case of taking into account the accidental eccentricity.

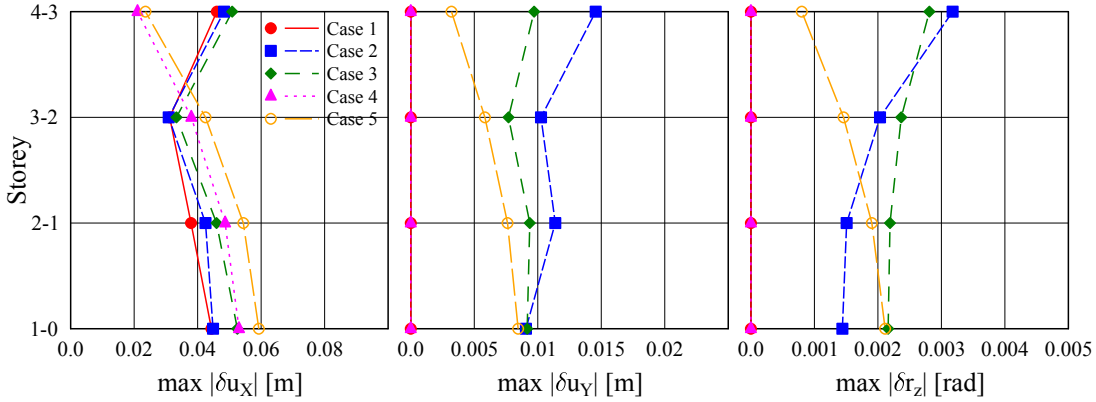


Figure 6. Peak absolute values of the deflections (two translational and one rotational) of the column C9 of the left building under the Kobe earthquake, for the five different cases regarding the mass eccentricity and the consideration of pounding.

6.2 Excitation with two orthogonal seismic components

Another aspect that cannot be examined in 2D simulations is the consideration of both horizontal components of the seismic action, which is obviously a more appropriate way to represent the real seismic event in numerical dynamic analyses of buildings. Therefore, the same buildings have been subjected to the longitudinal seismic record (PGA=0.821g) of Kobe 0KJMA along the X-axis and to the transversal seismic record (PGA=0.598g) along Y-axis. The results are compared with the two cases of having as excitation separately only one of the two components, which represents more or less the corresponding case of a 2D simulation. It is noted that in the case of the Y-only excitation no poundings occur. As previously, the deflections of column C9 of the left building are plotted for comparison in Figure 7 for the three cases. It is observed that the 2D simulations may provide a good approximation of the maximum deflections of the column in the two horizontal axes with negligible variations. However, the torsion that the column is subjected due to the rotational vibration of the building cannot be captured using single-component excitation and 2D analysis.

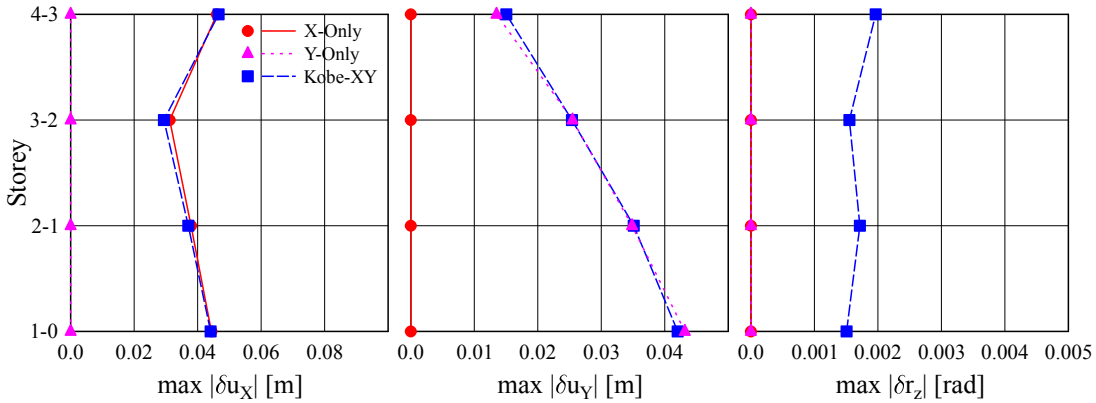


Figure 7. Peak absolute values of the deflections of the column C9 of the left building pounding against the right building under a single or both seismic components of the Kobe earthquake.

6.3 Effect of the excitation angle

Another ability that is provided through the presented methodology and the developed software application is the parametric investigation of the effect of the angle of the seismic excitation in respect to the global axes on the response of the adjacent buildings during pounding. The plots in Figure 8 present the maximum absolute values of the deflections of the column C9 of the left building during pounding, in terms of the excitation angle. For the analyses both seismic orthogonal components were used simultaneously. It becomes evident from the results that the direction of the excitation affects substantially the response during pounding and obviously is one important parameter that should be examine in more extent in future simulations and parametric studies in order to understand better the way it affects the response.

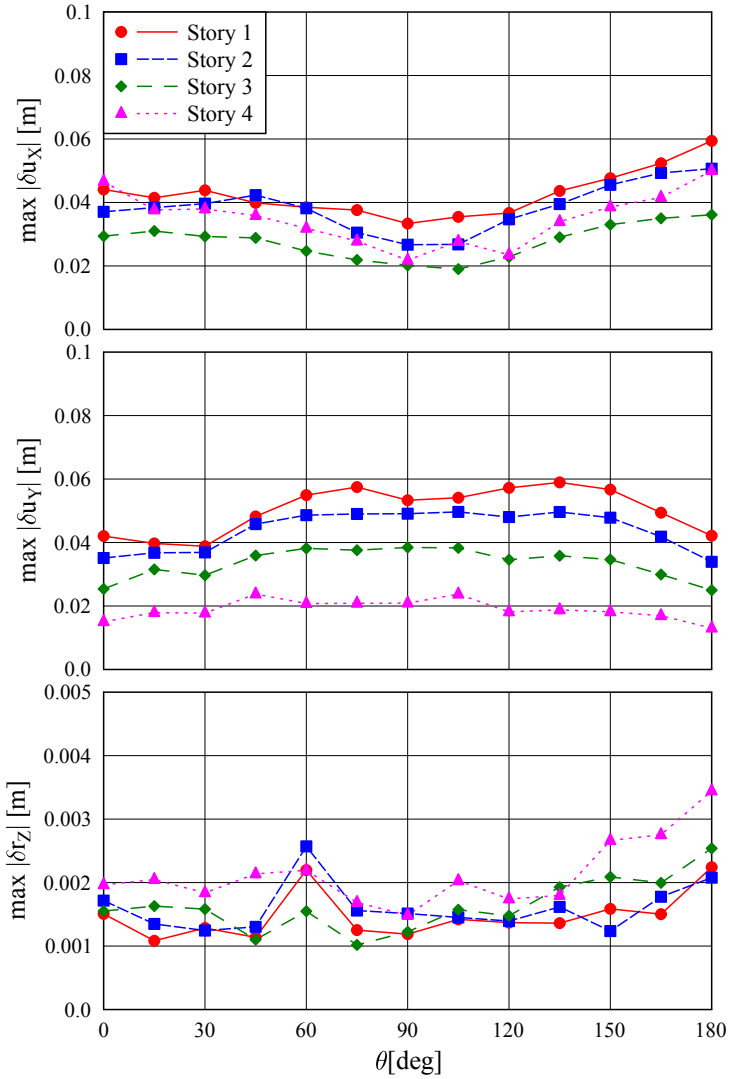


Figure 7. Peak absolute values of the deflections of the column C9 of the left building in terms of the excitation angle of the Kobe seismic record.

7 CONCLUSIONS

A new methodology for simulating earthquake induced pounding of buildings that are modeled as 3D-MDOF systems has been presented. Some significant disadvantages of the available impact models in the literature have led us to propose a new approach to the numerical problem of impact modeling. Specifically, following the 'penalty' method the impact

forces are calculated based on the area of the overlapping region, instead of the overlapping depth that is usually used in previous similar studies. This assumption takes into account the geometry at the vicinity of impact, a factor that was omitted in the case of using only the indentation depth. Another advantage of the proposed methodology is that the location of impacts is not known 'a priori' since the impact detection is based on the spatially arbitrary location of each of the rigid diaphragms that are at the same level. Therefore, there is no need for contact elements applied at certain locations of each diaphragm, which actually omit the location and the direction of the impact forces since in their majority such contact elements have only one dimension.

The methodology has been implemented in a specially developed software application that enables us to efficiently perform 3D dynamic analysis of buildings considering the case of pounding. In particular, the total time that is needed for a dynamic analysis such as the one described in the above example, which includes two buildings of four and three stories respectively, is about 50 sec, which is extremely fast compared to many other commercial FEM software applications. This efficiency provides the ability to easily perform large number of simulations in order to parametrically examine the effect of certain factors on the 3D response of buildings during earthquake induced pounding. A small example of such parametric investigation has been presented in the current paper. Nevertheless, more extensive investigation has to be performed in the future, in order to take into account more kinds of structures, different building arrangement, more earthquakes, and, in general, more other influencing factors that can be examined through 3D analyses.

ACKNOWLEDGEMENT

This work was carried out in the frames of the project with protocol number "ΔΙΔΑΚΤΩΡ/0609/39" which is co-funded by the European Regional Development Fund and the Republic of Cyprus through the Research Promotion Foundation.

REFERENCES

[1] S.A. Anagnostopoulos, Earthquake induced poundings: State of the art. *10th European Conference on Earthquake Engineering*, Duma (Ed.), Balkema, Rotterdam, 1995.

[2] V.V. Bertero, Observations on Structural Pounding. *Proceedings International Conference on Mexico Earthquakes*, ASCE, 264-278, 1987.

[3] Earthquake Engineering Research Institute (EERI), Loma Prieta Earthquake Reconnaissance Report, Rep. No. 90-01, Benuska, L., ed., EERI, Oakland, CA, 1990.

[4] Earthquake Engineering Research Institute (EERI), Kocaeli, Turkey, Earthquake of August 17, 1999 Reconnaissance Report, Publ. No. 00-03, Youd, T. L., Bardet, J-P., Bray, J. D., ed., EERI, Oakland, CA, 2000.

[5] Earthquake Engineering Research Institute (EERI), L'Aquila, Italy Earthquake Clearinghouse - Observations from-EERI/PEER team, 2009 (*http://www.eqclearinghouse.org/italy-090406/*).

[6] M. Papadrakakis and H. Mouzakis, Earthquake simulator testing of pounding between adjacent buildings. *Earthquake Engineering and Structural Dynamics*, **24**, 811–834, 1995.

[7] S.A. Anagnostopoulos, Pounding of buildings in series during earthquakes. *Earthquake Engineering and Structural Dynamics*, **16**, 443-456, 1988.

[8] Anagnostopoulos, S.A., Spiliopoulos, K.V. An investigation of earthquake induced pounding between adjacent buildings. *Earthquake Engineering and Structural Dynamics* 1992; **21**:289-302.

[9] P. Komodromos, P.C. Polycarpou, L. Papaloizou, MC. Phocas, Response of Seismically Isolated Buildings Considering Poundings. *Earthquake Engineering and Structural Dynamics*, **36**, 1605-1622, 2007.

[10] S. Mahmoud and R. Jankowski, Pounding-involved response of isolated and non-isolated buildings under earthquake excitation. *Earthquakes and Structures*; **1(3)**, 231-252, 2010.

[11] D.R. Pant, A.C. Wijeyewickrema, Structural performance of a base‐isolated reinforced concrete building subjected to seismic pounding. *Earthquake Engineering & Structural Dynamics*, **41(12)**, 1709–1716, 2012

[12] A.K. Chopra, *Dynamics of Structures: Theory and Applications to Earthquake Engineering*. (3rd Ed.) Prentice-Hall, Upper Saddle River, NJ, U.S.A., 2006.

[13] Fujino, Y., Abe, M. and Zhu, P. A 3D Contact-friction Model for Pounding at Bridges during Earthquakes. Earthquake Resisting Technologies for Civil Infrastructures. 3rd EQTAP Workshop, Nov. 28-30, Manila, Philippines, 2000.

[14] Zhu, P., Abe, M. and Fujino, Y. (2002) Modelling three-dimensional non-linear seismic performance of elevated bridges with emphasis on pounding of girders. Earthq. Eng. & Str. Dyn., 31:1891–1913.

[15] S. Goyal, E.N. Pinson and F.W. Sinden. Simulation of Dynamics of Interacting Rigid Bodies Including Friction II:Software System Design and Implementation. *Engineering with Computers*, **10**, 175-195, (1994)

[16] Guo, A., Li, Z. and Li, H. (2011). Point-to-Surface Pounding of Highway Bridges with Deck Rotation Subjected to Bi-Directional Earthquake Excitations. Journal of Earthquake Engineering, **15**, 274–302.

[17] Wei, X. X., Wang, L. X. and Chau, K.T. Nonlinear Seismic Torsional Pounding Between an Asymmetric Tower and a Barrier. Earthquake Spectra, **25(4)**, 899–925, 2009.

[18] Gong, L. and Hao, H. Analysis of Coupled Lateral-Torsional-Pounding Responses of One-Storey Asymmetric Adjacent Structures Subjected to Bi-Directional Ground Motions Part I: Uniform Ground Motion Input. Advances in Structural Engineering, **8(5),** 463-479, 2005.

[19] Goldsmith, W. *Impact: the theory and physical behaviour of colliding solids*, E. Arnold, London, UK, 1960.

[20] Johnson, K. L. *Contact mechanics*. Cambridge university press, 1987.

[21] M. Salman and H. Al-Amawee. The Ratio between Static and Dynamic Modulus of Elasticity in Normal and High Strength Concrete. Journal of Engineering and Development, **10 (2)**, 163-174, 2006.

COMPDYN 2013
4th ECCOMAS Thematic Conference on
Computational Methods in Structural Dynamics and Earthquake Engineering
M. Papadrakakis, V. Papadopoulos, V. Plevris (eds.)
Kos Island, Greece, 12–14 June 2013

PHENOMENOLOGICAL MODELING OF DEFORMATION OF POROUS AND CELLULAR MATERIALS TAKING INTO ACCOUNT THE INCREASE IN STIFFNESS BECAUSE OF THE COLLAPSE OF PORES

Vladimir M. Sadovskii, and Oxana V. Sadovskaya

Institute of Computational Modeling SB RAS
Akademgorodok 50/44, 660036 Krasnoyarsk, Russia
e-mail: {sadov,o_sadov}@icm.krasn.ru

Keywords: Cellular Material, Porous Metal, Expansion of Cavity, Incomplete Plasticity, Full Plasticity, Parallel Program System.

Abstract. *Mathematical model for the description of deformation of a porous material with a random distribution of pores is constructed on the basis of generalized rheological method taking into account the different resistance of a material to tension and compression. Phenomenological parameters of the model are determined by means of the approximate computations for the problem of static loading of a cubic periodicity cell with spherical cavities. Within the framework of this theory the fields of displacements and stresses around expanding cavity of spherical shape in a homogenious space are constructed. It is shown that the porosity does not change at the stage of elastic deformation. When the pressure increases, a zone of plastic compaction is formed in the vicinity of a cavity, and in a part of this zone the collapse of pores takes place. Engineering formulas for calculation of critical pressures of the elastic limit state and the limit state of a medium with open pores, and also the formulas for determining the radiuses of interfaces of zones of plasticity and compaction are obtained. A complex of parallel programs for numerical analysis of the dynamic deformation of porous materials on multiprocessor computer systems is worked out. By means of this complex a series of computations for deformation of the protection elements, made of metal foams, under the action of localized impulsive loads was performed. The random nature of distribution of the pores size is taken into account with the help of computer modeling. Computations allow one to estimate plastic dissipative part of the energy of impact.*

1 INTRODUCTION

A problem of modeling of porous and cellular materials has applications in many technical areas. One of these areas is related to the usage of porous metals (metal foams). Porous metals are new artificial materials, which can be widely used in engineering because of their low density and good damping properties [1]. The ability of porous metals to absorb the energy during plastic deformation opens prospect of their use for the production of car bumpers and the so-called "collapsible zones". They also can be applied in gearboxes and drives as destructible fuses, which dissipate the energy of dynamic impact, preventing the destruction of mechanical system.

At present the technologies of production of metal foams based on aluminum, copper, nickel, tin, zinc and other metals are well developed. According to the information published in Internet, professor A. Rabiei from the University of North Carolina (USA) in 2010 created a method of producing the most durable foam in the world. High strength of this material is achieved by ensuring that the surface of a thin-walled skeleton in the foam practically has no dislocations, i.e. defects that are initiators of the destruction. Extensive experimental researches of the mechanical properties of such materials are conducted. The diagrams of uniaxial tension and uniaxial compression on the example of an aluminum foam and of a porous copper were obtained in [2, 3]. The problems of durability and cyclic fatigue of porous metals are considered in [4], etc.

The main difficulties in mathematical modeling of the behavior of porous materials are related to the fact that their deformation properties are significantly different in tension and in compression, before and after the collapse of pores. In tension there are the stage of elastic deformation of a porous skeleton and the stage of plastic flow up to the fracture. In compression there are the stages of elastic and plastic deformation of a skeleton until the collapse of pores, and the subsequent stage of elastic or elastic-plastic deformation of a solid material without pores after the collapse. At small sizes of pores the collapse can occur on the elastic stage with the appearance of plasticity only under a sufficiently high level of load.

Theoretical questions of the constructing constitutive equations and of the analysis on this basis the spatial stress–strain state of structural elements of metal foams are poorly understood. At the level of physical and mechanical representations, the deformation of a metal foam is rather complex process. At high porosity the compression leads to elastic-plastic loss of stability of a metal skeleton, at low porosity the stable mechanism of collapse of pores is realized. The collapse is accompanied by a contact interaction of skeleton walls, which is difficult for modeling at the discrete level. Besides, it is necessary to consider the presence of compressed gas in closed pores. It is rather difficult to describe the process of shear when, according to experiments, the volume of a material changes. Even more difficult to construct a universal model of the spatial stress–strain state of a material under complex loading. The performance of adequate computations based on discrete models of a metal foam as a structurally inhomogeneous material is only possible with the use of multiprocessor systems with high productivity and large amount of random-access memory.

In this paper we construct a simple phenomenological model of a porous material, which takes into account the main qualitative and quantitative effects: a significant difference of diagrams of uniaxial deformation before and after the collapse of pores and a significant dissipation of energy at the stage of plastic flow of a material.

2 GOVERNING EQUATIONS

The porosity is defined as the ratio of the pore volume to the volume of a porous material: $\theta_0 = V_0/V$. If ρ denotes the density of a source (solid) metal then, ignoring the weight of the gas in the pores, the density of a porous metal can be calculated as follows: $\rho_0 = \rho\,(V - V_0)/V$. Therefore, $\theta_0 = (\rho - \rho_0)/\rho$. The volumetric strain of highly porous materials, caused by changing the volume of pores, is significantly higher than the volumetric strain of solid skeleton, hence, the pores disappear with the volumetric strain $\theta \approx ((V - V_0) - V))\,/V = -\theta_0$.

Rheological models of uniaxial stress–strain state of porous materials are constructed in [5]. A simple rheological scheme taking into account the main features of deformation of porous metals is shown in Fig. 1 *a*. The behavior of a material in tension and in compression before the collapse of pores is simulated by an elastic spring with the compliance modulus a, and the increase in stiffness after collapse is simulated by an additional spring with the compliance modulus b. A diagram of uniaxial tension–compression of a porous material is represented in Fig. 1 *b* as a two-segment broken line. Such scheme describes the elastic process that occurs without dissipation of mechanical energy.

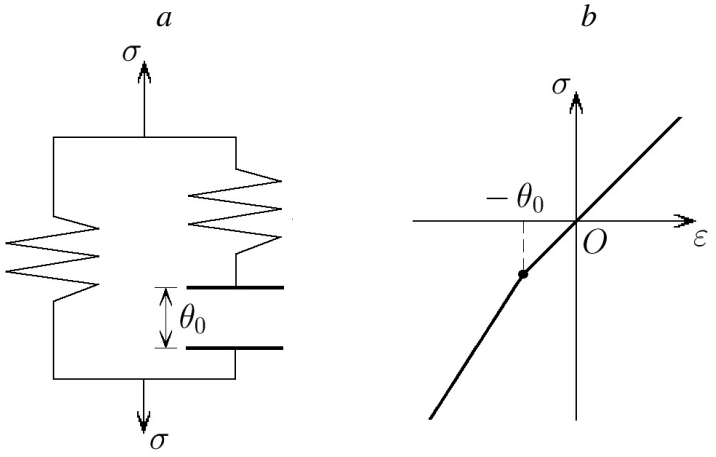


Figure 1: Rheological scheme (*a*) and diagram (*b*) of uniaxial elastic deformation.

More general rheological scheme with a plastic hinge is shown in Fig. 2 *a*. It is assumed that under the tensile stress σ_s^+ a sceleton goes into the state of plastic flow, and under the compressive stress $-\sigma_s^-$ the plastic loss of stability takes place. The stage of elastic-plastic deformation of a solid material after the collapse of pores is described by the rheological scheme of linear hardening. A diagram of uniaxial tension–compression is represented in Fig. 2 *b* as a four-segment broken line. In this model the specific dissipation of energy in the process of collapse can be evaluated by the product $\sigma_s^-\theta_0$.

In the case of spatial stress–strain state in accordance with rheological scheme in Fig. 2 the stress tensor σ is equal to the sum of the tensor σ^p of plastic stresses and the tensor σ^c of additional stresses, acting after the collapse of pores. Elastic compliance of a material is characterized by the fourth-rank tensors a and b, satisfying the usual conditions of symmetry and positive definiteness. Series connection of an elastic spring and a plastic hinge in the scheme corresponds to the Prandtl–Reuss theory of elastic-plastic flow. Constitutive relationships of this theory can be represented in the form of principle of maximum of the energy dissipation rate [5]:

$$(\tilde{\sigma} - \sigma^p) : (a : \dot{\sigma}^p - \dot{\varepsilon}) \geq 0, \qquad \tilde{\sigma},\ \sigma^p \in F. \tag{1}$$

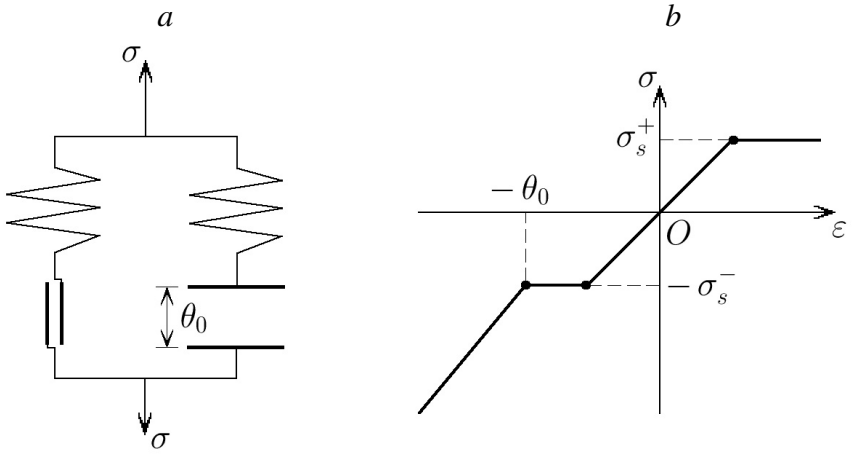


Figure 2: Rheological scheme (*a*) and diagram (*b*) of elastic-plastic deformation.

Here ε is the actual strain tensor, $\tilde{\sigma}$ is an arbitrary admissible variation of the stress, F is the convex set in the stress space, limited by the yield surface of a material. The conventional notations and operations of the tensor analysis are used: a colon denotes double convolution of tensors, a dot over a symbol denotes a derivative with respect to time.

The set F of admissible stresses is defined by means of the Tresca–Saint-Venant or von Mises yield condition. Assuming that the deformation of jumpers of a porous skeleton can be described by the rods model, this set can be approximated as follows:

$$F = \Big\{\sigma \;\Big|\; -\sigma_s^- \le \sigma_k \le \sigma_s^+,\;\; k = 1,2,3\Big\},$$

where σ_k are the principal values of the tensor σ.

Constitutive relationships of a rigid contact are formulated in the form of variational inequality [5]:

$$(\tilde{\sigma} - \sigma^c) : (\varepsilon^c + \varepsilon^0) \le 0, \qquad \tilde{\sigma},\ \sigma^c \in K. \tag{2}$$

Here $\varepsilon^c = \varepsilon - b : \sigma^c$ is the strain tensor of a porous skeleton, $\varepsilon^0 = \theta_0\,\delta/3$ is the spherical tensor of initial porosity (δ is the Kronecker delta), K is the convex cone in the stress space, which serves for modeling the transition from a porous state to a solid state of a material. Further K is the von Mises–Schleicher circular cone:

$$K = \Big\{\sigma \;\Big|\; \tau(\sigma) \le æ\, p(\sigma)\Big\},$$

where æ is the phenomenological parameter of dilatancy, $p(\sigma) = -\sigma : \delta/3$ is the hydrostatic pressure, $\tau(\sigma)$ is the intensity of tangential stresses, calculated via the deviator $\sigma' = \sigma + p(\sigma)\delta$ of stress tensor by the formula $\tau^2(\sigma) = \sigma' : \sigma'/2$.

The variational inequality (2) can be reduced to the next form:

$$(\tilde{\sigma} - \sigma^c) : b : (\sigma^c - s) \ge 0, \qquad \tilde{\sigma},\ \sigma^c \in K. \tag{3}$$

Here s is the conditional stress tensor, which is calculated by the law of linear elasticity taking into account initial strains, namely $b : s = \varepsilon + \varepsilon^0$. If this tensor is admissible, i.e. if $s \in K$, then by (3) the tensor σ^c is equal to s. If s is not admissible ($s \notin K$) and for any $\tilde{\sigma} \in K$ the inequality $\tilde{\sigma} : b : s \le 0$ is valid, which means that the sum $\varepsilon + \varepsilon^0$ of tensors belongs to the cone C of admissible strains, conjugate to K:

$$C = \Big\{\varepsilon \;\Big|\; \tilde{\sigma} : \varepsilon \le 0 \quad \forall\ \tilde{\sigma} \in K\Big\},$$

then $\sigma^c = 0$, as follows from (3). In the general case the variational inequality (3) allows to determine the tensor $\sigma^c = \pi_K(s)$ as the projection of s onto the cone K with respect to the Euclidean norm $|s| = \sqrt{s : b : s}$, and the considered above two variants are particular cases, when the projection coincides with the original tensor and when the projection is the vertex of the cone.

Third variant, when the projection belongs to the conical surface, is realized under the fulfillment of two conditions: $s \notin K$ and $\varepsilon + \varepsilon^0 \notin C$. For an isotropic material the elastic compliance tensor b is characterized by two independent parameters: the bulk modulus k and the shear modulus μ. Formulas for calculating the projection onto the conical surface are as follows [5]:

$$p(\sigma^c) = \frac{\mu\, p(s) + æ\, k\, \tau(s)}{\mu + æ^2 k}, \qquad (\sigma^c)' = æ\, p(s)\, \frac{s'}{\tau(s)}. \tag{4}$$

The cone C, conjugate to the von Mises–Schleicher cone, is defined as

$$C = \Big\{ \varepsilon \;\Big|\; æ\, \gamma(\varepsilon) \le \theta(\varepsilon) \Big\},$$

where $\theta(\varepsilon) = \varepsilon : \delta$ is the volumetric strain, $\gamma(\varepsilon) = \sqrt{2\, \varepsilon' : \varepsilon'}$ is the shear intensity. The condition $\varepsilon + \varepsilon^0 \in C$ means that a rigid contact in rheological scheme is open, i.e. that pores are in the open state. The limit condition of the collapse of pores $æ\, \gamma(\varepsilon) = \theta_0 + \theta(\varepsilon)$ describes the dilatancy of a porous material due to the shear deformation.

3 MATHEMATICAL MODEL

Mathematical model, describing the dynamic deformation of a porous material at small strains and rotations of elements, can be written in the form of the following system:

$$\begin{aligned} &\rho_0\, \dot v = \nabla \cdot \sigma + \rho_0\, f, \\ &(\tilde\sigma - \sigma^p) : (a : \dot\sigma^p - \nabla v) \ge 0, \qquad \tilde\sigma,\ \sigma^p \in F, \\ &b : \dot s = \frac{1}{2}\,(\nabla v + \nabla v^*), \qquad \sigma = \sigma^p + \pi_K(s). \end{aligned} \tag{5}$$

Here v is the velocity vector, f is the vector of body forces, ∇ is the vector of gradient with respect to spatial variables, the asterisk denotes transposition. This system consists of the equation of motion in vector form and the constitutive relationships, which follow from (1) and (2) taking into account the kinematic equation $2\,\dot\varepsilon = \nabla v + \nabla v^*$. The vector v and the tensors σ^p and s are unknown functions in this model.

Assuming $\tilde\sigma = 0$, one can derive from (5) the inequality of internal dissipation of energy:

$$\frac{1}{2}\,\frac{d}{dt}\Big(\rho_0 |v|^2 + \sigma^p : a : \sigma^p + \pi_K(s) : b : \pi_K(s)\Big) \le \nabla \cdot (\sigma \cdot v) + \rho_0\, f \cdot v.$$

The left-hand side of this inequality is the rate of change of kinetic and potential energy, the right-hand side is the power of internal surface forces and active body forces. The difference between right-hand side and left-hand side is equal to the power of plastic dissipation of energy, which can not be negative in accordance with the principles of irreversible thermodynamics.

The initial conditions, describing the natural (unstressed) state of a material, are as follows:

$$v\,\Big|_{t=0} = 0, \qquad \sigma^p\,\Big|_{t=0} = 0, \qquad s\,\Big|_{t=0} = b^{-1} : \varepsilon^0. \tag{6}$$

The boundary conditions can be given in velocities or stresses:

$$v\,\Big|_{\Gamma} = v^0(x), \qquad \sigma\,\Big|_{\Gamma} \cdot \nu(x) = q(x),$$

where ν is the normal vector to the boundary, v^0 and q are given functions. Mathematical correctness of the boundary conditions follows from the integral estimates of the difference between two solutions. Let us assume that in some space–time domain two sufficiently smooth solution v, σ^p, s and $\bar{v}$, $\bar{\sigma}^p$, $\bar{s}$ of the system (5) are defined. Substituting $\tilde{\sigma} = \bar{\sigma}^p$ in the variational inequality of (5) and $\tilde{\sigma} = \sigma^p$ in a similar inequality, characterizing the second solution, after summation of the results one can obtain

$$(\bar{\sigma}^p - \sigma^p) : a : (\dot{\bar{\sigma}}^p - \dot{\sigma}^p) \le (\bar{\sigma}^p - \sigma^p) : \nabla(\bar{v} - v).$$

With the help of a standard procedure of scalar multiplication of the equations of motion by the velocity vectors it can be shown that

$$\begin{aligned} \rho_0\,(\bar{v} - v) \cdot (\dot{\bar{v}} - \dot{v}) + (\bar{\sigma}^p - \sigma^p) : a : (\dot{\bar{\sigma}}^p - \dot{\sigma}^p) + \\ + \Big(\pi_K(\bar{s}) - \pi_K(s)\Big) : b : (\dot{\bar{s}} - \dot{s}) \le \nabla \cdot \Big((\bar{\sigma} - \sigma) \cdot (\bar{v} - v)\Big). \end{aligned} \tag{7}$$

As a result of integration of the inequality (7) over the domain of the type of a truncated cone, a priori estimates are obtained, guaranteeing the uniqueness of solution and the continuous dependence on the initial data for the Cauchy problem and for the boundary-value problems with dissipative boundary conditions. For a more general situation such estimates were obtained in the monograph [5]. Dissipativity of boundary conditions in this case means that in each point of the boundary the inequality

$$(\bar{\sigma} - \sigma) \cdot \nu(x) \cdot (\bar{v} - v) \le 0$$

is fulfilled. This inequality holds automatically for the mentioned above main types of boundary conditions.

4 RADIAL EXPANSION OF CAVITIES

The problem of expansion of a cavity in an infinite medium under the action of internal pressure is of great practical importance for applications on different scale levels in aerospace, marine and oil industries, in geomechanics and geodynamics. In classical formulation for isotropic and homogeneous continuum this problem was solved in [6, 7]. The problem for a porous medium has particular importance in the petroleum geophysics. Increasing the pressure in the well leads to the compression and collapse of pores, which impedes the filtration flow near the surface of the well until complete closing of hydrocarbons in a rock mass. In practice, it is important to estimate the size of the blocking zone as a function of pressure for given mechanical parameters of a geomaterial.

Let us describe the expansion of a cavity of the radius r_0 in an infinite porous space under the action of slowly increasing pressure p_0 in the framework of suggested model. In the case of spherical symmetry at elastic stage of the process the following system of equations is valid:

$$\begin{aligned} \frac{d\sigma_r}{dr} + 2\,\frac{\sigma_r - \sigma_\varphi}{r} = 0, \qquad \varepsilon_r = \frac{du_r}{dr}, \qquad \varepsilon_\varphi = \frac{u_r}{r}, \\ \sigma_r + 2\,\sigma_\varphi = 3\,k\,(\varepsilon_r + 2\,\varepsilon_\varphi), \qquad \sigma_\varphi - \sigma_r = 2\,\mu\,(\varepsilon_\varphi - \varepsilon_r). \end{aligned} \tag{8}$$

The solution of (8), satisfying the boundary condition on the surface of a cavity, is given by the formulas:

$$\sigma_r = -2\,\sigma_\varphi = -p_0\Big(\frac{r_0}{r}\Big)^3, \qquad u_r = \frac{p_0\,r_0^3}{4\,\mu\,r^2}. \tag{9}$$

The elastic state is realized up to the limit pressure $p_s = 4\,\tau_s/3$, determined by the Treska–Saint-Venant yield condition (τ_s is the yield point of a porous material under shear):

$$\sigma_\varphi - \sigma_r = 2\,\tau_s. \tag{10}$$

The plastic stage is described by a system which is obtained from (8) by replacing the last equation on the equation (10). From this system one can find

$$\sigma_r = -p_0 + 4\,\tau_s \ln\frac{r}{r_0}, \qquad \sigma_\varphi = 2\,\tau_s + \sigma_r. \tag{11}$$

The displacement in a plastic zone is determined from the equation of elastic change in volume

$$\frac{k}{r^2}\,\frac{d(r^2\,u_r)}{dr} = \frac{\sigma_r + 2\,\sigma_\varphi}{3} = \sigma_r + p_s,$$

the integration of which gives

$$3\,k\,u_r = -p_0\,r + 4\,\tau_s\,r\ln\frac{r}{r_0} + \frac{C_1}{r^2}. \tag{12}$$

At the interface between a zone of plastic deformation and an elastic zone the conditions of continuity of radial stress and radial displacement, and the additional condition of limiting elastic state are fulfilled. The solution in an elastic zone is given by the formulas (9), in which the radius r_0 of a cavity is replaced by the radius r_s of a plastic zone, and the acting pressure p_0 is replaced by the pressure p_s. So, we have

$$r_s = r_0\exp\frac{p_0 - p_s}{4\,\tau_s}, \qquad C_1 = \Big(\frac{k}{\mu} + \frac{4}{3}\Big)\tau_s\,r_s^3.$$

The expression for the displacement allows to determine the total strain in a plastic zone up to the moment of the pores collapse. Via the stresses (11) by means of Hooke's law one can find the elastic components ε_j^e of strains ($j = r, \varphi$), and then their plastic components $\varepsilon_j^p = \varepsilon_j - \varepsilon_j^e$. The critical pressure $p_c = p_s + k\,\theta_0$ of the collapse of pores on the surface of a cavity is calculated by the equality $\theta = -\theta_0$. This equality describes the collapse in the case of æ $= 0$, when a porous material has not the dilatancy.

Further increase in pressure leads to the formation near the cavity of a zone of compressed, non-porous material ($r < r_c$) within a zone of plastic compaction. According to the constitutive relationships (2), in this zone $\theta(\varepsilon^c) = -\theta_0$ and $\sigma_r^c = \sigma_\varphi^c = -q \le 0$. Thus, the total stresses in a zone of collapse are calculated via the stresses σ_j^p in a plastic element as $\sigma_r = \sigma_r^p - q$, $\sigma_\varphi = \sigma_\varphi^p - q$, where q can be interpreted as the additional pressure caused by the collapse.

Since $\sigma_\varphi - \sigma_r = \sigma_\varphi^p - \sigma_r^p$, then the continuity of radial stress in a plastic zone leads to the continuity of stresses σ_r and σ_φ, hence, the stresses in a whole space are defined by the formulas (11). The difference is only in formulas for strains. According to the rheological scheme, in a zone of collapse $\theta = -\theta_0 - q/k_0$, where k_0 is the bulk modulus of an elastic spring, which is in series connection with a rigid contact. On the other hand,

$$\theta = \frac{\sigma_r^p + 2\,\sigma_\varphi^p}{3\,k} = \frac{\sigma_r + 2\,\sigma_\varphi + 3\,q}{3\,k}.$$

Hence,

$$\Big(\frac{1}{k}+\frac{1}{k_0}\Big)q=-\theta_0-\frac{\sigma_r+2\,\sigma_\varphi}{3\,k}.$$

The volumetric strain satisfies the equation

$$\frac{k+k_0}{r^2}\,\frac{d(r^2\,u_r)}{dr}=-k_0\,\theta_0-p_0+p_s+4\,\tau_s\ln\frac{r}{r_0},$$

the integration of which gives

$$3\,(k+k_0)\,u_r=-(p_0+k_0\,\theta_0)\,r+4\,\tau_s\,r\ln\frac{r}{r_0}+\frac{C_2}{r^2}. \tag{13}$$

The constant C_2 and the radius r_c of a zone of collapse are obtained from the condition of continuity of displacement and from the condition $\theta=-\theta_0$ of collapse on the boundary of a plastic zone. The last condition gives

$$-k\,\theta_0=-p_0+p_s+4\,\tau_s\ln\frac{r_c}{r_0},\qquad r_c=r_0\exp\frac{p_0-p_c}{4\,\tau_s}.$$

The displacement in a plastic zone can be found from (12) after the replacing p_0 by p_c and r_0 by r_c. In a zone of collapse of pores the equation (13) is fulfilled. From the condition of continuity of u_r on $r=r_c$ it follows that

$$k\,C_2=-k_0\,p_s\,r_c^3+(k+k_0)\,C_1.$$

The equation (13) allows to find reversible and irreversible components of strains in this zone.

Typical graphs of distribution of the residual stresses and displacement around a spherical cavity of the radius $r_0=0.01\,\text{m}$ in an infinite porous medium after the increasing pressure to $p_0=0.3\,\text{GPa}$ and the complete unloading, in accordance with the elastic law, are shown in Fig. 3. Phenomenological parameters of a material were taken close to the parameters of a porous (cellular) aluminum [8]: $k=2$, $k_0=70$, $\mu=2.5$, $\tau_s=0.03\,\text{GPa}$. According to the exact solution, the residual stresses σ_r and σ_φ, which correspond to the curves 1 and 2 in Fig. 3 *a*, do not depend on the initial porosity. Three graphs of the residual displacement in Fig. 3 *b* were obtained for different values of the porosity $\theta_0=0$, $\theta_0=1$ and $\theta_0=10\,\%$ (curves 1, 2 and 3) at equal other parameters.

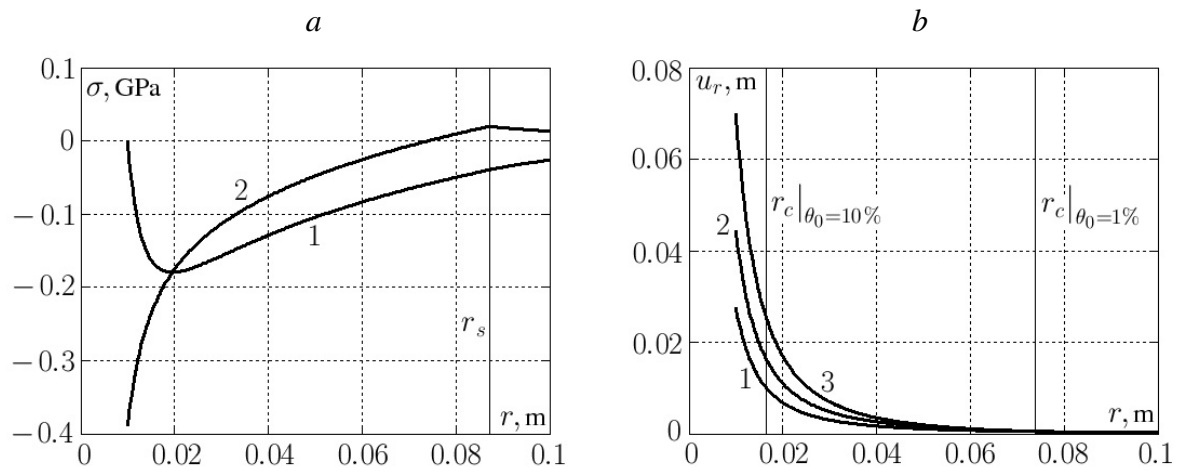


Figure 3: Residual stresses (*a*) and displacement (*b*) around a spherical cavity.

Similarly we obtain the solution of the problem of expansion of a cylindrical cavity in an infinite porous medium. It differs from the solution for a spherical cavity, because in the case of cylindrical symmetry after the appearance of a plastic zone of incomplete plasticity at the neighbourhood of a cavity appears a zone of full plasticity. With increasing pressure a zone of the collapse of pores can occupy some part of a zone of full plasticity or all points of this zone with some part of a zone of incomplete plasticity.

5 COMPUTATIONAL ALGORITHM

Within the framework of proposed mathematical model the parallel computational algorithm was worked out for numerical solution of the problems of dynamic deformation of porous materials. The system (5) is solved by means of the splitting method with respect to spatial variables. Variational inequality is solved by the splitting with respect to physical processes, which leads to a special procedure of solution correction in each node of the computational domain at each time step.

The technology of parallelization of computational algorithm is based on the method of two-cyclic splitting with respect to spatial variables [9]. For the solution of 1D systems of equations an explicit monotone finite-difference ENO–scheme of the "predictor–corrector" type with piecewise-linear distributions of velocities and stresses over meshes, based on the principles of grid-characteristic methods [10], is applied. The parallelizing of computations is carried out using the MPI library, the programming language is Fortran. The data exchange between processors occurs at step "predictor" of the finite-difference scheme by means of the function MPI_Sendrecv. At first each processor exchanges with neighboring processors the boundary values of their data, and then calculates the required quantities in accordance with the explicit finite-difference scheme. Mathematical models are embedded in programs by means of software modules that implement the constitutive relationships, the initial data and boundary conditions of problems. The universality of programs is achieved by a special packing of the variables, used at each node of the cluster, into large one-dimensional arrays. Computational domain is distributed between the cluster nodes by means of 1D, 2D or 3D decomposition so as to load the nodes uniformly and to minimize the number of passing data. Detailed description of the parallel algorithm one can found in [5].

Using this computational algorithm, we worked out the parallel program systems 2Dyn_Granular [11] and 3Dyn_Granular [12] for numerical solution of two-dimensional and three-dimensional dynamic problems, which can be applied particularly for modeling porous materials.

6 CONCLUSIONS

- Mathematical model of a spatial stress–strain state of a porous medium, taking into account the increase in stiffness of a material at the moment of the collapse of pores and the plastic energy dissipation during the deformation of a porous skeleton, was worked out.

- For the problem of expansion of a spherical cavity in an infinite porous medium under the action of internal pressure the exact solution was obtained, which allows to estimate the size of a zone of collapse and can be used for testing and verification of numerical algorithms and computer programs.

- On the basis of this model a software was worked out for multiprocessor computers of the cluster architecture. The developed parallel program system is intended for solving the problems of production of damping elements of constructions, made of porous metals.

ACKNOWLEDGMENTS

This work was supported by the Complex Fundamental Research Program no. 18 “Algorithms and Software for Computational Systems of Superhigh Productivity” of the Presidium of RAS and the Russian Foundation for Basic Research (grant no. 11–01–00053).

REFERENCES

[1] L.J. Gibson, Properties and applications of metallic foams. *Comprehensive Composite Materials, Chapt. 3.31*, 821–842, 2003.

[2] X. Badiche, S. Forest, T. Guibert, Y. Bienvenu, J.-D. Bartout, P. Ienny, M. Croset, H. Bernet, Mechanical properties and non-homogeneous deformation of open-cell nickel foams: application of the mechanics of cellular solids and of porous materials. *Mater. Sci. Eng. Ser. A: Struct. Mater.: Prop. Microstruct. Process.*, **289**(1–2), 276–288, 2000.

[3] J. Banhart, J. Baumeister, Deformation characteristics of metal foams. *J. Mater. Sci.*, **33**(6), 1431–1440, 1998.

[4] M.F. Ashby, Plastic deformation of cellular materials. *Encyclopedia of materials: science and technology*, 7068–7071, 2008.

[5] O. Sadovskaya, V. Sadovskii, *Mathematical modeling in mechanics of granular materials, Ser.: Advanced Structured Materials, Vol. 21*. Heidelberg – New York – Dordrecht – London, Springer, 2012.

[6] R. Hill, *The mathematical theory of plasticity*. Oxford, Clarendon Press, 1950.

[7] J.N. Sneddon, D.S. Berry, *The classical theory of elasticity*. Berlin – Göttingen – Heidelberg, Springer–Verlag, 1958.

[8] M.M. Carroll, A.C. Holt, Static and dynamic pore–collapse relations for ductile porous materials. *J. Appl. Phys.*, **43**, 1626–1636, 1972.

[9] G.I. Marchuk, *Splitting methods*. Moscow, Nauka, 1988 [in Russian].

[10] A.G. Kulikovskii, N.V. Pogorelov, A.Yu. Semenov, *Mathematical aspects of numerical solution of hyperbolic systems. Ser.: Monographs and Surveys in Pure and Applied Mathematics, Vol. 118*. Boca Raton – London – New York – Wasington, Chapman & Hall/CRC, 2001.

[11] V.M. Sadovskii, O.V. Sadovskaya, *Parallel program system for the solution of two-dimensional elastic-plastic problems of the dynamics of granular media (2Dyn_Granular)*. Certificate of State Registration of Computer Program no. 2012613989 from 28.04.2012. Moscow, FIPS, 2012 [in Russian].

[12] V.M. Sadovskii, O.V. Sadovskaya, *Parallel program system for the solution of three-dimensional elastic-plastic problems of the dynamics of granular media (3Dyn_Granular)*. Certificate of State Registration of Computer Program no. 2012613990 from 28.04.2012. Moscow, FIPS, 2012 [in Russian].

COMPDYN 2013
4th ECCOMAS Thematic Conference on
Computational Methods in Structural Dynamics and Earthquake Engineering
M. Papadrakakis, V. Papadopoulos, V. Plevris (eds.)
Kos Island, Greece, 12–14 June 2013

REAL-TIME ERROR CORRECTION IN FAST PSEUDODYNAMIC TESTING: A NUMERICAL STUDY

Ronald J. Gultom[1*], Quincy T. Ma[2]

[1,2]Department of Civil and Environmental Engineering,
The University of Auckland, Auckland, New Zealand
Private Bag 92019, Auckland Mail Centre, Auckland 1142, New Zealand
[1]rgul931@aucklanduni.ac.nz
[2]q.ma@auckland.ac.nz

Keywords: Fast Pseudodynamic Tests, Undershooting Error, Numerical Simulation

Abstract. *Undershooting error is a common error in fast pseudodynamic (PSD) tests as a result of inherent actuator lag. This type of systematic error introduces energy into a system, which if not monitored or controlled, can result in test instability and causes the response to grow exponentially. This leads to premature termination of a test and unreliable result. By considering the systematic error as negative damping in a structure, this paper proposes an intuitive error-correction scheme to compensate for the error. The key to this scheme is the introduction of a variable amount of viscous damping at every integration time step during the pseudodynamic test. The amount of time-varying viscous damping is derived by equating the magnitude of the energy error with that dissipated by the introduced damping at every integration time step. The accuracy and simplicity of the proposed error-correction scheme is demonstrated through numerical simulations of a linear-elastic SDOF structure and a two DOF structure subjected to sinusoidal ground motions.*

1 INTRODUCTION

The fast PSD test method is an improvement to the conventional PSD test method as it is able to directly replicate strain-rate dependent material effects and rate-sensitive behaviours [1]. A conventional PSD test numerically models the inertia and damping effects of a structure, allowing otherwise very large dynamic forces on the physical specimen to be applied at a slower rate or even pseudo-statically. A critical prerequisite of a conventional PSD test is that the effect of loading rate on the restoring force of the structure should be secondary. Although this assumption is generally valid for most conventional construction types, this is not the case for many new structural systems. These systems, such as structures with visco-elastic dampers and base-isolated structures, are highly rate dependent [2]. Thus, conventional PSD test is not suitable for simulating earthquake loads on such structures.

In a fast PSD test the specimen is loaded at or near real-time [3]. For example, if an earthquake event is 40 seconds long, then a fast PSD test may take 40 seconds of wall time to perform in real time, or 400 seconds at a 1/10 time scale. The fast PSD test imposes greater challenge in generating error-minimum test results, as every cycle in the test must be completed within a short interval (in the order of milliseconds). Each cycle of a PSD test involves 1) measuring the restoring force, 2) completing the necessary numerical integration, 3) data communication between the computer hosting the calculation and the computer controlling the actuator, and 4) moving the specimen to the target displacement using the actuator. Research shows minimising the errors in PSD tests, even for conventional PSD tests, is essential in ensuring reliable test results [4].

This paper presents a numerical simulation of a PSD test utilising a new intuitive compensation scheme, to minimise the effect of actuator control error in a fast PSD test where inaccurate displacements are applied to the specimen.

2 EXPERIMENTAL ERRORS IN PSD TEST

The PSD test method is a reliable alternative to the shake table test method provided errors are properly mitigated [1]. Experimental errors associated with inaccurate laboratory equipment control or inaccurate measurement should be given special attention as experimental data is intimately used in the step-by-step integration procedure. The effect of any small error in a single time step is compounded at each subsequent test cycle. Furthermore, if the errors are systematic in nature and occur at each time step, it could lead to a significant divergence from the true solution due to error accumulation from the large number of computation steps. Experimental errors can further be classified into random and systematic errors. Systematic errors have a regular pattern of occurrence and they have a greater detrimental effect on the accuracy of the solution and the stability of the solution process when compared to random errors. Random errors are irregular by nature and no specific effects on the solution can be anticipated [4, 5].

2.1 Systematic Displacement Control Error

One common and significant form of systematic errors is displacement control error. This occurs when the displacements applied to a specimen are systematically greater or smaller than the target displacements at the time when force measurements are required by the solution algorithm. Displacement control error commonly occurs to actuators under simple closed loop control and it can be a result of mis-calibration, poor control loop tuning, and truncation error in digital to analogue conversion amongst other causes. Displacement control error leads to one of two conditions, overshooting or undershooting. Overshooting occurs when the incremental displacement applied by the actuator is larger than the incremental displacement target. Conversely, undershooting occurs when the incremental displacement

applied by the actuator is less than the incremental displacement target. These conditions affect the energy balance in the system and affect the result of PSD tests [5, 6]

2.2 Effect of actuator delay

Undershooting error is more common in a fast PSD test due to the dynamic interactions between the structure and the test apparatus (servo-controller, servo valve and the hydraulic actuator). Due to these interactions, a time delay exists between when the displacement is commanded and when the specimen actually reaching the target displacement [7].

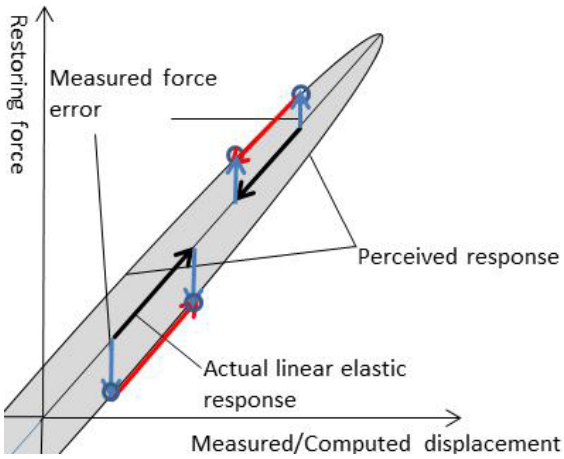


Figure 1: Idealised force-displacement response of systems with undershooting error

In a PSD test, the numerical integration algorithm calculates the time history response using the measured restoring forces from the test specimen and commanded (computed) displacements. This leads to an interesting conundrum as the commanded and measured displacements are not necessarily the same due to the presence of errors. Figure 1 shows a perceived force-deformation relationship of a linear-elastic structure where consistent undershooting errors are present. This results in the measured force lagging behind the command displacement. These errors can be thought as vertical departures of the restoring forces from the straight line. As a result, the system follows a counter-clockwise oval-shaped hysteretic response instead of the true linear response as shown by the bold straight line. This behaviour adds energy into the test specimen, represented by the shaded area of the plot [8]. Research by Horiuchi et al. [9] established that the effect of this response delay is equivalent to introducing negative damping to the system. Tests can become unstable if the negative damping is larger than the inherent structural damping. The paper also presented a method to negate this delay effect by using a simple polynomial extrapolation to predict displacement several time steps ahead to account for actuator delay, using computed displacements at current and several time steps before.

3 INTUITIVE ERROR COMPENSATION UTILIZING VARIABLE VISCOUS DAMPING

It is important that the negative damping from actuator delay is properly compensated to avoid instability and unintentional damage to the structures and the equipment. The proposed compensation scheme aims to dissipate the energy introduced into the structure by the delay error through additional viscous damping proportional to the amount of energy error introduced at every time step. The proposed scheme utilize previous research which has mathematically quantified the amount of energy error [6, 8].

3.1 Review of Hybrid Simulation Error Monitoring (HSEM)

The change in mechanical energy content in a dynamic structural system is the sum of the work done by the inertial, dissipative and elastic restoring components. This balances with the work done by the external force in lieu of any errors. This is expressed mathematically as Equation 1. This assumes the structural system is initially at rest and the system is elastic.

$$\int (\boldsymbol{M}\ddot{u})^T \, du + \int (\boldsymbol{C}\dot{u})^T \, du + \int \boldsymbol{R}^T \, du = \int \boldsymbol{F}^T \, du \tag{1}$$

where terms have their usual meaning.

The third term in Equation 1 represents the strain energy content. In a PSD test, this quantity depends on the measured restoring force from the test specimen. Any displacement control error will result in erroneous displacement and hence erroneous measured restoring force. This distorts the energy balance in the system described by Equation 1.

Mosqueda et al. [8] proposed an approach to calculate the energy error at each step based on the difference between the actual strain energy stored in the specimen and the strain energy in the specimen as perceived by the numerical integration process. Consider the system at time step *i*, the energy error is mathematically expressed as

$$\boldsymbol{E}_i^{er} = \boldsymbol{E}_i^{E} - \boldsymbol{E}_i^{BE} \tag{2}$$

where $\boldsymbol{E}_i^{E}$ is the vector of the change in strain energy across a time step in the deformed specimen as perceived by the numerical integration, while the actual change in strain energy in the specimen is given by $\boldsymbol{E}_i^{BE}$. $\boldsymbol{E}_i^{E}$ can be approximated using trapezoid rule, as

$$\boldsymbol{E}_i^{E} = \frac{1}{2}(\boldsymbol{R}_{i-1}^{m} + \boldsymbol{R}_i^{m})^T (u_i^{c} - u_{i-1}^{c}) \tag{3}$$

and $\boldsymbol{E}_i^{BE}$ can be approximated as

$$\boldsymbol{E}_i^{BE} = \frac{1}{2}(\boldsymbol{R}_{i-1}^{m} + \boldsymbol{R}_i^{m})^T (u_i^{m} - u_{i-1}^{m}) \tag{4}$$

In Equation 3 and 4, $\boldsymbol{R}$ and $\boldsymbol{u}$ represents the restoring force and displacements respectively, while the superscripts "*m*" and "*c*" denote "measured" and "computed" quantities respectively. Using the above expressions, Mosqueda et al. [8] proposed a means to monitor in real time, the accumulation of energy error in a PSD test to determine the reliability of the test. Hybrid Simulation Error Monitoring (HSEM) provides a timely warning when the accumulation of energy error in a PSD test exceeds a certain threshold, when the final result of the test would no longer be reliable and the test should be terminated and continued only after corrective measures are taken. Furthermore, this prevents damage to the specimen and/or equipment.

3.2 Calculating the artificial viscous damping

The amount of energy dissipated by viscous damping mechanism is given by the second term on the left-hand side of Equation 1. Using trapezoid rule, this integration can be approximated as

$$\boldsymbol{E}_i^{D} = \frac{1}{2}(\boldsymbol{C}\dot{u}_{i-1} + \boldsymbol{C}\dot{u}_i)^T (u_i^{c} - u_{i-1}^{c}) \tag{5}$$

where $\boldsymbol{E}^{D}$ is the energy dissipated by viscous damping mechanism from time step *i* to time step *i+1*. It is assumed that the viscous damping matrix $\boldsymbol{C}$ is constant throughout the simulation. For clarity, this constant viscous damping used here is the initial viscous damping matrix. The variable viscous damping matrix, represented by a new variable $\boldsymbol{C}^{cor}$, compensates for energy error $\boldsymbol{E}^{er}$ from time step *i* to time step *i+1* and can be derived from Equation 5, taking the form,

$$\boldsymbol{C}_i^{cor} = \frac{-2\boldsymbol{E}_i^{er}}{(\dot{u}_{i-1}+\dot{u}_i)^T(u_i^c-u_{i-1}^c)} \tag{6}$$

The energy balance between the structure and the external excitation, incorporating the errors in restoring forces and the new variable damping matrix is thus

$$\int(\boldsymbol{M}\ddot{u})^T\ du + \int(\boldsymbol{C}\dot{u})^T\ du + \int(\boldsymbol{R}^m)^T\ du + \int(\boldsymbol{C}^{cor}\dot{u})^T du = \int \boldsymbol{F}^T\ du \tag{7}$$

The term $\int(\boldsymbol{C}^{cor}\dot{u})^T du$ in Equation 7 compensates the energy error defined by Equation 2, which is inherent in the vector of restoring forces $\boldsymbol{R}^m$ (Equation 1).

It can be seen that similar to the HSEM procedure, the new compensation scheme proposed here only requires data that are readily available at every time step during a fast PSD test. The scheme does not require predicted displacement using polynomial extrapolation such as proposed that by Horiuchi et al. [9], thus eliminating the error associated with the extrapolation procedure.

3.3 Numerical verification

This section presents a series of numerical simulations for validating the proposed error compensation scheme. The simulation considers two systems, a single-degree-of-freedom (SDOF) system and a two DOF system, subjected to sweeping sinusoidal ground acceleration for 40 seconds. The structures emulate two simple shear buildings as shown in Figure 2, and the frequencies of the ground accelerations increases gradually from β = 0.75 to β = 4 in four equal steps. β is the ratio of the excitation frequency to the fundamental natural frequency of the structure. The numerical simulations used a time step size of 0.005 s. Table 1 listed the dynamic properties of both structures. Explicit Newmark integration method is utilized to solve the equation of motion of the structures.

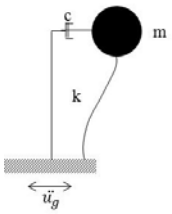


Figure 2a: SDOF structure

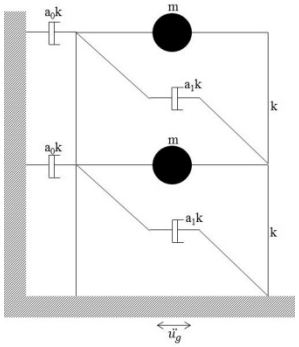


Figure 2b: Two DOF structure

m *(kg)*	1000	
k *(KN/m)*	158	
	SDOF	MDOF
Mass	m	$\begin{bmatrix} m & 0 \\ 0 & m \end{bmatrix}$
Stiffness	k	$\begin{bmatrix} 2k & -k \\ -k & k \end{bmatrix}$
Damping ratio	0.02	0.02 (all modes)
Natural period (sec)	0.5	$T_1 = 0.81$ $T_2 = 0.31$

Table 1: Properties of structures

In these numerical simulations, the restoring forces of the specimens are evaluated using the simulated stiffness for each specimen as shown in Table 1. Systematic undershooting errors are simulated at each step such that the restoring forces used for subsequent

computation are proportionally smaller than the ideal restoring forces according to the size of the displacement increments. Other common sources of errors in a PSD test, such as random noise in force and displacement measurements, or calibration errors in control and measurement devices, are not simulated here.

The results of the simulations where the errors are not compensated are shown in Figure 3 and 4 for the SDOF and the two DOF structures respectively. The figures show the response from the start of the excitation until instability occurs. The results emphasize the importance of compensating actuator delay to avoid such instabilities in real experiments.

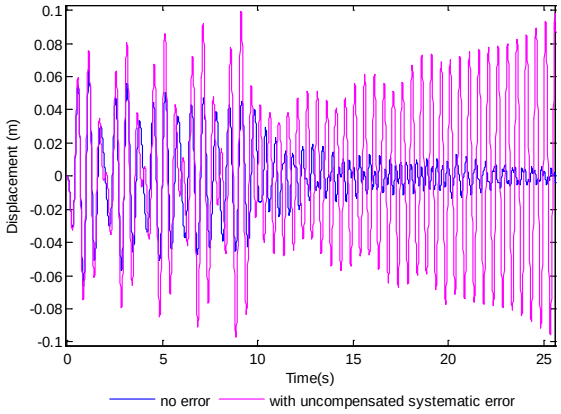
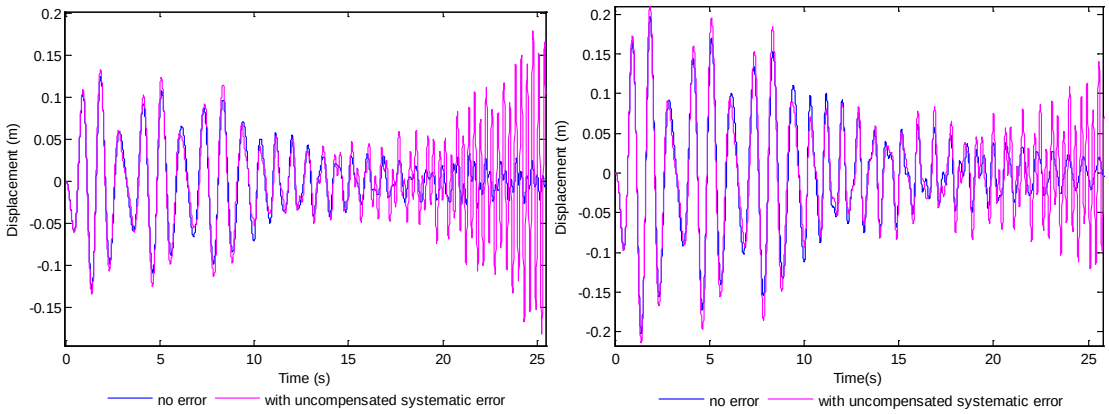


Figure 3: Displacement response of the SDOF structure without displacement error and uncompensated systematic displacement error



a b

Figure 4: Displacement response of the two DOF structure without displacement error and uncompensated systematic displacement error; a) lower storey response and b) upper story response

Figure 5 and 6 present the displacement response and the simulated force-deformation relationship for each structure, under the same excitation but with the proposed compensation scheme applied. It can be seen that the corrected responses accurately match the ideal response with no error for both structures. In Figure 6a and 6b, small hysteresis can be observed on the corrected force-deformation relationships compared to the linear relationships with no error. These small hysteresis exist as the proposed method does not completely eliminate all energy error at every time step, resulting in small cumulative residual error. The normalized maximum cumulative error, defined as the ratio of the maximum error to the maximum ideal displacement are 0.052 and 0.0445 for the lower and upper storey respectively for the two DOF structure, and 0.0105 for the SDOF structure. In the two DOF structure, the effect of the energy error is aggravated by the presence of a higher

second mode. This is because the rate of error propagation is proportional to the magnitude of the natural frequency.

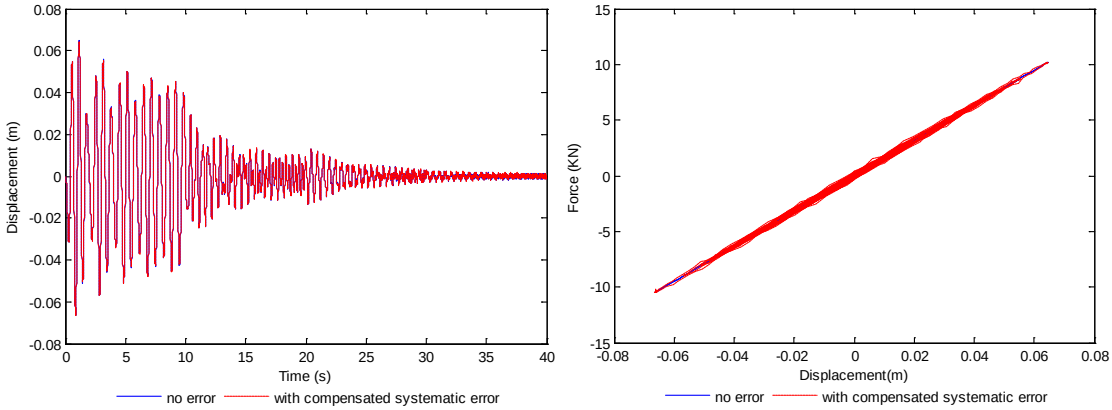
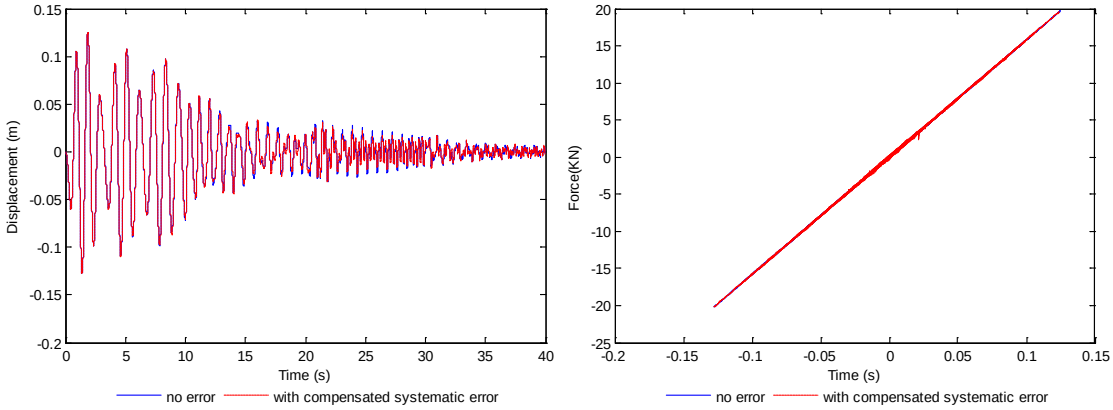
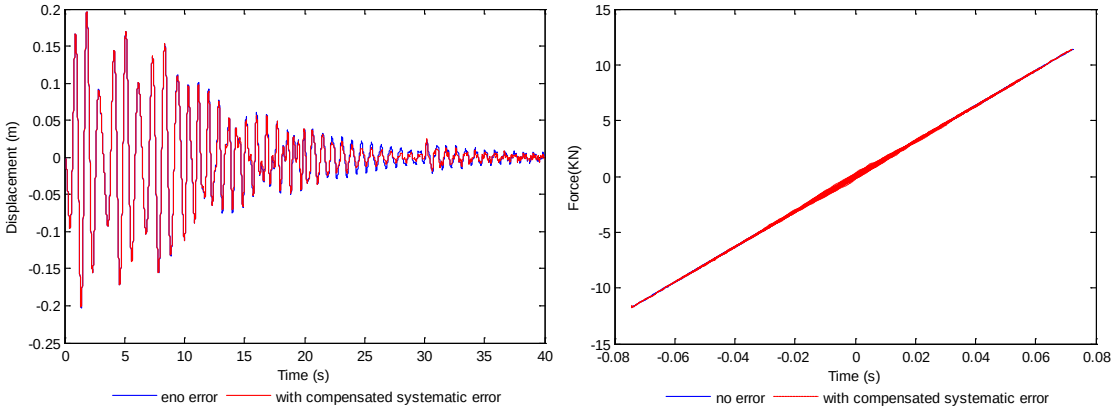


Figure 5: Displacement response and force-deformation relationship of the SDOF structure without displacement error and compensated systematic displacement control error



a



b

Figure 6: Displacement response and force-deformation relationship of the two DOF structure without displacement error and compensated systematic displacement error; a) lower storey and b) upper storey

4 CONCLUSION

This paper presents a new intuitive scheme to compensate for actuator delay in a fast PSD test. Compensation of actuator delay is essential to ensure a stable and accurate result of the

tests. The proposed compensation scheme dissipates the additional energy erroneously introduced into the system through a variable viscous damping matrix that is proportional to the energy error at every time step. Although some residual errors can still be observed, numerical simulations show that the scheme can accurately capture the exact response of the structures. The simplicity of the method can also be seen as it only requires data that is readily available during a fast PSD test at every time step, as in the case of HSEM scheme.

ACKNOWLEDGEMENT

The authors gratefully acknowledge the financial support from the Earthquake Commission (EQC) which has made the development and presentation of this work possible.

REFERENCES

[1] S.A. Mahin, P.B. Shing, Pseudodynamic method for seismic testing. *Journal of Structural Engineering*, **111**, 1482-503, 1985.

[2] M. Nakashima, H. Kato, E. Takaoka, Development of real-time pseudodynamic testing. *Earthquake Engineering and Structural Dynamics*, **21**, 79-92, 1992.

[3] G. Haussmann, Evaluation of openfresco and simcor for fast hybrid single site simulation. *Report CU-NEES-07-2* (University of Colorado, Boulder, Colorado, 2007).

[4] Y. Yamazaki, M. Nakashima, T. Kaminosono, Reliability of pseudodynamic test in earthquake response simulation. *Journal of Structural Engineering*, **115**, 2098-112, 1989.

[5] P.B. Shing, S.A. Mahin, Experimental error propagation in pseudodynamic testing. *Report UCB/EERC-83/12* (University of California, Berkeley, California, 1983).

[6] C.R. Thewalt, M. Roman, Performance parameters for pseudodynamic tests. *Journal of Structural Engineering*, **120**, 2768-81, 1994.

[7] J.E. Carrion, B. Spencer, B.M. Phillips, Real-time hybrid simulation for structural control performance assessment. *Earthquake Engineering and Engineering Vibration*, **8**, 481-92, 2009.

[8] G. Mosqueda, B. Stojadinovic, S.A. Mahin, Real-time error monitoring for hybrid simulation. Part I: Methodology and experimental verification. *Journal of Structural Engineering*, **133**, 1100-08, 2007.

[9] T. Horiuchi, M. Inoue, T. Konno, Y. Namita, Real-time hybrid experimental system with actuator delay compensation and its application to a piping system with energy absorber. *Earthquake Engineering and Structural Dynamics*, **28**, 1121-41, 1999.

COMPDYN 2013
4th ECCOMAS Thematic Conference on
Computational Methods in Structural Dynamics and Earthquake Engineering
M. Papadrakakis, V. Papadopoulos, V. Plevris (eds.)
Kos Island, Greece, 12–14 June 2013

A NUMERICAL INVESTIGATION INTO THE BEHAVIOR OF FLEXIBLE UPLIFTING STRUCTURES WITH SLIP-FRICTION CONNECTORS UNDER EARTHQUAKE LOADING

Wei Y. Loo, Pierre Quenneville, and Nawawi Chouw

Department of Civil and Environmental Engineering, University of Auckland
Symonds Street, Auckland, New Zealand
e-mail: wloo002@aucklanduni.ac.nz

Keywords: Slip-friction connector, uplift, rocking structure, earthquake engineering.

Abstract. *While there has been significant research into the behavior of uplifting (or rocking) rigid structures under seismic loading, far less attention has been paid to the behavior of flexible structures allowed to uplift. Recently, however, Acikgoz and DeJong [1] have shown that these types of structures have unique dynamic characteristics that arise from the interaction of rocking motion with elastic vibration. An understanding of the behavior of uplifting flexible structures is required in order to fully benefit from the damage avoidance potential of allowing uplift. This is because building structures are invariably flexible with a finite fundamental frequency, and it is the desire of the structural designer that the structures themselves remain elastic, even while displaying non-linear behavior in a global sense. This paper is concerned with the behavior of flexible uplifting structures adapted with slip-friction devices. These devices act as hold-down connectors resisting overturning moment. They have a definite force threshold at which sliding will occur, and exhibit close to perfect elasto-plastic behavior. The ability of shear walls to avoid damage through the use of slip-friction connectors has been previously demonstrated by Loo et al. [2]. The modeling of the slip-friction connectors, using a combination of elements commonly available in finite element software packages, and their verification is discussed. Both single-degree-of-freedom (SDOF) and multi-degree-of-freedom (MDOF) flexible structures were modeled with a single plastic deformable hinge at their bases, and their behavior under various earthquake simulations investigated. These flexible structures (both SDOF and MDOF) were then affixed at their bases to a rigid platform, with slip-friction connectors implemented at the ends of the platform, and then subjected to the same earthquake simulations. It was found that the maximum drifts of structures with slip-friction connectors compared favorably with their equivalent structures with a single plastic deformable hinge. With a small amount of vertical load, residual drifts were also found to be small. The performance of MDOF structures with slip-friction connectors was somewhat superior to that of the SDOF structures, with maximum drifts and residual drifts smaller than that of comparable SDOF structures.*

1 INTRODUCTION

In recent years there has been increasing interest in designing structures in earthquake prone areas that have the ability to avoid damage, and to re-centre after a seismic event. Earthquake resistant structures should thus allow not only for life preservation, but also avoid sacrificial damage.

One way of limiting damage on a structure during an earthquake is to allow it to uplift or to rock. Historically most of the research on rocking structures has concentrated on the behavior of rigid rocking blocks. However Acikgoz and DeJong [1] have recently written on the unique behavior of rocking flexible structures. This has applicability to the future design of rocking structures, because building structures are invariably flexible and not rigid, with a finite fundamental frequency of vibration.

An additional embellishment on the concept of a rocking flexible structure is the use of slip-friction dampers to provide damping and to cap earthquake induced forces on a structure below desired level. Slip-friction connectors (also commonly known as slotted-bolt connectors) can be fabricated in such a way that their hysteretic behavior approaches that of the idealized square shaped loops characteristic of a perfectly elasto-plastic substance.

In this paper a brief overview of slip-friction connectors is provided. These connectors are numerically implemented in models of flexible rocking structures, and their effectiveness in protecting both SDOF and MDOF structures from high base shears, and their performance in terms of maximum and residual drifts is demonstrated.

2 SLIP-FRICTION CONNECTORS: CONCEPT AND MODELING

2.1 Concept

Slip-friction connectors have in recent years been used or tested in both moment resisting frames and steel braced frames. Butterworth [3] describes their use in concentrically X-braced frames, and found from a preliminary time history analysis, that they had the ability to significantly increase the ductility of these frames. Butterworth et al. [4] also describe a particular type of slip-friction connector called the sliding hinge joint. The sliding hinge joint is used at the beam to column joint in moment resisting steel frames. During earthquake loading, the sliding hinge joint simulates yielding and plastic hinging by allowing sliding between steel plates – but without the concomitant permanent damage normally expected with traditional moment resisting steel frames after a design level seismic event.

Loo et al. [2], has demonstrated the performance advantages of the use of slip-friction connectors as hold-downs in timber shear walls. Base shears are limited to a predictable level, damage to the sheathing to framing nail connections is largely avoided, and re-centring performance found to be acceptable.

Slip-friction connectors are simple in configuration. The connector of Figure 1 has been proposed by the authors and consists of abrasion resistant steel plate sandwiched between outside plates of mild steel. The mechanism of sliding is symmetrical, in that the centre plate takes the connector force, F_{slip}, and each outside plate exactly $F_{slip}/2$.



Figure 1: Slip-friction connector

The connector force, F_{slip}, is a function of the number of bolts, n_b, clamping the plates of the connector together, the tension in each of the bolts, T_b, and the coefficient of friction, μ.

$$F_{slip} = 2n_b T_b \mu_{fr} \qquad (1)$$

In this paper slip-friction connectors are proposed for use as hold-downs for a rocking structure, and are implemented at the bottom corners of these structures.

2.2 Modeling

The behavior of a generic slip-friction connector can be readily modeled in most finite element software packages through using a multi-linear plastic nonlinear link, combined in parallel with a gap element. The multi-linear plastic element, by itself, would allow the model connector to displace upwards (positive displacement) and downwards (negative displacement) in an elasto-plastic manner.

However, for the bottom corners of a rocking structure, only uplift and its associated downward return motion is permitted – because the corner of the wall should not displace below its original level. Thus, the slip-friction connector must prevent displacement below the original position of the node to which it is attached. In order to do this a gap element is placed in parallel with the multi-linear plastic element. The initial 'gap' of the gap element is set to zero i.e. the gap is closed unless until there is a force causing uplift at its position. For positive displacement the stiffness is set to zero. For negative displacement a large value for stiffness is defined in order to keep any downward displacement to a negligible amount. To limit the amount of uplift, a hook element, is sometimes added to the connector assemblage. However for this study no limit was placed on uplift, thus allowing the maximum drifts that would naturally occur through rocking to be studied. Therefore the hook element was not required. The combined force displacement behaviors of the multi-linear plastic element and gap element produces hysteric behavior of the form shown in Figure 2 (taken from the SDOF slip-friction case of Section 3):

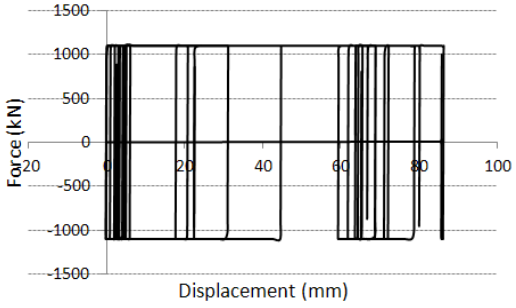


Figure 2: Force displacement behavior of numerically modeled slip-friction connector.

For a more detailed description of the modeling of slip-friction connectors, the reader is referred to Loo et al. [2].

3 EXPLORING THE BEHAVIOR OF STRUCTURES WITH SLIP-FRICTION CONNECTORS

3.1 Overview

In this section a set of results from a wider study carried out on SDOF and MDOF structures with slip-friction connectors is presented. The earthquake records used are first discussed, the modeling procedure described, and results are presented.

3.2 Acceleration records

The ground excitations used in the simulations were based on the design spectra adopted in Japan following the destructive 1995 Kobe earthquake. These spectra (5% damping) (see Figure 3) were used for this research because they have a distinct dominant frequency range, allowing relative ease in the interpretation of results. The return period for earthquake records used is 2500 years, which typically corresponds to a maximum considered event (MCE).

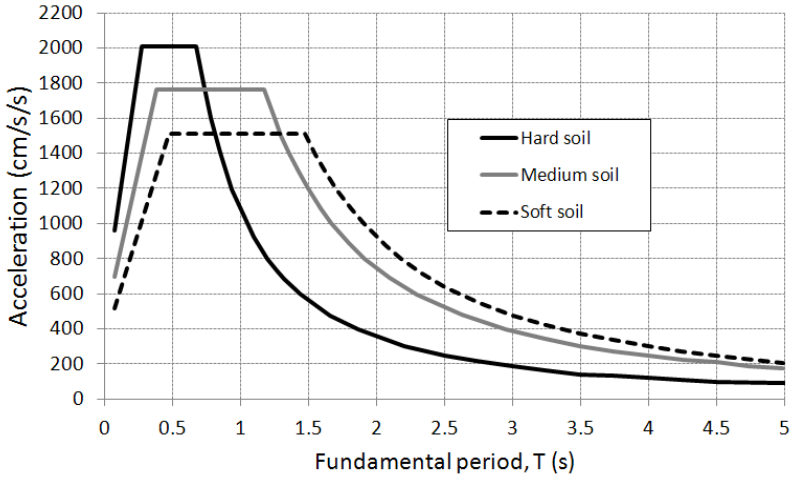


Figure 3: Japanese design spectra for soft, medium, and hard soil conditions.

Ninety ground acceleration records were used in this study; with thirty records for each of soft, medium, and hard soil conditions. In this paper, only the results for an SDOF and MDOF structure, both of fundamental period 0.55 s, and subjected to ground accelerations associated with medium soil conditions is presented.

3.3 Numerical modeling and results

For both the SDOF and MDOF cases, simulations were carried out on flexible structures with (1) a rigid joint at the base, then (2) a plastic deformable joint at the base, then (3) slip-friction connectors at the base, and finally (4) slip-friction connectors at the base and vertical loading applied to the top of the structure. The SDOF structures are modeled as a 9.6 m high flexible column with a single mass at the top of the column for the SDOF structures, while the MDOF structures have a total height of 16 m, with masses evenly distributed up the column (refer Figure 4).

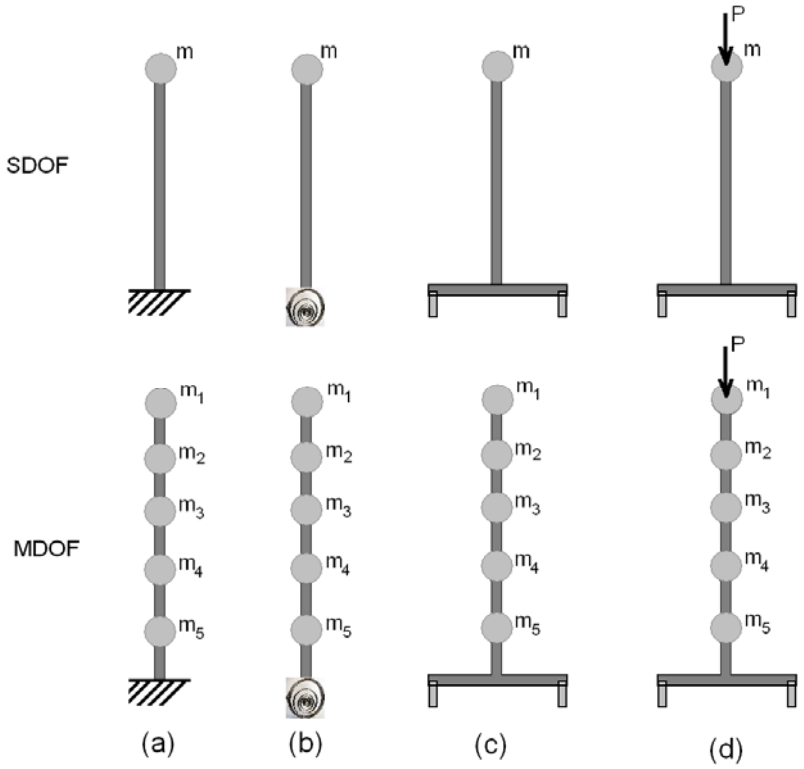


Figure 4: Modeling of SDOF structures (top row) and MDOF structures (bottom row): (a) fully elastic case, (b) ductile with plastic deformable hinge, (c) ductile with slip-friction connectors, and (d) ductile with slip-friction connectors and vertical load.

For the case considered, the Japanese design spectral response acceleration for a structure with fundamental period of 0.55 s is 17.6 m/s^2. For the SDOF case a mass of 125000 kg was used and the *EI* and length of the column adjusted to provide for the desired period of 0.55 s. For the MDOF case, masses of 25000 kg were provided at each level. The *EI* of the column was adjusted to provide a fundamental period of 0.55 s, with the length being 16 m.

For the SDOF structure, the expected base shear for the fully elastic case, V_{base} was found simply by multiplying the response acceleration by the lumped mass atop the column. Thus V_{base} was found to be 2163 kN. Subjecting this structure with a fully rigid joint at the base to earthquake excitations produced an average base shear of 2160 kN, very close to the expected.

For the SDOF structure with the plastic deformable hinge, a force reduction factor of R = 4 was adopted. Therefore the target V_{base} was 541 kN. Given that the model height adopted was 9.6 m, the maximum overturning moment M_o was thus 541 kN x 9.6 m = 5194 kNm. A multi-linear plastic link was used to model the behavior of this plastic deformable hinge, and its moment-rotation behavior defined. For the case with slip-friction connectors, the width of the rigid base of the structure was 4.8 m. Hence to resist overturning moment, the slip force, F_{slip}, of the connector was set to be M_o / 4.8 m = 1082 kN. The moment-rotation and force-displacement relationships for the plastic deformable hinge and the slip-friction connectors are shown in Figure 5.

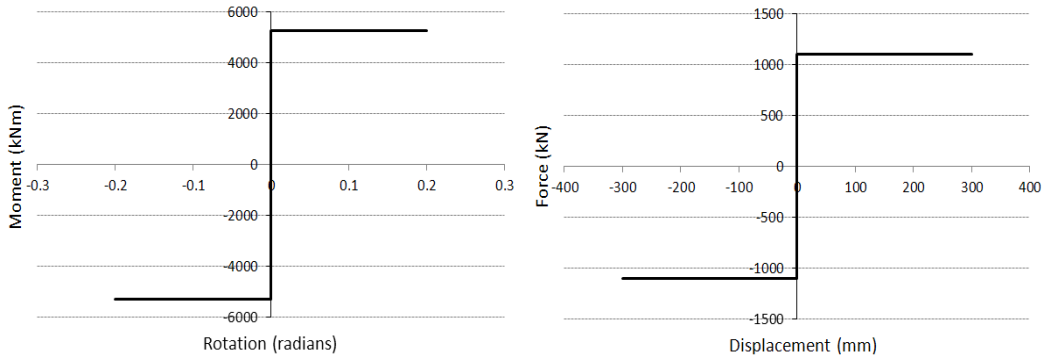


Figure 5: (a) Moment-rotation behavior of plastic deformable hinge, and (b) Force-displacement behavior of slip-friction connector.

For the case of the SDOF structure with vertical loading, it was decided to load the structure in such a way that the resistance to overturning moment provided by the vertical load would be 15% of the resistance to overturning moment provided by the slip-friction connectors. Thus a vertical load, P, of 287 kN was adopted, and the slip-friction connector force, F_{slip} set to 957 kN. Thus the moment resistance of the vertical load is 287 kN x 2.4 m = 689 kNm, while that of the slip-friction connectors is 957 kN x 4.8 m = 4594 kNm.

Figure 6 shows the base shears for the SDOF structure, with the fully elastic case shown first, and then the load limiting effects of the plastic deformable hinge, the slip-friction connectors by themselves, and finally the combination of slip-friction connectors with vertical load. It can be seen that for the ductile cases, the base shear is capped to the desired level of around 540 kN.

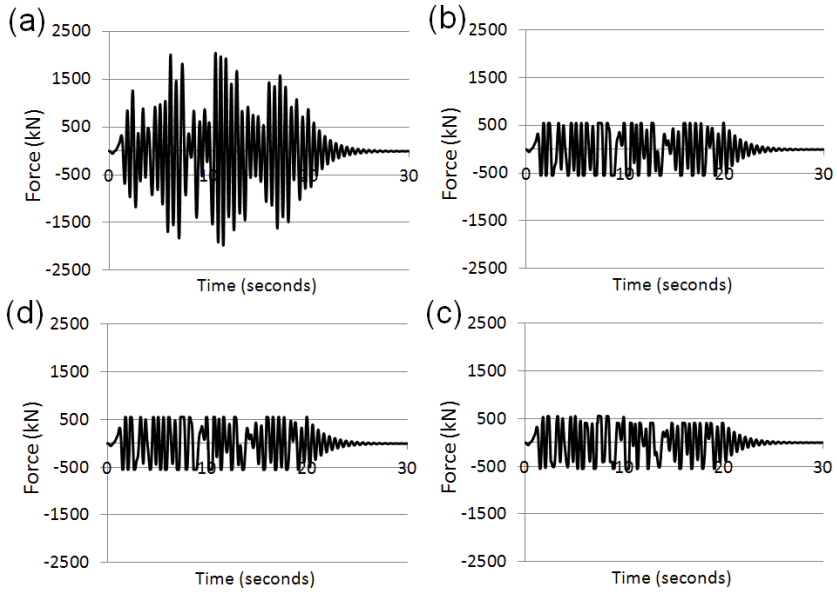


Figure 6: Base-shear time history of SDOF structures - (a) fully elastic case, (b) ductile with plastic deformable hinge, (c) ductile with slip-friction connectors, and (d) ductile with slip-friction connectors and vertical load.

When modeling the MDOF structures, a similar approach was taken to that of the SDOF case, except the column was lengthened from 9.6 m to 16 m, and the 125000 kg mass distributed over 5 levels. The 1st to 5th modes of vibration are shown in Figure 7.

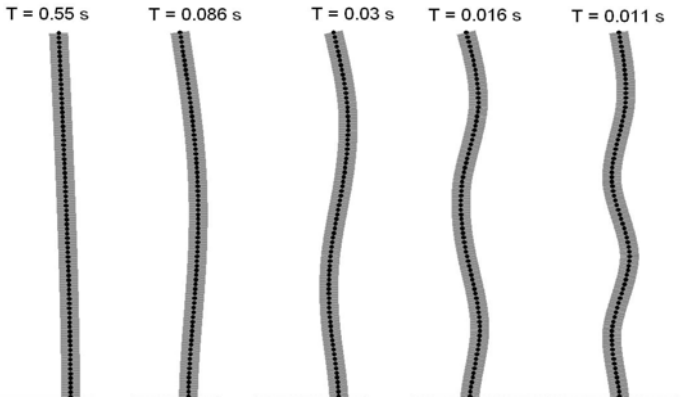


Figure 7: Modes of vibration for MDOF structure

Results for maximum horizontal and residual displacements at the top of the MDOF and SDOF structures, are now discussed. For the example presented in this paper, it can be seen that allowing ductile behavior, for both the MDOF and SDOF cases, results in displacements that are higher than that of the fully elastic cases (see Figure 8).

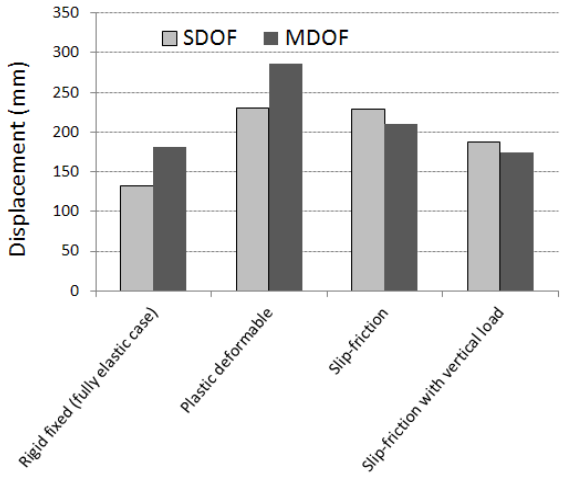


Figure 8: Maximum displacements at top of structure under earthquake loading.

This, however, is expected, as the fundamental period of 0.55 s for both types of structures is within the range where maximum inelastic displacements under earthquake loading are expected to exceed the elastic spectral displacements. From Figure 8 it can be seen that for both the MDOF and SDOF cases maximum drifts are less for structures in which base shears are capped by slip-friction connectors, compared with the case for those structures in which ductility is supplied by a plastic deformable hinge. Where slip-friction connectors are utilized, the drifts for the MDOF structure are slightly smaller than that of the equivalent SDOF structure.

For residual drifts, the application of vertical load to assist in resisting overturning moment appears to suppress residual drift to very low levels (see Figure 9). This is in spite of the fact that the moment resistance of the vertical loading was only 15% that of the moment resistance from the slip-friction connectors.

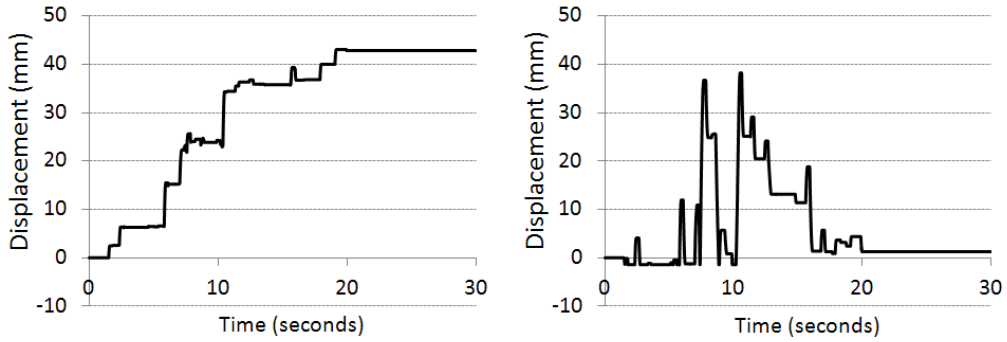


Figure 9: The effect of vertical loading on residual displacement (a) displacement time-history of structure without vertical loading and (b) with vertical load.

From Figure 10 it can be seen that for the case considered, slip-friction connectors provide for smaller residual drifts than the equivalent case with a plastic deformable hinge, and that the effect is more pronounced in the case of the MDOF structure.

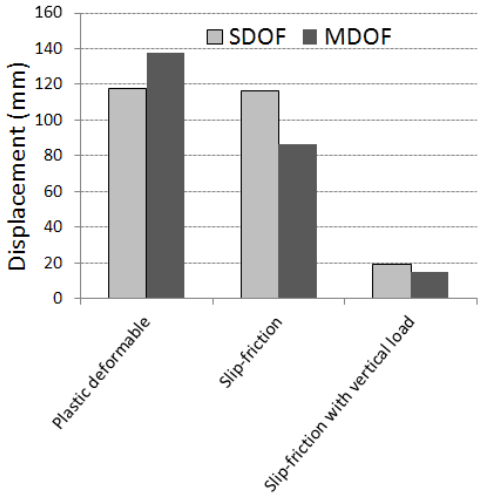


Figure 10: Residual drifts.

4 CONCLUSIONS

Some results from a wider study on the comparative performance of flexible SDOF and MDOF structures with slip-friction connectors are provided. For ductile structures, slip-friction connectors appear to have lower drifts in general, than that of the case where ductility is provided by a single plastic deformable hinge. Residual drifts are also smaller in the case of ductile structures with slip-friction connectors. The application of vertical loading has a relatively minor effect on reducing maximum displacement, but does significantly suppress residual displacements for both SDOF and MDOF structures. Residual drifts and maximum drifts for the MDOF structures appear to be less, under the same earthquake loadings, than those associated with comparable SDOF structures.

ACKNOWLEDGMENTS

The authors would like to thank the New Zealand Ministry for Primary Industries for the support of this research.

REFERENCES

[1] S. Acikgoz, M. J. DeJong, The interaction of elasticity and rocking in flexible structures allowed to uplift. *Earthquake Engineering and Structural Dynamics*, **41(15)**, 2177-2194, 2012.

[2] W. Y. Loo, P. Quenneville, N. Chouw, A numerical study of the seismic behaviour of timber shear walls with slip-friction connectors. *Engineering Structures*, **34(22)**, 233-243, 2012.

[3] J. Butterworth, Ductile concentrically braced frames using slotted bolted joints. *Journal of the Structural Engineering Society of New Zealand*, **13(1)**, 39-48, 2000.

[4] J. Butterworth, C. G. Clifton, G. MacRae, Developments in steel frame joints in New Zealand. *The Structural Engineer*, **86(16)**, 20-21, 2008.

COMPDYN 2013
4th ECCOMAS Thematic Conference on
Computational Methods in Structural Dynamics and Earthquake Engineering
M. Papadrakakis, V. Papadopoulos, V. Plevris (eds.)
Kos Island, Greece, 12–14 June 2013

MATH SIMULATION OF CONTACT INTERACTION DURING SPACECRAFT DOCKING AND ROBOTIC ASSEMBLY OPERATIONS

A. Yaskevich

Rocket Space Corporation "Energia"
Korolev city, Russia
Andrey.Yaskevich@rsce.ru

Keywords: Docking and berthing interfaces, Contact interaction, Real-time math simulation.

Abstract. *Contact interaction math models can be split into two classes depending on the character of the relative motion of assembly interface contacting elements.*

In the first-class models, one of contacting elements has several degrees of relative motion freedom. Therefore contact reaction forces must be taken into account in relative motion dynamics equations of a mechanical system. In this case the most efficient method of calculating such forces is based on the assumption of a contact penetration counteracted by contact stiffness. The penetration value is controlled; its maximal value determines the geometric contact simulation error. For the first-class contact models, basic principles of development and a classification of main pairs of interacting elements are presented; algorithms for calculation of penetration values, reaction unit vectors at contact points and contact forces are described.

In the second-class models, one of contacting elements has only one degree of freedom, and its relative displacement is counteracted by a spring. Here, a slight inertia of such an element does not influence the motion dynamics of mating interfaces, but it is only the spring force that is taken into account. Therefore contact reaction forces in the second-class models are calculated based on spring deformation only, without using contact penetration. In this case the geometric place of contact, which determines the spring deformation, is calculated by the iterative method with any given accuracy. This feature is particularly useful for simulating contact mechanisms that provide a stiff interface joint and have very small displacements. Models of this class are also used for describing the motion of capture latches.

Surfaces of the second and forth order (cone, torus) are approximated by more simple geometric elements of the first and third order respectively (segment, sphere) in contact models of both classes. As a result, a multiple use of simple analytical relations replaces a solution of a complex geometric problem. Calculation efficiency is ensured by the dichotomy method, as well as by a preliminary generation of the highest possible number of parameters that are just transformed during simulation into the coordinate system of the geometric problem solution.

The described algorithms provide a real-time simulation of contact interaction of different mating interfaces i.e. probe-cone type and androgynous peripheral docking units, specialized berthing devices.

1 INTODUCTION

Spacecraft docking or berthing represents an in-orbit mechanical assembly process that starts at the moment of their first contact and ends with a formation of a stiff joint. It is implemented with the use of active and passive docking assemblies that have mechanisms and interfaces with contacting surfaces. Forces and moments created by the spacecraft control system, mechanisms and contact reactions ensure a decrease of relative linear and angular misalignments at different phases of docking/berthing. A complex form of contacting surfaces can be represented by a group of elements whose geometry is described by equations of the first (line, plane) to forth (torus) order. Contact interaction math models can be split into two classes depending on the character of the relative motion of mating interface contact elements.

In the first-class models, it is considered that an interface element, e.g. a docking mechanism buffer link, has several degrees of freedom of a relative motion described by differential equations that involve contact reaction forces. To calculate these forces, the most efficient method is used, which is based on the admission of a contact penetration counteracted by contact stiffness. The penetration value is controlled; its maximal value determines the geometric contact simulation error.

In the second-class models, one of contacting elements has only one degree of freedom, and its relative displacement is counteracted by a spring. Here, a slight inertia of such an element does not influence the motion dynamics of mating interfaces, but it is only the spring tension considered that forces this element to take either its initial position (the spring is not deformed) or a position corresponding to a contact with the guide surface (the spring is deformed). This class includes the pairs *latch/sensor - guide surface* and *active – passive hook*. Contact parameters for this class pairs can be obtained in a basically different way, i.e. by iterative methods based on only geometric relations with any given accuracy that does not depend on the integration step value in the motion dynamic equations of mating spacecraft and docking mechanisms. This feature is particularly useful for simulating contact of mechanisms that provide a stiff interface joint and have very small displacements.

This research brings forward efficient calculation algorithms of analysis of contact conditions and determination of contact parameters for both classes of contacting elements based on simple analytical relations. They allow development of detailed and adequate models that can be computed real-time.

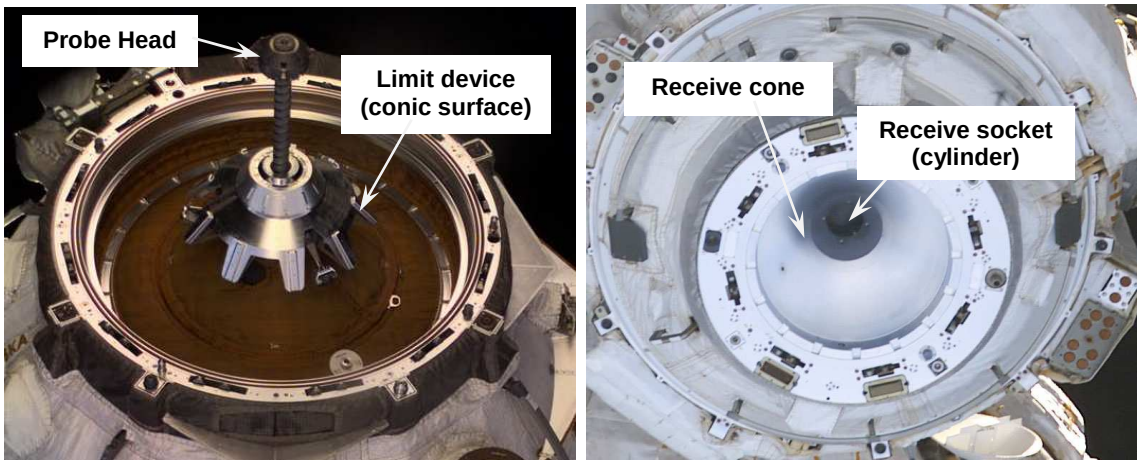
2 CONTACT ELEMENTS GEOMETRY DESCRIPTION

Development of a mathematical description of contact interaction of guide surface elements of docking assemblies is based on the following main points.

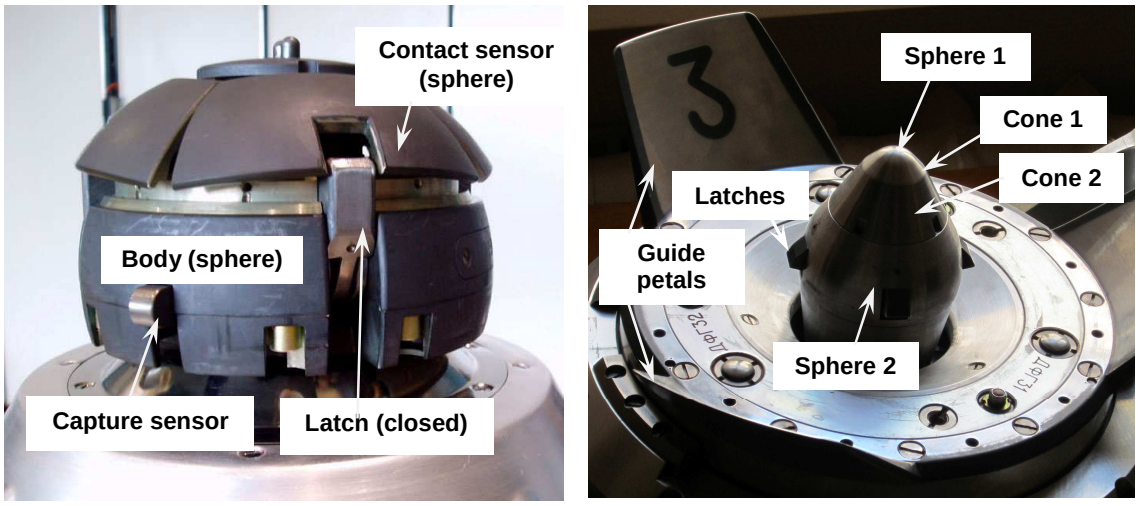
1. In a mathematical simulation each contact area is replaced by a single point. The number of contact points can be arbitrary, but must be finite.
2. Types of pairs of guide surface contacting elements make a finite set. Each of them is represented by a finite aggregation of geometric primitives, for which contact conditions and geometric parameters are determined by analytical expressions. As a result, a multiple use of simple analytical relations replaces a solution of a complex geometric problem.
3. Each analytical solution is developed subject to fulfillment of the designed allowable range of lateral and angular misalignments of docking assemblies. A violation of this range means an off-nominal course of the operation and leads to a termination of the simulation.

Structural analysis of different types of mating interfaces (see Fig. 1) allows sorting out the following pairs of contacting elements of guide surfaces:

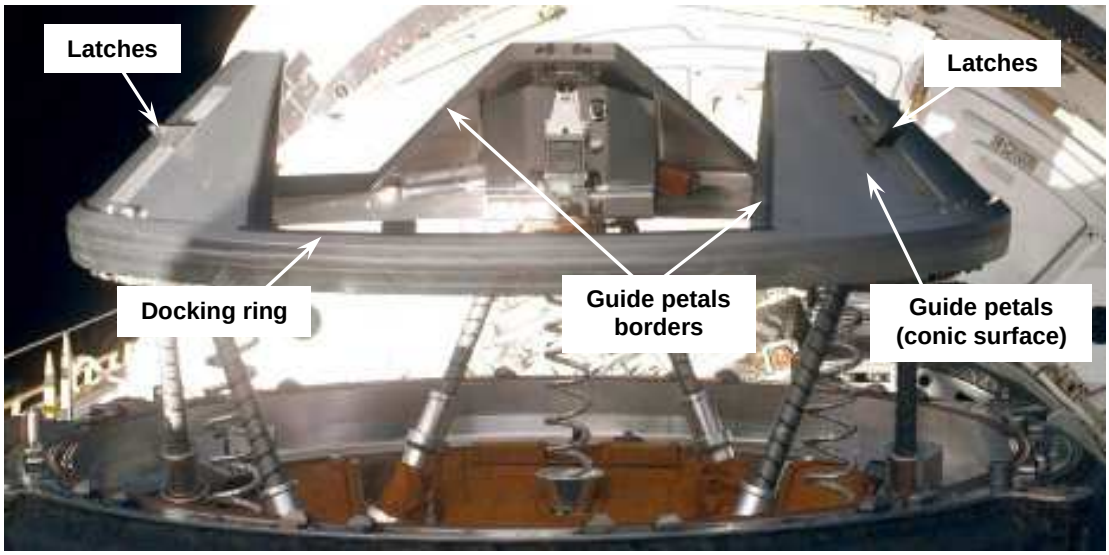
- spherical surface of the head and contact sensors of the probe - receiving cone surface;
- spherical surface of the probe head and contact sensors – receiving socket cylinder border;



a



b



c

Fig. 1. Types of contact surfaces of docking interfaces -Probe-Cone docking units (a);
Probe head and capture head of berthing unit (b), androgynous docking unit (c)

- spherical surface of the probe head and contact sensors – receiving socket cylinder surface;
- spherical surface of the probe head – receiving socket bottom;
- capture head conic surface base – receiving cone surface;
- capture head conic surface – receiving socket cylinder border (circle);
- capture head conic surface base – receiving socket cylinder surface;
- docking mechanism limit device – receiving cone base border;
- docking mechanism limit device extremity– receiving cone surface;
- aligning lever roller– receiving cone surface;
- latch extremity– receiving cone surface;
- latch and capture sensor on the probe head – receiving socket cylinder border;
- guide petal conic surface fragment – receiving cone base border;
- guide petals lateral borders of active and passive assemblies;
- guide petals border – receiving cone base border;
- torus surface of the lock head– conic receiving cone surface;
- torus surface of the lock head – receiving socket cylinder border (circle);
- torus surface of the lock head – receiving socket cylinder surface.

Guide petals are located at the periphery of docking assemblies, they are intended for decreasing lateral and angular misalignments during their axial approach. Geometrically they represent trapezoidal fragments of round conic surfaces with the angle between their axis and generatrix equal to 45^0. The inclined lateral borders of guide petals ensue from the sectioning of the conic surface by planes, i.e. lines of the second order, in particular hyperbolas. Despite this, they are represented by line segments; the accuracy of the math model is determined by their maximal distance from the surface. If a lateral border of the guide petal is a stiffening rib it can be specified by two segments as its contact borders. The dimensions and relative position of the guide petals allowed by initial approach conditions make their contact possible with their borders only, and with only one border for each petal.

The above mentioned pairs of guide surface contacting elements can be described by the following main pairs of geometric primitives, for which contact conditions and geometric parameters are determined by analytical expressions:

- sphere – truncated receiving cone;
- sphere – circle;
- sphere – cylinder;
- sphere – plane;
- point (extremity of a line segment) – truncated receiving cone;
- point (extremity of a line segment) – cylinder;
- line segment – line segment;
- line segment – plane;
- line segment – circle;
- inclined lateral borders of guiding petals.

More complex elements of contacting surfaces are represented by finite sets of geometric primitives. Thus, the surface of a truncated cone or its fragments contacting with a circle are replaced by a finite set of generatrix segments of a constant or variable length. Surface elements in the form of a torus are represented by a finite aggregation of spherical surfaces (spheres). The number of approximating geometric primitives is determined on the basis of the required accuracy.

3. FIRST CLASS MODELS FOR CONTACT FORCES CALCULATION

3.1 Taking into account unilateral constraints in first-class contact models

Contact of two and more bodies that include guide surfaces is hereinafter considered not as a shock characterized by instant change of velocities [1] but as a dynamic process, in which unilateral constraints are imposed on the motion of the bodies. Physically, such constraints are realized through relevant reaction forces. In a mathematical simulation these constraints can be taken into account in two ways – with a constraint equation or through a direct calculation of contact interaction forces.

If equations of temporarily imposed unilateral constraints are used they are to be written relative to accelerations

$$\mathbf{H}\ddot{\mathbf{q}} + \mathbf{h}(\mathbf{q}, \dot{\mathbf{q}}) = \mathbf{0} \tag{1}$$

and introduced into mechanical system dynamic equations

$$\begin{bmatrix} \mathbf{A}(\mathbf{q}) & \mathbf{H}^T \\ \mathbf{H} & \mathbf{0} \end{bmatrix} \begin{bmatrix} \ddot{\mathbf{q}} \\ \boldsymbol{\lambda} \end{bmatrix} = \begin{bmatrix} \mathbf{b}(\mathbf{q}, \dot{\mathbf{q}}) + \mathbf{Q} \\ -\mathbf{h}(\mathbf{q}, \dot{\mathbf{q}}) \end{bmatrix} \tag{2}$$

where $\mathbf{H} - (m \times n) -$ matrix; $\mathbf{q} - (n \times 1) -$ vector of generalized coordinates; $\boldsymbol{\lambda} - (m \times 1) -$ vector of Lagrange multipliers; $\mathbf{A}(\mathbf{q}) - (n \times n) -$ generalized inertia matrix; $\mathbf{b}(\mathbf{q}, \dot{\mathbf{q}}) - (n \times 1) -$ vector of generalized inertia forces; $\mathbf{Q} - (n \times 1) -$ generalized forces vector.

This method of constraint allowance has low computational efficiency for the following reasons. First, the system of equations (2) can be solved relative to $\ddot{\mathbf{q}}$ and $\boldsymbol{\lambda}$ only without linearly dependent lines in (1). In practice, the number of contacts can be great, and to fulfill this requirement decision algorithms for linearly dependent constraint equations are to be used. Second, the system of equations (2) is differential-algebraic. To solve it, methods [2-4], more complex than an explicit integration of dynamic equations without using (1) and (2), are to be applied.

Hereinafter we use a more computationally efficient method for motion constraint allowance based on a direct calculation of the contact reaction force using the simple relation $\mathbf{f}_R = (k_C \Delta_n + c_C \dot{\Delta}_n)\, \mathbf{n}_R$, in which the value of contact deformation Δ_n and its velocity $\dot{\Delta}_n$ are determined along the normal unit vector $\mathbf{n}_R$ which is common for the contacting surfaces; k_C and $c_C -$ contact rigidity and damping factor. This method is mathematically equivalent to the regularization method [2] that uses a virtual oscillator but does not require a calculation of coefficients and exclusion of dependent constraint equations or an integration of differential-algebraic equations. Contact reaction forces enter into the right part of the mechanical system dynamic equations.

Penetration of an active geometric primitive into a passive one along their common normal vector at the contact point determines the value of the contact reaction force in the mathematical model. The value of the contract penetration is controlled, if its allowable limit is exceeded the simulation process is terminated with a corresponding diagnostic message.

Geometric parameters of the contact point are its coordinates, components of the contact reaction force unit vector normal to the contacting primitives, and the value of the penetration along this vector; kinematic parameters are the penetration velocity and the unit velocity vector of the active contacting primitive relative to the passive one in the contact plane passing through the contact point. Dynamic parameters are components of the force applied at

the contact point, i.e. a normal component (penetration reaction) and a tangential one (friction force).

Expressions for contact conditions and parameters are built in the coordinate system $X_P Y_P Z_P$ of the passive assembly, where the X_P axis corresponds to the direction of approach. Parameters of active geometric primitives are expressed in the coordinate systems of the active assembly mechanism links and converted into $X_P Y_P Z_P$, and parameters of passive ones are constant values calculated once.

Given below are some main algorithms of calculation of geometric contact parameters. In the simplest ones, the active geometric primitive is a sphere with the radius R_S, which center P_S in $X_P Y_P Z_P$ is determined by the vector $\mathbf{r}_S^{(P)} = [\, x_S, y_S, z_S \,]^T$. This is specified by the symmetry of the sphere relative to its center and the axial symmetry of the counterpart geometric primitives, i.e. a truncated cone, a circle and a cylinder. Due to the equal probability of the directions of lateral and angular misalignments, X_P is the symmetry axis of geometric primitives of passive guide elements, i.e. a receiving cone, a cylinder and a circle. As the direction of this axis corresponds to the active vehicle approach, therefore:

- the vector from the base to the top of the receiving cone coincides with the direction of this axis (misalignments should decrease at approach);
- the contact reaction vector that reflects the impact of the active guide elements on the passive ones has a positive projection on this axis.

All the above mentioned geometric characteristics are taken into account when forming analytical expressions that determine contact conditions and parameters. The direction of the contact reaction unit vector $\mathbf{n}_R = [\, n_X,\, n_Y,\, n_Z \,]^T$ coincides with the direction of the sphere radius, and the position of the contact point is determined by the vector $\mathbf{r}_{P,k}^{(P)} = [\, x_S + n_X R_S,\, y_S + n_Y R_S,\, z_S + n_Z R_S \,]^T$.

3.2 Calculation of *sphere - truncated receiving cone surface* contact parameters.

Parameters of a passive truncated cone are radii R_{CB} and R_{CT} of the lower and upper bases, the α_C angle between the axis and the generatrix, and the P_T point of intersection of its generatrices, which is determined by the vector $\mathbf{r}_T^{(P)} = [\, x_T,\, 0,\, 0 \,]^T$ (see Fig. 2). To speed up calculations, a preliminary calculation of constant auxiliary parameters is made: $H_{CT} = R_{CT}\, ctg\, \alpha_C$ – the distance from P_T to the upper base of the receiving cone; $d_{TX,\min} = H_{CT} + R_S \sin\alpha_C$ and $d_{TX,\max} = d_{TX,\min} + (R_{CB} - R_{CT})\, ctg\, \alpha_C$ - minimal and maximal distances from the P_S point to the P_T point along the cone axis provided its contact with the sphere; $d_{L,\min} = R_{CT} - R_S \cos\alpha_C$ and $d_{L,\max} = d_{L,\min} + (R_{CB} - R_{CT})$ – minimal and maximal distances from the sphere center P_S to the cone axis provided its contact with the sphere; $n_{CX} = \sin\alpha_C,\ n_{CL} = \cos\alpha_C$ – constant axial and lateral components of the contact reaction unit vector normal to the cone surface.

Geometric contact parameters are calculated as follows.

1. From the sphere center P_S, the distances are calculated: $d_L = \sqrt{y_S^2 + z_S^2}$ to the axis, and $d_{TX} = x_T - x_S$ to the top of the receiving cone along its axis. When one of the conditions $d_L < d_{L,\min}$, $d_L > d_{L,\max}$, and $d_{TX} < d_{TX,\min}$ or $d_{TX} > d_{TX,\max}$ is met the search of a contact point of this type is terminated.

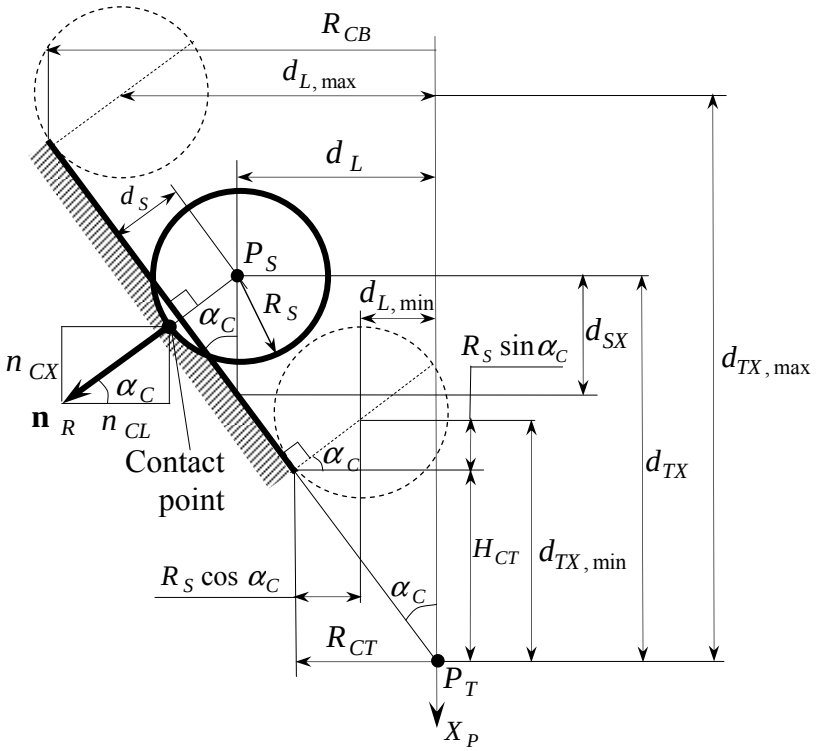


Fig 2. A sphere to a truncated cone surface contact model

2. The distance is calculated from the sphere center P_S to the cone surface along its axis $d_{SX} = d_{TX} - d_L\, ctg\,\alpha_C$ and along the normal to its surface $d_S = d_{SX} \sin\alpha_C$. If $d_S > R_S$ then a contact of this type is missing, and determination of its parameters is terminated.
3. The penetration value $\Delta_n = R_S - d_S$ is calculated along the normal to the cone surface. If it exceed the maximal allowable limit, i.e. $\Delta_n > \Delta_{n,\max}$, then the simulation is terminated with a corresponding diagnostic message.
4. If $0 < \Delta_n < \Delta_{n,\max}$ then a contact point between the sphere and the receiving cone is obtained. It is given a current number k. The reaction unit vector $\mathbf{n}_{R,k}^{(P)} = [\,n_{CX},\, n_Y,\, n_Z\,]^T$ has one constant component $n_X = \sin\alpha_C$ and two variable components $n_Y = n_{CL}\,(y_S / d_L)$ and $n_Z = n_{CL}\,(z_S / d_L)$.

Geometric contact parameters for the pair of geometric primitives *sphere – circle, sphere – cylinder, sphere – plane* are calculated similarly using preliminarily calculated characteristic distances from the sphere center corresponding to such contact types: to the axis of the circle, cone or cylinder, to the top of the cone or plane. Formulas for determining parameters of contact of individual points representing segment extremities with passive conic and cylindrical surfaces are derived from similar relations for the sphere, provided $R_S = 0$.

In the algorithms presented below for geometric primitives in a segment form, well-known formulas of analytical geometry are used [5]. In particular, a line passing through points $P_1 = (x_1, y_1, z_1)$ and $P_2 = (x_2, y_2, z_2)$ is described by the parametrical equation $x = x_1 + l\,t$, $y = y_1 + m\,t$, $z = z_1 + n\,t$, i.e. the initial point P_1 and the guide vector $\mathbf{L} = [\,l,\, m,\, n\,]^T$ with components $l = x_2 - x_1$, $m = y_2 - y_1$, $n = z_2 - z_1$. If this line crosses a plane

$A x + B y + C z + D = 0$ in a point P_C then the corresponding value of the parameter $t_C = -(A x_1 + B y_1 + C z_1 + D)/(A l + B m + C n)$, and the point P_C has coordinates $x_C = x_1 + t_C l$, $y_C = y_1 + t_C m$, $z_C = z_1 + t_C n$. It belongs to the segment between P_1 and P_2, provided $t_C \in [0, 1]$.

Parameters of the plane passing through a segment $\mathbf{L}_1$ parallel to another segment $\mathbf{L}_2$ and parameters of the plane passing through the segment $\mathbf{L}_1$ perpendicular to the plane $A x + B y + C z + D = 0$ are determined from structure-like equations

$$\begin{vmatrix} x - x_1 & y - y_1 & z - z_1 \\ l_1 & m_1 & n_1 \\ l_2 & m_2 & n_2 \end{vmatrix} = 0 \quad \text{and} \quad \begin{vmatrix} x - x_1 & y - y_1 & z - z_1 \\ l_1 & m_1 & n_1 \\ A & B & C \end{vmatrix} = 0 .$$

3.3 Calculation of a line segment to a circle line contact parameters.

A circle with a radius R_C and a center $P_B = (x_B, y_B, z_B)$ is the base of a truncated cone or cylinder. The top of the cone or the center of the other base of the cylinder are determined by the point $P_T = (x_T, y_T, z_T)$. The segment is represented by the vector $\mathbf{L}_i = [l_i, m_i, n_i]^T$ with the initial point $P_{1,i}$ (see Fig. 3).

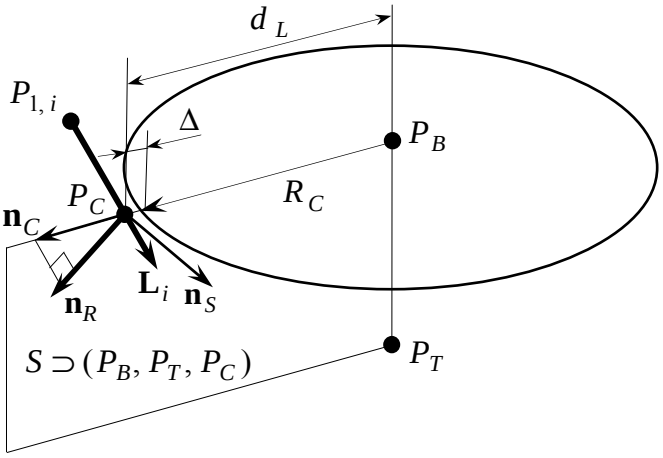


Fig. 3. A line segment and a circle line contact geometrical model

To determine the geometric contact parameters, the following items are calculated sequentially:

1. Parameters A, B, C, D of the circle plane passing through P_B perpendicular to the segment $P_B P_T$ of the cone axis or cylinder: $A = l = x_T - x_B$, $B = m = y_T - y_B$, $C = n = z_T - z_B$, $D_C = -(l x_B + m y_B + n z_B)$.
2. The parameter t_C corresponding to the cross point P_C of the pointed segment $\mathbf{L}_i$ and the circle plane; if $t_C \not\subset [0, 1]$ then the segment does not cross the circle plane, and determination of contact parameters of this type is terminated;

3. The coordinates of the point P_C and the distance d_L from it to the circle center P_B (if $d_L \le R_C$ then the segment does not cross the circle, and determination of its contact parameters of this type is terminated);
4. The components of the guide vector $\mathbf{n}_S = [\, A_S, B_S, C_S \,]^T$ of a plane S passing through three points P_C, P_B and P_T, i.e. the components of a vector parallel to a tangent to the circle in the point of its crossing the segment $P_B P_C$

$$A_S = (y_B - y_C)(z_T - z_C) - (y_T - y_C)(z_B - z_C),$$

$$B_S = -[(x_B - x_C)(z_T - z_C) - (x_T - x_C)(z_B - z_C)],$$

$$C_S = (x_B - x_C)(y_T - y_C) - (x_T - x_C)(y_B - y_C);$$

5. The unit vector $\mathbf{n}_R$ of the reaction in the contact point as a result of normalization of the components of the vector $\mathbf{L}_i \times \mathbf{n}_S$ with fulfillment of the condition $\mathbf{n}_{R,x} > 0$.
6. The unit vector $\mathbf{n}_C = [\, 0,\ y_C / d_L,\ z_C / d_L \,]^T$ of the circle radius passing through the point P_C allows to determine the contact penetration value $\Delta_n = (d_L - R_C)(\mathbf{n}_C^T \mathbf{n}_R)$ along the vector $\mathbf{n}_R$.

If $\Delta_n \le \Delta_{n,\max}$ then P_C is the contact point, otherwise the simulation is terminated with a corresponding diagnostic message.

3.4 Calculation of contact parameters for lateral borders of guide petals

Inclined lateral borders of guide petals are represented by pointed segments with initial points located on the lower bases of the petals. If the limitations on the initial contact conditions are met the extremity of the pointed segment $\mathbf{L}_\mathrm{A}$ of the active guide petal border is always outside the nearest passive petal, and does not go beyond the limits of the nearest lateral border of this petal (see Fig. 4.a).

This allows to implement the following algorithm of determining geometric parameters of contact of pointed segments $\mathbf{L}_\mathrm{A}$ and $\mathbf{L}_\mathrm{P}$ of the borders of the active and passive guide petals. First (see Fig. 4.b), sequentially, as follows below, goes the calculation of the parameters of

1. the plane $\mathbf{S}_{\mathrm{PP}}$ passing through $\mathbf{L}_\mathrm{A}$ parallel to $\mathbf{L}_\mathrm{P}$;
2. the plane $\mathbf{S}_{\mathrm{PA}}$ passing through $\mathbf{L}_\mathrm{P}$ parallel to $\mathbf{L}_\mathrm{A}$;
3. the plane $\mathbf{S}_{\mathrm{NP}}$ passing through $\mathbf{L}_\mathrm{A}$ normal to $\mathbf{S}_{\mathrm{PP}}$;
4. the plane $\mathbf{S}_{\mathrm{NA}}$ passing through $\mathbf{L}_\mathrm{P}$ normal to $\mathbf{S}_{\mathrm{PA}}$.
5. the parameter t_{CA} that corresponds, for the segment $\mathbf{L}_\mathrm{A}$, to the point C_A of its intersection with the plane $\mathbf{S}_{\mathrm{NA}}$
6. the parameter t_{CP} that corresponds for the segment $\mathbf{L}_\mathrm{P}$ to the point C_P of its intersection with the plane $\mathbf{S}_{\mathrm{NP}}$.

If $t_{\mathrm{CA}} \not\subset [\, 0, 1 \,]$ or $t_{\mathrm{CB}} \not\subset [\, 0, 1 \,]$ the segments do not cross, and the calculation of contact parameters is terminated. Otherwise, the segment $\mathrm{C_A C_P}$ crosses $\mathbf{L}_\mathrm{A}$ and $\mathbf{L}_\mathrm{P}$ and is normal to them. Its length is equal to the minimal distance between these segments.

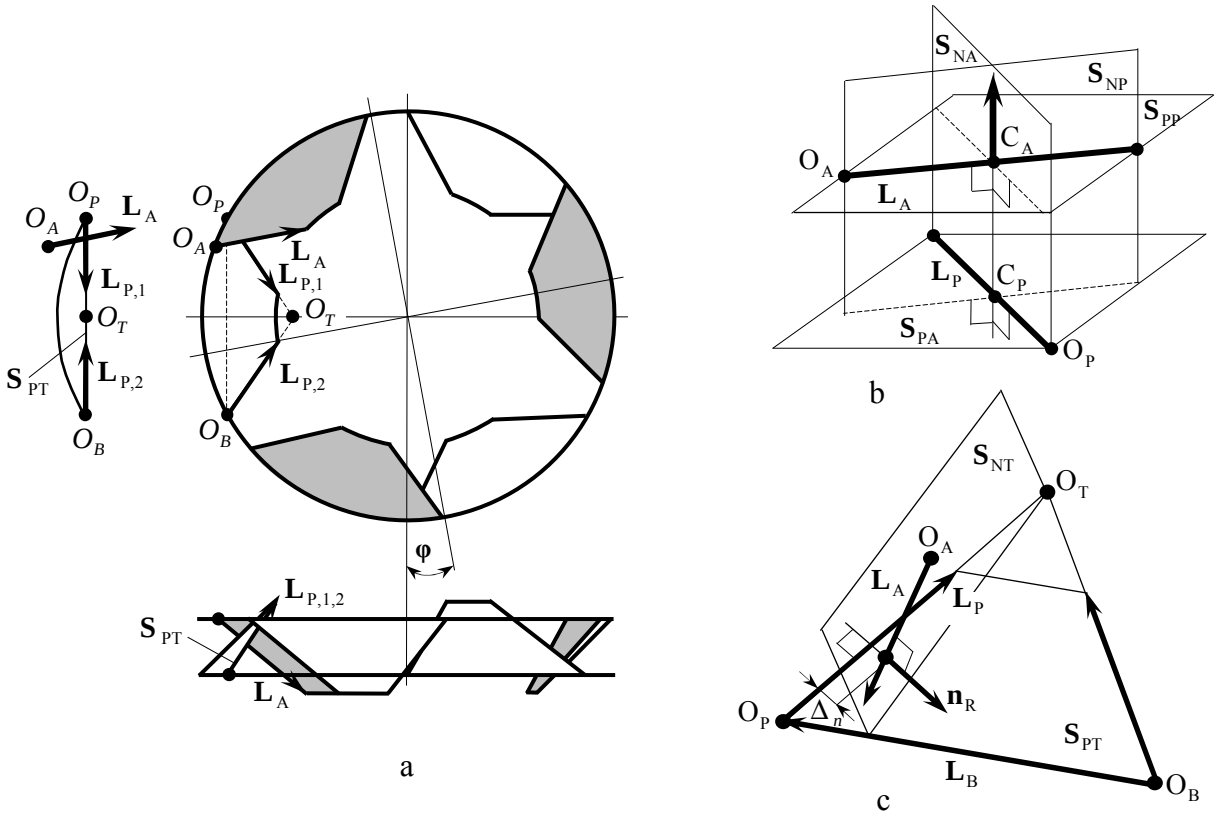


Fig. 4. Contact of lateral faces of guide petals
a – position of contacting faces relative to the guide petals surface with an axial turn of the ring;
b – building of the common normal to the line segments;
c – determination of penetration at the border contact

To determine the fact of contact penetration, an additional geometric element is used: an isosceles triangle formed by a continuation of the pointed segments of both borders of the passive guide petal until their intersection on the top O_T. Its base that joins the initial points of the border segments is specified by the pointed segment $\mathbf{L}_B$ with the initial point O_B (see Fig. 4c). The coordinates of the points O_T and O_B, the parameters of the plane $\mathbf{S}_T$ of the characteristic triangle and the segment $\mathbf{L}_B$, as well as the parameters of the border segments of the passive guide petal, are constant values in the coordinate system $X_P Y_P Z_P$.

To determine the fact of penetration, i.e. contact, sequentially, as follows below, goes the calculation of the parameters of

1. the line segment $\mathbf{L}_{TA}$ passing through the points O_T and C_A;
2. the plane $\mathbf{S}_{NT}$ passing through $\mathbf{L}_{TA}$ normal to $\mathbf{S}_T$;
3. t_{CB} that corresponds to the intersection point of the segment $\mathbf{L}_B$ with the plane $\mathbf{S}_{NT}$.

If $t_{CB} \not\subset [0, 1]$ then no contact is available. Otherwise, a contact penetration Δ_n occurs, its value is equal to the length of the segment $C_A C_P$. If it exceeds the allowable limit $\Delta_{n,\max}$ then the simulation process is terminated with a corresponding diagnostic message. Otherwise, the point C_A is considered a contact point, and the parameters of the normal

reaction line of action are calculated as $\mathbf{L}_{\mathrm{N}} = \mathbf{L}_{\mathrm{A}} \times \mathbf{L}_{\mathrm{P}}$. The contact reaction unit vector is determined as a result of normalization of the vector $\mathbf{L}_{\mathrm{N}}$, provided $\mathbf{L}_{\mathrm{N,x}} > 0$.

3.5 Calculation of contact interaction forces of guide surfaces.

In such a case contact interaction forces are determined by the value and velocity of penetration along the reaction unit vector, as well as the velocity of relative motion in the plane tangent to the contacting elements. All parameters of the contact points and contact interaction force are calculated in the coordinate system $X_P Y_P Z_P$ of the passive contacting surface. Primitives of the active surface elements may belong to one or several different links of the docking mechanism. In this case parameters of each primitive are expressed in one of moving coordinates $X_{A,k} Y_{A,k} Z_{A,k}$ and converted into $X_P Y_P Z_P$ with the direction cosine matrix $\mathbf{A}_{AP,\,k}$. The velocities of the passive and the active geometric primitives in a $i-th$ contact point are equal

$$\mathbf{v}_{PC,i}^{(P)} = \mathbf{v}_{P}^{(P)} + \boldsymbol{\omega}_{P}^{(P)} \times \mathbf{r}_{PC,i}^{(P)},$$

$$\mathbf{v}_{AC,i}^{(P)} = \mathbf{A}_{AP,k} (\mathbf{v}_{A}^{(A,k)} + (\boldsymbol{\omega}_{A}^{(A,k)} + \boldsymbol{\omega}_{A,i}^{rel(A,k)}) \times \mathbf{r}_{AC,i}^{(A,k)} + \mathbf{v}_{AC,i}^{rel(A,k)},$$

where $\mathbf{v}_{P}^{(P)}$, $\boldsymbol{\omega}_{P}^{(P)}$ и $\mathbf{v}_{A}^{(A,k)}$, $\boldsymbol{\omega}_{A}^{(A,k)}$ – absolute velocities $X_P Y_P Z_P$ and $X_{A,k} Y_{A,k} Z_{A,k}$; $\mathbf{r}_{PC,i}^{(P)}$ and $\mathbf{r}_{AC,i}^{(A,k)}$ – radius vectors of the contact point relative to $X_P Y_P Z_P$ and $X_{A,k} Y_{A,k} Z_{A,k}$, $\mathbf{v}_{AC,i}^{rel\,(A,k)}$, $\boldsymbol{\omega}_{A,i}^{rel\,(A,k)}$ – velocities of the active geometric primitive relative to $X_{A,k} Y_{A,k} Z_{A,k}$.

Velocity $\dot{\Delta}_{n,\,i}$ of penetration along the contact reaction vector $\mathbf{n}_{R}^{(P)}$, tangential velocity $\mathbf{v}_{T,\,i}^{(P)}$ in the contact point and its unit vector $\mathbf{n}_{T,\,i}^{(P)}$ are equal to

$$\dot{\Delta}_{n,\,i} = (\mathbf{v}_{AC,\,i}^{(P)} - \mathbf{v}_{PC,\,i}^{(P)})^{T}\, \mathbf{n}_{R}^{(P)},$$

$$\mathbf{v}_{T,\,i}^{(P)} = \mathbf{v}_{AC,\,i}^{(P)} - \mathbf{v}_{PC,\,i}^{(P)} - \dot{\Delta}_{n,\,i}\, \mathbf{n}_{R}^{(P)}, \qquad \mathbf{n}_{T,\,i}^{(P)} = \mathbf{v}_{T,\,i}^{(P)} / |\mathbf{v}_{T,\,i}^{(P)}|.$$

Respectively, forces $\mathbf{f}_{PC,i}^{(P)}$ and $\mathbf{f}_{AC,i}^{(P)}$ applied on the passive and active mechanisms in a $i-th$ contact point are determined by the relations

$$\mathbf{f}_{PC,\,i}^{(P)} = (k_{S,\,i}\, \Delta_{n,\,i} + c_{D,\,i}\, \dot{\Delta}_{n,\,i})(\mathbf{n}_{R}^{(P)} - k_{Fr,\,i}\, \mathbf{n}_{T,\,i}^{(P)}),$$

$$\mathbf{f}_{AC,\,i}^{(P)} = (k_{S,\,i}\, \Delta_{n,\,i} + c_{D,\,i}\, \dot{\Delta}_{n,\,i})(-\mathbf{n}_{R}^{(P)} - k_{Fr,\,i}\, \mathbf{n}_{T,\,i}^{(P)}),$$

where $k_{S,\,i}$, $c_{D,\,i}$ – contact stiffness and damping factors, $k_{Fr,\,i}$ – friction factor in the contact point.

Moments of these forces relative to $X_P Y_P Z_P$ and $X_{A,k} Y_{A,k} Z_{A,k}$ are modulo different even without the friction force due to the difference of the vectors $\mathbf{r}_{PC,i}^{(P)}$ and $\mathbf{r}_{AC,i}^{(A,k)}$.

4 REDUSING OF REDUNDAND CALCULATIONS, USAGE OF DICHOTOMY METHOD

Above, on describing the algorithms for different pairs of geometric primitives, the simplest method of increasing calculation efficiency was demonstrated, i.e. termination of calculations if required contact conditions are not met.

A more complex approach is based on a substantial analysis and elimination of incompatible types of contact. In particular, for a sphere to a receiving cone contact, it is not required to analyze interaction of the sphere with the inlet border (circle) and the receiving cone cylinder. It is not required to consider the second border of the guide petal if there is a contact with one border. Contact of the cone surface of one of the guide petals and the sphere of the counter receiving cone base excludes a similar type interaction for other guide petals of the same contact surface.

To determine contact points and parameters of surfaces represented by a finite set of geometric primitives, a direct search over the primitives can be avoided. For this, during initialization of the mathematical model, a description $2^n + 1$ of approximating geometric primitives – generatrix segments for a cone surface and spheres for a torus - is automatically generated in each of several sectors of these surfaces. The number n depends on the given accuracy of solution and determines the number of steps needed for a quick isolation of the approximating primitive, most distant from the axis of the receiving cone, circle or cylinder, using a dichotomy method [6] implemented in the following way.

At a successive iteration step, characteristic distances from the center of the counter line or axis of the second-order surface are determined for two extreme and one middle geometric primitives of the current sector with indexes i_B, i_E, i_M respectively. For generatrix segments of a cone surface these are distances between points of their intersection with the circle plane and the center of this circle; for spheres approximating a torus these are distances between the surfaces of the approximating sphere and the counter geometric primitive, i.e. a circle line, the surface of a cone or cylinder.

At the first iteration, the index values of the extreme and middle primitives are equal to $i_B = 1$, $i_E = i_B + 2^n$, $i_m = i_B + 2^{n-1}$. At the last iteration, among the three primitives with the indexes i_B, $i_M = i_B + 2^0 = i_B + 1$, and $i_E = i_B + 2^1 = i_B + 2$ one is selected with the maximal characteristic distance, contact parameters are determined for it, and the iteration process is terminated. The total number of its steps does not exceed n. Uniqueness of solution is secured by the convex form of as minimum one of the contacting elements and the linear form of the other.

If characteristic distances for all the three primitives are exactly equal it means that the axis of the cone surface or the torus coincides with the axis of the counter primitive. In this case the contact parameter is determined for the middle primitive. If this condition is not fulfilled two out of the three primitives are selected with maximal characteristic distances, the indexes i_B and i_E are assigned new values, and the search area is narrowed twice. An index $i_M = (i_B + i_E)/2$ is calculated for a new middle primitive, and the iteration process goes to a next step.

When determining contact parameters for any primitives with the maximal characteristic distance, penetration and contact may not be available. If a geometric primitive with the maximal characteristic distance is isolated at a boundary of a sector then a possibility must be analyzed for contact in the adjacent sector as well. If this primitive is interior then the rest of the sectors may not be considered.

Only those approximating geometric primitives of the surface element of the active assembly that are isolated with the dichotomy method are converted into the coordinate system $X_P Y_P Z_P$.

Fig. 5 shows a simplified example of only three iteration steps of the determination of the most circle center remote point of intersection of the circle plane and the generatrices of a truncated cone. At the first step the cone surface sector generatrices have indexes

$i_B(1), i_E(1), i_M(1)$. The characteristic distance for a $k-th$ iteration is equal to $\max\{d_B(k), d_M(k), d_E(k)\}$, where $d_B(k), d_M(k), d_E(k)-$ are distances between the center of a circle with the radius R and intersection points of the circle plane with segments of the truncated cone generatrices with indexes $i_B(k), i_E(k), i_M(k)$. The characteristic distance of the most center remote point of intersection is equal $d_M(3) < R$, which indicates absence of penetration and contact point.

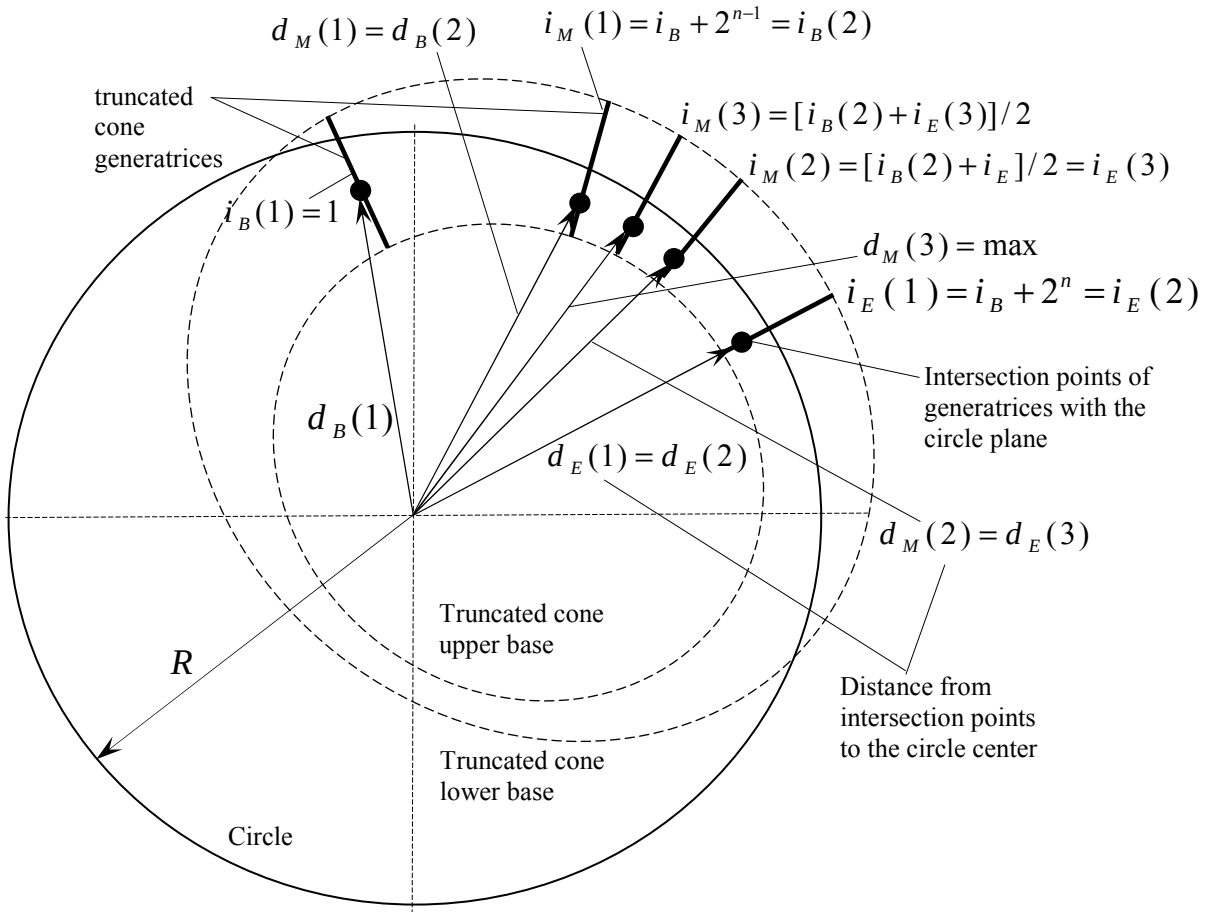


Fig. 5. Iterative determination of the most circle center remote point of intersection of the circle plane and the generatrix of the truncated cone (three iteration steps are shown).

Guide petals represent cone surface fragments, whose length of generatrix segments steadily changes in the areas of inclined lateral borders. Due to such a form of petals and presence of voids in the cone surface, it might exceed the bounds of the counter geometric primitive (circle). With that, generatrix lines in the areas of lateral faces may cross the circle, but their segments of a limited length will not contact the circle plane. Parameters of such a complex contact interaction are determined using the following modification of the above described algorithm for a next in turn guide petal.

At the first step, the dichotomy method is used to determine a generatrix segment with the index i_{Max} that has the maximal value of the characteristic distance Δ. If $\Delta <= 0$ then contact of the guide petal is impossible, and determination of its parameters is terminated. Otherwise, if for a segment with the index i_{Max} the parameter of intersection with the circle

plane meets the condition $t_C(i_{Max}) \in [0, 1]$ then contact parameters are calculated according the above described algorithm.

If $t_C(i_{Max}) > 1$ or $t_C(i_{Max}) < 0$ then the generatrix and the circle plane intersection point, which is most remote from the circle center, does not belong to the approximating segment of the guide petal. However in this case contact of adjacent approximating segments is possible.

For an identification of their contact, a sequential search is done in the direction of its possibility increase. The length of guide petal generatrix segments can change nly steadily; therefore, starting from a segment with index i_{Max}, sequentially selected are those whose t_C value decreases if $t_C(i_{Max}) > 1$, and it increases if $t_C(i_{Max}) < 0$. Contact is not available if

- for a next in turn segment the condition $t_C \in [0, 1]$ is met, but the characteristic distance $\Delta <= 0$ for its point of intersection with the circle plane;
- the extreme (first or last) approximating segment of the guide petal has been searched but no penetration into the circle identified.

If for a next in turn approximating segment of the generatrix the condition $t_C \in [0, 1]$ is met and penetration into the circle occurs then its contact parameters are determined according to the above described relations for a line segment and a circle line, and the analysis of the next guide petal is terminated.

This algorithm requires a significantly smaller scope of calculations than a direct search over all approximating segments of a guide petal cone surface.

5 METHOD OF REACTION FORCE DETERMINATION FOR SECOND CLASS CONTACT MODELS ILLUSTRATED ON MECHANICAL LATCHES

The contact reaction force in this case is determined by deformation of the spring acting on the contacting element that has one degree of freedom relative to the buffer link of the docking mechanism or docking assembly body. The notion of penetration is not used, which allows a precise fulfillment of geometric contact conditions.

The position of a spring-loaded element with one degree of freedom of a relative motion at contact is determined iteratively with the dichotomy method. But in this case a new search sector, after dichotomization of the previous one, is selected on the condition of a sign difference of the characteristic distances between contacting elements at its bounds.

The initial bounds of the solution search interval correspond to the element positions at the initial and the most deformed spring state. At the model initialization step, this interval is divided into 2^n equal parts corresponding to $2^n + 1$ intermediate positions. The number n is determined by a given solution accuracy that is limited theoretically only by real number representation accuracy in the computer. For a practically needed solution accuracy, the number of iterations is relatively small due to power dependence. For each possible position, the spring resistance force or moment, contacting element geometric parameters, and parameters of the reaction unit vector depending on the type of contact are calculated. That slightly increases the required memory size, but significantly increases the computation speed because during the iteration process pre-calculated parameters corresponding to possible positions of the element are just converted to the common calculation coordinate system. Therewith, only parameters for the positions selected during the dichotomy process are subject to conversion. Uniqueness of solution, as before, is secured by the form of contacting elements.

During simulation, for each spring-loaded element in the contacting pair within a given interval of its relative motion, characteristic distances to the counter element are calculated. If the characteristic distance for the unstrained spring position is negative then contact between

the elements does not occur. If at the extremities of the initial interval the characteristic distances have unlike signs then a position is searched, at which the characteristic distance is positive and within the required accuracy.

Algorithms of determination of distances between contacting elements are similar to the above described for guide surface simulation. For a calculated with a given accuracy relative latch position, the resistance force is already determined at the model initialization stage. For the pair of geometric primitives 'line segment – circle', pre-calculation is made for components of the reaction unit vector normal to the first characteristic segment of the latch. For the pair of geometric primitives 'point – conic surface', components of the reaction unit vector are determined in the same way as for contact between a sphere and a conic surface. It should be noted that, as for the calculation of contact parameters of guide surfaces, the algorithms are developed provided the presence of only those linear and angular docking mechanism misalignments that meet given limitations.

Contacting spring-loaded elements with one degree of freedom of relative motion are latches, contact sensors, passive hooks of the interface pressurization mechanism locks.

The geometry of a mechanical latch can be roughly described by two segments 1 and 2 corresponding to its direct and inverse surfaces. Segment 1 (direct surface) is contacting with counter elements before a latch operation, and segment 2 (inverse surface) is contacting with other counter elements after its operation. Latch operation conditions are expressed by inequalities that must be satisfied with the coordinates of the segment 1 extremity.

For a rotary-type latch (see Fig. 6), before its operation, the pairs of contacting geometric primitive are: *point (segment extremity) – conic surface, line segment – circle (receiving socket inlet border)*. To describe a translation-type latch, only one pair of primitives *point (segment extremity) – conic surface* is sufficient.

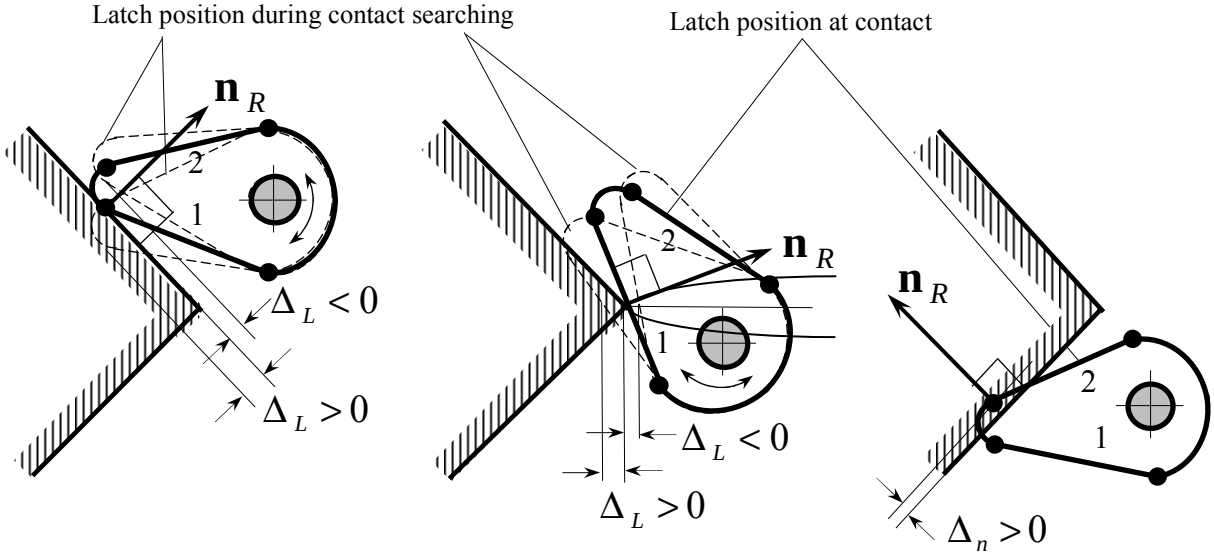


Fig. 6. Characteristic distances 1 and 2 for the description of rotary-type latch contacts:
Δ_L – characteristic distances calculated until latch operation when determining its contact with a cone or circle
Δ_n – penetration determined after its operation at contact with a mechanical stop

After latch operation (engagement), its direct rotation is impossible due to the absence of external forces applied to the direct surface (segment 1). Rotation in the inverse direction at a

contact of the inverse surface (segment 2) with a stop of the counter assembly is impossible due to the presence of the own mechanical stop of the latch. Due to the constant relative position of the latch, its contact parameters can be determined only using the penetration notion. In this case the pairs of contacting geometric primitives are: *point (segment extremity) – conic surface (of the counter element stop)* and *line segment – circle (border of the counter element stop)*. Algorithms for calculation of contact parameters for these cases are already described above.

Sensors contacting with guide surfaces and docking assembly bodies are also spring-loaded elements with one degree of freedom of relative motion. As well as latches, they can be rotary-type or translation-type. Their contacting surfaces can be represented accurately enough by a sphere. Their contact parameters are determined in the same way as for latches before engagement.

Similarly, the dichotomy iteration method can be used to determine contact parameters and reaction forces for interaction of each pair of hooks, i.e. the active controllable hook and the passive spring-loaded hook that has one degree of freedom. During rigid joining of docking assemblies, movements of these links have a lower amplitude, and the contacting surfaces have a more complex form that must be described much more accurately to assess engagement sensitivity to tight hook size tolerances. Models of such a contact interaction type are currently under development.

6 VERIFICATION OF CONTACT INTERACTION MATH MODEL

Verification includes a testing of algorithms and software operation, as well as a validation of geometric and dynamic parameters of the model.

Stand-alone testing of contact interaction simulation algorithms and software is performed before their integration into the general docking sequence model. However at this phase, it is very difficult to discover all behavioral features of the chosen analytical model. Therefore, the testing capability is also available during the dynamic process simulation. As the software code realizes a very complex model, utilization of a universal debugger is minimized. The simulation software has a capability of recording all model parameters into a file in a convenient format. To make the file size appropriate for analysis, the testing mode can be activated for any shortest possible time space, up to an individual integration step. Within this time space, individual indicators can be installed to initiate testing of a particular algorithm. Simulation can be abnormally terminated if the algorithm itself reveals a violation of contact condition limitations, allowable limit of the penetration value, or in case of a system error. Based on the simulation time of such occurrence and the error type, which are recorded in the simulation log, the testing time frame and indicators are selected for a repeated simulation and analysis. This method more than once gave information for a size correction of individual contacting elements even after a long-term use of the simulation software.

During the docking sequence, until a rigid connection of the assemblies, most contacts are damped by the docking mechanism that is more compliant than structural elements of the assemblies or the spacecraft. Therefore, it is sufficient to apply the design values of contact stiffness. For particular low-damping contacts, specific static and dynamic tests are done. A final model verification is done based on the results of a quasi-flight testing on a hybrid 6-DOF dynamic test facility with real docking assemblies and an approaching spacecraft motion math model. These test results are saved as time function measured forces and moments of contact interaction, spacecraft relative motion parameters, readings of mechanism sensors. During a real docking, sensor readings and spacecraft angular velocities are measured and recorded. The model performance criterion is a compliance of all this data with the design values.

7 CONCLUSION

Development of the above described algorithms started more than twenty years ago following the implementation of the new, at that time, approach to the description of docking mechanisms by rigid-body system dynamic equations. They ensure a real-time simulation of contact interaction for different types of docking interfaces: probe-cone, androgynous and specialized berthing units. Adequacy of these models used as part of integrated models of docking assemblies and sequences was repeatedly proved by the compliance of simulation results with ground and flight test data.

REFERENCES

[1] Course of theoretical mechanics: Course book for universities / V.I. Drong, V.V. Dubimnin, M.M. Ilyin et al.; Edited by K.S. Kolesnikov. 3-d edition, M.: MBSTU press, 2005.

[2] *J.W. Baumgarte,*. Stabilization of constraints and integrals of motion in dynamical systems.– Computer Methods in Applied Mechanics and Engineering, Vol.1, 1-16, 1972.

[3] *G.W. Gear,* Differential-algebraic Equations. – NATO ASI Series, Vol. 9. Computer Aided Analysis and Optimization of Mechanical System Dynamics./ Edited by E.J. Haug, Springer-Verlag, Berlin-Heidelberg, 1984.

[4] *L.R. Petzold,* Computational challenges in mechanical system simulation. – Computer-Aided Analysis of rigid and flexible Mechanical Systems, Kluwer Academic Publishers, Netherlands, 483-499, 1994.

[5] *M.Y. Vygodskiy,* Higher mathematics handbook. – M.: Technical-theoretical literature main press, 1956.

[6] *B.P. Demidovich, I.A. Maron,* Fundamental computational mathematics. – M.: Physmathgiz, 1963.

COMPDYN 2013
4th ECCOMAS Thematic Conference on
Computational Methods in Structural Dynamics and Earthquake Engineering
M. Papadrakakis, V. Papadopoulos, V. Plevris (eds.)
Kos Island, Greece, 12–14 June 2013

A PROCEDURE TO SELECT TIME-HISTORIES FOR SHAKING TABLE TESTS ON NONSTRUCTURAL COMPONENTS

Gennaro Magliulo[1], Giuseppe Maddaloni[2], Crescenzo Petrone[1]

[1] Department of Structures for Engineering and Architecture, University of Napoli Federico II
Via Claudio 21, 80125 Naples, Italy
e-mail: {gmagliul, crescenzo.petrone}@unina.it

[2] Department of Technology, University of Napoli Parthenope
Centro Direzionale, Isola C4, 80123 Naples, Italy
giuseppe.maddaloni@uniparthenope.it

Keywords: time-history definition, continuous plasterboard ceiling, full scale shaking table test, seismic performance, nonstructural components.

Abstract. *In the last years, the scientific community research effort is moving towards the investigation of the seismic behaviour of nonstructural components. In this paper, a procedure to select time histories to perform full-scale shaking table tests on nonstructural components is proposed. In particular, the experimental tests are designed and implemented to investigate the seismic behaviour of a typology of nonstructural components: the plasterboard continuous suspended ceilings.*
A set of five accelerograms, used as input for the shakings, are opportunely selected matching a target response spectrum or required response spectrum (RRS), provided by the USA code ICBO-AC156 "Acceptance criteria for seismic qualification testing of nonstructural components".
The RRS is obtained as a function of the design spectral response acceleration at short periods, SDS, depending on the site soil condition and the mapped maximum earthquake spectral acceleration at short periods. The selection procedure is performed, for a RRS corresponding to SDS=1.50g; the so obtained record is then scaled to match other four levels of the target spectrum (corresponding to SDS 0.30g, 0.60g, 0.90g and 1.20g).
These accelerograms, representative of different intensity levels, are then applied to a test setup opportunely designed and realized to perform the shaking table tests. Two typologies of continuous plasterboard ceilings are tested and three limit states (occupancy, damage and life safety limit state) are considered in this study to characterize the seismic response. The ceilings tested shows no damage at all intensity level (the acceleration on the ceiling ranges from 0.40g to 2.36g), resulting in a low fragility.

1 INTRODUCTION

The failure of ceiling systems has been one of the most widely reported types of nonstructural damage in buildings during past earthquakes [1, 2]. The recent L'Aquila earthquake, occurred on April the 6th, 2009, in central Italy, has widely confirmed the last assertion: the most part of the evacuated buildings showed undamaged structural elements and moderate-to-heavy damaged nonstructural components, especially ceiling systems [3].

The damage of the nonstructural components gives the largest contribution to the economic loss due to an earthquake. In fact, structural cost represents a small portion of the total one, corresponding to 18%, 13% and 8% for offices, hotels and hospitals respectively [4]. For these reasons, the knowledge of the seismic performance of nonstructural elements is essential.

Very limited studies were conducted in the past on the seismic behaviour of nonstructural components, even though they are very common both in residential and industrial buildings [5, 6]. The presence of nonstructural components may strongly influence the lateral stiffness of the portion of the structure in which they are inserted [7], and may also affect the regularity of the whole structural system [8-10]. For this reason systematic studies on their seismic behaviour are needed.

An extensive study aimed at the fragility curve evaluation of ceiling system composed of tiles supported by metallic grids was carried out in Buffalo via shake table test [2, 11]. Shaking table tests were also performed to investigate the seismic behaviour of plasterboard partitions in [12, 13].

In this paper, the seismic behaviour of plasterboard continuous suspended ceilings under strong earthquakes is investigated, focusing the attention on the definition of the input accelerogram time histories. The ceiling system differs from the systems of the previous studies for its "continuous" nature: it consists of a unique plasterboard panel obtained connecting few boards each other. The vulnerability evaluation of this particular plasterboard ceiling system is the main goal of the research. This aim is pursued via shake table tests: this experimental facility is particularly needed in this case since suspended ceiling systems are not amenable to traditional structural analysis.

A comparison with tests on a U.S. common ceiling system is also presented.

2 DESCRIPTION OF THE EXPERIMENTAL TESTS

Two typologies of plasterboard continuous suspended ceilings are tested: single frame ceiling (SFC) and double frame ceiling (DFC) systems. A schematic representation of the two used systems is shown in Figure 1(a) and Figure 1(b) respectively.

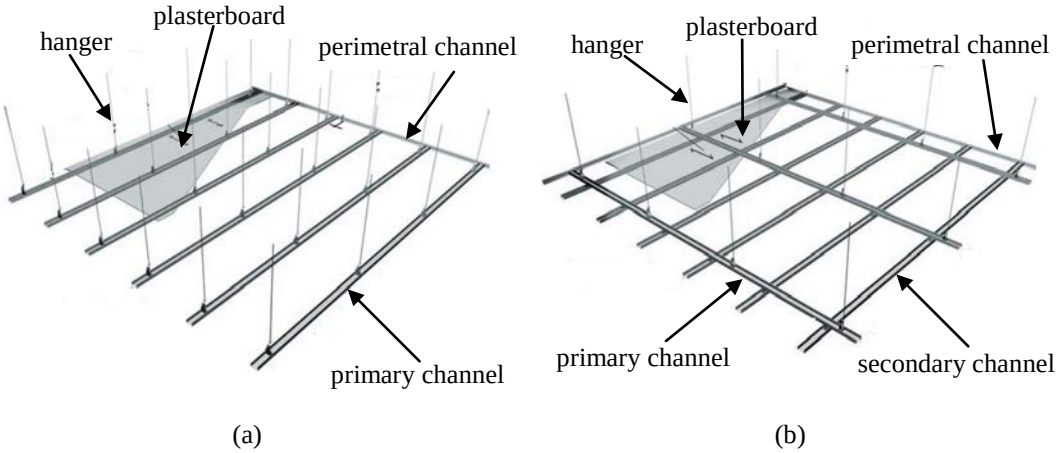


Figure 1: Suspended plasterboard continuous ceilings: (a) single frame ceiling (SFC); (b) double frame ceiling (DFC).

The seismic qualification of suspended ceiling is carried out by the earthquake simulator system available at the laboratory of Structural Engineering Department of University of Naples Federico II. The system consists of two 3 m x 3 m square shake tables but only is used in this experimental campaign.

With the purpose of simulating the seismic effects on the ceilings, a steel test frame is properly designed and built (Figure 2). The test frame is of S275 steel material with concentric V-bracings made of steel U-section (UPN160). The very stiff test frame is required in order to control the acceleration on the specimen and to avoid shake table – test frame – ceiling system double-resonance issues.

Two U-section profiles (UPN100) are welded around the perimeter of the test frame, at a distance of 20 cm and 50 cm from the roof; a 40 mm x 100 mm timber ledger is inserted in the U-section profile in order to easily laterally restrain the ceiling system. Indeed, the ceiling system plasterboards are connected along the perimeter of the frame to the timber ledger. Consequently, the light mass and the large stiffness of the timber-channel profiles system represent the typical boundary conditions of a ceiling on structural elements. The total weight of the test frame is equal to 19.2 kN.



Figure 2: Test frame installed on the shake table.

The tested specimen is composed by three plasterboards connected one another via stucco, both for SFC and DFC. The total dimension of the specimen is 2.20 m x 2.20 m.

Accelerometers and strain gauges are used to monitor the response of the test frame and plasterboard ceilings in both ceiling system configurations.

In order to adequately measure the seismic behaviour of the specimen, three triaxial accelerometers are installed at the centre and at the edges of the roof, as shown in Figure 3; one is also placed at the base of the frame, in order to verify the real input transmitted to the specimen from the shaking table. Further details are given in [14].

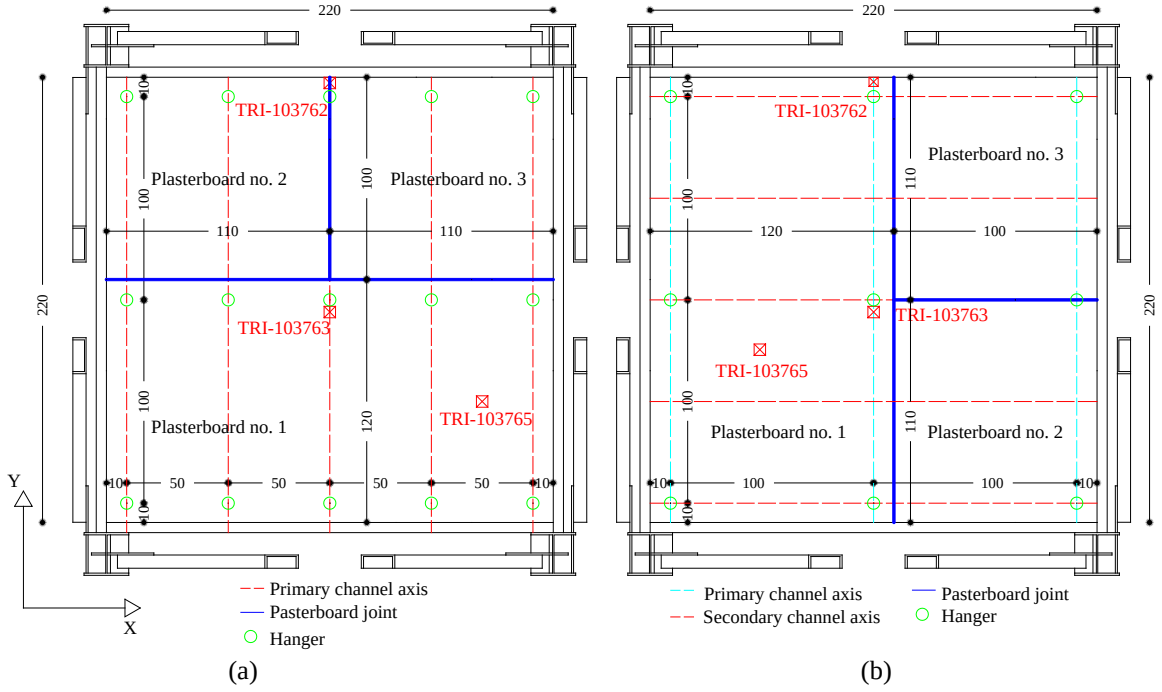


Figure 3: Triaxial accelerometers, plasterboard and hanger position in the case of single frame ceiling (a) and double frame ceiling (b) specimen.

3 DEFINITION OF THE INPUT MOTION

A set of five accelerograms, used as input for the shakings, are opportunely selected matching a target response spectrum or required response spectrum (RRS), provided by the ICBO-AC156 code "Acceptance criteria for seismic qualification testing of nonstructural components" [15].

The equipment earthquake effects are determined considering only horizontal load effects. The Required Response Spectra (RRS) for the horizontal direction are developed based on normalized response spectra shown in Figure 4 and the formula for the evaluation of the total design horizontal force, F_P.

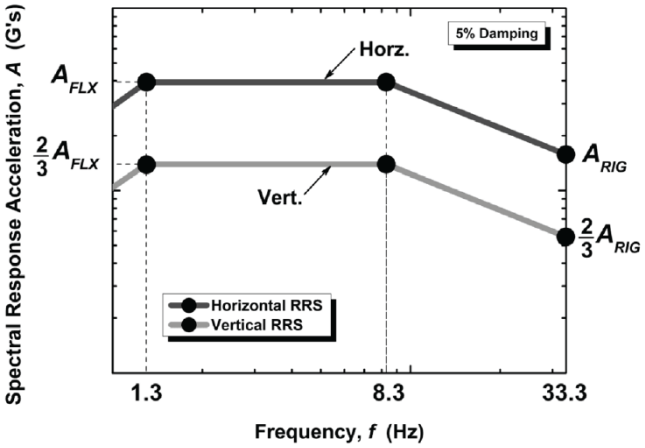


Figure 4: Normalized Required Response Spectrum for equipment and nonstructural components [15].

The RRS is defined using a damping value equal to 5 percent of critical damping. In case the building dynamic characteristics are not known or specified, the horizontal force requirements are determined using the following equation.

$$F_P = \frac{0.4 \cdot a_p \cdot S_{DS} \cdot W_P}{R_P / I_P} \left(1 + 2\frac{z}{h}\right) \tag{1}$$

The height factor ratio (*z*/*h*) accounts for above grade-level equipment installations within the primary supporting structure and ranges from zero at the base of the structure to one at roof level.

The site-specific ground spectral acceleration factor, S_{DS}, is taken from the design value maps. The S_{DS} factor is used to define the general design earthquake response spectrum curve and is used to determine the design seismic forces for the primary building structure. The ratio of R_p/I_p is a reduction factor to account for inelastic response of the component and the importance factor of the component. The ratio (R_p/I_p) is set equal to 1. The component amplification factor, a_p, acts as a force increase factor by accounting for probable amplification of response associated with the inherent flexibility of the non-structural component. The component amplification factor, a_p, is taken from the formal definition of flexible and rigid components. By definition, for fundamental frequencies less than 16.7 Hz the equipment is considered flexible (maximum amplification a_p = 2.5), which corresponds to the amplified region of the RRS. For fundamental frequencies greater than 16.7 Hz the equipment is considered rigid (minimum a_p = 1.0), which corresponds to the zero period acceleration. These results in two normalizing acceleration factors, that when combined, defines the horizontal equipment qualification RRS:

$$A_{FLX} = S_{DS} \cdot \left(1 + 2 \cdot \frac{z}{h}\right); A_{RIG} = 0.4 \cdot S_{DS} \cdot \left(1 + 2 \cdot \frac{z}{h}\right) \tag{2}$$

where A_{FLX} is limited to a maximum value of 1.6 times S_{DS}.

The input to the table is provided through acceleration time histories representative of expected/target ground motion; these time histories are selected with the aim of matching the target or required response spectrum of nonstructural components. Two artificial time histories, matching the nonstructural components spectra, are defined and used as drive motion for shaking table test, starting from the one characterised by the lowest intensity to the one characterised by the largest intensity.

The parameter selected to characterize the ground motion for input to the simulator is the spectral acceleration at 0,2 seconds, S_{DS}. For horizontal design-basis earthquake shaking, the

International Building Code [16] defines the short period design basis earthquake acceleration response as:

$$S_{DS} = \frac{2}{3} \cdot F_A \cdot S_s \tag{3}$$

where S_{DS} is the design spectral response acceleration at short periods, F_A is a site soil coefficient, and S_S is the mapped maximum considered earthquake spectral acceleration at short periods.

The target of shaking levels ranges from S_{DS} equal to 0.30 g to S_{DS} equal to 1.50 g in order to make the problem as general as possible, i.e. representative of general earthquake ground motions.

The earthquake excitations used for the qualification of the ceiling system are generated using a spectrum-matching procedure from the RSP Match program [17]. The values of the spectral acceleration of the response spectrum obtained with the matching procedure are scaled to envelope the target spectrum (ranging from S_{DS} equal to 0.30 g to 1.50 g) over the frequency range from 1 to 33 Hz. The low frequency content is removed from the scaled records for the purpose of not exceeding the displacement and velocity limits of the earthquake simulator. In the followings, the procedure used for the generation of the earthquake records used as acceleration input to the earthquake simulator is presented.

ICBO [15] requires that the response spectra associated with the earthquake histories used for qualification must envelope the required (or target) response spectrum (RRS) using a maximum one- third-octave bandwidth resolution over the frequency range from 1 to 33 Hz, or up to the limits of the simulator. The amplitude of each matched spectrum ordinate must be independently adjusted along each of the orthogonal axes until the response spectrum envelopes the RRS. The response spectrum ordinates must not be lower than 0.9 times RRS and larger than 1.3 times RRS (according to EC8 [18] and AC156 rules respectively). The earthquake histories used for the qualification and fragility testing of the ceiling systems were generated using the following procedure:

1. Select a baseline earthquake that defines the overall duration, the rise time, steady state, and decline time of the resultant acceleration record. The acceleration profile is interpolated to produce a time series.
2. The RSP Match software is applied by means of a time domain modification of the baseline earthquake of step1. in order to make it compatible with RRS (Required Response Spectrum) [17].

The baseline earthquake is defined according to requirements of code [15] according to the following characteristics:

- nonstationary broadband random excitations having an energy content ranging from 1.3Hz to 33.3Hz;
- multiple frequency random excitations, the amplitudes of which adjusted either manually or automatically based on multiple frequency bands;
- one sixth octave bandwidth resolution is used;
- the total duration of the input motion is 30seconds, with non-stationary character being synthesized by an input signal build hold decay envelope of 5 seconds, 20 seconds, and 5 seconds, respectively;
- the input duration of the time history tests contain at least 20 seconds of strong motion.

For the purpose of reaching the desired levels of shaking without exceeding the limits of the earthquake simulator, the maximum accelerations, velocities and displacements for the obtained records at all the shaking levels were calculated and were compared to the simulator

limits. In particular the earthquake simulator velocity and displacement limits are 100 cm/sec and ± 25.0 cm, respectively.

Acceleration limits have not been properly taken into account because the value of masses to be tested are small; in particular the mass allows reaching acceleration values of the earthquake simulator up to 5.0g. Then the matched record so obtained, is band passed filtered over the range of frequency 1 ÷ 33 Hz.

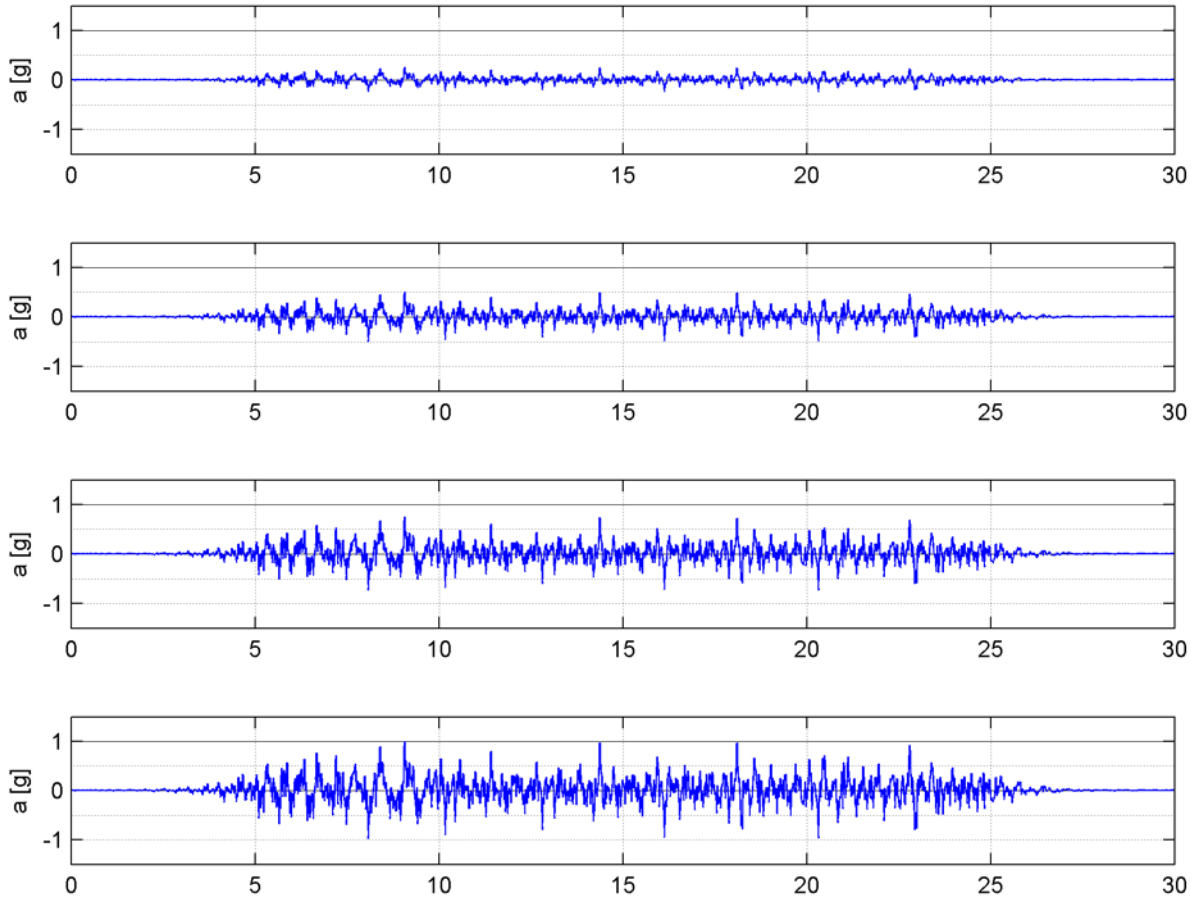
The low frequency content is eliminated from the scaled records for the purpose of not exceeding the displacement and velocity limits of the earthquake simulator.

Finally, the aforementioned procedure briefly consists of:

- defining a baseline earthquake;
- matching the required response spectrum;
- band – pass filtering over the frequency range 1 ÷ 33 Hz.

The procedure is performed for a Required Response Spectrum corresponding to SDS=1.50g; the so obtained record is then scaled to match the different levels of the target spectrum defined previously, i.e. SDS=0.30g, SDS=0.60g, SDS=0.90g, SDS=1.20g.

The input motion for the different intensities and the elastic spectrum are presented in Figure 5 and Figure 6.



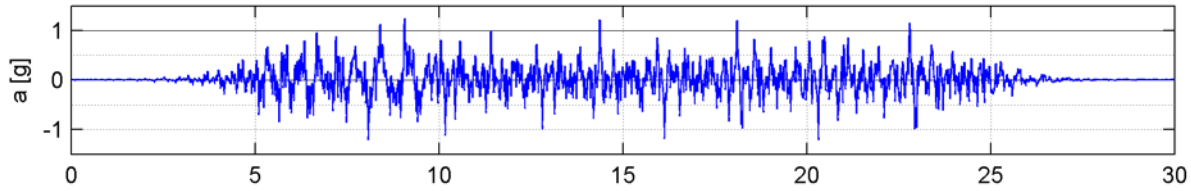


Figure 5: Input acceleration time histories for Y direction corresponding to SDS equal to 0.30g, 0.60g, 0.90g, 1.20g and 1.50g.

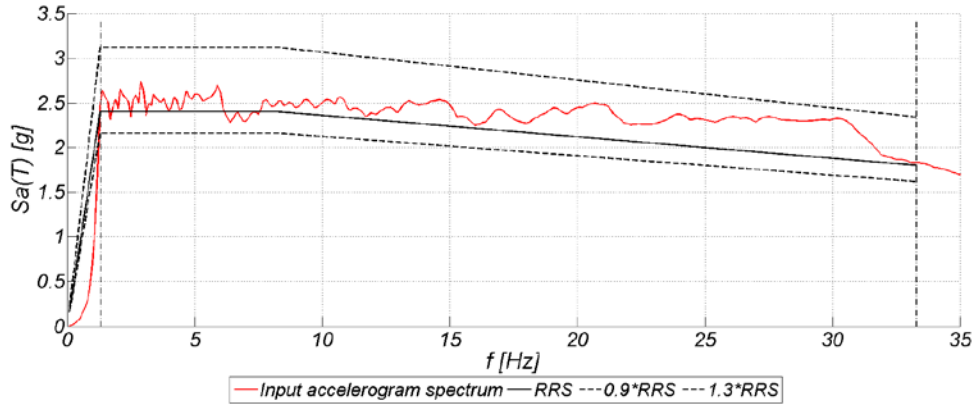
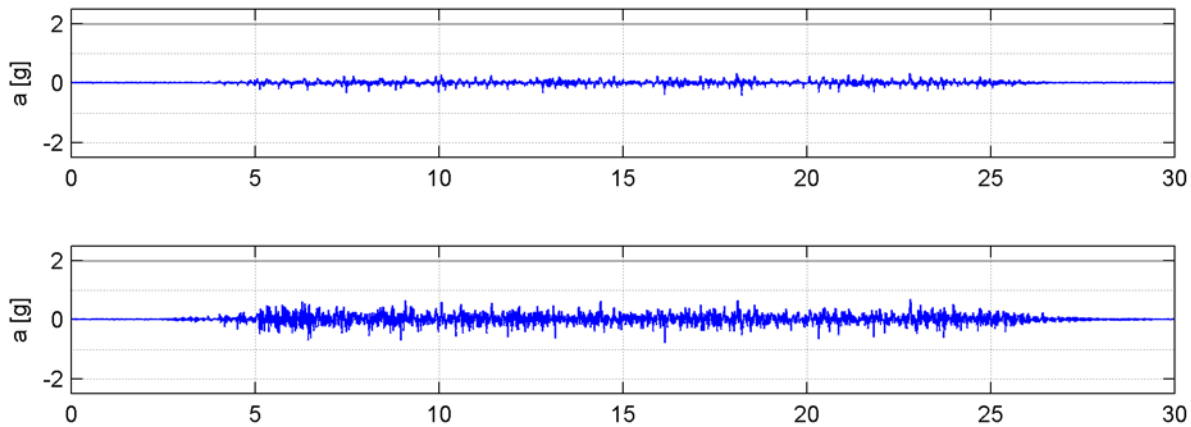


Figure 6: Input accelerogram spectrum, RRS (bold line), upper and lower matching limits (dashed line) for a level of shaking corresponding to S_{DS} equal to 1.50g.

4 RESULTS

Using the selected drive motions, five unidirectional shaking tests are performed for both ceiling systems. In Figure 7 the acceleration time history recorded on the ceiling is presented, while in Table 1 and Table 2 the maximum recorded values of acceleration on the ceilings and on the test frame roof are listed and compared to the maximum acceleration registered at the base of the shaking table. This comparison is done both for single (Table 1) and for double frame ceiling (Table 2). Values greater than 2.0g, due to dynamic amplifications in the specimen, are recorded on the ceiling. This aspect may be crucial when the build of a fragility curve is the main goal of the research. For this reason, the procedure described in [19], concerning the optimization of a signal recorded at desired locations, i.e. on the ceilings, will be taken into account in the next experimental campaigns.



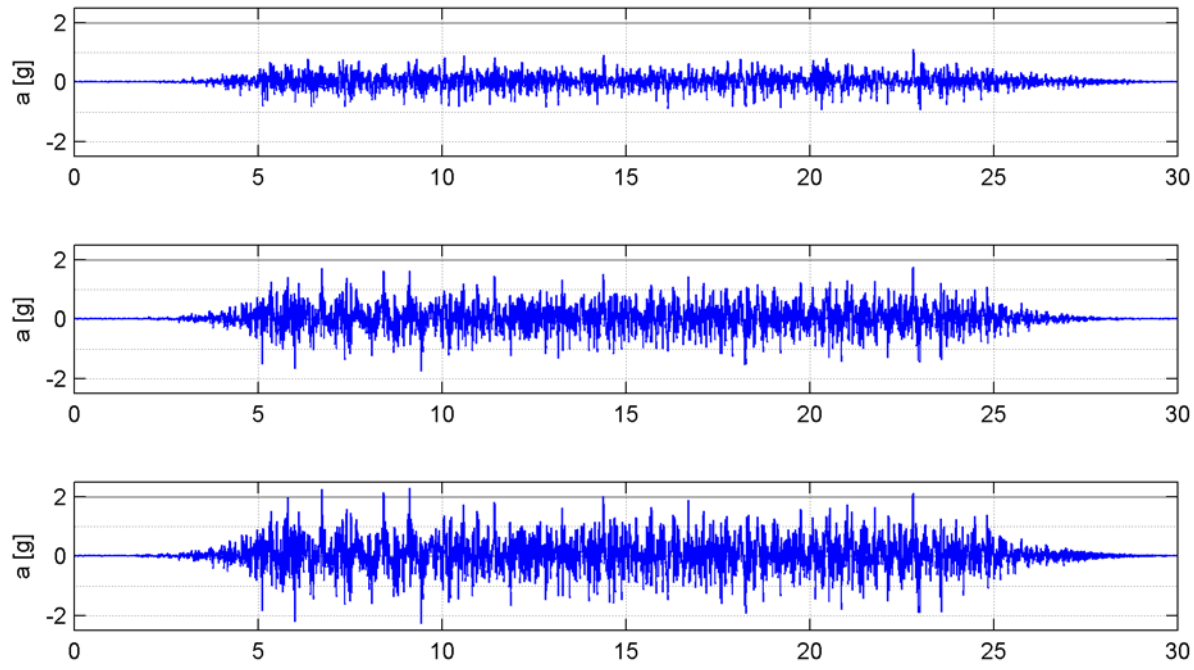


Figure 7: Acceleration time histories recorded on the ceiling (Accelerogram no. 103763) for single frame ceiling (SFC) for the intensity levels corresponding to SDS equal to 0.30g, 0.60g, 0.90g, 1.20g and 1.50g.

Position	Ceiling	Roof	Base
test no. 1	0.42g	0.45g	0.25g
test no. 2	0.78g	0.78g	0.50g
test no. 3	1.10g	1.15g	0.69g
test no. 4	1.79g	1.90g	1.04g
test no. 5	2.28g	2.51g	1.36g

Table 1: Maximum recorded accelerations at base, roof and ceiling level - single frame ceiling test.

Position	Ceiling	Roof	Base
test no. 1	0.42g	0.46g	0.28g
test no. 2	0.69g	0.75g	0.52g
test no. 3	1.07g	1.18g	0.75g
test no. 4	1.84g	2.06g	1.06g
test no. 5	2.36g	2.58g	1.35g

Table 2: Maximum recorded accelerations at base, roof and ceiling level - double frame ceiling test.

In this study, three limit states are considered in order to characterize the seismic response of suspended ceiling systems: (a) occupancy limit state (SLO); (b) damage limit state (SLD); (c) life safety limit state (SLV). The limit states are defined quantitatively by the number of

damaged components (indicated as percentage of damage). From the first to the third considered limit state the damage in the ceiling increases (10%, 30% and 50% damage respectively).

After each shaking level, damage is observed inspecting physical conditions of the components. Concerning the main components of the SFC system (see Figure 1(a)) indicated as primary and perimetral channels, hangers, plasterboards panels and connections, the number of damaged elements observed during the test performed with intensity level S_{DS} equal to 1.50g is indicated in Table 3. The table also reports for each component the total number of elements for the single frame ceiling system, the damage typology and the limit number of damaged elements required to reach a limit state. As clearly shown in the Table 3, no damage is recorded, though the high level of horizontal accelerations experienced. The same result is obtained for double frame ceiling system.

Elements	Number	Damage	SLO (10%)	SLD (30%)	SLV (50%)	Damaged elements
Hangers	15		2	5	8	0
Primary channels	5	buckling	1	2	3	0
		bending				0
Perimetral channels	4	buckling	1	1	2	0
		bending				0
Plasterboard-channel connections (screws)	87	shear	9	26	43	0
		tension				0
		punching shear				0
Plasterboards	3	collapse	-	-	1	0

Table 3: Form for recording damage observed during the test performed on single frame ceiling with intensity level SDS equal to 1.50g [14].

An interesting comparison with a previous vulnerability study performed by Badillo-Almaraz et al. [11] on typical U.S. ceiling system with discrete tiles is made. The tests were performed at the Structural Engineering and Earthquake Simulation Laboratory (SEESL) at the University of Buffalo.

In order to make a comparison, the fragility curve for ceilings with undersized tiles [11] in terms of PFA is considered (Figure 7). This fragility curve, at the acceleration equal to 1.35 g, which is the maximum acceleration of the shaking table (Table 1 and Table 2) attained during the tests performed in Naples, gives 100% probability of exceeding minor and moderate damage state and 29% probability of exceeding major damage state. As already said, the ceilings tested in Naples, instead, show no damage at all intensity levels of the tests, resulting in a lower fragility with respect to the ceiling systems tested in Buffalo. Three main reasons may be the cause of this different vulnerability: (a) the continuous nature of the tested ceiling, that improves the seismic behaviour with respect to the ceilings with tiles; (b) the dense steel channel grid (the “primary channel” span is 500 mm and 1000 mm for SFC and DFC systems respectively, the “secondary channel” span is 500 mm for DFC system), that connects one another the plasterboards in a unique horizontal element, ensuring high in plane stiffness and strength; (c) the large number of hangers that connects the ceiling system to the roof, ensuring an adequate out of plane stiffness and strength, avoiding any ceiling vertical movement; (d) the smaller dimensions of the specimen tested in Naples with respect to the specimen tested in

Buffalo (2.20m x 2.20m vs 4.88m x 4.88m), considering that very recent studies seem to show that specimen dimensions can affect the ceiling seismic response.

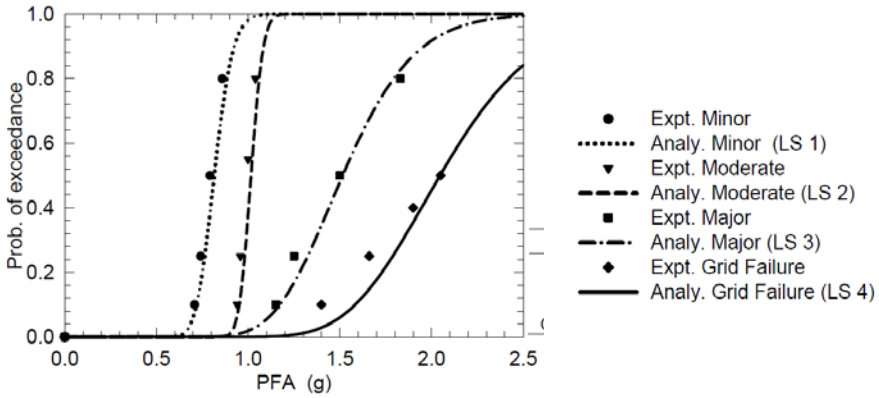


Figure 8: Ceiling fragility curve: ceiling with undersized tiles [11].

The tests are performed shaking the table only in one direction. No vertical excitation is applied to the specimen. For the tested continuous ceiling systems, this component is not assumed as crucial. Indeed, the continuous plasterboard is connected to the roof with many vertical steel hangers (span is equal to 1 m along both the horizontal directions) with a sufficient axial stiffness (for steel hanger design, a safety factor larger than 3 is considered). Hence, no failure due to earthquake vertical component is expected.

5 CONCLUSIONS

Shaking table tests are performed to investigate the seismic behaviour of plasterboard continuous suspended ceilings under strong earthquakes. Two typologies of continuous plasterboard ceilings (i.e. single frame ceiling (CSO) and double frame ceiling (CDO)) are tested. The ceilings tested shows no damage at all intensity level (the acceleration on the ceiling ranges from 0.40g to 2.36g), resulting in a low fragility.

A set of five accelerograms, used as input for the shakings, are opportunely selected matching a target response spectrum or required response spectrum (RRS), provided by the ICBO-AC156 code “Acceptance criteria for seismic qualification testing of nonstructural components”. The procedure for the selection of the accelerograms is described in details in the paper.

Three main reasons may be the cause of this low fragility: (a) the continuous nature of the tested ceilings; (b) the dense steel channel grid; (c) the large number of hangers that connects the ceiling system to the roof, avoiding any ceiling vertical movement.

Finally, an interesting comparison with a previous vulnerability study performed by Badillo-Almaraz et al. in 2007 on typical U.S. ceiling with tiles systems was performed. The comparison points out the lower fragility of continuous plasterboard ceiling systems, tested in Naples, with respect to the ceiling systems with discrete tiles, tested in the U.S.; however, this conclusion could be influenced by the smaller dimensions of the specimen tested in Naples with respect to the specimen tested in Buffalo.

ACKNOWLEDGEMENT

This research study has been funded both by Italian Department of Civil Protection in the frame of the national project DPC - ReLUIS 2010-2013 and by Siniat that also provided the ceiling components for the testing program.

REFERENCES

[1] H. Badillo-Almaraz, A.S. Whittaker, A. Reinhorn, G.P. Cimellaro, Seismic Fragility of Suspended Ceiling Systems, Report MCEER-06-0001. MCEER/SUNY/Buffalo, 2006.

[2] A. Gilani, A. Reinhorn, B. Glasgow, O. Lavan, H. Miyamoto, Earthquake Simulator Testing and Seismic Evaluation of Suspended Ceilings. *Journal of Architectural Engineering*, **16**, 63-73, 2010.

[3] G. Magliulo, V. Pentangelo, G. Manfredi, Danneggiamento delle controsoffittature a seguito del terremoto dell'Aquila dell'aprile 2009 V1.00, available on http://www.reluis.it (in Italian). 2009.

[4] S. Taghavi, E. Miranda, Response assessment of nonstructural building elements, PEER report 2003/05. College of Engineering, University of California Berkeley, USA. , 2003.

[5] G. Magliulo, G. Fabbrocino, G. Manfredi, Seismic assessment of existing precast industrial buildings using static and dynamic nonlinear analyses. *Engineering Structures*, **30**, 2580-2588, 2008.

[6] G. Magliulo, V. Capozzi, G. Fabbrocino, G. Manfredi, Neoprene-concrete friction relationships for seismic assessment of existing precast buildings. *Engineering Structures*, **33**, 535-538, 2011.

[7] T.B. Panagiotakos, M.N. Fardis, Seismic response of infilled RC frames structures. In: International Association on Earthquake Engineering, editor. Eleventh World Conference on Earthquake Engineering. Mexico. , 1996.

[8] G. Magliulo, V. Capozzi, R. Ramasco, Seismic performance of R/C frames with overstrength discontinuities in elevation. *Bulletin of Earthquake Engineering*, **10**, 679-694, 2012.

[9] G. Magliulo, G. Maddaloni, E. Cosenza, Extension of N2 method to plan irregular buildings considering accidental eccentricity. *Soil Dynamics and Earthquake Engineering*, **43**, 69-84, 2012.

[10] G. Magliulo, R. Ramasco, Seismic response of three-dimensional r/c multi-storey frame building under uni- and bi-directional input ground motion. *Earthquake Engineering and Structural Dynamics*, **36**, 1641-1657, 2007.

[11] H. Badillo-Almaraz, A.S. Whittaker, A.M. Reinhorn, Seismic fragility of suspended ceiling systems. *Earthquake Spectra*, **23**, 21-40, 2007.

[12] G. Magliulo, C. Petrone, V. Capozzi, G. Maddaloni, P. Lopez, G. Manfredi, Seismic performance evaluation of plasterboard partitions via shake table tests. *Bulletin of Earthquake Engineering*, (under review), 2013.

[13] G. Magliulo, C. Petrone, V. Capozzi, G. Maddaloni, P. Lopez, R. Talamonti, G. Manfredi, Shake Table Tests on Infill Plasterboard Partitions. *The Open Construction and Building Technology Journal*, **6**, 155-163, 2012.

[14] G. Magliulo, V. Pentangelo, G. Maddaloni, V. Capozzi, C. Petrone, P. Lopez, R. Talamonti, G. Manfredi, Shake table tests for seismic assessment of suspended continuous ceilings. *Bulletin of Earthquake Engineering*, **10**, 1819-1832, 2012.
[15] International Conference of Building Officials (ICBO), AC 156 Acceptance Criteria for the Seismic Qualification of Nonstructural Components. ICBO Evaluation Service, Inc., Whittier, California, USA, 2000.
[16] International Code Council (ICC), International Building Code, 2000 Edition (IBC 2000). Falls Church, Virginia, USA. , 2000.
[17] D.N. Grant, P.D. Greening, M.L. Taylor, B. Ghosh, Seed record selection for spectral matching with RSPMatch2005. Proceedings of 14th world conference on earthquake engineering. Beijing, China, 2008.
[18] G. Maddaloni, G. Magliulo, E. Cosenza, Effect of the seismic input on non-linear response of R/C building structures. *Advances in Structural Engineering*, **15**, 1861-1877, 2012.
[19] G. Maddaloni, K.P. Ryu, A.M. Reinhorn, Simulation of floor response spectra in shake table experiments. *Earthquake Engineering & Structural Dynamics*, **40**, 591-604, 2011.

COMPDYN 2013
4th ECCOMAS Thematic Conference on
Computational Methods in Structural Dynamics and Earthquake Engineering
M. Papadrakakis, V. Papadopoulos, V. Plevris (eds.)
Kos Island, Greece, 12–14 June 2013

AN IMPROVED METHODOLOGY FOR THE VIRTUAL POINT TRANSFORMATION OF MEASURED FREQUENCY RESPONSE FUNCTIONS IN DYNAMIC SUBSTRUCTURING

Maarten V. van der Seijs[1], Daniël D. van den Bosch[1], Daniel J. Rixen[2] and Dennis de Klerk[1]

[1]Delft University of Technology
Faculty of Mechanical, Maritime and Materials Engineering, Section of Engineering Dynamics
Mekelweg 2, 2628CD, Delft, The Netherlands
e-mail: m.v.vanderseijs@tudelft.nl

[2]Technische Universität München
Faculty of Mechanical Engineering, Institute of Applied Mechanics
Boltzmannstr. 15, D - 85748 Garching, Germany
e-mail: rixen@tum.de

Keywords: Frequency Based Substructuring, Experimental Substructuring, NVH, Virtual Point Transformation

Abstract. *Dynamic Substructuring methods play a significant role in the analysis of todays complex systems. Crucial in Dynamic Substructuring is the correct definition of the interfaces of the subsystems and the connectivity between them. Although this is straightforward practice for numerical finite element models, the experimental equivalent remains challenging. One of the issues is the coupling of the rotations at the interface points that cannot be measured directly. This work presents a further extension of the virtual point transformation that is based on the Equivalent Multi-Point Connection (EMPC) method and Interface Deformation Mode (IDM) filtering. The Dynamics Substructuring equations are derived for the weakened interface problem. Different ways to minimise the residuals caused by the IDM filtering will be introduced, resulting in a controllable weighting of measured Frequency Response Functions (FRFs). Also some practical issues are discussed related to the measurement preparation and post-processing. Special attention is given to sensor and impact positioning. New coherence-like indicators are introduced to quantify the consistency of the transformation procedures: sensor consistency, impact consistency and reciprocity.*

1 INTRODUCTION

Dynamic Substructuring (DS) has proven to be a powerful engineering tool for a wide variety of industries. It allows a complex dynamic system to be modelled and analysed as separate components or "substructures", building a bridge between the efforts of different suppliers and design groups. Also, components may be coupled from either numerical or experimental nature. The first class is often characterised by finite element models or reduced-order models, that tend to be relatively easy to assemble and highly controllable in terms of numerical accuracy. Substructuring methods associated with these models are numerous and have been well accepted over the last decades [2]. However, with increasing product complexity, the question rises how truthful some numerical models represent the actual behaviour of the components. Experimental identification of components is therefore often desired for the purpose of model validation.

In recent years though, an increasing amount of research has been devoted to substructuring with the experimental models themselves, leading to hybrid and very powerful modelling methodologies [4, 11]. Although the substructuring techniques themselves are formulated in a rather straightforward way (see for instance [5]), the largest challenges exist in the coupling of the measured components. To couple substructures properly, one requires a complete and accurate model of the dynamics at the interface for both translational and rotational degrees of freedom [8, 12, 13].

1.1 Modelling the interface problem

The DS algorithm requires that displacement compatibility and force equilibrium is explicitly satisfied on the interfaces of the connected substructures. In a discretised world, coupling could be fully determined by imposing this two conditions on the respective coupling nodes of the substructures.

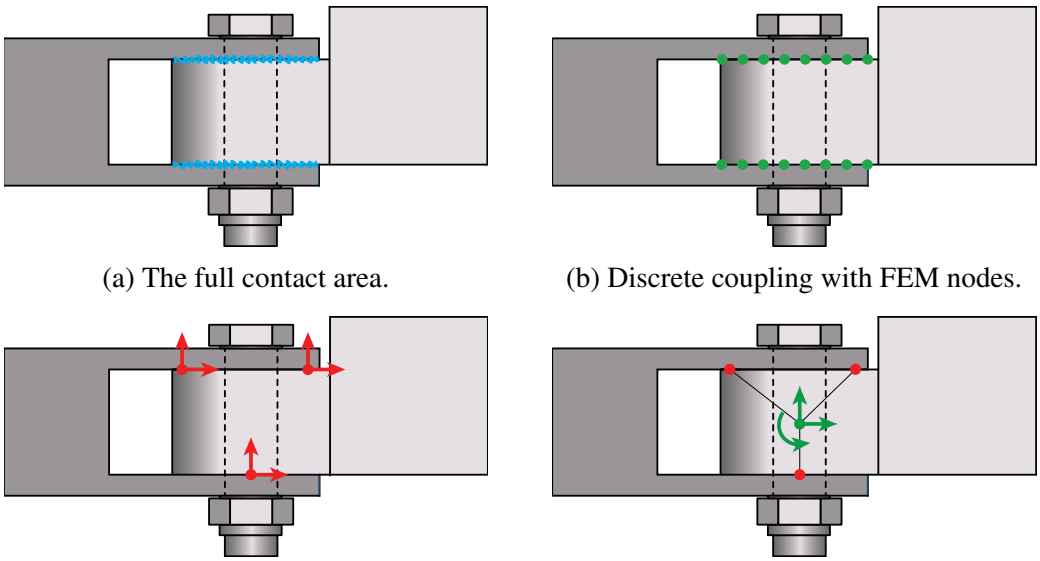
However in industrial practice components are often connected by bolts or welds, that physically show more resemblance to a line or surface connection than to a single point. Modelling a continuous contact surface or line is of course not feasible as one would theoretically need an infinite amount of DoFs. It is therefore common practice to reduce the interface problem to one or more connecting nodes.

Let us for example consider a substructure connection as illustrated in figure 1a. If both structures would be represented by an FE model, the substructuring task amounts to coupling the displacements and interface forces of the coinciding nodes (figure 1b). By coupling a sufficient number of nodes over a larger area, any rotational coupling is implicitly accounted for.

However in connecting experimental substructures very few guidelines exist. A simple triaxial translational Single-Point Connection (SPC) is simply inadequate to couple the rotational degrees of freedom (RDoFs). To overcome the RDoF problem, it was suggested by [6] and [14] to introduce an Equivalent Multi-Point Connection (EMPC) as illustrated by figure 1c. This method couples the translational directions of multiple points in the proximity of the interface which implicitly accounts for the rotations. In practice, a minimum of 3 triaxial accelerometers (not in line) is sufficient to fully determine the 6 DoF coupling, i.e. 3 translational and 3 rotational directions.

1.2 Weakening the interface conditions

Unfortunately it was observed that the 9 DoFs resulting from a 3-point coupling may even overdetermine the coupling problem. As the structure between the 3 connections point is typ-



(a) The full contact area.

(b) Discrete coupling with FEM nodes.

(c) Standard EMPC: multiple points, only translational directions (9 DoFs).

(d) Extended EMPC: One virtual point, 3 translations and 3 rotations (9 $\rightarrow$ 6 DoFs).

Figure 1: A bolted connection: three ways to model the interface problem.

ically very stiff, any discrepancy in motion (often due to measurement errors) will be over-compensated for in the DS coupling equations, resulting in unwanted "stiffening" and spurious peaks in the coupled FRFs [15].

In fact the local rigidness of the interface is the essential observation that leads to the concept of Interface Deformation Mode (IDM) filtering, as introduced in the same work. By defining 6 rigid IDMs per interface and projecting the 9-DoF (or more) receptance matrix onto this subspace, one only retains the dynamics that load the interface area in a rigid manner. When substructuring is performed with this "filtered" receptance, one only imposes the compatibility and equilibrium conditions on the motion of those 9 DoFs that obey local rigid behaviour, while the residual flexible motion is left uncoupled. In effect the interface problem is "weakened" and, due to the least-square reduction step, measurement errors are averaged out.

1.3 Virtual point description

More generally, one can look at this concept from a modal reduction point of view and simply describe the rigid interface dynamics using the generalised set of coordinates associated with the rigid IDMs. Doing so, one has in fact obtained a 6-DoF per node receptance model that is directly compatible for coupling with FE models. This is illustrated by figure 1d. Indeed, the nodal 6×6 receptance matrices describe the dynamic responses between the so-called *virtual point displacements* and *virtual point forces*: the receptance of the interface concentrated in a virtual point[1].

Interesting is now how to set up an experiment that leads to a complete and reciprocal 6×6 virtual point FRF matrix, including proper "driving-point" receptance on the diagonal. Various studies have dealt with problems related to driving-point measurements [10, 16] and the propagation of measurement errors into the coupled FRFs [7, 15].

[1]The point is said to be virtual, since no actual measurements have been done on this point and it can in fact be chosen anywhere in the proximity of the interface.

1.4 Paper outline

This paper discusses the virtual point transformation that translates the measured (impact) forces and displacements to virtual point receptance. The theoretical background on dynamic substructuring and the virtual point transformation is provided in section 2. Next, section 3 aims at providing some practical guidelines to set up an experiment and means to evaluate the results of the measurements in terms of consistency of the transformation and resulting reciprocity. The paper is concluded with a short summary in section 4.

2 THEORY

The Virtual Point Transformation is based on the theory of the Equivalent Multi-Point Connection (EMPC) method. This method was first presented by [6, 14, 17]. A physical derivation of the transformation and ways to construct IDM matrices for individual subsystems were suggested by [16]. In this work however, the virtual point transformation is approached slightly differently, namely from a Dynamic Substructuring point of view. Thereafter the physical derivation of the IDM matrices is discussed.

2.1 Dynamic Substructuring with weakened interface conditions

Dynamic substructuring connects substructures by imposing two conditions: compatibility of interface displacements and equilibrium of interface forces. For the derivation of the virtual point transformation, let us first consider a simple coupling problem of two substructures A and B, characterised by their FRF matrices $\mathbf{Y}^{\mathrm{A}}(\omega)$ and $\mathbf{Y}^{\mathrm{B}}(\omega)$. In summary, one can start with writing the dynamic equations of the uncoupled system using a block-diagonal receptance matrix $\mathbf{Y} = \mathrm{diag}(\mathbf{Y}^{\mathrm{A}}, \mathbf{Y}^{\mathrm{B}})$, such that the uncoupled responses $\mathbf{u} = [\mathbf{u}^{\mathrm{A}}; \mathbf{u}^{\mathrm{B}}]$ to some force loading $\mathbf{f}^{tot}$ are found by[2]:

$$\mathbf{u} = \mathbf{Y}\mathbf{f}^{tot} \tag{1}$$

The total forces $\mathbf{f}^{tot}$ are typically a combination of external loads $\mathbf{f}$ and interface forces $\mathbf{g}$. Let us for now imagine that the interface nodes of the two substructures coincide perfectly, such that the compatibility condition can be stated by equating the translational DoFs of the two substructure boundaries $\mathbf{u}_b^{\mathrm{A}} = \mathbf{u}_b^{\mathrm{B}}$ or $\mathbf{B}\mathbf{u} = \mathbf{0}$, using the signed boolean matrix notation (see [5]). The following coupled system of equations is then obtained:

$$\mathbf{u} = \mathbf{Y}(\mathbf{f} + \mathbf{g}) = \mathbf{Y}(\mathbf{f} - \mathbf{B}^T\boldsymbol{\lambda}) \tag{2a}$$

$$\mathbf{B}\mathbf{u} = \mathbf{0} \tag{2b}$$

where the interface forces are expressed using the same matrix $\mathbf{B}$ and a set of Lagrange multipliers $\boldsymbol{\lambda}$ that are yet unknown.

2.1.1 Interface reduction

Let us now imagine that one is interested in considering the interface displacements as rigid, or at least represented by some more general Interface Deformation Modes (IDMs) contained in the $N \times M$ matrix $\mathbf{R}$ with modal coordinates $\mathbf{q}$. As the number of IDMs is smaller than the number of interface DoFs ($M < N$), a residual on the displacements $\boldsymbol{\mu}$ is added:

$$\mathbf{u} = \mathbf{R}\mathbf{q} + \boldsymbol{\mu} \tag{3}$$

[2] In this derivation the explicit frequency dependency of $\mathbf{Y}(\omega)$, $\mathbf{u}(\omega)$ and $\mathbf{f}(\omega)$ is omitted for clarity.

To find $\mathbf{q}$ in a minimal sense, one could directly apply the (Moore-Penrose) pseudo-inverse of $\mathbf{R}$, minimising the norm of the residuals on the displacements. Instead one can also introduce a symmetric weighting matrix $\mathbf{W}$ that can be chosen to have the residual satisfying

$$\mathbf{R}^T\mathbf{W}\boldsymbol{\mu} = \mathbf{0} \tag{4}$$

such that the coordinate transformation and filtering process becomes:

$$\mathbf{R}^T\mathbf{W}\mathbf{u} = \mathbf{R}^T\mathbf{W}\mathbf{R}\mathbf{q} \tag{5a}$$

$$\mathbf{q} = \left(\mathbf{R}^T\mathbf{W}\mathbf{R}\right)^{-1}\mathbf{R}^T\mathbf{W}\mathbf{u} \tag{5b}$$

$$\tilde{\mathbf{u}} = \mathbf{R}\left(\mathbf{R}^T\mathbf{W}\mathbf{R}\right)^{-1}\mathbf{R}^T\mathbf{W}\mathbf{u} \tag{5c}$$

or short:

$$\mathbf{q} = \mathbf{T}\mathbf{u} \qquad \text{with} \qquad \mathbf{T} \triangleq \left(\mathbf{R}^T\mathbf{W}\mathbf{R}\right)^{-1}\mathbf{R}^T\mathbf{W} \tag{6a}$$

$$\tilde{\mathbf{u}} = \mathbf{R}\mathbf{T}\mathbf{u} = \mathbf{P}\mathbf{u} \qquad \text{with} \qquad \mathbf{P} \triangleq \mathbf{R}\left(\mathbf{R}^T\mathbf{W}\mathbf{R}\right)^{-1}\mathbf{R}^T\mathbf{W} \tag{6b}$$

Vector $\tilde{\mathbf{u}}$ denotes the physical displacements projected onto the IDM subspace. $\mathbf{P}$ is the $N \times N$ projection operator of reduced rank $M < N$.

Note that the above procedure is in fact a least-square projection minimising the squared error $\boldsymbol{\mu}^T\mathbf{W}\boldsymbol{\mu}$. If $\mathbf{W}$ is chosen to be identity, the pseudo-inverse is found, $\mathbf{T} = (\mathbf{R}^T\mathbf{R})^{-1}\mathbf{R}^T$, which leads to a minimisation of the error on the displacements. In general if $\mathbf{W}$ is a diagonal matrix, it gives weight to the individual displacements in the error minimisation such that one can control the importance of a certain DoF for the transformation. However if $\mathbf{W}$ is chosen to represent a (dynamic) stiffness matrix, one is nullifying some local residual energy. Alternative choices for $\mathbf{W}$ are beyond the scope of this paper.

2.1.2 Substructure assembly

The interface reduction as derived above allows us to assemble only the rigid behaviour of the interface ($\tilde{\mathbf{u}} = \mathbf{R}\mathbf{q}$) that was properly measured. The rest ($\boldsymbol{\mu}$) is left free, being either measurement noise or higher-order deformations that one could probably not measure correctly due to inaccuracies in impact and sensor locations.

Rewriting the dual DS equations of (2a) and (2b) for rigid interface coupling:

$$\mathbf{u} = \mathbf{Y}(\mathbf{f} + \mathbf{g}) \tag{7a}$$

$$\mathbf{B}\mathbf{q} = \mathbf{B}\left(\mathbf{R}^T\mathbf{W}\mathbf{R}\right)^{-1}\mathbf{R}^T\mathbf{W}\mathbf{u} = \mathbf{0} \tag{7b}$$

The boolean matrix $\mathbf{B}$ is different to the one of (2b) as it now couples the DoFs of the rigid IDMs, hence the rigid behaviour of $\mathbf{u}$. The forces $\mathbf{g}$ are still coupling forces in the unreduced domain but conjugate to the IDM conditions, namely:

$$\mathbf{g} = -\mathbf{W}^T\mathbf{R}\left(\mathbf{R}^T\mathbf{W}\mathbf{R}\right)^{-1}\mathbf{B}^T\boldsymbol{\lambda} = -\mathbf{T}^T\mathbf{B}^T\boldsymbol{\lambda} \tag{8}$$

and the coupled system becomes:

$$\mathbf{u} = \mathbf{Y}(\mathbf{f} - \mathbf{T}^T\mathbf{B}^T\boldsymbol{\lambda}) \tag{9a}$$

$$\mathbf{B}\mathbf{q} = \mathbf{B}\mathbf{T}\mathbf{u} = \mathbf{0} \tag{9b}$$

Writing now the first equation in the second and solving for $\boldsymbol{\lambda}$:

$$\mathbf{BTYf} - \mathbf{BTYT}^T\mathbf{B}^T\boldsymbol{\lambda} = \mathbf{0}$$

$$\boldsymbol{\lambda} = \left(\mathbf{BTYT}^T\mathbf{B}^T\right)^{-1}\mathbf{BTYf} \tag{10}$$

Putting everything together in (9a) gives us the dynamic equation for the reduced-interface coupling:

$$\mathbf{u} = \mathbf{Yf} - \mathbf{YT}^T\mathbf{B}^T\left(\mathbf{BTYT}^T\mathbf{B}^T\right)^{-1}\mathbf{BTYf} \tag{11}$$

The receptance matrix of the coupled system is given by

$$\mathbf{Y}^{ass} = \mathbf{Y} - \mathbf{YT}^T\mathbf{B}^T\left(\mathbf{BTYT}^T\mathbf{B}^T\right)^{-1}\mathbf{BTY} \tag{12}$$

such that we can simplify to $\mathbf{u} = \mathbf{Y}^{ass}\mathbf{f}$.

2.2 Dynamic Substructuring with virtual point DoFs

Equation (11) gives the coupled reduced-interface dynamic equations for the physical displacements and forces $\mathbf{u}$ and $\mathbf{f}$. However when coupling the experimental models to FE models or even to each other, it is probably more convenient to set up the substructuring equations using the virtual point DoFs directly. Let us therefore state the relation between measured and virtual displacements and forces once more:

$$\mathbf{q} = \left(\mathbf{R}^T\mathbf{WR}\right)^{-1}\mathbf{R}^T\mathbf{Wu} = \mathbf{Tu} \tag{13a}$$

$$\mathbf{f} = \mathbf{W}^T\mathbf{R}\left(\mathbf{R}^T\mathbf{WR}\right)^{-1}\mathbf{m} = \mathbf{T}^T\mathbf{m} \tag{13b}$$

The first equation was already defined by (5b). The second equation to obtain the virtual forces $\mathbf{f}$ uses the same $\mathbf{T}$ as the virtual displacements and therefore the same IDMs[3]. However a different $\mathbf{T}$ could easily be constructed, as long as the IDM coordinates match: the components in $\mathbf{m}$ are indeed a force or torque in the direction of the components of $\mathbf{q}$. More detail on how to obtain the IDMs for the sensors and impacts is found in section 2.3.

Combining equations (11), (13a) and (13b) gives us the coupled system equations in terms of the virtual point displacements $\mathbf{q}$ and forces $\mathbf{m}$:

$$\mathbf{q} = \mathbf{TYT}^T\mathbf{m} - \mathbf{TYT}^T\mathbf{B}^T\left(\mathbf{BTYT}^T\mathbf{B}^T\right)^{-1}\mathbf{BTYT}^T\mathbf{m} \tag{14}$$

Observes that compared to equation (11) the applied forces are now also filtered, so that only the resulting virtual forces corresponding to the IDM subspace are implied in the dynamic computations.

Substituting $\mathbf{H} = \mathbf{TYT}^T$ as a virtual point receptance matrix, we get:

$$\mathbf{q} = \mathbf{Hm} - \mathbf{HB}^T\left(\mathbf{BHB}^T\right)^{-1}\mathbf{BHm} \tag{15}$$

and as a result

$$\mathbf{H}^{ass} = \mathbf{H} - \mathbf{HB}^T\left(\mathbf{BHB}^T\right)^{-1}\mathbf{BH} \tag{16}$$

which has exactly the same form as the well-known Lagrange Multiplier FBS formula [5] but now for the virtual point dynamics. Indeed $\mathbf{H}(\omega)$ comprises the virtual point receptance relating the virtual point forces $\mathbf{m}(\omega)$ to virtual point displacements $\mathbf{q}(\omega)$. Due to the block-diagonal construction of the subsystem IDM matrices, we can also conclude that $\mathbf{H} = \mathrm{diag}(\mathbf{H}^{\mathrm{A}}, \mathbf{H}^{\mathrm{B}})$, showing that the virtual point receptance can be built up for the subsystems independently.

[3]This implies that the locations of the applied forces (hammer impacts or shaker excitations) should completely coincide with the corresponding measured responses (sensors).

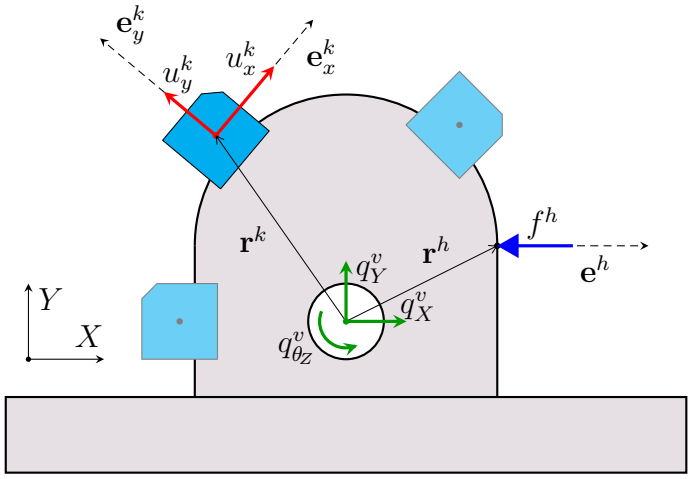


Figure 2: The IDMs associated with the virtual point (green) can be constructed from the positions and directions of the measured displacements (red) and impacts (blue).

2.3 Construction of the Interface Displacement Modes

In the derivation above it was shown that the virtual point transformation relies on a reduction in a modal sense, namely reducing the interface connectivity using a set of Interface Deformation Modes (IDMs) specified by $\mathbf{R}$. Let us now elaborate on how to obtain these IDMs for a single interface indicated in figure 2. Virtual point v is surrounded by $N_k = 3$ triaxial acceleration sensors, registering a total of 9 translational displacements[4] in the local (x, y, z) frame of the sensors. An impact is indicated by a thick blue arrow.

2.3.1 Displacements

Following equation (3) the sensor IDM matrix $\mathbf{R}$ translates the local frame displacements to 6 virtual point displacements and rotations plus a residual. Let us write out this equation for a triaxial sensor k. The orientation of the sensor is determined by its three measurement directions specified as the unit vectors $[\ \mathbf{e}_x^k\ \ \mathbf{e}_y^k\ \ \mathbf{e}_z^k\ ] = \mathbf{E}^k$ while the distance from the sensor to the virtual point is given by vector $\mathbf{r}^k$. The respective local displacements along these directions are denoted by $\mathbf{u}^k$. The 6 DoFs of virtual point v are contained in the set $\mathbf{q}^v$.

$$\begin{bmatrix} u_x^k \\ u_y^k \\ u_z^k \end{bmatrix} = \begin{bmatrix} e_{x,X}^k & e_{x,Y}^k & e_{x,Z}^k \\ e_{y,X}^k & e_{y,Y}^k & e_{y,Z}^k \\ e_{z,X}^k & e_{z,Y}^k & e_{z,Z}^k \end{bmatrix} \begin{bmatrix} 1 & 0 & 0 & 0 & r_Z^k & -r_Y^k \\ 0 & 1 & 0 & -r_Z^k & 0 & r_X^k \\ 0 & 0 & 1 & r_Y^k & -r_X^k & 0 \end{bmatrix} \begin{bmatrix} q_X^v \\ q_Y^v \\ q_Z^v \\ q_{\theta_X}^v \\ q_{\theta_Y}^v \\ q_{\theta_Z}^v \end{bmatrix} + \begin{bmatrix} \mu_x^k \\ \mu_y^k \\ \mu_z^k \end{bmatrix} \tag{17}$$

Introducing $\bar{\mathbf{R}}^{kv}$ as the 3×6 global frame matrix associated with sensor k and virtual point v, we can write:

$$\mathbf{u}^k = \mathbf{E}^{k^T} \bar{\mathbf{R}}^{kv} \mathbf{q}^v + \boldsymbol{\mu}^k \tag{18}$$

$$\mathbf{u}^k = \mathbf{R}^{kv} \mathbf{q}^v + \boldsymbol{\mu}^k \qquad \text{with} \qquad \mathbf{R}^{kv} = \mathbf{E}^{k^T} \bar{\mathbf{R}}^{kv} \tag{19}$$

[4] In fact the sensors measure accelerations but for simplicity of notation displacements are considered here.

For a typical problem having 3 sensors per virtual point and sorted in ascending virtual point order, the $\mathbf{R}^{kv}$ matrices can be stacked to form the following equations[5]:

$$\mathbf{u} = \mathbf{R}\mathbf{q} + \boldsymbol{\mu} \qquad \text{with} \qquad \mathbf{R} = \begin{bmatrix} \mathbf{R}^{1,1} & & & \\ \mathbf{R}^{2,1} & & & \\ \mathbf{R}^{3,1} & & & \\ & \mathbf{R}^{4,2} & & \\ & \mathbf{R}^{5,2} & & \\ & \mathbf{R}^{6,2} & & \\ & & \ddots & \\ & & & \mathbf{R}^{N_k,N_v} \end{bmatrix} \tag{20}$$

Alternatively one may prefer to describe the virtual point relation per measurement direction individually, such that a single displacement DoF u_i^k in the local direction $\mathbf{e}_i^k$ can be related to the associated set of virtual point coordinates in $\mathbf{q}^v$:

$$u_i^k = \begin{bmatrix} \mathbf{e}_i^{kT} & \left(\mathbf{r}_i^k \times \mathbf{e}_i^k\right)^T \end{bmatrix} \mathbf{q}^v + \mu_i^k = \mathbf{R}_i^{kv}\mathbf{q}^v + \mu_i^k \tag{21}$$

from which the full matrix $\mathbf{R}$ can be assembled row-wise per sensor channel i and column-wise for the different virtual points.

Regardless of the construction method the resulting IDM matrix $\mathbf{R}$ shall be block diagonal, or at least have IDMs that are uncoupled over the various virtual points and sensor groups (if a different ordering was used). Although not treated here, $\mathbf{R}$ may be augmented with flexible IDMs if desired. Note that in any case one should take care that $\mathbf{R}$ is at least full rank (but preferably overdetermined) such that a (generalised) inverse $\mathbf{T}$ can be computed by applying equation (13a):

$$\mathbf{q} = \left(\mathbf{R}^T\mathbf{W}\mathbf{R}\right)^{-1}\mathbf{R}^T\mathbf{W}\mathbf{u} = \mathbf{T}\mathbf{u}$$

2.3.2 Forces

The transformation of the forces can be performed in a similar step-wise way. Unlike displacements, forces are not uniquely defined by virtual point forces and moments (from here on simply called virtual forces). In fact the other way around is true, such that the following relation can be written for the set of virtual forces $\mathbf{m}^v$ as a result of an impact f^h in the direction of $\mathbf{e}^h$ at distance $\mathbf{r}^h$:

$$\begin{bmatrix} m_X^v \\ m_Y^v \\ m_Z^v \\ m_{\theta_X}^v \\ m_{\theta_Y}^v \\ m_{\theta_Z}^v \end{bmatrix} = \begin{bmatrix} 1 & 0 & 0 \\ 0 & 1 & 0 \\ 0 & 0 & 1 \\ 0 & -r_Z^h & r_Y^h \\ r_Z^h & 0 & -r_X^h \\ -r_Y^h & r_X^h & 0 \end{bmatrix} \begin{bmatrix} e_X^h \\ e_Y^h \\ e_Z^h \end{bmatrix} f^h \tag{22}$$

Now we like to use similar notation as (21), but to do so we need the transpose of $\mathbf{R}^{hv}$:

$$\mathbf{m}^v = \begin{bmatrix} \mathbf{e}^h \\ \mathbf{r}^h \times \mathbf{e}^h \end{bmatrix} f^h = \mathbf{R}^{hv^T} f^h \tag{23}$$

[5] it is easy to observe that if only translational information is desired for a certain virtual point (e.g. if one only used one sensor), the sensor rotation matrix can be used directly: $\mathbf{R}^{kv} = \mathbf{E}^{k^T}$.

Every impact adds a single column to the IDM matrix $\mathbf{R}^T$. Assuming 9 impacts per virtual point, the system for the complete set of DoFs is constructed as follows:

$$\mathbf{m} = \mathbf{R}^T\mathbf{f} \qquad \text{with} \qquad \mathbf{R} = \begin{bmatrix} \mathbf{R}^{1,1} & & & & \\ \vdots & & & & \\ \mathbf{R}^{9,1} & & & & \\ & \mathbf{R}^{10,2} & & & \\ & \vdots & & & \\ & \mathbf{R}^{18,2} & & & \\ & & \ddots & & \\ & & & \mathbf{R}^{N_h,N_v} \end{bmatrix} \tag{24}$$

Note that the transpose of the IDM matrix of the forces takes the same form as the IDM matrix of the displacements from equation (20). In fact if one decides to excite only on the sensor faces (which is generally not advised, see section 3.2), one has the exact same IDM matrix apart from some sign changes.

With more than independent 6 excitations per virtual point, equation (24) becomes underdetermined, which means that there is no unique combination of the impacts $\mathbf{f}$ from which a certain $\mathbf{m}$ can be constructed. Again the solution is found by using a generalised inverse, only this time a weighted "right inverse":

$$\mathbf{f} = \mathbf{W}^T\mathbf{R}\left(\mathbf{R}^T\mathbf{W}\mathbf{R}\right)^{-1}\mathbf{m} = \mathbf{T}^T\mathbf{m} \tag{25}$$

that can be shown to minimise the error on the residual impact forces weighted by $\mathbf{W}$. We can now see that the underdetermination of (24) in fact reflects an overdetermination of the inversed problem of (25), which again has advantageous properties for interface weakening and error suppression as discussed in section 2.1.

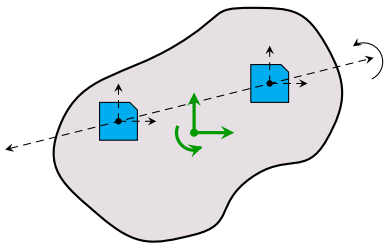
3 PRACTICE

This section will elaborate on some more practical issues related to virtual point modelling. Proper positioning of the sensors and impacts has to be taken into consideration. Much care should be taken to ensure that all 6 DoFs per virtual point can be described independently. This has implications for both sensor placement and impact positions. After measuring some careful post-processing needs to be done to come up with good results. The following preparation and post-processing steps are presented in the order as they may normally appear in time.

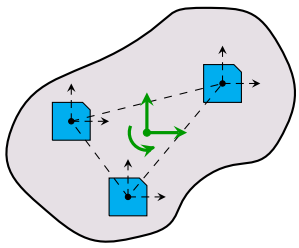
3.1 Sensor placement

The thought that two triaxial sensors (measuring two times 3 translations) can completely describe the 6 DoF virtual point, can be deceiving. When the responses of two triaxial sensors are transformed to a 6 DoF virtual point description, one linear dependence will always appear in the virtual points DoFs. This linear dependence is caused by the fact that the triaxial sensors are unable to describe the rotation over the axis spanned between both sensors as illustrated by figure 3a. This is regardless of the position of the sensors relative to the virtual point. Adding a third triaxial sensor, such that the three sensors span a surface (figure 3b), enables the three sensors with a total of 9 DoFs to describe all 6 DoFs of the virtual point.

The additional benefit of the third triaxial sensor is of course the overdetermination of the interface problem. Using the virtual point transformation as discussed in section 2 the effects of



(a) Two sensors spanning a line: one dependency between the rotational axes.



(b) Three sensors spanning a surface: all rotations fully determined.

uncorrelated measurement noise as well as errors due to misalignment of the sensor are reduced, which is generally considered a good practice [6, 9, 16]. The use of at least three triaxial sensors per virtual point can therefore be held as rule of thumb.

Finally, considering the rigid interface assumption, it seems evident that it would be best practice to place the sensors as close as possible to the virtual point. The smaller the distances are, the smaller the effects of flexible interface modes are compared to the rigid interface motion. On the other hand, for smaller distances, the virtual point transformation will get more sensitive to to absolute errors on the position. In general one should approach this matter with some engineering judgement or foreknowledge about the system.

3.2 Impact positions

Unlike the 6 displacements measured by 2 triaxial sensors, 6 well-positioned force impacts could in practice be sufficient to fully determine the 6 generalised forces at the virtual point. Still, for the same reason, it is wise to choose more excitation points that overdetermine the force transformation.

Similar to the sensor placement, three impacts in each direction (X, Y, Z) can be used as a rule of thumb. Also one should include excitations of which the direction normal ($\mathbf{e}^h$) does not point straight to the virtual point, in order to create "moment" along the rotational axes.

In some previous studies the sensor faces were chosen as possible impact locations [3, 16]. Depending on the chosen sensors this can have its advantages and disadvantages. Since the impact locations and directions are equal to the locations and orientations of the measured XYZ responses in the sensor, the same transformation matrix can be used for both transformations. However, practice shows that FRFs obtained at the driving point exhibit poor coherence, especially for the cross-directional FRFs of one sensor. Also, the sensor is easily driven in overload. As the virtual point transformation does not require physical driving-point receptance, this type of excitations should be avoided.

It seems logical to apply the impacts as close as possible to the virtual point in order to avoid inducing local deformation around the virtual point, but an the other hand one wants to be far enough to be less sensitive to errors in the impact location and orientation. The same reasoning as for the sensor placement holds here.

3.3 Post-processing

After measuring, the obtained FRF data should be organised into a matrix $\mathbf{Y}(\omega)$ such that the virtual point transformation can be performed:

$$\mathbf{H}(\omega) = \mathbf{T}\mathbf{Y}(\omega)\mathbf{T}^T$$

The transformation matrices $\mathbf{T}$ left and right from the receptance matrix denote respectively the sensor and impact transformation matrices as constructed from the IDMs[6]. In practice these steps involve accurate determination of the positions and orientations (directions) of both the sensors and impacts. Besides ruler and calliper measurement, optical measurement systems as well as CAD models of the components at hand may dramatically improve the accuracy of the position determination and with that the quality of the transformation. The use of such assisting systems is therefore strongly suggested.

3.4 Performance indicators

In section 2 the relation between measured and virtual displacements and forces was set up. The residuals that result from the least-square projection of the measured receptance data can be used to derive a meaningful value to evaluate the accuracy of the sensor and impacts positions.

3.4.1 Sensor consistency

In order to say something about the how the consistency of the sensor placement and the constructed IDMs, let us get back to the the interface reduction equation of (3):

$$\mathbf{u} = \mathbf{R}\mathbf{q} + \boldsymbol{\mu}$$

We define $\mathbf{f}_h$ as the "load case" resulting from a unit impact somewhere at the structure, reasonably far away from virtual point 1. Then the measured responses of the sensors associated with virtual point 1 due to the given load case are:

$$\mathbf{u}_1(\mathbf{f}_h) = \mathbf{Y}_1\mathbf{f}_h = \mathbf{Y}_{1h}$$

which is simply the receptance column corresponding to that impact. For substructure coupling, we are interested in the filtered responses $\tilde{\mathbf{u}}_1$ due to the transformation via $\mathbf{q}_1$:

$$\tilde{\mathbf{u}}_1(\mathbf{f}_h) = \mathbf{R}_{11}\mathbf{q}_1(\mathbf{f}_h) = \mathbf{R}_{11}\mathbf{T}_{11}\mathbf{u}_1(\mathbf{f}_h) = \mathbf{P}_{11}\mathbf{Y}_{1h}$$

Now, we are able to compare $\mathbf{u}_1$ with $\tilde{\mathbf{u}}_1$ using a formulation similar to the Modal Assurance Criterion [1]:

$$\rho^2_{\mathbf{u}_1} = \mathrm{MAC}\left(\tilde{\mathbf{u}}_1(\mathbf{f}_h), \mathbf{u}_1(\mathbf{f}_h)\right) = \mathrm{MAC}\left(\mathbf{P}_{11}\mathbf{Y}_{1h}, \mathbf{Y}_{1h}\right) \tag{26}$$

with

$$\mathrm{MAC}(\mathbf{a}, \mathbf{b}) \triangleq \frac{(\mathbf{a}^H\mathbf{b})(\mathbf{b}^H\mathbf{a})}{(\mathbf{a}^H\mathbf{a})(\mathbf{b}^H\mathbf{b})} \tag{27}$$

The value $\rho^2_{\mathbf{u}_1}$ is called the *sensor consistency* (in previous work *rigidness* [6, 16]) and gives a value between 0 and 1 that indicates how well the sensors of virtual point 1 can describe the dynamics (caused by a certain excitation) through the IDM modes. It is a frequency dependent indicator that can be evaluated for every virtual point and for each excitation separately[7]. Evaluating the sensor coherence for several impacts provides meaningful insights in the consequences of the transformation. Low sensor consistency can have the following causes:

[6] In general the two $\mathbf{T}$ matrices are different and depend on the sensor and impact locations, see section 2.3.

[7] An excitation $\mathbf{f}_2$ "far away" from the virtual point of interest is suggested because then one observes the global response to some force that brought the complete system in motion, rather then a response that may be highly affected by impact position differences in the vicinity of the virtual point of interest.

- The position and orientation of a sensor was not properly determined, such that the measured kinematics appear incompatible with the IDM kinematics. If for instance one sensor is rotated 90 degrees along the Z-axis, a rigid interface motion in the X, Y-plane will appear as a partly flexible motion. The effect will be visible as a low consistency over the full frequency range.
- The interface area spanned between the sensors is flexible, such that the rigid IDMs cannot fully describe the dynamics. This will mostly reflect in reduced consistency for increasing frequencies.
- If the rigidness is particularly low for a certain impact, one may question if this impact was either to soft (low signal-to-noise-ratio) or to strong (driving on or more sensors in overload). In such cases it is preferred to leave this impact (column of $\mathbf{Y}$) out of the transformation.

Note that the sensor consistency requires an overdetermination of the problem, otherwise it will just indicate a straight value of 1.

3.4.2 Impact consistency

Similar to the sensor consistency, it is possible to come up with a consistency measure for the applied forces. This value is especially valuable to assess the accuracy of the impact positions and by that the consistency of the force IDMs.

This time we are interested in the responses of a single sensor channel u_i to all the impacts of virtual point 1, which is equal to a row of the measured receptance matrix:

$$u_i(\mathbf{f}_1) = \big(u_i(f_1), u_i(f_2), \ldots, u_i(f_9)\big) = \mathbf{Y}_{i1}$$

The response to the filtered set of impacts, i.e. the combination of impacts that only result in a rigid load, is found by applying the projection matrix for the force IDMs:

$$u_i(\tilde{\mathbf{f}}_1) = \mathbf{Y}_{i1}\mathbf{P}_{11}$$

The *impact consistency* is then defined by:

$$\rho^2_{\mathbf{f}_1} = \mathrm{MAC}\left(u_i(\tilde{\mathbf{f}}_1), u_i(\mathbf{f}_1)\right) = \mathrm{MAC}\left(\mathbf{Y}_{i1}\mathbf{P}_{11}, \mathbf{Y}_{i1}\right) \tag{28}$$

Also, this value is limited between 0 and 1.

3.4.3 Reciprocity

Evaluating sensor and hammer impact consistency can be useful to find errors in the measurement setup, calibration, etc. However a high consistency does not guarantee reciprocity of virtual point FRFs. Reciprocity of the raw measurement data is often not meaningful as the location of sensors and impact positions do not coincide. Reciprocity of the virtual point receptance however should be reciprocal, and can therefore be used to assess the transformation quality.

Let i and j denote two different DoFs from the set of virtual point DoFs. Then a non-dimensional frequency dependent reciprocity value between 0 and 1 is defined by:

$$\chi_{ij} = \frac{(H_{ij} + H_{ji})({H_{ji}}^* + {H_{ji}}^*)}{2({H_{ij}}^* H_{ij} + {H_{ji}}^* H_{ji})} \tag{29}$$

This formula originates from the FRF input-output coherence function for the two measurements H_{ji} and H_{ij}. It shows the similarity in both amplitude and phase between the two virtual point FRFs.

4 SUMMARY

In this paper the theory behind the virtual point transformation is presented from a modal reduction perspective. We have shown that by weakening the interface problem, one only couples the rigid motion described by the IDMs, while the residual motion is left free. By assigning a certain weighting matrix, one can control this residual and with that the transformation. Ways to construct different IDMs from the sensor and impact positions are discussed.

Also some practical aspects were discussed that one may encounter when doing experimental substructuring. It appeared that sensor and impact positioning should be thought out carefully beforehand, but can still be evaluated afterwards on the basis of a number of non-dimensional performance indicators.

REFERENCES

[1] Randall J. Allemang. The modal assurance criterion twenty years of use and abuse. *Sound and Vibration*, pages 14–21, August 2003.

[2] R.R.J. Craig and M.C.C. Bampton. Coupling of substructures using Component Mode Synthesis. *AIAA Journal*, 6:1313–1319, 1968.

[3] D. de Klerk. *Dynamic Response Characterization of Complex Systems through Operational Identification and Dynamic Substructuring*. Phd thesis, Delft University of Technology, http://www.3me.tudelft.nl/live/pagina.jsp?id=73932050-a4ca-46b5-bd9b-d98b8a52dbe6, 2009.

[4] D. de Klerk, D.J. Rixen, and J. de Jong. The Frequency Based Substructuring Method reformulated according to the Dual Domain Decomposition Method. In *Proceedings of the XXIV International Modal Analysis Conference*. Society for Experimental Mechanics, 2006.

[5] D. de Klerk, D.J. Rixen, and S.N. Voormeeren. A General Framework for Dynamic Substructuring. History, review and classifcation of techniques. *AIAA Journal*, 46(8), 2008.

[6] D. de Klerk, D.J. Rixen, S.N. Voormeeren, and F. Pasteuning. Solving the RDoF problem in Experimental Dynamic Substructuring. In *Proceedings of the XXVI International Modal Analysis Conference, Orlando, FL*, Bethel, CT, 2008. Society for Experimental Mechanics.

[7] D. de Klerk and S.N. Voormeeren. Uncertainty Propagation in Experimental Dynamic Substructuring. In *Proceedings of the XXVI International Modal Analysis Conference, Orlando, FL*, Bethel, CT, 2008. Society for Experimental Mechanics.

[8] M.L.M Duarte and D.J. Ewins. Some Insights into the Importance of Rotational Degrees of Freedom and Residual Terms in Coupled Structure Analysis. In *Proceedings of the XIII International Modal Analysis Conference, Nashvill, TN*, pages 164–170, Bethel, CT, 1995. Society for Experimental Mechanics.

[9] T.S. Edwards. Implementation of Admittance Test Techniques for High-precision Measurement of Frequency Response Functions. In *Proceedings of the XXXI International Modal Analysis Conference*. Society for Experimental Mechanics, 2013.

[10] J. Harvie and P. Avitabile. Effects of precise FRF measurements for Frequency Based Substructuring. In *Proceedings of the XXXI International Modal Analysis Conference, Los Angeles, CA*, Bethel, CT, 2013. Society for Experimental Mechanics.

[11] B. Jetmundsen, R.L. Bielawa, and W. G. Flannelly. Generalized frequency domain substructure synthesis. *Journal of the American Helicopter Society*, 33(1):55–64, 1988.

[12] W. Liu and D.J. Ewins. The Importance Assessment of RDOF in FRF Coupling Analysis. In *Proceedings of the XVII International Modal Analysis Conference, Orlando, FL*, pages 1481–1487, Bethel, CT, 1999. Society for Experimental Mechanics.

[13] J.C. O'Callahan, I.W. Lieu, and C.M. Chou. Determination of Rotational Degrees of Freedom for Moment Transfers in Structural Modifications. In *Proceedings of the III International Modal Analysis Conference, Orlando, FL*, pages 465–470, Bethel, CT, January 1985. Society for Experimental Mechanics.

[14] F. Pasteuning. Experimental Dynamic Substructuring and its Application in Automotive Research. Master's thesis, TU Delft, Department of Engineering Mechanics, 2007.

[15] D.J. Rixen. How Measurement Inaccuracies Induce Spurious Peaks in Frequency Based Substructuring. In *Proceedings of the XXVI International Modal Analysis Conference, Orlando, FL*, Bethel, CT, 2008. Society for Experimental Mechanics.

[16] M.V. van der Seijs, D. de Klerk, D.J. Rixen, and S. Rahimi. Validation of current state Frequency Based Substructuring Technology for the characterisation of Steering Gear – Vehicle Interaction. In *Proceedings of the XXXI International Modal Analysis Conference, Los Angeles, CA*, Bethel, CT, 2013. Society for Experimental Mechanics.

[17] S.N. Voormeeren. Improvement of Coupling Procedures and Quantification of Uncertainty in Experimental Dynamic Substructuring Analysis; Application and Validation in Automotive Research. Master's thesis, TU Delft, 2007.

COMPDYN 2013
4th ECCOMAS Thematic Conference on
Computational Methods in Structural Dynamics and Earthquake Engineering
M. Papadrakakis, V. Papadopoulos, V. Plevris (eds.)
Kos Island, Greece, 12–14 June 2013

A SIMPLIFIED ALGORITHM FOR EVALUATING THE SEISMIC RETURN PERIOD OF STRUCTURAL CAPACITY

Domenico Raffaele[1], **Andrea Fiore**[1]

[1] DICATECh, Politecnico di Bari
address via Orabona, 4 - 70126 Bari (Italy)
d.raffaele@poliba.it, andrea.fiore@poliba.it

Keywords: Seismic Vulnerability Assessment, Return Period, Seismic Hazard, Structural Safety, Reference Life.

Abstract. *The modern technical rules define the proper seismic evaluation on the basis of reference period (reference life), established according to importance and use of the building. At the reference life is associated, to the different limit states, a return period for the seismic action. In Italy, seismic hazard maps were adopted, which by means of the geographical coordinates of the site allow to assess (for specific return periods) the elastic spectral shape, which defines the reference seismic action.*
Until now, the non-linear static methods, as the N2 method, allow to assess the seismic demand in terms of displacement starting precisely from the spectral shapes. However, it is difficult to quantify the seismic return period associated with the real strain capacity of the structure. In this paper is presented an algorithm based on the reverse application of the N2 method. The algorithm allows the assessment of the return period representing the seismic capacity of the structure (expressed in years), starting from the capacity curve of equivalent system. The capacity curve is defined once known the elastic stiffness, the yield and ultimate displacement at the limit state considered. The procedure is validated by comparison with the results of pushover analysis relating to an existing RC building obtained by locating it, respectively, in area at low, medium and high seismicity.

1 INTRODUCTION

The modern technique rules [1,2] use an approach based on performance for the design and verification of the structures. The seismic action to be considered in the design and verification is assessed by the "*local seismic hazard*" which is obtained by specific studies (based on statistical approaches) carried out on a national scale. The statistical studies provide three reference values (a_g, F_o, T_C^* [1]) relative to a ideal ground rigid type having horizontal topography ($v_{s,30}$>*800 m/s* [2]). This approach allows to take seismic actions that are calibrated, not only than on the seismic vulnerability of the site, but also on the years in which the structure has to be used in relation to the intended use and the importance that it has for the community (defined as "*life reference* - V_R" in [1]). The intensity of the seismic actions varies as a function of the limit state (LS) considered (that is connected to a "*probability of exceedance* - P_{VR}") which can probably be achieved during the service life of the structure. The parameter that regulates the seismic intensity is the return period (T_R), ie the time interval, expressed in years, between two earthquakes having equal intensity, which depends on the quantities defined above according to the relationship:

$$T_R = -\frac{V_R}{ln\left(1 - P_{V_R}\right)} \tag{1}$$

Consequently, the return period and the intensity of seismic action are directly proportional. The technical rules, therefore, define seismic actions closer to those that characterize the site of the structure so as to require structural performance which are functional also to the specific use during the service life. This way of defining the actions becomes very important in the case of safety assessment of the existing structures.

It should be noted that while by one side the recent seismic events have encouraged the development of new techniques for seismic assessment, they have also encouraged the diffusion of structural monitoring systems to be used already in the early stage of realization [3,4].

In accordance with the N2 method, [5] the seismic vulnerability assessment consist in verifying that the seismic demand associated with a given return period (therefore for a LS predetermined) is lower than the structural capacity. Obviously, the results become very reliable because they are based on survey methodologies in order to assess the performance of materials [6] and numerical models which take into account also of the effects of secondary elements [7,8]. Both parameters are usually expressed in terms of displacement or PGA (*peak ground acceleration*).

It should be pointed that, despite the primary role in the definition of the spectral shapes, the return period is quite completely absent in the explicit representation of the structural capacity and, consequently, in the overall judgment on the seismic vulnerability of the structure. Given the current tendency to try simplified methods to evaluate the seismic vulnerability of buildings and infrastructure with the help of few parameters of simple retrieval [9,10,11], the need to express the structural performance by means of same parameter that defines the seismic demand (ie the return period) becomes an information which can't be ignored. The return period of the earthquake on the real structural capacity (hereinafter as *return period "capacitive"* - $T_{R,\,SL}^{C}$), allows not only to quantify the safety levels and structural deficiencies differently and in a more quick impact (in terms of years), but also to assess the actual improvement after any retrofitting interventions carried out on the structure. The value is especially useful for existing buildings designed to withstand mainly to only vertical loads. For these structures becomes possible to uniquely assign a *Seismic Vulnerability Index* in order to build lists of priority on territorial scale of structures most seismically vulnerable. This index for a given LS is expressible by the following relationship:

$$I_{V,SL} = \frac{T_{R,SL}^{C}}{T_{R,SL}^{D}} \quad (2)$$

where, $T_{R,SL}{}^{D}$ is the return period of the earthquake that the structure would have to bear to the achievement of the SL predetermined. It's evident that the indices lower than 1, indicate the need to perform more extensive tests, and consequently, the greater distance from the unit value represents a direct measure of the urgency with which carrying out these checks. As regards the planning of structural interventions, to know the value of the period of return produces the effects certainly positive. In fact, the authorities responsible can engage the economic resources available in the most rational manner and in relation to actual needs.

From an analytical point of view, when the nonlinear response of the structure (pushover curve) for a LS predetermined and the geographical coordinates of the reference site are known, the algorithm to evaluating the return period associated with the displacement capacity, is iterative. The iteration is due to the fact that for Italian rules [1,12] the return period and some parameters related to ground types (such as the amplification coefficient stratigraphic) depend on factors that define the local seismic hazard. Consequently, to obtain a $T_{R,\,SL}{}^{C}$ adequate to the soil characteristics of the reference site must be assigned initial values of attempt for the aforesaid parameters. This paper proposes an iterative procedure to calculate the return period of the earthquake $T_{R,SL}{}^{C}$ associated with the displacement capacity of a generic structure in correspondence to a predetermined LS. The proposed algorithm is validated by benchmarks on a real case study.

The heart of the paper is introduced by a summary on the definition of the elastic spectral shapes, according to current rules, and by a description of the N2 method (because the inverse application is the base of the proposed algorithm).

2 SEISMIC ACTION ACCORDING TO THE MODERN STANDARD

Compared to the past, the rules [1,2] evaluate the seismic action with reference not to a single territorial zone (comprising several countries)), to a single spectral shape and to a return period predetermined and equal for all buildings, but site by site and structure by structure [12]. As mentioned in the introduction, the main change is the introduction of the concept of seismic hazard, intended as the probability, in a fixed time interval, that on the generic site occurs a seismic event of magnitude at least equal to a predetermined value. According to the NTC, 2008 [1], the time interval, expressed in years, is called the "*period or life reference*" V_R and the probability is called the "*probability of exceedance during the reference period*" P_{VR}. The first parameter is estimated using the following product:

$$V_R = V_N \cdot C_U \quad (3)$$

V_N is the nominal life. It's equivalent to the number of years in which the structure has to be used for the purpose for which it has been designed. For ordinary civil works must be at least ≥ 50 years.

C_U is the coefficient associated with the *Class of Use* of a building (also called *Importance Classes*). The factor depends from importance of the structure in the management of civil protection in case of a seismic event. Classes are 4 and its coefficient takes the values: *0.7*, *1.0*, *1.5*, *2.0* in order of importance.

The standard defines four LS reference for the definition of the seismic action: *LS of Operativity, LS of Damage limitation, LS of Severe damage* and *LS of near collapse*, to hereafter indicated as, respectively, SLO, SLD, SLC, SLC. To these correspond the following probability of exceedance (P_{VR}), respectively, equal to *81%*, *63%*, *10%* and *5%*. These percentages

remain unchanged whatever the importance class of the construction and by means of Eq. 1 assumes the values reported in Table 1:

LS		T_R
SLE	SLO	30 years < $0.60 \cdot V_R$
	SLD	V_R
SLU	SLV	$9.50 \cdot V_R$
	SLC	$19.50 \cdot V_R$

Table 1: $T_R=T_R(V_R,P_{VR})$ [1].

These parameters, together with the geographical coordinates and T_R, identify the single point in the grid which divides the whole national territory.

Having the geographical coordinates relative to the site of the construction and T_R value according to Eq. 1, the seismic hazard, and consequently the elastic response spectrum associated, is defined by the following three parameters that are uniquely determined:

a_g : design ground acceleration on type A ground;

F_o : maximum amplification factor of the horizontal acceleration spectra;

T_C^* : corner period at the upper limit of the constant acceleration region.

For the horizontal component of the seismic action, the elastic response spectrum $S_e(T)$ is defined by the following expressions [1]:

$$0 \le T \le T_B \quad \Rightarrow \quad S_e(T) = a_g \cdot F_o \cdot S_S \cdot S_T \cdot \left[\frac{T}{T_B} + \frac{1}{F_o}\left(1 - \frac{T}{T_B}\right)\right] \tag{4}$$

$$T_B \le T \le T_C \quad \Rightarrow \quad S_e(T) = a_g \cdot F_o \cdot S_S \cdot S_T \tag{5}$$

$$T_C \le T \le T_D \quad \Rightarrow \quad S_e(T) = a_g \cdot F_o \cdot S_S \cdot S_T \cdot \left(\frac{T_C}{T}\right) \tag{6}$$

$$T_D \le T \quad \Rightarrow \quad S_e(T) = a_g \cdot F_o \cdot S_S \cdot S_T \cdot \left(\frac{T_C \cdot T_D}{T^2}\right) \tag{7}$$

where, T is the vibration period of structure and S_e is the elastic response spectrum (spectral acceleration). S_S and S_T are the amplification stratigraphic coefficient and topographic amplification coefficient. S_T is equal to *1.4*, *1.2*, *1.2* and *1.4* respectively by category topographic T1, T2, T3 and T4 (see *Table 3.2.VI* - NTC 2008 [1]). In particular, S_S is expressible in the following form:

$$S_{S,min} < S_S = \gamma - \delta \cdot F_o \cdot \frac{a_g}{g} < S_{S,max} \tag{8}$$

where the factors $S_{S,max}$, $S_{S,min}$, γ and δ depend on the ground type.

T_B, T_C and T_D are, respectively, the lower limit of the period of the constant spectral acceleration branch, the upper limit of the period of the constant spectral velocity branch, the value defining the beginning of the constant displacement response range of the spectrum.

Should be noted that the period T_C is function of T_C^* (by means of two dimensionless parameters α and β). In turn, for geographic coordinates of the predetermined site, T_C^* is function of T_R. Table 2 collects the values of the parameters defined above for ground type.

As a example, the horizontal components of the elastic spectra corresponding to the city of Rome are shown below. The Figure 1a shows the variability of the spectral shape by varying the LS, while in Figure 1b by varying the ground type for SLV fixed.

	S_S				T_B $(=T_C/3)$		T_C $(=\alpha\cdot(T_C^*)^\beta)$		T_D
A	1				$0.33\cdot T_C^*$		T_C^*		
	$S_{S,min}$	γ	δ	$S_{S,max}$	$\alpha / 3$	β	α	β	
B	1.0	1.4	0.4	1.2	0.37	0.80	1.10	0.80	$4\cdot a_g\cdot g^{-1}+1.6$
C	1.0	1.7	0.6	1.5	0.35	0.67	1.05	0.67	
D	0.9	2.4	1.5	1.8	0.42	0.50	1.25	0.50	
E	1.0	2.0	1.1	1.6	0.38	0.60	1.15	0.60	

Table 2: S_S, C_C values and T_B, T_C, T_D fundamental periods.

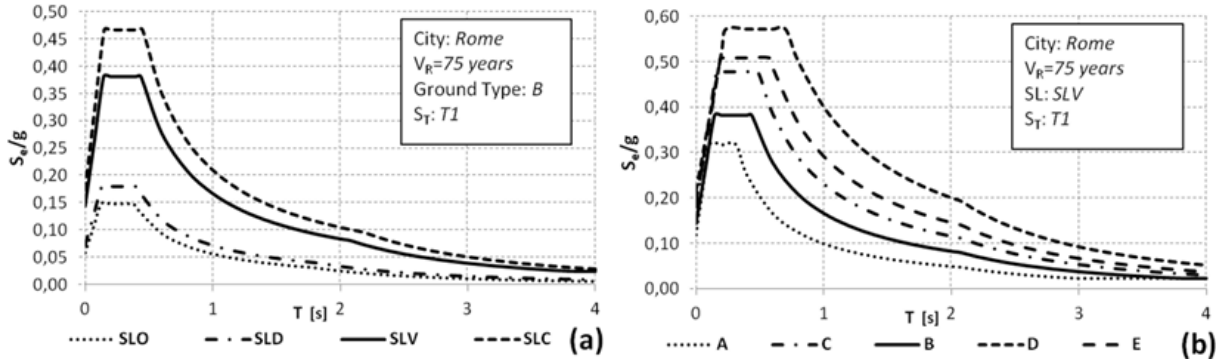


Figure 1: Elastic response spectra for city of Rome for reference life equal to 75 years, respectively, by varying the LS (a) by varying ground type for SLV (b).

3 ASSESSMENT OF STRUCTURAL PERFORMANCES: N2 METHOD

The N2 method [5,13] synthesizes in the same name two of its distinctive features

In fact, the letter "N" indicates that the method is Non-linear, whereas "2" refers to the use of two different computational models of the structure: a multi-degree of freedom (MDoF) model, on which a pushover numerical analysis is performed, and an "equivalent" single-degree of freedom (SDoF) system which is derived by the previous trough proper manipulations, and that is used for the analysis by the design response spectrum. The Method provides, as first step, the determination of the pushover curve of the MDoF system, which is obtained by loading the computational model with constant gravity loads and a proper distribution of horizontal static loads that are monotonically increased with the aim of "pushing" the structure into the non-linear field. The process is carried on until the ultimate limit condition of the structure is reached. Thence, the final output of the pushover analysis is represented by the relation between the base shear force V_b and the displacement D of a control point, usually taken at the centre of mass of the roof of the building. The distribution of the lateral forces to be used in the analysis is determined as:

$$F_{ij} = \Phi_{ij} \cdot m_j \tag{9}$$

with Φ_{ij} profile of displacements, m_j storey mass (the subscript "i" for the i-th profile of displacements and the subscript "j" for the j-th storey). The curve is then transformed in a elastic - perfectly plastic law characterized by resistance (V_{by}) and displacement (D_y) at yield by equivalence relationships. The SDOF system is obtained by dividing the above quantities for the "Modal Participation Factor - Γ_J ", defined below. The parameters obtained are equivalent values F_y^* and D_y^*.

$$\Gamma_J = \frac{\sum m_j \cdot \Phi_{ij}}{\sum m_j \cdot \Phi_{ij}^{\,2}} = \frac{m^*}{L^*} \tag{10}$$

The elastic period (T^*) of the SDoF system having mass m^* is defined as:

$$T^* = 2\pi \cdot \sqrt{\frac{m^* \cdot {D_y}^*}{{F_y}^*}} \tag{11}$$

The assessment of the seismic demand is graphically illustrated in Figure 2 for the generic LS, where the elastic spectrum and the capacity curve of the equivalent SDOF system are in the acceleration-displacement S_a-S_d format. When the elastic period (T^*) of the equivalent system is greater than T_C, the seismic demand (abscissa corresponding to "performance point - PP" identified on the bilinear curve of the SDoF system in the intersection with the inelastic spectrum) is equal to that obtained by the elastic system having equal period. Therefore, the seismic demand for the generic SL, it can be deduced directly by the elastic spectrum and calculated by Eq. 11.

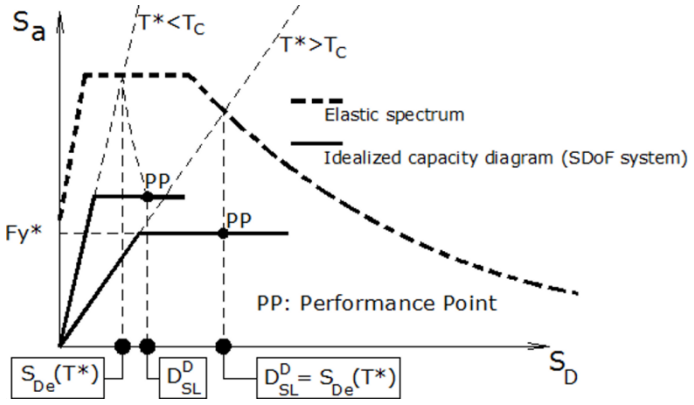


Figure 2: Assessment of seismic demand by the N2 method.

In cases where, instead, the T^* period is less than T_C, the seismic demand ${D_{SL}}^D$ is greater than the elastic displacement S_{De} and the value is analytically obtained by amplifying the elastic displacements as a function of reduction factor (q^*). This parameter is given by the ratio between the force that the SDoF system would suffer if it remained elastic and the force that causes the irreversible deformation of the structure (plastic phase). The equations that solve the method are the following:

$$T^* \geq T_C \quad \Rightarrow \quad D_{SL}^D = S_{De}(T^*) = \frac{T^{*2}}{4\pi^2} \cdot S_e(T^*) \tag{12}$$

$$T^* \leq T_C \quad \Rightarrow \quad D_{SL}^D = S_{De}(T^*) \cdot \frac{1}{k} \rightarrow \quad D_{SL}^D = S_{De}(T^*) \cdot \frac{1}{q^*}\left[1 + (q^* - 1)\frac{T_C}{T^*}\right] \tag{13}$$

where q^* is given by the following expression (by putting together Eq. 5 and ${F_y}^*$ equal to the product between elastic stiffness (${K_y}^*$) and yield displacement (${D_y}^*$):

$$q^* = \frac{S_e(T^*) \cdot m^*}{F_y^*} \Rightarrow q^* = \frac{a_g \cdot F_o}{D_y^*} \cdot S_S \cdot S_T \cdot \frac{4\pi^2}{T^{*2}} \tag{14}$$

The seismic verification is to check, for LS generic, if the following equation is satisfied.

$$D_{SL}^C \geq D_{SL}^D \tag{15}$$

Obviously, the Eq. 15 can also be expressed with reference to the MDoF system by multiplying both terms by the coefficient of modal participation factor Γ_J.

4 PROPOSED ALGORITHM

This paper proposes a procedure (Figure 3) which identifies, for any limit state, the elastic response spectrum associated with the structural capacity expressed in terms of displacement (D_{SL}^{C}). The return period of the earthquake relative to the elastic spectrum will be taken as: "capacitive" return period.

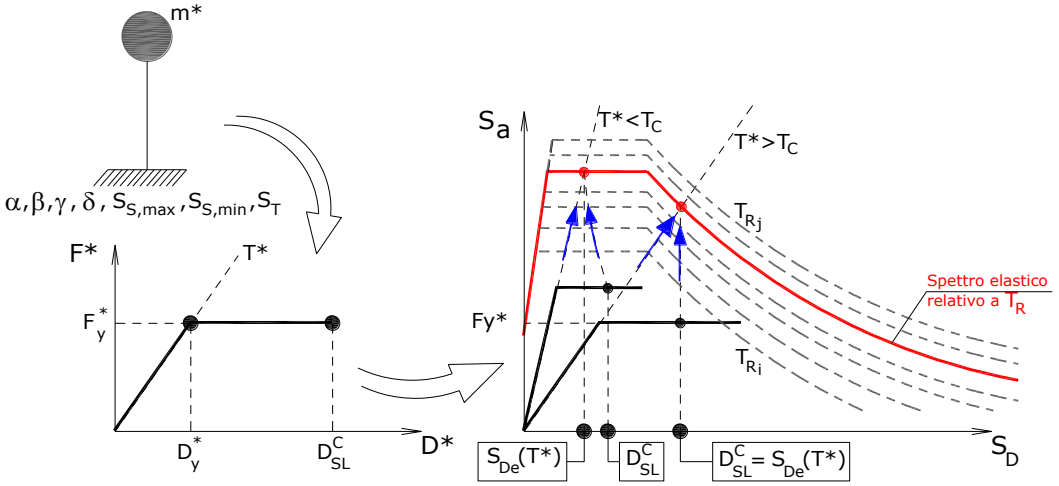


Figure 3: Graphical representation of the procedure.

The proposed procedure is based on an inverse application of the N2 method. For these reasons, it's possible to express the relationships that characterize the horizontal components of the elastic response spectrum (*§ 2* - Eqn. 5,6,7) as a function of the main parameters to the calculation of $T_{R,SL}^{C}$, and of the relations between seismic demand D_{SL}^{D} and elastic displacement $S_{DE}(T^{*})$, using the method N2 (*§ 3* - Eqn. 12,13,14). Of course, in the development of the N2 method, the capacity displacement D_{SL}^{C} instead of the seismic demand D_{SL}^{D} is indicated only for the purposes of the procedure. The convention is necessary because the aim of the research is the calculation of return period corresponding to the structural capacity.

- Substituting Eq. 5 into Eq. 13:

$$T^{*} \leq T_C \quad \Rightarrow \quad \left[a_g \cdot F_o\right] = \frac{k \cdot D_{SL}^{C}}{S_S \cdot S_T \cdot \frac{T^{*2}}{4\pi^2}} \tag{16}$$

- Substituting Eq. 6 into Eq. 12:

$$T_C \leq T^{*} \leq T_D \quad \Rightarrow \quad \left[a_g \cdot F_o \cdot T_C\right] = \frac{D_{SL}^{C} \cdot 4\pi^2}{S_S \cdot S_T \cdot T^{*}} \tag{17}$$

- Substituting Eq. 7 into Eq. 12:

$$T^{*} \leq T_D \quad \Rightarrow \quad \left[a_g \cdot F_o\right] = \frac{D_{SL}^{C} \cdot 4\pi^2}{S_S \cdot S_T \cdot T_C \cdot T_D} \tag{18}$$

$a_g{\cdot}F_o$ ed $a_g{\cdot}F_o{\cdot}T_C$ (the latter also expressed as $a_g{\cdot}F_o{\cdot}\alpha{\cdot}(T_C^{*})\beta$) are both monotonic increasing functions and uniquely determined when the geographic coordinates of the site and ground type were preliminarily fixed.

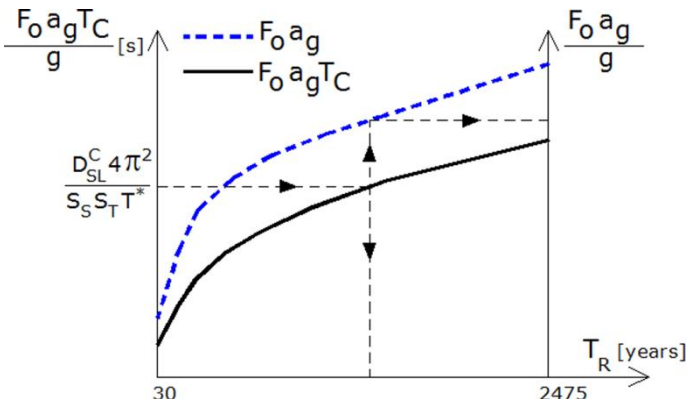


Figure 4: $a_g \cdot F_o = a_g \cdot F_o(T_R)$ and $a_g \cdot F_o \cdot T_C = a_g \cdot F_o \cdot T_C(T_R)$ functions.

According to foregoing, the assessment of the period of return is obtained by an iterative procedure which is summarized hereinafter in its fundamental steps (for B, C, D and E ground type to be developed entirely, while, by starting only from *step 2* for A soil type):

1) As initial assumption, a starting value must be assigned to the function $a_g' \cdot F_o'$. A good choice is to assume a value of the function that produces $S_{S,max}$ so as to reduce the number of iterations required to identify T_{SL}^C. Therefore, by Eq. 8:
2) Assuming that the elastic period of the SDOF system (T^*) is into constant spectral velocity branch, the value of the $a_g \cdot F_o \cdot T_C$ functions is evaluated with Eq. 17, which corresponds a relative return period T_R (see Figure 4).
3) With the return period T_R obtained in the previous step values of the parameters of seismic hazard (a_g, F_o, T_c^*) are evaluated. It's thus assessable the new value of the $a_g \cdot F_o$ function.
4) Having the value of T_C^*, the hypothesis assumed to step 2 for the period elastic T^* must be verified. When the hypothesis isn't more valid:
   - If $T^* < T_C$: value of the $a_g \cdot F_o$ function is given by Eq. 16;
   - If $T^* > T_D$: value of the $a_g \cdot F_o$ function is given by Eq. 18.
5) After determining the new value of the function, the value found is compared with that starting to control the convergence of the iteration. The procedure is considered completed when the convergence is reached. That is, when the difference between the values of two consecutive cycles is lower than a given tolerance (for the proposed procedure equal to 10^{-4} was assumed):

$$\left| a_g \cdot F_o - a_g' \cdot F_o' \right| \leq 10^{-4} \qquad (20)$$

   If Eq. 20 gives a negative result, the procedure must be repeated with the new value of $a_g \cdot F_o$ function, starting from step 2. Before however, the new value of the S_S coefficient must be checked because the new $a_g \cdot F_o$ value could vary S_S value and then to modify the ground type to starting. If the value of S_S coefficient corresponds to a ground type different by that set at the beginning, the procedure is ended and the return period is the last calculated.

The procedure just described is represented by the flowchart shown in the algorithm form in Figure 5. The same has been implemented in the numerical solver MatLab ®, in which a simple graphical user interface (Figure 6) *SEREP* called (short for SEismic REturn PEriod) was created. *SEREP* returns as output the value of the capacitive return period T_R^C (and the reference life associated with each LS) by inserting few input data (Figure 5).

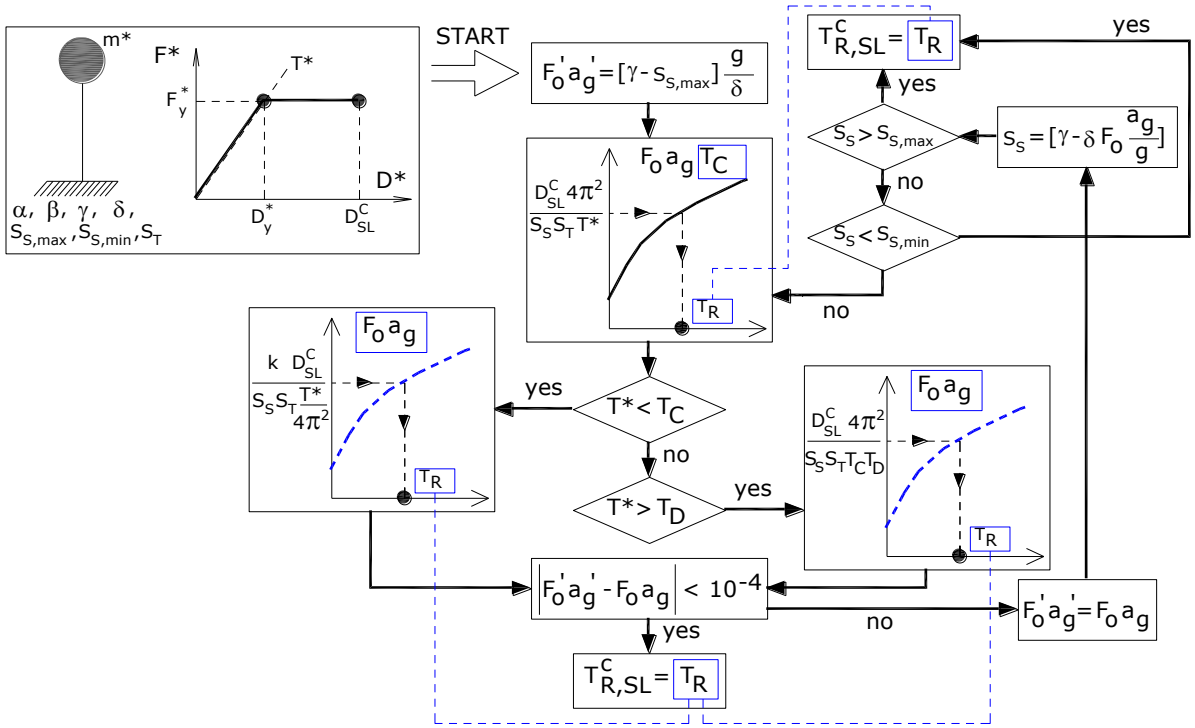


Figure 5: Flowchart

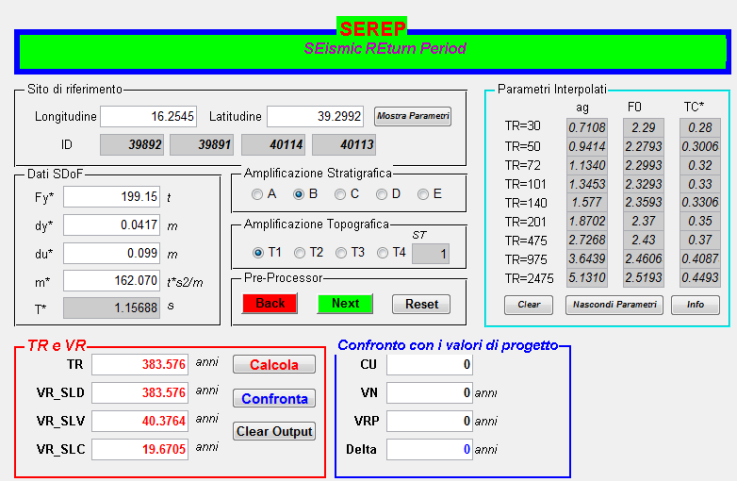


Figure 6. *SEREP* - Graphical user interface.

As highlighted in the introduction, the procedure is aimed at assessing the Seismic Vulnerability Index of the structure ($I_{V,SL}$)(*see Eq. 2*). If used on a regional scale, This index allows to identify the areas with the most vulnerable structures seismically in order to planning more detailed checks on them. Thus, the index helps the administrations which have the responsibility of the structural safety of the buildings because it allows to optimize the economic resources available.

Furthermore, given that the probability of exceeding (P_{VR}) in the reference life (V_R) must be the same, both for the demand spectrum and for capacity spectrum (design assumptions allowed by *Ministerial Circular 617/2009* [12]), Eq. 2 can be rewritten by the aid of Eqn. 1,3.

$$I_{V,SL} = \frac{T_{R,SL}^{C}}{T_{R,SL}^{D}} = \frac{\frac{V_{R,SL}^{C}}{\ln(1-P_{VR})}}{\frac{V_{R}^{D}}{\ln(1-P_{VR})}} = \frac{V_{R,SL}^{C}}{V_{R}^{D}} = \frac{V_{N,SL}^{C} \cdot C_U}{V_{N}^{D} \cdot C_U} \quad (21)$$

Where V_N^D is the *request life* to the structure in the design phase. Therefore by evaluating $T_{R,SL}^C$ and by applying indirectly the Eq. 21, it is possible to determine the "*current nominal life*" $V_{N,SL}^C$ that, in the case of $I_{V,SL}>1$ represents a direct measurement of the residual life of the structure.

5 NUMERICAL VALIDATION OF THE ALGORITHM

The numerical validation of the procedure by using the data contained in a previous work of the authors [14] was conducted. In [14] the data concerning to pushover analysis of different modelling of an existing RC building located in Calabria (southern Italy, an area of high seismic risk) are collected.

The main data of the SDoF system and starting parameters of the proposed algorithm are collected in Table 3. The data relate to pushover analysis in positive direction of thrust and along the larger dimension of the building plan. As purely descriptive information, the seismic verification to the limit state of near collapse (SLC) with the N2 method, is satisfied along the direction of analysis considered. The structural deficits, instead, in the orthogonal direction to that considered in hereinafter were observed. The building belongs to a Class of Use II ($C_U = 1$).

m^* *[t·s²/m]*	*162.07*	α	*1,10*	$S_{S,min}$	*1.0*
F_y^* *[t]*	*199.15*	β	*-0,20*	$S_{S,max}$	*1.2*
D_y^* *[m]*	*0.042*	γ	*1.40*	S_T	*1.0*
D_{SLC}^C *[m]*	*0.193*	δ	*0.40*		

Table 3: Parameters required to validate the algorithm proposed.

The algorithm is based on an inverse application of the N2 method, it was considered appropriate to validate the whole procedure by directly applying the same method. In other words, the numerical validation is to assess the "capacitive" return period $T_{R,SL}^C$ using the algorithm described in *§ 4* and summarized graphically in Figure 5. The value found defines the elastic response spectrum that it allows to get the seismic demand D_{SL}^D (in terms of displacement) by N2 method. Obviously the seismic demand corresponds to the seismic capacity D_{SL}^C of the SDoF system, neglecting, of course, the numerical approximations which are inherent to the same algorithm. Therefore, the validation consists in verifying the correspondence between two displacement values theoretically equal but which by different evaluation methods are obtained: the first, by directly applying the N2 method with the elastic spectrum (then, $T_{R,SL}^C$) by the algorithm proposed, the second, starting from the structural performance which provides the elastic spectrum, once again, by the same algorithm.

In brief, the validation comprises the following steps:

1) Assessment of return period ($T_{R,SL}^C$) corresponding to the structural capacity (D_{SL}^C) to a LS preliminarily fixed (see Figs. 3 and 5), starting from data relating to the generic case of study (Table 3). In the present paper the limit state of near collapse (SLC) was considered.
2) Definition of the elastic response spectrum (corresponding to the $T_{R,SL}^C$ value determined in step n.1) using the geographic coordinates of the site, the ground type, the

topographic class and limit state considered. The elastic spectrum can be obtained quickly by a commercial software commonly used to generate response spectra and accelerograms (for the case of study under examination SIMQKE_GR [15] software was employed);

3) Assessment of the seismic demand D_{SL}^{D} by N2 method;
4) Comparison of D_{SL}^{D} and D_{SL}^{C}, respectively, seismic demand valued by N2 method and structural capacity by pushover analysis. The algorithm can be considered reliable if the displacements are negligible, ie they are not very significant in terms of performance.

In order to expand the sample survey different structural performance were assumed to other things being equal. 7 different D_{SL}^{C} values by reducing by 10%, from time to time, the real starting value were considered. In Figure 7, the displacements as a function of the capacitive return period $T_{R,SL}^{C}$ evaluated by proposed algorithm are shown, while in Table 4, the absolute percentage errors are reported.

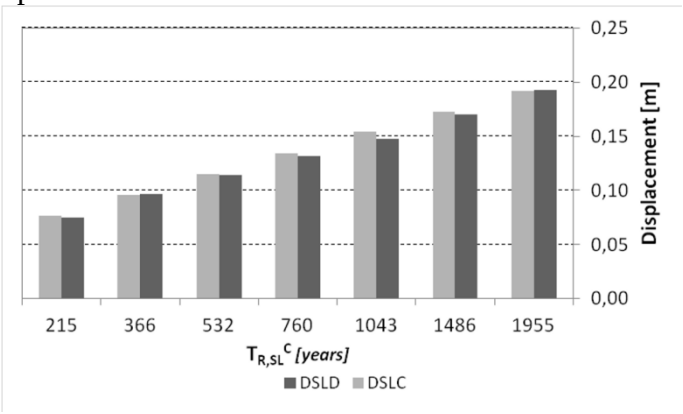


Figure 7: Comparison of demand and capacity in terms of displacement starting by return period capacitive T_{SL}^{C}, ie the elastic spectrum derived using the algorithm proposed.

$T_{R,SL}^{C}$ *[years]*	D_{SL}^{D} *[m]*	D_{SL}^{C} *[m]*	E_A *[%]*
1955	*0.193*	*0.192*	*0.56*
1486	*0.170*	*0.173*	*1.89*
1043	*0.148*	*0.154*	*3.71*
760	*0.132*	*0.134*	*1.90*
532	*0.114*	*0.115*	*1.30*
366	*0.097*	*0.096*	*0.56*
215	*0.075*	*0.077*	*3.25*

Table 4: Absolute percentage error (E_A).

The average percentage error is equal to *1.88%*. As can be seen by the values shown, there aren't significant difference. The overall outcome confirms the reliability of the procedure.

6 CONCLUSIONS

The newly developed technical standards assess the seismic action based on the seismic hazard of the national territory. However, if on one hand the seismic verification of an existing structure is immediate by the direct comparison between the seismic demand and capacity to oppose the same action, on the other hand, the seismic verification in terms of return period is much more difficult. Indeed, it's difficult to estimate the return period of the seismic action corresponding to the deformation capacity of the structure than to a predetermined limit state

(LS). The return period in question "capacitive" ($T_{R,SL}{}^{C}$) was called. The present study proposes an algorithm to calculate the return period having available the elastic period and the structural capacity for a given LS. The reference life is therefore directly determined for any LS considered. The algorithm is given by an iterative procedure which was implemented within a numerical solver. A GUI in MatLab code was created in a still poor format. *SEREP* (SEismic REturn Period) returns as output the return period "capacitive" after that the geographical coordinates of the site and some data of SDOF system were inserted. The numerical validation by using data relating to the structural response of an existing building was performed. The maximum percentage error obtained by calculating the return period with the proposed algorithm is of about *3%*. The error is very low and it doesn't affect the reliability of the algorithm.

AKCNOWLEDGEMENT

The research presented in this article was partially funded by the Department of Civil Protection, Project ReLUIS-DPC 2010-2013.

REFERENCES

[1] DM 14/01/2008. Norme Tecniche per le Costruzioni (NTC 2008). Gazzetta Ufficiale n.29. Roma; 2008 *(in Italian)*.

[2] CEN. Eurocode 8: design of structures for earthquake resistance. *Part 1: general rules. seismic actions and rules for buildings*. Brussels. Belgium; 2005.

[3] G. Uva, D. Raffaele, F. Porco, A. Fiore, G. Porco, Bridge monitoring by fiber optic deformation sensors: a case study. In: Biondini, Frangopol (eds) Proceedings of the 6th international conference on bridge maintenance, safety and management, Como, Italy, 8–12 July 2012. Taylor & Francis Group, London - ISBN: 978-0-415-62124-3.

[4] F. Porco, A. Fiore, G. Porco, G. Uva, Monitoring and safety for prestressed bridge girders by SOFO sensors, *Journal of Civil Structural Health Monitoring* **3**(1),3-18, 2013. DOI 10.1007/s13349-012-0029-9.

[5] P. Fajfar, P. Gaspersic, The N2 method for the seismic damage analysis of RC buildings. *Earthquake Engineering and Structural Dynamics*, **28**, 979–93,1996.

[6] G. Uva, F. Porco, A. Fiore, M. Mezzina, Proposal of a methodology of in-situ concrete tests and improving the estimate of the compressive strength, *Construction and Building Materials*, **38**(1):72-83, 2013 - DOI: 10.1016/j.conbuildmat.2012.08.025.

[7] G. Uva, F. Porco, A. Fiore, Appraisal of masonry infill walls effect in the seismic response of RC framed buildings: a case study. *Engeneering Structures*, **34**(1):514–26, 2012.

[8] G. Uva, F. Porco, D. Raffaele, A. Fiore, On the role of equivalent strut models in the seismic assessment of infilled RC buildings. *Engineering Structures*, **42**:83-94, 2012.

[9] H. Crowley, R. Pinho, J.J. Bommer, A probabilistic displacement-based vulnerability assessment procedure for earthquake loss estimation. *Bulletin of Earthquake Engineering*, **2**(2), 173-219, 2004.

[10] B. Borzi, R. Pinho, H. Crowley, Simplified Pushover-Based Vulnerability Analysis for Large Scale Assessment of RC Buildings. *Engineering Structures*, **30**(3), 804-820, 2007.

[11] D. Raffaele, F. Porco, A. Fiore, G. Uva, Simplified Vulnerability Assessment of RC Circular Piers in Multi-Span-Simply-Supported Bridges. *Structure and Infrastructure Engineering*, 2013 - DOI:10.1080/15732479.2013.772642.

[12] Circolare 2 febbraio 2009. n. 617 approvata dal Consiglio Superiore dei Lavori Pubblici. Istruzioni per l'applicazione delle "Nuove norme tecniche per le costruzioni" di cui al Decreto Ministeriale 14 gennaio 2008 – 2009 (*in Italian*).

[13] P. Fajfar, Capacity spectrum method based on inelastic demand spectra. *Earthquake Engineering and Structural Dynamics*, **28**, 979-993, 1999.

[14] A. Fiore, F. Porco, D. Raffaele, G. Uva, About the influence of the infill panels over the collapse mechanisms actived under pushover analyses: two case studies. *Soil Dynamics and Earthquake Engineering*, **39**,11-22, 2012.

[15] E.H. Vanmarcke, G.A. Fenton, E. Heredia-Zavoni, *SIMQKE-II Conditioned Earthquake Ground Motion Simulator, User's Manual*. *Version 2*. Princeton University; 1996.

COMPDYN 2013
4th ECCOMAS Thematic Conference on
Computational Methods in Structural Dynamics and Earthquake Engineering
M. Papadrakakis, V. Papadopoulos, V. Plevris (eds.)
Kos Island, Greece, 12–14 June 2013

A MULTI-DIRECTIONAL ABSORBING LAYERS FOR SEISMIC WAVE PROPAGATION IN UNBOUNDED DOMAIN BY USING HETEROGENEOUS MULTI-TIME STEP SUB-DOMAIN METHODS

Zafati E.[1], **Brun M.**[1], **and Irini DJ.M.**[1]

[1]INSA de Lyon
Batiment Coulomb 20, Avenue A. Einstein 69621 Villeurbanne cedex (France)
e-mail: eliass.zafati@insa-lyon.fr

Keywords: wave propagation, Rayleigh damping, sub domains, code coupling.

Abstract. *It is well known that the elastic wave propagation predicted by the FEM suffers from the difficulty to correctly reproduce the unbounded media: spurious waves are reflected at the FEM model at the artificial boundaries. Variant techniques may be introduced to reduce the spurious reflections at the boundaries, such as the infinite elements, the absorbing boundary conditions or the perfect matched layers. Nonetheless, the most efficient strategy, such as the perfect matched layer, leads to an important implementation effort in existing FE softwares. Recently, a simplified approach proposed by Semblat et al. (2010) consists in introducing classical Rayleigh formulation in a layer subdomain, surrounding the domain under investigation; the purpose of this artificial layer is to damp the incident seismic waves while minimizing the spurious reflected waves towards the studied domain. The objective of this work is to enhance this methodology by taking advantage of the subdomain methods. The GC method, proposed ten years ago by Combescure and Gravouil, enables to decompose a finite element mesh into several partitions and to use in each partition the suitable time integrator with its own time step. Therefore, the coupling method is heterogeneous, allowing to couple different time integrators and multi-time steps in the sense that very different time steps depending on the subdomains can be adopted. An external coupling software, based on the GC method, are developed to enable multi-time step explicit/implicit co-computations. It makes to interact in time an explicit FE code (Europlexus), associated with fine time step for the domain of interest, with an implicit FE code (Cast3m) handling the absorbing boundary layers by using a Rayleigh viscous damping matrix. Large time steps can be adopted for the absorbing boundary layers. The reduction of the spurious wave reflections at the interface has been optimized as well as the ability of the absorbing layers to damp the transmitted waves. The relevance and the numerical efficiency of the multi-time step implicit absorbing boundary layer strategy are compared with classical absorbing boundary conditions.*

1 Introduction

The simulation of the soil interaction problems [1] using the Finite Element method requires the modeling of an unbounded medium. Efficient numerical methods have to be set up, minimizing the number of operations while maintaining the accuracy of computation. For modeling the wave propagation in soils, we need a very huge mesh to avoid the artificial reflected waves at the boundaries of the domain of interest. However, such model becomes more costly in computation time, especially when we work with complex structures. To reduce the FE model for the domain of interest, several methods have been developed which consist in adding artificial conditions at the boundaries such as the PML (Perfect Matched Layers) [2], absorbing boundaries [3] or infinite elements [4]. The aim of these techniques is to absorb the energy coming from the field of interest without generating important spurious waves.

One technique for absorbing the incident waves is to introduce artificial layers at the boundaries. This method has been used in some problems by introducing the Rayleigh matrix [5] in elastic layers. The Rayleigh matrix is simply expressed as a linear combination of the mass matrix and the stiffness matrix. This method turns out to be efficient and easy to implement. However, the amount of spurious waves reflected at the boundaries is not easy to be predicted as well as the optimal thickness for minimizing the reflected waves while optimizing the damping in the Rayleigh medium.

The Rayleigh matrix has been generalized following the work of Caughey [6]. The use of the Rayleigh matrix for soil dynamics problems is not obvious because the behavior of the derived Rayleigh material can be viewed as unphysical. However, Semblat $et\ al.$ gives a rheological interpretation of this material and shows the similarity between this material and the Maxwell material [7].

As already mentioned, the optimization of the computation time is an important criterion to work with complex geometry problems. Subdomain methods with multi time steps depending on the subdomains can be good candidates for reducing the computation time. Gravouil and Combescure [8] proposed an efficient partitioning method, denoted as GC method, able to couple several time integration schemes from the Newmark family with different time steps. The method follows a dual Schur approach by ensuring the velocity continuity at the interface through Lagrange multipliers. The method is proved to be stable using the so-called energy method [9]. . It leads to the first order of accuracy when coupling second order accuracy time integration schemes due to a slight spurious dissipation at the interface as soon as different time steps are adopted. Implicit/Explicit multi-time step co-computations, using a coupling software based on the GC method, have been validated in comparison to full explicit computation for reinforced concrete structures subjected to earthquake loading [10].

In the present paper we suggest to:

1 - show the link between the Rayleigh damping and the Kelvin-Voigt viscoelastic material. We seek to obtain a strong from for wave propagation in the Rayleigh medium in order to determine the optimal conditions for minimizing the reflected waves between a non dissipative medium with a Rayleigh medium. These conditions will be determined for harmonic waves.

2 - Validate the previous optimal conditions at the interface by considering numerical examples: first without subdomain decomposition for a 1D wave propagation problem and second with the GC coupling method for the 2D Lamb's problem [11]. In this latter, two different Finite Element codes will be used into an Explicit/Implicit multi time step co-computation: Europlexus [12] based on the explicit scheme and Cast3m [13] based onthe implicit scheme.

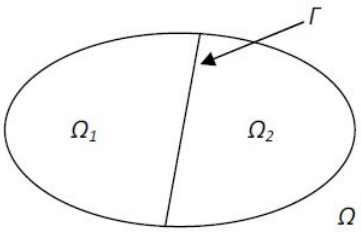


Figure 1: Domain Ω divided into two subdomains $\Omega_1$andΩ_2

2 Rayleigh damping

In this part, it is proposed to study a problem in a continuum medium divided into two subdomains separated by the interface denoted as Γ: the subdomain Ω_1 with a linear elastic behavior and the subdomain Ω_2 with a damping behavior defined later. A strong form for the wave propagation in the damped subdomain is proposed. It will be shown that the discretized form of the damped subdomain exactly corresponds to the introduction of the Rayleigh matrix into the classical discretized in space equation of motion. Once obtained the strong form for the wave propagation in the Rayleigh damping medium, the interface problem can be analytically studied, by writing for harmonic waves the continuity of displacements and the stress equilibrium at the interface.

Linear elastic behavior is assumed, with an infinitesimal strain tensor defined by:

$$\epsilon(u) = \frac{1}{2}(\nabla u + \nabla^t u) \tag{1}$$

u being the field displacement vector.

2.1 The boundary value problem (strong form)

Let Ω a bounded open set from $\mathbb{R}^3$ with a regular boundary. We assume that the domain is divided into two parts Ω_1 and Ω_2 illustrated in Figure 1 such as : $\Omega_1 \cap \Omega_2 = \varnothing$ and $\partial\Omega_1 \cap \partial\Omega_2 = \Gamma$.

Subdomain Ω_1 :

It is assumed that the medium Ω_1 is elastic linear characterized by the density ρ_1 and the Lame coefficients λ_1 and μ_1. We call E_1,ν_1 the Young's modulus and the Poisson's coefficient of this material. The displacement vector field u_1 is governed by the following equations:

$$\rho_1 \partial_t^2 u_1 = div(\sigma_1(u_1)) \tag{2}$$

$$\sigma_1 = \lambda_1 tr(\epsilon(u_1)) + 2\mu_1 \epsilon(u_1) \tag{3}$$

with the boundary conditions:

$$\sigma_1.n_1 = g_{1n} \ \ on \ \ \ \partial\Omega_{1n} \tag{4}$$

$$u_1 = u_{1d} \ \ on \ \ \partial\Omega_{1d} \tag{5}$$

Here $\partial\Omega_{1d}$ and $\partial\Omega_{1n}$ are subsets of the boundary with $\partial\Omega_{1n} \cup \partial\Omega_{1d} = \partial\Omega_1 \setminus \Gamma$ and $\partial\Omega_{1n} \cap \partial\Omega_{1d} = \varnothing$.

The initial conditions are:

$$u_1(x \in \Omega_1, t = 0) = 0 \tag{6}$$

$$\partial_t u_1(x \in \Omega_1, t = 0) = 0 \tag{7}$$

Subdomain Ω_2:

We assume that the displacement vector field u_2 is governed by the following equations:

$$\rho_2 \, \partial_t^2 u_2 + a \, \rho_2 \, \partial_t u_2 = div(\sigma_2(u_2)) \tag{8}$$

$$\sigma_2 = \lambda_2 \, tr(\epsilon(u_2)) + 2\mu_2 \epsilon(u_2) + b \, (\lambda_2 \, tr(\epsilon(\partial_t u_2)) + 2\mu_2 \, \epsilon(\partial_t u_2)) \tag{9}$$

with $a,\ b,\ \lambda_2,\ \mu_2$ being positive integers.

It is clear from the Eq. (9) that the material has the behavior of a Kelvin-Voigt viscoelastic material, with b corresponding to the characteristic time parameter. From Eq. (8), it can be seen that a dashpot, characterized by the damping coefficient $a\,\rho_2$, has been added as classically done for a damped oscillator. The parameters λ_2, μ_2 are called the Lame coefficients. Similarly, E_2 and ν_2 are the Young's modulus and the Poisson's ratio of the Kelvin-Voigt viscoelastic material.

Particular boundary conditions are given as follows:

$$\sigma_2.n_2 = 0 \; on \quad \partial\Omega_{2n} \qquad\qquad u_2 = 0 \; on \;\; \partial\Omega_{2d} \tag{10}$$

with

$$\partial\Omega_{2n} \cup \partial\Omega_{2d} = \partial\Omega_2 \setminus \Gamma \qquad\qquad \partial\Omega_{2n} \cap \partial\Omega_{2d} = \varnothing \tag{11}$$

The initial conditions are taken as:

$$u_2(x \in \Omega_2, t = 0) = 0 \qquad\qquad \partial_t u_2(x \in \Omega_2, t = 0) = 0 \tag{12}$$

The interface :

Figure 2 illustrates the conventional orientations of the normal vectors. The continuity of displacements and equilibrium of stresses are given by :

$$\sigma_2.n_2 = -\sigma_1.n_1 \quad on \quad \Gamma \qquad\qquad u_1 = u_2 \quad on \quad \Gamma \tag{13}$$

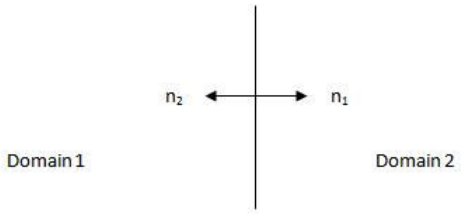


Figure 2: the normal vectors at the interface

2.2 The problem discretized in space

We assume that the problem presented above is well-posed ([16]). Through the weak formulation and the finite element approximation, it can be proved that the problem in the dicretized space is given by:

$$M_1\ddot{U}_1 + K_1U_1 + L_1^T\hat{\lambda} = F_1^{ext} \tag{14}$$

$$M_2\ddot{U}_2 + K_2U_2 + (a\ M_2 + b\ K_2)\dot{U}_2 + L_2^T\hat{\lambda} = 0 \tag{15}$$

$$L_1U_1 + L_2U_2 = 0 \tag{16}$$

Here U_1 and U_2 are the displacements vectors in the discretized space, M_i and K_i are the mass and the stiffness matrices related to the subdomain i, $i = \{1, 2\}$. The vector $\hat{\lambda}$ can be interpreted as the nodal forces at the interface. The operators L_1 and L_2 are defined as Boolean matrices which select the nodes belonging to the interface.

The Dirichlet and the Neumann conditions are given by:

$$U_1 = U_{1d}\ on\ \partial\Omega_{1d} \qquad\qquad U_2 = 0\ on\ \partial\Omega_{2d} \tag{17}$$

$$U_1(t=0) = \dot{U}_1(t=0) = 0\ on\ \Omega_1 \tag{18}$$

$$U_2(t=0) = \dot{U}_2(t=0) = 0\ on\ \Omega_2 \tag{19}$$

It can be observed that the term $a\ M_2 + b\ K_2$ appears in the Eq. (15) which corresponds to the Rayleigh matrix. Thus, it can be shown that the proposed strong from given in Eqs. (8) (9) corresponds to the introduction of the classical Rayleigh matrix $a\ M_2 + b\ K_2$ in the discrete in space equation of motion. In the following, the strong form is employed to obtain the optimal conditions for minimizing the reflections at the interface as well as better describing the damping properties in the Rayleigh medium.

2.3 The problem of the wave propagation

2.3.1 Wave propagation in the Rayleigh medium

We study in this part the problem of the wave propagation in a damping medium characterized by the Rayleigh matrix into the discrete in space equation of motion. We assume that the medium is infinite and the wave propagates in the direction of e_x (Figure 3).

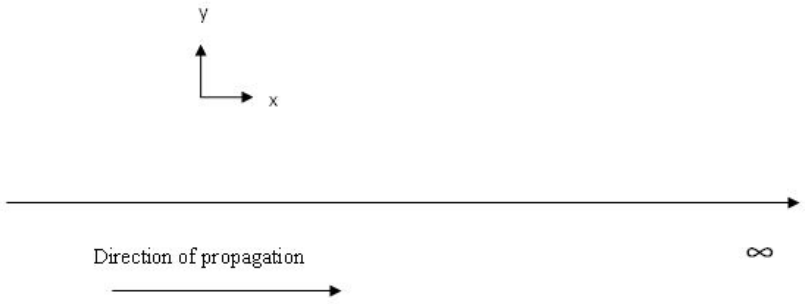


Figure 3: the problem of the wave propagation

Since the problem is 1D, the displacement can be put in the form: $u_2(x,t) = \widetilde{u}_2(x,t)\, e_x$ for P-waves or $u_2(x,t) = \widetilde{u}_2(x,t)\, e_z$ for S-waves.

The equation in the strong form Eq. (8) can be simplified as:

$$\rho_2\, \partial_t^2 \widetilde{u}_2 + a\, \rho_2\, \partial_t \widetilde{u}_2 = (\lambda_2 + 2\mu_2)\, \partial_x^2 \widetilde{u}_2 + b\, (\lambda_2 + 2\mu_2)\, \partial_x^2 \partial_t \widetilde{u}_2 \quad P - waves \tag{20}$$

$$\rho_2\, \partial_t^2 \widetilde{u}_2 + a\, \rho_2\, \partial_t \widetilde{u}_2 = \mu_2\, \partial_x^2 \widetilde{u}_2 + b\, \mu_2\, \partial_x^2 \partial_t \widetilde{u}_2 \quad S - waves \tag{21}$$

We consider an harmonic solution for the above equations in the following form:

$$\widetilde{u}_2(x,t) = T\ \exp(i(\omega_0\, t - k\, x)) \tag{22}$$

with k is the complex wave number such as: $Re(k) \geq 0$.

By introducing this solution into the previous equations, we obtain the following wave number:

$$k^2 = (\frac{\omega_0}{V_2})^2 \frac{1 - a\, b - i(\frac{a}{\omega_0} + b\, \omega_0)}{1 + b^2\, \omega_0^2} \tag{23}$$

with the phase velocity V_2 equal to $\sqrt{\frac{\lambda_2 + 2\mu_2}{\rho_2}}$ for P-waves or $\sqrt{\frac{\mu_2}{\rho_2}}$ for S-waves.

We remark that the expression of k is a complex number which depends on two parameters a and b. It is convenient to choose them as:

$$\frac{a}{\omega_0} = b\, \omega_0 = \xi \tag{24}$$

ξ being called the damping ratio.

We get:

$$\widetilde{u}_2(x,t) = T\ \exp(\frac{-\omega_0\,\xi\,x}{V_2\,\sqrt{1+\xi^2}})\ \exp(i(\omega_0\,t - \frac{\omega_0\,x}{V_2\,\sqrt{1+\xi^2}})) \tag{25}$$

Some interesting remarks can be done:

1. In order to have a logarithmic decrement of $\delta = \ln(\frac{|\widetilde{u}_2|(x)}{|\widetilde{u}_2|(x+\triangle x)})$, $\forall x$, the wave must travel a distance $\triangle x$ given by:
$$\triangle x = \frac{V_2}{\omega_0}\,\frac{\delta\,\sqrt{1+\xi^2}}{\xi} \tag{26}$$
We choose the largest value of V_2 (corresponding to the P-waves).
2. The phase velocity increases and becomes equal to $\sqrt{1+\xi^2}\,V_2$.

Next, we deal with non harmonic waves, by focusing on P-waves (the same results can be deduced for shear waves). Let us introduced $\widetilde{u}_2(x,t)$ the strong solution of the following problem:

$$\rho_2\,\partial_t^2\widetilde{u}_2 + a\,\rho_2\,\partial_t\widetilde{u}_2 = (\lambda_2+2\mu_2)\,\partial_x^2\widetilde{u}_2 + b\,(\lambda_2+2\mu_2)\,\partial_x^2\partial_t\widetilde{u}_2 \quad (x,\ t)\in]0,+\infty[\times\mathbb{R} \tag{27}$$

with the boundary conditions :

$$\widetilde{u}_2(x=0,t) = f(t) \quad \forall t\ \in\ [0,+\infty[\tag{28}$$

$$\widetilde{u}_2(x=0,t) = 0 \quad \forall t\ \in\ ]-\infty,0[\tag{29}$$

and the initial conditions:

$$\widetilde{u}_2(x,\ t=0) = 0 \quad \forall x\ \in]0,+\infty[\tag{30}$$

$$\partial_t\widetilde{u}_2(x,\ t=0) = 0 \quad \forall x\ \in]0,+\infty[\tag{31}$$

here f is a continuous map which satisfies the following conditions:

1. f is integrable on $\mathbb{R}$
2. the Fourier transform of f is integrable

The same expressions of a , b in Eq. (24) is adopted and we denote ω_0 as the dominant angular frequency. By applying the Fourier transform for Eq. (27), it can be shown that the solution is given by:

$$\widetilde{u}_2(x,t) = \frac{1}{2\pi}\int\limits_{\mathbb{R}}\ \hat{f}(\omega)\ \exp(i(\omega\,t - k(\omega)\,x))\,d\omega \tag{32}$$

with the complex wave number defined by:

$$k(\omega) = \frac{\omega}{V_{p2}}\ \sqrt{\frac{1-\xi^2-i\xi(\frac{\omega_0}{\omega}+\frac{\omega}{\omega_0})}{1+\xi^2\,\frac{\omega^2}{\omega_0^2}}} \tag{33}$$

Here $\hat{f}$ is the Fourier transform of f , V_{p2} is equal to $\sqrt{\frac{\lambda_2+2\,\mu_2}{\rho_2}}$.

Now we are able, thanks to Eq. (32), to predict the behavior of the wave traveling through the Rayleigh medium. The problem of the spurious reflections at the interface will be discussed in the next section.

2.3.2 1D wave propagation from an elastic medium to a Rayleigh medium

Let us consider a elastic linear medium Ω_1 and a Rayleigh medium Ω_2 (section 2.1). We assume there is an harmonic wave (P-wave or S wave), which propagates from Ω_1 toward Ω_2 as shown in Figure 4.

The wave propagation problem is 1D and the main purpose is to quantify the spurious waves created at the interface.

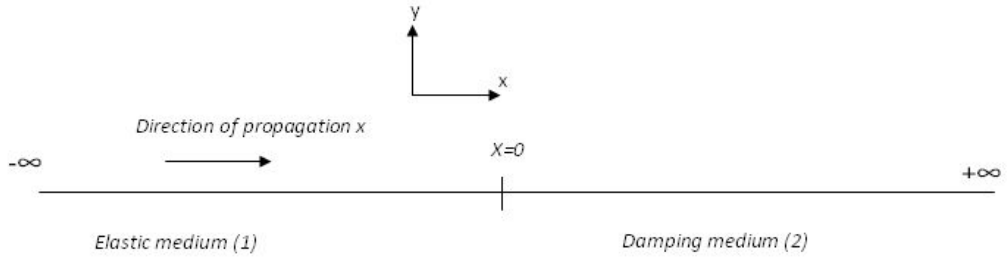


Figure 4: Wave propagation in two mediums separated by an interface $X = 0$

Let us called $\widetilde{u}_1$ is the incident wave, $\widetilde{u}_2$ the transmitted wave and $\widetilde{u}_R$ the reflected wave. Using the same values of the parameters a and b, we write:

$$\widetilde{u}_1(x,t) = A\ \exp(i\omega_0\,(t - \frac{x}{V_1})) \tag{34}$$

$$\widetilde{u}_2(x,t) = T\ \exp(\frac{-\omega_0\,\zeta\,x}{V_2\,\sqrt{1+\zeta^2}})\ \exp(i(\omega_0\,t - \frac{\omega_0\,x}{V_2\,\sqrt{1+\zeta^2}})) \tag{35}$$

$$\widetilde{u}_R(x,t) = R\ \exp(i\omega_0\,(t + \frac{x}{V_1})) \tag{36}$$

where $V_i\ \{i = 1, 2\}$ is the phase velocity and is equal to : $\sqrt{\frac{\lambda_i+2\mu_i}{\rho_i}}$ for P-waves and $\sqrt{\frac{\mu_i}{\rho_i}}$ for S-waves.

From the conditions (section 2.1) at the interface (continuity of displacements and equilibrium of stresses), we have :

$$\widetilde{u}_2(x=0,t) = \widetilde{u}_1(x=0,t) + \widetilde{u}_R(x=0,t) \tag{37}$$

$$\kappa_2\,\partial_x\widetilde{u}_2(x=0,t) = \kappa_1\,(\partial_x\widetilde{u}_1 + \partial_x\widetilde{u}_R)\,(x=0,t) \tag{38}$$

with $\kappa_i\ \{i = 1, 2\}$ being equal to $\lambda_i + 2\mu_i$ for P-waves or $2\mu_i$ for S-waves.

We focus on the reflected waves generated at the interface. The reflection coefficient is given by:

$$\frac{R}{A} = \frac{1 - \gamma \sqrt{1 + \xi^2}}{1 + \gamma \sqrt{1 + \xi^2}} \tag{39}$$

with the parameter γ defined by: $\gamma = \frac{\rho_2 V_2}{\rho_1 V_1}$

Now, we can give a condition under which the reflected P-waves and S-waves vanish as follows:

$$\gamma = \frac{1}{\sqrt{1 + \xi^2}} \tag{40}$$

For two subdomains, by choosing $\rho_1 = \rho_2$, the zero interface reflection coefficient condition writes as:

$$\begin{cases} \lambda_2 = \frac{\lambda_1}{1+\xi^2} & \mu_2 = \frac{\mu_1}{1+\xi^2} \\ E_2 = \frac{E_1}{1+\xi^2} & \nu_2 = \nu_1 \end{cases} \tag{41}$$

The results given by Eq. (41) show the relationships between the Young's modulus and Poisson's ratio for each material composing the subdomains. These results have been proved for harmonic waves and can be also used, as an approximation, for waves which have a dominant frequency.

In the following, non harmonic waves are considered. The incident wave is denoted $\widetilde{u}_1(x,t)$, satisfying $\widetilde{u}_1(x=0,t) = f(t)$ where f is the same function defined in (section 2.3.1.). We can write $\widetilde{u}_1(x,t)$ as:

$$\widetilde{u}_1(x,t) = \frac{1}{2\pi} \int_{\mathbb{R}} \hat{f}(\omega)\ \exp(i(\omega\, t - \frac{\omega}{V_{1p}}\, x)) \tag{42}$$

Let introduce $\widetilde{u}_2(x,t)$ the transmitted wave and $\widetilde{u}_R$ the reflected wave. Taking into account the conditions at the interface (section 2.1), we can prove that $\widetilde{u}_2(x,t)$ and $\widetilde{u}_R(x,t)$ have the following expressions:

$$\widetilde{u}_R(x,t) = \frac{1}{2\pi} \int_{\mathbb{R}} \frac{1 - \gamma \sqrt{1 + \zeta^2 - i\,\zeta\,(\frac{\omega_0}{\omega} - \frac{\omega}{\omega_0})}}{1 + \gamma \sqrt{1 + \zeta^2 - i\,\zeta\,(\frac{\omega_0}{\omega} - \frac{\omega}{\omega_0})}}\, \hat{f}(\omega)\ \exp(i(\omega\, t + \frac{\omega}{V_1}\, x))\, d\omega \tag{43}$$

$$\widetilde{u}_2(x,t) = \frac{1}{2\pi} \int_{\mathbb{R}} \frac{2}{1 + \gamma \sqrt{1 + \zeta^2 - i\,\zeta\,(\frac{\omega_0}{\omega} - \frac{\omega}{\omega_0})}}\, \hat{f}(\omega)\ \exp(i(\omega\, t - k(\omega)\, x))\, d\omega \tag{44}$$

The above expressions will be employed as reference results in the section devoted to numerical examples by using Discrete Fourier Transforms available in Matlab software. Derived reference results will be compared with numerical solutions obtained with finite element method along with a time integration scheme.

3 Numerical examples

Finite element method is employed for checking previous theoretical observations. We start by choosing a Ricker wave [14] R as an incident wave defined by :

$$R(t,\, t_p,\, t_s) = A\,(2\,\pi^2\,\frac{(t-t_s)^2}{t_p^2} -\, 1)\,\exp(-\pi^2\frac{(t-t_s)^2}{t_p^2}) \tag{45}$$

We observe that the Ricker wave depends on three parameters t_p, t_s and A chosen equal to $3,\ 3,\ 1$ respectively. The displacements are imposed at a given point according to the Ricker function, characterized by one dominant frequency equal to $\frac{1}{t_p}$ (Figure 5).

The first example deals with a 1D wave propagation in the damping Rayleigh medium. Numerical solution using an implicit time integration is validated against the reference results obtained by Discrete Fourier Transform and Discrete Inverse Fourier Transform using Matlab according to Eq. (32). Then, it will be shown that the condition in Eq. (40) minimizes the reflected waves by computing wave propagation from an elastic medium towards a damping Rayleigh medium separated by an interface. Finally, the 2D propagation problem from Lamb is dealt with the explicit/implicit multi-time step co-computations. An external coupling software is used, coupling the explicit FE code Europlexus with fine time step for the domain of interest with implicit FE code Cast3m with macro time step for the Rayleigh damping layer.

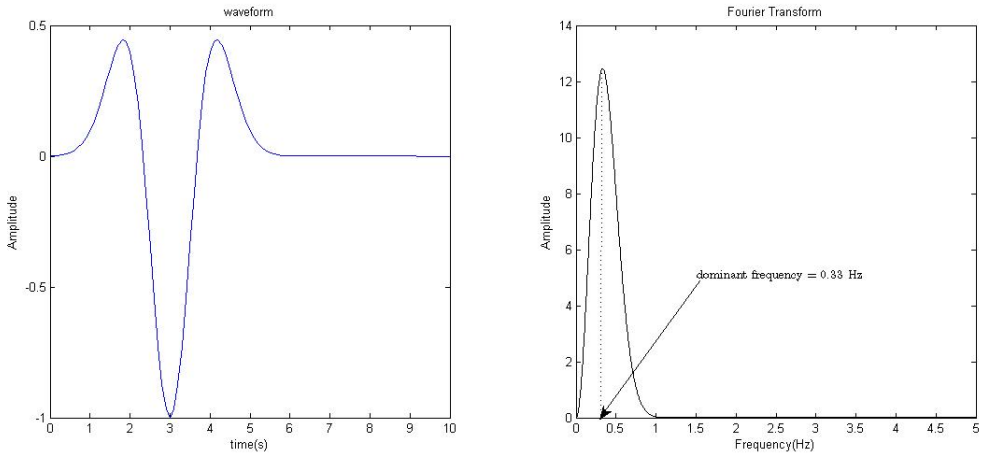


Figure 5: Input displacement (Ricker wavelet) and Amplitude of its Fourier transform

3.1 1D wave propagation in the Rayleigh damping material

In this part, we consider a problem of P-wave.The solution given by the finite element method will be computed using Castem software[13]. The semi-infinite layer is modeled using a bounded domain shown in Figure 6. A uniform finite element mesh of four-node rectangular elements, each one having the size of $\frac{\lambda}{50}$, is used to discretize the problem. From the displacement imposed point $x = 0$, the length of the mesh extends to a distance of 5λ (λ being the wave length of the Ricker wave). The mesh is chosen to be very large so as to avoid the interference between the incident wave and the reflected waves, which propagates back toward the displacement imposed point.

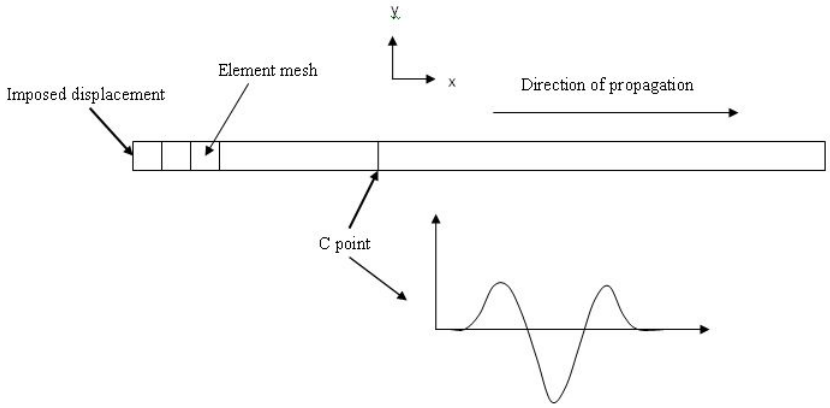


Figure 6: Homogeneneous damping layer of length 5λ

Finally, the displacement is imposed in the direction of x and we choose a point P at $x = 100\ m = 0.4\lambda$ to compare the time-history response predicted by the finite element code and the reference solution according to Eq. (32). In finite element code, an implicit time integration scheme has been adopted. Here, it has to be reminded that only one domain is considered.

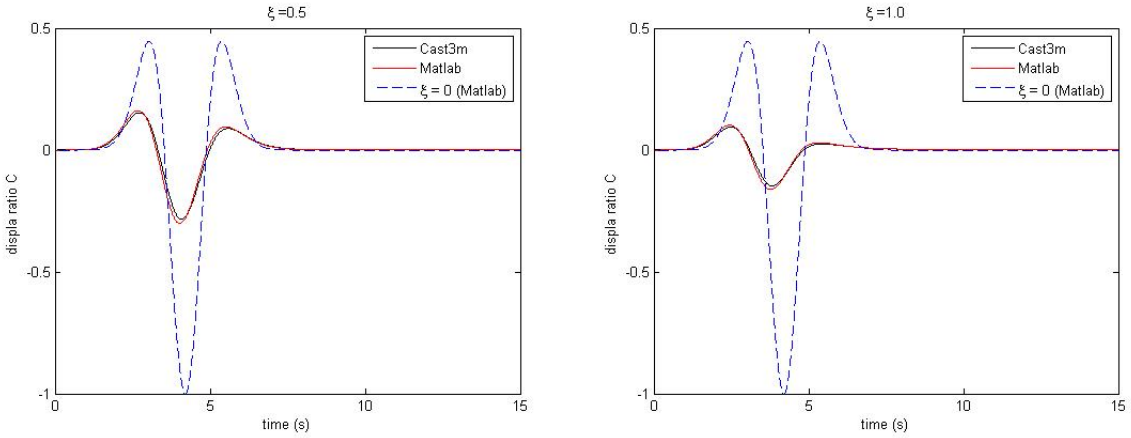


Figure 7: displacement in the point C, $\omega_0 = \frac{2\pi}{t_p} = 2.09$, $\xi = 0.5$ (left) , $\xi = 1$ (right)

Figure 7 presents the displacement ratio $(\frac{\widetilde{u}_2(x,t)}{A})$ computed at the point C using Cast3m and Matlab (reference results) against the solution without damping ($\xi = 0$), also computed using Matlab. The results obtained from Cast3m are very close to the reference results. From Figure 7, it can be verified that the numerical phase velocity in the Rayleigh damping domain is greater than the phase velocity in an undamped domain.

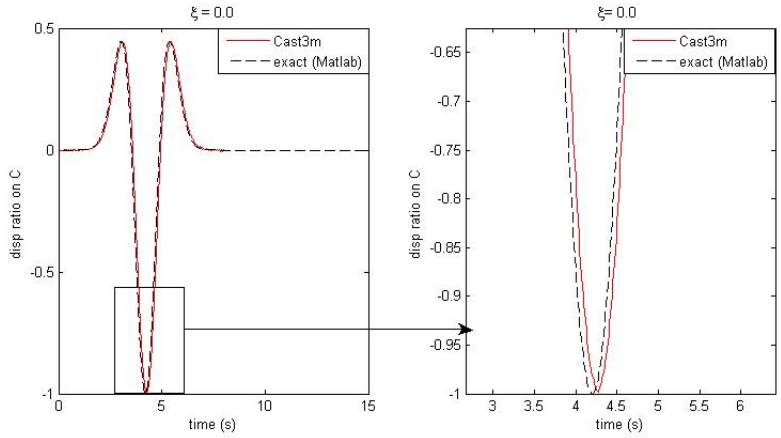


Figure 8: The difference between the numerical phase velocity and the exact phase velocity

From Figure 9, we observe that the numerical solution is more damped than the reference one. This remark can be justified by the following observations . Assuming a quasi harmonic wave, that is with a dominant frequency, it can be seen in Figure 8 that the numerical phase velocity V_{p2}^{num} without viscous damping is lower than the reference velocity V_{p2}^{real} without viscous damping. So, when considering Rayleigh damping medium with ξ the damping ratio, the following relationship between the logarithmic decrements can be written:

$$\delta^{real} = \frac{d\,\xi\,\omega_0}{V_{p2}^{real}\sqrt{1+\xi^2}} \leq \frac{d\,\xi\,\omega_0}{V_{p2}^{num}\sqrt{1+\xi^2}} = \delta^{num} \tag{46}$$

where d is a constant distance. It means that the numerical logarithmic decrement δ^{num} is greater than the reference logarithmic decrement δ^{real} underlined in Figure 9, where the displacemnt peaks of Figure 7 have been zoomed.

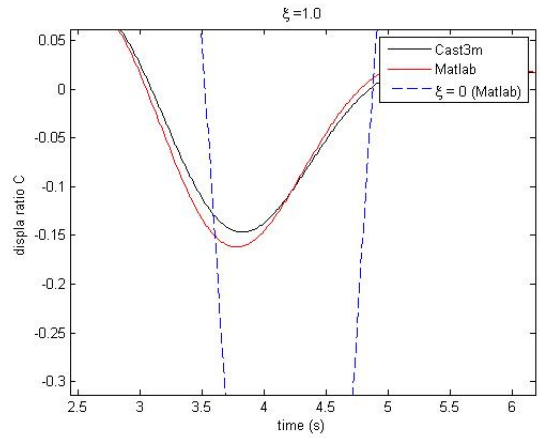


Figure 9: Zoom on the displacement computed on C for the case $\xi = 1$

3.2 1D wave propagation from an elastic medium towards the Rayleigh damping medium separated by an interface

In order to validate the theoretical results obtained in the section 2.3.2, we start by considering the problem illustrated in Figure 4. The characteristics of the two material are summarized in the following table :

	Domain 1 (Hooke material)	Domain 2 (Damping material)
Young's modulus (MPa)	10	Variable
Poisson's ratio	0.24	0.24
Element size	$\frac{\lambda}{50}$	$\frac{\lambda}{50}$
Type of element	rectangular (linear)	rectangular (linear)
Mesh length	5λ	5λ
Mass density (Kg/m^3)	1700	1700

Table 1: Characteristics of materials

We impose the displacement at the point $x = -5\lambda$ according to the same Ricker wave as previously. Then, we compute the displacement at the point C located at 0.4λ from the imposed displacement point. Here we can observe that the point C is far enough from the interface $x = 0$ to avoid the interference between the reflected wave and the incident wave. The Young's modulus of the domain 2, as given in Table 1, is dependent on the damping ratio as: $\gamma = \frac{1}{\sqrt{1+\xi^2}}$. The Figure 10 displays the comparison of results between the FE method using Cast3m with an implicit time integration scheme and the reference results using Matlab according to Eq. (43) for several values of ξ.

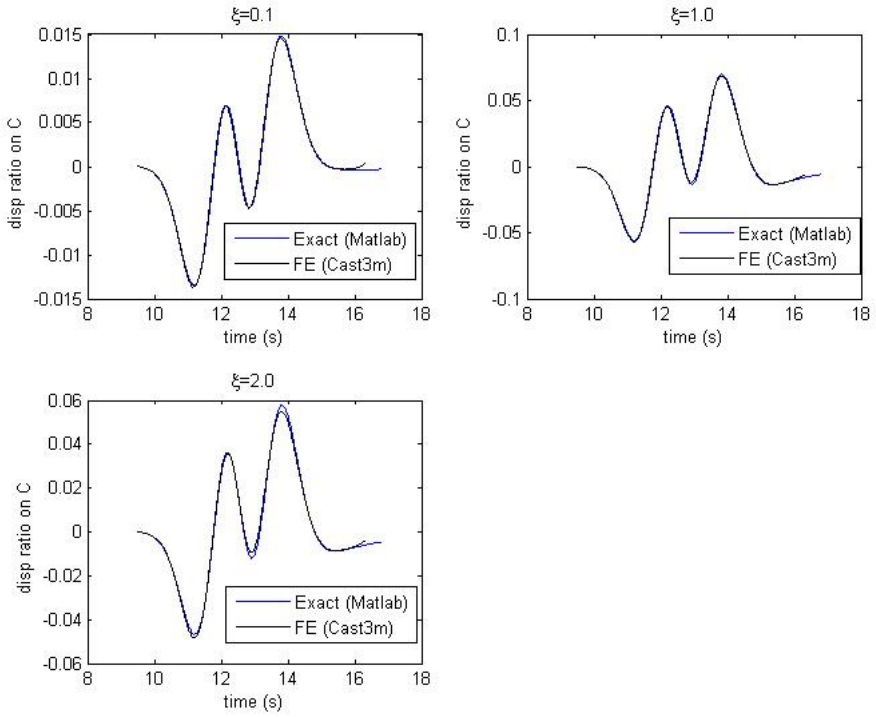


Figure 10: Refelected wave computed on point C, $\omega_0 = \frac{2\pi}{t_p} = 2.09$

From the Figure 10, we remark that both curves (numerical and reference results) are in very good agreement for different values of ξ. In the first case $\xi = 0.1$, the wave is reflected with a ratio of 1.5% which is much lesser than the other cases: $5,5\%$ for $\xi = 1$ and 6% for $\xi = 2$.

We want to check the condition about the Young modulus E_2 of the damping layer so as to minimize the reflected waves at the interface. For this purpose, we realize a simple test

using Cast3m in which we vary the value of E_2 within a range, ξ remaining constant as well as the parameters ν_2, ρ_2 equal to ν_1, ρ_1 respectively. For each value of ξ, the value of E_2 which minimizes the reflections at the interface is determined. In Figure 11, the identified optimal value of E_2 is compared with the theoretical condition, that is: $\gamma(\xi) = \frac{1}{\sqrt{1+\xi^2}}$. It can be seen that the numerical identified curve matches very well the theoretical curve. It is important to note that the condition $\gamma(\xi) = \frac{1}{\sqrt{1+\xi^2}}$ for minimizing the reflected waves at the interface has been obtained for harmonic waves. From Figure 11, it can be concluded that this condition provides a good approximation for non harmonic waves such as the ricker wave as well.

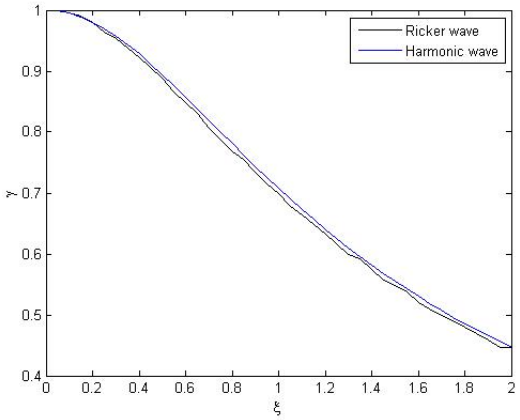


Figure 11: Values of γ miminizing the amplitude of the reflected waves for the both waves (theoretical curve with harmonic waves and numerical curve with a Ricker wavelet)

3.3 2D Lamb test using explicit/implicit multi-time step co-computations

The Lamb test consists in applying a concentrated load at the surface of a ground assumed to be infinite in the direction of both directions. A sensor is located at a distance $d = 10\,m$ from the load point for the purpose to recording the vertical and the horizontal displacements at this point (Figure 12). In 1904 Lamb [11] analytically calculated the displacements at a given point of the surface by assuming an isotropic linear elastic behavior of the soil. The theoretical solution shows the complexity of the problem since there are many types of waves traveling through the soil (P and S-waves, Rayleigh waves, etc). In this part, we will compute the numerical solution using the explicit/implicit multi time step GC method. Two FE codes are involved into the tho co-computations: Europlexus code based on a explicit time integration scheme for the domain of interest and implicit Cast3m code for the damping layers by adopting a large time step for reducing the time computation. The time step ratio between the macro time step (implicit FE code) and the micro time step (explicit FE code) is set to 50.

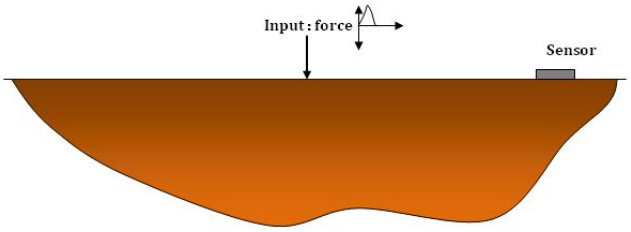


Figure 12: Lamb test

In order to use the GC method we have to divide the problem into 2 subdomains (Figure 13): subdomain 1 models the soil assumed to be linear elastic with $\rho_1 = 1700\ kg/m^3$, $E_1 = 10MPa$ and $\nu_1 = 0.24$ and the subdomain 2 models the Rayleigh damping medium with $\rho_2 = 1700\ kg/m^3$ and $\nu_2 = 0.24$. The Rayleigh matrix has the following parameters: $\xi = 0.1$ and $\omega_0 = \frac{2\pi}{t_p}$ according to Eq. (24). The soil is modeled by a rectangle surrounded by the damping layer of thickness e. A concentrate load is applied at the middle of the surface, defined by a Ricker wavelet with the parameters: $A = 1MN\ t_p = 3\ t_s = 3$. Figure 14 presents the meshes used for this simulation, the soil is modeled by Europlexus code (the symmetry is taken into account) using rectangular elements with size of $\frac{\lambda}{50}$ and the Rayleigh damping medium is modeled by Cast3m code using the same size of elements as in the subdomain 1.

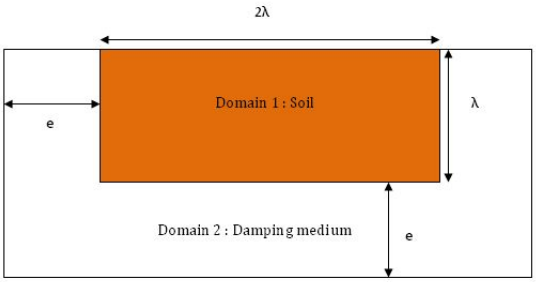


Figure 13: The shapes of the domains

The damping layer is defined by a logarithmic decrement target $\delta = \ln(10)$ leading to a thickness of $e = 914\ m = 3.6\ \lambda$ by using the condition in Eq. (26). Furthermore, we choose a point C close to the load point with a distance equal to $10\ m$ at which the horizontal and vertical displacements will be plotted.

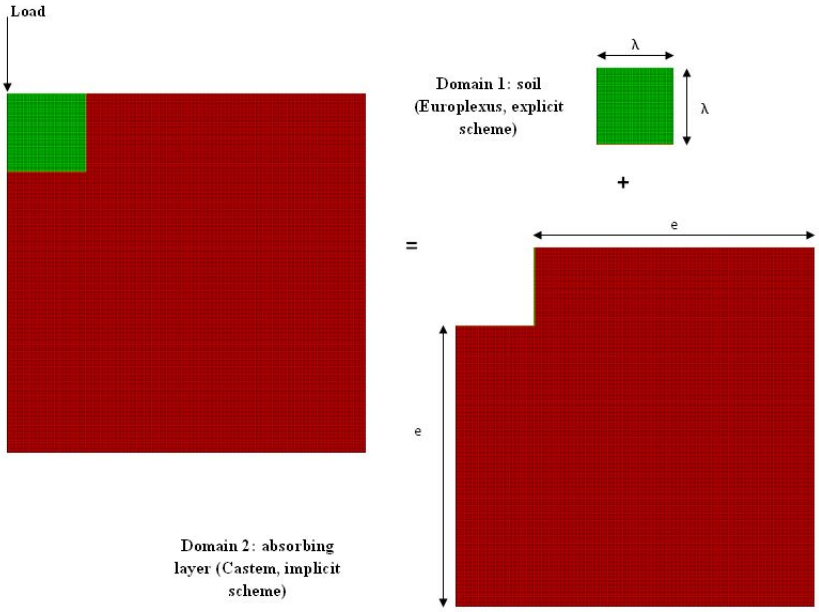
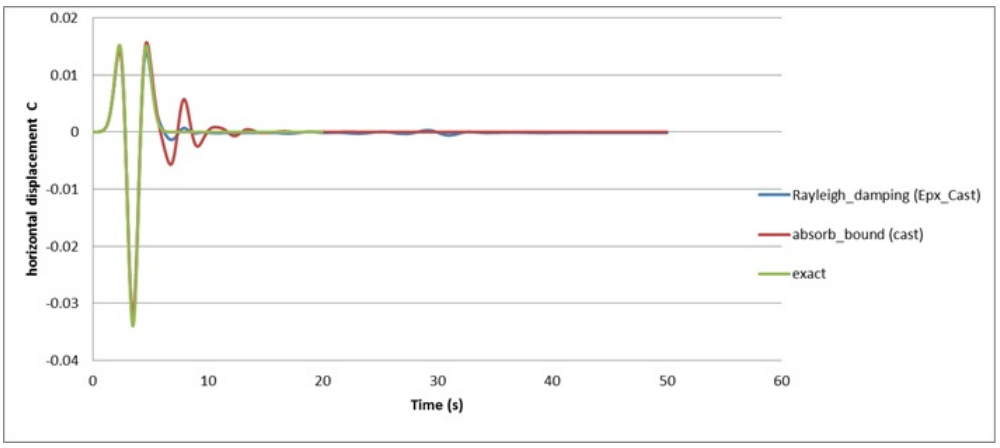


Figure 14: The mesh used for the GC method : domain 1 (soil) modeled by Europlexus and the domain 2 (absorbing medium) modeled by Castem

In Figure 15, the results computed at the point C using the Rayleigh damping layer are compared with Lamb analytical solutions using Matlab. An additional numerical solution is provided by using classical viscous dampers at the absorbing boundaries available in Cast3m code. An implicit time integration is adopted with this method, without considering subdomain decomposition. We remark that the results obtained by the absorbing boundary method are not accurate enough with respect to the exact solution (Matlab). It is due to artificial reflections at the interface. It has to be highlighted that our explicit/implicit multi-time step strategy with Rayleigh damping layers provides numerical results in very good agreement with respect to the reference solution. Consequently, it has been shown: 1- the approximate condition in Eq. (40) enables to efficiently minimize the reflected waves at the interface although this condition is strictly valid for harmonic waves with a normal incidence. 2- the multi-time step GC method is successively employed, enabling to gain computational performance by taking large time step in the Rayleigh damping layer. It is important to note that the GC method generates some spurious damping at the interface as soon as different time steps are employed for subdomains as proven in [8]. Thus, it can be concluded that this effect is not important in our simulation.



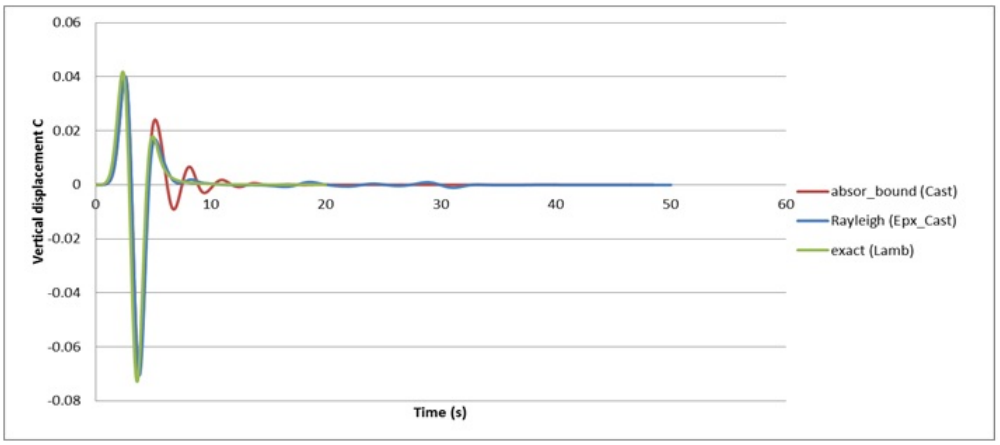


Figure 15: Horizontal and vertical displacements plotted on C obtained by Rayleigh damping (blue curve) , Absorbing boundaries (red curve) and the exact solution (Lamb) (green curve)

4 Conclusion

In this paper, a strong form for wave propagation in a damping Rayleigh medium is given. It has been shown that the proposed strong form exactly corresponds to the introduction of the Rayleigh matrix into the discretized equation of motion by the finite element method. This strong from is employed to derive optimal conditions for minimizing the reflected waves appearing at the interface between two media with different damping ratios in the case of harmonic waves. Analytical results using discrete Fourier transform in Matlab and numerical results using finite element code demonstrate the relevance of this optimal condition for a non harmonic Ricker wave. Explicit/implicit multi time step co-computations involving two FE codes (explicit for the domain of interest and implicit for the Rayleigh damping layers) have been successfully carried out. The proposed approach turns out to be very accurate in comparison to the reference results and the ability to choose a large time step in the Rayleigh damping layer enables to improve the computation performance of the proposed numerical strategy accounting for unbounded medium.

REFERENCES

[1] J.P. Wolf, *Dynamic Soil–Structure Interaction*, Prentice-Hall, Englewood Cliffs, NJ, 1985.

[2] Basu U, Chopra AK, Perfectly matched layers for time-harmonic elastodynamics of unbounded domains: theory and finite-element implementation. *Int J Numer Methods Eng*, 192 ,1337-1375, 2003.

[3] Engquist B, Majda A, Absorbing boundary conditions for the numerical simulation of waves. *Mathematics of Computation*, 31, 629-65, 1977.

[4] Bettess P, Infinite elements. *International Journal for Numerical methods in Engineering*, 11, 53-64, 1977.

[5] Semblat JF,Gandomzadeh A, Lenti L,A simple numerical absorbing layer method in elastodynamics. *C. R. Mecanique*, 338, 24-32, 2010.

[6] Clough RW, Penzien J, *Dynamics of stuctures*, McGraw-Hill Compagnies, 634 p,1975.

[7] Semblat JF, Rheological interpretation of Rayleigh damping. *Journal of Sound and Vibration*, 206, 741-744, 1997.

[8] Gravouil A, Une mthode multi-chelle espace-temps pour le calcul de la dynamique transitoire des structures, PhD Thesis, ENS Cachan, France, 2000.

[9] Hughes TJR, *The Finite Element Method: Linear Static and Dynamic Finite Element Analysis*, Prentice-Hall, Englewood Cliffs, NJ, 1987.

[10] Brun M, Batti B, Limam A, Combescure A, Implicit/explicit multi-time step co-computations for predicting reinforced concrete structure response under earthquake loading. *Soil Dynamics and Earthquakes Engineering*, 33, 19-37, 2012.

[11] Lamb H, On the propagation of tremors over the surface of an elastic solid. *Proceedings of the Royal Society of London*, 72, 128-130, 1903.

[12] Europlexus , *User's manual*, 2006 (www.europlexus.jrc.ec.europa.eu).

[13] Cast3m, *Presentation et utilisation de Cast3m*, 2011(www.cast3m.cea.fr).

[14] Semblat JF, Pecker A, *Waves and vibrations in soils*, IUSS Press, 499 p, 2009.

[15] Meza-Fajarado KC, Papageorgiou AS, A nonconvolutional, Split-Field, Perfectly matched layer for wave propagation in isotropic and anisotropic elastic media: stability analysis. *Bulletin of the Seismological Society of America*, 98, 1811-1836, 2008.

[16] Allaire G, *Analyse numrique et optimisation : Une introduction la modelisation mathmatique et a la simulation numerique*, Ecole Polytechnique, 459 p, 2005

COMPDYN 2013
4th ECCOMAS Thematic Conference on
Computational Methods in Structural Dynamics and Earthquake Engineering
M. Papadrakakis, V. Papadopoulos, V. Plevris (eds.)
Kos Island, Greece, 12–14 June 2013

PERFECTLY MATCHED LAYER (PML) FOR TRANSIENT WAVE PROPAGATION IN A MOVING FRAME OF REFERENCE

Stine S. Madsen[1], **Steen Krenk**[2] **and Ole Hededal**[1]

[1]Department of Civil Engineering / [2]Department of Mechanical Engineering
Technical University of Denmark
DK-2800 Kgs. Lyngby, Denmark
e-mail: sskk@byg.dtu.dk / sk@mek.dtu.dk / olh@byg.dtu.dk

Keywords: Absorbing boundaries, PML, Finite element, Moving load, Wave propagation.

Abstract. *In relation to the development of a Rolling Wheel Deflectometer (RWD), which is a non-destructive testing device for measuring pavement deflections, a finite element model for obtaining the soil/pavement response is developed. Absorbing boundary conditions are necessary in order to prevent reflections of the waves propagating through the soil due to the dynamic loading. The Perfectly Matched Layer (PML) has proven to be highly efficient when solving transient wave propagation problems in a fixed mesh. However, since the RWD is operating at traffic speeds, the load is moving with high speed and a formulation in a moving mesh is therefore more convenient. In this paper, a formulation of the PML is developed in the moving frame of reference. Numerical results are presented for a single layer and a double layer half space, respectively, subjected to a moving load of different velocities.*

1 INTRODUCTION

The Rolling Wheel Deflectometer (RWD) is a non-destructive testing device operating at traffic speed for measuring pavement deflections. The RWD is equipped with a heavy load on the rear-most axle under which the pavement deflections are measured. A 2D finite element model is developed in order to obtain the soil/pavement response from a transient dynamic load simulating the heavy load from the RWD. Absorbing boundary conditions are necessary in order to prevent reflections of the waves propagating through the soils due to the dynamic loading. As the load is moving at high speed, the use of a fixed mesh will require a very large computational domain in order to capture the response under the moving load before it leaves the domain. This can be quite costly and limit the analysis to a rather short time interval. A formulation in the moving frame of reference is therefore more convenient.

A local transmitting boundary condition formulated in convective coordinates developed by Krenk et al. [1, 2] has been used in transient vibration analysis of railway-ground system under fast moving loads [3]. The formulation is simple and computationally fast, essentially being equivalent to an oriented spring-damper configuration at the boundary nodes, based on planar waves with a single point of origin. In the moving coordinate system, the directions of propagation of P- and S-waves are modified to account for the translation of the frame of reference.

The radiation formulation can be made more general and robust by extending it to non-local form by using an additional attenuation layer around the computational domain, in the form of a Perfectly Matched Layer (PML) first proposed by Berenger [4] to electromagnetic waves. Later PML was formulated for the elastic wave equation in e.g. [5, 6, 7]. However, in this approach the solution for the displacements is dependent on computation of the strains in each time step. A simpler procedure, depending only on the displacements, using an artificially anisotropic material description of the PML layer, was recently proposed in [8]. Compared to the spring-damper configuration, the additional layer contains more information about propagation directions and has proven to be highly efficient when solving transient vibration problems in a stationary frame of reference [8]. The PML has not yet been formulated in the moving frame of reference.

In this paper, a formulation of the PML is developed in translating coordinates based on the PML formulation in [8]. Numerical results are presented for a half-space subjected to a moving load of different velocities and a half-space of multiple layers.

2 PERFECTLY MATCHED LAYER

The standard PML formulation of [8], valid for transient wave propagation in a stationary mesh, is generalized to a moving mesh. The key concept of the PML is a coordinate transformation in which the spatial variables are mapped onto complex space by a so-called complex stretching function. The mapping replaces propagating waves with exponentially decaying waves as the propagating waves passes the PML interface. The general equation of motion is written as

$$\nabla \boldsymbol{\sigma} + \boldsymbol{p} = \rho \ddot{\boldsymbol{u}} \tag{1}$$

$$\sigma = \boldsymbol{C}\boldsymbol{\varepsilon} = \boldsymbol{C}\nabla \boldsymbol{u} \tag{2}$$

where $\boldsymbol{u} = [u_1, u_2]^T$ is the displacement vector, $\boldsymbol{p} = [p_1, p_2]^T$ is the load vector, and $\dot{(\,)}$ denotes temporal differentiation. $\boldsymbol{\sigma}$ is the stress tensor defined by

$$\boldsymbol{\sigma} = \begin{bmatrix} \sigma_{11} & \sigma_{12} \\ \sigma_{21} & \sigma_{22} \end{bmatrix} \tag{3}$$

In the absorbing layer the original coordinate variables x_i, $(i = 1, 2)$ are replaced with the complex stretched coordinate variables $\tilde{x}_i$, defined by

$$\tilde{x_i} = \int_0^{x_i} s_i(\hat{x}_i, \omega) \mathrm{d}\hat{x}_i, \quad i = 1, 2 \tag{4}$$

where ω is the angular frequency and s_i are the stretched coordinate functions proposed in [9]

$$\frac{\partial \tilde{x}_i}{\partial x_j} = s_i(x_i, \omega) = 1 + \frac{\beta_i(x_i)}{i\omega}, \quad i = 1, 2 \tag{5}$$

where i denotes the imaginary unit and $\beta \geq 0$ is a real function which controls the attenuation of the wave propagation.

Applying the stretched coordinates to the equation of motion (1) in a frequency representation yields

$$\nabla_s \boldsymbol{\sigma} + \boldsymbol{p} = -\omega^2 \rho \, \boldsymbol{u} \tag{6}$$

where $u(t) = U(\omega)e^{-i\omega t}$, $\nabla_s = (\partial/\partial\tilde{x}_1, \partial/\partial\tilde{x}_2)^T$, and $\frac{\partial}{\partial \tilde{x}_i} = \frac{1}{s_i}\frac{\partial}{\partial x_i}$. Because the equations in the complex stretched coordinates are on the same form as those in the non-stretched coordinates, waves are passing through the PML interface without causing any reflections [10].

The introduction of the stretched coordinates yields an anisotropic formulation of the equation of motion, expressed by ∇_s. To keep the expressions of the divergence and the gradient in non-stretched coordinates, the anisotropy is moved to the material description by a modification of the constitutive relation, allowing for the use of the same kinematics in the computational domain and PML domain. Equation (6) is multiplied with the product $s_1 s_2$ and a new set of stress variables is introduced, defined in tensor form as

$$\tilde{\boldsymbol{\sigma}} = s_1 s_2 \begin{bmatrix} s_1^{-1} & 0 \\ 0 & s_2^{-1} \end{bmatrix} \boldsymbol{\sigma} = s_1 s_2 \boldsymbol{\Lambda} \boldsymbol{\sigma} \tag{7}$$

By substitution of equation (7) into (2) and modifying the constitutive relation, the equation of motion with the new stress variables can be written in non-stretched coordinates as

$$\nabla \tilde{\boldsymbol{\sigma}} + \boldsymbol{p} = -\rho\omega^2 s_1 s_2 \boldsymbol{u} \tag{8}$$

$$\tilde{\boldsymbol{\sigma}} = \tilde{\boldsymbol{C}} \nabla \boldsymbol{u} \tag{9}$$

where the constitutive relation is modified to

$$\tilde{C}_{ijkl} = \frac{s_1 s_2}{s_i s_k} C_{ijkl} \quad , \quad i, j, k, l = 1, 2 \tag{10}$$

with no summation over indices i and k. This formulation leads to an artificial anisotropic material description since $\tilde{C}_{1111} \neq \tilde{C}_{2222}$.

For a general FE-implementation, equation (9) is formulated in Voigt notation, and the constitutive law then reads

$$\begin{bmatrix} \tilde{\sigma}_{11} \\ \tilde{\sigma}_{22} \\ \frac{1}{2}\left(\tilde{\sigma}_{21}+\tilde{\sigma}_{12}\right) \\ \frac{1}{2}\left(\tilde{\sigma}_{21}-\tilde{\sigma}_{12}\right) \end{bmatrix} = \begin{bmatrix} \tilde{C}_{11} & C_{12} & & \\ C_{21} & \tilde{C}_{22} & & \\ & & \tilde{C}'_{66} & \tilde{C}''_{66} \\ & & \tilde{C}''_{66} & \tilde{C}'''_{66} \end{bmatrix} \begin{bmatrix} \frac{\partial}{\partial x_1} & 0 \\ 0 & \frac{\partial}{\partial x_2} \\ \frac{\partial}{\partial x_2} & \frac{\partial}{\partial x_1} \\ \frac{\partial}{\partial x_2} & -\frac{\partial}{\partial x_1} \end{bmatrix} \begin{bmatrix} u_1 \\ u_2 \end{bmatrix} \tag{11}$$

where $\tilde{C}_{11} = s_2 C_{11}/s_1$, $\tilde{C}_{22} = s_1 C_{22}/s_2$, and the shear-related parameters are given by

$$\tilde{C}'_{66} = \frac{C_{66}}{4}\left(\frac{s_1}{s_2}+\frac{s_2}{s_1}+2\right) \tag{12}$$

$$\tilde{C}''_{66} = \frac{C_{66}}{4}\left(\frac{s_1}{s_2}-\frac{s_2}{s_1}\right) \tag{13}$$

$$\tilde{C}'''_{66} = \frac{C_{66}}{4}\left(\frac{s_1}{s_2}+\frac{s_2}{s_1}-2\right) \tag{14}$$

Equation (11) can be written in the compact form $\tilde{\boldsymbol{\sigma}}_v = \tilde{\boldsymbol{C}}\boldsymbol{\partial}\boldsymbol{u}$ where subscript v indicates Voigt notation and the strain-displacement operator is

$$\boldsymbol{\partial} = \begin{bmatrix} \frac{\partial}{\partial x_1} & 0 \\ 0 & \frac{\partial}{\partial x_2} \\ \frac{\partial}{\partial x_2} & \frac{\partial}{\partial x_1} \\ \frac{\partial}{\partial x_2} & -\frac{\partial}{\partial x_1} \end{bmatrix} \tag{15}$$

The derived equations cover both the computational domain and the PML regions since $\beta_i = 0$ in the computational domain which leaves $s_i = 1$, resulting in the general formulation of the wave equation.

The frequency-dependent equation of motion (8) is transformed into the time domain using the inverse Fourier transform [11], yielding

$$\nabla\tilde{\boldsymbol{\sigma}}_v + \boldsymbol{p} = \rho\,\mathcal{D}_0(t)\boldsymbol{u} \tag{16}$$

$$\tilde{\boldsymbol{\sigma}}_v = \tilde{\boldsymbol{C}}\partial\boldsymbol{u} \tag{17}$$

where the operator $\mathcal{D}_0(t)$ is the inverse Fourier transform of $-\omega^2 s_1 s_2$, given by

$$\mathcal{D}_0(t) = \frac{d^2}{dt^2} + (\beta_1+\beta_2)\frac{d}{dt} + \beta_1\beta_2 \tag{18}$$

The modified constitutive relation is given by

$$\tilde{\boldsymbol{C}} = \boldsymbol{C} + \mathcal{F}_1(t)\boldsymbol{C}_1 + \mathcal{F}_2(t)\boldsymbol{C}_2 \tag{19}$$

where $\boldsymbol{C}$ is the non-stretched constitutive matrix and $\boldsymbol{C}_1$, $\boldsymbol{C}_2$ represent two stretched parts of the constitutive matrix, see the appendix. The operators $\mathcal{F}_1(t)$ and $\mathcal{F}_2(t)$ are the inverse Fourier transform of s_1/s_2 and s_2/s_1, respectively, given by

$$\mathcal{F}_1(t) = (\beta_1-\beta_2)e^{-\beta_1 t}, \quad t \geq 0 \tag{20}$$

$$\mathcal{F}_2(t) = (\beta_2-\beta_1)e^{-\beta_2 t}, \quad t \geq 0 \tag{21}$$

2.1 Convective coordinates

The formulation in a fixed coordinate system X_i, is transfered into a moving coordinate system x_i, via the relation [1]

$$x_i = X_i - Vt \tag{22}$$

where V is the velocity of the vehicle. The equilibrium equations are expressed in the moving coordinate system by introducing the partial differentiation operators

$$\left.\frac{\partial}{\partial X}\right|_t = \left.\frac{\partial}{\partial x}\right|_t , \qquad \left.\frac{\partial}{\partial t}\right|_X = \left.\frac{\partial}{\partial t}\right|_x - V\frac{\partial}{\partial x} \tag{23}$$

following from the relation (22) between the two coordinate systems.

Substitution of the operators into Equation (16) modifies the equilibrium equations to

$$\nabla\tilde{\boldsymbol{\sigma}}_v + \boldsymbol{p} = \rho\,\tilde{\mathcal{D}}_0\boldsymbol{u} \tag{24}$$

$$\tilde{\boldsymbol{\sigma}}_v = \tilde{\boldsymbol{C}}\partial\boldsymbol{u} \tag{25}$$

with the convected operator

$$\tilde{\mathcal{D}}_0 = \left(\frac{\partial}{\partial t} - V\frac{\partial}{\partial x}\right)^2 + (\beta_1+\beta_2)\left(\frac{d}{dt} - V\frac{d}{dx}\right) + \beta_1\beta_2 \tag{26}$$

The convolution equations related to (17) are not directly dependent on time, hence they remain unchanged. The transformation from fixed to moving coordinates only modifies the ordinary equation of motion, making it simple to implement in the PML formulation.

2.2 Finite element implementation

The principle of virtual work is used to obtain the weak formulation of the equation of motion (24), yielding

$$\int_\Omega (\delta\boldsymbol{u})^T\rho\,\tilde{\mathcal{D}}_0\boldsymbol{u}d\Omega + \int_\Omega (\partial\delta\boldsymbol{u})^T\tilde{\boldsymbol{\sigma}}_v d\Omega - \int_\Omega (\delta\boldsymbol{u})^T\boldsymbol{p}d\Omega - \int_\Gamma (\delta\boldsymbol{u})^T\boldsymbol{T}d\Gamma = 0 \tag{27}$$

The spatial variation of the actual and the virtual displacement fields are represented by shape functions as

$$\boldsymbol{u}(x,t) = \boldsymbol{N}(x)\boldsymbol{d}(t) \tag{28}$$

$$\widehat{\boldsymbol{u}}(x,t) = \widehat{\boldsymbol{N}}(x)\widehat{\boldsymbol{d}}(t) \tag{29}$$

with the shape functions $\boldsymbol{N}$ on the form

$$\boldsymbol{N} = \begin{bmatrix} N_1 & 0 & N_2 & 0 & \cdots & N_n & 0 \\ 0 & N_1 & 0 & N_2 & \cdots & 0 & N_n \end{bmatrix} \tag{30}$$

and $\widehat{\boldsymbol{N}}$ in a similar form. Separating the convolution terms in the operators $\mathcal{F}_1(t)$ and $\mathcal{F}_2(t)$ the following set of ordinary differential equations is obtained

$$\boldsymbol{M}\ddot{\boldsymbol{d}} + \boldsymbol{Z}\dot{\boldsymbol{d}} + \boldsymbol{K}\boldsymbol{d} + \tilde{\boldsymbol{g}} = \boldsymbol{f} \tag{31}$$

where $\boldsymbol{d}$ is the global displacement vector. $\boldsymbol{f}$ is the global force vector determined by

$$\boldsymbol{f}^e = \int_{\Omega^e} \boldsymbol{N}^T \boldsymbol{p} d\Omega \tag{32}$$

where only point loading on the free surface is assumed. The element mass, damping and stiffness matrices $\boldsymbol{M}^e$, $\boldsymbol{Z}^e$ and $\boldsymbol{K}^e$, are given by

$$\boldsymbol{M}^e = \int_{\Omega^e} \rho \widehat{\boldsymbol{N}}^T \boldsymbol{N} \mathrm{d}\Omega \tag{33}$$

$$\boldsymbol{Z}^e = \int_{\Omega^e} \left(\rho(\beta_1 + \beta_2) \widehat{\boldsymbol{N}}^T \boldsymbol{N} + \rho V \left(\widehat{\boldsymbol{N}}_x^T \boldsymbol{N} - \widehat{\boldsymbol{N}}^T \boldsymbol{N}_x \right) \right) \mathrm{d}\Omega \tag{34}$$

$$\boldsymbol{K}^e = \int_{\Omega^e} \left(\widehat{\boldsymbol{B}}^T \boldsymbol{C} \boldsymbol{B} + \rho \beta_1 \beta_2 \widehat{\boldsymbol{N}}^T \boldsymbol{N} \right) \mathrm{d}\Omega \tag{35}$$

$$+ \int_{\Omega^e} \left(-\rho V(\beta_1 + \beta_2) \widehat{\boldsymbol{N}}^T \boldsymbol{N}_x + V^2 \widehat{\boldsymbol{N}}_x^T \boldsymbol{N}_x \right) \mathrm{d}\Omega \tag{36}$$

where $\boldsymbol{B}$ denotes the strain-displacement matrix and $\boldsymbol{N}$ the shape functions with x-derivative $\boldsymbol{N}_x = \partial \boldsymbol{N} / \partial \boldsymbol{x}$. Assuming constant PML parameters inside each element the convolution vector $\tilde{\boldsymbol{g}}$ is given by

$$\tilde{\boldsymbol{g}}^e = \boldsymbol{K}_2^e \left(\mathcal{F}_1 * u(t) \right) + \boldsymbol{K}_1^e \left(\mathcal{F}_2 * u(t) \right) \tag{37}$$

where the element matrices $\boldsymbol{K}_1$ and $\boldsymbol{K}_2$ are given by

$$\boldsymbol{K}_p^e = - \int_{\Omega} \boldsymbol{B}^T \boldsymbol{C}_p \boldsymbol{B} \mathrm{d}\Omega \,, \quad p = 1, 2 \tag{38}$$

The convolution terms $\mathcal{F}_p * u(t)$ are defined on each element of the mesh and are discontinuous from one element to another since the PML parameters are assumed element-wise constant. The general appearance of the convolution term is

$$\mathcal{F}_p * u(t) = \int_0^t \mathcal{F}_p(\tau) u(t - \tau) d\tau = \int_0^t (\beta_p - \beta_{\bar{p}}) e^{-\beta_{\bar{p}} \tau} u(t - \tau) d\tau \tag{39}$$

with index $\bar{p}$ being the complement of p. When assuming $u(t)$ piece-wise constant in the time interval $[t_n,\ t_{n+1}]$, the solution can be reformulated to increment form via integration by parts, and the convolution integrals then only require information from the last time step.

The finite element equation system is solved for the displacements using bilinear elements with a Newmark-based time integration method, see e.g. [8].

3 NUMERICAL EXAMPLES

Two numerical examples are presented to demonstrate the absorbing properties of the suggested formulation in translating coordinates. The two examples involve a moving transient dynamic load traveling on the surface of a single layer half space and a double layer half-space, respectively, see Figure 1. The layers are indicated in Figure 1 as the areas Ω_1 and Ω_2 and the PML layer surrounds the computational domain indicated by a dashed line. The computational domain is 156m wide, corresponding to approximately two pressure wave lengths, and 78m deep. The material parameters of the two layers are listed in Table 1. The dynamic response is

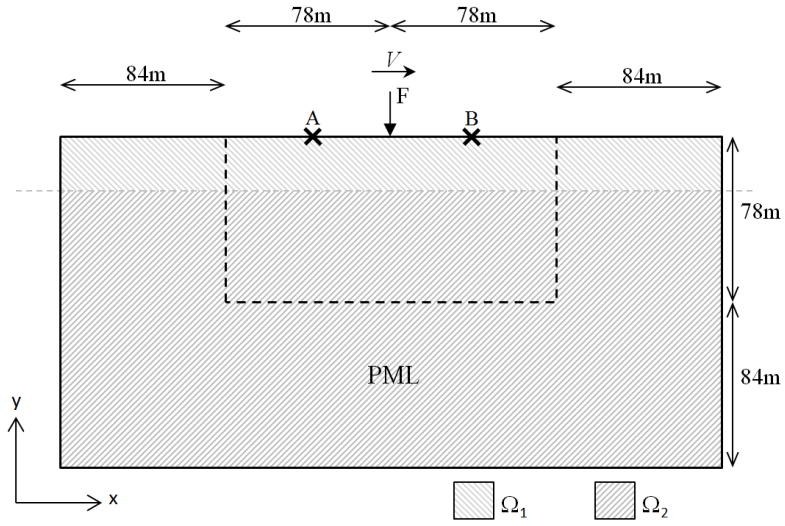


Figure 1: Illustration of numerical example. The observation points where the response is recorded is marked with two crosses. The interface between PML and the computational domain is indicated by a dashed line.

Table 1: Material parameters of the layered soil in Figure 1.

Material	E [MPa]	ν	ρ [kg/m^3]	c_p [m/s]	c_s [m/s]	c_r [m/s]
Ω_1	125	0.25	2000	273.9	158.1	145.5
Ω_2	250	0.25	2000	387.3	223.6	205.7

obtained from two observation points A and B placed on each side of the load at a distance of 39m corresponding to slightly more than one half pressure wave length. The load is defined as

$$F(x,t) = T(t)\delta(x - x^c) \tag{40}$$

where δ is the Dirac delta function and x^c is the location of the point source with temporal evolution $T(t)$ defined by

$$T(t) = \tau(1-\tau^2)^2, \quad -1 < \tau < 1 \tag{41}$$

where $\tau = 2t/T - 1$. The total duration of the pulse is $T = 0.2s$ and the dominant frequency of the pulse is $f = 1/T = 5Hz$. In the numerical examples, the maximum load is $F_{max} = 1$MN.

The spatial dependence of the PML parameter β_i in the x_i direction is chosen as in [8]

$$\beta_i = \beta_i^{max} \left(\frac{x_i^p}{d_i} \right)^{n_1+n_2} \tag{42}$$

in which x_i^p is measured from the interface to PML and d_i is the thickness of the PML layer. The coefficient β_i^{max} is given by [8]

$$\beta_i^{max} = -\frac{(1+n_1+n_2)c_p log_{10}(R_0)}{2d_i} \tag{43}$$

for $i = 1, 2$. Here R_0 is the theoretical reflection coefficient at normal incidence and c_p is the pressure wave velocity. In this example the following values for the parameters are chosen to: $R_0 = 10^{-8}$, $n_1 = 3$, $n_2 = 0$ and $d_i = 84$m corresponding to slightly more than two Rayleigh wave lengths.

3.1 Example 1: Single layer

In the single layer experiment the material parameters of the layers indicated in Figure 1 are equal, corresponding to material Ω_2 in Table 1. The element edge length is $\Delta x_1 = \Delta x_2 = 3.9$m corresponding to 20 elements per pressure wave length, and the time step is $\Delta t = 0.0071$s such that it meets the CFL condition defined by

$$\Delta t_c = \min\big[\Delta x_1, \Delta x_2\big]/c_p \tag{44}$$

The simulations run for 1.0 s, requiring 140 time steps. The load is traveling on the surface of the single layer half-space with the three different velocities $M = V/c_s = 0, 0.2, 0.4$. The responses are obtained at the two observation points A and B. The time evolutions are visualized in Figure 2 where the load signal is perfectly transported through the observation points without sending any reflections back from the boundaries. The pulse arrives at around 0.19s corresponding to the time of arrival for the Rayleigh wave, which is $39\,\mathrm{m}/205.7\,\mathrm{m/s} = 0.19\,\mathrm{s}$. Since the load is traveling from left to right the pulse delay increases with increasing velocity at point B while it decreases at point A. The response is seen to increase with velocity in front of the load, at point B, while it decreases behind the load, at point A.

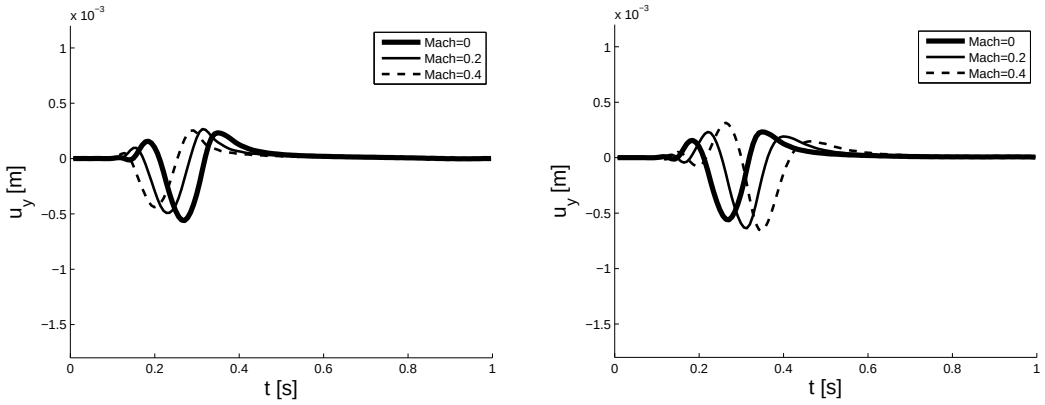


Figure 2: Single layer half-space: Vertical displacement response at two observation points A (left) and B (right) with velocity $M = 0.0, 0.2, 0.4$.

3.2 Example 2: Two layers

The material properties of the two layers are given by Ω_1 and Ω_2 as indicated in Figure 1. The top layer indicated by Ω_1 has a thickness of 7.8m and it is half as stiff as the bottom layer. Both the computational domain and the PML domain experience a change in material parameters at the interface between the two layers. The same element edge length and time step is used as in Example 1, where the time step $\Delta_t = 0.0071$ is determined based on the thicker bottom layer to ensure observance of the CFL condition in the entire domain. The time evolutions of the pulse obtained from observation point A and B are illustrated in Figure 3. The introduction of a softer surface layer causes a general increase in the response for all three velocities. It also becomes more clear that the response increases with velocity at point B, while it decreases at point A. However, in spite of the sudden material change at the interface between the top and bottom layers, the PML works very well for all three velocities. Only a slight disturbance is observed after the wave has passed. This may be avoided by adjusting the parameter β or by increasing the thickness of the PML layer.

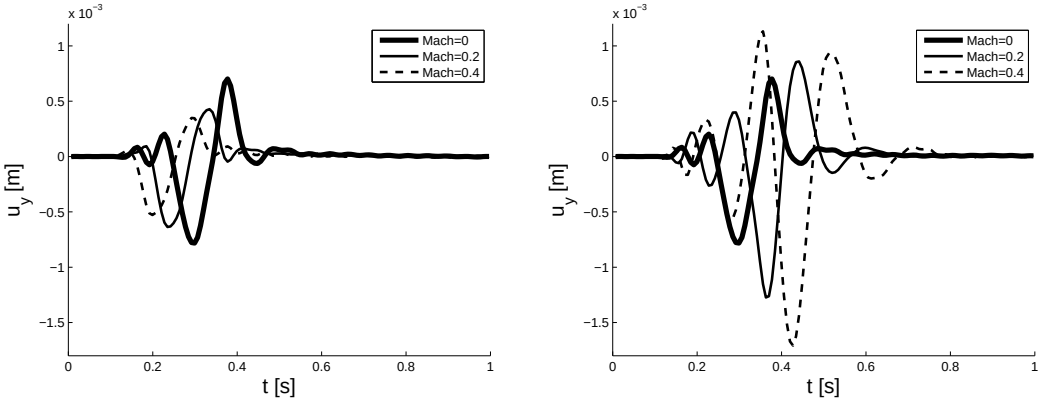


Figure 3: Two-layer half-space: Vertical displacement response at two observation points A (left) and B (right) with velocity $M = 0.0, 0.2, 0.4$.

4 CONCLUSION

The PML formulation for transient wave propagation has been generalized to a moving frame of reference. The transformation from fixed to moving coordinates only modifies the ordinary differential equation of motion and is therefore simple to implement in the PML equations. The applicability of the formulation was successfully tested on two numerical examples; a single layer and a double layer half-space, respectively.

REFERENCES

[1] S. Krenk, L. Kellezi, S. R. K. Nielsen, P. H. Kirkegaard, Finite elements and transmitting boundary conditions for moving loads, in: EURODYN'99, 4th European Conference on Structural Dynamics; Prague, June 7-10, 1999, Balkema, Rotterdam, 1999, pp. 447–452.

[2] S. Krenk, P. Kirkegaard, Local tensor radiation conditions for elastic waves, Journal of Sound and Vibration 247 (5) (2001) 875–896.

[3] W. Zhai, E. Song, Three dimensional fem of moving coordinates for the analysis of transient vibrations due to moving loads, Computers and Geotechnics 37 (1-2) (2010) 164–174.

[4] J.-P. Berenger, A perfectly matched layer for the absorption of electromagnetic waves, Journal of Computational Physics 114 (2) (1994) 185–200.

[5] U. Basu, A. Chopra, Perfectly matched layers for time-harmonic elastodynamics of unbounded domains: theory and finite-element implementation, Computer Methods in Applied Mechanics and Engineering 192 (11-12) (2003) 1337–1375.

[6] U. Basu, A. Chopra, Perfectly matched layers for transient elastodynamics of unbounded domains, International Journal for Numerical Methods in Engineering 59 (8) (2004) 1039–1074.

[7] U. Basu, Explicit finite element perfectly matched layer for transient three-dimensional elastic waves, International Journal for Numerical Methods in Engineering 77 (2) (2009) 151–176.

[8] R. Matzen, An efficient finite element time-domain formulation for the elastic second-order wave equation: A non-split complex frequency shifted convolutional PML, International Journal for Numerical Methods in Engineering 88 (10) (2011) 951–973.

[9] M. Kuzuoglu, R. Mittra, Frequency dependence of the constitutive parameters of causal perfectly matched anisotropic absorbers, IEEE Microwave and Guided Wave Letters 6 (12) (1996) 447–449.

[10] Y. Zheng, X. Huang, Anisotropic perfectly matched layers for elastic waves in cartesian and curvilinear coordinates anisotropic PML for elastic waves (1997) 1–18.

[11] R. N. Bracewell, The Fourier transform and its applications, McGraw-Hill, Boston, MA, 2000.

A CONSTITUTIVE MATRICES

The entries in the modified constitutive matrix $\tilde{\boldsymbol{C}}$ related to s_1/s_2 and s_2/s_1 are represented in the two stretched constitutive matrices $\boldsymbol{C}_1$ and $\boldsymbol{C}_2$, given by

$$\boldsymbol{C}_1 = \begin{bmatrix} 0 & 0 & 0 & 0 \\ 0 & \lambda+2\mu & 0 & 0 \\ 0 & 0 & \mu/4 & \mu/4 \\ 0 & 0 & \mu/4 & \mu/4 \end{bmatrix} \tag{A.1}$$

$$\boldsymbol{C}_2 = \begin{bmatrix} \lambda+2\mu & 0 & 0 & 0 \\ 0 & 0 & 0 & 0 \\ 0 & 0 & \mu/4 & -\mu/4 \\ 0 & 0 & -\mu/4 & \mu/4 \end{bmatrix} \tag{A.2}$$

The non-stretched constitutive matrix $\boldsymbol{C}$ is given by

$$\boldsymbol{C} = \begin{bmatrix} \lambda+2\mu & \lambda & 0 & 0 \\ \lambda & \lambda+2\mu & 0 & 0 \\ 0 & 0 & \mu & \mu \\ 0 & 0 & \mu & \mu \end{bmatrix} \tag{A.3}$$

in which μ, λ are the Lamé constants.

COMPDYN 2013
4th ECCOMAS Thematic Conference on
Computational Methods in Structural Dynamics and Earthquake Engineering
M. Papadrakakis, N.D. Lagaros, V. Plevris (eds.)
Kos Island, Greece, 12–14 June 2013

A COMPARISON OF TWO ELASTIC-PLASTIC APPROACHES TO CYCLIC SOIL MODELLING

Federico Pisanò[1], **Boris Jeremić**[2]

[1,2]1 University of California Davis
1 Shields Avenue 95616 Davis, California (USA)
e-mail: fpisano, jeremic@ucdavis.edu

Keywords: Geotechnical Earthquake Engineering, Soil Dynamics, Constitutive Modeling, Elasto-plasticity, Stiffness Degradation, Damping.

Abstract. *The choice of the soil constitutive relationship is an important step in the numerical modelling of many Geotechnical Earthquake Engineering problems. Although relevant results have been achieved in the field of elastic-plastic constitutive soil modelling, many practical problems are still tackled through 1D visco-elastic models, only based on shear modulus reduction and material damping curves. This is partly motivated by the usual lack of experimental data and the related difficulties in the calibration of advanced soil models. Even though the number of material parameters is kept low, multiple options exist in terms of theoretical framework for the model formulation. In this paper, the cyclic performances of two different kinematic hardening frictional models are compared. Both the models are characterized by a Drucker-Prager-type pressure-sensitiveness and non-associativeness, but, while the former is formulated as a standard elastic-plastic model with Armstrong-Frederick rotational hardening, the latter has been recently developed in the framework of bounding surface plasticity with vanishing elastic region. In particular, the bounding surface model allows for soil plastification at any load level, extending to frictional materials the previous cohesive version by Borja and Amies (1994).*

Although the two models are characterized by similar analytical structures and the same number of material parameters, the cyclic performance of the bounding surface model is apparently the most satisfactory in terms of simulated stiffness degradation and damping curves, which can be readily exploited for the calibration of the hardening parameters. The dissipation properties of both models are investigated in conjunction with an additional viscous mechanism, exploitable to improve the simulation of the experimental damping.

The effectiveness the bounding surface model is further analysed against the influence of the initial confining pressure. In particular, it is shown that the simple introduction of pressure-dependent hardening parameters readily allows to reproduce the soil cyclic response over a wide range of confining pressures.

1 INTRODUCTION

Geotechnical Earthquake Engineering (GEE) represents an important application field for Computational Dynamics methods, which have been increasingly employed in the last decades to analyse more and more challenging seismic soil-structure interaction (SSI) problems. Since SSI problems concern – by definition – both man-made structures and the interacting soil-like geomaterials, it is self-evident that no realistic results can be obtained from numerical simulations if the mechanical behaviour of all the materials involved is not properly described. In particular, modelling the mechanical response of soils is still a quite open issue because of the simultaneous presence of non-linearity, irreversibility, anisotropy and proneness to instability – especially when cyclic/dynamic loading conditions are applied to multiphase materials (i.e. filled with interstitial pore fluid(s)) [8].

The incorporation of suitable (multiaxial) constitutive relationships for soils into 3D SSI analyses is apparently a premise for reliable results to be obtained, but, on the other side, this also obstructs the routinary use of numerical methods for practical engineering purposes. Indeed, despite the huge steps forward taken in the elastic-plastic modelling of geomaterials, the most successful models in literature (overviews are given by [8, 13]) are usually characterized by rather complex analytical formulations and a quite high number of constitutive parameters: while the former aspect may result in cumbersome implementations into numerical codes and/or several computational difficulties, the latter prevents an easy model calibration on the basis of the few experimental data usually available. For these reasons, practitioners often prefer using so-called 1D equivalent linear visco-elastic models, only accounting for the dependence of the (secant) stiffness and the (viscous) damping on the cyclic strain amplitude [9].

The above considerations highlight the need for further research efforts in the field of soil cyclic modelling, not just aimed at conceiving new sophisticated constitutive relationships, but also at achieving reasonable accuracy with a minimum number of material parameters. In the present paper, this problem is addressed from a peculiar perspective, in order to point out how relevant is the choice of the theoretical/constitutive framework for the formulation of a specific soil model. For this purpose, two different elastic-plastic models are considered and compared in terms of analytical structure and resulting cyclic performance. Both the models are characterized by a Drucker-Prager-type pressure-sensitiveness and similar non-associated flow rules, but, while the former is formulated as a standard elastic-plastic model with Armstrong-Frederick rotational hardening, the latter has been recently developed in the framework of bounding surface plasticity with vanishing elastic domain [11]. In particular, the bounding surface model allows for soil plastification at the very onset of loading, extending to frictional materials a concept previously introduced by [2, 5] for the purely cohesive case.

Although the two models are characterized by similar analytical structures and – importantly – the same number of parameters, the bounding surface model appears to be preferable in terms of simulation of stiffness degradation and damping curves – here analytically implemented according to the proposal by [7]. The damping performance of both models is also investigated in conjunction with an additional viscous mechanism, exploitable to improve the simulation of the experimental damping. Finally, the initial version of the bounding surface model is slightly modified to accurately reproduce the soil cyclic response over a wide range of confining pressures.

2 CONSTITUTIVE FORMULATIONS

Hereafter, the analytical formulations of both the elastic-plastic models considered in this work are detailed. Then, the possibility of improving the purely frictional (elastic-plastic) dissipative performance through the coupling with a parallel viscous mechanism is illustrated.

Index tensor notation is henceforth used, along with the standard Einstein convention for repeated indices; the norm of any second–order tensor x_{ij} is defined as $\|x_{ij}\| = \sqrt{x_{ij}x_{ij}}$, whereas the deviatoric component can be extracted as $x_{ij}^{dev} = x_{ij} - x_{hk}\delta_{hk}\delta_{ij}/3$ (δ_{ij} is the Kronecker delta). In accordance with usual Solid Mechanics conventions, positive tensile stresses/strains are considered, whereas – as is done in Fluid Mechanics – only the isotropic mean pressure is positive if compressive. The usual symbols σ_{ij}, ϵ_{ij}, s_{ij} and e_{ij} are employed to denote the stress tensor, the strain tensor and the corresponding deviatoric components, while $p = -\sigma_{kk}/3$ and $\epsilon_{vol} = \epsilon_{kk}$ are the isotropic mean pressure and the volumetric strain, respectively.

2.1 Drucker-Prager kinematic hardening (DPkh) standard elastic-plastic model

As is well-known, the formulation of constitutive models in the framework of standard hardening elasto-plasticity requires the following ingredients: (i) elastic relationship, (ii) yield function, (iii) plastic flow rule and (iv) hardening law(s).

Under the usual elastic–plastic strain splitting, the incremental linear elastic Hooke's law is expressed as follows:

$$d\sigma_{ij} = D^e_{ijhk}\left(d\epsilon_{hk} - d\epsilon^p_{hk}\right) \tag{1}$$

where d is the differentiation operator, p stands for "plastic" and D^e_{ijhk} is the standard elastic stiffness tensor.

The yield locus $f = 0$ is of the same conical type described by [12, 10]:

$$f = \frac{3}{2}\left(s_{ij} - p\alpha_{ij}\right)\left(s_{ij} - p\alpha_{ij}\right) - k^2p^2 \tag{2}$$

in which α_{ij} is the so-called back-stress ratio tensor and k the yielding parameter. While this latter governs the opening angle of the cone, α_{ij} is a second–rank deviatoric tensor determining the rotation of the yield locus.

The plastic flow rule is in general expressed as:

$$d\epsilon^p_{ij} = d\lambda m_{ij} \tag{3}$$

where $d\lambda$ is the scalar plastic multiplier and m_{ij} rules the direction of the plastic flow. Here the following non–associated flow rule has been adopted:

$$m_{ij} = n^{dev}_{ij} - \frac{1}{3}D\delta_{ij} = \frac{\left(\partial f/\partial\sigma_{ij}\right)^{dev}}{\|\left(\partial f/\partial\sigma_{ij}\right)^{dev}\|} - \frac{1}{3}D\delta_{ij} \tag{4}$$

where the deviatoric unit tensor n^{dev}_{ij} is obtained from the deviatoric component of the yield function gradient (associated deviatoric plastic flow) and D represents the so-called dilatancy coefficient, expressed as suggested by suggested by [10]:

$$D = \xi\left(\alpha^d_{ij} - \alpha_{ij}\right)n^{dev}_{ij} = \xi\left(\sqrt{\frac{2}{3}}k_d n^{dev}_{ij} - \alpha_{ij}\right)n^{dev}_{ij} \tag{5}$$

The definition (5) introduces two further constitutive parameters, namely k_d and ξ: the former relates to the stress obliquity for the transition from contractive to dilative responses; the latter quantitatively governs the volumetric plastic strain rate.

Finally, the evolution law for the back-stress tensor α_{ij} is given according to the well-known Armstrong-Frederick approach [1] (see also [10]):

$$d\alpha_{ij} = \frac{2}{3} h_a de^p_{ij} - c_r \alpha_{ij} \sqrt{\frac{2}{3} de^p_{rs} de^p_{rs}} \tag{6}$$

where h_a and c_r are two hardening constitutive parameters. The incremental relationship (6) yields a saturation–type evolution and the existence of a limit back–stress ratio α^{lim}_{ij} measured by the following tensor norm:

$$\left\| \alpha^{lim}_{ij} \right\| = \sqrt{\frac{2}{3}} \frac{h_a}{c_r} \tag{7}$$

Accordingly, all the feasible stress states lie within an outer surface determined both by α^{lim}_{ij} and the opening parameter k in (2). The external bounding locus is in this case a Drucker–Prager (Lode angle-insensitive) cone: the limit stress obliquity M can be derived for triaxial loading conditions and shown to be equal to $M = k + h_a/c_r$ (both in compression and extension). As a consequence, the material shear strength is ruled by the ratio h_a/c_r, whereas c_r determines the evolution rate of α_{ij}.

2.2 Drucker-Prager kinematic hardening bounding surface (DPbs) model with vanishing elastic region

The DPbs constitutive relationship being presented is in essence a frictional effective–stress update of the cohesive model by [2] (improving the former work by [5]). While an exhaustive description is given in [11], the key-points of the analytical formulation are hereafter reported.

The DPbs model is chiefly characterized by the introduction of a vanishing elastic region: as a consequence, while the same Hooke's elastic law (1) is still used, plastic/irreversible strains take place at the very onset of loading (as is pointed out by many experimental evidences).

Starting from the same yield function definition (2), the following relationship ensures mutually consistent evolutions of the stress state and the back-stress when $k \to 0$:

$$\lim_{k \to 0} f = 0 \Rightarrow s_{ij} = p \alpha_{ij} \Rightarrow ds_{ij} = d\alpha_{ij} p + \alpha_{ij} dp \tag{8}$$

The same plastic flow relationships (3), (4) and (5) are employed for the DPbs model as well, with the exception of the manner in which the deviatoric unit tensor n^{dev}_{ij} is obtained. Specifically, the combination of a Prager-type translation rule for α_{ij} ($d\alpha_{ij} = \|d\alpha_{ij}\| n^{dev}_{ij}$) with the constraint (8) leads to:

$$n^{dev}_{ij} = \frac{ds_{ij} - \alpha_{ij} dp}{\|ds_{ij} - \alpha_{ij} dp\|} \tag{9}$$

Since the direction of the deviatoric plastic strain increment ($de^p_{ij} = d\lambda n^{dev}_{ij}$) depends on the stress increment through n^{dev}_{ij}, the model is intrinsically – and spontaneously – "hypoplastic" [6].

As was done by [2], an incremental hardening relationship is here directly established between the increments of the deviatoric second invariant q and the incremental deviatoric plastic strain (see [11]):

$$dq = \sqrt{\frac{2}{3}} H \| de^p_{ij} \| \tag{10}$$

where H is the so-called hardening modulus. Following a typical bounding surface plasticity approach, H is related to the tensorial distance between the current stress state and its projection onto an *ad hoc* bounding locus $f_{bs} = 0$. In particular, provided a Drucker-Prager bounding locus (set $\|\alpha_{ij}\| = 0$ and $k = M$ in (2)), the hardening modulus is given by:

$$\begin{aligned} H &= p\left(h\beta^m\right) \\ \beta \in \mathbb{R}^+ : \frac{3}{2}\bar{s}_{ij}\bar{s}_{ij} - M^2\bar{p}^2 &= 0, \\ \bar{\sigma}_{ij} &= \sigma_{ij} + \beta\left(\sigma_{ij} - \sigma^0_{ij}\right) \end{aligned} \tag{11}$$

in which h and m are two hardening parameters, whereas σ^0_{ij} embodies the stress tensor at the last load reversal. Since a standard yield locus is missing, the loading/unloading criterion is alternatively defined according to the approach by [2]: to ensure an instantaneous elastic response at the onset of unloading, σ^0_{ij} is set equal to the current stress tensor whenever $d\beta > 0$, so that $\sigma^0_{ij} = \sigma_{ij} \Rightarrow \beta \to \infty$ and therefore $H \to \infty$. In contrast, the fulfilment of $\lim_{\beta\to 0} H = 0$ guarantees the occurrence of failure when the distance coefficient β is nil.

A notable flexibility stems from the fact that the $H\left(\beta\right)$ relationship can be modified without affecting the analytical structure (and the computer implementation), so that the DPbs model can be in principle adapted to reproduce a large variety of experimental results.

2.3 Constitutive parameters and calibration

Both the above models require the calibration of seven constitutive parameters. Two material constants – e.g. the Young modulus E and the Poisson's ratio ν – are needed to characterize the elastic behaviour, usually investigated by means of *in situ* tests and/or laboratory dynamic tests at very small strains.

Then, the two parameters ξ and k_d must be identified to describe the soil volumetric behaviour for a given relative density – or for a narrow range around the calibration value (the use of any density-dependent state parameter has been here avoided for the sake of simplicity).

The remaining three parameters can be set on the basis of a single datum concerning the shear strength (friction angle) and, for instance, the modulus reduction and damping curves (these are in many cases the only available information concerning the cyclic response). In the DPbs model the shear strength is independently governed by the M parameter (opening of the bounding surface), so that the hardening parameters h and m can be selected to get the best match between numerical and experimental cyclic curves. In contrast, hardening and failure properties are not decoupled in DPkh case, this implying the need for a simultaneous identification of k, h_a and c_r.

2.4 Coupling frictional and viscous energy dissipations

The dissipative performance of an elastic-plastic model can be improved via an additional viscous damping mechanism. This means that the global stress state on the soil solid skeleton

can be split into two parallel components ($\sigma_{ij} = \sigma^f_{ij} + \sigma^v_{ij}$), namely a frictional contribution σ^f_{ij} given by thr elastic-plastic behaviour and a viscous term σ^v_{ij}, e.g. of the following form:

$$\sigma^v_{ij} = D^v_{ijhk}\dot{\epsilon}_{hk} \tag{12}$$

where the dot stands for time derivation and D^v_{ijhv} is the fourth-rank tensor of viscous moduli. In standard finite element computations, the additional viscous mechanism (12) is often introduced through the following calibration of the so-called Rayleigh parameters [4] for the damping matrix $\mathbf{C}$:

$$\mathbf{C} = a_0\mathbf{M} + a_1\mathbf{K}^e, \tag{13}$$
$$a_0 = 0 \qquad a_1 = \frac{2D_{min}}{\omega}$$

ensuring a damping ratio D_{min} for a given circular frequency ω at very small strains. As could be readily shown [3, 11], the main effects of coupling frictional and (linear) viscous dissipations are: (i) an apparent smoothing of stress-strain loading cycles, avoiding the sharp transitions at stress reversals usually exhibited by purely elastic–plastic responses [3]; (ii) higher material damping, given by the sum of the frictional and the viscous components. While at very low strains the damping ratio approaches the purely viscous limit D_{min}, both the frictional and the viscous components contribute to the global damping at progressively larger strains; suitably, the stiffness modulus reduction results to be unaffected by viscosity.

3 REFERENCE MODULUS REDUCTION AND MATERIAL DAMPING CURVES

The DPkh/DPbs models will be mainly evaluated by comparing their capability of reproducing shear modulus reduction (G/G_{max}) and damping (D) curves. Therefore, reference cyclic curves are needed for the parameter calibration (see section 2.3) and, in this work, the family of normalized curves proposed by Darendeli [7] is taken into account for two reasons: (i) stiffness reduction and damping curves are provided analytically, with particular convenience for their implementation and use in parametric analyses; (ii) the recent development of Darendeli's curves gives sufficient confidence about the absence of "accuracy problems in material damping measurements arising from the use of older generation cyclic triaxial equipment employed in previous studies" [7]. While the reader can refer to the original work [7] for conceptual/operational details, the main aspects concerning the use of Darendeli's curves are hereafter summarized.

As far as the shear modulus reduction is concerned, a modified hyperbolic expression is adopted:

$$\frac{G}{G_{max}} = \frac{1}{1 + (\gamma/\gamma_r)^a} \tag{14}$$

in which γ_r and a are the so-called "reference strain" and "curvature coefficient", respectively. Then, the following relationship for the damping ratio D – defined as usual [9] – is assumed:

$$D = D_{min} + b * \left(\frac{G}{G_{max}}\right)^{0.1} * D_{Masing} \tag{15}$$

where b is a "scaling coefficient", D_{min} the limit damping ratio at very low shear strain ($\lim_{\gamma\to 0} D = D_{min}$) and D_{Masing} the material damping evaluated from the corresponding G/G_{max} trend by assuming the validity of the well-known Masing loading/unloading criterion [9].

The practical use of equations (14) and (15) requires the identification of four material parameters (γ_r, a, b and D_{min}). Based on a significant sample of experimental data, they have been conveniently related to few physical/loading indices through the following empirical formulas:

$$\begin{aligned} \gamma_r &= \left(\phi_1 + \phi_2 * PI * OCR^{\phi_3}\right) * p_0^{\phi_4} \\ a &= \phi_5 \\ D_{min} &= \left(\phi_6\phi_7 * PI * OCR^{\phi_8}\right) * p_0^{\phi_9} * \left[1 + \phi_{10} * ln\left(f\right)\right] \\ b &= \phi_{11} + \phi_{12} * ln\left(N\right) \end{aligned} \tag{16}$$

where:

p_0: mean effective confining pressure [atm]

PI: soil plasticity index [%]

OCR: overconsolidation ratio [-]

f: loading frequency [Hz]

N: number of loading cycles [-]

The values of the twelve constants ϕ_i are not reported here for the sake of brevity but can be found in [7].

4 DPkh and DPbs SIMULATION OF THE SOIL CYCLIC RESPONSE

In this section the cyclic performances of the DPkh and DPbs models are compared by using the above Darendeli's curve as a good analytical approximation of real experimental results. As is implied by Equations (16), G/G_{max} and D damping curves are obtained on the basis of few relevant mechanical/loading parameters. In what follows – unless differently stated – $p_0 = 1$ atm, $OCR = 1$ and $PI = 0$ %, while – as suggested by [7], $f = 1$ Hz, $N = 10$ cycles have been set to approximate typical seismic loading in "single frequency" shear tests.

The plastic volumetric behaviour of the soil is neglected in this study, in order to avoid the complex interaction between soil dilatancy behaviour and the kinematic constraints characterizing many experimental devices [11]. Therefore, the $\xi = 0$ parameter in (5) will be always set to zero (i.e. $d\epsilon_{vol} = 0$), this implying shear strain-controlled cyclic tests to be performed at constant mean pressure $p = p_0$.

While typical values have been selected for the elastic and strength parameters – $E = 10$ MPa, $\nu = 0.25$, $M = 1.2$ (30 deg friction angle), the calibration of the hardening parameters is discussed in more detail, as they mainly affect the resulting G/G_{max} and D curves.

4.1 DPkh simulations

As any standard plasticity model, the DPkh model predicts a purely elastic pre-yielding response and strain-independent cyclic curves for shear strains less than the yielding strain γ_y. Based on this consideration and the above DPkh constitutive equations, the following calibration procedure has been followed:

1. once chosen the amplitude of the elastic range, the opening of the yield locus has been obtained as $k = \sqrt{3\left(G_{max}\gamma_y/p_0\right)^2}$ (the influence of both the elastic shear modulus G_{max} and p_0 should be noted);

2. in order to prescribe a given shear strength M, the hardening and yielding parameters must be related as $h_a = c_r\,(M - k)$;

3. c_r has been varied to modify the overall hardening response.

It is especially worth remarking that, within an elastic-plastic modelling framework, G/G_{max} and D are interdependent: this means that the constitutive parameters must be calibrated to achieve at the same time the best agreement with both the experimental cyclic curves.

In Figure 1 DPkh and Darendeli's curves are compared for two different DPkh yielding strains (γ_y =2.2E-4, 1E-2 %). Darendeli's average curves (blue lines) are given along with the uncertainty ranges derived from the corresponding standard deviations (black dashed lines) [7], while the DPkh D curves have been obtained in both the purely frictional and frictional/viscous versions. The plots in Figure 1 lead to the following conclusions:

- the singularity at the elastic/elastic-plastic transition prevents the DPkh G/G_{max} curves to follow the concavity exhibited by Darendeli's curves;

- the smaller γ_y, the more difficult is to reproduce the experimental trend over the whole strain range. For medium/large γ_y reasonable G/G_{max} ratios are obtained at medium/large strains: this kind of calibration may be acceptable for applications in which the small-strain behaviour (assumed to be linear elastic) is not very important;

- the trend of DPkh D curves is markedly non-monotonic as a consequence of the peculiar interaction between hardening evolution (stiffness degradation) and the cyclic loading/unloading behaviour (determining the shape of the stress-strain cycles);

- the introduction of the parallel viscous mechanism is effective only to reproduce the small-strain damping (neglected by the purely frictional formulation), with no effect on the aforementioned non-monotonicity.

The influence of the hardening behaviour is further explored in Figures 2 and 3, where the simulations in Figure 1 have been repeated for different c_r values (only the purely frictional curves are shown). Expectedly, since c_r governs the shape of the hardening stress-strain branches, it directly affects the decay of the secant shear modulus, as well as the damping ratio. However, regardless of γ_y, obtaining a satisfactory agreement does not appear to be an easy task. Different trends may be obtained by varying at the same time both h_a and c_r, but this would in general modify the prescribed shear strength.

4.2 DPbs simulations

The same Darendeli's curves for $p_0 = 1$ atm have been approximated by using the DPbs model. Figure 4 shows the overall good DPbs performance (much better than the DPkh one), with an almost perfect G/G_{max} match and a qualitatively good agreement in terms of material damping as well. Because of the vanishing yield locus, no elastic/elastic-plastic transition takes place, so that the resulting curves are smooth and easier to be adapted on the experimental trends. However, to author's experience, optimising the agreement in terms of modulus reduction usually prevent very satisfactory damping curves to be obtained. As is shown in Figure 5, better results can be achieved by attempting a "trial-and-error" calibration to reasonably match both G/G_{max} and D curves. Figure 5 also illustrates the beneficial effect of the viscous damping in the small strain range, while it leads to some damping overestimation at larger strains:

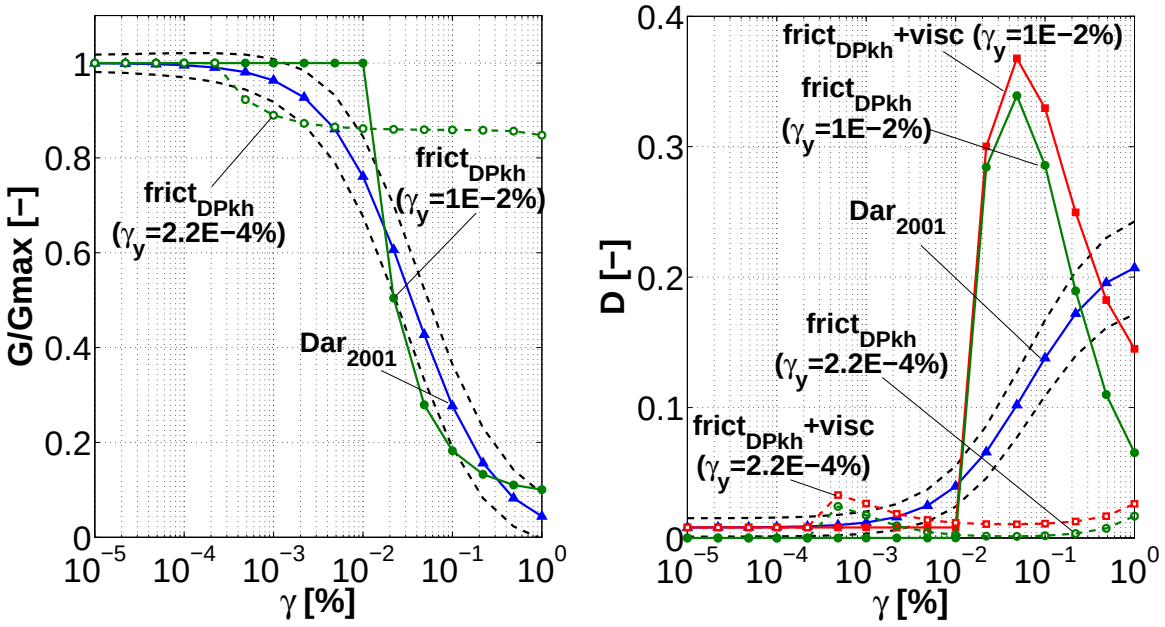


Figure 1: Darendeli-DPkh comparison for $p_0 = 1$ atm and two (γ_y, c_r) couples (γ_y =1E-2% and c_r =10, γ_y =2.2E-4% and c_r =600)

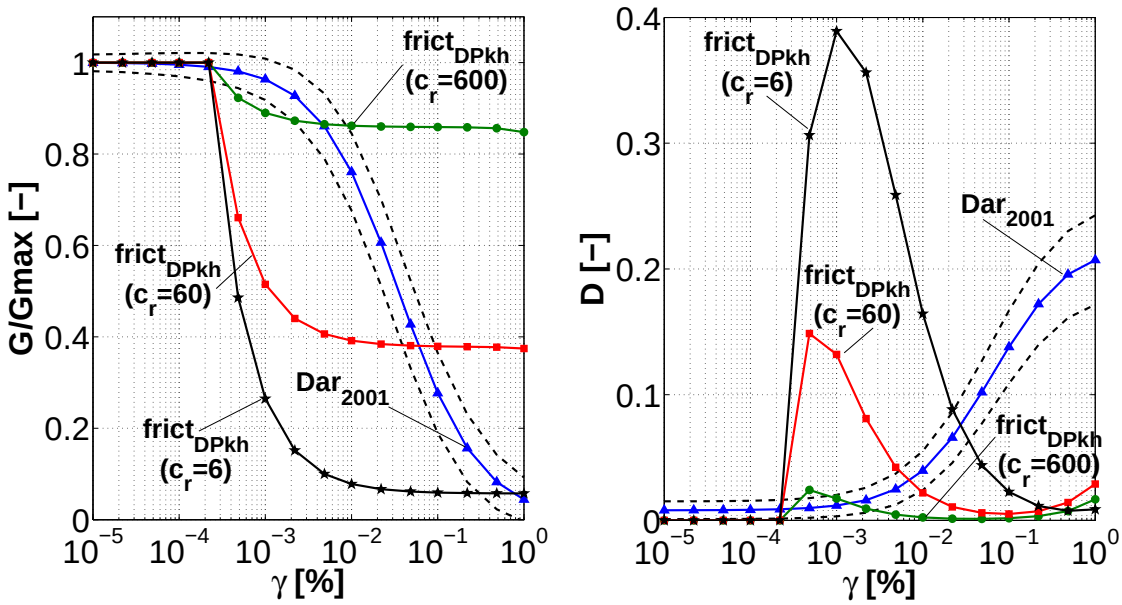


Figure 2: Darendeli-DPkh comparison for $p_0 = 1$ atm, γ_y =2.2E-4% and c_r =6, 60, 600

depending on the specific application, the value of D_{min} can be varied as an additional free parameter to improve the accuracy for a given strain interval.

Figures 6 and 7 exemplify the influence of the hardening parameters h and m, giving the chance to significantly vary the shapes of the predicted curves. Whenever no satisfactory agreement is reached by simply varying h and m, the option of modifying the $H(\beta)$ relationship (11)

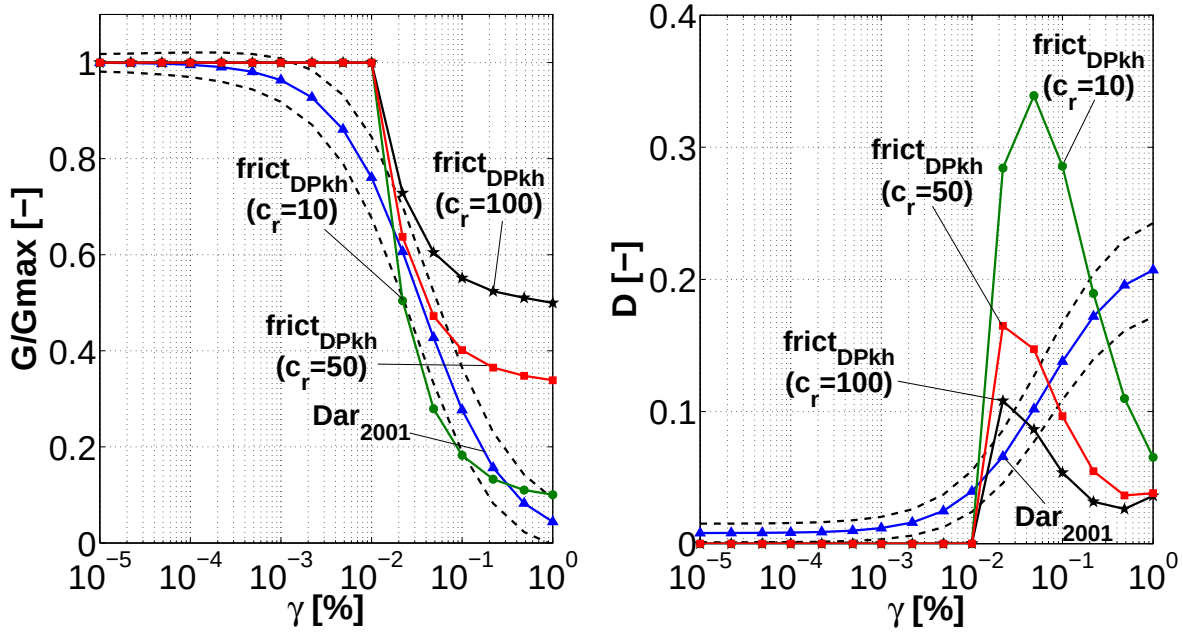


Figure 3: Darendeli-DPkh comparison for $p_0 = 1$ atm, γ_y =1E-2% and c_r =10, 50, 100

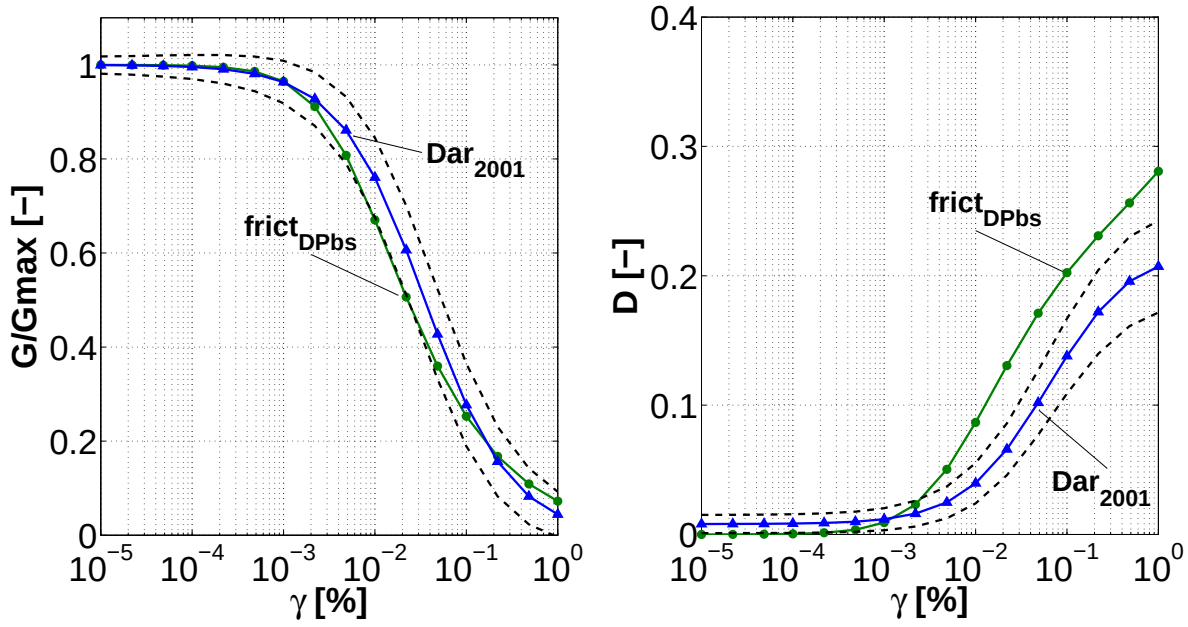


Figure 4: Darendeli-DPbs comparison for $p_0 = 1$ atm (h =0.15, m =1.34)

is always possible with no substantial changes in the structure and the implementation of the model.

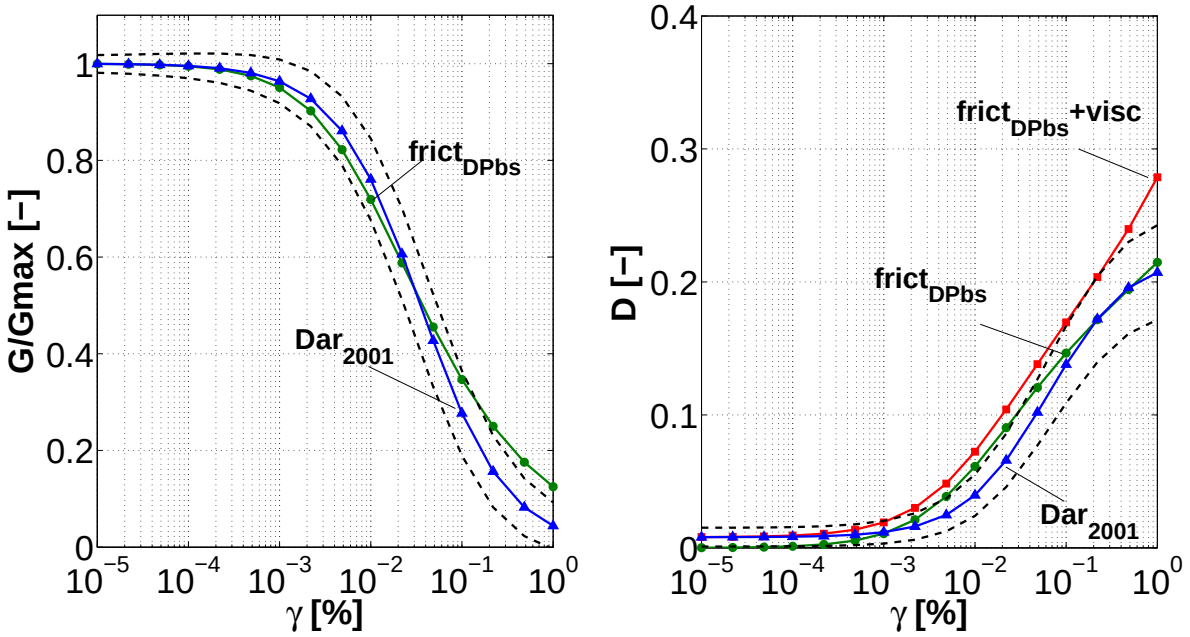


Figure 5: Darendeli-DPbs comparison for $p_0 = 1$ atm (h =1.4, m =1)

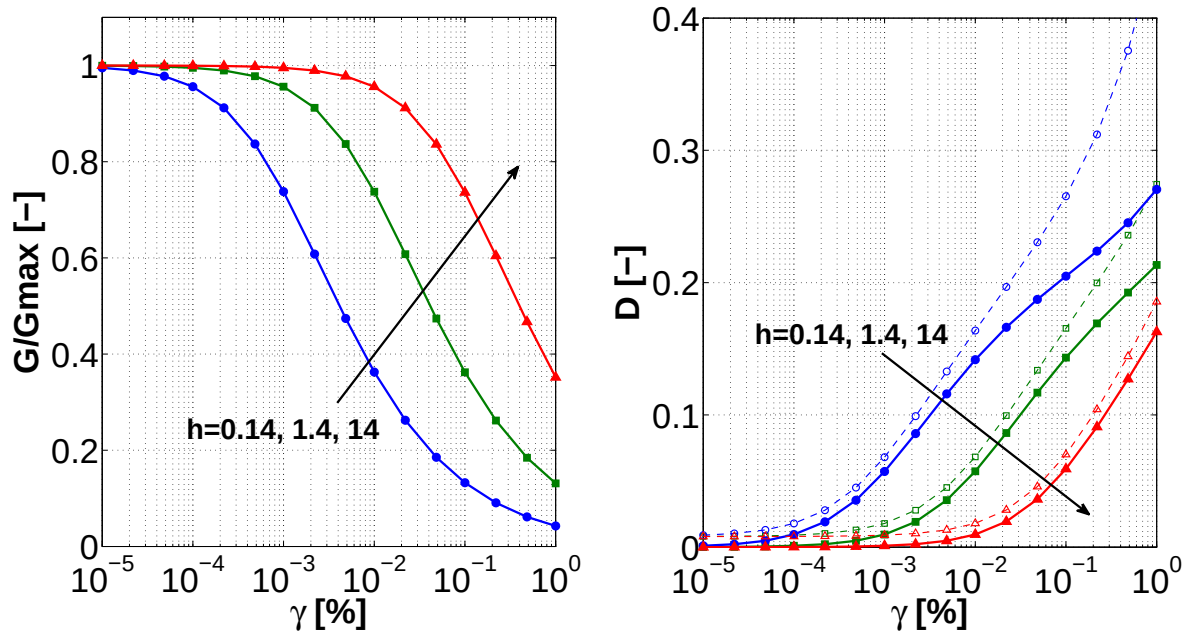


Figure 6: DPbs parametric analyses: $p_0 = 1$ atm, Simulazione 1 atm, m =1, h variable (dashed lines include both frictional and viscous dissipation)

5 DPbs MODELLING OF PRESSURE-SENSITIVE CYCLIC BEHAVIOUR

The mechanical behaviour of frictional materials is considerably pressure-sensitive and, as many experimental evidences confirm, both shear modulus reduction and damping curves are affected by the value of the confining pressure. Accounting for pressure-dependence can be

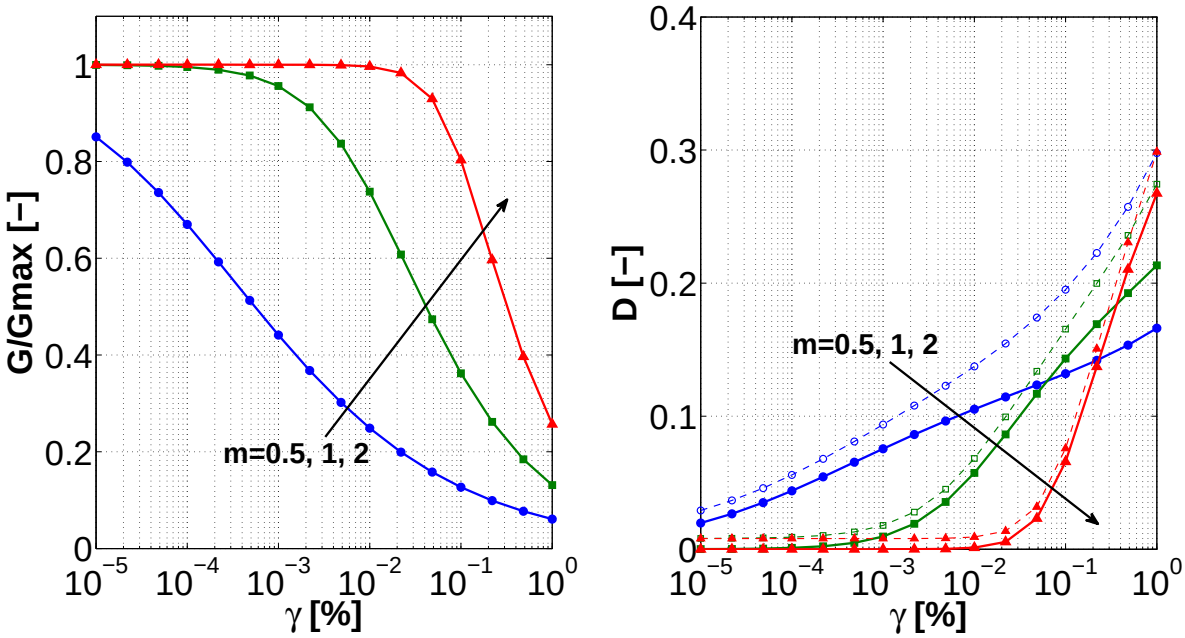


Figure 7: DPbs parametric analyses: $p_0 = 1$ atm, h =1.4, m = variable (dashed lines include both frictional and viscous dissipation)

particularly important in practical applications, especially when the computational soil model involves large depth ranges.

Darendeli's cyclic formulation takes explicitly into account the influence of the initial mean pressure p_0 and can be exploited to check how accurately the DPbs model reproduces this mechanical aspect. Figure 8 illustrates the cyclic pressure-sensitiveness predicted by Darendeli's formulas over the 0.25–16 atm pressure range for the values $OCR = 1$, $PI = 0\%$, $f = 1$ Hz and $N = 10$ cycles. The same simulations have been performed by using the DPbs model and the corresponding outcomes plotted in Figure 9 (frictional mechanism only). As is evident, the DPbs model calibrated for $p_0 = 1$ atm (the material parameters are given in the figure caption) overestimates the effect of the confining pressure and a rather unsatisfactory Darendeli-DPbs agreement results.

A possible simple approach to improve the DPbs performance over a wide pressure range is to introduce p_0-dependent hardening parameters and small-strain damping, requiring two or more calibrations for h, m and D_{min}[1]. Here, four distinct (h, m, D_{min}) triplets have been first set for $p_0 = 0.25, 1, 4, 16$ atm on the basis of Darendeli's formulas and then the following interpolating power laws have been identified:

$$\begin{aligned} h &= 1.2762 * p_0^{-1.95} \\ m &= 0.9952 * p_0^{0.0691} \\ D_{min} &= 0.008 * p_0^{-0.29} \end{aligned} \tag{17}$$

Owing to the convenient formulation of the DPbs model, the introduction of pressure-dependent hardening parameters does not imply any additional analytical/computational difficulty, so that

[1]the pressure-dependence of the elastic moduli has been neglected with no substantial effect on the suitability of the approach proposed

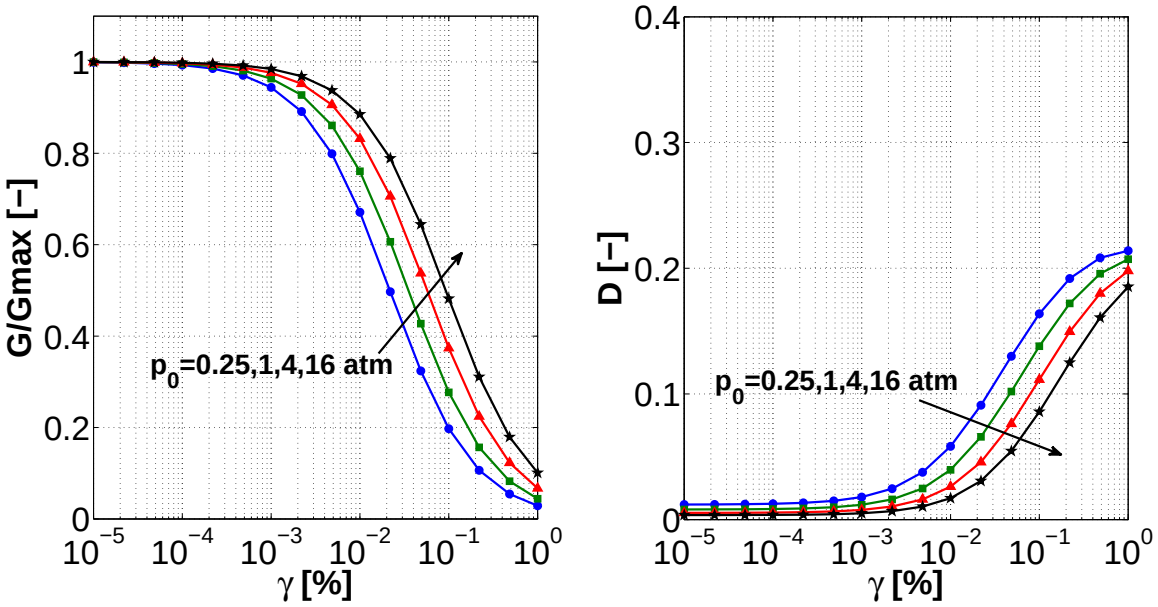


Figure 8: Pressure-sensitiveness of G/G_{max} and D curves predicted via Darendeli's formulas

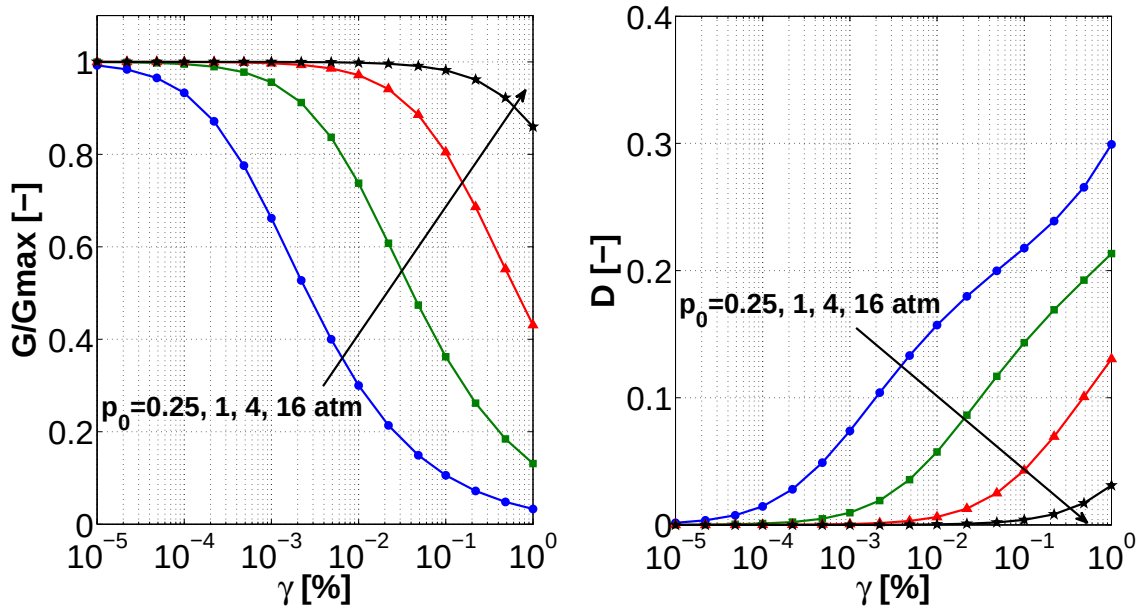


Figure 9: Pressure-sensitiveness of G/G_{max} and D curves predicted via the DPbs model with constant hardening parameters ($E = 10$ MPa, $\nu = 0.25$, $M = 1.2$, $h = 1.4$, $m = 1$)

this slight modification can be readily implemented. Provided the satisfactory Darendeli-DPbs agreement – here not shown – at the calibration pressures ($p_0 = 0.25, 1, 4, 16$ atm), the effectiveness of the interpolation procedure is proven in Figure 10 for the different pressure $p_0 = 8$ atm. Even in this case the contribution of the viscous mechanism is particularly needed at medium/low strains, while it leads to some damping overestimation at higher strain levels: as in the previous cases, some adjustment is possible to get a reasonable match over the whole strain

range.

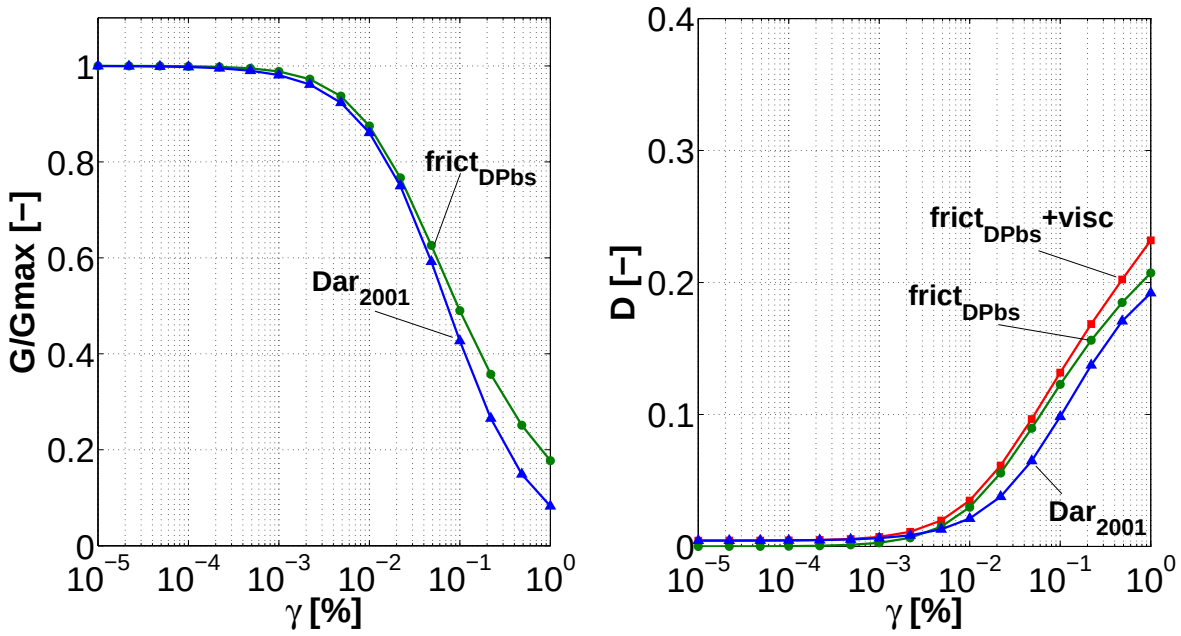


Figure 10: Comparison between Darendeli's and DPbs cyclic curves for $p_0 = 8$ atm

6 CONCLUSIONS

Two elastic-plastic kinematic hardening Drucker-Prager models were formulated and compared in terms of cyclic performance, i.e. simulation of the modulus reduction and damping curves usually employed in the GEE practice. While the former model (DPkh) is a standard elastic-plastic with an Armstrong-Frederick evolution law for the back-stress tensor, the latter (DPbs) was developed within the framework of bounding surface plasticity with vanishing elastic region.

For practical purposes, both the models were formulated by using the same low number of constitutive parameters and including the most essential mechanical characteristics of frictional materials, i.e. pressure-sensitive shear strength and non-associated plastic flow. Despite the apparent similarities, the two models produce very different outcomes and highlight that passing from standard 1D visco-elastic approaches to multiaxial plasticity modelling requires attention on the choice of the specific elastic-plastic framework. Specifically, the DPbs bounding surface approach appeared to work much better than the DPkh one, owing to the absence of the usual elastic/elastic-plastic transition and the easily modifiable relationship for the hardening modulus. In particular, the latter feature was exploited to introduce pressure-dependent DPbs hardening parameters and thus extend the predictive effectiveness over a wide range of confining pressures. The beneficial effect of introducing an additional viscous damping mechanisms was also explored, allowing to precisely reproduce energy dissipation at very low strains and, in general, to remedy some accuracy lack of the purely frictional model.

Further work is currently in progress to investigate the influence of the modelling framework in dynamic boundary value problems, especially in the presence of hydro-mechanical coupling.

REFERENCES

[1] P. Armstrong, C. Frederick, A mathematical representation of the multiaxial Bauschinger effect. Technical Report RD/B/N/ 731, C.E.G.B., 1966.

[2] R.I. Borja, A.P. Amies, Multiaxial cyclic plasticity model for clays. *Journal of Geotechnical Engineering*, **120**, 1051–1060, 1994.

[3] R.I. Borja, C. Lin, K. Sama, G. Masada Modelling non-linear ground response of non-liquefiable soils. *Earthquake Engineering and Structural Dynamics*, **29**, 63–83, 2000.

[4] A.K. Chopra, *Dynamics of structures. Theory and application to Earthquake Engineering*. Prentice Hall, 2000.

[5] Y.F. Dafalias, E. Popov, Cyclic loading for materials with a vanishing elastic region. *Nuclear Engineering and Design*, **41**, 293–302, 1977.

[6] Y.F. Dafalias, Bounding surface plasticity. I: Matematical foundations and hypoplasticity. *ASCE Journal of Engineering Mechanics*, **112**, 966–987, 1986.

[7] M.B. Darendeli, *Development of a new family of normalized modulus reduction and material damping curves*. Ph.D. thesis, University of Texas at Austin.

[8] C.G. di Prisco, D.M. Wood, *Mechanical behaviour of soils under environmentally-induced cyclic loads*. Springer, 2012.

[9] S.L. Kramer, *Geotechnical Earthquake Engineering*. Prentice Hall, 1996.

[10] M.T. Manzari, Y.F. Dafalias, A critical state two-surface plasticity model for sands. *Géotechnique*, **47**, 255–272, 1997.

[11] F. Pisanò, B. Jeremić , Coupling multiaxial plasticity and viscous dissipation for cyclically loaded granular materials. Submitted to *Soil Dynamics and Earthquake Engineering*, 2012.

[12] J.H. Prevost, A simple plasticity theory for frictional cohesionless soils. *International Journal of Soil Dynamics and Earthquake Engineering*, **4**, 9–17, 1985.

[13] O.C. Zienkiewicz, A.H.C. Chan, M. Pastor, B.A. Schrefler, T Shiomi, *Computational Geomechanics with special reference to Earthquake Engineering* . Wiley and Sons, 1999.

COMPDYN 2013
4th ECCOMAS Thematic Conference on
Computational Methods in Structural Dynamics and Earthquake Engineering
Kos Island, Greece, 12–14 June 2013

AN INSIGHT INTO THE INFLUENCE OF THE CONSTRUCTION METHODS ON THE LATERAL LOAD CAPACITY OF DRILLED DEEP FOUNDATIONS

Assistant. Prof. Dr. N. Özgür Bezgin

İstanbul University, Avcılar Campus
Civil Engineering Department, 34320, Avcılar, Istanbul, Turkiye
ozgur.bezgin@istanbul.edu.tr

Keywords: Deep-foundations, drilling methods, drill rig, soil-structure interaction, seismic loads.

Abstract. *Deep foundations are frequently employed in the construction of structures where the loads of the superstructure have to be transferred in an economical way to geotechnical strata that rest beyond the reach of shallow foundations. The operation of drilled deep foundation construction equipment frequently employs pressurized fluids or mechanical rotary actions to agitate and remove the soil. The design of a deep foundation element under lateral loads relies on the "as in place" properties of soil. However, it has been observed that the construction method to drill a foundation frequently changes the properties of the soil as well as the surface interaction of the soil with deep foundation element. This influence changes the lateral support stiffness of the soil on the deep foundation element and the surface contact conditions between the deep foundation element and the soil. Such changes heavily influence the lateral load behavior of the deep foundation due to the lack of lateral soil support or reduced lateral soil stiffness as a result of the construction activity.*

The construction of a deep-foundation is not an isolated process and there is a difference between the "as-conceived" and the "as-built" foundation. Therefore an estimate has to be made regarding what this influence could be before the design of the deep-foundation is complete. In this paper, two case studies relating to the construction of deep foundations of two high rise buildings in New York City will be presented that highlight the effects stated in the previous paragraphs. An experimental study will also be presented that will be reinforced with an analytical finite element investigation to represent the influence of the construction operations on the lateral load capacities of drilled deep foundations.

Introduction:

Deep-foundations transfer structural loads through a weak soil layer into a strong soil layer or into bedrock. A drilled-shaft (shaft) is a type of deep-foundation element. The construction projects presented in this paper focus on 50 cm diameter shafts drilled with pressurized drilling methods and embedded in bedrock. These shafts consist of a cage composed of reinforcing bars centered within a steel shell that is filled with concrete. The supports for these shafts are rock sockets that extend into competent bedrock after the termination of the steel shell. The installation of the shafts involved the drilling of a steel shell through weak soil layers into competent bedrock. During this process, the soil was simultaneously drilled and removed as the steel shell was advanced into the ground. Once the competent bedrock was reached, the steel shell was drilled into bedrock to establish a seal with the bedrock. The steel shell terminated at the competent bedrock where a rock socket extended further than the casing by the use of a high-frequency air-hammer. After the rock socket reached the sufficient design depth, the interior of the casing and the socket was cleaned of any accumulated debris and a cage of steel reinforcing-bars was lowered and centered in the cylindrical hole which was later filled with structural concrete.

The vertical load transfer mechanism of shafts embedded in a rock socket involves end bearing and side friction within the rock socket whereas the lateral load transfer mechanism of shafts is related to the relative value of the flexural stiffness of the shaft and axial stiffness of the soil surrounding the shaft. In certain cases where the shaft slenderness is low and the embedded soil is weak, the end moments at the rock socket could also resist the lateral loads. This paper concentrates on the effect of the procedure to drill the steel-casing of a shaft until it reaches the rock.

There is an abundance of theoretical and experimental information related to the behavior of deep-foundations under lateral loads within soil media. One simple equation that is presented here is for deep-foundations embedded in cohesionless soils where the soil modulus can vary linearly with depth. Equation 1 presents the relative rigidity factor (T) between the rigidity of the deep-foundation and the rate of change of elastic modulus of the soil with depth (n_h). [2,4,7,14].

$$T = \left(\frac{EI}{n_h} \right)^{1/5} \qquad (1)$$

Determination of an allowable structural displacement requires the determination of the displacement of the super-structure with respect to the deep-foundation element ($\Delta 1$) plus the displacement of the deep-foundation element with respect to the ground surface ($\Delta 2$). Thus the total displacement is: $\Delta 1+\Delta 2$. This value becomes important if there are neighboring structures next to the proposed structure. Another importance arises due to seismic loads since the deep-foundation displacement, which is an indicator of its stiffness, modifies the natural period of the super structure, which in return modifies the seismic lateral load effective on the superstructure.

Effect of installation procedures on the soil properties:

The advance of the steel shell requires the removal of the soil within the shell in order to allow the rebar cage and the concrete to be placed into the shell. The methods used in the removal of the soil within the casing influences the soil strength and the soil continuity around the shaft. The variation of displacements along a shaft is influenced by its interaction with the surrounding soil. The relativity of the rotational stiffness of the shaft and the translational stiffness of the soil are critical in the determination of this lateral capacity. Thus any change in the relative stiffness will have an effect on lateral capacity. The installation procedures for the shafts disturb the soil surrounding the shaft. Determination of the extent and the parametric evaluation of the soil disturbance need to be included in the assessment of the lateral load capacity of the shaft. A correct shaft design requires an estimate or a consideration of the post-installation soil properties around the shaft. The designer must make sure he or she is aware of the state of the soil the shaft is embedded within, in order to make a correct assessment of the soil-structure interaction.

Case studies:

In urban construction projects that require deep foundations such as those in crowded cities like New York City, shaft diameters up to 90-cm are common. The drill rigs for such diameters can be transported to and maneuvered within tight urban construction sites and the shafts can be drilled by pressurized drilling methods. Two case studies will be presented that involve the installation of 50 cm diameter shafts in granular soil media.

Case study - 1:

The construction took place in Downtown Manhattan/New York. The planned structure was a 25-story hotel building. The soil profile was granular and consisted of 1 meter fill layer and 13 meter sand and trace silt-sand layer above bedrock. The drilled-shafts used 15 meter long casings that were 50 cm in diameter.

The drilling methodology used pressurized water-polymer mix through the casing as the casing was rotated and pushed into the ground by a drill-rig. The use of polymer in water increased the viscosity of the water and enabled the water to drag soil particles. The high-pressure water-polymer mix served two purposes: 1) to push the soil through the casing and 2) to transport this soil along the sides of the casing from a certain depth within the ground to the ground surface. Water mixed with polymer was collected from a pit by a pump and transferred to the drill rig. As the casing was rotated and pushed into the ground, the soil was pushed out of the casing by the water pressure applied through the casing and traveled to the ground surface along the sides of the casing carrying with it the soil particles. As the run-off water that drained back into the pit was pumped back into the drill-rig the soil that accumulated within the pit was removed by an excavator at regular intervals. This procedure continued until the casing was properly sealed into the bedrock. After the casing was sealed into the bedrock a rock socket was drilled into the bedrock by a high frequency oscillating hammerhead.

During the advancement of the casing towards the bedrock, the soil around the casing was disturbed and the soil was affected in two ways: 1) Gaps formed around the casing and the soil support was removed or 2) Soil stiffness was reduced and the soil support was weakened. The

accumulation of the soil gaps and weakened soil layers were concentrated around the casing closer to the ground surface. The reason for this concentration was that the effective soil pressures became lower closer to the ground surface. Thus any gap formed around the casing either remained open or was refilled with the collapsing soil in an un-compacted state and therefore the soil was permanently weakened after the drilling process was complete.

Figure 1 shows the casings ready for drilling. Figure 2 shows the collecting pit in the foreground, the pump in the middle and the rig in the background. The site was sloped by the contractor such that the water-polymer mix flowed back into the pit along the right side of the rig. Figure 3 shows a 15 meter long and 50 cm diameter casing attached and ready to be installed. Figure 4 and figure 5 shows runoff water from the sides of the casing flowing back into the pit. Figure 6 shows the gaps formed around the casing after the casing is terminated in bedrock. The gaps were found to extend approximately 2.5 meters into the ground, which is approximately 5 times the diameter of the casing.



Figure 1 – Steel casings ready to be drilled.



Figure 2 – Water drilling set-up.



Figure 3 – Drill rig in place ready to drill the casing.



Figure 4 – Water-polymer mix flowing out of the casing at low pressure.



Figure 5 – Water-polymer mix flowing back into the pit.



Figure 6 –The gaps formed around the casing after the drilling operation.

Another influence of the installation method on the soil was observed during the drilling operation. As the casing was rotated and advanced into the ground, an extent of soil around the casing was disturbed due to the vortex created by the high-pressure water-polymer mix and due to the rate of revolution of the casing. The end result was that the soil within this volume was highly disturbed and liquefaction occurred. During the operation, the soil around the casing did not have sufficient bearing capacity to step on, therefore the rig was approached to a distance of

50 cm by stepping on a wood plank and a steel reinforcing bar was penetrated into the soil to observe the soil resistance. Within a distance of 50 cm from the casing, the rebar penetrated the soil without any resistance. The resistance increased with the increasing distance from the casing face and diminished around 3 times the diameter of the casing. The granular nature of the soil in this particular site was an important contributor to this observed behavior. Figure 7 shows the extension of the influence zone around the casing. Figure 8 and 9 shows the state of the perimeter soil around the shaft after the installation. Notice the gap around the perimeter and the reduction of the soil slope with the increasing distance from the casing.

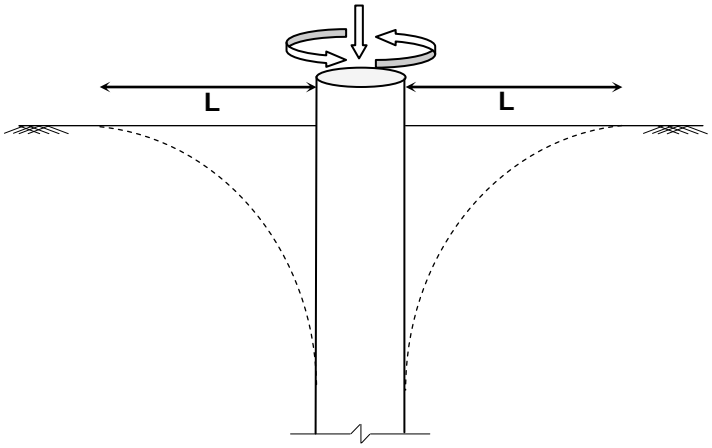


Figure 7 – Soil disturbance caused by the drilling of the casing.



Figure 8 – Disturbed soil around the casing perimeter during the operation.



Figure 9 – Influence zone around the casing perimeter during drilling.

Acknowledgement of this behavior is important before the installation of drilled-shaft next to existing structures. Figure 10 shows the operation next to an existing three-story 75-year-old masonry building that was supported on shallow foundations bearing approximately 1 meter below the ground surface.



Figure 10 – Installation of a casing close to an existing structure.

The face of drilled shafts was originally located 30 cm away from the face of the wall. After the influence of the drilling methodology was observed, the shafts were relocated 1 meter away from the face of the wall in order to prevent loss of bearing pressure underneath the footings of the existing building. This relocation created an eccentricity with respect to the super-structure columns and the shaft caps had to be redesigned. The shafts along the perimeter were coupled to the surrounding shafts by deep grade beams in order to distribute the extra moment generated by this relocation.

Case study – 2:

The construction took place in midtown Manhattan/New York. The soil profile consisted of 2 meter of clay-sand, 5 meter of clay, and 7 meters of sand-silt above bedrock. The drilled casings were 15 meters long and 50 cm in diameter. The planned structure was a 50-story residential building.

The drilling methodology used high-pressure air through the casing as the casing was drilled into the ground. In this method, the soil within the casing was removed by an air operated high frequency oscillating hammerhead inside the casing that was flush with the tip of the casing. The oscillating hammerhead was also used to drill the rock socket after the casing was sealed into bedrock. The diameter of the hammerhead was smaller than the interior diameter of the casing, such that there was sufficient gap between the two for some part of the soil to pass through. The soil that was hammered through was then blown out by high-pressure air at certain depth intervals along the interior and the exterior of the casing.

The soil disturbance created around the casing due to removal of the soil by pressurized air was observed not to be as high as the soil disturbance when water-polymer mix was used to remove the soil within the casing. However, unlike the pressurized water-polymer drilling method, the effect of the drilling procedure was also observed at locations further away from the casing due to the weakening of the soil through a process called “piping” that occurs when the high-pressure air finds a way within the ground to the surface of the ground.

Figure 11 shows the drill rig in the middle, an excavator in the background and a crane in the foreground (Note the air hoses attached at the back of the rig which are attached to the compressors not shown in the photograph). Figure 12 shows a rig in position to drill a casing. Figure 13 shows the hammerhead and figure 14 shows the hammerhead attached to a series of rods, which is inside the casing. Figure 15 shows the soil particles released internally from the casing by high-pressure air as the casing is drilled. The neighboring building were supported by piles bearing on bedrock, therefore the perimeter shafts were able to be drilled 25 cm away from the face of the wall.



Figure 11 – Air drilling set-up.



Figure 12 – Drill rig in place to drill a casing.



Figure 13 – Oscillating hammerhead.

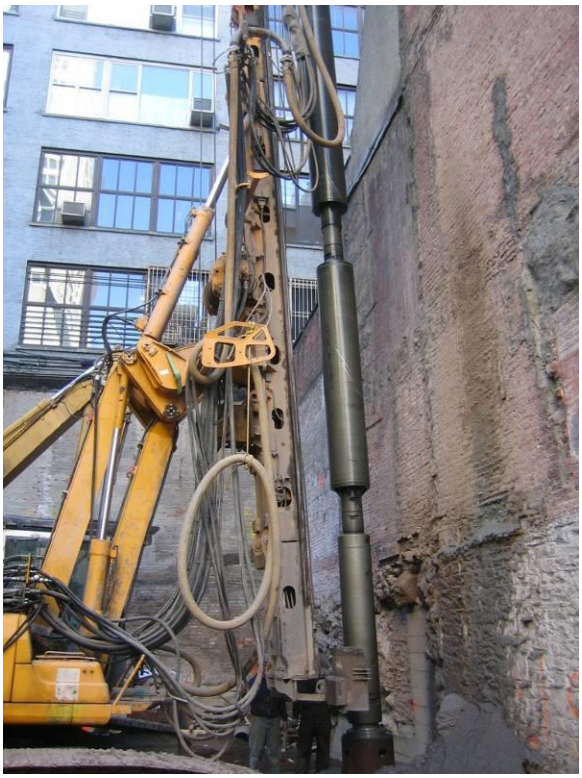


Figure 14 –Extension rods for the hammerhead that will be inserted within the casing.



Figure 15 –Soil that is hammered and then blown out.

Experimental study:

Tests were conducted on the foundation element of a bridge that was being constructed. (N., Gucunski, M., Balic, 2002). The name of the bridge is Doremus Avenue Bridge which is located in Newark, NJ. The bridge foundations are concrete drilled-shafts with steel casing that has the following properties:

Concrete
Class B
$f_c' = 20$ MPa
$E_c = 21{,}000$ MPa
$\rho = 2{,}400$ kg/m^3

Steel
$E_s = 200{,}000$ MPa
$\rho = 7{,}800$ kg/m^3

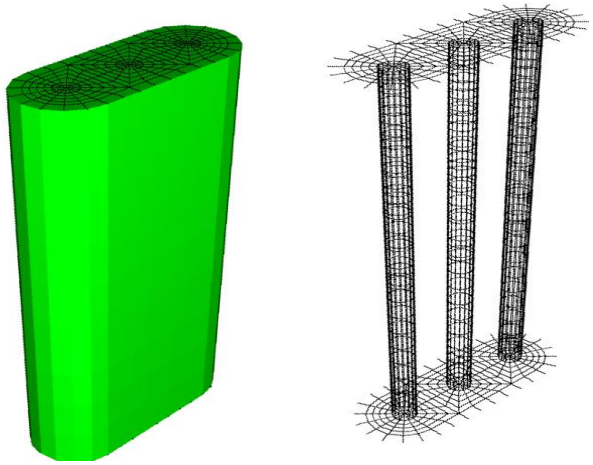
The shafts were 25 meters in depth and extended 3 meters into the bedrock. The concrete diameter was 1.196 meters with a 0.012-meter thick steel casing. The center-to-center spacing of the shafts was 3.75 meters. The soil was removed by augers and a kelly and the casing was advanced gradually through a diameter slightly larger than the casing.

Balic M. under the direction of Prof. Gucunski N. from Rutgers, the State University of New Jersey (2002) conducted on-site lateral load tests on the drilled shafts during the construction stage of the deep foundations, which involved the use of a shaker that applied sinusoidal loads at specified frequencies.

Soil-shaft interaction modifies shaft stiffness, which makes the shaft response dependent on the frequency of the loading. Shaft-soil system stiffness depends on the relative stiffness of the shaft and the soil, slenderness ratio of the shaft, shaft support condition and the variation of soil properties with the depth [9,10]. The stiffness of the SSI system is also affected by the

disturbance zone around the shaft, as well as the accumulated shaft-soil interface separations caused by repetitive loading in granular soils for soil depths that extend up to five times the shaft diameters below the ground level.

A detailed finite element model of the shaft group was created that analyzed the interaction of the foundation elements with the surrounding soil [1]. Figure 16 shows the three dimensional solid and wireframe views of the group shafts. The use of steel shell around the concrete has the effect of increasing the bending stiffness of the shafts as well as modifying the interface friction with the soil.



(a) Solid (b) Wireframe

Figure 16 - Solid and wireframe views of the Doremus group shaft.

Figure 17 shows the plan view of the model showing the concrete core and the steel shells around the concrete cores.

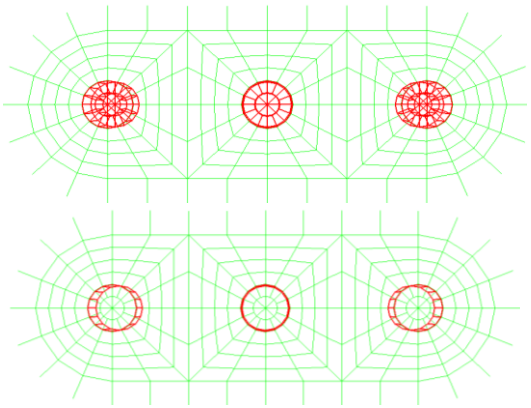


Figure 17- Plan view of the components of the shafts (a) Concrete cores, (b) Steel shells.

Figure 18 shows the soil profile and the stiffness parameters associated with the soil types along the profile. Table 1 is the soil stiffness parameters obtained by through shear wave testing. Shear wave velocity within a soil layer and the shear modulus of the soil layer are given in equation (2).

$$\text{shear wave velocity}: v_s = \sqrt{\frac{G}{\rho}} \qquad \text{shear modulus}: G = \frac{E}{2(1+\nu)} \tag{2}$$

G=Shear modulus
E=Elastic modulus
υ=Poisson's ratio
ρ=density

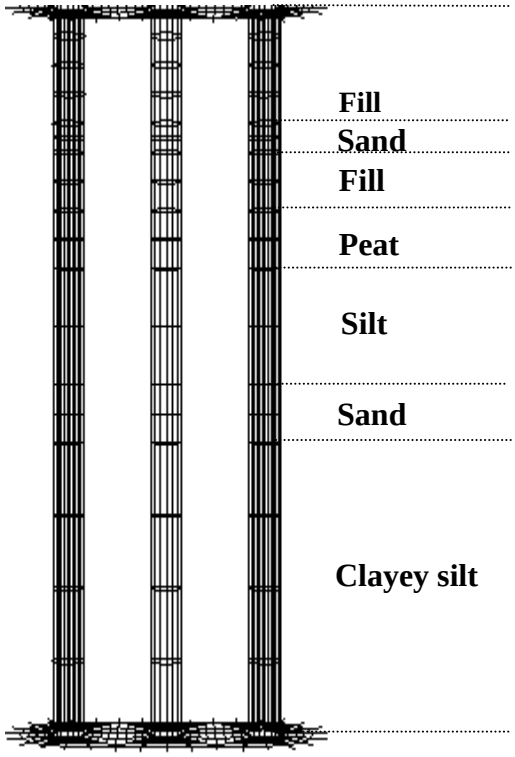


Figure 18 – Soil profile.

Table 1- Soil profile at Doremus group shaft location.

depth (m)	soil type	unit weight (kN/m^3)	density (kg/m^3)	friction angle (^{o})	velocity (m/sec)	S. Modulus (kN/m^2)	E. Modulus (kN/m^2)
0	fill	19	1937	32.5	139	37,421	93,552
4	sand	19.6	1998	35	267	142,433	356,082
5	fill	9	917	32.5	170	26,514	66,284
7	peat	11.8	1203	0	183	40,282	100,706
9	silt	18.9	1927	0	256	126,262	315,655
13	sand	19.6	1998	35	360	258,936	647,339
15	clay/silt	18.9	1927	0	320	197,284	493,211
25	bedrock						

The shafts were excited harmonically using an APS Model 400 electromagnetic shaker. The shaker was suspended on a frame and attached to the drilled shaft through a steel section

anchored into the shaft. The force on the shaker was controlled by a signal generator and amplifier, and measured using a load cell placed between the arm of the shaker and the steel section. The response of the loaded and adjacent shafts was measured using triaxial Mark Products L-4C-3D geophones, placed on the top of the shaft and along the shaft at depths of 4-ft, 9-ft, 14-ft and 20-ft. The test setup is shown in figure 19 that basically illustrates the components of the setup.

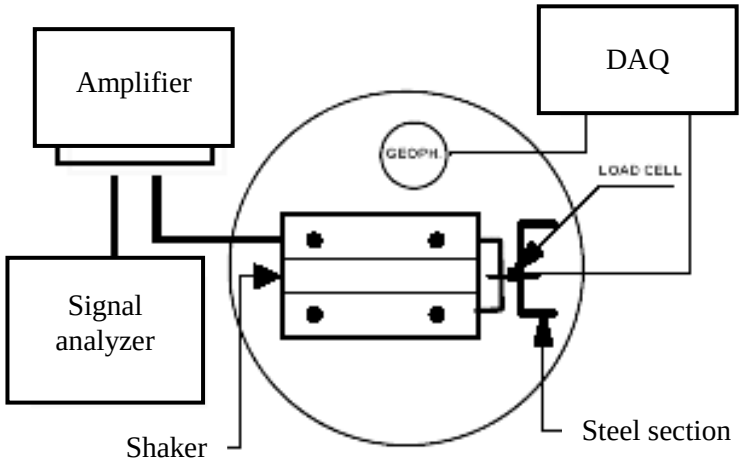


Figure 19 – Plan view of the experimental setup.

Figure 20 shows the forcing function applied by the shaker. The experimental results for 5 Hz and 8 Hz are investigated through analytical modeling. The displacements obtained through experimental testing and analytical modeling is shown in figure 21.

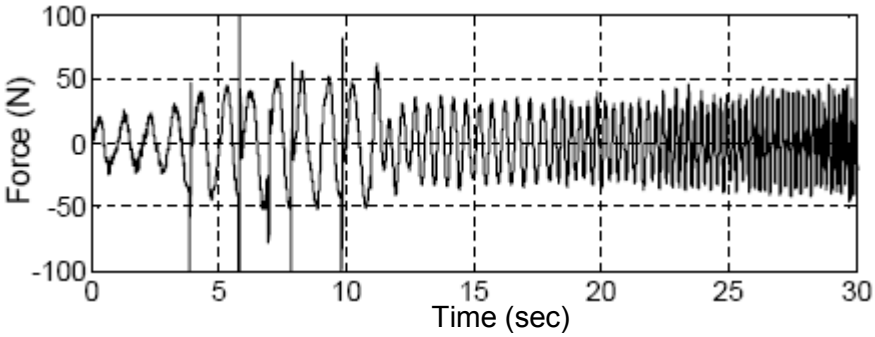


Figure 20 – Loads applied by the electromagnetic shaker.

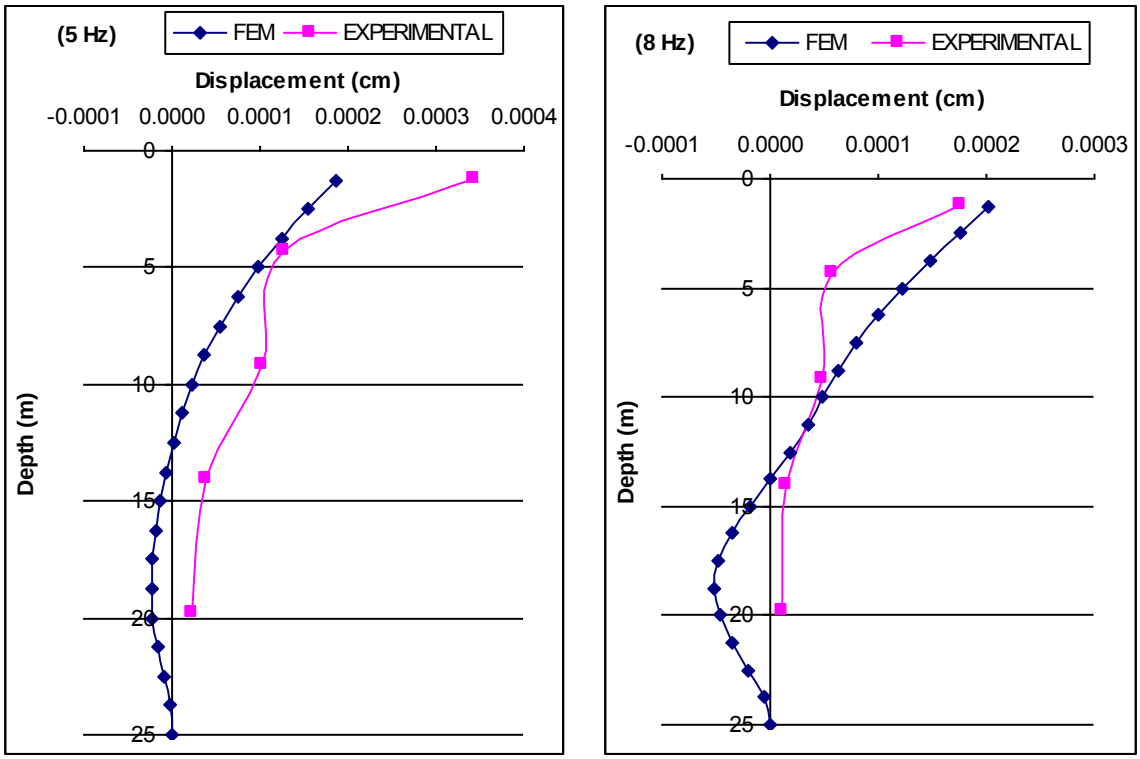


Figure 21- Comparison of the experimental and the analytical results for shafts with continuous soil support under 5 Hz and 8 Hz excitation frequencies.

The effect of soil support is visible in the analytical shaft response both in the magnitude of the displacements and the displaced shape of the shaft. However the experimental results do not show a clear effect of the lateral soil support other than the differences measured in displacement. The reasons could be that, since the loading value is low, the soil is not mobilized sufficiently to provide a lateral resistance and also, the soil support to the shaft extending a certain depth into ground may have been reduced or completely eliminated due to the drilling operation and therefore the shaft may have been exposed to lateral loading without any soil support.

Further investigation into the site conditions where the tests were conducted resulted in the findings and verbal confirmation that there were shaft-soil surface separations as well as random fillings along a depth that extended a certain distance below the ground surface that couldn't be quantified at the time of testing. Drilling of the steel casing that extends the full depth of the shaft may have caused a significant reduction in the soil strength in close proximity to the shaft, as well as widening the hole beyond the design diameter. The impact of such a process would be to significantly reduce or completely diminish the soil support to the shaft under lateral loadings.

The finite element model had to be modified to incorporate such effects that were believed to be the cause of the differences between the experimental and the analytical results presented in figure 21. However, between the time when this test was conducted and the model was developed the bridge was constructed and the physical means for any measurement of this detached zone around the shaft was not possible. Therefore an assumption had to be made regarding the extent of the depth of soil that was thought to have no contribution to lateral load capacity of the shaft. However, instead of changing the depth of this detached soil zone around the shaft to make the experimental and analytical numbers fit, the interaction between the shaft and the soil was

completely removed and the model was re-analyzed. The variation of the displacements with depth for the re-analyzed models with the soil support completely removed is shown in figure 22.

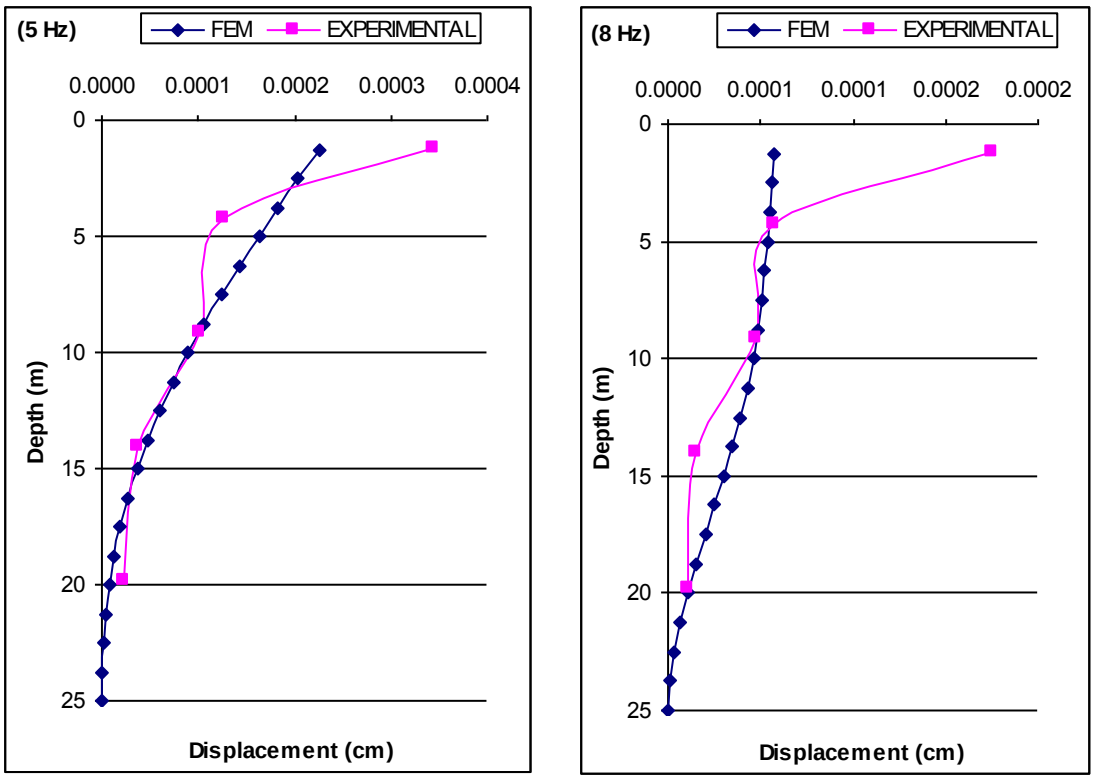


Figure 22 - Comparison of the experimental and the analytical results for shafts with the soil support completely removed for the analytical model under 5 Hz and 8 Hz excitation frequencies.

Figure 22 can be compared with figure 21, where the analytical lateral shaft responses are shown with continuous soil support along the shaft. The removal of soil support for the analysis shown in figure 22 resulted in analytical results in better correlation with experimental results. The analytical model has predicted the variation of the response of the shaft to cyclic loading similar to the experimentally obtained results. In the figures presented, due to the low natural frequency of the shaft, the lateral displacement for higher frequencies (8 Hz) is lower.

Analytical study:

Soil data obtained from undisturbed soil samples are frequently used in the design of foundation elements. However, installation procedures of the drilled deep foundations results in soil disturbance around the perimeter of the foundation element up to a certain depth that weakens or completely removes the soil support to the foundation element. The case studies previously presented indicate the weakening effect of drilling procedures on the soil structure interaction capacity of a drilled foundation element. In order to investigate the effect of drilling procedures on the post-installation properties of drilled shaft, a finite element model [1] was developed for a drilled shaft 30 meters long with 1.5 meter diameter that takes into account the radial weakening of soil properties up to a depth of five times the shaft diameter. The soil is non-

cohesive soil with linearly varying elastic modulus with depth with a coefficient of subgrade reaction of n_h= 13.55 N/cm^3. Figure 23 shows the finite element model for the drilled shaft and Figure 24 shows a qualitative cross-sectional view of a deep foundation element and extent of soil that is weakened due to drilling methods. Four weakened soil conditions have been analyzed due to drilling procedures were: Case 1: 15 cm weakened soil extension (L) with 10% of the elastic modulus value of undisturbed soil (E).
Case 2: 15 cm of L with 50% of E
Case 3: 25 cm of L with 10% of E
Case 4: 25 cm of L with 50% of E

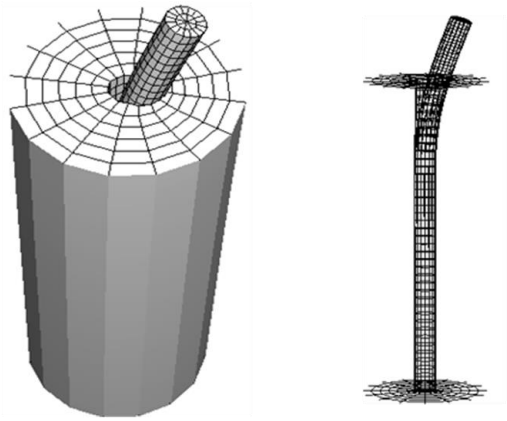


Figure 23- Finite element model of a laterally loaded drilled shaft.

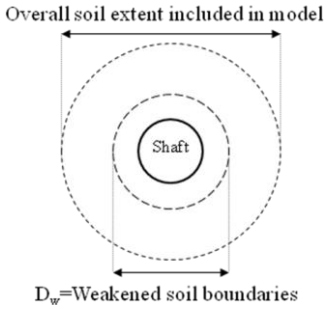


Figure 24- Weakened soil layers along the perimeter of the drilled shaft.

The weakened soil extensions of 15 cm and 25 cm are 10% and 17% of the shaft diameter respectively. Under the application of 222 kN lateral load, the variation of displacement and moment are shown in Figure 25 and Figure 26 for the weakened soil conditions. The percentage increase in displacement and moment for the four cases with respect to the "undisturbed" case are as follows:

Displacement: Case1: 53%, Case2: 8%, Case3: 71%, Case4: 11%.
Moment: Case1: 7%, Case2: 2%, Case3: 10%, Case4: 3%.

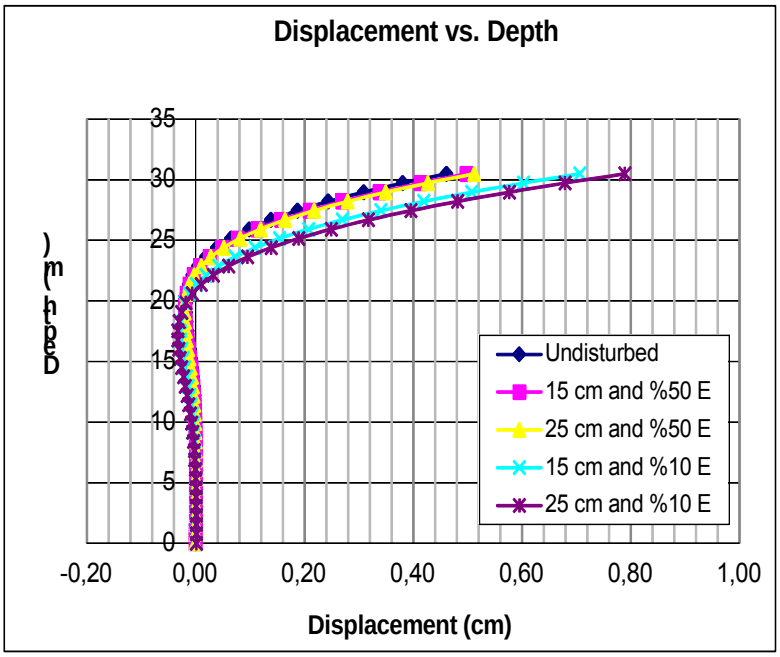


Figure 25- Variation of displacement with depth.

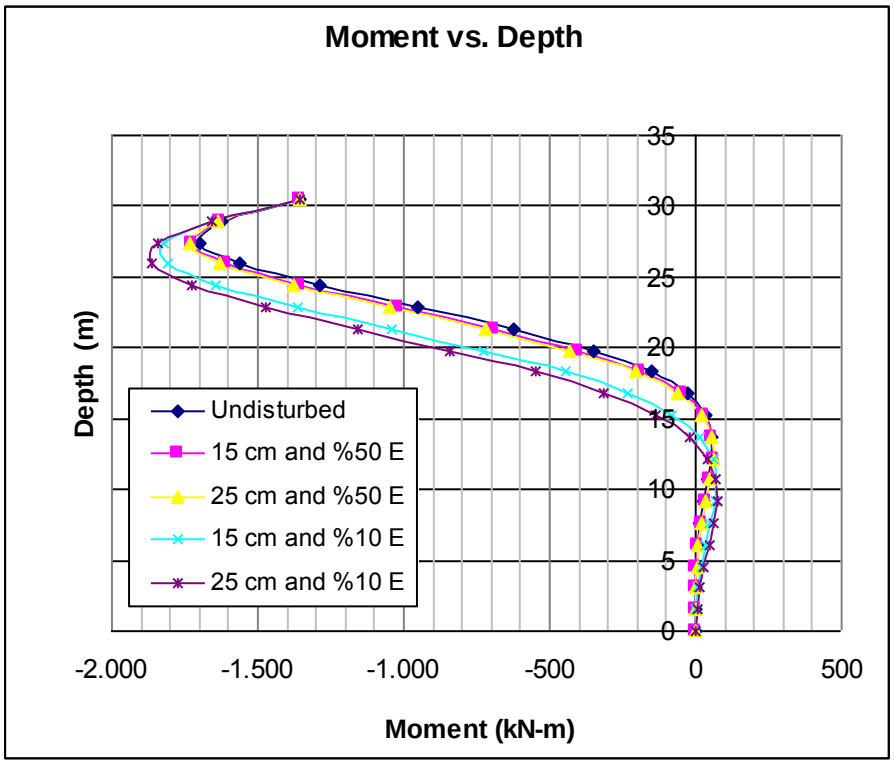


Figure 26- Variation of moment with depth.

Conclusion:

Soil-structure interaction of laterally loaded deep-foundations is an indeterminate problem. The type of soil, the type of foundation element and the construction methodology cause this indeterminacy. Reduction in the number of unknowns has to be made in order to render the problem solvable. However, the number of parameters that need to be incorporated into design and analysis that are thought to have an effect on the lateral response of a deep-foundation depends on the clear judgment of the engineer. The stiffness of the deep-foundation and the surrounding soil and the continuity of this stiffness around the deep-foundation are three variables that are commonly used to measure the lateral displacement along a deep-foundation element. The literature on the issue of response of deep foundation to lateral loads show that the soil layers close to the ground surface that extend 5-8 diameters along the depth of a deep-foundation element provide the effective soil support.

The two case studies presented in this paper involved 50 cm diameter shafts that were pressure drilled, during which the soil was continuously drilled and removed either by pressurized high viscosity water or by pressurized air. The case studies resulted in the finding that the granular soil support around a drilled-shaft was either weakened or completely removed along a depth up to 5 times the diameter of the drilled-shaft. Unlike the case studies, the experimental study involved the installation of a 120 cm shaft by drilling and removal of the soil in two separate mechanical processes and advancing the casing at discrete intervals. However, the analytical investigation of the experimental study also indicated the presence of a weakened soil zone around the shaft.

Pressure drilling is a single-continuous process that mechanically removes and transports the soil. During this process the penetrated soil in the vicinity of the shaft is highly disturbed. It is suggested that prior to design of a drilled-shaft, a "free-length" design concept is implemented and an allowance is made for weakened and gapped soil layers. The free length value will depend on the type of soil and the type of installation process. By the use of a free-length value, the soil support for the drilled-shaft design with respect to lateral loads should begin below a certain depth from the ground surface. For pressure drilled-shafts installed in what could be characterized as granular soil, the author of this paper uses 5 times the diameter of the drilled-shaft for the "free-length" value for shaft diameters up to 50 cm.

There are many other types of drilled-shafts that are outside the scope of this paper. Drilled-shafts with diameters as large as 250 cm are not uncommon. The installation of these shafts typically involves separate mechanical processes for the drilling and removal of the soil and the advancement of the casing at discrete time intervals. The disturbance of the soil due to drilling and the disturbance due to soil removal are mostly confined within the casing. Therefore the free-length for such large diameter shafts would be expected to be lower than 5 times the diameter. On the other hand, deep-foundations with such large diameters could have high rotational stiffness values such that the contribution of the soil stiffness to shaft-soil lateral response could be neglected. Under such circumstances, it would not matter whether any gaps have formed between the shaft surface and the soil interface.

The post-installation behavior of other types of drilled-shafts that require the casing to be removed after the placement of the concrete would be different than what has been discussed up to now, since the workable concrete within the steel shell would flow and penetrate into the porous spaces in the soil surrounding the casing generated by the drilling and removal of the soil within the casing. The effect of the seepage of the structural concrete penetration could result in

stiffer soil environment. The lateral load capacity could not only be enhanced due to this soil stiffness increase but also due to the soil-concrete interface interlocking that results in increased shear and friction.

For pressurized water-polymer drilling method, it was observed that the soil was completely transported through the exterior perimeter of the casing and for pressurized air drilling method the soil was observed to be transported both through the exterior perimeter and the interior of the casing. In the pressurized air-drilling method it was observed that as the depth of penetration of the casing into the ground was increased, the amount of soil that was transported through the casing interior also increased. The effect of the mechanical disturbance due to the transport of soil on the lateral load capacity of a drilled shaft depends on how the soil is transported after the soil is drilled. In pressure drilling methods, the adverse effect of this transport along the shaft-soil interface, to the lateral shaft support was observed.

The construction of a deep-foundation is not an isolated process and there is a difference between the "as-conceived" and the "as-built" foundation. Therefore an estimate has to be made regarding what this influence could be before the design of the deep-foundation is complete.

Acknowledgements:

I would like to thank Prof. Dr. Feyza Çinicioglu and Prof. Dr. Mustafa Karaşahin of Istanbul University, Civil Engineering Department, Prof. Dr. Husam Najm, Prof. Dr. Hani Nassif, Prof. Dr. Nenad Gucunski, Prof. Dr. Ali Maher of Rutgers, the State University of New Jersey, Civil Engineering Department and Prof. Dr. Magued Iskander of Polytechnic Institute of New York University, Civil Engineering Department.

I would also like to thank the **Turkish Precast Concrete Association** for supporting my contribution.

I would like to give my love and respects to my mother Nurhayat Bezgin, to my father Mustafa Bezgin and to my lovely wife Selin Üstün Bezgin.

REFERENCES

[1]. ABAQUS Standard/Explicit Manuals Versions 6.3 and 6.4.

[2]. Bowles, J. E. (1997), *Foundation Analysis and Design*, 5th Edition McGraw-Hill, New York

[3]. American Petroleum Institute (API), (1993), "*Recommended Practice for Planning and Designing, and Constructing Fixed Offshore Platforms*," *API Recommended Practice* 2A (RP2A), 20th Edition, Washington, D.C.

[4]. Bogard, D., and Matlock, H. (1983), "Procedures for Analysis of Laterally Pile Groups in Soft Clay,", *Proceedings of Specialty Conference of Geotechnical Engineering in Offshore Practice, ASCE* pp. 499-535.

[5]. Brinch Hansen, J. (1961), "The Ultimate Resistance of Piles Against Transversal Forces," *Bulletin No. 12 , Danish Geotechnical Institute*, Copenhagen, Denmark, 5-9.

[6]. Broms, B. B., (1964), "Lateral Resistance of Piles in Cohesive Soils,", *Journal of Soil Mechanics and Foundation Division,* Vol. 90, No. 2, pp. 27-64.

[7]. Budek, A., M., Priestly, M.J.N., and Benzoni, G.," Inelastic Seismic Response of Bridge Drilled-Shaft RC Piles/Columns,", Journal of Structural Engineering, ASCE, Vol. 126, No.4, April 2000, pp. 510-517.

[8]. Burdette, E., G., Pezeshk, S., Deatherage, H., and Goodpasture, D.," Comparisons of Static and Dynamic Lateral Stiffnesses of Driven Piles,", Journal of Bridge Engineering, ASCE, Vol. 6, No.2, Mar-April 2001, pp. 13.

[9]. Das, B., *Principles of Foundation Engineering*, 4th Edition, PWS Publishing 1999.

[10]. Kumar, Kort, D., Hosin A., and Chong, S. (2004) "Lateral Load Tests on Small Diameter Drilled Piers", EJGE, Vol. 9, Bundle C.

[11]. Matlock, H., and Reese, L.C., (1960), "Generalized Solutions for laterally Loaded Piles,", Journal of the Soil Mechanics and Foundations Division, ASCE, Vol.86, No SM5, Proc.Paper 2626, pp.63-91.

[12]. Matlock, Reese, (1960). Generalized Solutions for laterally Loaded Piles, Journal of the Soil Mechanics and Foundations Division, ASCE, Vol.86, No SM5, Proceedings Paper 2626, pp.63-91

[13]. Poulos, H. G., (1971a), " Behavior of Laterally Loaded Piles, Part I: Single Piles,", *ASCE Journal of Soil Mechanics and Foundation Division,* 97(SM5), pp. 711-731.

[14]. Prakash, S., and Sharma, H., *Pile Foundations in Engineering Practice,* John Wiley and Sons, Inc.1990.

[15]. Reese, L.C., and Matlock, H., (1956), "Non-Dimensional Solutions for Laterally Loaded Piles with Soil Modulus Assumed Proportional to Depth,", Proceedings, Eighth Texas Conference on Soil Mechanics and Foundation Engineering.

[16]. Reese, L.C., and Matlock, H., (1956). "Non-Dimensional Solutions for Laterally Loaded Piles with Soil Modulus Assumed Proportional to Depth", Proceedings, Eighth Texas Conference on Soil Mechanics and Foundation Engineering.

COMPDYN 2013
4th ECCOMAS Thematic Conference on
Computational Methods in Structural Dynamics and Earthquake Engineering
M. Papadrakakis, N.D. Lagaros, V. Plevris (eds.)
Kos Island, Greece, 12–14 June 2013

THREE-DIMENSIONAL FINITE ELEMENT MODELLING OF DYNAMIC PILE–SOIL–PILE INTERACTION IN TIME DOMAIN

G. Kouroussis[1], I. Anastasopoulos[2], G. Gazetas[2] and O. Verlinden[1]

[1] University of Mons (UMONS), Faculty of Engineering, Department of Theoretical Mechanics, Dynamics and Vibrations
Place du Parc 20, 7000 Mons (BELGIUM)
georges.kouroussis@umons.ac.be

[2] National Technical University of Athens (NTUA), School of Civil Engineering, Laboratory of Soil Mechanics
Iroon Polytechneiou 9, 15780 Athens (GREECE)
e-mail: ianast@civil.ntua.gr

Keywords: 3-D Piles analysis, Pile group response, Soil–pile interaction, Finite element analysis, Seismic waves.

Abstract. *Dynamic analysis of embedded foundations like pile groups have received considerable attention in the past. Most existing approaches are established in the frequency domain, not allowing the simulation of material and geometric nonlinearities. In this paper, transient analyses are conducted to calculate the impedance of piles and pile groups, using a full three-dimensional numerical model for both the soil and the structure. Based on a combined viscous boundary and infinite elements, defining an efficient non-reflecting boundary, a finite element model is developed. Modelling guidelines, in terms of domain and element size, are presented and appear to be less severe in time domain than in frequency analysis. The proposed three-dimensional model can be processed with no excessive computational resources. Besides boundary efficiency, wave propagation effects are studied through dispersion diagrams in the case of homogeneous and layered soil. In particular, dissipative conditions are described, with the emphasis on the proper representation of wave propagation. These analyses thoroughly validate the proposed modelling approach for transient excitations. Viscoelastic model of soils are therefore developed including piles group considered as concrete material. A decay function is chosen for the excitation defined in the time domain, allowing a large covering of the input force spectral content. The implementation and validation of the numerical model for predicting the dynamic stiffness and damping of pile groups are presented. Vertical and lateral pile and pile group impedance examples are given and compared to a published analytical model. The proposed analysis methodology provides a convincing example of the capability of the finite element method to reproduce foundation response to dynamic loading.*

1 INTRODUCTION

With the growing development of society, the construction of buildings is increasingly affected by the soil constitution and becomes problematic in some circumstances (soft soil, lack of space, large design loads, ...). Significant research has been reported on the static and dynamic analysis of deep foundations, and especially the pile groups, in order to master the soil–structure interaction and to propose pile designs adapted to the soil configuration. Foundations relying on driven piles often have groups of piles connected by a pile cap (a large concrete block into which the heads of the piles are embedded) to distribute loads which are larger than one pile can bear.

Dynamic analysis of piles and pile groups interaction with soils has received considerable attention in the past. The main difficulty is to represent a large structure with finite dimensions coupled to a medium considered as infinite. The challenge is not only to define the accurate interaction properties in the pile–soil contact surface but also the transmission of static and dynamic loads from the concrete structures and the ground wave propagation generated by their kinematics. The dynamic pile–soil interaction can be typically associated with a problem of ground wave propagation. Several procedures to model soils used in the various soil dynamics fields (traffic ground vibration, blasting, earthquake studies) can be applied to the pile–soil–pile systems. Most of the existing approaches contribute to the understanding of ground vibration behaviour and provide interesting findings. Nevertheless, dynamic soil–structure interaction is difficult to take into account for complex structure geometries, advanced mechanical behaviour models and realistic soil configurations. The objective is to define an approach which represents the structure in a rigorous manner, while still using a reasonable number of degrees of freedom.

Soil dynamics analysis is often defined as a problem where the region of interest is small compared to the surrounding medium, which is considered as unbounded. The first modelling approaches were based on Winkler's formulation largely used in many geotechnical applications due to its implementation simplicity. Gazetas [1] provided a detailed description of these models for soil–foundation interaction problems. The main difficulty is obviously the identification of model parameters, often obtained by fitting results from numerical or experimental studies. In the case of pile–soil–pile configurations, this formulation is not able to purely represent the associated interaction but it is possible to make a reasonable assessment of the dynamic stiffness, as these proposed by Dai and Roesset [2] with approximate expressions for horizontal loading in pile groups or by Gazetas et al. [3] for their beam–on–dynamic–Winkler–foundation model.

Because of the rapid progress of computers, the numerical models abound in literature today and are considered as one of the most attractive tools for the soil–structure interaction problems. The finite element method (FEM) is efficient in dealing with complex geometries and numerous heterogeneities but it requires special local boundaries in order to mimic the geometrical radiation to infinity. Numerical models of soils have received particular attention in recent times with important contributions to the modelling of the radiation conditions. Lou et al. [4] mentioned in their review the many possible ways to define efficient radiation conditions for application in FEM. Boundary element methods (BEMs) have proved their efficiency to solve the problem with infinite dimensions but they are limited to weak heterogeneities and simple constitutive laws, and require extra mathematical developments. For example, Batista de Paiva and Trondi [5] used a BEM formulation for solving capped and uncapped pile groups, representing each pile by a polynomial function. The combination of the two methods, well known as FEM/BEM approach [6–8], allows an accurate description of the near field (FEM model) and

a reliable estimation of the far-field (BEM model). Researchers have also proposed the use of finite difference method (FDM) [9], the infinitesimal finite element cell method (CIFECM) [10] or the finite layer theory [11].

The dynamic behaviour of the piles strongly depends on the characteristics of the pile itself but also on the soil characteristics (rigidity, half-space, layered medium, material damping, ...). The use of the numerical soil modelling initially developed by Kouroussis et al. [12, 13] for railway–induced ground vibrations could be an interesting example of the capacity of the FEM to reproduce the response of foundations to dynamic loads. This paper presents the implementation and the validation of a similar model for predicting the dynamic stiffness and the damping of piles groups. The purpose of this study is to compare the numerical results with those obtained by a published simple analytical method. After a brief review of this method, an overview of the existing boundaries conditions associated to the FEM is presented, also mentioning the associated mesh rules in frequency and in time domain. The dispersion properties are checked for typical homogeneous and layered soil examples. Numerical impedances are afterwards introduced, with the corresponding findings.

2 REVIEW OF THE SIMPLE ANALYTICAL MODEL

In 1988, Dobry and Gazetas [14] presented an original simple method for predicting the dynamic impedance of pile groups. This method requires as input the related dynamic impedance of a single pile (which can be easily found in the literature) and three soil parameters: the shear waves velocity c_S, the Poisson's ratio ν and the hysteretic damping η. The geometrical dimensions (spacing S, length L, and radius r_0) are shown in Figure 1.

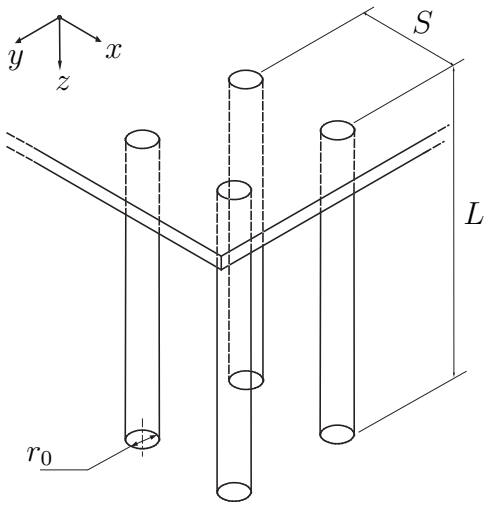


Figure 1: Typical dimensions of a pile group

The studied problem has as assumption that the single pile impedance is known, by any of several available numerical methods or from experimental tests. The impedance of the pile group is defined as the ratio between force F^G and displacement w^G at the head of the pile group (the cap is assumed to be massless and rigid):

$$K_a^G = F^G / w^G = k_a^G + j a_0 c_a^G \,, \tag{1}$$

the terms k_a^G and c_a^G being interpreted as equivalent spring and dashpot coefficients at the head of the pile group ($a = v$ or h for vertical and horizontal motions respectively). The proposed

method defines interaction factors

$$\alpha_a(\omega) = \frac{w_{qp}}{w_{qq}} = \frac{\text{additional displacement of pile } q \text{ caused by pile } p}{\text{additional displacement of pile } q \text{ under own dynamic load}} \tag{2}$$

and expresses for each motion type as a function of the circular frequency ω [14]:

$$\alpha_v(\omega, S) = \sqrt{\frac{r_0}{S}}\, e^{-\eta\omega S/c_S}\, e^{-j\omega S/c_S} \tag{3}$$

$$\alpha_h(\theta, \omega, S) = \sqrt{\frac{r_0}{S}}\, e^{-\eta\omega S/c_{La}}\, e^{-j\omega S/c_{La}} \cos^2\theta + \alpha_v(\omega, S)\sin^2\theta\,. \tag{4}$$

As seen, the horizontal motion depends on the angle θ between the line of the two piles and the direction of the applied force. The velocity c_{La} is the so-called Lysmer analogue velocity, equal to $3.4c_S/(\pi(1-\nu))$. The motion of each group is calculated by accounting for all possible interactions between piles. Table 1 summarizes the various applications developed by the authors, assuming the knowledge of the single pile impedance K_a^S.

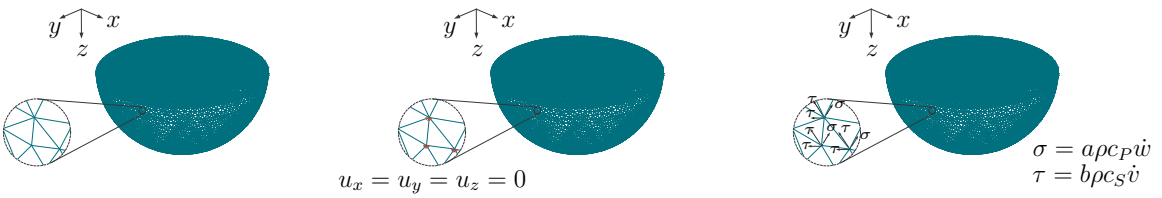
Pile group	axial impedance K_v^G	horizontal impedance K_h^G
1×2 piles	$\frac{2K_v^S}{1+\alpha_v(S)}$	
2×2 pile group	$\frac{4K_v^S}{1+2\alpha_v(S)+\alpha_v(\sqrt{2}S)}$	$\frac{4K_h^S}{1+\alpha_v(S)+0.5\alpha_v(\sqrt{2}S)+\alpha_h(0^o,S)+0.5\alpha_h(0^o,\sqrt{2}S)}$

Table 1: Examples of dynamic stiffness functions of various pile groups

3 FINITE ELEMENT MODELLING

3.1 Modelling seismic wave propagation

Soil dynamics analysis is often defined as a problem where the region of interest is small compared to the surrounding medium, which is considered unbounded. Compared to the BEM, the FEM presents an interesting alternative only if absorbing boundary conditions to avoid spurious reflections are well defined. These conditions are known as transmitting boundaries, which are sub-categorised by Wang et al. [15] as elementary boundaries (Figures 2(a) and 2(b)), local boundaries (Figure 2(c)) or consistent boundaries (typically the infinite elements). The goal is to obtain an accurate description of the near field, including eventual complex geometries or nonlinear behaviours, and an accurate radiation condition estimating the far field.



(a) Free boundary conditions (b) Fixed boundary conditions (c) Viscous boundary conditions

Figure 2: Classical boundary conditions

3.2 On the use of combined viscous boundary and infinite elements

Many local boundary formulations exist but the viscous boundary proposed by Lysmer and Kuhlemeyer [16, 17] is the most commonly used in this case, consisting of dashpots attached to the boundaries. The authors have investigated different possibilities for expressing an efficient boundary condition analytically and have found that the most promising way is to express it by the conditions

$$\sigma = a\rho c_P \dot{w} \tag{5}$$

$$\tau = b\rho c_S \dot{v} \tag{6}$$

where σ and τ are respectively normal and shear stresses, depending on the normal and tangent velocities $\dot{w}$ and $\dot{v}$ of the boundary (Figure 3). Parameters a and b are dimensionless and can both vary from 0 (defining in this way a free boundary) to ∞ (rigid boundary). In accordance with [16, 17], a and b are chosen equal to 1; these values give maximum absorption, in the case of body wave reflections. Physically, Eq. (5) and (6) define a border supported on infinitesimal dashpots with normal and tangential orientations with respect to the boundary. The study of Rayleigh waves is more complex. Lysmer and Kuhlemeyer showed that, in the case of steady–state problems, the damping, constant for body waves, depends on the depth of the soil for Rayleigh waves.

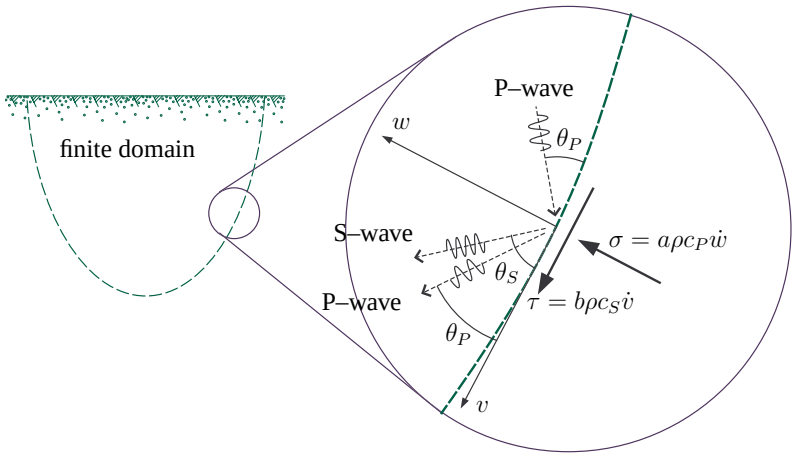


Figure 3: Reflection on the viscous boundary

In this study, an infinite/finite element model is used under the ABAQUS software, with a mix of local and consistent boundaries. Since the software does not present a procedure to implement this boundary condition through its mesh library, an individual MatLab script has been developed to edit the ABAQUS input file. A spherical geometry form is chosen allowing a convex shape at the border, for easy meshing and to guarantee the condition of non-crossing infinite elements (in order to avoid non-unique mappings). Figure 4 shows a typical model based on the aforementioned conditions.

3.3 Meshing rules

Classical rules exist [18], concerning the element size T_e and the domain dimension T_d: a minimum of 10 elements per Rayleigh wavelength λ_R and a domain size T_d greater than at least $3\lambda_R$. The number N_e of elements depends therefore on these two parameters. In soil dynamic

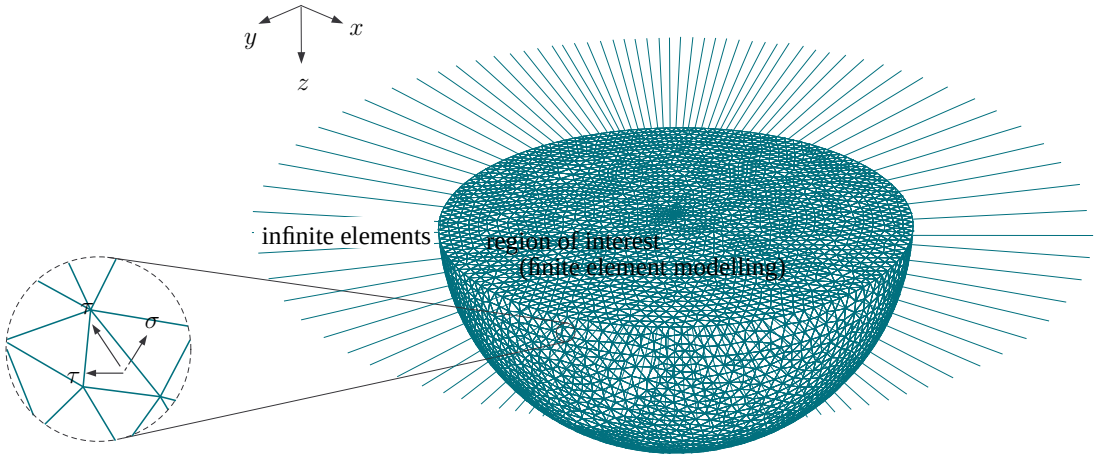


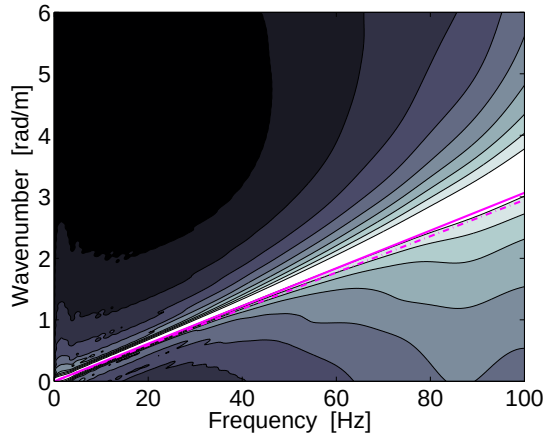
Figure 4: Combined viscous boundary conditions / infinite elements

analysis, the frequency range reaches up to $100\,\mathrm{Hz}$, implying an excessive number of elements (more than 10^9 for a three-dimensional analysis). The well-known condition about element size is critical and must be kept. To make the FEM model practicable on usual computers, it is necessary to reduce the domain dimension. Recently, Kouroussis et al. [12] have shown that the time domain simulation gives the possibility to work with a reduced domain dimension. The influence of the domain dimension was investigated, considering a mesh adapted to the problem yet without loss of accuracy nor excessive number of elements.

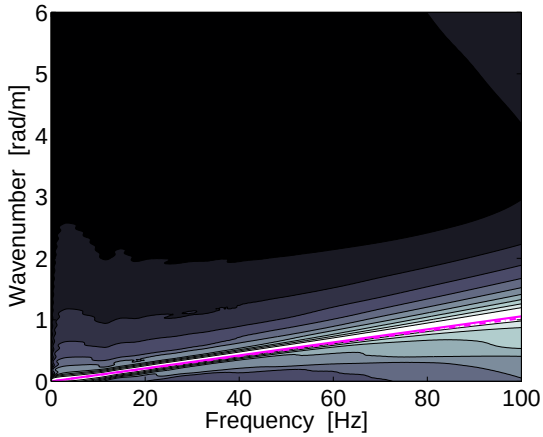
4 ANALYSIS OF DISPERSION CHARACTERISTICS

In [13], a detailed validation of a finite element model working in the time domain was performed through the physical modelling of the generation and propagation of ground vibration. The obtained results were compared to elementary boundary conditions for various domain sizes. It turned out that the residual reflected wave energy is less than 5% in all domain dimension cases. Additional results are presented in this section and, complementing this previous study, additional results from checking the wave types are presented in this section.

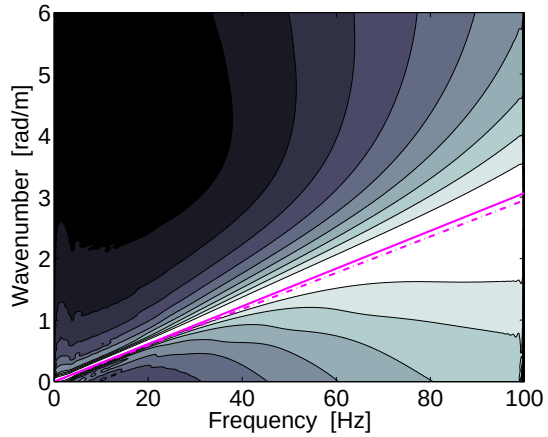
The dispersion diagram is a useful tool to analyse the propagating modes of the ground as a function of frequency. If the wavenumber k for each mode is plotted as a function of frequency, the dispersion curve for the wave type is generated. Such a curve is generally identified by analytical methods [19] but an alternative method is to calculate the Fourier transformed displacements generated by a load for different frequencies and wavenumbers. With a transient force adjusted so as to realistically represent an impulse load, the ground surface is excited by a uniform magnitude in a large frequency range. Figure 5 presents dispersion diagrams for four examples of soil configuration where the shear velocity c_S and the viscous damping parameter β vary. The response at each frequency is normalized to the maximum value at that frequency, as proposed by Triepaischajonsak et al. [20], allowing an easy identification of the associated wavenumbers. The maximum indicates the modal wave numbers that are vertically excited and follows straight lines (from the origin to the point on its dispersion curve at that frequency) corresponding to the inverse of wave speed. For each case, expected results are found in the frequency range $[0 - 100\,\mathrm{Hz}]$. Figures 5(a) to 5(c) show the waves modes for homogeneous soil configuration. Only a single propagating mode exists with a wave speed close to that of the Rayleigh waves. The effect of soil rigidity and damping is also depicted. Figure 5(d) presents the results for the layered soil configuration. It can be seen that the high frequency



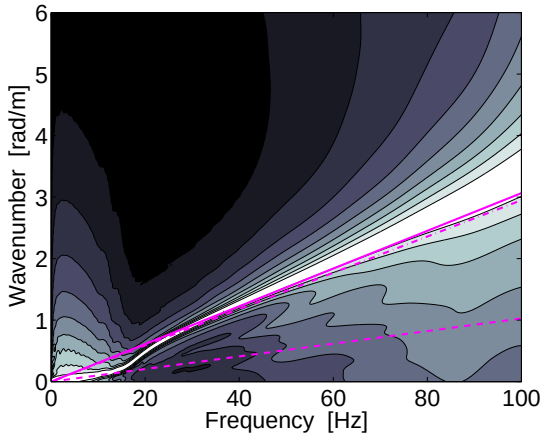
(a) Homogeneous soil configuration — $c_S = 213\,\mathrm{m/s}$; $\beta = 0.0004\,\mathrm{s}$



(b) Homogeneous soil configuration — $c_S = 612\,\mathrm{m/s}$; $\beta = 0.0004\,\mathrm{s}$



(c) Homogeneous soil configuration — $c_S = 213\,\mathrm{m/s}$; $\beta = 0.001\,\mathrm{s}$



(d) Layered soil configuration — $c_{S_1} = 213\,\mathrm{m/s}$; $c_{S_2} = 612\,\mathrm{m/s}$; $\beta = 0.0004\,\mathrm{s}$; $d = 5\,\mathrm{m}$

Figure 5: Dispersion diagrams (light=high amplitude; solid line: Rayleigh wave speed of upper layer, dash-dot line: shear wave speed of upper layer, dashed line: shear wave speed of the substratum)

content follows the characteristics of the upper layer while the low frequencies are associated to the substratum. The passage between the two reference lines corresponds to the oscillation frequency of the soil surface, characterized by [21]

$$f_{layer} = \frac{c_P}{4d} \tag{7}$$

where c_P is the compression wave velocity of the first layer of depth d. This frequency is equal to $20\,\mathrm{Hz}$ for the example proposed in Figure 5(d).

These results confirm the potentiality of the FEM model in time domain to capture the modal phenomena of soils. It can be applied to the characterisation of the pile–soil dynamic impedance.

5 APPLICATION TO THE SOIL–PILE INTERACTION

The numerical determination of dynamic impedance has rarely been performed with a 3D FEM model, due to the difficulty of modelling simultaneously the infinite conditions of soil

and the three-dimensional nature of the problem. With the developed approach (time domain simulation), the numerical model can be easily built.

We consider the following dimensions for the pile :

$$2r_0 = 1\,\mathrm{m} \;\; ; \quad L = 15\,\mathrm{m}$$

and the spacing is $S = 10\,\mathrm{m}$ for a 2×2 group. The single pile is also modelled separately, to obtain its dynamic impedance (note that the results of Dobry and Gazetas are in dimensionless form, where the group impedance is normalized by the sum of the static stiffnesses of the individual single piles).

Table 2 gives the dynamic parameters of the soil and piles (considered as concrete material). The ratio E_s/E_p is equal to 1000. Subscripts p and s denote the pile and the soil, respectively.

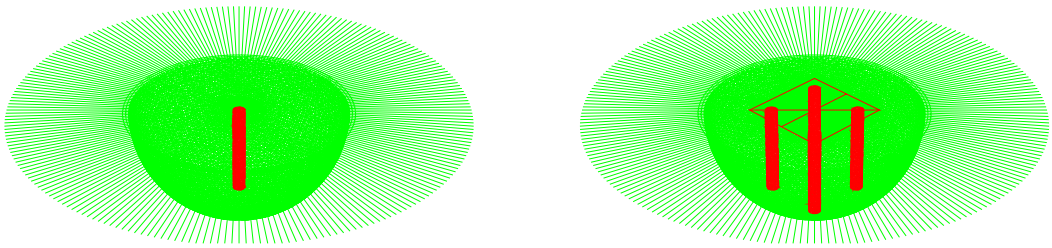
	Soil (subscript s)	Pile (subscript p) — concrete material
Young's modulus E	$30\,\mathrm{MN/m}$	$30\,\mathrm{GN/m}$
Poisson's ratio ν	0.30	0.20
Density ρ	$2000\,\mathrm{kg/m^3}$	$2500\,\mathrm{kg/m^3}$
Viscous damping β	$0.0004\,\mathrm{s}$	*no damping*

Table 2: Soil and pile dynamic parameters

Figure 6 displays the model established for the simulation, considering a single pile and a 2×2 pile group configuration. A half-sphere containing the piles is used to model the soil. Tie constraints are imposed at the surface contact between soil and pile parts to assemble them. In this way, the FEM model of the soil subsystem consists of $200{,}000$ and $550{,}000$ finite/infinite elements, for the single and 2×2 pile configurations, respectively (that is $215{,}000\,dof$ for a single pile problem and $410{,}000\,dof$ for a 2×2 pile group, a pile needing around $15{,}000$ elements). The area around the piles, where the forces are applied, is finely described. The analysis is performed in the time domain, considering the following decay function for the excitation:

$$f_{\mathrm{excitation}}(t) = \begin{cases} 0 & \text{if } \; t < t_0 \\ A\, e^{[-(t-t_0)/t_d]} & \text{if } \; t \geq t_0 \end{cases} \tag{8}$$

with $A = 1\,\mathrm{N}$, $t_0 = 0.05\,\mathrm{s}$ and $t_d = 0.001\,\mathrm{s}$.



(a) Single pile configuration (b) 2×2 pile group configuration

Figure 6: Modelling of piles under ABAQUS

5.1 Vertical response

The first analysed results are related to the vibrations of the pile–soil system at various instants after the load described by Eq. (8) is applied vertically on the pile cap. With our approach, the dimension of the soil (i.e. the radius of the half-sphere) is reduced to $20\,\mathrm{m}$.

Figure 7 gives the time history of the vertical displacement of the cap, for the two studied cases. It clearly and naturally appears that the maximum value is divided by nearly four in the 2×2 pile group, compared with the single pile group maximum. The curve shape is moreover different, with additional oscillations after the first maximum. They are stemming from the pile–to–pile interaction induced by low–frequency waves, which are enable by the large inter–pile spacing of $S/r_0 = 20$. For this spacing, the pile group cannot be considered as an isolated embedded foundation.

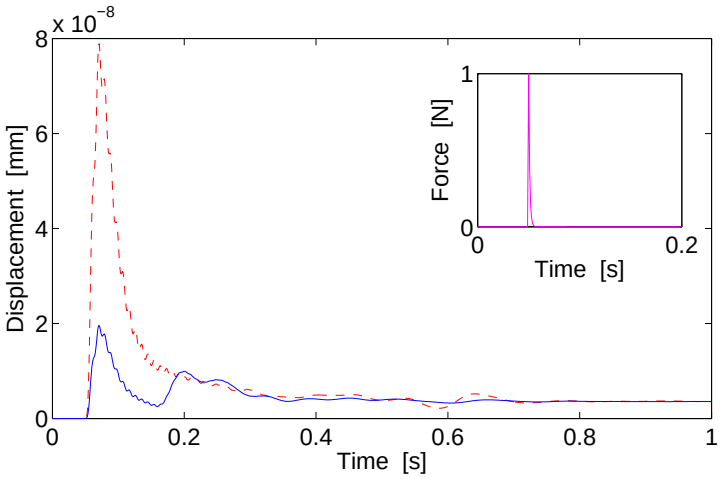


Figure 7: Time history of the vertical displacements obtained with ABAQUS (dash line: single pile; solid line: 2×2 pile group)

5.2 Horizontal response

In the same way, we analyse the horizontal vibrations. Specific boundary conditions are imposed to the cap to allow only the horizontal motion along the x–direction. It is worth mentioning that the horizontal and rocking degrees of freedom of a pile are coupled. For the free field, we impose only the horizontal motion (rocking motion is locked).

Figure 8 displays the time history of the horizontal displacement of the cap, for the two studied cases. As previously, the same observation can be made with the decrease of the maximum amplitude: the maximum value of the single pile group is divided by approximately four in the 2×2 pile group. Some comments can be made regarding the shape of the curve. Although in the preceding results (for the vertical motion), the two curves reach up to the same value after $t = 0.2\,\mathrm{s}$, the curves have more deviations from each other. The next section presents the results in the frequency domain for a deeper understanding of the problem.

5.3 Comparison with a simple analytical model

The analytical method proposed by Dobry and Gazetas needs damping in the form of the hysteretic parameter η. Unfortunately, the time domain simulation performed for our numerical model limits the intrinsic damping to the Rayleigh type, usually defined as a combination of the

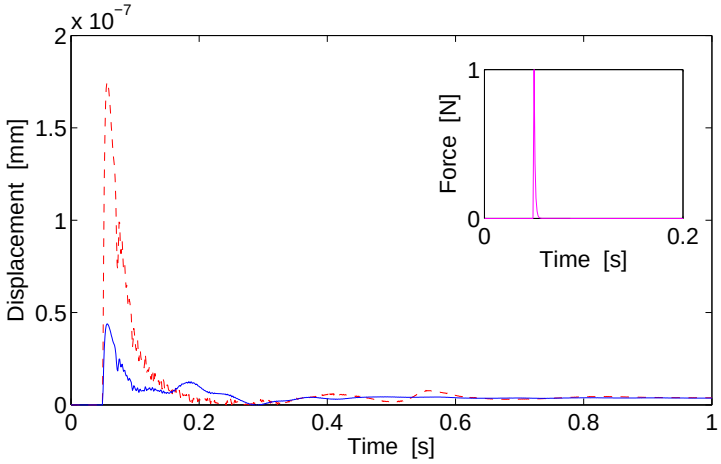


Figure 8: Time history of the horizontal displacements obtained with ABAQUS (dash line: single pile; solid line: 2×2 pile group)

mass $\mathbf{M}$ and stiffness $\mathbf{K}$ matrices of the system

$$[\mathbf{C}] = \alpha\,[\mathbf{M}] + \beta\,[\mathbf{K}]\ . \tag{9}$$

In this formulation, coefficients α and β are usually chosen so as to match the damping ratio at two specific frequencies. Viscous Kelvin–Voigt damping β can be used in the two methods since $\eta = \beta\omega$ in the frequency domain (α is therefore equal to 0). To compare the results in the frequency domain, a discrete Fourier transform is applied on the time history of pile responses.

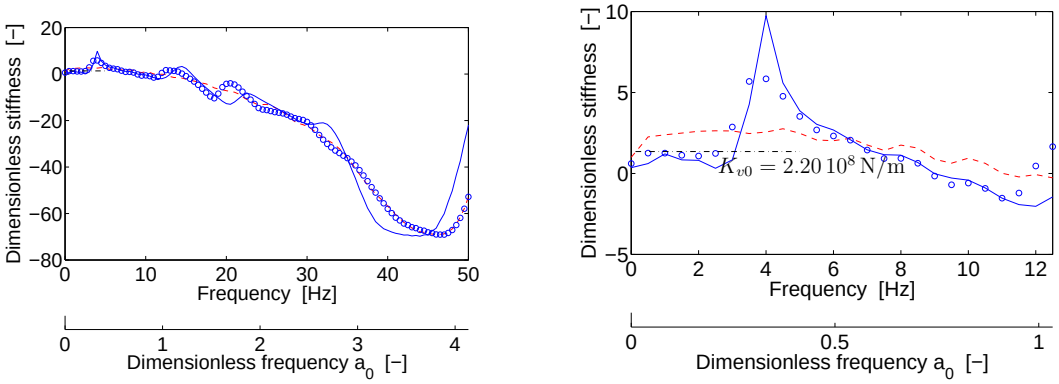
The dynamic stiffnesses are decomposed in the standard manner as described in Eq. (1). Dynamic stiffness and dashpot group factors are defined as the ratio of the spring k_a and damping coefficient c_a to the sum of the static stiffnesses K_{a0}^S of the individual single piles. These curve are plotted in function of the frequency parameter

$$a_0 = \frac{\omega L}{c_S} \tag{10}$$

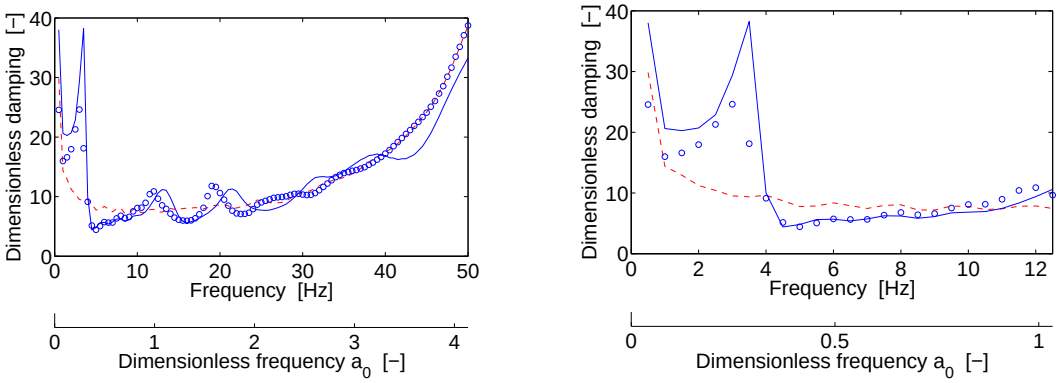
for the vertical and horizontal motions, in Figures 9 and 10. Single pile and 2×2 pile group are analysed. To make the deviation more visible, the curves are replotted enlarged in the low frequencies (up to $a_0 = 1$). The solutions of Dobry and Gazetas, denoted analytical solutions, are also on the same figures, considering viscous damping. Good agreement is obtained between simple analytical model results and the numerical values for the 2×2 pile group. Several comments can be highlighted from the results of these figures:

- The sum of the static stiffnesses of the individual piles is larger than the static stiffness of the pile group. The magnitude of the dynamic stiffness of the pile group for a specific frequency can be smaller or larger than that of the sum of the contributions of the individual piles. For dynamic loads, pile–soil–pile interaction is caused by the waves emitted from each pile and propagating to the neighbouring piles with resulting refractions and reflections. The pile group dynamics is strongly frequency dependent.

- The comparison with analytical results is not straightforward, because the viscous damping β intervenes only in the imaginary part although the whole dynamic stiffness K_a is multiplied by $1 + 2j\eta$ in the case of hysteretic damping.



(a) Real part (b) Real part (zoom in)



(c) Imaginary part (d) Imaginary part (zoom in)

Figure 9: Vertical dynamic stiffness and damping group factors as a function of frequency (∘: analytical solution; dash line: single pile; solid line: 2×2 pile group)

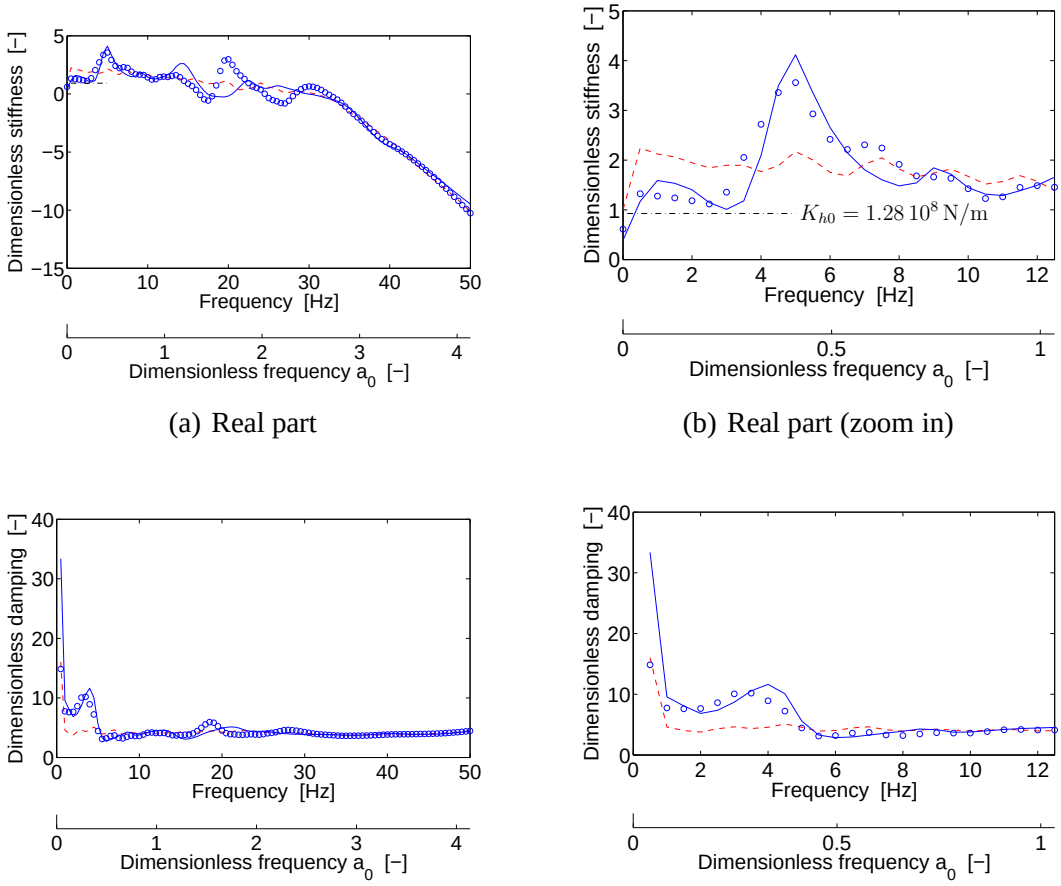
- For the 2×2 pile group, the analytical solution uses the numerical one pile results. The agreement with this approximative solution is good. To make the deviations more visible, real and imaginary parts are plotted in the frequency range $[0 - 12\,\mathrm{Hz}]$, which represents the realistic range of the pile study.

Despite the fact that a reference result for the single pile motion is not available, it is possible to make a reasonable assessment of the static value. The static stiffnesses of a pile in a homogeneous halfspace is given by [22]:

$$K_{v0} = 3.8 r_0 E_s \left(\frac{L}{4r_0}\right)^{0.67} \tag{11}$$

$$K_{h0} = 2 r_0 E_s \left(\frac{E_p}{E_s}\right)^{0.21} \tag{12}$$

for the vertical and horizontal motion, respectively. The cone model allows obtaining results for the vertical motion in $17.5 E_s r_0$ and for the horizontal motion in $7.4 E_s r_0$. Figures 9(b) and 10(b) display these static values, showing a good correspondence with the numerical results, both for the vertical value and the horizontal one.



(a) Real part

(b) Real part (zoom in)

(c) Imaginary part

(d) Imaginary part (zoom in)

Figure 10: Horizontal dynamic stiffness and damping group factors as a function of frequency (○: analytical solution; dash line: single pile; solid line: 2×2 pile group)

6 CONCLUSIONS

In the past, to analyse the dynamic behaviour of a group of vertical piles with their heads connected by a rigid cap, the interaction of the individual piles via the soil was taken into consideration with the help of analytical solutions. BEM has also been used but to a limited extent due to the complex geometry. With the developed FEM in time domain simulation, a new kind of solution can be easily computed, as proposed in this paper. The wave propagation is underlined in the results, showing the performance of the non-reflecting boundary (viscous boundary and infinite elements) attenuating the reflected waves to the maximum.

The limitation imposed by the time domain is not restrictive since the obtained results from a Fourier transform of an “impulse” response are very satisfactory and encouraging, through the validation of dispersive characteristics. Interesting results are obtained and it all leads to believe that advanced analyses could be performed with the proposed FEM approach, as well in pile dynamics as well as in other applications in geotechnics.

REFERENCES

[1] G. Gazetas. Analysis of machine foundation vibrations: state of the art. *Soil Dynamics and Earthquake Engineering*, 2(1):2–42, 1983.

[2] W. Dai and J. M. Roesset. Horizontal dynamic stiffness of pile groups: Approximate expressions. *Soil Dynamics and Earthquake Engineering*, 30(9):844–850, 2010.

[3] G. Gazetas, K. Fan, and A. Kaynia. Dynamic response of pile groups with different configurations. *Soil Dynamics and Earthquake Engineering*, 12(4):239–257, 1993.

[4] M. Lou, H. Wang, X. Chen, and Y. Zhai. Structuresoilstructure interaction: Literature review. *Soil Dynamics and Earthquake Engineering*, 31(12):1724–1731, 2011.

[5] J. B. de Paiva and R. R. Trondi. Boundary element analysis of capped and uncapped pile groups. *Advances in Engineering Software*, 30(9-11):715–724, 1999.

[6] L. A. Padrón, J. J. Aznárez, and O. Maeso. Dynamic analysis of piled foundations in stratified soils by a BEM-FEM model. *Soil Dynamics and Earthquake Engineering*, 28(5):333–346, 2008.

[7] J. Mulliken and D. C. Rizos. A coupled computational method for multi-solver, multi-domain transient problems in elastodynamics. *Soil Dynamics and Earthquake Engineering*, 34(1):78–88, 2012.

[8] M. A. Millán and J. Domínguez. Simplified BEM/FEM model for dynamic analysis of structures on piles and pile groups in viscoelastic and poroelastic soils. *Engineering Analysis with Boundary Elements*, 33(1):25–34, 2009.

[9] E. M. Comodromos, M. C. Papadopoulou, and I. K. Rentzeperis. Pile foundation analysis and design using experimental data and 3-D numerical analysis. *Computers and Geotechnics*, 36(5):819–836, 2009.

[10] P. K. Emani and B. K. Maheshwari. Dynamic impedances of pile groups with embedded caps in homogeneous elastic soils using CIFECM. *Soil Dynamics and Earthquake Engineering*, 29(6):963–973, 2009.

[11] H. H. Zhang and J. C. Small. Analysis of capped pile groups subjected to horizontal and vertical loads. *Computers and Geotechnics*, 26(1):1–21, 2000.

[12] G. Kouroussis, O. Verlinden, and C. Conti. Ground propagation of vibrations from railway vehicles using a finite/infinite-element model of the soil. *Proc. IMechE, Part F: J. Rail and Rapid Transit*, 223(F4):405–413, 2009.

[13] G. Kouroussis, L. Van Parys, O. Verlinden, and C. Conti. Prediction of environmental vibrations induced by railway traffic using a three-dimensional dynamic finite element analysis. In B.H.V. Topping and Y. Tsompanakis, editors, *Proceedings of the Thirteenth International Conference on Civil, Structural and Environmental Engineering Computing*, Chania (Greece), 2011. Civil-Comp Press.

[14] R. Dobry and G. Gazetas. Simple method for dynamic stiffness and damping of floating pile groups. *Géotechnique*, 38(4):557–574, 1988.

[15] J. Wang, X. Zeng, and D. A. Gasparini. Dynamic response of high-speed rail foundations using linear hysteretic damping and frequency domain substructuring. *Soil Dynamics and Earthquake Engineering*, 28(4):258–276, 2008.

[16] J. Lysmer and R. L. Kuhlemeyer. Finite dynamic model for infinite media. *Journal of the Engineering Mechanics Division, Proceedings of the ASCE*, 95(EM4):859–877, 1969.

[17] G. Kouroussis, O. Verlinden, and C. Conti. Finite-dynamic model for infinite media: corrected solution of viscous boundary efficiency. *Journal of Engineering Mechanics*, 137(7):509–511, 2011.

[18] O. Laghrouche and D. Le Houédec. Soil–railway interaction for active isolation of traffic vibration. In B. H. V. Topping, editor, *Advances in Simulation and Interaction Techniques*, pages 31–36, Edinburgh (Scotland), 1994. Civil–Comp Ltd.

[19] X. Sheng, C.J.C. Jones, and M. Petyt. The fourier transformed stationary and moving dynamic flexibility matrices of a layered ground. Technical report, Technical Memorandum 873, Institute of Sound and Vibration Research, University of Southampton, 1999.

[20] N. Triepaischajonsak, D. J. Thompson, C. J. C. Jones, J. Ryue, and J. A. Priest. Ground vibration from trains: experimental parameter characterization and validation of a numerical model. *Proc. IMechE, Part F: J. Rail and Rapid Transit*, 225(2):140–153, 2011.

[21] D. V. Jones and M. Petyt. Ground vibration in the vicinity of a strip load: An elastic layer on a rigid foundation. *Journal of Sound and Vibration*, 152(3):501–515, 1992.

[22] J. P. Wolf. *Foundation Vibration Analysis Using Simple Physical Models*. Prentice–Hall, New Jersey (USA), 1994.

COMPDYN 2013
4th ECCOMAS Thematic Conference on
Computational Methods in Structural Dynamics and Earthquake Engineering
M. Papadrakakis, V. Papadopoulos, V. Plevris (eds.)
Kos Island, Greece, 12–14 June 2013

PERFORMANCE-BASED SEISMIC DEMAND OF SOIL-FOUNDATION-STRUCTURE SYSTEMS

Anna Karatzetzou [1], Dimitris Pitilakis [2]

[1] Department of Civil Engineering, University of Thessaloniki
P.O.B. 424, 54124, Thessaloniki, GREECE
e-mail: akaratze@civil.auth.gr

[2] Department of Civil Engineering, University of Thessaloniki
P.O.B. 424, 54124, Thessaloniki, GREECE
e-mail: dpitilak@civil.auth.gr

Keywords: soil compliance, seismic demand, FEMA440, effective foundation motion

Abstract. *Seismic demand of soil-foundation-structure systems is evaluated herein in the light of performance-based design approaches, accounting for soil-foundation compliance effects. Due to kinematic and inertial interaction, structural response may be substantially different from the traditionally calculated fixed-base-structure-on-free-field approach. When soil-foundation-structure interaction (SFSI) is accounted, seismic demand of a system is identical to the notion of performance point, the latter being unique for every linear elastic SFSI system. We evaluate seismic demand using three distinct approaches: a) the traditional fixed-base-on-free-field approach, b) a finite element numerical code and c) the analytical approach proposed in FEMA440. In the current study, we utilize the exact ground motion at the foundation level and we propose a practical method to account for soil-foundation-structure interaction effects on seismic structural performance. We then highlight and quantify the discrepancies between our approach and the traditional approach and FEMA440 methodology. We propose use of effective foundation motion (EFM), which is affected by both kinematic and inertial interaction. Until now, no such index has been proposed, since relevant notions, such as the foundation input motion proposed in FEMA440, do not take into account both inertial and kinematic interaction. Moreover, EFM is measurable directly from actual records and field measurements. Using the graphical capacity spectrum method, intersection of the spectrum, expressed in acceleration-displacement format, that results for the acceleration time-history at the foundation level with the radial, which refers to the SFSI structural period, gives good estimation of structural response, compared to the direct method. Finally, for systems affected by interaction, FEMA440 seems to become un-conservative compared to numerical solutions and the deviation of EFM compared to the free-field motion can be from -60% up to +35%.*

1 INTRODUCTION

When analyzing the structural seismic response it is common in practice to assume the base of the structure to be fixed, which is only an assumption since in most cases the foundation soil is flexible. Recent earthquakes showed and highlighted the importance of SFSI to actual structural response [1]. The assumption of a fixed-base structure is realistic only when the structure is founded on solid rock. In all other cases, compliance of the soil can induce two distinct effects on the response of the structure, that is the modification of the free-field motion at the base of the structure (kinematic interaction), and the introduction of deformation from dynamic response of the structure into the supporting soil (inertial interaction). There are two main ways to analyze the SFSI phenomenon: the direct approach, in which the whole SFSI system is modeled in one step, and the substructure approach [2], in which the SFSI problem is divided in two distinct mechanisms, notably the inertial and the kinematic interaction.

The aim of this paper is to elucidate the effects of SFSI on system response, in context of performance-based design. Performance-based design is the design or assessment of a structure, to meet a specified performance level. The performance level is affected by several and important parameters and one of them is certainly the soil foundation structure interaction. So, a realistic consideration of interaction phenomenon is in some cases unavoidable.

One of the widely used methods to evaluate structural response in the light of performance-based design is the capacity spectrum method, originally developed by Freeman, 1998 [3] and extended later by Fajfar and Gaspercic, 1996 [4]. In both approximations, performance of a structure is evaluated as the intersection of the capacity curve with the demand spectrum in Acceleration-Displacement Response Spectrum (ADRS) coordinates. The capacity curve is obtained by standard nonlinear static procedures. The demand spectrum is usually estimated from free-field motion recordings. The above-mentioned methodologies have been used mainly to predict the structural performance ignoring the SFSI effects.

Most of the available methodologies to account the SFSI effects propose the increase of the structural period and the increase of the damping of the system. The available methodologies are based on response spectrum approach [5]. Based on the shape of the design spectra that are proposed by the codes for normal structures (i.e. structures not responding at very low periods), the SFSI effects work in favor of the structure's response. However, The ADSR spectra that result from actual records are not smooth in shape like the ones proposed in building codes and have spikes at the predominant response periods [3]. Aviles and Perez Rocha, 2003 [6] proposed that for structures with fixed-base periods, shorter than the soil resonant periods, a detailed study of the SFSI effects is needed.

Kinematic interaction effects, and thus the effect of SFSI on FIM (foundation input motion), in most of the abovementioned studies are neglected. When kinematic effects are neglected, FIM is equal to the FFM (free-field motion). However, there are two available simple approximations in order to consider the effect of kinematic interaction on structural response. Kim and Stewart, 2003 [7] proposed a methodology for shallow foundations, while Kurimoti and Iguchi, 1995 [8] proposed a methodology for both shallow and embedded foundations. The method proposed by Kurimoti and Iguchi is taking the weighted average of the free-field displacements along the foundation interface, adding the displacements caused by the resultant force and moment associated with the free-field tractions along with this surface. The abovementioned methods are easy to implement when the substructure method is used. Foundation input motion (FIM) is not probably a proper index of the whole soil foundation structure interaction phenomenon [9]. According to Iguchi et al. 2001 [10], an appropriate index that expresses the effects of SFSI effects on seismic input is the effective input motion

(EIM) that will be named as effective foundation motion (EFM) in this study. This motion includes effects of both inertial and kinematic interaction, and thus can be an index of the whole SFSI phenomenon. Effective foundation motion is really useful when studying SFSI using actual earthquake records at the level foundation, or when the whole SFSI phenomenon is being simulated with a one-step method (direct method). According to Iguchi et al. 2001 [10], the magnitude of the horizontal effective input motion greatly depends on the frequency content included in the free-field motion. The numerical evaluation of the effective foundation motion seems to be in good agreement with the records from field observations. Recently, Givens et al., 2012 [11] study kinematic interaction effects by comparing field tests with simplified analytical solutions.

The main objective of this paper is to highlight effects of SFSI on structural response for the simplest case of linear systems. For linear elastic systems, soil-foundation compliance affects directly seismic demand. Moreover, as it will be further explained, for flexible-base linear elastic structures, spectral demand and performance are notions practically identical, as only one pair of demand spectral coordinates exists, a unique performance point for any soil-foundation-structure system.

2 EVALUATION OF ELASTIC PERFORMANCE OF STRUCTURES

In the following paragraphs three different approaches are presented for the estimation of seismic performance of structures. All three methods have been used herein.

2.1 Fixed-base structure with free-field motion

In engineering practice, seismic demand to dynamic excitation is calculated directly from the free-field motion (FFM). Free-field response is not influenced by the presence of structures and thus the demand for all systems is the same irrespectively the dynamic characteristics of the soil-foundation-structure system. Such an approximation is irrelevant for structures founded on actual soil profiles. This approximation is relevant only when the structure is founded on solid rock which in most cases is far from reality.

2.2 Direct FEM

Direct finite-element approach can be used to calculate the response at the foundation level in a single step. The performance point of the flexible-base system is estimated from the intersection of the demand curve resulting from the time-history response at the foundation level with the radial line that concerns effective period of the system T_{SFSI}. It is worth mentioning here that something important is the T_{SFSI} value and the way this value is estimated. Moreover, using the direct method the structural response at the top can be estimated directly as output of the analysis.

When considering the SFSI effects, spectral demand and performance are notions practically identical and the performance point is unique for any soil-foundation-structure system. The demand curve changes its shape when the superstructure's characteristics change. This is the main difference between direct FEM and the traditional fixed-base system approach.

2.3 FEMA440 methodology

A simplified approach for including SFSI effects in seismic assessment is proposed in FEMA440 [12]. More specifically, kinematic interaction and foundation damping effects are approximately taken into consideration in estimating the FIM. Inertial interaction effects are partially addressed in FEMA356 [13] and ATC 40 [14] procedures for including foundation stiffness and strength of the geotechnical components of the foundation in the structural anal-

ysis model. It is important to mention that the FEMA440 methodology does not consider the effect of inertial interaction on FIM. However, in reality the foundation level response changes comparing to free-field motion due to both inertial and kinematic interaction.

3 SOIL-FOUNDATION-STRUCTURE SYSTEM

A set of dynamic analyses is performed in order to investigate the effect of soil structure interaction on seismic demand evaluation. As first step, dynamic analysis is performed for the soil system only, and in a second step for the complete soil-foundation-structure system.

Elastic demand spectra that result from the obtained free-field motion and the response at the foundation level are then depicted in the same graph, together with the demand spectrum that results when following the methodology proposed by FEMA440 for accounting SFSI effects. All demand spectra are presented graphically by elastic spectra with equivalent viscous damping ratio equal to 5%. The performance points that result for the fixed-base - free-field system and the complete systems are then compared.

Soil-foundation-structure system is modeled using the finite element method. The soil domain is homogeneous with thickness of H=50m. The soil deposit is simulated by 4 node linear elastic elements. The elastic bedrock is simulated using Lysmer-Kuhlemeyer, 1969 [15] dashpots at the base of the soil profile. The bedrock has shear wave velocity equal to V_s=1500m/s and density equal to ρ=2400kg/m^3. Plane strain conditions are assumed for both soil and bedrock. The foundation is a surface, rigid foundation and simulated by 4 node linear elastic elements and its width is equal to 2B. The structure represents a typical single-column bridge pier having a cylindrical cross section, which is a common choice for bridges in both in Europe and other areas. The structure is simulated by linear elastic beam elements and its height is equal to 6m.

The structure's mass is assumed to be lumped at the top of the pier. The damping for both soil and structure is five per cent for the first mode of both structure and soil profile (Rayleigh damping). The properties and the geometry of the studied models are depicted in Fig. 1. The concrete elasticity modulus is equal to E=32GPa for all models. The soil's density in all cases is stable and equal to ρ=2000kg/m^3 and the Poisson's ratio equal to ν=0.333. All models are triggered at the level of bedrock by the Northridge 1994 earthquake record (NGA_1011) with fundamental period T_p=0.16s and peak ground acceleration equal to a_{max}=0.95m/s^2.

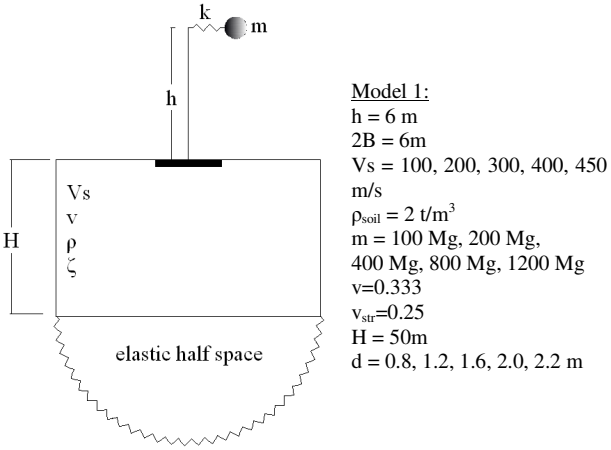


Figure 1: Soil foundation structure systems studied

4 CONCEPTUAL EXAMPLE

We consider for example Model 1 with shear wave velocity V_s=300m/s^2, mass at the top of the structure equal to m= 400Mg and pier diameter d= 2.2m. The elastic demand spectra that occur from the obtained free-field motion from analysis of the soil profile only (FFM) and the SFSI motion at the foundation level using the direct method (EFM) are depicted at the same graph, together with the demand spectrum that occurs when following the FEMA440 methodology. All demand spectra are depicted graphically by elastic spectra with an equivalent viscous damping ratio equal to 5%. Fig. 2 depicts the performance points (PP) which are the intersection of the following curves:

- PP1 is the intersection of the free-field demand spectrum with fixed-base structural period T_{FIX}.
- PP2 is the pair of values of the total (maximum) acceleration and displacement relative to the foundation that result directly at the top of the structure from the analysis. This pair of values gives also T_{SFSI} from Eq. 1. It is worth mentioning here that PP2 is almost identical to the one that results using the capacity spectrum method with the demand curve being the EFM curve and the radial the effective period of the system that stems from the division of the Fourier spectrum at the top of the structure to the one at the level of foundation. This combination of demand curve and effective period gives in all studied cases a very good approximation of the performance results using the direct method where the pairs of acceleration-displacement values are estimated directly from the analysis.
- PP3 is the intersection of the FFM demand spectrum with T_{SFSI}.
- PP4 represents the PP which is the intersection of the demand curve that results after utilizing the FEMA440 methodology with the T_{SFSI}.

For each analysis the output is in terms of accelerations and displacements at the top of the structure, at free-field and at the level of foundation. Moreover u_t (total displacement), u_{FFM}(displacement at free-field conditions), u_{fnd} (foundation's displacement), u_θ (displacement due to foundation's rocking) and u_{sb} (displacement due to structural bending) are also estimated (Fig.3). Most of the results of this study are depicted in terms of u_{str}, which is the displacement at the top of the structure relative to the foundation level, and it is the sum of the displacements due to rocking of the foundation and structural bending. Finally, each analysis gives the results in terms of drift values at the top and foundation's rotation values.

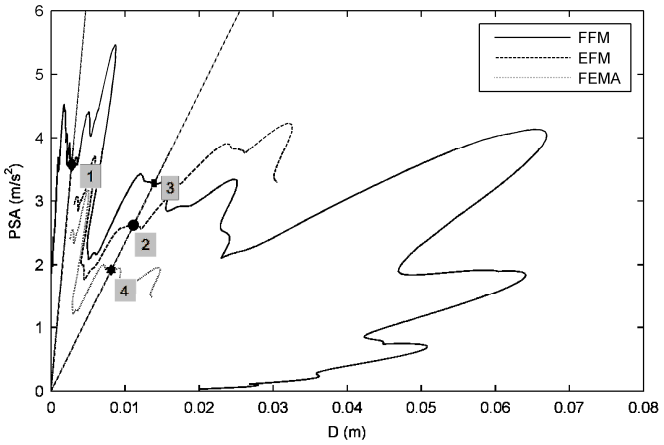


Figure 2: Performance points using different approximations. PP1 concerns the performance of the structure when using the traditional approach, PP2 concerns the performance when using the direct method for the whole SFSI system, PP3 is the structure's performance when considering demand curve for free-field conditions with the effective period of the system T_{SFSI}.

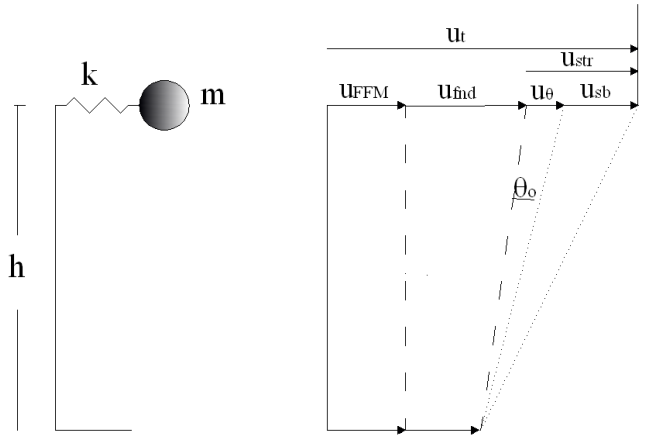


Figure 3: Response at the top of the structure when considering soil-foundation-structure interaction effects in terms of displacements.

5 RESULTS

The results of the parametric study conducted herein are depicted in Fig. 4 to Fig.8. The results are expressed in terms of relative soil to structure stiffness ratio $1/\sigma$ (Eq. 2) and normalized mass ratio m_{norm} (Eq. 3), and concern the same value for the normalized height ratio $h_{norm}=h/B=2$.

Fig. 4 shows the resulted effective to fixed-base period (T_{SFSI}/T_{FIX}) values, in three (Fig4a) and two (Fig4b) dimensional plot, in terms of $1/\sigma$ and m_{norm}. As expected, the T_{SFSI}/T_{FIX} ratio is increasing with either decreasing the soil stiffness or increasing the slenderness of the structure. As stems from the graphs, for actual soil profiles the effective period of the system including SFSI is up to 4 times the fixed-base period. This is a value that stems also from literature for bridge piers and normalized height equal to $h_{norm}=2$ [16].

Another important point to mention is what exactly the effective period of the system represents when estimated by different approaches. More specifically in Fig.5 the resulting from Eq.1 values of effective period T_{SFSI} are compared with three different approximations (a) the effective period the occurs when dividing the Fourier spectrum at the top of the structure by the one at the level of foundation, (b) the effective period that results when dividing the Fourier spectrum at the top of the structure to the one at free-field conditions and (c) the effective period that results from theoretical expressions that exist in literature [17]. It seems that T_{SFSI} is in good agreement with $T_{SFSI(FOUND)}$, while $T_{SFSI(FFM)}$ is in good agreement with $T_{SFSI(THEO)}$. This could be explained by the fact that T_{SFSI} and $T_{SFSI(FOUND)}$ include only to the relative to the foundation level displacement at the top u_{str} (Fig.3), while $T_{SFSI(FFM)}$ and $T_{SFSI(THEO)}$ include also the horizontal displacement of the footing u_{fnd} (Fig.3).

$$T_{SFSI} = 2 \cdot \pi \cdot \sqrt{\frac{u_{str}}{\ddot{u}_{str}}} \tag{1}$$

$$1/\sigma = \frac{h}{T_{FIX} \cdot V_S} \tag{2}$$

$$m_{norm} = \frac{m}{B^3 \cdot \rho} \tag{3}$$

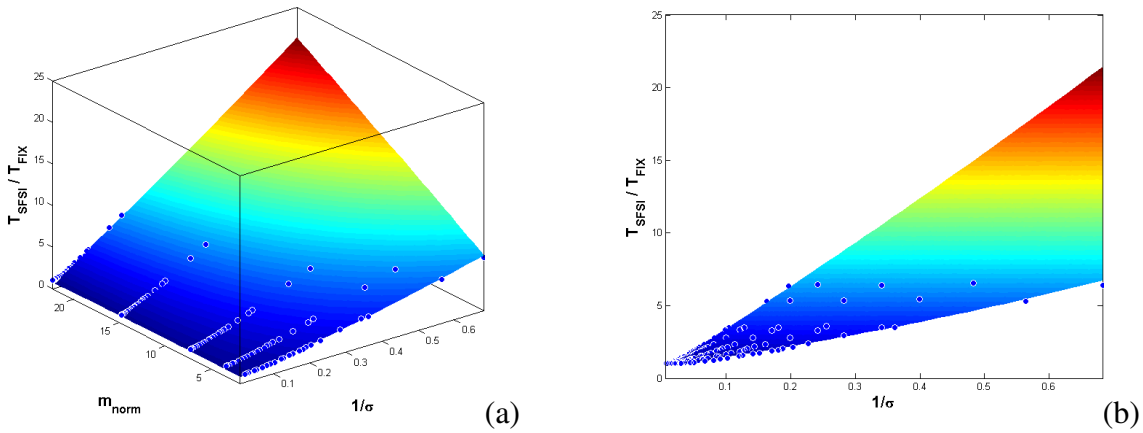


Figure 4: Effective system's period to fixed-base period (T_{SFSI}/T_{FIX}) values in terms of soil to structure stiffness ratio $1/\sigma$ and normalized mass m_{norm} in (a) three dimensions plot and (b) two dimensions plot.

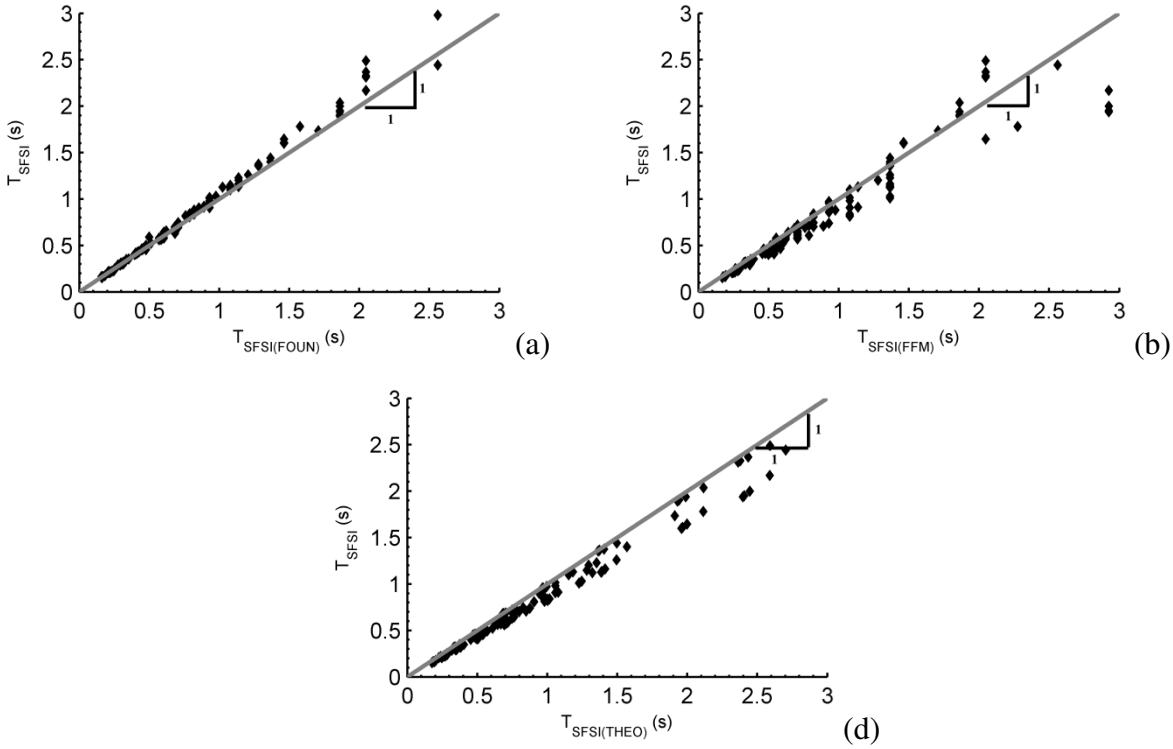


Figure 5: Effective period T_{SFSI} compared with three different approximations (a) the effective period the occurs when dividing the Fourier spectrum at the top of the structure to the one at the level of foundation $T_{SFSI(FOUND)}$, (b) the effective period that results when dividing the Fourier spectrum at the top of the structure to the one at free-field conditions $T_{SFSI(FFM)}$ and (c) the effective period that results from theoretical expressions that exist in literature $T_{SFSI(THEO)}$.

Fig. 6 shows the maximum acceleration values at the top of the structure that occur when using the direct method ($\ddot{u}_{str}$) together with the maximum acceleration values that result by the intersection of free-field demand curve with T_{SFSI} radial line ($\ddot{u}_{strf}$). Additionally, in the same graph it is depicted the 1:1 radial line and the radial line that results after linear regression of the results. In most cases the acceleration value at the top of the structure for the SFSI system ($\ddot{u}_{str}$, see PP2 in Fig. 2) is smaller than the acceleration at the top of a structure with

effective period equal to T_{SFSI} triggered by the free-field motion ($\ddot{u}_{strf}$, see PP3 in Fig. 2). After linear regression the $\ddot{u}_{str}/\ddot{u}_{strf}$ ratio is equal to 0.7573 (Fig. 6). The relation between $\ddot{u}_{str}$ and $\ddot{u}_{strf}$ gives more or less the relation between the EFM and the FFM motion in terms of spectral values at the effective period of the system.

The displacement at the top of the structure (u_{str}) is composed by two parts the displacement due to foundation's rocking (u_θ) and the displacement due to structural bending (u_{sb}). Fig. 7 and Fig. 8 show in two and three dimensional plot the u_θ/u_{str} and u_{sb}/u_{str} ratios respectively in terms of $1/\sigma$ and m_{norm} ratios. As the soil becomes softer and the structural mass value greater the u_θ/u_{str} values are greater (Fig. 7). This in other words means that for very soft soil profiles the structure's response is defined mainly by rocking. On the other hand, as the soil becomes softer the u_{sb}/u_{str} values are smaller.

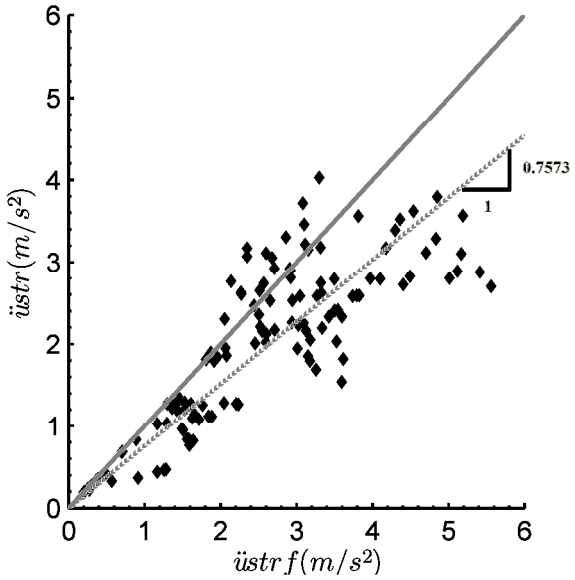


Figure 6: Maximum acceleration at the top of a structure with T_{SFSI} subjected to EFM ($\ddot{u}_{str}$) and to FFM ($\ddot{u}_{strf}$).

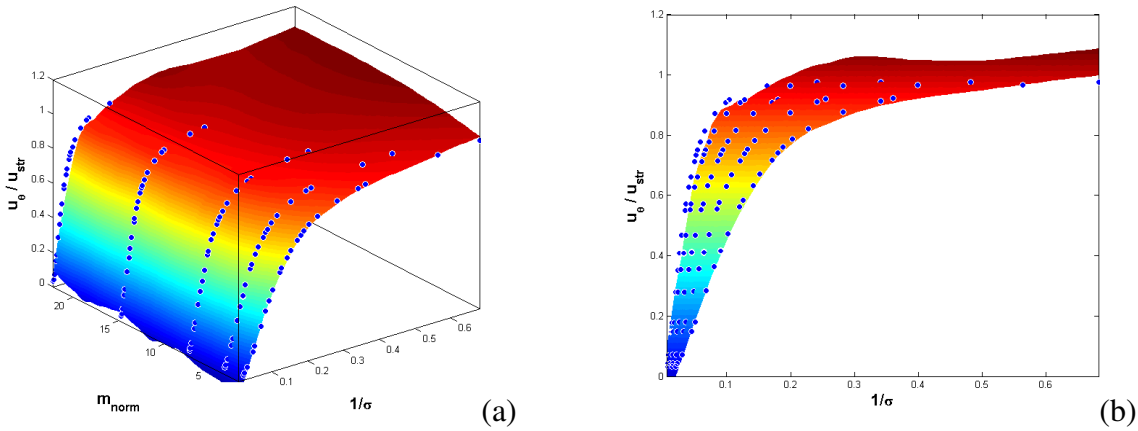


Figure 7: Rocking to relative displacement ratio u_θ/u_{str} in terms of soil to structure stiffness ratio $1/\sigma$ and normalized mass m_{norm}.

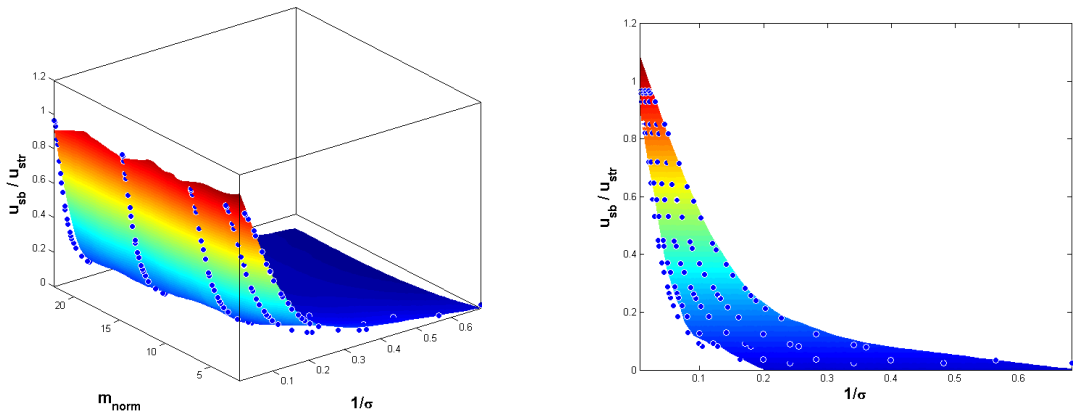


Figure 8: Structural bending to relative displacement ratio u_{sb}/u_{str} in terms of soil to structure stiffness ratio 1/σ and normalized mass m_{norm}.

6 PROPOSED METHODOLOGY AND ITS APPLICATION

The methodology that is proposed herein could be described by the following steps:

1. Estimate the dynamic and geometrical characteristics h, m, Vs, 2B of the soil and structure and soil response acceleration at free-field conditions.
2. Evaluate 1/σ, m_{norm}, T_{FIX}, h_{norm} using the Eq.2 and the Eq.3.
3. Estimate the T_{SFSI}/T_{FIX} ratio in terms of 1/σ and m_{norm} (Fig. 4).
4. Estimate $\ddot{u}_{str}$ using the proposed in terms of $\ddot{u}_{strf}$ modification value (Fig. 6).
5. Calculate u_{str} from the T_{SFSI} period value combined with the $\ddot{u}_{str}$ value.

The u_{str} value is the sum of the u_θ and u_{sb}. The values of both two parts could be estimated by the proposed curves in Fig. 7 and Fig. 8. The resulting values, when applying the proposed methodology, are in a very good agreement with the ones from the time history analysis.

As an example for the model described in paragraph 4, m_{norm}=7, 1/σ=0.113, T_{FIX}=0.176s. For these values according to Fig.4, T_{SFSI}/T_{FIX}=2.36 and thus T_{SFSI}=0.42s. The intersection of T_{SFSI} with the FFM demand curve gives the $\ddot{u}_{strf}$ value that is equal to 3.27m/s^2. According to Fig.6, $\ddot{u}_{str} = 0.7573 \cdot 3.27 = 2.48 \text{m/s}^2$. From Eq.1 u_{str} is estimated equal to 0.011m and using Fig.7 and Fig.8, the rocking displacement is equal to 0.009m and the displacement at the top due to structural bending is equal to 0.002m. These values are in a very good agreement with the ones resulted from the time history analysis.

The main advantage of the proposed methodology is that, in order to calculate the structure's response considering SFSI effects (kinematic and inertial), one needs only to know the main characteristics of the system and the ground response at free-field conditions.

7 COMPARISON BETWEEN FEMA AND FEM

The comparison of PP2 and PP4 for all the analyses in terms of per cent acceleration modification factor $(PP_{FEMA}-PP_{FEM})/PP_{FEM}$ % are depicted in Fig. 9. The trend line shows that for stiff soil profiles (1/σ<0.1) FEMA440 gives from 0% up to 50% higher values, while for soft soil profiles FEMA440 gives up to 100% smaller values comparing to the direct methodology that is proposed herein. In other words, FEMA440 seems to be un-conservative when 1/ σ > 0.1 and this could be attributed to the fact that when T_{SFSI}/T_{FIX} takes values greater than two, normal values for bridge piers that are characterized by important masses, the FEMA440

overestimates system's damping. The FEMA440 methodology is more appropriate for buildings.

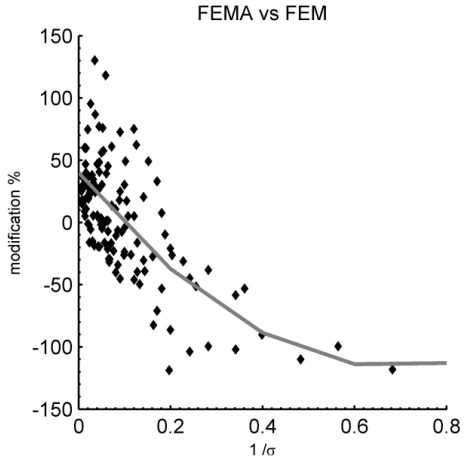


Figure 9: Comparison between FEMA440 and FEM methodologies in terms of per cent spectral acceleration modification.

8 CONCLUSIONS

Based on the results presented the following conclusions could be deducted:

- For the SFSI system we propose the demand curve calculated from the effective foundation motion combined with the $T_{SFSI(FOUN)}$ that stems from the division of the Fourier spectrum at the top of the structure with the one at the level of foundation. This combination gives results in good agreement with the response from the direct method. The abovementioned seismic performance concerns total relative to the foundation level lateral displacement at the top. However, both parts of total displacement are easily evaluated by the proposed methodology. Final performance depends on the limit state to be considered.
- Structural response can be calculated only if the main characteristics of the system and the motion at free filed conditions are known. The final result considers both kinematic and inertial interaction.
- T_{SFSI}/T_{FIX} values are up to 4 for actual soil profiles.
- The maximum acceleration values at the top of the structure that occur when using the direct method ($\ddot{u}_{str}$) divided to the maximum acceleration values that result by the intersection of free-field demand curve with T_{SFSI} radial line ($\ddot{u}_{strf}$) give after linear regression a ratio equal to 0.7573.
- For very soft soils the main part of u_{str} is u_{θ}, while for stiff soils and slender structures the main part of u_{str} is u_{sb}.
- For typical soil profiles, FEMA seems to be un-conservative and overestimates damping when SFSI effects are important.

ACKNOWLEDGEMENTS

Part of this work was performed in the framework of the European project "Performance-based approach to earthquake protection of cultural heritage in European and Mediterranean countries (PERPETUATE)", Grant agreement 244229, as well as in the framework of the European project "Seismic engineering research infrastructures for European synergies (SERIES)", Grant agreement 227887.

REFERENCES

[1] G. Mylonakis, G. Gazetas, Seismic soil-structure interaction: beneficial or detrimental? *Journal of Earthquake Engineering*, Vol. 4, no. 3, pp. 277-301, 2000.

[2] JP Wolf, *Dynamic Soil–Structure Interaction*. Prentice-Hall: New Jersey, 1985.

[3] S.A. Freeman, The Capacity Spectrum Method as a Tool for Seismic Design, *Proceedings of the 11th European Conference on Earthquake Engineering*, Paris, France, 1998b.

[4] P. Fajfar, P. Gaspersic, The N2 method for the seismic damage analysis for RC buildings. *Earthquake Engineering & Structural Dynamic*. 25(1):23–67, 1996.

[5] J. P. Stewart, S. Kim, J. Bielak, R. Dobry, M. S. Power, Revisions to soil structure interaction procedures in NEHRP design provisions. *Earthquake Spectra*, Vol. 19, no. 3, pp. 677-696, 2003.

[6] J. Aviles, LE Perez-Rocha, Soil-structure Interaction in Yielding Systems. *Earthquake Engineering and Structural Dynamic*, 32: 1749–1771, 2003.

[7] S. Kim, J. P. Stewart, Kinematic soil-structure interaction from strong motion recordings. *J. Geotech.. & Geoenv. Engrg.*, ASCE, 129 (4), 323-335, 2003.

[8] O. Kurimoto and M. Iguchi, Evaluation of foundation input motion based on observed seismic waves. *Journal of Structural Construction Engineering (in Japanese)*, AIJ, Vol. 472, pp. 67-74, 1995.

[9] D. Pitilakis, A. Karatzetzou, Soil-foundation-structure interaction effects on seismic performance of systems (submitted to SDEE for possible publication).

[10] M. Iguchi, Y. Yasui, C. Minowa, On Effective Input Motions: Observations and Simulation Analyses. *Proc. of the Second U.S.-Japan Workshop on Soil-Structure Interaction*, Building Research Institute, Ministry of Land, Infrastructure and Transport of Japan, 2001: pp75-87, 2001.

[11] M. J. Givens, A. Mikami, T. Kashima, J. P. Stewart, Kinematic soil-structure interaction effects from building and free-field seismic arrays in Japan. *9th International Conference on Urban Earthquake Engineering/ 4th Asia Conference on Earthquake Engineering*, March 6-8, 2012, Tokyo Institute of Technology, Tokyo, Japan., 2012.

[12] Federal Emergency Management Agency (FEMA), Improvement of nonlinear static seismic analysis procedures. *Report FEMA 440*, Washington, DC, 2005.

[13] American Society of Civil Engineers (ASCE), *FEMA-356-Pre-standard and commentary for the seismic rehabilitation of buildings*, Washington, DC, 2000.

[14] Applied Technology Council (ATC), ATC 40 – *The seismic evaluation and retrofit of concrete buildings*, vol I & II. ATC, Redwood, 1996.

[15] J. Lysmer, A.M. Kuhlemeyer, Finite dynamic model for infinite media. *Journal of the Engineering Mechanics Division*, ASCE, 95, 859-877, 1969.

[16] CC. Spyrakos, Seismic behavior of bridge piers including soil – structure interaction. *Comput Struct 1992*;4(2):373 – 84, 1992.

[17] A. S. Veletsos, J. Meek, Dynamic behaviour of building-foundation systems. *Earthquake Engineering and Structural Dynamics*, 3, 121-138, 1974.

COMPDYN 2013
4th ECCOMAS Thematic Conference on
Computational Methods in Structural Dynamics and Earthquake Engineering
M. Papadrakakis, V. Papadopoulos, V. Plevris (eds.)
Kos Island, Greece, 12–14 June 2013

STRUCTURE-SOIL INTERACTION FOR FRAMED STRUCTURES UNDER DYNAMICS LOADING CAUSED BY RECIPROCATING COMPRESSOR

E. VIANA[1*], **D. ROEHL**[2]

[1] Petróleo Brasileiro S.A. – PETROBRAS
Av. Almirante Barroso, 81, Centro - Rio de Janeiro, RJ - Brazil - 20031-004
eduardo.arreguy@petrobras.com.br

[2] Pontifícia Universidade Católica do Rio de Janeiro – PUC-RIO
Rua Marquês de São Vicente, 225, Gávea - Rio de Janeiro, RJ - Brazil - 22451-900
droehl@puc-rio.br

Keywords: Vibration, structure-soil interaction, spring stiffness, finite element model, sprig-mass model, effective velocity (*rms*), natural frequency.

Abstract. *Gas compressors are key components of industrial plants in oil refining, mainly acting as mechanical energy suppliers to chemical processes. Among the types of compressors, the reciprocating ones are highlighted. Due to mandatory demands of chemical process and industrial arrangement, such equipment is commonly installed on framed structures. This condition and the typical movement of mechanical parts of the compressors generate dynamic loads which frequently cause unacceptable vibrations. The work aim at evaluate the dynamic behavior of a system consisting of a framed structure, a reciprocating compressor, foundation in piles and the soil itself. For this purpose, parametric study is developed from a finite element model and field measurements. The parametric study goal is to establish ranges of local soil parameters within which the dynamic behavior of a system can be understood and measured. The parameters so-called constant coefficient of horizontal reaction (n_h) of natural soil which typically occurs in an industrial area located in Araucária, Paraná state, Brazil, are then evaluated. The evaluation of the dynamic behavior of the system through the developed models is benchmarked by field measurements of effective velocity of vibration in the actual structure, obtained by instrumentation. The soil parameters are obtained by back analysis of tests results by using a model widely used in design offices: model proposed by Miche[1]. It takes into account the variation of the soil parameters with depth. Yet the other goal is to evaluate the influence of the soil parameters obtained by static and cyclic horizontal loading tests, the later ones being proposed to simulate the dynamic effect on the soil. Finally, the article presents comparisons of the results provided by the finite element model in terms of natural frequencies of vibration.*

1 INTRODUCTION

During the first studies of vibrations in structures and machine foundations, simple calculation methods considered the dynamic effects simply as an amplified static loading, that is, a factor known as Dynamic Factor was applied over the value of static loads, which often led to larger loads than the actual dynamic loading and thus the design became very conservative.

By the increasing size of equipments as the ones found at an industrial plant, which began operating under conditions more and more severe, a deeper analysis regarding dynamic loads became necessary and fundamental. Among these equipment, we highlight the large reciprocating compressors, which have as main function to provide mechanical energy to chemical processes. Reciprocating compressors, due to requirements of chemical process and industrial arrangement, are commonly installed on framed structures, which are no rarely under unacceptable vibrations caused by dynamic loads. This condition motivates special attention during design phase.

Furthermore, the cost associated with equipment shutdowns in industrial plants due to mechanical failures and poor performance is significantly higher than the cost associated with a well developed design, which justifies every effort to ensure that the appropriate behavior during the future operation be achieved.

The dynamic interaction between soil and structures embedded in it is still a field where researchers are looking for answers to various problems. As an example, the soil is modeled as a linear spring on the theory of elastic half-space, which by hypothesis is considered as a linear isotropic medium, which indeed is not.

In the analysis of the dynamic response of foundations, soil can be treated in several ways. These treatments include finite element method, boundary element method, analytical solutions developed from the solution of the wave equation and simplified mechanical models. The finite element method allows the evaluation of the underground complex configurations, but requires significant computational effort. Yet analytical solutions are generally limited to very simple conditions and are not always applicable to real conditions, especially when nonlinearities and complex boundary conditions are involved [2].

In this work, we studied the typical soil parameters of an industrial area, located in Araucaria, Paraná state, Brazil, which in general belongs to the geological formation so-called Guabirotuba.

This parametric study aimed at establishing ranges of local soil parameters within which the dynamic behavior of a framed piled structure supporting a reciprocating compressor could be completely understood.

The numerical evaluation of the dynamic behavior of the system was fitted by measured values of velocities in the actual structure obtained by data acquisition. The spring coefficient km and the horizontal reaction constant n_h were assessed.

These parameters were obtained by back analysis from field loading tests considering a model widely used in design offices, which was proposed by Miche [1]. It considers the soil parameters varying along depth.

The article also seeks to evaluate the influence of soil parameters obtained by testing static load and obtained through cyclic static loading tests on piles, the last one proposing to simulate the dynamic effect on the soil.

Finally, comparisons between the results provided by the simplified models and the finite element model in terms of natural frequencies of vibration were done.

2 INTERACTION AMONG MACHINE, STRUCTURES AND SOIL

In general, a problem of machine foundations corresponds to an interaction among machines, supporting structures and underground, all of them directly or indirectly subjected to dynamic loads.

The dynamic interaction between a reciprocating compressor, a concrete supporting structure, its foundation and subsoil is covered in this paper. As will be shown, the movement of the pistons inside the cylinders of the compressor generates transient forces and moments on the structure and, consequently, on its foundations.

2.1 Machines

Typically, the basic oscillating mechanism shown in Figure 1 consists of a piston moving in a cylinder guide, a connection bar fixed at a piston and the rotating element (crank), which rotates around its axis (crankshaft) with angular frequency ω. The piston movement can be horizontal or vertical depending on the design of the equipment.

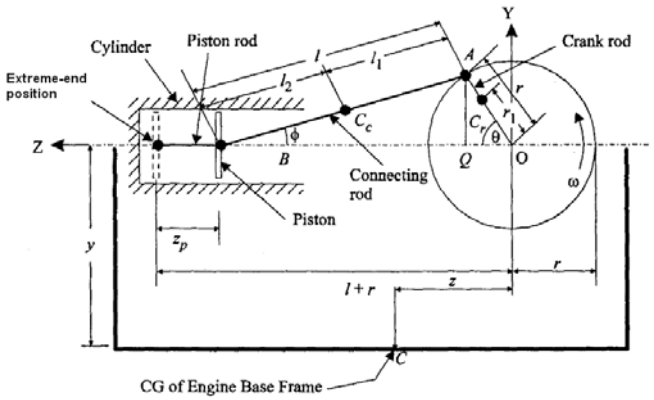


Figure 1: Typical arrangement of reciprocating compressor 1 cylinder [4]

The components of the mechanical system of the reciprocating compressor shown above are described in table 1.

Crank mass	m_r
Crank lengh	r
Crank gravity center	C_r
Conection rod gavity center	C_c
Rotational axis	O
Lengh between C_r and O	r_1
Rotational velocity	ω
Conection point at crank	A
Conection point at piston	B
Concetion rod mass	m_c
Concetion rod lengh	l
Distance between C_c and A	l_1
Distance between C_c and B	l_2
Piston mass	m_p

Table 1: Mechanical elements of a reciprocating compressor

The force generated at point *B* can be expressed by the following equation.

$$F_B = m_B r\omega^2(\cos\omega t) + m_B r\omega^2\left(\frac{r}{l}\cos 2\omega t\right) \quad (1)$$

The term m_B in equation *1* can be written as $m_B = m_r(\frac{l_1}{l}) + m_p$.

2.2 Structure and soil

The complete understanding of a problem of dynamic loading on a structure and its foundation due to a mechanical equipment or even due to earthquakes can be achieved only when it is analyzed as a whole unique system. For instance, by ignoring the effect of the soil, treating it as undeformable, the response of the structure can vary significantly.

The consideration of soil as a deformable elastic element leads to the coupling between soil and structure stiffness, which changes the overall behavior of the system. Also, what if the foundation of a structure is placed directly on the ground, what if it is supported on piles, what if it is embedded in the soil, what if the soil layers are laminated, all these features are capable of influencing the behavior of a system.

3 PHYSICAL MODEL

This chapter presents all the physical characteristics of the problem of soil-structure interaction-equipment studied, namely geometry and material of the structure-foundation system, soil physical properties and mechanical equipment operating data.

There are also shown the results of the horizontal loading test conducted in the field, the values of the soil physical property (spring coefficient) obtained through the test results and back analysis, besides the results of field measurements of vibration velocities at specific points of the structure.

3.1 Structure

The supporting system is formed by a concrete framed structure over block-pile foundation, as shown in figures below.

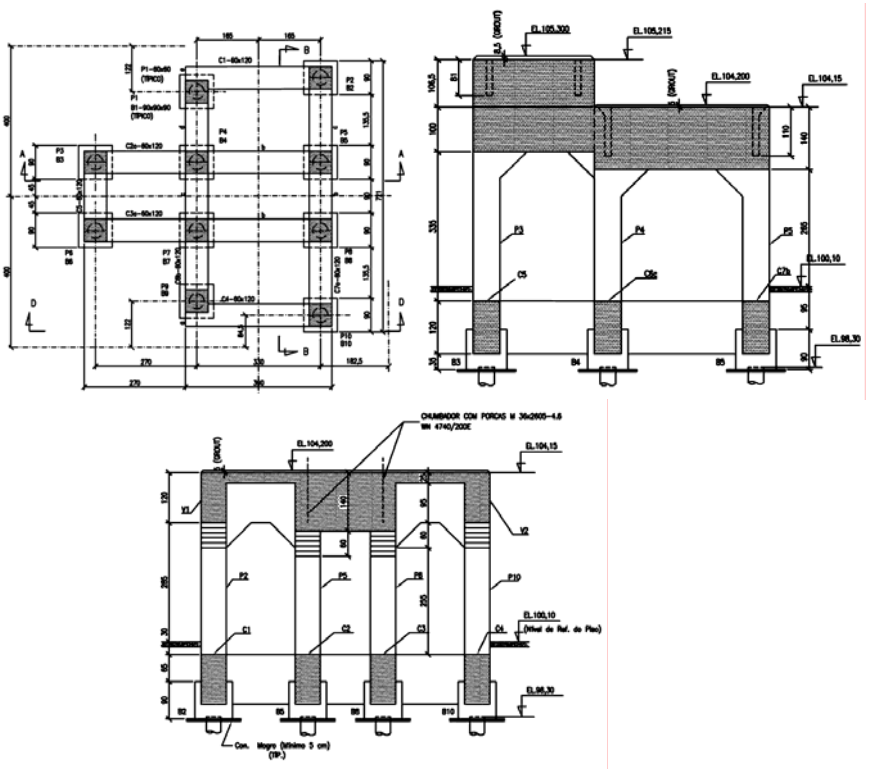


Figure 2: Assessed structure – Plan and Views

3.2 Equipment

The set of equipment that belongs to the mechanical system consists primarily of gas compressor, electric motor and accessories in general.

The compressor is reciprocating with horizontal cylinders, manufactured by the *Neuman & Esser*, operating at frequency of 590 *rpm*. The following images show some of its components.



Figure 3: Overview of motor-compressor coupling and parts of mechanical system

Amplitude of dynamic loadings transmitted by the compressor is shown on the table below.

Direction	Dynamic forces (N)	Dynamic torsion (N.m)
Horizontal	20788	35287
Vertical	0	9542

Table 2: Mechanical elements of a reciprocating compressor

The magnitude of the dynamic forces generated by the electric motor is small and hence its contribution to the dynamic response of the system is negligible [5]. Therefore, in the developed model, the electric motor only participates with its mass.

In this case, the allowable vibrating velocity on the top of the supporting structure (settling of skids) was limited to 2.00 mm/s.

3.3 Soil constitutive model

The typical geological formation of the region where the assessed equipment is installed consists of two phases well highlighted. The first and most superficial is known as Tinguis formation. The second and deeper is known as Guabirotuba formation, consisting generally the layer in which foundations elements are embedded.

Figure 4 shows a typical geotechnical profile obtained through two SPT tests. On this figure, the horizontal lines are spaced one meter along the depth of the borehole.

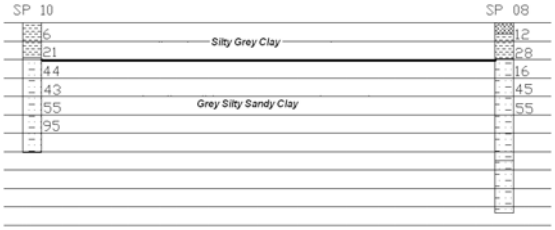


Figure 4: Geotechnical profile of the local subsoil

In this study, the soil was considered as a discrete component, linear, mass less, acting independently in two orthogonal horizontal directions as a spring coefficient km. Each spring is applied at one point (node) of foundations (piles).

Considering the data above and in order to define the constitutive model of soil, field test (horizontal static loading) was performed on two piles of the same diameter (40.0 cm) and close to the region where the compressors are installed. The tests followed the Brazilian standard ABNT NBR 12131 [3] and American standard ASTM D3966 [6].

The following table summarizes the test results.

Pile tag	**E-16**	**E-3**
Bore-hole	SP-13	SP-10A
Max load test (kN)	84	65
Max displacement (mm)	20,4	31,31

Table 3: Results of horizontal static loading test

Also, cyclic loading tests were performed, whose applied load versus displacement curves for each cycle are presented below.

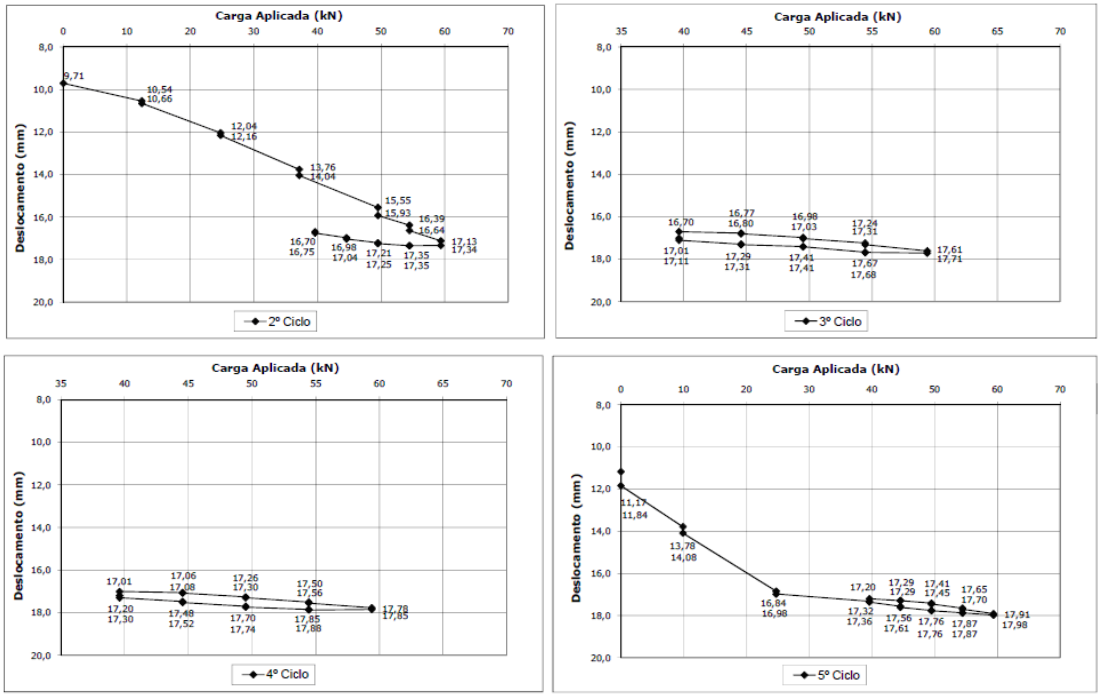
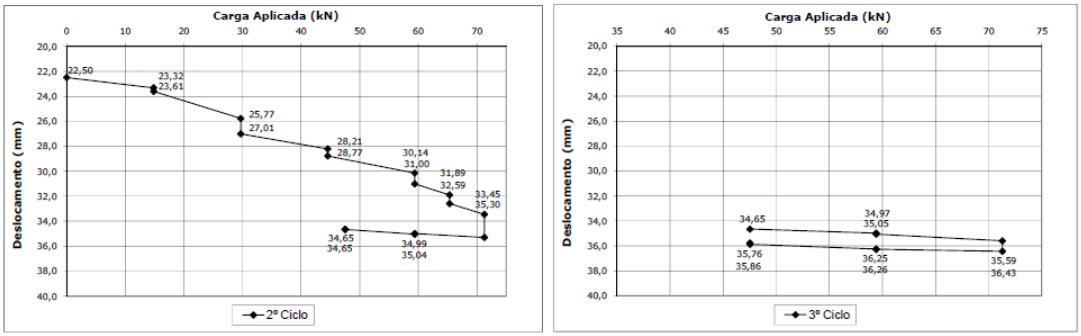


Figure 5: Cyclic loading test results – Pile E-16



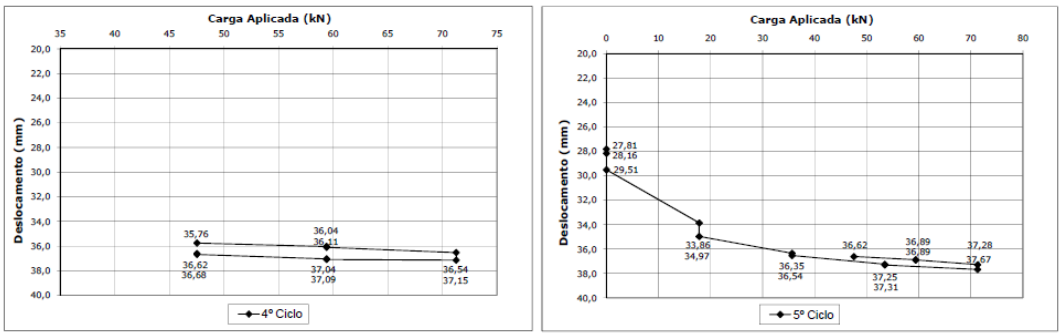


Figure 6: Cyclic loading test results – Pile E-03

The results of these cyclic tests were used to calculate the soil dynamic parameters.

In order to obtain soil parameters values (static and cyclic), a back calculation procedure was used by means of Miche [1] method. This method deals with horizontal interaction between a pile element embedded in subsoil and subjected to horizontal loads.

Miche [1] analyzed the problem of piles immersed in an elastic medium with horizontal soil parameter growing linearly with depth, subjected to a horizontal force on its top. The constant of this linear behavior is called n_h and can be written as follows.

$$n_h = \sqrt[3]{\left(\frac{2{,}4F}{y}\right)^5 (EI)^2} \tag{2}$$

In this equation parameters E and I are known, which depend on the material of the pile and its geometry, and the values F and y, which are obtained from the horizontal loading test cited above.

For the static case, considering pile E-16, the soil parameter n_h achieved 5087.99 kN/m^3.

For the cyclic case, also considering pile E-16, the results are shown below for each cycle.

	Cycle 1	Cycle 2	Cycle 3	Cycle 4	Cycle 5	Cycle 6
n_h (kN/m^3)	170776,2606	69712,6988	166058,8790	94779,7101	191974,2753	107239,9283
n_h/D	426940,6515	174281,7471	415147,1976	236949,2751	479935,6882	268099,8206

	Cycle 7
n_h (kN/m^3)	157227,3290
n_h/D	393068,3226

Table 4: Soil parameter n_h for cyclic loading – Pile E-16

Considering Pile E-03, for the static case, the soil parameter n_h achieved 1624.98 kN/m^3.

For the cyclic case, also considering pile E-03, the results are shown below for each cycle.

	Cycle 1	Cycle 2	Cycle 3	Cycle 4
n_h (kN/m^3)	34222,4094	183437,5885	82482,4884	326398,0336
n_h/D	85556,0235	458593,9713	206206,221	815995,084

Table 5: Soil parameter n_h for cyclic loading – Pile E-03

4 ACTUAL VIBRATION DATA

Figure below shows the amplitude of vibration (*rms* – root means square) in terms of velocity (mm/s). The measurements were taken on the support structure of the compressor. The data collection points were located in all columns of the structure, more precisely at 2.00 m

from ground level. The following rectangles represent columns cross section and containing the amplitude values of vibration velocity.

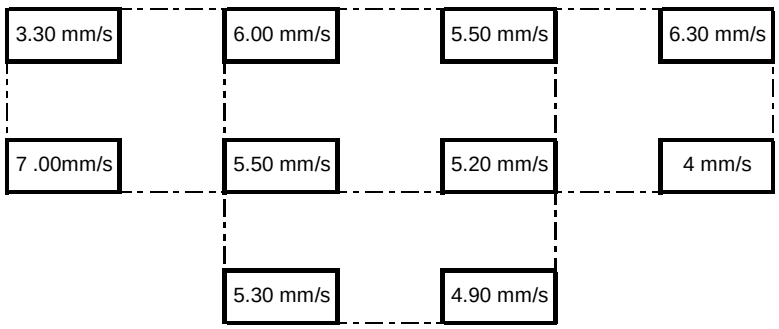


Figure 7: Velocities amplitude of vibration in columns (mm/s)

In the present work, the model had the root mean square of velocity as a parameter of calibration.

5 NUMERICAL MODEL

5.1 General

This chapter aim at presenting the numerical model used to understand the structure-soil-equipment behavior under dynamics loading. For this purpose, a computational 3D Finite Element model was developed by using ABAQUS® software, which was calibrated by field measurements.

A modal superposition was driven in the dynamics analysis.

The structure was modeled with two distinct elements. Once they have massive aspect, bases were modeled with C3D4 type elements (linear tetrahedral solid with 4 nodes). Columns and beams were modeled with linear beam elements (B31).

Pile foundations and its interaction with the soil were modeled considering the piles as linear beam elements and the soil as a set of linear springs (SPRING 1) acting in both perpendiculars directions to the pile.

The modeling of equipment takes into account the concentration of masses in their respective centers of gravity and its connection to the structure by rigid mass less beam elements [7]. Besides acting as dynamic loading, the mechanical system also affects the dynamic behavior of the model since it contributes to the mass matrix of the equations of motion. Figure 8 shows the FE Structure-Foundation-Soil-equipment model.

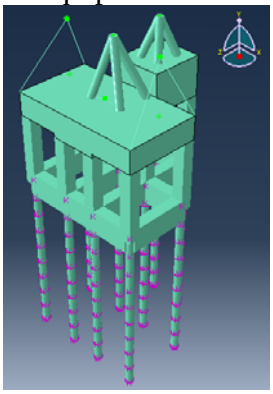


Figure 8: FE model on ABAQUS®

The main model input data are shown on tables 6 and 7 below.

Sub Systems	Elements	Geometry (m)			Type of Finite Element
		Section		Diameter	
		a	b		
Structure	Beam underground	0,6	1,2	-	Beam
	Columns	0,6	0,6	-	Beam
	Bases	-	-	-	Solid 4 nodes linear
Foundation	Piles	-	-	0,4	Beam
	Soil	-	-	-	Linear spring

Table 6: Model data (a)

Sub Systems	Elements	Material	Physical Properties			
			Elasticity Modulus (N/m^2)	Poisson Coefficient	Specific Weight (N/m^3)	Spring Constant (N/m)
Structure	Beam underground	Reinforced concrete	21287367145,8	0,2	25000	-
	Columns					
	Bases					
Foundation	Piles					
	Soil	-	-	-	-	See tests

Table 7: Model data (b)

5.2 Loadings

The static loading is considered herein to be the weight of all components of the system.

The forces and torsion generated by reciprocating compressor are provided by the equipment manufacturer. The amplitudes of the primary and secondary excitation loads, as well as corresponding excitation frequencies are presented below.

Forces	F0x1	17865	N
	F0x2	2923	N
Torsion	T0x1	31667	N.m
	T0x2	3620	N.m
	T0y1	9542	N.m
	T0y2	0	N.m
Excitation	w	9,83	Hz

Table 8: Machine loading data

Either forces or torsions act in direction x and y under the same excitation frequency.

6 PARAMETRIC ANALYSIS

This chapter describes the parametric studies conducted from the finite element model of the interactive system structure-soil-foundation and analyzes the influence of the soil parameter in the dynamic behavior of such system, that is, vibration velocity and natural frequencies (eigenvalues). The constant of horizontal reaction coefficient n_h obtained by back analysis is then used as the soil parameter.

6.1 Assessment 1 - n_h static case

From figure 9, it is observed that the calculated velocities fall into two distinct narrow limits, the first between the actual speed of 3.2 mm/s and 4.0 mm/s, and the second between 5 mm/s and 5.5 mm/s, whereas values of n_h between 1600 kN/m^3 and 65000 kN/m^3. For lower values of n_h , approximately between 1600 and 5000 kN/m^3, the velocities behave more in a random pattern, and for values above 5000 kN/m^3, there is a tendency for smaller influence of n_h on the system dynamic response.

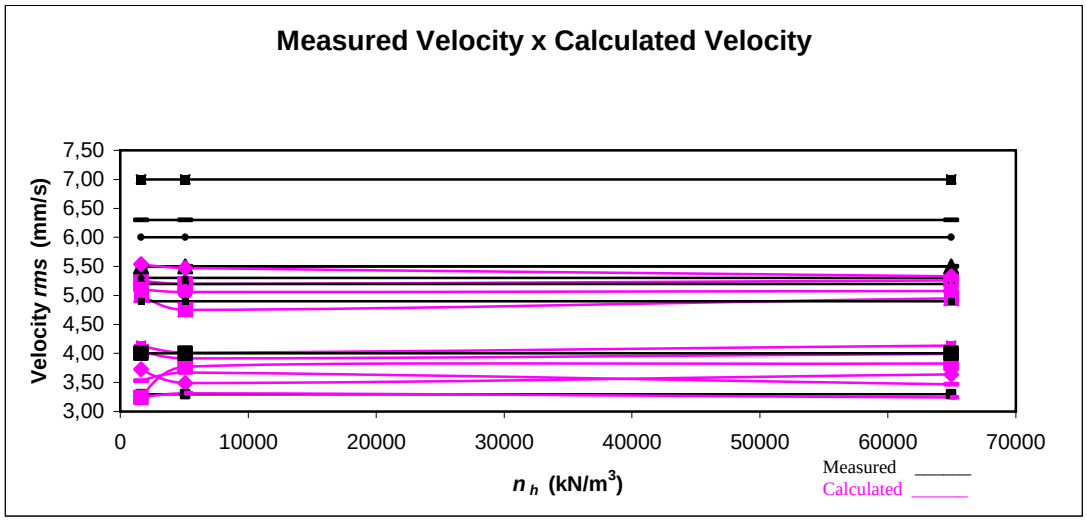


Figure 9: Comparisons between measured and calculated velocities

For the n_h values within the typical range of these soils, it is observed that the natural frequencies exhibit significant variation. Practically, only the natural frequencies corresponding to modes 8 and 9 showed variation less than 20%, thus inferring that the parameter nh obtained under static conditions is not suitable to represent the soil models when one wishes to obtain the eigenvalues of the structure- foundation-soil interactive system.

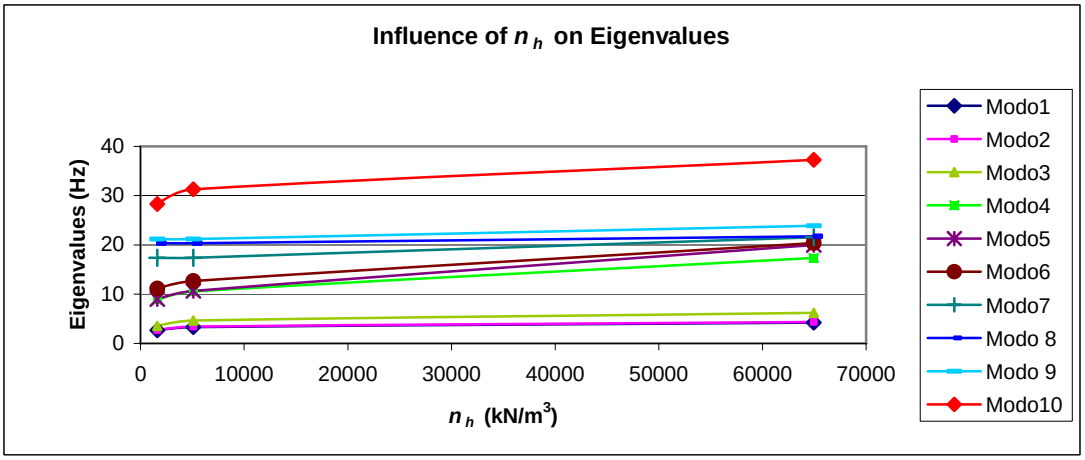


Figure 10: Curves eigenvalue versus n_h

6.2 Assessment 2 - n_h cyclic case

From figure 11, it is noted that the calculated velocities are predominantly underestimated for n_h parameter values within the range of 34000 to 326,000 kN/m^3.

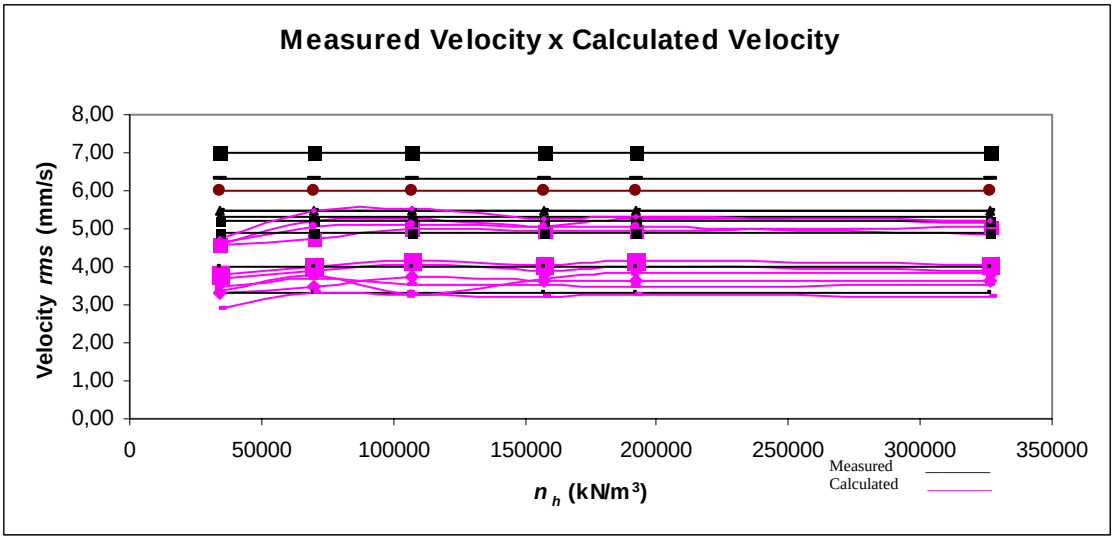


Figure 11: Comparisons between measured and calculated velocities

For the first six modes of vibration, the percentage deviation was no greater than 3.5% when varying the n_h value of approximately 64% (n_h between 69,000 kN/m^3 and 192,000 kN/m^3). In contrast, the percentage deviation of the natural frequencies from the seventh vibration mode, when varying the value of n_h, was approximately 28%.

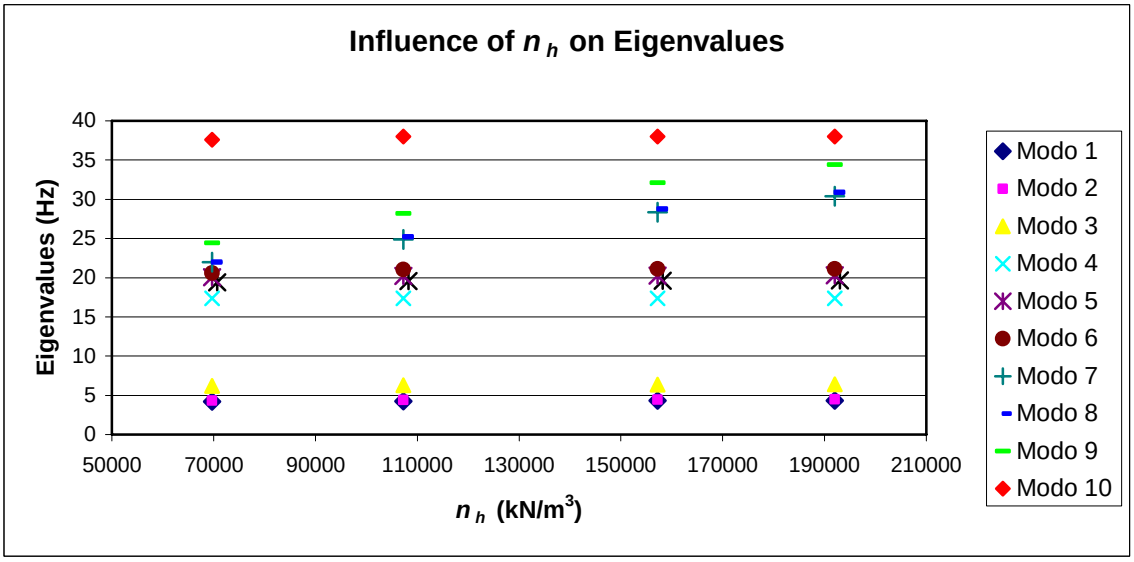


Figure 12: Curves eigenvalue versus n_h

7 CONCLUSIONS

When using soil parameters obtained under static conditions, there is distinct ranges of n_h where the dynamic response of the system is sometimes overestimated and sometimes underestimated. For values of static n_h within the typical range of these soils, it is observed that the

natural frequencies exhibit significant variation. Practically, only the natural frequencies corresponding to modes 8 and 9 showed variation less than 20%, thus alerting on the need for careful choice of soil parameter so as not to provide misinterpretation of the system resonance condition.

When using soil parameters obtained under cyclic conditions, there is also distinct ranges of n_h where the dynamic response can be underestimated or overestimated. In relation to natural frequencies, it appears that from the seventh mode of vibration, there is significant variability in its magnitude as a function of n_h. For cases of compressors with high operating frequency, the choice of soil parameter must be careful to avoid misinterpretation of the resonance condition. However, the first six vibration modes undergo little variation due to the increased stiffness caused by dynamic loading. This fact motivates the completion of field trials with a larger number of charge cycles.

The study of the interaction between equipment, structures, foundations and soil is a vast field and inherently with many uncertainties, which often forces the specialists involved in the design to assume parameter values that can lead to either success or failure of machine performance.

In this context, complementary studies have been carried out in order to improve knowledge in this subject, for example: testing the effect on the dynamic response of the system by using non-linear spring as a representative parameter of soil; testing the effect on the dynamic response of the system in relation to the use of springs associated with viscous dampers and evaluating the effect of the soil stiffness degradation due to the dynamic loading.

REFERENCES

[1] R. J. Miche *Investigation of piles subject to horizontal forces. Application to quay walls*. Journal of the School of Engineering, n. 4, Giza, Egipt, 1930, apud Velloso, 2010.

[2] T. Nogami *Simplified subgrade model for three-dimensional soil-foundation interaction analysis*, Soil Dynamics and Earthquake Engineering, Elsevier, Volume 15, number 7, pp. 419-429, 1996.

[3] ASSOCIAÇÃO BRASILEIRA DE NORMAS TÉCNICAS. *NBR 12131: Estacas – prova de carga estática – Método de ensaio, 2006*.

[4] K. G. Bathia *Foundations for industrial machines*, D-CAD Publishers, New Delhi, 2008.

[5] S. C. Arya; M. W. O'neill; G. Pincus *Design of Structures and Foundations for Vibrating Machines,* Gulf Publishing Company, USA, 4th edition, 1979.

[6] AMERICAN SOCIETY FOR TESTING AND MATERIALS. *ASTM D3966 - 07: Standard test methods for deep foundations under lateral load*, 2007.

COMPDYN 2013
4th ECCOMAS Thematic Conference on
Computational Methods in Structural Dynamics and Earthquake Engineering
M. Papadrakakis, N.D. Lagaros, V. Plevris (eds.)
Kos Island, Greece, 12–14 June 2013

A PROCEDURE FOR EVALUATING THE SOIL-STRUCTURE INTERACTION EFFECTS ON THE SYSTEM PERIOD AND DAMPING OF PILE-SUPPORTED STRUCTURES

Cristina Medina[1], Juan J. Aznárez, Luis A. Padrón, and Orlando Maeso

Instituto Universitario de Sistemas Inteligentes y Aplicaciones Numéricas en Ingeniería (SIANI).
Universidad de Las Palmas de Gran Canaria
Edificio Central del Parque Científico y Tecnológico del Campus Universitario de Tafira. Las Palmas de Gran Canaria. España.
e-mail: cmedina[1], jjaznarez, lpadron, omaeso@siani.es

Keywords: soil-structure interaction, piled foundations, effective period, effective damping.

Abstract. *Soil-structure interaction involves kinematic and inertial effects that affect the dynamic behaviour of the structures. Thus, a proper assessment of their dynamic response requires the development of models that incorporate, in a rigorous manner, the interaction between the structure and the soil on which it is founded. These interaction phenomena depend on factors such as: the foundation type, its geometry and embedment depth, the soil type and stratigraphy as well as the characteristics of the structure. In line with other authors' studies for shallow [7] and embedded foundations [15], a simple substructuring model of soil-structure interaction in the frequency domain is proposed herein to evaluate the influence of these factors on the dynamic response of structures founded on pile groups when subjected to seismic loads. A BEM-FEM coupling model [5] is used to compute the impedance functions and the kinematic interaction factors. A simple and stable procedure is developed in order to estimate the period and damping of structures supported by different configurations of pile groups considering soil-structure interaction. For this purpose, several modifications are introduced in the strategy presented by Avilés and Pérez-Rocha [15] for embedded foundations. A diagonal impedance matrix that takes into account the cross-coupled impedances of pile groups, which allows getting manageable equations, is obtained in the lines of Maravas et al. [16] in the case of single piles. All equations are expressed in terms of dimensionless parameters. An analysis of the influence of some of the main characteristics of the foundation affecting the system response is accomplished. The results show that cross-coupled impedances and soil-structure interaction effects should not be neglected.*

1 INTRODUCTION

The dynamic characteristics of the interacting system, as well as the ground motion around the foundation, are both influenced by kinematic and inertial effects associated to soil-structure interaction (SSI). The exact analysis of this interaction for building structures may be implemented through a substructuring methodology, which enables, moreover, to accomplish parametric analysis in the broad sense with low computational effort. It is common knowledge that two fundamental problems have to be solved in these models in order to carry out a SSI harmonic analysis: the evaluation of the impedance functions and the input motion (kinematic interaction) of the foundation. Then soil-structure system is analized through a rigid-base structure over springs and dashpots representing the soil-foundation system and subjected to a base excitation due to the kinematic interaction factors obtained for the type of foundation analized.

On the other hand, direct approaches, modelling simultaneously the main aspects of the problem and their mutual interactions more rigorously [1–5], are both more complex and more demanding from the computational point of view, and are consequently not frequently used for the analysis of this kind of problems. Even so, these methods are specially competitive in the analysis of interaction phenomena among nearby structures, and in problems involving nonlinearities.

The effects of SSI on the effective period and damping of soil-structure systems have been extensively studied either for surface-supported foundations (e.g. [6–12]) or for embedded foundations [13, 14]. However, they have been examined at the exclusion of the kinematic interaction. Avilés et al. [15] evaluate the effects of foundation embedment on the effective period and damping and the response of soil-structure systems, considering both kinematic and inertial interaction. Among other simplifying assumptions, all these solutions neglect the cross-coupled stiffness and damping terms.

On the other hand, there are few studies in the scientific literature that analyse the dynamic characteristics of pile-supported structures. In this line, Maravas et al. [16] presented an approximate iterative procedure placing the reference system at a depth such that a diagonal impedance matrix is obtained. This procedure allows to study the SSI effects on single-pile supported one-storey shear structures considering the influence of cross-coupled impedances on their dynamic response.

The aim of this work is to evaluate the influence of SSI on the period and damping of structures founded on square pile groups, in homogeneous viscoelastic half-spaces subjected to vertically incident S waves. The analysis is performed by a substructuring model in the frequency domain that takes into account both kinematic and inertial interaction effects. In order to do this, a simplified, stable and accurate procedure is proposed herein. This procedure allows to determine the dynamic characteristics of an equivalent viscously damped single-degree-of-freedom (SDOF) oscillator, which being subjected to the free-field ground motion, causes the same response in terms of shear force at the base of the structure as the coupled system involving kinematic and inertial interaction with the foundation ground within the range where the peak response occurs.

All equations are expressed in terms of the main dimensionless parameters of the problem which considerably facilitates the analysis of their influence on the system dynamic response.

In this study, the harmonic response of the soil-structure system is computed by making use of impedance functions and kinematic interaction factors, which are both frequency-dependent functions, computed by a BEM-FEM coupling model [5].

Finally, results for different piles configurations are presented. The influence of some of the

parameters involved (mass density ratio, fixed-base struture damping, pile-soil Young's modulus ratio, number of piles) are studied over practical ranges of interest.

2 PROBLEM DEFINITION

A model consisting of a single-degree-of-freedom system in its fixed-base condition, as the one represented in Figure1, is used in this paper to study the dynamic behaviour of linear shear structures. This model may represent either one-storey buildings or one mode of vibration of multi-storey multi-mode structures. The structure is considered to be founded on a square pile group embedded in a homogeneous, viscoelastic and isotropic half-space. The pile cap that constrains the pile heads is assumed to be a rigid square plate of negligible thickness which is not in contact with the half-space. The columns of the structure are supposed to be massless and axially inextensible. Both the foundations mass and the structural mass are considered to be uniformly distributed over square areas. The pile group configuration, which is illustrated in Figure 1, is defined by foundation halfwidth b, centre-to-centre spacing between adjacent piles s, length L and sectional diameter d of piles, cap mass m_o and cap moment of inertia about a horizontal axis passing through the centre of gravity of the cap I_o. The dynamic behaviour of the structure can be defined by its fixed-base fundamental period T, the height h of the resultant of the inertia forces for the first mode, the mass m participating in this mode, the moment of inertia of the vibrating mass I, the structural stiffness k, and the viscous damping ratio ξ.

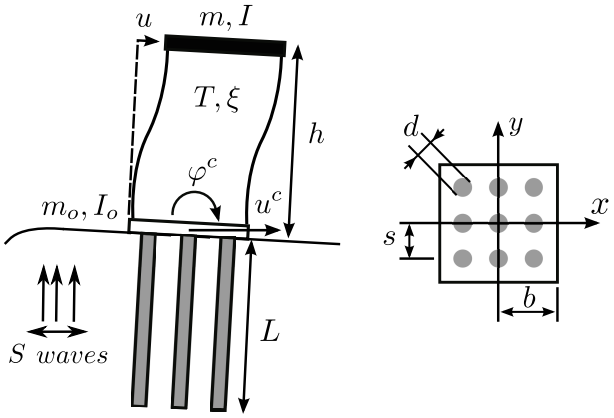


Figure 1: *Problem definition.*

The system response, when soil-structure interaction is considered, can be approximated by that of a three-degree-of-freedom system defined by the structural horizontal deflection u together with the foundation horizontal displacement u^c and rocking φ^c. Vertical and torsional motions are neglected in this study.

3 SUBSTRUCTURE MODEL

This problem can be studied using the substructure methodology which provides accurate results for this kind of problems and at the same time allows performing parametric analysis with very little computational effort. For this purpose the system is subdivided into *soil-foundation* stiffness and damping, represented by means of springs and dashpots (see Figure 2), and *building-cap* superstructure. The solution can be broken into three steps, as proposed by Kausel and Roësset [17]. In the case under study, the first step consist in the determination of

the frequency dependent kinematic interaction factors which represent the horizontal (u_g) and rocking (φ_g) motions of the massless pile cap when subjected to the same input motion as the total solution. In the present case of deep foundations, even vertically incident S waves in a halfspace (for which the free-field motion at the ground surface is exclusively horizontal) generate rocking kinematic response at the pile cap. The second step is to obtain the impedances whose mathematical representation is $K_{ij} = k_{ij} + \mathrm{i}a_o c_{ij}$. The dimensionless frequency is defined as $a_o = \omega b/c_s$; where ω is the excitation circular frequency, $c_s = \sqrt{\mu_s/\rho_s}$ the speed of propagation of shear waves in the halfspace, and ρ_s and μ_s the soil mass density and shear modulus of elasticity, respectively. These complex-valued frequency-dependent functions (k_{xx}, c_{xx}), $(k_{\theta\theta}, c_{\theta\theta})$ and $(k_{x\theta}, c_{x\theta})$ represent the stiffness and damping of the soil in the horizontal, rocking and cross-coupled horizontal-rocking vibration modes,respectively. When computed numerically, the cross-coupled terms $(k_{x\theta}, c_{x\theta})$ and $(k_{\theta x}, c_{\theta x})$, which should be identical, are not exactly equal to one another. Given that this difference is not significant for practical purposes, they are considered identical in this approach. Lastly, the response of the structure supported on springs and subjected to the motion computed in the first step is computed at each frequency.

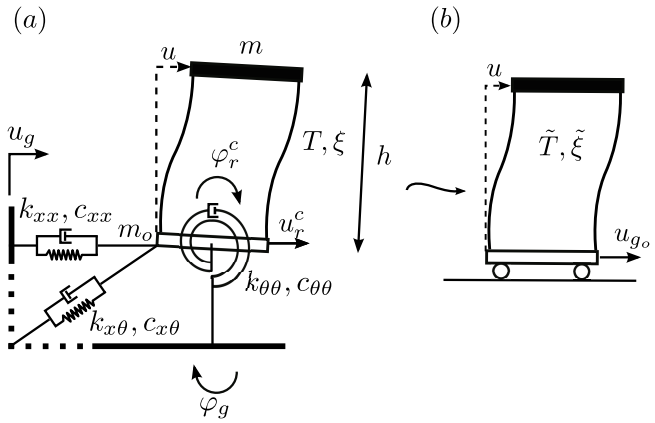


Figure 2: *(a) Substructure model of a one-storey structure. (b) Equivalent single-degree-of-freedom oscillator*

Hence, the equations of motion of the system depicted in Figure 2(a), assuming small displacements, can be expressed in terms of relative motions, as

$$m \cdot [\ddot{u} + \ddot{u}_r^c + \ddot{u}_g + h(\ddot{\varphi}_g + \ddot{\varphi}_r^c)] + K \cdot u = 0 \tag{1}$$

$$m_o \cdot [\ddot{u}_r^c + \ddot{u}_g] + K_{xx} \cdot u_r^c + K_{x\theta} \cdot \varphi_r^c - K \cdot u = 0 \tag{2}$$

$$\begin{aligned} &m \cdot h[\ddot{u} + \ddot{u}_r^c + \ddot{u}_g + h(\ddot{\varphi}_g + \ddot{\varphi}_r^c)] + I(\ddot{\varphi}_r^c + \ddot{\varphi}_g) \\ &+ K_{\theta x} \cdot u_r^c + K_{\theta\theta} \cdot \varphi_r^c + I_o(\ddot{\varphi}_r^c + \ddot{\varphi}_g) = 0 \end{aligned} \tag{3}$$

where eq. (1) represents the horizontal force equilibrium of the structure, eq. (2) the horizontal force equilibrium of the soil-foundation system and eq. (3) the moment equilibrium of the

structure-foundation system about the centre of gravity of the pile cap. This set of equations can be expressed in a matrix form as

$$\left\{ \begin{bmatrix} K & 0 & 0 \\ -K & K_{xx} & K_{x\theta} \\ 0 & K_{\theta x} & K_{\theta\theta} \end{bmatrix} - \omega^2 \begin{bmatrix} m & m & mh \\ 0 & m_o & 0 \\ mh & mh & m\,h^2 + I_o + I \end{bmatrix} \right\} \cdot \cdot \begin{bmatrix} u \\ u_r^c \\ \varphi_r^c \end{bmatrix} = \omega^2 \left\{ \begin{bmatrix} m \\ m_o \\ mh \end{bmatrix} u_g + \begin{bmatrix} mh \\ 0 \\ m\,h^2 + I_o + I \end{bmatrix} \varphi_g \right\} \tag{4}$$

where $K = k + \mathrm{i}2\omega_n m\xi\omega$, being $\omega_n = 2\pi/T$ the fixed-base natural frequency of the superstructure, and motions have been assumed to be time-harmonic of the type $u(t) = u\, e^{i\omega t}$. Once the foundation input motion is computed and the right-hand vector and the coefficient matrix are known, the structural deflection and foundation relative motions can be computed for every frequency.

4 DIMENSIONLESS PARAMETERS

A set of dimensionless parameters, covering the main features of SSI problems, has been repeatedly used in the related literature to perform parametric analyses [7, 8, 13, 15]. Following these authors, the parameters that will be used herein to characterize the soil-foundation-structure system are:

- The wave parameter $\sigma = c_s T/h$, measuring the soil-structure relative stiffness.
- The structural slenderness ratio h/b, measuring the relation between structure height and foundation half-width.
- The mass density ratio $\delta = m/(4\rho_s b^2 h)$ between structure and supporting soil.
- The foundation-structure mass ratio m_o/m.
- The dimensionless fixed-base natural frequency of the structure, that can be expressed by means of the ratio $\lambda = \omega_n/\omega$.
- The fixed-base structure damping ratio ξ.
- The dimensionless excitation frequency $a_o = \omega b/c_s = (b/d)(\omega d/c_s)$.
- The Poisson's ratio ν_s and damping ratio ξ_s of the soil.

On the other hand, the following dimensionless parameters are considered regarding the pile foundations:

- The pile spacing ratio s/d, expressed as the ratio between the centre-to-centre spacing between adjacent piles and their sectional diameter.
- The embedment ratio L/b, measuring the relation between pile length and foundation half-width.

- The pile slenderness ratio L/d, measuring the relation between length and sectional diameter of piles.
- The pile-soil Young's modulus ratio E_p/E_s, measuring the pile-soil relative stiffness.
- The soil-pile densities ratio ρ_s/ρ_p.
- The size of the square pile group.
- The dimensionless frequency a_o.

5 DIMENSIONLESS SYSTEM EQUATIONS

It can be shown that the equation of motion of the system (eq. (4)) can be expressed as a function of the dimensionless parameters already defined, as follows

$$\left\{ \begin{bmatrix} \lambda^2+2\lambda\xi\mathrm{i} & 0 & 0 \\ 0 & \lambda^2\sigma^2\frac{1}{16\pi^2}\frac{h}{b}\frac{1}{\delta}\tilde{K}_{xx} & \lambda^2\sigma^2\frac{1}{\delta}\frac{1}{16\pi^2}\tilde{K}_{x\theta} \\ 0 & \lambda^2\sigma^2\frac{1}{\delta}\frac{1}{16\pi^2}\tilde{K}_{\theta x} & \lambda^2\sigma^2\frac{1}{16\pi^2}\frac{b}{h}\frac{1}{\delta}\tilde{K}_{\theta\theta} \end{bmatrix} - \begin{bmatrix} 1 & 1 & 1 \\ 1 & 1+\frac{m_o}{m} & 1 \\ 1 & 1 & 1+\frac{b^2}{3h^2}\left(1+\frac{m_o}{m}\right) \end{bmatrix} \right\} \begin{bmatrix} \omega_n^2 u/\omega^2 u_{g_o} \\ \omega_n^2 u_r^c/\omega^2 u_{g_o} \\ \omega_n^2 h\varphi_r^c/\omega^2 u_{g_o} \end{bmatrix} = \\ -\lambda^2 \left\{ \begin{bmatrix} 1 \\ 1+\frac{m_o}{m} \\ 1 \end{bmatrix} I_u + \frac{h}{b} \begin{bmatrix} 1 \\ 1 \\ 1+\frac{b^2}{3h^2}\left(1+\frac{m_o}{m}\right) \end{bmatrix} I_\varphi \right\} \tag{5}$$

Equation (5) is obtained by introducing the structural stiffness and damping expressions, that corresponds to a viscous damping model, into the equation (4); adding the two firsts rows of the equation so that the second equation represents the horizontal balance of the whole; replacing the structural stiffness by its expression $k = \omega_n^2 m$; extracting the structural mass m, as a common factor, from both sides of the equation and adding the matrices of the first term of the equation; extracting ω^2/ω_n^2 as a common factor from de first term of the equation; dividing by h the third row of the equation and the third column of the system matrix; replacing the rotational inertias I_o and I by their expressions $I_o = m_o b^2/3$ and $I = mb^2/3$, respectively; normalizing the kinematic interaction factors and the impedance functions; and expressing the later ones in a dimensionless form.

The impedance functions are normalized as follows: $\tilde{K}_{xx} = K_{xx}/\mu_s b$, $\tilde{K}_{\theta\theta} = K_{\theta\theta}/\mu_s b^3$ and $\tilde{K}_{x\theta} = K_{x\theta}/\mu_s b^2$, and the kinematic interaction factors are normalized with the free-field motion at the surface u_{g_o}, being $I_u = u_g/u_{g_o}$ and $I_\varphi = \varphi_g b/u_{g_o}$, both being functions of the dimensionless frequency a_o.

Negligible differences were obtained from the comparison between the results computed by using this model and those reported by Veletsos [7] for shallow foundations, and Avilés and Pérez-Rocha [15] for embedded foundations.

6 SOLUTION STRATEGIES

The objective is to find the dynamic characteristics of an equivalent viscously damped single-degree-of-freedom (SDOF) oscillator, as that shown in Fig. 2 (b), which being subjected to the free-field ground motion, causes the same response in terms of shear force at the base of the

structure as the coupled system involving kinematic and inertial interaction with the foundation ground within the range where the peak response occurs. This SDOF system can be defined by its undamped natural period $\tilde{T}$ and its damping ratio $\tilde{\xi}$.

A procedure based on finding the eigenvalue $\tilde{\lambda}$ of the 3DOF system is proposed in this paper to determine the dynamic characteristics of the equivalent SDOF system. This procedure is similar to that proposed by Avilés and Pérez-Rocha [15] for embedded foundations. However, contrary to what they do, herein the cross-coupled horizontal-rocking terms and the high-order terms involving products of damping coefficients are considered. Neglecting the cross-coupled stiffness and damping terms $k_{x\theta}$ and $c_{x\theta}$ is not acceptable for pile foundations, not even for certain configurations of embedded foundations, even though such assumption has been extensively used by many authors [6–14].

In order to obtain manageable approximated expressions for the period and damping of the interacting system while keeping all the impedances, the soil-foundation interaction is condensed to a point at a certain virtual depth $D(\omega) = -K_{x\theta}/K_{xx}$ (see Figure 3) such that the impedance matrix becomes diagonal, as some authors propose [16, 18]. If, in addition, m_o, I and I_o are neglected as usual (see, for instance [15]), eq. (5) becomes

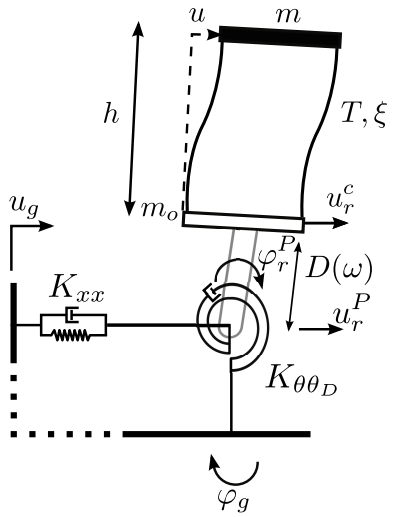


Figure 3: *Equivalent model with diagonalized impedance matrix*

$$\left\{ \lambda^2 \begin{bmatrix} (1+\mathrm{i}2\xi') & 0 & 0 \\ 0 & \alpha_{xx}^2(1+\mathrm{i}2\xi_{xx}) & 0 \\ 0 & 0 & \alpha_{\theta\theta}^2(1+\mathrm{i}2\xi_{\theta\theta}) \end{bmatrix} - \begin{bmatrix} 1 & 1 & 1 \\ 1 & 1 & 1 \\ 1 & 1 & 1 \end{bmatrix} \right\} \cdot \begin{bmatrix} \omega_n^2 u/\omega^2 u_{g_o} \\ \omega_n^2 u_r^P/\omega^2 u_{g_o} \\ \omega_n^2 (h+D)\varphi_r^c/\omega^2 u_{g_o} \end{bmatrix} = -\lambda^2 \left(I_u + \frac{h}{b} I_\varphi \right) \begin{bmatrix} 1 \\ 1 \\ 1 \end{bmatrix} \tag{6}$$

where,

$$\xi' = \frac{\omega}{\omega_n}\xi \tag{7}$$

$$\alpha_{xx}^2 = \sigma^2 \frac{1}{16\pi^2} \frac{h}{b} \frac{1}{\delta} \tilde{k}_{xx} \tag{8}$$

$$\xi_{xx} = \frac{\tilde{c}_{xx}}{2\tilde{k_{xx}}} \tag{9}$$

$$\alpha_{\theta\theta}^2 = \sigma^2 \frac{1}{16\pi^2} \frac{h}{b} \frac{1}{\delta} \, Re\left[\frac{b^2}{(h+D)^2} \tilde{K}_{\theta\theta_D}\right] \tag{10}$$

$$\xi_{\theta\theta} = \frac{Im\left[\frac{b^2}{(h+D)^2} \tilde{K}_{\theta\theta_D}\right]}{2Re\left[\frac{b^2}{(h+D)^2} \tilde{K}_{\theta\theta_D}\right]} \tag{11}$$

being $\tilde{K}_{xx} = \tilde{k}_{xx} + \mathrm{i}\tilde{c}_{xx}$ and

$$\tilde{K}_{\theta\theta_D} = \frac{1}{\mu_s b^3} \left(K_{\theta\theta} - \frac{K_{\theta x}^2}{K_{xx}}\right) \tag{12}$$

$$\frac{b^2}{(h+D)^2} = \left(\left(\frac{h}{b}\right)^2 - 2\left(\frac{h}{b}\right) \frac{\tilde{K}_{\theta x}}{\tilde{K}_{xx}} + \left(\frac{\tilde{K}_{\theta x}}{\tilde{K}_{xx}}\right)^2\right)^{-1} \tag{13}$$

Solving the complex system of algebraic equations given in (6) for $\omega_n^2 u / \ddot{u}_{g_o}$ yields the following expression for Q, which represents the ratio of the shear force at the base of the structure to the effective earthquake force [19].

$$Q(\lambda) = \left| \frac{I_u(\lambda) + \frac{h}{b} I_\varphi(\lambda)}{A(\lambda) + \mathrm{i}\, B(\lambda)} \right| \tag{14}$$

where

$$A(\lambda) = 1 - \frac{1}{\lambda^2} - \frac{1 + 4\xi_{xx}\xi'}{\lambda^2 \alpha_{xx}^2 (1+4\xi_{xx}^2)} - \frac{1 + 4\xi_{\theta\theta}\xi'}{\lambda^2 \alpha_{\theta\theta}^2 (1+4\xi_{\theta\theta}^2)} \tag{15}$$

$$B(\lambda) = 2\left[\xi' - \frac{\xi' - \xi_{xx}}{\lambda^2 \alpha_{xx}^2 (1+4\xi_{xx}^2)} - \frac{\xi' - \xi_{\theta\theta}}{\lambda^2 \alpha_{\theta\theta}^2 (1+4\xi_{\theta\theta}^2)}\right] \tag{16}$$

The first root λ' of equation (15) leads to a SDOF system whose peak response does not always lead to an acceptable approximation for the 3DOF system peak response. However, better resuts are obtained by neglecting all second-order damping terms, which leads to the following approximate expression for A

$$A(\lambda) = 1 - \frac{1}{\lambda^2} - \frac{1}{\lambda^2 \alpha_{xx}^2} - \frac{1}{\lambda^2 \alpha_{\theta\theta}^2} \tag{17}$$

The dimensionless undamped natural frequency of the SDOF system $\tilde{\lambda} = \omega_n / \tilde{\omega}_n$ can be found as the root of the equation (17). This is equivalent to the resolution of the eigenvalue problem from equation (6), without considering damping.

As, in this case, $\tilde{\xi} = 1/(2Q(\tilde{\lambda}))$, and taking the expression for $Q(\tilde{\lambda})$ obtained from taking equations (15) and (16) as values of A and B, the effective damping ratio $\tilde{\xi}$ can be written as follows

$$\tilde{\xi} = \left| \left(I_u + \frac{h}{b} I_\varphi \right)^{-1} \left[\frac{\xi'}{\tilde{\lambda}^2} + \frac{1}{\tilde{\lambda}^2} \left(\frac{\xi_{xx}}{\alpha_{xx}^2 (1 + \mathrm{i}2\xi_{xx})} + \frac{\xi_{\theta\theta}}{\alpha_{\theta\theta}^2 (1 + \mathrm{i}2\xi_{\theta\theta})} \right) \right] \right| \tag{18}$$

The obtained values of the dynamic characteristics, effective system period $\tilde{T}$ and damping $\tilde{\xi}$, are used to build modified response spectra that include SSI effect which allow to obtain more accurate design criteria for building structures.

7 RESULTS

Herein, the described procedure is applied to several configurations of pile supported structures in order to perform parametric studies of the influence of SSI effects on their dynamic response. In this paper, some conclusions are drawn from analysing the influence of the variation of parameters such as the size of the pile group, the fixed-base structure damping ratio ξ, the mass density ratio δ, the pile-soil Young's modulus ratio E_p/E_s, the wave parameter σ and the structural slenderness ratio h/b.

Different pile group configurations, for which the values of the dimensionless parameters are listed in Table 1, are analysed. All configurations follow the pattern represented in Figure 4.

Table 1: *Pile groups configurations*

L/b	L/d	s/d		
		2×2	3×3	4×4
1	7.5	7.5	5	3.75
	15	15	10	7.5
2	7.5	3.75	2.5	1.875
	15	7.5	5	3.75
	30	15	10	7.5
4	15	3.75	2.5	1.875
	30	7.5	5	3.75

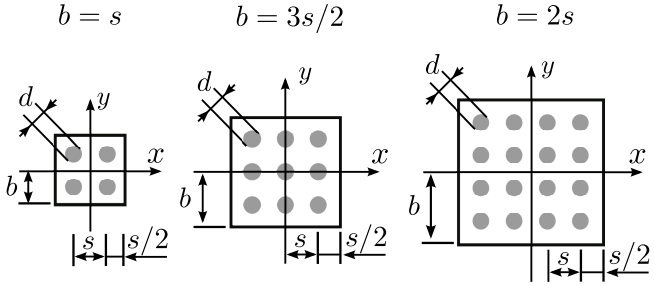


Figure 4: *Geometric configuration of groups of* 2×2 *,* 3×3 *and* 4×4 *piles*

It is assumed that $m_o/m = 0$; $\xi = 0.05$; $\xi_s = 0.05$ and $\nu_s = 0.4$. These values are representative for typical buildings and soils [15]. Moreover $\rho_s/\rho_p = 0.7$.

7.1 Impedances and kinematic interaction factors

In this paper, all impedance functions and kinematic interaction factors are computed using a boundary element (BEM)- finite element (FEM) coupling model [5]. Piles are modelled directly using FEM as beams according to the Bernoulli hypothesis, while soil is modelled using BEM as a linear, isotropic, homogeneous, viscoelastic medium. Welded boundary contact conditions at the pile-soil interfaces are assumed and the pile heads are constrained by a rigid pile-cap which is not in contact with the half-space.

Figures 11 to 15 show the impedances of the pile groups under investigation. On the other hand, Figures 12 to 16 present their kinematic interaction factors (see appendix).

7.2 Influence of the mass density ratio δ

Figure 5 illustrates the relevant influence that the mass density ratio between structure and supporting soil has on the system response. This response can be represented in terms of effective period $\tilde{T}/T$ and damping $\tilde{\xi}$ and maximum shear force at the base of the structure per effective earthquake force unit $Q_m = \mathrm{Max}[|\omega_n^2 u/\omega^2 u_{g_o}|]$. An increase of δ implies a decrease of the system stiffness which results in greater values of $\tilde{T}/T$ and $\tilde{\xi}$. Thus, lower values of Q_m are achieved. The influence of the aforementioned effects becomes more remarkable for increasing values of h/b. For the results provided below, the value of this parameter is taken as $\delta = 0.15$ because it is representative for typical buildings and soils and has been used in previous works (e.g. [7, 15]).

7.3 Influence of the fixed-base structure damping ratio ξ

Figure 6 shows how the variation of the fixed-base structure damping ratio influences the effects of SSI on the system dynamic response. It can be observed that this parameter has no influence on the system effective period $\tilde{T}/T$. However, as it is expected, it affects to the system effective damping $\tilde{\xi}$ that reaches greater values as ξ increases. This effect becomes more remarkable for greater values of the wave parameter σ. By contrast, its influence is negligible when $1/\sigma \geq 0.4$. These variations on the system effective damping leads to increasing values of Q_m for decreasing values of the fixed-base structure damping ratio ξ. Furthermore, greater values of the structural slenderness ratio h/b implies a wider range of the parameter σ where the variation of ξ has a significant influence.

For the results provided in this paper, the value of this parameter is taken as $\xi = 0.05$ because it is representative for typical buildings and has been used in previous works (e.g. [7, 15]).

7.4 Influence of the pile-soil Young's modulus ratio E_p/E_s

As it can be seen in Figures 17 to 22, the variation of the pile-soil Young's modulus ratio affects to impedance functions and kinematic interaction factors. Consequently, SSI effects on the system dynamic response are also influenced.

In order to analyse the influence of E_p/E_s on the dynamic characteristics of the system, Figure 7 presents the results considering two different values of this parameter.

Considering constant properties for the material of piles, lower values of E_p/E_s imply an increase of the soil stiffness which leads to greater values of the system effective period $\tilde{T}/T$ and lower values of the effective damping $\tilde{\xi}$. Consequently, higher values of Q_m are reached. This effect is more remarkable for greater values of the pile slenderness ratio L/d.

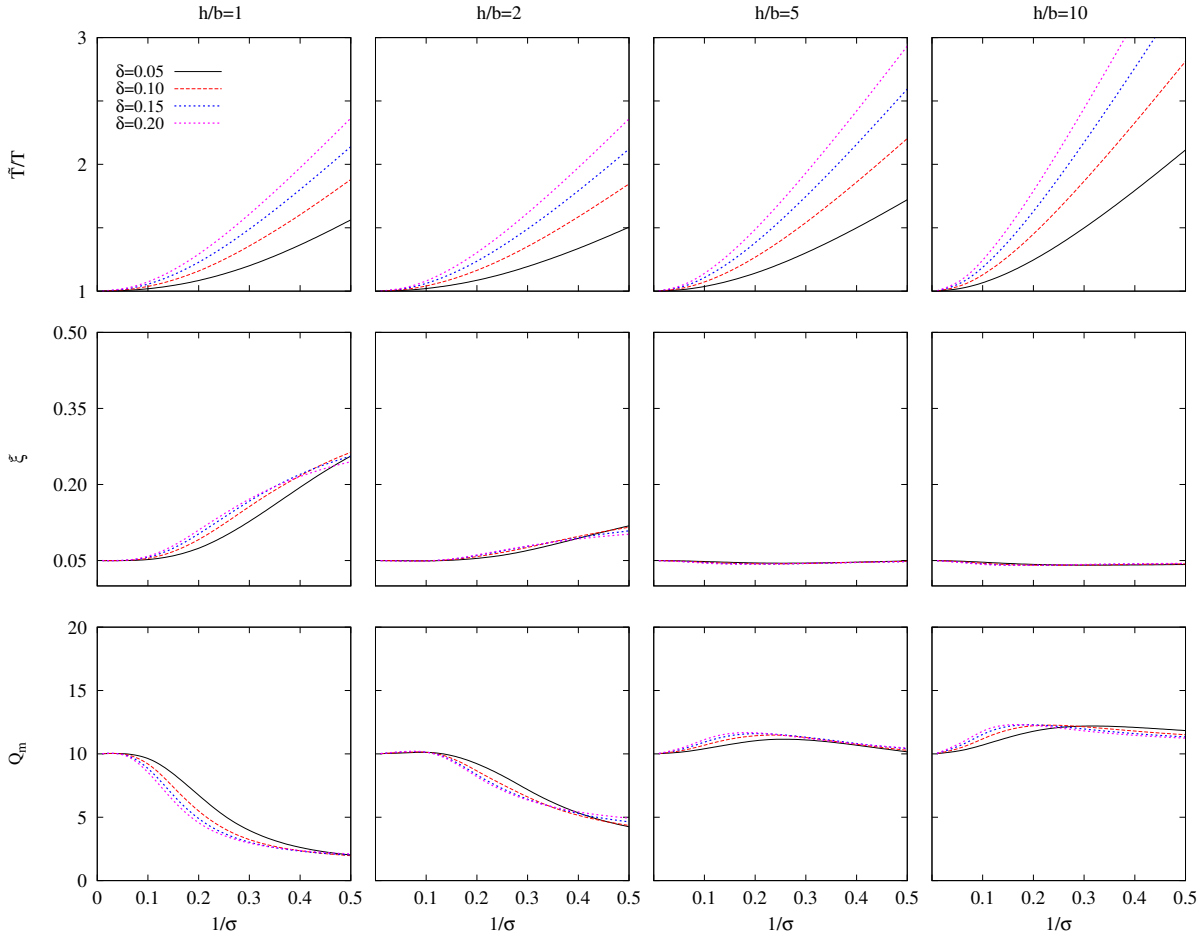


Figure 5: *Effective period $\tilde{T}/T$, damping ratio $\tilde{\xi}$ and maximum structural response value Q_m for a 3×3 pile group with $L/d = 7.5$, $L/b = 1$, $\xi = 0.05$, $Ep/Es = 10^3$ and $\xi_s = 0.05$. Influence of the mass density ratio δ*

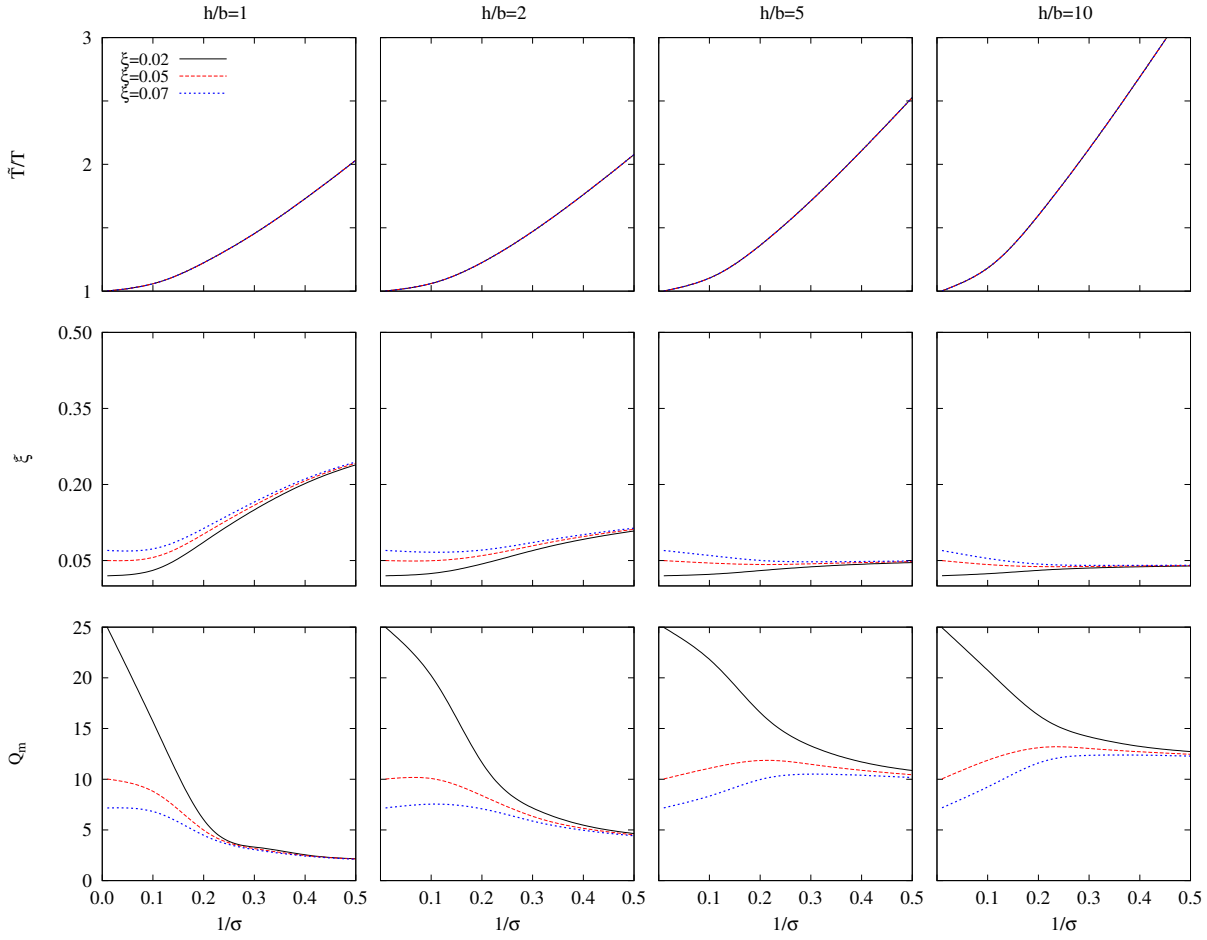


Figure 6: *Effective period $\tilde{T}/T$, damping ratio $\tilde{\xi}$ and maximum structural response value Q_m for a 3×3 pile group with $L/d = 30$, $L/b = 2$, $\delta = 0.15$, $Ep/Es = 10^3$ and $\xi_s = 0.05$. Influence of the fixed-base structure damping ratio ξ*

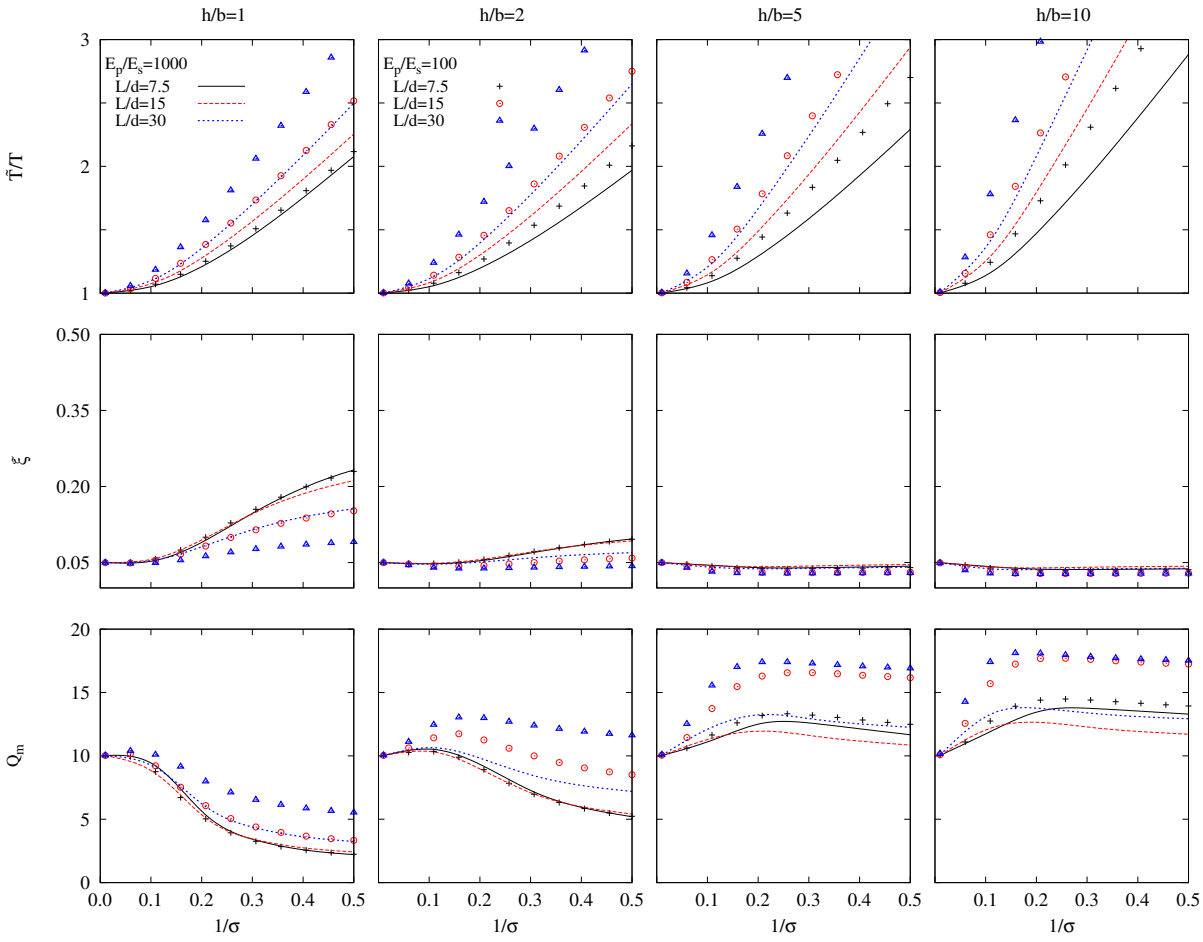


Figure 7: *Effective period $\tilde{T}/T$, damping ratio $\tilde{\xi}$ and maximum structural response value Q_m for 2×2 pile groups with $L/b = 2$, $\delta = 0.15$, $\xi = 0.05$ and $\xi_s = 0.05$. Influence of the pile-soil Young's modulus ratio E_p/E_s*

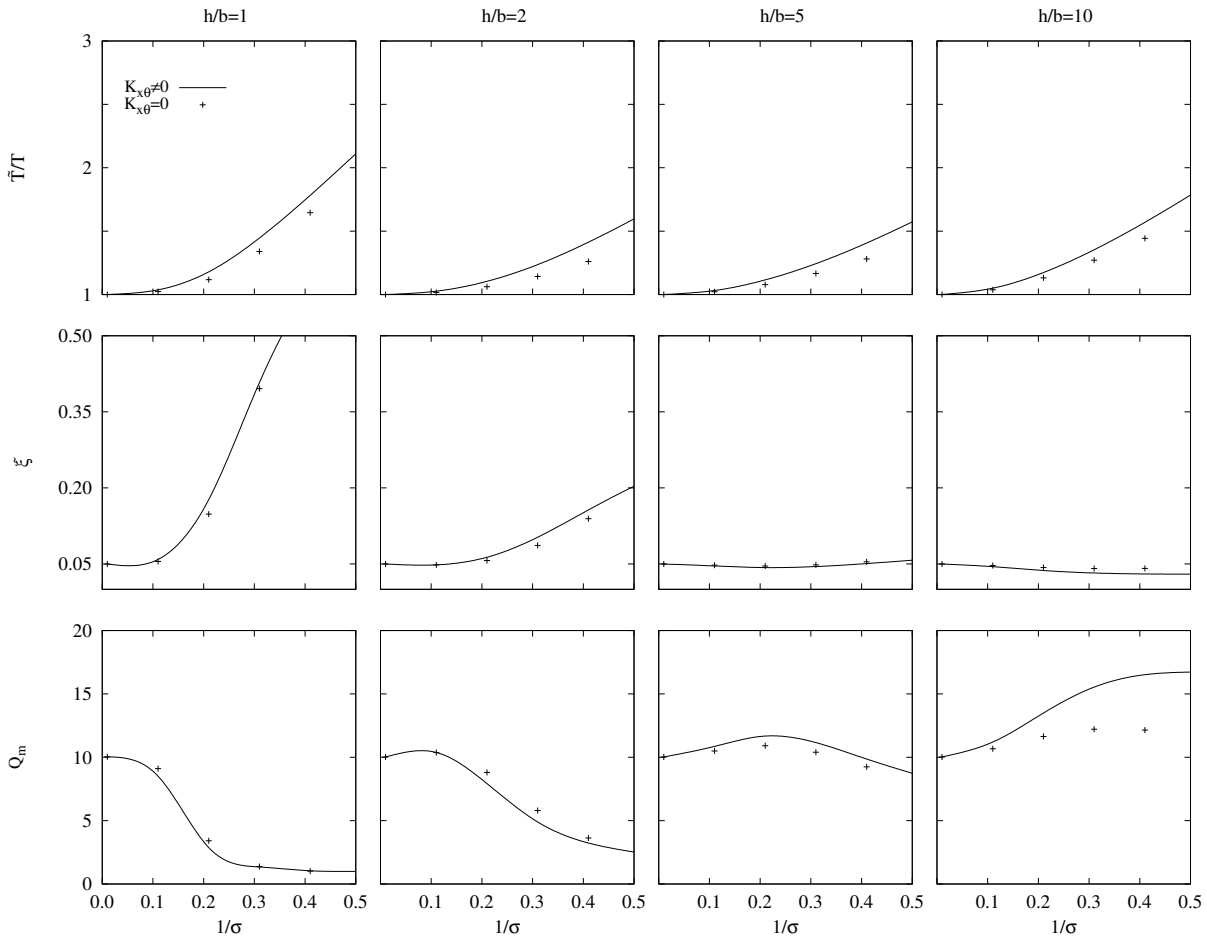


Figure 8: *Effective period $\tilde{T}/T$, damping ratio $\tilde{\xi}$ and maximum structural response value Q_m for 4×4 pile groups with $L/d = 15$, $L/b = 4$ and $\xi_s = 0.05$. Influence of cross-coupled impedances*

7.5 Influence of cross-coupled impedances

Figure 8 illustrates the influence of the cross-coupled impedances on the system dynamic response. As it can be seen, for configurations with $h/b \geq 5$ the system dynamic response in terms of Q_m is subestimated when these elements of the matrix of impendances are neglected. The relative error, in terms of Q_m, committed by neglecting the cross-coupled impedances, could reach a 40%. Therefore, all the results presented in this paper are obtained considering all the elements of the matrix of impedances.

7.6 Influence of kinematic interaction factors

In order to show how kinematic interaction influences the system dynamic response, Figure 9 presents the results involving total soil-structure interaction (both kinematic and inertial interaction) or only inertial interaction. The system effective period $\tilde{T}/T$ is not affected by kinematic interaction. However, generally, the effective damping $\tilde{\xi}$ decreases when these factors are considered. Therefore, the results for the system dynamic response computed without taking

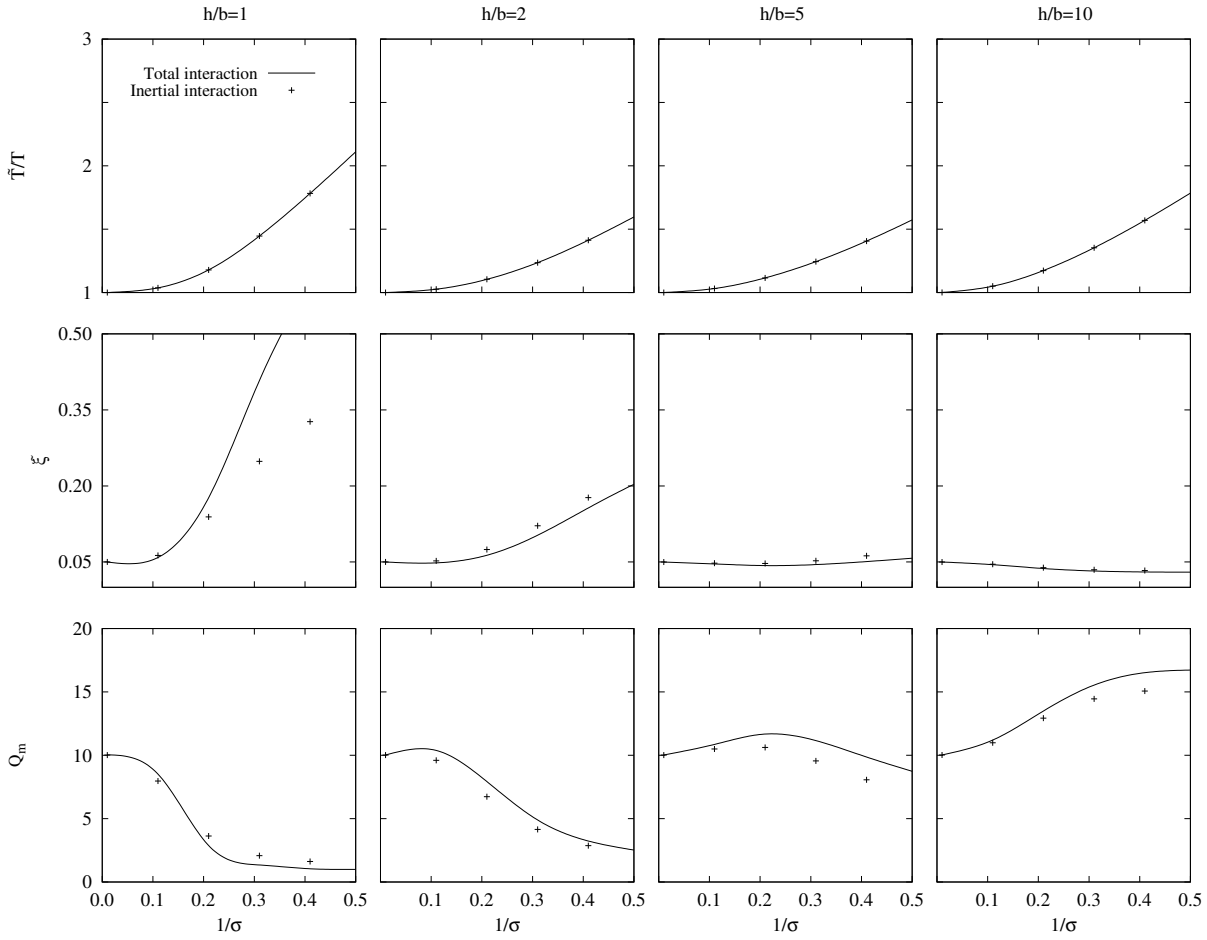


Figure 9: *Effective period $\tilde{T}/T$, damping ratio $\tilde{\xi}$ and maximum structural response value Q_m for 4×4 pile groups with $L/d = 15$, $L/b = 4$ and $\xi_s = 0.05$. Influence of kinematic interaction factors*

kinematic interaction effects into account are not on the side of safety except for non-slender structures $h/b \leq 1$, in which case this trend could be reversed.

7.7 Influence of pile group size

A decrease of the number of piles leads to a reduction of the system stiffness, which implies an increase of the effective period that becomes more remarkable for greater values of h/b, as it can be seen in Figure 10. Regarding the effective damping $\tilde{\xi}$, for $h/b \leq 2$, it reaches greater values as the number of piles increases which leads to smaller values of Q_m.

8 CONCLUSIONS

In this paper, several parametric analysis are presented in order to study the influence of SSI on the dynamic characteristics of structures founded on square pile groups, in homogeneous viscoelastic half-spaces subjected to vertically incident S waves. The analysis is performed by a substructuring model in the frequency domain that takes into account both kinematic and inertial

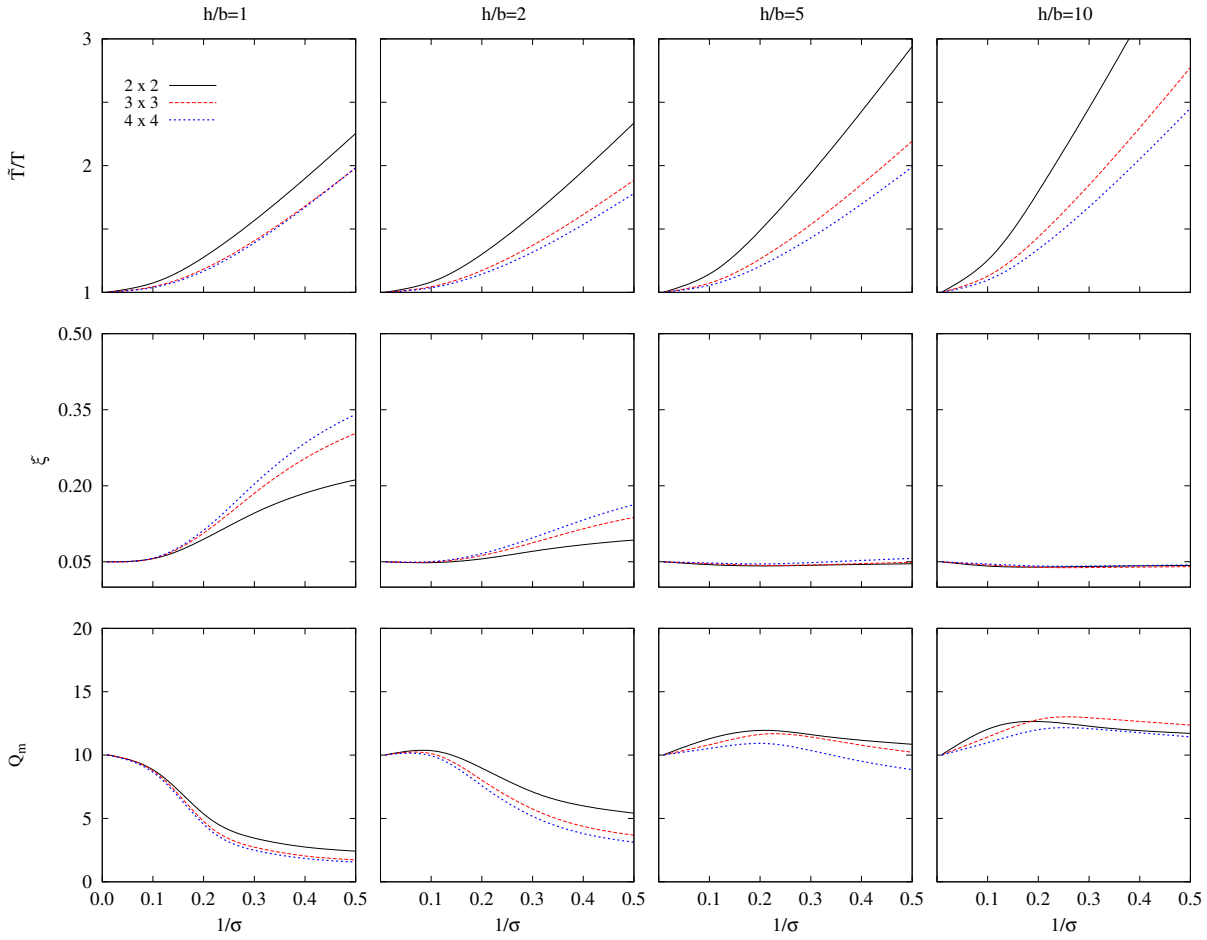


Figure 10: *Effective period $\tilde{T}/T$, damping ratio $\tilde{\xi}$ and maximum structural response value Q_m for pile groups with $L/d = 15$, $L/b = 2$ and $\xi_s = 0.05$. Influence of pile group size*

interaction effects. In order to do this, a simplified, stable and accurate procedure is proposed herein. This procedure allows to determine the effective period and damping of an equivalent viscously damped single-degree-of-freedom (SDOF) oscillator, which being subjected to the free-field ground motion, causes the same response in terms of shear force at the base of the structure as the coupled system involving kinematic and inertial interaction with the foundation ground within the range where the peak response occurs.

All the results provided herein have a dimensionless character, thus their physical interpretation must be carefully done and requires a specific data processing taking into account the influence of every dimensionless parameter.

The main conclusions are summarised below.

- The kinematic interaction does not influence the system effective period but leads to lower values of the system damping, except for non-slender structures.
- Increasing values of the number of piles result in an increase of the foundation stiffness which leads to lower values of $\tilde{T}/T$ and greater values of $\tilde{\xi}$.
- In the same line, lower values of the pile-soil Young's modulus ratio E_p/E_s result in an increase of the foundation stiffness which leads to lower values of the effective period and greater values of the effective damping.
- An increase of the mass density ratio implies greater values of the system effective period and damping.
- The effective period is not affected by variations of the fixed-base structure damping ratio ξ. However, the influence of this variation on the effective damping is more important as the wave parameter increases.
- For slender buildings, the system effective damping remains close to that corresponding to fixed-base condition or lower.

Soil-structure interaction effects significantly influences the system response. Period and damping curves have been obtained considering these effects and they show noticeable differences in relation to those obtained considering fixed-base condition. These effects are more decisive for pile foundations than for embedded or surface-supported foundations and its influence depends substantially on the configuration of the foundation.

9 ACKNOWLEDGEMENTS

This work was supported by the Ministerio de Investigación, Ciencia e Innovación of Spain (MICINN) and FEDER through research project BIA2010-21399-C02-01 and also by the Agencia Canaria de Investigación, Innovación y Sociedad de la Información (ACIISI) of the Government of the Canary Islands and FEDER through research project ProID20100224. C. Medina is a recipient of a fellowship from the Program of predoctoral fellowships of the University of Las Palmas de Gran Canaria (ULPGC). The authors are grateful for this support.

10 APPENDIX

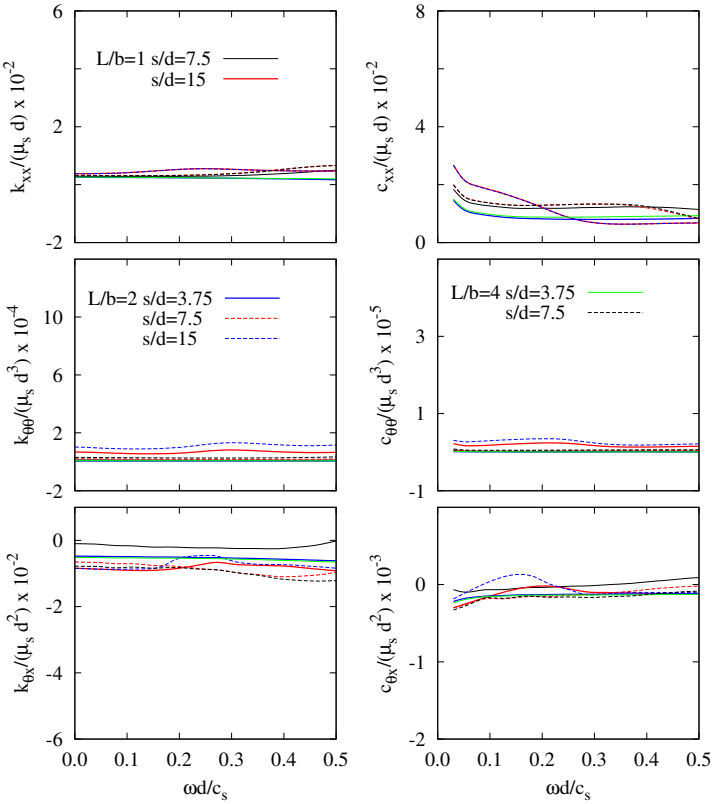


Figure 11: *Impedance functions of different* 2×2 *pile groups;* $E_p/E_s = 10^3$ *and* $\xi_s = 0.05$.

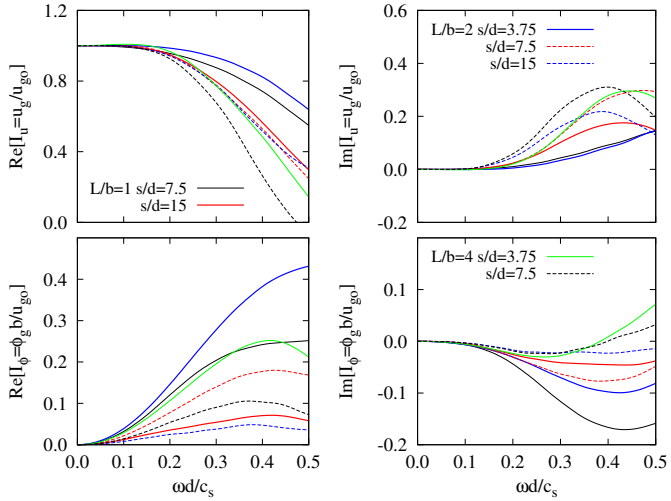


Figure 12: *Kinematic interaction factors of different* 2×2 *pile groups;* $E_p/E_s = 10^3$ *and* $\xi_s = 0.05$.

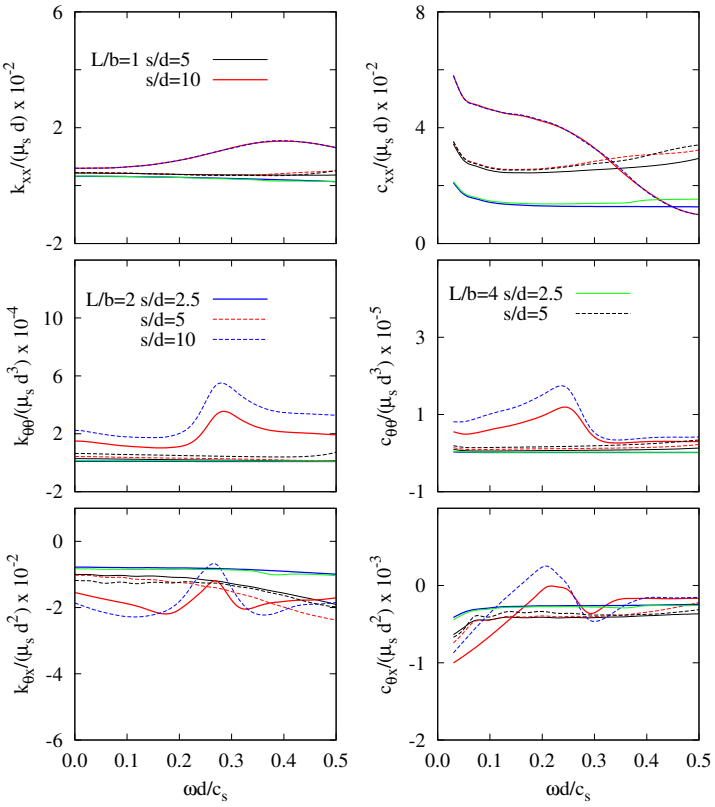


Figure 13: *Impedance functions of different* 3×3 *pile groups;* $E_p/E_s = 10^3$ *and* $\xi_s = 0.05$.

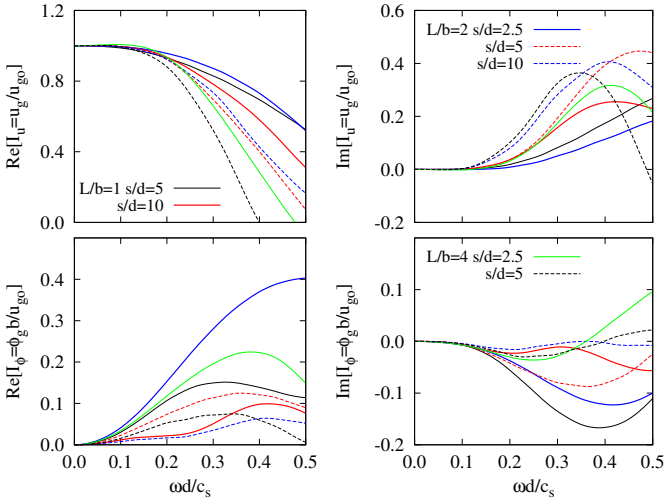


Figure 14: *Kinematic interaction factors of different* 3×3 *pile groups;* $E_p/E_s = 10^3$ *and* $\xi_s = 0.05$.

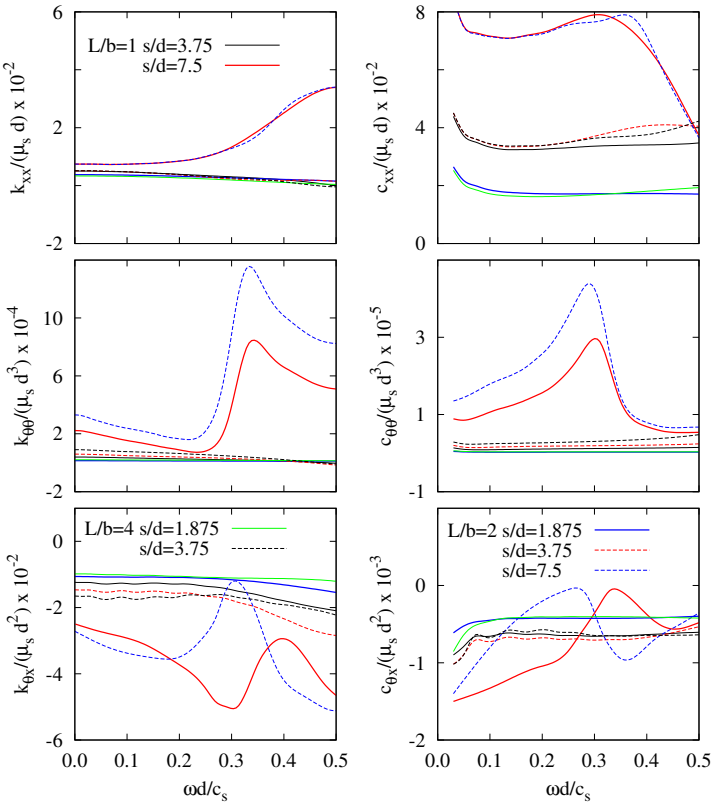


Figure 15: *Impedance functions of different* 4×4 *pile groups;* $E_p/E_s = 10^3$ *and* $\xi_s = 0.05$.

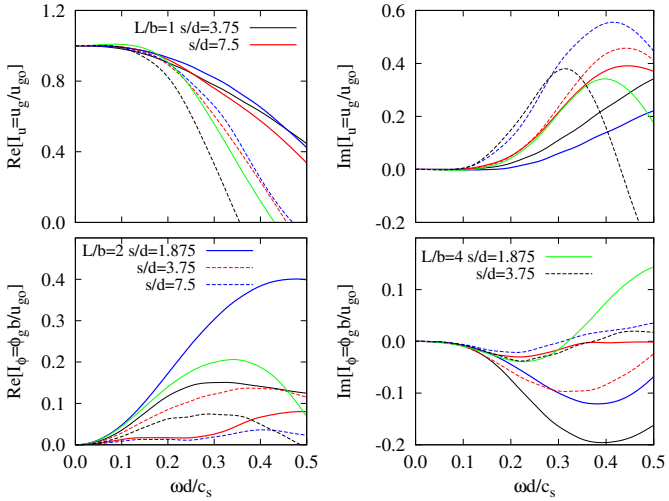


Figure 16: *Kinematic interaction factors of different* 4×4 *pile groups;* $E_p/E_s = 10^3$ *and* $\xi_s = 0.05$.

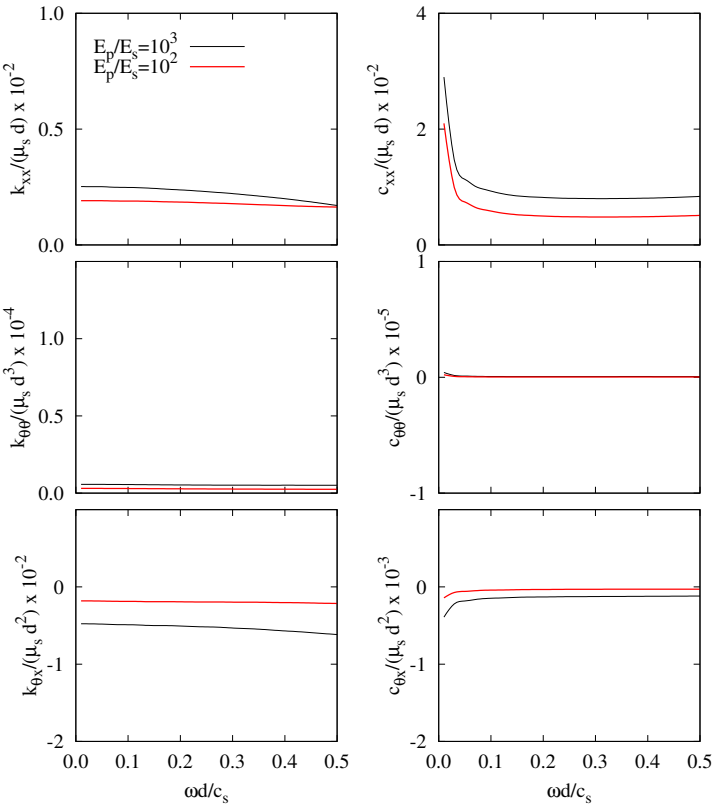


Figure 17: *Impedance functions for a* 2×2 *pile group with* $L/d = 7.5$, $L/b = 2$ *and* $\xi_s = 0.05$. *Influence of the pile-soil Young's modulus ratio* E_p/E_s

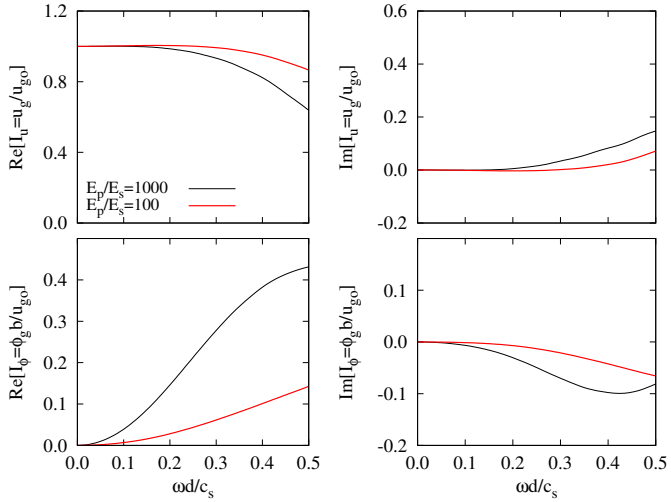


Figure 18: *Kinematic interaction factors for a* 2×2 *pile group with* $L/d = 7.5$, $L/b = 2$ *and* $\xi_s = 0.05$. *Influence of the pile-soil Young's modulus ratio* E_p/E_s

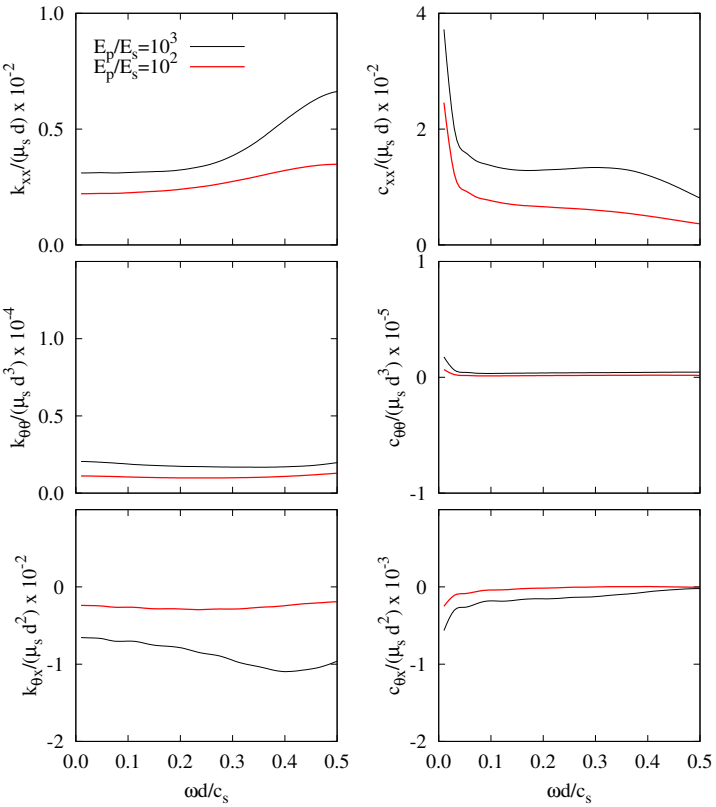


Figure 19: *Impedance functions for a* 2×2 *pile group with* $L/d = 15$, $L/b = 2$ *and* $\xi_s = 0.05$. *Influence of the pile-soil Young's modulus ratio* E_p/E_s

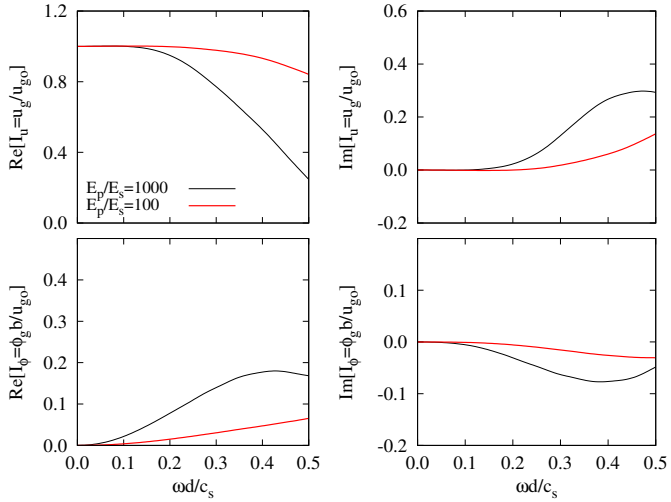


Figure 20: *Kinematic interaction factors for a* 2×2 *pile group with* $L/d = 15$, $L/b = 2$ *and* $\xi_s = 0.05$. *Influence of the pile-soil Young's modulus ratio* E_p/E_s

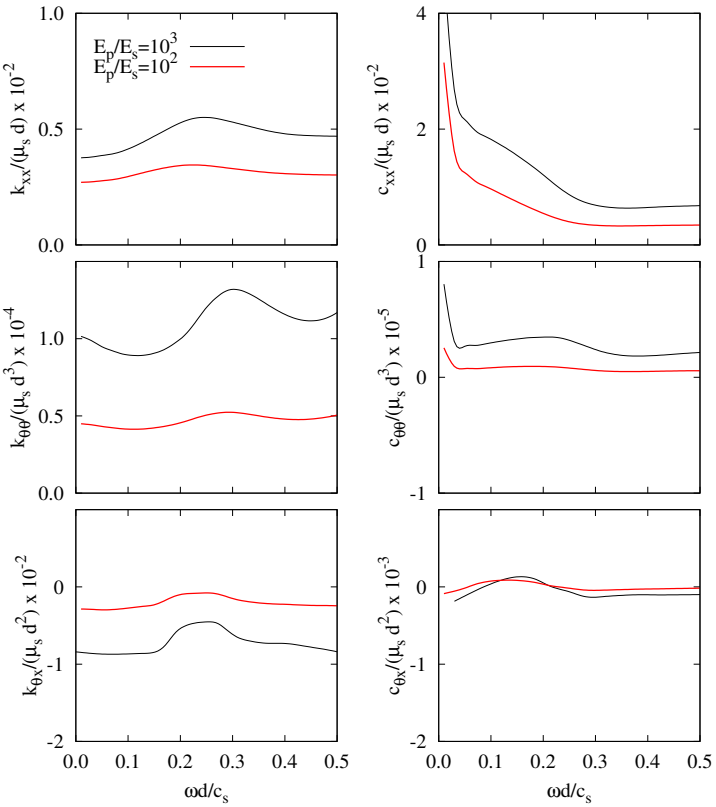


Figure 21: *Impedance functions for a* 2×2 *pile group with* $L/d = 30$, $L/b = 2$ *and* $\xi_s = 0.05$. *Influence of the pile-soil Young's modulus ratio* E_p/E_s

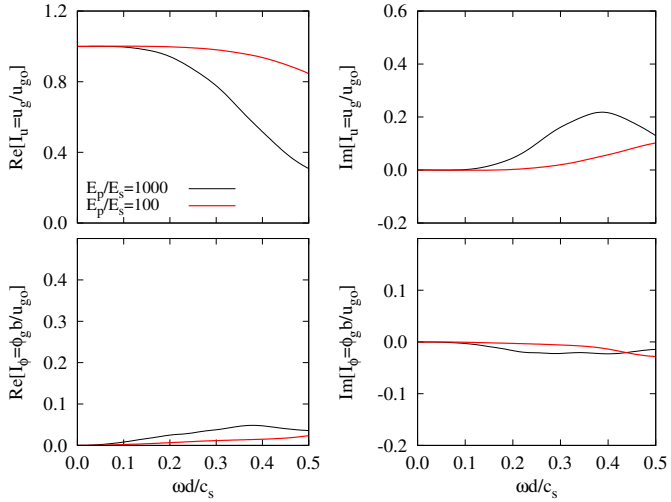


Figure 22: *Kinematic interaction factors for a* 2×2 *pile group with* $L/d = 30$, $L/b = 2$ *and* $\xi_s = 0.05$. *Influence of the pile-soil Young's modulus ratio* E_p/E_s

REFERENCES

[1] J. Guin, P. K. Banerjee, Coupled soil-pile-structure interaction analysis under seismic excitation, *J Struct Eng*, **124**, 434–444, 1998.

[2] K. K. Koo, K. T. Chau, X. Yang, S. S. Lam, Y. L. Wong, Soil-pile-structure interaction under SH wave excitation, *Earthquake Eng Struct Dyn*, **32**, 395–415, 2003.

[3] M. A. Millán, J. Domínguez, Simplified BEM/FEM model for dynamic analysis of structures on piles and pile groups in viscoelastic and poroelastic soils, *Eng Anal Bound Elem*, **33**, 25–34, 2009.

[4] L. A. Padrón, J. J. Aznárez, O. Maeso, Dynamic structure-soil-structure interaction between nearby piled buildings under seismic excitation by BEM-FEM model, *Soil Dyn Earthquake Eng*, **29**, 1084–1096, 2009.

[5] L. A. Padrón, J. J. Aznárez, O. Maeso, 3-D boundary element - finite element method for the dynamic analysis of piled buildings, *Eng Anal Bound Elem*, **35**, 465–477, 2011.

[6] P. C. Jennings, J. Bielak, Dynamics of building-soil interaction, *Bull Seismol Soc Am*, **63**, 9–48, 1973.

[7] A. S. Veletsos, J. W. Meek, Dynamic behaviour of building-foundation systems, *Earthquake Engng Struct Dyn*, **3**, 121–138, 1974.

[8] A. S. Veletsos, V. V. D. Nair, Seismic interaction of structures on hysteretic foundations, *J Struct Div, ASCE*, **101**, 109–129, 1975.

[9] J. Bielak, Modal analysis for building-soil interaction, *J Engng Mech Div ASCE*, **102**, 771–786, 1976.

[10] J. E. Luco, *Linear soil-structure interaction*, Technical Report UCRL-15272, Lawrence Livermore National Laboratory, Livermore, California, 1980.

[11] J. E. Luco, Soil-structure interaction and identification of structural models, in: *Proc. ASCE Speciality Conf. in Civil Engineering and Nuclear Power*, Knoxville, Tennessee, 1980.

[12] J. P. Wolf, *Dynamic soil-structure interaction*, Englewood Cliffs, (NJ); Prentice-Hall, 1985.

[13] J. Avilés, L. E. Pérez-Rocha, Evaluation of interaction effects on the system period and the system damping due to foundation embedment and layer depth, *Soil Dyn Earthquake Engng*, **15**, 11–27, 1996.

[14] J. Bielak, Dynamic behaviour of structures with embedded foundations, *Earthquake Engng Struct Dyn*, **3**, 259–274, 1975.

[15] J. Avilés, L. E. Pérez-Rocha, Effects of foundation embedment during building-soil interaction, *Earthquake Engng Struct Dyn*, **27**, 1523–1540, 1998.

[16] A. Maravas, G. Mylonakis, D. Karabalis, Dynamic characteristics of simple structures on piles and footings, in: *Proc. of 4th Int Conf on Earthquake Geotech Eng*, no. 1672, Thessaloniki, Greece.

[17] E. Kausel, J. M. Roësset, Soil-structure interaction for nuclear containment, in: *Electric Power and Civil Engineer. Power Div. ASCE Specialty Conf*, Boulder, Colorado, pp. 469–498, 1974.

[18] E. Kausel, *Structures in seismic regions*, Technical Report, Technische universitt Berlin and MIT, 1984.

[19] A. K. Chopra, Dynamic of structures. *Theory and applications to earthquake engineering.*, Prentice-Hall (NJ), 2001.

[20] G. Gazetas, K. Fan, T. Tazoh, K. Shimizu, M. Kavvadas, N. Makris, Seismic pile-groupstructure interaction, *Geothec Spec Publ, ASCE*, **34**, 56–93, 1992.

[21] K. Fan, G. Gazetas, A. M. Kaynia, E. Kausel, S. Ahmad, Kinematic seismic response of single piles and pile groups, *J Geothec Eng Div, ASCE*, **117(12)**, 1860–1879, 1991.

[22] S. Nikolaou, G. Mylonakis, G. Gazetas, T. Tazoh, Kinematic pile bending during earthquakes: Analysis and field measurements, *Géothecnique*, **51(5)**, 425–440, 2001.

COMPDYN 2013
4th ECCOMAS Thematic Conference on
Computational Methods in Structural Dynamics and Earthquake Engineering
M. Papadrakakis, V. Papadopoulos, V. Plevris (eds.)
Kos Island, Greece, 12–14 June 2013

NON-LINEAR DYNAMIC ANALYSIS OF MASONRY TOWERS UNDER NATURAL ACCELEROGRAMS ACCOUNTING FOR SOIL-STRUCTURE INTERACTION

Siro Casolo[1] **and Giuseppina Uva**[2]

[1]Dipartimento ABC. Politecnico di Milano
P.za L. da Vinci 32, 20133 Milano, Italy
e-mail: siro.casolo@polimi.it

[2]Dipartimento Dicatech, Politecnico di Bari
Via E.Orabona 4, 70125 Bari, Italy
e-mail: g.uva@poliba.it

Keywords: Keywords: Masonry towers; Seismic assessment; Nonlinear dynamic analysis; natural accelerograms; vertical accelerograms; Soil-structure Interaction.

Abstract. *The object of the paper is the influence of the soil-structure interaction on the dynamic response of masonry towers, for which a high level of stress is involved already in the static field. The relevant deformations and displacements at the base of the tower suggest that a significant volume of ground is engaged into the overall dynamic response, both as a participating mass and as a potential carrier of energy dissipation. In order to investigate this aspect and assess the sensitivity of the dynamic response of the soil-structure system to different soil characteristics, the non linear dynamic response of a case study is analysed, by including in the model a significant volume of foundation soil and considering two different ground types. The numerical model is based on a specific Rigid Body and Springs approach, in which the structure is idealized as a mechanism made of rigid elements connected each to the other by axial and shear springs. The nonlinear behaviour is lumped into the springs assigning proper constitutive laws able to model the significant inelastic aspects of the constitutive behaviour and the meso-scale damage mechanisms with a moderate computational effort. Two types of foundation soil have been considered in order to perform the dynamical analysis accounting for the soil-structure interaction: rock and deposits of compact gravel. For both models, non-linear dynamic analyses have been performed adopting natural records having different characteristics (with regard to the frequency content; distance from the epicentre and type of soil). Some interesting considerations are derived from this comparative study about a problem that is very actual for those who deal with non linear dynamics of structures, but yet is not much explored.*

1 INTRODUCTION

The paper deals with the non linear dynamic modelling and analysis of slender masonry bell-towers with a specific focus on two aspects which have a fundamental influence over the structural seismic response of this specific typology: investigation of the non-linear dynamic response under natural accelerograms, including the vertical component; effect of the soil-structure interaction.

A main issue in the seismic behaviour of slender masonry towers is the influence of the axial stresses induced by gravity loads, which are often close to the compression strength limit of the masonry material. Considering that historical masonry is typically characterized by complex geometry, irregularities and a high degree of inhomogeneity, stress concentrations can easily occur, which could even trigger a local collapse. Thence, the structural failure can be driven even by a moderate increase in the stress level, which can occur under seismic events or under long term loads. It is clear, therefore, that masonry towers are vulnerable also to low-intensity earthquakes, since static vertical loads combine with the dynamic loads induced by the ground motion.

In Italy, bell towers are a quite widespread architectural element, with peculiar morpho-typological characters, according to the geographic area. The examination of the documentation about the damage caused by the 1976 Friuli earthquake [1] points out that in isolated bell towers damage patterns tend to be distributed all along the height, although it is frequently more severe at the base. This suggests the need of further investigations about the combined effects of flexural and axial actions, as well as the incorporation into the model of the higher vibration modes, which seem to be have a relevant role in the damage of the upper part, especially the tower crown and belfry [2].

Moreover, during strong earthquakes shear damages are also often observed, and in this case the loss of validity of the Eulero–Bernoulli hypothesis of plane cross-section can significantly affect the overall response of the structure. Specific approaches are needed on order to deal with these aspects, and in particular it is paramount to model the non-symmetry in tension and compression that characterise the masonry material of which these structures are composed.

Finally, the investigation of the response to very strong earthquakes requires to describe the effects of the damages that cause a remarkable reduction of the material stiffness, as well as the energy dissipation through plastic deformation [3]. When the tower is not particularly slender, and depending on the frequency content of the forcing actions, a material model which is capable to describe both the axial and the shear response and damage under cyclic loading is also required in order to investigate the global shear damage effects [4, 5].

In the literature, there are several research studies dealing with the seismic assessment and the vulnerability analysis of masonry towers, with regard to different aspects: mechanical and numerical analysis by computational or simplified approaches [2, 6, 7, 8, 9]; experimental testing methods and structural identification [10, 11] A significant case is that of the Civic Tower of Pavia, Italy (about 900 years old), suddenly collapsed on 17 March, 1989 [12], which has drawn the attention of the scientific community on the high vulnerability of masonry towers also to low-intensity earthquakes, since static vertical loads combine with the dynamic loads induced by the ground motion. The examination of the documentation about the damage caused by the 1976 Friuli earthquake [1] has pointed out that, in isolated bell towers, damage patterns tend to be distributed all along the height, although it is frequently more severe at the base. This suggests the need of further investigations about the combined effects of flexural and axial actions, as well as the incorporation into the model of the higher vibration modes, which seem

to be have a relevant role in the damage of the upper part, especially the tower crown and belfry [2, 7]. Moreover, during strong earthquakes, shear damages are often observed, and in this case the reduction of the section stiffness (i.e. the loss of validity of the EuleroBernoulli hypothesis of plane cross-section) can significantly affect the overall response of the structure. When the tower is not particularly slender, and depending on the frequency content of the forcing actions, a material model which is capable to describe both the axial and the shear response and damage under cyclic loading is required in order to investigate the global shear damage effects [4, 6]. Even if great attention has been devoted to the theme (the mentioned references are a limited part of the available literature) the dynamic analysis of masonry structures in the presence of the interaction with the foundation soil is still unexplored. A first approach to the problem is presented in the paper, by proposing a direct modelling of the soil-foundation-structure system.

2 THE NUMERICAL MODEL: RIGID BODY AND SPRING APPROACH

Analyses are performed by means of a specific mechanistic model, made by rigid masses and springs, (RBSM) which considers only the in-plane dynamics. This model is capable of describing higher vibration modes, as well as the combined axial and shear deformation and damage of the material by means of a simplified heuristic approach, which has been developed both for the out-of-plane behaviour [5, 13, 14] and for the in-plane behaviour [4, 5] here applied. The application of the herein described RBSM model is particularly effective since it allows to considerably reduce the computational burden while keeping, at the same time, the information about the meso-scale effects of the masonry behaviour. It has been , in fact, fruitfully employed both for the analyses of complex, real buildings [15, 16, 17, 18] and when it is used to perform a large number of analyses for calibrating simplified macro-models of masonry panels [19, 20].

The elements are quadrilateral and have the kinematics of rigid bodies with two linear displacements and one rotation, as shown in Figure 1(b). Three springs devices connect the common side between two rigid elements or the restrained sides, as shown in Figure 1(c). These connections are two axial springs k^P and k^R, placed in the point P and R separated by a distance $2b$, and one shear device k^Q placed in the middle of the side. A volume of pertinence V^P, V^Q and V^R is assigned to each connection point. The elastic characteristics of the connecting devices are assigned with the criterion of approximating the strain energy of the corresponding volumes of pertinence in the cases of simple deformation.

The conceptual core of this model is the macroscopic unit cell defined by four quadrilateral rigid elements connected to each other as shown in Figure 1(a). The cell size should be equal or larger than the minimum representative volume (RVE)of the heterogeneous solid material. In particular, the orthotropy of the shear response and the local mean rotation of the blocks, which depend on the different geometric arrangement of the vertical and horizontal material joints as well as the shape and size of the original blocks, are features that can be accounted at the macro-scale [21].

Out-of the linear elastic field, the main macroscopic constitutive aspects are: the very low tensile strength; the significant post-elastic orthotropy combined with the texture effects; the dependence of the shear strength on vertical compression stress; the progressive mechanical degradation during repeated loading; and the energy dissipation capability. To do this, a simplified heuristic approach is proposed, based on the phenomenological consideration of the main in-plane damage mechanisms that can be described at the meso–scale by adopting specific separate hysteretic laws for the axial and shear deformation between the elements. This separation reduces the computational effort, even though a Coulomb-like law is adopted in order to relate the strength of the shear springs to the vertical axial loading.

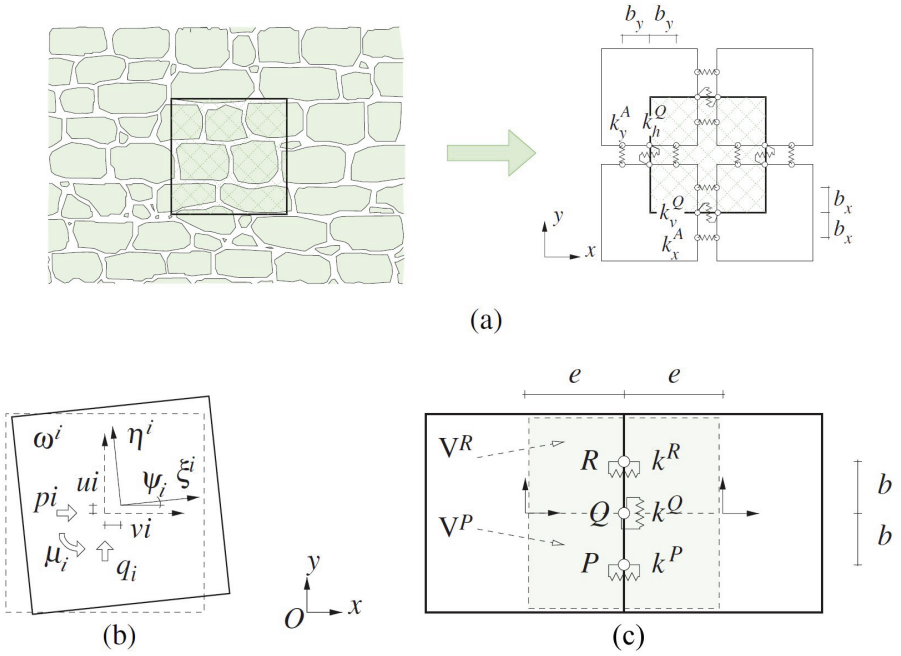


Figure 1: Scheme of a unit cell defined by four rigid elements(a), kinematics (b), disposition of the connecting spring-devices between a couple of rigid elements (c) for macroscale modelling of a representative volume of masonry [5, 21].

Two axial, one symmetric shear, and two in-plane flexural loadings are considered for the parameter identification. The monotonic and hysteretic constitutive laws are assigned to the connecting devices adopting a phenomenological approach and separate phenomenological descriptions of the hysteresis behaviour of the axial and shear connections, as schematically shown in Figure 2. These laws are based on experimental monotonic and cyclic tests available in literature, and should be assigned to rigid elements whose size is approximately comparable to the test specimens in order to limit the problems with size effect. The plastic response of each axial connection is independent from the behaviour of any other connection, while the shear strength is related to the stresses of the axial connections according with Coulomb criterion.

It is worth noting the true discrete character of this model. In fact, during loading, relative motion between two adjacent elements always occurs, with overlapping, separation or sliding between two adjacent rigid elements; numerically, this means compression, tension or shear in the volume of pertinence of the connecting devices. This notwithstanding, the initial contacts do not change during the analysis and the global mechanism maintains the initial connectivity in order to reduce the computational effort.

3 THE REFERENCE TOWER

An idealized case study has been considered [7], in order to assess some basic and common features of the structural response to seismic actions and to appraise the performance of the approach proposed for the modelling. Such a reference model has been supposed to be structurally independent, i.e. with no adjacent interacting construction, and characterized by geometrical regularity both in plan and in elevation (Fig. 3, 4). The dimensions (see Table 1) were chosen by looking at a number of significant examples [1, 9, 8], in order to represent an average masonry bell tower located in seismic zones of Northern Italy, without the intent,

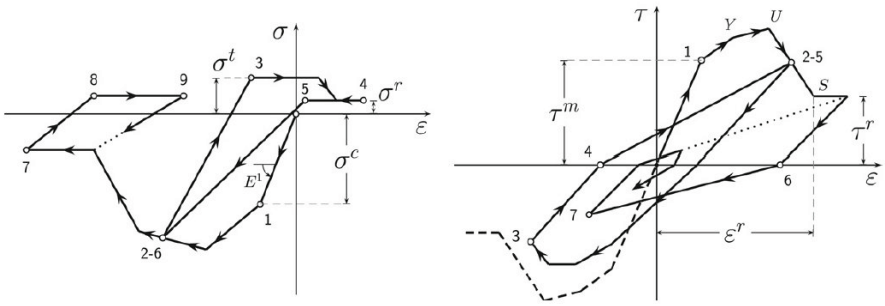


Figure 2: Schematic representation of the hysteretic rules for the axial (on the left), and the shear connecting springs (on the right).

of course, to cover all the possible situations. The geometry of the model was simplified by disregarding the typical structural details, like – for example – the presence of internal vaults.

On the basis of these observations, it was designed an ideal tower having a 5.30 x 5.30 m square base, with a wall thickness varying from 1.00 m at the base to 0.85 m at the top, and having a total height of 28.50 m. In Figures 3 and 4, the 3D drawings and the schematic sections and plans of the tower are shown, and the geometrical characteristics are summarized in Table 1.

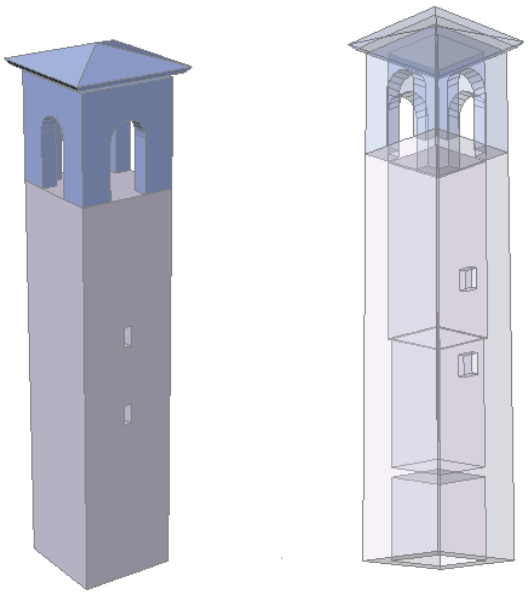


Figure 3: 3D drawing of the reference tower.

3.1 Mechanical parameters of the masonry material

According to the constitutive model adopted for the axial and shear springs (Par. 2), a set of parameters are needed in order to define the corresponding skeleton curves and hysteretic rules

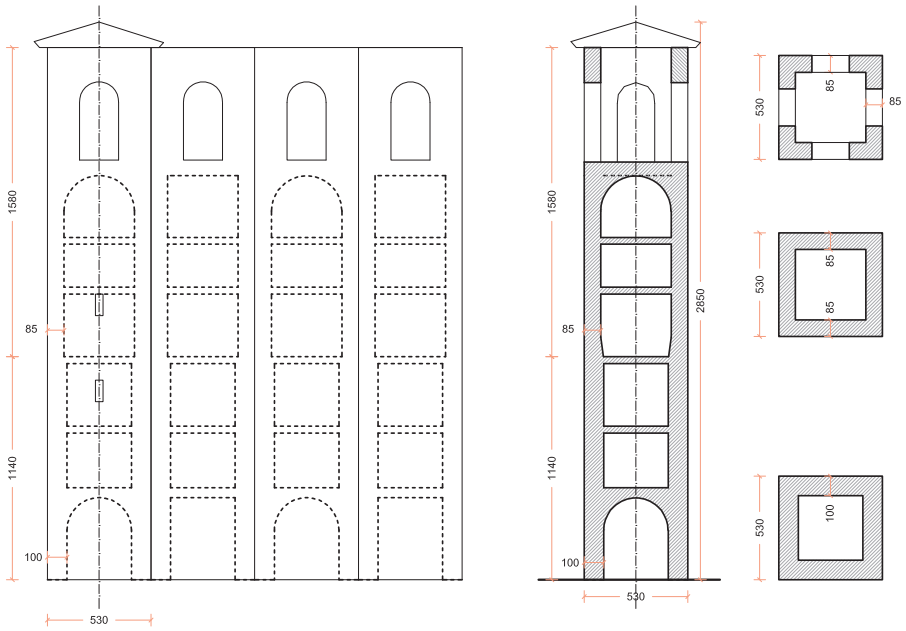


Figure 4: Schematic prospects, section and plan views of the idealized case study.

Table 1: Geometrical characteristics of the reference tower.

Total height (H)	$28.50\ m$
Base (LxL)	$5.30\ m$ x $5.30\ m$
Base wall Thickness (t)	$1.00\ m$
Wall mass density (ρ)	$1900\ kg/m^3$
Damping (ξ)	0.05

[4].

The values assigned to the relevant parameters to define the masonry material of the reference tower are: compressive stress at the elastic limit: $1\ MPa$; peak compressive strength: $2\ MPa$; residual compressive strength: $0.2\ MPa$; peak tensile strength: $0.2\ MPa$; residual tensile strength: $0.02\ MPa$; shear value at the elastic limit: $0.88\ MPa$; peak shear strength on the horizontal plane: $0.097\ MPa$; peak shear strength on the vertical plane: $0.165\ MPa$; residual shear strength: $0.02\ MPa$ friction coefficient on the horizontal plane: 0.25; friction coefficient on the vertical plane: 0.05.

3.2 The model of the foundation soil

3.2.1 Mechanical parameters of the soil

Two types of foundation soil have been considered in order to perform the dynamical analysis accounting for the soil-structure interaction: rock (type A ground) and a type B ground. Since the study is oriented at appraising the interaction effects in the structural dynamic response, only the elastic part of the constitutive behaviour of the soil is actually relevant in the performed

analyses. The elastic moduli adopted for the two soils are, respectively: $E_A = 1400\ MPa$; $G_A = 584\ MPa$; $E_B = 700\ MPa$; $G_B = 292\ MPa$.

3.2.2 Choice of the significant volume of soil

The choice of the significant volume of soil to be introduced in the numerical model is an important question. Clearly, it is necessary to consider a volume large enough to include the pressure bulb under the foundation system. This volume will also represent a mass of soil that participates in the dynamic response of the system. On the other side, the choice cannot be casual, because a possible effect of wave propagation, and in particular of resonance and multiple reflections within the domain, could arise. In order to minimize this eventuality, it was chosen to limit the width of the soil volume under the value of $1/4$ of the length $\lambda^{2\ Hz}$ of the waves "s" secundae corresponding to the frequency of the first mode of the tower (which is about $2\ Hz$). Thence, for the two considered ground types, we have:

$$\nu_s = \sqrt{\frac{G}{\rho}}; \quad G_A = 584\ MPa \rightarrow \lambda^{2\ Hz} = 285\,m; \quad G_B = 292\ MPa \rightarrow \lambda^{2\ Hz} = 198\,m; \quad (1)$$

In Fig. 5, the mesh adopted for the numerical analyses of the case study is shown. The elements coloured in brown represent the foundation of the tower, and the mechanical parameters of masonry are assigned to them. The elements coloured in dark green represent the soil (for each of the two considered ground types, the proper mechanical parameters - see Par. 3.2 are assigned), and are $41\ m$ deep, in order to model the actual thickness of the participant soil mass. In order to reduce the problem of the wave reflection within the domain, two vertical strips (light green colour) with a reduced stiffness of the vertical shear springs ($1/10$ of the stiffness of vertical shear springs) have been introduced in the mesh. In the same figure, the two control points A and B are also shown.

4 Dynamic analyses with natural accelerograms accounting for soil-structure interaction

Two numerical models of the reference tower have been analysed (see Fig. 5) by using the two soil types defined in Par. 3.2. In the following paragraphs, the discussion of the case study will be made with reference to the models with the soil volume: Type A soil (rock) and B type soil (compact gravel). It should be remarked that, in the context of the present paper, attention is focused on the response of the tower and on the alteration induced by the interaction with the soil on the natural vibration modes and damage mechanisms, whereas the strictly geotechnical aspects (advanced modelling of the non linear constitutive behaviour and failure of the ground) are not treated. For the dynamic analyses, a set of natural accelerograms has been chosen in order to represent the ground motions. Actually, the aim of the paper is not to perform an engineering safety assessment of the tower, nor to perform a statistical analysis on the base of a large number of analyses. The objective is rather to perform a preliminary investigation for improving the current framework about the seismic assessment of historical towers, by analysing two problems: use of natural accelerograms, including the vertical component; effect of the soil-structure interaction.

Starting from the idea that non linear dynamics is the most complete and realistic method for the structural analysis under seismic actions, particularly for special types of buildings like these, it is necessary to overcome a number of drawbacks, that actually make the application

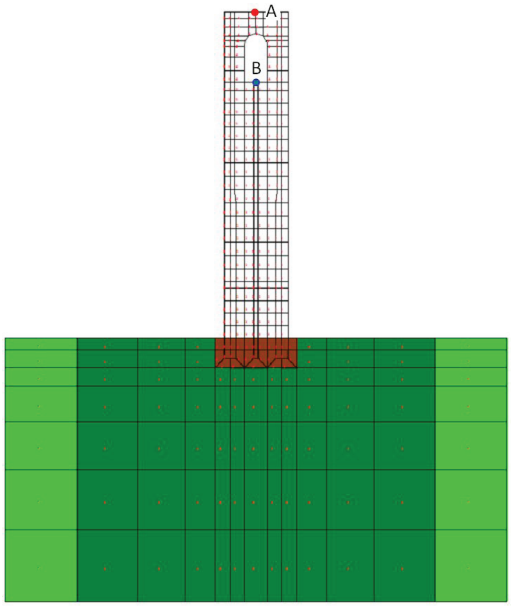


Figure 5: Mesh of the tower with the significant volume of soil included in the model, and location of the control points A and B.

of the approach quite limited. The two above mentioned points (which are not much investigated) are indeed critical, since concerns some of the major criticisms raised against non linear dynamic analyses: proper choice of the accelerograms in order to be truly representative of the seismic hazard (in this sense, the use of artificial accelerograms is often considered to be a purely conventional "domesticated" option); sensitivity of the method to the presence of large soil masses participating to the motion. With regard to the second point, it has been shown in [22] that the different characteristics of the ground have important effects on the structural response of the tower under the dynamic seismic loads both on the distribution of the damage and on the related failure mechanisms. Thence, the incorporation of the soil volume in the dynamic numerical model has a great importance with regard to the structural performance and should has been considered in the models assumed in the present study.

4.1 Choice of the natural records

On the basis of the above mentioned remarks, a relatively limited groups of accelerograms has been used (6), leaving apart the specific requirements of the Building Codes with respect to the deviation from the design spectrum. The idea, instead, was of considering a set of case studies representing a real, coherent seismic event. The records used in the analyses are listed in Table 2.

4.2 Numerical results

For each of the two models, the registrations of three seismic events at three stations have been considered, as shown in Table 2. For each of them, three records are available: horizontal component in the North-South direction (NS); horizontal component in the West-East direction (WE); vertical component (UP).

Since the problem is analyzed by means of a plane model, a group of accelerogram shall be composed of two components, a horizontal one plus the vertical one. Thence, the available

Table 2: Selected station and recordings [23, 24].

Event station/EC8 soil	component	Date / UTC time	Event code	R_{epi} [km]	PGA [cm/s^2][cm/s]
Friuli 3^{rd} shock	NS				258
FRC (Forgaria)	WE	1976-09-15 / 03:15:18	FR2-76b	17.3	211
soil B	UP				96
Umbria-Marche $1^{st} shock$	NS				332
CLF (Colfiorito)	WE	1997-09-26 / 00:33:12	UMM-97a	2.8	284
soil D	UP				236
Umbria-Marche $1^{st} shock$	NS				486
NCR (Nocera Umbra)	WE	1997-09-26 / 00:33:12	UMM-97a	13.1	263
soil E	UP				143

registrations have been combined in order to obtain 6 different groups of accelerograms to be applied to each of the two computational models of the tower (Type A soil - "Mat3b"; Type B soil - "Mat4b"). In order to appraise the effects of the presence of the vertical component of the accelerogram, all the analyses have been also performed by considering the horizontal component only. A total number of 12 nonlinear dynamic analyses has been therefore performed for each of the two soil cases.

In this paragraph, due to space limitations, the most interesting and representative results have been selected. In the Figures 6, 8, 10, 7, 9, 11, results are reported in terms of deformed shape, map of the shear deformation E_{12} and E_{21}, map of the S_{22} stress component (all plotted at the end of the time history) for the two cases: combination of the horizontal and vertical components simultaneously applied (bottom of the figure); horizontal component alone (top of the figure). In the center, the two displacement histories are plotted and compared in the same graph.

5 DISCUSSION OF THE RESULTS AND FINAL REMARKS

Among the whole set of analyses, the results relative to three groups of accelerograms have been selected, all belonging to 2 distinct events (Friuli Earthquake, 1976, third shock, Forgaria Cornino Station; UmbriaMarche Earthquake, 1997, first shock, Station of Nocera Umbra):

C1. Fr2-76b FRC NS (with and without the vertical component "UP");

C2. Fr2-76b FRC WE (with and without the vertical component "UP");

C3. UMM-97a NCR NS (with and without the vertical component "UP").

It is possible at this point to perform some interesting observations for the cases of analysis of mentioned, comparing for each of them the results obtained with or without the presence of the vertical component of the recording. A further element of comparison is then represented by the results for the same series of analyses made for the second category of soil, through which are highlighted specific aspects of soil structure interaction analysis in nonlinear dynamics.

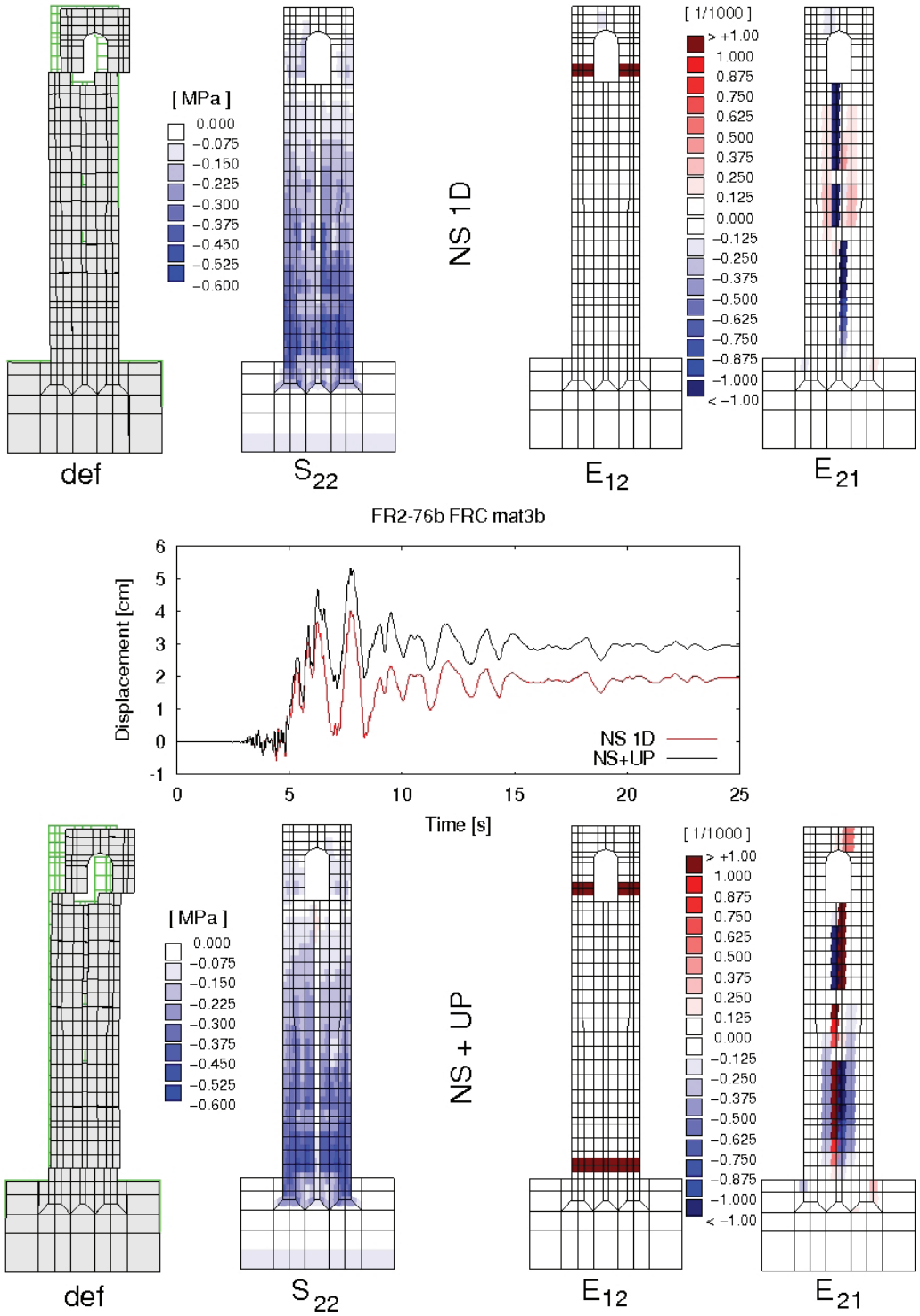


Figure 6: Results of the non linear dynamic analyses for the model: soil A rock; accelerogram Friuli, Forgaria Cornino, 3^{rd} shock; NS horizontal component (mat3b FR2-76b FRC NS).

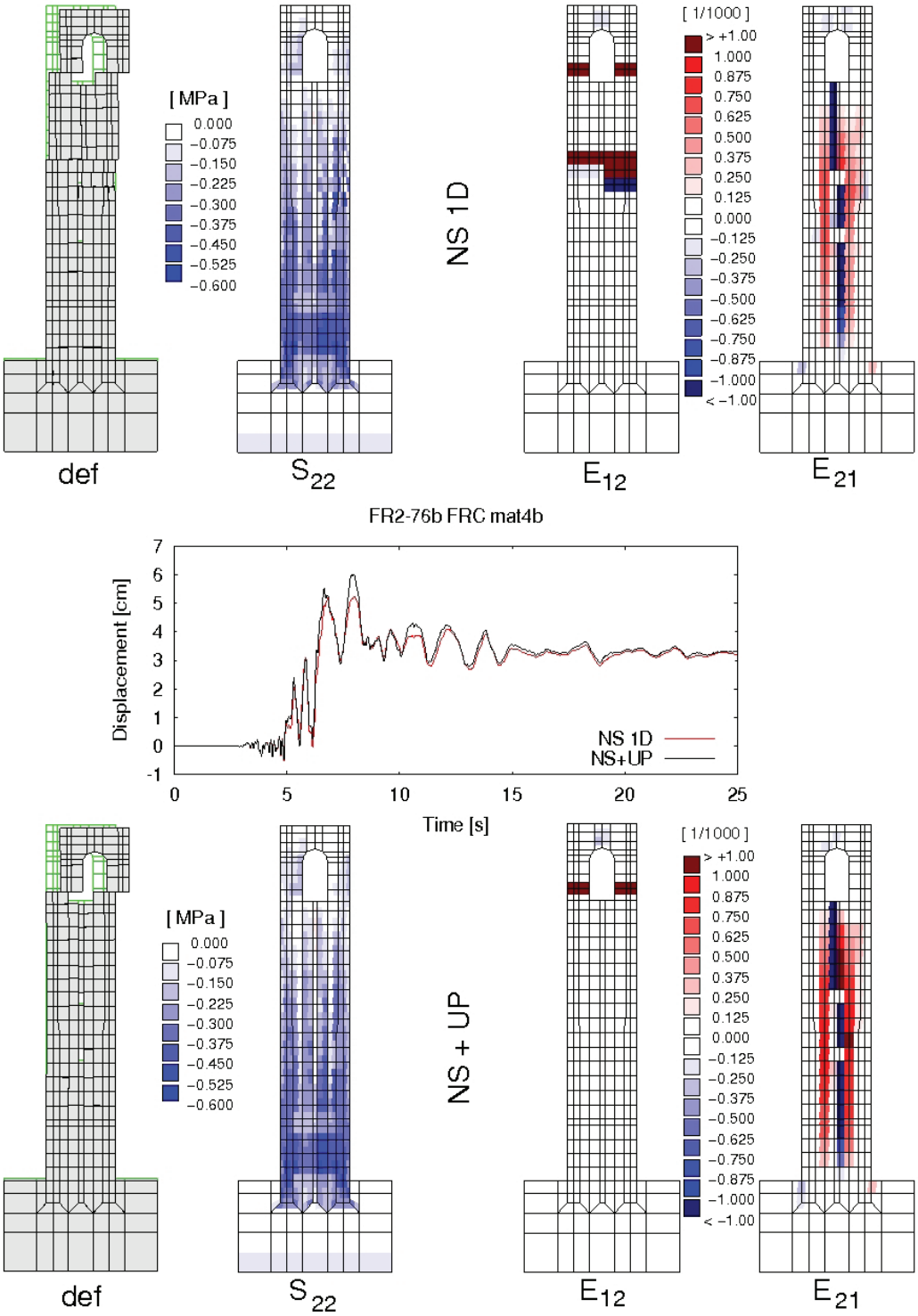


Figure 7: Results of the non linear dynamic analyses for the model: soil B; accelerogram Friuli, Forgaria Cornino, 3^{rd} shock; NS horizontal component (mat4b FR2-76b FRC NS).

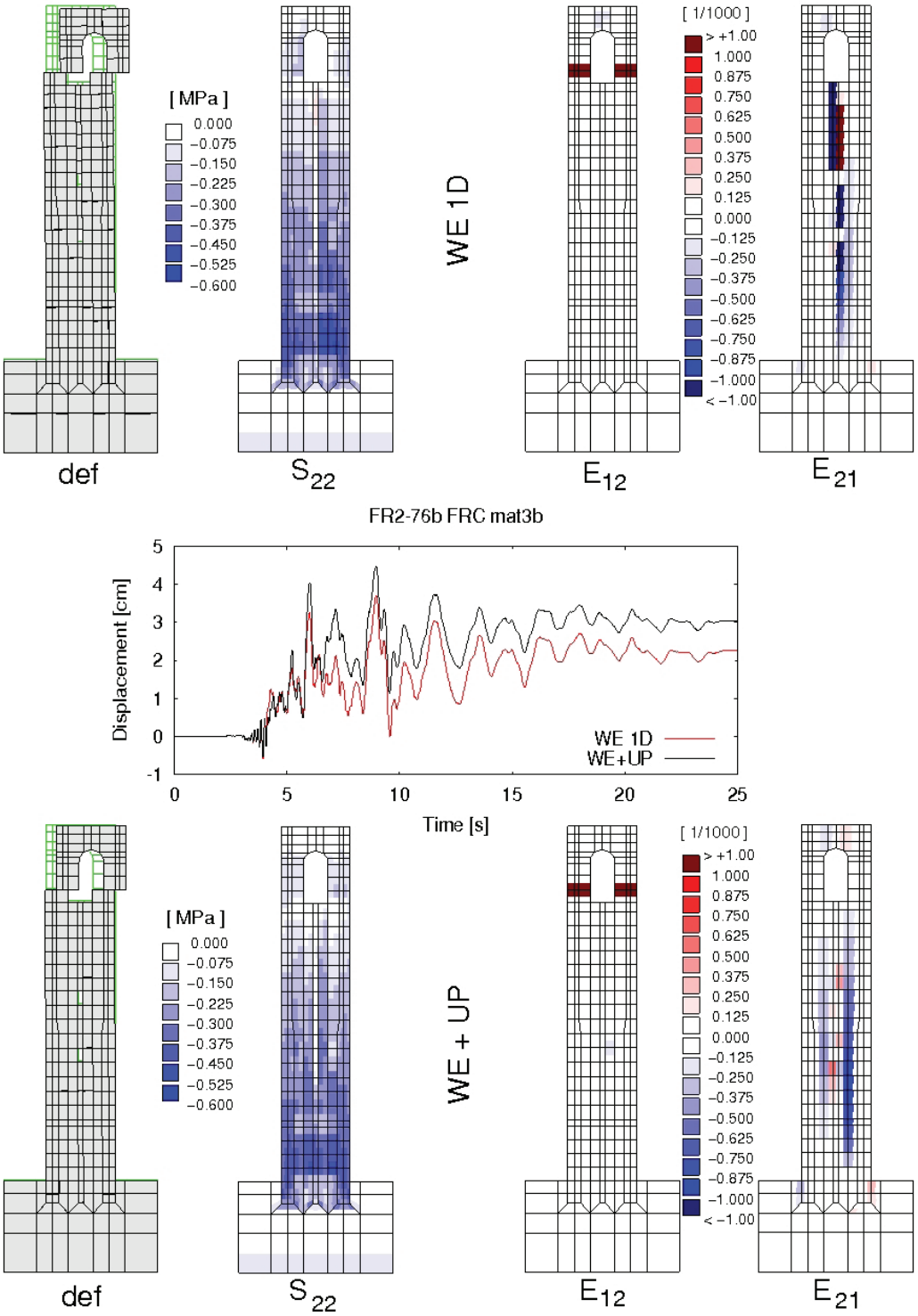


Figure 8: Results of the non linear dynamic analyses for the model: soil A; accelerogram Friuli, Forgaria Cornino, 3^{rd} shock; WE horizontal component (mat3b FR2-76b FRC WE).

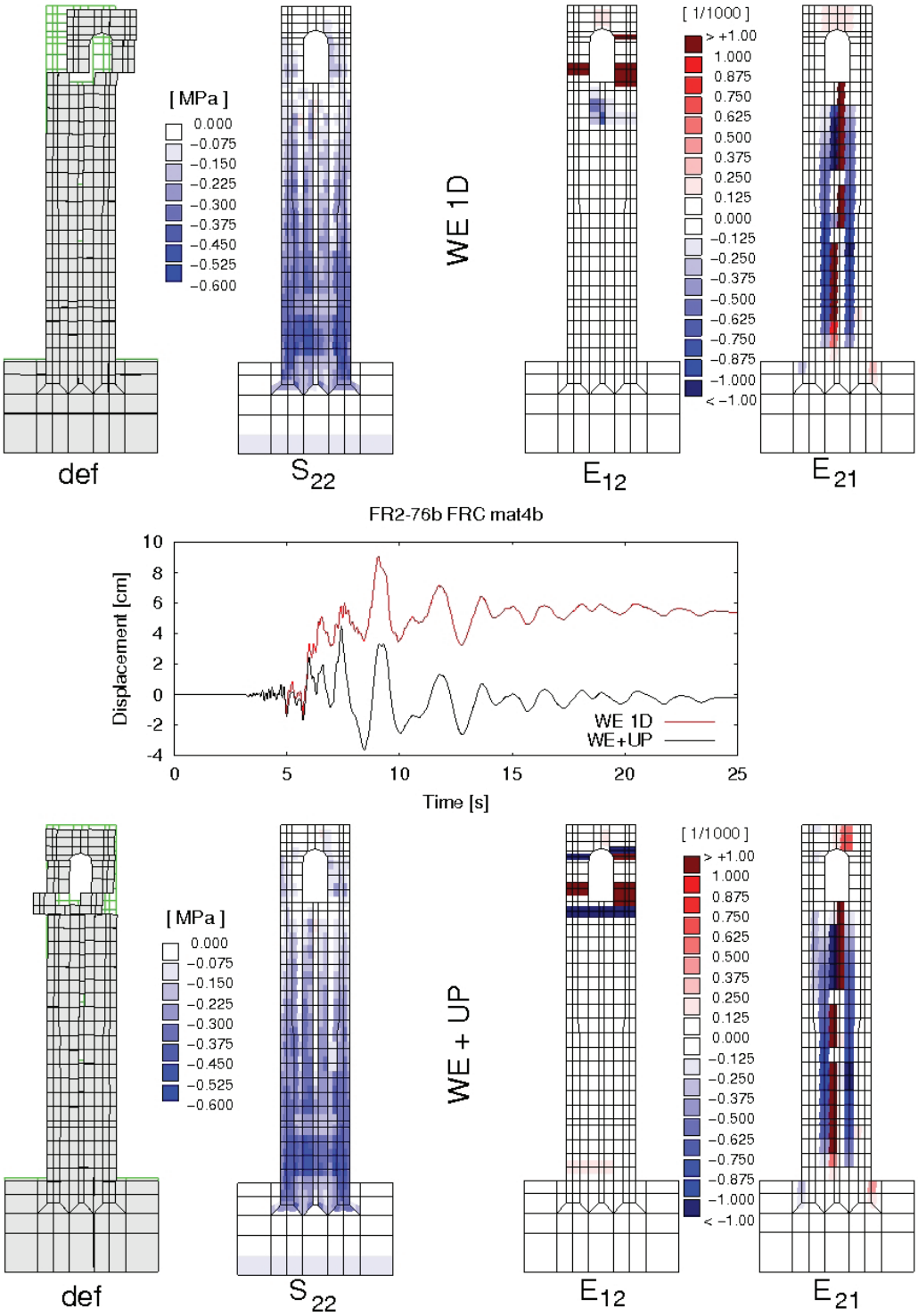


Figure 9: Results of the non linear dynamic analyses for the model: soil B; accelerogram Friuli, Forgaria Cornino, 3^{rd} shock; WE horizontal component (mat4b FR2-76b FRC WE).

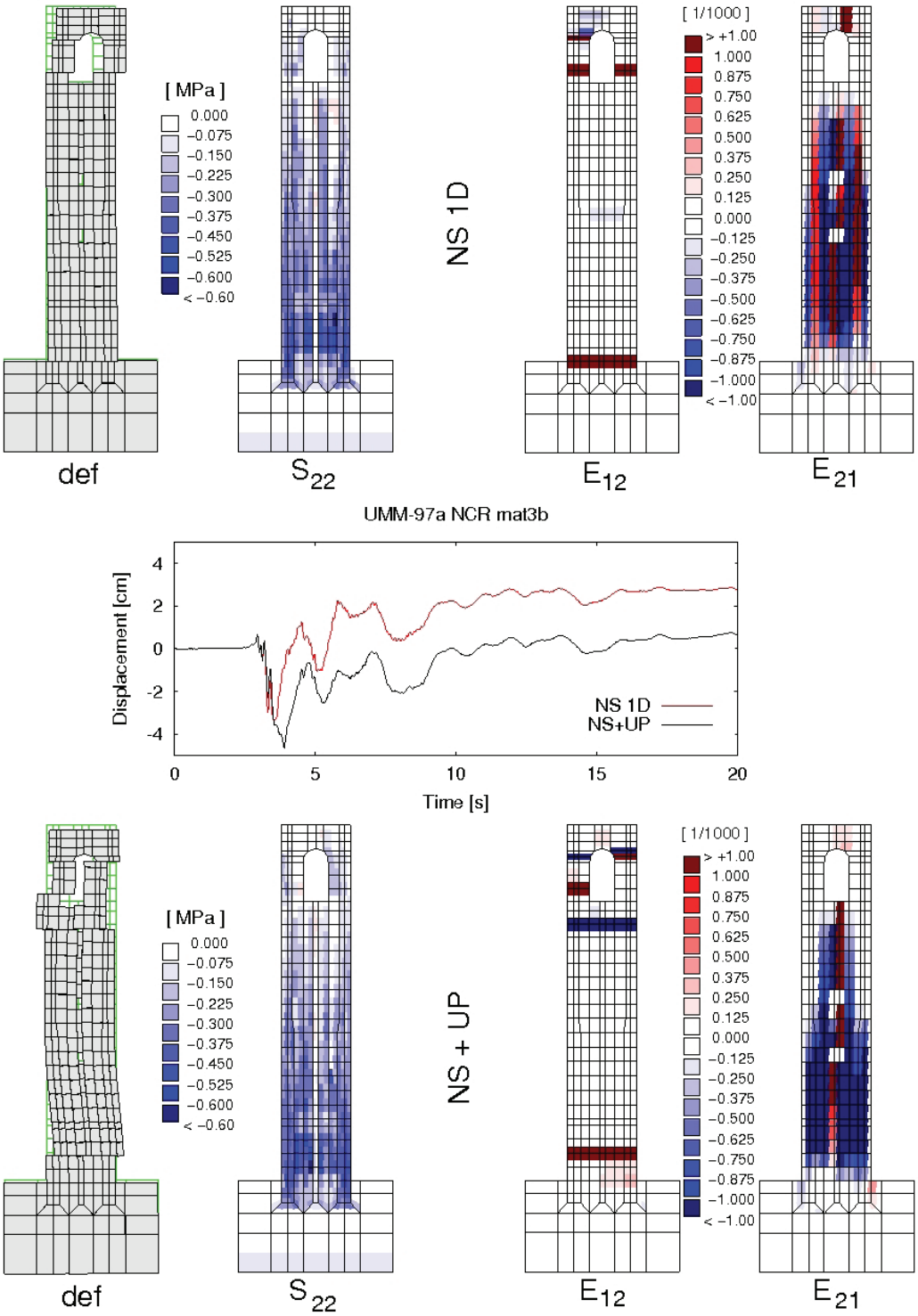


Figure 10: Results of the non linear dynamic analyses for the model: soil A; accelerogram Umbria-Marche, Nocera Umbra; NS horizontal component (mat3b UMM-97a NCR NS).

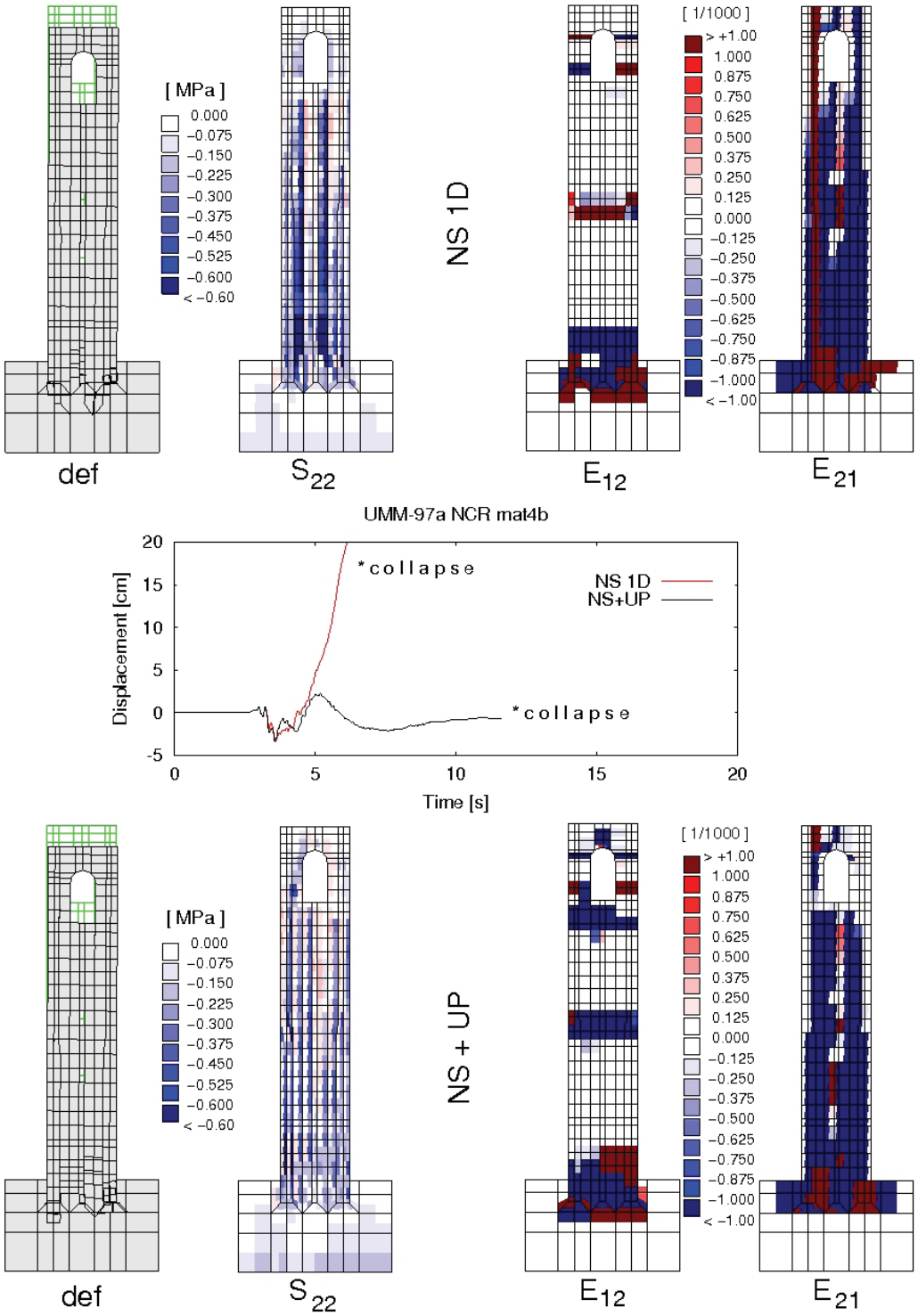


Figure 11: Results of the non linear dynamic analyses for the model: soil B; accelerogram Umbria-Marche, Nocera Umbra; NS horizontal component (mat4b UMM-97a NCR NS).

5.1 Combination C1

Soil type A

The results for the this combination, which is relative to the seismic event Fr2-76-b (NS component + UP component), are reported in Figure 6.

The analysis performed under the horizontal component indicates the presence of a global shear mechanism: the tower tends to be split into two separate vertical portions (see Fig.6, E_{21} map). This is accompanied by a local damage mode involving the belfry, with damage clustered at the base of the belfry (Fig. 6, E_{12} map), and sliding of the whole belfry (Fig. 6, final deformed shape).

When the vertical component of the accelerograms is included in the analysis, it can be observed that, qualitatively, the failure modes engaged are the same but global displacements and the damage level are increased. Moreover, an additional global collapse mechanism is engaged: sliding of the tower, with damage clustered at the base section (see Fig. 6 final deformed shape, E_{21} map and E_{12} map).

Soil type B

In this situation, a damping of the displacement response with respect to the previous case is observed, with a substantially unchanged value of the final displacement. The alterations induced by the presence of the vertical component on the displacement history are negligible, whereas the damage distribution of tensions and the damage pattern are different. The local collapse of the belfry is quite the same, and so the global shear (see Fig. 7 $S22$ map and E_{21} map). An additional partial collapse mechanism is engaged, with the sliding of the upper part of the tower, above the level of the upper window (see Fig. 7, final deformed shape, E_{12} map).

5.2 Combination C2

Soil type A

The results for the this combination, which is relative to the seismic event Fr2-76-b (WE component + UP component), are reported in Figure 8. In this case, there are two failure mechanisms, at the end of the analysis: global shear mechanism (very similar to that of combination C1 (see Fig. 8, E_{21} map); local collapse of the belfry, with damage clustered at the base of the belfry (see Fig. 8, E_{12} map). The behaviour in the presence of the vertical component is qualitatively the same, with an increase of the displacement. The distribution of damage is not significantly altered and, indeed, the global shear damage is even lower, whereas the damage is more concentrated in the local belfry mechanism, whereas the global shear damage (see Fig. 8, E_{21} map and S_{22} map).

Soil type B

What happen, this time, is different than in combination C1. If only the horizontal component is considered, the presence of the softer soil significantly increases the displacements and the damage level. It is interesting to observe, then, the behaviour in the presence of the vertical component. The displacement history is apparently "regularized". Actually, this is related to the modification of the local mechanism of the belfry, that is much more damaged (see Fig. 9, final deformed shape and E_{12} map), with two sections subjected to sliding. The global damage level, concerning a shear type failure, is increased.

5.3 Combination C3

Soil type A

The results for the this combination, which is relative to the seismic Event UMM-97a (NS component + UP component), are reported in Figure 10. The analysis has revealed some peculiar and interesting features. Despite a displacement range that is not much large, a sever damage is suffered by the tower, and almost all the possible failure modes previously observed are simultaneously present: global shear with sliding at the tower base, local collapse of the belfry at different sections (base of the upper pillars, base of the belfry, lintel; see Fig. 10: final displacement, E_{12} and E_{21} maps).

Soil type B

This time, there is a full structural collapse (see Fig. 11, displacement history and tensional maps). The severe level of damage is mainly related to the global shear mode and collapse at the tower base, whereas the belfry damage is more limited. The situation is quite similar with or without the vertical component, even if the vertical component actually accentuates a failure at the mid section of the tower and at the belfry base, more then at the shear mechanism (see Fig. 11, E_{12} and E_{21} maps).

5.4 Final Remarks

The range of possibilities which have been observed is quite diversified. Even if a clear, univocal trend cannot be identified, it should be observed that the incorporation of the vertical components of the accelerograms in the seismic analysis is very important, since it induces relevant effects on the structural response and on the final damaged configuration. Indeed, it significantly influences the seismic safety verification. The most important remark to be done, however, is that it cannot a-priori established if the effect is significantly worse for the structure and above all, which structural part and local mechanisms will be involved. The final situation will depend on the frequency content of the accelerograms and must be specifically examined case by case. It can therefore be concluded, on the basis of this set of analyses, that for the specific typology considered (historical, slender masonry towers), it is highly recommend to resort to put into the field an advanced and complete method of analysis like the nonlinear dynamics in order to have the possibility of capturing the complexity and variability of the structural response. The present paper offers a first glimpse over the issue, which shall be further investigated in two directions: providing a wider set of results with regard to a statistically significant number of input accelerograms; considering a wider range of examples, also concerning real cases of towers collapsed after seismic events.

REFERENCES

[1] F. Doglioni, A. Moretti and V. Petrini (eds.), *Le Chiese e il Terremoto* Lint Press, Trieste, 1994.

[2] E. Curti, S. Lagomarsino, S. Podest, Dynamic Models for the Seismic Analysis of Ancient Bell Towers. P.B. Lourenço, P. Roca, C. Modena, S. Agrawal eds. *Structural Analysis of Historical Constructions (SAHC 2006)*, New Delhi, India, November, 2006.

[3] G. Magenes, GM. Calvi, Cyclic behaviour of brick masonry walls. *Proceedings of the 10th World Conference on Earthquake Engineering*, Madrid, 1992.

[4] S. Casolo, F. Peña, Rigid element model for in-plane dynamics of masonry walls considering hysteretic behaviour and damage. *Earthquake Engineering and Structural Dynamics*, **36**:8, 1029–1048, 2007- DOI: 10.1002/eqe.670

[5] S. Casolo, Macroscale modelling of the micro-structure damage evolution by a rigid body and spring model. *Journal of Materials and Structures*, **4**:3 (551–570), 2009.

[6] F. Peña, P.B. Lourenço, N. Mendes, D:V: Oliveira, *Numerical models for the seismic assessment of an old masonry tower*, **32**:5, 1466 1478 2010.

[7] S. Casolo, G. Uva, Seismic vulnerability assessment of masonry towers: full non-linear dynamics vs pushover analyses, *Proc. COMPDYN 2011 – ECCOMAS Thematic Conference on Computational Methods in Structural Dynamics and Earthquake Engineering*, Corfu, Greece, 2011. (CD-ROM).

[8] G. Milani, S. Casolo, A. Naliato, A.G. Tralli, Seismic assessment of a medieval masonry tower in Northern Italy by limit, nonlinear static, and full dynamic analyses, *International Journal of Architectural Heritage*, **6**:5, 489-524, DOI = 10.1080/15583058.2011.588987, 2012

[9] S. Casolo, G. Milani, G. Uva, C. Alessandri, Comparative seismic vulnerability analysis on ten masonry towers in the coastal Po Valley in Italy, *Engineering Structures*, **49**, 465-490, DOI = 10.1016/j.engstruct.2012.11.033, 2013.

[10] L. Binda, L. Zanzi, M. Lualdi, P. Condoleo, P., The use of georadar to assess damage to a masonry bell tower in Cremona, Italy. *NDTE International*, **38**, 171179, 2005.

[11] S. Ivorra, F. J. Pallares, Dynamic investigations on a masonry bell tower, *Engineeering Structures*, **28**, 660-667, 2006.

[12] L. Binda, G. Gatti, G. Mangano, C. Poggi, G. Sacchi Landriani, The collapse of the civic tower of Pavia: a survey of the materials and structure. *Masonry International*, **6** (1), 11–20, 1992.

[13] S. Casolo, G. Milani, A simplified homogenization-discrete element model for the non-linear static analysis of masonry walls out-of-plane loaded *Engineering Structures*, **32**:8,2352-2366, 2010 - DOI: 10.1016/j.engstruct.2010.04.010

[14] S. Casolo, G. Milani, Simplified out-of-plane modelling of three-leaf masonry walls accounting for the material texture, *Construction and Building Materials*, **40**, 330-351, 2013 DOI: 10.1016/j.conbuildmat.2012.09.090

[15] S. Casolo, C.A. Sanjust, Seismic investigation on the cathedral of Syracuse by finite elements and by a specific rigid body and spring model, *Structural Studies, Repairs and Maintenance of Heritage Architecture X, WIT Transactions on the Built Environment*, **95**, 535-54 DOI = 10.2495/STR070501, 2007

[16] S. Casolo, C.A. Sanjust, Seismic analysis and strengthening design of a masonry monument by a rigid body spring model: The "Maniace Castle" of Syracuse, *Engineering Structures*, **31**:7, 1447-1459, DOI = 10.1016/j.engstruct.2009.02.030, ISSN = 0141-0296, 2009.

[17] S. Casolo, G. Uva, Out-of-plane seismic response of masonry façades some comparisons among full dynamic and pushover analysis, *Ingegneria Sismica*, **27**:3, 33-54, ISSN = 03931420, 2010.

[18] S. Casolo, G. Uva, Nonlinear analysis of out-of-plane masonry façades: Full dynamic versus pushover methods by rigid body and spring model, *Earthquake Engineering and Structural Dynamics*, **42**, 499521, DOI = 10.1002/eqe.2224, 2013.

[19] A. Fiore, F. Porco, D. Raffaele, G. Uva, About the influence of the infill panels over the collapse mechanisms actived under pushover analyses: two case studies, *Soil Dynamics and Earthquake Engineering*, **39**, 11-22, DOI = 10.1016/j.soildyn.2012.02.004, 2012.

[20] G. Uva, F. Porco, D. Raffaele, A. Fiore, On the role of equivalent strut models in the seismic assessment of infilled RC buildings, *Engineering Structures*, **42**, 83-94, DOI = 10.1016/j.engstruct.2012.04.005, 2012.

[21] S. Casolo, Macroscopic modelling of structured materials: relationship between orthotropic Cosserat continuum and rigid elements. *International Journal of Solids and Structures*, **43** (3–4), 475–496, 2006.

[22] G. Uva, S. Casolo, G. Milani, M. Acito, An evaluation of the soil-structure interaction in the non-linear dynamic analysis of masonry towers *Proc.* 15^{th} *World Conference on Earthquake Engineering*, Lisbon, September 2012.

[23] ITACA(2010)-Working-Group, *Data Base of the Italian strong motion records*, http://itaca.mi.ingv.it, 2010.

[24] F. Pacor, R. Paolucci, L. Luzi, F. Sabetta, A. Spinelli, A. Gorini, M. Nicoletti, S. Marcucci, L. Filippi, M. Dolce, Overview of the Italian strong motion database ITACA 1.0, *Bulletin of Earthquake Engineering*, **9**:6, 1723-1739, 2011.

COMPDYN 2013
4th ECCOMAS Thematic Conference on
Computational Methods in Structural Dynamics and Earthquake Engineering
M. Papadrakakis, V. Papadopoulos, V. Plevris (eds.)
Kos Island, Greece, 12–14 June 2013

GENERATION OF INCOHERENT GROUND MOTIONS FOR SOIL-STRUCTURE INTERACTION APPLICATIONS

Ph. Tran[1], **F. Wang**[1], **and D. Clouteau**[2]

[1]CEA, DEN, DM2S, SEMT, EMSI
F- 91191 Gif-sur-Yvette , France
phuong.tran@cea.fr, fan.wang@cea.fr

[2] Dept. of Civil Engineering, Ecole Centrale Paris
F-92295 Châtenay-Malabry, France
didier.clouteau@ecp.fr

Keywords: Soil-Structure Interation, Seismic Ground Motions, Seismic Hazard, Seismic Spatial Variability, Earthquake Engineering

Abstract. *This paper aims to present a new method for generating incoherent seismic ground motions on the basis of the stochastic deconvolution technique and the spectral representation method. The generated free field motion satisfies the imposed statistical properties on the free surface and is composed of elementary plane waves of types SH, P-SV incoming from all directions. This will allow 3D soil-structure interaction analyses to be performed with spatially varying seismic motions in the case of structure with embedded foundation. Eventually, structural non-linearity can be accounted for when the SSI analysis is performed in the time domain.*

1 INTRODUCTION

The term 'Seismic spatial variability' refers to the non-uniform ground motion during the earthquake. This phenomenon has an important effect on the response of large superstructures, such as dams, tunnels, bridges and nuclear power plants [1, 2, 3]. The spatial variability of ground motion was studied at the first time in the 1960's and then was extensively investigated by researchers after the installations of dense seismograph arrays, such as the El Centro at the Imperial Valley [4], SMART-1 [5], LSST [6]... Many effects due to the incoherent ground motions on the response of structure were revealed. In general, the seismic spatial variability reduces the translational response but creates torsional and rocking effects [7, 8], moreover for extended structures such as pipelines, bridges, tunnels, the differential displacement at the structure supports may cause additional stress on the structure. The causes of seismic spatial variations are multiple, they are always related to the mechanics of fault, the complex pattern of seismic wave propagation, the variations of site conditions and wave passage effect. From recordings at the dense seismograph arrays, researchers have tried to model the incoherent field which is used in engineering application as seismic inputs. Many methods of generation of the incoherent field have been developed in the last two decades [9, 10, 11, 12, 13, 14, 15, 16]. However, due to the lack of recordings at the depth, the previous methods concentrate on the generation of the motion on the surface of the free field and their applications are limited for the extended structures with surfacing supports. In order to perform a SSI analysis of the superstructures with massive embedded foundation accounting for the non-linearity of the structure, the incoherent free field must be generated in the soil and the compatible traction must be extracted at the boundary of full FEM model of structures and its vicinity soil.

The method presented here is based on the propagation of plane waves of types SH, P-SV through the layered elastic soil. To satisfy the statistical properties which are known on the surface of the free field, the incident elementary waves are assumed to income from all directions but independents of each others. Each elementary wave is characterized by its power spectral density function which must be computed. The details of the method are shown in the later sections.

The paper is structured as follows: section 2 presents the description of seismic spatial variability, section 3 summarizes the stochastic deconvolution technique of seismic ground motions developed initially by Kausel [17, 18], section 4 discusses about the generation of incoherent ground motion method, conclusions and perspectives are given in section 5.

2 SEISMIC SPATIAL VARIABILITY

The seismic spatial variability can be studied by examining the cross-correlation function of displacement which shows the statistical properties of the displacement field in both space and time domain. Consider the motion at a point $\mathbf{x}$ and at time t to be the stochastic process $\mathbf{U}(\mathbf{x}, t)$, the cross-correlation function between any two points can be defined as follows:

$$\mathbf{C}(\mathbf{x}, \mathbf{x}', t, t') = \mathbb{E}\left[\mathbf{U}(\mathbf{x}, t) \times \mathbf{U}(\mathbf{x}', t')\right] \tag{1}$$

where $\mathbb{E}$ denotes the mathematical expectation.

Because of the limited amount of available data and for simplicity, one need to use the assumptions of stationarity, homogeneity and ergodicity of the displacement field, then the previous equation can be rewritten in the following:

$$\mathbf{C}(\mathbf{x}, \mathbf{x}', t, t') = \mathbf{C}(|\mathbf{x}' - \mathbf{x}|, t, t + \tau) = \mathbf{C}(|\mathbf{x}' - \mathbf{x}|, \tau) \tag{2}$$

The power spectral density and the cross-power spectral density can be defined as the Fourrier transformation of the auto-correlation function and the cross-correlation function respectively:

$$\mathbf{S}(\omega) = \int_{-\infty}^{+\infty} \mathbf{C}(\tau) e^{i\omega\tau} d\tau \tag{3}$$

$$\mathbf{S}(|\mathbf{x}' - \mathbf{x}|, \omega) = \int_{-\infty}^{+\infty} \mathbf{C}(|\mathbf{x}' - \mathbf{x}|, \tau) e^{i\omega\tau} d\tau \tag{4}$$

The previous cross PSD function already describes the full joint statistical properties at two different points of the free field. However, in engineering practice, one works with the coherency function which is obtained from the cross spectral density function normalized with respect to the corresponding power spectra :

$$\gamma(\mathbf{x}, \mathbf{x}', \omega) = \frac{\mathbf{S}(\mathbf{x}, \mathbf{x}', \omega)}{\sqrt{\mathbf{S}(\mathbf{x}, \mathbf{x}, \omega)\mathbf{S}(\mathbf{x}', \mathbf{x}', \omega)}} \tag{5}$$

Another form of coherency function usually used in the literature can be expressed as follows:

$$\gamma(\mathbf{x}', \mathbf{x}', \omega) = |\gamma(\mathbf{x}, \mathbf{x}', \omega)| \exp\left[i\phi(\mathbf{x}, \mathbf{x}', \omega)\right] \tag{6}$$

Where :

$$|\gamma(\mathbf{x}, \mathbf{x}', \omega)| = \frac{|\mathbf{S}(\mathbf{x}, \mathbf{x}', \omega)|}{\sqrt{\mathbf{S}(\mathbf{x}, \mathbf{x}, \omega)\mathbf{S}(\mathbf{x}', \mathbf{x}', \omega)}} \; ; \quad \phi(\mathbf{x}, \mathbf{x}', \omega) = \tan^{-1}\left(\frac{\mathbf{Im}(\mathbf{S}(\mathbf{x}, \mathbf{x}', \omega))}{\mathbf{Re}(\mathbf{S}(\mathbf{x}, \mathbf{x}', \omega))}\right)$$

The absolute value $|\gamma(\mathbf{x}, \mathbf{x}', \omega)|$ is named the lagged coherency function. Its value tends to unity when ω or the separation distance $|\mathbf{x}' - \mathbf{x}|$ tends to zero and it tends to zero when ω or the separation distance $|\mathbf{x}' - \mathbf{x}|$ tends to infinity. The lagged coherency refers to the stochastic sources of seismic spatial variability such as mechanic of faults, scattering wave effects, local site effects. However, the phase $\phi(\mathbf{x}, \mathbf{x}', \omega)$ refers to the systematic source of seismic spatial variability which is the so called wave passage effect. Many coherency models have been developed in the literature [9, 6, 19, 20, 3]. Among these models, a model of Luco and Wong [1] is the most used in the literature.

$$|\gamma(|\mathbf{x}' - \mathbf{x}|, \omega)| = e^{-(\frac{\nu\omega|\mathbf{x}' - \mathbf{x}|}{c_\alpha})^2} \tag{7}$$

$$\nu = \mu \left(\frac{R}{r_o}\right)^{1/2}$$

where c_α is the wave velocity in the random medium, R is the distance in the random medium travelled by the wave, r_o is the length scale of random inhomogeneities along the path, μ is a measure of the relative variation of the elastic properties of the random medium. However there are few models describing ground motion at depth [21] due to the lack of recordings at downhole arrays.

3 STOCHASTIC DECONVOLUTION OF EARTHQUAKE MOTION

This section gives a summary of stochastic deconvolution method. For more details one can refer to the original paper [17]. This method is based on the wave propagation theory with several assumptions on the wave field and the medium as follows:

- The soil is a semi infinite homogeneous horizontally layered medium.
- The motion at any point is a result of the superposition of plane waves incoming from all directions. The elementary waves are stationary uncorrelated body waves of types SH and P-SV.

Let $\mathbf{U}(\mathbf{r},z,t) = \begin{pmatrix} \mathbf{u}(\mathbf{r},z,t) \\ \mathbf{v}(\mathbf{r},z,t) \\ \mathbf{w}(\mathbf{r},z,t) \end{pmatrix}$ be the displacement vector at an arbitrary point $\mathbf{x}$ in the soil at time t . This motion can be expressed as follows:

$$\mathbf{U}(\mathbf{r},z,t) = \frac{1}{8\pi^3} \iint \tilde{\mathbf{U}}(\mathbf{k},z,\omega) e^{i(\omega - \mathbf{k}\cdot\mathbf{r})} d\mathbf{k} d\omega \tag{8}$$

in which $\mathbf{k} = (k_x, k_y)$ is the wavenumber vector, $\mathbf{r} = (x,y)$, $d\mathbf{k} = dk_x dk_y$, and $\mathbf{k}\cdot\mathbf{r} = k_x x + k_y y$. Thus, $\tilde{\mathbf{U}}(\mathbf{k},z,\omega)$ is the Fourier transform in wave-number frequency domain of the displacement $\mathbf{U}(\mathbf{r},z,t)$.

In the wave-number frequency domain, one can compute the motion at depth z from the motion on the free surface by means of Transfer Matrix $\mathbf{T}(\mathbf{k},z,\omega)$ [22, 23]:

$$\tilde{\mathbf{U}}(\mathbf{k},z,\omega) = \mathbf{T}(\mathbf{k},z,\omega)\tilde{\mathbf{U}}(\mathbf{k},0,\omega) \tag{9}$$

The cross-correlation matrix at depth z can be defined as follows:

$$\mathbf{C}(\mathbf{r},\mathbf{r}',z,t,t') = \mathbb{E}\left[\mathbf{U}(\mathbf{r},z,t)\mathbf{U}^T(\mathbf{r}',z,t')\right] \tag{10}$$

where the superscript T stands for transposed vector. Under the assumption of the stationarity and horizontal homogeneity of the wave field, the cross-correlation matrix depends only on the separation distance $|\mathbf{r}' - \mathbf{r}|$ and the time lag τ. Thus, Eq. 10 can be rewritten in the following:

$$\mathbf{C}(|\mathbf{r}' - \mathbf{r}|,z,\tau) = \mathbb{E}\left[\mathbf{U}(\mathbf{r},z,t)\mathbf{U}^T(\mathbf{r}',z,t')\right] \tag{11}$$

The cross PSD matrix is obtained by the Fourier transform of Eq. 11:

$$\hat{\mathbf{S}}(\mathbf{k},z,\omega) = \mathcal{F}_{\mathbf{k}\omega}\left[\mathbb{E}\left[\mathbf{U}(\mathbf{r},z,t)\mathbf{U}^T(\mathbf{r}',z,t')\right]\right] \tag{12}$$

On the free surface $z = 0$, the cross PSD matrix can be expressed as:

$$\hat{\mathbf{S}}(\mathbf{k},0,\omega) = \mathcal{F}_{\mathbf{k}\omega}\left[\mathbb{E}\left[\mathbf{U}(\mathbf{r},0,t)\mathbf{U}^T(\mathbf{r}',0,t')\right]\right] \tag{13}$$

Finally, substituting Eqs. 8 and 9 into the Eqs. 12 and 13, one can obtain the relation between the cross PSD on the free surface and the one at depth z :

$$\hat{\mathbf{S}}(\mathbf{k},z,\omega) = \mathbf{T}(\mathbf{k},z,\omega)\hat{\mathbf{S}}(\mathbf{k},0,\omega)\mathbf{T}^T(\mathbf{k},z,\omega) \tag{14}$$

4 GENERATION OF INCOHERENT WAVE FIELD

4.1 Stationary incoherent wave field

4.1.1 General assumptions

In this section, one shows the method of generation of stationary incoherent wave field. Before entering into the details of the method, the main assumptions should be reminded:

- The medium is the homogeneous layered half-space elastic / visco-elastic.
- The motion at an arbitrary point in the ground is the result of the superposition of the plane waves incoming from all incident directions. One supposes the seismic waves propagate from the source to the site inside of the plane $\mathbf{Oxz}$. The incident waves are of types SH, P-SV. Each elementary wave is a stationary and independent stochastic process which is characterized by its power spectra $\mathbf{S}^{SH}(\omega,\theta)$, $\mathbf{S}^{P}(\omega,\theta)$ or $\mathbf{S}^{SV}(\omega,\theta)$ where θ stands for the incident angle with respect to the vertical axis. Thus, the anti-plane motion $\mathbf{Oy}$ is attributed to the SH waves, the in-plane motion in $\mathbf{Ox}$ and $\mathbf{Oz}$ direction is attributed to P-SV waves.
- The statistical properties of the free field are known only on the free surface and characterized by the coherency function. Moreover, the power spectra of the motion on the free surface is supposed identical, i.e. $\mathbf{S}(\mathbf{x},\mathbf{x},\omega)=\mathbf{S}(\mathbf{x}',\mathbf{x}',\omega)=\mathbf{S}_0(\omega)$, then the coherency function in Eq. 5 can be written in the following form:

$$\gamma(d_x,0,\omega)=\frac{\mathbf{S}(d_x,0,\omega)}{\mathbf{S}_0(\omega)} \tag{15}$$

So,

$$\mathbf{S}(d_x,0,\omega)=\gamma(d_x,0,\omega)\mathbf{S}_0(\omega) \tag{16}$$

$$\hat{\mathbf{S}}(k_x,0,\omega)=\hat{\gamma}(k_x,0,\omega)\mathbf{S}_0(\omega) \tag{17}$$

Where d_x stands for separation distance of two points in $\mathbf{Ox}$ direction.

Remark: in spite of the assumption that the incident waves are independent, the motion in $\mathbf{Ox}$ and $\mathbf{Oz}$ direction are correlated but these ones are uncorrelated with the motion in $\mathbf{Oy}$ direction. Thus, one can study the case of SH waves and P-SV waves separately. In the next two subsections, one shows the details of the novel method of generation of incoherent field on the basis of the stochastic deconvolution technique [17] and the spectral representation method [24].

One prefers to start with the simplest case: SH-wave and P-SV propagating through elastic half-space. The advantage is that one has the analytical formulas of wave transfer function (or transfer matrix $\mathbf{T}(\mathbf{k},z,\omega)$) therefore the numerical errors can be limited. In the case of stratified medium, the transfer matrix $\mathbf{T}(\mathbf{k},z,\omega)$ can be computed by means of Thomson-Haskell method [22, 23].

4.1.2 Case of SH waves

Let $a_j^{SH}(t)$ be the time history of the elementary incoming wave and $\mathbf{S}_0^{SH}(\theta_j,\omega)$ its power spectra. According to the spectral representation method [24], the j^{th} incoming wave can be generated as follows:

$$a_j^{SH}(t)=\sum_{i=1}^{\mathbf{K}}\sqrt{\mathbf{S}_0^{SH}(\theta_j,\omega_i)\,\Delta\omega}\;e^{i\varphi_j^{SH}(\omega_i)}\,e^{i\omega_i t} \tag{18}$$

and its Fourier amplitude:

$$\tilde{a}_j^{SH}(\omega)=\sqrt{\mathbf{S}_0^{SH}(\theta_j,\omega)}\;e^{i\varphi_j^{SH}(\omega)} \tag{19}$$

where $\varphi_j^{SH}(\omega)$ is a uniformly distributed random variable on the interval $[0, 2\pi)$. The out-of-plane motion in $\mathbf{Oy}$ direction at a point $\mathbf{x} = (x, y, z)$ in the medium is the result of the superposition of $\mathbf{N}$ incoming waves and the reflected waves by the free surface:

$$\tilde{\mathbf{v}}(x, y, z, \omega) = \sum_{j=1}^{\mathbf{N}} \sqrt{\mathbf{S}_0^{SH}(\theta_j, \omega)\ \Delta\theta}\, e^{i\phi_j(\omega)}\, (e^{-ik_{xj}x - ik_{zj}z} + e^{-ik_{xj}x + ik_{zj}z}) \tag{20}$$

in which

θ_j is of the interval $[-\frac{\pi}{2}, \frac{\pi}{2}]$
c_s is the shear wave velocity
$k_{xj} = \frac{\sin\theta_j}{c_s}\omega$ is the horizontal wave-number in $\mathbf{Ox}$ direction
$k_{zj} = \frac{\cos\theta_j}{c_s}\omega$ is the vertical wave-number in $\mathbf{Oz}$ direction

Because one considers only the out-of-plane waves in the plane $\mathbf{Oxz}$, the coordinate y is omitted for convenience. The cross PSD function of two arbitrary points in the medium is expressed as follows:

$$\mathbf{S}_{\mathbf{vv}}(x, x', z, z', \omega) = \mathbb{E}\left[\tilde{\mathbf{v}}(x, z, \omega)\tilde{\mathbf{v}}^*(x', z', \omega)\right] \tag{21}$$

where $*$ denotes the complex conjugate.

$$\begin{aligned}\mathbf{S}_{\mathbf{vv}}(x, x', z, z', \omega) = \sum_{j=1}^{\mathbf{N}} \mathbf{S}_0^{SH}(\theta_j, \omega)\, \Delta\theta\, (&e^{-ik_{xj}(x-x') - ik_{zj}(z-z')} + e^{-ik_{xj}(x-x') - ik_{zj}(z+z')} \\ &+ e^{-ik_{xj}(x-x') + ik_{zj}(z+z')} + e^{-ik_{xj}(x-x') + ik_{zj}(z-z')})\end{aligned} \tag{22}$$

Under the hypothesis of the homogeneous medium and the hypothesis of the independent elementary waves, one has:

$$\begin{aligned}\mathbf{S}_{\mathbf{vv}}(dx, z, z', \omega) = \sum_{j=1}^{\mathbf{N}} \mathbf{S}_0^{SH}(\theta_j, \omega)\, \Delta\theta\, e^{ik_{xj}dx}(&e^{-ik_{zj}(z-z')} + e^{-ik_{zj}(z+z')} \\ &+ e^{ik_{zj}(z+z')} + e^{ik_{zj}(z-z')})\end{aligned} \tag{23}$$

One can deduce the cross PSD function between 2 points of the same horizontal plane. On the free surface where $z = z' = 0$:

$$\mathbf{S}_{\mathbf{vv}}(d_x, 0, \omega) = 4\sum_{j=1}^{\mathbf{N}} \mathbf{S}_0^{SH}(\theta_j, \omega)\, e^{ik_{xj}dx}\, \Delta\theta \tag{24}$$

At the depth $z = z'$:

$$\mathbf{S}_{\mathbf{vv}}(d_x, z, \omega) = \sum_{j=1}^{\mathbf{N}} \mathbf{S}_0^{SH}(\theta_j, \omega)\, \Delta\theta\, e^{ik_{xj}d_x}(2 + e^{-2ik_{zj}z} + e^{2ik_{zj}z}) \tag{25}$$

The continuous form of Eq. 24 is given in the following:

$$\mathbf{S_{vv}}(d_x, 0, \omega) = 4 \int_{-\pi/2}^{\pi/2} \mathbf{S}_0^{SH}(\theta, \omega)\, e^{ik_{xj}d_x}\ d\theta \tag{26}$$

Then Eq. 26 can be written in the wave-number domain as follows:

$$\hat{\mathbf{S}}_{\mathbf{vv}}(k_x, 0, \omega) = \frac{4\, c_s}{\omega}\, \mathbf{S}_0^{SH}(\theta, \omega)\, \frac{1}{\sqrt{1 - \left(\frac{k_x c_s}{\omega}\right)^2}} \tag{27}$$

One has:

$$\mathbf{S}_0^{SH}(\theta, \omega) = \hat{\mathbf{S}}_{\mathbf{vv}}(k_x, 0, \omega) \frac{\omega}{4c_s} \sqrt{1 - \left(\frac{k_x c_s}{\omega}\right)^2} \tag{28}$$

Where $\theta = \arcsin(\frac{k_x c_s}{\omega})$ is the incident angle which is deduced by previous definition.

By substituting Eq. 17 into Eq. 28, the relation between the power spectra of the elementary waves with the coherency function on the free surface can be obtained:

$$\mathbf{S}_0^{SH}(\theta, \omega) = \hat{\gamma}_{\mathbf{vv}}(k_x, 0, \omega)\, \mathbf{S_{vv0}}(\omega)\, \frac{\omega}{4c_s} \sqrt{1 - \left(\frac{k_x c_s}{\omega}\right)^2} \tag{29}$$

This shows that the power spectra of the elementary waves can be computed from the given coherency function $\hat{\gamma}(k_x, 0, \omega)$ and the power spectra of the motion $\mathbf{S}_0(\omega)$ on the free surface, thus the out-of-plane motion at any point in the medium is readily obtained by means of Eq. 20.

4.1.3 Case of P-SV waves

In this case, the elementary waves are of types **P** and **SV** waves incoming with incident angle θ_j with respect to the vertical axis. Its time histories are $a_j^P(t)$, $a_j^{SV}(t)$. The elementary waves are mutually independent. The in-plane motion in the **Ox** and **Oz** directions are the summation of the projection of each elementary wave on these axis. The motion in the **Ox** and **Oz** direction can be decomposed as follows:

$$\mathbf{u} = \sum_{j=1}^{\mathbf{N}} \mathbf{u}_j^P + \mathbf{u}_j^{SV} \tag{30}$$

$$\mathbf{w} = \sum_{j=1}^{\mathbf{N}} \mathbf{w}_j^P + \mathbf{w}_j^{SV} \tag{31}$$

Moreover,

$$\begin{aligned}
\mathbf{u}_j^P &= \mathbf{u}_j^{+PP} + \mathbf{u}_j^{-PP} + \mathbf{u}_j^{-PS} \\
\mathbf{u}_j^{SV} &= \mathbf{u}_j^{+SS} + \mathbf{u}_j^{-SS} + \mathbf{u}_j^{-SP} \\
\mathbf{w}_j^P &= \mathbf{w}_j^{+PP} + \mathbf{w}_j^{-PP} + \mathbf{w}_j^{-PS} \\
\mathbf{w}_j^{SV} &= \mathbf{w}_j^{+SS} + \mathbf{w}_j^{-SS} + \mathbf{w}_j^{-SP}
\end{aligned}$$

in which

$+$ and $-$ denote the upcoming and downgoing wave
PP and SS stand for P and SV wave
PS and SP stand for the conversion mode of P and SV

Let $\mathbf{S}_0^P(\theta_j,\omega)$ and $\mathbf{S}_0^{SV}(\theta_j,\omega)$ be the power spectra of the P and SV elementary waves. On the basis of spectral representation method [24], the motion at any point in the medium can be generated as follows:

$$\tilde{\mathbf{u}}^P(x,z,\omega) = \sum_{j=1}^{\mathbf{N}} \sqrt{\mathbf{S}_0^P(\theta_j,\omega)\,\Delta\theta}\; e^{i\varphi_j^P(\omega)}\; e^{-i\omega p_j x}((e^{-i\omega\gamma_{pj}z} + A_{PP}\, e^{i\omega\gamma_{pj}z})\, p_j c_p + A_{PS}\, e^{i\omega\gamma_{sj}z}\, \gamma_{sj} c_s) \tag{32}$$

$$\tilde{\mathbf{w}}^P(x,z,\omega) = \sum_{j=1}^{\mathbf{N}} \sqrt{\mathbf{S}_0^P(\theta_j,\omega)\,\Delta\theta}\; e^{i\varphi_j^P(\omega)}\; e^{-i\omega p_j x}((-e^{-i\omega\gamma_{pj}z} + A_{PP}\, e^{i\omega\gamma_{pj}z})\, \gamma_{pj} c_p - A_{PS}\, e^{i\omega\gamma_{sj}z}\, p_j c_s) \tag{33}$$

$$\tilde{\mathbf{u}}^{SV}(x,z,\omega) = \sum_{j=1}^{\mathbf{N}} \sqrt{\mathbf{S}_0^{SV}(\theta_j,\omega)\,\Delta\theta}\; e^{i\varphi_j^{SV}(\omega)}\; e^{-i\omega p_j x}((e^{-i\omega\gamma_{sj}z} + A_{SS}\, e^{i\omega\gamma_{sj}z})\, \gamma_{sj} c_s + A_{SP}\, e^{i\omega\gamma_{pj}z}\, p_j c_p) \tag{34}$$

$$\tilde{\mathbf{w}}^{SV}(x,z,\omega) = \sum_{j=1}^{\mathbf{N}} \sqrt{\mathbf{S}_0^{SV}(\theta_j,\omega)\,\Delta\theta}\; e^{i\varphi_j^{SV}(\omega)}\; e^{-i\omega p_j x}((e^{-i\omega\gamma_{sj}z} - A_{SS}\, e^{i\omega\gamma_{sj}z})\, p_j c_s + A_{SP}\, e^{i\omega\gamma_{pj}z}\, \gamma_{pj} c_p) \tag{35}$$

in which A_{PP}, A_{SS}, A_{PS}, A_{SP} are the reflection and transmission coefficients of $\mathbf{P}$ and $\mathbf{SV}$waves by the free surface and that are given in annex.

The cross PSD matrix can be computed readily:

$$\mathbf{S}(x,x',z,z',\omega) = \begin{pmatrix} \mathbf{S_{uu}}(x,x',z,z',\omega) & \mathbf{S_{uw}}(x,x',z,z',\omega) \\ \mathbf{S_{wu}}(x,x',z,z',\omega) & \mathbf{S_{ww}}(x,x',z,z',\omega) \end{pmatrix} \tag{36}$$

Under the hypothesis of spatial homogeneity, the PSD function depends only on the horizontal separation distance. The previous equation can be rewritten in the following:

$$\mathbf{S}(d_x,z,z',\omega) = \begin{pmatrix} \mathbf{S_{uu}}(d_x,z,z',\omega) & \mathbf{S_{uw}}(d_x,z,z',\omega) \\ \mathbf{S_{wu}}(d_x,z,z',\omega) & \mathbf{S_{ww}}(d_x,z,z',\omega) \end{pmatrix} \tag{37}$$

where:

$$\mathbf{S_{uu}}(d_x,z,z',\omega) = \mathbb{E}\left[\tilde{\mathbf{u}}(x,z,\omega)\,\tilde{\mathbf{u}}^*(x',z',\omega)\right] \tag{38}$$

$$\mathbf{S_{uu}}(d_x,z,z',\omega) = \mathbb{E}\left[(\tilde{\mathbf{u}}^P(x,z,\omega) + \tilde{\mathbf{u}}^{SV}(x,z,\omega))\,(\tilde{\mathbf{u}}^{*P}(x',z',\omega) + \tilde{\mathbf{u}}^{*SV}(x',z',\omega))\right] \tag{39}$$

$$\mathbf{S_{uu}}(d_x, z, z', \omega) = \mathbb{E}\left[\tilde{\mathbf{u}}^P(x, z, \omega)\, \tilde{\mathbf{u}}^{*P}(x', z', \omega)\right] + \mathbb{E}\left[\tilde{\mathbf{u}}^{SV}(x, z, \omega)\, \tilde{\mathbf{u}}^{*SV}(x', z', \omega)\right] \quad (40)$$

$$\mathbf{S_{uu}}(d_x, z, z', \omega) = \mathbf{S}^P_{\mathbf{uu}}(d_x, z, z', \omega) + \mathbf{S}^{SV}_{\mathbf{uu}}(d_x, z, z', \omega) \quad (41)$$

$$\mathbf{S_{ww}}(d_x, z, z', \omega) = \mathbf{S}^P_{\mathbf{ww}}(d_x, z, z', \omega) + \mathbf{S}^{SV}_{\mathbf{ww}}(d_x, z, z', \omega) \quad (42)$$

$$\mathbf{S_{uw}}(d_x, z, z', \omega) = \mathbf{S}^P_{\mathbf{uw}}(d_x, z, z', \omega) + \mathbf{S}^{SV}_{\mathbf{uw}}(d_x, z, z', \omega) \quad (43)$$

$$\mathbf{S_{wu}}(d_x, z, z', \omega) = \mathbf{S}^P_{\mathbf{wu}}(d_x, z, z', \omega) + \mathbf{S}^{SV}_{\mathbf{wu}}(d_x, z, z', \omega) \quad (44)$$

On the free surface $z = z' = 0$,

$$\mathbf{S}(d_x, 0, 0, \omega) = \begin{pmatrix} \mathbf{S_{uu}}(d_x, 0, 0, \omega) & \mathbf{S_{uw}}(d_x, 0, 0, \omega) \\ \mathbf{S_{wu}}(d_x, 0, 0, \omega) & \mathbf{S_{ww}}(d_x, 0, 0, \omega) \end{pmatrix} \quad (45)$$

The statistic properties on the surface of the free field are given by the coherency function and power spectra function of the horizontal and vertical motion $\gamma_{\mathbf{uu}}(d_x, \omega)$, $\gamma_{\mathbf{ww}}(d_x, \omega)$, $\mathbf{S_{uu0}}(\omega)$, $\mathbf{S_{ww0}}(\omega)$ and in the wave-number frequency domain. One has :

$$\hat{\mathbf{S}}^P_{\mathbf{uu}}(k_x, 0, \omega) = \mathbf{S}^P_0(\theta, \omega)\, \mathbf{H}^P_{\mathbf{uu}}(\theta, \omega)$$

$$\hat{\mathbf{S}}^P_{\mathbf{ww}}(k_x, 0, \omega) = \mathbf{S}^P_0(\theta, \omega)\, \mathbf{H}^P_{\mathbf{ww}}(\theta, \omega)$$

$$\hat{\mathbf{S}}^{SV}_{\mathbf{uu}}(k_x, 0, \omega) = \mathbf{S}^{SV}_0(\theta, \omega)\, \mathbf{H}^{SV}_{\mathbf{uu}}(\theta, \omega)$$

$$\hat{\mathbf{S}}^{SV}_{\mathbf{ww}}(k_x, 0, \omega) = \mathbf{S}^{SV}_0(\theta, \omega)\, \mathbf{H}^{SV}_{\mathbf{ww}}(\theta, \omega)$$

$$\begin{pmatrix} \mathbf{H}^P_{\mathbf{uu}}(\theta, \omega) & \mathbf{H}^{SV}_{\mathbf{uu}}(\theta, \omega) \\ \mathbf{H}^P_{\mathbf{ww}}(\theta, \omega) & \mathbf{H}^{SV}_{\mathbf{ww}}(\theta, \omega) \end{pmatrix} \begin{pmatrix} \mathbf{S}^P_0(\theta, \omega) \\ \mathbf{S}^{SV}_0(\theta, \omega) \end{pmatrix} = \begin{pmatrix} \hat{\gamma}_{\mathbf{uu}}(k_x, 0, \omega)\mathbf{S_{uu0}}(\omega) \\ \hat{\gamma}_{\mathbf{ww}}(k_x, 0, \omega)\mathbf{S_{ww0}}(\omega) \end{pmatrix} \quad (46)$$

where $\mathbf{H}^P_{\mathbf{uu}}(\theta, \omega)$, $\mathbf{H}^{SV}_{\mathbf{uu}}(\theta, \omega)$, $\mathbf{H}^P_{\mathbf{ww}}(\theta, \omega)$, $\mathbf{H}^{SV}_{\mathbf{ww}}(\theta, \omega)$ are given in annex.

By means of Eq. 46, the PSD of each elementary wave can be computed from the given coherency functions and PSD of the vertical and horizontal motion on the free surface. Thus, the motion at any point in the medium is readily obtained by means of Eqs. 32,33,34 and 35.

4.2 Example Applications

This section shows an example to illustrate the proposed method. The soil is an elastic half-space whose S wave velocity is 489 m/s, P wave velocity is 2054 m/s and the mass density is 2420 kg/m^3. The coherency function on the free surface is the Luco et al 's model [1]

$$|\gamma_{\mathbf{uu}}(d_x, \omega)| = e^{-(\frac{\nu\omega d_x}{c_\alpha})^2} = e^{-(\alpha_{\mathbf{uu}}\omega d_x)^2} \quad (47)$$

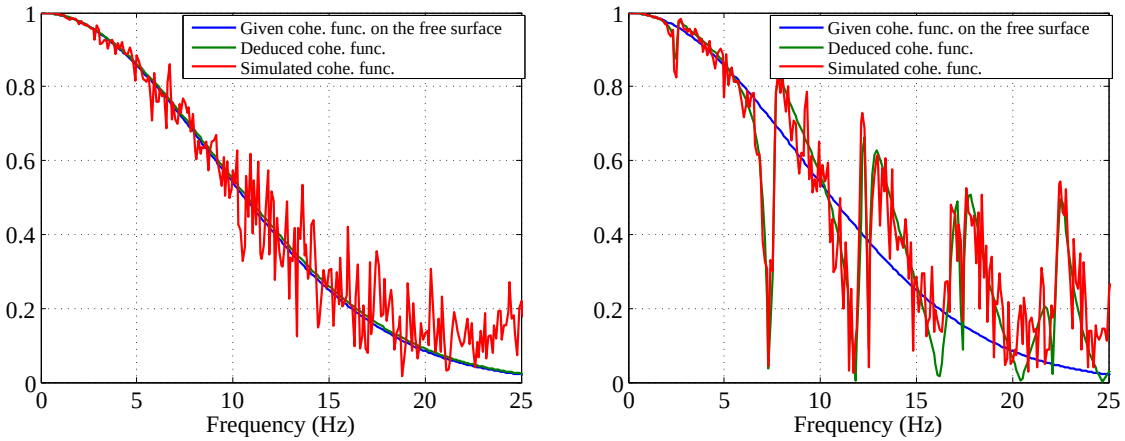
$$|\gamma_{\mathbf{vv}}(d_x, \omega)| = e^{-(\frac{\nu\omega d_x}{c_\alpha})^2} = e^{-(\alpha_{\mathbf{vv}}\omega d_x)^2} \quad (48)$$

$$|\gamma_{\mathbf{ww}}(d_x, \omega)| = e^{-(\frac{\nu\omega d_x}{c_\alpha})^2} = e^{-(\alpha_{\mathbf{ww}}\omega d_x)^2} \quad (49)$$

By assuming that the vertical motion is more coherent than the horizontal motion, we adopt the following parameters: $\alpha_{\mathbf{uu}} = \alpha_{\mathbf{vv}} = 0.00025$, $\alpha_{\mathbf{ww}} = 0.0002$. The PSDs on the free surface are $\mathbf{S_{uu0}}(\omega) = \mathbf{S_{vv0}}(\omega) = \mathbf{S}_{CP}(\omega)$, $\mathbf{S_{ww0}}(\omega) = \frac{2}{3}\mathbf{S}_{CP}(\omega)$ where $\mathbf{S}_{CP}(\omega)$ is the Clough-Penzien model [25] given in the following equation:

$$\mathbf{S}_{CP}(\omega) = S_0 \frac{1 + 4\zeta_g^2(\frac{\omega}{\omega_g})^2}{[1-(\frac{\omega}{\omega_g})^2]^2 + 4\zeta_g^2(\frac{\omega}{\omega_g})^2} \frac{(\frac{\omega}{\omega_f})^4}{[1-(\frac{\omega}{\omega_f})^2]^2 + 4\zeta_f^2(\frac{\omega}{\omega_f})^2} \tag{50}$$

The parameters of the Clough-Penzien spectrum are: $\omega_g = 5\pi$ rad/sec, $\omega_f = 0.5\pi$ rad/sec, $\zeta_g = \zeta_f = 0.6$, $S_0 = 1$ cm^2/sec^3.



(a) The coherency function on the free surface

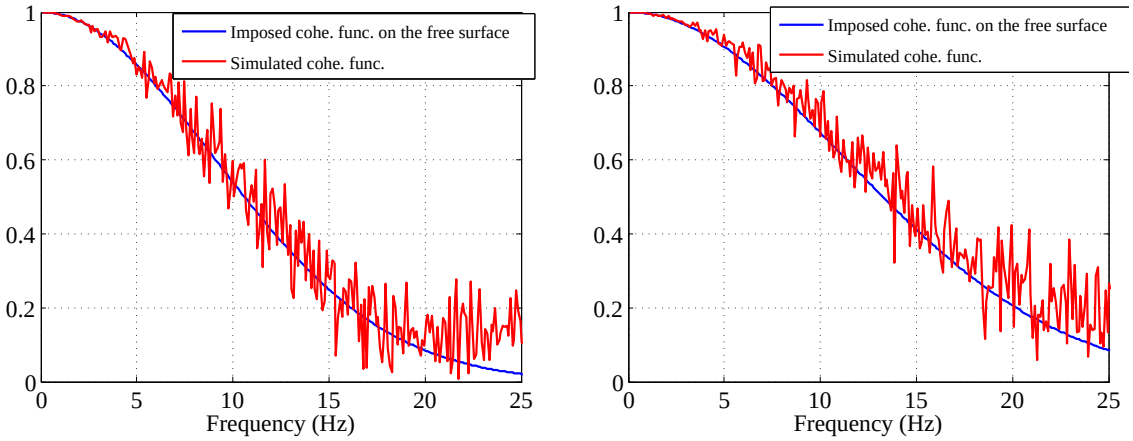
(b) The coherency function at 50 m in depth

Figure 1: The coherency function of out-of-plane the motion with 50 m of horizontal separation distance

Figure 1 shows the horizontal coherency funtion of the out-of-plane motion between two point separated by 50 m on the free surface on the left part (a) and at 50 m in depth on the right part (b). The red curve is the simulated coherency function computed by means of Eq. 5 from 50 simulations. The green curve is the coherency function obtained analytically by means of Eqs. 5 and 17. The simulated coherency function on the free surface converges to the imposed coherency function which is represented by the blue curve on Fig.1(a). On Fig. 1(b), one can note that the coherency function at depth is reduced at certain frequencies. The same remarks can be made from Fig.3. This figure shows the coherency function computed between two vertically separated points. This effect is due to the interference of the incoming and the reflected waves at the resonance frequencies corresponding to the 1, 3, 5 ... times of f_o.

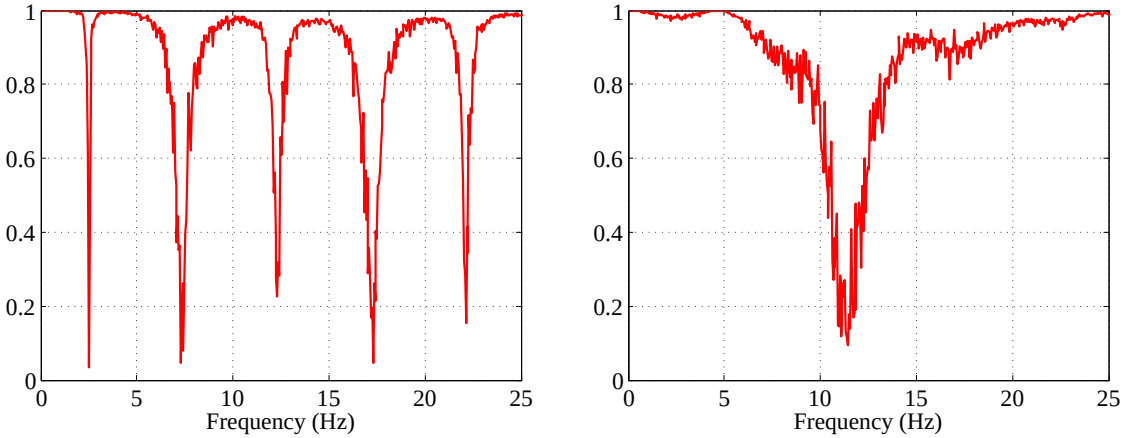
$$f_o = \frac{v}{4H} \tag{51}$$

where $v = c_s$, $v = c_p$ in the case of shear wave or P wave respectively and , H is the soil layer thickness. On Fig.3, one can note that the resonance frequency of the vertical motion is greater than the that of the horizontal motion because the vertical motion is due essentially to the P incoming waves whereas the horizontal motion is dominated by SV waves. The same conclusion can be found in [6] where the author has ploted the experimental vertical coherency function.



(a) The in-plane horizontal motion (b) The in-plane vertical motion

Figure 2: The coherency function of the horizontal and the vertical motion in the on the free surface with 50 m of horizontal separation distance



(a) The in-plane horizontal motion (b) The in-plane vertical motion

Figure 3: The coherency function of horizontal and vertical motion between 2 points vertically separated with distance = 50 m

4.3 Generation of non-stationary incoherent field

In the previous section, the method of generation of stationary incoherent field is shown. In order to perform a SSI analysis in time domain, the generated free field in the section 4.1 is transformed into the time domain by the Fourier transform. Of course, this free field satisfies the statistic properties on the free surface but it is still stationary. The full non-stationary incoherent field may be computed by the knowledge of the cross-correlation function of the

motion between any points of the medium. However, these cross-correlation functions are not available yet because of the lack of recordings. By using the coherency function to generate the incoherent wave field one implies the homogeneity of the medium and of the stationarity of the signals. This proposed method is in the same case. But the non-stationarity characteristic of seismic signals is essential in the structural dynamic engineering while performing response-history analyses. A method of generation of non-stationary incoherent field is proposed here by giving more "degree" of non-stationarity to the initial stationary incoherent field. In the literature, there are different ways to obtain a non-stationary incoherent field such as by using an evolutionary PSD function [9] or by fitting the incoherent field with the time histories at several reference points [10, 26]. The use of the evolutionary PSD function or the real time histories depends on the available data-bases and on the goals of each analysis. Discussion on this subject can be found in [27, 28] and the references therein. In this paper, one shows how to fit the stationary incoherent field with a given signal at a reference point.

Physically, in the present method, the stochastic spatial variability is represented by the summation of the incident waves incoming from all directions but their Fourier amplitude and phase are unknown. The varying incident wave field is the result of all phenomena such as the source effect, the scattering effect, the wave passage effect. The topology effect is accounted for only by considering the stratified soil. The Fourier amplitude of the elementary wave is computed from the coherency function on the free surface and their phase is supposed to be a random variable. In the time domain, the motion at any point can be considered as the superposition of a set of deterministic wave incoming with random time lag. Thus, if the motion at the reference point is fixed with a given signal, the non-stationary information of the given signal propagates through the medium. Surely, one can not obtain the full non-stationary field by this way because of the use of the stationary coherency model. In addition, the zero padding technique is used to avoid the overlapping phenomenon. In the case of SH wave, one supposes the signal at a point $\mathbf{O}(x_0, y_0, z_0)$ is $\mathbf{v}_0(\omega)$, the Fourier amplitude of the motion at any point is given as follows:

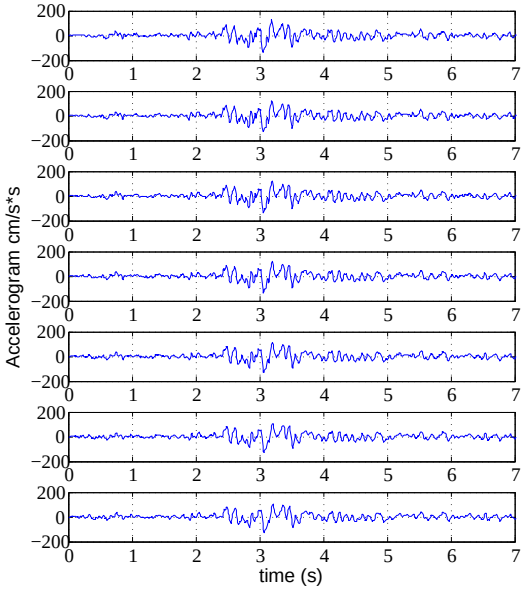
$$\bar{\mathbf{v}}(x, y, z, \omega) = \tilde{\mathbf{v}}(x, y, z, \omega) \frac{\mathbf{v}_0(\omega)}{\tilde{\mathbf{v}}(x_0, y_0, z_0, \omega)} \tag{52}$$

In the case of P-SV waves, because of the correlation between the vertical and horizontal motions of the chosen signals, one can not apply simultaneously the normalisation to the vertical and the horizontal motion. The estimation of the statistic properties obtained from several simulations and the fact that one applies the normalisation sequentially to the vertical and horizontal motion do not affect the statistic properties of the free field. Let $(\mathbf{u}_0(\omega), \mathbf{w}_0(\omega))$ be the real signal at the reference point $\mathbf{O}(x_0, y_0, z_0)$, the motion at the other points is computed as follows:

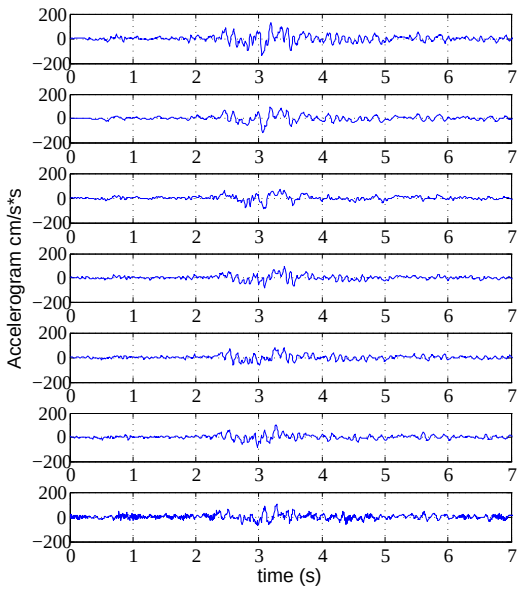
$$\bar{\mathbf{u}}(x, y, z, \omega) = \tilde{\mathbf{u}}(x, y, z, \omega) \frac{\mathbf{u}_0(\omega)}{\tilde{\mathbf{u}}(x_0, y_0, z_0, \omega)} \tag{53}$$

$$\bar{\mathbf{w}}(x, y, z, \omega) = \tilde{\mathbf{w}}(x, y, z, \omega) \frac{\mathbf{w}_0(\omega)}{\tilde{\mathbf{w}}(x_0, y_0, z_0, \omega)} \tag{54}$$

Figures 4 and 5 show the generated horizontal and the vertical in-plane motions on the free surface and in the downhole. The wave passage effect is not taken into account. The accelerogram at the reference point is fitted with a real signals.

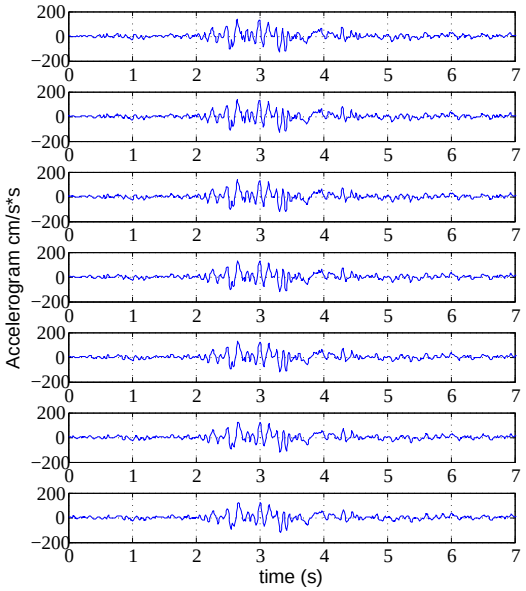


(a) The accelerogram on the surface at points of 0 m, 25 m , 50 m, 75 m, 100 m, 125 m, 150 m from referecne point

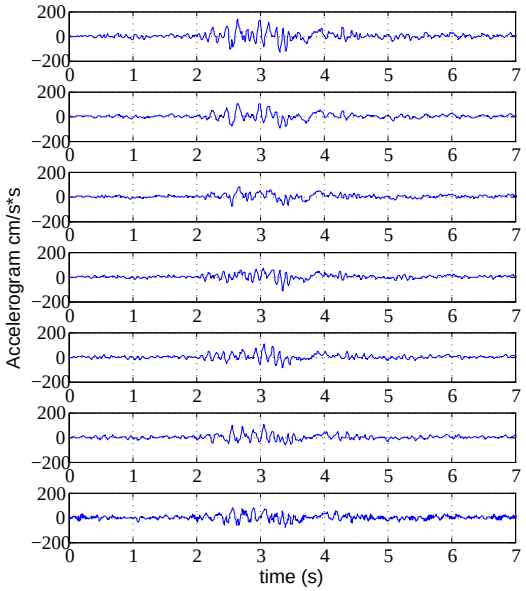


(b) The accelerogram in the downhole at 0 m, -25 m, -50 m, - 75 m, -100 m, -125 m, -150 m

Figure 4: The generated acceleration of the horizontal motion (case of P-SV incident wave)



(a) The accelerogram on the surface at points of 0 m, 25 m , 50 m, 75 m, 100 m, 125 m, 150 m from referecne point



(b) The accelerogram in the downhole at 0 m, -25 m, -50 m, - 75 m, -100 m, -125 m, -150 m

Figure 5: The generated acceleration of the vertical motion (case of P-SV incident wave)

5 CONCLUSION

An approach for generation of non-stationary incoherent seismic wave field is shown. The advantages are that the incoherent field satisfies the imposed coherency model on the free surface and fitted with the real signal at reference point. Moreover, the wave field is generated in time domain and is based on the wave propagation theory thus the traction and the velocity field at any point can be readily extracted and used as seismic input loading for a Finite Element model. This will allow 3D soil-structure interaction analyses to be performed with spatially varying seismic motions in the case of structure with embedded foundation. Eventually, structural non-linearity can be accounted for when the SSI analysis is performed in the time domain.

The drawbacks are that this approach is based on the strong hypotheses of stationarity and homogeneity of the wave field but in the points of view of the earthquake engineering these hypotheses are reasonable.

In the case of viscoelastic medium, the hysteretic damping of the medium is accounted for by using the complex Lamé coefficients.

ANNEX

Reflection coefficients by the free surface of P-SV waves:

$$A_{PP} = \frac{-(\frac{1}{c_s^2} - 2p^2)^2 + 4p^2\gamma_s\gamma_p}{(\frac{1}{c_s^2} - 2p^2)^2 + 4p^2\gamma_s\gamma_p}$$

$$A_{PS} = \frac{4\kappa p\gamma_p(\frac{1}{c_s^2} - 2p^2)}{(\frac{1}{c_s^2} - 2p^2)^2 + 4p^2\gamma_s\gamma_p}$$

$$A_{SP} = \frac{4\frac{1}{\kappa}p\gamma_s(\frac{1}{c_s^2} - 2p^2)}{(\frac{1}{c_s^2} - 2p^2)^2 + 4p^2\gamma_s\gamma_p}$$

$$A_{SS} = \frac{(\frac{1}{c_s^2} - 2p^2)^2 - 4p^2\gamma_s\gamma_p}{(\frac{1}{c_s^2} - 2p^2)^2 + 4p^2\gamma_s\gamma_p}$$

where

$$\kappa = \frac{c_p}{c_s}$$

$$p = \frac{\sin\theta_s}{c_s} = \frac{\sin\theta_p}{c_p}$$

$$\gamma_s = \sqrt{1 - p^2}$$

$$\gamma_p = \sqrt{1 - \kappa^2 p^2}$$

$$\mathbf{S}^P_{\mathbf{uu}}(d_x, z, z', \omega) = c_p^2 \int_{-\pi/2}^{\pi/2} \{\mathbf{S}_0^P(\theta, \omega)\, e^{i\omega p d_x}[e^{-i\omega\gamma_p(z-z')}p^2 + e^{-i\omega\gamma_p(z+z')}\, p^2\, A^*_{PP}$$
$$+e^{-i\omega(\gamma_p z+\gamma_s z')}\, p\, A^*_{PS}\, \gamma_s^* \frac{1}{\kappa} + e^{i\omega\gamma_p(z+z')}\, A_{PP}\, p^2 + e^{i\omega\gamma_p(z-z')}\, p^2\, A_{PP} A^*_{PP}$$
$$+e^{i\omega(\gamma_p z-\gamma_s z')}\, A_{PP}\, p\, A^*_{PS}\, \gamma_s^* \frac{1}{\kappa} + e^{i\omega(\gamma_s z+\gamma_p z')}\, A_{PS}\, \gamma_s \frac{1}{\kappa} p \;+\; e^{i\omega(\gamma_s z-\gamma_p z')} A_{PS}\gamma_s \frac{1}{\kappa} A^*_{PP} p$$
$$+e^{i\omega\gamma_s(z-z')}\, A_{PS}\, \gamma_s\, A^*_{PS}\, \gamma_s^* \frac{1}{\kappa^2}]\}d\theta \qquad (55)$$

$$\mathbf{S}^{P}_{\mathbf{ww}}(d_x,z,z',\omega) = c_p^2 \int_{-\pi/2}^{\pi/2} \{\mathbf{S}^{P}_0(\theta,\omega)\, e^{i\omega p d_x}[e^{-i\omega\gamma_p(z-z')}\gamma_p\gamma_p^* - e^{-i\omega\gamma_p(z+z')}\,\gamma_p\gamma_p^*\,A^*_{PP}$$
$$+e^{-i\omega(\gamma_p z+\gamma_s z')}\,\gamma_p\,A^*_{PS}\,p\frac{1}{\kappa} - e^{i\omega\gamma_p(z+z')}\,A_{PP}\,\gamma_p\gamma_p^* + e^{i\omega\gamma_p(z-z')}\,A_{PP}\gamma_p\,A^*_{PP}\gamma_p^*$$
$$-e^{i\omega(\gamma_p z-\gamma_s z')}\,A_{PP}\,\gamma_p\,A^*_{PS}\,p\frac{1}{\kappa} + e^{i\omega(\gamma_s z+\gamma_p z')}\,A_{PS}\,p\frac{1}{\kappa}\,\gamma_p^* - e^{i\omega(\gamma_s z-\gamma_p z')}\,A_{PS}p\frac{1}{\kappa}A^*_{PP}\gamma_p^*$$
$$+e^{i\omega\gamma_s(z-z')}\,A_{PS}\,p^2\,A^*_{PS}\,\frac{1}{\kappa^2}]\}d\theta \tag{56}$$

$$\mathbf{S}^{SV}_{\mathbf{uu}}(d_x,z,z',\omega) = c_p^2 \int_{-\pi/2}^{\pi/2} \{\mathbf{S}^{SV}_0(\theta,\omega)\, e^{i\omega p d_x}[e^{-i\omega\gamma_s(z-z')}\gamma_s\gamma_s^*\frac{1}{\kappa^2}$$
$$+e^{-i\omega\gamma_s(z+z')}\,\gamma_s\gamma_s^*\,A^*_{SS}\,\frac{1}{\kappa^2} + e^{-i\omega(\gamma_s z+\gamma_p z')}\,\gamma_s\,A^*_{SP}\,p\frac{1}{\kappa} + e^{i\omega\gamma_s(z+z')}\,A_{SS}\,\gamma_s\gamma_s^*\frac{1}{\kappa^2}$$
$$+e^{i\omega\gamma_s(z-z')}\,A_{SS}\gamma_s\,A^*_{SS}\gamma_s^*\frac{1}{\kappa^2} + e^{i\omega(\gamma_s z-\gamma_p z')}\,A_{SS}\,\gamma_s\,A^*_{SP}\,p\frac{1}{\kappa} + e^{i\omega(\gamma_p z+\gamma_s z')}\,A_{SP}\,p\frac{1}{\kappa}\,\gamma_s^*$$
$$+\,e^{i\omega(\gamma_p z-\gamma_s z')}\,A_{SP}p\frac{1}{\kappa}A^*_{SS}\gamma_s^* + e^{i\omega\gamma_p(z-z')}\,A_{SP}\,p^2\,A^*_{SP}]\}d\theta \tag{57}$$

$$\mathbf{S}^{SV}_{\mathbf{ww}}(d_x,z,z',\omega) = c_p^2 \int_{-\pi/2}^{\pi/2} \{\mathbf{S}^{SV}_0(\theta,\omega) e^{i\omega p d_x}[e^{-i\omega\gamma_s(z-z')}p^2\frac{1}{\kappa^2} - e^{-i\omega\gamma_s(z+z')}\,p^2\,A^*_{SS}\frac{1}{\kappa^2}$$
$$+e^{-i\omega(\gamma_s z+\gamma_p z')}\,p\,A^*_{SP}\,\gamma_p^*\frac{1}{\kappa} - e^{i\omega\gamma_s(z+z')}\,A_{SS}\,p^2\,\frac{1}{\kappa^2} + e^{i\omega\gamma_s(z-z')}\,p^2\,A_{SS}A^*_{SS}\frac{1}{\kappa^2}$$
$$-e^{i\omega(\gamma_s z-\gamma_p z')}\,A_{SS}\,p\,A^*_{SP}\,\gamma_p^*\frac{1}{\kappa} + e^{i\omega(\gamma_p z+\gamma_s z')}\,A_{SP}\,\gamma_p\frac{1}{\kappa}\,p$$
$$-e^{i\omega(\gamma_p z-\gamma_s z')}\,A_{SP}\gamma_p\frac{1}{\kappa}A^*_{SS}p + e^{i\omega\gamma_p(z-z')}\,A_{SP}\,\gamma_p\,A^*_{SP}\,\gamma_p^*\}d\theta \tag{58}$$

$$\mathbf{S}^{P}_{\mathbf{uw}}(d_x,z,z',\omega) = c_p^2 \int_{-\pi/2}^{\pi/2} \{\mathbf{S}^{P}_0(\theta,\omega)e^{i\omega p d_x}[-e^{-i\omega\gamma_p(z-z')}p\gamma_p^* + e^{-i\omega\gamma_p(z+z')}p\,A^*_{PP}\,\gamma_p^*$$
$$-e^{-i\omega(\gamma_p z+\gamma_s z')}p^2A^*_{PS}\frac{1}{\kappa} - e^{i\omega\gamma_p(z+z')}A_{PP}p\gamma_p^* + e^{i\omega\gamma_p(z-z')}A_{PP}pA^*_{PP}\gamma_p^*$$
$$-e^{i\omega(\gamma_p z-\gamma_s z')}A_{PP}pA^*_{PS}p\frac{1}{\kappa} - e^{i\omega(\gamma_s z+\gamma_p z')}A_{PS}\gamma_s\frac{1}{\kappa}\gamma_p^*$$
$$+e^{i\omega(\gamma_s z-\gamma_p z')}A_{PS}\gamma_s\frac{1}{\kappa}A^*_{PP}\gamma_p^* - e^{i\omega\gamma_s(z-z')}A_{PS}\gamma_s A^*_{PS}p\frac{1}{\kappa^2}]\}d\theta \tag{59}$$

$$\mathbf{S}^{SV}_{\mathbf{uw}}(d_x,z,z',\omega) = c_p^2 \int_{-\pi/2}^{\pi/2} \{\mathbf{S}^{SV}_0(\theta,\omega)e^{i\omega p d_x}[e^{-i\omega\gamma_s(z-z')}\gamma_s p\frac{1}{\kappa^2} - e^{-i\omega\gamma_s(z+z')}\gamma_s p\frac{1}{\kappa^2}$$
$$+e^{-i\omega(\gamma_s z+\gamma_p z')}\gamma_s\frac{1}{\kappa}A^*_{SP}\gamma_p^* + e^{i\omega\gamma_s(z+z')}A_{SS}\gamma_s\frac{1}{\kappa^2}p - e^{i\omega\gamma_s(z-z')}A_{SS}\gamma_s A^*_{SS}p\frac{1}{\kappa^2}$$
$$+e^{i\omega(\gamma_s z-\gamma_p z')}A_{SS}\gamma_s\frac{1}{\kappa}A^*_{SP}\gamma_p + e^{i\omega(\gamma_p z+\gamma_s z')}A_{SP}p^2\frac{1}{\kappa} - e^{i\omega(\gamma_p z-\gamma_s z')}A_{SP}pA^*_{SS}p\frac{1}{\kappa}$$
$$+e^{i\omega\gamma_p(z-z')}A_{SP}pA^*_{SP}\gamma_p\}d\theta \tag{60}$$

when $z = z' = 0$

$$\hat{\mathbf{S}}^{P}_{\mathbf{uu}}(k_x, 0, \omega) = \mathbf{S}^{P}_{0}(\theta, \omega)\, \mathbf{H}^{P}_{\mathbf{uu}}(\theta, \omega)$$

$$\hat{\mathbf{S}}^{P}_{\mathbf{ww}}(k_x, 0, \omega) = \mathbf{S}^{P}_{0}(\theta, \omega)\, \mathbf{H}^{P}_{\mathbf{ww}}(\theta, \omega)$$

$$\hat{\mathbf{S}}^{SV}_{\mathbf{uu}}(k_x, 0, \omega) = \mathbf{S}^{SV}_{0}(\theta, \omega)\, \mathbf{H}^{SV}_{\mathbf{uu}}(\theta, \omega)$$

$$\hat{\mathbf{S}}^{SV}_{\mathbf{ww}}(k_x, 0, \omega) = \mathbf{S}^{SV}_{0}(\theta, \omega)\, \mathbf{H}^{SV}_{\mathbf{ww}}(\theta, \omega)$$

where:

$$\mathbf{H}^{P}_{\mathbf{uu}}(\theta, \omega) = c_p^2[p^2 + p^2\, A^*_{PP} + \, p\, A^*_{PS}\, \gamma^*_s \frac{1}{\kappa} + \, A_{PP}\, p^2 + \, p^2\, A_{PP} A^*_{PP}$$
$$+ A_{PP}\, p\, A^*_{PS}\, \gamma^*_s \frac{1}{\kappa} + \, A_{PS}\, \gamma_s \frac{1}{\kappa} p \, + \, A_{PS} \gamma_s \frac{1}{\kappa} A^*_{PP} p + \, A_{PS}\, \gamma_s\, A^*_{PS}\, \gamma^*_s \frac{1}{\kappa^2}] \frac{1}{\omega \gamma_p} \tag{61}$$

$$\mathbf{H}^{P}_{\mathbf{ww}}(\theta, \omega) = c_p^2[\gamma_p \gamma^*_p - \, \gamma_p \gamma^*_p\, A^*_{PP} + \, \gamma_p\, A^*_{PS}\, p \frac{1}{\kappa} - \, A_{PP}\, \gamma_p \gamma^*_p + \, A_{PP} \gamma_p\, A^*_{PP} \gamma^*_p$$
$$- A_{PP}\, \gamma_p\, A^*_{PS}\, p \frac{1}{\kappa} + \, A_{PS}\, p \frac{1}{\kappa}\, \gamma^*_p \, - \, A_{PS} p \frac{1}{\kappa} A^*_{PP} \gamma^*_p + \, A_{PS}\, p^2\, A^*_{PS}\, \frac{1}{\kappa^2}] \frac{1}{\omega \gamma_p} \tag{62}$$

$$\mathbf{H}^{SV}_{\mathbf{uu}}(\theta, \omega) = c_p^2[\gamma_s \gamma^*_s \frac{1}{\kappa^2} + \, \gamma_s \gamma^*_s\, A^*_{SS}\, \frac{1}{\kappa^2} + \, \gamma_s\, A^*_{SP}\, p \frac{1}{\kappa} + \, A_{SS}\, \gamma_s \gamma^*_s \frac{1}{\kappa^2} + \, A_{SS} \gamma_s\, A^*_{SS} \gamma^*_s \frac{1}{\kappa^2}$$
$$+ A_{SS}\, \gamma_s\, A^*_{SP}\, p \frac{1}{\kappa} + \, A_{SP}\, p \frac{1}{\kappa}\, \gamma^*_s \, + \, A_{SP} p \frac{1}{\kappa} A^*_{SS} \gamma^*_s + \, A_{SP}\, p^2\, A^*_{SP}] \frac{1}{\omega \gamma_s} \tag{63}$$

$$\mathbf{H}^{SV}_{\mathbf{ww}}(\theta, \omega) = c_p^2[p^2 \frac{1}{\kappa^2} - \, p^2\, A^*_{SS} \frac{1}{\kappa^2} + \, p\, A^*_{SP}\, \gamma^*_p \frac{1}{\kappa} - \, A_{SS}\, p^2\, \frac{1}{\kappa^2} + \, p^2\, A_{SS} A^*_{SS} \frac{1}{\kappa^2}$$
$$- A_{SS}\, p\, A^*_{SP}\, \gamma^*_p \frac{1}{\kappa} + \, A_{SP}\, \gamma_p \frac{1}{\kappa} p \, - \, A_{SP} \gamma_p \frac{1}{\kappa} A^*_{SS} p + \, A_{SP}\, \gamma_p\, A^*_{SP}\, \gamma^*_p] \frac{1}{\omega \gamma_s} \tag{64}$$

REFERENCES

[1] J.E. Luco, and H.L. Wong, Response of a Rigid Foundation to a Spatially Random Ground Motion. *Earthquake Engineering and Structural Dynamics*, 14(6): 891-908, 1986.

[2] A. Zerva, Effect of spatial variability and propagation of seismic ground motion on the response of multiply supported structures. *Probabilistic Engineering Mechanics*, Vol. 6,212–221,1991.

[3] R. Kassawara and L. Sandell, Program on Technology Innovation: Effects of Spatial Incoherence on Seismic Ground Motions. *Electric Power Research Institute Report*, December 2007.

[4] Bycroft, G. Noel, El Centro, California, Differential Ground Motion Array. *United States Geological Survey Open-File Report*, 80–919, 1980.

[5] B. A. Bolt, *Preliminary Report on the SMART 1 Strong Motion Array in Taiwan*. University of California, Earthquake Engineering Research Center, 1982.

[6] N. Abrahamson, J. F. Schneider, and J.C. Stepp, Spatial Coherency of Shear Waves from the Lotung, Taiwan Large-scale Seismic Test. *Structural Safety*, 10(1-3): 145-162, 1991.

[7] F. Wang, Effect of seismic spatial variability on the floor response. *Report DMT* SEMT/EMSI/RT/99–064/A.

[8] D. M. Ghiocel, F. Ostadan, Seismic Ground Motion Incoherency Effects on Soil-Structure Interaction Response of NPP Building Structures. *Proceedings of 19th Conference on Structural Mechanics in Reactor Technology*, Toronto, August 2007.

[9] H. Hao, C.S. Oliveira, and J. Penzien, Multiple-station Ground Motion Processing and Simulation Based on Smart-1 Array Data. *Nuclear Engineering and Design*, 111(3): 293310, 1989.

[10] N.A. Abrahamson, Generation of Spatially Incoherent Strong Motion Time Histories . *Proceedings of Tenth World Conference on Earthquake Engineering*, ISBN : 90 5410 060 5, Balkema, Rotterdam, 1992.

[11] H.E. Vanmarcke, E. Heredia–Zavoni, and G.A. Fenton, Conditional Simulation of Spatially Correlated Earthquake Ground Motion. *Journal of Engineering Mechanics*, 119(11): 2333-2352.

[12] H. Kameda, H. Morikawa, Conditioned Stochastic Processes for Conditional Random Fields. *Journal of Engineering Mechanics*, 120(4): 855875, 1994.

[13] L. S. Katafygiotis, A. Zerva, An Efficient Approach for the Simulation of Spatially Variable Motions for the Seismic Response of Lifelines. *Proceedings of 13th Engineering Mechanics Conference*, ASCE, Baltimore, MD 1999.

[14] T. Sato, H. Imabayashi, Real Time Conditional Simulation of Earthquake Ground Motion. *Earthquake Engineering and Engineering Seismology*, Vol. 1, Num. 1, 27–38,1999.

[15] I. Zentner, Proposition d'une méthode pour prendre en compte la variabilité spatiale du champ sismique incident. *EDF report*, H-T61-2006-02165-FR. In french

[16] A. Chakraborty, and B. Basu, Nonstationary Response Analysis of Long Span Bridges Under Spatially Varying Differential Support. *Motions Using Continuous Wavelet Transform. Journal of Engineering Mechanics*, 134(2): 155-162, 2008.

[17] E. Kausel, A. Pais, Stochastic Deconvolution of Earthquake Motions. *Journal of Engineering Mechanics*, 113(2): 266-277, 1987.

[18] D. Zendagui, M.K. Berrah, and E. Kausel, Stochastic Deamplification of Spatially Varying Seismic Motions. *Soil Dynamics and Earthquake Engineering*, 18(6): 409-421,1999.

[19] A.D. Kiureghian, A Coherency Model for Spatially Varying Ground Motions. *Earthquake Engineering and Structural Dynamics*, 25(1): 99-111, 1996.

[20] N. Laouami, and P. Labbe, Analytical Approach for Evaluation of the Seismic Ground Motion Coherency Function. *Soil Dynamics and Earthquake Engineering*, 21(8): 727-733, 2001.

[21] H . Nakamura, Depth-dependent Spatial Variation of Ground Motion based on Seismic Array Records. *Proceedings of Eleventh World Conference on Earthquake Engineering*, paper no. 731, ISBN : 0 08 042822 3.

[22] W.T. Thomson, Transmission of Elastic Waves Through a Stratified Solid Medium. *Journal of Applied Physics*, 21(2): 89-93, 1950.

[23] N.A. Haskell, The Dispersion of Surface Waves on Multilayered Media. *Bulletin of the Seismological Society of America*, 43(1): 17-34, 1953.

[24] M. Shinozuka, C.-M Jan, Digital Simulation of Random Processes and Its Applications. *Journal of Sound and Vibration*, 25(1): 111-128, 1972.

[25] P.W. Clough, J. Penzien, *Dynamics of Structures*, McGraw-Hill, Inc.,New York, NY, 1975.

[26] I. Zentner, Simulation of Non-stationary Conditional Ground Motion Fields in The Time Domain. *Georisk: Assessement and Management of Risk for Engineering Systems and Geohazards*, 7:1, 37–48, 2013.

[27] C.B. Haselton, A.S Whittaker, A. Hortacsu, J.W. Baker, J.Bray, Selecting and Scaling Earthquake Ground Motions for Performing Response-History Analyses. *Proceedings of Fifteenth World Conference on Earthquake Engineering*, Lisboa, Portugal, 2012.

[28] E. Kalkan, A.K Chopra, Practical Guidelines to Select and Scale Earthquake Records for Nonlinear Response History Analysis of Structures. *U.S Geological Survey Open-File Report*, 113p, 2010.

COMPDYN 2013
4th ECCOMAS Thematic Conference on
Computational Methods in Structural Dynamics and Earthquake Engineering
M. Papadrakakis, V. Papadopoulos, V. Plevris (eds.)
Kos Island, Greece, 12–14 June 2013

DYNAMIC SOIL-STRUCTURE INTERACTION ANALYSIS OF A TELESCOPE AT THE JAVALAMBRE ASTROPHYSICAL OBSERVATORY

Stijn François[1], Pedro Galvín[2], Pedro Museros[3], Geert Lombaert[1] and Geert Degrande[1]

[1] KU Leuven, Department of Civil Engineering, Kasteelpark Arenberg 40, B-3000 Leuven, Belgium

[2] Universidad de Sevilla, Escuela Técnica Superior de Ingenieros, Camino de los Descubrimientos, 41092 Sevilla, Spain

[3] Universidad de Granada, Departamento de Mecánica de Estructuras, Escuela Técnica Superior de Ingenieros de Caminos, 18071 Granada, Spain

e-mail: stijn.francois@bwk.kuleuven.be

Keywords: Dynamic soil-structure interaction, pile foundations, vibrations

Abstract. *This paper reports on the dynamic soil-structure analysis of a telescope pier of an astrophysical laboratory in the Sierra de Javalambre, Teruel (Spain). Vibration control in the design stage is of prime concern, since astrophysical observations may be hindered by mechanical vibration of the sensitive optics of the telescope. These vibrations may result from wind loading on the telescope dome, transferred through the foundation to the telescope. Therefore, the manufacturer of the telescope has imposed a minimal resonance frequency of 10 Hz for the supporting structure. For a massive construction such as a telescope pier, this resonance frequency may be significantly influenced by the effects of dynamic soil-structure interaction. The telescope is mounted on a concrete pier with a height of 15.25 m, founded on 73 reinforced concrete micro-piles with a diameter of 0.40 m. The dynamic soil characteristics at the site have been determined by means of a down-hole test. The effect of dynamic soil-structure interaction is studied using a coupled finite element - boundary element model of the telescope pier - foundation soil system. The response of the telescope is computed for harmonic loading at the top of the telescope pier. Results demonstrate that the effect of dynamic soil-structure interaction is significant. An analysis that disregards dynamic soil-structure interaction results a predicted resonance of 14.28 Hz while a fully coupled analysis predicts a resonance frequency of 11.2 Hz.*

1 INTRODUCTION

This paper reports on the dynamic response of a telescope pier of an astrophysical laboratory in the Sierra de Javalambre, Teruel (Spain). From early in the design stage, vibration control has been of prime concern, since astrophysical observations may be hindered by mechanical vibration of the sensitive optics of the telescope. These vibrations are expected to result from wind loading on the telescope dome, transferred through the foundation to the telescope [7].

In order to avoid the mechanical vibration of the sensitive optics of the telescope, the telescope manufacturer has imposed that the resonance frequency of the telescope pier should be higher than 10 Hz. For a massive construction such as a telescope pier, this resonance frequency may be significantly lowered by the effects of dynamic soil-structure interaction. On the other hand, dynamic soil-structure interaction allows for the dissipation of energy through wave propagation in the soil, mitigating resonance peaks.

This paper investigates the effects of dynamic soil-structure interaction on the resonance frequency of the telescope pier by means of a coupled finite element - boundary element model of the telescope pier - foundation - soil system.

The paper is outlined as follows. In section 2, the dynamic soil characteristics at the site of the Javalambre astrophysical observatory are discussed. The geometry and material properties of the structure are summarized in section 3. In section 4, the coupled finite element - boundary element model of the telescope is outlined. The response of the telescope pier is discussed in section 5, where the effect of dynamic soil-structure interaction is investigated.

2 SITE CHARACTERIZATION

The Javalambre astrophysical observatory is located at the top of the Pico del Buitre, 1957 m above sea level, close to the village of Arcos de las Salinas (Teruel, Spain).

An extensive geotechnical site characterization of the construction site has been carried out [7]. This has revealed an intense ground fracturing combined with density changes in the rock matrix up to a depth of 7 m (figure 1).

A down-hole test has been performed at the test site [3] to determine the shear wave velocity C_s and dilatational wave velocity C_p as a function of depth (table 1). The material damping ratio of the soil as a function of depth is not available from the down-hole test, and an identical value for shear and volumetric deformation $\beta_\mathrm{s} = \beta_\mathrm{p} = 0.01$ will be assumed in the following. The intense fracturing of the top rock matrix has been confirmed by the down-hole test and results in low wave speeds in the top layers.

3 GEOMETRY AND MATERIAL PROPERTIES

The telescope is mounted on a concrete pier with a height of 15.25 m, founded on 73 reinforced concrete micro-piles with a diameter of 0.40 m (figures 2 and 3). The upper part of the pier is a truncated cone with an outer radius of 1.4 m at the top and 3.5 m at the base. The lower part of the telescope pier consists of a concrete cylinder with a constant outer radius of 3.5 m, reinforced with 7 radial ribs. The overall thickness of the pier is 0.6 m.

The telescope pier is supported by a ring-shaped pile cap with an external radius of 5 m and an internal radius of 1.2 m. The pile cap has a thickness of 1.5 m. The opening in the pile cap acts as an elevator pit for the telescope lens lift.

The concrete used for the pier and the pile cap is referred to as HA-35 and has a Young's modulus $E = 35\,\mathrm{GPa}$, a Poisson's ratio $\nu = 0.2$ and a density $\rho = 2500\,\mathrm{kg/m^2}$. For the micro-piles, a high-strength concrete HA-45 is used, with a Young's modulus $E = 37.5\,\mathrm{GPa}$,

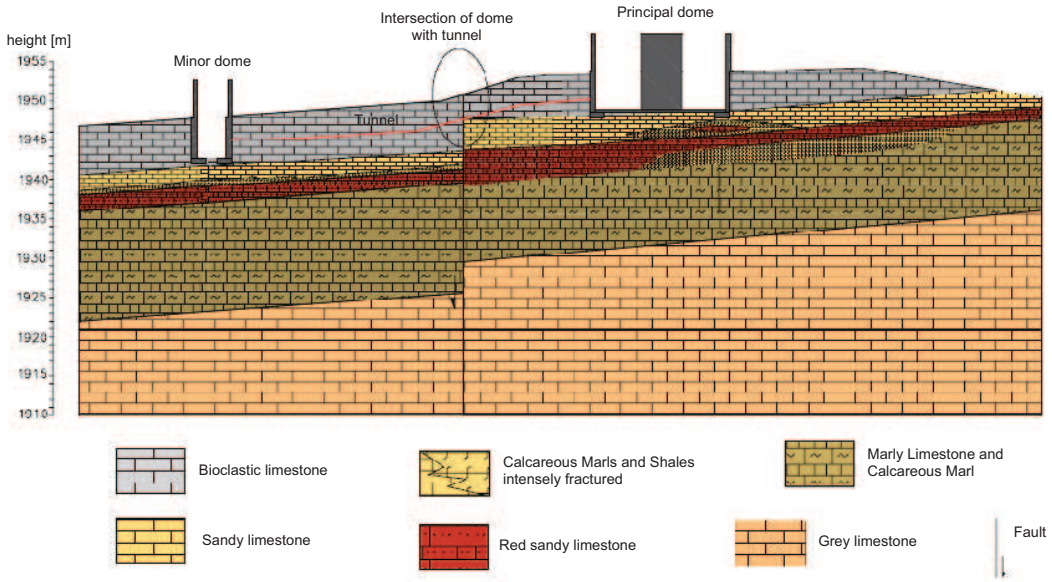


Figure 1: Geological layering at the construction site.

Depth [m]	C_s [m]	C_p [m]	ρ [kg/m^3]
1	407	646	2700
2	403	903	2700
3	446	937	2700
4	490	815	2670
5	520	937	2670
6	520	1190	2250
7	555	1229	2250
8	974	3195	2250
9	1056	3409	2250
10	961	1811	2250
11	1100	2335	2650
12	1064	2670	2650
13	2055	3335	2650
14	1764	2647	2650
15	2150	3164	2650
16	2294	3759	2650
17	1629	3505	2650
18	1383	2635	2650

Table 1: Dynamic soil properties at the site of the Javalambre Astrophysical Observatory.

a Poisson's ratio $\nu = 0.2$ and a density $\rho = 2500\,\mathrm{kg/m^2}$. In addition, a material damping ratio $\beta_\mathrm{c} = 0.02$ is assumed for the concrete.

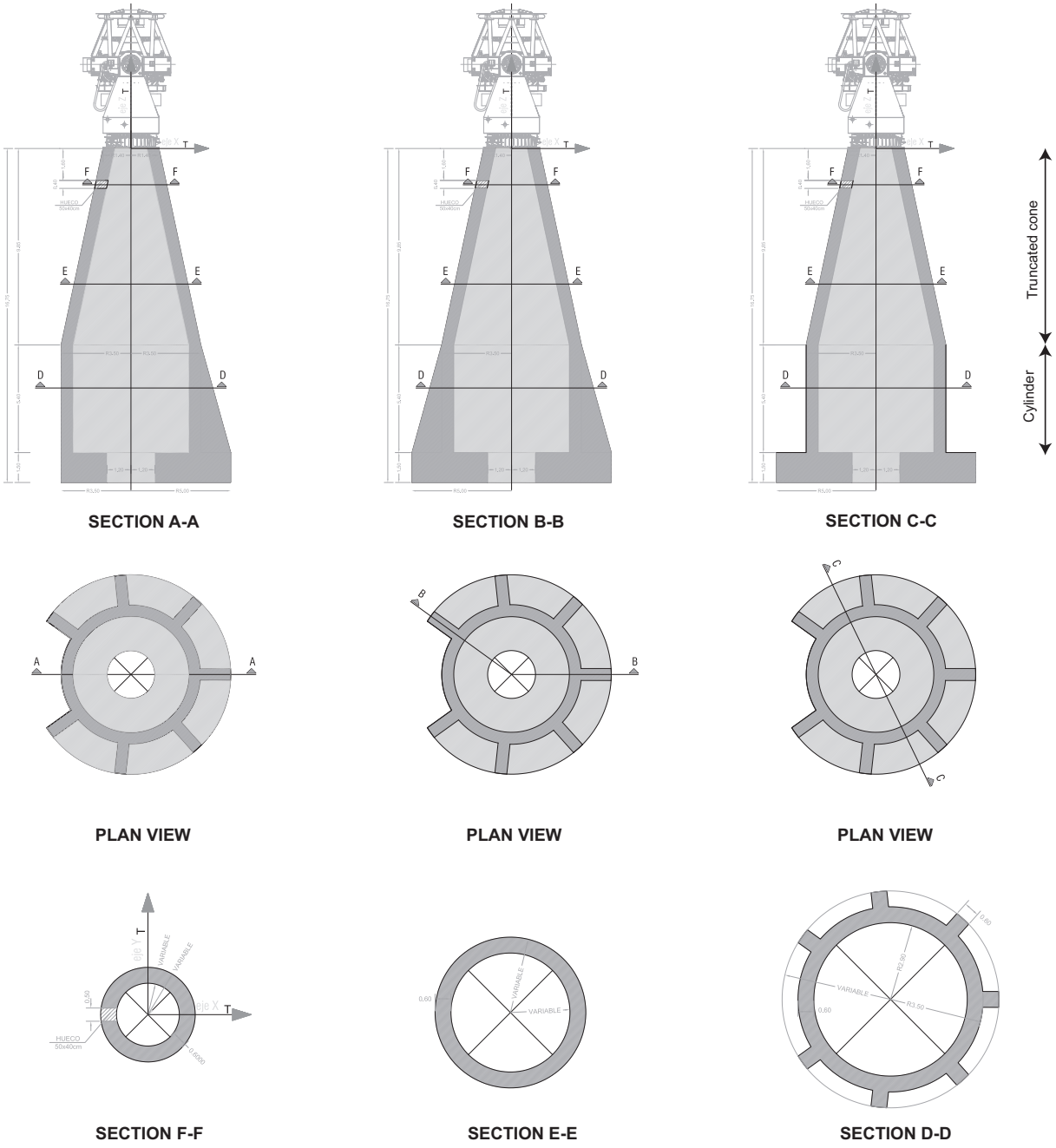


Figure 2: Layout of the telescope.

4 NUMERICAL MODEL

4.1 Finite element model

The finite element (FE) model of the telescope pier, the pile cap, the micro-piles and a cylindrical soil region with a radius of 5 m and a depth of 7.5 m is shown in figure 4. The origin of the right-handed Cartesian frame of reference (x, y, z) is considered at ground level, with the x-axis along the center line of the notch in the pile cap and the z-axis ponting upwards.

The FE model is shown in figure 4. The telescope pier is meshed in Ansys with 1206 8-node rectangular shell elements with a thickness of 0.6 m. The shell elements use Mindlin-Reissner shell theory for bending, accounting for first order shear deformation theory. The pile cap and

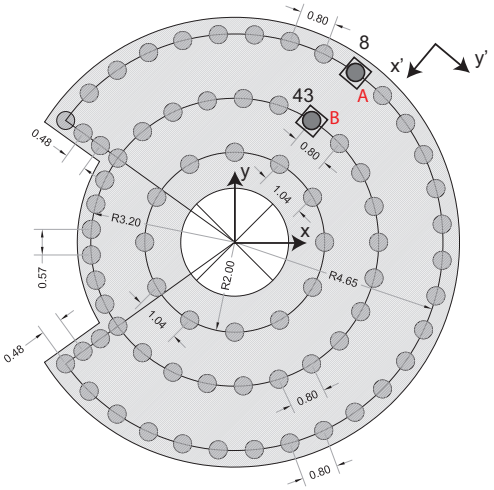


Figure 3: Layout of the pile foundation.

the cylindrical soil region are modelled with 20-node (quadratic) solid elements, employing 1720 and 3200 elements, respectively. The micro-piles are modelled with 584 beam elements, connected to the solid elements for the cylindrical soil region. The maximum element size equals 1 m.

The telescope is represented as a rigid mass of 45000 kg, located at a distance of 3.15 m above the top of the pier. This is modelled as a concentrated mass in an auxiliary node with 6 degrees of freedom at the point ($x = 0$, $y = 0$, $z = 19.9\,\mathrm{m}$). Constraint equations are employed, coupling six rigid body modes of the top ring of the pier to the respective degrees of freedom of the concentrated mass.

The structure has been meshed using Ansys, whereas the Matlab toolbox StaBIL [5] is used to assemble the stiffness and mass matrices $\mathbf{K}$ and $\mathbf{M}$. The FE model (telescope pier, pile cap, pile foundation, and soil) has 25898 nodes, 6711 elements, and 90888 degrees of freedom.

4.2 Boundary element model

As the soil has been excavated prior to construction of the telescope, the first five soft layers in table 1 are not considered. The soil is modelled as a horizontally layered halfspace (figure 5), where the properties of the layers correspond to layers 6 to 18 of the down-hole test in table 1. The underlaying homogeneous halfspace has a shear wave velocity $C_\mathrm{s} = 2000\,\mathrm{m/s}$, a dilatational wave velocity $C_\mathrm{p} = 3650\,\mathrm{m/s}$, and a density $\rho = 2650\,\mathrm{kg/m^3}$. The latter properties are average values from a secondary down-hole test at larger depths [7].

In order to account for the interaction between the layered soil and the FE model, a boundary element (BE) model that conforms with the FE mesh of the cylindrical soil volume is employed (figure 6), where 8-node serendipity boundary elements are used with 6×6 Gaussian integration points per element.

The BE system matrices are computed with the Matlab toolbox BEMFUN [6]. These BE system matrices allow to compute displacement and traction vectors at the BE nodes. At the edge of the bottom and side of the cylindrical soil volume, double nodes are used to account for double traction vectors on the corners.

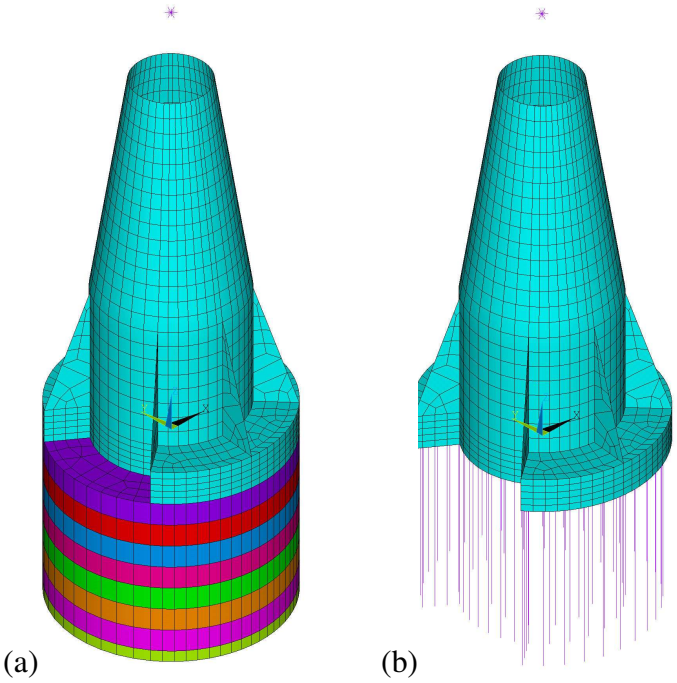


Figure 4: FE mesh of (a) the telescope pier, the pile cap, the soil and the micro-piles, and (b) the telescope pier, the pile cap, and the micro-piles. Different materials are indicated with different colors.

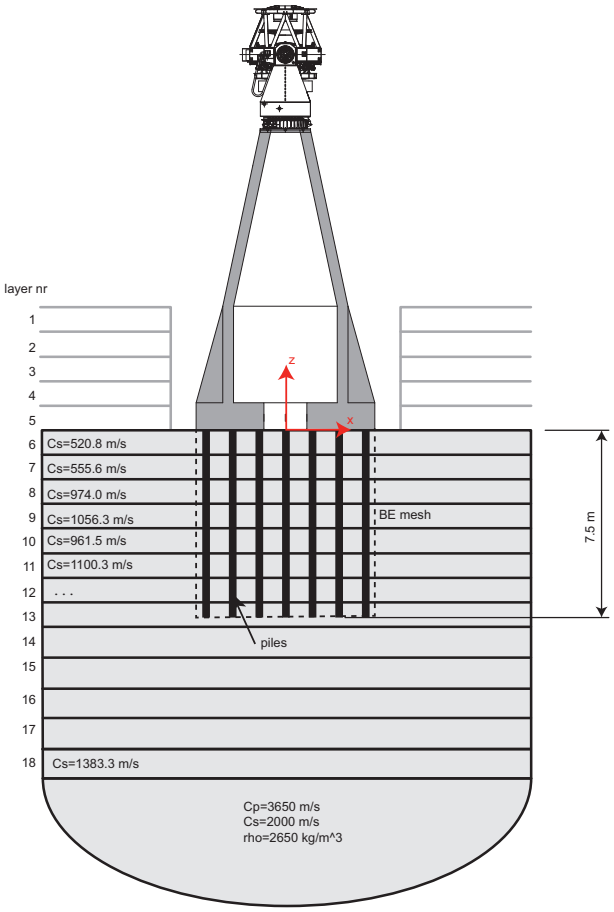


Figure 5: Layout of the coupled FE-BE model.

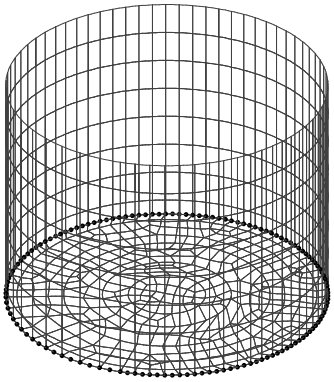
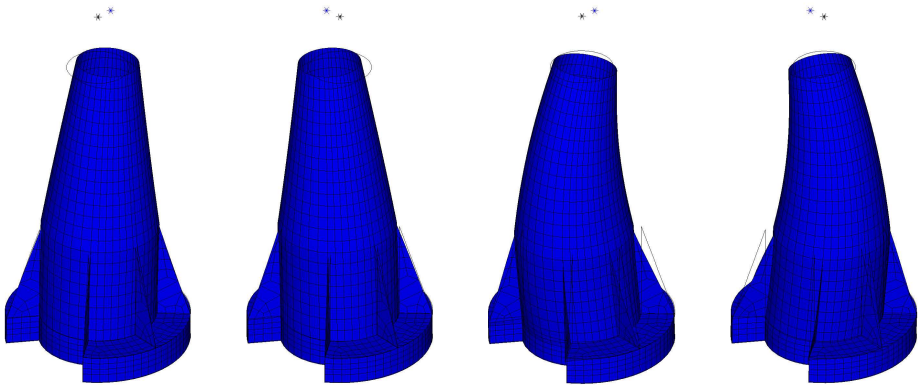


Figure 6: BE mesh conforming with the FE mesh of the cylindrical soil volume surrounding the micro-piles. The double corner nodes (black dots) are also indicated.

5 NUMERICAL RESULTS

5.1 Reference analysis disregarding dynamic soil-structure interaction

As a reference, the response of the telescope pier fixed at the base is computed. Figure 7 shows the first 4 mode shapes. The first eigenfrequency of the structure equals 14.28 Hz, which is well above the limit of 10 Hz imposed by the telescope manufacturer to avoid malfunctioning of the equipment.



(a) Mode 1 at 14.28 Hz. (b) Mode 2 at 15.06 Hz. (c) Mode 3 at 41.74 Hz (d) Mode 4 at 42.42 Hz

Figure 7: Eigenmodes of the structure fixed at its base.

A unit harmonic point load in the x-direction is applied at the concentrated mass of 45000 kg that represents the telescope. Figure 8 shows the displacement of the concentrated mass in the direction of the loading. The response is dominated by the first structural mode.

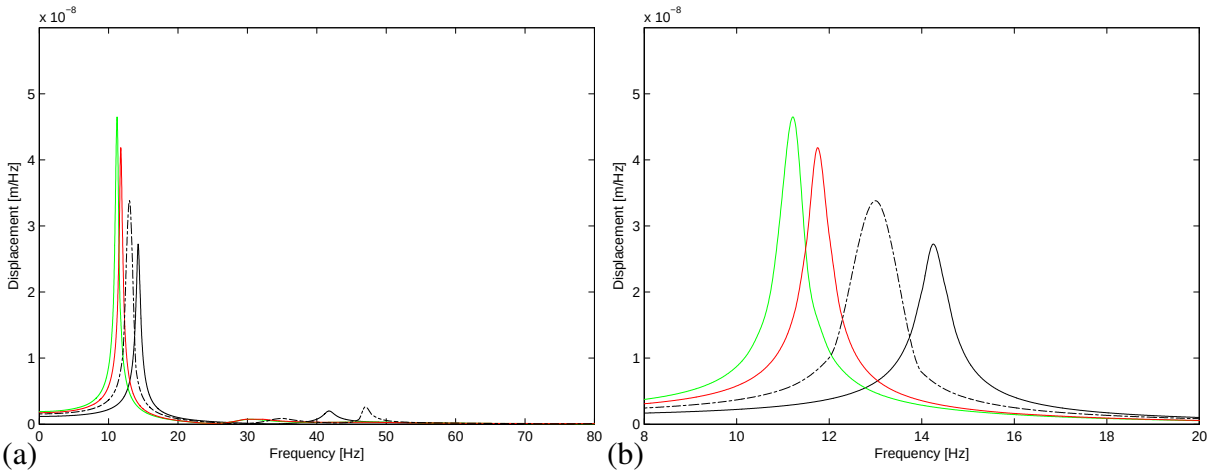


Figure 8: (a) Modulus of the displacement of the top of the telescope due to a unit harmonic horizontal load applied at the concentrated mass, and (b) zoom around the resonance peak. Results are plotted for an analysis without dynamic soil-structure interaction (solid black line), an analysis including dynamic soil-structure interaction (green line) and including dynamic soil-structure interaction with a rigid pile cap (red line) and a simplified approach (dash-dotted line).

5.2 Dynamic soil-structure interaction analysis

Next, a complete dynamic soil-structure interaction analysis is performed, The response of the telescope pier due to a unit harmonic point load in the x-direction applied at the concentrated mass of 45000 kg is computed.

Figure 8 shows the displacement of the concentrated mass in the direction of the loading. The response of the telescope, loaded by a harmonic point load at the top, is dominated by a resonance peak corresponding to the first bending mode of the telescope pier. Due to the effect of dynamic soil-structure interaction, the peak response occurs at 11.2 Hz, which is above the limit imposed by the telescope manufacturer to avoid malfunctioning of the equipment. The amplitude at the peak response is larger than the resonance frequency of the telescope pier fixed at its base, due to the lower eigenfrequency. This is partially compensated for by the additional radiation and material damping in the soil. The corresponding radiated wave field at 20, 40, 60 and 80 Hz is plotted in figure 9.

A modal analysis is not performed, since the presence of the soil stiffness of the layered halfspace renders the dynamic stiffness matrix frequency dependent and strongly damped.

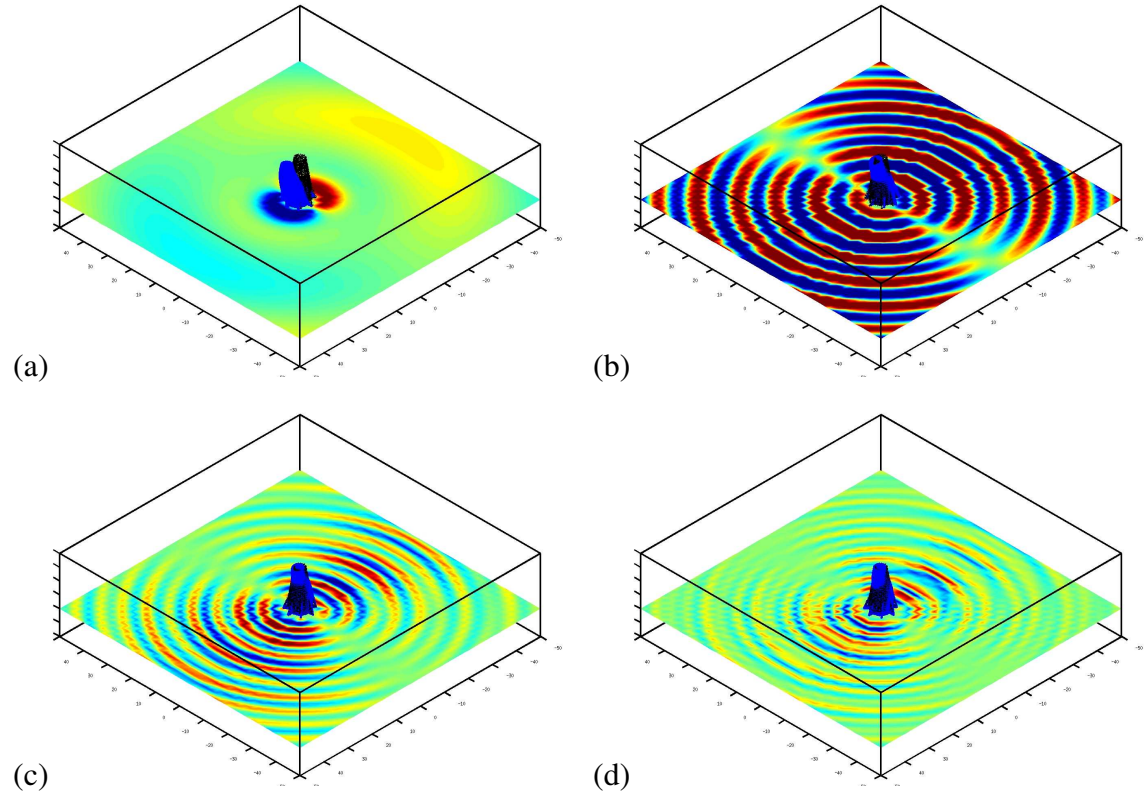


Figure 9: Real part of the vertical soil displacement at (a) 20 Hz, (b) 40 Hz, (c) 60 Hz, and (d) 80 Hz due to a horizontal harmonic load at the top of the telescope.

5.3 Dynamic soil-structure interaction analysis with a rigid pile cap

The assumption of a rigid pile cap allows the use of impedance functions [1, 4, 10] in a dynamic soil-structure interaction analysis. The frequency dependent elements $S_{mn}(a_0)$ of the 6×6 impedance matrix of a rigid foundation are commonly written in the following dimensionless form [10]:

$$S_{mn}(a_0) \quad = \quad K^{\mathrm{s}}_{mn} \left[K_{mn}(a_0) + i C_{mn}(a_0) \right] \tag{1}$$

where the subscripts m and n denote the horizontal (h), vertical (v), rotational (r) and torsional (t) degree of freedom, while the static stiffness coefficients K^{s}_{mn} are defined as $K^{\mathrm{s}}_{\mathrm{hh}} = K^{\mathrm{s}}_{\mathrm{vv}} = \mu R$, $K^{\mathrm{s}}_{\mathrm{rr}} = K^{\mathrm{s}}_{\mathrm{tt}} = \mu R^3$ and $K^{\mathrm{s}}_{\mathrm{hr}} = \mu R^2$, with $\mu = {C^{\mathrm{ref}}_{\mathrm{s}}}^2 \rho$ the (reference) shear modulus of the soil. The dimensionless stiffness and damping coefficients $K_{mn}(a_0)$ and $C_{mn}(a_0)$ depend on the dimensionless frequency $a_0 = \omega R / C^{\mathrm{ref}}_{\mathrm{s}}$ where R is the radius of the embedded cylindrical foundation.

It is noted that the imaginary part of the dynamic stiffness matrix is sometimes plotted in the literature after division by a_0. This is interesting in simple cases where the imaginary part remains more or less linear, such as for rigid surface foundations. In the case of a pile group this is not relevant and this practice is not followed in the present report.

Figure 10 shows the dimensionless stiffness and damping coefficients for the pile foundation with a rigid massless pile cap, where an average shear wave speed $C^{\mathrm{ref}}_{\mathrm{s}} = C^{\mathrm{av}}_{\mathrm{s}} = 890\,\mathrm{m/s}$ and a density $\rho = 2400\,\mathrm{kg/m^3}$ are considered to compute the dimensionless foundation characteristics.

The results are compared to results obtained with a simplified model developed by Taherzadeh et al. [11] (figure 11). Parameters are provided for floating pile groups and for end-bearing pile groups. Floating pile groups are pile groups embedded in a homogeneous halfspace while end-bearing pile groups are embedded in a soft layer on top of a bedrock. Results are only given for the horizontal component K_{hh} and rocking component K_{rr} of the dynamic stiffness matrix, which dominate the response of the pile cap. The simplification consists of a lumped parameter model, composed of masses, springs and dampers. The properties of the components are determined by the parametrization:

$$\lambda_0 \left(\frac{R}{H} \right)^{\lambda_1} \left(\frac{L_0}{s} \right)^{\lambda_2} \left(\frac{\rho_{\mathrm{b}} C^{\mathrm{b}}_{\mathrm{s}}}{\rho_{\mathrm{l}} C^{\mathrm{l}}_{\mathrm{s}}} \right)^{\lambda_3} \tag{2}$$

where R is the pile cap radius, H is the thickness of the top soil layer, $L_0 = \left(E_{\mathrm{p}} I_{\mathrm{p}} / E_l \right)^{0.25}$ the critical pile length, s the pile separation. ρ_{b} and ρ_{l} are the density of the bedrock (b) and the soil layer (l), respectively. Similarly, $C^{\mathrm{b}}_{\mathrm{s}}$ and $C^{\mathrm{l}}_{\mathrm{s}}$ are the shear wave velocities of the bedrock and the soil layer. The parameters λ_0 to λ_3 have been tuned for each of the components in the simplified model, against the results of coupled FE-BE calculations for a regular grid of piles supported by a rectangular, rigid pile cap.

The parametrization (2) reduces to the model of a floating pile group if the properties of the bedrock and the soil layer correspond ($\rho_{\mathrm{b}} = \rho_{\mathrm{l}}$ and $C^{\mathrm{l}}_{\mathrm{s}} = C^{\mathrm{b}}_{\mathrm{s}}$). The model accounts for the effect of friction along the pile through the factor $\left(\rho_{\mathrm{b}} C^{\mathrm{b}}_{\mathrm{s}} / \left(\rho_{\mathrm{l}} C^{\mathrm{l}}_{\mathrm{s}} \right) \right)^{\lambda_3}$, which is considered to contribute significantly to the overall vertical impedance in the present study.

Figure 10 compares the dynamic stiffness and damping coefficients obtained with both models. The correspondance is very good for the horizontal impedance at low frequencies, but deviates at higher frequencies. The rocking stiffness and damping are overestimated by the

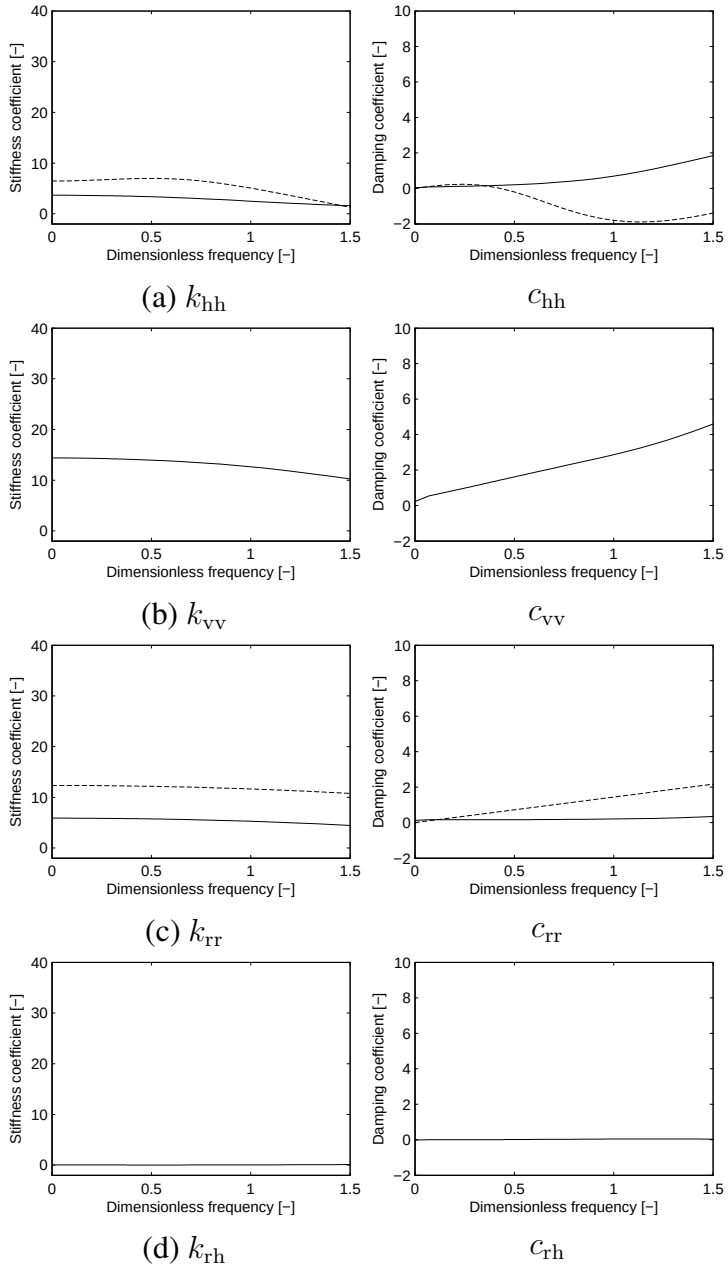


Figure 10: Stiffness (left) and damping (right) coefficients of the pile group with a rigid massless cap for the (a) horizontal, (b) vertical, (c) rocking and (d) horizontal-rocking deformation. The results obtained with the coupled FE-BE model (solid line) are compared with results obtained with a simplified model by Taherzadeh et al. [11] (dashed line) for the horizontal and rocking motion.

simplified model. This is attributed to the fact that the foundation is not rectangular, that the pile separation is not constant and that the top soil layers and the bedrock are not homogeneous.

The dynamic soil stiffness of the massless, rigid pile cap is added to the FE model using constraint equations, imposing a rigid body displacement to the base of the pile cap.

Figure 8 shows the displacement of the concentrated mass in the direction of the loading. The resonance related to the first bending mode occurs at a frequency of 11.7 Hz. The increase of the frequency with respect to the model in with a flexible pile cap (11.2 Hz) is due to the assumption of a rigid pile cap, resulting in a higher dynamic soil stiffness.

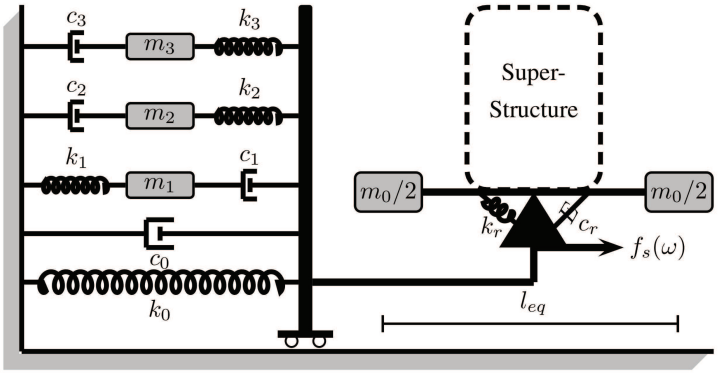


Figure 11: Lumped parameter model for the soil, consisting of a set of masses, springs and dampers [11].

Figure 8 also shows the response as computed with the dynamic soil stiffness from the simplified pile cap model. Since the simplified pile cap model overestimates the dynamic stiffness of the pile group, the corresponding resonance is located at a higher frequency of about 13 Hz. The damping coefficient is underestimated, resulting in a larger response at resonance.

6 CONCLUSIONS

In this paper, the dynamic behavior of a telescope pier of an astrophysical laboratory in the Sierra de Javalambre, Teruel (Spain), has been considered.

In order to quantify the effects of dynamic soil-structure interaction, a coupled FE-BE model of the telescope pier on the pile foundation embedded in the soil has been employed. The telescope pier, the foundation cap, the micro-piles and a cylindrical soil volume have been meshed with finite elements. The surrounding layered halfspace has been modelled with boundary elements.

A first analysis that disregards dynamic soil-structure interaction has been performed, where the telescope pier is fixed at its base. The response of the telescope, loaded by a harmonic point load at the top, is dominated by the bending modes of the telescope pier. The first eigenfrequency of the telescope pier equals 14.28 Hz.

A coupled FE-BE model is next used to compute the response of the telescope pier, fully accounting for dynamic soil-stucture interaction. The response of the telescope, loaded by a harmonic point load at the top, is dominated by a resonance peak corresponding to the bending mode of the telescope pier. Due to the effect of dynamic soil-structure interaction, the peak occurs at 10.7 Hz. This demonstrates that the effect of dynamic soil-structure interaction is significant.

A simplified approach is next used where the FE model of the telescope pier is coupled to the pile cap impedance of a rigid pile cap, accounting for dynamic soil-structure interaction in a simplified way. The resulting foundation stiffness and damping coefficients have been validated by means of impedance curves for pile groups, as published in the literature [11]. The dynamic soil stiffness of the massless, rigid pile cap is added to the FE model using constraint equations, imposing a rigid body displacement to the base of the pile cap. Due to the assumption of a rigid pile cap, the dynamic soil stiffness is higher than in the case of a flexible pile cap, and the resonance related to the first bending mode of the telescope pier occurs at 11 Hz. This demonstrates that the flexibility of the pile cap has only a minor effect on the resonance frequency of the telescope pier.

7 ACKNOWLEDGEMENTS

The results presented in this paper have been obtained in collaboration with the University of Granada. The first author is a postdoctoral fellow of the Research Foundation - Flanders (FWO). All financial support is hereby gratefully acknowledged.

REFERENCES

[1] R.J. Apsel and J.E. Luco. Impedance functions for foundations embedded in a layered medium: an integral equation approach. *Earthquake Engineering and Structural Dynamics*, 15:213–231, 1987.

[2] M. Bonnet. *Boundary integral equation methods for solids and fluids*. John Wiley and Sons, Chichester, United Kingdom, 1995.

[3] B.G.H. Consulting. Reconocimiento geofísico básico mediante sísmica de refracción, tomografía eléctrica, down-hole, cross-hole y sondeo eléctrico vertical (SEV). Observatorio Astrifísico del Pico del Buitre. Technical report, B.G.H., 2009.

[4] R. Dobry and G. Gazetas. Simple method for dynamic stiffness and damping of floating pile groups. *Géotechnique*, 38:557–574, 1988.

[5] D. Dooms, G. De Roeck, G. Degrande, and S. François. Een interactieve en adaptieve toepassing voor de statische en dynamische analyse van structuren (StaBIL). Technical Report BWM-2009-21, Department of Civil Engineering, KU Leuven, October 2009.

[6] S. François, M. Schevenels, and G. Degrande. BEMFUN: MATLAB toolbox for boundary elements in elastodynamics. Version 2.1 Build 16. User's guide BWM-2009-26, Department of Civil Engineering, KU Leuven, December 2009.

[7] Geodeser. Estudio geológico-geotécnico. Observatorio Astrifísico del Pico del Buitre. Technical report, Geodeser, 2009.

[8] L. Pyl, D. Clouteau, and G. Degrande. A weakly singular boundary integral equation in elastodynamics for heterogeneous domains mitigating fictitious eigenfrequencies. *Engineering Analysis with Boundary Elements*, 28(12):1493–1513, 2004.

[9] H.A. Schenck. Improved integral formulation for acoustic radiation problems. *Journal of the Acoustical Society of America*, 44:41–58, 1968.

[10] J.-G. Sieffert and F. Cevaer. *Handbook of impedance functions. Surface foundations*. Ouest Editions, Presses Académiques, Nantes, 1992.

[11] R. Taherzadeh, D. Clouteau, and R. Cottereau. Simple formulas for the dynamic stiffness of pile groups. *Earthquake Engineering and Structural Dynamics*, 38(15):1665–1685, 2009.

COMPDYN 2013
4th ECCOMAS Thematic Conference on
Computational Methods in Structural Dynamics and Earthquake Engineering
M. Papadrakakis, V. Papadopoulos, V. Plevris (eds.)
Kos Island, Greece, 12–14 June 2013

ACCOUNTING FOR NONLINEAR DYNAMIC SOIL-STRUCTURE INTERACTION IN EARTHQUAKE ENGINEERING

A. Nieto Ferro[1], N. Greffet[1], G. Devésa[1] and D. Clouteau[2]

[1]Électricité de France R&D and LaMSID (UMR EDF/CNRS/CEA 8193)
Avenue du Général de Gaulle 1, 92141 Clamart, France
e-mail: {alex.nieto-ferro,nicolas.greffet,georges.devesa}@edf.fr

[2] LMSSMat (CNRS UMR 8579), École Centrale Paris
Grande Voie des Vignes, 92295 Châtenay-Malabry, France
e-mail: {didier.clouteau}@ecp.fr

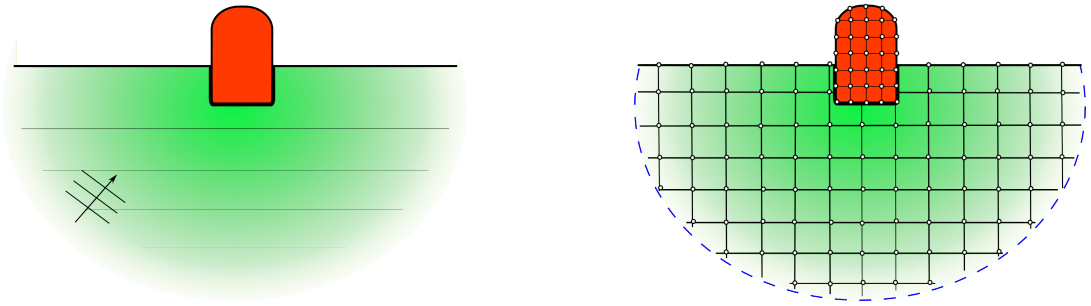
Keywords: Dynamic soil-structure interaction, impedance matrix, Hybrid Laplace-Time domain Approach, Convolution Quadrature Method, nonlinear analysis.

Abstract. *Dynamic soil-structure interaction problems are usually solved by a sub-structuring technique where the soil-structure system is decomposed into two sub-domains: the nonlinear superstructure and the linear visco-elastic unbounded soil. The superstructure might include, in addition to the actual structure, a part of soil showing a nonlinear behaviour. To address this problem, a BEM-FEM coupling strategy is adopted in this work. On one hand, the superstructure is modelled by a FE method which allows to take into account nonlinear constitutive laws as well as complex geometries in a straightforward way. Besides, the problem within the superstructure is formulated in the time domain. On the other hand, the interaction forces coming from the linear unbounded soil are represented by means of an impedance operator defined on the soil-superstructure interface and computed with a Laplace-domain BE method. A semi-industrial application is used to illustrate the effect of nonlinear soil (the Hujeux law) in soil-structure interaction analysis.*

1 INTRODUCTION

Given the recent new insight on seismic hazard in France and other countries, Électricité de France (EDF), the main electricity operator in France and the principal funder of this research work, needs to provide new seismic risk assessment of the entire power production sites. In this framework, the Research and Development (R&D) division of EDF is interested in the development of efficient procedures to solve three-dimensional nonlinear dynamic soil-structure interaction (SSI) problems in the time domain.

Dynamic SSI problems in earthquake engineering can be commonly summarized by Fig. 1a where the soil-structure system is subjected to an incident field displacement that represents the seismic waves. To solve these problems, the most predominant numerical methods in the literature can be divided into two categories. The first category deals with the so-called direct method. This method classically uses spatial discretization techniques based on finite elements (FE). The FE method is well-adapted to bounded domains showing complex nonlinear behaviour and geometry but for the modelling of unbounded domains, artificial boundaries (AB) satisfying transmitting conditions are also required (see Fig. 1b). Different types of AB are used in wave propagation problems such as Lysmer elements, Perfectly Matched Layers or paraxial elements [1, 2, 3]. However, the main disadvantage of these methods are not only the imperfection of the absorbing boundaries but also the considerable computational requirements of such calculations.



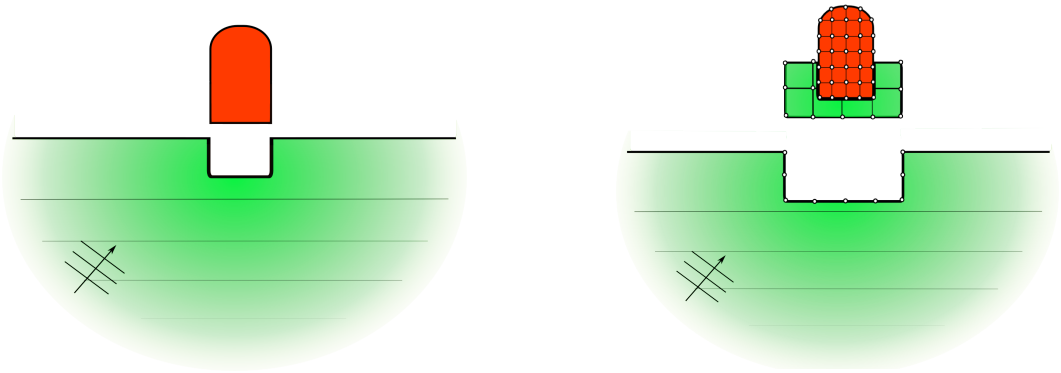
(a) (b)

Figure 1: (a) Simplified model of a SSI system in earthquake engineering. (b) The whole SSI system, bounded by an artificial boundary (dashed blue line), is discretized using a FE-based method.

The second category deals with domain decomposition techniques. In this case, the problem is decomposed into two sub-domains: the nonlinear superstructure and the linear (visco)-elastic unbounded soil (see Fig. 2a). This decomposition allows the use of different numerical techniques for each of the domains enhancing thus the advantages of the FE method while its main drawbacks get reduced. The most popular approach combines the FE method for the modelling of the bounded superstructure with the Boundary Element (BE) method for the unbounded –but linear– domain of soil. Indeed, the BE method relies on the use of Green's functions which implicitly satisfy radiation conditions at infinity. However, when nonlinear analysis is carried out, the coupled problem must be solved in the time domain but transient Green's functions are not always available or difficult to compute.

To overcome last problem, substructuring approaches based on soil impedances can be employed. In particular, the spring method [4] where the soil impedance, assumed as a set of frequency-independent spring and dashpots, is assembled to the structural domain. Although this approach may result attractive from a computational point of view, it does not perform well neither for embedded foundations nor for complex soils with relevant frequency dependency.

Alternatively to the spring method, frequency-time domain couplings can be done [5, 6]. In these cases, the nonlinear domain, which includes the structure and the surrounding soil exhibiting nonlinear behaviour (see Fig. 2b), is formulated in the time domain using FE. The far-field soil is assumed linear and thus, it can be solve in the frequency domain by means, for instance, of a BE method. Following the same principle, recent works have employed Laplace-time domain couplings [7, 8, 9].



(a) (b)

Figure 2: (a) Domain decomposition technique: the bounded superstructure and the unbounded domain of soil. (b) The superstructure, which also includes a surrounding part of nonlinear soil, is modelled with FE whereas the rest of the soil is solved with a BE method.

The present work relies on the so-called Hybrid Laplace-Time domain Approach (HLTA) [10, 11]. To address this problem, the nonlinear FE code (*Code_Aster* [12], developed at EDF R&D) is coupled in the time domain to a BE formulation of the soil impedance matrix in the Laplace domain (computed using code MISS3D [13], developed at École Centrale Paris).

Within the framework of a linear soil and a nonlinear structure, previous research works [11] showed that the use of HLTA leads to satisfactory results when compared to a full-FE solution, at least in terms of spectra responses and damage assessments. The effect of nonlinearities in the soil, in addition to those in the structure, is thus the scope of the present study.

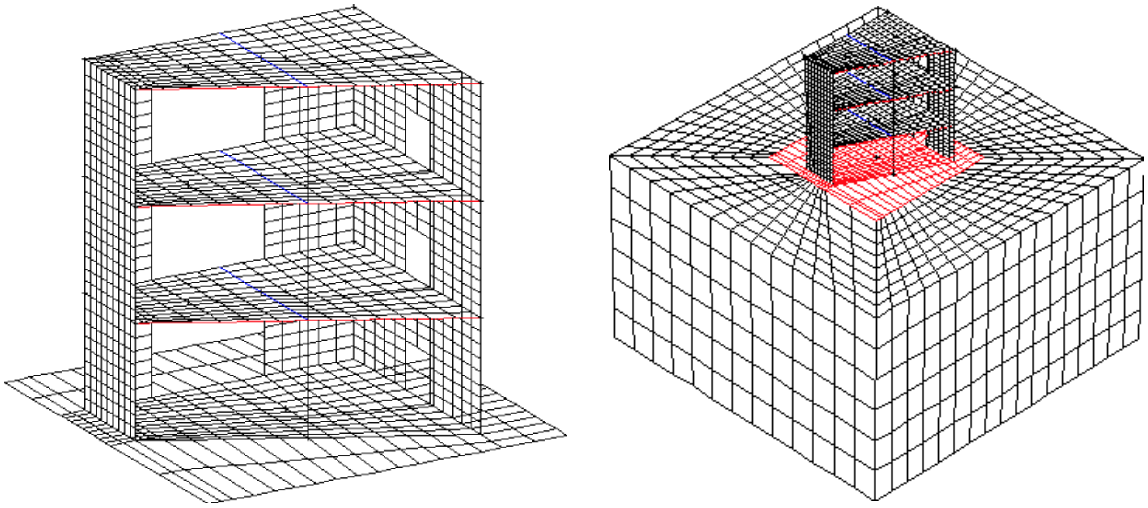
2 NUMERICAL MODEL

The numerical nonlinear model chosen for the structure is the one used in the international SMART-2008 project [14], where it was compared to experimental results obtained on the CEA/EMSI shaking table Azalée. In order to build up a dynamic SSI system, this structure has been completed with a concrete slab and a bounded domain of soil (see Fig. 3) modelled in *Code_Aster*. As a result, the HLTA applies on the boundary of this FE domain of soil, allowing the rest of the unbounded domain of soil to be accounted for by a BE impedance matrix computed by MISS3D. In the following, the building is assumed to be nonlinear. However, two types of calculation are considered and compared in Sec. 3: one where the FE region of soil exhibits a nonlinear behaviour and the other, where the soil behaves entirely linear.

Some properties of the considered numerical model are briefly reviewed in next subsections but the reader can refer to [11] for further details.

2.1 The structural domain

The building is modelled in *Code_Aster* using shell elements (floors and walls) except for a multi-fiber beam going from the bottom to the top the structure. The corresponding FE model



(a) (b)

Figure 3: FE model of the SMART building with an additional (a) base-slab and (b) a bounded domain of soil.

consists of $1\,500$ nodes and thus $9\,000$ degrees-of-freedom. For shell elements, reinforced concrete showing a global damage law known as GLRC-DM [15] is used. The squared base-slab, which shows a side length of 4m, is also modelled with shell elements and introduces 332 nodes.

	Bending 1	Bending 2	Torsional	Pumping
Eigenfrequencies [Hz]	9.0	15.9	31.6	32.3

Table 1: First eigenfrequencies of the base-clamped SMART building.

The first eigenfrequencies corresponding to the structure satisfying zero displacement at the base, which are given in Tab. 1, provide some insight on dynamic properties of the SMART building. A modal damping of 2% over frequencies $5\,Hz$ and $15\,Hz$ has been used in order to calibrate the equivalent Rayleigh damping model used for the structure domain.

2.2 The soil domain

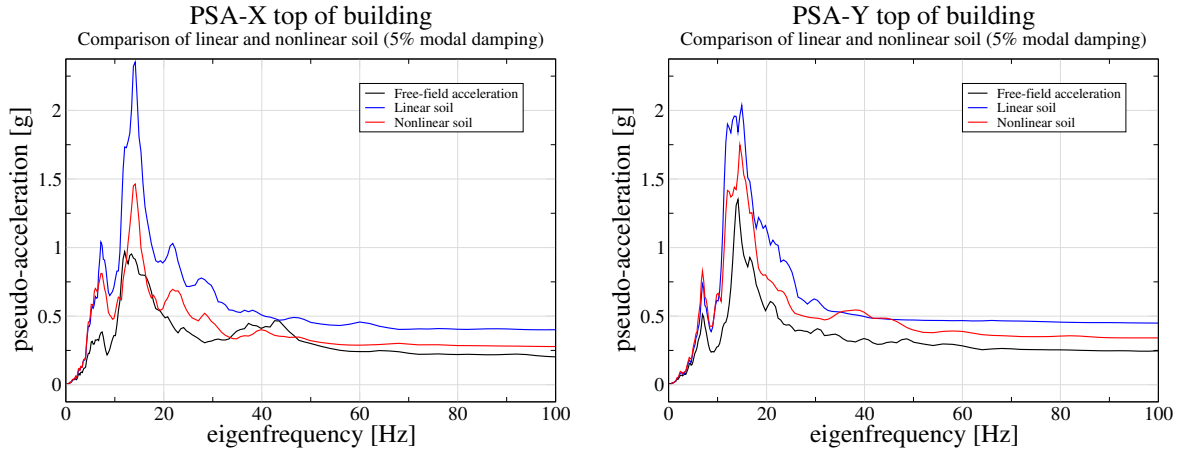
The unbounded domain of soil is assumed to be horizontally stratified, in particular, seven layers of soil are considered over the bedrock. However, the bounded domain of soil modelled in FE, which measures $10\,$m of side length and $6\,$m of depth, remains within only the first layer of soil. The interface between the unbounded soil has $3\,500$ degrees-of-freedom and hence, a modal reduction technique [16] is recommended. In the present study, the kinematics of the SSI interface are represented by means of 240 interface eigenmodes, a sufficient number of modes to ensure the convergence of the solution.

The unbounded soil, since it is accounted by a BE method in the frequency domain, is assumed to be modelled with hysteretic damping. Nevertheless, a hysteretic damping does not ensure causality properties in the time domain and hence, it cannot be used for nonlinear transient analysis. As a consequence, an equivalent Rayleigh model has been calibrated for the FE region of nonlinear soil.

It has already been mentioned that the case of both linear and nonlinear soils are considered in the following. The Hujeux model of soil [17], which allows to take into account nonlinear ground-borne phenomena, is assumed for the nonlinear case whereas a visco-elastic constitutive law is alternatively used.

3 NONLINEAR TRANSIENT ANALYSES

The response of the building accounting for nonlinear soil-structure interaction under seismic loading is addressed in this section. Three different accelerograms, in x, y and z directions, are applied to the model. Within the HLTA, an unconditionally stable Newmark's time integration scheme is used for the resolution of the FE equations. Two SSI models are considered: one where the soil domain behaviour is modelled by the Hujeux law and the other, where the soil remains fully linear during the whole calculation. Recall that in both cases, the GLRC_DM damage law is used for the building. The comparison is made in terms of response spectra, in particular, the pseudo-acceleration in x and y directions are plotted in Fig. 4.

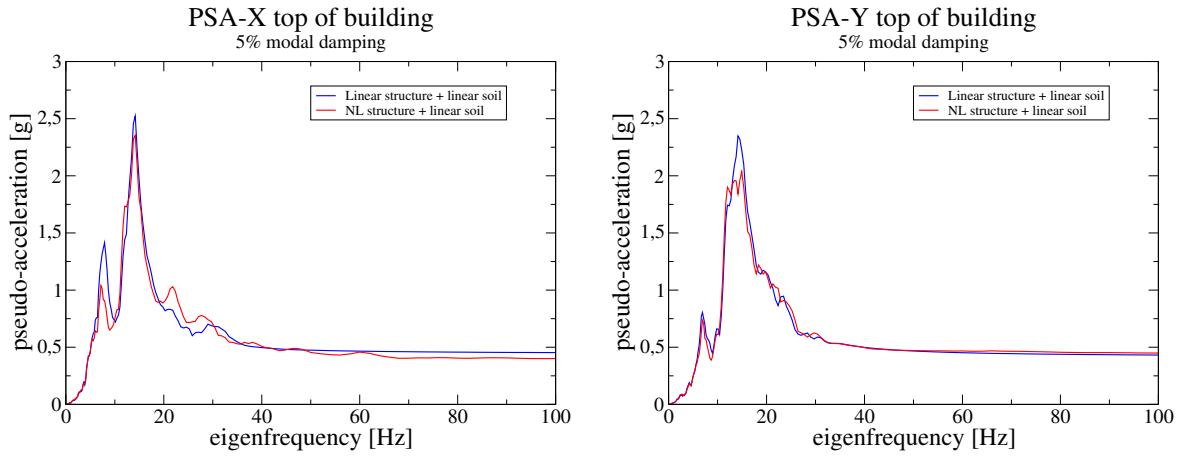


(a) (b)

Figure 4: Pseudo-acceleration at the top of the building in x and y directions, for the free-field accelerogram (black) and for models showing a linear (blue) and nonlinear soil (red).

Because of the asymmetry of the SMART building, differences are observed between x and y responses. Nevertheless, the overall impression is that accounting for nonlinear phenomena in the soil results in lower Peak Ground Accelerations (PGA) at the top of the building. In fact, the PGA in the y-direction is almost lowered of 19% and for x-direction, the reduction rises to almost 32%. Also the amplitude of the pseudo-acceleration at lower frequencies decreases when a nonlinear soil is considered. In fact, the peak around $15\,Hz$ is reduced in both directions, particularly, in the x-direction where the amplitude descends from $23.4\,m.s^{-2}$ to $14.6\,m.s^{-2}$. On the other hand, the peak around $8\,Hz$ is slightly amplified in the y-direction. Other local amplifications can be observed in this direction around $40\,Hz$. These amplifications, even if not significant, are probably the reason of getting lower PGA reductions in the y-direction than in the x-direction when comparing to the PGA of a linear soil model.

It is interesting to remark that when the Hujeux model is used, plastic deformation appears by just applying the weight of the structure. Indeed the nonlinear character that the soil exhibits from the beginning of the calculation, increases the amount of seismic energy dissipated before reaching the building, yielding thus to more attenuated responses at the top of the structure. This argument can still be reinforced by observing Fig. 5, where pseudo-accelerations corresponding to a linear soil model and a fully linear model (i.e. not only the soil but also the structure shows an elastic behaviour) are plotted. Notice that the use of the GLRC_DM law reduces indeed global pseudo-acceleration levels but not as much as when soil nonlinearities are modelled in the surroundings of the structure.



(a) (b)

Figure 5: Pseudo-acceleration at the top of the building in x and y directions, for the case of a fully linear model (blue) and a model showing nonlinear behaviour within the structural domain but not within the soil (red).

Regarding the dynamic properties of the coupled system, it may be concluded that the inelastic deformation considered in the soil is not enough to introduce important differences on the resonant frequencies of the dynamic SSI system.

4 CONCLUSIONS AND PERSPECTIVES

This work presents the numerical results obtained when nonlinear soil-structure interaction analysis is performed using an efficient BE-FE coupling based on the Hybrid Laplace-Time domain Approach (HLTA). The SMART building numerical model has been chosen for this application, where the FE code of *Code_Aster* is used for modelling nonlinear domains and the BE code of MISS3D, for the computation of the impedance matrix that accounts for the linear unbounded domain of soil.

It has been observed that inelastic deformation (Hujeux model) arising in the soil attenuates acceleration responses at the top of the building, significantly more than only with a damage model (GLRC_DM law) in the structure. It has to be noticed that this conclusion is particular to the SMART model considered and should not be generalized.

The obtained results have been presented from a qualitative point of view. Further research has to be done in order to validate these results. In particular, a reference solution should be obtained when the Hujeux soil model is used, this is for instance a full-FE solution.

In addition to this, different nonlinear constitutive laws of the soil should be tested in order to evaluate their influence on the structural response. Also the size of the volume of soil that has to be meshed using FE should be studied so that SSI modelling criteria could be identified.

5 ACKNOWLEDGEMENTS

This work has been funded by Électricité de France (EDF), the LaMSID and the French ANRT. The first author gratefully acknowledges their support as well as the supervision of École Centrale Paris.

REFERENCES

[1] J. Lysmer and R.L. Kuhlemeyer, Finite dynamic model for infinite media, *Journal of the Engineering Mechanics Division, Proc. ASCE*, **95** (EM4), 859–876, 1969.

[2] J. Berenger, A perfectly matched layer for the absorption of electromagnetic waves, *Journal of Computational Physics*, **114** (2), 185–200, 1994.

[3] F. De Martin, H. Modaressi and H. Aochi, Coupling of FDM and FEM in seismic wave propagation, *4th International Conference on Earthquake Geotechnical Engineering*, Greece, 2007.

[4] Calcul sismique des bâtiments - Règles RCC-G, Annexe A.

[5] J. P. Wolf, *Soil-Structure-Interaction Analysis in Time Domain*. Prentice-Hall, USA, 1988.

[6] S. François, *Nonlinear modelling of the response of structures due to ground vibrations*, PhD Thesis, Katholieke Universiteit Leuven, Belgium, 2008.

[7] M. Schanz and H. Antes, Aplication of 'Operational Quadrature Methods' in Time Domain Boundary Element Methods, *Meccanica*, **32** (3), 179–186, 2006.

[8] W. Moser, H. Antes and G. Beer, Soil-structure interaction and wave propagation problems in 2D by a Duhamel integral based approach and the convolution quadrature method, *Computational Mechanics*, **36**, 431–443, 2005.

[9] A. Pereira and G. Beer, Interface dynamic stiffness matrix approach for three-dimensional transient multi-region boundary element analysis. *International Journal for Numerical Methods in Engineering*, **80**, 1463–1495, 2009.

[10] A. Nieto Ferro, D. Clouteau, N. Greffet and G. Devésa, On a hybrid Laplace-time domain approach to dynamic interaction problems, *European Journal of Computational Mechanics*, **21** (3-6), 290–299, 2012.

[11] A. Nieto Ferro, *Nonlinear Dynamic Soil-Structure Interaction in Earthquake Engineering*, PhD Thesis, École Centrale Paris, France, 2013.

[12] *http://www.code-aster.org*.

[13] *http://www.mssmat.ecp.fr/cms/lang/en/mssmat/moyens/moyens_techniques_logiciels/miss*.

[14] S. Lermitte, T. Chaudat, T. Payen, D. Vandeputte and E. Viallet, SMART 2008: Seismic design and best-estimate methods assessment for RC buildings subjected to torsion, *The 14th World Conference on Earthquake Engineering*, China, 2008.

[15] D. Markovic, P. Koechlin and F. Voldoire, Reinforced concrete structures under extreme loading: Stress resultant Global Reinforced Concrete Models (GLRC), *Proceedings of ECCOMAS Thematic Conference, COMPDYN2007*, Greece, 2007.

[16] E. Balmes, Use of generalized interface degrees of freedom in component mode synthesis. *International Modal Analysis Conference*, 204–210, 1996.

[17] J.C. Hujeux, *Une loi de comportement pour le chargement cyclique des sols*. Génie Parasismique, Presses ENPC, Davidovici V. & al., 287–302, 1985.

COMPDYN 2013
4th ECCOMAS Thematic Conference on
Computational Methods in Structural Dynamics and Earthquake Engineering
M. Papadrakakis, V. Papadopoulos, V. Plevris (eds.)
Kos Island, Greece, 12–14 June 2013

BLAST RESPONSE OF FIELD OBJECTS

A.Chen[1], L.A. Louca[2], and A.Y. Elghazouli[2]

[1] Imperial College London
South Kensington, London
e-mail: anqi.chen07@imperial.ac.uk

[2] Imperial College London
South Kensington, London
l.a.louca@imperial.ac.uk, a.elghazouli@imperial.ac.uk

Keywords: Blast load, ABAQUS, Uncoupled and coupled Eulerian – Lagrangian, Pressure – Impulse diagram, Forensic study, Buncefield Incident,

Abstract. *During the last few decades, several major industry accidents occurred across the world. These include the Buncefield event in the United Kingdom (UK) back in 2005. There were a number of steel switch boxes in the site located within the area covered by the vapour cloud. The present work reports numerical studies on the steel boxes covering both detonation and deflagration scenarios and assessing the response of those boxes in order to aid the investigation of the explosion. New Eulerian capabilites in ABAQUS has are together with existing Lagrangian formulations to create three numerical models with increasing complexity: (1) Pure Lagrangian model; (2) Uncoupled Eulerian – Lagrangian model; (3) Coupled Eulerian – Lagrangian model. Results from different modelling approaches are discussed and parametric studies are carried out based on Pure Lagrangian models to investigate the response of the switch box to a series of combination of pressures and impulses. Findings from the parametric study are summarised in the form of pressure – impulse diagrams and residual deformation of selected boxes are presented. The results confirmed the estiamted minimum overpressure level of 200kPa and it can also be concluded that the overpressure wave inside the cloud is most likely to be of a deflgrative form. The forensic study described in this paper has gives a good insight into the likely loading scenarios. The study presents a systematic approach for analysing the response of small objects to various blast loadings and the results have shown sthat the forensic studies can be undertaken by using the pressure – impulse diagrams in conjunction with damaged residual deformations.*

1 INTRODUCTION

During the last few decades, a number of major industrial accidents have occurred around the world. These include the Buncefield event in the United Kingdom back in 2005 where the explosion of 240000 m3 of vapour cloud resulted in considerable damage to business and residential properties in the surrounding area [1]. The explosion generated much higher overpressure than would usually be expected from a typical vapour cloud explosion. The severity of the explosion would not have been anticipated in any major hazardous assessment of oil storage depots before the incident.

A cloud of combustible vapour in the atmosphere can explode under certain conditions, which is usually referred to as a vapour cloud explosion (VCE). In the combustible-air mixture a flame could propagate through the entire cloud by two different mechanisms: (i) deflagration, where the propagation of the flame is caused by heat transfer from the reacted region to the fresh mixture. Deflagration is easy to initiate, but only generates relatively low peak overpressures in an unconfined, uncongested area. (ii) If the flame is coupled with a shock wave which compresses and heats the mixture in front then a detonation event can be identified. Detonation in a vapour cloud could be very destructive but difficult to initiate. It produces a shock wave of high overpressure.

For the purpose of assessing the overpressure history across the incident site, evidence relating to overpressure is important as part of the forensic studies. It was found that there were many small objects such as steel switch boxes distributed across the site and nearby areas. These field objects could be used as overpressure indicators, as the final deformation of these objects can provide an indication of possible overpressure at their location after the passage of blast waves. Figure 1 shows three damaged steel switch boxes found within the vapour cloud. One of the main objectives of the work presented in this paper is to carry out numerical analyses covering both detonation and deflagration scenarios with a range of overpressures and impulses, in order to examine more realistically the possible blast characteristics experienced at Buncefield.



Figure 1 Damaged steel switch boxes in the vapour cloud (Courtesy of HSE)

A recent release of the advanced finite element program ABAQUS [13] provides an Eulerian modelling capability and a contact algorithm for interaction between Lagrangian and Eulerian formulations. The validity of the Eulerian capabilities in ABAQUS has been recently examined in detail by Mougeotte and Carlucci [3, 4]. The present work uses the numerical approaches provided by ABAQUS to analyse the response of steel switch boxes to a range of explosions leading to the generation of Pressure-Impulse diagrams. These diagrams provide an insight into the relationship between blast characteristics and structural damage, and could be used for forensic assessments as well as design considerations.

2 NUMERICAL APPROACHES

Most blast problems usually involve the following phases: (i) the explosion phase where the source produces higher pressure and high temperature gases that propagate outwards and generates pressure waves in the medium (air), (ii) the propagation phase where the pressure waves travel in the surrounding medium (air) towards the target, (iii) the interacting phase between the travelling pressure waves and the target, (iv) the final phase where the target responses to the impinging pressure waves.

In general, the propagation of pressure waves and structural responses are treated separately. The pressure waves can be determined simply by using of empirical charts in manuals such as those included in UFC – 3 – 340 – 02 [8]. Alternatively it can be generated by an Eulerian model such as that in ABAQUS [3, 4] if the target is of complex geometry. Regarding the structural response, a simple system is often reduced into a single degree of freedom (SDOF) model based on Bigg's method [10]. There are also improved models which take into account the catenary actions [11]. For a more complex system the SDOF is not applicable hence a Lagrangian finite element model can be used to calculate the response to blast loadings. In reality, the movement of a structure is often directly coupled with the surrounding fluid due to the interaction between the response and fluid motion. Therefore, in ABAQUS the Eulerian model of blast can be coupled with as Lagrangian model of the structure to capture such interaction. This numerical technique is referred as coupled Eulerian – Lagrangian modelling.

A typical switch box shown in Figure 1 has dimensions of 300mm ×300mm ×150mm, with wall thickness of 1mm. There are two supporting methods: one is supported vertically along the edges of the box back panel, and the other is supported at the box bottom. The box is modelled by S4R reduced integration shell elements in ABAQUS, and two hinge type connectors were used to represent the actual steel hinge. Several coupon tests were carried out to determine the material properties of the box, and a yield stress of 300 MPa was found to be representative of the material. A Johnson – Cook plasticity and stain – rate model was employed for the modelling, such that:

$$\sigma_Y = \left[A + B\left(\varepsilon_{eff}^{p}\right)^{N}\right]\left[1 + C\ln\frac{\dot{\varepsilon}}{\dot{\varepsilon_0}}\right] \tag{1}$$

where in the strain hardening part: the nominal yield stress A = 300 MPa, the strain hardening constant B = 200Mpa and the hardening exponential constant N=0.228. For the strain rate dependence: the rate constant C=0.017 and the reference strain rate $\dot{\varepsilon_0}$=1/s. The two variables are the effective plastic strain ε_{eff}^{p} and strain rate $\dot{\varepsilon}$.

The combination of Eulerian and Lagrangian capabilities in ABAQUS provides three possible modelling approaches:

Lagrangian analysis (LC and LI)

This approach only has a Lagrangian finite element model of the switch box. Blast waves are implemented as pressure loadings on the surfaces of the box, incident or reflected where appropriate. Two methods were used to determine the load – time histories: one is from the CONWEP data base built in ABAQUS (referred to as model LC) and the other is from analytical calculation (which is an idealised pressure profile referred to as model LI). The difference is that the idealised pressure profile takes into account the pressure relief effect for a finite dimension target for calculating the reflected pressure where CONWEP does not give a reflected pressure from an infinite surface.

Uncoupled Eulerian – Lagrangian analysis (UEL)

The UEL approach involves three steps. The first step is a one dimensional Eulerian modelling to produce the required pressure waves by specifying a triangular particle velocity inflow boundary condition. The Eulerian model is grade meshed to maximise the computing efficiency. Figure 2 (a) shows a schematic of the one dimensional Eulerian model.

Once the applied particle velocity triangle can generate the required pressure waves, this velocity profile is used in the second step and applied on a three dimensional Eulerian model with an empty volume, as shown in Figure 2 (b). The empty volume is the space occupied by the box and in this second step the pressure wave interacts with the box volume and the pressure loading on each surface is recorded. Pressure waves from the three dimensional Eulerian model can be seen in Figure 2 (c), and for comparison corresponding pressure waves predicted by CONWEP and analytical method (idealised) are also included.

The last step in this approach is the Lagrangian modelling. The pressure loadings recorded in the second step are now applied on the Lagrangian model of the box as surface pressure loads where appropriate.

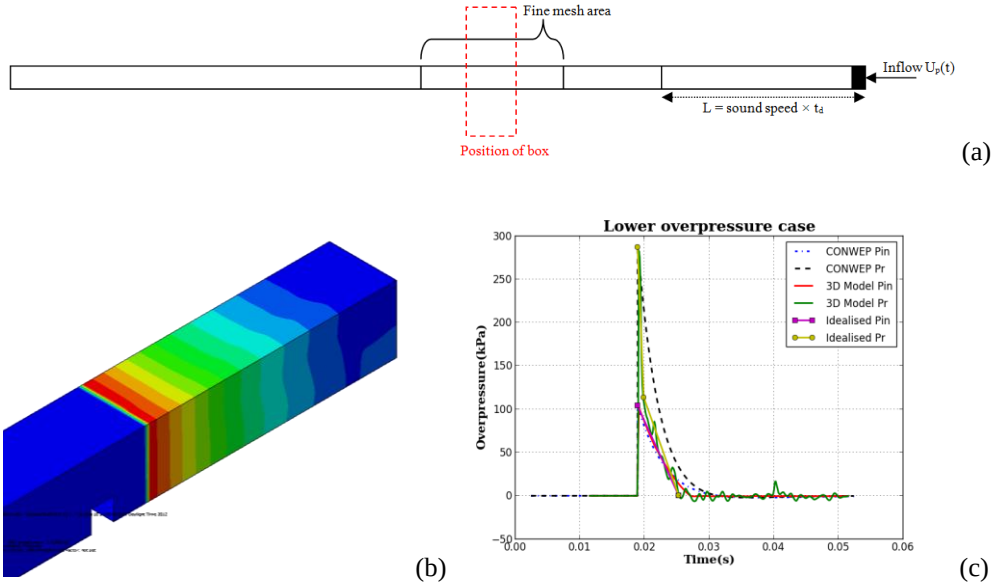


Figure 2 (a) schematic of one dimensional Eulerian model (b) numerical Eulerian model with pressure waves (reflected value) and box volume (c) pressure waves predicted by different tools

Coupled Eulerian – Lagrangian analysis (CEL)

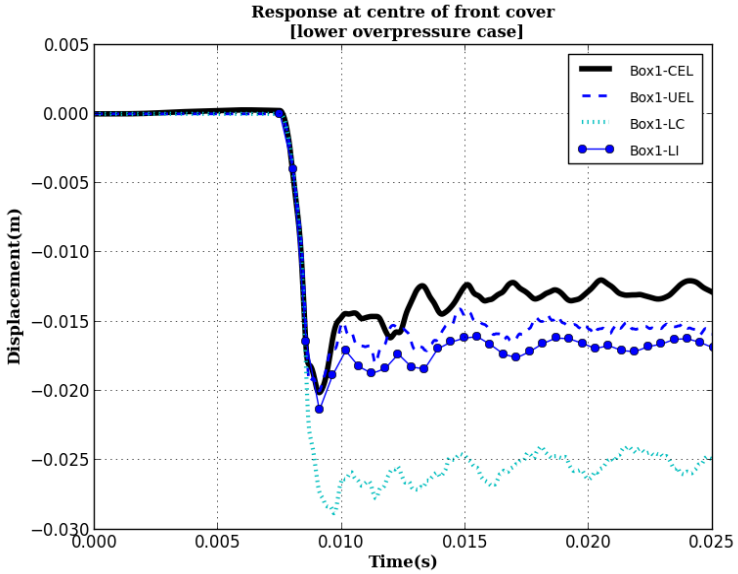
The coupled method uses the determined particle velocity profile in the first step of the uncoupled approach. The inflow particle velocity is applied at the inlet Eulerian boundary. The explicit general contact definition automatically implements the interaction between the Eulerian and the Lagrangian parts.

In the previous paragraphs we introduced various numerical simulation approaches were introduced above. To compare these afore mentioned approaches for the purpose of performing parametric studies, the explosion scenarios need to be specified and subsequently the response of the boxes can be studied. Limited experimental data is available in the report produced by HSE [1], and based on those data, two explosion scenarios are specified: the first one is a relatively low overpressure detonation with incident overpressure of 100 kPa (reflected 274 kPa) and duration of 8ms. The second is a relatively high overpressure detonation with

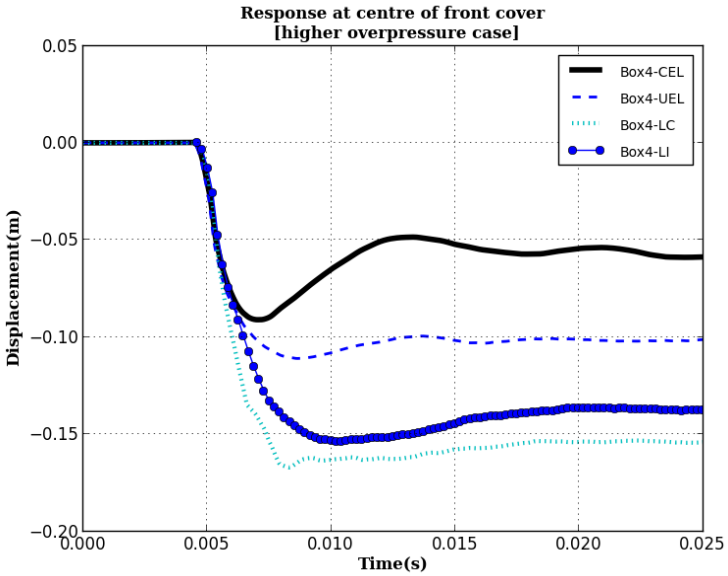
incident overpressure of 400 kPa (reflected 1665) and duration of 4ms. Figure 2 (c) shows the reflected pressure – time profile predicted by different tools for the lower overpressure case.

Comparative assessments

Having defined the explosion scenarios, the responses of the box can now be studied. The study is mainly focused on the deflection at the centre of the box front panel. For the lower overpressure case, the maximum deflection predicted by the Lagrangian model with idealised pressure profile model (LI) is in good agreement with the UEL and CEL models, as shown in Figure 3(a), although the discrepancy is larger at the residual deformation. However, in the case of relatively high overpressure, the maximum deflections predicted by LI and UEL models are apparently different to the results from the CEL model, as shown in Figure 3(b). In both cases, the model LC produces the largest maximum deflections.



(a)



(b)

Figure 3 Displacement – time histories of the centre of the box front surface

It is important to note that in Figure 3, the order of the maximum deflection of the box front panel predicted by the different models is generally as following: LC > LI > UEL > CEL. Results of CEL models are discussed in the next paragraph while the order between LC, LI and UEL can be explained by referring to Figure 2(c), in which the peak reflected pressures are the same for all three types of loads: CONWEP (for LC model), 3D Eulerian (for UEL model) and Idealised (for LI model). However, the reflected impulses from those pressure loadings are different with CONWEP producing the largest impulse and the 3D Eulerian producing the least. With the same pressure levels, the pressure loading with the largest impulse produces the greatest deflection response. This explains why the Lagrangian model with CONWEP load (LC) predicted much larger deflection than UEL and LI models.

In Figure 4(b), the results of the Lagrangian model with idealised pressure (LI) deviated significantly from the CEL model compared with other boxes. Since the pressure relief effect is inherent in the CEL model, the discrepancy could be explained by the impulse reduction due to the movement of the target surface. The reflected pressures of the idealised profile and UEL were determined based on a rigid surface which was stationary throughout the loading duration. However, in the CEL model, the reflected pressure was affected by the movement of the front surface of the box model. For the CEL models, the average velocities at the centre of the front surface up to maximum dynamic deflection were determined as: 14.9 m/s for low pressure case and 41.8 m/s for high pressure case. The differences in peak deflection between the Lagrangian model with idealised pressure (LI) and the CEL models were determined as: 10% for low pressure case and 68% for high pressure case. The higher velocity of movement of the front surface resulted in a higher discrepancy and thus more impulse reduction. Similar observations were made by Borvik [5] on the movement of the reaction surface where more impulse has been reduced at the reaction wall with higher velocities.

The results indicate that the accuracy of the Lagrangian (LI) model appears to reduce at incident pressures above 400 kPa. Further consideration showed that the velocity at the deflected surface played an important role. The velocity of the deflected surface of Box 4 in CEL model was high enough to reduce significantly the impulse imparted on it. The combination of pressure and impulse determined the response of the surface including the average velocity to maximum deflection. At the same level of damage, a combination of high pressure with low impulse would result in a higher velocity of response than a combination of low pressure with high impulse. Accordingly, the Pressure-Impulse studies presented below were limited to a maximum incident pressure of 400 kPa (reflected pressure of 1665 kPa for an ideal blast wave) in order to keep the response velocity low and hence ensure the validity of the Lagrangian model. The HSE report [2] has briefly reviewed 9 previous significant vapour cloud explosion incidents for which detailed data is available. The work indicates that most of the major incidents experienced overpressure of 100 kPa or less within the cloud. The exception is the Flixborough incident in which the overpressure was estimated to be 1000 kPa. Therefore, this limiting pressure level of 400 kPa is notably higher than the lower bounds suggested from the Buncefield investigation and also adequate for most of the incidents.

As a result of the study of the response of boxes to two different explosion scenarios, it has been decided that the following parametric studies is best performed based on the Lagrangian model with idealised pressure loading profiles and a maximum incident overpressure of 400kPa (reflected value of 1665 kPa).

3 PRESSURE – IMPULSE DIAGRAMS

In order to study the possible overpressure experienced at the Buncefield event, it is necessary to examine a wide range of overpressure and impulses. In all P – I diagram studies in the

present work, the overpressure and impulse ranged from 10 – 400 kPa (reflected pressure: roughly 20 kPa – 1665 kPa) and 10 – 10000 Pa.s respectively. The positive duration of overpressure ranged from 2ms to 2000ms at incident pressure of 10 kpa and from 0.05ms to 50ms at incident pressure of 400 kPa. Three shapes of blast waves were also used in the parametric studies.

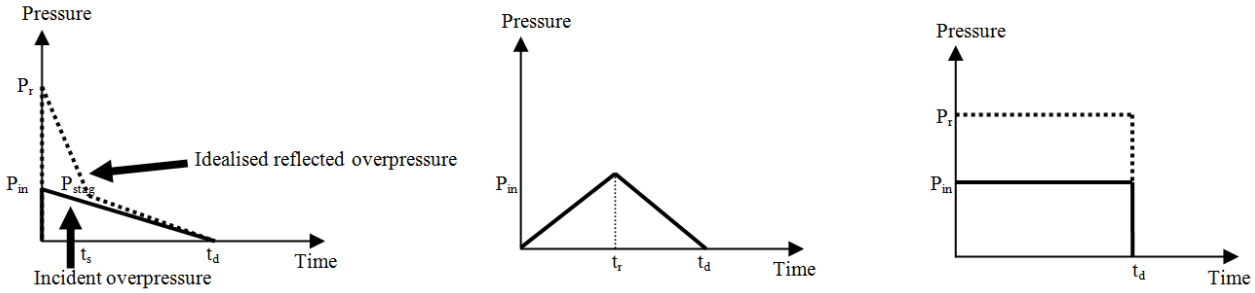


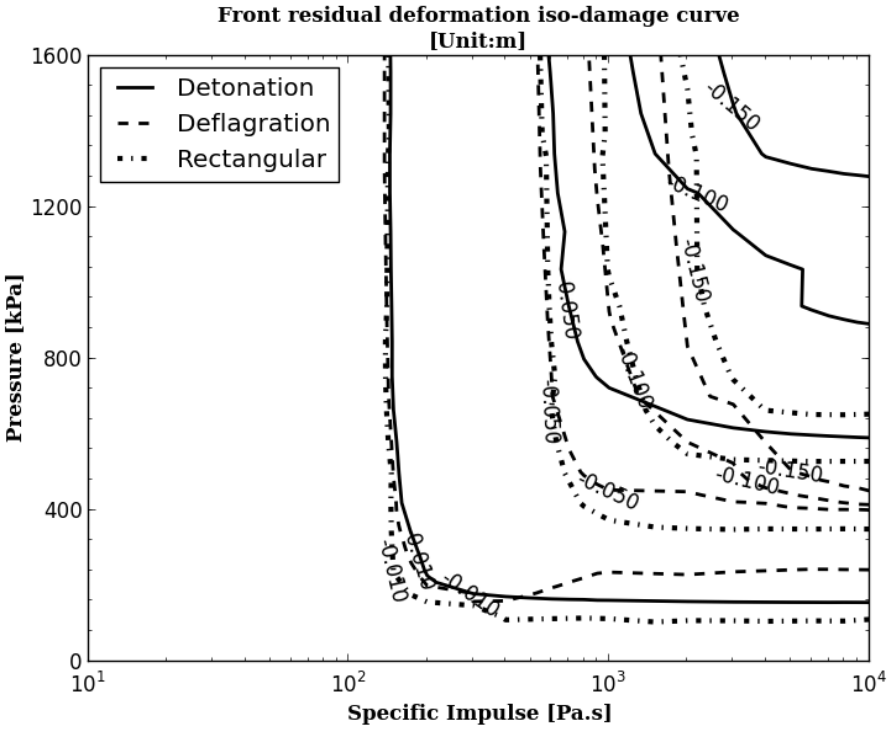
Figure 4 Pressure load types: left – detonation; middle – deflagration; right – rectangular

The three types of pressure loadings are: detonation, deflagration and rectangular, as depicted in Figure 5. For detonation and rectangular types of loads, the front surface of the box will be subjected to reflected pressures (Pr) and the other surfaces were subjected to incident pressures (Pin). It is important to note that for detonation pressure loadings, the reflected pressure is the idealised reflected pressure which takes into account the pressure relief effect of a finite dimension target.

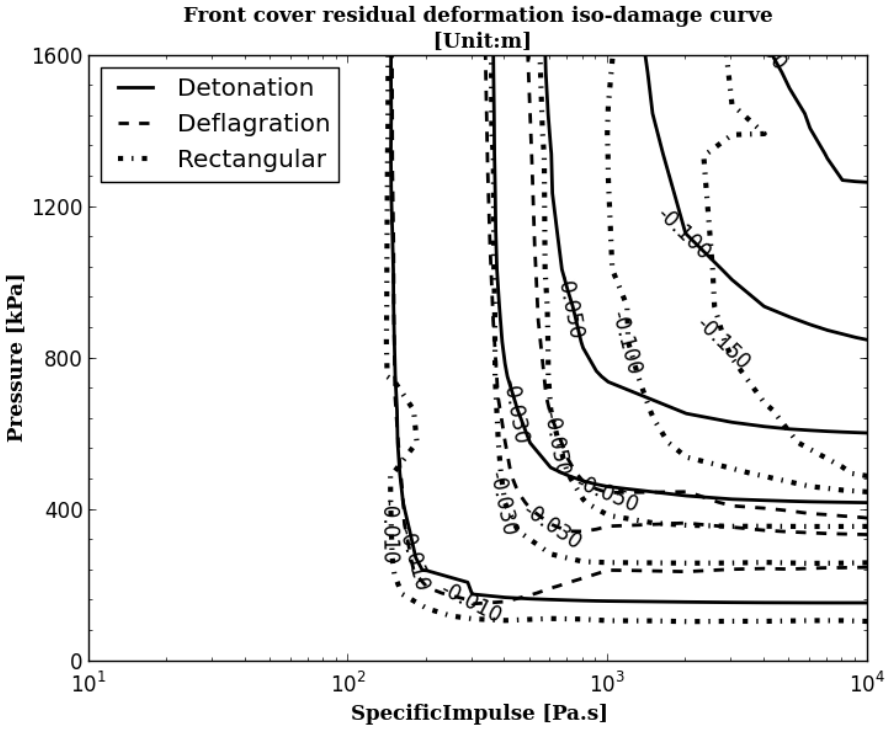
For the deflagration type of loading, only one type of pressure loading was used and applied on all the surfaces of the box model. This is due to the consideration that for a deflagration blast wave, the Rankine – Hugonoit relationship is no longer applicable, so the reflected pressure cannot be readily calculated. The rise of overpressure for deflagration takes a finite time, the pressure relief may start before the peak is reached, and the stagnation pressure would also have a finite rise time. The loading form the non-ideal blast wave is strongly related to the dimension of the target and the blast parameters. As a result, the reflection enhancement of a deflagration will be significantly reduced compared with an ideal blast wave of the same overpressure level [6]. Therefore no effect is made to distinguish the reflected pressure from incident in the case of a deflagration pressure wave. Although when interpreting the results and if we recognise the pressure on the front surface to be a reflected value, the results will become conservative as other surfaces are subjected to the reflected pressures as well.

Structural response

The structural responses of the box model are presented in terms of two pressures – impulse diagrams in Figure 5. In order to have direct visual assessment of the response of boxes, a group of selected residual shapes in the quasi – static regions are presented in Figure 6. In Figure 5, the iso – damage curves were plotted based on residual deflection at the centre of the front surface. Responses for three different types of loads are superimposed.



(a)



(b)

Figure 5 Pressure – impulse diagrams (a) box model constrained vertically at back (b) box model constrained at bottom

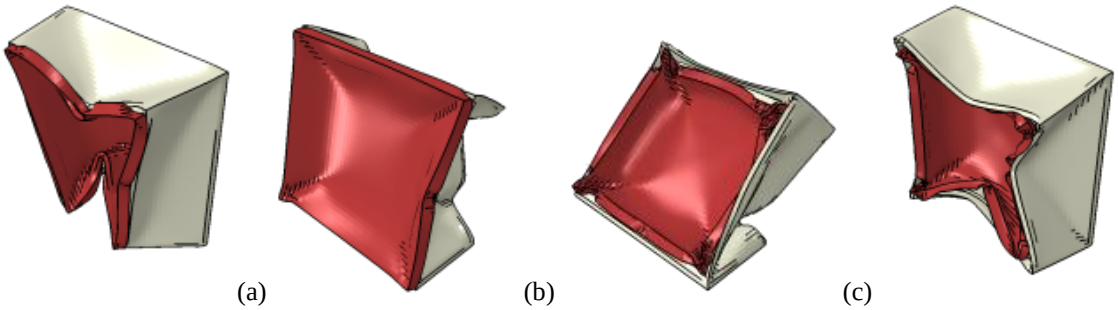
Damage levels are shown together with the iso – damage curves and it is worthy of noting that at lower damage level such as -0.01m the curves are approximately the same for boxes of two different supporting conditions. However at higher damage level the curves are quite dif-

ferent and this is mainly due to the supporting boundaries which results in a different response at higher damage levels. It can be observed from the -0.01m damage curves of Figure 5 (a) that the quasi – static asymptote ranges from approximately 100 kPa to 240 kPa for all load types, which is a relatively wide range. The impulse asymptote ranges from 137 Pa.s to 144 Pa.s, which is a relatively small range. It can be concluded that damage level of -0.01m is sensitive to the impulse and relatively insensitive to peak applied pressure. This observation holds true for other damage levels as well but overall the sensitivity is reduced with increased damage. The iso – damage curves for all three load cases tend to converge in the impulsive region as expected as the shape of the load is not important in this region.

It should be noted that in the dynamic and quasi – static region of the -0.01m damage curve for deflagration load case is of a different shape than for the other load forms. The quasi – static asymptote of the damage curve is shifted upward slightly when compared to other load cases. This is a well understood phenomenon and is due to the finite rise time at the beginning of the deflagration load curve. In Figure 5 (a), in the dynamic and quasi – static region, rectangular loads produce more damage than the other two as for a fixed impulse it requires lower peak pressure to produce the same level of deformation at the centre of the front panel. Beyond damage level of -0.05m, deflagration produces the worst damage to the front panel as at given peak pressure and impulse it produces the most damage to the front surface. The buckling of the top side of the box (as shown in Figure 6 (a)) significantly promotes the deformation in the centre of the front panel. It is the reason that the iso – damage curves of deflagration load is positioned very closely in the quasi – static region while curves for the other two load cases are relatively evenly spread over the diagram.

The general features of plots (b) in Figure 5 are very similar to plot (a) discussed above. Responses of front surfaces are sensitive to peak applied pressures in the quasi – static region for deflagration, due to the buckling of the side wall promoting deformation in the front panel as shown in Figure 6 (b). Moreover, the buckling of side wall near the bottom (shown in Figure 6 (c)) occurs for rectangular load cases in the quasi – static region. This has a significant effect on the deformation of front surfaces and leads to the damage curves of -0.1m and -0.15m approaching each other.

Three residual deformation levels for the box model subject to deflagration and rectangular types of loading are presented in Figure 6. They are selected in the quasi – static region with specified impulse of 10000 Pa.s. This is to examine the residual shape of the box under pressure loadings of long durations. In each of the three deformed shapes, buckling of the box occurred at different positions. However, the overpressure level at which the buckling occurred was similar. For deflagration case in Figure 6 (a) and (b) of different supporting conditions, the overpressures are 440 and 420 kPa. It has been assumed that no reflection is considered for deflagration load cases to calculate the responses, as the reflection enhancement of deflagration is significantly reduced. With the due consideration of the reduced reflection when interpreting the results we should recognise the overpressure on the front surface to be the reflected one. Hence roughly with an assumed reflection factor of 2 for a non-ideal blast wave the incident overpressures of deflagration to cause buckling on the walls are approximately to be 220 and 210 kPa. And Figure 6 (c) and (d) show that buckling of the box occurred at incident overpressure of 160 kPa for rectangular and 280kPa for detonation. The supporting conditions in Figure 6 are: (a) supported at back, (b) supported at bottom, (c) supported at bottom and (d) supported at back.



(a) (b) (c) (d)

Figure 6 Residual shape of box in quasi – static region I=10000 Pa.s (a) deflagration – 440 kPa (b) deflagration – 420 kPa (c) rectangular – 497(incident 160) kPa (d) detonation – 1035(incident 280 kPa)

The damage is mostly focused on the front covers of the boxes when subjected to detonation and rectangular load, while when the buckling of wall occurs near the bottom, the body of the box seems to be bent around the fixed bottom. Due to the reduced reflection enhancement, deflagration loads produce more symmetric deformed shape than detonation and rectangular load types. The residual shapes of boxes from the quasi – static series predicted by applying deflagration loads (Figure 6 (b)) compare more favorably with Figure 1. These observations suggest that within the vapour cloud the overpressure wave is most likely to be of a deflagrative form. Studies of the buckling features of the boxes suggest the level of overpressure should be at least 200 kPa. This is in agreement with the conclusion of the incident investigation carried out by HSE. Without the measurements of the damage boxes in the incident, the actual level of overpressure is difficult to determine accurately. Nevertheless, the forensic study described above gives an insight into the likely loading scenarios.

4 CONCLUSION

In this study three numerical approaches have been used to analysing the response of a switch junction box to various blast loadings, namely: (a) Pure Lagrangian, (b) Uncoupled Lagrangian – Eulerian, and (c) Coupled Eulerian – Lagrangian. The deformation responses from uncoupled and coupled Eulerian – Lagrangian approaches were found to be less pronounced compared to a pure Lagrangian simulation with pressure load calculated by the CONWEP function in ABAQUS. However, the pure Lagrangian model with idealised pressure load profile can produce acceptable results compared to the coupled Eulerian – Lagrangian approach. With consideration of both accuracy and computational efficiency, a pure Lagrangian model with idealised load has been adopted in a parametric study of the response of the box to combinations of pressures and impulses. In the parametric study, the maximum incident pressure was limited to 400 kPa (reflected pressure of 1665kPa) in order to minimise the impulse reduction on the front face of the box hence to ensure the validity of the Lagrangian model. The present work demonstrated a systematic approach for analysing the response of a small object to various blast loading scenarios. Studies of small objects other than steel switch boxes examined in this study could be based on Lagrangian approaches. However, as shown in this investigation, the possible reduction in impulse would need to be taken into consideration to ensure the accuracy of numerical models.

Results of the parametric studies carried out on the Lagrangian model were summarised in the form of pressure – impulse diagrams. Iso – damage curves were plotted based on the deflection of the front surface of the box. Residual deformations of representative models in quasi – static regions in the pressure – impulse diagrams were also presented in this paper. Through the studies on the switch boxes, it was found that the minimum require pressure level to cause the damage observed at Buncefield Incident is about 200 kPa. This is based on com-

paring the buckling deformation of the wall of the box models to the damage pattern of the boxes recovered on site. From a qualitative point of view, by comparing the residual shapes of the numerical models with the damaged boxes it can be concluded that the blast within the vapour cloud in the Buncefield Incident was deflagration. Exact estimation of the overpressure level is difficult since the deformation measurements of the damaged junction boxes are not available, therefore a meaningful quantitative comparison cannot be conducted.

This study has shown that forensic studies of the response of the junction box can be undertaken by using the pressure – impulse diagrams in conjunction with residual shapes. With the measurements of the damaged box, the pressure – impulse diagrams can be used to determine the blast parameters which caused the observed level of damage. While measurements are not readily available, the presented residual shapes can be used to identify similar deformation features such as buckling of the wall and then determine the pressure levels required to initiate such damage. This methodology can be used for future forensic studies on other similar objects and structures damaged in explosion accidents.

ACKNOWLEDGMENTS

The work presented in this paper was funded by the UK Health and Safety Executive (HSE). The technical input and suggestions provided by Drs Graham Atkinson, Laurence Cusco and Bob Simpson from HSE as well as Dr Bassam Burgan from the Steel Construction Institute (SCI) are gratefully acknowledged.

REFERENCES

[1] OPSI (2008). The Buncefield Incident 11 December 2005, Final Report of the Major Incident Investigation Board, Volume 1.

[2] OPSI (2008). The Buncefield Incident 11 December 2005, Final Report of the Major Incident Investigation Board, Volume 1.

[3] HSE (2009). Buncefield Explosion Mechanism Phase 1, Volumes 1 and 2, Research Report RR718, Health and Safety Executive.

[4] Mougeotte, C., Carlucci, P., Recchia, S. and Ji, H. (2010) Novel approach to conducting blast load analyses using Abaqus/Explicit – CEL, SIMULIA Customer Conference

[5] Carlucci, P., Mougeotte, C., and Ji, H. (2010) Validation of Abaqus Explicit – CEL for classes of problems of interest to the U.S. Army, SIMULIAN Customer Conference.

[6] Borvik, T., Hanssen, A.G., Langseth, M. and Olovsson, L. (2009) Response of structures to planar blast loads – a finite element engineering approach. Journal of computers and structures 87 507-520.

[7] Needham, C.E., (2010) Blast waves, Springer-Verlag, Berlin.

[8] UFC (2008). Structures to resist the effects of accidental explosions, Unified Facilities Criteria, UFC 3-340-02, US Army Corps of Engineers.

[9] van den Berg, A.C. (1985) The multi-energy method: a framework for vapour cloud explosion blast prediction. Journal of hazardous materials, 12, 1-10.

[10] Biggs, J.M. (1964) Introduction to structural dynamics. McGraw-Hill Inc, New York.

[11] FABIG (1999). Technical Note 7. Technical note and worked examples to supplement the interim guidance notes for the design and protection of topside structures against explosion and fire, Fire and blast information group (FABIG), Steel Construction Institute, 1999.

[12] Luccioni, B., Ambrosini, D. and Danesi, R. (2006) Blast load assessment using hydrocodes. Journal of Engineering Structures 28, 1736-1744.

[13] Remennikov, A.M. and Rose, T.A. (2005) Modelling blast loads on buildings in complex city geometries. Journal of Computers and Structures 83 (2005) 2197-2205.

[14] ABAQUS, ABAQUS Analysis User's Manual, Simulia, Dassault systems, 2010

[15] Borvik, T., Hanssen, A.G., Langseth, M. and Olovsson, L. (2009) Response of structures to planar blast loads – a finite element engineering approach. Journal of computers and structures 87 507-520.

[16] Kinney, G.F. and Graham, K.J (1985) Explosive shocks in air, Springer-Verlag, New York

[17] Introduction to Python, ABAQUS Scripting User's Manual, Simulia, Dassault systems, 2010

COMPDYN 2013
4th ECCOMAS Thematic Conference on
Computational Methods in Structural Dynamics and Earthquake Engineering
M. Papadrakakis, N.D.Lagaros, V. Plevris (eds.)
Kos Island, Greece, 12–14 June 2013

COMPARATIVE ASSESSMENT OF BUILDINGS WITH PURE STEEL OR STEEL-CONCRETE COMPOSITE COLUMNS USING STRUCTURAL DESIGN OPTIMIZATION

Georgios S. Papavasileiou*, Nicolas Nicolaou, Dimos C. Charmpis

Department of Civil and Environmental Engineering, University of Cyprus,
75 Kallipoleos Str., P.O. Box 20537, 1678 Nicosia, Cyprus,
papavasileiou.georgios@ucy.ac.cy, nicolaou.a.nicolas1@ucy.ac.cy, charmpis@ucy.ac.cy

Keywords: Composite steel-concrete, structural optimization, seismic design

Abstract. *The present work investigates the cost-effectiveness of fully encased composite columns and concrete filled tubes as an alternative to pure steel I-shaped columns. In order to achieve objectiveness in the comparison of the three methods, the designs assessed are obtained by a structural optimization procedure. Thus, any subjectivity which would result from the designer's experience is avoided. The Evolution Strategies optimization algorithm is employed to minimize structural cost subject to constraints associated with: (a) Eurocode 4 provisions for safety of composite column-members, (b) Eurocode 3 provisions for safety of steel structural members and (c) structural system resistance. Furthermore, the assessment is performed for a variety of seismic intensities, as it provides important information on the ability of each method to meet high performance criteria and the total cost increase such requirements would lead to. The results obtained provide an insight to the advantages of partially substituting steel as a main structural material with concrete, in composite column sections, and demonstrate the effectiveness of the proposed optimization approach.*

1 INTRODUCTION

Steel-concrete composite elements are intended to fill the gap between reinforced concrete elements and pure steel elements. The utilization of steel-concrete composite elements is not a new concept, since they have gradually gained popularity during the course of the 20th century mainly in North America, Japan and Europe, while early applications of such elements at the end of the 19th century have been recorded. Over the past few decades, numerous steel-concrete composite structures have been erected worldwide. This form of construction is seen as an alternative mainly to constructing pure steel structures. The increasing preference in composite elements can be primarily attributed to the fact that concrete, a significantly less expensive material compared to steel, is utilized in an effort to cost-effectively replace a percentage of the required steel sections area. This way, overall material cost in a structure can be reduced and, at the same time, better lateral support and fire protection of the steel elements can be achieved, since concrete (which usually covers steel elements) as a material exhibits a much better performance at high temperatures than steel.

Although the incorporation of steel-concrete composite elements in a structure is nowadays regarded as established design and construction practice, a formal and extensive investigation on the conditions under which such practice is more cost-effective than other alternatives has not been conducted yet. The purpose of the present work is to comparatively assess multi-storey buildings with pure steel or steel-concrete composite columns with respect to their cost effectiveness and seismic performance. In order to ensure that comparisons are made in an objective manner, the structures considered are designed in a way that optimal usage of the available materials and cross-sectional geometries is achieved. Thus, the structural designs attained do not depend on a particular designer's experience and subjectivity, but are the outcome of an objective automatic design optimization procedure.

In the framework of this paper, structural optimization is applied for the design of buildings with steel-concrete composite columns, which consist of: (a) steel members with standard I-shaped sections (HEB) fully encased in concrete or (b) concrete-filled steel tubes with standard hollow sections (CHS or RHS). Moreover, buildings with pure steel columns are optimally designed using the above mentioned standard steel sections. Steel beams with standard I-shaped sections (IPE) and (optional) steel bracings with standard L-shaped sections are considered for all design cases (using either composite or pure steel columns). All buildings assessed are required to satisfy the provisions of Eurocode 4 for the steel-concrete composite members and Eurocode 3 for the pure steel members. Seismic actions are taken into account using a displacement-controlled nonlinear static pushover analysis to the targeted top displacement, as it is defined in FEMA-440.

Optimal structural designs are identified for a variety of seismic intensities by means of an Evolution Strategies optimization algorithm. The optimization results allow for an objective comparison of various designs in terms of required material cost and achieved capacity to withstand earthquake actions.

2 OPTIMIZATION PROBLEM

The Evolution Strategies optimization algorithm [2,7] used in this work, in order to determine the most cost-effective design for each scenario considered, has been found to be suitable for structural optimization problems [8]. As an optimization problem, its aim is to minimize the objective function, by systematically selecting combinations of the independent variables and checking the satisfaction or not of the defined constraints.

2.1 Objective Function

Since the objective of this paper is to assess the cost-effectiveness of different design methods, the objective function used was the total cost of the materials of the structural elements. In common engineering practice, the estimation of the structural cost incorporates several parameters which depend on the region where the works will take place. Such parameters are the total labor cost, the availability of the materials on the market, the characteristics of the soil, etc. In this work all the aforementioned were considered to be incorporated into the cost P_C and P_S of the concrete and steel, respectively. Additionally, all structural parts and details which can be designed separately, such as the slabs, the beam-column connections, the bracings' connections and the foundation scheme (including the column base connections) were excluded from the total cost calculation. However, their contribution to the structural performance was taken into account in the structural modeling process. Taken all these into consideration, it becomes obvious that, in this work, the term total cost refers to the cost of the materials for beams, columns and bracings only. Furthermore, because the beams and bracings in all designs are simulated as pure steel sections only, one can understand that the cost of concrete refers specifically to the steel-concrete composite columns. The total material cost could be simply calculated as:

$$P_{tot} = P_C \cdot V_C + P_S \cdot V_S \tag{1}$$

where

P_{tot}: the total cost calculated in local currency
P_C : the total cost for the concrete in local currency per m^3
P_S : the total cost for the steel in local currency per m^3
V_C: the total volume of concrete (m^3)
V_S : the total volume of steel (m^3)

In Equation 1 the total cost is calculated in monetary units, so its actual value should be constantly altered in order to be consistent with the current prices. Therefore, one can understand that, after any change to the prices of the materials, the currency exchange rate or the labour cost, this work would be rendered outdated. In order to avoid this implication, a more robust equation had to be used. Instead of using the average current prices of the materials, the total cost was calculated in equivalent steel weight. Such an assessment was made possible by introducing the ratio of concrete cost over steel cost, in order to convert the total volume of concrete to equivalent steel volume. Finally, the total equivalent steel volume was converted into weight by multiplying by the density of steel. in order to provide the final value in equivalent tons of steel. The final form of the objective function used is described in Equation 2:

$$\frac{W_{tot}}{\gamma_{\text{steel}}} = V_{tot} = CR \cdot V_C + V_S \tag{2}$$

where

W_{tot} : the total material cost calculated in equivalent steel weight (tn of steel)
γ_{steel}: the density of steel (tn/m^3)
C_R: the ratio of the concrete cost to the steel cost ($CR = P_C/P_S$)
V_C: the total volume of concrete on the storey (m^3)
V_S : the total volume of steel on the storey (m^3)

2.2 Design Variables

Use of structural optimization implies a large number of structural simulations which need to take place, until the optimization algorithm converges to an optimum solution. Additionally, all designs simulated during the procedure, are evaluated using specific performance criteria.

In order to significantly reduce to the total time required for the whole optimization procedure to acceptable limits, one needs to reduce the number of design variables as much as possible. It was noticed in previous works [10,11] that the division of the columns into four groups, as they are described in Paragraph 3, was effective in limiting the computational effort and, at the same time, allowing the algorithm to reduce the total structural cost significantly, comparing to using the same section for all columns.

At this point, it has to be noted that the rest of the design parameters such as the dimensions of the buildings and the mechanical properties of the materials of both the column and the beam sections were the same for all scenarios. Also, the concrete cover of the fully encased composite columns had been found to have a minimal effect to the total performance of the structure, so its value also remained the same for all designs.

Six design variables were defined for this particular optimization problem: four variables for the steel sections of the columns, one for the beams and one for the bracings. Standard IPE sections were used for the beams, while the columns' database consisted only of HEB sections for the fully encased composite columns and various RHS and SHS sections for the concrete filled tubes. For the bracings, specific L type sections were used.

2.3 Performance Criteria & Constraints

All the constraints of the optimization problem are defined by the design codes and methodology used. They can be categorized into two groups: one consisting of provisions related to the overall structural behaviour, and another comprising of the individual member checks. The two groups differ mainly in the way they affect the optimization procedure. The overall performance criteria define the number and type of analyses required in order to evaluate each design. On the other hand, the individual member criteria refer to the structural elements' capacity, so they need to be checked during all analyses.

2.3.1. Overall Performance Criteria

Naturally, earthquakes are events with a probability of occurrence; therefore a probabilistic approach of the problem and use of various accelerograms would be required in order to simulate more accurately the seismic actions. However such an assessment would increase dramatically the computational time needed for an optimization and would deviate from the objectives of this paper. Hence, the nonlinear static pushover analysis with deterministic criteria was used instead.

Two displacement-controlled pushover analyses up to the targeted top displacement described in F.E.M.A. 440 [1,5], needed to take place [12], one for each direction on the horizontal plane. The feasibility criterion used was the maximum inter-storey drift, which was calculated for each pair of analyses.

$$\Delta_{target} = C_0 \cdot C_1 \cdot C_2 \cdot C_3 \cdot \frac{S_a}{\omega^2} \tag{3}$$

where

Δ_{target}: the targeted top displacement of a M.D.O.F. system to be used in the pushover analysis

C_i: coefficients used in order to convert the S.D.O.F. to M.D.O.F. displacement

Sa: the design pseudo-acceleration defined for a S.D.O.F. system with fundamental period T
ω: the fundamental frequency of the structure (= 2π/T)

2.3.2. Individual Member Checks

The structural elements of the buildings were checked independently during both analyses per design for the capacity criteria defined in the Eurocodes. EN1993 [3] was used to check all beams, bracings and columns which were designed as pure steel sections. They were checked for all types of actions: bending moment, shear and axial force, as well as the respective buckling types that might occur as a result of these actions. It has to be noted that the bracings are subjected only to axial force, so they do not need to be checked for the other types of actions. The steel section capacities are calculated by:

$$M_{Rd} = \frac{f_{yk} \cdot W_{el}}{\gamma_{M0}} \tag{4}$$

$$V_{Rd} = \frac{f_{yk} \cdot A_V}{\gamma_{M0}} \tag{5}$$

$$N_{c,Rd} = \frac{f_{yk} \cdot A_{tot}}{\gamma_{M0}} \tag{6}$$

where
M_{Rd}, V_{Rd}, $N_{c,Rd}$: the design bending moment, shear and axial force capacity respectively
W_{el}: the elastic moment of resistance of the steel section
A_V: the effective shear area for each direction
A_{tot}: the total area of the section
f_{yk}: the nominal yielding stress of the steel category used
γ_{M0}: the safety factor used for sections of category 1 to 3

All fully encased steel and concrete composite sections and concrete filled tubes were checked for all design actions mentioned for the beams, according to the EN1994 [4]. The axial shear force criterion, used in order to determine the number and diameter of the required shear headed stud connectors in composite columns, was also checked during the analysis procedure, however it was found not to render a solution unfeasible at any case, so one could ignore it in order to speed up the optimization procedure, as long as there is a preliminary check which confirms that all sections available have the dimensions required for the installation of the headed studs. Considering that the composite operation of the columns ensured, their total capacity can be calculated as the sum of the respective concrete and steel part capacities:

$$M_{Rd,tot} = M_{C,Rd} + M_{S,Rd} \tag{7}$$

$$V_{Rd,tot} = V_{C,Rd} + V_{S,Rd} \tag{8}$$

$$N_{Rd,tot} = N_{C,Rd} + N_{S,Rd} \tag{9}$$

where

$M_{Rd,tot}$, $V_{Rd,tot}$, $N_{Rd,tot}$: the design bending moment, shear and axial force capacity of the composite section

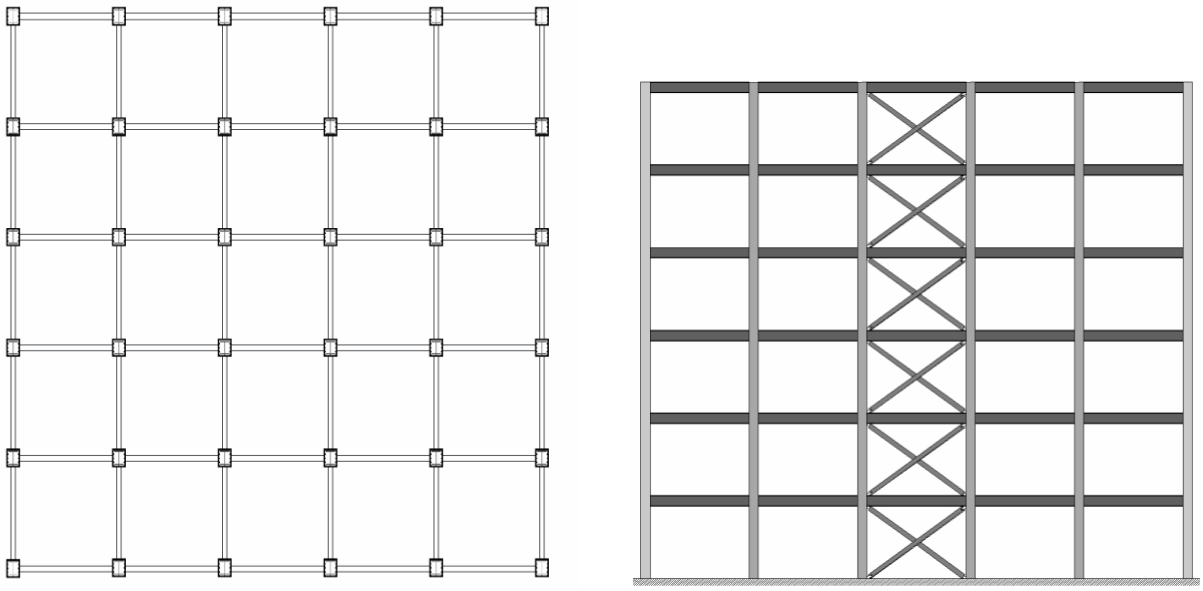
$M_{C,Rd}$, $V_{C,Rd}$, $N_{C,,Rd}$: the design bending moment, shear and axial force capacity provided by the concrete part of the section

$M_{S,Rd}$, $V_{S,Rd}$, $N_{S,Rd}$: the design bending moment, shear and axial force capacity provided by the steel part of the section

3 STRUCTURAL SIMULATION

The reference building simulated was a six-storey symmetrical building of 5 bays per direction. Its dimensions were 5.00m for each beam's span, in both directions, and 3.50m for the height of each storey. Bracings were used in the middle bay at each of the four sides. In Figure 1 is illustrated the horizontal and vertical layout of the elements, in an indicative floor plan and side view respectively.

All structural members were modeled with fibber elements. This element type is considered to be suitable for analyses where brittle types of failure are not expected to occur. As described in Section 2.2, the columns were divided into four groups regarding their location in the floor layout: group 1 includes all design variables associated with the corner columns, groups 2 and 3 refer to all side columns in x-direction and y-direction, respectively, and group 4 involves all internal columns.



(a) **(b)**

Figure 1: (a) Floor plan and (b) side view of the reference building

All gravitational loads from the slabs were modeled directly as distributed loads on the beams. Nonlinear static analysis under the combination of dead and live loads would take place before the implementation of the horizontal displacements. All structural simulations were performed using the OpenSEES software (Open System for Earthquake Engineering Simulation) [9]. The effect of the slabs to the structural performance was simulated by the definition of a rigid diaphragm on each floor level. Also, all columns were considered to be fixed on their base. Finally, the beam-to-column connections were modeled both as hinges and fixed connections. The first scenario would provide the maximum bending moment in the beam's span and, consequently define the minimum required beam section. The fixed connec-

tion results in transfer of an amount of the beam's bending moment to the columns, increasing the capacity demands on bending moment for the columns.

4 NUMERICAL RESULTS

The aim of this work is to examine the advantages and disadvantages of the three different columns types in the context of design against earthquake. In order to define the capabilities of each design methodology, an investigation of their cost-effectiveness in increased horizontal deformation demands was performed. This was achieved by introducing the coefficient δ [10] in the calculation of the targeted top displacement defined in Equation 3.

$$\Delta_{target} = \delta \cdot C_0 \cdot C_1 \cdot C_2 \cdot C_3 \cdot \frac{S_a}{\omega^2} \tag{10}$$

It becomes obvious that, values of δ higher than 1.0 simulate increased ductility demands, i.e. more strict design codes. So, for δ = 1.50, the structure is required to reach 50% further on the horizontal plane, remaining, however, at the same performance level. Eight values of δ ranging from 0.50 to 2.0 were used for the purposes of this research. Also, an extra optimization for gravitational loads only took place for each design method, in order to define the actual increase to the total cost due to the seismic requirements. All structures were required to perform within the collapse prevention limit state. The results obtained from the optimizations are illustrated in Figure 2.

It has to be noted here that the placement of the bracings in the middle bay of the structure was not an arbitrary decision, but it came as a result of preliminary structural optimizations. These analyses had shown that this option allows the optimization algorithm to provide more cost-effective solutions than installing them in the corner bays. The later option failed specially for low values of δ, which for the minimum bracings section was required, as it resulted in use of twice as much the steel as the scheme finally adopted.

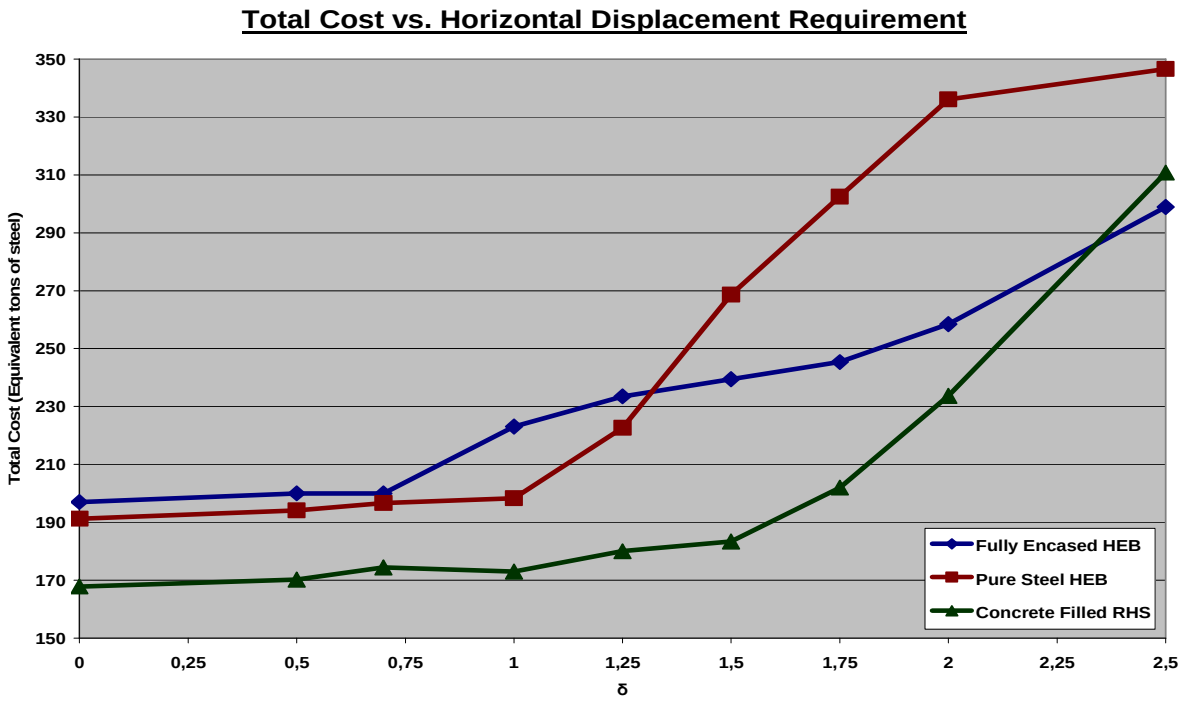


Figure 2: Optimized designs' total cost versus horizontal displacement capacity demand

	y-y'		z-z'			y-y'		z-z'	
	K_s/K_{tot}	K_c/K_{tot}	K_s/K_{tot}	K_c/K_{tot}		K_s/K_{tot}	K_c/K_{tot}	K_s/K_{tot}	K_c/K_{tot}
HE100B	26,4%	73,6%	11,7%	88,3%	**HE340B**	60,3%	39,7%	31,1%	68,9%
HE120B	32,4%	67,6%	14,8%	85,2%	**HE360B**	61,2%	38,8%	31,1%	68,9%
HE140B	37,5%	62,5%	17,5%	82,5%	**HE400B**	62,4%	37,6%	30,7%	69,3%
HE160B	42,0%	58,0%	20,0%	80,0%	**HE450B**	63,5%	36,5%	30,4%	69,6%
HE180B	45,6%	54,4%	22,3%	77,7%	**HE500B**	64,5%	35,5%	30,1%	69,9%
HE200B	48,7%	51,3%	24,3%	75,7%	**HE550B**	64,6%	35,4%	29,1%	70,9%
HE220B	51,4%	48,6%	26,1%	73,9%	**HE600B**	64,7%	35,3%	28,3%	71,7%
HE240B	53,6%	46,4%	27,7%	72,3%	**HE650B**	64,8%	35,2%	27,5%	72,5%
HE260B	54,9%	45,1%	28,5%	71,5%	**HE700B**	65,0%	35,0%	26,9%	73,1%
HE280B	56,1%	43,9%	29,3%	70,7%	**HE800B**	64,4%	35,6%	25,2%	74,8%
HE300B	57,7%	42,3%	30,5%	69,5%	**HE900B**	64,5%	35,5%	24,3%	75,7%
HE320B	59,3%	40,7%	31,1%	68,9%	**HE1000B**	64,0%	36,0%	23,0%	77,0%

Table 1: Stiffness contribution of each material to the composite section (fully encased sections)

	Dimensions (mm)			y-y'		z-z'			Dimensions (mm)			y-y'		z-z'	
	h	b	t	K_s/K_{tot}	K_c/K_{tot}	K_s/K_{tot}	K_c/K_{tot}		h	b	t	K_s/K_{tot}	K_c/K_{tot}	K_s/K_{tot}	K_c/K_{tot}
1	200	100	5	75,7%	24,3%	82,3%	17,7%	**26**	300	300	10	76,9%	23,1%	76,9%	23,1%
2	200	200	5	70,5%	29,5%	70,5%	29,5%	**27**	400	200	10	75,7%	24,3%	82,3%	17,7%
3	200	100	8	84,7%	15,3%	89,7%	10,3%	**28**	200	200	16	91,4%	8,6%	91,4%	8,6%
4	250	150	6	73,2%	26,8%	78,6%	21,4%	**29**	250	150	16	90,6%	9,4%	93,4%	6,6%
5	220	220	6	72,5%	27,5%	72,5%	27,5%	**30**	300	200	12,5	83,6%	16,4%	86,8%	13,2%
6	200	100	10	88,2%	11,8%	92,5%	7,5%	**31**	250	250	12,5	84,6%	15,4%	84,6%	15,4%
7	300	200	6	68,0%	32,0%	72,7%	27,3%	**32**	260	260	12	83,2%	16,8%	83,2%	16,8%
8	250	250	6	69,5%	30,5%	69,5%	30,5%	**33**	350	350	10	73,6%	26,4%	73,6%	26,4%
9	260	260	6	68,6%	31,4%	68,6%	31,4%	**34**	300	200	16	87,6%	12,4%	90,3%	9,7%
10	250	150	8	79,3%	20,7%	84,0%	16,0%	**35**	250	250	16	88,5%	11,5%	88,5%	11,5%
11	200	200	8	80,6%	19,4%	80,6%	19,4%	**36**	500	300	10	68,9%	31,1%	74,7%	25,3%
12	220	220	8	78,7%	21,3%	78,7%	21,3%	**37**	400	400	10	70,5%	29,5%	70,5%	29,5%
13	200	100	12,5	91,2%	8,8%	94,7%	5,3%	**38**	260	260	16	87,9%	12,1%	87,9%	12,1%
14	300	300	6,3	66,3%	33,7%	66,3%	33,7%	**39**	450	250	12,5	77,0%	23,0%	82,6%	17,4%
15	250	150	10	83,5%	16,5%	87,6%	12,4%	**40**	350	350	12,5	78,4%	21,6%	78,4%	21,6%
16	220	220	10	83,0%	17,0%	83,0%	17,0%	**41**	400	200	16	84,7%	15,3%	89,7%	10,3%
17	300	300	8	72,0%	28,0%	72,0%	28,0%	**42**	300	300	16	85,7%	14,3%	85,7%	14,3%
18	400	200	8	70,6%	29,4%	78,0%	22,0%	**43**	400	400	12	74,7%	25,3%	74,7%	25,3%
19	200	200	12,5	88,1%	11,9%	88,1%	11,9%	**44**	500	300	12,5	74,1%	25,9%	79,4%	20,6%
20	300	200	10	79,4%	20,6%	83,1%	16,9%	**45**	400	400	12,5	75,6%	24,4%	75,6%	24,4%
21	250	250	10	80,6%	19,4%	80,6%	19,4%	**46**	450	250	16	81,9%	18,1%	86,8%	13,2%
22	220	220	12	86,0%	14,0%	86,0%	14,0%	**47**	350	350	16	83,1%	16,9%	83,1%	16,9%
23	260	260	10	79,8%	20,2%	79,8%	20,2%	**48**	500	300	16	79,3%	20,7%	84,0%	16,0%
24	450	250	8	66,7%	33,3%	73,5%	26,5%	**49**	400	400	16	80,6%	19,4%	80,6%	19,4%
25	350	350	8	68,4%	31,6%	68,4%	31,6%								

Table 2: Stiffness contribution of each material to the composite section (hollow sections)

An upper and a lower cost limit are defined, which differ for each curve. The upper limit is related to the availability of sections in the databases used. In other words, it is the total cost of a building designed with the largest sections available for the simulated structural members. On the other hand, the lower limit is defined by the total cost of an optimized structure, which was designed for gravitational loads only, i.e. for $\delta = 0$.

An initial investigation of the results shows that, for low values of δ, all optimized designs' cost curves converge to their lower limit. Even though, it is logical to assume that a building designed only for gravitational loads also has a capacity for horizontal deformation, one would expect it to be minimal. However, it can be noticed that this capacity seems to be significant enough and, by the means of structural optimization, it could meet the current code requirements with negligible increase to its total material cost.

Each of the three curves, depicting the correlation between the total material cost and the horizontal displacement requirements, seems to be of a different type. In particular, the cost versus δ curve for the fully encased composite steel-concrete sections seems to have a mainly linear behavior. On the other hand, the one for the pure steel sections can be defined as bilinear, as its gradient changes dramatically for a δ value between 1.00 and 1.25. Finally, the behavior of the concrete filled tubes' curve could be characterized something between the two aforementioned types. One can notice that it is definitely not linear, since its gradient increases significantly for large values of δ. However, it is not bilinear either, as this change takes place smoothly. At any case, it is similar to the one of the pure steel columns curve.

In order to explain this type of behaviour, one needs to calculate the contribution of each material to the total section stiffness. This can provide an estimation of the behaviour to which a composite section is more similar. Tables 1 and 2, present this ratio for each material, for the fully encased HEB sections and the composite hollow sections. Taking into consideration that only HE200B or larger sections have been used in the first scenario, the contribution of concrete to the total stiffness ranges from 35.0% to 51.3% around the y-y' axis, and from 23% to 31% around the z-z' axis. In other words, the HEB sections' stiffness is increased from 53.8% up to 105.3% when they are encased in concrete. On the other hand, in the composite hollow sections, steel seems to be the dominant material. Its stiffness ranges from 86.3% to 91.4% and from 66.3% to 94.7% on the y-y' and z-z' axes respectively. Therefore, it becomes clear that the hollow sections' behavior is expected to be more similar to the pure steel design, than to the fully encased sections.

Also, what is remarkable is that designs which would seem unfeasible otherwise, satisfying the desired performance criteria, become available without a significant increase to the materials cost (61.2% for the fully encased sections). This observation is indicative of the efficiency of the optimization method, when it is used on structural design. It should also be noted that, in all feasible design scenarios, the usage ratio of the shear capacity of the columns ranged from 10% to 20%. Therefore, the assumption made during modelling that no brittle failure of the simulated structural members is expected to occur is verified.

5 CONCLUSIONS

- The application of optimization algorithms on structural design [6] has been proven a powerful tool which allows engineers to reduce significantly the total cost, without any compromise in the quality of the buildings.
- Structural design optimization enables the improvement of structural performance, far beyond their conventional limits, without excessive increase on their total cost.

- As the design codes become more demanding, in an effort to protect the structures against more dangers, optimization algorithms are expected to become necessary to designer engineers.
- Further decrease to the total cost of structures designed for high demands is feasible by further division of the element groups (e.g. by storey). However it results in significantly increased computational cost, therefore the engineer needs to determine the optimum configuration of the optimization problem.
- Steel-concrete composite design becomes more advantageous than pure steel design for increased demands, as it enables the definition of more cost-effective solutions. The increased cost-effectiveness is achieved by appropriately using concrete in order to partially replace the contribution of steel.
- Not being susceptible to buckling failure, concrete filled tubes are able to provide more cost-effective designs than fully encased I-shaped sections, for low horizontal displacement requirements. However, having a performance which is more similar to pure steel sections, due to the high contribution of steel, they lose this advantage, as the demands increase.
- An engineer's decision on the most preferable design scheme cannot be based only on the cost-effectiveness of the method. More parameters need to be taken into consideration, such as the applicability of the design method or its practicality regarding the building use.
- Increased fire resistance of the fully encased composite sections, thanks to the surrounding concrete, is an aspect which was not taken into consideration in the present paper; however it is important for a designer engineer in practice.

REFERENCES

[1] A.S.C.E., "*Seismic Rehabilitation of Existing Buildings*", *A.S.C.E. Standard A.S.C.E./S.E.I. 41-06, including Supplement No. 1*, American Society of Civil Engineers, Reston, Virginia, 2006.

[2] Beyer H.G. and Schwefel H.P.. "*Evolution Strategies: A Comprehensive Introduction.*" *Journal Natural Computing*, 1(1):3–52, 2002.

[3] Comité Européen de Normalisation (CEN), "*Eurocode 3: Design of steel structures (ENV 1993)' Part 1-1/1992 General rules and rules for buildings*", CEN Publications, Brussels, Belgium, 2003.

[4] Comité Européen de Normalisation (CEN), "*Eurocode 4: Design of composite structures (ENV 1994)' Part 1-1/1992 General rules and rules for buildings*", CEN Publications, Brussels, Belgium, 2003.

[5] F.E.M.A., "*Improvement of nonlinear static seismic analysis procedures (FEMA.440)*", Federal Emergency Management Agency, Washington D.C., 2005.

[6] Fradiadakis M., Lagaros N.D., Papadrakakis M. "*Performance based earthquake engineering using structural optimization tools*", International Journal of Reliability and Safety, 2006.

[7] Ingo Rechenberg, *"Evolutionsstrategie – Optimierung technischer Systeme nach Prinzipien der biologischen Evolution" (PhD thesis),* 1971.

[8] Lagaros, N. D., Papadrakakis, M. and Kokossalakis, G. *"Structural optimization using evolutionary algorithms". Computers & structures*, 80(7), 571-589, 2002.

[9] McKenna, F., Fenves, G. L., & Scott, M. H.. *"OpenSees: Open system for earthquake engineering simulation."* Pacific Earthquake Engineering Center, University of California, Berkeley, CA., http://opensees. berkeley. edu., 2006.

[10] Papavasileiou G.S. and Charmpis D.C., *"Maximizing the collapse resistance of composite steel and concrete structures", 10th World Congress on Computational Mechanics*, Sao Paulo, Brazil, 2012.

[11] Papavasileiou G.S., Charmpis D.C. and Lagaros N.D., *"Optimized Seismic Retrofit of Steel-Concrete Composite Frames", 3rd International Conference on Computational Methods in Structural Dynamics and Earthquake Engineering*, Corfu, Greece, 4573-4586, 2011.

[12] Spacone E., El-Tawil S., "Nonlinear Analysis of Steel-Concrete Composite Structures: State of Art", *Journal of Structural Engineering, Vol. 130, No. 2*, 159-168, A.S.C.E., 2004.

COMPDYN 2013
4th ECCOMAS Thematic Conference on
Computational Methods in Structural Dynamics and Earthquake Engineering
M. Papadrakakis, V. Papadopoulos, V. Plevris (eds.)
Kos Island, Greece, 12–14 June 2013

GRAPHICAL MODAL ANALYSIS AND EARTHQUAKE STATICS OF LINEAR ONE-WAY ASYMMETRIC SINGLE-STORY STRUCTURE

M. Faggella[1]

[1] Sapienza University of Rome
Via Eudossiana 18, Rome, Italy
e-mail: marco.faggella@uniroma1.it

Keywords: Graphical statics, graphical dynamics, earthquake response, modal analysis, torsionally coupled structures.

Abstract. *Graphical Static methods were developed in 1800s by European engineers and were a fundamental practice for generations of structural designers. Today they remain generally a valuable tool for representing and visualizing problems of structural mechanics that are governed by linear equations and rigid body kinematics, i.e. beam section analysis, mechanics of rigid bodies, etc. In this work we explore an application of graphical methods to the static earthquake response and vibrations of a single story elastic structure with a rigid-body diaphragm and a one-way asymmetry. We show that, based on involutory relations with respect to the floor ellipse of elasticity it is possible to graphically determine the lateral deflection under bi-directional earthquake loads, and the vibrational mode shapes. The method proves effective to gain insight into parameters that govern the earthquake response, and may be further explored to study more complex and general structures.*

1 INTRODUCTION

The use of graphics to solve static problems is found from some sketches made by Leonardo Da Vinci to some more systematic applications by Varignon and Poncelet [1]. A robust graphical static theory was first introduced in the 1800s by the work of Culmann [2], and further developed by other European engineers. Graphical methods became then an important tool for design of structures. Among them, the theory of the ellipse of elasticity was further developed by Ritter [2] and was used to solve elastic problems of beam and frame analysis, [4, 5]. The theory applies to any structural system that is elastic and whose kinematics can be described by rigid body deformations. This assumption is normally made for the cross section of a beam or for a building with rigid floor diaphragms. In some works of the literature of the last century [6] the ellipse of elasticity of a foundation block on an elastic soil was used to derive the stiffness matrix for vibrational analysis. The theory of the ellipse of elasticity can also be applied to the multi-directional and torsionally coupled response of three-dimensional frame structures, such as buildings under horizontal earthquake loads.

As it was observed after earthquake events the torsionally coupled behavior of irregular and plan-asymmetric structures can result in unbalanced demand on structural components and non-optimal or poor earthquake performance. Several authors have studied the behavior of torsionally coupled one-way asymmetric linear systems [7], and proposed methods for estimating the multidirectional nonlinear response or gave recommendations on how to approach the nonlinear response of one-way and two-ways eccentric torsionally coupled structures [8,9,10].

In this paper we highlight some graphical properties of the static earthquake response of an elastic single-story structure with a one-way plan asymmetry, that are useful to gain insight into the torsionally coupled behavior and into some key parameters that govern the seismic response. We introduce a graphical dynamic application of the theory of the ellipse of elasticity for dynamic modal analysis. We show that the static earthquake response can be handled through antipolarity relations based on the shear-type floor ellipse of elasticity. An additional antipolarity with respect to the circle of mass gyration is used for the modal analysis. We then introduce a simple graphical method to compute the modes of vibration, and use the properties of the ellipse of elasticity to obtain the modal frequencies.

2 GRAPHICAL EARTHQUAKE STATICS

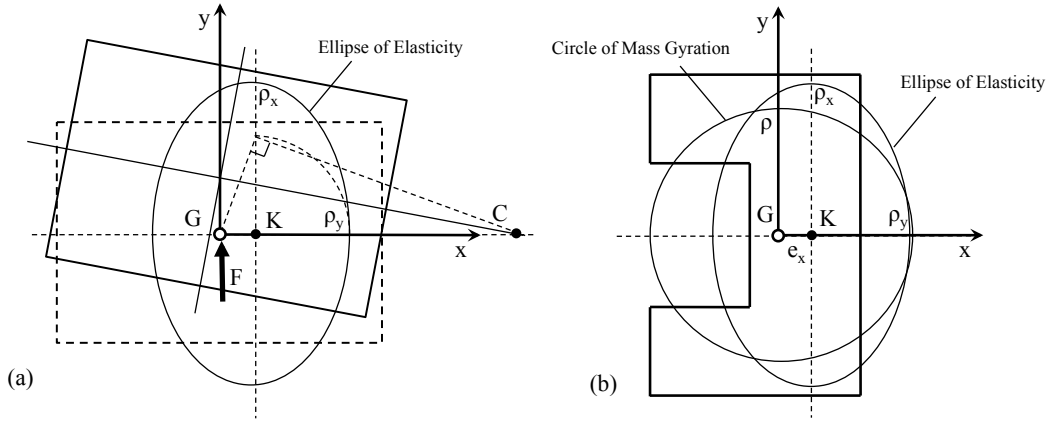


Figure 1: One-way eccentric torsionally coupled structures, (a) static analysis through the ellipse of elasticity. (b) Ellipse of elasticity and circle of mass gyration for a structure with a C-shaped geometry and a one-way asymmetry.

We consider herein a general single-story elastic structure with a one-way asymmetry. Both the center of mass G and the shear-type center of stiffness K are located on a principal axis. Therefore one of the three modes of vibrations has the direction of the eccentricity, i.e. along the principal axis that connects the floor center of mass with the center of shear-type stiffness. Without loss of generality, we will consider this principal axis as the X-axis, and restrict our analysis to a 2DOFs rigid diaphragm structure loaded in the Y-direction.

We select as DOFs the displacement in the Y-direction and rotation of the center of mass, and then we express them as a function of the rotation angle θ and of the position of the center of rotation x_c. This leads to decoupling the shape (represented by the position) from the amplitude, represented by the rotation angle. Also the force vector is expressed in term of the intensity of the external force F and of the distance x_F of the force from the center of stiffness. The static equations become

$$\mathbf{F}_e = \mathbf{K}\mathbf{u} = \begin{bmatrix} k_y & e_x k_y \\ e_x k_y & e_x^2 k_y + k_\theta \end{bmatrix} \begin{Bmatrix} -x_c \\ 1 \end{Bmatrix} \theta = \begin{Bmatrix} 1 \\ x_F \end{Bmatrix} F \tag{1}$$

Where k_y is the stiffness in the Y direction, k_θ is the rotational stiffness about the center of stiffness K, e_x is the eccentricity. A graphical static method of analysis can be used based on the ellipse of elasticity that is defined by its center K, and by the two principal semi-diameters

$$\begin{aligned} \rho_x &= \sqrt{k_\theta / k_x} \\ \rho_y &= \sqrt{k_\theta / k_y} \end{aligned} \tag{2}$$

The circle of mass gyration, which will be used later in the graphical dynamic analysis, can be defined through its radius ρ using the floor mass m and the polar moment of inertia I_p

$$\rho = \sqrt{I_p / m} \tag{3}$$

Figure 1a illustrates the graphical static analysis. The floor deformation for effect of a force F applied in the center of mass G and acting in the Y direction is identified by the position of the center of rotation C, and by the angle of rotation θ. According to the theory of the ellipse of elasticity the center of rotation is the antipole of the line of action of the force F with respect to the ellipse of elasticity. In this case the center C is the conjugated antipole of the vertical line passing through the center of mass G, and can be found graphically applying the involutory relation following the steps: 1) we rotate the X semi-diameter ρ_y of the ellipse by 90 degrees, 2) we draw a line from G to the end point of the ρ_y segment along the vertical line that passes through G, 3) we then draw from this point an orthogonal line whose intersection with the X-axis is the center of rotation. The points G and C are in mutual correspondence therefore the procedure can be inverted and used to determine the forces associated to a given deformation.

Figure 2 depicts the general case of a rotational displacement field and the relevant graphical determination of the elastic forces in the structure based on the properties of the ellipse of elasticity.

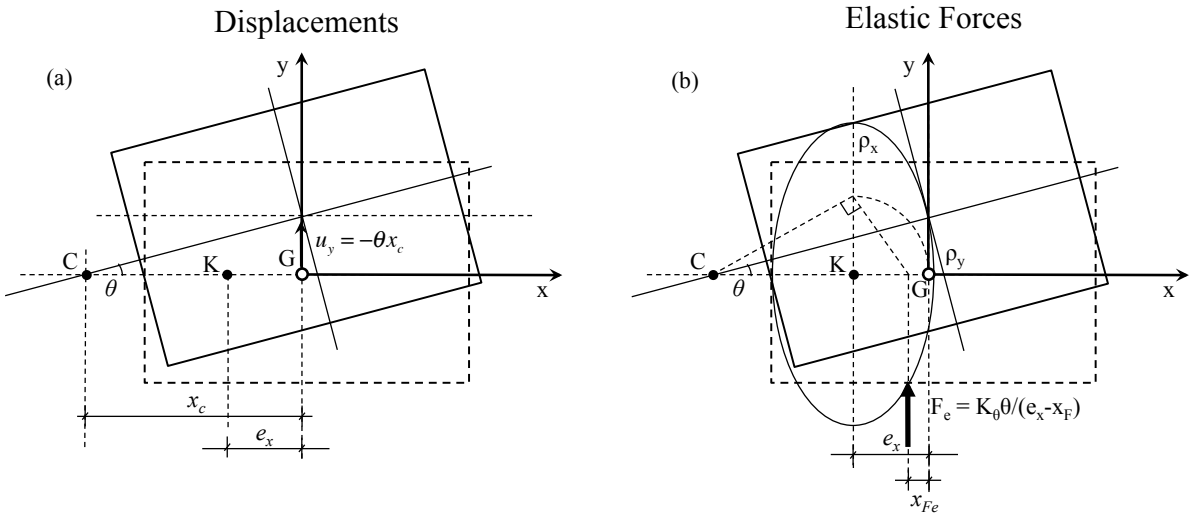


Figure 2: DOFs of one-way symmetric structure loaded with seismic forces orthogonal to a principal axis. (a) Rotational rigid-body displacements, (b) corresponding elastic forces F_e based on the antipolarity with respect to the ellipse of elasticity.

By using the equations (1) we can find the analytical confirmation of the antipolarity that allows to expresses the center of rotation as the antipole of the line of action of the force with respect to the ellipse of elasticity:

$$-(x_c - e_x) = \frac{\rho_y^2}{(x_{Fe} - e_x)} \tag{4}$$

Equation (4) represents an involutory relation from which x_c can be obtained, once x_F is known and vice-versa. The same static equations give the value of the floor rotation as a function of the intensity of the force, in terms of the rotational stiffness k_θ about the center of stiffness K.

$$\theta = \frac{F}{k_\theta}(x_{Fe} - e_x) \tag{5}$$

It can be noted that the equation (5) is one of the properties of the ellipse of elasticity, and k_θ represents the inverse of the so-called "elastic weight" encountered in the theory of the ellipse of elasticity.

3 GRAPHICAL DYNAMICS

Under dynamic undamped free vibration conditions the systems of the elastic forces $\mathbf{F}_e$ and of the inertial forces $\mathbf{F}_m$ must be in equilibrium. The equations of the free vibration of the structure are described by the previously defined stiffness matrix and by the mass matrix:

$$\mathbf{F}_m + \mathbf{F}_e = \mathbf{M}\ddot{\mathbf{u}} + \mathbf{K}\mathbf{u} = \mathbf{0} \tag{6}$$

The total response vector can be expressed in terms of modal contributions as a summation of the products of each mode shape function times the relevant time-dependent function:

$$\mathbf{u}(t) = \sum \Phi_n(x)\theta_n(t) = \sum \begin{Bmatrix} -x_{c,n} \\ 1 \end{Bmatrix} \theta_n(t) \tag{7}$$

The system of equations can then be written expressing both the modal rotational accelerations and displacements in terms of the positions of the modal centers of rotation and of the rotational displacement and acceleration angles:

$$m\begin{bmatrix} 1 & 0 \\ 0 & \rho^2 \end{bmatrix}\sum\begin{Bmatrix} -x_{c,n} \\ 1 \end{Bmatrix}\ddot{\theta}_n(t)+\begin{bmatrix} k_y & ek_y \\ ek_y & e^2k_y+k_\theta \end{bmatrix}\sum\begin{Bmatrix} -x_{c,n} \\ 1 \end{Bmatrix}\theta_n(t)=\begin{Bmatrix} 0 \\ 0 \end{Bmatrix} \tag{8}$$

The use of rotational kinematic degrees of freedom allows to decouple the shape from the rotational amplitude, therefore: 1) the mode shapes can be univocally identified through the positions $x_{c,n}$ of their centers of rotation, and their position remains fixed throughout the free vibration response; 2) the time-dependent functions are the time functions $\theta_n(t)$ of the modal angles of rotation.

Figure 3a shows a generic modal displacement and acceleration field. The latter is represented by a rigid body rotational acceleration about the center of rotation C_n, and is used to define the inertial forces that can be obtained through the terms of the mass matrix, as shown in Figure 3b. It is important to note that the moment of the inertial forces about the center of mass is equivalent to that generated by a force equal to $m\rho d^2\theta_n/dt^2$ applied at a distance from the center of mass G equal to the radius of gyration ρ.

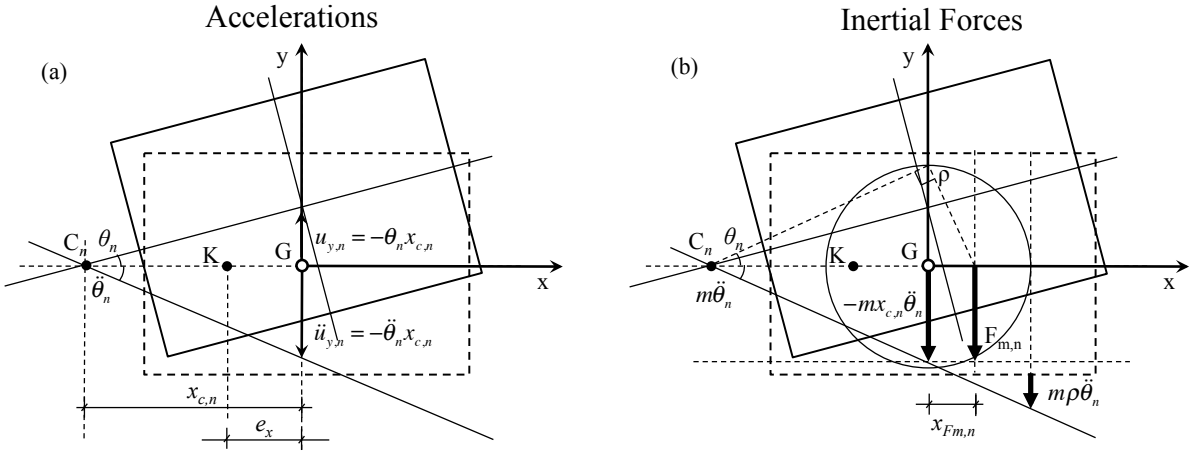


Figure 3: Definition of the floor accelerations based on rotational kinematics for a single modal component of the response (a), corresponding inertial forces F_m (b) expressed in terms of antipolarity with respect to the circle of mass gyration.

This is equivalent to saying that the line of action of the modal inertial force is the antipolar line of the center of rotation C_n with respect to the circle of mass gyration, as we can find from the inertial contribution of the equations (8) that yields the involutory relation:

$$-x_{c,n}=\frac{\rho^2}{x_{F_m,n}} \tag{9}$$

Therefore we have found that both the elastic forces and the inertial forces can be determined graphically using the involutory properties of the ellipse of elasticity and of the circle of mass gyration respectively. This allows the introduction of a graphical modal analysis method. Considering that the vectors of the modal inertial forces must be in equilibrium with the elastic forces, and since the modal centers of rotation are fixed, we can say that each mode's elastic and inertial forces must act on the same line. If we write both equations (4) and (7) for the modal centers of rotation we can find the following important property: the modal

centers must be mutually conjugated in both the antipolarity with respect to the ellipse of elasticity and in the antipolarity with respect to the circle of mass gyration. This implies that also the two directions of the modal and inertial forces are mutually conjugated in both the antipolarites. In other terms, in the graphical representation, the property of orthogonality of the mode shapes with respect to both the mass matrix and the stiffness matrix, can be translated into the property of mutual graphical/involutory conjugation of the centers and of the lines of action of the forces with respect to the circle of mass gyration and to the ellipse of elasticity respectively.

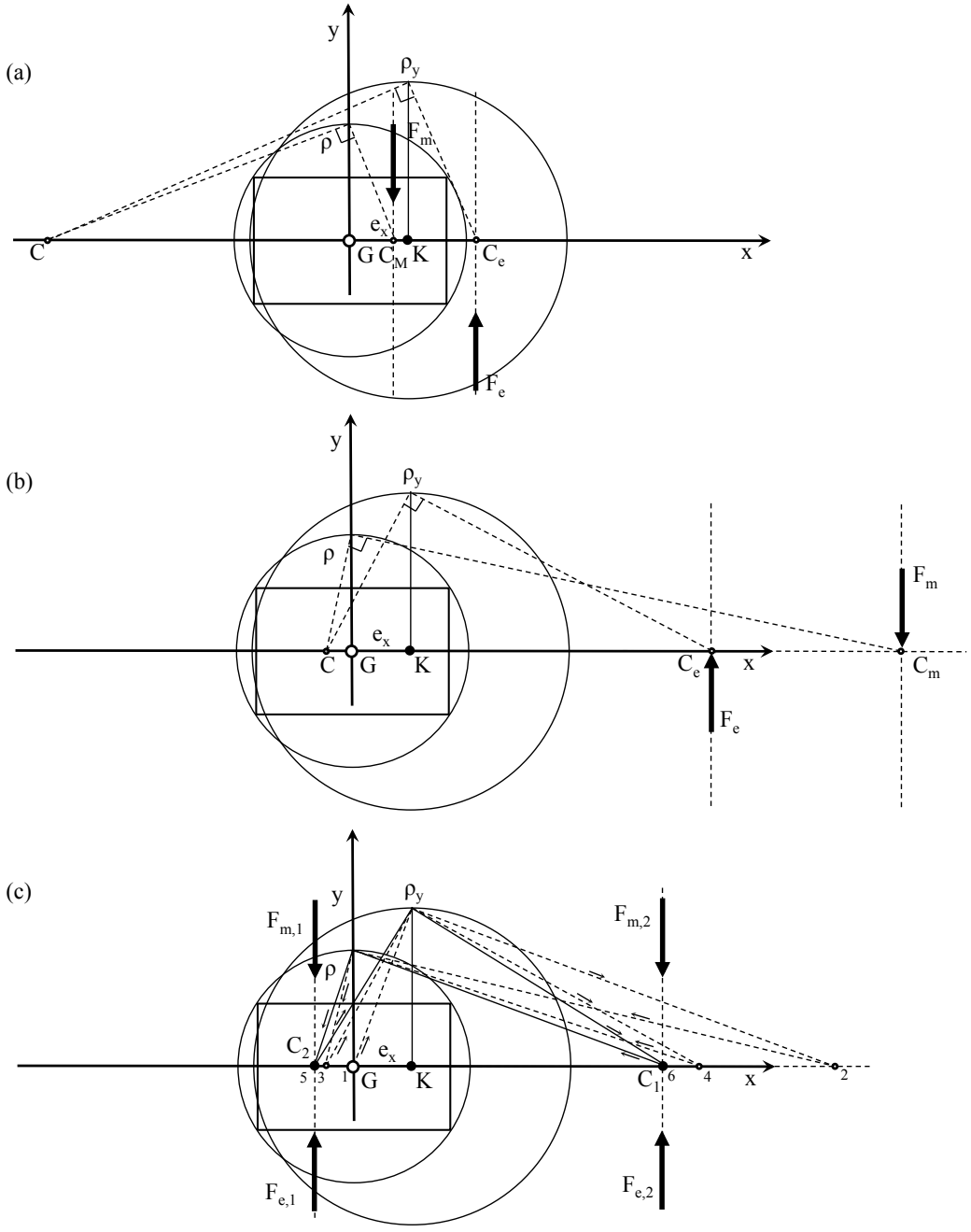


Figure 5: For a general deformed shape of center C there is an offset (a) between the inertial force and the elastic force; (b) the forces reverse as the center of rotation C approaches the center of mass; the offset is zero in correspondence of the modal centers of rotation. (c) Recursive graphical determination of C_1 and C_2 starting from the center of mass.

This leads to a convenient method to search and locate the modes of vibration through their centers of rotation, allowing a graphical procedure for modal analysis. Normally the mode shapes can be determined by matrix analysis finding the eigenvectors of the system of dynamic free vibration equations. In other cases they can be determined by direct methods choosing a starting displacement vector and recursively generating force vectors, such as in the Ritz method.

Here we present a graphical recursive approach for finding the mode shapes. In Figure 5 the ellipse of elasticity is for ease of description omitted and replaced by the circle of radius ρ_y.

This is done without losing generality since the X-axis is a principal axis and both the vibrations of the reference points K and G and the forces are in the Y direction. Therefore the centers of rotation are contained in the X-axis. Figure 5a shows that if a trial point that is external to both the ellipse of elasticity and the circle of mass gyration is chosen as center of deflection/acceleration, in general there is an offset between the corresponding inertial forces and elastic forces, as shown by the graphical forces determination. Therefore the corresponding forces cannot be in equilibrium, and the elastic forces fall beyond the corresponding inertial forces with respect to the center of rotation.

Figure 5b shows that if a trial deformation is chosen with center of rotation internal to both the circle and the ellipse and close enough to the center of mass G, there is again an offset between the inertial and elastic forces. However in this case the outer-most force is the inertial force. This means that as the trial center of rotation moves on the X axis approaching the center of mass, there is a position corresponding to which the offset is zero and the two forces act on the same line. Such middle zero-offset or reversal point is one of the two modal centers of rotation. Figure 5c shows the graphical procedure for finding the modal centers of rotation C_1 and C_2. The procedure consists of recursively generating elastic and inertial force vectors by applying the antipolarity with respect to the mass and to the stiffness, until convergence is achieved. Any trial point can be assumed as starting center of rotation. In this case we start from a rotational deflected shape centered in the center of mass G, labeled as 1. The conjugate point of 1 with respect to the stiffness is point 2, whose conjugate point with respect to the mass does is not point 1 but point 3. Then the conjugate of 3 with respect to the stiffness is found in point 4, and so on. At the step corresponding to point 6 we find that the procedure falls very close to a convergence loop represented by the double mutual antipolarity (conjugated points and directions) of points C_1 and C_2 that are the modal centers of rotation sought. The line of action of the Mode 2 inertial and elastic forces is the vertical line passing through C_1, and vice-versa the line of action of the Mode 1 inertial and elastic forces is the vertical line passing through C_2.

Finally the mode shapes are represented in Figure 6. It can be noted that from the analytical standpoint the procedure described above is equivalent to applying alternatively equations (4) and (9), therefore the convergence points C_1 and C_2 can be also found analytically, i.e. finding the values of x_c that satisfy both equations. This yields the two solutions

$$x_{c1,2} = \frac{(\rho^2 - d^2) \pm \sqrt{(\rho^2 - d^2)^2 + 4e_x^2\rho^2}}{2e_x} \tag{10}$$

Where d is the segment that connects the center of mass G with the end of the semi-axis ρ_x oriented along a vertical line

$$d = \sqrt{e_x^2 + \rho_y^2} \tag{11}$$

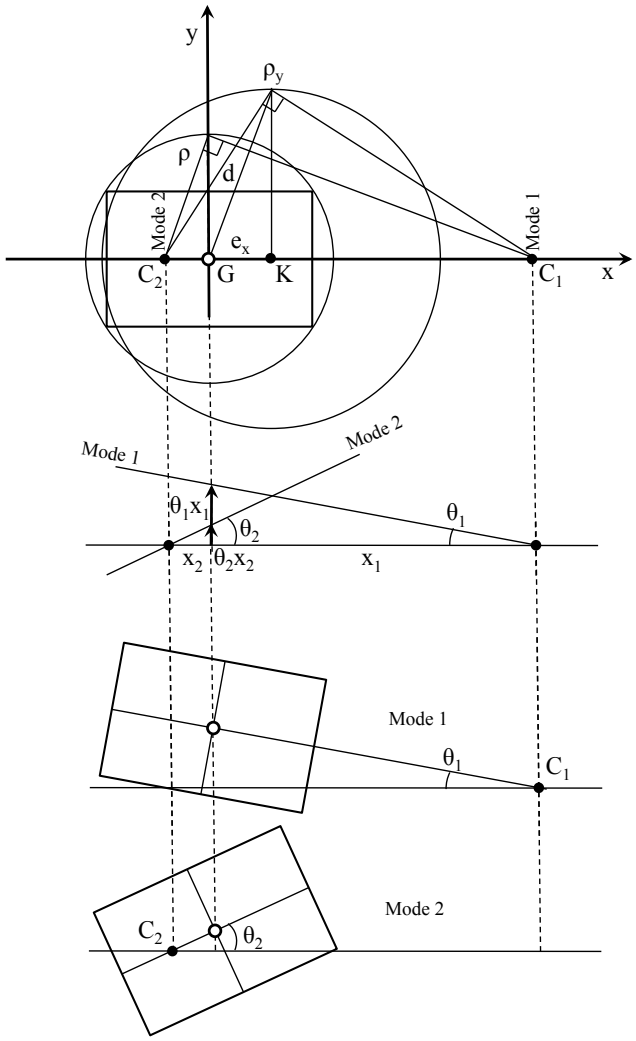


Figure 6: Torsionally coupled mode shapes. The centers C_1 and C_2 are double-conjugated in both the antipolarity with respect to the ellipse of elasticity and the antipolarity with respect to the circle of mass gyration.

Once the positions x_{c1} and x_{c2} are known, due to the equilibrium we can impose for each mode the equal intensity of the modal inertial forces and of the modal elastic forces, and compute the rotation amplitudes according to the properties of the ellipse of elasticity. This yields the values of the two frequencies of vibration (12) as a function of x_{c1} and x_{c2}, of the semi-diameters ρ and ρ_y, and of the other structural properties.

$$\omega_1^2 = \frac{k_y}{m}\frac{\rho_y^2}{(\rho^2 + e_x x_{c1})}$$
$$\omega_2^2 = \frac{k_y}{m}\frac{\rho_y^2}{(\rho^2 + e_x x_{c2})} \tag{12}$$

We can also note that the mode shapes and frequencies can be normally found solving the corresponding eigenproblem. However the use of rotational kinematic DOFs for modal displacements and the inherent decoupling of the shape (centers) from the amplitude (rotation) leads to a simplification of the equations so that they can easily be solved by substitution, and gives the chance to introduce the involutory relations on which the graphical procedure described here is based.

4 CONCLUSIONS

We presented the application of graphical static methods to the dynamics of one-way symmetric torsionally coupled elastic single-story structures, provided that the positions of the center of mass and of the center of stiffness are known, and given the ellipse of elasticity and the floor mass radius of gyration. In alternative to static analysis thorough the stiffness matrix, and in analogy with the method used in sectional analysis for determination of the neutral axis, we introduce rigid body rotational kinematics to solve the statics of the structure under horizontal loads using the involutory properties of the antipolarity with respect to the ellipse of elasticity. After introducing the dynamic equations of free vibrations, we find that the antipolarity with respect to the circle of radius equal to the floor gyrator of the mass can be used to graphically determine also the inertial forces. Therefore both the dynamic inertial forces and the static elastic forces can be determined based on the ellipse and on the circle. These properties are used to introduce a graphical method for direct determination of the mode shapes through a recursive generation of the lines of action of the elastic forces and of the inertial forces. The modal frequencies are then determined using the other properties of the ellipse of elasticity imposing the equilibrium of the modal inertial forces and elastic forces. Instead of regular eigenvector analysis, the graphical procedure described here relies on a number of graphical static analyses to obtain the modal frequencies, the mode shapes and the intensity and lines of action of the modal forces. The method is effective to gain insight into properties and parameters that govern the dynamic earthquake response, and its application to more complex structures can be object of further investigation.

REFERENCES

[1] E. Benvenuto, La Scienza delle Costruzioni e il suo sviluppo storico, Edizioni di Storia e Letteratura, Roma, 2006. (In Italian).

[2] K. Culmann, Die Graphische Statik, 1865. (In german).

[3] W. Ritter, Anwendungen der Graphischen Statik, **3**, (Appendix), Zurich, 1865. (In German).

[4] O. Belluzzi, Scienza delle Costruzioni, Bologna: Zanichelli, 1942. (In Italian).

[5] V. Franciosi, Fondamenti di Scienza delle Costruzioni, vol. **III** Teoria delle Strutture, Napoli, Liguori ed., 1988. (In Italian).

[6] A. Galli, Su di una applicazione dinamica dell'ellisse di elasticità. *Ricerche di Ingegneria*, **2**, 106-109, 1934. (In Italian).

[7] T.L. Trombetti, J.P. Conte, New insight into and simplified approach to seismic analysis of torsionally coupled one-story, elastic systems, *Journal of Sound and Vibration*, **286**, 265-312, 2005.

[8] A.K. Chopra, R.K. Goel. A modal pushover analysis procedure to estimate seismic demands for un-symmetric-plan buildings*, Earthquake Engineering and Structural Dynamics*, **33**, 903-927, 2004.

[9] J.L. Lin, K.C. Tsai, Seismic analysis of two-way asymmetric building systems under bi-directional seismic ground motions, *Earthquake Engineering and Structural Dynamics*, **37**, 305-328, 2008.

[10] J.C. Reyes, E. Kalkan. Relevance of Normal-Fault and Maximum Components of Ground-Motions on Nonlinear Behavior of Symmetric and Asymmetric Buildings in Near Fault Sites. *15WCEE, 15th World Conference in Earthquake Engineering*. Lisbon, Portugal, 2012.

COMPDYN 2013
4th ECCOMAS Thematic Conference on
Computational Methods in Structural Dynamics and Earthquake Engineering
M. Papadrakakis, V. Papadopoulos, V. Plevris (eds.)
Kos Island, Greece, 12–14 June 2013

COMPUTATIONAL MODELING OF THE WAVES PROPAGATION IN A BLOCK MEDIUM WITH VISCOELASTIC INTERLAYERS

Oxana V. Sadovskaya, Vladimir M. Sadovskii, and Mariya P. Varygina

Institute of Computational Modeling SB RAS
Akademgorodok 50/44, 660036 Krasnoyarsk, Russia
e-mail: {o_sadov,sadov,vmp}@icm.krasn.ru

Keywords: Block Medium, Cosserat Continuum, Viscoelasticity, Rotational Motion, Resonance Frequency, Parallel Program System.

Abstract. *In the framework of mathematical model of a block medium with elastic blocks interacting through compliant viscoelastic interlayers and its approximation on the basis of equations of the Cosserat continuum, the problems of periodic perturbation of a layer and of a half-space under the action of distributed and localized surface loads are solved numerically. The simple formulas are suggested to determine the elasticity coefficients of the moment continuum by given characteristics of the materials of blocks and interlayers, which provide a good correspondence of the wave fields received by means of the exact and approximate models. Parallel computational algorithms, based on models of the inhomogeneous elasticity theory and the Cosserat elasticity theory, are applied to the analysis of propagation of elastic waves in geomaterials with layered and block microstructure. These algorithms are realized as parallel program systems for GPUs (using CUDA technology) and for multiprocessor computers of the cluster type (using MPI library). Monotone grid-characteristic schemes with a balanced number of time steps in elastic layers or blocks and in viscoelastic interlayers are used. By the analysis of numerical solutions it is shown that the multiblock medium has a resonant frequency of rotational motion of blocks, and this frequency does not depend on the size of a massif and on the boundary conditions at its surface.*

1 INTRODUCTION

Many natural materials, such as rocks and soils, are characterized by inhomogeneous block-hierarchical structure. The block structure is observed at different levels of scale: from the size of crystal grains to large blocks of a rock body, separated by faults. The blocks are connected to each other by means of interlayers of a rock with substantially more compliant mechanical properties [1]. One of the most important technological problems of coal mining is to forecast the sudden collapse of the roof of coal mines. This process is preceded by the weakening of mechanical contact between blocks: the rock becomes weakened microstructure. This state of a material can be found by exciting elastic waves of small amplitude and recording the response to these perturbations, which can be used in the development of special technical devices for timely prediction and prevention of emergencies.

The theory of inhomogeneous media with layered and block microstructure is the field of mechanics, intensively developing during more than half a century. By present time the efficient analytical methods in this field are developed [2, 3, 4], numerical algorithms for the solution of quasi-static and dynamic problems are worked out by means of the finite element and finite difference approximation of continuous models. However such methods are practically unsuitable for the problems on propagation of high-frequency waves in block media, lengths of which are comparable with the size of blocks and layers. This is because of the methodological errors, caused by the approximation viscosity, which are comparable with the physical viscosity. It is necessary to perform computations on fine grids, the mesh size of which is consistent with the characteristic size of the blocks. For these computations it is appropriate to use modern multiprocessor computer systems.

The works [5, 6] are devoted to experimental and theoretical study of low-frequency oscillations of the blocks caused by the propagation of short single impulses of pressure in block media (the so-called pendulum waves). One-dimensional computations of the longitudinal waves of pendulum type on the basis of the equations of a layered medium are carried out in [7]. The purpose of this paper is to work out two-dimensional and three-dimensional models for numerical analysis of the propagation of waves. Computations, performed by means of these models, allow to analyze resonant motion of a block medium due to accounting rotational degrees of freedom of the blocks.

2 EQUATIONS OF A BLOCK MEDIUM

Let us consider the state of plane strain of a block medium, formed by square elastic blocks with sides of the length h, parallel to the coordinate axes x_1, x_2 of a Cartesian coordinate system, and thin interlayers of the thickness δ. Blocks are numbered by pairs of indices k_1 and k_2, taking the values from 1 to N_1 and N_2, respectively. The system of equations of a homogeneous isotropic elastic medium

$$\begin{aligned}
&\rho\,\dot v_1 = \sigma_{11,1} + \sigma_{12,2},\\
&\rho\,\dot v_2 = \sigma_{12,1} + \sigma_{22,2},\\
&\dot\sigma_{11} = \rho\,c_1^2(v_{1,1} + v_{2,2}) - 2\rho\,c_2^2\,v_{2,2},\\
&\dot\sigma_{22} = \rho\,c_1^2(v_{1,1} + v_{2,2}) - 2\rho\,c_2^2\,v_{1,1},\\
&\dot\sigma_{12} = \rho\,c_2^2(v_{2,1} + v_{1,2})
\end{aligned} \tag{1}$$

is fulfilled inside of each block. Here v is the velocity vector, σ is the symmetric stress tensor, ρ is the density of a material, c_1 and c_2 are the velocities of longitudinal and transverse elastic

waves, the dot over the symbol and indices after the comma denote the derivatives with respect to time and spatial variables.

Elastic interlayer between neighboring blocks with the numbers (k_1, k_2) and $(k_1 + 1, k_2)$ in the horizontal direction is described by ordinary differential equations, taking into account its mass and the longitudinal and transverse rigidities:

$$\begin{aligned} \rho' \frac{\dot{v}_1^+ + \dot{v}_1^-}{2} &= \frac{\sigma_{11}^+ - \sigma_{11}^-}{\delta}, \quad \frac{\dot{\sigma}_{11}^+ + \dot{\sigma}_{11}^-}{2} = \rho' c_1'^2 \frac{v_1^+ - v_1^-}{\delta}, \\ \rho' \frac{\dot{v}_2^+ + \dot{v}_2^-}{2} &= \frac{\sigma_{12}^+ - \sigma_{12}^-}{\delta}, \quad \frac{\dot{\sigma}_{12}^+ + \dot{\sigma}_{12}^-}{2} = \rho' c_2'^2 \frac{v_2^+ - v_2^-}{\delta}. \end{aligned} \tag{2}$$

Elastic interlayer between blocks with the numbers (k_1, k_2) and $(k_1, k_2 + 1)$ in the vertical direction is described by the equations:

$$\begin{aligned} \rho' \frac{\dot{v}_2^+ + \dot{v}_2^-}{2} &= \frac{\sigma_{22}^+ - \sigma_{22}^-}{\delta}, \quad \frac{\dot{\sigma}_{22}^+ + \dot{\sigma}_{22}^-}{2} = \rho' c_1'^2 \frac{v_2^+ - v_2^-}{\delta}, \\ \rho' \frac{\dot{v}_1^+ + \dot{v}_1^-}{2} &= \frac{\sigma_{12}^+ - \sigma_{12}^-}{\delta}, \quad \frac{\dot{\sigma}_{12}^+ + \dot{\sigma}_{12}^-}{2} = \rho' c_2'^2 \frac{v_1^+ - v_1^-}{\delta}. \end{aligned} \tag{3}$$

Here the quantities with superscripts relate to the boundary meshes of interacting blocks. Similar equations were used in [7] for the one-dimensional model of a layered medium. It can be shown that these equations are thermodynamically consistent with the system of equations (1), i.e. for a regular block structure the energy conservation law is fulfilled, in which the sum of kinetic and potential energy is the sum of kinetic and potential energies of blocks and interlayers separately.

When taking into account the viscoelastic strains in interlayers, the equations (2), (3) are replaced by more general equations depending on the rheological scheme of a material [7]. For numerical solution of the equations (1) – (3) and the system, which takes into account the viscoelastic properties of interlayers on the basis of rheological schemes by Maxwell, Kelvin–Voigt and Poynting–Thomson, the parallel computational algorithm is worked out. In this algorithm the Godunov discontinuity decay method is realized for equations of the elasticity theory on a uniform grid with a choice of the maximum permissible time step according to the Courant–Friedrichs–Levy condition. At smaller time step a piecewise-linear ENO–reconstruction of the second order of accuracy is used [8]. The method of two-cyclic splitting with respect to spatial variables is applied for the solution of two-dimensional problems. Splitting method leads to a series of one-dimensional problems, solved by means of a monotone ENO–scheme. Parallelization of the algorithm is performed for computer systems on graphics accelerators using the CUDA technology. Study of the effectiveness of parallel implementation of the algorithm showed acceleration of the program up to 50 times compared to the sequential version.

Created programs are used to solve a series of one-dimensional and two-dimensional problems on the propagation of waves, caused by the influence of short and long (periodic) localized loads at the boundary of a layered (block) medium. Numerical solutions, obtained on the basis of the equations (1) – (3) and in the framework of complete formulation, are compared for Lamb's problem on the action of concentrated force on a surface of massif of a block medium with elastic interlayers. In the complete formulation the interlayers are modeled using the equations of plane theory of elasticity with the pasting together conditions at interfaces. Computations in the complete formulation are performed by means of the 2Dyn_Granular program [9] on the MVS-100K cluster of the Joint Supercomputer Center of RAS. Numerical results for

both models are in good correspondence. However, because of a large dimension of the finite-difference grid in interlayers, the computations on the cluster using MPI require on the order more time than the computations on the GPUs using CUDA by simplified model (1) – (3).

In Figs. 1 and 2 one can see the graphs of velocity on the spatial coordinate for the one-dimensional problem on the action of Λ–shaped impulse of a pressure on boundary of a layered medium composed of 512 layers of a rock with microfractures elastic interlayers of a ground [7]. Computations were carried out after reduction of the system of equations to dimensionless variables with the following parameters: $\delta/h = 0.027$, $\rho'/\rho = 0.76$, $a'/a = 7.17$ ($a = 1/(\rho\, c^2)$ and $a' = 1/(\rho' c'^2)$ are the elastic compliances of materials). A uniform finite-difference grid in layers consists of 16 meshes. One mesh is used within each interlayer. Choice of the integer parameters in the form of powers of two is related to the specific features of programming and memory allocation in CUDA. Computations were performed on the eight-core computer with graphics card Tesla C2050.

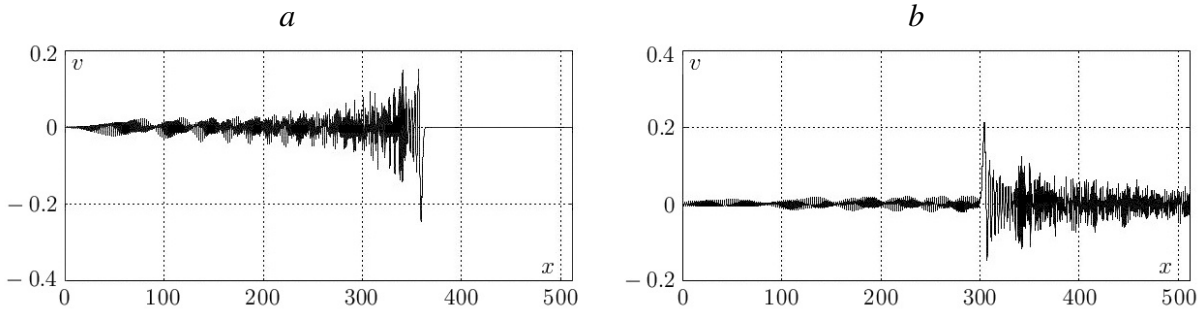


Figure 1: Velocity distribution behind the front of the incident wave (*a*) and the reflected wave (*b*), caused in a layered medium by the influence of a short impulse.

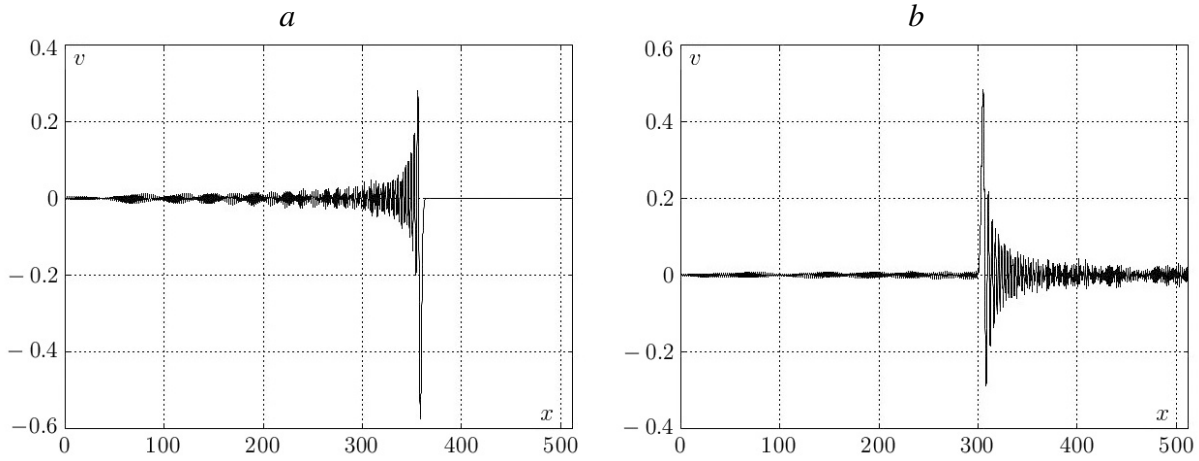


Figure 2: Velocity distribution behind the front of the incident wave (*a*) and the reflected wave (*b*), caused in a layered medium by the influence of a long impulse.

Fig. 1 corresponds to the impulse duration which is equal to the time of passage of elastic wave through one layer, Fig. 2 corresponds to the duration which is two and a half times greater. The impulse of unit amplitude acts on the left boundary of computational domain, the right boundary is fixed. In Figs. 1 *a* and 2 *a* the velocity profiles are shown at the moment when the incident wave goes about 370 layers (6000-th time step of the basic scheme). In Figs. 1 *b* and 2 *b* the reflected wave goes in the opposite direction about 200 layers (12000-th time step

of the basic scheme). These results demonstrate a qualitative difference of the wave pattern in layered media as compared with a homogeneous medium. At the initial stage this difference is the appearance of waves reflected from the interlayers – the characteristic oscillations behind the front of loading wave as it passes through the interface. With time, after multiple reflections behind the front of a head wave appears stationary wave pattern, the so-called pendulum wave, whose existence was predicted in [5, 6].

A comparison of Figs. 1 and 2 show that with an increase in impulse duration the amplitude of a head wave increases up to unity, and the amplitude of oscillations behind the front decreases and tends to zero. This is due to the fact that waves, which lengths are considerably greater than the thickness of the interlayer, are practically not reflected from the interlayers. Thus, it is possible to detect a weakened microstructure of layered or block medium only with the help of sufficiently short waves.

Fig. 3 presents the results of two-dimensional computations within the framework of the model in complete formulation. Computations for block media consisting of 6 blocks (Figs. 3 *a* and 3 *b*) and 15 blocks (Figs. 3 *c* and 3 *d*) were performed on a cluster system. The thickness of interlayers is 5 times smaller than the thickness of blocks. The following parameters of materials are used: $\rho = 3700$, $\rho' = 1200\,\text{kg/m}^3$, $c_1 = 3500$, $c_2 = 2100$, $c_1' = 1500$, $c_2' = 360\,\text{m/c}$. In Fig. 3 *a* and 3 *c* the level curves of the stress σ_{11} for Lamb's problem on the action of a normal force, concentrated in the central point of upper boundary of a half-plane, are shown. In Fig. 3 *b* and 3 *d* the level curves of the stress σ_{12} for similar problem on the action of a concentrated tangential force are shown (the x_1 axis is directed downwards, deep into the massif, and the x_2 axis is in the horizontal direction).

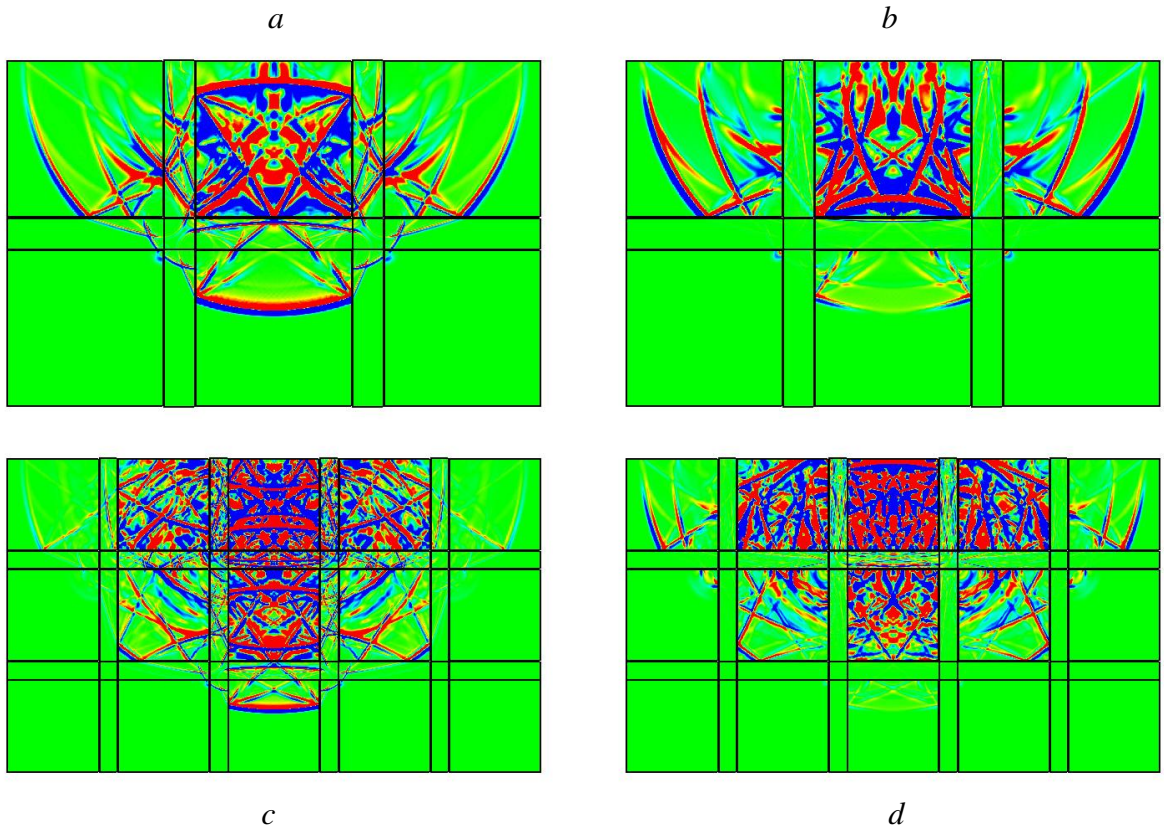


Figure 3: Lamb's problem for a block medium with thick elastic interlayers: level curves of normal stress (*a*, *c*) and tangential stress (*b*, *d*).

Under the action of a impulse load there are formed incident longitudinal and transverse waves, conical transverse waves, propagating deep into the massif with time, and also the Rayleigh surface waves, rapidly damped with depth. Moreover, a series of waves, reflected from interfaces, and a series of surface waves, generated under the arrival of reflected waves on the boundary of a half-plane, appear because of the presence of compliant interlayers.

In Fig. 4 one can see computational results for a multiblock medium (Lamb's problem on the action of a concentrated tangential force), performed on the basis of a simplified model (1) – (3). Computational domains consist of 4×2 blocks of a rock with 10 interlayers of a ground in Fig. 4 *a*, of 8×4 blocks with 52 interlayers in Fig. 4 *b*, of 16×8 blocks with 232 interlayers in Fig. 4 *c*, and of 32×16 blocks with 976 interlayers in Fig. 4 *d*. Computations showed that the increase of the number of blocks and a proportional decrease of the parameters h and δ lead to the appearance of a diffuse wave front, caused by the rotational motion of blocks, behind the front of an incident transverse wave. It is a confirmation of intuitive representation that a multiblock medium with compliant interlayers can be approximated by a generalized continuum. The asymmetry of stress tensor, caused by the rotational motion of blocks, and the couple stresses, associated with the curvature of a regular block structure due to the inhomogeneity of rotations, are taken into account in the equations of a generalized continuum.

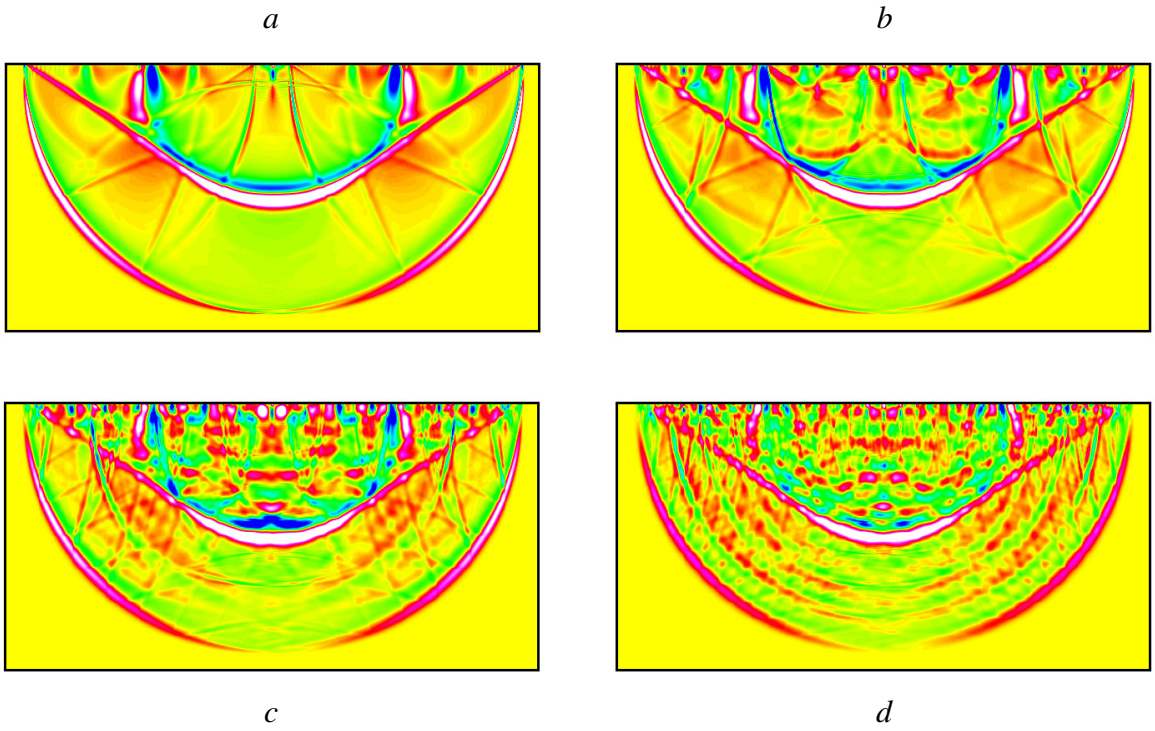


Figure 4: Lamb's problem for a block medium with thin elastic interlayers: level curves of tangential stress; 4×2 blocks of a rock with 10 interlayers of a ground (*a*), 8×4 blocks with 52 interlayers (*b*), 16×8 blocks with 232 interlayers (*c*), 32×16 blocks with 976 interlayers (*d*).

3 A BLOCK MEDIUM AS THE COSSERAT CONTINUUM

Known property of layered and block media, tested many times experimentally and by means of numerical computations (see, for example, [6, 7]), is that the waves of small amplitude, the length of which is larger than the size of layer or block, move in such a medium almost as in a homogeneous medium with some effective elastic moduli. Strictly speaking, this applies only

to the waves of translational motion. Perturbation of rotational motion of the blocks leads to the appearance of new types of waves. Let us describe the propagation of long waves in a multiblock medium by means of the system of equations of the Cosserat continuum, which is widely used in the modeling of structurally inhomogeneous materials at different scale levels [10, 11, 12]. To do this, assuming that the block size is small compared with the size of all massif, let us calculate the phenomenological parameters of the moment continuum via the elasticity parameters of materials of blocks and interlayers.

One of the simplest ways of recalculation is connected with the requirement of correspondence between models in the special schemes of quasistatic or dynamic deformation [13, 14, 15, 16]. The scheme of deformation of a block medium, in which blocks rotate by a small angle φ, and their centers of mass remain fixed, is shown in Fig. 5 *a*. The deformation of blocks can be neglected taking into account the compliance of interlayers. In this approximation, the interlayers are in a state of pure shear with the angle of shear $\gamma = h\,\varphi/\delta$. The corresponding tangential stress $\tau = \mu'\gamma$ ($\mu' = \rho' c_2'^2$ is the shear modulus for a material of interlayer) is proportional to the rotation angle. The proportionality coefficient $f_\alpha = \tau/\varphi = \mu' h/\delta$ is one of the phenomenological parameters of the Cosserat continuum.

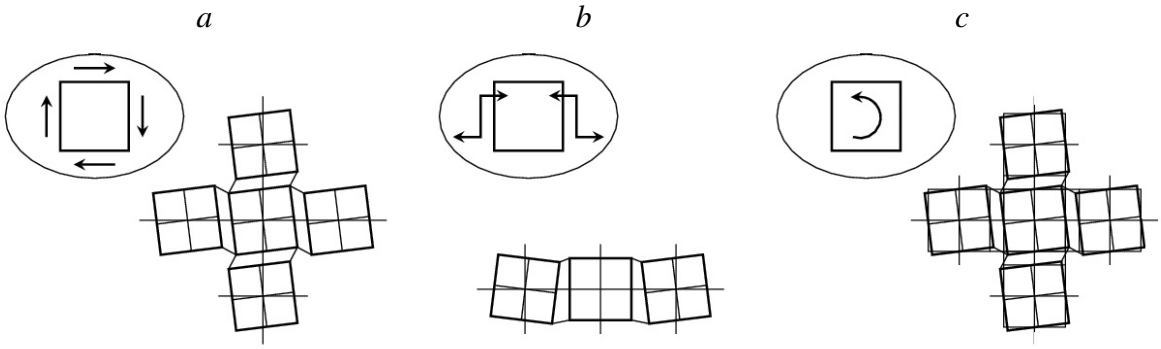


Figure 5: Schemes of deformation of a block medium: uniform rotation of blocks (*a*), nonuniform rotation with formation of curvature (*b*), uniform torsion (*c*).

In the scheme, represented in Fig. 5 *b*, the displacements of centers of mass are also absent. The curvature æ $= \partial\varphi/\partial x$ is formed because of the counter rotation of neighboring blocks. It can be estimated by the formula: æ $= \varphi/(h+\delta)$. Linear distribution of the strain $\varepsilon = -\varphi\, y/\delta$ and the normal stress $\sigma = E'\varepsilon$ appears in the interlayer. Here x and y are the horizontal and vertical coordinates, $E' = \rho' c_2'^2(3c_1'^2 - 4c_2'^2)/(c_1'^2 - c_2'^2)$ is the Young modulus of a material of interlayer. Action of the stress is reduced to the action of the bending moment $m = E'\varphi\, h^3/(12\delta)$. Consequently, one more parameter of the Cosserat continuum can be defined by the formula: $f_\beta = E'(h+\delta)h^3/(12\delta)$.

In Fig. 5 *c* one can see the scheme of uniform torsion of a block medium around the axes passing through the fixed centers of mass of blocks perpendicular to the plane of the figure. In this state the stresses in interlayers are determined by solving the problem of elastic torsion. Projections of the displacement vector in interlayer onto horizontal and vertical axes are expressed by formulas: $u_x = -y\,\varphi\, z/\delta$ and $u_y = x\,\varphi\, z/\delta$. According to Hooke's law, the tangential stresses $\tau_x = \mu'\partial u_x/\partial z$ and $\tau_y = \mu'\partial u_y/\partial z$ are found. The torsional moment is defined

as the integral

$$M = \int\limits_{-h/2}^{h/2}\int\limits_{-h/2}^{h/2} (x\,\tau_y - y\,\tau_x)\,dx\,dy = \frac{\mu'\varphi}{\delta}\int\limits_{-h/2}^{h/2}\int\limits_{-h/2}^{h/2} (x^2+y^2)\,dx\,dy = \frac{\mu'\varphi\,h^4}{6\delta}.$$

The torsion $æ_0 = \partial\varphi\partial z$ is estimated using the above formula for the curvature. Therefore the phenomenological parameter $f_\kappa = M/æ_0$, which equals the ratio of torsional moment to torsion, can be calculated by the formula: $f_\kappa = \mu'(h+\delta)h^4/(6\delta)$.

In the spatial state the elastic properties of an isotropic moment continuum are characterized by six independent parameters. Recalculation of three of them is performed via f_α, f_β and f_κ. One more parameter can be found from the condition of realizability of a generalized plane stress state. It turns out that in general case the constitutive equations of the Cosserat elasticity theory do not allow simultaneous equality to zero of the projections of the angular velocity vector and the components of the couple stress tensor, which are absent in this state.

The complete system of equations for description of the dynamics of the Cosserat continuum in terms of components of the linear velocity vector v_p, the angular velocity vector ω_p, the asymmetric stress tensor σ_{pq} and the couple stress tensor m_{pq} can be represented in the next form [17, 18]:

$$\begin{aligned}
&\rho_0\,\dot v_p = \sigma_{1p,1} + \sigma_{2p,2} + \sigma_{3p,3}\,,\\
&\dot\sigma_{pp} = \Big(k + \frac{4\mu}{3}\Big)v_{p,p} + \Big(k - \frac{2\mu}{3}\Big)(v_{q,q} + v_{r,r})\,,\\
&\dot\sigma_{pq} = (\mu+\alpha)\,v_{q,p} + (\mu-\alpha)\,v_{p,q} - 2\alpha\,\omega_r\,,\\
&\dot\sigma_{qp} = (\mu-\alpha)\,v_{q,p} + (\mu+\alpha)\,v_{p,q} + 2\alpha\,\omega_r\,,\\
&j_0\,\dot\omega_p = m_{1p,1} + m_{2p,2} + m_{3p,3} + \sigma_{qr} - \sigma_{rq}\,,\\
&\dot m_{pp} = \Big(\kappa + \frac{4\eta}{3}\Big)\omega_{p,p} + \Big(\kappa - \frac{2\eta}{3}\Big)(\omega_{q,q} + \omega_{r,r})\,,\\
&\dot m_{pq} = (\eta+\beta)\,\omega_{q,p} + (\eta-\beta)\,\omega_{p,q}\,,\\
&\dot m_{qp} = (\eta-\beta)\,\omega_{q,p} + (\eta+\beta)\,\omega_{p,q}\,.
\end{aligned} \tag{4}$$

Here the indices p, q and r take the values $1, 2, 3$ and besides $q = p{+}1 \bmod 3$, $r = q{+}1 \bmod 3$. The symbol j_0 denotes the inertial characteristic of a material, which is equal to the product of the moment of inertia of a block and the number of blocks in a unit volume:

$$j_0 = jN, \quad j = \rho\,\frac{h^5}{6}, \quad N = \frac{1}{(h+\delta)^3}.$$

Comparing the equations of the system (4) and the equations for stresses and couple stresses, coefficients of which are the parameters f_α, f_β and f_κ, one can obtain the following conversion formulas:

$$\alpha = \frac{f_\alpha}{2} = \frac{\mu' h}{2\delta}, \quad \eta+\beta = \frac{f_\beta}{h} = \frac{E'(h+\delta)h^2}{12\delta}, \quad \kappa + \frac{4\eta}{3} = \frac{f_\kappa}{h^2} = \frac{\mu'(h+\delta)h^2}{6\delta}. \tag{5}$$

In a generalized plane stress state, which is realized in the layer of the thickness h loaded in the plane with lateral surfaces $x_3 = 0$ and $x_3 = h$ free from stresses, the quantities $v_{1,3}$, $v_{2,3}$, $v_{3,1}$, $v_{3,2}$, ω_1, ω_2, $\omega_{3,3}$ and $\sigma_{13} = \sigma_{31}$, $\sigma_{23} = \sigma_{32}$, σ_{33}, m_{31}, m_{32}, m_{33} are identically zero. Such variant is allowed by the system (4) only if the parameters η and β are equal between

themselves. Otherwise, $\omega_{3,1} = \omega_{3,2}$ follows from the equations for the couple stresses m_{31} and m_{32}, i.e. nonuniform rotation of the blocks in a generalized plane stress state is impossible. Thus, the parameters conversion formulas (5) are closed by the equality $\eta = \beta$.

Parameters, characterizing the compliance of a material in tension–compression and in shear, are determined from the condition of coincidence of velocities of plane longitudinal and transverse elastic waves for a block medium and for an effective homogeneous material. In the directions of coordinate axes the waves in a block medium move with the average velocities:

$$\bar{c}_1 = c_1\, c_1' \,\frac{h+\delta}{h\, c_1' + \delta\, c_1}, \quad \bar{c}_2 = c_2\, c_2' \,\frac{h+\delta}{h\, c_2' + \delta\, c_2}.$$

Taking into account the expressions for velocities of longitudinal and transverse waves in the Cosserat medium, the phenomenological parameters k and μ are calculated as follows:

$$\mu = \rho_0\, \bar{c}_2^{\,2} - \alpha, \quad k = \rho_0\, \bar{c}_1^{\,2} - \frac{4\mu}{3}, \quad \rho_0 = \frac{\rho\, h + 3\rho'\delta}{(h+\delta)^3}. \tag{6}$$

For example, let us consider a block medium with parameters of materials, presented in section 1, and with thicknesses of blocks and interlayers, characteristic for a brick masonry: $h = 0.05$ and $\delta = 0.01$ m. Calculation of the parameters of the Cosserat continuum for this medium by formulas (5), (6) gives:

$$k = 16.9, \;\; \mu = 3.07, \;\; \alpha = 0.389 \text{ GPa}, \quad \kappa = 7.92, \;\; \eta = \beta = 286 \text{ kN}.$$

The material density is $\rho_0 = 2560$ kg/m^3, the inertial inertial characteristic of rotation is $j_0 = 0.892$ kg/m. Velocities of longitudinal, transverse, rotational and torsional waves for these parameters are:

$$\bar{c}_1 = \sqrt{\frac{k + 4\mu/3}{\rho_0}} = 2864, \;\; \bar{c}_2 = \sqrt{\frac{\mu + \alpha}{\rho_0}} = 1163,$$

$$\bar{c}_3 = \sqrt{\frac{\eta + \beta}{j_0}} = 800, \;\; \bar{c}_4 = \sqrt{\frac{\kappa + 4\eta/3}{j_0}} = 660 \text{ m/s}.$$

The natural frequency of the rotational motion, which is calculated by the period of natural oscillations $T = \pi\sqrt{\alpha/j_0} = 15.05$ ms, is equal to $\nu_* = 1/T = 6.645$ kHz.

It should be noted that since in the model of the Cosserat continuum the particles of a material microstructure are considered as undeformable, the approximation of a block medium by means of a moment continuum is possible only if the elastic compliance of interlayers is significantly more compared with the compliance of blocks, and if, in addition, the thickness of interlayers is not too small compared with the size of blocks. Incorrectness of the approximation manifests, ultimately, in violation of the inequalities

$$k,\; \mu,\; \alpha > 0, \quad \kappa,\; \eta,\; \beta > 0.$$

If these inequalities are fulfilled, then potential energy of the Cosserat continuum is a positive definite quadratic form [18], and it provides the hyperbolicity of the system of equations (4).

4 RESONANCES IN A BLOCK MEDIUM

Resonant excitation of a medium due to the perturbation of rotational motion of blocks is modeled on the basis of equations of the Cosserat continuum. In Fig. 6 the graphs of dependence of the modulus of amplitude of tangential stress on the frequency are shown, which are obtained from the solution of a problem on uniform cyclic shear of viscoelastic layer of the thickness H. Phenomenological parameters of a material are pointed at the end of previous section. The tangential stress belongs to the rigidly fixed lower side of the layer. At the upper side the linear velocity varies on periodic law with the frequency ν. the layer thickness is varied. The similar graphs for ideal inviscid media have a system of resonant peaks with infinite amplitudes. Viscosity is used as a smoothing mechanism. The process of shear is described by equations (4), in which, according to the Boltzmann viscoelasticity theory, the products of parameters of a medium on the characteristics of the strain state are replaced by the convolutions of relaxation kernel corresponding to these parameters on the same characteristics.

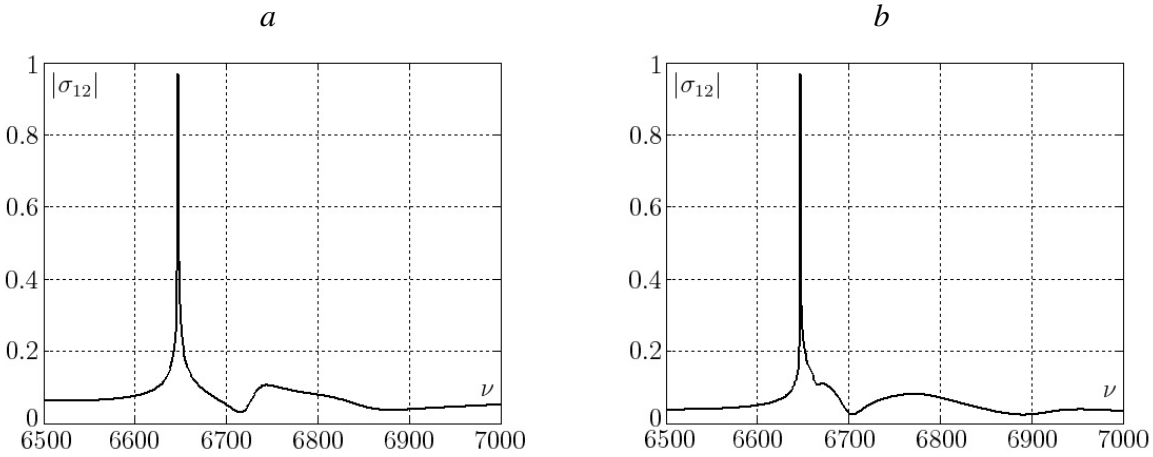


Figure 6: Amplitude-frequency characteristics of a viscoelastic layer: $H = 0.5\,\mathrm{m}$ (*a*) and $H = 1\,\mathrm{m}$ (*b*).

Assume that the axis x_1 of a Cartesian coordinate system is directed deep into the layer, and the axis x_2 is directed horizontally. The system of equations of plane shear waves with rotation of the particles, moving in a moment continuum in the direction x_1, has the form:

$$\begin{aligned} &\rho_0\,\dot v_2 = \sigma_{12,1}\ , && j_0\,\dot\omega_3 = m_{13,1} + \sigma_{12} - \sigma_{21}\ ,\\ &\dot\sigma_{12} = (\mu+\alpha) * v_{2,1} - 2\,\alpha * \omega_3\ , && \dot\sigma_{21} = (\mu-\alpha) * v_{2,1} + 2\,\alpha * \omega_3\ ,\\ &\dot m_{31} = (\eta-\beta) * \omega_{3,1}\ , && \dot m_{13} = (\eta+\beta) * \omega_{3,1}\ . \end{aligned} \tag{7}$$

From the system (7) one can obtain the amplitude equations:

$$\begin{aligned} &2\pi i\,\nu\rho_0\,\hat v_2 = \hat\sigma_{12,1}\ , && 2\pi i\,\nu j_0\,\hat\omega_3 = \hat m_{13,1} + \hat\sigma_{12} - \hat\sigma_{21}\ ,\\ &2\pi i\,\nu\,\hat\sigma_{12} = (\hat\mu+\hat\alpha)\,\hat v_{2,1} - 2\hat\alpha\,\hat\omega_3\ , && 2\pi i\,\nu\,\hat\sigma_{21} = (\hat\mu-\hat\alpha)\,\hat v_{2,1} + 2\hat\alpha\,\hat\omega_3\ ,\\ &2\pi i\,\nu\,\hat m_{31} = (\hat\eta-\hat\beta)\,\hat\omega_{3,1}\ , && 2\pi i\,\nu\,\hat m_{13} = (\hat\eta+\hat\beta)\,\hat\omega_{3,1}\ . \end{aligned}$$

Consequently,

$$\begin{aligned} &4\,\pi^2\nu^2\rho_0\,\hat v_2 + (\hat\mu+\hat\alpha)\,\hat v_{2,11} - 2\,\hat\alpha\,\hat\omega_{3,1} = 0\ ,\\ &4\,(\pi^2\nu^2 j_0 - \hat\alpha)\,\hat\omega_3 + (\hat\eta+\hat\beta)\,\hat\omega_{3,11} + 2\,\hat\alpha\,\hat v_{2,1} = 0\ . \end{aligned}$$

Hence, $A\,\hat{v}_{2,1111} + 4\,B\,\hat{v}_{2,11} + 16\,C\,\hat{v}_2 = 0$, where

$$A = (\hat{\mu}+\hat{\alpha})(\hat{\eta}+\hat{\beta}),\;\; B = \hat{\alpha}^2+\pi^2\nu^2\rho_0(\hat{\eta}+\hat{\beta})+(\pi^2\nu^2 j_0-\hat{\alpha})(\hat{\mu}+\hat{\alpha}),\;\; C = \pi^2\nu^2\rho_0(\pi^2\nu^2 j_0-\hat{\alpha}).$$

Let λ_1 and λ_2 be the roots of biquadratic characteristic equation

$$\frac{\lambda_{1;2}^2}{2} = \frac{-B \pm \sqrt{B^2 - 4AC}}{A}.$$

Then general solution for the amplitude of linear velocity depends on four constants:

$$\hat{v}_2 = A_1\, e^{\lambda_1 x_1} + A_2\, e^{-\lambda_1 x_1} + B_1\, e^{\lambda_2 x_1} + B_2\, e^{-\lambda_2 x_1}.$$

The Fourier transform of angular velocity takes the form:

$$2\,\hat{\alpha}\,\hat{\omega}_3 = -\,\frac{æ_1}{\lambda_1}\Big(A_1\, e^{\lambda_1 x_1} - A_2\, e^{-\lambda_1 x_1}\Big) - \frac{æ_2}{\lambda_2}\Big(B_1\, e^{\lambda_2 x_1} - B_2\, e^{-\lambda_2 x_1}\Big),$$

where $æ_{1;2} = 4\,\pi^2\nu^2\rho_0 + \lambda_{1;2}^2\,(\hat{\mu} + \hat{\alpha})$.

Boundary conditions for the layer are formulated in terms of the velocities v_2 and ω_3:

$$v_2\Big|_{x_1=0} = v_0\, e^{2\,\pi i\,\nu\, t}, \quad \omega_3\Big|_{x_1=0} = 0, \quad v_2\Big|_{x_1=H} = \omega_3\Big|_{x_1=H} = 0.$$

They lead to a system of four linear algebraic equations for finding the constants of integration:

$$\begin{aligned}
&A_1 + A_2 + B_1 + B_2 = v_0, \quad æ_1(A_1 - A_2) + æ_2(B_1 - B_2) = 0,\\
&A_1\, e^{\lambda_1 H} + A_2\, e^{-\lambda_1 H} + B_1\, e^{\lambda_2 H} + B_2\, e^{-\lambda_2 H} = 0,\\
&æ_1\Big(A_1\, e^{\lambda_1 H} - A_2\, e^{-\lambda_1 H}\Big) + æ_2\Big(B_1\, e^{\lambda_2 H} - B_2\, e^{-\lambda_2 H}\Big) = 0.
\end{aligned}$$

Solution of the system can be written in explicit form, but it is not included in this paper because of the cumbersome expression. The amplitude of tangential stress at the lower boundary of the layer is calculated by formula:

$$2\,\pi i\,\nu\,\hat{\sigma}_{12} = \frac{(\hat{\mu} + \hat{\alpha})\lambda_1^2 - æ_1}{\lambda_1}\Big(A_1\, e^{\lambda_1 H} - A_2\, e^{-\lambda_1 H}\Big) + \frac{(\hat{\mu} + \hat{\alpha})\lambda_2^2 - æ_2}{\lambda_2}\Big(B_1\, e^{\lambda_2 H} - B_2\, e^{-\lambda_2 H}\Big).$$

The Kelvin–Voigt viscoelasticity theory is used in calculations, according to which the complex moduli are linear functions of the frequency, in particular $\hat{\mu} = \mu + 2\pi i\,\nu\tilde{\mu}$. Imaginary parts of the complex moduli are chosen so as to achieve the necessary smoothing of solutions.

Comparing the graphs in Fig. 6, obtained for the thicknesses $H = 0.5$ and $H = 1\,\text{m}$, one can see that the resonance peak at the frequency $6.645\,\text{kHz}$, equal to the natural frequency of rotational motion of the particles, is present regardless of the layer thickness.

5 LOCALIZED PERTURBATIONS

In the computations of impulsive action on a block elastic medium on the basis of two-dimensional and three-dimensional equations of the Cosserat continuum the specific low-frequency pendulum waves, caused not by translational motion (as in the original paper [5]) but the rotation of blocks, were found. The method of solving the problem on high-performance cluster systems and some results of computations are presented in the monograph [18].

Numerical results for 2D Lamb's problem on the normal action of a concentrated impulsive load on the boundary of an elastic block are represented in Fig. 7. Fig. 7 *a* shows the level curves of normal stress for a homogeneous elastic medium (in the framework of the classical theory of elasticity), and Fig. 7 *b* shows the level curves of normal stress for the Cosserat medium. Computations were performed on 15 processors of a cluster, the uniform difference grid consists of 1000×500 meshes. In both figures one can see the incident longitudinal and transverse waves, conical transverse waves and the Raleigh surface waves, moving from the loading point inside the computational domain. The essential difference between Figs. 7 *a* and 7 *b* is that in a moment medium behind the front of the transverse wave an additional system of low-frequency waves, caused by rotational motion of the particles, is observed. Oscillations behind the front of the transverse wave have the period T. The corresponding wavelength is evaluated by the velocity of transverse waves as $\bar{c}_2\,T$.

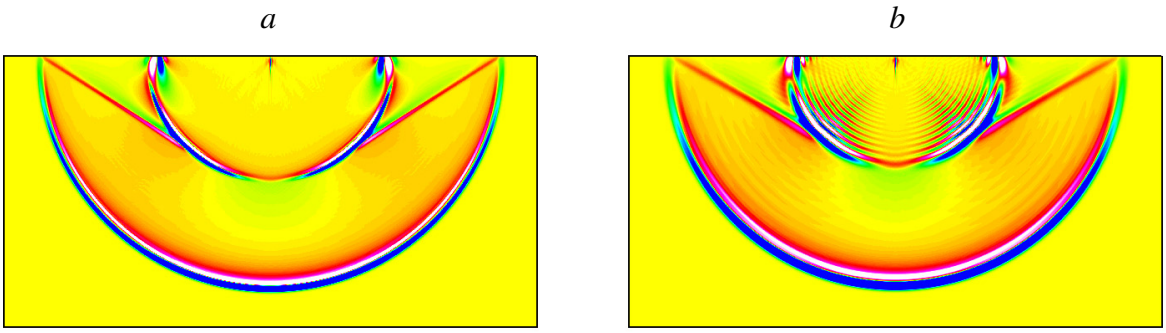


Figure 7: 2D Lamb's problem for a homogeneous elastic medium (*a*) and for the Cosserat elastic medium (*b*): level curves of normal stress.

More accurate expression for the phase velocity c of the pendulum wave of rotational motion can be obtained using the dispersion equation of plane shear waves with rotation of the particles [17, 18]:

$$\left(1-\frac{\bar{c}_2^2}{c^2}\right)\left(\pi^2\nu^2\left(1-\frac{\bar{c}_3^2}{c^2}\right)-\frac{\alpha}{j_0}\right)=\frac{\alpha^2}{\rho_0\,j_0\,c^2}.$$

For $\nu=\nu_*$ this equation gives

$$c=\bar{c}_2\left(1+\frac{\alpha}{\rho_0\,\bar{c}_3^2}\right)^{-1}.$$

It turns out that $c\approx\bar{c}_2$ only for small values of the parameter α and for relatively high velocities $\bar{c}_3$. If the velocity $\bar{c}_3$ is low, then c is also low. Thus, in the model of a reduced Cosserat continuum, where the couple stress tensor is zero, the waves of this type are standing waves.

Computations of 3D problems have confirmed the main qualitative difference of the wave field in the Cosserat continuum as compared with the classical elasticity theory, which consists in the appearance of oscillations of the rotational motion of particles on the wave fronts. Comparative calculations with different values of scale of the microstructure of a material were performed in [18]. A direct proportional dependence of the period of natural oscillations from this scale was found numerically.

In Fig. 8 one can see results for the problem on the action of a concentrated rotational moment, periodic in time, obtained by means of the 3Dyn_Cosserat program [19]. Computations were performed for a material with the above parameters on 64 processors of the MVS-100K cluster of the Joint Supercomputer Center of RAS. The loading scheme (Fig. 8 *a*), and level

surfaces of the angular velocity ω_2 for the resonance frequency $\nu = \nu_*$ (Fig. 8 *b*) and for the nonresonance frequency $\nu = 1.75\,\nu_*$ (Fig. 8 *c*) at different moments of time are represented. The maximum amplitude of oscillations of the angular velocity is achieved at the point of load application, and the wavelength depends essentially on the frequency. Comparison of the graphs shows that for the frequency of external action, equal to the natural frequency ν_* of rotational motion of the particles, the growth of amplitude with time occurs and a more smooth decay of oscillations with increasing the distance from the point of load application, characteristic of the acoustic resonance, takes place (Fig. 8 *b*). It should be noted that if normal stress or tangential stress, linear velocity or angular velocity, concentrated in space, acts at the boundary point of a computational domain, then the resonance excitation of a medium does not take place.

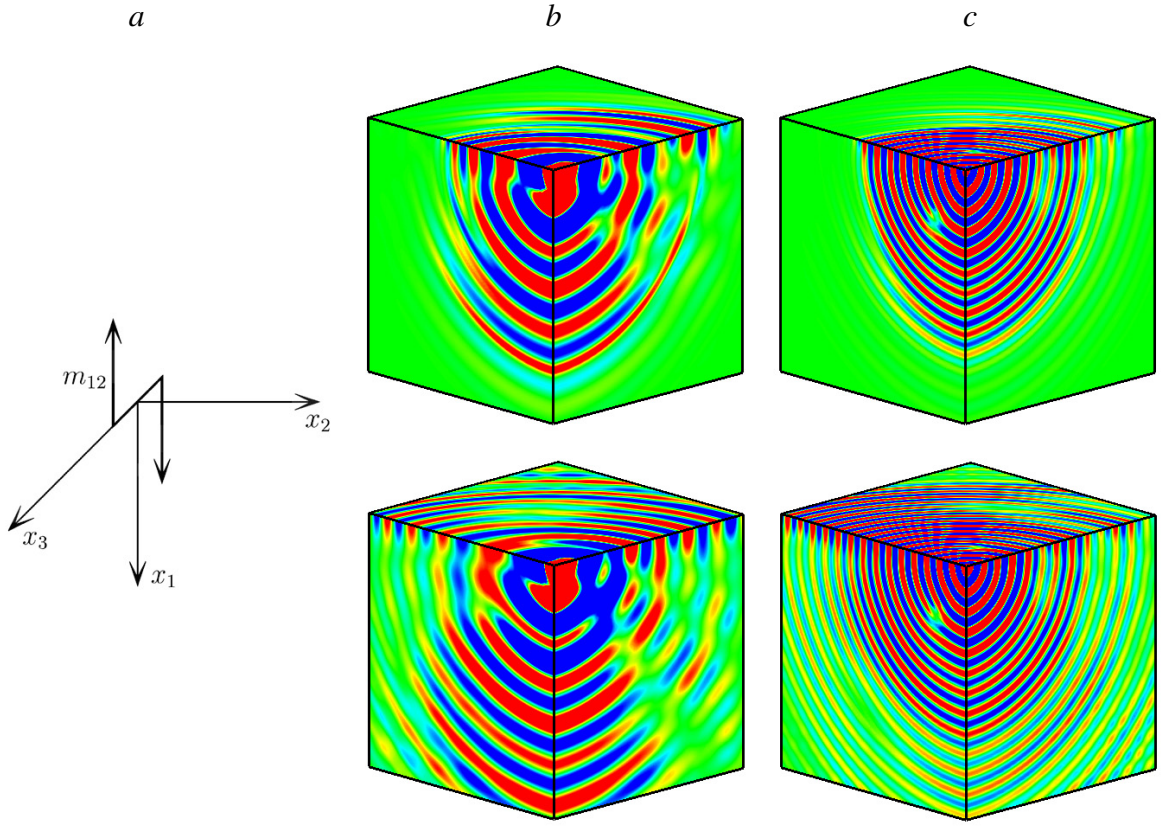


Figure 8: 3D problem on the periodic action of concentrated rotational moment: loading scheme (*a*), level surfaces of angular velocity for the resonance frequency (*b*) and for the nonresonance frequency (*c*); $t = 1.5$ ms (*above*), $t = 2.10$ ms (*below*).

The existence of resonance frequency in the Cosserat continuum model, which does not depend on the size of a sample and is essentially a phenomenological parameter of a material, was found in [17, 18]. It was shown in [20] that the resonance frequency, connected with rotational motion of particles in the microstructure of a material, is also present in the models of micropolar elastic thin shells.

6 CONCLUSIONS

- To describe the wave processes in a multiblock medium with elastic blocks interacting through compliant viscoelastic interlayers, the simplified mathematical model, received

by averaging the equations of deformation of the interlayers in thickness, and the model of the Cosserat continuum, in which the independent rotations of the blocks are taken into account along with the translational degrees of freedom, were applied.

- From a comparison of the velocities of elastic waves and the coefficients of elastic resistance of a medium to rotation and torsion of the blocks, the formulas for recalculation of phenomenological parameters of the Cosserat continuum by given characteristics of materials of the blocks and the interlayers were obtained.
- Algorithms and parallel programs are worked for numerical realization of considered models on multiprocessor computer systems of the cluster type and on the systems with GPUs.
- Parallel computational algorithms, based on models of the inhomogeneous elasticity theory and the Cosserat elasticity theory, are applied to the analysis of propagation of elastic waves in geomaterials with layered and block microstructure.
- The results of analysis of the oscillation processes show that the Cosserat medium possesses the eigenfrequency of acoustic resonance, which appears under certain conditions of perturbation and depends only on the inertial properties of the microstructure particles and the elasticity parameters of a material.

ACKNOWLEDGMENTS

This work was supported by the Complex Fundamental Research Program no. 18 “Algorithms and Software for Computational Systems of Superhigh Productivity” of the Presidium of RAS and the Russian Foundation for Basic Research (grant no. 11–01–00053).

REFERENCES

[1] M.A. Sadovskii, Natural lumpiness of a rock. *Dokl. Akad. Nauk SSSR*, **247**(4), 829–831, 1979 [in Russian].

[2] I.A. Kunin, *Elasticity theory for media with microstructure*. Moscow, Nauka, 1975 [in Russian].

[3] L.M. Brekhovskikh, *Waves in layered media*. New York, Academic Press, 1970.

[4] S.V. Goldin, *Seismic waves in anisotropic media*. Novosibirsk, Izd. SO RAN, 2008 [in Russian].

[5] M.V. Kurlenya, V.N. Oparin, V.I. Vostrikov, Formation of elastic wave packages in block media under impulse excitation. Pendulum-type waves. *Dokl. Akad. Nauk SSSR*, **333**(4), 3–13, 1993 [in Russian].

[6] N.I. Aleksandrova, E.N. Sher, A.G. Chernikov, Effect of viscosity of partings in block-hierarchical media on propagation of low-frequency pendulum waves. *J. of Mining Science*, **44**(3), 225–234, 2008.

[7] M.P. Varygina, M.A. Pokhabova, O.V. Sadovskaya, V.M. Sadovskii, Numerical algorithms for the analysis of elastic waves in block media with thin interlayers. *Numerical Methods and Programming: Advanced Computing*, **12**(2), 190–197, 2011 [in Russian].

[8] A.G. Kulikovskii, N.V. Pogorelov, A.Yu. Semenov, *Mathematical aspects of numerical solution of hyperbolic systems. Ser.: Monographs and Surveys in Pure and Applied Mathematics, Vol. 118*. Boca Raton – London – New York – Wasington, Chapman & Hall/CRC, 2001.

[9] V.M. Sadovskii, O.V. Sadovskaya, *Parallel program system for the solution of two-dimensional elastic-plastic problems of the dynamics of granular media (2Dyn_Granular)*. Certificate of State Registration of Computer Program no. 2012613989 from 28.04.2012. Moscow, FIPS, 2012 [in Russian].

[10] E. Cosserat, F. Cosserat, *Théorie des corps deformables. In: Chwolson's Traité Physique*. Paris, Librairie Scientifique A. Hermann et Fils, 1909, 953–1173.

[11] V.I. Erofeev, *Wave processes in solids with microstructure*. New Jersey – London – Singapore – Hong Kong – Bangalore – Taipei, World Scientific Publishing, 2003.

[12] H. Altenbach, J. Altenbach, W. Kissing, *Mechanics of composite structural elements*. Berlin, Springer, 2004.

[13] S. Diebels, H. Steeb, T. Ebinger, Volume and surface based homogenization procedures for Cosserat continua. *Proc. Appl. Math. Mech.*, **3**, 266–267, 2003.

[14] I.S. Pavlov, A.I. Potapov, Structural models in the mechanics of nanocrystal media. *Doklady Physics*, **421**(3), 408–412, 2008.

[15] D. Branke, J. Brummund, G. Haasemann, V. Ulbricht, Obtaining Cosserat material parameters by homogenization of a Cauchy continuum. *Proc. Appl. Math. Mech.*, **9**, 425–426, 2009.

[16] F.D. Reis, J.-F. Ganghoffer, *Construction of micropolar continua from the homogenization of repetitive planar lattices. In: Mechanics of Generalized Continua (ed. by H. Altenbach, G.A. Maugin, V. Erofeev), Ser.: Advanced Structured Materials, Vol. 7*. Berlin – Heidelberg, Springer, 2011, 193–217.

[17] O.V. Sadovskaya, V.M. Sadovskii, Analysis of rotational motion of material microstructure particles by equations of the Cosserat elasticity theory. *Acoustical Physics*, **56**(6), 942–950, 2010.

[18] O. Sadovskaya, V. Sadovskii, *Mathematical modeling in mechanics of granular materials, Ser.: Advanced Structured Materials, Vol. 21*. Heidelberg – New York – Dordrecht – London, Springer, 2012.

[19] V.M. Sadovskii, O.V. Sadovskaya, M.P. Varygina, *Parallel program system for the solution of three-dimensional dynamic problems of the Cosserat elasticity theory (3Dyn_Cosserat)*. Certificate of State Registration of Computer Program no. 2012614824 from 30.05.2012. Moscow, FIPS, 2012 [in Russian].

[20] S.O. Sarkisyan, The general theory of micropolar elastic thin shells. *Physical Mesomechanics J.*, **14**(1), 55–66, 2011 [in Russian].

COMPDYN 2013
Proceedings of the
4th International Conference on
Computational Methods in Structural Dynamics and Earthquake Engineering

M. Papadrakakis, V. Papadopoulos, V. Plevris (Eds)

First Edition, February 2014

ISBN: **978-960-99994-2-7**



Institute of Structural Analysis and Antiseismic Research
National Technical University of Athens, Greece